JOURNAL OF THE ELECTROCHEMICAL SOCIETY

ELECTROCHEMICAL SCIENCE
— AND TECHNOLOGY —

JANUARY
1983

The Structure of the Double Layer at the Mercury-Phosphoric Acid Interface from Studies of Adsorption of Thiourea and Its Implications on Oxygen Reduction Kinetics

E. R. Gonzalez,* K-L. Hsueh,* and S. Srinivasan*

Los Alamos National Laboratory, Los Alamos, New Mexico 87545

ABSTRACT

Because the efficiency loss of phosphoric acid fuel cells is determined mainly by the slow kinetics of the oxygen reduction reaction, there is evidently a need for understanding why this reaction is slower in concentrated phosphoric acid than in aqueous solutions of strong acids. In this work, the structure of the double layer at the interface mercury-concentrated phosphoric acid is examined at room temperature by using thiourea as a probe species. For this purpose, the differential capacity of the interface was measured as a function of the electrode potential in 95% phosphoric acid and in the same electrolyte with nine concentrations of added thiourea. Analysis of the results indicates that thiourea adsorbs with the positive end of the dipole toward the metal; the amount adsorbed is sufficiently small and can be described by a Henry's law type of isotherm. Analysis of the inner layer parameters shows that in this region the permittivity has similar values to those found in water, but the distance from the metal to the outer Helmholtz plane is much larger. Thus, slower oxygen reduction kinetics can be rationalized in terms of a wider barrier for the rate-determining electron transfer step.

Of the several fuel cell systems now being considered for power generation and transportation applications, the phosphoric acid fuel cell is in the most advanced state of development. The factor limiting the efficiency of this fuel cell system is the high overpotential (300-400 mV) for the oxygen reduction reaction. On platinum, this reaction is considerably slower in phosphoric acid than in aqueous strong acids, such as trifluoromethanesulfonic acid, in which electrolyte the rates are two orders of magnitude faster (1, 2). More than one factor may be responsible for this difference in reaction kinetics, but undoubtedly one of the main reasons, which has been neglected so far, is the difference in properties of the double layer of the electrode with concentrated phosphoric acid on the one hand and with aqueous solutions of strong acids on the other. Thus, it seemed worthwhile to carry out double layer studies at the electrode-phosphoric acid interface in order to elucidate its effect on oxygen reduction kinetics.

By a revised analysis of the experimental results of Schapink *et al.* (3) for the adsorption of thiourea on mercury from 0.1M solutions of NaF, Parsons (4) showed that thiourea can be used as a probe species to gain knowledge of double layer properties, such as the thickness and the average permittivity value. Since then, this approach has been employed to obtain information on the characteristics of the electrode-solution interface in several nonaqueous solvents such as methanol (5), formamide (6), dimethylformamide (7), ethylene carbonate (8), and ethanol (9).

In this work, it was decided to use thiourea as a probe species to study the properties of the double layer at the electrode-concentrated phosphoric acid interface. As a first step, mercury was chosen as the electrode material because of the many advantages that this metal offers for interfacial studies, particularly when used as a dropping electrode. Further, most studies have shown that many of the characteristics of the double layer on mercury can be extended to solid metals. The electrolyte used in these studies was 95% phosphoric acid, which is close to the concentration in fuel cells being developed for power generation and on-site integrated energy systems. This concentration was chosen because it is the highest possible one before the formation of pyrophosphoric acid at room temperature takes place (10). It must, however, be noted that at the concentrations (~100%) and operational temperatures (~180°C) prevailing in phosphoric acid fuel cells, pyrophosphoric acid is expected to be a major component of the electrolyte. Examination of the interfacial properties of this species will be the object of a separate study.

* Electrochemical Society Active Member.
Key words: metals, electrode, organic, chemisorption.

Experimental

Phosphoric acid (85%, Mallinckrodt, AR) was treated with H_2O_2, concentrated to 95% by evaporation, and finally pre-electrolyzed for 3 hr at a potential of 1.5V between two platinum electrodes. Thiourea (Eastman Kodak) was used as received. The cell, working and counterelectrodes, and electrical equipment used for the measurement of the differential capacity have already been described (11). Potentials of zero charge (E_z) were measured using the streaming electrode technique (12). All potentials were measured using a dynamic hydrogen electrode as reference. Differential capacities were measured at 25° ± 0.1°C as a function of potential for the interface of the mercury electrode with the pure 95% phosphoric acid and with this acid containing the following concentrations of thiourea: 0.017, 0.1, 0.178, 0.251, 0.355, 0.501, 0.708, 1.0, and 1.413. Because no dependence of the capacity on frequency was observed in the range 50-400 Hz, measurements were done at 200 Hz. It was found that thiourea hydrolyzes in the 95% phosphoric acid. However, this process is so slow at room temperature that it can be neglected in the time range needed to perform the experiments.

Results and Discussion

Preliminary observations from capacitance measurements.—Figure 1 shows the capacity curves for the

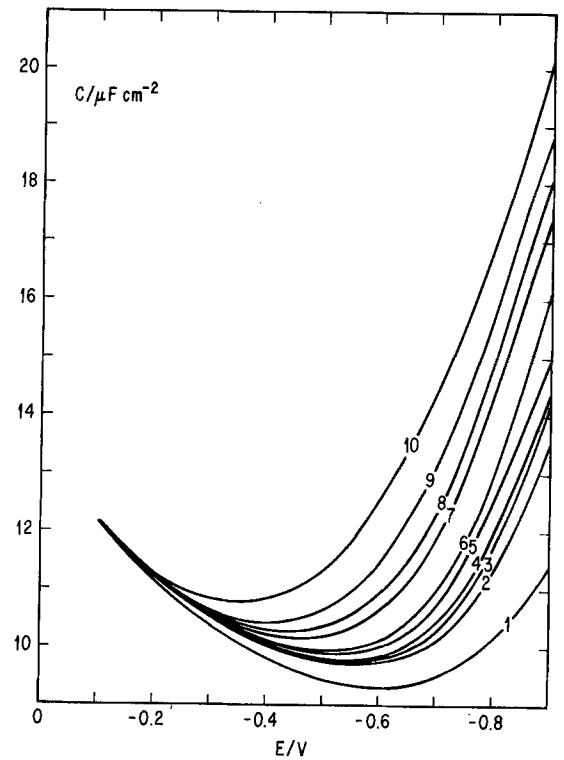

Fig. 1. Differential capacity-potential plots at 25° for Hg in 95% H_3PO_4. Concentration of thiourea: (curve 1) 0, (curve 2) 0.071, (curve 3) 0.1, (curve 4) 0.178, (curve 5) 0.251, (curve 6) 0.355, (curve 7) 0.501, (curve 8) 0.708, (curve 9) 1.0, and (curve 10) 1.413M.

control electrolyte (95% phosphoric acid) and for this electrolyte with nine concentrations of thiourea. The cathodic limit of the curves corresponds to potentials very near E_z and was imposed by the onset of hydrogen evolution. On the positive side, the limit was determined by an anodic current whose magnitude was a function of the concentration of thiourea. This current is probably due to the oxidation of thiourea although mercury dissolution cannot be discarded. Because of this current, solutions more concentrated than 1.5M in thiourea could not be used. It is important to observe that in order to obtain an appreciable effect on the capacity, concentrations of thiourea had to be larger than those used in water (3).

It is interesting to note that the addition of up to 1M KH_2PO_4 to 95% H_3PO_4 did not produce any change in the capacity-potential relation as observed for the control electrolyte. This means either that KH_2PO_4 is not dissociated in the 95% phosphoric acid (which is not probable) or that the diffuse layer capacity is already much larger than the inner layer capacity so that no effect is observed when the ionic concentration in the bulk is increased. The values of the total capacity are much smaller than in water, which means that in phosphoric acid the dielectric constant of the inner layer is smaller or that the double layer is thicker, or both. This point is further discussed below.

On addition of thiourea to a 95% phosphoric acid solution, E_z shifts to more positive values, indicating that the thiourea dipole is oriented with the positive end toward the metal. This orientation is opposite to the one observed in water and in nonaqueous solvents (4-9). To some extent this is surprising because the orientation with the negative end of the dipole toward the metal is favored by the strong mercury-sulfur atom interaction. However, it should be expected that in the concentrated phosphoric acid the thiourea is protonated precisely on the sulfur atom, which in this situation cannot interact with the mercury surface. This possibility has been suggested previously (13).

The adsorption characteristics of thiourea.—Following the thermodynamic treatment of the double layer, the capacity curves were integrated twice with respect to the potential, first to obtain the charge density on the metal (q) and then the surface tension (γ). For this purpose the control electrolyte curve (*i.e.*, without thiourea) was first integrated anodically from E_z to a potential of −0.12V, where all the curves coincide. The value of the charge density and of γ (assumed arbitrarily as being zero at E_z for the control electrolyte because only changes in γ are relevant) determined at −0.12V were used as constants for the cathodic integration of the capacity curves recorded in the presence of thiourea. The integrations were performed numerically using Simpson's rule for two subintervals with the aid of suitable computer programs (14). The values of q and γ were combined to obtain Parson's function $\xi = qE + \gamma$ from which the surface excesses of thiourea (Γ) at constant charge on the electrode were obtained through the expression (4)

$$\Gamma = \frac{1}{RT}\left(\frac{\partial \xi}{\partial \ln c}\right)_q \qquad [1]$$

where c is the concentration of thiourea in the bulk of the solution. Differentiations were performed numerically with improved procedures that make use of cubic spline functions (14).

Figure 2 shows the values of Γ as a function of the electrode charge for the different concentrations of thiourea. In comparison with the results reported in water (3), the values of Γ are small, being significant only over a restricted range of q values. It is clear that Γ increases as q is made more negative, while thiourea appears to be desorbed for charges on the electrode more positive than 5 μC cm^{-2}.

The smaller values of Γ obtained in phosphoric acid as compared with water could be explained by the differing strengths of interaction between the thiourea and the electrode surface when the molecule presents opposite orientations. On the other hand, this could also be due to phosphoric acid species being more strongly attached than the water molecule to the metal

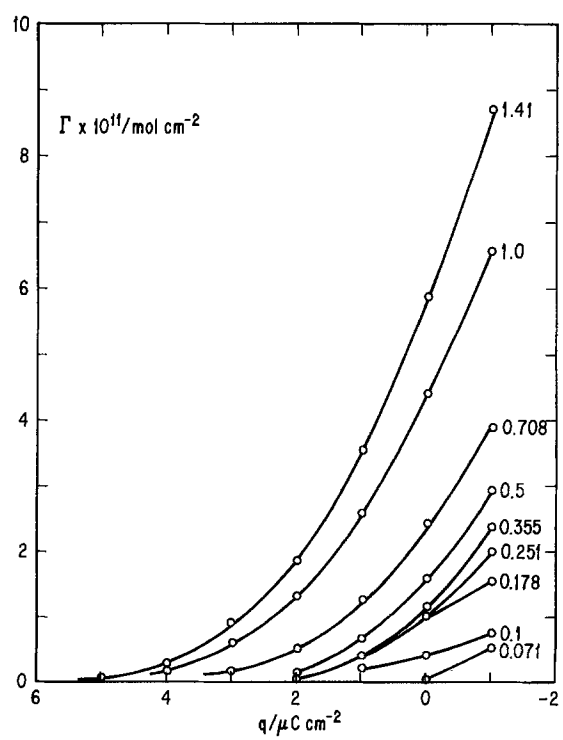

Fig. 2. Surface excess of thiourea as a function of the electrode charge density. Figures on the lines indicate the molar concentration of thiourea.

surface. Studies of the adsorption of $H_2PO_4^-$ on mercury in aqueous solutions (15) show that the anion is only weakly adsorbed. However, the situation could well be different in the concentrated acid used here.

The characteristics of the inner layer.—The inner layer properties were determined by analyzing the potential drop across the inner double layer (ϕ_{m-2}) as a function of the surface excess of thiourea. In order to obtain ϕ_{m-2}, it was necessary to calculate the potential ϕ_2 of the outer Helmholtz plane (o.H.p.) with the aid of the diffuse layer theory (16). This calculation involves the use of the bulk dielectric constant of the solvent, for which a value of 20 was taken (17) and of the bulk ionic concentration. The magnitude of the latter was evaluated considering only the first dissociation of phosphoric acid. From the work of Munson (18) the concentration of univalent species was taken as 0.37M. This value is subject to error but, in any case, values differing by ±50% from the one given, produce differences of only ±10% in ϕ_2. Furthermore, in the range of electrode charges considered here (−1 to 4 μC cm^{-2}) the values of ϕ_2 are small, varying from −7 to 27 mV. Thus, ϕ_2 does not have a significant influence on the value of ϕ_{m-2}.

The potential drop across the double layer was then obtained by subtracting ϕ_2 from the electrode potential. Thus, ϕ_{m-2} includes the potential drop between the reference electrode and the solution, which presents no problem because only changes in ϕ_{m-2} are of interest.

Figure 3 shows ϕ_{m-2} plotted as a function of Γ at constant values of q. As in water (4), a set of reasonably straight lines is obtained, but the slope has the opposite sign. The lines are not parallel, and a least squares analysis shows that the slope increases from 1.26×10^9 to 1.45×10^9 V cm^2 mol^{-1} when q increases from −1 to +2 μC cm^{-2}.

The potential drop across the double layer can be considered a function of q and Γ and can formally be divided into two contributions so that

$$\phi_{m-2} = \frac{q}{K^i} + \frac{\Gamma}{D} \qquad [2]$$

where K^i is an integral capacity of the inner layer at constant amount of thiourea adsorbed. Assuming a uniform permittivity (ϵ) in the inner layer

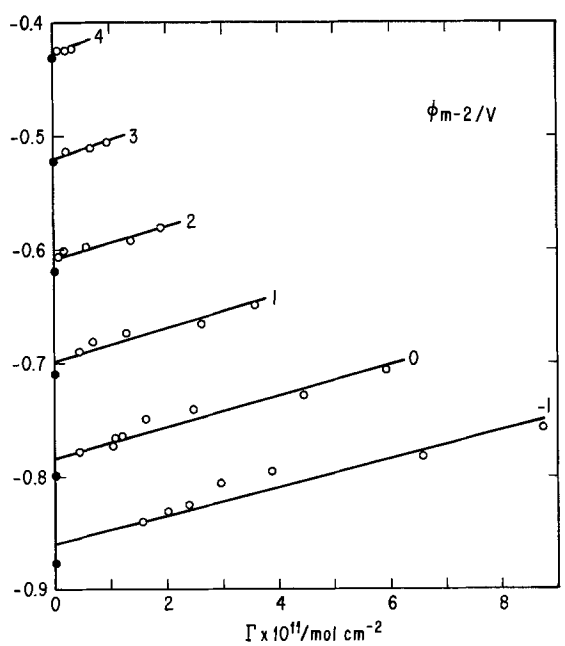

Fig. 3. Potential drop across the inner layer as a function of the surface excess of thiourea. Figures on the lines indicate the electrode charge density in μC cm^{-2}. (●) values correspond to the control electrolyte.

$$K^i = \frac{\epsilon}{4\pi x_2} \qquad [3]$$

where x_2 is the distance between the metal and the o.H.p.

In Eq. [2], D is the equivalent of an integral capacity of the inner layer at constant electrode charge. Assuming again that ϵ is uniform

$$D = \frac{\epsilon}{4\pi\mu} \qquad [4]$$

where μ is the effective dipole moment of the adsorbed thiourea molecules.

Because the lines in Fig. 3 are not parallel, it follows that ϵ and probably x_2 are dependent on the amount of thiourea adsorbed. An approximate analysis can be made by disregarding this dependence in the range $-1 \leq q \leq 2$ μC cm^{-2} and by taking an average slope equal to 1.40×10^9 V cm^2 mol^{-1}. With this value, ϵ could be calculated from Eq. [4]. However, it must be taken into account that the effective dipole moment of the adsorbed thiourea is

$$\mu = \mu^o + \alpha E \qquad [5]$$

where μ^o is the permanent dipole moment, α the polarizability, and E the effective electric field at the site of adsorption. For ethylene carbonate (8), E was evaluated using the two position model of Levine *et al.* (19). However, in the present case necessary parameters such as the polarizability of phosphoric acid, the relative contributions of the two possible orientations of the solvent molecules, and the effective coordination number of the thiourea molecule with its solvent neighbors are unknown.

It is interesting to note that if the average value of E in the inner layer calculated for different values of q is used the term αE does not exceed a few percent of the value of μ^o and hence can be ignored. As a first approximation, it will then be assumed that $\mu \simeq \mu^o$. Using $\mu^o = 4.89D$ (20) and the calculated value of D in Eq. [4], it is found that $\epsilon = 8$. This value is somewhat smaller but not much different from the value found in aqueous solutions (4). It indicates a high degree of saturation of the solvent molecules in the inner layer. However, the change from bulk conditions, where $\epsilon \simeq 20$, is not as large as in the case of water.

The integral capacity K^i, related to the separation of the lines in Fig. 3 at a given Γ, is evidently a function of Γ. Figure 4 shows a plot of q *vs.* ϕ_{m-2} at $\Gamma = 0$, constructed by using the least squares intercepts of the lines in Fig. 3. From the slope of this plot $K^i = 11.8$ μF cm^{-2}. With this value, and the previously determined value of ϵ, it is determined from Eq. [3] that $x_2 = 6$Å. A comparison with the values of x_2 obtained in water (~4Å) shows that the double layer is much

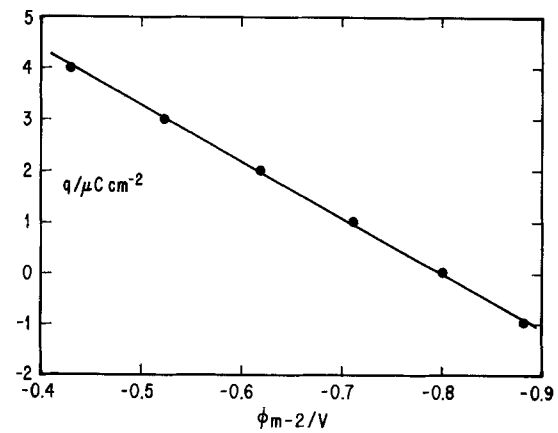

Fig. 4. Electrode charge density as a function of the potential drop across the inner layer for $\Gamma = 0$.

thicker in phosphoric acid. This is reasonable in view of the relative sizes of the phosphoric acid (21) and the water molecules.

With regard to the approximation involved in using the permanent dipole moment of the thiourea molecule, it must be pointed out that in cases where the effective dipole moment could be calculated (8, 9) it was found that μ is 1.5-2 times larger than μ^o. This means that the values of ϵ and x_2 calculated above must be considered as lower limits. If it were assumed that $\mu = 1.5\mu^o$, it would be found that $\epsilon = 12$ and $x_2 = 9$Å. These values are still reasonable for the conditions prevailing in the inner layer in the presence of phosphoric acid.

The adsorption isotherm for thiourea.—In many of the systems studied previously, the adsorption of thiourea on mercury has been described by a virial isotherm, which for the present case can be written as

$$\Gamma \exp(2B\Gamma) = c \exp(-\Delta G^o/RT) \quad [6]$$

where B is the second virial coefficient and ΔG^o the standard free energy of adsorption. The isotherm is usually determined using Parson's procedure (4) of plotting the surface pressure at a constant charge on the electrode $\Phi = \xi^o - \xi$ where ξ^o is the value for the control electrolyte, as a function of log c, and superimposing the different segments. However, the procedure could not be applied in this case due to the small values of Φ obtained. A virial equation was then tested by plotting log (Γ/c) *vs.* Γ at constant q, but the plots were far from being linear. It was then thought that a simple Henry's law isotherm (*i.e.*, a virial equation with $B = 0$) could be more appropriate in view of the low values of Γ. Figure 5 shows a plot of Γ *vs.* c for different values of q. Taking into account that the uncertainty in the values of Γ increases as Γ becomes smaller, it can be stated that Henry's law is a good approximation for the adsorption of thiourea from phosphoric acid on mercury. The isotherm can then be written

$$\Gamma = c \exp(-\Delta G^o/RT) \quad [7]$$

From the slopes of the lines in Fig. 5, ΔG^o can be obtained as a function of q. In particular, $\Delta G^o(q = 0) = -76.3$ kJ mol^{-1} (for standard states of 1 mol liter^{-1} in the solution and 1 molecule cm^{-2} on the surface). The applicability of a Henry's isotherm means that lateral repulsion between adsorbed thiourea molecules is negligible. For most of the experimental range, $\Gamma < 5 \times 10^{-11}$ mol cm^{-2}, which corresponds to an available area of more than 300Å^2 per molecule. Because the area covered by a thiourea molecule is about 30Å^2 (4), adjacent adsorbed molecules are expected to be separated by at least two phosphoric acid units. Thus, repulsion between adsorbed molecules can hardly be significant. The value of $\Delta G^o(q = 0)$ is lower than the value obtained in water (−96.1 kJ mol^{-1} (4)), which evidently points to the weaker interaction between the mercury and the thiourea molecule when the positive end of the dipole is directed toward the metal.

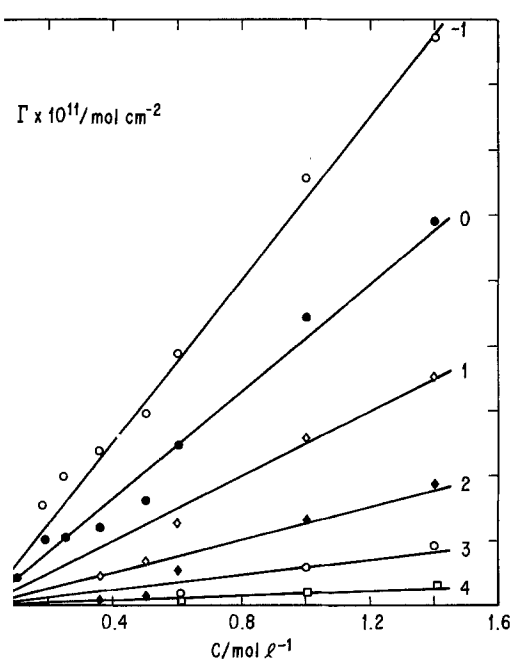

Fig. 5. Surface excess of thiourea as a function of its concentration in the bulk. Figures on the lines indicate the electrode charge density in μC cm^{-2}.

Rationale for slow oxygen reduction kinetics in H_3PO_4.—From the point of view of the oxygen reduction kinetics, a thicker double layer means that the electron transfer has to occur over greater distances from the metal surface to the plane of the reaction in concentrated phosphoric acid than in aqueous electrolytes. At the same time, the adsorption of intermediates of the reaction will be more difficult when phosphoric acid species have to be dislocated from the electrode surface. The present study provides a semiquantitative interpretation, based on double layer structure, for the slower oxygen reduction kinetics in concentrated phosphoric acid than in aqueous solutions of strong acids.

Acknowledgments

This work was performed under the auspices of the U.S. Department of Energy. E. R. Gonzalez thanks CNPq, Brazil, for a scholarship during his sabbatical leave from the Instituto de Física e Química de São Carlos, USP. The contribution of K-L. Hsueh to this work will be in partial fulfillment toward his Ph.D. degree from the Department of Chemical Engineering, Clarkson College of Technology, Potsdam, New York.

Manuscript submitted Jan. 25, 1982; revised manuscript received July 12, 1982. This was Paper 102 presented at the Denver, Colorado, Meeting of the Society Oct. 11-16, 1981.

Any discussion of this paper will appear in a Discussion Section to be published in the December 1983 JOURNAL. All discussions for the December 1983 Discussion Section should be submitted by Aug. 1, 1983.

Publication costs of this article were assisted by Los Alamos National Laboratory.

REFERENCES

1. A. J. Appleby and B. S. Baker, *This Journal*, **125**, 404 (1978).
2. W. E. O'Grady. E. J. Taylor, and S. Srinivasan, *J. Electroanal. Chem. Interfacial Electrochem.* **132**, 137 (1982).
3. F. W. Schapink, M. Oudeman, K. W. Lee, and J. N. Halle, *Trans. Faraday Soc.*, **56**, 415 (1960).
4. R. Parsons, *Proc. R. Soc. London, Ser. A*, **261**, 79 (1961).
5. J. D. Garnish and R. Parsons, *Trans. Faraday Soc.*, **63**, 1754 (1967).
6. E. Dutkiewicz and R. Parsons, *J. Electroanal. Chem. Interfacial Electrochem.*, **11**, 196 (1966).
7. I. M. Ganzhina and B. B. Damaskin, *Elektrokhimiya*, **6**, 1715 (1970).
8. W. R. Fawcett and M. D. Mackey, *J. Chem. Soc. Faraday Trans.*, **70**, 947 (1974).
9. R. V. Ivanova and O. G. Ivanova, *Elektrokhimiya*, **15**, 1474 (1979).
10. A-L. Huhti and P. A. Gartagania, *Can. J. Chem.*, **34**, 785 (1956).
11. E. R. Gonzalez, *J. Electroanal. Chem. Interfacial Electrochem.*, **90**, 431 (1978).
12. D. C. Grahame, R. P. Larsen, and M. A. Poth, *J. Am. Chem. Soc.*, **71**, 1978 (1949).
13. R. Narayan and N. Hackerman, *This Journal*, **118**, 1426 (1971). See also discussion by A. N. Frumkin and N. B. Grigoryev, *ibid.*, **119**, 1695 (1972).
14. A. Batana, R. C. Rocha, L. A. Avaca, and E. R. Gonzalez, *J. Computational Chem.*, **2**, 221 (1981).
15. R. Parsons and F. R. G. Zobel, *J. Electroanal. Chem. Interfacial Electrochem.*, **9**, 333 (1965).

16. P. Delahay, "Double Layer and Electrode Kinetics," Interscience, New York (1965).
17. J. H. Christensen, A. J. Smith, R. B. Reed, and K. L. Elmore, *J. Chem. Eng. Data*, **11**, 60 (1966).
18. R. A. Munson, *J. Phys. Chem.*, **68**, 3374 (1964).
19. S. Levine, G. M. Bell, and A. L. Smith, *ibid.*, **73**, 3534 (1969).
20. W. D. Kumler and G. M. Fohlen, *J. Am. Chem. Soc.*, **64**, 1944 (1942).
21. S. Furberg, *Acta Chem. Scand.*, **9** 1557 (1955).

Morphological Studies on the Li-Al Electrode in Fused Salt Electrolytes

Albert K. Fischer and Donald R. Vissers*

Argonne National Laboratory, Chemical Engineering Division, Argonne, Illinois 60439

ABSTRACT

Well-functioning Li-Al electrodes in Li-Al/FeS cells have an open, coral-like structure. Occasionally, a coalesced zone develops that is believed to cause a decline in capacity. Comparative morphology experiments suggest that β-Li-Al, as well as α-Li-Al, is involved in the development of coalescence in Li-Al electrodes operating in fused salt electrolytes. The course of developing coalescence is viewed as a sintering process; it is hypothesized that there is a contribution to this process from electrochemically formed diffusive pathways that develop between particles of β-Li-Al. Local overpotential is regarded as important in forming these pathways. A significant impact on the rate of coalescence is expected from the high lithium vacancy concentration and chemical diffusion coefficient in β-Li-Al. There is a clear correlation between coalescence and charging of the electrode. Variation of current density and electrolyte composition alone did not, within the range of the experiments, prevent coalescence.

Lithium-aluminum alloy, the electroactive material in negative electrodes in cells for high temperature lithium/iron sulfide batteries, develops several morphological features during cycling. The main characteristic of well-functioning electrodes is an open, interconnected network structure. However, another feature, a kind of coalescence, sometimes appears in certain developmental cells that use these electrodes (1). An example is shown in Fig. 1. The phenomenon has practical significance in these cells because the densified regions are believed to hinder movement of lithium into and out of the electrode and therefore are expected to contribute to capacity decline. Work reported here shows that a capacity decline process (probably at least partially related to coalescence) does occur in the negative electrode, but leaves open the possibility that in a complete Li-Al/FeS cell, additional processes to diminish overall cell capacity could occur elsewhere, such as in the iron sulfide electrode.

The coalesced condition is not the result of an instantaneous, calamitous event. Rather, the coalescence is the result of a sequential process that in various stages will show differing degrees of densification. The technological process that has been studied extensively and which the coalescence process closely resembles, if it is not identical to, is sintering. This process and the relevant theory have been the subject of much study and have recently been reviewed by Waldron and Daniell (2). Neck formation and growth is observed as the first stage of coalescence in the comparative morphology experiments described in this paper. The connected porous (or skeletal) structure that is regarded as advantageous for a functioning Li-Al electrode in developmental cells (3) and that also is found in our current experiments may be hypothesized, in our view, as a stage in the coalescence process subsequent to neck formation, a stage in which open porosity exists but is probably declining. The ultimate coalesced state is regarded as having advanced to a condition with, probably, some closed porosity. However, since at least a steady-state morphological condition is reached in well-functioning engineering cell electrodes, and since such electrodes can be formed from massive aluminum, we propose to regard the morphology development of the Li-Al electrode in terms of a composite of processes and concepts, which include (*i*) sintering, (*ii*) electrochemical processes that help establish the initiating and propagating conditions for interparticle growth (4), and (*iii*) surface energy effects that can lead not only to larger bodies but to finer ones as well. We present evidence for the view that both the α- and β-phases of the Li-Al system (5) are influential in coalescence. Earlier views were centered on the role of the α-phase (3).

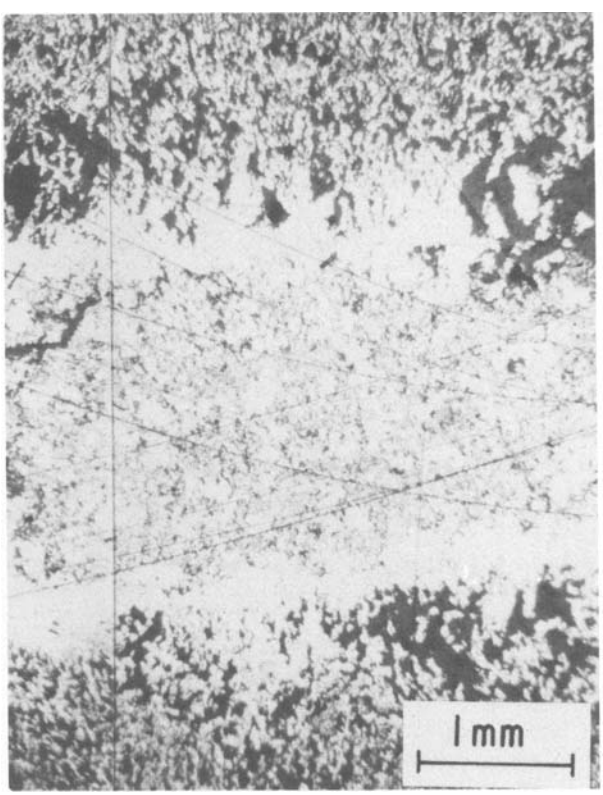

Fig. 1. Agglomeration occurring in negative electrodes of multiplate engineering cells. Photomicrograph available through courtesy of Dr. J. E. Battles, Argonne National Laboratory.

* Electrochemical Society Active Member.
Key words: alloy, anode, growth, overvoltage.

Experimental and Results

The objective of this study was to compare the effects of current density and electrolyte composition on coalescence. We developed a technique to make controlled comparisons of the morphological effects of these two variables against a baseline condition of morphology. The technique uses small, deep bed (~2 cm) porous electrodes. Earlier examinations of engineering cells (electrode thickness up to ~0.8 cm) had suggested a correlation between agglomeration and thickness of electrode. Hence, by using deep bed electrodes in the present study, the likelihood was enhanced for the occurrence of a zone favorable for coalescence. Also, the time required for the development of the baseline condition turned out to be conveniently short. All of our experiments lasted one week, much less than the several months that a developmental test cell usually runs. Our technique uses two electrodes cycled counter to each other. Geometrically, they were identical right circular stainless steel cylinders with 325 mesh stainless steel screens on the bottom. In the initial condition for an experiment, one electrode was loaded with ($\alpha + \beta$)-Li-Al [17.45 weight percent (w/o) lithium, 0.451 atomic fraction lithium, corresponding to about 96.3 mol percent (m/o) β-Li-Al]. The initial condition of the other electrode was pure aluminum. Both electrodes were sealed at the top after loading.

Electroactive material in the particle size range of −60 to +100 mesh was loaded in both electrodes to provide the initial state, but because of differences in particle shape the materials packed differently. The brittle ($\alpha + \beta$)-Li-Al (Kawecki-Berylco) consisted of irregularly shaped angular particles resulting from grinding, whereas the aluminum (Alcoa) was in the form of irregular globules resulting from the commercial blow-forming process. The volume fraction of vibratorily loaded ($\alpha + \beta$)-Li-Al was 0.56 and of the aluminum, 0.43. The loading density of the aluminum particles was 1.16 g/cm^3. In regions where the initially pure aluminum electrode was converted to β-Li-Al in the course of the experiment, the local volume fraction of active material is calculated to have become about 0.8-0.9. This loading is greater than that typical of negative electrodes in engineering cells (about 0.6). Thus, a prototypic range of loading volume fraction would have been traversed in the operation of the electrode. Although the electrodes used in these experiments differ in some respects from those of engineering cells, the morphologically determinative processes may reasonably be expected to be common to both systems. Thus, the study of the morphology in our electrodes would bear on the morphology found in the large-scale systems.

Experiments were performed in furnace wells attached to a high purity helium-atmosphere glove box. The cylindrical electrodes were immersed vertically in the molten salt electrolyte with the screens facing down, together with a reference electrode of similar construction and loaded with ($\alpha + \beta$)-Li-Al. The electrodes were filled with electrolyte (polarographic grade from Anderson-Physics Laboratories) by immersion in molten electrolyte under vacuum, with a gradual return of the furnace well to atmospheric pressure. After cycling, the electrodes were sectioned along the longitudinal axis, mounted, ground, and polished for metallographic study.

Table I lists the baseline experimental conditions. In addition to the baseline current density of 50 mA/cm^2, current densities of 25 and 150 mA/cm^2 were selected. In addition to the baseline electrolyte of LiCl-KCl eutectic (58.2 m/o LiCl-41.8 m/o KCl), two other electrolytes, "LiCl-rich" (67 m/o LiCl-33 m/o KCl) and all-lithium cation electrolyte (22 m/o LiF-31 m/o LiCl-47 m/o LiBr) were investigated. Two additional experiments to aid in the interpretation of the findings were (*i*) a blank experiment in which no current was passed but which otherwise incorporated baseline conditions, and (*ii*) a unidirectional current experiment at 25 mA/cm^2 with no cycling and in which lithium was only charged into the originally aluminum electrode and discharged out of the originally ($\alpha + \beta$)-Li-Al electrode.

Table I. Baseline experimental conditions

Particle size	−60 to +100 mesh in each electrode
Mass loading	1.128 A-hr of 17.45 w/o Li-Al (one electrode) 1.460g Al (other electrode)
Electrolyte	LiCl-KCl eutectic
Electrode geometry	2 cm depth, 0.78 cm^2 area, 1.56 cm^3 volume
Current density	51 mA/cm^2
Temperature	450°C
Cutoff voltages	0.2V, *IR*-included, both directions
Total duration of cycling	1 week

Under the baseline conditions, extensive coalescence developed in the electrode that was initially pure aluminum. In addition to the coalesced zone, a region of striated material developed that was aligned parallel to the direction of current flow in the electrode; see Fig. 2. These stria, which are longer than the average particle size of unreacted materials, are contiguous and joined to coalesced material, a situation that suggests that the stria are involved in the coalescence process. In the original Li-Al electrode of the baseline experiment, some striation was evident, but the coalescence was not of the degree that is considered deleterious. As the originally pure aluminum electrode is cycled, the aluminum is converted to β-Li-Al. This conversion results in a nearly twofold volume expansion and causes interparticle crowding to develop. In contrast, in the electrode originally composed of Li-Al the interparticle crowding is at its greatest in the as-fabricated condition before cycling occurs (the normal condition in a practical cell).

The blank experiment, where no current was passed, revealed no signs of coalescence in either electrode. At the end of the one-week experiment, the open-circuit cell emf was 0.194V. From Wen *et al.* (6), this potential would correspond to a composition on the electroactive surfaces in the originally aluminum electrode of about 3 atomic percent (a/o) Li in Al, a composition in the α-Li-Al region. The Li-Al reference electrode (described above), which was used for many of the experiments, also showed no signs of particle coalescence. Essentially no current passed through this electrode by virtue of its function; it did, however, experience freeze-thaw cycling between experiments. Particle coalescence in an electrode environment appears, therefore, to require the passage of current either as a preparatory step (for example, to clean the surfaces) or as an integral mechanistic component contributing electrochemical and mechanical features (for example, critical overpotential and expansion effects, respectively) to the ongoing morphological process.

The unidirectional current experiment revealed extensive particle coalescence in the reaction zone where β-Li-Al was formed in the originally aluminum electrode; see Fig. 3. In the upper zone of this electrode where the composition of the material was α-Li-Al, only a minor degree of reaction was achieved. Interparticle contacts and necking in this region were found, although the necking was much less extensive than in the β-Li-Al region. At 200× magnification, the necks in the α-Li-Al particles showed a retained line of grain boundary pores; the coalescence was not as advanced in this respect as among the β-Li-Al particles in the electrode. In the originally ($\alpha + \beta$)-Li-Al electrode, where only the discharge process occurred, no evidence for particle coalescence was found. The unidirectional current experiment suggested, therefore, that the sintering process is associated at least in part with charging of the electrode.

From the morphological data for the experiments covering the current density and electrolyte variables,

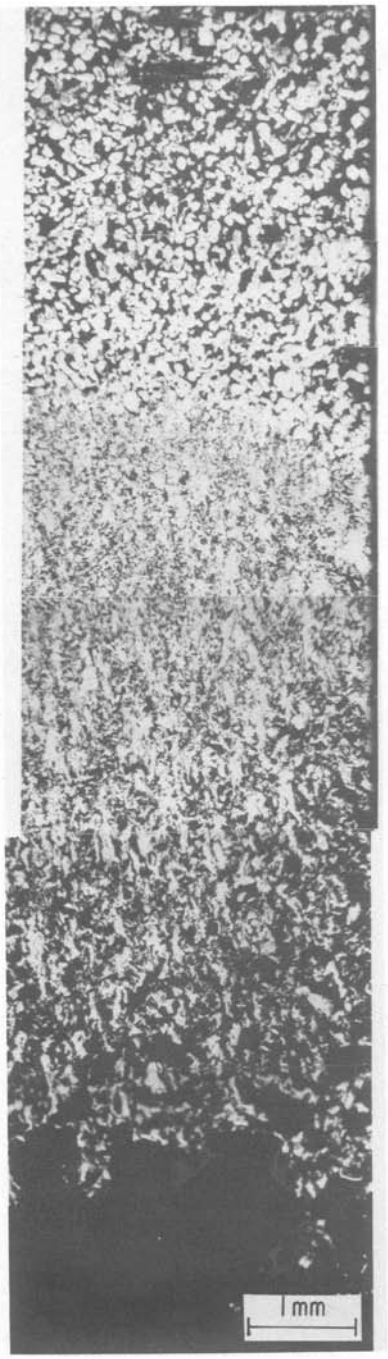

Fig. 2. Morphology observed in originally aluminum electrode under baseline conditions; includes coalescence and striation. Unreacted zone is at top.

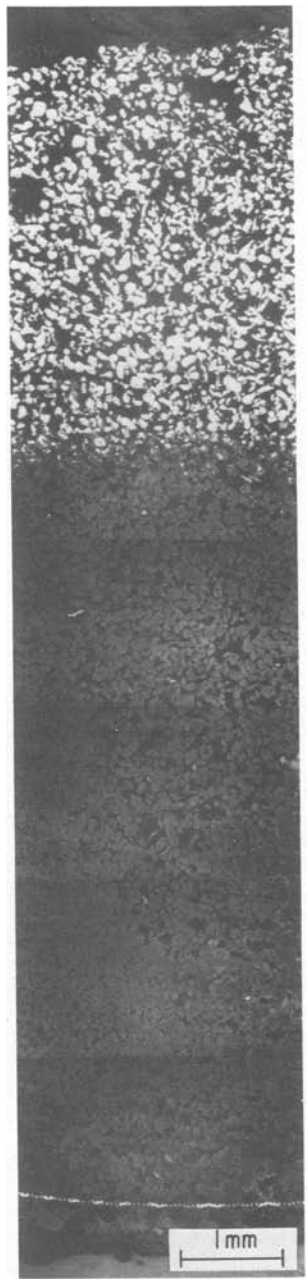

Fig. 3. Morphology observed in originally aluminum electrode that was only charged (unidirectional current experiment). Darker, tarnished zone of lower 3/4 of electrode is reaction zone.

summarized in Table II, it is apparent that electrolyte composition alone (in respect to lithium ion concentration) is not the key to preventing coalescence. The all-lithium cation electrolyte, the extreme case of lithium-ion richness, does not provide freedom from coalescence although in other aspects it showed favorable performance, such as in ease of electrode break-in. Similarly, the nominal current density does not seem to be a single determinative variable, though it is indicated below that local overpotential, and hence the related local current density, at particle surfaces within the electrode is important.

It is interesting to note that for the 50 mA/cm^2, all-lithium cation case, see Fig. 4, a striation zone occurs deeper (higher in the figure) in the reaction zone, close to the advancing reaction front as well as closer to the screen. The stria close to the reaction front appear more conspicuously aligned and developed than in most other cases; material both ahead of and behind the stria is coalesced.

Despite the substantial density change when a mass of β-Li-Al is discharged to α-Li-Al (about 1.7 to 2.7 g/cm^3 leading to about 52% predicted contraction) the outline of the body does not seem to change or shrink noticeably in a single discharge. In the unidirectional current experiment, the polished sample of the electrode originally composed of LiAl was treated with ethylene glycol to remove electrolyte. At 200$\times$ magnification, the discharged particles showed a fine-grained granularity believed to reflect porosity that developed during the β-to-α conversion. In the electrode originally composed of aluminum, after the ethylene glycol treatment, examination under a stereomicroscope showed a lava-like interconnectedness of electroactive material. This lava-like pattern has been described previously (1).

Examination of particles at the front edge of the reaction zone revealed few instances where the conversion of material proceeded inward from all surfaces

Table II. Findings from comparative morphology experiments*

Current density / Electrode / Electrolyte	25 mA/cm²		50 mA/cm²		150 mA/cm²	
	Li-Al	Al	Li-Al	Al	Li-Al	Al
Al-Li+	Only few cycles but deep RZ. No C. No S.	Few cycles. 14 mm RZ. Some C. No S.	Most of electrode reacted. Slightly advanced C. S at top of RZ.	15 mm RZ plus 1 mm strong S zone close to advancing edge of main RZ. C in main part of RZ with moderate S. Very little F.	Moderate C. S, F.	12 mm RZ. Moderate C. S less aligned than in baseline. Same F.
LiCl-rich	No C. No S.	12 mm RZ, with lower half showing considerable granularity and F. Upper half showing extensive C in early stage.	No C. Some S.	13-15 mm RZ. Strongly bulged screen. C, F, S.	Pronounced uniform F. No C. Slight S.	5 mm RZ. Pronounced uniform F. Incipient C at reaction front.
			Baseline case			
LiCl-KCl eutectic	No C. Some S and F near screen.	Fairly shallow RZ, about 5 mm. C, S,	S.	13 mm RZ. C, S.	No C. Slight F.	Shallow RZ, about 3 mm. S, F.

* C, coalescence; S, striation; F, fineness; RZ, reaction zone.

in contact with electrolyte. Instead, a zone of reaction product was frequently seen starting at a point on the particle surface and advancing toward the interior of the particle, or through the particle, leaving other parts of the surface unreacted. An example is shown in Fig. 5. Sometimes reaction sites on a particle could be seen, even on the side away from the screen. This observation will probably have kinetic implications for models that assume that particles react uniformly on their surfaces to form shells of reaction product around a core of unreacted material (7).

The cycled electrodes often showed development of "fines" and a thinning out of material density at the bottom, close to the screen. An example is shown in Fig. 6. Assuming interparticle connectedness was retained, it is not likely that this material simply fell through the screen. However, it is possible that a process occurs analogous to that reported by Szpak *et al.* (8) whereby stria of material are undercut electrochemically, with the resulting fragments migrating in the electrolyte by a displacement mechanism or by an electrophoretic process. If such a process occurs, it could be the means for transfer of material toward the electrode interior, contributing to densification there. An additional fragmentation hypothesis based on surface energy effects is discussed in the next section.

Although the primary purpose of the comparative morphology experiments was an examination of coalescence conditions, we also gained information related to electrode capacity. The lithium content of each electrode was determined for the end of each half-cycle as the product of current and duration of the half-cycle. Plots of these data have been published elsewhere (9). Comparing curves showing the amounts of lithium retained after a discharge with curves showing the amount present after a charge (the difference being a measure of capacity) indicates that a capacity decline phenomenon is associated with the Li-Al electrode. Although the emphasis of this study is on the coalesced state of morphology as a likely cause for capacity decline, evidence was found that suggests development of fines is likely to be an additional cause for capacity decline. This is most clearly borne out by the 150 mA/cm² case in LiCl-rich electrolyte, shown in Fig. 6. The photomicrograph shows only slight or incipient coalescence at the reaction front, but pronounced and uniform fineness throughout the reaction zone. The lithium inventory curves, published in Ref. (9), show an increasing retention of lithium on discharge. Fines in the electrode could account for some of this diminution of electroactive lithium if they become electrically disconnected from the bulk of the electrode or if their remaining connections become highly resistive.

Discussion

In the comparative morphology experiments, the lack of coalescence in most cases of the originally Li-Al electrode is noteworthy. It might be expected that the tendency to join particles would be less in these electrodes because the initially Li-Al particles are most crowded at the start and alternate between this state and a less crowded one on discharge. Even if interparticle pressure promotes coalescence, this effect is minimized in the initially Li-Al electrode. Nevertheless, exceptions to the lack of coalescence in initially Li-Al electrodes were observed in the middle and high current cases with all-lithium cation electrolyte. In addition to coalescence, striation was also observed. In these electrodes, even with lessened pressure between particles, coalescence still occurs.

We hypothesize that the development of striations is an example of an early stage of sintering involving β-Li-Al protrusion growth on particles, extension of a protrusion to contact a neighboring particle, neck formation, and coalescence of particles into a stranded configuration. In support of the protrusion hypothesis we recall our earlier observations of β-Li-Al protrusion growth on massive aluminum surfaces where lithium was electrodeposited (9). The directionality of the striations is expected to be a consequence of this interparticle protrusion growth and bridge development (or neck growth, in sintering terminology) that is favored along lines of current flow. Protrusion growth, being influenced by diffusional flow to the protrusion, is strongly correlated with the current flow since it is known that diffusive lines are parallel to current lines (4). In addition to initiating a diffusion pathway between particles when contact is made, the points of protrusions also are expected to be sites of local high pressure if external compression forces develop to force particles together. Such a process would further favor coalescence.

In a consideration of the atomic motions that would be needed to join particles, it can be seen that certain properties of β-Li-Al are unusual and are expected to contribute to its role in the coalescence process. They are the very high lithium vacancy concentration (up

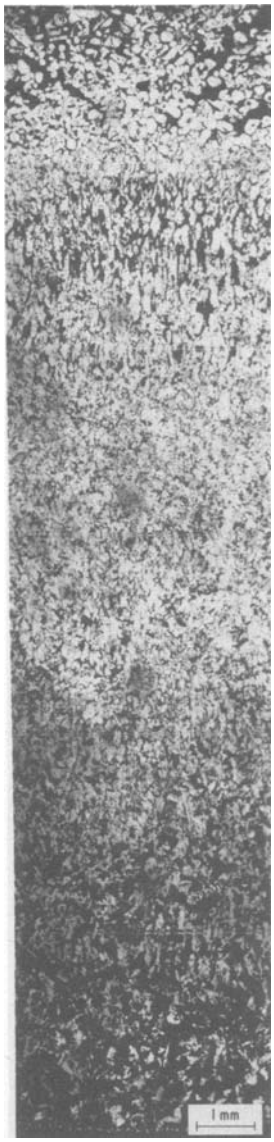

Fig. 4. Morphology observed in originally aluminum electrode cycled at 50 mA/cm^2 in all-lithium cation electrolyte. Only a small unreacted zone is at top. Note striation near top of reaction zone.

to about 3%) that occurs mainly in the lithium sublattice (10, 11) and the high lithium chemical diffusion coefficient that at $\sim 10^{-5}$ cm^2/sec approximates that in liquids (6). These two properties would significantly influence the sinterability of β-Li-Al, considering that in crystalline metals and ceramics the mass transport in sintering is generally by bulk diffusion (3).

In β-Li-Al, at 450°C, aluminum probably diffuses more slowly than lithium. At room temperature and below, the aluminum atoms are essentially immobile (10). However, at 450°C, which is about ¾ of the absolute melting point of β-LiAl and is well above the Tammann temperature, it is likely that aluminum becomes mobile. However, aluminum, in the development of interparticle bridges, may not move exclusively by a diffusion process. For example, lithium depositing on the tip of a β-Li-Al protrusion will result in a local composition that is in the lithium-rich part of the β-phase field and will establish a lithium activity gradient in the protrusion. This is possible because the β-Li-Al single phase field in the Li-Al phase diagram covers approximately a 50-fold range of lithium activity (6). The driving force of this activity gradient causes lithium to diffuse rapidly through the β-Li-Al protrusion to the aluminum-rich base. There, the

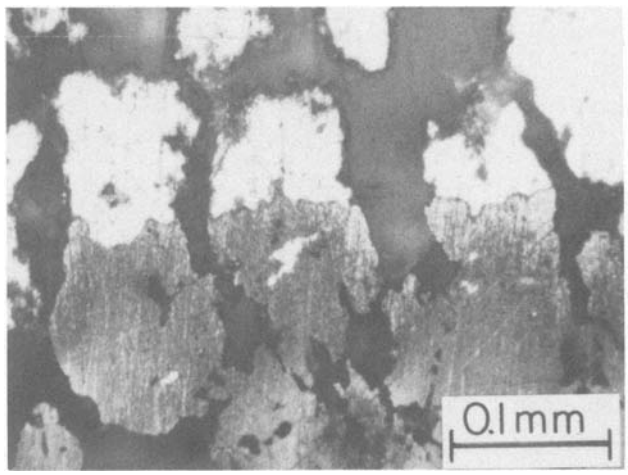

Fig. 5. Example of reaction zone advancing through a particle rather than forming a shell. Unreacted portion is in upper portion of particles.

reaction to form the less dense β-Li-Al from α-Li-Al would cause the protrusion to grow from the base and to carry its aluminum content with it. The progression of lithium into aluminum-rich material at the base, or anywhere the α-to-β conversion is taking place, is, thus, not limited by the relatively slow bulk diffusion of lithium in α-Li-Al. [The chemical diffusion coefficient of lithium in aluminum is of the order of 10^{-10} cm^2/sec

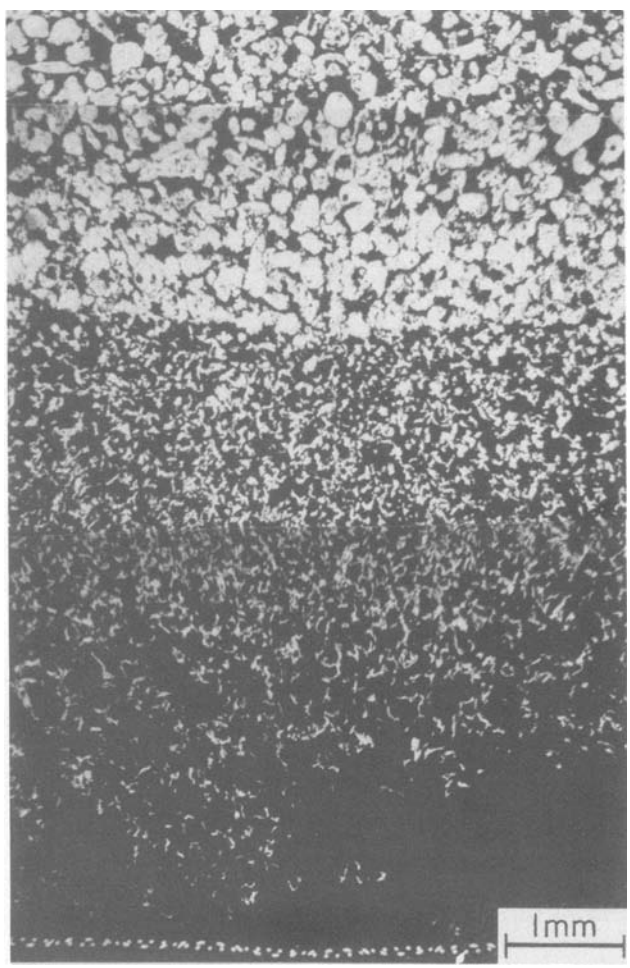

Fig. 6. Fine-textured reaction zone formed in experiment in LiCl-rich electrolyte at 150 mA/cm^2. The reacted portion in the lower two-thirds of the figure is to be compared with the corresponding portion of the baseline case shown in Fig. 2.

(12).] Instead, the α-Li-Al structure at the reaction interface is broken up from one side, at least to the degree of forming a β-like reaction intermediate of monolayer dimensions. The movement of lithium, to complete the conversion to β-Li-Al, through such a loosened structure can be expected to be more rapid than movement through bulk α-Li-Al.

For the initially Li-Al electrodes in all-lithium cation electrolyte, we note that coalescence occurred in the middle and high current-density cases and to a degree that was worse for the high-current case than for the middle-current case. In the LiCl-rich electrolyte studies, striation (but no extensive coalescence) appeared in the middle- and high-current density cases. This dependence of the striation-sintering process on current density can be understood in terms of protrusion growth, which in other cases is known to be dependent on overpotential and current density (4).

Protrusions are augmented surface irregularities; the phenomenology and related theory have been treated by numerous workers and were reviewed by Despić and Popov (4). The general equation [Eq. [29] of Ref. (4)] of this theoretical development was applied to the present case. We emphasize, however, that the theoretical development, as given by Despić and Popov, was for electrodeposition of a single component, a process that can be expected to differ from the more complex deposition-diffusion reaction process in the Li-Al electrode. Our application of the equation is intended as an analogy to rationalize the observed morphological dependences on current density; the numbers are illustrative, and are not suggested to be the actual values pertinent to this system. Thus, a curve calculated for the growth rate of protrusions as a function of overpotential, using reasonable values for parameters in the Despić and Popov equation, is fairly flat until a critical region of overpotential (about 10-30 mV) is reached. At higher overpotentials the protrusion growth rate increases rapidly. Also, the growth rate as a function of tip size is a flat maximum for tip radii in the approximate range 10^{-5}-10^{-3} cm and falls off significantly for smaller and larger tips. Though it is known that morphology strongly depends on overpotential, an evaluation of overpotentials in the experiments is difficult at this time because local values of activities inside the electrodes cannot be determined in order to calculate local reversible potentials. Other experimentation designed to measure critical overpotentials for protrusion growth is needed.

Comparing the initially Li-Al electrode from the unidirectional current experiment with that from the baseline experiment (these experiments were identical except that one was cycled and the other was not), we found that the Li-Al electrode that was only discharged showed no striations, but the cycled Li-Al electrode showed striations. The development of striations appears, therefore, to be associated with the charging process. This result is consistent with the suggested occurrence of β-Li-Al protrusion growth, a process that would occur during charging. In the originally Li-Al electrodes, furthermore, there is negligible interparticle pressure development during cycling, as already discussed, so that striation development from such pressure (if it is a cause) would also be negligible.

The initially aluminum electrode from the unidirectional current experiment, besides showing that coalescence proceeds during charging, also provides insight into the active participants in the coalescence process. In this electrode, shown in Fig. 3, the initial interparticle contacts would probably have been α-to-α, or possibly occasional β-to-β contacts, as lithium deposition started. The extent of coalescence produced from α-to-α contacts during the experiment may be judged from the upper portion of the electrode (α-Li-Al region). Compared with α-to-α neck development in this region, we might expect the degree of coalescence through α-to-α contacts in the lower region to be less because the formation of β-Li-Al in the lower region would have shortened the existence time of α-material. The more extensive coalescence (in terms of numbers of contacts and degree of advancement) observed among the β-Li-Al bodies in the lower part suggests that additional interparticle contacts developed as the particles expanded toward each other as a result of the α-to-β conversion and that the earlier α-to-α joins were converted to β-necks. The new contacts would have been β-to-β or β-to-α in composition. Therefore, the coalescence process would be dominated in this region by a mechanism involving β-Li-Al, but in coexistence with a mechanism involving α-Li-Al. However, it is not implied from the observation of coalescence during charging that coalescence cannot continue during a discharge of the electrode or during an open-circuit period; the consolidating processes initiated during a charge of a cycled electrode do not necessarily stop immediately and reverse when the next discharge starts. Such processes might include diffusion along sintering pathways or pressure-induced sintering under pressure generated by expansive forces due to β-Li-Al formation, or, in engineering cells, under pressure due to expanding positive electrodes.

In the comparative morphology experiments, the electrode potentials of either electrode, under the cutoff conditions of ±0.200V *IR*-included cell voltage, never reached values that would have permitted a liquid Li-Al phase to form. The most negative *IR*-free potential ever applied to an electrode was only 104 mV more negative than the reference electrode. To form liquid phase would have required an electrode potential at least 230 mV (*IR* free) more negative than (α + β)-Li-Al (6). The absence of such a liquid phase rules out the possibility of a role for liquid Li-Al coalescence.

Universally in the comparative morphology experiments, and usually in engineering cells (3), the coalesced region is found in the interior of the electrode and not at the screen. Closer to the screen, the morphology is more finely textured. Where fineness is pronounced, it is reflected in Table II by the notation "fineness." Insight for the location of coalesced zones can be found in the theories and phenomenology related to augmented surface irregularities in electrodeposition in the above-mentioned review (4). From this background, it is known that the roles of local overpotential, current density, and induction time in the initiation and growth of an asperity are interrelated. Under conditions of constant current charging, the applied potential increases with time. The portion of the *IR* drop between the electrodes remains essentially constant, assuming an essentially constant interelectrode cell resistance. The increase in applied potential as it influences local overpotential, then, must be accommodated within the electrodes, more so deeper inside the porous structure than near the screen. In this way, the local overpotential increasing in the interior may be expected to reach the levels required for substantial increases in the growth rate of irregularities on particle surfaces at interior sites.

More detailed profiles of conditions in an electrode have been calculated in the mathematical modeling of the porous electrodes in the Li-Al/FeS battery by Pollard and Newman (7). The Pollard-Newman treatment supports belief in the generally increasing local overpotentials within the electrode. According to their model, composition shifts for the electrolyte (hence, one deduces, local overpotential shifts) inside the electrode are predicted to be substantial, leading to precipitation of KCl, for example, in zones within the Li-Al electrode during charging. They also predict precipitation in the FeS electrode. Experimental observations of such intraelectrode precipitation have been reported for the charged FeS positive electrode by Martin *et al.* (13). Also, an electrolyte concentration gradient in the electrolyte in the separator between electrodes of an Li-Al/electrolyte/Li-Al cell has been demonstrated experi-

mentally by Braunstein *et al.* (14) so that the expectation of localized overpotential changes within the electrodes, brought about by electrolyte concentration shifts and perhaps by precipitation, appears well supported.

The more broken-up strandedness and generally finer texture that develop near the screen can be rationalized by several processes; at our present level of understanding all of these may be assumed to occur to various degrees. One involves the possibility of electrochemical fragmentation and undercutting as reported by Szpak *et al.* (8). Another would be a possibility for a process analogous to powder formation during electrodeposition (4); in this case, even higher overpotentials than those allowing protrusions to grow would, presumably, need to be invoked. For a third process we hypothesize that surface energy changes for different parts of a body as the body's composition changes (*e.g.*, between α- and β-LiAl) will favor separation of these parts. Details of the analysis will be presented elsewhere, but the general situation for cylindrical systems with parts of different compositions is that the drive to diminish surface energy will facilitate separation of parts from very slender bodies with any reasonable combination of assumed surface energies for the parts, but for squat bodies, surface energy differences will not favor separation. The critical length-to-diameter ratio for favored separation is diameter dependent, and for a critical size ratio there is a critical ratio of surface energies, too, if separation is to be allowed. Thus when an electrode is cycled and various parts of the particles change composition and, hence, surface energy, conditions are set up which satisfy the separation criteria to various degrees. With the establishment of a thermodynamic driving force for separation, kinetic factors will then influence the degree to which fragmentation actually occurs. In this way, a rationale based on surface energy and geometric considerations contributes further to an understanding of the development of fines in the Li-Al electrode.

Conclusions

We have presented evidence for a role for β-Li-Al in the coalescence process in Li-Al electrodes and recognize the likelihood for a role for α-Li-Al as well. The coalescence process is associated at least in part with charging of the electrode.

Current density or initial electrolyte composition alone, in the range studied, are not variables by which one may prevent coalescence. Striated morphology, regarded as an intermediate stage in the sintering progression, is seen as resulting from β-Li-Al protrusion formation and bridging between particles. The high lithium vacancy concentration and the high chemical diffusion coefficient of lithium in β-Li-Al are expected to have deep significance for the electrochemical behavior and morphological development of this system. Local overpotential is regarded as important in determining the initiation and growth of morphological features. Surface energy effects are considered influential in the development of fine texture in an Li-Al electrode. A liquid Li-Al phase was not involved in the coalescence in these experiments. A model to rationalize comprehensively the electrochemical performance and morphological development of the electrode would need to deal with the time dependence of (*i*) local overpotential effects as they are influenced by local composition shifts for electroactive material and electrolyte (conductivity and transport number changes in the electrolyte will probably be interrelated) and (*ii*) local mechanical effects from pressure changes due to electrolyte solidification and redissolution and to density changes in electroactive material.

If vacancy concentration and lithium diffusivity bear on sintering, it appears desirable to modify the solid-state chemistry of the Li-Al system with additives. However, it is possible that gains in a stabilized morphology might come at some sacrifice in electrochemical kinetics and performance. Some experiments have been performed to explore the effect of additives and will be reported elsewhere.

Acknowledgment

We are grateful for the use of the metallographic facilities extended us by Dr. J. E. Battles and for the technical assistance of W. R. Lehman, as well as for the encouragement given by Dr. Duane Barney and Dr. R. K. Steunenberg. This work was supported by the U.S. Department of Energy under Contract W-31-109-Eng-38.

Manuscript submitted Dec. 14, 1981; revised manuscript received July 22, 1982.

Any discussion of this paper will appear in a Discussion Section to be published in the December 1983 JOURNAL. All discussions for the December 1983 Discussion Section should be submitted by Aug. 1, 1983.

Publication costs of this article were assisted by Argonne National Laboratory.

REFERENCES

1. F. C. Mrazek and J. E. Battles, Argonne National Laboratory Report ANL-79-39, p. 50.
2. M. B. Waldron and B. L. Daniell, "Sintering," Chap. 2, Heyden, London (1978).
3. J. E. Battles, F. C. Mrazek, and N. C. Otto, Argonne National Laboratory Report ANL-80-130, p. 20.
4. A. R. Despić and K. I. Popov, in "Modern Aspects of Electrochemistry," Vol. 7, B. E. Conway and J. O'M. Bockris, Editors, p. 199, Plenum Press, New York (1972).
5. K. M. Myles, F. C. Mrazek, J. A. Smaga, and J. L. Settles, Argonne National Laboratory Report ANL-76-8, p. B-69 (1976).
6. C. J. Wen, B. A. Boukamp, R. A. Huggins, and W. Weppner, *This Journal*, **126**, 2258 (1979).
7. R. Pollard and J. Newman, *ibid.*, **128**, 491, 503 (1981).
8. S. Szpak, C. T. Gabriel, and T. Katan, *ibid.*, **127**, 1063 (1980).
9. A. K. Fischer and D. R. Vissers, in "Symposium on Lithium Batteries," H. V. Venkatasetty, Editor, p. 442, The Electrochemical Society Softbound Proceedings Series, Pennington, NJ (1981).
10. H. E. Schone and W. D. Knight, *Acta Metall.*, **11**, 179 (1963).
11. K. Kishio and T. O. Brittain, *J. Phys. Chem. Solids*, **40**, 933 (1979).
12. C. J. Wen, W. Weppner, B. A. Boukamp, and R. A. Huggins, *Met. Trans.*, **11B**, 131 (1980).
13. A. E. Martin, M. F. Roche, and Z. Tomczuk, Argonne National Laboratory Report ANL-75-1, p. 108 (July 1975).
14. J. Braunstein, S. Cantor, and C. E. Vallet, ORNL/TM-7639 (March 1981).

Effective Conductivities of a Positive Electrode in an Li-Al/FeS Cell at Different States of Charge

M. Hiroi[1] and H. Shimotake*

Chemical Engineering Division, Argonne National Laboratory, Argonne, Illinois 60439

ABSTRACT

Effective conductivities of porous electrodes containing FeS as the initial active material and 54 weight percent (w/o) LiCl-KCl electrolyte were experimentally determined at 450°C for different states of charge by means of an a-c impedance bridge. The effective conductivity of the fully charged FeS electrode was found to be approximately 7 $\Omega^{-1} \cdot cm^{-1}$, about four times higher than the conductivity of the electrolyte. This high effective conductivity is considered to be one of the superior features of the FeS cells because such high conductivity results in high power density without the addition of conductive material. The change of the electrode effective resistance during the discharge is discussed in connection with both the electrode reactions and the results of metallographic examinations.

An Li-Al/FeS cell operating at temperatures ranging from 430° to 500°C has been under development for electric-vehicle propulsion and stationary energy-storage applications (1). Experimental results indicate that the resistance of the Li-Al/FeS cell increases with discharge (2, 3). Efforts to lower the cell resistance are being made in order to increase its power capability. However, at present, detailed knowledge of the resistance as a function of state of charge is lacking. To help understand this cell-resistance behavior, separate determinations of effective conductivities of each positive and negative electrode, respectively, are needed.

In this study, polarization-free effective conductivities of porous electrodes containing FeS as the active material were determined. Typical electrodes were measured in the 54 weight percent (w/o) LiCl-KCl (67.4 mol % LiCl-KCl) electrolyte at 450°C for different states of charge by means of an a-c impedance bridge. The FeS electrode demonstrated high conductivity in the first stage of discharge and significant decline of the electrode resistance at the final stage of discharge. This unique behavior is discussed in connection with the electrode reactions and the results of metallographic examinations.

Experimental Procedure

The test cell, shown in Fig. 1, consisted of an FeS working electrode, an Li-Al counterelectrode, and a reference electrode. These electrodes were immersed in about 80 ml of 54 wt % LiCl-KCl (67.4 mol % LiCl-KCl) (LiCl-rich) electrolyte contained in a 200 ml molybdenum beaker, which also served as an electrode for the impedance measurements. The distance between the surface of the FeS electrode and the bottom of the molybdenum beaker was kept at 0.5 cm with a boron nitride spacer, which is not shown in the figure. The 54 wt % LiCl-KCl (polarographic grade) was obtained from Anderson Physics Laboratory, and the FeS was obtained from Great Western Inorganic. Prior to mixing, both the FeS and LiCl-KCl were ground and sieved to −50, +120 mesh. The mixture was then loaded into a set of dies and pressed into a cylindrical pellet with a hand press. The cell was operated at 450°C in a furnace well which was attached to a helium-atmosphere glove box. An Ni/Ni_3S_2 reference electrode, whose potential is 1.364V against the Li-Al electrode at 450°C when nickel and stainless-steel terminals are used (4), was used for monitoring the FeS electrode. A sheathed Chromel-Alumel thermocouple was inserted into the cell. Boron nitride (supplied by Union Carbide Corporation) was used to make an electrode housing which had a cavity of 0.63 cm diam and 0.4-0.75 cm depth. The pressed mixture of active material containing 82.7 wt % FeS and 17.3 wt % electrolyte, corresponding to a loading density of 1.4 A · hr/cm³ or 55% porosity, was placed in the cavity. This working electrode was covered with fine stainless steel screen (325 mesh) for both particle retention and constraint of volume change during cell reaction.

The FeS electrode was brought to a desired state of discharge by discharging slowly at a current density of 10 mA/cm² or less. When the closed circuit voltage of the FeS electrode reached −0.2V *vs.* Ni/Ni_3S_2, the discharge was terminated, and a subsequent charge was made at the same current density. The impedance of the FeS electrode was measured by interrupting the discharge or charge current and applying an a-c cur-

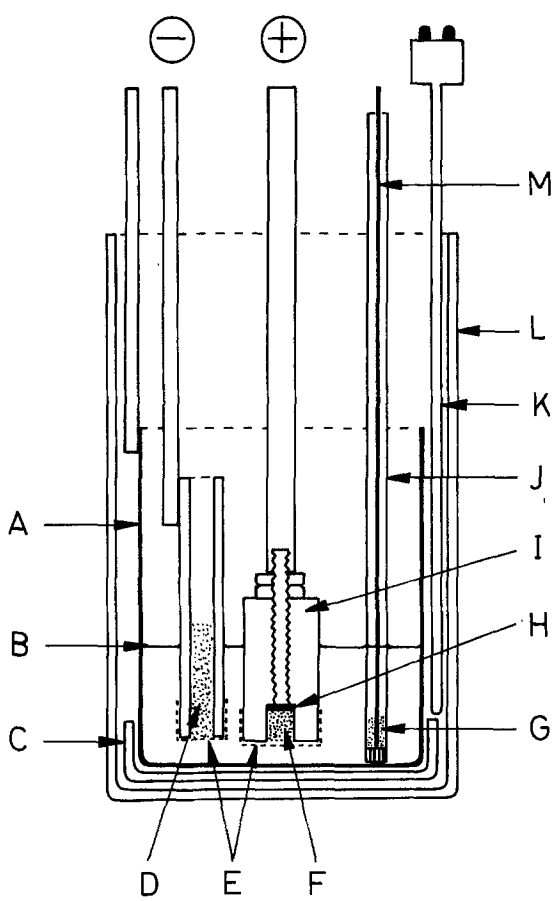

Fig. 1. Cell assembly. A—molybdenum beaker, B—electrolyte level, C—Pyrex beaker, D—Li-Al, E—stainless steel mesh, F—positive active mass, G—Li_2S, H—steel current collector, I—boron nitride housing, J—Ni/Ni_3S_2 reference electrode, K—thermocouple, L—Al_2O_3 crucible, M—Ni wire.

* Electrochemical Society Active Member.

[1] Present address: Kobe University of Mercantile Marine, Higashi-nada, Kobe 658 Japan.

Key words: cathode, conductivity, molten salt, impedance, iron sulfide.

rent with an impedance bridge; the circuit for the bridge is shown in Fig. 2. The impedance measurements were begun several minutes after interrupting current because the impedance changed little even after 3 hr of open circuit; at a peak resistance, 0.90-0.88Ω in 3 hr. The polarization-free resistance was determined from extrapolation to infinite frequency of the observed ohmic resistance against $f^{-1/2}$, where f is frequency in Hz. The impedance measurements were made over a frequency range of 200-20,000 Hz. Cell constants were determined from the resistance values obtained by using the unloaded electrodes (I in Fig. 1) in the electrolyte at 450°C and the conductivity of the electrolyte, 1.83 $\Omega^{-1} \cdot cm^{-1}$ (5). The electrolyte dissolves small amounts of cell components, such as FeS (6), Li_2S (6, 7), and Li from the Li-Al anode during discharge and charge. The dissolution causes change in conductivity of the electrolyte. The conductivity measurement at fully-discharged state showed that the conductivity increased by 1.5-5%. This change was considered small and negligible.

Results and Discussion

Typical changes in the effective specific resistance of a 0.4 cm thick FeS electrode during the first cycle at different states of discharge and charge are shown in Fig. 3. The impedance of the FeS electrode is related to the state of charge (SOC) on both discharge and charge. The electrode resistance initially decreases with discharge, then rapidly increases. After the discharge has reached about 70-80% utilization of the theoretical capacity, the electrode resistance reverses its trend and starts to decrease. During charge, the resistance values are lower than those during discharge at all states of charge. At full charge, the resistance does not completely return to its initial value, which is always higher than any resistance value obtained after the cell has been activated.

Figure 4 shows the resistance change during the second cycle. The resistance pattern, which includes a resistance peak, is similar to the pattern of the first cycle. Similar behavior is also observed with FeS electrodes of different thicknesses, as shown in Fig. 5. No increase in the specific resistance was observed when the electrode thickness increased from 4 to 6 mm. However, a significant increase in the effective specific resistance was observed when the thickness was increased from 6 to 7.5 mm, particularly at the peak resistance in the latter stage of the discharge, indicating that perhaps in a thick electrode, distribution of the reaction phase is less uniform. The pattern of the effective specific resistance *vs.* utilization curve changed with current density. The resistance peak shifted to lower utilization as the discharge current density increased. For example, the resistance peak shifted to about 50% utilization at 80 mA/cm^2. However, at current densities lower than 10 mA/cm^2 the identical relationship could be obtained.

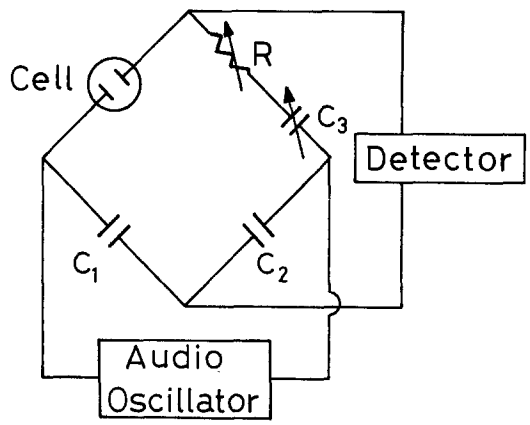

Fig. 2. Circuit diagram of the bridge. $C_1 = C_2 = 0.5$ μF, $C_3 =$ 0.1-1,000 μF, $R =$ 0.2-100Ω.

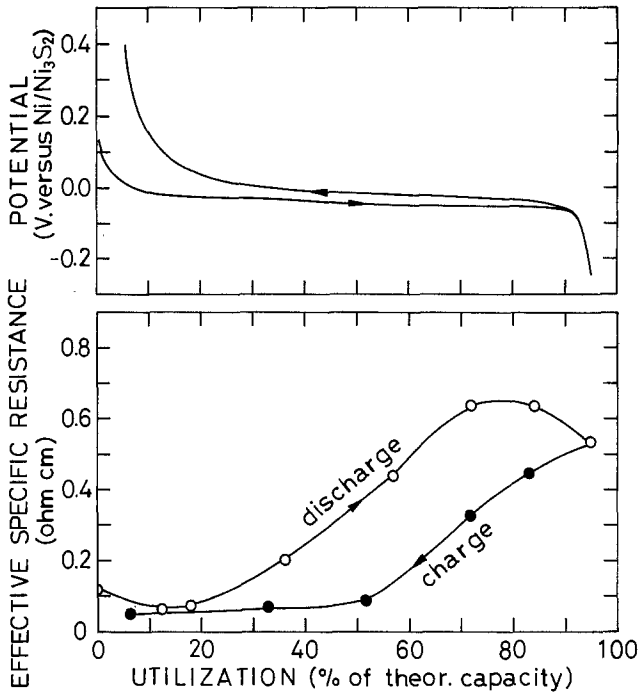

Fig. 3. Change of the effective specific resistance of an FeS electrode at the first cycle. The electrode thickness was 4 mm and its porosity was about 55%.

The initial values of the effective specific resistance of an electrode vary somewhat from electrode to electrode, ranging from 0.11 to 0.5 Ω · cm. The variation in the initial resistance values of the FeS electrode can be attributed to difficulties in preparing completely homogeneous mixtures and in uniform pressing.

Effective conductivities of heterogeneous systems such as FeS dispersed in molten salt can be calculated from the equation developed by Meredith and Tobias (8). The equation that deals with effective conductivities of heterogeneous systems for two-phase mixtures containing spherical particles is as follows

$$K_m = \left[\frac{2(K_d + 2) + 2(K_d - 1)v}{2(K_d + 2) - (K_d - 1)v}\right] \times \left[\frac{(2 - v)(K_d + 2) + 2(K_d - 1)v}{(2 - v)(K_d + 2) - (K_d - 1)v}\right] \quad [1]$$

where $K_m = k_m/k_c$, $K_d = k_d/k_c$, and v is the volume fraction of the dispersed phase (*i.e.*, FeS); k_m is the specific conductivity of the mixture; k_d is the specific conductivity of the dispersed phase; and k_c is the specific conductivity of the continuous phase (*i.e.*, molten salt). The specific conductivity, k_d, of FeS was estimated from Eq. [1] to be more than 2.1 Ω^{-1} cm^{-1} from our experimental values of $k_m = 2.0 - 9.1$ Ω^{-1} cm^{-1}, using 1.83 $\Omega^{-1} \cdot cm^{-1}$ as the value of k_c, and 0.45 as the value for v. The range of the values is consistent with the reported value of 3.6 $\Omega^{-1} \cdot cm^{-1}$ (9), which was experimentally measured for a cast bar of FeS at 450°C. This result indicates that a typical FeS electrode in Li-Al/FeS cell at a fully charged state has a high effective specific conductivity.

For a given configuration of the FeS electrode, the effective specific conductivities of the dispersed phases, which include Fe, FeS, Li_2S, and intermediate phases such as $LiK_6Fe_{24}S_{26}Cl$ (J phase) electrode. Although the thermodynamic and chemical equilibrium relationships among the cell reactants are still not completely understood, the following reactions have been identified as probable reactions (10-13)

$$6Li^+ + 26FeS + 6KCl + 6e^- = LiK_6Fe_{24}S_{26}Cl\,(J\ phase) + 2Fe + 5LiCl \quad [2]$$

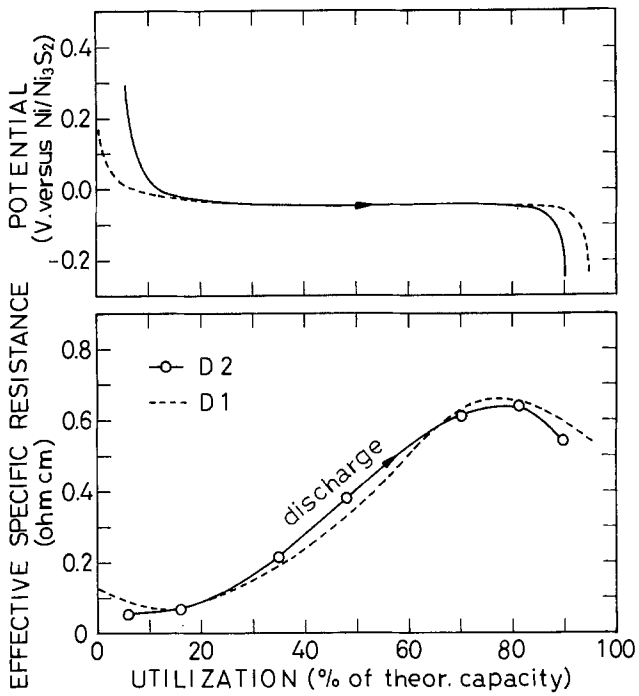

Fig. 4. Change of the effective specific resistance of the FeS electrode on the second discharge.

$$20Li^+ + J + 5LiCl + 20e^- = 13Li_2FeS_2\ (X\ phase) + 11Fe + 6KCl \quad [3]$$

$$2Li^+ + 2FeS + 2e^- = X + Fe \quad [4]$$

$$2Li^+ + X + 2e^- = 2Li_2S + Fe \quad [5]$$

When an FeS electrode is cathodically discharged, the J phase starts to form at the surface of FeS particles according to Eq. [2], accompanied by the production of iron. A part of the J phase is, in turn, chemically converted to X phase by one or more of the following chemical reactions (6, 14, 15), while the rest of J phase reacts according to Eq. [3]

$$J + 20Li_2S + 5LiCl = 23X + Fe + 6KCl \quad [6]$$

$$J + 5LiCl = 3X + 20FeS + Fe + 6KCl \quad [7]$$

$$J + 5LiCl = 23FeS + 3Li_2S + Fe + 6KCl \quad [8]$$

$$FeS + Li_2S = X \quad [9]$$

In the LiCl-rich electrolyte, the chemical formation of J phase is suppressed to an insignificant level, as has been confirmed by metallographic examinations (13). Thus, in an FeS electrode containing the LiCl-rich electrolyte, the contribution to the resistance increase by J phase should be insignificant. In such a case, the X phase is believed to be the predominant intermediate in the FeS electrode containing LiCl-rich electrolyte, accounting for as much as 50% of the theoretical capacity.

The results of the present study indicate that the contribution of the X phase of the resistance increase is small, as shown in Fig. 6 by the flat curve during the first 50% of discharge. This result is further supported by the electrode-resistance change of an FeS electrode containing LiCl-LiBr-LiF electrolyte. In this electrolyte where the lithium ion is the only cation, the formation of J phase is completely eliminated due to the absence of the potassium ion; X phase is formed according to Eq. [4], then discharged to Li_2S and Fe according to Eq. [5] (12). In Fig. 6, the first 50% discharge corresponds to the reaction described by Eq. [4]. During this reaction, the electrode resistance remains relatively flat at a low level, indicating that the formation of X phase does not affect the electrode resistance. The increase in the electrode resistance is observed when the formation of Li_2S occurs according to Eq. [5] as the X phase is cathodically discharged. This was confirmed by impedance measurements of an electrode containing X phase as the starting material. The results shown in Fig. 7 indicate that the resistance of the electrode containing the X phase as the starting material is higher from the start than the resistance of the electrode containing FeS and immediately begins to increase as the electrode is discharged. In Fig. 7, the resistance value is plotted from 50% theoretical capacity (which is based on FeS) because the X phase can be considered to be the material in the FeS electrode which has been discharged 50%. However, the porosity and composition of the X-phase electrode are perhaps not exactly the same as those of the actual FeS electrode at the 50% discharged state, since at 50% discharge an FeS electrode contains some Fe according to Eq. [4] and a small amount of unreacted FeS and J phase according to Eq. [6]-[8].

It is significant that the resistance of the FeS electrode reaches a peak value and starts to decrease at the final stage of discharge. This behavior can be considered to be one of the characteristics of the FeS electrode. Typical polished sections of the FeS elec-

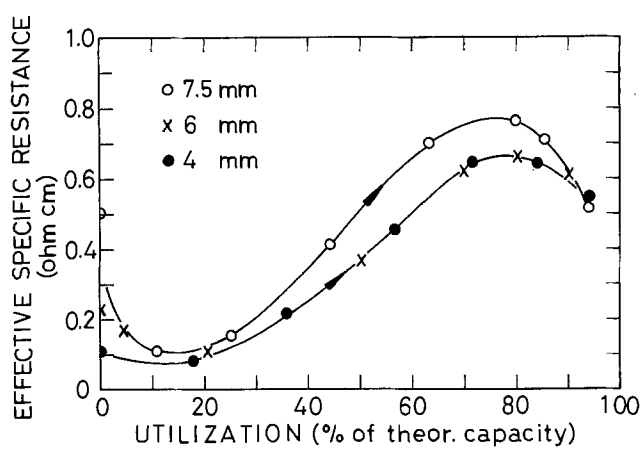

Fig. 5. Effect of electrode thickness on the electrode resistance during first discharge.

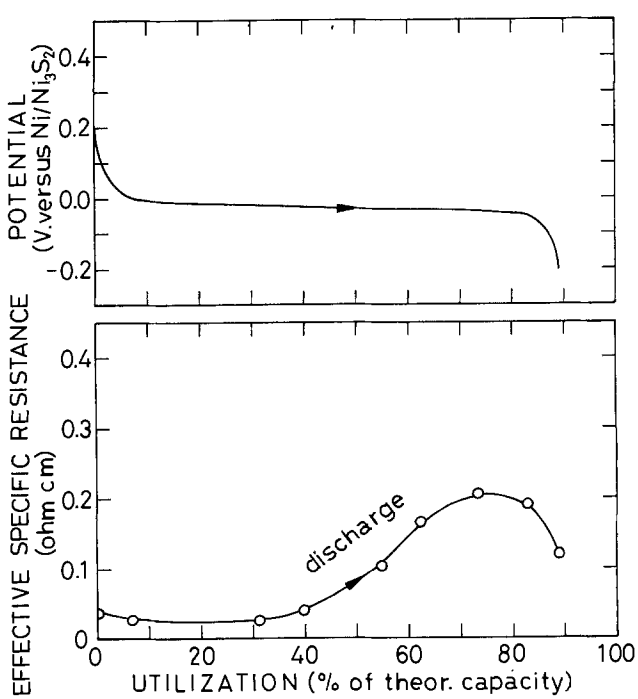

Fig. 6. Change of the effective specific resistance in LiCl-LiBr-LiF electrolyte at 450°C.

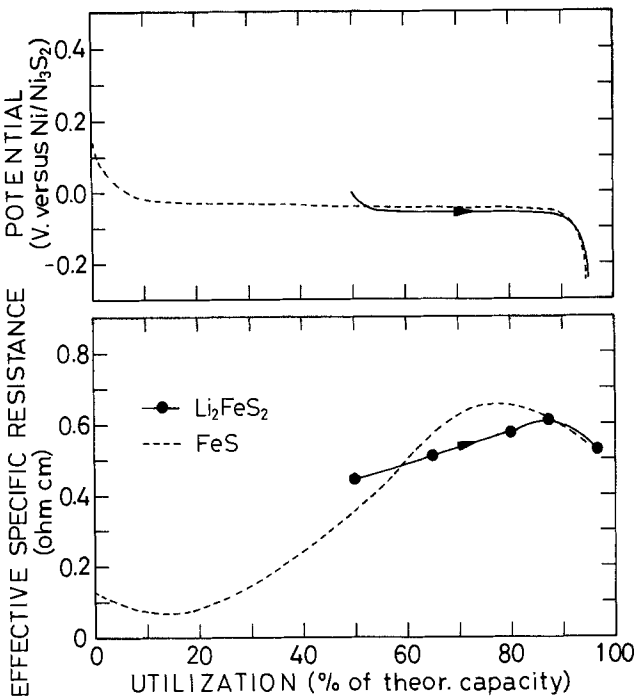

Fig. 7. Change of the effective specific resistance of a 4 mm thick electrode containing Li_2FeS_2 (X phase) as starting material in LiCl-rich electrolyte.

trode at the maximum resistance and at the end of discharge during the first cycle are shown in Fig. 8(a) and (b). This figure shows a significant increase in the population of the coarse iron particles as the electrode goes from the maximum resistance (Fig. 8a) to the end of discharge (Fig. 8b). As the discharge progresses, the population of coarse iron particles increases. At the end of discharge, corresponding to about 95% discharge [Fig. 8(b)], approximately 12% of the cross-sectional area of a typical electrode is occupied by the coarse iron particles (white area) with this area increasing from about 7% at the 75% depth results in the reduction of the effective resistivity, as observed by the present work. In some areas, the coarse iron particles appear to form a connected chain structure as shown in Fig. 8(b). This connected chain provides good conductance, thus further contributing to the reduction of the effective resistivity of the electrode. Metallographic examination shows that the decrease is attributed to the connected chain of iron formed during this period.

At the start of charge of the discharged FeS electrode, and X phase forms, according to Eq. [5], consuming Li_2S and Fe (12). The X phase provides a large porous electrode area with a high conductivity by reducing the volume occupied by nonconductive Li_2S. Since the surface of Li_2S is first converted to the X phase, this surface conversion should result in a significant reduction of the resistivity of the electrode. The experimental results show much lower resistance during charge than during discharge (see Fig. 3). At the state of charge corresponding to about 50% theoretical capacity, the formation of FeS is believed to start. As expected, the resistance of this region is low, as is shown in Fig. 3.

Conclusion

The present study revealed two unique features of the porous FeS electrode related to its ohmic impedance characteristics. The first feature is related to its high conductivity, particularly at the beginning of discharge. Such high conductivity potentially yields high power density. The second feature is the unique characteristic involving declining resistance of the

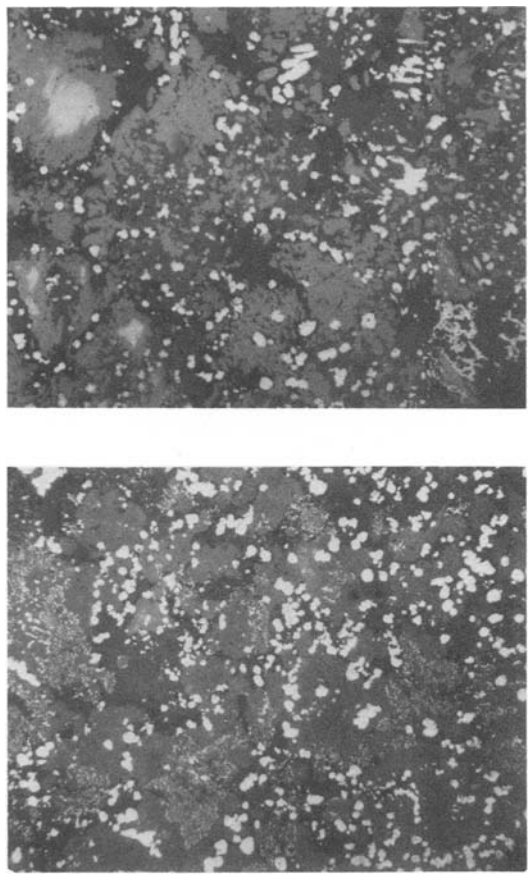

Fig. 8. Polished sections of the electrode at the maximum resistance (a, top) and at the end of discharge (b, bottom).

FeS electrode in the last stage of discharge due to the formation of iron particles. These features represent important information for the design and optimization of the FeS electrode, particularly for high-performance battery applications.

Acknowledgments

The authors wish to express their appreciation to Z. Tomczuk and J. R. Selman for helpful discussions, to F. C. Mrazek for metallographic analyses, and E. Gay and L. Burris for their encouragement. This work was conducted under the auspices of the U.S. Department of Energy.

Manuscript submitted Feb. 1, 1982; revised manuscript received Aug. 13, 1982.

Any discussion of this paper will appear in a Discussion Section to be published in the December 1983 JOURNAL. All discussions for the December 1983 Discussion Section should be submitted by Aug. 1, 1983.

Publication costs of this article were assisted by the Argonne National Laboratory.

REFERENCES

1. D. L. Barney *et al.*, Progress Report for the period October 1978-September 1979, Argonne National Laboratory Report No. ANL-79-94 (1980).
2. H. Shimotake and M. Fitzgibbon, Argonne National Laboratory Report No. ANL-79-94 (1980).
3. L. G. Bartholme, E. C. Gay, and H. Shimotake, Abstract 110, p. 298, The Electrochemical Society Extended Abstracts, Hollywood, Florida, October 5-10, 1980.
4. L. Redey, Argonne National Laboratory Report No. ANL-79-39, p. 59 (1979); Argonne National Laboratory Report No. ANL-79-94, p. 121 (1980); Private communications; L. Redey and D. R.

Vissers, *This Journal*, **128**, 2703 (1981).
5. H. Ohno, Private communication.
6. M. L. Saboungi, J. J. Marr, and M. Blander, *This Journal*, **125**, 1567 (1978).
7. C. H. Liu, A. J. Zielen, and D. M. Gruen, *ibid.*, **120**, 67 (1973).
8. R. E. Meredith and C. W. Tobias, "Advances in Electrochemistry and Electrochemical Engineering," Vol. 2, P. Delahay and C. W. Tobias, Editors, Chap. II, Interscience, New York (1962).
9. W. Savelsberg, Z. *Elektrochem.*, **46**, 379 (1940).
10. C. A. Melendres, C. C. Sy, and B. Tani, *This Journal*, **124**, 1060 (1977).
11. D. R. Vissers, Z. Tomczuk, K. E. Anderson, and M. F. Roche, U.S. Pat. 4,156,758 (1979).
12. Z. Tomczuk and M. F. Roche, Argonne National Laboratory Report No. ANL-79-94, p. 142 (1980).
13. Z. Tomczuk, S. K. Preto, and M. F. Roche, *This Journal*, **128**, 760 (1981).
14. R. A. Sharma, *ibid.*, **123**, 448 (1976).
15. F. C. Mrazek and J. E. Battles, *ibid.*, **124**, 1556 (1977).

Self-Discharge Behavior of Engineering-Scale LiAl/FeS Cells

Reinhard Knödler*

Brown, Boveri and Cie AG, Central Research Laboratory, 6900 Heidelberg, Germany

ABSTRACT

The self-discharge rate of LiAl/FeS cells at different state of charge was determined by operating the cells for prescribed periods of time at open circuit and then recharging them. The rate was shown to be minimal in a semicharged state (<0.5% capacity loss per day) and to be inversely proportional to the A-hr efficiency. When cycled after being at open circuit, a temporary change in utilization was observed which could be attributed to a change in cell resistance. One cause for self-discharge in LiAl/FeS cells may be the electronic conductivity of the electrolyte.

The lithium aluminum alloy/iron sulfide (LiAl/FeS) and the beta (Na/S) batteries are the most promising candidates among the advanced high-temperature batteries which are suitable for electric-vehicle and stationary energy-storage applications (1, 2). The LiAl/FeS cells show a low self-discharge rate, whereas the Na/S cells show no self-discharge because of the impermeable β-Al_2O_3 solid electrolyte. The former behavior can be seen from the fact that the coulombic efficiency is always slightly below 100%, typically 99.5%. Measurements on laboratory-scale cells (6 A-hr capacity) showed that the self-discharge rate is in the range of 1% per day and decreases with time, if the cell is left on open circuit for extended periods of time (3). However, no data are available on engineering-scale cells and nothing is known about the dependence of the self-discharge rate on the state of charge and on thermal cycling. Therefore, the following measurements were made to provide data on these properties.

Experimental

The investigations were carried out with two LiAl/FeS multiplate cells (MKII 152 and 157), which were manufactured by Eagle-Picher Industries, Joplin, Missouri. These prismatic cells have four negative and three positive electrodes with boron nitride (BN)-felt separators and a theoretical capacity of 395 A-hr. The electrolyte is "LiCl-rich," *i.e.*, 66.7 mol percent (m/o) LiCl-33.3 m/o KCl (liquidus temperature = 425°C). The operating temperature generally was 470°C. In the charged state the negative electrode consisted of LiAl (~ 48 atom percent [a/o] Li) and the positive electrode consisted of FeS. The negative-to-positive capacity ratio was about 1.3:1.0; therefore the cell capacity was limited by the positive electrode. The cells were operated in a helium-atmosphere glove box. They were discharged to 1V at a constant current of 70A and were charged at first at a constant current of 40A to 1.56V and then at constant voltage until the current had decreased to 10A ("tapering"). With an overall surface area of approximately 1900 cm^2, 10A corresponds to a current density of about 5 mA/cm^2.

The self-discharge rate at a certain state of charge was determined by the following procedure:

1. Cycle several times.
2. Discharge to the desired depth of discharge (DOD) (no discharge if DOD is to be 0%).
3. Leave on open circuit for 20-40 hr. Record the voltage behavior.
4. Recharge at the same current using the same cutoff voltage and the same procedure (tapering) as during initial cycling.
5. Calculate the self-discharge rate, S (in percent capacity loss per day), from the amount of excess recharge capacity, ΔC, (identical to the recharge capacity in case of 0%) by the following equation

$$S = \frac{2400 \cdot \Delta C}{C \cdot T} \qquad [1]$$

where C is the nominal cell capacity in A-hr and T the time in hr on open circuit.

6. Repeat steps 2 to 5 at least once more.
7. Repeat steps 1 to 6 (reproducing the results).

Results

One of the two cells was run for 99 cycles and during this time underwent 2 freeze/thaw cycles, 5 open-circuit periods after charge, one period after medium state of charge, and 3 periods after discharge. The utilization dropped from 84 to 78%. The other cell was run for 59 cycles and underwent one freeze/thaw cycle, 3 open-circuit periods after charge, 2 periods after medium state of charge, and 1 period after discharge. The utilization dropped from 84 to 80%. Both cells failed from short circuits.

Figure 1 shows the voltage change after opening the circuit in the fully charged state (run 1) and after recharge and opening again (run 2). It was observed that in every first open circuit after cycling, the self-discharge rate was higher than that in the following runs where the cell was not cycled but only recharged. In Fig. 2 the self-discharge rate (values taken from run 2) is shown at different depths of discharge. Although the performance of the two cells was almost identical, the absolute values of the self-discharge rates were somewhat different. In both cells, minimum values were observed somewhere between the fully charged and the fully discharged states. Therefore, by leaving a cell on open circuit in the fully charged or the fully discharged state, a rate of about 1% per day has to be expected; for the semicharged state the rate is about

* Electrochemical Society Active Member.

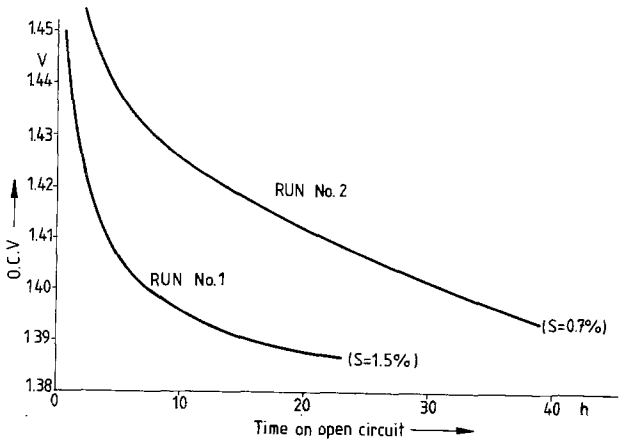

Fig. 1. Run 1, open-circuit voltage of cell MK II 152 after charging to 1.56V. Run 2, after recharging.

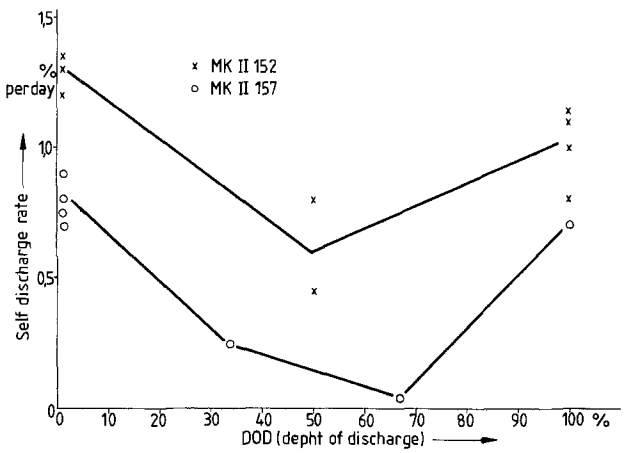

Fig. 2. Self-discharge rate at different depths of discharge

0.5% per day or less. If the temperature is increased 15°C (to 485°C), about the same values are observed. The open-circuit voltage in this case, however, is 10-20 mV higher. After thermal (freeze/thaw) cycling, both cells show essentially the same self-discharge rates as before. This result shows that thermal cycling does not affect the self-discharge behavior.

From the measurements of the dependence of open-circuit voltage on time, the open-circuit voltage with respect to the actual DOD can be calculated. Let S be the self-discharge rate in percent per day, C the nominal capacity and I_L the "leakage current" due to self-discharge. Then

$$I_L = \frac{S \cdot C}{2400} \qquad [2]$$

For instance, for $S = 1\%$ per day, one obtains $I_L = 140$ mA, meaning that the open-circuit voltage *vs.* time curves are equivalent to open-circuit voltage *vs.* DOD curves. Because the currents are so small, IR drops are negligible. Therefore, knowing the leakage current, I_L, the emf as a function of DOD can be calculated, using voltage-time curves at different self-discharge rates (*e.g.*, runs 1 and 2 in Fig. 1). In this way one gets information on the emf at very small deviations from the fully charged state.

The slowly decreasing coulombic efficiency of one cell (from cycle 86 to 99) due to an internal short circuit allowed the determination of the relationship between the coulombic efficiency, η, and the self-discharge rate, S, (in the charged state). The points in Fig. 3 show that there is an almost linear correlation between these two properties. Therefore, the self-discharge rate can be predicted if the coulombic efficiency is known. For practical applications, rates of more than about 5% per day are intolerable. This

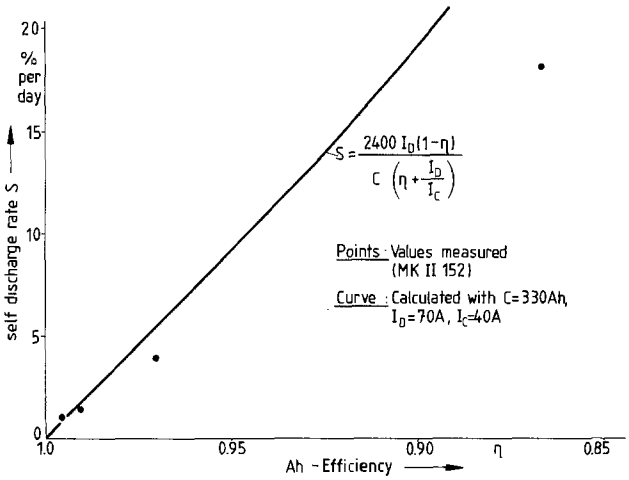

Fig. 3. Correlation between self-discharge rate and coulombic efficiency.

means a coulombic efficiency of about 96%. A theoretical expression for the relationship between η and S can be derived as follows: let C_C and C_D be the capacities and I_C and I_D the currents for charging and discharging, respectively. The self-discharge rate, S, in percent per day is

$$S = \frac{2400 \cdot I_L}{C} \qquad [3]$$

Assuming that C_D and C_C are independent of I_C and I_D (in a practical cell the utilization usually drops somewhat with increasing current), the discharge and charge capacity, respectively, will be

$$C_D = C - I_L \frac{C_D}{I_D} \quad \text{or} \quad C_D = \frac{CI_D}{I_D + I_L} \qquad [4]$$

$$C_C = C + I_L \frac{C_C}{I_C} \quad \text{or} \quad C_C = \frac{CI_C}{I_C - I_L} \qquad [5]$$

Thus, the coulombic efficiency η becomes

$$\eta = \frac{C_D}{C_C} = \frac{I_D(I_C - I_L)}{I_C(I_D + I_L)} \quad \text{or} \quad I_L = \frac{(1-\eta)I_D I_C}{I_C\eta + I_D} \qquad [6]$$

From this

$$S = \frac{2400\, I_D(1-\eta)}{C\left(\eta + \frac{I_D}{I_C}\right)} \qquad [7]$$

Figure 3 shows that this equation fits the experimental data only at high coulombic efficiencies. For lower values the self-discharge rate is lower than calculated. This means that opening the circuit obviously slows down the process that leads to the final short circuit.

When the cells were left on open circuit after charge for at least 50 hr (with a recharge in between) and then cycled again, a distinct drop in the utilization was observed. After several cycles the utilization reached its initial value again. When the same procedure was carried out for the discharged state, an increase in utilization was observed. Figure 4 shows this effect for different depths of discharge. Because the times on open circuit were different for each experiment (from 50 to 80 hr), the capacity changes in Fig. 4 were all interpolated to a time of 60 hr (assuming a linear relationship between time on open circuit and capacity change). The figure shows that there is an almost linear relationship. According to this curve, at about 75% DOD there will be no capacity change. This corresponds somewhat to Fig. 5, which shows the open-circuit voltage after discharging to different values of DOD. At 66% DOD the open-circuit voltage remains constant, whereas at all other DOD's the open-circuit voltage drops slowly. If the cell is oper-

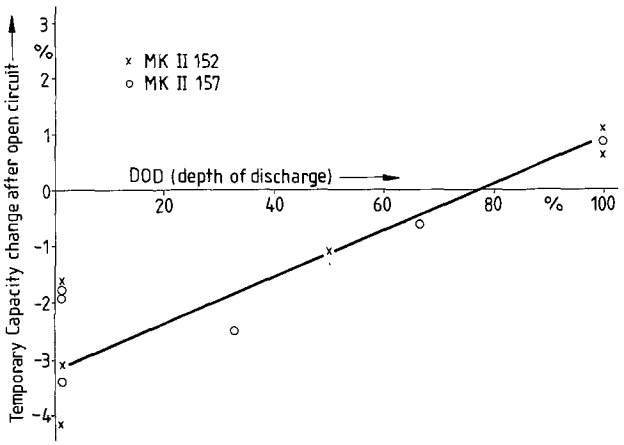

Fig. 4. Temporary capacity change after 60 hr open circuit for different depths of discharge.

ated at 485°C, no capacity change at zero DOD is observed.

Figure 6 shows points calculated from different open-circuit runs of the two cells. At 485°C the capacities are increased by about 2 A-hr at a given voltage, which corresponds well to the overall increase in capacity, which is about 2 A-hr higher at 485°C than at 470°C. Figure 7 shows the open-circuit voltage after 24 hr of open circuit over the whole capacity range as measured by both cells, including the data from Fig. 6.

By using the values for the open-circuit voltage, E_o, (Fig. 6 and 7), the d-c resistance R can be calculated from the discharge/charge curves by

$$R = \text{abs}\left(\frac{E_o - E}{I}\right) \qquad [8]$$

It turns out that during charge R is almost constant (between 1.6 and 1.8 mΩ), but during discharge it increases considerably (Fig. 8). In Fig. 9 the section at small deviations from the charged state is shown in

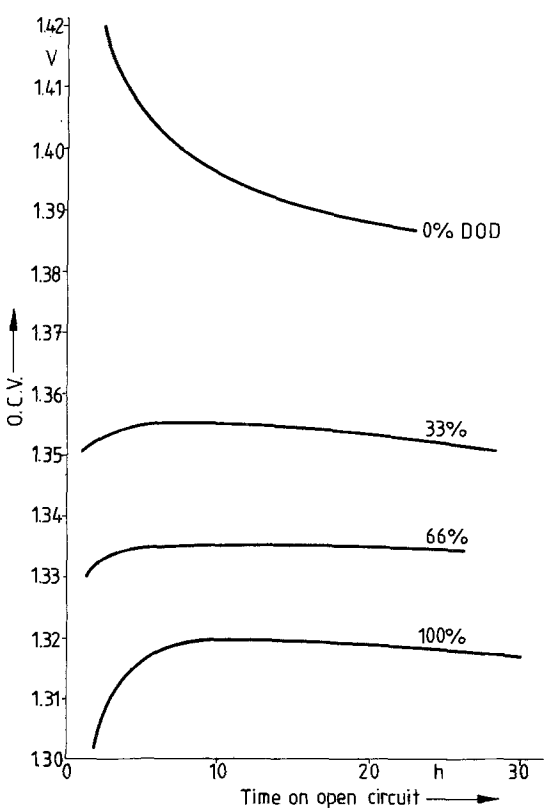

Fig. 5. Open-circuit voltage of cell MK II 157 after discharging to different depths of discharge.

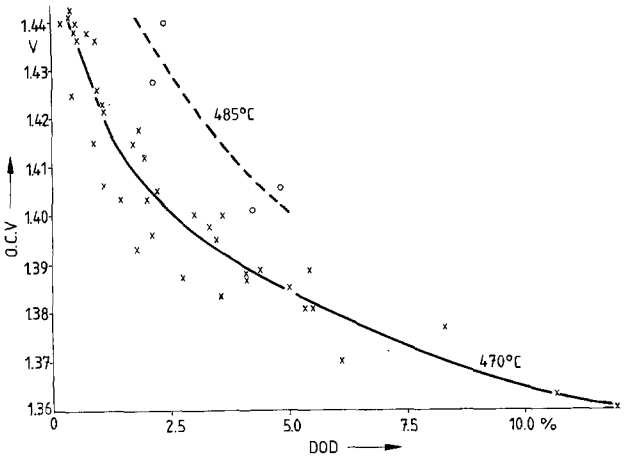

Fig. 6. Open-circuit voltage vs. depth of discharge. Calculated from the self-discharge vs. time curves (MK II 152 + 157).

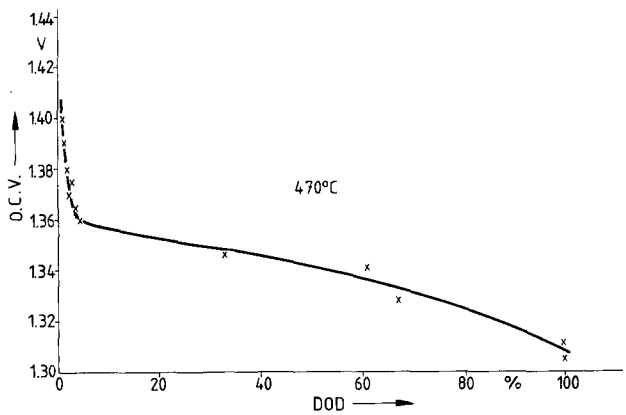

Fig. 7. Open-circuit voltage vs. depth of discharge

detail. The minimum resistance is at 6% DOD. This corresponds to the rapid change in the open-circuit voltage (Fig. 7) in the region between 0 and 4% DOD. Figures 8 and 9 further indicate that the resistance increased when the cell was discharged after it had been on open circuit in the charged state for some time. In contrast to this, the resistance was lower when the cell was discharged after being on open circuit in the discharged state. This behavior corresponds well to the changes in capacity after different types of open circuits, shown in Fig. 4.

Discussion

The data presented in this work show that there is self-discharge in LiAl/FeS cells. However, more in-

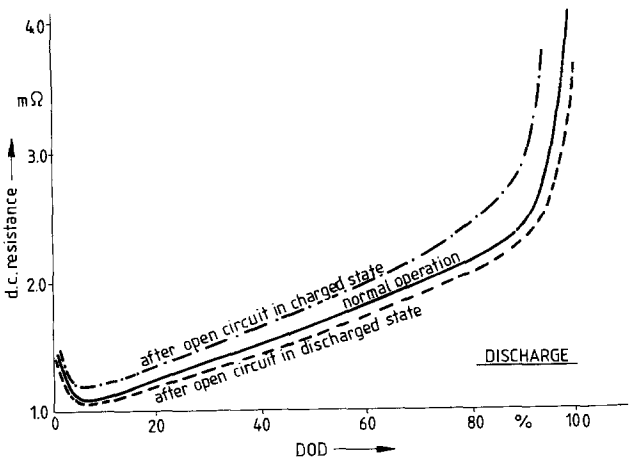

Fig. 8. Cell resistance during discharge with 70A at different depths of discharge (MK II 157).

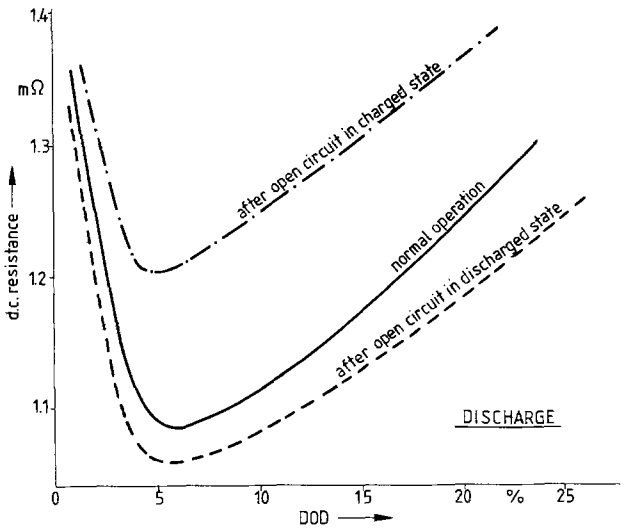

Fig. 9. Cell resistance during discharge with 70A at different depths of discharge (MK II 157).

formation is needed in order to explain the results satisfactorily. In the following, some preliminary conclusions are drawn.

The most likely explanation for a self-discharge reaction might be the electronic conductivity of the molten electrolyte. Measurements with blocking electrodes (7) yielded a value of about $\rho = 10^4$ Ωcm for the electronic conductivity of KCl/LiCl melts. However, this value will depend on the lithium activity of the electrodes. The "electronic resistance" can be calculated by

$$R_e = \rho \cdot \frac{d}{A}$$

Assuming an average electrode distance of $d = 4$ mm and an electrode area A, of 2000 cm^2, an "electronic resistance" of about 2Ω will result. This would lead to an electronic self-discharge current of about 650 mA, or a self-discharge rate 4.7% per day. The fact that the measured rate is considerably smaller suggests that self-discharge by electronic conduction might be possible in principle, but that the size of the effect is suppressed, because of a low lithium activity in the LiAl electrode.

The temporary capacity loss of the cells after being on open circuit in the fully charged state is due to an increased resistance, as is shown by Fig. 8 and 9. It is possible that this increase is caused by processes occurring in the electrodes during the open-circuit period (*e.g.*, crystal growth, agglomeration in the negative electrode). This lowers the actual electrode surface area, thus enhancing the resistance. The temporary capacity gain of the cells after being on open circuit in the discharged state may be attributed to a lower cell resistance, as indicated in Fig. 8 and 9. No explanation based on experimental evidence can be given for this now. One might speculate that the Li_2S in the positive electrode, formed during discharge, needs some time to distribute uniformly within the electrode and it may rearrange in such a way that the resistance will be decreased (*e.g.*, due to a higher specific surface area).

The drop in the voltage after opening the circuit in the fully charged state could have various causes: it may result from a diffusion overvoltage which was built up during the final stage of charging, or it may have its origin in a recombination of species created during the final charging. In the first case it is not necessary to assume self-discharge in order to explain the voltage drop after opening the circuit, because a diffusion overvoltage will disappear after the electrodes have become homogeneous; this process (the voltage drop) will, however, proceed according to the square root of time. This was shown not to be the case in our experiments. Relaxation processes caused by diffusion are described in literature (5, 6). Measurable effects (partial freezing of electrolyte, capacity decline, diffusion overvoltage) were observed only at relatively high current densities of about 100 mA/cm^2. Below 10 mA/cm^2 no diffusion relaxation was observed (5). Since in our experiments described above, charging was done by tapering the current until it reached a density as low as 5 mA/cm^2, diffusion-controlled processes can be ruled out. Processes, that like precipitation of electrolyte because of local changes in its composition, are not going on below 20 mA/cm^2 (8). Therefore, a more likely explanation for the drop in voltage after opening the circuit in the fully charged state, is that the voltage in this region is determined by species which were formed in the final course of charging, and which recombine during open circuit. However, due to the lack of additional data (especially metallurgical) these explanations can only be preliminary. Other causes of the observed effects may be possible as well.

Conclusions

The following conclusions can be drawn from the experiments and considerations described above.

1. The self-discharge rate of full-scale LiAl/FeS cells is about 1% per day in the charged and discharged states and is below 0.5% in medium states of charge.
2. A possible cause for self-discharge is the electronic conductivity of the electrolyte.
3. A temperature increase to 485°C and thermal cycling have no influence on the self-discharge rate.
4. The coulombic efficiency of a cell is directly related to the self-discharge rate.
5. A temporary capacity loss, which can be attributed to an increase in cell resistance, is observed after an open circuit in the charged state. A capacity gain occurs (decrease in cell resistance) after an open circuit in the discharged state.

Acknowledgments

This study was carried out during a stay at Argonne National Laboratory. The author is grateful to D. L. Barney, P. A. Nelson, H. Shimotake, and L. Bartholme for their support and to F. Gross for giving him the opportunity to carry out this investigation at ANL.

Manuscript submitted April 6, 1982; revised manuscript received Aug. 10, 1982.

Any discussion of this paper will appear in a Discussion Section to be published in the December 1983 JOURNAL. All discussions for the December 1983 Discussion Section should be submitted by Aug. 1, 1983.

Publication costs of this article were assisted by Brown, Boveri and Cie AG.

REFERENCES

1. D. L. Barney *et al.*, U.S. DOE report ANL-80-128, Argonne National Laboratory, February 1981.
2. W. Fischer, *Solid State Ionics*, **3/4**, 413 (1981).
3. (a) R. Knödler, G. Bohme, and W. Borger, *This Journal*, **127**, 1311 (1980); (b) R. Knödler, G. Bohme and H. Heide, BMFT-Forschungsbericht BMFT-FB-T80-031, July 1980.
4. Z. Tomczuk, S. K. Preto, and M. F. Roche, *This Journal*, **128**, 760 (1981).
5. N. J. Willars, J. G. Smith, and R. W. Glazebrook, *J. Appl. Electrochem.*, **11**, 335 (1981).
6. C. E. Vallet, D. E. Heatherley, and J. Braunstein, *This Journal*, **127**, 1 (1980).
7. R. J. Heus and J. J. Egan, *J. Phys. Chem.*, **77**, 1989 (1973).
8. R. Pollard and J. Newman, *This Journal*, **128**, 503 (1981).

The Molten Carbonate Carbon Dioxide Concentrator: Cathode Performance at High CO_2 Utilization

John L. Weaver and Jack Winnick*

Georgia Institute of Technology, Atlanta, Georgia 30332

ABSTRACT

Representative cathode half-cell polarization data at low inlet cathode CO_2 concentrations are presented for the MCCDC operated in the fuel-cell mode. A mathematical model is used to correlate the cathode data and to explain the observed behavior, especially at high CO_2 utilization. Also presented are representative cathode removal and current efficiency data.

With the advent of manned space stations, men will be residing in space for extended periods of time. Since the passenger cabin will be a closed unit, the air must be recycled due to the isolation of the station. The methods presently used to remove carbon dioxide from the air on manned spacecraft (*e.g.*, Skylab) include a cyclic adsorption bed utilizing commercial zeolites (1). Future missions require that the CO_2 partial pressures in the cabin be 0.0039 atm or lower. At these low partial pressures the zeolite system is inefficient, resulting in a high system-equivalent weight.

The aqueous, alkaline fuel cell has been successfully converted into a CO_2 concentrator for use in manned spacecraft (2-4). The aqueous concentrator utilizes Cs_2CO_3 as the electrolyte, which limits the air relative humidity to a minimum of 60% (2). At lower humidities drying occurs and $CsHCO_3$ precipitates at the anode. The humidity limits of the aqueous concentrator can be reduced by using TMAC (tetramethylammonium carbonate) (5) or the proprietary electrolytes of Life Systems, Incorporated, LSI-B (6), or LSI-D (7), but with reduced efficiency.

The molten carbonate fuel cell (MCFC) is undergoing extensive research and development as a power producer (8-10). It could prove to be even more desirable as a CO_2 concentrator than the aqueous cell. The MCFC converts reducing gas to electric power by oxidizing the fuel gas components, mainly H_2 and CO, electrochemically, at the anode

$$H_2 + CO_3^{2-} \rightleftarrows H_2O + CO_2 + 2e^- \quad [1]$$

$$CO + CO_3^{2-} \rightleftarrows 2CO_2 + 2e^- \quad [2]$$

The anode effluent gas is recycled and mixed with the air intake to the cathode where this gas is electrochemically reduced

$$CO_2 + \tfrac{1}{2}\, O_2 + 2e^- \rightleftarrows CO_3^{2-} \quad [3]$$

The MCFC typically operates with 30% CO_2 in the oxidant gas, and as much as 80% H_2 in the fuel gas.

Preliminary investigations (11, 12) have shown that the MCFC can be successfully converted into a molten carbonate carbon dioxide concentrator (MCCDC). In the fuel-cell mode H_2 (fuel gas) is supplied to the anode. CO_2 and air (simulated cabin air) are sent to the cathode where

$$CO_2 + \tfrac{1}{2}\, O_2 + 2e^- \rightleftarrows CO_3^{2-} \quad [3]$$

The anode reaction is

$$H_2 + CO_3^{2-} \rightleftarrows CO_2 + H_2O + 2e^- \quad [1]$$

The MCCDC has several advantages over the aqueous concentrator. First, any humidity, from 0 to 100% appears to be tolerable. Second, noble electrodes are not necessary. Nickel and nickel/chrome alloy electrodes work efficiently. Finally, higher power densities are possible. These advantages must be weighed against the problems inherent in a device which operates near 800 K.

The cathode reaction [3] is approximately zero order in carbon dioxide (13). This suggests that, theoretically, the MCCDC, with an inlet CO_2 partial pressure of 0.0039 atm should have power densities of the same order as the MCFC, which has inlet CO_2 partial pressures around 0.30 atm. However, in a working MCCDC, oxidant gas flow would be kept at a minimum. This is due to the energy inefficiency in regenerative heat exchange with the high temperature stream. Low flows will require high CO_2 utilizations, so that exit CO_2 concentrations will be 1-5% of the inlet, orders lower than at the MCFC cathode. Therefore, the achievable power density of the MCCDC depends on the diffusional limitations of the reactants and products and on equilibrium considerations (Nernst losses), in addition to the chemical and electrochemical kinetic limitations.

It is anticipated that with the proper cell design and component usage the MCCDC will achieve the same anodic polarization with respect to current density as the MCFC. This is assumed because both cells have anode gases which have high inlet reactant (hydrogen) concentrations. Cathode polarization is not anticipated to be the same because of the CO_2 concentration difference.

To date, half-cell polarization studies have not been conducted on the MCCDC. We attempt here to perform an experimental study of the cathode performance at typical expected gas concentrations. We also describe the behavior in terms of standard electrochemical kinetic analysis.

Theory

The total current-generating processes of the MCCDC are represented by the following reactions: at the cathode the gas mixture is electrochemically reduced to form carbonate ion

$$\tfrac{1}{2}\, O_2 + CO_2 + 2e^- \rightleftarrows CO_3^{2-} \quad [3]$$

The actual reaction mechanism on a gold wire in free electrolyte has been analyzed in detail by Appleby and Nicholson (26, 27). A rather complex scheme was found in which the reaction order for CO_2 was -1.0, due to its equilibrium with ionic oxygen species in solution: *e.g.*, $O_2 + 2CO_3^{2-} \rightleftarrows 2\, O_2^{2-} + 2CO_2$. They predicted, however, that at porous electrodes this effect would be overcome by the need for high fluxes of CO_2 for oxide neutralization at the high current densities. The net effect on porous NiO has been found to be a zero reaction order in CO_2 (13). At the anode, H_2 is electrochemically oxidized to form water and CO_2

$$H_2 + CO_3^{2-} \rightleftarrows H_2O + CO_2 + 2e^- \quad [1]$$

Therefore the overall cell reaction is

$$H_2 + \tfrac{1}{2}\, O_2 \rightleftarrows H_2O \quad [4]$$

The open-circuit or equilibrium potential can be predicted for the cathode half-cell reaction with re-

* Electrochemical Society Active Member.

Key words: cathode, mathematical model, exchange current density, limiting current.

spect to a reference O_2/CO_2 electrode, using the Nernst equation. The activity (a) of carbonate ions is taken to be unity. The predicted cathode equilibrium potential is

$$E_{e,ca} = (RT/n\mathbf{F}) \ln [(a_{co_2}a_{o_2}^{1/2})_{ca}/(a_{co_2}a_{o_2}^{1/2})_{ref}] \quad [5]$$

where the activities will be here replaced with partial pressures.

The cathode overpotential is the result of impedances (or resistances) caused by: (i) the cathode reactions (charge transfer and associated chemical reactions), (iia) gas-phase transport of reactants and products to and from the electrolyte, (iib) transport in the electrolyte of dissolved reactants and products, and (iii) transport in the electrolyte of ionic species between the electrodes and between the gas/electrolyte interface and the electrodes.

The total overpotential is

$$\eta = E - E_e + IR \quad [6]$$

where the concentrations in the bulk phase are the same at equilibrium and under load. Under the actual operating conditions of the MCCDC and MCFC there is not an infinite reservoir of gas, therefore the bulk phase concentrations change with current. The contribution to overpotential, Nernst loss, is due to the change in the bulk phase compositions and the subsequent effect on the equilibrium potential. These concentration changes increase the absolute magnitude of the respective half-cell overpotentials.

Since the equilibrium potential of the cell cannot be measured when the cell is under load, the equilibrium potential must be estimated using the compositions that are present under load with the half-cell Nernst equation, Eq. [5]. Nernst loss (ΔE_N) therefore, is the difference between the actual equilibrium potential and the equilibrium potential that would exist with the concentrations present under load

$$\Delta E_N = (RT/n\mathbf{F}) \ln [(P_{co_2}P_{o_2}^{1/2})_e/(P_{co_2}P_{o_2}^{1/2})_i] \quad [7]$$

Therefore, the overpotential corrected for Nernst loss can be defined as

$$\eta = E - E_e + \Delta E_N + IR \quad [8]$$

where E_e is the measured equilibrium potential.

A mathematical model for correlating cathode performance with temperature, flow rates and gas compositions is considered here. If the reaction kinetics can be represented by the Butler-Volmer equation, an expression for mixed control (activation and diffusion) can be represented by a modified Butler-Volmer equation (14)

$$i = i_o[(C_{p,x=0}/C_p^o) \exp(\overleftarrow{\alpha}\mathbf{F}\eta/RT) - (C_{r,x=0}/C_r^o) \exp(-\overrightarrow{\alpha}\mathbf{F}\eta/RT)] \quad [9]$$

$C_{i,x=0}/C_i^o$ is the ratio of concentration of the limiting species at the electrode to that in the bulk phase, where the subscript p represents the product and the subscript r represents the reactant. The ratio $C_{i,x=0}/C_i^o$ is dependent on current.

The relative importance of CO_2 and O_2 diffusion in the gas and electrolyte phases can be estimated by considering the appropriate molar flux equation and the resulting limiting apparent current densities (i_L). These i_L are based on the superficial electrode area. The limiting currents due to diffusion of O_2 and CO_2 in the flow channel can be predicted with the following flux equation

$$i_L = -k_g n\mathbf{F}C^o \quad [10]$$

where the molar flux is given by

$$J_D = -k_g(C^o - C_{x=0}) = i/n\mathbf{F} \quad [11]$$

and $C_{x=0}$ is zero at the limiting current.

Winnick *et al.* (12) showed that mass transfer to a flat plate describes the mass transfer characteristics of the sub-scale MCCDC at low flow rates. Mass transfer coefficients for laminar flow over a flat plate can be predicted with the following equation (15)

$$(N_{SH})_{in} = k_g L/D_{AB} = 0.646 N_{Re,L}^{1/2} N_{Sc}^{1/3} \quad [12]$$

At 923 K, limiting currents are calculated using Eq. [10] and [12] for 1.0% and 0.3% CO_2, and 20% O_2 at flow rates of 100 cm³/min and 2000 cm³/min. The length of the flow channel is taken to be 7.4 cm (7.92 cm² area cell)[1] and the velocity of the gas is given by

$$V = Q/A_{cs} \quad [13]$$

where the cross-sectional area (A_{cs}) of the flow channel is 0.97 cm². These limiting currents are listed in Table I.

Limiting currents for diffusion of O_2 and CO_2 through the electrolyte can be calculated only if its morphology on the electrode is assumed. We here use the thin-film model, where the active area of electrode is covered with a thin film of electrolyte through which diffusion of the active species must occur. These limiting currents are estimated using average values for the thickness, δ, of this film

$$i_L' = -D_{AB}n\mathbf{F}C^o/\delta \quad [14]$$

where i_L' is based on the actual electrode area and the molar flux is given by

$$J_D' = i'/n\mathbf{F} = -D(C^o - C_{x=0})/\delta \quad [15]$$

Concentrations at the gas/electrolyte interface (C_i^o) can be estimated using Henry's law constants

$$C_i^o = H \cdot P_i \quad [16]$$

At 923 K, the Henry constant for CO_2 is 1.17×10^{-5} mol/cm³-atm in the ternary carbonate melt (16). The solubility of O_2, however, is dependent on the CO_2 pressure (16a). At a CO_2 pressure of 0.01 atm, the apparent Henry constant for O_2 is about 4.8×10^{-7}; at 0.003 atm CO_2 it is about 8.8×10^{-7} mol/cm³-atm. The diffusion coefficients of O_2 and CO_2 are estimated to be 4.65×10^{-5} and 3.9×10^{-5} cm²/sec, respectively (16). While we are not using the ternary carbonate eutectic, the purpose of the following calculations is a semiquantitative comparison of diffusional resistances and order of magnitude estimates are sufficient.

The effective thickness of the electrolyte film (δ) is estimated to be between 0.1 and 0.5 μm (17). Assuming that the electrode is 0.076 cm thick and complete wetting occurs, the actual area to superficial area is about 300 cm²/cm² based on a specific surface area of 0.21 m²/g (18). The values of i_L' calculated from Eq. [14] are thus multiplied by 300 to arrive at i_L for liquid phase diffusion. The limiting currents for diffusion in the electrolyte are listed in Table I at the same partial pressures used to calculate gas-phase-limiting currents.

Although the limiting current due to oxygen diffusion can be lower in the electrolyte than in the gas phase it is not the limiting specie because the limiting current due to CO_2 diffusion in the gas phase is much smaller than that due either to O_2 or CO_2 diffusion in

[1] This cell is described later.

Table I. Estimated limiting currents

			i_L (mA/cm²)			
	Gas phase concentrations (%)		Gas phase flow rate (cm³/min)		Electrolyte film thickness (μm)	
Component	CO_2	O_2	100	2000	0.5	0.1
CO_2	1.0	20.0	120	500	5,300	26,000
	0.3	20.0	40	160	1,600	8,000
O_2	1.0	20.0	2,400	10,600	5,200	26,000
	0.3	20.0	2,400	10,600	9,500	47,000

the electrolyte. With CO_2 pressures an order or two higher, as in the MCFC, this is likely not the case.

Note that gas phase diffusion in the pores of the electrode is not considered here. If it were the limiting currents due to gas phase diffusion would be even lower than those shown in Table I, which gives further support to the premise that gas phase diffusion of CO_2 is the limiting diffusion process.

The following assumptions are made in order to derive the final working equation: (*i*) Diffusion of O_2 in the gas phase and in the electrolyte[2] is not limiting. (*ii*) Diffusion limitations of CO_2 in the electrolyte are negligible. (*iii*) Diffusion limitations of carbonate ion (product) is accounted for in the *IR* drop. $C_{p,x=0}/C_p^o$ is taken to be unity, since the overpotentials to be used are *IR* free. (*iv*) Reaction occurs at the interface of the electrode and electrolyte tile. (*v*) The overpotential in addition to being *IR* free is also Nernst-loss free. Therefore, this model directly takes into account only the effects of diffusion of CO_2 in the gas phase and of activation.

The ratio $C_{CO_2,x=0}/C^o_{CO_2}$ is determined by considering the zones of gaseous diffusion. In the first zone (flow cavity) the molar flux is described by the following equation

$$J_D = i/n\mathbf{F} = -k_g(C^o - C^*) \quad [17]$$

where C^* is the concentration of CO_2 at the entrance of the pore. In the second zone (the pore) the molar flux is represented by the following equation

$$J_D = i/n\mathbf{F} = -D_{eff}(C^* - C_{x=0})/\delta_g \quad [18]$$

The effective diffusivity (D_{eff}) is defined as follows

$$D_{eff} = D_{AB}\epsilon/\tau \quad [19]$$

Since the flux in the cavity is equal to the flux in the pore, Eq. [17] and [18] are solved simultaneously to eliminate C^* yielding the ratio $C_{x=0}/C^o$

$$C_{x=0}/C^o = 1 + (i/n\mathbf{F}C^o)(1/k_g + \tau\delta_g/D_{AB}\epsilon) \quad [20]$$

The limiting current when $C_{x=0}$ is equal to zero is

$$i_L = -n\mathbf{F}C^o/(1/k_g + \tau\delta_g/D_{AB}\epsilon) \quad [21]$$

Substituting Eq. [20] and [21] into Eq. [9] in conjunction with the stated assumptions yields the final working equation

$$i = i_o[\exp(\overleftarrow{\alpha}\mathbf{F}\eta/RT) - (1 - i/i_L)\exp(-\overrightarrow{\alpha}\mathbf{F}\eta/RT)] \quad [22]$$

Equipment and Procedure

To test the application of the MCFC to the removal of low-levels of CO_2, state-of-the-art components were used. An assembly was made which conformed as closely as possible to that used at Argonne National Laboratory (8).

The electrochemical cell consists of two cell housings, anode and cathode half-cells, through which the process gases flow. The housings, Fig. 1, are made of 316 stainless steel. Inlet and outlet ports are provided, through which the process gas enters and leaves the housing. A third port is provided to allow insertion of a thermocouple for monitoring the cell temperature. For the cathode housing a fourth port is available for insertion of the reference electrode. Baffles, 0.152 cm deep, are incorporated into the cell.

Two different size cells were used in these tests. The basic cell design remains the same, though the baffle configuration is different for the two cell sizes. Figure 1 shows the configuration for the 3.18 cm diameter cell (electrode diameter), which was used during runs No. 1, 2, and 3. A 5.72 cm diameter cell was used for run No. 4.

Sintered nickel electrodes were used in these tests. Sheets of 80% porous nickel of 0.0762 cm thickness with

[2] The most recent work of Smith (16b) gives somewhat higher oxygen solubilities in the Li-K binary than those assumed here. This reinforces this assumption.

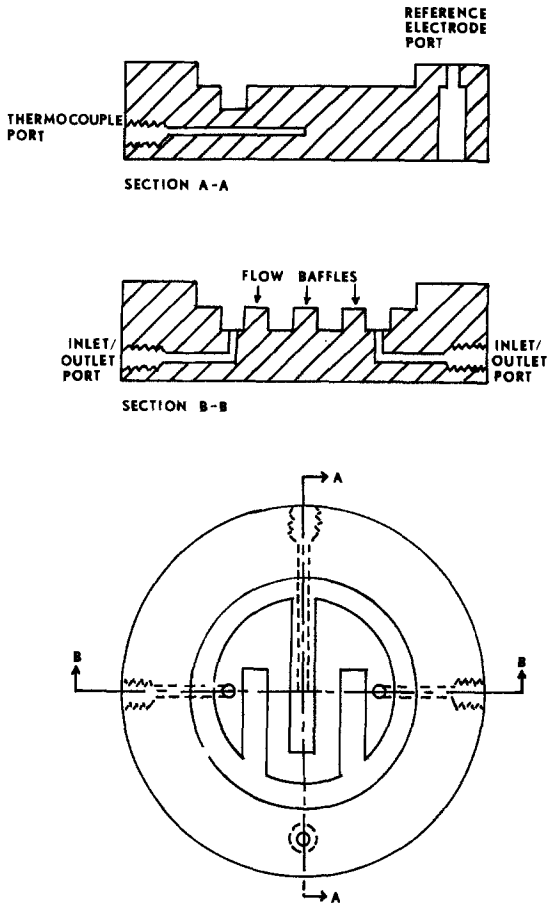

Fig. 1. Cell housing

nickel screen for structural support were purchased from Gould, Incorporated. The mean pore diameter of the cold nickel is 10 microns. Upon heating, the cathode electrode oxidizes *in situ* to nickel oxide. The anode electrode remains nickel during operation.

Electrolyte tiles were provided by Argonne National Laboratories and the General Electric Company. The tiles are a mixture of electrolyte eutectic, 55% by weight, and lithium aluminum oxide ($LiAlO_2$), 45% by weight. The electrolyte eutectic is a mixture of potassium carbonate (K_2CO_3), 38% by mol fraction, and lithium carbonate (Li_2CO_3), 62% by mol fraction. The $LiAlO_2$ is the supporting matrix. Retention of electrolyte eutectic by capillarity and prevention of process gas crossover is due to the small pore size in the matrix.

The melting temperature of the electrolyte limits the minimum operating temperature of the MCCDC. This carbonate eutectic melts at 763 K.

A reference electrode is inserted into the reference electrode port (Fig. 1). The reference electrode, Fig. 2, consists of a gold wire, alumina tubes for gas transport and insulation, and a stainless steel tube for structural support. The coiled end of the gold wire (coiling is done to assure adequate surface area) is immersed in a well containing the lithium and potassium carbonate eutectic. A standard gas of CO_2 and air is bubbled into the electrolyte well.

Figure 3 shows a diagram of the cell assembly. The electrodes are cut so that they fit snugly in the housing, resting on the baffles.

The major electronic component in testing the MCCDC is the Potentiostat-Galvanostat (PAR 371) used in conjunction with a PAR Model 178 Electrometer.

Steady-state potentials are measured with Simpson 460 Digital Multimeters. Current is monitored with a Westinghouse ammeter. A Bailey Instruments, Incorporated, BRY-1 Recorder is used to monitor the cell

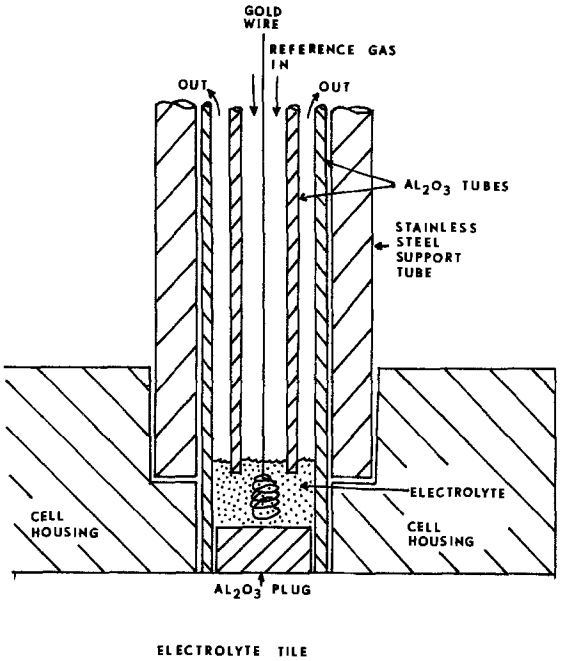

Fig. 2. Reference electrode

potential and cathode CO_2 outlet concentration during approach to steady-state.

A Tektronix 5111 Storage Oscilloscope with a SA19N Differential Amplifier and a 5810N Time Base Amplifier is used to record potential as a function of time during current interruption.

The cell *IR* drop can be estimated using a current-interruption technique utilizing the a-c component (19). The ohmic overpotential decays much more rapidly than the other types of overpotential; thus its magnitude is measured as the initial portion of the potential decay curve. The ohmic resistance is given by the following equation

$$R = \Delta E/\Delta I \qquad [23]$$

A Barber-Coleman 121-B Temperature Controller is used to control the furnace air temperature to ±2°C of the desired temperature. Thermo Electric Company, iron-constantan 24 gauge thermocouples are used to monitor each half-cell temperature.

Cathode carbon dioxide concentrations are measured with a Beckman 864 Infrared Analyzer which is tuned to the adsorption frequency of CO_2 only. Measurements can be performed either continuously or on demand. A four-way valve allows the passage of gas from a point downstream of the cell to the Beckman analyzer and back to the same point. Calibration of the analyzer is checked daily using the cathode process gas.

The cell was heated at a rate of 50°-100°C per hr. During heat-up the process gases were flowing through the cell. About 100 cm³/min of CO_2 in air and H_2 were sent to the cathode and anode, respectively. A standard reference gas of CO_2 and air was sent to the reference electrode. After the operating temperature was reached the cell was allowed to stabilize for two or three days. During this time open-circuit was maintained and the cathode electrode oxidized *in situ*.

Steady-state polarization was obtained by the following method: After the cell reached the desired operating temperature, between 818 and 923 K, the cell was allowed to stabilize. Upon stabilization the desired flow rates were set. Cathode flow rates ranged from 100 to 2000 cm³/min. Anode flow rates were usually held constant at approximately 32 cm³/min. Recycle flow rates, when used, ranged from 1000 to 2000 cm³/min.

After the flow rates were set the cell was allowed to equilibrate, normally one day. Upon equilibration outlet concentrations and half-cell potentials were measured. Current was then drawn from the cell galvanostatically. The cell was allowed to reach steady-state; normally 1-2 hr, minimum, or a day, maximum, was necessary. Approach was observed using the strip-chart recorder. After steady state was reached, concentrations and potentials were again measured.

The current was incremented in 10, 20, or 50 mA steps until the cathode removal reached 90-95% or the current efficiency dropped to approximately 100%.

In addition to the steadv-state polarization measurements. ohmic loss was also measured at each current drawn from the cell.

Results

A total of four runs (experiments) were performed. Each run required assembly and disassembly of the cell and introduction of new electrodes and electrolyte tile. New electrodes and tile were necessary for each run due to their destruction on disassembly. Termination was generally due to mechanical failure encountered after several hundred hours of operation. About half of the tiles failed due to gas crossover.

The cathode removal efficiency is the difference of the cathode inlet and outlet CO_2 concentrations divided by the cathode inlet concentration, multiplied by 100. All concentrations are listed in volume percent.

The current efficiency (Ca Current Eff) is the ratio of the mols of CO_2 removed to the theoretical mols that could be removed by two faradays of current. The current efficiency is related to the CO_2 removal rate $(\dot{m}_{CO_2})$ (cm³/min) and current (I) (amp)

$$\text{Ca Current Eff} = \dot{m}_{co_2} n\mathbf{F}\rho/I = \dot{m}_{co_2}/7.6I \qquad [24]$$

where ρ (mol/cm³) is the density of CO_2 at room temperature. The cathode removal rate used for the current efficiency is based on the inlet cathode flow rate.

Typical cathode overpotentials (*IR* free) are plotted in Fig. 4 and 5. These figures show the dependence on cathode flow rate and cathode inlet CO_2 concentrations. Typical carbon dioxide removal efficiencies are plotted

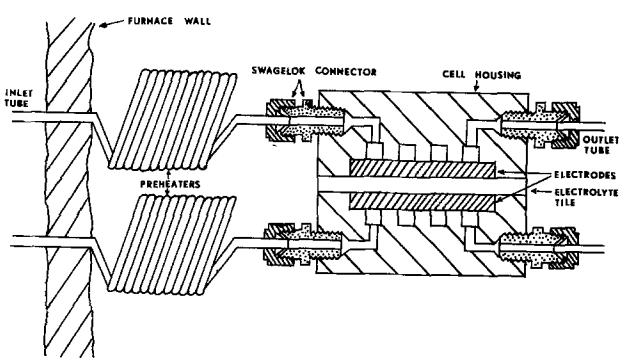

Fig. 3. Cell assembly

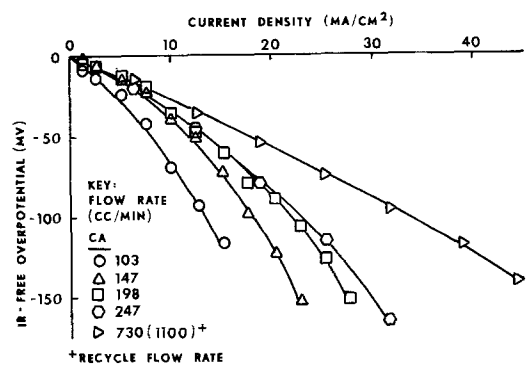

Fig. 4. Cathode overpotentials *vs.* current density for run No. 1; inlet $[CO_2] = 1.00\%$, temp. $\doteq$ 923 K.

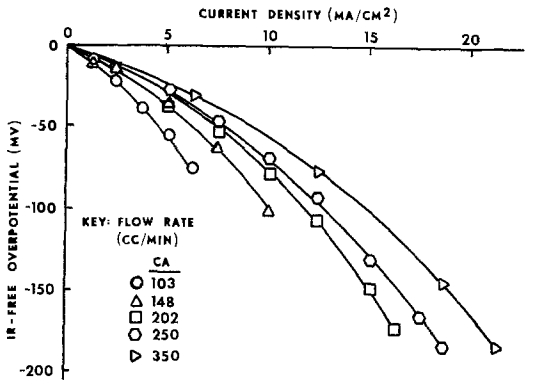

Fig. 5. Cathode overpotential vs. current density for run No. 2, tests C through G; inlet $[CO_2] = 0.50\%$, temp. $\doteq$ 915 K.

in Fig. 6. Note the dependence of removal efficiency on flow rate and the approximately linear relationship with respect to current density.

Typical current efficiencies as a function of current density are plotted in Fig. 7. Note the asymptotic behavior at zero current density approaching infinite efficiency and the approach to 100% efficiencies at high current densities.

Typical cathode CO_2 removal rates as a function of flow rate are presented in Fig. 8 and 9. Complete results are shown by Weaver (20).

Treatment of Data

Polarization data were treated by first removing the estimate of ohmic loss and calculated Nernst losses. Nernst loss (ΔE_N) is calculated using Eq. [7]. The partial pressures used are based on the log mean average of the inlet and outlet concentrations at equilibrium and under load. Transport and kinetic parameters for the cathode half-cell reaction [3] were estimated by fitting Eq. [22] to the experimental data using a nonlinear least-squares computer program. Certain parameter values were assumed while others were allowed to vary to give the best fit. The cathodic transfer coefficient was assumed to be 0.60. This is the value found by Winnick and Ross (13) and it agrees with the value determined graphically from Allen-Hickling plots (20). The effective diffusion layer was assumed to be equal to the electrode thickness, 0.076 cm. The porosity was taken to be the value of the cold nickel, 0.80. The diffusion coefficient of CO_2 in air was esti-

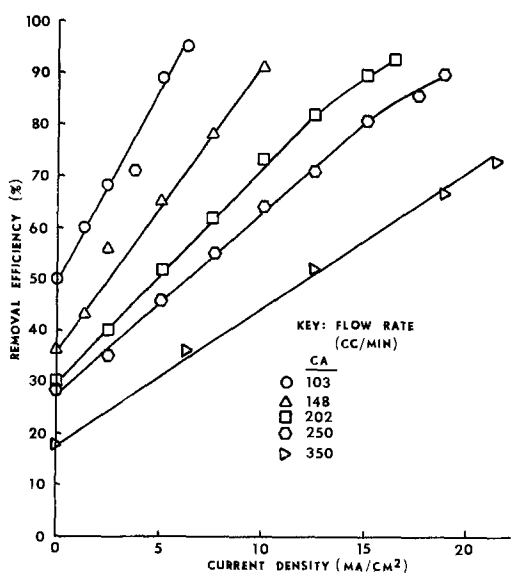

Fig. 6. Removal efficiency as a function of current density for run No. 2, tests C through G; inlet $[CO_2] = 0.50\%$, temp. $\doteq$ 915 K.

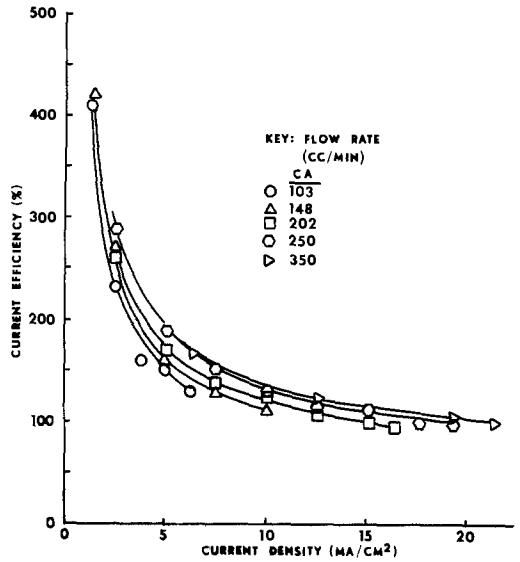

Fig. 7. Current efficiency as a function of current density for run No. 2, tests C through G; inlet $[CO_2] = 0.50\%$, temp. $\doteq$ 915 K.

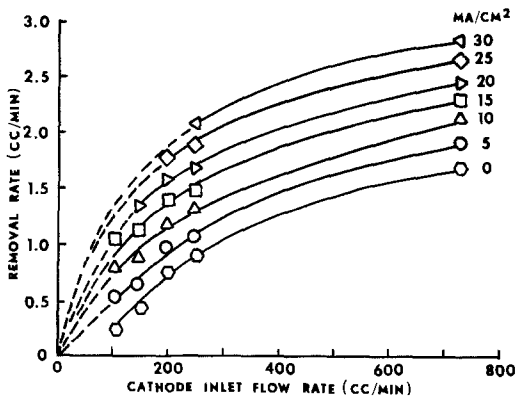

Fig. 8. CO_2 removal rate as a function of flow rate for run No. 1; inlet $[CO_2] = 1.00\%$, temp. $\doteq$ 923 K.

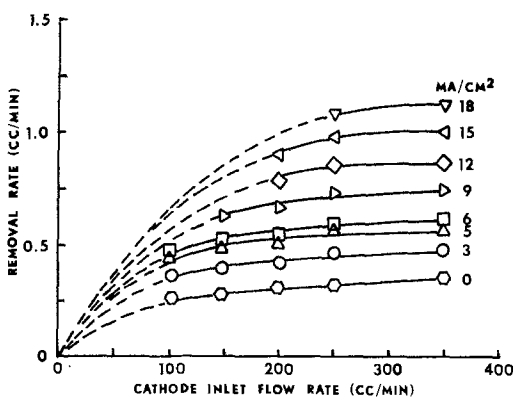

Fig. 9. CO_2 removal rate as a function of flow rate for run No. 2, tests C through G; inlet $[CO_2] = 0.50\%$, temp. $\doteq$ 915 K.

mated using the Wilke and Lee modification of the equation of Hirschfelder, Bird, and Spotz (21)

$$D_{AB} = BT^{3/2}\sqrt{(1/M_{CO_2}) + (1/M_{Air})}\; Pr^2_{CO_2\text{-}Air} I_D \quad [25]$$

where

$$B = [1.0 - 2.46\sqrt{(1/M_{CO_2}) + (1/M_{Air})}] \times 10^{-4}$$

and r is the collision diameter and I_D is the collision integral for diffusion.

The viscosity of the gas mixture is taken to be the viscosity of air, which is found in Perry and Chilton (21). The value used for $C°$, the bulk-phase concentration of CO_2, is the log mean average of the inlet

CO_2 concentration and the outlet CO_2 concentration at 99% removal. This means of determining C° gives limiting currents, Eq. [21], under conditions of high CO_2 utilization and thus limits the usefulness of Eq. [22] to high utilizations.

Gas flow in the cell is assumed to be turbulent, even though Reynolds numbers are less than 300, due to the tortuous nature of the flow channel. Therefore it is assumed that the mass transfer coefficient (k_g) is proportional to the Reynolds number taken to the 0.8 power (15)

$$k_g = B'(N_{Re})^{0.8} \qquad [26]$$

where

$$N_{Re} = r_{H\rho}Q/A_{cs}\mu$$

and B' is a constant.

B', τ, and i_0 are the parameters used to fit Eq. [22] to the experimental data.

The parameters τ and i_0 were allowed to float for each run, but are held constant for all tests within the run.[3] Each run has a different τ and i_0 because they are a function of the contact between the electrode and the electrolyte tile (electrode wetting). This wetting is an experimental parameter that is difficult to predict or duplicate and is therefore assumed to be different for each run.

Table II lists the values of the parameters that were estimated by the computer program. The standard error of the model estimate is 6.5 mV.

Typical cathode overpotentials (*IR* and Nernst loss free) as functions of current density were predicted, and plotted in Fig. 10 and 11 using the estimated parameters and Eq. [22] and [26]. These curves were predicted using the same flow rates and temperatures as the experimental data. Also plotted in Fig. 10 and 11 are predicted polarization curves as i_L approaches infinity (activation) and where k_g approaches infinity (activation and electrode diffusion). All experimental data were correlated with the same degree of fit as shown here.

Discussion of Results

Evaluation of the cell at equilibrium and under load indicates performance is as expected from preliminary results (11, 12). Good agreement with the MCFC is also seen.

Ohmic losses during these runs ranged from 10 times (run No. 1) to 50 times (run No. 4) greater than ohmic losses typically found in the MCFC. Specific conductivities ranged from 0.063 $(\Omega\text{-cm})^{-1}$ to 0.012 $(\Omega\text{-cm})^{-1}$. These are considerably lower than those found in the MCFC (22) which average 0.6 $(\Omega\text{-cm})^{-1}$. This discrepancy is probably due to poor electrode/electrolyte tile contact for the MCCDC. Gorin and Recht (23) found that measured resistance can be 10 times greater than that predicted due to gas formation between the electrolyte and electrode.

High values of measured *IR* might also be due to oxide precipitation at the electrode-electrolyte interface. However, this would occur during operation with depleted CO_2, the resistance increasing with the elapsed time of such operation. No such time dependence was seen in these experiments.

[3] During run No. 4 there was a change in cell performance between the two tests at 500 cm³/min, tests A and B, performed early in the run, and the two tests at higher flow rates, tests C and D, performed at the end of the run. This is assumed to be because of a change in electrode wetting. Therefore tests A and B, and tests C and D were each assigned a τ and i_0.

Table II. Estimated parameters for mathematical model

B' = 0.28 cm/sec

Run	Temp (K)	τ	i_0 (mA/cm²)
1	923	0.36	23
2	915	0.76	17
3	910	0.32	15
4 A, B	818	1.54	8.3
4 C, D	818	0.62	6.2

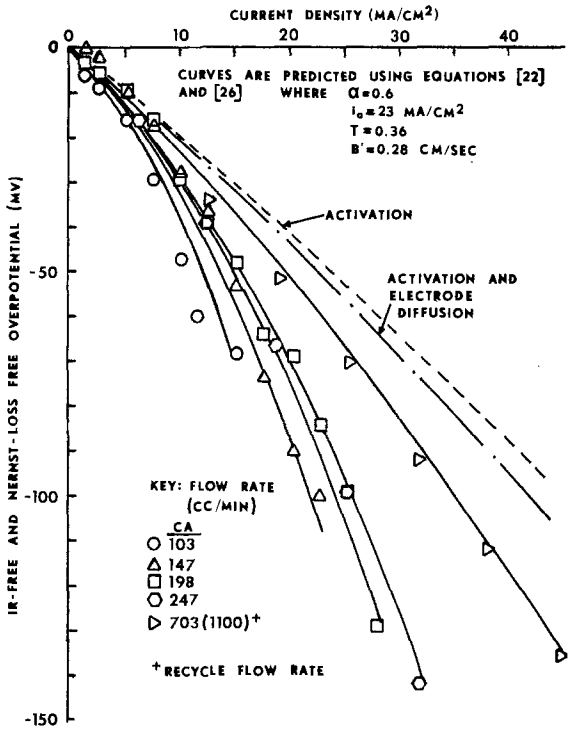

Fig. 10. Cathode overpotential as a function of current density for run No. 1; $[CO_2] = 1.00\%$, temp. $\doteq$ 923 K.

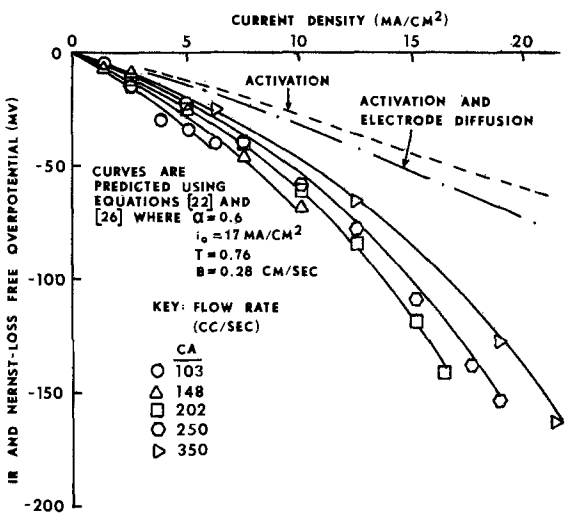

Fig. 11. Cathode overpotential as a function of current density for run No. 2, tests C through G; inlet $[CO_2] = 0.50\%$, temp. $\doteq$ 915 K.

Typical cathode half-cell overpotentials (*IR* free), Fig. 4 and 5, show the dependence of the overpotential on flow rate and CO_2 inlet concentration. It is seen that the cathode overpotential at constant current density decreases with increasing CO_2 inlet partial pressures and flow rate.

The mathematical model used to correlate these data gives some insight into explaining the behavior. As noted earlier there are three parameters used to fit the data to Eq. [22]. Two parameters, the mass transfer coefficient and tortuosity, are used to correlate the diffusion overpotential and the third parameter, exchange current density, along with the transfer coefficient are used to correlate the activation overpotential. Mass transfer is thought to be controlled by gas phase diffusion of CO_2 in the flow cavity and pores (see Table I).

Tortuosity, which was allowed to vary for each run, is a function of the electrode wetting, and is listed in Table III for each run. It is observed that all but one tortuosity are less than one. From physical considera-

Table III. Cathode limiting currents

Test	Flow rate (cm^3/min) single-pass/ recycle	CO_2 inlet conc. (%)	Temp (K)	Mass transfer coeff. (cm/sec)	Limiting current (mA/cm^2)
1A	103	1.0	923	2.2	35
1B	147	1.0	923	2.9	45
1C	198	1.0	923	3.7	56
1D	247	1.0	937	4.4	66
1E	730/1080	1.0	937	14.0	168
2A	251	1.0	915	4.5	59
2B	320	1.0	916	5.4	68
2C	103	0.5	917	2.2	16
2D	148	0.5	918	2.9	20
2E	202	0.5	913	3.8	26
2F	250	0.5	914	4.5	29
2G	350	0.5	910	5.8	36
3	500/1320	0.3	910	17.0	59
4A	500	0.3	817	8.2	18
4B	480	1.0	818	7.9	60
4C	500/1560	1.0	817	20.0	150
4D	2200	1.0	819	27.0	170

tions it is known that τ cannot be less than one since a value of one would indicate a cylindrical pore (24). From Eq. [21] it is seen that τ is used to fit the term $\tau\delta_g/\mathcal{D}_\epsilon$ to the data. Since the same electrode material is used for each run τ should be a constant. The reason τ is less than one and is different for each run is because the effective diffusion layer is less than the electrode thickness and is different for each run. This indicates that a certain amount of wetting has occurred, that the degree of wetting is different for each run, and the active reaction zone is closer to the electrode/bulk-gas-phase interface than originally assumed.

The parameter τ, therefore is not a true tortuosity but is a parameter which includes tortuosity and the effective diffusion layer. In addition to the above, τ is also a function of the active electrode area since the diffusion of CO_2 is both normal and parallel to the pore walls, whereas diffusion of CO_2 was visually assumed to be only normal to the reaction zone.

Using the mass transfer coefficients predicted with Eq. [26], and the tortuosities from Table II limiting currents for each run are calculated using Eq. [21] and are listed in Table III.

The limiting currents calculated in this way are comparable to those estimated in Table I, for CO_2-gas-phase diffusion. For example, test 1A, with 1% CO_2, shows a limiting current of 35 mA/cm^2 compared with 120 mA/cm^2 estimated at this flow rate and composition. The approximately threefold difference is due to the effects of pore diffusion and the high CO_2 utilization in the experiments. Neither was included in the estimation for Table I but both are used in developing Eq. [21] and [22]. The same threefold difference is seen for test 4D, with 170 mA/cm^2 found from the test results and 500 estimated in Table I. The tests with 0.3% CO_2 (3 and 4A) are also about a factor of three below the estimates of Table I. These comparisons tend to verify that gas-phase diffusion of CO_2 is, in fact, the controlling process at these low CO_2 pressures.

The limiting currents listed in Table IV are those due to diffusion of CO_2 under conditions of high utilization. The overall cathode reaction [3] has a complicated reaction mechanism (26, 27). At 100% CO_2 utilization, current will still flow due to the following reaction

$$\tfrac{1}{2}\,O_2 + 2e^- \rightleftarrows O^{2-} \qquad [27]$$

This results in a continuous-smooth overpotential curve and will proceed until depletion of carbonate ions in the electrolyte occurs. Thus, operation at currents higher than these values does not result in immediate infinitely high overpotential.

Table II lists the values of i_o for each run. The values of the exchange current density are approximately a factor of 4 or 5 lower than the values found by Winnick and Ross (13). For example, at 923 K and an O_2 concentration of 20%, Winnick and Ross found the exchange current density to be 103 mA/cm^2 (superficial area), and at 818 K, they found an i_o of 45 mA/cm^2. The Winnick and Ross correlation for exchange current density is

$$i_o\ (\text{superficial area}) = (1.5 \times 10^2)$$
$$P_{CO_2}{}^0 P_{O_2}{}^{0.5} \exp\,(-6 \times 10^3)/(T + 273) \qquad [28]$$

The activation energy for the reaction mechanism is given by

$$\Delta E_A = R\Delta(\ln i_o)/\Delta(1/T) \qquad [29]$$

For a temperature range of 923-818 K the activation energy for Eq. [28] is 11.7 kcal/g mol. Using the average values of i_o (listed in Table II) at 916 K, 0.018 mA/cm^2, and at 818 K, 0.072 mA/cm^2, the activation energy for the above temperature range is 13.9 kcal/g mol. This is in fairly good agreement with Winnick and Ross and indicates that the difference in the performance of their cell and the cells used in this experiment is the active electrode area. This assumption is supported by the high ohmic losses found, which indicates poor electrode wetting (small active area) due to insufficient electrode/electrolyte tile contact.

Wilemski *et al.* (17), using their semi-empirical model, were successful correlating IGT cathode half-cell overpotentials (22). They found an i_o of 0.35 mA/cm^2 (actual area) for 15% O_2 and 30% CO_2 at 923 K. The actual area to superficial area they used for the cathode was 320 cm^2/cm^2 (16), resulting in an i_o of 112 mA/cm^2 (superficial area). This corresponds reasonably well with the value calculated from Eq. [28], 87 mA/cm^2 (superficial area).

By taking the ratio of 112 mA/cm^2 to the i_o found for run No. 1, 23 mA/cm^2 (superficial area), the ratio of the active areas of the IGT MCFC and the MCCDC is found to be 4.9. A rough comparison of the IGT MCFC data with the MCCDC can be made by multiplying the MCCDC current densities by 4.9. At 100 mA/cm^2 (20 mA/cm^2 for the MCCDC) the MCFC has a cathode overpotential of 45 mV while the MCCDC has an overpotential of 55 mV (Test IE). At 200 mA/cm^2 (40 mA/cm^2 for the MCCDC) the MCFC has an overpotential of 85 mV and the MCCDC has an overpotential of 118 mV. The agreement is good, which suggests that the major differences between the two cells is in the wetting characteristics.

Comparison of the MCCDC's anode current-overpotential performance with IGT's anode data also showed good agreement when the comparison is based on the ratio of the exchange current densities (superficial area) using the exchange current density found by Wilemski (17, 20).

The temperature dependence of the cathode overpotential is controlled by the temperature dependence of the exchange current density and the effect of temperature on the exponential terms in Eq. [22].

The combined effects of diffusion in the flow cavity and the pores, and activation is seen in the predicted cathode polarization curves, Fig. 11. The overpotential is both *IR* and Nernst-loss free. The dependence of the cathode overpotential on flow rate and CO_2 inlet concentration is described above and is seen in this figure.

Cathode CO_2 Removal Efficiency

The goal of high removal efficiencies of CO_2 from simulated cabin gas with low CO_2 partial pressures ($P_{CO_2} \leq 7.6$ mm Hg) has been achieved during these runs. For an inlet CO_2 concentration of 1.0% CO_2 removal efficiencies of at least 95% were achieved at flow rates as high as 200 cm^3/min. For 0.5% CO_2, removal efficiencies greater than 80% were obtained at 500 cm^3/min at temperatures of 637° and 545°C. From Fig. 6 it is seen that a removal efficiency of 95% was reached for 0.5% CO_2 at 103 cm^3/min.

During several tests, 1A, 1B, and 2C, the outlet CO_2 concentrations of the cathode gas were reduced to ambient levels (0.03%). For all other tests, the outlet CO_2 concentrations were below 0.1%.

As evident from Fig. 6 and 7, the removal efficiency is approximately a linear function of current density over the range tested. Since the CO_2 removal rate is proportional to the CO_2 removal efficiency, the CO_2 removal rate is also linear with respect to current over the range tested.

Cathode Current Efficiency

The MCCDC achieves high removal efficiencies at high current efficiencies. The lowest current efficiency recorded was 80%. At most current densities, for all runs, current efficiencies were above 100%.

Typical current efficiencies as a function of current density are shown in Fig. 8. Current efficiencies at low current densities approach infinity. This is because of the open-circuit removal of CO_2. At high current densities the current efficiencies approach 100%.

The phenomenon of open-circuit CO_2 removal and current efficiencies above 100% is discussed by Winnick *et al.* (12) and Stepanov (29). Under normal operating conditions the ratio of cathode to anode flow rates will be approximately 50 whereas experimental ratios of 3 to 22 were used. At these low ratios open-circuit CO_2 removal occurs due to diffusion of CO_2 and reaction with the excess hydrogen (12, 28). In an operating cell, efficiencies of 100% will be seen even at the low current densities.

Conclusions

The cathode of a molten carbon fuel cell has been found to perform quite well at extremely low carbon dioxide partial pressures. Current densities appear to be limited by gaseous diffusion of CO_2 to the reaction zone.

The high current efficiencies, current densities, and removal efficiencies achievable make the MCCDC attractive for manned space applications. The penalties associated with such a high-temperature device, however, would have to be considered in any design.

Acknowledgments

We thank P. D. Quattrone and the National Aeronautics and Space Administration who supported this work under Contract No. NAG 2-11. Special thanks are due to P. N. Ross and Franz Schubert for comments during the preparation of this paper. The electrolyte tiles were generously donated by the Direct Energy Conversion Program of the General Electric Company. We also thank A. J. Appleby and W. M. Vogel for their helpful comments during review.

Manuscript submitted March 22, 1982; revised manuscript received Aug. 27, 1982.

Any discussion of this paper will appear in a Discussion Section to be published in the December 1983 JOURNAL. All discussions for the December 1983 Discussion Section should be submitted by Aug. 1, 1983.

Publication costs of this article were assisted by the Georgia Institute of Technology.

LIST OF SYMBOLS

a	Activity
A_{cs}	Cross-sectional area (cm^2)
B'	Constant for Eq. [26] (cm/sec)
C	Concentration (g mol/cm^3)
C^o	Bulk phase concentration (g mol/cm^3)
C^*	Concentration at entrance of pore (g mol/cm^3)
D_{AB}	Diffusivity (cm^2/sec)
D_{eff}	Effective diffusivity (cm^2/sec)
E	Potential (V)
ΔE_N	Nernst loss (V)
ΔE_A	Activation energy (cal/g mol)
$\mathbf{F}$	Faraday
H	Henry's constant (mol/cm^3-atm)
R	Gas constant (cm^3-atm/g mol K)
r_H	Hydraulic radius (cm)
r	Collision diameter
T	Temperature (K)
V	Velocity (cm/sec)
i	Current density (mA/cm^2)
i_L	Limiting current density (mA/cm^2)
i_o	Exchange current density (mA/cm^2)
I	Current (A)
I_D	Collision integral for diffusion
I^R	Ohmic loss (V)
J_D	Molar flux (g mol/cm^2 sec)
k_g	Mass transfer coefficient (cm/sec)
L	Length (cm)
m_{co_2}	CO_2 removal rate (cm^3/min)
M	Molecular weight
n	Mols of electrons transferred per mol of reactant
(N_{sh})ln	Log mean Sherwood number
N_{Re}	Reynolds number
N_{Sc}	Schmidt number
P	Pressure (atm)
R	Resistance (Ω)
Q	Volumetric flow rate (cm^3/min)

Greek Letters

$\overrightarrow{\alpha}$	Cathodic transfer coefficient
$\overleftarrow{\alpha}$	Anodic transfer coefficient
δ	Effective thickness (cm)
ϵ	Porosity
η	Overpotential (V)
η_d	Diffusion overpotential (V)
ρ	Density (g mol/cm^3)
τ	Tortuosity
μ	Viscosity (g/cm sec)

Subscripts

ca	Cathode
ref	Reference
$x = 0$	Electrode/electrolyte interface
P	Product
R	Reactant
e	Equilibrium
g	Gas phase
i	Specie i
i	Under load

REFERENCES

1. L. Dell'Osso, J. Ruder, and J. Winnick, *I/EC Proc. Dev.*, **8**, 477 (1969).
2. J. Winnick, R. D. Marshall, and F. A. Schubert, *ibid.*, **13**, 59 (1974).
3. C. H. Lin and J. Winnick, *ibid.*, **13**, 63 (1974); C. H. Lin, M. L. Heinemann, and R. M. Angus, *ibid.*, **13**, 261 (1974).
4. Life Systems, Inc., NAS CR1S2250, May 1979.
5. J. C. Huddleston and J. R. Aylward, Final Report Contract NAS 9-13679, NASA, Johnson Space Center, Houston, Texas, May 1975.
6. R. R. Woods, F. H. Schubert, and T. M. Hallick, Final Report, Contract NAS-9-14301, NASA, Johnson Space Center, Houston, Texas, Oct. 1975.
7. F. H. Schubert, *et al.*, NASA CR-166141, Final Report, Dec. 1981.
8. Argonne National Laboratories, Contract W-31-109-ENG-38 Progress Report ANL-78-71, Aug. 1978.
9. United Technologies Corporation, EPRI EM-856, Project 114-2, Dec. 1978.
10. Institute of Gas Technology, Project 9105, Final Report, April 1979.
11. O. E. Abdel-Salam and J. Winnick, Paper No. 70-ENAs-2 Intersociety Conference on Environmental Systems, San Diego, CA, July 1978.
12. J. Winnick, H. Toghiani, and P. Quattrone, *AIChE J.*, **28**, 103 (1982).
13. J. Winnick and P. N. Ross, Jr., *This Journal*, **128**, 5 (1981).
14. A. J. Bard and L. R. Faulkner, "Electrochemical Methods," John Wiley and Sons, New York (1980).
15. A. H. P. Skelland, "Diffusional Mass Transfer," John Wiley and Sons, New York (1974).
16. Institute of Gas Technology, Project 8984, Quarterly Report, Jan.-March 1977.
16. (a) A. J. Appleby and Van Drunen, *This Journal*, **127**, 1655 (1980); (b) S. W. Smith, W. M. Vogel, and S. Kapelner, *ibid.*, **129**, 1668 (1982).
17. G. Wilemski, T. Wolf, D. Bloomfield, M. L. Finson,

E. R. Pugh, and K. L. Wray, Physical Sciences, Inc., Final Report, DOE Contract DE-AC-03-79ET11322, July 1979.
18. Argonne National Laboratories, Contract W-31-109-ENG-38 Progress Report ANL-77-56, June 1977.
19. S. Schuldiner and R. E. White, *This Journal*, **97**, 433 (1950).
20. J. Weaver, Masters Thesis, Georgia Institute of Technology (1981).
21. R. H. Perry and C. H. Chilton, "Chemical Engineers Handbook," 5th ed., McGraw-Hill, New York (1973).
22. Institute of Gas Technology, Project 8984, Final Report, Vol. I, Vol. II, Sept. 1977.
23. E. Gorin and H. L. Recht, *Ind. Eng. Chem.*, **52**, 306 (1960).
24. C. G. Hill, Jr., "An Introduction to Chemical Engineering Kinetics and Reactor Design," John Wiley and Sons, New York (1977).
25. J. O'M. Bockris and A. K. N. Reddy, "Modern Electrochemistry," Plenum Press, New York (1970).
26. A. J. Appleby and S. Nicholson, *J. Electroanal. Chem. Interfacial Electrochem.*, **53**, 105 (1974).
27. A. J. Appleby and S. Nicholson, *ibid.*, **83**, 309 (1977).
28. G. K. Stepanov and A. M. Trunov, Electrochemistry of Molten and Solid Electrolytes, **3**, 74, Consultation Bureau, New York (1966).

Electrochemical Studies of Photocorrosion of n-CdSe

Karl W. Frese, Jr.*

SRI International, Menlo Park, California 94025

ABSTRACT

Rotating-ring-disk studies of the photoelectrochemical corrosion of n-CdSe (1120) have been made. Flatband potentials for CdSe as a function of light intensity and redox potential were determined. The studies focused on the role of the Se corrosion layer. Evidence is presented to show that the nominally Se layer is a good hole conductor with an active energy level for holes at +0.76V *vs.* SCE. The Marcus-Gerischer reactivity pattern was found by an analysis of stabilization efficiency with various reducing agents.

The use of semiconductors, such as GaAs or CdSe, in contact with redox electrolytes to convert radiant energy to electrical or chemical energy will continue to be a widely pursued research objective. The nature of these photoelectrochemical devices is such that corrosion of the electrode material is a major concern. Therefore, we (1, 2) and others (3) have made attempts to describe the corrosion process as well as the competitive electron transfer from redox species in the electrolyte.

This paper deals with several aspects of our studies of the photoelectrochemical corrosion of n-CdSe. We have applied various measurement techniques including capacitance-voltage (C/V), monochromatic quantum yield, and the rotating ring-disk electrode, RRDE.

We have determined the bandedge energy levels of illuminated CdSe using capacitance/voltage (C/V) analysis and compared this value with the kinetically determined energy level for holes, E_h, in a nominally selenium corrosion layer. We used quantum yields *vs.* wavelength to show that the corrosion layer on CdSe is a good hole conductor. We have also demonstrated the utility of applying homogeneous electron transfer rate data to problems in semiconductor electrode kinetics such as the problem discussed here, namely, the competition between corrosion and electrode redox reactions.

Experimental Details

All samples of CdSe (Cleveland Crystals) (11$\bar{2}$0) were first chemomechanically etched and polished using a 1% Br_2/CH_3OH(v/v) solution. Before each experiment, the samples were cleaned with 1% Br_2/CH_3OH mixed 50% by volume with 1M HCl using a wet cotton tip applicator. Finally, the samples were rinsed for ~10 sec with 1M HCl, followed by a 20 sec rinse in flowing deionized water. After such treatment, the samples were always bright and hydrophobic.

A Bausch and Lomb high-intensity grating monochromator was used in the spectral experiments. Light intensities were measured with an Eppley thermopile.

A rotating ring-disk electrode was assembled with a 5 mm diam CdSe disk and a glassy carbon ring. The collection efficiency was found to be 0.30. A Pine RDE-3 bi-potentiostat was used to control the ring and disk electrode potentials. The rotation speed, 1000 rpm, was high enough to avoid diffusion limitation. The measured currents were independent of rotation speed in the same speed range and above.

Capacitance measurements were made using a lock-in amplifier set up at a constant a-c voltage of ~10 mV amplitude. The parallel capacitance C_p is measured in our arrangement. The measuring frequency was 10 kHz. Previous measurements (4) on the same crystals used here showed no frequency dispersion in the frequency range 1 kHz to 100 kHz.

Flatband Potential Measurements

We have previously discussed (4) our results on the measurements of dark flatband potentials of n-CdSe (11$\bar{2}$0). The results were interpreted by assuming interface state charging by redox couples in the dark. When such interface states are present, the flatband potential can differ between light and dark due to the effect of light in causing electronic transitions, that lead to a different state of charge in the interfacial region. For example, holes may be captured on negatively charged acceptor states. Our earlier results on CdSe showed clearly that interface states contribute a major role in the C^{-2}/V behavior in the dark in the presence of various redox couples. We therefore investigated the effect of illumination on the flatband potential using three different redox couples. Typical results are shown in Fig. 1 where we show sample Mott-Schottky (10 kHz) plots at various light intensities with 0.05M each $[Fe(II)DTPA]^{=}/[Fe(III)DTPA]^{-}$ as the redox couple ($E^o = -0.21$V *vs.* SCE). DTPA is diethylenetriaminepentacetic acid. The anodic current varied from 10^{-8} (dark) to 1×10^{-3} A/cm^2 at the highest light intensity. The Mott-Schottky slopes are parallel at each light intensity, yielding donor densities of 1.5×10^{17} cm^{-3} in both dark and light. We can therefore say that bulk hole trapping is not an important effect in these experiments. As shown in Fig. 1, the flatband potential is strongly dependent on light intensity. A positive shift that eventually saturates at $V_{fb} = -0.40$V *vs.* SCE

* Electrochemical Society Active Member.

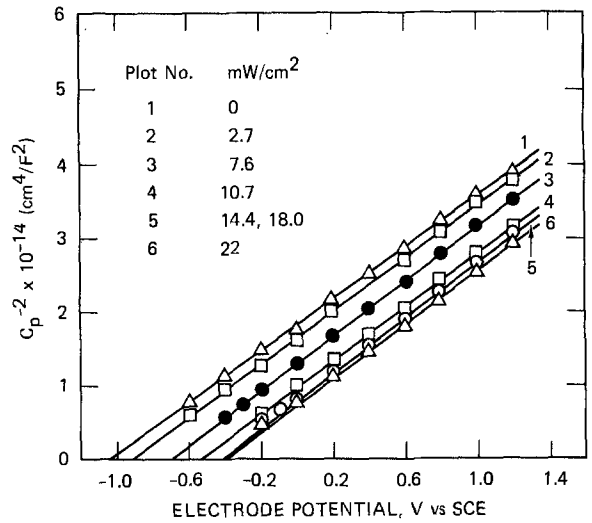

Fig. 1. Mott-Schottky plots for n-CdSe (1120) at various light intensities. Tungsten-halogen lamp. Electrolyte: 0.05M each Fe^{2+}/Fe^{3+} in 0.5M DTPA, pH 8.5.

is observed. If the illumination is removed, the M-S plot returns to the original dark value. The CdSe is relatively unstable if the photocurrent exceeds 1×10^{-3} A/cm^3 under the conditions in Fig. 1. In this case, the Mott-Schottky plot does not return to the original dark condition.

Similar measurements were made with $Fe(CN)_6^{4-/3-}$ ($E^\circ = +0.12$V *vs.* SCE) and [Fe EDTA]$^{-/=}$ ($E^\circ = -0.12$V *vs.* SCE) as the redox couples. The effect of illumination was very similar in these cases. The results of V_{FB} *vs.* light intensity are summarized in Fig. 2. In each of the three cases investigated, V_{FB} saturates at the same potential, namely, −0.40V *vs.* SCE. In the dark, the flatband potential depends on the redox couple in agreement with previous results (4). The results in Fig. 2 show another interesting feature. As the redox couple becomes more reducing, a higher hole flux is needed to shift V_{FB} to the saturation value. This may indicate that holes neutralize negative charge in acceptor interface states (4). The amount of negative charge depends on the reducing power of the redox couple.

We emphasize that the above measurements were made on freshly etched crystals, in which case we can expect a thin corrosion layer of Se. Just how thin these layers are is not clear. A film of 10-15Å is not unreasonable in view of the 10-15Å residual SiO_2 film found after HF/H_2O etching of silicon (5, 6). Some unpublished Auger spectroscopy results from our laboratory do indicate that the freshly etched CdSe surface (1% Br_2/CH_3OH:1M HCl) is rich in Se.

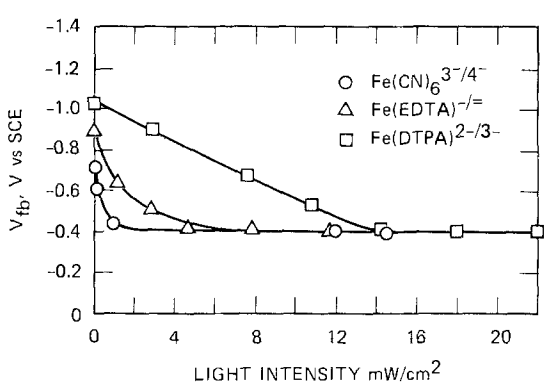

Fig. 2. Flatband potential *vs.* light intensity for n-CdSe (1120) in contact with various redox electrolytes. Electrolyte compositions: 0.25M each $K_3Fe(CN)_6/K_4Fe(CN)_6$ 0.01M DTPA, pH 8.5; 0.2M each Fe^{2+}/Fe^{3+} in 0.5M Na_4EDTA, pH 6.5, 0.05M each Fe^{2+}/Fe^{3+} in 0.5M DTPA, pH 8.5.

Optical Properties of Corrosion Layer

The effect of the corrosion layer of CdSe on the quantum efficiency, Φ, at short circuit is shown in Fig. 3. The quantum efficiency is calculated by dividing the observed short-circuit current density by the monochromatic photon flux in current density units. In these experiments low light intensities were used so that the current density at the CdSe electrode was always less than 50 μA/cm^2. The corresponding current density at the large area Pt counterelectrode was ≤ ~5 μA/cm^2. The electrolyte contained 0.1M $K_4Fe(CN)_6$ and a small amount of $K_3Fe(CN)_6$. The concentration of the reduced form was high enough to ensure a very high electrode stability at ≤50 μA/cm^2 photocurrent while the concentration of $K_3Fe(CN)_6$ was kept low to minimize light absorption in the electrolyte. The measured currents were not affected by stirring.

The Φ *vs.* wavelength, λ, relation was first determined for the as etched electrode. Quantum efficiencies were ~0.85 over most of the λ range. The decrease in Φ at ~440 nm is caused by light absorption by the $K_3Fe(CN)_6$.

In subsequent experiments the CdSe was photocorroded at 100 μA/cm^2 photocurrent in a separate cell containing 1M Na_2SO_4, pH 7. Following earlier work on CdSe and CdS (7), we assumed that the corrosion reaction caused the release of Cd^{2+} ions into the electrolyte while the Se deposited in elemental form on the CdSe surface. Our Auger results on anodized surfaces again showed the corrosion layer was >95% Se. With this assumption we calculate that a corrosion photocurrent of 100 μA/cm^2 is equivalent to an Se growth rate of 55 Å/min.

Proceeding in the above fashion, we grew Se layers that were 60-3600Å thick, as listed in Fig. 3. The 2400 and 3600Å thick layers showed film colors with the characteristic red of amorphous selenium ($E_g = 2.05$ eV) (8). The Φ *vs.* λ was determined as shown by the remaining plots in Fig. 3. The growth of the first 60Å caused Φ to increase over much of the wavelength range. This effect could be related to an improvement in surface conditions that led to lower recombination and/or more effective light absorption. In a recent paper (9), the improvement in solar cell efficiency of polycrystalline CdSe caused by short photoanodic etching has been demonstrated.

Some quantum efficiencies in Fig. 3 exceeded unity by at most 10%. We attribute this to a systematic error in light flux measurement. Ultimately, we wish to calculate the apparent absorption coefficient of the corro-

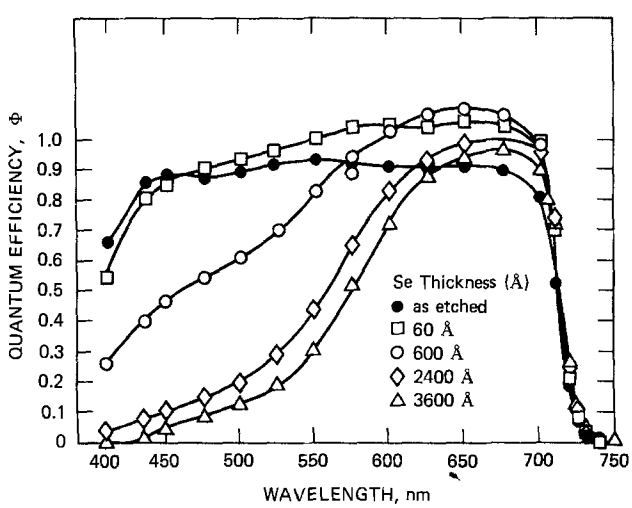

Fig. 3. Short-circuit quantum efficiency *vs.* wavelength for n-CdSe (11$\bar{2}$0) in 0.1M $K_4Fe(CN)_6$ 0.1M Na_2 EDTA, pH = 8.5. Samples were anodized in 1M Na_2SO_4, pH = 7, for various times.

sion layer so that only relative Φ values are important. We used the 60Å Φ *vs.* λ as the "base line" zero light absorption curve. Other curves at 600, 2400, and 3600Å were compared with the 60Å at each λ. From the relative Φ referred to the 60Å curve, the apparent adsorption coefficient, α, cm^{-1} was obtained by solving the following equation

$$\ln [\Phi/\Phi_{60Å}] = \alpha t \qquad [1]$$

where t is the thickness of Se calculated from the photocorrosion time data. The apparent α for three thicknesses is shown in Fig. 4 where the data are compared with one set of literature α values for amorphous Se (10). In view of the uncertainties in our method, the agreement is good, indicating that the corrosion layer behaves optically very much like an Se light filter. The implications of these results are discussed later.

Determination of Rearrangement Energies

In our corrosion-redox competition model (2), a parameter of major importance is the most probable level of the reducing agent E_{red}. This level (11) is related to the redox potential, E_F^{redox} according to

$$E_{red} = E_F^{redox} - \lambda_{el} \qquad [2]$$

where λ_{el} is the reorganization energy (12, 13) for a heterogeneous (electrode) reaction. It is evident that λ_{el} values must be evaluated to understand the corrosion process.

A large body of data on homogeneous electron transfer reactions in solution exists in the chemical literature. In general, two types of reactions have been studied. Type one consists of electron exchange reactions between redox species that only differ in their oxidation state, such as $Fe^{2+} + {}^*Fe^{3+}$. The second group is made up of cross reactions, *e.g.*, $Ce^{4+} + Fe(CN)_6^{4-}$.

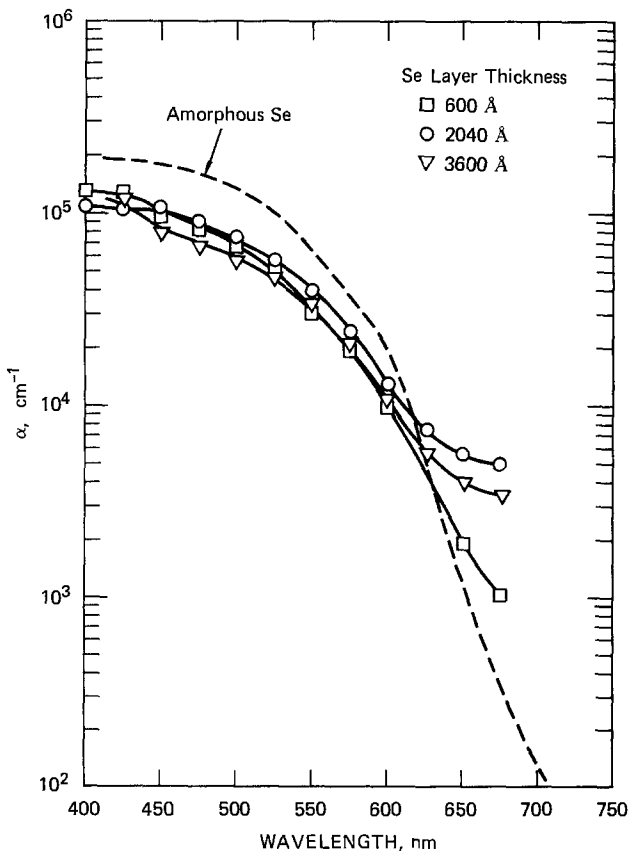

Fig. 4. Comparison of absorption coefficient calculated from loss of photocurrent for various Se layer thicknesses with literature value for amorphous Se.

We have recently analyzed rate constant data for about 50 such reactions using the Marcus theory (12, 13).

The analyses provide good experimentally based values for λ_{el}.

For the first case of the simple exchange reaction with rate constant, k_x, we have

$$k_x = Ze^{-(\Delta G_t^* + \lambda_x/4)/kT} M^{-1} sec^{-1} \qquad [3]$$

where Z is a collision number ($\sim 10^{11}$ M^{-1} sec^{-1}) and ΔG_t^* ($\sim$0.05 eV) is the work associated with transfer of the reacting species to their transition state separation, and λ_x is the reorganization energy of the environment. This λ_x contains contributions from both the oxidized and reduced forms of the couple. According to Marcus (13)

$$\lambda_{el} \cong \frac{\lambda_x}{2} \qquad [4]$$

In the case of cross reactions we have

$$k = Ze^{-[(\Delta G^0 + \lambda)^2/4\lambda kT]} M^{-1} sec^{-1} \qquad [5]$$

when the work terms are negligible. In this equation (13)

$$\lambda \simeq \frac{\lambda_x^1}{2} + \frac{\lambda_x^2}{2} \simeq \lambda_{el}^1 + \lambda_{el}^2 \qquad [6]$$

where λ_x refers to the simple exchange reaction, Eq. [3], and the superscripts refer to the two different redox couples in the cross reaction. The term ΔG^0 is the standard free energy change of the electron transfer reaction. Table I summarizes some of the results for rearrangement energies for reducing agents expressed as λ_{el}. These λ_{el} values will be used in Eq. [8] in the kinetic analysis below.

Rotating Ring-Disk Data

In the insert of Fig. 5 the concentration dependence of the stabilization efficiency, S, with $K_4Fe(CN)_6$ as the reducing agent is shown. The stabilization efficiency is the hole current to the reducing agent, *e.g.*, $Fe(CN)_6^{4-}$ divided by the total photocurrent. The potentials of the ring and disk were -0.6 and $+0.6$V *vs.* SCE, respectively. During these experiments an Se corrosion layer formed as evidenced by the blue color of the transparent film on the electrode surface. The color of a freely corroding CdSe electrode passes from metallic to blue to pale gold to red as the corrosion layer grows. Auger analysis of such films showed they are >95% Se. Thus, the colors are likely to be interference colors associated with the Se layer.

S increases rapidly as the concentration of the reducing agent increases. These data were tested to see how well they conform to the theory (2) by plotting log $[j_pS^2/1 - S]$ *vs.* log C (see Eq. [7] below). The quantity, j_p, is the observed photocurrent. The predicted slope is 2 and the experimental value from the linear plot in Fig. 5 is 1.8 ± 0.2. In unpublished similar work in our laboratory on CVD GaAs, an experimental slope of 2.0 was found. Other tests of the theory may be found in Ref. (1-3).

Table I. Experimentally derived values[a] of λ_{el} (eV) for several reducing agents

$IrCl_6^{3-}$	0.65
[Fe(II)DTPA]≡	0.69[b]
$Fe(CN)_6^{4-}$	0.72,[c] 1.15[d]
[Fe(II)EDTA]=	0.72[b]
[Fe(II)CyEDTA]=	0.81
$[Fe(H_2O_6)^{2+}]$	1.18
Ce^{3+}	1.31[c]

[a] See Ref. (12).
[b] See Ref. (2) also.
[c] pH > 5.
[d] 0.5M H_2SO_4.
EDTA = ethylenediaminetetraacetic acid.
CyEDTA = cyclohexane EDTA.

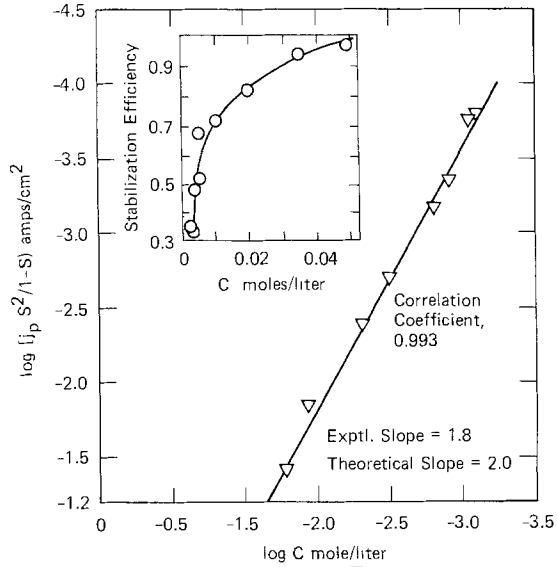

Fig. 5. Dependence of stabilization efficiency on concentration of $Fe(CN)_6^{4-}$ for n-CdSe ($11\bar{2}0$). Photocurrent, 1 mA/cm^2 ± 10%. Electrolyte contained 0.1M Na_2EDTA, pH 8.5. Data also plotted in linear form according to theory. (See text.)

Stabilization efficiency data *vs.* redox couple and time are shown in Fig. 6. The disk was held at +0.6V *vs.* SCE and the ring potential varied with the reducing agent. In all cases the ring potential chosen was sufficiently cathodic to ensure a saturation current. In each case the concentration of reducing agent was 0.02M and the photocurrent was kept at 1.0 mA/cm^2. We were careful to work at ring potentials where Cd^{2+} (a corrosion product) was not reduced. In all the experiments except for the case of $IrCl_6^{3-}$, a large excess of complexing agent was present. In the case of $Fe(CN)_6^{4-}$, 0.1M Na_2EDTA was used as the background electrolyte. Blank runs were made without the reducing agents added, and no Cd^{2+} reduction was observed in the ring potential region in which the oxidized forms of the couples are reduced.

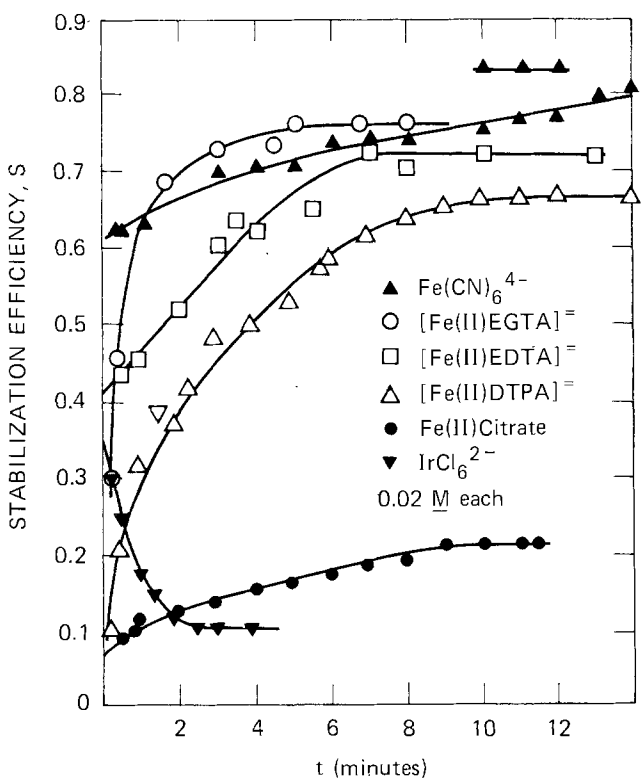

Fig. 6. Stabilization efficiency vs. time for n-CdSe (1120) for various reducing agents. Photocurrent: 1 mA/cm^2; concentration: 0.02M; pH range: 6-9.

One interesting feature in Fig. 6 is that S changed with time and reached a saturation value in times ranging from 2 to 14 min. After each S *vs.* time run, the electrode was covered with a blue or red transparent film. We have given substantial evidence here and elsewhere (4) that this film is elemental selenium. It is reasonable to associate the change in S with the growth of an Se film. In the case of $Fe(CN)_6^{4-}$, the same rise in S as in Fig. 6 was observed if the Se layer was grown in a separate cell with 1M Na_2SO_4 electrolyte, pH 7, exactly as described earlier in the optical measurements. In this case, the initial value of S in the ring disk experiment was considered. The same saturation value of $S = 0.85$ was observed in both cases of corrosion in $Fe(CN)_6^{4-}$ or Na_2SO_4 solution.

An interesting observation is that S increased with time for all redox systems in Fig. 6 except for $Ir(Cl)_6^{3-}$ which is the weakest reducing agent shown. The decrease of S in the case of $Ir(Cl)_6^{3-}$ shows that the increases in S are not simply due to a retardation of the Cd^{2+} ionic current (corrosion current) caused by film growth at constant electrode potential. A similar decrease in S (not shown) was observed with 0.02M I^{3-} at pH = 4.5. However, the stabilization efficiency dropped to values too low to accurately measure. Note that I^{3-} like $Ir(Cl)_6^{3-}$, is a weak reducing agent. Finally, no electron transfer reaction could be detected with $Ru(bipyridyl)_3^{2+}$ or $Fe(phenantholein)_3^{2+}$ as the reducing agent. That is, these ions are extremely poor stabilizing agents on CdSe.

If the saturation values of S in Fig. 6 are plotted *vs.* redox potential, a peak is found at $E^0_{redox} = \sim 0.0$V *vs.* SCE. A more exact kinetic analysis of this effect is given below.

Analysis and Discussion

For the analysis to follow, it is necessary to discuss the results bearing on the hole conductivity of the corrosion layer. We believe we have good evidence that the anodically grown Se layer has high hole conductivity. The evidence is as follows: First, in the constant current photocorrosion of n-CdSe at 100 μA/cm^2 the anodization cell voltage remains constant at −0.4V *vs.* Pt (pH 7, in $NaSO_4$) even though films thicker than 1000Å are grown. For constant current photoanodization of n-GaAs or n-Si where insulating films form, a linear rise in cell voltage *vs.* time is observed (14). Second, the quantum yields for the short-circuit current in Fig. 3 are not very sensitive to the presence of the Se layer at any thickness for wavelengths between the bandgaps of Se (605 nm) and CdSe (740 nm), although 90% of the current at 500 nm has been lost for films ~ 3000Å thick. From the results of experiments on evaporated Se films (15), we do not expect any sizable photocurrent due to holes generated by light absorbed in the Se layer. Apparently, strongly bound electron-hole pairs are formed in this material that require fields > 10^7 V/cm for efficient free hole-electron generation (15). Because of the similar chemical nature of our films, as well as the reasonable agreement of the apparent absorption coefficients with literature values and the evidence cited above, we conclude that the Se layer allows holes generated in the CdSe to be transmitted to the electrolyte while filtering the light according to its absorption spectrum.

Additional evidence discussed elsewhere (16) has been obtained to support the conducting p-Se layer model. In these experiments, Se layers were grown up to 8000Å thick in Na_2SO_4 as described above. Then, the j_p-V curve was obtained in alkaline $Fe(CN)_6^{4-/3-}$ redox electrolyte using the AM2 solar light flux. As expected, the short-circuit current j_{sc}, dropped as the Se layer thickened. For a thickness of 8000Å, j_{sc} had dropped to ~ 0.44 of its initial value of 10 mA/cm^2. By means of the apparent absorption coefficients for

the corrosion layer (Fig. 4) and tables of the monochromatic AM2 solar spectrum, the photon current was calculated at each wavelength and the resulting distribution was integrated. The predicted relative $j_{sc}/j_{sc}^{t=0}$ was in excellent agreement with experiment up to 8000Å of Se. We concluded that the photocurrent is limited only by the light flux even in the presence of thick Se layers.

In summary, these results at high photocurrent (4-10 mA/cm^2) are in very good agreement with the quantum yield measurements in Fig. 3, which were obtained at a photocurrent of about 10 μA/cm^2. We can now say that in analyzing the ring-disk data for S in the presence of a corrosion layer, the holes pass readily through the layer, and so we may inquire what is the redox-active hole energy level, E_h, associated with these films.

The kinetic analysis is based on the corrosion-redox competition model previously derived (1, 2). Several expressions relating the stabilization efficiency, S, to the photocurrent, j_p, and the current to the reducing agent, j_3, were given. The simplest expression to use is

$$\frac{1}{S} = 1 + \frac{\alpha j_3}{C^2_R} \qquad [7]$$

where $j_3 = Sj_p$, α is a composite rate constant, and C_R is the concentration of reducing agent. An equivalent, but more complex, form relating S to j_p, α, and C^2_R has been given (1). In Eq. [7], α is a composite rate constant of the form

$$\frac{1}{\alpha} = K \langle q\sigma_3 v d_3 \rangle^2 \frac{kT}{\pi\lambda} e^{-(E_h - E_{red})^2/2\lambda kT} \qquad [8]$$

where K contains rate constants for the solid-state hole capture processes and hole transport in the corrosion layer. The meaning of the other symbols has been discussed before (2).

The final saturation values of S were used to calculate α using Eq. [7]. E_{red} values were calculated from Eq. [2] using λ_{el} from Table I. Finally, a plot of $\lambda/\alpha(\sigma d)_3^2$ *vs.* E_{red} was constructed and is shown in Fig. 7. The ordinate in Fig. 7 is a quantity proportional to the rate constant for hole capture by the reducing agent. Both the cross section, σ, and reaction length, d, were estimated from the size of the ions. Because of the constancy of λ at $\sim$ 0.7 eV for several ferrous complexes, a value of 0.72 was assumed for the case of ferrous citrate and ferrous EGTA ions. The curve drawn through the derived values of $\lambda/\alpha(\sigma d)_3^2$ appears to conform to the Marcus-Gerischer reactivity pattern. That is, the rate of reaction of holes at a fixed energy level passes through a maximum as the energy level of the reducing agent is varied. The decrease in stability as E_{red} increases (less positive potential) corresponds to the "inverted region" in homogeneous electron transfer kinetics. The inverted region reflects the decrease in rate constant of a reaction when the exothermic free energy change exceeds the reorganization energy.

The value of E_{red} corresponding to the peak yields the energy level for the holes at the Se surface. Thus, the kinetically determined energy level is +0.76V *vs.* SCE on the electrode potential scale.

It is of interest to compare this level with the valence bandedge of CdSe determined under illumination (Fig. 2). Using the bandgap of 1.74 eV for CdSe and $V_{FB} = -0.40$V and assuming $E_{CB} - E_F = 100$ mV, we obtain $E_{VB} = +1.24$V *vs.* SCE (pH 6.5-8.5). It is reasonable to assume the Helmholtz potential drop is the same for as-etched (thin Se layer) the corroded CdSe (thick Se layer) surfaces. Therefore, the energy level for holes in the presence of the Se corrosion layer is $\sim$0.5V above the valence band of CdSe. This difference in energy level is consistent with the model that holes move through the Se layer in a distinct set of states.

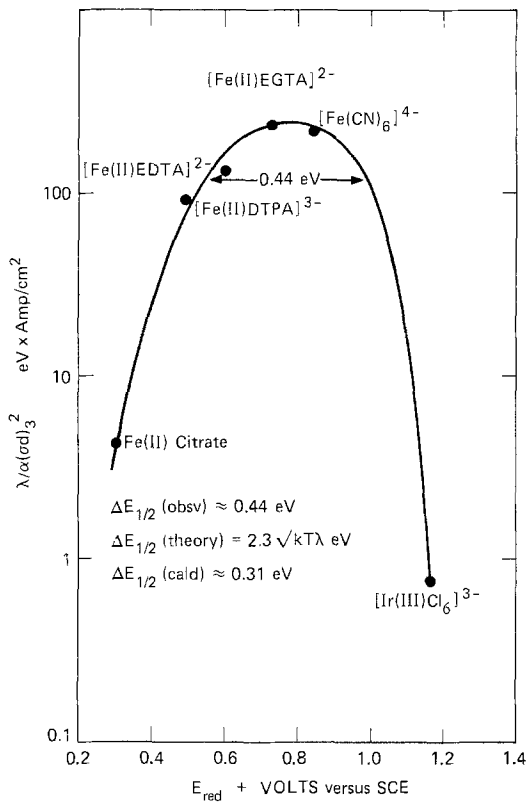

Fig. 7. Log plot of $\lambda/\alpha(\sigma d)^2$ *vs.* the most probable level of the reducing agent, E_{red}. This plot is suggested by the corrosion-redox competition theory. (See text.)

The highest filled levels in Se form a nonbonding valence band (17). Holes moving in a nonbonding band are not expected to corrode the material which contains them. However, we do not intend to imply that the Se corrosion layer is stable under all conditions. At higher positive cell voltages the layer is probably oxidized to soluble forms such as $SeO_3^=$. The very existence of elemental Se films on CdSe produced under photoanodic conditions suggests the possibility of hole conduction in a nonbonding band.

Finally, we compare the bandedges of CdSe and Se as determined by vacuum photoemission. Swank (18) found a value of 6.62 eV for the bandedge on CdSe. Nielsen (19) gives a value of 6.20 $\pm$ 0.05 eV for Se layers evaporated on Al substrates. The difference of these vacuum levels, 0.42 eV, agrees very well with the 0.48 eV (1.24-0.76V *vs.* SCE) difference determined in our photoelectrochemical studies. Our model for the CdSe/Se PEC cell is summarized in Fig. 8. We show no potential drop in the Se layer under anodic current flow due to the high concentration of holes that must be present (ohmic drop is neglected). The holes are injected into a nonbonding band that overlaps with the next (bonding) band (17).

The phenomena described here are related to the general problem of surface passivation in PEC cells using conducting polymer layers. It is likely that the Se layer is amorphous and thus its structure resembles evaporated Se layers; that is, it is made up of polymer chains and possibly rings. As in the case of Se, the electronic band structure of the polymer films could be a very important factor in determining the stability of such films. The injection of holes into favorable nonbonding levels in these films would be desirable.

In conclusion, we have measured many properties of the n-CdSe/Se corrosion layer/redox electrolyte system. We have shown that V_{FB} depends on light intensity and that saturation V_{FB} under illumination seems to be a meaningful energy level. By measuring the stabilization efficiency *vs.* known energy levels, we demonstrated the Marcus-Gerischer reactivity pattern

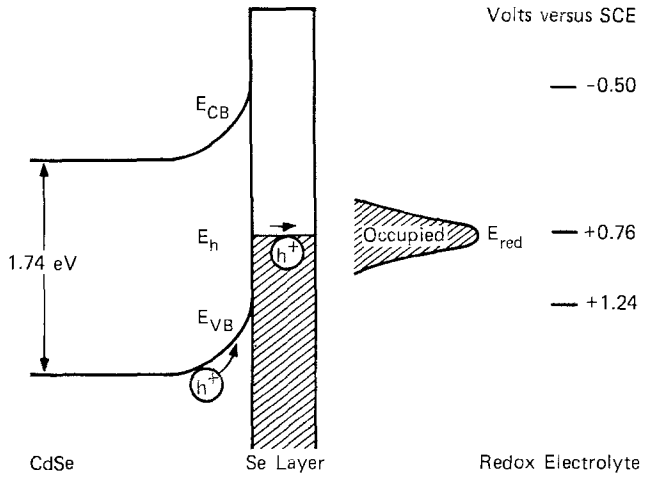

Fig. 8. Band diagram for CdSe/Se/redox electrolyte system with anodic photocurrent flow. Kinetically determined hole energy level is +0.76V vs. SCE. The shaded region in the Se layer corresponds to the nonbonding (uppermost) and bonding valence bands. (See text.) The position of the various bandedges are indicated.

for photogenerated holes. Available evidence suggests that the Se layer is a good hole conductor and that the holes occupy a band about 500 mV above the valence band of CdSe.

Acknowledgment

This work was sponsored by the Solar Energy Research Institute under contract XP-9-8002-6.

Manuscript submitted Nov. 16, 1981; revised manuscript received July 15, 1982. This was Paper 489, 490 presented at the Denver, Colorado, Meeting of the Society, Oct. 11-16, 1981.

Any discussion of this paper will appear in a Discussion Section to be published in the December 1983 JOURNAL. All discussions for the December 1983 Discussion Section should be submitted by Aug. 1, 1983.

Publication costs of this article were assisted by SRI International.

REFERENCES

1. K. W. Frese, Jr., M. J. Madou, and S. R. Morrison, *J. Phys. Chem.*, **84**, 3172 (1980).
2. K. W. Frese, Jr., J. Madou, and S. R. Morrison, *This Journal*, **128**, 1527 (1981).
3. W. Gomes, F. Van Overmeire, F. Van Maekelbergh, F. Vanden Kerchove, and F. Cardon, in "Photoeffects at Semiconductor Electrolyte Interfaces," A. J. Nozik, Editor, ACS Symposium Series No. 146 (1981).
4. K. W. Frese, Jr., *J. Appl. Phys.*, **53**, 1571 (1982).
5. R. J. Archer, *J. Opt. Soc. Am.*, **52**, 970 (1962).
6. B. H. Loo, K. W. Frese, Jr., and S. R. Morrison, *Surf. Sci.*, **109**, 75 (1981).
7. H. Gerischer and W. Mindt, *Electrochim. Acta*, **13**, 1329 (1968).
8. E. A. Davis, *J. Non-Cryst. Solids*, **4**, 107 (1970).
9. R. Tenne and G. Hodes, *Appl. Phys. Lett.*, **37**, 428 (1980).
10. J. L. Hartke and P. J. Regensburger, *Phys. Rev.*, **139A**, 970 (1965).
11. H. Gerischer, in "Physical Chemistry, An Advanced Treatise," Vol. IX-A, H. Erying, D. Henderson, W. Jost, Editors, Academic Press, New York. (Also see references cited therein.)
12. K. W. Frese, Jr., *J. Phys. Chem.*, **85**, 3911 (1981).
13. R. A. Marcus, *J. Chem. Phys.*, **43**, 679 (1965).
14. K. W. Frese, Jr. and S. R. Morrison, *Appl. Surf. Sci.*, **8**, 266 (1981).
15. D. M. Pai and R. C. Enck, *Phys. Rev. B*, **11**, 5163 (1975).
16. K. W. Frese, Jr., *Appl. Phys. Lett.*, **40**, 275 (1982).
17. M. Kastner, *Phys. Rev. Lett.*, **28**, 355 (1972).
18. R. W. Swank, *Phys. Rev.*, **153**, 153 (1967).
19. P. Nielsen, *ibid.*, **136**, 3739 (1972).

A New Type of Separator for High Temperature Water Electrolyzers

O. Teschke*

Laboratório de Hidrogênio, Institute de Fisica, Universidade Estadual de Campinas, 13 100 Campinas, São Paulo, Brazil

and F. Galembeck

Instituto de Química, Universidade Estadual de Campinas, 13 100 Campinas, São Paulo, Brazil

ABSTRACT

Perforated nickel sheets can be covered with polytetrafluoroethylene (PTFE Teflon) and used as diaphragms in water electrolyzers. The technique used consists of filling the sheet holes with camphor, spraying PTFE latex on them, and allowing the solid camphor to evaporate. Since the holes are left unclogged, the membrane has good ionic conductivity. However, electronic transport, because the nickel surface is covered by Teflon, is negligible. The hydrophobicity imparted by PTFE to the metal surface has a beneficial effect on gas bubble release during electrolysis. Insulating characteristics of the PTFE coating make this diaphragm adequate for use in sandwich arrangements for bipolar cells.

To improve alkaline water electrolyzer performance, it is necessary to increase its operating temperature to 200°C. This leads to the search for new separation materials for the diaphragm, since asbestos, the conventional separator, decomposes in an alkaline medium above 80°C. The diaphragms have to allow for ionic conduction but they have also to maintain the gases generated in the cell well separated.

Some authors have recently suggested the use of porous metallic diaphragms as separators in alkaline water electrolyzers (1, 2). The materials are resistant to corrosion and, once soaked with solution, they have low gas permeabilities and high ionic conductivity. The major problem with this type of diaphragm is its high electronic conductivity. When current passes through the cell, a potential difference arises across the porous metal diaphragm so that electrochemical reactions may occur, resulting in production of an explosive gas mixture (3). Besides that, the conductivity of these membranes puts stringent conditions on the mechanical design of the bipolar structure. It is necessary to carefully separate the anode and cathode from the membrane, otherwise the membrane can operate as a cathode or anode.

By covering perforated nickel plates with a PTFE layer the membrane is insulated and the above draw-

* Electrochemical Society Active Member.
Key words: nickel sheet, diaphragm, bipolar cells.

backs are avoided. The insulated nickel plate becomes a promising separator for alkaline water electrolyzers.

In the absence of electrolysis, the electrolyte resistance between the cathode and anode is approximately the resistance of the volume of electrolyte in between the parallel plates. During electrolysis the experimentally determined resistance is always larger. Obviously, the additional resistance is caused by coverage or screening of the electrodes and diaphragm surface by adhering bubbles and also by the gas bubbles in the electrolyte. The effect of bubbles in the electrodes will be treated at a later time (4).

Potential difference measurements in the electrolyte can give us insight into the effect of the bubbles on the ohmic resistance of the electrolyte and may lead to an optimal diaphragm structure. The gas flux is determined by the current, which at a given potential difference depends on the electrical resistance of the liquid-gas electrolyte mixture. The resistance fluctuates as a result of the bubble formation. If the bubble population at the electrode increases, the overall resistance increases and so does the heat evolution.

Experimental

The new separator was prepared by covering perforated nickel sheets with a layer of PTFE. Commercially available, 0.1 mm thick, nickel sheets were used. These have a hole density of 1444 cm^{-2} and are fabricated by electroerosion. A cross section of the membrane is shown in Fig. 1a. The detailed hole geometry is shown in Fig. 1b.

The PTFE coating procedure for the nickel plates was the following: the perforated nickel sheets were soaked in a concentrated (*ca.* 10%) ethanolic solution of camphor; the ethanol was evaporated under air, leaving the sheet holes filled with solid camphor. The flat sheet surfaces were then wiped with a razor blade and a detergent-free PTFE aqueous dispersion (*ca.* 1%) was sprayed on them. Water and the remaining camphor were evaporated under air and the PTFE-covered plates were heated to 370°C to improve PTFE adhesion to the metal. Other diaphragms were prepared as above except for omitting the camphor treatment.

The result of this procedure is shown in Fig. 2a, an optical micrograph of a perforated nickel plate treated

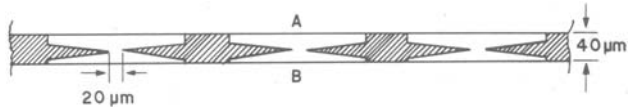

Fig. 1a. Cross-sectional view of the perforated nickel plates, showing in detail the hole structure.

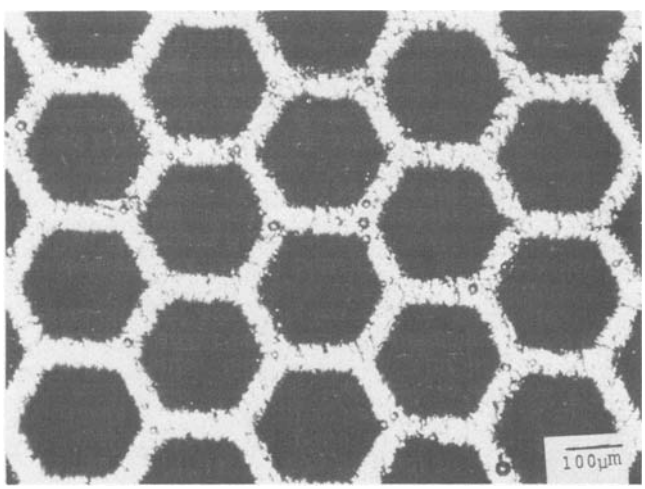

Fig. 1b. Optical micrograph of the nickel plate

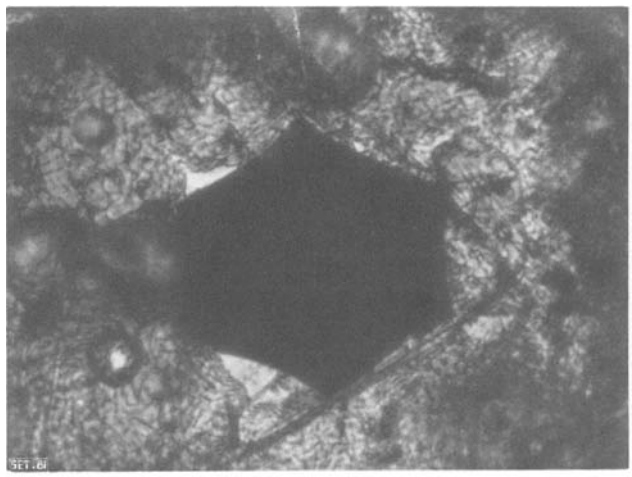

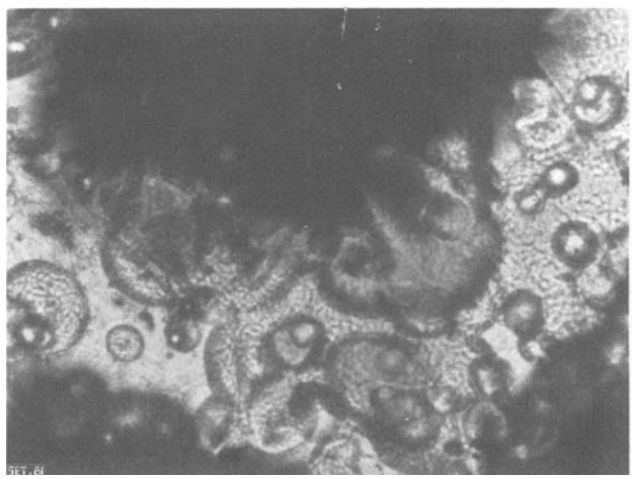

Fig. 2. Optical micrographs of Teflon-coated nickel plates. Nickel surface has a light color, Teflon coating is identified by a colorful, irregular pattern. (a, top) Inner hole in a plate previously treated with camphor (144×); (b, bottom) outer hole in a plate untreated with camphor (200×).

with camphor and covered with Teflon. The irregular pattern observed corresponds to the Teflon layer and the dark area is the unclogged hole (region B in Fig. 1). Figure 2b shows region A (Fig. 1) of a nickel plate sprayed with Teflon latex without camphor treatment. Penetration of the hole by the Teflon is obvious, leading to clogging. Specific resistance of the camphor-treated diaphragms was *ca.* 20% of those prepared without using camphor; the latter were thus discarded.

The characterization of the diaphragms was done by measuring the voltage drop of the cell electrolyte and of the diaphragms during electrolysis, under different conditions.

To measure this voltage drop an assembly of reference electrodes was used. The schematic diagram of the circuit used for the voltage drop measurements is shown in Fig. 3. The reference electrodes were Hg/HgO; Luggin capillary tubing made the electrical connection between the reference electrodes and the electrolysis cell components.

Figure 4 shows the electrolysis cell, which was made of a Pyrex glass container and a Teflon electrode frame: the cell was thermostated, the electrodes were platinum sheets soldered to a copper wire. This wire connection was insulated with silicone rubber. The platinum plate in the cathode was covered with black platinum by the usual method. The anode was not subjected to any special treatment. In order to simulate conditions similar to those existing inside an electrolyzer, membranes with an area of 10 cm^2 were

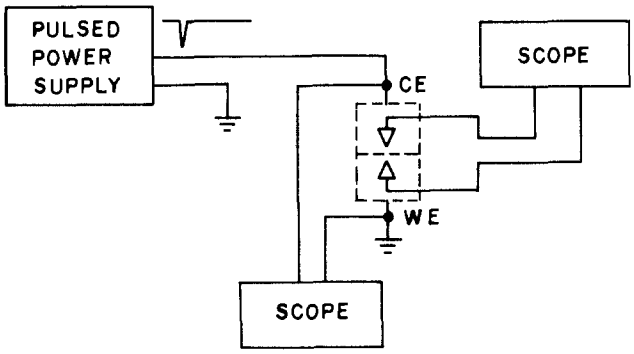

Fig. 3. Schematic diagram of the circuit used for *IR*-drop measurements.

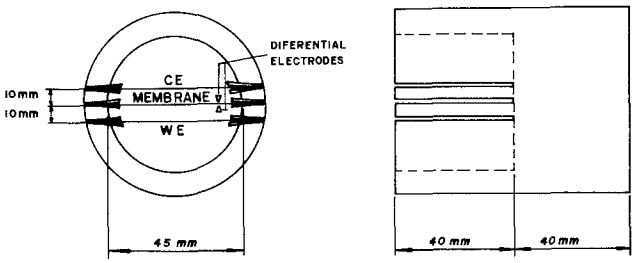

Fig. 4. Schematic diagram of the test cell

used. Experimental conditions were 80°C, KOH 30% w/v. The electrolyte flowed by thermal convection, anolyte and catholyte being separated by the perforated nickel plate.

The test cell was operated galvanostatically during the experiments. The counterelectrode was interrupted using a pulse generator and a current amplifier. The working electrode-to-reference electrode potential was recorded on an oscilloscope set to a 20 μsec span. Repeated measurements were made at each of several current densities. Two Hg/HgO electrodes formed a differential pair and the d-c voltage drop was measured across the membrane for various current densities.

The voltage measured by the differential pair was compared to the one obtained by the current-interruption technique. When the electrolyte concentration gradient within the cell was negligible, both measurements were in good agreement.

Results and Discussion

The voltage drops across the cell and the diaphragm were measured during the electrolytic gas evolution. The results are shown in Fig. 5 and 6, respectively. First of all, we noticed excellent behavior of the diaphragm compared to the asbestos sheet (2). The

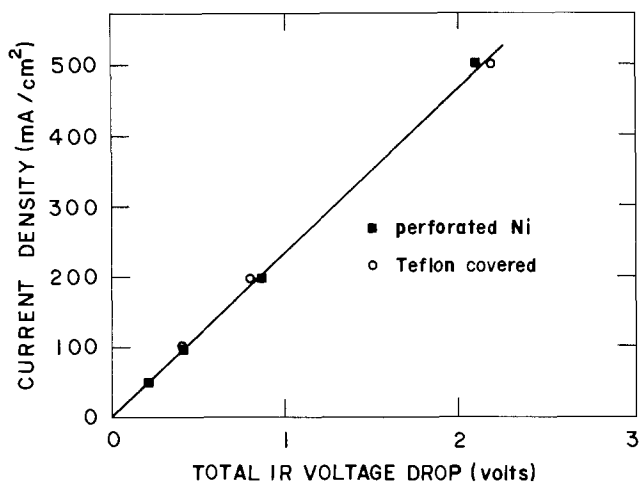

Fig. 5. $I \times V$ (cathode to anode) measurements

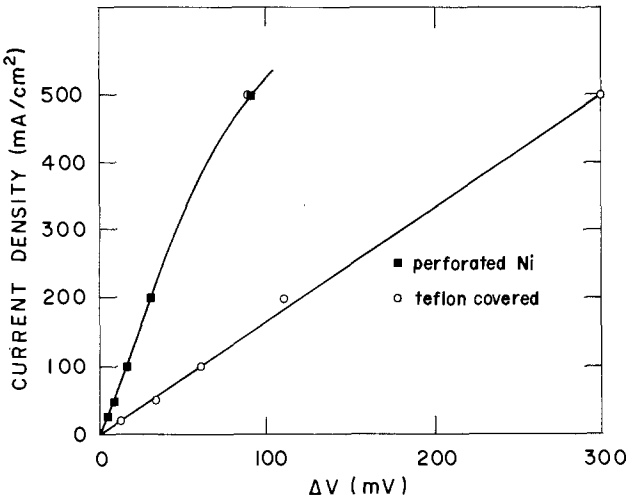

Fig. 6. $I \times V$ (across to diaphragm) measurements

total voltage drop across the electrolyte using nickel sheets, both uncovered and Teflon-covered, is practically the same. There is, however, a significant difference between the voltage drops across the uncovered and covered sheets, as shown in Fig. 6. The larger voltage drop across the covered sheets results partially from the inadequate nickel plate geometry which is asymmetric (Fig. 1). Some Teflon material ends up covering part of the shallow hole. This happens because the camphor has to cover the shallow hole but not the external part of the sheet, a condition which is not completely met. This problem should not arise in sheets containing uniform, cylindrical holes.

Nevertheless, the total voltage drop between cathode and anode, which includes both the electrolyte and diaphragm voltage drops, is the same in both cases. There is consequently a lower *IR* drop in the electrolyte for the same current density in the case of the Teflon-coated diaphragm. This is ascribed to a surface effect of the Teflon coating as described below.

Since both the electrolyte and the diaphragm are passive elements the change of the resistance, for a given temperature, results from bubble formation and the difference in ionic concentration produced by the electrolysis across the membrane. Both effects are reflected as an increase in the voltage drop across the cell. Due to the very small size of the bubbles (bubble radius ~10 μm) they do not have enough buoyancy and fill the volume between the electrodes and diaphragm. The current density diminishes due to loss in the electrolyte and loss of contact in the diaphragm interface.

The Teflon coating helps to solve this problem because it creates within the cell an additional gas-bubble-coalescing region due to increased surface-liquid contact angle. On this surface the bubbles will grow until they have sufficient buoyancy to leave the interelectrode space.

The Teflon hydrophobicity will thus result in a scavenging action on the gases. Moreover, the bubbles adhering to the diaphragm surface are outside the ionic current paths; for this reason, they do not contribute to power dissipation within the cell. The Teflon coverage results then in an appreciable decrease in the voltage drop across the electrolyte as shown by comparison of Fig. 5 and 6.

Figure 6 also shows that the Teflon-coated diaphragms have a constant specific resistance within the region of measured current densities.

Conclusion

A procedure for Teflon coating of perforated nickel plates was developed. The Teflon coating works as a bubble-scavenging region, which results in a lower *IR* drop across the electrolyte. The coating also works

as an insulation element between the electrolyzer elements. Its chemical resistance is excellent.

Optimization of the diaphragms is still necessary, which includes a more appropriate shape for the holes used in the metal plate. However, it has been shown that an insulating coating may be obtained that does not clog the plate holes and that helps in decreasing power consumtion within the system.

Manuscript submitted Jan. 28, 1982; revised manuscript received July 16, 1982.

Any discussion of this paper will appear in a Discussion Section to be published in the December 1983 JOURNAL. All discussions for the December 1983 Discussion Section should be submitted by Aug. 1, 1983.

Publication costs of this article were assisted by the Physics Institute-UNICAMP.

REFERENCES

1. P. Perroud, *Rev. Generale d'Electricité*, **85**, 627 (1976).
2. P. Perroud and G. Terrier, in Proc. 2nd World Hydrogen Energy Conf., Zurich, Switzerland, Aug. 21-24, 1978, Vol. 1, pp. 241-245.
3. R. Alkire, *This Journal*, **120**, 900 (1973).
4. To be submitted to *This Journal*.

Preparation of Anthrasol Blue IBC by Anodic Oxidation

Han Yong Hui

Shanghai Third Dyestuff and Chemicals Factory, Shanghai, China

ABSTRACT

The use of anodic oxidation for preparation of Anthrasol Blue IBC eliminates totally the oxidant lead dioxide and results in the solution of the complicated problems arising in the fields of oxidant recovery and environmental protection. The use of a mesh lead dioxide electrode as an anode increases the mechanical strength of the electrode. The operation and maintenance of the electrolytic cell are described.

Anthrasol Blue IBC (7, 16-dichlor-indanthrone-5, 9, 14, 18-tetrasulfuric acid ester salt) is a solubilized vat dyestuff with brilliant hue and excellent fastness; it has found wide application in the dyeing and printing industries and has been used for more than fifty years. The technical process of preparation by oxidation with lead dioxide has remained unaltered in this period. Only freshly prepared lead dioxide (1) can be used for the preparation, and the resulting lead monoxide must be removed from the reaction mixture completely in order to give a high quality dye; recovery of the lead dioxide is also important in lowering the cost and avoiding pollution.

In order to overcome this disadvantage, various other materials have been tried as oxidants, *e.g.*, silver oxide, nickel oxide (2), ferrate (3), ozone and other metallic oxides (4), but the result has been disappointing because of the difficulties encountered in the recovery of the raw materials. Unsuccessful results have also been reported with sodium hypochlorite (5), hydrogen peroxide, sodium perborate, catalytic air oxidation (6) as oxidation agents. In order to circumvent these difficulties, electrolytic oxidation was studied and found to be a suitable method for preparing Anthrasol Blue IBC. The conditions parallel those reported earlier in a patent (7) and are reported here.

The original method is summarized below by the following reaction

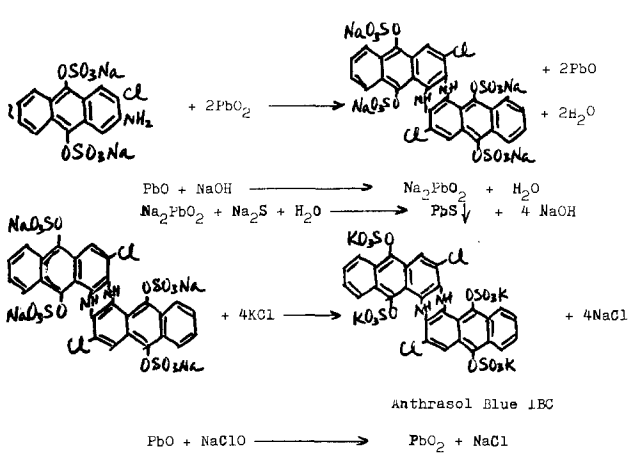

In the anodic oxidation, the manipulation involving lead dioxide and lead oxide are eliminated.

Anode for Electrolytic Production of Anthrasol Blue IBC

The lead dioxide electrode has been used extensively in electroorganic synthesis due to its advantages of a high oxygen overvoltage, inertness to most chemical reagents, and low cost. Numerous reports and patents have appeared in the literature (8-10) for the preparation of lead dioxide electrodes. According to some reports (11), the alpha-crystal form of lead dioxide is obtained from an alkaline electrolyte and has been found to be superior in quality to the beta-crystal form obtained from an acidic electrolyte. As the maintenance of high Pb(II) concentration in an alkaline electrolyte is complicated, in general the deposition of lead dioxide is done in an acidic electrolyte.

The plate-form electrode was used first, but was found susceptible to cracks or breakdowns during the electrochemical process because of large electrode area and the stress resulting from expansion and contraction caused by temperature variations. By adopting a titanium mesh as a base for electrodeposition, the resulting lead dioxide electrode has proved to be far less susceptible to crack or breakdown and possesses a greater mechanical strength than the plate-form anodes. Although the mesh-type electrode has less area than the plate-type electrode, it has the advantage of allowing the electrolyte to circulate through the mesh openings from one anode to another; the electrolytic unit can be assembled, therefore, with one cathode above two anodes and results in a simplified cell construction.

The nitric acid produced in the electrodeposition of lead dioxide has to be neutralized with the gradual addition of lead monoxide in order to maintain a constant concentration of lead nitrate. The addition of sodium fluoride improves the quality of lead dioxide coating. Absorption of fluoride ion on the surface of anode increases the oxygen overvoltage and stops the production of oxygen which would lead to a coating of inferior quality. A copper layer was spray-coated by a plasma torch onto the upper 80 mm of the anode after sandblasting the titanium mesh surface and reduced the contact electrical resistance.

Important Factors in Electrolytic Production of Anthrasol Blue IBC

The product in the oxidative ring closure process is a mixture of two isomers (A) and (B) in a ratio of 6:4, that can be separated by use of the different solubilities in methanol. The solubility of isomer (B) in methanol is larger than that of isomer (A); isomer (B) therefore remains in the filtrate after salting out

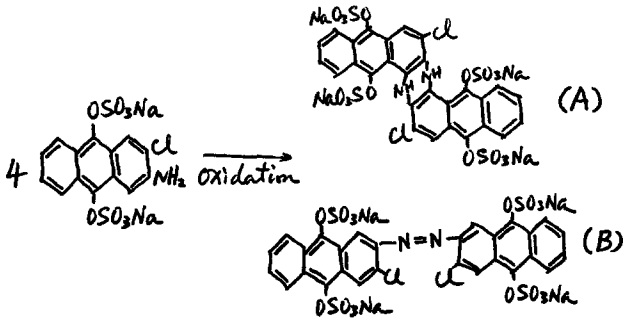

The suitable range of current density is 0.8-1.2 A/dm². If the anodic current density is larger than 1.5 A/dm², the amount of isomer (B) in the mixture increased markedly and the yield of the final product was low.

Over-oxidation, according to a report (13), causes the hydrolysis of the sulfuric acid ester group. The ideal method would be to take the anolyte out of the cell after incomplete oxidation and to separate the starting material from the product; the starting material could be returned to the cell. Since the physical properties of disulfuric acid ester (starting material) and tetrasulfuric acid ester (product) are very similar, no suitable separation method has been devised; the only way to avoid over-oxidation is to limit the reaction time to about 5.5 hr.

Electrolytic Cell

The press-type cell has been widely applied in the industrial electro-organic synthesis in cases where the frequency of lead dioxide electrode replacement is high, and the life of the diaphragm is short. The convenience of electrode and membrane replacement is the prime basis for the design of the electrolytic cell; the top of the cell is open so that the electrolytic process can be carried on without interruption during the replacement of damaged electrode or membrane. The concentration of caustic soda in the catholyte does not change significantly during the operation; only a slight addition of water is made once each week. It was not necessary therefore to recycle the catholyte during the reaction. Each cell was divided into seven isolated sections, a removable box with a cation-exchange membrane on one side was placed in every section and

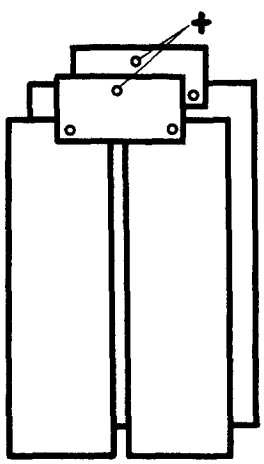

Fig. 1. The connection of lead dioxide anode

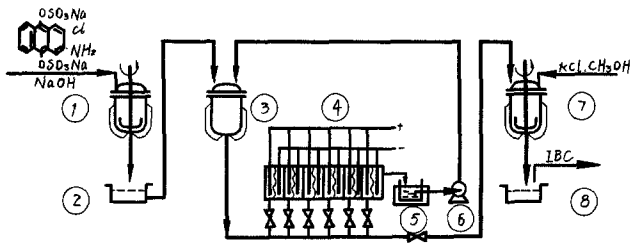

Fig. 2. Diagram for the anodic oxidative preparation of Anthrasol Blue IBC. 1, Dissolving kettle; 2 and 8, filter; 3, recycling kettle; 4, electrolytic cell; 5, intermediate storage kettle; 6, gear pump; 7, salting out kettle.

served as the cathode chamber which could be easily removed for the replacement of membrane. The remaining space in every section serves as the anode chamber. The lead dioxide anodes as prepared are connected as a single unit and a combination of two such pairs serve as the anode (Fig. 1, Table I). The cathode was a copper plate; the anolyte was pumped from the bottom of the recycling kettle into the lower part of every anode chamber and overflowed from the upper part of this chamber to an intermediate storage kettle, which was connected to the recycling kettle by a gear pump (Fig. 2, Table II).

Batch Process

Altogether ten electrolytic cells were connected in two parallel trains, each with five cells connected in series. Thus, there were 70 electrolytic units (Fig. 3, Table III) in ten cells with a total of 70 cathodes and 280 anodes on 70 multiplate lead dioxide anodes.

Table I. The operating conditions of lead dioxide electrodeposition

Cell:
- Anode base: 1 mm thick titanium mesh (expansion 30%)
- Base dimension: 540 mm high × 170 mm wide
- Cathode: two carbon rods, 43 mm thick × 70 mm wide × 580 mm high placed on the sides of the anode at a distance of 40 mm each
- Base pretreatment: sand blast the base surface with a mixture of sand and quartz (ratio of sand and quartz was 4:1) and then rinse with water

Electrolyte:		
	lead nitrate (C.P.)	150-200 g/liter
	nitric acid (C.P.)	5-20 g/liter
	sodium fluoride (A.R.)	0.5-1 g/liter
	deionized water	(free Cl^-, Fe^{+++})

Heating: 2 kW electroheater
Agitation: bubbling with oil-free compressed air
Temperature: 75°C
Anodic current density: 10 A/dm² for 2 hr followed by 7.5 A/dm² 5 hr
Flow rate of electrolyte: 5 liters/min
Weight of base: 280g
Weight of lead dioxide deposit: 1800-2000g
Thickness of deposit: about 2 mm
The chemical reaction during electrodeposition may be represented by

$$2Pb(NO_3)_2 + H_2O \rightarrow PbO_2 + Pb + 4HNO_3$$

Table II. The detail of the cell construction

Cell dimension: 385 mm wide × 630 mm long × 545 mm high
Cell material: 10 mm polypropylene sheet
Total anode area: 4000 dm²
Membrane: nonreinforced sulfonated polyphenylene ether cation-exchange membrane
Anode dimension (coating): 170 mm wide × 460 mm high × 3 mm thick
Cathode dimension: 300 mm wide × 400 mm high × 2 mm thick

Table III. Operating conditions

Anolyte:		
	2-chloro-3-aminoanthraquinone-9,10-sulfuric acid ester (100%)	120 kg
	Caustic soda 30%	65 liters
	diluted with water to	600 liters

Catholyte: caustic soda 6%
Temperature: 65°-70°C
Voltage: (single cell) 2.8V (initial), 3V (final)
Anodic current density: 0.8 A/dm²
Rate of flow: 2.5 liters/sec (3 cm/sec)
Current efficiency: 75.9% [including isomer (B)]
Energy consumption: 0.7 kW-hr/kg Anthrasol Blue IBC

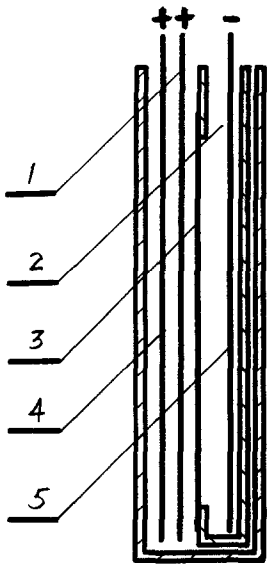

Fig. 3. 1, 4, Lead dioxide anode; 2, cathode chamber; 3, cation-exchange membrane; 5, cathode.

Procedure

The anolyte was prepared in a 500 liter dissolving kettle by heating with stirring until complete solution, and then filtering to remove impurities. The filtrate or anolyte was transferred into the recycling kettle and then fed simultaneously into every anode chamber of the cell. As soon as the cells were filled, electrolysis was started with an anode current density of 0.8 A/dm^2 for 5.5-6 hr at 65°-70°C. Upon completion of the reaction, the reaction liquor was filtered and the filtrate was transferred into the salting out kettle, where methanol was added and the solution was heated to 50°C. Salting out was carried out by the addition of potassium chloride in an amount of 18 weight percent of the total volume. The solution was maintained at 50°C for half an hour, cooled to 20°C, and after 2 hr was filtered.

The filter cake was mixed with Glauber's salt, urea, and dicyandiamide in certain concentrations, dissolved in water, and spray dried. The final product was pure Anthrasol Blue IBC and proved to be satisfactory in the textile industry applications.

Manuscript submitted Nov. 10, 1980; revised manuscript received *ca.* Aug. 10, 1982.

Any discussion of this paper will appear in a Discussion Section to be published in the December 1983 JOURNAL. All discussions for the December 1983 Discussion Section should be submitted by Aug. 1, 1983.

REFERENCES

1. B.I.O.S. Report No. 960.
2. Kuhlmann Co., British Pat. 577,167 (1941).
3. W. B. Hardy and R. B. Fortenbaugh, U.S. Pat. 2,659,727 (American Cyanamid Co.) (1952).
4. B. E. Rogovik, T. B. Gerebkako, S. E. Pohela, B. L. Plakegin, and B. E. Alekazayef, USSR Pat. 330,-753 (1977). B. E. Rogovik, T. B. Gerebyako, C. F. Sofronova, and C. E. Pohela, USSR Pat. 466,262 (1975).
5. J. Haller and G. Roesch, German Pat. 580,013 (IG) (1933).
6. K. Helmut, B. Hans, M. Udo, and O. Andreas, German Pat. 2,138,931 (1973).
7. J. Haller, French Pat. 779,890 (IG) (1934).
8. T. Osuga and K. Sugino, *This Journal*, **104**, 448 (1957).
9. H. C. Miller and J. C. Grigger, U.S. Pat. 2,872,405 (Pennsalt Chemicals Co.) (1955).
10. G. H. Kelsall, British Pat. 277,425 (Electricity Council Research Centre, Capenhurst, England) (1977).
11. N. G. Bakhchisaraits'yan and E. A. Dzhafarov, *Doklady Akad. Nauk Azerbaijan SSSR*, **17**, 785 (1961).
12. Y. Bausho, K. L. Huang, S. Suzuki, and I. Saito, *Kogyo Kagaku Zasshi* (Japan), **64**, 1066 (1961).
13. K. Vankataraman, "The Chemistry of Synthetic Dyes," Vol. V, p. 190, Academic Press, New York and London (1971).

Regenerative Photoelectrochemical Cells Using Polymer-Coated n-GaAs Photoanodes in Contact with Aqueous Electrolytes

K. Rajeshwar*

Department of Electrical Engineering, Colorado State University, Fort Collins, Colorado 80523

and M. Kaneko and A. Yamada

The Institute of Physical and Chemical Research, Wako-shi, Saitama 351 Japan

ABSTRACT

Short-term (up to ~2 hr) stabilization of n-GaAs photoanodes in aqueous electrolytes has been accomplished by coating them with polymer films comprising polystyrene with pendant $Ru(bpy)_3^{2+}$ complexes (bpy = 2,2'-bipyridyl). The electrolytes contained the $Fe^{2+/3+}$, I^-/I_3^-, S^{2-}/S_x^{2-}, $[Fe(CN)_6]^{3-/4-}$, and $Fe^{2+/3+}$ EDTA (EDTA = ethylenediamine-tetraacetic acid) redox couples. The best photoelectrochemical response was observed in the presence of the $Fe^{2+/3+}$ redox couple and an AM 1 optical-to-electrical conversion efficiency of ~12% was reached in nonoptimized systems. The possible role of the Ru complex in the mode of charge transport across the polymer-coated n-GaAs/electrolyte interface is finally discussed.

A key problem in the use of photoelectrochemical (PEC) systems for conversion and storage of solar energy concerns electrode stability (1). Of the various approaches that have been undertaken to circumvent this problem, the use of polymeric coatings on the photoelectrode surface deserves special mention. Thus, previous authors have described the protection of narrow bandgap semiconductor photoanodes with electrochemically generated polypyrrole films (2-6), while more recent studies report an enhanced degree of stabilization by incorporation of thin metal films, in combination with the polymer overlayer (5, 6). A recent report also describes the intriguing application of

* Electrochemical Society Active Member.

o-phenylene diamine polymerization for passivation of surface states on n-WSe_2 photoelectrodes (7). Studies oriented toward solar energy storage include the use of poly (benzyl viologen) coatings on p-Si electrodes to catalyze the photoassisted evolution of H_2 from water (8), and polymer pendant $Ru(bpy)_3^{2+}$ complexes (bpy = 2,2'-bipyridyl) on inert substrates for the photoreduction of methyl viologen (9, 10).

In this paper, we describe the performance and characterization of n-GaAs photoanodes coated with films of polystyrene pendant $Ru(bpy)_3^{2+}$ complexes (hereafter called "PSt-bpy-Ru complex"). This coating was developed by one of the present authors (M.K.) for the aforementioned studies on photochemical conversion of sunlight (9, 10). On the other hand, the results described herein pertain to PEC systems of the regenerative type [*i.e.*, those designed for the conversion of sunlight into electricity (1)]. The PSt-bpy-Ru coated n-GaAs photoanodes were tested in aqueous redox electrolytes in which the bare counterparts are known to be photoelectrochemically unstable (11).

Experimental

The PSt-bpy-Ru complex was prepared as follows. γ-picoline was coupled by Raney Ni catalyst in excess reactant to yield 4,4'-dimethyl-2,2'bipyridine, which was then lithiated by n-butyllithium and hydroxymethylated by HCHO gas to yield 4-methyl-4'hydroxymethyl-2,2'-bipyridine. This product was dehydrated by reaction in dry xylene in the presence of P_2O_5 to give 4-methyl-4'-vinyl-2,2'-bipyridine (Vbpy). Vbpy was copolymerized with styrene in dioxane in the presence of 0.2% azobisisobutyronitrile initiator for 120 hr to yield the backbone copolymer. The copolymer was reacted with cis-$Ru(bpy)_2Cl_2$ in n-butylalchohol/xylene (1/4 v/v mixture) under reflux for 48 hr to give PSt-bpy-Ru. The composition and structure of this material was determined by methods described previously (9, 10) to be the following

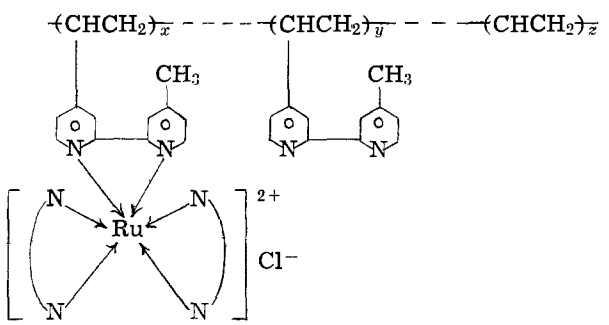

N⌒N = 2,2'-bipyridine

$x = 0.048$, $y = 0.047$, $z = 0.905$

The PSt-bpy-Ru complex as prepared is soluble in organic solvents but insoluble in water. (By way of contrast, monomeric $Ru(bpy)_3Cl_2$ is soluble in water and insoluble in organic solvents except alcohols.) The hydrophobic nature of the PSt-bpy-Ru complex aids in its persistent attachment to the electrode surface during use in the PEC cell (see below). Polished wafers of Si-doped n-GaAs (<100> orientation) were obtained from commercial sources. The doping density as quoted by the manufacturer was 4.5×10^{16} cm^{-3} for these samples. Electrodes were fashioned out of these massive wafers after providing them with ohmic contacts as described elsewhere (12). The electrodes were pretreated as follows. An initial 15 sec etch in 3:1:1 H_2SO_4-30%H_2O_2-H_2O was followed by a 30 sec etch in 6M HCl. A rinse in deionized water was followed by a wash in acetone and vacuum drying. The pretreated electrodes were then coated with PSt-bpy-Ru complex by dropping a predetermined amount of solution[1] of an organic solvent (dimethyl formamide or chloroform)[2] onto the n-GaAs surface with a microsyringe, followed by air-drying for 15-20 min and oven-drying at ~50°C under reduced pressure for 1-2 hr. The resultant electrodes had a markedly dull surface (as opposed to the mirror-like appearance of the starting material) and geometric surface areas ranging from 0.09 to 0.24 cm^2.

Redox electrolytes were prepared from Analar® grade chemicals and deionized water. Ferrous salt of ethylenediaminetetraacetic acid (EDTA) was prepared by dissolving ferrous perchlorate in 0.1M disodium salt of EDTA. In this case as well as for the $[Fe(CN)_6]^{3-/4-}$ couple the *p*H of the electrolyte was adjusted either with NH_4OH or with HCl. Polysulfide electrolytes were prepared from mixtures of varying quantities of Na_2S, S, and NaOH in deionized water. Polyiodide electrolytes were prepared in similar fashion from KI and I_2. Electrolytes containing the $Fe^{2+/3+}$ redox couple were prepared from solutions of ferrous ammonium sulfate and the ferric salt in acidic (*p*H = ~2) media. In most cases, the cells were continually purged with inert gas during measurements to preclude air oxidation of the reduced redox species.

Standard three-electrode geometry was used in all cases for the PEC systems reported here. Pt foil was the counterelectrode. All potentials are quoted with reference to the saturated calomel electrode (SCE). The instrumentation used for the PEC measurements was the same as that described previously (12). Illumination of the electrodes was by ELH quartz-iodine projection lamps. Light intensities were measured on an Ealing Corporation Model LIMS 920 radiometer/photometer. The intensities reported herein are not corrected for reflection and absorption losses from the cell wall and the electrolytes. The electrodes, however, were positioned as close to the cell wall as possible to minimize light absorption by the electrolyte.

Results and Discussion

Figures 1 and 2 illustrate steady-state current-voltage (I-V) characteristics of modified n-GaAs photoanodes in contact with aqueous electrolytes containing the

[1] A typical Ru^{2+} concentration of 1 mM was employed in the organic solvent. The nominal solution volume was 4 μl/cm^2 of electrode surface yielding a film thickness of 1430Å for unity density.
[2] No influence of the specific organic solvent on the PEC performance of the corresponding electrodes was noted.

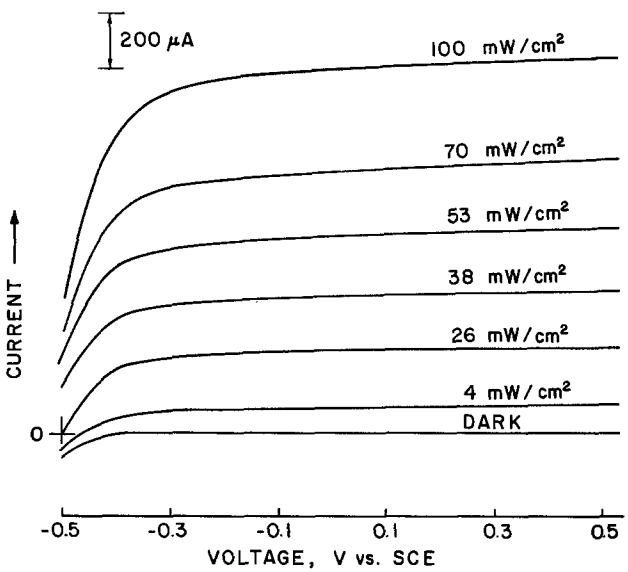

Fig. 1. Steady-state current-voltage (I-V) characteristics (scan rate: 100 mV/sec) of a representative polymer-coated n-GaAs photoanode (electrode area: ~0.09 cm^2) in contact with aqueous $Fe^{2+/3+}$ redox electrolyte (*p*H = ~2). The electrolyte was magnetically stirred and contained 0.1M each of reduced and oxidized species.

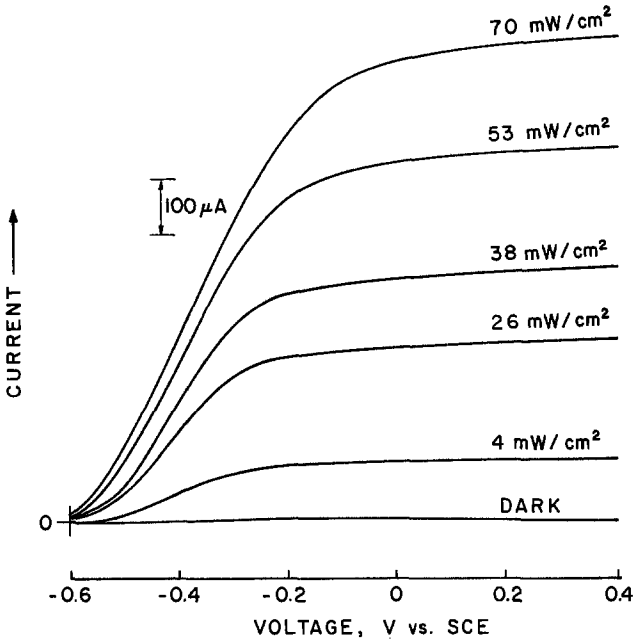

Fig. 2. Steady-state I-V characteristics (scan rate 100 mV/sec) of a polymer-coated n-GaAs photoanode (same electrode as that used in the experiments in Fig. 1) in contact with iron-EDTA redox electrolyte (pH = ~5). The Fe(II) ion concentration was 0.01M and the electrolyte was magnetically stirred.

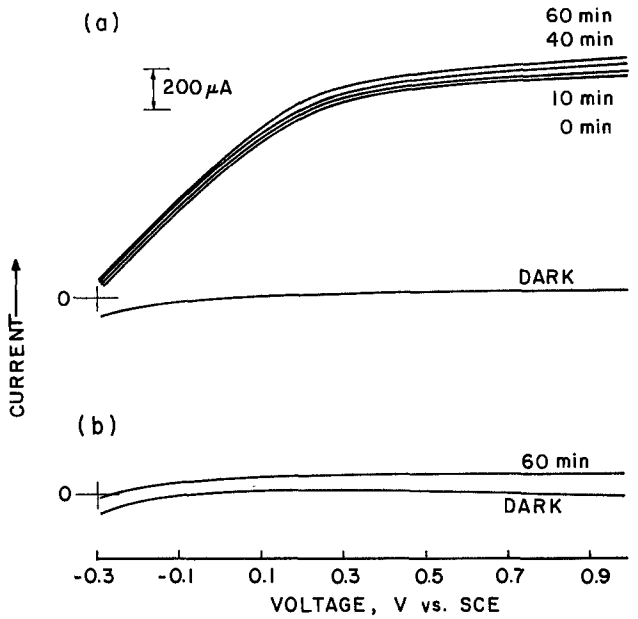

Fig. 3. Time dependence of steady-state I-V behavior (scan rate: 100 mV/sec) for (a) polymer-coated n-GaAs electrode (area: ~0.1 cm^2) and (b) bare n-GaAs photoanode in contact with the I_3^-/I^- (0.5/0.5M) redox electrolyte (pH = ~5). The illuminated electrode (light intensity 53 mW/cm^2) was maintained at approximately short-circuit condition (0.3V vs. SCE) for the duration shown, after which the potential scans were initiated. The initial level of the I-V curve for the bare electrode was close to that seen at 0 min for the coated sample (Fig. 1a). The electrolyte was stirred in all cases.

$Fe^{2+/3+}$ and $Fe^{2+/3+}$-EDTA redox couples, respectively. The electrolytes were magnetically stirred in these experiments. The behavior shown in these diagrams is fairly representative of the polymer-coated material and only very minor differences in the magnitude of current densities (possibly caused by morphological and thickness variations in the polymer films) were noted in a series of runs on these modified electrodes. The main criteria chosen to evaluate PEC stability in experiments such as those illustrated in Fig. 1 and 2 were constancy in the shape of the steady-state I-V curve, and in the value for the onset potential (V_{on}) for photoanodic current flow. The behavior exemplified by the data in Fig. 1 and 2 could be reproduced through several repetitive cycles at the 100 mV/sec scan rate nominally employed for these runs. On the other hand, bare n-GaAs photoanodes showed a rapid deterioration in the magnitude of the photoeffect over a comparable time scale. Figure 3 illustrates this trend for the I^-/I_3^- redox electrolyte. The upper frame in Fig. 3 shows the time-dependent behavior of the polymer-coated photoanode, whereas the data illustrated in Fig. 3b underscore the contrasting performance of a bare electrode. For these experiments, the dark I-V characteristics were first established after which the electrodes were illuminated with white light (53 mW/cm^2) at approximately the short-circuit condition. The steady-state I-V behavior was then traced at various time intervals as shown in the figure. The initial increase in the magnitude of the photoeffect for the polymer-coated electrode is worthy of note and may be caused by slow equilibration of the polymer layer with the redox electrolyte. The I-V characteristics in this case did not show a further change after 1 hr during ten repetitive scans at 100 mV/sec at 5 min intervals. By way of contrast, photoeffects on the bare electrode had diminished considerably after 1 hr irradiation from an initial level which approximated that observed on the polymer-coated electrode.

While the conclusion is firm on the short-term (~2 hr) PEC stability of these polymer coatings, long-term stability (>2 hr) is presently a problem. Gradual peeling of the polymer coating has been observed in experiments run for periods longer than 2 hr and this effect seems to originate at the edges of the photoanode. Optimization of the coating thickness and parameters associated with the coating procedure is presently in progress.

Figure 4 illustrates further data contrasting the behavior of polymer-coated electrodes vis-à-vis the bare samples. These experiments utilized the S^{2-}/S_x^{2-} redox couple in which bare n-GaAs electrodes have been shown to be photoelectrochemically unstable (11). A gradual transition from a single photoprocess to an oxidation involving two distinct steps appears in the I-V characteristics for the bare photoanode with increasing light intensity (Fig. 4a). The first wave is a diffusion-controlled process as evidenced in experiments with varying concentrations of Na_2S whereas the plateau region for the second wave is independent of the S^{2-} concentration. In accord with these results, the first wave is attributed to the PEC oxidation of S^{2-} ions, whereas the second wave represents the photoanodic corrosion of n-GaAs. A similar behavior has been noted by previous authors (13, 14) for n-CdS, although the two-step I-V characteristics for n-GaAs does not seem to appear in previous reports on the PEC behavior of this material.

Of more direct relevance to the present study, however, is the steady-state I-V behavior of polymer-coated electrodes in contact with the S^{2-}/S_x^{2-} redox couple (Fig. 4b). Note the complete absence of multiple waves in the anodic polarization region in this case, even at light intensities much higher than that employed in the previous case (Fig. 4b). The plateau levels in this case are also sensitive to the effective redox concentration at each light intensity (varied, for example, by changes in electrolyte stirring rate). These experiments demonstrate that the photogenerated holes are being effectively channeled into the route involving oxidation of reduced redox species in the presence of the polymer coating. Note the shift in the potential for photoanodic current flow in the case of the coated electrodes (cf. Fig. 4b) relative to the bare samples (Fig. 4a). This positive shift (which is confirmed by capacity measurements) in our belief, reflects the decreased negative surface charge on the n-GaAs surface

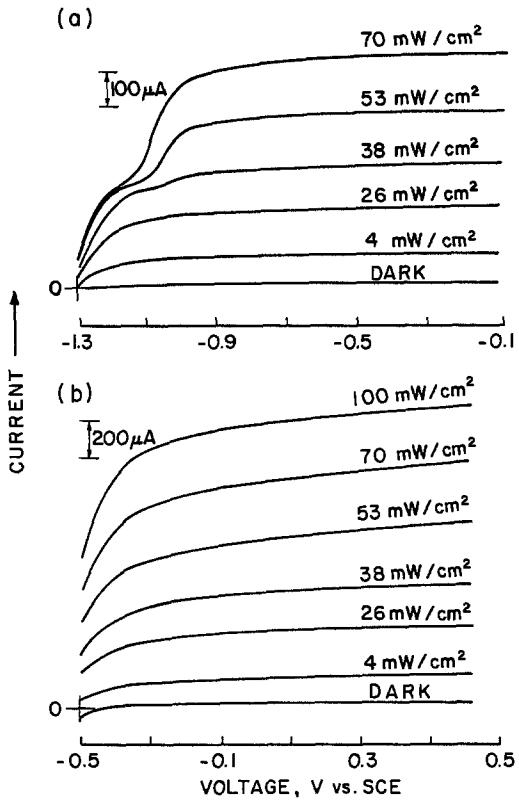

Fig. 4. Steady-state I-V characteristics (scan rate: 100 mV/sec) for (a) bare and (b) polymer-coated n-GaAs photoanodes in contact with the polysulfide (0.5M Na_2S, 0.5M S) redox electrolyte (pH = ~9). The coated electrode sample same as that described in Fig. 1 and 2.

[caused possibly by specific adsorption of S^{2-} species, cf. Ref. (15)] brought about by the intervening polymer layer. An unfortunate consequence of this shift is that no photovoltage is gained at the coated n-GaAs/polysulfide electrolyte interface.

In order to further probe the nature of the modified electrode/electrolyte interface, the photovoltage obtained with the various redox couples was examined as a function of their corresponding equilibrium potentials, V_{redox}. Figure 5 illustrates the correlation between the two parameters. Note that variations in V_{redox} span almost the entire bandgap of the semiconductor. The observed correspondence between the open-circuit voltage, V_{oc}[3] and V_{redox} (the slope of the straight-line plot in Fig. 5 is approximately unity) implies the absence of Fermi level pinning (16) at the interface. This, in turn, is suggestive of modifications in the nature and role of surface states at the n-GaAs/electrolyte interface brought about by the polymer coating (see below). A similar behavior seems to have been observed by previous authors (2) for n-GaAs photoanodes coated with polypyrrole although detailed correlations were not presented. There is also precedence in the literature for passivation of surface states on semiconductor electrodes in the presence of polymer films (7).

Further evidence for the near ideality of the modified electrode/electrolyte interface is provided by an examination of light intensity effects. Figure 6 illustrates typical data for the $Fe^{2+/3+}$ couple. The linear dependence of the short-circuit current density, J_{sc}, on light intensity, I_L, shows that the rate of supply of minority carriers (holes) to the surface is not limited by the availability of reduced redox species at the interface and the kinetics of charge transfer across it. The logarithmic dependence of V_{oc} on light intensity is predicted by the relationship (17)

$$V_{oc} \simeq \frac{nkT}{q} \ln \frac{J_{sc}}{J_o} \qquad [1]$$

under conditions where $J_{sc} \propto I_L$ and $J_{sc} >> J_o$ (J_o is the reverse saturation current density). A plot of V_{oc} *vs.* ln I_L should yield a straight line according to Eq. [1], the slope of which then permits an estimation of the junction ideality factor, n. The inset in Fig. 6 shows such a plot whose slope of 75 mV corresponds to an n value of 1.3. Ideality factors close to unity are typical of semiconductor/electrolyte (or metal) interfaces wherein carrier recombination losses (mediated by surface states) are negligible (18). Our previous studies of semiconductor/electrolyte interfaces (*e.g.*, n-GaAs/room temperature molten salt (19) and n-CdSe/aqueous polysulfide systems (18) have revealed much higher n values (close to 2) in keeping with the various loss mechanisms that have been identified (20) in these cases. On the other hand, the present PEC systems comprising polymer-coated n-GaAs photoanodes show how the presence of a polymer coating can drastically minimize deleterious surface-state effects.

Figure 7 illustrates typical Mott-Schottky (M-S) plots for polymer-coated n-GaAs electrodes in contact with $Fe^{2+/3+}$, $[Fe(CN)_6]^{3-/4-}$, $Fe^{2+/3+}$-EDTA, and I^-/I_3^- redox electrolytes. The data are shown only for an a-c signal frequency of 10 kHz since minimal frequency dispersion was observed in the measured

[3] V_{oc} is taken here as the difference between V_{on} and V_{redox}.

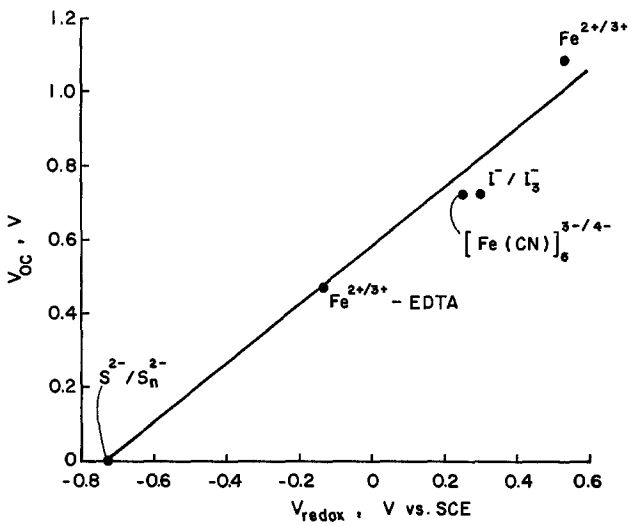

Fig. 5. Correlation between the open-circuit voltage, V_{oc} (see text for definition) and the equilibrium redox potential, V_{redox} for PEC systems employing various redox couples.

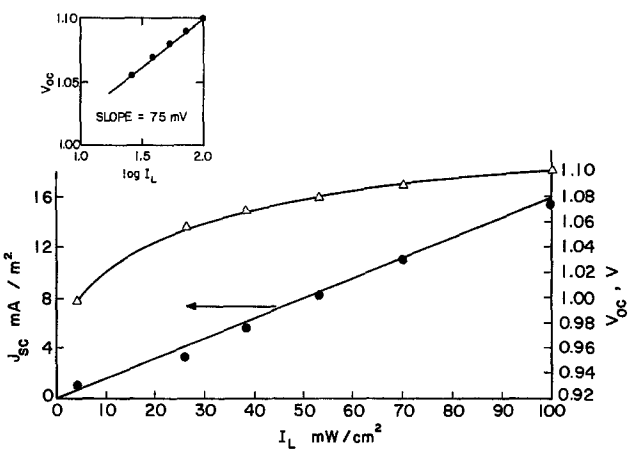

Fig. 6. Dependence of short-circuit current density, J_{sc} and V_{oc} on light intensity, I_L for polymer-coated n-GaAs photoanodes in contact with the $Fe^{2+/3+}$ redox couple. Parameters same as those described in Fig. 1. Inset: Plot showing the logarithmic dependence of V_{oc} on I_L.

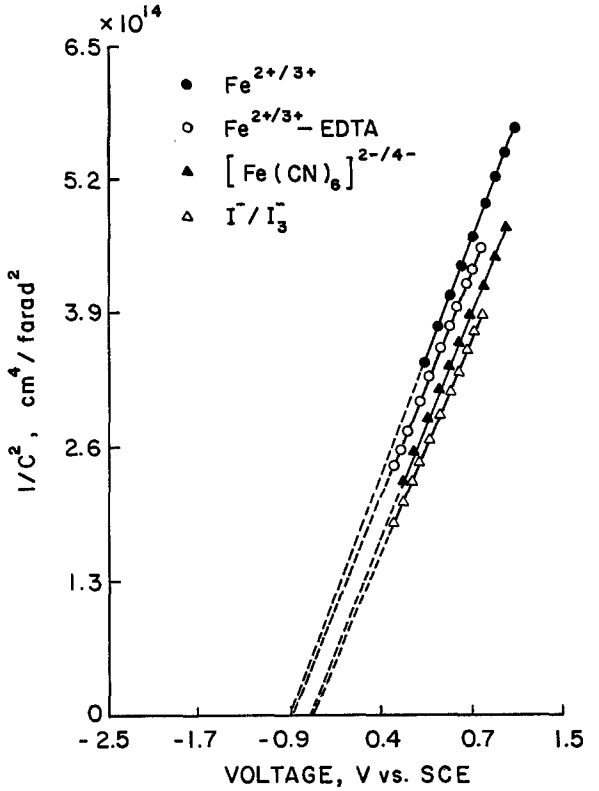

Fig. 7. Mott-Schottky plots for an a-c signal frequency of 10 kHz for polymer-coated n-GaAs photoanodes in contact with aqueous redox electrolytes. The solution pH was ~5 in all the cases except for the $Fe^{2+/3+}$ couple (~2).

capacitance values. The average of the slopes of the M-S plots in Fig. 7 yields a donor density value of 4.9 (±0.2) × 10^{16} cm^{-3} in good agreement with the manufacturer-quoted value (see above). The flatband potentials (V_{FB}) deduced from the M-S plots are −0.89, −0.73, −0.91, and −0.45V respectively for the $Fe^{2+/3+}$, $[Fe(CN)_6]^{3-/4-}$, $Fe^{2+/3+}$-EDTA, and I^-/I_3 redox electrolytes. The above variations in V_{FB} are outside the range of experimental error (mean deviation in measured V_{FB} is ±0.05V as borne out by duplicate measurements) and reflect subtle effects in the interfacial region. The V_{FB} values for the bare and coated electrodes were comparable for the above cases. A similar invariance of V_{FB} in the presence of a polymer film has been noted by previous authors (2) for polypyrrole-coated n-GaAs electrodes.

For a given semiconductor in contact with a series of redox electrolytes, V_{oc} should track the difference between V_{FB} and V_{redox}. For the systems studied here, this is roughly the case with the most positive redox couple, $Fe^{2+/3+}$ showing the maximum V_{oc}. Exact correspondence between $V_{on} - V_{redox}$ and $V_{FB} - V_{redox}$, however, is precluded by the aforementioned affects on V_{FB} caused by features in interfacial chemistry unique to each individual redox system.

Finally, typical performance parameters are assembled in Table I for regenerative PEC cells based on polymer-coated GaAs photoanodes. Of the redox electrolytes included for this study, the $Fe^{2+/3+}$ couple by far yielded the best PEC response in keeping with the positive value (0.53V) of its equilibrium potential. It is noted that the efficiencies listed in Table I were obtained for systems in which no attempts were made to optimize either cell geometry and operational parameters (*e.g.*, redox concentration, solution *p*H) or variables associated with electrode fabrication.

General Discussion

The role of $Ru(bpy)_3^{2+}$ species in the present polymer films merits further discussion. Definitive conclusions on their effects on PEC performance, however, cannot be made on the basis of the data described in the preceding discussion. It is unlikely that the anodic photoeffects observed for the polymer-coated n-GaAs photoanodes (cf. Fig. 1-3) are due to electron injection from the photoexcited Ru complex into the n-GaAs conduction band because: (*i*) Such a mode of charge transport would require a nontrivial activation energy in all the cases except possibly in the case of the I_3^-/I^- redox system since the n-GaAs conduction bandedge is located at a potential more negative (cf. Fig. 7) than the maximum in the distribution function for occupied levels of the $*Ru(bpy)_3^{2+}/Ru(bpy)_3^{3+}$ system (−0.6V) (21). (*ii*) Current flow in background electrolytes for the polymer-coated electrodes is orders-of-magnitude lower in the absence of regenerative redox couples such as the ones employed here. Mediation of $Ru(bpy)_3^{2+}$ species in the transfer of photogenerated holes to the reduced redox species, however, is a possibility, for example, by a scheme such as that shown in Eq. [2]-[5]

Table I. Typical performance parameters[a] of regenerative PEC systems based on polymer-coated n-GaAs photoanodes

Redox couple	V_{oc}[b] (V)	J_{sc} (mA/cm²)	P_{max} (mW/cm²)	FF	η (%)
$Fe^{2+/3+}$	1.09 (1.10)[c]	10.89 (15.11)	8.41 (11.54)	0.71 (0.69)	12.0₁ (11.5₄)
$Fe^{2+/3+}$-EDTA	0.47	8.33	1.07	0.27	1.5₈
I^-/I_3^-	0.72	11.67	2.33	0.28	3.3₈

V_{oc} = open-circuit voltage, J_{sc} = short-circuit current density, P_{max} = maximum power output, FF = fill-factor, η = optical-to-electrical conversion efficiency.
[a] Light intensity: 70 mW/cm².
[b] Taken as the difference between the potential onset of photocurrent and equilibrium redox potential (see text).
[c] Parameters in parentheses correspond to AMI illumination (~100 mW/cm²).

$$\text{n-GaAs} \xrightarrow{h\nu} e^-_{CB} + h^+_{VB} \quad [2]$$

$$h^+_{VB} + Ru(bpy)_3^{2+} \rightarrow Ru(bpy)_3^{3+} \quad [3]$$

$$Ru(bpy)_3^{3+} + \text{red} \rightarrow Ru(bpy)_3^{2+} + \text{ox} \quad [4]$$

$$\text{ox} + e^- \xrightarrow{\text{dark}} \text{red} \quad [5]$$

Here, e^-_{CB} = photogenerated electron in the conduction band in n-GaAs, h^+_{CB} = photogenerated hole in n-GaAs valence band, red = reduced redox species and ox = oxidized redox species. Note that in the above reaction scheme, ground-state $Ru(bpy)_3^{2+}$ species are implicated.

An alternative pathway (as pointed out by a reviewer) to reactions [3] and [4] is photoexcitation of $Ru(bpy)_3^{2+}$ species followed by reductive quenching by reduced redox species (cf. Eq. [6]-[8])

$$Ru(bpy)_3^{2+} \xrightarrow{h\nu} *Ru(bpy)_3^{2+} \quad [6]$$

$$*Ru(bpy)_3^{2+} + \text{red} \rightarrow Ru(bpy)_3^{+} + \text{ox} \quad [7]$$

$$Ru(bpy)_3^{+} \rightarrow Ru(bpy)_3^{2+} + e^-_{CB} \quad [8]$$

Reaction [7] is favored thermodynamically in that the V_{redox} values for all the couples included in this study are more negative than the standard potential of the $*Ru^{2+}/Ru^+$ couple (0.62V) (22).

Similarly, reaction [8] is energetically favored by the placement of the Ru^+/Ru^{2+} couple (−1.5V) (22) with respect to the n-GaAs conduction bandedge (−0.45 to −0.91V, see Fig. 7).

It must be pointed out that competition between the hole transfer routes schematized by Eq. [2]-[8] and the direct photo-oxidation of reduced redox species, namely Eq. [9]

$$h^+_{VB} + \text{red} \rightarrow \text{ox} \quad [9]$$

cannot be ruled out on the basis of the data presented here. That the PSt-bpy-Ru complex is quite efficient in mediating electron transfer, however, is clearly brought out by recent results on coated graphite electrodes (23). In these experiments, photoinduced electron relay to solution species (*e.g.*, methyl viologen) was quite facile via the excited state of the PSt-bpy-Ru complex.

A factor which merits further study is the role of $Ru(bpy)_3^{2+}$ and 2,2'-bipyridyl pendant groups in modifying the electronic conductivity of PSt films. The role of aromatic and heterocyclic ring structures in this respect is well recognized (24).

Experiments to address the above issues are in progress in these laboratories.

Acknowledgments

The authors would like to thank Rakesh Thapar for assistance in some of the experiments reported herein. We also thank one of the referees for pointing out the possibility of mediated hole transfer via reductive quenching. A major portion of the work reported herein was done during M.K.'s visit to CSU which was made possible by financial assistance from the National Science Foundation U.S.-Japan Cooperative Science Program.

Manuscript submitted May 17, 1982; revised manuscript received Aug. 24, 1982.

Any discussion of this paper will appear in a Discussion Section to be published in the December 1983 JOURNAL. All discussions for the December 1983 Discussion Section should be submitted by Aug. 1, 1983.

Publication costs of this article were assisted by Colorado State University.

REFERENCES

1. K. Rajeshwar, P. Singh, and J. Dubow, *Electrochim. Acta*, **23**, 1117 (1978).
2. R. Noufi, D. Tench, and L. F. Warren, *This Journal*, **127**, 2310 (1980).
3. R. Noufi, D. Tench, and L. F. Warren, *ibid.*, **128**, 2596 (1981).
4. R. Noufi, A. J. Frank, and A. J. Nozik, *J. Am. Chem. Soc.*, **103**, 1849 (1981).
5. T. Skotheim, I. Lundstrom, and J. Prejza, *This Journal*, **128**, 1625 (1981).
6. F. F. Fan, B. L. Wheeler, A. J. Bard, and R. N. Noufi, *ibid.*, **128**, 2042 (1981).
7. H. W. White, H. D. Abruna, and A. J. Bard, *ibid.*, **129**, 265 (1982).
8. H. D. Abruna and A. J. Bard, *J. Am. Chem. Soc.*, In press.
9. M. Kaneko, S. Nemoto, A. Yamada, and Y. Kurimura, *Inorg. Chim. Acta*, **44**, L289 (1980).
10. M. Kaneko, A. Yamada, and Y. Kurimura, *ibid.*, **45**, L73 (1980).
11. See, *e.g.*, A. B. Ellis, J. M. Bolts, S. W. Kaiser, and M. S. Wrighton, *J. Am. Chem. Soc.*, **99**, 2848 (1977).
12. P. Singh, K. Rajeshwar, J. DuBow, and R. Job, *ibid.*, **102**, 4676 (1980).
13. T. Inoue, T. Watanabe, A. Fujishima, and K. Honda, *Bull. Chem. Soc. Jpn.*, **52**, 1243 (1979).
14. H. Minora and M. Tsuiki, *Electrochim. Acta*, **23**, 1377 (1978).
15. P. Singh, R. Singh, R. Gale, K. Rajeshwar, and J. DuBow, *J. Appl. Phys.*, **51**, 6286 (1980).
16. A. J. Bard, A. B. Bocarsly, F. F. Fan, E. G. Walton, and M. S. Wrighton, *J. Am. Chem. Soc.*, **102**, 3671 (1980).
17. K. Rajeshwar, L. Thompson, P. Singh, R. C. Kainthla, and K. L. Chopra, *This Journal*, **128**, 1744 (1981).
18. E. H. Rhoderick, "Metal-Semiconductor Contacts," p. 7, Clarendon Press, Oxford (1978).
19. P. Singh and K. Rajeshwar, *This Journal*, **128**, 1726 (1981).
20. K. Rajeshwar, *ibid.*, **129**, 1003 (1982).
21. See, *e.g.*, E. Bogarello, J. Kiwi, E. Pelizzetti, M. Visca, and M. Gratzel, *J. Am. Chem. Soc.*, **103**, 6324 (1981) and references therein.
22. R. Memming, *Surf. Sci.*, **101**, 551 (1980).
23. M. Kaneko, A. Yamada, and N. Oyama, Submitted.
24. J. Mort, *Science*, **208**, 819 (1980).

Electrophoretically Deposited CdS and CdSe Anodes for Photoelectrochemical Cells

Yasusada Ueno, Hideki Minoura, Takeshi Nishikawa, and Masayasu Tsuiki

Department of Industrial Chemistry, Faculty of Engineering, Gifu University, Yanagido, Gifu 501-11, Japan

ABSTRACT

The electrophoretic deposition of CdS, CdSe, and their mixtures has been studied for the preparation of thin film anodes for photoelectrochemical cells. These films were obtained in a homogeneous state on SnO_2-coated glass substrates from the suspensions using polar organic dispersion media. Prior to photoelectrochemical experiments, the thin film anodes were thermally treated for 3 hr at 400°-600°C. An energy conversion efficiency of 2% was observed for the photoelectrochemical cells using these film anodes in S^{2-}/S_x^{2-} electrolytes.

Cadmium chalcogenides such as CdS, CdSe, and their mixtures are important materials for the anode of photoelectrochemical cells. Recently, the techniques of thin film growth of these compounds have become of interest in fabricating low cost photocells. These films have been obtained by vacuum deposition, painting, spray pyrolysis, chemical deposition, and electrodeposition (1-5). Electrophoretic deposition also seems to be a simple and inexpensive method for fabricating semiconductor films. It brings about a reduction in time of the film formation, saving of source material, and prevention of pollution owing to the avoidance of a vaporization procedure. No photoelectrochemical study of electrophoretically deposited semiconducting films has been given so far. This paper describes our results on preparing the thin films of CdS, CdSe, and CdS_xSe_{1-x} by the electrophoretic deposition. The photoanodic characteristics of these film electrodes are also shown.

Key words: semiconductor, photovoltaic, films, cell.

Experimental

Commercially available CdS (4*N*) and CdSe (3*N*) powders were used as starting materials. To determine the size of these particles, an electron microscope (Japan Electron Optics Limited, JEM T-8) was used: these powders were dispersed with distilled water under ultrasonic vibration, and the resulting suspensions were dropped onto copper grids with polyvinyl formal film.

Applying the electrophoretic deposition technique to inorganic solid particles, a mixture of polar organic liquids has been recommended as a dispersion medium (6). The basis of solvent choice is attributable to the fact that the desirable throwing power is obtained by mixing two suspensions using separate medium which gives the different deposition rates. The selected medium in CdS deposition was an equivolume mixture of acetone and isobutyl alcohol, whereas for the CdSe deposition, propylene carbonate was an excellent medium which was chosen on the basis of some preliminary tests. The suspensions for the electrophoretic deposition were prepared by the addition of CdS or CdSe powder to the medium under ultrasonic vibration. The dispersed CdS or CdSe particles in each system usually exhibit negative charges and have nearly the same size range of about 0.5-3 μm as that of the starting materials. Since most of particles in the suspension tend to sediment within 12 hr, the ultrasonic vibration is needed prior to repeated use.

The electrophoretic deposition experiments were performed in a 100 ml beaker containing 40 ml of suspension as shown in Fig. 1. An SnO_2-coated glass anode (effective area was about 10 mm $\times$ 15 mm) and a Pt plate cathode of nearly the same area were assembled at 15 mm distance in the cell.

The electrophoretic deposition of semiconductor particles onto SnO_2-coated glass substrates was performed anodically by application of d-c voltage from 30 to 800V. The films deposited in this way were dried, weighed, and then thermally treated in a furnace for 3 hr at 400°-600°C in a stream of purified nitrogen gas. The surface morphology and the composition of the deposited CdS or CdSe anodes were determined by scanning electron microscope and an x-ray microanalyzer (Hitach Horiba, EMAX 8000). A copper wire was attached at the end of each anode with silver epoxy and all the surface except for a portion on the facing surface of 0.5-1.0 cm^2 was insulated with epoxy resin as shown in Fig. 2. The three-electrode system including the electrophoretically deposited CdS or CdSe anode, and a Pt plate cathode, and a saturated calomel reference electrode was used for the polarization measurement. A 500W Xe arc lamp was used as a light source and the spectral distribution of photocurrent was determined by using a monochromator. The light intensity was measured with a calibrated thermopile (Kipp and Zonen CA1) placed at the same position as semiconductor electrodes.

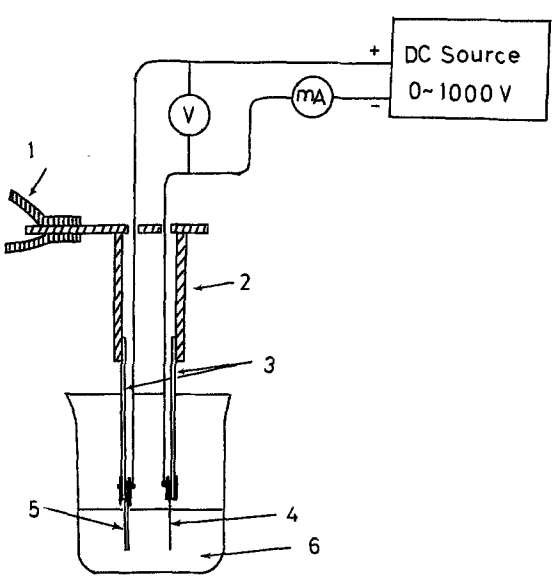

Fig. 1. Experimental setup for electrophoretic deposition. 1, Clamp; 2, plastic plate; 3, glass plate; 4, Pt cathode; 5, SnO_2-coated glass plate; 6, suspension.

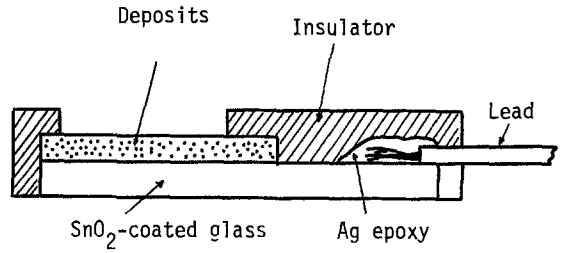

Fig. 2. Photoanode

Results and Discussion

Electrophoretic deposition of CdS.—Figure 3 shows the TEM photographs of particles in starting materials which have partially coalesced. The particle sizes were found to be 0.5-1 μm for CdS (Fig. 3a) and 0.5-3 μm for CdSe, respectively (Fig. 3b). These ranges of particle sizes are suitable because colloidal sizes give low deposition rates (7) and coarser particles than 5 μm lead to uneven coating.

Figure 4 shows the relationship between the applied voltage and the deposition rate of CdS expressed as the weight of the CdS deposited per unit area in 1 min. These measurements were done with deposits from a freshly prepared suspension. In such a condition the experimental data gave a linear relation. The relationship between deposition rate and concentration of CdS particles in suspension is shown in Fig. 5. In this case each deposition rate was measured using a shorter deposition period of 30 sec with care to avoid sedimentation of particles in the freshly prepared concentrated suspension. The result thus obtained also follows a linear relation, as expected from Eq. [1] given by Zhuravlev (6)

$$W = \frac{X\zeta\epsilon\tau SC}{6\pi\eta} \qquad [1]$$

where W is the weight deposited, X the potential gradient, ζ the electrokinetic potential, ϵ the dielectric constant of the medium, τ the time of deposition, S the electrode area, C the concentration of particles, and η the viscosity of the medium. Since no special additive affecting the electrokinetic potential is in-

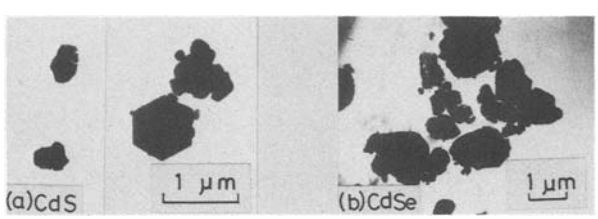

Fig. 3. Electron micrographs of CdS (a) and CdSe (b) powder

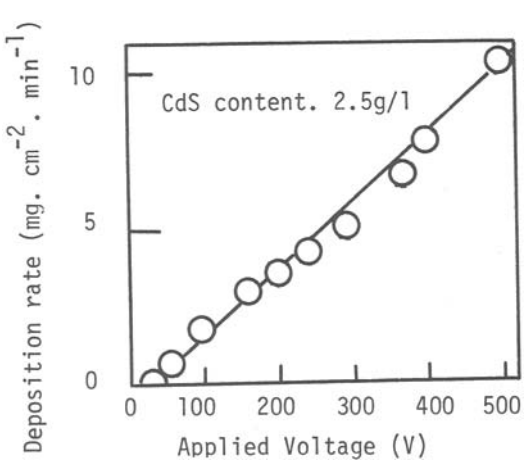

Fig. 4. Dependence of the deposition rate on the applied voltage

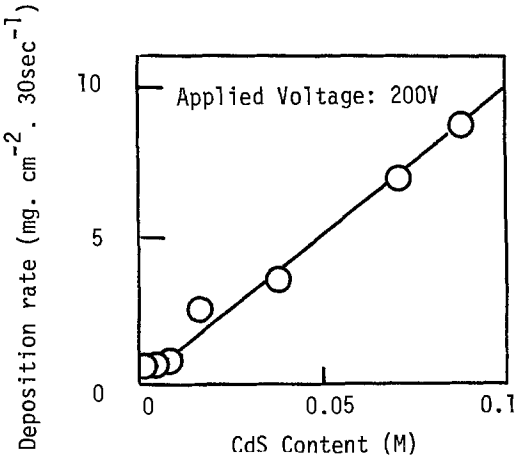

Fig. 5. Dependence of deposition rate on the CdS content in suspension.

volved in this case, all the quantities except for X or C in the right-hand side of Eq. [1] are regarded as constant. Consequently, the weight of electrophoretically deposited CdS from the fresh suspension, *i.e.*, the product of the deposition rate and τ, s can be described by Eq. [1].

In the case of successive coating on separate anodes in one suspension, however, the above dependence of the deposition rate on the concentration was no longer observed except for the early stage, as shown in Fig. 6. Thus depositing CdS on an SnO_2-coated glass anode becomes increasingly difficult for repeated runs. Such a deterioration of the process may be attributed to the electrolytic disappearance of ionic species which contributed to the negative charging of particles. To confirm the assumption, it is necessary to investigate how to suppress the deposition rate in the suspension prepared by use of pre-electrolyzed medium. The results obtained for this experiment are shown in Fig. 7. It is found that the lowering of the deposition rate is dependent on the charge passed through the medium and is associated with exhaustion of ionic species in the medium. Therefore, the use of additives was attempted to allow the repeated deposition of CdS films from the same suspension. Among the additives investigated (ammonium thyocyanate, potassium iodide, and cadmium chloride), a small amount of $CdCl_2$ was found to be most effective.

Figure 8 shows the effects of Cl′ on the maintenance of repeated deposition from the same suspension expressed as relations between cumulative deposition weight and the sum of charge through unit area of individual substrates. Although the deposition rate

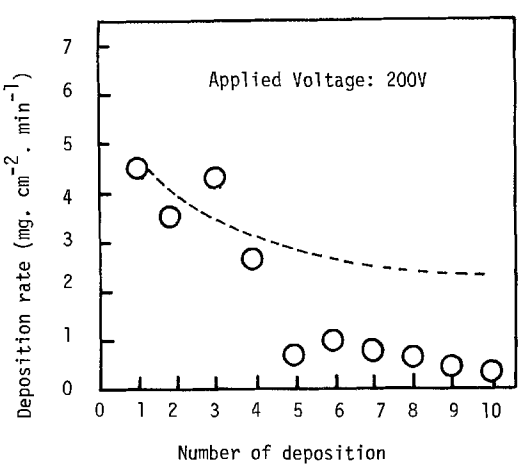

Fig. 6. Changes of the deposition rate for successive coats on separate anode in one suspension. – – – –; expected value from the CdS content in suspension.

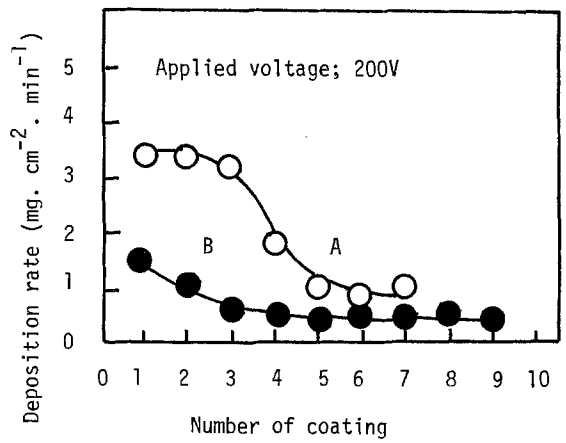

Fig. 7. Changes of deposition rate with repetition of coating. Charge passed through the medium before preparation of suspension: A, 228 mC/40 ml, B, 492 mC/40 ml.

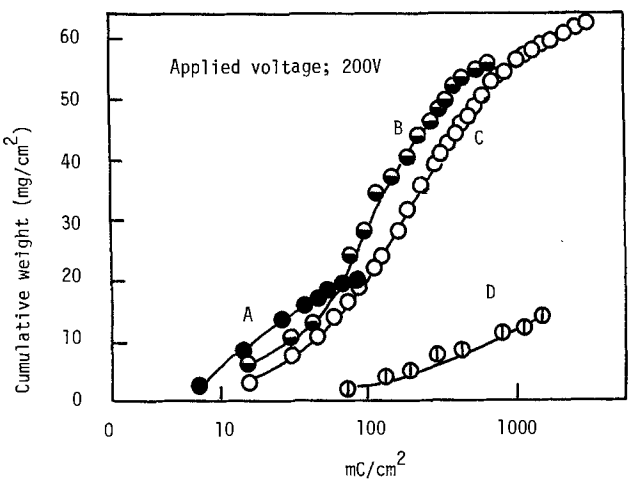

Fig. 8. Effects of chloride ion addition successive coats of CdS on separate anodes in one suspension. Cl′, A, 0; B, 1×10^{-6}; C, $1 \times 10^{-4.5}$; D, $1 \times 10^{-2.6}$ eq/l. Initial content of CdS: 100 mg in 40 ml of acetone-isobutyl alcohol mixture.

from the suspension containing 1×10^{-6}-3.2×10^{-5} equiv./liter of Cl′ was suppressed at the initial stage compared with additive-free suspension, it is possible to deposit all the dispersed particles in the course of repeated runs. Furthermore, the addition of Cl′ was found to be effective for the improvement of adhesion and throwing power of the electrophoretic deposits. In this case, Cl′ may be specifically adsorbed on the surface of CdS particles by forming a double layer. This brings about the increase of effective charge of particles. Under these conditions, the electrophoretic deposition proceeds smoothly giving adherent deposits. However, the presence of large amounts of Cl′ (2.5×10^{-3} equiv./liter) in the suspension is responsible for slower deposition of CdS. When the Cl′ concentration exceeds the optimum value for the formation of the double layer, the excess additive remains in the form of solute, and it is quite likely that the electrolysis of the additive occurs.

Electrophoretic deposition of CdSe and CdS_xSe_{1-x}.— Electrophoretic deposition of CdSe from the propylene carbonate system requires higher applied voltages compared to CdS deposition. Figure 9 shows cumulative deposition weights on separate anodes as a function of the sum of the charge through the unit area of individual substrates. Adherent and uniform CdSe films could be obtained from suspensions containing a relatively high concentration of $CdCl_2$ (2×10^{-3} equiv./liter. In this case, the existence of $CdCl_2$ in electrophoretic films was confirmed by x-ray analysis. This

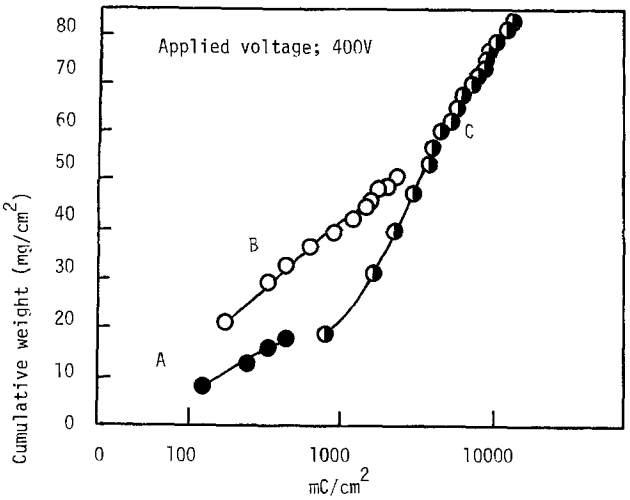

Fig. 9. Effects of chloride ion addition for successive coats of CdSe on separate anodes in one suspension. Cl', A, 0; B, 2 × 10^{-4}; C, 2 × 10^{-3} eq/l. Initial content of CdSe: 100 mg in 40 ml of propylene carbonate.

$CdCl_2$ has two effects in the formation of n-type semiconductor films (5). First, by dissolving the outer layer of CdSe particles and subsequently by vaporizing off during sintering process, the $CdCl_2$ binds particles to each other and thus it provides a more adherent film on the substrate. It also enhances the mutual diffusion of atoms in deposited CdSe particles and hence the growth of large grains. The evidence for such grain growth is shown in Fig. 10 using SEM pictures taken before and after thermal treatment. From these pictures it is found that the average final particle size is increased and there is flattening of the surface morphology as a result of sintering. In addition, the chloride can act as an n-type dopant for the most II-VI compound semiconductors (8). Therefore, the addition of $CdCl_2$ to the propylene carbonate medium is reasonable even at concentration as high as 10^{-3} equiv./liter.

To obtain mixed coating of CdS and CdSe, a mixture of these materials was dispersed in acetone-isobutyl alcohol (A) containing 3.2 × 10^{-5} eq/l of $CdCl_2$ or in propylene carbonate (B) containing 1 × 10^{-3} eq/l of $CdCl_2$. Codeposition of CdSe in this case is due to mechanical collision and coalescence with CdS particles of higher mobility in the electric field. Electrophoretic deposition was performed using an applied d-c voltage of 200V for (A) and 400V for (B). Figure 11 shows the relations between CdSe content in initial deposit and CdSe content in the dispersed mixture of semiconductor particles in suspension. The CdSe content in deposits from (A) or (B) was found to be comparable with the composition in the suspension. The concentrations shown in Fig. 11 were determined by x-ray diffraction intensities of (0002) reflections for mixed crystal phases. The deposit from medium (B) is much better in homogeneity and adherence to the substrate than that from the medium (A).

Photoelectrochemical behavior of electrophoretically deposited films.—Figure 12 gives the photocurrent

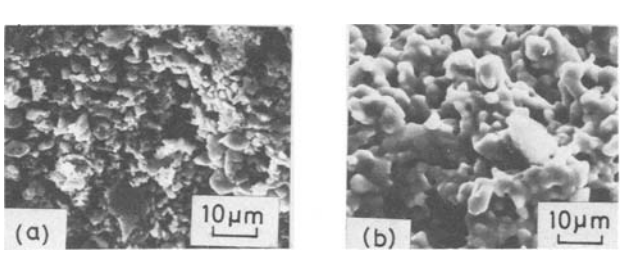

Fig. 10. Scanning electron micrographs of electrophoretically deposited CdSe films: (a) as deposited film (b) after sintering.

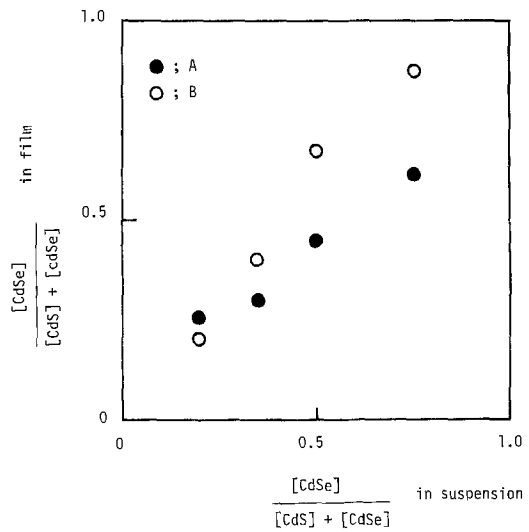

Fig. 11. Composition of deposits and suspension. A, Acetone-isobutyl alcohol, applied voltage: 200V, Cl' 1 × $10^{-4.5}$ equiv./liter; B, propylene carbonate, applied voltage: 400V, Cl' 2 × 10^{-3} equiv./liter.

action spectra for the CdS, CdSe, and CdS_xSe_{1-x} thin film electrodes prepared by electrophoretic deposition in the electrolyte containing 1M NaOH and 1M Na_2S. The photoresponse of electrophoretically deposited CdS and CdSe electrodes was observed at wavelengths shorter than 520 and 720 nm, respectively, while the photoresponse of the CdS_xSe_{1-x} electrode appeared at a wider range of wavelength due to the formation of solid solution by sintering. The existence of solid solution in the sintered film of mixed deposits has been also confirmed by x-ray analysis data and the application of Vegard's rule (9). If a solid solution completely formed, a sharp change in photoresponse would be expected in the vicinity of the wavelength corresponding to its bandgap. But in our mixed specimens, the action spectrum consists of the overlapping photoresponse from the three components containing a small CdSe peak, which may be presumably due to the inadequate thermal treatment.

Quantum yields for anodic photocurrents of electrophoretically deposited CdS and CdSe photoanodes at −0.7V *vs.* SCE are shown in Fig. 13. In the favorable photoresponse region, quantum yields exceed 0.6 and they are appropriate values for polycrystalline thin film electrode though did not reach unity as for a single crystal electrode (10). The main reason for quantum yields lower than unity can be attributed to the recombination of photogenerated electrons and holes. Recombination centers in electrophoretically deposited films are presumably due to the fine grain size in addition to lattice defects and impurities contaminated from the suspension.

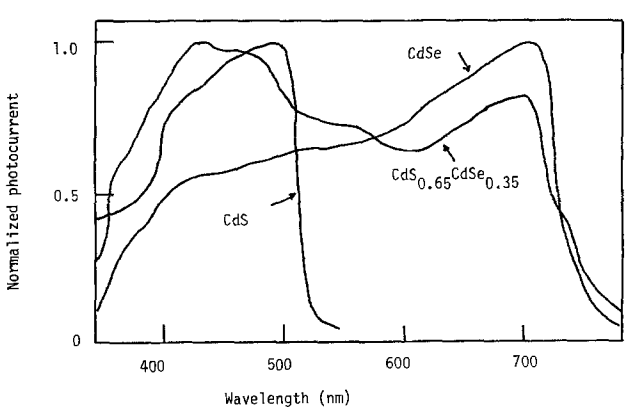

Fig. 12. Action spectra of photocurrent at three types of photoanodes.

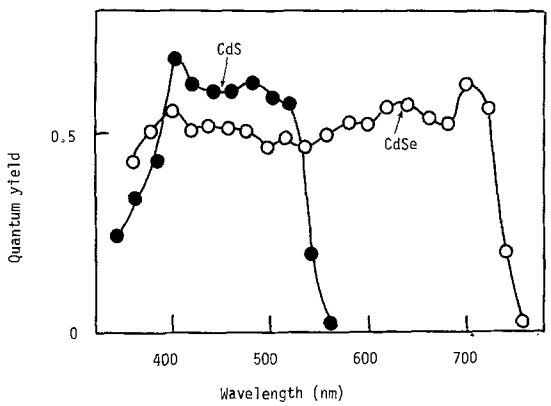

Fig. 13. Quantum yields of electrophoretic deposition CdS and CdSe vs. incident light wavelength.

The current-voltage characteristics of photocells using above three types of photoanodes are shown in Fig. 14 (a) and (b), for irradiation near 50 mW/cm^2. The results in Fig. 14 (a) refer to the front illumination cell in which anodes are illuminated through a quartz window of the cell wall and a layer of the electrolyte of about 1 mm thickness, whereas, Fig. 14 (b) is the result obtained from the rear illumination cell avoiding the light absorption in the colored electrolyte (3). For CdS, CdS_xSe_{1-x}, and CdSe photoanodes, fill factors in (a) were 0.36, 0.43, and 0.33 and energy conversion efficiencies were 1.4, 1.6, and 1.3%, respectively. Recently, conversion efficiencies of the photocell with a vacuum codeposited film anode (11-12) or a spray pyrolyzed thin film photoanode (13) of CdSe were reported to be in the range 4.3-6.4%. Our results on the output characteristics of CdSe photoelectrochemical cell, as shown in Fig. 14(a), fall below these values. The best conversion efficiency in (b) type cell was 2%, which was superior to those in (a). This result as shown in Fig. 15, can be explained on the basis of the action spectra of CdSe photoanodes in the two types of electrolyte with and without S_x^{2-} ion and of the absorption spectrum of S_x^{2-}. Although the CdSe photoanodes used in this experiment exhibit a significant photoresponse at wavelengths shorter than 720 nm in the colorless sulfide solution, they do not respond to the light of wavelengths shorter than 520 nm in the colored polysulfide solution, as demonstrated in the figure. Therefore, the use of a rear illumination cell avoiding the influence of the colored solution is found to be effective for the improvement of energy conversion efficiency. As the similar results may be expected for CdS-CdSe mixed or solid solution photoanodes, several measurements were attempted for CdS_xSe_{1-x} photoanodes using the rear illumination cell. But the conversion efficiencies to date are not

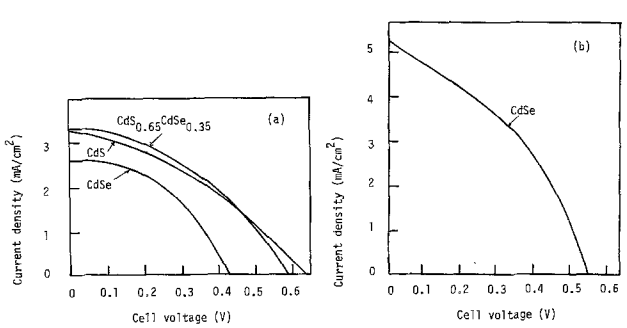

Fig. 14. Current-voltage characteristics of photoelectrochemical cell. (a) Front illumination. Light intensity: 55 mW/cm^2 for CdS and CdS_xSe_{1-x}, 44 mW/cm^2 for CdSe. (b) Rear illumination. Light intensity: 55 mW/cm^2 for CdSe. Electrolyte: 1M NaOH, 1M Na_2S for CdS, 1M NaOH, 1M Na_2S, 1M S for CdS_xSe_{1-x} and CdSe.

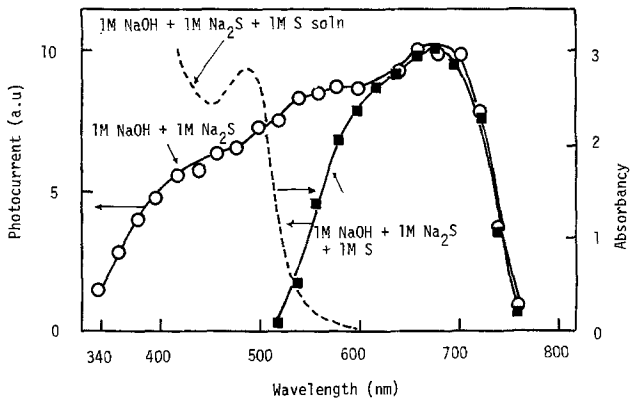

Fig. 15. Action spectra of CdSe photoanodes in the two electrolytes and photoabsorption of S_x^{2-} ion.

higher than the values for CdSe based photoelectrochemical cell. These will be improved in further investigation of deposition and sintering conditions for the CdS-CdSe film. More detailed studies are needed and are now in progress.

Conclusions

The present work demonstrates that;

1. An electrophoretic deposition technique can be applied for thin film deposition of CdS, CdSe, and mixtures onto SnO_2-coated glass substrates.
2. The addition of Cl^- to the suspensions for the electrophoretic deposition of CdS or CdSe is effective in obtaining adherent and smooth deposits.
3. The electrophoretically deposited layer of CdS and/or CdSe can be used as the photoanode in an electrochemical photocell.
4. An energy conversion efficiency of 2% under white light illumination was obtained with the electrochemical photocell using these film anodes.

Acknowledgment

A part of this work was supported by a Grant in Aid for Scientific Research from the Ministry of Education of Japan.

Manuscript submitted March 1, 1982; revised manuscript received Aug. 21, 1982.

Any discussion of this paper will appear in a Discussion Section to be published in the December 1983 JOURNAL. All discussions for the December 1983 Discussion Section should be submitted by Aug. 1, 1983.

Publication costs of this article were assisted by Gifu University.

REFERENCES

1. M. Tsuiki, Y. Ueno, T. Nakamura, and H. Minoura, *Chem. Lett.*, **1978**, 289.
2. M. Tsuiki, H. Minoura, T. Nakamura, and Y. Ueno, *J. Appl. Electrochem.*, **8**, 523 (1978).
3. I. Kaur, D. K. Pandya, and K. L. Chopra, *This Journal*, **127**, 943 (1980).
4. G. Hodes, D. Cahen, J. Manassen, and M. David., *ibid.*, **127**, 2252 (1980).
5. M. S. Kazakos and B. Miller, *ibid.*, **127**, 2378 (1980).
6. G. I. Zhuravlev, "Tainetsu Mukihimaku no Kagaku to Shorigijutsu," p. 67, Nichi-So Tsushinsha, Wakayama, Japan (1980).
7. C. P. Gutierrezt, J. R. Mosley, and T. C. Wallace, *This Journal*, **109**, 923 (1962).
8. A. G. Milnes and D. L. Feucht, "Heterojunctions and Metal-Semiconductor Junction," p. 8, Academic Press, New York and London (1978).
9. P. Cherin, F. L. Lind, and E. A. Davis, *This Journal*, **117**, 233 (1970).
10. A. Heller, K. C. Chang, and B. Miller, *ibid.*, **124**, 697 (1977).
11. M. A. Russak and J. Reichman, *ibid.*, **129**, 542 (1982).
12. M. A. Russak and J. Reichman, *ibid.*, **128**, 2025 (1981).
13. C. J. Liu and J. H. Wang, *ibid.*, **129**, 719 (1982).

Molten Carbonate Fuel Cell Performance Model

Thomas L. Wolf and Gerald Wilemski*

Physical Sciences Incorporated, Andover, Massachusetts 01810

ABSTRACT

A two-dimensional numerical model is developed to simulate nonisothermal performance of molten carbonate fuel cells. The model takes account of gas stream utilization due to electrochemical reaction, conductive heat transfer between cell hardware and gas streams, energy transfer accompanying mass addition to the bulk streams, convective heat transfer by the bulk streams, and inplane heat conduction through the cell hardware. Individual porous electrode models are used to predict the local dependence of current density on cell temperature and gas composition. Calculated results are compared with experimental data for 94 cm^2 isothermal cells with crossflow geometry for various fuel and oxidant compositions, total gas pressures, and cell temperatures. Excellent agreement is obtained. Calculated distributions of current density and cell temperature are also presented for 1 m^2 nonisothermal cells for cross-, co-, and counterflow geometries. Current density and cell temperature distributions are found to be highly coupled. Calculated temperature differences on the order of 200 K are observed across the face of a cell operating at maximum load.

Numerical modeling of a molten carbonate fuel cell (MCFC) is worthwhile for several reasons. With a model, reliable predictions of cell current-voltage characteristics can be made over a wide range of operating conditions. Beyond predicting overall performance, a numerical model can also be used to study the variation in local quantities (*e.g.*, current density, temperature) within a simulated operating cell. In this respect, a model provides a deeper level of interpretation of experimental data because inference of local behavior is not possible from the gross cell observables typically measured.

In modeling small laboratory cells (less than 100 cm^2), heat transfer effects are unimportant and to a good approximation the cell may be treated as isothermal. For larger cells with commercially realistic dimensions (about 1 m^2), the isothermal approximation is no longer appropriate, as temperature differences of several hundred degrees kelvin may be attained across the plane of a single cell operating at maximum load. From the standpoint of predicting performance, it is important to accurately compute the cell temperature distribution because local current density is temperature dependent. Prediction of the cell temperature distribution is also useful in anticipating such cell engineering problems as the differential expansion arising from large temperature gradients and electrolyte evaporation losses at high local cell temperature.

The predominant heat transfer mechanisms treated in our model of nonisothermal MCFC performance are conductive heat transfer between the cell hardware and gas streams, energy exchange associated with mass transfer, conductive heat transfer between adjacent cells in a stack, and heat conduction in the plane of the cell hardware. Separate anode and cathode porous electrode models (1) are used to calculate the current density as a function of the local gas composition and temperature at each point in the cell. In this respect, as well as in its comprehensive treatment of heat transfer effects, our model is more versatile in its predictive capabilities than the fuel cell model recently reported on by Sampath, Sammells, and Selman (2), which was restricted to small isothermal cells and relied on empirical fits of experimental data to obtain current density overpotential relations for the electrodes.

Other aspects of the present treatment resemble the earlier work (2). Changes in gas composition arising from electrochemical half-reactions are taken account of in a similar fashion, although molar, rather than volume, gas flow rates are used here in order to automatically account for the effect of volume changes in the gas flow associated with nonisothermal operation. As in the earlier study, either equilibrium or frozen chemistry is assumed in the anode stream; no finite-rate gas phase kinetic effects are considered.

In the present study primary emphasis is placed on crossflow geometry, and the majority of numerical results presented are for that case. Extension of the analysis to other flow geometries is straightforward, and this capability (for coflow and counterflow) has been built into our computer code. Presentation of numerical results for these alternative geometries is limited.

Restrictions and Assumptions

The analysis developed in this study is strictly applicable to design configurations that satisfy the following structural requirements:

1. The gas streams flow in narrow smooth-walled channels of constant cross section.
2. The cell operates in an effectively infinite stack of identical cells separated by thermally conducting boundaries (end effects are not considered).
3. The edges of the stack hardware are thermally insulated.

In addition to the foregoing restrictions, we make use of the following approximations.

1. Finite-rate kinetics are not considered; the water-gas shift and methanation reactions may either remain in equilibrium or be frozen in the anode stream. Experimental evidence (3) indicates that water-gas shift equilibrium is maintained, while methane remains approximately inert. Results are presented for this case.
2. Thermal properties of the gas streams are independent of temperature and pressure and are evaluated at 923 K and 1 atm using numerical values listed in Ref. (4). This approximation is reasonable over the expected range of conditions. Gas stream properties are evaluated as functions of local mixture composition, using the approximate method of Brokaw (5) to evaluate gas mixture thermal conductivities.
3. Radiative heat transfer between hardware and the gas streams is neglected, because the gas streams are optically thin. For the gas compositions of interest over the expected range of temperatures and pressures, this approximation is reasonable, although we may be underestimating heat transfer coefficients somewhat at high pressure ($\approx$ 10 atm) if local CO_2 and H_2O mol fractions become large.
4. The cell operates at constant voltage, independent of position in the plane of the cell. This approximation is justified by the high electrical conductivity of the current collectors and separator plates, which are placed in good electrical contact with each other and the porous electrodes.
5. Profiles of velocity and temperature remain fully developed in the gas streams. In the case of the velocity profile, this approximation is justified for the

* Electrochemical Society Active Member.
Key words: fused salts, fuel cell, current density, transport.

low Reynolds number flows typically envisioned in commercial cells; streamwise changes in boundary conditions occur slowly compared with flow response time. Full development of the temperature profile follows from similarity considerations, because the Prandtl number is of order unity in the gas streams.

6. The gas composition is uniform across the channel depth. This approximation has been examined in detail in a separate study (6) which made use of the exact solution for species diffusion between parallel plates with a fully developed velocity profile. It was concluded from this work that concentration gradients are appreciably only for very dilute species in cells operating at high current density.

7. At a given location in the plane of the cell, the hardware assumes a uniform local temperature. This approximation was rigorously justified by numerically evaluating temperatures of the various hardware components over the expected range of gas temperatures and local current density, using an equivalent thermal network to represent a given location in the cell plane. This calculation demonstrated that hardware temperatures never differ by more than a few kelvins from the uniform temperature based on neglecting hardware thermal resistance in the direction perpendicular to the cell plane. It is therefore unnecessary to treat heat release or absorption at individual electrodes (7).

It should be mentioned that the assumption of negligible hardware resistance is not as accurate for the case of a single cell operating adiabatically. In the stacked configuration thermal coupling between the electrodes is due primarily to heat conduction through the highly conductive current collectors and separator plates. For a single cell the only thermal path between the electrodes is through the less conductive electrolyte tile.

Theoretical Development

Mass balance equations.—The overall electrode half-reactions are

$$CO_2 + \frac{1}{2}O_2 + 2e^- = CO_3^= \quad \text{(cathode)} \qquad [1]$$

and

$$H_2 + CO_3^= = H_2O + CO_2 + 2e^- \quad \text{(anode)} \qquad [2]$$

Although only H_2 is considered to undergo direct electrochemical conversion, anode CO and CH_4 act as fuels by supplying H_2 via the water-gas shift and methane reforming reactions, that is

$$CO + H_2O \rightleftarrows H_2 + CO_2 \qquad [3]$$

$$CH_4 + 2H_2O \rightleftarrows 4H_2 + CO_2 \qquad [4]$$

We define a fuel flow rate $\dot{n}_F$ to be the molar flow rate of H_2 plus the number of mols of H_2 potentially available via reactions [3] and [4]. Depending on which reactions are considered, $\dot{n}_F$ is defined by

$$\dot{n}_F = \dot{n}_{H_2} \qquad [5a]$$

$$\dot{n}_F = \dot{n}_{H_2} + \dot{n}_{CO} \qquad [5b]$$

$$\dot{n}_F = \dot{n}_{H_2} + \dot{n}_{CO} + 4\dot{n}_{CH_4} \qquad [5c]$$

where Eq. [5a] corresponds to CO and CH_4 frozen, [5b] to only CH_4 frozen, [5c] to reactivity of both species. Definitions [5b] and [5c] assume that water is present in sufficient quantity to convert all of the available CO and CH_4.

In the gas stream, we define fuel and oxidant species utilization parameters

$$u_\alpha = (\dot{n}_\alpha^\circ - \dot{n}_\alpha)/\dot{n}_\alpha^\circ \qquad [6]$$

where α = H_2, CO, CH_4, CO_2, or F. In this expression $\dot{n}_\alpha$ is the molar flow rate (per unit channel width) of species α and superscript o denotes an inlet quantity.

From mass balance considerations and inspection of Eq. [1] and [2], we can write the local relations

$$\partial u_F/\partial x = j/(2F\dot{n}_F^\circ) \quad \text{(anode)} \qquad [7]$$

$$\partial u_{CO_2}/\partial y = j/(2F\dot{n}_{CO_2}^\circ) \quad \text{(cathode)} \qquad [8]$$

where x and y are the anode and cathode flow directions, and j is the local current density.

If reactions [3] and [4] are in equilibrium in the anode stream, we have the equilibrium constraints

$$K_s = \frac{x_{H_2}x_{CO_2}}{x_{H_2O}x_{CO}} = K_s\,(u_{H_2}, u_{CO}, u_{CH_4}, \dot{n}_i^\circ) \qquad [9]$$

$$K_m = \frac{x_{CO_2}x_{H_2}^4P^2}{x_{CH_4}x_{H_2O}^2} = K_m\,(u_{H_2}, u_{CO}, u_{CH_4}, \dot{n}_i^\circ) \qquad [10]$$

where x is a mole fraction based on the bulk gas stream composition and P is the pressure. As indicated, the equilibrium expressions can be written in terms of the anode utilizations and the inlet molar flow rates of the constituents $\dot{n}_i^\circ$ (the inlet flow rates must satisfy equilibrium). Given K_s and K_m, with u_F obtained from integration of Eq. [7], Eq. [5], [9], and [10] can be solved for the anode utilizations u_{H_2}, u_{CO}, and U_{CH_4}.

Local current density.—The local current density j at any point in the cell can be calculated by solving the local potential balance equation

$$j = (E - V - \eta_a + \eta_c)/Z_\Omega \qquad [11]$$

Here, V is the cell operating voltage, E is the local open-circuit potential given by the Nernst equation, and Z_Ω is the local ohmic impedance of the cell. The anodic and cathodic overpotentials η_a and η_c are complex functions of j, the local gas compositions, and the local temperature. They are calculated using the electrode models presented in another paper (1). Because of the difficulty in modeling the contact resistances between cell components, Z_Ω was taken simply to be given by the equation

$$Z_\Omega = t/\kappa \qquad [12]$$

where κ is the conductivity of the bulk electrolyte $(\Omega\ \text{cm})^{-1}$ and t is an effective tile thickness chosen by demanding that Z_Ω yield the measured cell resistance. Equation [12] could, in principle, contain a tortuosity/porosity correction factor; however this refinement only results in a redefinition of t. In the calculations for nonisothermal cells, Z_Ω is computed from the equation $Z_\Omega = Z^{923}\kappa(923\ \text{K})/\kappa(T)$ with Z^{923} equal to the impedance of an isothermal cell at 923 K.

With the assumption of uniform composition across the channel depth, the composition terms of the Nernst equation may be expressed in terms of the bulk gas stream mole fractions. The local open-circuit voltage E can then be written in the usual way as

$$E = E^\circ(T_l) + (RT_l/2F)\ln\left([x_{O_2}{}^{1/2}x_{CO_2}]_c[x_{H_2}/x_{H_2O}x_{CO_2}]_a\right) + (RT_l/4F)\ln P$$

The bulk gas stream mol fractions are easily expressed in terms of the utilizations u_i (2). A single local cell temperature T_l has been assumed for both electrodes, as explained previously.

Hardware energy balance.—The magnitude of the heat flux transferred locally to the gas streams is equal to the sum of local heat release $\dot{Q}$ and the net heat flow convergent on a given point due to inplane conduction $\dot{Q}_{ip}$. Defining a gas/hardware thermal convection coefficient h, the equation governing the local hardware temperature T_l is then

$$\dot{Q} + \dot{Q}_{ip} = A_a\bar{h}_a\,(T_l - T_{ma}) + A_c\bar{h}_c\,(T_l - T_{mc}) \qquad [13]$$

The A's are local ratios of gas/hardware interface area to cell area and are assigned the value $A_a = A_c = 2$ in subsequent calculations. The local mean gas temperature T_m is defined for a constant heat capacity incompressible flow by $T_m = \int vTdA / \int vdA$, where v and T are the local gas velocity and temperature, and the integral is taken over the channel area. The thermal convection coefficient can be expressed in terms of a local Nusselt number, $Nu = \bar{h}d/k$, where d is the channel depth and k is the gas mixture thermal conductivity. With our assumption of a fully developed gas temperature profile in a constant cross-sectional gas channel, Nu is a constant determined by the gas channel geometry alone (8). In our calculations, the values $Nu = 3$ and $d = 0.2$ cm are used. For a given channel geometry, $\bar{h}$ is then a local function of k only.

The inplane conduction term $\dot{Q}_{ip}$ is given by

$$\dot{Q}_{ip} = \Sigma\,(L_n\lambda_n)\,\nabla^2 T_l \qquad [14]$$

where λ is a thermal conductivity and L is a thickness. The summation is over all hardware components to give an effective hardware inplane thermal conductivity, that is

$$\Sigma(L_n\lambda_n) = L_a\lambda_a + L_c\lambda_c + L_t\lambda_t + L_{sp}\lambda_{sp} + \gamma_{ka}L_{ka}\lambda_{ka} + \gamma_{kc}L_{kc}\lambda_{kc} \qquad [15]$$

where subscripts t, sp, and k denote electrolyte tile, separator plate, and current collector, respectively. The fractional ratios γ_{ka} and γ_{kc} depend on current collector geometry and are chosen such that the last two terms represent effective current collector inplane thermal conductivities. The values $\gamma_{ka} = \gamma_{kc} = 1/2$ were used in subsequent calculations. Other hardware-dependent parameters were assigned the numerical values listed in Table I.

The net heat release $\dot{Q}$ includes the net electrochemical heat release (subscript e) and the net heat release due to chemical reaction (subscript r) in the anode stream, so that

$$\dot{Q} = \dot{Q}_{ae} + \dot{Q}_{ce} + \dot{Q}_{ar} = \dot{Q}_e + \dot{Q}_{ar} \qquad [16]$$

where $\dot{Q}_e$ is related to the current density by

$$\dot{Q}_e = -j\,(\Delta H_{H_2O}(T_l)/2F + V) \qquad [17]$$

and $\dot{Q}_{ar}$ is proportional to the rate at which reactants are used up in the anode stream

$$\dot{Q}_{ar} = \frac{d\dot{n}_{CO}}{dx}\Delta H_s(T_l) + \frac{d\dot{n}_{CH_4}}{dx}\Delta H_m(T_l) \qquad [18]$$

Here, ΔH_{H_2O} is the heat of formation of H_2O, ΔH_s and ΔH_m are the enthalpy changes (per mole CO, CH_4) for the water-gas shift and methanation reactions (Eq. [3] and [4]). Because these reactions are presumably catalyzed by the Ni electrode surface, the heat is evolved at the local hardware temperature T_l.

Energy addition to gas stream.—Thermal energy exchange between the cell and either gas stream is due to the combined effect of conductive heat transfer and a mass transfer contribution associated with exchange of reacting species at the cell temperature. An expression relating the mean gas temperature to these heat and mass fluxes can be derived.

Consider a multicomponent gas stream flowing in the x direction at local mean temperature T_m, with mass added at temperature T_l. We denote the molar flow rate (per unit channel width) as $\dot{n}_i$ and the molar heat capacity of species i as c_{pi}. Let ΔT_m be the change in the mean gas temperature over a distance Δx, and $\Delta\dot{n}_i$ be the corresponding change in $\dot{n}_i$ due to mass addition. The conductive heat flux $\dot{q}_k$ heats the initial bulk stream from T_m to $T_m + \Delta T$, while the added mass changes temperature from T_l to $T_m + \Delta T$

$$\sum_i \dot{n}_i \int_{T_m}^{T_m+\Delta T} c_{pi}dT + \sum_i \Delta\dot{n}_i \int_{T_l}^{T_m+\Delta T} c_{pi}dT = \int_x^{x+\Delta x} \dot{q}_k dx \qquad [19]$$

As $\Delta T \to 0$, and $\Delta x \to 0$, we can write $\Delta T = (dT/dx)dx$, and $\Delta\dot{n}_i = (d\dot{n}_i/dx)dx = g_i dx$ where g_i is the molar flux of species i entering the stream. We then obtain the following relation for the energy balance

$$\sum_i \dot{n}_i c_{pi}\frac{dT_m}{dx} + \sum_i g_i \int_{T_l}^{T_m} c_{pi}dT = \dot{q}_k \qquad [20]$$

If we express the conductive heat flux as $\dot{q}_k = A\bar{h}(T_l - T_m)$, treat c_{pi} as constant, and introduce the bulk heat capacity $c_p = \dot{n}^{-1}\Sigma\dot{n}_i c_{pi}$, Eq. [20] can be written as

$$\partial(\dot{n}c_pT_m)/\partial x = A\bar{h}(T_l - T_m) + \sum_i g_i c_{pi}T_l \qquad [21]$$

where the derivative is in the conservative form used in the numerical procedure.

The mass transfer accounted for by the molar fluxes g_i arises in both streams from electrochemical reaction at the electrode surfaces, but in the anode stream, there is an additional contribution associated with the heterogeneous chemistry of the water-gas shift and methanation reactions.

Table I. Numerical values for cell hardware thermal conductivities (λ) and thicknesses (L) used in calculation of effective hardware in-plane thermal conductivity, Eq. [15]

Component	Material	λ (W/cm-K)	L (cm)
Separator plate	Stainless steel	0.22	0.03
Anode current collector	Stainless steel	0.22	0.2
Cathode current collector	Stainless steel	0.22	0.2
Anode	Ni	0.78	0.08
Cathode	NiO	0.009	0.04
Tile	Molten salt and $LiAlO_2$ matrix	0.02	0.18

Numerical Solution

Approach.—The interdependence of temperature and current density distributions is sufficiently weak to permit a partially decoupled solution technique. The distribution of current density can be evaluated subject to prescribed cell and gas temperature and vice versa; these distributions are computed in alternating fashion and the procedure is iterated to convergence.

Evaluation of the current density distribution (given a prescribed temperature distribution) requires integration of Eq. [7] and [8]. Because the gas composition dependence of the local current density is complex, we are restricted to a simple marching solution here. This is accomplished without iteration for crossflow and coflow geometries. For counterflow geometry an iterative approach is used in which an initial current density distribution is guessed. Gas compositions corresponding to this distribution are then determined by marching (independently at the anode and cathode) in the directions of the gas flows. From these, a new current density distribution is computed, and so on to convergence.

Evaluation of the cell and gas temperature distributions (given a prescribed current density distribution) requires integration of Eq. [13] and [21]. Knowledge of the current density distribution enables the equations to be effectively linearized by evaluating the coefficients $\bar{h}$, $\dot{n}$, c_p, g, and $\dot{Q}$. (To be precise, g and $\dot{Q}$ also have a weak temperature dependence, but for numerical purposes these can be evaluated using the cell temperature from a previous iteration.) Because the inplane conduction term makes Eq. [13] elliptic

in structure, solution for the entire cell temperature field is indicated for the sake of computational efficiency. Moreover, because all three temperature equations are strongly coupled, simultaneous solution for the entire cell and gas temperature field is necessary. This is accomplished by expressing the temperature equations in finite difference form, yielding a system of linear algebraic equations which is solved through a matrix inversion.

Computational scheme.—The foregoing ideas are incorporated into the numerical computation scheme outlined below. Given a prescribed temperature distribution (initially assumed isothermal), the mass balance equations are integrated over an $N \times N$ mesh by marching forward in the direction of the gas flows. At each mesh point local anode utilizations satisfying the equilibrium constraints are computed with the equilibrium constants evaluated at the local anode stream temperature. Local current density is then computed from the potential balance relation.

In solving the temperature equations, all of the nonlinear coefficients ($\dot{n}$, g, $\bar{h}$, c_p, $\dot{Q}$) are evaluated at each mesh point using the previously computed distributions of current density, utilization, and temperature. The system of linear equations corresponding to the finite difference representations of the differential equations is then solved, using standard matrix techniques, to compute new distributions of T_l, T_{ma}, T_{mc}. The entire procedure is iterated until converged distributions of temperature and current density are obtained. The computer code used in making the calculations reported in this paper has been described and documented in detail elsewhere (9).

Finite difference equations.—The mass balance and heat transfer equations are written in a conservative form, consistent with the trapezoid rule for integration. This procedure is accurate to second order.

The anode mass balance equation has the representation

$$u_F(L,M) - u_F(L,M-1) = (\Delta x/4\dot{n}_F^\circ)\,(j(L,M) + j(L,M-1)) \quad (M = 2,\ldots,N;\ L = 1,\ldots,N) \quad [22]$$

where L and M label mesh points $(1,\ldots,N)$ in the y and x directions, respectively. A similar equation is used for the cathode utilization, u_{CO_2}, with differencing appropriate to the particular flow geometry.

The anode convective heat transfer equation takes the form

$$e(L,M) - e(L,M-1) = (\Delta x/2)\,(S(L,M) + S(L,M-1)), \quad (M = 2,\ldots,N;\ L = 1,\ldots,N) \quad [23]$$

where e and S denote the groupings

$$e = \dot{n} c_p T_m \quad [24]$$

$$S = A\bar{h}(T_l - T_m) + \sum_i g_i c_{pi} T_l \quad [25]$$

Again, a similar equation is used for the cathode. Finally, the hardware energy balance equation is

$$\begin{aligned} H(L,M) = {} & \dot{Q}(L,M) \\ & + (L_n\lambda_n)\,\{(\Delta x)^{-2}\,[T_l(L,M+1) \\ & - 2T_l(L,M) + T_l(L,M-1)] \\ & + (\Delta y)^{-2}\,[T_l(L+1,M) - 2T_l(L,M) \\ & + T_l(L-1,M)]\} \quad (L,M = 1,\ldots,N) \end{aligned} \quad [26]$$

where H denotes the collection of terms

$$H = A_a\bar{h}_a(T_l - T_{ma}) + A_c\bar{h}_c(T_l - T_{mc}) \quad [27]$$

For co- and counterflow geometries only a one-dimensional treatment is required.

Boundary conditions.—Insulating boundary conditions are used for the cell edges ($T_l(0,M) = T(2,M)$ etc.), and the cathode gas temperature is fixed at a constant value T_c° along the inlet edge. In principle, the anode stream should be treated similarly, but difficulties arise in practice if this is done. The need for high fuel utilization results in a slowly flowing anode stream whose effective heat capacity is much smaller than the cathode's. As a consequence, the anode gas heats rapidly from its cool inlet temperature to within a few degrees of cell temperature over a small fraction of the gas channel length. In order to accommodate accurately this small length-scale phenomenon on the coarse numerical mesh (10×10) used in practical calculations, the anode stream temperature is set equal to the cell temperature at the anode inlet edge and the power needed to heat the incoming gas from its true inlet temperature T_{ma}° to the cell edge temperature is subtracted from $\dot{Q}$ at the anode inlet edge. That is, $\dot{Q}(L,1)$ in Eq. [26] is replaced by $\dot{Q}(L,1) - n_a^\circ c_{pa}(T_{ma}(L,1) - T_{ma}^\circ)/(\Delta x/2)$, where the factor of 2 appears because edge quantities represent averages over a half-interval. Detailed numerical studies show that the resulting error in the cell edge temperature is at most 10 K, which is inconsequential for performance predictions. Overall gas stream energy balance is satisfied to better than 0.2% in all calculations to date.

Mesh size and execution speed.—For crossflow, use of an $N \times N$ mesh requires the solution of $3N^2$ temperature equations. To hold execution time to reasonable values, the choice $N = 10$ was made. A typical point on a constant utilization V *vs.* j curve for crossflow takes about 15 cpu minutes on our Prime 400 computer.

Because co- and counterflow geometries require only one-dimensional treatment, much finer meshes can be used. Results calculated for $N = 37$ and 100 were virtually identical. Results for $N = 10$ were also in good overall agreement with those for the finer meshes, although peak temperatures were found to be low by roughly 10 K. A typical calculation of current density for prescribed utilizations takes about 5-10 cpu minutes ($N = 37$).

Calculations with constant flow rates are accomplished more quickly regardless of flow geometry.

Calculation with prescribed fuel and oxidant utilizations.—In the numerical procedure outlined in the previous section inlet gas flow rates are specified, and fuel and oxidant flow rates emerge as outputs. It is straightforward to compute cell performance at prescribed utilizations, although considerably more computational effort is required. With one flow rate varied at a time, utilization varies monotonically with inlet flow rate, so that no convergence problems are encountered. The secant method for finding roots is used.

It is worth mentioning that performance curves based on constant utilization never attain the open-circuit voltage based on inlet gas composition; the cell operating voltage can never exceed the minimum local open-circuit voltage at any point in the cell, which will be based on maximum gas stream utilization (roughly speaking). In a numerical calculation, it is necessary to verify that this condition has been satisfied in order to ensure that a physically reasonable cell operating voltage has been prescribed.

Comparison with Experimental Results

A number of performance curves have been measured at IGT (10) on 94 cm² isothermal cells for a variety of fuel and oxidant mixtures, pressures, and temperatures. Our calculated results are compared with these data in Fig. 1, 2, and 3. None of the electrode model parameters (1) were changed in computing the curves shown in these figures. Because measured cell resistances vary from run to run, the tile thickness t in Eq. [12] is chosen so that measured

and calculated resistances agree. We emphasize that t is adjusted not to give agreement between predicted and observed cell performance, but between calculated and measured cell resistance.

In Fig. 1 we plot performance at constant utilization (75% H_2, 50% CO_2) at 923 K for three different fuel and oxidant combinations. To roughly bracket the performance range, we compared high and low BTU fuel mixtures against the standard oxidant, and we considered the low BTU fuel with the noble oxidant. Precise gas compositions are given in Table II. All three curves were calculated with CH_4 inert but with water-gas shift equilibrium maintained. In general, considering that no electrode model parameter adjustments were made, the agreement is very good.

In Fig. 2 we compare calculated gains in performance with increased pressure for the high BTU fuel with standard oxidant. In contrast to the curves in the preceding figure, these curves and data are for constant inlet gas flow rates. The flow rates were set to achieve 75% H_2 and 50% CO_2 utilization at 200 mA/cm^2. Again we see that agreement is very good over the entire range. The cell on which these data were taken had a measured resistance of about 4.6 mΩ at 5 atm and 5.2 mΩ at 10 atm, so we accordingly adjusted our tile thickness to 0.60 cm at 5 atm and to 0.68 cm at 10 atm in order to increase calculated cell resistance to about these levels. The symbol • denotes a data point taken from the constant utilization curve (75% H_2, 50% CO_2) for this cell at 1 atm. The increase in performance is evident.

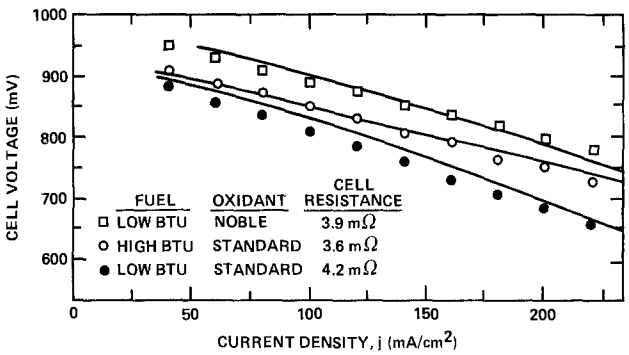

Fig. 1. Calculated (———) and measured (□, ○, ●) cell performance at constant 75% H_2 and 50% CO_2 utilization, 1 atm, and 923 K for various fuel-oxidant combinations. [Measurements from Ref. (10).] Calculations made with fuel gas in shift equilibrium, but with CH_4 inert; effective tile thicknesses used in calculations: 0.47 cm (3.6 mΩ), 0.51 cm (3.9 mΩ), 0.55 cm (4.2 mΩ).

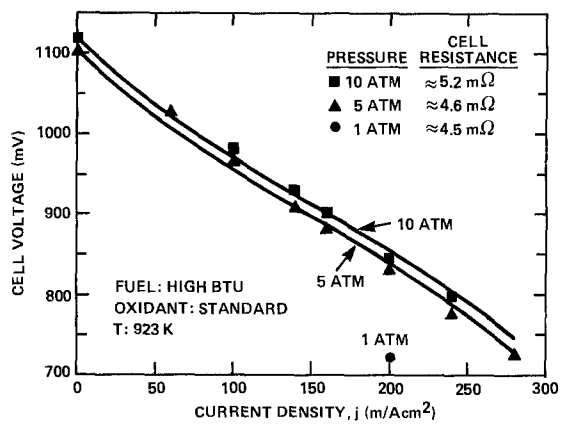

Fig. 2. Effects of pressure on constant flow rate polarization. Calculated (———), measured (■, ▲, ●). [Measurements from Ref. (10).] Flow rates set to achieve 75% H_2 and 50% CO_2 utilization at 200 mA/cm^2. Fuel gas in shift equilibrium. Effective tile thicknesses used in calculations: 0.60 cm (4.6 mΩ), 0.68 cm (5.2 mΩ).

Table II. Fuel and oxidant gas compositions used in performance calculations. All fuel compositions are in water-gas shift equilibrium at 923 K. Fuel compositions at different temperatures were obtained by putting the listed composition into shift equilibrium at the required temperature.

Fuel	H_2	CO_2	H_2O	CO	N_2
	(mol percent)				
Low BTU-air blown gasifier output	18.6	11.4	7.8	14.0	48.2
High BTU-methane steam	60.0	7.4	22.6	10.0	0.0

Oxidant	O_2	CO_2	N_2	H_2O
	(mol percent)			
Standard	14.6	29.1	53.4	2.9
Noble	32.0	65.0	0.0	3.0

The theoretical gains in cell open-circuit potential at 923 K for 5 and 10 atm are 32 and 46 mV. Our calculated gains in IR-free cell voltage at 200 mA/cm^2 are 96 and 126 mV. These are roughly triple the Nernst gains and are in good agreement with what is observed. In addition to the purely thermodynamic gains, this extra performance arises principally from reduced activation overpotential via increased exchange current densities with pressure and from decreased concentration overpotential at the anode as limiting currents increase with pressure (solubility). (Concentration overpotential at the cathode is calculated to be small in our model.)

In Fig. 3 calculated effects of temperature on cell voltage are compared with measurements on a cell using high BTU fuel and standard oxidant. The calculated curve shows a somewhat higher performance level than that measured at low temperatures, but agrees reasonably well at higher temperatures. Our model has three principal sources of temperature dependence: cell resistance, open-circuit potential, and the Butler-Volmer equations used in the electrode models (1). The temperature dependence of the cell resistance agrees well with that measured at IGT (10). The open-circuit potential is rigorously prescribed by simple thermodynamic calculations. This leaves the temperature dependence of the electrode kinetics as the prime focus for improving the model.

The parameter values used for these calculations were identical to those used for the high BTU fuel case plotted in Fig. 1. Because the temperature and gas composition dependence are only weakly coupled, it seems unnecessary to make further comparisons of the temperature dependence with other gas mixtures, particularly since we have convincingly demonstrated the model's capability to predict isothermal composition dependence.

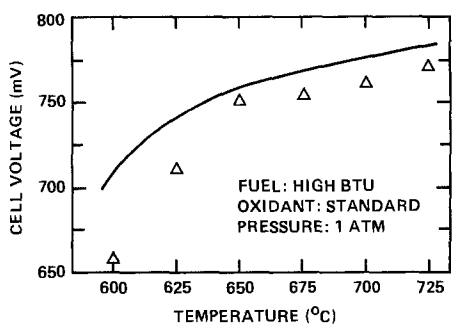

Fig. 3. Effects of temperature on cell voltage at 200 mA/cm^2, 75% H_2 and 50% CO_2 utilization. Calculated (———), measured (▲). [Measurements from Ref. (10).] Fuel gas in shift equilibrium. Effective tile thickness used varies from 0.50 cm at 600°C to 0.46 cm at 725°C.

Operating Characteristics of Nonisothermal Cells

In this section we examine the essential features of computed nonisothermal cell current density and temperature distributions. The discussion primarily concerns cells with crossflow geometry because complex two-dimensional distributions arise for this case. The one-dimensional distributions characteristic of cells with co- and counterflow geometries are simpler and do not require such extensive description. They are briefly treated at the end of this section. In another article (11), we discuss several other examples of nonisothermal cell behavior.

Effect of utilization.—In cells operating with high gas stream utilizations, current density distributions can become extremely nonuniform solely because of changes in gas stream composition. Utilization effects are especially pronounced at high cell voltage where the difference between the local open-circuit potential and cell voltage may not vary substantially over much of the cell; variations in local open-circuit potential then have increased leverage on current density via the potential balance relation, Eq. [11]. Variations in cell temperature tend to moderate utilization effects, so that the most severe current maldistribution is seen in isothermal cells.

The current density distribution presented in Fig. 4 exemplifies the effect of high utilization in cells with crossflow geometry. The calculation corresponds to an isothermal cell with fuel and oxidant utilizations 75% and 50%, respectively. Cell voltage is 0.875V, which is about 25 mV less than the maximum attainable voltage under these conditions. Operating conditions are those of Fig. 1 for high BTU fuel. Maximum current density is achieved at the inlet corner, where both gas streams are fresh. Minimum current densities are achieved at the anode outlet/cathode inlet corner, and at the anode inlet/cathode outlet corner and not (as might be expected) at the anode outlet/cathode outlet corner. The substantial depletion that occurs as either gas stream traverses the high current density region in the vicinity of the inlet corner is responsible for this effect.

Effect of nonisothermal operation.—With incorporation of heat transfer effects, cell temperature distributions in large cells (≈ 1 m^2) become severely nonisothermal, and corresponding distributions of current density differ substantially from their isothermal counterparts. Typical examples of nonisothermal operation

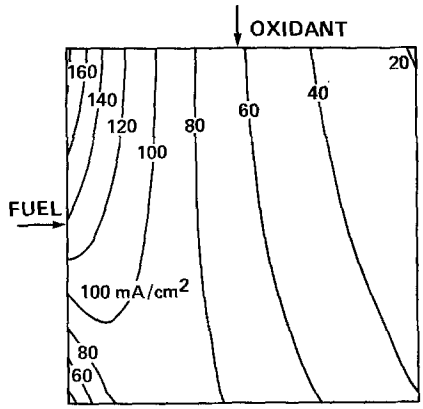

Fig. 4. Calculated current density distribution for isothermal cell. $T = 923°$, $p = 1$ atm, $V = 0.875$V, $j_{avg} = 71$ mA/cm^2. High BTU fuel maintained in water-gas shift equilibrium, but with CH_4 inert. Standard oxidant.

with crossflow geometry are presented in Fig. 5 for 1 m^2 cells. In these figures, calculated distributions of current density and cell temperature are presented for three cell voltages separated by 100 mV increments. These examples were arbitrarily chosen to illustrate major features of nonisothermal operation that remain qualitatively similar for all of the cases investigated. These features can be identified as follows:

1. The nonisothermal current density distribution is more uniform than its isothermal counterpart. In an approximate sense nonisothermal operation tends to offset nonuniformities due to utilization effects; utilization effects tend to move maximum current densities toward the gas stream inlets, whereas convective heating of the gas streams tends to move maxima toward regions of high temperature at the gas stream outlets.

2. A pronounced ridge of maximum cell temperatures runs approximately down the center of the cell, with peak temperatures appearing at the cathode outlet side. In a separate calculation in which the full temperature dependence of the local current density was not considered and inplane heat conduction was neglected, this maximum was also observed (somewhat closer to the anode inlet) although the distribution of current densities was substantially different. This indicates that the presence of this temperature maximum is attributable primarily to convective heat

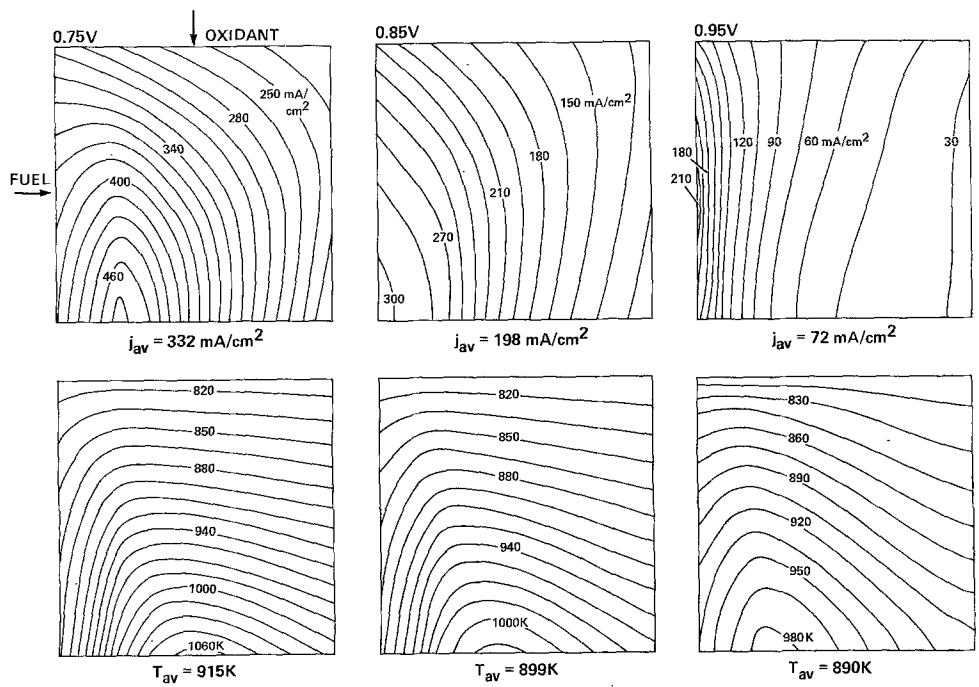

Fig. 5. Calculated distributions of current density and cell temperature for 1 m^2 nonisothermal cell with crossflow geometry corresponding to points on a constant utilization (75% fuel, 25% oxidant) performance curve. Fuel: low BTU with shift equilibrium. Oxidant: standard. Inlet gas temperatures: 800 K. $Z^{923} = 0.5$ Ωcm^2.

transfer in the gas streams, and only secondarily to nonuniformities in the current density distribution. The temperature maximum arises in the anode inlet region because here the thermal conductivity of the fresh (hydrogen-rich) anode gas is high relative to the cathode stream, and its effective heat capacity is low. High gas conductivity causes most of the heat generated in the anode inlet region to be absorbed by the anode stream, low heat capacity gives rise to steep temperature gradients in the streamwise direction. Farther downstream the cell and the anode stream lose heat to the cathode stream, which is slightly cooler by virtue of its high effective heat capacity and because it has traversed the region of relatively low current density/heat release far downstream of the anode inlet.

3. Maximum current densities are approximately coincident with maximum cell temperatures, although utilization effects tend to move the location of maximum current densities upstream in the gas flow directions, particularly at high cell voltage (see "Effect of utilization," above). The net effect of high local cell temperature is to increase current density, although this effect is partially offset by a decrease in the local open-circuit voltage caused by the reduction of $E°$ with increasing temperature. This mutual dependence of current density and temperature might appear to give rise to an instability, but inplane conduction can be shown to have a stabilizing influence.. This effect is most easily seen by considering transient response to local nonuniformities. A local hot spot increases temperature, hence current density in the adjacent cell area. Increased current density upstream in the gas flows reduces local current density due to gas stream depletion. Also, high local current densities deplete the gas flows downstream, reducing downstream current densities, hence downstream heat release and temperature, which reduces local temperature due to increased inplane heat conduction.

4. As expected, average cell temperature is diminished at high voltage because low current densities result in smaller heat release. For the present case of equal inlet gas stream temperatures, the cell tends toward isothermal operation, so that utilization effects begin to become more significant in this regime.

Comparison of flow geometries.—To provide some comparison among the various flow geometries, cell performance was calculated at 0.85V using co- and counterflow geometries, with utilizations and inlet gas temperatures and compositions held equal to the conditions of Fig. 5. Resulting distributions of current density and cell temperatures are shown in Fig. 6. Additional comparisons are given elsewhere (11).

Average computed current densities at 0.85V were 189, 198, and 227 mA/cm^2 for co-, cross-, and counterflow, respectively. These results can be used to give a relative measure of performance efficiency (on a voltage basis) by realizing that performance curves at constant utilization are approximately parallel in the neighborhood of these computed current densities. By extrapolation to points of equal average current density, we see that operating cell voltage and, hence, efficiency increase in the order cited above.

In a separate calculation (not shown) of isothermal performance of cross-, co-, and counterflow cells, it was found that average current densities vary only slightly among the three geometries. We may conclude from this observation that utilization effects are unimportant in a comparison of relative efficiencies, but that thermal effects play a dominant role. It is not surprising, then, that average cell temperatures for co-, cross-, and counterflow are 888, 899, and 935 K, respectively, corresponding to the relative ranking of cell performance.

With coflow geometry, a maximum in current density occurs in the vicinity of inlet, where both gas

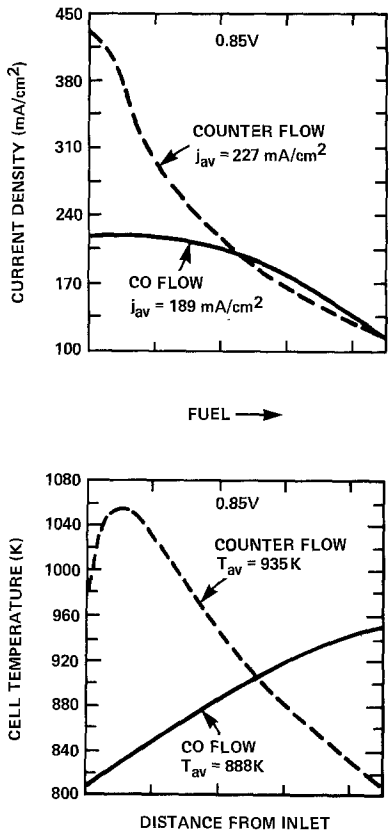

Fig. 6. Calculated distributions of current density and cell temperature at $V = 0.85V$ for 1 m^2 nonisothermal cell with coflow (———) and counterflow (– – –) geometry. Utilizations: 75% fuel, 25% oxidant. Fuel: low BTU with shift equilibrium. Oxidant: standard. Inlet gas temperatures: 800 K. $Z^{923} = 0.5$ Ωcm^2.

streams are fresh. Cell temperatures are seen to increase monotonically in the direction of gas flow. This helps maintain high current density as the gas streams become depleted. With counterflow geometry, the fresh anode inlet and hot cathode outlet coincide, giving rise to pronounced current density and temperature maxima. The temperature maximum is displaced slightly from the cell edge because the low anode inlet gas temperature (relative to average cell temperature) reduces the local edge temperature.

Conclusions

Our model accounts for utilization of fuel and oxidant gases with or without gas phase equilibria under isothermal and nonisothermal operating conditions. In order to predict cell performance under nonisothermal conditions, the coupling between the current density and temperature distributions must be accounted for. This is accomplished through treatment of conductive heat transfer between cell hardware and gas streams, energy transfer accompanying mass addition to the bulk streams from electrochemical reactions, convective heat transfer by the bulk streams, and in-plane heat conduction through the cell hardware.

Predicted isothermal cell performance agrees well with that measured experimentally using crossflow geometry for various fuel and oxidant compositions, total gas pressures, and cell temperatures. The only parameter varied in these calculations was the effective tile thickness, in order to bring measured and calculated cell resistances into agreement. This is a reasonable adjustment to make because measured resistances vary irregularly from cell to cell and from run to run. On the basis of these results, it appears that our model has attained high predictive capability in calculating cell performance.

Nonisothermal performance of 1 m^2 cells with cross-flow geometry was predicted for a variety of operating conditions. In general, the cell temperature distribution deviates from an isothermal distribution most strongly at lower voltages. Current density distributions in nonisothermal cells are generally more uniform than in isothermal cells. The current density distribution is coupled to the temperature distribution; current densities are maximized in and near regions of high temperature. Cells will have to be run at low ($\approx 25\%$) cathode utilizations to avoid the occurrence of local extreme temperature maxima (> 1100 K) that are very detrimental to cell life.

A limited comparison of various flow geometries was accomplished by evaluating performance of 1 m^2 cross-, co-, and counterflow cells at a prescribed set of operating conditions (fuel and oxidant utilizations, voltage, inlet gas compositions, and temperatures). The best performance was achieved with counterflow geometry, followed by cross- and coflow, respectively. More severe temperature gradients and higher peak temperatures were observed in cross- and counterflow than in coflow.

Acknowledgments

We thank D. Bloomfield, M. Finson, A. Gelb, P. F. Lewis, E. Pugh, and K. L. Wray for helpful discussions. This work was supported by the U.S. Department of Energy under Contract No. DE-AC-03-79ET11322 and by Argonne National Laboratory (under DOE Contract No. 31-109-Eng-38).

Manuscript submitted June 23, 1981; revised manuscript received *ca.* July 14, 1982. This was Paper 140 presented at the Los Angeles, California, Meeting of the Society, Oct. 14-19, 1979.

Any discussion of this paper will appear in a Discussion Section to be published in the December 1983 JOURNAL. All discussions for the December 1983 Discussion Section should be submitted by Aug. 1, 1983.

Publication costs of this article were assisted by Physical Sciences Incorporated.

REFERENCES

1. G. Wilemski, *This Journal*, **130**, 117 (1983).
2. V. Sampath, A. F. Sammells, and J. R. Selman, *ibid.*, **127**, 79 (1980).
3. C. A. Reiser, C. R. Schroll, S. J. Szymanski, and R. F. Buswell, in Abstracts of the National Fuel Cell Seminar, Bethesda, MD, p. 130 (1979).
4. F. Kreith, "Principles of Heat Transfer," Intext Press, New York (1973).
5. R. C. Reid, J. M. Prausnitz, and T. K. Sherwood, "The Properties of Gases and Liquids," McGraw-Hill Book Co., New York (1977).
6. T. L. Wolf, N. H. Kemp, and G. Wilemski, In preparation.
7. T. Jacobsen and G. H. J. Broers, *This Journal*, **124**, 207, 210 (1977); G. Wilemski, *J. Chem. Phys.*, **72**, 369 (1980) and in "Second International Symposium on Molten Salts," J. Braunstein and J. R. Selman, Editors, The Electrochemical Society Softbound Proceedings Series, Pennington, NJ (1981).
8. W. M. Kays and A. L. London, "Convective Heat and Mass Transfer," McGraw-Hill Book Co., New York (1965).
9. T. Wolf, W. J. Robins, and G. Wilemski, "Code Documentation for Molten Carbonate Fuel Cell," TR-194, Physical Sciences Inc., Woburn, MA (1979).
10. "Fuel Cell Research on Second Generation Molten-Carbonate Systems," Vol. I, Project 8984 Final Status Report, Institute of Gas Technology, Chicago, IL (1977).
11. G. Wilemski, A. Gelb, and T. L. Wolf, in "Symposium on Molten Carbonate Fuel Cell Technology," J. R. Selman and T. Claar, Editors, The Electrochemical Society Softbound Proceedings Series, To be published.

Electrochemical Solar Cells Using CdSe Thin Film Electrodes

Xu-Rui Xiao[1] and H. Ti Tien

Department of Biophysics, Michigan State University, East Lansing, Michigan 48824

ABSTRACT

Electrochemical photocells consisting of a CdSe thin film anode and a Pt cathode immersed in 1M Na_2S-NaOH-S solution have been studied. CdSe thin films were formed on Ti, Cr, Mo, SnO_2, glassy carbon, and graphite substrates by coating an aqueous mixture of CdSe, $ZnCl_2$, and surfactant, subsequently sintering at 400°-500°C in air. The current-voltage (I-V) relations, output power efficiency, open-circuit voltage, and short-circuit current were measured. 7% power conversion efficiency was obtained at 20 mW/cm^2 light intensity after photoetching. The monochromatic I-V curves were analyzed.

A variety of electrochemical photocells have been investigated for transducing solar energy into electricity [for reviews see Ref. (1-5)]. For practical applications, such cells must be competitive with solid-state photovoltaic devices. Although as yet no practical electrochemical photocells have been developed, several photoelectrochemical (PEC) cells appear to be promising (6-8). Among these is the CdSe-based cell studied by a number of workers (9-11). The properties of direct optical transitions and suitable band-gap energy (1.7 eV) of CdSe offer the possibility of higher conversion power efficiency. Another advantage of CdSe is that it is capable of being formed as thin film electrodes by various methods with high power efficiency and at low cost. To date, the power conversion efficiency of some thin film Cd(Se, Te) photocells is approaching that of single crystal solar cells (12).

In this paper we report the results of CdSe thin film electrodes formed on various substrates using the painting method (13). This technique which has been used to manufacture film-type electronic circuit elements such as resistors, capacitors, transistors (14) has been applied by Hodes and his colleagues to prepare thin film electrodes for photoelectrochemical cells (13, 15). The painting method is simple, inexpensive, and potentially feasible to fabricate large electrode areas. To prepare a thin film electrode, an appropriate substrate has to be chosen to receive the photoactive semiconducting layer. The substrate should be a passive and good conducting material with good film adherence. It should also be stable during fabrication processes and withstand post heat-treatment. We have prepared the CdSe thin film on metal substrates such as Ti, Cr, Mo, and nonmetal substrates SnO_2, glassy

[1] Permanent address: Institute of Photographic Chemistry, Academia Sinica, Beijing, China.

Key words: photoelectrochemistry, electrochemical cells, energy conversion, thin film electrodes, photoanodes.

carbon, and pyrolytic graphite by a simple procedure and examined the photoelectrochemical and physical characteristics of these film electrodes.

Experimental

The CdSe thin films were prepared by coating a slurry containing 50 mg CdSe powder (99.999%, Alfa Chemical Company), 2% $ZnCl_2$ (analyzed reagent, Baker), and 50 μl of 5% Triton X-100 aqueous solution on a substrate surface such as Ti, Mo, Cr, SnO_2, glassy carbon, or pyrolytic graphite (usually a sheet of 0.5 cm^2, with a thickness 0.2 mm for Ti, 0.25 mm for Mo, 1 mm for Cr, 2.5 mm for glassy carbon, 3 mm for pyrolytic graphite, and 3 mm for a glass substrate coated with 1.5 μm SnO_2. After drying in air the semiconducting CdSe layer was activated by heat-treatment at 400°-500°C for 30-60 min in air. After cooling to room temperature, an adherent CdSe film electrode was obtained with film thickness ~20 μm, as determined by scanning electron microscope (SEM). Lead wires were attached to the electrode in the usual manner. Chemical etching and photoetching were employed for the film electrode before testing. Chemical etching consisted of dipping the electrode in 2% HNO_3 aqueous solution for 2-3 sec followed by rinsing with distilled water. Photoetching was performed under illumination with 75 mW/cm^2 intensity of white light by connecting the CdSe film electrode to a carbon electrode (2 cm^2) in 1M $ZnCl_2$ aqueous solution (pH = 1.5) for a few minutes, then rinsing with distilled water. The cell was constructed with a CdSe film electrode as photoanode and a platinum electrode (1 cm^2) as counterelectrode. A saturated calomel electrode (SCE) was used as reference electrode for potential measurements. The electrolyte was composed of 1M Na_2S, 1M NaOH, and 1M S. Nitrogen was bubbled into the solution continually during tests.

The current-potential measurements were carried out by cyclic voltammetry (Model CV-1B, Bioanalytical Systems, Incorporated) at a scan rate of 25 mV/sec and recorded on an X-Y recorder (Houston Instruments). The short-circuit current (I_{sc}), open-circuit voltage (V_{oc}), and conversion power were measured with a Keithley Model 177 Microvolt Electrometer in conjunction with a decade resistance box. A 500W tungsten lamp was used as light source.

Results and Discussion

Figure 1 shows the representative photocurrent-potential curves for CdSe thin films coated on Mo substrates and subjected to heat-treatment at several temperatures. It was found that the optimum heat-treatment condition for most of the substrates used (except chromium) was 1 hr at 500°C. When the temperature was either lower or higher than 500°C, the photocurrent was reduced at the potential sweep ranging from −1.3 to −0.6V as shown in Fig. 1. The film tended to peel off if the heat-treatment was carried out at 600°C for longer than 30 min. For Cr substrates the temperature had to be about 400°C. At higher temperatures a blue oxide film with high resistance was formed on the Cr substrate surface, which reduced the photocurrent of the CdSe electrode significantly. Figure 2 shows SEM photographs of the thickness and surface of CdSe thin film electrodes on Ti substrate before etching.

The photocurrent-potential (I-V) behavior of CdSe electrode coated on various substrates and the power conversion performance of these thin film electrode-based PEC cells are shown in Fig. 3 and Fig. 4, respectively. These data were obtained after etching the electrodes in 2% HNO_3 for 2-3 sec. The I-V curves shown in Fig. 3 were obtained by potential scanning over the range −1.3 to −0.6V *vs.* SCE. There are six curves in Fig. 3 corresponding to the different substrates. In each case, a clear trend in the I-V behavior is noted. No anodic dark current was observed over the scanned

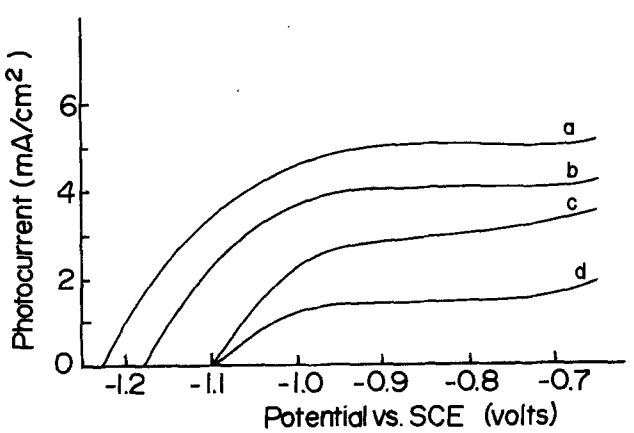

Fig. 1. Photocurrent vs. applied potential for CdSe thin film electrodes annealed at different temperatures on Mo substrate. (a) 500°C, 1 hr; (b) 400°C, 1 hr; (c) 600°C, 5 min; (d) 600°C, 30 min. The film electrodes were etched in 2% HNO_3 for 2-3 sec before measurements. Irradiance: 50 mW/cm^2.

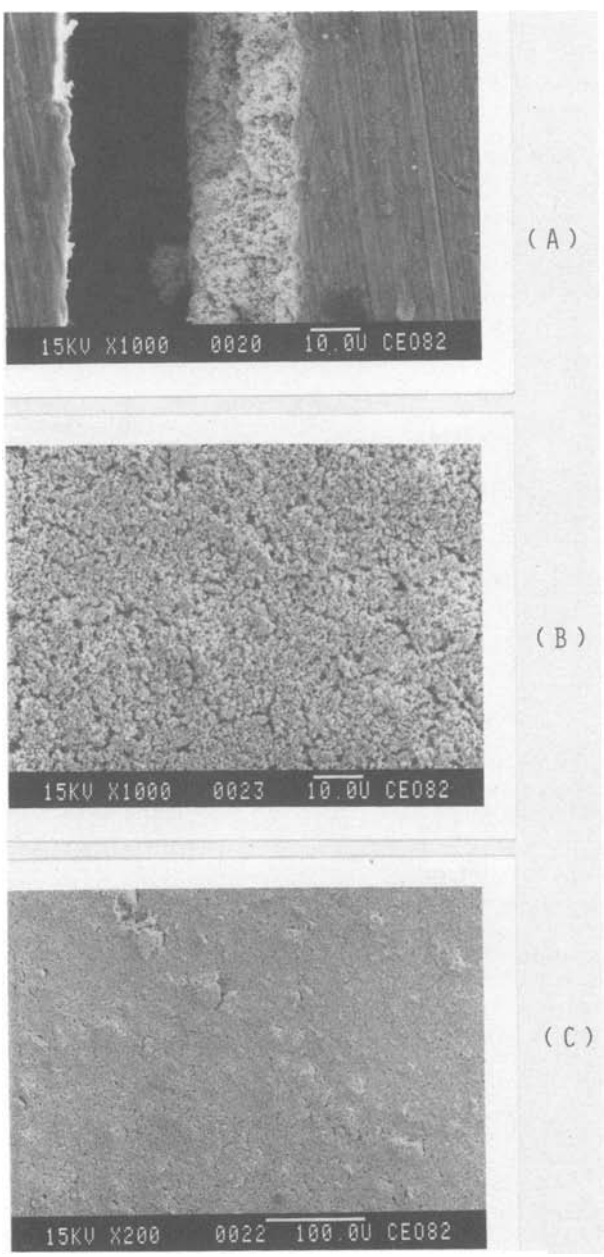

Fig. 2. Scanning electron micrographs of CdSe thin film electrode on Ti before etching (a) the thickness of thin film, (b), (c) two magnifications of the surface of thin film.

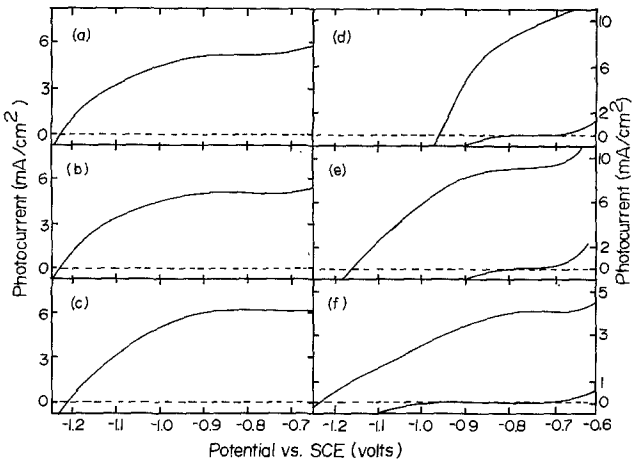

Fig. 3. Photocurrent *vs.* applied potential of CdSe thin film electrodes on Ti, Mo, Cr, SnO_2, glassy carbon, and graphite substrates. Irradiance: 50 mW/cm² (a) Cr, (b) Mo, (c) Ti, (b) SnO_2, (e) graphite, (f) glassy carbon. In each case, the electrode was etched in 2% HNO_3 for 2-3 sec before testing.

potential range, but a large cathodic current flow was detected at more negative potentials. Additionally, an anodic dark current was present at more positive potentials for film electrodes on glassy carbon and pyrolytic graphite substrates. The onset of anodic photocurrent was at -1.23 ± 0.05 *vs.* SCE, which is the estimation of the flatband potential. Table I gives the data of open-circuit voltage, short-circuit current of various CdSe thin film electrodes.

The energy conversion performance of CdSe thin film electrodes on various substrates is illustrated in Fig. 4. To measure the optical to electrical energy conversion power a variable decade resistance was used as an electrical load which was connected in series with

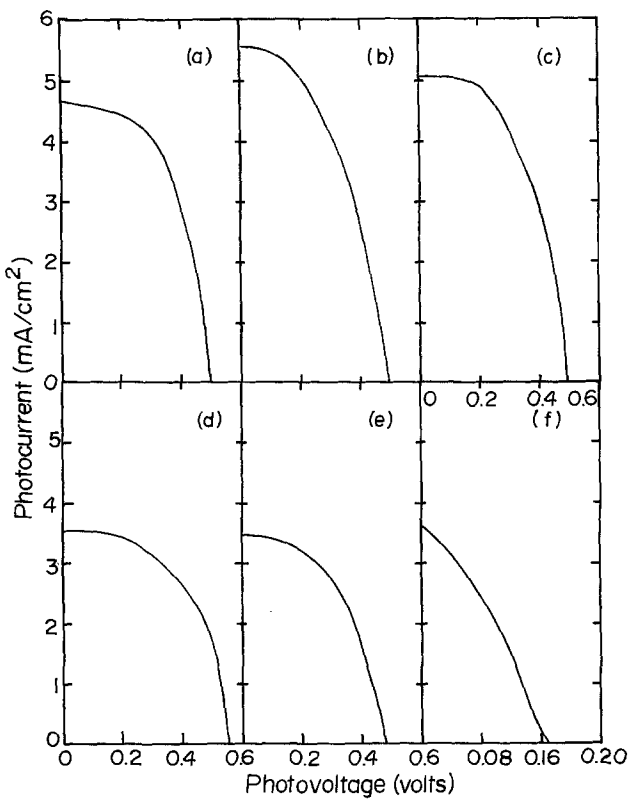

Fig. 4. Output power curves of CdSe thin film electrodes on Ti, Mo, Cr, SnO_2, glassy carbon, and graphite substrates. Incident light intensity is 20 mW/cm². The electrodes were etched in 2% HNO_3 for 2-3 sec before testing. (a) Cr, (b) Mo, (c) graphite, (d) Ti, (e) glassy carbon, (f) SnO_2.

Table I. Open-circuit voltage (V_{oc}), short-circuit current (I_{sc}) of CdSe thin film electrode, under illumination 50 mW/cm²

Electrode	V_{oc} *vs.* SCE (mV)	I_{sc} (mA/cm²)
Mo	460	10.5
Ti	474	5.2
Cr	512	5.3
SnO_2	348	2.3
Glassy-carbon	505	4.0
Graphite	402	10.8

the external circuit. The incident light intensity at the CdSe electrode surface was about 20 mW/cm². Photovoltages of the cells were measured directly by the electrometer and photocurrents calculated from the variable resistance of external circuit. The conversion power efficiency and fill factor (F.F.) were determined from the photocurrent *vs.* photovoltage curves (Fig. 4) as summarized in Table II.

It can be seen from these results that pyrolytic graphite is a good substrate for CdSe thin film electrodes. There is also an economic advantage of this low cost material over that of metal substrates. For these reasons, pyrolytic graphite may be more suitable for practical CdSe solar cell systems. The conversion efficiency is quite respectable and comparable with that of metal substrate electrodes.

Since the photoresponse of CdSe electrodes can be improved considerably by chemical etching and subsequently photoetching (12, 15), we have studied the effect of both etchings on the power output of CdSe film electrode on pyrolytic graphite substrate. The results shown in Fig. 5 indicate that both the short-circuit current and open-circuit voltage are increased, resulting in an increase of conversion power efficiency from 4.6% (without chemical etching) to 6.2% (with HNO_3 etching), and to 7% (with photoetching in 1M $ZnCl_2$). Table III gives the power conversion efficiency and fill factor of several samples of CdSe thin film electrodes on pyrolytic graphite substrate before and after the etching treatment. It can be seen that the power conversion efficiency increased by 1-2%, but the fill factor remained unchanged in this case. The photoetching was performed in 1M $ZnCl_2$ (*p*H 1.5) solution and was controlled by the appearance of the dark blue color on the CdSe film surface. The solution was selected as electrolyte for photoetching as it is more favorable than strong acid solutions such as H_2SO_4 or

Table II. Energy conversion power efficiency of CdSe thin film electrode based PEC cells (incident light intensity 20 mW/cm²)

Substrate of electrode	Power efficiency (%)	Fill factor (F.F.)
Mo	6.2	0.46
Ti	5.3	0.69
Cr	6.3	0.56
SnO_2	1.3	0.43
Glassy carbon	4.2	0.15
Graphite	6.2	0.50

Table III. The effect of surface etching on CdSe thin film electrodes (pyrolytic graphite substrate) on the power conversion efficiency (incident light intensity 20 mW/cm²)

Sample	Conversion power efficiency (%)			Fill factor (F.F)		
	No etching	2% NHO_3 etching	1M $ZnCl_2$ photoetching	No etching	2% HNO_3 etching	1M $ZnCl_2$ photoetching
1	4.0	5.5	6.2	0.50	0.51	0.47
2	5.6	5.9	6.4	0.49	0.51	0.50
3	4.5	6.1	6.5	0.50	0.52	0.50
4	4.5	5.0	5.7	0.51	0.52	0.52
5	3.7	3.9	5.0	0.44	0.45	0.51
6	4.6	6.2	7.0	0.48	0.50	0.49

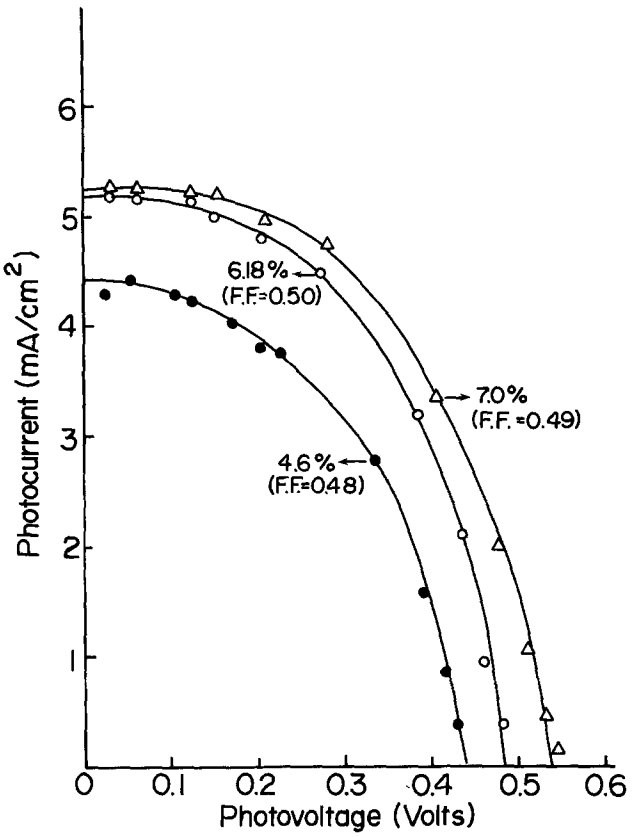

Fig. 5. The effect of surface etching on output conversion power of CdSe thin film electrodes on graphite substrate at 20 mW/cm² incident light intensity: (●) without surface etching, (○) surface etching in 2% HNO_3 2-3 sec, (△) photoetching in 1M $ZnCl_2$ (pH = 1.5) ≃ 3 min.

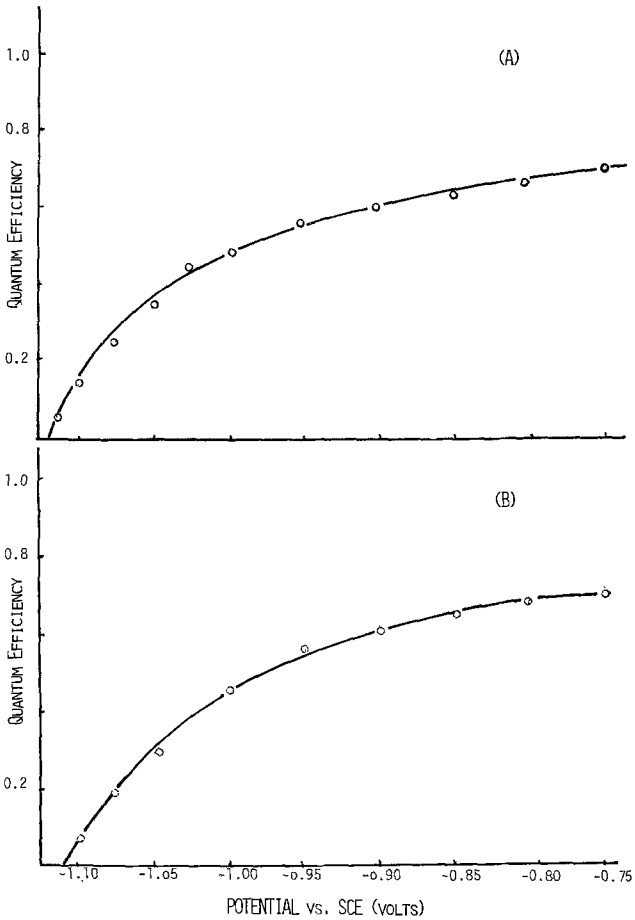

Fig. 6. Plots of quantum efficiency of CdSe thin film electrodes on graphite substrate as a function of applied potential at monochromatic light 650 nm wavelength. The two solid lines in (A) and (B) are the computer fitting curves of two electrodes A and B, respectively, using Butler equation and the experimental data. Points (○) are experimental data of these two electrode after chemical etching in 2% HNO_3 2-3 sec.

HCl. Undoubtedly, the power efficiency was improved and the deterioration of the thin film was avoided during photoetching.

In order to understand better the characteristic of this CdSe film electrode, we have applied the Butler equation (17) to our system. Equation [1] is based on the assumption that the semiconductor-electrolyte interface is a Schottky barrier. The equation, describing the dependence of photocurrent (J) on applied potential (V), flatband potential (V_{FB}), diffusion length (L_p), optical absorption (α), and depletion width (W_o), may be expressed as follows

$$J = qN\left[1 - \left\{\frac{\exp\left[-\alpha W_o (V - V_{FB})^{1/2}\right]}{1 + \alpha L_p}\right\}\right]$$

where α is the absorption coefficient at the wavelength of monochromatic light, q is the electronic charge, N is the number of incident photons. A nonlinear least squares computer program (Kinfit) was used to solve the equation and to fit the experimental photocurrent-potential data obtained by monochromatic light at the wavelength of 650 nm by using the experimental parameters N and V_{FB} (the potential of the onset of anodic photocurrent in the I-V curves). α was taken from the data given by Parsons *et al.* (16). L_p and W_o were adjusted until the calculated value approached the experimental results.

The experimental data and the theoretical curves of the two samples are shown in Fig. 6. There is a good agreement between the experimental points and theoretical curves. The adjustable parameters L_p and W_o are given in the final results of the curve fitting program. Table IV presents the data of two electrodes. These parameters can be used to characterize the CdSe thin film electrodes. Hole diffusion length is quite small compared to the depletion layer, implying that the photoresponse of this electrode is caused by the carriers generated in the depletion layer, and any decrease in power efficiency is due primarily to the recombination of photo-generated carriers within the depletion layer. For direct bandgap semiconductor with short absorption length, the requirement of depletion layer is not severe. In this case, the larger carrier density is profitable for maximizing the efficiency of semiconductor by lowering the resistivity. From Table IV which shows the width of the depletion layer obtained for this electrode, one can estimate the carrier density which is in the order of 10^{13} cm^{-3}. This indicates that the CdSe thin film electrode here is characterized by low carrier density and high resistivity, which results in a considerable resistive loss and consequently reduces overall efficiency. In order to improve the power efficiency, it is necessary to minimize the resistive losses. We have also examined the doping of Cu and Li and the annealing of CdSe film in Se atmosphere which were expected to introduce acceptor-like impurities and Cd-vacancies in CdSe lattice for decreasing the resistivity and raising the photosensitivity (19). However, these efforts were not successful. The thin films peeled off after annealing in Se atmosphere. Probably a variety of recombination cen-

Table IV. L_p and W_o of two CdSe thin film electrodes on pyrolytic graphite substrate

	L_p (μm)	W_o (μm)
Electrode A (Fig. 6 a)	0.030	6.1
Electrode B (Fig. 6 b)	0.038	6.8

ters in the depletion layer plays a more important role for limiting the efficiency of these types of electrodes.

In summary, CdSe thin film electrodes on various substrates (Ti, Cr, Mo, SnO_2, glassy carbon, and pyrolytic graphite) have been fabricated successfully by a simple painting method and tested as photoanodes in the following cell arrangement: CdSe(substrate)/Na_2S, NaOH, S (all 1M)/Pt. CdSe thin films on pyrolytic graphite electrodes were studied in some detail, and showed good stability and power conversion efficiency for possible practical use. From the I-V curves of these electrochemical photocells, the results are analyzed in terms of a Schottky barrier model. A good agreement has been found between the model and experimental data.

Acknowledgments

This work was supported by a grant (DE-FG02-80CS83101) from the Department of Energy.

Manuscript submitted March 26, 1982; revised manuscript received July 22, 1982.

Any discussion of this paper will appear in a Discussion Section to be published in the December 1983 JOURNAL. All discussions for the December 1983 Discussion Section should be submitted by Aug. 1, 1983.

Publication costs of this article were assisted by the Michigan State University.

REFERENCES

1. J. R. Bolton, Editor, "Solar Power and Fuels," Academic Press, New York (1977).
2. K. Rajeshwar, P. Singh, and J. DuBow, *Electrochim. Acta*, **23**, 1117 (1978).
3. H. Gerischer, *Top. in Appl. Phys.*, **31**, 115 (1979).
4. R. Hautala, R. B. King, and C. Kutal, Editors, "Solar Energy: Chemical Conversion and Storage," The Humana Press, Inc., Clifton, NJ (1979).
5. F. Cardon, W. P. Gomes, and W. Dekeyser, Editors, "Photovoltaic and Photoelectrochemical Solar Energy Conversion," Plenum Press, New York (1981).
6. G. Hodes, J. Manassen, and D. Cahen, *Nature*, **261**, 697 (1976).
7. A. B. Ellis, S. W. Kaiser, and M. W. Wrighton, *J. Am. Chem. Soc.*, **98**, 1635 (1976).
8. A. Heller, R. G. Vadimsky, W. D. Johnston, Jr., K. E. Strege, H. J. Leamy, and B. Miller, in 15th IEEE Photovoltaic Specialists Conf., May 12-16, 1981, pp. 1-6.
9. G. Hodes, J. Manassen, and D. Cahen, *This Journal*, **127**, 544 (1980).
10. K. T. L. deSilva, D. J. Miller, and D. Haneman, *Sol. Energy Mater.*, **4**, 233 (1981).
11. U. Nashimoto, S. Fuyuki, T. Akutagawa, and S. Hayakawa, *Jpn. J. Appl. Phys.*, **20**, 565 (1981).
12. G. Hodes, *Nature*, **285**, 29 (1980).
13. G. Hodes, D. Cahen, J. Manassen, and M. David, *This Journal*, **127**, 2252 (1980).
14. Y. T. Sikvoneu, S. G. Parker, and D. R. Boyd, *ibid.*, **114**, 96 (1967).
15. R. Tenne and G. Hodes, *Appl. Phys. Lett.*, **37**, 428 (1980).
16. R. B. Parsons, W. Wardzynski, and A. D. Yoffe, *Proc. R. Soc., London, Ser. A*, **262**, 120 (1961).
17. M. A. Butler, *J. Appl. Phys.*, **48**, 1914 (1977).
18. D. Haneman, D. J. Miller, K. T. L. deSilva, and J. F. McCann, *J. Electroanal. Chem. Interfacial Electrochem.*, **118**, 101 (1981).
19. Y. Kokubun, H. Hatano, and M. Wada, *Jpn. J. Appl. Phys.*, **18**, 1947 (1979).

Preparation of Dispersed Platinum on Conductive Tin Oxide and Its Catalytic Activity for Oxygen Reduction

M. Watanabe,*,[1] S. Venkatesan,[2] and H. A. Laitinen*

Department of Chemistry, University of Florida, Gainesville, Florida 32611

ABSTRACT

An investigation was carried out to find the optimum conditions for pretreatment of SnO_2 coatings and for chemisorption from aqueous platinum solution. An alkaline pretreatment, using 10M NaOH, caused an increasing Pt uptake rate up to a limiting value that was reached after relatively short soaking at elevated temperature. A platinizing solution, containing 1000 ppm Pt(IV) + 0.135*M* Na_2HPO_4 + 0.5*M* NaCl was the most effective found so far in achieving chemisorption. Platinized electrodes were electroreduced after preheating at 200°C. Platinum analysis by RBS showed a linear increase of Pt content with platinizing time. A monolayer equivalent Pt was reached in several hours soaking at 90°C. Dispersion, defined as the ratio of surface Pt atoms determined electrochemically to total Pt atoms determined by RBS, reached very high values ($\geq$0.9) for Pt loadings of 0.2 to 1 μg/app cm^2. The prepared electrodes showed a higher activity than that of metallic platinum electrodes in catalyzing oxygen reduction in alkaline solution.

It has been demonstrated that platinized tin oxide surfaces exhibit a high catalytic activity in electrochemical oxidation of methanol (1-3). Andrew *et al.* (4) electrodeposited Pt and Sn on gold foil from $SnCl_4$ and H_2PtCl_6 and found that the catalytic activity was larger than that of electrodeposited platinum black by a factor of 50, an observation which is in agreement with an earlier study by Cathoro (5). They concluded that this increased activity was not a result of greater platinum dispersion. This conclusion is supported clearly by the results on enhancement effects by tin adatoms on catalytic activities of platinum for the oxidation of methanol, formaldehyde, formic acid, and carbon monoxide (6-8); *i.e.*, tremendous enhancement is obtained, although the adatoms never increase the surface area of platinum.

Increased catalytic activity of Pt-Sn catalysts has been observed toward reactions other than the electrochemical oxidation of organic compounds. γ-alumina-supported Pt-Sn catalysts are used as industrial reforming catalysts and have increased selectivity and stability (9). Strong interaction between group VIII metals dispersed on metal oxides, in particular those metal oxides that can be chemically reduced, and the support have been shown to make profound changes in the catalytic and chemisorption properties of the dispersed metals (10). Such an interaction, which has been postulated to involve electron transfer between substrate and metal, might be expected for tin oxide and platinum. Tseung and Dhara (11) found that the

* Electrochemical Society Active Member.
[1] Present address: Laboratory of Electrocatalysts for Fuel Cells, Faculty of Engineering, Yamanashi University, Takeda-4, Kofu, Japan
[2] Present address: Energy Conversion Devices, Incorporated, Troy, Michigan 48084.
Key words: chemisorption, electrocatalysis, antimony-doped tin oxide.

addition of small amounts of platinum to antimony-doped tin oxide electrodes significantly increases the activity toward the reduction of O_2 in 85% H_3PO_4.

It is well known now that platinum can have an extraordinary catalytic activity in the presence of tin oxide. Watanabe and Motoo have proved that monolayer catalysts on substrates have almost the same activity as bulk catalysts for the oxidation of organic compounds (8, 12-13). Atomically dispersed platinum on a tin oxide substrate may also be expected to show an activity similar to that of bulk platinum for oxygen reduction.

Whatever preparation is being used for making supported platinum catalysts in general one has to consider the relative rates of nucleation and growth. With electrochemical preparation the indications are that growth of crystallites is preferred over nucleation (14). This suggests that a monolayer equivalent of platinum would consist of widely separated crystallites as is usually observed in vapor deposition methods (15-16). An electrode platinized by thermal decomposition of platinum (II) acetylacetonate dissolved in ethylenediamine and methyl alcohol showed evidence of whisker growth and larger platinum crystals easily visible with an electron microscope (17), because of nucleation being relatively forbidden compared to growth. Therefore, it is important to seek methods that would not have those steps.

Chemisorption of zinc ions has been observed on several metal oxide surfaces through the formation of chelates between the hydrated oxide surfaces and zinc ions (18). Seiyama *et al.* (19) applied this phenomenon to the fixation of Cu(II) and Pd(II) complex ions on tin oxide substrates to prepare catalysts for propylene oxidation.

It has been shown (20) that an alkaline pretreatment of SnO_2 causes the *p*H response of the electrode to be enhanced, evidently through a superficial hydration, *i.e.*, the formation of an —Sn—OH surface by hydrolysis of —Sn=O bonds. There is evidence for enhanced chemisorption on SnO_2 by the pretreatment. Specific adsorption of certain cations, such as Fe(III) or Pb(II), occurs on the hydrated surface presumably by replacement of Sn—OH protons (21). Specific adsorption of anions, notably bromide and iodide (22), occurs on SnO_2 only on surfaces which have been hydrated.

On the basis of this background we sought to make a highly dispersed platinum catalyst on tin oxide through chemisorption phenomena. For experimental convenience a spray hydrolysis method was used for the preparation of a tin oxide film on Pyrex glass. For practical purposes, a chemical vapor deposition method can be used, in principle, to prepare this deposit onto a suitable support. Ghoshtagore has described the mechanisms of several chemical vapor deposition reactions for tin oxide films (23).

Experimental

Chemical, electrolytes, and cells.—Reagent grade chemicals were used without further purification. Electrolytes were purified by pre-electrolysis with platinum gauze until the occupation of Pt sites by impurities became less than 3% of total Pt sites even after the potential of a smooth platinum electrode was kept at 0.4V for 10 min. Cells consisted of three compartments for working, counter, and reference electrodes, respectively, and potentials were referred to a hydrogen electrode in the same solution.

SnO_2 films.—We have followed a procedure described in a patent issued to Corning Glass Company (24), in which an aqueous solution of 3M $SnCl_4$, 1.5M HCl, and 0.03M $SbCl_3$ is sprayed in intermittent bursts onto a Pyrex surface heated to temperatures of the order of 450°C. The product is a film of *ca.* 1 μm thickness, which is polished by means of alumina powder.

Alkali pretreatment.—Prior to platinization of SnO_2 electrodes they were presoaked in 10M NaOH solution and investigated for optimum conditions of chemisorption of platinum compounds, *i.e.*, temperature and time. Presoaking at 90°C in 10M NaOH solution for 30 min was finally adopted as the optimum conditions for developing the full catalytic activity of platinum. After the soaking the electrodes were washed to remove excess sodium hydroxide with several portions of distilled water under ultrasonic agitation and soaked in distilled water before use.

Platinization.—The following solution was the most effective found so far in achieving chemisorption. Chloroplatinic acid was mixed with ammonium chloride, and the resulting precipitate was dissolved in Na_2HPO_4 solution, evaporated almost to dryness to expel most of the free ammonia and taken up with 0.5 NaCl and then made up to 1000 ppm platinum (IV) with distilled water.

The optimum *p*H region of the solution for soaking was investigated in advance by changing the concentrations of Na_2HPO_4 and found to be from 7.3 to 7.7. Therefore, chemisorption was studied by exposing a series of alkali pretreated electrodes for varying temperatures and times to the platinizing solution of *p*H 7.4. After the soaking they were washed with several portions of distilled water and dried at room temperature.

Preheating and developing of Pt compounds.—Platinum activity was developed by electrochemical reduction of the compounds chemisorbed on SnO_2 surface. It was soon found that preheating as well as alkali pretreatment is essential to fully develop platinum activity prior to the electroreduction. It is believed that heating is required to remove residual coordinated chloride by thermal decomposition. Therefore samples were first heated at 200°C in air for 15 min. Then they were reduced potentiostatically at 0.05V until triangular potential sweeps between 0.5 and 1.1V in 0.5M NaOH solution deaerated by bubbling Ar gas showed well developed and steady hydrogen desorption peaks. This behavior indicates the complete reduction of platinum compounds to metallic platinum.

Evaluation of activity for oxygen reduction.—As a standard procedure for measuring activities, an air-saturated 0.1M NaOH solution was used and a preliminary anodic scan was used as a cleanup procedure at room temperature. Then the electrode potential was scanned in the cathodic direction with a scan rate of 100 mV/sec; the oxygen reduction current at 0.8V, corrected for residual current in the absence of oxygen, was then taken as a measure of catalytic activity. This potential corresponds to a point part way up the oxygen reduction region. Kinetic control is dominant in this region, because little change of the current is observed by stirring the solution.

Determination of S_{Pt}, T_{Pt}, and D.—The amount of surface platinum exposed to electrolyte (S_{Pt}) was determined electrochemically by the desorption of hydrogen from Pt-H sites prepared by transient electrolysis in the hydrogen predeposition region in deaerated 1M H_2SO_4 solution, based on the fact that the tin oxide substrate does not adsorb hydrogen in that potential region.

The amount of total platinum on the SnO_2 surface (T_{Pt}) was determined by Rutherford backscattering of alpha particles (RBS) as reported previously (25). The dispersion is given by the ratio S_{Pt}/T_{Pt}.

The former method is sensitive to 0.01 $\mu g/cm^2$ of exposed platinum, and the latter to 0.3 mg/cm^2 of platinum regardless of the chemical form of platinum on the substrate surface (25). If platinum crystallites of conventional type are present, the dispersion D should decrease with increasing size of crystallites, and if platinum atoms disperse on SnO_2 surface in a monolayer or submonolayer, it should be unity.

Results and Discussion

All steps of the preparation of platinized electrodes are interrelated. We will discuss them in order, but anticipating results of later steps in describing the optimization of each step.

Alkali pretreatment.—Figure 1 shows the effect of pretreatment with alkali on the activity of platinized electrodes. Tin oxide electrodes were soaked in 10M NaOH solution under ultrasonic agitation. They were platinized at 50°C for 6.5 hr, washed, and then heated at 200°C prior to electrochemical reduction. With alkaline pretreatment the catalytic activity could be increased up to a limiting value with increase of deposited platinum. This limiting value was reached upon relatively prolonged soaking (>5 hr) at 50°C.

The presoaking time can be shortened even without ultrasonic agitation by elevating the soaking temperature, *i.e.*, the limiting value was reached after soaking at 80°C (1 hr) or 90°C (30 min) as shown in Fig. 2. Even at 90°C, the SnO_2 coating itself was not noticeably attacked, but unprotected glass showed etching after longer exposure. In the following a 30 min, 90°C pretreatment was used.

Platinization.—The platinizing solution was prepared by the method mentioned in the Experimental section. Chemisorption was studied by exposing a series of alkali pretreated SnO_2 samples using varying concentrations of Na_2HPO_4 in the platinizing solutions at 25°C for 15 hr under ultrasonic agitation. The chemisorbed platinum was developed electrochemically after preheating at 200°C. It is clear in Fig. 3 that chemisorption occurs in a concentration region lower than 0.2M Na_2HPO_4. Figure 4 shows the relation between *p*H and the concentration of Na_2HPO_4 in the solutions. The upper limit 0.2 M/liter Na_2HPO_4 corresponds to *p*H 7.7.

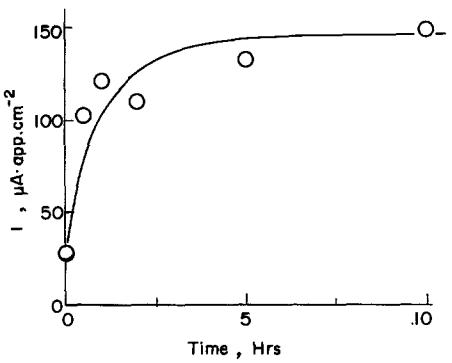

Fig. 1. The effect of pretreatment with alkali on the activity of platinized electrodes. Conditions: in 10M NaOH at 50°C under ultrasonic agitation. Electrodes were heated at 200°C for 15 min prior to electroreduction.

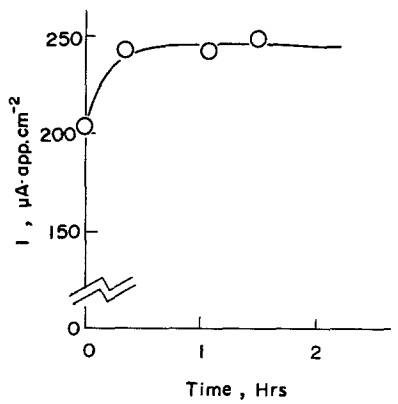

Fig. 2. The effect of pretreatment with alkali on the activity of platinized electrodes. Conditions: in 10M NaOH at 90°C without ultrasonic agitation. Electrodes were heated at 200°C for 15 min prior to electroreduction.

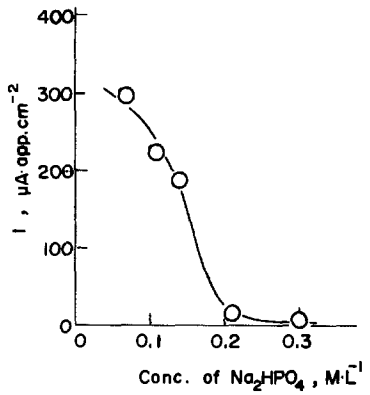

Fig. 3. The effect of concentration of Na_2HPO_4 on the activity (or chemisorption) of Pt compounds. Conditions: in platinizing solution at 25°C for 15 hr under ultrasonic agitation. Other conditions were similar to those of Fig. 2.

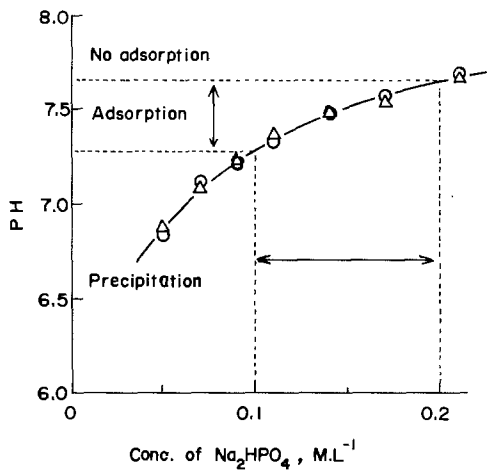

Fig. 4. The relation between the concentration of Na_2HPO_4 and *p*H of the platinizing solution. ○, Before soaking samples; △, after soaking samples.

On the other hand, at a lower concentration of Na_2HPO_4, a small amount of colloidal precipitate was formed with time in the stock solution. A *p*H of 7.3 was found as a lower limit. Sodium chloride was dissolved additionally into the solution in order to stabilize it. In all subsequent experiments, the platinizing solution contained 1000 ppm Pt(IV), made up to be 0.135*M* in Na_2HPO_4 and 0.5*M* in NaCl, at a *p*H of 7.4.

Chemisorption was again studied by soaking a series of SnO_2 samples for varying times in the platinizing solution. Platinum analyses showed a linear increase of platinum content with time. By soaking at 50°, a platinum content of about 0.35 $\mu g/cm^2$ was achieved in 40 hr (Fig. 5), while at 90°, a similar platinum content was reached in 3 hr (Fig. 6). In both cases, quite negligible amounts of platinum were detected on just Pyrex glass. This result proves that the primary deposition occurs through the chemisorption of the platinum compound on functional groups of SnO_2.

It was expected that platinum deposition would level off with saturation of surface functional groups. With longer exposure to the platinizing solution, the total platinum concentration continued to increase, but the catalytic activity leveled off as is shown below, so that platinum loadings beyond 1 $\mu g/app\ cm^2$ were essentially ineffective in catalytic activity. This loading would be about equivalent to a close-packed monolayer if a roughness factor of 2.5 were assumed. It is believed that loadings of several micrograms are the result of condensation reactions between primarily chemisorbed Pt compounds and solution species, to yield platinum

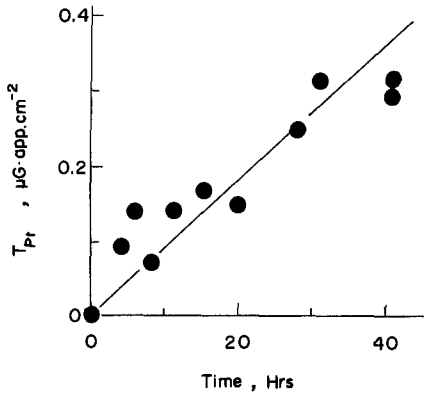

Fig. 5. The dependence of chemisorbed Pt content upon platinizing time. Conditions: platinized at 50°C without agitation. Other conditions were similar to those of Fig. 2.

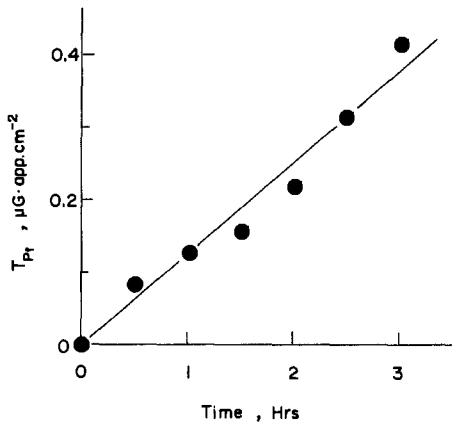

Fig. 6. The dependence of chemisorbed Pt content upon platinizing time. Conditions: platinized at 90°C without agitation. Other conditions were similar to those of Fig. 2.

crystallites of increasing size. As is shown below, the dispersion decreases with Pt loading in this range.

Thermal treatment.—We tried the direct electrochemical reduction of platinized surfaces after thorough washing but the reduction was not successful. Figure 7 shows the effect of preheating temperature on the electroreduction. Each sample was platinized at 90°C for 3.5 hr and electroreduced at 50 mV for 30 sec after the preheating. Filled circles stand for T_{Pt}, and open circles for S_{Pt} determined electrochemically. The nonpreheated sample, or S_{Pt} at 25°C in the figure, indicates that direct electroreduction is very difficult. By preheating at higher than 150°C, the reduction becomes easier, and a maximum value of S_{Pt} was obtained at higher than 200°C, probably by the complete decomposition of platinum compounds.

A temperature of about 200°C was found to be critical; at this temperature (or at 300°C) a short heating (15 min) was sufficient to fully "activate" the platinum as shown in Fig. 8.

Catalytic activity for oxygen reduction.—Figure 9 shows a plot of catalytic activity (expressed as the apparent current density for oxygen reduction) as a function of total platinum loading. Beyond a loading of about 1 μg/app cm^2 the catalytic activity leveled off at a value corresponding to that of metallic platinum foil.

In Fig. 10, the catalytic activity per unit of surface platinum is plotted against total Pt loading. Such a normalization procedure permits a direct comparison between catalyzed oxygen reduction and electrochemical reoxidation of chemisorbed hydrogen, regardless of roughness factor or dispersion. The "loading" for a 0.2

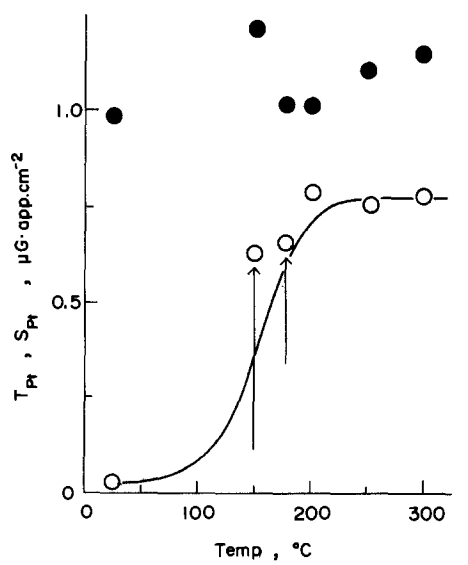

Fig. 7. The effect of preheating temperature on the electrochemical reduction of chemisorbed Pt compounds. Electrodes were platinized at 90°C for 3.5 hr and reduced at 0.05V for 30 sec potentiostatically after the preheating. ●, T_{Pt}; ○, S_{Pt}.

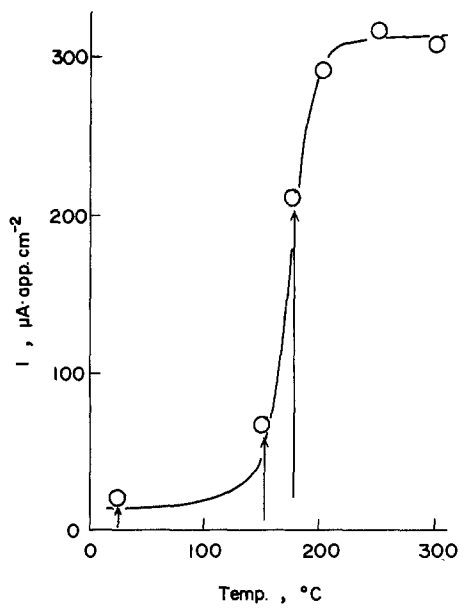

Fig. 8. Activity expressed as μA/app cm^2 at potential of 0.8V (vs. RHE) in air-saturated 0.1N NaOH at scan rate of 100 mV/sec.

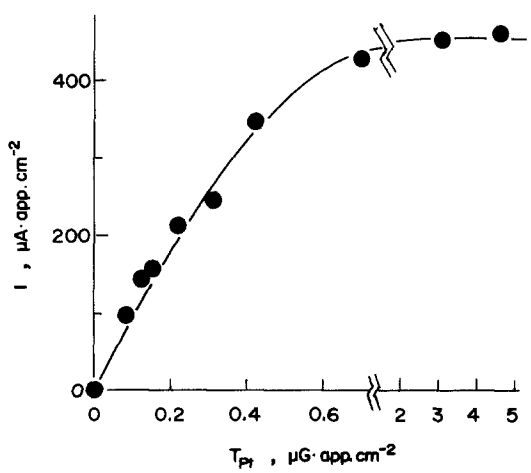

Fig. 9. The dependence of activity on deposited Pt content. Refer to Fig. 6 for the preparation of electrodes and Fig. 8 for test conditions.

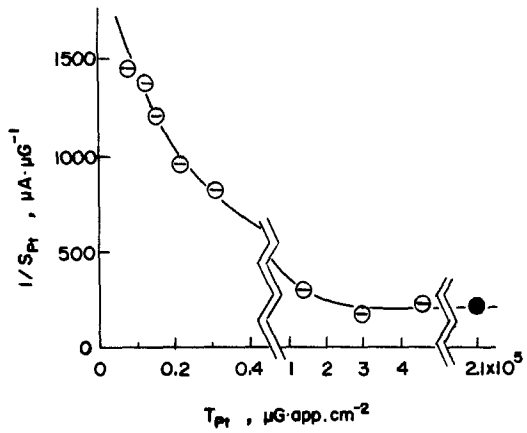

Fig. 10. The change of specific activity with deposited Pt content, corresponding to Fig. 9.

mm foil, or roughness factor 2.5, would be 2.1×10^5, which is plotted as a full circle in Fig. 10. It is clear that the first fractional monolayer atoms are much more effective catalytically than surface atoms of metallic platinum crystallites or bulk metal. Evidently the catalytic activity is enhanced by the SnO_2 substrate.

Dispersion.—Dispersion for 50° and 90°C chemisorptions were plotted against the total platinum contents in Fig. 11 and 12, respectively. The results show that

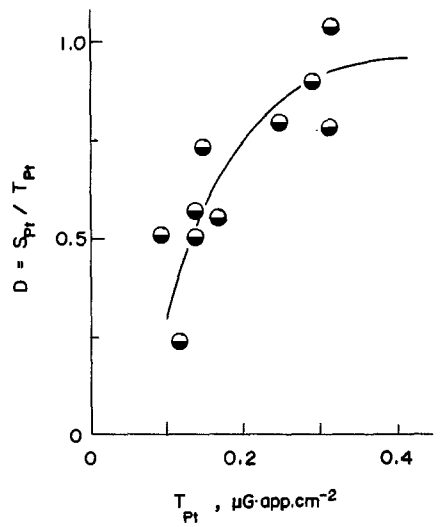

Fig. 11. The dependence of dispersion on deposited Pt content, refer to Fig. 5 for the preparation of electrodes.

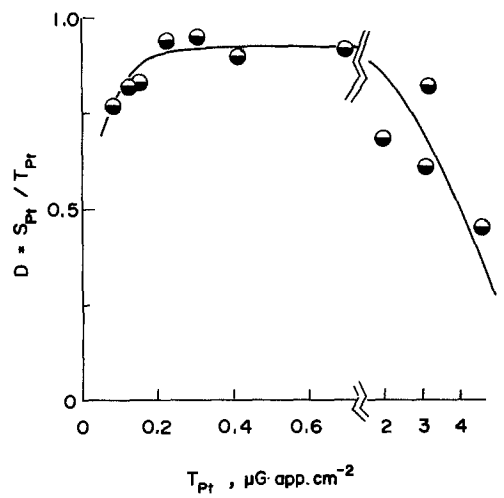

Fig. 12. The dependence of dispersion on deposited Pt content, refer to Fig. 6 for the preparation of electrodes.

very high values of D (of the order of 0.9) are obtained both at 50° and 90°C, if T_{Pt} approaches 0.4 μg/app cm^2 for the former and 0.2 μg/app cm^2 for the latter. In the 50°C experiments, the remarkable result was that lower D was found at lower Pt loadings. This is just opposite to the trend observed for electrochemically deposited platinum, and what would be expected if smaller crystallites formed at lower loading. Both the inverse trend of D, and its high value, suggest that perhaps substrate-catalyst interactions are enhancing catalytic activity. In the 90°C experiments, D is nearly constant covering the region from 0.2 μg to 1 μg/app cm^2, suggesting an optimum support catalyst in a range of 20-100% of a close-packed monolayer equivalent. Of course a close-packed monolayer is not expected actually. The D is decreased with increasing platinum loading for more than 1 μg Pt, presumably because of crystal growth.

Summary and Conclusions

Quite highly dispersed platinum can be prepared on conductive SnO_2 by the chemisorption mentioned above. The dispersion can exceed 90% at small amounts of loading, and the activity per unit of surface Pt is higher than that of metallic platinum, perhaps being enhanced through substrate-catalyst interactions (10). Thus the Pt-SnO_2 system presents many possibilities as a replacement for platinum metal as a catalyst. Further investigations on a simplification of the preparation method and on the stability of the catalyst upon heating and upon standing in electrolyte will be required.

Acknowledgment

The authors gratefully thank Professor H. A. Van Rinsvelt, the University of Florida, for the use of RBS and Mr. J. T. Sanders for carrying out the analysis for platinum by RBS. This work was supported by the National Science Foundation, No. CHE 78-08423.

Manuscript submitted Jan. 20, 1982; revised manuscript received *ca.* July 26, 1982. This was Paper 20 presented at the Hollywood, Florida, Meeting of the Society, Oct. 5-10, 1980.

Any discussion of this paper will appear in a Discussion Section to be published in the December 1983 JOURNAL. All discussions for the December 1983 Discussion Section should be submitted by Aug. 1, 1983.

REFERENCES

1. M. M. P. Janssen and J. Moolhuysen, *Electrochim. Acta*, **21**, 861 (1976).
2. M. R. Andrew, B. D. McNicol, R. T. Short, and J. S. Drury, *J. Appl. Electrochem.*, **7**, 153 (1977).
3. M. M. P. Janssen and J. Moolhuysen, *Electrochim. Acta*, **21**, 869 (1976).
4. M. R. Andrew, J. S. Drury, B. D. McNicol, C. Pinnington, and R. T. Short, *J. Appl. Electrochem.*, **6**, 99 (1976).
5. K. J. Cathro, *Electrochem. Technol.*, **5**, 441 (1967).
6. S. Motoo and M. Watanabe, *J. Electroanal. Chem. Interfacial Electrochem.*, **69**, 429 (1976).
7. S. Motoo, M. Watanabe, and N. Furuya, Extended Abstract 234, 27th Meeting of I.S.E.-Zürich, Switzerland (1976).
8. S. Motoo, M. Shibata, and M. Watanabe, *J. Electroanal. Chem. Interfacial Electrochem.*, **110**, 103 (1980).
9. R. R. Cecil, W. S. Kmak, J. H. Sinfelt, and L. W. Chambers, *Oil Gas J.*, **7**, 50 (1972); E. M. Blue, *Hydrocarbon Processes*, **48**, 141 (1969).
10. S. J. Tauster, S. C. Fung, R. T. K. Baker, and J. A. Horsley, *Science*, **211**, 1121 (1981).
11. A. C. C. Tseung and S. C. Dhara, *Electrochim. Acta*, **19**, 845 (1974).
12. M. Watanabe and S. Motoo, *J. Electroanal. Chem. Interfacial Electrochem.*, **60**, 259 (1975); *ibid.*, **60**, 267 (1975).
13. S. Motoo and M. Watanabe, Abstract 7F311, 26th IUPAC Congress, Tokyo (1977).
14. M. Yokoyama and H. A. Laitinen, Unpublished paper.

15. M. Chen and L. D. Schmidt, *J. Catal.*, **55**, 348 (1978).
16. L. A. Harris and J. A. Hugo, *This Journal*, **128**, 1203 (1981).
17. M. Hayes, A. T. Kuhn, and W. Grant, *J. Catal.*, **53**, 88 (1978).
18. A. Kozawa, *This Journal*, **106**, 552 (1959); *J. Inorg. Nuclear Chem.*, **21**, 315 (1961); in "Oxide-Electrolyte Interface," R. B. Alwitt, Editor, pp. 72-90, The Electrochemical Society Softbound Proceedings Series, Princeton, NJ (1973).
19. T. Kaji, H. Yamazoe, and T. Seiyama, *Nippon Kagaku Zassi*, **7**, 1088 (1980).
20. H. A. Laitinen and T. M. Hseu, *Anal. Chem.*, **51**, 1550 (1979).
21. H. A. Laitinen and N. H. Watkins, *ibid.*, **47**, 1352 (1975); *This Journal*, **123**, 804 (1976).
22. H. Yoneyama and H. A. Laitinen, *J. Electroanal. Chem. Interfacial Electrochem.*, **75**, 647 (1977); *ibid.*, **79**, 129 (1977).
23. (a) R. M. Ghoshtagore, *This Journal*, **125**, 110 (1978); (b) B. T. Baliga and S. K. Ghandhi, *ibid.*, **123**, 941 (1976).
24. J. M. Mochel, U.S. Pat. 2,564,707 (1951).
25. J. Rosenfarb, H. A. Laitinen, J. T. Sanders, and H. A. Van Rinsvelt, *Anal. Chim. Acta*, **108**, 119 (1979).

Electrochemical Behavior of Li_2S in Fused LiCl-KCl Electrolytes

D. Warin

Laboratoire Central, De Recherches, Thomson-CSF, France

and Z. Tomczuk* and D. R. Vissers*

Argonne National Laboratory, Chemical Engineering Division, Argonne, Illinois 60439

ABSTRACT

Cyclic voltammetric studies of lithium sulfide in LiCl-KCl electrolytes have shown that the voltammograms obtained in a large range of potentials with an inert, glassy carbon electrode were dependent on Li_2S concentration, temperature, and LiCl-KCl electrolyte composition. Voltammograms suggest three successive sulfide ion oxidation stages and a complex reduction electrochemistry. A detailed analysis of the results allows postulation of different possible redox mechanisms, but because numerous ionic sulfur species can exist in molten salts, an overall definitive mechanism, based solely on these electrochemical measurements, cannot be proposed. The diffusion coefficient of S^{2-} and the solubility of Li_2S have also been investigated as a function of electrolyte composition at temperatures between 400° and 450°C. The diffusion coefficient of S^{2-} is $(5.2 \pm 1) \times 10^{-5}$ cm^2 sec^{-1} in the electrolytes used; the solubility of Li_2S is 950 ± 100 ppm at 454°C in the eutectic LiCl-KCl electrolyte and increases with increasing LiCl concentration.

Rechargeable lithium/iron-sulfur batteries with high specific energy are currently being developed by Argonne National Laboratory and its industrial subcontractors for use in off-peak energy storage and electric-automobile applications (1). The possibility of using an FeS_2 positive electrode in these high temperature batteries has caused considerable interest in the electrochemical properties of sulfides and polysulfides in molten salt systems, because one of the main difficulties encountered with batteries of this type is the loss of sulfur from the positive electrode through vaporization and through the formation of sulfides that are soluble in the molten salts. These sulfur loss mechanisms limit the lifetime and capacity of the cells.

Because basic information was needed to further improve the sulfur electrode, many studies have been conducted on the electrochemical behavior of sulfur and sulfide ion in molten salts (2). Many investigators (3-19) have suggested various identities for the sulfide species present in the LiCl-KCl eutectic electrolyte and various sequences for the redox mechanism for S^{2-}. Initial studies have indicated a single step for the oxidation of S^{2-} to sulfur (3-5) and also a direct reduction transition of sulfur to sulfide (6-8). The observed blue color of the molten solution was ascribed to polysulfide ions, formed by a chemical reaction between sulfur and sulfide (9), or to the hypersulfide ions S_2^- (10); the yellowish color of the frozen melt was found to be due to the dimerization of S_2^- to S_4^{2-}. These results were partly supported by the work of Bernard *et al.* (11) who asserted that a polysulfide S_n^{2-} and a supersulfide S_n^- were involved in the calcium sulfide oxidation.

Kennedy and Adamo (12) and Cleaver *et al.* (13) have carried out cyclic voltammetric studies on sulfur and on sodium or potassium sulfides in the LiCl-KCl eutectic. Their voltammograms showed two anodic and two cathodic peaks. The authors proposed the following mechanism $S_n^{2-} \rightleftarrows S_n^- + e^-$, $S_n^- \rightleftarrows nS + e^-$ where $n > 2$, but the peak positions from the two sets of their experiments were different. A cyclic voltammetry study of lithium sulfide by Birk and Steunenberg (14) also showed two stages of oxidation leading to sulfur, and two or three stages of reduction going back to sulfide, depending on the Li_2S concentration, the temperature, and the potential scan rate. The redox mechanism was postulated to be $2S^{2-} \rightleftarrows S_2^{2-} + 2e^-$, $S_2^{2-} \rightleftarrows 2S + 2e^-$; the third cathodic intermediate step $S_2^- + e^- \rightarrow S_2^{2-}$ was found to occur when the conditions were favorable to the formation of the S_2^- ion by the hypothetical chemical reaction $3S + S^{2-} \rightleftarrows S_4^{2-} \rightleftarrows 2S_2^-$. These results agreed in general with the work reported by Raleigh *et al.* (15) who, nevertheless, indicated an important distortion in the cyclic voltammograms when different types of indicator electrodes (graphite, molybdenum, platinum) were used. Under these conditions, the choice of the carbon electrode used by Birk and Steunenberg appeared questionable, due to the inherent porosity of the material, especially when an insoluble product such as sulfur could be retained on the electrode.

Kam and Johnson (16) have indicated three oxidation steps of S^{2-} leading to the formation of S_2, on the first scan of the cyclic voltammogram; the subsequent scans were found to be different from the first scan and the authors invoked another mechanism with four electrochemical steps including the reaction $2S^{2-} \rightarrow S_2^{3-} + e^-$. These authors were the only ones to mention such a modification of the redox mechanism when scanning and, based on the other works, the formation of the ion S_2^{3-} appears very unlikely. A bibliographic study by Santarini (17) has indeed suggested that

* Electrochemical Society Active Member.
Key words: battery, fused salts, voltammetry.

the more likely sulfur ions existing in the eutectic LiCl-KCl at 450°C are S^{2-}, S_4^{2-}, S_2^-, S_3^-, and S_8^-.

Thus, the electrochemical behavior of sulfide ions is still uncertain with regard to the species existing in the LiCl-KCl eutectic and to the number of redox processes. The purposes of this work were to characterize the electroactive species involved in the redox reactions of sulfide, and to study the kinetics of these processes as functions of temperature, Li_2S concentration, and LiCl-KCl electrolyte composition.

Experimental

All operations were performed inside a glove box under a dry helium atmosphere. The test cell, an alumina beaker 4.5 cm diam and 12 cm long, contained a weighed amount (130g) of LiCl-KCl salt and three electrodes. The working and counterelectrodes were glassy carbon rods (0.6 cm diam) from the Fluoro-Carbon Corporation with working electrode areas of 1.0 cm^2. The reference electrode employed a two-phase (α + β)-LiAl alloy (42 a/o Li) from KBI Incorporated which was loaded into an Al_2O_3 tube (3.2 mm diam) that served as the insulator housing with an Al_2O_3 plug at the bottom of the tube; a nickel wire inside the Al_2O_3 tube ensured electrical contact with the Li-Al powder. The role of the Al_2O_3 plug was to create a diffusion barrier effective enough to prevent the contact and possible chemical reduction of the soluble species by the Li-Al alloy. The electrolyte in the test cell was polarographic-grade LiCl-KCl eutectic (58.2 m/o LiCl) from Anderson Physics Laboratory. Variations in electrolyte composition were accomplished by the addition of either LiCl (Anderson Physics Laboratory) or KCl (Baker, reagent grade) in order to shift the composition to "LiCl-rich" (66.0 m/o LiCl) or "KCl rich" (54.0 m/o LiCl). The Li_2S concentration in the test cell was controlled by adding weighed known quantities of Li_2S (Eagle-Picher Industries, Incorporated, > 99% purity) to the LiCl-KCl electrolyte. In order to ensure that the Li_2S contained no free sulfur, the Li_2S was heated under a dry helium atmosphere for several hours before it was added to the electrolyte. The simple design of the cell prevented questions about possible unwanted side reactions (15, 18) because alumina and vitreous carbon were the only materials in contact with the electrolyte.

The test cell was placed in a tubular, vertical Lindberg furnace where the temperature was regulated with an appropriate selection of Variac settings and measured with a Chromel-Alumel thermocouple located between the outside of the cell and the furnace. The electrolyte temperature was controlled to within 1°C in the range 400°-460°C. The upper end of the furnace well was closed by a cap equipped with a number of Swagelok fittings through which the electrodes were inserted and the apparatus could be evacuated or flushed with helium.

Cyclic voltammetry was performed with a Princeton Applied Research Potentiostat equipped with a Model 179 Digital Coulometer and a Model 175 Universal Programmer. The data were recorded on a Hewlett-Packard Model 7045 A X-Y recorder. The usual voltage range was 1.1-2.8V *vs.* the Li-Al reference electrode; the voltage, however, was often restricted to smaller ranges in order to permit study of particular transitions. The scan rates were varied from 10 to 1000 mV/sec. The usual procedure consisted of repeated anodic and cathodic sweeps to obtain steady-state voltammograms for each of the different experimental conditions. The starting potential was chosen to be the point where no current passed through the cell ($V_i \simeq 1.2V$) and the first sweep was anodic. The electrodes were immersed directly in the molten salt a few minutes before cyclic voltammograms were begun. The purity of the initial LiCl-KCl melt was checked by obtaining a clean blank voltammogram on the carbon electrode all along the scanned voltage range. (The residual current density was less than 1 mA/cm^2 at the highest scan rate of 1 V/sec.) After each addition of Li_2S, the solution was stirred; complete dissolution of the Li_2S, which occurred after several hours, was indicated by stable and reproducible voltammograms over a long period of time.

Results and Discussion

Essentially three different types of studies were conducted, in which the cyclic voltammograms were obtained at various Li_2S concentrations (Fig. 1), temperatures (Fig. 4), and LiCl-KCl electrolyte compositions (Fig. 6). In each type of study, the conditions of the cyclic voltammetry (potential scan-rate, range of potentials) were widely varied to study the characteristics of the redox processes and the stability of the different species.

Eight different Li_2S additions were made to provide concentrations ranging from 80 to 2200 ppm. The data shown in Fig. 1 are typical of the evolution of the voltammograms at a scan rate of 50 mV/sec and a temperature of 454°C when the concentration of Li_2S was increased. The peak currents increased to constant values which were reached when the amount of added Li_2S became greater than the solubility limit. The main features of these voltammograms in Fig. 1 are the two anodic peaks, which occur at 1.88 and 2.16V, and the two cathodic peaks, which occur at 2.07 and 1.65V, regardless of the Li_2S concentration. The coulombic efficiency was only ~30%, which was mainly because high and unstable charging current was observed at potentials greater than 2.4V during both anodic and cathodic scans. When the maximum cutoff voltage was decreased (Fig. 2), the first anodic peak, designated I_a, could be associated with the last cathodic peak III_c, and peak III_a could be associated with peak I_c, although the shapes of these two peaks were

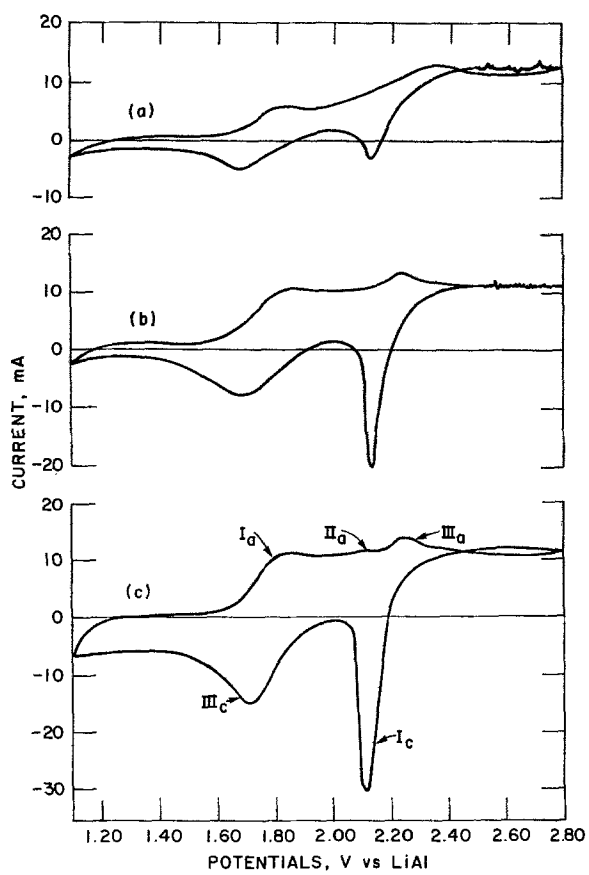

Fig. 1. Voltammograms (50 mV/sec) of sulfide ion in LiCl-KCl eutectic electrolyte at 454°C with the following Li_2S concentration: (a) 230 ppm, (b) 450 ppm, (c) saturated.

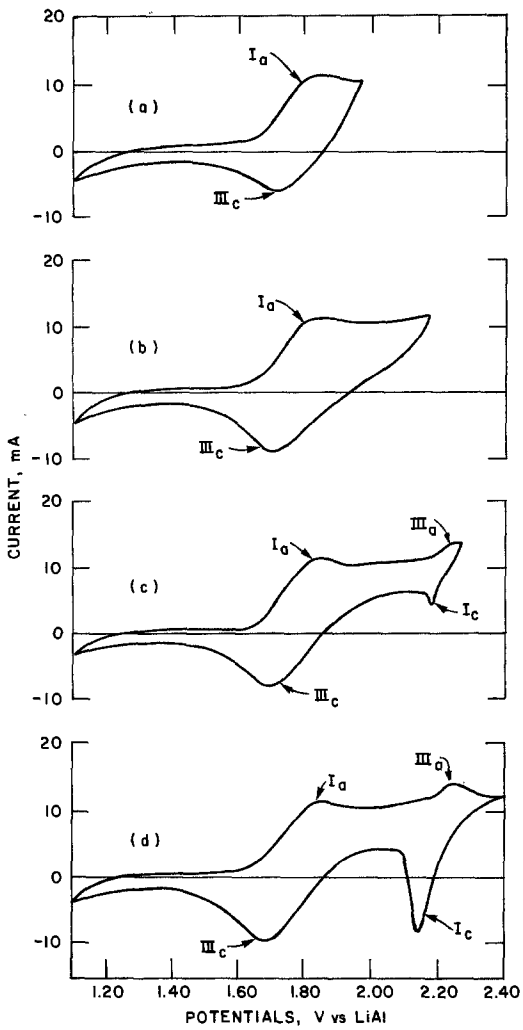

Fig. 2. Voltammograms (50 mV/sec) of sulfide ion in Li_2S-saturated LiCl-KCl eutectic electrolyte at 454°C, for voltage ranges between (a) 1.10 and 1.95V, (b) 2.17V, (c) 2.25V, and (d) 2.40V.

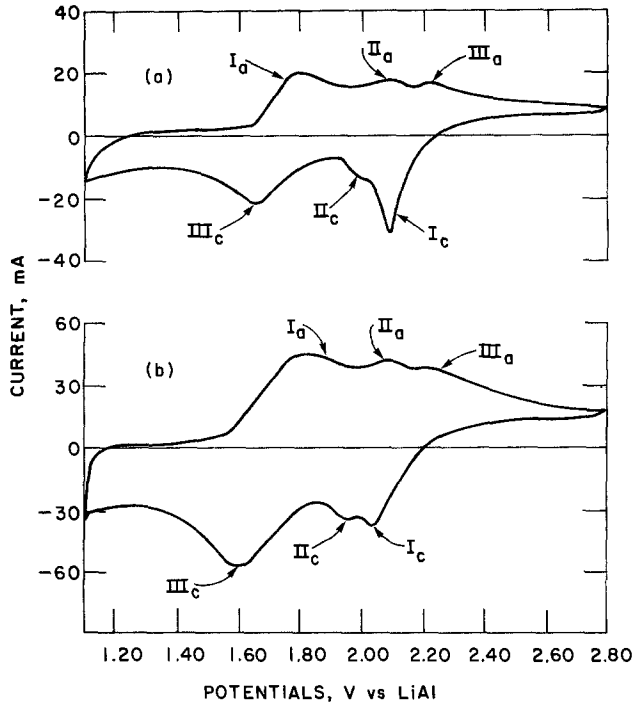

Fig. 3. Voltammograms of sulfide ion in Li_2S-saturated LiCl-KCl eutectic electrolyte at 454°C with (a) ν = 200 mV/sec and (b) ν = 1000 mV/sec.

very different. On closer examination, an intermediate anodic peak II_a with a peak potential, E_p, of ~2.10V, could barely be seen at a scan rate of 50 mV/sec with Li_2S-saturated electrolyte (Fig. 1c); this peak was more clearly observed when the scan rate was faster than 50 mV/sec (Fig. 3). The high anodic current, obtained between peaks I_a and III_a when other conditions were used, leads to the conclusion that a third anodic intermediate transition is always present, even if the peak corresponding to this transition is not clearly observed. Thus, these data indicate the existence of three steps for the oxidation of S^{2-} at temperatures close to 450°C.

In an attempt to characterize the kinetics of the first anodic transition, I_a, occurring at E = 1.88V, different scan rates ranging from 10 mV/sec to 500 mV/sec were used between 1.1 and 1.95V. The peak potential was found to be independent of the sweep rate, ν, and the peak current increased as the square root of the sweep rate increased. These results indicate that a Nernstian equilibrium is maintained at the electrode surface and that the reaction is simply diffusion controlled (20). Furthermore, the shape factor of the peak, $E_p - E_{p/2}$ (where E_p is the peak potential and $E_{p/2}$ is the potential at the half-peak height), can be used to determine the number of electrons transferred; its value is 130 ± 5 mV. For a simple diffusion-controlled reversible reaction followed or not by a slow chemical reaction, the theoretical value of the shape factor is 140 mV per electron transferred at 450°C in the case of soluble products (15, 16, 26). Because of the agreement between the experimentally obtained and the theoretically predicted shape factors, $E_p - E_{p/2}$, it can be concluded that the first stage of oxidation of S^{2-} corresponds to the transfer of one e^-, thus forming S^-.

The second anodic transition, II_a, is more difficult to characterize because only the upper part of the peak was observed and the peak width could not be measured. Nevertheless, the peak position was not shifted when the sweep rate was increased, and the evolution of the peak current with the sweep rate was similar to the variation of peak I_a (Fig. 3). The poor resolution of the peak suggested also that the peak was relatively broad and was characteristic of a one-electron transfer reaction because a two-electron transfer reaction or a reaction of the type 2 Red $\rightleftarrows$ Ox + $2e^-$ would correspond to a narrower and better resolved peak. Depending on the rate of the likely chemical reaction $2S^- \rightarrow S_2^{2-}$ which follows the first electrochemical reaction, the species which is oxidized in reaction II_a can be either S^- or S_2^{2-}; the existence of S_2^{2-} is generally admitted in the literature (8-15, 19). The electrochemical reaction II_a is then assigned to be the oxidation of one of these species $S^- \rightarrow S + e^-$ or $S_2^{2-} \rightarrow S_2^- + e^-$.

As with transitions I_a and II_a, the peak potential of the last anodic stage, III_a, did not vary when the sweep rate was increased (Fig. 3), but the proportionality between the peak current and the square root of the scan rate observed for the first two transitions was not as definitive for the transition III_a. The shape factor can be roughly estimated to be 70 ± 10 mV; this value corresponds to the theoretical value (21, 22) of a two-electron transfer reaction between two soluble species ($E_p - E_{p/2}$ = 69 mV, at 450°C). As there is no evidence of peaks between 2.30 and 3.50V, it is assumed that the product formed by the last anodic reaction, III_a, is free sulfur. Depending on the species which is oxidized, reaction III_a can be one of the three steps involving two electrons and leading to free sulfur $S_2^{2-} \rightarrow S_2 + 2e^-$, $S_3^{2-} \rightarrow S_3 + 2e^-$, $S_4^{2-} \rightarrow S_4 + 2e^-$. Prior to the electrochemical reaction S_2^{2-} can be formed chemically by the dimerization reaction $2S^- \rightarrow S_2^{2-}$, as suggested above, or by the reaction $S^{2-} + S \rightarrow S_2^{2-}$

if sulfur is formed by transition II_a; S_3^{2-} can also be formed by two possible chemical reactions $S + S_2^{2-} \rightarrow S_3^{2-}$ or $S^- + S_2^- \rightarrow S_3^{2-}$; S_4^{2-} can be formed by the dimerization reaction $2S_2^- \rightleftarrows S_4^{2-}$ (9, 20), S_2^- coming from the electrochemical reaction II_a or from two possible chemical reactions $S + S^- \rightarrow S_2^-$ or $3S + S^{2-} \rightarrow 2S_2^-$ (14).

The features of the voltammograms observed during the cathodic sweeps imply that the discharge electrochemistry is as complex as the charge electrochemistry. The first cathodic peak, I_c, in Fig. 2 is clearly associated with the peak III_a. Nevertheless, the peak current of the transition, I_c, increased when the maximum cutoff voltage was increased from 2.40 to 2.80V, which is a potential region where no anodic transition was observed (Fig. 1c, 2d). Furthermore, the peak current, I_c, increased only very slightly when the scan rate was increased from 50 to 1000 mV/sec. The normalized peak current, $I/\nu 1/2$, decreased (Fig. 1c, 3b), although peak III_a increased almost as the square root of the scan rate increased. Under these conditions, it appears that the reaction I_c is not the inverse process of reaction III_a. Since the shape factor of the peak was not constant for the different scan rates, it is difficult to assign with certainty an electrochemical reaction to this step. Nevertheless, based on the voltammograms at scan rates less than 1000 mV/sec, the shape factor is between 35 and 45 mV. This value corresponds to the expected value for a 4-electron transfer mechanism for the reduction of soluble species; it also corresponds to the theoretical value for a 1-electron process for the reduction of an insoluble species (23). These two possibilities have to be considered because free sulfur is known to be virtually insoluble in the LiCl-KCl eutectic but its solubility has been found to increase in LiCl-KCl electrolytes containing sulfide ions (24); in addition, the current instabilities seen above 2.50V in Fig. 1 are probably indicative of the formation, buildup, and erratic dissolution of the small amount of sulfur generated at the end of the anodic scan. For these reasons, it cannot be determined if the sulfur species is dissolved or not. So, a possible reaction for peak I_c, in the case of soluble sulfur, can be $S_4 + 4e^- \rightarrow S_4^{4-}$; the species S_4^{4-} is then dissociated to form the more stable polysulfide S_2^{2-}. In the case of insoluble sulfur, reaction I_c is $S + e^- \rightarrow S^-$, and the dimerization reaction $2S^- \rightarrow S_2^{2-}$ leads also to the formation of the polysulfide ions.

At a scan rate of 50 mV/sec, only a second cathodic peak, III_c, was observed. Its characteristics lead to the conclusion that it represents a diffusion-controlled reaction of the type $Ox + 2e^- \rightarrow 2\,Red$ (21). Comparisons of the first and subsequent scans show that the anodic peaks do not change significantly, suggesting that the initial electroactive sulfide species was reformed at the end of the reduction sweep. All these data lead to the conclusion that reaction III_c is $S_2^{2-} + 2e^- \rightarrow 2S^{2-}$. When a scan rate faster than 50 mV/sec was used (Fig. 3), an intermediate cathodic transition, II_c, appeared at a peak potential of 1.95V; the normalized peak current, I_c, concurrently decreased, and the last cathodic transition, III_c, was not affected. Two mechanisms can be proposed to explain this result. First, since this transition, II_c, is enhanced with a rapid scan rate, it can be representative of the reduction of the species S_4^{2-} formed during the anodic scan and not completely oxidized during the following step III_a. This hypothesis that the polysulfide ions, S_4^{2-}, are not fully consumed by oxidation III_a implies a diminution of the concentration of the sulfur species, S_4, and explains why the reduction peak of S_4 (I_c) was reduced when peak II_c was observed. Under these conditions, the assigned reaction for the peak II_c is postulated to be $S_4^{2-} + 2e^- \rightarrow 2S_2^{2-}$. A second possible mechanism is that the species S^- formed by the reaction, I_c, reacts rapidly with the still-existing sulfur species to chemically form S_4^{2-} ($2S + 2S^- \rightarrow S_4^{2-}$); less sulfur is available for reaction, I_c, while reaction, II_c, $S_4^{2-} + 2e^- \rightarrow 2S_2^{2-}$ becomes more important. We can conclude that the possible overall mechanism in the LiCl-KCl eutectic electrolyte at 450°C is one of the following possibilities

Anodic

(I_a) $S^{2-} \rightarrow S^- + e^-$, $2S^- \rightarrow S_2^{2-}$

(II_a) $S^- \rightarrow S + e^-$, $S + S^{2-} \rightarrow S_2^{2-}$
or $S + S_2^{2-} \rightarrow S_3^{2-}$
or $S + S^- \rightarrow S_2^- \rightarrow 2S_4^{2-}$
or $3S + S^{2-} \rightarrow S_4^{2-}$

or

$S_2^{2-} \rightarrow S_2^- + e^-$, $S_2^- + S^- \rightarrow S_3^{2-}$
or $2S_2^- \rightarrow S_4^{2-}$

(III_a) $S_n^{2-} \rightarrow S_n + 2e^-$ with $n = 2, 3,$ or 4.

Cathodic:

(I_c) $S_4 + 4e^- \rightarrow S_4^{4-}$, $S_4^{4-} \rightarrow 2S_2^{2-}$

or

$S + e^- \rightarrow S^-$, $2S^- \rightarrow S_2^{2-}$ or
$2S + 2S^- \rightarrow S_4^{2-}$

(II_c) $S_4^{2-} + 2e^- \rightarrow 2S_2^{2-}$

(III_c) $S_2^{2-} + 2e^- \rightarrow 2S^{2-}$

In addition to the cyclic voltammetry studies at 450°C, experiments have been performed at several temperatures between 400° and 450°C. The data presented in Fig. 4 are typical of the evolution of the voltammograms when the temperatures were 399°, 418°, and 428°C at a scan rate of 50 mV/sec. When the

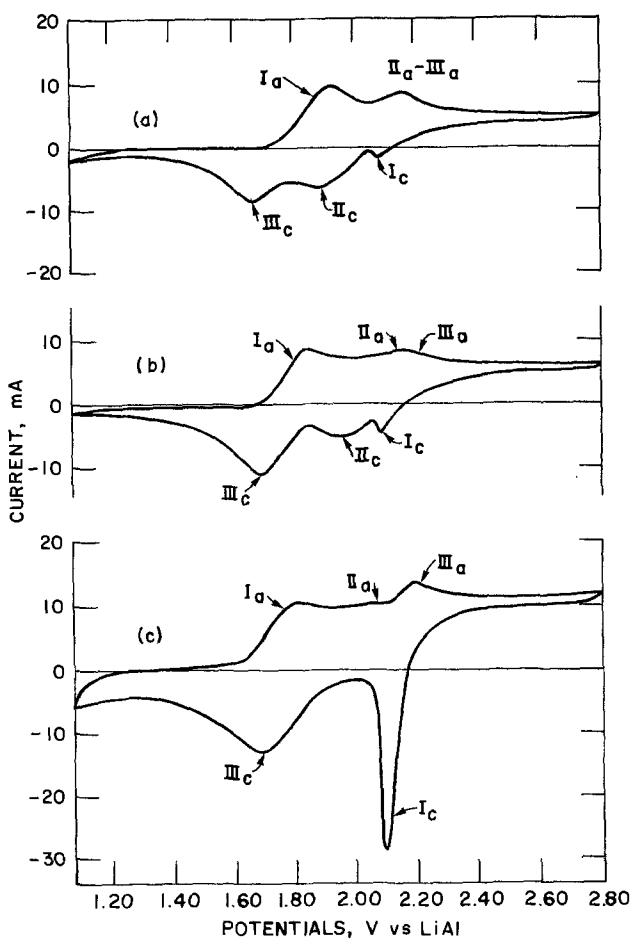

Fig. 4. Voltammograms (50 mV/sec) of sulfide ion in Li_2S-saturated LiCl-KCl eutectic electrolyte at (a) $T = 399$°C, (b) $T = 418$°C, and (c) $T = 428$°C.

temperature was less than 428°C (Fig. 4a, 4b) only two anodic peaks were observed upon oxidation instead of the three observed at 450°C. However, this result does not imply a two-step oxidation mechanism for S^{2-} at lower temperatures because the two last anodic peaks, II_a and III_a, obtained at 450°C can form the single broad peak designated II_a-III_a at 400°C. This hypothesis is consistent with the fact that the cathodic scan showed the same three peaks at both 400° and 450°C. Nevertheless, at 400°C, the intermediate peak, II_c, is much more important; it was observed even with the slowest sweep rate and it increased when the temperature decreased, whereas an inverse evolution was seen for the peak I_c. This result probably signifies that the species S_4^{2-}, responsible for the transition II_c, becomes more stable at lower temperatures. The use of different maximum cutoff voltages (Fig. 5) confirms that peak II_a-III_a is a doublet, as suggested above, since it can be clearly associated with the two different cathodic peaks, I_c and II_c.

An analysis of the different peaks, similar to the study made earlier on the voltammogram taken at 450°C, reveals that the shapes and evolutions of the anodic and cathodic peaks at different sweep rates are identical at 450° and 400°C, except for the first anodic transition. This first oxidation stage occurred at a high potential ($E = 1.75$V) and its shape factor was 110 ± 10 mV, which corresponds to the value for a mechanism of the type 2 Red $\rightleftarrows$ Ox + $2e^-$, at 400°C (23). Under these conditions, the possible oxidation mechanisms at temperatures less than 428°C are proposed to be

Anodic

(I_a) $2S^{2-} \rightarrow S_2^{2-} + 2e^-$

(II_a) $S_2^{2-} \rightarrow S_2^- + e^-$, $2S_2^- \rightarrow S_4^{2-}$

(III_a) $S_n^{2-} \rightarrow S_n + 2e^-$ with $n = 2$ or 4

The cathodic sequence is the same as at 450°C, with the second step always occurring.

In a final series of experiments, the concentrations of LiCl or KCl in the electrolyte were varied (Fig. 6). The voltammograms obtained in the LiCl-rich or KCl-rich LiCl-KCl electrolytes were very similar to those obtained with the eutectic electrolyte. Voltammograms were recorded in both cases with several Li_2S concentrations at different temperatures; their evolutions as a result of these conditions were identical to those described above for the eutectic electrolyte, except that the intermediate cathodic peak, II_c, was slightly reduced with both LiCl-rich and KCl-rich electrolytes (the stability of the intermediate polysulfide species responsible for this transition may be dependent on the LiCl:KCl ratio of the electrolyte). Thus, the redox mechanism of the sulfide ion suggested for the eutectic composition of the molten salt is thought to correspond also to the behavior of S^{2-} over a wide range of compositions of the LiCl-KCl electrolyte.

A plot of the normalized peak current *vs.* the Li_2S concentration leads to an estimation of the diffusion coefficient of S^{2-} and of the solubility of Li_2S in the different electrolytes. As can be seen in Fig. 7, the height of peak I_a increases linearly with the concentration of Li_2S and becomes practically constant when the concentration of S^{2-} in solution is constant, regardless of the added amount of Li_2S, which indicates that the solubility limit is reached. For instance, the solubility limit was 950 ± 100 ppm Li_2S in the LiCl-KCl eutectic electrolyte at 454°C. The variations of the solubility of Li_2S in the different electrolytes tested between 400° and 450°C are given in Fig. 8. In this range of temperatures, the solubility increased with increasing LiCl concentration of the LiCl-KCl electrolyte. This result confirms the theoretical calculations of Saboungi *et al.* (26, 27) who have also calculated an increase in the solubility of Li_2S with the LiCl concen-

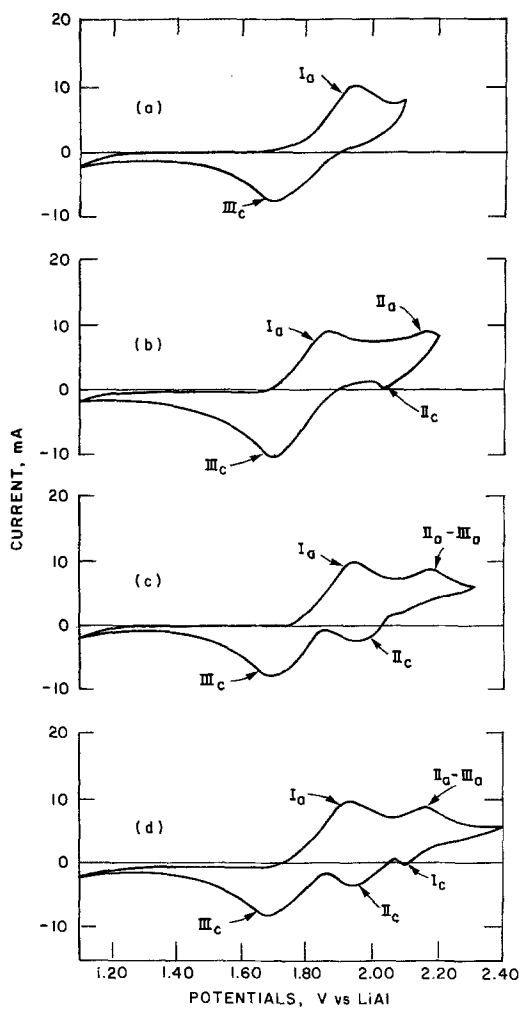

Fig. 5. Voltammograms (50 mV/sec) of sulfide ion in Li_2S-saturated LiCl-KCl eutectic electrolyte at $T = 399$°C for voltage ranges between (a) 1.10 and 2.10V, (b) 2.20V, (c) 2.30V, and (d) 2.40V.

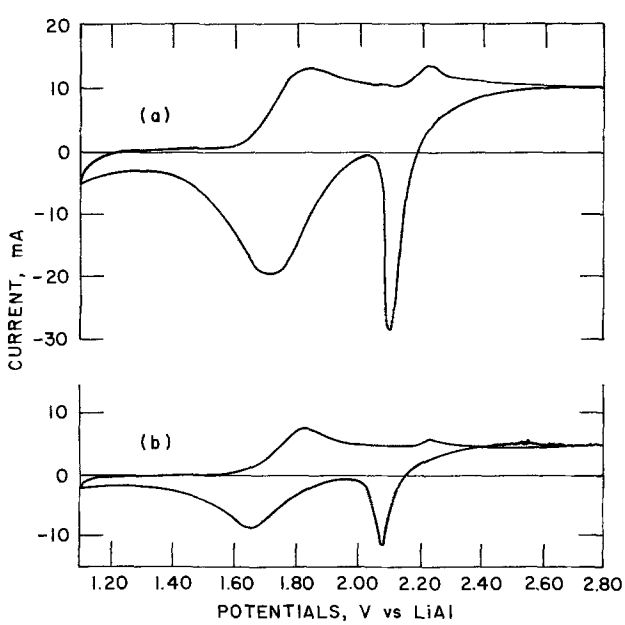

Fig. 6. Voltammograms (50 mV/sec) of sulfide ion in Li_2S-saturated (a) 66 m/o LiCl-34 m/o KCl and (b) 54 m/o LiCl-46 m/o KCl electrolytes at $T = 450$°C.

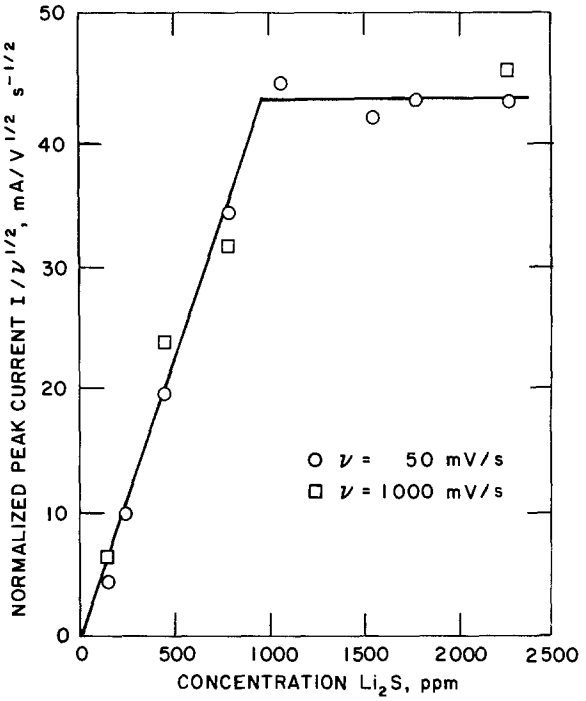

Fig. 7. Dependence of the normalized peak currents $I/\nu^{1/2}$ on Li_2S concentration in the LiCl-KCl eutectic for peak I_a at 454°C.

tration. In order to calculate the diffusion coefficient of S^{2-}, it is assumed that the first oxidation step is only diffusion controlled and that it involves the transfer of one electron per atom of sulfur, which has been suggested by the analysis of the voltammograms. For a purely diffusion-controlled one-electron reaction, the laws of diffusion lead to the linear relationship (22, 28) between the peak current and the concentration

$$\frac{I_p}{A\nu^{1/2}} = 0.446 \frac{F^{3/2}}{R^{1/2}T^{1/2}} D^{1/2} C^\circ$$

where I_p is the peak current (mA), A the area of the electrode (cm^2), ν the scan rate (V/sec), D the diffusion coefficient (cm^2/sec), and C° the concentration in the bulk of the solution (mol/liter). Under these conditions, the value of D can be determined. The experimental slope of the line for the anodic peak, I_a, (Fig. 7), gives a value of the diffusion coefficient of S^{2-} in the LiCl-KCl eutectic electrolyte: $D = (5.2 \pm 1) \times 10^{-5}$ cm^2 sec^{-1}, at 454°C. A similar value was also found with the LiCl-rich or KCl-rich LiCl-KCl electrolytes between 400° and 450°C. These results are in good agreement with the previous data of Cleaver *et al.* (13) and Weaver *et al.* (19) who had reported values of 5.7×10^{-5} cm^2 sec^{-1} and $(3.5 \pm 1) \times 10^{-5}$ cm^2 sec^{-1}, respectively, for the diffusion coefficient of S^{2-} in the LiCl-KCl eutectic electrolyte. The concordance of these results also supports the likely correctness of the postulated mechanism of the first anodic step.

Conclusion

Cyclic voltammetric studies in LiCl-KCl electrolytes containing Li_2S have shown that the electrochemistry of sulfide is sharply dependent on temperature in the range 400°-450°C. Systematic experiments performed under a wide range of experimental conditions were necessary to characterize the three oxidation steps and the two or three reduction steps of the system. The fact that the redox mechanism of the sulfide-sulfur system varies when the different parameters, especially the temperature, are changed partly explains the discrepancies among the results of previous work, since the authors have usually carried out their studies under fixed experimental conditions. In many cases, our measurements are in good (but partial) agreement with other studies. Nevertheless, we cannot propose, at this point, a detailed overall mechanism; further study, using analytical techniques which should allow the determination of the sulfur species formed, is required to address this problem and to propose, among the different possibilities that we have presented, the definitive correct sequence of reactions.

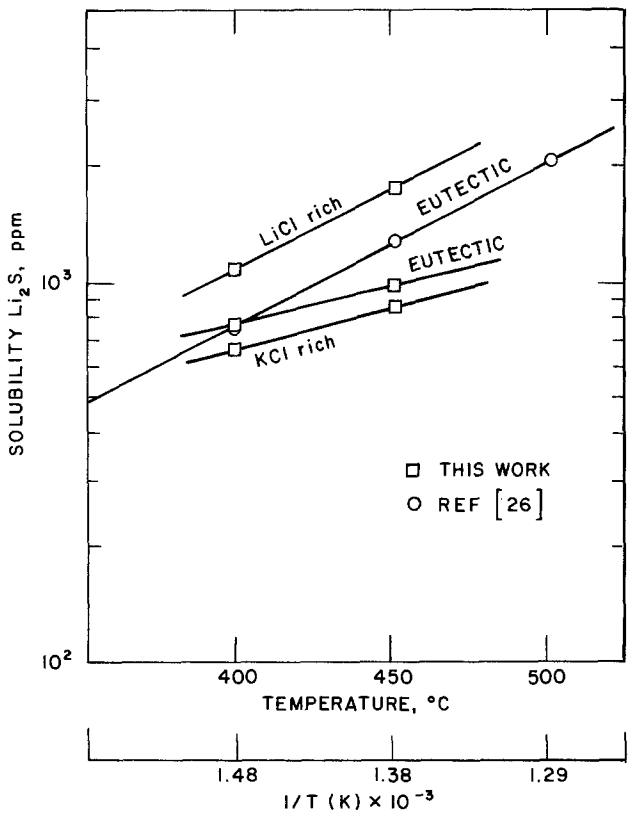

Fig. 8. Effect of electrolyte composition on solubility of Li_2S

The results that we have obtained, concerning the electrochemical behavior of sulfide ions in the LiCl-KCl molten salts, are also expected to be helpful for the study of metal sulfide redox processes in solution; better understanding of these processes could lead to an improvement of the FeS_2 electrode for high-temperature battery cells.

Acknowledgments

This work was conducted under the auspices of the Department of Energy.

Manuscript submitted Sept. 8, 1981; revised manuscript received *ca.* Feb. 22, 1982.

Any discussion of this paper will appear in a Discussion Section to be published in the December 1983 JOURNAL. All discussions for the December 1983 Discussion Section should be submitted by Aug. 1, 1983.

Publication costs of this article were assisted by Argonne National Laboratory.

REFERENCES

1. D. L. Barney *et al.*, Argonne National Laboratory ANL-79-94 (1979).
2. R. P. Tischer and F. A. Ludwig, *Adv. Electrochem. Electrochem. Eng.*, **10**, 391 (1977).
3. G. Delarue, *Bull. Soc. Chim. Fr.*, 1654 (1960).
4. G. Delarue, *ibid.*, 906 (1960).
5. R. Marassi, G. Mamantov, and J. Q. Chambers, *This Journal*, **123**, 1128 (1976).
6. F. G. Bodewig and J. A. Plambeck, *ibid.*, **116**, 607 (1969).
7. K. A. Paulsen and R. A. Osteryoung, *J. Am. Chem. Soc.*, **98**, 6866 (1976).
8. A. deGuibert, V. Plichon, and J. Badoz-Lambling, *This Journal*, **126**, 1902 (1979).
9. D. M. Gruen, R. L. McBeth, and A. J. Zielen, *J. Am.*

Chem. Soc., **93**, 6691 (1971).
10. W. Giggenbach, *Inorg. Chem.*, **10**, 1308 (1971).
11. J. P. Bernard, A. DeHaan, and H. Van der Poorten, *C. R. Acad. Sci. Paris*, **276**, 587 (1973).
12. J. H. Kennedy and F. Adamo, *This Journal*, **119**, 1518 (1972).
13. B. Cleaver, A. J. Davies, and D. J. Schiffrin, *Electrochim. Acta*, **18**, 747 (1973).
14. J. R. Birk and R. K. Steunenberg, *Adv. Chem. Ser.*, **740**, 786 (1975).
15. D. O. Raleigh, J. T. White, and C. A. Ogden, *This Journal*, **126**, 1087 (1979).
16. K. W. Kam and K. E. Johnson, *J. Electroanal. Chem. Interfacial Electrochem.*, **115**, 53 (1980).
17. G. Santarini, *C. R. Acad. Sci. Paris*, **288**, 457 (1979).
18. C. H. Liu, A. J. Zielen, and D. M. Gruen, *This Journal*, **120**, 67 (1973).
19. M. J. Weaver and D. Inman, *Electrochim. Acta*, **20**, 929 (1975).
20. R. S. Nicholson and I. Shain, *Anal. Chem.*, **36**, 706 (1964).
21. D. S. Polcyn and I. Shain, *ibid.*, **38**, 370 (1966).
22. C. P. Andrieux, L. Nadjo, and J. M. Saveant, *J. Electroanal. Chem. Interfacial Electrochem.*, **26**, 147 (1970).
23. G. Mamantov, D. L. Manning, and J. M. Dale, *ibid.*, **9**, 253 (1965).
24. R. C. Vogel *et al.*, Argonne National Laboratory ANL-7775, 120 (1971).
25. M. S. Shuman, *Anal. Chem.*, **41**, 142 (1969).
26. M. L. Saboungi, J. J. Marr, and M. Blander, *This Journal*, **125**, 1567 (1978).
27. M. L. Saboungi, J. J. Marr, and M. Blander, *Metall. Trans.*, **10B**, 477 (1979).
28. T. Berzins and P. Delahay, *J. Am. Chem. Soc.*, **75**, 555 (1953).

Oxygen Transfer on Substituted ZrO_2, Bi_2O_3, and CeO_2 Electrolytes with Platinum Electrodes

I. Electrode Resistance by D-C Polarization

M. J. Verkerk,[1] M. W. J. Hammink, and A. J. Burggraaf

Twente University of Technology, Department of Chemical Engineering, Laboratory of Inorganic Chemistry and Materials Science, 7500 AE Enschede, The Netherlands

ABSTRACT

The electrode behavior of Pt-sputtered and PT-gauze electrodes on ZrO_2-Y_2O_3, Bi_2O_3-Er_2O_3, and CeO_2-Gd_2O_3 solid electrolytes was investigated by means of d-c measurements in the temperature region of 770-1050 K and in the oxygen partial pressure region of 10^{-5} – 1 atm O_2 using N_2-O_2 mixtures. On these different materials the same electrode morphology was realized and was preserved during the subsequent experiments. The electrode process is strongly influenced by the nature of the electrolyte. The electrode resistance for Pt electrodes on Bi_2O_3-Er_2O_3 was found to be many times lower than on ZrO_2-Y_2O_3 and CeO_2-Gd_2O_3. On zirconia- and ceria-based materials diffusion of atomic oxygen on the Pt electrode is the rate-determining step in the electrode process, whereas for bismuth sesquioxide-based materials diffusion on the oxide surfaces is rate determining.

There is a considerable interest in solid electrolytes for use in oxygen sensors, oxygen pumps, and high temperature fuel cells. In these applications the electrode polarization and the electrolyte resistance both play an important role. These effects influence the response of an oxygen sensor and give rise to energy losses and therefore to a decreased efficiency of oxygen pumps and fuel cells. Many studies are performed on electrode processes. However, the dominant elementary steps of the overall process are still unknown in most cases.

The kinetics of the electrode process is strongly influenced by the electrode structure (1-6), electrode material (4, 5, 7-9), and the electrolyte (4, 5, 7). Information about the role of the electrolyte in the electrode process is very scarce and is limited to the role of the dopant. Schouler (4) found that the oxygen partial pressure dependence of the electrode resistance of a sputtered platinum electrode depends on the Y_2O_3 content of the ThO_2 electrolyte. Fabry and Kleitz (7) found that the activation energy of the electrode resistance of a point electrode on calcia-stabilized zirconia is higher than that on yttria-stabilized zirconia. Wang and Nowick (5) reported that the exchange current of a Pt-paste electrode is not influenced by the nature and the concentration of the dopant of the CeO_2 electrolyte.

Even less attention is paid to the influence of the nature of the electrolyte on the overall electrode process. From model considerations this influence has to be expected if particular elementary steps are dominant. In most studies reported in the literature the measurements are performed under different circumstances and using different and badly characterized electrode structures and consequently the results can hardly be compared.

Therefore, we studied the influence of the electrolyte conductivity and electrolyte composition on the electrode kinetics using different oxygen ion conductors. An important condition is that on these different materials the same electrode morphology has to be realized. Sputtered and gauze electrodes, subjected to several treatments, can meet this condition. The comparison of a sputtered and a gauze electrode on the same electrolyte may be a tool for investigating the rate-determining step.

The following systems were investigated:

$(ZrO_2)_{0.83}(YO_{1.5})_{0.17}$ (ZY17)

$(CeO_2)_{0.90}(GdO_{1.5})_{0.10}$ (CG10)

$(Bi_2O_3)_{0.80}(Er_2O_3)_{0.20}$ (BE20)

$(Bi_2O_3)_{0.70}(Er_2O_3)_{0.30}$ (BE30)

$(Bi_2O_3)_{0.60}(Er_2O_3)_{0.40}$ (BE40)

The bulk conductivity of the stabilized bismuth sesquioxides is 10-100 times higher than that of the stabilized zirconias and the substituted cerias (10, 11). Besides, bismuth oxide compounds are used as oxidation catalysts and a relative rapid transfer of oxygen on the solid-gas interface is suggested. For these reasons, we

[1] Present address: Philips Research Laboratories, Eindhoven, The Netherlands.

Key words: electrode resistance, solid electrolytes, Pt electrodes, electrode morphology.

investigated the idea whether the electrode resistance on the bismuth-based materials might be lower than that on the zirconia- and ceria-based materials.

Special attention is paid to the possibility of using the above-mentioned materials as a solid electrolyte in an oxygen pump. Therefore, the measurements were performed at relatively low temperatures and high oxygen partial pressures.

In this paper a phenomenological description of the influence of the nature of the electrolyte on the electrode process is given (d-c study). In part II of this study (12) the observed influence of the electrolyte is analyzed with respect to its critical steps by means of a frequency dispersion study.

Experimental

Sample preparation and characterization are given in Table I. The composition of the samples was checked with x-ray fluorescence. The diameter of the samples was 5-10 mm and the thickness 0.7-1.5 mm.

Measurements were performed in the temperature range 770-1050 K and with N_2-O_2 mixtures in the oxygen partial pressure range of 10^{-5}-1 atm O_2. The oxygen partial pressures in the range of 10^{-2}-1 atm were obtained by mixing appropriate O_2/N_2 mixtures and in the range of 10^{-5}-10^{-2} atm by an oxygen pump (15, 16). The oxygen partial pressure is measured using an oxygen sensor based on stabilized zirconia. The gases were supplied at a rate of 600 cm³/min.

The electrical circuit used in the d-c experiments is shown in Fig. 1. A Wenking potentiostat was used. The current was measured by the voltage drop across the reference resistor. The voltages were measured with an HP 3465A multimeter. The electrode resistance R_{el} was measured using a voltage of 1-10 mV across the sample and calculated according to

$$R_{el} = \left(\frac{dV}{dI}\right)_{I\to 0} - R_b \qquad [1]$$

The total bulk resistance R_b was obtained from a-c impedance measurements (13).

The complex impedance measurements were performed in the frequency range 10^6-10^{-3} Hz using a Solartron 1174 Frequency Response Analyzer with a sample voltage of 10 mV. The circuit is described in Ref. (13).

Electrode Preparation and Characterization

Platinum electrodes with a thickness of 0.75 μm were sputtered onto the polished samples. The sintering of the electrode during thermal treatments is influenced by the nature of the electrolyte. To obtain the same electrode morphology on different electrolytes a sintering temperature in the region of 1200-1400 K was necessary (2-4 hr). To be sure that no visible changes in the electrode morphology take place during the measurements, the system was equilibrated for 48 hr at the highest measuring temperature, and an a-c current treatment (1 kHz, 1V, 5 min) was applied. A typical scanning electron microscope (SEM, JEOL JSMU 3) picture is given in Fig. 2a. The morphology of the electrode is characterized by the length of the three-phase line and the surface area of the interfaces: electrolyte/electrode, electrolyte/gas, and electrode/gas. These data are given in Table II. The maximum measuring temperature is restricted by the requirement that the morphology of the electrode does not change in time. This condition is satisfied if the maximum measuring temperature is kept 150-200 K below the sintering temperature of the metal electrode. At every temperature the electrode was equilibrated for 16 hr before a measurement was performed.

Table I. Preparation and characterization of the samples

System	Preparation method	Sintering temperature (K)	Density (%)	Grain size (μm)
ZY17	Alkoxide synthesis (13)	1673	99	2.5
CG10	Citrate synthesis (14)	1773	96	5
BE20	Solid-state reaction (10)	1198	95	30
BE30	Solid-state reaction (10)	1273	96	30
BE40	Solid-state reaction (10)	1323	95	30

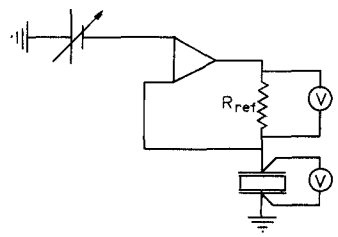

Fig. 1. Electrical circuit for the d-c measurements

Platinum gauze electrodes (200 meshes/cm²) were plastically deformed before use to obtain a reproducible contact surface. An overall picture of the gauze electrode is shown in Fig. 2b and its characteristic data are given in Table II. Figure 2c shows a representative part of the contact surface of a gauze electrode used on ZY17 or CG10 and Fig. 2d shows the same for BE20, BE30, and BE40. From these figures it is clear that because of the roughness of the contact surface oxygen molecules can penetrate this interface. Therefore, the actual three-phase line will be much larger than calculated on the basis of the circumference of the oval flattened parts of the gauze electrode. The gauze electrode was held with a constant pressure on the sample. Before the measurements were performed the above-described thermal and current treatments were applied.

After performing the d-c measurements (1-10 mV) and subsequently the a-c measurements [reported in part II of this study (12)], the electrode resistance was again measured by d.c. (1-10 mV). The total measuring time was about 600 hr. The electrode resistance of the Pt-sputtered electrode on BE20 was increased by a factor of two. Some Er_2O_3 particles could be detected on the electrode surface by means of SEM and x-ray diffraction. The R_{el} for the other combinations was not significantly changed during the measuring period. SEM pictures showed no changes in the morphology of the electrodes. Afterward the same samples were used for d-c experiments in the region of 0-2V.

Reproducibility of the electrode resistance of sputtered and gauze electrodes was checked on three nominally equal electrodes applied on ZY17. The electrode resistance falls in the region of log R_{el} ± log 1.2 and log R_{el} ± log 2 for sputtered and gauze electrodes, respectively.

Preliminary experiments on ZY17 with grain sizes of 0.5, 2.5, and 20 μm showed that the electrode resistance is not influenced by the grain size of the electrolyte.

Theory

In this section the relevant theory for the interpretation of the experimental data is given.

Table II. Characteristic data of the morphology of the sputtered (sp) and the gauze (g) electrode

Electrode	Three-phase line length (m/m²)	Electrolyte/electrode contact surface (m²/m²)	Electrolyte/gas contact surface (m²/m²)	Electrode/gas contact surface (m²/m²)
sp	1.2×10^6	0.64	0.36	0.8
g	$1.4 \times 10^{3*}$	0.64	0.96	1.6
Ratio $\frac{g}{sp}$	860	16	0.38	0.50

* Determined from the circumference of the oval flattened parts of the electrode.

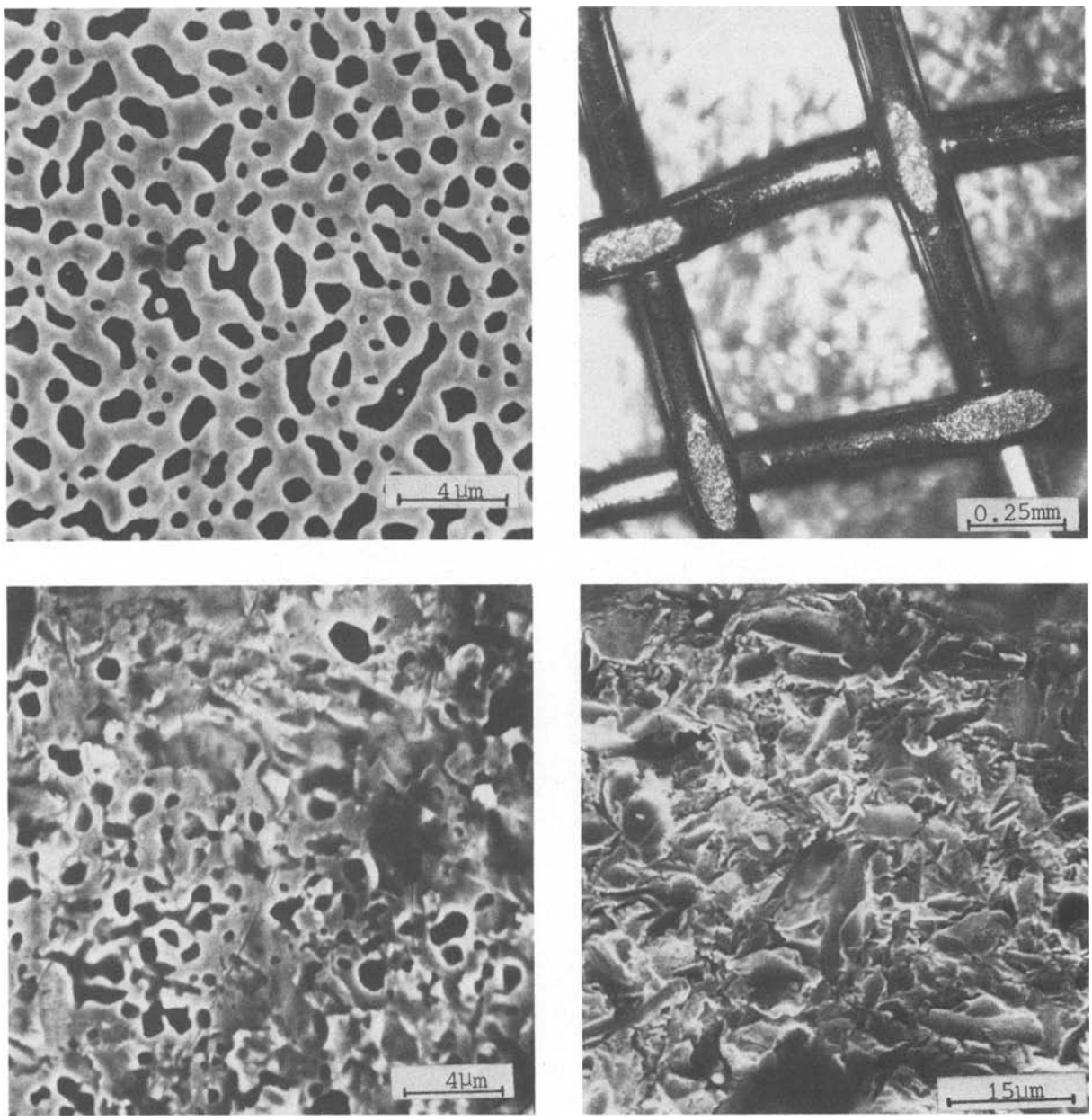

Fig. 2. Morphology of the platinum electrodes used in this study. Sputtered electrode (a, upper left), gauze electrode (b, upper right), contact surface of a gauze electrode after use on a ZY17 or CG10 sample (c, lower left), and contact surfaces of a gauze electrode after use on a BE20, BE30, or BE40 sample (d, lower right).

The elementary adsorption step in the electrode process is given by

$$O_2(g) + 2V_{ads} \leftrightarrows 2\,O_{ads} \qquad [2]$$

where V_{ads} is a vacant adsorption site and O_{ads} is an adsorbed oxygen atom. The mass action relation for this reaction can be written as (Langmuir adsorption)

$$\theta_{ads}/(1 - \theta_{ads}) = K_1(T) \times [P_{O_2}]^{1/2} \qquad [3]$$

The equilibrium constant is given by

$$K_1(T) = K_1^{o} \exp(\Delta H_{ads}/RT) \qquad [4]$$

where ΔH_{ads} is the heat of adsorption.

The adsorption step is followed by diffusion to the reaction site

$$O_{ads} + V_{rs} \leftrightarrows O_{rs} + V_{ads} \qquad [5]$$

where V_{rs} and O_{rs} are a vacant and occupied reaction site, respectively.

At the reaction site the charge transfer process takes place (given in Kröger-Vink notation)

$$O_{rs} + 2e' + V_O^{\cdot\cdot} \rightleftarrows O_o^{x} + V_{rs} \qquad [6]$$

If the charge process is rate limiting the relation between the current I and the overpotential η is given by the Butler-Volmer equation (17)

$$I = I_o[\exp(\alpha_a n V^*) - \exp(-\alpha_c n V^*)] \qquad [7]$$

$$V^* = \eta \mathbf{F}/RT \qquad [8]$$

where α_a and α_c are the anodic and cathodic transfer coefficients, respectively, V^* is a dimensionless potential, I_o the exchange current, and n number of charges transferred.

However, if the anodic or cathodic process is limited by mass transport the following equation holds (17)

$$I = [\exp(\alpha_a n V^*) - \exp(-\alpha_c n V^*)]/$$
$$[I_o^{-1} + I_{la}^{-1} \exp(\alpha_a n V^*) + I_{lc}^{-1} \exp(-\alpha_c n V^*)] \qquad [9]$$

where I_{la} and I_{lc} are the anodic and cathodic limiting current, respectively, and are defined positive. At low overpotentials, $|nV^*| << 1$, ohmic behavior is obtained

$$I = nV^*/(I_o^{-1} + I_{la}^{-1} + I_{lc}^{-1}) \qquad [10]$$

Using [8] we find

$$R_{el} = \frac{\eta}{I} = R_{ct} + R_{la} + R_{lc} \quad [11]$$

with $R_{ct} = \frac{RT}{nF} \cdot \frac{1}{I_o}$, $R_{la} = \frac{RT}{nF} \cdot \frac{1}{I_{la}}$, and $R_{lc} = \frac{RT}{nF} \cdot \frac{1}{I_{lc}}$.

From Eq. [9]-[11] it is clear that for I_{la}, $I_{lc} >> I_o$ the electrode process is determined by the charge transfer and for $I_o >> I_{la}$, I_{lc} by mass transport.

The oxygen atoms for the electrode process can be supplied by dissociated adsorption of oxygen molecules at the electrode or the electrolyte and the charge transfer will take place near the triple line (this will be further discussed below). Now we assume a model where the limiting current originates from diffusion of atomic oxygen from the adsorption site at $x = \delta$ to the reaction site at $x = 0$. At $x = \delta$ the concentration oxygen atoms is constant [see part II of this study (12)]. We can write then for I_c and I_a

$$I_c = -D_o nF \frac{C_o(\text{ads}) - C_o(\text{rs})}{\delta'} \quad [12]$$

$$I_a = D_o nF \frac{C_o(\text{rs}) - C_o(\text{ads})}{\delta''} \quad [13]$$

where D_o and C_o are the diffusion coefficient and the concentration of the oxygen atoms. I_c and I_a are given per surface unit of reaction area. A cathodic and anodic limiting current is observed for $C_o(\text{rs}) \rightarrow 0$ and $C_o(\text{rs}) \rightarrow C_o'(\text{rs})$, respectively, and are given by

$$I_{lc} = D_o nF \frac{C_o(\text{ads})}{\delta'} \quad [14]$$

$$I_{la} = D_o nF \frac{C_o'(\text{rs}) - C_o(\text{ads})}{\delta''} \quad [15]$$

where $C_o'(\text{rs})$ is the surface concentration of oxygen atoms for $\theta = 1$.

Results and Discussion

Pt electrodes on ZY17.—For all samples the I-V relation at small voltages shows an ohmic behavior, as shown in Fig. 3 for ZY17. Due to a small d-c voltage of 0-1 mV, probably originating from thermoelectric effects, the curves do not pass through the origin. The determination of the electrode resistance according to Eq. [1] is not influenced by this small voltage.

The electrode resistance R_{el} measured as a function of temperature for P_{O_2} is equal to 1, 0.21, 1.6×10^{-2}, and 9×10^{-4} atm O_2, respectively. Values of the activation energy E_a and the pre-exponential term log R_o are given in Table III. The results for a sputtered and a gauze electrode at $P_{O_2} = 1.6 \times 10^{-2}$ atm are shown

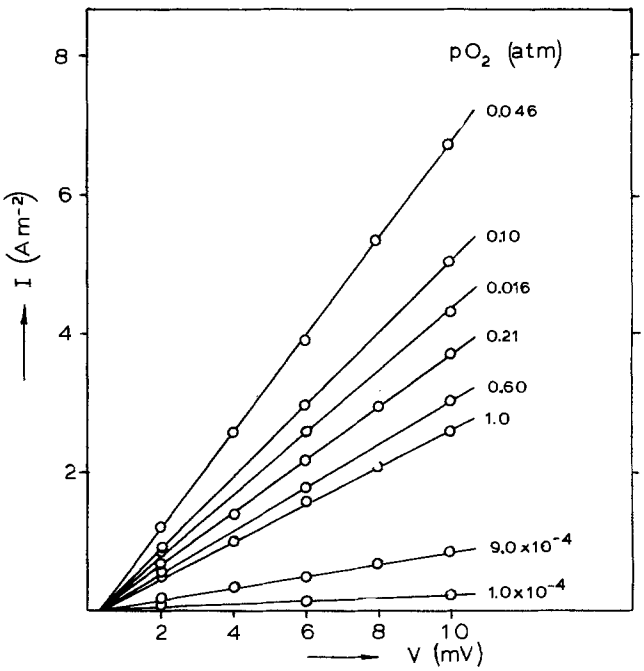

Fig. 3. Current-voltage characteristics for ZY17 at $T = 983$ K using Pt-sputtered electrodes.

in Fig. 4. At about 960 K a bend in the Arrhenius plot of R_{el} is observed and E_a changes from about 75 kJ mol^{-1} (high temperature part) to about 250 kJ mol^{-1} (low temperature part). This bend is correlated with a change from the regime where $R_{el} \sim P_{O_2}^{-1/2}$ to the regime where $R_{el} \sim P_{O_2}^{+1/2}$ (see below). Its position on the temperature scale depends on the P_{O_2} pressure and its position on the P_{O_2} scale on the temperature (Fig. 5).

Figure 5a gives R_{el} as a function of P_{O_2} at 983 K. For comparison the R_{el}-P_{O_2} relation calculated from Table III for 908 K is also given in this figure. A minimum in the R_{el}-P_{O_2} curve is observed at a value of $P_{O_2}^{\text{min.}}$. For both sputtered and gauze electrodes at $P_{O_2} < P_{O_2}^{\text{min.}}$ one finds $R_{el} \sim P_{O_2}^{-1/2}$ and from Fig. 4 and Table III it follows that in this region E_a has a value of 75-100 kJ mol^{-1}. Whereas $P_{O_2} > P_{O_2}^{\text{min.}}$ one finds $R_{el} \sim P_{O_2}^{+1/2}$ and in this region E_a has a value of about 250 kJ mol^{-1}. The value of $P_{O_2}^{\text{min.}}$ shifts to higher values with increasing temperature.

These results are in good agreement with literature data concerning platinum electrodes on stabilized zirconia. However, the reported experimental literature data are incomplete and only parts of the picture described above were measured. A minimum in the

Table III. Activation energies and log R_o of the electrode resistance of sputtered (sp) and gauze (g) electrodes on several electrolytes. The deviation is given in the 65% reliability interval.

	1 atm O_2		0.21 atm O_2		1.6×10^{-2} atm O_2			9×10^{-4} atm O_2		
System	$-\log R_o$ (Ωm^2)	E_a (kJ mol^{-1})	$-\log R_o$ (Ωm^2)	E_a (kJ mol^{-1})	Range (K)	$-\log R_o$ (Ωm^2)	E_a (kJ mol^{-1})	Range (K)	$-\log R_o$ (Ωm^2)	E_a (kJ mol^{-1})
ZY17 (sp)	16.9 ± 0.9	270 ± 15	16.5 ± 0.4	260 ± 7	<970	15.3 ± 0.6	230 ± 10	<925	9.8 ± 0.5	145 ± 10
					>970	6.6 ± 0.6	72 ± 10	>925	5.6 ± 0.5	70 ± 10
ZY17 (g)	13.8 ± 0.6	245 ± 10	15.8 ± 0.7	280 ± 10	<960	9.9	167		5.5 ± 0.1	98 ± 5
					>960	4.9 ± 0.4	75 ± 10			
CG10 (sp)	14.8 ± 0.5	230 ± 10	14.9 ± 0.5	321 ± 9	<970	16.0 ± 0.1	245 ± 3	<930	10.3 ± 0.1	148 ± 1
					>970	7.7 ± 0.3	91 ± 6	>930	5.4 ± 0.3	61 ± 4
CG10 (g)	12.3 ± 0.3	212 ± 6	12.3 ± 0.3	208 ± 6	<940	12.1	203		5.5 ± 0.2	96 ± 4
					>940	5.1 ± 0.3	77 ± 5			
									2.2 × 10^{-4} atm O_2	
BE20 (sp)	11.8 ± 0.4	145 ± 6	9.6 ± 0.1	115 ± 2		10.0 ± 0.3	129 ± 5		7.1 ± 0.3	101 ± 6
BE20 (g)	9.7 ± 0.3	133 ± 5	9.8 ± 0.4	137 ± 7		8.1 ± 0.4	116 ± 6		5.6 ± 0.6	83 ± 10
BE30 (sp)	11.1 ± 0.1	138 ± 2	10.0 ± 0.3	125 ± 5		9.2 ± 0.2	121 ± 3		6.8 ± 0.6	99 ± 10
BE30 (g)	8.3 ± 0.3	112 ± 5	7.9 ± 0.4	108 ± 6		6.3 ± 0.3	87 ± 4		3.4 ± 0.4	45 ± 7
BE40 (sp)	10.3 ± 0.4	129 ± 7	8.8 ± 0.5	110 ± 8		9.6 ± 0.3	125 ± 5		5.7 ± 1.1	75 ± 20
BE40 (g)	8.3 ± 0.4	119 ± 7	7.7 ± 0.5	110 ± 8		6.9 ± 0.2	102 ± 3		3.3 ± 0.3	45 ± 6
BE20 (gold, sp)			11.2 ± 0.9	150 ± 15						

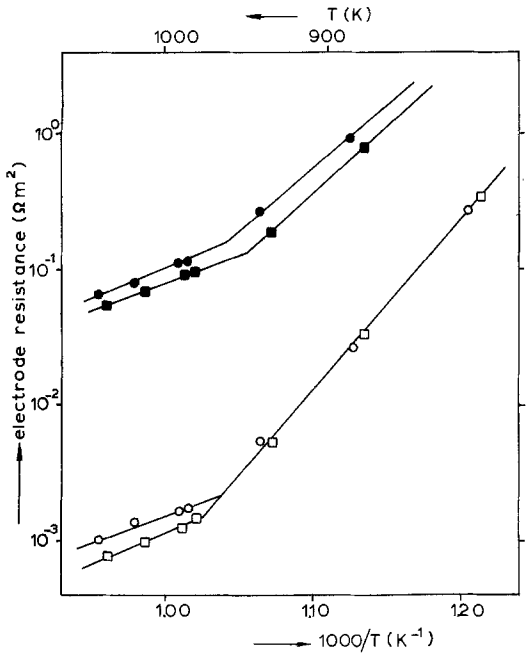

Fig. 4. Electrode resistance as a function of temperature for $P_{O_2} = 1.6 \times 10^{-2}$ atm O_2. ○, Pt-sputtered electrode on ZY17; ●, Pt-gauze electrode on ZY17; □, Pt-sputtered electrode on CG10; ■, Pt-gauze electrode on CG10.

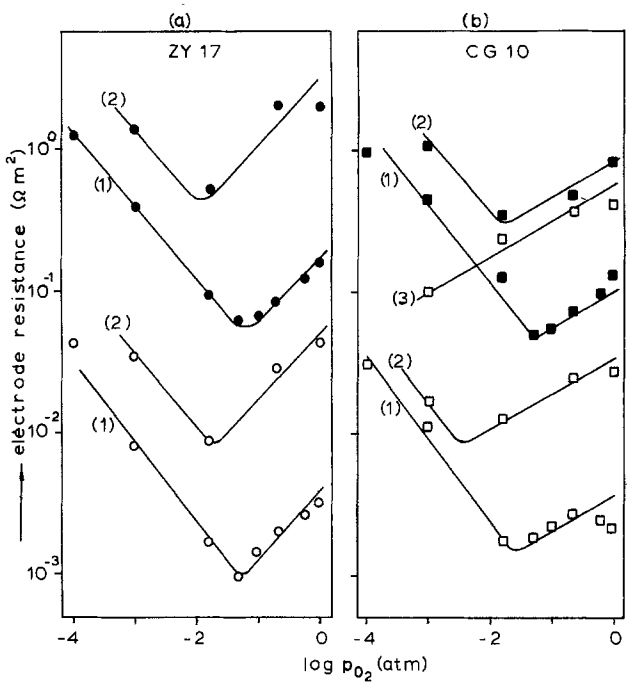

Fig. 5. (a) Electrode resistance as a function of the oxygen partial pressure at 983 K, 1; 908 K, 2; and 833 K, 3. Pt electrodes on ZY17. The drawn lines represent a $P_{O_2}^{-1/2}$ and $P_{O_2}^{+1/2}$ dependence respectively. (b) Pt electrodes on CG10. The drawn lines represent a $P_{O_2}^{-1/2}$ and $P_{O_2}^{+1/4}$ dependence respectively. Open points: sputtered electrodes. Closed points: gouze electrodes.

R_{el}-P_{O_2} curve was reported by Schouler (4) for Pt-sputtered and Pt-paste electrodes on $(ZrO_2)_{0.83}(YO_{1.5})_{0.17}$ and by Hartung (6) for Pt-paste electrodes on $(ZrO_2)_{0.82}(YO_{1.5})_{0.10}(MgO)_{0.08}$. According to Bauerle (2) at 1073 K, $R_{el} \sim P_{O_2}^{-0.64}$ at low oxygen partial pressures and becomes constant at high oxygen partial pressures (0.21-1.00 atm O_2) for Pt-sputtered electrodes on yttria-stabilized zirconia (YSZ). In the opinion of the authors the experimental data permit the following interpretation: $P_{O_2}^{min.}$ has a value of 0.21-1.00 atm O_2 and for $P_{O_2} < P_{O_2}^{min.}$ $R_{el} \sim P_{O_2}^{-0.5}$. For Pt electrodes on YSZ an activation energy of about 100 kJ mol^{-1} was reported in Ref. (4 and 7) in the region where $R_{el} \sim P_{O_2}^{-1/2}$ and a value of about 250 kJ mol^{-1} in Ref. (2 and 4) in the region where $P_{O_2} > P_{O_2}^{min.}$.

The observed phenomena were ascribed by Schouler (4) to oxidation of the platinum surface. This hypothesis may be a good explanation for the high activation energy found at high P_{O_2}. The observed relationship $R_{el} \sim P_{O_2}^{+1/2}$ at $P_{O_2} > P_{O_2}^{min.}$ cannot be explained with the formation of an oxidized Pt surface because it is well known that this is catalytically less active.

In our opinion the observed phenomena can be explained in the following way. The oxygen atoms for the electrode process are supplied by dissociative adsorption of oxygen molecules at the Pt electrode. The overall electrode reaction is rate determined by diffusion of the oxygen atoms from the adsorption site to the reaction side (see section on Theory). At $P_{O_2} < P_{O_2}^{min.}$, θ_{ads} is low and mass transport limitation occurs at the cathode. At $P_{O_2} > P_{O_2}^{min.}$, $\theta_{ads} \approx 1$ and mass transport limitation occurs at the anode. This hypothesis is discussed in the following.

As shown by Wang and Nowick (5) the electrode resistance varies as the $-1/4$ or $+1/4$ power of P_{O_2} if the electrode process is determined by charge transfer (see following section). The experimentally found powers of $-1/2$ and $+1/2$ point to mass transfer limitation and can be derived from Eq. [14] and [15]. For $\theta_{ads} << 1$ holds $(1 - \theta_{ads}) \approx 1$ and assuming that $\delta' \approx \delta''$ we find $I_{1a} >> I_{1c}$. From Eq. [3] it follows that $\theta_{ads} = K_1(T) \times [P_{O_2}]^{1/2}$ and using Eq. [10], [11], and [14] it is found that

$$R_{el} = R_{1c} \sim \frac{\delta}{D_o\sqrt{K_1}} P_{O_2}^{-1/2} \qquad [16]$$

For $\theta_{ads} \approx 1$ we find that $I_{1c} >> I_{1a}$ and $(1 - \theta_{ads}) = K_1(T) \times [P_{O_2}]^{-1/2}$ and this results in

$$R_{el} = R_{1a} \sim \frac{\delta\sqrt{K_1}}{D_o} P_{O_2}^{+1/2} \qquad [17]$$

According to Eq. [16] at $P_{O_2} < P_{O_2}^{min.}$ (*i.e.*, $\theta_{ads} << 1$) mass transport limitation of oxygen atoms occurs at the cathode and according to Eq. [17] at $P_{O_2} > P_{O_2}^{min.}$ (*i.e.*, $\theta_{ads} \approx 1$) mass transport limitation of oxygen atoms occurs at the anode. The surface coverage of oxygen atoms decreases with increasing temperature and this is in a good agreement with the observed change of $P_{O_2}^{min.}$ as a function of T. From Eq. [16] and [17] it follows that in the region where R_{el} varies with $P_{O_2}^{-1/2}$ and $P_{O_2}^{+1/2}$ the activation energy of R_{el} is given by $E_a(R_{el}) = \Delta H_d - 1/2\Delta H_{ads}$ and $E_a(R_{el}) = \Delta H_d + 1/2\Delta H_{ads}$, respectively, where ΔH_d is the activation enthalpy for diffusion. In literature no precise data are known of ΔH_d and ΔH_{ads} as a function of the coverage. Supposing that ΔH_d and ΔH_{ads} are not strongly dependent on the coverage, we calculate from the experimental values of $E_a(R_{el})$ for ΔH_d and ΔH_{ads} values of 170 and 160 kJ mol^{-1}, respectively. These calculated data are in reasonable agreement with literature data concerning ΔH_d and ΔH_{ads} of oxygen on platinum. Lewis and Gomer (19) found a surface diffusion enthalpy of 145 kJ mol^{-1} for oxygen atoms on platinum at $T >$ 500 K. The values of the enthalpy of adsorption found by different authors scatter. Brennan *et al.* (21) reported that ΔH_{ads} decreases with increasing surface coverage from 285 to 150 kJ mol^{-1} (300 K). Netzer and Gruber (18) reported for high surface coverages a value for ΔH_{ads} of 135 kJ mol^{-1} (670-770 K). Finally, ΔH_{ads} can be calculated from the temperature dependence of $P_{O_2}^{min.}$. According to the Langmuir equation a minimum in R_{el} is predicted for $\theta = 1/2$ and with Eq. [3] this results in $K_1(T) \times P_{O_2}^{min.} = 1$. From Schouler's (4) data it follows that $\Delta H_{ads} = 280 \pm 15$ kJ mol^{-1} and from our data $\Delta H_{ads} = 160 \pm 30$ kJ mol^{-1}.

Additional evidence that the oxygen atoms for the electrode process are supplied by dissociative adsorption on the Pt electrode and not on the electrolyte comes from the following data. First, $P_{O_2}^{min.}$ has about the same value for Pt electrodes on ZY17 and on CG10 (compare Fig. 5a and b) while with other electrode materials no $P_{O_2}^{min.}$ is observed and E_a has a quite different value (4, 9). Finally, the work of Kleitz (8) strongly suggests that adsorbed oxygen atoms on the stabilized zirconia surface are practically immobile.

The proposed hypothesis for the mechanism of the electrode reaction on ZY17 gives a good explanation for the limiting current observed by Gür (20) at low voltages ($\leq$ 300 mV). Gür performed measurements on the cell

$$(-)P_{O_2}, Pt|ZrO_2 - Sc_2O_3|Pt, air\ (+)$$

in the temperature region of 873-1173 K and P_{O_2} region of 10^{-6}-1 atm. The limiting current was observed below 1073 K and was independent of the oxygen partial pressure at the cathode. Gür (20) assumed that the anodic polarization of the cell was negligible. However, as discussed above, at $T < 1073$ K, $\theta_{ads} \approx 1$ in air. At a high surface coverage of oxygen atoms the electrode process is limited by mass transport at the anode, see Eq. [15]. According to Gür (20) the limiting current has an activation energy of about 250 kJ mol^{-1} and this value is in a good agreement with the value found in this study for $E_a(R_{el})$ at $\theta_{ads} \approx 1$. Therefore, we can conclude that the limiting current at these high P_{O_2} values and low temperatures has to be correlated with mass transport limitation at the anode.

The location of the reaction site is discussed in the following. The difference in electrode resistance between a gauze and sputtered electrode ($R_{el}(g)/R_{el}(sp) \approx 50$) cannot be simply correlated with the size of the electrolyte/electrode two-phase area or the length of the three-phase line. An additional experiment was performed to determine whether the size of the electrolyte/electrode two-phase area or the length of the three-phase line plays a role in the magnitude of R_{el}. On three identical samples a 0.3 μm thick Pt electrode was sputtered and subjected to different thermal treatments resulting in strongly different electrode morphologies. The characteristic data are summarized in Table IV. The shape of the frequency dispersion diagrams is not influenced by the size of the Pt grains. This is a strong indication that the mechanism of the electrode process is not influenced by the particle size of the Pt grains. As shown in Table IV the electrode resistance increases strongly with increasing particle size. With increasing particle size the size of the electrolyte/electrode two-phase area is nearly constant whereas the length of the three-phase line decreases. We can conclude that the reaction area is correlated with the length of the three-phase line. The width of the three-phase line area (perpendicular on this line) is small in comparison with the smallest Pt particles used.

Pt electrodes on CG10.—The data of sputtered and gauze electrodes on CG10 are summarized in Fig. 4 and 5 and in Table III. The characteristics of Pt electrodes on CG10 show a large similarity with that of Pt electrodes on ZY17 and are therefore briefly discussed.

Table IV. Characteristic data of a Pt-sputtered electrode on ZY17, treated at different temperatures

Thermal treatment temperature (K)	Size of the Pt-grains (μm)	Length of the three-phase line (m/m^2)	Electrolyte/electrode contact surface (m^2/m^2)	Electrode resistance (O_2, 823K) (Ωm^2)
973	$\leq$0.1	$\geq 1.5 \times 10^7$	0.99	0.95
1173	0.5	3×10^6	0.93	6.25
1273	1.0	1.5×10^6	0.85	10.5

In the R_{el}-P_{O_2} relation a minimum is observed. For $P_{O_2} > P_{O_2}^{min.}$ it is found that $R_{el} \sim P_{O_2}^{1/4}$ and $E_a(R_{el}) \approx 230$ kJ mol^{-1}, whereas in the region where $P_{O_2} < P_{O_2}^{min.}$, $R_{el} \sim P_{O_2}^{-1/2}$ and $E_a(R_{el}) \approx$ 75-100 kJ mol^{-1}.

In the region of $P_{O_2} > P_{O_2}^{min.}$ there is a good agreement with the data of Wang and Nowick (5) for Pt-paste electrodes on CeO_2-CaO [1-15 mol percent (m/o)] and CeO_2-Y_2O_3 (6 m/o). The power 1/4 points to charge transfer limitation, as shown by Wang and Nowick (5). The exchange current is given by

$$I_o \sim K_{ct}[\theta(1-\theta)]^{1/2} \quad [18]$$

where K_{ct} is the charge transfer reaction constant. If the electrode reaction is determined by the charge transfer and the oxygen for this process is supplied through adsorbed oxygen atoms on the electrode, it is derived from Eq. [3], [10], and [18] that for $P_{O_2} > P_{O_2}^{min.}$ (*i.e.*, $\theta \approx 1$) $R_{ct} \sim P_{O_2}^{+1/4}$. The activation energy is given by $E_a(R_{el}) = E_a(ct) + \Delta H_{ads}/4$ (5), where $E_a(ct)$ is the activation energy of the charge transfer. Using the experimental values $E_a(R_{el})$ and $\Delta H_{ads} =$ 160 kJ mol^{-1} the value of $E_a(ct)$ is calculated to be 190 kJ mol^{-1}.

In the region of $P_{O_2} < P_{O_2}^{min.}$ Wang and Nowick (5) found that $R_{el} \sim P_{O_2}^{-1/4}$ and $E_a(R_{el}) \approx 95$ kJ mol^{-1}. The power $-1/4$ can be derived from Eq. [3], [10], and [18] assuming that the electrode process is determined by the charge transfer and $\theta << 1$ (5). However, in this study we found that $R_{el} \sim P_{O_2}^{-1/2}$, pointing to mass transport limitation. In our opinion this difference can be explained in the following way. For ceria-based materials with a porous electrode I_o is of the same order of magnitude as I_{lc}. Depending on the electrode morphology, the electrode process will be dominated by I_o or I_{lc}. The electrodes studied by Wang and Nowick (5) have larger metal grain sizes than used in this study. The influence of the morphology of the Pt electrode is clearly illustrated by the fact that for Pt foil electrodes on substituted ceria diffusion along the electrolyte/electrode interphase is rate determining, as shown by Wang and Nowick (9).

Pt electrodes on BE20, BE30, and BE40.—The electrode resistance of a Pt-sputtered and Pt-gauze electrode on BE20, BE30, and BE40 was measured as a function of T in the oxygen partial pressure range 1.0-2.2 $\times$ 10^{-4} atm O_2. Values of $E_a(R_{el})$ and log R_o are given in Table III. Figure 6 gives R_{el} for sputtered and gauze electrodes as a function of temperature. The electrode resistance increases with increasing Er content. $E_a(R_{el})$ for sputtered and gauze electrodes has a value of about 125 kJ mol^{-1} in the region of $P_{O_2} =$ 1-1.6 $\times$ 10^{-2} atm O_2 and is independent of the Er content. For $P_{O_2} = 2.2 \times 10^{-4}$ atm, $E_a(R_{el})$ varies in the region of 50-100 kJ mol^{-1}.

$E_a(R_{el})$ is slightly higher than the activation energy of the bulk conductivity at $T < 820$ K [$E_a(b) \approx 115$ kJ mol^{-1}] and both the bulk and electrode resistance increase with increasing Er content. Yet, the electrode resistance cannot be directly correlated with bulk effects. For the sample BE20 $E_a(b)$ changes at 870 K from 115 kJ mol^{-1} (low temperature part) to 62 kJ mol^{-1} (high temperature part) and this change is not reflected in the R_{el}-T^{-1} curve.

Figure 7 gives the electrode resistance of sputtered and gauze electrodes on BE20 and BE40 as a function of P_{O_2} (the values for BE30 are omitted for clarity reasons). For sputtered electrodes the relation $R_{el} \sim P_{O_2}^{-1/2}$ is found, pointing to mass transport of atomic oxygen as the rate-limiting step (see section on Pt electrodes on ZY17). For gauze electrodes the relation $R_{el} \sim P_{O_2}^{-3/8}$ is found. As shown by Wang and Nowick (9) the 3/8 power can be derived if the charge transfer takes place on the electrolyte/electrode interface and diffusion along this interface is rate determining. As shown in part II of this study (12), R_{el} consists of a parallel combination of two resistances. Therefore, in

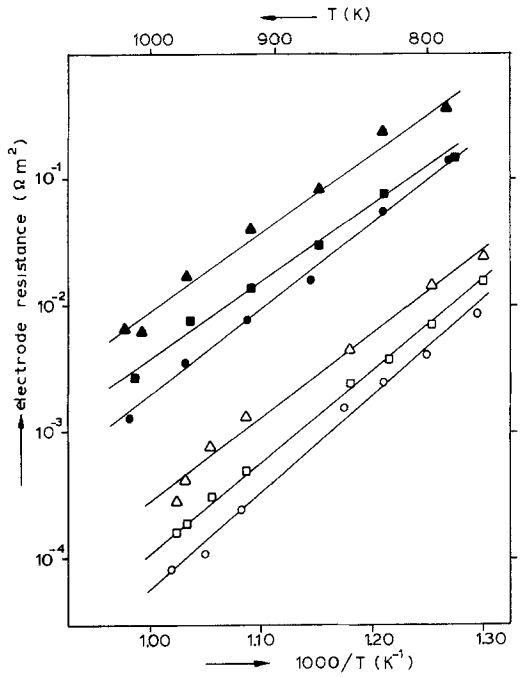

Fig. 6. Electrode resistance of platinum electrodes on BE20 (circles), BE30 (squares), and BE40 (triangles) as a function of the temperature in O_2 (1 atm). Open points: sputtered electrodes. Closed points: gauze electrodes.

this case the observed P_{O_2} dependency is the result of two other dependencies. This will be further discussed in part II (12).

In contrast with the data for Pt electrodes on ZY17 and CG10 (see Fig. 5) no minimum in the R_{el}-P_{O_2} relation for Pt electrodes on Bi_2O_3-based materials is observed (see Fig. 7). In the section on Pt electrodes on ZY17 it was concluded that for ZY17 and CG10 the oxygen atoms for the electrode process are supplied by dissociative adsorption of oxygen molecules on the Pt electrode. Therefore, we must conclude that for the Bi_2O_3-based materials this adsorption step on Pt does not play a dominant role here. This conclusion is supported by the magnitude of $E_a(R_{el})$ on Bi_2O_3-based materials, which strongly deviates from what one expects for adsorption and diffusion on Pt. Consequently, adsorption and diffusion on the electrolyte plays a dominant role on Bi_2O_3-based materials. Additional evidence comes from the observation that $E_a(R_{el})$ is not or only slightly changed if a gold-sputtered electrode is used on BE20 (see Table III) whereas for gold electrodes on zirconia- and ceria-based materials $E_a(R_{el})$ is significantly higher (4, 9). The active site for this adsorption is probably correlated with the Bi^{3+} ion, because with decreasing amount of Bi^{3+} ions the amount of adsorption sites decreases, which results in a higher electrode resistance (it is assumed, see above, that the increased bulk electrolyte resistance does not play an important role).

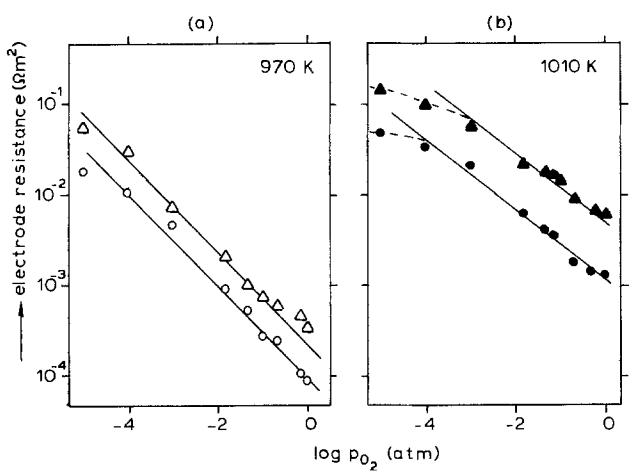

Fig. 7. Electrode resistance of Pt-sputtered electrodes (a) and Pt-gauze electrodes (b) as a function of the oxygen partial pressure. In (a) the drawn lines represent a $P_{O_2}{}^{-1/2}$ dependence and in (b) a $P_{O_2}{}^{-3/8}$ dependence. BE20: circles. BE40: squares.

The electrode resistance of a sputtered electrode on Bi_2O_3-based materials is 10-30 times lower than that of a gauze electrode. This suggests that the charge transfer takes place on the electrolyte/electrode interface (see Table II). However, due to the fact that it is questionable whether the electrode mechanism is the same for a sputtered and gauze electrode, these data are not further used to determine the reaction site.

Comparison of the Different Electrolytes

The combination of the electrolyte material, electrode material, and electrode morphology determines whether the dominating adsorption, dissociation, or diffusion step takes place at the electrolyte, electrode, or at the electrolyte/electrode interface. As shown above, there are large differences between the adsorption behavior of, on the one hand, ZY17 and CG10 and, on the other hand, the electrolytes BE20, BE30, and BE40, both groups in combination with porous Pt electrodes. In case of ZY17 and CG10 the oxygen atoms for the electrode process are supplied by the platinum electrode, whereas for the Bi_2O_3-based materials the oxygen atoms are supplied by the electrolyte surface. Therefore, it can be expected that there are large differences in the polarization of Pt electrodes on ZY17 and CG10, on the one hand, and Bi_2O_3-based materials, on the other hand.

Table V summarizes the values of the electrode resistance for Pt-sputtered and Pt-gauze electrodes on several electrolytes. The data for $P_{O_2} = 1$ atm lie in the region where θ_{ads} on Pt is about one and the data for $P_{O_2} = 9 \times 10^{-4}$ atm O_2 in the region where θ_{ads} (Pt) $<< 1$. As expected, the electrode resistance for Pt electrodes on ZY17 and CG10 is similar. However, the electrode resistance for Pt electrodes on Bi_2O_3-based materials is much smaller. In the region where $\theta_{ads}(Pt) << 1$ the resistance of sputtered and gauze electrodes on BE20 is respectively 4 and 20 times smaller than that of similar electrodes on ZY17.[2] In the region where $\theta_{ads}(Pt) \approx 1$ the electrode resistance on BE20 at 974 K is 40 (sputtered electrode) and 80 (gauze electrode) times smaller than on ZY17 and at 873 K these values are 250 and 400 times smaller, respectively. These data show clearly the influence of the electrolyte on the electrode resistance of Pt/Bi_2O_3-

[2] It must be noticed that the microscopic structure of a gauze electrode on ZY17, CG10, and on BE20, 30, 40 differ (see section on Electrode Preparation and Characterization).

Table V. Electrode resistance for platinum-sputtered electrodes (sp) and platinum-gauze electrodes (g) on several electrolytes

System	Electrode resistance (10^{-3} Ωm²) 1 atm O_2 873 K	1 atm O_2 973 K	9×10^{-4} atm O_2 973 K
ZY17 (sp)	184	4.1	14.5
CG10 (sp)	93	3.7	7.6
BE20 (sp)	0.76	0.098	3.9
BE30 (sp)	1.43	0.20	5.5
BE40 (sp)	2.65	0.43	6.7
ZY17 (g)	7370	230	550
CG10 (g)	2470	125	460
BE20 (g)	18.3	2.8	22*
BE30 (g)	25.6	5.2	44*
BE40 (g)	66.7	12	95*

* These values were calculated from the R_{el}-P_{O_2} plot at 1073 K shown in Fig. 7b, assuming $E_a = 120$ kJ mol^{-1}.

based systems, an effect which becomes larger with increasing P_{O_2} and lower temperatures.

For Pt electrodes with the same morphology, at $P_{O_2} > P_{O_2}^{min.}$ the electrode process on ZY17 is determined by mass transfer (see section on Pt electrodes on ZY17), whereas for CG10 by charge transfer (see section on Pt electrodes on CG10). Due to a similar electrode morphology I_{la} will have the same value for CG10 and ZY17 and therefore we can conclude that on CG10 I_0 is smaller (and becomes rate determining) than on ZY17.

Oxygen ion conductors may be used in devices in which pumping of oxygen plays an important role, *i.e.*, oxygen pumps for the enrichment of air. For comparing the different materials as a potential candidate for the solid electrolyte, current-overpotential relations for Pt electrodes were measured in air. The results for sputtered and gauze electrodes are shown in Fig. 8a and b.[3] The current that can be drawn at $\eta = 600$ mV is for BE20 using sputtered electrodes about 5 times higher than for ZY17 and for gauze electrodes about 10 times higher. This shows that the Bi_2O_3-based materials are superior to the other materials with respect to its electrochemical characteristics. For a better understanding of these current-overvoltage curves, the anodic and cathodic contributions to the polarization have to be separated by using a reference electrode.

[3] Remark that Fig. 8 cannot be calculated from Fig. 5 due to different experimental conditions (Fig. 8: high voltage/currents resulting in different electrode morphology and additional processes).

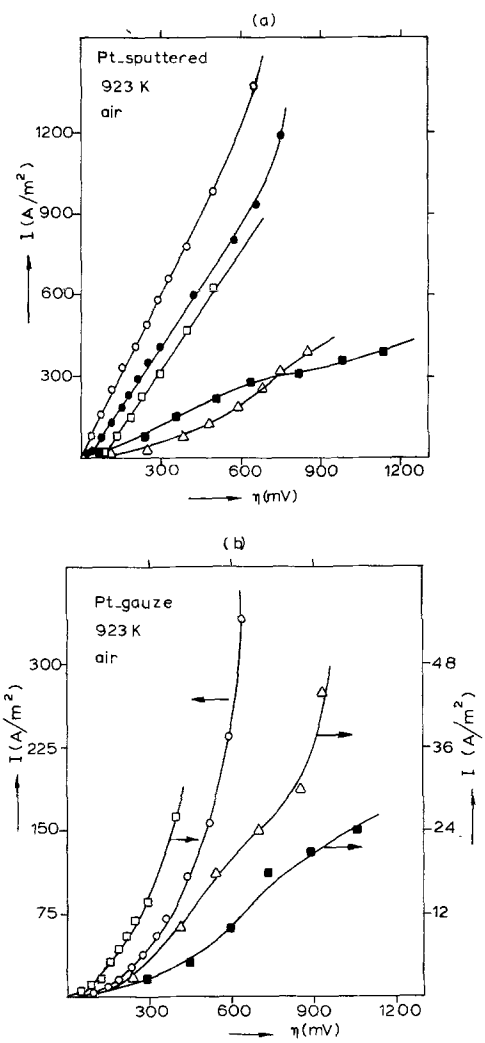

Fig. 8. Current-overvoltage curves for Pt-sputtered electrodes (a) and Pt-gauze electrodes (b) for several electrolytes in air at 923 K. ○, BE20; ●, BE30; □, BE40; ■, ZY17; △, CG10.

Conclusions

1. The combination of electrolyte and electrode material determines whether the dominating adsorption or diffusion step takes place on the electrolyte or on the electrode.

2. For ZY17 and CG10 the oxygen atoms for the electrode process are supplied by dissociative adsorption of oxygen molecules on the Pt electrode. For low temperatures and high oxygen partial pressures the surface coverage of oxygen atoms on the Pt electrode is about one and in this region we find that $R_{el} \sim P_{O_2}{}^{+n}$. For ZY17 mass transport at the anode is rate determining ($n = \frac{1}{2}$) and for CG10 the charge transfer ($n = \frac{1}{4}$). If the surface coverage of oxygen atoms on the electrode is low we find for ZY17 and CG10 that $R_{el} \sim P_{O_2}{}^{-\frac{1}{2}}$, showing that mass transport of atomic oxygen at the cathode is rate determining.

3. For Bi_2O_3-based materials adsorption and diffusion on the solid electrolyte determines the behavior of R_{el}. The electrode process is determined by mass transport at the cathode. The electrode resistance increases with increasing amount of substituent.

4. The electrode resistance for electrodes with the same morphology is for Bi_2O_3-based materials many times lower than for materials based on ZrO_2 and CeO_2.

Acknowledgments

We would like to thank Mr. J. M. Paauwe for experimental assistance and Dr. K. J. de Vries and Mr. H. Kruidhof for supplying the CeO_2-Gd_2O_3 sample. Financial assistance from Philips N. V. (Elcoma) is gratefully acknowledged.

Manuscript submitted Jan. 27, 1982; revised manuscript received July 20, 1982.

Any discussion of this paper will appear in a Discussion Section to be published in the December 1983 JOURNAL. All discussions for the December 1983 Discussion Section should be submitted by Aug. 1, 1983.

Publication costs of this article were assisted by the Twente University of Technology.

REFERENCES

1. R. J. Brook, W. L. Peltzmann, and F. A. Kröger, *This Journal*, **118**, 185 (1971).
2. J. E. Bauerle, *J. Phys. Chem. Solids*, **30**, 2657 (1969).
3. S. V. Karpachev and Yu Ovchinnikov, *Sov. Electrochem.*, **5**, 181 (1969).
4. E. Schouler, Ph.D. Thesis, Grenoble (1979).
5. Da Yu Wang and A. S. Nowick, *This Journal*, **126**, 1155 (1979).
6. R. Hartung, *Z. Phys. Chem.*, **260**, 259 (1979).
7. P. Fabry and M. Kleitz, *Electroanal. Chem. Interfacial Electrochem.*, **57**, 165 (1974).
8. M. Kleitz, Ph.D. Thesis, Grenoble (1968).
9. Da Yu Wang and A. S. Nowick, *This Journal*, **128**, 55 (1981).
10. M. J. Verkerk, K. Keizer, and A. J. Burggraaf, *J. Appl. Electrochem.*, **10**, 81 (1980).
11. M. J. Verkerk and A. J. Burggraaf, *This Journal*, **128**, 75 (1981).
12. M. J. Verkerk and A. J. Burggraaf, *ibid.*, **130**, 78 (1983).
13. M. J. Verkerk, B. J. Middelhuis, and A. J. Burggraaf, *Solid State Ionics*, **6**, 159 (1982).
14. M. A. C. G. van de Graaf, T. van Dijk, M. A. de Jongh, and A. J. Burggraaf, "Science of Ceramics," Vol. 9, K. J. de Vries, Editor, p. 75, Sterwin Rivers, Ltd., Cobridge, England (1977).
15. D. Yuan and F. A. Kröger, *This Journal*, **116**, 594 (1969).

16. Y. K. Agrawal, D. W. Short, R. Gruenke, and R. A. Rapp, *ibid.*, **121**, 354 (1974).
17. H. R. Thirsk and J. A. Harrison, "A Guide to the Study of Electrode Kinetics," Academic Press, London and New York (1972).
18. F. P. Netzer and H. L. Gruber, *Z. Phys. Chem. N.F.*, **85**, 159 (1973).
19. R. Lewis and R. Gomer, *Surf. Sci.*, **12**, 157 (1968).
20. T. M. Gür, I. D. Raistrick, and R. A. Huggins, *This Journal*, **127**, 2620 (1980).
21. D. Brennan, D. O. Hayward, and B. M. W. Trapwell, *Proc. R. Soc. London, Ser. A*, **256**, 81 (1960).

Oxygen Transfer on Substituted ZrO_2, Bi_2O_3, and CeO_2 Electrolytes with Platinum Electrodes

II. A-C Impedance Study

M. J. Verkerk[1] and A. J. Burggraaf

Twente University of Technology, Department of Chemical Engineering, Laboratory of Inorganic Chemistry and Materials Science, 7500 AE Enschede, The Netherlands

ABSTRACT

An equivalent electrical circuit that describes the electrode processes on different electrolytes, using porous Pt electrodes, is given. Diffusional processes are important and have to be presented by Warburg components in the circuit. The overall electrode process is rate limited by diffusion of atomic oxygen on the electrode surface for stabilized zirconia and substituted ceria (low P_{O_2}). On stabilized bismuth sesquioxide diffusion of atomic oxygen on the electrolyte surface is rate limiting at high P_{O_2} while at low P_{O_2} another process, probably diffusion of electronic species in the electrolyte, is dominant. One of these processes plays a role too on substituted ceria at high P_{O_2}, where a charge transfer process is dominant. These results are consistent with the mechanisms developed in part I of this paper.

In part I of this paper (1) a d-c study was performed on solid electrolytes based on ZrO_2, CeO_2, and Bi_2O_3 with platinum electrodes. It was concluded that for ZrO_2- and CeO_2-based materials the oxygen atoms for the electrode process are mainly supplied by dissociative adsorption of oxygen molecules at the Pt electrode, followed by transport to the reaction site where the charge transfer occurs. For Bi_2O_3-based materials the dominant adsorption and diffusion steps (in the high P_{O_2} and low temperature region) take place on the electrolyte. This different adsorption behavior is the origin of the lower electrode resistance of a Pt electrode on Bi_2O_3-based materials in comparison with that on ZrO_2- and CeO_2-based materials. Frequency dispersion analysis is a powerful tool for studying in detail the mechanism of the electrode process on these electrolytes (2-4).

Various authors studied the frequency behavior of Pt electrodes on a solid electrolyte. Generally, for Pt-paste and Pt-sputtered electrodes on stabilized zirconia the part of the frequency dispersion diagram which corresponds to the electrode process consists of a depressed semicircle (2, 5-9). This is interpreted in terms of a parallel combination of a resistance and a double layer capacity (2). A Warburg-type behavior, which is characteristic for diffusion limitation, is sometimes observed at high temperatures and low oxygen partial pressures (5, 8, 10). For Pt-paste electrodes on substituted ceria Braunshtein *et al.* (11) found that the overall process consists of a parallel combination of a resistance and a Warburg impedance. However, Wang and Nowick (12) observed for a Pt-paste electrode on substituted ceria a depressed semicircle, which interpretation is not very clear. The electrode process on (porous) Bi_2O_3 was studied using Au-paste electrodes (13, 14). The experimental results are interpreted in terms of a parallel combination of a resistance and Warburg impedances. The Warburg impedances are correlated with diffusion on the oxide surface and on the metal surface (14). These data can hardly be used for obtaining insight on the influence of the electrolyte on the electrode process because the measurements were performed under different experimental conditions and using different electrode morphologies, which are sometimes badly characterized.

The object of this paper is to study in detail the mechanism of the electrode process on different electrolytes using frequency dispersion analysis and to support the models of the electrode process developed in part I of this study. With the frequency dispersion technique an equivalent electrical circuit of the electrode process can be achieved and resolved in its components and a further insight in the influence of the electrolyte on the electrode process can be obtained.

The following systems were studied:

$(ZrO_2)_{0.83}(YO_{1.5})_{0.17}$ (ZY17),

$(CeO_2)_{0.90}(GdO_{1.5})_{0.10}$ (CG10),

$(Bi_2O_3)_{1-x}(Er_2O_3)_x$ with $x = 0.20$, 0.30, and 0.40 (BE20, BE30, and BE40). Electrodes with the same morphology were realized on these electrolytes and this morphology was preserved during the subsequent experiments. The electrode preparation and characterization is thoroughly described in part I of this study. Experimental details concerning the preparation and characterization of electrolytes and the electrical measurements are given in Ref. (1). The procedure to determine the individual components of the equivalent electrical circuit is described elsewhere (27).

Theory

In part I of this study it was concluded that the rate-limiting step in the electrode process on ZY17, CG10 ($P_{O_2} < P_{O_2}^{min.}$), BE20, BE30, and BE40 is mass transport of oxygen atoms. In this section the relevant theory for the frequency dispersion behavior of a mass transport controlled reaction is given.

When a d-c current passes through the electrolyte the oxygen atoms for the electrode process are supplied or removed by diffusion of oxygen atoms on the electrode surface and/or electrolyte surface. The oxygen atoms diffuse over a characteristic length δ from $x = \delta$ to the triple line at $x = 0$, where the charge transfer

[1] Present address: Philips Research Laboratories, Eindhoven, The Netherlands.

Key words: electrode resistance, solid electrolytes, oxygen transfer mechanism, complex impedance.

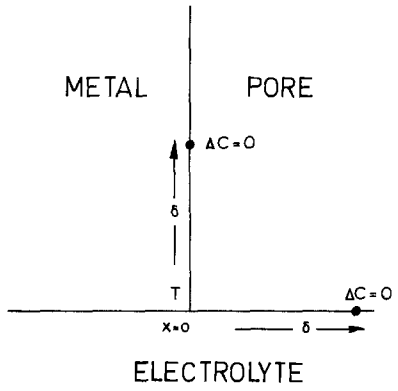

Fig. 1. Schematic picture of the diffusion process of oxygen atoms from $x = \delta$ to triple line T at $x = 0$.

takes place. The situation is depicted in Fig. 1. At $x \geq \delta$ the concentration of adsorbed oxygen atoms is constant. The production or removal of oxygen atoms is so small that the equilibrium concentration at $x \geq \delta$ is not changed during the experiments or for $x \geq \delta$ the exchange of oxygen molecules with the gas phase is large enough to keep the concentration of oxygen atoms at $x \geq \delta$ constant. It is assumed that across the distance δ the exchange of oxygen molecules with the gas phase has an ignorable effect on the concentration distribution in this area (δ is small in comparison with the size of the electrode particles).

In the case that an a-c current passes the electrolyte the "penetration depth" λ of the concentration perturbation, due to the production or removal of oxygen atoms at the triple line, is given by $\sqrt{2D_o/\omega}$, where D_o is the diffusion coefficient of oxygen atoms and ω is the frequency $\omega = 2\pi f$. For $\lambda < \delta$ the diffusion process occurs in a semi-infinite medium. For small frequencies the penetration depth will be limited by $\lambda_{max} = \delta$. The calculation of the impedance of this diffusion process for a comparable situation is given by Broers (15) for an electrode in aqueous solutions and molten salts and is summarized below.

The one-dimensional diffusion equation is given by

$$\frac{\partial \Delta C}{\partial t} = D_o \frac{\partial^2 \Delta C}{\partial x^2} \qquad [1]$$

where $\Delta C = C(x,t) - C_o$ and C_o is the equilibrium concentration. The boundary conditions are given by

$$x = \delta \quad \Delta C = 0 \qquad [2]$$

$$x = 0 \quad D_o \left(\frac{\partial \Delta C}{\partial x} \right)_{x=0} = \frac{i}{n\mathbf{F}} \qquad [3]$$

where n is the number of electrons involved in the electrode process. Assuming Nernst reversibility, the solution of the diffusion Eq. [1] using the boundary conditions [2] and [3] and the additional condition $|\Delta C| << C_o$ (which implies small overvoltages), is given by (14, 15)

$$Z_w = \frac{RT\delta}{n^2\mathbf{F}^2 C_o D_o} \times \frac{\tanh\,[\beta(1+j)]}{\beta(1+j)} \qquad [4]$$

where

$$\beta = \delta \sqrt{\frac{\omega}{2D_o}} \qquad [5]$$

A graphical representation of [4] is given in Fig. 2a and the admittance diagram correlated with this process is given in Fig. 2b.

If $\beta \geq 3$, *i.e.*, the penetration depth λ is small with respect to the length δ, the diffusion occurs in an effectively semi-infinite medium and Eq. [4] is reduced to a classical Warburg impedance

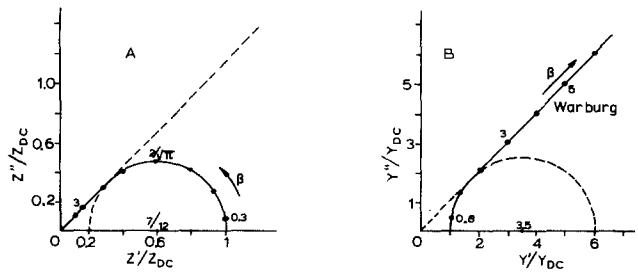

Fig. 2. Normalized impedance (A) and admittance (B) plots of the R-type Warburg impedance (Eq. [4]). [After (14, 15).]

$$Z_w = K_w \omega^{-1/2} \times (1 - j) \qquad [6]$$

where

$$K_w = \frac{RT}{n^2\mathbf{F}^2 C_o \sqrt{2D_o}} \qquad [7]$$

K_w is called the Warburg constant.

On the other hand, if $\beta \leq 0.3$, *i.e.*, the penetration depth is limited by $x = \delta$, where $\Delta C = 0$, we find from [4]

$$Z_w = \frac{RT\delta}{n^2\mathbf{F}^2 C_o D_o} \qquad [8]$$

$$Z''/\omega = \frac{3RT}{n^2\mathbf{F}^2 C_o \delta} = \frac{1}{C_{LF}} \qquad [9]$$

where C_{LF} is the low frequency capacity.

For the maximum value of the imaginary component of [4] $\beta = 2/\sqrt{\pi}$ (see Fig. 2a). Using Eq. [5] the magnitude of $\delta/\sqrt{D}$ can be calculated without knowledge of the electrode area and the value of C_o and we find

$$\beta = 2/\sqrt{\pi} = \delta \sqrt{\frac{\omega_{max}}{2D_o}} \qquad [10]$$

where ω_{max} is the value of the frequency at the maximum value of the imaginary component of [4].

At low frequencies this type of Warburg behavior is like a resistance and is called "*R*-type Warburg impedance" (14).

Pt Electrodes on ZY17

Pt-sputtered electrodes.—In part I it was shown that in the relation between the electrode resistance R_{el} and the oxygen partial pressure a minimum in R_{el} appears at $P_{O_2} = P_{O_2}^{min.}$. Above and below $P_{O_2}^{min.}$ the electrochemical characteristics of R_{el} are quite different. At 983 K $P_{O_2}^{min.}$ has a value of about 4.5×10^{-2} atm O_2.

Figure 3 shows the complex impedance diagram at 983 K of sputtered electrodes on ZY17 as a function of the oxygen partial pressure. At $P_{O_2} > P_{O_2}^{min.}$ a single semicircle is observed (Fig. 3a). For $P_{O_2} \approx P_{O_2}^{min.}$ two overlapping semicircles are observed (Fig. 3b and c), indicating that two processes (connected in series) play a role. For $P_{O_2} < P_{O_2}^{min.}$ (Fig. 3d) the frequency dispersion diagram is interpreted in terms of a distorted Warburg impedance. It is shown (27) that interpretation of Fig. 3d in terms of two strongly overlapping semicircles is not correct. The development of the frequency dispersion diagrams as a function of the oxygen partial pressure was quite reproducible (using porous sputtered electrodes). The total equivalent electrical circuit is given in Fig. 4a. W_a is connected with diffusion at the anode. Generally, for W_a the condition $\beta \leq 0.3$ holds over the whole frequency range investigated and W_a is reduced to a resistance R_a (Eq. [8]). This is discussed below. R_a varies with $P_{O_2}^{+1/2} \cdot W_c$ is connected with diffusion at the cathode and Z_{W_c} ($\omega \to 0$) $\sim P_{O_2}^{-1/2}$. This is discussed in the following.

At $P_{O_2} > P_{O_2}^{min.}$ the resistance R_a is large in comparison with the resistance of the Warburg impedance

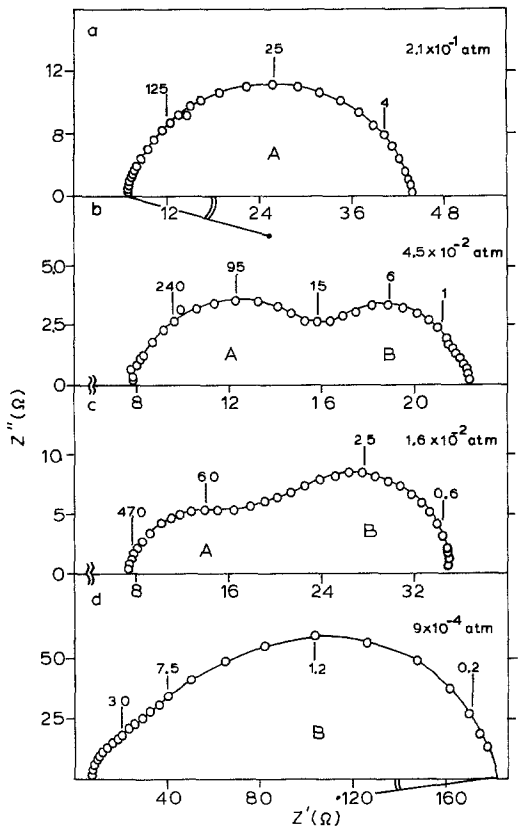

Fig. 3. The frequency dispersion diagrams of Pt-sputtered electrodes on ZY17 at 2.1 × 10^{-1} atm O_2 (a), 4.5 × 10^{-2} atm O_2 (b), 1.6 × 10^{-2} atm O_2 (c), and 9 × 10^{-4} atm O_2 (d). The temperature is 983 K. The frequency is given in Hz and is indicated by figures on the curves.

W_c. Therefore in this region the equivalent circuit can be simplified to that shown in Fig. 4b and the frequency dispersion diagram is a semicircle, see Fig. 3a. The depression of the semicircle is independent of the oxygen partial pressure and the temperature and has a value of about 10°-20°. The capacity C_{dl} is independent of the oxygen partial pressure and the temperature (see Table I) and is therefore correlated with the double layer and has a value of about 2.8 F/m². From the frequency dispersion measurements it follows that $R_a \sim P_{O_2}{}^{+1/2}$ and $E_a(R_a)$ has a value of about 250 kJ mol^{-1}. This was already found in part I.

In part I of this study R_a was correlated with diffusion from the reaction site to the desorption site at $x = \delta$ (anodic process) and it was derived that $R_a \sim P_{O_2}{}^{+1/2}$ ($\theta \approx 1$). This result is supported by the experimental frequency dispersion diagram, which showed only resistive behavior in this case. The Warburg impedance given by Eq. [4] is reduced to a resistance if the condition $\beta \leq 0.3$ holds in the investigated frequency range. In our opinion this condition holds indeed at 983 K but not at lower temperatures. At 923 K in air the high frequency part of the frequency dispersion diagram deviates from a semicircle. The tangent of the high frequency part has an angle with the real axis of about 55° whereas the semicircle is depressed with 10°. This can be explained in the following way. At lower temperatures D_o is smaller and therefore the condition $\beta = \delta\sqrt{\omega/2D_o} \leq 0.3$ does only hold at low frequencies. At high frequencies this condition does not hold and the impedance of the diffusion process does not correspond with a simple resistance and the observed deviation appears.

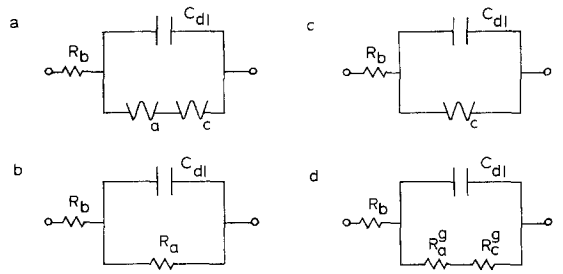

Fig. 4. Equivalent electrical circuits for Pt electrodes on ZY17. (a) Complete circuit for Pt-sputtered electrodes, (b) circuit for Pt-sputtered electrodes in the region of $P_{O_2} > P_{O_2}{}^{min.}$, (c) circuit for Pt-sputtered electrodes in the region of $P_{O_2} < P_{O_2}{}^{min.}$, (d) complete circuit for Pt-gauze electrodes. R_b, bulk resistance; C_{dl}, double layer capacity; W_a, Warburg impedance at the anode; W_c, Warburg impedance at the cathode; R_a, diffusion resistance at the anode (see text); $R_a{}^g$, diffusion resistance at the anode for gauze electrodes; $R_c{}^g$, diffusion resistance at the cathode for gauze electrodes.

At $P_{O_2} < P_{O_2}{}^{min.}$ the resistance R_a is small in comparison with the resistance of the Warburg impedance W_c. Therefore, in this region the equivalent circuit can be simplified to that shown in Fig. 4c and the experimental frequency dispersion diagram is shown in Fig. 3d. Figure 5 shows the complex impedance and admittance diagram at $P_{O_2} = 9 \times 10^{-4}$ atm O_2 after elimination of the bulk resistance and the double layer capacity from the circuit of Fig. 4c.

The diagrams shown in Fig. 5 have the same shape as those shown in Fig. 2a and b and are therefore correlated with a diffusion process. The experimentally found angle of the high frequency part of the diagrams with the real axis is 35°-37° instead of the theoretical value of 45°. The frequency dispersion diagram in $P_{O_2} = 1 \times 10^{-4}$ atm (not shown), after eliminating R_b and C_{dl}, has the same shape as that shown in Fig. 5. The values of C_{dl} and K_w are given in the Tables I and II, respectively.

Table I. Double layer capacity and low frequency capacity measured for the different electrode/electrolyte combinations

Material	Electrode	T (K)	Double layer capacity (F/m²)* 1.00 atm	0.60 atm	0.21 atm	0.10 atm	4.5 × 10^{-2} atm	1.6 × 10^{-2} atm	9 × 10^{-4} atm	10^{-4} atm
ZY17	Pt (sp)	1023			3.0					
		983	2.6	2.8	2.9	2.8	4.1	3.9	1.8	1.5
		923			3.9					
	Pt (g)	1023			10.9 × 10^{-2}					
		983	5.3 × 10^{-2}	6.8 × 10^{-2}	6.4 × 10^{-2}	9.2 × 10^{-2}	4.3 × 10^{-2}	7.3 × 10^{-2}	7.5 × 10^{-2}	7.4 × 10^{-2}
		923			5.5 × 10^{-2}					
CG10	Pt (sp)	983							0.8	1.0
BE30	Pt (sp)	973				10.4	11.4			33.8
BE40	Pt (sp)	973					14.6		10.4	7.0
			Low frequency capacity (F/m²)*							
ZY17	Pt (sp)	983					34	22	15	13

* The capacities are given per unit area of electrolyte and are not corrected for the size of the actual electrolyte/electrode contact surface. The values in this table are given for the two electrodes together.

Table II. Warburg constant for several systems as a function of the oxygen partial pressure

System	Temperature	Electrode	Kw (Ωm^2 $sec^{-1/2}$) 1 atm O_2	6×10^{-1} atm O_2	2.1×10^{-1} atm O_2	9×10^{-4} atm O_2	10^{-4} atm O_2
ZY17	983	sp				2.5×10^{-2}	3.5×10^{-2}
CG10	983	sp	1.2×10^{-2}	1.2×10^{-2}	1.4×10^{-2}	2.0×10^{-2}	2.3×10^{-2}
BE20	973	sp			4.9×10^{-4}		
	823	sp			9.5×10^{-4}		
BE40	973	sp			3.6×10^{-4}		
	823	sp			8.8×10^{-4}		

The low frequency resistance Z_{W_c} ($\omega \to 0$) varies with $P_{O_2}^{-1/2}$ and this agrees well with the results reported in part I, where it was concluded that the electrode resistance in this P_{O_2} region was correlated with diffusion of atomic oxygen from the adsorption site to the reaction site (cathodic process) and it was derived that the electrode resistance varies with $P_{O_2}^{-1/2}$ ($\theta << 1$).

For $P_{O_2} \approx P_{O_2}^{min.}$ both R_a and W_c play a role. At low frequencies the frequency dispersion diagram is determined by W_c whereas at high frequencies by R_a and C_{dl}, resulting in two overlapping semicircles.

The existence of two series connected processes, as given in the equivalent circuit in Fig. 4a, was not recognized before in literature (6, 9, 16).

Pt-gauze electrodes.—The complex impedance diagram for Pt-gauze electrodes on ZY17 consists of a depressed semicircle over the whole oxygen partial pressure range. The total equivalent electrical circuit is given in Fig. 4d with $R_a^g \sim P_{O_2}^{+1/2}$ and $R_c^g \sim P_{O_2}^{-1/2}$. For $P_{O_2} > P_{O_2}^{min.}$ the total electrode resistance is determined by R_a^g · R_a^g shows the same P_{O_2} dependence and the same value of E_a as R_a for sputtered electrodes and is therefore correlated with the same process, *i.e.*, diffusion limitation at the anode.

For $P_{O_2} < P_{O_2}^{min.}$ the total electrode resistance is determined by R_c^g. R_c^g has the same P_{O_2} dependence as Z_{W_c} ($\omega \to 0$) for sputtered electrodes and about the same value for the activation energy is found (see part I). Therefore, it is plausible that R_c^g represents the same process as W_c, *i.e.*, diffusion at the cathode. Due to the difference in electrode morphology between a sputtered and a gauze electrode the condition $\beta \leq 0.3$ holds for gauze electrodes (resulting in a depressed semicircle) to higher frequencies than for sputtered electrodes where a typical "Warburg-type behavior" is observed.

We conclude that the mechanism of the electrode reaction for gauze and sputtered electrodes is the same.

Diffusion path.—The diffusion paths correlated with W_a and W_c (R_a^g and R_c^g, respectively, for gauze electrodes) are now discussed. The processes W_a and W_c are correlated with an R-type Warburg impedance and therefore the condition $\Delta C = 0$ holds at $x = \delta$. This condition holds for the situation depicted in Fig. 1, where diffusion of atomic oxygen proceeds over a distance δ to the triple line. According to the preceding paper (part I) in the case of Pt electrodes on ZY17 the diffusion process should proceed on the Pt electrode.

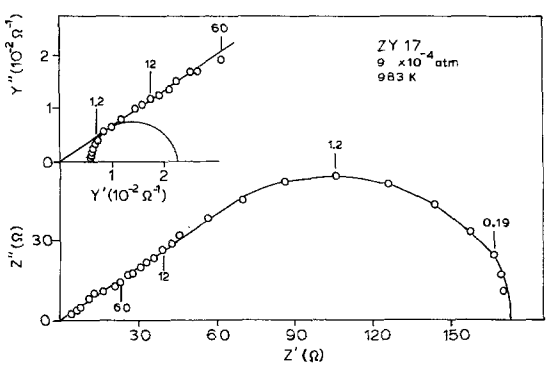

Fig. 5. Complex impedance diagram and complex admittance diagram for Pt-sputtered electrodes on ZY17 at $P_{O_2} = 9 \times 10^{-4}$ atm O_2 (983 K) after elimination of R_b and C_{dl}. The frequency is given in Hz.

The investigated frequency range, for the diffusion process underlying W_a, holds that $\beta \leq 0.3$. Using $\omega = 1000$, this condition is equivalent to $\delta/\sqrt{D_o} \leq 1.4 \times 10^{-2}$ $sec^{+1/2}$ (Eq. [5]). Lewis and Gomer (17) measured the surface diffusion of oxygen on (100)- and (111)-oriented Pt field emitters for $T > 500$ K and for low surface coverages. In the absence of better information we used these data to calculate D_o at 983 K and found a value of 1.2×10^{-11} m^2/sec. For the effective diffusion distance δ a value of ≤ 50 nm is calculated, which seems a reasonable value in view of the electrode morphology (particle size $\approx$ 1000 nm).

At $P_{O_2} < P_{O_2}^{min.}$ a value of $\delta/\sqrt{D_o}$ can be calculated according to Eq. [10] using ω_{max}. This value is estimated to be 0.58 and 1.16 $sec^{+1/2}$ at 9×10^{-4} and 10^{-4} atm O_2, respectively. Using the above-discussed value of $D_o = 1.2 \times 10^{-11}$ m^2/sec (19), δ is estimated to be 2 and 4 μm (at 9×10^{-4} and 10^{-4} atm O_2, respectively. These δ-values are too large taking into account the morphology of the electrode. Although there is a large uncertainty in the value of D_o, comparison of the δ-values at high P_{O_2} and at low P_{O_2} suggest that δ decreases with increasing P_{O_2} (18, 21).

According to Cahen (14) the condition $\Delta C = 0$ at $x = \delta$ holds also for a diffusion path between the two electrodes and the diffusion proceeds then on the oxide grains between the electrodes. This model can be applied for porous samples but is not very probable for our sample with a relative density of 99%. Furthermore, for our samples this diffusion process should proceed via the grain boundaries, whereas it was shown in part I that grain boundaries in pure ZY17 do not play a role in the electrode process. Braunstein *et al.* (11) concluded that a Warburg behavior should result from diffusion on the electrolyte/electrode interface (from the triple line). However, the current distribution assumed in their very simplified model is in contradiction with the distribution calculated on the basis of a physically more reasonable model (24). Furthermore, a recent analysis of Broers (23) showed that if the correct current distribution is taken into account, no Warburg behavior is found. Consequently, the electrolyte/electrode interface is not the dominant diffusion path.

Pt electrodes on CG10.—The frequency dispersion diagrams and the equivalent electrical circuit for Pt electrodes on CG10 are briefly discussed. The R_{el}-P_{O_2} relation for Pt electrodes on CG10 shows at 983 K a minimum in R_{el} for $P_{O_2} = 1.6 \sim 4.5 \times 10^{-2}$ atm O_2 (part I). For sputtered electrodes at $P_{O_2} > P_{O_2}^{min.}$ the frequency dispersion diagram consists of a quarter circle (comparable with Fig. 7a and b), at $P_{O_2} \approx P_{O_2}^{min.}$ of two overlapping semicircles (comparable with Fig. 3b and c) and at $P_{O_2} < P_{O_2}^{min.}$ of a distorted Warburg impedance (comparable with Fig. 3d). The total equivalent electrical circuit for sputtered electrodes is given in Fig. 6a. Experimentally R_{ct} is found to vary with $P_{O_2}^{+1/4}$ and Z_{W_c} ($\omega \to 0$) with $P_{O_2}^{-1/2}$. This is in a good agreement with the results of the d-c measurements, where R_{ct} was interpreted as a charge transfer resistance and Z_{W_c} ($\omega \to 0$) as a diffusion resistance at the

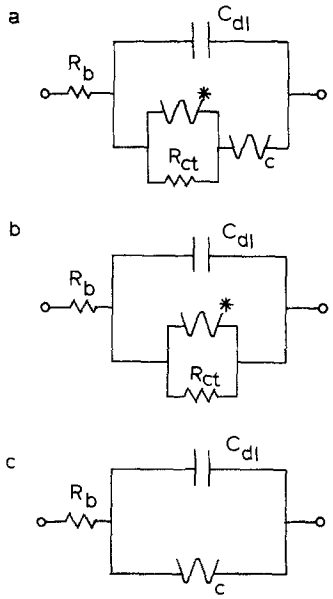

Fig. 6. Equivalent electrical circuit for Pt electrodes on CG10. (a) Complete circuit for Pt-sputtered electrodes, (b) circuit for Pt-sputtered electrodes in the region of $P_{O_2} > P_{O_2}^{min.}$, (c) circuit for Pt-sputtered electrodes in the region of $P_{O_2} < P_{O_2}^{min.}$, R_{ct}, charge transfer resistance; W^*, Warburg impedance. The meaning of the other symbols is given in the caption of Fig. 4.

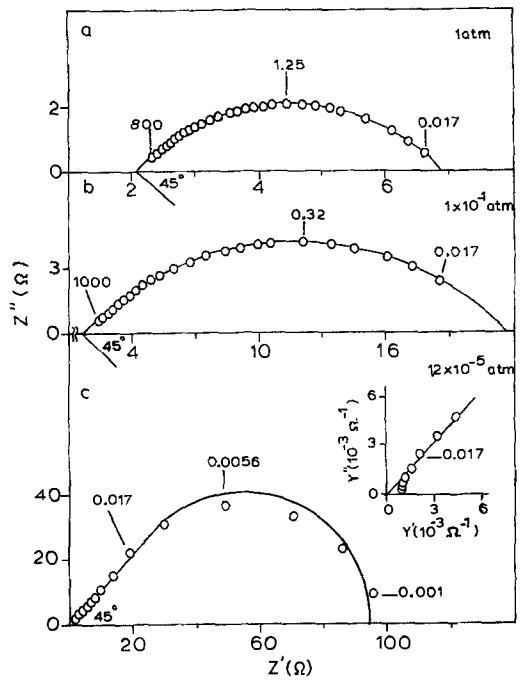

Fig. 7. Complex impedance diagrams for Pt-sputtered electrodes on BE20 at 1 atm O_2 (a), 1×10^{-1} atm O_2 (b), and 1.2×10^{-5} atm O_2 (c). The temperature is 973 K. In the impedance diagram shown in (c) the drawn line gives the theoretical plot for R-type Warburg behavior according to Eq. [4]. In (c) the admittance diagram is also given. The frequency is given in Hz.

cathode (part I). The equivalent circuit is now discussed.

At $P_{O_2} > P_{O_2}^{min.}$, R_{ct} is large in comparison with the impedance of W_c and the circuit is reduced to that shown in Fig. 6b; the impedance diagram consists of a quarter circle. (The influence of C_{dl} is only measurable at $P_{O_2} \leq P_{O_2}^{min.}$. W^* is semi-infinite over the frequency range measured and the K_w-value is given in Table II.

At $P_{O_2} \approx P_{O_2}^{min.}$ the frequency dispersion diagram is determined at low frequencies by W_c and at high frequencies by R_{ct}, W^*, and C_{dl} and this results in two overlapping semicircles.

At $P_{O_2} < P_{O_2}^{min.}$, R_{ct} is small compared with W_c and the circuit is reduced to that shown in Fig. 6c and results in a Warburg-type behavior. The values of K_{W_c} are summarized in Table II.

For Pt-gauze electrodes on CG10 the electrical equivalent circuit is also given by Fig. 6 and is discussed further elsewhere (25).

The P_{O_2} dependence and activation energy of Z_{W_c} ($\omega \to 0$) of Pt electrodes on CG10 is similar with that of Pt electrodes on ZY17. Furthermore for K_w the same value is found as on ZY17 (see Table II). Therefore we conclude that, similar to Pt electrodes on ZY17, W_c is correlated with diffusion on the Pt electrode.

At high P_{O_2} an additional Warburg impedance W^* was measured, which is parallel to R_{ct}. This impedance was not found for Pt electrodes on ZY17. This Warburg impedance W^* may be correlated with diffusion of atomic oxygen on the electrolyte or diffusion of electronic charge carriers through the electrolyte (which probably plays a role for Pt electrodes on stabilized Bi_2O_3, see below). More study is necessary to elucidate the origin of W^*.

Pt Electrodes on BE20, BE30, and BE40

Pt-sputtered electrodes.—Figure 7 shows the complex impedance behavior for Pt-sputtered electrodes on BE20 as a function of the oxygen partial pressure. The complete equivalent electrical circuit for sputtered electrodes on BE20, BE30, and BE40 is shown in Fig. 8a and is discussed. The double layer capacities were determined with the method described in Ref. (25) and its numerical values are summarized in Table I.

For BE20 the double layer capacity (in comparison with R and W) was too small to be measured. The double layer capacities measured for BE30 and BE40 are in good agreement with the values measured by Harwig (13) and Cahen (14) for gold-paste electrodes on pure Bi_2O_3 and are higher than found in this study for ZrO_2- and CeO_2-based materials. Consequently, the magnitude of C_{dl} is dominated by a process connected with the electrolyte.

At oxygen partial pressures in the range of $1\text{-}10^{-2}$ atm O_2 a perfect quarter circle is observed (Fig. 7a and b), representing a parallel combination of a resistance K and a Warburg impedance W. In the measured frequency range (10^3-10^{-2} Hz) the Warburg process is semi-infinite, *i.e.*, $\beta \geqq 3$. Therefore, in this range the d-c resistance of the parallel R-W combination is determined by R because Z_w ($\omega \to 0$) is much larger than R. From the a-c study it follows that $R \sim P_{O_2}^{-1/2}$ and this is in a good agreement with the results of the d-c study (part I), where it was found additionally that $E_a(R) \approx 125$ kJ mol^{-1}.

At lower oxygen partial pressures ($< \omega^{-2}$ atm O_2) deviations appear at the low frequency part. These

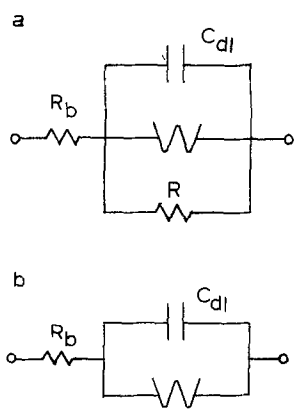

Fig. 8. (a) Complete equivalent electrical circuit for Pt electrodes on Bi_2O_3-based materials, (b) equivalent electrical circuit at low P_{O_2}. R, diffusion resistance; W, Warburg impedance. The meaning of the other symbols is given in the caption of Fig. 4.

deviations are due to the fact that under these circumstances the Warburg impedance is no longer semi-infinite. At $P_{O_2} = 1.2 \times 10^{-5}$ atm O_2 the electrode process is fully determined by the warburg impedance, as shown in Fig. 7c and the equivalent circuit is reduced to that shown in Fig. 8b. In this range the d-c resistance is determined by Z_w ($\omega \rightarrow 0$), which is characterized by an activation energy of about 50-90 kJ mol^{-1} (part I).

The value of the Warburg constant is not strongly dependent on the erbium concentration (27). K_w^{-1} varies with about $P_{O_2}^{1/4}$ and has an activation energy of about 35 kJ mol^{-1} (25).

Sputtered gold electrodes were not studied in detail. Frequency dispersion measurements showed that the equivalent electrical circuit is also given by Fig. 8a. At high oxygen partial pressures the impedance of the parallel R-W combination is determined by R. In part I it was shown that the E_a and P_{O_2} dependence of R for gold electrodes was the same as for platinum electrodes, which points to processes connected dominantly with the electrolyte.

These results support the conclusion of the preceding paper (part I) that R originates from diffusion of atomic oxygen on the oxide at the cathode [θ(oxide) $<< 1$].

Pt-gauze electrodes.—Figure 9a shows the complex impedance behavior for a Pt-gauze electrode on BE20 in oxygen and Fig. 9b shows the admittance behavior after eliminating the bulk resistance. The complete equivalent electrical circuit is given in Fig. 8a. The diagrams shown in Fig. 9 are representative of the diagrams in the oxygen partial pressure range of 1-10^{-5} atm O_2 and the shape is not influenced by the Er_2O_3 content.

The solid line in Fig. 9a gives the theoretical plot of the Warburg impedance. The deviation of the experimental data from this theoretical plot is caused by the resistance parallel to the Warburg impedance. The Warburg impedance is not semi-infinite and therefore the d-c resistance of the parallel R-W combination is determined by both R and W. As a consequence the experimentally found activation energy and P_{O_2} dependence is not characteristic for one process but is a combination of that belonging to R and W. Fitting procedures are necessary to separate the contribution of these components.

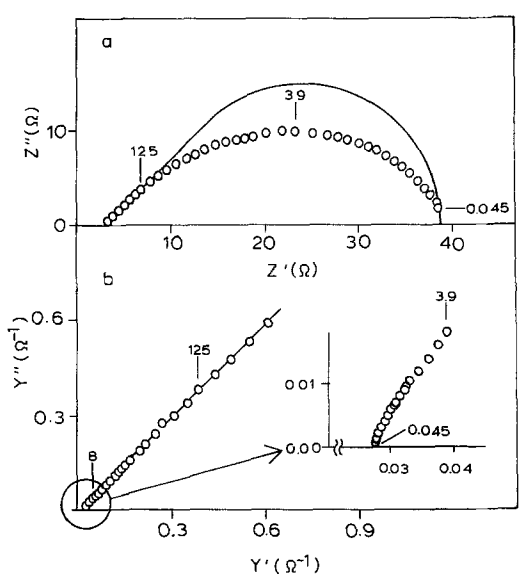

Fig. 9. (a) Complex impedance diagram for a Pt-gauze electrode on BE20 in oxygen at 1010 K. The solid line gives the theoretical plot for an R-type Warburg impedance after Eq. [4]. (b) Complex admittance plot after elimination of the bulk resistance. The frequency is given in Hz.

In our opinion, R varies with $P_{O_2}^{-1/2}$ and Z_w ($\omega \rightarrow 0$) varies with $P_{O_2}^{-1/4}$.[2] At high P_{O_2} the $-1/2$ power will dominate whereas at low P_{O_2} the $-1/4$ power will dominate. This interpretation is in a good agreement with the experimental data (see Fig. 7b from part I) and is confirmed by the good agreement of E_a(sp) and E_a(g) in the different regions (Table III, part I). This is also supported by the P_{O_2} dependence of K_w. For gauze electrodes we found that $K_w^{-1} \sim P_{O_2}^{1/4}$ (27). By comparing Eq. [7] and [8] we conclude that Z_w ($\omega \rightarrow 0$) also varies with $P_{O_2}^{-1/4}$.

We conclude that the mechanisms of the electrode reaction for gauze and sputtered electrodes on Bi_2O_3-Er_2O_3 is the same whereas the actual contribution of the different processes is influenced by the morphology of the electrode.

Diffusion path.—The resistance R in the equivalent electrical circuit shown in Fig. 8a is connected with the electrolyte. The conclusion drawn in part I, that R is a diffusion resistance of atomic oxygen on the oxide surface, could not be explicitly proved by frequency dispersion. As discussed above the impedance of a diffusion process reduces to a resistive behavior for $\beta \leq 0.3$.

The Warburg impedance W cannot be correlated with diffusion of adsorbed oxygen atoms on the Pt surface because according to Eq. [7] we should have to find $K_w^{-1} \sim P_{O_2}^{1/2}$. Furthermore, if W is correlated with diffusion of oxygen atoms on the Pt surface the value of K_w should be independent of the electrolyte. However ,at 10^{-4} atm O_2 (973 K) K_w has a value of 2.4×10^{-3} Ωm^2 sec$^{-1/2}$ for BE20 and this is about 10 times lower than for ZY17 and CG10 (see Table II). We can conclude that the Warburg impedance W does not find its origin in diffusion of oxygen atoms on surfaces. The power 1/4 suggests that hole conduction plays a role. It may be that transport of holes from the electrode to electrolyte/gas interface is rate determining and that on this interface the charge transfer takes place,according to

$$O_{ads} \leftrightarrows O^{2-} + 2h^+ \qquad [11]$$

where h denotes a hole and $C_h \sim P_{O_2}^{1/4}$.

According to Eq. [7] and [8], $E_a(Z_w$ ($\omega \rightarrow 0$)) are given by $E_a(C_h) + 1/2\Delta H_{Dh}$ and $E_a(C_h) + \Delta H_{Dh}$, respectively, with $E_a(C_h)$ the formation enthalpy of free holes and ΔH_{Dh} the diffusion enthalpy for holes. From the experimental data for $E_a(K_w)$ and $E_a(Z_w$ ($\omega \rightarrow 0$)) it follows that $E_a(C_h)$ is small and we find for ΔH_{Dh} a value of about 80 kJ mol^{-1}. This value is, however, lower than the activation energy measured for the hole conductivity of stabilized Bi_2O_3, which should have a value of 106 kJ mol^{-1} (24).

More study is necessary to elucidate the origin of Warburg impedance W. Up to this moment it is clear that W is typically for Bi_2O_3-based solid electrolytes and is not found for zirconia. In ceria-based electrolytes a Warburg component may play some role at high P_{O_2}.

Conclusions

1. The diffusion path which actually occurs in the electrode process on Pt/solid electrolyte combination is strongly influenced by the type of solid electrolyte.

2. For Pt electrodes on ZY17 frequency dispersion measurements showed that the rate-limiting steps are diffusion processes that are connected in series. At $P_{O_2} > P_{O_2}^{min.}$ ($\theta \approx 1$) diffusion of atomic oxygen at the anode (W_a) is rate determining and at $P_{O_2} < P_{O_2}^{min.}$ ($\theta << 1$) diffusion of atomic oxygen at the cathode (W_c) is rate determining. In part I it was concluded that these diffusion steps occur on the electrode surface. This study showed that diffusion on the electrolyte surface and through the electrolyte plays no significant role.

[2] Simulation shows that using a parallel combination of a $-1/2$ and $-1/4$ power yields a $-3/8$ power over 5 decades.

3. For Pt electrodes on CG10 frequency dispersion measurements showed that at $P_{O_2} < P_{O_2}^{min.}$ ($\theta << 1$) the electrode process is determined by diffusion at the cathode (W_c). This diffusion process shows the same characteristics as for Pt electrodes on ZY17. Therefore it was concluded that this diffusion process occurs on the electrode too. At $P_{O_2} > P_{O_2}^{min.}$ the electrode process is determined by a resistance, which is correlated with a charge transfer process (R_{ct}). Parallel to this resistance is a Warburg impedance, which is proposed to be correlated with the electrolyte: diffusion of oxygen atoms on the oxide surface or electronic conductivity through the electrolyte.

4. For Pt electrodes on BE20, BE30, and BE40 frequency dispersion measurements showed that two processes play a role, a resistance R and a Warburg impedance W which are connected parallel. From a comparison with other electrolyte-electrode combinations it is concluded that R is correlated with diffusion of atomic oxygen on the electrolyte surface at the cathode. The Warburg impedance is typically for Bi_2O_3-based materials and it is suggested that electronic charge carriers in the electrolyte are the diffusing species in this process.

At high P_{O_2} the d-c resistance of the electrode process is determined by the resistance R (diffusion on the electrolyte) and a low P_{O_2} by the Warburg impedance (diffusion through the electrolyte).

5. The magnitude of the double layer capacities C_{dl} are dependent on the nature of the solid electrolyte. For the Bi_2O_3-based materials they reach the very large value of about 15 F/m^2 for sputtered electrodes, whereas for substituted zirconia or ceria values of about 1-3 F/m^2 are found.

Acknowledgments

We would like to thank Mr. M. W. J. Hammink and Mr. J. M. Paauwe for experimental assistance and Dr. K. J. de Vries and Mr. H. Kruidhof for supplying the CeO_2-Gd_2O_3 sample. Prof. Dr. G. H. J. Broers is thanked for the stimulating discussions concerning Warburg impedance. Financial assistance from Philips N.V. (Elcoma) is gratefully acknowledged.

Manuscript submitted Jan. 27, 1982; revised manuscript received July 20, 1982.

Any discussion of this paper will appear in a Discussion Section to be published in the December 1983 JOURNAL. All discussions for the December 1983 Discussion Section should be submitted by Aug. 1, 1983.

Publication costs of this article were assisted by Twente University of Technology.

REFERENCES

1. M. J. Verkerk, M. W. J. Hammink, and A. J. Burggraaf, *This Journal*, **130**, 70 (1983).
2. J. E. Bauerle, *J. Phys. Chem. Solids*, **30**, 2657 (1969).
3. J. R. Macdonald, *J. Chem. Phys.*, **61**, 3977 (1974).
4. D. R. Franceschetti and J. R. Macdonald, *J. Electroanal. Chem. Interfacial Electrochem.*, **82**, 271 (1977).
5. E. Schouler, M. Kleitz, and C. Déportes, *J. Chim. Phys.*, **70**, 923 (1973).
6. E. Schouler, Ph.D. Thesis, Grenoble (1979).
7. S. H. Chu and M. A. Seitz, *J. Solid State Chem.*, **23**, 297 (1978).
8. S. P. S. Badwal and H. J. de Bruin, *Phys. Status Solidi A*, **49**, 261 (1979).
9. T. M. Gür, I. D. Raistrick, and R. A. Huggins, *Solid State Ionics*, **1**, 251 (1980).
10. H. Peters and K. H. Radeke, *Monats Ber. Det. Akad. Wiss. Berlin*, **10**, 819 (1968).
11. D. Braunshtein, D. S. Tannhauser, and I. Riess, *This Journal*, **128**, 82 (1981).
12. D. Y. Wang and A. S. Nowick, *ibid.*, **126**, 1166 (1979).
13. H. A. Harwig, Ph.D. Thesis, State University, Utrecht (1977).
14. H. T. Cahen, Ph.D. Thesis State University, Utrecht (1980).
15. G. H. J. Broers and M. Schenke, Proc. Int. Conf. on Fuel Cells, p. 299, Akademie Verlag, Dresden (1967).
16. T. M. Gür, Ph.D. Thesis, Stanford University (1978).
17. R. Lewis and R. Gomer, *Surf. Sci.*, **12**, 157 (1968).
18. M. Kleitz, Ph.D. Thesis, Grenoble (1968).
19. P. Fabry and M. Kleitz, *J. Electroanal. Chem. Interfacial Electrochem.*, **57**, 165 (1974).
20. J. Fouletier, P. Fabry, and M. Kleitz, *This Journal*, **123**, 204 (1976).
21. J. Fouletier, H. Seinera, and M. Kleitz, *J. Appl. Electrochem.*, **5**, 177 (1975).
22. I. V. Murygin and V. N. Chebotin, *Elektrokhimiya*, **15**, 1647 (1979).
23. G. H. J. Broers, Private communication.
24. T. Takahashi, T. Esaka, and H. Iwahara, *J. Appl. Electrochem.*, **7**, 303 (1977).
25. M. J. Verkerk, Ph.D. Thesis, Twente University of Technology, The Netherlands (1982).

Separation by Electrosorption of Organic Compounds in a Flow-Through Porous Electrode

I. Mathematical Model for One-Dimensional Geometry

Richard C. Alkire* and Ronald S. Eisinger*,[1]

Department of Chemical Engineering, University of Illinois, Urbana, Illinois 61801

ABSTRACT

An engineering model of potential-dependent adsorption of organic compounds in a flow-through porous electrode was derived from fundamental principles. A one-dimensional geometry was considered in which the counterelectrode was located downstream. Potential was controlled at the end of the porous electrode nearest the counterelectrode. The model considered convective mass transfer, ohmic resistance, charging of the electrical double layer, and a potential-dependent adsorption isotherm. Electrosorption can be an efficient cyclic separation process if the full change in adsorption capacity of the adsorbent is utilized in minimum cycle time. For one-dimensional geometry, the model predicted conditions under which efficient operation could be achieved.

Adsorption from solution onto solids is widely used as a separation process, usually in a cyclic manner in which the adsorption phase is followed by renewal of the adsorbent. Typically, and depending on the scale of operation, renewal involves either installation of fresh adsorbent or regeneration of spent adsorbent by washing with solvent or by heating. An electrochemical analog, known as electrosorption, can be used to control the adsorption of material from ionically conducting solutions onto conductive solids. In electrosorption, both adsorption and regeneration may be accomplished by judicious control of an electric potential.

Electrosorption is a surface phenomenon in which the amount of adsorption is determined by forces acting within a few atomic diameters of the adsorbent surface. Faradaic reaction need not accompany electrosorption. Usually, maximum adsorption is limited to monolayer surface coverage. Potential-dependent adsorption has been observed for both charged and neutral species. Explanations of potential dependence in the adsorption of neutral species have been proposed by Frumkin (1), Butler (2), and Bockris *et al.* (3). Potential dependence in the adsorption of organic compounds on mercury had been observed even prior to publication of Gouy's extensive results in 1906 (4). While numerous scientific studies have been carried out on mercury, relatively few studies have been reported on solid adsorbents of high surface area. The thorough review of electrosorption on solid adsorbents by Damaskin *et al.* (5) primarily dealt with low surface-area metals.

Electrosorption may hold promise for practical applications such as separation of small quantities of organic species from process or effluent streams, either for the purpose of concentration and recovery, or for removal. These applications would require high surface-area adsorbents, and the process would be similar in many respects to that of conventional adsorption in packed beds. However, design of the process must also consider electrochemical factors. The use of high surface-area electrodes further increases the complexity of the process. The purpose of this paper is to develop a mathematical model of electrosorption of neutral compounds in a flow-through porous electrode. The model is compared with experimental data in the paper which follows (6).

No engineering model of electrosorption of neutral species has to date been reported, although many salient features have previously been addressed in the literature of conventional adsorption and of porous electrode processes. The earliest models were directed toward analogous heat-transfer applications (7), including prediction of the temperature of gas leaving a blast furnace (8). Application of the foregoing concepts to adsorption phenomena was carried forward by Klotz (9), Hougen and Marshall (10), and Mickley *et al.* (11). Amundson and Lapidus (12-14) obtained elegant but complex analytical solutions for adsorption in packed beds in which several of the assumptions of previous workers had been relaxed.

Modeling of transient behavior of porous electrodes was reviewed by de Levie (15) and, more recently, by Newman and Tiedemann (16). Johnson and Newman (17) give an approximate analysis for charging of a porous electrode during electrosorption of salt on activated carbon. A similar analysis of electrochemical desalination was reported by Schmidt (18). A Soviet application of the process reported power consumption of 0.35 kW-hr/kg of salt removed at a current efficiency of 65% (19). Electrosorption of uncharged species, for which the adsorption isotherm and its potential dependence are radically different than for ions, has not previously been modeled.

Theoretical Model

A mathematical model for electrosorption of an uncharged adsorbate onto a flow-through porous electrode was formulated from fundamental principles in order to predict the amount adsorbed as a function of time and to identify parameters by which behavior may be correlated.

Physical representation of the phenomenon.—A diagram of the geometry under consideration is shown in Fig. 1. The electrode is a conductive packed bed of particles (adsorbent) through which flows solution containing electrolyte and neutral adsorbate species. The counterelectrode is located downstream from the

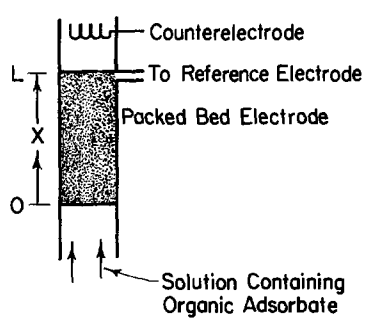

Fig. 1. One-dimensional flow-through porous electrode

* Electrochemical Society Active Member.

[1] Present address: Research and Development Department, Union Carbide Corporation, South Charleston, West Virginia 25303.

Key words: mass transfer, ohmic resistance, charging of double layer, adsorption isotherm.

packed bed. This arrangement results in parallel flow of solution and of electrical current through the bed.

Prior to initiating the act of adsorption, the adsorbent is maintained at a desorbing potential, ϕ_D, for which the amount of adsorbate held by the packed bed is small. Then, at time $t = 0$, the potential at the downstream end[2] of the packed bed ($x = L$) is changed suddenly to an adsorbing potential, ϕ_A. The sudden change of potential sets into motion two processes: charging of the electrical double layer on the surface of the adsorbent and removal of species from solution filling the porous bed.

The charging of the double layer to the new potential requires passage of electrical current through the solution within the pores and through the conductive packed bed. Because of solution resistivity, the region of porous electrode nearest the counterelectrode becomes charged more rapidly than regions farther away. That is, the electrical charging process moves through the bed as a wave. Ideally, faradaic reactions would not occur, and the current which flows would be only that needed to charge the double layer.

Because the adsorption isotherm is potential dependent, it should be clear that, at any instant during charging of the bed, the local driving force for electrosorption will depend on the potential at that particular location. Therefore removal of species from solution by electrosorption also occurs as a wave which moves through the bed. The actual rate of electrosorption depends on the mass transfer of adsorbable species from the solution, flowing through the pores, to the surface of the adsorbent. Eventually, the entire bed becomes charged to the new potential, the quantity of adsorbate held by the bed increases to the equilibrium amount according to the adsorption isotherm, and further removal of adsorbate from solution ceases.

Assumptions.—The six primary assumptions in the development of the model were: (*i*) adsorption was mass-transfer limited, (*ii*) faradaic reactions were negligible, (*iii*) radial gradients were negligible, (*iv*) solution conductivity remained constant, (*v*) conductivity of the adsorbent was much greater than that of the solution, and (*vi*) differential capacitance was constant.

According to numerous studies in the literature, most adsorption processes exhibit very rapid kinetics so that adsorption rates are usually mass-transfer limited. With appropriate choice of adsorbent and of range of potential, current caused by faradaic reaction can be made insignificant compared to capacitive charging current. The potential gradient in the radial direction can be ignored when, for bed radius R_B and bed length L, the term R_B^2/L^2 is much less than one. Since large concentrations of electrolyte were needed in all studies, their concentration, and hence the solution conductivity, remained constant during electrosorption. The final assumption, that differential capacitance was constant, was the most questionable assumption. In general, differential capacitance may vary considerably with surface coverage and with potential. In the case of the experiments described in the following paper, however, the variation over most of the range of potential used for electrosorption was less than 10% from the median value.

Mathematical representation.—The equation of transient convective diffusion in the presence of mass-transfer limited adsorption is

$$\epsilon \frac{\partial c_A}{\partial t} + v \frac{\partial c_A}{\partial x} = \epsilon D \frac{\partial^2 c_A}{\partial x^2} - \epsilon k a (c_A - c_A^s) \quad [1]$$

[2] It is important that the end of the bed at which the potential is controlled (the location of the reference electrode) be the end nearest the counterelectrode. If the potential were controlled at the opposite end (upstream in Fig. 1) then a change in potential would temporarily send the potential near the counterelectrode to an extreme value where electrolysis would occur.

On the left-hand side appear transient and convective terms. The concentration of adsorbate in solution is c_A, ϵ is porosity of the packed bed, and v is the superficial velocity. The first term on the right-hand side accounts for both molecular diffusion and for axial dispersion. The coefficient D consists of two terms

$$D = \left(\frac{2\epsilon}{3 - \epsilon}\right) D_A + \frac{v d_p}{2\epsilon} \quad [2]$$

The molecular diffusion coefficient D_A is corrected for tortuosity in a packed bed (20). The second term is given by Sherwood *et al.* (21) for axial dispersion in a bed of particles of diameter d_p. The diffusion-dispersion term is usually a minor factor in flow-through porous electrodes. The last term in Eq. [1] accounts for mass transfer between the fluid and the porous electrode. The mass transfer coefficient is symbolized by k (cm/sec), and a is the interfacial area per volume of solution (cm^{-1}). In this work, the mass transfer correlation of Wilson and Geankoplis (22) was used

$$k = \frac{1.09\, D_A}{\epsilon d_p} \mathrm{Pe}^{1/3} \quad [3]$$

In Eq. [3], Pe is the particle Peclet number, $d_p v/D_A$.

Boundary conditions for Eq. [1] are:

at

$$t = 0, \text{ all } x: \quad c_A = c_{Ao} \quad [4]$$

at

$$x = 0, \text{ all } t: \quad c_A = c_{Ao} + \frac{D}{v} \frac{\partial c_A}{\partial x} \quad [5]$$

at

$$x = L, \text{ all } t: \quad \frac{\partial c_A}{\partial x} = 0 \quad [6]$$

While not exact, the last boundary condition was found by Wehner and Wilhelm (23) to be a very good approximation.

Under the assumption that the solution concentration at the adsorbent surface, c_A^s, was in equilibrium with adsorbate adsorbed on the surface of the adsorbent, a relationship for c_A^s can be obtained from an adsorption isotherm. The relationship between c_A^s and fractional surface coverage, θ, is frequently expressed in the form

$$K' c_A^s = f(\theta) \quad [7]$$

Potential dependence in the adsorption isotherm manifested itself in the adsorbability constant, K'.

A differential mass balance yielded the relation needed to close the convective-diffusion equation

$$\Gamma_m \frac{\partial \theta}{\partial t} = k(c_A - c_A^s) \quad [8]$$

Monolayer surface coverage is symbolized by Γ_m (mol/cm²). The left-hand side of Eq. [8] corresponds to the amount of adsorbate taken up by the adsorbent, and the right-hand side represents the loss of adsorbate from solution. At $t = 0$, the adsorbent was partially covered by adsorbate with fractional coverage θ_o, giving the initial condition at

$$t = 0, \ \theta = \theta_o \quad [9]$$

The transient potential distribution resulting from charging of the double layer in porous electrodes has been derived by several researchers (17, 24-26). Resistance in the electrode phase was neglected. The one-dimensional equation for charging of the double layer may then be written

$$\frac{\partial \phi}{\partial t} = \frac{\kappa}{aC} \frac{\partial^2 \phi}{\partial x^2} \quad [10]$$

The potential ϕ is the difference between potentials in the metal and in adjacent solution, $\phi_M - \phi_S$. The differential capacitance is C (F/cm^2) and the effective conductivity of solution in porous media, κ (Ω-cm)$^{-1}$, is (20)

$$\kappa = \left(\frac{2\epsilon}{3-\epsilon}\right)\kappa_0 \quad [11]$$

where κ_0 is the specific conductivity of the solution.

Initially, the bed is held at a desorbing potential:
at

$$t = 0, \text{ all } x: \quad \phi = \phi_D \quad [12]$$

At $t > 0$, the potential is changed to an adsorbing potential and held constant thereafter; the potential change is accomplished by a linear scan over the rise time $t_R = (\phi_A - \phi_D)/\dot{\phi}$, where $\dot{\phi}$ is the scan rate of the applied potential:
at

$$x = L, \ t > 0: \quad \phi = \phi_A + \left[1 - \frac{t}{t_R}\right][1 - U(t - t_R)]\,(\phi_D - \phi_A) \quad [13]$$

No current flows in the solution phase at the end of the packed bed furthest from the counterelectrode:
at

$$x = 0, \ t > 0: \quad \frac{\partial \phi}{\partial x} = 0 \quad [14]$$

Dimensionless equations.—The equation for the charging of the double layer, Eq. [10] may be written in dimensionless form

$$\frac{\partial \Phi}{\partial \tau} = \frac{\partial^2 \Phi}{\partial X^2} \quad [15]$$

where

$$\Phi = \frac{\phi - \phi_A}{\phi_D - \phi_A} \quad [16]$$

$$X = x/L \quad [17]$$

and

$$\tau = t/(aCL^2/\kappa) = t/\tau_{DL} \quad [18]$$

The corresponding boundary conditions, Eq. [12], [13], and [14] are:
at

$$\tau = 0, \text{ all } X: \quad \Phi = 1 \quad [19]$$

at

$$X = 1, \ \tau > 0: \quad \Phi = \left[1 - \frac{\tau}{\tau_R}\right][1 - U(\tau - \tau_R)] \quad [20]$$

at

$$X = 0, \ \tau > 0: \quad \frac{\partial \Phi}{\partial X} = 0 \quad [21]$$

The time constant for charging of the double layer, τ_{DL}, is an RC time constant which characterizes the time required for the potential to change to its new value throughout the bed.

The convective-diffusion equation and adsorption isotherm, Eq. [1] and [7], can be made dimensionless with use of the time constant, τ_{DL}

$$\epsilon\frac{\partial C_A}{\partial \tau} + \frac{vaCL}{\kappa}\frac{\partial C_A}{\partial X} = \frac{\epsilon DaC}{\kappa}\frac{\partial^2 C_A}{\partial X^2} - \frac{\epsilon kaCL^2}{\kappa}\left[C_A - \frac{f(\theta)}{c_{A_0}K'}\right] \quad [22]$$

where the adsorbate concentration has been made dimensionless by use of the feed concentration, c_{A_0}

$$C_A = c_A/c_{A_0} \quad [23]$$

The dimensionless boundary conditions are:
at

$$\tau = 0, \text{ all } X: \quad C_A = 1 \quad [24]$$

at

$$X = 0, \text{ all } \tau: \quad C_A = 1 + \frac{D}{vL}\frac{\partial C_A}{\partial X} \quad [25]$$

at

$$X = 1, \text{ all } \tau: \quad \frac{\partial C_A}{\partial X} = 0 \quad [26]$$

Additionally, Eq. [8] can be written in dimensionless form

$$\frac{\partial \theta}{\partial \tau} = \frac{aCL^2kc_{A_0}}{\kappa\Gamma_m}C_A - \frac{aCL^2k}{\kappa\Gamma_m K'}f(\theta) \quad [27]$$

with the initial condition, at

$$\tau = 0: \quad \theta = \theta_0 \quad [28]$$

Method of Solution

The mathematical model consisted of three parabolic partial differential equations. In addition, algebraic equations were used to describe the adsorption isotherm, the mass transfer correlation, and the potential dependence of the adsorbability constant. The nonlinear adsorption equations, Eq. [22] and [27], were coupled to the equation for charging of the double layer through the potential dependence of K'. Additional coupling was avoided by assuming a constant differential capacitance. Because diffusion/dispersion was relatively unimportant, the term accounting for it in the upstream boundary condition, Eq. [25], was ignored during calculations. Solution of the system of equations employed several mathematical techniques, the key technique being the solution of the convective-diffusion equation by the method of finite difference. An implicit back-difference scheme proved to be stable for calculating adsorbate concentration at each location. Specific details and a computer program are available (27). Adsorbate concentration, fractional surface coverage, potential distribution, and charging current were calculated by the computer program. The dimensionless space increment, ΔX, was 1/60; the dimensionless time increment, initially at 1/6 $(\Delta X)^2$, was increased during the simulation.

Potential distribution and charging current were determined independently of adsorbate concentration. An analytical solution for the potential distribution, adapted from Carslaw and Jaeger (28), was

$$\Phi = \frac{4}{\pi}\sum_{j=0}^{\infty} e^{-(2j+1)^2\pi^2\tau/4}\cos[(2j+1)\pi X/2]\frac{(-1)^j}{(2j+1)} \quad [29]$$

Determination of potential allowed calculation of the potential-dependent adsorbability constant at each location in the bed. The charging current density was calculated from

$$i = -\kappa\left(\frac{\partial \phi}{\partial x}\right)_{x=L} \quad [30]$$

Note that all variation in potential occurs in the solution phase and that ϕ_M is constant. Error in numerically approximating the derivative was usually negligible, but was as high as 20% at the maximum current.

All calculations were carried out on a CDC Cyber 175. The program required 11,400 words. The program was terminated when effluent adsorbate concentrate returned to within 2% of its initial value. Execution time varied considerably with different input parameters, ranging from 200 to 400 sec.

Model Results and Discussion

Input Parameters

Parameters for the model were based on one particular adsorbent/adsorbate system, the adsorption of

Table I. Fixed parameters for modeling electrosorption of β-naphthol on glassy carbon

Parameter	Value
a = interfacial area	3400 cm²/cm³
A = cross-sectional area of bed	1.85 cm²
C = differential capacitance	8.2×10^{-6} F/cm²
c_{Ao} = adsorbate concentration in feed	1.95×10^{-5} mols/cm³
D_A = adsorbate diffusion coefficient	8.95×10^{-6} cm²/sec [Ref. (30)]
d_p = particle diameter	0.0036 cm
ϵ = porosity	0.38
ϕ_A = adsorbing potential	−0.26V
ϕ_D = desorbing potential	−1.26V
$\dot{\phi}$ = scan rate	10 V/sec
Mass transfer correlation	Equation [3]
Adsorption isotherm (modified Langmuir)	Ref. (6), Eq. [1]
Γ_m = monolayer surface coverage	2.5×10^{-10} mols/cm²
n = number of water molecules replaced by one adsorbate molecule	6
c_w = water concentration	0.055 mols/cm³
Potential dependence of adsorbability constant, K	Ref. (6), Eq. [2]

β-naphthol on microspheres of glassy carbon. Experiments with this system are reported in the following paper (6). Fixed parameters and properties used in the model are listed in Table I. Parameters which were varied in model calculations are listed in Table II. The values of the parameters for the base case, as well as the range of values, are given. The superficial velocities corresponded to a range of Re_p from 0.025 to 0.58.

Results of Model Simulations

Potential distribution.—A dimensionless plot of the transient potential variation within the bed is shown in Fig. 2 for several locations. The bed was initially at a desorbing potential, $\Phi = 1$, throughout. At $\tau = 0$, the potential suddenly changed to an adsorbing potential (at a scan rate of 10 V/sec in this example). Charging of the double layer proceeded in a wavelike manner through the bed. The region closest to the counterelectrode ($X = 1.0$) became charged most rapidly, while the region furthest from the counterelectrode ($X = 0.0$) lagged behind. In fact, it may be seen that regions far from the counterelectrode experienced a delay period before they even began charging. Also, at a time equal to τ_{DL}, the bottom of the bed achieved ~90% of the total potential change. If the differential capacitance is constant, the one-dimensional potential distribution for charging of the double layer depends solely on τ_{DL}.

Capacitive charging current.—A dimensionless plot of the charging current density as a function of time is shown in Fig. 3 for the parameters given in Table I. The current increased quickly to a peak at the end of the potential scan and decreased thereafter while the potential was held constant. The peak in current density increased with increasing values of κ, $(\phi_D - \phi_A)$, and τ_{DL}. The numerical errors in computing the current density were a maximum (20%) in the vicinity of the peak and negligible elsewhere, *i.e.*, to within the width of the line shown in Fig. 3.

Adsorption within the bed.—Adsorption results should more appropriately be presented as a function of a characteristic adsorption time than of τ_{DL}. The breakthrough time, τ_{BT}, was therefore defined

$$\tau_{BT} = \frac{(\theta_A - \theta_D)\Gamma_m a \epsilon L}{c_{Ao} v} \quad [31]$$

The values θ_A and θ_D correspond to equilibrium surface coverage at potentials ϕ_A and ϕ_D, respectively. The breakthrough time was the time required to saturate the adsorbent if all adsorbate entering the bed before the onset of saturation were adsorbed.

Fractional surface coverage as a function of bed location is plotted for several time intervals in Fig. 4. Parameters for the base case were used. At small values of t/τ_{BT}, when t/τ_{DL} was also small, θ had not changed from its initial value, 0.30, in the lower part of the bed because the potential there had not yet changed. At intermediate times, after appreciable change in potential had occurred throughout the bed, increased values of θ at the lower and upper ends of the bed were caused by adsorption-isotherm and potential-dependent effects, respectively. Adsorption-isotherm effects refer to the increased adsorption observed at higher solution concentrations. By $t/\tau_{BT} = 1.0$, shortly before breakthrough, charging of the double layer had been completed. At this time, an adsorption wave was progressing toward the top of the bed in the same manner as for simple adsorption. Propagation of the adsorption wave may also be observed from the adsorbate concentration in solution. Figure 5 shows the chronological history of adsorbate concentration for several locations along the bed. Wavelike propagation of adsorption became evident at $x/L > 0.5$. The curve at $x/L = 1.0$ corresponded to adsorbate concentration in the effluent.

Velocity, solution conductivity, and bed length.—The effects of velocity, solution conductivity, and bed length on effluent adsorbate concentration are shown in Fig.

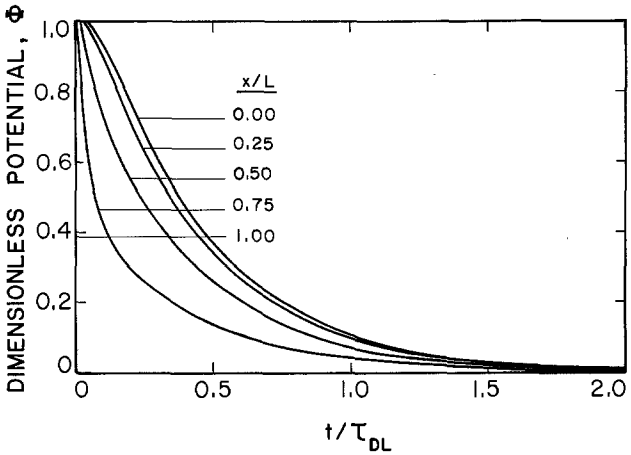

Fig. 2. Decay of potential at several locations in packed bed during charging of the double layer.

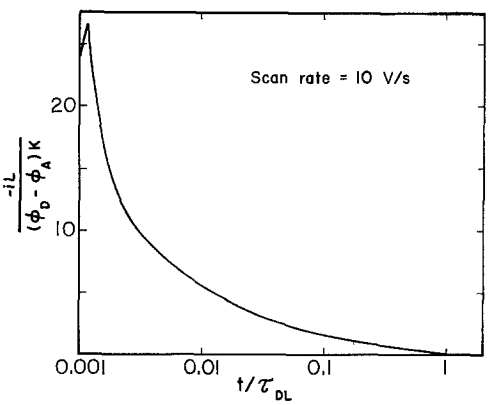

Fig. 3. Capacitive charging current, base case

Table II. Base case values and range of variable parameters

Parameter	Units	Base case value	Range
v = velocity	cm/sec	0.177	0.063-1.45
L = bed length	cm	8.5	3.0-24.3
κ_o = specific conductivity of solution	$(\Omega\text{-cm})^{-1}$	0.0815	0.01-0.0815

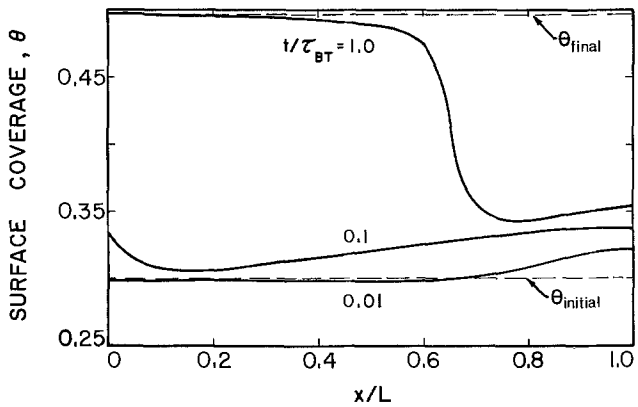

Fig. 4. Surface coverage distribution, base case

6. Each plot used parameter values for the base case, except for the parameter being varied. In all cases, the effluent concentration fell very rapidly in the first few tenths of a second. However, the concentration never dropped below 30% of its initial value, in accord with the adsorption isotherm. Therefore, breakthrough always occurred at values of $t/\tau_{BT} > 1$.

At the lowest velocity in Fig. 6a, the dimensionless concentration remained fairly constant at a value of 0.34 until breakthrough. The flat concentration profile, followed by a steep breakthrough curve, would be desirable in a practical application of electrosorption. However, for simulations at higher velocities, which would increase separation per unit time, the flat profile was lost. At intermediate velocities, following the initial rapid decline, adsorbate concentration climbed, then dipped again before leveling off. At highest velocities, breakthrough commenced before the second concentration dip could occur. The breakthrough curve broadened at higher velocities.

The only effect of altering solution conductivity in the model was to change the capacitive charging time. However, the effect on adsorbate concentration caused by decreasing conductivity was similar to the effect caused by increasing velocity. When an electrolytic solution with a specific conductivity of 0.0815 $(\Omega\text{-cm})^{-1}$, corresponding to 0.5*M* K_2SO_4, was considered, a nearly flat concentration profile was observed. At a conductivity of 0.0397 $(\Omega\text{-cm})^{-1}$, corresponding to 0.2*M* K_2SO_4, the level region in the concentration profile had nearly disappeared. At the two lowest conductivities, for which $\tau_{DL} > \tau_{BT}$, the breakthrough curve became very broad. At these two lowest conductivities, capacitive effects in the diffuse double layer would probably decrease the overall double layer capacitance. The effect of a smaller capacitance, which would reduce

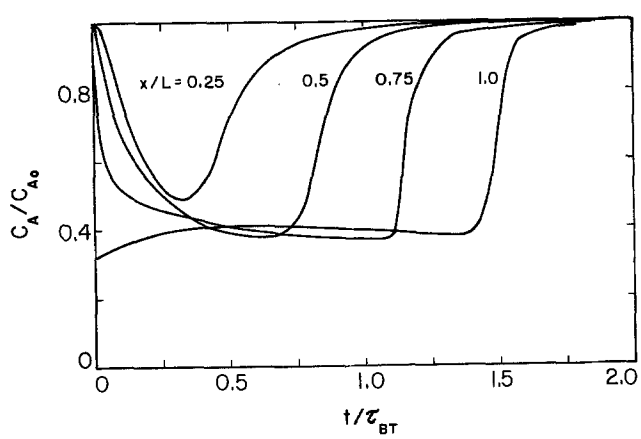

Fig. 5. Adsorbate concentration *vs.* time at several locations, base case.

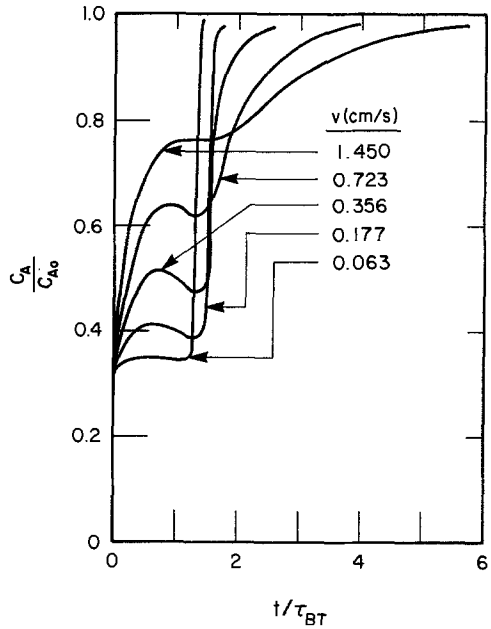

Fig. 6a. Predicted effect of velocity on effluent adsorbate concentration.

the double layer charging time, was not considered in Fig. 6b.

Larger bed lengths increased both the breakthrough time and the double layer charging time. The effect of bed length on effluent concentration, shown in Fig. 6c, was similar to the effects observed for velocity and for conductivity changes. A flat effluent concentration profile only occurred at the lowest length, 3 cm. Since τ_{DL} increased with the square of length and τ_{BT} increased only with the first power of length, increased length resulted in less desirable profiles. The effect of bed length on effluent concentration suggested formidable scale-up problems for a one-dimensional geometry.

The similar patterns observed in Fig. 6 suggested that a single dimensionless parameter might describe all variations in velocity, solution conductivity, and bed length. A characteristic observation was that broadening of the breakthrough curve occurred when the double layer charging time exceeded the breakthrough time. A dimensionless parameter that could account for

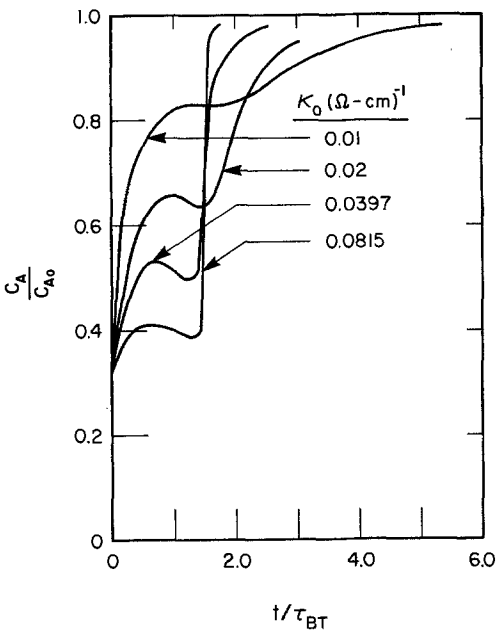

Fig. 6b. Predicted effect of solution conductivity on effluent adsorbate concentrations.

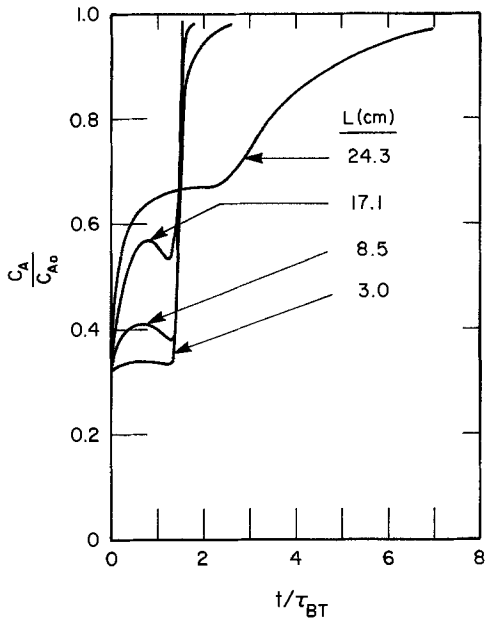

Fig. 6c. Predicted effect of bed length on effluent adsorbate concentration.

the broadening effect was the ratio of the two characteristic times

$$\frac{\tau_{DL}}{\tau_{BT}} = \frac{vc_{Ao}CL}{(\theta_A - \theta_D)\Gamma_m \varepsilon \kappa} \quad [32]$$

Pairs (and in one case, a trio) of model simulations which used different variable parameters, but in which the ratio of characteristic times was the same, were compared (27). The simulations for each ratio were nearly coincident and qualitative trends matched. A flat concentration profile was obtained for $\tau_{DL}/\tau_{BL} < 1.0$. The simulations for ratios at or above unity reflected incomplete adsorption at the time that breakthrough was expected. Because the adsorbing potential had not penetrated the entire bed, the breakthrough curve was extended in time until charging of the double layer was complete. The rise in adsorbate concentration immediately after the initial drop in concentration was caused by saturation of the top of the bed before the adsorbing potential had reached lower into the bed.

Similarity among the curves computed at the same values of τ_{DL}/τ_{BL} permitted the establishment of a general dimensionless correlation, shown in Fig. 7. The general correlation was not exact and has not been tested beyond the range of parameter values listed in Table II. Also, its validity for different values of the fixed parameters has not been considered. Nevertheless, the correlation accounted for the behavior of three important parameters over a useful range of values. More important, the correlation worked in regimes of very different behavior. Therefore, the results of Fig. 7 represented the most important contribution of the mathematical model.

Application of the model simulation to the desorption cycle is discussed in the following paper (6).

Adsorption isotherm.—It was found in this work (27) that the manner of electrode pretreatment affected the magnitude of the dimensionless adsorbability constant $K = K'c_w$ without changing the form of the adsorption isotherm. For several values of K relative to the experimental value, K_o, simulation of the effluent adsorbate concentration *vs.* time is presented in Fig. 8, under base-case conditions. Usually, the flat region of effluent concentration was at a lower concentration at higher values of K. However, the concentration in the flat region for $2 \times K_o$ was slightly higher than for K_o.

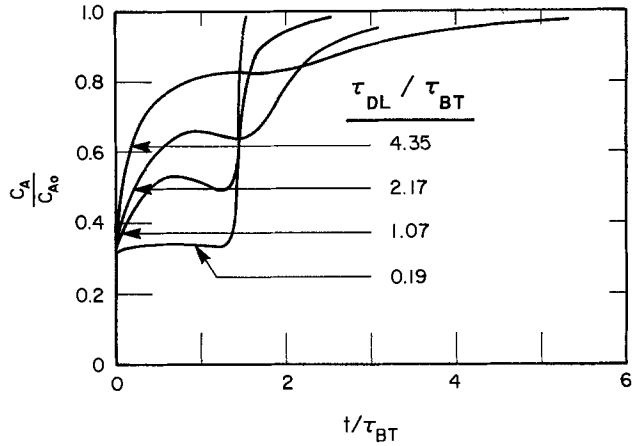

Fig. 7. Dimensionless correlation for electrosorption in a flow-through porous electrode.

Coincidentally, K_o may have represented an optimal value for electrosorption.

The effect of potential dependence could not be generalized because the form of the dependence may vary with each adsorbate/adsorbent system. The effect of changing c_{Ao} was partially considered in Fig. 7 by its inclusion in τ_{BT}. Adsorption generally increases with lower temperature. However, little, if any benefit would accrue in the case of electrosorption at low temperature because the amount of adsorption at ϕ_D would also increase.

Mass transfer and dispersion.—The correlations used in the model to determine the coefficients of mass transfer and of dispersion were not very accurate. The model's sensitivity to these two coefficients was tested by reducing the mass transfer coefficient to 1/4 of its original magnitude and by increasing the dispersion coefficient by a factor of 4. Correlations for dispersion (21) in the appropriate range of Peclet number suggested the factor of 4. The lower mass transfer coefficient reduced the rate of change of effluent concentration during the first few tenths of a second and, to a lesser extent, during breakthrough. Overall, the effect of changing the mass transfer coefficient was minor for the conditions of the base case. Changing the dispersion coefficient had negligible effect on effluent concentrations.

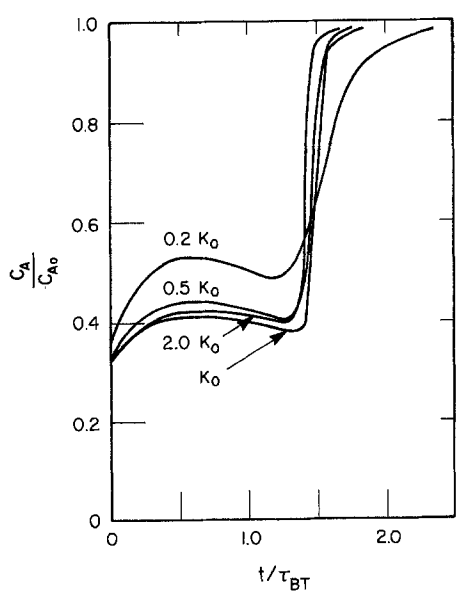

Fig. 8. Predicted effect of adsorbability on effluent adsorbate concentration.

Practical Implications for One-Dimensional Geometry

Cycle time.—Two broad objectives must be met in optimizing a practical, cyclic, electrosorption process. In order to increase the amount of adsorbate separated per unit time, the cycle time should be minimized, as by increasing flow velocity. In addition, utilization of the adsorbent capacity per cycle should be maximized. Unfortunately, the constraint that must be satisfied to meet these objectives, $\tau_{DL}/\tau_{BT} < 1.0$, limits scale-up of the one-dimensional flow-through porous electrode. Consider, for example, methods to minimize $\tau_{DL} = aCL^2/\kappa$. Since charging time increases with the square of bed length, the greatest reduction in τ_{DL} would result from decreasing L. But then, scale-up to larger beds must consider a two-dimensional geometry. Highly conductive solutions allow more flexibility in scale-up. Increased temperature may increase conductivity by about 2%/°C. However, reduced temperature would be more effective in systems exhibiting excessive faradaic current. Gagnon (29) found that the differential capacitance of nickel was unchanged at low temperatures. Differential capacitance ought to be smaller in solvents of low dielectric. Increasing the interfacial area permits some degree of scale-up without affecting the ratio, τ_{DL}/τ_{BT}. However, an order of magnitude increase in specific surface area from that on glassy carbon would change the limiting rate of adsorption from convective mass transfer to pore diffusion.

Effluent concentration.—In some applications considered for electrosorption, the goal might be maintenance of adsorbate concentration below a certain level. It was found that neither longer beds nor slower velocities had much effect on the minimum adsorbate concentration in the effluent. Minimum effluent concentration is determined by the potential-dependent adsorption isotherm. Within certain limits, potential can be changed to provide a suitable effluent concentration. In order to achieve much lower concentrations in a one-dimensional flow-through configuration, placement of two or more independent flow-through porous electrodes in series would be necessary.

Energy consumption.—The energy required of an electrosorption process, exclusive of pumping costs, is that needed to charge the double layer. The two mandatory components of energy consumption are the energy stored in the double layer and the energy dissipated in the interstitial solution of the porous electrode during charging of the double layer. These two components are equal in magnitude. Additional energy is dissipated in the separator between the working and counterelectrodes. Energy consumption during each half-cycle will be independent of the utilization of adsorbent surface area for adsorption, unless increased surface coverage changes the differential capacitance.

Energy stored in the double layer, analogous to the storage of energy in a capacitor, is

$$E_{DL} = \frac{1}{2} aC(\Delta\phi)^2 AL \qquad [33]$$

for a porous electrode of cross-sectional area A and bed length L. Energy dissipated within the interstitial volume of a porous electrode is

$$E_{inter} = \int_0^\infty \int_0^L [i(x,t)/\kappa] dx dt \qquad [34]$$

The energy dissipated in the separator is

$$E_{sep} = \int_0^\infty I(x = L, t)^2 R_{sol}\, dt \qquad [35]$$

If the working and counterelectrodes are separated by a porous glass frit of thickness L_F having the same cross-sectional area as that of the porous electrode, the solution resistance, R_{sol}, becomes $L_F/\kappa A$. Equations [34] and [35] were solved by finite difference, with the upper time limit replaced by τ_{DL} because the charging current I becomes negligible at τ_{DL}.

Components of energy consumption of an electrode per half-cycle are given in Table III under conditions of several model simulations. The tabulations assumed values of $L_F = 1$ cm and $A = 1.85$ cm^2. Solution conductivity, bed length, and specific surface area were varied. In spite of different calculational procedures, the magnitudes of E_{DL} and E_{inter} were nearly the same. No significant change in energy consumption resulted from varying solution conductivity. Energy dissipated in the interstitial solution was proportional to bed length and to specific surface area. Energy dissipated in the separator was also proportional to specific surface area, but E_{sep} increased only slightly with bed length.

Total energy consumption per half-cycle was calculated on the basis that the counterelectrode was a second flow-through porous electrode operating in the opposite sorption mode

$$E_{total} = E_{sep} + 2E_{inter} + E_{DL} \qquad [36]$$

The double layer storage term was not doubled, even though the two electrodes were considered, because, in principle, half of the double layer energy can be recovered during discharge by using it to charge partially the second electrode. In practice, less than half of the stored energy would be recovered if rapid charging and discharging were required. Tabulation of total energy consumption per g-mol of adsorbate in Table III assumed full use of adsorption capacity between θ_D and θ_A. Energy consumption, about 0.2 kW-hr/g-mol of adsorbate, was unaffected by changes in solution conductivity and specific surface area. The small decrease in energy consumption per amount adsorbed at larger bed lengths reflected the reduced influence of separator resistance. At conditions corresponding to the base case, energy consumption was 1.43 kW-hr/kg of β-naphthol. For comparison with desalination by electrosorption, Soviet workers (19) reported energy usage of 0.35 kW-hr/kg of salt.

Conclusions

A mathematical model was developed to describe electrosorption of uncharged compounds in a flow-

Table III. Energy consumption

Variables			Energy consumption				
			Components: per half-cycle per electrode			E_{total}	
L (cm)	κ_0 $(\Omega\text{-cm})^{-1}$	Specific surface area (cm^2/g)	E_{DL} (W-sec)	E_{inter} (W-sec)	E_{sep} (W-sec)	Per half-cycle (W-sec)	Per amount adsorbed (kW-hr/g-mol)
8.5	0.0815	1510	0.219	0.215	0.131	0.780	0.206
8.5	0.0397	1510	0.219	0.216	0.137	0.789	0.208
8.5	0.0200	1510	0.219	0.217	0.142	0.795	0.208
3.0	0.0815	1510	0.077	0.073	0.107	0.330	0.245
8.5	0.0815	1510	0.219	0.215	0.131	0.780	0.206
24.3	0.0815	1510	0.627	0.622	0.145	2.016	0.186
8.5	0.0815	1510	0.219	0.215	0.131	0.780	0.206
8.5	0.0815	3020	0.438	0.432	0.274	1.576	0.208
8.5	0.0815	6040	0.877	0.868	0.566	3.179	0.209

through porous electrode. The model treated the case of downstream placement of the counterelectrode and control of potential at the end of the porous electrode nearest the counterelectrode. Rate of adsorption was assumed to be limited by convective mass transfer. The mathematical model predicted amount adsorbed, effluent adsorbate concentration, transient potential distribution, and flow of current under various operating conditions.

The most important result of the model was that rapid and efficient adsorption occurred when the ratio of double layer charging time to breakthrough time was below unity. This ratio specified operating constraints on flow rate, solution conductivity, and bed length. The model also showed that the adsorption isotherm, rather than engineering variables, determined the minimum effluent concentration of adsorbate.

For use as an industrial separation process, electrosorption must be carried out on a considerably larger scale than in laboratory experiments. In particular, larger flow rates, specific surface areas of adsorbents, and adsorbent beds would be necessary. The mathematical model developed for one-dimensional electrosorption characterized the limitations on scale-up and also enabled identification of future areas of study.

While augmentation of adsorption rate and capacity can be achieved by increasing fluid velocity or bed length, it should be recognized that these parameters also influence the double layer charging time with respect to the breakthrough time. Excessive scale-up by velocity or bed length may therefore have an adverse effect upon cycle time. Increases in capacity can also be achieved by increasing bed diameter, which has no influence on the characteristic time constants, although mechanical limitations and fluid-flow channeling may impede performance of large-diameter systems.

Placement of the counterelectrode in positions other than the downstream arrangement studied here should be explored further. In particular, flow-by geometry appears attractive where electrical current flows perpendicular to the direction of fluid flow within the packed adsorption bed.

Practical applications of electrosorption would favor use of porous adsorbent particles rather than the nonporous microspheres used in this fundamental study. Porous particles would permit increased specific surface area while maintaining low fluid pressure drop. Models of porous particle adsorbents, however, would need to be developed to account for pore-diffusion-limited adsorption.

Note Added in Proof: An error in these two papers (*This Journal*, **130**, 85, 93) has been discovered. In the equation for the charging of the double layer in the first paper, Eq. [10], the right hand side should be divided by the porosity, ϵ. The omission of ϵ does not change the results qualitatively. However, in comparison of theory and experiment, correction of the equation will reduce the calculated characteristic time for charging of the double layer by 62%. The quantitative effect of the correction is a much better agreement between calculated and measured decay of potential and of current with time. The corrected forms of the double-layer charging time, τ_{DL}, and of the ratio of charging to breakthrough times, τ_{DL}/τ_{BT}, become

$$\tau_{DL} = \epsilon a C L^2/\kappa$$

$$\tau_{DL}/\tau_{BT} = v c_{A_0} CL/[(\theta_A - \theta_D)\Gamma_m \kappa$$

Acknowledgments

This work was funded by grants NSF ENG 76-83379 and NSF CPE 80-08947. Fellowship assistance from Union Carbide Corporation, American Oil Company, General Electric Company, and Exxon Education Foundation, was deeply appreciated.

Manuscript submitted Jan. 10, 1982; revised manuscript received July 1, 1982.

Any discussion of this paper will appear in a Discussion Section to be published in the December 1983 JOURNAL. All discussions for the December 1983 Discussion Section should be submitted by Aug. 1, 1983.

Publication costs of this article were assisted by the University of Illinois.

LIST OF SYMBOLS

a	interfacial area per unit volume of solution, cm^{-1}
A	cross-sectional area of bed, cm^2
c_A	adsorbate concentration, mol/cm^3
c_{A_0}	initial adsorbate concentration, mol/cm^3
c_A^s	adsorbate concentration at adsorbent surface, mol/cm^3
c_w	concentration of water, mol/cm^2
C	differential capacitance, F/cm^2
C_A	dimensionless adsorbate concentration $= c_A/c_{A_0}$
d_p	particle diameter, cm
D	sum of effective diffusion and dispersion coefficients, cm^2/sec
D_A	diffusion coefficient of adsorbate, cm^2/sec
E_{DL}	energy stored in the capacitive double layer during a half-cycle, W-sec
E_{intcr}	energy dissipated in the interstitial solution within a porous electrode during a half-cycle, W-sec
E_{sep}	energy dissipated in the solution within the separator during a half-cycle, W-sec
E_{total}	energy consumed per half-cycle, using two porous electrodes, W-sec
i	current density, A/cm^2
I	current, A
k	mass transfer coefficient, cm/sec
K	potential-dependent adsorbability constant, dimensionless
K_o	experimental value of K
K'	K/c_w, cm^3/mol
L	bed length, cm
L_F	thickness of glass frit, cm
n	number of solvent molecules displaced by one organic adsorbate molecule
Pe	particle Peclet number $= d_p v/D_A$
R_B	radius of bed, cm
R_{sol}	effective solution resistance, Ω
Re_p	particle Reynolds number $= d_p v/\nu$
t	time, sec
t_R	rise time of potential scan, Eq. [13]
$U(t - t_R)$	unity step function equal to 0 (when $t < t_R$) or 1 (when $t > t_R$)
v	superficial velocity (the velocity obtained at the same flow rate in a column without packing), cm/sec
x	distance, cm
X	dimensionless distance $= x/L$

Greek letters

Γ_m	amount of organic compound adsorbed per unit area at monolayer surface coverage, mol/cm^2
ϵ	porosity of packed bed
θ	fractional surface coverage
θ_A	fractional surface coverage at adsorbing potential
θ_D	fractional surface coverage at desorbing potential
θ_o	fractional surface coverage at $t = 0$, generally $= \theta_D$
κ	effective solution conductivity, $(\Omega\text{-cm})^{-1}$
κ_o	specific conductivity of solution, $(\Omega\text{-cm})^{-1}$
ν	kinematic viscosity, cm^2/sec
τ	dimensionless time $= t/\tau_{DL}$
τ_{BT}	breakthrough time $= (\theta_A - \theta_D)\Gamma_m a\epsilon L/(vc_{A_0})$, sec
τ_{DL}	double layer charging time $= aCL^2/\kappa$, sec
τ_R	dimensionless rise time $= t_R/\tau_{DL}$
ϕ	potential difference between electrode and adjacent solution, V
ϕ_A	adsorbing potential, V
ϕ_D	desorbing potential, V
ϕ_M	potential of metal phase, V
ϕ_S	potential in solution adjacent to electrode, V
$\dot{\phi}$	scan rate of potential, V/sec
Φ	dimensionless potential $= (\phi - \phi_A)/(\phi_D - \phi_A)$

REFERENCES

1. A. Frumkin, *Z. Physik*, **35**, 792 (1926).
2. J. Butler, *Proc. R. Soc. London, Ser. A*, **122**, 299 (1929).
3. J. Bockris, M. Devanathan, and K. Muller, *ibid.*, **274**, 55 (1963).
4. G. Gouy, *Ann. Chim. Phys.*, **8**, 291 (1906).
5. B. Damaskin, O. Petrii, and V. Batrakov, "Adsorption of Organic Compounds on Electrodes," E. Uvarov, Translator, Plenum Press, New York (1971).
6. R. S. Eisinger and R. C. Alkire, *This Journal*, **130**, 93 (1983).
7. T. Schumann, *J. Franklin Inst.*, **208**, 405 (1929).
8. C. Furnas, *Trans. AIChE.*, **24**, 142 (1930).
9. I. Klotz, *Chem. Rev.*, **39**, 241 (1946).
10. O. Hougen and W. Marshall, *Chem. Eng. Progr.*, **43**, 197 (1947).
11. H. Mickley, T. Sherwood, and C. Reed, "Applied Mathematics in Chemical Engineering," 2nd ed., p. 303, McGraw-Hill, New York (1957).
12. L. Lapidus and N. Amundson, *J. Phys. Chem.*, **54**, 812 (1950).
13. L. Lapidus and N. Amundson, *ibid.*, **56**, 984 (1952).
14. N. Amundson, *Ind. Eng. Chem.*, **48**, 26 (1956).
15. R. de Levie, in "Advances in Electrochemistry and Electrochemical Engineering," Vol. 6, P. Delahay and C. Tobias, Editors, Interscience, New York (1967).
16. J. Newman and W. Tiedemann, in "Advances in Electrochemistry and Electrochemical Engineering," Vol. 11, H. Gerischer and C. Tobias, Editors, John Wiley & Sons, Inc., New York (1978).
17. A. Johnson and J. Newman, *This Journal*, **118**, 510 (1971).
18. T. Schmidt, Ph.D. Thesis, Illinois Institute of Technology, Chicago (1973).
19. N. Zhumagulov and E. Matskievich, *Nauch. Osn. Tekhnol. Ochist., Vody.*, (1973), p. 39 from Ref. Zh. Khim, 1973, Abstract No. 17I392.
20. G. Neale and W. Nader, *AIChE J.*, **19**, 112 (1973).
21. T. Sherwood, R. Pigford, and C. Wilke, "Mass Transfer," p. 136, McGraw-Hill, New York (1975).
22. E. Wilson and C. Geankoplis, *Ind. Eng. Chem. Fundam.*, **5**, 9 (1966).
23. J. Wehner and R. Wilhelm, *Chem. Eng. Sci.*, **6**, 89 (1956).
24. O. Ksenzhek and V. Stender, *Dokl. Acad. Nauk SSSR*, **106**, 487 (1956).
25. F. Posey and T. Morozumi, *This Journal*, **113**, 176 (1966).
26. J. McCallum, R. Hardy, and R. Redmond, Report AFAPL-TR-66-31, Battelle Memorial Institute, Columbus, OH (1966).
27. R. S. Eisinger, Ph.D. Thesis, University of Illinois (1981).
28. H. Carslaw and J. Jaeger, "Conduction of Heat in Solids," 2nd ed., p. 101, Oxford University Press, London (1959).
29. E. Gagnon, *This Journal*, **121**, 512 (1974).
30. L. McCune and R. Wilhelm, *Ind. Eng. Chem.*, **41**, 1124 (1949).

Separation by Electrosorption of Organic Compounds in a Flow-Through Porous Electrode

II. Experimental Validation of Model

Ronald S. Eisinger*,[1] and Richard C. Alkire*

Department of Chemical Engineering, University of Illinois, Urbana, Illinois 61801

ABSTRACT

The use of potential-dependent adsorption to separate an organic compound from solution was demonstrated experimentally. Isotherms for the adsorption of β-naphthol on glassy carbon were obtained over a range of potential of 1.0V. Adsorption of β-naphthol, in dilute concentration, from aqueous electrolytic solution was also carried out in a flow-through porous electrode consisting of nonporous microspheres of glassy carbon. A counterelectrode was located downstream and the potential was controlled at the end of the porous electrode nearest to the counterelectrode. Analysis of measurements of the transient potential distribution along the length of the porous electrode and of the current showed that each arose from charging of the electrical double layer. Profiles of effluent adsorbate concentration during both adsorption and desorption confirmed a theoretical model of electrosorption in a flow-through porous electrode. Cyclic electrosorption was experimentally demonstrated.

Potential-dependent adsorption is a novel means of separating adsorbable compounds from electrolytic solutions. The process appears to be particularly applicable to the adsorption of organic compounds that are present in dilute concentrations in process streams. For such applications, electrosorption is an inherently low-energy-consumption process. In cyclic operation, absorbate can be removed from a solution while the adsorbent is held at one potential, then desorbed into another solution at a second potential. The key to achieving a high rate of separation per unit amount of adsorbent is a short cycle time.

In this work, electrosorption of an organic compound in a flow-through porous electrode was carried out experimentally. The experimental program consisted of the following steps:

1. Measurement of physical properties of an appropriate adsorbate/adsorbent system.
2. Measurement of adsorption isotherms over a wide range of potential.
3. Determination of differential capacitance.
4. Evaluation of electrosorption during the adsorption cycle in a flow-through porous electrode.

The fourth step included the measurement of the transient responses of effluent adsorbate concentration, axial potential distribution, and capacitive charging current following a step change in applied potential. The measurements were compared with predictions of a one-dimensional mathematical model (1).

Separation of organic compounds from solution by electrosorption has not been practiced commercially. In fact, even laboratory studies of electrosorption on adsorbents of sufficient surface area to be of commercial interest are sparse. Perhaps the earliest demonstration of charge-dependent adsorption of an organic compound on a high-surface-area adsorbent was an

* Electrochemical Society Active Member.
[1] Present address: Union Carbide Corporation, Research and Development Department, South Charleston, West Virginia 25303.
Key words: adsorption, desorption, potential distribution.

elegant experiment described by Frumkin and Obrutsheva in 1926 (2). To a solution of silver nitrate containing the adsorbate caprylic acid, varying amounts of potassium iodide were added. The resulting silver iodide precipitate, the adsorbent, was positively charged until an excess of potassium iodide had been added. Then, the silver iodide became negatively charged. The concentration of caprylic acid exhibited a sharp decrease (corresponding to increased adsorption on the silver iodide) very near the titration point where no net charge existed on the silver iodide.

Barradas and Conway (3) were the first to obtain potential-dependent adsorption data on moderately high-surface-area material. Using spectrophotometry, they measured the adsorption of quinoline on silver gauze over a range of nearly 400 mV, observing greater adsorption at more negative potentials. Lee and Kirwan (4) published limited data on the electrosorption of enzymes on porous carbon including one case of reversible adsorption over a range of 800 mV. Strohl and Dunlap (5) used a flow-through column of graphite particles to concentrate quinones selectively at different potentials, but did not determine adsorption isotherms. The excellent review of adsorption of organic compounds on solid electrodes by Damaskin *et al.* (6) predominantly discussed metallic adsorbents. The adsorption of β-naphthol on graphite (7), studied over a range of 1.27V, represented the only thorough tabulation of potential-dependent adsorption isotherms on an adsorbent of industrial interest. No evaluation of engineering parameters for electrosorption of uncharged (*i.e.*, many organic) compounds has been published. The closest approaches to such an endeavor were the analyses of desalination by electrosorption (8-10).

Experimental

Materials.—The adsorption of β-naphthol from aqueous solution onto glassy carbon was studied. The choice of adsorbate was based on its ability to be adsorbed from very dilute solution, on the considerable potential dependence exhibited in its adsorption, on its stability with respect to redox reactions, and on its high molar extinction coefficient, permitting measurement by ultraviolet spectroscopy. The β-naphthol was purified grade (Baker and Adamson) with a melting point of 120.0-121.0°C. Electrolytic solution consisted of 0.5 or 0.2*M* K_2SO_4, containing in either case a phosphate buffer of the following composition: 0.0125*M* KH_2PO_4 (Baker Reagent), 0.0125*M* Na_2HPO_4 (Fisher Certified A.C.S.), and $10^{-3}M$ H_2SO_4 (du Pont A.C.S.). Potassium sulfate (Mallinckrodt Analytical Reagent) was recrystallized from water. Water was deionized-distilled, then distilled in glass from alkaline potassium permanganate. Electrolytic solutions were filtered and then deaerated with Prepurified Grade nitrogen (Linde) which had been presaturated in a bubbler containing electrolytic solution. During flow studies, adsorbate concentration in the electrolytic solution was $1.95 \times 10^{-5}M$ β-naphthol.

Glassy carbon microspheres were chosen as the adsorbent because of their sufficiently high electrical conductivity, the minimal faradaic reaction that occurred on them over a wide range of potential, and the well-defined mass transfer characteristics of spheres. Glassy carbon, also called vitreous carbon, is an amorphous form of carbon characterized by very low values of porosity and permeability to gases. It is much harder and chemically more inert than graphite. Glassy carbon microspheres were fabricated at Oak Ridge National Laboratory by heating 0.0040-0.0088 cm particles of Dowex 50W × 8, a sulfonated cationic exchange resin, in a fluidized bed at 2800°C until all sulfur was removed. Under microscopic investigation, the glassy carbon powder appeared as smooth spheres. Measured physical properties of the microspheres are given in Table I.

Table I. Physical properties of glassy carbon microspheres

Range of particle diameters	0.0014-0.0050 cm
Average particle diameter	0.0036 cm
Density	1.38 g/cm³
Packed bed porosity, ϵ	0.38
Electrical conductivity of packed bed	0.7 $(\Omega\text{-cm})^{-1}$
Specific surface area	
Geometric	1210 cm²/g
Based on adsorption	1510 cm²/g

Apparatus.—Cells, tubing and wetted surfaces of pumps, fittings, and storage containers were nearly exclusively constructed from borosilicate glass or inert fluorocarbons. Cylindrically shaped cells, into which adsorbent powder could be packed, were used for four purposes: determining adsorption isotherms, evaluating differential capacitance, measuring potential distribution and charging current, and performing flow studies. Each of the cells shared the same cell assembly. The cells were constructed from "Ace-Thred" glass columns (Ace Glass, Incorporated), connected with threaded Teflon adapters, and sealed with O-rings of Viton® or FETFE fluorocarbon elastomer. A diagram of the cell assembly common to all four purposes is shown in Fig. 1.

Adsorbent powder was held in place with medium-porosity glass frits (Porosity D) at either end of the cell. A current-collecting lead was passed through a hole drilled in the lower frit and was extended the entire length of the adsorbent bed. The portion of the lead below the lower frit, but within the cell assembly, was isolated from solution by a length of glass capillary tubing. Reference electrode taps were constructed by drilling 3 mm holes in the glass cell.

Adsorption isotherms and differential capacitance measurements were carried out in the recirculating system shown in Fig. 2. A 1.36 cm ID, 2.05 cm long cell and 30 cm³ capacity mixing compartment were used. A metering pump (Model RP-SY-1CSC or RP-D-1-CSC, Fluid Metering, Incorporated) in which only Teflon and the head of the ceramic piston contacted solution, pumped solution through the cell and into a mixing compartment, from which the solution was recirculated. The counterelectrode compartment was separated from the mixing compartment by Nafion 125, a Teflon-based cation-exchange membrane (du Pont). The current-collecting lead was a 0.27 cm OD, vitreous carbon rod (VC-10, Atomergic Chemetals) with a specific conductivity of 160 $(\Omega\text{-cm})^{-1}$.

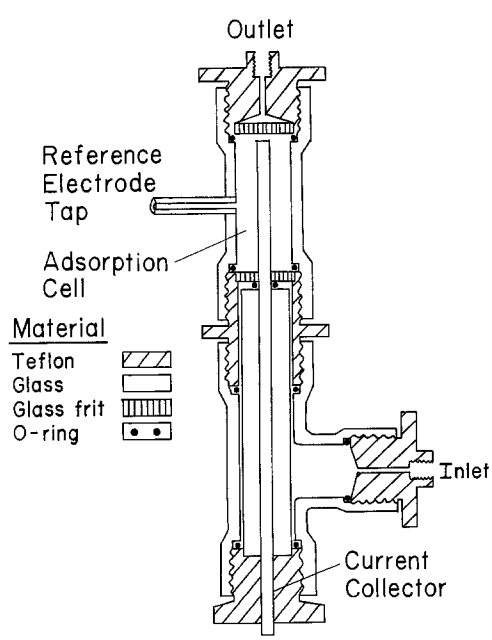

Fig. 1. Adsorption cell assembly

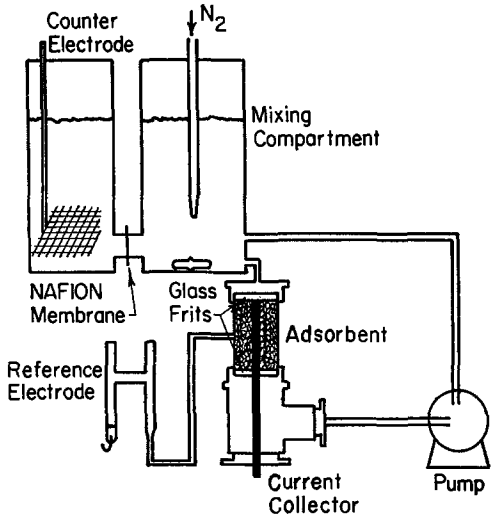

Fig. 2. Recirculating flow system used for measurement of adsorption isotherm and differential capacitance.

The flow system, in which charging current, potential distribution, and flow-through electrosorption studies were carried out, is shown in Fig. 3. Three or six reference electrode taps were located along the length of the cell, each rotated 45° or 90° from the adjacent one. Two 1.56 cm ID cells were used, one with a packed-bed length of 3.2 cm, the second with a length of 8.5 cm. The current-collector lead in the shorter cell was a vitreous carbon rod, and a similar OD graphite rod (Grade ECV, Union Carbide), with a specific conductivity of 610 $(\Omega\text{-cm})^{-1}$, was used in the longer cell. In order to maintain the bed of adsorbent at the height of the highest reference electrode tap, the space between the tap and the upper glass frit was filled with glass beads of average diameter 0.0050 cm (Superbrite No. 130-5005, 3M Company). The adsorbent and glass beads were separated by a disk-shaped filter, made from Teflon, of coarse porosity (Chemplast). A stainless steel pulse dampener (Fluid Metering, Incorporated) reduced pressure oscillations to <10%. During flow studies, effluent from the cell flowed through a 40 cm length of 0.082 cm ID Teflon tubing into an ultramicro flow cell (Varian) having a volume of 0.08 cm^3, in a Model 11 Cary u.v. spectrophotometer.

Platinum served as a counterelectrode in all studies. Potentials were measured and are reported with respect to the mercury/mercurous sulfate couple, in saturated (0.68*M*) potassium sulfate and $10^{-2}M$ H_2SO_4. The potential of this reference electrode was calculated to be +0.686V with respect to the normal hydrogen electrode.

Control of potential was maintained with a potentiostat built in-house. Slow and fast voltage scans were provided by a Motorpotentiometer MP 165 (Brinkmann Instruments) and by a Model 175 Universal Programmer (Princeton Applied Research), respectively. When adsorption isotherms were measured, the potential of the working electrode was monitored with a Model 602 Electrometer (Keithley Instruments) in which the internal impedance was $10^{14}\Omega$. The Y-axis of a Model 2000 X-Y Recorder (Houston Instruments) recorded the signal proportional to current from the potentiostat. Two three-pen strip chart recorders (Linear Instruments), each having internal impedances of $2.5 \times 10^6\Omega$, monitored potentials along the length of the cell.

Procedure.—The glassy carbon microspheres were initially cleaned in 0.5*M* NaOH, then in 6*M* HCl. The microspheres were regenerated *in situ* after each adsorption experiment to remove adsorbate and to restore the same level of adsorbability (11). Regeneration was accomplished by maintaining the packed bed of microspheres at a potential of +0.40V *vs.* Hg/Hg_2SO_4 (in 1.5*M* H_2SO_4) while pumping a solution of 1.5*M* H_2SO_4 through the bed. A plot of current density, based on actual surface area, *vs.* potential for the glassy carbon microspheres in electrolyte, shown in Fig. 4, illustrates the wide range of potential, from +0.6 to −1.4V, over which electrosorption may be studied. Outside this range, water was electrolyzed. The range of potentials on the positive side was further limited by the oxidation of β-naphthol. The magnitude of the current peak at −0.7V depended on the extent of deaeration.

Adsorption isotherms were obtained by increasing incrementally the adsorbate concentration while the adsorbent, a 2.5g sample of glassy carbon, was held at constant potential. The amount of β-naphthol adsorbed was calculated from the change in concentration in the bulk solution. An initial charge of 22 ml of buffered 0.5*M* K_2SO_4 was recirculated through the glassy carbon. Samples were analyzed, then replaced, 15 min after the first addition of adsorbate, and 10 min after subsequent additions. Concentrations of β-naphthol from 2×10^{-7} to $3 \times 10^{-5}M$ were linearly related to optical density at a wavelength of 224 nm. Reproducibility of the readings of the spectrophotometer was ±1%, and overall accuracy of the measured concentration was estimated to be ±3%. In an adsorption test without adsorbent, the rate of loss of adsorbate was 10^{-10} mol/min. At the low adsorbate concentrations studied, steady-state adsorption on glassy carbon microspheres was reached quickly and reproducibly.

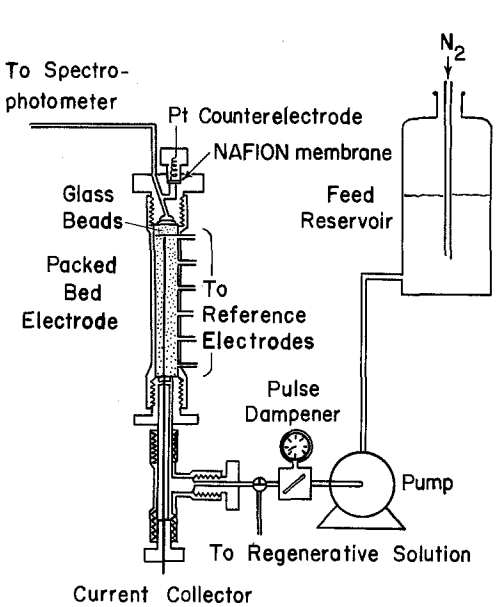

Fig. 3. Flow system used for flow-through electrosorption studies

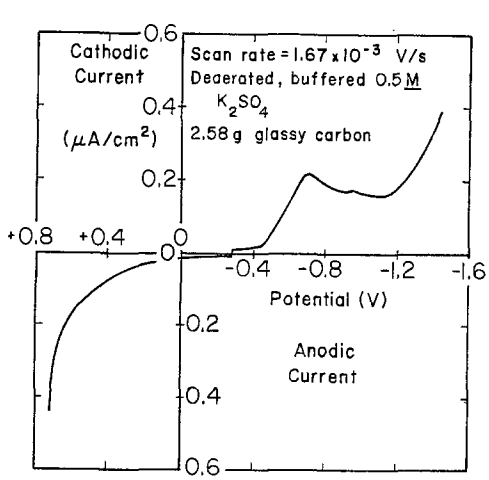

Fig. 4. Current-potential curve on glassy carbon

Overall, the experimental error in determining the amount of β-naphthol adsorbed was about ±5%. Uncertainty in the actual surface area of the glassy carbon was considerably larger. Because of the low faradaic current on glassy carbon, the variation of potential (ϕ) with bed location was calculated to be no more than ±8 mV from that at the center of the bed.

Capacitive charging currents were measured during application of ramp potentials at constant scan rates of 1.67×10^{-3} or 0.56×10^{-3} V/sec. The product of adsorbent surface area and differential capacitance of the adsorbent/electrolytic solution interface was then determined as a function of potential by dividing the charging current by scan rate. Absolute values of the differential capacitance were based on surface area determined from adsorption behavior.

Flow experiments permitted evaluation of the effects of flow rate, solution conductivity, and cell length on electrosorption. To prepare for flow studies, the packed bed of adsorbent was brought to the desorbing potential, −1.26V, while deaerated electrolytic solution was being pumped through it. While the packed bed was maintained at −1.26V, the feed stream was switched to a deaerated electrolytic solution containing $1.95 \times 10^{-5}M$ β-naphthol. Saturation of the adsorbent was complete when the effluent concentration of adsorbate reached its initial value. The adsorption was then initiated by changing the potential at the top of the packed bed, at a rate of 10 V/sec, to the adsorbing potential of −0.26V. Flow rates were measured with graduated cylinder and stopwatch. Effluent concentration of adsorbate, capacitive charging current, and potential distribution along the length of the packed bed were continuously monitored.

Results and Discussion

Adsorption isotherm.—The amount of β-naphthol adsorbed on glassy carbon, Γ (mol/cm²), is plotted *vs.* solution concentration over a range of potential from −0.26 to −1.26V in Fig. 5. Only very dilute concentrations of β-naphthol, up to $2.5 \times 10^{-5}M$, were studied. Even so, with Γ calculated on the basis of a specific surface area of adsorbent of 1510 cm²/g, fractional surface coverage reached 0.5. The data were fitted with a Langmuir adsorption isotherm modified for displacement of solvent molecules (12)

$$\frac{\theta[\theta + n(1-\theta)]^{n-1}}{(1-\theta)^n n^n} = Kc_A/c_w \qquad [1]$$

where c_A is the solution concentration (mol/cm³) of organic adsorbate, c_w is the water concentration, 0.055 mol/cm³, and K is the potential-dependent adsorbability constant. The fractional surface coverage θ equals Γ/Γ_m. Values chosen for n, the number of water molecules displaced from the adsorbent surface by an organic molecule, and Γ_m, the amount of adsorption corresponding to monolayer surface coverage, were those found for the β-naphthol/graphite system (7), 6 and 2.5×10^{-10} mol/cm², respectively. An excellent fit with the modified isotherm was obtained at all potentials when using a specific surface area of 1510 cm²/g, 25% greater than the geometric specific surface area. Including data points for solution concentrations up to $2 \times 10^{-5}M$, coefficients of determination, r^2, were in excess of 0.999 for all potentials. Adsorption monotonically increased with increasingly positive potential. The potential dependence of the adsorbability constant, shown in Fig. 6, was described by the parabolic equation

$$K = 4.66 \times 10^5\phi^2 + 14.30 \times 10^5\phi + 13.41 \times 10^5 \qquad [2]$$

The adsorbability constant for adsorption of β-naphthol on graphite (7) also increased monotonically with more positive potential, but was roughly twice as large as for adsorption on glassy carbon.

Differential capacitance.—Differential capacitance C was determined on glassy carbon microspheres in buffered solutions of both 0.5 and 0.2M K_2SO_4. The specific surface area required to fit adsorption results, 1510 cm², was assumed. Reproducibility varied from 3 to 20%, being worse at the most negative potentials where faradaic currents were relatively high. Differential capacitances for both concentrations, shown in Fig. 7, were nearly identical in both magnitude and potential dependence. The electrolyte concentration apparently was sufficiently high at 0.2M K_2SO_4 that the diffuse double layer did not contribute measurably to the total double layer capacitance. The differential capacitance ranged from 6.7 μF/cm² at −0.12V to 9.3 μF/cm² at −0.76V. A local minimum occurred at

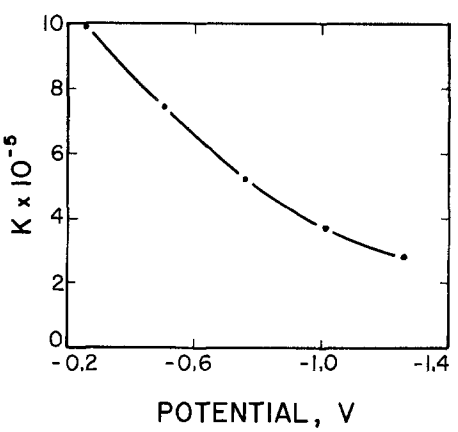

Fig. 6. Potential dependence of adsorbability constant for adsorption of β-naphthol on glassy carbon.

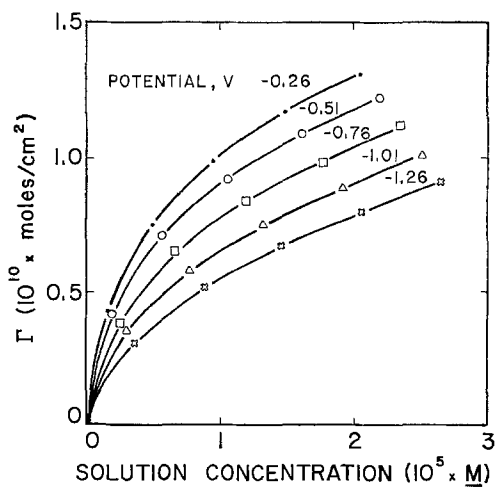

Fig. 5. Adsorption of β-naphthol on glassy carbon as a function of potential.

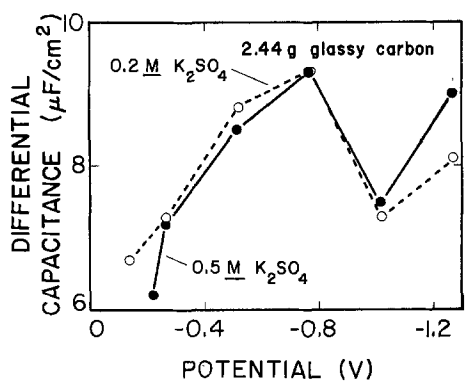

Fig. 7. Differential capacitance of glassy carbon as a function of potential.

−1.0V. Adsorption of β-naphthol barely affected differential capacitance on glassy carbon.

Potential distribution and charging current.—Potential distributions and charging currents were measured on glassy carbon during six flow-through electrosorption experiments. Values for the superficial velocity v, bed length L, and effective solution conductivity within the packed bed κ in each experiment are listed in Table II. In each experiment, the potential at the top of the bed ($x/L = 1.0$) was changed from −1.26 to −0.26V at a scan rate of 10 V/sec. Transient potential and current were characterized by the time required for charging of the electrical double layer, τ_{DL}

$$\tau_{DL} = aCL^2/\kappa \qquad [3]$$

where a is the interfacial area per unit volume of solution (cm^{-1}). Good reproducibility was usually found for measured potentials and current when different experiments employing the same value of τ_{DL} were compared. Typical results are shown in Fig. 8, 9, and 10, for run 08, which was carried out with buffered 0.5*M* K_2SO_4 in the 8.5 cm bed. For these experimental conditions, the calculated value of τ_{DL} was 85 sec. In Fig. 8, the transient potential is shown for six locations along the length of the bed. In Fig. 9 and 10, the potential distribution and the transient current, respectively, are compared with predictions of a model for charging of the electrical double layer (1).

In each experiment, the potential at the top of the bed changed almost immediately to the final potential, −0.26V. However, the time required to reach the final potential became greater at locations further down the bed. Near the bottom of the bed, at $x/L = 0.07$, a time in the order of 100 sec was required for the potential to attain 90% of the final potential. The measured current in each experiment jumped to about 100 mA in the first few tenths of a second, then rapidly decayed toward zero.

Observed charging times for different values of bed length and solution conductivity, shown in the last column of Table II, followed trends predicted for τ_{DL}. In all six experiments, the model prediction of slower decay of potential at lower values of x/L was experimentally observed. In addition, quantitative agreement between measured and calculated potential decay at $x/L = 0.81$ was usually excellent. However, at lower locations, the experimental potential decayed more rapidly than in model simulations. The discrepancy between measured and predicted potential, in the worst case, was about 40%.

Qualitative trends of the charging current were similar for experiment and model. Also, the two curves of current *vs.* time often coincided during the first few seconds. However, the experimental current was consistently lower, often by as much as 40%, for much of the charging period. When charging was nearly completed, charging current was small and faradaic reaction had a relatively large effect on the measured current. Therefore, toward the end of most experiments, the measured current reached and sometimes surpassed the level predicted by the model.

Potential distribution and charging current measurements exhibited two areas of disagreement with the model. Potentials decayed too quickly at the lower locations along the bed and current was smaller than predicted. Three factors may explain these disagree-

Table II. Parameter values for flow-through experiments

Run number	v (cm/sec)	L (cm)	κ (Ω-cm)$^{-1}$	τ_{DL} (calc) (sec)	τ_{DL} (obs.)* (sec)
06	0.063	8.5	0.0236	85	73
08	0.18	8.5	0.0236	85	101
10	0.29	8.5	0.0236	85	62
11	0.070	8.5	0.0115	175	169
12	0.17	8.5	0.0115	175	170
14	0.19	3.2	0.0115	25	24

* Time required for potential at $x/L = 0.07$ to achieve 90% of final potential.

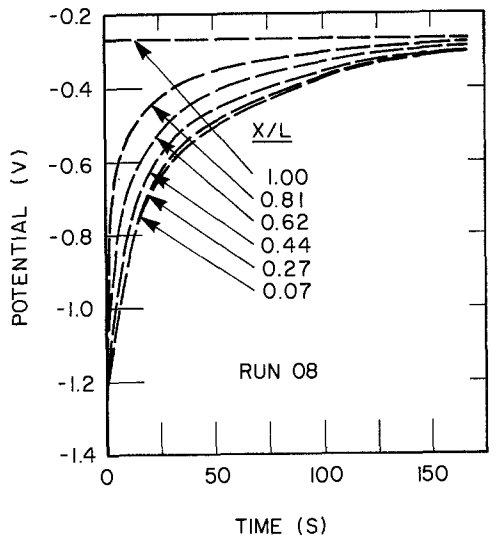

Fig. 8. Experimental potential distribution, run 08. Experimental conditions are described in Table II.

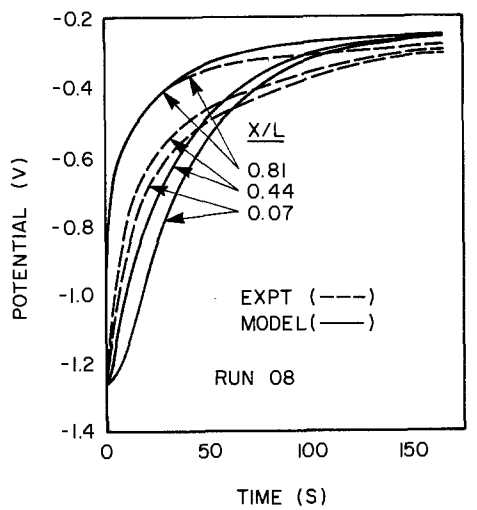

Fig. 9. Comparison of experimental and model potential distributions, run 08. Experimental conditions are described in Table II.

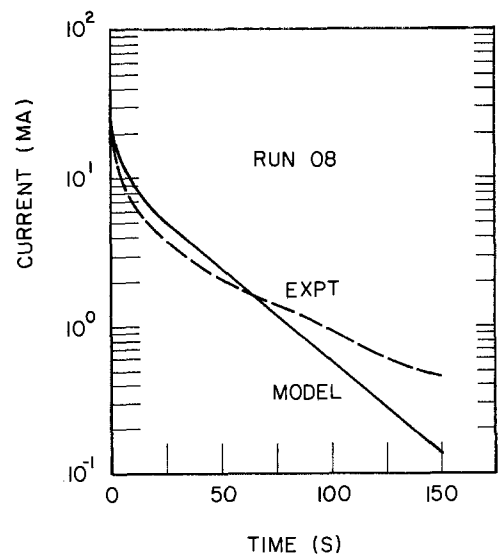

Fig. 10. Comparison of experimental and model charging currents, run 08. Experimental conditions are described in Table II.

ments. First, the initial potential along the bed was not uniformly at −1.26V. Rather, faradaic current resulting from oxygen reduction and, to a lesser extent, from hydrogen evolution, caused a potential gradient. The rate of oxygen reduction depended on flow rate, and at the highest flow rate studied, steady-state currents of nearly 1 mA occurred. Prior to the potential scan, measured voltage drops between $x/L = 1$ and $x/L = 0.07$ ranged from 0.06V for run 06 to 0.23V for run 12. Nor was the potential uniform at −0.26V at the end of each experiment, although voltage drop did not exceed 0.04V at the end. Nonuniform potentials qualitatively explained the disagreements in both potential distribution and current. The measured voltage drops would account for about a 25% decrease in the calculated potential at $x/L = 0.07$, and a 15% decrease in calculated current, roughly half of the observed discrepancies.

A second factor was the neglect of variation in differential capacitance. At certain potentials, an error of at least 10% in the value of the capacitance will be incurred. However, the choice of a median value for the capacitance should reduce its effect on discrepancies in potential and current to less than 10%. The third factor, a possibly excessive estimate of τ_{DL}, could have a significant effect on the predictions of both potential distribution and current. However, there was little reason to change the estimate. While error in the interfacial area could be as high as 25%, error in the product, aC, ought to be much smaller. A higher value for κ would reduce the discrepancy in potential distribution, but would increase the predicted value of the charging current. The tortuosity factor used by Newman and Tiedemann (13), which was 20% smaller than the one used in the model, would have reduced the discrepancy in the current.

Taken together, the three factors could account for nearly all of the observed discrepancies. An additional experimental potential distribution, measured on graphite over a range of potential where faradaic reaction was negligible, matched a calculated distribution even at low values of x/L. Therefore, the equation for the charging of the double layer was probably the correct one for describing the transient potential distribution and charging current.

Adsorption in a flow-through porous electrode.— Electrosorption in a flow-through porous electrode was carried out by changing the potential from −1.26 to −0.26V while pumping electrolytic solution containing $1.95 \times 10^{-5}M$ β-naphthol (c_{Ao}) through a packed bed of glassy carbon microspheres. Values chosen for variables in these experiments are given in Table II. Actual flow rates ranged from 0.12 to 0.54 ml/sec, and corresponding particle Reynolds numbers (vd_p/ν) ranged from 0.025 to 0.12. Adsorbate concentration in the effluent is plotted as a function of time for two representative experiments, runs 06 and 12, and for model simulations of them in Fig. 11 and 12. Both experiments were carried out in the 8.5 cm bed. Run 06 was performed in $0.5M$ K_2SO_4 at a superficial velocity of 0.063 cm/sec. In run 12, the concentration of K_2SO_4 was $0.2M$ and the superficial velocity was 0.17 cm/sec.

Comparison of experimental adsorption results with model simulations focused on three areas: the amount of β-naphthol adsorbed, effluent concentration levels, and trends in effluent concentration profiles. The amount of β-naphthol that should have been adsorbed during each experiment, calculated from the change in surface coverage, $(\theta_A - \theta_D)$, is

$$N_{calc} = (\theta_A - \theta_D)\,\Gamma_m a \epsilon L A \qquad [4]$$

where the amount adsorbed, N_{calc}, has units of mols and A is the cross-sectional area of the bed. The actual amount adsorbed, N_{expt}, was determined by measuring the area between c_{Ao} and c_A in plots of effluent adsorbate concentration *vs.* time, such as Fig. 11 and 12. Calculated values are compared with actual adsorption in Table III. In each experiment, less adsorbate was adsorbed than expected. Two trends in the discrepancy were observed. First, the discrepancy was larger at higher flow rates. Second, packed beds with greater solution-phase resistance betwen the ends of the bed experienced greater discrepancies. A major source of the discrepancy was in the determination of the adsorption isotherm. The adsorption isotherm was measured in a sample of glassy carbon that had been exposed to a variety of chemical environments to determine proper cleaning procedures. A subsequent adsorption isotherm test on a fresh sample of glassy carbon exhibited 10% less adsorption. Another contribution to the discrepancy was the nonuniform potential distribution before the start of the potential scan. Larger potential gradients followed the same trends as increasing discrepancy, occurring at higher flow rates, lower solution conductivity, and larger bed length. For

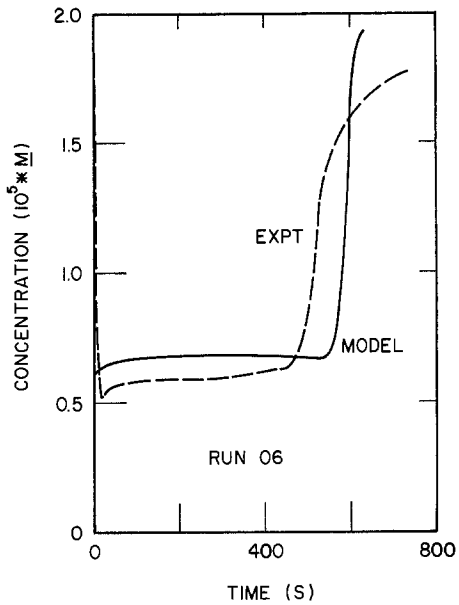

Fig. 11. Effluent adsorbate concentration *vs.* time, experiment, and model, run 06. Experimental conditions are described in Table II.

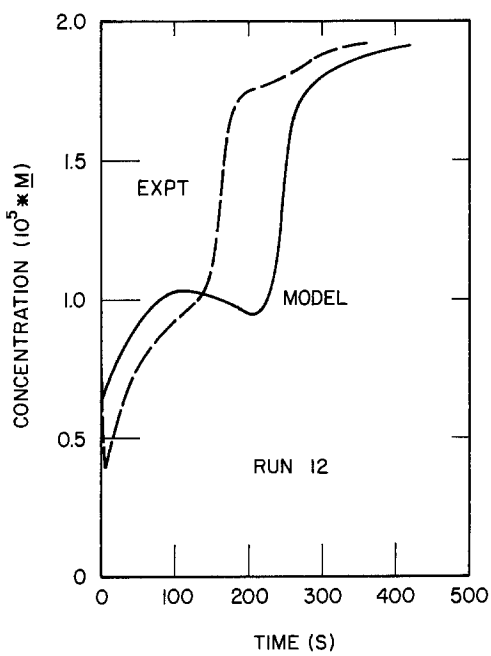

Fig. 12. Effluent adsorbate concentration *vs.* time, experiment, and model, run 12. Experimental conditions are summarized in Table II.

Table III. Predicted and actual adsorption of β-naphthol

Run number	N_{calc} (μmols)	N_{expt} (μmols)	Discrepancy (%)
06	1.06	0.90	15
08	1.06	0.64	39
10	1.05	0.75	29
11	1.05	0.89	16
12	1.05	0.67	37
14	0.38	0.36	6

two of the experiments, the amount of β-naphthol adsorbed at −1.26V was measured prior to the potential scan and was about 5 and 20% greater than expected for a uniform potential along the bed. Thus, because the average change in bed potential following the potential scan was less than 1.0V, the change in surface coverage was less than calculated.

Effluent adsorbate levels measured for each experiment were generally within 10% of model predictions. No systematic error was observed between measured and predicted levels. Adsorbate concentration during experiments, initially at $1.95 \times 10^{-5}M$, generally dropped to about $0.6\text{-}0.8 \times 10^{-5}M$, indicating that 60-70% of the β-naphthol in solution was being adsorbed before breakthrough. Both experimental results and model simulations showed that the minimum adsorbate concentration in the effluent could not be changed significantly by altering engineering variables (flow rate, bed length, or solution conductivity), if the flow-through configuration were used.

The most obvious lack of agreement in a comparison of effluent concentration profiles was in the earlier breakthrough observed in experiments. The lack of agreement was caused by the discrepancy in amounts adsorbed. A minor source of disagreement was the experimental rate of decline in effluent concentration following the potential scan, which was slower than predicted. Even at higher velocities, several seconds, rather than several tenths of a second, were required for the concentration to bottom out. The slow rate of decline was ascribed to backmixing of the effluent in the layer of glass beads and in the glass frit. Additional, but probably minor dispersion may have occurred in the 40 cm length of tubing between the cell assembly and spectrophotometer.

The most critical comparison of experiment and model involved sets of experimental conditions in which different mechanisms limited the amount or rate of adsorption. In the least restrictive mechanism, adsorption was controlled only by the adsorption isotherm. In this situation, the effluent concentration would drop to its minimum level and stay at that level until the adsorbent was saturated. A steep breakthrough curve would follow. The adsorption-isotherm-controlling situation would be ideal for practical applications because the full adsorption capacity of the adsorbent can be utilized in the shortest possible cycle time. The length of time required for adsorption can be characterized by a breakthrough time, τ_{BT}, which may be defined for electrosorption as

$$\tau_{BT} = \frac{(\theta_A - \theta_D)\Gamma_m a \epsilon L}{c_{Ao} v} \qquad [5]$$

The value of τ_{BT} is the time required to saturate the adsorbent if all adsorbate entering the bed before the onset of saturation were adsorbed. According to the model, the adsorption-isotherm-controlling situation occurred when the ratio, τ_{DL}/τ_{BT}, was less than one. In run 06, shown in Fig. 11, where $\tau_{DL}/\tau_{BT} = 0.19$, the flat concentration profile and the steep breakthrough curve predicted by the model were also observed experimentally.

A second limiting mechanism was the charging of the electrical double layer, which controlled the time required to change the potential along the length of the bed. This mechanism was expected to predominate when $\tau_{DL}/\tau_{BT} \geq 1$. Its effect on the effluent concentration profile is illustrated in run 12, shown in Fig. 12, where $\tau_{DL}/\tau_{BT} = 1.07$. A predicted sharp increase in effluent concentration immediately after the initial drop in concentration was observed experimentally. The more gradual breakthrough observed, reflecting incomplete charging of the double layer, also agreed with model predictions. Because the ratio, τ_{DL}/τ_{BT}, is proportional to vL/κ, the experiments confirmed that operation at minimum cycle time in a one-dimensional configuration cannot be attained following scale-up to high flow rates or long beds, or in poorly conductive solution.

In Fig. 11, the breakthrough curve was very steep because of the rapid rate of convective mass transfer. If an industrially more appealing, high-surface-area adsorbent, such as activated carbon, were used, breakthrough would have occurred more slowly. In this case, a third limiting mechanism, mass transfer by pore diffusion, would also have to be considered.

In summary, experimental charging current, potential distribution, and effluent concentration were predicted qualitatively over a range of experimental conditions in which controlling mechanisms changed. Quantitative agreement was usually reasonable, and where it was only fair, faradaic current and differences in the adsorption isotherm for different carbon samples accounted for most of the discrepancy. The most remarkable aspect of the agreement between experiment and model was that no parameters of the model were adjusted to improve the fit with experimental data.

Desorption.—In order to examine the desorption behavior of β-naphthol on glassy carbon, and also to evaluate the predictive power of the model for desorption, a desorption experiment was carried out under the conditions of run 14. A solution of buffered $0.2M$ K_2SO_4 containing 1.95×10^{-5}M β-naphthol was pumped through a 3.2 cm long bed at a flow rate of 0.35 ml/sec. The direction of potential change was reversed, changing from −0.26 to −1.26V, in order to cause desorption.

The effluent concentration during desorption, shown in Fig. 13, immediately rose from 1.95×10^{-5} to $3.7 \times 10^{-5}M$. After beginning to decrease, the concentration rose again, reaching $4.3 \times 10^{-5}M$ about 25 sec after the potential was changed. Completion of desorption at −1.26V, signaled by the return of the effluent concentration to the initial feed concentration, required 100

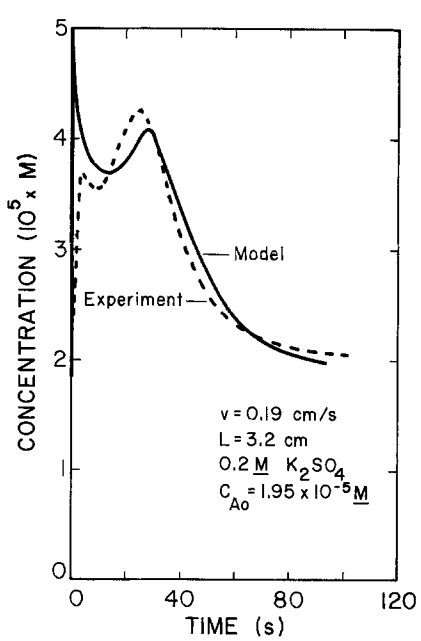

Fig. 13. Desorption under a potential change from −0.26 to −1.26V. Experimental conditions are given in Table II.

sec, about the same length of time as required for adsorption under the same conditions.

The model used for adsorption was also employed to simulate the desorption experiment. Two problems associated with the use of the model for desorption ought to be noted. First, adsorption of aromatics on carbon is usually affected by hysteresis. Second, the adsorption isotherm for β-naphthol/glassy carbon was only determined for solution concentrations up to $2 \times 10^{-5}M$, and the modified Langmuir isotherm was not valid at higher concentrations. Nevertheless, agreement between theory and experiment in Fig. 13 was excellent. Even the unusual appearance of two desorption peaks was predicted. The only quantitative disagreement was in the magnitude of the initial peak. The model simulation predicted a value of $5.0 \times 10^{-5}M$, whereas the experimental peak only reached $3.7 \times 10^{-5}M$. However, the initial peak predicted by the model attained its maximum value in less than 0.2 sec. Backmixing in the glass beads and frit of the experimental system would have prevented the full height of such a sharp peak from being observed.

Cyclic electrosorption.—Practical application of electrosorption requires that the adsorbent sustain repeated cycles of adsorption and desorption. A cyclic electrosorption experiment was carried out with use of the same feed stream for both half-cycles. Conditions were those discussed in the desorption experiment: $v = 0.19$ cm/sec, $0.2M$ K_2SO_4, and $L = 3.2$ cm. Potential was cycled between −1.26 and −0.26V every 102 sec. The effluent concentration is displayed for the duration of the experiment, 3 1/2 cycles, in Fig. 14.

The most remarkable observation was the reproducibility of each cycle. Slightly more β-naphthol was adsorbed in the first adsorption half-cycle, but the amount stabilized in subsequent adsorption half-cycles. The desorption half-cycles were similarly reproducible. Also, the magnitude of the peak current after the first potential scan did not vary by more than 2% from half-cycle to half-cycle. The experiment demonstrated that the adsorption capacity of the carbon adsorbent can be reproducibly regenerated for at least three cycles by application of electrical potential.

Conclusions

Potential-dependent adsorption was demonstrated for adsorption of β-naphthol on glassy carbon. Model predictions of the transient potential distribution and current, based on charging of the electrical double layer, were confirmed, on glassy carbon. With the use of a flow-through porous electrode of glassy carbon, both adsorption and desorption behavior were shown to obey model simulations. In particular, the long time required for changing the potential through the entire packed bed was experimentally confirmed as a major scale-up limitation for a one-dimensional geometry. Faradaic reaction was identified as a principal source of reduced performance during electrosorption. The adsorption capacity of glassy carbon can be restored by periodic application of a desorbing potential.

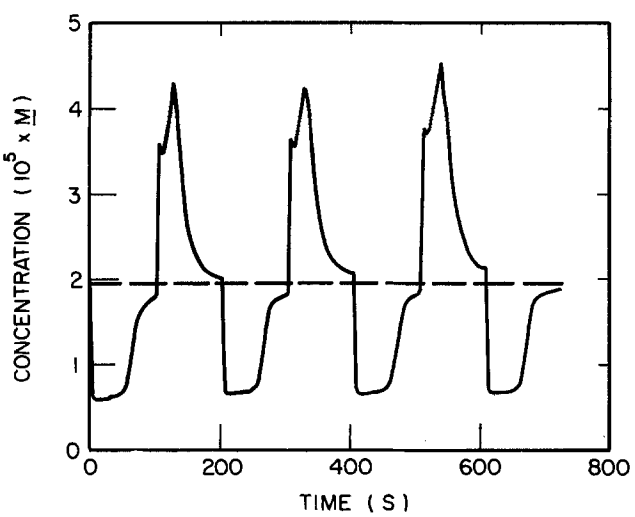

Fig. 14. Cyclic electrosorption between −1.26 and −0.26V every 102 sec. Other experimental conditions the same as Fig. 13.

Acknowledgments

This work was funded by grants NSF ENG 76-83379 and NSF CPE 80-08947. Fellowship assistance from Union Carbide Corporation, American Oil Company, General Electric Company, and Exxon Education Foundation was deeply appreciated.

Manuscript submitted Jan. 10, 1982; revised manuscript received July 1, 1982.

Any discussion of this paper will appear in a Discussion Section to be published in the December 1983 JOURNAL. All discussions for the December 1983 Discussion Section should be submitted by Aug. 1, 1983.

Publication costs of this article were assisted by the University of Illinois.

LIST OF SYMBOLS

a	interfacial area per unit volume of solution, cm^{-1}
A	cross-sectional area of bed, cm^2
c_A	adsorbate concentration, mol/cm^3
c_w	concentration of water, $= 0.055$ mol/cm^3
C	differential capacitance, F/cm^2
d_p	particle diameter, cm
K	potential-dependent adsorbability constant, dimensionless
L	bed length, cm
n	number of solvent molecules displaced by one organic adsorbate molecule
N_{calc}	amount of organic compound adsorbed, calculated, mol
N_{expt}	amount of organic compound adsorbed, experimental, mol
v	superficial velocity, cm/sec
x	distance, cm

Greek Letters

Γ	amount of organic compound adsorbed per unit area, mol/cm^2
Γ_m	amount of organic compound adsorbed per unit area at monolayer surface coverage, mol/cm^2
ϵ	porosity of packed bed
θ	fractional surface coverage
θ_A	fractional surface coverage at adsorbing potential
θ_D	fractional surface coverage at desorbing potential
κ	effective solution conductivity, $(\Omega\text{-cm})^{-1}$
ν	kinematic viscosity, cm^2/sec
τ_{BT}	breakthrough time, sec
τ_{DL}	double layer charging time, sec
ϕ	potential difference between electrode and adjacent solution, V

REFERENCES

1. R. C. Alkire and R. S. Eisinger, *This Journal*, **130**, 85 (1983).
2. A. N. Frumkin and A. Obrutsheva, *Nature*, **117**, 790 (1926).
3. R. Barradas and B. E. Conway, *J. Electroanal. Chem. Interfacial Electrochem.*, **6**, 314 (1963).
4. K. Lee and D. Kirwan, *Ind. Eng. Chem. Fundam.*, **14**, 279 (1975).
5. J. Strohl and K. Dunlap, *Anal. Chem.*, **44**, 2166 (1972).
6. B. Damaskin, O. Petrii, and V. Batrakov, "Adsorption of Organic Compounds on Electrodes," E. Uvarov, Translator, Plenum Press, New York (1971).
7. R. Eisinger and R. Alkire, *J. Electroanal. Chem. Interfacial Electrochem.*, **112**, 327 (1980).
8. A. Johnson and J. Newman, *This Journal*, **118**, 510 (1971).
9. T. Schmidt, Ph.D. Thesis, Illinois Institute of Tech-

nology, Chicago (1973).
10. N. Zhumagulov and E. Matskievich, *Nauch. Osn. Tekhnol. Ochist. Vody.*, p. 39 (1973), from Ref. Zh. Khim., 1973, Abstract No. 171392.
11. R. Eisinger, Ph.D. Thesis, University of Illinois, Urbana (1981).
12. J. Bockris and D. Swinkels, *This Journal*, **111**, 736 (1964).
13. J. Newman and W. Tiedemann, "Advances in Electrochemistry and Electrochemical Engineering," Vol. 11, H. Gerischer and C. Tobias, Editors, John Wiley & Sons, Inc., New York (1978).

Conductivity of the Mixed Organic Electrolyte Containing Propylene Carbonate and 1,2-Dimethoxyethane

Yoshiharu Matsuda,* Masayuki Morita, and Kenji Kosaka

Department of Industrial Chemistry, Faculty of Engineering, Yamaguchi University, Tokiwadai, Ube, Yamaguchi, Japan

ABSTRACT

Electrolytic conductivity of the organic solution dissolving $LiClO_4$ has been studied at 30°C in the mixed system of propylene carbonate and 1,2-dimethoxyethane. The variation of the conductivity with the solvent composition was explained on the basis of the changes in the dielectric constant and the viscosity of the solvent. With increasing the concentration of 1,2-dimethoxyethane, the viscosity of the solvent lowers and then the ionic mobility increases, while the decrease in the dielectric constant tends to cause ion association. The critical distance for ion-pair formation in Bjerrum's model was calculated for the mixed system, and the degree of ion association was estimated for each solution of the different solvent compositions. The mixing effect of the solvents on the conductivity was substantially accounted for by these parameters. It was also pointed out that ion-solvent and solvent-solvent interactions contribute to the improvement of the conductance to some extent.

Mixed organic solutions of propylene carbonate (PC) with 1,2-dimethoxyethane (DME), γ-butyrolactone (BL) with tetrahydrofuran (THF), and the like have been used as the solvent of the electrolytic solution in lithium cells (1-4). One of the reasons for using them is that the conductivity of the electrolyte can be improved with mixing the solvents (5, 6). In previous papers (7-11), electrolytic conductivity, vapor pressure, viscosity, dielectric constant, and laser Raman spectrum were studied in the PC-THF, PC-DME, and BL-THF systems, and the mixing effect of the solvents was discussed. From the data under infinite dilution condition, it was suggested that the solvent-solvent and ion-solvent interactions play an important part in the mixing effect on the conductance (10). For a moderately concentrated solution (*e.g.* 1 mol dm^{-3} $LiClO_4$), however, the synergistic effect on the conductivity seems to be produced mainly by a desirable combination of the high dielectric constant of PC (or BL) and the low viscosity of DME (or THF) (7-9, 11).

In the present work, electrolytic conductivity of the mixed PC-DME system dissolving $LiClO_4$ was mainly studied in connection with the viscosity and the dielectric constant (relative permittivity), in the course of a research and development of lithium cells. The results were discussed from the viewpoints of ionic mobility and ion association. Though the latter concept is rather classical compared with a modern treatment using statical mechanics, it is convenient for understanding the conductivity in such complex systems as mixed PC-DME solution. Therefore, Bjerrum's model (12) was adopted for the ion association in the present system. Then the degree of the association was correlated to the variation of the conductivity.

Experimental

The solvents were purified by the methods described previously (6, 13). PC was dehydrated with molecular sieves and distilled under the reduced pressure of 1-1.5 Torr at 65°-70°C. DME was refluxed with metallic sodium for 12 hr, followed by the atmospheric distillation at 83°C. Water contents in the resulting solvents were below 80 mg dm^{-3} for PC and 50 mg dm^{-3} for DME. The lithium perchlorate ($LiClO_4$) as a supporting electrolyte was an extra pure reagent by Ishizu Pharmaceutical Company Limited. It was used after drying under reduced pressure at 170°C for 24 hr.

The electrolytic conductivity of the solution was measured with an impedance bridge using 10 kHz a.c. The viscosities of the solvents and the solutions were measured with a modified Ostwald viscometer. The dielectric constant of the solvent was determined by a bridge method using 10 kHz a.c. These measurements were carried out at 30°C. In the present work, the solvent composition will be represented by the concentration volume percent (v/o) of DME for convenience, though it should be strictly described with the mol fraction in a thermodynamic sense. For the present mixed system, the conclusive discussion obtained in the former case would be little different from that obtained in the latter, because the ratio of density to molecular weight in PC is almost the same as that in DME.

Results

Figure 1 shows the variation in the molar conductivity, Λ, of $LiClO_4$ with the solvent composition. The molar conductivity in the mixed solvents is much higher than that in the pure solvents, and maximum conductivity is obtained in the range of 50-75 v/o DME. In a qualitative sense, this is due to that both the high dielectric constant of PC and the low viscosity of DME contribute to the electrolytic conductivity in the mixed system. Such a variation of the conductivity has been also observed in the analogous systems of PC-THF (8) and BL-THF (11). However, the mixing ratio of the solvents providing the maximum conductivity slightly depends on not only the constituent solvents but also the concentration of the electrolyte (11). In the present system, the maximum are situated at *ca.* 65 and 55% DME for 1.0 mol dm^{-3} and 0.1 mol dm^{-3} $LiClO_4$ solution, respectively.

The viscosities, η, of the mixed PC-DME with and without 1.0 mol dm^{-3} $LiClO_4$ are shown in Fig. 2. The correlation between the viscosity of the solvent and the solvent composition is not linear, which implies that the system is not an ideal solution in a thermodynamic sense. The negative deviation from the straight line is related to the fact that the associated structure of pure PC is destroyed by addition of DME (9, 10). Furthermore, it is considered that the struc-

* Electrochemical Society Active Member.
Key words: lithium cell, mixed solvent, conductance, ion association.

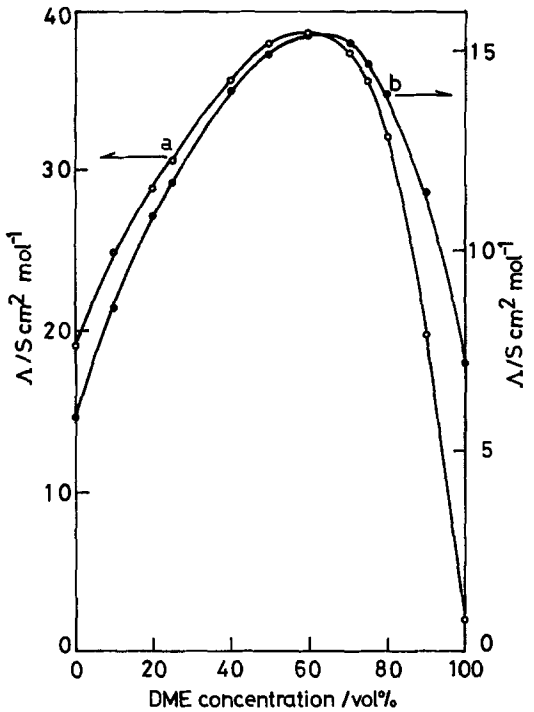

Fig. 1. Molar conductivity of $LiClO_4$ in mixed PC-DME system, a: 0.1 mol dm^{-3}, b: 1.0 mol dm^{-3}.

ture change in the solvated Li^+ caused by the DME addition influences the viscosity characteristics in the $LiClO_4$ solution. These solvent-solvent and ion-solvent interactions have been also supported by the data on the laser Raman spectra and the vapor pressure as discussed previously (10).

The dielectric constant (or relative permittivity), ϵ_r, of the mixed solvent is shown in Fig. 3. The values of the pure solvents were well consistent with those in literatures (14, 15). The dielectric constant varies almost linearly with the solvent composition, in contrast to the changes in the viscosities. This means that the solvent-solvent interactions affecting the viscosities and the vapor pressure in the mixed system are little reflected in the dielectric constant. Thus, the dielectric

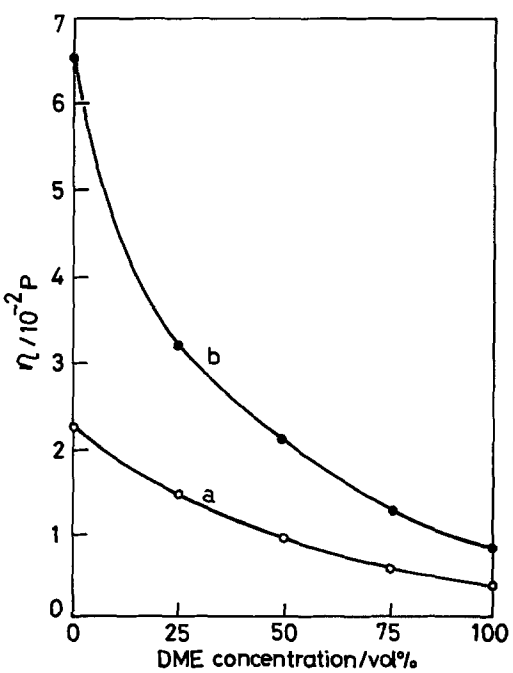

Fig. 2. Viscosities of the solvent and the solution in mixed PC-DME system, a: solvent, b: solution (1.0 mol dm^{-3} $LiClO_4$).

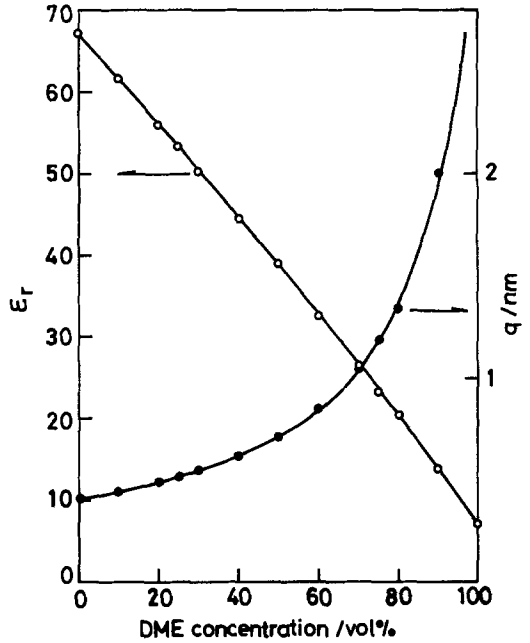

Fig. 3. Dielectric constant (○) and critical distance for ion-pair formation (●) in mixed PC-DME system.

constant of the mixed solvent is practically established by an additive property of each solvent.

Discussion

Up to the present, the effects of viscosity and dielectric constant of the solvent on the electrolytic conductivity have been widely discussed. For example, in the Onsager equation, Eq. [1], they are comprehended in the limiting conductivity, Λ_0, and the parameters B_1 and B_2 (16)

$$\Lambda = \Lambda_0 - (B_1\Lambda_0 + B_2)\sqrt{C} \qquad [1]$$

However it is really complicated to describe quantitatively such variation of the conductivity as shown in Fig. 1 by analyzing these parameters. For the sake of convenience, the following model would be introduced into the present system.

If the viscosity only lowers and the dielectric constant does not change with increasing the DME concentration in the solvent, the molar conductivity would increase monotonously because of the rise in ionic mobility. Since the measured conductivity has a maximum value, it is possible to regard the deviation from the monotonous increase as the effect induced from the actual lowering of the dielectric constant. Thus, the formation of an associated ion-pair was considered according to Bjerrum's treatment (12). The critical distance for the ion pair formation, q, is given by Eq. [2]

$$q = \frac{|z_i z_j| e^2}{8\pi\epsilon_0\epsilon_r kT} \qquad [2]$$

where ϵ_0 is the permittivity of a vacuum, z's are charge number of ions, e is the charge of electron, and k is the Boltzmann constant. The calculated values for a 1:1 electrolyte in the PC-DME system are shown in Fig. 3, together with the dielectric constant. The critical distance for the ion-pair formation increases steeply in the concentration range of 60-80% DME or above. This suggests that ion association is liable to occur in this region. The degree of association is represented by Eq. [3] (12, 17)

$$1 - \alpha = 4\pi n_i \int_a^q \exp\left(\frac{|z_i z_j| e^2}{4\pi\epsilon_0\epsilon_r kT} \cdot \frac{1}{r}\right) r^2 dr \qquad [3]$$

where α is the degree of dissociation, a is the distance of closest approach of the two ions, n_i is the number of

ions i per unit volume, and r is the distance from the center of ion j. By using the relation of

$$n_i = Nc/1000 \quad [4]$$

where N and c are the Avogadro constant and the molar concentration, respectively, one can rewrite Eq. [3] as follows

$$1 - \alpha = \frac{4\pi Nc}{1000}\left(\frac{|z_i z_j|e^2}{4\pi\epsilon_0\epsilon_r kT}\right)^3 Q(b) \quad [5]$$

where

$$Q(b) = \int_2^b X^{-4}\exp(X)dX \quad [6a]$$

$$b = \frac{|z_i z_j|e^2}{4\pi\epsilon_0\epsilon_r kTa} = \frac{2q}{a} \quad [6b]$$

$$X = -\frac{z_i z_j e^2}{4\pi\epsilon_0\epsilon_r kTr} \quad [6c]$$

The function $Q(b)$ was calculated algebraically in the range of b = 2-80. Then the degree of association was evaluated as a function of a/q or the distance of closest approach, a. The results in the case of $|z_i| = |z_j| = 1$ and c = 1 mol dm^{-3} are shown in Fig. 4 and 5. Since Eq. [3] includes some artificiality in the case of a/q or a being very small, strict values of $1 - \alpha$ would not be expected especially in such a region. Except for this, however, the curves in Fig. 4 and 5 essentially show the actual condition of the ion association in the present system. While it is practically difficult to determine the distance of closest approach, it may be estimated by using some assumptions as follows: (*i*) The sum of the crystallographic radii of Li^+ and ClO_4^- ions corresponds to the distance of closest approach. One obtains a = 0.26 nm by using Pauling's ionic radii (18). (*ii*) The distance of closest approach equals to that between Li^+ and ClO_4^- in crystalline $LiClO_4$. In this case, however, the lattice parameters

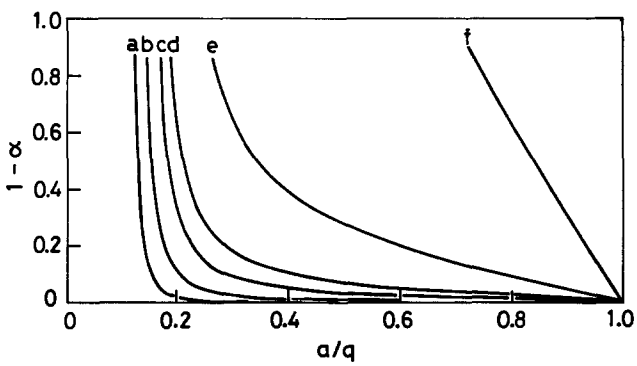

Fig. 4. Variation in degree of association with a/q in mixed PC-DME system, a: DME 0%, b: 50%, c: 70%, d: 80%, e: 90%, f: 100%.

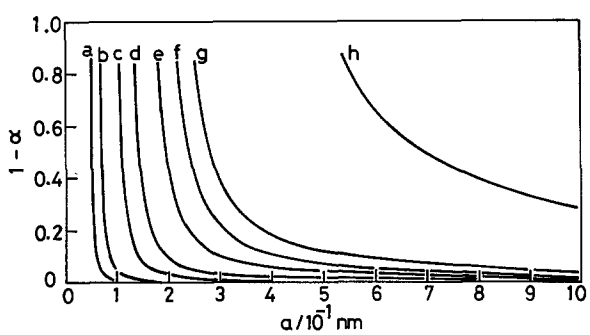

Fig. 5. Variation in degree of association with distance of closest approach in mixed PC-DME system, a: DME 0%, b: 25%, c: 50%, d: 60%, e: 70%, f: 75%, g: 80%, h: 90%.

of $LiClO_4 \cdot 3H_2O$ are only available because of the lack of data on anhydrous $LiClO_4$ (19). This leads a = 0.42 nm. (*iii*) The distance is equivalent to the sum of Stokes' radii which correspond to the radii of solvated ions in solution. The Stokes' radii in the mixed PC-DME system were found to be 0.41-0.42 and 0.35-0.40 nm for Li^+ and ClO_4^-, respectively (10), then the distance is estimated to be 0.76-0.82 nm.

Figure 6 shows the molar conductivities expected from the degree of ion association which were calculated by using a's in the above assumptions, (*i*)-(*iii*). The conductivity curve with complete dissociation (curve a) was estimated from the viscosity curve of the solution by applying Walden's law, Eq. [7]

$$\Lambda\eta = \text{constant} \quad [7]$$

which is only approximately valid even in such a high concentration solution. In spite of quantitative disagreement, these calculated curves are fairly analogous to the observed one in the manner of variation. This suggests that the variation of the conductivity in the mixed PC-DME system is explicable by the viscosity and the ion association to some extent. Comparing the observed conductivity with the calculated ones, it is considered that the distance of closest approach is rather short. On the other hand, curve e in Fig. 6 is an imaginary one calculated by a different assumption where the distance of closest approach is a function of the critical distance for ion-pair formation, q in Fig. 4, *i.e.*, $a = 0.2 \cdot q$. The good correspondence of the curve e to the observed curve f is very interesting though it depends on only the assumption and there is not the theoretical basis in this stage. It might be better to consider the state of closest approach varying with the solvent composition than the definite distance of closest approach. This is probably correlated with the fact that both solvent-separated and contact ion-pairs may be formed in a certain system (20). The behavior of the conductivity would be also affected by a specific solvation of Li^+ ion with DME in the mixed PC-DME system (10). In an extensive sense, not only ion-solvent but also solvent-solvent interactions make a significant contribution to the variation in the conductivity. However, the main factors determining the conductivity of the mixed solution are viscosity of the solution and the dielectric constant of the solvent in a solution with relatively high concentration of electrolytic salts. Similar results were obtained on PC-DME containing

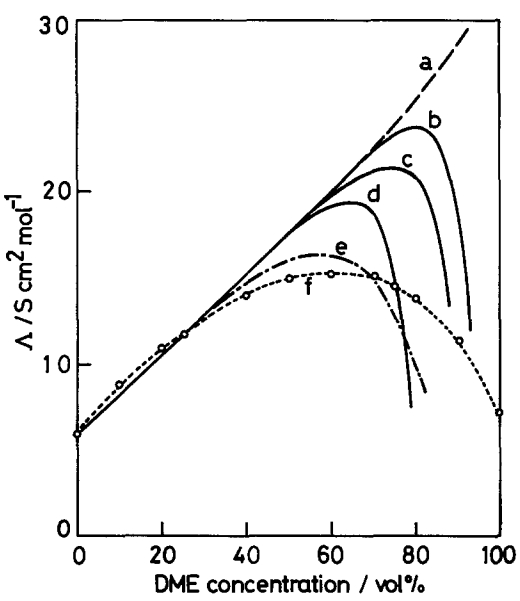

Fig. 6. Molar conductivity calculated by using the ion association model, a: completely dissociated, b: a = 0.81 nm, c: a = 0.42 nm, d: a = 0.26 nm, e: a/q = 0.2 (this assumption is explained in the text), f: observed conductivity.

$NaClO_4$ by calculation using the data of physical properties and conductivity of the system (9, 10), and these sustain the discussion.

Acknowledgment

The authors are grateful to the Grants in Aid for Scientific Research No. 555313 and for Energy Research No. 505577 by Japan Ministry of Education for partial support of this research. They are also indebted to Mitsubishi Petrochemical Company, Limited for supplying DME.

Manuscript submitted Feb. 16, 1982; revised manuscript received ca. July 15, 1982.

Any discussion of this paper will appear in a Discussion Section to be published in the December 1983 JOURNAL. All discussions for the December 1983 Discussions Section should be submitted by Aug. 1, 1983.

Publication costs of this article were assisted by Yamaguchi University.

REFERENCES

1. H. Ikeda, T. Saito, and H. Tamura, *Denki Kagaku*, **45**, 314 (1977).
2. H. Ikeda, S. Ueno, T. Saito, S. Nakaido, and H. Tamura, *ibid.*, **45**, 391 (1977).
3. K. Nakamura, T. lijima, and M. Fukuda, Preprint of 16th Battery Symposium, Japan, p. 46 (1975).
4. M. Broussely, U.S. Pat. 4,129,691 (1978).
5. R. Jasinski, *Electrochem. Technol.*, **6**, 28 (1968).
6. T. Saito, H. Ikeda, Y. Matsuda, and H. Tamura, *J. Appl. Electrochem.*, **6**, 85 (1976).
7. Y. Matsuda, Extended Abstract of 3rd Japan-USSR Seminar on Electrochemistry, p. 173 (1978).
8. Y. Matsuda and H. Satake, *Denki Kagaku*, **47**, 743 (1979).
9. Y. Matsuda and H. Satake, *This Journal*, **127**, 877 (1980).
10. Y. Matsuda, H. Nakashima, M. Morita, and Y. Takasu, *ibid.*, **128**, 2552 (1981).
11. Y. Matsuda, Y. Yamamoto, and M. Morita, *Denki Kagaku*, **49**, 653 (1981).
12. N. Bjerrum, *K. Danske Vidensk. Selk.*, **7**, No. 9 (1926); R. A. Robinson and R. H. Stokes, "Electrolyte Solutions," p. 392, Butterworths, London (1959).
13. Y. Matsuda, Y. Ouchi, and H. Tamura, *J. Appl. Electrochem.*, **4**, 53 (1974).
14. C. Carvajal, K. J. Tölle, J. Smid, and M. Szwarc, *J. Am. Chem. Soc.*, **87**, 5548 (1965).
15. G. J. Janz and R. P. T. Tomkins, "Nonaqueous Electrolytes Handbook," Vol. 1, p. 33, 62, Academic Press, New York (1972).
16. R. M. Fuoss and L. Onsager, *J. Phys. Chem.*, **61**, 668 (1957); T. Shedlovsky, *J. Am. Chem. Soc.*, **54**, 1405 (1932); R. A. Robinson and R. H. Stokes, "Electrolyte Solutions," p. 143, Butterworths, London (1959).
17. G. H. Nancollas, "Interactions in Electrolyte Solutions," p. 16, Elsevier, New York (1966).
18. L. Pauling, "Nature of the Chemical Bond," Cornell University Press, Ithaca, New York (1945); C. M. Criss and M. Salomon, in "Physical Chemistry of Organic Solvent Systems," A. K. Covington and T. Dickinson, Editors, Chap. 2, p. 261, Plenum Press, London (1973).
19. "Kagaku Binran (Handbook on Chemistry, 2nd Edition)," The Chemical Society of Japan, Editor, p. 78, Maruzen, Tokyo (1975).
20. R. Fernández-Prini, in "Physical Chemistry of Organic Solvent Systems," A. K. Covington and T. Dickinson, Editors, Chap. 5, p. 525, Plenum Press, London (1973).

Resistive Behavior of Thin Gold Film Electrodes under Direct Current Polarization

R. I. Tucceri and D. Posadas

Instituto de Investigaciones Fisicoquímicas, Teóricas y Aplicadas (INIFTA), 1900 La Plata, Argentina

ABSTRACT

The potential drop along thin gold film electrodes together with the current was measured as a function of the applied overpotential for a pure charge transfer control and a mixed control electrochemical process. These were the hydrogen evolution reaction (HER) and the reduction of Fe(III), respectively. The results show that the potential drop along the electrode follows a simple Ohm's law type in agreement with the theoretical predictions.

In recent years, thin film electrodes have been applied in a variety of electrochemical studies, mostly in the field of spectroelectrochemistry and in the measurement of electrode conductivity [see, for instance, Ref. (1, 2)].

Since thin film electrodes are resistive electrodes, it is important to ascertain the magnitude of the potential drop developed within the film as a consequence of the electrochemical process occurring at its surface. Several theoretical treatments are available for calculating the potential distribution along a resistive electrode (3-11), including those related to conductivity in porous electrodes, reviewed in Ref. (12). A simple Ohm's law behavior is predicted when the electrochemical currents are not too large (11). None of these treatments have been, to our knowledge, experimentally tested for resistive electrodes. Though the measurement of the potential distribution along the electrode poses some experimental difficulties, the total potential drop along it is an easily accessible quantity. The latter, however, would not provide a definitive test of the theory, but it would permit ascertainment as to whether the approximations involved are reasonable.

In the present work the potential drop along thin gold film electrodes together with the polarization current is measured as a function of the applied overpotential. Two cases are considered: (*i*) charge transfer controlled processes for which the hydrogen evolution reaction from H_2SO_4 aqueous solutions was studied and (*ii*) a mixed, charge transfer-convective diffusional, controlled process. In this case the reduction of Fe(III) from aqueous acid solution was studied.

Key words: electrode resistivity, thin metal film electrodes, electrode potential distribution.

Experimental

The thin film metal electrodes were obtained by vacuum deposition of evaporated gold onto optically polished Pyrex glass at room temperature. The electrical contacts were made *via* two or three aligned platinum wires of 0.5 mm diam previously fused into a glass disk of about 5 cm diam. Film thicknesses of approximately 25 ± 1 nm were used throughout. They

were determined by weighing samples obtained at the same time, *i.e.*, under the same evaporating conditions, as the electrode. These values agreed within 5% with those calculated from the deposition conditions (13). The source-substrate distance was about 10 cm and the evaporation rate was 0.1 nm sec^{-1}. Electrodes of rectangular shape 0.2 × 2 cm were obtained through the use of appropriate masks. The resistance in air of all the electrodes was approximately 13.0 ± 1.0Ω. At times, half-length films were employed. In this case the resistance was about 6.5 Ω.[1]

The electrolytic cell (Fig. 1) was of a design similar to that used by previous workers (14). The NHE reference electrode was located in a separate compartment. The platinum foil counterelectrode was located in the same compartment as the working electrode.

Triply distilled water, H_2SO_4 (Merck), and $FeCl_3$ (Mallinckrodt) analytical reagent grade, were used in preparing the electrolytic solutions.

A PAR Model 173 potentiostat together with a PAR Model 175 function generator were used for the potentiodynamic and the stationary polarization experiments. The potential drop at the extremes of the film was measured with a Keithley Model 160 voltmeter.

All the experiments were carried out at room temperature. The resistivity changes of the thin film electrodes were measured applying the three-contact method (11, 14). In this method a current is fed through two contacts at the extremes of the electrode while the third one, the central contact, is connected to the current follower of the potentiostat. The voltage difference at the extremes of the film is directly proportional to the resistance, and thus to the resistivity of the electrode if the side effects of the faradaic current passing through the electrode can be neglected (11). It has been shown (11) that for an electrochemical reaction having an exchange current density smaller than $i_o < 10^{-2}$ A cm^{-2} this occurs when the contacts at the ends of the electrode are symmetrically placed with respect to the central one. Let the distances of the end contacts to the central one be l_1 and l_2, then a factor g can be defined as

[1] Generally, the value in air decreased about 10-15% when the electrode was brought in contact with the electrolyte solution.

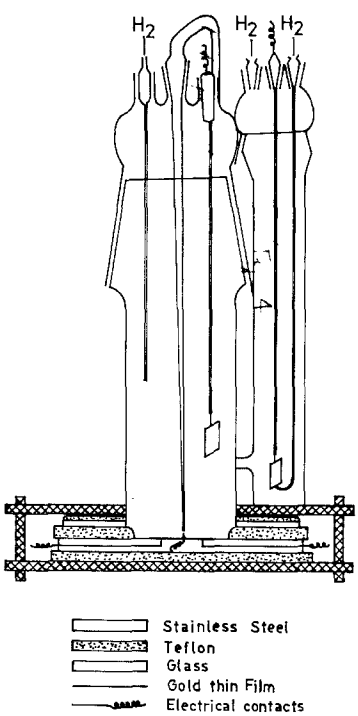

Fig. 1. Side view of the electrolytic cell

$$g = \frac{l_1 - l_2}{l_1} \qquad [1]$$

which takes into account the symmetry of the electrical contacts. In the present design $g = 0.003$ resulting from the l_1 and l_2 values measured with a traveling microscope with a precision of 10^{-4} cm.

The electric circuitry employed for measuring the resistance of the electrodes was essentially the same as that reported by previous workers (14).

Results

The hydrogen evolution reaction on gold was studied through both stationary and potentiodynamic ($v = 10^{-3}$ V sec^{-1}) polarization curves with simultaneous measurement of the potential difference at the extremes of the film, V_p (Fig. 2). The measured electrochemical current I_p was plotted as a function of V_p (Fig. 3). Good straight lines of inverse slope approxi-

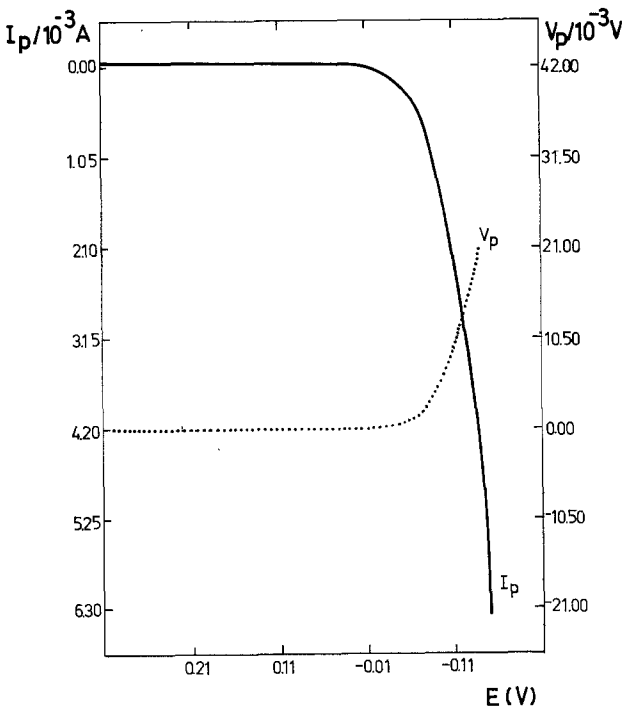

Fig. 2. Potentiodynamic current/potential (—) and V_p/potential (···) curves for the HER $v = 10^{-3}$ V sec^{-1}.

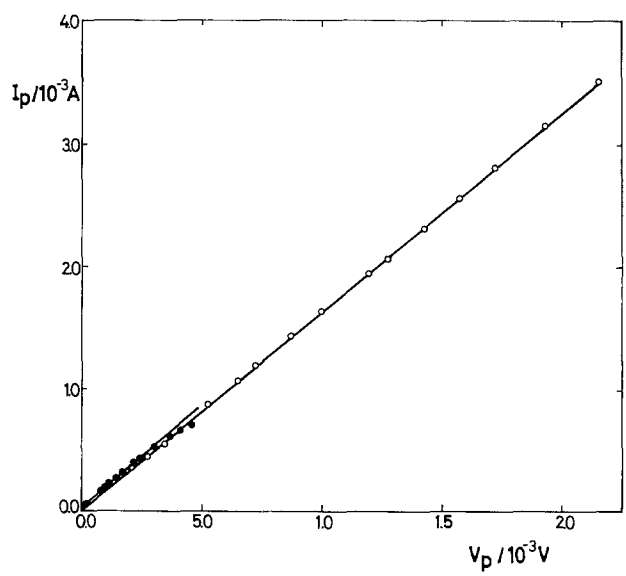

Fig. 3. I_p vs. V_p curves for (○) potentiodynamic, $R_{exp} = 12.5\Omega$, and (●) stationary, $R_{exp} = 14.5\Omega$.

mately equal to half the initial resistance in solution were obtained over the overpotential range studied.

Both potentiodynamic and steady-state polarization curves as well as simultaneous recording of V_p were also carried out for the electrochemical reduction of Fe(III) in quiescent solutions of 0.1M $FeCl_3$ and 0.5M H_2SO_4 in water (Fig. 4). As in the case of the HER the corresponding I_p *vs.* V_p plots give a straight line of inverse slope equal to half the electrode resistance (Fig. 5). The uncertainty in the limiting currents was about ±5%.

Discussion

The experimental results of Fig. 3 and 5 can be interpreted, in a first approximation, with the help of the theory developed previously (11, 12). Accordingly, the potential drop, V_p, along a homogeneous, finite, resistive electrode is

$$V_p = \frac{a}{b}\left(1 - \frac{1}{\cosh al}\right) \quad [2]$$

where a is the current density in the absence of resistive effects. For pure charge transfer control

$$a = i = i_o\left[\exp - \left(\frac{\alpha_a F\eta}{RT}\right) - \exp\left(-\left(\frac{\alpha_c F\eta}{RT}\right)\right)\right] \quad [3]$$

and

$$b = \frac{i_o F}{RT}\left[\alpha_a \exp\left(\frac{\alpha_a F\eta}{RT}\right) - \alpha_c \exp\left(-\frac{\alpha_c F\eta}{RT}\right)\right] \quad [4]$$

whereas for a mixed, charge transfer-convective diffusional, controlled process

$$i = a = \frac{\left[\exp\left(\frac{\alpha_a F\eta}{RT}\right) - \exp\left(-\frac{\alpha_c F\eta}{RT}\right)\right]}{\left[\frac{1}{i_o} + \frac{1}{i_a^l}\exp\left(\frac{\alpha_a}{RT}\right) - \frac{1}{i_c^l}\exp\left(-\frac{\alpha_c}{RT}\right)\right]} \quad [5]$$

and

$$b = \frac{F}{RT}\left\{\frac{a'\left[\frac{\alpha_c}{i_c^l}\exp\left(-\frac{\alpha_c F\eta}{RT}\right) - \frac{\alpha_a}{i_a^l}\exp\left(\frac{\alpha_a F\eta}{RT}\right)\right] - \left[\alpha_c \exp\left(-\frac{\alpha_c F\eta}{RT}\right) - \alpha_a \exp\left(\frac{\alpha_a F\eta}{RT}\right)\right]}{\frac{1}{i_o} + \frac{1}{i_a^l}\exp\left(\frac{\alpha_a F\eta}{RT}\right) - \frac{1}{i_c^l}\exp\left(-\frac{\alpha_c F\eta}{RT}\right)}\right\} \quad [6]$$

where η is the overpotential, i_o is the exchange current density, α_a and α_c are the transfer coefficients for the anodic and cathodic reactions, i_a^l and i_c^l are the anodic and cathodic limiting currents, respectively, and R, $\mathbf{F}$, and T are the gas constant, the Faraday constant, and the temperature. l is the length of the electrode and α is defined as (11, 14)

$$\alpha^2 = \frac{\rho D b}{A} \quad [7]$$

where ρ is the resistivity, D the width, and A the cross sectional area of the thin film electrode.

It has been shown (11) that for $\alpha l < 1$ (b small) the term in cosh αl in Eq. [2] can be expanded in series. Retaining up to the second term, it yields

$$V_p \cong \frac{a}{b}\left(\frac{\alpha^2 l^2}{2} + \frac{\alpha^4 l^4}{24} + \ldots\right) = \frac{I_p R}{2} + \frac{I_p R^2}{24} Dbl + \ldots \quad [8]$$

where the resistance, R, has been defined as

$$R = \frac{\rho l}{A} \quad [9]$$

The total electrochemical current (11), I_p, is given by

$$I_p \simeq aDl \quad [10]$$

when $\alpha l < 1$. According to Fig. 4 in Ref. (11) for not too high overpotentials, only the first term is important in Eq. [8]. Then

$$V_p \simeq \frac{I_p}{2} R \quad [11]$$

and the results of Fig. 3 and 5 can be straightforwardly explained. Since the measurement of the resistivity change of the gold electrode in the potential range considered does not show important variations of ρ (see Fig. 6), Eq. [11] can be applied. Accordingly, the slope of the V_p *vs.* I_p plot is approximately equal to half the value of the total resistance.

For the Fe(III) reduction reaction on gold, the i_o reported in the literature is about 0.7×10^{-3} A cm^2 (15). Taking this value into consideration, αl is smaller than 0.5 for $\eta > -0.3$V [see Fig. 4, Ref. (11)]. Under these conditions the approximation given by Eq. [10] is valid. Consequently, the current density was calculated from the measured current divided by the geometrical area of the electrode. This is tantamount to assuming the absence of resistive effects in the polarization curve. Since the higher experimental V_p value is smaller than 5×10^{-3}V (see Fig. 4), it is clear that

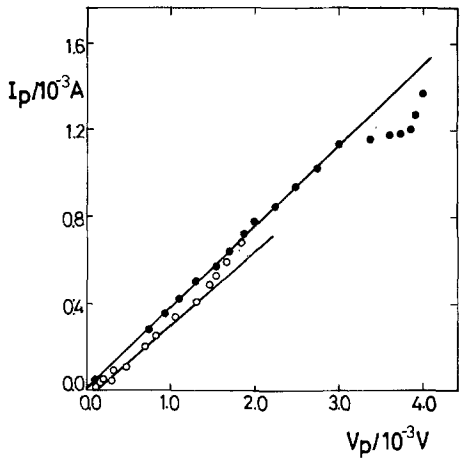

Fig. 5. I_p *vs.* V_p curves for (●) potentiodynamic, $R_{exp} = 5.3\Omega$, and (○) stationary, $R_{exp} = 5.5\Omega$, runs for the reduction of Fe(III).

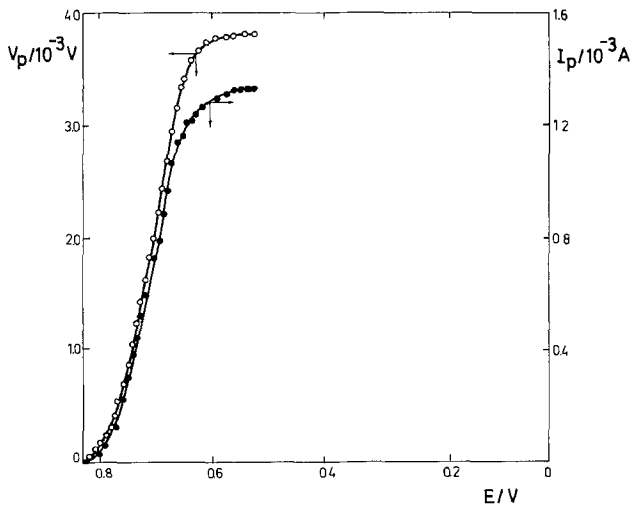

Fig. 4. Potentiodynamic I_p/potential (●) and V_p/potential (○) curves for the reduction of Fe(III) $v = 10^{-3}$ V sec^{-1}.

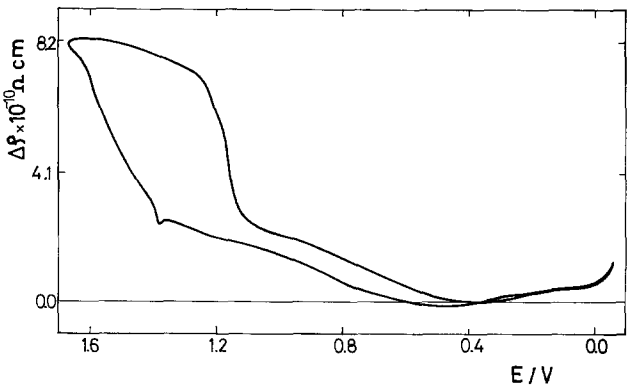

Fig. 6. Potentiodynamic electrode resistance/potential curve for the reduction of gold film in ϕN H_2SO_4, $v = 5 \times 10^{-2}$ V sec^{-1}.

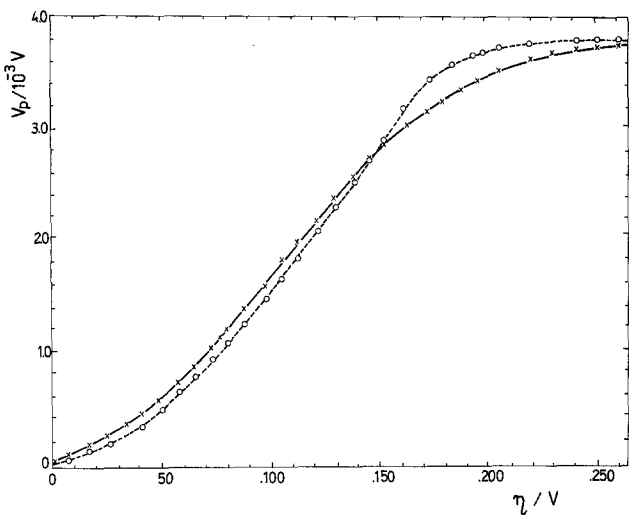

Fig. 7. Comparison between the experimental (○) and the calculated (×) V_p values as a function of overpotential.

in the overpotential range studied the kinetic parameters determined from the experimental polarization curve will be practically equal to those determined in the absence of resistive effects. With this approximation the kinetic parameters α and i_o were obtained from an η *vs.* $\ln|(i_c^l - i)/i|$ plot (Table I). The values of α and i_o obtained in this way are in good agreement with those obtained with the linear relationship

$$\frac{1}{i} = \frac{\alpha_a}{i_a^l} + \frac{RT}{F}\left(\frac{1}{i_o} + \frac{1}{i_a^l}\right)\frac{1}{\eta} \qquad [12]$$

obtained from Eq. [5] by assuming η small, $i << i_c^l$, and $\alpha_a + \alpha_c = 1$.

The values assembled in Table I were employed to calculate the overpotential dependence of V_p applying Eq. [2]. In Fig. 7 the experimental and calculated values of V_p as a function of the overpotential are shown. The agreement is good.

Conclusions

The experimental results for both the hydrogen evolution reaction and the reduction of Fe(III) on thin gold electrodes show that the equations for the potential distribution along a thin metal film electrode in the presence of a faradaic process are fulfilled. The potential drop along the electrode follows Ohm's law in terms of the average current. The calculated overpotential dependence of V_p compares reasonably well with the experimental results.

Table I. Experimental kinetic parameters for the reaction $Fe^{3+} + e \rightleftarrows Fe^{2+}$ on thin gold films at room temperature

i_o (A cm^{-2})	i_c^l (A cm^{-2})	i_a^l (A cm^{-2})	α_c	α_a
7.2×10^{-4}	1.2×10^{-3}	8.9×10^{-4}	0.48	0.52

Acknowledgments

The authors wish to thank Professor A. J. Arvía for valuable discussion and suggestions. R.I.T. thanks the CONICET for a fellowship during the period in which this work was carried out. INIFTA is sponsored by the Consejo Nacional de Investigaciones Científicas y Técnicas, the Universidad Nacional de La Plata, and the Comisión de Investigaciones Científicas (Provincia de Buenos Aires). This work is partially supported by the Regional Program for the Scientific and Technological Development of the Organization of The American States.

Manuscript submitted March 2, 1981; revised manuscript received *ca.* Feb. 15, 1982.

Any discussion of this paper will appear in a Discussion Section to be published in the December 1983 JOURNAL. All discussions for the December 1983 Discussion Section should be submitted by Aug. 1, 1983.

Publication costs of this article were assisted by Case Western Reserve University.

REFERENCES

1. T. Kuwana, in "Electroanalytical Chemistry," Vol. 1, A. J. Bard, Editor, Chap. 3, Ronald Press.
2. J. P. Ganon, C. Nguyen Van Huong, and J. Clavilier, *Surf. Sci.*, **79**, 245 (1979).
3. C. W. Tobias and R. Wijsman, *This Journal*, **100**, 459 (1953).
4. S. Zaromb, *ibid.*, **109**, 912 (1962).
5. W. W. Harvey, *ibid.*, **109**, 638 (1962).
6. B. E. Conway, E. Gileardi, and H. G. Oswin, *Can. J. Chem.*, **41**, 2447 (1963).
7. S. K. Rangarayan, M. J. Dignam, and B. E. Conway, *ibid.*, **45**, 422 (1967).
8. R. C. Alkire, *This Journal*, **118**, 1935 (1971).
9. R. C. Alkire and A. Tvarusko, *ibid.*, **119**, 340 (1972).
10. I. V. Tolkashev, *Sov. Electrochem.*, **15**, 130 (1979).
11. R. I. Tucceri and D. Posadas, *This Journal*, **128**, 1478 (1981).
12. R. de Levie, *Adv. Electrochem. Engr.*, **6**, 329 (1967).
13. K. L. Chopra, "Thin Film Phenomena," McGraw-Hill Book Co., New York (1969).
14. T. Dickinson and P. R. Sutton, *Electrochim. Acta*, **19**, 427 (1974).
15. D. Galizzioli and S. Trasatti, *J. Electroanal. Chem. Interfacial Electrochem.*, **44**, 367 (1973).

Electrosynthesis of N_2O_5 by Controlled-Potential Oxidation of N_2O_4 in Anhydrous HNO_3

J. E. Harrar* and R. K. Pearson

Chemistry and Materials Science Department, Lawrence Livermore National Laboratory, University of California, Livermore, California 94550

ABSTRACT

The anodic oxidation of N_2O_4 in aqueous and anhydrous HNO_3 has been investigated by controlled-potential techniques and found to be an excellent method for the preparation of solutions of N_2O_5 in anhydrous HNO_3. The product solutions can be used directly for the nitrolysis of organic compounds. The oxidation is carried out at approximately +1.85V *vs.* SCE (aq) at platinum or titanium-supported iridium oxide anodes. Up to 40g quantities of N_2O_5 have been prepared with good energy efficiency in a laboratory-scale, divided cell with a porous Vycor or Nafion separator. Complete oxidation of the N_2O_4 occurs in a region of low solvent background current; however, the overall current efficiency is reduced to ~65%, apparently because of transport losses of N_2O_4 and N_2O_5 to the catholyte. Several of the species resulting from the dissociation of N_2O_4 and N_2O_5 in the solutions have been identified by Raman spectroscopy.

Interest in the use of solutions of N_2O_5 in anhydrous HNO_3 for the nitrolysis of organic compounds has prompted us to reexamine the preparation of this reagent by the electro-oxidation of N_2O_4. The basic process was first described in a 1910 German patent (1). Zawadski and Bankowski, in work published in 1948 (2), also evaluated this reaction on the laboratory scale using a two-electrode cell with a platinum anode and demonstrated good yield and energy efficiency in the production of N_2O_5. Using controlled-potential techniques, we have further characterized the oxidation of N_2O_4 electrochemically and have found it to be a very convenient, facile synthesis that is a promising alternative to the usual method of preparation of N_2O_5, *i.e.*, the dehydration of HNO_3 with P_2O_5.

Experimental

Electrolysis equipment.—Three sizes of electrolysis cells were used for the N_2O_5 preparations, each designed as shown in Fig. 1. The counterelectrodes (cathodes) and working electrodes (anodes) for most of the experiments were Engelhard grade E2C (>99.95%) platinum gauze. Iridium oxide-coated titanium (obtained from the Diamond Shamrock Corporation as a DSA-Type TIR-2000 coating) was also tested as a working electrode material. The working electrodes were folded to a double thickness to give the configuration shown. As shown in Fig. 1, most of the experiments were done with Corning Glass No. 7930 porous Vycor as the separator material; du Pont Nafion perfluorinated polymer membrane was also tested briefly. The three electrosynthesis cells were constructed with working-electrode planar areas, solution capacities, and separator tube diameters as follows: 68 cm^2, 25 ml, 1 cm; 124 cm^2, 125 ml, 1.5 cm; and 180 cm^2, 225 ml, 1.5 cm.

The cell for voltammetry and Tafel-plot measurement was a 25 ml cell similar in design, except that the working electrode was a wire sealed in heat-shrinkable Teflon tubing and positioned in the center of the cell. The principal electrode materials used in these measurements were platinum and IrO_x. The platinum electrode was Johnson-Matthey spectrographically standardized 1 mm diam wire. The IrO_x electrode was prepared by Diamond Shamrock using Materials Research Corporation Marz-grade 1 mm titanium wire. Other electrode materials examined briefly were of comparable purity. The cell used for controlled-potential coulometry of milligram amounts of N_2O_4 has been described previously (3, Fig. 22).

The reference electrode used for all of the cells was a Fisher Scientific Catalog No. 13-639-210 aqueous saturated calomel electrode whose potential was checked occasionally against a laboratory-prepared standard. The salt bridge tube (Fig. 1) was terminated in a tip containing an asbestos fiber. The tip was drawn out to ~1 mm diam and positioned ~1 mm from the working electrode. Both the salt bridge tube and the counter-electrode compartment were filled with anhydrous HNO_3.

EG&G Princeton Applied Research Corporation Models 371 and 173 potentiostats were used for the controlled-potential electrosyntheses and Tafel-plot measurements. An EG&G PAR Model 364 polarographic analyzer with recorder was used for the voltammetry. Instrumentation designed at this laboratory (4) was used for the low level coulometry. An ECO (Amel) Model 731 digital integrator was used to integrate the current during the electrosynthesis experiments. For currents >2A, a 2X current shunt was used. The specific energy consumption was calculated by integrating the product of the total cell voltage and current over the period of the electrolysis.

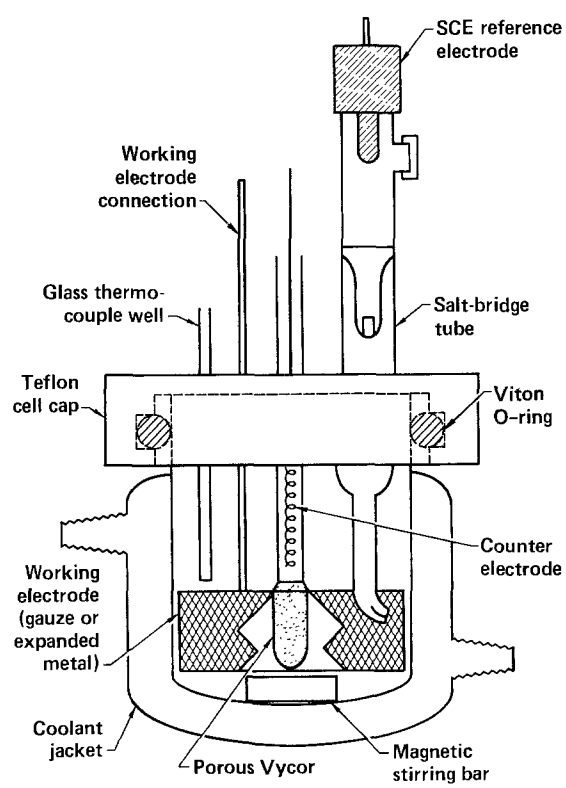

Fig. 1. Electrolytic cell for the synthesis of N_2O_5 in anhydrous HNO_3.

* Electrochemical Society Active Member.

Key words: inorganic, electrode, analysis, voltammetry, coulometry.

Reagents.—The anhydrous nitric acid was prepared by distillation from a mixture of reagent grade 90% HNO_3 and fuming (20% free SO_3) H_2SO_4 (1:1.16 v/v) in a glass apparatus at ~50 Torr pressure and 40°-50°C. The 90% HNO_3 was pretreated by adding 0.4 weight percent (w/o) urea and sparging with air until colorless. NMR analyses verified that the water content of the distilled acid did not exceed 0.4%, the equilibrium concentration present in nominally anhydrous acid (5). The N_2O_4 was Air Products & Chemicals, Incorporated CP grade.

Procedures.—Solutions in the range of 5-20% N_2O_4 in HNO_3 were prepared by weight from the anhydrous HNO_3 and liquid N_2O_4 cooled in an ice bath. The less concentrated solutions for voltammetry and coulometry were obtained by volumetric dilution.

During the electrosynthesis experiments, the control potential was generally set to a value ~100 mV less positive than the final value, and then raised gradually as the electrolysis proceeded to maintain a more nearly constant rate of electrolysis and tighter temperature control. The control potential reported for these experiments is the nominal final control potential uncorrected for uncompensated resistance. Power consumption was calculated from periodic measurements of the cell current and total voltage.

The Tafel-plot data were obtained with the wire electrodes in stirred solutions by stepwise, manual adjustment of the control potential. After a short period of time to reach steady state, the current was then recorded, except for the return sweep at the platinum electrode, for which the surface conditions were quite transient. The Tafel-plot data are corrected for an uncompensated resistance of 1.6Ω, calculated from measurements of the total cell resistance, 17Ω, and the cell transfer function attenuation (3) in the 5-50 kHz frequency range.

Chemical analysis methods.—The initial solutions and solutions produced by electrolysis were examined by two different analytical techniques: high resolution Raman and NMR spectrometry. Raman spectra were obtained by means of a laser-Raman system incorporating a Spectra Physics 1-M double monochromator. NMR measurements were made with a Nicolet Model NT-200 FT-NMR spectrometer.

Quantitative determinations of the concentrations of N_2O_5 produced by the electrolyses were performed using a method developed by Happe and Whitaker (6). The method is based on measurement of the proton chemical shift resulting from the presence of NO_3^- ions in the anhydrous HNO_3. This shift is believed to be caused by hydrogen bonding between HNO_3 and NO_3^- to produce a solvated nitrate ion. As described by Addison (5) and as shown by the Raman spectra to be discussed below, pure, anhydrous nitric acid is slightly dissociated into water, nitronium cation, and nitrate anion

$$\underset{}{2HNO_3} \leftrightarrows \underset{0.4}{H_2O} + \underset{1.1}{NO_2^+} + \underset{1.5\ \text{w/o}}{NO_3^-} \qquad [1]$$

Dinitrogen pentoxide also dissociates as follows (5)

$$N_2O_5 \leftrightarrows NO_2^+ + NO_3^- \qquad [2]$$

Thus, if the dissociation of N_2O_5 is complete in the concentration range of interest, and no N_2O_4 is present, measurement of the nitrate ion concentration relative to that in pure HNO_3 would yield the concentration of N_2O_5 (and NO_2^+) produced in the electrosynthesis.

An experiment was carried out in which a highly concentrated solution of N_2O_5 in HNO_3 (produced by electrolysis of N_2O_4) was successively diluted with HNO_3 and the resulting solutions analyzed by NMR. The results are shown in Table I. The initial N_2O_5 concentration of 23.2 w/o and the observed concentrations of N_2O_5 in the diluted solutions were based on the chemical shifts of standard solutions of KNO_3 in HNO_3 (6). These solutions and the final solutions of the electrolyses were also analyzed by Raman spectrometry to verify the absence of N_2O_4. The good agreement between the calculated and observed concentrations of N_2O_5, and confirmation of the species existing in the solutions by Raman spectroscopy indicated that NMR is a valid technique for this analysis.

Table I. NMR analyses of diluted solutions of N_2O_5 in anhydrous HNO_3

Calculated conc. N_2O_5 (w/o)	Observed conc. N_2O_5 (w/o)	Proton chem. shift *vs.* anhydr. HNO_3 (ppm)
23.2	23.2	1.867
16.8	17.7	1.369
12.6	12.2	0.929
8.4	9.0	0.663
4.9	5.2	0.368

Results and Discussion

In addition to smooth platinum, as employed by previous investigators (1, 2), we initially tested a number of other materials as candidates for the oxidation of N_2O_4 in HNO_3. Found to be inactive were gold, glassy carbon, magnetite (Fe_3O_4), tantalum, tungsten, and titanium, the latter three acquiring a poorly conducting film in the required potential region. Figure 2 shows voltammetric curves for the reaction at smooth platinum and IrO_x-coated titanium electrodes. For the same geometric area, the IrO_x electrode is much more active than smooth platinum, both for the oxidation of N_2O_4 and the decomposition of the HNO_3. High electrocatalytic activity was also found for RuO_x-coated titanium (7) and platinized platinum. Thus, as has been found for the chlorine evolution reaction (7, 8), the apparent high activity is probably a combination of increased microscopic surface area and the electrocatalytic properties of the conducting noble metal oxides.

The catalytic nature of this reaction is also illustrated by the controlled-potential electrolysis curves shown in Fig. 3. At the beginning of the electrolysis, the current decreases slowly and is relatively insensitive to the rate of mass transfer, but as the N_2O_4 is consumed and its concentration decreases, the overall electrolytic rate constant increases. Coulometry at this concentration level yields coulometric n-values near 2.00 which are expected for the overall process in the oxidation of N_2O_4 to N_2O_5.

Tafel plots for the oxidation of N_2O_4 in the concentration range suitable for electrosynthesis are shown in Fig. 4 and 5, again revealing the marked contrast in platinum and IrO_x as anode materials. As indicated in Fig. 4, considerable hysteresis is exhibited in the current-potential curves of platinum. Polarization of the electrode at the high positive potentials increases its activity; however, this increased activity is rapidly lost

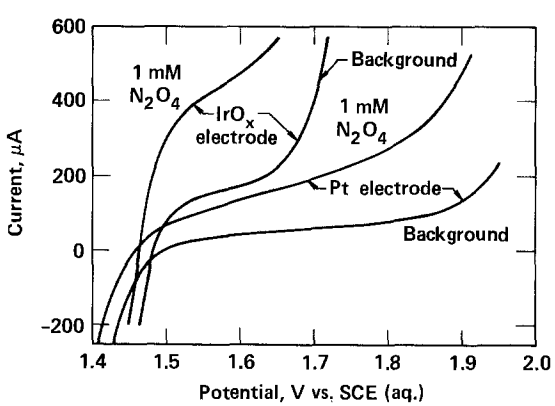

Fig. 2. Stirred-solution voltammetric curves for the oxidation of N_2O_4 in anhydrous HNO_3 (300 mV/min scan rate).

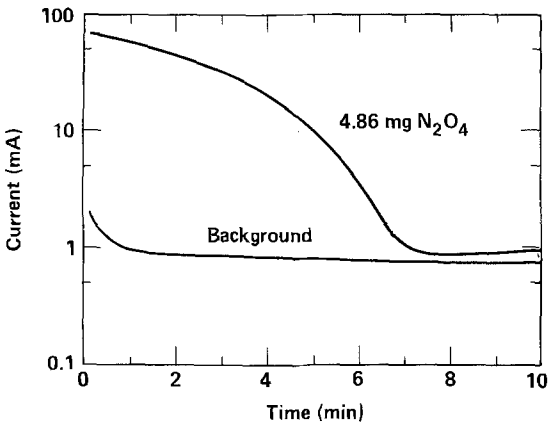

Fig. 3. Current-time curve for the controlled-potential oxidation of N_2O_4 in anhydrous HNO_3 (25 ml cell).

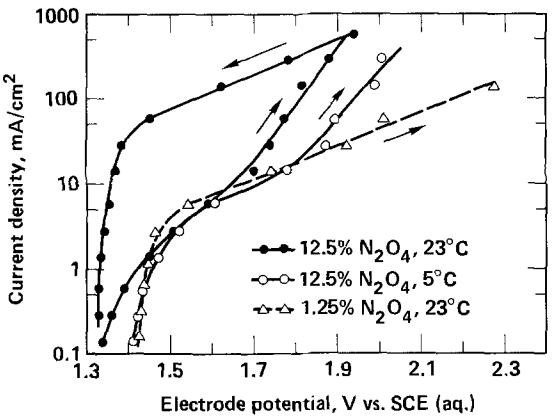

Fig. 4. Tafel plots for the oxidation of N_2O_4 at a platinum electrode in anhydrous HNO_3. (Potentials corrected for uncompensated resistance.)

as the electrode is used at the lower potentials. This effect was nearly absent in the case of the IrO_x electrode. With the possible exception of the positive-scan curves for platinum, there are no clearly defined Tafel regions, and these slopes are quite high (>150 mV/dec). The cathodic reaction, which is the reduction of HNO_3 to N_2O_4, influences the curves at low overpotentials, especially those of the IrO_x electrode. In the current density range of 50-200 mA/cm², the overpotential for the oxidation of N_2O_4 is ~0.4V lower for IrO_x than for platinum; this should permit correspondingly lower cell voltages for the electrosynthesis.

Figure 6 is a typical current-time curve for the electro-oxidation of N_2O_4 to N_2O_5 at high concentrations. At control potentials more negative than that of the decomposition of the HNO_3 (~2.0V), the current is nearly

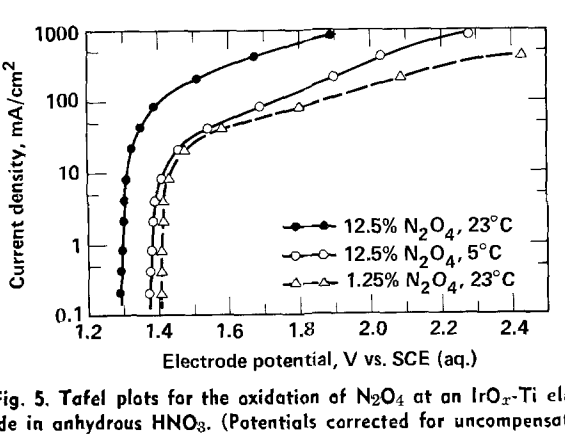

Fig. 5. Tafel plots for the oxidation of N_2O_4 at an IrO_x-Ti electrode in anhydrous HNO_3. (Potentials corrected for uncompensated resistance.)

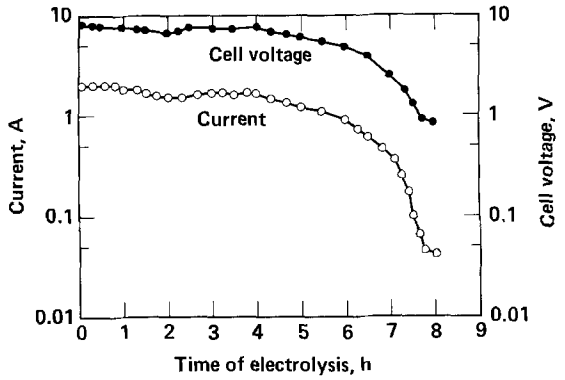

Fig. 6. Cell current and voltage during oxidation of 22.7g N_2O_4 (12.5% solution) in anhydrous HNO_3 at a platinum electrode [125 ml cell; E = +1.78 to +1.85V vs. SCE (aq.)].

constant for about 80% of the time, and then drops to a relatively low value when all of the N_2O_4 has been consumed.

Figure 7 shows Raman spectra of the solution during various stages of the electrolysis. Figure 7a is the spectrum of pure, anhydrous HNO_3, showing the peaks of NO_2^+ and NO_3^- from the dissociation of HNO_3. Figure 7b is the spectrum of the starting solution of the electrolysis; this includes a peak due to the nitrosyl cation, NO^+, which arises from the dissociation of N_2O_4 (5)

$$N_2O_4 \leftrightarrows NO^+ + NO_3^- \quad [3]$$

In the spectrum of the partially electrolyzed solution, Fig. 7c, the peaks of NO_2^+, NO^+, and the undissociated HNO_3 are present. Finally, at the end of the electrolysis, Fig. 7d, the NO^+ peak is virtually absent and the large, sharp peak of NO_2^+ is dominant. Some of the peak positions shift slightly as the composition of the solution changes. These high resolution spectra are qualitatively similar to those obtained by Odokienko *et al.* (9) for mixtures of N_2O_5 and HNO_3.

Table II summarizes the characteristics of the electrosynthesis of N_2O_5 as determined for a range of values of the operating parameters. For each of the experiments listed in Table II, the electrolysis of N_2O_4 was carried out to completion, as indicated by the electrolysis current decaying to the background value (see Fig. 6). At present, the electrolytic preparation has been investigated extensively only with a platinum anode. Up to 40g quantities of N_2O_5 have been prepared. In these electrolyses, the principal reaction in the cathode compartment of the cell is the reduction of HNO_3 to N_2O_4, which at temperatures above ~20°C, vigorously distills out of the catholyte.

In Table II, the N_2O_5/N_2O_4 mol ratios were calculated from the concentrations of N_2O_5 in the final solutions, as determined by NMR, and the quantity of N_2O_4 in the initial solution. A significant fraction of the anolyte solution was lost during the electrolysis, most likely as a result of both electro-osmosis and consumption of the HNO_3 in the electrolysis. Thus the mol ratios are somewhat lower than if based on the true amount of N_2O_5 produced. The quantity of HNO_3 lost from the anolyte is given as a percentage in Table II; it is usually highest at the most positive control potentials and highest current densities.

The specific energy consumption of the process is generally very good, especially for the larger cell and low temperature electrolysis. Unexpectedly, the experiment at 6°C had the best characteristics overall. In this experiment, significantly lower cell voltages were required, which we suspect was due to better performance of the cathode/catholyte half-cell. In contrast to the higher temperature electrolyses, which were carried out above the boiling point of N_2O_4, at low temperatures there was little gas evolution or loss of catholyte. Thus there was no blockage of the cathode by

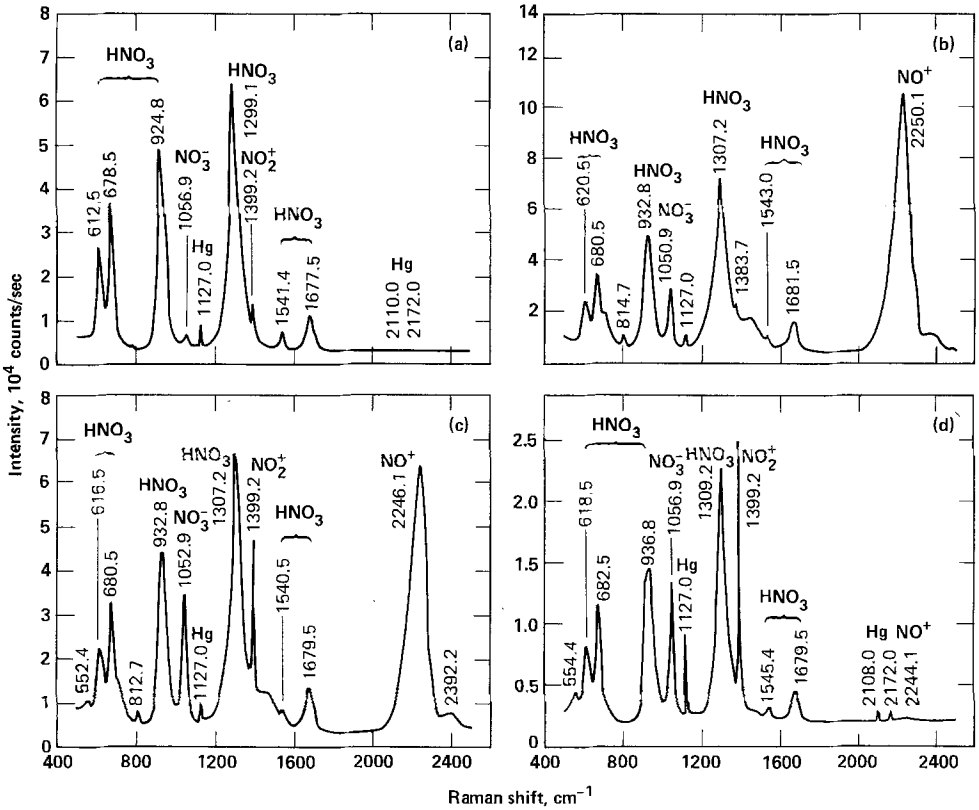

Fig. 7. Raman spectra of solutions of anhydrous HNO_3, N_2O_5, and N_2O_4. (a) Pure anhydrous HNO_3; (b) 20.5% N_2O_4 in HNO_3; (c) partially electrolyzed N_2O_4 in HNO_3; (d) N_2O_5 in HNO_3 (N_2O_4 completely electrolyzed). Mercury calibration lines also shown.

gas bubbles and probably a lower resistance catholyte. A preliminary experiment with Nafion perfluorinated polymer membrane in place of the porous Vycor revealed that it could afford a further reduction in cell resistance, voltage, and specific energy consumption. The use of large-scale industrial-type cells for this process would undoubtedly result in even lower specific energies.

Several experiments were performed to ascertain the effect of water on the electrochemistry of this process. Up to 3% water was found to have no effect on either the shapes of the voltammetric curves for low concentrations of N_2O_4, or the decomposition potential of the HNO_3. In the electrosyntheses, the only apparent effect of water is to consume the N_2O_5 produced until all of the water has reacted; the electrolysis current behavior is unaffected. Red fuming nitric acid, which contains ~1.5% H_2O (5), and N_2O_4 in white fuming nitric acid (containing 11% H_2O) were also used as the reactants, with reduced yields of N_2O_5.

The overall stoichiometry of the reaction has one prominent feature that cannot yet be explained. It is clear from the N_2O_5/N_2O_4 mol ratios that 1 mol of N_2O_5 is produced per mol of N_2O_4 consumed (see Table II). However, as the initial concentrations of N_2O_4 are increased, the quantity of electricity consumed becomes less than expected, leading to n-values of ~1.5. Within the ranges of the variables studied, this phenomenon is independent of the control potential, current density, temperature, time of electrolysis, and cell size (solution volume:electrode area ratio and mass transfer rate). An experiment was performed using the 25 ml cell to test whether N_2O_4 volatilized from the solution, decomposed, or diffused into the cathode compartment during the period of an electrolysis, which would cause a negative error in the n-value. In this experiment, anolyte containing 24% N_2O_4 was stirred for 7 hr, without electrolysis, and analyzed for N_2O_4 before and afterward. No loss of N_2O_4 was found, but this leaves open the possibility, discussed below, of the electromigration of reacting species during the electrolysis. Electrolysis with an IrO_x anode in the 225 ml cell gave virtually the same result as platinum: oxidation of a 12.1% N_2O_4 solution

Table II. Representative results of the synthesis of N_2O_5 by controlled-potential oxidation of N_2O_4 in anhydrous HNO_3 at a platinum electrode

Initial N_2O_4 conc. (w/o)	Temp (°C)	Final control potential (*V vs.* SCE)	Peak current (A)	Time of electrolysis (hr)	Final N_2O_5 in anolyte (mmols)	Final conc N_2O_5 (w/o)	Mol ratio $\frac{N_2O_5}{N_2O_4}$	HNO_3 loss (%)	n (F/mol N_2O_4)	Product current efficiency (%)†	Specific energy (kW-hr/mol N_2O_5)
21.4*	24	1.80	4.0	6	317	22.8	0.79	14.5	1.49	53	0.49
20.5	24	1.85	0.8	7.5	98.5	23.7	0.95	6.0	1.57	60	0.85
13.9	14	1.80	0.8	5	69.5	15.7	0.97	0.5	1.48	65	0.68
12.5*	23	1.80	2.0	7	235	14.6	0.94	8.9	1.50	63	0.50
12.5*	6	1.85	2.0	7.5	238	14.7	0.97	5.9	1.52	64	0.29
10.8*	25	1.90	1.9	7	175	11.1	0.80	8.6	1.46	55	0.42
10.5*	25	1.95	3.5	3	179	12.0	0.87	12.6	1.40	62	0.67
9.8	22	1.78	0.7	4	43.3	11.75	1.03	1.4	1.54	67	0.55
5.1	24	1.79	0.6	2.5	26.9	6.05	1.01	0.0	1.57	65	0.86
1.57	25	1.80	0.28	2.5	7.9	1.85	1.01	0.0	1.73	59	0.48
1.59	25	1.56	0.10	7	7.8	1.82	0.98	0.0	1.73	57	0.77
0.50	24	1.75	0.10	2	—	—	—	—	1.93	—	—
0.04	24	1.78	0.10	0.2	—	—	—	—	1.97	—	—

* 125 ml cell; other experiments with 25 ml cell.
† Assuming equivalent weight of N_2O_5 = molecular weight.

yielded an N_2O_5/N_2O_4 ratio of 0.98 and an n-value of 1.59.

Zawadski and Bankowski (2) proposed for this process the overall reaction

$$N_2O_4 + 2NO_3^- \rightarrow 2N_2O_5 + 2e^- \quad [4]$$

which corresponds to $N_2O_5/N_2O_4 = 2$ and $n = 2$. However, since these workers did not control the electrode potential in their experiments, it is possible that there was considerable concomitant oxidation of the HNO_3. We carried out an oxidation of the HNO_3 alone at a potential of +2.37V *vs.* SCE (aq) and a current of 0.55A for 7 hr and found that the resulting solution contained 5.6% N_2O_5. Considerable evolution of gaseous oxygen was also observed. Thus excursions of the control potential to more positive values in the N_2O_4 electro-oxidation should increase the product yield but decrease the current efficiency.

In the more concentrated solutions, where undissociated N_2O_4 and NO_2 are present (5), the electrode reaction may be represented as

$$NO_2 \rightarrow NO_2^+ + e^- \quad [5]$$

corresponding to the same ratio of N_2O_5/N_2O_4 and n-value as Eq. [4]. Because it appears that in theory one faraday of electricity is consumed for each mol of N_2O_5, the product current efficiencies given in Table II have been calculated on this basis. The lower values that we observe for these parameters may be attributed in part to electrodialysis effects. Because the predominant cations in these solutions are the NO^+ and NO_2^+ ions, there is probably a loss of these species from the anolyte by electromigration through the separator. (Raman spectroscopy showed the presence of NO_2^+ in the catholyte after the electrolysis.) Loss of the NO^+ ion would decrease the n-value, while loss of either NO^+ or NO_2^+ ion would decrease the yield of N_2O_5. The influence of electrodialysis on this process could be tested by carrying out electrolyses in the presence of inert salts. As suggested for the aqueous oxidation of nitrate ion (10), this reaction also probably involves interaction with the oxide layer on the metal anode. Further speculation on the mechanism of this process must await additional electrochemical studies and perhaps experiments with isotopically labeled compounds.

The N_2O_5 solutions produced in the electrosyntheses carried out here have proved to be excellent reagents for the preparation of the explosive HMX (1,3,5,7-tetranitro-1,3,5,7-tetraazacyclooctane) by reaction with the compounds 1,3,5,7-tetraacetyl-1,3,5,7-tetraazacyclooctane and 1,5-diacetyl-3,7-dinitro-1,3,5,7-tetraazacyclooctane. The utility of the electrosynthesis and the accuracy of the chemical analyses were validated by the fact that the ultimate HMX yields were 81 ± 1% when N_2O_5 was prepared either by electrolysis or by dehydration with P_2O_5 (11, 12).

As a laboratory-scale batch synthesis procedure, the anodic oxidation of N_2O_4 to N_2O_5 is relatively inexpensive to implement, and the electrolysis itself is very easy to monitor and control. The low resistivity (30 Ω-cm) and viscosity of the anhydrous HNO_3 make it an excellent nonaqueous solvent. Optimization for scale-up should include a further investigation of IrO_x and platinum-clad alloys as anode materials, alternative separator materials, different cathode materials that would maintain low cell voltages and power dissipation, and a process for recovery of the N_2O_4 generated at the cathode for use as a reactant at the anode. For practical cells, noble-metal oxide and platinum-clad materials would probably also be the best for the cathode, although corrosion resistant metals such as tantalum, titanium, and zirconium might be suitable if their overvoltages for the cathode reactions are not too high.

Acknowledgments

Helpful discussions and support of this study by C. L. Coon and R. R. McGuire are gratefully acknowledged. The anhydrous HNO_3 was prepared by R. N. Swansiger, the Raman spectrochemical analyses were done in collaboration with F. P. Milanovich, and J. A. Happe performed the NMR determinations. The possible effect of electrodialysis in the synthesis was suggested by W. G. Grot of E. I. du Pont de Nemours.

This work was performed under the auspices of the U.S. Department of Energy under Contract No. W-7405-ENG-48.

Manuscript submitted Feb. 1, 1982; revised manuscript received July 20, 1982.

Any discussion of this paper will appear in a Discussion Section to be published in the December 1983 JOURNAL. All discussions for the December 1983 Discussion Section should be submitted by Aug. 1, 1983.

Publication costs of this article were assisted by the Lawrence Livermore National Laboratory.

REFERENCES

1. German Pat. 231,546 (1910).
2. J. Zawadski and Z. Bankowski, *Roznicki Chem.*, **22,** 233 (1948); *Chem. Abstr.*, **43,** 8906b (1949).
3. J. E. Harrar, in "Electroanalytical Chemistry," Vol. 8, A. J. Bard. Editor, Chap. 1, Marcel Dekker, New York (1975).
4. J. E. Harrar and E. Behrin, *Anal. Chem.*, **39,** 1230 (1967).
5. C. C. Addison, *Chem. Rev.*, **80,** 21 (1980).
6. J. A. Happe and A. G. Whittaker, *J. Chem. Phys.*, **30,** 417 (1959).
7. S. Trasatti and G. Lodi, in "Electrodes of Conductive Metal Oxides," S. Trasatti, Editor, Part A, Chap. 7, Elsevier, Amsterdam (1980).
8. J. Mozota and B. E. Conway, *This Journal,* **128,** 2142 (1981).
9. S. S. Odokienko, N. V. Latypov, I. N. Shokhar, Yu. A. Federov, and E. N. Vishnevskii, *Zh. Prikl. Khim.*, **51,** 683 (1978).
10. A. A. Yakovleva, R. K. Bairamov, and V. I. Veselovskii, *Soviet Electrochem.*, **11,** 482 (1975).
11. C. L. Coon, Private communication.
12. V. I. Siele, M. Warman, J. Leccacorvi, R. Hutchinson, R. Motto, and E. E. Gilbert, Tech. Rept. ARLCD-TR-78008, p. 41, ARRADCOM, Dover, NJ (1979).

Technical Notes

Lithium Cycling Behavior in 2-Methyltetrahydrofuran with Alcohol Additives

Paul G. Giugla

Department of Chemical Engineering, University of Colorado, Boulder, Colorado 80309

It is generally agreed that the key technical problem preventing the realization of high energy density, ambient temperature secondary lithium batteries is the unacceptable cycling behavior of the lithium electrode (1-4). Koch *et al.* (4) have identified the 2-methyltetrahydrofuran lithium hexafluoroarsenate electrolyte (MeTHF-$LiAsF_6$) as a promising liquid organic electrolyte for secondary lithium batteries. Koch states that the advantage of this electrolyte over other candidates is its low reactivity to lithium metal. The purpose of this study was to improve the MeTHF-$LiAsF_6$ electrolyte by altering the lithium metal/electrolyte interface. It was hoped that an additive to the electrolyte could be found that would form a protective layer between the lithium metal and the electrolyte. This would reduce the rate of attack on the lithium from the solvent by adding a diffusional barrier in series with the kinetic barrier.

A successful additive must be more reactive to lithium than is MeTHF, but yet inert to the electrolyte. This would insure that the protective film would be formed from additive molecules and not from an unknown parasitic reaction. Furthermore, the resulting film must be ionically conductive to be stable during the plating and stripping operations. A series of alcohols were tested as additives since they are logically more reactive to lithium than is MeTHF. Alcohols containing ether groups were of particular interest since poly(ethylene glycol) has been reported to be a weak ionic conductor (5). These new electrolytes were evaluated on their ability to plate and strip lithium efficiently.

Experimental

All procedures subsequent to distillation and the electrochemical experiments were conducted at ambient temperature under an argon atmosphere in a Vacuum-Atmosphere Corporation dry box equipped with a Model HE-493 Dri-Train and a Cryotrap.

Materials.—The lithium hexafluoroarsenate ($LiAsF_6$) (ALFA) was used as received. Lithium foil was obtained from Foote Mineral Company sealed under argon.

All of the remaining compounds except for 1-dodecanol and 1-hexadecanol were purified by distillation. 1-Dodecanol and 1-hexadecanol were not purified because their high boiling points made distillation difficult. The distillation column demonstrated 54 theoretical plates with the methanol/water system. The temperature at the top of the column was controlled by adjusting the total pressure. This temperature was less than 90°C for all of the distillations. The reflux ratio was set at 13:1. All compounds were distilled from 3A molecular sieves. The sieves had been washed with acetone and dried at 300°C under moderate vacuum prior to use. The product was collected in 10-15 receiver flasks. Only those portions that were collected at constant temperature (±0.05°C) were retained.

All of the compounds were tested for purity with gas chromatography. Samples with >0.02% (area %) impurities were rejected. The only samples to fail this test after distillation were a few samples of MeTHF that had been stored in the dry box for more than three months.

A blank solution of 0.5M $LiAsF_6$ in MeTHF was prepared and stored in the dry box. All of the solutions with additives were prepared from this blank. The initial concentration of additive was 2% (m/o) for all tests.

Cells and the cycling experiment.—The electrochemical cell consisted of a 15 ml cylindrical glass vial and a sealed vial cover. Up to six electrodes could be mechanically attached to the vial cover. Sealed electrical connections were also incorporated in the vial cover. Generally, three electrodes were incorporated in every cell, a working, counter, and a reference. The working electrode was fabricated from 2 mm diam. nickel wire. Shrink fit Teflon tubing was used to define the electrode area. The counter and the reference electrodes were prepared by crimping lithium foil to nickel wires and were identical. The cells were connected to the electronics, which were outside the dry box, by a 36 line electrical cable that ran through the dry box wall.

Cycle efficiencies were determined from a deep cycling experiment. A cycle consisted of a galvanostatic plating of lithium on the working electrode at 1.5 mA/cm^2 for 20 min followed by a potentiostatic stripping of the working electrode at 70 mV. 70 mV was chosen as the control voltage in the stripping procedure because it produced currents of less than 2 mA/cm^2 on the working electrode. All of the electrochemically active lithium was removed from the working electrode in the stripping procedure. The potentiostats, galvanostats, and switching apparatus were constructed in-house. Voltages and currents were recorded every 15 sec. The efficiency of a cycle was computed by integrating the recorded currents. The total number of coulombs of lithium stripped per cycle was compared to the total number of coulombs of lithium plated per cycle.

Results and Discussion

Table I is a summary of the effects of a series of 14 additives. An initial plateau of good behavior was observed in the tests where efficiencies and number of cycles are quoted. The number of cycles quoted in the table indicates the duration of the plateau. The efficiency indicates the average efficiency of the cycles in the plateau. In all cases swiftly deteriorating behavior occurred after the plateau.

Each cycle in the plateau can be characterized as follows. When the constant current plating operation was initiated, the voltage of the working electrode with respect to the reference assumed a relatively

Key words: organic electrolyte, lithium electrode.

Table I. Electrolyte additives and their effect. 2% (m/o) additive was used in all solutions

Additive	Effect
1. None	35 cycles at 79% efficiency
2. Ethanol	Heavy gasing with difficulty plating
3. 2-Propanol	Heavy gasing with difficulty plating
4. 1-Butanol	Slight gasing with difficulty plating
5. 1-Hexanol	25 cycles at 68% efficiency
6. 1-Heptanol	25 cycles at 70% efficiency
7. 1-Octanol	28 cycles at 71% efficiency
8. 1-Decanol	30 cycles at 73% efficiency
9. 1-Dodecanol	35 cycles at 76% efficiency
10. 1-Hexadecanol	35 cycles at 76% efficiency
11. 1-Methoxy-2-petanol	10 cycles at 72% efficiency
12. 3-Methoxy-1-butanol	10 cycles at 70% efficiency
13. 2-Methoxy-ethanol	900 cycles at 85% efficiency
14. Diethylene glycol, monomethyl ether	40 cycles at 80% efficiency
15. Triethylene glycol, monomethyl ether	35 cycles at 78% efficiency

large value. This voltage decayed to a voltage that is reflective of the cell resistance within 30 sec and remained at that value for the duration of the plating. The initial voltage was typically one and one-half times the steady-state plating voltage. When the constant voltage stripping operation was initiated, the initial current assumed a relatively small value. Within 120 sec the current increased to a value reflective of the cell resistance. The stripping current remained constant until the store of lithium became depleted. At this point the current decayed to zero over a 2 to 3 min time span. This pattern was observed for all of the successful electrolytes including the control solution.

The cells and cycling procedure used in this test were not optimized to produce maximum cycling efficiencies. The procedures outlined here were designed to indicate the relative merits of a series of electrolytes. As a result the blank solution did not perform as well as was reported in the literature (4). It is assumed that the behavior of all of the solutions tested here would improve with fine tuning. It is also assumed that the fine tuning would not change the ranking of any of the solutions.

The premise and motivation for this study is based on the belief that a protective film can be built that will enhance lithium cycling behavior. Initial current delays in plating and stripping are commonly used as evidence for protective film formation. Furthermore, mirror-like lithium surfaces swiftly become dull in these solutions. However, this is not conclusive evidence for the existence of protective films and the basis for lithium stability in these solutions remains unknown.

By far the most successful additive was 2-methoxyethanol. The lithium cycling efficiency was significantly improved over the blank. Furthermore, the electrode life was extended by a factor of 25. The electrode history (efficiency *vs.* cycle number) is shown in Fig. 1. This test was repeated three times. Identical behavior was observed in all four cells.

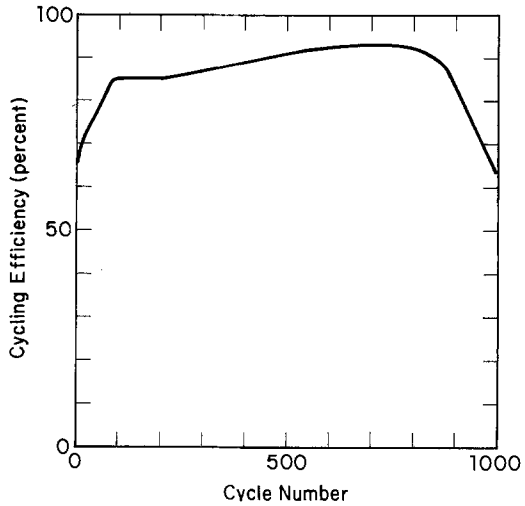

Fig. 1. Efficiencies of cycling Li on an Ni substrate in 0.5M $LiAsF_6$/2-methyltetrahydrofuran electrolyte with 2 m/o 2-methoxyethanol added.

It is the opinion of the author that the additive, 2-methoxyethanol, is superior to the other additives because it improves the protective layer on the lithium. However, no evidence of changes in the character of the protective layer was observed in the plating or stripping behavior. Current delays in the 2-methoxyethanol test were similar to current delays in all the other tests. The explanation of improved behavior must be left to future queries.

Acknowledgments

The author gratefully acknowledges the General Electric Company for the support and encouragement. Special thanks goes to Dr. Roy Thornton for freely sharing his thoughts and experience in battery technology.

Manuscript submitted July 8, 1982; revised manuscript received Aug. 14, 1982.

Any discussion of this paper will appear in a Discussion Section to be published in the December 1983 JOURNAL. All discussions for the December 1983 Discussion Section should be submitted by Aug. 1, 1983.

REFERENCES

1. M. S. Whittingham, *Science*, **192**, 1176 (1976).
2. D. W. Murphy and P. E. Christian, *ibid.*, **205**, 657 (1979).
3. J. Jorne and C. W. Tobias, *J. Appl. Electrochem.*, **5**, 279 (1975).
4. J. L. Goldman, R. M. Mank, J. H. Young, and V. R. Koch, *This Journal*, **127**, 1461 (1980).
5. M. B. Armand, J. M. Chabagno, and M. J. Duclot, in "Fast Ion Transport in Solids," P. Vashishta, J. N. Mundy, and G. K. Shenoy, Editors, pp. 131-136, Elsevier-North Holland, Inc., New York (1979).

Interpretation of Log *i*-Log *t* Relationships for Nickel Passivation

B. MacDougall*

National Research Council of Canada, Division of Chemistry, Ottawa, Ontario, Canada K1A OR9

The kinetics of passive film growth on metals is often investigated by following the decay of the anodic current, i_a, with time, t, upon polarization into the passive potential region (1-5). If the current efficiency (C.E.) for oxide film growth is a constant, independent of film thickness, then the anodic charge, Q_a, is proportional to the film thickness. The rate of film growth at a constant potential generally decreases with increasing thickness and an expression of the form, $i = A \exp(-Q/B)$, *i.e.*, $-\log i \propto Q$, is obtained. For logarithmic growth of the oxide film, $Q \propto \log t$, so that a plot of log i *vs.* log t should give a straight line.

* Electrochemical Society Active Member.
Key words: defects, corrosion, films, current efficiency.

When such a relationship is observed, it has sometimes been suggested that a place-exchange mechanism applies, with the activation energy for oxide growth increasing linearly with film thickness (2, 3). Inverse logarithmic kinetics, which are very similar to direct logarithmic kinetics, are associated with high field oxide growth (5), and linear log i-log t relationships have also been interpreted in terms of a high field mechanism (5). It is generally considered that nonlinearity between log i and log t begins when the rate of oxide film growth has decreased to the point where it is comparable to the rate of oxide chemical dissolution. In the present work, the kinetics of passive film growth and development on nickel have been studied at different potentials, temperatures, and solution pH's, and it is shown that a linear log i-log t relation can persist over an extensive time period even when the C.E. for oxide growth is very low. These results are discussed in terms of a model which considers the defect character of the oxide film.

Current-Time Relationships as a Function of Potential

Electropolished nickel electrodes (6) were cathodically reduced in pH 4.0 Na_2SO_4 solutions at 20 μA cm^{-2} for 5 min, then the potential was stepped into the passive region and the decay of i_a with t followed. The results are shown in Fig. 1 for potentials of 0, 0.4, and 0.6V;[1] the extent of linearity of log i *vs.* log t is indicated by extrapolating the initial readings to longer polarization times. At each potential, the current eventually deviates from the linear behavior, with the deviation starting earlier and being greater the lower the anodic potential. (At 0V, the currents begin to deviate at about 10 sec, while at 0.6V, the deviation does not begin until about 300 sec.)

[1] Potentials are measured *vs.* an Hg/Hg_2Cl_2 reference electrode whose potential is 0.245V with respect to the standard reversible hydrogen electrode.

Current-Time Relationships as a Function of Temperature and pH

The influence of temperature and pH on the decay of i_a with t is shown in Fig. 2 and 3, respectively. At 5°C, it takes a longer time for the oxide to form and block active metal dissolution so that during the first 10 sec there is no linearity between log i and log t (Fig. 2b). At the lower solution temperature, linearity when observed extends over three decades of time and deviation does not occur until after $\sim 10^4$ sec. At 25°C, the current begins to deviate from the linear log i-log t relationship after only ~ 30 sec (Fig. 2a). Figure 3 shows the log i-log t plots at 0.3V for both pH 2.0 Na_2SO_4 and pH 7.65 borate buffer solution. For the former, deviation from linearity begins after ~ 20 sec and the current decay has practically ceased after $\sim 10^5$ sec, *i.e.*, under these conditions the current eventually reaches an almost constant value. On the other hand, in the pH 7.65 borate solution the linear decrease of log i with log t continues for times $> 10^5$ sec. This result is not due to the fact that the anodic potential is effectively 0.34V higher in the borate solution because of the higher pH; indeed, the same linear decrease of log i with log t over $\sim 10^5$ sec is observed at a potential of -0.04V in the borate solution. The results thus indicate that the cutoff time for the linear decrease of log i with log t increases with decreasing solution aggressiveness.

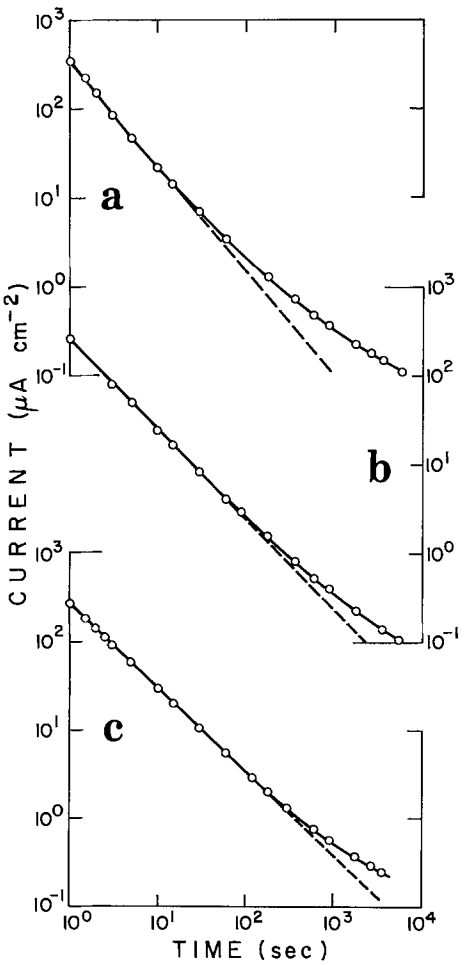

Fig. 1. Decay of anodic current with time in pH 4.0 Na_2SO_4 (25°C) after stepping the potential to various values in the passive region: (a) 0V; (b) 0.4V; (c) 0.6V. (Before the potential step, the prior oxide on electropolished nickel was cathodically reduced at 20 μA cm^{-2} in the same solution.)

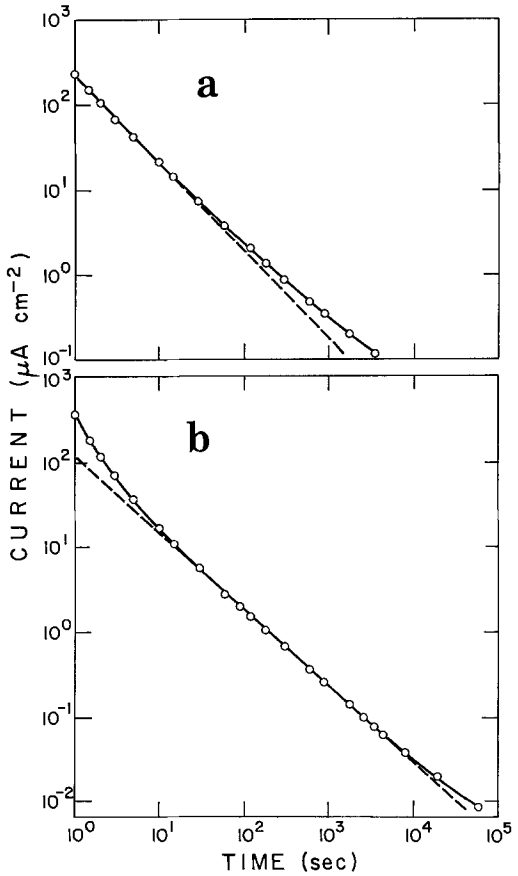

Fig. 2. Decay of anodic current with time at 0.2V in pH 4.0 Na_2SO_4 at (a) 25°C and (b) 5°C. (In both cases, the prior oxide on electropolished nickel was cathodically reduced at 20 μA cm^{-2} in the same solution.)

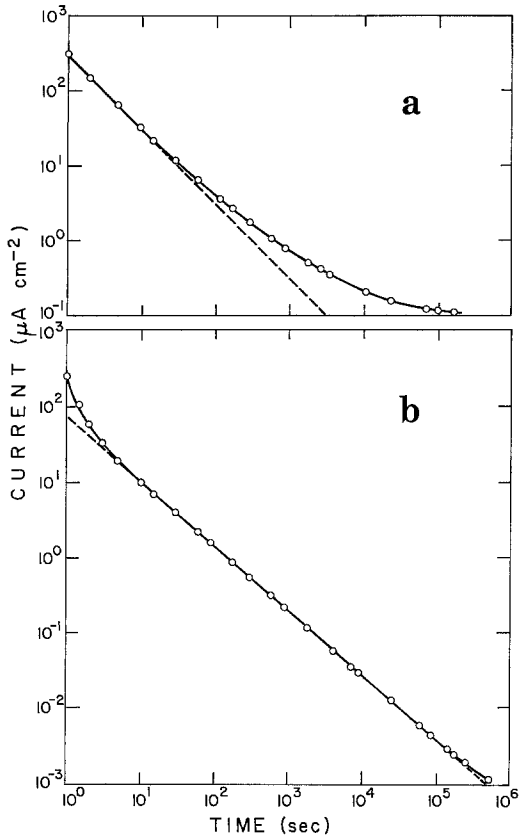

Fig. 3. Decay of anodic current with time at 0.3V and 25°C in (a) pH 2.0 Na_2SO_4 and (b) pH 7.65 borate buffer solution. (In both cases, the prior oxide on electropolished nickel was cathodically reduced at 20 μA cm^{-2} in the same solution.)

Anodic Charge/Current Efficiency (C.E.)

Solution analysis for Ni^{2+} (by atomic absorption spectrophotometry) showed that > 80% of the anodic charge which flows after the first second of anodic polarization can be accounted for by Ni^{2+} in solution. This result applies at every potential, pH, and temperature under study and indicates that only a small part of the measured anodic current is due to oxide growth. The result is supported by both x-ray emission and Auger spectroscopic analysis which shows that the thickness of the oxide does not increase substantially after the first few seconds of polarization at each potential. Oxide growth is obviously a very inefficient process (C.E. < 20%), with most of the long-term anodic charge being accounted for by a side reaction such as chemical dissolution of the nickel oxide. The situation, however, is more complicated than just having an oxide chemical dissolution reaction which limits the C.E. for oxide growth, since it has been shown in a number of previous papers that both the oxide growth C.E. and the maximum oxide film thickness are practically independent of solution pH (from 2.0 to 8.4) and temperature (from 5° to 45°C) (6-10). Such changes in pH and temperature have a profound influence on the aggressiveness of the solution and should therefore have a major influence on the rate of oxide chemical dissolution.

Model for Passive Oxide Film Development

The fact that a linear log i-log t relationship holds even at very low (< 20%) oxide growth C.E., *i.e.*, when the apparent rate of oxide chemical dissolution is much greater than the rate of film growth, suggests that neither the standard high field oxide growth mechanism nor the place-exchange mechanism is applicable. The results can, however, be explained in terms of the defect model of the oxide film (11-15). According to this model, the anodic current which passes after the first few seconds of passivation is mainly associated with breakdown at local weak points in the oxide film (*e.g.*, by oxide chemical dissolution, $NiO + 2H^+ \rightarrow Ni^{2+} + H_2O$) and subsequent anodic repassivation. Repassivation involves both reformation of the oxide ($Ni + H_2O \rightarrow NiO + 2H^+ + 2e$) and parallel nickel dissolution ($Ni \rightarrow Ni^{2+} + 2e$). Since this current is a measure of the resistance of the oxide toward local breakdown, its logarithmic decrease with time suggests a logarithmic increase in the state of perfection of the oxide film. In the borate buffer solution, as in the sulfate solution at 5°C, this logarithmic increase in oxide perfection persists over a very long time period; however, in the more aggressive solutions, perfecting of the oxide slows down and may eventually stop altogether if the time is long enough and/or the solution is sufficiently aggressive (Fig. 3a).

To explain the present results, it is suggested that oxide perfection occurs at local defect sites and that this perfection (*i.e.*, increase in stability toward breakdown) requires the oxide to reside locally on the surface for a certain period of time. The lifetime of the oxide at these local sites is determined by the solution aggressiveness (the driving force for oxide dissolution) and the anodic potential (the driving force for oxide formation and therefore repair). To explain the logarithmic increase in film stability with time, it is further suggested that the local oxide lifetime required for an increase in film perfection increases rapidly as the oxide becomes more perfect. In the early stages of passivation, the oxide is able to perfect itself quite easily, even in aggressive solutions, because the lifetimes required for an increase in local stability are short. However, the oxide soon reaches a state of perfection where substantially longer dwell times are required for a further increase in perfection to occur. These longer dwell times prevail in the less aggressive solutions, such as the borate buffer, and the oxide can achieve a very high state of perfection. Deviation from linear log i-log t behavior is thus only observed after extremely long times of polarization (Fig. 3b). However, in more aggressive solutions localized chemical dissolution of the oxide is rapid and the local dwell times are therefore short. This leads to a slowing down of the increase in oxide perfection and therefore deviation from linear log i-log t behavior. Eventually a steady state may be reached where no further increase in perfection can occur and the anodic current is thus constant with time (Fig. 3a).

Regarding the anodic potential, the higher its value, the higher is the driving force for localized oxide formation. Thus, with increasing anodic potential the oxide dwell time at defect sites increases, and this leads to the achievement of a higher state of oxide perfection before chemical dissolution begins to limit the increase in film stability. The anodic potential referred to here is in the passive region; at potentials in the transpassive or oxygen evolution regions, the passive film deteriorates (15) and other reactions such as metal dissolution and/or growth of a thick porous oxide (16, 17) control the anodic current. In this potential region, no linearity would be found between log i and log t. The most stable anodic oxide films on nickel would therefore be produced in the least aggressive electrolyte at the highest anodic potential that is still within the passive region.

Important Properties of Passive Oxide Films

The precise property of the oxide film that changes with time of anodization and is responsible for the change in stability is open to speculation. As mentioned earlier, oxide film thickness measurements indicate little change in this parameter with time of anodization, the thickness being 10 ± 1Å (at 0.3V) over the pH range 2.0-7.65. While film thickness changes within this 2Å range could have an influence on the local defect character of the film, it is more likely that the de-

fect distribution is influenced by a change in other film properties such as lattice parameter, strain, oxide misorientation, stoichiometry, particle size, bound water, and/or hydrogen content of the film. Whatever the reason, the defect density has a profound influence on the stability of the oxide since the defect sites essentially control both the stability and reactivity of the oxide. The importance of local sites within the oxide on the thermal oxidation of metals has been recognized for many years. For example, Evans (18) developed models explaining logarithmic growth on the basis of a changing density of defects within the film. These ideas have been expanded by Smeltzer *et al.* (19) and Graham *et al.* (20) to consider the importance of oxide grain boundaries as easy diffusion paths during high temperature oxidation, and the exponential decrease with time of the effectiveness of these paths. This is somewhat analogous to the present work where local defect sites control the stability of the oxide, which increases logarithmically with time.

In summary, the existence of a linear log i-log t relationship when the C.E. for oxide growth is very low ($<20\%$) indicates that neither the standard high field oxide growth mechanism nor the place-exchange mechanism applies. The results are understandable, though, in terms of the defect model of the oxide film where film perfection increases logarithmically with time. The solution aggressiveness and the anode potential determine the upper limit of film stability and therefore the extent of linearity between log i and log t. While the present results were obtained with nickel, a somewhat similar mechanism may well apply to passive oxide film development on other metals such as iron and the stainless steels.

Acknowledgment

The author wishes to thank Dr. M. J. Graham for helpful discussions and Dr. D. F. Mitchell and Mr. G. I. Sproule for measurements of oxide film thickness.

Manuscript received March 1, 1982.

Any discussion of this paper will appear in a Discussion Section to be published in the December 1983 JOURNAL. All discussions for the December 1983 Discussion Section should be submitted by Aug. 1, 1983.

Publication costs of this article were assisted by the National Research Council of Canada.

REFERENCES

1. M. Nagayama and M. Cohen, *This Journal*, **109**, 781 (1962).
2. G. M. Bulman and A. C. C. Tseung, *Corros. Sci.*, **12**, 415 (1972).
3. N. Sato and M. Cohen, *This Journal*, **111**, 512 (1964).
4. S. Asakura and K. Nobe, *ibid.*, **118**, 536 (1971).
5. M. Stern, *ibid.*, **106**, 376 (1959).
6. B. MacDougall and M. Cohen, *ibid.*, **121**, 1152 (1974).
7. B. MacDougall, *ibid.*, **127**, 789 (1980).
8. B. MacDougall and M. Cohen, *ibid.*, **123**, 191 (1976).
9. B. MacDougall and M. J. Graham, *Electrochim. Acta*, **26**, 705 (1981).
10. B. MacDougall, D. F. Mitchell, and M. J. Graham, *Corrosion*, **38**, 85 (1982).
11. B. MacDougall and M. Cohen, *Electrochim. Acta*, **23**, 145 (1978).
12. B. MacDougall and M. Cohen, in "Passivity of Metals," R. P. Frankenthal and J. Kruger, Editors, p. 827, The Electrochemical Society, Princeton, NJ (1978).
13. B. MacDougall, D. F. Mitchell, and M. J. Graham, *Israel J. Chem.*, **18**, 125 (1979).
14. B. MacDougall, *This Journal*, **125**, 1883 (1978).
15. B. MacDougall and M. Cohen, *ibid.*, **124**, 1185 (1977).
16. B. MacDougall, D. F. Mitchell, and M. J. Graham, *ibid.*, **127**, 1248 (1980).
17. B. MacDougall and M. J. Graham, *ibid.*, **128**, 2321 (1981).
18. D. E. Davies, U. R. Evans, and J. N. Agar, *Proc. R. Soc. London, Ser. A*, **225**, 443 (1954); U. R. Evans, "The Corrosion and Oxidation of Metals," Edward Arnold, London (1960).
19. W. W. Smeltzer, R. R. Haering, and J. S. Kirkaldy, *Acta Metall.*, **9**, 880 (1961).
20. M. J. Graham, D. Caplan, and M. Cohen, *This Journal*, **119**, 1265 (1972).

Simple Porous Electrode Models for Molten Carbonate Fuel Cells

Gerald Wilemski*

Physical Sciences Incorporated, Andover, Massachusetts 01810

Individual porous electrode models for the anode and cathode of a molten carbonate fuel cell are described in this note. These models are used to calculate local cell overpotential and current density in an integral cell model (1) that predicts overall current density and voltage of scaled-up isothermal and nonisothermal cells. The analysis is based on the thin film cylindrical pore model (2, 3). In this model all electrochemical activity is assumed to occur on film covered walls of the larger gas filled pores. Smaller flooded pores are treated as electrochemically inert. The principal deficiency of this model, besides the oversimplified pore structure assumed, is the lack of measured values for film areas and film thicknesses, forcing these parameters to be treated empirically. The main justification for using this model is pragmatic: it is the simplest model that predicts current densities equal to or greater than those already being measured (4). Whether or not one fully trusts the microscopic pictures embodied in the models, the models are successful in accurately calculating electrode current density as a function of overpotential for both anodes and cathodes over a wide range of gas compositions. They thus afford the large scale predictions (1) with a measure of flexibility and accuracy that would otherwise be difficult to attain.

The specific task of the models is to calculate the rate at which the overall half-reactions

$$H_2 + CO_3^{=} \rightarrow H_2O + CO_2 + 2e^- \qquad \text{(anode)}$$

$$CO_2 + \tfrac{1}{2}\,O_2 + 2e^- \rightarrow CO_3^{=} \qquad \text{(cathode)}$$

proceed for a given electrode potential. The general mathematical analysis using the thin film model is well known (2, 3), so only a brief outline is given here. The treatment includes the effects of the finite electrolyte conductivity and diffusion of dissolved gas species in the electrolyte film. Gas phase diffusion and electrode conductivity are much less limiting, so these phenomena are not treated.

The analysis consists of numerically integrating the equation

$$d^2\eta(z)/dz^2 = (\kappa\delta'')^{-1} i(\eta(z)) \qquad [1]$$

* Electrochemical Society Active Member.
Key words: fused salts, current density, overvoltage.

from $z = 0$ to $z = l$ (the film length). The boundary conditions are $\eta(0) = \eta_o$ and $d\eta(z)/dz = 0$ at $z = 0$. The measurable overpotential η and current density j can be directly computed as

$$\eta = \eta(l) \quad [2]$$

$$j = (\pi\delta''\kappa/2R_p)\,(d\eta/dz)_{z=l} \quad [3]$$

In Eq. [1]-[3], κ is the electrolyte conductivity, i is the transfer current density (per unit area of pore wall), R_p is the pore radius, and $\delta'' = \delta(1 - \delta/2R_p)$ where δ is the film thickness.

For the anode, i is computed from the expressions

$$i(\eta) = i_o\{f_{H_2}{}^{1/2} \exp[\beta\eta\mathbf{F}/RT] - f_{H_2}{}^{-1/2} f_{CO_2} f_{H_2O} \exp[(\beta - 2)\eta\mathbf{F}/RT]\} \quad [4]$$

$$i_o = i_a{}^o p_{H_2}{}^{(1-\beta)/2} (p_{CO_2} p_{H_2O})^{\beta/2} \quad [5]$$

and for the cathode from

$$i(\eta) = i_o\{f_{O_2}{}^s f_{CO_2}{}^t \exp[\alpha\eta\mathbf{F}/RT] - f_{O_2}{}^u f_{CO_2}{}^v \exp[(\alpha - n)\eta\mathbf{F}/RT]\} \quad [6]$$

$$i_o = i_c{}^o p_{O_2}{}^\sigma p_{CO_2}{}^\tau \quad [7]$$

The assumptions implicit in Eq. [4]-[7] will be discussed shortly. The quantity f_k denotes the ratio $c_k/c_k{}^e$ where c_k is the concentration of species k "at" the electrode surface under load and $c_k{}^e$ is the equilibrium (open circuit) value. For the thin film model, f_k is expressible as

$$f_k = 1 - i/i_k \quad [8]$$

where i_k is the limiting current for species k. $i_k = \pm n_k\mathbf{F}D_k c_k{}^e/\delta'$. ($D_k$ is the diffusion constant, n_k is the number of electrons transferred per molecule of species k destroyed(+) or produced(−), and $\delta' = -R_p \ln(1 - \delta/R_p)$.)

Transfer Current Density Equations

The generalized Butler-Volmer equation for the anode is based on the mechanism proposed by Ang and Sammells (5) to explain the reaction of H_2 on Ni wire electrodes. The quasi-equilibrium assumption was used for all reactions preceding and following the rate-determining step. In addition, only the low coverage limit of the H_2 adsorption equilibrium was considered, variations in $CO_3{}^{2-}$ activity in the film were neglected, and Henry's law was assumed to describe the dissolution of gases in the melt. Evaluation of the transfer coefficient β and the standard exchange current $i_a{}^o$ is treated below.

For the cathode, no suitable mechanism has been found on which to base a derivation of i. So the general theoretical form given by Eq. [6] was used. For simplicity of computation with Eq. [1], i and η were both taken to be positive for a net cathodic process. The cathodic transfer coefficient α; total number of electrons transferred n; reaction orders at constant potential s, t, u, and v; and reaction orders at constant overpotential σ and τ are not all independent. Assuming that the equilibrium potential is governed by the Nernst equation, $E = E^o + (RT/2\mathbf{F}) \ln(p_{O_2}{}^{1/2} p_{CO_2})$, and that the solubilities of molecular O_2 and CO_2 obey Henry's law relationships, the following relationships hold

$$\sigma = s - \alpha/4 = u + (n - \alpha)/4 \quad [9]$$

$$\tau = t - \alpha/2 = v + (n - \alpha)/2 \quad [10]$$

Assuming an overall two-electron transfer ($n = 2$), it is only necessary to determine values of α, σ, and τ to fix the values of s, t, u, and v. The evaluation of parameters is discussed below.

Evaluation of parameters.—Physical properties.— Electrolyte conductivities κ and diffusion constants D of dissolved gas species were prescribed as functions of temperatures by fitting the values listed in several IGT reports (6, 7) to Arrhenius type expressions. The parameters are listed in Tables I and II. Gas solubilities were treated using Henry's law: $c^e = Kp$. The Henry law constants were fitted to Arrhenius type expressions using Broers' (8) solubility data as presented in an IGT report (6). They are listed in Table III. Use of Henry's law appears to be justified for H_2 and CO_2. Because little is known about H_2O solubility it was set equal to the H_2 solubility following the practice elsewhere (6). In the absence of data, it is impossible to assess the accuracy of the approximation. As seen from Eq. [4] and [8], the H_2O solubility affects i only through f_{H_2O} and, because of its location in Eq. [4], this quantity's influence is negligible at high overpotentials. At low overpotentials, the H_2O solubility would have to be an order of magnitude lower than estimated here in order to significantly affect i. Total oxygen solubility is complicated by the various $O_2/CO_3{}^=$ equilibria occurring in the melt (9, 10) but the thermodynamics of dilute solutions guarantees that the solubility of molecular oxygen will be proportional to its partial pressure. The approximation employed here is to overestimate the concentration of dissolved molecular oxygen by using the "constant" K_{O_2} appropriate to the total amount of dissolved oxygen.

No account was given to the variation of solubility or diffusivity with melt composition because of the unavailability of data.

Thin film and pore properties.—Pore lengths were set equal to the electrode thickness, 0.5 mm. The cylindrical pores were assumed to be packed in a square array and using the experimental internal/external area ratio (6) of 320, the average pore radius was calculated to be $R_p = 2.5$ μm. No account was given for possible changes in porosity at the cathode with oxidation to NiO.

Values for the film length l and the film thickness δ were found by fitting the theoretical expression for the initial slope of the η-j curve (*i.e.*, the polarization resistance Z) to the experimentally determined values from polarization curves for single electrodes (11). Equations [1] and [4] or [6] result in the following expression for Z

$$Z = [(\pi/2R_p)\,\delta''\kappa K \tanh(Kl)]^{-1} \quad [11]$$

where K is the inverse utilization depth

Table I. Values of electrical conductivity parameters for two molten alkali carbonate mixtures

$\kappa L = \kappa_O \exp(-E_K/T)$, units: $(\Omega\text{-cm})^{-1}$

Electrolyte (m/o)	ln κ_O	E_K (K^{-1})
$62Li_2CO_3/38K_2CO_3$	3.594	3016
$43.5Li_2CO_3/31.5Na_2CO_3/25K_2CO_3$	3.541	2918

Table II. Values of diffusivity parameters for dissolved gas species

$D = D_O \exp(-E_D/T)$, units; 10^{-5} cm²/sec

Species	ln D_O	E_D (K^{-1})
H_2	6.413	5500
H_2O	6.221	5476
CO_2	5.822	5432
O_2	6.068	5503

Table III. Values of solubility parameters for dissolved gases

$K = K_O \exp(-E_S/T)$, units, 10^{-7} mol/(cm³-atm)

Species	ln K_O	E_S
H_2, H_2O	3.345	−658.8
CO_2	5.154	364.6
O_2	9.592	7589

$$K^2 = \left[(RT/n\mathbf{F})\kappa\delta'' \left(1/i_o - \sum_k (\nu_k/i_k) \right) \right] \quad [12]$$

and ν_k is the signed stoichiometric coefficient of species k in the overall electrode half-reaction for the transfer of n electrons (12). For each electrode, one set of values of l and δ were sought that would bring Z into agreement with the measured value when i_o was specified in rough accordance with experimental measurements on smooth and wire electrodes.

At the anode the i_o values lie roughly in the range 25-50 mA/cm^2 (5). For the cathode, exchange current densities on the order of 0.1 mA/cm^2 at 923 K can be inferred from recent work (13, 14) on gold electrodes. Measured values (11) of Z for both electrodes are on the order of 0.5 Ω-cm^2 (see Fig. 1-4). Values chosen for δ and l are listed in Tables IV and V.

Electrode kinetic parameters.—For the anode transfer coefficient β, the value reported by Ang and Sammells (5) $\beta = 0.7$, was used. The standard exchange current density i_a^o in Eq. [5] was evaluated by requiring that calculations of anode polarization agree with measurements for one gas mixture (11) (shown in Fig. 1). For the temperature dependence of i_o the activation energy reported by Ang and Sammells (5) was used to write i_a^o in the form

$$i_a^o = k_a^o \exp\left(E_a(T - T_{923})/T_{923}T\right) \quad [13]$$

where $T_{923} = 923$ K. The anode parameters are summarized in Table IV.

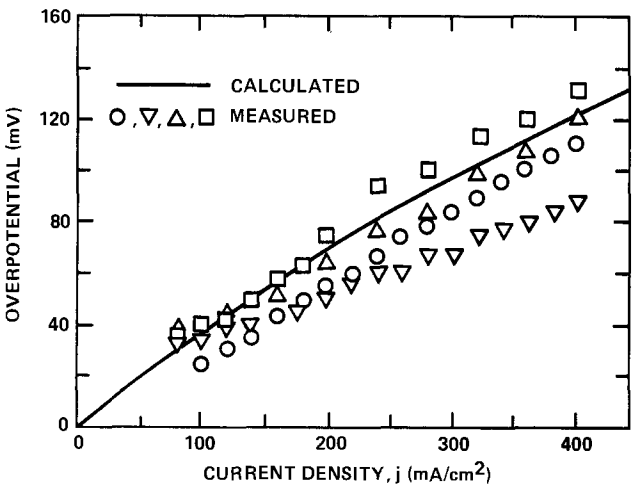

Fig. 1. Small cell (3 cm^2) anode performance. Gas composition listed in Table VI. Measurements from Ref. (11).

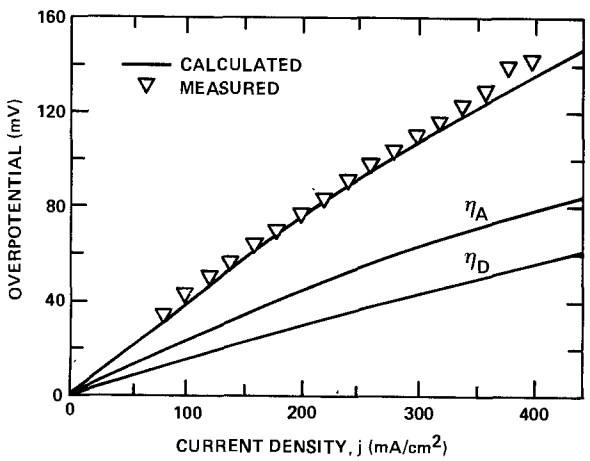

Fig. 2. Small cell (3 cm^2) anode performance. Also shown are calculated activation, η_A, and diffusion η_D, overpotentials. Gas composition listed in Table VI. Measurements are from Ref. (11).

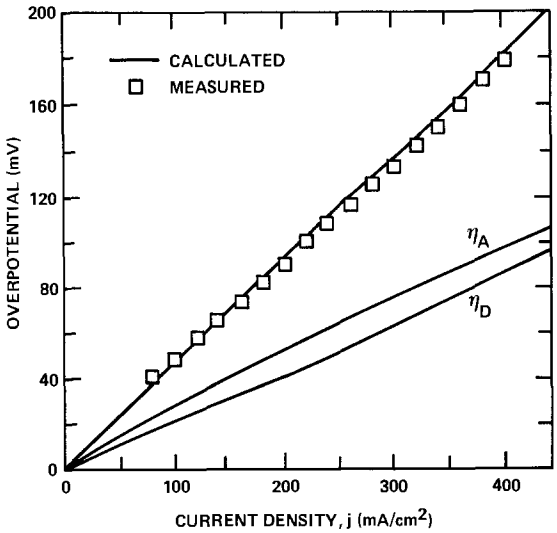

Fig. 3. Small cell (3 cm^2) anode performance. Also shown are calculated activation, η_A, and diffusion η_D, overpotentials. Gas composition listed in Table VI. Measurements are from Ref. (11).

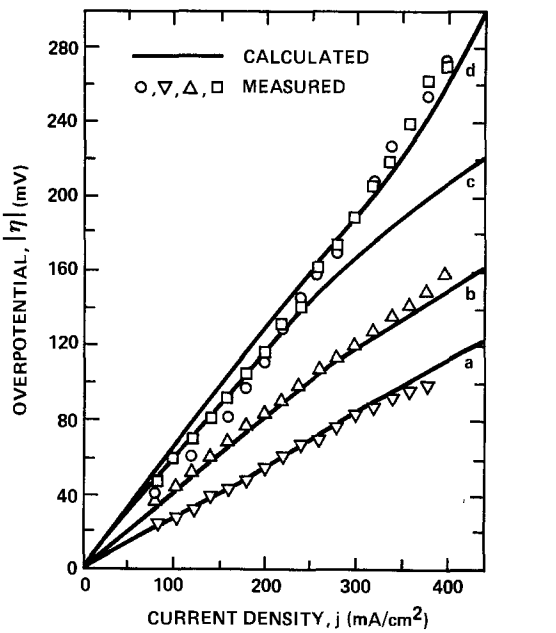

Fig. 4. Small cell (3 cm^2) cathode performance. Correspondence between calculations and measurements: a—▽, b—△, c—○, d—□. Gas compositions are listed in Table VII. Measurements are from Ref. (11).

For the cathode, most of the available data (11) had a fixed p_{CO_2}/p_{O_2} ratio of 2, it was not possible to unambiguously determine σ and τ separately. Best results were found using $\alpha = 0.75$ and $\sigma + \tau = 0.4$. The arbitrary choice $\sigma = \tau = 0.2$ was made in order to evaluate s, t, u, and v, although no experimental or theoretical information was available to support or disprove this choice. Recent work (15, 16) with different gas compositions suggests that the partial pressure dependence may be better described by $\sigma \approx 0.4$, $\tau \approx 0.0$, and these values are recommended if further use is made of this model. The standard exchange current density i_c^o was determined analogously to i_a^o; data (11) at $p_{O_2} = 0.33$ atm and $p_{CO_2} = 0.67$ atm were used for the evaluation. The temperature dependence for i_o was prescribed by the equation

$$i_c^o = k_c^o \exp\left(E_c(T - T_{923})/T_{923}T\right) \quad [14]$$

where E_c was inferred from the limited exchange current density data of Appleby and Nicholson (14) for the first wave reaction in the binary Na/K carbonate

Table IV. Values of anodic pore, film, and kinetic parameters used in calculations; i_a^o in Eq. [5] is given by Eq. [13]

R_p	2.5 μm
l	5.0 μm
δ	0.1 μm
β	0.7
k_a^o	315 mA/cm²
E_a	3350 K

Table V. Values of cathodic pore, film, and kinetic parameters used in calculations; i_c^o in Eq. [7] is given by Eq. [14]

R_p	2.5 μm
l	0.5 mm
δ	0.5 μm
α	0.75
σ, τ	0.2
k_c^o	0.78 mA/cm²
E_c	5800 K

melt. Cathode electrode kinetic parameters are summarized in Table V.

Comparison of calculated and experimental results.—A limited number of individual anode and cathode polarization curves have been reported (11) for different gas compositions at 1 atm and 923 K in the 62/38 m/o Li_2CO_3-K_2CO_3 binary electrolyte. Comparisons of calculated and measured are shown in Fig. 1-3 for anodes and in Fig. 4 for cathodes. Numerical integration of Eq. [1] was done with a standard fourth-order Runge-Kutta scheme. For the anode computations, gas compositions in water-gas shift equilibrium were derived from the reported initial compositions. Because the measurements were made with small 3 cm² cells at low utilizations (7½% fuel and 15% oxidant), they may be directly compared with calculations based on the single electrode models. Gas compositions are listed in Table VI and VII, as are the corresponding calculated values of i_o.

It is important to emphasize that only one set of parameter values was used in all computations for a given electrode. Individual adjustments were not made to enhance agreement or alter the computed shape of the curve. These calculations constitute relatively successful model predictions of single electrode performance.

A significant feature of the anode results, in Fig. 1-3, is how well the partial pressure dependence is predicted, even at relatively high current densities of 400 mA/cm². Because of the short, thick film used, ohmic losses in the film are extremely small and j can be calculated directly as $j = (\pi l/2R_p)i$. Calculated total overpotential consists solely of activation (η_A) and diffusion ($\eta_D = -(RT/2F)\ln[f_{H_2}/(f_{H_2O}f_{CO_2})]$) overpotential in roughly comparable amounts, as indicated in Fig. 2 and 3. Despite the high values for i_o, the activation overpotential is still high because the active electrode area is only increased by a factor of π over the external electrode area for the film and pore parameters used ($2\pi R_p l/(4R_p^2) = \pi$ with values of Table IV).

Table VI. Anode gas mixture compositions and calculated exchange current densities. Both the nominal composition and that satisfying water-gas shift equilibrium are listed. Equation [5] was used to calculate i_o.

Figure	Nominal m/o H_2 / CO_2 / N_2			Shifted m/o* H_2 / H_2O / CO_2 / N_2				i_o (mA/cm²)
1	80	20	0	66	14	6	0	55.6
2	40	20	40	29	11	9	40	52.0
3	20	20	60	12	8	12	60	45.1

* Balance of the mixture is CO.

Table VII. Cathode gas mixture compositions and calculated exchange current densities. Equation [7] was used to calculate i_o. The symbols ▽, △, □, ○ denote experimental results (Ref. (11)) in Fig. 4.

Symbol	ITG exp. No.	Composition (m/o) O_2 / CO_2 / N_2			i_o (mA/cm²)
▽	4	33	67	0	0.58
△	1	15	30	55	0.42
□	5	5	10	85	0.27
○	6	10	5	85	0.27

The cathode model calculations also agree well with experiment. The composition of a latter mixture was 5 m/o CO_2/10% O_2. No explanation is apparent for the trivial difference in performance recorded for the 5% CO_2/10% O_2 and 10% CO_2/5% O_2 mixtures, but it is clearly at odds with the model calculations as well as with other recent work (15, 16).

Success in reproducing the observed partial pressure dependence of each electrode is evident. However, this success should not distract attention from the inadequacies of the cylindrical pore-thin film model. Several major criticisms of the electrode models can be made: they lack realistic pore structure; there is no experimental confirmation that the primary mode of wetting of the electrode is by films; there is no direct evidence that films of 0.1-0.5 μm in thickness can exist within porous electrodes.

Work on a more realistic model that alleviates these criticisms for the cathode is nearing completion (17).

Acknowledgment

The author thanks W. J. Robins for help with computing.

This work was supported by the U.S. Department of Energy, under Contract No. DE-AC-03-79ET11322.

Manuscript submitted June 23, 1981; revised manuscript received *ca.* July 14, 1982. This was Paper 140 presented at the Los Angeles, California, Meeting of the Society, Oct. 14-19, 1979.

Any discussion of this paper will appear in a Discussion Section to be published in the December 1983 JOURNAL. All discussions for the December 1983 Discussion Section should be submitted by Aug. 1, 1983.

Publication costs of this article were assisted by Physical Sciences Incorporated.

REFERENCES

1. T. L. Wolf and G. Wilemski, *This Journal*, **130**, 48 (1983).
2. S. Srinivasan and H. D. Hurwitz, *Electrochim. Acta*, **12**, 495 (1967).
3. D. T. Wasan, T. Schmidt and B. S. Baker, *Chem. Eng. Prog. Symp. Ser.*, **63**(77), 16 (1967).
4. J. R. Selman, H. C. Maru, V. Sampath, and I. G. Marianowski, in "Electrode Materials and Processes for Energy Conservation and Storage," J. D. E. McIntyre, S. Srinivasan, and F. G. Will, Editors, p. 656, The Electrochemical Society Softbound Proceedings Series, Princeton, NJ (1977).
5. P. G. P. Ang and A. F. Sammells, *This Journal*, **127**, 1287 (1980).
6. Project 8984 Quarterly Status Report for January-March 1977, Institute of Gas Technology, Chicago, IL.
7. Vol. II, Project 8984 Quarterly Report for 1 July-30 September, 1976, Institute of Gas Technology, Chicago, IL.
8. G. H. J. Broers, Internal Rept. No. 69-0667/1272-7211. Apeldoorn, Netherlands: Centraal Technisch Institut TNO (1969).
9. R. E. Andresen *This Journal*, **126**, 328 (1979).
10. A. J. Appleby and C. Van Drunen, *ibid.*, **127**, 1655 (1980).
11. Vol. II, Project 8984 Final Report for 1 July 1976-30 September 1977, Institute for Gas Technology, Chicago, IL.
12. A. C. Riddiford, *J. Chem. Soc. (London)*, 1175 (1960).
13. A. J. Appleby and S. B. Nicholson, *J. Electroanal.*

Chem. Interfacial Electrochem., **112**, 71 (1980).
14. A. J. Appleby and S. Nicholson, *ibid.*, **53**, 105 (1974); *ibid.*, **83**, 309 (1977).
15. T. E. Tang, J. R. Selman, T. D. Claar, and L. G. Marianowski, Abstract 127, p. 347, The Electrochemical Society Extended Abstracts, Vol. 80-2, Hollywood, Florida, October 5-10, 1980.
16. J. Winnick and P. N. Ross, Jr., *This Journal*, **128**, 991 (1981).
17. J. Mitteldorf and G. Wilemski, In preparation.

Polythiazyl Films: Preparation and Use as Electrodes in Aqueous Solution

Judith F. Rubinson,*,[1] Thomas D. Behymer,[2] and Harry B. Mark, Jr.*

Department of Chemistry, University of Cincinnati, Cincinnati, Ohio 45221

and R. J. Nowak

6130 Naval Research Laboratory, Washington, DC 20375

Electrodes constructed from single crystals of the polymeric conductor polythiazyl, $(SN)_x$, have been studied in aqueous solution (1, 2). Depending on the choice of electrolyte, the background currents are smooth over a wide range, from greater than +0.9V to greater than −1.2V *vs.* SCE at the other extreme. The use of these electrodes is of considerable interest because of strong interaction of the material with cations (1) and in terms of producing $(SN)_x$ surface modified electrodes (2). Applications of such modified electrodes for the photoinduced reduction of water (3) and the direct reduction of acetylene (4) have been reported. As the small surface areas possible for single crystal electrodes (1, 2) are a limiting factor in their practical use at catalysts, application of polythiazyl films as electrodes are of interest.

We report the behavior in aqueous solution of electrodes constructed from polythiazyl films and the effects of variation of such factors as *p*H, nature of the cation in solution, and ionic strength. The ferri/ferrocyanide couple was examined as a test redox couple.

Experimental

The $(SN)_x$ crystals and films were prepared by a method based on that of MacDiarmid and co-workers (3). Crystals of $(SN)_x$ were heated *in vacuo* to 158°C, gradually increasing the temperature from ambient to that level over a period of about 4-5 hr. The sublimed $(SN)_x$ was trapped on Mylar® sheets at 15°-20°C. Attachment of the Mylar to a cold finger was accomplished with double-sided tape. Total adherence of the Mylar to the cold thumb surface is necessary to obtain a uniform $(SN)_x$ film. After two days, the heat was removed and pumping was continued for 15 hr. The two-day sublimation period produced films thick enough to be opaque to transmitted light. The sublimed films on the Mylar substrate were cut to the desired size and fashioned into electrodes as shown in Fig. 1. The most effective masking material for the silver paste contact was dental sticky wax. Glass was investigated as a substrate for the $(SN)_x$ films, but on even short electrolysis, the films flaked off. This occurred even when the glass was etched previously with HF. Metal substrates were even less stable on electrolysis. For film electrodes, the chain axis of the $(SN)_x$ is parallel to the substrate surface and, hence, the solution interface (5). Thus, no significant number of chain ends are exposed to the solution.

Cyclic voltammetric experiments were carried out using a system made up of an MFE Plotamatic 815 recorder, a PAR 173 Potentiostat/Galvanostat equipped with a Model 176 current to voltage converter, a Hewlett-Packard 3310B function generator, and a Nicolet Explorer III oscilloscope.

All chemicals were reagent grade and the water was distilled, then further purified by passing through a carbon and/or demineralization cartridge before use. Solutions were deaerated with argon which had been scrubbed for oxygen. A saturated calomel reference electrode and a platinum gauze auxiliary electrode were used in conjunction with the $(SN)_x$ film working electrode. Initial electrode areas were approximately 1 cm^2.

Results and Discussion

Scanning electron microscopic investigation of the $(SN)_x$ films produced by the described method are shown in Fig. 2. The surfaces differ markedly not only from those described previously (5), but also differences occur between films deposited on glass as opposed to Mylar®. The films deposited on the latter are much flatter, with little surface structure, other than tiny cracks, even at very high magnifications (1-200,000×).

The variation in background behavior due to changes in the nature of the cation are shown in Fig. 3 and 4 for the series Li^+, Na^+, and K^+. As is the case for $(SN)_x$ crystal electrodes (1), the background currents are lowest with the smallest cation, Li^+, and increases as going from sodium to potassium. It is interesting to note, however, that the hysteresis observed at break-

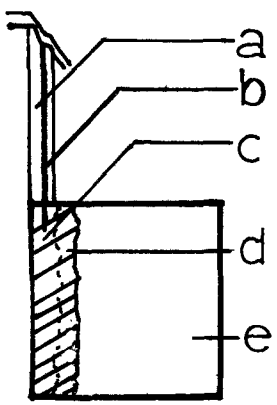

Fig. 1. Assembly of $(SN)_x$ film electrodes. (a) Pyrex tubing, (b) silver wire, (c) silver paste contact, (d) dental sticky wax, (e) $(SN)_x$ film on Mylar®.

* Electrochemical Society Active Member.
[1] Present address: C. F. Kettering Research Laboratory, Yellow Springs, Ohio 45387.
[2] Present address: Department of Chemistry, Indiana University, Bloomington, Indiana 47465.
Key words: polythiazyl, film electrodes, polymeric conductor, surface modified electrodes, electrocatalysis.

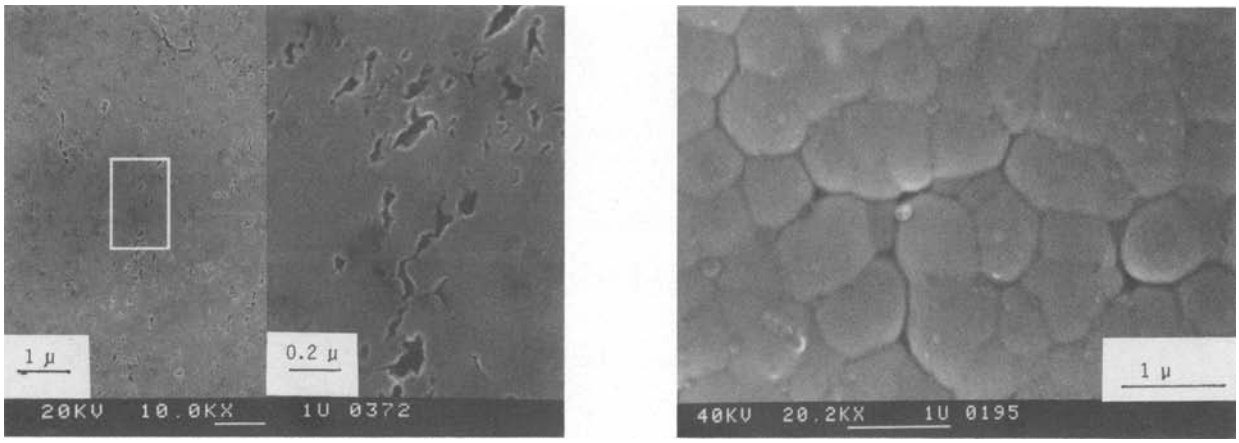

Fig. 2. Scanning electron micrographs of $(SN)_x$ films deposited on (a, left) glass, and (b, right) Mylar® (0.005 in.)

down for single crystal electrodes does not occur at the voltages scanned for the film electrode. Variation of the anion of the supporting electrolyte had no effect on the background cyclic voltammograms.

As shown in Fig. 5 and 6, the background currents with $CaCl_2$ are not as low as that reported for the single crystal electrodes (1), but the same variation in surface reduction waves occurs, with the lower ionic strength solution resulting in two irreversible waves prior to breakdown and the higher in only one broad irreversible wave. The origin of these peaks is still not fully understood.

The effect of variation of acidity of the background electrolytes was investigated by means of solutions of H_2SO_4 in combination with Na_2SO_4, thus keeping the ionic strength approximately constant. As seen in Fig. 7, the variation of acidity of the solution does have an effect on the magnitude of the background currents at the film electrodes, but not as pronounced as that for single crystal electrodes (Fig. 8). Also, hysteresis was not always present for the film electrodes, which is not understood. When hysteresis is observed, the point at which the negative breakdown began shifted to more negative potentials as the solution acidity increased. In cases in which hysteresis did not occur, a slight overall decrease in background current occurs at lower *p*H. At positive potentials, the acidity did not appreciably affect the onset of the breakdown potential. However, the magnitude of the breakdown currents increased with increasing acidity after breakdown occurred.

The ferro/ferricyanide couple was used to assess the quality of the electrodes using the same experi-

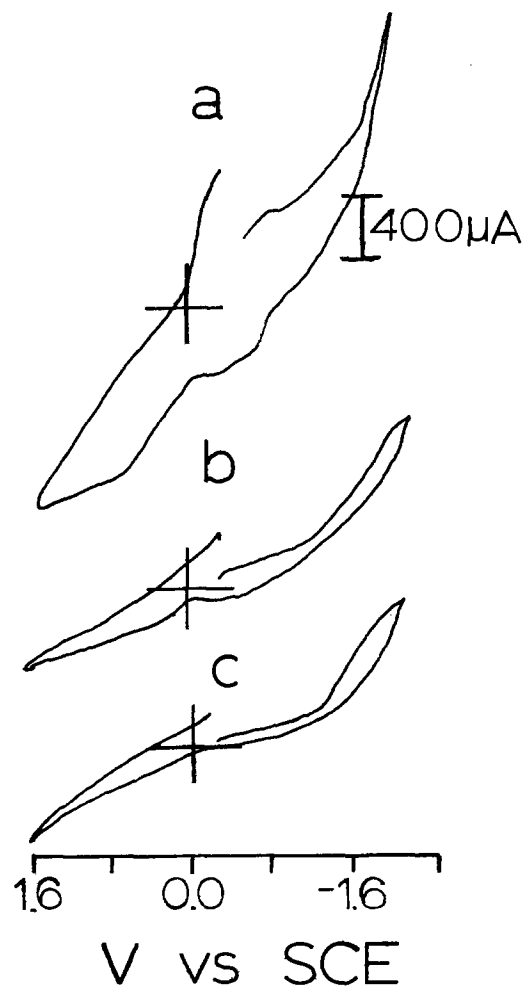

Fig. 3. Variation in background currents at $(SN)_x$ film electrode with nature of the cation of the supporting electrolyte. (a) KCl, (b) NaCl, (c) LiCl. All solutions 3M. Scan rate: 38 mV/sec.

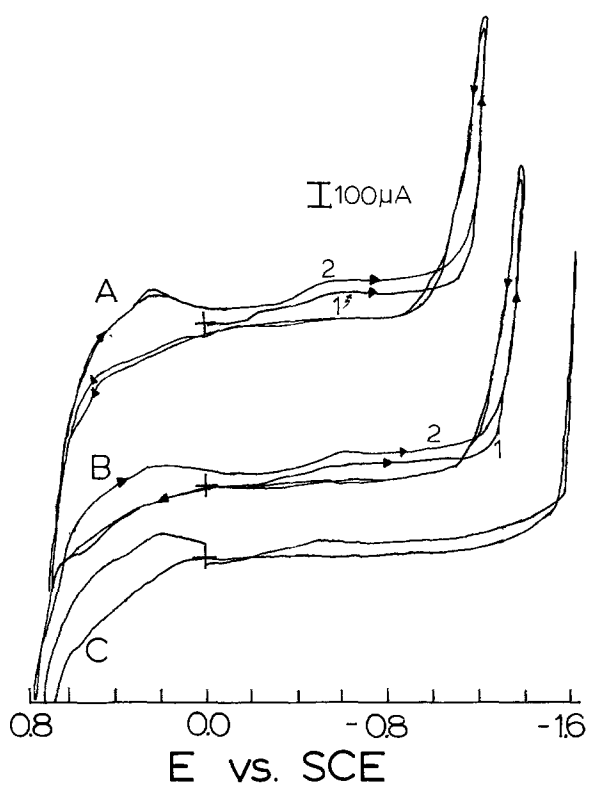

Fig. 4. Variation in background currents at a parallel $(SN)_x$ crystal electrode with nature of the cation of the supporting electrolyte. (a) KCl, (b) NaCl, (c) LiCl. Scan rate: 0.02 V/sec.

mental condition as previously used (1). Oxidation and reduction waves do appear at the potentials expected, but the peak separation is quite large (2-300 mV) even at scan rates as low as 10 mV/sec (Fig. 9).

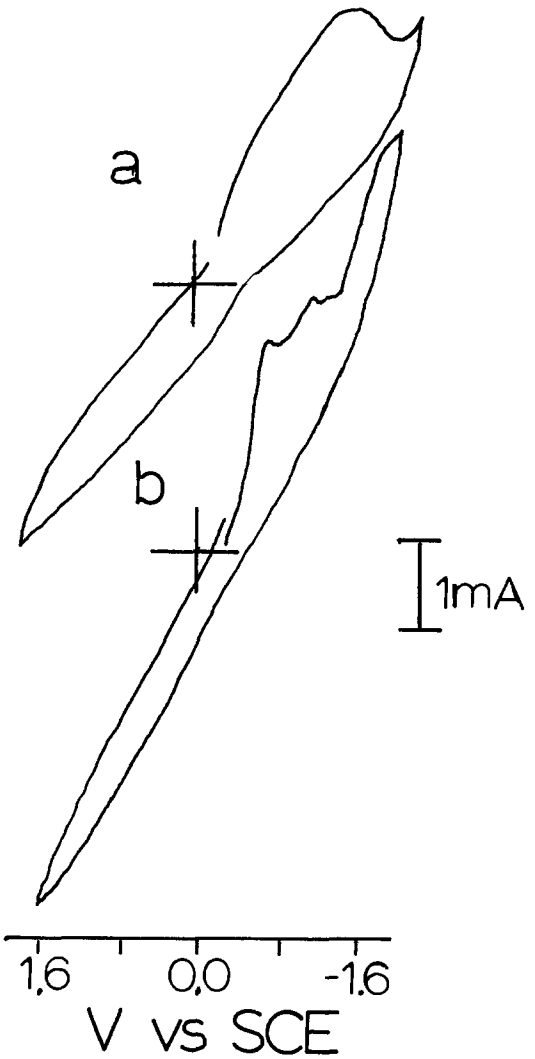

Fig. 5. Variation in background currents at $(SN)_x$ film electrode with concentration of $CaCl_2$ supporting electrolyte. (a) 2M $CaCl_2$, (b) 1.2M $CaCl_2$. Scan rate: 37 mV/sec.

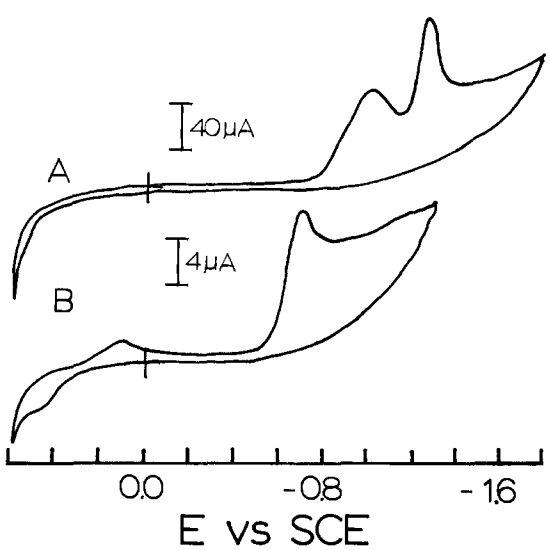

Fig. 6. Variation in background currents at $(SN)_x$ crystal electrode with concentration of $Ca(NO_3)_2$ supporting electrolyte. (a) 1M, (b) 5M. Scan rate: 0.050 V/sec.

Part of this is undoubtedly due to contact and film resistance.

Conclusions

Although the magnitude of background currents for $(SN)_x$ film electrodes are higher on an absolute basis, as would be expected, than those for crystal electrodes, in general the background is still smooth over a larger potential range. For example, with the single crystals, breakdown voltages more negative than −1.2V *vs.*

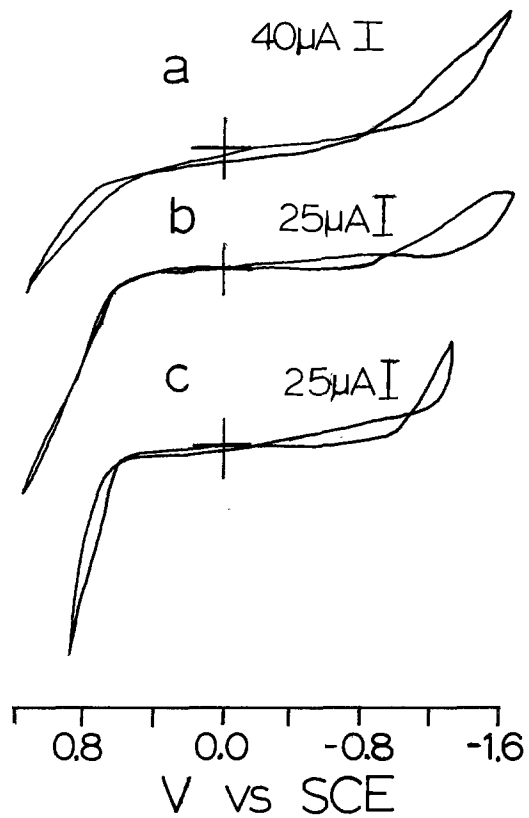

Fig. 7. Variation in background currents with acidity at $(SN)_x$ film electrode. (a) pH 5 (scan rate: 30 mV/sec), (b) pH 3 (scan rate: 30 mV/sec), (c) pH 1 (scan rate: 23 mV/sec). All solutions 1M in SO_4^{2-} with appropriate amounts H_2SO_4 in Na_2SO_4.

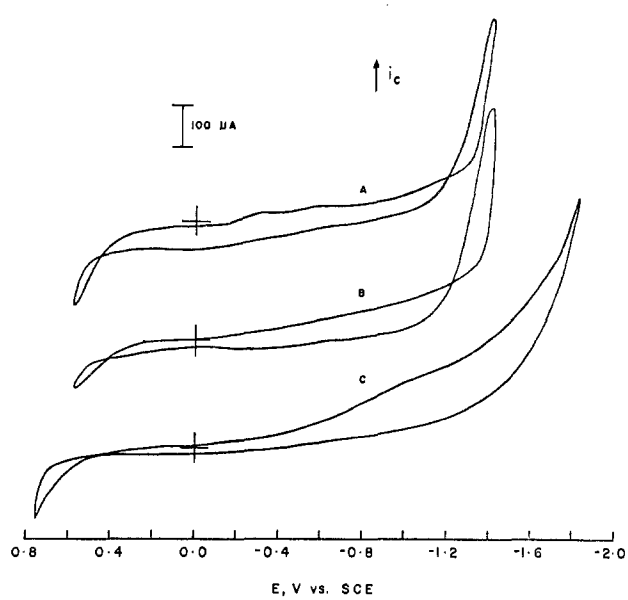

Fig. 8. Cathodic current breakdown dependence on solution acidity at $(SN)_x$ crystal electrode. (a) 0.5M Na_2SO_4, (b) 0.45M Na_2SO_4 + 0.05M H_2SO_4, (c) 0.5M H_2SO_4. Scan rate: 0.05 V/sec.

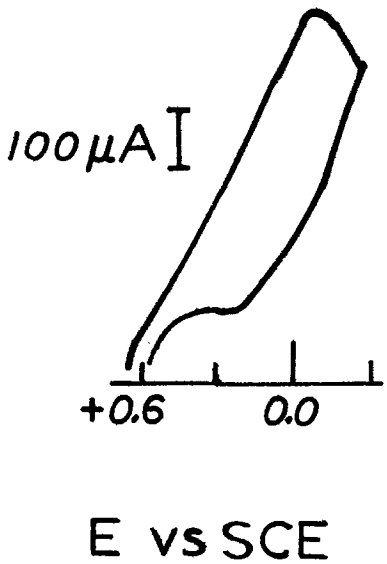

Fig. 9. Ferri-ferrocyanide couple at $(SN)_x$ film electrode. Concentration: 50 mM in 2M Na_2SO_4. Scan rate: 15 mV/sec.

SCE were possible only with certain background electrolytes (1, 4); but this range is apparently exceeded with the systems investigated here for film electrodes. The breakdown processes are corrosion of the $(SN)_x$ rather than the electrolysis of water (1), but the nature of the reaction breakdown processes is not known at this time. It is obvious that the film electrodes behave only somewhat differently than either parallel or perpendicular single crystal $(SN)_x$ electrodes. The most serious problem at present is the durability of the films themselves, as they still tend to separate from the Mylar® substrate after extended periods of immersion (one or two days) under electrolysis. Further investigation to produce more stable film-substrate interactions are in progress.

In conclusion, films of $(SN)_x$ can be utilized as electrodes in aqueous solution, thereby providing a means of obtaining larger electrode surface areas than are possible with crystal electrodes while retaining essentially the same overall general behavior. However, the minor differences in behavior indicate that a simultaneous detailed study of single crystal and film electrodes under identical conditions is necessary before extrapolating single crystal to film response (or vice versa) for the same system. The acetylene reduction on film electrodes and both parallel and perpendicular electrodes are essentially the same except for available surface area of the electrodes (4). However, the photo-induced reduction of water at ruthenium modified electrodes is observed only at perpendicular electrodes and it may not be possible to extend these experiments to that system.

Acknowledgments

The authors gratefully acknowledge financial assistance received through the National Science Foundation, grant number NSF CHE76-04321. We also thank Dr. Harry Calvert of Kettering Research Laboratory, Yellow Springs, Ohio for the scanning electron microscopic studies.

Manuscript submitted April 19, 1982; revised manuscript received *ca.* Aug. 23, 1982.

Any discussion of this paper will appear in a Discussion Section to be published in the December 1983 JOURNAL. All discussions for the December 1983 Discussion Section should be submitted by Aug. 1, 1983.

Publication costs of this article were assisted by the University of Cincinnati.

REFERENCES

1. R. J. Nowak, W. Kutner, H. B. Mark, Jr., and A. G. MacDiarmid, *This Journal*, **125**, 232 (1978).
2. R. J. Nowak, W. Kutner, J. F. Rubinson, A. Voulgaropoulos, H. B. Mark, Jr., and A. J. MacDiarmid, *ibid.*, **128**, 1927 (1981).
3. H. B. Mark, Jr., A. N. Voulgaropoulos, and C. A. Meyer, *J. Chem. Soc., Chem. Comm.*, **1981**, 1021.
4. J. F. Rubinson, T. D. Behymer, and H. B. Mark, Jr., *J. Am. Chem. Soc.*, **104**, 1224 (1982).
5. C. M. Mikulski, P. J. Russo, M. J. Saran, A. G. MacDiarmid, A. F. Garito, and A. J. Heeger, *ibid.*, **97**, 6358 (1975).

JOURNAL OF THE ELECTROCHEMICAL SOCIETY

SOLID-STATE SCIENCE AND TECHNOLOGY

JANUARY 1983

Current-Voltage Characteristics Of Metal-Gallium Phosphate-Gallium Arsenide Capacitors

Chien-Sheng Su and Wayne W. Grannemann

Department of Electrical and Computer Engineering, University of New Mexico, Albuquerque, New Mexico 87131

ABSTRACT

Thin film gallium phosphate capacitors have been fabricated on gallium arsenide substrates using an electron beam evaporation technique. The effects of both $GaPO_4$ deposition conditions and post-deposition annealing on the current-voltage (I-V) characteristics of the dielectric films have been investigated. Our results show that films deposited with oxygen back-filling exhibit better I-V characteristics than those deposited in vacuum. Furthermore, annealing of these films in hydrogen ambient at low temperatures reduces the leakage current. Best resistivities of about 10^{14}-10^{15} Ω-cm and an average dielectric strength of about $(1\text{-}4)\times10^6$ V/cm have been obtained in these films. Results are also presented on the effect of different substrates like p-type GaAs and Si on the I-V characteristics of the $GaPO_4$ deposited films.

Because of the interface and surface charges, the most critical use for high quality dielectric films on semiconductor substrates is for passivation. In many applications, semiconductor devices benefit from surface dielectric insulators which act as barriers to deleterious environmental influences, and so improve their stability and performance.

Thermally grown SiO_2 and chemical vapor deposited Si_3N_4 films have resulted in the highest quality dielectric layers and have made silicon the main substrate for integrated circuit fabrication. Several material properties of GaAs, including a large energy bandgap and a high electron mobility, make it more attractive than silicon for high-speed and high-temperature device applications. In the past few years, considerable attention has been focused on growing high quality dielectric films on GaAs substrates. Various growth techniques like anodic oxidation (1-4), thermal oxidations (4-9), plasma oxidation (10-13), chemical vapor deposition (2, 14, 15), sputtering (16-18), and reactive vacuum evaporation (19) have been investigated. However, surface passivation has not been as successful for GaAs MIS devices as for silicon devices.

In our laboratory, considerable effort has been expended in obtaining high quality dielectric films on GaAs substrates. Our previous studies (20) on the thermal oxidation of $GaAs_{1/2}P_{1/2}$ have indicated that the oxide compound $GaPO_4$ is stable and of high quality. This led us to the investigation of the electrical properties of $GaPO_4$ films. This paper presents the current-voltage characteristics of $GaPO_4$ films grown on GaAs and Si substrates using an electron beam evaporation technique under different evaporation conditions.

Experimental

GaAs substrates were of (100) orientation, n-(Te-doped) and p-type (Zn-doped) single crystals with carrier concentrations of 4×10^{16} and 2×10^{17} cm^{-3}, respectively. Just prior to deposition, the substrates were cleaned and degreased in trichloroethylene, acetone, and deionized water. A chemical etch in 10 NH_4OH:1H_2O_2:1H_2O at room temperature then followed to remove the native oxide layer and surface damage. Gallium phosphate was evaporated from a hot-pressed target of polycrystalline powder using an electron beam. The depositions were carried out under three different conditions: (*i*) type A films were deposited in high vacuum (2×10^{-7} Torr), (*ii*) type B films were deposited in the presence of oxygen (10^{-4}-10^{-5} Torr), with the substrates exposed to oxygen before evaporation, and (*iii*) type C films were formed under conditions similar to type B films, except that oxygen was back-filled when the evaporation started. The substrate temperature was maintained at 200°-250°C during the evaporation. Sample annealing was done in ultrahigh purity Ar, O_2, and H_2 ambients at various temperatures for times varying from 1 min to 17 hr.

The MIS capacitors were then completed by the thermal evaporation of chromium dots of 39 mil diameter on the films and coating of silver on the back side of the substrates. The use of a large area metal dot of this size can minimize the electrical noise and ensure correct current readings. Two systems were used for I-V characteristic measurements of MIS devices. The first system used a Keithley Model 600A electrometer to measure the current as a function of voltage by adjusting the series-connected power supply output. The second system consisted of a Fluke 1720 instrument control with all current data taken from an HP Model 4140PA meter. Results from both measurements agreed well within the experimental error limit. All the MIS devices under test were enclosed in a light-shielded box to eliminate light-stimulated generation carriers.

Results

Gallium phosphate films grown by electron-beam evaporation technique were amorphous as determined by x-ray diffraction analysis. Even films as thick as 2 μm showed no crystalline structure. Annealing at elevated temperatures (≧750°C) in different ambients *viz.* H_2, O_2, or Ar converted the films into crystalline β-Ga_2O_3 with (100) preferred orientation.

Typical forward I-V characteristics for as-deposited films of type A, B, and C are shown in Fig. 1. For n-type MIS devices, the forward voltage indicated that the voltage applied on the gate metal was positive with respect to the semiconductor. At low voltages, the current was ohmic varying linearly with voltage. Above

Key words: dielectrics, current, evaporation.

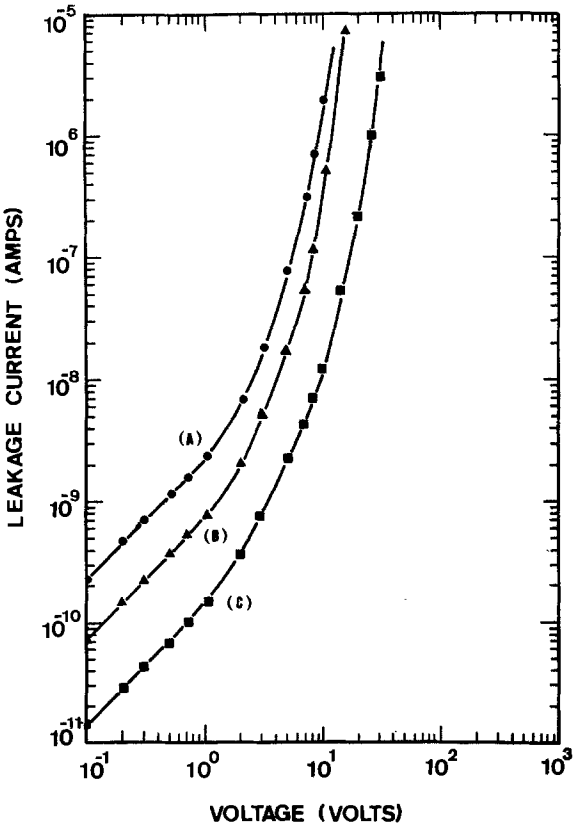

Fig. 1. Current-voltage characteristics of unannealed GaPO films grown on n-GaAs ($n = 4 \times 10^{16}$ cm^{-3}) substrates: (a) type A film, (b) type B film, and (c) type C film. Film thickness = 600Å.

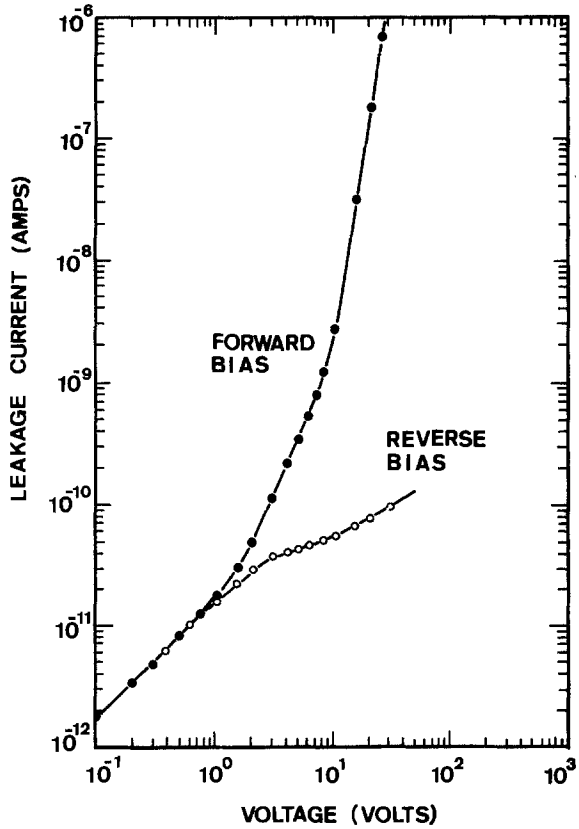

Fig. 2. Forward and reverse current-voltage characteristics of annealed type C film on n-GaAs substrate ($t = 600$Å).

the transition voltage, however, the current increased more rapidly. Further increase in the gate voltage led to dielectric breakdown of the devices. It is seen in Fig. 1 that type C film showed the lowest leakage current level, whereas type A film showed the highest. The estimated resistivity was approximately 5×10^{11} Ω-cm for type A film and 7.9×10^{12} Ω-cm for type C film. As far as the device fabrication yield and aging are concerned, type C films had a yield of about 85% and had stable properties lasting for more than 6 months. The better properties of type C films led us to further investigation of these films.

In this study, type C films were annealed in various ambients, such as hydrogen, argon, and oxygen. Films annealed in argon and oxygen ambients showed little or no improvement in their electrical properties. Figure 2 shows both forward and reverse I-V characteristics of a typical low-temperature hydrogen-annealed type C film. The voltage dependence of the leakage current was about the same for both annealed and unannealed films but the resistivities of the annealed films were apparently at least an order of magnitude higher than those of unannealed ones. Best resistivities of low-temperature H_2-annealed films were in the range of 10^{14}-10^{15} Ω-cm.

The reverse I-V characteristic shown in Fig. 2 was different from the forward characteristic. At low voltages, the ohmic region was identical. As the gate voltage became more negative, the I-V curve showed a reverse-biased diode characteristic. Another interesting feature was that the transition voltage (about 0.7V) from the ohmic region to the nonohmic region was almost same for both curves. Similar I-V characteristics have been reported earlier by Brown and Grannemann for electron-beam evaporated titanium oxide films on silicon (21).

Figure 3 illustrates the I-V characteristics for films annealed in hydrogen at various temperatures. The leakage current remained unchanged for films annealed below 300°C. Annealing at 450°C resulted in an increase in leakage current by one order of magnitude. With further increase in the annealing temperature, the leakage current drastically increased and eventu-

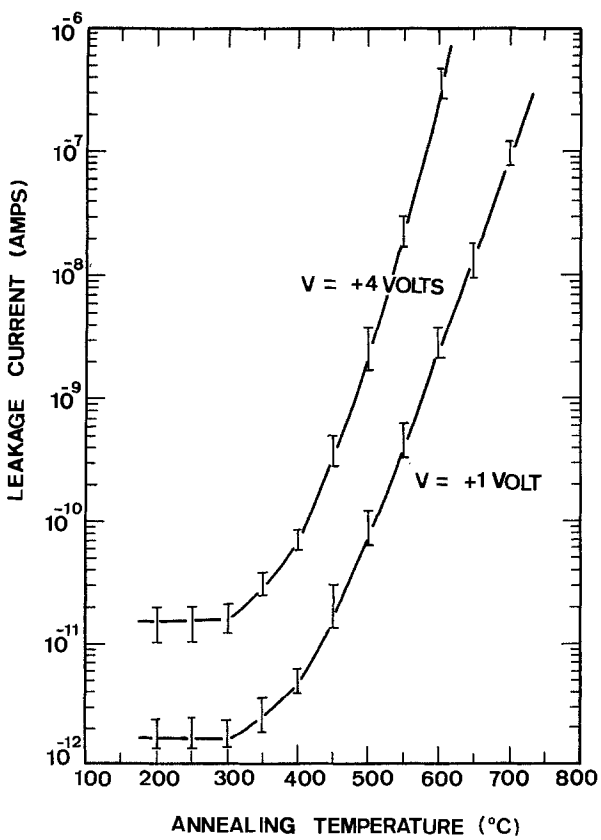

Fig. 3. Leakage current vs. annealing temperature for type C films at $V_G = +1$V and $+4$V. Films ($t = 1000$Å) were annealed in H_2 ambient for 25 min.

ally caused the dielectric breakdown to occur at lower voltages.

Figure 4 shows the I-V characteristics for type C films of various thicknesses ranging between 500 and 2000Å. The transition voltage, which was thickness dependent, was higher for thicker films. In addition, the leakage current decreased with increase in film thickness.

The variation in leakage current with applied voltage at various temperatures is shown in Fig. 5 for a film thickness of 1000Å. All I-V curves had the same general shape. At higher temperatures, the leakage current was more significant and a lower breakdown voltage was observed.

In order to determine the influence of the substrate conductivity type on the device electrical properties, several MIS capacitors were fabricated on p-type substrates. The general shapes of all I-V curves and the leakage current level were similar to those obtained on n-type devices (Fig. 1 and Fig. 2).

In addition, n-type silicon substrates were also used for MIS structures to investigate the effect of different substrate materials on the I-V characteristics. All the fabrication and annealing procedures used for GaAs devices were applied to silicon devices, except that gold was used for substrate ohmic contact and a subsequent sintering at 350°C was used after metallization for better eutectic bonding.

Figure 6 shows the forward I-V characteristic for an annealed n-type silicon MIS structure. The transition from the low-voltage ohmic region to the nonohmic region was very short. The reverse I-V curve, like that of GaAs devices, also showed a reverse-biased p-n diode characteristic but the shapes of I-V curves for Si devices were different from those of GaAs devices. The best resistivity estimated from the ohmic region was of the order 10^{13} Ω-cm.

Another interesting feature was that n-type GaAs devices always showed higher breakdown voltages (about $1 \sim 3$V) for negative polarity than for positive. For p-type devices, however, positive polarity exhibited higher breakdown voltages than for negative. In general, the average dielectric strength was about (1-4) $\times$ 10^6 V/cm for annealed type C films on GaAs and 1×10^6 V/cm for those on silicon.

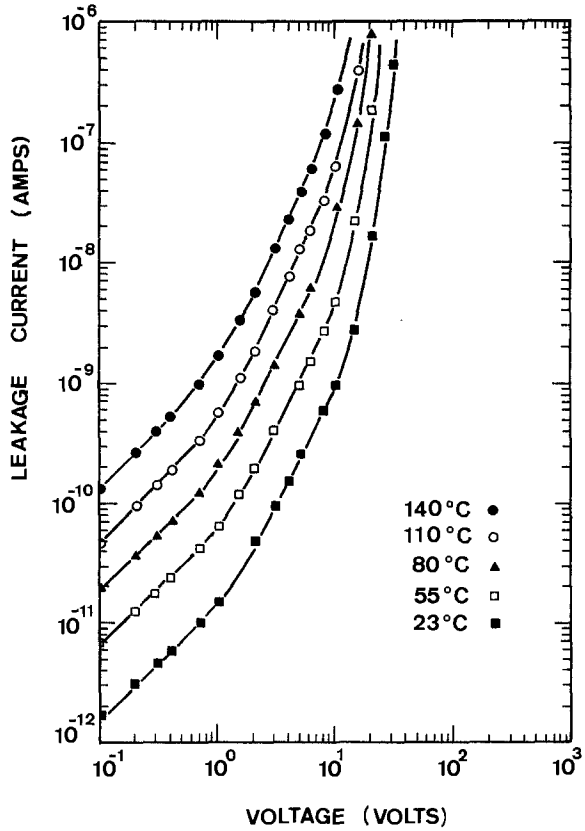

Fig. 5. Current-voltage characteristics of type C $GaPO_4$ films on n-GaAs substrates measured at various temperatures (t = 1000Å).

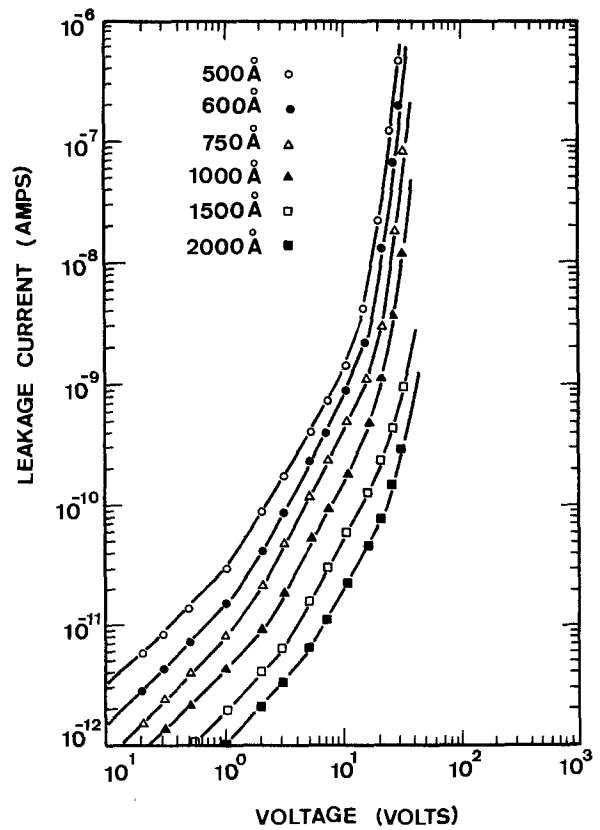

Fig. 4. Current-voltage characteristics of annealed type C films for various thicknesses.

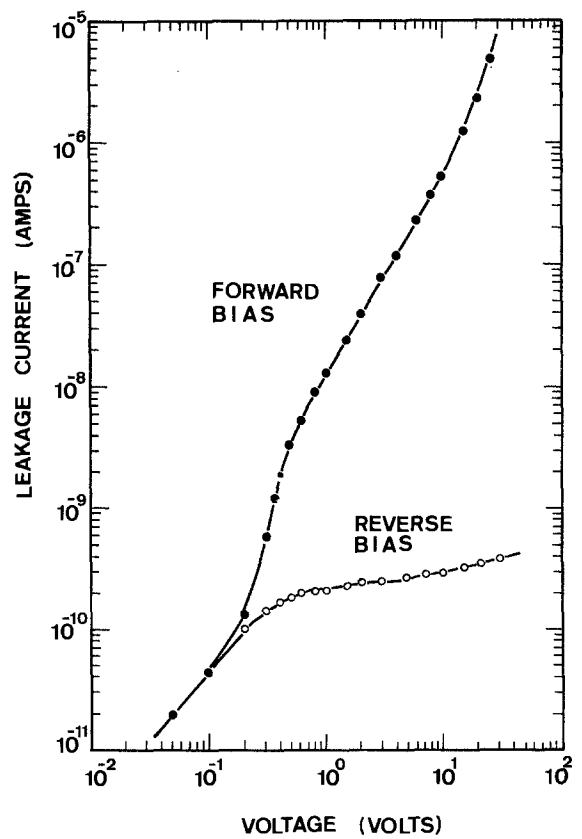

Fig. 6. Forward and reverse current-voltage characteristics of $GaPO_4$ film (t = 750Å) on n-Si ($n = 2 \times 10^{16}$ cm^{-3}) substrates.

Discussion

From these measurements it is clear that the electrical properties of the deposited $GaPO_4$ films are influenced by the deposition conditions and post-deposition annealing treatments. The x-ray diffraction studies revealed that the as-deposited films were amorphous. This structure is desired for semiconductor surface passivation because there are no grain boundaries, which tend to cause higher leakage current. Further, the results indicate that type C films have better electrical properties than type A and type B films.

The compositions of these films were analyzed using Auger and *IR* techniques (22). Auger profile analysis revealed that type A films were predominantly Ga_2O_3 with only a small amount (about 5%) of phosphorus at the insulator-semiconductor interface. Type C films were mainly of $GaPO_4$ composition with a small amount of Ga_2O_3. For type C films, the *IR* spectrum had absorption peaks occurring at about 1100 cm^{-1} (strong, broad), corresponding to the presence of $GaPO_4$, and at about 560 cm^{-1} (weak) and 310 cm^{-1} (weak), corresponding to the presence of small amount of Ga_2O_3. The low concentration of phosphorus in type A films, as compared to type C films, is due to the dissociation of phosphate during evaporation. By introducing oxygen into the deposition system, phosphorus will be able to recombine with oxygen and reduce its loss in the deposited films. The higher percentage of Ga_2O_3 in type B films is probably due to the reaction of oxygen with the heated GaAs substrates prior to evaporation.

Thin films of Ga_2O_3 grown on GaAs are reported to have resistivities of 10^9-10^{12} Ω-cm (19). Unfortunately, there are no data available on the resistivities of $GaPO_4$ films for comparison. The present results, however, indicate that $GaPO_4$ films have better insulating properties than Ga_2O_3, the native oxide of GaAs.

The different I-V characteristics of the forward and reverse voltages may mean that there is a heterojunction between the $GaPO_4$ film and the GaAs substrate. At larger reverse voltages the depletion region is wider, and consequently the number of transported carriers becomes less. For low-temperature hydrogen-annealed films, the improvement in the resistivities is attributed to the reduction in the dangling bonds at the interface and to the better uniformity of the insulating films.

At elevated temperatures, the deposited $GaPO_4$ films may dissociate and become nonstoichiometric. The increase in leakage current for films annealed above 300°C is probably due to their nonstoichiometric nature. Scanning electron microscopy x-ray energy dispersive analysis has revealed that insulating films lost phosphorus completely after annealing at 750°C (25 min). Lesser changes in film composition probably occur at lower temperatures.

The activation energy (ΔE), which corresponds to the position of the dominant trapping level below the conduction bandedge of the insulator, was calculated using the relation $I = A \exp(\Delta E/kT)$. A plot of log leakage current *vs.* reciprocal temperature at 0.6V (Fig. 5) gave a value of ΔE of about 0.42 eV.

The similarity in the I-V characteristics for p-type and n-type GaAs MIS devices suggests that the conductivity type of the substrate has very little effect on the electrical properties. However, the different dependence of the current on the voltage between GaAs and Si MIS devices (Fig. 2 and Fig. 6) is probably due to the different properties of deposited films at the interface and the bulk regions. Related high-frequency capacitance-voltage measurements on these devices indicated that the GaAs devices had a minimum surface state density of about 2×10^{11} eV^{-1} cm^{-2} while Si devices had a value of about 5×10^{10} eV^{-1} cm^{-2}. The different surface chemistry of the compound semiconductor GaAs and elemental Si may result in different properties. Since $GaPO_4$ films were deposited on different materials, the trap densities and distribution in these films might also be different. These factors may cause different I-V curves for GaAs and Si devices.

For n-type GaAs devices, the reason that higher breakdown voltages are observed for negative polarity than for positive is explained as follows. At high negative voltages, the n-type semiconductor is in deep depletion, and the density of minority carriers is very low. As a result, the space-charge region is much wider than it is at positive voltages, where the semiconductor is in the accumulation region. The effective voltage across the insulator near the breakdown is lower for negative polarity because a larger portion of the applied voltage is across the depletion region than for positive polarity.

Conclusion

The current-voltage characteristics of gallium phosphate films deposited on gallium arsenide substrates by the electron-beam evaporation technique have been studied by using MIS structures. Type C films, deposited in the presence of oxygen which was back-filled when the evaporation started, had the best electrical properties. Low-temperature annealing (300°C for less than 1 hr) in hydrogen improved film properties. High-temperature annealing should be avoided because it causes film dissociation and results in a higher leakage current. Films deposited on p-type GaAs substrates show similar properties as those on n-type GaAs substrates. The different characteristics of GaAs and Si MIS devices is attributed to the difference in the film properties at the interface and bulk region.

Manuscript submitted Jan. 5, 1982; revised manuscript received May 25, 1982.

Any discussion of this paper will appear in a Discussion Section to be published in the December 1983 JOURNAL. All discussions for the December 1983 Discussion Section should be submitted by Aug. 1, 1983.

Publication costs of this article were assisted by The University of New Mexico.

REFERENCES

1. H. Hasegawa, K. E. Forward, and H. L. Hartnagel, *Appl. Phys. Lett.*, **26**, 567 (1975).
2. C. R. Zeisse, L. J. Messick, and D. L. Lile, *J. Vac. Sci. Technol.*, **14**, 957 (1977).
3. G. Sixt, K. H. Zeigler, and W. R. Fahrner, *Thin Solid Films*, **56**, 107 (1979).
4. C. W. Wilmsen, *J. Vac. Sci. Technol.*, **19**, 279 (1981).
5. H. T. Minden, *This Journal*, **109**, 733 (1962).
6. M. Rubenstein, *ibid.*, **133**, 540 (1966).
7. S. P. Muraka, *Appl. Phys. Lett.*, **26**, 180 (1975).
8. D. N. Butcher and B. J. Sealy, *Electron. Lett.*, **13**, 558 (1977).
9. D. N. Butcher and B. J. Sealy, *J. Phys. D.*, **11**, 1451 (1978).
10. R. P. H. Chang and A. K. Sinha, *Appl. Phys. Lett.*, **29**, 56 (1976).
11. C. C. Chang, R. P. H. Chang, and S. P. Muraka, *This Journal*, **125**, 481 (1978).
12. R. P. H. Chang, *Thin Solid Films*, **56**, 89 (1979).
13. A. Matsuzawa, T. Itoh, Y. Ishikawa, and Yanagida, *J. Vac. Sci. Technol.*, **17**, 793 (1980).
14. J. E. Foster and J. M. Swartz, *This Journal*, **117**, 1410 (1970).
15. J. A. Cooper Jr., E. R. Ward, and R. S. Schwartz, *Solid-State Electron.*, **15**, 1219 (1972).
16. Hariu, N. Suzuki, K. Matsushita, and Y. Shibata, IEEE 1978 International Electron Device Meeting, Washington, D.C., Dec. 4-6, 598 (1978).
17. L. G. Meiners, R. P. Pan, and J. R. Sites, *J. Vac. Sci. Technol.*, **14**, 961 (1977).
18. L. G. Meiners, *ibid.*, **15**, 1402 (1978).
19. T. Hariu, S. Sasaki, H. Adachi, and Y. Shibata, *Jpn.*

J. Appl. Phys., **16**, 841 (1977).
20. D. H. Phillips, W. W. Grannemann, L. E. Coerver, and G. J. Kuhlmann, *This Journal*, **120**, 1087 (1973)
21. W. D. Brown and W. W. Grannemann, *Thin Solid Films*, **51**, 119 (1978).
22. C. S. Su, Ph.D. dissertation, University of New Mexico, 1982.

A Novel Polyimide Film Preparation and Its Preferential-Like Chemical Etching Techniques for GaAs Devices

Yasoo Harada, Fumio Matsumoto, and Takashi Nakakado

Sanyo Electric Company, Research Center, Limited, 1-18-13 Hashiridani, Hirakata, Osaka 573, Japan

ABSTRACT

A novel chemical etching technique using etchants composed of hydrazine hydrate and ethylene diamine to generate V-shape grooves in thick polyimide films through photoresist masks has been developed. The etching characteristics, in terms of etch rate, side etched width and taper angle, have been found to depend strongly on (*i*) preparation condition of the films, especially baking temperature, and (*ii*) the composition and temperature of the etchants. In order to achieve preferential etching behavior, the polyimide films have been fabricated by repeating 3 times a coating process, which consists of a spin coating followed by two sequential bakings. An optimized baking condition has been found to be 15 min at 150°C in air for each prebaking and 2 min and 30 min at 185°C in N_2 for the first two and the last postbaking, respectively. An optimized condition of the etchants has also developed. Under the optimized condition, a side etched width less than 20% of the film thickness and a constant taper angle of about 35° has been achieved. The size of the V-shape grooves has been controlled by both the opening width in the photoresist masks and the side etch rate. The taper angle of the grooves has been determined by the film preparation condition itself, and is independent of the etching time even when the films are over-etched.

Significant progress in GaAs device technologies such as ion implantation and epitaxial growth by molecular beam epitaxy or metalorganic chemical vapor deposition has been made. An excellent insulating film such as thermally oxidized SiO_2 on Si, however, has not been developed yet. A polyimide film as an insulator has excellent electrical characteristics such as a low dielectric constant of approximately 3.5, and a thermal stability up to 400°C (1). By using the polyimide film, a beam lead GaAs mixer diode for use in a super high frequency band and a liftoff technique, developed for fabricating Si LSI, have been reported (1-3). In the latter case, a sputtering method through metal masks has been employed for etching the polyimide film. A chemical etching technique of the polyimide film for GaAs device fabrication, however, has not been reported.

The photoresist masked chemical etching technique is simpler than the dry etching through metal masks. Since photoresist has a good optical transparency, the mask alignment process in the chemical etching is straightforward. However, preparation conditions of the polyimide film for a successful chemical etching are more restricted than that for the dry one, since they strongly affect the adhesion of the photoresist and the etching characteristics. The baking temperature in the film preparation for the chemical etching is more important than the baking time and should be kept below the cure temperature of the polyimide film.

In this paper, we describe an optimized baking process which provides good chemical etching results. An optimized condition of the etchant composed of hydrazine hydrate and ethylene diamine also has been developed. The chemical etching characteristics of the thick polyimide films such as the etch rate, side etched width, and taper angle as functions of the film preparation and etchant conditions have been discussed. And it has been demonstrated that V-shape grooves produced in GaAs or Si by means of preferential etching techniques (4, 5) can be formed in the polyimide films reproducibly. An optimized condition for producing the V-shape groove with a taper angle of about 35° is established.

Key words: polyimide, chemical etching, taper angle, hydrazine hydrate-ethylene diamine system.

Experimental Procedure

Polyimide coating.—A special polyimide has been synthesized for semiconductor devices (1). A prepolymer solution of polyimide was spun onto GaAs wafers and then baked. This process was repeated 3 times in order to evaporate diluent in the polyimide film as much as possible. Etch baking process was done at a temperature (T_L) and subsequently at a higher temperature (T_H).

The T_L and T_H were varied from 50° to 185°C and from 150° to 400°C, respectively. The prebaking time t_L at each step and the postbaking time at first and second steps (t_{H1}, t_{H2}) were 15 and 2 min, respectively. The last postbaking time t_{H3} was varied from 5 to 180 min. These processing and conditions are summarized in Table I. Typical film thickness prepared was 6.5 ± 0.5 μm.

Etching mask.—The masks employed were negative photoresists such as Waycoat IC resist (Philip A. Hunt Chemical Corporation), which were spun onto the baked polyimide films and photoengraved by the conventional technique. A typical width at the opening was 20 μm.

Table I. Preparation processing and conditions of the polyimide films in this experiment. The films were prepared with repeating 3 times a step which consists of a spin coating followed by two sequential bakings.

PROCESS / STEP	(1) SPIN-COAT	(2) PRE-BAKING			(3) POST-BAKING		
		TEMP. T_L(°C)	TIME t_L(MIN)	AMBIENCE	TEMP. T_H(°C)	TIME t_H(MIN)	AMBIENCE
1st	5000 rpm	150 (50~185)*	15	AIR	185 (150~400)*	$T_{H1,2}$=2	N_2
2nd							
3rd						t_{H3}=30 (5~180)*	

*. PARAMETERS IN THIS EXPERIMENT.

Etching.—The etchant used was the mixed solution composed of hydrazine hydrate (H_2NNH_2 H_2O; purity 80.0%) and ethylene diamine ($NH_2CH_2CH_2NH_2$; 99%).

The composition α, which is the volume ratio of ethylene diamine to the solution, and the temperature were varied from 0° to 1°C and 20° to 70°C, respectively. The etching was carried out in a slowly stirred solution.

Measurement.—Minimum etching time, being defined as the time when the surface of GaAs wafers is exposed, can be determined precisely by visual means (within 1 sec), since just before the surface was exposed, optical fringes could be easily observed on the wafers. The width of the openings in the photoresist mask, as well as of the top and the bottom of the grooves in the polyimide films, were measured by a microscope (maximum magnification: × 1000 and accuracy: ±0.2 μm).

After removing the mask, the film thickness was measured by an interference microscope (accuracy: ±500Å). By using these measured values, the etch rate, normalized side etched width W, and taper angle θ were calculated. A definition of these terms and schematic cross section of an etched groove in the polyimide films are described in Fig. 1.

Results and Discussion

Etchant composition dependence of the etch rate.—The following results were obtained by utilizing the polyimide films prepared with $T_L = 150°C$, $T_H = 185°C$, and $t_{H3} = 30$ min. The etchant temperature was kept at 35°C. The dependence of the average etch rate, normalized side etched width W, and taper angle θ on the etchant composition α are shown in Fig. 2. The etch rate increased with increasing α and reached a maximum value of about 9.5 μm/min at $\alpha = 0.75$-0.8. Beyond these points, the etch rate decreased rapidly. A minimum W ($\lesssim 0.2$) and maximum θ (~35°) were also obtained around the same compositions.

W of less than 1 and θ of more than 22° were obtained over a wide composition range from 0.35 to 0.95. Therefore, the etched profiles in the polyimide films prepared with an optimized condition can be controlled by the composition.

Etching temperature dependence.—The polyimide films employed were also prepared under the above mentioned conditions. Figure 3(a) shows a relation between the etching temperature and the etch rates in the etchants with α of 0.6 and 0.83. These etch rates increased exponentially with the etching temperature but changed at the temperature of around 40°C. The activation energies obtained below 40°C were larger than those above as described in Table II. W and θ at each composition α were also changed drastically between 40° and 50°C as shown in Fig. 3(b). The smallest W and largest θ at each composition α were obtained at temperatures below 40°C. Above this temperature, the taper width increased rapidly. Since the adhesion of the photoresist to the polyimide films degraded with increased chemical reactivity of the etchants, θ became small. Therefore, the etching temperature should be kept below 40°C.

Prebaking temperature dependence.—Etching was carried out by using an etchant with $\alpha = 0.6$ at 35°C and the polyimide films prepared with varying only

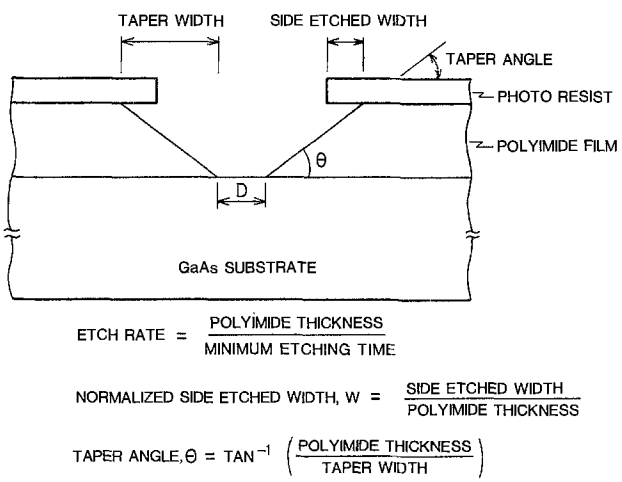

Fig. 1. Schematic cross section of the etched groove in the polyimide films, and measured and calculated parameters.

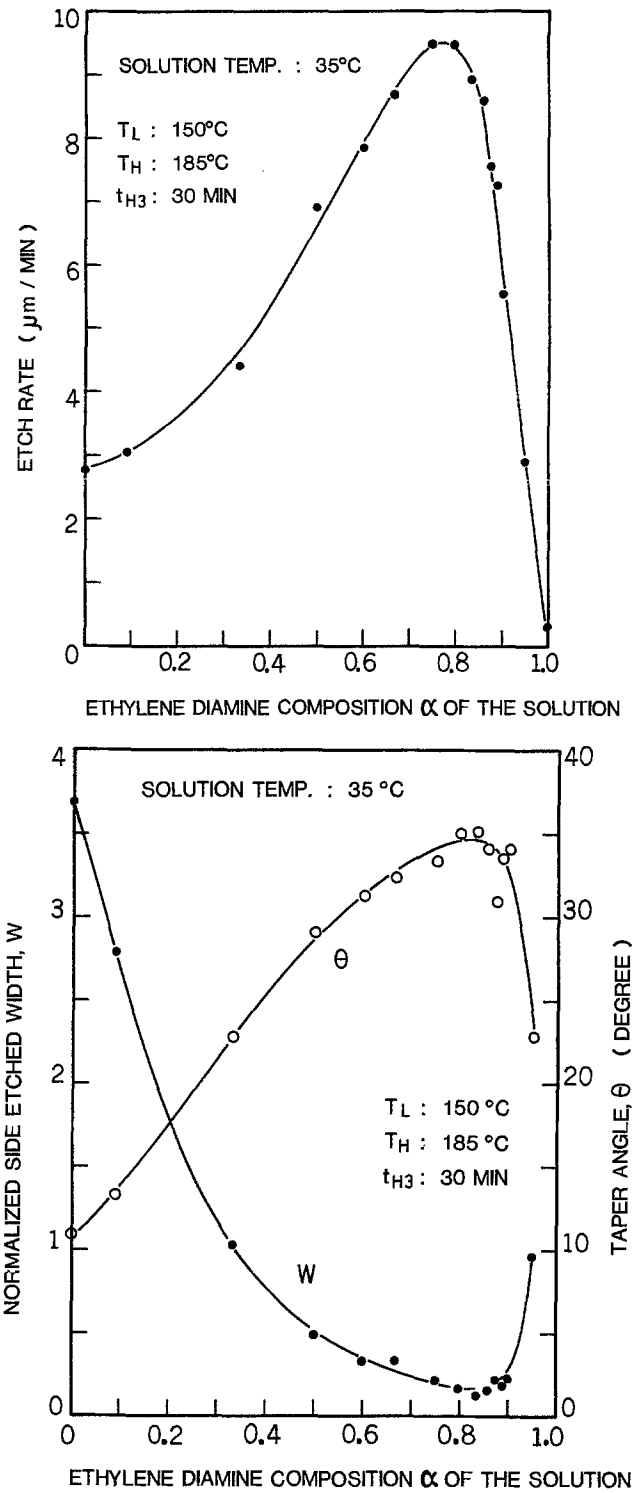

Fig. 2. Ethylene diamine composition of the etchants at 35°C vs. the etch rate, normalized side etched width and taper angle in the polyimide films prepared with an optimized baking condition; (a, top) = the etch rate; (b, bottom) = the side etched width and taper angle.

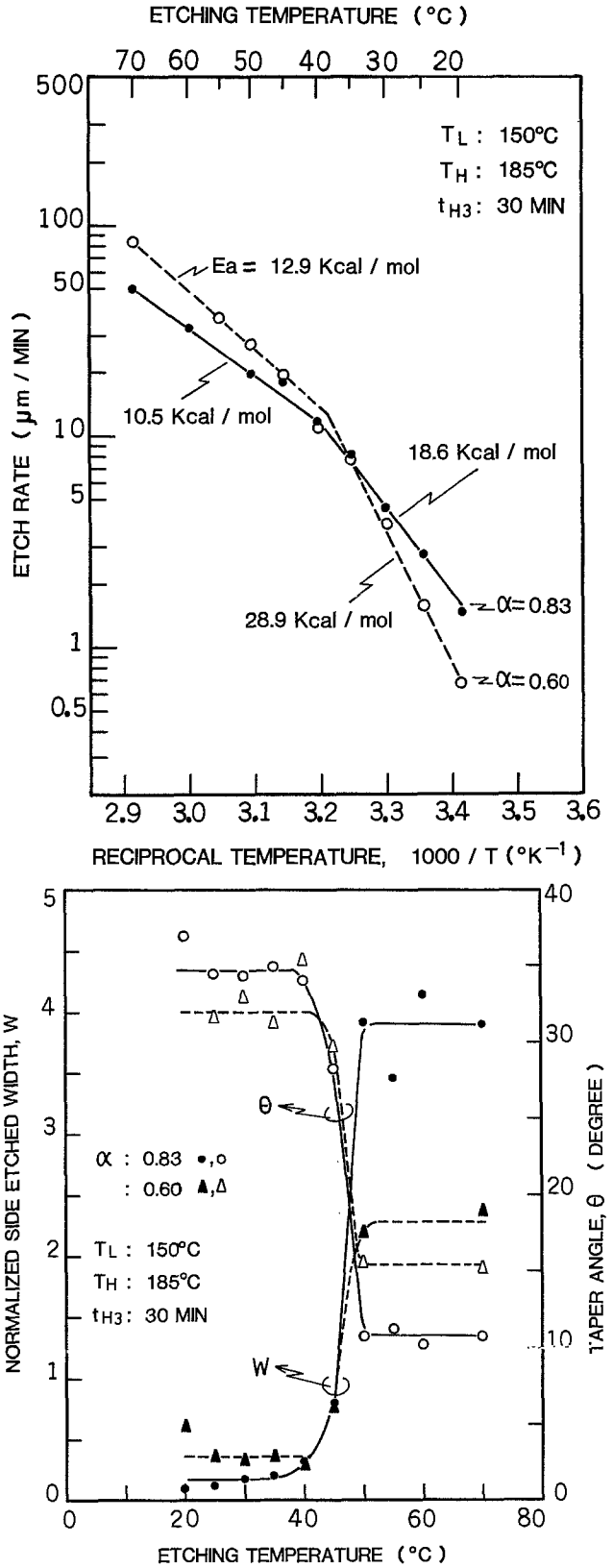

Fig. 3. Etching temperature of the etchants with ethylene diamine composition α = 0.6 and 0.83 *vs.* the etch rate, normalized side etched width and taper angle in the polyimide films prepared under an optimized baking condition; (a, top) = the etch rate; (b, bottom) = the side etched width and taper angle.

the prebaking temperature T_L ranging from 50 to 185°C. The dependence of the etch rate, W and θ on T_L are shown in Fig. 4(a) and (b). These three terms depended strongly on T_L. A minimum and maximum values of W and θ respectively were about 0.37 and 35° at T_L = 150°C at which a maximum etch rate of about 8.9 μm/min was observed. The dashed line in Fig. 4(a)

Table II. Activation energies of the etchants with ethylene diamine composition α of 0.6 and 0.83

COMPOSITION α	0.6		0.83	
ETCHING TEMP. (°C)	$\lesssim 40$	$\gtrsim 40$	$\lesssim 40$	$\gtrsim 40$
ACTIVATION ENERGY (Kcal / mol)	28.9	12.9	18.6	10.5

shows the side etch rate having a constant value of about 3.7 μm/min, which was measured on the surface of the polyimide films; so W can be controlled by the etch rate. However, from the fact that θ cannot be estimated by using the etch rate and the side etch rate, we think, θ is determined by the film preparation condition itself, that is, only the T_L in this case. The details will be described later.

The dependence of these three terms on the prebaking time as a function of T_L was also investigated, but they merely depended on the time up to 45 min at least. The temperature rather than the time of the prebaking is important for preparing suitable films. The typical prebaking condition described in Table I, *i.e.*, T_L = 150°C for 15 min, produced good results.

The reasons for the occurrence of maximum etch rate at T_L = 150°C, we suppose, are as follows. Polyimides are obtained by heating a prepolymer solution (called polyimide precursor) whose diluent is dimethylacetamide with a boiling temperature of 165°C.

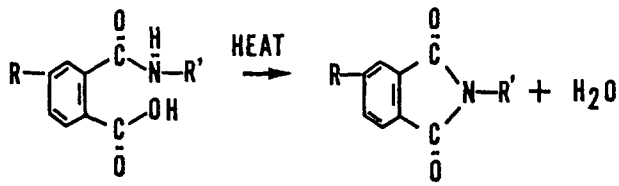

POLYIMIDE PRECURSOR **POLYIMIDE**

This dehydration reaction causes an increase in the imide bond and cyclization of the polymer chain.

An infrared spectrum analysis of spin-coated polyimide films exposed to evaporated temperature indicates that this dehydration (*i*) occurs at temperatures as low as 50°C, (*ii*) increases steeply at temperatures of 100°-150°C, and (*iii*) is essentially completed above 250°C (1).

Polyimide films are soluble in the etchant due to scission of the polymer chain at the imide bond. So, the etch rate is determined by two competing processes of increase in the imide bond and the cyclization.

Since the polymer chain will not cyclize extensively until the boiling temperature of diluent is reached (6), the etch rate increases with an increase in the imide bond. Although further increasing T_L (> 150°C) causes an increase in the imide bond, the cyclization will occur extensively due to increase in the evaporation of diluent, which causes a decrease in the scission rate of the polymer chain and the etch rate. Therefore, the etch rate maximum occurs. The temperature giving the etch rate maximum is closely related to the boiling temperature of diluent and the film baking processes to evaporate diluent. T_L = 150°C, including the postbaking temperature of 185°C, corresponds to the boiling temperature of diluent used.

Postbaking temperature dependence.—The experiments were done by using the etchant with α = 0.6

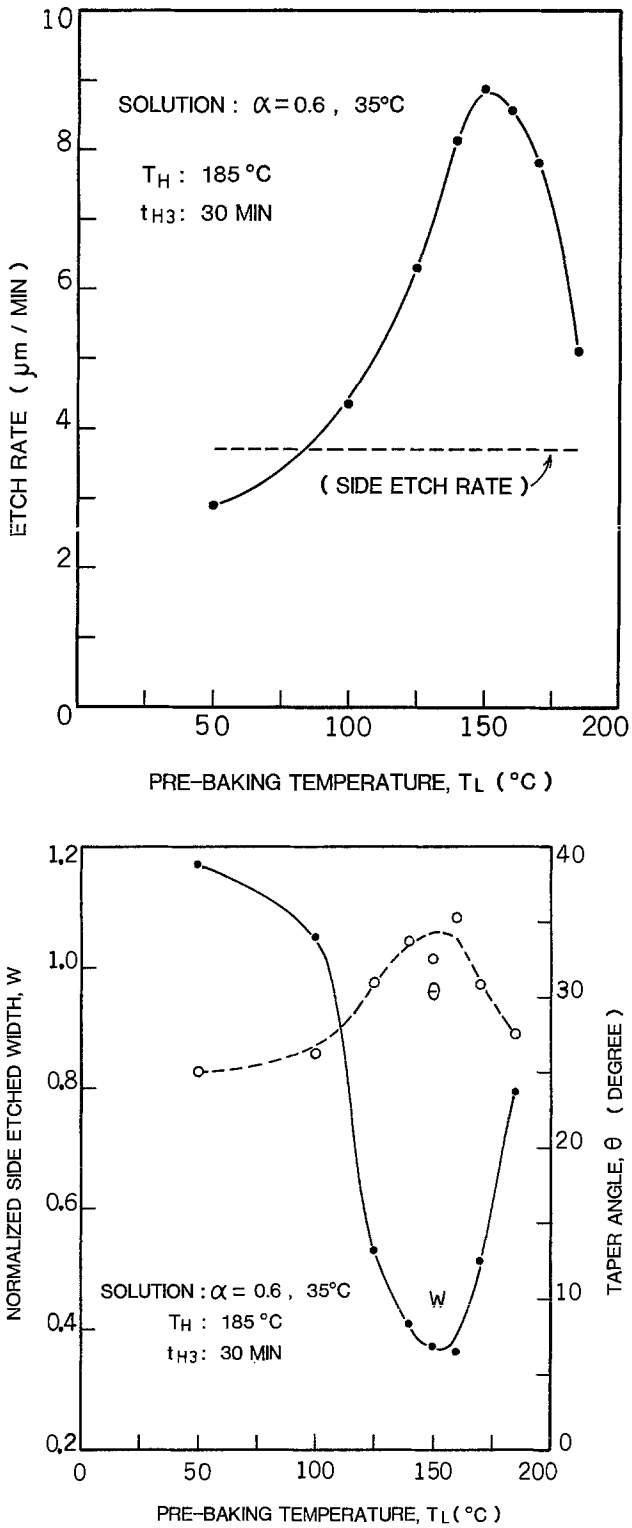

Fig. 4. Prebaking temperature of the polyimide film vs. the etch rate, normalized side etched width and taper angle. The etching was carried out in the etchants with ethylene diamine composition α = 0.6 at 35°C; (a, top) = the etch rate; (b, bottom) = the side etched width and taper angle.

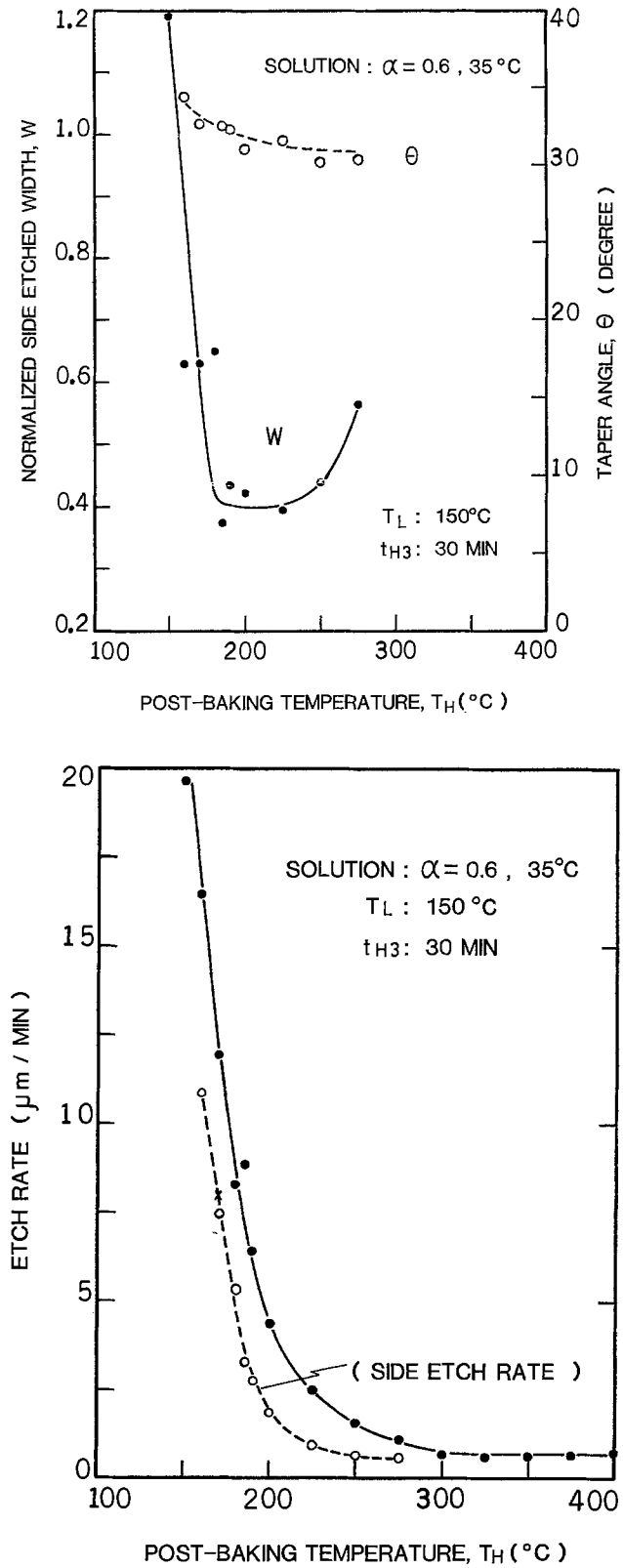

Fig. 5. Postbaking temperature dependence of the etch rate, normalized side etched width and taper angle. The etching was done in the etchants with ethylene diamine composition α = 0.6 at 35°C; (a, top) = the etch rate; (b, bottom) = the side etched width and taper angle.

at 35°C and the polyimide films prepared with varying only the postbaking temperature T_H over a range from 185° to 400°C. Figure 5(a) shows the etch rate decreased rapidly with increasing T_H and reached a constant value of about 0.6 μm/min above 300°C which is nearly equal to cure temperature of the polyimide (1). As shown in Fig. 5(b), W varied with T_H and had a minimum value of about 0.4 between 185° and 225°C, but θ varied little, which was different from the results of T_L dependence. However, θ could not be also estimated by utilizing the etch rate and side etch rate.

W and θ could not be measured exactly above 280°C, since an adhesion of the photoresist masks to the film degraded during a long etching time. In order to minimize side etching T_H should be kept between 185° and 225°C.

Last postbaking time t_{H3} dependence.—The films were prepared varying only the last postbaking time t_{H3} over a range of 5-180 min and etched in the etchant

with $\alpha = 0.6$ at 35°C. Figure 6(a) shows the etch rate varied strongly with t_{H3}, especially below 30 min. W and θ, however, varied little with t_{H3} above 15 min and had a constant value of about 0.31 and 33°C, respectively. This result indicates that it is better for a precise etching control to keep t_{H3} as long as possible where the preparation time of the polyimide films in device fabrication process is not important. The 30 min baking time t_{H3} was enough for achieving reproducible results.

Overetching time dependence.—Figure 7 shows the dependence of W and θ on the normalized overetching time τ which is defined as a ratio of the etching time to the minimum etching time. The films were prepared with the typical condition, and etched in an etchant with $\alpha = 0.83$ at 35°C. W increased linearly with increasing τ, and was less than 1 up to $\tau = 4$. θ decreased little as τ increased. This is, we suppose, due to a slight degradation of the photoresist adhesion during a long etching. The fact that θ was approximately constant even when overetched, also indicates that it is determined by the film preparation condition itself.

Cross section of V-shape groove.—The cross section of the grooves formed in the polyimide films is shown in Fig. 8. The V-shape etched grooves have the following features: (*i*) The size of the groove is controlled by the width of the opening in the photoresist mask. When the width is relatively small compared with the polyimide thickness, a completely V-shape groove is formed; (*ii*) the bottom size of the groove at minimum etching time is always smaller than the opening width; and (*iii*) the taper angle is almost independent of the opening width and the etching time, and has a constant value which is determined by the film preparation condition.

These features are similar to the preferential etching characteristics of the single crystal such as GaAs or Si (4, 5). The V-shape grooves in the polyimide films, however, can be formed with no need of aligning the opening in the masks with a particular direction and with no restriction on the opening figures available for the masks.

Based on these results, we propose that the V-shape grooves are produced by the following mechanism: (*i*) the etching proceeds with a constant taper angle which is determined by the film preparation condition itself; and (*ii*) the grooves with a constant taper angle are controlled by the side etch rate when both side walls

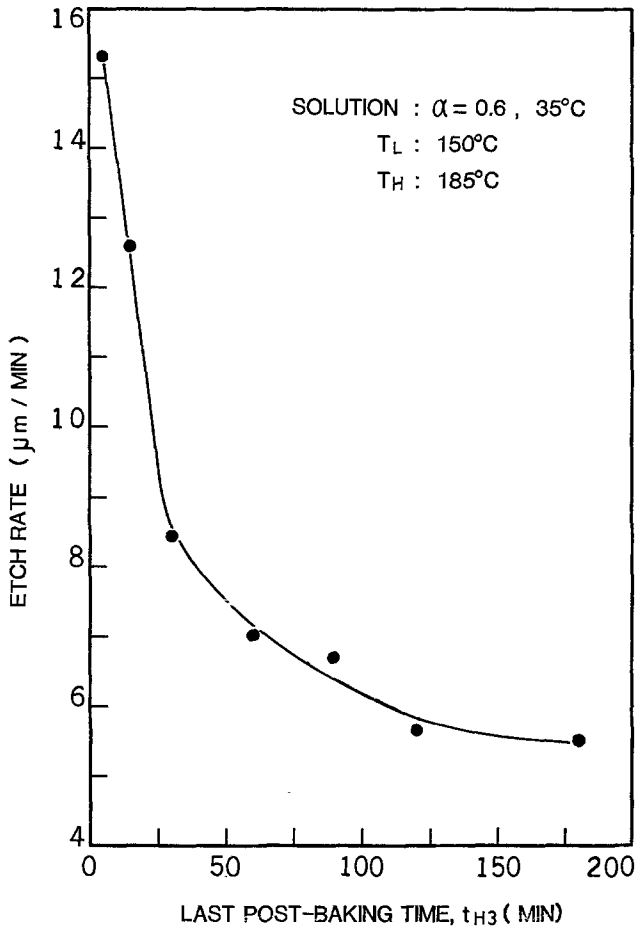

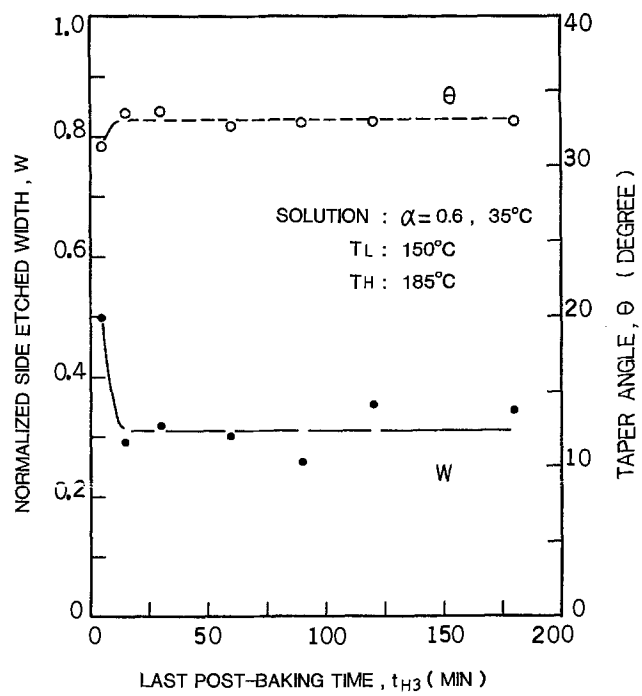

Fig. 6. The etch rate, normalized side etched width and taper angle vs. the last postbaking time t_{H3} at the 3rd coating step of the polyimide film preparation process. The etching was carried out in the etchants with ethylene diamine composition $\alpha = 0.6$ at 35°C; (a, top) = the etch rate; (b, bottom) = the side etched width and taper angle.

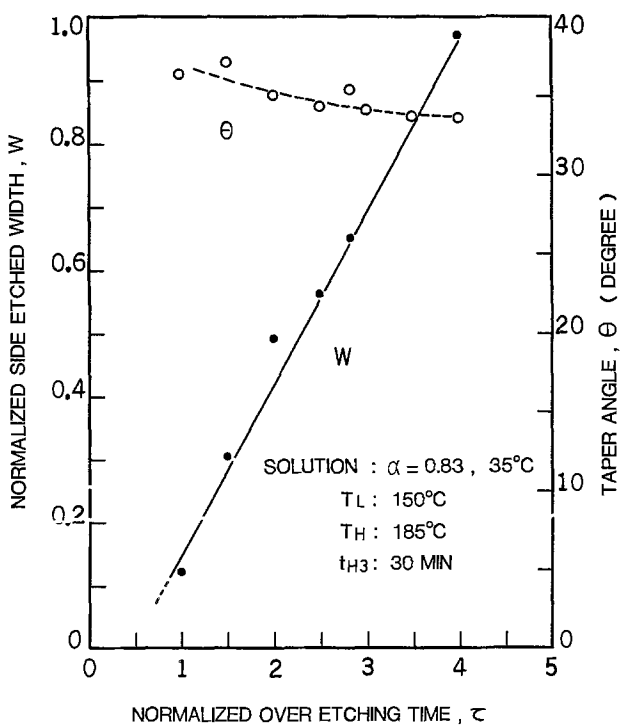

Fig. 7. Overetching time dependence of the normalized side etched width and taper angle. The polyimide films were prepared under an optimized baking condition, and etched in the etchants with ethylene diamine composition $\alpha = 0.83$ at 35°C.

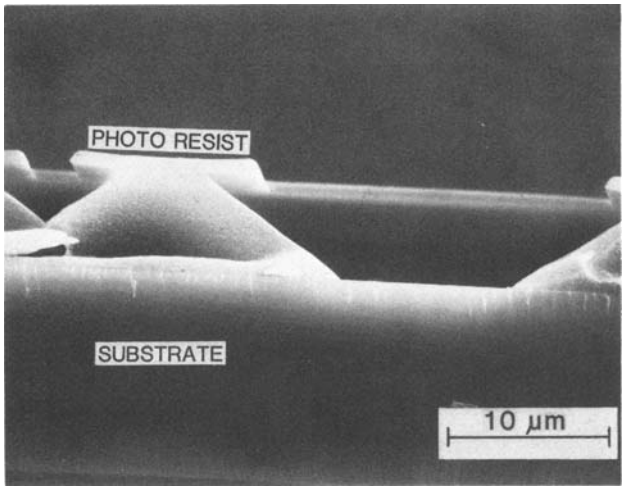

Fig. 8. Cross section of the V-shape grooves produced in the polyimide films through photoresist mask in cases of L (mask opening) $>> H$ (polyimide thickness) and $L \lesssim H$.

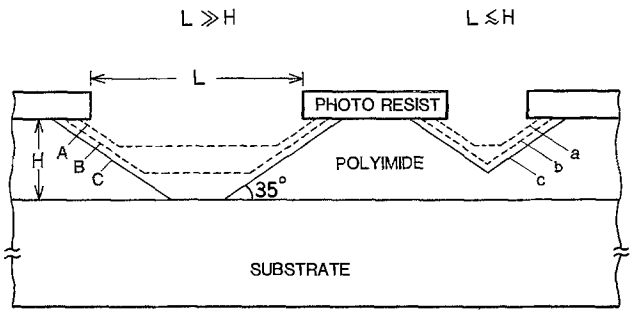

Fig. 9. Proposed etched profiles in the polyimide films. The dashed lines show them formed before minimum etching time and the solid lines show them at minimum etching time.

in the profiles intersect before exposing the surface of the wafers, or when the surface is exposed. Figure 9 schematically shows the etched profiles with a constant taper angle (~35°) in the case of L (width of the photoresist opening) $>>H$ (polyimide thickness) and $L \lesssim H$. At the beginning of the etching, the profile A and a produced at the same etching time have the same etched depth which is determined by the etch rate.

After further etching, the profile B and b are formed. The side walls in B do not intersect each other. But in b they do intersect and a complete V-shape profile is formed. The etched depth in b is shallower than that in B due to the slow side etch rate. The profile C and c are the etched profiles at minimum etching time. The surface of the substrate is exposed in the case of $L >>$ H, but is not in $L \lesssim H$. The complete V-shape profile c becomes larger than the profile b by the side etch width. When overetched, the sizes of the profiles in both cases are controlled by the side etch rate and the taper angle is kept constant. Therefore, for a successful preferential-like chemical etching of the polyimide films, it is essential to keep the large ratio of the etch rate to the side etch rate.

Compatibility with GaAs processing.—The alkaline etchant composed of hydrazine hydrate and ethylene diamine did not erode GaAs wafers and negative type photoresists (Waycoat IC, NMR, or OMR), but eroded positive photoresists such as AZ-1350J or OFPR-800. On the other hand, the polyimide films were not eroded in the alkaline GaAs etchants such as the $NaOH$-H_2O_2 system and in the J-100 photoresist remover. Therefore, our chemical etching technique of the polyimide films gives much flexibility to GaAs device fabricators.

Conclusions

A novel chemical etching technique for generating V-shape grooves in spin-coated thick polyimide films has been developed by employing the etchants composed of hydrazine hydrate and ethylene diamine.

A three-step coating process containing pre- and postbakings is used for the thick film preparation. Optimizing these baking temperatures is very important for a successful preferential-like chemical etching.

The etchants with a higher composition of ethylene diamine and a temperature below 40°C have provided good results. The side etch rate and the width of the photoresist opening have played a very important role for controlling the size of the groove with a constant taper angle. The taper angle has been determined by the film preparation condition itself and is approximately independent of the etching time.

Acknowledgments

The authors would like to thank Drs. M. Yamano, managing director of the company, and E. Komatu for their continuous guidance, and H. Fukuda for suggesting this work and for stimulating interest in it. Thanks are also due to members of the laboratory for their cooperation.

Manuscript submitted Jan. 18, 1982; revised manuscript received *ca.* May 24, 1982.

Any discussion of this paper will appear in a Discussion Section to be published in the December 1983 JOURNAL. All discussions for the December 1983 Discussion Section should be submitted by Aug. 1, 1983.

Publication costs of this paper were assisted by the Sanyo Electric Company, Limited.

REFERENCES

1. Y. Harada and H. Fukuda, *IEEE Trans. Electron. Dev.*, **ed-26,** 1799 (1979).
2. Y. Homma, H. Nozawa, and S. Harada, *ibid.*, **ed-28,** 552 (1981).
3. P. Shah, D. Laks, and A. Wilson, *IEDM Tech. Dig.*, 465 (1979).
4. Y. Tarui, Y. Komiya, and Y. Harada, *This Journal,* **118,** 118 (1971).
5. R. M. Finne and D. L. Klein, *ibid.*, **114,** 965 (1967).
6. C. E. Sroog, A. L. Endrey, S. V. Abramo, C. E. Berr, W. M. Edwards, and K. L. Olivier, *J. Polym. Sci.: Part A,* **3,** 1373 (1965).

Thermal Stress in CVD PSG and SiO_2 Films on Silicon Substrates

M. Shimbo* and T. Matsuo*

Toshiba R & D Center, Komukai Toshiba-cho, Kawasaki, Japan

ABSTRACT

Stress-temperature relationships of APCVD and LPCVD SiO_2 and PSG films on silicon substrates were measured with the Newton ring method up to 1000°C. Compressive stress in PSG films at room temperature reduces and turns to tension above 100°C. Stress-temperature curves of PSG have a maximum at about 500°C regardless of film compositions and deposition conditions. Heat-treatment of APCVD PSG films at constant temperatures below or above the stress maximum temperature causes an increase or decrease of stress. Stress in APCVD SiO_2 on heating up to 1000°C is tensile while that in LPCVD SiO_2 film changes from compression to tension on heating though both films have the same stress maximum temperature. Stress of the films is attributed to swelling or shrinking caused by water adsorption or desorption up to the stress maximum temperature above which sintering and stress release take place. The stress maximum temperature corresponds to the solidus line in the SiO_2-P_2O_5 binary system.

Silicon dioxide (SiO_2) and phosphosilicate glass (PSG) films prepared with chemical vapor deposition (CVD) are widely used on IC and LSI circuits for protection or passivation of aluminum interconnect lines. One of the serious problems in this application is stress formation in the films. Since the stress causes cracks that reduce the reliability of circuits, several investigations have been carried out, and many factors such as composition of the films, deposition conditions, and humidity in surroundings are known to affect the stress (1-5). Above all, the effect of heat-treatment is important not only for optimization of the circuit fabrication process but also for investigation of the stress propagation mechanism (6). However, most of the former research efforts were based on room temperature measurement which includes stress developed during cooling.

In this work, stress-temperature relationships of SiO_2 and PSG films with various phosphorus concentrations and different preparation methods were investigated by using a convenient apparatus with which a curvature of wafers in a heating furnace can be directly measured up to 1000°C with the Newton ring method (7).

Direct measurement of the thermal stress in SiO_2 films was reported by Sinha *et al.* (8).

Recently, Sintani *et al.* (9) have reported *in situ* measurement of stress-temperature relationships of CVD PSG and SiO_2 films by using x-ray diffraction, and they discussed the results in relation to water adsorption or desorption and high temperature creeping. Their report is consistent with our work basically, but more refined measurements are presented in this paper; and the stress propagation mechanism is qualitatively discussed.

Experimental

SiO_2 and PSG films of 500-1200 nm in thickness were formed on (100) silicon plane wafers at 3 in. diam and 0.45 mm thick with atmospheric CVD (APCVD) and low pressure CVD (LPCVD) at 0.1-0.2 Torr. Deposition temperatures were 380° and 500°C for APCVD and 430°C for LPCVD. Deposition rates of the films are 500 Å/min for APCVD and 50 Å/min for LPCVD. In both cases, the O_2/SiH_4 ratio was kept constant (12 and 2.5) and PH_3 diluted with N_2 was introduced in the reactor as the phosphorus source. Phosphorus content in the films was determined by x-ray fluorescence analysis. All samples before measurement were stored for 1-3 weeks at room temperature without humidity control.

An apparatus designed for stress measurement is shown schematically in Fig. 1. A sample wafer 22 mm in diameter, which was cut from an initial 3 in. wafer, was placed on an optically flat plate of quartz glass in a vertical electric furnace of about 30 mm internal diameter. Interference fringes of reflected light between the wafer and the quartz glass surface were detected through a half-mirror and a telescope using a sodium lamp as the light source, and the radius of curvature of the wafer was calculated (7). Temperature of the furnace was increased and decreased at the rate of 250°C/hr. Before this experiment, direction and magnitude of curvature of the wafers were measured with a laser flatness tester (Cannon Corporation, LSF-500). Sensitivity of this experiment is limited by (*i*) uncertainty of center position of the samples and (*ii*) anisotropic deformation of the curvature. The error caused by (*i*) could be minimized to less than one-half of the wavelength by careful measurements, but a discrepancy of more than 20% in curvature between two perpendicular directions of wafers took place in some samples. Mean values were chosen in these cases.

The stress was calculated from the following formula reported by Jacodine *et al.* (10)

$$\sigma = \frac{1}{6}\frac{E}{1-\nu}\frac{1}{R}\frac{t_s^2}{t_g}$$

where σ is the stress in the film, E and ν are Young's modulus and Poisson ratio of silicon, respectively, t_g and t_s are thickness of films and wafers, respectively, and R is the radius of curvature.

Results

Stress-temperature relationships.—Figure 2 shows the stress-temperature relationships of APCVD films

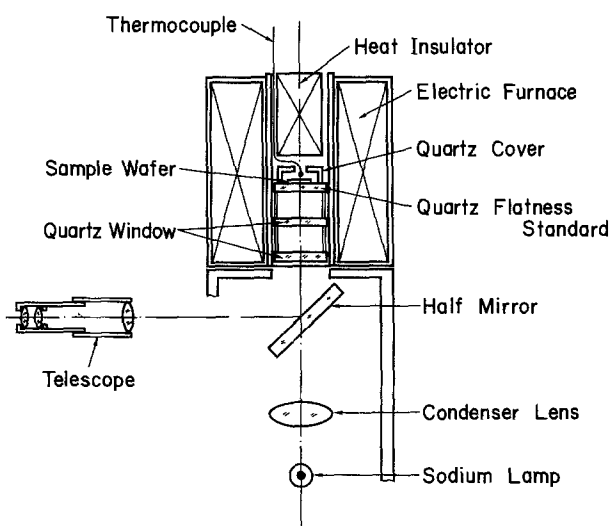

Fig. 1. Schematic view of experimental apparatus

* Electrochemical Society Active Member.

Key words: stress-temperature relationship, heat-treatment, stress propagation mechanism.

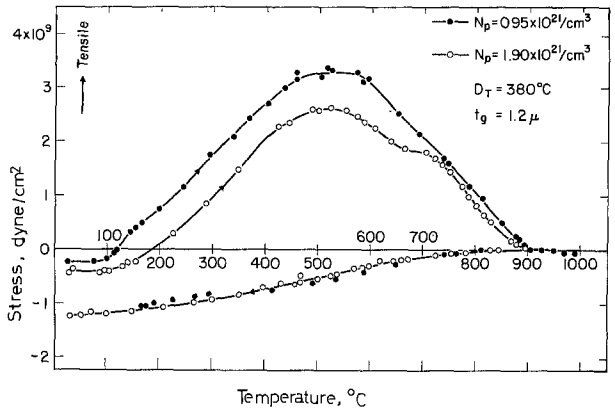

Fig. 2. Stress-temperature relationship of APCVD PSG films deposited at 380°C.

deposited at 380°C. The initial stress before heating is compressive. This may be caused by the long storage time of samples, as is shown below. Above 100°C, the stress decreases and changes to tensile with increasing temperature. The stress reaches a maximum at about 500°C, then decreases, and completely disappears above 900°C. On cooling, compressive stress develops below about 700°C and increases with decreasing temperature. A small hump at about 700°C is observed in some samples though we failed to connect it to any sample preparation process or composition.

Figure 3 also shows the stress-temperature relationship of APCVD PSG and SiO_2 films deposited at 500°C. Similar results can be observed except for SiO_2 film where the initial stress is tensile, and the tensile stress remains until 1000°C. The stress maximum temperature of the SiO_2 film is about 700°C. When phosphorus content is above 2.8×10^{21} atoms/cm³ ($\simeq$6 mol percent P_2O_5) no significant stress can be observed at any temperature.

Figure 4 shows stress of LPCVD films of various phosphorus concentrations in relation to temperature. In contrast to APCVD films, initial stress of SiO_2 films is compressive although the stress maximum temperature is approximately the same as that of APCVD films. In the case of PSG films, behavior of stress is similar to that of APCVD.

Stress maximum temperature and maximum stress are shown in Fig. 5 in relation to phosphorus concentration in the films. Maximum stress of APCVD decreases with increasing phosphorus concentration, but only a slight decrease of the stress is observed in LPCVD PSG films. On the other hand, the stress maximum temperature of PSG films is constant regardless of deposition method or phosphorus content.

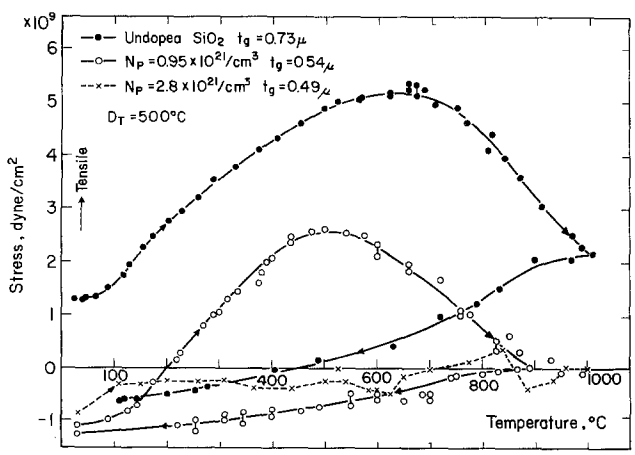

Fig. 3. Stress-temperature relationship of APCVD SiO_2 and PSG films deposited at 500°C.

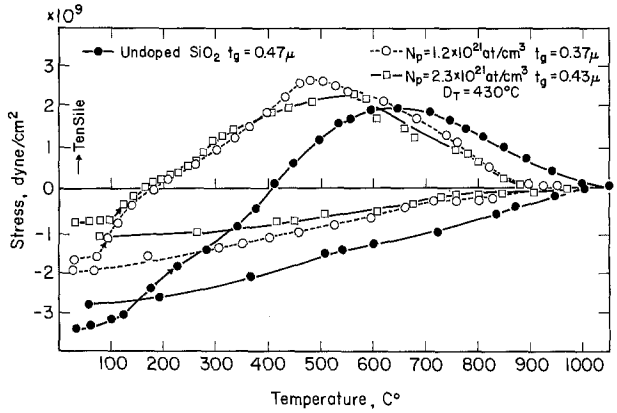

Fig. 4. Stress-temperature relationship of LPCVD SiO_2 and PSG films.

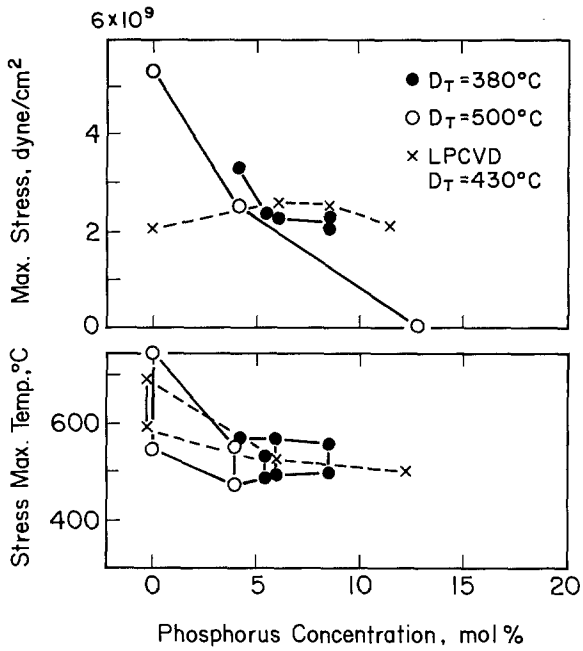

Fig. 5. Maximum stress and stress maximum temperature of APCVD and LPCVD PSG films in relation to phosphorus concentration.

Effect of heat-treatment.—Figures 6 and 7 show stress-temperature relationships of APCVD films under various heating cycles. When the films are kept at constant temperature near, but below or above, the stress maximum temperature, stress increases or decreases with time, respectively. On cooling, stress decreases monotonously. Further decrease in stress is observed after storage at room temperature, if heat-treatment temperature is limited below the stress maximum temperature, though its rate is small. When the sample was reheated, the stress increased nearly parallel to the cooling curve up to the initial heating temperature. Above that temperature, the stress-temperature curves change similar to that shown in Fig. 2 and 3. Similar stress-temperature loops are observed on LPCVD PSG films.

Time dependence of the stress in APCVD PSG films heat-treated at constant temperature is shown in Fig. 8. Stress increases or decreases with time when the heat-treatment temperature is below or above the stress maximum temperature.

Change of stress after deposition.—Figure 9 shows change of stress in APCVD PSG films stored at room temperature in relation to the phosphorus concentrations. Stress in films just after deposition is tensile, but it decreases or turns to compression after one week.

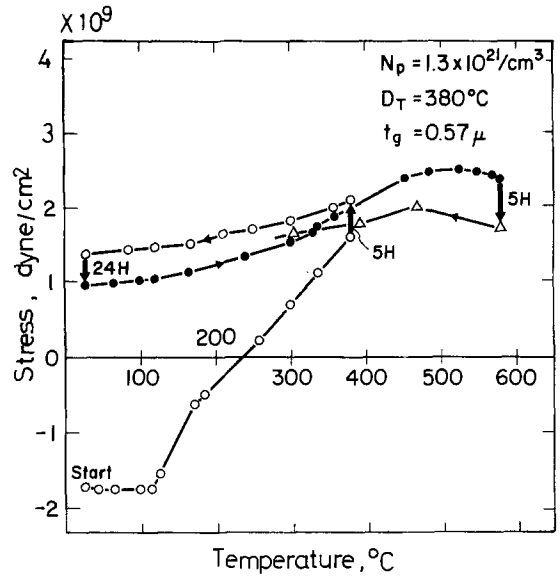

Fig. 6. Stress-temperature relationship of APCVD PSG films under various heat-treatments.

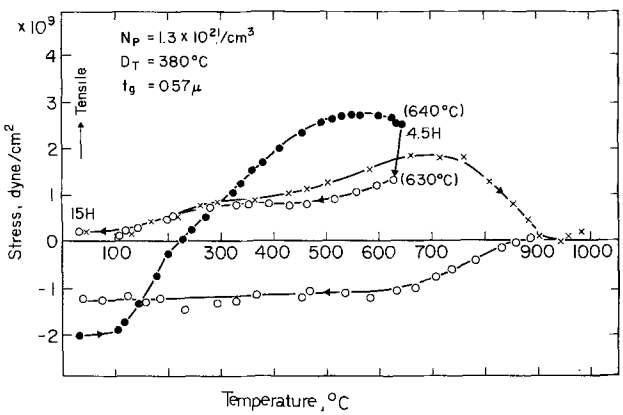

Fig. 7. Stress-temperature relationship of a APCVD PSG film heat-treated above the stress maximum temperature.

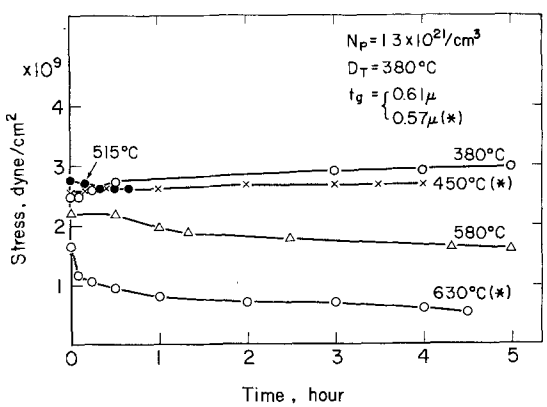

Fig. 8. Stress in APCVD PSG films in relation to heating time at various temperatures.

Similar results have been reported by Sunami (5). These phenomena are explained as the swelling of films with adsorption of water.

Discussion

Pulker (6) reported that the total stress developed in films originates from (*i*) redistribution of incomplete structural order, (*ii*) the chemical and physical incorporating materials, and (*iii*) thermal expansion difference between the films and substrates. The total stress in CVD PSG and SiO_2 films can be explained by

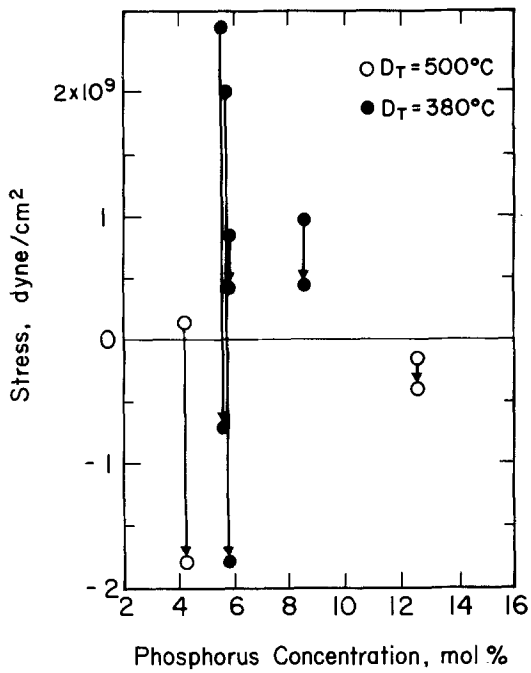

Fig. 9. Change of stress in APCVD PSG films at room temperature after deposition in relation to phosphorus concentration in the films.

using similar mechanisms. Quantitative separation of the above factors, however, is quite difficult in our experiment because they are supposed to be correlated with each other, and many physical constants of the films (ν, E, etc.) are unknown. Therefore the dominant process contributing to the total stress will be qualitatively proposed.

Stress-temperature relationships up to the stress maximum temperature can be explained if we assume that CVD films are porous in nature like silica gel or porous glass, and water molecules are absorbed or desorbed to reach an equilibrium determined with temperature and humidity (11, 12). LPCVD SiO_2 films which absorb much water (9) swell to propagate compressive stress at room temperature, while tensile stress develops on APCVD SiO_2 films in which swelling with water is not sufficient to compensate shrinkage which may be based on the above mechanism (*i*) according to Pulker. In the case of PSG films, behavior of stress is similar to that of LPCVD SiO_2 but sign and magnitude of initial stress depend on their composition and deposition conditions together with the storage time under humidity. Above 100°C, all films shrink with dehydration up to the stress maximum temperature.

Some irreversible dehydration polymerization may proceed in this temperature range because the stress reducing rate of the films heat-treated below the stress maximum temperature is small at room temperature (cf. Fig. 6). But change of the maximum stress could not be detected after annealing the films below the stress maximum temperature. Above the stress maximum temperature, the total stress reduces with sintering and creeping of films (9).

The stress maximum temperature of PSG films is constant, and is consistent with the solidus line in the SiO_2-P_2O_5 phase diagram (13). The phase diagram also shows that the stable phase of PSG films may be a mixture of SiO_2 and low melting phosphosilicates.

Segregation of constituents in some PSG films during deposition is plausible because the high temperature hump shown in Fig. 2 coincides with the stress maximum temperature of SiO_2 films shown in Fig. 3. PSG films completely melt and flow above 900°C, and stresses caused by thermal expansion difference between substrates and films develop below the strain

temperature (about 700°C for PSG films) during cooling. Cooling curves of the stress shown in Fig. 6 and 7 suggest that reduction of stress in annealed films on cooling is also caused mainly by the thermal expansion difference. But change of the stress in these films was larger than that in the remelted films under the same temperature change. This suggests that the mechanical constants (E and ν) or the thermal expansion coefficient of annealed and sintered films are not equal.

Conclusion

Stress of APCVD SiO_2 films on heating is tensile (from room temperature to 1000°C) and has a maximum at about 700°C, while that of LPCVD SiO_2 changes from compression to tension, though its maximum temperature coincides with the former. In the case of PSG, the stress temperature curves resemble that of LPCVD SiO_2, but have a maximum at about 500°C regardless of film compositions and preparation conditions.

Stress of films is attributed to swelling or shrinking caused by water adsorption or desorption up to the stress maximum temperature above which sintering and stress release with creep proceed. The stress maximum temperature from which sintering proceeds corresponds to the solidus line in SiO_2-P_2O_5 binary system. Segregation of constituent in some PSG films between SiO_2 and low melting glass before heat-treatments is plausible.

Acknowledgment

The author wishes to thank Dr. T. Kishii of Toshiba R & D Center for useful suggestions about this experimental method. The author also wishes to acknowledge M. Hirai for the x-ray fluorescence analyses.

Manuscript submitted April 12, 1982; revised manuscript received July 19, 1982. This was Paper 313 presented at the Hollywood, California, Meeting of the Society, Oct. 5-10, 1980.

Any discussion of this paper will appear in a Discussion Section to be published in the December 1983 JOURNAL. All discussions for the December 1983 Discussion Section should be submitted by Aug. 1, 1983.

Publication costs of this article were assisted by Toshiba R & D Center.

REFERENCES

1. G. L. Schnable, W. Kern, and R. B. Comizzoli, *This Journal*, **122**, 1092 (1975).
2. W. Kern, G. L. Schnable, and A. W. Fisher, *RCA Rev.*, **37**, 3 (1976).
3. W. Kern, *ibid.*, **37**, 55 (1976).
4. W. Kern, *Vac. Sci. Technol.*, **14**, 1082 (1977).
5. H. Sunami, Y. Itoh, and K. Sato, *J. Appl. Phys.*, **41**, 5115 (1970).
6. H. K. Pulker, *Appl. Optics*, **18**, 1969 (1979).
7. D. S. Campbell, "Handbook of Thin Film Technology," Chap. 12, McGraw-Hill, New York (1970).
8. A. K. Sinha, H. J. Levinstein, and T. E. Smith, *J. Appl. Phys.*, **49**, 2423 (1978).
9. A. Shintani, S. Sugai, and H. Nakashima, *ibid.*, **51**, 4197 (1980).
10. R. J. Jacodine and E. A. Schelgel, *ibid.*, **37**, 2429 (1966).
11. R. K. Iler, "The Colloid Chemistry of Silica and Silicate," Cornell University Press, Ithaca, NY (1955).
12. P. J. Sereda and R. F. Feldman, "The Solid Gas Interface," Vol. 2, p. 729, Marcel Dekker, New York (1967).
13. T. Y. Tien and F. A. Hummel, *J. Am. Ceram. Soc.*, **45**, 424 (1962).

Kinetics of Changes in N_f and D_{it} at the Si-SiO_2 Interface under Long-Term Positive as well as Negative Bias-Temperature Aging

Noboru Shiono, Osaake Nakajima, and Chisato Hashimoto

Nippon Telegraph and Telephone Public Corporation, Musashino Electrical Communication Laboratory, Musashino-shi, Tokyo, 180 Japan

ABSTRACT

The kinetics of changes in fixed oxide charge density, N_f, and interface trap density, D_{it}, under bias-temperature (BT) stress aging has been determined for poly Si-thin SiO_2 (40-50 nm)-silicon structures formed by three gate oxidation methods; dry O_2, steam, and HCl oxidation. Positive BT aging, that is the aging with a positive voltage applied to the gate at an elevated temperature, causes D_{it} generation in the upper half of the bandgap. Here, a peak appears at around 0.7 eV above the valence bandedge. Negative BT aging causes a negative flatband voltage V_{FB} shift accompanied by D_{it} generation. Here, a D_{it} broad peak appears at around 0.4 eV above the valence bandedge. Time, temperature, and oxide field dependence for V_{FB} shifts and D_{it} generation are investigated for three oxides. Comparing the amount of changes in N_f and D_{it} under BT aging in ±3 MV/cm, 250°C, and 2000 hr, HCl oxides are found to be the most stable and steam oxides the most unstable.

It is well known that fixed oxide charges and interface trapped charges are generated at the Si-SiO_2 interface under negative bias-temperature (BT) stress aging, that is the aging with a negative voltage applied to the gate at an elevated temperature. This is the so-called slow trapping instability, and is potentially a major threat to the reliability of p-channel MOSFET devices (1-9). Few experimental results other than mobile ion effects, however, have been reported on changes in interface properties of the Si-SiO_2 interface under positive BT stress aging. Such results are important for estimating the reliability of n-channel MOSFET devices, which are widely used.

Key words: MOS devices, reliability, interface stability, fixed oxide charge, interface trapped charge.

It has been reported recently that interface trapped charges are generated under long-term positive BT aging, without an increase in fixed oxide charges (10). This effect has also been reported to cause a positive threshold voltage shift in n-channel MOSFET's (11). The object of the present work has been to obtain more detailed information on the kinetics of changes in fixed oxide charges and interface trapped charges under positive, as well as negative, bias-temperature stress aging of poly Si-thin SiO_2- p-Si capacitors. Special focus is placed on the influence of gate oxide formation methods. Dry O_2 oxides, steam oxides, and HCl oxides are chosen for comparing the effects on the interface stability of the Si-SiO_2 interface.

Experimental

Sample preparations.—Polysilicon (phosphorus doped)-thin SiO_2-silicon capacitors were fabricated using the standard silicon gate technology with applied LOCOS process (12) as previously described (10). (100) oriented p-type silicon substrates with 2-5 Ω · cm resistivity were used. After the LOCOS process, a thin gate silicon dioxide layer, with a 40-50 nm thickness, was grown by dry O_2 oxidation, steam oxidation, and HCl oxidation. Dry O_2 oxidation was carried out at 1000°C. Steam oxidation was performed by the direct reaction of H_2 and O_2 in a pyrogenic system at 900°C. For HCl oxidation, a 5% HCl/O_2 (volume percent) ambient was used. After oxidation for 20 min at 1150°C to a thickness of about 120 nm, the oxides were thinned to about 50 nm by etching, using a dilute HF solution. This preparation method was used to obtain good passivation effect against mobile ions in HCl oxides. This referred to Rohatgi's result (13), as complete passivation was accomplished by adequate oxidation in high HCl concentration ambients at high temperature, such as in 4% HCl/O_2 at 1150°C for 30 min. Phosphorus-doped polysilicon was then grown to form gate electrodes. After the polysilicon was etched out from regions other than the gate and interconnects, a thick CVD SiO_2 layer was deposited for surface passivation. Contact windows were defined and CVD SiO_2 was etched. Aluminum was then evaporated to prepare bonding pads on the field oxides. These pads are intended to exclude such damage on the thin gate SiO_2 as might be caused by bonding stress. Finally, the wafers were annealed in forming gas at 450°C to reduce fixed oxide charges and interface trapped charges. Dicing chips were mounted on TO-5 headers by alloying gold silicon. After aluminum wires were bonded between the bonding pads and the posts of TO-5 packages, the chips were encapsulated in a dry N_2 ambient.

The gate oxide formation method was a variable process parameter. Dry O_2, steam, and HCl oxidation were chosen for preparing thin gate oxides. Although the oxidation temperature varied depending on the oxidation method, the oxidation conditions employed were the most suitable for obtaining good controlability and reproducibility in preparing thin gate oxides, and for realizing each oxide's quality.

Aging method and measurements.—Bias-temperature stress aging was carried out under various stress conditions. A positive or negative oxide field, ranging from 2 to 6 MV/cm, was applied to the gate electrode with respect to the silicon substrate at an elevated temperature of from 150° to 300°C, and aging time was extended to 2000 hr. Here, the oxide field was defined simply as the applied gate voltage divided by the gate oxide thickness.

Flatband voltage V_{FB} shift and change in interface trap density D_{it} distribution were estimated after BT aging. The V_{FB} shift was obtained from high-frequency (1 MHz) *C-V* measurements. Interface trap density, as a function of relative surface potential, was obtained through the quasi-static *C-V* technique, and measured by means of a computerized *C-V* analysis system. The quasi-static *C-V* method allows an accurate determination of interface trap density between about 300 mV above the valence bandedge and about 300 mV below the conduction bandedge in the forbidden gap. The accuracy of the interface trap density measurement was about 1×10^{10} cm^{-2} eV^{-1} at midgap.

Results and Discussion

Initial characteristics.—Table I shows the initial state of flatband voltage V_{FB}, fixed oxide charge density N_f, and interface trap density D_{it} at midgap. These values were obtained from measurement of about 50 samples for each oxide. Since the initial values of N_f and D_{it} were less than 4×10^{10} cm^{-2} and 2×10^{10} cm^{-2} eV^{-1}, respectively, for all MOS capacitors, these oxides were verified to be of good quality. Mobile ionic charge density in the oxides was also below 5×10^9 cm^{-2}, because the V_{FB} shift after positive BT aging was within 10 mV, which is the experimental accuracy.

Table I. Initial characteristics of flatband voltage, fixed oxide charge density, and interface trap density

Gate oxide formation method	Gate oxide thickness t_{ox} (nm)	Concentration of acceptor impurities N_A (cm^{-3})	Flatband voltage V_{FB} (V)	Fixed oxide charge density N_f* (10^{10} cm^{-2})	Interface trap density D_{it} (10^{10} cm^{-2} eV^{-1})
Dry O_2	40	1.5×10^{15}	-0.88 ± 0.01	~1	<2
Steam	40	3.5×10^{15}	-0.89 ± 0.01	~1	<2
HCl	50	9.0×10^{15}	-1.00 ± 0.01	~4	<2

* For calculating this value, we use $\Phi_{ms} = -0.55 - \Psi_F$ (14).

Representative C-V curves.—Figure 1 shows typical *C-V* curves in the initial state and after positive BT aging. Figure 2 shows changes in the interface trap density distribution that correspond to the *C-V* curves shown in Fig. 1. There were three main features in the positive BT aging. (*i*) The initially single minimum in the quasi-static *C-V* curve was split into two minima which occurred at a significantly higher C/C_{ox}. This splitting resulted from an increase in D_{it}, which had a peak around 0.7 eV above the valence bandedge, as shown in Fig. 2. (*ii*) The high frequency *C-V* curve shifted to more positive values, indicating positive V_{FB} shifts for steam oxides. For dry O_2 oxides and HCl oxides, however, the curve did not shift, although a positive V_{FB} shift was observed after aging in an oxide field higher than 5.5 MV/cm. (*iii*) Strong inversion voltage, namely threshold voltage V_T, shifted to more positive values, as indicated by the vertical arrows in Fig. 1. This was due to the increase in acceptor-

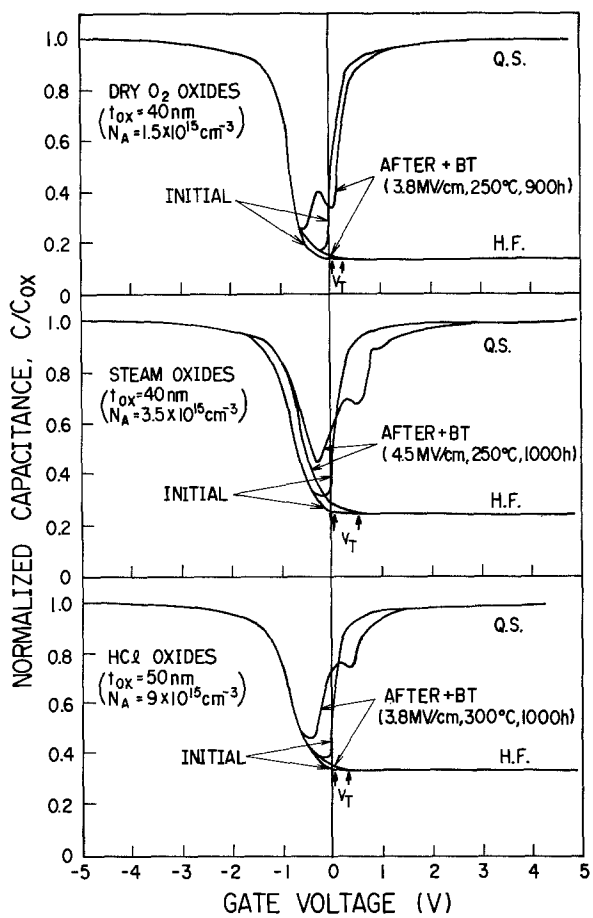

Fig. 1. Typical changes in high frequency (H.F.) *C-V* curves and quasi-static (Q.S.) *C-V* curves due to positive BT aging.

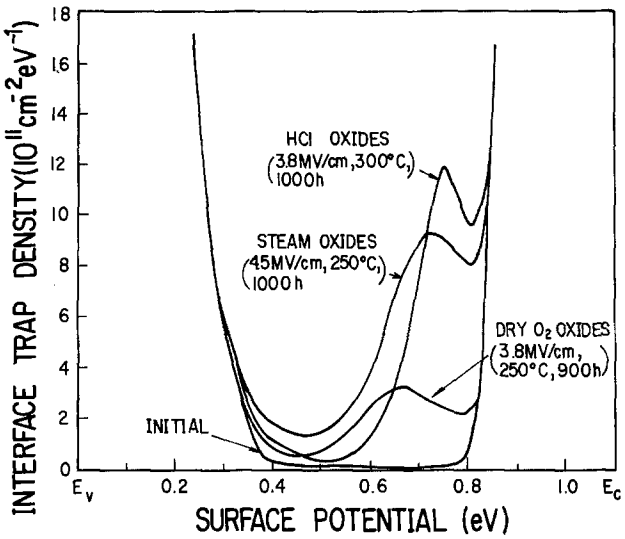

Fig. 2. Changes in interface trap density D_{it} distribution due to positive BT aging, derived from quasi-static C-V curves shown in Fig. 1.

type interface trapped charges in the upper half of the bandgap (11).

Figure 3 shows typical C-V curves in the initial state, and after negative BT aging. Interface trap density distributions corresponding to these C-V curves are shown in Fig. 4. There were also three main features in negative BT aging. (*i*) The high frequency C-V curve shifted to more negative values, indicating a negative V_{FB} shift for all oxides. This shift was in the opposite direction to that induced by positive BT aging. (*ii*) Interface trap density increased over the entire bandgap. For dry O_2 and steam oxides, a broad but readily identifiable peak in D_{it} at around 0.4 eV above the valence bandedge was observed after high temperature or long aging. Such a distinct peak, however, could not be observed for HCl oxides. The D_{it} peak at around 0.4 eV above the valence bandedge is similar to the results reported by Goetzberger (3) and Saminadayer (5) observed by negative BT aging on metal gate MOS capacitors. (*iii*) Strong inversion voltage shifted little, as compared to an amount of negative V_{FB} shift. Under high stress aging conditions, V_T shifted to more positive voltages in spite of negative V_{FB} shift, indicating the increase in acceptor-type interface trapped charges.

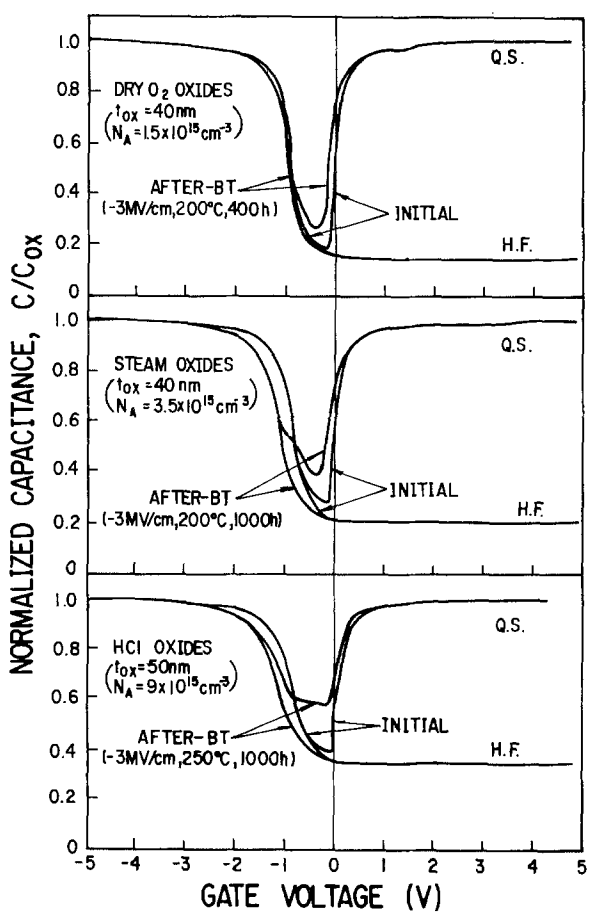

Fig. 3. Typical changes in high frequency C-V curves and quasi-static C-V curves due to negative BT aging.

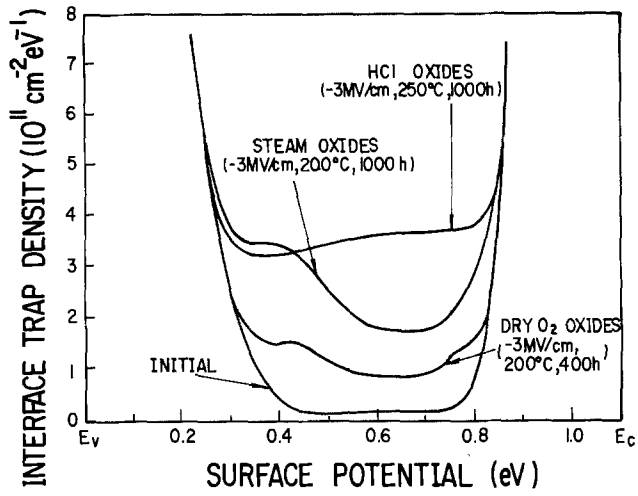

Fig. 4. Changes in interface trap density distribution due to negative BT aging, derived from quasi-static C-V curves shown in Fig. 3.

Kinetics of V_{FB} shifts.—Kinetics measurements on the V_{FB} shift were made under positive and negative BT aging. Figure 5 shows positive V_{FB} shift *vs.* aging time observed under positive BT aging, given as a function

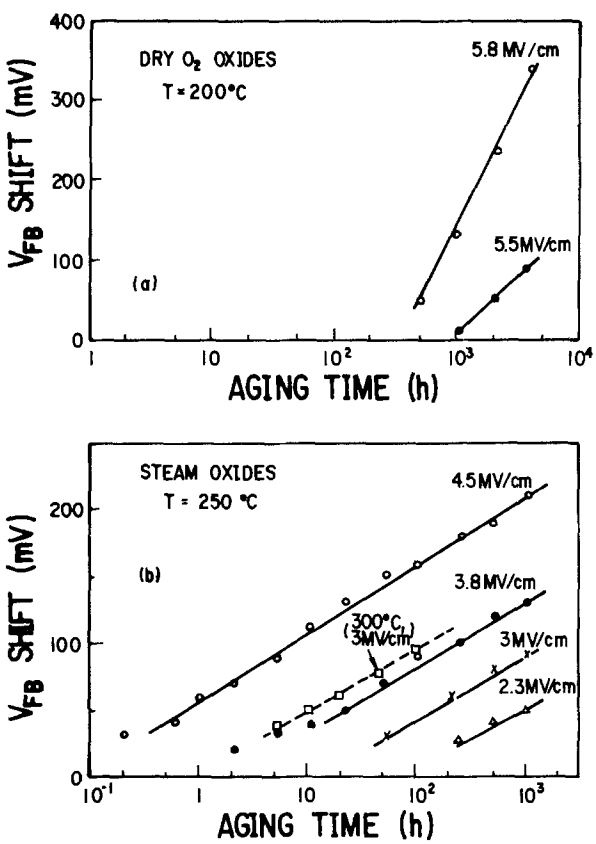

Fig. 5. Time dependence for flatband voltage V_{FB} shifts during positive BT aging. (a) For dry O_2 oxides. (b) For steam oxides.

of oxide fields and of temperatures. For dry O_2 oxides, a positive V_{FB} shift was observed after a high oxide field aging at 5.5 MV/cm and 200°C for 1000 hr. At standard aging conditions employed in the experiment, 3 MV/cm, 250°C, and 2000 hr, however, V_{FB} did not shift for dry O_2 and HCl oxides.

For steam oxides, a positive V_{FB} shift appeared under relatively weak stress conditions, when compared to the stress for dry O_2 and HCl oxides. V_{FB} shifted logarithmically with aging time. It is thus possible to express the V_{FB} shift approximately in the following relationship

$$\Delta V_{FB} \sim 50 \log (t/t_0) \quad [1]$$

where ΔV_{FB} is the V_{FB} shift in mV units, t is the aging time in hour units, and t_0 is the starting time for the V_{FB} shift in hour units. The oxide field dependence for t_0^{-1} can be expressed as exponential form $t_0^{-1} \propto \exp(AE_{OX})$, where A is determined from the plots of log (t_0^{-1}) *vs.* the oxide fields. Combining this field dependence with a temperature dependence for t_0^{-1}, which can be determined from the Arrhenius plots of log (t_0^{-1}) *vs.* the inverse aging temperatures, it is possible to express t_0^{-1} in the following simple form

$$t_0^{-1} \sim 1.0 \times 10^{13} \exp(-1.35/kT + 3.0\,E_{OX}) \quad [2]$$

where E_{OX} is the oxide field in MV/cm units and kT is the thermal voltage at the aging temperature in eV units.

Figure 6 shows the time dependence of the negative V_{FB} shift under negative BT aging, given as a function of aging temperatures. Negative V_{FB} shifts appeared faster than positive V_{FB} shift induced by positive BT aging, when compared to the same stress conditions other than bias polarity. For steam oxides the V_{FB} shift tended to saturate after several tens of hours aging. For dry O_2 and HCl oxides, however, the V_{FB} shift did not saturate even after 1000 hr aging at 300°C. These experimental facts are contrary to previously reported results, where negative V_{FB} shift tends to saturate after two hours at −10V and 300°C aging for steam oxide capacitors that are about 100 nm thick gate oxides on (111) Si (1).

Figure 6 indicates that under shorter aging time of less than 100 hr, the magnitude of the negative V_{FB} shift for steam oxides was two or three times larger than that for dry O_2 and HCl oxides. On the other hand, under a longer aging period, the negative V_{FB} shift for HCl oxides increased faster than that for dry O_2 and steam oxides.

For dry O_2 and steam oxides, V_{FB} shifted logarithmically with time, irrespective of aging temperatures. Thus, the negative V_{FB} shift before saturation under a −3 MV/cm field can be expressed approximately as follows, by referring to the Arrhenius plots for the starting time t_0^{-1} for the V_{FB} shift *vs.* the inverse aging temperatures

Dry O_2 oxides: $\Delta V_{FB} \sim -25 \log (t/t_0)$

$$t_0^{-1} \sim 6.7 \times 10^{12} \exp(-1.1/kT) \quad [3]$$

Steam oxides: $\Delta V_{FB} \sim -80 \log (t/t_0)$

$$t_0^{-1} \sim 1.9 \times 10^{15} \exp(-1.5/kT) \quad [4]$$

where the units of the quantities are the same as in Eq. [1] and [2].

For HCl oxides, V_{FB} shifted with the time dependence of t^n, but n varied from temperature to temperature. n was 0.31 at 300°C aging, 0.25 at 250°C, and 0.20 at 200°C aging. Therefore, time dependence for the V_{FB} shift cannot be summarized in a simple form. It is noticeable that time dependence parameter n becomes large with raising aging temperatures.

Kinetics of D_{it} increase.—The development for D_{it} peak which appeared at around 0.7 eV above the valence bandedge was examined under positive BT aging. Figure 7 shows D_{it} increase *vs.* aging time for the three

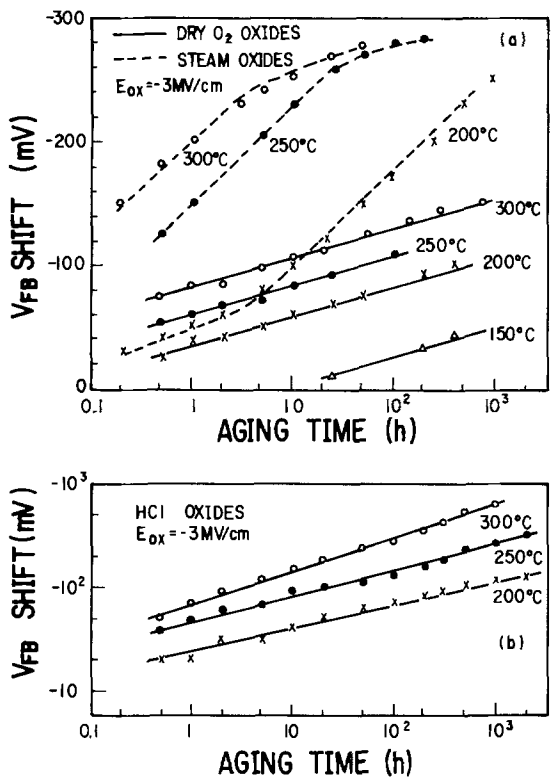

Fig. 6. Time dependence for V_{FB} shifts during negative BT aging in a −3 MV/cm oxide field, given as a function of aging temperatures. (a) For dry O_2 oxides and steam oxides. (b) For HCl oxides.

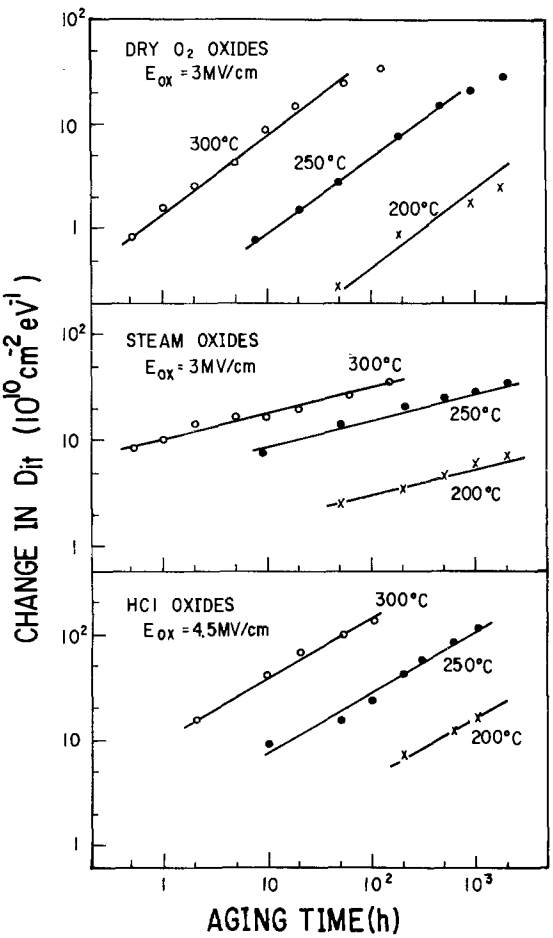

Fig. 7. Time dependence for increase in interface trap density D_{it} peak at around 0.7 eV above the valence bandedge during positive BT aging.

oxides, given as a function of aging temperatures. D_{it} peak was found to increase in proportion to nth power of aging time, where n is 0.67 for dry O_2 oxides, 0.25 for steam oxides, and 0.57 for HCl oxides. The rate of D_{it} increase was also found to increase exponentially with the reciprocal temperatures and exponentially with the square root of the oxide fields as shown in Fig. 8. Thus, time, temperature, and field dependence for D_{it} increase can be expressed as a simple form for each oxide

Dry O_2 oxides:

$$\Delta D_{it} \sim 9.1 \times 10^5 \exp(-1.0/kT + 4.0\sqrt{E_{ox}})t^{0.67} \quad [5]$$

Steam oxides:

$$\Delta D_{it} \sim 4.1 \times 10^3 \exp(-0.58/kT + 3.3\sqrt{E_{ox}})t^{0.25} \quad [6]$$

HCl oxides:

$$\Delta D_{it} \sim 6.1 \times 10^{-1} \exp(-0.82/kT + 6.7\sqrt{E_{ox}})t^{0.56} \quad [7]$$

where ΔD_{it} is the increase in the D_{it} peak in 10^{10} cm^{-2} eV^{-1} units, E_{ox} is the applied oxide field in MV/cm units, t is the aging time in hour units, and kT is the thermal voltage at the aging temperature in eV units.

Time evolution for the broad D_{it} peak at around 0.4 eV above the valence bandedge was examined under negative BT aging for an oxide field of −3 MV/cm. The results are plotted in Fig. 9, where the increase in D_{it} at 0.4 eV above the valence bandedge is also plotted for HCl oxides. D_{it} generation under negative BT aging appeared quickly in comparison with that induced by positive BT aging, when comparison was made under the same stress conditions except for bias polarity. D_{it} was found to increase with time dependence of t^n, where n was 0.20 for dry O_2 oxides, 0.17 for steam oxides, and 0.57 for HCl oxides. The D_{it} increases, thus, can be approximately expressed in the following simple forms

Dry O_2 oxides: $\Delta D_{it} \sim 3.5 \times 10^3 \exp(-0.28/kT)t^{0.20}$ [8]

Steam oxides: $\Delta D_{it} \sim 7.8 \times 10^3 \exp(-0.29/kT)t^{0.17}$ [9]

HCl oxides: $\Delta D_{it} \sim 1.4 \times 10^4 \exp(-0.45/kT)t^{0.57}$ [10]

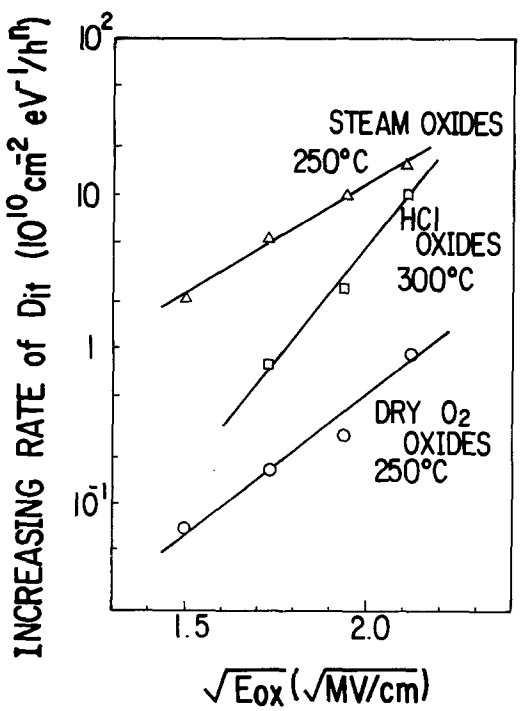

Fig. 8. Increasing rate of interface trap density peak plotted in relation to square root of oxide field. Time dependent parameter n is 0.67 for dry O_2 oxides, 0.25 for steam oxides, and 0.56 for HCl oxides.

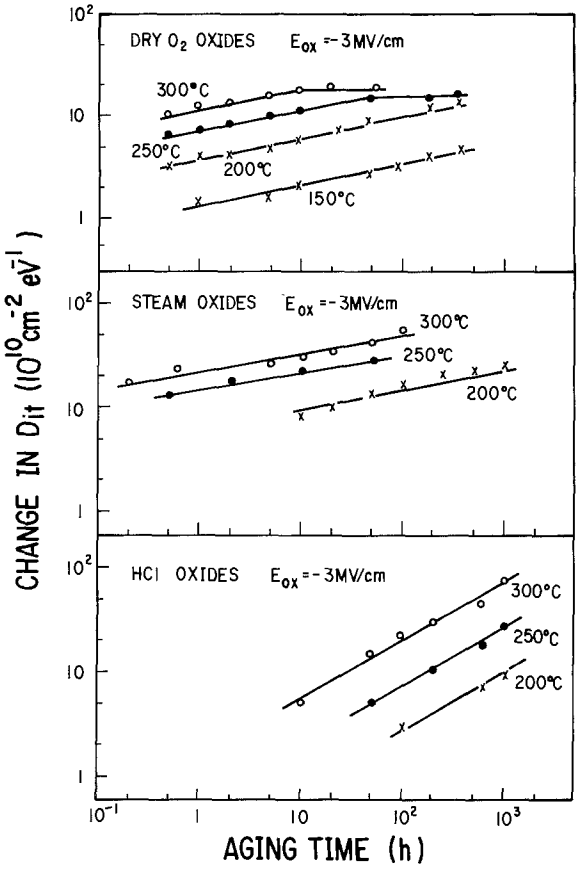

Fig. 9. Time dependence for increase in interface trap density at around 0.4 eV above the valence bandedge, during negative BT aging, given as a function of aging temperatures.

where the units of the quantities are the same as in Eq. [5]-[7].

From these results, it was verified that steam oxides showed fast D_{it} increase, whereas HCl oxides showed slow D_{it} increase, when compared to the same stress aging conditions for three oxides.

Discussion on BT aging behavior.—The negative V_{FB} shift, accompanied by an increase in D_{it}, induced by negative BT aging has been known as a slow trapping instability. This instability has been attributed to field-temperature induced structural rearrangements at the $Si-SiO_2$ interface (4). Breaking strained Si-O bonds of a partially ionized Si atom, or Si-H or Si-OH bonds near the interface, results in the generation of positive fixed oxide charges and of interface trapped charges (4, 6). Since steam oxides would contain more Si-H and Si-OH bonds near the interface than other oxides (15), a large negative V_{FB} shift and fast D_{it} increase could be observed. On the other hand, HCl oxides contain more Si-Cl bonds in place of Si-H, Si-OH bonds, and dangling bonds near the interface. The Si-Cl bonds are believed to be more stable than Si-H or Si-OH bonds, since high temperature oxidation above 1150°C was carried out to incorporate Cl into the oxides. This explains the experimental fact that HCl oxides showed small V_{FB} shifts and D_{it} increase at a low aging temperature or under short aging period. Large V_{FB} shift and D_{it} increase were observed, however, at such a high temperature as 300°C and under longer aging time than several tens of hours. This may be accounted for by the breaking of Si-Cl bonds and strained Si-O bonds near the interface under a high stress aging condition, as has been reported by Hess (7).

Interface trapped charge generation in the upper half of the bandgap under positive BT aging seems to be caused by field-temperature induced structural modification at the $Si-SiO_2$ interface, especially breaking or

stretching of Si-O bonds. This is because, as Sakurai (16) has pointed out, energy levels of weak Si-O bonds at the Si-SiO_2 interface appear at the upper half of the forbidden gap.

HCl oxides showed small D_{it} increase under positive BT aging, compared to other oxides. This is believed to be caused by the oxide quality formed at an extremely high temperatures as 1150°C and stable Si-Cl bonds near the interface.

Positive V_{FB} shifts appeared for steam oxides under positive BT aging in relatively low oxide fields. This is believed to be due to electron trapping at the water-related centers in the oxides which may be contained in steam oxides (17, 18). A very small amount of electrons would inject from silicon into the oxides under positive gate bias at a high temperature, although it was not measurable because of the very small current level. On the other hand, for dry O_2 oxides, a considerable positive V_{FB} shift was observed under aging in an oxide field higher than 5.5 MV/cm. This oxide field corresponded to about 10^{-10} A/cm^2 Fowler-Nordheim current at 200°C. This positive V_{FB} shift, therefore, can be attributed to electron trapping in oxide trap centers, induced by current flowing into the oxides.

Summary and Conclusion

The kinetics of changes in V_{FB} and D_{it} have been investigated for polysilicon gate MOS capacitors having three kinds of gate oxides; dry O_2, steam, and HCl oxides.

Positive BT aging causes an increase in D_{it} which peaks at around 0.7 eV above the valence bandedge. This effect is responsible for a positive threshold voltage shift of MOSFET's. This aging also causes a positive V_{FB} shift, which appears under a relatively low oxide field aging for steam oxides. For dry O_2 oxides, on the other hand, it appears under only high stress aging in an oxide field higher than 5.5 MV/cm.

Comparing stability among the three oxides under the same stress aging conditions, HCl oxides turn out to be most stable, and steam oxides least stable.

It is hypothesized that interface trapped charges are generated by field-temperature induced dissociation of such weak bonds as strained Si-O bonds, Si-H bonds, Si-OH bonds, and Si-Cl bonds, that are near the Si-SiO_2 interface. The difference in stability among the oxides causes the difference in the number of weak bonds and in the ease of bond breakage. However, the exact physical origin for field-temperature induced interface instability remains uncertain.

Acknowledgments

The authors would like to thank M. Kondo, J. Kato, H. Ikawa, and S. Muramoto for their advice and encouragement. They are also indebted to E. Watanabe for measurements, and the members of the Semiconductor Memory Technology Section for sample preparations.

Manuscript submitted July 30, 1981; revised manuscript received March 17, 1982.

Any discussion of this paper will appear in a Discussion Section to be published in the December 1983 JOURNAL. All discussions for the December 1983 Discussion Section should be submitted by Aug. 1, 1983.

Publication costs of this article were assisted by Nippon Telegraph and Telephone Public Corporation.

REFERENCES

1. B. E. Deal, M. Sklar, A. S. Grove, and E. H. Snow, *This Journal*, **114**, 266 (1967).
2. S. R. Hofstein, *Solid-State Electron.*, **10**, 657 (1967).
3. A. Goetzberger, A. D. Lopez, and R. J. Strain, *This Journal*, **120**, 90 (1973).
4. B. E. Deal, *ibid.*, **121**, 198C (1974).
5. K. Saminadayer and J. C. Pfister, *Solid-State Electron.*, **20**, 891 (1977).
6. K. O. Jeppson and C. M. Svensson, *J. Appl. Phys.*, **48**, 2004 (1977).
7. D. W. Hess, *This Journal*, **124**, 740 (1977).
8. A. K. Sinha, H. J. Levinstein, L. P. Adda, E. N. Fuls, and E. I. Povilonis, *Solid-State Electron.*, **21**, 531 (1978).
9. A. K. Sinha and T. E. Smith, *This Journal*, **125**, 743 (1978).
10. N. Shiono and T. Yashiro, *Jpn. J. Appl. Phys.*, **18**, 1087 (1979).
11. N. Shiono and C. Hashimoto, *IEEE Trans. Electron Dev.*, **ed-29**, 361 (1982).
12. J. A. Appels, E. Kooi, M. M. Paffen, J. J. H. Schatorje, and W. H. C. G. Verkuylen, *Philips Res. Rep.*, **25**, 118 (1970).
13. A. Rohatagi, S. R. Butler, and F. J. Feigl, *This Journal*, **126**, 149 (1979).
14. F. Faggin and T. Klein, *Solid-State Electron.*, **13**, 1125 (1970).
15. K. H. Beckmann and N. J. Harrick, *This Journal*, **118**, 614 (1971).
16. T. Sakurai and T. Sugano, *J. Appl. Phys.*, **52**, 2889 (1981).
17. E. H. Nicollian, A. Goetzberger, and C. N. Berglund, *Appl. Phys. Lett.*, **15**, 174 (1969).
18. E. H. Nicollian, C. N. Berglund, P. F. Schmidt, and J. M. Andrews, *J. Appl. Phys.*, **42**, 5654 (1971).

Dry Etch Resistance of Organic Materials

H. Gokan, S. Esho, and Y. Ohnishi

Nippon Electric Company, Limited, Basic Technology Research Laboratories, Takatsuku Kawasaki 213, Japan

ABSTRACT

The dry etch resistance of metal-free organic materials, mainly resist materials, has been studied. Etch rates have been measured under argon ion-beam, oxygen ion-beam, and oxygen plasma etching conditions. It is found that the etch rate under ion bombardment has a linear dependence on the "$N/(N_c-N_o)$ factor" of the etched materials, where N, N_c, and N_o denote the total number of atoms in a monomer unit, the number of carbon atoms in a monomer unit, and the number of oxygen atoms in a monomer unit, respectively. The results indicate that the dry etch resistance under ion bombardment is determined by the effective carbon content in a material. The etch rates of the polymers in an oxygen plasma condition have no simple correlation with the effective carbon content in a material. This implies that etching mechanism under ion bombardment differs from the etching mechanism by radical species.

Dry etching techniques have been applied to the fabrication of a wide variety of devices. These techniques produce precise and reproducible etching. However, since the mask material or resist material is simultaneously eroded during etching, the resist material is required to be highly resistant to the etching process.

Consequently, dry etch resistance as well as sensitivity and resolution capability has become one of the

Key words: dry etch resistance, ion-beam etching, resists.

most important factors in the development of resist materials for microfabrication.

Taylor *et al.* (1) reported that the etch rate for positive electron beam resists is proportional to the Gs value, the efficiency of chain scission per 100 eV of absorbed high energy radiation, in an oxygen plasma reactor system. Helbert *et al.* (2) studied the dry etch resistance of various vinyl resist polymers with a wide range of side chain substituents. Empirically, aromatic polymers are known to be highly resistant to the dry etching process (3). However, the relationship between dry etch resistance and polymer structure has not yet been clarified.

Among various etching techniques (4, 5), accelerated ions and radicals are the most important factors. The ion-bombardment effect is prevalent in ion-beam etching, and the radical effect is prevalent in plasma etching. In reactive ion etching, which has become the most widely used technique in manufacturing semiconductor devices, both accelerated ions and radicals play important roles in controlling pattern profiles.

In this paper, metal-free organic polymer resistance to ion bombardment and oxygen radicals is discussed. Since ion bombardment is an essential factor for anisotropic or precise etching in microfabrication, the results would provide a fundamental understanding on polymer resistance to dry etching process.

Experimental

Etch rates for various metal-free polymers have been measured under argon ion-beam incidence, oxygen ion-beam incidence, and oxygen plasma flow conditions.

A Kaufman type 3 in. ion-gun (Veeco) and a 10 in. diffusion pumping system were used in argon or oxygen ion-beam etching. As an etching gas, argon or oxygen was introduced through a gas inlet port, which is attached to the top end of the gun. Etching samples, coated on silicon wafers, are mounted on a water-cooled rotary stage using a heat sink material. Thus sample bulk temperature is kept below 40°C during etching. Etching chamber pressure was 2×10^{-4} Torr (2.7×10^{-2} Pa) for argon or oxygen. Conventional barrel plasma reactor PR501 (made by Yamato Kagaku), with a 140 mmϕ $\times$ 300 mm Al etch tunnel, was used in oxygen plasma etching. In this system, substrate temperature cannot be controlled independently of plasma heating. The effect of a change in temperature during etching has been avoided by using the same procedure that was proposed by Battey (6). First, the temperature is set somewhat higher than the desired operating (equilibrium) temperature by preheating the reactor without sample loading. Then, the reactor is opened to insert the sample. Next, the power is turned on just when temperature has subsided to the desired temperature.

All the polymers examined in the present experiment are listed in Table I.

Table I. List of organic polymers examined in the present experiment

	Name	Remarks
SEL-N		Somar Manufacturing
PMMA	Poly(methyl methacrylate)	
COP	Poly(glycidyl methacrylate-co-ethyl acrylate)	Mead Associates
CP-3	Poly(methacrylate-co-t-butyl methacrylate)	t-BMA 30%
EBR-9	Poly(α-chloro-trifluoro ethylacrylate)	
PBzMA	Poly(benzyl methacrylate)	
FBM	Poly(hexa fluorobutyl methacrylate)	
FPM	Poly(fluoro propyl methacrylate)	
PMIPK	Poly(methyl isopropenyl ketone)	
PS	Poly styrene	
CMS	Chloromethylated polystyrene	
PαMS	Poly(α-methyl styrene)	
PVN	Poly(vinyl naphthalene)	
PVB	Poly(vinyl biphenyl)	
AZ1350J		Shipley Co., Inc.
CPB	Cyclized polybutadiene	

Results and Discussions

Figure 1 shows the etched depth for several polymers *vs.* etching time, measured under the condition of 2×10^{-4} Torr (2.7×10^{-2} Pa) argon pressure, 500 eV acceleration energy, and about 0.9 mA/cm^2 ion current density. The polymer film thicknesses were measured with a stylus instrument (a Talystep made by Taylor-Hobson). Note that the etch rate for certain polymers decreases after etching for several minutes. The etch rate decrease was observed for PMMA, CP-3, EBR-9, COP, and FPM. It was found that decrease in etch rate was almost the same for these polymers, 280 Å/min for PMMA, 265 Å/min for EBR-9, 284 Å/min for CP-3, 286 Å/min for COP, and 300 Å/min for FPM, although the initial etch rates are different from each other. The surface roughness increase was observed for these materials, as is typically shown in Fig. 2. This may be attributed to the outgassing from the polymers due to surface temperature rise. On the contrary, no change in etch rate was observed during etching for all the

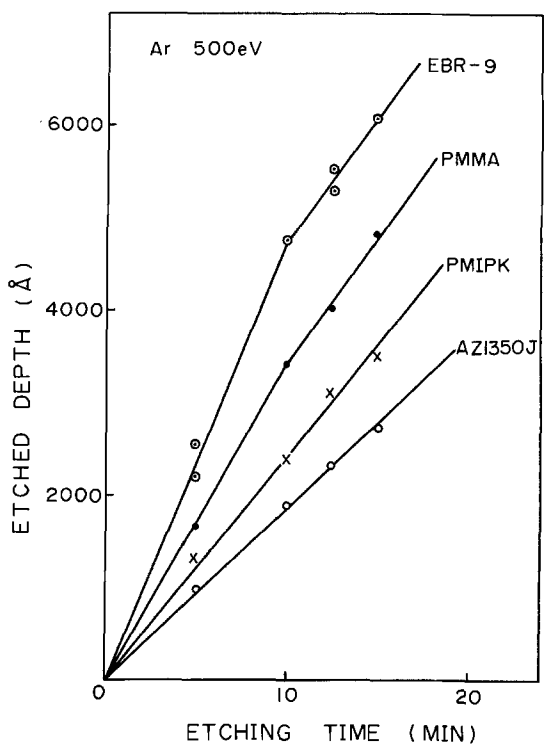

Fig. 1. Etched depth for typical polymers *vs.* etching time measured under 2×10^{-4} Torr (2.7×10^{-2} Pa) argon pressure and 500 eV acceleration energy.

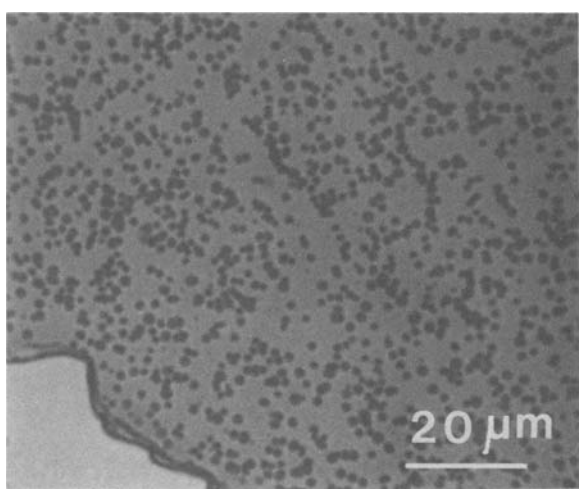

Fig. 2. Surface roughness observed in PMMA after 500 eV argon ion-beam etching.

materials examined under the condition of 300 eV acceleration energy and about 0.3 mA/cm^2 current density. No surface roughness was observed, even after etching polymers down to the same depth that was examined under the 500 eV etching condition.

The etch rate of the various polymers may be considered to be due to sputtering. The main atoms in metal free polymers are carbon, hydrogen, and oxygen atoms. Since carbon has a small sputtering yield, it is reasonable to pay attention to carbon content in the polymer structure. Since the etching of the carbon will be the slowest, and hence rate-determining step, the etch rate V is assumed to be inversely proportional to the carbon content in a unit volume. The number of carbon atoms in a unit volume is given by

$$\frac{\rho}{M} N_c = \frac{\rho}{\bar{M}} \cdot \frac{N_c}{N} \qquad [1]$$

where ρ is the density of polymer; M, the molecular weight in a monomer unit; N, the total number of atoms in a monomer unit; N_c, the carbon atoms in a monomer unit, and $\bar{M}$, the average atomic weight in a monomer unit. Since $\rho/\bar{M}$ is empirically almost constant for metal-free organic polymers, etch rate V is given by

$$V \propto \frac{N}{N_c} \qquad [2]$$

Although the etch rate revealed a fairly good correlation with N/N_c, the etch rate was higher than expected for polymers having large N/N_o value, where N_o represents the number of oxygen atoms in a monomer unit. This suggests that oxygen atoms in the polymer structure influence the etch rate. Then, Eq. [2] is modified as follows

$$V \propto \frac{N}{N_c - N_o} \qquad [3]$$

Figure 3 shows the etch rate under 300 eV argon ion-beam etching condition *vs.* $N/(N_c - N_o)$. The etch rate for electron-beam evaporated carbon film is shown for comparison. It is found that the etch rate is directly proportional to the "$N/(N_c - N_o)$ factor." Figure 4 shows the etch rate under 500 eV argon ion-beam etching condition *vs.* $N/(N_c - N_o)$. Since the etch rate is not constant during etching for certain polymers, etch rates for such polymers are represented in a range in the figure. The correlation between the etch rate and

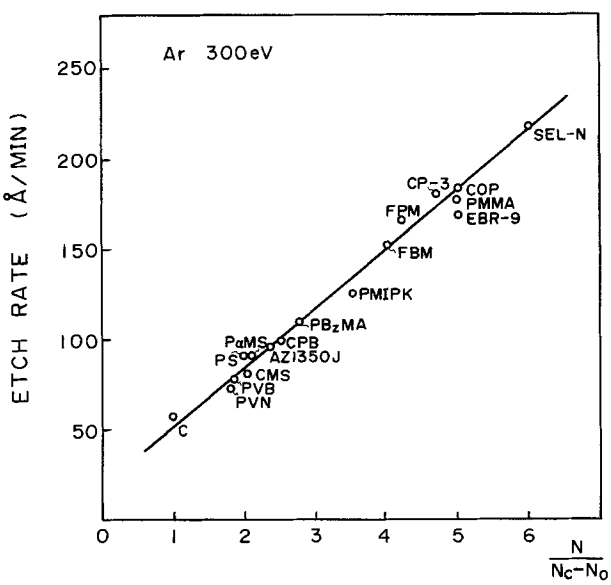

Fig. 3. Etch rate under 300 eV argon ion-beam etching condition *vs.* $N/(N_c - N_o)$.

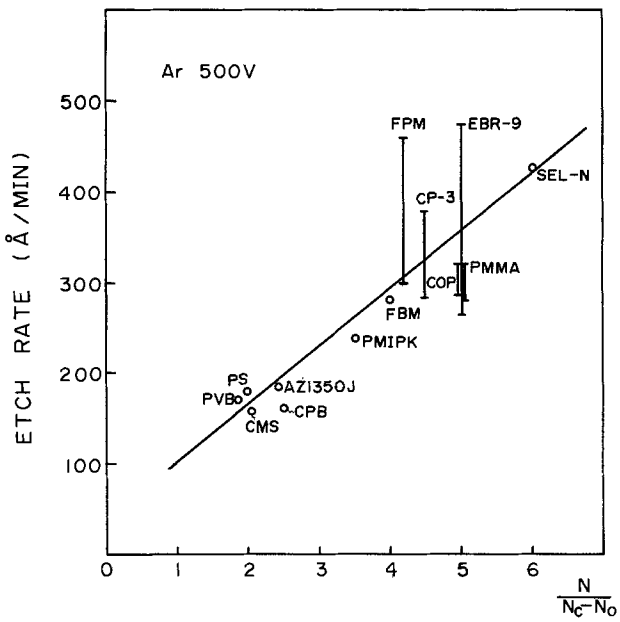

Fig. 4. Etch rate under 500 eV argon ion-beam etching conditions *vs.* $N/(N_c - N_o)$.

the $N/(N_c - N_o)$ factor is not as good as that obtained under 300 eV argon ion-beam etching conditions. This may be interpreted as that a deteriorated thin layer is formed under 500 eV argon ion-beam etching conditions (7). This is supported by the fact that, although the etched surface layer was hard to dissolve in any solvents, it dissolved easily after a slight oxygen plasma treatment for a surface layer.

Under the oxygen ion-beam etching condition, etch rates were measured for both 500 and 300 eV acceleration energy. The etched depth increases linearly with etching time for all the polymers examined. Figure 5 shows etch rate under 300 and 500 eV acceleration energy conditions *vs.* $N/(N_c - N_o)$ factor. Although etch rate under oxygen ion bombardment is 15 times larger than the rate under argon ion bombardment, it should be noted that there exists a linear relation between these etch rates. The etch rate enhancement under oxygen ion bombardment is considered to be caused by an ion-assisted chemical etching effect (8). Only EBR-9 has a somewhat higher value than expected.

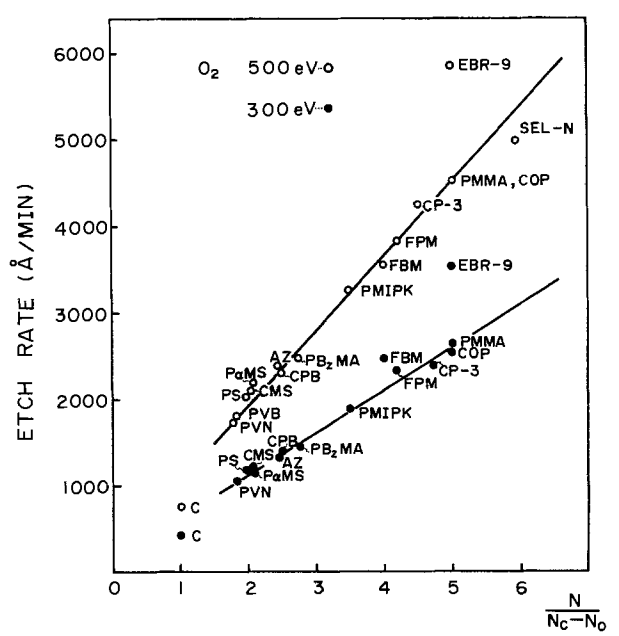

Fig. 5. Etch rate under 300 and 500 eV oxygen ion-beam etching conditions *vs.* $N/(N_c - N_o)$.

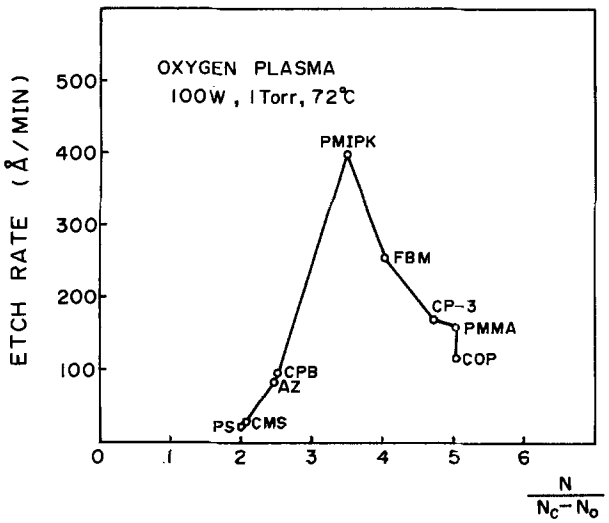

Fig. 6. Etch rate under oxygen plasma condition vs. $N/(N_c - N_o)$. Etching conditions were 100W incident power, 155 cm³/min oxygen flow rate, and 1 Torr (133 Pa) chamber pressure.

This may be explained by the fact that Cl incorporation to the site in the main chain structure enhances the polymer degradation in oxygen plasma (2).

These results reveal that, under an ion-bombardment condition, the etch rate is empirically determined by the "effective" carbon content in the polymer. The "effective" term means subtracting the number of oxygen atoms from that of carbon atoms in the polymer. This implies that C-O or C=O groups have much higher sputtering yield than does carbon. The fact that the etch rate has a linear dependence on $N/(N_c - N_o)$ implies that all the -CHx-($x = 1 \sim 3$) components in a polymer structure have the same sputtering yield. It is interesting that there seems to be no significant difference in etch resistance between polymers composed only by C, O, and H atoms and polymers having Cl, F, or N atoms in a polymer structure, with the exception of EBR-9. Chemical bond strength may not be an important factor with respect to etch resistance. This is because incident ion energy is much higher than the bond energy under an ion-beam etching condition.

Etch rates were also measured under oxygen plasma etching conditions. The etching conditions were 100W incident rf power, 155 cm³/min oxygen flow rate, and 1 Torr (133 Pa) chamber pressure. The substrate temperature was 72°C during etching. Both ion and electron bombardment onto the etching samples are eliminated, using an Al etch tunnel. Figure 6 shows etch rate under oxygen plasma condition *vs.* $N/(N_c - N_o)$. There seems to be no simple correlation between etch rate and effective carbon content in the polymer. The result suggests that the etching mechanism in oxygen plasma etching is quite different from that under ion bombardment. It is noted that, in PMIPK there exists marked difference between etch resistance to ion bombardment and etch resistance to oxygen radicals.

Conclusion

The dry etch resistance of metal-free polymers has been measured. It is found that the etch rate under argon or oxygen ion-beam etching linearly depends on the $N/(N_c - N_o)$ factor. This result indicates that etch rate under an ion bombardment condition is inversely proportional to the effective carbon content in the polymer.

Acknowledgment

The authors would like to thank T. Furuoya, S. Fujiwara, K. Matsumi, and K. Yoshimi for their encouragement. They also thank M. Suzuki and K. Tanigaki for useful discussions and M. Mukainaru for technical assistance.

Manuscript submitted March 8, 1982; revised manuscript received Aug. 10, 1982.

Any discussion of this paper will appear in a Discussion Section to be published in the December 1983 JOURNAL. All discussions for the December 1983 Discussion Section should be submitted by Aug. 1, 1983.

Publication costs of this article were assisted by Nippon Electric Company, Limited.

REFERENCES

1. G. N. Taylor and T. M. Wolf, Tech. Papers, SPE Reg. Techn. Conf., "Photopolymers Principles—Process and Materials," p. 174, Ellenville, New York, Oct. 10-12 (1979).
2. J. N. Helbert, M. A. Schmidt, and J. H. Lai, *Organic Coatings Plastic Chem.*, **43**, 258 (1980).
3. L. F. Thompson, L. E. Stillwagon, and E. M. Doerries, *J. Vac. Sci. Technol.*, **15**, 938 (1978).
4. S. Smoekh, *ibid.*, **13**, 1003 (1976).
5. C. M. Melliar-Smith, *ibid.*, **13**, 1008 (1976).
6. J. Battey, *IEEE Trans. Electron Devices*, **ed-24**, 140 (1977).
7. H. I. Smith, J. Melngailis, R. C. Williamson, and W. T. Brogan, Ultrasonic Symp. Proc., 558 (1973).
8. J. W. Coburn and Harold F. Winters, *J. Vac. Sci. Technol.*, **16**, 391 (1979).

Boriding of Nickel and Other Metals at Temperatures below 670°C

Koichiro Koyama,[1] H. Shimotake,* and F. C. Mrazek

Argonne National Laboratory, Chemical Engineering Division, Argonne, Illinois 60439

ABSTRACT

A method has been developed to boronize nickel and other metals at temperatures below 670°C. Metals including nickel, cobalt, iron, molybdenum, tantalum, titanium, niobium, and Hastelloy B were immersed in the KBF_4, KBF_4-KF (25 m/o) $NaBF_4$, $NaBF_4$-KBF_4 (10 m/o) molten salt systems containing dispersed borides at temperatures between 500° and 670°C. Metal borides including NiB, FeB, MnB_2, CrB_2, ZrB_{12}, and GdB_6 were shown to be effective boron sources; NiB was the most effective. A 46 μm thick layer of boride was successfully formed on a nickel substrate in the KBF_4-KF (25 m/o) molten salt system in less than 24 hr at a temperature as low as 550°C.

The development of the Li-Al/FeS_2 cell with molten salt electrolyte is underway at Argonne National Laboratory for use in batteries for electric vehicle propulsion. At present, molybdenum metal is considered to be the only metal suitable for the positive current collector of Li-Al/FeS_2 cells (1). However, because of the high cost and poor fabricability of molybdenum metal, efforts have been made to find alternative materials for positive-electrode current collectors. An electronically conducting ceramic coating on an inexpensive metallic substrate is considered to be an attractive possibility. Koura *et al.* (2) tested iron current collectors coated with iron borides. In their method, the iron boride coating was prepared by electrolysis in a molten salt bath at 900°C. The test results in FeS_2 cells at 450°C showed poor corrosion resistance. Bandyopadhyay *et al.* (3) also performed static corrosion tests on iron substrates coated with iron borides (prepared by the powder boriding method) and titanium diboride (prepared by the chemical vapor deposition method). Both the iron boride and titanium diboride coatings showed poor stability in the mixture of FeS_2 and LiCl-KCl at 500°C. A possible cause for the unfavorable results is that the differences in the thermal expansion coefficients of the metal boride layers and their metal substrates may have caused microcracks to develop in the protective coating, thus reducing the apparent corrosion resistance. In the case of titanium diboride, incomplete adhesion between the titanium diboride layer and the substrate metal was observed (3). To minimize the development of microcracks in the coating layer, the boriding should be performed at the lowest practical temperature.

At present, boriding of metals is commonly done by one of the following processes: (*i*) immersion in a molten salt bath without applied potential, (*ii*) chemical vapor deposition, (*iii*) electrolysis in a molten salt bath, and (*iv*) powder boriding (4). All of the processes are carried out at high temperatures (typically between 850° and 1000°C). More recently, for iron and steel, Komatsu *et al.* (5) prepared an iron boride coating at temperatures as low as 600°C by the powder boriding method using the mixture of ferroboron and KBF_4. However, a process for boriding of nickel at temperatures below 700°C has not been previously demonstrated. This paper discusses a method that we developed for boriding of metals at temperatures below 670°C. Our method involves immersion of a metal substrate in a molten salt bath containing dispersed borides without applied potential. The boride layer then forms electrolessly. We found that boriding is possible even at 550°C if the substrate metals are immersed in the KBF_4-KF [25 mol percent (m/o)] molten salt bath with dispersed NiB as a boron source.

Experimental

Test samples of metal sheets were boronized by immersion in molten salt baths containing dispersed boron or borides. The molten salt systems tested were KBF, KBF_4-KF (25 m/o), $NaBF_4$, and $NaBF_4$-KBF_4 (10 m/o). These molten salt systems were chosen because they were expected to dissolve boron-containing compounds to some extent as Na_3AlF_6 dissolves Al_2O_3.

In the experiments, reagent grades of KBF_4, KF, and $NaBF_4$ were used. Table I lists the boron and the borides used in these tests. These boron-containing solids were ground to 325 mesh before mixing with the salts and loaded into an AISI Type 304 stainless steel crucible (ID, 25 mm; height, 60 mm), which was then placed in a stainless steel beaker.[2] The metal samples tested were nickel, iron, cobalt, titanium, molybdenum, tantalum, niobium, and Hastelloy B. They were polished with No. 5 emery paper, degreased by acetone, placed in the various salt baths, and then heated at a desired temperature in an argon atmosphere for 24 hr. After boriding, the metal samples were subjected to x-ray diffraction analysis, and the borides formed were identified on the basis of the JCPDS cards. The thickness and uniformity of the boride layer were examined with an optical microscope. The distribution of boron in the boride layer was measured by an ion microprobe analyzer. The deposition into the boride layers of the metal elements from the borides used as boron sources was examined by x-ray fluorescence analysis (x-ray energy dispersive fluorescence analyzer).

Results and Discussion

Boron sources and boride layers.—The boride coatings formed on the nickel substrates in molten KBF_4 baths containing various boron sources at 670°C are listed in Table II. Those baths containing CrB_2, MnB_2, FeB, NiB, ZrB_{12}, and GdB_6 as boron sources gave boride layers of 40, 52, 35, 80 ~ 120, 46, and 35 μm thickness, respectively. These thicknesses were greater than the 23 μm thickness obtained on nickel in the bath

[2] The crucible was protected from the molten salt corrosion by the boride layer formed on the crucible wall.

Table I. Boron sources used

Major constituent	Impurity*	Major constituent	Impurity*
B		NiB	Ni_4B_3
B_4C		ZrB_2	
AlB_{12}		ZrB_{12}	ZrB_2
B_4i	Other B-Si phase	NbB	Nb_3B_2
B_6i	B_4Si, Si	NbB_2	
TiB_2		Mo_2B	MoB
VB_2		MoB	
CrB		MoB_2	Mo_2B_5
CrB_2		Mo_2B_5	
MnB		TaB_2	
MnB_2		W_2B_5	
Fe_2B	FeB, Fe	CaB_6	
FeB	Fe_2B	BaB_6	
Co_3B, Co_2B		CeB_6	
Ni_3B		GdB_6	
Ni_2B			

* Analyzed by supplier using x-ray powder diffraction analysis.

* Electrochemical Society Active Member.
[1] Present address: Himeji Institute of Technology, 2167, Shosha, Himeji, Hyogo 671-22, Japan.
Key words: coatings, fused salts, electroless, ceramics.

Table II. Summary of boride coatings formed on nickel substrates (670°C)

No.	Boron source: Compound	Boron source: Concentration** (w/o)	Thickness (μm)	Borides present*: Ni_3B	Borides present*: Ni_2B	Borides present*: Ni_4B_3	Remarks
1	B	7.9	23	W	S	—	
2	B_4C	5	23	W	S	—	
3	AlB_{12}	7.7	29	VW	S	—	
4-1	B_6Si	5	17	W	S	—	Ni_2Si, Ni_5Si_2
4-2	B_6Si	5	23	—	S	—	Ni_2Si, Ni_5Si_2
5	TiB_2	7.5	12	M	M	—	
6	VB_2	7.5	0	—	—	—	Unk
7-1	CrB	7.5	nil	M	M	—	
7-2	CrB_2	7.5	40	—	S	—	
8-1	MnB	7.5	6	M	M	—	
8-2	MnB_2	7.5	52	—	S	—	
9-1	Fe_2B	7.5	3	M	M	—	
9-2	FeB	11	35	VW	S	—	
10	Co_3B, Co_2B	15	12	M	M	—	
11-1	Ni_3B	9.8	nil	W	—	—	
11-2	Ni_2B	9.8	9	M	M	—	
11-3	NiB	10 ~ 20	80 ~ 120	—	S	W	
12-1	ZrB_2	14	23	W	S	M	
12-2	ZrB_{12}	7.4	46	W	S	VW	
13-1	NbB	14	6	—	M	—	Unk
13-2	NbB_2	9.8	0	—	—	—	Unk
14-1	Mo_2B	15	0	—	—	—	
14-2	MoB	14	0	—	—	—	
14-3	MoB_2	7.5	29	W	S	—	
14-4	Mo_2B_5	7.5	6	M	M	—	
15	TaB_2	9.8	6	—	—	—	Unk
16	W_2B_5	17.5	23	W	S	—	
17	CaB_6	7.5	12	W	S	—	
18	BaB_6	10	17	W	S	—	
19	CeB_6	10	23	S	M	—	
20	GdB_6	16	35	W	S	—	

* S, strong; M, medium; W, weak; VW, very weak; Unk, additional unknown compounds. All identified by x-ray diffraction analysis.
** Concentration of boron-containing compound.

containing boron metal as the boron source, suggesting that the boron compounds described above are more effective boron sources than boron metal. Figure 1 shows the optical microstructures of the boride layers that were obtained with the baths containing CrB_2, MnB_2, FeB, NiB, ZrB_{12}, and GdB_6, respectively. The boundaries between the nickel substrates and the boride layers show intimate interlocking. No evidence of cracks was observed at magnifications up to 500×. An apparent two-phase boride layer consisting of Ni_2B and Ni_4B_3 was formed in the bath containing the NiB boron source, as shown in Fig. 2a, while an ap-

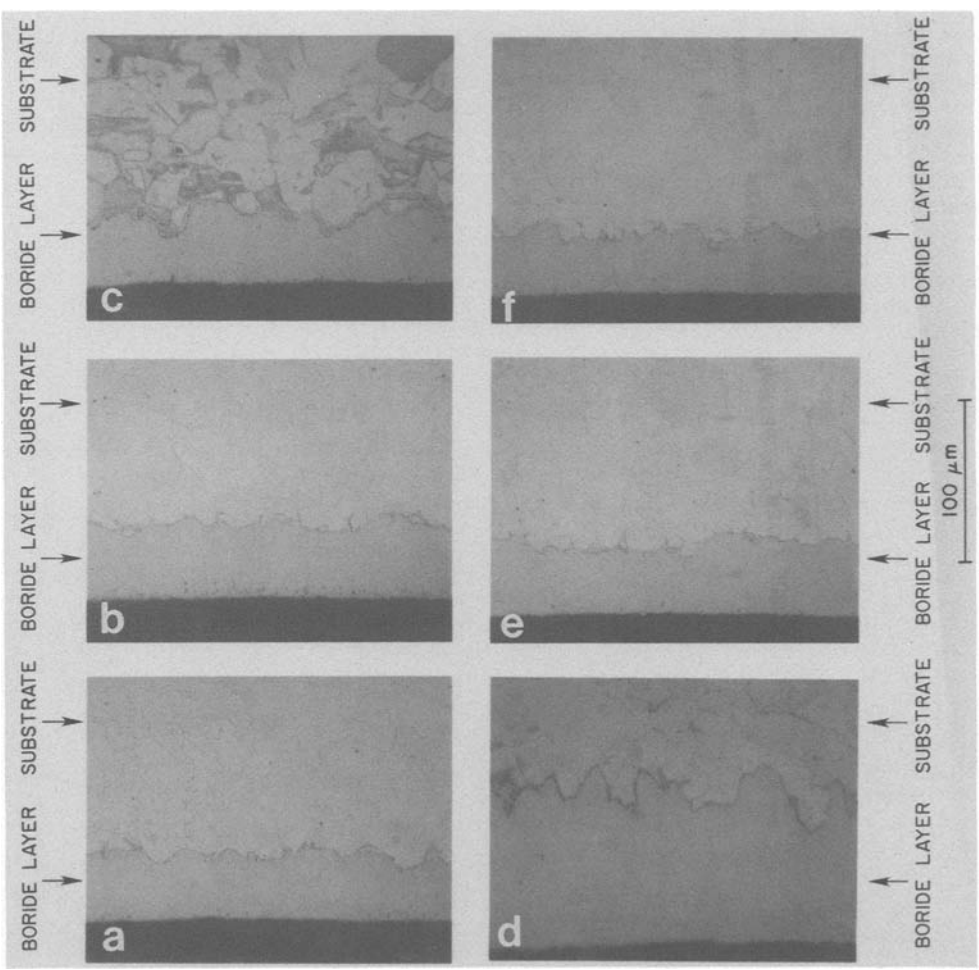

Fig. 1. Microstructures of boronized layers produced on nickel substrates. (a) Sample No. 7-2 (from CrB_2), (b) sample No. 8-2 (from MnB_2), (c) sample No. 9-2 (from FeB), (d) sample No. 11-3 (from NiB), (e) sample No. 12-2 (from ZrB_{12}), and (f) sample No. 20 (from GdB_6), etched with 5% NaCN-5% $(NH_4)_2S_2O_8$ solution.

parent one-phase boride layer consisting of Ni_2B was formed from either the CrB_2 or MnB_2 boron source, as shown in Fig. 2b and c. Figure 3 shows the result from the ion microprobe analyzer for an apparent two-phase layer consisting of the Ni_2B and Ni_4B phases. This result suggests either of the following ideas: (*i*) the Ni_2B and Ni_4B_3 phases were distributed randomly through the boride layer or (*ii*) the thin Ni_4B_3 phase existed only on the surface as an outer layer, although the ion microprobe analysis could not show its existence because the thickness of this Ni_4B_3 layer was smaller than the beam diameter (6 μm). In order to determine which is true, about 5 μm of the surface of the boride layer was removed by polishing the boronized sample on an emery paper. The sample was then resubmitted for x-ray diffraction analysis. The result obtained showed that the Ni_4B_3 phase was no longer present in the boride layer. Therefore, we conclude that the Ni_4B_3 phase was only present as an outer layer, and its thickness was 5 μm or less. Furthermore, it was highly possible that the Ni_3B phase existed as the most inner layer in the boride coatings of specimens 4-2, 7-2, 8-2, and 11-3, but was not detected by x-ray diffraction because of the thick boride coatings. When the outer layers of the boride coatings were gradually removed with an emery paper and resubmitted for x-ray diffraction analysis, the Ni_3B phase was clearly detected in all the specimens except for specimen 4-2, in which the presence of the Ni_2Si and Ni_5Si_2 phases made it difficult to identify the Ni_3B phase. Therefore, it was concluded that the Ni_3B phase had been present as an inner layer.

The boriding reaction for the formation of an Ni_2B layer on the nickel substrate using boron metal as the boron source can be expressed by the following reaction

[3] The values of standard free energies of formation for Ni_2B, Ni_3B, FeB, and Fe_2B were obtained by extrapolating the data reported by Omori *et al.* (6, 7).

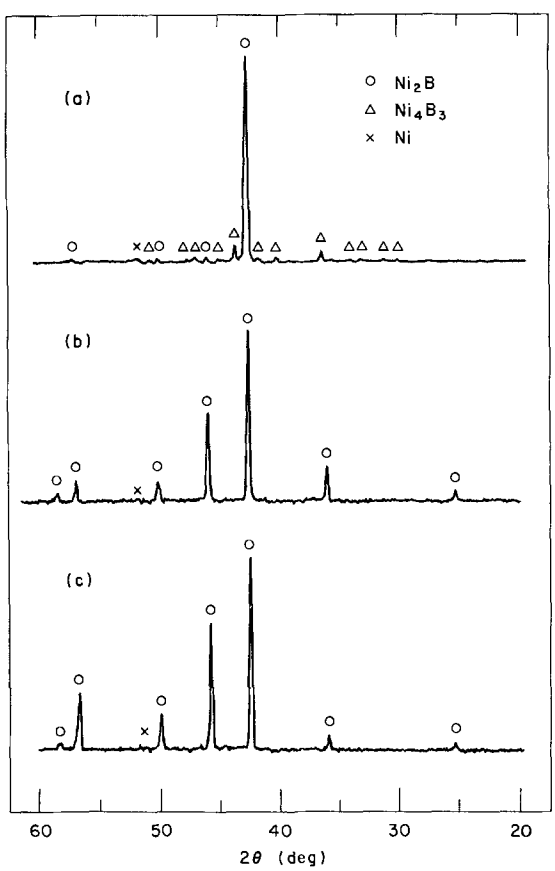

Fig. 2. X-ray diffraction patterns obtained from boride layers and nickel substrates (CuKα). (a) Sample No. 11-3 (from NiB), (b) sample No. 7-2 (from CrB_2), and (c) sample No. 8-2 (from MnB_2).

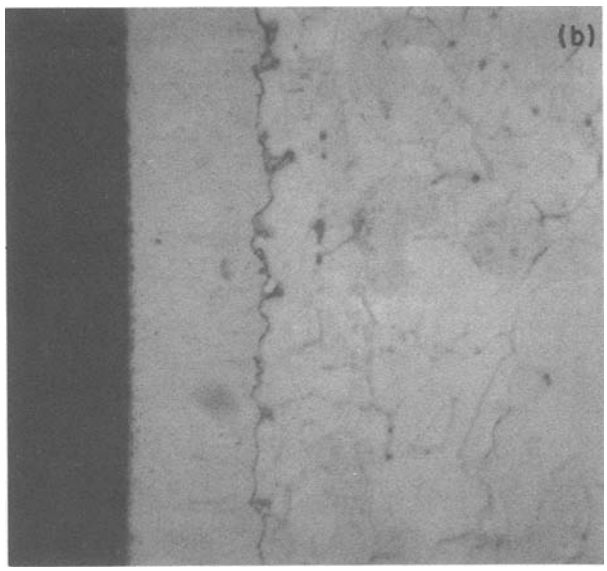

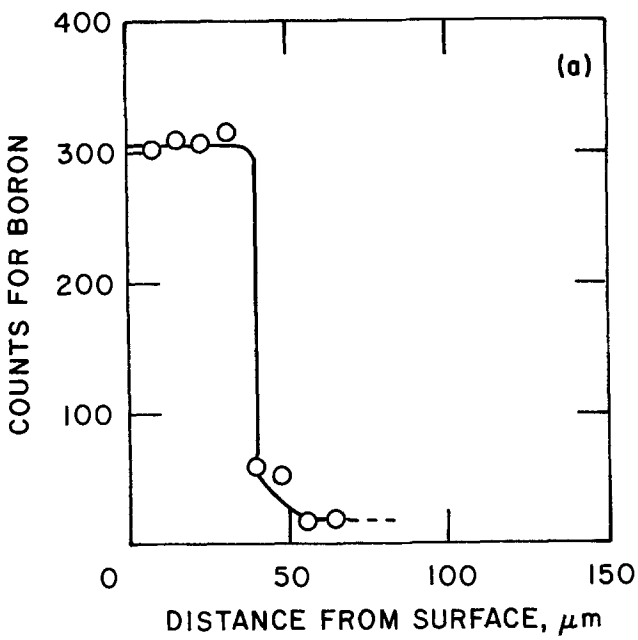

Fig. 3. (a) Distribution of boron from ion microprobe analysis. Counts show the five time average for 5 sec. Beam diameter, 6 μm; beam current, 0.1 $\times$ 10^{-9} A. (b) Optical micrograph.

$$2Ni + B = Ni_2B,\ \Delta G = -79{,}900J \text{ at } 900\ K^{3} \quad [1]$$

where ΔG denotes the change in the Gibbs free energy for the reaction. Similarly, for the formation of the Ni_3B layer we can write

$$3Ni + B = Ni_3B,\ \Delta G = -93{,}000J \text{ at } 900\ K^{3} \quad [2]$$

When FeB instead of boron is used as the boron source, the following boriding reactions can occur

$$2Ni + FeB = Ni_2B + Fe,\ \Delta G = -8{,}500J^{3} \quad [3]$$

$$2Ni + 2FeB = Ni_2B + Fe_2B,\ \Delta G = -20{,}000J^{3} \quad [4]$$

$$3Ni + FeB = Ni_3B + Fe,\ \Delta G = -21{,}600J^{3} \quad [5]$$

$$3Ni + 2FeB = Ni_3B + Fe_2B,\ \Delta G = -33{,}500J \text{ at } 900\ K^{3} \quad [6]$$

If Fe_2B is used

$$3Ni + Fe_2B = Ni_3B + 2Fe,\ \Delta G = -9{,}700J \text{ at } 900\ K^{3} \quad [7]$$

Similarly, when NiB is used

$$2Ni + 4NiB = Ni_2B + Ni_4B_3 \quad [8]$$

$$2Ni + 4NiB = \underline{Ni_4B_3} + Ni_2B \quad [9]$$

$$8Ni + 9NiB = \underline{2Ni_4B_3} + 3Ni_3B \quad [10]$$

$$3Ni + 2NiB = \underline{Ni_3B} + Ni_2B \quad [11]$$

The underlines denote the boride layers formed on the nickel substrate. Reliable data for the free energies of formation for NiB and Ni_4B_3 are not available.

Similarly, when Ni_2B is used

$$2Ni + 2Ni_2B = \underline{Ni_3B} + Ni_3B, \Delta G = -106{,}000J \text{ at } 900\ K^{3} \quad [12]$$

Similar reactions can be obtained for the other boron sources. For the spontaneous proceeding of a reaction, it is necessary that ΔG for the reaction be negative. Therefore, for example, in case of the boron source of Fe_2B, the following reaction is not expected to take place

$$2Ni + Fe_2B = Ni_2B + 2Fe, \quad \Delta G = -106{,}000J \text{ at } 900\ K^{3} \quad [13]$$

However, the formation of Ni_2B was detected by x-ray diffraction analysis, as can be seen from Table II, No. 9-1, implying that probably the reagent grade Fe_2B used in the experiment contained some FeB as an impurity (as listed in Table I). Similarly, in case of the boron source of Ni_3B, the following reaction will not take place

$$Ni + \underline{Ni_3B} = Ni_3B + Ni, \quad \Delta G = 0J \quad [14]$$

However, the formation of Ni_3B was detected by x-ray analysis although the layer was extremely thin, as can be seen from Table II, No. 11-1. This is probably due to the supply of boron coming not from the Ni_3B added but from the boride layer attached to the inside surface of the stainless steel crucible which had been used in experiment No. 11-3.

We can see from Table II that the borides in the coatings tend to become higher borides when higher borides are used as the boron sources (comparison of No. 4-1 and 4-2, 7-1 and 7-2, 8-1 and 8-2, 9-1 and 9-2, 11-1, 11-2 and 11-3, 12-1 and 12-2). The reason for this can be shown by the following thermodynamic equations:

The boriding reaction can be written as

$$B_{\text{in boron source}} = B_{\text{in boride layer}} \quad [15]$$

The free energy change for the above reaction is

$$\Delta G = RT \ln \alpha_{B \text{ in boride layer}} - RT \ln \alpha_{B \text{ in boron source}} \quad [16]$$

and for the spontaneous reaction, the following condition must be met

$$\alpha_{B \text{ in boride layer}} < \alpha_{B \text{ in boron source}} \quad [17]$$

where α is the activity of the species in the indicated phases. This means that the activity of the boron in the boride layer is smaller than that of the boron in a boron source. Therefore, we can say that when a higher boride having a higher boron activity is used as the boron source, a higher boride is formed in the boride layer. Similarly, Table II shows that the thickness of the boride layers increases when higher borides are used as boron sources. This can be attributed to the increased boron activity at the surface of the metal substrate, providing a higher driving force for the boriding reaction.

Because the activities of boron in CrB_2, MnB_2, FeB, NiB, ZrB_{12}, and GdB_6 are less than unity, the ΔG's of the boriding reactions in which these compounds are used as boron sources are less negative than the ΔG of the boriding reaction where boron metal is used as the boron source. The experimental results, however, show that these compounds are superior to boron metal as boron sources. This suggests a low solubility of boron metal in the KBF_4 bath (solubility data for this system is not available). Among the higher borides tested, VB_2, TaB_2, NbB_2, and Mo_2B_5 were found either ineffective or only slightly effective. This is perhaps due to their low solubility in the KBF_4 molten salt.

The metal elements deposited from the borides used as the boron sources were examined by x-ray fluorescence analysis. Table III shows the results of these analyses. Metal elements including iron, silicon, manganese, chromium, molybdenum, zirconium, cerium, and aluminum were identified in the boride coatings while tungsten, tantalum, and gadolinium were not detected. It is worth noting that silicon was easily included in the boride layer; the silcon was included as silicides (Ni_2Si and Ni_5Si_2).

The effects of bath composition and temperature.—The effects of the bath composition and temperature on the boride layer were investigated; Table IV shows the results. At 600°C, the KBF_4 bath produced a 51 μm thick boride layer and at 550°C, a 12 μm thick layer. At 550°C, the bath did not appear to be completely melted. The 25 m/o addition of KF lowered the melting point of the KBF_4 bath to 460°C (8) and resulted in a thick boride layer, 46 μm, when the bath temperature was brought back to 550°C. The low melting point of the KBF_4-KF (25 m/o) bath and KF addition have probably resulted in the increased solubility of NiB. The $NaBF_4$ and $NaBF_4$-KBF_4 (10 m/o) baths gave thin boride layers, 11 μm at 550°C and 4 μm at 500°C, despite their low melting points, 408° and 398°C, respectively (8, 9). These results seem to support the effectiveness of adding KF to the bath as a boriding aid.

Metal substrates and boride layers.—Cobalt, iron, molybdenum, tantalum, titanium, niobium, and Hastelloy B were used as metal substrate for our boriding process. This result can be explained by the difference in the diffusion rates of boron in the boride layers (Ni_3B, Ni_2B, Ni_4B_3, Fe_2B, FeB, Co_2B, CoB). The reliable data of the diffusivities of boron are unavailable for these borides at the experimental temperatures. Titanium metal became brittle and disintegrated during the boriding process. Molybdenum metal was hardly bo-

Table III. Metals deposited in the boride layers from the boron sources

Boron source	Element	Content* (w/o)
FeB	Fe	0.6
B_6Si	Si	17
MnB_2	Mn	2.6
CrB_2	Cr	0.7
MoB_2	Mo	0.2
ZrB_{12}	Zr	0.05
W_2B_5	W	Not detected
CeB_6	Ce	1.2
AlB_{12}	Al	0.2
TaB_2	Ta	Not detected
GdB_6	Gd	Not detected

* Determined by x-ray fluorescence analysis.

Table IV. Boride coatings on Ni substrate formed in different molten salt baths

Molten salt	Temp. (°C)	Thickness (μm)	Borides present*		
			Ni_3B	Ni_2B	Ni_4B_3
KBF_4	670	81	—	S	W
	600	51	—	S	W
	550	12	—	S	W
KBF_4-KF (25 m/o) (Eutectic composition)	550	46	—	S	W
	500	4	—	S	W
$NaBF_4$	550	11	—	S	W
	500	4	—	S	W
$NaBF_4$-KBF_4 (10 m/o) (Composition of minimum point)	550	11	—	S	W
	500	4	—	S	W

Nickel was boronized in the molten salts for 24 hr using NiB as a boron source.
* S, strong; W, weak. Identified by x-ray diffraction analysis.

ronized, and tantalum metal and niobium metal could not be boronized at all at 600°C. A uniform coating formed on Hastelloy B, although it was thin (5 μm).

Summary

A method has been developed to boronize nickel and other metals at low temperatures. Metals including nickel, iron, cobalt, titanium, molybdenum, tantalum, niobium, and Hastelloy B were immersed in the molten salt bath containing the various borides at temperatures between 500° and 670°C. The borides used as boron sources include B_4C, AlB_{12}, B_4Si, B_6Si, TiB_2, VB_2, CrB, CrB_2, MnB, MnB_2, Fe_2B, FeB, Co_3B, Co_2B, Ni_3B, Ni_2B, NiB, ZrB_2, ZrB_{12}, NbB, NbB_2, Mo_2B, MoB, MoB_2, Mo_2B_5, Ta_2B_2, W_2B_5, CaB_6, BaB_6, CeB_6, and GdB_6. The molten salts used were the KBF_4, KBF_4-KF (25 m/o), $NaBF_4$, and $NaBF_4$-KBF_4 (10 m/o) systems. The results can be summarized as follows:

1. NiB, FeB, MnB_2, CrB_2, ZrB_{12}, and GdB_6 were found to be effective boron sources for boronizing nickel; NiB, especially, was useful.
2. Boriding of nickel was found to be possible at a temperature as low as 550°C when the KBF_4-KF (25 m/o) molten salt bath containing NiB as a boron source was used.
3. Nickel was more easily boronized than either cobalt or iron. Molybdenum metal was barely boronized, and tantalum metal and niobium metal could not be boronized at 600°C.

Acknowledgment

The authors wish to thank B. S. Tani and E. T. Kucera for their x-ray diffraction and fluorescence analyses work. This work was supported by the Department of Energy.

Manuscript submitted Nov. 13, 1981; revised manuscript received Aug. 17, 1982.

Any discussion of this paper will appear in a Discussion Section to be published in the December 1983 JOURNAL. All discussions for the December 1983 Discussion Section should be submitted by Aug. 1, 1983.

Publication costs of this article were assisted by Argonne National Laboratory.

REFERENCES

1. J. E. Battles, "Critical Materials Problems in Energy Production," C. Stein, Editor, p. 801, Academic Press, New York (1976).
2. N. Koura, N. P. Yao, and J. Kincinas, *Denki Kagaku*, **46**, 395 (1978).
3. G. Bandyopadhyay, Argonne National Laboratory Report No. ANL-78-94, 144 (1978).
4. A. P. Epik, in "Boron and Refractory Borides," V. I. Matkovich, Editor, p. 597, Springer-Verlag, New York-Heidelberg (1977).
5. N. Komatsu, M. Obayashi, and J. Endo, *J. Jpn. Inst. Metals*, **38**, 481 (1974).
6. S. Omori and Y. Hashimoto, *ibid.*, **40**, 601 (1976).
7. S. Omori and J. Moriyama, *Trans. JIM*, **21**, 790 (1980).
8. C. J. Barton, L. O. Gilpatrick, J. A. Bornmann, H. H. Stone, T. N. Macvay, and H. Insley, *J. Inorg. Nucl. Chem.*, **33**, 337 (1971).
9. C. J. Barton, L. O. Gilpatrick, J. A. Bornmann, T. N. Macvay, and H. Insley, *ibid.*, 345 (1971).

Kinetic Study Of Zirconium-Iodine Reaction By Modulated Molecular Beam Mass Spectrometry

M. Balooch and D. R. Olander

Materials and Molecular Research Division of the Lawrence Berkeley Laboratory, and the Department of Nuclear Engineering, University of California, Berkeley, California 94720

ABSTRACT

The reaction of molecular iodine with polycrystalline zirconium was studied by modulated molecular beam-mass spectrometric methods. The reaction was investigated in the temperature range 400-1400 K and equivalent iodine pressures of 10^{-5}-10^{-4} Torr. ZrI_4 was identified as the sole detectable reaction product at low temperatures (<850 K), achieving a maximum reaction probability at about 600 K. At high temperatures, molecular dissociation and atomic desorption of iodine play a predominant role in the gas-surface reaction. The molecular beam data, in conjunction with Auger and ESCA analysis of the surface after the experiment, support a reaction model involving a thin scale of a lower iodide present on the surface at low temperatures during the reaction. The kinetics of the reaction are governed by the diffusional properties and the reactivity of this scale with respect to adsorbed iodine atoms. At high temperatures the reaction mechanism consists of adsorption and dissociation of I_2 on the metal partially covered with the iodide scale followed by desorption of atomic iodine.

It is generally believed that the failure of zirconium cladding in light water-cooled reactor (LWR) fuel elements is due to stress corrosion cracking (SCC) induced by one or more fission products (1, 2). Iodine, an abundant fission product, has long been known to promote SCC of Zircaloy at reactor operating temperatures and is one of the prime suspects as the chemical substance involved in this type of cladding failure (2, 3). Notwithstanding the controversial nature of the issue of iodine SCC in fuel elements (4), understanding of the chemistry of zirconium-iodine system is an essential part of the complex iodine-induced stress corrosion cracking mechanism. The thermochemical aspect of this problem has been considered in detail by Cubicciotti and co-workers and progress in this area is reported in several recent publications (5-8). Another aspect of the chemistry that needs further investigation is the kinetics of the reaction between iodine and zirconium, which is the subject of the present study.

In connection with the iodine refining of zirconium, several investigators (9-11), have investigated the kinetics of reaction of zirconium in the range 400-800 K and at iodine pressures of the order of a few Torr. Shelest *et al.* (11) studied the effect of temperature and pressure on the rate of iodination of metallic zirconium using a quartz spiral balance. They found the overall order of the reaction to be 0.77 and an activation energy of ~9 kcal/mol. Busol (12) studied the rate of reaction of gaseous ZrI_4 with zirconium metal filings and found the rate of disappearance of gaseous ZrI_4 to be parabolic with time in the temperature range of 600-800 K. Cubicciotti *et al.* (13) also studied the formation of iodide products from reaction of Zr with gaseous ZrI_4 which they found to obey cubic kinetics.

Key words: iodide films, diffusion, rate constant, sticking probability.

In the present work, the kinetics of the zirconium-iodine system were investigated by modulated molecular beam techniques in the temperature range 400-1400 K and of equivalent iodine pressures between 10^{-5} and 10^{-4} Torr. A reaction mechanism was deduced from the amplitudes and phases of the reaction product signals in the molecular beam experiment. Analysis of the reaction surfaces by ESCA and Auger electron spectroscopy provided supporting evidence for the mechanism.

Experimental

The molecular beam apparatus, which is a slightly modified version of one described previously (14), is shown in Fig. 1. It consists of three differentially-pumped chambers separated by collimating orifices. The first chamber contains the iodine molecular beam source and the chopper motor. This chamber is pumped by a 6 in. oil diffusion pump with the speed of 1500 liter/sec. Iodine from a constant temperature bath is conducted through a heat tube to a small cell at the source tip where the temperature is controlled by a miniature furnace. The tube is kept at a slightly higher temperature than that of the reservoir to ensure that effusion from the system is controlled by reservoir temperature (and hence iodine pressure). The tube has an orifice with diameter of about 1 mm through which the molecular beam issues. The flux calculated from the reservoir pressure compares well with that computed from the in-line pressure measurement, using the appropriate geometries to estimate conductances of the line and of the orifice.

The polycrystalline zirconium specimen is mounted on the end of a tube containing a filament which heats the target by radiation and by electron bombardment. The surface temperature is measured by an infrared pyrometer. The specimen surface is 4 cm from the molecular beam source. The target chamber is pumped by a well-trapped 6 in. oil diffusion pump. A typical pressure of this chamber is $\sim 1 \times 10^{-9}$ Torr.

A portion of scattered iodine and reaction products are detected by a quadrupole mass spectrometer mounted in the detector chamber. The distance from the specimen surface to the mass spectrometer ionizer is 4 cm. This chamber is pumped by a 200 liter/sec ion pump to about 1×10^{-10} Torr pressure.

The output from mass spectrometer is processed by a PAR HR-8 lock-in amplifier with a two-phase accessory to yield the first Fourier components of the periodic signals for the scattered reactant and desorbed products. The apparent reaction probability ϵ (the ratio of the amplitudes of the product and reactant signals, corrected for ionization efficiencies of the mass spectrometer) and the phase lag ϕ, which is the difference between the product and the reactant phase angles, are obtained from the information provided by the lock-in amplifier (15).

Results

Figure 2 shows that iodine reacts vigorously with zirconium (reaction probabilities >0.1) at temperatures as low as 420 K. Below ~850 K, zirconium volatilization is the principal reaction. Zirconium-containing ions observed in the mass spectrometer were ZrI_3^+, ZrI_2^+, ZrI^+, and Zr^+. The signals at these masses all had the same phases and the same temperature dependence. The cracking pattern of a ZrI_4 beam scattered from the zirconium target at room temperature matched that of the experimental reaction product fragments. Therefore, it was concluded that the sole zirconium-bearing product of the reaction was ZrI_4. The atomic iodine signal detected at high temperature (<850 K) had to be extracted from I^+ signals arising from cracking in the ionizer of the mass spectrometer of whatever ZrI_4 product was emitted from the surface and of scattered reactant I_2. The effects of frequency and beam intensity variations on ϵ and ϕ are shown in Fig. 3-5. The curves on these graphs are best fits from the model discussed later.

Knowledge of the chemical state of the surface during bombardment by the iodine beam is essential for the development of a kinetic model. Cubicciotti and Scott (13) studied the reaction of zirconium with gaseous ZrI_4 in the temperature range 600-800 K and examined the solid zirconium iodides that formed on the zirconium surface by scanning electron microscopy. Initially, ZrI_4 attack formed isolated clusters of ZrI crystals which subsequently covered the whole surface. In a later stage, a layer of the diodide was observed to form on the top of the monoiodide. Further attack produced material of approximately the composition of ZrI_3 on the top surface.

Due to geometrical difficulties, we were unable to utilize Auger electron spectroscopy (AES) to monitor the surface *in situ* while conducting the experiments. Attempts were made to analyze the surface by AES and ESCA in different chambers after an experiment but iodine was not observed, probably due to contamination by atmospheric gases during transfer. To avoid

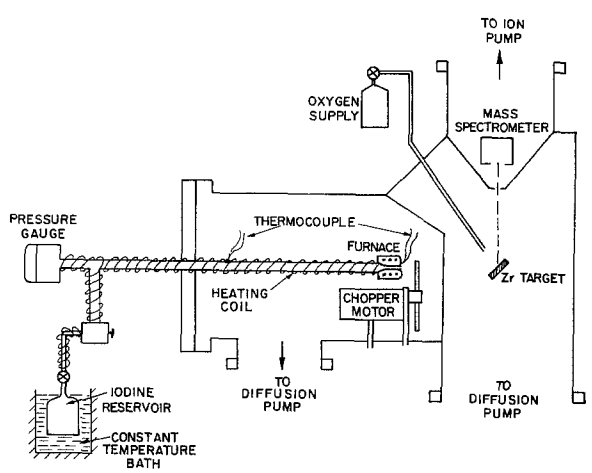

Fig. 1. Schematic of apparatus with iodine inlet system and oxygen doser.

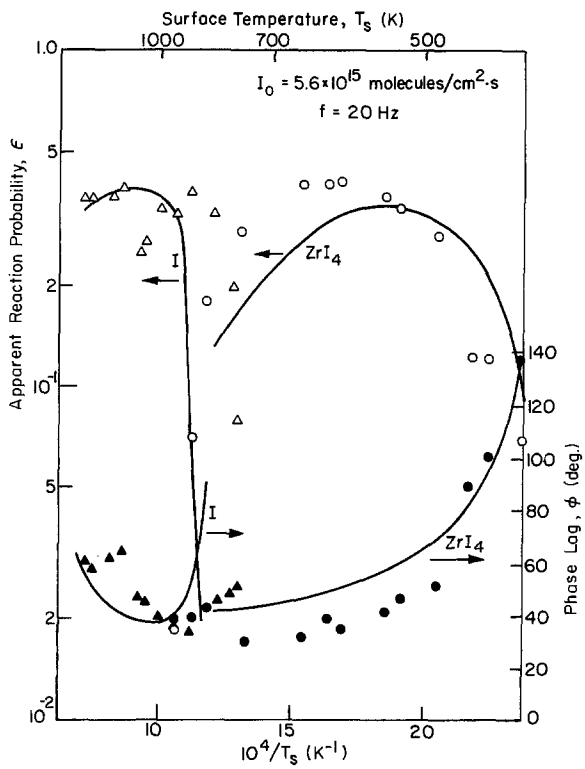

Fig. 2. Apparent reaction probabilities and phase lags of ZrI_4 and I as functions of zirconium target temperature.

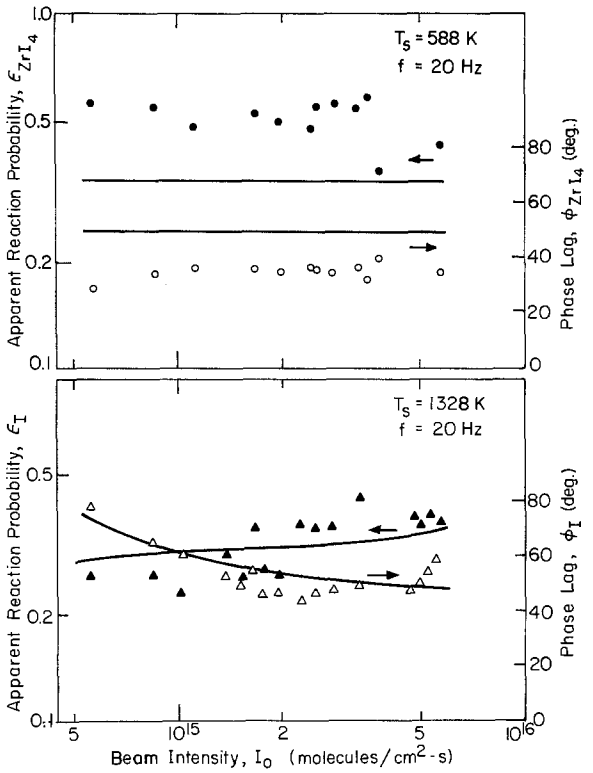

Fig. 3. Effect of beam intensity on the production of ZrI_4 and I at fixed temperature and modulation frequency.

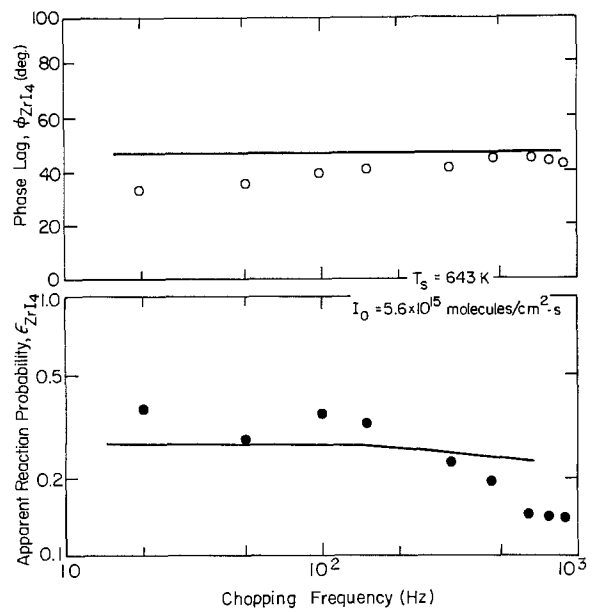

Fig. 4. Modulation frequency dependence of the ZrI_4 reaction probability and phase lag at fixed beam intensity and surface temperature.

loss of an iodide scale during transport, the reacting surface at 580 K was simultaneously coated with platinum supplied by a hot filament located in front of the target. Deposition was continued until the ZrI_4 signal was reduced to ~10% of its initial value, which required approximately 20 monolayers of platinum. The sample was then removed and depth-profile-analyzed by ESCA and AES. The upper curve of Fig. 6 is the ESCA spectrum of the reacted surface which had not been protected by platinum. It shows oxygen and carbon lines from air exposure as well as zirconium peaks, but no iodine. The lower spectrum in Fig. 6, which followed ~20Å sputtering, shows ~2% iodine and 16% platinum on the surface. AES spectra of the sample for three different sputter removal depths are

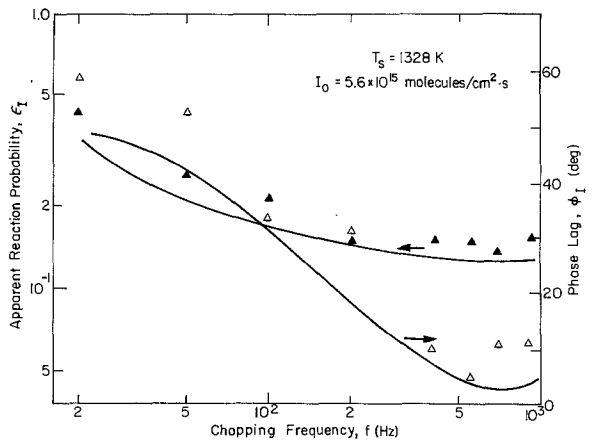

Fig. 5. Modulation frequency dependence of the atomic iodine reaction product vector at fixed beam intensity and surface temperature.

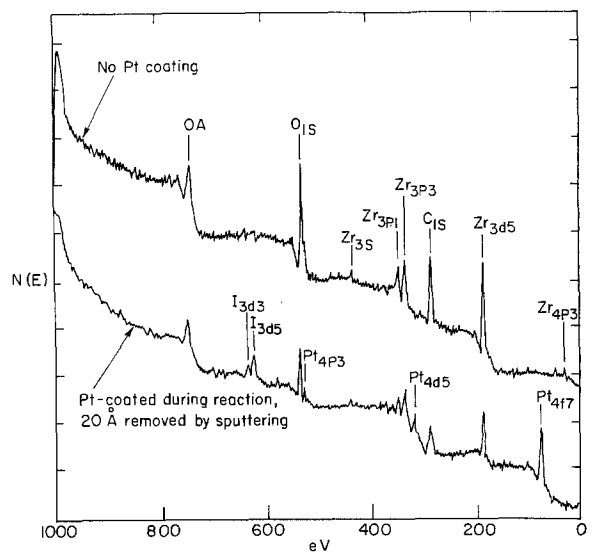

Fig. 6. ESCA analysis of zirconium surface exposed to an iodine beam (upper spectrum) and of a zirconium surface coated with platinum during reaction with iodine (lower spectrum). 20Å of the surface were removed by sputtering before recording the lower spectrum. Reaction with iodine and surface analysis were conducted in separate vacuum systems.

shown in Fig. 7. Although the peaks due to oxygen and iodine nearly coincide, they could be clearly resolved after removal of ~100Å of surface. These analyses confirm the existence of a nonvolatile iodide layer on the reacting surface. However, it was not possible to bury the iodide layer beneath a uniform coat of platinum, which would have permitted removal of the metal coat to expose an intact iodide scale amenable to analysis of the I/Zr ratio by ESCA or AES. First, the co-impingement technique used to deposit the platinum during reaction caused the metal coat to be incorporated into the iodide scale. Second, platinum deposits on graphite in isolated patches at this temperature (16); if similar island deposition also occurs on zirconium, not all of the iodide scale is exposed at a definite sputter-removal depth.

In an attempt to investigate the effect of an oxidized surface on reaction, a beam of oxygen was directed at a 600 K target along with a beam of iodine of intensity 6×10^{15} molecules/cm^2-sec. No change in apparent reaction probability or phase lag of ZrI_4 was observed up to an intensity of ~10^{16} oxygen molecules/cm^2-sec striking the same spot as the iodine impingement. However, when the beam of iodine was turned off for about 10 min while the oxygen beam was on, no reaction product was detected when I_2 impingement was resum-

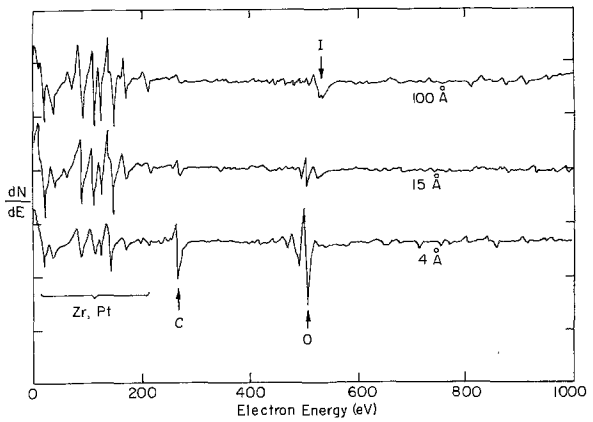

Fig. 7. Auger electron spectra of a zirconium surface which had been platinum-coated during reaction with iodine and subsequently etched to depths of 4, 15, and 100Å by sputtering. Reaction with iodine and surface analysis were conducted in separate vacuum systems.

ed. Then both beams were turned off and the sample was annealed in vacuum for 4 min at about 1200 K, after which the surface temperature was brought back to 600 K and the beam of iodine was turned on. The resulting reaction probability and phase lag of ZrI_4 are shown as triangles in Fig. 8. By repeating the 1200 K heat-treatment for another 7 min the magnitude of reaction probability and phase lag of ZrI_4 approached those characteristic of the fresh zirconium surface (circles in Fig. 8). No oxyiodide was detected during these experiments. These tests demonstrated that the 1200 K annealing is sufficient to dissolve a thin oxide scale in the substrate metal. Partial dissolution evidently occurs in 4 min, and complete removal is accomplished in the second 7-min treatment.

Reaction Mechanism

The following inferences from the data serve as guidelines for construction of a kinetic model of the surface reactions:

1. An iodide scale is present on the zirconium surface during reaction at low temperatures. Although the I/Zr ratio of this scale could not be determined quantitatively by ESCA or AES, its presence is consistent with the observations of multiple scales with variable I/Zr ratios at I_2 pressures much higher than those used in the present work (13).

2. Figure 2 indicates that a distinct change in the reaction mechanism occurs at ~850 K, where the signals of both I and ZrI_4 change precipitously. This behavior is best explained by the disappearance of the lower iodide scale from the surface at this temperature, and suggests that ZrI_4 is formed by I_2 reaction with the ZrI_x solid scale but that the bare metal which is present at high temperatures serves principally to dissociate impinging I_2.

3. The slow change of the phase lag of ZrI_4 with modulation frequency (Fig. 4) suggests that bulk diffusion, probably through the lower iodide scale on the surface, is an important step in the mechanism (15).

4. The reduction of the ZrI_4 reaction probability at temperatures below ~500 K and the observation of phase lags larger than 90° in the same temperature range (Fig. 2) indicates a mechanism consisting of series steps prior to product desorption (15).

5. Production of ZrI_4 is linear in the reactant beam intensity while atomic iodine exhibits an apparent reaction order greater than unity (Fig. 3).

6. The indication of a minimum in the response of the iodine atom phase lag to modulation frequency (Fig. 5) is indicative of a branched process (*i.e.*, two independent parallel paths (15)) for dissociating I_2 on the surface to form the atomic iodine product. Minima in the iodine phase data are also observed when the

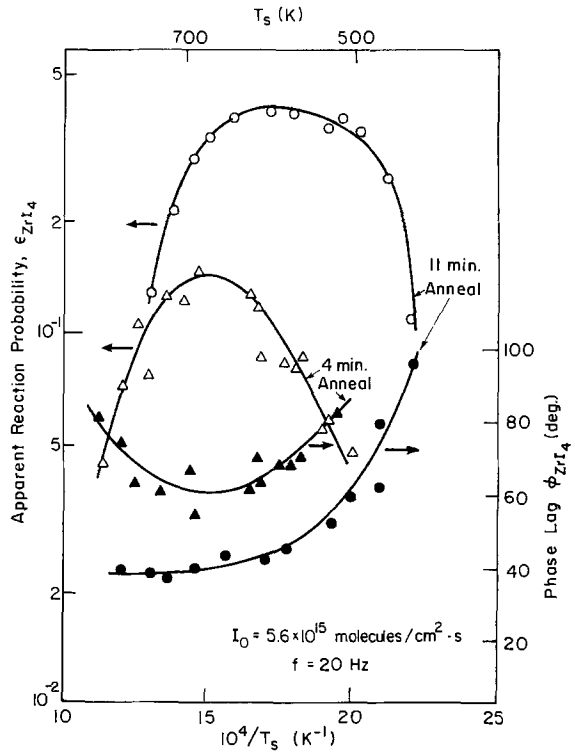

Fig. 8. Effect of annealing of a pre-oxidized zirconium specimen at 1200 K on ZrI_4 production at 600 K; 4 min anneal (triangles) and an additional 7 min anneal (circles).

temperature is varied (Fig. 2), and for the high-temperature beam intensity plot (Fig. 3).

Low temperature ($T < 850$ K).—The following reaction mechanism for surface temperatures below 850 K closely resembles that determined for the fluorine-tantalum system (14). The surface is assumed to be covered with a uniform scale of a lower iodide of zirconium. To simplify the analysis, the I/Zr ratio of the scale is assumed to be unity, corresponding to the lowest iodide of zirconium observed by Cubicciotti *et al.* (5-8). The elementary steps in the reaction model are

$$I_2(g) \xrightarrow{\eta_1} 2I(ads) \quad [1]$$

$$ZrI + I(ads) \xrightarrow{k_1} ZrI_2 \quad [2a]$$

$$ZrI_2 + 2I(ads) \xrightarrow{\text{fast}} ZrI_4(ads) \quad [2b]$$

$$I(ads) \overset{H}{\rightleftharpoons} I(bulk, surface) \quad [3]$$

$$I(bulk, surface) \xrightarrow{D} I(bulk, interface) \quad [4]$$

$$I(bulk, interface) + Zr \xrightarrow{\text{fast}} ZrI \quad [5]$$

$$ZrI_4(ads) \xrightarrow{k_2} ZrI_4(g) \quad [6]$$

$$I(ads) \xrightarrow{k_3} I(g) \quad [7]$$

The model contains no provision for evaporation of lower zirconium iodides or for surface recombination of I(ads) to form I_2, since there is no experimental evidence for the formation of these products.

Reaction [1] represents the dissociative chemisorption of molecular iodine on the surface of the ZrI scale exposed to the impinging reactant beam.

Reaction [2] represents the production of ZrI_4 by reaction between absorbed I atoms and the ZrI scale.

Production of ZrI_2, with rate constant k_1, is assumed to be the limiting step in production of ZrI_4 on the surface; addition of I atoms to ZrI_2 is assumed to be rapid.

Steps [3]-[5] provide a mechanism for regenerating the ZrI scale which is consumed at its upper surface by reaction [2]. The adsorbed I atoms dissolve into the top surface of the scale with a solubility coefficient H (step [3]), then diffuse through the scale to the metal-scale interface (step [4]), where they rapidly and irreversibly react to form fresh scale (step [5]). Diffusion in the scale demodulates the product signal and reduces its fundamental mode component, to which the detection system responds.

Reactions [6] and [7] account for the desorption of adsorbed ZrI_4 and I species for which the rate constants are k_2 and k_3, respectively. Reaction [6] could be a limiting step at low temperatures. As the surface temperature increases above ~600 K, desorption of I(ads) (reaction [7]) causes a decrease in ZrI_4 production.

Numerical implementation of the kinetic model based on reactions [1]-[7] begins with determination of the thickness of the ZrI scale. At steady state, the rate at which the scale is removed by reaction [2] is equal to the rate at which it is produced by the combination of steps [3]-[5]. The thickness of the scale is (14)

$$\xi = \frac{DH}{k_1} \qquad [8]$$

The balance on iodine atoms adsorbed on the ZrI scale is

$$\frac{dm}{dt} = 2\eta_1 I_0 g(t) - (3k_1 + k_3)m + D\left(\frac{\partial C}{\partial z}\right)_{z=0} \qquad [9]$$

where m is the adsorbed iodine atom concentration, I_0 is the iodine beam intensity, and $g(t)$ is the gating function of the beam. The first term on the right-hand side of this equation represents the source of I atoms from the incident I_2 beam. The second term is the loss due to desorption of I atoms and production of ZrI_4. The last term on the right-hand side represents loss of I atoms from the surface by solution and diffusion into the scale, where C is the concentration of iodine in the ZrI scale (in excess of the nominal I/Zr ratio of unity). The diffusion coefficient of iodine atoms in the ZrI scale is denoted by D.

Diffusion of iodine in the scale is governed by Fick's law

$$\frac{\partial C}{\partial t} = D\frac{\partial^2 C}{\partial z^2} \qquad [10]$$

where z is the coordinate perpendicular to the surface. The boundary conditions at the scale/metal interface is

$$C(z = \xi) = 0 \qquad [11]$$

The second boundary condition can be expressed in terms of solubility coefficient, H, relating the surface concentration of I atoms to the bulk concentration of excess iodine in the upper surface of the scale

$$C(z = 0) = Hm \qquad [12]$$

The mass balance on ZrI_4(ads), with concentration of p, is

$$\frac{dp}{dt} = k_1 m - k_2 p \qquad [13]$$

To solve this system of equations for the first Fourier components of the product waveforms (which were measured experimentally), the following forms are assumed

$$g = \tfrac{1}{2}(1 + g_1 e^{i\omega t}) \qquad [14]$$

$$\left.\begin{aligned} m &= m_0 + \bar{m}e^{i\omega t} \\ p &= p_0 + \bar{p}e^{i\omega t} \\ C &= C_0 + \bar{C}e^{i\omega t} \end{aligned}\right\} \qquad [15]$$

Equation [14] is the beam modulation function which is periodic with a frequency ω rad/sec and $i = \sqrt{-1}$. In Eq. [15] the subscript o denotes the steady component of the beam and the overbar denotes complex quantities possessing amplitude and phase. Simultaneous solution of Eq. [9], [10], and [13] gives

$$\epsilon_{ZrI_4} e^{-i\phi_{ZrI_4}} = \frac{4k_2\bar{p}}{I_0 g_1} = \frac{4\eta_1}{\left(1 + i\frac{\omega}{k_2}\right)\left[\left(3 + \frac{k_2}{k_1}\right) + i\frac{\omega}{k_1} + \frac{\alpha DH}{k_1}\frac{1 + e^{-2\alpha\xi}}{1 - e^{-2\alpha\xi}}\right]} \qquad [16]$$

and

$$\epsilon_I e^{-i\phi_I} = \frac{k_3\bar{m}}{I_0 g_1} = \frac{\eta_1}{i\frac{\omega}{k_3} + \left(1 + \frac{3k_1}{k_3}\right) + \frac{\alpha DH}{k_3}\frac{1 + e^{-2\alpha\xi}}{1 - e^{-2\alpha\xi}}} \qquad [17]$$

where

$$\alpha = \left(\frac{\omega}{D}i\right)^{1/2}$$

High temperatures (T > 850 K).—At high temperature the ZrI scale breaks down to a partially-covered zirconium surface and I_2 dissociation by the bare metal provides a second route to atomic iodine. Under these conditions the mechanism involves reactions [1] and [7] on the ZrI-covered portion surface and the following steps on the bare metal

$$I_2(g) + 2Zr \xrightarrow{\eta_2} 2ZrI \qquad [18]$$

$$ZrI \xrightarrow{k_4} Zr + I(g) \qquad [19]$$

Reaction [18] represents dissociative chemisorption of molecular iodine followed immediately by reaction of the adsorbed I with zirconium to produce ZrI. The ZrI so formed decomposes with rate constant k_4. However, the balance between production of ZrI by reaction [18] and removal by reaction [19] results in a partial coverage of the surface by ZrI. Molecular iodine dissociatively adsorbs on and atomically desorbs from the ZrI-covered portion of the surface with the same sticking probability and rate constants which characterize reactions [1] and [7] in the low-temperature regime. If the surface density of ZrI maintained by Eq. [18] and [19] is denoted by n molecules/cm^2 the fraction of the total surface covered by this species is $n\sigma$, where σ is the projected area of a ZrI molecule. The adsorbed ZrI may be sufficiently surface mobile to cluster into islands, leading to a discontinuously covered surface. The surface balance for ZrI is

$$\frac{dn}{dt} = 2\eta_2 I_0 g(t)\,(1 - n\sigma) - k_4 n \qquad [20]$$

The first term on the right-hand side of Eq. [20] represents the production of ZrI(ads) from I_2 gas striking the bare metal surface. The second term shows the loss of ZrI(ads) due to dissociation of this species, desorbing I and leaving Zr behind. The mass balance on iodine atoms adsorbed on ZrI clusters with surface concentration m can be represented by

$$\frac{dm}{dt} = 2\eta_1 I_0 g(t)\,(n\sigma) - k_3 m \qquad [21]$$

The first term on the right-hand side of Eq. [21] represents the rate of dissociative adsorption on ZrI(ads). The second term represents the loss of iodine atoms due to desorption. This equation is the same as Eq. [9] in the limit where the coverage of ZrI is unity (*i.e.*,

$n\sigma \to 1$) and tetraiodide production and bulk solution-diffusion are negligible.

The reaction product vector for iodine atom production can be shown to be

$$\epsilon_I e^{-i\phi_I} = \frac{\eta_2(1-\sigma n_o)}{\left(1+\frac{\eta_2 I_o \sigma}{k_4}\right)+\frac{\omega}{k_4}i} \sigma\eta_1 n_o + \frac{I_o\eta_1\sigma}{2k_4}\left\{\frac{\eta_2(1-\sigma n_o)}{1+\frac{\eta_2 I_o\sigma}{k_4}+\frac{\omega}{k_4}i}\right\} + \frac{}{1+\frac{\omega}{k_3}i} \quad [22]$$

where

$$n_o = \frac{\eta_2 I_o}{k_4 + \eta_2 I_o \sigma} \quad [23]$$

Curves representing the theoretical apparent reaction probabilities and phase lags of the products I and ZrI_4 are compared with the data in Fig. 2-5. Such comparison requires selection of all the physicochemical parameters describing each elementary step of the model, which include the sticking probabilities η_1 and η_2, the rate constants k_1 through k_4, the solution diffusion properties of the scale H and D, and the projected area of adsorbed ZrI, σ. The parameters H and D always appear as the product H^2D in the model and σ is estimated to be 1.6×10^{-15} cm^2 from the cross sections of iodine and zirconium atoms (18). Five parameters ($k_1 - k_4$, H^2D) are assumed to exhibit Arrhenius-type temperature dependences but the sticking probabilities are considered to be temperature-independent. Thus 12 parameters were obtained by fitting the model to the complete set of data in Fig. 2-5. The best values are chosen by an optimization routine which has been modified to accept complex numbers for comparing molecular beam data with the theoretical reaction model (18). The results are summarized in Table I.

Discussion

The restriction of the reaction products to atomic iodine and the tetraiodide is consistent with thermodynamic data for the Zr/I_2 system obtained by Kleinschmidt *et al.* (5). At a total reactive species pressure of 10^{-8} atm (close to the equivalent iodine beam pressures used in the present study), they showed that ZrI_4 and I are the principal vapor components, the former dominant below ~800 K and the latter replacing it at higher temperatures. The close connection between the results of the equilibrium thermochemical study of Ref. (5) and the present nonequilibrium kinetic system can be seen by comparing Fig. 4 of the former with Fig. 2 of this paper. This qualitative link between thermodynamics and product formation in a kinetic system has been placed on quantitative terms by the "quasi-equilibrium model" of chemical kinetics (19). This model is generally in good agreement with the observed product distributions in most halogen-metal reactions, and would appear to be applicable to the present system. However, quantitative application of the quasi-equilibrium model to the zirconium-iodine reaction is hampered by the lack of sufficiently accurate free energy data for the various solid and gaseous zirconium iodides. Nevertheless the abrupt shift in product from ZrI_4 to I as the temperature passes ~850 K can be viewed in a thermodynamic sense as high-temperature instability of ZrI_4. This view of the reaction in no way vitiates the utility of the proposed reaction mechanism, some of the features of which are discussed below.

Table I. Parameters of the Zr-I_2 surface reaction

Parameter	Pre-exponential factor	Activation energy (kcal/mol)
η_1	1.0	—
η_2	0.8	—
k_1	1.6×10^{0} s^{-1}	15
k_2	1.4×10^{14} s^{-1}	24
k_3	1.7×10^{13} s^{-1}	50
k_4	1.7×10^{8} s^{-1}	13
H^2D	1.3×10^{10} s^{-1}	21

The near-unity sticking probabilities of iodine on both ZrI and Zr are essential for the explanation of the vigorous reaction between iodine and zirconium.

The activation energy of the parameter k_3 represents desorption of iodine atoms from the ZrI scale. The value 50 kcal/mol shown in Table I compares satisfactorily with the value of 58 kcal/mol for equilibrium reaction [20]

$$ZrI_2(s) \to ZrI(s) + I(g)$$

which closely resembles reaction [7].

The pre-exponential for desorption of I and ZrI_4 (k_2 and k_3) are consistent with vibrational frequencies of adsorbed species. The low pre-exponential factor for formation of ZrI_2 and decomposition of ZrI(ads) (with rate constants of k_1, k_4) often characterize reaction-controlled surface steps (21).

Interpretation of the results with a model which assumes formation of lower iodide scale on the substrate is consistent with many observations of metal-halogen reactions. Early work by McKinley (22-24) demonstrates the existence of a scale on the reaction of nickel with bromine, chlorine, and fluorine. The assumption of scale formation by Machiels and Olander (14) in the reaction between fluorine and tantalum was later confirmed by Nordine (25) in his study of the kinetics of fluorine reactions with iridium, platinum, and tantalum using transonic flow reactor techniques. Another example of scale formation in low pressure halogen-metal reactions is the iron-chlorine system (26).

The molecular beam reaction response of the system depends only on the product H^2D while according to Eq. [8], the scale thickness requires knowledge of HD. Thus the thickness of the scale cannot be determined from the model unless the diffusion coefficient of I in the scale or the solubility coefficient is known. Assuming $D = 10^{-15}$ cm^2/sec at 600 K gives a scale thickness $\xi = 10$Å, while for $D = 10^{-13}$ cm^2/sec, a thickness of 100Å is predicted.

Acknowledgments

This work was supported by the Director, Office of Energy Research, Office of Basic Energy Sciences, Materials Sciences Division of the U.S. Department of Energy under contract No. DE-AC03-76SF00098.

Manuscript submitted July 20, 1982; revised manuscript received Sept. 15, 1982.

Any discussion of this paper will appear in a Discussion Section to be published in the December 1983 JOURNAL. All discussions for the December 1983 Discussion Section should be submitted by Aug. 1, 1983.

Publication costs of this article were assisted by the University of California.

REFERENCES

1. J. H. Davies *et al.*, in Proc. ANS Topical Meeting Water Reactor Fuel Performance, p. 230, St. Charles, Illinois, May 9-11, 1977.
2. J. T. A. Roberts, E. Smith, N. Fuhrman, and D. Cubicciotti, *Nucl. Technol.*, **35**, 131 (1977).
3. J. T. A. Roberts, "Structural Materials in Nuclear Power Systems," pp. 77-85, Plenum Press (1981).
4. D. R. Olander, *J. Nucl. Mater.*, To be published.
5. P. D. Kleinschmidt, D. Cubicciotti, and D. L. Hildenbrand, *This Journal*, **125**, 1543 (1978).
6. D. Cubicciotti, D. L. Hildenbrand, K. H. Lau, and P. D. Kleinschmidt, in "High Temperature Metal Halid Chemistry," D. L. Hildenbrand and D.

Cubicciotti, Editors, p. 217, The Electrochemical Society Softbound Proceedings Series, Princeton, New Jersey (1978).
7. D. Cubicciotti, K. H. Lau, and M. J. Farrante, *This Journal*, **125**, 975 (1978).
8. D. Cubicciotti and K. H. Lau, *ibid.*, **128**, 196 (1981).
9. Z. M. Shapiro, in "Metallurgy of Zirconium," B. Lustman and F. Kerze, Editors, Chap. 5, McGraw-Hill, New York (1955).
10. R. M. Horton and R. L. Kinney, in "Metal Slag Gas Reactions and Processes," Z. A. Foroulis and W. W. Smeltzer, Editors, p. 317, The Electrochemical Society Softbound Proceedings Series, Princeton, New Jersy (1975).
11. L. N. Shelest, E. K. Safronov, and A. S. Mikhailova, *Russ. J. Inorg. Chem.*, **18**, 9 (1973).
12. F. I. Busol, *Russ. J. Phys. Chem.*, **33**, 799 (1959).
13. D. Cubicciotti and A. C. Scott, *J. Less-Common Met.*, **77**, 241 (1981).
14. A. J. Machiels and D. R. Olander, *Surf. Sci.*, **65**, 325 (1977).
15. R. H. Jones, D. R. Olander, W. J. Siekhaus, and J. A. Schwartz, *J. Vac. Sci. Technol.*, **9**, 1429 (1972).
16. D. R. Olander and M. Balooch, *J. Catal.*, **60**, 41 (1979).
17. J. B. Mann in "Recent Developments in Mass Spectroscopy," K. Ogata and T. Hayakawa, Editors, p. 814, University Park Press, Baltimore (1970).
18. A. J. Machiels and D. R. Olander, *High Temp. Sci.*, **9**, 3 (1977).
19. J. C. Batty and R. E. Stickney, *J. Chem. Phys.*, **51**, 4475 (1969).
20. D. Cubicciotti, R. L. Jones, and B. C. Syrett, Paper presented at ASTM Fifth Conference on "Zirconium in Industry" (1980).
21. R. C. Baetzold and G. A. Somorjai, *J. Catal.*, **45**, 94 (1976).
22. J. D. McKinley, *J. Chem. Phys.*, **40**, 120 (1964).
23. J. D. McKinley, *ibid.*, **40**, 576 (1964).
24. J. D. McKinley, *ibid.*, **45**, 1690 (1966).
25. P. C. Nordine, *This Journal*, **125**, 498 (1978).
26. M. Balooch, W. Siekhaus, and D. R. Olander, To be published.

Rapid Determination of Apparent Activation Energies in Chemical Vapor Deposition

G. Leyendecker, H. Noll, and D. Bäuerle

Angewandte Physik, Johannes Kepler Universität, 4040 Linz, Austria

and P. Geittner and H. Lydtin

Philips Forschungslaboratorium, 5100 Aachen, Germany

ABSTRACT

Laser induced chemical vapor deposition is a powerful tool for rapid determination of apparent chemical activation energies. The method is demonstrated for the case of pyrolytic carbon which was deposited from C_2H_2 at various gas pressures, and we find apparent activation energies of 51 ± 2 kcal/mol.

The deposition rates which can be achieved in the kinetically controlled regime in chemical vapor deposition (CVD) and gas phase epitaxial processes are determined by apparent chemical activation energies which characterize the rate-determining step in the chain of chemical reactions involved in the deposition process. The determination of such activation energies by using normal CVD techniques is very time consuming and problematic because a number of parameters, such as substrate temperature, gas velocity, gas mixture, etc., must be held constant over long periods of time, generally several hours, and only small numbers of data points can be generated (1).

In this paper we will show that laser-induced chemical vapor deposition (LCVD), which is based on local substrate heating by the visible light of a laser (2), is a powerful tool for rapid and accurate determination of apparent chemical activation energies. The method allows the simultaneous quasi-continuous measurement of the deposition rates and the local temperatures which are achieved within the focus of the laser during continuous growth of the cylindrical rods which were described in Ref. (2). We outline the procedure for the example of pyrolytic graphite which was deposited from C_2H_2 by using the visible light of an Ar^+ laser for local heating. The experiments were performed at various pressures of C_2H_2.

Experimental

The experimental setup which allows the simultaneous measurement of local temperatures, deposition rates, and gas pressures is schematically shown in Fig. 1.

The temperature in the growing region of the carbon rods, *i.e.*, at the tip of the rod, was measured pyrometrically. The alignment of the pyrometer was almost parallel to the incident laser beam. Laser plasma lines which are especially strong in the spectral region of the pyrometric measurements near $\lambda = 650$ nm, were eliminated by an interference filter with a 30Å pass band.

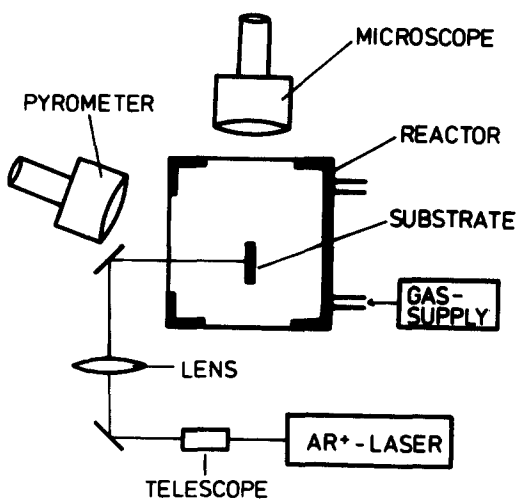

Fig. 1. Experimental setup

Key words: CVD, laser, activation, carbon.

The laser light which is reflected from the tip of the growing rod, and which can produce fluorescence in the internal filters of the pyrometer, was blocked by a long wave pass dichroic filter placed in front of the pyrometer. The calibration of the pyrometer was checked by means of a calibrated tungsten band lamp. The error in calibration was $\lesssim \pm 10$ K.

The hot tip of the growing rod produced a disk shaped pyrometer image with a diameter between about one to seven times the diameter of the pyrometer reference wire. Within this disk we always determined the highest value of temperature at the center. The reproducibility of the pyrometer readings under these conditions was ±20 K. Because of reflection losses at the windows of the reaction chamber and the additional filters these temperature readings must be corrected. Systematic errors arise from uncertainties in the value of the coefficient of emissivity ϵ of carbon at 650 nm, which varies with temperature and surface quality of the region of growth. Assuming $\epsilon = 0.87 \pm 0.05$ (3), the resulting error was estimated to be about ±15 K. Furthermore, because of the temperature gradient on the tip of the growing rod, the measured temperature might be somewhat lower than the actual temperature in the center of the rod, *i.e.*, at $r = 0$. This error was estimated to be $\lesssim$ 40 K in the worst case. The procedure and accuracy of the temperature measurement was checked during similar experiments on the deposition of polycrystalline Si from SiH_4 (4). In this case, the melting point of Si, which is strongly indicated by the step-like increase in laser light intensity reflected from the tip of the rod, was reproduced within ±10 K. Note that all temperatures, T, henceforth used within this paper, refer to the maximum temperature value within the center of the tip of the growing rod.

Deposition was performed from pure C_2H_2 without using a carrier gas. The gas pressure was measured with a standard baratron (capacitance manometer). The accuracy in the pressure measurements was about ±0.5%.

Results

The determination of the activation energy requires an exact definition of a deposition rate which is uniquely correlated to the temperature which is measured according to the procedure described above. While this correlation is trivial in the case of normal CVD where the substrate is held at a uniform temperature, the situation is less obvious in our case where deposition occurs at the tip of the growing rod, which naturally shows a strong temperature gradient. In fact, because the temperature is measured only at $r = 0$, only the growth rate here is uniquely determined by the temperature. We will see, in the next section, that this growth rate is equivalent to the rate of increase of length of the rod. In the following section we present Arrhenius plots for the deposition of C at various C_2H_2 pressures.

Growth velocities.—In Fig. 2a we show a polished longitudinal section of a typical rod, in which can be seen a set of cracks which follow the surface of the rod at different times, and an orthogonal set of striations, which are due to the columnar structure typical of pyrolytic graphite. It is usual to take the direction of growth as being parallel to the columnar structure (8); thus we may define the growth rate v as the rate of translation of a surface element along its perpendicular. It is clear from the shape of the rod that the growth rate is a maximum at the center of the tip, and decreases monotonically away from the tip; in Fig. 2b we plot the growth rate $v(r)$, and also its vectorial representation in the basis of axial $v_a(r)$ and lateral $v_l(r)$ growth rates. Both v and v_a show maxima at $r = 0$ where, by symmetry, v_l vanishes; it follows that $v(r = 0)$ and $v_a(r = 0)$ are identical with the rate of increase of length of the rod, $w(T)$, and, since the

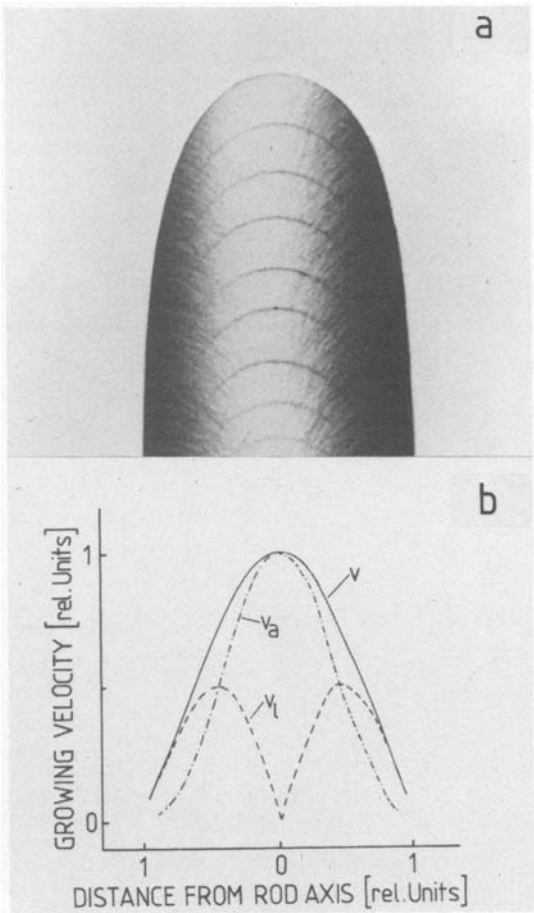

Fig. 2. (a) Polished longitudinal section of carbon rod. (b) Growth rate v (full line) and component growth velocities v_a and v_l (broken lines).

temperature is measured in the center of the rod, uniquely determined by T. We may therefore define the deposition rate by

$$w(T) = \frac{\Delta l}{\Delta t} \equiv v_a(r = 0, T) \equiv v(r = 0, T) \qquad [1]$$

The growth in length, Δl, can be measured very precisely by means of the microscope as shown in Fig. 1. Care must be taken that the time interval for measurement, Δt, is small. In our experiments $\Delta t \lesssim 20$ sec. During this short time of measurement $\Delta l << L$, where L is the length of the laser focus. Typical values of Δl and L were $\lesssim 100$ μm and $\gtrsim 1$ mm, respectively. Under these experimental conditions, the effective laser irradiance, and thereby the temperature T, remained constant within the interval Δt, and within accuracy of measurements. When measuring Δl and T quasi-continuously during the growth of the rod along the total length of the laser focus, L, a large number of data points can be obtained with quasi-continuous changes in temperature. Figure 3 shows directly the range of reproducibility of the data. To cover the range of temperatures plotted, the laser power had to be changed a few times. This was done in such a way that the corresponding irradiances, and thereby the temperature regimes, overlapped considerably.

Arrhenius plots.—For a thermally activated process the deposition rate should follow an Arrhenius type relation of the form

$$w = w_0 e^{-\Delta E/kT} \qquad [2]$$

where ΔE is the apparent activation energy, and w_0 is a constant when the concentrations of the reacting

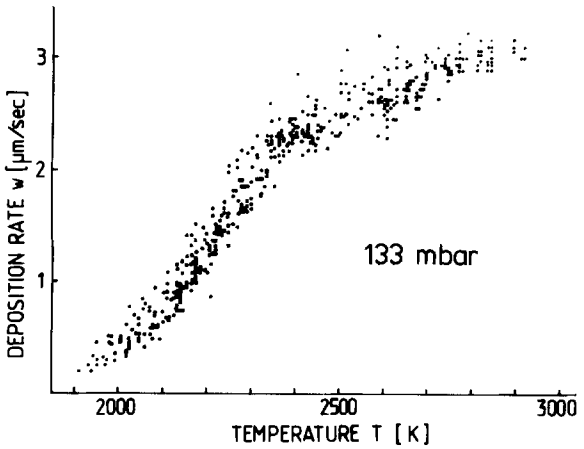

Fig. 3. Dependence of deposition rate on temperature measured quasi-continuously.

species are constant. Figure 4 shows the experimental results in an Arrhenius plot according to Eq. [2], assuming w_0 to be independent of temperature, for various pressures of C_2H. Each data point marked was obtained by averaging about 30 single data points measured according to the technique described above. The error bars represent the standard error.

In the low temperature regime, the slope of the curves is, within the accuracy of measurement, independent of pressure, and corresponds to an apparent activation energy of $\Delta E = 47 \pm 2$ kcal/mol. However, because the gas concentration within the reaction zone is not constant, but depends on temperature according to the ideal gas law, we make the ansatz $w_0 \propto T^{-1}$. Taking this ansatz into account, we still obtain in the low temperature regime of the Arrhenius plot a straight line, within accuracy of measurements, the slope of which is slightly increased and yields an actual apparent activation energy of $\Delta E = 51 \pm 2$ kcal/mol. This value is within the range of activation energies which were derived from the thermal decomposition of acetylene (5). At high temperatures, the curves deviate below the straight lines; this effect becomes more pronounced at low pressures. Note that for the lowest pressures the deposition rate in the "high" temperature regime increases only very slightly with temperature.

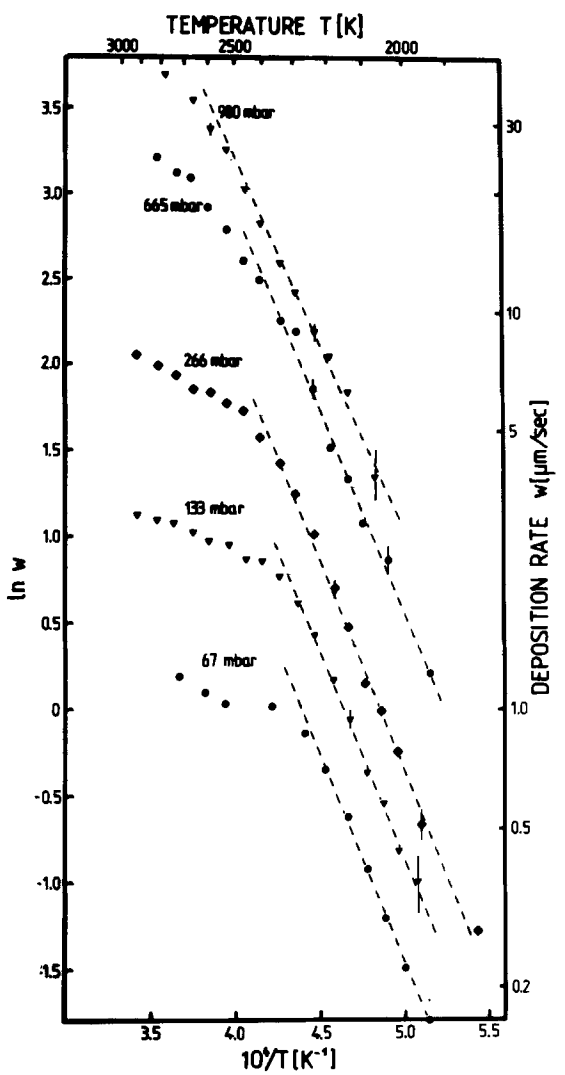

Fig. 4. Arrhenius plot for laser-induced deposition of carbon from C_2H_2.

Discussion

The method described above is reasonably simple and allows an accurate and rapid determination of apparent chemical activation energies in chemical vapor deposition processes. The reasons are as follows: Because the relevant temperature is directly measured *in situ, i.e.,* during the deposition process, rather than derived indirectly from, for example, the effective laser irradiance (6, 7), a number of errors which may arise from possible changes in the diameter and/or the length of the laser focus, from changes in the position of the focal plane with laser power etc., will not affect the experimental accuracy. Furthermore, because of the strong localization of the heated area, typically 10^{-3} mm^2, the reactor can be held at a well-defined ("low") temperature even at very high local temperatures. Therefore, no problems arise with deposition elsewhere than the localized hot spot, even at pressures of several hundred mbar. As a consequence of the much higher pressures that can be used in the LCVD experiments, the deposition rates are higher by 10^2-10^3 than those reported for conventional CVD. For this reason data points can be obtained quasi-continuously, Δl is "reasonably" large and thereby easily measurable even for short time intervals, and the statistics can therefore be very much improved. The strong localization of heating allows three dimensional diffusion of molecules into/out of the reaction zone and is therefore responsible for the much wider extension of the kinetically controlled regime in which the slope of the curve is independent of pressure, reactor geometry, etc. In other words, the break in slope indicating the so-called "diffusion limited" regime occurs at much higher temperatures than in normal CVD experiments, in which, due to the large area slab geometry, only one dimensional diffusion is effective. The marked decrease in slope at higher temperatures may indicate that the deposition becomes limited by transport. However, we cannot rule out the possibility that this change in slope is also influenced by an onset of particle formation, by different chemical reaction pathways, or by H_2 enrichment near the growing surface. H_2 enrichment could arise due to thermodiffusion because of the strong temperature gradient near the tip of the rod, and it could limit the transport of reactive species.

Acknowledgment

Two of us (G. L. and D. B.) wish to thank the Fonds zur Förderung der wissenschaftlichen Forschung in Österreich for financial support.

Manuscript submitted June 14, 1982; revised manuscript received Sept. 3, 1982.

Any discussion of this paper will appear in a Discussion Section to be published in the December 1983 JOURNAL. All discussions for the December 1983 Discussion Section should be submitted by Aug. 1, 1983.

Publication costs of this article were assisted by Johannes Kepler Universität.

REFERENCES
1. See e.g.: J. Bloem and L. J. Giling, "Current Topics in Materials Science," Vol. 1, E. Kaldis, Editor, p. 147, North Holland Publishing Company (1978).
2. G. Leyendecker, D. Bäuerle, P. Geittner, and H. Lydtin, *Appl. Phys. Lett.*, **39**, 921 (1981), and references therein.
3. "CRC Handbook of Chemistry and Physics," 59th ed., Robert C. Weast, Editor, CRC Press MC, West Palm Beach, Florida (1978).
4. D. Bäuerle, P. Irsigler, G. Leyendecker, H. Noll, and D. Wagner, *Appl. Phys. Lett.*, **41**, 819 (1982).
5. H. B. Palmer and C. F. Cullis, *Chem. Phys. Carbon*, **1**, 265 (1965).
6. V. Baranauskas, C. I. Z. Mammana, R. E. Klinger, and J. E. Greene, *Appl. Phys. Lett.*, **36**, 930 (1980).
7. J. Mazumder and S. D. Allen, *SPIE*, **198**, 73 (1979).
8. J. C. Bokros, *Chem. Phys. Carbon*, **5**, 1 (1969).

Practical Limiting Efficiencies for Crystalline Silicon Solar Cells[1]

James A. Amick* and Amal K. Ghosh

Exxon Research and Engineering Company, Linden, New Jersey 07036

ABSTRACT

A review is given of the factors governing the conversion efficiency for crystalline silicon solar cells at AM1 and of the practical limits on cell efficiencies. Included are losses due to reflection, shadowing, carrier diffusion length, and I^2R dissipation. The influence of polycrystalline grain size on conversion efficiency is also discussed. For conventional cells having a planar junction, a practical limiting efficiency in production appears to be about 17% in the absence of sunlight concentration.

The theoretical efficiency for crystalline silicon solar cells has been calculated as about 22% for operation at AM1 (1). For currently manufactured cells, efficiencies of only 12-14% are achieved, one-half to two-thirds the theoretical value. Reasons for the divergence between theory and practice have been discussed in the literature and the loss mechanisms are largely understood (2). With new technology, efficiencies are continually being raised, but there are limits to the efficiencies that can be achieved. It is the purpose of this paper to reexamine the loss mechanisms operative in crystalline silicon solar cells and to estimate the practical upper limits for achievable efficiency.

Assumptions

For the purposes of this analysis, several assumptions and constraints are made: (*i*) The cell is constructed from a single crystal or polycrystalline silicon sheet with a continuous junction in (or on) one major surface of the cell. (Interdigitated back contact cells, for example, are not considered). (ii) To collect current, a conductive metal network is present on the front surface. This network consists of a grid line array of parallel, constant width lines plus a bus pattern. Losses for the network are minimized by the optimization procedure described in a previous paper (3). (*iii*) The power density for AM1 sunlight is taken as 100 mW/cm^2, a number that is subject to some uncertainty because of uncontrolled and uncontrollable atmospheric conditions, such as haze, humidity, pollutants, that vary from day to day and from season to season. (*iv*) The spectral distribution and density of photons in AM1 sunlight and corresponding analytic expressions representing this distribution are taken from DeVos (4). (*v*) The solar cell obeys a classical diode equation (5) which can be written in simplified form as

$$J = J_o(e^{qV/nkT} - 1) \qquad [1]$$

where J = current density in A/cm^2, J_o = reverse saturation current density for the diode in the dark in A/cm^2, q = electronic charge, V = voltage across the diode (cell) in volts, k = Boltzmann constant, T = temperature in K, n = "diode quality factor," typically unity at higher voltages, and $q/kT = 38.46\text{V}^{-1}$ at $T = 300$ K (room temperature).

Approach

Historically, the output of a solar cell is represented as the product of three parameters: short-circuit current (I_s), open-circuit voltage (V_{oc}), and fill factor (FF). For estimating efficiency, the product of these three parameters is found. This product is then divided by the total incident power and multiplied by 100. If the short-circuit current density (J_{sc}) for AM1 illumination is known, the efficiency can be simply expressed as

$$\eta = (J_{sc})\ (V_{oc})\ (FF) \qquad J_{sc} \text{ in mA/cm}^2$$

since the incident power density is taken as 100 mW/cm^2. Each of these parameters will be considered in turn.

Short-Circuit Current Density

The short-circuit current density is a key parameter since it is influenced by many factors. The open-circuit voltage changes only slowly with changes in short-circuit current, and the fill factor is essentially fixed by the diode equation. The short-circuit current density is therefore treated first in this discussion.

Incident light intensity.—The primary factor governing short-circuit current density is the availability in sunlight of photons having an energy suitable for absorption by crystalline silicon. For AM1, this number is not completely defined. Figure 1 shows the data from

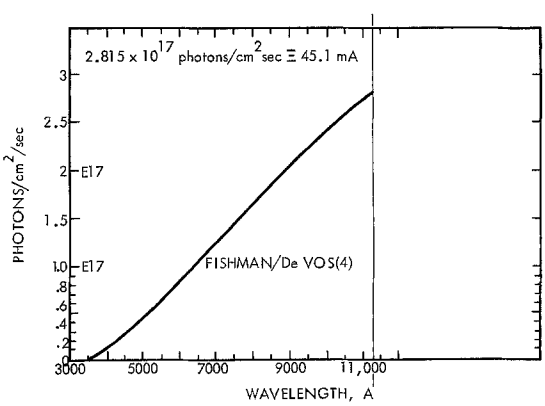

Fig. 1. Photon density vs. wavelength for AM1

* Electrochemical Society Active Member.

[1] A more detailed treatment will be found in "Proceedings of the Symposium on Materials and New Processing Technologies for Photovoltaics," Vol. 81-3, J. A. Amick, E. Sirtl, P. Rai-Choudhury, and J. P. Dismukes, Editors, The Electrochemical Society Softbound Proceedings Series, Pennington, New Jersey (1981).

Key words: current density, diffusion, reflection.

DeVos (4) which covers the energy range of interest for solar cells. Upon integrating the photon density from 1.1 eV (the bandgap of silicon) to infinite energy, a value of $\sim 2.8 \times 10^{17}$ photons/cm^2 sec is obtained.[2] Assuming that every photon creates a carrier pair and that all carriers are collected, this translates to a current density (no loss) of about 45 mA/cm^2. This value is an upper bound for for short-circuit current density in a crystalline silicon device. A recent calculation with SERI AM1 spectra yields a value of 45.8 MA/cm^2.

Diffusion length for carriers.—As shown by Ghosh, Fishman, and Feng (5), the short-circuit current for a practical crystalline silicon cell is less than 45 mA/cm^2 because of finite thickness (hence limited absorption of photons) and finite diffusion length (hence limited carrier collection). The limited thickness implies that wavelengths that are poorly absorbed in silicon, *i.e.*, the red region of the spectrum, will partly pass through the silicon without being absorbed.[3] The finite diffusion length implies that carrier pairs created deep within the interior of the cell cannot all reach the junction before they recombine. For these two constraints of thickness and diffusion length, the ideal short-circuit current can be determined, employing the energy distribution of sunlight and the optical absorption characteristics of crystalline silicon. Results of this calculation were shown in Fig. 10 of Ref. (5) and are replotted here to show short-circuit current density as a function of wafer thickness with diffusion length as the independent parameter (Fig. 2).

As can be seen from Fig. 2, the short-circuit current density begins to fall substantially if the cell thickness decreases below about 250 μm (0.010 in.). A cell thickness of 150 μm (0.006 in.) lowers the short-circuit current by about 6% compared with a thickness of 300 μm (0.012 in.) and for a diffusion length of 200 μm. For a cell 150 μm thick, there is virtually no advantage to raising the diffusion length beyond this 200 μm value. On this basis, we conclude that future photovoltaic cells should be made from silicon at least 250 μm (0.010 in.) and up to 400 μm (0.016 in.) thick, especially as techniques for increasing the diffusion length are developed.

As is well known, the diffusion length is dependent on two fundamental parameters, carrier mobility and lifetime. In general, if the quality of the starting silicon decreases, or if impurities are inadvertently introduced during processing, the lifetime falls more rapidly than the mobility. For solar cells currently being manufactured, mobilities approach the ideal values; lifetimes are typically in the range of 10-100 μsec. This places the diffusion length in the vicinity of 100-500 μm. A lifetime of 100 μsec is probably an upper bound for a practical silicon device (7). This would give a diffusion length of about 500 μm for a production cell.

For a single crystal silicon solar cell, taking into account just the thickness and diffusion length limitations, and assuming a thickness of 300 μm and a diffusion length of 500 μm, the ideal current density of 45 mA/cm^2 is reduced to about 38 mA/cm^2. While not truly fundamental, this appears to us as a loss of 15% which is unavoidable in practical cells.

For polycrystalline wafers, the diffusion length will be further reduced. As shown by Ghosh *et al.* (6), the diffusion length is a function of grain size. Mobility and lifetime are both affected by decreasing the size of grains. Practical cells will require grain sizes of at least 100 μm (0.004 in.). To approach the performance of single crystal cells, grain sizes of 0.5 cm or larger will be needed. Such grain sizes can be obtained for polycrystalline silicon by slow cooling of a melt (8). It is consequently anticipated that efficiencies for polycrystalline cells will closely approach those for single crystal devices, given equivalent quality of the starting silicon.

From this analysis of diffusion length and thickness limitations, we conclude that cell thickness in the range 0.009-0.020 in. will be used in future production cells, with the larger thicknesses favored as the cost of silicon decreases and the technology for increasing diffusion length improves. It also appears that polycrystalline silicon with large grain sizes will be available and that the efficiencies for cells formed in such polycrystalline material will closely approach the efficiencies for single cells. It nevertheless appears that an unavoidable loss of short-circuit current density of perhaps 15% will be encountered for crystalline silicon cells due to the finite thickness and the finite diffusion length for silicon.

Reflection losses.—A second factor controlling short-circuit current density is the reflection of incident light from the front surface of the cell. This reflection loss is a fundamental characteristic of a discontinuous change in refractive index and, for a single discontinuity in nonabsorbing materials, is determined by the equation

$$R = \frac{(n_1 - n_2)^2}{(n_1 + n_2)^2} \qquad [2]$$

where R = the fraction of light reflected and n_1 and n_2 are optical indexes of refraction for two different media.

For crystalline silicon, the index of refraction is about 3.9 at a wavelength of 6600A (9). This leads to a reflection loss of about 35% for light traveling from air into an optically polished silicon surface. Reflection losses well below this value can be obtained by (*i*) surface texturing, (*ii*) antireflection coating with interference-thickness films, and (*iii*) optical index matching. Surface texturing is normally achieved for (100) oriented silicon wafers by treatment in hot caustic (10). Such treatment can reduce the reflection loss to a few percent, but has the disadvantage that not all crystal orientations are suitable. Especially for polycrystalline silicon wafers, in which the grains tend to be randomly oriented, this type of surface texturing is unsatisfactory. Antireflection coatings are capable of lowering the reflection loss in selected, narrow wavelength ranges for silicon, but must be carefully controlled in thickness and in refractive index. Unfor-

[2] There is uncertainty in the literature whether the number 2.8 $\times$ 10^{17} photons/cm^2 sec corresponds to 100 mW/cm^2 of incident sunlight. This uncertainty could modify the conclusions about limiting cell efficiency by as much as 15% and needs to be resolved.

[3] A reflective back contact can conceptually increase the effective cell thickness by up to a factor of 2 or more, but may place constraints on cell processing that may not be achievable in practice.

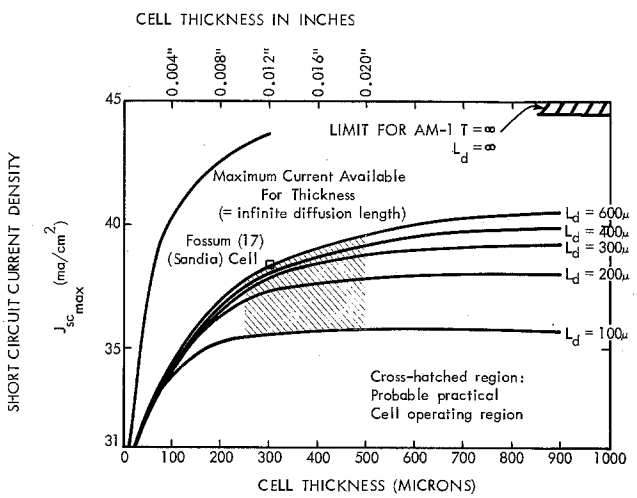

Fig. 2. Maximum short-circuit current for crystalline silicon solar cells in AM1 sunlight vs. cell thickness (for various diffusion lengths of minority carriers). (No shadowing, reflection, surface recombination, I^2R losses.)

tunately, the band of wavelengths available from sunlight is broad enough so that losses on either side of the minimum are substantial. Matching of optical indexes for multiple layers is possible by selecting a series of gradually decreasing optical index layers from 3.5 to 1. By properly grading the index, for 3 to 4 layers, reflection losses can be held below about 5% over the spectral range of interest.

Unfortunately, there appears to be an unavoidable loss of about 4% for an encapsulated solar cell due to the mismatch between the uppermost glass or plastic layer and air. Techniques for texturing glass to reduce this loss are known (11), but the surfaces produced are fragile. Upon exposure to weathering conditions and pollutants, the beneficial effects of the texturing processes can be lost. We, therefore, conclude that there is an approximate 5% loss by reflection which is unavoidable in production.

Shadowing loss.—The metal grid overlying the photosensitive surface contributes a further loss of incident photons. Unfortunately, the metal grid is required because of the relatively high sheet resistivity for the diffused junction formed in a conventional solar cell. Even for the heterojunctions formed with tin oxide deposits, sheet resistivities are in the neighborhood of 100 Ω/sq. While the sheet resistivity for a diffused junction can be lowered by deeper diffusion, the resulting heavily doped surface region has poor lifetime and the improvement obtained with lower sheet resistivity is more than offset by the loss of carriers in the surface region of the device. For the foreseeable future, it is anticipated that a metal grid will be required. As described in an earlier paper (3), for practical metallization systems and cell diameter, there is at least a 5% shadowing (*i.e.*, short-circuit current density) loss,[4] which is unavoidable for production cells. It may be difficult to achieve this magnitude of shadowing loss within any reasonable low cost process.

Recombination in the front surface.—At one time, the junctions in solar cells were deep enough so that appreciable optical absorption occurred in the heavily doped surface region formed by diffusion. Since recombination in this region is rapid, carrier loss was significant. With the advent of shallow junction devices, this loss mechanism decreased greatly in importance (12). Fishman (13) has calculated the absorption of AM1 photons in a region of silicon 0.1 μm thick as this region is moved from the front surface to the back surface of a wafer. Assuming 100% carrier collection efficiency, *i.e.*, infinite diffusion length, this data can be converted into the current contribution from each 0.1 μm thick slab of silicon as shown in Fig. 3. For junctions 2500A deep, the total current contribution from the region on the surface side of the junction is about 5 mA/cm². In actual cells, most of this current appears to be collected, and recombination in the front surface constitutes a loss of only a couple of percent. Some loss by this mechanism is unavoidable in diffused junction cells, but heterojunction cells are apparently free from this loss. Because of the small contribution, this loss is neglected in the estimation of practical cell efficiency.

Summary of losses in short-circuit current density.—From the discussions above, it appears that the short-circuit current density for practical production cells made from single crystal silicon will be substantially lower than the 45 mA/cm² which represents the no-loss case. The thickness/diffusion length loss will be about 15%, the reflection loss will be about 5%, and the shadowing loss will be about 5%. This combination effectively reduces the 45 mA/cm² to about 34.5 mA/cm². While this number is not a fundamental limit, it will be very difficult to exceed in production, For small diameter cells, particularly those without a metal grid pattern, values up to 36-37 mA/cm² can be expected. However, production cells with areas of 25-100 cm² or more cannot achieve the higher current levels without introducing concomitant I^2R losses that more than offset the gain from the increased current. We, therefore, anticipate that production cells will exhibit short-circuit currents ≤ 35 mA/cm².

[4] With another 5% loss due to the I^2R dissipation in the metal grid, as discussed in more detail below.

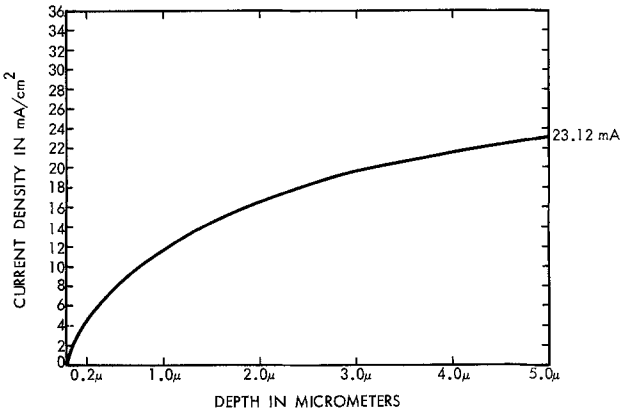

Fig. 3. Cumulative current in 0.1 thick slabs *vs.* depth of slab

Reverse Saturation Current Density and Open-Circuit Voltage, (V_{oc})

The open-circuit voltage for a diode is not an independent parameter. For a diode obeying Eq. [1], the reverse saturation current density, in combination with the short-circuit current density, determines the open-circuit voltage. The short-circuit current density was calculated above. The reverse saturation current density is made up of three components (14), but in a well-behaved diode, the dominant saturation current density is usually the J_{01} given by the diffusion-limited current. Typical dark characteristics for a silicon solar cell are plotted schematically as the logarithm of the current density *vs.* voltage in Fig. 4. Such plots usually exhibit two distinct slopes. At lower voltages, the n-value (diode quality factor) is two or more; at higher voltages, the n-value is near unity. The higher n-value is normally associated with recombination in the junction region of the device; extrapolation of this line-segment to zero voltage gives the current density intercept J_{02}. The segment having unity slope is asso-

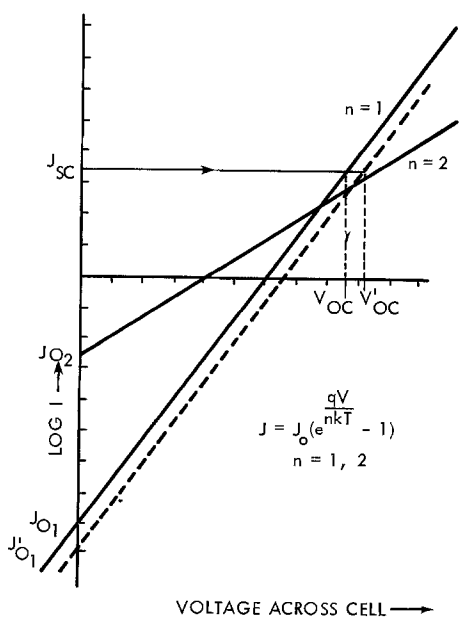

Fig. 4. Dark current-voltage characteristics for solar cell

ciated with diffusion-limited current density arriving at the junction from the bulk; extrapolation of this line segment gives the intercept J_{01}. These intercepts represent currents arising from different processes and can vary independently. In real cells, both are governed by the presence of impurity states typically of uncontrolled and undefined origin.

If the saturation current density from either process (at zero voltage) is altered, *e.g.*, by using a higher purity silicon, the corresponding J_0 is lowered (*e.g.*, J_{01} to J_{01} in Fig. 4), and the corresponding line segment for that process is moved parallel to itself, as shown. The open-circuit voltage for a cell can be found by extending the expected short-circuit current density (*e.g.*, 35 mA/cm^2) parallel to the voltage axis until it intercepts one of the two line segments. For practical cells, the intercept lies near the cross-over point for the two line segments, but usually intercepts the $n = 1$ slope region. For future cells, it is assumed that the junction recombination current density will be decreased and that the open-circuit voltage will be determined by intercept with the $n = 1$ line segment.

Reduction of J_{01} and J_{02} leads to higher open-circuit voltages as shown in Fig. 4, but J_{01} appears to be the more fundamental limit. An estimate of J_{01} for a practical cell can be made following the approach of Hall (15). For a simple diode with a metal back contact (recombination velocity infinite) and a diffused thin front junction, he gives the saturation current density (the values of the parameters are given in Table I)

$$J_{01} = \frac{qD_e n_i^2}{N_A L_e} \coth (W/L_e) \qquad [3]$$

Similarly, for a back surface field (BSF) cell, where carriers are reflected from the back contact (recombination velocity = zero), he gives

$$J_{01} = \frac{qD_e n_i^2}{N_A L_e} \tanh (W/L_e) \qquad [4]$$

From Fig. 2 it can be anticipated that the ratio W/L_e will lie in the range $0.3 < W/L_e < 3$. Insertion of the values for each parameter allows calculation of the expected saturation current densities for each type of cell as shown in Table II.

There are other theories which account for the back surface field. Reference to these theories can be found in a recent publication by Dhariwal and Kulshreshtha (16).

From Table II, it is seen that the saturation current densities, J_{01}, are all in the range 10^{-12}-10^{-13} A/cm^2. From Eq. [1], using $J_{sc} = 0.035$ A/cm^2, the corresponding open-circuit voltages are: $J_{01} = 10^{-12}$ A/cm^2, $V_{oc} = 0.63$V; $J_{01} = 10^{-13}$ A/cm^2, $V_{oc} = 0.69$V.

Table I. Values of parameters

$q = 1.6 \times 10^{-19}$C	where: q	= electronic charge
$D_e = 35.1$ cm^2/sec	D_e	= electron diffusion coefficient
$n_i = 1.35 \times 10^{10}$/cm^3	n_i	= intrinsic electron concentration
$N_A = 10^{17}$ atoms/cm^3	N_A	= acceptor atoms in base region
$L_e = 100\text{-}500 \times 10^{-4}$ cm	L_e	= diffusion length of electrons in the base
$W = 0.038$ cm = 0.015 in.	W	= cell thickness

Table II. Saturation current density (J_{01}) for solar cells

	Eq. [3]		Eq. [4]	
	Simple cell, metal back		Back surface field cell	
W/L_e	coth (W/L_e)	J_{01} (A/cm^2)	tanh (W/L_e)	J_{01} (A/cm^2)
0.3	3.4	1.8×10^{-12}	0.3	1.6×10^{-13}
1	1.3	7.1×10^{-13}	0.76	4.1×10^{-13}
3	1	5×10^{-13}	0.99	5×10^{-13}

Within ± 5%, we anticipate that the open-circuit voltage will be 0.64V for production cells; with lower quality starting silicon, hence higher concentrations of inadvertent impurities, the voltages will tend to be lower. Green and co-workers (17) have reported V_{oc} of 0.64V in MINP structures.

It should be noted that the same parameters that control the major short-circuit current loss, *i.e.*, diffusion length and cell thickness, also control the reverse current and hence the open-circuit voltage.

The uncertainty in this value is greater than for the short-circuit current density. From the treatment of Rose (18), for saturation current limited by radiative recombination, an open-circuit voltage of about 0.75V is calculated. With present-day silicon, recombination is dominated by impurities. How and whether the impurity concentration can be decreased to approach the radiative-recombination-limited J_{01} is not known. It is not likely to occur in the near future. Accordingly, we anticipate that production cells will have an open-circuit voltage < 0.64V.

Fill Factor

The fill factor for a silicon solar cell can be calculated from the ideal diode curve as 0.83-0.84 (19). Present-day cells have fill factors in the range of 0.72-0.76. Departure from the ideal value may be due to metallization resistance, interfacial (contact) resistance, limitations in sheet resistance on the front surface, and/or resistances within the bulk of the cell. Although these resistances can probably be reduced, they cannot be entirely eliminated. A practical fill factor of about 0.8 appears reasonable for production cells as the technology improves.

I^2R Losses in the Metal Network

The flow of current through the metal network on the front surface of the cell leads to an additional I^2R loss due to the finite resistance of the bus and grid metallization. From the optimization procedure described in Ref. (3), and as mentioned in the section on shadowing loss, an estimated 5% of the power available from the cell is lost. Since the conductivity of these metal grids is finite, it is estimated that a loss of this magnitude will be present in future production cells.

Estimated Efficiency for Production Cells

The effects of the losses described in the preceding sections are combined as follows for cells meeting the constraints of section on Assumptions:

Overall efficiency

$$\eta = (J_{sc} \times V_{oc} \times FF)(1 - I^2R \text{ loss})$$
$$= 34.5 \text{ mA/cm}^2 \times 0.64\text{V} \times 0.8 \times 0.95$$
$$= 16.78 \text{ at } 28^\circ\text{C}$$

This value may be in error by 5 to 10%, but we conclude that the practical upper limit for efficiency of crystalline silicon cells will probably lie between 16 and 18%. Values in this range have already been reported by Fossum for his back surface field cells (20).[5]

The single most important loss component is the 15% loss due to limited thickness/diffusion length in silicon. This loss could theoretically be reduced by 10% by increasing the thickness of the silicon to 0.025-0.030 in. with diffusion lengths of 500-1000 μm. The increment in output is small, however, compared with the increasing cost of the silicon used in the wafer and will probably not be cost justified. Increased efficiency could also be obtained by reducing the area per cell, hence lowering losses due to the (optimized) metal grid, at the expense of increasing the cost of assembly of the module and increasing the number of cell inter-

[5] See also a recent theoretical paper by C. H. Henry concerning ideal cells (21).

connections required for a given power output from the module.

Conclusions

From a practical standpoint, the manufacturer of solar cells is not concerned with absolute efficiency. His concern is with dollars per peak watt of output power (system cost). Efficiency calculations are of value principally to the research worker who seeks to improve solar cells and to understand mechanisms that limit performance. By considering the loss mechanisms in detail, the reasons for less than optimum cell performance should be definable. Once the principal loss mechanisms are understood, steps can be taken to improve cell performance.

Although the efficiency range of 16-18% appears to represent a rational goal for production cells, we conclude that, for crystalline silicon, efforts to exceed these efficiencies will be counterproductive. The increase from 12-14% to 16-18% represents an improvement of perhaps 1/3 in efficiency and translates to a corresponding decrease in cost per peak watt for the finished modules, assuming that the added cost of the processes required to achieve the greater efficiency is negligible. At today's module prices of about $10 per peak watt, this represents a saving of almost $2.50 per peak watt, a major step toward the goal of low cost power from photovoltaics.

Manuscript submitted Aug. 14, 1981; revised manuscript received Aug. 17, 1982.

Any discussion of this paper will appear in a Discussion Section to be published in the December 1983 JOURNAL. All discussions for the December 1983 Discussion Section should be submitted by Aug. 1, 1983.

Publication costs of this article were assisted by Exxon Research and Engineering Company.

REFERENCES

1. P. Rappaport, *RCA Rev.*, **20**, 373 (1959).
2. See, for example, "Solar Cells," C. E. Backus, Editor, IEEE Press, New York (1976).
3. J. Amick, in "Symposium on Materials and New Processing Technology," J. Amick, P. Rai-Choudhury, E. Sirtl, and J. P. Dismukes, Editors, The Electrochemical Society Softbound Proceedings Series, Pennington, NJ (1981).
4. A. DeVos, *Energy Convers.*, **16**, 67 (1976); see also A. K. Ghosh, C. Fishman, and T. Feng, *J. Appl. Phys.*, **50**, 3454 (1979).
5. A. K. Ghosh, C. Fishman, and T. Feng, *ibid.*, **50**, 3454 (1979).
6. A. K. Ghosh, C. Fishman, and T. Feng, *ibid.*, **51**, 446 (1980).
7. See, for example, K. Graff and H. Fischer, in "Topics in Applied Physics," Vol. 31, B. O. Seraphin, Editor, pp. 173ff, Springer Verlag, Berlin (1979).
8. See, for example, F. Schmid and C. Khattak, quarterly reports from Crystal Systems, Inc., Contract DOE/JPL 954373 80/15.
9. R. Hulthen, *Phys. Scri.*, **12**, 342 (1975).
10. C. R. Baraona and H. W. Brandhorst, in "11th IEEE Photovoltaic Specialists Conference," pp. 44 ff (1975).
11. S. M. Thomsen, U.S. Pat. 2,490,662 (1949); also Motorola Quarterly Reports under DOE/JPL Contract NAS-7-100-955387, E. Pastirik, principal investigator. See also R. J. H. Lin, H. Mar, and R. E. Peterson, Abstract 309, p. 789, The Electrochemical Society Extended Abstracts, Philadelphia, Pennsylvania, May 8-13, 1977.
12. J. Lindmayer and J. F. Allison, COMSTAT Tech. Rev., **3**, 1 (Spring, 1973).
13. C. Fishman, Private communication.
14. M. Wolf and H. Rauschenbach, *Adv. Energy Conversion*, **3**, 455 (April-June 1963).
15. R. N. Hall, *Solid State Electron.*, **24**, 595 (1981).
16. S. R. Dhariwal and A. P. Kulshreshtha, *ibid.*, **24**, 1161 (1981).
17. M. A. Green, A. W. Blakers, M. R. Willison, T. Szbitalak E. M. Keller, E. Gauja, and P. J. Hart, "15th IEEE PV Specialist Conference," p. 1405 (1981).
18. A. Rose, *J. Appl. Phys.*, **31**, 1640 (1960), and Private communication.
19. M. Wolf, *Proc. IRE*, **48**, 1246 (1960).
20. J. G. Fossum, R. Nasby, and E. L. Burgess, Energy Res. Abstracts, (1978), 3(20), Abstract 47077.
21. C. H. Henry, *J. Appl. Phys.*, **51**, 4494 (1980).

Solutal Diffusion Coefficient for Liquid PbTe-SnTe

I. O. Clark, A. L. Fripp, W. J. Debnam, Jr., R. K. Crouch, and W. D. Brewer

NASA Langley Research Center, Hampton, Virginia 23665

ABSTRACT

The solutal diffusion coefficient has been determined for liquid lead telluride-tin telluride using a modified shear cell technique. Postdiffusion concentration profiles are presented for several diffusion couples. The best analytical curve fit to the data gives a composition-dependent diffusion coefficient of $(3/7)^C \times 1.4 \times 10^{-4}$ cm²/sec, where C is the PbTe concentration. In addition, data are presented to show the importance of solutal convection in the lead-tin-telluride system.

The solutal diffusion coefficient is one of the thermophysical properties that enters into the theory of crystal growth of alloys by directional solidification. Tiller, Jackson, Rutter, and Chalmers (1) have shown that the length of crystal needed to reach steady-state, compositionally unvarying growth, with a system in which no mixing occurs other than solutal diffusion, is dependent on the growth rate, segregation coefficient, starting composition, and the solutal diffusion coefficient of the liquid. Maintaining interfacial stability and avoiding constitutional supercooling also requires knowledge of the solutal diffusion coefficient (2). Ostrach (3), in an article on solutal convection in fluid systems, has shown that the liquid diffusion coefficient enters into the equation which predicts the onset of convective fluid flow. Hence, the diffusion coefficient must be known before directional solidification crystal growth conditions can be reliably set by other than trial and error techniques.

There is a noticeable dearth in the literature of values of high-temperature liquid diffusion coefficients. This is probably due to several factors which make these types of experiments difficult. One of the problems is in obtaining reliable data on the distribution of the solute in the melt or in the solid after quenching. Another difficulty is that several of the semiconductor materials studied in crystal growth are quite corrosive to thermocouples and other experimental apparatus. A third problem area is that for a material which has a lens-shaped phase diagram there is compositional segregation during the solidification which

Key words: semiconductor, diffusion, liquid, convection.

can affect the distribution of solute even when the diffusion couples are quenched. Undercooling the melt before solidification begins can also affect the solute distribution. Finally, these materials can undergo dendritic growth which will affect the distribution profiles. This paper presents data obtained by the modified shear cell technique on the pseudobinary PbTe-SnTe system, obtains a value for the solutal diffusion coefficients, and discusses some possible effects the aforementioned difficulties may have on the results.

Experimental

The modified shear cell technique used in this research was first used by Broome and Walls to measure self-diffusion in liquid mercury (4) and liquid gallium (5). Figure 1 shows a conceptual drawing of the apparatus and the location of the materials before, during, and after diffusion was allowed to take place. The experiment was conducted by melting the two components and sliding the SnTe upper half-cells over the PbTe lower half-cells to form a diffusion couple. After allowing diffusion to proceed for a predetermined time, the couples are sheared apart to neutral positions such that no upper and lower sections are in contact and the apparatus is removed from the furnace and allowed to cool.

The shear cell apparatus was machined from high-purity graphite. The capillaries are split cylindrical sleeves which facilitate easy sample removal and allow the use of various capillary diameters in the same base and slide units. The diameters of the capillaries used in these experiments were 2.00 or 2.25 mm, and the half-cell lengths were 14 mm. The bottom half-cells were always overfilled such that the initial shearing action produced a fresh surface at the shear plane. The top half-cells could not be completely filled due to both the vapor loss at the upper surface and settling of the material at melting. A fresh surface for the diffusion couples was produced by the shearing action. Manipulation of the shear cell apparatus was done by means of fused quartz push rods which extended through the end cap of the furnace tube.

In a typical run, the diffusion shear cell is assembled and loaded in a glove box filled with either an inert or reducing atmosphere. The diffusion apparatus is then passed into the furnace tube through a connecting port in the glove box. After further purging in the furnace tube, the preheated split furnace is opened to pivot the tube into the furnace cavity. Approximately 30 min are allowed for the system to reach thermal equilibrium after closing the furnace and then the half-cells are sheared to form the diffusion couples. After 10 min, the apparatus is again manipulated so that the diffusion couples are sheared but the upper and lower half-cells are not exposed to material wiped off earlier. The furnace is opened immediately and the tube is pivoted out to cool.

A thermal time history of the shear cell during cooling was determined for each run by means of optical pyrometer readings of the graphite boat. These optical pyrometer readings were calibrated by taking similar readings with thermocouples placed within the empty diffusion cells. The diffusion temperature for all runs except one was 990°C. In one run, couple 5, for which the diffusion cell was not sheared, the temperature was 940°C.

Since the pseudobinary, PbTe-SnTe is single phase and fully miscible over the entire range of compositions, the distribution was determined with a wavelength-dispersive electron microprobe equipped with on-line data reduction capability. The effective spot size was less than 2 μm in diameter and the translation resolution was 1 μm. The microprobe data was taken by using standards of PbTe and elemental Sn. A sample of PbSnTe with a known composition was then checked to make sure that the system was giving consistent values. The data on the compositions have an uncertainty of about $\pm 1\%$. Unless otherwise noted, the data presented are from the as-quenched surface. An advantage of the microprobe analysis over a chemical or other bulk technique is that in addition to the composition, information can be obtained about the microscopic distribution and some of the mechanisms which have an effect on the distribution can be studied on the interior of the couples.

The possible occurrence of either thermal or solutal convection must be considered in liquid diffusion measurements. In order to avoid convection, horizontal density gradients must be eliminated and any vertical density gradients must either be in a stabilizing orientation or below the critical value for convective onset in the destabilizing orientation. Detailed treatments of convection and convective onset may be found in articles by Verhoeven (6) and Ostrach (3). In order to avoid thermal convection, the furnace controls were set such that the temperature profile of the empty furnace tube in the furnace was maintained uniform to within 0.1°C over the region occupied by the shear cell apparatus during diffusion. The high-thermal conductivity of the graphite apparatus would further damp out any temperature variations that might exist. To help eliminate solutal convection, all runs were made with the capillary axes parallel to the gravity vector and, with one exception, the less dense SnTe on top. In one run the more dense PbTe was placed in the upper half-cell in order to observe solutal convection effects.

Results and Discussion

Figure 2 presents the data for the solutally unstable configuration, *i.e.*, the PbTe on top and the SnTe in the bottom half-cell. These data clearly demonstrate the strength of solutal convection in this material system. The difference in density between PbTe, 7.35 g/cm^3, and SnTe, 5.74 g/cm^3, at 990°C causes complete mixing in the liquid in a 2.25 mm diameter capillary in this solutally unstable configuration. The Pb/Sn ratio

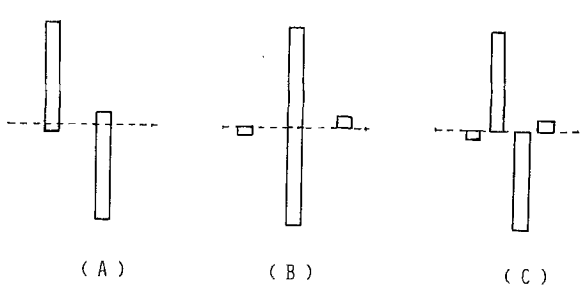

Fig. 1. The modified shear cell concept. (a) Preheat. (b) Diffusion couple. (c) Sheared and quench position.

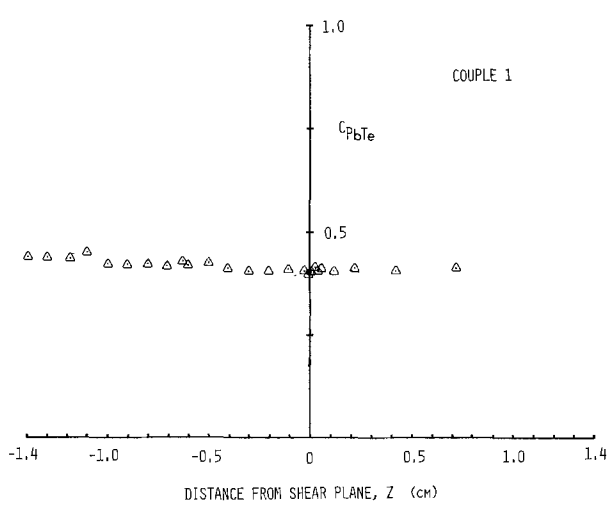

Fig. 2. Concentration distribution for solutally unstable, couple 1

is not 50/50 because the top diffusion half-cell does not contain as much material as the bottom half-cell. In the other diffusion runs where material from one half-cell did not reach the end of the other half-cell this difference has no effect on the analysis. The composition as a function of position in the interior of the couple exhibited large variations over very small distances in both the axial and radial directions.

The following implications are drawn from the data for this sample:

1. The outside surface of the sample is essentially an isothermal surface. This is indicated by the distribution along the surface of the sample in Fig. 2, which was mixed due to the solutal convection. Since this sample had a constant composition, it only had one solidification temperature. Therefore, if a temperature gradient had been imposed along the axial direction, a compositional variation would have occurred due to the segregation upon solidification.

2. Dendritic growth is taking place from the surface to the interior of the sample. This is indicated by the large compositional variations over very small radial distances. These two observations indicate that the area least affected by segregation during solidification is the outer surface of the couples.

In the couples with a nonuniform composition, the first to freeze will have the highest concentration of PbTe (pure PbTe has a T_s of about 925°C) and the last to freeze will have the highest concentration of SnTe (pure SnTe has a T_s of about 810°C). This will result in a directional solidification along the diffusion couple even in an isothermal temperature furnace. By using the microprobe to analyze only the outer surface for the diffusion coefficients, the effects of the segregation during solidification will be minimized.

The data in Fig. 3 show that the lead distribution is neither continuous nor symmetrical across the shear plane interface. The lack of continuity across the interface is due in part to the fact that the melt does not immediately solidify at the end of the 10 min run but that approximately another 90 sec are needed before the PbSnTe is completely solidified. Hence, solutal diffusion continues after the couple is sheared; and, since the concentration gradient upon shearing will be steepest at the shear plane, the greatest change will occur in this region.

If both species diffused at the same rate, the number of lead telluride molecules that crossed the plane would be the same as the number of tin telluride molecules that cross the plane in the opposite direction. In that case the distribution would be symmetric; however, if the lead component moved more rapidly in the SnTe then the tin component in the PbTe, the 50/50 ratio would shift towards the PbTe side of the couple. Also, according to the theory of Tiller (1), there will be an SnTe enrichment in the bottom half-cell in the last to freeze. There will also be the possibility of an enriched SnTe content in the first to freeze of the top couple. These effects will affect the distribution in the region of the interface. The asymmetry of the data seems to be consistent with this sort of explanation.

Analytical interpretation of the data in Fig. 3 requires consideration of both a concentration-dependent diffusion coefficient and finite source diffusion for the diffusion that takes place after the couple is sheared, but before the final solidification. Note, however, that experimental conditions permit the assumption of an infinite couple.

Attempts were made to fit analytically-generated, constant diffusion coefficient curves to the data. Figure 3 presents the data from the sheared diffusion couples. The curves were obtained by starting with a standard finite difference technique (6, 7) as applied to Fick's second law. Each curve was generated by assuming an infinite diffusion couple existed for 10 min. Then, due to the shearing action, a distributed source diffusion occurred for the additional 90 sec diffusion time during cooling. The concentration array obtained at the end of the first 10 min was shifted 0.5 mm towards the PbTe side to account for the aforementioned asymmetries.

The data in Fig. 4 are overlaid with an analytical curve generated by using the slowly varying concentration-dependent diffusion coefficient given by $D(C) = D_1^C D_2^{1-C}$, where C = molecular concentration of PbTe, D_1 = diffusion coefficient chosen for dilute SnTe in PbTe, and D_2 = diffusion coefficient chosen for dilute PbTe in SnTe. Values of 6.0×10^{-5} cm²/sec and 1.4×10^{-4} cm²/sec were chosen for D_1 and D_2, respectively. These values optimized the fit of the curve to the data. This results in a concentration-dependent diffusion coefficient of $D(C) = (3/7)^C \times 1.4 \times 10^{-4}$ cm²/sec. This diffusion couple was solidified in place without shearing. Hence, the analysis of these data did not require working with the distributed source case.

Figure 5 shows an analytical curve generated when the slowly varying concentration-dependent diffusion coefficient given above is overlaid on the data from the shear cells. The curve shows remarkable agreement with the data, especially in the knee areas of the curves. This is the region least affected by the spurious effects of the supercooling, the post-shearing diffusion, and the last to freeze region described by Tiller (1).

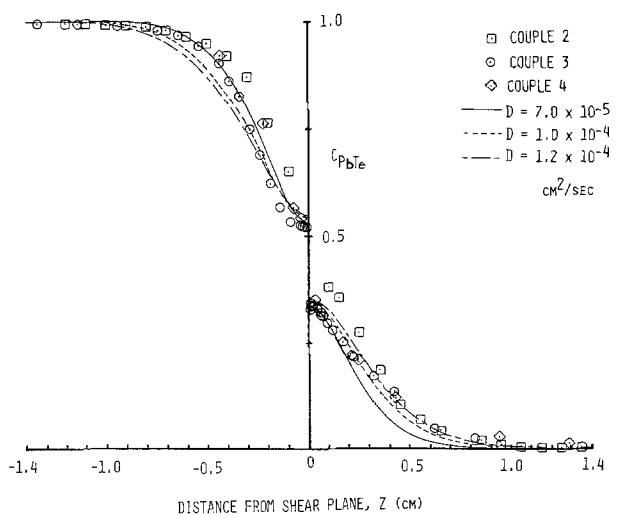

Fig. 3. Concentration distribution curves as determined by finite difference techniques overlaid on concentration distributions for couples 2, 3, and 4.

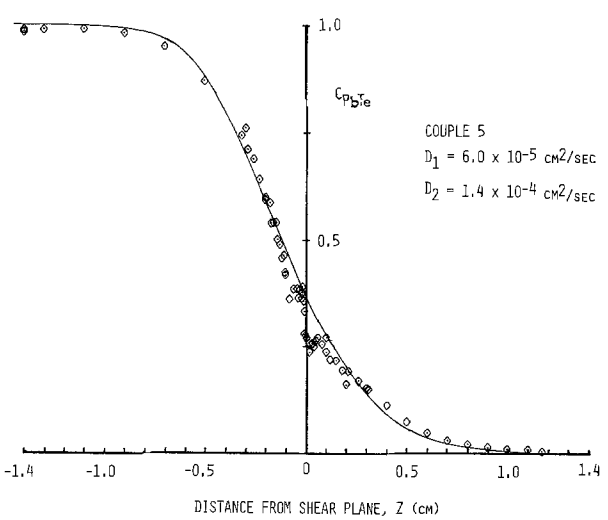

Fig. 4. Concentration distribution for couple 5 overlaid with concentration distribution curves obtained for variable diffusion coefficient.

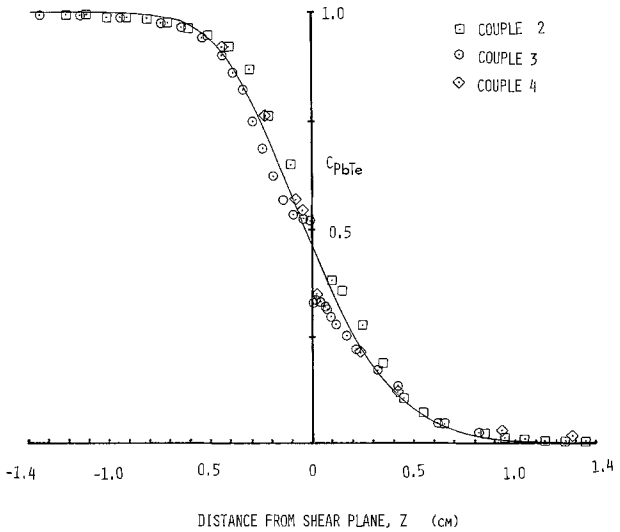

Fig. 5. Concentration distribution for couples 2, 3, and 4 overlaid with concentration distribution curve obtained for variable diffusion coefficient.

It is important to note the limitations that may be present in the data and the possible problems involved in the reduction of the data in order to put these results in their proper perspective. As noted previously, the following phenomena will have an impact on the solute distribution in the solid and consequently may affect the results of the analysis. First, it has been found that a solution of lead-tin-telluride will undergo a certain amount of supercooling before it starts to solidify. Since the result of this cooling can lead to a compositional anomaly, *i.e.*, a SnTe-rich solid, the first to freeze composition in the upper half-cell containing the SnTe with the in-diffused PbTe may appear to have slightly more SnTe at the couple interface than was present in the melt. Since there is no way to monitor the temperature accurately during the quench, this amount could not be determined quantitatively by the tests carried out here. However, it is known that this would affect only a narrow band near the interface. Also, as noted earlier, there would be no such effect in the PbTe couple since the first to freeze here would be the pure PbTe. Second, the segregation in the couple during solidification was found in these experiments to be primarily in the radial direction. This is shown by the fact that the completely mixed sample which was solutally unstable did not show a normal freezing curve along the axial direction. When this sample was cross sectioned and examined however, there were large variations in the composition along the radial direction. This structure is compatible with a pattern of dendritic growth where the dendrites are pointing towards the center of the couple. For these reasons, only the compositional profiles measured at the surface were used for the calculations in this paper. Third, there will be an enrichment in the SnTe content in the last to freeze portion of the PbTe half-cell. This again would affect only a small portion of the couple near the interface between the two couples. This effect cannot be quantized from this series of tests.

Concluding Remarks

Composition profiles have been measured for PbTe-SnTe diffusion couples obtained from a modified shear cell technique. By using both convectively stable and unstable solutal orientations, the importance of convection due to solutally unstable configuration has been demonstrated. Although data were obtained for diffusion at two different temperatures, the solutal diffusion coefficient did not show a strong temperature dependency. The best analytical curve fit to the data gives a composition-dependent diffusion coefficient of $D(C) = (3/7)^C \times 1.4 \times 10^{-4}$ cm²/sec, where C = concentration of PbTe. Several complications in the study of this type of material are pointed out but it is considered that the values of the diffusion coefficient presented here are representative of the system. It is also acknowledged that much more work must be done in this area before the values can be precisely determined. Since these are the only data reported to date in the open literature, it is presently the best available estimate of the solutal diffusion coefficients for this system of materials.

Acknowledgments

The authors would like to thank Todd N. Solberg of VPI and SU for assistance in determining the concentration distributions.

Manuscript submitted Oct. 7, 1981; revised manuscript received Aug. 10, 1982.

Any discussion of this paper will appear in a Discussion Section to be published in the December 1983 JOURNAL. All discussions for the December 1983 Discussion Section should be submitted by Aug. 1, 1983.

Publication costs of this article were assisted by the Langley Research Center.

REFERENCES

1. W. A. Tiller, K. A. Jackson, J. W. Rutter, and B. Chalmers, *Acta Metall.*, **1**, 428 (1953).
2. W. W. Mullins and R. F. Sekerka, *J. Appl. Phys.*, **35**, 444 (1964).
3. S. Ostrach, *Prog. in Astronaut. and Aeronaut.*, **52**, 3 (1977).
4. E. F. Broome and H. A. Walls, *Trans. Metall. Soc. AIME*, **242**, 2177 (1968).
5. E. F. Broome and H. A. Walls, *ibid.*, **242**, 739 (1968).
6. J. D. Verhoeven, *ibid.*, **242**, 1937 (1968).
7. J. Crank, "The Mathematics of Diffusion," 2nd ed., Clarendon Press, Great Britain (1975).
8. J. R. Welty, C. C. Wicks, and R. E. Wilson, "Fundamentals of Momentum, Heat and Mass Transfer," John Wiley and Sons, Inc., New York (1969).
9. V. M. Glazov, S. N. Chizhevskaya, and N. N. Glagoleva, "Liquid Semiconductors," Plenum Press, New York (1969).

A Quantitative Model for Carbon Incorporation in Czochralski Silicon Melts

Torbjörn Carlberg

Royal Institute of Technology, Department of Casting of Metals, 100 44 Stockholm, Sweden

ABSTRACT

A quantitative model for carbon incorporation in silicon melts during crystal growth by the Czochralski technique is presented. The rate-determining step has been identified to be the transport from the graphite parts in the furnace to the melt surface. Experimental results support the theoretical conclusions, and techniques to control the carbon level, based on the theory, are discussed.

The effects of carbon in silicon have not been investigated as thoroughly as the effects of oxygen. However, in several papers (1-5) it has been shown that high carbon concentration has an impact on thermal donor activity and on oxygen precipitation and, thereby, on point defects. The diode characteristics have also been shown to degrade at carbon levels above 1 parts per million atomic (ppma) (6). It is therefore of vital importance to control the carbon level in the production of silicon for electronic applications.

The thermodynamics of carbon and oxygen in silicon have been studied (7-10), and the equilibrium data between the phases involved, *e.g.*, silicon melt, ambient atmosphere, silicon crucible, and graphite furnace parts, are known. On the other hand, the information on carbon distributions in grown silicon crystals is very limited (11-13).

It is well known that carbon in silicon melts originates both from the starting material and from the graphite hot-zone components (7-13), but any theoretical treatments of the rate of incorporation have not been done. In this paper a treatment of the kinetics of carbon transport in a Czochralski growth system is made. Calculations are performed, which are based on known thermodynamic data, to identify the rate-determining steps, and to formulate a quantitative model for the transport. The purpose is to establish a knowledge of the factors influencing the carbon distribution in silicon crystals.

Theoretical Approach

The carbon level in a silicon crystal rises from the seed end to the tang end. There are two reasons for that; one is the segregation, which easily can be accounted for by the normal freeze relation, and the other is the constant incorporation through the ambient atmosphere originating from the graphite hot-zone parts. The latter transport is treated in the following sections, and subsequently an analysis of the melt concentration as a result of carbon fluxes through the system will be made.

To identify the rate-determining step in carbon transport, several possibilities have to be considered. The consecutive steps in the overall reaction are; (*i*) reactions at the graphite parts, (*ii*) transport of CO from the graphite/silica interface to the melt surface, (*iii*) reactions at the melt furnace, and (*iv*) transport of dissolved carbon from the melt surface into the bulk melt.

In the first step at the graphite parts, several different reactions and equilibria are involved, but in an analysis of Schmid *et al.* (9) the major source of CO was concluded to be the following two reactions

$$3C + SiO_2 = SiC + 2CO \qquad [1]$$

$$C + SiO_2 = SiO + CO \qquad [2]$$

Key words: semiconductor, thermodynamics, kinetics, mass transport.

This conclusion was made on the basis of both thermodynamic data and experiments, which showed that direct contact between silica and graphite was a necessary condition for a heavy product of SiC. In a Czochralski growth system for silicon the silica liner is supported by a graphite retainer, thus forming the necessary contact between silica and graphite for the reactions to come into equilibrium. The pressure of CO in equilibrium with graphite and SiO_2 can therefore be obtained from the standard free energy of reaction [2]. CO is the only important carbon containing gaseous component involved at these temperatures, where the pressure of CO_2 can be neglected.

The reactions at the melt surface have been investigated (10) and the standard free energy for the equilibrium between dissolved carbon and oxygen in the melt and the pressure of CO in the ambient atmosphere is well known. In a situation where the reacting species are allowed to adjust their concentration to the equilibrium point, the carbon and oxygen levels are dependent on each other, *i.e.*, a low oxygen concentration gives a high carbon concentration. However, this is only valid as long as the CO pressure at the melt surface is high enough to keep up with the transport of carbon into the bulk melt. If the transport rate from the surface (*iv*) is faster than to the surface (*ii*) the equilibrium never will be reached and step (*ii*) will be rate determining. To check this, the following calculations are made.

From Fick's 1st law the rate at which carbon is transported from the melt surface into the melt is obtained as

$$\frac{dm}{dt} = A_s k_m (C^e - C) \qquad [3]$$

where A_s is the surface area, C^e the carbon concentration in equilibrium with the atmosphere, C the carbon concentration in the bulk, and k_m the mass transfer coefficient. From expression [3] the rate of carbon incorporation into the melt can be expressed as

$$\frac{dC}{dt} = \frac{A_s}{V} k_m (C^e - C) \qquad [4]$$

where V is the melt volume. The only problem in this case is to find a value of the mass transfer coefficient. In a recent paper (14) an analysis of oxygen transport to the free surface in Czochralski silicon growth was made. It was found that k_m values between 0.12 and 0 53 cm/sec could account for oxygen distributions corresponding to experimental data. A comparison between oxygen and carbon transport can be made through the application of the penetration theory (15), which describes the mass transfer between two fluid phases. From the theory an expression for the mass transfer coefficient can be obtained

$$k_m = 2\sqrt{\frac{D}{\pi \cdot t}} \qquad [5]$$

where D is the diffusion coefficient, and t the time a certain volume element of the melt is in contact with the gas phase, *i.e.*, t is in inverse proportion to the convection in the melt. For systems of the same size the t values are the same and transport to or from the surface makes no difference. A value for k_m can therefore be obtained for the carbon transport from Eq. [5] by comparing the diffusion coefficient for carbon and oxygen in silicon. With the limiting k_m values (0.12 to 0.53) from (14) and a difference of a factor of two (16) between the diffusion coefficients ($D_o = 2D_c$) the range of k_m values for the carbon transport will be 0.08-0.37. In Fig. 1 the two limiting curves are shown for the rise in carbon concentration relative to the equilibrium value C^e, calculated with Eq. [4] for a normal size (10 cm crystal, 25 cm crucible) Czochralski system. It can be seen that, even for the lowest value of k_m, concentrations close to the equilibrium are reached after only a few minutes, indicating that the transport from the surface into the melt is not a limiting step. Instead, it can be concluded that the carbon concentration at the surface in equilibrium with the ambient atmosphere C^e is governing the carbon level in the melt. The C^e value is dependent on the CO pressure in the atmosphere, which is a function of the CO transport from the graphite parts to the melt surface, *i.e.* step (*ii*) is rate determining and will be treated in the following section.

From Fick's law and under the assumption that the CO concentration at the melt surface is zero (all CO reaching the surface is transported into the melt immediately) the following equation for the carbon transport to the melt is obtained

$$\dot{n}_s = A_s k_g C^g \qquad [6]$$

where C^g is the equilibrium carbon concentration in the atmosphere at the graphite/silica interface and k_g is the mass transfer coefficient for the transport through the ambient atmosphere.

To formulate an expression for the carbon level in the melt, the difference between the flux entering the melt and the flux leaving the melt has to be considered

$$\dot{n}_m = \dot{n}_s - \dot{n}_c \qquad [7]$$

where $\dot{n}_c$ is the carbon flux entering the crystal

$$\dot{n}_c = A_c \cdot v \cdot k^o \cdot C \qquad [8]$$

and A_c is the area of the crystal cross section, v is the linear growth velocity, and k^o is the equilibrium partition coefficient. The carbon accumulation in the melt, n_m, can be obtained as a function of the melt volume, $V(t)$, (which is a function of time) and of the derivative of the concentration

$$\dot{n}_m = V(t) \frac{dC}{dt} \qquad [9]$$

By combining Eq. [6]-[9]

$$\frac{dC}{dt} = \frac{A_s \cdot k_g \cdot C^g}{V(t)} - \frac{A_c \cdot v \cdot k^o}{V(t)} C \qquad [10]$$

Solving Eq. [10] gives an expression for the carbon concentration in the melt as a function of time. Different sizes and geometries of the growth system can be accounted for through the constants and through the time dependence of the volume.

Discussion

In applying Eq. [10], the mass transfer coefficient, k_g, for the transport of CO in the atmosphere is the only unknown parameter. k_g depends on several factors such as the gas flow pattern in the furnace, the pressure level, and the distance between the melt surface and the graphite parts. Factors like these cannot be accounted for in a theoretical analysis. A value of k_g must therefore be experimentally determined for every single crystal growth furnace. In a paper by Baker (11), the carbon content in the seed ends of crystals as a function of the time the silicon had been molten was reported. From those data a value of k_g can be estimated by combination of Eq. [6] and [9]. Unfortunately, the crucible size was not reported, but as the crystals grown had a diameter of 3 cm, a good estimate of the crucible diameters would be 7.5 cm (3 in.). With a value for C^g of 0.16 atm (9), (from the standard free energy of reaction [2] at 1430°C), a value of the mass transfer coefficient of $9 \cdot 10^{-4}$ cm/sec is obtained. Making use of Eq. [10] the carbon content in the melt now can be calculated as a function of the melt fraction solidified. This has been done for a 3 cm crystal grown from a 7.5 cm crucible, and the results are shown in Fig. 2. The concentrations in the liquid have been converted to concentrations in the solid with a partition coefficient of 0.07 (7). Average results (11) from measurements of the carbon concentration in the seed ends and tang ends of several crystals grown in the same puller are also shown in the figure. The starting positions of the curves are dependent on the concentration of the starting material and on the time the silicon has been molten before the pulling starts. The calculated curve has been drawn from zero, but if the increase along the crystal is compared to the experimental data a very good agreement is found, thus proving the validity of the model.

The calculations above were made for an older system with an argon pressure around 1 atm and at

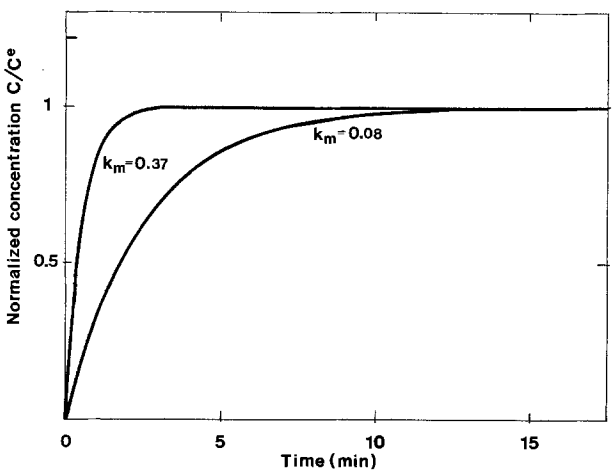

Fig. 1. Calculated rate of carbon transport from the surface to the bulk melt.

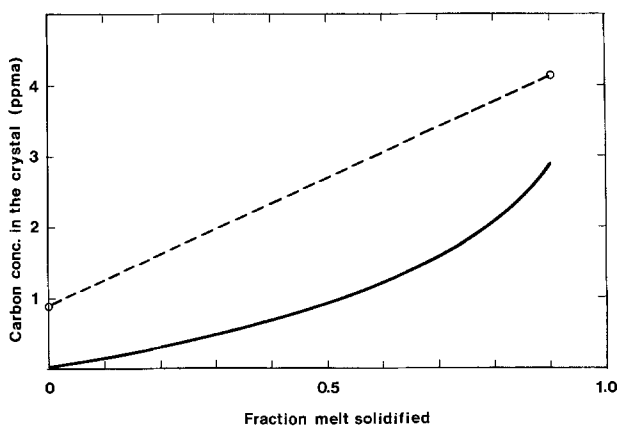

Fig. 2. Calculated carbon distribution in a 3 cm crystal grown from a 7.5 cm crucible. $k_g = 9 \cdot 10^{-4}$ cm/sec. Dashed line combines seed end and tang end average concentrations measured on several crystals.

growth of crystals with only 3 cm diam. In a modern crystal growth system the working pressure is reduced to about 10 Torr and the crystal and crucible sizes are often much larger. The mass transfer coefficient will therefore be different; also, the equilibrium CO pressure at the graphite parts will be different due to a higher temperature at the crucible wall. If a temperature of 1460°C is assumed at the contact interface between the crucible wall and the surrounding graphite cup the equilibrium CO pressure, C^g, is 0.33 atm (9). In Fig. 3 results are presented from calculations by Eq. [10] of axial carbon distributions in Czochralski crystals. The calculations were performed for a 10 cm crystal grown from a 25 cm crucible with a pull rate of 10 cm/hr. The starting concentration in the melt was assumed to be $1 \cdot 10^{17}$ at/cm^3, the partition coefficient was assumed 0.07, and the mass transfer coefficient was used as a parameter ranging from $1 \cdot 10^{-4}$ to $1 \cdot 10^{-3}$ cm/sec.

The curves show the expected increase in concentration towards the tang end of the crystals as a result of the combined effects of the incorporation from the atmosphere and the segregation. The sensitivity to the mass transfer coefficient is clear, thus showing the importance of controlling the gas flow pattern in the furnace. It is only for mass transfer coefficients of $1 \cdot 10^{-4}$ cm/sec and smaller, that the entire crystal has a carbon content below 1 ppma, which has been regarded to be the upper limit for a material free of defects due to carbon (6). The sensitivity of the carbon content in the melt to the conditions in the ambient atmosphere has been clearly shown experimentally. Baker (11) showed that small additions of CO_2 to the argon purge heavily increased the carbon content in the crystals and in a paper by Liaw (12) the carbon content was plotted as a function of the total pressure in the furnace, showing decreased concentrations with increasing pressure. These facts are strongly supporting the conclusions of this paper, that the rate-determining step is the transport in the atmosphere and not the transport from the liquid surface to the bulk melt. It is also interesting to note that these facts are opposite to the conditions for oxygen concentration. For oxygen it has been concluded that the rate-determining step at the liquid/gas interaction is the transport in the liquid (14), and consequently it has been shown experimentally that atmospheric conditions do not influence the oxygen concentration (8, 17).

Any quantitative test of the calculated curves is not possible, due to the lack of experimental data adequately reported in the literature. There are only two papers (12, 13) reporting carbon distributions from modern crystal growth systems, but in both cases neither the sizes of the systems nor the growth conditions were revealed. However, in Fig. 3 the experimental curves are added with dashed lines as a comparison to the theoretical. Curves (i) and (ii) are from (12), where (i) is the result from one crystal and (ii) is the average from measurements in the seed end and tang end of many crystals. Curve (i) has a parabolic shape, which is in contradiction to the theoretical results. The parabolic shape can be explained if the mass transfer coefficient, k_g, and/or the equilibrium CO pressure, C^g, at the graphite parts decrease during the crystal growth run. This is in fact likely to occur. As the crystal is pulled the crucible is lifted, to maintain the same absolute level of the melt surface. The distance between the surface and the graphite parts will therefore increase and the crucible wall will more effectively shield the interior of the crucible from the outer graphite parts. This will result in a successive lowering of the mass transfer coefficient. As the crucible and its surrounding graphite cup are lifted, the temperature at the rim will decrease, and with it, the equilibrium partial pressure, C^g. Curve (i) in Fig. 3 covers only the first half of the crystal and it is likely that at the end, where the effects of the segregation and the accumulation are stronger, the curve shape will change to exponential due to the dominance of the latter effects. This is the case for curve (iii), which shows a typical carbon distribution from a modern crystal growth system (13). The shape of the curve is in very good agreement with the theoretical curve calculated with a mass transfer coefficient of $1 \cdot 10^{-4}$ cm/sec.

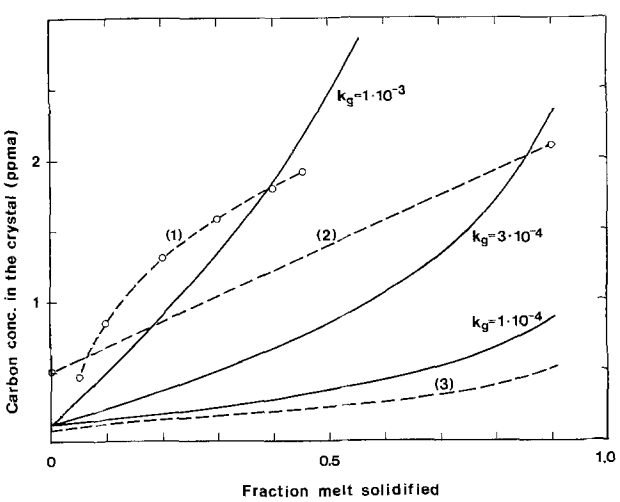

Fig. 3. Calculated carbon distributions in 10 cm crystals grown from 25 cm crucibles. Dashed lines show experimental results (12, 13).

To decrease the carbon level in the melt, it is obvious that the flow path from the graphite parts to the melt surface have to be controlled. This is automatically achieved in reduced pressure systems, where the vacuum pump is connected to an outlet in the bottom of the furnace. Although the main purpose in using this kind of arrangement is to eliminate SiO precipitates at the crucible wall, a positive effect on the carbon level is also achieved. If a further decrease of the carbon level is desired, a possibility would be to shield the melt from the graphite parts by means of a higher crucible, or with the top of the crucible bent out over the graphite cup. The most effective way, of course, would be to replace the graphite parts with another material such as molybdenum (9) and, especially, eliminate the direct contact between the graphite cup and the SiO_2 crucible. Another factor influencing the carbon level is the size of the melt surface which is directly proportional to the carbon concentration (Eq. [10]).

Conclusions

A model, describing the carbon concentration in the melt during crystal growth of silicon by the Czochralski technique has been developed. The model has been shown to be in good agreement with available experimental results. The rate-determining step of the carbon incorporation has been shown to be the transport in the gas phase from the graphite furnace parts to the melt surface. Therefore, it can be concluded that attempts to control the carbon level should be focused on the flow pattern in the furnace atmosphere and not at convection in the melt. Elimination of the source of carbon, *i.e.* the graphite parts, is of course also a possibility, as well as a decrease in the melt surface.

Acknowledgment

This work was sponsored by the Swedish Board for Space Activities.

Manuscript submitted April 19, 1982; revised manuscript received Aug. 28, 1982.

Any discussion of this paper will appear in a Discussion Section to be published in the December 1983 JOURNAL. All discussions for the December 1983 Discussion Section should be submitted by Aug. 1, 1983.

Publication costs of this article were assisted by the Royal Institute of Technology.

LIST OF SYMBOLS

C	carbon concentration in the bulk melt
C^e	carbon concentration in the melt in equilibrium with the ambient atmosphere
C^g	carbon concentration in the atmosphere in equilibrium with graphite and silica
$\dot{n}_s$	carbon flux from graphite parts to melt surface
$\dot{n}_c$	carbon flux from melt to crystal
$\dot{n}_m$	net carbon flux entering the melt
A_s	area of the free surface of the melt
A_c	area of the interface between the crystal and the melt
k_m	mass transfer coefficient for transport from melt surface to bulk melt
k_g	mass transfer coefficient for transport from graphite parts to melt surface
k^o	equilibrium partition coefficient for carbon between crystal and melt
V	melt volume
v	crystal growth velocity
D	diffusion coefficient of carbon in the melt

REFERENCES

1. A. R. Bean and R. C. Newman, *J. Phys. Chem. Solids*, **33**, 255 (1972).
2. Y. Matsushita, S. Kishino, and M. Kanamori, *Jpn. J. Appl. Phys.*, **19**, L101 (1980).
3. D. Helmreich and E. Sirtl, in "Semiconductor Silicon 1977," H. R. Huff and E. Sirtl, Editors, p. 626, The Electrochemical Society Softbound Proceedings Series, Princeton, NJ (1978).
4. R. A. Craven, Abstract 200, p. 508, The Electrochemical Society Extended Abstracts, Minneapolis, Minnesota, May 10-15, 1981.
5. C.-C. Hsu, B.-K. Sun, S.-N. Jiang, W.-N. Wang, and C.-Y. Sung, Abstract 201, p. 511, *ibid.*
6. T. Abe, K. Kikuchi, S. Shirai, and S. Muraoka, Abstract 187, p. 477, *ibid.*
7. T. Nozaki, Y. Yatsurugi, and N. Akiyama, *This Journal*, **117**, 1566 (1970).
8. D. M. Coldwell, *High Temp. Sci.*, **8**, 309 (1976).
9. F. Schmid, C. P. Khattak, T. G. Digges, and L. Kaufmann, *This Journal*, **126**, 935 (1979).
10. Y. Endo, Y. Yatsurugi, Y. Terai, and T. Nozaki, *ibid.*, **126**, 1422 (1979).
11. J. A. Baker, in "Semiconductor Silicon 1969," R. R. Haberecht and E. L. Kern, Editors, p. 566, The Electrochemical Society Softbound Proceedings Series, New York (1969).
12. M. Liaw, *Solid State Technol.*, **22**, 71 (Oct. 1979).
13. A. C. Bonora, Microelectronic Manufacturing and Testing, p. 44 (Sept. 1980).
14. T. Carlberg, T. B. King, and A. F. Witt, *This Journal*, **129**, 189 (1982).
15. R. Higbie, *Trans. Am. Inst. Chem. Eng.*, **31**, 365 (1935).
16. C. E. Wakefield, *This Journal*, **127**, 1139 (1980).
17. H. Hirata and K. Hoshikawa, *Jpn. J. Appl. Phys.*, **19**, 1573 (1980).

The Depreciation of $Na_3Ce_{0.65}Tb_{0.35}(PO_4)_2$ in Low Pressure Discharge Lamps

W. Lehmann, F. M. Ryan,* and A. S. Manocha

Westinghouse Research and Development Center, Pittsburgh, Pennsylvania 15235

and W. McAllister*

Westinghouse Electric Corporation, Lamp Business Unit, Bloomfield, New Jersey 07003

ABSTRACT

The phosphor $Na_3Ce_{0.65}Tb_{0.35}(PO_4)_2$ depreciates rapidly in fluorescent lamps. Its high sodium content leads one to suspect severe depreciation due to an interaction with mercury from the discharge. We find that while a mercury interaction does indeed occur, it plays a minor role compared to ion-electron recombination induced depreciation. The ion recombination process produces a nonluminescent layer whose thickness is approximately proportional to $(\text{time})^{1/2}$. Surface analytical studies (x-ray photoelectron spectroscopy) failed to reveal chemical alterations in the "dead" layer, although optical diffuse reflectance measurements indicate that it may be accompanied by a conversion of Ce^{+3} to Ce^{+4}. A tentative model for the structure of the "dead" layer is proposed and further experiments are suggested.

In a low pressure mercury discharge lamp there are many processes occurring that can lead to phosphor depreciation, such as color center formation, ion recombination damage, and mercury interaction. As each phosphor system possesses an individual ability to withstand the effects of these several processes, phosphors are depreciated to varying degrees by each. In this study we investigated the phosphor $Na_3Ce_{0.65}Tb_{0.35}(PO_4)_2$ which has been reported to exhibit very rapid depreciation in a low pressure mercury discharge (1, 2). Its high sodium content leads one to suspect that its rapid depreciation might be due to an interaction with mercury from the discharge, forming light absorbing sodium-mercury complexes on the surface of the phosphor. We chose this compound for investigation, as we thought that it would be an ideal candidate for studying the nature of the interaction of mercury with certain phosphors. To our surprise we found that, although some interaction with mercury did occur, the rapid depreciation observed was due instead to ion-electron recombination at the surface of the phosphor particles.

During the operation of a discharge, radial cataphoresis occurs in which electrons from the plasma diffuse out to the phosphor layer at the lamp wall, setting up a so-called "sheath" potential (3). This potential grows until an equilibrium is reached with positive ions attracted to the surface of the phosphor, where ion-electron recombination occurs. The high energy released in the recombination process (10.2 eV for $Hg^+ + e^- \rightarrow Hg$, 14 eV for $Ar^+ + e^- \rightarrow Ar$) may break chemical bonds in the phosphor. This may re-

* Electrochemical Society Active Member.

Key words: inorganic, luminescence.

duce the efficiency of the phosphor by a number of processes, such as changing the valence state of the activator ions, introducing large defect concentrations into the lattice, or even changing the lattice structure itself. If diffusion of this damage occurs, a nonluminescent layer may be formed whose thickness increases with time.

In this investigation we attempted to determine the character of the nonluminescent layer formed by ion recombination on $Na_3Ce_{0.65}Tb_{0.35}$ $(PO_4)_2$.

Experimental

Phosphor synthesis.—Samples of the approximate composition $Na_3Ce_{0.65}Tb_{0.35}$ $(PO_4)_2$ were formulated using 1.5 mols sodium carbonate, 2.0 mols basic ammonium phosphate, 0.65 mol cerium oxide (CeO_2), and 0.0875 mol terbium oxide (Tb_4O_7). The rare earths were of 99.99% purity, the other raw materials analytical reagent grade. This combination was ground thoroughly in an ethanol slurry, dried, and fired in nitrogen at 400°C for 0.5 hr, 600°C for 4 hr, and 1300°C for 6 hr with grinding between firings. Finally the phosphor was fired in N_2-10% H_2 at 1300°C for 6 hr and the structure of this end product confirmed by x-ray diffraction.

Depreciation measurements.—Screens of the phosphor were prepared on glass slides using an organic binder. Following lehring of the screens, they were placed in the demountable discharge tube shown in Fig. 1. They were depreciated in both pure argon and in argon-mercury discharges for varying lengths of time. The tube has cold aluminum electrodes and contains not a static but a slowly flowing argon atmosphere, Argon purity: 99.995%, from a tank. Hg is picked up from a little boat in the lamp and was omitted for tests in plain argon. The current through the discharge was adjusted to provide a "wall loading" or incident flux on the phosphor samples equivalent to the "wall loading" in a T-12 40W fluorescent lamp. Before and after aging, the samples were measured for 254 nm excited efficiency. *In situ* efficiency measurements were also performed using the discharge as the excitation source. The two sets of efficiency measurements were in good agreement.

Two types of samples were prepared as shown in Fig. 2. One type completely exposed the phosphor screen to the discharge so that the phosphor was exposed to the complete environment in the interior of the lamp, including ion recombination at the surface of the phosphor. The other type of sample had thin magnesium fluoride windows covering the screens so that only ultraviolet (down to 120 nm) could reach the phosphor surface and not ions.

Cathodoluminescence measurements.—Cathodoluminescence was excited by a d-c E beam of varied voltage. Brightnesses were measured of 2 samples placed side by side, one previously aged in the demountable lamp, the other unaged. The brightness ratio aged/unaged is multiplied by the beam voltage and the product plotted as function of beam voltage. Any dead layer on the aged sample which is not present on the unaged shows up as a dead voltage. From known relationship dead voltage/physical thickness (4), the thickness of the dead layer, if present, can be estimated.

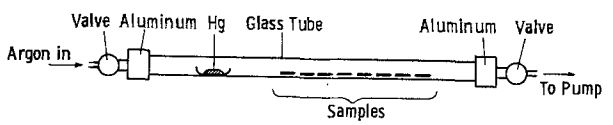

Fig. 1. The demountable fluorescence lamp. Power (60 Hz) is applied to the two aluminum end fittings from a current-limited (18 mA) neon transformer.

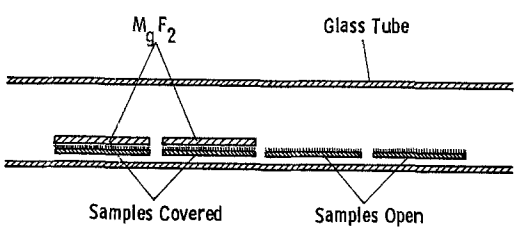

Fig. 2. Samples in demountable lamp, open or covered with MgF_2. The gap between phosphor and MgF_2 is less than a mm.

Surface analytical measurements.—X-ray photoelectron measurements were performed in a GCA-McPherson/36 photoelectron spectrometer, using a magnesium anode as a primary x-ray source (1253.6 eV). Low resolution survey scans were performed to determine the surface compositions and changes in these compositions during depreciation. High resolution scans were then performed on all of the elements detected in the survey scans, both on the virgin surfaces and following argon etching of the surfaces. The high resolution scans were performed in an attempt to detect chemical state changes induced by depreciation such as valence or bonding alterations.

Results

Typical depreciation results (expressed as percent maintenance) are summarized in Table I for exposed and MgF_2 covered samples, in both Ar and Ar + Hg discharges. It can be seen that depreciation occurs only when ions are incident on the phosphor surface and that an argon discharge is as effective as an argon-mercury discharge in depreciating the phosphor. No measurable depreciation was observed for the samples covered by MgF_2, demonstrating that u.v. induced degradation is not an important damage mechanism for these phosphors.

X-ray photoelectron spectroscopy (XPS) measurements performed on the depreciated phosphors showed that samples that are open to the discharge and that are depreciated in mercury-argon, do indeed interact to some degree with mercury. Approximately 5% of the surface atoms of such samples are mercury, following 140 hr of depreciation. While this deposit certainly does contribute to depreciation, it is a minor effect compared to ion induced depreciation, as equally severe depreciation occurs when no mercury is present in the discharge.

In order to obtain some information on the nature of the ion recombination induced damage of the phosphors, depreciated phosphors were placed in a demountable CRT and their cathodoluminescent intensities were measured as a function of incident voltage to determine their "dead" voltages. The "dead" voltage correlates with the presence of a nonluminescent layer on the surface of the phosphor. Data are shown in Fig. 3 and summarized in Table II. Ion recombination

Table I. Maintenance of $Na_3Ce_{0.65}Tb_{0.35}(PO_4)_2$ subjected to various discharge conditions

Sample	Discharge	4 hr % maint.	20 hr % maint.	140 hr % maint.
Open	Ar + Hg	70	60	22
MgF_2 cover	Ar + Hg	~100%	~100%	~100%
Open	Ar	75	63	25
MgF_2 cover	Ar	~100%	~100%	~100%

Table II. Data relating to Fig. 3

Sample	Aging condition in lamp	Maintenance (%)	Dead voltage (kV)	Thickness of dead layer (A)
A	1/4 hr, open	91	~0.4	~30
B	4 hr, open	70	~1.4	~250
C	4 hr, covered	100	0	0

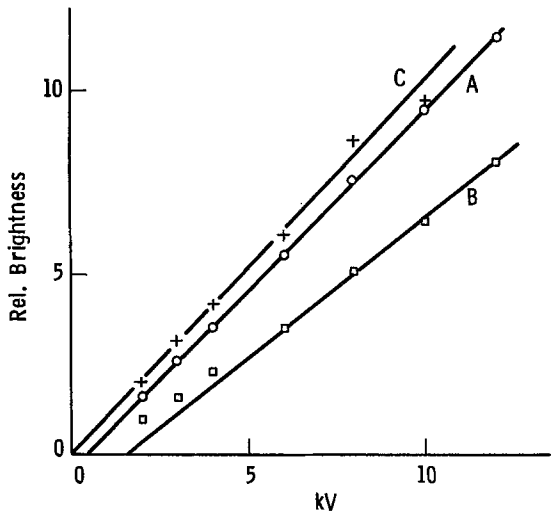

Fig. 3. Relative (compared to an unaged standard) brightness of cathodoluminescence of three samples aged in demountable lamp in Ar + Hg. A: 1/4 hr, open. B: 4 hr, open. C: 4 hr, covered with MgF_2. For data see Table II.

produces a nonluminescent layer whose depth increases with time of depreciation, approximately proportional to (time)½. For this nonluminescent layer to be responsible for the reduction in photoluminescent efficiency, one would expect that the phosphor brightness would therefore decrease with time according to the relationship

$$\beta = \beta_0 \exp(-\sqrt{t/\tau})$$

assuming that a uniform nonluminescence producing absorption is present in the "dead" layer. In Fig. 4 it can be seen that this relationship does hold, as a log plot of the brightness *vs.* (time)½ yields a straight line.

Diffuse optical reflectance shows that depreciation induces additional optical absorption in the samples as shown in Fig. 5 where an induced absorption can be observed from 320 to 450 nm (the absorption at shorter wavelengths such as 254 nm is already so high in undepreciated samples that additional induced absorption is difficult to detect). This induced absorption is present only on the surface of the phosphor immediately adjacent to the discharge. The phosphor surface away from the discharge shows no discoloration. Also shown in Fig. 5 are the diffuse reflectance spectra of CeO_2 and a phosphor sample heated in air to 600°C. These suggest that the depreciation induced optical

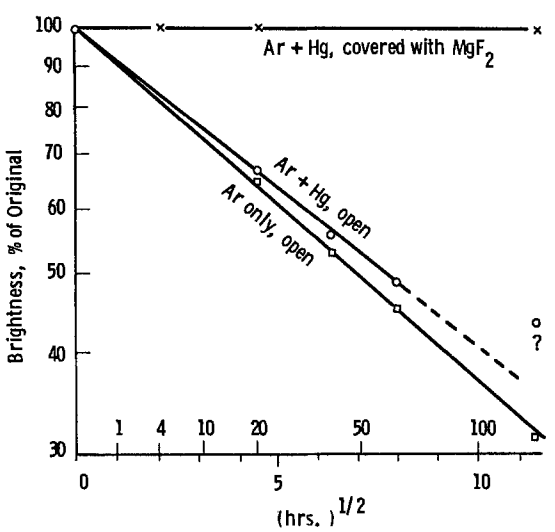

Fig. 4. Brightness of photoluminescence under excitation by 254 nm u.v. outside of the demountable lamp. Hours refer to depreciation time in the lamp.

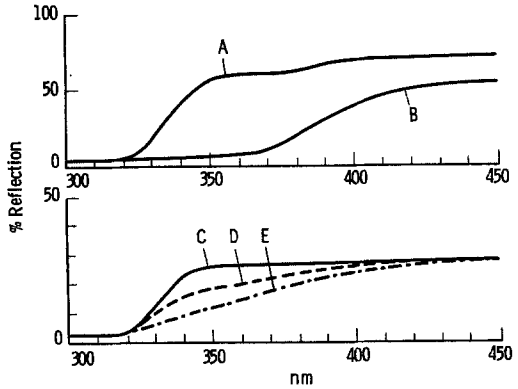

Fig. 5. Optical reflection spectra of powders. A: Thick phosphor layer, not lehred or aged. B: Thick layer of pure CeO_2. C: Thin phosphor layer, lehred 400°C, before aging. D: Sample C after aging in demountable lamp to 59% of original. E: Thin phosphor layer, lehred 600°C, not aged. Brightness about 34% of sample D. All lehrings in air, 15 min.

absorption and loss of brightness may be due to the conversion of Ce^{+3} to Ce^{+4} (additional conversion of Tb^{+3} to Tb^{+4} is also a possibility). The tendency of Ce^{+3} to oxidize to Ce^{+4} is well known for many phosphors, $Ca_3(PO_4)_2$:Ce for example (5). Infrared absorption measurements, however, failed to reveal any conversion of Ce^{+3} to Ce^{+4}.

The observed spectra were typical of orthophosphates with strong P-O stretches at 1050 cm^{-1} and O-P-O deformations at 575 cm^{-1}. Further, splitting of these *IR* modes were characteristic of the asymmetric nature of PO_4^{-3} ligands. Any shifts in the PO_4^{-3} peaks due to the incorporation of a more positively charged cation or relative intensities due to changes in the crystal structure can be ruled out on the basis of the observed spectra down to 200 cm^{-1}. Sulfate ions for instance show all the expected differences when cerium oxidation changes from Ce^{+3} to Ce^{+4} (6). In analogy to the sulfates one would have expected to see similar results for the phosphates. It may therefore be concluded that the chemical structures were unaltered by the depreciation.

High resolution XPS measurements were then performed on the depreciated phosphors. In particular, we looked very carefully for evidence of conversion of Ce^{+3} to Ce^{+4}, Tb^{+3} to Tb^{+4}, or changes in bonding strengths of the atoms in the depreciated layer, indicative of chemical modifications in the nonluminescent layer. These data are summarized in Table III. No significant XPS shifts were observed, leading one to believe that no substantial chemical alterations occur in the depreciated layers.

In general, the rare earths do not show large chemical shifts per unit change in oxidation state with the exception of Eu^{2+} compounds (7). Since +3 is the most prevalent state, chemical shifts in going from one compound to another are not very significant. XPS spectra of rare earths are, however, complexed

Table III.

Sample	XPS binding energies and (FWHM) (eV)					
	Na (Auger)	Na-1s	P-2p	O-1s	Tb-4d	Ce-4d
Fresh	990.6 (2.5)	1070.6 (7.0)	132.7 (2.3)	530.9 (2.3)	153.8 (10.2)	111.2, 107.6 (7.2)
Depreciated	990.5 (2.8)	1070.4 (7.0)	132.8 (2.2)	531 3 (2.5)	154.4 (10.5)	111.4, 107.3 (7.2)

Binding energies were calibrated with adventitious Cls peak at 284.6 eV.
Instrument linearity was checked and found to be accurate to ±0.2 eV in 50-1800 eV range.
Reported binding energies are accurate to ±0.3 eV.

by many satellite features adding to many more peak components which make qualitative distinctions rather obvious. One such feature is the shake up satellite observed with the 3d electrons (8, 9), another being the 4d photohole electrostatic interaction with the 4f orbitals (10).

In the present case, we were not able to get enough photoelectrons from 3d levels in the fixed retardation ratio mode (the only mode McPherson instrument operates in) and had, therefore, to rely on the information obtained from the 4d levels. Since the multiplet structure of the 4d levels depends on the number of electrons in the ionized species, therefore along with a small observable core-level shift, we expected to see changes in the overall shape of the 4d level associated with a redox phenomena. Not only did we not see any differences between the fresh and aged samples, argon ion sputtering (with 7 keV ions and 20 $\mu A/cm^2$) failed to show any differences in the Ce 4d current density and P2p levels. Normally, these ions are energetic enough to convert a higher oxidation state to a lower oxidation state (11) (in our case Ce^{+4} to Ce^{+3}) and higher oxides to lower oxides, for instance PO_4^{3-} to PO_3 to P^{3-}. The data therefore suggest that the present system is not only inert to oxidation but also to reductions under the conditions of our present experiments.

Discussion

Our analytical measurements were unfortunately of limited assistance in determining the exact nature of the depreciation damage. Subject to the qualifications stated previously concerning the interpretation of our XPS measurements, we can only conclude that the depreciation is not due to certain mechanisms. That is, it is not due to the conversion of Ce^{+3} or Tb^{+3} to the four valent state, and it is not due to a chemical decomposition of the phosphor. Our high resolution XPS measurements show that the depreciated layer still consists of $Na_3Ce_{0.65}Tb_{0.35}(PO_4)_2$. In the absence of additional analytical information, we can therefore only speculate on the exact nature of the damaged layer. A reasonable model however, would be the following.

The energy released in the ion recombination (10.2 eV for Hg and 14 eV for Ar) is more than adequate to break the chemical bonds in the phosphor. To our knowledge, the exact process by which this may occur on the surface of solids has not been determined. Argon ion recombination on silicon surfaces has been shown to release Na atoms bound to surface states (12). The Na atoms then diffuse into the bulk of the crystal. Our tentative picture is similar in that we view the ion recombination at the surface as breaking chemical bonds, perhaps the type of sodium-oxygen bond that exists at the surface. The defects thus produced, interstitials and/or vacancies, would then diffuse into the crystal. We assume that above a certain defect concentration C_1 the phosphor is nonluminescent. In order to determine how the depth to which C_1 is achieved increases as a function of time (the thickness of the "dead" layer), we use the special solution of the diffusion equation (13)

$$C(x,t) = \frac{C_o}{2}\left[1 + \text{erf}\left(\frac{x}{2\sqrt{Dt}}\right)\right]$$

where $C(x, t)$ = the defect concentration as a function of depth and time, C_o = constant = defect production rate at the surface, D = diffusion coefficient here assumed to be independent of C. The boundary conditions are: $x = 0$ is the surface of the phosphor and $C_o = 0$ at $t = 0$ and constant at $t > 0$. The phosphor is semi-infinitely thick.

In this equation every defect concentration (including C_1) moves in from the surface at a rate proportional to $\sqrt{Dt}$. This expected variation is in agreement with our experimentally observed variation of the increase in thickness of the nonluminescent layer with time.

What remains unanswered is the exact nature of these defects and the mechanism(s) by which they reduced the luminescent efficiency of the phosphor. Two possible mechanisms are: (*i*) by the formation of color centers that can absorb either the 254 nm excitation or the fluorescence of the phosphor or, (*ii*) by removing the long range order of the phosphor lattice and producing an amorphous structure in which the pathway of energy transfer from the absorption of 254 nm to the Tb^{+3} ions is destroyed. In order to choose between these two, it would be necessary to perform electron spin resonance measurements to detect the generation of color centers, or low energy electron diffraction to detect the loss of long range order. Both of these techniques require single crystals however, and no crystals were available to us for such studies.

An unsuccessful attempt to detect the presence of an amorphous phase was made by looking for a broadening of x-ray diffraction patterns following depreciation. This is not a very sensitive technique for determining small amounts of disorder on the surfaces of powders however, and the failure to detect diffraction pattern broadening is inconclusive. In the absence of better analytical data, the exact nature of the damage must remain undetermined.

Manuscript submitted June 7, 1982.

Any discussion of this paper will appear in a Discussion Section to be published in the December 1983 JOURNAL. All discussions for the December 1983 Discussion Section should be submitted by Aug. 1, 1983.

Publication costs of this article were assisted by the Westinghouse Research and Development Center.

REFERENCES

1. J. Fava *et al.*, *J. Lumin.*, **18/19,** 389 (1979).
2. C. Fouassier and G. LeFlem, University of Bordeaux, Personal communication.
3. F. M. Ryan, *J. Lumin.*, **24/25,** 827 (1981).
4. J. D. Kingsley and J. S. Prener, *J. Appl. Phys.*, **43,** 3073 (1972).
5. H. C. Froelich and J. M. Margolis, *This Journal,* **98,** 400 (1957).
6. R. A. Nyquist and R. O. Kagel, "Infrared Spectra of Inorganic Compounds," p. 283, Academic Press, New York (1971).
7. T. A. Carlson, "Photoelectron and Auger Spectroscopy," pp. 213, 367, and 368, Plenum Press, New York (1975).
8. G. K. Westheim, R. L. Cohen, A. Rosencwaig, and H. J. Guggenheim, "Electron Spectroscopy," D. A. Shirley, Editor, p. 813, North Holland, Amsterdam (1972).
9. A. Plateau and S. K. Karlsoon, "The Rare Earths in Modern Science and Technology," Vol. 2, pp. 487-488, Plenum Press, New York (1980).
10. A. J. Signorelli and R. G. Hayes, *Phys. Rev. B,* **8,** 81 (1973).
11. K. S. Kim, W. E. Baitinger, J. W. Amy, and N. Winograd, *J. Electron Spectros.*, **5,** 351 (1974).
12. D. V. McCoughan *et al.*, *Phys. Rev. Lett.*, **30,** 614 (1973).
13. P. G. Shewmon, "Diffusion in Solids," pp. 12-13, McGraw-Hill, New York (1963).

Energy Levels and Crystal Field Parameters of ZnS:Tm^{3+}

Yves Charreire and Pierre Porcher

Laboratoire des Eléments de Transition dans les Solides, E.R. 210 du C.N.R.S., 92190 Meudon Bellevue, France

ABSTRACT

For various samples of ZnS doped with Tm^{3+}, different in structure and charge compensations, it has been possible to identify a point site symmetry with a T_d symmetry for Tm^{3+}. The analysis of the emission spectra measured at different temperatures and under different excitation sources (u.v. and cathode-ray) permits the partial identification of the experimental splittings for $^1D_2$, $^1G_4$, $^3H_4$, $^3F_4$, $^3H_5$, and $^3H_6$ levels. The energy level scheme deduced from the spectra is reasonably simulated by a set of free ion and crystal field parameters $E_1 = 6800\ cm^{-1}$, $E_2 = 34.2\ cm^{-1}$, $E_3 = 661\ cm^{-1}$, $\xi = 2625\ cm^{-1}$, $\alpha = 18\ cm^{-1}$ (fixed), $\beta = -630\ cm^{-1}$ (fixed), $\gamma = 2000\ cm^{-1}$ (fixed), $B_0^4 = 136\ cm^{-1}$, and $B_0^6 = 180\ cm^{-1}$.

Fluorescent properties of rare earth doped ZnS were extensively studied during the sixties. The main purpose of these works was to optimize the synthesis methods for phosphors and to study the energy transfer properties ZnS → Ln^{3+} (1) by using coactivators such as Cu-Ln^{3+} or Cu-Li-Ln^{3+} (2). More recently, the electroluminescent properties of the rare earth doped material were studied in relation to inclusion of "lumocen" centers such as fluorides (3, 4) or oxysulfides (5, 6).

Optical studies considering the rare earth ion as a local structural probe were not so decisive. One can note:

1. In 1960, a study by Ford *et al.* (7) yielded a C_{3v} point site symmetry for Dy^{3+} located in substitutional positions, exhibiting a strong vibronic coupling with the network.
2. In 1963-1964 Ibuki and Langer (8, 9) identified several point sites for Tm^{3+} in ZnS, the most predominant one having a T_d symmetry. But, performed before the work of Larach (1) giving the conditions for alkaline coactivations, this work showed a too complex fluorescence spectrum to permit a realistic attribution of the observed lines.
3. In 1979 a study by Yu (10) of ZnS with ionic implantation of Er^{3+} showed that it was possible to identify two main cubic point sites, corresponding to an interstitial and to a substitutional position of Er^{3+}.

In our work, because of the impossibility of inserting the best local structural probe, Eu^{3+}, at its normal valence (11), we chose Tm^{3+} ion because: (*i*) the $4f^{12}$ configuration is relatively simple and the even number of electrons allows the observation of small symmetry distortions through the number of experimental lines; (*ii*) the diffusion of Tm^{3+} in ZnS is good; and (*iii*) the number of fluorescence lines, sharp and well resolved at low temperature ($T < 60$ K) is large.

In a preliminary work, we studied the configuration for the activation of ZnS by Tm^{3+}. The diffusion method was applied on cubic (powder and single crystals) and on hexagonal (powder) type ZnS. The first method employed was the one previously described by Larach (1). The activation is obtained by the simultaneous action of $TmCl_3$ and LiCl at 1150°C under H_2S flux. By this method, a great number of different sites are observed by Tm^3 spectroscopy, and a mass spectroscopy analysis (12) underlines that the amount of Li^+ is about ten times that of Tm^{3+}. The great number of sites observed has to be related to the variety of possible charge compensation position. The second method used the diffusion of $LiTmS_2$, with the same experimental procedure. The spectrum then observed is simple, showing two or three point sites occupied by the Tm^{3+} ion. The third method used the diffusion of $ZnTm_2S_4$. In such a case, the rough analysis of the spectrum showed that the Tm^{3+} ion occupied probably one site, with a charge compensation not located in the first neighborhood, allowing us to consider T_d as point site symmetry occupied by Tm^{3+}. The purpose of this work is to analyze as far as possible the spectrum obtained.

Nature of the Point Site in ZnS

Sites without charge compensation in the immediate neighborhood.—This case has been extensively studied by EPR or optical techniques with divalent ions of the iron series as dopant (13). Four types of sites have been recognized: one site T_d (AN), one site C_{3v} (PS), and two axial sites (AS and PN). The occurrence of these sites depends on both the dominant structure of the crystal (cubic or hexagonal) and the stacking faults always encountered for the doped crystals. Moreover, because of the stacking faults, polytypes with axial sites (PN and AS) are created in the same quantity. For our fluorescent crystals case, the transition 3C-6H often is observed showing stackings as [in Roth's notations (14)]

Stacking	ABC	ABCACB	ABC
Structure	3C	6H	3C
Sites	AN	AN-PN-AS	AN

Sites with charge compensation in the immediate neighborhood.—To our knowledge there are no conclusive studies on this possibility. However, by EPR studies of Er^{3+} doping ZnS, Watt *et al.* (15) have observed two sites in substitutional positions, one pure cubic site and one axial site, the last corresponding to a very small distortion of the cubic one. Other sites, one axial and one orthorhombic site, have been also observed but in hexagonal crystals doped by diffusion.

We performed some experiments for insertion of Gd^{3+} in our samples in order to perform EPR studies. We noted a large absorption band, characteristic of Gd^{3+}, but situated in an aggregate form (6). We think the conditions for diffusion of a rare earth ion of the beginning of the series such as Gd^{3+} are unknown, such implantations appear to be really possible only for rare earth with smaller ionic radius (Er, Tm, Yb).

In a previous work (12), the importance of the synthesis conditions on the number of sites occupied by Tm^{3+} had been underlined. For this study, cubic crystals have been prepared, showing only two distinct sites. One of these sites is predominant, for the other, we have identified fluorescence lines only for the $^1G_4 \rightarrow {}^3H_6$ transition, *i.e.*, the most intense lines of the spectrum. Moreover, we have prepared an hexagonal powder of ZnS:Tm^{3+}, without any alkaline coactivator. In such a case, the number of sites observed is also limited to two or three. These different syntheses allow us to identify a predominant site, common for all structures, for all kinds of compensating charges. The aim of this work is exclusively the study of this predominant site. The identification of the energy level scheme is not so evident, because of the

lack of absorption data due to the low concentration of Tm^{3+} optically active in ZnS (10^2-10^3 ppm). Only emission spectra measured at different temperatures and under different excitation sources (u.v. and cathode-ray) are available to determine the experimental energy level scheme, the nature of the site, and to compute the phenomenological spectroscopic parameters.

Theoretical Background

Simulation of the spectra.—The Tm^{3+} ion has $4f^{12}$ as the ground configuration. Then, the degeneracy of the configuration is 91:7 terms and 13 free ion $^{2S+1}L_J$ levels. The phenomenological method of simulation used hereafter is classical. We consider the total hamiltonian of the system as a sum of elementary hamiltonians.

For the part of the hamiltonian simulating free ion interactions, we consider only the two-body interaction, that is the electrostatic repulsion characterized by the Racah parameters E_k (k = 0-3) and the configuration interactions whose strength is given by the α, β, and γ parameters. We take also into account spin-orbit coupling. The total number of parameters involved is then 7. The number of spectroscopic terms being also 7, the simulation of barycenter positions has to be considered with care. It is best to set the $\alpha\beta\gamma$ parameters to values determined for other rare earths as indicated by the literature (16). Other interactions, such as three-body interactions, represented by Judd's parameters T^λ do not exist for the $4f^{12}$ configuration case.

The crystal field hamiltonian is written in the formalism described by Wybourne (17). For the case of ZnS:Tm^{3+}, the point site symmetry considered is T_d, and we choose to describe the hamiltonian with respect to the ternary axis, because a small distortion of the symmetry eventually would reduce the point site to C_{3v}. Then, the crystal field hamiltonian can be written as

$$H_{C.F.} = B_0^4\left[C_0^4 - \frac{\sqrt{70}}{7}(C_{-3}^4 - C_3^4)\right] + B_0^6\left[C_0^6 + \frac{\sqrt{210}}{24}(C_{-3}^6 - C_3^6) + \frac{\sqrt{231}}{24}(C_{-6}^6 + C_6^6)\right]$$

In order to simulate the spectrum, the secular determinant takes into account simultaneously all the interactions of the free ion, together with the crystal field effect, that is, also including the J-mixing.

Ab initio calculation of the crystal field parameters.—By using the PCEM model, it is possible to perform *ab initio* calculations of crystal field parameters. Even if the model is known to be over simplified (18), it is possible to have the magnitude of the influence on crystal field parameters of the distortion of the cubic site, when the different possible structures or polytypes are considered. Such calculations were performed for the wurtzite and polytype 6H structures, which appear to be the most frequent distortion encountered from the ideal blende structure. Table I summarizes the results obtained. One can remark that:

1. For the wurtzite and the 6H polytype structure, the ratios B_0^4/B_3^4, on one hand, and of B_0^6/B_3^6 and B_0^6/B_6^6, on the other hand, are not far from the theoretical cubic ratios of the blende structure. This fact indicates that we may keep the ratio of crystal field parameters to their cubic values in our simulations, as a first good approximation.

2. The signs for B_0^4 and B_0^6 are both positive. It is also known that, even if the order of magnitude for such parameters is not always satisfactory in this type of calculations, the sign is however always quite good. So, we shall choose these signs for the phenomenological parameters.

3. Results for B_0^2 are not significant, because we do not use the complete *ab initio* calculation model, which also includes polarizabilities of ions and screening factors (18). These corrections can have the same order of importance as pure PCEM calculations.

In any case, the small absolute value calculated for B_0^2 and the small distortion for crystal field parameters of rank 4 and 6 around cubic ratios, allow us to start simulations of crystal field splitting of the experimental levels by considering a T_d symmetry, an approximation confirmed by the literature cited here.

Experimental

Detection of the emission spectra of ZnS (Tm^{3+}) has been performed at various temperatures between 4.2 and 77 K, through a 0.5m Jobin and Yvon monochromator equipped with a holographic grating with 1200 l/mm. The resolution essentially depends on the wavelength range and on the intensity of fluorescence: $\Delta\lambda/\lambda \simeq 10{,}000$ in the blue region ($^1G_4 \rightarrow {}^3H_6$ and $^1D_2 \rightarrow {}^3H_5$) and 2000 in the near-infrared ($^1G_4 \rightarrow {}^3F_4$ and $^3H_4 \rightarrow {}^3H_6$). Excitation of the fluorescence is obtained by either classical u.v. lamps (UVL or UVS) or a cathode-ray excitation previously described (11). The use of these two types of excitation sources permit us to separate without ambiguity the emitting levels $^1G_4$ and $^1D_2$. Under UVL excitation only $^1G_4$ emits while both $^1G_4$ and $^1D_2$ emit under cathode-ray excitation (Fig. 1).

For lifetimes and time resolved measurements, the electron beam is modulated by polarization in square signals of the Venelt. Then, the signal is recorded through a boxcar integrator. This type of measurement permits the attribution without ambiguity of the emitting levels when transitions are superimposed like $^1G_4 \rightarrow {}^3F_4$ and $^3H_4 \rightarrow {}^3H_6$ ($\simeq 12{,}500\ cm^{-1}$).

Analysis of the Spectra

In the analysis of the spectra observed, transitions between Stark levels are assigned by supposing that the symmetry of the main point site is T_d. When an ion is embedded in a crystal, the free ion energy levels are split into Stark levels. The number and the type of perturbated levels for each value of the J quantum

Table I. Crystal field parameters calculated from PCEM method for ZnS (Tm^{3+}). Radial integrals $\langle r^k \rangle$ are taken from Ref. (19).

Parameters (cm^{-1})	Blende	6H	Wurtzite	Theoretical ratios	Blende	6H Ratios	6H Deviation (%)	Wurtzite Ratios	Wurtzite Deviation (%)
B_0^2		30	88						
B_0^4	250	250	263	$B_0^4/B_3^4 = -0.837$	−0.836	−0.769	8.1	−0.800	4
B_3^4	−300	−326	−329	$B_0^6/B_3^6 = 1.655$	1.655	1.787	8	1.838	11
B_0^6	80	80	82	$B_0^6/B_6^6 = 1.579$	1.579	1.580	0	1.594	1
B_3^6	48.3	45	44.7						
B_6^6	50.8	51	51.4						

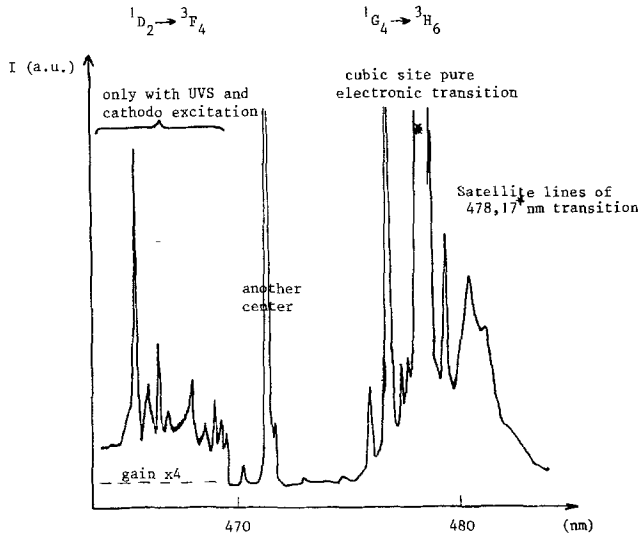

Fig. 1. Blue emission of ZnS (Tm^{3+}) at 77 K with different excitations.

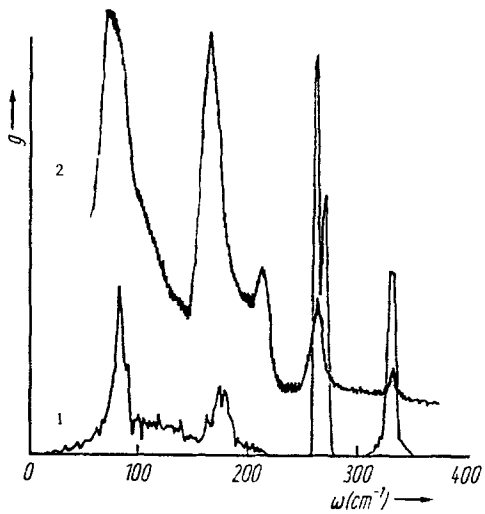

Fig. 2. 1. Phonon density of states corresponding to the best models calculated for 913 points of the reduced Brillouin zone by Kunk et al. (22). The main maxima are at 83, 175, 179, 263, 271, 331, and 335 cm^{-1}. Gaps from 220 to 258 and 278 to 308 are observed inside the optical band. 2. Fluorescence spectrum with the same scale, the origin of the x-axis is centered at 20.919 cm^{-1} (the pure electronic line).

number, depends on an isomorphism with the irreducible representation of the point group T_d. The number and the type of perturbation level can be found in the Prather monography (19).

At low temperature in the $^1G_4 \rightarrow {}^3H_6$ emission region near 478.0 nm, Ibuki and Langer have observed two types of transitions on each side of the main line (478.17 nm : 20,913 cm^{-1}). Toward the high energies ($\nu > 20{,}913$ cm^{-1}) these authors have classified a large number of sharp lines ($\Delta\nu \simeq$ 1-3 cm^{-1}). We have shown that they are due in fact to a great number of different sites for Tm^{3+} and that it is possible to make most of them disappear by using $ZnTm_2S_4$ as an activator for ZnS. On the other energy side ($\nu < 20{,}913$ cm^{-1}) we observe some diffuse and wide lines ($\Delta\nu \simeq$ 10-30 cm^{-1}) which are not affected by the nature of charge compensation. The position and intensity of these lines essentially depend on the sample structure. By analogy with previous observations on $LaAlO_3$ (Ln^{3+}) (20) we attribute these lines to a vibronic coupling associated with the purely electronic $^1G_4 \rightarrow {}^3H_6$ transition.

We have estimated experimentally at 4.2 K the values of the Huang-Rhys parameter S_0 by the ratio of the 0-phonon line intensity (for T_d site) to the total emission intensity. We thus find $S_0 = 0.35$ (cubic structure) and $S_0 = 0.25$ (hexagonal structure). Although weak these values are much greater than those generally reported for rare earth compounds ($S_0 \simeq 0.05$) as measured by Auzel in rare earth fluoride (21).

This last result is not very surprising since the $A_{II}B_{VI}$ compounds and more precisely ZnS usually exhibit a very strong electron-phonon coupling both in emission and absorption processes for all the activators in the iron series. The same characteristic seems to be true for rare earth activators.

A proof of the vibronic origin of some lines is generally given by the comparison of absorption and emission spectra. The vibronic structure appearing on the high energy side (with respect to the purely electronic line) in absorption measurements is an exact replica trough, a mirror plane of the vibronic structure seen on the low energy side by emission. In our case, such a proof is not attainable since the Tm^{3+} concentration is too low to permit the observation of absorption spectra.

Nevertheless we have several arguments justifying our interpretation:

1. There exists a strong analogy between the fluorescence spectrum and the theoretical curves of phonon density (22). In Fig. 2 we have superposed with the same energy scale the theoretical curve and the fluorescence spectrum of Tm^{3+} in one cubic sample. We observe first that the positions of the maxima correspond well to the main phonons (acoustic and optic) commonly described in the literature, and second that there exist two zones without emission whose wavelengths agree with the two gaps between 220-258 and 278-308 cm^{-1} of the theory.

2. In this spectral region we noted a displacement toward the low energies when the temperature is increasing, this fits well with the augmentation of transition probabilities involving higher energy phonons.

3. The first results on the generalization of the present work on ZnS with terbium as an activator show some analogy in the fluorescence spectrum indicating the same influence of electron-phonon coupling.

Transitions observed from $^1D_2$.—These transitions are only observed under cathode-ray or UVS excitations. The transition to $^3H_6$ (Fig. 3) is not very useful because, even at low temperature, we observe only one relatively wide line ($\simeq$ 80 cm^{-1} at half-width). The evolution with temperature ($4.2 < T < 60$ K) does not change the spectrum. Then, probably, the $^1D_2$ level has a small splitting; it means that the absolute value of B_0^4 is small. The transition to $^3F_4$ exhibits a better resolution, showing the splitting of $^1D_2$ ($\simeq$ 8 cm^{-1}) and allowing a complete attribution of the $^3F_4$ Stark levels.

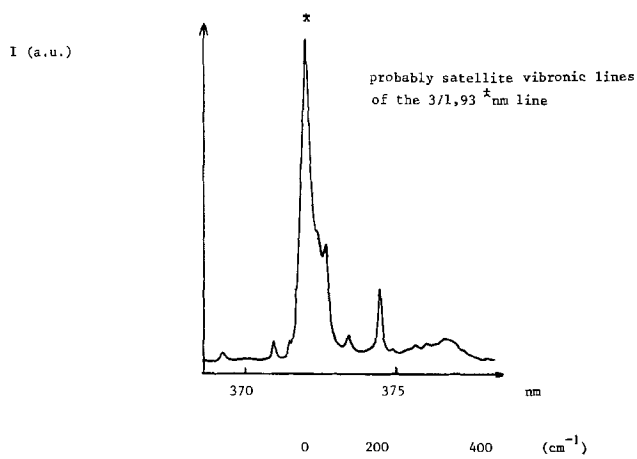

Fig. 3. $^1D_2 \rightarrow {}^3H_6$ emission of ZnS (Tm^{3+}) at 10 K

Transitions observed from $^1G_4$.—$^1G_4$ is the main emitting level in ZnS:Tm^{3+}. At 4.2 K, about 80% of the total emission is concentrated in one transition between Stark levels of $^1G_4 \rightarrow {}^3H_6$ (transition located at 20,913 cm^{-1}). Nevertheless, another transition has been assigned to another Stark level of $^3H_6$. The other lines observed in the $^1G_4 \rightarrow {}^3H_6$ area were attributed, and analyzed as vibronic transitions (20) (Fig. 4). Considering there are only two lines for $^1G_4 \rightarrow {}^3H_6$ zero phonon electronic transitions at 4.2 K, the dipolar electronic transition rules indicate that the irreducible representation of the lowest Stark level of $^1G_4$ is A_1.

Other transitions were observed from $^1G_4$ to $^3F_4$ and $^3H_5$. At 4.2 K, the number of lines observed for $^1G_4 \rightarrow {}^3F_4$ (Fig. 5) and $^1G_4 \rightarrow {}^3H_5$ (Fig. 6) transitions is also compatible with an A_1 irreducible representation for the lowest $^1G_4$ Stark level, if we admit a double character (magnetic and electric dipolar) for these transitions.

For all transitions observed, the evolution of the spectra *vs.* the temperature allow the identification of a first excited Stark level for $^1G_4$ located at 70 cm^{-1} above A_1; when the temperature increases we observe a second one located at 104 cm^{-1}. But it is not possible to attribute to these levels irreducible representations, by using selection rules, because of the broadening of the lines and the increase of the number of lines observed.

Transitions observed from $^3H_4$.—The only transition observed from this level is $^3H_4 \rightarrow {}^3H_6$. Although the wavelength range is the same that for $^1G_4 \rightarrow {}^3F_4$, lifetime measurements and time resolved spectroscopy allow the identification of the emitting level. This transition exhibits also satellite vibronic lines whose frequencies are similar to those of the $^1G_4 \rightarrow {}^3H_6$ satellites. The evolution of the spectra with temperature suggests a first excited Stark level for $^3H_4$ located at 25 cm^{-1} above the ground level. Figure 7 shows the spectrum at 10 K when the first excited Stark level of $^3H_4$ begins to be populated.

Energy level scheme.—The analysis of the emitting levels gives positions for some Stark levels. The comparison of transitions having different emitting levels and the same final level gives a partial knowledge of the splitting of the final states $^3H_6$, $^3H_5$, and $^3H_4$. Then, it is possible to partially construct the energy level scheme (Table II). For all levels, the total amplitude of splittings is rather small, a fact which probably indicates small absolute values of crystal field parameters. When compared to the literature, the barycenters of the ^3H_J levels are well positioned, but we note a quite important lowering of the barycenters for the $^3F_4$, $^1G_4$, and $^1D_2$ levels (Fig. 6). However, because of the missing Stark levels, the computation of the barycenter positions will be, in the present case, only tentative.

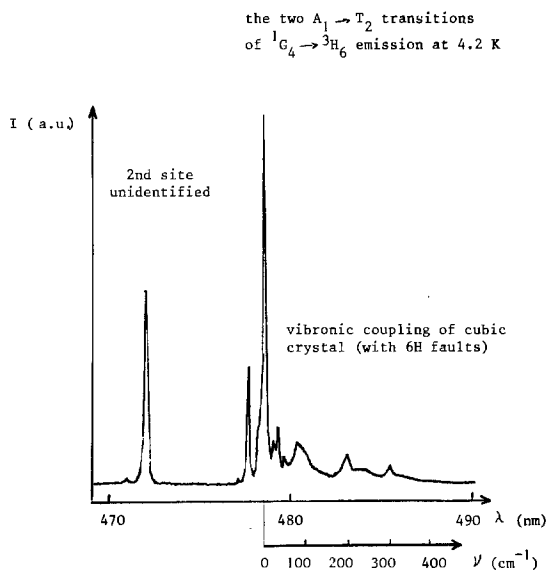

Fig. 4. Blue emission of ZnS (Tm^{3+}) crystal of cubic structure at 4.2 K excited by UVL Hg lamps (365 nm).

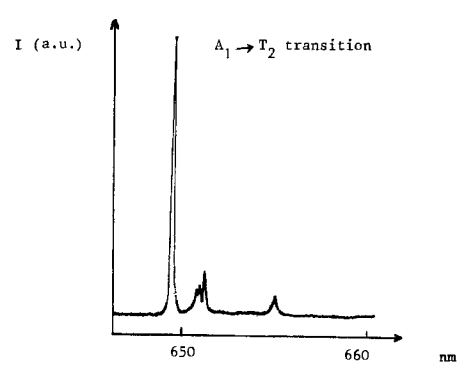

Fig. 5. $^1G_4 \rightarrow {}^3F_4$ emission of ZnS (Tm^{3+}) crystal at 4.2 K

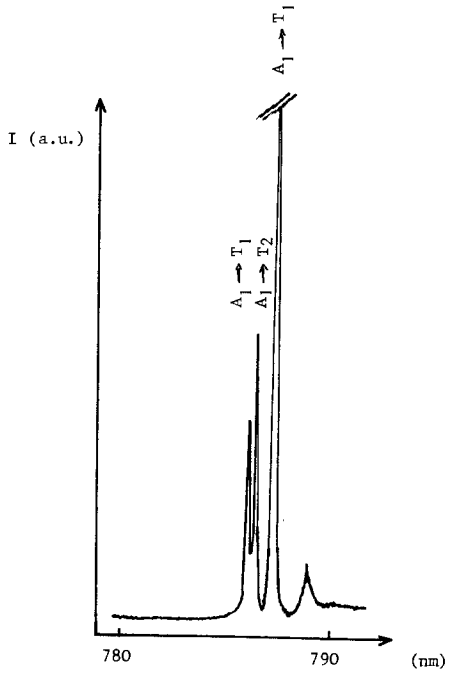

Fig. 6. $^1G_4 \rightarrow {}^3H_5$ emission of ZnS (Tm^{3+}) crystal at 4.2 K with UVL (365 nm) excitation.

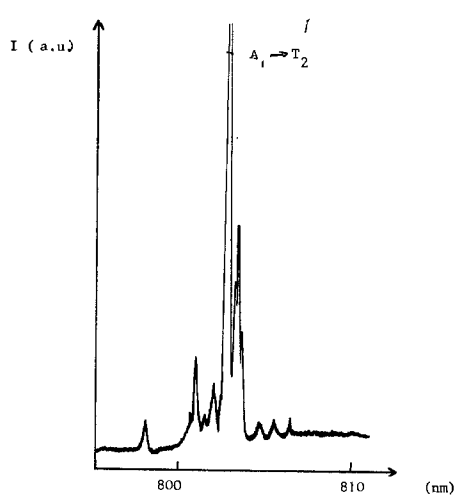

Fig. 7. $^3H_4 \rightarrow {}^3H_6$ emmission of ZnS (Tm^{3+}) crystal at 10 K with UVL (365 nm) excitation.

Table II. The energy of the electronic transitions observed in the emission spectrum of ZnS (Tm^{3+})

Transition	Assignment	Energy without correction (cm^{-1})	Temperature 40 K	Temperature 10 K	Relative intensities
$^1D_2 \rightarrow {}^3H_6$		27,083	x	x	2
		26,956	x	x	6
		26,915	x	x	4
		26,887	x	x	100
		26,856	x	x	9
$^1D_2 \rightarrow {}^3F_4$	$T_2 \rightarrow T_2$	21,492	x	x	
	$E \rightarrow T_2$	21,488	x	x	100
	$T_2 \rightarrow T_2$	21,464	x	x	
	$E \rightarrow T_2$	21,458	x	x	21
	$T_2 \rightarrow A_1$	21,432	x	x	36
$^1G_4 \rightarrow {}^3H_6$	$T_1 \rightarrow T_2$	21,033	x		17
	$T_2 \rightarrow T_2$	21,018	x		17
	$T_2 \rightarrow E$	20,993	x		17
	$T_2 \rightarrow T_2$	20,986	x		21
	$A_1 \rightarrow T_2$	20,956	x	x	10
	$T_2 \rightarrow T_1$	20,942	x		6
	$A_1 \rightarrow T_2$	20,913	x	x	100
$^1G_4 \rightarrow {}^3F_4$	$T_2 \rightarrow T_2$	15,467	x		45
	$T_2 \rightarrow T_1$	15,431	x		18
	$A_1 \rightarrow T_2$	15,398	x	x	100
	$T_2 \rightarrow T_2$	15,378	x		7
$^1G_4 \rightarrow {}^3H_5$	$T_1 \rightarrow T_2$	12,838	x		
	$T_2 \rightarrow T_2$	12,875	x		
	$A_1 \rightarrow T_1$	12,728	x	x	28
	$A_1 \rightarrow T_2$	12,722	x	x	35
	$A_1 \rightarrow T_1$	12,707	x	x	100
	Vibronic (?)	12,682	x	x	4
$^3H_4 \rightarrow {}^3H_6$	—	12,555		x	3
	—	12,517		x	2
	$T_2 \rightarrow T_2$	12,509		x	10
	—	12,482		x	8
	$A_1 \rightarrow T_2$	12,486		x	100
	—	12,480		x	15
	—	12,471		x	15
	—	12,454		x	2
	—	12,432		x	2
	—	12,405		x	2

Simulation of the Energy Level Scheme

Because of the nature and of the number of transitions experimentally observed, we cannot vary freely both free ion and crystal field parameters. So, we separate the simulation into two steps: first, estimation of the crystal field parameters, with free ion parameters fixed to reasonable values (16), and second, estimation of the free ion parameters.

The crystal field splittings in the T_d symmetry depend only on two parameters: it is easy to make a systematic exploration of the two dimensional space B_0^4, B_0^6, *i.e.*, $-1200\ cm^{-1} < B_0^k < +1200\ cm^{-1}$. Experimental arguments suggest that:

1. A small splitting for $^1D_2$ means a small absolute value for B_0^4 since, in the first-order interactions, B_0^6 does not operate on this level.
2. An A_1 irreducible representation for the lowest Stark level of $^1G_4$ means $B_0^4 > 0$.
3. *Ab initio* calculations suggest B_0^4 and B_0^6 are positive.
4. There is a splitting of 70 and 25 cm^{-1} for the first excited Stark levels of $^1G_4$ and $^3H_4$, respectively, as shown by the evolution of the spectra *vs.* the temperature.

With this information, and from the estimated splittings of the levels of the ground multiplet, the best fit is obtained with $B_0^4 = 136 \pm 10\ cm^{-1}$ and $B_0^6 = 180 \pm 10\ cm^{-1}$ (Fig. 8).

When crystal field parameters are adjusted we can get the positions of the barycenters. But, only four terms (six J-levels) are available. It is not possible to vary simultaneously all free ion parameters, we chose to adjust only the Racah parameters E_k, and the spin orbit coupling constant ξ, keeping $\alpha\beta\gamma$ to their expected values. The ξ-value is rapidly estimated, because we have the positions in the multiplet ^3H_J ($J = 4, 5, 6$). On the other hand, when variations for Racah parameters are individually performed, it can be seen that, in the first order, E_3 does not affect

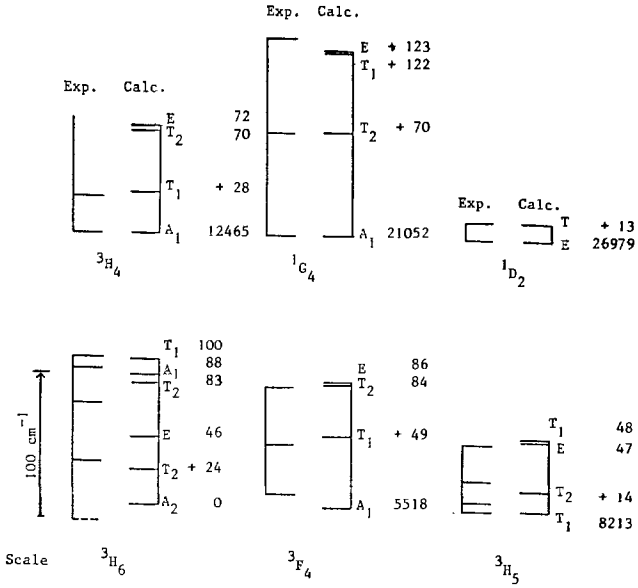

Fig. 8. Comparison of the experimental and calculated splittings of ZnS (Tm^{3+}).

the position of $^1D_2$, E_1 modifies equally the $^1D_2$ and $^1G_4$ barycenters, and E_2 displaces them in the opposite direction. Taking this into account, the free ion parameters were estimated to be $E_0 = 10{,}965\ cm^{-1}$, $E_1 = 6800\ cm^{-1}$, $E_2 = 34.2\ cm^{-1}$, $E_3 = 661\ cm^{-1}$, $\xi = 2625\ cm^{-1}$, $\alpha = 18\ cm^{-1}$ (fixed), $\beta = -630\ cm^{-1}$ (fixed), and $\gamma = 2000\ cm^{-1}$ (fixed). One can notice that the values for Racah parameters are quite different from the classical ones. This fact cannot be really interpreted because of the relatively small number of terms effectively experimentally observed. But it can be connected to the experimental remake upon a lowering of the Slaters integrals when the number of the coordinate decreases. The coordinate 4 not usual for the rare earth bonding rules in this sense.

Conclusion

By using an original synthesis method, it has been possible to insert Tm^{3+} in ZnS. Samples in powder or crystalline form were obtained for fluorescence studies. It appears that the Tm^{3+} ion mainly occupies a site with T_d symmetry. The analysis of the fluorescence spectra as a function of the temperature and of the excitation source allowed us to construct a partial energy level scheme. The estimation of the spectroscopic parameters shows that the crystal field strength is relatively small. Its influence on the splittings of the J-levels is less important than even for the rare earth trichlorides (23). Naturally this fact depends on the considered matrix, but it must be also associated with the lowering of the barycenter positions which is more curious. This latter fact contributes to Racah parameter values located at the frontier of the classical range, for such an ion. Unfortunately, the relative scarcity of the energy levels does not allow a precise estimation of these parameters and, as a consequence, a reasonable explanation of this fact.

Manuscript submitted July 30, 1981; revised manuscript received June 1, 1982.

Any discussion of this paper will appear in a Discussion Section to be published in the December 1983 JOURNAL. All discussions for the December 1983 Discussion Section should be submitted by Aug. 1, 1983.

Publication costs of this article were assisted by Laboratoire des Elements de Transition dans les Solides.

REFERENCES

1. S. Larach, Proc. Int. Conf. Luminescence Budapest, p. 1549 (1966).

2. J. Kingley, J. Prener, and H. Aven, *Phys. Rev. Lett.*, **14**, 136 (1965).
3. D. Krupka and D. Mahoney, *J. Appl. Phys.*, **43**, 2314 (1972).
4. J. Benoit and P. Benalloul, *Phys. Status Solidi*, **15**, 67 (1973).
5. J. Benoit, Thèse de Doctorat ès-Sciences Physiques, Université de Paris VI (1978).
6. Y. Charreire, Thèse de Doctorat ès-Sciences Physiques, Université de Paris VI (1980).
7. R. Ford and M. Williams, *Spectrochim. Acta*, **16**, 721 (1960).
8. S. Ibuki and D. Langer, *Appl. Phys. Lett.*, **2**, 95 (1963).
9. S. Ibuki and D. Langer, *J. Chem. Phys.*, **40**, 796 (1964).
10. C. Yu and F. Bryant, *J. Luminescence*, **18/19**, 841 (1979).
11. Y. Charreire and J. Loriers, *C.R. Acad. Sci. Paris*, **284**, 475 (1977).
12. Y. Charreire, H. Dexpert, and J. Loriers, *Mater. Res. Bull.*, **15**, 657 (1980).
13. B. Lambert, J. Buch, and A. Geoffroy, *Solid State Commun.*, **12**, 147 (1973).
14. W. Roth, in "Physics and Chemistry of II-VI Compounds," Chap. 3, North Holland Publishing (1967).
15. R. Watts and W. Holton, *Phys. Rev.*, **173**, 417 (1968).
16. See for instance, J. M. O'Hare and V. L. Donlan, *Phys. Rev. B*, **14**, 3732 (1976); D. E. Wortman, C. A. Morrison, and R. P. Leavitt, *ibid.*, **12**, 4780 (1975).
17. B. G. Wybourne, "Spectroscopic Properties of Rare Earth Ions," Interscience Publishers, New York (1965).
18. M. Faucher, J. Dexpert-Ghys, and P. Caro, *Phys. Rev. B*, **21**, 3689 (1980).
19. J. L. Prather, "Atomic Energy Levels," M.B.S. Monography No. 19 (1961).
20. C. Delsart, *C.R. Acad. Sci. Paris*, **263**, 744 (1966).
21. F. Auzel, *Phys. Rev. B*, **13** (7), 2809 (1976).
22. K. Kunk, M. Balkanski, and M. Jusimovici, *Phys. Status Solidi*, **41**, 491 (1970).
23. J. B. Gruber, R. P. Leavitt, and C. A. Morrison, *J. Chem. Phys.*, **74**, 2705 (1981).
24. A. J. Freeman and R. E. Watson, *Phys. Rev.*, **127**, 2058 (1962).

Properties of Cross-Linked Positive Acting X-Ray Resists Fabricated on the Basis of Poly(methylmethacrylate-co-methacrylyl Chloride)

F. Asmussen

Fraunhofer-Institut für Festkörpertechnologie, München, Germany

H. Betz

Fritz Haber-Institut der Max Planck-Gesellschaft, Berlin-Dahlem, Germany

J.-T. Chen

Fritz Haber-Institut der Max Planck-Gesellschaft, Berlin-Dahlem, Germany

A. Heuberger and S. Pongratz

Fraunhofer-Institut für Festkörpertechnologie, München, Germany

H. Sotobayashi

Fritz Haber-Institut der Max Planck-Gesellschaft, Berlin-Dahlem, Germany

and W. Schnabel

Hahn-Meitner-Institut für Kernforschung GmbH, Berlin-Wannsee, Germany

ABSTRACT

Copolymers of methylmethacrylate (MMA) and methacrylyl chloride (MACl) were cross-linked under various conditions, in order to obtain intermolecularly cross-linked polymeric networks having different cross-linking densities (β). These materials were irradiated with x-rays generated by an electron-storage ring or a conventional x-ray tube. The results showed that there is a critical dose for total solubilization, which can be used to determine the radiation sensitivity of cross-linked resists. Both the critical dose and the sensitivity (D_S) obtained from conventional exposure curves depend strongly on β. Optimum sensitivity values were obtained with slightly cross-linked material produced from copolymers with about 4 m/o MACl. In this case, D_S was up to five times lower than in the case of PMMA. The contrast factor, however, was not significantly affected. The technological properties of this resist were investigated by evaluating influences upon stability due to ion milling, plasma etching (CF_4), and HF etchant, as well as by performing adhesion-sensitive electroplating experiments. The results indicate that this material is at least as good as PMMA resist with regard to etch stability, and that it is superior as concerns adhesion behavior. The storage instability of the uncured (not yet cross-linked) material, caused by the gradually proceeding hydrolysis of acid-chloride groups, leads to some problems in practical applications. It was found that reproducible resist performance can only be obtained (after controlled partial conversion of the acid chloride groups) if the material is stored and cross-linked under total exclusion of water.

The importance of highly sensitive resists for x-ray lithography in connection with the production of VLSI devices has been pointed out in several articles (1-12). Some years ago, cross-linked positive-acting resists consisting of copolymers of methylmethacrylate (MMA) and methacrylyl chloride (MACl) were de-

Key words: critical dose for total solubilization, technological properties, storage stability.

veloped by Roberts (13). These copolymers, which are thermally cross-linked in the presence of small amounts of water prior to irradiation, received attention for their excellent adhesive properties.

The present paper concerns property studies aiming at the assessment of the applicability of MMA/MACl resists for practical purposes.

Our attention has been directed to some points that have not been dealt with in earlier works (13). These points concern technological properties, such as etch resistance and adhesion as well as the solubility behavior and the determination of the optimal chlorine content, with the aim of achieving better long-term stability of the resist material.

With respect to liquid developing procedures for cross-linked positive-acting resists, it is to be pointed out that total solubilization of the irradiated material is a prerequisite. This implies the destruction of the three-dimensional network structure of the cross-linked resist by x-ray irradiation, which is accomplished only if the absorbed dose D exceeds a critical value D_{crit}. If $D \leq D_{crit}$, part of the irradiated resist layer remains insoluble.

D_{crit} depends on the cross-linking density, β (the number of cross-links per repeating unit), as well as on the radiation-chemical yield of main-chain scissions G(S) (scissions per 100 eV absorbed by the polymer). At absorbed doses higher than D_{crit}, cross-linked resists exhibit a behavior similar to noncross-linked resists.

Experimental Procedure

Synthesis of copolymers and determination of their properties.—Copolymerization.—The copolymerization was carried out as a free radical process in a methylethyl-ketone solution at 72°C for 4 hr. The total concentration of comonomers was about 10 v/o. The initiator was benzoylperoxide (concentration: 0.5 g/liter). N_2 was bubbled through the solution until the polymerization was interrupted by the addition of excess petrol ether. The copolymer thus precipitated was then reprecipitated from the methylethyl-ketone solution at a copolymer concentration of 10 g/liter. The copolymer composition was determined by selecting appropriate comonomer concentration ratios. Details are given in Table I, where the copolymers used in this study are listed.

Determination of copolymer composition.—The copolymer composition was determined through chlorine-content measurements. For this purpose, the copolymers were subjected to melt decomposition using Na_2O_2 (14). The melt was then dissolved in water and, following acidification with HNO_3, the chlorine content was measured using a Cl specific electrode (Orion, Cat. No. 94-1700).

Determination of molecular weights.—Weight-average molecular weights were determined with a low-angle laser light-scattering photometer (Chromatix, KMX-6) and with a gel-permeation chromatography apparatus (Waters).

Preparation and cross-linking of copolymer layers.—Solutions of the copolymers in chlorobenzene (concentration *ca.* 12 w/o) were spin dried. Prior to use, chlorobenzene was dried with P_2O_5 and fractionally distilled. The thickness of the polymer layer varied between 0.5 and 1 μm, depending on the polymer concentration and the molecular weight. The samples were prebaked for 15 min at temperatures between 100° and 150°C. For this purpose, a special oven was constructed which allowed a temperature control of ±0.05°C.

Table I. List of copolymers

Copolymer	f^{M}_{MACl}* (m/o)	f^{P}_{MACl}** (m/o)	$M_{w,o}$
CP-A	1.5	5.3	1.4×10^5
CP-B	1.5	3.8	1.9×10^5
CP-C	6.0	13.2	1.4×10^5
CP-D	6.0	13.8	1.4×10^5

* Fraction of MACl in monomer mixture.
** Fraction of MACl in copolymer, as determined immediately after polymerization.

Irradiation of the samples.—The exposure experiments were carried out using synchrotron radiation delivered from the electron storage ring DORIS at Desy (Hamburg), as well as using the monochromatic radiation ($\lambda = 8.34$Å) of an aluminum x-ray tube. The electron energy ($E = 1.5$ GeV) of the storage ring (magnetic radius 12.12m) was chosen in such a manner that the maximum of the spectral distribution ($\lambda = 8.4$Å) corresponded with the wavelength of the monochromatic source. The vacuum window of the exposure chamber (7.5 μm Kapton) cut away the long wavelength portion ($\lambda \geq 15$Å) of the synchrotron radiation, so that the entire emission was concentrated in the wavelength region between 5 and 15Å.

The different spectra of the two sources lead to no significant change in the shape of the absorbed dose in the resist. The absolute radiation power reaching the resist, however, is about 30 times higher in the case of synchrotron radiation near the maximum of the spatial distribution (*ca.* 15 mW/cm², average electron current *ca.* 60 mA, source-wafer distance 27m), in comparison to the x-ray tube (10 kW primary electrical power, 18 cm resist/source distance).

Development of irradiated resists.—The developer consisted of a 50/50 (w/w) mixture of methylethylketone and 2-propanol. The samples were developed at 23°C for up to 6 min. The choice of the developer mixture and development temperature were made in such a manner as to achieve an approximate optimization of the dissolution rate in the exposed resist area, together with a tolerable dissolution rate in the unexposed area.

Etching and electroplating.—Etching as well as electroplating tests were made in order to evaluate the stability against semiconductor-specific technological processes. The resist was therefore subjected to argon ion milling, to a CF_4 plasma in a barrel reactor, and to a wet etching process using HF as well. The adhesion was tested by a gold electroplating process.

Experimental Results and Discussion

Chemical alterations during storage of uncured resist material, and their implications for cross-linking.—The performance of a cross-linked resist system depends on whether the cross-linking conditions are controllable (and therefore reproducible), and also on whether reliable development conditions are available.

Table I shows a list of copolymers which were prepared for our experiments.

Typical dissolution curves, indicating the development performance of cross-linked nonirradiated resists, are shown in Fig. 1. In order to convert the linear copolymers into cross-linked networks, the samples were heated on glass supports for 15 min at various temperatures, as indicated in Fig. 1. An inspection of the curves clearly indicates the following tendencies: (*i*) In all cases, a certain fraction of the copolymer remains soluble, indicating incomplete cross-linking. (*ii*) The soluble fraction becomes smaller as the reaction temperature is increased, indicating an increase in the degree of cross-linking (β). (*iii*) Freshly synthesized copolymers require higher cross-linking (prebaking) temperatures than copolymers stored for several months, if the same degree of cross-linking is to be attained. (*iv*) Higher MACl contents allow lower prebake temperatures to attain equal degrees of cross-linking.

Prevention of the gradual conversion of acid-chloride groups, under practical storage conditions, would be essential for defining easily controllable cross-linking conditions.

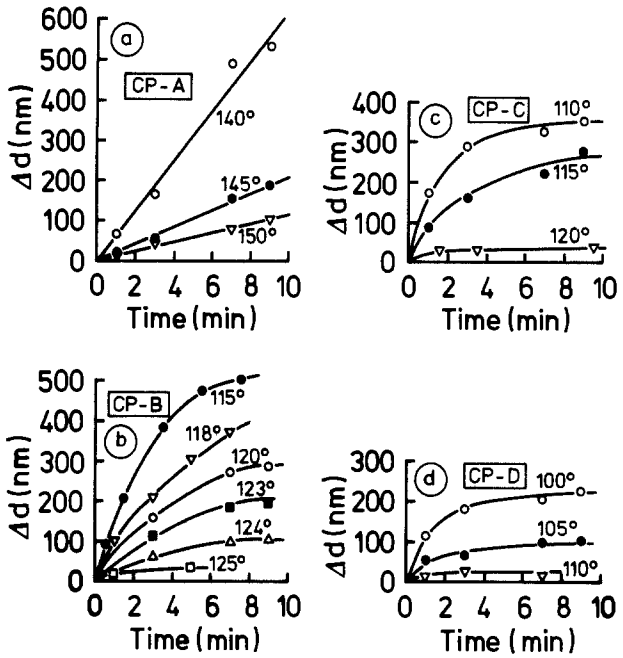

Fig. 1. Solubility tests on cross-linked nonirradiated copolymers (removed resist thickness Δd as a function of developing time).

Copolymers	MACL content (m/o)	Storage time
a CP-A	5.3	One week
b CP-B	2.6	14 months
c CP-C	13.2	One week
d CP-D	12.1	7 months

Initial resist thickness d_0: ca. 0.9 μm; developer: methylethyl-ketone/isopropanol = 50/50 (w/w).

Critical absorbed dose for total solubilization.—The critical dose for total solubilization is of decisive importance in determining the sensitivity of cross-linked positive resists. For the irradiation experiments, samples having various degrees of cross-linking (β) were used. It was found that the critical dose for total solubilization increases with an increasing degree of cross-linking. Typical results are shown in Fig. 2, where the solubility performance of two resist samples, having low (Fig. 2a) or high (Fig. 2b) degrees of cross-linking, is illustrated. In the case shown in Fig. 2a, the critical dose is lower than $D^{exp} = 95$ mJ/cm². Whereas the nonirradiated samples only dissolve partly ($\Delta d/d_0 = 0.20$), all irradiated samples are completely soluble. In the case shown in Fig. 2b, the critical exposure dose is much higher, *i.e.*, between 248 and 287 mJ/cm². Table II lists typical values. It is obvious

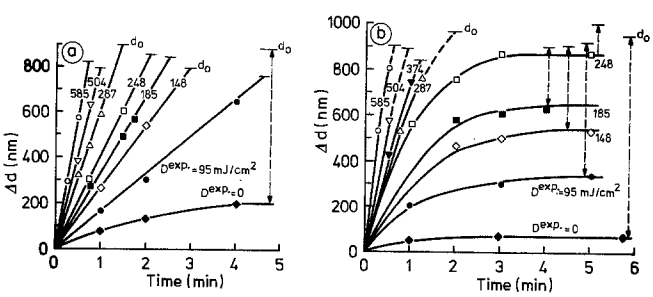

Fig. 2. Solubility tests on the cross-linked irradiated copolymers CP-B(a) and CP-D(b) (removed resist thickness Δd as a function of developing time). Cross-linking (prebake) temperatures: 120°C (CP-B) and 105°C (CP-D). The exposure doses (in mJ/cm²) of synchrotron irradiation and the initial resist thicknesses d_0 are indicated at the curves. Developer: methylethyl-ketone/isopropanol = 50/50 (w/w).

Table II. Dependence of the critical dose for total solubilization on the degree of cross-linking. Higher cross-linking (prebake) temperatures correspond to higher degrees of cross-linking

Copolymer	Cross-linking (prebake) temperature (°C)	D_{crit}^{exp} (mJ/cm²)
CP-C	120	390
	125	550
CP-D	105	280
	110	440
CP-B	120	≦95
CP-A	145	≦248

that the lowest critical-dose values correspond to the resist samples that are the least cross-linked. This can be achieved by a low cross-linking temperature (Table II), as well as by a low fraction of MACl (Table I and II). For practical applications, in this case, the rather high solubility of the nonirradiated resist material must be taken into account. It is noteworthy that highly cross-linked copolymers, when irradiated with doses higher than the critical dose, dissolve in the developer at higher rates that slightly cross-linked copolymers irradiated with the same dose.

Sensitivity and contrast factor.—Figure 3 shows typical exposure curves obtained for copolymer CP-B; for comparison, the exposure curve a for polymethylmethacrylate (PMMA) is also shown. It can be seen that although the contrast factor (γ) remains nearly constant, the D_S values vary significantly, up to a factor of 2.2. A comparison of curves b and c indicates the strong influence which the cross-linking density has on D_S. Again, one clearly sees the importance of both the chemical composition, *i.e.*, the chlorine content, and the choice of the cross-linking conditions, especially the prebaking temperature. The observed difference in sensitivity between PMMA and copolymer CP-B is not merely an apparent effect, but is in fact a genuine one, since the absorbed dose, due to the difference in chemical composition, is less than 10%.

Technological properties.—In addition to the sensitivity and the contrast, the factor of resolution is a further important criterion in the evaluation of a photoresist. The resolution obtained, in our experiments with the polymer in question, indicates that there is no limitation concerning the transfer of sub-μm features down to 0.5 μm. However, the factor of technological stability in regard to etching processes,

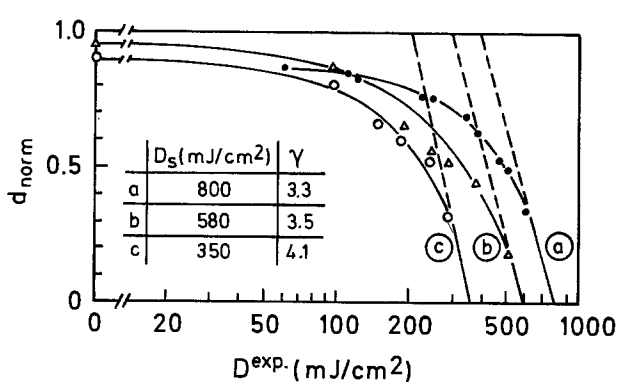

Fig. 3. Exposure curves for synchrotron irradiation

Resist	Cross-linking (prebake) temperature (°C)
a PMMA (EPMF-1)	150
b copolymer CP-B	124
c copolymer CP-B	120

d_{norm}: normalized remaining resist thickness; initial resist thickness d_0: ca. 1 μm; prebake time: 15 min; developer: methylethyl-ketone/isopropanol = 50/50 (w/w); development time: 60 sec.

as well as that of resist adhesion on various substrates, are the decisive parameters for the evaluation of a resist in semiconductor technology.

Ion milling.—The ion-etching experiments were conducted using a Veeco unit, Model 7760. The argon pressure was $8 \cdot 10^{-5}$ Torr, the voltage was *ca.* 500V, and the current was 55 mA. The resist was subjected before etching to a postbake at 90°C for 15 min. Under these conditions, the etch rate of this resist was 2000 Å/min, which is better by a factor of 2 in comparison to PMMA, which has an etch rate of 4000 Å/min under the same etching conditions. In Fig. 4, for the example of an etched gold structure (thickness 0.4 μm), the structural-transfer quality which is attainable using this resist can be seen. The 60° slope of the walls, which is normally produced by this kind of ion-etching procedure (15), is also visible.

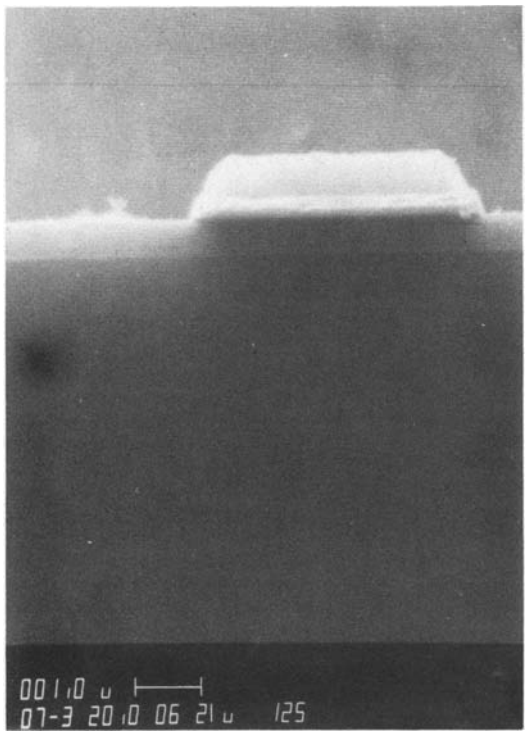

Fig. 4. Ion milling test of CP-C on gold layer (thickness 0.4 μm). Initial resist thickness: *ca.* 1 μm; postbake at 90°C for 15 min; etching time: 2 min.

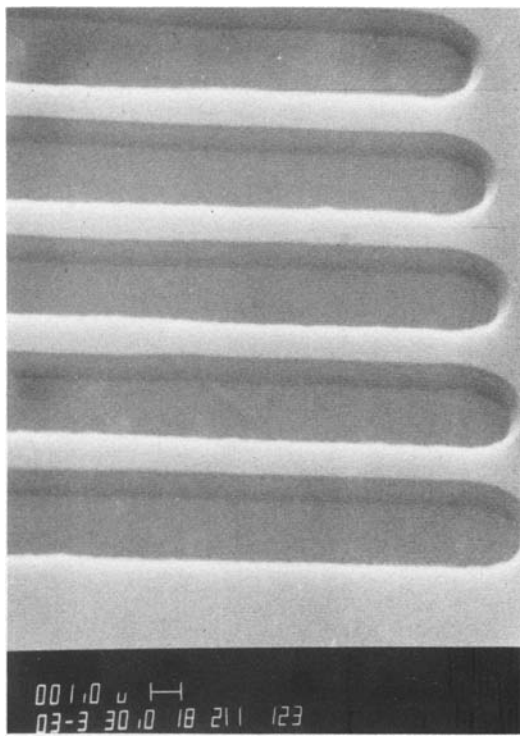

Fig. 6. HF etching test of CP-B on silicon oxide (0.5-0.6 μm) after lift-off procedure. Initial resist thickness: 0.95 μm; postbake at 90°C for 15 min; etching time: 4 min.

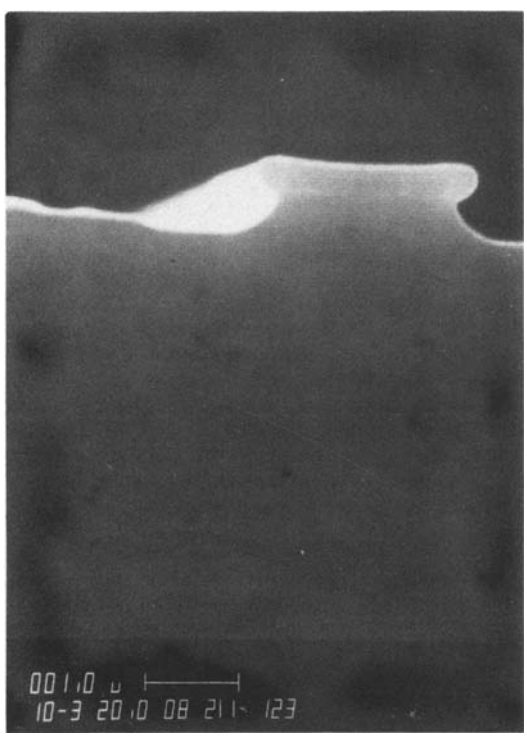

Fig. 5. CF_4-plasma etching test of CP-A on silicon oxide. Initial resist thickness: *ca.* 1 μm; postbake at 90°C for 15 min; etching time: 60 min.

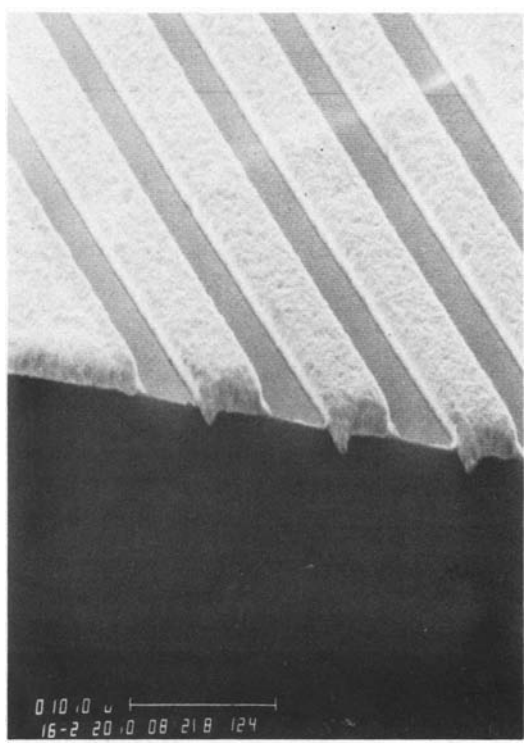

Fig. 7. Resist adhesion test of CP-A by gold plating after lift-off procedure. 0.5 μm high Au structure with a width of 3 μm.

CF_4-plasma etching.—In order to carry out silicon-oxide etching, a CF_4 plasma was produced in a barrel reactor manufactured by LFE. Etching was done for 60 min at an rf power of 100W, a reflected power of 0.2-1.5W, and a constant gas flow. Prior to this, the 1 μm thick resist was postbaked at 90°C for 15 min. The etch rate of the resist, 120 Å/min, is relatively low and corresponds to the behavior of PMMA. Figure 5 shows the result, using the example of an etched oxide structure. The considerable underetching is due to the isotropic etching behavior of the barrel reactor.

HF etching.—For the purpose of silicon-oxide etching using buffered HF, the resist was likewise postbaked at 90°C for 15 min. The etching temperature was 22°C. Under these conditions, the resist reached an etch rate of 1000 Å/min, which corresponds approximately to the etch rate for PMMA. In Fig. 6 (for the resist-free case), a considerable underetching can also be seen, caused again by the isotropic characteristics of a wet etchant.

Gold plating.—To test the resist's adhesion properties on the substrate, a fine-grain gold electrolyte was deposited. The deposition-bath temperature was 57°C; the process was carried out using a charge of $Q = 12.7$ As and a pulsed current of $I = 15$ mA (pulse duration: 30 msec, interval duration: 10 msec). As opposed to the case of PMMA, no underplating could be seen. This implies a very strong adhesion of the MMA/MACl resist material to the substrate. Figure 7 shows (for the resist-free case) a 0.5 μm high Au structure with a width of 3 μm, which is an exact reproduction of the structure produced in the resist.

Conclusion

In conclusion, cross-linked copolymers of MMA and MACl possess a significantly higher sensitivity than PMMA while retaining the same good contrast, provided that the cross-linking density is sufficiently low. The poor adhesion behavior of PMMA, which leads to considerable underplating in a gold electroplating process, is completely eliminated in the case of the chlorine-containing copolymer. The etch stability, which has been tested against a wet etchant (buffered HF), a CF_4 plasma, as well as against ion milling, is appreciably better than in the case of PMMA. The resist described in this paper is therefore well suited for semiconductor applications, if one pays the necessary attention to the critical storage conditions.

Manuscript submitted March 22, 1982; revised manuscript received Aug. 19, 1982.

Any discussion of this paper will appear in a Discussion Section to be published in the December 1983 JOURNAL. All discussions for the December 1983 Discussion Section should be submitted by Aug. 1, 1983.

Publication costs of this article were assisted by the Fraunhofer-Institut für Festkörpertechnologie.

REFERENCES

1. M. Hatzakis, Applied Polymer Symposium No. 23, 73-86 (1974).
2. M. J. Bowden and L. F. Thompson, *J. Appl. Polym. Sci.*, **17**, 5211 (1973); *This Journal*, **120**, 1722 (1973) and **121**, 1620 (1974).
3. T. Hirai, Y. Hatano, and S. Nonogaki, *This Journal*, **118**, 669 (1971).
4. H.-J. Queisser, Editor, "Topics of Applied Physics," Vol. 22, Springer, Berlin (1977).
5. E. Spiller and R. Feder, in "Topics of Applied Physics," Vol. 22, H.-J. Queisser, Editor, Chap. 3, Springer, Berlin (1977).
6. L. F. Thompson, L. E. Stillwagen, and E. M. Doerris, *J. Vac. Sci. Technol.*, **15**, 938 (1978).
7. M. J. Bowden and L. F. Thompson, *Solid State Technol.*, **22**, 72 (1979).
8. M. Hatzakis, *J. Vac. Sci. Technol.*, **16**, 1984 (1979).
9. A. R. Neureuther, in "Synchrotron Radiation Research," H. Winick and S. Doniach, Editors, Chap. 7, Plenum Press, New York (1980).
10. A. Heuberger, H. Betz, and S. Pongratz, *Adv. Solid State Phys.*, **20**, 259 (1980).
11. W. D. Grobman, in "Handbook on Synchrotron Radiation," Vol. 1, E. E. Koch, D. E. Eastman and Y. Farge, Editors, North Holland, Amsterdam (1980).
12. G. N. Taylor, *Solid State Technol.*, **23**, 73 (1980).
13. E. D. Roberts, *ACS Div. Org. Coatings Plast. Chem. Preprints*, **35**, 281 (1975) and **37**, 36 (1977); Ger. Offen. 2362 092 (1974).
14. R. Bock, "Aufschlußmethoden der anorganischen und organischen Chemie," Verlag Chemie, Weinheim (1972).
15. D. Bollinger and R. Fink, *Solid State Technol.*, **23**, 97 (1980).

Junction Depth Measurement for VLSI Structures

S. Prussin*

TRW Defense Systems and Space Group, Redondo Beach, California 90278

ABSTRACT

A method has been developed for accurately and rapidly measuring submicron junctions, utilizing a conventional commercial groover and profilometer. Junctions are indicated on a tapered groove, using conventional staining techniques. Direct depth measurements made at stain indications exhibit a reproducibility of 200Å.

Modern integrated circuits, designed to consist of multiple layers of shallow pn junctions, are being fabricated with ever greater spatial density. The increase in the number of components or logic gates per packaged unit has held at a factor of four every two years (Moore's law) for the past two decades. This has required correspondingly closer junction spacing. The need for a fast, accurate method for the determination of shallow junctions has become increasingly apparent.

* Electrochemical Society Active Member.

Key words: semiconductor, integrated circuits, doping, ion implantation.

A traditional method for junction depth determination has been the use of angle lapping and staining and measurement with an interference microscope. Two years ago, Wu and his co-workers (1) evaluated the various techniques available for measuring shallow junctions. They pointed out the limitations of such techniques as spreading resistance probe traverses, C-V determinations, and successive anodization and stripping, and concluded that the optimum method was an adaption of the traditional lapping and staining technique which permitted the delineation of a junction depth to an accuracy of ± 200Å.

The use of an interference microscope permits us to make a direct measurement of junction depth, but since each fringe is approximately 3000Å, the precision leaves much to be desired for junctions of less than 1 μm. The technique developed by Wu and his coworkers measures the junction distance along a shallow lapped angle and then converts this distance into the actual depth by measuring the tangent of the angle. Care is required to obtain the necessary accuracy. The lapping jig must be massive to eliminate rocking and insure a planar lapped surface. SiO_2 must be deposited on the silicon surface prior to lapping to avoid edge rounding of the silicon and to help delineate the surface. A laser reflection system is used to determine the exact angle of the lapping each time a specimen is prepared.

Recently Sheng and Marcus (2) described a method of delineating shallow junctions in silicon by using transmission election microscopy on cross-section samples. This method, while exhibiting a high degree of accuracy and reproducibility, requires a relatively lengthy time for preparation.

In this paper a method is described for accurately, reproducibly, and rapidly measuring the multiple junction depths in closely spaced bipolar structures.

Technique

The method recommended here utilizes two instruments frequently found in semiconductor processing laboratories, a cylindrical wafer groover and a profilometer.

The groover is conventionally used for junction depth determination by grooving, staining, and measuring both the groove width and the exposed substrate (3). The junction depth is given by the expression

$$x_j = \left[R^2 - \left(\frac{W_2}{2}\right)^2\right]^{1/2} - \left[R^2 - \left(\frac{W_1}{2}\right)^2\right]^{1/2} \quad [1]$$

where R is the cylinder radius, W_1 the width of the groove, and W_2 the width of the exposed substrate. Major sources of error appear to be the assumption that the groove is exactly cylindrical and the difficulty in accurately determining the edge of the groove. These are exaggerated by the need for very shallow grooves required for the shallow junctions being studied.

One of the bases of our technique is the use of a tapered groove. This was simplified by the fact that the equipment used in this study[1] was designed with set screws to level the wafer holding chuck. These could be easily adjusted to introduce a slight fixed taper in the grooves produced. Figure 1 illustrates the stained groove typical of a shallow four layer structure. The cotangent of the taper angle of 6.89′ yields a multiplication factor, m, of 498.8 along the bottom of the groove. It is not necessary to measure this factor as it is not used in the calculation of the junction depths which are measured directly. The stain used here was the conventional HF plus nitric with intense light which darkens the p regions.

[1] Model 2015C, Philtec Instrument Company, Philadelphia, Pennsylvania.

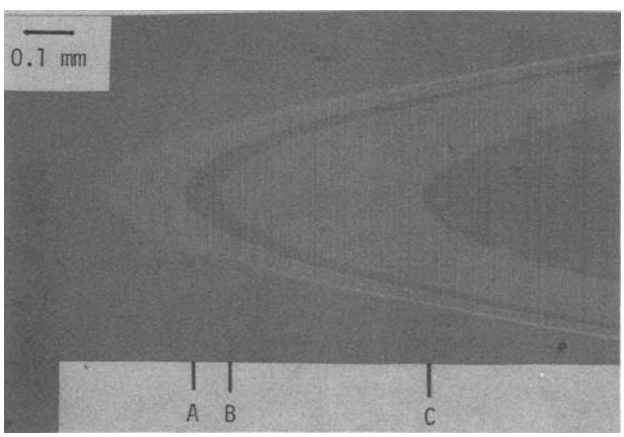

Fig. 1. Photomicrograph of stained tapered groove of shallow four layered structure. Pn junctions at A, B, and C. Taper magnification factor = 498.8.

Positions A, B, and C represent the three pn junctions of the shallow four layer structure. Measurement of the depth of the groove at these points yields the value of the junction depth.

We investigated two methods for reading the depth of the groove at these points. The first method was analogous to that conventionally used, measuring the groove width, W, at the junction and calculating the junction depth, x_j, by the relation

$$x_j = \frac{m+1}{m}\left(R - \left[R^2 - \left(\frac{W}{2}\right)^2\right]^{1/2}\right) \quad [2]$$

The factor $(m + 1)/m$ takes into account the effect of the taper which makes the groove curvature slightly elliptical.

We also find that x_j can be given very closely for the high magnification factors and the shallow junctions studied, by the relation

$$x_j = W^2/8R \quad [3]$$

The value of R is taken from the given diameter, 1.5 in., of the grooving spindle; the value of W is obtained by measurement either from a photomicrograph of the groove such as Fig. 1 or directly from the grooved specimen by the use of an optical microscope with a filar eyepiece.

The second method, which we felt exhibited greater accuracy, utilized a profilometer to obtain a direct reading of the groove depths at the three pn junctions A, B, and C, as marked in Fig. 1. Typical profiles of these junctions are shown in Fig. 2.

The accuracy of the first method is dependent upon how closely Eq. [2] describes the cross section of the groove. In this case, W represents the width of the groove at a distance x above the bottom of the groove.

In Fig. 3 we have repeated the profile of the groove taken at point A but with the horizontal magnification increased from 50 to 500×. The superimposed points were obtained from Eq. [2] utilizing 1.5 in. as the diameter. We find that Eq. [2] fits the groove very closely except at the wafer surface where there ap-

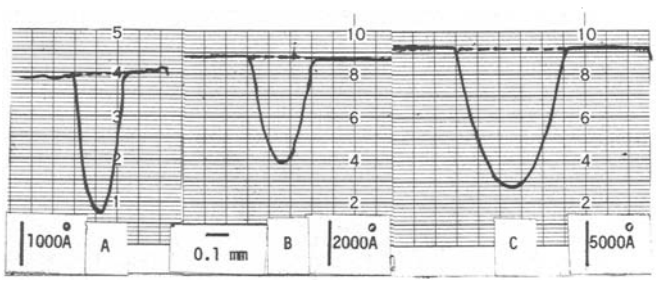

Fig. 2. Profile of tapered groove of shallow four layered structure at junction A, vertical scale 1000Å per cm, at junction B, vertical scale 2000Å per cm, and at junction C, vertical scale 5000Å per cm. Horizontal magnification 50× before reduction.

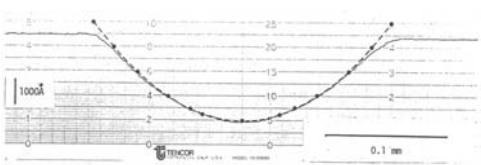

Fig. 3. Profilometer trace of tapered groove at junction A. Vertical scale 1000Å per cm, horizontal magnification 500×, before reduction. Dashed line corresponds to Eq. [2] with $x = 0$ at the bottom of the groove.

pears to be a decided rounding of the groove edges. We recognize that it is necessary to correct the measured length of the groove width at the surface in order to calculate an accurate value for the junction depth from Eq. [2].

The manufacturer of the Philtec groover suggests the use of a filar eyepiece to measure W and recommends use of a table relating x to W to obtain values of x_j. The x values in this table appear to be calculated from Eq. [4]

$$x = R - \left[R^2 - \left(\frac{W - 20}{2}\right)^2\right]^{1/2} \quad [4]$$

This is similar to Eq. [2] but includes a correction of 20 microns subtracted from each W value, no matter how large or small. This becomes particularly significant for calculating shallow junctions. While the 20 micron correction represents a decrease of 5.8% for a 3 μm junction, it represents a reduction of 18% for a 3000Å junction. The 20 micron correction may be valid for deep grooves used for deeper junctions. Our profilometer measurements suggest that the correction for shallow grooves should be somewhat less.

The manufacturer recommends for shallow junctions, *i.e.*, less than 1 μm, that the groove be cut into a surface covered with oxide. Otherwise, because the angle of the groove with the surface is very slight, he notes that it is extremely difficult to accurately measure the width of the groove.

The use of a direct reading profilometer eliminates the error inherent in assuming perfectly cylindrical grooves and in measuring the width of shallow grooves.

Experiment

This technique was evaluated by means of several hundred measurements made by two newly trained technicians on four layered monitor wafers. These had accompanied wafer lots through a sequence of operations for all but the photoresist steps. In this process the starting p-type wafers had been subjected to three implantations interspersed between various furnace operations. As a result of the processing, three pn junctions were generated.

One set of monitor wafers was given to each technician with instructions to determine the grooving conditions which he found gave the most consistent results. The grooving variables were the diamond particle size and the groove taper.

One set of wafers was prepared with implantations of 1.5×10^{13} P cm^{-2} at 60 keV, 3×10^{14} B cm^{-2} at 90 keV, and 5×10^{15} As cm^{-2} at 50 keV. The processing chosen gave three pn junctions that were nominally 0.35, 0.50, and 1.60 μm deep. The technician carrying out studies on these wafers chose 1 μm diamond particle size for the groover and a groove taper corresponding to a magnification factor of 500 as giving the most consistent results. A series of ten profilometer traverses was made at each of the three junctions shown as A, B, and C in Fig. 1 on two stained tapered grooves on a wafer of this series. The instrument used was the Alpha-step profiler (Tencor Instruments, Mountain View, California). Typical traverses are shown in Fig. 3, where the junction depth at A is 3,230Å, the junction depth at B is 4,950Å, and the junction depth at C is 16,500Å. The mean junction depth and standard deviation values are listed in Table I.

Table I. Junction depth measurements on two tapered grooves on the same monitor wafer

Groove	Values	Junction A (Å)	Junction B (Å)	Junction C (Å)
1	Mean	3390	4816	16,140
	Std. deviation	102	95	156
2	Mean	3349	5288	15,998
	Std. deviation	127	170	175

The second set of wafers with implantations of 1.5×10^{13} P cm^{-2} at 60 keV, 1.35×10^{14} B cm^{-2} at 90 keV, and 3×10^{15} As cm^{-2} at 50 keV was processed to result in three pn junction that were nominally 2500, 4000, and 9200Å deep. Here the 0.25 μm diamond particle size was chosen together with a taper having a magnification factor of 200 as giving the most consistent results. Standard deviation values within the ranges listed in Table I were obtained. We recognize that the junction depths characteristic of each set of test wafers did not differ greatly. The fact that similar precision was obtained under different test conditions suggests that the choice of angle and particle size is not too critical.

Discussion

We recognize that cur junction depth measurements are characterized by accuracies falling into three categories, as given below.

Reproducibility of measurement.—Here we are comparing the depth values measured by successive traverses across a single stained junction. This accuracy is dependent both on the profilometer and the way it is used. The particular instrument used was designed for the accurate measurement of step heights. To use it for groove depth measurement, it was necessary to use it in the manual mode. The scan speed used was 0.1 mm/sec. A slower speed might result in more accurate response of the stylus to the groove surface. For the experimental conditions, the standard deviation for all three junction depth measurements was in the range of 100-200Å.

Reproducibility of junction indication.—Here we are examining the reproducibility of the stain. We assume that the junction depths on a single monitor wafer are uniform, and that comparing the depth values obtained from separately stained grooves gives us a measure of the reproducibility of the staining process. We find from Table I that values obtained from two separate grooves for the junctions at A, B, and C, differ within 200Å from their mean.

Significance of junction indication.—The displacement of an HF stained junction from the metallurgical junction position has been shown to occur if light of insufficient intensity is used (1). This has been attributed to an unstained depletion zone whose width can be approximated from the concentration gradient at the junction (4). The SUPREM II-5 diffusion model was used to predict the profiles for the submicron junctions and the corresponding depletion widths. These suggest that the discrepancies in junction depth measurement on this account are limited to 12%. Another potential discrepancy is the "wedge effect" suggested by Wu (1). For low angle lapped surfaces such as we are using there may be an insufficient number of dopant ions to result in a true staining of the pn junction. This would tend to give us shallower junction depth values than actually exist.

Acknowledgments

We wish to acknowledge the significant contribution of Boris Hikin who pointed out the advantage of using a groove of varying depth.

David Margolese and Tim Hersh carried out the numerous measurements necessary to evaluate this technique.

This work was supported by the Naval Electronic System Command, under contract N-00039-81-C-0414.

Manuscript submitted March 15, 1982; revised manuscript received July 22, 1982.

Any discussion of this paper will appear in a Discussion Section to be published in the December 1983 JOURNAL. All discussions for the December 1983 Discussion Section should be submitted by Aug. 1, 1983.

Publication costs of this article were assisted by TRW Defense Systems and Space Group.

REFERENCES
1. C. P. Wu, E. C. Douglas, C. W. Mueller, and R. Williams, *This Journal*, **126**, 1982 (1979).
2. T. T. Sheng and R. B. Marcus, *ibid.*, **128**, 881 (1981).
3. B. McDonald and A. Goetzberger, *ibid.*, **109**, 141 (1962).
4. S. M. Sze, "Physics of Semiconductor Devices," p. 92, John Wiley & Sons, New York (1969).

Reactive Ion Etching Resistant Negative Resists for Ion Beam Lithography

Yasuo Wada,* Kozo Mochiji, and Hidehito Obayashi

Hitachi, Limited, Central Research Laboratory, Kokubunji, Tokyo 185 Japan

ABSTRACT

Exposure characteristics and mesh mask pattern replication of two negative resists, AZ1350J and IPS (iodinated polystyrene), by hydrogen ion beam are reported. A 180 keV hydrogen ion beam exposure followed by a flood u.v. light exposure makes it possible to use AZ1350J as a negative ion beam resist (IDER: ion desensitization of photosensitive resist). The sensitivity and contrast factor of IDER are 3×10^{-6} C/cm^2 and 2.0, respectively, while 3×10^{-7} C/cm^2 and 3.0 for IPS, respectively. The mesh mask patterns are neatly replicated on these resists, and suggest the potential high resolution of these resists. Reactive ion etching of an SiO_2 layer through the patterns are performed. Both resists show good resistance against reactive ion etching, which is an indispensable tool for the coming submicrometer technology age.

Current technological innovation has brought the semiconductor industry to the stage where submicrometer lithography technology will become generally required within five years (1). Ion beam lithography has attracted attention recently for its capability in submicrometer pattern fabrication (2-4). Dry etching resistant ion beam resists (5), which are indispensible for the coming submicrometer processing technologies, have not necessarily demonstrated their capability in patterning and sensitivities to the ion beam. This paper reports ion beam exposure characteristics of two reactive ion etching resistant negative "ion beam" resists, AZ1350J and IPS (iodinated polystyrene).

AZ1350J (Shipley) is generally known as a positive photoresist. Recently, ELDER (electron desensitization of photosensitive resist) processing for negative electron beam resists was reported, and they were shown to be resistant to reactive ion etching (6). This paper reports that AZ1350J is also desensitized by an ion beam, and that it can be used as a negative resist for ion beam lithography.

IPS (Hitachi) has been developed as an electron beam resist (7), which also shows good resistance against reactive ion etching. The sensitivity of IPS to an electron beam is in the order of 10^{-6} C/cm^2, suggesting that it should be very sensitive to an ion beam (8).

The exposure characteristics of these resists and the mesh pattern replication by hydrogen ion beam, as well as the resist pattern transfer to an oxide layer by reactive ion etching is reported.

Experimental Procedures

A p-type, (100) oriented silicon wafer was used as a substrate. The resist was spun on the substrate to a thickness of approximately 0.9 μm. An ion implanter was used to expose the resist layer by hydrogen ions. The energy range utilized in the experiment was between 30 and 180 keV. The dose rate was low enough so that substrate heating did not affect the exposure characteristics of the resists (9).

After exposure to a hydrogen ion beam, these samples were developed, rinsed, and dried. In the case of AZ1350J, the flood u.v. light exposure after ion beam exposure was on the order of 30 mJ/cm^2, and the resist layer was developed by immersing the sample in a 40% MF312 (Shipley) developer for 90 sec followed by rinsing in water. IPS was developed in a methyl-ethyl-ketone and ethanol mixture, with a 10:1 volume ratio, then rinsed in a methyl ethyl ketone and ethanol mixture with a 6:1 volume ratio. Residual resist thickness after development was measured by an ellipsometer, a film thickness analyzer, and/or DEKTAK (Sloan), and the possible error of these measurements were within 5%. Ion dose dependence of the residual resist thickness was derived from these results. A 25 μm pitch (5 μm in width) copper mesh stencil mask was used to form patterns in these resists. The typical exposure stage is schematically shown in Fig. 1, where the half shadow, δ, is around 1 μm in the current experimental conditions. Reactive ion etching was carried out to form patterns in SiO_2 through the resist mask (11).

The samples thus prepared were evaporated with gold to a thickness of several tens of nanometers. An SEM was used to observe the patterns, with a magnification between 1,000 and 20,000. The typical electron acceleration energy was 20 keV.

Results and Discussions

AZ1350J (IDER).—AZ1350J is desensitized and can be used as a negative ion beam resist, as shown in Fig. 2. In the figure, hydrogen ion dose dependence of residual resist thickness is depicted. The ion beam exposed regions become insoluble to the developer, where due to the following flood u.v. light exposure, the regions unexposed to ion beam become soluble to the developer. The mechanism of this ion desensitization of photosensitive resist (IDER) is the same as in the case of electron exposure (ELDER). The u.v. sensitive inhibitor, containing N ≡ N bond, is decomposed by the irradiated charged particles (6), and becomes insensitive to the following u.v. flood exposure; hence, negative tone appears due to the novolak resin.

The main exposure mechanism of conventional electron or ion beam resists are either scission of main chain or cross-linking, depending on positive or negative resists, respectively. The sensitivities of conventional resists to a hydrogen ion beam are almost one to two orders of magnitude higher than to an electron beam. This phenomenon is mainly due to the higher interaction of ions than electrons with resists (8).

The appropriate dose range for ELDER is reported to be around 10^{-5} C/cm^2 (6). As shown in Fig. 2, it is in the order of 10^{-6} C/cm^2 for IDER. These results indicate that AZ1350J is also one order of magnitude

* Electrochemical Society Active Member.
Key words: semiconductor, SEM, ion beam lithography, resist.

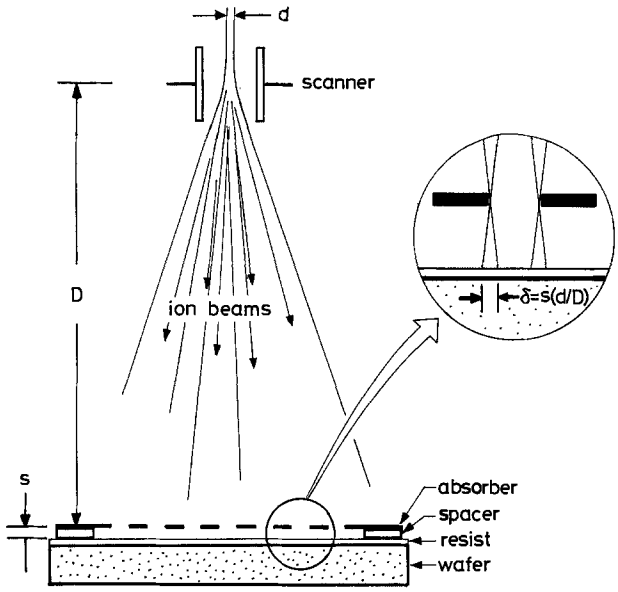

Fig. 1. Schematic representation of a mesh mask pattern replication by hydrogen ion beam using an ion implanter.

more sensitive to an ion beam than to an electron beam. The main exposure mechanism is the decomposition of N ≡ N bond, which would occur through electronic excitation. The calculated electronic and nuclear energy loss of a 180 keV hydrogen ion beam shows that hydrogen ions transfer their energy mainly through electronic energy loss (10). The higher acceleration energy and smaller projected range of an ion beam than to an electron beam contribute to the higher energy transfer to the exposed resist layer. This fact explains the higher sensitivity of AZ1350J to a hydrogen ion beam than to an electron beam.

The refractive index increase of AZ1350J is also shown in Fig. 2 by a broken line. It increases from 1.5 to 1.9 with the increase of hydrogen ion dose. This phenomenon could be partly due to the decomposition of C—H bond by the hydrogen ion beam, and partly due to the decomposition of N ≡ N bond, which is the desensitization mechanism itself.

The thickness reduction of AZ1350J by a 120 keV phosphorus ion beam exposure was within the experimental error up to the dose range of 10^{-4} C/cm², as depicted in Fig. 3. Therefore, the residual resist thickness is almost the same as the applied resist thickness under appropriate exposure conditions. This effect suggests good characteristics of IDER for practical

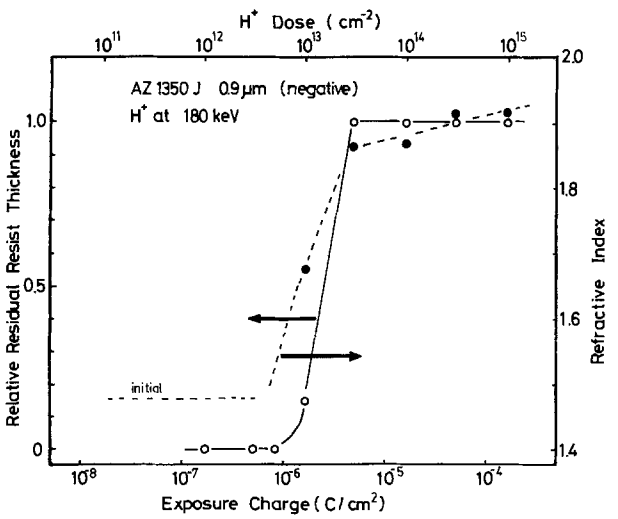

Fig. 2. A 180 keV hydrogen ion beam exposure characteristics of AZ1350J.

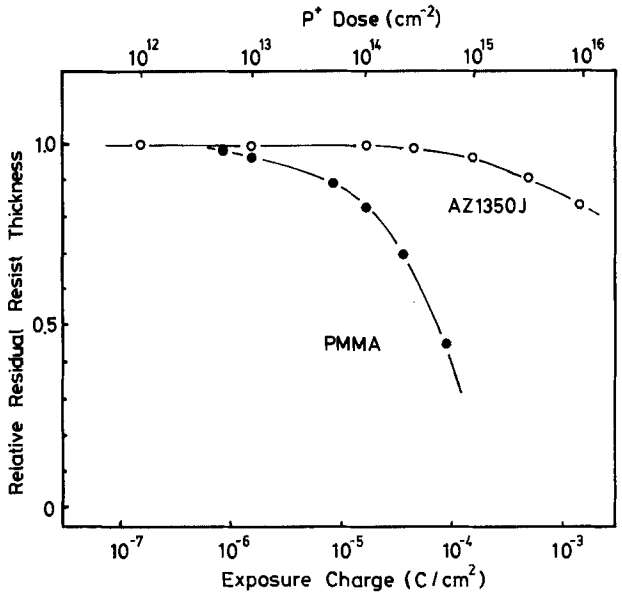

Fig. 3. Thickness reduction of AZ1350J and PMMA by heavy ion dose.

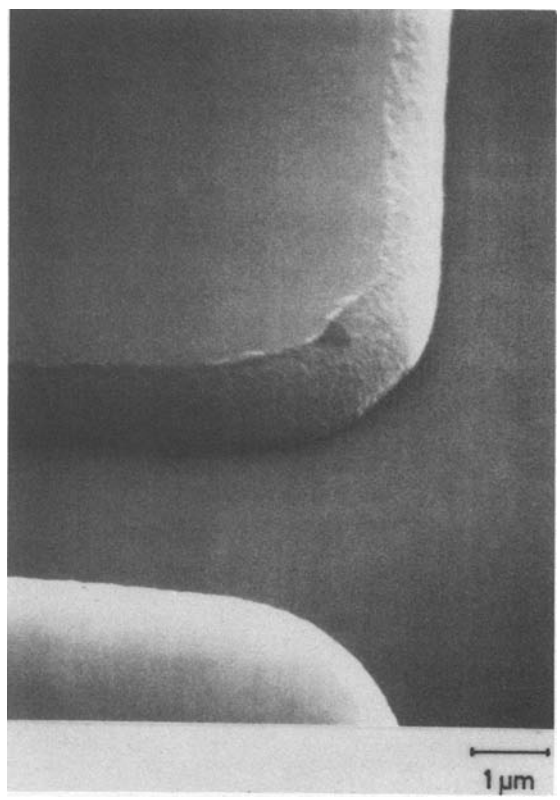

Fig. 4. SEM micrograph of mesh mask patterns replicated on AZ1350J by a 180 keV hydrogen ion beam.

applications, such as ion implantation. In the figure, the ion dose dependence of thickness reduction of PMMA is also shown for a comparison. It clearly indicates that PMMA is an unacceptable resist when exposed to an ion beam.

The mesh patterns replicated on AZ1350J by a 180 keV hydrogen ion beam is shown in Fig. 4, where sharp resist edge profile is clearly shown, despite the 1 μm wide half shadow depicted in Fig. 1. This phenomenon is due to the relatively high contrast factor, γ, of around 2.0, of AZ1350J as shown in Fig. 2.

IPS (iodinated polystyrene).—IPS is a very sensitive negative electron resist with good reactive ion etching resistance. Figure 5 shows a 180 keV hydrogen ion dose

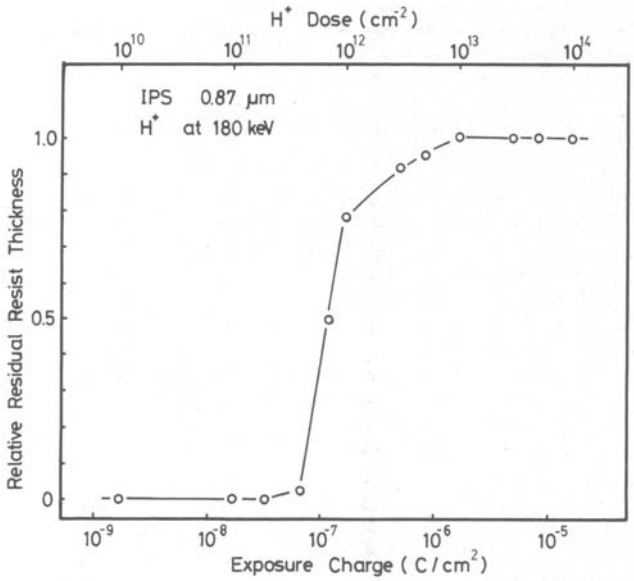

Fig. 5. A 180 keV hydrogen ion beam exposure characteristics of IPS.

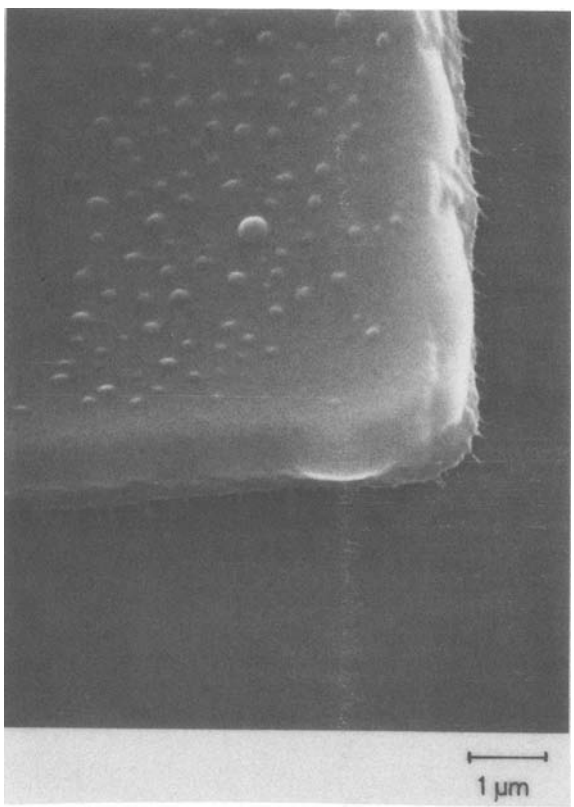

Fig. 6. SEM micrograph of mesh mask patterns replicated on IPS by a 180 keV hydrogen ion beam.

dependence of residual resist thickness after development. The sensitivity of IPS is around 3×10^{-7} C/cm^2 under these experimental conditions, and is also almost one order of magnitude more sensitive than to an electron beam. The contrast factor, γ, is 3.0, which suggests that a steep resist profile is expected. Figure 5 also indicates that a hydrogen ion dose of around 2×10^{-6} C/cm^2 is required to fully expose the whole resist layer. However, since negative electron resists are usually used with a residual resist thickness of around 70-80% of the applied thickness, the low gradient of the relative residual resist thickness between 80-100% does not degrade the resolution, nor increase the appropriate dosage.

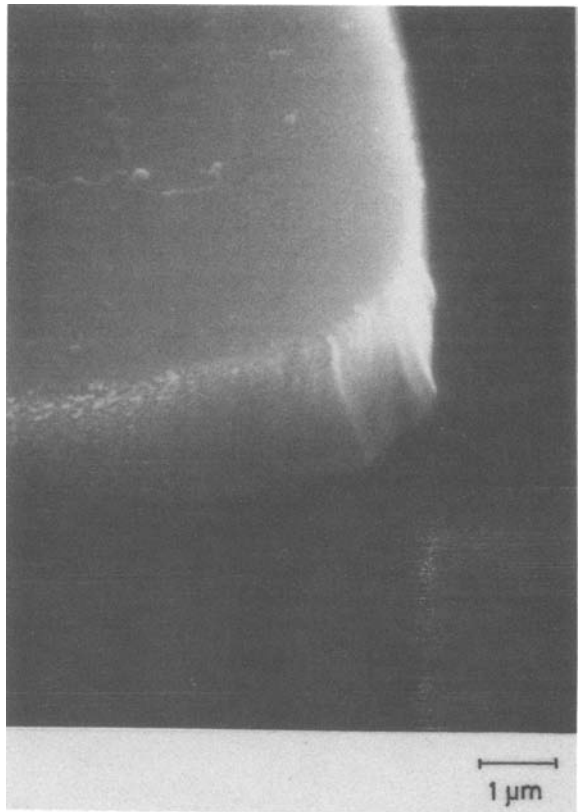

Fig. 7. SEM micrograph of a 0.6 μm thick SiO_2 layer, reactive ion etched through IPS mask.

Figure 6 shows the replicated mesh mask patterns on IPS by a 180 keV hydrogen ion beam. In the figure, the hydrogen ion dose to the sample is 3×10^{-7} C/cm^2. The slope of the resist edge is more than 80 degrees, despite the half shadow of 1 μm as depicted in Fig. 1. The exposure stage shown in Fig. 1 and the ion dose dependence of residual resist thickness shown in Fig. 5 suggest that the width of the half shadow actually obtained in IPS should be around 0.3 μm (1 μm × 1/3), assuming that the hydrogen ion dosage that the resist layer receives is linearly decreased from the fully exposed region to the shadow. Figure 6 shows that the half shadow is around 0.2 μm, and that these assumptions can be applied. This effect shows that the contrast factor plays an important role in forming a pattern with a steep resist profile.

IPS also shows a good reactive ion etch resistance. A typical SEM micrograph is shown in Fig. 7, where a 0.6 μm thick thermally grown silicon dioxide layer was reactive ion etched through the IPS mask. The steep edge profile of the resist is neatly replicated in the oxide layer, which indicates sufficient resistance of IPS to reactive ion etching.

Conclusions

The hydrogen ion beam exposure characteristics of two negative ion beam resists, AZ1350J and IPS, were reported. Dose dependence of these resists indicates high contrast factor, which suggests their capability in fine pattern formation. Combined with their reactive ion etching resistance, it has been shown that these resists can be applied to ion beam lithography as useful negative resists.

Acknowledgments

The authors wish to express their thanks to Drs. T. Tokuyama and M. Migitaka for their continuous encouragements and fruitful discussions. Drs. Y. Kawamoto and H. Shiraishi are acknowledged for valuable discussions on dry etching and on resist characterization, respectively. SEM micrographs taken by Y. Yoneda are gratefully appreciated.

Manuscript submitted Nov. 13, 1981; revised manuscript received Aug. 11, 1982.

Any discussion of this paper will appear in a Discussion Section to be published in the December 1983 JOURNAL. All discussions for the December 1983 Discussion Section should be submitted by Aug. 1, 1983.

Publication costs of this article were assisted by Hitachi, Limited.

REFERENCES

1. G. E. Moor, Paper 1-3 IEEE Int. Electron Device Meeting, Washington, D.C. (Dec. 1975).
2. D. B. Rensch, R. L. Seliger, G. Csanky, R. D. Olney, and H. L. Stover, *J. Vac. Sci. Technol.*, **16**, 1897 (1979).
3. G. Stengl, P. Wolf, R. Kaitna, H. Loschner, and R. Sacher, *ibid.*, **16**, 1883 (1979).
4. L. Csepregi, F. Iberl, and P. Eichinger, *Appl. Phys. Lett.*, **37**, 630 (1980).
5. T. M. Hall, A. Wagner, and L. F. Thompson, *J. Vac. Sci. Technol.*, **16**, 1889 (1979).
6. K. Mochiji, Y. Maruyama, F. Murai, S. Okazaki, Y. Takeda, and S. Asai, *Jpn. J. Appl. Phys. Suppl. 20-1*, 63 (1981).
7. H. Shiraishi, Y. Taniguchi, S. Hirozome, and S. Nonogaki, *Polym. Eng. Sci.*, **20**, 1054 (1980).
8. R. G. Brault and L. J. Miller, *ibid.*, **20**, 1064 (1980).
9. Y. Wada, H. Usui, and M. Ashikawa, *Jpn. J. Appl. Phys.*, **14**, 1351 (1975).
10. L. Karapiperis, I. Adesida, C. A. Lee, and E. D. Wolf, in Proc. Electron, Ion and Photo Sci. Technol., Dallas (1981).
11. Y. Kawamoto, S. Okudara, and Y. Shimomoto, *J. Met. Finish. Soc. Jpn*, **30**, 508 (1979).

Defect Characteristics and Generation Mechanism in a Bird Beak Free Structure by Sidewall Masked Technique

R. C. Y. Fang, K. Y. Chiu,* and J. L. Moll

Integrated Circuit Laboratory, Hewlett-Packard Company, Palo Alto, California 94304

ABSTRACT

The fabrication of the bird beak free device isolated with vertical sidewalls masked with Si_3N_4 film has been investigated. The oxidation condition and combination of the second Si_3N_4 and SiO_2 are studied to investigate the defect mechanism for (100) silicon substrate. The characteristics of dislocations are examined by Secco etching, x-ray topography, transmission electron microscopy, copper decoration, infrared and micrography. Two different mechanisms, responsible for dislocation generation, are identified where dislocations are introduced either by the intrinsic stress of the second Si_3N_4 or due to the mechanical damage at the corners of the island pedestal. Edge dislocations are found close to the island edges and mainly located outside the active device area. The dislocation lines are long and straight with the simple 60 deg type dislocation in <011> direction, on (111) and ($1\bar{1}1$) planes or in <011> direction on ($11\bar{1}$) and ($\bar{1}11$) planes. The unique characteristics of the generated dislocations are described.

VLSI technology has been progressing rapidly in a drive toward higher packing density and better circuit performance. Device isolation is one of the major obstacles for scaling device geometries at or below 1 micron range. Local oxidation of silicon (LOCOS) has been widely used as the isolation technology of silicon integrated circuits, due to its simplicity and compatibility with existing LSI processing techniques (1-2).

Unfortunately, the encroachment inherent in the LOCOS severely limits the scalability of this isolation technology, especially when the device geometries are scaled down to micrometer and submicrometer range. A new isolation technology is needed that can provide the smallest pattern transfer difference between mask and device geometries without the requirement of scaling down the isolation oxide thickness. It is desirable that the new technology be compatible with the existing LSI fabrication techniques and without increasing the number of masking steps.

Recently, several modified local oxidation technologies have been proposed as a potential isolation approach for VLSI circuit fabrication (3-5). A sealed interface local oxidation technique was proposed by using a thin thermal Si_3N_4 film in intimate contact with the silicon surface (3). Sidewall masked isolation techniques, which used a 2nd Si_3N_4 film to protect the etched sidewalls, were also explored (4-5). Although the new techniques could achieve thick field oxide with small and even zero transition region, there are difficulties in controlling the process related defect generations associated with the new bird beak free process. The defects, usually edge dislocations, are likely to cause excessive junction leakage current, device degradation, and reliability problems by providing deep recombination centers, especially by attracting heavy metal impurities. Therefore, it is important to determine and clarify the correlation of this process induced imperfection and the new isolation structures.

This paper reports the defect generation mechanisms associated with the bird beak free process by a sidewall masking technique with a 2nd Si_3N_4 film. Two types of defect generation mechanisms are identified and discussed. One is due to the intrinsic stress of the 2nd Si_3N_4 on the sidewalls of the etched island. The other mechanism responsible for the defect generation is due to the oxide intrusion under the 2nd Si_3N_4 film and the island region. The defects observed are generally long edge dislocations of the simple 60 deg type dislocation. The characteristics of these defects are analyzed by Secco etching, x-ray topography, copper decoration, and infrared micrograph methods.

Experimental Procedures

The samples used in this experiment are P-type (100) oriented, 16-24 Ω-cm Czochralski grown silicon wafers. Initial thermal oxide of 450Å is grown and LPCVD Si_3N_4 of 1000Å is deposited by chemical reaction of SiH_2Cl_2 and NH_3 at 800°C. The sample is then patterned and dry etched. The dry etching is performed in a C_2F_6/He mixture for anisotropic oxide and nitride etching. The etched edge profile is vertical with no loss of the island dimensions. The unmasked silicon substrates are subsequently dry etched to a depth of approximately half the designated oxide thickness where the etched silicon depth is normally 0.3 μm in this work.

* Electrochemical Society Active Member.
Key words: sidewall masking oxidation, birds beak, defect density, LOCOS.

The vertical silicon sidewalls are etched with an anisotropic etching process in CCl_4/C_2F_6 gas mixture. The wafers are then cleaned and the second stress relief oxide (SRO) is grown before the deposition of the second Si_3N_4 film. The thicknesses of the SRO and Si_3N_4 films are in the ranges of 0-450Å and 200-1000Å, respectively. The last step is to remove the second Si_3N_4 in the field region by anisotropic dry etching. The final structure is the island plateau from the silicon etching surrounded by the second Si_3N_4 film and SRO on the sidewalls. The wafers are then cleaned and oxidized locally for different thicknesses at temperatures from 900° to 1100°C in steam. The total thermal history of all samples are: initial oxidation at 900°C, field oxidation at 900°-1100°C, gate oxidation at 900°C, source and drain oxidation and annealing at 900°C, LPCVD oxide deposition and final annealing at 900°C with fast and slow cool. Figure 1(a) shows an example of the oxide edge profile from the sidewall masking technique with a thick second Si_3N_4 film of 1000Å. The sidewall nitride film is not removed in this SEM picture. The grown oxide is seen to have small lateral growth under the thick nitride film. On the other hand, oxide grows and extends into the island region if a thin nitride film is used on the silicon sidewalls. An example is shown in Fig. 1(b) where the second nitride thickness is 220Å. After removing all the films the oxidation induced defects are investigated by Secco etching (6). The defect, shown as an etch pit, can be observed easily by means of an optical microscope and the defect density can be counted. The techniques of copper decorating, inspection by infrared microscope, TEM (transmission electron microscopy), and x-ray topography are also used to investigate the characteristics of the defect generations in the studied structure (7-8).

Characteristics of Defects

The defects generated from the sidewall masking technique are studied for different combinations of second Si_3N_4 and SRO at various oxidation temperatures. The observed defects are mainly edge dislocations which originate from the island edges and terminate at the same edges. The detailed shapes of these dislocation lines will be discussed later. The correlations of the observed defect density and the corresponding sidewall structure are first shown in Table I. The general trend is that more defects are observed for wafers with a thicker second SRO and a thinner second Si_3N_4 film. The best results are obtained from wafers with a thick Si_3N_4 film and thin or even zero SRO thickness. These results cannot be simply explained due to the stress of the Si_3N_4 film on the sidewalls of the island edges.

Two different mechanisms responsible for the defect generation with the sidewall masked wafers have been identified. The first mechanism is due to the tensile stress of the thick Si_3N_4 film on silicon sidewalls. Although the subject of Si_3N_4 stress and defect generation is not new, there are unique features of the defect characteristics for the studied structures. The second mechanism is due to the silicon mechanical damage from the oxide intrusion under the Si_3N_4 masked sidewalls.

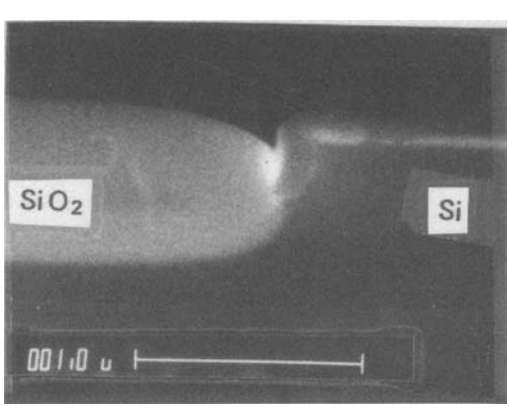

Fig. 1(a). Cross section of the oxide edge profile with 0.3 μm silicon etched depth and 1000Å of second Si_3N_4 and 300Å of SRO.

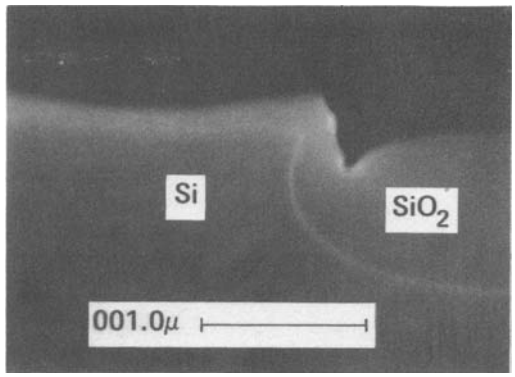

Fig. 1(b). Cross section of the oxide edge profile with 0.3 μm silicon etched depth and 220Å of second Si_3N_4 film.

Generation of dislocations due to the tensile stress of the thick second Si_3N_4 film.—It is well known that thick Si_3N_4 film directly on silicon substrate, with or without a thin SRO, can produce stress in the substrate and generate dislocations along the island edges (9). When a second Si_3N_4 film is used to protect the island sidewall, the thickness of the second nitride in the direction perpendicular to substrate is actually very thick and is equal to the summation of the first Si_3N_4 film thickness, the first SRO thickness, and the etched silicon depth. Therefore, it forms a rigid film in that direction if the second Si_3N_4 is fairly thick, such as 1000Å or thicker. The stress gradient is maximum at both ends of the long Si_3N_4 film. This is similar to the stress in a conventional structure with thick Si_3N_4 on silicon where the maximum stress gradient is at the nitride boundaries. The stress gradient is relatively smaller in the direction parallel to the substrate for the second Si_3N_4 film thinner than 1000Å. It could be expected that the dislocations will be generated mainly at the corners of the patterned island, just like dislocations are generated at the island edges masked by a thick Si_3N_4 film without SRO or with a thin SRO in a conventional local oxidation process.

Figure 2(a) shows the observed etch pits in a contact chain test pattern with dimensions of 10 μm by 30 μm. The squares are islands with two circular contact holes on each island. Most of the etch pits are at the corners of the islands. These dislocation lines are generally on the longer side of the island, emerging out at both ends at a short distance away from the island edges. The detail features of the dislocation lines can be seen from the TEM picture of Fig. 2(b). The sample has been etched 1 min in Secco etchant which removes approximately 1.2 μm thick of silicon. In this picture, the dark areas are islands and the etch pits are shown as the white areas. Dislocation lines are seen parallel to the island edge in <011> direction. Since electrons can

Table I. Relative defect densities in a sidewall masked island edge for various thickness combinations of SRO and the second Si_3N_4 films at different oxidation temperatures. The notations of S, M, and L represent small, medium, and large quantities in the etch pit counts.

Wafer No.	SRO-II (Å)	Si_3N_4-II (Å)	Temp (°C)	Relative defect density
1	0	500	925	M
2	0	1000	925	S
3	150	250	950	L
4	150	250	1000	L
5	150	450	1000	L
6	450	750	1100	L
7	450	1000	1100	M

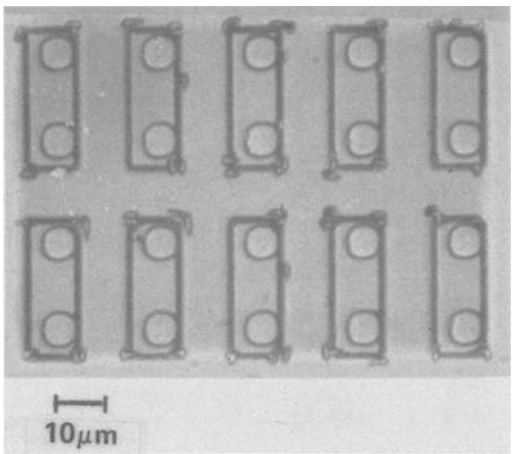

Fig. 2(a). Appearance of dislocation pits of samples with 1000Å of second Si_3N_4 film and no SRO. The sample is oxidized at 925°C.

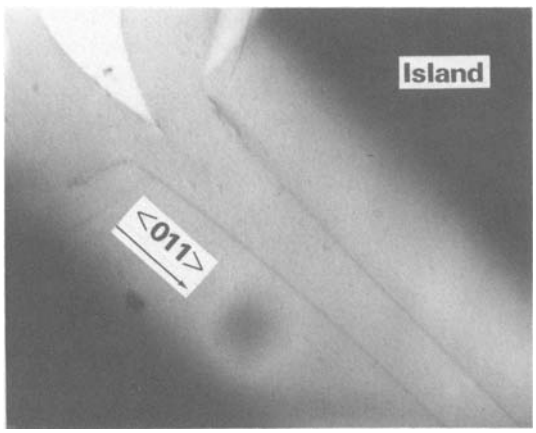

Fig. 2(b). Transmission electron micrograph of the dislocation lines in the silicon substrate having a thick second Si_3N_4 film of 1000Å. The sample was etched in Secco etchant for 1 min before the sample preparation for TEM measurement.

penetrate no more than 0.5 μm at 125 keV in the TEM measurement, the depth of the generated dislocations are less than 2 μm from the silicon surface. We also observed that no dislocations could be found in smaller patterns with island length less than 6 μm. This suggests that the thick sheet of the second Si_3N_4 films on the sidewalls should be relatively long in order to exert enough stress to form dislocations in the silicon substrate. This is consistent to the findings that strains are higher at the long edges of islands than those of the shorter edges and dislocations are more likely to form at these long edges (10). Since these dislocation lines generally locate outside the active device regions, the junction leakage current of a large diode with this type of dislocation defect is found comparable to that of the standard local oxidation technique. However, the diodes tend to degrade much faster and become a reliability problem. The electrical properties of the junction diode are discussed later.

It is also well known that Si_3N_4 stress to the silicon substrate can be reduced by inserting a thin SRO between Si_3N_4 and silicon substrate. The stress is reduced by the viscoelastic behavior of SRO (11, 12). Empirical rule indicates that a sufficiently thick SRO can be used to minimize the probability of dislocation generations. For the sidewall masked structure, Table I shows that greater dislocation density is observed for structures with thicker SRO thickness in general. This cannot be simply explained due to the intrinsic stress of Si_3N_4 film on the sidewalls. On the other hand, it can be explained by the mechanical damage in the silicon substrate from the oxide volume expansion and intrusion under the island regions.

Generation of dislocations due to the oxide volume expansion and intrusion under the island regions.—A schematic diagram of the studied sidewall masking technique is shown in Fig. 3. The strains associated with the overhang of the silicon island from the oxide intrusion can be estimated under the following assumptions:

1. No oxide viscous-flow occurs for the grown oxide in the field regions. This is true at oxidation temperatures of 965°C or less (12).
2. The intruded oxide under the island can expand only upward instead of sideways or downward, since the substrate is very thick and rigid and the island width is much wider than the etched silicon depth. The strains in the silicon overhang of thickness t can be calculated from the following equation

$$\text{Strain} = \frac{y' - y}{t} = 0.532\,\frac{y'}{t}$$

where t is the etched silicon depth, y' is the oxide thickness in the vertical direction under the island area, and y is the consumed silicon in growing y' thick of oxide. y' is 60/28 times y according to the difference in the molecular weight of SiO_2 and Si. It is straightforward to estimate the oxide thickness y' for the stress to exceed the yield stress of the silicon crystal in the island edges. Assuming the yield strain of silicon is 1% and the etched silicon step height is 0.3 μm, y' is equal to 507A.

We have observed good correlations between the thickness of the intruded oxide and the etch pit density for the sidewall masked structures with thin Si_3N_4 film. This is shown in Fig. 4, where the etch pit density and the intruded oxide thickness are shown as functions of the field oxide thickness for sidewalls masked with SRO and Si_3N_4 of 150 and 220Å, respectively. Here the encroached oxide thickness is defined as the depth of the intruded oxide in the lateral direction from the second SRO edge. The quantitative values are obtained from the SEM measurements of the oxide edge profile.

From the previous analysis, it is expected that defect generation is inevitable as long as there is intruded oxide under the island region. The general trend is that more dislocations are observed for wafers with a thicker field oxide or with deeper intruded oxide thickness. This characteristic is contrary to that of the conventional local oxidation, where it was reported that the generated defect density in silicon does not depend on the oxidation time for more than 20 min (13).

The defect characteristics are quite unique in the sidewall masked structure with defect generation due to the oxide intrusion. Figure 5 shows an example of such structure after Secco etching. The dislocation etch pits can be observed over the entire island edges and also in the extended areas beyond the island edge in

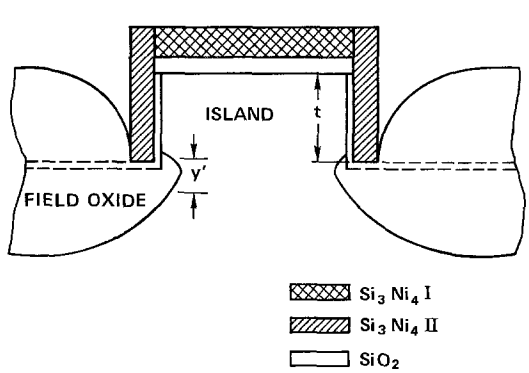

Fig. 3. A schematic illustration of the oxide intrusion under the islands for samples with a thick SRO and a thin second Si_3N_4.

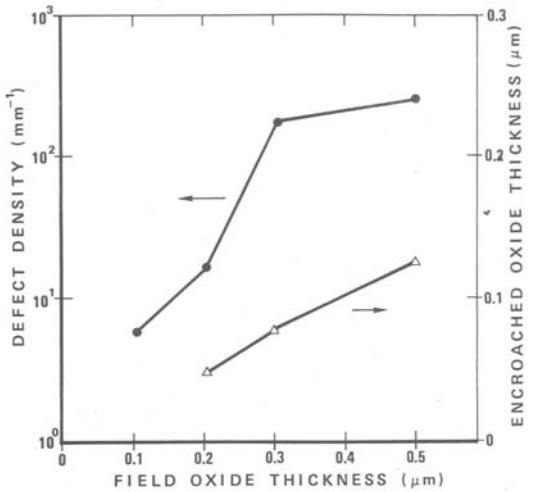

Fig. 4. Dislocation pit density and the intruded oxide thickness under the islands vs. the field oxide thickness. The samples have second Si_3N_4 and SRO of 220 and 150Å, respectively, and are oxidized at 900°C.

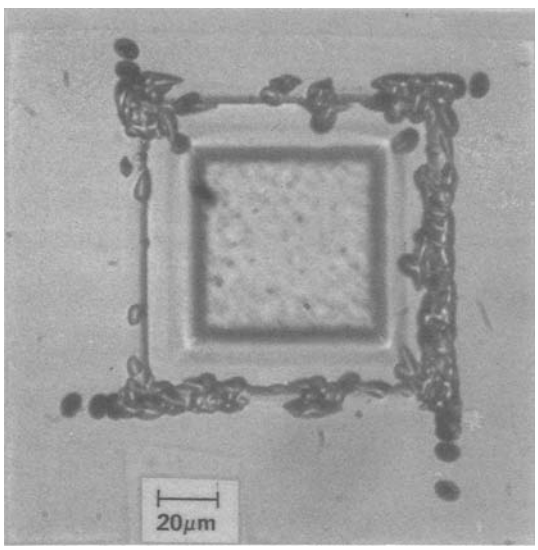

Fig. 5. Optical micrograph of defect pattern revealed by Secco etching for samples with 220Å of second Si_3N_4 and no SRO. The samples are oxidized at 900°C to a thickness of 0.3 μm.

the directions of <011> or <01$\bar{1}$>. The long dislocation lines are randomly distributed at the island corners. Some island corners do not have the extended dislocation pits, while some have the dislocation pits in both directions. It is seen that dislocation pits of a sidewall masked structure locate mainly outside of the island region. This is also contrary to the defect pattern of the conventional local oxidation technique, where dislocation pits are more uniformly distributed on both sides of the island region (13). The effect of this particular defect characteristic on the junction leakage current is discussed in the following section.

Nature of Stress and Dislocation

Figure 5 indicates that the etch pits are irregularly distributed along <011> and <01$\bar{1}$> directions. A cross-sectional view of the Secco etched wafer shows that the dislocation lines are the <01$\bar{1}$>, 60 deg type dislocations. The dislocation lines lie on the (111) or ($1\bar{1}\bar{1}$) planes and originate from the island edges as shown by the merged point of (111) and ($1\bar{1}\bar{1}$) in Fig. 6. A similar cross section, parallel to the <01$\bar{1}$> direction, reveals the dislocation lines in <011> direction and on (11$\bar{1}$) and ($1\bar{1}$1) planes. These dislocation lines

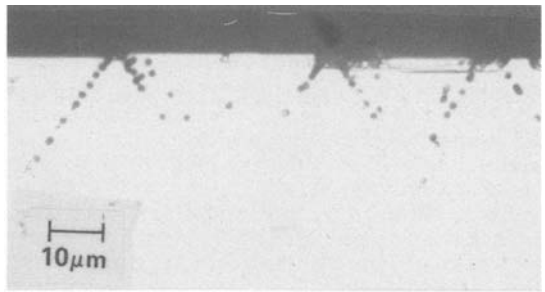

Fig. 6. Cross-sectional view of the dislocation pits. The dislocations lie on the (111) and ($1\bar{1}\bar{1}$) planes and originate from the island edge.

can be as deep as 150 μm from the wafer surface, but seldom from the top surface to the substrate back surface.

These long dislocations can also be revealed by copper decoration and inspected in an infrared microscope. The substrate back surface is coated with copper nitride and annealed at 950°C for 20 min in an argon ambient. The samples are then rapidly cooled to room temperature to produce copper precipitation along the dislocation lines. Figure 7 shows an infrared micrograph of copper decorated dislocations on the die scribe lines. The dislocations generally start from some points on the island edge and extend from surface to surface in <011> or <01$\bar{1}$> direction. Long dislocation lines can emerge to the surface beyond the island region and form a straight line of etch pits such as shown in Fig. 5.

Similar characteristics of the dislocations can be seen from the transmission x-ray topography picture shown in Fig. 8 (8). The dislocations are shown as dark lines along the die scribe lines. The dislocation source appears to be irregular on the island edges. A structural representation of the dislocations in the sidewall

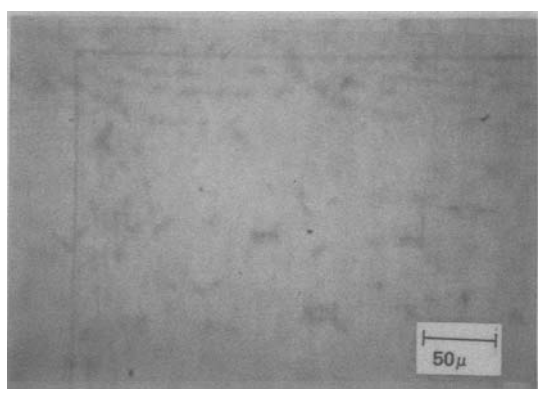

Fig. 7. Infrared photomicrograph of copper decorated dislocation lines along the die scribe line. The dislocation lines revealed from copper precipitation are in the <011> direction.

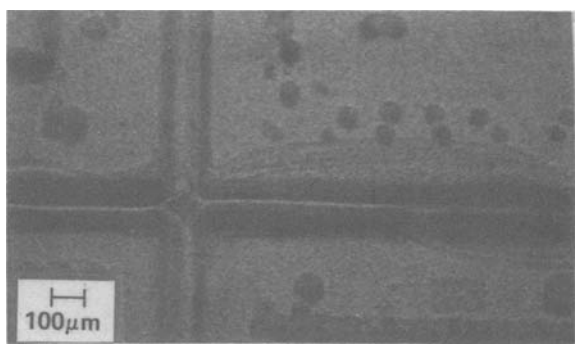

Fig. 8. X-ray topograph of dislocation lines along the die scribe line.

masked structure is shown in Fig. 9. Dislocations originate from some points on the island edge, presumably at the corners of the etched island plateau due to the oxide intrusion, lying on either (111) or ($1\bar{1}\bar{1}$) plane. The dislocation line generally extends from one corner of the island to another for a small island area, and it can extend several millimeters long for a large island or on the scribe lines.

Figure 10 shows the schematic diagram of the sidewall masked structure with an Si_3N_4 film and the components of the compressive stresses associated with the silicon substrate. The horizontal and vertical components of the compressive stresses in the substrate are mainly due to the tensile stress of the thick Si_3N_4 film on the island sidewalls. However, any oxide intrusion under the island region contributes far more compressive stress than that from the intrinsic stress of the Si_3N_4 film on the sidewalls, especially the vertical component of the stress in the over-hung island foot.

It is believed that the vertical stress is responsible for the dislocation generation on the island edges when a thin nitride film is used for masking the silicon sidewalls. The evidence is based on the observation of the similarity of the defect densities among islands with different areas and side lengths. For sidewalls masked by a thin Si_3N_4 film of 300Å or less or a thick Si_3N_4 with thick SRO, the stress from the intrinsic stress of the Si_3N_4 film is relatively small. On the other hand, the vertical component of the compressive stress, due to the oxide intrusion at the foot of the island, is a function of the oxide thickness and the etched silicon depth, not the function of the island size. The large compressive stress due to the oxide intrusion is generally much higher than the silicon yield stress at lower oxidation temperature. Increasing the oxidation temperature can reduce the silicon mechanical damage to some degree through the oxide viscous flow. However, we have observed that the compressive stress in the silicon substrate is still higher than the silicon yield stress at a temperature up to 1100°C. In the case of thick nitride film on sidewalls, the lateral oxide growth is completely suppressed such as shown in Fig. 1(a). The defect generation is mainly due to the nitride stress instead of the vertical compressive stress from the lateral oxide intrusion under the island regions.

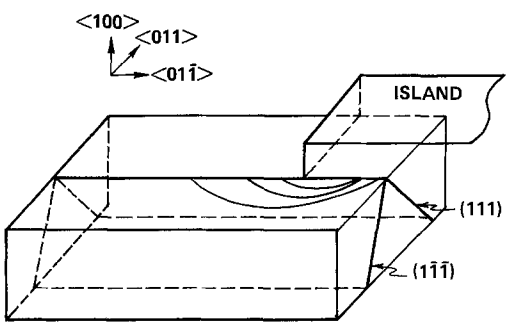

Fig. 9. Schematic illustration of the preferred slip planes of (111) and ($1\bar{1}\bar{1}$) planes for dislocation generation in a sidewall masked structure.

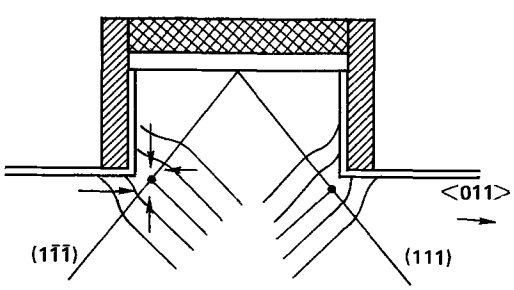

Fig. 10. A schematic illustration of the dislocation configuration and the compressive component stresses in the substrate.

Effects of the Oxidation Temperature on the Defect Generation

It was discovered that thermally grown SiO_2 has a viscous flow at a temperature of 960°C and higher (12). Severe mechanical damage to the silicon substrate can be expected to be reduced at a higher oxidation temperature through the viscous flow of SRO. However, the stress yield strength of the silicon substrate is also reduced at higher temperature (14). Experiments show that the stress in the silicon substrate cannot be completely relieved at a temperature up to 1100°C, and there are comparable defect densities observed for the studied structure at oxidation temperature from 900° to 1100°C. At oxidation temperatures higher than 1050°C, defects consist not only of edge dislocations but occasionally oxidation induced stacking faults. Also, the higher process temperatures are not compatible with the standard integrated circuit fabrication process.

Electrical Measurements

The junction leakage current of a large diode is measured in order to evaluate the new process for the device and circuit fabrication. A flat diode with a size of 500 μm by 500 μm and a finger diode with the same total flat areas, but different sidewall areas, are used to separate the components of the leakage current in the plane and sidewall junction. The results are shown in Fig. 11, where the leakage current of the sidewall masked structure is seen comparable to that of the conventional local oxidation technique, if a slow cooling rate of 0.2°C/min is performed during the last thermal process.

Without using the slow cooling process, the distribution of the diode leakage current becomes highly irregular among the diodes and the leakage currents are generally much higher than wafers annealed with the slow cooling process. As shown in Fig. 12 is the comparison of the leakage current histogram of two samples with the same structure but with or without the slow cooling process. The effect of the cooling rate on the junction leakage current can be explained by the fact that crystal defects, such as dislocations, are

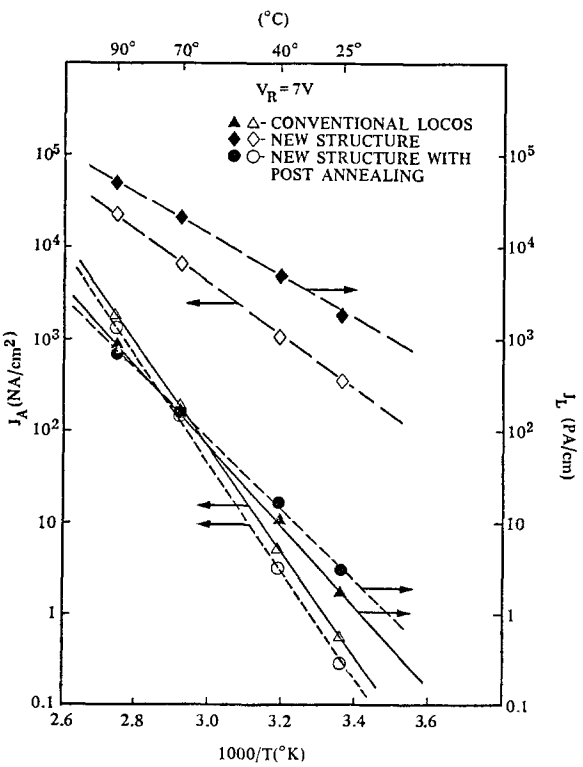

Fig. 11. Leakage current density of flat (JA) and sidewall (JL) junctions for conventional diode and sidewall masked diode with or without slow-cool annealing.

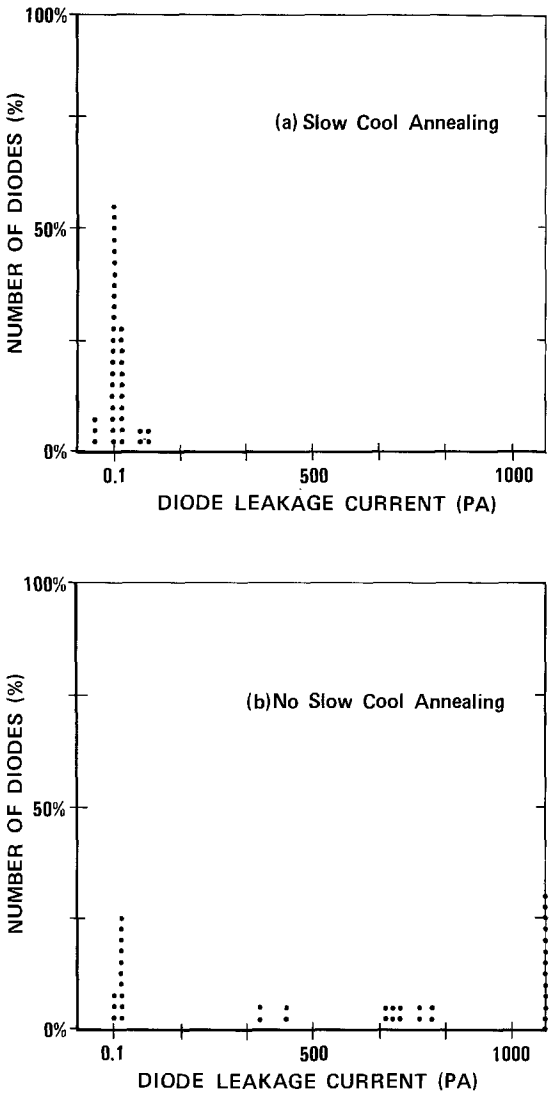

Fig. 12. Histograms of the distribution of the large finger diode leakage current with or without using the slow-cool process at 5V and at room temperature.

favorable for impurity precipitation at a fast cooling rate. On the other hand, the impurity precipitation in these defect sites are greatly reduced with a slow cooling process. That is, both the dislocations and the metal precipitation in these defect sites are responsible for the excessive leakage current and the nonuniform distribution observed for large diodes with the sidewall masking technique.

An interesting experiment also shows that the interactions of impurities and dislocations are reversible with respect to the cooling rate in the final annealing operation. Two groups of wafers are processed with slow and fast-cool annealing. The first group of wafers is annealed at 900°C and cooled down to 700°C with a slow cooling rate of 0.2°C/min. The second group of wafers is annealed at 900°C and pulled out the quartz tube at a regular pulling rate of 10 cm/min. After testing the diode leakage current, the metal electrodes are stripped and wafers are cleaned in aqua regia in order to reduce the metal contamination from the metal stripping operation. The wafers are then annealed with a reversed cooling process and repatterned with Al-Si(2%). The junction leakage current is measured and compared to the original values. The results show that the magnitudes and the spreads in the current distributions are reversible with respect to the cooling rate of the annealing process. The leakage currents are two to three orders larger after a second fast-cool annealing and with a wider spread in the current distribution among the tested diodes. This comparison is shown in Fig. 12(a) and 13(a). On the contrary, the leakage current is greatly reduced with a second slow-cool following the initial fast-cool annealing. This is shown in Fig. 12(b) and 13(b). In this experiment a third group of defect-free wafers by the standard local oxidation method is also processed and served as the controlled wafers with both fast-cool annealings. The tested results show little change in the leakage current, which indicates no metal contaminations from the metal stripping operation. The experiment of T-B (temperature bias) stress also indicates one to two orders higher junction degradation for the sidewall masked structure of having edge dislocations, as compared to the conventional local oxidation structures.

Conclusions

The generation mechanisms of dislocations in the sidewall masked silicon substrate have been investigated. Defect characterizations are performed for structures with different Si_3N_4 and SRO combinations at various oxidation conditions. Based on these observations several conclusions can be made.

1. For sidewalls consisting of thick Si_3N_4 film, with or without thin SRO, the defect generation is due to the intrinsic stress of the thick Si_3N_4. For sidewalls consisting of a thin Si_3N_4 film with a thick SRO, the defect generation is due to the mechanical damage to the silicon substrate from the oxide intrusion at the foot of the island pedestal.

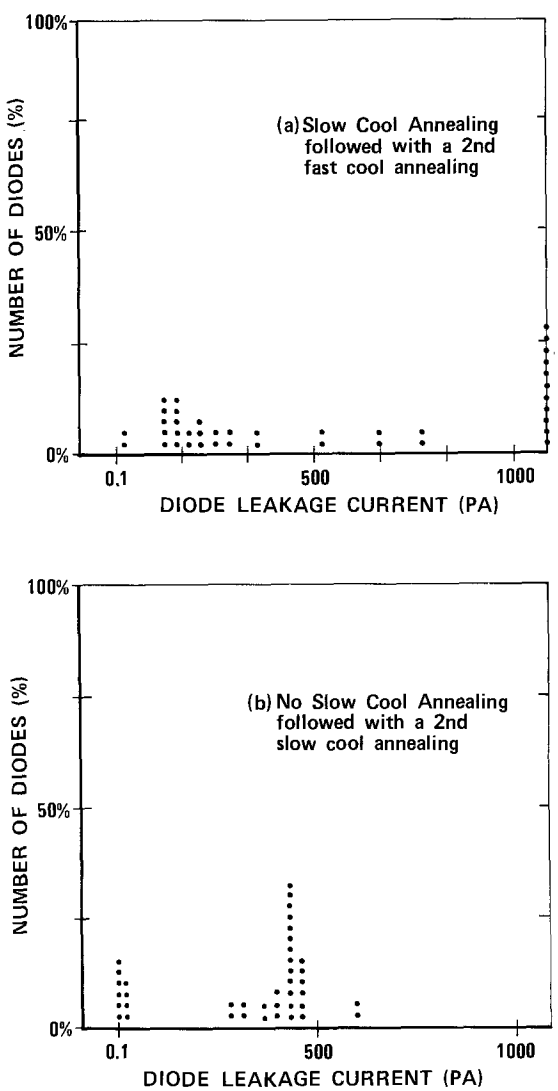

Fig. 13. Histograms of the current distributions of the large finger diodes annealed with a reversed cooling process from that of Fig. 12.

2. Dislocations observed in the silicon substrate are of the 60 deg type, generated along the <011> direction on the (11$\bar{1}$) and (1$\bar{1}$1) slip planes and <01$\bar{1}$> direction on the (111) and ($\bar{1}\bar{1}\bar{1}$) planes for a (100) substrate surface.

3. Dislocations that are the result of nitride stress are normally long and straight and extend from corner to corner in the islands. The dislocations are also shallow in the silicon substrate. The etch pits generally locate a few micrometers from the island edges. The junction leakage current in the sidewall masked structure is found comparable to that of the conventional local oxidation method, when a slow cooling process is used in the final thermal step. The effect of slow cooling is conjectured to be associated with the reduced metal precipitation around the dislocations in the vicinity of the device junction regions.

4. Dislocations that are caused by oxidation encroachment under the silicon island randomly locate near the island edge. The dislocations are also deep in the silicon substrate and can be found a few hundred micrometers away from the island edges. The electrical behavior is similar to the dislocations caused by nitride stress.

5. Due to the strong stress in the corner region of the island pedestals, the stress in the silicon substrate cannot be completely relieved through the viscous flow property of SRO under the second Si_3N_4 film at temperatures up to 1100°C for the studied structures with several combinations of SRO and Si_3N_4 thicknesses. However, defect-free structures can still be obtained for small island patterns. In order to achieve both defect and bird beak free isolation technique, alterations in structural details and processing conditions are required (15).

Acknowledgments

The authors gratefully acknowledge M. Scott for taking the x-ray picture, T. Cass for taking the TEM picture, and the I.C. Process Laboratory for the process support.

Manuscript submitted March 30, 1982; revised manuscript received July 23, 1982.

Any discussion of this paper will appear in a Discussion Section to be published in the December 1983 JOURNAL. All discussions for the December 1983 Discussion Section should be submitted by Aug. 1, 1983.

Publication costs of this article were assisted by The Hewlett Packard Company.

REFERENCES

1. J. A. Appels and M. M. Paffen, *Philips Res. Rep.*, **26**,157 (1971).
2. E. Bassous, H. N. Yu, and V. Maniscalco, *This Journal*, **123**, 1729 (1976).
3. J. Hui, T. Y. Chiu, S. Wong, and W. G. Oldham, *Electron. Lett.*, **EDL-2**, 244 (1981).
4. D. Kahng, T. A. Shankoff, T. T. Sheng, and S. E. Hazko, *This Journal*, **127**, 2468 (1980).
5. K. Y. Chiu, J. Moll, and J. Manoliu, *IEEE Trans. Electron. Devices*, **ED-29**, 536 (1982).
6. F. Secco d Aragona, *This Journal*, **119**, 948 (1972).
7. W. C. Dash, *J. Appl. Phys.*, **27**, 1193 (1956).
8. A. R. Lang, *ibid.*, **30**, 1748 (1959).
9. S. Isomae, M. Nanba, Y. Tamaki, and M. Maki, *Appl. Phys. Lett.*, **30**, 564 (1977).
10. G. Franz and W. Hartmann, *Appl. Phys.*, **23**, 107 (1980).
11. S. Isomae, Y. Tamaki, A. Yajima, M. Nanba, and M. Maki, *This Journal*, **126**, 1014 (1979).
12. E. P. EerNisse, *Appl. Phys. Lett.*, **30**, 290 (1977).
13. K. Shibata and K. Taniguchi, *This Journal*, **127**, 1383 (1980).
14. T. Suzuki and H. Kojima, *Acta Metall.*, **14**, 913 (1966).
15. K. Y. Chiu, R. Fang, J. Lin, and J. L. Moll, Presented at a 1982 symposium on VLSI Technology, Kanagawa, Japan.

Contamination-Free High Temperature Treatment of Silicon or Other Materials

Paul F. Schmidt

Bell Laboratories, Allentown, Pennsylvania 18103

ABSTRACT

It has been shown that the contamination picked up during high temperature treatments of silicon stems from the diffusion of impurities from the outside of the quartz furnace tube and into the material being heat-treated. This contamination can be prevented by placing the quartz tube into a protective atmosphere of HCl in dry oxygen, *i.e.*, by passing a dry O_2-HCl mixture through the annulus of a double-walled quartz tube. Silicon wafers oxidized in such a tube at 1000°C were found to be uncontaminated at the sensitivity afforded by neutron activation analysis. It is suggested that many transition group metals diffuse preferentially along incipient grain boundaries in vitreous quartz at high temperatures, the grain boundaries in turn stemming from the devitrifying action of sodium vapors in the furnace. The double-wall tube arrangement thus not only prevents transition group metals from diffusing into and through the quartz of the inner wall, but also prevents sodium from initiating the devitrification process thus rendering the quartz more opaque to transition group metal diffusion.

The deleterious effects of contamination of silicon devices with transition group metals or with alkali are well known. Minority carrier lifetimes are degraded through recombination-regeneration processes, junction leakage is increased by metal precipitates as a result of transition group metal contamination, and flatband voltage shifts are caused by the presence of alkalis. The starting silicon substrates, if properly prepared, can be essentially free of contamination (1, 2). Most of the contamination introduced during device processing is due to high temperature furnace treatments, with the level of contamination increasing strongly with temperature (1).

The normal procedure in the semiconductor industry is to getter the contaminants toward the end of processing by a variety of gettering procedures (phosphorus diffusions, backsurface damage by laser irradiation, sandblasting, etc.). Special preprocess treatments have also been introduced to lessen the sensitivity of the silicon front surface layers by reducing or preventing the formation of oxidation-induced stacking faults, *e.g.* by formation of an oxygen denuded zone (3, 4). Gettering treatments, however, are rarely 100% effective unless applied to very high quality silicon, *i.e.*, epitaxial silicon or oxygen de-

nuded zones; impurities already precipitated at crystal defects are hard to getter.

The prevention of cantamination would thus be preferable to a reliance on gettering only. A well-known means of preventing contamination during oxidation in dry oxygen is to add a low percentage of HCl (or other chlorine-bearing organic species) to the oxygen. Transition group metal chlorides are mostly quite volatile at high temperatures;[1] thus the chlorine present in the gas phase combines with the transition or alkali metals, diffusing through the walls of the quartz furnace tube before they can reach and diffuse into the silicon wafers being oxidized. Unfortunately, this treatment is not applicable to the important case of oxidations in steam, or when bare silicon surfaces are exposed.

The protection afforded by chlorine at high temperatures is not unique to silicon surfaces, but applies equally well to SiO_2 (in fact, silicon wafers must have an SiO_2 film in order not to be attacked by the chlorine). A preventive method not limited to any particular process step thus consists in the use of a double-walled quartz tube with a small percentage of HCl (or other chlorine-bearing species) in oxygen, flowing only in the annulus between the inner and outer tubes, as shown schematically in Fig. 1. The use of a double-walled quartz tube with high purity nitrogen flowing in the annulus only was already employed by Irene (5) to prevent penetration of moisture through the quartz in oxidation studies of silicon in extremely dry O_2. In the present case, the chlorine in the jacket of the tube prevents alkali or transition group metals from diffusing into the wall of the inner quartz tube; thus any material placed into the inner tube is protected against contamination (except with hydrogen or possibly chlorine), without any limitation on the kind of process step that may be carried out in the inner tube. The impurities contained in high purity quartz are present at such low concentrations that the quartz itself cannot serve as a source of contamination for any length of time.

Table I shows contamination picked up during steam oxidation in a conventional single-wall quartz furnace tube (case A), and during steam oxidation in a double-wall quartz furnace tube, with a 1% HCl in dry O_2 mixture flowing in the annulus only at a rate of 1 liter/min (case B). The amounts of impurities, copper and zinc, present on the starting substrates (all wafers were cut from the same ingot) have been subtracted in both cases as indicated there, to show the contamination due to the oxidation step. The single-wall tube was operated in an exceptionally clean ambient surrounding the tube, the double-wall tube was operated in a normal production ambient. Contamination is absent in wafers processed in the double-walled tube, but quite significant when the single-wall tube is used. The difference between the two cases would have increased still more, if the experiment had not been limited to a single oxidation but had been carried out for a series of process steps. It is also important to remember that transition group metals in heat-treated silicon wafers are invariably strongly enriched in the surface-near layers; thus the moderate concentrations in atoms/wafer given here translate into much higher concentrations if expressed in atoms/cm^3 of the surface-near layers.

[1] An exception are the chlorides of gold or the platinum group metals; these, however, are not normally contaminants picked up during furnace treatments.

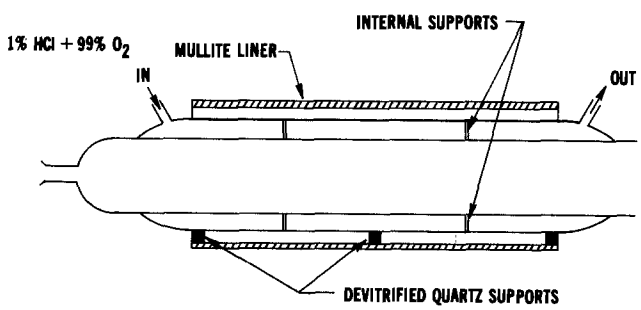

Fig. 1. Sketch of a double-walled quartz furnace tube with HCl-O_2 mixture flowing in the space between inner and outer walls. The tube is shown resting on devitrified quartz supports which do not bond to vitreous quartz.

Table I. Contamination introduced into silicon wafers by steam oxidation at 1000°C for 1 hour. Concentration in atoms/3"ϕ silicon wafer.

	A Conventional single-wall quartz furnace tube	B Double-wall quartz furnace tube with 1% HCl-99% O_2 in annulus only
Cu	3.2E14	None detected
Fe	3.3E14	None detected
Co	2.1E12	None detected
Ni	3.0E14	None detected
Cr	7.4E13	None detected
Zn	3.0E13	None detected
Zr	4.6E14	None detected
Ta	1.4E14	None detected
Na	5.0E13	None detected

The wafers used in this run had a significant copper contamination of 5.6E13/wafer and a small zinc contamination of 8.3E12. Copper was a surface contamination only, zinc was a bulk contaminant. The background concentrations quoted for Cu and Zn have been subtracted in both columns.

The detection limits for the isotopes listed, under the given experimental conditions were: Cu, 4.5E12 atoms/wafer; Fe, 8.0E13 atoms/wafer; Co, 5.0E10 atoms/wafer; Ni, 4.8E13 atoms/wafer; Cr, 1.7E12 atoms/wafer; Zn, 7.7E11 atoms/wafer; Zr, 1.4E14 atoms/wafer; and Ta, 5.2E10 atoms/wafer.

Sodium (6) and copper (7) are known to be very fast diffusers in, and to cause devitrification of, vitreous quartz (8). It was shown in the two papers of Ref. (8) that the crystal modification of SiO_2 resulting depends on the type of alkali ion present, as well as on the temperature at which devitrification occurs. Thus lithium at 850°C will cause quartz to form, but at 950°C, cristobalite, while sodium at 950°C produces both cristobalite and tridymite, potassium only tridymite.

Crystallization has also been observed for SiO_2 films on silicon, especially for steam-grown SiO_2 films (9, 10), in which case the crystalline silicon substrate apparently acts as the nucleation site, since crystallization has always been shown to begin at the Si/SiO_2 interface. The initially puzzling fact that various observers reported different modifications of crystalline SiO_2 as present in the films is readily explainable along the lines of Ref. (8). All of the work on the Si/SiO_2 system was done by glancing angle electron diffraction, and the films showed only incipient crystallization, with amorphous material still present.

Figure 2 shows concentrations of various transition group metals in silicon wafers having undergone a 1 hr oxidation in a relatively new single-wall quartz furnace tube. The existing temperature profile in the furnace tube was utilized for this experiment, *i.e.*, wafers were placed at positions of slightly different temperatures in a furnace whose temperature setting had not been changed for a period of about two months. In other words, the positions of higher temperature had been at the higher temperature for two months, as had been the positions of lower temperature. The ordinate of the graph is a sliding logarithmic scale in order to display concentrations different by several orders of magnitude on the same graph. The highest concentration for each line is shown in the inset next to the impurity corresponding to the various symbols. The fully unexpected result of this experiment was an increase in concentration by two orders of magnitude

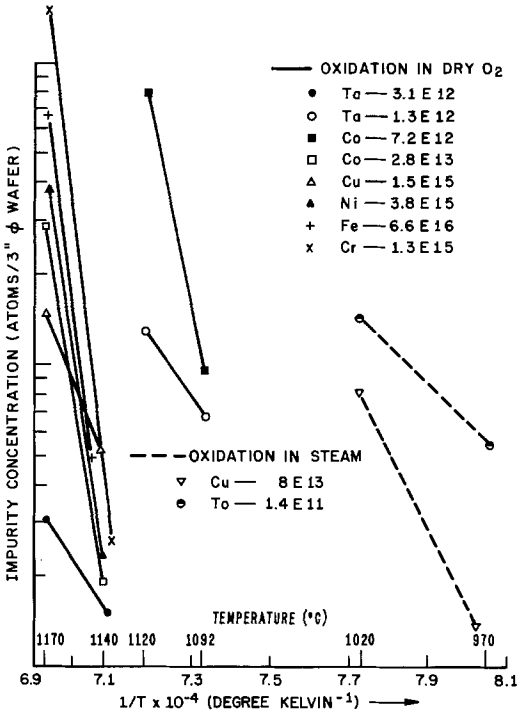

Fig. 2. Arrhenius plot of the impurity concentrations on silicon wafers oxidized simultaneously for 1 hr in sections of different temperature of a quartz furnace tube. The scale of the ordinate is logarithmic. The concentration shown in the inserts refer to the highest concentration for any given line.

for a temperature change of only some 30°C for the elements Cr, Fe, Co, and Ni, while the concentrations increased much less for Cu and Ta.

Since the time of diffusion was the same for all curves, one can regard the impurity concentrations as a measure of the diffusivity of the impurities in the quartz, in which case the graph would correspond to an Arrhenius plot of diffusion coefficient *vs.* inverse temperature. However, a two hundredfold concentration increase over a temperature difference of only 30°C would obviously lead to an impossibly large activation energy, if all of the effect were to be attributed only to the difference in temperature during the actual diffusion run. A much more likely explanation is that the long anneal at high temperature during the two months preceding the experiment has caused some kind of a change in the quartz of the tube, the change being more pronounced at those positions that were at the higher temperature.

We believe that this postulated change in the quartz may consist of a better development of grain boundaries in the quartz at the positions of higher temperature. The outer surface of a quartz furnace tube is usually visibly crystalline, but the crystallization does not extend all the way through the thickness of the wall of the tube, which otherwise would already have become useless. It appears likely that the devitrification observable by electron diffraction in aged SiO_2 films on Si is a precursor of complete devitrification that would eventually follow (especially at high temperature). The structure of a quartz tube operated at high temperature over a prolonged period of time may thus consist of a crystalline layer at its outer surface, gradually changing to a mixture of crystalline and amorphous material with depth into the wall of the tube. This mixture of crystalline and amorphous SiO_2 we have referred to as incipient grain boundaries. These incipient grain boundaries may be expected to be preponderant at locations of higher temperature of the tube.

Enhanced diffusivity, and reduced activation energy for diffusion at grain boundaries are a well-known fact in polycrystalline materials (11, 12). Why grain boundaries in a matrix of vitreous quartz should also be paths of enhanced diffusivity as compared to the fully vitreous material is not immediately obvious, but not illogical in view of the wide-open channel structure of the SiO_2 network, for instance, in quartz along the c-axis.

An additional but probably lesser enhancement of diffusivity would also result just from the incorporation of sodium (and of lithium)[2] into the fused quartz; lattice dilation due to the rupture of Si-O-Si bonds is well known to occur.

The strong enhancement of the diffusivity observed at positions of higher temperatures may thus be a consequence of several superimposed factors: a decreased activation energy E, an increased frequency factor D_0 for diffusion at grain boundaries in the standard equation $D = D_0e^{-E/kT}$, and perhaps also a larger supply of impurities liberated from the liner or furnace material at the positions of higher temperature (though convection and diffusion in the gas phase should keep concentration gradients there small). Since copper is a fast diffuser even in vitreous SiO_2, its diffusivity should not be increased as much by the availability of easy diffusion paths as that of the slow diffusers in SiO_2: Cr, Fe, Co, and Ni; this is as actually observed. Tantalum appears to remain a slow diffuser even in the presence of easy diffusion paths for other ions, perhaps because of the high charge on the ion.

Additional support for this model comes from a run in which the wall of a single-wall tube was driven into strong devitrification by holding it at 1250°C for three days inside of a new mullite liner, which at this temperature is an ample source of both sodium and of transition group elements. The concentration of the transition group elements detected on silicon wafers placed into the tube after three days, but while still at 1250°C, increased by 2-3 orders of magnitude compared to the levels normally seen at 1000° for the same duration of 1 hr. The temperature was then lowered to 1000°C, and was kept at 1000°C for six weeks; silicon wafers oxidized in the tube during these ensuing six weeks showed contamination levels equivalent to those observed at 1250°C, actually even increasing somewhat with time. Since the quartz of the tube cannot continue to function as a constant source of strongly enhanced contamination for a period of six weeks, and since out-diffusion from the liner also could not have become stronger than normal at 1000°C, the experiment again points to increased diffusivity in the quartz due to devitrification.

The function of a double-walled quartz tube with dry O_2-HCl mixture in the annulus thus appears to be twofold: not only does the chlorine "getter" the transition group metals before they can diffuse into the wall of the inner tube, but it removes sodium as well, thus preventing devitrification of the inner tube and preserving its quality.

The absence of contamination during oxidation at 1000°C in a double wall tube (Table I, case B) was continually demonstrated during three weeks of continuous monitoring, and has since been duplicated for a longer period of time at another Bell Laboratories facility. Thus most of the contamination due to high temperature furnace treatments can be eliminated by this simple arrangement.

Contamination can also be introduced during other processing steps, during polishing, ion implantation, epitaxy, or plasma etching, but in these cases can be avoided or at least drastically reduced by taking common sense precautions. A protective shield is necessary during high temperature treatments in furnace tubes permeable to impurity diffusion.

[2] Since neutron irradiation of lithium does not produce a gamma-ray active isotope, its concentrations remained unknown in this work.

While the use of a protective dry O_2-HCl shield would eliminate contamination problems, it would pose problems of its own due to the corrosive nature of HCl. A simple solution to this problem would be to recirculate the dry O_2-HCl mixture of the double-wall tube. The total amount of chlorides formed will be small compared to the amount of HCl present in the annulus of the tube; thus there would be little need to replenish the HCl, perhaps on a weekly basis. This would reduce corrosion or environmental problems. The metal chlorides would be swept out of the hot zone by the circulating gas and would deposit in cool regions where they are harmless. Teflon-coated chemical pumps etc. for handling of the HCl are readily available.

Acknowledgment

The author is indebted to one of the reviewers for bringing Ref. (5) to his attention, and also for useful discussions on other points.

Manuscript submitted Jan. 28, 1982; revised manuscript received *ca.* July 26, 1982.

Any discussion of this paper will appear in a Discussion Section to be published in the December 1983 JOURNAL. All discussions for the December 1983 Discussion Section should be submitted by Aug. 1, 1983.

Publication costs of this article were assisted by Bell Laboratories.

REFERENCES

1. P. F. Schmidt and C. W. Pearce, *This Journal*, **128**, 630 (1981).
2. H. G. Riotte, U. Herpers, and W. Weber, *Radiochem. Radioanal. Lett.*, **30** (4), 311 (1977).
3. G. A. Rozgonyi, R. P. Deysher, and C. W. Pearce, *This Journal*, **123**, 1910 (1967); C. W. Pearce and G. A. Rozgonyi, in "Semiconductor Silicon 1977," H. Huff and E. Sirtl, Editors, p. 606 ff, The Electrochemical Society Softbound Proceedings Series, Princeton, NJ (1977).
4. S. M. Hu, *Appl. Phys. Lett.*, **27**, 165 (1974); L. Y. Tan, L. L. Wu, and W. K. Tice, *ibid.*, **29**, 765 (1976).
5. E. A. Irene, *This Journal*, **121**, 1613 (1974).
6. G. H. Frischat, *Ber. Dtsch. Keram. Ges.*, **47**, 313 (1970).
7. L. E. Katz, P. F. Schmidt, and C. W. Pearce, *This Journal*, **128**, 620 (1981).
8. O. W. Flörke, *Geologie*, **3**, 71 (1954); O. W. Flörke, *Fortschr. Mineral.*, **44** (2), 181 (1967).
9. T. Sugano, K. Hoh, K. Kudo, and N. Hishinuma, *Jpn. J. Appl. Phys.*, **7** (7), 715 (1968).
10. J. Drobek, Private communication.
11. J. C. Fisher, *J. Appl. Phys.*, **22**, 74 (1951).
12. R. Smoluchovski, *Phys. Rev.*, **87**, 482 (1952).

Laser Diffusion in Silicon from Spin-On Arsenic Glass

Schyi-yi Wu*

Motorola, SPS, Process Technology Laboratory, SRDL, Phoenix, Arizona 85008

ABSTRACT

Diffusion from spin-on arsenic glass by laser melting was investigated. Antireflection effect is exhibited by spin-on arsenic glass densified at as low as 210°C. Measured sheet resistance is a cosine-like function of glass thickness. Production throughput and process lattitude are greatly enhanced by effective use of the antireflection effect that is related to the efficiency of laser energy absorption. Laser energy absorption efficiency is related to glass thickness, glass densification temperature, and source concentration. Sirtl etch showed no crystalline defects in the diffused or melted layer. Diffused surface is rough but excellent back contact characteristics were obtained for n-type silicon substrates.

In the fabrication of semiconductor devices, the conventional solid-state diffusion is accomplished by heating the entire wafers at about 1000°C in a furnace. In contrast, liquid-state diffusion can be accomplished by localized laser melting of the near surface while the bulk of the wafer remains at about room temperature. The laser diffusion process allows one to prevent thermal stress-induced damage to large thin wafers. Small, closely spaced junctions should be able to be formed by laser diffusion without photolithography. In addition, metal deposition and the associated patterning steps can be performed in a surface area of a wafer before laser diffusion in the other surface area. A practical application is "ohmic contact diffusion" on the back side of thinned wafers after metal deposition and the associated patterning steps are completed on the front side of thick wafers. Processing on thick wafers is desired to minimize yield loss due to wafer breakage. Laser diffusion allows one to do this and offers greater advantages over the conventional solid-state diffusion. In the conventional process, the ohmic contact diffusion by solid-state diffusion as well as the subsequent metal deposition and the associated patterning must be performed on thinned wafers.

Laser diffusions from elemental aluminum (1), elemental phosphorus (2, 3), and boric acid (3) sources have been reported in the literature. Most recently, laser diffusions from spin-on glasses doped with oxides of antimony, arsenic, and phosphorus were demonstrated by Smith and Thompson (4). In this paper, the author reports on the antireflection effect exhibited by spin-on arsenic glass and the dependence of arsenic diffusion on wafer clean, source concentration and source bake temperature.

* Electrochemical Society Active Member.
Key words: semiconductor, contacts, doping.

Experimental

Arsenic source.—The arsenic concentration in the glass is controlled by the weight ratio of arsenic oxide to TEOS (tetraethylorthosilicate). The viscosity of the arsenic glass solution, and thus the thickness of the spun film, are controlled by the weight ratio of TEOS to solvent. The arsenic concentration, C_s, was calculated assuming complete glass densification to SiO_2 and an ideal solid solution of arsenic oxide and SiO_2. Except where noted, $C_s = 4.5 \times 10^{21}$ cm^{-3}. The formulation is reported elsewhere (5).

Silicon wafers.—Wafers were CZ grown, boron-doped, 7-17 $\Omega \cdot$ cm, <111> crystal. The diameter is 3 in.

Wafer clean.—Except where noted, wafers were cleaned by 1 min 10 H_2O:1HF (49%) at room temperature, rinsed in ultrapure deionized H_2O, spin rinsed, and spin dried. In the exception, the H_2O/HF step was replaced by 10 min $7H_2SO_4$:$3H_2O_2$ at 110°C.

Source application.—The wafer was placed on a Headway EC101 spinner, and the arsenic glass solution was applied to the surface. The wafers were spun

at various speeds, ω, for 10 sec to achieve the desired thickness and baked at 150°C for 1 hr in N_2 or 400°C for 30 min in air. Bake temperature is represented by T_b. Thickness of glass after bake, X_s, was measured by an IBM FTA Film Thickness Analyzer using the Cauchy refractive index equation for thermal oxide

$$n = 1.45076 + 317410.7/\lambda^2 \quad [1]$$

where n is the refractive index, and λ is the measurement wavelength in angstroms. The relationship between glass thickness (for $T_b = 400$°C) and the spin speed (1-8 krpm) is

$$X_s \propto 1/\omega^{\alpha} \quad [2]$$

where α has a value of 0.4631 ± 0.0205. This is a reasonable value considering the volatility and evaporation of solvent during the spin process (6).

Diffusion.—Diffusion was performed in a Model 610 Epitherm laser system. The laser consists of a CW-pumped, repetitively Q-switched Nd:YAG laser with a wavelength of 1.064 μm. In this work, the wavelength was converted to 0.532 μm by a second harmonic generator. The beam is focused by an objective lens and travels over a rotating platen. The motion of the beam over the rotating wafers generates a spiral path that results in coverage of the entire wafer surface. The platen can hold six 4 in. wafers or nine 3 in. wafers. Five adjustable variables are beam diameter (S) defined at $1/e$ peak power from 60 to 220 μm, laser power (P) up to 1W, pulse repetition rate (f) from 0.1 to 10 kHz, radial spot to spot spacing (R), and tangential spot to spot spacing (θ).

The pulse energy (E) in joules is defined by

$$E = P/f \quad [3]$$

The energy density (I) in J/cm^2 is defined by

$$I = E/(\pi S^2/4) = 4P/(\pi f S^2) \quad [4]$$

It can be shown that the throughput (A) in cm^2/sec can be expressed by

$$A = (4P/\pi I)G_tG_r \quad [5]$$

where G_t and G_r are spot to spot overlapping factors ($G_r = R/S$ and $G_t = \theta/S$).

Evaluations.—After diffusion wafers were etched in dilute HF solution. Melted spot size was measured on a micrograph with 256× magnification. The largest dimension of the melted spot was considered as the melted spot diameter even though the melted spot was elliptical. Sheet resistance was measured by four-point probes. Five points were measured on each wafer: center and four equi-spaced peripheral points, one-third of an inch from the wafer edge. Junction depth was measured by grooving, staining, and fringe counting with an interferometer. Surface roughness was measured by Dektak Surface Profile Measuring System. Crystalline quality of the diffused or melted layer was examined by microscope at 1010× magnification after 15° bevel and 5 sec Sirtl etch (7). Dopant profile was determined by secondary ion mass spectrometry (SIMS) (8).

Results and Discussion

Antireflection effect.—It can be seen from Eq. [5] that given the maximum power available and the spot-to-spot overlapping required, the throughput is inversely proportional to the energy density required for the process. The required energy density depends on the threshold energy density for melting silicon, which can be a function of glass thickness due to an antireflection effect. From the Gaussian distribution of the energy density within a pulse, it can be shown that

$$I = I_{th} \exp[(d_t/S)^2] \quad [6]$$

where I_{th} is the apparent melting threshold energy density and d_t is the melted spot diameter. In Eq. [6], the quantities I and I_{th} can be replaced by P and P_{th}, respectively, since I is proportional to P. The average apparent threshold power (P_{th}) for a given thickness was determined by four sets of P and d_t at a given S according to Eq. [6]. The plots of log P *vs.* $(d_t)^2$ are shown in Fig. 1 for three thicknesses of glass baked at 210°C. The scatter of the data was essentially due to the variability of the laser pulse since variation in melted spot size was observed under identical process conditions. Nevertheless, Fig. 1 shows that the energy density distribution can be considered Gaussian at least to the first approximation. It is worth mentioning that the melted spots are irregular or not well defined if the laser power is only slightly higher than the threshold power.

Figure 2 shows threshold power as a function of glass thickness. These data are generated from Fig. 1. Three arsenic glass solutions were used to cover the thickness range up to 3000Å. These solutions have the same concentration ratio of arsenic oxide to TEOS but differ in dilution. The cosine-like curve shows that the effect of the antireflection coating is produced by spin-on arsenic glass baked at a temperature as low as 210°C. The sheet resistance variation with thickness of glass baked at 400°C is shown in Fig. 3. These two data were produced from arsenic glass solutions with the same concentration ratio of arsenic oxide to TEOS but with different dilution factors. The cosine-like curve shows that the antireflection has a direct effect on diffusion. Note that lower sheet resistance indicates higher efficiency of absorption of laser energy by silicon or higher transmission efficiency of laser energy through the glass. The maximum absorption efficiency occurs at about 800 and 2500Å obtained from the 45% solution and the 100% solution, respectively.

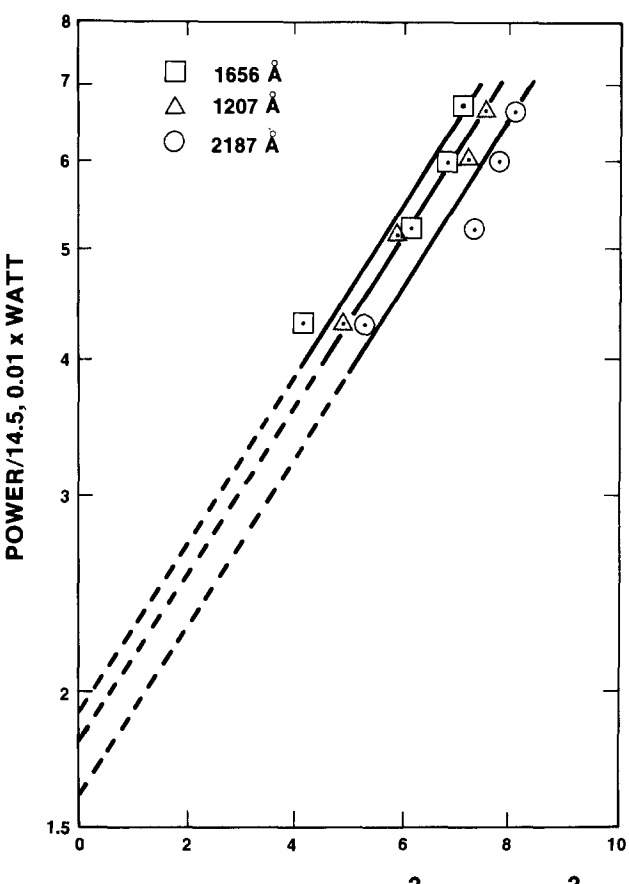

Fig. 1. Melted spot diameter as a function of laser power. T_b = 210°C, f = 5 kHz, S = 76 μm.

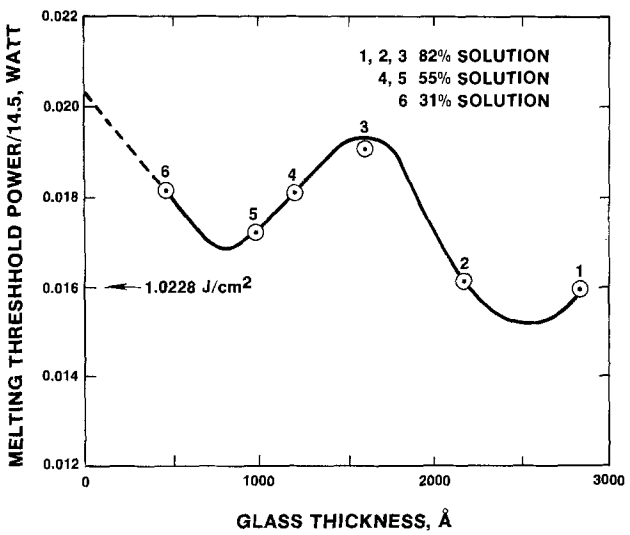

Fig. 2. Melting threshold power as a function of glass thickness. $T_b = 210°C$, $f = 5$ kHz, $S = 76$ μm.

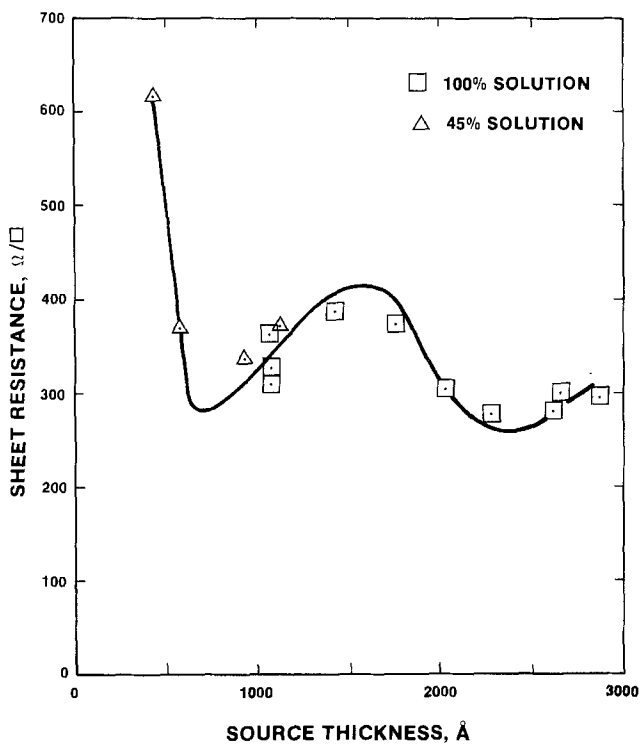

Fig. 3. Measured sheet resistance as a function of glass thickness. $T_b = 400°C$, $f = 3$ kHz, $S = 168$ μm, $I = 1.53$ J/cm^2, $R = \theta = 81.28$ μm.

Source concentration.—Sheet resistance data for two source concentrations are shown in Fig. 4. Lower sheet resistance was obtained from higher concentration source ($C_s = 5.5 \times 10^{21}$ cm^{-3}). This is at least in part due to higher energy transmission efficiency, as evidenced by larger melted spots, associated with the higher concentration source. The difference in sheet resistance may not be due to source concentration. In fact, a specially formulated source with $C_s = 4.5 \times 10^{21}$ cm^{-3}, tested under identical conditions, gave almost the same sheet resistance values as the source with $C_s = 5.5 \times 10^{21}$ cm^{-3}. For this specially formulated source, the average junction depths are 0.405 and 0.27 μm corresponding to a source thickness of 483 and 299Å, respectively. In all cases, the melted spot size was decreased as the source thickness was decreased.

Wafer clean.—The small amount of oxide grown during the piranha clean may perhaps be a diffusion barrier. Figure 5 shows the sheet resistance data obtained on wafers cleaned by piranha and H_2O/HF solution. The H_2O/HF clean resulted in lower sheet resistance than the piranha clean. Examination of the melted spots showed no difference in sizes. Thus, the small amount of oxide, ~30Å, formed from the piranha clean appears to be a significant diffusion barrier.

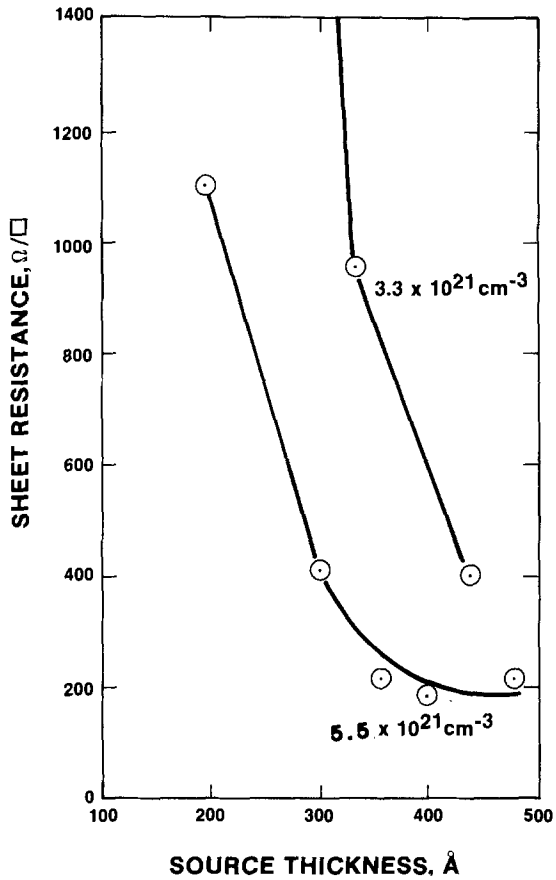

Fig. 4. Effect of source concentration on sheet resistance. $T_b = 400°C$. $R = \theta = 81.28$ μm, $S = 168$ μm, $f = 3$ kHz, $I = 1.53$ J/cm^2.

Glass densification.—The sheet resistance obtained from two wafers coated with the same source and spun at same speed, but baked at two temperatures is shown in Table I. The source thickness and concentration were the same after spin for both wafers. The 400°C bake, however, gave lower sheet resistance than the 150°C bake (224 *vs.* 272 Ω/□). This is at least in part due to the difference in energy absorption efficiency

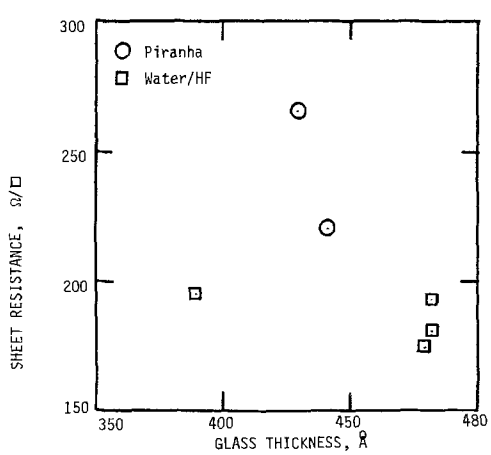

Fig. 5. Effect of wafer clean on sheet resistance. $T_b = 400°C$. $R = \theta = 81.28$ μm, $S = 168$ μm, $f = 3$ kHz, $I = 1.53$ J/cm^2.

Table I. Effect of source bake temperature on sheet resistance. Substrate was p-type, 1.5-2.0 Ω · cm, 3 in. diam. Spin speed was 4 krpm. Laser conditions were: $R = \theta = 50.8$ μm, $S = 108$ μm, $f = 5$ kHz, $I = 1.75$ J/cm².

Bake temperature	Thickness (Å)	R_s (Ω/□)	2σ (%)
400°C, 30 min, air	1574	224.06	8.59
150°C, 60 min, N_2	2376	272.40	5.30

based on melted spot size comparison. Data for thinner glass (~500Å) showed the same effect.

Surface quality.—The sample with the lowest sheet resistance obtained was evaluated for surface roughness and the diffused or melted layer quality. The surface was rough due to rapid localized melting and freezing. The maximum step height was 1 μm. Sirtl etching showed no crystalline defects in the diffused or melted layer.

Estimated diffusivity.—A sample diffused with 85 nsec pulse of 1.9 J/cm² was analyzed by SIMS (8) for the arsenic concentration profile. The profile, as shown in Fig. 6, can be approximated by an erfc distribution with a diffusion length, $2\sqrt{Dt} = 1.34 \times 10^{-5}$ cm. Assuming a reasonable diffusion time, $t = 120$ nsec, an estimated diffusivity, D, of 3.75×10^{-4} cm²/sec was obtained. This is consistent with the reported literature value: $(3.3 \pm 0.9) \times 10^{-4}$ cm²/sec (9). The erfc distribution implies that the surface concentration is constant during melting. If this is true, the ohmic contact resistance would be independent of the pulse duration. Affolter *et al.* (3) investigated diffusion from elemental phosphorus source for ohmic contact application and found no significant dependence of resistance on wavelength, pulse energy, or pulse duration over a certain range of parameters. Thus a constant surface concentration model is consistent with the data reported by Affolter *et al.*

Device application.—The most efficient source was used for ohmic contact diffusion in the fabrication of devices utilizing n-type silicon substrates. This was done on the back side of wafers thinned after metal deposition and the associated patterning step were completed on the front side of the thick wafers. The throughput is greater than 1081 cm²/hr. The ohmic contact produced by laser diffusion is at least as good as that produced by the conventional solid-state diffusion from PH_3 source, based upon I-V characteristics under forward bias.

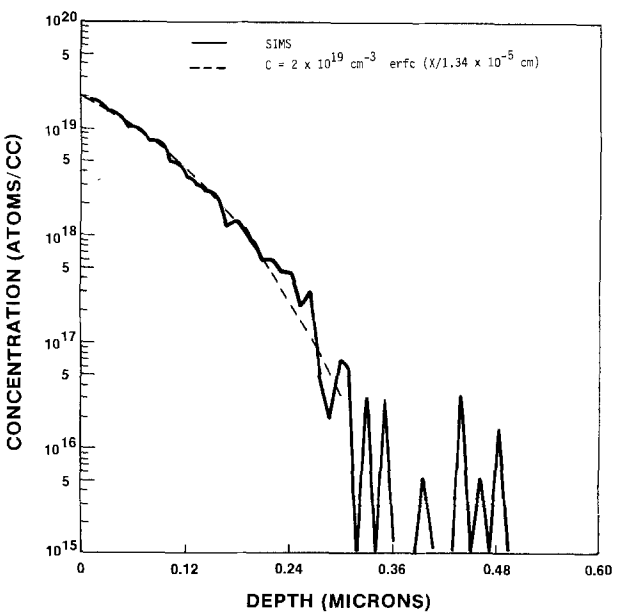

Fig. 6. Arsenic concentration profile. $T_b = 400$°C, $S = 120$ μm, $I = 1.923$ J/cm², $f = 5$ kHz, $R = \theta = 78.74$ μm.

Summary and Conclusions

Gaussian distribution of the energy density of a laser pulse is a useful basis for the determination of the relative melting threshold power. The threshold power for melting silicon is a cosine-like function of glass thickness for glass densified at as low at 210°C. That is, an antireflection effect is exhibited by spin-on arsenic glass densified at as low as 210°C. Antireflection has a direct effect on diffusion in terms of melted area coverage and depth. For glass densified at 400°C, the most effective doping occurs at about 800 and 2500Å due to the most efficient absorption of laser energy by silicon. The laser energy absorption efficiency is also related to the glass densification temperature and source concentration. Glass densified at 400°C gave lower sheet resistance than glass densified at 150°C. At a given densification temperature, sheet resistance is a function of arsenic concentration of the densified film which is determined by the weight ratio of dopant to TEOS in the liquid solution. The small amount of oxide, ~30Å, produced by the piranha clean, is a significant diffusion barrier. The diffusivity value estimated from the dopant profile is consistent with the mechanism of liquid state diffusion.

By the use of the most efficient glass, a viable and efficient production process of laser diffusion yielding excellent ohmic contact characteristics has been instituted.

Acknowledgments

The author wishes to acknowledge A. Chavez for the preparation of arsenic glass solutions, R. Peterson for diffusion processing and evaluation, R. Stoltenberg for the melted spot size measurements, and M. Gibbs for typing this report.

Manuscript submitted March 31, 1982; revised manuscript received July 20, 1982. This was Paper 389 presented at the Denver, Colorado, Meeting of the Society, Oct. 11-16, 1981.

Any discussion of this paper will appear in a Discussion Section to be published in the December 1983 JOURNAL. All discussions for the December 1983 Discussion Section should be submitted by Aug. 1, 1983.

Publication costs of this article were assisted by Motorola Semiconductor Products, Incorporated.

REFERENCES

1. F. E. Harper and M. I. Cohen, *Solid State Electron.*, **13**, 1103 (1970).
2. J. M. Fairfield and G. H. Schwuttke, *ibid.*, **11**, 1175 (1968).
3. K. Affolter, W. Luthy, and M. von Allmen, *Appl. Phys. Lett.*, **33** (2), 185 (1978).
4. J. N. Smith and A. D. Thompson, Private communication.
5. K. Ritchie, U.S. Pat. 3,832,202 and 3,789,023 (1974).
6. J. H. Lai, *Polymer. Eng. Sci.*, **19**, 1117 (1979).
7. E. Sirtl and A. Adler, *Z. Metalkd.*, **52**, 529 (1961).
8. Charles Evans & Associates, California.
9. H. Kodera, *Jpn. J. Appl. Phys.*, **2**, 212 (1963).

Gas Phase Reactions and Transport in Silicon Epitaxy

T. Aoyama, Y. Inoue, and T. Suzuki

Hitachi Limited, Hitachi Research Laboratory, Hitachi, Ibaraki, 319-12, Japan

ABSTRACT

Gas phase transport in Si epitaxial growth has been investigated by means of *in situ* mass spectrometry measurements. of reaction gas concentration profiles. Five species, $SiCl_4$, $SiHCl_3$, SiH_2Cl_2, $SiCl_2$, and HCl are observed in the reaction gas. Not only $SiCl_4$ (source gas) but the other Si chlorides as well contribute to the surface growth reaction. The primary reaction species shifts from $SiCl_4$ to the other Si chlorides with decreasing gas velocity and with increasing temperature and position along the susceptor.

Gas phase reactions and transport phenomena in Si epitaxial growth have been studied extensively by a number of authors and reaction models deduced from an equilibrium viewpoint (1-5). However, the actual reaction is not in equilibrium, but rather quasi-equilibrium (6), and the Si epitaxial reaction is difficult to describe by a theoretical model, It is necessary to observe the reaction gas species by *in situ* measurements in a reactor. Recently such measurements have been made and reaction models proposed. Ban and Gilbert observed the reaction gas profiles in a reactor by using mass spectrometry and reported that $SiCl_4$ and only a small amount of $SiCl_2$ were found (7, 8). A reaction mechanism was proposed in which $SiCl_4$ was transported to the substrate surface by diffusion and the source gas decomposed into solid Si and HCl by-product. The following heterogenous reaction occurred at the surface

$$SiCl_4(g) + 2H_2(g) \rightarrow Si(s) + 4HCl(g)$$

Sedgwick and Smith observed reaction gas concentration profiles using laser Raman spectroscopy in Si epitaxy with SiH_2Cl_2 as source material (9). The SiH_2Cl_2 decomposed into $SiCl_2$ in the gas phase, and then $SiCl_2$ was transported to the surface where the epitaxial layer grew

$$SiH_2Cl_2 \rightarrow SiCl_2 + H_2 \quad \text{(gas phase)}$$

$$SiCl_2 + H_2 \rightarrow Si + 2HCl \quad \text{(substrate surface)}$$

Nishizawa and Nihira observed reaction gas profiles by using infrared absorption spectroscopy and found $SiCl_4$, $SiHCl_3$, SiH_2Cl_2, and HCl species (10). They proposed the following models

$$SiCl_4 + H_2 \rightleftarrows \begin{matrix} SiHCl_3 \\ SiCl_2 \\ SiH_2Cl_2 \end{matrix} \rightleftarrows Si + HCl$$

Duchemin also investigated Si epitaxial reactions extensively by observing reaction gas profiles in a vertical type reactor (11).

Recently, Pollard and Newman have reported a model in which multicomponent mass transfer was considered (12). However, they used calculated gas concentration profiles for the calculation of growth rates. We have observed the reaction gas concentration profiles by *in situ* measurements using mass spectrometry while changing the growth parameters. It is apparent that the three models mentioned above are likely to describe only a part of the actual reaction. In this paper, it is proposed that all the Si chlorides, $SiCl_4$, $SiHCl_3$, SiH_2Cl_2, and $SiCl_2$, participate in the surface reaction, and the primary surface reaction species which contributes to the growth rate is suggested to shift with changing gas velocity, substrate temperature, and position along the susceptor.

Key words: gas phase diffusion, silicon chlorides, growth rate.

Experimental

Figure 1 shows the *in situ* reaction gas concentration measuring system. Two kinds of reactor tubes (rf heated horizontal type) were used. One reactor tube had the dimensions of 5.4 cm (height) × 7.9 cm (width) × 110 cm (length) and an effective cross-sectional area of 21 cm^2. The other had the dimension of 5.2 cm (height) × 7.5 cm (width) × 83 cm (length) and an effective cross-sectional area of 24 cm^2. The respective silicon graphite susceptors were 37 and 24 cm long. The former susceptor was tilted at an angle of 1.3°. Above the susceptor, hydrogen was used as the carrier gas at various velocities of 6.2-34 cm/sec (at room temperature). Silicon tetrachloride was used as source material. During the growth of the epitaxial layer a constant $SiCl_4$ gas concentration introduced into the reactor tube was monitored by the infrared spectrometer (13). Doping gases were not used. Temperature measurements were made during the deposition using a calibrated optical pyrometer and corrected for the emissivity of silicon and for the reactor tube walls. The substrates were chemical-mechanical polished Czochralski-grown silicon wafers with (111) orientation. Reaction gas was sampled through a quartz capillary (50 μm diam) inserted into the reactor tube. The sampling system was usually pumped to 130 Pa (~1 Torr) and a portion of the gas was introduced into the mass spectrometer (quadrupole type: QMS). The pressure of the sampling line was changed from 13 Pa (~0.1 Torr) to 1300 Pa (~10 Torr) to examine whether the reactant species might change before the detection in QMS. The capillaries were set in the reactor tube by the use of bellows. Reaction gas at an arbitrary height could be sampled by moving the capillary up or down. Reaction gas at an arbitrary position along the susceptor could be sampled by moving the susceptor upstream or downstream and selecting the capillary position. Argon was added to the carrier H_2 as reference gas (0.25%). Because of the mass separation effect (11), calibration curves were prepared beforehand to determine the concentrations of the reactants, $SiCl_4$, $SiHCl_3$, SiH_2Cl_2, $SiCl_2$, and HCl. The concentration of $SiCl_2$ was determined by decomposing SiH_2Cl_2 in He and by comparing SiH_2Cl_2 concentration as follows

$$[SiCl_2] = [SiH_2Cl_2] \times \frac{\Sigma I_i(SiCl_2)}{\Sigma I_j(SiH_2Cl_2)}$$

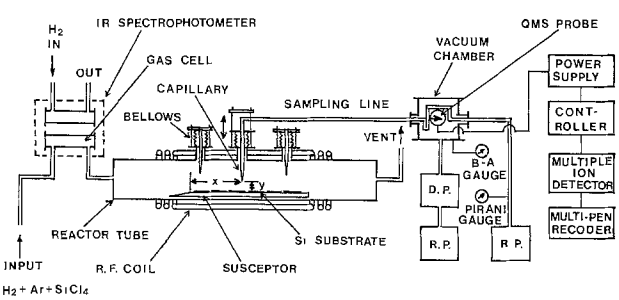

Fig. 1. The *in situ* reaction gas concentration measuring system

where $I_i(s)$ = intensity of peak in mass spectrum at m/e = i from the source s.

Results

Figure 2 shows typical reactant concentration profiles in the y direction (y: height above the susceptor). Five species, $SiCl_4$, $SiHCl_3$, SiH_2Cl_2, $SiCl_2$, and HCl were detected in the reactor. The concentration of $SiCl_4$ is constant in the upper region of the gas (constant concentration region). Not only $SiCl_4$, but $SiHCl_3$, and SiH_2Cl_2 also have concentration gradients towards the substrate surface in the vicinity of the substrate. This result indicates that all Si chloride species diffuse toward the substrate surface and contribute to the epitaxial growth. Furthermore the fact that Si by-products diffuse toward the substrate indicates that these species are formed in the gas phase. The HCl has a concentration gradient from the susceptor and diffuses from it. No apparent dependency of the pressure is obtained as to the concentration profiles when the pressure of the sampling line is changed.

Figure 3 shows $SiCl_4$ concentration profiles along the susceptor. The concentration of $SiCl_4$ in the upper region above the susceptor decreases slightly in the downstream direction, while near the susceptor, it decreases significantly downstream. The decrease in $SiCl_4$ concentration along the gas stream becomes larger as the substrate temperature is increased. Gas phase transport of $SiCl_4$ to the susceptor is assumed to change with changing temperature and position along the gas flow.

Figure 4 shows $SiHCl_3$ concentration profiles along the susceptor. Near the susceptor surface the concentration of $SiHCl_3$ decreases significantly downstream.

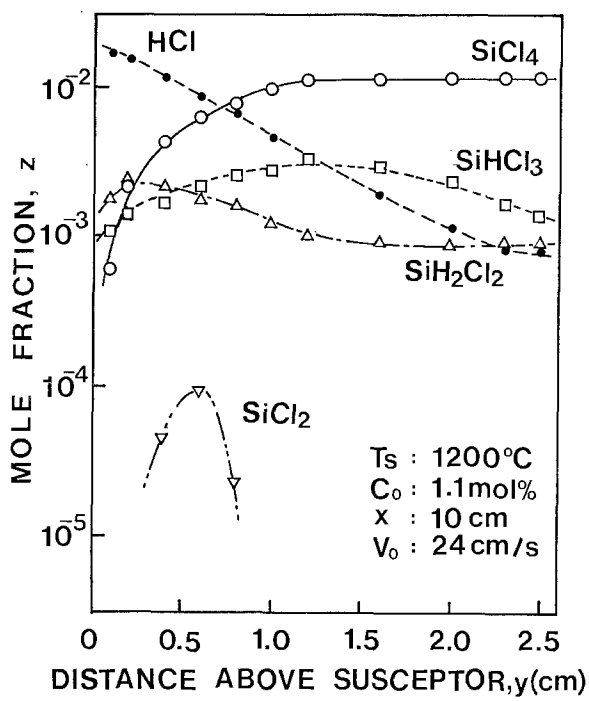

Fig. 2. Typical reactant concentration profiles

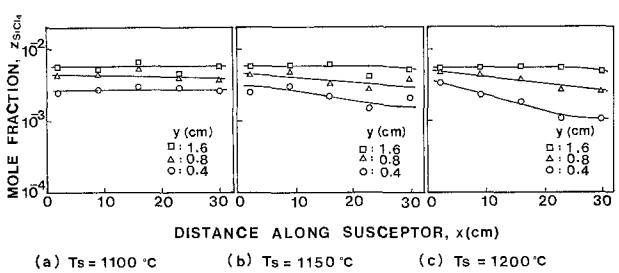

Fig. 3. $SiCl_4$ concentration profiles

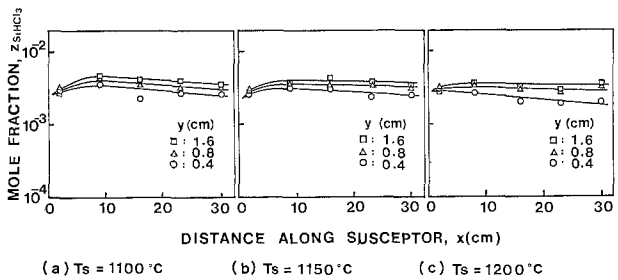

Fig. 4. $SiHCl_3$ concentration profiles

The $SiHCl_3$ concentration profiles at the top region of the susceptor are reduced. This may be due to the fact that the amount of $SiHCl_3$ decomposed from $SiCl_4$ is still small because of an insufficient rise in gas temperature. The decrease in $SiHCl_3$ concentration downstream may be caused by decomposition of $SiHCl_3$ into SiH_2Cl_2 and $SiCl_2$.

Figure 5 shows HCl concentration profiles along the susceptor. The concentration of HCl increases with an increase of temperature and position along the susceptor. This is explained by the increase in temperature which causes increase in epitaxial growth rate and in the by-product, HCl concentration. The HCl in the upstream region flows downstream and increases the HCl concentration there.

Figure 6 shows concentration profiles at three positions along the susceptor. Both the concentration and the concentration gradient of $SiCl_4$ in the vicinity of the susceptor decrease in the downstream direction. Transport of $SiCl_4$ to the susceptor seems to decrease with an increase of position along the gas flow. The $SiHCl_3$ concentration in the diffusion region decreases, but the concentration gradient is almost constant in the gas flow direction. The SiH_2Cl_2 also has a concentration gradient toward the substrate surface ($y < 0.2$ cm) but no specific effect of position along the susceptor on the concentration gradient could be determined. The HCl has a concentration gradient from the susceptor and the concentration gradient increases with an increase of position along the susceptor. Transport of

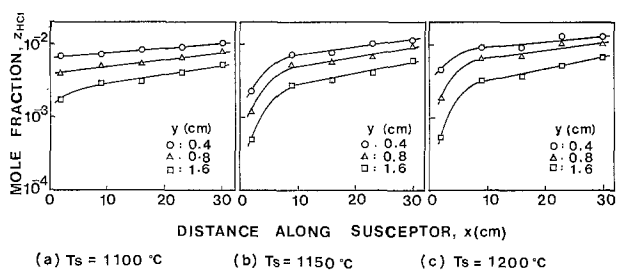

Fig. 5. HCl concentration profiles

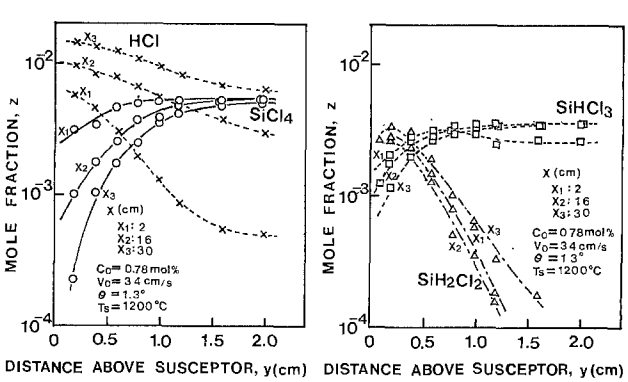

Fig. 6. Concentration profiles at three positions along the susceptor.

HCl from the susceptor appears to increase with an increase of position along the gas flow.

Figure 7 shows gas concentration profiles for distance above the susceptor at three substrate temperatures. Both the concentration and the concentration gradient of $SiCl_4$ in the vicinity of the susceptor decrease with an increase in the substrate temperature. The concentration of $SiHCl_3$ decreases, but the concentration gradient is almost constant in the vicinity of the susceptor with increasing temperature. Both the concentration and the concentration gradient of HCl from the susceptor increase with increase of substrate temperature. Transport of $SiCl_4$ to the susceptor and that of HCl from it seem to increase with an increase in temperature.

Figure 8 shows the effect of gas velocity on the concentration profles for distance above the susceptor. Both the concentration and the concentration gradient of $SiCl_4$ and $SiHCl_3$ in the diffusion region increase with an increase in the gas velocity. Transport of both $SiCl_4$ and $SiHCl_3$ to the susceptor seems to decrease with an increase in gas velocity. The concentration of SiH_2Cl_2 in the upper region above the susceptor decreases with an increase in gas velocity. It is likely that the concentration of $SiCl_4$ and $SiHCl_3$ decrease while the concentrations of other Si chlorides increase with a decrease in gas velocity because the gas temperature increases with a decrease in gas velocity and the $SiCl_4$ and $SiHCl_3$, when heated enough, decompose into other Si chlorides to reach the growing surface.

Discussion

When the results of thermodynamic calculations (2, 5) are compared with the above concentration profiles, two trends are evident, firstly, in equilibrium the concentration of $SiHCl_3$ is always higher than that of $SiCl_4$, and secondly, $SiCl_2$ is the main species in high temperature region (or in the vicinity of the susceptor). This implies the possibility that in the above experiments, while $SiCl_2$ is sampled and transferred to the detector, it might change into SiH_2Cl_2 though no apparent result is obtained from the experiments made in changing sampling pressure.

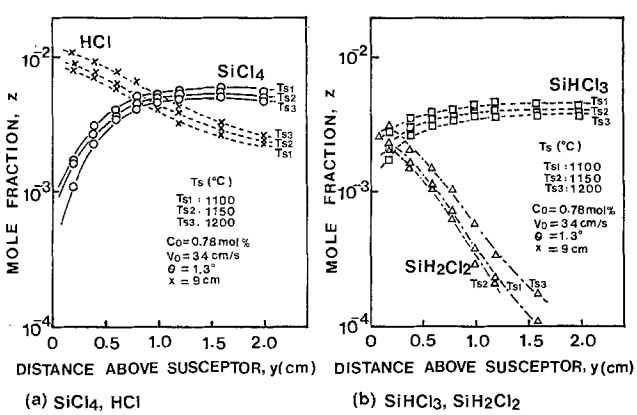

Fig. 7. Gas concentration profiles for distance above the susceptor

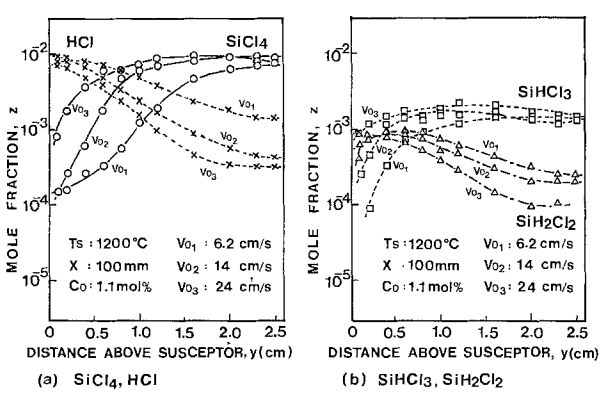

Fig. 8. The effect of gas velocity on the concentration profiles

As the growth parameters are changed, the concentration gradients of Si chlorides toward the growing surface change; the primary reaction species which contribute to the growth rate are also likely to change. It is a necessary condition for epitaxial growth that reaction species reach the substrate surface. By calculating diffusion fluxes, transport of molecules to the substrate or total flows of molecules from gas phase to solid phase can be evaluated. We compared the growth rates with those calculated from the concentration gradients.

There are seven species; $SiCl_4$, $SiHCl_3$, SiH_2Cl_2, $SiCl_2$, HCl, Ar, and H_2 in the reactor. In a multicomponent mixture the Stefan-Maxwell equation is satisfied for one dimensional concentration diffusion toward the substrate surface (12).

$$\nabla z_i = \sum \frac{1}{cD_{ij}} (z_i N_j - z_j N_i) \qquad [1]$$

where z_i = mol fraction of i; c = number of mols of gas in a unit volume; D_{ij} = binary diffusivity; N_i = diffusion flux relative to stationary coordinates. If we use the effective binary diffusivity D_{im} and approximate this by D_{iH_2}, the one dimensional diffusion flux N_i is expressed as the following

$$N_i = -cD_{iH_2} \nabla z_i \qquad [2]$$

If a term for thermal diffusion (13) is added to Eq. [2], then

$$N_i = -cD_{iH_2} \left(\nabla z_i + \frac{\alpha z_i dT}{T dy} \right) \qquad [3]$$

where α = thermal diffusivity. The binary diffusivity D_{iH_2} is given as follows (13)

$$D_{iH_2} = D_{iH_2O} \left(\frac{T}{273} \right)^k \qquad [4]$$

where we used $k = 1.67$. In order to evaluate N_i, the concentrations at the substrate surface were estimated by extrapolating the concentration profiles, and the gradients at the surface were approximated by those between 0.2 cm and the surface. The growth rate is written as

$$G = \frac{M_{Si}}{\rho} \sum N_i \qquad [5]$$

$$= -\frac{M_{Si}}{\rho} \sum cD_{iH_2} \left(\nabla z_i + \frac{z_i dT}{T dy} \right) \qquad [6]$$

where M_{Si} = molecular weight of Si; ρ = density of solid Si.

Figure 9 makes a comparison of observed and calculated growth rates along the susceptor. Two calculations were made. In calculation [1], only $SiCl_4$ was

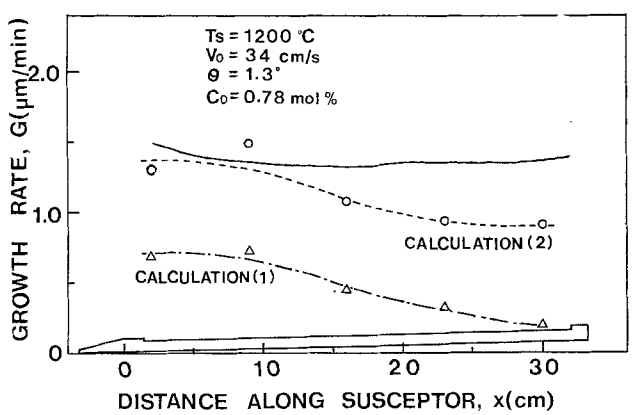

Fig. 9. Comparison of growth rates

taken as the diffusing species. In calculation [2], both $SiCl_4$ and $SiHCl_3$ were taken as the diffusing species. The contribution of SiH_2Cl_2 and $SiCl_2$ could not be calculated because of the uncertainty in their concentration gradients at the substrate surface. The results in calculation [1] do not agree with the observed growth rate. However, calculation [2] values almost coincide with the observed growth rate in the upstream region. Therefore, it is concluded that $SiCl_4$ and $SiHCl_3$ contribute mainly to the growth rate upstream. It seems that the contributions of $SiCl_4$ and $SiHCl_3$ decrease with the increase of position along the susceptor since calculation [2] does not agree with the observed growth rate in the downstream region. This discrepancy may be due to the contribution of SiH_2Cl_2 and $SiCl_2$.

Figure 10 is a plot of calculated and observed growth rates at three substrate temperatures. The contribution of $SiCl_4$ to the growth rate decreases with an increase in the substrate temperature (calculation [1]). The discrepancy between the observed and calculated growth rates for $SiCl_4$ and $SiHCl_3$ seems to come from the contribution of SiH_2Cl_2 and $SiCl_2$ (calculation [2]).

The probable transport models are shown in Fig. 11. The silicon source $SiCl_4$ is the primary contributor to the growth rate in the case of a large gas velocity, low substrate temperature, and upstream position along the gas flow. The primary reaction species shifts from $SiCl_4$ to the other Si chlorides with the decrease of gas velocity and with the increase of substrate temperature and position along the susceptor.

Conclusion

Gas phase transport in Si epitaxial growth was investigated by means of *in situ* mass spectrometry measurements while changing growth parameters. Five, species, $SiCl_4$, $SiHCl_3$, SiH_2Cl_2, $SiCl_2$, and HCl were observed in the reaction gas. Not only $SiCl_4$ but the other Si chlorides contribute to the surface growth reactions. The primary reaction species shifts from $SiCl_4$ to the other Si chlorides with decreasing gas velocity and with increasing substrate temperature and position along the susceptor.

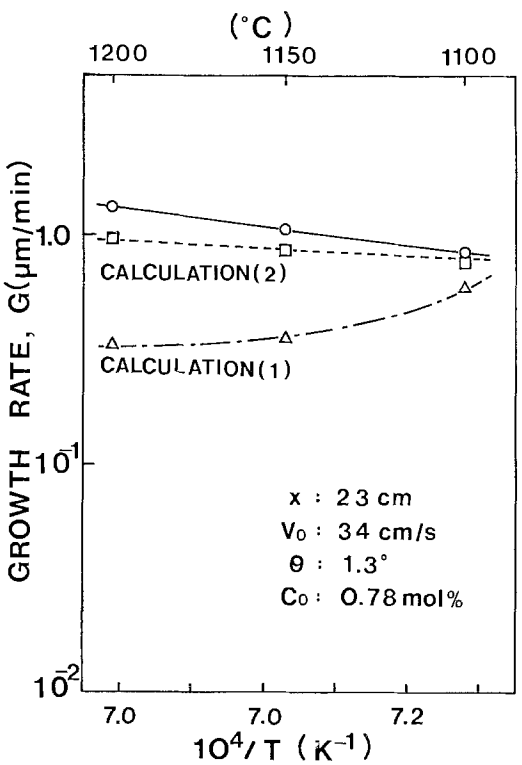

Fig. 10. Plot of calculated and observed growth rates

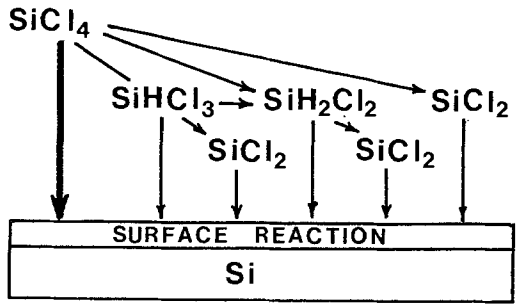

(a) gas velocity: large, substrate temperature: low, position along the susceptor: upstream,

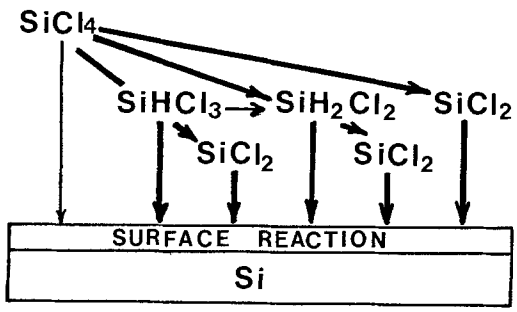

(b) gas velocity: small, substrate temperature: high, position along the susceptor: downstream.

Fig. 11. Probable transport models

Acknowledgments

The authors would like to thank Drs. T. Takasuna, Y. Takeda, M. Okamura, and Y. Sugita, and also Mr. M. Maki. Mr. T. Tokai, and Prof. J. Nishizawa for their helpful discussions and encouragement.

Manuscript submitted May 5, 1982; revised manuscript received Sept. 14, 1982. This was Paper 211 presented at the Minneapolis, Minnesota, Meeting of the Society, May 10-15, 1981.

Any discussion of this paper will appear in a Discussion Section to be published in the December 1983 JOURNAL. All discussions for the December 1983 Discussion Section should be submitted by Aug. 1, 1983.

Publication costs of this article were assisted by Hitachi Limited.

REFERENCES

1. E. G. Bylander, *This Journal*, **109**, 1171 (1962).
2. R. F. Lever, *IBM J. Res. Dev.*, **8**, 460 (1964).
3. J. Bloem, *This Journal*, **117**, 1397 (1970).
4. K. J. Sladek, *ibid.*, **118**, 654 (1971).
5. L. P. Hunt and E. Sirtl, *ibid.*, **119**, 1741 (1972).
6. T. O. Sedgwick, *ibid.*, **111**, 1381 (1964).
7. V. S. Ban and S. L. Gilbert, *ibid.*, **122**, 1382 (1975).
8. V. S. Ban and S. L. Gilbert, *J. Cryst. Growth*, **31**, 284 (1975).
9. T. O. Sedgwick and J. E. Smith, Jr., *This Journal*, **123**, 254 (1976).
10. J. Nishizawa and H. Nihira, *J. Cryst. Growth*, **45**, 82 (1978).
11. J. P. Duchemin, *Extrait de la Revue Technique* THOMSON-CSF **9**, No. 1 (1977).
12. R. Pollard and J. Newman, *This Journal*, **127**, 744 (1980).
13. T. Suzuki, Y. Inoue, M. Ura, and T. Ogawa, *J. Cryst.*

Growth, **45**, 109 (1978).
14. S. Yamazaki, M. Taki, and Y. Fujitani, *Jpn. J. Appl. Phys.*, **18**, 2191 (1979).
15. R. B. Bird, W. E. Stewart, and E. N. Lightfoot, "Transport Phenomena," John Wiley & Sons, Inc., New York (1960).
16. P. D. Putte, L. J. Giling, and J. Bloem, *J. Cryst. Growth*, **31**, 299 (1975).

TEM Observation of Precipitates of Cd-Phosphides in Cd-Diffused InP: A Correlation with the Previously Proposed Diffusion Models

B. V. Dutt* and D. Brasen

Bell Laboratories, Murray Hill, New Jersey 07974

ABSTRACT

Cadmium-diffused InP was studied by transmission electron microscopy. The surface regions of the samples, in which Cd was diffused on the P-rich side, showed several precipitate phases. Some of these could be identified as the phosphides, Cd_3P_2 and Cd_7P_{10}. No evidence of precipitate formation was observed in samples when Cd was diffused at relatively low phosphorus vapor pressures or on the In-rich side. These results are explained semiquantitatively on the basis of the recent thermodynamic data of the Cd-phosphides. Previously proposed interstitial-substitutional diffusion models are also discussed in light of the present evidence of second-phase precipitates. The proposal, that on the P-rich side, the diffusing interstitial is doubly ionized and that most of Cd is incorporated in its neutral substitutional form is consistent with the present data.

A study of Cd diffusion in undoped n-type InP using elemental mixtures of (Cd, In) and (Cd, P) as starting sources has been reported recently (1, 2). In an attempt to gain a better understanding of the InP: Cd system, some of the samples studied in Ref. (2) are evaluated by transmission electron microscopy (TEM), and these results constitute the present paper. The samples in which the cadmium was diffused from (Cd, In) alloys showed no precipitates or second-phase formation in the TEM analysis. However, the InP samples in which Cd was diffused on the P-rich side showed a variety of precipitates in the surface regions of the samples. Some of these were identified to be Cd_3P_2 and Cd_7P_{10}. In the following, a quantitative analysis of the precipitate formation is attempted using the currently available thermodynamic data (3, 4). The mechanisms of incorporation and diffusion of Cd and InP are reexamined taking into consideration the coexisting phase of phosphides of cadmium as precipitates.

Background

For completeness, a brief summary of the previous work (1, 2) is presented here. Cd was shown to be an acceptor in InP (5) and was thus expected to form p-n junctions in n-type InP. However, two junctions were delineated (1) on chemically staining with A-B etch (6). EBIC profiling suggested that the two junctions were p^+p^- and p^-n^- with the p^- region being the depletion region in a p^+-p^--n^- junction formation (1). In order to understand the mechanism of the diffusion of Cd in InP, the junction depth variations were investigated as a function of the cadmium activity and the amount of P (2). On the P-rich side, the data suggested the formation of Cd-phosphides which appear to be the actual diffusion sources, although the starting sources were elemental mixtures of (Cd, P). The diffusion of Cd has been interpreted on the basis of an interstitial-substitutional model. In this model, Cd rapidly diffuses through the interstitial lattice and dissolves substitutionally on the In-lattice. The substitutional Cd is relatively immobile and does not directly transport Cd. The diffusion data of Ref. (2) are reproduced here in Fig. 1. Based on the variations of the diffusion coefficient, D_{Cd}, with a_{Cd}, the activity of Cd in the (In, Cd) alloy, and the amount of phosphorus, W_P shown in Fig. 1(a) and (b), it was proposed that the charge states of the fast diffusing interstitial species and the substitutionally dissolved Cd depend on the diffusion conditions. The junction depth variations of Fig. 1 are consistent with the interpretation that, on the In-rich side, at $a_{Cd} < 0.4$ the diffusing interstitial is neutral and Cd is mostly present as a monovalent acceptor. At $a_{Cd} > 0.4$ the diffusing interstitial is doubly ionized and Cd is present as a monovalent acceptor. On the P-rich side, assuming that the principal phosphides, Cd_3P_2, CdP_2, and CdP_4, are the diffusion sources for Cd, the data are consistent with an interstitial-substitutional mechanism with the assumption that the interstitial is doubly ionized and Cd is largely present in its neutral substitutional form.

Experimental

The details of the diffusion anneals are described elsewhere (2). Briefly, Cd was diffused in sealed ampuls, into undoped (001)-oriented, n-type InP substrates using elemental mixtures of (Cd, In) and (Cd, P) as starting sources. The ampul volume and the amount of Cd were held constant at 5 cm^3 and 3.5 mg, respectively, while the amount of In or P was varied.

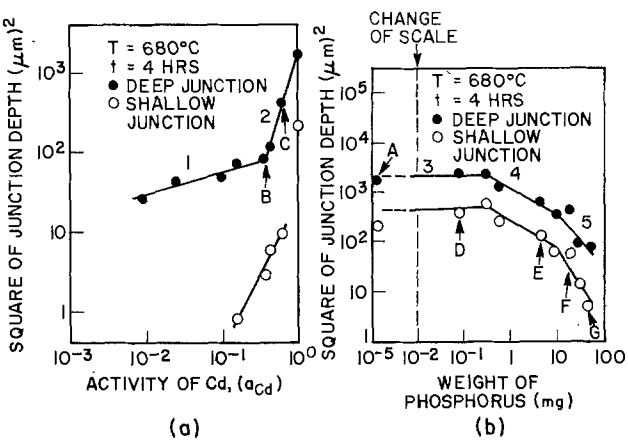

Fig. 1. Square of junction depth as a function of the activity of Cd on the In-rich side and the weight of phosphorus on the P-rich side are shown, respectively, in (a) and (b). The various regions marked 1 to 5 are the same as those listed in column 4 of Table I. Arrows A, B, . . ., G indicate the region and the diffusion history. See column 2 of Table I for ampul contents. All diffusions were done at 680°C for 4 hr.

* Electrochemical Society Active Member.
Key words: III-V compounds, defects, thermodynamics.

Table I. Summary of TEM results, diffusion history, and proposed models

Sample* ID	Weight of excess In (mg)	Weight of excess P (mg)	Region of Fig. 1 where the diffusion data of sample falls	D_{Cd} vs. a_{Cd} dependence of the region	Proposed models for diffusion and incorporation of Cd (2)	TEM results	Upper limit of $p(P_1)$ assuming all added P goes into vapor, atm†
A	0	0	2	a_{Cd}^3	$Cd_i^{\cdot\cdot}$, Cd_{In}'	No precipitates	10^{-3}
B	3.4	0	2	a_{Cd}^3	$Cd_i^{\cdot\cdot}$, Cd_{In}'	No precipitates	10^{-3}
C	13.8	0	1	$a_{Cd}^{1/2}$	Cd_i^x, Cd_i'	No precipitates	10^{-3}
D	0	0.10	3	a_{Cd}	$Cd_i^{\cdot\cdot}$, Cd_{In}^x	No precipitates in matrix, but decorated dislocations. No additional phases observed.	1.3×10^{-2}
E	0	4.75	4	a_{Cd}	$Cd_i^{\cdot\cdot}$, Cd_{In}^x	Cd_3P_2 identified	0.6
F	0	19.5	5	a_{Cd}	$Cd_i^{\cdot\cdot}$, Cd_{In}^x	Cd_3P_2 identified	2.5
G	0	47.7	5	a_{Cd}	$Cd_i^{\cdot\cdot}$, Cd_{In}^x	Cd_7P_{10} identified	6.0

* Weight of Cd in 5 cm³ ampuls is 3.5 mg in all cases.
† For samples, A, B, and C, the upper limit is taken as the dissociation pressure of InP.

The diffusion anneals were carried out for 4 hr with the sample at 680°C and the diffusion source at 675°C. After the anneals, the ampuls were rapidly quenched to room temperature.

Samples for transmission electron microscopy were prepared by thinning down from the back side of the wafers to about 10 mils thickness, using a chemical-mechanical polishing technique. Disks, 3 mm diam, were then cut ultrasonically from the wafers. They were further thinned down from the back side with a 1.5% bromine-methanol solution, while protecting the diffused side. The samples, approximately 2000Å thick, were examined in a JEM 200 transmission electron microscope operating at 200 kV.

Results

A total of seven samples was examined by transmission electron microscopy. These are labeled A to G and are marked by corresponding arrows A,B,...,G on Fig. 1 to indicate their diffusion anneal history. Table I summarizes the details of the diffusion anneals. The variation of the diffusion coefficient, D_{Cd}, with a_{Cd} generated by the data from each sample is also given in Table I. Sample A, in which Cd was diffused with no excess In or P added to the ampul, and samples B and C, with excess In, indicated by arrows A, B, C in regions I and II of Fig. 1, showed no evidence of precipitates. This suggests that the activity of the dissolved Cd has not approached the value necessary for the formation of a second phase, such as Cd-phosphides. In other words, under these conditions, Cd is incorporated at bona fide lattice sites and the concentration of Cd is within the solubility limit, which is a function of the temperature and the activities of the three constituents In, Cd, and P.

On the other hand, the samples D to G in which Cd was diffused under P-rich conditions show many interesting features. Figure 2 shows transmission electron micrographs obtained from sample D. Figure 2a was taken using a two-beam diffraction condition, while Fig. 2b shows a quasi-kinematical situation. Comparison of (b) with (a) suggests that the dislocations are probably decorated with impurities or microprecipitates. Further examination of the sample revealed that the impurities only seem to precipitate out along dislocations, while no precipitates appear in the matrix. Due to their fine structure and the low density of the dislocation clusters, the corresponding diffraction patterns did not reveal any additional phases. Hence the nature of these precipitates could not be determined.

Samples E and F showed similar features and we shall therefore discuss our findings on sample F as they apply to both. Figure 3 shows the micrographs of sample F. Figure 3(a) and (b) show, respectively, an area viewed using bright and dark field diffraction conditions. Figure 3c shows the corresponding diffraction pattern. It is clear from Fig. 3(a) and (b) that fine precipitates, approximately 50-150Å in size are formed in InP. The diffraction pattern in Fig. 3c shows extra planes which do not belong to the matrix. A comparison of the d-spacings of these planes with those of the phosphides of Cd given in Table II reveals that the precipitates are Cd_3P_2 crystallites. A

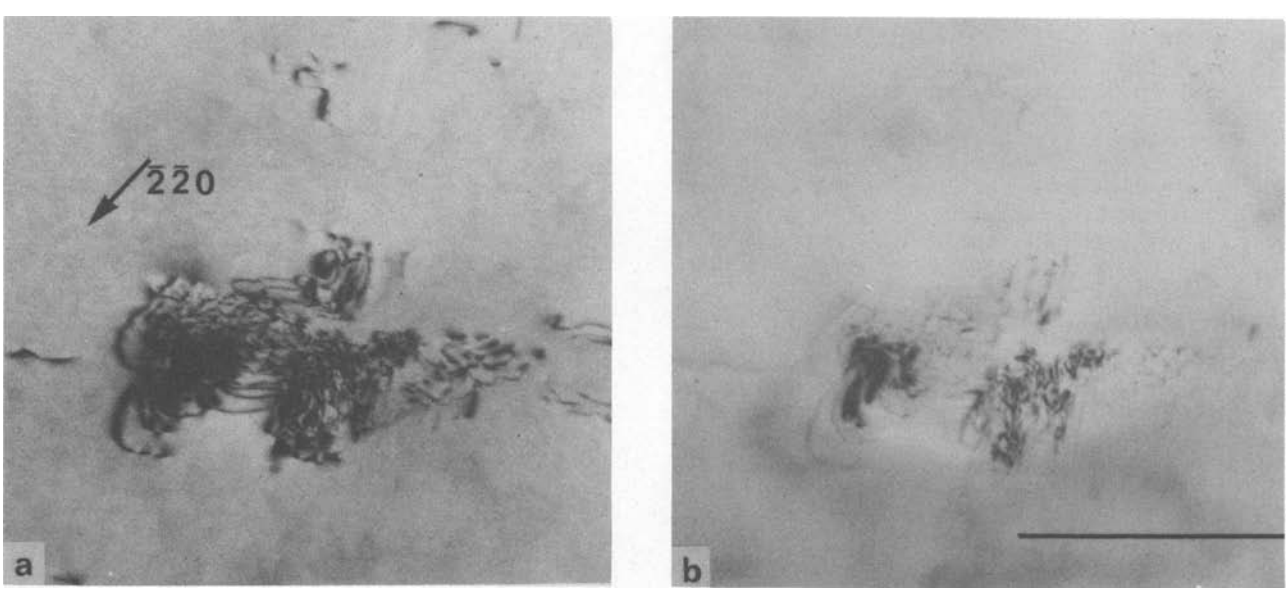

Fig. 2. TEM micrographs of sample D of Table I. (a) Shows dislocations using (220) reflections, (b) shows microprecipitates visible under quasi-kinematical condition. Marker = 0.5 μm.

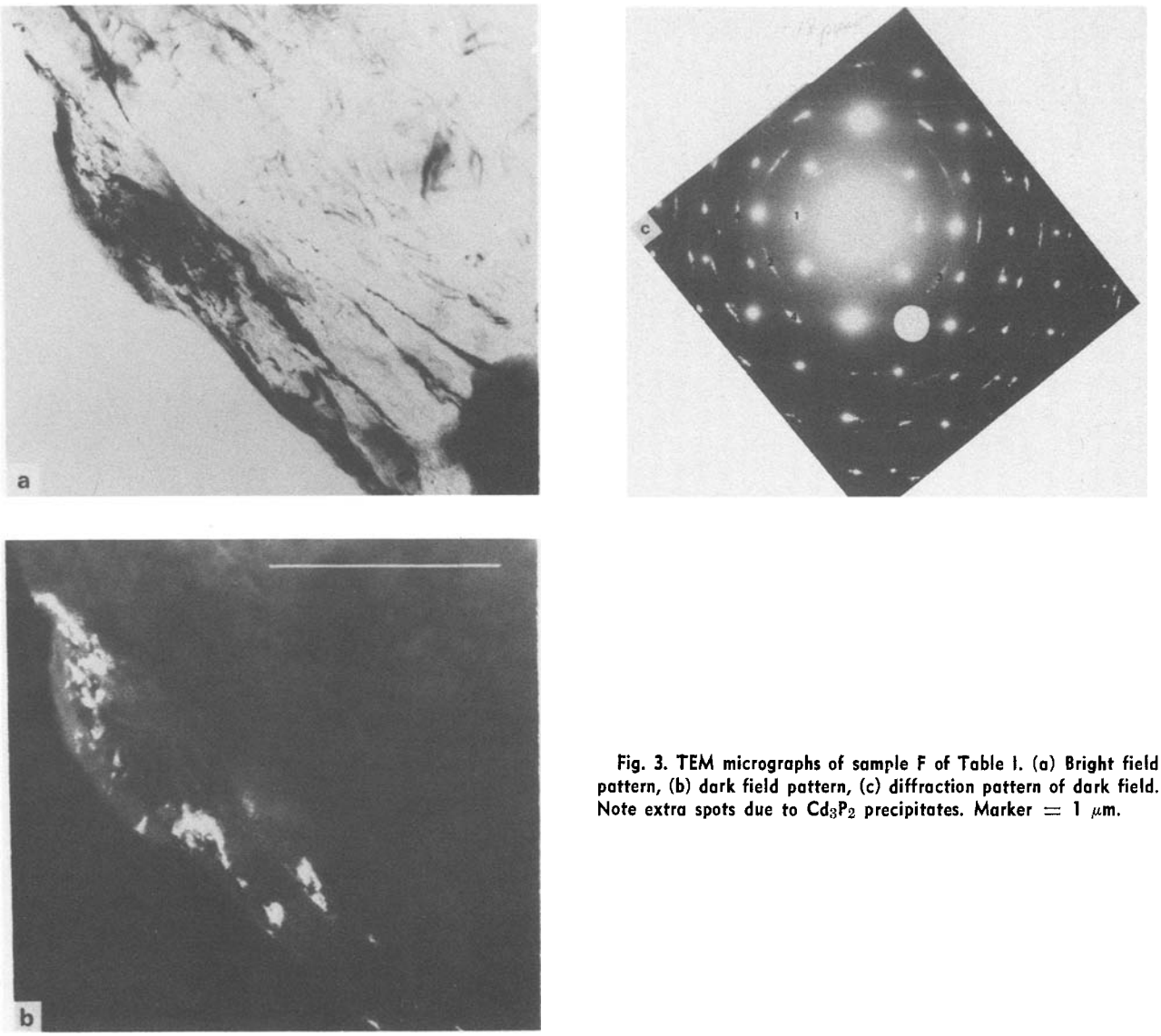

Fig. 3. TEM micrographs of sample F of Table I. (a) Bright field pattern, (b) dark field pattern, (c) diffraction pattern of dark field. Note extra spots due to Cd_3P_2 precipitates. Marker = 1 μm.

closer examination of the diffraction micrograph shown in Fig. 3c indicates that the Cd_3P_2 crystallites are oriented with their (010) plane parallel to the (001) plane of the InP matrix. However, since the crystallites appear to be rotated about their (010) axis, it is difficult to assess their growth orientation.

As the amount of phosphorus added to the ampuls was increased, new phases became evident. Figures 4 and 5 show electron micrographs of sample G prepared with 47.66 mg of P. Note how the crystallites have grown and are now better defined. However, the resulting diffraction patterns, Fig. 4c and 5c, have become very complex. In order to determine the nature of some of these crystallites, it was again necessary to at least partially index the diffraction patterns. A comparison of the d-spacings of the unknown planes with those of the known Cd-P compounds, as can be seen in Table III, shows that some of these crystallites can be identified as Cd_7P_{10}. In addition, the corresponding interplanar angles were calculated and compared with those which were measured from the micrographs. The results, in Table IV, confirm these crystallites to be Cd_7P_{10}. Hence as the amount of excess phosphorus is increased, the precipitated Cd-phosphides seem to become richer in phosphorus.

The zone axes of Cd_7P_{10} crystals identified in Fig. 4 and 5 were determined to be (211) and (001), respectively. Due to the complexity of the diffraction patterns, it was not possible to measure any angular relationships between the InP matrix and the Cd_7P_{10}

Table II. Comparison of measured d-spacings of extra planes with the known d-spacings of Cd_3P_2

d-Spacing (A)			
Point No.	Measured	ASTM File of Cd_3P_2	Plane
1	3.59	3.56	(202)
2	2.15	2.157	(401)
3	2.05	2.06	(402)
4	1.78	1.78	(404)
5	1.50	1.50	(203)
6	1.36	1.37	(407)
7	1.18	1.19	(606)

Table III. Comparison of measured d-spacings of planes of some of the crystallites with known d-spacings of Cd_7P_{10}

	d-Spacing (A)			
	Point No.	Measured	ASTM file of Cd_7P_{10}	Plane
Fig. 4	1	5.36	5.30	(240)
	2	3.24	3.08	(351)
	3	2.71	2.653	(480)
	4	2.33	2.23	(222)
	Zone axis is $(2\bar{1}\bar{1})$			
Fig. 5	1	4.13	4.26	(620)
	2	3.06	3.44	(800)
	3	2.88	2.883	(080)
	4	2.66	2.562	(860)
	Zone axis is (001)			

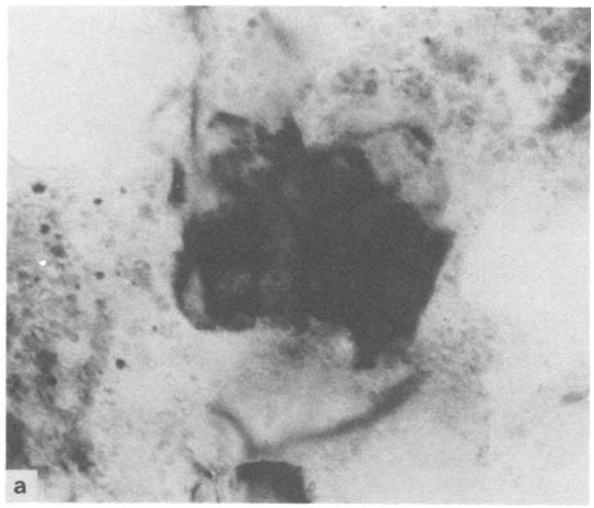

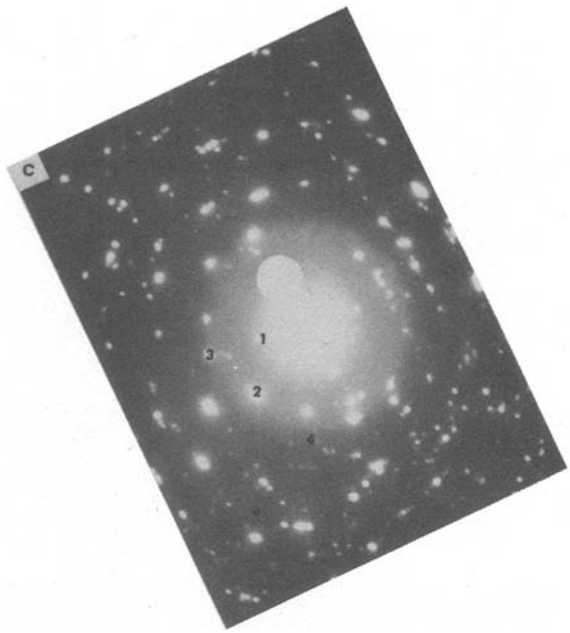

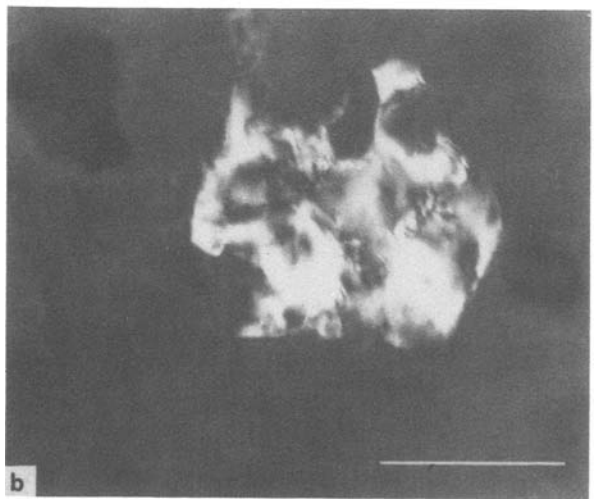

Fig. 4. TEM micrographs of sample G. (a) Bright field pattern, (b) dark field pattern, (c) diffraction pattern of dark field. Some planes indexed as belonging to Cd_7P_{10} crystallites. Marker = 2000Å.

crystallites. Hence, the complete growth orientation is not known. However, since in Fig. 5 it was known that the InP matrix had a zone axis of (001), it can be assumed that the (001) planes of InP are parallel to the (001) planes of at least some of the Cd_7P_{10} crystals.

Discussion

We shall now make an attempt to explain the observed precipitate formation in terms of the available thermodynamic data (3, 4). In addition, the previously proposed diffusion models will be reexamined in light of the coexisting second phase of Cd-phosphides as precipitates.

Table IV. Comparison of the calculated and measured interplanar angles of Cd_7P_{10} crystallites

	Planes	Interplanar angles (degrees) Measured	Calculated
Fig. 5	(240)∧(351)	41	41.87
	(240)∧(480)	0	0
	(240)∧(222)	76.5	76.02
	(351)∧(480)	41	41.87
	(351)∧(222)	35.5	34.15
	(480)∧(222)	76.5	76.02
Fig. 6	(620)∧(800)	21.7	21.72
	(620)∧(080)	68.5	68.28
	(620)∧(860)	19.5	20.15
	(800)∧(080)	90	90
	(800)∧(860)	41.2	41.86
	(080)∧(860)	49.5	48.14

Case 1: In-rich side.—Consider the incorporation of Cd in InP from liquid (In, Cd) alloy through the following reaction

$$Cd\,(In, Cd)_{alloy} + V_{In}^{x} \rightarrow Cd_{In}' + h \qquad [1]$$

The corresponding law of mass action is

$$K_{Cd} = [Cd_{In}']p/a_{Cd}[V_{In}^{x}] \qquad [1a]$$

For an extrinsic semiconductor regime, given by $[Cd_{In}'] \simeq p$, $[Cd_{In}], p \sim a_{Cd}^{1/2}[V_{In}^{x}]^{1/2}$ or since $[V_{In}^{x}] \sim a_{In}^{-1}$, $[Cd_{In}'] \sim a_{Cd}^{1/2}a_{In}^{-1/2}$. Here p denotes hole concentration. In (In, Cd) alloys, a_{Cd} is inversely proportional to a_{In}. Thus for large a_{In}, a_{Cd} is small and vice versa. Further, a_{In} and $p(P_4)$ are related through the dissociation constant of InP; a large a_{In} corresponds to a low $p(P_4)$. Therefore, on the In-rich side, a_{Cd} and $p(P_4)$ will be too small to lead to Cd-P compound formation, *i.e.*, Cd is present only homogeneously in the InP and no second phase is present (2). Proof of presence of Cd as a single ionized acceptor Cd_{In}', as proposed in Ref. (2), needs further data on the solubility of Cd as a function of a_{Cd} and a_{In}.

Case 2: P-rich side.—The observation of precipitates in the Cd-diffused samples on the P-rich side raises a difficult question. Are the precipitates formed and

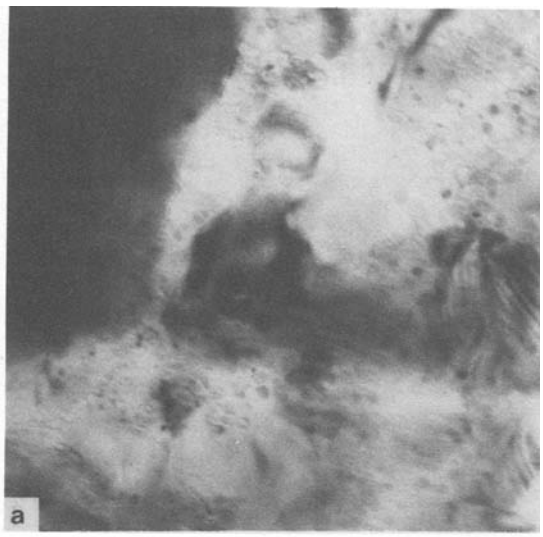

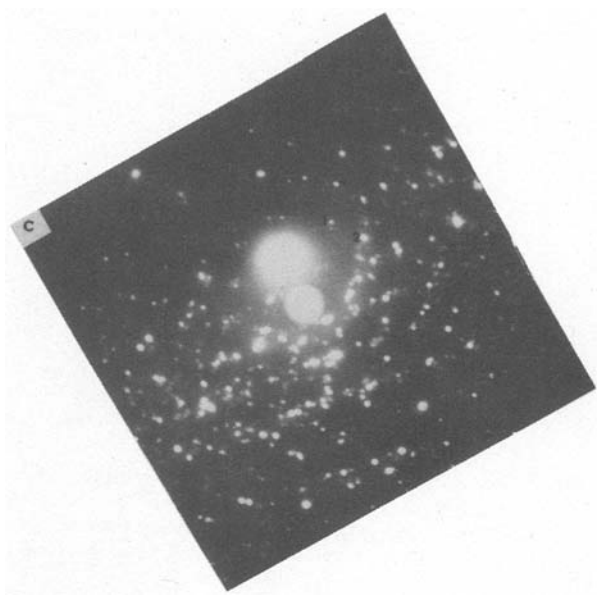

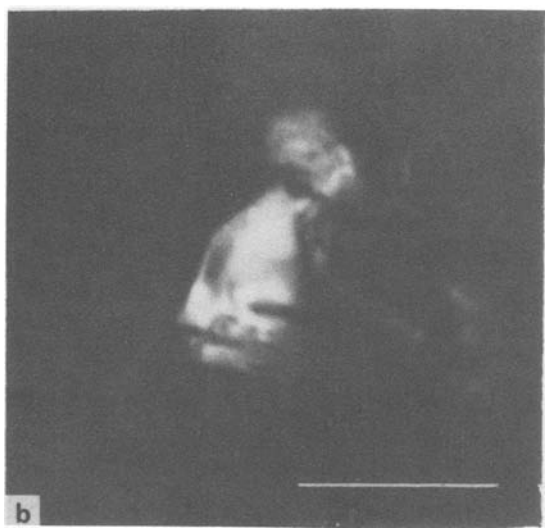

Fig. 5. TEM micrographs of a second region of the sample G shown in Fig. 4. (a) Bright field pattern, (b) dark field pattern, (c) diffraction pattern of dark field. Some planes indexed as belonging to Cd_7P_{10} crystallites.

present in the samples at the diffusion temperature of 680°C or do they form as a result of the quench from the high temperature to the room temperature? We believe that the quenching technique we adopted of dropping the ampuls into an ethylene glycol bath after the diffusion anneal is sufficiently rapid to freeze the high temperature defect equilibrium, thus preventing any atomic rearrangements necessary for precipitate formation during the quench. It is therefore assumed that the precipitates were formed and present at the diffusion temperature of 680°C itself.

The behavior of the In-Cd-P ternary system on the P-rich side can best be interpreted with the aid of the schematic ternary phase diagram shown in Fig. 6 and the activity diagram, Fig. 7, where the activity of a_{Cd} is plotted as a function of $p(P_4)$. In Fig. 6, four phases coexist in regions 1, 2, 3, 4, etc., with all activities fixed inside these regions. These regions appear as points in Fig. 7. The 4-phase regions are separated by 3-phase regions, in which a_{Cd}, $p(P_4)$, and a_{In} vary. In Fig. 7 the 3-phase transition regions are the sections between the points x_1, x_2, x_3, and x_4. At low partial pressures of phosphorus, $p(P_4)$, or equivalently, at a high activity of Cd, InP may coexist with liquid Cd. As $p(P_4)$ is increased InP may coexist with the various phosphides of Cd. At a particular value of $p(P_4)$, say point x_1, three condensed phases coexist: InP(s), Cd(l), and Cd_3P_2(s). Similarly at points x_2, x_3, and x_4 corresponding to different values of $p(P_4)$, the following phases coexist: Cd_3P_2(s), CdP_2(s), and InP(s) at x_2; CdP_2(s), CdP_4(s), and InP(s) at x_3; CdP_4(s), InP(s), and P(s) at x_4. For lack of sufficient thermodynamic data, we omitted Cd_7P_{10} from Fig. 6 and 7, although it is identified as one of the phosphides in our InP:Cd samples. The discussion here is merely restricted to the forms of phosphides for which thermodynamic data have recently become available (3, 4). The activity of cadmium and the partial pressure of phosphorus at x_1, x_2, x_3, and x_4 can be estimated

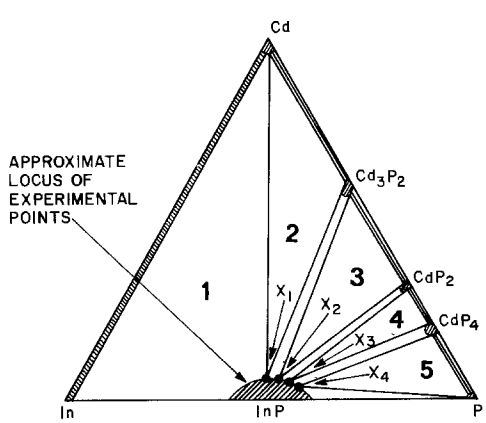

Fig. 6. Schematic of In-Cd-P ternary with exaggerated view of the region around InP to indicate the position of points x_1, x_2, x_3, and x_4 (see text).

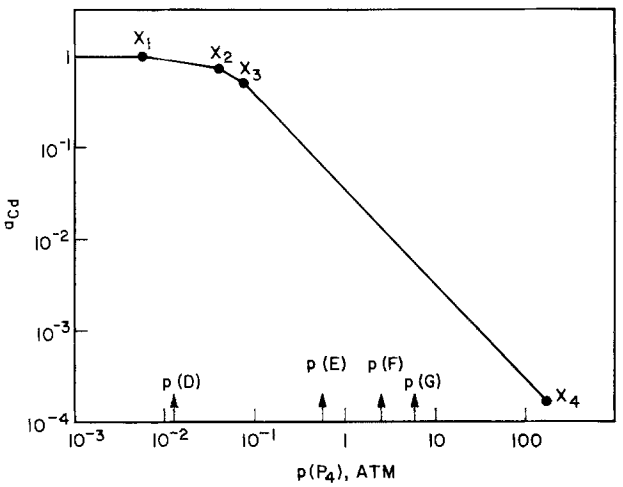

Fig. 7. Graphical representation of the experimental locus through points x_1, x_2, and x_4 plotted as Cd-activity vs. phosphorus vapor pressure. Arrows $p(D)$, $p(E)$, $p(F)$, $p(G)$ indicate estimated upper limit of the phosphorus vapor pressure using ideal gas law (see text).

from the known values of dissociation constants of the phosphides (3, 4) and the saturated vapor pressures of Cd and P as a function of temperature (6, 7). The dissociation constants, $K_{Cd_3P_2}$, K_{CdP_2}, and K_{CdP_4} correspond to the following reactions and the respective mass action relations; thus

$$Cd_3P_2(s) \rightarrow 3Cd(g) + 1/2P_4(g) \quad [2]$$

$$K_{Cd_3P_2} = p^3(Cd)p^{1/2}(P_4) \quad [2a]$$

$$CdP_2(s) \rightarrow Cd(g) + 1/2P_4(g) \quad [3]$$

$$K_{CdP_2} = p(Cd)p^{1/2}(P_4) \quad [3a]$$

$$CdP_4(s) \rightarrow CdP_2(s) + 1/2P_4(g) \quad [4]$$

$$K_{CdP_4} = p^{1/2}(P_4) \quad [4a]$$

The following values of the constants are obtained by Lazarev *et al.* (3, 4)

$$\log_{10}(K_{Cd_3P_2}/atm^{7/2}) = -\frac{(24{,}940 \pm 480)}{T} + (23.70 \pm 0.39) \quad [5]$$

$$\log_{10}(K_{CdP_2}/atm^{3/2}) = -\frac{(11{,}420 \pm 130)}{T} + (10.69 \pm 0.14) \quad [6]$$

$$\log_{10}(K_{CdP_4}{}^2/atm) = -\frac{(4{,}950 \pm 150)}{T} + (4.04 \pm 0.17) \quad [7]$$

The saturated vapor pressure of Cd, $p_{Cd}{}^o$ is given by [6]

$$p_{Cd}{}^o = 1.7 \times 10^5 \exp\left(-\frac{1.08\ eV}{kT}\right) atm \quad [8]$$

The vapor pressure of commercial grades of phosphorus is given by (7)

$$\ln p(P_4) = -\frac{(10.8 \pm 0.4) \times 10^3}{T} + (16.5 \pm 0.6) \quad [9]$$

from Eq. [5] to [9], at the diffusion temperature of 680°C, we obtain

$$K_{Cd_3P_2} = 3.39 \times 10^{-3}\ atm^{7/2} \quad [10a]$$

$$K_{CdP_2} = 5.10 \times 10^{-2}\ atm^{3/2} \quad [10b]$$

$$K_{CdP_4}{}^2 = 7.01 \times 10^{-2}\ atm \quad [10c]$$

$$p_{Cd}{}^o = 0.36\ atm \quad [10d]$$

$$p(P_4) = 175.5\ atm \quad [10e]$$

Using the numerical estimates [10(a-e)], an approximate locus of the experimental data passing through the points x_1 to x_4 can be constructed. Figure 7 shows this locus represented graphically as an activity diagram showing log a_{Cd} *vs.* log $p(P_4)$. For example, the position of x_1, where Cd(l), InP(s), and Cd_3P_2(s) are presumed to coexist, is determined from $p(P_4) \approx K_{Cd_3P_2}{}^2/p_{Cd}{}^{o\,6} = 5.64 \times 10^{-3}$ atm, giving the coordinates of x_1, as $a_{Cd} \approx 1$ and $p(P_4) \simeq 5.64 \times 10^{-3}$ atm. Similarly, [10(a) and (b)] yield the coordinates of x_2 as $a_{Cd} \simeq 0.72$ and $p(P_4) \simeq 3.92 \times 10^{-2}$ atm, and so on. It should be understood, however, that an estimation of the actual partial pressures of Cd, P, and In in the diffusion ampul is not an easy task. Such a task is even more complicated with the possibility of Cd-phosphide formation. A rough estimate of the upper limit of the phosphorus partial pressure can be made with a simple-minded assumption that all the excess amount of phosphorus added to the ampul is present as P_4 in the vapor. The estimate may be too high because some P is dissolved in InP or present as Cd_mP_n(s). It may be too low because P_2 is also present. Thus the arrows $p(D)$ to $p(G)$ marked in Fig. 7 indicate these estimated upper limits based on ideal gas law. The actual vapor pressures will be lower than these limits and will be expected to fall to the left side of the arrows $p(D)$ to $p(G)$. It is apparent that the samples A, B, and C represented by arrows $p(A)$, $p(B)$, and $p(C)$ in Fig. 1 fall to the left of X_1 in Fig. 7 and are therefore not shown. Thus the phosphorus vapor pressure at which samples A, B, and C were annealed is not high enough for Cd-phosphide formation. The arrow $p(D)$ corresponds to sample D. As seen from Table I, sample D shows dislocations decorated with precipitates; thus it is in a three-phase region. The $p(P_4)$ estimate places it in the region InP + Cd_3P_2 + vapor (with Cd_3P_2 as the precipitates). However, samples E, F, and G with fairly large amounts of phosphorus have a high probability of forming Cd-phosphides as seen from their position on Fig. 7. These fall to the right of x_3, *i.e.*, in the three-phase region InP + CdP_4 + vapor with a $p(P_4)$ larger than expected for InP + Cd_7P_{10} + vapor which should have a $p(P_4)$ between x_1 and x_3. The identification of Cd_7P_{10}, however, is certain. There are other precipitate forms observed which we could not identify. These may include CdP_2 and CdP_4 as expected from the predictions of Fig. 7.

Consider the incorporation of Cd in InP from Cd-phosphide, Cd_mP_n present as an external phase (diffusion source); this occurs via the reaction

$$Cd_mP_n \rightarrow mCd_{In}{}^x + nP_P{}^x + (m-n)V_P{}^x \quad [11]$$

The corresponding law of mass action is given by

$$K_{mn} = \frac{[Cd_{In}{}^x]^m[V_P{}^x]^{m-n}}{[a(Cd_mP_n)]} \quad [11a]$$

since the site fraction $[P_P{}^x] \simeq 1$. The dissociation reactions of phosphides of In and Cd lead to the following relations between the partial pressures of Cd, P, and In

$$InP(s) = In(l) + \frac{1}{4}P_4(g) \quad [12]$$

$$K_{InP}(s) = a_{In}p_{(P_4{}^{1/4})}/a_{InP} \quad [12a]$$

$$Cd_mP_n = mCd(l) + \frac{n}{4}P_4(g) \quad [13]$$

$$K_{Cd_mP_n} = a_{CdP}{}^{m\,n/4}(P_4)/a(Cd_mP_n) \quad [13a]$$

Taking $a(Cd_mP_n)$, $a(InP) \simeq 1$, for coexistence between InP and Cd_mP_n, the phosphorus vapor pressure

over them is the same: thus from [12a] and [13a] we get

$$p(P_4) = K_{InP}{}^4 a_{In}{}^{-4} = K_{Cd_mP_n}{}^{4/n} a_{Cd}{}^{-4m/n} \quad [14]$$

Therefore for equilibrium between coexisting phases of InP and Cd_mP_n, the activities of In and Cd are related by

$$a_{In}{}^{-4} a_{Cd}{}^{4m/n} = K_{Cd_mP_n}{}^{4/n} K_{InP}{}^{-4} \quad [15]$$

Depending on the phosphorus to Cd ratio of the phosphides, m and n take different values; thus for Cd_3P_2, CdP_2, and CdP_4, respectively, we obtain the relations [16], [17], and [18]

$$a_{In}{}^{-4} a_{Cd}{}^{6} = K_{Cd_3P_2}{}^2 K_{InP}{}^{-4} = K_1 \quad [16]$$

$$a_{In}{}^{-4} a_{Cd}{}^{2} = K_{CdP_2}{}^2 K_{InP}{}^{-4} = K_2 \quad [17]$$

$$a_{In}{}^{-4} a_{Cd}{}^{1} = K_{CdP_4} K_{InP}{}^{-4} = K_3 \quad [18]$$

For a concentration-dependent dissociative diffusion mechanism, it has been shown (8) that the effective diffusion coefficient is given by

$$D_{eff} = D_i \partial C_i / \partial C \quad [19]$$

where C_i = interstitial Cd concentration and C = total Cd concentration in the sample. On the phosphorus side it has been shown (2) that the assumption of $[Cd_{In}'] \simeq p$ and $[Cd]_{tot} \simeq [Cd_{In}{}^x]$ leads to

$$[Cd_{In}'], p \sim a_{Cd}{}^{1/2} a_{In}{}^{-1/2} \quad [20a]$$

$$[Cd_{In}{}^x] \simeq [Cd]_{tot} \sim a_{Cd} a_{In}{}^{-1} \quad [20b]$$

$$[Cd_i{}^{\cdot\cdot}] \sim a_{Cd}{}^2 a_{In}{}^{-1} \quad [20c]$$

Note that in our model (2) $C_i = Cd_i{}^{\cdot\cdot} \sim a_{Cd}{}^2 a_{In}{}^{-1}$ and $C = [Cd]_{tot} = [Cd_{In}{}^x] \sim a_{Cd} a_{In}{}^{-1}$, thus

$$D_{eff} = D_i \frac{\partial C_i}{\partial C} = D_i \frac{\partial C_i}{\partial a_{Cd}} \frac{\partial a_{Cd}}{\partial C} \quad [21]$$

For equilibrium between Cd_3P_2 and InP, using the relationship given by Eq. [16] between a_{Cd} and a_{In} and substituting in [20(b) and (c)] and [21] it can be seen that $D_{eff} \sim a_{Cd}$. Similarly for coexistence of CdP_2 and CdP_4 we get $D_{eff} \sim a_{Cd}$ from Eq. [17]-[21]. Thus the previous proposals of models discussed in Ref. (2) for the Cd diffusion and incorporation appear to hold good even when there is a second-phase precipitation.

Figure 7 indicates that in the wake of Cd-phosphide precipitation, a_{Cd} gradually decreases with increasing phosphorus vapor pressure, $p(P_4)$; this corresponds to a lower a_{In}. This suggests that the solubility of Cd, as measured by $[Cd]_{tot} \simeq [Cd_{In}{}^x]$ or the precipitates will be expected to decrease, exhibiting a functional dependence on phosphorus vapor pressure, similar to that of a_{Cd} on $p(P_4)$.

A decreasing solubility of Zn in InP with an increasing phosphorus vapor pressure, reported by Tuck and Hooper (9), may similarly be attributed to the precipitation of Zn-phosphides. Tien and Miller (5) proposed a neutral Cd-complex, the concentration of which rapidly varies along the diffusion profile. This complex may not be identified as the second phase of Cd-phosphides. A complex refers to species present in solid solution, a second phase is a precipitate. The results, however, can be re-interpreted on the basis of a second-phase formation. Tuck and Hooper (9) and Tien and Miller (5) proposed that the fast diffusing interstitial is neutral. This proposal was based on the P-rich side data. Since the concentration of the neutral interstitial is proportional to a_{Cd} and the total concentration, approximated by $[Cd_{In}{}^x]$ varies as $a_{Cd} a_{In}{}^{-1}$, the effective diffusion coefficient, as seen from Eq. [16]-[21], would be expected to vary as $D_{Cd} \sim a_{Cd}{}^{\alpha}$, α being 3/2 or 1/2 or 1/4 depending on the coexisting phases of Cd_3P_2, CdP_2, and CdP_4, respectively. However, the observed behavior of D_{Cd} with phosphorus vapor pressure, shown in Fig. 1(b) has been interpreted as an indication of the rapid formation of the Cd-phosphides, which then act as diffusion sources. In region 3, liquid Cd was assumed to be in equilibrium with Cd_3P_2 and InP, thus maintaining a constant $a_{Cd} \approx 1$, and hence a constant D_{Cd}. The approximate D_{Cd} variations of $W_P{}^{-1/2}$ and $W_P{}^{-1}$ in regions 4 and 5, respectively, were assumed to represent the stability regions of CdP_2 and CdP_4. On this basis, the three regions of Fig. 1(b) have been interpreted as an indication of a linear $D_{Cd} \sim a_{Cd}$ behavior. But, for equilibrium between CdP_2 and CdP_4 with InP, relations [17] and [18] always apply, irrespective of whether the Cd-phosphides are present as precipitates inside InP, or present as external diffusion sources only. Strictly, the activities of Cd, In, and P are related via the Gibbs-Duhem equation, and the assumptions made here are questionable. Nevertheless, the observation of the strong variation of $D_{Cd} \sim a_{Cd}{}^3$ on the In-rich side and the $D_{Cd} \sim a_{Cd}$ on the P-rich side, appear to suggest a charged interstitial. From the simple picture presented here, and in Ref. (2), a doubly ionized interstitial is indicated.

The diffusion studies of Ref. (2) and (5) based on p-n junction depths fall into the realm of chemical diffusion and not iso-concentration diffusion. Thus the question of the specific charge state of the diffusing species may be resolved by carefully controlled tracer diffusion experiments. A comprehensive analysis of the In-P-Cd system from the point of view of defect chemistry may be worth looking into when more data become available.

Summary

Transmission electron microscopic examination of Cd-diffused samples under P-rich conditions showed Cd-phosphide precipitates. A semi-quantitative analysis based on the currently available thermochemical data is in reasonable agreement with the observed precipitate formation under P-rich conditions.

The previous proposal (2) of interstitial-substitutional diffusion mechanism with a doubly ionized interstitial as the fast diffusing species with most Cd dissolved in a neutral substitutional form via precipitated Cd-phosphides appears to be in satisfactory agreement with the present data.

Acknowledgments

We thank A. K. Chin for help with the diffusion depth measurements and EBIC profiling. We are indebted to W. A. Bonner for InP wafers. S. Mahajan has contributed by stimulating our interest with helpful discussions. We gratefully acknowledge several stimulating comments and suggestions of Professor F. A. Kroger, of the University of Southern California, on the manuscript. We thank O. G. Lorimor for a critical reading of the manuscript. We thank A. A. Bergh and G. Y. Chin for constant encouragement and support.

Manuscript submitted April 14, 1982; revised manuscript received July 12, 1982.

Any discussion of this paper will appear in a Discussion Section to be published in the December 1983 JOURNAL. All discussions for the December 1983 Discussion Section should be submitted by Aug. 1, 1983.

Publication costs of this article were assisted by Bell Laboratories.

REFERENCES

1. A. K. Chin, B. V. Dutt, H. Temkin, W. A. Bonner, and D. D. Roccasecca, *Appl. Phys. Lett.*, **36**, 924 (1980).
2. B. V. Dutt, A. K. Chin, and W. A. Bonner, *This Journal*, **128**, 2014 (1981).
3. V. B. Lazarev, J. H. Greenberg, V. J. Shevchenko, S. F. Marenkin, and S. E. Kozlov, *J. Chem. Thermodyn.*, **8**, 61 (1976).

4. V. B. Lazarev, Ya. Kh. Grinberg, S. F. Marenkin, and S. Kh. Samiev, *Izv. Akad. Nauk SSR* (English Translation *Inorganic Matls*)., **15** (7), 901 (1979).
5. P. K. Tien and B. I. Miller, *Appl. Phys. Lett.*, **34**, 701 (1979).
6. H. R. Vydyanath, *J. Appl. Phys.*, **47**, 4993 (1976).
7. K. J. Bachmann and E. Buehler, *This Journal*, **121**, 835 (1974).
8. F. C. Frank and D. Turnbull, *Phys. Rev.*, **104**, 617 (1956).
9. B. Tuck and A. Hooper, *J. Phys. D: Appl. Phys.*, **8**, 1806 (1975).

A Quantitative Study of the Relationship Between Interfacial Carbon and Line Dislocation Density in Silicon Molecular Beam Epitaxy

J. H. McFee, R. G. Swartz, V. D. Archer, and S. N. Finegan

Bell Laboratories, Holmdel, New Jersey 07733

and L. C. Feldman

Bell Laboratories, Murray Hill, New Jersey 09074

ABSTRACT

Silicon layers grown by molecular beam epitaxy on (100) silicon substrates were depth-profiled for carbon and oxygen by secondary ion mass spectrometry (SIMS). The same epitaxial layers were subjected to a defect etch to reveal dislocation density. A strong correlation is found between the carbon concentration at the substrate-epitaxy interface and the line dislocation density of the epitaxial layer. Layers with interfacial carbon concentration $\approx 10^{21} cm^{-3}$ exhibit line dislocation densities $\geq 10^{7} cm^{-2}$, while layers with interfacial carbon concentration $\leq 10^{19} cm^{-3}$ ($\leq$0.01 monolayer carbon) have line dislocation densities $\leq 10^{4} cm^{-2}$. In contrast, no correlation is found between interfacial oxygen (as revealed by SIMS) and the line dislocation density of the epitaxial layers.

It is known that carbon contamination at the substrate-epitaxy interface is an influential parameter in the growth of silicon molecular beam epitaxy (MBE) (1-3). For example, Joyce *et al.* (2) have reported that carbon coverage of approximately 0.01 monolayer at the silicon substrate is sufficient to cause three-dimensional growth from nuclei rather than the desired two-dimensional step-wise growth which results in smooth epilayers of high crystalline perfection. The present study confirms and quantifies the effects of carbon as an interfacial contaminant in Si-MBE. Measurements were made on a dozen different samples, each of which represents a different MBE growth run. These runs took place over a span of nearly one year and thus encompass a wide variety of growth conditions. Consequently, in this group of samples the interfacial carbon contamination varied over a wide range. We subsequently studied the perfection of these samples by subjecting them to a defect etch which reveals the density of various defect structures via etch pit count. The same samples were depth profiled by secondary ion mass spectrometry (SIMS) to reveal the amount of carbon present at the substrate-epilayer interface. In the case of the most heavily contaminated samples, Rutherford backscattering (RBS) channeling experiments were used to relate the quality of the interface to the carbon contamination.

Epitaxial Layer Growth

The epitaxial layers were grown in a Si-MBE system designed and built by Ota (4). The stainless steel UHV growth chamber is evacuated with ion and titanium sublimation pumps, and is equipped with a mass analyzer for residual gas analysis. After pump down and overnight bakeout at $\sim$ 130°C an ambient pressure of $\sim 1 \times 10^{-9}$ Torr was routinely obtained in the growth chamber. The most prominent peak in the mass spectrum of the residual gas in the chamber before growth was at mass number $M = 16$, and is believed to be methane. During growth, the ambient pressure in the growth chamber rose to the mid-10^{-8} Torr range. The epitaxial layers were deposited via E-beam evaporation onto (100) oriented substrates of 1 × 3 in. rectangular shape. These were clamped at the short ends and resistively heated via an applied current. During growth the substrate temperature was in the range 700°-800°C.

Prior to insertion into the growth chamber the substrates received a chemical clean consisting of solvent degreasing, followed by immersion in a heated solution of 1:1 H_2SO_4:H_2O_2. Then, after a 50:1 H_2O:HF dip and deionized water rinse, a thin protective oxide layer was grown on the substrate using a heated mixture of 1:1:1 NH_4OH:H_2O_2:H_2O. This oxide layer remains on the substrate during transfer to the MBE growth chamber, pump down, and bakeout; it is desorbed just prior to growth when the substrate temperature is raised briefly (~45 sec) to 1100°-1200°C. Experience has shown that care must be taken during this critical operation. For many of the samples in this study a deposition-blocking shutter was positioned in front within a few cm of the substrate during the thermal preclean. In this condition the ambient pressure in the growth chamber rose into the mid-10^{-7} Torr range when the substrate temperature was cycled to 1100°-1200°C. Films grown after such pretreatment exhibited line dislocation densities ranging from 10^4 cm^{-2} to 10^8 cm^{-2}. If, on the other hand, the blocking shutter was pulled away from the substrate, the ambient pressure did not rise above low-10^{-8} Torr during the thermal cleaning cycle. In this case the subsequently grown epitaxy consistently exhibited a line dislocation density in the 10^3-10^4 cm^{-2} range.

We consider it probable that when the deposition-blocking shutter is positioned in front of the wafer during the thermal clean, the shutter together with the wafer and any nearby surfaces (*e.g.*, wafer clamps) forms a partially enclosed oven. All surfaces within this oven are heated to high temperatures, resulting in voluminous outgassing. This is responsible for the relatively high pressures observed during the thermal clean cycle. As the wafer cools following this procedure, the ambient gaseous impurities within the volume enclosed by the shutter and wafer condense and redeposit on the wafer, thereby contaminating its

Key words: semiconductor, defects, growth, contamination.

surface in an uncontrolled manner. These impurities are subsequently trapped at the epitaxy/substrate interface following MBE growth.

The epitaxial layers grown for this study ranged in thickness from 0.3 μm to 2.5 μm. Most of the epilayers were purposely made less than 1 μm thick to facilitate probing of the epitaxy-substrate interface via Rutherford backscattering and SIMS. Most layers were not intentionally doped (N $\approx 10^{14}$ cm^{-3}). A few layers were lightly doped with boron or arsenic (P or N $\approx 10^{16}$ cm^{-3}) during growth via low energy ion implantation (4, 5). In all samples the substrates were heavily doped (N or P $\approx 10^{19}$ cm^{-3}) so that they could be resistively self-heated.

Analysis

Defect etch.—Each MBE-grown silicon epitaxial sample was evaluated using a wet-chemical defect etch. Standard etching techniques using a dilute Schimmel defect etch (6) (one part 0.75M CrO_3, two parts 49% HF, and 1.5 parts DI water) were used on samples having epitaxial layer thickness greater than 2 μm. An "etch-through" technique (7) was developed for the analysis of epitaxial layers less than 2 μm thick using the same dilute Schimmel etch. This technique exploited our use of heavily doped substrates with lightly doped epitaxy, and allowed the same samples purposely grown thin for RBS and SIMS analysis to be defect etched and to yield defect density data as well. The predominant etch artifacts observed were random line dislocations which extend through the epitaxy to the substrate, although other defects and defect arrays were present. The flash heating technique used to clean the substrate just before epitaxial growth induced some slip. Partial dislocations were also observed in the MBE-grown epitaxy, but the layers evaluated were of insufficient thickness to determine whether or not these were associated with stacking faults. A graininess of the etched epitaxial surface of some samples is resolved into small "saucer" pits by the scanning electron microscope, but these are not included in our etch pit count. Unlike the line dislocations, they are thought to be localized defect structures not associated with the epitaxy-substrate interface. Inasmuch as the remaining etch pits are primarily line dislocations, we use the term "line dislocation density" to refer to the quantitative data obtained from chemical etching. The line dislocations and slip were distributed such that the center of the 1 by 3 in. wafers was consistently the best quality silicon in each sample. Quantitative etch pit data were taken from this portion of the wafer.

Secondary ion mass spectrometry (SIMS).—SIMS analysis of our samples was provided as a service by Charles Evans and Associates (8) The SIMS measurements were performed on a CAMECA IMS-3f Ion Microanalyzer using Cs^+ ion bombardment for sensitive carbon and oxygen analyses. Depth profiles of ^{12}C and ^{16}O were run on each sample. The data were furnished in the form of ^{12}C and ^{16}O concentration (cm^{-3}) *vs.* sputtering depth (Fig. 1). The sputtering rate was determined to be ~50 Å/sec and the depth resolution specified as 100-200Å at a depth of 1 μm. In each case the measurement profile extended through the epilayer into the substrate so that ^{12}C and ^{16}O concentration at the interface was examined.

Rutherford backscattering (RBS).—Many of our samples were also examined by RBS. An incident beam of 1.8 MeV $^4He^+$ ions was used. RBS spectra were taken with the incident beam randomly oriented and also with the beam aligned parallel to the (100) direction (substrate normal) to give a "channeling" spectrum. The ratio of the channeling spectrum to the random spectrum, χ_{min}, is a measure of the crystalline quality of the epitaxial layer. All of the samples examined showed $\chi_{min} = 3.1$-3.3%, which is indistinguishable from high quality single-crystal silicon. However, in the case of those samples which had the largest amounts of interfacial carbon contamination, an anomalous silicon peak was observed in the RBS channeling spectrum (Fig. 3), at a backscattered energy corresponding to the position of the epitaxy-substrate interface. The area under this peak can be interpreted quantitatively in terms of the number of displaced silicon atoms (cm^{-2}) (9).

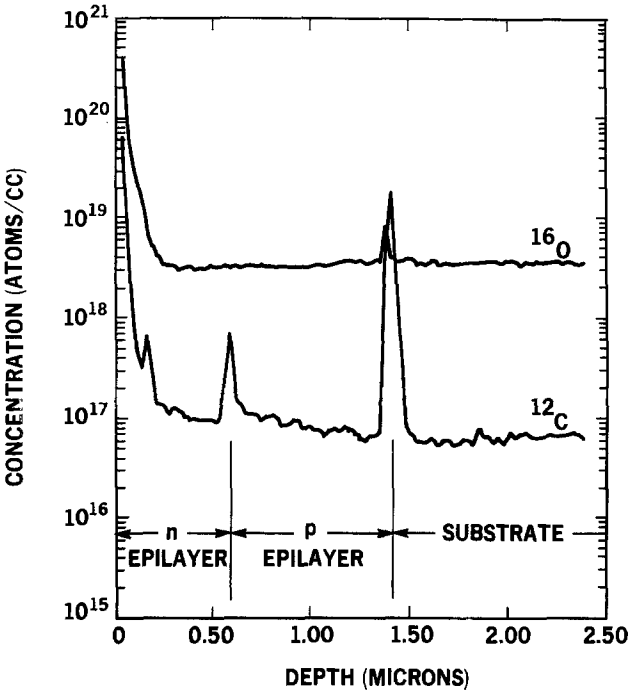

Fig. 1. SIMS depth profile of ^{12}C and ^{16}O concentration. The substrate-epilayer interface is at a depth of 1.5 μm in this sample. At 0.6 μm depth, growth was interrupted for a few minutes in order to change from p to n doping. At 0.2 μm depth, the growth rate was decreased from 10 Å/sec to 3 Å/sec.

Results

As an example of the SIMS results, Fig. 1 shows the depth profile obtained from one of our samples. The substrate-epilayer interface lies at a depth of 1.5 μm in this particular case. At this depth the ^{12}C concentration increases from a background level $\approx 10^{17}$ cm^{-3} to a peak value $\approx 2 \times 10^{19}$ cm^{-3}. The ^{16}O concentration also increases noticeably at the interface, but its increase is less than that of ^{12}C, an observation true in general. The peak ^{12}C concentration at the substrate-epitaxy interface was obtained from the SIMS depth profiles of eleven other samples, each representing a different MBE growth run. Figure 2 plots the line dislocation density for each of the same twelve samples *vs.* the peak ^{12}C concentration at the substrate-epitaxial layer interface, as determined from the SIMS data. A strong correlation is evident in Fig. 2 between these two parameters. At one extreme of the plot is a sample with a line dislocation density of 10^8 cm^{-2} and peak ^{12}C concentration of 10^{21} cm^{-3}. At the other extreme are samples with line dislocation densities of less than 10^4 cm^{-2} and peak ^{12}C concentrations of less than 10^{19} cm^{-3} at the interface. The solid line plotted in Fig. 2 is a least mean squares linear fit to the carbon-defect data on the log-log plot. The slope of this line indicates that the line dislocation density varies approximately as the three-halves power of the peak carbon concentration at the epitaxy-substrate interface. We cannot presently offer a physical explanation for this empirical result. For comparison to the ^{12}C data, the SIMS ^{16}O concentration at the interface is also plotted in Fig. 2. In contrast to the carbon results, no correlation between interfacial ^{16}O and line dislocation density is evident.

As mentioned above, in the case of the three samples having the greatest interfacial carbon concentrations

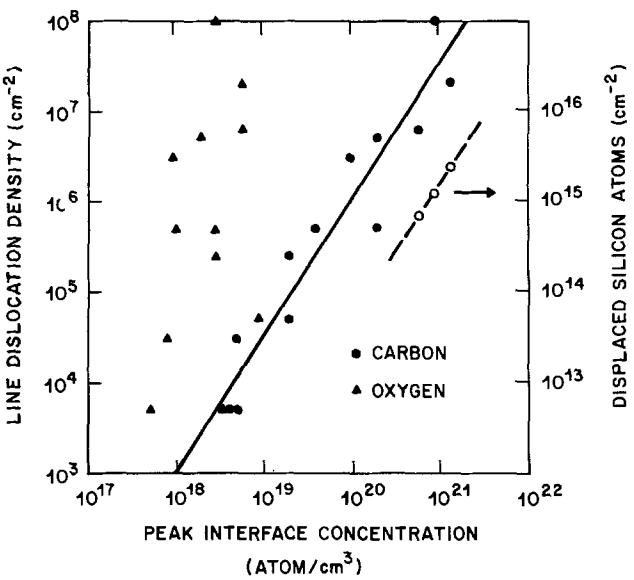

Fig. 2. Line dislocation density vs. peak carbon and oxygen concentration at substrate-epilayer interface for twelve different MBE-grown samples. The solid line plotted is a least mean squares fit to the carbon data. Also shown (open circles) is the number of displaced silicon atoms/cm^2 at the interface as derived from RBS data. These three points refer to the samples having the highest concentration of interfacial carbon.

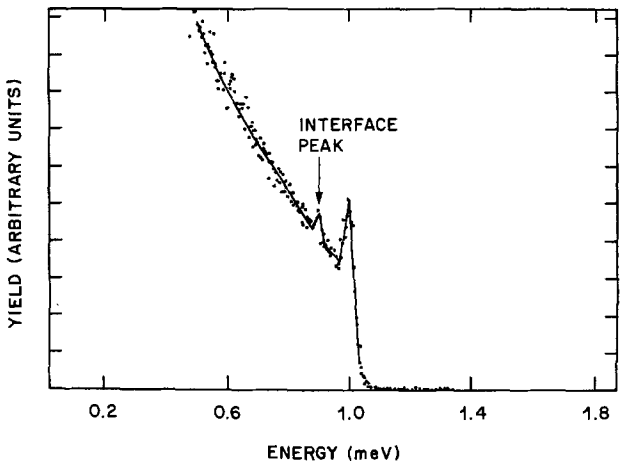

Fig. 3. RBS channeling spectrum showing the anomalous interface peak from a sample with interfacial carbon concentration of 10^{21} cm^{-3}. This peak represents increased backscattering at the epitaxy-substrate interface. Epitaxial layer thickness is 0.3 μm.

an anomalous silicon peak was observed in the RBS channeling measurements. The RBS data, in terms of displaced silicon atoms/cm^2, is also plotted in Fig. 2 *vs.* the peak carbon at the interface as determined by SIMS. Note that the RBS scattering increases monotonically with the carbon concentration. This agreement suggests that the interfacial carbon is responsible for the anomalous RBS peak. The RBS data of Fig. 2 indicate that there is approximately one monolayer (10^{15} cm^{-2}) of displaced silicon present at the interface in the case of the most heavily contaminated samples. It is possible to estimate the carbon coverage by integrating the SIMS ^{12}C data over the width of the interface peak which has a typical half-amplitude width of 200Å. We thus find that a peak carbon concentration of 10^{21} cm^{-3} corresponds to an area density of approximately 10^{15} cm^{-2}. Since the ion scattering peak corresponds to 10^{15} cm^{-2} displaced silicon atoms, there is approximately one displaced silicon atom for each carbon atom present at the interface.

Conclusion

A quantitative relationship between interfacial carbon concentration and defect density in Si-MBE has been demonstrated (Fig. 2). This result strongly suggests that a major cause of defects in Si-MBE layers is carbon contamination present on the substrate surface at the beginning of epitaxial growth. In our silicon MBE system, severe carbon contamination resulted from the presence of a deposition-blocking shutter in front of the substrate during a high temperature cleaning treatment. In other MBE systems, sources of carbon contamination may be quite different. Our results indicate, however, that if the carbon contamination is reduced to 0.01 monolayer or less, epitaxy with line dislocation density of order 10^4 cm^{-2} can be produced. Epitaxy of this quality is already suitable for many integrated circuit applications. Since the starting substrates used in this study typically had etch pit counts of 10^3-10^4 cm^{-2}, better quality starting material is probably necessary in order to achieve Si-MBE with line dislocation density significantly less than 10^4 cm^{-2}.

For the samples plotted in Fig. 2 the interfacial oxygen concentration is in the range 10^{18}-10^{19} cm^{-3}, and is generally small compared to the carbon concentration. The absence of any correlation between interfacial oxygen and line dislocation density in Fig. 2 leads us to conclude that interfacial oxygen is not an important contaminant in Si-MBE, at least for the types and quantities of defects studied here.

Acknowledgment

We are happy to acknowledge the assistance of P. J. Silverman in the RBS analysis.

Manuscript submitted June 17, 1982; revised manuscript received Aug. 30, 1982. This was Paper 135 presented at the Montreal, Canada, Meeting of the Society, May 9-14, 1982.

Any discussion of this paper will appear in a Discussion Section to be published in the December 1983 JOURNAL. All discussions for the December 1983 Discussion Section should be submitted by Aug. 1, 1983.

Publication costs of this article were assisted by Bell Laboratories.

REFERENCES

1. B. A. Joyce, *Rep. Prog. Phys.*, **37**, 363 (1974).
2. B. A. Joyce, J. H. Neave, and B. E. Watts, *Surf. Sci.*, **15**, 1 (1969).
3. T. Sakamoto, T. Takahashi, E. Suzuki, A. Shoji, H. Kawanami, Y. Komiya, and Y. Tarui, *ibid.*, **86**, 102 (1979).
4. Y. Ota, *J. Appl. Phys.*, **51**, 1102 (1980).
5. R. G. Swartz, J. H. McFee, A. M. Voshchenkov, S. N. Finegan, and Y. Ota, *Appl. Phys. Lett.*, **40**, 239 (1982).
6. D. G. Schimmel, *This Journal*, **126**, 479 (1979).
7. V. D. Archer, *ibid.*, **129**, 2074 (1982).
8. Charles Evans and Associates, 1670 South Amphlett Boulevard, Suite 120, San Mateo, California.
9. Wei-Kan Chu, J. W. Mayer, and Marc-A. Nicolet, "Backscattering Spectrometry," pp. 255-261, Academic Press, New York (1978).

Optical Techniques for Implant Process Diagnosis In GaP

David R. Myers and Paul L. Gourley

Sandia National Laboratories, Albuquerque, New Mexico 87185

ABSTRACT

This paper discusses the relative merits of two quick, nondestructive optical techniques, namely, photoluminescence and Raman spectroscopy at room temperature, for the characterization of ion-implanted GaP. Raman scattering from energies near that of the LO-phonon mode is found to provide a sensitive probe for initial ion dose, lattice recovery during annealing, and impurity activation during annealing. On the other hand, while the photoluminescence spectrum disappears upon implantation, it recovers on annealing, but changes that occur do not correlate with electrical activation of the implanted ions. These results suggest that Raman scattering would be especially useful for the diagnosis and development of implantation technologies in the III-V compound semiconductors.

Often in the development of new device technologies, and especially in compound semiconductors, a need arises for rapid, nondestructive techniques for the evaluation of various process alternatives. Ideally, these techniques would be useful not only for process development, but also as monitors for existing processes. In this regard, room-temperature optical techniques appear to be ideal, as they are noncontacting and nondestructive, can probe surface areas with lateral dimensions of tens of micrometers, and can sample depths comparable to those of active devices. In the work reported here, we examine the relative merits of two optical techniques, namely, room-temperature photoluminescence and Raman spectroscopy, as applied to the development of an implantation technology (1) for the fabrication of GaP diodes for high temperature operation.

Physical Background

When photons enter a semiconductor, two optical processes are of interest for our purposes (2). The photon can be absorbed and re-emitted at a significantly reduced energy, or the light can scatter inelastically, *e.g.*, from a lattice vibration. The first process, photoluminescence, is a sensitive probe of electronic energy levels; the second process, Raman scattering, is a sensitive probe of the vibrational properties of the system. In principle, both techniques can be used to measure the effects of damage, strain, or doping. Also, both techniques can provide useful information at room temperature, where experiment setup time is minimal. In a typical photoluminescence experiment, light with energy above that of the bandgap is absorbed by excitation of carriers across the forbidden energy gap. The excited carriers then diffuse and recombine. Consequently, the photoluminescence from a given region can be dependent on absorption coefficient, carrier diffusion length, and recombination mechanisms. Radiative recombination competes with nonradiative processes occurring at surface, defects, or impurities. A further complication is that the resulting recombination spectra can be difficult to interpret (3).

Raman spectroscopy determines the energy loss of the scattered light associated with the creation or destruction of a well-defined excitation of the crystal. The dominant first-order scattering in semiconductors is due to optical phonons. At room temperature, phonon creation is usually favored over phonon annihilation (4, 5) and is easily measured.

Symmetry considerations determine which phonon scattering events are allowed. In a zinc-blende crystal, first-order Raman scattering for either the longitudinal optical (LO) phonon or the transverse optical (TO) phonon is allowed from the following faces: (111), TO and LO allowed; (110), only TO allowed; and, (100) LO only. In practice, however, crystals are often cut $\sim$ 5 degrees off axis for convenience in vapor-phase growth; this slight misorientation is usually enough to allow weak scattering by the forbidden phonon. The value of Raman spectroscopy as a diagnostic technique comes not from identifying a peak in the spectrum of scattered light as being that of a particular phonon, but rather from interpreting the changes in the phonon frequencies that occur as a result of processing.

By changing the elastic properties of the crystal through stress (6) or disorder (7), one can change the energy of the phonons that satisfy the conservation requirements and thus shift the location of the peak in the spectrum of the scattered light (Fig. 1). This feature of Raman spectroscopy is useful not only for estimation of implanted ion dose, but also for the detection of residual stress in an implanted layer following annealing. Changes in the spectrum can also occur if phonons couple to other elementary excitations of the crystal. In particular, the free carriers in a semiconductor form a plasma, with a characteristic excitation frequency ω_p, which is proportional to the square root of the free carrier density (4). This plasma oscillation is a space charge wave with a longitudinal electric field. In polar semiconductors, the electric field of the LO phonon (of frequency ω_{LO}) interacts with the longitudinal electric field of the plasma oscillation (plasmon). Thus the LO phonon mode and the plas-

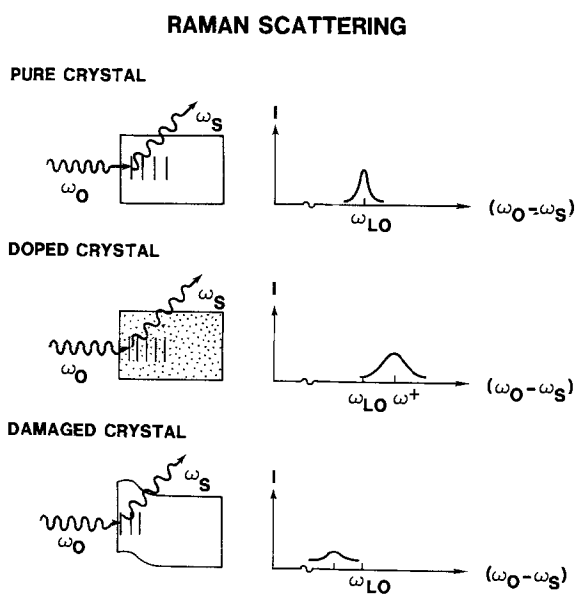

Fig. 1. Schematic illustration of Raman scattering from the LO phonon in GaP. Top: Raman scattering from a pure, undoped sample. Light scattered from the sample loses energy by creating a phonon of frequency ω_{LO}. Middle: Raman scattering from a doped GaP crystal. Coupling of the LO phonon to the free carrier plasma produces a peak in the spectrum of scattered light shifted to higher Raman energies from that of the undoped crystal. Bottom: Light scattered from a damaged crystal surface produces a peak in the spectrum of scattered light at lower Raman energies than that of the undoped crystal.

mon are replaced by coupled plasmon-phonon modes ω_+ and ω_- (8, 9). It has been found experimentally in GaP that the ω_- mode is too strongly damped to be observed in the low photoexcitation limit (9). Alternatively, the ω_+ line is observed in GaP, and over the entire range of feasible doping ($\sim 10^{15}$-10^{19} cm^{-3}), the ω_+ line is shifted up to 6 cm^{-1} from that of the uncoupled LO phonon mode ω_{LO} (9). Thus, by adding carriers to the compound semiconductors (10), the Raman peak near that of the LO phonon will shift and broaden (9) due to the increase in the plasma frequency of the free carriers, thereby allowing contactless measurement of the free carrier density. The exact amount of broadening and shifting of the line depends on the damping rate of the free carrier plasma. This extra parameter can be obtained from a fit to the spectral lineshape (11).

The transverse optical phonons are not accompanied by a long-range electric field; thus, the TO phonons do not couple directly to the plasma oscillations, and are unaffected by changes in the doping level (8). The TO phonons are shifted, however, by strain (as are the LO phonons); so that examination of both the TO and LO phonon scattering can provide unambiguous determination of removal of lattice strain and activation of implanted dopants following the annealing of compound semiconductors.

As already described, determination of the volume probed by photoluminescence is complicated by several factors, whereas the volume probed by Raman spectroscopy is determined solely by the absorption length of the incident and scattered light. By changing the incident wavelength, one can readily adjust the probe depth. This ability to probe different depths of the sample is especially useful. For composite structures, the presence of surface layers of vastly different carrier concentrations [such as "dead layers" often produced in implanted surfaces by damage or compensation (12)] can be detected as a sharp discontinuity in the lineshape of the scattered light. This discontinuity arises from the superposition of the narrow uncoupled phonon line and the coupled phonon-plasmon lines.

Finally, although not a factor in this study, the manner of surface preparation can affect the linewidth through the formation of residual strain in the layers (13), in a manner similar to implantation-induced damage.

Experimental Procedure

Two different n-type GaP substrates were used in these studies. The first was cut from an ingot doped with tin to a density of $\sim 3 \times 10^{17}$ cm^{-3}; while the second consisted of a ~ 5 μm layer of nominally undoped GaP ($\sim 5 \times 10^{16}$ net donors/cm^3) grown by liquid phase epitaxy on sulfur-doped GaP substrates with nominal doping levels of 3×10^{17} cm^{-3}. In each case, the substrates were cut 5 degrees off <100> toward <110> (14). The bulk substrates were polished in a bromine-methanol solution; the epitaxial layers were examined and processed with the as-grown surfaces. These precautions were taken to prevent poor surface preparation from affecting the phonon lineshapes due to residual strain. Implantations of 150 keV $^{12}C^+$ or 260 keV $^{24}Mg^+$ were performed in a minimum channeling alignment (15) at room temperature at doses ranging from 10^{11} to 10^{15} cm^{-2}. Anneals were performed for 10 min at selected temperatures between 800° and 900°C, using either proximity annealing (16) or controlled atmosphere annealing (1).

Optical spectra were obtained at room temperature with 50 mW of 457.9 nm wavelength light from a CW argon laser, focused to a 50 μm diameter spot. Light from the sample was analyzed in a near 90 degree geometry with a Spex 1404 double monochromator and an RCA C31034 photomultiplier tube. The Raman spectra, as well as the luminescence spectra and its associated decay, were obtained using multichannel scaling techniques (for luminescence decays, the CW excitation was mechanically chopped at 1 kHz). The spectra were collected with a multichannel analyzer for ease in data analysis. Typical Raman and photoluminescence spectra were acquired in less than 1 min with peak counts in excess of 1000.

Results

Photoluminescence from ion-implanted GaP disappears rapidly with implantation fluence, probably due to the introduction of nonradiative trapping centers. At the same time, the excitation volume decreases significantly due to the bombardment-induced increase in optical absorption (17). In contrast, Raman spectra were observed up to doses near those needed to produce a continuous amorphous layer. Examination of the dose dependence of the LO phonon peak (Fig. 2) demonstrates a continuous shift of that peak to lower Raman energies with narrowing of the line. At doses between 10^{12} and 10^{13} cm^{-2}, the lineshape exhibits two components: a broad weaker component at high energies, most likely from the undamaged substrate; and a strong, narrow component at lower Raman energies, associated with a damaged surface layer of effective carrier removal. At the highest doses, the spectra broaden considerably, consistent with other spectra from ion bombarded surface layers (18).

Measuring the Raman shift of the ω_+ peak and assuming a carrier damping rate equal to that of the specimens examined in Ref. (9) allow contactless measurement of the carrier density in the unimplanted substrate. Both the location of the ω_+ peak and the full width at half maximum (FWHM) provide an estimate of the free carrier density in the unimplanted substrate of $\sim 4 \times 10^{17}$ cm^{-3}, which corresponds well to the value $(3 \pm 1) \times 10^{17}$ cm^{-3} measured on these wafers by capacitance-voltage profiling. The ability to measure ion dose and uniformity is presently an area of great concern (19). The sensitivity of Raman scattering to the ion damage in combination with the high lateral resolution (tens of micrometers) of the probe beam implies this spectroscopic technique may hold great potential for the measurement of these parameters.

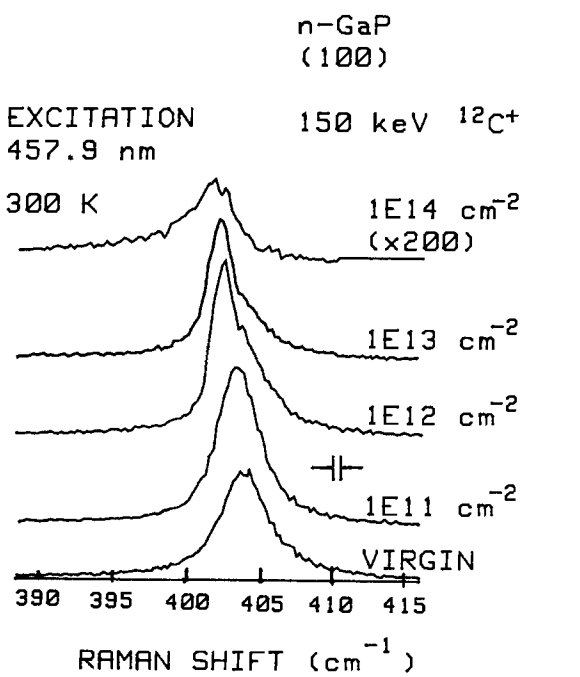

Fig. 2. Raman scattering from (100)-oriented n-type GaP (3×10^{17} cm^{-3}) ion implanted with 150 keV $^{12}C^+$ to the fluences indicated. The spectrum from the sample implanted to 1×10^{14} cm^{-2} has been magnified 200×.

The above results have demonstrated that Raman spectroscopy can provide a useful monitor of the initial ion dose. Of more immediate concern to the development of an implantation technology is the removal of lattice damage by annealing and the subsequent electrical activation of the implanted dopants. Raman spectra near the LO phonon taken from various stages of process development are illustrated in Fig. 3. The lowest spectrum is from an unimplanted, unannealed epitaxial layer (n-type, mid 10^{16} cm^{-3}), and is shown for reference. Following implantation of 260 keV $^{24}Mg^+$ to a fluence of 7×10^{13} cm^{-2}, this peak shifts to lower Raman energies, similar to the spectra of Fig. 2 (but not illustrated in Fig. 3). Proximity annealing at 800°C for 10 min recovers this line to very nearly its initial frequency and to its initial FWHM. This spectrum indicates that annealing was sufficient to remove most of the lattice damage, but not to activate the implanted species. The incomplete recovery of the peak location is probably due to some residual damage that may also be responsible for the carrier removal implied by the slight narrowing of the lineshape. For samples annealed in a controlled atmosphere at 900°C for 10 min, the shift of the peak to higher Raman energies and the broadening of the phonon line due to plasmon-phonon coupling is unequivocable evidence for successful activation of the implanted ions (upper trace in Fig. 3). Since the density of implanted ions is highly nonuniform (and to first order follows a gaussian), one determines "averaged" doping concentrations by this technique. Since the optical penetration depth (~ 5 μm) far exceeds the depth of the implant (~ 1.0 μm), the Raman spectra observed in the top trace of Fig. 3 result from a superposition of scattering from the undamaged substrate with that from the implanted layer. Because the substrate signal is known (bottom trace, Fig. 3), it can be subtracted from the upper trace to yield the signal from the implanted layer. This method produces an ω_+ peak at 405 cm^{-1}, which corresponds to a free carrier density of $\sim 8 \times 10^{17}$ cm^{-3} (9). Alternatively, since the width of the ω_+ peak is far greater than that of the uncoupled LO phonon peak, by measuring the FWHM and assuming a damping identical to that of Ref. (9), one can estimate an "optically averaged" doping density of 5×10^{17} cm^{-3}. Since the average density obtained by either method far exceeds the doping density of the epitaxial layer, these results would predict diode formation by the implanted magnesium acceptors, as was verified for these samples by metallization and testing (1). If one assumes that the implanted ion distribution can be approximated by a uniformly doped region of a width equal to twice the projected standard deviation of 0.0994 μm [calculated for this implant using the TRIM code (20)], one obtains an estimated electrical activation of 14%. This value is in excellent agreement with the activation of 8-18% found for 900°C encapsulated anneals of Mg-implants into semi-insulating GaP (21). Again, verification of impurity activation took 50 sec of real time to determine by Raman spectroscopy.

Room temperature photoluminescence was also used to characterize the recovery of the implanted layers, as is illustrated in Fig. 4 and 5 for implants performed into the tin-doped substrates. The red luminescence (associated with deep recombination centers) from the unimplanted, unannealed substrate (trace 1) appears to arise from two overlapping bands. The time decay of this luminescence is characterized by an initial

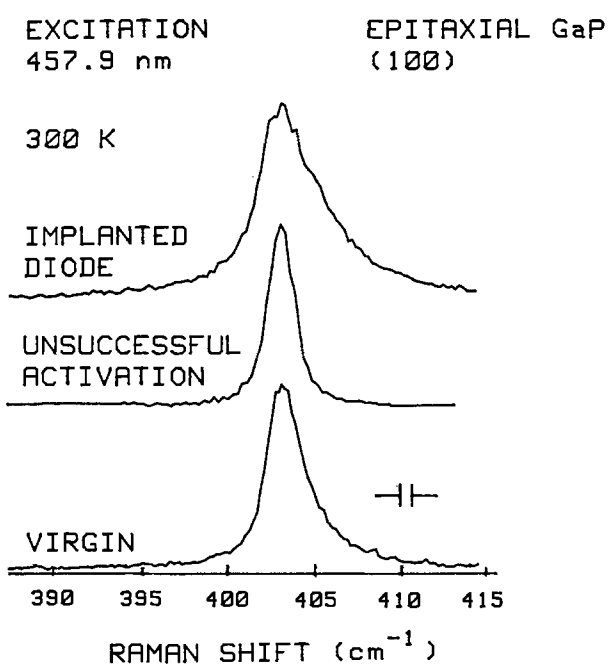

Fig. 3. Raman scattering from (100)-oriented n-type, epitaxial GaP ($\sim 3 \times 10^{16}$ cm^{-3}) implanted with 7×10^{13} cm^{-2}, 260 keV $^{24}Mg^+$. Bottom, before implantation; middle, unsuccessful activation; top, successful activation. These spectra demonstrate that Raman spectroscopy can be used as a contactless measure of carrier density.

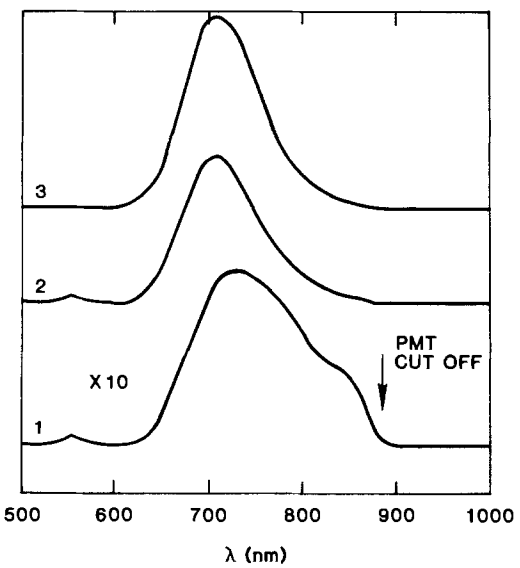

Fig. 4. Room temperature photoluminescence spectra from: 1, virgin substrate (GaP, 3×10^{17} Sn doping); 2, substrate proximity annealed at 875°C; 3, substrate that has been implanted with 150 keV C^+ to a dose of 1.0×10^{14} cm^{-2}. The cutoff in photomultiplier response occurs at 890 nm.

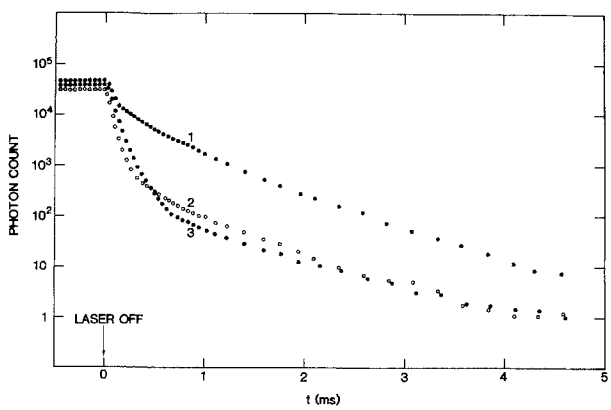

Fig. 5. Time decays of the photoluminescence at 710 nm from the three samples corresponding to the spectra in Fig. 1. The initial and (final) lifetimes (in μsec) of the three decays are: 1, —, (700); 2, 60, (700); 3, 90, (1050).

rapidly decaying component followed by a slower decaying component. Proximity annealing alone (without implantation) eliminates the longer wavelength band and simultaneously reduces the relative magnitude of the slower decay component (trace 2 of Fig. 4). Implantation and successful activation produce identical spectral shapes and very similar decay rates to those produced by annealing alone (trace 3 of Fig. 4).

Thus, while the shift and broadening of the Raman signal near the LO phonon frequency provides conclusive evidence of successful activation of the implanted species, changes in the photoluminescence spectra do not correlate with impurity activation, and appear to be related to the heat-treatment only.

Conclusions

Raman scattering from frequencies near that of the LO phonon is shown to be an excellent diagnostic for implantation damage effects, their recovery by annealing, and the successful activation of the implanted ions consistent with diode fabrication from the annealed material. In contrast, changes in the room temperature photoluminescence spectra occur independent of the activation of the implanted species. The success of Raman spectroscopy as a diagnostic is based on the sensitivity of the LO phonon frequency to strain, damage, and the free carrier plasma. Since these same physical effects also occur in the other III-V compound semiconductors, Raman spectroscopy may find even wider application to process diagnosis, as has been independently suggested by others (22-24), but has been demonstrated here.

A significant advantage of Raman spectroscopy is that these physical effects can be readily monitored at room temperature. In contrast, photoluminescence would provide more information if the samples were held at cryogenic temperatures, since only the ground states of impurities would be occupied and thermalization and phonon broadening effects would be minimized (3). The use of cryogenic temperatures, however, would greatly increase the time required for the measurement, and thus no longer be production compatible as a real-time monitor. Furthermore, situations exist where photoluminescence even at low temperatures would not provide the desired information about carrier activation. This is especially true for implanted Be in the III-V compound semiconductors, where electrical activation of the implanted species occurs for annealing temperatures below those required to activate Be-related photoluminescence (25), while Raman scattering, being sensitive to the free carrier density from the activated acceptors, does not suffer this limitation.

Acknowledgments

The authors wish to thank P. Peercy for providing the implantations and for many useful discussions; R. M. Biefeld for the controlled atmosphere annealing; L. R. Dawson for the epitaxial GaP; T. E. Zipperian for device fabrication; and M. E. Wilkins, R. N. Chavez, C. E. Robinson, T. A. Plut, and J. B. Snelling for technical assistance. One of the authors (DRM) also wishes to acknowledge R. A. Forman and M. I. Bell of the National Bureau of Standards, and J. Comas and R. L. Schmidt of the Naval Research Laboratory for useful discussions.

This work performed at Sandia National Laboratories supported by the U.S. Department of Energy, Office of Basic Energy Sciences, Division of Material Science (KC020105) under contract number DE-AC04-76DP00789.

Manuscript submitted March 26, 1982; revised manuscript received July 18, 1982. This was Paper 343 presented at the Denver, Colorado, Meeting of the Society, Oct. 11-16, 1981.

Any discussion of this paper will appear in a Discussion Section to be published in the December 1983 JOURNAL. All discussions for the December 1983 Discussion Section should be submitted by Aug. 1, 1983.

Publication costs of this article were assisted by Sandia National Laboratories.

REFERENCES

1. D. R. Myers, R. M. Biefeld, T. E. Zipperian, and L. R. Dawson, *Electron. Lett.*, **18,** 323 (1982).
2. J. I. Pankove, "Optical Processes in Semiconductors," Prentice-Hall, Englewood Cliffs, N.J. (1971).
3. R. Z. Bachrach, *J. Electron. Materials*, **3,** 645 (1974).
4. W. Hayes and R. Loudon, "Scattering of Light by Crystals," John Wiley & Sons, New York (1978).
5. H. W. Lo and A. Compaan, *J. Appl. Phys.*, **51,** 1565 (1980).
6. I. Balslev, *Phys. Status Solidi B*, **61,** 207 (1974).
7. J. F. Morhange, R. Beserman, and M. Balkanski, *ibid., A*, **23,** 383 (1974).
8. A. Mooradian and A. L. McWhorter, in "Light Scattering Spectra of Solids," G. B. Wright, Editor, p. 297, Springer Verlag, New York (1968).
9. B. Kh. Bairamov, V. D. Timofeev, V. V. Toporov, and Sh. B. Ubaidullaev, *Sov. Phys. Solid State*, **20,** 1916 (1978).
10. It should be noted that this mechanism does not occur in elemental semiconductors, such as silicon. Instead, doping variations in these semiconductors affect the elastic constants, to produce a shift in the phonon frequencies with doping opposite to that due to the coupling of the plasmon to the LO phonon in the compound semiconductors [*e.g.*, F. Cerdiera and M. Cardona, *Phys. Rev.*, **B5,** 1440 (1972)].
11. M. V. Klein, B. N. Ganguly, and P. J. Colwell, *Phys. Rev.*, **B6,** 2380 (1972).
12. P. M. Asbeck, J. Tandon, B. M. Welch, C. A. Evans, Jr., and V. R. Deline, *IEEE Electron Device Letters*, **edl-1,** 35 (1980).
13. D. J. Evans and S. Ushioda, *Phys. Rev.*, **B9,** 1638 (1974).
14. R. M. Biefeld, *J. Cryst. Growth*, **56,** 382 (1982).
15. D. R. Myers, R. G. Wilson, and J. Comas, *J. Vac. Sci. Technol.*, **16,** 1892 (1979).
16. D. R. Myers and P. L. Gourley, Abstract 343, p. 835, The Electrochemical Society Extended Abstracts, Vol. 81-2, Denver, Colorado, Oct. 11-16, 1981.
17. T. Shimada, Y. Kato, Y. Shiraki, and K. F. Komatsubara, *J. Phys. Chem. Solids*, **37,** 305 (1976).
18. P. S. Peercy, *Appl. Phys. Lett.*, **18,** 574 (1971).
19. J. N. Gan and D. S. Perloff, *Nucl. Instrum. Methods*, **189,** 265 (1981).
20. J. P. Biersack and L. G. Haggmark, *ibid.*, **174,** 257 (1980).
21. D. J. Lank, B. C. Dobbs, and Y. S. Park, *J. Appl. Phys.*, **50,** 1318 (1979).
22. G. Abstreiter, E. Bauser, A. Fisher, and K. Plogg, *Appl. Phys.*, **16,** 345 (1978).
23 R. Tsu, *SPIE Proc.*, **276,** 78 (1981).
24. P. P. Yaney, W. E. Baird, Jr., and Y. S. Park, *ibid.*, **276,** 84 (1981).
25. J. P. Donnelly, *Nucl. Instrum. Methods*, **182,** 553 (1981).

Low Temperature Electrosynthesis of Tantalum and Niobium Monocarbides

A. J. Hockman

Department of Chemistry and Chemical Engineering, Stevens Institute of Technology, Hoboken, New Jersey 07030

and R. S. Feigelson

Center of Materials Research, Stanford University, Stanford, California 94305

ABSTRACT

A method has been developed for electrolytically synthesizing TaC and NbC at 750°C from a molten salt solution containing $Na_2B_4O_7$, Na_2CO_3, NaF, KF, and Ta_2O_5 or Nb_2O_5. Carbide formation was possible on both graphite and silver cathodes with deposition potentials in the range of −0.45 to −0.7V. The melt composition must be carefully controlled so that borides do not codeposit. In TaC electrosynthesis, thermally-generated cubic crystals formed on the cathode when the Ta_2O_5 concentration was too high. A similar phase was found during NbC deposition.

The monocarbides of tantalum and niobium are highly refractory materials with the cubic NaCl structure. Both are hard, brittle compounds with TaC being a gold-colored metalloid which melts at 3915° ± 75°C while NbC is gray-black with a melting point of 3600° ± 50°C. Several methods have been used to synthesize these compounds including; (*i*) solid-state reaction of the elements in vacuum or H_2 [1600°-2300°C] (1, 2), (*ii*) reaction of the metal hydride or oxide with carbon black [2200°C] (2), (*iii*) fusion, and (*iv*) reaction of the metal with a hydrocarbon gas [>1800°C] (4). Most of these methods involve very high temperatures and produce metal-rich carbides of the form TaC_{1-x} and NbC_{1-x}.

The preparation of single crystals of these compounds by fusion methods is made difficult by their extremely high melting temperatures and decomposition problems at elevated temperatures, principally the loss of carbon. Several methods, some of which utilize lower temperatures, have been developed including: (*i*) flux growth from molten aluminum [1300°-1500°C] (5), (*ii*) thin film deposition by vacuum evaporation [1300°-2000°C] (6), (*iii*) crystal pulling from an NbC_{1-x} melt formed in an argon-helium plasma arc stream (7), and (*iv*) the growth of TaC fibers by an a-c arc discharge method [250°-650°C] (8).

Electrolytic methods for the synthesis of some refractory metal carbides from molten salt solutions at temperatures near 800°C have been reported in the literature (9, 10). Table I summarizes some of the experimental conditions used by Andrieux and Weiss (11) to prepare W, Mo, and Fe carbides. All involved the use of Na_2CO_3 as the source of carbon and an oxide for the metallic constituent. These low melting solvents contained $NaBO_2$ and LiF (a viscosity modifier). No previous work on the electrolytic preparation of TaC and NbC has been reported.

Kunnmann (10) stated that "materials electrochemically precipitated from fused melts can almost always be obtained in the form of reasonably large crystals when sufficiently low current densities are employed." The low temperature electrolytic method would, therefore, clearly be an advantage for the growth of single crystals of TaC and NbC.

This paper describes the conditions necessary to synthesize TaC and NbC by molten salt electrolytic techniques.

Experimental Procedure

TaC and NbC were electrolytically synthesized from a melt containing reagent grade $Na_2B_4O_7$, Na_2CO_3, NaF, and KF as the solvent phase (12) and Ta_2O_5 or Nb_2O_5 (purity 99.9%) respectively as the solute. The Na_2CO_3 also doubled as the source of carbon. The synthesis conditions are given in Table II. The melt composition was similar to Andrieux and Weiss (11) except that $Na_2B_4O_7$ was used instead of $NaBO_2$ and a low melting eutectic of NaF and KF was substituted for the LiF. The solidified NaF-KF mixture is more soluble in aqueous solutions than LiF-based solvents, and any which solidifies on the electrodeposit can be easily dissolved away. Because they pick up moisture, the fluorides were baked in a vacuum furnace for 8 hr at 350°C before weighing.

The furnace used in these experiments was a converted silicon crystal puller (Fig. 1). The crystal seed rod was converted to a cathode holder. Two different cathode materials were used: graphite, in the form of 3 mm diam rods, 8 cm in length, or silver strips 1 cm wide, 0.2 mm thick, and 7 cm long. An amorphous carbon crucible was used as the anode. Electrical connection to the anode was made by use of a carbon rod contacting the bottom of the crucible. The crucible was surrounded by a graphite heater with a thermocouple placed between the heater and crucible. The charge, after it was loaded into the crucible, was placed immediately into the furnace and purged with argon for at least ½ hr prior to heating. The argon atmosphere was maintained throughout electrosynthesis. The cathodes were immersed in the molten salt solution to a depth of approximately 1 cm and rotated during electrolysis. Electrodeposition in the temperature range 750°-960°C was explored.

The applied potential for electrodeposition was provided by a Princeton Applied Research (PAR) Model 173 potentiostat. This unit, in conjunction with a PAR Model 175 programmer and an X-Y chart recorder, was used to plot current *vs.* applied potential (I-V) curves for determining minimum decomposition poten-

Table I. Previous methods for electrolytic synthesis of refractory metal carbides*

Carbide	Melt composition	T° (C)	Voltage (V)	Current (A)	Time (min)
Fe_3C	$2NaBO_2$, $3Na_2CO_3$, 4LiF 1/10 Fe_2O_3	815	2	20	15
WC	$2NaBO_2$, $2Na_2CO_3$, 4.5LiF 1/6 WO_3	780-800	2	20	30
W_2C	$2NaBO_2$, $3Na_2CO_3$, 4.5LiF 1/2 WO_3		Similar range		
MoC	$2NaBO_2$, $2Na_2CO_3$, 4.5LiF 1/1 5 MoO_3		Similar range		
Mo_2C	$2NaBO_2$, $2Na_2CO_3$, 4.5LiF 1/3 MoO_3	780-800	2.5	20	20

* Andrieux and Weiss (11).

Key words: ceramics, refractories, electrodeposition synthesis.

Table II. Synthesis conditions for TaC and NbC

Experimental conditions	TaC			NbC
	Initial	Intermediate	Improved	
Melt composition (m/o)				
$Na_2B_4O_7$	19.2	13.7	13.9	13.9
Na_2CO_3	19.1	27.1	27.4	27.4
NaF	38.9	37.3	37.7	37.7
KF	20.6	19.8	20.0	20.0
Ta_2O_5	2.2	2.1	1.1	1.1
$Na_2CO_3/Na_2B_4O_7$	$\simeq 1$	1.97	1.98	1.98
Na_2CO_3/Ta_2O_5	8.6	12.9	25	25
Charge weight (g)				
Solvent	44.4	44.4	44.4	44.4
Ta_2O_5	5.0	5.0	2.5	2.5
Temperature (°C)	960	750	750	750
Applied potential (V)	−0.51	−0.2 to −0.6	−0.4 to −0.7	−0.6
Current (mA)	40	2-40	1.7-6	40
Current density (mA/cm²)	43-93	3-50	1-8	44 (final)
Cathode	Graphite	Graphite	Graphite or Ag	Graphite
Anode (crucible)	Amorphous carbon	Amorphous carbon	Amorphous carbon	Amorphous carbon
Deposition time (hr)	2-27	2-17	15-25	18
Cathode products	TaC, TaB, and cubic crystals	TaC and cubic crystals	TaC (some free C)	NbC and small quantity of NbB

tials. Deposition potentials ranged from −0.2 to −0.7V in this investigation. A PAR Model 379 coulometer was used to measure the number of coulombs passed during electrodeposition. Deposition times of up to 27 hr were studied.

Electrodeposits were analyzed using x-ray diffraction, scanning electron microscopy, electron microprobe, and optical microscopy techniques.

Discussion of Results

In the initial synthesis experiments (Table I) an Na_2CO_3/Ta_2O_5 ratio (C/Ta) of 8.7 was used with a corresponding $Na_2CO_3/Na_2B_4O_7$ ratio (C/B) near 1. A potential of −0.51V produced a current of 40 mA at 960°C which was much lower than reported in previous carbide electrosynthesis experiments (11). At 960°C the melt was not completely homogeneous, with some undissolved material observable at the bottom of the crucible. Evaporation losses from the melt at this temperature, primarily the fluoride constituents, were about 1.1% per hr.

The initial experimental conditions yielded small quantities of both TaC and TaB on the cathode (as confirmed by x-ray analysis) together with a cluster of relatively large crystals of cubic morphology (Fig. 2a, b). In some experiments these crystals grew to 3-4 mm on an edge. Their color varied from colorless to dark blue-black and they were very insoluble in acids. The color variations were probably due to deviations from stoichiometry. Figure 2a shows the extent and morphology of the crystals attached to the cath-

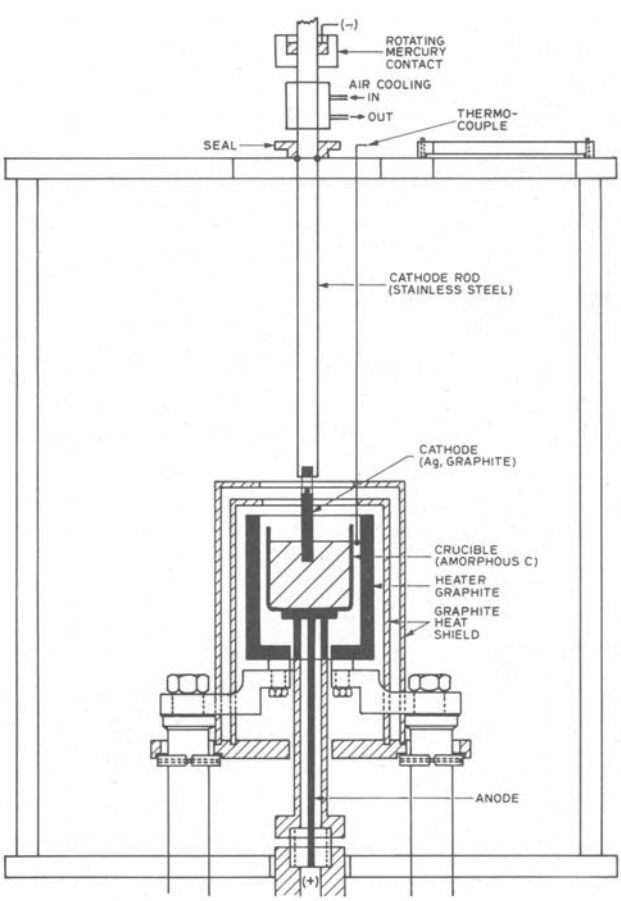

Fig. 1. Schematic diagram of the electrodeposition furnace used for TaC and NbC synthesis.

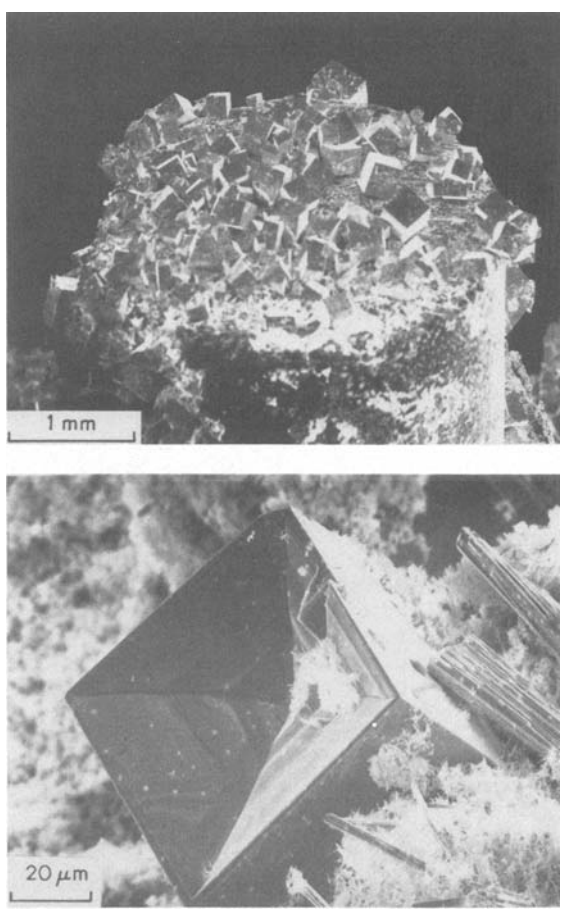

Fig. 2. SEM photographs of a TaC electrodeposit prepared on graphite using the initial synthesis conditions given in Table II. (a, top) Tip of cathode, (b, bottom) higher magnification showing the coexistence of three phases; TaB, TaC, and cubes of unknown composition.

ode rod, and at higher magnification (Fig. 2b), all three cathode products formed during electrodeposition are distinguishable: TaB, TaC, and the cubic crystals.

To eliminate the TaB phase from the electrodeposit, several changes in experimental conditions were made as given in Table II, column 2. The $Na_2CO_3/Na_2B_4O_7$ molar ratio was increased from 1 to 1.97 and the Na_2CO_3/Ta_2O_5 ratio was allowed to increase from 8.6 to 12.9 since the solvent/Ta_2O_5 ratio was kept essentially constant. The electrodeposition temperature was lowered to 750°C to reduce evaporation losses (1.1-0.125%/hr).

The modified conditions used were successful in eliminating the boride phase. Figure 3 shows the resulting cathode deposit. The TaC electrodeposited in a cluster of small crystallites forming a dendritic-like structure. It was still surrounded by the cubic phase which we also wanted to eliminate.

While the exact composition of the cubic crystals was not completely determined, they were found to contain Na, Ta, and oxygen, and their x-ray pattern compared closely to those of $Na_{0.95}TaO_{0.295}F_{0.05}$ (13), TaF_3, and TaO_2F. The undissolved material remaining at the bottom of the crucible had an identical x-ray pattern to that of the cubic crystals on the cathode. Since it was unlikely that these crystals were electrochemically formed, it was suspected that they nucleated and grew on the cathodes by a thermally driven process. This was verified by repeating the synthesis procedure in all details but without an applied potential across the electrodes. Under these conditions the crystals formed as before.

Since the composition of the undissolved material on the crucible bottom appeared to be the same as the crystals found on the cathode rod, the most likely mechanism for nucleation and crystal growth is a gradient transport process. When the cathode rod is inserted into the melt surface it acts as a heat sink, lowering the temperature of the melt in its vicinity. Since the melt at the bottom of the crucible is at a higher temperature, the undissolved phase, which is more soluble at the higher temperatures, is transported to the cathode due to the concentration gradient created by the temperature gradient. As electrodeposition proceeds the cubic crystals continue to nucleate and grow and become interspersed with the electrodeposited products.

Improved conditions for TaC electrosynthesis are given in Table II column 3. The amount of Ta_2O_5 was reduced by half, to 1 m/o. This increased the Na_2CO_3/Ta_2O_5 ratio to 25. The $Na_2CO_3/Na_2B_4O_7$ ratio was kept at 2 to prevent the formation of TaB and the temperature at 750°C to reduce evaporation losses. Under these conditions the melt was completely transparent and homogeneous (no undissolved solid was present) and the cubic crystals did not form.

Figures 4a and 4b show electrodeposits of TaC on graphite at two different potentials. At −0.7V (Fig. 4a) small, poorly formed crystallites were observed. At −0.55V (Fig. 4b) larger crystallites were formed. Figures 5a and 5b show deposits on silver at −0.05V. The coverage was continuous but the crystallites were smaller and less well formed than on graphite.

The $Na_2CO_3/Na_4B_4O_7$ ratio in the melt was very critical for TaC synthesis. If the Na_2CO_3 content was too high, excess carbon or graphite was formed at the cathode, usually as a very fluffy black powder, some of which floated off into the melt during electrodeposition and upon removing the cathode from the melt. If the melt contained too much $Na_2B_4O_7$ (such as an equimolar concentration of $Na_2B_4O_7$ and Na_2CO_3), then TaB formed. A convenient melt composition for TaC deposition was 31 w/o $Na_2B_4O_7$, 33 w/o Na_2CO_3, 18 w/o NaF, and 13 w/o KF. With this melt composition, TaC could be electrodeposited on the Ag cathode at cell potentials of between −0.04 to −0.07V. At greater than −0.4V, graphite was the dominant phase to form and at −0.7V TaB codeposited with TaC. The best results were obtained with a cell potential of −0.05, both for graphite cathodes, where the current density was approximately 4 mA/cm², and for Ag cathodes (7.5 mA/cm²). In most experiments the current dropped during the first few hours and then remained almost constant as the electrodeposition process proceeded.

Electrodeposited TaC was a crystalline, bronze-colored powder. Crystallite morphology was poorly developed except in a few cases where well-defined prisms were observed (Fig. 4). The maximum crystallite size was about 10 μm. The powder x-ray diffraction

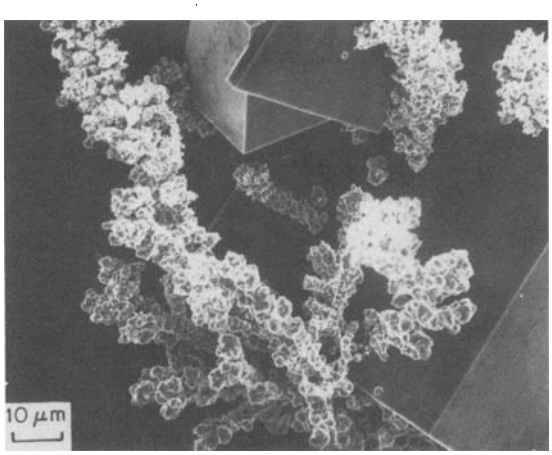

Fig. 3. An SEM photograph of TaC crystallites formed during electrodeposition on graphite using the intermediate synthesis conditions given in Table II. Crystals of the cubic phase were still present.

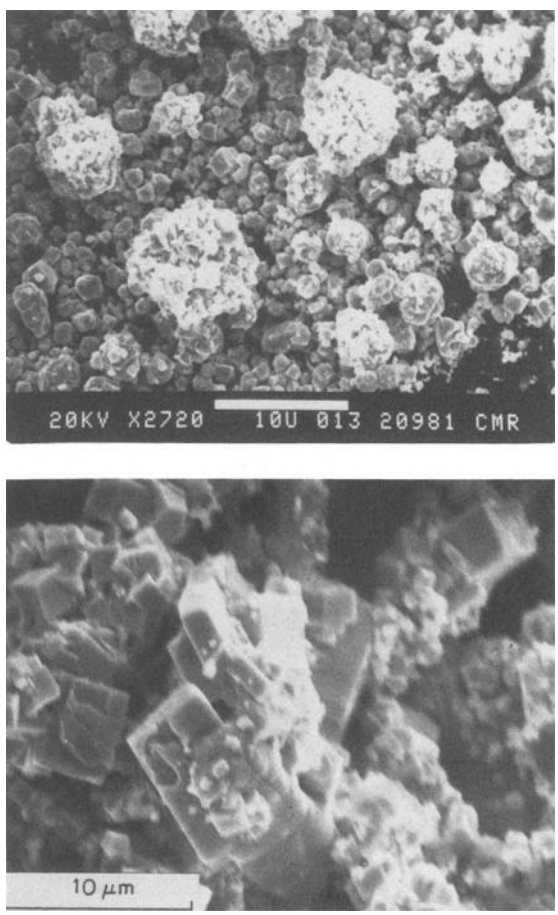

Fig. 4. SEM photographs of single phase TaC crystallites prepared on graphite using the improved synthesis conditions given in Table II. (a, top) Deposition potential −0.7V, (b, bottom) deposition potential −0.55V.

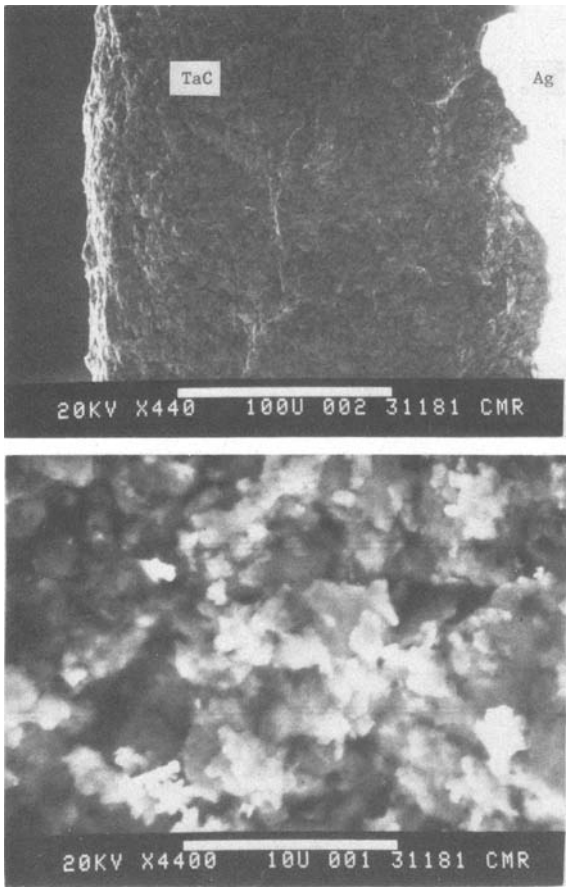

Fig. 5. SEM photographs showing a TaC electrodeposit on a silver cathode at —0.05V (a, top) overall morphology of deposit, (b, bottom) morphology of crystallites.

data agree very well with published literature results. The deposits were not very adherent to either the silver or graphite cathodes and could be easily removed.

The major contaminants in the TaC deposits were Fe (0.5%), B (1.5%), and Si (0.8%). The other impurities were Ca, Al, Pb, and Mg. The Fe impurity was most likely derived from the stainless steel cathode holder, the B from $Na_2B_4O_7$, and Si from the starting material. The starting materials used were not particularly pure and no effort was made to pre-electrolyze the bath prior to TaC electrodeposition. The stoichiometry of the TaC prepared by this method has not yet been determined.

Similar results were obtained for the electrosynthesis of NbC. The experimental parameters are given in Table II. Only a few experiments were undertaken to verify the feasibility of NbC electrosynthesis. An analogous thermally deposited phase also appeared on the cathode if the Nb_2O_5 concentration was too high. The crystallite morphology of the electrodeposited NbC was not as well defined as in the TaC electrodeposits. A small quantity of NbB was present in these electrodeposits and the $Na_2CO_3/Na_2B_4O_7$ ratio should be increased to generate single phase NbC.

Conclusions

Tantalum and niobium carbide can be electrodeposited as essentially single phase products under a narrow range of experimental conditions. TaC can be synthesized at 750°C with deposition potentials between —0.45 to 0.70 on graphite or Ag electrodes. NbC can be similarly synthesized. If the $Na_2B_4O_7$ to Nb_2CO_3 ratio or the deposition potential is too high, borides form and if the Ta_2O_5 (or Nb_2O_5) concentration is too high, a complex tantalum (or niobium) compound forms on the cathode by a thermal process. At low deposition potentials, or if the Na_2CO_3 content is too high, excess C will be present. Low temperatures (about 750°C) are desirable to prevent excessive evaporation of fluoride constituents from melt. The TaC and NbC electrodeposits were in the form of submillimeter crystallites. It may be possible to increase their size by more careful control of the deposition parameters or with the use of seed crystals.

Acknowledgments

We would like to thank Pamela Focia for her assistance in carrying out some of the experiments in this program, and Wayne Kway for his helpful advice. This work was supported by the NSF-MRL Program through the Center for Materials Research at Stanford University.

Manuscript submitted April 26, 1982; revised manuscript received *ca.* Sept. 24, 1982. This was Paper 540 presented at the Denver, Colorado, Meeting of the Society, Oct. 11-16, 1981.

Any discussion of this paper will appear in a Discussion Section to be published in the December 1983 JOURNAL. All discussions for the December 1983 Discussion Section should be submitted by Aug. 1, 1983.

Publication costs of this article were assisted by Stanford University.

REFERENCES

1. A. L. Bowman, T. C. Wallace, J. L. Yarnell, R. G. Wenzel, and E. K. Storms, *Acta Cryst.*, **19,** 6 (1965).
2. E. K. Storms and N. H. Kirkorian, *J. Phys. Chem.*, **64,** 1471 (1960).
3. L. B. Dubrovskaya, G. P. Shveykin, and P. V. Geld, *Fiz. Metal Metalloved,* **17,** 73 (1964).
4. B. H. Eckstein and R. Forman, *J. Appl. Phys.*, **33,** 82 (1962).
5. I. Higashi, Y. Takahashi, and T. Atoda, *J. Cryst. Growth,* **33,** 207 (1976).
6. N. Terao, *Jpn. J. Appl. Phys.*, **9,** 1263 (1970).
7. Y. M. Goryacher, I. A. Podchernyaeva, N. I. Siman, V. S. Sinelinikova, I. I. Timofeeva, and G. S. Burkhanov, *Sov. Phys. Tech. Phys.*, **23,** 321 (1978).
8. T. Takahashi and K. Sugiyama, *This Journal,* **121,** 714 (1974).
9. A. Wold and D. Bellavance, "Preparative Methods in Solid State Chemistry," p. 279, P. Hagenmuller, Editor, Academic Press, New York (1972).
10. W. Kunnmann, "Preparation and Properties of Solid State Materials," p. 1, R. A. Lefever, Editor, Dekker, New York (1971).
11. J. L. Andrieux and G. Weiss, *C.R. Acad. Sci.*, **219,** 550 (1944).
12. H. J. Heinen, D. H. Baker, Jr., and J. M. Gomes, U.S. Pat. 3,375,180 (1968).
13. J-P. Chaminade, M. Pouchard, and P. Hagenmuller, *Rev. Chim. Miner.*, **9,** 381 (1972).

Technical Notes

Evaluation of a Process for Achieving Low Between-Metal Contact Resistance in Plasma Etched Polyimide Vias

P. K. Smith, T. O. Herndon, and R. L. Burke

MIT Lincoln Laboratory, Lexington, Massachusetts 02173

and D. R. Day and S. D. Senturia

MIT Cambridge, Massachusetts 02139

Polyimide (PI) is finding increasing application as an intermetal insulator in integrated circuits. A potential problem is that high contact resistance can occur at the bottom of vias etched in PI. Various techniques such as argon sputtering (1) and sulfamic acid treatment (2) have been recommended for preventing this high contact resistance, but the detailed origin of the effect has only recently been elucidated. Day and Senturia (3), using scanning Auger analysis of plasma-etched vias in PI over aluminum, have suggested that the high contact resistance is due to the combined effect of a thick aluminum oxide layer on the first-level metal and a thin etch-resistant carbonaceous film over the oxide which is redeposited from the PI or photoresist during the oxygen plasma etching of the via. They recommend a three-step procedure: finish etching with a low-pressure plasma (50 mTorr) to remove the carbonaceous film, dip in buffered HF to thin the aluminum oxide, and sinter the contacts after deposition of second-level metal. The goal of this paper is to evaluate each of the steps in this sequence, and to compare this procedure with other widely used techniques.

Experimental Procedures

Five silicon wafers with 4800Å of thermal silicon dioxide were used as substrates for this study. Following cleaning of the substrates, 3800Å of 94% Al, 5% Cu, and 1% Si (Al-Si-Cu) were deposited using a Varian sputter gun at a pressure of 1 mTorr and a deposition rate of 800 Å/min. This first-level metal was patterned by plasma etching with BCl_3 in a parallel plate reactor (4). A 5:1 dilution of du Pont PI-2555 and T9035 thinner was spun on the wafers at 8,000 rpm, producing a 10,000Å dry film thickness. The PI was cured by baking at 125°C in a convection over for 1 hr, followed by a bake on a hot plate at 300°C for 1 hr, and then a sinter in a furnace tube under forming gas (97% nitrogen, 3% hydrogen) at 400°C for 5 min. This produced a fully cured 7000Å PI film.

A 1.8 μm thick AZ-1350J photoresist layer was spun onto the PI, the wafers were exposed, developed, and then either plasma etched or reactive ion etched in oxygen. All etching was done in a parallel plate reactor, using the pressure and power levels indicated in Table I. Wafer A received the procedure recommended by Day. For wafer B, the low pressure finishing of the plasma etch was omitted. Two of the wafers received additional treatment in the form of argon sputter (wafer C) or a 1 min dip in a 20% by weight aqueous solution of sulfamic acid (wafer D), whereas wafer E was only reactive-ion etched. The resist was stripped in acetone.

Each of the wafers was then immersed halfway in a buffered HF dip for 4 sec. Pure aluminum was then deposited using the Varian sputter gun at a rate of 680 Å/min and a pressure of 1 mTorr. The second-level metal was patterned by BCl_3 plasma, and the photoresist was stripped by dipping the wafers in acetone for 2-3 min. The wafers were then divided prior to sintering, and half of each sample was sintered for 5 min at 400°C in 97% N_2, 3% H_2. Thus each wafer produced four differently treated quadrants: no HF dip or sinter, HF dip only, sinter only, and both HF dip and sinter.

Within each wafer quadrant were a total of 32 contact chains, 16 chains with large vias (7.5 μm × 7.5 μm) and 16 chains with small vias (2.5 μm × 2.5 μm). Each chain contained 40 contacts. Thus, for each via size, a total of 640 contacts was tested for each variation of the process. A typical via cross section is shown in Fig. 1.

Results

The effect of HF dip and sinter.—Figure 2 compares the results for wafer A (the Day procedure) with and without the HF dip. The figure contains a histogram of the number of 40-contact chains that showed a given average contact resistance (grouped to the nearest 0.1Ω average contact resistance). For the large vias, in the absence of the HF dip, there is wide scatter in the data, whereas, with the HF dip, all but one of the via chains has an average resistance of either 0.2 or 0.3 Ω/contact. It was found that each quadrant showed at least one open contact chain at the edge where the wafers were broken. We feel that these open chains are damage related rather than process related; however, for completeness, they are reported here as "open." Results for the small via chains are similar. Without the HF dip, most of the chains were open.

Table I. Parameters for various etch conditions and via treatments

Wafer	Process	Pressure (mTorr)	Etch time	Power (W)
A	Plasma etched	200	3 min	350
		50	30 sec	340
B	Plasma etched	200	3 min	350
C	Plasma etched	200	3 min	350
	Argon sputter	10	3 min*	100
D	Plasma etched	200	3 min	350
	Sulfamic acid	200	1 min	350
E	Reactive ion etched	10	3 min	100

* Sputter rate 100 Å/min.

Key words: multilevel, interconnect, via, resistance, polyimide, plasma etching.

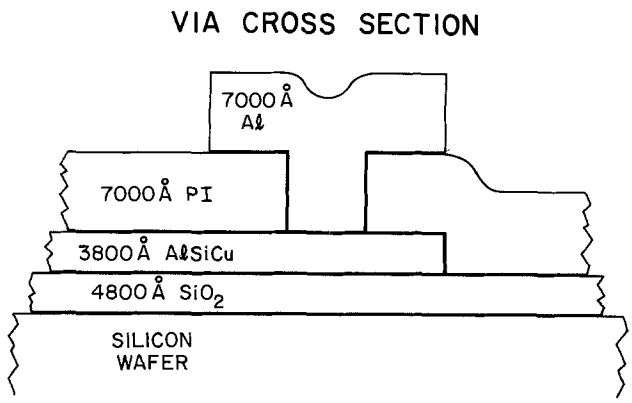

Fig. 1. Via cross section

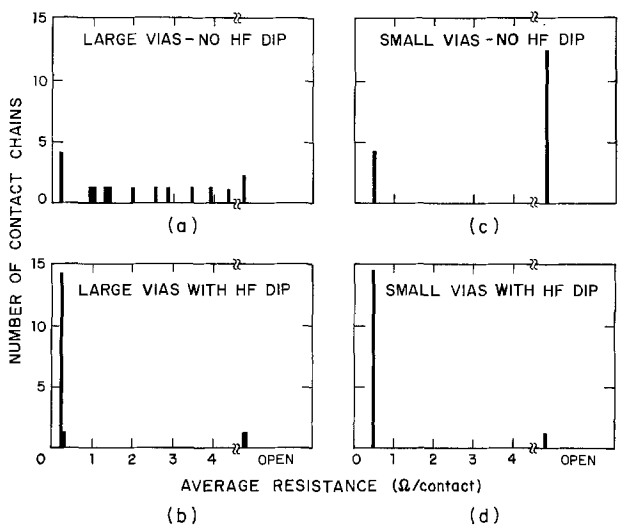

Fig. 2. The effect of HF dip on sintered samples from wafer A, the Day procedure (200 mTorr plasma plus 50 mTorr plasma).

With the HF dip, all but one showed an average resistance of 0.4 Ω/contact. For the other wafers, the effect of HF dip was similar. That is, comparisons of sintered wafers with and without the HF dip showed that the HF dip systematically improved the average contact resistance.

The effect of sinter was also to improve the average contact resistance. That is, for samples subjected to HF dip but not sintered, the results were worse than for those receiving both HF dip and sinter. The quantitative data in this case, while statistically clear, are not particularly important, in view of the fact that sintering is virtually always used in integrated circuit processing.

Given that the results on wafer A demonstrate the value of the HF dip in combination with sintering, results on the comparison of various etch procedures

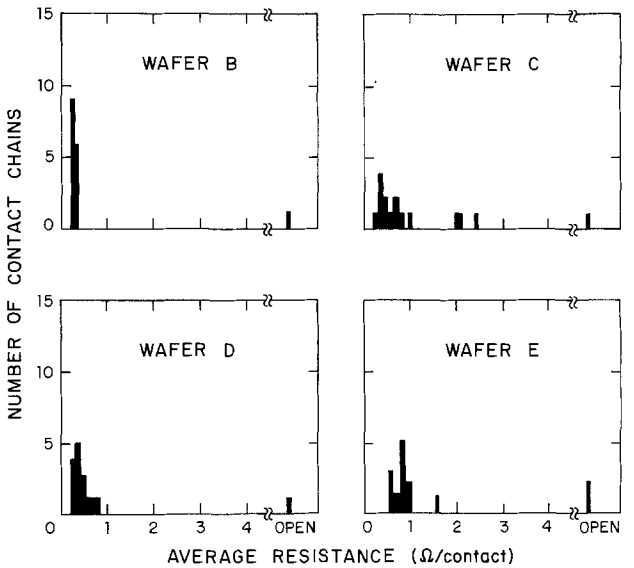

Fig. 3. Data for large vias showing the effects of various etch procedures and via treatments on samples subjected to both the HF dip and sinter steps.

and via treatments are reported only for the wafer quadrant that received both the HF dip and sinter steps. These results are presented below.

The effect of etch procedures and via treatments.— The comparison between various etch procedures and via treatments is summarized in Fig. 3 (large vias), Fig. 4 (small vias), and Table II (average contact resistances).

The data for wafer B, which received the standard 200 mTorr plasma etch but no finishing step at 50 mTorr, show contact resistances almost as low as the Day procedure (wafer A, Fig. 2b and 2d). In Ref. (3), Day reports that the thickness of the deposited carbonaceous film begins to increase as the pressure in the oxygen plasma increases above a critical threshold value. In our reactor, this threshold value happens to be at about 200 mTorr, as measured by Day (3). Thus wafer B represents nominally "clean" vias which, nevertheless, are not quite as low in resistance as those subjected to the low-pressure finishing step. Since the threshold pressure for clean vias may also depend on such variables as the precise substrate temperature during the etch, the results on wafer B suggest that the low-pressure finishing step is valuable even if one is working at the redeposition threshold.

The data for wafers C, D, and E show significantly worse contact resistances than wafer A. The argon sputter and sulfamic acid via treatments actually produce worse contacts than straight plasma etching at the redeposition threshold pressure (wafer B), and reactive ion etching yielded poor results, particularly in the small vias. Clearly, the procedure represented

Table II. Summary of results for sixteen 40-contact via chains for each via size subjected to HF dip and sinter
Open chains are not included in averages and standard deviations

Wafer	Large vias (55 μm²)			Small vias (6 μm²)		
	Avg resistance (Ω/contact)	Std dev (Ω)	Open chains	Avg resistance (Ω/contact)	Std dev (Ω)	Open chains
A: Plasma 200 mTorr Plasma 50 mTorr	0.21	0.03	1	0.40	[a]	1
B: Plasma 200 mTorr	0.24	0.05	1	0.40	0.07	1
C: Plasma 200 mTorr Argon sputter	0.85	0.72	1	0.68	0.30	1
D: Plasma 200 mTorr Sulfamic acid	0.45	0.15	1	0.73	0.17	1
E: Reactive ion	0.85	0.25	2	2.16	0.93	1

[a] No observable dispersion in the data.

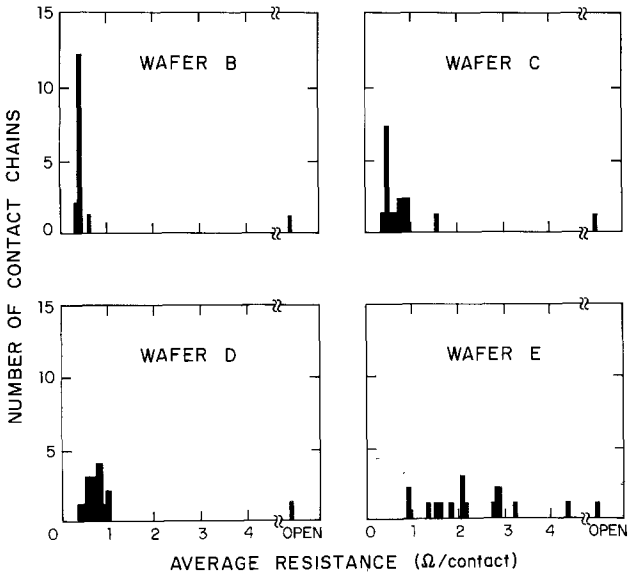

Fig. 4. Data for small vias showing the effects of various etch procedures and via treatments on samples subjected to both the HF dip and sinter steps.

by wafer A produces the most consistent results, and the lowest average contact resistance of the procedures tested.

Discussion

From a purely empirical point of view, the results described above are clear. The Day procedure works well; straight plasma etching can work nearly as well; other via treatments appear to do more harm than good. In more fundamental terms, the results support the explanation proposed by Day, namely, that the exposure of the first-level metal to the oxygen plasma produces a relatively thick aluminum oxide layer which must be chemically thinned with HF to achieve good contacts. Furthermore, the redeposition of a carbonaceous film during plasma etching coats the aluminum oxide with an etch-resistant layer, protecting it from the oxide-thinning effects of the HF dip.

It will be interesting to examine whether similar results will be found in wet-etched polyimide. There, one should not encounter plasma induced thickening of the aluminum oxide. These experiments are in progress, and will be reported separately.

The Day procedure has been used at MIT Lincoln Laboratory on approximately 2 dozen experimental MNOS memory wafers containing in excess of 50,000 vias per wafer with consistently good results. In addition, a number of other double level interconnect wafers have been processed in this fashion with low via contact resistance.

Acknowledgments

One of the authors (PKS) wishes to acknowledge the support of the MIT Lincoln Laboratory Summer Program for Engineers and Scientists.

This work was sponsored by the Department of the Air Force, and in part by the Office of Naval Research.

Manuscript submitted Feb. 22, 1982; revised manuscript received *ca.* May 24, 1982.

Any discussion of this paper will appear in a Discussion Section to be published in the December 1983 JOURNAL. All discussions for the December 1983 Discussion Section should be submitted by Aug. 1, 1983.

Publication costs of this article were assisted by the Massachusetts Institute of Technology.

REFERENCES

1. T. O. Herndon and R. L. Burke, Paper presented at Kodak Microelectronics Seminar, New Orleans, LA, 1979.
2. Hitachi Corporation, Chemical Data Sheet, Y-082, March 1978.
3. D. R. Day and S. D. Senturia, Paper presented at Electronic Materials Conference, Santa Barbara, CA, June 1981.
4. T. O. Herndon and R. L. Burke, Paper presented at Kodak Microelectronics Seminar, Monterey, CA, 1977.

Heat-Treatment Effects in Neutron Transmutation Doped Epitaxial Silicon

John W. Cleland*

Oak Ridge National Laboratory, Solid State Division, Oak Ridge, Tennessee 37830

Chemical vapor deposition (CVD) of silicon from a gaseous silicon compound onto a heated silicon substrate may be used to deposit an epitaxial Si layer and to obtain an electrical p-n junction. The dopant concentration in the epi-Si layer is a function of the gaseous dopant ion content, flow rate, temperature gradient, and any migration of impurities (autodoping) from the heated substrate (1). Neutron transmutation doping (NTD) may also be used to introduce a desired and highly uniform concentration of n-type phosphorous dopant into Si ingots, wafers, or epi-Si wafers (1-3). However, annealing is required to remove radiation damage and to obtain the anticipated carrier concentration in NTD Si, and a number of defect-impurity interactions can occur in either Si or NTD Si as a consequence of various heat-treatments (4-5). Autodoping may also occur in NTD epi-Si during annealing to remove radiation damage.

This technical note describes some results of carrier concentration, mobility, and resistivity measurements on small (0.5 cm^2) epi-Si samples using the van der Pauw (vdP) technique. The samples were cut from wafers of epi-Si, before or after irradiation (to introduce an estimated 2×10^{14} cm^{-3} ^{31}P in the epi-Si layer), followed by heat-treatment for 30 min at either 750° or 900°C to remove radiation damage. The epi-layer was n-type, P-doped, 60 Ω-cm resistivity, 0.01 cm thick, deposited on a p-type, Ga-doped, 0.05 Ω-cm, 0.03 cm thick substrate cut from a Czochralski (CZ)-grown Si ingot.[1] The initial carrier concentration and mobility values were $\sim 1.1 \times 10^{14}$ cm^{-3} and 1300 cm^2 V^{-1} sec^{-1} for the epi-layer and $\sim 1.1 \times 10^{18}$ cm^{-3} and 85 cm^2 V^{-1} sec^{-1} for the substrate. The irradiation conditions and annealing procedures are described in previous papers (4, 5).

Extended ($\geqq$ 100 hr) annealing at 450°C can introduce $\sim 10^{16}$ cm^{-3} oxygen-related donors in CZ Si that contains $\sim 10^{18}$ cm^{-3} interstitial oxygen (O_i) initially (4, 5). The initial O_i content was not determined in the

* Deceased.

[1] The author is indebted to C. W. Pearce, Western Electric Company, Allentown, Pennsylvania, for supplying the epi-Si wafers.

substrates used here, but the apparent acceptor concentration in the substrate portion of several samples was reduced from $\sim$ 1.1 to 0.7 $\times$ 10^{18} cm^{-3} by annealing for 180 hr at 450°C. The apparent donor concentration remained at $\sim$ 1.1 $\times$ 10^{14} cm^{-3} in the epi-layer of these samples, so no evidence of either O donor formation in the epi-layer or of O donor migration from the substrate was observed in these annealing experiments.

It has been shown in our earlier work that heat-treatment for 30 min at 750°C is sufficient to obtain the anticipated carrier concentration in NTD Si, taking the separate effect of O donor formation into account (6). However, a significant concentration (10^{14}-10^{15} cm^{-3}) of an impurity (presumably Li), which can be activated as a donor by short term (30 min) heat-treatment at $\geq$ 650°C, is present in some commercially available float zone (FZ) refined, CZ-grown, or NTD Si (4, 5). Figure 1 indicates the initial carrier concentration of two samples of unirradiated epi-Si, samples 1 and 2, the estimated initial carrier concentration of two samples after irradiation, samples 3 and 4, and the change in carrier concentration at room temperature of the samples after heat-treatment for 30 min at 750° or 900°C. These data indicate that $\sim$ 10^{16} cm^{-3} donors were activated in sample 1 at 750°C and that $\geq$ 98% of them became inactive within a few hours at room temperature. More than 2 $\times$ 10^{16} cm^{-3} donors were activated in sample 2 at 900°C and again $\geq$ 98%

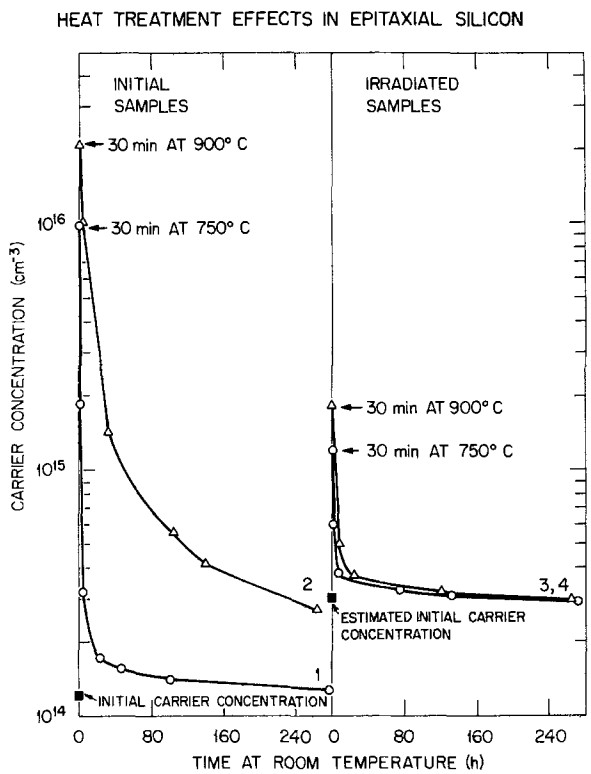

Fig. 1. Heat-treatment effects in epitaxial silicon

were inactive after 250 hr at room temperature. Samples 1 and 2 were given a second identical heat-treatment (data not shown) and the apparent donor concentration increased to $\geq$ 10^{16} cm^{-3} in both samples. Most (99%) of the donors were inactive in sample 1 after 100 hr at room temperature, but 20% of the donors remained in sample 2 after 5 months at room temperature. These data indicate that the higher temperature (900°C) heat-treatment may introduce lattice defects that interact with Li to form a stable donor.

Only 1-2 $\times$ 10^{15} cm^{-3} donors were activated in the NTD epi-Si samples 3 and 4 after heat-treatment for 30 min at 750° or 900°C, respectively (Fig. 1). Most of these donors became inactive within a few hours at room temperature. Previous experiments (4) have indicated that Li can form a stable donor if associated with fast-neutron induced lattice defects (D_f) in NTD Si and that heat-treatment for 20 hr at 900°C is required to remove most of these Li-D_f donors. In the present experiments the source of the inactive donor impurity is not known, but it is probably Li from the substrate, since all of the samples were from the same epi-Si wafers and were heated under identical conditions. The fact that $\sim$ 10^{16} cm^{-3} donors were activated in the unirradiated samples as compared to $\sim$ 10^{15} cm^{-3} donors in the irradiated samples may indicate that extensive autodoping by Li from the substrate can occur as a consequence of heat-treatment of epi-Si, unless the simultaneous presence of D_f impedes Li migration in NTD epi-Si.

Acknowledgments

The author is indebted to D. H. Lowndes for a careful review of the manuscript. This research was sponsored by the Division of Materials Sciences, U.S. Department of Energy under contract W-7405-eng-26 with Union Carbide Corporation.

Manuscript submitted Feb. 24, 1982; revised manuscript received *ca.* June 15, 1982.

Any discussion of this paper will appear in a Discussion Section to be published in the December 1983 JOURNAL. All discussions for the December 1983 Discussion Section should be submitted by Aug. 1, 1983.

Publication costs of this article were assisted by the Oak Ridge National Laboratory.

REFERENCES

1. S. Prussin and J. W. Cleland, *This Journal*, **125**, 350 (1978).
2. "Proceedings of the Third International Conference on Neutron Transmutation Doped Silicon," Jens Goldberg, Editor, Plenum Press, New York (1981).
3. "Proceedings of the Second International Conference on Neutron Transmutation Doping in Semiconductors," Jon Meese, Editor, Plenum Press, New York (1979).
4. J. W. Cleland, *J. Nucl. Mater.*, In press.
5. J. W. Cleland, *This Journal*, In press.
6. J. W. Cleland and N. Fukuoka, in "Proceedings of the Third International Conference on Neutron Transmutation Doped Silicon," Jens Goldberg, Editor, Plenum Press, New York (1981).

Mercury Pressure-Induced LPE Growth of HgCdTe

H. Ruda, P. Becla,[1] J. Lagowski,* and H. C. Gatos*

Massachusetts Institute of Technology, Cambridge, Massachusetts 02139

Present state-of-the-art epitaxial layers of HgCdTe (ideally suited for infrared imaging systems) are fabricated by LPE; however, it is necessary to provide a continuous control of the Hg pressure (1) during growth. In this communication a new modified method of LPE is proposed which utilizes an Hg pressure differential

* Electrochemical Society Active Member.
[1] Present address: Institute of Physics, Technical University of Wroclaw, Wroclaw, Poland.

as the sole driving force to initiate and sustain growth. Growth is performed from Te-rich solutions under strictly isothermal conditions. The mechanism responsible for growth involves the generation of excess Hg in the vapor (from an Hg reservoir) which is then incorporated into the solution, thereby providing an effective supersaturation in the solution leading to growth.

The principle of the present approach is illustrated in Fig. 1. Consider the system initially in equilibrium when the Hg reservoir is held at temperature T_1 and the solution at temperature T. The partial pressure of Hg is identical over the solution and the reservoir. Upon raising the temperature of the reservoir to a new higher temperature T_2, while maintaining the solution at its original temperature, T, a flux of Hg from the reservoir to the solution is generated. The excess Hg is incorporated into the solution, and the new Hg pressure becomes $P_{(f)}$ over the whole system. In this way, the solution undergoes a transition (i) → (f), *i.e.*, it becomes supersaturated leading to growth.

Experiments to establish the validity of this growth principle were made using Te-rich source material over a wide range of temperatures and with a wide range of pressure differentials. The apparatus consisted of a boron nitride tipping boat positioned at one end of a sealed quartz ampul and an Hg reservoir at the other end (Fig. 1). The solution and the reservoir were separated by a quartz volume spacer reducing the free volume in the ampul to about 8 cm³. The end of the ampul containing the boat remained in an isothermal configuration throughout the experiment. The temperature of the reservoir zone was controlled independently of the boat zone, being ramped up to its new temperature for growth by applying a temperature differential, ΔT.

About 3g of solution were placed at one end of the boat, and a polished and oriented wafer of (111)A CdTe was placed at the other end. The temperature was raised to T_1 (determined by phase diagram data) and contact was established by tipping the apparatus through a small angle, the solution thickness was about 3 mm. The system was then allowed to equilibrate; a period of 15-30 min was found to be sufficient. After the desired growth the solution was separated from the epilayer again by tipping the apparatus. Layers about 40 μm thick and with x values between 0.16 and 0.28 were grown (see Table I). Typical growth velocities were higher than those typical of ramp-cooled LPE (2-5).

A distinct advantage of the present method is that it requires no "wiping" of the solution after growth, which in practice introduces limitations regarding the dimensions of the substrate area. Furthermore, it permits *in situ* post-growth annealing under controlled Hg pressure.

Hall measurements on layers which were prepared by the present method are given in Table I. Mobilities of up to 43,000 cm²/V sec are reported with relatively low carrier concentrations. These values compare favorably with layers reported in the literature for conventional LPE processes (1, 5). In addition, the surface morphology was satisfactory, although the method as employed was still in its early stages of development.

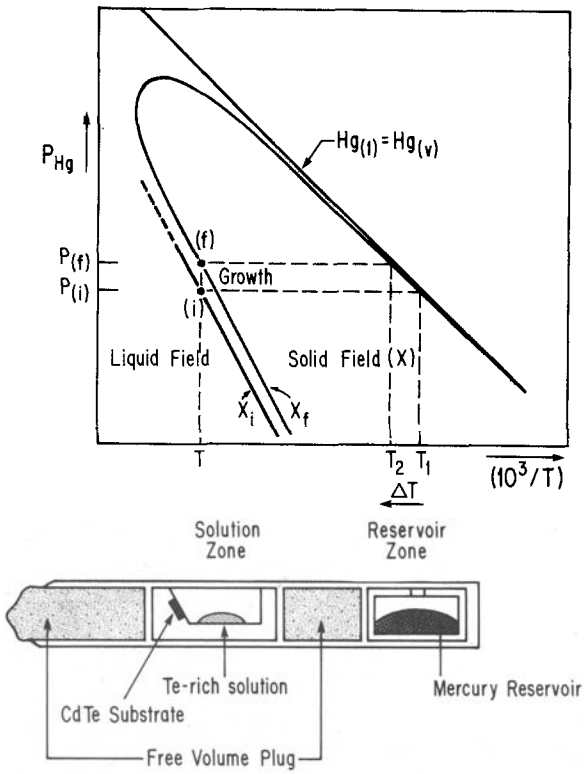

Fig. 1. Schematic diagram of apparatus for Hg pressure-induced LPE of HgCdTe and illustration of the growth principle; a temperature increase, ΔT, of the mercury reservoir causes a supersaturation of the solution (held at constant temperature) leading to growth. x_i is the initial composition at equilibrium T_1, and x_f is the composition of the growing layer.

Some qualitative predictions on the type of growth behavior one might expect are presented below. The growth velocity should reflect two distinct stages: an initial transient stage (stage I in Fig. 2) in which the solution attains its maximum incorporation of the excess Hg generated, followed by a supersaturation stage II. Stage I is directly related to the incorporation kinetics at the solution-vapor interface. Stage II should be analogous to the kinetics of growth from supersaturated solution as in the case of step-cooled LPE. That is, the velocity should follow $t^{-(1/2)}$ in stage II (6-8). The solution thickness is an important factor which affects the Hg gradient in the solution, and thus the mercury transport to the growth interface. It is apparent that this Hg concentration gradient leading to growth is larger the thinner the solution.

Table I. Characteristics of layers grown by Hg pressure-induced LPE: growth parameters

Sample code	Growth temperature (°C)	$T_1 - T_2$ (°C) (Hg reservoir)	Growth time (min)	Layer thickness (μm)	Composition x-value	$\lvert N_d - N_a \rvert$ (cm^{-3})	Mobility (cm²/Vsec)
PI-12	578	350-358	45	26	0.28	2.3×10^{16} (p)	3.2×10^{2}*
PI-18	569	350-365	45	34	0.27	—	—
PI-19	476	240-251	25	20	0.16	6.5×10^{16} (n)	4.3×10^{4}**
PI-21	478	243-265	30	39	0.18	7.6×10^{16} (n)	2.1×10^{4}**
PI-32	547	300-318	45	24	0.21	5.0×10^{16} (n)	4.5×10^{3}**

* As grown.
** Annealed *in situ*.

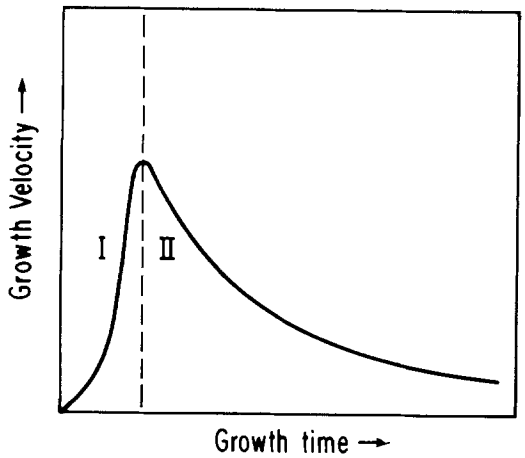

Fig. 2. Schematic illustration of growth velocity vs. time: I—initial transient state; II—supersaturation stage.

The effects of the isothermal growth temperature can best be understood on the basis of the Gibbs phase rule for a three component liquid in equilibrium with its vapor and solid. There are two degrees of freedom. Therefore, for a given solution composition, by setting the isothermal growth temperature, the composition of the solid, x, is uniquely determined. Thus, the higher the growth temperature, the higher the component solubilities, and the larger the fraction of CdTe in the solid, x. Figure 3 shows an experimental plot of the solidus, where the data is taken from Table I. It is seen that indeed x increases with increasing temperture. As ΔT is increased, more Hg is incorporated into the solution, and the effective supersaturation of the solution increases. Thus we would expect greater growth rates for a larger value of ΔT at a given growth temperature and solution composition. Comparing experiments PI-19 and PI-21 in Table I (carried out at approximately the same temperature) it is seen that the grown thickness, over about the same growth time (25 to 30 min), is practically double for an increase of the differential, ΔT by about a factor of two.

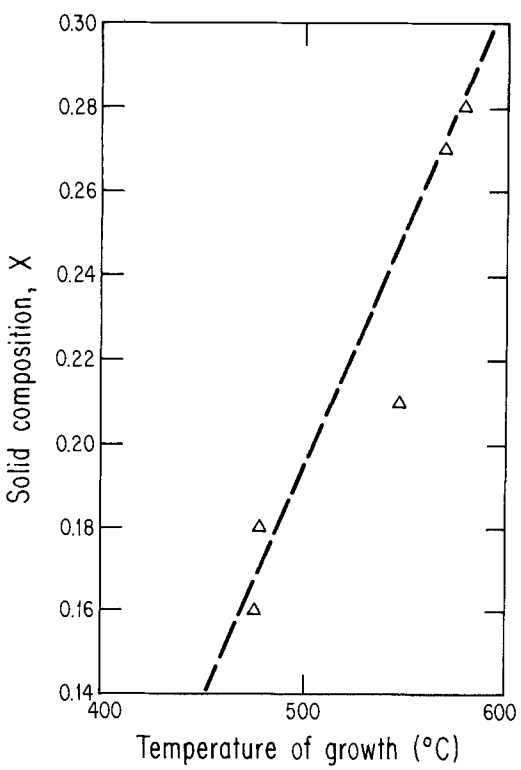

Fig. 3. Experimental solidus data

Referring back to the growth velocity as illustrated in Fig. 2, we may infer that over the relatively long growth periods employed in these experiments, stage II behavior is expected to dominate the principal part of the growth kinetics, *i.e.*, the grown layer thickness is expected to vary to good approximation, as $t^{(1/2)}$. The maximum thickness of the epitaxial layer is limited by the depletion of cadmium and tellurium in the solution.

One factor that might be anticipated to limit the achievement of a maximum thickness is spontaneous nucleation in the solution, by removing the solute from the already-dilute solution. This effect should be most pronounced in the early stages of growth (stage I), when the instantaneous supersaturation across the solution is maximum. However, no such behavior was observed, and thus the initial kinetics are believed to be sufficiently rapid to dissipate such constitutional gradients across the solution. Therefore, constitutional supercooling is not anticipated to be a significant problem. A full theoretical treatment of the thermodynamics and kinetics of pressure-induced growth is currently being pursued.

Acknowledgment

The authors are grateful to the Defense Advanced Research Projects Agency for financial support.

Manuscript submitted April 13, 1982; revised manuscript received July 26, 1982.

Any discussion of this paper will appear in a Discussion Section to be published in the December 1983 JOURNAL. All discussions for the December 1983 Discussion Section should be submitted by Aug. 1, 1983.

Publication costs of this article were assisted by the Massachusetts Institute of Technology.

REFERENCES

1. T. C. Harman, *J. Electron. Mater.*, **10**, 1069 (1981); *ibid.*, **9**, 945 (1980).
2. J. A. Mroczkowski and H. R. Vydyanath, *This Journal*, **128**, 655 (1981).
3. J. E. Bowers, J. L. Schmit, C. J. Speerschneider, and R. B. Maciolek, *IEEE Electron. Dev.*, **ed-27**, 24 (1980).
4. C. C. Wang, S. H. Shin, M. Chu, M. Lanir, and A. H. B. Vanderwyck, *This Journal*, **127**, 175 (1980).
5. J. L. Schmit and J. E. Bowers, *Appl. Phys. Lett.*, **35**, 457 (1979).
6. J. J. Hsieh, *J. Cryst. Growth*, **27**, 49 (1974).
7. M. B. Small and J. F. Barnes, *ibid.*, **5**, 9 (1969).
8. D. L. Rode, *ibid.*, **20**, 13 (1969).

JOURNAL OF THE ELECTROCHEMICAL SOCIETY

ACCELERATED

—BRIEF COMMUNICATIONS—

JANUARY 1983

Construction of Reference Electrodes for Long-Term Testing of Compact Li-Al/FeS Cells

L. Redey* and D. R. Vissers*

Argonne National Laboratory, Chemical Engineering Division, Argonne, Illinois 60439

The $Ni/Ni_3S_2/S^{2-}$ and $(\alpha + \beta)Li\text{-}Al/Li^+$ reference electrodes (1,2) have proven to be excellent investigative tools for evaluating Li-Al/FeS cell performance (3). These electrodes have been used to investigate the polarization characteristics of electrodes in compact cells and to carry out a variety of electrochemical studies in experimental laboratory cells. The compact cell designation is used here to refer to cells constructed with high specific energy and high specific power. At present, the compact Li-Al/FeS cells we test have a capacity range of 20-400 Ah.

Basic Principles of Construction

Investigations with reference electrodes, especially electrode polarization studies, require that the chemical and physical characteristics of the reference electrode and cell construction be meticulously selected. Also, the proper placement of the electrodes and the location of the electrolytic junction point (opening of the Luggin capillary) to its surroundings require careful consideration. The basic principles of the Luggin-capillary tip construction and its placement to avoid error in electrode potential measurements for laboratory cells are well known (4-6). Such laboratory cells are designed for the special purpose of the measurement (7); consequently, flexibility in the cell design is provided to allow the selection of various configurations for reference electrode work. In compact cells, on the other hand, because the geometry is fixed and the current path and the mass transfer effects must be disturbed as little as possible, the options for reference electrode design and placement are limited. The consequences of the high temperature and the reactive environment impose further limitations on the electrochemically active and inactive components of the electrode; these limitations have been described in an earlier paper (2). The construction materials for the reference electrodes must withstand molten salt electrolyte and the effects of dissolved lithium metal and S^{2-} ions up to 500°C as well as endure thermal cycling between room temperature and the cell upper working-temperature.

Our state-of-the-art Li-Al/FeS compact cells can undergo several hundreds of cycles (100-1000) equivalent to testing periods of 50-500 days; a reference electrode consequently must have a useful life at least this long or longer.

Typical Designs

The chemistry of our $(\alpha+\beta)Li\text{-}Al/Li^+$ and $Ni/Ni_3S_2/S^{2-}$ reference electrodes can be symbolized by the following half cells:

$$\underset{T_1}{Ni\text{-}Ni}/(\alpha+\beta)Li\text{-}Al/LiCl\text{-}KCl \quad \underset{T_2}{} \qquad [1]$$

$$\underset{T_1}{Ni\text{-}Ni}/Ni_3S_2/LiCl\text{-}KCl,\ Li_2S(s) \quad \underset{T_2}{} \qquad [2]$$

where T_1 is the temperature of the glovebox and T_2 is the cell temperature. In this reference electrode work, the $(\alpha+\beta)Li\text{-}Al$ electrode has been taken as the primary standard and thus its potential is defined as zero at any temperature (2). Consequently, combining the two electrodes described above forms a calibration cell whose emf is the potential of the $Ni/Ni_3S_2/S^{2-}$ reference electrode on this "standard" potential scale. The temperature dependence of the emf (E in mV) of this cell (2) is found to be:

$$E = 1367.5 + 0.097\ (T-700) \qquad [3]$$

where T is the cell temperature in K. Recent studies (8) indicate the above cell voltage is independent of the Li^+/K^+ ion ratio in the electrolyte. The construction of these electrodes will be described below.

To date, high-purity, high-density beryllia ceramic is the best material for the reference electrode housing in terms of meeting the chemical requirements detailed in the preceeding section. The design details of a typical reference electrode are shown in Fig. 1.

Key words: reference electrode, nickel sulfide, Li-Al alloy, molten salt

*Electrochemical Society Active Member.

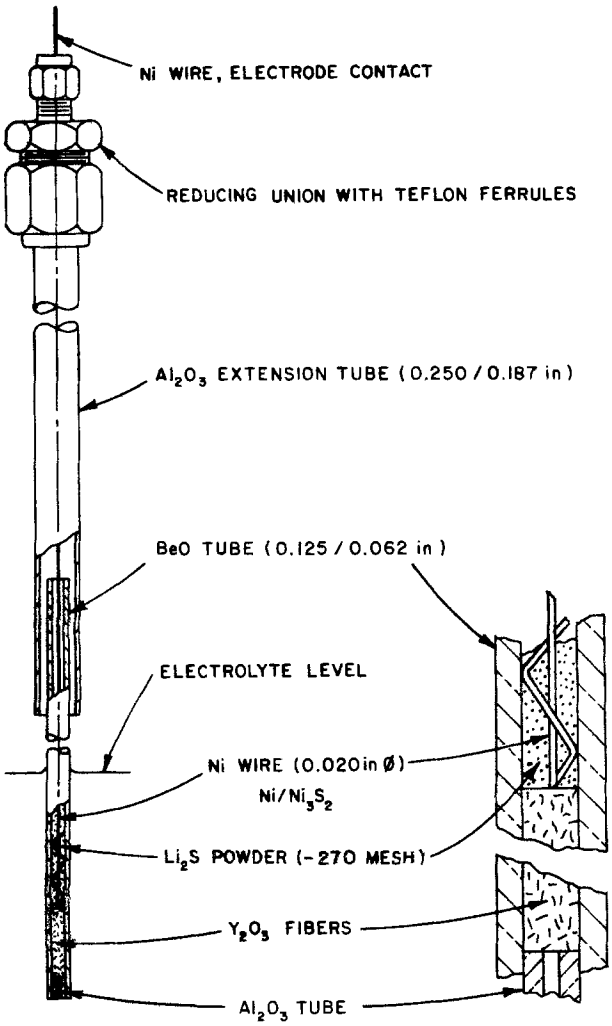

Fig. 1. Ni/Ni_3S_2 Reference Electrode with Beryllia Tube Housing.

The BeO tube (3M Company, Technical Ceramics Div., Type ALSIMAG 794) is 178 mm (7 in.) in length and has a 3.2 mm (1/8 in.) OD and a 1.6 mm (1/16 in.) ID. The spring action of the saw-toothed loop of the nickel wire (Ni 200, nominally 99.5% Ni; 0.5 mm, 20 mil ϕ) fixes the BeO housing in place, thus eliminating the need for an undesirable rigid connection between the electrode holder assembly (reducing union and Al_2O_3 extension tube) and BeO tube. The Y_2O_3 plug diffusion barrier is formed by vibrating fibers of yttria felt (Zircar Products Inc.) into the BeO tube. This barrier is readily wetted by the electrolyte and develops a resistance of 7-10 kohm/cm. The short Al_2O_3 tube, held in place by friction at the tip of the reference electrode, serves as support for the yttria diffusion barrier. In preparing the electrodes approximately 20 mg of high purity (>99%) Li_2S powder (particle size $\lesssim$2 μm, -270 mesh) is vibratorily loaded into the lower 2-3 cm portion of the BeO tube. Because of the low solubility of Li_2S in the electrolyte (500-1700 ppm in the working temperature range of the cell) a small quantity of Li_2S can maintain the electrolyte in the electrode cavity saturated for more than a year if an adequate diffusion barrier is provided.

The major disadvantage in the use of BeO is the dimensional limitations of the available products. Because of the high toxicity of the BeO powder and dust, any alteration in shape of a commercial item is very difficult to implement. At present, the 1/8 in. OD high-density BeO tube appears to be available only in lengths of 7 in. or less.

Thermodynamically, Al_2O_3 is not stable in electrolyte media of unit Li° activity. However, our experimental work has shown high-purity, high-density alumina materials (like McDanel Refractory Co., 998 Alumina) to be stable as reference electrode housings in Li-Al/FeS cell environments for several years without significant chemical or mechanical deterioration. The only change noted was the formation of a harmless thin, grey surface layer. The major advantage in the use of Al_2O_3 is its ready availability as tube in a wide variety of lengths and ID and OD dimensions.

Diffusion barriers are made by inserting a short (10-15 mm) solid piece of Al_2O_3 rod into the Al_2O_3 tube. End sections of both the rod and the tube are polished to make a near perfect fit. The friction holds this plug firmly in place and the narrow gap between the two pieces forms a fine capillary which creates an excellent liquid junction with an approximately 5 kohm resistance and thus a very low diffusion rate.

Because a reference electrode operates at the temperature of its surroundings and its potential is temperature dependent, knowledge of its exact temperature is essential. Therefore, for precise measurement, we have developed a bifunctional sensor (Ni/Ni_3S_2 reference electrode and thermocouple combination). A schematic diagram of this sensor is shown in Fig. 2.

Our typical sensor utilizes a 3.2 mm OD, 1.6 mm ID (0.125/0.062 in.) Al_2O_3 tube of the required length (long enough for the upper end to be at room temperature) and a Ni 200 tube (with 1.0 mm OD and 0.5 mm ID, 0.040/0.020 in.) with its lower end closed by electron beam welding. This Ni tube serves as sheathing for a 0.25 mm (0.010 in.) OD Omega chromel-alumel thermocouple (type TJ 36-SCASS-010U) and at the same time as the base metal for Ni_3S_2 formation (2).

Manuscript submitted May 10, 1982; revised manuscript received ca. Sept. 7, 1982.

Publication costs of this article were assisted by Argonne National Laboratory.

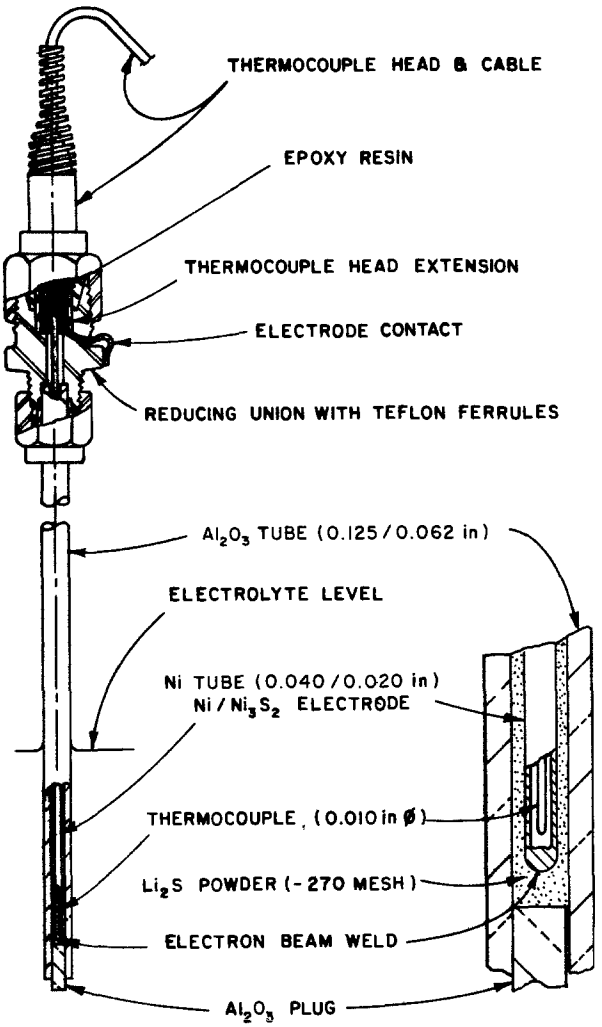

Fig. 2. Ni/Ni_3S_2 Reference Electrode - Thermocouple Bifunctional Sensor with Alumina Tube Housing.

Because of the small masses of its active components and housing, the sensor system (Ni/Ni_3S_2 reference electrode plus thermocouple) responds rapidly to temperature changes. The corresponding new voltage values of the thermocouple and the electrode stabilize within a minute after a step temperature change providing excellent opportunity for monitoring these variables. Typical response-time values for 90% of the total change (starting from sensor temperatures below the melting point of the electrolyte) are 12 s and 18 s for the temperature and electrode potential measurements respectively. The potential approaches the final mean value to within 1 mV in 50 s.

Li-Al/Li^+ reference electrodes can be used as well in Li-Al/FeS cell systems. Construction of these electrodes is similar to that just described for the Ni/Ni_3S_2 electrode except finely powdered ($\alpha + \beta$)-phase Li-Al alloy replaces the Li_2S. In another version, the alloy is formed in situ electrochemically (2) using a fine aluminum wire (1-10 mg, 0.125 mm, 5 mil ϕ) wound around the tip of the nickel sheathing.

A decision whether to use the Ni/Ni_3S_2 or the Li-Al reference electrode depends on the purpose of the experiment in question. The Ni_3S_2 system is more stable and less sensitive to impurities. On the other hand, an ($\alpha + \beta$)-phase Li-Al alloy reference electrode directly indicates potential values on the proposed "standard" scale (2). Outward diffusion of either nickel and sulfide ions or the strongly reducing solution of dissolved lithium metal through the diffusion barrier of the reference electrode can cause minor polluting effects on the tested system, and might be a criterion for selecting the appropriate electrode from the two alternatives.

The above described simple Ni/Ni_3S_2 and Li-Al/Li^+ reference electrodes possess well-defined potentials of excellent stability. These electrodes function well even after many thermal cycles between 500°C and room temperature. Most of our Ni/Ni_3S_2 reference electrodes have performed well for more than a year of continuous service in Li-Al/FeS cell testing, thus proving their chemical stability and compatibility.

Acknowledgement

This work was performed under the auspices of the U. S. Department of Energy. We thank Drs. D. L. Barney and R. K. Steunenberg for their encouragement and support of our work.

References

1. L. Redey and D. R. Vissers, Extended Abstracts of Electrochem. Soc. Meeting, Boston, MA, May 6-11, 1979, Abstract No. 371.

2. L. Redey and D. R. Vissers, J. Electrochem. Soc., 128, 2703 (1981).

3. D. L. Barney, et al., High Performance Batteries for Electric Vehicle Propulsion and Stationary Energy Storage, Progress Report for the Period October 1978 - September 1979, ANL-79-94, Argonne National Laboratory (1980).

4. R. Piontelli and G. Bianchi, Gass. Chim. Ital. 8, 581 (1950).

5. R. Piontelli G. Bianchi and R. Aletti, Z. Elektrochem. 56, 86 (1952).

6. B. R. Sundheim, J. Electrochem. Soc., 115, 158 (1968).

7. B. D. Cahan, Z. Nagy and M. A. Genshaw, J. Electrochem. Soc., 119, 64 (1972).

8. Z. Tomczuk, L. Redey and D. R. Vissers, article to be published in this journal.

Vapor Phase Deposition of Aluminum Film on Quartz Substrate

D. R. Biswas, C. Ghosh, and R. L. Layman

ITT Electro-Optical Products Division, Roanoke, Virginia 24019

Sputtering (1), vacuum evaporation (2), and conventional chemical vapor deposition (CVD) (3) are the major processes by which aluminum film can be deposited onto a flat substrate. Sputtering and vacuum evaporation normally cannot be used for producing a uniform coating on an irregular substrate and the CVD usually produces large grains or growth cones on the substrate surface. In order to produce a uniform, fine grained film on any desired substrate surface, a surface controlled heterogeneous (4) nucleation and growth process is currently being used. In this process, the substrate surface is preferentially heated to a reaction temperature by induction heating or by any other means keeping the reactant vapor temperature lower than that of the reaction temperature. Therefore, the reaction can take place heterogeneously at the substrate surface. An application of this deposition method is being considered to deposit aluminum films on fused quartz substrates.

A metallorganic compound of aluminum namely trimethyl aluminum (TMA)* was used for the deposition of an aluminum film on quartz substrates. Fused quartz samples were fabricated from a commercial** T08 rod by cutting, polishing and properly cleaning the surface. The samples were placed on a graphite susceptor inside the deposition chamber as shown in Fig. 1. The chamber was flushed with ultrapure hydrogen and then the susceptor was heated by using RF induction to the desired deposition temperature and was allowed to equilibriate for an hour before injecting the chemicals. The susceptor was rotated continuously to achieve uniform deposition. Ultra pure hydrogen was used as a carrier gas for TMA and introduced from the top of the chamber. The flow rate of hydrogen through TMA was 0.1 ℓ/min and the TMA was kept at 25°C. A total flow rate of 5 ℓ/min through the reactor was maintained throughout the experiment. The deposition temperature was varied from 350°C to 550°C for a fixed concentration of TMA. Since the deposition can take place wherever the vapor is in contact with the hot substrate, any desired shape of quartz substrate can be used for uniform aluminum deposition.

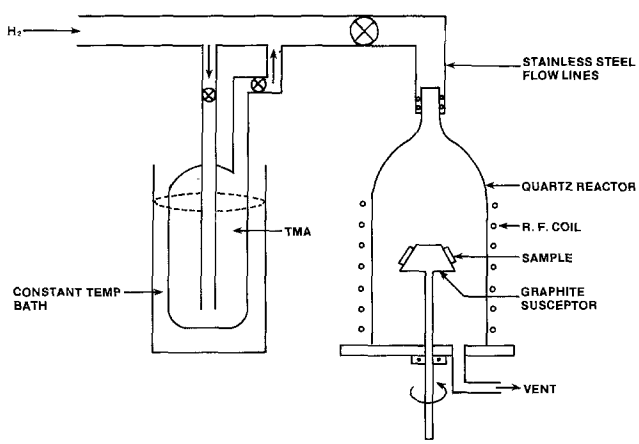

Fig. 1. A schematic diagram of metallorganic deposition chamber.

*Alfa Products. Thiokol/Ventron Division, Danvers, MA.
**Hereaeus-Amersil, Sayreville, NJ.
Key words: deposition, metallorganic, aluminum, quartz

The deposition rate is plotted as a function of temperature in Fig. 2, which indicates that the rate of aluminum deposition increases with increase in temperature up to around 500°C and then levels off. A higher deposition rate can be obtained by increasing the TMA concentration. Uniform aluminum films ranging from 500 Å to several micron thick on fused quartz were deposited. Excellent adhesion of Al film on quartz was observed from the SEM micrograph as shown in Fig. 3. No pinholes were detected at 30,000X. The reflectivity was found to be about 87% and the resistivity of the film was $\sim 1 \times 10^{-5}$ Ω-cm.

Therefore, a low resistive, highly reflecting defect-free aluminum coating on fused quartz substrate can be obtained at low temperature by the metallorganic decomposition method. A protective coating of aluminum on any desired shaped substrate materials can be obtained without damaging the substrate surface by this method.

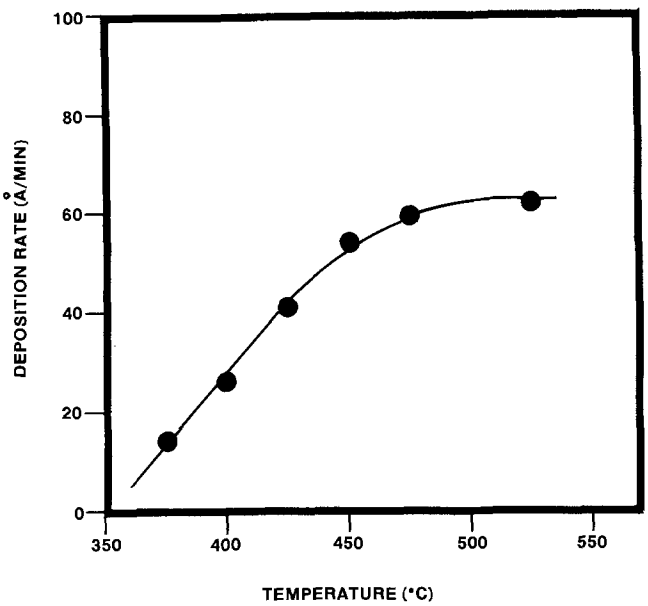

Fig. 2. A plot of deposition rate of aluminum film on flat polished quartz disc samples as a function of temperature.

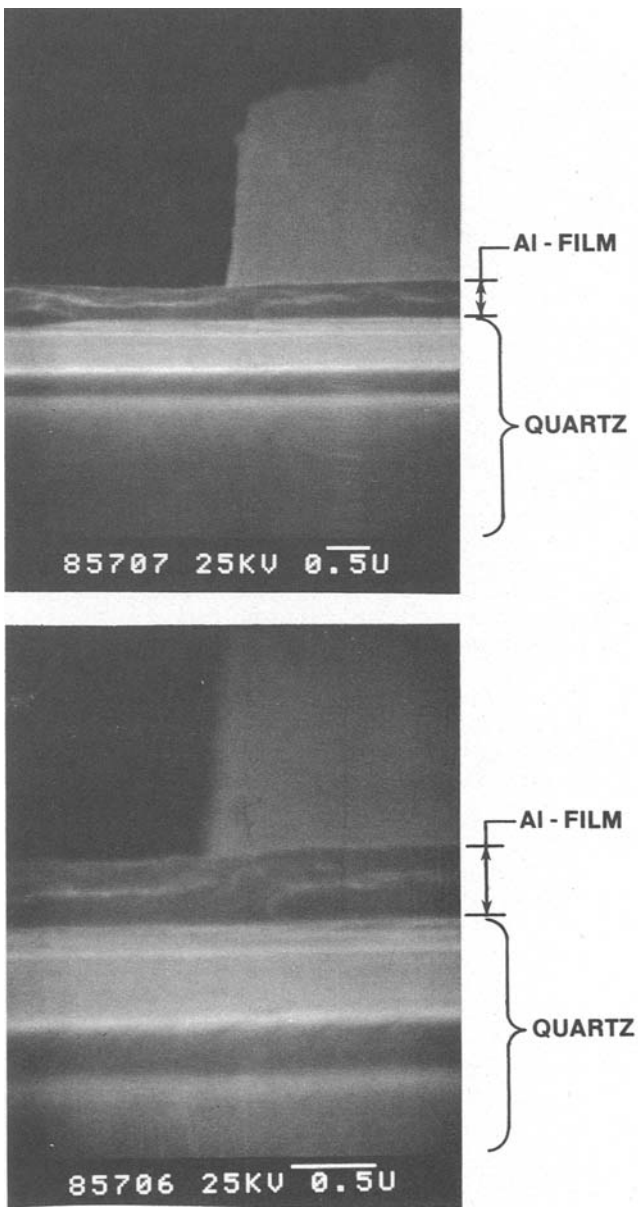

Fig. 3. Typical SEM micrographs showing the adhesion of pinhole-free aluminum film on quartz substrate at low and at high magnifications.

ACKNOWLEDGEMENT

The authors would like to acknowledge ITT Electro-Optical Products Division for permission to publish this communication.

REFERENCES

1. G. K. Wehner and G. S. Anderson, "Handbook of Thin Film Technology," ed. by L. I. Maissel and R. Glang., Chap. 3, McGraw-Hill, New York (1970).

2. R. W. Berry, P. M. Hall and M. T. Harris, "Thin Film Technology," Chap. 3, D. van Nostrand Co. Inc., New Jersey (1968).

3. C. F. Powell, "Vapor Deposition," ed. by C. F. Power, J. H. Oxley and J. M. Blocher, Jr., Chap. 10, John Wiley & Sons, Inc., New York (1966).

4. R. N. Ghoshtagore, This Journal, 125, 110 (1978).

Manuscript submitted July 19, 1982; revised manuscript received Oct. 7, 1982.

Publication costs of this article were assisted by International Telephone and Telegraph Corporation.

Laser-Induced Photoelectrochemical Transients at a Dye Solution-SnO_2 Interface

A. Frippiat, A. Kirsch-De Mesmaeker,* and J. Nasielski

Université Libre de Bruxelles, Faculté des Sciences, Service de Chimie Organique, B-1050 Bruxelles, Belgique

Richardson, Perone et al (1) and Gottesfeld et al (2) have developed a technique to measure laser-induced photoelectrochemical transients generated in absorbing semi-conducting electrodes. We now present an extension of this method to systems where the light is absorbed by a dye solution in contact with a transparent semi-conducting electrode. The technique consists in irradiating the solution with an 8 ns dye laser pulse through the electrode and to measure the open-circuit photopotential relaxation of the corresponding PEC cell. The measurements were performed in a cell composed of a small, highly doped (10^{19}-10^{20} donors/cc) transparent SnO_2 electrode, a large Pt counter-electrode and a Rhodamine B solution without or with hydroquinone (HQ).

The light pulse induces a rapid charging of the capacitance associated with the semi-conductor space-charge (1, 2); in the case of the SnO_2/Rhodamine B interface, the excited dye either decays to the ground state (reaction 1) or injects an electron into the SnO_2 conduction band (reaction 2) inducing thus a negative shift of the SnO_2 potential.

$$R \longrightarrow R^* \qquad I_a$$

$$R^* \longrightarrow R \qquad (1)$$

$$R^* \longrightarrow R^+ + e_{CB}^- \qquad (2)$$

$$R^+ + e_{CB}^- \longrightarrow R \qquad (3)$$

$$R^+ \longrightarrow P \qquad (4)$$

$$R^+ + HQ \longrightarrow R + HQ_{ox} \qquad (5)$$

Reaction scheme (3, 4) for semi-conductor supersensitization. R = Rhodamine B.

Just after the pulse, depending on the external resistance between the SnO_2 and the Pt counter-electrode, the SnO_2 capacitance discharges through the external load or through a leak resistance, characteristic of faradic reactions at the electrode. With a 1 MΩ external resistance, the capacitance has to discharge through the leak resistance; in other words, in these conditions, the capacitance discharges by the back electron transfer tunnelling through the thin SnO_2 space charge layer from the conduction band to the oxidized dye (reaction 3). This process will cause the relaxation of the open-circuit SnO_2 photopotential after the pulse.

Figure 1 shows, in a time-scale of a few tens of nS, the rise of the open-circuit photopotential, induced by a laser pulse of 8 nS at 556 nm, the rise-time depending on the RC constant of the electrical device (1, 2), i.e. on the cell resistance R ($\leq 200\Omega$) and the combined values of the cables capacitances and input capacitance of the oscilloscope (typically less than 100 pF). It has to be noted that in the absence of dye or by illuminating the cell at a

---

*Electrochemical Society Active Member; Chercheur Qualifié of the Fonds National de la Recherche Scientifique.

Key words : Photoelectrochemistry, Photosensitization, Rhodamine B, Semiconductor electrochemistry.

wavelength where Rhodamine B does not absorb, no photopotential rise is observed.

Figure 2 gives, in a longer timescale, the relaxation of the open-circuit photopotential for different HQ concentrations. The initial photopotential value does not depend on the HQ concentration (if HQ $\leq 10^{-3}$M) but, with increasing reductant, the final potential value after relaxation increases and is reached more rapidly. It means that, with increasing HQ, more photoelectrochemically produced oxidized dye R^+ is trapped by HQ to regenerate the dye (reaction 5), which leads to a less important relaxation by process 3. Figure 2 shows also that without HQ, the potential does not relax entirely to its dark initial value. This can be explained by a reaction of R^+ into a product, P, which is not reducible (reaction 4) or by desorption of R^+ during the relaxation, both processes competing with the back electron transfer (reaction 3). The relaxation curves of figure 2 are exponential, except the one without HQ.

One can calculate an expression for the time evolution of the photopotential $\Delta V(t)$, taking into account reactions 3 to 5 and assuming that the kinetic rate constants and the SnO_2 capacitance (C) are constant during the discharge. This is reasonable since the pulse intensity is adjusted in order to keep a moderate potential jump : $\Delta V \leq 25$ mV. In these conditions and if all the species of the reaction scheme are adsorbed on the SnO_2 (3,4), one can write in the open-circuit situation, the expression of the faradic current of discharge :

$$i_F = -SF\, k_3 \left[R_o^+\right] e^{-\alpha t} \qquad 1$$

with $\alpha = k_3 + k_4 + k_5\,[HQ]$ and where S is the electrode area, F the Faraday constant and $\left[R_o^+\right]$ the superficial concentration of R^+, just after the laser pulse. The faradic current being equal to the capacitive current, we may write :

$$\frac{d\Delta Q}{dt} = -SF\, k_3 \left[R_o^+\right] e^{-\alpha t} \qquad 2$$

which, by replacing ΔQ by $C\Delta V$ and by integrating, leads to the expression of the measured open-circuit photopotential $\Delta V(t)$ as a function of time

$$\Delta V(t) = \frac{k_3}{\alpha}\,\Delta V_o\, e^{-\alpha t} + \Delta V_o\left(1-\frac{k_3}{\alpha}\right) \qquad [3]$$

The calculated expression [3] of $\Delta V(t)$ is exponential with time, in agreement with the experimental results. Identical relaxation curves as those of figure 2 are obtained when the experiments are performed with Rhodamine B chemically bound by an ester linkage, to the SnO_2, indicating that a kinetic treatment with the adsorbed species only, is reasonable.

Plotting the arguments α of the exponentials versus the HQ concentration for HQ $\leq 10^{-3}$M, it is found that $k_5 = 3.10^6\ M^{-1}S^{-1}$ and $\frac{1}{k_3+k_4} \equiv \tau(R^+) = 200\ \mu S$; $k_5\tau(R^+)$ being equal to 600 M^{-1}, in agreement with the value found previously (4) from the supersensitization experiments under continuous illumination. These results show that laser pulsed excitation allows to study easily the photoelectrochemical kinetics in a short time scale since in this case, k_5 and $\tau(R^+)$ have been determined independently whereas under continuous illumination, only the product $k_5\tau(R^+)$ could be determined (4) ; this method seems thus promising to investigate detailed aspects of the photoelectrochemical processes.

Figure 2 shows an additional interesting feature; for HQ concentrations $\geq 10^{-2}$M, the photopotential, instead of relaxing, increases slowly with time during a few mS after the pulse. We attribute this to the photochemical production, during the pulsed illumination, of an electroactive species which would slowly charge the electrode. That this electroactive entity originates from the adsorbed dye is evidenced by the fact that the same slow potential increase is observed also with Rhodamine chemically bound to the SnO_2 and in contact with the supporting electrolyte 10^{-2}M in HQ.

It may be possible that the electroactive species originates from the quenching by HQ of the excited singlet state of adsorbed Rhodamine B. Although we have no evidence yet for this photoreaction in the adsorbed layer, this quenching would be in agreement with the decrease of ΔV_o observed from 10^{-2}M in HQ. Moreover, the fact that the photopotential relaxations remain exponential at least up to 10^{-3}M in HQ and that only ∿3% of the Rhodamine B fluorescence is quenched in solution by HQ 10^{-3}M (4), indicate that the ΔV relaxation for HQ $\leq 10^{-3}$M are not contaminated by the charging process occurring for HQ $\geq 10^{-2}$M, resulting from photoreactions between the excited dye and HQ.

ACKNOWLEDGEMENTS

One of us (A.F.) thanks the "Institut pour l'Encouragement de la Recherche Scientifique dans l'Industrie et l'Agriculture" (IRSIA) for a fellowship.

REFERENCES

(1) S.P. Perone, J.H. Richardson, S.B. Deutscher, J. Rosenthal, and J.N. Ziemer, This Journal, 127, 2580 (1980); J.H.Richardson, S.P. Perone, and S.B. Deutscher, J. Phys. Chem., 85, 341 (1981); S.B. Deutscher, J.H. Richardson, S.P. Perone, J. Rosenthal, and J. Ziemer, "Faraday Discussion 70-70/2", p.35 (1980).

(2) Z. Harzion, N. Croitoru, and S. Gottesfeld, This Journal, 128, 551 (1981).

(3) H. Gerischer and F. Willig, Topics Curr. Chem., 61, 31 (1975).

(4) A. Kirsch-De Mesmaeker, P. Leempoel, and J. Nasielski, Electrochim. Acta, 23, 605 (1978).

Manuscript submitted Sept. 9, 1982; revised manuscript received Oct. 29, 1982.

Publication costs of this article were assisted by Universite Libre de Bruxelles.

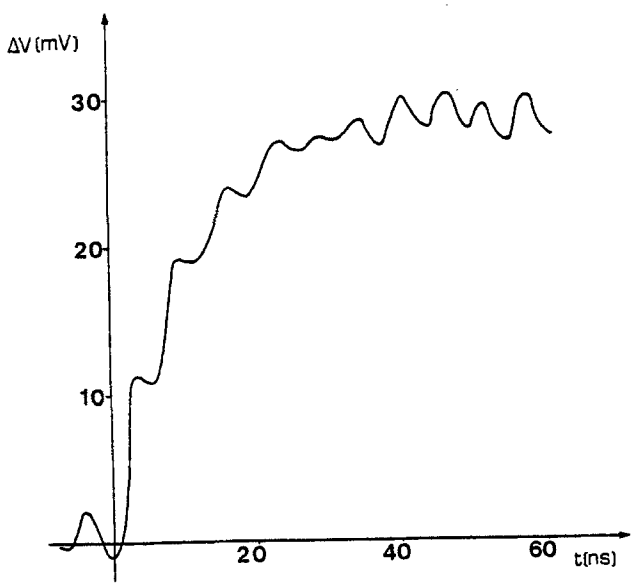

Fig. 1. Rise of the open-circuit photopotential after the laser pulse, 1 MΩ external load. Rhodamine B concentration = 10^{-4}M. Acetate buffer 5.10^{-2}M, pH 4.5.

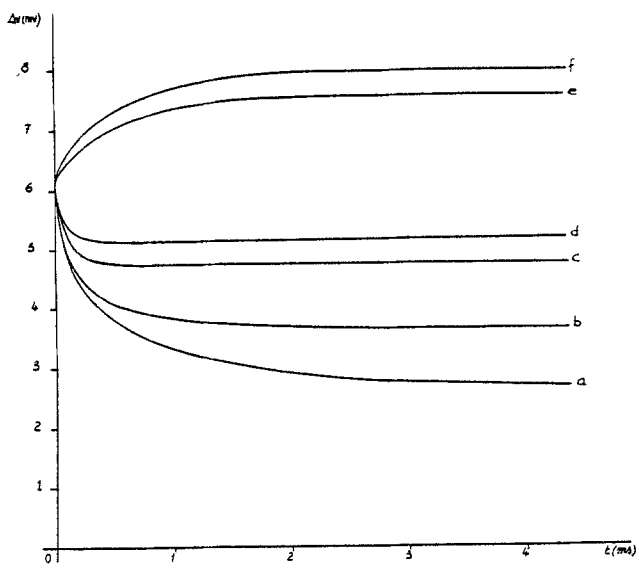

Fig. 2. Relaxation of the open-circuit photopotential after the laser pulse, 1 MΩ external load. Rhodamine B concentration = 10^{-4}M. Acetate buffer 5.10^{-2}M, pH 4.5. (a) : HQ=0 ; (b) 10^{-4}M ; (c) 5.10^{-4}M; (d) 10^{-3}M ; (e) 10^{-2}M ; (f) 2.10^{-2}M.

EXAFS Study of the Passive Film on Iron

Gabrielle G. Long, Jerome Kruger,* David R. Black*, and Masao Kuriyama

Center for Materials Science, National Bureau of Standards, Washington, D.C. 20234

Recent Mössbauer studies (1,2) of the passive film on iron have emphasized the important role of water in the structure of the in situ thin film. In these experiments, the "disorder" in the structure of the film was shown to be very similar to that of "amorphous" iron (III) oxide or hydroxide. Ex situ measurements using electron diffraction (3) have generally concluded that the main protective film on iron was crystalline Fe_3O_4 at the metal-oxide interface and γFe_2O_3 at the oxide-air interface. These results taken together can be understood if the vacuum environment of the ex situ experiments caused water to be removed from the films, causing their crystallization.

Laboratory-EXAFS (extended x-ray absorption fine structure) measurements (4) were undertaken in an attempt to determine the structure of the passive film using a direct method that avoids the need for a vacuum environment. (Background references on EXAFS are given in (4)). These exploratory measurements, while not in situ, did not require exposure of the films to a vacuum environment, and can be considered as intermediate, non-equilibrium results with respect to possible water in the film. These are the first results for the short range order parameters in the passive film, derived from measurements in a non-vacuum environment. Such information cannot be obtained directly from Mössbauer measurements.

The samples were 5 nm thick iron films vapor deposited on glass. They were passivated by immersing them in either a potassium chromate (0.005M) or a sodium nitrite (0.1M) passivating solution. Films formed this way have been shown (3,5) to have the structure, composition, and formation kinetics of the passive layers that form in Fe^{++}-free solutions by anodic oxidation.

The passive film experiment, which is a fluorescence-EXAFS measurement, utilizes a photocathode x-ray ionization chamber described earlier (6,7). The detector collects electrons emitted from the sample and amplifies them through field-intensified ionization in helium gas.

Transmission-EXAFS measurements were performed on (greater than 98% pure) finely powdered Fe_3O_4, γFe_2O_3, and $\gamma FeO(OH)$, and on (99.998% pure) bulk iron. These were then used as model compounds for the determination of phase shifts in the analysis of the thin films.

The iron-to-oxygen bond distances which were derived for the passive films are 1.91± 0.05 and 1.99±0.05 Å for for the nitrite-passivated and the chromate-passivated films respectively. These values are in the middle of the range of Fe-O and Fe-OH bond

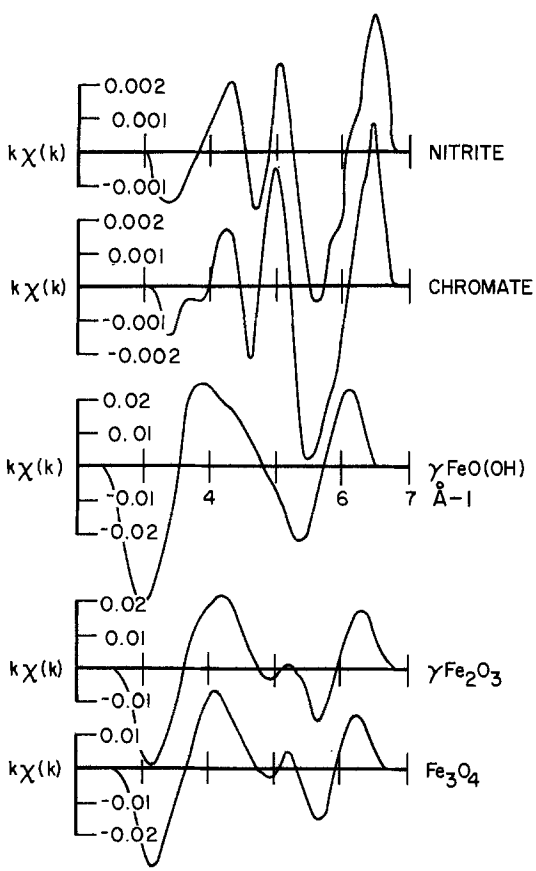

Figure 1. EXAFS signals ($k\chi(k)$) for γFe_2O_3, Fe_3O_4, $\gamma FeO(OH)$ and the passive films. Note that only $\gamma Feo(OH)$ has two oscillations over this region in k-space.

*Electrochemical Society Active Member.

lengths derived for the model compounds. The first iron-to-iron distances derived for the passivated films are shorter than those for Fe_3O_4 and γFe_2O_3, and similar to that for $\gamma FeO(OH)$. It is useful to examine the EXAFS signal directly. Since Fe_3O_4 and γFe_2O_3 are both cubic spinels, where the latter is a defect version of the former, the EXAFS signals from these compounds should be quite similar. The FeO(OH) compounds are orthorhombic with a tetramolecular unit cell, and thus their EXAFS signals should be different from the spinel-like iron oxides. The EXAFS signal, $k\chi(k)$, over the range from $k \approx 3$ to $k \approx 7$ A^{-1} for the two sets of passive films are compared to those for the model compounds in Figure 1. The EXAFS signatures of the thin films are different from that of $\gamma FeO(OH)$, whereas they bear some resemblance to the signatures of the cubic spinels.

The magnitudes of the inverse Fourier transforms are shown for the crystalline iron oxides and iron hydroxide in Figure 2, and those for the passive films are shown in Figure 3. As indicated above, the positions of the first peaks (related to the Fe-O distance) in the passive films are very similar to positions for the crystalline compounds, whereas the positions of the second peaks (Fe-Fe distance) are different. Further, the amplitude ratios of the first to the second peak for the passive films are unlike

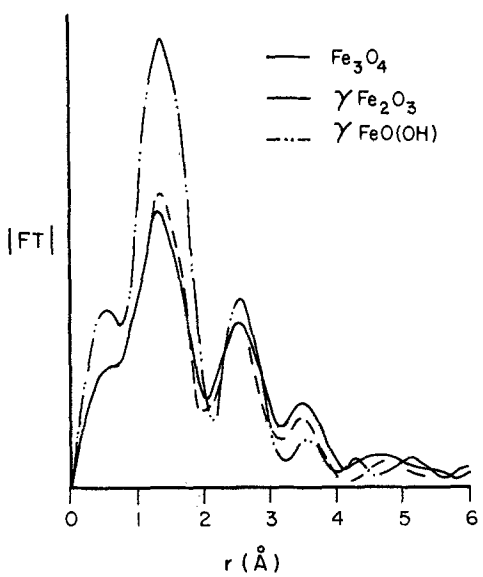

Figure 2. The magnitude of the inverse Fourier transform as a function of the radial distance, r, from the iron atom for the model crystalline compounds.

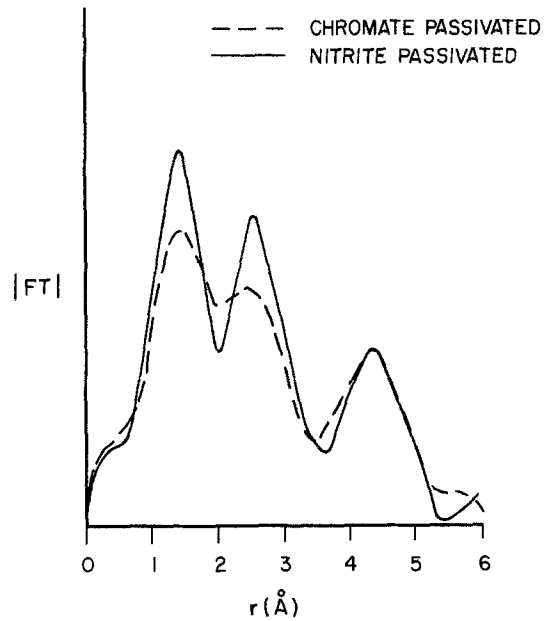

Figure 3. The magnitude of the inverse Fourier transform as a function of the radial distance, r, from the iron atom for the two passive films. The origin of the third peak is explained in Ref. 10.

those for the crystalline compounds. Since the data range in k-space used was as nearly identical as possible, this alteration in amplitude ratio may indicate a relative change in the number of nearest neighbors as well. This demonstrates that the passive film on iron is either different from these model compounds or a random mixture of many crystalline forms.

Although it has been shown that the structures of the nitrite-passivated and the chromate-passivated films are quite similar, the first two peaks in r-space are better resolved for the nitrite-formed film. This suggests that there may be a greater range of structures in the chromate-formed film, indicating greater disorder for this case. If the two films had the same structure in an aqueous environment, then the evident disorder in the chromate-passivated film could be the result of the improved stability of that film in the helium environment due to the inclusion of chromium (8). It was found, using a comparison of the fluorescence intensities at the chromium and the iron K-absorption edges, that more than 12% of

the cations in the film were chromium.

Furthermore, the absorption edge shift, as measured from the position of the K-edge of pure iron, was greatest for γFe_2O_3. If the passive films consist only of iron (III) compounds, the smaller edge shifts measured for the films would be evidence of a greater degree of covalency in the bonding (9). Another interpretation is that there may be both Fe^{++} and Fe^{+++} oxidation states present in the passive film, with the possibility of greater covalency as well. The smallest edge shift was found for the chromate-passivated film. This result taken together with the detection of Cr in this film suggests that it is the more vitreous of the two (8).

In conclusion, the EXAFS signatures of the passive films measured here resemble those of the cubic spinel ferric oxides. The sharpness of the peaks, however, is different, and at least the chromate-formed film may be more vitreous than the model crystalline compounds.

A complete account of the experiment and data analysis is to be published (10).

ACKNOWLEDGMENT

The contribution of J. Kruger was supported by the Office of Naval Research under contract NAONR 18-69 NR036-082.

REFERENCES

1. W. E. O'Grady, This Journal 127, 555 (1980).
2. J. Eldridge, M. E. Kordesch and R. W. Hoffman, J. Vac. Sci. Tech. 20, 934 (1982).
3. C. L. Foley, J. Kruger and C. J. Bechtoldt, This Journal 114, 994 (1967).
4. G. G. Cohen, D. A. Fischer, J. Colbert and N. J. Shevchik, Rev. Sci. Inst. 51, 273 (1980).
5. J. Kruger, This Journal 110, 654 (1963).
6. N. J. Shevchik and D. A. Fischer, Rev. Sci. Inst. 50, 577 (1979).
7. D. A. Fischer, G. G. Cohen and N. J. Shevchik, J. Phys. F 10, L139 (1980).
8. A. G. Revesz and J. Kruger, Passivity of Metals, R. P. Frankenthal and J. Kruger, Eds., The Electrochemical Society, Princeton, NJ, 137 (1978).
9. I. A. Ovsyannikova, S. S. Batsanov, L. I. Nasanova, L. R. Batsanova, and E. A. Nekrasova, Bull. Acad. Sci. USSR, Phys. Ser. (English translation) 31, 936 (1967).
10. Proceedings of the "International Conference on the Electronic and Molecular Structure Of the Electrode-Electrolyte Interface, held in Logan, Utah, July 25-30, 1982. To be published in J. Electroanal. Chem.

Manuscript submitted Aug. 31, 1982; revised manuscript received Sept. 17, 1982.

Publication costs of this article were assisted by the National Bureau of Standards.

Secondary Lithium Cells Employing Vanadium Tungsten Oxide Positive Electrodes

R. J. Cava, D. W. Murphy,* and S. M. Zahurak

Bell Laboratories, Murray Hill, New Jersey 07974

Reversible topochemical reactions involve a host lattice into which a guest species may be inserted and withdrawn without major structural reorganization. When the reaction involves oxidation-reduction, as is the case for reactions of lithium with many transition metal oxides and chalcogenides, it can form the basis of the positive electrode reaction for nonaqueous, high energy density, ambient temperature, secondary batteries (1). Lithium insertion reactions of ReO_3 and crystallographic shear (CS) structures derived from it in the vanadium-oxygen chemical system (e.g. V_6O_{13}) have been reported (2). On Li insertion into ReO_3 itself, the 3/4 CCP host anion array undergoes a twist to an HCP anion array in $LiReO_3$ and Li_2ReO_3. This twist creates octahedral sites for lithium (3). This structural transformation gives rise to a large activation energy and a decrease in the rate of reaction. The compound FeV_3O_8, which exhibits extensive CS, readily yields $Li_2FeV_3O_8$, which does not show severe structural distortion, and accommodates lithium in five-coordinate, square pyramidal sites of the host (4). We have undertaken the study of Wadsley-Roth phases to determine the minimum amount of CS necessary to stabilize open ReO_3 like structures against twisting and thus maintain high reaction rates and low activation energies. The Wadsley-Roth phases (5) generally with stoichiometries between MO_2 and MO_3, occur extensively in chemical systems involving Nb_2O_5. We will report the results of our studies of lithium insertion in the Nb_2O_5-TiO_2, Nb_2O_5-WO_3 and Nb_2O_5-NbO_2F chemical systems in a subsequent publication. The most promising lithium insertion reactions we have found in this class of compounds occur, however, in compounds in the WO_3-VO_2-V_2O_5 ternary system. In this report, we present the results of chemical lithium insertion reactions and preliminary test cell data for $WV_2O_{7.5}$ and $W_{.2}V_{2.8}O_7$.

The basic structural units of the Wadsley-Roth phases are blocks consisting of distorted MO_6 octahedra sharing corners, which are joined to adjacent blocks either through edge sharing or a combination of edge sharing and tetrahedrally coordinated metal atoms at the block corners. The blocks are infinite in 1 dimension, and thus the structures are built of $n \times m \times \infty$ ReO_3 type units, where n and m are the numbers of MO_6 octahedra along the length and width of the blocks. Such structures generally display open tunnel like regions bound by regions of extensive edge sharing. The two presently well characterized tungsten vanadium oxides in this class, $WV_2O_{7.5}$ and $W_{.6}V_{2.4}O_7$, are $4 \times 4 \times \infty$ and $3 \times 3 \times \infty$ m-niobia like Wadsley-Roth phases, respectively (6-8). The structure of $WV_2O_{7.5}$ is presented in figure 1; $W_{.6}V_{2.4}O_7$ has a smaller block size with the same type of crystallographic shear present.

*Electrochemical Society Active Member.

The $WV_2O_{7.5}$ and $W_{.2}V_{2.8}O_7$ employed in this study were prepared by heating mixtures of VO_2, V_2O_5 and WO_3 powders at 650°C in sealed, evacuated quartz tubes for 40 hours with 1 intermediate grinding. The products were identified as single phase by powder X-ray diffraction. We verify the reported range (6) of stoichiometry for m-niobia type $W_xV_{3-x}O_{7.5}$, $0.8 \leq X \leq 1.2$, and find an apparent range of stoichiometry for m-niobia like $W_xV_{3-x}O_7$ of approximately $0.2 \leq X \leq 0.5$ under the present synthesis conditions. At the previously reported $X = .6$ composition we found a mixture of the M_3O_7 type phase and V_2O_5 related $V_5W_3O_{20}$. We were unable to syntheses a compound at the composition $WV_2O_{7.3}$, whose existence was previously reported (6); powders at that composition were mixtures of the M_3O_7 and $WV_2O_{7.5}$ phases.

Preliminary cycle data for representative Li/$LiAsF_6$, propylene carbonate (PC)/$WV_2O_{7.5}$,graphite and Li/$LiAsF_6$, PC/$W_{.2}V_{2.8}O_7$,graphite test cells (9) are presented in figures 2 and 3 respectively. The positive electrode comprises 50% graphite by weight, as well as the tungsten vanadium oxides,

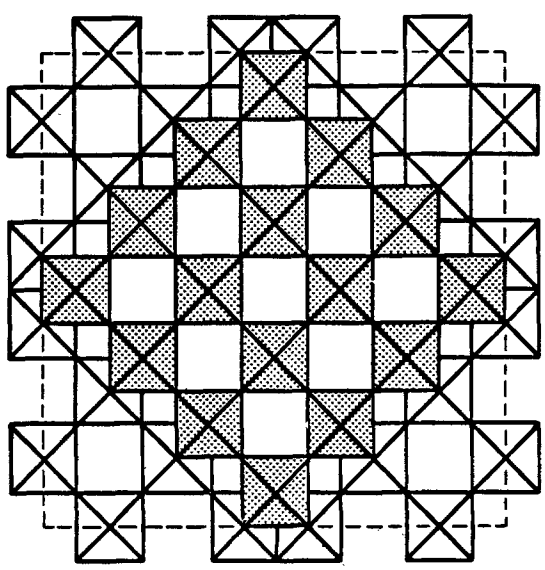

Figure 1. Idealized $4 \times 4 \times \infty$ m-niobia type structure of $WV_2O_{7.5}$, viewed down the tetragonal *c* axis. Structural units are MO_6 octahedra. Shaded octahedra are at a level ½ *c* from level of unshaded octahedra, resulting in edge sharing along the block perimeters. The unit cell is indicated by a dashed line.

to increase their conductivities. Cells were cycled at .2 mA (6-10 hours discharge for the sizes used). Test cells employing $WV_2O_{7.5}$ type cathodes have capacities over 10 cycles of between .5 and .9 Li/metal at potentials between 3.2 and 1.7 volts. The vanadium rich composition $W_{.8}V_{2.2}O_{7.5}$ behaves in our test cells somewhat better than $WV_2O_{7.5}$. Test cells employing $W_{.2}V_{2.8}O_7$ cathodes have capacities between .6 and 1.0 Li/metal between potentials of 3.2 and 2 volts. ($W_{.6}V_{2.4}O_7$ cathodes have capacities over 10 cycles of .6 and .7 Li/metal between potentials 3.2 and 1.6 volts.) No self discharge of the cells was noted over periods of several weeks.

Chemical lithiation of the tungsten vanadium oxides was performed by treatment with n-butyllithium in hexane. Stoichiometries of $Li_{3.5}WV_2O_{7.5}$, 1.2 Li/metal, and $Li_{3.7}W_{.2}V_{2.8}O_7$, 1.2 Li/metal, are obtained in that manner. The fully lithiated compounds were found by differential scanning calorimetry to undergo changes suggesting decomposition at approximately 150°C for $Li_{3.5}WV_2O_{7.5}$ and 225°C for $Li_{3.7}W_{.2}V_{2.8}O_7$. Powder X-ray diffraction patterns for both lithiated compounds are quite similar to those for the starting materials, but with significant changes in the unit cell dimensions. The cell parameters, compared to the original tetragonal cells, are presented in Table 1. The X-ray powder patterns are presented in Table 2. We note the significant (9.7% and 8.8%) increases in the *c* axes, parallel to the infinite dimensions of the ReO_3 type blocks. This relatively large expansion in one direction, parallel to the infinite block dimension (usually a monoclinic *b* or tetragonal *c* axis) has been noted in several other oxide insertion compounds, and has been observed by us in general in the Wadsley-Roth phases on lithiation. The great similarity of the unit cell dimensions and powder pattern intensities of the lithiated and unlithiated compounds suggests that there has not been extensive distortion of the host lattice on Li insertion, accounting for the good rechargability observed in the electrochemical test cells. Analysis of the 4×4 and 3×3 m-niobia like structures indicates 1.7 and 1.33 ReO_3-like cavities (some of which are capped by additional oxygen atoms) per formula unit for $WV_2O_{7.5}$ and $W_{.2}V_{2.8}O_7$, respectively. At the stoichiometries obtained in the butyllithium reactions, an occupancy of approximately 2 Li/cavity is therefore suggested for the $WV_2O_{7.5}$ structure type, and approximately 2.8 Li/cavity for the $W_{.2}V_{2.8}O_7$ structure type. Such stoichiometries are not unusual for lithium inserted metal oxide shear structures such as V_6O_{13} and FeV_3O_8 (2,4), and we have found them to occur also for the Nb_2O_5 based Wadsley-Roth phases we have studied.

The theoretical energy density of the $Li/WV_2O_{7.5}$ cell, based on the n-butyllithium stoichiometry of 1.2 Li/metal and the average voltage of 2.2 volts, is approximately 420 whr/Kg (2.18 whr/cc). Similarly, the theoretical energy density for the $Li/W_{.2}V_{2.8}O_7$ cell is approximately 594 whr/Kg (2.36 whr/cc). These energy densities are comparable to those of other cells presently being considered for use as ambient temperature secondary lithium batteries. Graphite must be added to the positive electrode, however, for satisfactory cell performance due to the relatively low

TABLE I: Comparison of Unit Cell Dimensions for Lithiated and Host Tungsten Vanadium Oxides

Compound	a_o (Å)	c_o (Å)	Volume (Å^3)
$WV_2O_{7.5}$	19.50	3.70	1406.9
$Li_{3.5}WV_2O_{7.5}$	20.016 (5)	4.059 (4)	1626.2
$W_{.2}V_{2.8}O_7$	14.01	3.72	730.2
$Li_{3.7}W_{.2}V_{2.8}O_7$	14.414 (6)	4.049 (3)	841.2

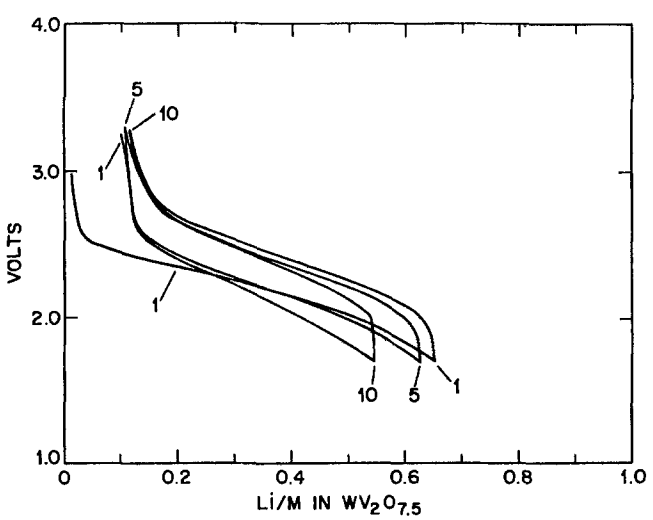

Figure 2. Voltage of an Li/1*M*LiAsF$_6$,PC/$WV_2O_{7.5}$ cell containing 10.15 mg $WV_2O_{7.5}$ and an equal weight of graphite cycled at 0.2 ma. Cell constructed as in reference 9. Cycle numbers indicated.

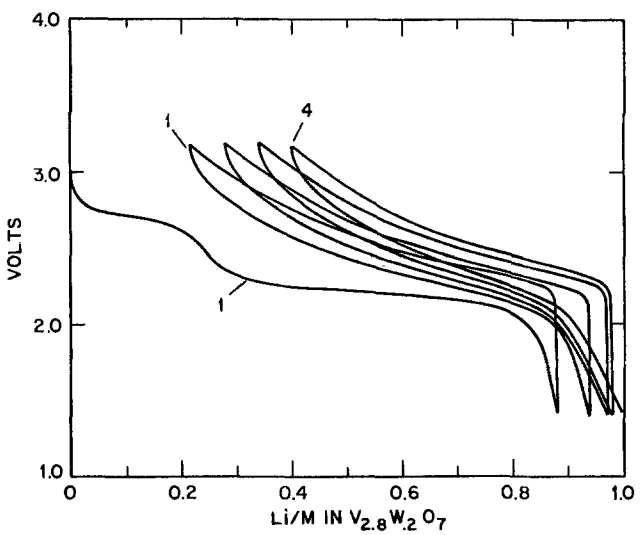

Figure 3. Voltage of an Li/1*M*LiAsF$_6$,PC/$W_{.2}V_{2.8}O_7$ cell containing 4.3 mg $W_{.2}V_{2.8}O_7$ and an equal weight of graphite, cycled at 0.2 ma. Cycle numbers indicated.

TABLE II: Powder X-ray Diffraction Patterns for Lithiated Tungsten Vanadium Oxides

$Li_{3.5}WV_2O_{7.5}$

h	k	l	d_{obs}	d_{calc}	I/I_o
2	2	0	7.098	7.077	20
3	3	0	4.730	4.718	100
1	0	1	3.986	3.978	80
2	1	1	3.699	3.697	20
4	4	0	3.542	3.538	90
4	3	1	2.848	2.850	90
5	2	1	2.740	2.741	10
8	0	0	2.499	2.502	10
7	0	1	2.338	2.338	30
7	7	0	2.022	2.022	90
9	2	1	1.913	1.914	10
10	4	0	1.860	1.858	20
11	3	0	1.755	1.756	20
6	0	2	1.732	1.734	10
10	3	1			
8	7	1	1.707	1.708	10
11	4	1	1.574	1.576	10
8	0	2		1.576	
9	9	0		1.573	
14	0	0	1.430	1.430	30

$Li_{3.7}W_{.2}V_{2.8}O_7$

h	k	l	d_{obs}	d_{calc}	I/I_o
1	1	0	10.202	10.192	100
2	0	0	7.219	7.207	20
2	2	0	5.107	5.096	80
3	1	0	4.567	4.558	20
1	0	1	3.897	3.898	20
3	3	0	3.402	3.397	60
3	2	1	2.840	2.845	20
5	1	0	2.821	2.827	20
4	1	1	2.646	2.646	10
4	4	0	2.549	2.548	20
5	5	0	2.038	2.038	90
0	0	2	2.026	2.025	40

electrical conductivity of the tungsten vanadates. The results of the present study indicate that tungsten vanadium oxides deserve further consideration as positive electrode materials for lithium batteries. They further show that the presence of a large amount of crystallographic shear is not necessary to stabilize ReO_3 structure based oxide CS structures against extensive structural distortion (and the resultant decrease in reaction rate) during lithium insertion. In the Wadsley-Roth CS structures where intersecting shear planes form ReO_3 type blocks of finite extent in 2 of their 3 dimensions, our studies of tungsten-vanadium oxide and niobium oxide based compounds have demonstrated structural stability on lithium insertion for compounds with the largest block sizes (and least crystallographic shear) presently known.

Acknowledgement

The assistance of D. J. Kleinman in the preparation of some of the tungsten vanadium oxides employed in this study is greatfully acknowledged.

REFERENCES

1. See, for instance, M. S. Whittingham, Prog. Sol. St. Chem., *12*, 41 (1978).
2. D. W. Murphy, P. A. Christian, F. J. DiSalvo and J. N. Carides, J. Electrochem. Soc., *128*, 2053 (1981).
3. R. J. Cava, A. Santoro, D. W. Murphy, S. Zahurak and R. S. Roth, J. Sol. St. Chem., *42*, 251 (1982).
4. R. J. Cava, A. Santoro, D. W. Murphy, S. Zahurak and R. S. Roth, Sol. St. Ionics, *5*, 323 (1981).
5. S. Andersson and A. D. Wadsley in *Perspectives in Structural Chemistry* Vol. 3, Dunitz and Ibers, eds., John Wiley and Sons, New York, 1970.
6. S. Launay-Mondet, Rev. Chim. Min., *8*, 391 (1971).
7. L. Kihlborg and M. Israelson, Acta. Chem. Scand., *22*, 1685 (1968).
8. J. Darriet and J. Galay, J. Sol. St. Chem., *4*, 357 (1972).
9. D. W. Murphy, J. N. Carides, F. J. DiSalvo, C. Cros, and J. V. Waszczak, Mat. Res. Bull., *12*, 825 (1977).

Manuscript received Oct. 1, 1982.

Publication costs of this article were assisted by Bell Laboratories.

Work Function Changes Due To the Coadsorption of Water with Oxygen and Bromine on Cu(110)

D. E. Grider,* K. Bange, and J. K. Sass

Fritz-Haber-Institut der Max-Planck-Gesellschaft, Faradayweg 4-6, D-1000 Berlin 33, Germany

Despite its relevance in double layer modelling (1), very little is as yet known about the orientation of water molecules at the metal-electrolyte interface. Recently, it has been suggested that by adsorption of electrochemically relevant species onto clean, well defined metal surfaces under ultra-high vacuum conditions important complementary information on the microscopic structure of the double layer may be obtained (2). Due to the rapid advances in experimental methods and theoretical concepts in surface science, a detailed characterization at the molecular level of adsorption processes has now become possible. In contrast, traditional electrochemical techniques, particularly differential capacity measurement, can only provide information on macroscopic averages such as, for example, excess charge and potential drop across the interface.

In this brief communication, results of work functions measurements, as part of an extensive investigation with a variety of surface-sensitive methods, are reported on the adsorption of water on Cu(110) predosed with either oxygen or bromine. Experiments were performed in a stainless steel chamber at base pressures of $\sim 10^{-10}$ torr. The sample temperature was ~110 K. Oxygen was dosed through the chamber, whereas bromine was evolved from a silver bromide solid cell (3). Both gases adsorb dissociatively on Cu(110) at 110 K. Water exposures were obtained from a microcapillary array molecular beam doser. The vibrating capacitor (Kelvin) method was used to monitor the work function changes $\Delta\phi$ due to gas adsorption. A detailed description of the experimental procedures will be given elsewhere (4).

The results of this study are shown in Figs. 1 and 2. Upon exposure of either oxygen or bromine to the clean Cu(110) surface, an increase of the work function is observed. The saturation values of $\Delta\phi$ for oxygen and bromine dosing are ~450 and ~1100 mV, respectively. The saturation coverage for both adsorbates, corresponding to these $\Delta\phi$-values, is 0.5 monolayers (4). The $\Delta\phi$ vs. exposure curves (lines without crosses in Figs. 1 and 2) exhibit an initial linear slope which is characteristic of a constant sticking coefficient at low exposures where the adsorbate atoms do not interact. At higher exposures, the sticking coefficient rapidly decreases towards saturation coverage. The work function changes due to water exposure to either oxygen- or bromine-predosed Cu(110) are shown by the lines with crosses in Figs. 1 and 2. The clean surface behaviour is shown for comparison. It is seen that the work function decreases induced by the water are qualitatively very similar in their strong dependence on the amount of coadsorbate present on the surface. This is true not only for the saturation values of $\Delta\phi$ at higher H_2O exposures, but also for the initial slopes of these curves which provide information on the effect of fractions of a monolayer of water arriving at the surface.

The close correlation between the electrode potential in electrochemistry and the work function in surface science has been extensively discussed (1,2). The work function increases, for example, when a layer of dipoles is formed with the negatively charged ends pointing away from the metal surface. Three contributions to the work function change from an adsorbate layer may

*Present address: Phys. Chem. Dept., Donnan Labs, Grove Street, P.O.Box 147, Liverpool L69 3BX, England

Key words: Gas phase adsorption, work function, water orientation, specific adsorption, double layer

be distinguished:

(i) preferential orientation of adsorbed molecules with a permanent dipole moment
(ii) charge transfer between metal and adsorbate
(iii) modification of the metal surface electron density distribution

The water molecule posesses a large dipole moment of ∿1.8 Debye and it may be safely assumed that the variations in the water-induced $\Delta\phi$-curves in Figs. 1 and 2 with coadsorbate coverage, and compared to the clean surface, are predominantly orientational in origin. The largest work function decrease is then, of course, expected if adsorption occurs via the oxygen with the molecular axis perpendicular to the surface. On the basis of these considerations, we have calculated the perpendicular component $\mu_\perp$ of the initial dipole moment of water molecules adsorbed with oxygen or bromine from the slopes at low H_2O exposures in Figs. 1 and 2. The result, shown in Fig. 3, demonstrates very clearly that at low coadsorbate coverages $\mu_\perp$ is substantially larger than for the clean surface, but decreases rapidly with surface concentration of either one of the electronegative species. This would agree with recent experimental evidence (5,6) that the molecular axis of water is inclined when adsorbed in the form of hydrogen-bonded clusters on clean metal surfaces, but more perpendicular to the surface when small amounts of oxygen are present.

In electrochemical terms, the coadsorption of water with bromine or oxygen may be thought of as a model system for the case of specific adsorption of anions. The water arriving on the predosed surface is attracted by the negative charge on the adsorbate and forms a surface solvation shell. The degree of solvent dipole orientation in this shell, our study would seem to indicate, must be expected to vary strongly with anion coverage. This aspect and other electrochemical implications will be elaborated upon in more detail elsewhere (4).

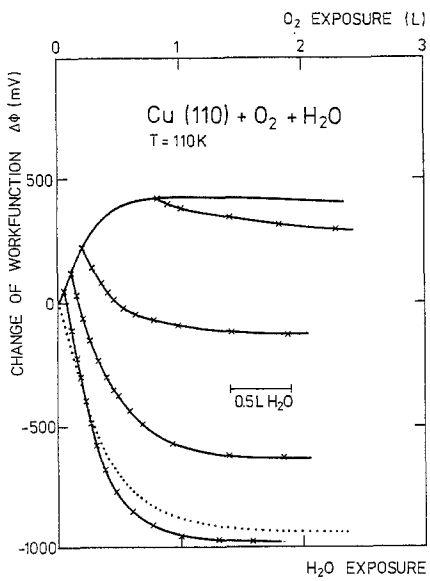

Fig. 1. Work function changes $\Delta\phi$ as a function of oxygen exposure (1L = 10^{-6} torr•sec), shown by the upper curve without crosses, and subsequent exposure of water at four different predoses of oxygen (lines with crosses). The decrease of the work function due to water exposure to the clean surface is shown for comparison (dotted line).

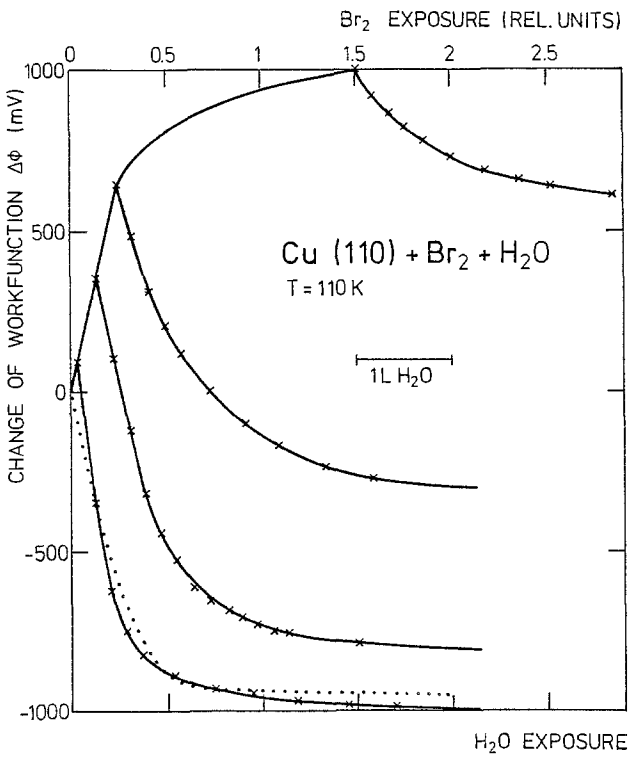

Fig. 2. Same as Fig. 1, but with the copper surface dosed with bromine instead of oxygen. Bromine exposures are given in relative units, derived from the charge passed through the AgBr solid electrochemical cell. Note the different scales for water exposure used in Figs. 1 and 2.

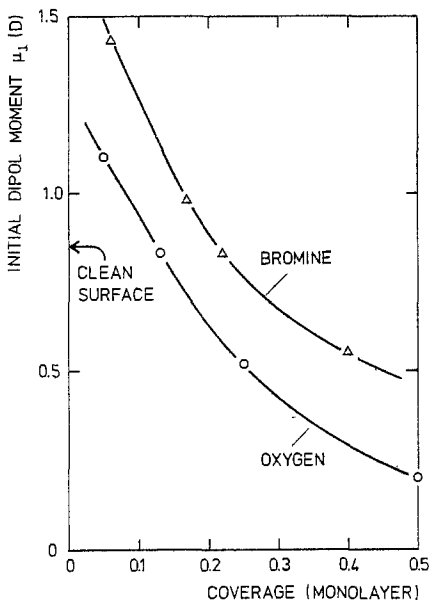

Fig. 3. Perpendicular component of the dipole moment of water molecules adsorbed onto the metal surface, with different predoses of either oxygen or bromine, calculated from the initial slopes of the $\Delta\phi$-curves in Figs. 1 and 2 (see text for details).

ACKNOWLEGEMENT

The authors would like to thank E. Piltz for expert technical assistance and R. Unwin for his advice and generous help during the experiments. Valuable discussions with S. Holloway and T. E. Madey are gratefully acknowledged. This work has been supported by the Deutsche Forschungsgemeinschaft through Sonderforschungsbereich 6.

REFERENCES

1. S. Trasatti, in "Modern Aspects of Electrochemistry", B. E. Conway and J. O'M. Bockris, Editors, vol. 13, p. 81, Plenum Press, New York (1979)
2. J. K. Sass, K. Kretzschmar, and S. Holloway, Vacuum, 31, 483 (1981)
3. N. V. Richardson and J. K. Sass, Surf. Sci., 103, 496 (1981)
4. K. Bange, D. Grider, and J. K. Sass, to be published.
5. T. E. Madey and F. P. Netzer, Surf. Sci., 117, 549 (1982)
6. K. Kretzschmar, J. K. Sass, A. M. Bradshaw, and S. Holloway, Surf. Sci., 115, 183 (1982)

Manuscript received Oct. 5, 1982.

Publication costs of this article were assisted by Fritz-Haber-Institut der Max-Planck-Gesellschaft.

Photoelectrochromic Behavior of Prussian Blue-Modified TiO_2 Electrodes

David W. DeBerry* and Alfred Viehbeck*

SumX Corporation, Austin, Texas 78758

There has been a considerable interest in new electrooptic display devices employing reversible electrochemical processes [1]. As recently demonstrated, the redox properties and corresponding color changes of thin Prussian blue (PB) films on metal or transparent substrates could form the basis of electrochromic [2] or bichromic [3] display devices. Neff [4] first reported the chemical preparation of PB films on Pt and Au, and the redox behavior of PB coated electrodes. Itaya et al. [2] later described an electrochemical method for depositing thin PB films and discussed their electrochemical properties. In the present report we describe the photoelectrochromic characteristics of thin Prussian blue films on both single crystal and polycrystalline TiO_2 electrodes.

Single crystal TiO_2 electrodes were prepared by cutting disks (2 mm thick) from a rutile boule that was reduced in an H_2 atmosphere at 650°C for 30 min. Ohmic contacts were made using a Ga-In alloy. Polycrystalline TiO_2 electrodes were made by first etching a Ti electrode in a solution of HF/ HNO_3/ H_2O (1:4:5) and then potentiodynamically growing an anodic film at 50 mV/sec from -0.60 V to 3.00 V vs SCE in a 1M KCl solution adjusted to pH 3.45 with HCl. The thickness of the anodic TiO_2 films formed in this manner were estimated to be ca. 10 nm [5]. The PB films were galvanostatically deposited under cathodic conditions in a 0.02 M $FeCl_3$/ 0.02 M $K_3Fe(CN)_6$ solution. After this treatment the PB modified electrode was thoroughly rinsed with distilled water and then placed in a 1M KCl (pH 3.45) solution in which all electrochemical characterizations were conducted. All potentials are reported with respect to SCE.

As deposited, the film is blue and in the PB form. On Pt the cathodic scan exhibits a reduction peak with a simultaneous loss of the blue color and on scan reversal there is an anodic peak accompanying the return of the blue surface coloration. This redox process (centered at 0.20 V) corresponds to the reduction of PB to the colorless Prussian white (PW) and the reoxidation back to PB. The excellent stability of these films under repetitive potential cycling (> 10^6 cycles) over the potential region of the PB and PW redox couple has been observed by other workers [2]. There is also a redox process near 0.90 V attributed to the oxidation of PB to Prussian green, PG (Berlin Green), which is less stable than the PB form.

The PB reduction for a PB modified (2.4 mC/cm^2) TiO_2 single crystal electrode occurs at ca. -0.35 V with no corresponding reoxidation peak on the anodic scan in the dark. Thus, on the subsequent cathodic scan following the anodic excursion only a small cathodic response is detected near the PB reduction potentials. Since O_2 was excluded from the cell this response is attributed to either some residual unreduced PB or a leakage current by the n-type electrode positive of the flat-band potential.

If however, the PB modified TiO_2 electrode is illuminated with UV light during the anodic scan following PB reduction, an anodic photocurrent is detected at potentials positive of - 0.35 V. Figure 1a shows anodic potential scans under irradiation ($200 < \lambda < 400$ nm, @ 20 mW/cm^2) to increasing potential limits and the subsequent cathodic sweep in the dark. The more positive a scan reversal limit is reached, the more PW that is oxidized, as demonstrated by the increase in cathodic response on each successive cycle. The photooxidation potentials of PW are quite negative of the PB redox potential for a modified Pt electrode (E° = 0.20 V). The dependence of the current density at the peak maximum is linear versus sweep rate over the range 5 to 500 mV/sec which indicates a rapid electron transfer process involving a surface confined redox specie.

*Electrochemical Society Active Member.

Key words: Prussian blue films, photoelectrochromic device, titanium dioxide, chemically modified electrodes.

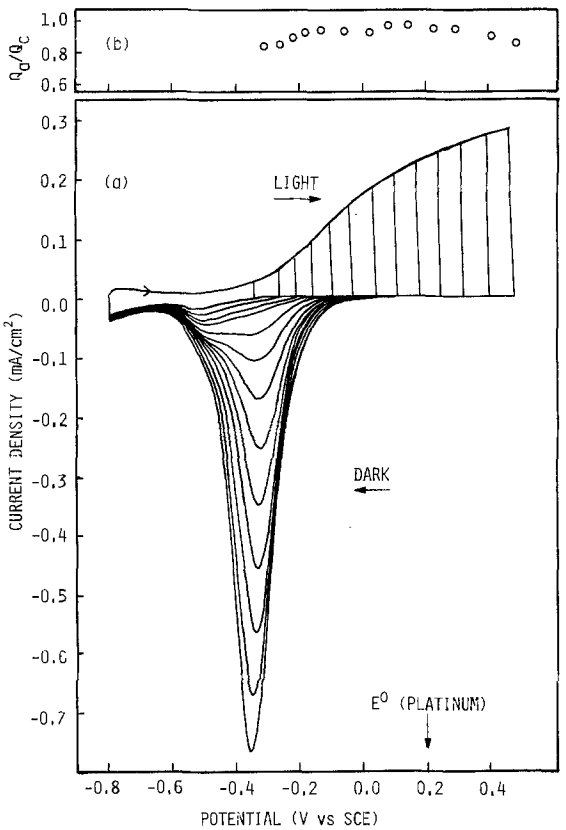

Fig. 1. (a) Cyclic voltammograms for PB modified TiO_2 single crystal electrode at a sweep rate = 50 mV/sec. (b) Ratio of anodic photocharge to cathodic reduction charge.

The ratio of the total quantity of anodic photocharge to corresponding cathodic reduction charge (Fig. 1b) shows that the average charge storage efficiency is nearly 95 percent for the oxidation of PW under illumination. However, once the anodic photocharge exceeds the PW oxidation charge, the storage efficiency decreases and a second reduction peak develops on the cathodic scan at ca. -0.20 V. The total charge that can be stored in the film amounts to almost twice the initial PB deposition charge. The additional charge is attributed to the oxidation of PB to PG which results in the doublet (representing the two step reduction of PG to PW) on the cathodic sweep profile.

The photooxidation of PW to PB can also occur for a PB modified Ti metal electrode with an anodically grown TiO_2 film. In Fig. 2, the increase in the cathodic responses is due to longer UV illumination periods (given in sec) while the electrode is held at 0.10 V. The amount of photocharge stored is directly proportional to the illumination time up to approximately 90 sec under these conditions. The intensity of the blue color also increases with irradiation time. After a sufficient light "on" time the maximum charge that can be stored in the film is again double the original deposition charge. These results demonstrate the large underpotentials for photooxidation of PW to PB and also PB to PG (at least 800 mV for the latter process) that is induced by an illuminated n-type semiconductor electrode.

The photoelectrochromic imaging response of a PB modified (7.2 mC/cm^2) anodized Ti plate (4 x 4.5 cm) is illustrated in Fig. 3. The initial blue color following the PB deposition is first stripped by polarizing to -0.60 V. The image shown in Fig. 3 was produced by exposing a capital sigma-shaped region on the plate to light from a 150 W Xe lamp at an electrode potential of 0.15 V. The resulting blue colored sigma is in good contrast with the gray-white background of the anodized Ti plate. The imaging rate (image contrast) can be controlled by varying the electrode potential, irradiation time,

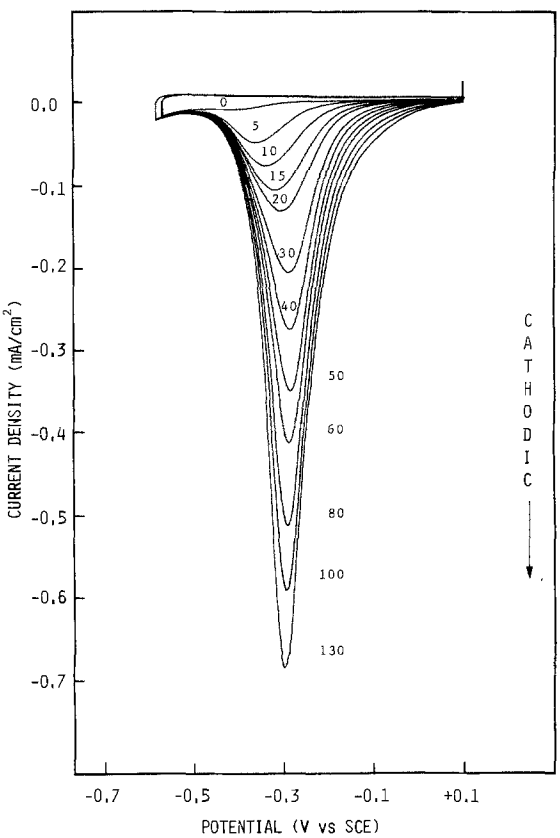

Fig. 2. Cathodic response for a PB modified anodized Ti electrode (2.4 mC/cm^2) during the negative scan following an irradiation period at 0.10 V. Sweep rate = 50 mV/sec.

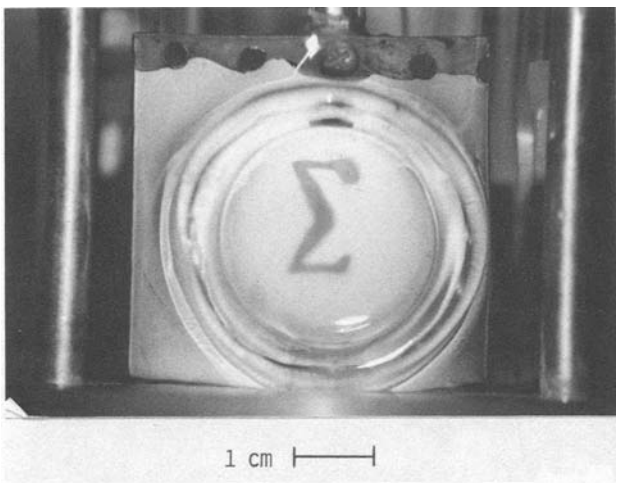

Fig. 3. Picture of an electrochemical cell containing a PB modified anodized Ti plate (7.2 mC/cm^2) on which an image has been activated by UV irradiation at an electrode potential of 0.15 V.

light intensity or quantity of PB initially deposited. The image is stabilized at open circuit potential, erased by cathodic polarization and readily regenerated under anodic conditions as described above. In situations where portions of the image were overexposed a green color or gray color appeared due to PB oxidation to PG or in the latter case loss of the film caused by the decomposition of PG; Berlin green has been found to slowly degrade in KCl solutions [2].

The practical application of electrochromic displays requires low switching voltage, low power consumption, good contrast, good open-circuit memory and high cycling stability [1, 6]. Several imaging devices employing photographic processes based on light induced metal deposition on semiconductor electrodes have been described [7]. Bard et al. [8] have also investigated a photoelectrochromic display involving the reduction of heptyl viologen bromide at an irradiated p-GaAs electrode. Such a system could be activated with a light beam as in a raster display. An advantage of a raster system compared to the usual devices is the simplified electrical addressing system requiring only two contacts instead of the numerous leads needed for a multi-character display.

The results given here in combination with previous studies of thin PB films suggest a number of possible applications for PB modified semiconductor electrodes. The use of polycrystalline substrates and the ease of PB deposition affords the production of inexpensive large screen devices. The advantages of this system as compared to other photoelectrochromic displays includes good color contrast between the anodized Ti electrode and PB, long cycling stability, and the possibility of bichromic display. Since the system can be addressed by UV light and the reaction rates across the immobilized PB layer are fast it might be used in a raster type device as described above [8]. Another possible application is as a reversible optical storage system which, as shown here, can remember the amount of light at a given spot as well as the light exposure event and which can be interrogated either optically or electrically. Research on the photoelectrochemical properties of PB-semiconductor systems and their applications is continuing in this laboratory.

ACKNOWLEDGMENT

This work was supported by SumX Corporation.

REFERENCES

1. a) B. Reichman, and A. J. Bard, This Journal, 126, 583 (1979). b) J. Bruinink, C. G. A. Kregting, and J. J. Ponjee, This Journal, 124, 1854 (1977). c) S. Gottesfeld, and J. D. E. McIntyre, This Journal, 126, 742 (1979). d) R. C. Cieslinski and N. R. Armstrong, This Journal, 127, 2605 (1980). e) F. B. Kaufman, A. H. Schroeder, E. M. Engler, and V. V. Patel, Appl. Phys. Lett., 36, 422 (1980).
2. a) K. Itaya, T. Ataka and S. Toshima, J. Am. Chem. Soc., 104, 4767 (1982), J. Appl. Phys., 53, 804(1982). b) D. Ellis, M. Eckhoff V. D. Neff, J. Phys. Chem., 85, 1225 (1981).
3. H. Kellawi and D. R. Rosseinsky, J. Electroanal. Chem., 131, 373 (1982).
4. V. D. Neff, This Journal, 125, 886(1978).
5. J. F. McAleer and L. M. Peter, Faraday Disc. Royal Soc. Chem., 70, 286 (1980).
6. B. W. Faughan, and R. S. Crandall, "Display Devices,"Springer-Verlag, Berlin (1980).
7. a) G. L. McLeod, Photogr. Sci. Eng., 13, 93 (1979). b) F. Mollers, H. J. Tolle, and R. Memming, This Journal, 121, 1160 (1974). c) T. Inoue, A. Fujishima, and K. Honda, Chem. Lett., 11, 1197 (1978).
8. B. Reichman, Fu-Ren F. Fan, and A. J. Bard, This Journal, 127, 333 (1980).

Manuscript received Oct. 18, 1982.

Publication costs of this article were assisted by SumX Corporation.

Epitaxial Growth of $Hg_{1-x}Cd_xTe$ by Chemical Vapor Transport

Heribert Wiedemeier and Andrius E. Uzpurvis

Department of Chemistry, Rensselaer Polytechnic Institute, Troy, New York 12181

The desirable electro-optical properties of $Hg_{1-x}Cd_xTe$ (with $x \gtrsim 0.2$) are based on the formation of a continuous series of solid solutions between the binary compounds HgTe and CdTe (1,2). The vapor pressures of the constituent elements of these materials differ by orders of magnitude (3). Owing to the wide homogeneity range of HgTe (4), these differences are reflected in the thermochemical properties of the ternary alloys $Hg_{1-x}Cd_xTe$ which yield significantly different partial pressures of the elements over wide temperature and composition ranges (4-7). These general characteristics have been known for several years from various internally consistent studies (4,8,9), even before the detailed investigations were carried out (5-7). In view of the above it is not surprising that the growth of $Hg_{1-x}Cd_xTe$ crystals of a given composition from the vapor phase requires an appropriate adjustment of the vapor pressures of the source materials employed. This can be done by using separate source reservoirs of the elements and/or compounds (10). More recently, metal-organic compounds of the elements Te and Cd were used for epitaxial growth of $Hg_{1-x}Cd_xTe$ (11). Uniform layers of HgCdTe on CdTe substrates were obtained under isothermal conditions from a Te-rich HgTe source making use of the vapor pressure dependence of the source material on its stoichiometry (12). Bulk type single crystals of $Hg_{1-x}Cd_xTe$ (with $x \gtrsim 0.2$) were grown in this laboratory by chemical vapor transport in closed ampoules using HgI_2 as a transport agent (13). The good chemical and crystallographic homogeneity of these materials (13) suggested the application of this technique to the growth of $Hg_{1-x}Cd_xTe$ layers which has not been reported previously. This communication is concerned with the successful growth of such layers on CdTe substrates by the above technique (13) in closed ampoules. For this purpose, well-defined ternary alloy source material, HgI_2 transport agent, and a temperature gradient were employed.

The source materials used in these experiments had the composition $Hg_{0.8}Cd_{0.2}Te$; the uncertainties in terms of Hg were between 0 and -0.3 at%, those of Cd and Te were negligibly small. The synthesis of the source material and of HgI_2 from high purity elements is discussed earlier (13). The substrates were (100) oriented CdTe single crystal wafers ($\rho > 10^8$ Ω·cm) of about 1 mm thickness and 0.5 cm edge length. They were mechanically polished on one side. The transport ampoules of fused silica were 8 cm in length and 1.5 cm inner diameter with a constriction close to one end to hold the source material in place during manipulation of the ampoule. The pretreated ampoule (13) was loaded with source material, transport agent, and the substrate and sealed under a residual pressure of about 10^{-5} torr. The substrate was then positioned at the tube end opposite the source material with the unpolished side resting flat on the ampoule wall. The experiments were performed in a transparent, two-zone, tubular resistance furnace made of fused silica tubing which allowed direct visual observation. The temperature of the source region was 590°C and that of the deposition zone 535°C with a nearly sigmoidal shaped profile between the end temperatures, which were maintained within ± 0.5°C using proportional temperature controllers. The furnace and ampoule were in a horizontal position. After termination of the growth experiment the residual gas phase was quenched in the source region. Under the experimental conditions reported here deposition occurred only on the substrate and no crystal growth was observed on the walls of the ampoule.

The amounts of HgI_2 transport agent in these experiments corresponded to initial HgI_2 partial pressures of 0.06-0.08 atm. The chemical reactions in this system are complex. Exploratory studies suggested that under present conditions the mass transport is controlled by diffusion of transport species (HgI_2, CdI_2, Te_2) through the gas phase which consists predominantly of Hg vapor. This is consistent with systematic transport studies (13) and a thermodynamic analysis of the $Hg_{1-x}Cd_xTe$-HgI_2

system (14). Preliminary studies of the deposition rates as a function of time yielded the minimum time required to achieve steady-state conditions. Based on the combined information it is reasonable to assume that for the epitaxial growth experiments reported here the growth rate is gas phase limited.

During the initial growth period of the $Hg_{1-x}Cd_xTe$ epitaxial layers on CdTe, the substrate surface changed visibly from specularly reflective to a dull greyish after about five minutes to become specularly reflective again after about 25 min of growth. This appearance did not change for the remainder of the growth period. In some cases, the original substrate was cut yielding two adjacent edges which were not polished afterwards. This caused polycrystalline deposition on these edges and considerably higher growth rates than for the polished surface of the substrate. The other two smooth edges revealed a much smaller number of platelet-type polycrystals. This reflects the importance of surface treatment. It is interesting to note that the polycrystalline deposition along the edges did not propagate to any extent into the (100) face of the substrate.

A typical area of the surface of the $Hg_{1-x}Cd_xTe$ layer, using Nomarski contrast illumination, after a growth time of five hours is shown in Fig. 1. The layer reveals a slightly wavy surface with the "troughs" of the waves about 50-200 μm apart. The thickness of the epitaxial layer after 5 hr under present growth conditions is about 18 μm. The height of the waves is less than 0.1 μm. It was observed that the degree of surface smoothness increases considerably with layer thickness. It is worthwhile noting that the "troughs" of the waves are nearly parallel to the temperature (density) gradient of the ampoule. This observation could indicate a possible interaction between fluid flow and surface morphology. Besides these "troughs," there were no well-defined crystallographic defects visible on the layer surface.

The Laue x-ray diffraction pattern (back reflection mode) of a $Hg_{1-x}Cd_xTe$ layer (growth time 5 hr, thickness about 18 μm) in Fig. 2 reveals the two-fold symmetry of the (100) oriented epitaxial layer. The overall appearance of the diffraction pattern and Laue spots indicates that the epitaxial layer is single crystalline. This aspect will be further investigated through detailed diffraction studies of different layers.

The optical photomicrograph of a substrate/layer cross-section under Nomarski contrast illumination is shown in Fig. 3 for a growth time of 11 hr and a layer thickness of about 38 μm. The photograph reveals the uniform thickness of the epilayer and the well-defined interface between the substrate (left-hand side of the photograph) and the epitaxial layer. The pattern of slightly curved lines across the epitaxial layer is caused mechanically by cutting the substrate/layer with a diamond tipped scribe without subsequent polishing of the cross-sectional area.

In summary, the chemical vapor transport technique was applied for the first time to the growth of $Hg_{1-x}Cd_xTe$ epitaxial layers on CdTe substrates using a preannealed source material of $Hg_{0.8}Cd_{0.2}Te$. Present characterization data indicate nearly uniform thickness and single crystallinity of the epitaxial layer. These results are very promising for a more detailed investigation of the chemical and crystallographic homogeneity of different epitaxial layers. This work as well as a thermodynamic analysis of the system and electrical characterization of the epilayers are in progress.

ACKNOWLEDGEMENTS

The authors are pleased to acknowledge the partial support of this work by the National Aeronautics and Space Administration.

REFERENCES

1. D. Long and J. L. Schmit, Semiconductors and Semimetals, Vol. 5, p. 175, Ed.: R. K. Willardson and A. C. Beer, Academic Press, New York, 1970.
2. R. Dornhaus and G. Nimitz, Solid State Physics, Vol. 78, p. 1, Springer-Verlag, Berlin, 1977.
3. D. R. Stull and G. C. Sinke, Advan. Chem. Series, 18, 64, 129, 201 (1956).
4. R. F. Brebrick and A. J. Strauss, J. Phys. Chem. Solids, 26, 989 (1965).
5. J. P. Schwartz, A Thermodynamic Investigation of the Ternary Alloy $(Hg_{1-x}Cd_x)_yTe_{1-y}$, Ph.D. Dissertation, Marquette University, 1977.
6. J. P. Schwartz, Tse Tung, and R. F. Brebrick, This Journal, 128, 438 (1981).
7. Tse Tung, L. Golonka, and R. F. Brebrick, This Journal, 128, 451 (1981).
8. J. L. Schmit and C. H. Speerschneider, Infrared Physics, 8, 247 (1968).

9. J. Steininger, J. Electron. Mater., 5, 299 (1976).

10. D. K. Hohnke, H. Holloway, E. M. Logothetis, and R. C. Crawley, J. Appl. Phys., 42, 2487 (1971).

11. S. J. C. Irvine and J. B. Mullin, J. Crystal Growth, 55, 107 (1981).

12. P. Becla, J. Lagowski, and H. C. Gatos, This Journal, 129, 1103 (1982).

13. H. Wiedemeier and D. Chandra, Z. Anorg. Allg. Chem., 488, 137 (1982).

14. H. Wiedemeier and D. Chandra, to be published.

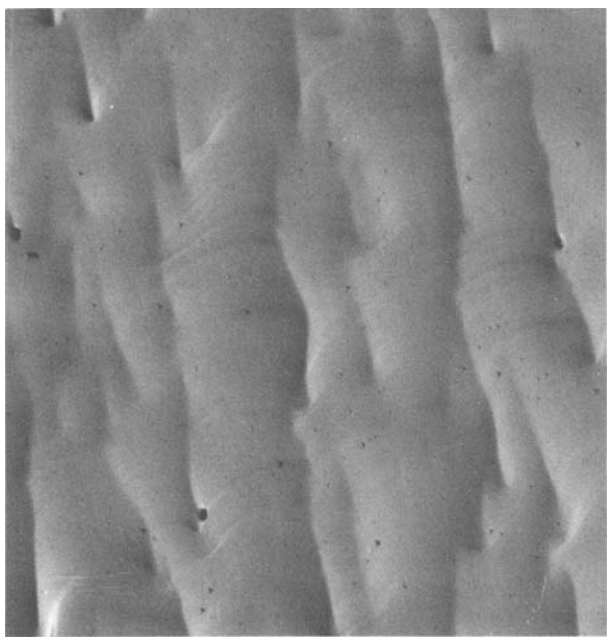

Fig. 1. Optical photomicrograph (Nomarski contrast illumination) of the surface of a $Hg_{1-x}Cd_xTe$ epitaxial layer after a growth time of 5 hr. Magnification 1 cm = 100 μm.

Key words: $Hg_{1-x}Cd_xTe$, epitaxy on CdTe, chemical vapor transport.

Manuscript received Oct. 25, 1982.

Publication costs of this article were assisted by Rensselaer Polytechnic Institute.

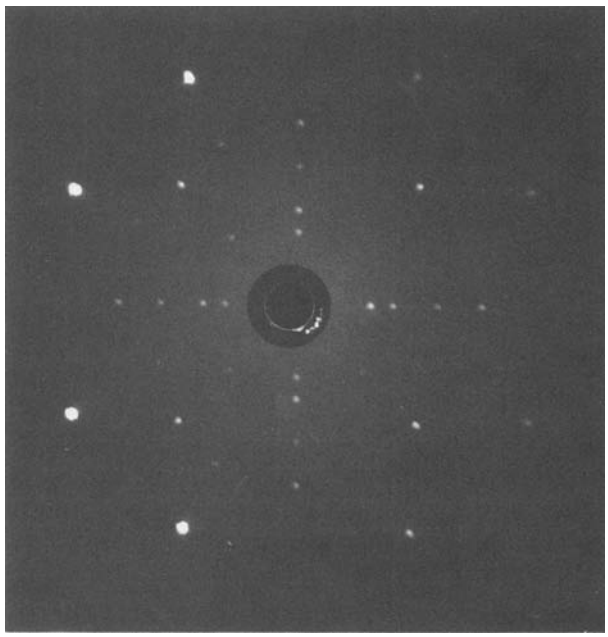

Fig. 2. Laue x-ray diffraction pattern (back reflection) of a $Hg_{1-x}Cd_xTe$ epitaxial layer of about 18 μm thickness. Ni-filtered CuKα radiation.

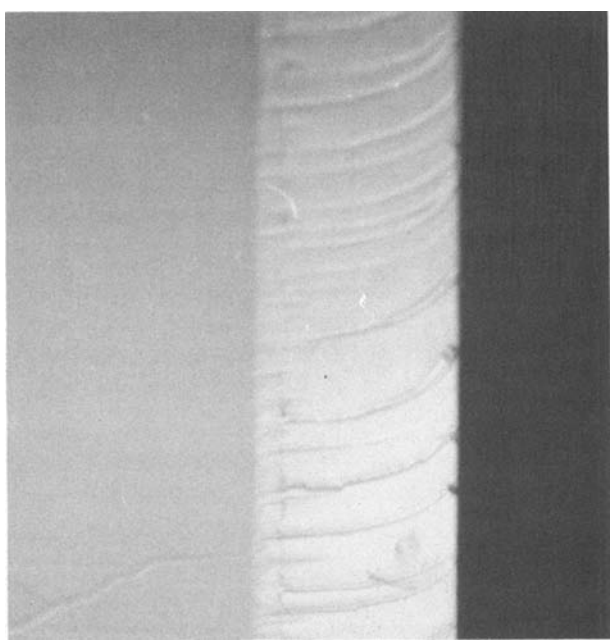

Fig. 3. Optical photomicrograph (Nomarski contrast illumination) of a substrate/layer cross-section. CdTe substrate on left-hand side, $Hg_{1-x}Cd_xTe$ layer (center) of about 38 μm thickness.

JOURNAL OF THE ELECTROCHEMICAL SOCIETY

ELECTROCHEMICAL SCIENCE
AND TECHNOLOGY

FEBRUARY
1983

Cross-Linked Polyvinyl Alcohol Films as Alkaline Battery Separators

Dean W. Sheibley,* Michelle A. Manzo,* and Olga D. Gonzalez-Sanabria*

National Aeronautics and Space Administration, Lewis Research Center, Cleveland, Ohio 44135

ABSTRACT

Cross-linking methods have been investigated to determine their effect on the performance of polyvinyl alcohol (PVA) films as alkaline battery separators. The following types of cross-linked PVA films are discussed: *(i)* PVA-dialdehyde blends post-treated with an acid or acid periodate solution (two-step method, and *(ii)* PVA-dialdehyde blends cross-linked during film formation (drying) by using a reagent with both aldehyde and acid functionality (one-step method). Laboratory samples of each cross-linked type of film were prepared and evaluated in standard separator screening tests. Then pilot-plant batches of films were prepared and compared to measure differences due to the cross-linking method. The pilot-plant materials were then tested in nickel oxide-zinc cells to compare the two methods with respect to performance characteristics and cycle life. Cell test results are compared with those from tests with Celgard.

The use of polyvinyl alcohol (PVA) as a separator in various alkaline battery applications is well known. PVA film separators are used because of their insolubility and high ionic conductivity in alkaline electrolytes. Further, PVA film is easily fabricated on a commercial scale from aqueous solution and presents neither a health hazard to personnel nor a pollution threat to the environment.

Cross-linking PVA makes it water insoluble, increases its mechanical strength, and improves its oxidation resistance (1). Methods of cross-linking PVA have been reported by Philipp and Hsu (2) with applications for use in alkaline electrolytes. More recently, low-molecular-weight PVA films cross-linked by using dialdehydes, aldehydes with acid functional groups, and polysaccharides (aldehyde precursors) were evaluated as alkaline battery separators by Hsu and Sheibley (3). This work showed that cross-linked PVA films exhibit acceptable properties in comparative separator screening tests and perform in an acceptable manner as separators in silver oxide-zinc (Ag-Zn) and nickel oxide-zinc (Ni-Zn) cells from the standpoints of cycle life and cell performance.

This paper compares the effect of two cross-linking methods on PVA film properties measured for alkaline battery separators. One cross-linking method involves a two-step process: first, the film is made; then the dry film is treated with acidic solutions to achieve the desired cross-linking. The second method is a one-step method developed at the NASA Lewis Research Center to cross-link PVA films during commercial production operations. The PVA film is cross-linked during conventional oven drying; thus no further treatment is required.

Separator properties were measured for films made by the two-step method where the cross-linking reaction is catalyzed by either acid or acid periodate solutions. Two dialdehyde cross-linking reagents were compared. Then the effect on separator properties of glyoxylic acid (the reagent used to convert the two-step method into a one-step method) was evaluated in both methods.

Finally films made on pilot-plant equipment were evaluated to measure the effect of the two cross-linking methods on separator properties. These films were then performance characterized and cycle tested in small Ni-Zn cells to compare the two cross-linking methods and to compare the cross-linked PVA films to Celgard.

* Electrochemical Society Active Member.

Key words: alkaline batteries, separators, cross-linked polyvinyl alcohol, nickel oxide-zinc cells.

Materials and Procedure

Materials

A commercially available polyvinyl alcohol (PVA), Elvanol 71-30, a medium-viscosity-grade PVA, was used for this work. This material is greater than 99% hydrolyzed. A 4% aqueous solution has a viscosity of 28-32 cP. The 1,2 diol content was 3.99 groups per 100 monomer units.

The furan 2,5-dialdehyde (DAF) was supplied by Quaker Oats Chemical Company. The terephthaldehyde (TPA) was obtained from Fisher Scientific. The structural formulas of DAF and TPA are shown in Table I. The glyoxylic acid (GOA) also came from Fisher (a 50% solution in water). The structural formula of GOA is shown in Table II. The sucrose was cane sugar. The filler materials, shown in Table III, came from commercial sources. The (143) filler combination was 7.9 volume percent (v/o) SiO_2 (Cab-O-Sil M, Cabot Corporation) and 92.1 v/o 200-mesh white pine wood flour (Wood Flour, Incorporated). The (144) filler combination was 7.8 v/o SiO_2 and 92.2 v/o calcium zirconium silicate (TAM Products, Hightstown, New Jersey). The acid cross-linking solution contained 20 mliters of concentrated H_2SO_4 and 200g of Na_2SO_4 dissolved in 1 liter of water. The acid periodate solution contained 30g of KIO_4, 50 mliters of concentrated H_2SO_4, and 200g of Na_2SO_4 dissolved in 1 liter of water.

General Procedure for Preparation of Aldehyde Cross-Linked PVA Membrane Separators

Two-step cross-linking method.—A quantity of the dialdehyde or aldehyde precursor is added to an aqueous solution of 10 weight percent (w/o) Elvanol 71-30 in order to achieve the theoretical amount[1] of cross-linking desired (usually 2-10% cross-linker). The solution is well mixed. Entrapped air bubbles are removed

[1] The theoretical amount of cross-linker desired is the percentage of cross-linking reagent required to chemically react with all the hydroxyl groups present in the PVA; *e.g.*, 2% cross-linking would be 0.02 times the amount required to react with 100% of the PVA hydroxyl groups, assuming one aldehyde group per two hydroxyl groups.

Table I. Results of treating PVA[a]-dialdehyde blends with acid and acid periodate solutions

Cross-linker (%)[b]	Method	Volume[c] resistivity (Ω-cm)	Zinc dendrite[c] penetration rate (cm/min)	Zincate[c] diffusivity (mols/cm² min)
2 DAF[d]	Acid	10	1.0×10^{-4}	2.6×10^{-7}
2 DAF	Periodate	102	$<9.0 \times 10^{-5}$	2.2×10^{-7}
2 TPA[e]	Acid	20	1.1×10^{-4}	1.2×10^{-6}
2 TPA	Periodate	54	5.8×10^{-5}	7.2×10^{-8}
None	Uncross-linked	43	4.2×10^{-5}	9×10^{-8}

[a] Medium-viscosity grade Elvanol 71-30.
[b] Percentage of theoretical amount required to react with all hydroxyl groups in PVA.
[c] Wet film thickness ranged from 0.013 to 0.017 cm.

[d] Furan 2,5-dialdehyde

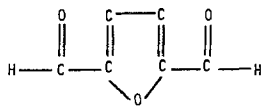

[e] Terephthaldehyde—1,4-(CHO)

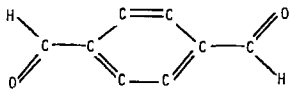

Table II. Effect of glyoxylic acid in polyvinyl alcohol on resistivity and zincate diffusivity (acid periodate cross-linked)

GOA[a] content in film (%)[b]	Volume resistivity (Ω-cm)	Zincate diffusivity[c] (mols/cm² min)
10	24	5.5×10^{-7}
25	21	3.9×10^{-7}
50	13	6.2×10^{-7}
100	4	2.0×10^{-6}

[a] GOA-glyoxylic acid

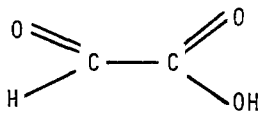

[b] Percentage of theoretical amount required to react with all hydroxyl groups in PVA.
[c] Wet film thickness ranged from 0.013 to 0.017 cm.

Table III. Comparison of films made with two- and one-step cross-linking methods

Cross-linker[a] (%)	Volume resistivity (Ω-cm) Two-step method	Volume resistivity (Ω-cm) One-step method	Zincate diffusivity (mols/cm² min) Two-step method	Zincate diffusivity (mols/cm² min) One-step method
2 DAF	21	40	6.8×10^{-7}	3.1×10^{-7}
2 TPA	21	20	1.2×10^{-6}	4.7×10^{-7}
2 DAF+ 5 w/o fillers (143)	5	17	1.6×10^{-6}	3.0×10^{-7}
2 DAF+ 5 w/o fillers (144)	7	23	3.8×10^{-6}	6.9×10^{-7}

[a] Percentage of theoretical amount required to react with all hyroxyl groups present in PVA.

by placing the solution in a bell jar under a vacuum. The solution is cast on a smooth, clean, glass plate by using a Gardner blade. The cast film is air dried at room temperature, usually overnight. For films with the dialdehyde cross-linking reagent, cross-linking is achieved by immersing the dry film in a solution of sulfuric acid (pH, 4-5) saturated with sodium sulfate and then gradually increasing the temperature to 90°C over a period of 4-16 hr. The films are then rinsed in water to remove the sodium sulfate. The treated film is immersed in boiling water; if it is cross-linked, it will not dissolve. This is a qualitative test for cross-linking.

For films containing an aldehyde precursor (*e.g.*, polysaccharides) or where cleavage of the 1,2-diol units of the PVA is desired, cross-linking is achieved by immersing the film in the acid periodate solution (pH, 4-5). The same heat-treatment and rinsing step and the boiling water test for cross-linking are performed on the film.

One-step cross-linking method.—A quantity of dialdehyde is added to an aqueous solution of 10 w/o Elvanol 71-30 in order to achieve the theoretical amount of cross-linking desired, and the solution is well mixed. Then, a quantity of acid-aldehyde reagent, glyoxylic acid, is added to attain the theoretical amount of reaction desired, and the solution is well mixed. The amount added is sufficient to produce a pH value below 5. The entrapped air bubbles are removed by vacuum. The film is then cast on a clean, smooth, glass plate by using a Gardner blade. The film is cast before the mixture begins to gel. At a solution temperature of 120°F, gelation starts about 45 min after addition of the GOA. After the film is cast and air dried, the glass plate is placed in an oven for a period of time, the length of which depends on the drying temperature. Time ranges from 4 hr at 90°C to 5 min at 160°C. The film is placed in boiling water to check for cross-linking.

Screening tests of cross-linked PVA separators.—The cross-linked PVA films were evaluated by determining their ionic resistivity (d-c method), zinc dendrite penetration rate, and zincate ion diffusivity according to methods described in Ref. (4).

Cell test evaluation of cross-linked PVA separators.—Cell test evaluation of the cross-linked PVA film separators was performed in nickel oxide-zinc (Ni-Zn) cells of approximately 7.2 A-hr capacity. The electrolyte was 35 w/o KOH. Ampere-hour efficiency leveled out after 3-5 formation cycles. Overcharge was limited to 10% of the nominal capacity. The Ni-Zn cell electrode configuration was Ni-Zn-2Ni-Zn-Ni. Electrode sizes were 7.3 × 9.4 cm with thickness ranging from 0.075 cm for the nickel electrode to 0.225 cm for the zinc oxide electrodes. The ratio of active material was ~3:1 Zn to Ni. The nickel electrodes were contained in an absorber bag of beater-treated fuel cell grade asbestos (6), while the zinc electrodes each received two wraps of the film separator (the PVA or the Celgard). Performance was characterized at discharge rates of C/8 (the 8 hr rate, the current required to discharge the cell capacity in 8 hr), C/4, C/2, C, and 2C. Midpoint voltage (the voltage after 3.6 A-hr of capacity was removed) was recorded as was the ampere-hour capacity above 1V.

Cycle testing consisted of 8 hr cycles [6 hr of charge (C/12 rate) and 2 hr of discharge (C/4 rate)]. The discharge current density was approximately 7 mA/cm². The cells were charged and discharged under constant current conditions. The testing was continuous: three cycles per day, 7 days per week. Depth of discharge was 50% on the basis of the nominal 7.2 A-hr capacity. Cell failure was determined to occur when the cell would no longer deliver 50% of its nominal capacity above 1.0V for three consecutive cycles.

Results and Discussion

The two-step method of cross-linking PVA uses either an acid solution or an acid periodate solution. The acid solution is used when a dialdehyde is incorporated in the film. The acid catalyzes the acetalization reaction and this leads to cross-linking. The acid periodate method is used to cross-link PVA under several conditions. It can be used to cross-link PVA alone

through oxidative cleavage of its 1,2-diol units in order to form aldehyde groups that react with the secondary alcohol groups of PVA (1). The addition of aldehyde precursors (polysaccharides such as sucrose or alginic acid) to PVA requires the acid periodate treatment to cleave the saccharide ring structure, resulting in aldehyde formation and cross-linking of PVA (5). Dialdehydes can also be used in the acid periodate method.

The effects of the acid and acid periodate catalysis methods were compared in Ref. (3) for cross-linked PVA films made from low viscosity PVA. Results indicated that periodate-treated PVA films exhibited higher ionic resistivity but longer cycle life in Ag-Zn and Ni-Zn cells than did acid-treated films.

Two-Step Cross-Linking Methods

Table I compares the two-step cross-linking method using either acid or acid periodate and two cross-linking reagents: furan 2,5-dialdehyde (DAF) and terephthaldehyde (TPA) in medium-viscosity PVA. Properties measured were volume resistivity, zinc dendrite penetration rate, and zincate diffusivity. The data show that resistivity is increased by use of acid periodate treatment. However, periodate treatment results in a longer time for zinc dendrite penetration and a lower zincate diffusion rate. From these data it appears that the cross-linked films generally have comparable properties to uncross-linked PVA used as an alkaline separator. Cross-linked films should have greater oxidation resistance than the uncross-linked PVA and thus lead to an increased cycle life.

The data presented in Table II show the effect of incorporating GOA into the PVA. The reagent contains both an aldehyde and a carboxylic acid group. The carboxylic acid group affects the resistivity and zincate diffusion. The reaction of the aldehyde with PVA can follow two routes: either form the cyclic acetal with PVA (the intramolecular reaction) and/or cross-link it (the intermolecular reaction). The films were cast with the solutions buffered to a *p*H of 7 with ammonia solution. The dry films were then treated with the acid periodate solution according to the method described in the procedure section. The extent of cross-linking as compared with cyclic acetal formation with the GOA is not known. The percentage of GOA shown in Table II represents the percentage of the theoretical amount needed to cross-link all the OH groups on the PVA.

As the amount of GOA in the film increases, the volume resistivity decreases with a corresponding increase in zincate diffusion rate. Between 10 and 50% GOA, the resistivity is halved (24-13 Ω-cm) while the zincate diffusion rate increases approximately 10%. The use of smaller amounts of GOA appears to represent a method of resistivity control with minimal change in zincate diffusion.

The effect of GOA on lowering resistivity is very pronounced in the data shown in Table IV. The films contained 2 w/o sucrose in PVA with the amounts of GOA required to achieve the percentages of the theoretical amount to react with all the PVA. The film-casting solution was buffered with ammonia solution to a *p*H of 7. The dry film was then treated with acid periodate solution to cross-link the PVA through the tetra aldehyde fragments resulting from oxidative cleavage of the sucrose ring structure (5). The resistivity is decreased significantly (approximately 90%) over the range 10-35% GOA. However, zincate diffusivity increases approximately 20 times over the same range. But the zincate diffusivity does not approach the 2×10^{-6} mol/cm² min value of commercially available film separators (6) until about 70% GOA in the film is reached.

One-Step Cross-Linking Method

The two-step methods of cross-linking were judged not commercially desirable because the dry films when immersed in the acid treatment solutions lost much of their strength. They tore easily when handled. The use of machine processing appeared very unlikely. An evaluation of a batch-processing method to achieve cross-linking showed that a wound roll of uncross-linked PVA film required a layer of material to separate the layers of PVA film to permit penetration of the acid-treating solution and to prevent "adhesion" of adjacent film layers of PVA because of the cross-linking reaction. Further, batch processing would lead to nonuniform cross-linking as a result of varying solution concentration and temperature.

An apparent manufacturing method was found when the one-step cross-linking method described in the procedure section was worked out. The GOA, selected as the model reagent, was used to convert the cross-linking method to a one-step film-manufacturing process. The GOA contains the necessary acid to catalyze the cross-linking reactions; and since GOA reacts chemically with PVA, it leaves no residual products in the film that need to be rinsed out. The only constraints on the film-casting process are time and temperature. The film has to be cast before gelation starts in order to prevent casting a film containing domains of cross-linked product. As temperature is lowered, the time to gelation increases.

The acid periodate cross-linking treatment does not appear easily adaptable to the one-step method. The oxidation-reduction reaction involving the hydroxyl and the periodate leaves an iodine reaction product in the membrane. This can be removed by rinsing with water but involves an additional treatment step. This approach was not pursued.

In Table III the effect of the cross-linking methods (two step *vs.* one step) on resistivity and zincate diffusivity is measured for two cross-linking reagents (DAF and TPA) and on films with 2 w/o DAF and 5 w/o fillers. The one-step method generally results in a cross-linked film having a higher (but acceptable) resistivity and a lower zincate diffusion rate.

Evaluation of Pilot-Plant Materials

Two pilot-plant batches of film materials were processed. The purpose was to establish the feasibility of the one-step method on a PVA-film-casting machine. The compositions of the two materials are shown in Table V. The major difference in composition was the 13 w/o GOA (manufacturer error, should have been 10%) added to the one-step material to cross-link it

Table IV. Comparison of polyvinyl alcohol films with varying glyoxylic acid content (Sucrose content, 2 w/o; wet film thickness, 0.014-0.018 cm; acid periodate cross-link)

GOA content in film (%)[a]	Volume resistivity (Ω-cm)	Zincate diffusivity (mols/cm² min)	Zinc dendrite penetration rate (cm/min)
0	122	2.3×10^{-8}	$<4 \times 10^{-5}$
10	28	3.1×10^{-7}	6×10^{-5}
35	14	5.5×10^{-7}	9×10^{-5}
70	12	3.9×10^{-6}	2×10^{-4}

[a] Percentage of theoretical amount required to react with all hydroxyl groups present in PVA.

Table V. Composition of pilot-plant films[a] (film drying temperature, 350°F; line speed, 25-30 ft/min; dry film thickness, ~1.5 mils)

Component	Two-step method	One-step method
	Composition (%)	
DAF	2.3	2.0
GOA	0	13.0
Triton X-100	0.7	0.6
Zelec UN	0.56	0.5
Film color	Yellow	Clear

[a] Elvanol 71-30.

Table VI. Pilot-plant materials: measured properties of cross-linked PVA compared with those of Celgard and Cellophane

	Dry film thickness (cm)	Area resistivity (Ω-cm^2)	Volume resistivity (Ω-cm)	Zinc dendrite penetration rate (cm/min)	Zincate diffusivity (mols/cm^2 min)	OH diffusivity (mols/cm^2 min)	H_2O diffusivity (mols/cm^2 min)
PVA (one-step method)	0.0044	0.038	8.6	2.0×10^{-4}	7.1×10^{-7}	2.6×10^{-4}	4.3×10^{-4}
PVA (two-step method)	0.0036	0.037	10.3	1.1×10^{-4}	6.8×10^{-7}	3.0×10^{-4}	3.1×10^{-4}
Celgard 3401	0.0025	0.078	31.0	8.5×10^{-4}	29.4×10^{-7}	2.4×10^{-4}	2.5×10^{-4}
Cellophane	0.0025	0.051	20.0	0.4×10^{-4}	22.9×10^{-7}	2.3×10^{-4}	—

during the drying process. The one-step material came off the line as a cross-linked product. The two-step material was processed and dried and subsequently cross-linked by using the acid treatment procedure.

The two cross-linked films were then compared. The data on the two-step film in Table VI are quite similar to the 2 w/o DAF two-step data in Table III. The area resistivity of 0.037 Ω-cm^2 shown in Table VI is quite close to the 0.04 Ω-cm^2 value for the laboratory-prepared sample. The 6.8×10^{-7} mol/cm^2 min zincate diffusion values are identical. Comparing the measured separator properties of the PVA films in Table VI shows no significant difference in properties when films are made on pilot-plant equipment. Table VI also contains measured properties of Celgard 3401 and Cellophane, which are commercially available alkaline battery separators. The PVA films exhibit lower resistivity values, lower zincate diffusion rates, and equivalent hydroxyl diffusion rates. The measured rate of water diffusion was approximately 50% higher in the one-step cross-linked PVA than in Celgard.

The two PVA films were compared with Celgard in cycle tests in 7.2 A-hr Ni-Zn cells. A plot of discharge voltage as a function of ampere-hour capacity is shown in Fig. 1 for the two types of cross-linked PVA films and Celgard. The ampere-hour capacity was measured to a 1V cutoff. The C/2 discharge rate was 3.6A (approximately 14 mA/cm^2 current density) for a constant current discharge. An examination of Fig. 1 shows that although the ampere-hour capacities did not vary much for the cells, the PVA films showed a midpoint voltage that was approximately 50 mV higher than that of the Celgard film. The plots in Fig. 1 were taken from cycle 6, the C/2 rate performance characterization cycle.

Results of cycle testing in Ni-Zn cells are shown in Fig. 2. The PVA film from the one-step method was cycle tested in cells built by two suppliers (A and B).

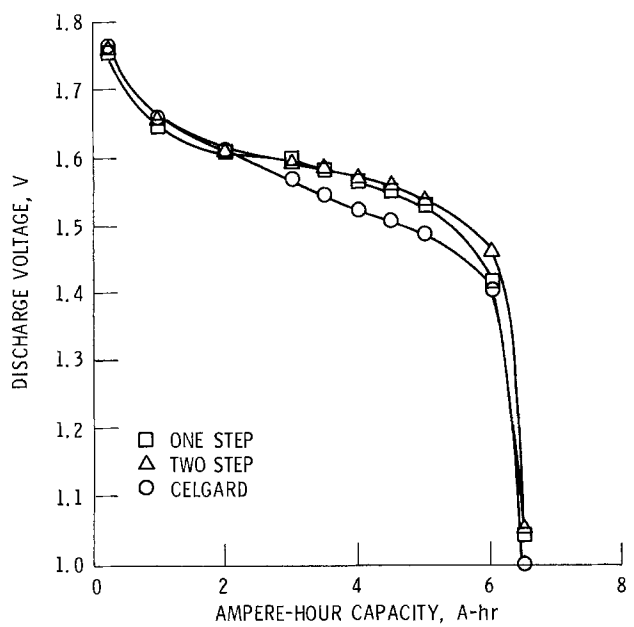

Fig. 1. Comparison of discharge voltage at C/2 rate pilot-plant-made PVA cross-linked film and Celgard.

The average (and standard deviation) of two cells built by supplier A was 117 (±4) cycles; the average of three cells from supplier B was 116 (±10) cycles. A combined (A + B) average of 116 (±8) is shown in Fig. 2. The average cycle life for the two-step method was 108 (±4) cycles based on three cells from supplier A. The 82-cycle result for Celgard is based on three cells from supplier A.

From the results of performance characterization and cycle life tests in small Ni-Zn cells, the one-step method of cross-linking provides essentially the same results as the two-step method. Hence it appears that cross-linked PVA film made on commercial production equipment has acceptable separator properties and performs at least as well as the commercially available separators to which it was compared.

Concluding Remarks

The development work on cross-linked polyvinyl alcohol (PVA) films for use as alkaline battery separators has produced the following results:

1. Chemically cross-linked PVA films generally exhibited comparable separator properties to uncross-linked PVA.
2. The introduction of carboxylate functional groups to the cross-linked film reduced resistivity and, when used in smaller amounts (<35% theoretical), did not appear to alter other film properties significantly.
3. A one-step cross-linking method appears adaptable to the commercial PVA film production process.
4. Cross-linked films produced on pilot-plant equipment by the one-step method did not exhibit significant differences from films similarly made by a two-step process.

These films are now under further development by W. R. Grace & Company, Columbia, Maryland, under a cost-sharing contract with NASA (Contract NAS 3-22223). Producing a cross-linked film in a one-step process during conventional film drying opens up other areas for separator development. An obvious approach would be to apply the separator directly to the electrode as a result of a multiple dipping operation, using

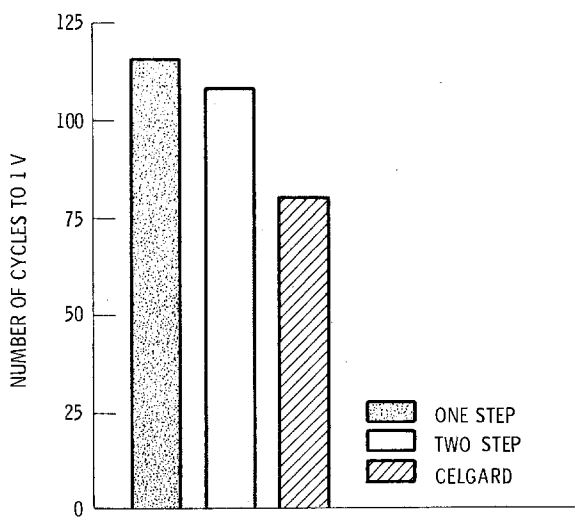

Fig. 2. Results of cycle life tests of pilot-plant-made PVA cross-linked film and Celgard 7.2 A-hr Ni/Zn cells.

drying steps between dipping steps to achieve a satisfactory, defect-free separator.

Manuscript submitted April 23, 1982; revised manuscript received Sept. 14, 1982. Part of this paper was Paper 95 presented at the Hollywood, Florida, Meeting of the Society, Oct. 5-10, 1980.

Any discussion of this paper will appear in a Discussion Section to be published in the December 1983 JOURNAL. All discussions for the December 1983 Discussion Section should be submitted by Aug. 1, 1983.

Publication costs of this article were assisted by the National Aeronautics and Space Administration.

REFERENCES

1. W. H. Philipp, L. C. Hsu, and D. W. Sheibley, U.S. Pat. 4,154,912 (1979).
2. W. H. Philipp and L. C. Hsu, "Three Methods for In Situ Crosslinking of Polyvinyl Alcohol Films for Application as Ion-Conducting Membranes in Potassium Hydroxide Electrolyte," National Aeronautics and Space Administration, Washington, D.C., NASA TP-1407 (1979).
3. L. C. Hsu and D. W. Sheibley, Paper 122 presented at The Electrochemical Society Meeting, Los Angeles, California, Oct. 14-19, 1979.
4. J. E. Cooper and A. Fleischer, Editors, "Characteristics of Separators for Alkaline Silver Oxide-Zinc Secondary Batteries: Screening Methods," Air Force Aero Propulsion Lab, Air Force Systems Command, Wright-Patterson AFB, Ohio (1964).
5. L. C. Hsu, D. W. Sheibley, and W. H. Philipp, U.S. Pat. 4,272,470 (1981).
6. D. W. Sheibley, M. A. Manzo, and O. D. Gonzalez-Sanabria, Paper 96 presented at The Electrochemical Society Meeting, Hollywood, Florida, Oct. 5-10, 1980.
7. L. C. Hsu and D. W. Sheibley, "Inexpensive Crosslinked Polymeric Separators Made from Water Soluble Polymers," National Aeronautics and Space Administration, Washington, D.C., NASA TM-82619 (1979).

Electrolyte Film Structure on Battery Separator and Electrode Materials

H. F. Bittner* and C. C. Badcock*

The Aerospace Corporation, Chemistry and Physics Laboratory, El Segundo, California 90245

ABSTRACT

Structural properties of alkaline electrolyte films on battery electrode and separator materials are investigated. Thermodynamic principles that affect film formation are presented, and a model is developed that predicts the wetting-dewetting transition, for a network of fibers, as a function of electrolyte volume and fiber network compactness. Film characteristics on single fibers and networks of fibers of a variety of materials are studied by a laser diffraction technique and by conductivity measurements. Materials studied include nickel, cadmium, nylon, polypropylene, and Teflon. Wetting characteristics of actual separator materials are studied in a simulated battery environment. Experimental results yield good agreement with the model.

The operation of battery cells depends critically on the characteristics of the electrolyte as it contacts the electrodes and separator material. Sealed battery cells, such as spacecraft nickel-cadmium (NiCd) cells, are usually operated in an electrolyte-starved state, which permits gas generated during overcharge to be easily recombined at an electrode. Consequently, the electrolyte exists as films on the battery separator material and on the electrode surfaces. These films transport both mass and charge to the electrodes, and are therefore required for the charge and discharge processes in the cell. A study of the properties and dynamics of electrolyte films permits better understanding of cell operation and better specification of separator and other cell components.

In this study, properties of electrolyte films on single fibers of separator and electrode materials were investigated. These studies were then extended to three-dimensional networks of fibers. Factors that determine wetting and electrolyte distribution in a battery cell configuration were considered and a model was developed that describes conditions for wetting. Good agreement was found between experimental results and the model.

Experimental

An apparatus for creating and monitoring electrolyte film on single fibers and fiber networks (cylindrical meshes of fibers) was constructed. The electrolyte was a 33% solution of potassium hydroxide (KOH). The apparatus, depicted in Fig. 1, consisted of a Plexiglas housing with a bubbler in a bath of electrolyte at the bottom to maintain a humid environment. Fibers studied were nylon (Textron, Incorporated), Pellon 2505 (Pellon, Incorporated), polypropylene (Hercules, Incorporated), and Teflon (Tetko, Incorporated). The fiber or fiber network was suspended between two small (3 cm^3) Plexiglas reservoirs, 0.5 cm apart, by means of holes in the reservoirs through which the ends of the fiber or network passed. The reservoirs could be filled with or drained of electrolyte by means of tubes connected to burettes outside the Plexiglas housing. This arrangement permitted measuring the effects on electrolyte film thickness of different volumes (levels) of electrolyte in the reservoirs.

The impedance of the electrolyte film was measured by means of platinum electrodes (1 cm^2) in each well that were connected in series with an oscillator and a current-sensing resistor. Voltages were measured through operational amplifiers. To calibrate the plati-

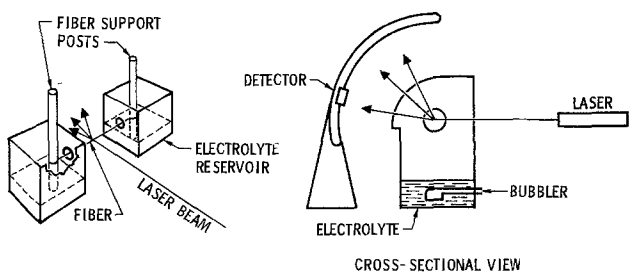

Fig. 1. Experimental apparatus for creating and monitoring electrolyte films on single fibers.

* Electrochemical Society Active Member.
Key words: interfaces, cell, thermodynamics, conduction.

num electrodes, they were placed in the same electrolyte-filled well and their impedance was measured as a function of frequency. Impedance measurements were subsequently made where reactance resulting from inductances and capacitances was minimal, at a frequency less than 10 kHz. The effects of different volumes (heights) of electrolyte in the reservoir were included in the calibration and were found to be negligible. The cross-sectional area A of the film was calculated by means of the following equation

$$A = l/\rho R \quad [1]$$

where l is fiber-mesh length, ρ is specific conductivity (0.65 Ω^{-1} cm^{-1} for 33% KOH) (1), and R is total resistance. Films on metal fibers could not be measured by this technique. The same circuit as above was used to oxidize the metal fibers, which were connected directly to one platinum electrode. An increasing d-c bias was applied until the fibers were passivated.

Diameters of single fibers and electrolyte-coated fibers were measured by laser diffraction. The Plexiglas housing contained a small Brewster window through which laser light ($\lambda = 6.238 \times 10^{-5}$ cm) entered and illuminated the fiber perpendicular to its axis. The resulting scattered light exited the box through a window that formed a 100° arc of a cylinder concentric about the fiber, so that the scattered light was not refracted. The scattering pattern was monitored by a detector that scanned through a 100° arc.[1] The apparatus was both designed and constructed to obtain measurements of high precision.

Fibers and fiber networks were pretreated by being soaked overnight in a KOH solution, rinsed with distilled water, and then dried in a dessicator. Fiber surfaces were analyzed by optical and electron microscopy. To estimate contact angles for 33% KOH on nylon, polypropylene, and Teflon, a flat sheet of each material was partially immersed in a beaker of the solution, after which the angle of the sheet relative to the surface of the liquid was changed until the surface of the liquid was flat. This angle was taken to be the contact angle. The experiments were performed so that the liquid advanced onto a dry substrate rather than receded from a wet substrate (3).

Wetting characteristics of Pellon separator (nylon 6) material were measured in an actual battery cell configuration. Cells were fabricated from nonwoven Pellon 2505 separator material sandwiched between discharged Ni and Cd electrodes. Cells consisted of three pieces of separator and either four electrodes or two electrodes and two Ni current collectors. These cells were placed between two Plexiglas plates that were connected by screws, so that compression could be applied to the cells as the screws were tightened. A hole was cut in the top plate and the top Plexiglas support to admit electrolyte, and each cell pack was placed horizontally in a covered glass dish capable of being purged with nitrogen.

For one set of experiments, electrolyte was injected incrementally into each cell pack from a microburette; it flowed onto the separator through the hole in the top Ni plate. After each addition, the cell was allowed to equilibrate for 24 hr, and then resistances between each plate were measured by a Hewlett-Packard Model 4328A milliohmeter. After the experiment, the components of each cell were weighed and the electrolyte distribution between the plates and the separator was calculated. A second set of experiments was performed to determine the effects of cycling on electrolyte distribution. For these experiments, electrolyte was added to the cells all at once. Cells were charged at 0.1A for 1 hr, and then cycled through a series of 0.8A discharge to 1.6V, which was followed by a 0.5A charge for 2 hr. At the end of cycling, electrolyte distribution among plates and separator was measured.

[1] The mathematical techniques used to extract structure information from the scattering patterns are summarized in the Appendix to Ref. (2).

Model Development

Equilibrium properties of wetting for a three-phase system (solid, liquid, and vapor) can be described by three interfacial interactions: the surface tensions of the liquid-vapor interface γ_{LV}, the solid-liquid interface γ_{SL}, and the solid-vapor interface γ_{SV} [see, for example, Ref. (3, 4)]. These surface tensions are defined in terms of free energy G by

$$\gamma_n = (\partial G/\partial A_n)_{T,\mu_i} \quad [2]$$

where n is the interface, A the area of the interface, T the temperature, and μ_i the chemical potential of each component in the phases present. The contact angle θ, a directly measurable quantity, may be described in terms of the interfacial tensions

$$\cos\theta = (\gamma_{SV} - \gamma_{SL})/\gamma_{LV} \quad [3]$$

For most systems γ_{SV} is small (2), and for a completely wetted substrate there is no solid-vapor interface ($A_{SV} = 0$).

Single fibers.—The change in system free energy with changing film volume on a uniformly covered cylindrical substrate can be calculated, if one ignores gravity and edge effects at the ends of the cylinder, by

$$\frac{dG}{dV} = -(\partial G_{SL}/\partial V)_{T,\mu_i} + (\partial G_{SL}/\partial V)_{T,\mu_i} \quad [4]$$

where the volumes can be expressed in terms of film thickness or interfacial area. Once the surface is uniformly covered by several monolayers of film, $\partial G_{SL}/\partial V$ becomes small; because $\partial G_{LV}/\partial V$ is positive, work must then be done on the system to effect an increase in film thickness. However, the most stable configuration might consist of spherical beads of film on the cylindrical substrate. Figure 2 shows the change in free energy with increasing volume of 33% KOH for a uniform film and for liquid beads on a nylon cylinder of radius 8 μm and a polypropylene cylinder of radius 13 μm. These calculations were performed by means of Eq. [4], with the film volume defined in terms of interfacial areas; the free energy at each volume of solution is the sum of the interfacial free energies of the liquid-solid and liquid-vapor interfaces. In these calculations γ_{SV} was assumed to be small and was ignored (3). At low volumes the beaded state is the more stable, whereas at higher volumes the film is more stable.

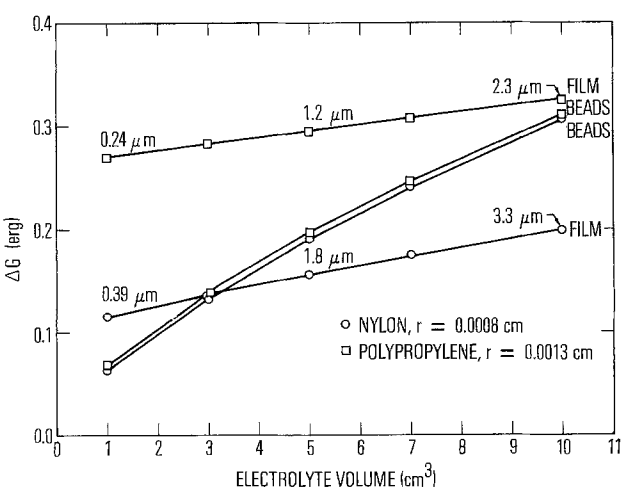

Fig. 2. Calculated free-energy change of wetting vs. electrolyte volume (33% KOH) for continuous film and bead states on nylon and polypropylene fibers. Bead states were calculated for an assumed four spherical electrolyte beads.

In the above calculations, edge effects were not included. However, energy considerations arising from edge effects can actually dominate the system free energy. Consider a cylindrical substrate with ends immersed in reservoirs containing liquid to coat the substrate. If the system is designed so that the liquid in the reservoirs can apply a pressure on the film along the axis of the cylindrical substrate, this pressure will "do work" on the system and effect a thicker film on the substrate. If the system is designed so that the pressure on the liquid is produced by gravity acting on the liquid in the reservoirs, Eq. [4] then becomes

$$\frac{dG}{dV} = -(\partial G_{SL}/\partial V)_{T,\mu_i} + (\partial G_{LV}/\partial V)_{T,\mu_i} - 2\rho g h \qquad [5]$$

where ρ is the density of the liquid, g the acceleration of gravity, and h the height of the liquid above the level of the substrate.

Surface roughness of the substrate will affect the film's characteristics. The effect may be expressed in terms of an observed contact angle θ' for the rough surface, compared to the true contact angle θ

$$r = \cos\theta'/\cos\theta \qquad [6]$$

where r is the roughness factor and is usually significantly greater than 1.0 (3). The magnitude of the interfacial tensions is not dependent on surface roughness or shape, but the area of the interface is. Hence a rough surface has a larger solid-liquid interface, which is a stabilizing interaction, and therefore wets more readily than a smooth surface. Similarly, a spherical bead of liquid at the junction of two crossed fibers will have a lower system free energy than the same bead on a single fiber.

Fiber networks.—Calculations for three-dimensional fiber networks extend from the above considerations. Again ignoring the relatively small solid-vapor interaction, the free energy of the system can be calculated from Eq. [4]. Substrate configurations that increase the solid-liquid interfacial area relative to the liquid-vapor interfacial area will stabilize the system (provide greater wettability), whereas increasing the liquid-vapor interfacial area relative to the solid-liquid interface will destabilize the system. For a separator, wetting will be increased if its surface area is maximized, which can be accomplished by means of small-diameter fibers that are densely packed or woven.

From these considerations, it is possible to develop a model that predicts wetting and dewetting, for a particular separator material, as a function of volume of electrolyte and compactness of the separator material. For an actual battery cell, the model predicts the volume of electrolyte required to ensure complete wettability, and it also defines the effect on wettability of compressing the separator in the plate stacks. The model consists of a pseudophase diagram constructed from thermodynamic considerations.

The pseudophase diagram is constructed in the following manner. An idealized configuration of a regular cubic lattice of separator material fibers is assumed, so that the compactness of the separator material can be described by the length of the side of a cube in the lattice, or the distance between adjacent fibers in the lattice. The model is shown in Fig. 3. The free energy of wetting is taken to be the difference between the free energy of a sphere of electrolyte of given volume at the fiber junction (Fig. 3a) and the free energy of the same volume of electrolyte in a wetted configuration on the separator junction. The latter free energy is calculated by means of Eq. [4] and liquid-vapor surface areas according to the following model. At low electrolyte volumes, the electrolyte is assumed to exist as spheres at the fiber junctions, with cones extending along the fibers in all directions; the base of each cone is coincident with the face of a cube that just fits inside the sphere, and the height of the cone is such that the tip of one cone meets the tip of another cone from an adjacent junction (see Fig. 3b). This configuration provides that the fibers are completely wetted at any electrolyte volume. At high electrolyte volumes, the surface area of the electrolyte is taken to be that of a void sphere inside each cube of the separator (Fig. 3c); increasing electrolyte volume corresponds to decreasing void sphere volume, until the separator lattice is saturated with electrolyte and the liquid-vapor interfacial area goes to zero. The crossover point between the low- and high-electrolyte-volume models is taken to occur where the free energies of both models cross. These calculations were performed for 33% KOH on Pellon, polypropylene, and Teflon, at various degrees of compression or junction-junction distances. Results are shown for Pellon in Fig. 4. The liquid-vapor surface tension for 33% KOH was extrapolated from data for more dilute concentrations (5) to be $\gamma_{LV} = 91$ erg/cm^2; the contact angle for 33% KOH on nylon was measured

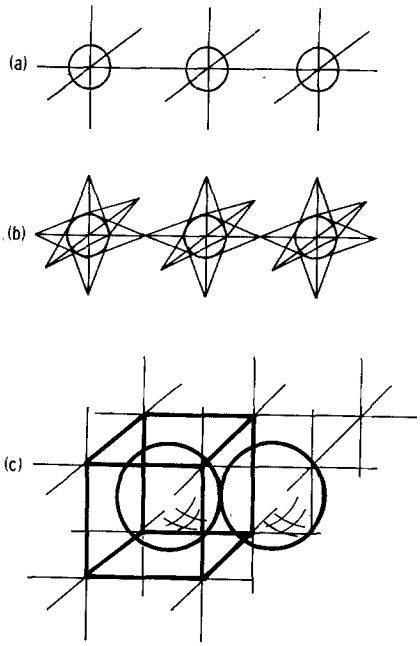

Fig. 3. Geometric model of wetting. (a) Initial state where electrolyte exists as spheres of equal volume at junctions of fibers in cubic lattice; (b) wetted state for low electrolyte volume, where electrolyte is modeled as cones extending along fibers away from fiber lattice junctions; tips of cones meet at midpoint of adjacent junctions, and bases of cones are coincident with faces of cubes that just fit inside spheres at fiber junctions; (c) wetted state for high electrolyte volumes, where electrolyte fills lattice everywhere except spherical voids within each cube of fiber lattice.

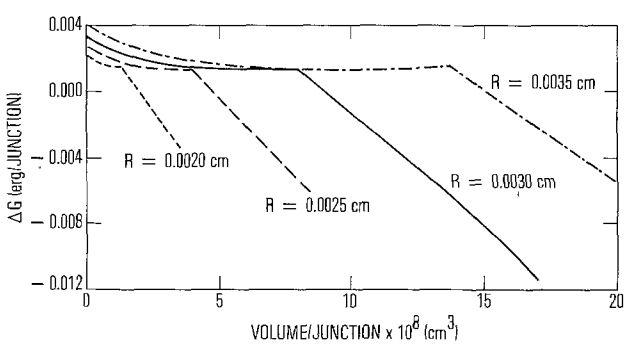

Fig. 4. Calculated free-energy change of wetting vs. electrolyte volume (33% KOH) for Pellon fiber of radius $r = 0.0008$ cm, at various degrees of compactness of separator lattice.

to be 55°, and γ_{SL} was calculated from Eq. [3] to be -49 erg/cm^2 (assuming $\gamma_{SV} \cong 0$). Similarly, plots were made for polypropylene and Teflon from the following experimentally determined values: for polypropyene, $\theta = 73°$ and $\gamma_{SL} = -27$ erg/cm^2; for Teflon, $\theta = 83°$ and $\gamma_{SL} = -15$ erg/cm^2. The pseudophase diagrams, shown in Fig. 5 for Pellon, polypropylene, and Teflon, are constructed from $\Delta G = 0$ points in these plots. The resulting curves are the equilibrium lines separating the wetted and dewetted regions.

Results and Discussion

Single fibers.—Experiments were performed involving electrolyte coatings on single fibers of Ni, Cd, nylon, and polypropylene. The metals were studied both in their virgin and oxidized states, the latter as they occur in battery cells. Two nylon materials were studied, nylon filament and Pellon 2505, a battery separator material. The polypropylene fiber studied had been kinked for use in separator materials. Diameters of the uncoated materials were obtained by laser diffraction, then electrolyte was added to the reservoirs and directly onto the fibers, and new diameters were obtained. Results are compiled in Table I; values presented for the metal and polypropylene fibers are averages of at least eight measurements. Values presented for the nylon fibers were calculated by means of a scattering-theory approach, which yields the highest precision.

The data indicated that films on metal fibers were thin or nonexistent. The precision of the technique used to determine the film thicknesses (± 1.3% of the metal fiber diameter) was insufficient to measure these films. However, metals and oxides have large surface energies and should have been wetted by the electrolyte. If films did form on these substrates, they were less than 2 μm thick.

Diffraction patterns were obtained for the nylon filament in two positions approximately 0.4 cm apart (at either end of the fiber). The diameter of the base fiber was virtually identical at both ends. However, one position exhibited a coating about 1.0 μm thick, while the other position showed a coating about 0.3 μm thick; this is consistent with resistance measurements, which give an average thickness weighted toward the minimum, and indicate a coating 0.3 μm thick. The Pellon fiber exhibited, by means of laser diffraction, an electrolyte film about 0.7 ± 0.4 μm thick, whereas the resistance measurement indicated a film only 0.1 μm thick. These results suggest that the films were not uniform in thickness along the length of the fiber. Scanning electron microscopy showed that the fiber surfaces were not smooth; surface irregularities might account for the nonuniform film thicknesses.

Attempts at forming a coating on polypropylene were unsuccessful. Beading of the electrolyte was observed, and resistance measurements indicated no continuous coating had formed. A comparison of this result and the nylon results with the theoretical results

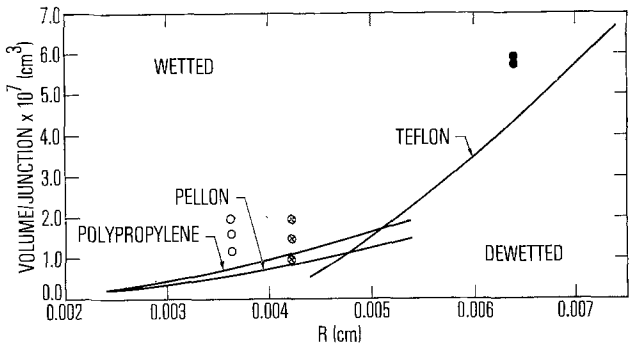

Fig. 5. Calculated pseudophase diagrams (solid lines) and experimental points for polypropylene (⊗), Pellon (○), and Teflon (●). *R* represents the distance between adjacent fibers in the idealized fiber lattice.

in Fig. 2 shows good agreement. Those calculations predicted that films on nylon fibers were more stable than beads at these film thicknesses, whereas for polypropylene the beaded state was more stable. Both the type of material and the fiber radius differ in this comparison, and both factors contribute to the stability differences shown in Fig. 2.

Fiber networks.—Fibers of Pellon, polypropylene, and Teflon were fashioned into cylindrical networks and placed in the apparatus; electrolyte was then added to the reservoirs. The level of electrolyte was changed in the reservoirs and the corresponding change in impedance along the fiber mesh was monitored. Calculated cross-sectional areas of KOH at different electrolyte levels are given in Table II. Results indicate that for Pellon, the lowest level of electrolyte in the wells effected wetting sufficiently to just fill the void space, whereas the highest level filled the void space and formed a coating exterior to the fiber mesh. For polypropylene and Teflon, results indicate somewhat less wetting than for Pellon.

The degree of wetting in each case, as indicated in Table II by the calculated cross-sectional area of KOH, was dependent on three factors: (*i*) the inherent wettability of the fiber material; (*ii*) the compactness of the fiber mesh; and (*iii*) the level of electrolyte in the reservoirs, which corresponds to work done on the system. Comparison of these results with the model is shown in Fig. 5, where the solid lines are the calculated pseudophase diagrams for the three materials, and the circles are the experimental results calculated from values in Table II. The experimental points represent conditions where the fiber networks were wetted, and in general the points lie within regions where the pseudophase diagrams indicate wetting would occur (one point for polypropylene lies slightly into the dewetted region). For Teflon, the lowest level of electrolyte in the reservoirs did not effect wetting, as indicated by a high impedance along the fiber network. The

Table I. Laser diffraction and conductivity results for aqueous KOH electrolyte (33%) films on single-fiber substrates. The electrolyte level in the reservoirs was 0.8 cm above the fibers

Material	Starting diameter × 10^2 (cm)	Diameter with electrolyte coating × 10^2 (cm)	Coating thickness	
			By diffraction (μm)	By conductivity (μm)
Ni, virgin	1.23 ± 0.01	1.22 ± 0.02	•	—
Ni, oxidized	1.23 ± 0.02	1.24 ± 0.02	•	—
Cd, virgin	2.47 ± 0.03	2.51 ± 0.03	•	—
Cd, oxidized	2.51 ± 0.02	2.53 ± 0.03	•	—
Nylon, filament	Pos. 1 1.175 ± 0.002	1.181 ± 0.002	0.3 ± 0.2	0.3
	Pos. 2 1.176 ± 0.002	1.195 ± 0.002	1.0 ± 0.2	0.3
Nylon, Pellon	0.172 ± 0.002	0.186 ± 0.003	0.7 ± 0.4	0.1
Polypropylene	0.24 ± 0.03	0.23 ± 0.01	0.0••	No coating

• Coating was smaller than precision of technique, ~2 μm.
•• Beading noted.

Table II. Cross-sectional areas of electrolyte and corresponding percent of void space filled for KOH electrolyte (33%) on various substrate networks

Well height (cm)	Pellon (r = 0.0008 cm)		Polypropylene (r = 0.0013 cm)		Teflon (r = 0.0038 cm)	
	Cross-sectional area KOH $\times 10^3$ (cm^2)	Void space filled (%)	Cross-sectional area KOH $\times 10^3$ (cm^2)	Void space filled (%)	Cross-sectional area KOH $\times 10^3$ (cm^2)	Void space filled (%)
0.1	1.0	83	2.2	25	—	—
0.5	1.3	108	3.9	44	1.6	67
0.8	1.6	133	4.7	53	1.7	69

volume of electrolyte in the fiber mesh in a dewetted condition cannot be calculated by resistance measurements and is therefore not included in Table II or Fig. 5. However, the volume of electrolyte would be less than the volume represented by the two other points for Teflon shown in Fig. 5 and would therefore lie toward, if not into, the dewetted region predicted by the pseudophase diagram.

Increasing the level of electrolyte in the reservoirs "does work" on the system by producing a pressure along the electrolyte film. From Eq. [5], the system is thereby stabilized and can therefore support a film with a larger liquid-vapor surface area relative to the solid-liquid surface area. When comparing the experimental results with the pseudophase diagrams in Fig. 5, one must realize that the theoretical curves were calculated with the assumption that no work was done, and that the experiments were conducted so that work was done on the system. Quantifying the amount of work done by the electrolyte height in the reservoirs would stretch the model beyond its usefulness.

Experiments were performed to measure the dewetted-wetted transition for Pellon separator material at three different degrees of compactness (compressions). A battery cell configuration was used so that results could be directly compared to those of an actual battery. Three cells were fabricated, as described in the experimental section, from one discharged Ni electrode and one Cd electrode sandwiched between two Ni plates, with pieces of Pellon material separating each component. The cells were compressed to three different degrees: 0%, 31%, and 43%; these values correspond to percent volume compression. For comparison with the model, a regular cubic lattice array of fibers was assumed as before, and the distance between each adjacent fiber was calculated to yield the same percent volume compression: 6.00×10^{-3}, 5.28×10^{-3}, and 4.95×10^{-3} cm, respectively. Electrolyte was added incrementally to each cell pack and resistances were measured after equilibration. Wetting was assumed to have occurred when the total cell resistance did not change appreciably with further addition of electrolyte. After the experiment, the components of each cell were weighed and the electrolyte distribution between the plates and separator was calculated. Approximately 65% of the electrolyte was found in the separator.

Because the plates had an apparently much higher affinity for electrolyte than did the separator, it was assumed that the plates saturated first. The amount of electrolyte in the separators was taken to be the total amount of electrolyte added minus the amount in the saturated plates. Results are shown in Fig. 6. The horizontal bars indicate the cell resistance at each incremental volume of electrolyte, translated into volume of electrolyte per fiber junction in the separator material. The solid line is the calculated pseudophase diagram.

The experimentally determined dewetted-wetted transitions occurred at somewhat higher electrolyte volumes than were predicted by the pseudophase diagram; however, the general characteristics of the curve defined by the experimental results and the theoretical curve are similar. In actual NiCd cells, postmortem analysis indicates that only 20-35% of the electrolyte is found in the separators (6), a range of values significantly lower than the 65% found in these cells. One of the differences between the actual postmortemed cells and the cells in this experiment was that the actual cells had been cycled through charge and discharge.

A second set of experiments was performed to determine the effects of cycling on electrolyte distribution. For these experiments, cells were constructed as before, except that four electrodes were used instead of two, and the outer Ni plates were omitted. Two cells were cycled simultaneously, one at 0% compression and one at 31%. Cells were cycled according to the schedule in the experimental section. The electrolyte distribution after cycling apparently was independent of the degree of compression; the amount of electrolyte was sufficient to effect wetting at both compressions. Results are given in Table III for the 31% compressed cells; one result from a previous two-plate experiment is included for comparison.

The volume of electrolyte added was not consistent among all the tests because each test originally had a different purpose. The volume of electrolyte added to those cells cycled 2 and 39 times was identical, although electrolyte was lost during the latter test through evaporation. Despite this loss, the absolute amount of electrolyte in the plates cycled 39 times was higher than in the other tests. These results indicate that a higher amount of electrolyte is found in the plates after modest cycling ($<$ 39 cycles). This suggests that between 2 and 39 cycles are required to establish equilibrium, if a change in concentration (because of evaporation) is not the driving force. The plates apparently have a much greater affinity for electrolyte than do the separators, so that the plates will retain their maximum amount of electrolyte consistent

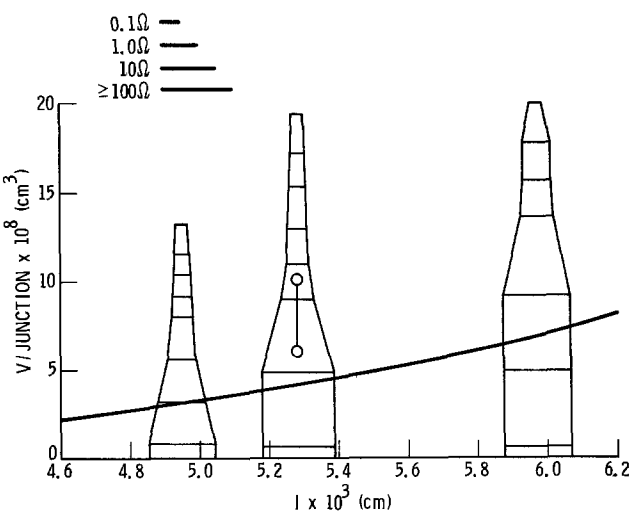

Fig. 6. Pseudophase diagram for Pellon separator and experimental results indicating cell resistances as a function of electrolyte volume for three different cell compressions. The points designated (○) indicate the 20-35% range of electrolyte absorption in the separators for an actual NiCd cell. A flooded separator corresponds to a volume/junction of about 1.2×10^{-7} cm^3.

Table III. Electrolyte distribution in simulated NiCd cells as a function of charge-discharge cycling. Percent electrolyte in separators is normalized to a ratio of separators to plates of 23/22

Number of electrodes	Number of cycles	Total electrolyte (g)	Electrolyte in plates (g)	Electrolyte in separators (g)	Electrolyte in separators, normalized (%)
2	0	8.5	2.5	6.0	61
4	0	7.4	4.1	3.3	53
4	2	10.3	4.9	5.4	60
4	39	6.6	5.5	1.1	21

with their degree of cycling, and any remaining electrolyte will reside in the separators.

The points indicated in Fig. 6 that correspond to an actual NiCd cell were calculated according to characteristics for a 30 A-hr cell, and with the assumption that 20-35% of the electrolyte goes into the separator (6). The results in Fig. 6 indicate that the 20% figure lies near the wetted-dewetted transition, and therefore represents nearly the minimum amount of electrolyte consistent with a wetted configuration.

Conclusions

A number of conclusions can be drawn regarding the fundamental properties of electrolyte films on battery electrode and separator materials. The structure of aqueous electrolyte films on single-fiber substrates depends primarily on fiber diameter and surface roughness, and to a lesser degree on substrate material. These parameters determine whether either a continuous film or a beaded state is favored. However, edge effects can dominate these considerations by "doing work" on the system. For a three-dimensional system, the structure of the fiber network is critical to its wettability. A pseudophase diagram for any system may be constructed to predict the volume of electrolyte required to ensure wetting, as a function of compactness of the substrate material, if the interfacial surface tensions are known for that system.

The most significant conclusion from this work is that the wettability of a separator depends primarily on the structure of the separator. The basic parameters of wetting discussed here could be used to design a separator structure with optimal wetting characteristics for particular battery applications. This finding may lead to the investigation and use of new separator materials that are better suited for alkaline-cell environments than materials that are presently used.

Acknowledgment

The assistance of Albert Zimmerman, R. L. Brittain, T. Fitzmaurice, and E. Shon is gratefully acknowledged.

Manuscript received May 16, 1982. This was Paper 435 presented at the Montreal, Quebec, Canada, Meeting of the Society, May 9-14, 1982.

Any discussion of this paper will appear in a Discussion Section to be published in the December 1983 JOURNAL. All discussions for the December 1983 Discussion Section should be submitted by Aug. 1, 1983.

Publication costs of this article were assisted by The Aerospace Corporation.

REFERENCES

1. G. W. Heise and N. Corey Cahoon, Editors, "The Primary Battery," Vol. 1, p. 180, John Wiley & Sons, Inc., New York (1971).
2. H. F. Bittner, C. C. Badcock, R. L. Brittain, T. Fitzmaurice, and E. Shon, "The Structure of Electrolyte Films on Battery Separators and Electrodes," ATR-81(8426)-1, The Aerospace Corp. (1982).
3. W. A. Zisman, in "Contact Angle, Wettability, and Adhesion," Robert F. Gould, Editor, American Chemical Society, Washington, D.C. (1964).
4. J. F. Padday, Editor, "Wetting, Spreading, and Adhesion," Academic Press, London (1978).
5. R. C. Weast, Editor, "Handbook of Chemistry and Physics," p. F28, The Chemical Rubber Co., Cleveland, Ohio (1970).
6. C. C. Badcock and P. Riley, Aerospace Technical Memorandum No. 81(6409-13)-3, The Aerospace Corp. (1981).

Reactions of FeS_2, CoS_2, and NiS_2 Electrodes in Molten LiCl-KCl Electrolytes

S. K. Preto,* Z. Tomczuk,* S. von Winbush,*,[1] and M. F. Roche*

Argonne National Laboratory, Chemical Engineering Division, Argonne, Illinois 60439

ABSTRACT

The electrochemistry of the FeS_2, CoS_2, and NiS_2 electrode phases in molten LiCl-KCl electrolyte at 400°C was studied using cyclic voltammetry at sweep rates of 0.02-1 mV/sec. Emf's, polarization characteristics, and nucleation overpotentials were obtained for each major electrode reaction; the anodic nucleation overpotentials increased with emf for all three electrodes. The disulfide electrodes lost sulfur during the extended cyclic-voltammetry tests. These losses appear to be associated with a nonequilibrium species that is involved in the electrochemical formation of the disulfides from their precursors.

Lithium-alloy/iron-sulfide secondary batteries for electric vehicles and stationary energy storage systems are being developed at Argonne National Laboratory and at a number of industrial firms (1). Much of this development program has concentrated on the 1.34V Li-Al/FeS cell, which employs molten LiCl-KCl as the electrolyte and is operated at 400°-500°C. In this type of cell, the current collectors are made of iron and the electrode separators are made from BN felt. Iron disulfide may be used instead of FeS as the positive electrode (1-6) if a more noble current collector such

* Electrochemical Society Active Member.
[1] Present address: State University of New York/College at Old Westbury, Old Westbury, Long Island, New York, 11568.
Key words: electrode, fused salts, cathode, voltammetry.

as molybdenum is employed. The Li-Al/FeS_2 cell, which has two major voltage plateaus at 1.75 and 1.34V, has a higher specific energy than the Li-Al/FeS cell, but has generally exhibited a lower cycle life (1, 6). The capacity decline of Li-Al/FeS_2 cells has been attributed to the loss of sulfur from the FeS_2 electrode (6, 7). The sulfur forms a dense deposit of Li_2S crystals in the BN separator near the Li-Al electrode; precipitates of iron are associated with these Li_2S crystals (7). Dense deposits of Li_2S crystals have also been found at the Li-Al electrodes of Li-Al/NiS_2 cells (8). In this case, the Li_2S is not associated with metallic deposits, and the cells have long cycle lives (6). In an earlier Argonne program, lithium sulfide deposits were found on the negative electrodes of Li/S cells; the proposed transport mechanism involved highly soluble intermediates formed in the cycling of the sulfur electrode (9). The above sulfur-transport problems do not exist in Li-Al/FeS cells, which accounts for their superior capacity retention and cycle life.

A variety of other transition metal sulfides are also employed as positive electrodes (3, 6, 10) or as performance-improvement additives in the iron sulfide electrodes (6, 11, 12). For example, CoS_2 has been used as an electronic conduction additive in FeS_2 and NiS_2 electrodes (6). It is of interest to compare the electrochemistry of FeS_2, CoS_2, and NiS_2 because of their similar structures (pyrite) and similar thermochemical properties. From available thermodynamic data (13-17), the theoretical specific energies of the LiAl/MS_2 (M = Fe, Co, or Ni) cells can be readily calculated for the following overall reaction

$$4LiAl + MS_2 \rightleftarrows 4Al + M + 2Li_2S \qquad [1]$$

For all three disulfides, the theoretical specific energy at 425°C is about 650 W-hr/kg, and all three electrodes are potentially of interest for high performance cells.

The discharge of FeS_2, CoS_2, and NiS_2 is more complicated than reaction [1] indicates because of the occurrence of intermediate phases. According to the Fe-S, Co-S, and Ni-S phase diagrams (18, 19), the intermediate binary phases at 400°C are: FeS for FeS_2; Co_3S_4 and Co_9S_8 for CoS_2; and NiS, Ni_7S_6, and Ni_3S_2 for NiS_2. Considering only these binary phases, FeS_2 seems to be the least complicated electrode. However, ternary phases are also formed in FeS_2 electrodes (20, 21). For example, the FeS_2 electrode phases include $Li_3Fe_2S_4$ and a solid-solution phase $Li_{2+x}Fe_{1-x}S_2$ that extends from $x = 0$ to $x = 0.33$ (21). Even more complex phases are possible; for example, $LiK_6Fe_{24}S_{26}Cl$, which is a common phase in FeS electrodes (22, 23), is also found in FeS_2 electrodes (21). Thus, the phases in FeS_2 electrodes are more complex than is suggested by the Fe-S phase diagram; the phases in CoS_2 and NiS_2 electrodes have not been previously determined.

In the present study, cyclic voltammograms were obtained for FeS_2, CoS_2, and NiS_2 electrodes in LiCl-KCl electrolyte at 400°C. Cyclic voltammograms were also obtained for Li_2S, a discharge product common to all three disulfide electrodes. The phases in CoS_2 and NiS_2 electrodes were identified by x-ray diffraction and metallographic analysis of positive electrodes taken from small cells.

Experimental

The electrolyte was polarographic grade LiCl-KCl of eutectic composition [58 mol percent (m/o) LiCl, mp 352°C], which was obtained from Anderson Physics Laboratory (APL). Off-eutectic compositions were prepared from the eutectic by adding either APL polarographic grade LiCl or Baker reagent grade KCl, which had been vacuum dried at 400°C.

The negative electrodes were prepared using lithium aluminum [48 atom percent (a/o) Li] from KBI, Incorporated, aluminum (>99%) demister wire from Otto H. York, Incorporated, and lithium from Lithcoa. The positive electrodes contained FeS_2 (>99%) from Gould Incorporated, CoS_2 from Cerac/Pure Incorporated, or NiS_2 from Alpha Inorganics. Chemical and metallographic analyses showed that the CoS_2 contained about 20 m/o Co_3S_4 and that the NiS_2 contained about 20 m/o NiS. Other positive-electrode materials included 99% pure Co_9S_8 and NiS from Great Western Inorganics, and Li_2S (approximately 97% pure) from Eagle Picher Industries, Incorporated.

The cells for the cyclic voltammetry experiments consisted of Li-Al reference and counterelectrodes positioned above the sulfide working electrode in about 200g of electrolyte. The Li-Al electrodes employed cylindrical iron housings that were wrapped in 325-mesh Type 304 stainless steel screens. The ratio of LiAl powder to aluminum demister wire was such that the final lithium concentration was about 42 a/o. The resulting mixture of two lithium-containing phases (α-Al and β-LiAl) has a fixed potential of 303 mV *vs.* liquid lithium at 400°C (17). The reference electrode (1.5 cm^2 × 2 cm) had a capacity of about 1 A-hr, and the counterelectrode (10 cm^2 × 1 cm) had a capacity of about 6 A-hr. The working electrode employed a molybdenum housing (1 cm^2 × 0.5 cm). About 1 mmol of the sulfide powder was vibrated into a 1 cm^2 × 0.5 cm piece of vitreous carbon foam (Chemtronics International Incorporated) that was held within the molybdenum housing; the electrode face was then covered with zirconia cloth and molybdenum screens.

The cells that were operated to identify the sulfide phases employed 4 A-hr negative electrodes and 1 A-hr positive electrodes. The negative electrodes were either Li-Al or liquid lithium. The Li-Al electrodes were like those used in the cyclic voltammetry; the liquid lithium electrodes have been described previously (2). The positive electrodes contained about 1g of the transition metal disulfide powder placed in the cavity (4.6 cm^2 × 0.7 cm) of a cylindrical graphite housing. A porous disk of graphite (PG-60, Union Carbide Corporation) was graphite-cemented to the face of the housing to retain the active material within the cavity.

Procedures.—The cells were operated at temperatures of about 400°C in furnace wells that were attached to helium-atmosphere glove boxes. The helium was continuously purified (<3 ppm O_2 and H_2O) by a combination of molecular sieves and cold traps. A furnace controller maintained the temperature within 1°C of the preselected value during cell operation; the temperature was monitored with a calibrated Chromel-Alumel thermocouple.

The instrumentation for the cyclic voltammetry experiments was a PAR 175 universal programmer, a PAR 173 potentiostat, a PAR 179 coulometer, a Fluke 8000 A digital voltmeter, and an HP 7045A X-Y recorder. The procedure consisted of repeated cathodic and anodic sweeps at each potential sweep rate to obtain steady-state voltammograms. The sweep rate was varied from 0.02 to 1 mV/sec, and the potential range was usually 1.0-2.0V *vs.* Li-Al. A broader potential range was employed at the higher sweep rates, and narrower ranges were employed when associating specific cathodic peaks with their anodic analogs.

The instrumentation for galvanostatic cycling of the phase-identification cells consisted of an HP 620B constant-current power supply, a Fluke 8000A digital voltmeter, and an HP 7100B strip chart recorder. The power supply was equipped with a voltmeter-controlled relay system that reversed the direction of cell current at appropriate charge and discharge cutoff voltages (for example, 2.0V on charge and 1.0V on discharge). The cells were cycled repeatedly at current densities ranging from 12 to 60 mA/cm^2 and were then stopped at various states of charge for subsequent phase studies. The positive electrodes were removed from the cells, sectioned, and analyzed by x-ray diffraction and metallographic techniques (23).

Results and Discussion

Cyclic voltammograms at low sweep rates and the electrode phases.—Cyclic voltammograms are shown in Fig. 1-3 for the FeS_2, CoS_2, and NiS_2 electrodes, respectively, operated at a temperature of 400°C in the LiCl-KCl eutectic electrolyte. The potential sweep rate was 0.02 mV/sec and the potential range was 1.0-2.0V.[2] This combination of rate and range corresponds to about one cycle per day, which is comparable to the cycling rate of the phase-identification cells. At such a low rate, cyclic voltammetry is equivalent to coulometry. For example, the summed areas of either the anodic or cathodic peaks in Fig. 1-3, when converted to coulombs per mmol, exceeded 85% of the theoretical capacity (386 C/mmol) based on reaction [1].

The dominant features in Fig. 1-3 are labeled with Roman numerals that are the same, except for subscript, for an anodic (a) peak or band and its cathodic (c) counterpart. The labeling was checked by

[2] All electrode potentials are with respect to the two phase (α + β) Li-Al reference electrode.

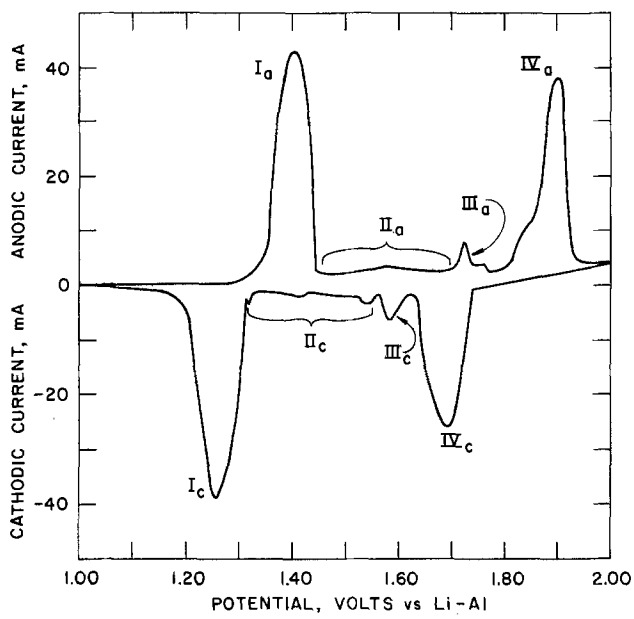

Fig. 1. Cyclic voltammogram of FeS_2 at 400°C in LiCl-KCl eutectic electrolyte (sweep rate, 0.02 mV/sec).

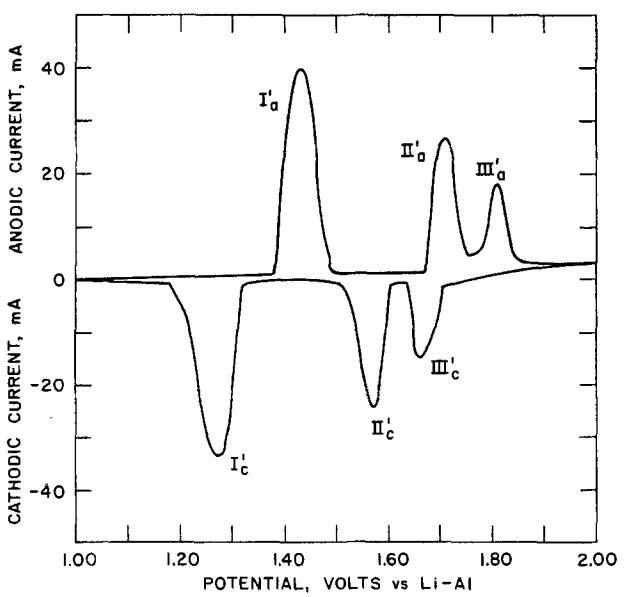

Fig. 2. Cyclic voltammogram of CoS_2 at 400°C in LiCl-KCl eutectic electrolyte (sweep rate, 0.02 mV/sec).

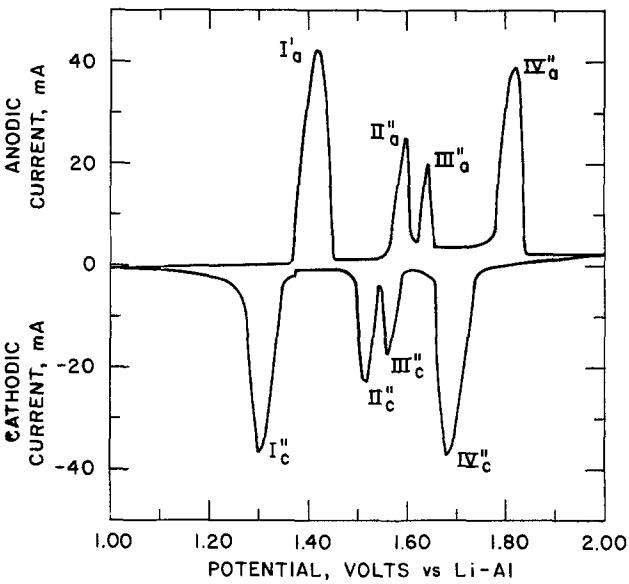

Fig. 3. Cyclic voltammogram of NiS_2 at 400°C in LiCl-KCl eutectic electrolyte (sweep rate, 0.02 mV/sec).

narrow-voltage-range sweeps centered on each pair of peaks. In these sweeps, the areas of the individual peaks were unchanged from those in Fig. 1-3, and, in most cases, the peaks were located at nearly the same potential. A notable exception was peak IV_a of the FeS_2 electrode (Fig. 1), which shifted to significantly lower potentials on narrowing the potential range. Figure 4 illustrates this effect and also shows that the anodic peak has a very complex structure.

The x-ray diffraction and metallographic studies of positive electrodes taken from the phase-identification cells at various states of charge showed that, in addition to the electrolyte, the CoS_2 electrodes contained CoS_2 at full charge and Co plus Li_2S at full discharge. At intermediate states of charge, Co_3S_4 and Co_9S_8 were found. The NiS_2 electrodes contained NiS_2 at full charge and Ni plus Li_2S at full discharge. At intermediate states of charge, NiS, Ni_7S_6, and Ni_3S_2 were found. Thus, no ternary phases were detected in these electrodes; they contained Li_2S throughout their charge and either Co-S or Ni-S phases. The x-ray diffraction measurements did not rule out the possibility of small solubility effects between phases. For example, the NiS phase in the NiS_2 electrode may have been either $Ni_{1-x}S$ (19) or $Ni_{1-x}S$ containing a small amount of Li_2S (24); these materials have very similar crystallographic parameters.

The phase sequences for the CoS_2 and NiS_2 electrodes, which are derived from the above phase data, are compared in Fig. 5 with the phase sequence for

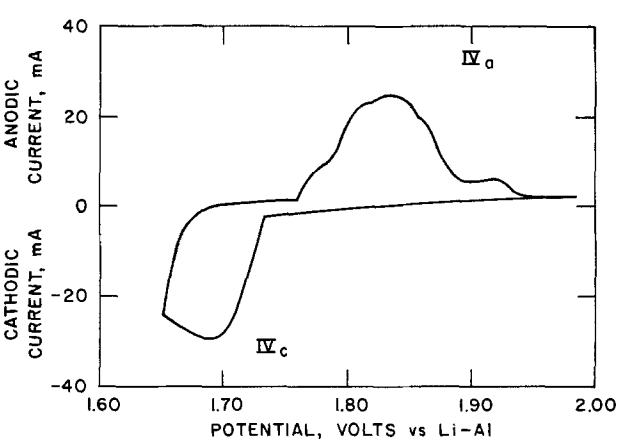

Fig. 4. Cyclic voltammogram of FeS_2, peak IV_a, at 400°C in LiCl-KCl eutectic electrolyte (sweep rate, 0.02 mV/sec).

$$FeS_2 \underset{IV_a}{\overset{IV_c}{\rightleftharpoons}} Li_3Fe_2S_4 \underset{III_a}{\overset{III_c}{\rightleftharpoons}} Li_{2.2}Fe_{0.8}S_2 \text{ and } Fe_{1-x}S \underset{II_a}{\overset{II_c}{\rightleftharpoons}} Li_2FeS_2 \underset{I_a}{\overset{I_c}{\rightleftharpoons}} Fe \text{ and } Li_2S$$

$$CoS_2 \underset{III'_a}{\overset{III'_c}{\rightleftharpoons}} Co_3S_4 \text{ and } Li_2S \underset{II'_a}{\overset{II'_c}{\rightleftharpoons}} Co_9S_8 \text{ and } Li_2S \underset{I'_a}{\overset{I'_c}{\rightleftharpoons}} Co \text{ and } Li_2S$$

$$NiS_2 \underset{IV''_a}{\overset{IV''_c}{\rightleftharpoons}} NiS \text{ and } Li_2S \underset{III''_a}{\overset{III''_c}{\rightleftharpoons}} Ni_7S_6 \text{ and } Li_2S \underset{II''_a}{\overset{II''_c}{\rightleftharpoons}} Ni_3S_2 \text{ and } Li_2S \underset{I''_a}{\overset{I''_c}{\rightleftharpoons}} Ni \text{ and } Li_2S$$

Fig. 5. Sequence of phases in FeS_2, CoS_2, and NiS_2 electrodes and associated voltammetry peaks from Fig. 1-3.

the FeS_2 electrode, which is taken from Ref. (21) (minor amounts of potassium-containing phases were omitted from the FeS_2 sequence). The connecting arrows in Fig. 5 indicate the occurrence of an electrode reaction, and each arrow is labeled with a voltammetry peak from Fig. 1-3. The labeling is quite straightforward because of the coulometric aspects of the low-sweep-rate voltammograms. However, no detailed reaction mechanism is implied by the labels; they serve merely to indicate the equilibrium phases associated with each voltammetry peak.

Note in Fig. 5 that Li_2S is present at all states of charge up to full charge in both the CoS_2 and NiS_2 electrodes, but appears in the FeS_2 electrode only during the $Li_2FeS_2 \rightleftarrows Fe + Li_2S$ reaction. Although Li_2S is not observed as a distinct phase in the other FeS_2 electrode reactions, its activity is substantial. For example, the Li_2S activity of Li_2FeS_2 is 0.86 from the $\Delta G°(400°C)$ for the chemical reaction: $Li_2S + FeS \rightarrow Li_2FeS_2$ (23). Therefore, it is appropriate to consider the possible competition between Li_2S reactions and those of FeS_2, CoS_2, and NiS_2.

Lithium sulfide voltammetry and sulfur losses from the disulfide electrodes.—Successive voltammograms for Li_2S, in the same type and size of housing as was used for the disulfide electrodes, are shown in Fig. 6 for a sweep rate of 0.05 mV/sec. There is a prominent cathodic peak at 1.74V and an anodic peak at 1.9-1.8V. The electrochemical reaction assigned by Birk and Steunenberg (9) to these peaks can be written as

$$2LiAl + Li_2S_2 \rightleftarrows 2Al + 2Li_2S \qquad [2]$$

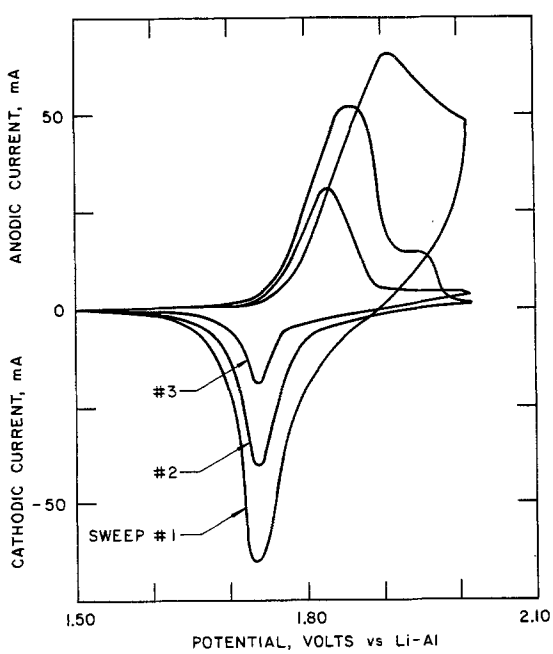

Fig. 6. Cyclic voltammograms of Li_2S (2 mmol) at 400°C in LiCl-KCl eutectic electrolyte (sweep rate, 0.05 mV/sec).

The successive voltammograms in Fig. 6 indicate a rapid loss of sulfur from the voltammetry electrode; 100% of the sulfur was lost in one day. With a sweep rate of 0.01 mV/sec, all the sulfur was lost in the first anodic sweep, and there were no peaks in subsequent cathodic and anodic sweeps. This effect, which could not be observed in the earlier study of Li_2S solutions (9), was readily detected in the present study because of the large volume of unsaturated electrolyte surrounding the voltammetry electrode. The dissolution of Li_2S in this electrolyte must have contributed to some extent to the sulfur loss; electrolyte saturation at 400°C requires about twice as much lithium sulfide as was present in the voltammetry electrode (25). However, the dissolution and transport of Li_2S are relatively slow processes. For example, FeS voltammetry electrodes, which are operated below the potential for reaction [2], retain their Li_2S for hundreds of hours at 400°C (23). [At 481°C, they lose about 12% of their sulfur per day *via* Li_2S dissolution (23).] Thus, the present study suggests that the formation of Li_2S_2 causes the rapid loss of sulfur shown in Fig. 6; this direct correlation between a specific charge product and sulfur losses was not possible in the earlier voltammetry study (9).

The FeS_2, CoS_2, and NiS_2 voltammetry electrodes lost sulfur like the Li_2S voltammetry electrode, but at a much lower rate. The sulfur losses were detected when successive voltammograms of the type shown in Fig. 1-3 were accummulated at a rate of about one cycle per day over a period of two to three weeks. In these voltammograms, the lower voltage peaks of each electrode had constant areas (and capacities), but the highest voltage peaks exhibited an approximately linear decrease in area (and capacity) with time. As the highest voltage peaks decreased, the FeS_2, CoS_2, and NiS_2 electrodes were gradually converted to FeS, Co_3S_4, and NiS electrodes, respectively. Thus, the transition metals were retained by the electrodes but their sulfur-to-metal ratios declined. The rates of decrease in the initial peak areas at a sweep rate of 0.02 mV/sec (about one cycle per day) were 2% per day for the FeS_2 peaks IV_a and IV_c (Fig. 1), 10% per day for the CoS_2 peaks III'_a and III'_c (Fig. 2), and 4.5% per day for the NiS_2 peaks IV''_a and IV''_c (Fig. 3). These rates are far lower than the 100% per day loss for the Li_2S electrode (Fig. 6). The flux of sulfur from each electrode was calculated from the above data. For FeS_2, CoS_2, NiS_2, and Li_2S, respectively, the sulfur fluxes were 0.005, 0.012, 0.014, and 0.5 $\mu g/cm^2/sec$. The effect of sweep rate was investigated for the CoS_2 electrode; the sulfur flux increased from 0.012 to 0.028 $\mu g/cm^2/sec$ when the sweep rate was increased from 0.02 mV/sec (about one cycle per day) to 0.1 mV/sec (about 5 cycles per day), indicating a strong dependence of the sulfur flux on cycling rate.

Note that the formation and discharge of FeS_2, CoS_2, and NiS_2 occur at approximately the same potential as the formation and discharge of Li_2S_2 (compare the highest voltage peaks in Fig. 1-3 with Fig. 6). Since Li_2S is present in the CoS_2 and NiS_2 electrodes during their formation from Co_3S_4 and NiS, respectively (see

Fig. 5), it is clear that the Li_2S reaction [2] must occur in competition with the formation of CoS_2 and NiS_2. This competing reaction may account for the sulfur flux from these electrodes being 2-3% of the flux from the Li_2S electrode. Lithium sulfide is not present as a distinct phase during the formation of FeS_2 from $Li_3Fe_2S_4$ (see Fig. 5), but it is still expected to have a substantial activity; an activity of 0.3 is estimated from thermodynamic data (13-17, 26, 27). Thus, reaction [2] also competes with the formation of FeS_2 and may account for the sulfur flux from this electrode being about 1% of the flux from the Li_2S electrode.

Equilibrium potentials and nucleation potentials.—The majority of the electrode reactions, which are indicated simply by arrows in Fig. 5, are given as a series of consecutive Li-Al/MS_2 cell reactions and their thermodynamic equilibrium potentials in Table I. The two Li-Al/FeS_2 cell potentials given in Table I were measured (23, 26, 27); no thermodynamic data were available for the two intermediate reactions in this cell, which are omitted from the table. The Li-Al/CoS_2 and Li-Al/NiS_2 cell potentials were computed from available thermodynamic data (13-17, 26).

The assignments of the voltammetry peaks in Fig. 5 are consistent with the equilibrium potentials in Table I since the anodic peaks are located at a higher potential and the cathodic peaks are located at a lower potential; this test is often used to check reaction assignments (23, 28, 29). Linear extrapolation of the peak's leading edge (left edge for anodic peaks; right edge for cathodic peaks in Fig. 1-3) to zero current gives an estimate of the potential at which a new phase begins to nucleate (29). For anodic peaks, this potential is called the anodic nucleation potential, V_{an}; for cathodic peaks, it is called the cathodic nucleation potential, V_{cn}. The differences between these nucleation potentials and the emf are attributed to nucleation overpotentials (29).

In Table II, the nucleation potentials obtained from the leading edges of the peaks in Fig. 1-3 are compared with the equilibrium potentials from Table I. The differences between V_{an} and V_{cn} are also given, with a larger difference implying a greater probability of the anodic and cathodic reaction mechanisms being different. In nearly every case, V_{cn} in Table II is slightly smaller than the emf and V_{an} is slightly larger. However, there are two reactions where V_{cn} is slightly larger than the emf; these emf's were calculated and could be in error. To determine if the leading edges of the voltammetry peaks coincided with an emf in the absence of nucleation overpotentials, the potential sweep range was narrowed to leave some of the electrode material unreacted. This unreacted material provided nucleation sites during the subsequent sweep. One example was shown in Fig. 4. In this test, traces of FeS_2 remained after peak IV_c, causing the leading edge of peak IV_a in Fig. 4 to be 75 mV closer to the emf (1.755V) than it was in Fig. 1.

Table I. Thermodynamic equilibrium potentials of Li-Al/MS_2 cell reactions at 400°C

Cell reaction	Emf (V)
$2FeS_2 + 3LiAl \rightleftarrows Li_3Fe_2S_4 + 3Al$	1.755[a]
$Li_2FeS_2 + 2LiAl \rightleftarrows Fe + 2Li_2S + 2Al$	1.334[b]
$3CoS_2 + 4LiAl \rightleftarrows Co_3S_4 + 2Li_2S + 4Al$	1.701
$3Co_3S_4 + 8LiAl \rightleftarrows Co_9S_8 + 4Li_2S + 8Al$	1.639
$Co_9S_8 + 16LiAl \rightleftarrows 9Co + 8Li_2S + 16Al$	1.372
$NiS_2 + 2LiAl \rightleftarrows NiS + Li_2S + 2Al$	1.741
$7NiS + 2LiAl \rightleftarrows Ni_7S_6 + Li_2S + 2Al$	1.586
$3Ni_7S_6 + 8LiAl \rightleftarrows 7Ni_3S_2 + 4Li_2S + 8Al$	1.552
$Ni_3S_2 + 4LiAl \rightleftarrows 3Ni + 2Li_2S + 4Al$	1.365

[a] Ref. (27).
[b] Ref. (23, 26).
[c] This potential is computed for formation of $Ni_{1-x}S$ from NiS_2 using data in Ref. (13). Between 1.741 and 1.586V the $Ni_{1-x}S$ is converted to NiS.

Table II. Equilibrium and nucleation potentials for electrode phases at 400°C

Electrode phases[a] (peaks)	V_{cn}[b] (V)	Emf[c] (V)	V_{an}[b] (V)	$V_{an} - V_{cn}$ (V)
$FeS_2 \rightleftarrows Li_3Fe_2S_4$ (IV)	1.744	1.755	1.845[d]	0.101
$Li_2FeS_2 \rightleftarrows Fe$ and Li_2S (I)	1.310	1.334	1.345	0.035
$CoS_2 \rightleftarrows Co_3S_4$ and Li_2S (III')	1.709	1.701	1.774	0.065
$Co_3S_4 \rightleftarrows Co_9S_8$ and Li_2S (II')	1.605	1.639	1.670	0.065
$Co_9S_8 \rightleftarrows Co$ and Li_2S (I')	1.317	1.372	1.378	0.061
$NiS_2 \rightleftarrows NiS$ and Li_2S (IV")	1.740	1.741	1.775	0.035
$NiS \rightleftarrows Ni_7S_6$ and Li_2S (III")	1.591	1.586	1.618	0.027
$Ni_7S_6 \rightleftarrows Ni_3S_2$ and Li_2S (II")	1.545	1.552	1.563	0.018
$Ni_3S_2 \rightleftarrows Ni$ and Li_2S (I")	1.358	1.365	1.368	0.010

[a] Phases and associated voltammetry peaks are from Fig. 5.
[b] From Fig. 1-3.
[c] From Table I.
[d] This value is for the major anodic peak IV_a. The value for the minor peak on its leading edge is 1.805V.

Other voltammograms which illustrate this shift effect for most of the electrode reactions are given in Fig. 7-9. In these voltammograms, the sweep rate was 0.05 or 0.1 mV/sec, which is higher than that used for Fig. 1-3 (0.02 mV/sec). However, the leading-edge potentials were insensitive to sweep rate up to at least 0.2 mV/sec. Four of the cathodic peaks in Fig. 7-9 are labeled to show how their leading edges shifted toward the emf between sweep No. 1 and sweep No. 2. In these instances, cathodic sweep No. 1 was preceded by a complete anodic sweep while sweep No. 2 was preceded by the truncated anodic sweep shown in Fig. 7-9. The other voltammetry peaks shown in Fig. 7-9 have leading edges closer to their emf's than in Fig. 1-3, but the shifts that occurred during successive sweeps are not shown. Generally, the leading edge of each anodic (or cathodic) peak shifted toward the emf after the trailing edge of its cathodic (or anodic) counterpart was clipped by the potential limit.

The voltammograms in Fig. 7-9 demonstrate the reversibility of the electrode reactions in the absence of nucleation overpotentials, and the equilibrium potentials can be estimated from the nearly coincident leading edges of the anodic and cathodic peaks. These estimated emf's are listed in Table III; the uncertainties are the small differences in the anodic and cathodic leading-edge potentials in Fig. 7-9. Where comparison is possible, the estimated emf's seem to be reasonably accurate. For example, the value of 1.365V, which is given for $Ni_3S_2 \rightleftarrows Ni$ plus Li_2S in Table III,

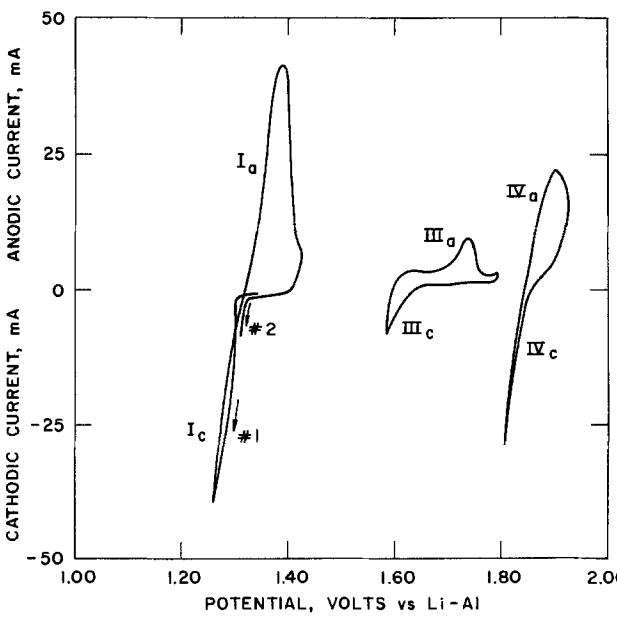

Fig. 7. Cyclic voltammograms of FeS_2 at 400°C in LiCl-KCl eutectic electrolyte (sweep rate, 0.05 mV/sec for peaks I and III; 0.1 mV/sec for peak IV).

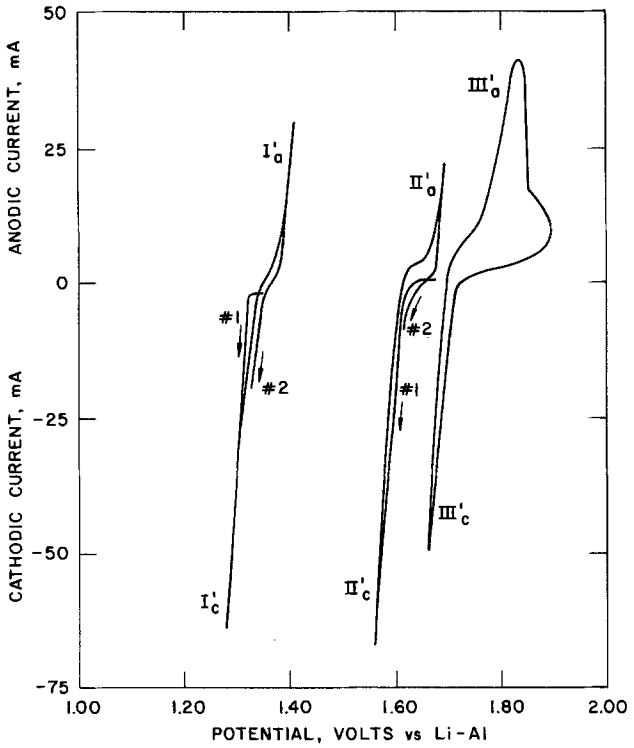

Fig. 8. Cyclic voltammograms of CoS_2 at 400°C in LiCl-KCl eutectic electrolyte (sweep rate, 0.1 mV/sec).

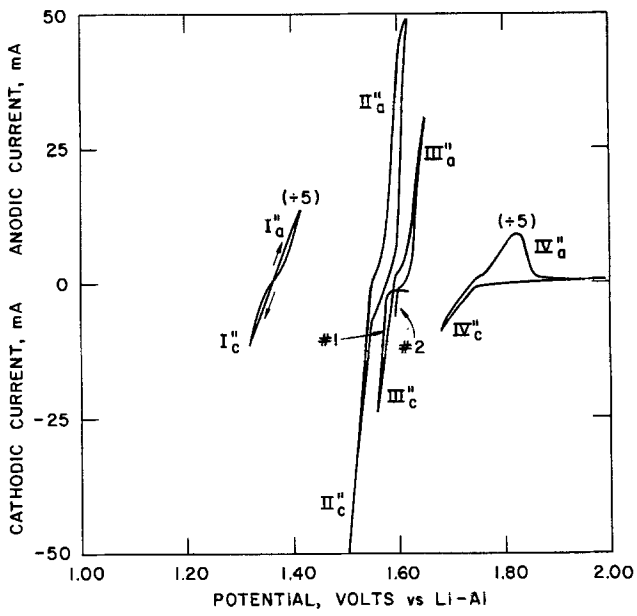

Fig. 9. Cyclic voltammograms of NiS_2 at 400°C in LiCl-KCl eutectic electrolyte (sweep rate, 0.1 mV/sec).

is in excellent agreement with recently reported (30) emf measurements (1.3649V). The other estimated emf's in Table III are generally in good agreement with the values shown in Table I. For calculating nucleation overpotentials, we prefer the estimated emf's of Table III since they are obtained in the same way as the nucleation potentials of Table II.

The anodic nucleation overpotential

$$\eta_{an} = V_{an} - \text{emf} \qquad [3]$$

and the cathodic nucleation overpotential

$$\eta_{cn} = \text{emf} - V_{cn} \qquad [4]$$

were derived from the estimated emf's in Table III and the nucleation potentials in Table II and are also listed

Table III. Equilibrium potentials and nucleation overpotentials at 400°C from cyclic voltammograms

Electrode phases[a] (peaks)	Emf[b] (mV)	η_{cn}[c] (mV)	η_{an}[d] (mV)
$FeS_2 \rightleftarrows Li_2Fe_2S_4$ (IV)	1750 ± 5	6	95[e]
$Li_2Fe_2S_4 \rightleftarrows Li_{2-2x}Fe_{0.8}S_2$ and $Fe_{1-x}S$ (III)	1660 ± 10	~30	~50
$Li_2FeS_2 \rightleftarrows Fe$ and Li_2S (I)	1328 ± 5	18	17
$CoS_2 \rightleftarrows Co_9S_8$ and Li_2S (III')	1718 ± 5	9	56[e]
$Co_3S_4 \rightleftarrows Co_9S_8$ and Li_2S (II')	1620 ± 5	15	50
$Co_9S_8 \rightleftarrows Co$ and Li_2S (I')	1373 ± 5	56	5
$NiS_2 \rightleftarrows NiS$ and Li_2S (IV")	1748 ± 5	8	27[e]
$NiS \rightleftarrows Ni_7S_6$ and Li_2S (III")	1605 ± 5	14	13
$Ni_7S_6 \rightleftarrows Ni_3S_2$ and Li_2S (II")	1559 ± 5	14	4
$Ni_3S_2 \rightleftarrows Ni$ and Li_2S (I")	1365 ± 2	7	3

[a] Phases from Fig. 5 (voltammetry peaks from Fig. 7-9).
[b] Estimated from Fig. 7-9.
[c] Cathodic nucleation overpotential (emf-V_{cn}).
[d] Anodic nucleation overpotential (V_{an}-emf).
[e] These are lower limits; nonequilibrium species have been detected (see text).

in Table III. Note that the anodic nucleation overpotentials increase with state of charge for each electrode. Vermilyea (31), in his review of anodic film formation on metal substrates, has noted this general trend for other electrodes. For example, the formation of PbO from Pb requires a nucleation overpotential of 10 mV while the formation of PbO_2 from PbO requires a nucleation overpotential of 300 mV (31). The cathodic nucleation overpotentials in Table III do not display a similar systematic trend. However, there is an interesting trend in the ratio of anodic to anodic-plus-cathodic overpotentials. As shown in Fig. 10, the anodic fraction of the total nucleation overpotential increases in a similar manner with emf for all three electrodes. Unfortunately, the scatter in these data is large (the error bars in Fig. 10 result from the uncertainties in the estimated emf's in Table III). Nevertheless, the data suggest that the overpotential ratios are controlled by some process common to all three electrode materials.

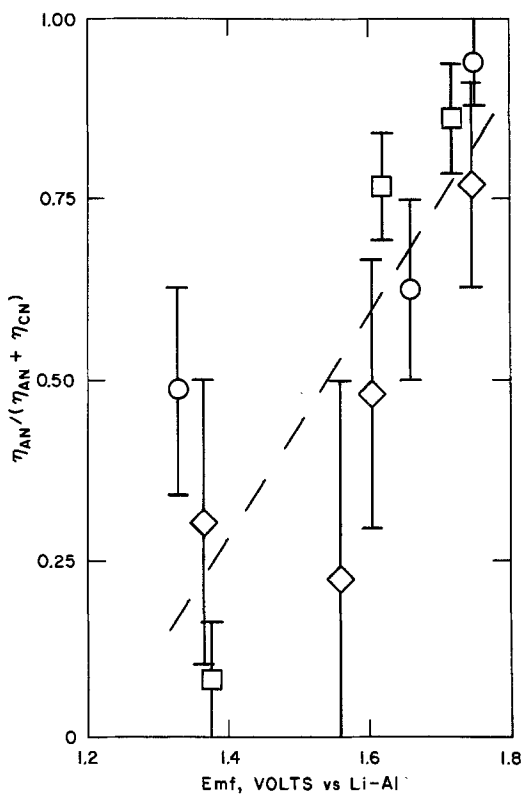

Fig. 10. Ratio of anodic to total nucleation overpotential for FeS_2 (○), CoS_2 (□), and NiS_2 (◇) reactions. The dashed line is included to indicate the apparent trend in the data.

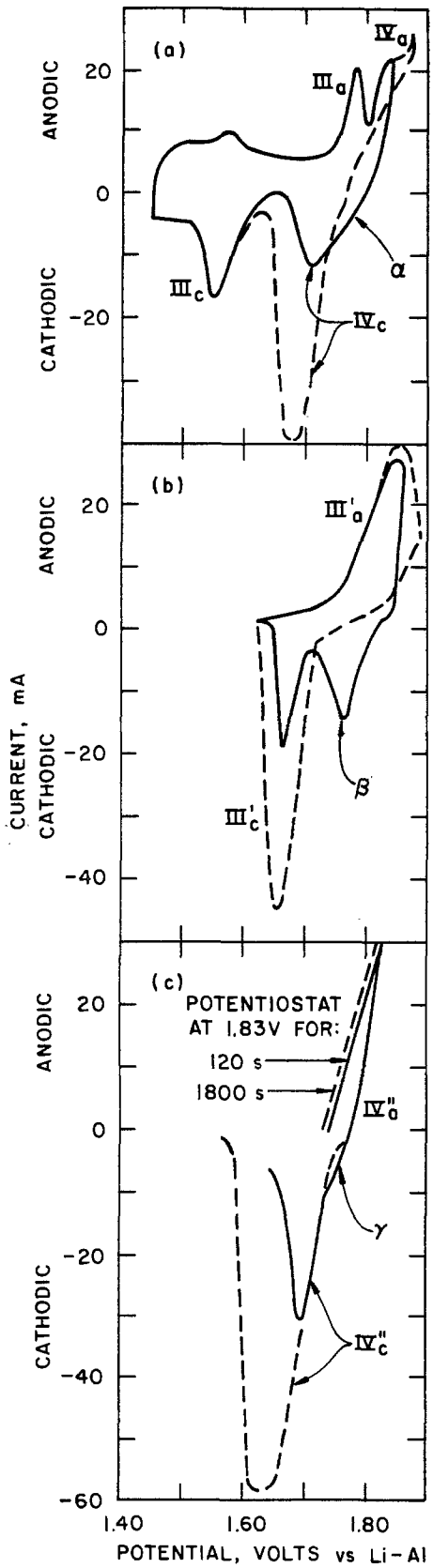

Fig. 11. Detection of nonequilibrium species α, β, and γ, associated with (a) FeS_2 peak IV_a, (b) CoS_2 peak III'_a, and (c) NiS_2 peak IV''_a (sweep rate, 0.1 mV/sec). Note that increased anodic sweep potential, which is equivalent to increased time, eliminates α- and β-peaks in (a) and (b), respectively, while increased time at 1.83V eliminates γ-peak in (c).

Peak assignments and nonequilibrium species.—There are three peaks in Fig. 1-3 that are not adequately described by the reactions in Table I; nonequilibrium species are detected along the leading edge of the highest voltage anodic peak of each electrode. As indicated in Fig. 11, the nonequilibrium species are detected cathodically after sweeping into the leading edge of the anodic peaks. The results are clearest for the CoS_2 electrode, where a distinct cathodic peak, β, precedes peak III'_c. With the FeS_2 and NiS_2 electrodes, the nonequilibrium species, α and γ, respectively, are detected as slight distortions of the leading edges of cathodic peaks IV_c and IV''_c. Note that the β peak in Fig. 11(b) is located at the same voltage and has the same shape as the Li_2S_2 cathodic peak in Fig. 6. Thus, the β-peak is probably due to reduction of Li_2S_2. The smaller α- and γ-peaks may also be due to reduction of Li_2S_2 since this species should form in the FeS_2 and NiS_2 electrodes (see section on Lithium sulfide voltammetry). Because nonequilibrium species are associated with the leading edges of peaks IV_a (FeS_2), III'_a (CoS_2), and IV''_a (NiS_2) in Fig. 1-3, the η_{an} values given in Table III for these peaks may be low.

For the other peaks in Fig. 1-3, nonequilibrium species were not detected at sweep rates up to 0.1 mV/sec. Consequently, the equilibrium phases in Fig. 5 and the cell reactions in Table I give a reasonably complete description of these low-sweep-rate peaks.

Effects of higher sweep rates.—Voltammograms for sweep rates of up to 1 mV/sec are shown in Fig. 12-14 for FeS_2, CoS_2, and NiS_2, respectively. There is little to be gained by further increasing the rate. The peaks already overlap to a significant extent at the higher rates shown in each figure because the width of the peaks increases with the scan rate. This peak broadening is due primarily to the resistive nature of the electrodes; the peak widths, currents, and potentials in Fig. 12-14 all tend to be proportional to the square root of the scan rate, which is the expected behavior under ohmic control (23, 32).

Another cause of peak broadening is evident in Fig. 12-14. The peaks in Fig. 12 (FeS_2) exhibit a more complex structure as the scan rate increases, suggesting the presence of additional reactions. The peaks in Fig. 13 (CoS_2) are less complex than those in Fig. 12 (FeS_2), but peak I'_a of Fig. 13 does exhibit a detectable bowing along its trailing edge at 0.5 mV/sec, which suggests the presence of an additional reaction. Likewise, the trailing edges of peaks I''_a and II''_c in Fig. 14 (NiS_2) show more structure as the scan rate increases, which again suggests the presence of additional reactions at the higher rates. The central anodic and cathodic peaks (II" and III") in Fig. 14 increase

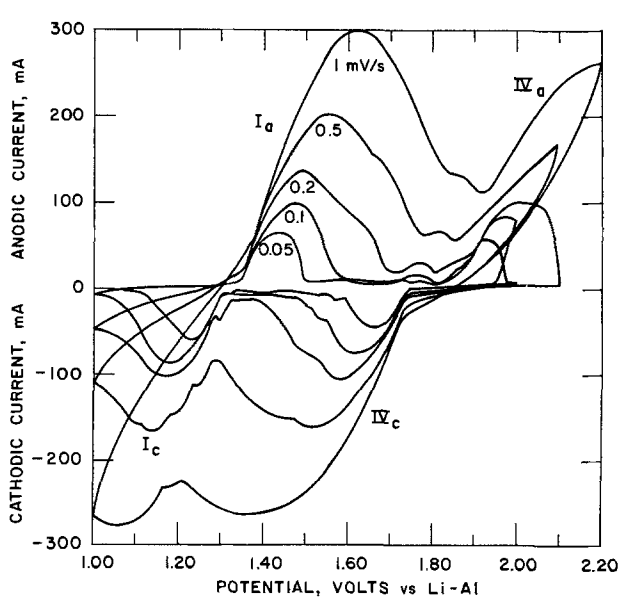

Fig. 12. Cyclic voltammograms of FeS_2 at 400°C in LiCl-KCl eutectic electrolyte at sweep rates of 0.05, 0.1, 0.2, 0.5, and 1 mV/sec.

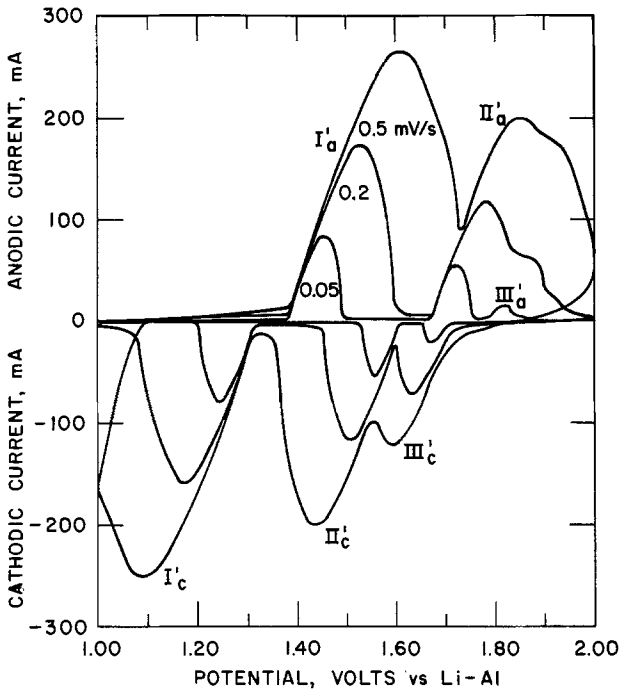

Fig. 13. Cyclic voltammograms of CoS_2 at 400°C in LiCl-KCl eutectic electrolyte at sweep rates of 0.05, 0.2, and 0.5 mV/sec.

in height, not as the square root of the scan rate, $\nu^{0.5}$, but as $\nu^{0.7}$. This unusual behavior may reflect the occurrence of additional reactions, or it may be due to peak overlap since the neighboring peaks (I″ and IV″) are large. Thus, we are unable to make unequivocal reaction assignments at sweep rates above 0.1 mV/sec; each peak may well contain several reactions at the higher sweep rates.

Plots of the peak currents *vs.* peak potentials for each major voltammetry peak (ignoring any fine structure) are shown in Fig. 15. Where the data are linear, slopes are given in ohms (actually Ω-cm², since the electrode area is 1 cm²). If no slope is given, the data are nonlinear. Note that data points are given at zero current on each horizontal axis in Fig. 15 (a), (b), and (c). These are the leading-edge or nucleation potentials of each peak (from Table II) where the reactions may go to completion at an extremely low sweep rate,

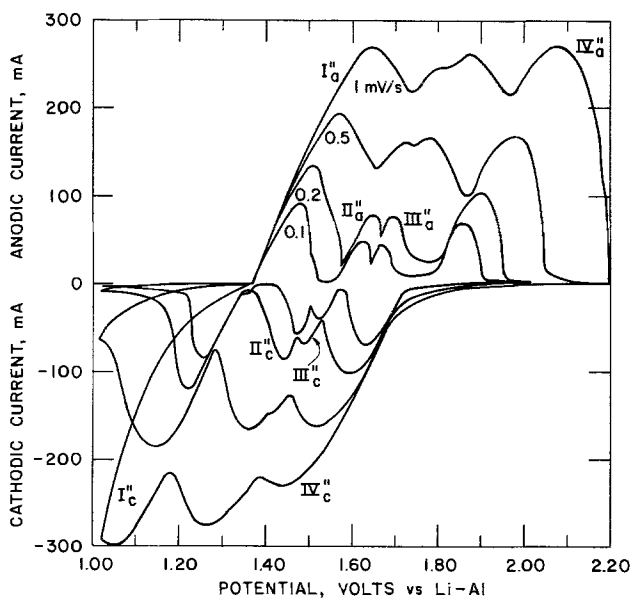

Fig. 14. Cyclic voltammograms of NiS_2 at 400°C in LiCl-KCl eutectic electrolyte at sweep rates of 0.05, 0.1, 0.2, 0.5, and 1 mV/sec.

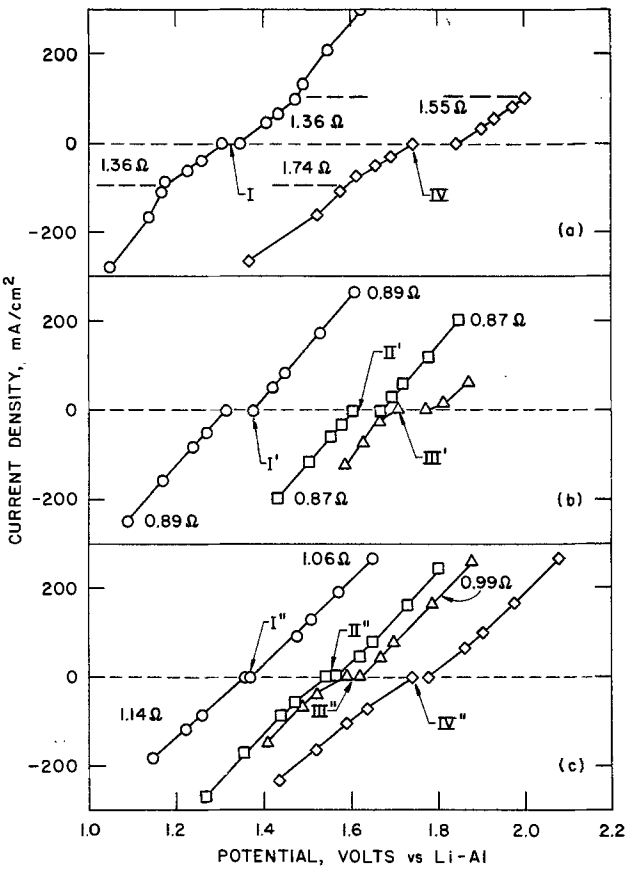

Fig. 15. Peak current *vs.* peak potentail from cyclic voltammograms in Fig. 1-3 and 12-14 for (a) FeS_2, (b) CoS_2, and (c) NiS_2. Polarization slopes are given for linear data, and Roman numerals show locations of equilibrium potentials from Table III.

at least in principle. Also indicated on each horizontal axis are the locations of the emf's which are taken from Table III.

The polarization slopes in Fig. 15 are seen to be significantly larger for the FeS_2 electrode reactions, indicating poorer electronic conduction. There is also a sudden onset of curvature in the FeS_2 data above a peak current density of 100 mA/cm², which corresponds to a sweep rate of 0.1 mV/sec. Above this sweep rate, each major peak has more than one component (see Fig. 12), and only the coordinates of the highest current components are plotted in Fig. 15(a). A weighted average of the coordinates of all the components of these peaks would probably continue along the linear polarization curves.

The CoS_2 polarization data in Fig. 15(b) are quite linear for reactions I′ and II′, while for reaction III′ there is significant curvature. This curvature may be caused by increasing amounts of the nonequilibrium species associated with the β-peak [see Fig. 11(b)].

The NiS_2 polarization data in Fig. 15(c) are linear for three of the peaks, but show various degrees of nonlinearity for the other peaks. In the case of reaction IV″ the nonlinearity may be caused by increasing amounts of the nonequilibrium species associated with the γ-peak [see Fig. 11(c)]. The nonlinearities in reactions II″ and III″ may be due to increasingly complex reactions, or, as discussed previously, to peak distortions caused by the neighboring I″ and IV″ peaks.

Effects of variation in electrolyte composition.—We have examined the effects of varying the electrolyte composition at 400C over the range 55-61 m/o LiCl (the eutectic is 58 m/o LiCl). A cyclic voltammogram for FeS_2 in the presence of eutectic electrolyte was shown in Fig. 4 and is repeated in Fig. 16 for comparison with the voltammograms using LiCl-rich electrolyte (61 m/o LiCl) and KCl-rich electrolyte (55

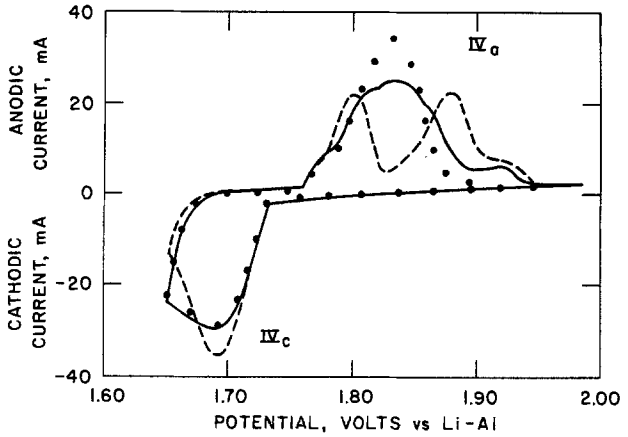

Fig. 16. Cyclic voltammograms of FeS_2, peak IV_a, at 400°C in three LiCl-KCl electrolytes (sweep rate, 0.02 mV/sec). Eutectic electrolyte: 58 m/o LiCl ———; LiCl-rich electrolyte: 61 m/o LiCl ● ● ●; KCl-rich electrolyte: 55 m/o LiCl – – –.

m/o LiCl). These voltammograms show that peak IV_c, which is the cathodic reaction

$$2FeS_2 + 3LiAl \rightarrow Li_3Fe_2S_4 + 3Al \quad [5]$$

is unaffected by the change in electrolyte composition, but peak IV_a displays a very complex structure. In LiCl-rich electrolyte this anodic peak is the reverse of reaction [5], or

$$Li_3Fe_2S_4 + 3Al \rightarrow 2FeS_2 + 3LiAl \quad [6]$$

However, the anodic peak splits into two distinct components in KCl-rich electrolyte. Since $KFeS_2$ has been identified as the intermediate phase (21), we assume that the two anodic components in the presence of KCl-rich electrolyte are

$$Li_3Fe_2S_4 + Al + 2KCl \rightarrow 2KFeS_2 + LiAl + 2LiCl \quad [7]$$

and

$$KFeS_2 + Al + LiCl \rightarrow FeS_2 + LiAl + KCl \quad [8]$$

If the potentials of reactions [6]-[8] are presumed to be identical in the LiCl-rich electrolyte, the difference between the potentials of [7] and [8] in KCl-rich electrolyte is given by

$$\Delta E = \frac{3RT}{F} \ln \frac{a_{LiCl}(\text{LiCl rich}) \cdot a_{KCl}(\text{KCl rich})}{a_{LiCl}(\text{KCl rich}) \cdot a_{KCl}(\text{LiCl rich})} \quad [9]$$

Using the known activities of LiCl and KCl (33), this equation yields a ΔE of 93 mV. The peak potentials of the two anodic components are separated by about 80 mV in the presence of the KCl-rich electrolyte (see Fig. 16), which is in reasonable agreement with the calculated value. The calculated ΔE in eutectic electrolyte is only 46 mV. Thus, the complex structure of peak IV_a in eutectic electrolyte can be explained as a combination of the closely spaced reactions [6], [7], and [8].

The voltammograms of CoS_2 and NiS_2 in the KCl-rich and LiCl-rich electrolytes were identical to those in Fig. 2 and 3, respectively. This suggests that potassium-containing phases are not present in these electrodes, at least over the narrow range of LiCl concentrations employed in this study (55-61 m/o).

Conclusions

The electrochemistry of the FeS_2 electrode is more complex than that of the CoS_2 and NiS_2 electrodes. Nevertheless, the three electrodes have quite similar properties. For example, they all tend to lose sulfur during extended cycling tests, and a nonequilibrium species is involved in the electrochemical formation of the three disulfides from their precursors. All three electrodes exhibit similar trends in their nucleation overpotentials; the anodic nucleation overpotentials increase with emf in each system.

With its comparatively small nucleation overpotentials and relatively simple polarization characteristics, the NiS_2 electrode is superior to FeS_2 and CoS_2, but it remains an extremely complex electrode because of its multiple reactions. The FeS_2 electrode exhibited a lower rate of sulfur loss than CoS_2 and NiS_2, and this may be a more important consideration than the differences in polarization characteristics.

The major problem to be solved in the development of Li-Al/MS_2 cells is elimination of their tendency to lose high-voltage capacity during extended cycling because of the sulfur losses from the positive electrode. This problem is under continuing investigation at General Motors Research Laboratories (34) and Argonne National Laboratory (35).

Acknowledgments

This work was conducted under the auspices of the U.S. Department of Energy. The metallographic analyses were conducted by A. E. Martin and N. C. Otto. The x-ray diffraction analyses were provided by B. S. Tani.

Manuscript submitted May 11, 1982; revised manuscript received Sept. 9, 1982. This was Paper 337 presented at the Pittsburgh, Pennsylvania, Meeting of the Society, Oct. 15-20, 1978.

Any discussion of this paper will appear in a Discussion Section to be published in the December 1983 JOURNAL. All discussions for the December 1983 Discussion Section should be submitted by Aug. 1, 1983.

Publication costs of this article were assisted by Argonne National Laboratory.

REFERENCES

1. E. C. Gay, W. E. Miller, R. F. Malecha, and R. C. Elliott, Proc. 13th IECEC, pp. 690-696, Society of Automotive Engineers, Inc., Warrendale, PA (1978).
2. D. R. Vissers, Z. Tomczuk, and R. K. Steunenberg, *This Journal*, **121**, 665 (1974).
3. L. A. Heredy, S. C. Lai, L. R. McCoy, and R. C. Saunders, in "New Uses of Sulfur," J. R. West, Editor, pp. 203-215, Advances in Chemistry Series 140, American Chemical Society, Washington, DC (1975).
4. E. C. Gay, D. R. Vissers, F. J. Martino, and K. E. Anderson, *This Journal*, **123**, 1591 (1976).
5. E. J. Zeitner, Jr., and J. S. Dunning, Proc. 13th IECEC, pp. 697-701, Society of Automotive Engineers, Inc., Warrendale, PA (1978).
6. F. J. Martino, T. D. Kaun, H. Shimotake, and E. C. Gay, Proc. 13th IECEC, pp. 709-716, Society of Automotive Engineers, Inc., Warrendale, PA (1978).
7. J. E. Battles, F. C. Mrazek, and N. C. Otto, "Post-Test Examinations of Li-Al/FeS_x Secondary Cells," Argonne National Laboratory Report No. ANL-80-130 (December 1980).
8. J. E. Battles, "Failure Mechanisms," in Argonne National Laboratory Report ANL-79-94 (March 1980), p. 100.
9. J. R. Birk and R. K. Steunenberg, in "New Uses of Sulfur," J. R. West, Editor, pp. 186-202, Advances in Chemistry Series 140, American Chemical Society, Washington, DC (1975).
10. Z. Tomczuk, K. E. Anderson, D. R. Vissers, and M. F. Roche, *This Journal*, **127**, 1881 (1980).
11. W. J. Walsh, C. C. McPheeters, N. P. Yao, and K. Koura, U.S. Pat. 3,992,222 (1976).
12. R. K. Steunenberg, Z. Tomczuk, and A. E. Martin, U.S. Pat. 3,941,612 (1976).
13. P. H. Ribbe. Editor, "Sulfide Mineralogy," Southern Printing Co., VA (1974).
14. K. C. Mills, "Thermodynamic Data for Inorganic Sulfides, Selenides. and Tellurides," Butterworth and Co., London (1974).
15. D. R. Stull and H. Prophet. "JANAF Thermochemical Tables," NSRDS-NBS-37 (1971).
16. R. Hultgren, P. D. Desai, D. T. Hawkins, M. Gleiser,

and K. K. Kelley, "Selected Values of the Thermodynamic Properties of the Elements," American Society of Metals, Metals Park, OH (1973).
17. C. J. Wen, B. A. Boukamp, and R. A. Huggins, *This Journal*, **126**, 2258 (1979).
18. M. Hansen and K. Anderko, "Constitution of Binary Alloys," McGraw-Hill Book Co., New York (1958).
19. R. P. Elliot, "Constitution of Binary Alloys, First Supplement," McGraw-Hill Book Co., New York (1965).
20. R. A. Sharma, *This Journal*, **123**, 448 (1976).
21. Z. Tomczuk, B. Tani, N. C. Otto, M. F. Roche, and D. R. Vissers, *ibid.*, **129**, 925 (1982).
22. F. C. Mrazek and J. E. Battles, *ibid.*, **124**, 1556 (1977).
23. Z. Tomczuk, S. K. Preto, and M. F. Roche, *ibid.*, **128**, 760 (1981).
24. M. Laffitte and J. Rey, *J. Phys. Chem. Solids*, **27**, 277 (1966).
25. M. L. Saboungi, J. J. Marr, and M. Blander, *This Journal*, **124**, 1060 (1978).
26. Z. Tomczuk, M. F. Roche, and D. R. Vissers, *ibid.*, **128**, 2255 (1981).
27. P. A. Nelson *et al.*, "High-Performance Batteries for Stationary Energy Storage and Electric-Vehicle Propulsion, Progress Report for the Period October-December 1976," Argonne National Laboratory Report No. ANL-77-17 (April 1977).
28. D. D. MacDonald and B. Roberts, *Electrochim. Acta*, **23**, 781 (1978).
29. D. E. Williams and G. A. Wright, *ibid.*, **21**, 1009 (1976).
30. L. Redey and D. R. Vissers, *This Journal*, **128**, 2703 (1981).
31. D. A. Vermilyea, in "Advances in Electrochemistry and Electrochemical Engineering," P. Delahay, Editor, Interscience, New York (1963).
32. A. J. Calandra, N. R. deTacconi, R. Pereiro, and A. J. Arvia, *Electrochim. Acta*, **19**, 901 (1974).
33. J. Lumsden, "Thermodynamics of Molten Salt Mixtures," Academic Press, New York (1966).
34. R. N. Seefurth and J. S. Dunning, "General Motors Research Laboratories," in Argonne National Laboratory Report ANL-81-65 (February 1982) p. 89.
35. D. M. Warin and Z. Tomczuk, "FeS_2 Electrode Development," *ibid.*, p. 18.

Mixed Mn,Na-Sulfate Reactions in Low Temperature Hot Corrosion

R. L. Jones*

Chemistry Division, Naval Research Laboratory, Washington, D.C. 20375

ABSTRACT

The formation and low temperature hot corrosion (LTHC) effects of Mn,Na mixed sulfates (eutectic mp 645°C) at 725°C were studied. Mixed sulfate formation by reaction of 50 mol percent Mn_2O_3-Na_2SO_4 (simulating Mn oxide-Na_2SO_4 gas turbine deposits) with equilibrated SO_3-SO_2 in air was slow compared to Co,Na or Ni,Na sulfate formation, but molten sulfates were produced within 100 hr under as little as 160 ppm SO_3 (350 ppm total SO_x). Rapid LTHC resulted when molten Mn,Na sulfates were formed on Nickel 200, Rene 80, or CoCrAlY blade coating alloy. Evidence was obtained for Co,Mn,Na and Ni,Mn,Na ternary sulfate formation, along with indication that Mn oxide contaminants might induce or increase LTHC in Ni or Ni-base alloys, but not necessarily affect LTHC of cobalt-containing alloys.

A low temperature mode of hot corrosion (LTHC) where severe corrosion can occur at blade temperatures of only 600°-750°C has been identified in marine gas turbines (1). This corrosion is caused principally by molten Co,Na mixed sulfates (eutectic mp 575°C) that form by reaction of engine gas SO_3 with cobalt oxide-Na_2SO_4 deposits on the blade surface (1-4). Molten Ni,Na or ternary Co,Ni,Na sulfates may be involved as well (1, 5).

Other oxides may occur on turbine blades, however, which also yield low melting mixed sulfates and thus could affect LTHC. One such oxide is manganese oxide (Mn_2O_3). Significant amounts of a water-soluble Mn species have been detected in the sulfate salt remaining on the surface of prototype Navy blade alloys, which contain small ($< 1\%$) percentages of manganese, after low temperature (704°C) burner rig testing (6). This Mn species is most likely a mixed sulfate from the $MnSO_4$-Na_2SO_4 system (eutectic mp 645°C) (7), and the question is raised as to whether such Mn,Na sulfates might reduce the LTHC performance of the prototype alloys.

The experiments described below were undertaken to determine the SO_3 partial pressure required for molten $MnSO_4$-Na_2SO_4 formation and to assess the corrosion effects that molten Mn,Na sulfates might have if formed. The results should be relevant also to those cases where manganese is used in smoke suppressant additives for gas turbine fuels, since this may produce deposits of manganese oxide on the turbine blade surfaces.

* Electrochemical Society Active Member.
Key words: coatings, fused salts, sulfidation.

Experimental

The general procedures and experimental apparatus have been described previously (4, 5). Controlled concentrations of SO_2 or equilibrated SO_3-SO_2 in air were passed over the test specimens contained in porcelain boats in a quartz-lined, catalytically inert constant temperature zone furnace, with the exhaust air analyzed for SO_2 and SO_3 concentrations. All experiments were run at 725° ± 5°C. The gas concentrations ranged from 200 to 1000 ppm (2×10^{-4} to 1×10^{-3} atm) SO_x, where $SO_x = SO_2 + SO_3$, and were controlled to ± 10% as verified by the gas analysis. An air flow rate of 200 ml/min was used.

Two principal types of experiments were run: (*i*) "$MnSO_4$-Na_2SO_4 formation" experiments to determine the sulfation kinetics and $MnSO_4$-Na_2SO_4 compositions obtained, and (*ii*) "$MnSO_4$-Na_2SO_4 corrosion" experiments where the corrosion effects produced by the generation of molten mixed $MnSO_4$-Na_2SO_4 on different metals were analyzed. For (*i*), 250 ± 3 mg mixtures of 50 mol percent (m/o) MnO_2-Na_2SO_4 were spread evenly in porcelain boats (Coors 6A, 97 × 16 × 10 mm OD) and exposed to different concentrations of SO_3-SO_2 or SO_2 at 725°C with periodic weighing. For (*ii*), small deposits of 50 m/o MnO_2-Na_2SO_4 (~ 0.5 mm thickness and 2 mm diam) were placed on Nickel 200, Rene 80, or CoCrAlY blade coating specimens and exposed under the same conditions as (*i*) with periodic inspection to determine when the deposit became molten and the extent of apparent corrosion.

Reagent grade chemicals and anhydrous SO_2 (Matheson 99.98%) were used in all experiments. Because it could be obtained in high purity (Puritronic grade,

Johnson Matthey Chemicals), MnO_2 was used in preparing the Mn oxide-Na_2SO_4 mixtures. However, our x-ray diffraction analysis revealed that MnO_2 is quickly converted to Mn_2O_3 on heating in air at 725°C with a corresponding 9% loss in weight. The weight gain readings were corrected therefore to account for this reaction.

The composition of the CoCrAlY coating was 20.9Cr, 12.9Al, 0.32Y, and balance Co weight percent (w/o) according to the supplier. D-C argon plasma atomic emission analysis indicate the Nickel 200 to be 98.85Ni, 0.33Zn, 0.31Mn, 0.25Fe, 0.08Co, 0.05Cr, and 0.01Cu, (w/o). The Rene 80 was not analyzed, but should be near alloy specifications, *i.e.*, 14Cr, 9.5Co, 5.0Ti, 4.0 Mo, 4.0W, 3.0Al, 0.17C, 0.03Zr, 0.015B, balance Ni (w/o). The metal specimens were washed with hot water and detergent and rinsed with methanol before use. The corrosion specimens were mounted in epoxy without rinsing and dry polished to prevent loss of water soluble salts from the corrosion surface. A specimen tilt angle of 20° was used in the scanning electron microscopy/energy dispersive x-ray analysis (SEM/EDXA) examinations, with palladium rather than gold (to avoid possible Au interference with the sulfur x-ray peak) being used for the anti-charging coating.

Results and Discussion

Mixed $MnSO_4$-Na_2SO_4 formation.—The formation is considered to proceed with MnO_2 first rapidly converted to Mn_2O_3 at temperature

$$2MnO_2 \rightarrow Mn_2O_3 + 1/2\ O_2 \qquad [1]$$

and Mn_2O_3 then sulfated by the reaction

$$Mn_2O_3 + 2SO_3 \leftrightarrows 2MnSO_4 + 1/2\ O_2 \qquad [2]$$

As $MnSO_4$ is generated, it is taken into solution (solid solution initially and then liquid solution) by Na_2SO_4

$$MnSO_4 + Na_2SO_4 \leftrightarrows MnSO_4\text{-}Na_2SO_4 \qquad [3]$$

Since the Mn_2O_3-SO_3-$MnSO_4$-Na_2SO_4 system is bivariant, some equilibrium concentration of $MnSO_4$ in Na_2SO_4 will be formed for each SO_3 concentration, even for sub-ppm levels of SO_3. This is in contrast to the univariant Mn_2O_3-SO_3-$MnSO_4$ system, where for a given temperature, no $MnSO_4$ will form until the "decomposition" SO_3 partial pressure is exceeded, and then there will be complete conversion to $MnSO_4$. Complete sulfation of 250 mg of 50 m/o Mn_2O_3-Na_2SO_4 via reactions [1]-[3] produces a 79 mg weight gain. By noting the weight gain, it is possible to calculate the mol percent of $MnSO_4$ formed at any time.

Figure 1 shows representative weight gain behavior under different sulfur oxide concentrations. Except for the 1000 ppm SO_2 run, the tests were made with a platinum catalyst upstream in the 725°C zone of the furnace, and thus with essentially equilibrated SO_2-SO_3 (within ± 10%). This was confirmed by comparing the analyzed SO_3/SO_2 ratios with the 0.84 theoretical SO_3-SO_2 ratio for SO_2-SO_3 in air (0.21 atm O_2) at 725°C (8). The weight gains for 225 ppm SO_3 (500 ppm SO_x) and 160 ppm SO_3 (350 ppm SO_x) are substantially higher than for 1000 ppm SO_2, indicating that SO_3 is critical in the formation of $MnSO_4$-Na_2SO_4. This is similar to earlier results, where SO_3 was shown to be critical in $CoSO_4$- and $NiSO_4$-Na_2SO_4 formation (4, 5).

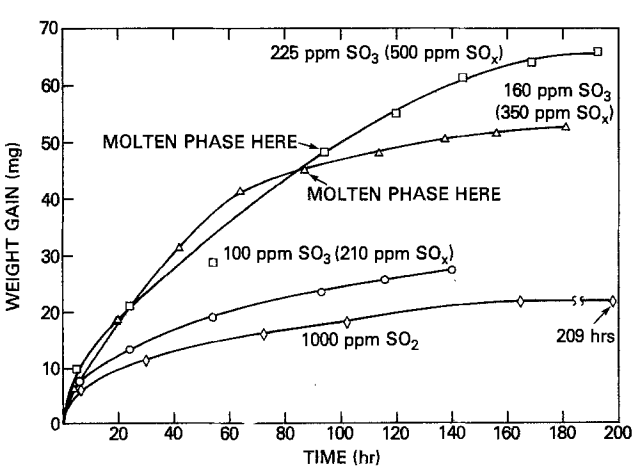

Fig. 1. Weight gain for 50 m/o Mn_2O_3-Na_2SO_4 (250 mg specimens) exposed under SO_2 or equilibrated SO_3-SO_2 in air at 725°C.

The sulfate phases in Fig. 1 began to become partially molten after weight gain of ~ 45 mg, which corresponds to formation of 36 m/o $MnSO_4$ in Na_2SO_4. The only $MnSO_4$-Na_2SO_4 phase diagram available (Fig. 2) indicates the sulfate to be completely molten at 725°C at ≧ 42 m/o $MnSO_4$, but does not show the lower boundary of the concentration region where solid solution and liquid $MnSO_4$-Na_2SO_4 exist simultaneously. Our findings suggest this boundary should be at ~ 36 m/o $MnSO_4$, giving the region a breadth of about 6 m/o which is close to the breadth of the equivalent regions shown in the $NiSO_4$-Na_2SO_4 (9) and $CoSO_4$-Na_2SO_4 (10) diagrams. There is good agreement therefore between the $MnSO_4$-Na_2SO_4 phase diagram and the mixed $MnSO_4$-Na_2SO_4 formation reactions depicted in Fig. 1.

X-ray diffraction was applied to the deposits produced by the 225 ppm SO_3, 160 ppm SO_3, and 1000 ppm SO_2 runs in Fig. 1 to identify the mixed sulfates formed. X-ray diffraction was applied also to a fourth "calibration" specimen consisting of 250 mg of 50 m/o $MnSO_4$-Na_2SO_4 which was heated for 7 hr at 725°C under 1000 ppm SO_2, and then quenched and ground just the same as the Fig. 1 deposits. The resulting patterns were poor, with only 7-8 peaks detected (Table I). However, the patterns were the same for the three deposits from Fig. 1 and the calibration specimen and appeared to be derived from the high temperature $Na_2Mn(SO_4)_2$ pattern, although many lines were missing or had incorrect relative intensities. The deposits produced in Fig. 1 are therefore indicated to be mixed sulfates and at least partially $Na_2Mn(SO_4)_2$, although the x-ray identification was not as good as would be desired.

Although $MnSO_4$-Na_2SO_4 is formed under "pure" 1000 ppm SO_2 in air in Fig. 1, the actual reaction prob-

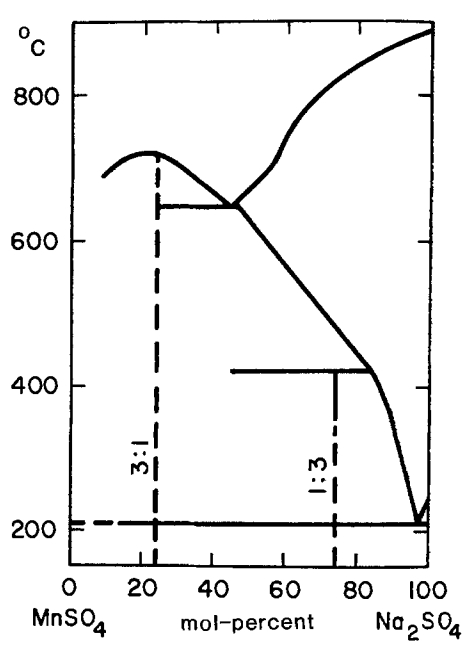

Fig. 2. $MnSO_4$-Na_2SO_4 phase diagram. [G. Calcagni and D. Marotta (7), reprinted from the "Phase Diagrams for Ceramists" by permission of The American Ceramic Society, Incorporated.]

Table I. Identification of x-ray patterns from $MnSO_4$-Na_2SO_4 deposits

β-$Na_2Mn(SO_4)_2$ (JCPDS 20-1126)* d (I/I₁)	Mn_2O_3 (JCPDS 10-69)* d (I/I₁)	1000 ppm SO_3 deposit d (I/I₁)	160 ppm SO_3 deposit d (I/I₁)	225 ppm SO_3 deposit d (I/I₁)	50 m/o $MnSO_4$-Na_2SO_4 d (I/I₁)
4.58 (25)				5.55 (30)	
4.38 (20)					
3.84 (100)	3.84 (25)	3.83 (100)	3.84 (100)	3.83 (100)	3.81 (100)
3.74 (100)		3.70 (20)	3.76 (25)	3.73 (15)	3.72 (50)
3.21 (25)					
3.10 (25)		3.05 (20)	3.05 (20)	3.06 (20)	
2.92 (20)			2.91 (25)		
2.89 (50)					2.88 (30)
2.85 (40)		2.85 (70)	2.86 (75)	2.87 (75)	
2.796 (50)			2.81 (20)		2.80 (25)
	2.72 (100)	2.71 (30)	2.72 (25)	2.73 (20)	
2.567 (50)		2.58 (35)	2.58 (50)	2.59 (50)	2.56 (35)
2.534 (45)			2.55 (20)		2.53 (25)
	2.35 (11)				
2.169 (15)					
1.915 (10)		1.92 (25)	1.92 (20)	1.92 (20)	1.91 (25)

* Lines with I/I_1 of 10 and below omitted.

ably involves SO_3 produced by Mn_2O_3 catalysis of the reaction, $SO_2 + 1/2\ O_2 \leftrightarrows SO_3$, at the Mn_2O_3-Na_2SO_4 mix surface. Catalysis by Co_3O_4 and NiO to produce SO_3 and promote mixed sulfate formation was seen previously (4, 5). To examine the suspected catalytic activity of Mn_2O_3, tests were made using equivalent volumes (weight/density) of Co_3O_4, NiO, and Mn_2O_3 with 500 ppm SO_2 in air which gave SO_3/SO_2 ratios of 0.44, 0.39, and 0.32, respectively. These are not quantitative data since the conditions were not rigorously standardized, but they confirm that the oxides are all clearly catalytic (blank runs without oxides yielded SO_3/SO_2 ratios below 0.05). It is reasonable to expect, therefore, that substantial SO_3 is formed at the metal oxide-sodium sulfate mix surface. This idea was investigated earlier by Reid *et al.* for Fe_2O_3-Na_2SO_4 (11), who also used S^{35}-tagged SO_3 and SO_2 to show that SO_3 is 30,000 times more reactive than SO_2 in the formation of Fe,Na mixed sulfates.

Finally, the reaction kinetics for mixed $MnSO_4$-Na_2SO_4 formation in Fig. 1 are distinctly slower than those seen for mixed $CoSO_4$- or $NiSO_4$-Na_2SO_4 formation (4, 5). For the latter sulfates at 725°C (cf. Fig. 3), the equilibrium sulfate compositions are reached within ~ 10 hr, whereas the Mn,Na sulfates are not clearly in equilibrium even after 100+ hr. However, despite the slow kinetics, molten Mn,Na sulfate phases are produced ultimately after approximately 100 hr under 225 ppm SO_3 (500 ppm SO_x) and 160 ppm SO_3 (350 ppm SO_x), but not under 100 ppm SO_3 (210 ppm SO_x). The critical partial pressure of SO_3 for molten Mn,Na sulfate at 725°C is thus indicated to be $\sim 1.5 \times 10^{-4}$ atm. This is somewhat more than the P_{SO_3} required for molten $CoSO_4$-Na_2SO_4 formation ($\sim 1 \times 10^{-4}$ atm) (1, 4), but less than that necessary for liquid $NiSO_4$-Na_2SO_4 production ($\sim 5 \times 10^{-4}$ atm) (1, 5).

Mixed $(Mn,Ni)SO_4$- and $(Mn,Co)SO_4$-Na_2SO_4 formation.—Some tests were also made (Fig. 3) to indicate effects Mn_2O_3 might have in reactions with preformed Ni,Na or Co,Na sulfates on turbine blade surfaces. The procedure was to bring 250 mg specimens of 50 m/o NiO-Na_2SO_4 or Co_3O_4-Na_2SO_4 to constant weight under 500 ppm equilibrated SO_2-SO_3 at 725°C, make 44 mg additions of Mn_2O_3, and follow the resultant weight gain behavior. Complete sulfation of Mn_2O_3, assuming no other change in the sulfate mixture, would yield a 40 mg weight gain.

As Fig. 3 shows, the NiO-Na_2SO_4 and Co_3O_4-Na_2SO_4 came to limiting weight gains corresponding to formation of 12 m/o $NiSO_4$ and 34 m/o $CoSO_4$, respectively. These results are consistent with earlier work (4, 5). Neither composition represents the full 50 m/o MSO_4 formation possible, and in the case of NiO-Na_2SO_4, the mixed sulfate is not molten and therefore noncorrosive (5). The sulfation of Mn_2O_3 after addition appears to proceed virtually independently of the presence of NiO or Co_3O_4. However, comparison with Fig. 1 (where twice the weight of Mn_2O_3 was involved) suggests that in fact the sulfation of Mn_2O_3 may be somewhat promoted in NiO-$NiSO_4$-Na_2SO_4 and retarded in Co_3O_4-$CoSO_4$-Na_2SO_4.

From a corrosion standpoint, the important facts brought forth by Fig. 3 are (*i*) that when Mn_2O_3 occurs with NiO or Co_3O_4 in Na_2SO_4 deposits, more total mixed sulfate can be formed (*i.e.*, the amount of potential corrodent is increased) for a given SO_3 partial pressure than with any one of the oxides alone, and (*ii*) that molten corrosive mixed sulfates may be produced on Na_2SO_4 deposited nickel-based metals by the presence of Mn_2O_3 under P_{SO_3} levels where normally only solid noncorrosive sulfates would be formed.

Corrosion of CoCrAlY by $MnSO_4$-Na_2SO_4 deposits.—To determine if molten $MnSO_4$-Na_2SO_4 itself would be corrosive, small deposits (approximately 0.5 mm thick by 2 mm diam) of 50 m/o $MnSO_4$-Na_2SO_4 were placed on CoCrAlY coating specimens, which then were exposed under flowing air at 725°C. As the deposits came to temperature, they melted and flowed, wetting the surface well, and then darkened as the $MnSO_4$-Na_2SO_4 underwent thermal decomposition and reaction with the underlying CoCrAlY. When the specimens were metallurgically cross sectioned and examined, they were found to have suffered areas of localized corrosion (Fig. 4) which displayed the typical LTHC morphology (1). The extent of corrosion was signifi-

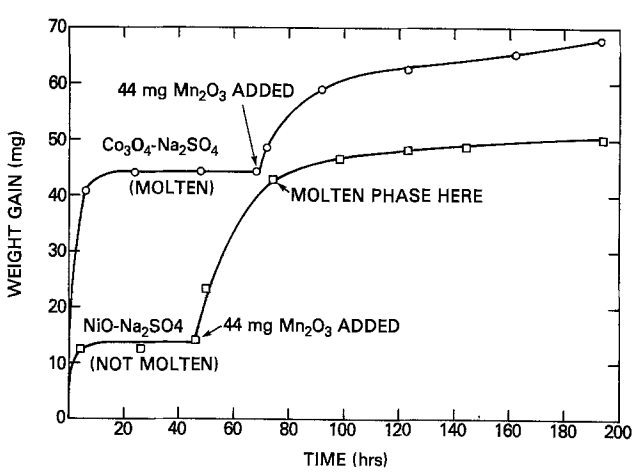

Fig. 3. Weight gain for 250 mg specimens of 50 m/o Co_3O_4-Na_2SO_4 and NiO-Na_2SO_4 under 225 ppm SO_3 (500 ppm SO_x) in air at 725°C, with 44 mg additions of Mn_2O_3.

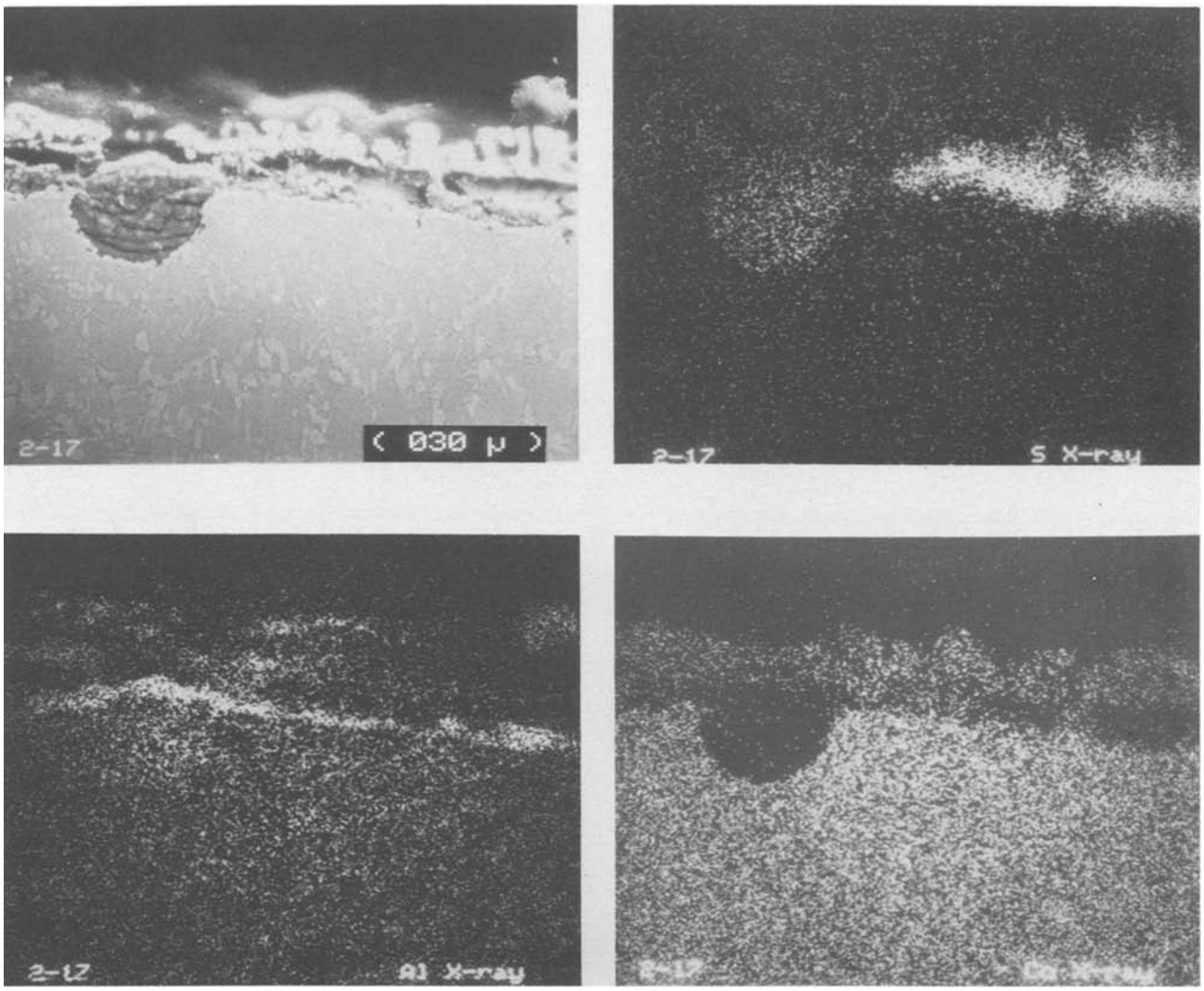

Fig. 4. SEM micrograph and S, Al, and Co x-ray maps of corrosion of CoCrAlY by 50 m/o $MnSO_4$-Na_2SO_4 after 19 hr under air at 725°C

cantly less however (although larger pits than the one shown in Fig. 4 could be found) than with similar experiments in earlier work with $CoSO_4$-Na_2SO_4 and $NiSO_4$-Na_2SO_4 deposits (4, 5). This difference in corrosivity has not been unequivocally explained. When molten $NiSO_4$- and $CoSO_4$-Na_2SO_4 react with CoCrAlY, bubbles form in the liquid deposits, and the most severe LTHC is found beneath the bubble sites (4). Little if any bubbling was evident with the $MnSO_4$-Na_2SO_4 deposits. The bubbles are presumably SO_3 (although possibly containing SO_2 also), and the SO_3 pressure is thus inferred to be higher in the molten Ni,Na and Co,Na sulfates than Mn,Na sulfate. However, simple thermal decomposition of the mixed sulfates cannot produce a P_{SO_3} higher than that required for their formation. The SO_3 (or SO_2) bubbles must thus result from some aspect of the molten sulfate/CoCrAlY reaction, and it is not certain whether the evolved gases play a significant corrosive role, or are merely products indicating a greater (unspecified) attack by the Ni,Na and Co,Na mixed sulfates.

Some clues to the possible corrosion initiation mechanism can be seen in Fig. 4. As the micrograph and sulfur x-ray map show, the sulfate film is essentially still present on the unattacked CoCrAlY areas (at the right of the pit) even after 19 hr at temperature, but it is gone above the corrosion pit, with sulfur however showing in the pit corrosion product. Also, the Al x-ray map indicates a band of aluminum concentration on the CoCrAlY surface under the sulfate film (and extending over the corrosion pit) which could represent a "protective" layer of Al_2O_3. This morphology suggests that the CoCrAlY was protected from molten $MnSO_4$-Na_2SO_4 attack by a surface Al_2O_3 layer, with corrosion being initiated only at sites where either the P_{SO_3} from the $MnSO_4$-Na_2SO_4 reaction (or other attack) was especially high, or the Al_2O_3 layer was weak. Since the Al_2O_3 layer still exists over the corrosion pit, it is likely that the layer was penetrated, rather than being substantially dissolved away by, *e.g.*, reaction with SO_3. The nature of the penetrating species is uncertain, but the Mn x-ray map (not shown) gave little evidence of Mn in the pit corrosion product, indicating that penetration by $MnSO_4$-Na_2SO_4 per se was probably limited. The manganese was mostly concentrated in the columnar particles on top of the sulfate film, which are probably at least partially manganese oxide produced by thermal decomposition of the original $MnSO_4$-Na_2SO_4. However, notice that these particles also contain cobalt (Co x-ray map of Fig. 4), which suggests that cobalt from the CoCrAlY substrate was taken into and transported through the $MnSO_4$-Na_2SO_4 film while it was molten at temperature. The "$MnSO_4$-Na_2SO_4" film may therefore have actually contained a sizable $CoSO_4$ component during the corrosion process.

Corrosion of Nickel 200 by Mn_2O_3-Na_2SO_4 under SO_2-SO_3.—Small deposits (~0.5 mm thick by 2 mm diam) of 50 m/o Mn_2O_3-Na_2SO_4 were placed on Nickel 200, Rene 80, and CoCrAlY coating alloy specimens and exposed under 500 ppm equilibrated SO_x (225

ppm SO_3, 275 ppm SO_2) to (*i*) show the effect of the substrate metal composition, and (*ii*) elucidate the different molten sulfate formation and LTHC processes. With Nickel 200, molten sulfate deposits were formed after ~ 48 hr with corrosion resulting as shown in Fig. 5. Little corrosion occurred until the Mn_2O_3-Na_2SO_4 surface deposits became molten. The corrosion in Fig. 5 has proceeded by a sulfidation-oxidation attack, *i.e.*, where metal sulfides were formed but then oxidized, with the released sulfur penetrating further into the metal to produce new oxidation-susceptible sulfides. The x-ray maps of Fig. 5 show an Mn-S phase, probably a sulfide, at the sulfidation front. At higher magnification, globular MnS phases could be detected in the metal in advance of the sulfidation front. Our Nickel 200 stock contains 0.31 w/o Mn, and it is not certain that the Mn in the MnS phases comes exclusively from the original Mn_2O_3-Na_2SO_4 surface deposit. However, examination of the morphology (micrograph and Mn x-ray map in Fig. 5) suggests that this is likely, particularly for the MnS at the sulfidation front. Presumably therefore, molten $MnSO_4$-Na_2SO_4 formed on the Nickel 200 surface and reacted with the metal, creating a manganese sulfide phase which diffused inward with the corrosion front.

Whether formation of the MnS phase increases the sulfidation-oxidation rate is not known, but it does appear to affect the overall corrosion morphology. In equivalent experiments with NiO-Na_2SO_4 on the same Nickel 200 stock (5), liquid eutectic Ni-Ni_3S_2 formed beneath and then broke through the surface oxide, producing distinctive spheres of Ni-Ni_3S_2 on the Nickel 200 surface which subsequently oxidized to NiO. No spheres of NiO were detected here, which suggests that the MnS prevented formation of liquid nickel-nickel sulfide phases (MnS is thermodynamically more stable than either Ni_3S_2 or NiS). However, the SO_3 concentration was higher in the NiO-Na_2SO_4 experiments (1100 ppm SO_3 at 750°C), and the absence of liquid nickel sulfide here may result simply from the lower SO_3 partial pressure. Further study is needed to understand the MnS *vs.* NiS formation processes.

Corrosion of Rene 80 by Mn_2O_3-Na_2SO_4 under SO_2-SO_3.—Corrosion experiments under the same conditions as with Nickel 200 gave the characteristic LTHC morphology for Rene 80, *i.e.*, a clean corrosion front, absence of advance sulfide phases in the metal, and transport of nickel outward from the corrosion pit (Fig. 6). There was pronounced spalling of the corrosion product, as commonly seen with Rene 80, with some suggestion that alternate spalling layers composed predominantly of nickel and chromium oxide were involved (Ni and Cr x-ray maps in Fig. 6). The Mn x-ray map (not shown) indicated that the Mn concentration was low and mostly in the outer corrosion product. On the other hand, the Co x-ray map (not shown) revealed significant cobalt in the corrosion product above the attack site, with the distribution of cobalt being essentially the same as that

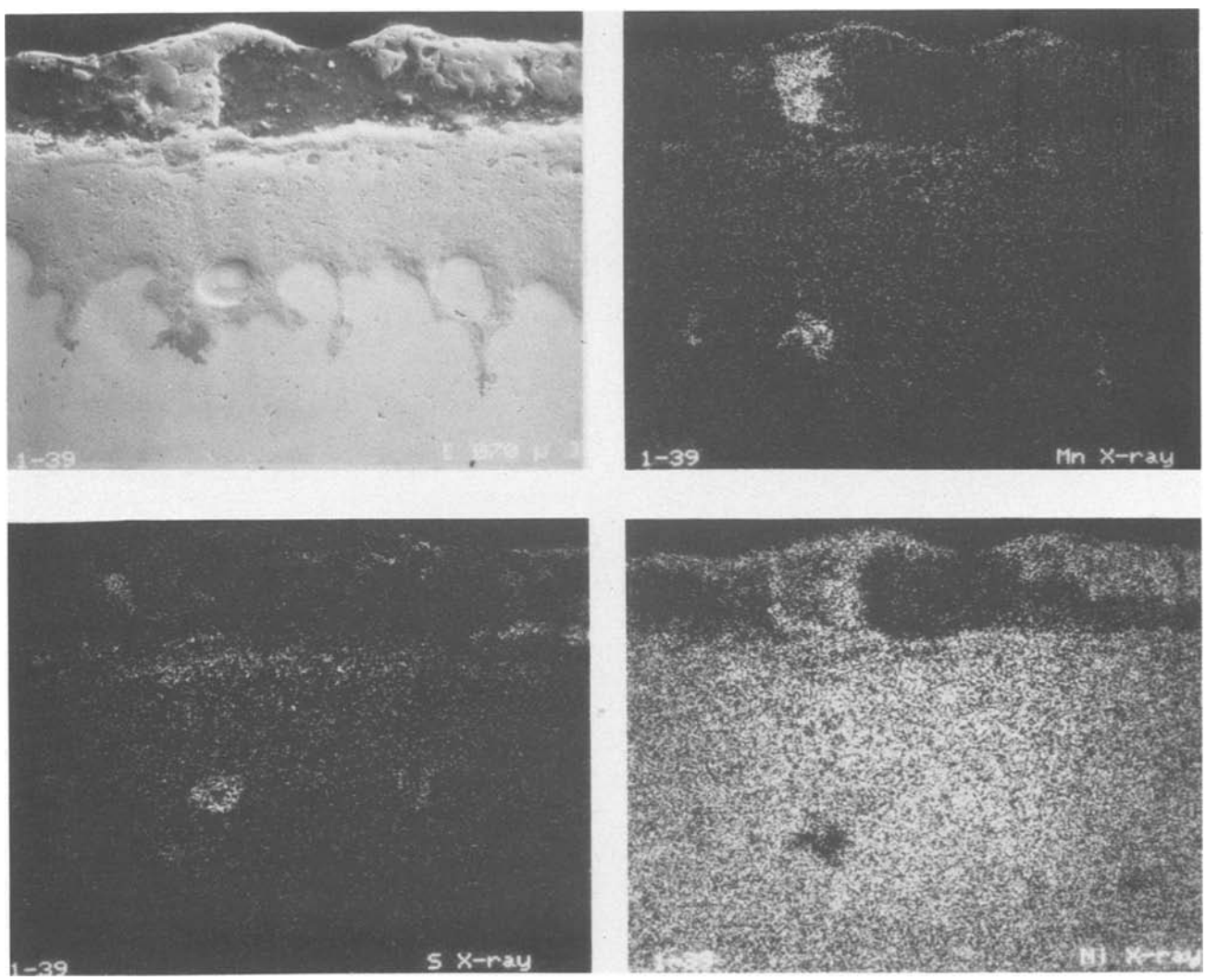

Fig. 5. SEM micrograph and Mn, S, and Ni x-ray maps of corrosion of Nickel 200 by 50 m/o Mn_2O_3-Na_2SO_4 after 46 hr under 225 ppm SO_3 (500 ppm SO_x) in air at 725°C.

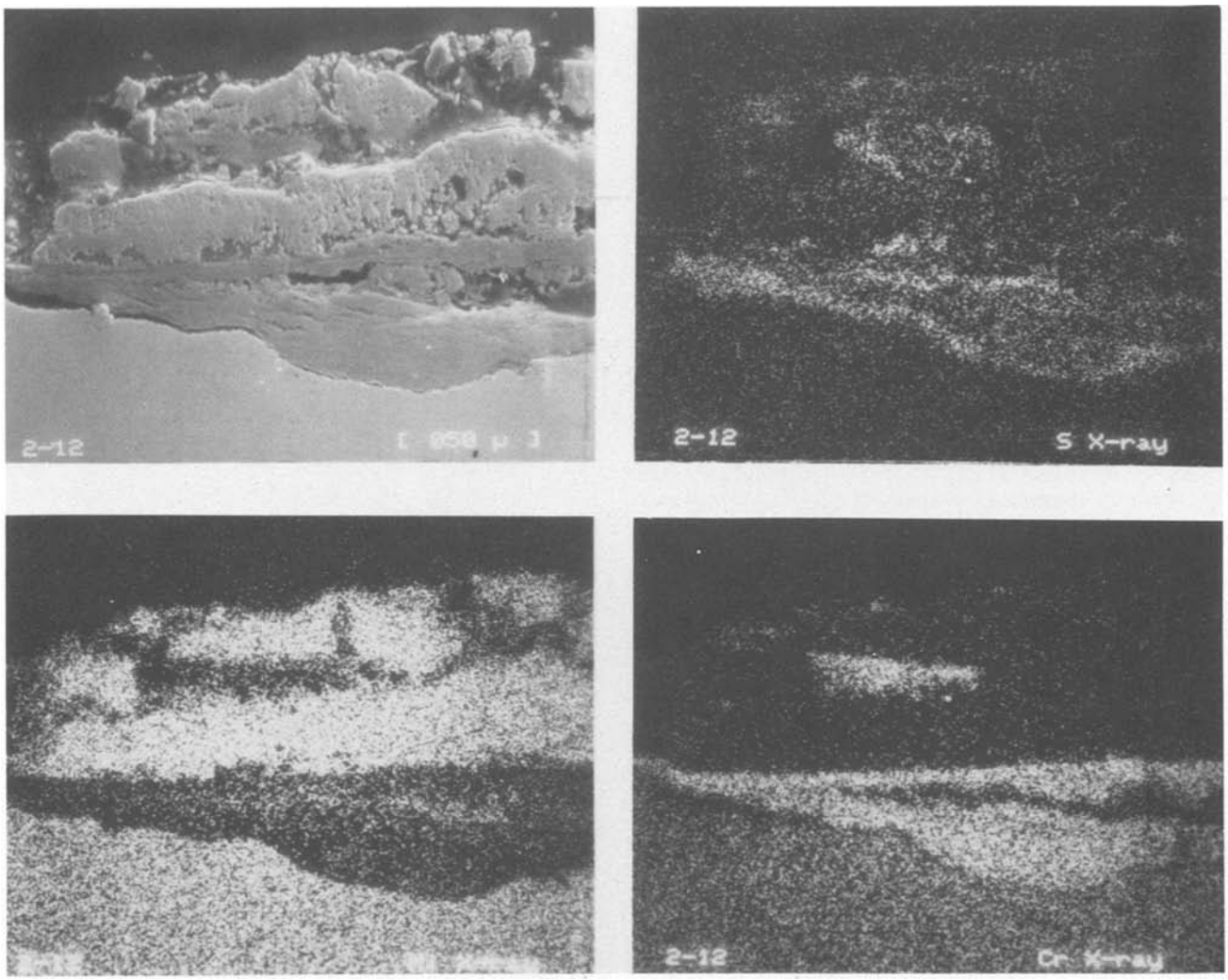

Fig. 6. SEM micrograph and S, Ni, and Cr x-ray maps of corrosion of Rene 80 by 50 m/o Mn_2O_3-Na_2SO_4 after 91 hr under 225 ppm SO_3 (500 ppm SO_x) in air at 725°C.

shown for nickel in the Ni x-ray map in Fig. 6. Rene 80 contains ~9 w/o cobalt, and finding of cobalt in the outer corrosion product suggests that a molten Co,Na or Co,Ni,Na sulfate may have formed under the 225 ppm SO_3 present, and initiated LTHC without any major participation by the manganese.

Corrosion of CoCrAlY by Mn_2O_3-Na_2SO_4 under SO_2-SO_3.—Extensive LTHC occurred after only 41 hr (Fig. 7) when CoCrAlY with 50 m/o Mn_2O_3-Na_2SO_4 deposits was exposed under 225 ppm SO_3 at 725°C. The distributions of sulfur and cobalt shown in Fig. 7 are characteristic for LTHC of CoCrAlY (1), with heavy transport of cobalt into the outer corrosion layer. The manganese has remained mostly above the original CoCrAlY surface and penetrated little if any into the corrosion pit (Mn x-ray map in Fig. 7). The manganese also appears to have never wetted the CoCrAlY surface; that is, it appears that a fully molten $MnSO_4$-Na_2SO_4 phase was never formed to give the type of strong wetting seen with 50 m/o $MnSO_4$-Na_2SO_4 (cf. Fig. 4). Considering the high concentration of cobalt available, and the apparently slow kinetics of $MnSO_4$-Na_2SO_4 formation, it is likely that the molten phase formed here to initiate LTHC, as probably with Rene 80 above, was predominantly $CoSO_4$-Na_2SO_4 rather than $MnSO_4$-Na_2SO_4.

This idea was supported by a subsequent experiment where a CoCrAlY specimen deposited with Na_2SO_4 alone developed a molten $CoSO_4$-Na_2SO_4 phase and suffered equivalent LTHC in essentially the same time (55 hr), when exposed under the same 225 ppm SO_3 and 725°C conditions as the Mn_2O_3-Na_2SO_4 deposited CoCrAlY.

Conclusions

Molten $MnSO_4$-Na_2SO_4 can be formed under as little as 1.6×10^{-4} atm (160 ppm) of SO_3 in air at 725°C, as compared with $\sim 1 \times 10^{-4}$ atm of SO_3 for $CoSO_4$-Na_2SO_4 (1, 4) and $\sim 5 \times 10^{-4}$ atm of SO_3 for $NiSO_4$-Na_2SO_4 (1, 5).

The sulfation of Mn_2O_3-Na_2SO_4 mixtures by SO_3 appears to be substantially slower (at least 10×) than the equivalent sulfation of Co_3O_4- or NiO-Na_2SO_4 mixtures. This is of potential scientific and technological importance and merits further investigation.

Sulfur trioxide is clearly more reactive than SO_2 in Mn_2O_3-Na_2SO_4 sulfation, and may in fact be critical for the reaction. However, Mn_2O_3 catalyzes the $SO_2 \rightarrow SO_3$ oxidation and will produce SO_3 at the mix surface even when the gas stream contains only SO_2.

Ternary sulfates are formed by the sulfation of Mn_2O_3 by SO_3 in the presence of NiO-Na_2SO_4 or Co_3O_4-Na_2SO_4. Detailed study of these (and like) ternary systems could aid in predicting their properties and possible roles in LTHC.

Thermal decomposition/reaction of molten $MnSO_4$-Na_2SO_4 causes LTHC of CoCrAlY, but not to the extent of $NiSO_4$-Na_2SO_4 or $CoSO_4$-Na_2SO_4. The reason for this difference in corrosivity is not clear at this time.

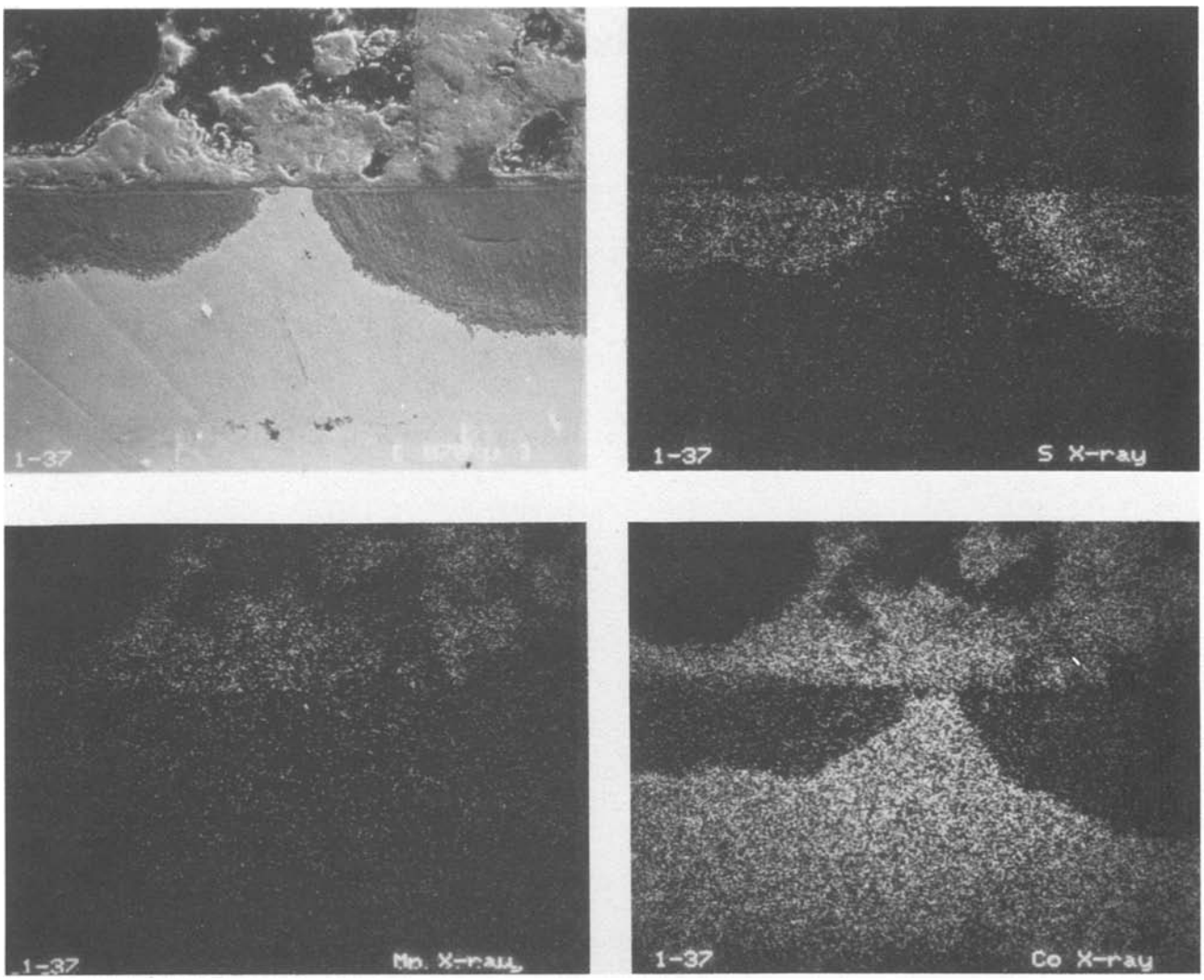

Fig. 7. SEM micrograph and S, Mn, and Co x-ray maps of corrosion of CoCrAlY by 50 m/o Mn_2O_3-Na_2SO_4 after 41 hr under 225 ppm SO_3 (500 ppm SO_x) in air at 725°C.

On the basis of the present experiments, Mn_2O_3 would not be expected to significantly accelerate the LTHC of gas turbine alloys containing 8-9 w/o and upward of cobalt. However, occurrence of Mn_2O_3 on blades constructed of superalloys not containing cobalt (*e.g.*, 713C) could conceivably promote LTHC.

These experiments simulate the deposition of Mn_2O_3 on blade surfaces and may not necessarily relate to Mn as an alloying element. For example, in the original burner rig testing (6), the ratio of the w/o of water soluble Mn in the surface salt to the w/o Mn in the alloys was approximately 10 times the equivalent ratio for cobalt, indicating that Mn was preferentially transported into and/or retained in the surface sulfate. Manganese may still have unrecognized properties, therefore, that require caution in its applications in marine gas turbines.

Acknowledgments

This research was funded under the Naval Sea Systems Command Program for Advanced Marine Gas Turbine Materials, and the support is gratefully acknowledged. We also wish to thank Dr. J. A. Goebel, of Pratt & Whitney Aircraft Group, who furnished the CoCrAlY and Rene 80 specimens, and Dr. Rm. Panayappan of NRL, who performed the analysis of the Nickel 200 stock.

Manuscript submitted June 2, 1982; revised manuscript received Aug. 9, 1982. This was Paper 28 presented at the Montreal, Quebec, Canada, Meeting of the Society, May 10-14, 1982.

Any discussion of this paper will appear in a Discussion Section to be published in the December 1983 JOURNAL. All discussions for the December 1983 Discussion Section should be submitted by Aug. 1, 1983.

Publication costs of this article were assisted by the Naval Research Laboratory.

REFERENCES

1. K. L. Luthra and D. A. Shores, *This Journal*, **127**, 2202 (1980).
2. G. H. Meier, F. S. Pettit, and K. T. Chang, in International Conference on High Temperature Corrosion, San Diego, 1981, NACE, To be published.
3. R. H. Barkalow and G. W. Goward, in International Conference on High Temperature Corrosion, San Diego, 1981, NACE, To be published.
4. R. L. Jones, in International Conference on High Temperature Corrosion, San Diego, 1981, NACE, To be published.
5. R. L. Jones and S. T. Gadomski, *This Journal*, **129**, 1613 (1982).
6. L. F. Aprigliano, Report DTNSRDC/SME-81/33, August 1981, David W. Taylor Naval Ship R&D Center, Annapolis, Md.
7. G. Calcagni and D. Marotta, *Gazz. chim. ital.*, **45 II**, 373 (1915).
8. K. H. Stern and E. L. Weise, Natl. Stand. Ref. Data Ser., Natl. Bur. Stand., No. 7 (Sulfates) (1966).
9. K. A. Bol'shakov and P. I. Fedorov, *Zhur. Obsch. Khim.*, **26**, 349 (1956).
10. K. A. Bol'shakov and P. I. Fedorov, *ibid.*, **26**, 348 (1956).
11. H. H. Krause, A. Levy, and W. T. Reid, *Trans. ASME J. Eng. for Power*, **90**, Series A, 38 (1968).

Optical Anisotropy and Electrostriction in the Anodic Oxide of Molybdenum

D. J. DeSmet

Department of Physics and Astronomy, The University of Alabama, University, Alabama 35486

and

J. L. Ord

Department of Physics, University of Waterloo, Waterloo, Ontario, Canada N2L 3G1

ABSTRACT

The anodic oxidation of molybdenum in acetic acid electrolyte is studied using a self-nulling ellipsometer to follow field-induced changes in the optical properties of the oxide film. When oxidized at constant field, the oxide exhibits the greatest optical anisotropy of any oxide studied thus far. When the field is removed, the oxide retains more than half of its original anisotropy. The oxide film thickness increases when the field is applied, and the dependence of strain on field is linear at low fields. There is a corresponding decrease in the dielectric constant of the film when the film thickness increases. The zero-field optical anisotropy is not removed by an electrochromic conversion cycle.

When oxide films are grown on valve metals by anodic oxidation at constant current density, the electric field in the growing film remains constant at several million V/cm. Optical measurements made with ellipsometers which can follow the growth process have shown that most valve-metal oxides are optically anisotropic under these conditions. The oxides of tantalum (1), niobium (2-4), and tungsten (5) have been reported to lose this anisotropy when the anodizing field is removed, but vanadium oxide appears to retain significant optical anisotropy at zero field (6). Optical anisotropy in amorphous and nonpolar crystalline oxides is thought to be due to electrostriction, the universal second-order effect which couples the electrical and mechanical properties of the oxide. Although electrostrictive effects are expected to vanish at zero field, oxides grown in a high field experience a stress when the field is removed, and may retain some degree of optical anisotropy at zero field if the stress does not relax.

Interest in electrostriction in anodic oxides was sparked by the surprising observation that instead of decreasing slightly due to "condenser pressure," the oxide film thickness actually increases by more than a tenth of a percent when the field is applied. Examination of the theory of electrostriction shows that the sign of the field-induced strain is dictated by the sign of the strain dependence of the dielectric constant (7). The experimental results can only be explained if the dielectric constant also has an explicit field dependence of opposite sign which dominates the strain dependence. This conclusion, required by energy conservation, is just as surprising as the original observation of an increase in film thickness, and calls for further experimental verification.

In this paper we present the results of study of optical anisotropy and electrostriction in the anodic oxide of molybdenum. *A priori* we expect molybdenum to behave more like vanadium (and to a lesser extent tungsten) than like tantalum or niobium.

Experimental

The ellipsometer used in this study is a modified version (8) of the self-nulling instrument which has been in use at the University of Waterloo for many years (9). Quadrature Faraday modulation is decoded by a two-phase lock-in amplifier and the d-c error signals are fed back to the stepping motor drives through voltage-to-frequency converters. The sine-cosine quadrature drives have a nominal resolution of 1/1600th of a degree, and under typical operating conditions the instrument has a response time of a few tenths of a second and a resolution of a few thousandths of a degree. A helium-neon laser is the light source, and all refractive indexes quoted in this paper are for a wavelength of 6328Å. The hollow equilateral glass prism used as a cell requires an angle of incidence of 60 deg. The cell has standard-taper joints through which the electrode holder, a platinum counterelectrode, a reference electrode, and a gas dispersion tube are inserted. The cell was filled with acetic acid electrolyte containing 2% water and saturated with sodium borate. A platinum wire is used as a reference electrode with this electrolyte, and all experiments were performed at room temperature (22°C).

The circuitry used with the cell is operated by the HP 2114B process-control computer which logs the optical data and operates the on-line displays (two storage oscilloscopes and an X-Y plotter). The current source consists of a digital-to-analog converter connected to a high voltage operational amplifier, and a second amplifier follows the potential of the reference electrode relative to the working electrode which is held at virtual ground. A programmable amplifier interfaces the follower to a 16-bit analog-to-digital converter with a 25 microsecond conversion time.

The cylindrical working electrode, prepared from a single crystal of molybdenum, exposes a vertical surface 1.45 cm^2 in area to the electrolyte when it is clamped between Teflon washers in a glass electrode holder. The optical measurements are made on a flat ground on one side of the cylinder. Between experiments the electrode is stored with an oxide film on its surface, and all that is required to prepare the surface for an experiment is to dissolve the oxide film by rinsing the electrode in distilled water.

Results and Discussion

The results of an experiment in which molybdenum is oxidized anodically at a current density of 345 $\mu A/cm^2$ are shown in Fig. 1 and Fig. 2. A plot of potential *vs.* time is shown in the lower portion of Fig. 1, and the locus traced out by the null settings of the ellipsometer are shown on a polarizer-analyzer plot in the upper portion. Figure 2 shows the time dependence of the potential and the polarizer null setting for region A-B in Fig. 1. The potential increases slowly at first, and the polarizer null setting exhibits an arrest for approximately 100 sec before undergoing the rapid S-shaped change shown in Fig. 2. In the thin-film region, the change in polarizer null setting is approximately proportional to

Key words: capacitance, dielectrics, ellipsometry.

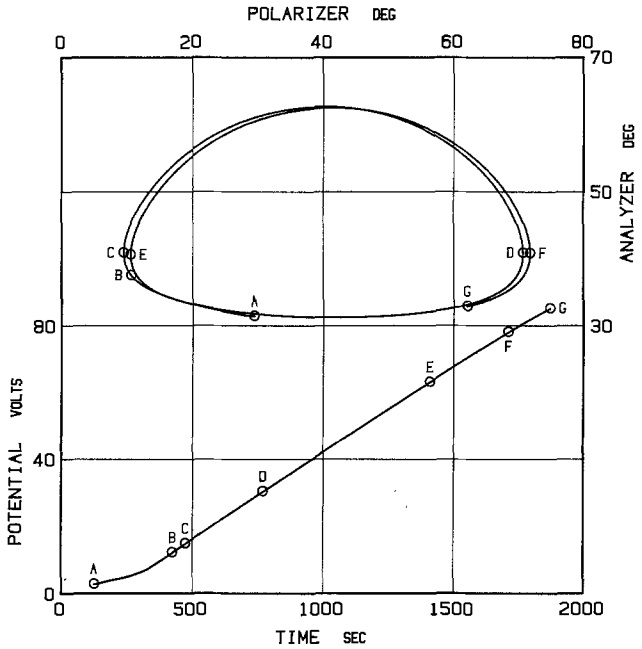

Fig. 1. Potential-time and polarizer-analyzer data for the anodic oxidation of molybdenum at a current density of 345 $\mu A/cm^2$ in acetic acid electrolyte. The labels identify corresponding points in the two data sets.

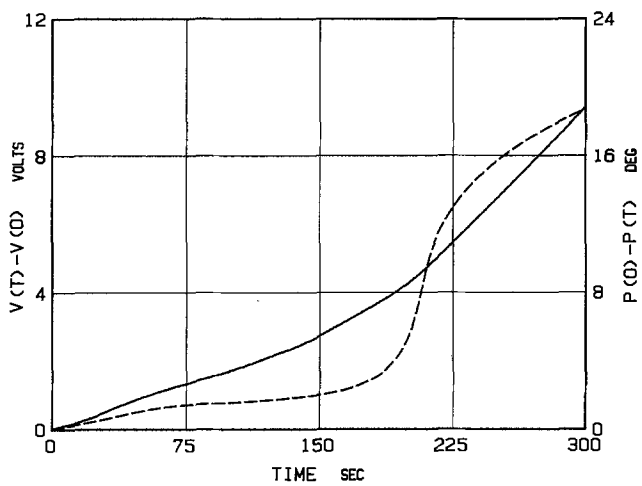

Fig. 2. The time dependence of the change in potential (solid curve) and the change in polarizer null setting (broken curve) for region A-B of the experiment plotted in Fig. 1.

the change in film thickness, and the curves shown in Fig. 2 are characteristic of a passivation process which proceeds by a dissolution-precipitation mechanism. The length of the dissolution plateau and the height of the subsequent precipitation rise are strong functions of both the current density and the water content of the electrolyte. The anodic oxidation process requires the presence of water in the electrolyte, but if too much water is present the electrode will not passivate. We found a 2% water electrolyte to be optimum for our experimental conditions. In all of our experiments except the one shown in the first two figures, we passivate the electrode at 690 $\mu A/cm^2$ in order to minimize dissolution effects, then reduce the current density by a factor of four to make it easier for the ellipsometer to follow the film growth.

After the initial passivation, the potential rises linearly to about 80V before curvature becomes significant, signifying a change in the oxidation process. The corresponding optical data in the upper portion of Fig. 1 trace out two similar loops, the second diplaced slightly to the right of the first. This optical behavior is characteristic of the growth of a transparent anisotropic film with a lower refractive index for light polarized perpendicular to the surface (Nz) than for light polarized parallel to the surface (Nx). For transparent isotropic films the second loop superimposes on the first, and for absorbing films the second loop spirals outward from the first. The field-dependent data (shown below in Fig. 3) require the film to be optically anisotropic, so there is little point in trying to model the film as a superposition of isotropic layers with differing indexes, even though such a model might be made to fit the data in Fig. 1. If we compare the optical data in Fig. 1 with data obtained on other valve metals under similar conditions, we see that all valve metals have the second optical loop displaced to the right of the first, and that molybdenum has the largest displacement of any of the metals studied thus far.

There are two different approaches one can follow when analyzing anisotropic optical data. In the first approach one uses a program which varies Nz, Nx, and the substrate index to minimize the deviation between the theoretical curve and optical data such as that in Fig. 1. This process converges fairly quickly because the spacing between the loops (C-E and D-F) essentially determines the difference between Nx and Nz, and the width of the loops (C-D and E-F) determines Nx. The substrate index must be varied slightly because one is not sure how thick a film is present initially on the nominally bare surface. This is the approach which was used in the vanadium study (6), and is the approach we will use here.

In the second approach, the field is removed at intervals during the experiment, and the zero-field data are fitted first using a program which varies the substrate index and the index of an isotropic film (N). The field-up data are then fitted by varying two parameters, either Nz or Nx and the ratio $(N-\bar{N}z)/(N-Nx)$, usually referred to as beta. Beta is determined by requiring the degree of anisotropy to be independent of thickness (an assumption which is necessary in both approaches). Beta is then assumed to remain constant as the field changes, and only one parameter, Nz or Nx, remains to be varied when analyzing the field dependence. This is the approach which has been followed in

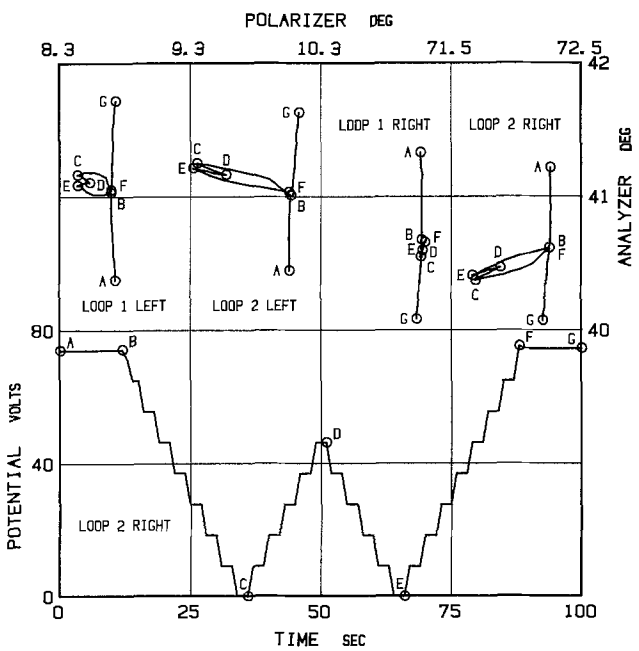

Fig. 3. Plot of a potential-stepping transient and expanded-scale plots of the corresponding optical changes at the left (upper left) and right (upper right) ends of the first two optical loops. The initial current density was 173 $\mu A/cm^2$ when the transients were applied, and the potential transient plotted is the one applied at the right end of the second loop.

all of the other studies, and is the logical approach to follow when there is no significant offset between the zero-field data obtained on different loops. When the offset is significant, as was found for vanadium, either the second approach must be modified or the first approach must be used.

The experiment we use to study the field-dependence of optical anisotropy in the molybdenum system is shown in Fig. 3. The potential is stepped to zero when the optical data reach the left and right ends of the first two loops (points C, D, E, and F in Fig. 1). The data obtained in regions C-E and D-F are shown on expanded scales in the upper left and upper right of Fig. 3, and a typical potential-stepping transient is shown in the lower portion of the figure. The potential is stepped to zero in eight equal steps of three-second duration, then it is stepped up five steps, down five steps, and back up eight steps producing a W-shaped transient. The first step is somewhat rounded by the software routine used to step the potential, but the remaining steps are sharper than is indicated in the figure (the lines connect points recorded at one-second intervals). When the potential is stepped, the polarizer and analyzer null settings change, but the changes are less than the displacement between the loops, and the zero-field data from the two loops do not lie on the same curve. The slow dissolution of the oxide in the 2% water electrolyte causes the W-shape of the potential transient to be reflected in the optical data.

In analyzing the optical data in Fig. 3 following the first of the approaches outlined above, we make up data sets for the nine potential steps, then analyze each set separately using a common substrate index. One can include all of the data obtained at a particular potential in the data set, or one can average the data at a common potential within each W-transient. Since the transients are symmetric, the averaging process eliminates the effect of film dissolution as well as any up-stepping *vs.* down-stepping hysteresis. We will use the averaged data in what follows in order to reduce the complexity of the figures.

Figure 4 shows the results of the anisotropic analysis on an Nx *vs.* Nz plot. The values labeled both sides were obtained using all four points in each analysis, and the values labeled left side were obtained using the same substrate index but just the two left-end data points. As the figure shows, both sets of results lie on straight lines, and hence can be expressed in terms of the parameters N and beta. The reciprocals of the slopes of the lines in Fig. 4 give the beta values directly, and the N values are given by the intersections of the lines with the isotropic line with Nx = Nz.

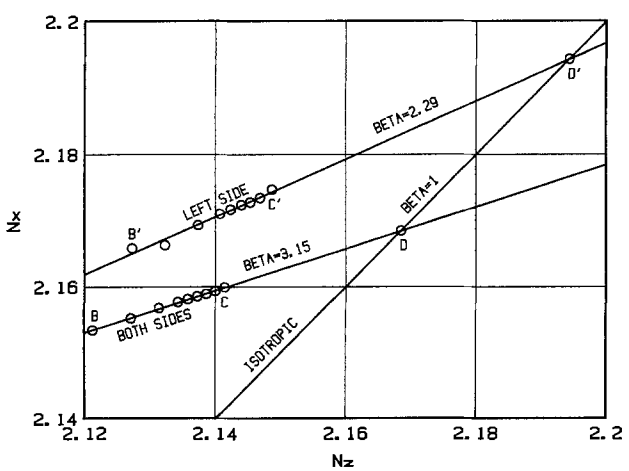

Fig. 4. The results of anisotropic analysis of the optical data in Fig. 3. The both sides results are fitted to data from all four transients, whereas the left side results are fitted to only the two transients in the upper left of Fig. 3. The beta values are the reciprocals of the slopes of the lines in the figure.

The difference between the sets of results is a consequence of the sensitivity of the analysis to any factor such as substrate topography which can change as the film grows and cause the optical data to drift to the right or left on a P-A plot. The theoretical curves all have approximately the same displacement between loops at the left and right ends, and so does the experimental curve in Fig. 1, but the data in Fig. 3 have a significantly larger displacement at the left end than at the right. We can get more nearly equal displacements by repeating the experiment, but we have no electrochemical reason for rejecting the data in Fig. 3, and we regard the uncertainties in the analylsis apparent in Fig. 4 as typical for a system with a soluble oxide and a dissolution-precipitation passivation process. It is interesting to note that although the left and right end displacements may vary somewhat, the field-switching displacements do not change, and hence they may provide a better starting point for anisotropic data analysis.

Both of the analyses whose results are plotted in Fig. 4 support our contention that the molybdenum system exhibits the greatest optical anisotropy of any of the valve-metal systems studied so far, and show that the residual anisotropy at zero field is more than half the anisotropy at the anodizing field. The left side analysis (whose beta-value is closer to that found in other systems) has a difference between Nx and Nz of 1.8% with the field applied, and 1.2% with the field removed, whereas the vanadium system has a difference of only 0.9% at a slightly higher anodizing field, and the tantalum and niobium systems exhibit much lower anisotropy at substantially higher anodizing fields.

The significance of the lines in Fig. 4 and their intersections is apparent in Fig. 5 where we show the theoretical curves determined by the left-side analysis superimposed on the averaged experimental data. The curve through the field-up data has Nx = 2.166 and Nz = 2.127 and the corresponding curve through the zero-field data has Nx = 2.175 and Nz = 2.149. The isotropic curve has N = 2.194. All nine averaged data points are shown for the second loop, but the first-loop data overlap, and not all of the points are shown in the figure. Had we taken the other approach to the anisotropic optical analysis, we would have done our geometry in Fig. 5 rather than Fig. 4. The problem would have been to extrapolate B-C to find a point D on an isotropic curve which gives the same BC/BD ratio for both loops. This ratio is 1/3 for the data in Fig. 5, and is consistent with the 1/3 reduction in anisotropy (from 1.8 to 1.2%) found in Fig. 4 when the field is removed.

The optical analysis gives film thicknesses for each of the points plotted in Fig. 5, and hence we can cal-

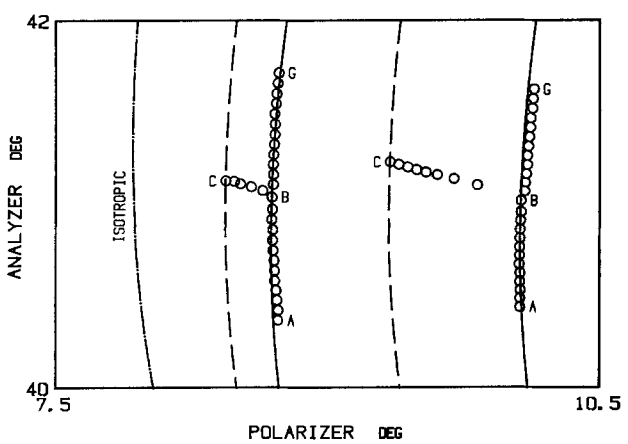

Fig. 5. Theoretical curves from the left-side analysis in Fig. 4 superimposed on averaged data from the two transients in the upper left of Fig. 3.

culate both the field in the film and the strain induced by the field. The field in the oxide film is 2.645×10^6 V/cm at an anodizing current density of 173 μA/cm^2, and the strain induced by the field is plotted as a function of field in Fig. 6 for the second loop data from Fig. 5. The strain is positive, indicating that the film thickness increases when the field is applied, just as it does in the other valve-metal systems, and the dependence on field, linear at low fields, increases sharply as the anodizing field is approached. The overall increase in thickness of just over half a percent is about the same as the overall percentage decrease in Nx, and hence measurements at normal incidence will find that the optical thickness is essentially independent of the electric field.

The technique we use to study the dielectric constant variation associated with electrostriction uses a W-shaped transient similar in shape to the one used for the optical measurements, but without steps, and of two to three orders of magnitude shorter duration. The transient is produced by applying a constant current and switching its sign at appropriate points in order to produce a W of the type shown in Fig. 7. A detailed description of the circuitry and the algorithm used to apply the transient can be found elsewhere (10). Note that the duration of the transient is just over a tenth of a second, and that the effect of electrolyte resistance is apparent when the current is reversed. The sweeping current density was 173 μA/cm^2 for the transient in Fig. 7, and the initial steady-growth current density was one-sixteenth of this value.

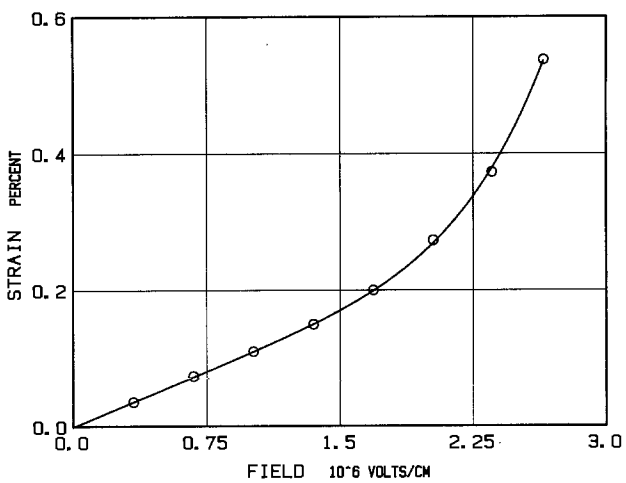

Fig. 6. A plot of the strain in the oxide film *vs.* the applied field for the second-loop optical data in Fig. 5. The positive strain shows that the film thickness increases when the field is applied.

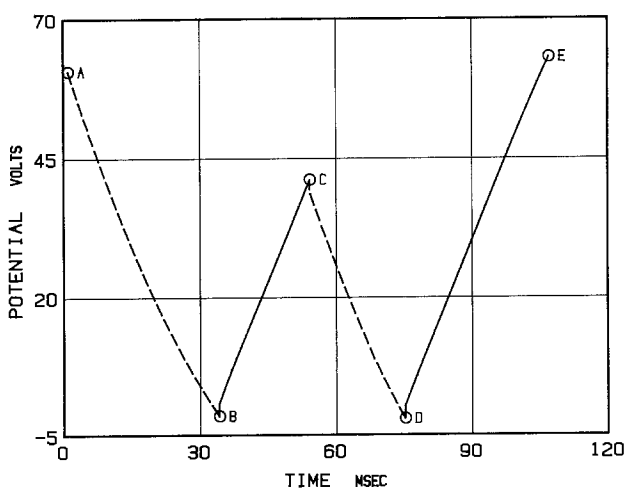

Fig. 7. A galvanostatic charging transient produced by reversing the current at intervals in order to produce a W whose central potential is 5/8ths of the initial potential. The charging current density, 173 μA/cm^2, is sixteen times the initial oxidation current density. Anodic segments of the transient are shown as solid curves, and cathodic segments are shown as broken curves.

The V-Q charging curve derived from the W-transient in Fig. 7 is shown in Fig. 8. The charge is calculated by integrating the current (corrected for the effect of the ionic current at high potentials) and extrapolating to a potential origin where the optical thickness data extrapolate to zero. There are some uncertainties involved in the origin extrapolation, but the experimental conditions are chosen to minimize the effect of any uncertainty in how the ionic current depends on potential. The general features of the charging curve are similar to those for the tungsten system (10). The discharge segments exhibit pronounced upward curvature, and the charging segments are approximately linear except for some downward curvature near the origin and near point E. What appears common in most valve-metal systems is the upward curvature of the discharge segments and the substantial charge-discharge hysteresis. The curvature of the charging segments is a second-order effect which depends on the difference between the two first-order effects, and its sign can be either positive or negative depending on the system studied and the current density used.

The interpretation of the charging curve in Fig. 8 is greatly complicated by the fact that the hysteresis effect is just as large as any effect of dielectric constant variation. A proper treatment of the data in Fig. 8 would require an analysis of polarization kinetics somewhat similar to that used by Taylor and Dignam in their study of ion current transients (11). We do not wish to undertake such an analysis here. Instead we will simply average the data in much the same way as we averaged the optical data, and assume that the dielectric constant values we calculate in this manner give a reasonable indication of the steady-state dependence of dielectric constant on electric field. The results of this calculation are shown in a plot of Ko/K *vs.* field in Fig. 9. The decrease in dielectric constant observed when the field is applied (increase in Ko/K) agrees with what is found in other valve-metal systems. If the dielectric constant varied with density in the manner predicted by the Clausius-Mossotti relation, the precentage change in Ko/K would be Ko/3 times the percentage strain plotted in Fig. 6. The observed overall change in Ko/K is three times that predicted from the overall strain, and although both Ko/K and the strain have a linear component in their field-dependence, their curvature is of opposite sign.

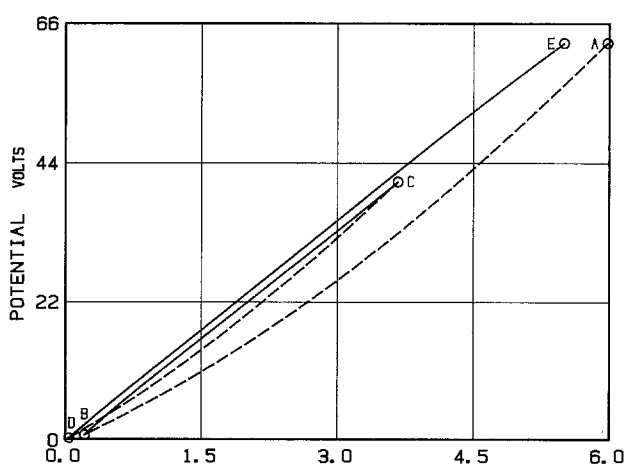

Fig. 8. Potential-charge plot for the transient in Fig. 7. Corresponding points have the same labels in the two figures. Solid curves represent anodic segments and broken curves represent cathodic segments.

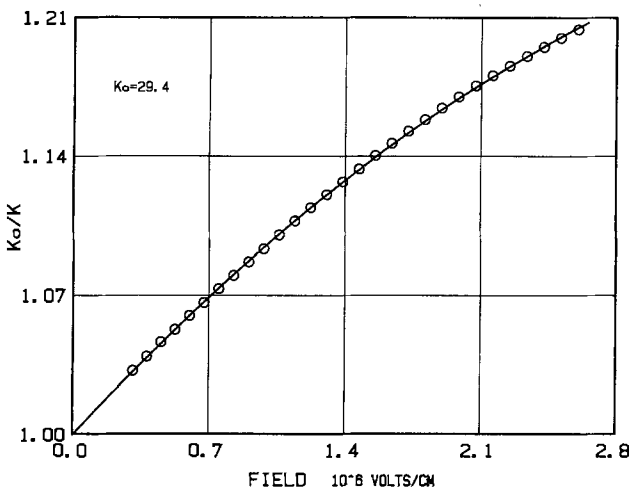

Fig. 9. Plot of K_o/K vs. field obtained by averaging data from the initial cathodic and final anodic segments of the charging curve in Fig. 8. Ko, the zero-field value of the dielectric constant, is found by extrapolating the data to zero field.

The theory of electrostriction (7) predicts an E^2 dependence for both the strain and Ko/K at low fields. Failure to observe this dependence in anodic oxides is explained by noting that the theory assumes that the stress in the film goes to zero when the field is removed, whereas anodic oxides will be more nearly free of stress at the anodizing field than at zero field if the atomic movement involved in the ionic conduction process is a major stress-relaxation mechanism. Although there is nothing quantitative in this explanation, it does predict a more nearly linear dependence of strain on field for oxides with high zero-field stress. The molybdenum system, with its residual anisotropy indicating a high zero-field stress, and strain varying linearly with field at low fields, certainly fits this pattern.

We can test the assumed link between residual anisotropy, high zero-field stress, and a linear dependence of strain on field, if we can find a way to relax the zero-field stress. It is usually assumed that the relaxation process is driven by the passage of ionic current through the film, and if the ionic current depends exponentially on the field, there will be no significant ionic current at low fields. There is a process which involves the passage of substantial ionic current at low fields, and that is the conversion of oxide to oxy-hydroxide which colors the film (12) and classes molybdenum oxide as an electrochromic material. The oxy-hydroxide can be converted back to an oxide by application of an anodic current, and we might hope that after such a cycle the zero-field stress would be substantially reduced.

Figure 10 shows the results of an experiment in which electrochromic conversion is used to try to relax zero-field stress. The electrode was passivated at 690 μA/cm^2, and at point B the current density was reduced to 173 μA/cm^2. The current was made cathodic at point C, and was switched back to anodic at point D. The optical data exhibit a definite structure at the end of the reconversion process, and do not return to point C, but the offset is in the direction of higher anisotropy, not lower. Under continued film growth, the offset decreases steadily, and the optical data asymptotically approach the original growth curve. The offset at C is

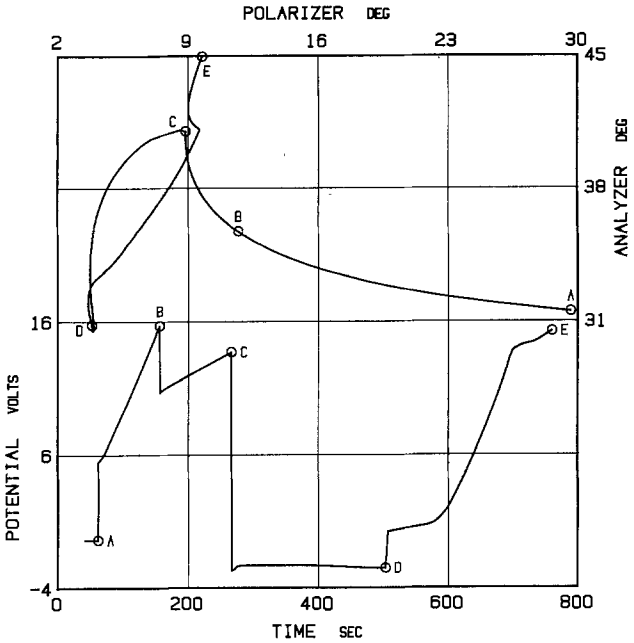

Fig. 10. An anodic oxidation experiment with an electrochromic conversion cycle at the left end of the first loop. The current density is 690 μA/cm^2 from A to B, 173 from B to C, −173 from C to D, and 173 from D to E.

more likely due to a structural change in the oxide than to a change in its anisotropy, and says more about the processes involved in electrochromism than about the processes we are studying here. For the present we will have to leave the connection between residual anisotropy, zero-field stress, and a linear dependence of strain on field as an untested hypothesis.

Acknowledgments

This work received partial support from the Natural Sciences and Engineering Research Council Canada under Grant No. A-1151.

Manuscript submitted March 26, 1982; revised manuscript received July 28, 1982.

Any discussion of this paper will appear in a Discussion Section to be published in the December 1983 JOURNAL. All discussions for the December 1983 Discussion Section should be submitted by Aug. 1, 1983.

Publication costs of this article were assisted by the University of Waterloo.

REFERENCES

1. W. D. Cornish and L. Young, *Proc. R. Soc. London Ser. A*, **335**, 39 (1973).
2. K. K. Yee and L. Young, *Appl. Opt.*, **14**, 1316 (1975).
3. W. P. Wang, Thesis, University of Waterloo (1975).
4. J. L. Ord and E. M. Lushiku, *This Journal*, **126**, 1374 (1979).
5. J. L. Ord, J. C. Clayton, and K. Brudzewski, *ibid.*, **125**, 908 (1978).
6. J. C. Clayton and D. J. DeSmet, *ibid.*, **123**, 1886 (1976).
7. J. L. Ord, *ibid.*, **127**, 2682 (1980).
8. J. L. Ord, *SPIE Proc.*, **112**, 58 (1977).
9. J. L. Ord, *Surf. Sci.*, **16**, 155 (1969).
10. J. L. Ord, *This Journal*, **129**, 2038 (1982).
11. D. F. Taylor and M. J. Dignam, *ibid.*, **120**, 1299 (1973).
12. D. J. DeSmet, *Electrochim. Acta*, **21**, 1137 (1976).

Optical Anisotropy and Electrostriction in the Anodic Oxide of Niobium

C. G. Matthews, J. L. Ord,* and W. P. Wang*

Department of Physics, University of Waterloo, Waterloo, Ontario, Canada N2L 3G1

ABSTRACT

The anodic oxidation of niobium in sulfuric acid electrolyte is studied using a self-nulling ellipsometer to follow the optical changes that occur when the field in the oxide film is switched. The oxide is optically anisotropic with the anodizing field applied, and the degree of anisotropy, the ratio between index changes parallel and transverse to the field, is found to equal 2.2 by a procedure that requires consistency from the analysis of field-switching transients for a wide range of oxide film thicknesses. The film thickness increases and its refractive index values decrease when the field is applied. The dependences are not the parabolic dependences predicted by the theory of electrostriction, and the significance of this finding is discussed. Although the galvanostatic charge-discharge transients that are used to study the changes in the low-frequency dielectric constant exhibit significant hysteresis, they show that the decrease in dielectric constant with increasing field observed at optical frequencies occurs also at low frequencies. The results are compared with the dependence of dielectric constant on field deduced from open-circuit transient analysis, and the significance of the discrepancy is discussed. It is concluded that the possibility that the oxide film has a significantly polar structure remains an open question.

The anodic oxides of most valve metals appear to be optically anisotropic during anodization. The uniaxial negative anisotropy disappears when the field is removed from tantalum (1) and niobium (2-4), but substantial anisotropy remains at zero field for vanadium (5) and molybdenum (6). The associated changes in the low-frequency dielectric constant are in the same direction as at optical frequency, and the fractional changes are considerably larger at low frequency. The thickness of the oxide film is found to increase when the field is applied, and the change is of about the magnitude required by the Clausius-Mossotti relation to account for the dielectric constant changes.

The changes in film thickness and dielectric constant are thought to be due to electrostriction, the universal second-order effect which couples strain and field in nonpolar materials. In the theory of electrostriction, the dielectric constant depends on strain in much the same way as in the Clausius-Mossotti relation, and the sign of the electrostrictive coefficient determines both how the dielectric constant depends on the strain and how the strain depends on the field. When we compare the experimental results with the theory, we see that it is possible to fit the strain data by choosing a sign for the electrostrictive coefficient that is opposite to the sign in the Clausius-Mossotti relation, but neither sign can fit the dielectric constant data. If the dielectric constant data are valid, the theory can be shown to violate energy conservation (7), and it must either be modified to make the dielectric constant an explicit function of the field, or the oxide films must be assumed to be polar. Since it is the behavior of the dielectric constant that is critical in this regard, we recently developed a technique for studying dielectric constant variation under conditions where the requirements of energy conservation can be tested directly (8), and the results confirmed our earlier findings.

The functional form of the field dependence should distinguish clearly between a first-order effect in a polar material and a second-order effect in a nonpolar material. Parabolic dependences characteristic of electrostriction have been reported for both tantalum (1) and niobium (2), but all of the measurements made in our laboratory have found dependences that have been between linear and parabolic. We have thus far interpreted these results as indicating that the stress in the film does not go to zero when the anodizing field is removed, but we cannot rule out the possibility that the films have some polar characteristics, although a first-order polar effect would normally be expected to dominate completely any second-order effect.

In view of the difficulties involved in trying to relate theory to experiment, and the fact that measurements made in different laboratories agree on little beyond the sign of the effect, we decided to reexamine the experimental evidence for electrostriction in anodic oxides. In a previous paper (6) we extended the measurements to include the molybdenum system and dealt with the problems involved in anisotropic analysis in systems with substantial zero-field anisotropy. In a subsequent paper we will report the results of a study of the tantalum system where the effects are very small, but a great deal of work has been done on relaxation processes (9, 10). In this paper we report the results of a study on the most extensively studied system, the niobium system. The niobium system has many features which make it ideal for electrostrictive measurements. The oxide can be grown with 100% current efficiency and is insoluble in sulfuric acid electrolyte. Although the anodizing field is lower than in tantalum or tungsten, the dielectric constant of the oxide is higher, and the electrostrictive effects are relatively large. Perhaps the most important factor for the optical analysis is the considerable thickness that can be attained before the oxide breaks down or there is a change in the growth process. The niobium system is also one of the ones that exhibits no significant anisotropy at zero field, and this further simplifies the analysis.

The present study has three specific objectives. We first look in detail at the factors that enter into the determination of the degree of field-induced anisotropy. We then determine dependence of the film thickness and refractive index on the applied field. Finally we use galvanostatic charging curves to study the associated changes in the low-frequency dielectric constant and compare the results with those obtained using open-circuit transients (4).

Experimental

The ellipsometer used in this study is a modified version (11) of the self-nulling instrument which has been used in this laboratory for many years (12). Quadrature Faraday modulation is decoded by a two-phase lock-in amplifier and the d-c error signals are fed back to the stepping motor drives through voltage-to-frequency converters. The sine-cosine quadrature drives have a nominal resolution of 1/1600th of a degree, and under typical operating conditions the instrument has a response time of a few tenths of a second and a resolution of a few thousandths of a degree. A helium-neon laser is the light source, and all refractive indexes quoted in this paper are for a wavelength of 6328Å. The hollow equilateral glass prism

* Electrochemical Society Active Member.

Key words: capacitance, dielectrics, ellipsometry.

used as a cell requires an angle of incidence of 60 degrees. The cell has standard-taper joints through which the electrode holder, a platinum counterelectrode, a mercury-mercurous sulfate reference electrode, and a gas dispersion tube are inserted. The cell was filled with 0.1 molar sulfuric acid electrolyte, and all experiments were performed at 22°C.

The circuitry used with the cell is operated by the HP 2114B process-control computer which logs the optical data and operates the on-line displays (two storage oscilloscopes and an X-Y plotter). The current source consists of a digital-to-analog converter connected to a high-voltage operational amplifier, and a second amplifier follows the potential of the reference electrode relative to the working electrode which is held at virtual ground. A programmable amplifier interfaces the follower to a 16-bit analog-to-digital converter with a 25 μsec conversion time.

The cylindrical working electrode, prepared from a single crystal of niobium, exposes a vertical surface 1.2 cm^2 in area to the electrolyte when it is clamped between Teflon washers in a glass electrode holder. The optical measurements are made on a flat ground on one side of the cylinder. The surface was prepared for optical measurements by electropolishing in an electrolyte consisting of 1 part hydrofluoric acid to 9 parts sulfuric acid. Between experiments the electrode was stored with a thick oxide film on its surface, and the surface was freshly polished before each experiment.

Results and Discussion

The type of experiment used to grow oxide films on niobium and to study their electrostrictive properties is shown in Fig. 1. Potential is plotted *vs.* time in the lower portion of the figure, and the corresponding locus traced out by the polarizer and analyzer null readings is shown in the upper portion. The potential plotted is actually an overpotential with its zero at the potential where the optical analysis indicates that the film thickness goes to zero. The 0.204 mA/cm^2 anodizing current is applied at point A, and the oxide is allowed to grow until the optical data reach the left end of the first loop at point B1. At this point the potential is stepped at 3 sec intervals down 8 steps to C1, up 5 to D1, down 5 to E1, and back up 8 to F1 where the anodizing current is reapplied. The stepping sequence is carried out under program control, and the potential reached at points C1 and E1 is high enough to avoid the Faradaic processes associated with electrochromism and hydrogen evolution. After the current is reapplied, the oxide is allowed to continue growing until the right end of the first optical loop is reached at B2 where the stepping process is repeated. The experiment continues in this manner until stepping data have been obtained at the left and right ends of three optical loops.

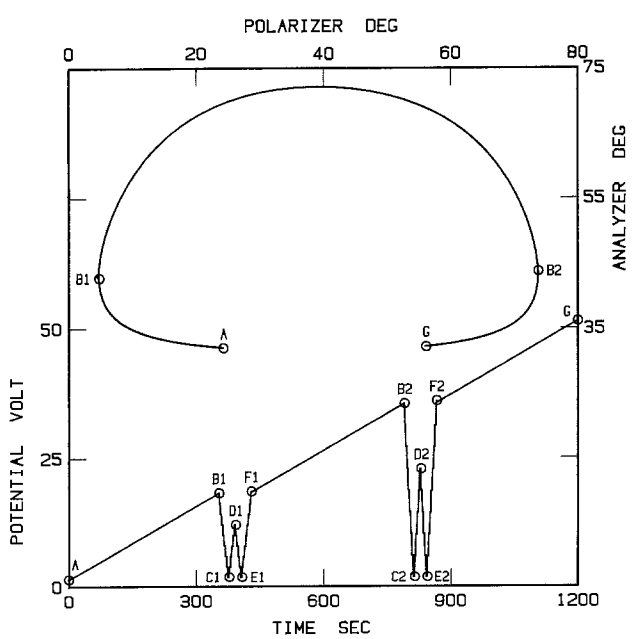

Fig. 1. Anodic oxidation of niobium at 0.204 mA/cm^2 in 0.1M sulfuric acid with stepped-potential transients applied at the points where the polarizer null reading of the ellipsometer passes through its minimum and maximum values.

The optical data recorded in the regions where the potential is stepped are shown on greatly expanded scales in Fig. 2. The progressive offset to higher polarizer readings characteristic of uniaxial negative anisotropy shows up clearly on these scales. The nomenclature used to describe the potential-switching transients is the same as in Fig. 1, and the six transients are numbered in order of increasing film thickness. The points plotted are those recorded at 1 sec intervals during film growth, and at 3 sec intervals on all potential steps except the first (where the ionic current is still appreciable).

The anlysis of optical anisotropy is essentially an analysis of the geometry of the curves in Fig. 2. On completion of the stepping sequence the data return to their respective growth curves with very little overshoot. The growth curves are clearly defined, and the interloop spacing is approximately constant and the same at both ends. The field-down ends of the stepping data lie approximately on a common growth curve, and hence the oxide film has no significant anisotropy with the field removed. At the right end, the first and second loops bracket the field-down curve and narrow the range of any extrapolation to zero field. The sixth stepping transient is the only one which deviates significantly from a common zero-field curve. The stepping transients themselves are clearly defined with parallel up-stepping and down-stepping segments which have a small offset proportional to film thickness. A proportionate offset of this type in the direction of greater film thickness is characteristic of a relaxation process rather than a growth process. What hysteresis there is in the stepping transients does not show up on a plot of this type.

The two approaches that have been used previously to analyze data similar to that in Fig. 2 both regard the approximately constant interloop spacing as the geometric feature that determines the anisotropy. In the first approach, one varies the refractive indexes in the field direction (Nz) and transverse to the field (Nx) to find the best fit to the growth curve at the anodizing field. The fitting procedure must also vary

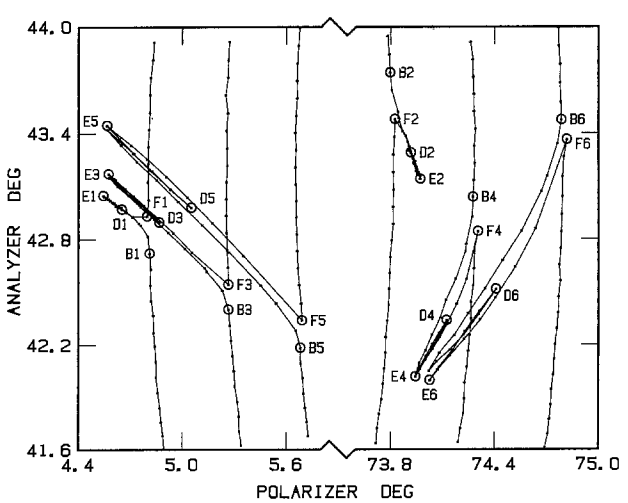

Fig. 2. Optical data in the region of the stepped-potential transients for three cycles of the experiment plotted in Fig. 1. The B-C-D-E-F labeling identifies corresponding points in Fig. 1 and 2.

the substrate index over a narrow range to deal with the uncertainty in the initial film thickness, but by using average loop width and average interloop spacing as parameters one can set up a procedure which converges rapidly to give Nx and Nz. This is the approach which was used in the vanadium study (5), and an extension of this approach was used recently in work on molybdenum (6). The extension involves fitting data in the same manner at a sequence of lower fields in order to determine the field-dependence of Nx and Nz. An Nz-Nx plot of the values determined in this manner showed a linear relation between Nz and Nx in the molybdenum system.

In the second approach, one begins by finding the isotropic index which gives the best fit to the approximately common curve traced out by zero-field data. One then assumes a linear relation between Nz and Nx, and uses the interloop spacing along with the offsets from the isotropic curve to find the constants in the relation. At zero field, Nz and Nx are both equal to the isotropic index, and the Nz-Nx slope, beta, is a measure of the degree of anisotropy induced by the field. This approach can be applied directly to systems like tantalum (1) and niobium (2) which have insignificant zero-field anisotropy, and the approach can be extended to deal with a small amount of residual anisotropy, but the extrapolations involved become rather large when it is applied to the vanadium or molybdenum systems.

The assumption underlying both of the approaches described above is that the refractive index of the oxide film depends on the field in it but not on its thickness. Both approaches also implicitly assume that the refractive index of the substrate remains constant as the film grows. These assumptions are very reasonable, and there would be no need to question them were it not for the extremely expanded scales used in the analysis and the large difference in film thickness at the points where the interloop spacing is determined. During extended film growth the topography of the metal-oxide interface may change to a greater or lesser extent depending on how the surface was prepared, and this change in topography shows up in ellipsometry as an apparent change in substrate index. As the film thickness and potential both increase, so does the possibility that pre-breakdown effects may be modifying the structure of the film and changing its index slightly. Although one cannot guard against such effects completely, one can try to use an analysis approach that is less sensitive to their influence than the approaches described above.

The approach we will use here to analyze the data in Fig. 2 is based on our observation that although particular interloop spacings may vary considerably from experiment to experiment, the field-switching transients do not change their shape if the same switching sequence is used. We begin the analysis by determining the fractional changes in index and thickness associated with each transient for a range of assumed values of beta. We then plot our results as a function of beta to find the value at which the fractional changes in index and thickness are most nearly independent of film thickness. Although this procedure involves a number of steps, the results obtained are not sensitive to any of the assumptions required. In particular, the results at any fixed value of beta are not sensitive to the location assumed for the isotropic curve, and hence are not sensitive to the substrate index or the isotropic layer index, nor are they sensitive to the data segment used in the analysis provided the ionic current is low enough to avoid significant film growth or relaxation. Here we take the lower five-eighths of the first down-stepping segment, and use a least-squares fitted function to extrapolate to zero field and interpolate to a field of 2.7×10^6 V/cm. We then plot the fractional changes in index and film thickness over this field range as a function of beta for all six transients.

The strain curves calculated by the above procedure are shown in Fig. 3, and the standard deviation from the average at each beta is shown in Fig. 4 along with comparable data for the fractional change in index Nx. Note that it is the curves from transients at the right end, 2, 4, and 6, which intersect at the steepest angles and hence determine the value of beta in this procedure. The index data behave similarly, and the curves in Fig. 4 have their minima at approximately the same point, the point where beta has a value of 2.2. Previous studies have reported values of 1.6 (2) and 2.07 (3) for beta. As Fig. 3 shows, our data give strain values which differ by more than an order of magnitude at a beta value of 1.6. Data from left-end transients 3 and 5 superimpose over a broad region spanning the optimum beta, and the combination of high resolution with low beta sensitivity make transient 5 the best one to use in determining the field dependence of the index and the strain.

Once we have determined beta we can see how our analysis procedure deals with the interloop spacings at the anodizing field. Since the analysis is based on index changes rather than absolute indexes, we must first calculate a value for Nz at the anodizing field by averaging the values which fit points B1 through B6. With an isotropic index of 2.3375 and substrate optical

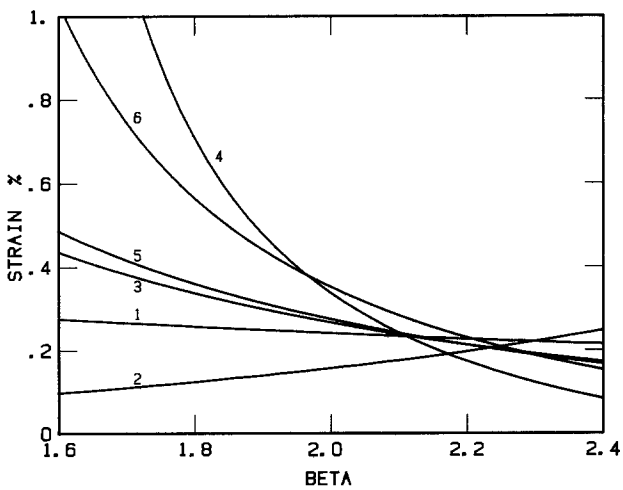

Fig. 3. Calculated strain values for each of the six transients in Fig. 2 for different assumed values of beta, the degree of anisotropy. The strain is calculated from the thicknesses at 2.7×10^6 V/cm and at zero field on the initial down-stepping segment of the potential transient.

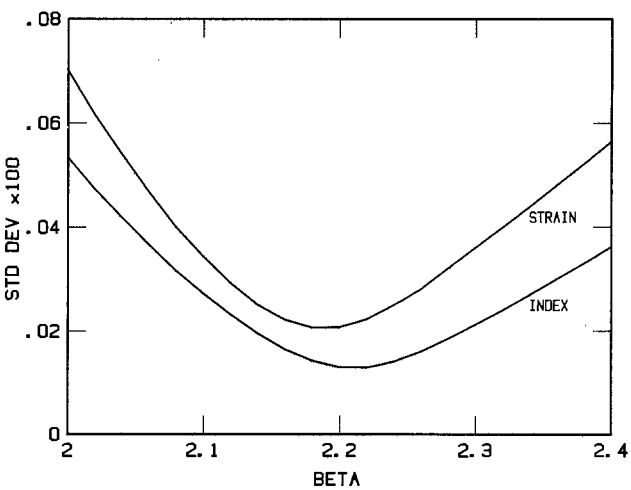

Fig. 4. Standard deviation of the strain values plotted in the right half of Fig. 3 along with the corresponding deviation in the refractive index Nx.

constants $N = 3.3447$ and $K = 3.7516$, we calculate a value for Nz of 2.30548 at an anodizing field of 4.3×10^6 V/cm. Curves calculated using these values are plotted in Fig. 5 on the same scales used in Fig. 2. The fit, although reasonable, is far from perfect. Although we cannot be certain, we think we know why the fit is not better, and we present our opinion here to help make our earlier comments about approaches to data analysis more specific. What appears to be wrong with the geometry in Fig. 2 and 5 is the width of the third loop. It is too far left at the left end and right at the right end to fit constant index growth of an anisotropic film. Optical expansion of the third loop can be produced either by increasing the index or by introducing a slight amount of absorption. Physically these effects could result from a slight modification in the structure of the film which occurs at high voltage and leads eventually to breakdown. If the data in Fig. 2 are offset to compensate for the expansion of the third loop, the low-field ends of the transients exhibit a regular offset indicative of residual anisotropy at zero field. Although we believe that the data exhibit effects characteristic of structural modification at high voltage and residual anisotropy at zero field, this is only an opinion, and we do not argue that the data warrant such a conclusion.

The fractional changes in film thickness and Nx which occur during the course of the 5th transient are plotted *vs.* field in Fig. 6. Thickness data at the anodizing field require film growth corrections and are not included in the figure. The increase in thickness and decrease in index with increasing field agree with previous work and appear to be nearly universal characteristics of valve-metal oxides. The curvature is away from the field axis, but neither slope goes to zero at zero field, so the dependences on field are not parabolic. The index curve exhibits some hysteresis, but the strain curve exhibits very little. Since the form of the field dependence and the amount of hysteresis it exhibits both can depend on the history of the oxide, it is important to specify just how the experiment was performed. In the present study, the history of the oxide and the transient switching sequence are defined clearly in Fig. 1, and the results in Fig. 6 pertain to an oxide film with this history. Although the scale factors in Fig. 6 are sensitive to the accuracy with which beta is determined by the optical analysis, the shape of the curves in the figure is determined mainly by the spacing between data points on a polarizer-analyzer plot and can be shown to be reproducible over a wide thickness range without elaborate analysis. The strain scale factor gives a magnitude for the strain

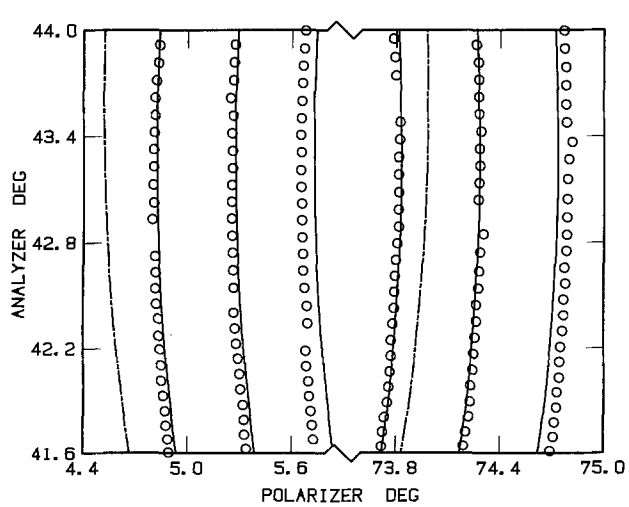

Fig. 5. The optical data at the anodizing field in Fig. 2 along with theoretical curves for an isotropic film with index 2.3375 (broken curve) and for a related anisotropic film with a beta of 2.2 and an Nx of 2.30548 (solid curve).

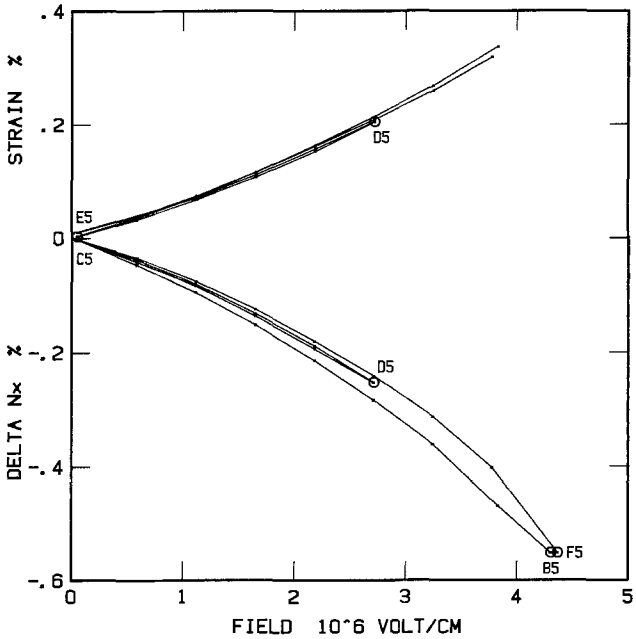

Fig. 6. Fractional changes in film thickness and refractive index transverse to the field as a function of the electric field in the oxide film for the fifth potential-stepping transient in Fig. 2.

which is intermediate between the values reported in previous studies (2, 3). Note that the fractional decrease in Nx is slightly larger than the fractional increase in thickness, and hence normal incidence optical measurements would indicate a slight decrease in optical thickness when the field is applied.

In our original study of electrostrictive effects in valve metals (13), we used an a-c technique to study the field dependence of the low-frequency dielectric constant. More recently (4, 14, 15) we have used open-circuit transient analysis for this purpose. The objective of the open-circuit analysis has been more to test the hypothesis that the ionic current is controlled by an effective field proportional to the dielectric constant than it has been to measure the field dependence of the dielectric constant itself. When it became apparent that a decrease in the dielectric constant with increasing field has serious implications for the theory of electrostriction (7), we developed a technique for studying dielectric constant variation under conditions which simplify comparison with the theory (8). The theory requires V-Q charging curves to curve toward the Q-axis, not away from it, and the experimental technique is designed to produce such curves directly using a computer-controlled constant current source. The W-shaped potential-time transient has the same turning points as the transient used for the optical measurements, but it is of much shorter duration, and has no steps.

A galvanostatic W-transient is shown in Fig. 7. The anodizing current, initially 0.204 mA/cm^2, was reduced by a factor of 16 and the overshoot was allowed to die away before the transient, which uses a 0.204 mA/cm^2 charge-discharge current, was applied. The factor of 16 reduces the uncertainty introduced by the ionic current correction, and this is the reason it is used, but it also appears to affect the time constant of relaxation processes, and hence affects the shape of the transient. The charging curve derived from the W-transient is shown in Fig. 8. The discharge segments of the transient exhibit significant upward curvature, but the charging segments are close to linear, with barely discernible upward curvature at lower potentials, and definite downward curvature as point F is approached. Clearly the average curvature is upward, but since hysteresis and curvature effects are of the same order, a proper analysis of the field dependence of the dielectric con-

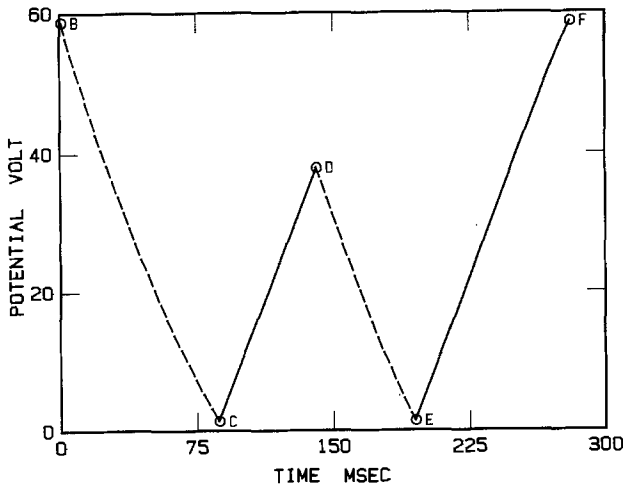

Fig. 7. Galvanostatic W-transient with alternating cathodic (broken curve) and anodic (solid curve) segments. The charge-discharge current density, 0.204 mA/cm², is sixteen times the initial galvanostatic oxidation current density.

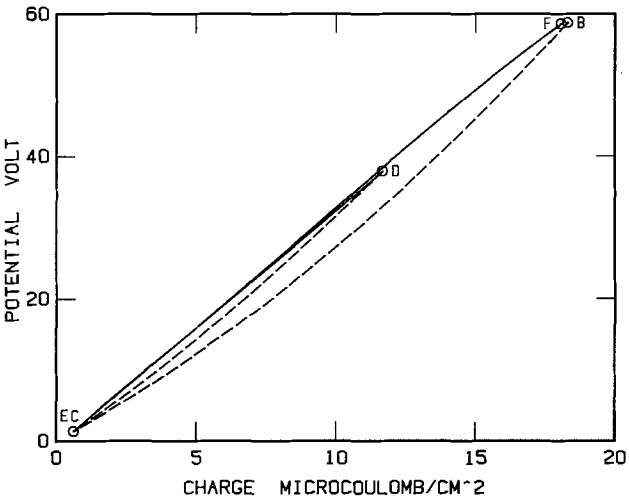

Fig. 8. Charging curve deduced from the W-transient in Fig. 7. Corresponding points in the two figures have the same labels. Broken curves indicate cathodic segments, solid curves anodic segments.

stant must involve an analysis of polarization kinetics somewhat similar to that used by Taylor and Dignam in their analysis of ionic conductivity variations (9). We will not undertake such an analysis in this paper. Instead, we will see what sort of dielectric constant variation is required to account for the shape of the first discharge segment, and we will compare the results with the dielectric constant variation deduced from open-circuit transient analysis. Although the discharge conditions are rather different, we expect the results to show some similarity.

Figure 9 shows how the reciprocal of the dielectric constant depends on the field for segment B-C of the transient plotted in Fig. 7 and 8. A reciprocal plot is used because it gives a simpler functional dependence on field. Curve R-S in the figure is the dependence of dielectric constant on field previously determined by open-circuit transient analysis (4). Aside from a positive slope, the two curves have nothing in common. At the anodizing field, the W-transient gives a value of 53 for the dielectric constant, whereas the open-circuit transient gives 130, a value which does not appear physically meaningful.

In second-order open-circuit transient analysis one is faced with the problem of analyzing the small residue left after the first-order analysis, and unfortunately the results obtained are quite sensitive to the functional dependence of dielectric constant on field used in the parameter variation process. If we regard curve B-C in Fig. 9 as approximately linear over the range of an open-circuit transient, and use this functional form in the open-circuit analysis, we get just as good a fit to the data for the dependence R'-S' as was obtained previously using R-S. The two curves are well separated, and the new value for the dielectric constant at the anodizing field is 78, a more meaningful value than the 130 obtained previously.

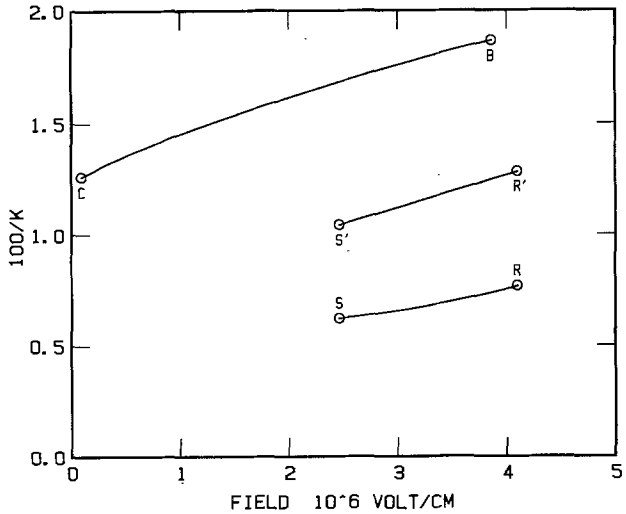

Fig. 9. Plot of reciprocal dielectric constant vs. field in the oxide film for segment B-C of the charging curve in Fig. 8. Curve R-S is the dependence previously determined by open-circuit transient analysis. Curve R'-S' is the dependence obtained from open-circuit analysis by assuming a linear dependence of reciprocal dielectric constant on field.

We have used second-order open-circuit transient analysis primarily to test the effective-field hypothesis, not to measure dielectric constant variation. What is really needed to test the hypothesis is an analysis of the hysteresis in Fig. 8 that enables one to predict the dielectric constant variation which will occur under open-circuit conditions. The open-circuit analysis can then use this disposable-parameter-free prediction to test whether or not the dielectric constant enters into the field that controls the ionic current.

The basic question as to whether the effects observed are purely electrostrictive or partially polar in nature remains unanswered by the results we have presented here. The theory of electrostriction, even when modified to account for the sign of the dielectric constant variation, is inherently second order and requires a parabolic field dependence. We have argued previously that the observed field dependence may result from the fact that the stress in the film does not go to zero at zero field as it does in the usual theoretical models. Although the present results can be interpreted as indicating some residual anisotropy at zero field, the effect appears to be too small for there to be sufficient zero-field stress to alter the field dependence to the extent observed. In all our measurements, we use galvanostatic oxidation as the reference state at which out transients begin and end, and the structure of the film may be partially polar under these conditions. It may be that the parabolic dependences which have been reported (1, 2) have been obtained under experimental conditions that reduce the size of the polar component, but since even film capacitors have been reported to retain a polar "memory" of the anodization process (16), we regard this as an open question at present.

Acknowledgments

This work received partial support from the Natural Sciences and Engineering Research Council Canada under Grant No. A-1151.

Manuscript submitted May 3, 1982; revised manuscript received July 28, 1982.

Any discussion of this paper will appear in a Discussion Section to be published in the December 1983 JOURNAL. All discussions for the December 1983 Discussion Section should be submitted by Aug. 1, 1983.

REFERENCES

1. W. D. Cornish and L. Young, *Proc. R. Soc. London, Ser. A*, **335**, 39 (1973).
2. K. K. Yee and L. Young, *Appl. Opt.*, **14**, 1316 (1975).
3. W. P. Wang, Thesis, University of Waterloo (1975).
4. J. L. Ord and E. M. Lushiku, *This Journal*, **126**, 1374 (1979).
5. J. C. Clayton and D. J. DeSmet, *ibid.*, **123**, 1886 (1976).
6. D. J. DeSmet and J. L. Ord., *ibid.*, **130**, 280 (1983).
7. J. L. Ord, *ibid.*, **127**, 2682 (1980).
8. J. L. Ord, *ibid.*, In press.
9. D. F. Taylor and M. J. Dignam, *ibid.*, **120**, 1299 (1973).
10. L. Young and D. J. Smith, *ibid.*, **126**, 765 (1979).
11. J. L. Ord, *SPIE Proc.*, **112**, 58 (1977).
12. J. L. Ord, *Surf. Sci.*, **16**, 155 (1969).
13. J. L. Ord, M. A. Hopper, and W. P. Wang, *This Journal*, **119**, 439 (1972).
14. J. L. Ord, J. C. Clayton, and W. P. Wang, *ibid.*, **124**, 1671 (1977).
15. J. L. Ord, J. C. Clayton, and K. Brudzewski, *ibid.*, **125**, 908 (1978).
16. P. W. Wyatt, *ibid.*, **122**, 1660 (1975).

Kinetics of Formation of Passive Oxide Films on Corrosion-Resistant Fe-Cr Thin Films

Boniface A. Okorie[1] **and Welville B. Nowak**

Northeastern University, Boston, Massachusetts 02115

ABSTRACT

The transient electrochemical behavior of chromium-containing amorphous and amorphous/microcrystalline iron-alloy thin films in near-neutral 1M NaCl solutions has been investigated and compared with the behavior of "bulk" amorphous and bulk crystalline specimens of comparable compositions. The films have been deposited onto Ebrite (Fe-Cr) substrates by the ion-plating technique. The transient current-decay behavior upon application of a positive voltage step from the specimen rest potential is reported here. This voltage-step technique has revealed several distinct regions in the behavior of current with time. Initially, there is an exponential decay region, with current relaxation time constant (τ_0) of 0.5-0.8 sec. Then follows another exponential decay with $\tau_1 \simeq$ 5-10 sec. The next region of current decay can be described by a power law: $i = At^{-n}$, with n in the range of 0.6-0.7 for the ion-plated films and the "bulk" amorphous Fe-Cr alloy (Metglas 2826A), and 1.0 for the bulk polycrystalline alloy (Ebrite). Finally, there is a relatively slow exponential decay region with time constant (τ_2) of 200 sec to over 1000 sec for low and intermediate values of the voltage step, ΔV. For high values of ΔV, this region is approximately exponential over limited periods of time, with τ_2 increasing monotonically from a few hundred seconds to over 6000 sec. The overall results strongly suggest that different mechanisms are operative at various intervals during the formation of the passive oxide layer.

The superior corrosion resistance of amorphous Fe-Cr and Fe-Ni-Cr alloys has been studied by several workers in recent years (1-12). These alloys are produced by liquid-quenching techniques (1-3) or by vapor-quenching techniques such as thermal evaporation, sputtering (4, 9, 11), and ion plating (10, 12). These techniques involve rapid deposition of the alloys onto highly conducting substrates. Because of the need for very rapid heat transfer (desirable cooling rates are of the order of 10^6 K/sec), the specimen dimension normal to the substrate surface will necessarily be very small. Thus, melt-spun "bulk" amorphous alloys are only available in the form of thin ribbons or wires. Sputtered and ion-plated amorphous alloys, on the other hand, are in the form of thin metallic films on bulk substrates and can therefore be very useful as corrosion-resistant coatings to protect more reactive substrates. Moreover, these low pressure techniques offer the prospect of progressive buildup of amorphous metallic materials. Previous work on the electrochemical potentiodynamic behavior of vacuum-deposited amorphous and amorphous/microcrystalline thin films (4, 9-11) showed that these films exhibit a Tafel-like (linear) behavior in the lower passive region, whereas crystalline Ebrite (Fe-26Cr-1Mo; Airco Incorporated, Berkeley, California) and melt-spun "bulk" amorphous Metglas 2826A (32Fe-36Ni-14Cr-12P-6B; Allied Chemical Corporation, Morristown, New Jersey) showed a constant, low current passive behavior in this potential region. Investigation revealed that this was partly due to the scan rate (0.020 V/min), and has led to studies of transient current decay behavior upon application of: (*i*) a voltage "hold" part way through a potentiodynamic scan, and (*ii*) a positive voltage step from the specimen rest potential. Results obtained from the progressive "voltage-hold" technique have previously been reported (12), and the present paper reports on phenomena observed using the voltage-step technique. The purpose of this paper is to investigate the kinetics of passive layer formation and compare their differences among Ebrite, Metglas 2826A, and Fe-Cr alloy ion-plated films.

Experimental Details

The thin films employed for this study were fabricated by ion plating in an argon glow discharge established between an alumina-coated tungsten crucible and a negatively biased (~ -2 kV) substrate. The argon pressure was maintained at 4.7 Pa (35 mTorr), and the substrates were polished Ebrite disks (Fe-26Cr-1Mo). About 0.5g of appropriate source material was evaporated from the resistance-heated crucible. The source material used for the experiments reported here was Metglas 2826A. The substrate-to-source distance was 6.7 cm. The substrates were ultrasonically degreased in acetone and then placed in an aluminum holder that was cooled either with Dry Ice and methanol, or with liquid nitrogen. Just prior to ion plating, the substrates were sputter-cleaned for 5-10 min at -1.8 kV. Film thicknesses were measured by interference microscopy and were about 1 μm; average rates of deposition were about 0.2 μm/min.

[1] Present address: Box 14, Okpafe Mbaise P.A., Iwo State, Nigeria.

Key words: films, metal, polarization, transients.

The "bulk" amorphous Metglas 2826A specimens were available in ribbon form. For electrochemical measurements, the thin ribbons were mounted in a polycarbonate holder exposing 1 cm^2. The substrates with ion-plated films were also mounted in a polycarbonate holder exposing a circular area of 1 cm^2.

Three specimen types [polished Ebrite disks, ion-plated films (on Ebrite substrates), and "bulk" Metglas 2826A] were used for voltage-step transient electrochemical measurements in near-neutral 1M NaCl, air saturated at room temperature. Each specimen was left in solution for 45-60 min in order to attain equilibrium for the rest potential V_r. The corrosion cell was connected to the potentiostat through a switch which permitted the cell to be electrically detached from the potentiostat while the desired value of applied anodic potential, V_a, was set on the potentiostat. When the cell was switched back to the potentiostat circuit, the working electrode (specimen) encountered a sudden voltage step ΔV ($\Delta V = V_a - V_r$). The behavior of corrosion current with time was then plotted on an X-t recorder. Separate specimens were used for each voltage step.

Results

The structure of the ion-plated films was evaluated by scanning electron microscopy, transmission electron microscopy, and selected area transmission electron diffraction. The diffraction patterns show the diffuse halos that are characteristic of amorphous materials. Differential scanning calorimetry (DSC) of the films also shows exothermic reaction peaks that indicate transition from disordered high energy phases (amorphous) to more stable equilibrium crystalline (or metastable crystalline) phase. Scanning electron microscopy revealed that the films have a cobblestone surface with a few isolated nodules. Chemical analysis of the various films showed that the chromium content ranged from 15 to 40 atom percent. In general there was chromium enrichment in the films as compared to the source material. Adhesion of the film to their substrates was very strong.

The typical behavior of a corrosion specimen upon application of a voltage step ($V = 0.7V$, $\Delta V = 0.75V$) is shown in Fig. 1. This technique has revealed five distinct current decay regions (13).

1. Initially there is a region of very rapid decay. Analysis of oscillograms showing the current-time response (Fig. 2a) shows that this region exhibits an approximately exponential behavior, with time constant (τ_0) of about 0.5-0.8 sec. The oscillogram shows two different signals: a 60 Hz signal within a 10 Hz signal. The 60 Hz signal was probably from room

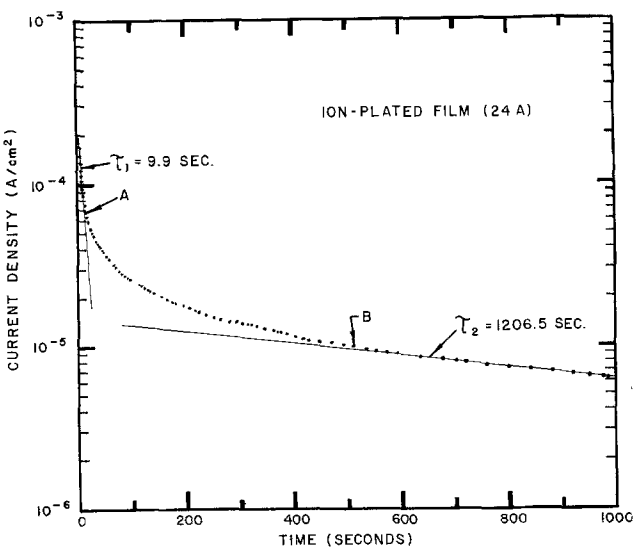

Fig. 1. Behavior of current with time following application of a 0.8V step. Ion-plated film IP-24.

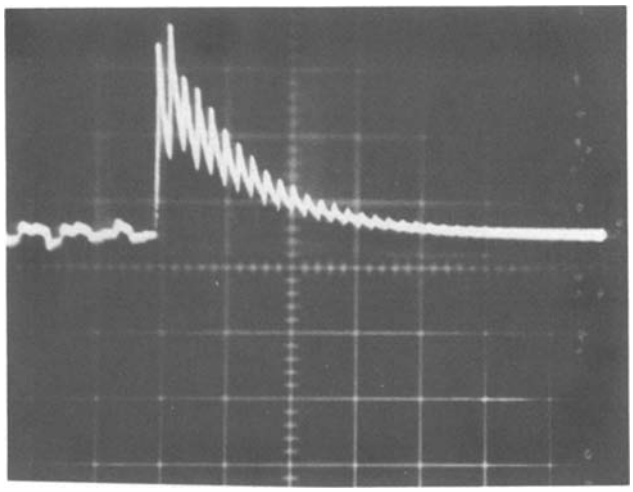

Fig. 2. (a) Typical oscillogram showing initial transient (τ_0 region). Vertical axis: specimen current density (arbitrary units); horizontal axis: time (0.5 sec/div).

pickup. To check the source of the 10 Hz signal, a resistance-capacitance circuit having nearly the same time constant as that calculated from an oscillogram such as Fig. 2a was connected in place of the corrosion cell. The $V_R - t$ oscillogram resulting from this experiment is shown in Fig. 2b. The absence of the 10 Hz signal from this oscillogram indicates that this signal is from the corrosion cell. Experiments with a dummy cell indicate that the transient associated with τ_0 is due to the passive layer buildup and not to stray capacitances in the measurement apparatus.

2. The τ_0 region is followed by one of rapid decay which could be traced on an X-t graphical recorder. This region shows an approximately exponential behavior with time constant (τ_1) of 5-10 sec for most of the specimens studied. For Ebrite, relatively high τ_1 values (15-20 sec) are encountered for very low potential steps.

3. A clearly nonexponential decay behavior follows immediately after the τ_1 region. Data from this region (A to B in Fig. 1) fall along a straight line on a double logarithmic scale, so that the region can be described by a power law

$$i = At^{-n} \qquad [1]$$

where A and n are constants. The value of n lies between 0.5 and 1.0 for most specimens.

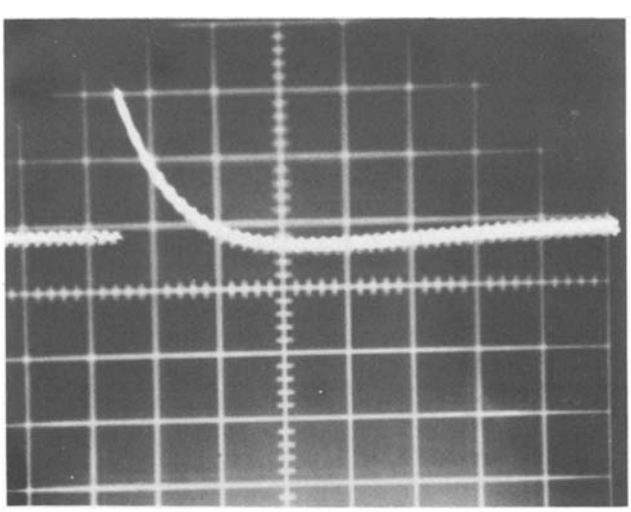

Fig. 2. (b) Response of equivalent RC circuit. Vertical axis: "specimen" current density (arbitrary units); horizontal axis: time (1.0 sec/div).

4. After the power-law decay region, another exponential decay region is observed with time constant (τ_2) of 200 to over 1000 sec for most of the specimens.

5. At low values of the voltage step ΔV, the τ_2 decay behavior is continued until the current falls to the constant "passive" value of about 2×10^{-7} A/cm^2. At high values of ΔV, τ_2 shows a time dependence for some specimens, varying monotonically from a few hundred seconds to over 6000 sec.

Very similar decay curves were reported by Sato *et al.* (14) for passive film formation on iron. However, these authors did not comment on the nature of the curves. Figures 3, 4, and 5 show the experimental current decay curves (log i *vs.* t) for Ebrite, an ion-plated film (IP-31), and "bulk" amorphous Metglas 2826A, respectively, for various values of ΔV. During each voltage-step experiment the recorder was automatically reset to the start each time it reached the end of the scale until the decay was fully recorded; but for clarity, only the first traverse to the end of the scale is presented in each case. However, most of the useful information is available in the portions of the curves presented. The constant current density values at about 1.6×10^{-7} A/cm^2 shown in Fig. 3, 4, 5, and 7 are not due to an instrumental limitation but are the dynamic equilibrium passive current. The equipment noise level is about 10^{-8} A/cm^2 for our 1 cm^2 specimens. Tables I, II, and III show the values of the current decay constants for the specimens Ebrite, ion-plated film, and Metglas 2826A, respectively. These constants have been determined from Fig. 3, 4, and 5.

It may be noted in general that the value of n approximates 0.67 for ion-plated Fe-Cr films and 1.0 for Ebrite in the passive potential region. The absence of a power-law region for the melt-spun Metglas, except in very high potential regions (0.9V and above) is also noteworthy. For the Metglas, τ_2 is remarkably low (20-45 sec) in the 0.5-0.7V potential region; relaxation to equilibrium current value is very rapid below 0.5V. The observed values of n for this specimen are 0.62 at 0.9V and 0.41 at 0.95V.

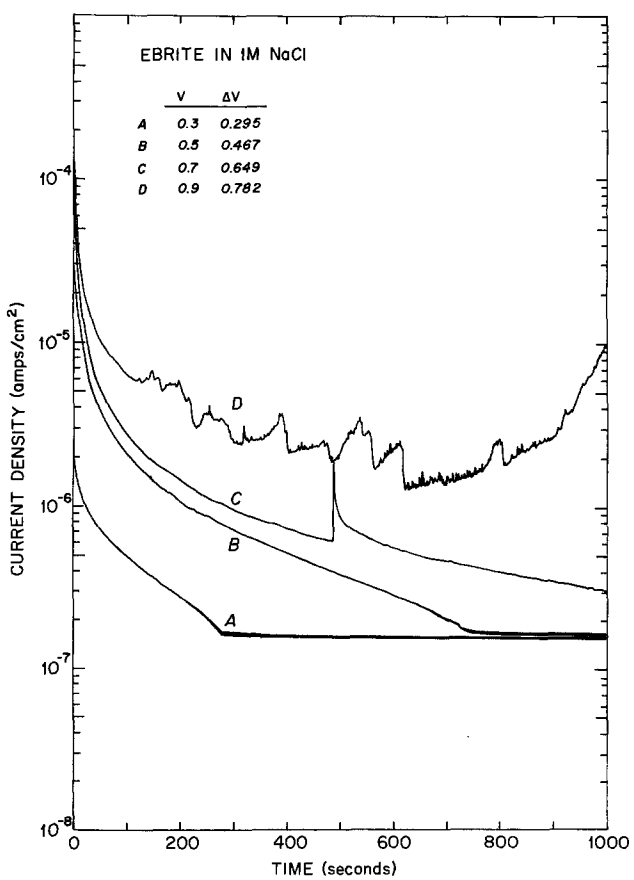

Fig. 3. Current relaxation curves for Ebrite following application of various voltage steps.

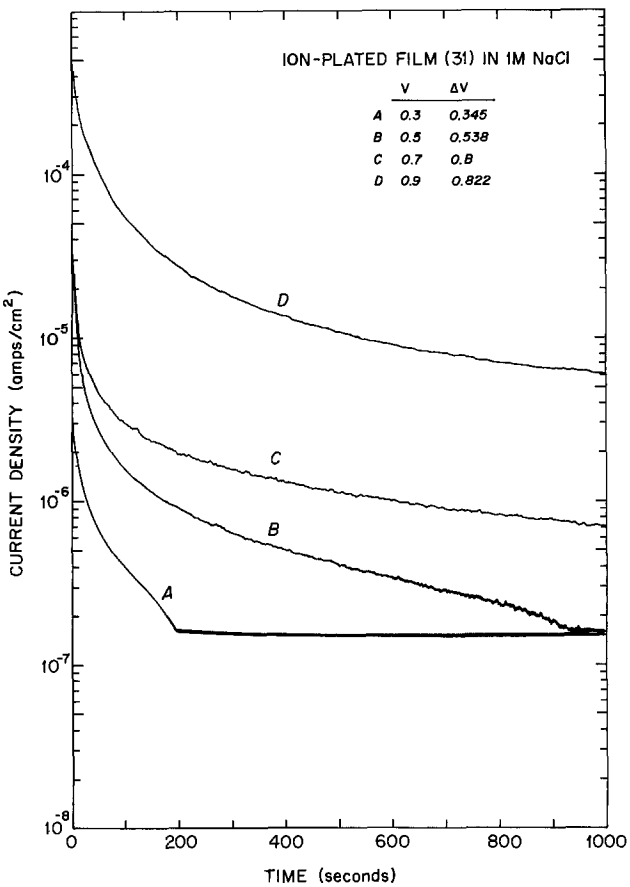

Fig. 4. Current relaxation curves for ion-plated film following application of various voltage steps.

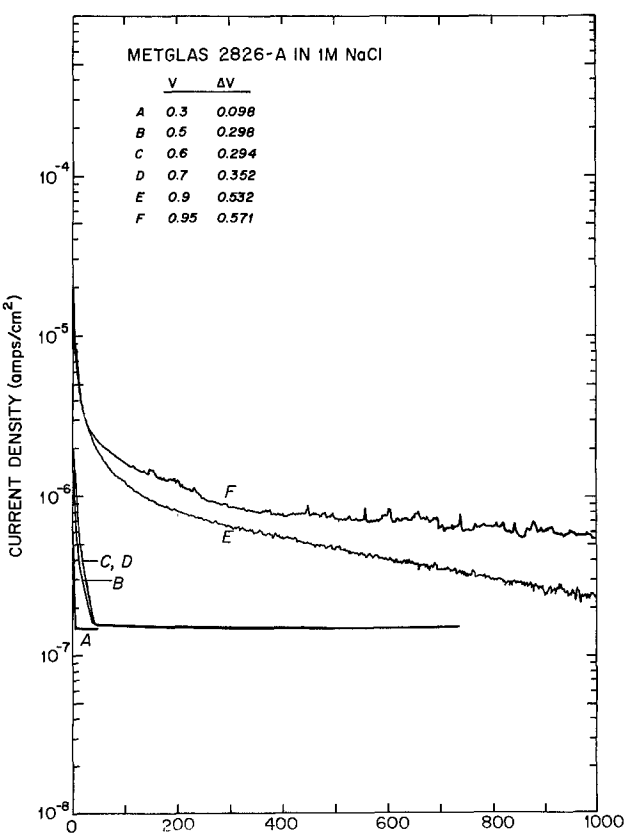

Fig. 5. Current relaxation curves for Metglas 2826A following application of various voltage steps.

Table I. Values of current decay constants for Ebrite in 1M NaCl*

V	ΔV	τ_1	n	τ_2
0.3	0.295	18	0.46	214
0.5	0.467	16	0.90	420
0.7	0.649	7	0.94	920
0.9	0.782	4	0.72	BKDN

* V = applied potential (V *vs.* SCE), τ = time constant (sec), BKDN = breakdown, ΔV = voltage step above rest potential = applied potential − rest potential (V).

Table II. Values of current decay constants for ion-plated Fe-Cr film in 1M NaCl

V	ΔV	τ_1	n	τ_2
0.3	0.345	7	0.64	135
0.5	0.538	8	0.73	665
0.7	0.800	7	0.60	1500*
0.9	0.822	1.6	1.0	1700**

* τ_2 changes with time to 2200 sec.
** τ_2 changes with time to 6500 sec.

Table III. Values of current decay constants for Metglas 2826A in 1M NaCl

V	ΔV	τ_1	n	τ_2
0.3	0.098	—	—	—
0.5	0.298	9	NA*	42
0.6	0.294	7	NA	28
0.7	0.352	7	NA	23
0.9	0.532	6	0.62	870

* NA = Not applicable.

The mean values (and extreme variations) of the rest potentials were +0.052 (±0.057), −0.065 (±0.031), and +0.285 (±0.083)V (SCE) for Ebrite, ion-plated, and Metglas specimens, respectively. The differences in V_r for Ebrite and ion-plated films were judged to be not significant in view of the magnitude of the voltage steps and the observed trends in the data. Although the V_r differences led to differences in the initial currents, only minor variations were observed in the kinetic behavior. Additionally, changes in the nature of the passive layer for these Fe-Cr alloys seem related more to the absolute voltage (SCE) than to the voltage step (12). Therefore uniform values of absolute voltage were applied rather than uniform values of ΔV. While the general kinetics of Metglas is similar to the others, more care is needed to match the behavior with an appropriate ΔV. For example, Metglas at 0.9V may be expected to behave approximately as the ion-plated films at 0.5V.

Table IV lists the amount of charge passed during each of the various current relaxation stages. The table shows that apparently most of the charge is passed during the power-law and τ_2 stages. The data also show relatively small amounts of charge for the bulk amorphous specimen (Metglas 2826A).

If one assumes that Cr_2O_3 is the major constituent of the passive layer, and that a negligibly small number of cations go into solution, then the passage of 10^{-4} C/cm^2 would correspond to a passive layer thickness of 0.1 nm. Thus, at 0.5V the total charges shown in Table IV indicate passive layer thicknesses of 1.0, 1.0, and 0.01 nm for Ebrite, ion-plated, and Metglas samples, respectively. At 0.7V, the corresponding thicknesses are 2.0, 3.0, and 0.02 nm. The Metglas thicknesses seem dubiously small and the other values also seem small. It is quite possible that in the τ_0 region there is an average current density of about 10^{-3} A/cm^2 for about 1 sec [see also Ref. (3)]. This would result in an additional charge of 10^{-3} C/cm^2 and would add 1 nm thickness to all layers, thus bringing the thickness for Metglas to a more reasonable value and reducing the differences among the materials to factor of only 2 or 3. The very large charge of the ion-plated film at 0.9V may be associated with cations going into solution. As ΔV is increased, the time interval taken by the power-law region increases and that taken by the τ_1 region decreases. Figure 6 shows a bar representation of the time intervals taken by the various decay regions. Values of the decay constants are indicated in the appropriate locations in the chart. The unmarked gaps at the end of some of the τ_2 intervals correspond to transition intervals.

While most of the ion-plated films exhibit the behavior reported above, others have been produced that are identical to the melt-spun Metglas both in potentiodynamic voltage *vs.* log i behavior at 0.020 V/min (Fig. 7) and in either voltage-hold or voltage-step current-time response. The latter films have been made by increasing the substrate-to-source distance, d, in the ion-plating equipment from 6.7 to 13 cm. Transmission electron microscopy and selected area electron diffraction appear to show no difference between the films. The films are either completely amorphous or a mixture of microcrystalline and amorphous material. However, scanning electron microscopy shows that, while most of the films with d = 6.7 cm have a relatively coarse cobblestone surface, films with d = 13 cm have relatively smooth surfaces with extremely fine surface texture. No cracks were observed on any of the films.

Discussion of Results

In the exponential decay region, the current is given by

$$i = k \exp(-t/\tau) \quad [2]$$

so that the charge passed in time t is

$$Q = \int_0^t i\,dt$$

$$= k\tau[1 - \exp(-t/\tau)] \quad [3]$$

One should note that, although the thickness, X, of the growing passive layer may be proportional to Q, X cannot be quantitatively related to Q until further information is available as to the proportion of Q that goes into oxide layer formation and the proportion that corresponds to cations going into solution (15). However, assuming a direct relation between X and Q, ex-

Table IV. Amount of charge passed in various current decay regions (μC)

	Ebrite			Ion-plated film			Metglas 2826A		
V	Q_1	Q_p	Q_2	Q_1	Q_p	Q_2	Q_1	Q_p	Q_2
0.3	11	80	78	10	78	38	—	—	—
0.5	134	840	190	73	650	250	5.7	—	7.3
0.6	—	—	—	—	—	—	7.6	—	11
0.7	226	1360	411	152	1650	1410*	10.3	—	11.6
0.9	306	1750+	BKDN	1320	31900	2520**	28.5	461	404

+ Charge measured only up to middle of power-law region owing to film breakdown.
* τ_2 changed from 1500 to 2200 sec; 500 μC was measured in the τ_2 = 1500 sec region, and 910 μC in the τ_2 = 2000 sec region.
** τ_2 changed from 1700 to 6500 sec. Value of charge given is measured in τ_2 = 1700 sec region only.

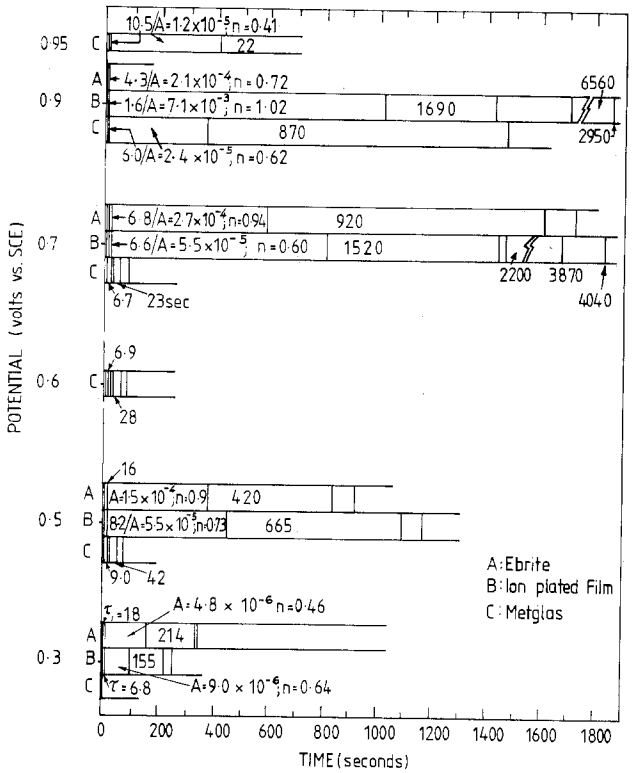

Fig. 6. Bar representation of time intervals taken by various current decay regions.

perimental data from the exponential decay regions indicate an asymptotic growth law for the passive layer, given by

$$X = K\,[1 - \exp\,(-t/\tau)] \qquad [4]$$

The rate of layer growth is then

$$\frac{dX}{dt} = \frac{K}{\tau}\exp\,(-t/\tau)$$

$$= \frac{K}{\tau} - \frac{X}{\tau}$$

$$= A - BX \qquad [5]$$

where $A = K/\tau$ and $B = 1/\tau$ are constants.

In the power-law region, we have

$$i = A_1 t^{-n} \qquad [6]$$

and

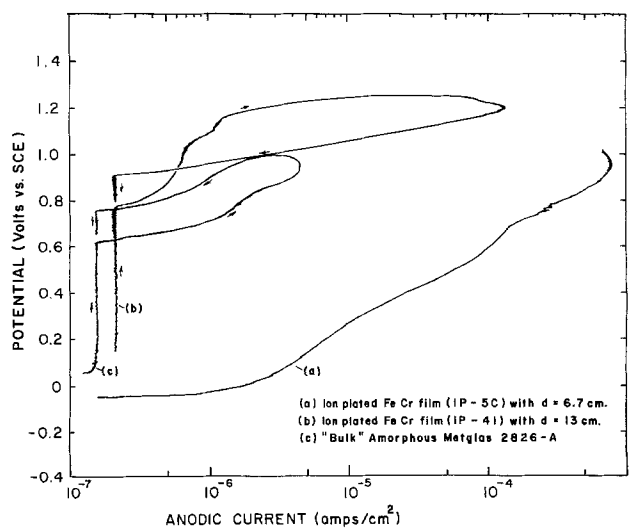

Fig. 7. Polarization curves for ion-plated films and Metglas 2826A.

$$\frac{dX}{dt} = B_1 t^{-n} \qquad [7]$$

For Ebrite in 1M NaCl, $n \approx 1$. Thus from Eq. [6]

$$i = A_1/t$$

Since i is proportional to the rate of growth of the oxide layer we have

$$i = C\frac{dX}{dt}$$

Thus

$$\frac{dX}{dt} = \frac{C'}{t} \qquad [8]$$

Integration of [8] gives the logarithmic oxidation equation

$$X = a + b \log t \qquad [9]$$

In the general case where $n \neq 1$, integration of Eq. 7 gives

$$X^{\left(\frac{1}{1-n}\right)} = \left(\frac{B_1}{1-n}\right)^{\left(\frac{1}{1-n}\right)} \cdot t$$

or

$$X^{n'} = K_p \cdot t \qquad [10]$$

where $K_p = (B_1 n')^{n'}$ and $n' = \dfrac{1}{1-n}$.

When $n \approx 0.67$ (such as for the ion-plated films, or for Metglas 2826A specimen at 0.9V), Eq. [10] gives the cubic oxidation relation

$$X^3 = K_p t \qquad [11]$$

where $K_p = 27B_1^3$. Also, when $n \approx 0.5$ (such as for Metglas 2826A at ~0.95V), we obtain the parabolic oxidation law

$$X^2 = K_p t \qquad [12]$$

where $K_p = 4B_1^2$.

Our observed transients indicate that no single model is adequate for explaining the full range of current decay behavior exhibited by the specimens. The passive layer thickens by asymptotic growth kinetics in all the regions except that of power law (16). The data in the τ_1 region also fit a logarithmic growth law as well as the modified form of the inverse logarithmic law due to Ghez (17). In the power-law region, the passive layer thickens by logarithmic, cubic, or parabolic kinetics. The amorphous Metglas 2826A obeys either a parabolic or a cubic kinetic law, the ion-plated Fe-Cr film obeys a cubic kinetic law, and the crystalline Ebrite (Fe-Cr alloy) obeys logarithmic kinetics.

Four major models have been suggested for interpreting film growth on metals, and various investigators have attempted to fit their kinetic data to these models [see, for example, the review paper of Brusic (18) and the more recent work of Lukac *et al.* (19)]. These models are: (*i*) that of Mott and Cabrera (20) wherein $1/X = A - B \ln t$ [X = film thickness, t = time, A and B are constants]; (*ii*) modification of (*i*) by Ghez (17) wherein $1/X = A' - B' \ln [(t + t_o)/X^2]$ (*iii*) Sato and Cohen (21) wherein $X = C + D \ln (t + t_o)$; and (*iv*) Fehlner and Mott (22) wherein a different mechanism of growth than that of Sato and Cohen is postulated but leads to the same functional relationship of X to t.

Because our data give reasonably good fits to more than one of these functions over portions of the current decay it is not possible to select a preferred model. Lukac *et al.* (19) (for passive films on iron in a borate solution at pH 8.6) found a similar situation with respect to choice of model, although they did not observe the multiple regions reported here. They also encountered inconsistencies between the models and

their observed temperature and potential effects. Their conclusion was that either the existing models do not postulate the correct mechanism or they are in need of modification.

A Model for Passive Film Formation

The observation of five distinct passive layer growth regions may be modeled as follows. It is assumed that, at the rest potential, there are one or two monolayers of metal oxide/hydroxide on the metal surface. Upon application of a voltage step, oxide nucleation takes place by the growth of discrete oxide islands on top of the initial layers just discussed. It is assumed that a large number of nuclei, N_o, is formed initially, and growth proceeds by planar diffusion parallel to the surface of the specimen. The current-time relation for "instantaneous" nucleation and growth is given by (17, 23, 24)

$$i = q_{mon}\pi\theta^2 D \exp(-\pi\theta^2 D N_o t) \quad [13]$$

or

$$i = i_o \exp(-kt) \quad [14]$$

where θ is a constant dependent on the potential, the molecular weight M, and density ρ of the oxide; D is the diffusion coefficient of the metal cation, and

$$q_{mon} = \frac{z\mathbf{F}l\rho}{M}$$

equals the charge involved in the formation of a monolayer (coulombs cm^{-2}) where l = height of edge, cm. The τ_o region corresponds to the "instantaneous" formation of a very large number of discrete nuclei (N_o) on the specimen surface immediately following the application of a voltage step, where the term k in Eq. [14] is equal to $1/\tau_o$.

The passive layer next thickens by field-assisted diffusion and high field migration of cations. In this region, the current density, i, depends on the rate of cation transport through the diffusion layer away from the electrode surface into bulk solution

$$i = z\mathbf{F}\frac{dN}{dt} \quad [15]$$

where z = number of electrons removed from a metal atom as it is oxidized, $\mathbf{F}$ = the Faraday constant, and dN/dt = number of mols reacting in unit time. The reaction rate is governed by the cation diffusion. From Fick's first law, we have, assuming concentration polarization

$$\frac{dN}{dt} = -DS\frac{C_o - C}{\delta^*} \quad [16]$$

where D = diffusion coefficient of cation, S = surface area of specimen, C_o and C are the cation concentrations at the electrode and in bulk solution, respectively, and δ^* is the boundary (diffusion) layer thickness.

The reaction rate, dN/dt, is equal to the increase in cation concentration in a solution of volume, v. Thus

$$\frac{dN}{dt} = -v\frac{d(C_o - C)}{dt} \quad [17]$$

Thus

$$i = -z\mathbf{F}v\frac{d(C_o - C)}{dt} \quad [18]$$

From Eq. [16], [17], and [18]

$$\frac{di}{dt} = -z\mathbf{F}\frac{DS}{\delta^*}\cdot\frac{d(C_o - C)}{dt} = -\frac{DS}{\delta^* v}\cdot i \quad [19]$$

Integration of Eq. [19] gives

$$i = i_o \exp\left(-\frac{SD}{\delta^* v}\cdot t\right) \quad [20]$$

which is of the form

$$i = i_o \exp(-k't) \quad [21]$$

where

$$k' = \frac{SD}{\delta^* v} = \frac{1}{\tau_1}$$

Equation [20] has been obtained by assuming concentration polarization, but is also valid for polarization due to an activation overpotential.

Owing to the very high rate of passive layer growth in the τ_1 decay region just discussed, the layer formed in this region is not well developed, but has a porous, loose structure. The amount of porosity in the initially formed passive layer depends on values of the potential step. Muller's model for passivity (25) helps to explain the mechanism of pore formation during the initial stages (τ_o stages) of layer building. According to this model, the passive layer is nucleated at certain points and extends outward over the metal surface as a layer of uniform thickness. The degree of coverage of the metal surface depends on the number of nucleation sites on the metal surface during the τ_o stage, and the uncovered areas give rise to a network of pores which become trapped as the layer thickens in the τ_1 region. High electric field strengths exist in the vicinity of the pores, and at some characteristic layer thickness corresponding to time τ_1, the activation energy for oxide growth in the pores (leading to pore filling) becomes less than that for the continued thickening of the layer by the diffusive movement of cations to the film-solution interface, which is limited by the rate of diffusion through the boundary layer. Thus the pore-filling mechanism becomes dominant, leading to the power-law relation

$$i = At^{-n}$$

In time, the passive layer becomes less porous as a result of: (*i*) pore filling, and (*ii*) decrease in pore density with increase in thickness in accordance with the relation (26-28)

$$N_p = AX^{-m}$$

where N_p = pore density (pores cm^{-2}), X = film thickness, and A and m are constants with $m \simeq 2$ to 3.

The pore-filling mechanism becomes less important as the passive layer becomes less porous, and a field-assisted diffusion and ion migration mechanism becomes dominant resulting in a new exponential decay (τ_2 region). Variation of τ_2 with time for high values of the anodic voltage could be due to an increase in the activation energy for ion transfer with increasing thickness of the passive layer in this region, possibly due to change in layer composition.

The experimental results show that the power-law region is absent in the case of "bulk" amorrphous Metglas, and the ion-plated film at 13 cm substrate-source distance, at low values of the anodic voltage. This might be explained by the high reactivity of the amorphous structure and the surface morphology. For low values of anodic voltage, the relatively small field in the film results in a modest growth rate so that all surface nucleation and growth sites are fully activated. Since virtually every surface site is a nucleation site on the highly reactive surface, a dense, relatively pore-free passive layer develops from the very start. On the other hand, for high values of anodic voltage, a high growth rate results from the relatively high electric field and high current density. Passive layer growth at the most active nucleation sites may be so rapid that the development of other sites is bypassed. This would lead to a porous structure for the initial passive layer (τ_o and τ_1 regions). In the case of crystalline Ebrite, the specimen surface is less reactive and fewer nucleation centers may be expected both for low and for high values of anodic voltage. A considerable level of porosity should therefore exist in the passive layer formed at low as well as high voltages, and this may be associated with observation of the power-law region for all the values of voltage steps.

Summary and Conclusions

The transient data from the voltage-step technique reveal several distinct regions in the behavior of current with time. The results indicate that the process of passive layer formation can be very complex and cannot be fully explained by a single mechanism. The various regions have been attributed to different mechanisms that successively become dominant. The regions may be modeled in terms of: (*i*) the nucleation of a large number of oxide islands and lateral growth of these islands (τ_0 region); (*ii*) initial rapid growth of a three-dimensional layer with a porous structure (τ_1 region); (*iii*) pore filling together with continued film thickening leading to a denser, well-developed layer (power-law region); and (*iv*) thickening of the dense passive layer by a field-assisted diffusion mechanism (τ_2 region). The τ_2 region may exhibit a time constant that increases with time (at high values of the voltage step) that might be due to changes in activation energy for diffusion in the oxide film as the film thickens. The experimental data in all the regions (except the power-law region) obey an asymptotic growth law; the data in the τ_1 region also fit the logarithmic growth law as well as a modified form of the inverse logarithmic law. In the power-law region, the growth kinetics are logarithmic for the Ebrite substrate, parabolic for the ion-plated Fe-Cr films, and parabolic or cubic for the amorphous alloy (Metglas 2826A).

The mechanisms of passive layer formation and their associated kinetics depend on the morphology of the surface. It has been found possible to reproduce the excellent corrosion resistance of certain "bulk" amorphous metal alloys by their vapor-deposited (ion-plated) film counterparts provided the film is sufficiently smooth.

Manuscript submitted June 25, 1981; revised manuscript received *ca.* July 15, 1982. This was Paper 225 presented at the Los Angeles, California, Meeting of the Society, Oct. 14-19, 1979.

Any discussion of this paper will appear in a Discussion Section to be published in the December 1983 JOURNAL. All discussions for the December 1983 Discussion Section should be submitted by Aug. 1, 1983.

REFERENCES

1. M. Naka, K. Hashimoto, and T. Masumoto, *J. Jpn. Inst. Met.*, **38**, 835 (1974); also *Corrosion*, **32**, 146 (1976).
2. K. Asami, K. Hashimoto, T. Masumoto, and S. Shimodaira, *Corros. Sci.*, **16**, 909 (1976).
3. K. Hashimoto, K. Osada, T. Masumoto, and S. Shimodaira, *ibid.*, **16**, 71 (1976).
4. W. B. Nowak, *Mater. Sci. Eng.*, **23**, 301 (1976).
5. R. B. Diegle and J. E. Slater, *Corrosion*, **32**, 155 (1976).
6. T. M. Devine, *Scri. Metall.*, **10**, 309 (1976).
7. T. M. Devine, *This Journal*, **124**, 38 (1977).
8. M. Naka, K. Hashimoto, and T. Masumoto, *J. Non-Cryst. Solids*, **28**, 403 (1978).
9. R. B. Diegle, D. M. Lineman, and W. K. Boyd, Interim Technical Report, ONR, Report No. ONR-00014-770048 (1978).
10. W. B. Nowak and M. F. Collins, in "Rapidly Quenched Metals III," Vol. 2, B. Cantor, Editor, Book No. 198, The Metals Society, London (1978).
11. R. B. Diegle, *Corrosion*, **35**, 250 (1979).
12. W. B. Nowak and B. A. Okorie, in "Proceedings of International Conference on Ion-Plating and Allied Techniques, London, July, 1979," p. 153, CEP Consultants Ltd., Edinburgh (1979). Also accepted for publication in *Corrosion*, Journal of National Association of Corrosion Engineers, Houston, Texas.
13. W. B. Nowak and B. A. Okorie, Abstract 255, p. 662, The Electrochemical Society Extended Abstracts, Los Angeles, California, Oct. 14-19, 1979.
14. N. Sato, T. Noda, and K. Kudo, *Electrochim. Acta*, **19**, 471 (1974).
15. V. M. Novakovski and Y. A. Likhachev, *ibid.*, **12**, 267 (1967).
16. B. A. Okorie, Ph.D. Dissertation, Northeastern University (1980).
17. R. Ghez, *J. Chem. Phys.*, **58**, 1838 (1973).
18. V. Brusic, in "The Anodic Behavior of Metals and Semiconductor Series, Oxides and Oxide Films," Vol. I, J. W. Diggle, Editor, Marcel Dekker, New York (1973).
19. C. Lukac, J. B. Lumsden, S. Smialowska, and R. W. Staehle, *This Journal*, **122**, 1571 (1975).
20. N. Cabreta and N. F. Mott, *Rep. Prog. Phys.*, **12**, 163 (1948).
21. N. Sato and M. Cohen, *This Journal*, **111**, 512 (1964).
22. F. P. Fehlner and N. F. Mott, *Oxid. Met.*, **2**, 59 (1970).
23. H. R. Thirsk and J. A. Harrison, "A Guide to the Study of Electrode Kinetics," pp. 115-135, Academic Press, London and New York (1972).
24. F. C. Frank, *Proc. R. Soc. A*, **201**, 586 (1950).
25. R. D. Armstrong and J. A. Harrison, *This Journal*, **116**, 328 (1969).
26. W. J. Muller, *Trans. Faraday Soc.*, **27**, 737 (1931).
27. M. Clarke, in "Properties of Electrodeposits: Their Measurement and Significance," R. Sard, H. Leidheiser and F. Ogburn, Editors, pp. 122-141, The Electrochemical Society Softbound Proceedings Series, Princeton, NJ (1975).
28. R. Kerr, R. M. Angles, and K. W. Caufield, *J. Soc. Chem. Ind.*, **66**, 5 (1947).

On The Limiting Rate Of Magnetoelectrolytic Deposition Via Pulsed Current

Thomas Z. Fahidy*

Department of Chemical Engineering, University of Waterloo, Waterloo, Ontario, Canada N2L 3G1

ABSTRACT

Peak currents observed in magnetically assisted pulsed current electrolysis are compared to peak currents observed in the absence of magnetic fields and with theoretical current ratio relationships. The magnetic enhancement effect, which has a minimum at an intermediate frequency, is interpreted in terms of a magnetohydrodynamic model; a comprehensive theory is not available at present for quantitatively accurate predictions.

In recent years, a number of researchers carried out studies of electrolysis via pulsating potential or current in the mass transport-controlled regime, especially from the viewpoint of efficiency with respect to d-c electrolysis. Despic (1) and Popov *et al.* (2) used the unidimensional unsteady-state diffusion equation with appropriate boundary conditions as their model, in terms of an effective current and potential defined as a time-averaged value over the pulsation cycle. Cheh (3) employed the concept of a diffusion layer thickness at the end of one pulse (0.01-0.1 mm, on an average, for cycles of 1-100 sec duration, respectively); later, Ibl (4) analyzed the efficiency of pulsed electrolysis in terms of the pulsed diffusion layer thickness-to-Nernst diffusion layer thickness ratio. His treatment leads to results quantitatively similar to Cheh's, although numerical discrepancies between the two approaches may be as high as 30%, with respect to Cheh's model, at large pulse durations and on-times. The comprehensive theoretical analysis of Cheh (3) yields a relatively simple relationship between $(i_p)_L$, the limiting current density in pulsed electrolysis and $(i_{dc})_L$, the limiting current density in d-c electrolysis

$$R_L \equiv \frac{(i_p)_L}{(i_{dc})_L} = \frac{1}{1 - \frac{8}{\pi^2}\phi(\theta, \theta_2)} \qquad [1a]$$

where

$$\phi \equiv \sum_{n=1}^{\infty} \frac{1}{(2n-1)^2} \cdot \frac{\exp[(2n-1)^2 a\theta_2] - 1}{\exp[(2n-1)^2 a\theta] - 1} \qquad [1b]$$

assuming perfect mixing and a 100% cathode current efficiency of metal deposition. Comparison with experimental data obtained by Cheh in gold deposition indicates moderate to good agreement with theory, at least in the systems so far investigated.

The question of relative efficiency of pulsed electrolysis becomes even more interesting in magnetoelectrolysis where a (uniform) magnetic field is superimposed transversally on the pulsed potential or current. It has been recently demonstrated (5) that in the instance of half-rectified sine-wave potentials the larger the magnetic field strength, the larger the ratio of peak currents (observed in the presence of the magnetic field with respect to the absence of the magnetic field), but as the frequency is increased, this ratio approaches unity; in other terms, past a certain frequency the magnetic field effect becomes minimal. Similar results were obtained (6) with rectified square-wave pulses; moreover, there appears to be a definite relationship between frequency, magnetic field strength and the potential drop between electrodes beyond which hydrogen evolution at the cathode prevents the formation of a good-quality metal deposit. These results create a considerable incentive for a thorough analysis of the maximum allowable (*i.e.*, limiting) deposition rates in pulsed magnetoelectrolysis, with obvious potential gains for industrial electroplating.

* Electrochemical Society Active Member.

Key words: pulsed current, magnetoelectrolysis, copper deposition.

Experimental

Aqueous acidified copper sulfate solutions were electrolyzed using a pulsed electric field with a peak voltage range of 1-3.2V and a frequency range of 1-1000 mHz, obtained from a conventional signal generator/amplifier assembly. The magnetic field was generated by a 5 kW Walker regulated d-c electromagnet whose strength varied between 4 (residual flux density) and 685 mT at the applied pole-face separation. The electrolytic cell was an open-top 8 cm long rectangular Plexiglas box where two vertical copper electrodes, with active area of 2.5 × 1.46 cm were placed in grooves 5.8 cm apart. A typical current-potential variation, shown in Fig. 1, indicates the magnetic field effect in d-c electrolysis (used as reference condition); the limiting current density observed in the residual field, 489 A/m^2 differs only by about 7% from the theoretically (7) computed value of 526 A/m^2. In the relatively strong magnetic field of 685 mT, however, no clear limiting current plateau can be observed, as shown in earlier work, *e.g.*, (8). Here, the limiting current density (point L in Fig. 1) is defined as the largest value i_L at which bright deposits can be produced. In Fig. 2 the combined effect of magnetic field strength and pulse frequency is demonstrated: as the

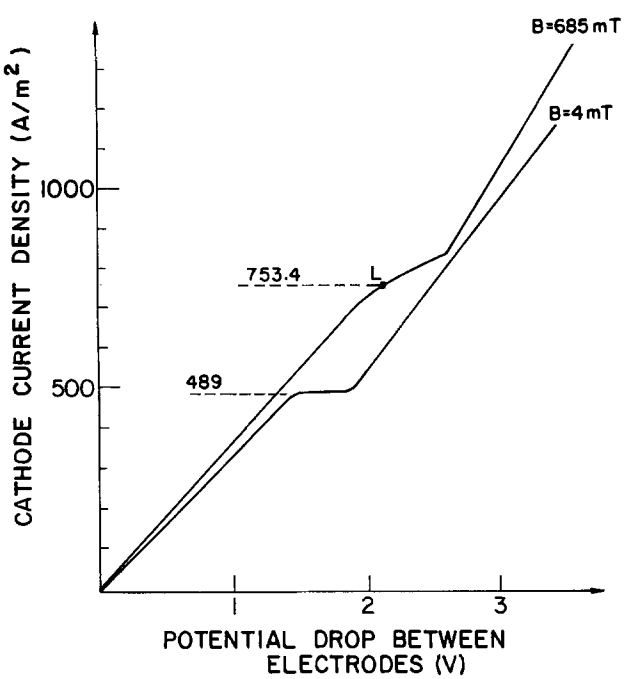

Fig. 1. Typical current-potential variations under d-c conditions ($CuSO_4$:0.511 mol/L; H_2SO_4:1.057 mol/L; T = 28°C).

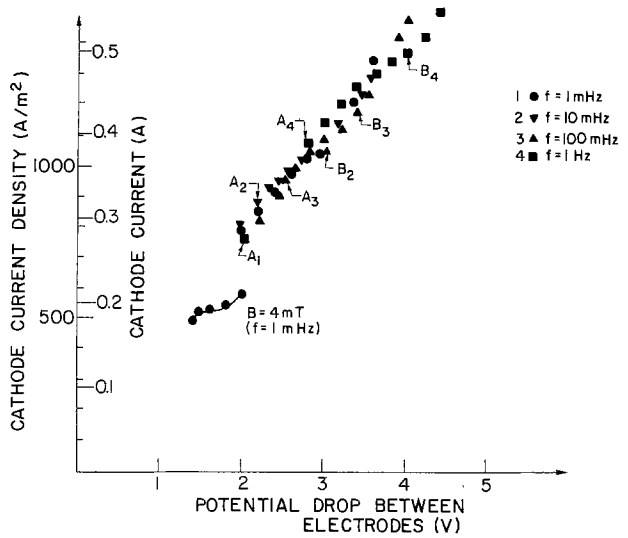

Fig. 2. The effect of pulsation frequency on a magnetoelectrolytic copper deposition (A_i: max. potential drop at which bright deposits can be obtained; B_i: onset of visible H_2 evolution at cathode).

frequency is increased, both the maximum voltage drop allowed for producing bright deposits, V_m, and the onset voltage for visible H_2 evolution increase. Voltage drops between points A_i and B_i corresponding to the same frequency constitute a zone of indeterminacy, where the relatively good quality of the copper deposit is not consistently reproducible. From a technical standpoint V_m is an important design parameter for such a magnetoelectrolytic cell, since it represents the largest practical voltage drop imposable between the two electrodes. As demonstrated in Fig. 3, V_m is essentially a linear function of the magnetic flux density at a fixed pulsation frequency and its value can be considerably higher than under d-c conditions.

Analysis

In order to compare the efficiency of pulse magnetoelectrolysis to pulsed-current electrolysis in the absence of a magnetic field, it is beneficial to return to Eq. [1] and to consider the specific instance where the off-time and on-time periods are equal. Since $\theta_2 = \theta/2$, Eq. [1b] takes the degenerate form

$$\phi(\theta) = \sum_{n=1}^{\infty} \frac{1}{(2n-1)^2} \cdot \frac{\exp\left[\tfrac{1}{2}(2n-1)^2 a\theta - 1\right]}{\exp\left[(2n-1)^2 a\theta - 1\right]} \qquad [2a]$$

which may be rearranged to read

$$\phi(\theta) = \frac{1}{2} \sum_{n=1}^{\infty} \frac{1}{(2a-1)^2} \cdot \frac{1 - \exp\left[-\tfrac{1}{2}(2n-1)^2 a\theta\right]}{\sinh\left[\tfrac{1}{2}(2n-1)^2 a\theta\right]} \qquad [2b]$$

At infinitesimally small values of θ, the limiting values are

$$\lim_{\theta \to 0} \phi = \frac{\pi^2}{16}$$

and

$$\lim_{\theta \to 0} R_L = 2$$

On the other hand, as θ increases indefinitely, the limiting values become

$$\lim_{\theta \to \infty} \phi = 0$$

and

$$\lim_{\theta \to \infty} R_L = 1$$

In the intermediate range the infinite series may be truncated to its first term without significant loss of accuracy, when $a\theta \geq 1.0$, *e.g.*, when $a\theta = 1$ the rigorous value of $\phi = 0.75786$ compares favorably with the single-term approximation of 0.75542. In consequence, Eq. [1] may be approximated at a good accuracy by

$$R_L \cong \frac{1}{1 - \frac{4}{\pi^2} \cdot \frac{1 - \epsilon^{-\frac{1}{2}a\theta}}{\sinh\left(\frac{1}{2}a\theta\right)}} \qquad [3]$$

In Fig. 4 the variation of the theoretical peak current with the $(a\theta)$ parameter is compared to experimentally observed values in the absence of a magnetic field and at the highest magnetic flux density attainable in the experimental apparatus. The numerical value at $a = 0.01224\ s^{-1}$ was computed from estimated values of the diffusion layer thickness ($\delta = 0.339$ mm) and the diffusion coefficient ($D = 5.7 \times 10^{-6}$ cm²/s) of the electrolyte. It is interesting to note that although the electrolyte was not stirred, the experimental ratios of $B = 4$ mT do not differ appreciably more from the theoretical relationship than Cheh's experimental observations in well-stirred gold plating solutions. On the other hand, experimental R_L values in the presence of a transverse magnetic field exhibit a strong positive deviation from Cheh's model at high frequencies and seem to approach theoretical $(i_p)_L/(i_{dc})_L$ ratios pertaining to $(\theta - \theta_2)/\theta < 0.5$ conditions. As shown by Cheh (3), for the general case of an asymmetric pulse

$$\lim_{a\theta \to 0} R_L = \frac{\theta}{\theta - \theta_2} \qquad [4]$$

hence the low-$a\theta$ tendency at $B = 685$ mT in Fig. 4 suggests a roughly equivalent behavior of the $\frac{\theta - \theta_2}{\theta} \cong 0.3$, $B = 0$ case.

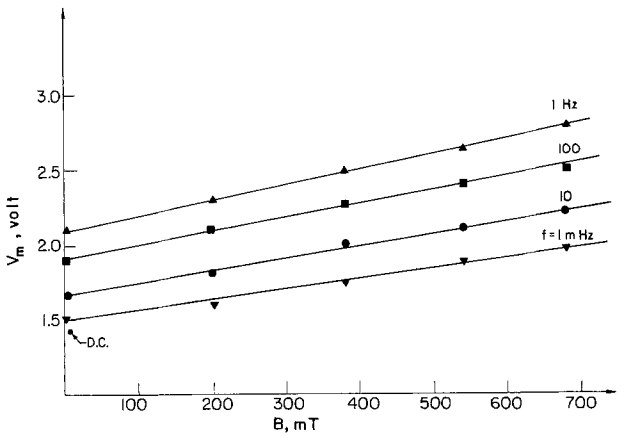

Fig. 3. The variation of the maximum allowable voltage drop for producing bright cathode deposits in a magnetoelectrolytic cell with magnetic field strength and pulsation frequency.

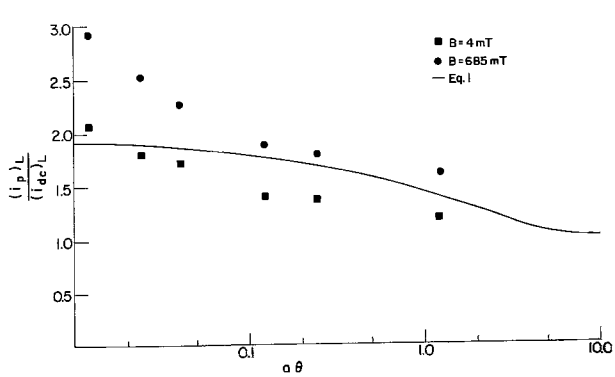

Fig. 4. Comparison of theoretical and experimental current peak ratios (the latter refer to associated V_m values).

It is instructive at this point to compare the results so far obtained to Ibl's previously quoted work (4). In the specific case of $\theta_2 = \theta/2$, Ibl's method yields in this instance

$$R_L = \frac{2}{\sqrt{\frac{D\theta}{2\delta_n^2} + 1}} \quad [5a]$$

$$= \frac{2}{0.04955\sqrt{\theta + 1}} \quad [5b]$$

As shown in Table I, the discrepancy between Cheh's and Ibl's model increases gradually as the pulsation period becomes larger; at $\theta < \sim 3$ sec the discrepancy is practically negligible but both models severely underestimate R_L values observed experimentally in the presence of magnetic fields.

In the foregoing analysis the d-c limiting current was used as the reference quantity, following Cheh's and Ibl's approach. Further insight is obtained, however, if peak currents observed at various frequencies but in the absence of the magnetic field are compared to peak currents observed at the same frequencies, but in superimposed magnetic fields the peak current ratio

$$R_p = \frac{(i_p)_{L,m}/(i_{dc})_L}{(i_p)_L/(i_{dc})_L}$$

$$= \frac{\text{Limiting current at } V_m, \text{ in the presence of a magnetic field}}{\text{Limiting current in pulse electrolysis, in the absence of a magnetic field}} \quad [6]$$

represents directly the magnetic field effect in pulse electrolysis without reference to d-c conditions. Figure 5 compares experimental values of R_p and the $(i_p)_{L,m}/(i_{dc})_L$ ratio with the theoretical variation of R_L as the $a\theta$ parameter is varied. The curves indicate that although the relative increase in current amplitude with respect to magnetic field-free d-c electrolysis diminishes as $a\theta$ is increased, the magnetic field effect on limiting current in pulse electrolysis reaches a relative minimum at an intermediate $a\theta$ value (*i.e.*, at an intermediate frequency). The latter finding cannot be explained quantitatively at the present time by means of a fundamental physical model due to our incomplete understanding of all processes involved, but a qualitative interpretation in terms of magnetohydrodynamic (MHD) principles can be offered.

The starting point is the effect of the MHD force generated by the interaction of the pulsed electric and the uniform magnetic field. If the pulsed current is represented by its Fourier expansion with amplitude i_p and if B_o is the magnitude of the magnetic flux density, an MHD body force per unit electrolyte volume

$$F_d = \frac{i_p B_o}{2} + \frac{2 i_p B_o}{\pi} \sum_{n=0}^{\infty} \frac{(-1)^n}{2n+1} \cos\left[(2n+1)\pi \frac{t}{\theta}\right] \quad [7]$$

is generated in the vector direction mutually perpendicular to the direction of the electric and of the magnetic field. This pulsating lateral force field has a nonzero vector curl (9, 10) and according to Kelvin's theorem

$$\text{curl}\,[(\mathbf{i} \times \mathbf{B})/\rho] = \frac{1}{\rho}\text{curl}\,(\mathbf{i} \times \mathbf{B}) + \frac{1}{\rho^2}(\mathbf{i} \times \mathbf{B})\,\text{grad}\,\rho \quad [8]$$

it will generate a vorticity field $\boldsymbol{\omega} = \text{curl}\,\mathbf{v}$ due to its rotational nature.

$$\frac{D}{Dt}\left(\frac{\boldsymbol{\omega}}{\rho}\right) - \left(\frac{\boldsymbol{\omega}}{\rho}\right) \cdot \text{grad}\,\mathbf{v} = \frac{1}{\rho}\text{curl}\left(\frac{\mathbf{i} \times \mathbf{B}}{\rho}\right) \quad [9]$$

Consider first the frequency zone to the right of the R_p minimum in Fig. 5. In this low frequency range the pulsating force and vorticity field possess a relatively large penetration distance parallel to the electrode surfaces in the associated boundary layer, resulting in a concentration gradient field where each principal component (*i.e.*, each gradient element in the three Cartesian directions) is represented by a non-negligible magnitude. The measured current is determined in the limiting range by the concentration gradient component normal to the electrode surface, $\partial C/\partial y$. In order to compute this quantity, the convective-diffusion equation (strictly correct only at very low active ion concentrations)

$$\frac{\partial C}{\partial t} + \mathbf{v} \cdot \text{grad}\,C = D\,\text{divgrad}\,C \quad [10]$$

would have to be solved with appropriate boundary conditions, if they, and the velocity field $\mathbf{v}$ were accurately known. As the frequency is increased the vorticity field generates increasingly larger $\partial C/\partial x$ and $\partial C/\partial z$ components, hence the current through the electrodes becomes relatively smaller (with respect to pulsation in the absence of the magnetic field) as $\partial C/\partial y$ becomes relatively smaller, hence R_p decreases. As the frequency of the pulsating field is increased to values shown to the left of the R_p minimum in Fig. 5, the MHD force field begins to oscillate at smaller amplitudes, consequently the generated vorticity field will produce $\partial C/\partial x$ and $\partial C/\partial z$ gradient components with decreasing amplitudes; the $\partial C/\partial y$ component becomes relatively stronger and current through the electrodes, hence R_p begins to increase. It is important to remember that R_p is not a direct measure of $\partial C/\partial y$ in the magnetic field, in as much as the denominator in Eq. [5], also varies with frequencies; R_p is a measure of the relative variation of $\partial C/\partial y$ in a magnetic field with respect to $\partial C/\partial y$ in the absence of a magnetic field, at a given frequency.

The foregoing analysis is based on purely MHD-oriented arguments, without considering kinetic aspects of cathodic deposition. As shown by the theory of cyclic

Table I. Comparison of R_L values at various lengths of the pulsation period

θ s	R_L $B = 0$ Cheh's model (Eq. [1])	R_L $B = 0$ Ibl's model (Eq. [5])	R_L Experimental (B = 685 mT)
0.5	1.94	1.93	3.20
1.0	1.92	1.91	2.92
2.0	1.89	1.87	2.53
3.33	1.85	1.83	2.27
10	1.77	1.73	1.88
20	1.68	1.64	1.80
100	1.38	1.34	1.63
1000	~1.00	0.78	1.58

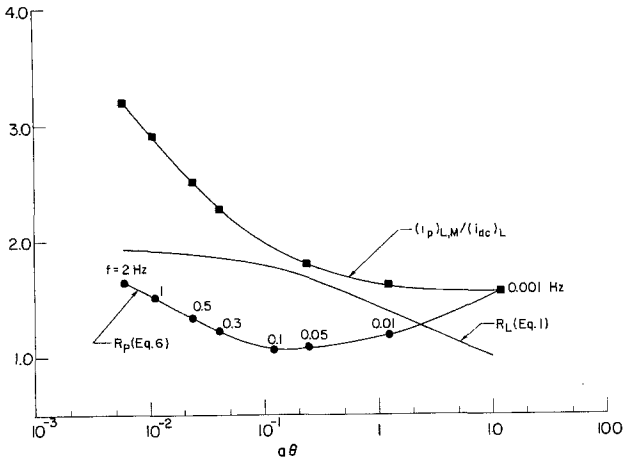

Fig. 5. The variation of current peak ratios in the presence and the absence of a magnetic field of B_o = 685 mT.

electroanalytical processes (11, 12), interaction with kinetic parameters becomes signficant only at much higher pulsation frequencies, unless the electrode-kinetic rate is extremely slow. In the case of the electronation of cupric ions and within the pulsation frequency range of this work MHD-based arguments appear to be entirely adequate, although a quantitative MHD model cannot yet be proposed at this stage.

Concluding Remarks

Experimental data so far obtained and the preceding treatment of observations in magnetically assisted pulsed current electrolysis demonstrate the beneficial effect of a magnetic field on transport rates in the process. Although the exact mechanism governing the effect of pulsation frequency on the relative transport enhancement is not well understood, the approach presented here represents the first step towards a comprehensive study of pulse-magnetoelectrolysis. Fast electroplating is one particular technology where such results might be potentially important.

Manuscript submitted April 26, 1982; revised manuscript received *ca.* Aug. 27, 1982.

Any discussion of this paper will appear in a Discussion Section to be published in the December 1983 JOURNAL. All discussions for the December 1983 Discussion Section should be submitted by Aug. 1, 1983.

Publication costs of this article were assisted by the University of Waterloo.

LIST OF SYMBOLS

a	diffusion parameter in Cheh's analysis: $a = \pi^2 D/4\delta^2$
$\mathbf{B}$	magnetic flux density vector; B_0 its magnitude (unit employed is the millitesla with symbol mT)
C	electrolyte concentration
D	electrolyte diffusivity
$\mathbf{i}$	current density vector
$(i_{dc})_L$	limiting current density under d-c conditions, and in the absence of a magnetic field
i_p	current density amplitude in pulsed current electrolysis
$(i_p)_L$	limiting current density in pulsed current electrolysis, and in the absence of a magnetic field
$(i_p)_{L,m}$	as $(i_p)_L$, but in the presence of a magnetic field, corresponding to V_m
R_L	ratio of $(i_p)_L$ to $(i_{dc})_L$; Eq. [1]
R_p	defined in Eq. [5]
t	time
V	potential drop imposed between electrodes; V_m its maximum value allowed for bright cathode deposition
$\mathbf{v}$	velocity vector
x	Cartesian coordinate along the electrode height
y	Cartesian coordinate normal to the electrode surface
Z	Cartesian coordinate parallel to the electrode surface
δ	thickness of the diffusion layer (d-c conditions)
θ	pulsation period; θ_2 off-time (half of the pulsation period)
ρ	electrolyte density
$\boldsymbol{\omega}$	vorticity vector; $\boldsymbol{\omega} = \text{curl } \mathbf{v}$

REFERENCES

1. A. R. Despic and K. I. Popov, *J. Appl. Electrochem.*, **1**, 275 (1971).
2. K. I. Popov, D. N. Keca, S. I. Vidojkovic, B. J. Lazarevic, and V. B. Milojkovic, *ibid.*, **6**, 365 (1976).
3. H. Y. Cheh, *This Journal*, **118**, 551, 1132 (1971).
4. N. Ibl, *Metalloberflache*, **33**, 51 (1979).
5. M. S. E. Abdo, M. S. Quraishi, and T. Z. Fahidy, Proceed. 2nd World Congress of Chem. Eng., pp. 214-216, Montreal, Canada, October 4-9, 1981.
6. M. S. E. Abdo and T. Z. Fahidy, Paper presented at ACHEMA Meeting, Frankfurt am Main, Germany, June 6-12, 1982.
7. J. S. Newman, in "Electrochemical Systems," Chap. 17, Prentice Hall, Englewood Cliffs, NJ (1973).
8. S. Mohanta and T. Z. Fahidy, *Can. J. Chem. Eng.*, **50**, 248 (1972).
9. J. A. Shercliff, "A Textbook of Magnetohydrodynamics," Section 4.11, Pergamon Press, Inc., Elmsford, NY (1965).
10. T. Z. Fahidy, *Electrochim. Acta*, **18**, 607 (1973).
11. Z. Galus, "Fundamentals at Electrochemical Analysis," Chap. 17, 18, Wiley-Holsted, New York (1976).
12. A. J. Bard and L. R. Faulkner, "Electrochemical Methods," Chap. 6, 9, John Wiley and Sons, Inc., New York (1980).

Electrodeposition of Tantalum Carbide Coatings from Molten Salts

Kurt H. Stern* and Stanley T. Gadomski

Chemistry Division, Naval Research Laboratory, Washington, D.C. 20375

ABSTRACT

Adherent tantalum carbide coatings have been deposited on nickel substrates from a ternary (Li, Na, K)F eutectic containing a few percent each of K_2TaF_7 and K_2CO_3.Tantalum and carbon are deposited simultaneously on the nickel cathode where they react to form the carbide at 750°-800°. The coatings are highly resistant to abrasion and are thermally stable to ~600°.

The need in a variety of technologies to protect metals from mechanical degradation caused by wear and erosion at increasingly higher temperatures has led to much recent activity in attempting the deposition of various coatings to serve this purpose. Refractory carbides, because of their great hardness and good oxidation resistance, have become prominent candidates for such applications.

Thus far, however, all of the deposition methods employed have drawbacks. Most of the methods which have been used for the preparation of carbides (1) produce the bulk material and thus are not suitable for coatings. Deposition from the gas phase, either by reaction of halogenides with carbon-containing gases or by decomposition of carbonyls, appears to be a promising method for applying coatings, but has not yet been fully exploited. Currently, the most successful commercial method appears to be plasma processing, in which finely divided carbides impinge directly on the surface to be coated. However, the method, which has so far been applied mainly to tungsten carbide deposition, requires very high temperatures and is line-of-sight.

Electrodeposition from molten salts, in contrast, offers the potential advantages of lower temperatures, the ability to coat complex shapes, and the fine control

* Electrochemical Society Active Member.
Key words: ceramics, electrode.

that can be applied to electrical variables. Weiss and Andrieux (2, 3) were probably the first to show that refractory carbides could be prepared by electrodeposition. Carbides of molybdenum and tungsten were produced by the electrolysis of melts containing B_2O_3, Na_2O, or Li_2O, LiF, an oxide of the metal, and Na_2CO_3 or Li_2CO_3 as the source of the carbon. The borate melt evidently served to dissolve the oxide. Small crystals were produced whose stoichiometry primarily depended on the carbonate/oxide ratio. More recently Gomes and Wong (4) reported the deposition of WC from an NaCl melt containing Na_2WO_4, a graphite anode serving as the source of carbon. However, their purpose was to produce the material rather than a coating; and in fact the deposit did not have the properties desirable in a protective coating.

Early work on the electrodeposition of refractory metals from molten salts similarly did not lead to adherent coatings. Mellors and Senderoff (5), who cite much of the earlier literature, seem to have been the first to produce satisfactory coatings. The key features of their process include (*i*) fluoride as the only anion, (*ii*) 15-75% of the cation to be K^+, Rb^+, or Cs^+, and (*iii*) the absence of any oxyanion with which the metal to be plated could complex. To fill these requirements the ternary eutectic of LiF-NaF-KF (FLINAK) is very satisfactory. Operating temperature is 750°-800°, and the current density is 10-100 mA/cm^2. The valence of the cation to be plated is evidently fairly critical. For example, for tungsten it is +4.5, which is obtained by reacting $WF_6(g)$ with W in the melt prior to electrolysis. For tantalum it is +5, which is easily obtained by dissolving K_2TaF_7 in the melt.

We considered it possible that the method of Senderoff and Mellors might form the basis for the electrodeposition of refractory carbides. If carbon could be codeposited with the metal, and if the metal and carbon would then react on the substrate, an adherent deposit of carbide might form. Major questions were: (*i*) whether metal and carbon would react below 800°, since the reaction between the elements in bulk typically occurs near 1400°, (*ii*) whether the carbonate serving as the source of carbon, being an oxyanion, would interfere with the metal deposition, and (*iii*) whether carbonate reduction in FLINAK would yield carbon.

As regards the last point, Bartlett and Johnson (6) have calculated $E°$ for the electrolysis of pure alkali metal carbonates as a function of temperature. They find that although the anodic reaction is always

$$CO_3^{2-} = CO_2 + \tfrac{1}{2}\,O_2 + 2e \qquad [1]$$

there are four possible cathodic processes

$$CO_3^{2-} + 4e^- = C + 3\,O^{2-} \qquad [2]$$

$$CO_3^{2-} + 2e^- = CO + 2\,O^{2-} \qquad [3]$$

$$M^{n+} + ne = M \qquad [4]$$

$$2CO_3^{2-} + 10e^- = C_2^{2-} + 6\,O^{2-} \qquad [5]$$

Which of these processes occurs is known for the pure carbonates, but is unknown for a dilute solution of carbonate in FLINAK. For our method to be feasible [2], (or conceivably [5]) must occur.

Since the preparation of a melt containing $W^{+4.5}$ is experimentally somewhat difficult, we decided to begin with tantalum, whose required valence of +5 is easily obtained by the addition of commercially obtainable K_2TaF_7 powder.

To our knowledge there has been no previous work on the electrodeposition of tantalum carbide in any form, and no successful electrodeposition of any refractory carbide coating.

Experimental

Materials.—Reagent grade LiF, NaF, and KF were individually vacuum dried at 450° for several days. K_2TaF_7 (Alfa) was used without pretreatment. Reagent-grade anhydrous K_2CO_3 was oven dried at 120° and stored in a desiccator.

Tantalum anodes were obtained as ¼ in. diam rods from Materials Research Corporation. The material is stated to be 99.996% pure. Carbon anodes were ¼ in. spectroscopic carbon. They were ultrasonically cleaned in propanol to remove loose carbon particles and oven dried.

Rectangular cathodes, 5 × 0.8 cm, were cut from Nickel sheet 200 (Huntington Alloys), an alloy of 98.85% Ni, and polished with 600 grit SiC paper. (However, in later experiments polishing was found to be unnecessary.) They were welded onto long steel rods at their narrow end for immersion into the melt. Before immersion they were etched for 30 sec in a solution of HNO_3, H_2SO_4, H_3PO_4, and acetic acid (3:1:1:5), washed with H_2O, methanol, and dried.

Procedure.—All plating experiments were carried out in a gas-tight, cylindrical Inconel reactor, 6 in. in diameter and 18 in. long, positioned in an electric furnace. At the upper end, a water-cooled annular brass flange was welded onto the Inconel reactor. The top was closed with a brass plate, bolted to the flange. Four brass tubes were screwed into threaded holes in the top of the plate. Electrodes and an alumina-sheathed Chromel-Alumel thermocouple passed through these tubes into the reactor and were electrically insulated from the reactor with Nylon Swagelok fittings. Needle valves in the top of the reactor permitted evacuation of the reactor or the passage of gases into and out of it.

The melt was contained in a crucible, 3½ in. diam, 5 in. high, positioned on a stand within the reactor. In early experiments the crucible was made of Inconel, but the fluoride melt leached chromium out of the alloy. Subsequent experiments were therefore conducted in crucibles made of Nickel 200.

The predried melt components were weighed and mixed in a dry box to give the composition of the ternary eutectic (FLINAK) KF-LiF-NaF (42-46.5-11.5 mol percent, mp 457°), transferred to the crucible and placed in the reactor. Approximately 800g FLINAK were used.

The temperature was slowly raised with the reactor under vacuum, for 2-3 days. When the temperature had reached ~500°, a flow of dried and deoxygenated argon was substituted for the vacuum. At this point various purification procedures were tried. If no additional purification was carried out, the subsequent deposits were of poorer quality, less adherent, and the current efficiency was low. Since voltammetric curves indicated the presence of reducible impurities, an electrochemical purification step was introduced. The melt was electrolyzed at 2-3V between carbon electrodes, the current and total charge passed being monitored by an ammeter and coulometer, respectively. During the electrolysis the current dropped continuously until it reached a final value of 1/3 of its initial value after ~0.2 equivalent of charge had passed. Solid deposits (not further analyzed) were visible on the cathode. For electrolysis at 3V the cathode evolved gas when immersed in water, indicating the deposition of alkali metal. No change was obvious on the anode. Both preelectrolysis electrodes were removed immediately after electrolysis. 5-10 weight percent (w/o) K_2TaF_7 and the desired amount of K_2CO_3 were then added to the melt. (At higher temperatures K_2CO_3 appeared to decompose before dissolving.) Electrodes were then inserted in the melt and the temperature raised to 750°-770°. Usually the OCV was monitored with an electrometer (Princeton Applied Research Model 136) until the voltage stabilized. The effect of the purification on the current-voltage curve and the effect of temperature on the purified melt are shown in Fig. 1.

Electrolyses were carried out with either a potentiostat (PAR Model 173) equipped with a plug-in Model 179 coulometer, or (at currents > 1A), a Hewlett-

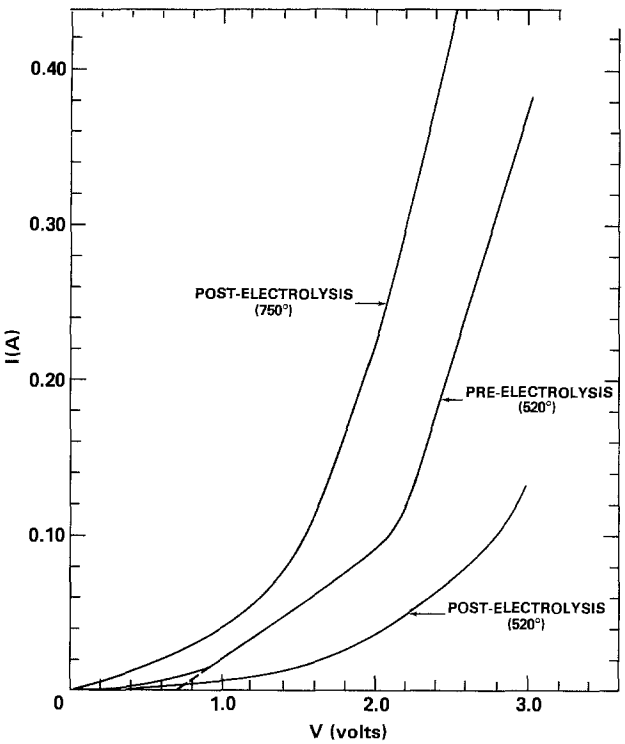

Fig. 1. The effect of electrolysis and temperature on current-voltage behavior of FLINAK. Graphite electrodes.

Packard Model 6264B Power Supply and Koslow Model 541 Coulometer. Both constant current and constant voltage electrolyses were tried, but, after it was noticed that the *I-V* relation was not unique, being dependent on factors such as the size of the anode, electrolyses were run at constant voltage since it is the driving force for the reaction that is expected to control the nature of the deposition reaction. In general, 0.02 equivalents of charge were passed, which was small compared to the total amount of carbonate present.

After electrolysis, electrodes were freed of adherent frozen melt by ultrasonic cleaning and weighed to determine the current efficiency. Coatings which appeared sound in a low power optical microscope were further examined in a scanning electron microscope (AMR Model 1000). The composition of the deposit was determined by x-ray diffraction using a Norelco goniometer x-ray diffraction apparatus with Ni-filtered $CuK_{\alpha 1}$ radiation. Selected coating specimens were epoxy mounted and metallographically polished to produce cross sections of the coating/substrate, which were examined by SEM/EDXA (energy dispersive x-ray analysis) to establish the nature of the coating-substrate interface and the disposition of the metals (by x-ray mapping).

Mechanical and thermal tests were also done. For this, the cathode was cut with a carbide saw into 2-3 pieces so that all tests could be performed on the same sample.

The apparatus used to obtain friction values was a "stick-slip" machine which utilizes a sphere sliding on a plane surface. The slider in the "stick-slip" apparatus is attached to an elastically restrained friction arm, and the sample is clamped to a sliding platform so that the disk moves under the steel (52100) slider. Two pairs of resistance strain gauges, bonded to the arm, measure the normal and tangential forces (load and friction).

The sample was cleaned ultrasonically in acetone and then rinsed with isopropanol. The sliders were cleaned by refluxing benzene in a Soxhlet extractor, stored in toluene, and when needed, removed and then rinsed with copious amounts of acetone and then isopropanol.

Measurements were done dry-sliding in air, with the arm loaded with a force of 9.8N. Unilateral traverses were made at a sliding speed of 0.1 mm/sec.

Hardness measurements were made on a Tukon Microhardness heater, using loads ranging from 50 to 1000g on a portion of the coating which had been polished to allow measurements of the small indents. Selected samples were tested for thermal stability by hanging them into the hot zone of a furnace in quiet air and measuring the weight change on a Cahn Model 1000 recording microbalance while the temperature was raised over a period of several days. Weight changes of 0.1 mg are easily detected.

Results

Several kinds of preliminary experiments were carried out to ascertain whether the process, as envisaged, was feasible. (A) To determine whether the carbide would form, tantalum was plated between a Ta anode and a carbon cathode from a melt containing dissolved Ta^{+5} (added as K_2TaF_7). Examination of the Ta-C interface by Auger analysis showed the presence of carbidic carbon. (B) The role of the anode in the electrolytic reduction of CO_3^{2-} seemed at first somewhat ambiguous. In early experiments carbon anodes were generally consumed, consistent with the results of Gomes and Wong (4) who used carbon anodes as the only source of carbon in the electrolytic formation of WC from a chloride melt. However, when the fluorides were more carefully dried, carbon anodes no longer lost weight, even when carbonate was absent from the melt and no carbide formed. It seems likely that carbon reacts electrochemically to form fluoromethanes (7), but only in the presence of moisture. There is also an "anion effect" on graphite electrodes in melts (8) but, the objective of this study being carbide formation, fluoride electrochemistry was not pursued further. It seems evident, however, that, since no carbide formed during tantalum plating from shorted tantalum and graphite anodes when the melt contained no carbonate, the anode did not serve as a carbon source.

In early experiments it seemed that this arrangement produced better deposits, but as the purification of the melt improved, the carbon anode seemed to serve no useful purpose and the final arrangement consisted of tantalum as the only anode.

To gain some insight into the current-voltage-composition relations of the deposition process, current-voltage curves were run for the cells Ta|FLINAK + K_2TaF_7|Ni and C|FLINAK + K_2CO_3|Ni. To avoid exceeding the 1A limit of the potentiostat the cathode consisted of a Ni wire, 1.6 mm diam, immersed to a depth of 5 cm. Figure 2 shows the current-voltage curve for several concentrations of Ta^{+5}. The reasons for the crossing of the lines at low applied voltages is not clear, but at higher voltages the current increases with increasing Ta^{+5} concentration, as expected. A more informative view is shown in Fig. 3, which gives the current as a function of Ta^{+5} concentration at various voltages. Particularly at higher voltages, limiting currents are reached beyond which additional solute does not lead to increased current, presumably because the current is limited by the reduction kinetics at the cathode surface. The limiting concentration is reached between 5-10 w/o, the concentration range suggested by Mellors and Senderoff (5) for Ta plating. Corresponding curves for the carbonate reduction are shown in Fig. 4 and 5. Even at the highest voltages the limiting concentration lies below 0.5%. The deposit formed was carbon, showing that reaction [2] occurred and indicating that one prerequisite for carbide formation was met. On the basis of these curves it was expected that very low carbonate concentrations would be sufficient to yield an adequate amount of carbon for carbide deposition, *i.e.* for a fixed Ta-Ni potential difference the Ta^{+5} and CO_3^{2-} concentrations could be adjusted to yield approximately equal partial currents

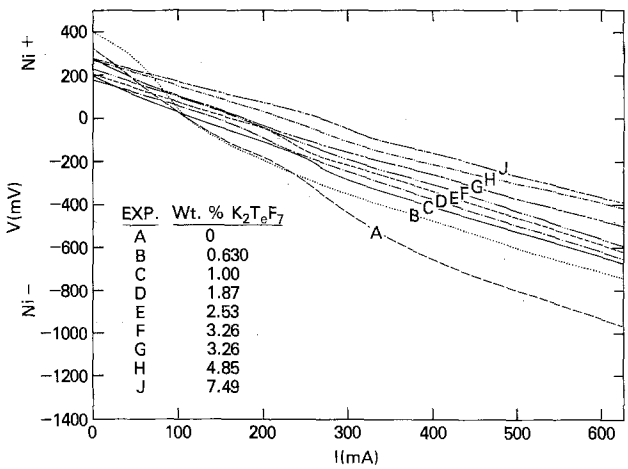

Fig. 2. Current-voltage behavior of the cell Ta|FLINAK + K_2TaF_7|Ni for various K_2TaF_7 concentrations at 750°.

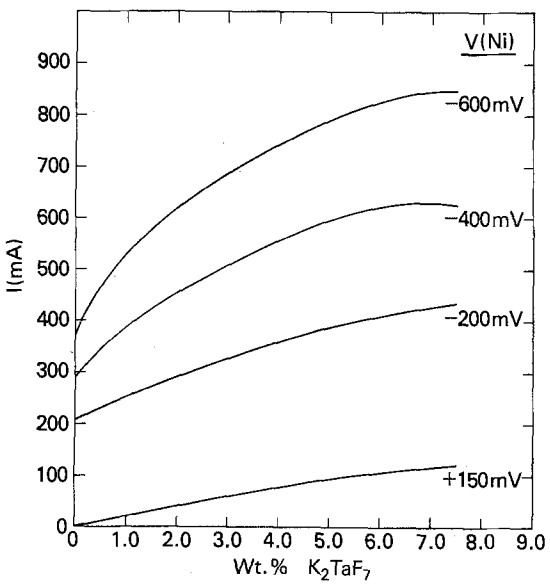

Fig. 3. Current-concentration curves at various voltages for the data in Fig. 2.

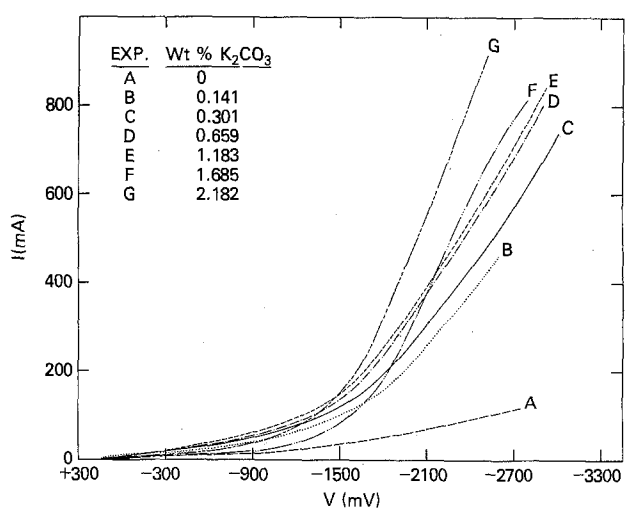

Fig. 4. Current-voltage behavior of the cell C|FLINAK + K_2CO_3|Ni for various K_2CO_3 concentrations at 750°.

for the two processes. However, this turned out not to be the case and much larger carbonate concentrations were required to yield carbide deposits (cf. Fig. 6).

Numerous plating experiments were run in a somewhat Edisonian fashion, to find conditions which would

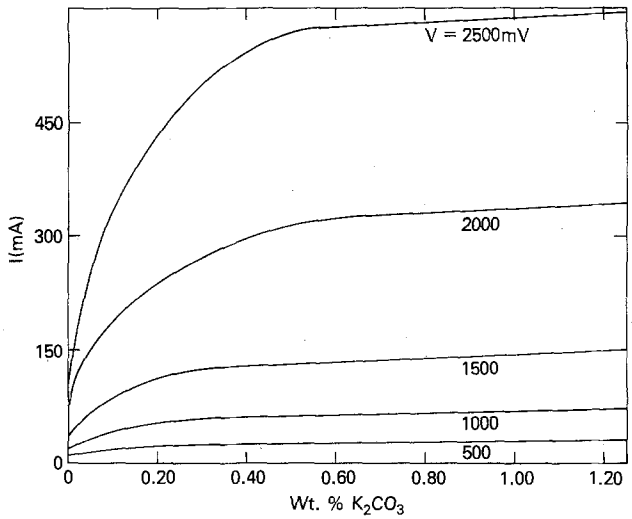

Fig. 5. Current-concentration curves at various voltages for the data in Fig. 4.

lead to carbide formation. The concentrations were at first selected on the basis of Fig. 2-5 which show that (*i*) the limiting concentration for tantalum plating is reached near 7.5 w/o K_2TaF_7, *i.e.*, higher solute concentrations do not lead to higher current and Mellors and Senderoff had found this concentration to be suitable for tantalum plating; and (*ii*) the limiting current for carbon deposition (CO_3^{2-} reduction) is reached at much lower concentrations and high oxyanion concentrations were reported (5) to interfere with tantalum reduction. Since 5 electrons are required for tantalum plating and 4 electrons for CO_3^{2-} reductions, concentrations of K_2TaF_7 and K_2CO_3 were chosen in the region around equal partial currents of the two processes. To limit the number of variables the K_2TaF_7 concentration was kept constant in all experiments at 7.5 w/o. Since the driving force for the deposition of carbon is provided by the voltage, the composition of the deposit might also be expected to vary with voltage. For tantalum deposition this is not the case since a tantalum anode was used.

Figure 6 is a map showing deposits obtained at various voltages and K_2CO_3 concentrations. Several symbols at a particular coordinate indicate that either x-ray lines of more than one material were observed from a single deposit, or that different deposits were obtained in different experiments under nominally the same conditions. As regards this last point, it must be emphasized that the carbonate concentration is based

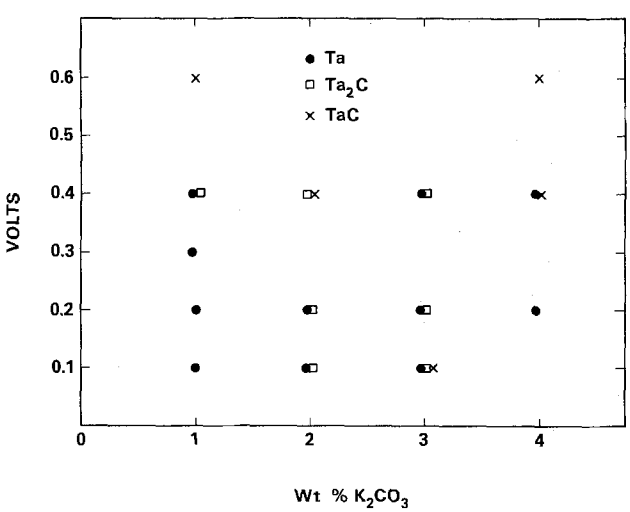

Fig. 6. Dependence of coating composition on voltage and carbonate concentration.

on the weighed quantities of K_2CO_3 only, and there is now no good method for allowing for decomposition, if any, and loss of material by plating, since current efficiencies are never 100%. Nevertheless, it can be seen from Fig. 6 that (*i*) no carbide is deposited at low voltages and low carbonate concentration, contrary to what would be expected from the current-voltage curves in Fig. 2-5; (*ii*) TaC is formed only at high voltages and carbonate concentrations of 3-4%; and (*iii*) Ta_2C, either alone or in combination with Ta and TaC is formed over a fairly wide range of conditions and is the carbide usually observed. We have no way at present of apportioning the contribution of each constituent (Ta, Ta_2C, TaC) in any particular deposit.

Another important parameter in electrodeposition is current efficiency. For pure Ta deposition this is as high as 85% even at 1% K_2CO_3 and 100 mV, but drops as the voltage (and therefore the current) is increased. For mixed deposits the current efficiency cannot be calculated exactly, although it can be estimated since the weight of deposit/0.1 equiv. is 0.360g for Ta, 0.258g for Ta_2C, and 0.200g for TaC. In general, the C.E. decreases with increasing carbonate concentration and voltage. For example, for Ta_2C deposited at 1% K_2CO_3 and 0.4V, C.E. = 57%, but for the mixed Ta_2C-TaC deposit at 3% K_2CO_3 and 0.5V, the C.E. is only 10%. Thus, from a practical view point, the present method is most suited to the deposition of Ta_2C.

Deposits were examined in two additional ways: SEM pictures were taken of the surface, and metallurgical cross sections of the coating/substrate were examined by SEM/EPXA. Figure 7a shows the surface of a Ta_2C-coated nickel coupon at a magnification of 2000×. The dense and hole-free nature of the deposit is clearly evident. Figure 7b shows an optical view, and Fig. 7c and d the Ta and Ni x-ray maps, respectively, of the coating cross section. The deposit, which is ~10 μm thick consists of two zones: (a) a region near the Ni-coating interface containing both Ni and Ta, probably a Ni-Ta alloy formed by diffusion and (b) a zone further out, which constitutes the true carbide coating. An Auger Microprobe profile of the diffusion zone shows that nickel decreases and tantalum increases with distance from the substrate surface. It is probably this diffusion zone which is responsible for the excellent adherence of the coating.

Mechanical tests.—Figure 8 shows the coefficient of friction of a typical Ta_2C coating. The plot of coefficient of friction *vs.* number of unilateral traverses shows that after 25 passes, the friction coefficient has risen to 0.34 from an initial value of 0.18. The initial value of 0.4 is probably caused by a protruding grain. (In some samples there was no change at all.) The coating is very durable, with no visible signs of the coating flaking off the sample. No "stick-slip" behavior was observed.

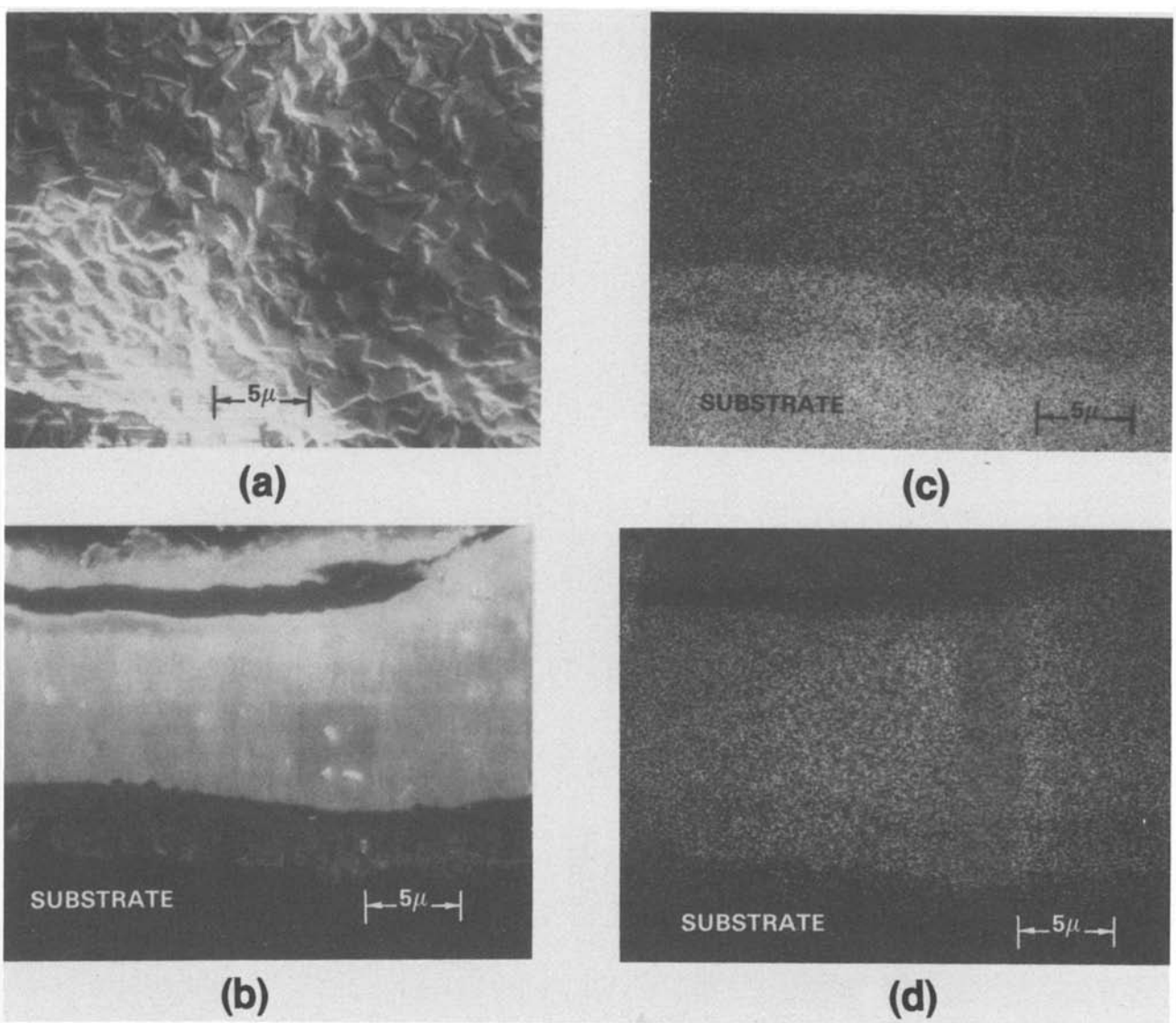

Fig. 7. Typical tantalum carbide coating (a) surface, (b) cross section, (c) nickel x-ray map of cross section, (d) tantalum x-ray map of cross section.

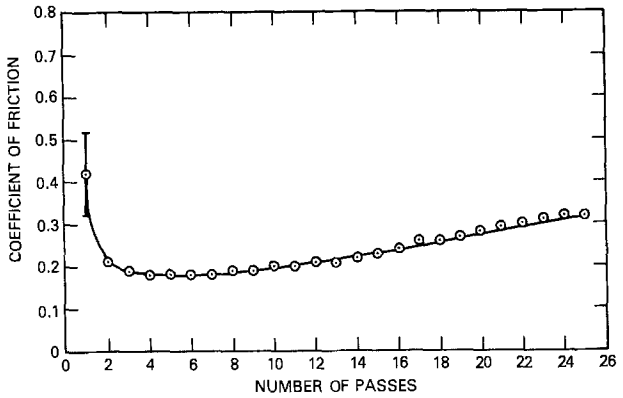

Fig. 8. Friction coefficient of tantalum carbide coating on nickel

Profilometry on the resulting sample was performed with a Taylor-Hobson Talysurf 4. No measurable wear had taken place on the coating surface, either perpendicularly measured across the track or in the track itself. The original surface is somewhat rough and grainy, so that minute material losses were unobservable on the scale required by the recorder.

The results of a typical hardness test are shown in Fig. 9. At a depth into the coating of 0.7 μm, hardness values in the ranges of 1600-1800 kg/mm^2 were obtained. Measurements on the polished nickel substrate were 120 kg/mm^2 at 200g loads.

Thermal tests.—The time-temperature behavior of all the samples tested was the same in its main features, although some differences were observed which we have not been able to correlate with coating structure. Up to 400° no weight change is observed. Between 400° and 500° the weight increases by a few milligrams (for a 1.5g sample) over a period of several hours to 2-3 days. Above 500° this weight gain becomes more rapid, although this varies from sample to sample. A few showed no weight change to 650°. At temperatures between 550° and 700° weight gain is rapid, subsequent to which weight loss occurs stepwise, corresponding to spalling of coating particles. The final product is pale yellow, identified from its x-ray powder pattern as Ta_2O_5. Since weight gains from the oxidation of nickel are negligible over this temperature range, the entire weight gain can be attributed to the oxidation of tantalum, the weight loss caused by the oxidation of carbon being small by comparison.

Discussion

This work constitutes, to our knowledge, the first electrochemical synthesis of tantalum carbide and also the first electrochemical deposition of dense, abrasion-resistant coatings of this material. The method consists of co-depositing tantalum and carbon by the simultaneous reduction of Ta^{+5} and CO_3^{2-} from a (Li, Na, K)F eutectic at 750°-800°C, and the subsequent reactions of the elements to form the carbide

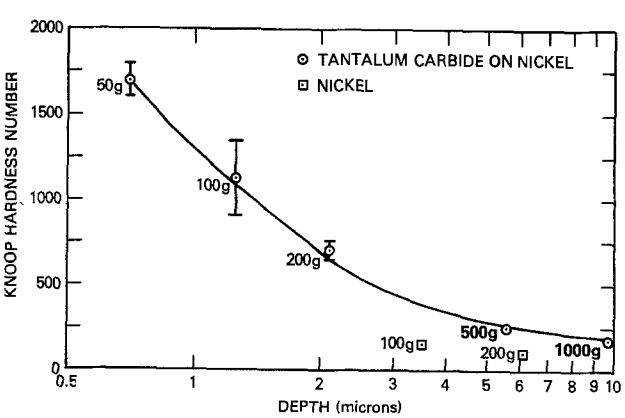

Fig. 9. Hardness of tantalum carbide coating on nickel

$$Ta^{+5} + 5e^- = Ta^0 \quad [6]$$

$$CO_3^{2-} + 4e^- = C + 3\,O^{2-} \quad [2]$$

$$Ta + C = TaC \quad [7a]$$

$$2Ta + C = Ta_2C \quad [7b]$$

Because of its general applicability, this method, appropriately modified, should lead to the electrodeposition of other refractory carbide coatings. Tungsten carbide coatings have already been prepared and will be reported soon. Work on other carbides is in progress.

Although the process described has resulted in tantalum carbide coatings, the detailed chemistry of the process is not well understood. Senderoff and Mellors (5) studied tantalum deposition from alkali metal fluoride metals by chronopotentiometry and describe the overall process [6] in terms of two successive reactions: (a) the diffusion-controlled, reversible reduction of Ta^{+5} to a slightly soluble form of Ta^{+2}

$$[TaF]_7^{2-} + 3e \rightarrow TaF_2(s) + 5F^- \quad [8]$$

(b) less is known of the second step, which is irreversible

$$TaF_2(s) + 2e \rightarrow Ta + 2F^- \quad [9]$$

For example, it is not clear whether TaF_2 is deposited on the cathode and reduced there, or whether TaF_2 diffuses away from the cathode into the melt saturated with it and is subsequently reduced.

Nothing is known of the mechanism of carbonate reduction in fluoride melts although a good deal of work has been reported on the mechanism of reaction [2] in molten carbonates (9, 10) and KCl-NaCl (11). Such studies, as well as kinetic work on the simultaneous reduction of Ta and C, would aid in understanding the mechanism of carbide formation and lead to better control of the coating composition, which is evidently related to both compositional and electrochemical variables.

Acknowledgments

We would like to thank Dr. Robert L. Jones for helpful advice, particularly that related to the identifications of the coatings, Russell Jeffries for the mechanical tests, Marianne Bernett and Elaine Shafrin for Auger analyses, and Dr. M. L. Deanhardt for helpful suggestions and experimental work related to melt purification.

Manuscript received May 20, 1982.

Any discussion of this paper will appear in a Discussion Section to be published in the December 1983 JOURNAL. All discussions for the December 1983 Discussion Section should be submitted by Aug. 1, 1983.

Publication costs of this article were assisted by the Naval Research Laboratory.

REFERENCES

1. T. I. Kosalopova, "Carbides," Plenum Press, New York (1971).
2. G. Weiss, *Ann. Chim.*, **1** [12], 424 (1946).
3. J. L. Andrieux and G. Weiss, *Bull. Soc. Chim. Fr.*, 598 (1948).
4. J. M. Gomes and M. M. Wong, *U.S. Bur. Mines Rept. Invest. 7247* (1969).
5. S. Senderoff and G. W. Mellors, *Science*, **153**, 1475 (1966); *This Journal*, **112**, 266, 841 (1965); **113**, 60, 66 (1966).
6. H. E. Bartlett and K. E. Johnson, *Can. J. Chem.*, **44**, 2119 (1966).
7. S. Nagase, *Fluorine Chemistry Rev.*, **1**, 77 (1967).
8. G. Kortüm, "Treatise on Electrochemistry," 2nd ed., p. 538, Elsevier, Amsterdam (1965).
9. M. D. Ingram, B. Baron, and G. J. Janz, *Electrochim. Acta*, **11**, 1629 (1966).
10. H. E. Bartlett and K. E. Johnson, *This Journal*, **114**, 457 (1967).
11. Yu. K. Delimarskii, V. I. Shapoval, and V. A. Vasilenko, *Russ. J. Electrochem.*, **7**, 1255 (1970).

Electrodeposition of Nickel by an Asymmetric Periodically Reversed Step Current

O. Teschke* and D. Menez Soares

Instituto de Física, Laboratório Hidrogênio, UNICAMP, C.P. 6165, 13.100 Campinas, SP, Brasil

ABSTRACT

We report the investigation of high current density (~0.15 A/cm²) nickel electrodeposition with a periodically reversed step current and the characterization of the surface morphology of the coatings thus produced. The deposits show microstructure coherency, characteristics of columnar growth, diameter and shape of growth features, and porosity, which are current controlled. For the same total deposited mass, the deposit thickness is shown to be a function of periodically reversed step current parameters. The control of deposit layers allows the fabrication of nickel coatings with well-defined mechanical and electrocatalytic properties.

Metal plating under steady current density may result in an irregular morphology of the deposit due to the depletion of ions at the cathode. Methods involving agitation or air sparging may reduce this problem by decreasing the thickness of the diffusion layer, but pulse techniques have been shown to provide the best method of obtaining good filling and coherency of the deposit (1).

It is known that metal deposition with high current density results in a greater uniformity of the layer thickness if the electrodeposition is performed by a pulse technique 1-3). The potentialities of reversing current in plating practice have been investigated by several workers (4-8). They have shown that operating current densities can, in some cases, be considerably increased compared with normal d-c deposition, and ductile deposits can also be obtained. A detailed survey of the effects of pulsed current on various processes of plating and dissolution is given by Despic and Popov (9). In the present work a periodically reversed step current with different cathodic and anodic magnitudes was used. The anodic periods were shorter than the cathodic ones, and were adjusted in such a way that all deposits have the same amount of nickel. The deposits show microstructure coherency, columnar growth characteristics, diameter and shape of growth features, and porosity which are current controlled. This control of microstructures of the deposit layer in a precise manner allows the fabrication of nickel deposits with well-defined mechanical and electrocatalytic properties.

The basic principles of the periodically reversed step technique used in this study, are schematically illustrated in Fig. 1, where the operating parameters of the periodically reversed current signal are defined. This signal is characterized by the cathodic (deposition) current density, I_+, and the anodic (dissolution) current density, I_-, as well as by the time periods, t_+ and t_-, during which current flows in the cathodic and anodic directions, respectively. Naturally, $t_+ > t_-$ and $t_+ + t_- = T$ represents the full period of the current cycle.

Experimental Method

The cell with the electrode arrangement used for the electroplating experiments is shown in Fig. 2. The plating substrate, a grid, was rotated about its axis at a constant speed (20 rpm) in order to smooth out local electric field differences.

All grid substrates used were prepared from the same brass piece. The brass grid was initially washed in a detergent solution, mechanically scrubbed, and then cleaned in the following sequence: (*i*) degreasing in methanol for 15 min; (*ii*) washing in an alkaline bath (KOH 10%) for 5 sec; (*iii*) rinsing in distilled water; (*iv*) washing in an acid bath (H_2SO_4 5%) for 5 sec; (*v*) washing in distilled water.

All cleaning solutions were at 25C.

The nickel-plating solution consisted of the following compounds dissolved in distilled water: $NiSO_4 \cdot 6H_2O$, 300 g · l^{-1}, $NiCl_2 \cdot 6H_2O$, 45 g · l^{-1}, and H_3BO_3, 30 g · l^{-1}. This solution was stirred at 80°C in a Pyrex beaker. The counterelectrode was a nickel sheet. The solution was heated to 80°C prior to each experiment. The total nickel plating time was 12 min. After plating, the brass meshes were washed with distilled water and dried. Small pieces were then cut from the central area of the meshes and mounted in a mechanical support for observation under optical and electron microscopes.

During the first deposition (Fig. 4a) the current density was approximately 0.10 A/cm². No insulating material was used for edge protection during electroplating.

The following conditions were studied: (*i*) steady-state galvanostatic plating (Fig. 4a); (*ii*) periodically reversed step plating with $T = 1$ sec, t_+ and t_- variable (Fig. 4b, 4c, and 4d). The total charge was iden-

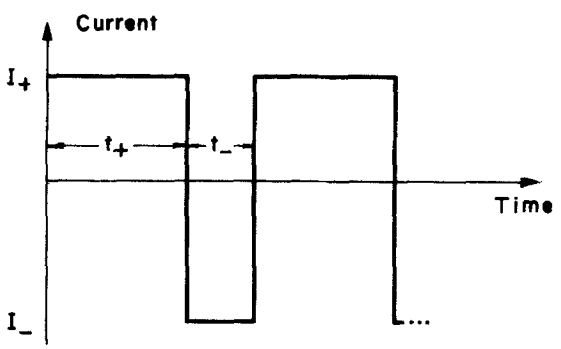

Fig. 1. Time dependence of current

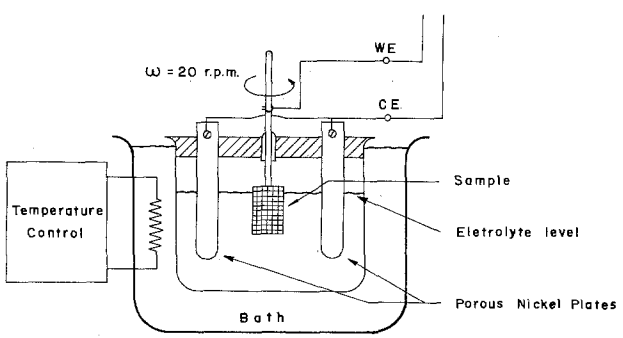

Fig. 2. Illustration of the electrode arrangement used for the electrodeposition.

* Electrochemical Society Active Member.

Key words: microfeatures, asymmetric reversed current, nickel electrodeposition.

tical in both steady-state and periodically reversed step (PRS) plating.

Typical cathode efficiency curves for the nickel plating bath are given by Wesley and Roehl (10). The measured pH of the plating solution was 4.5 which corresponds to a cathode efficiency higher than 90% at 80°C.

Results

Scanning electron microscope (SEM) photographs of portions of the grid, Fig. 3 and 4(a)-(d), show differences in three dimensional morphology of the electrodeposits.

In the PRS mode experiments constant current pulses were applied between the electrodes. The voltage pulses displayed showed a rapid initial charging of the double layer and a linear voltage increase during the plating. The pulse width was chosen so as to maintain the current efficiency high, keeping the charging and discharging of the double layer at a low level. The deposition period was one second and the current was applied for 12 min.

Figure 3 shows a low magnification (400×) SEM photograph of a portion of the deposit obtained by using the PRS mode. The picture reveals a columnar microstructure of the deposit; it has a light gray color. At such low magnification all deposits with pulsed current show a similar structure. Higher magnification SEM photographs are necessary to analyze the microstructure in more detail.

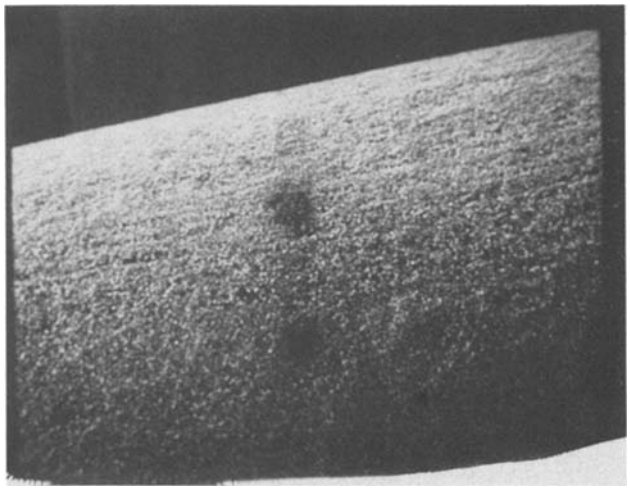

Fig. 3. Typical scanning electron micrograph (400×) taken from a brass mesh electroplated with nickel using current reversal.

The deposit shown in Fig. 4(a) was obtained by applying a constant plating current. The average cathodic current density in this sample was about 0.10 A/cm^2. The deposit has a poor quality. It has an incoherent and irregular columnar microstructure. The microfeatures are randomly oriented and the deposit is porous with a faulty structure. Figures 4(b),

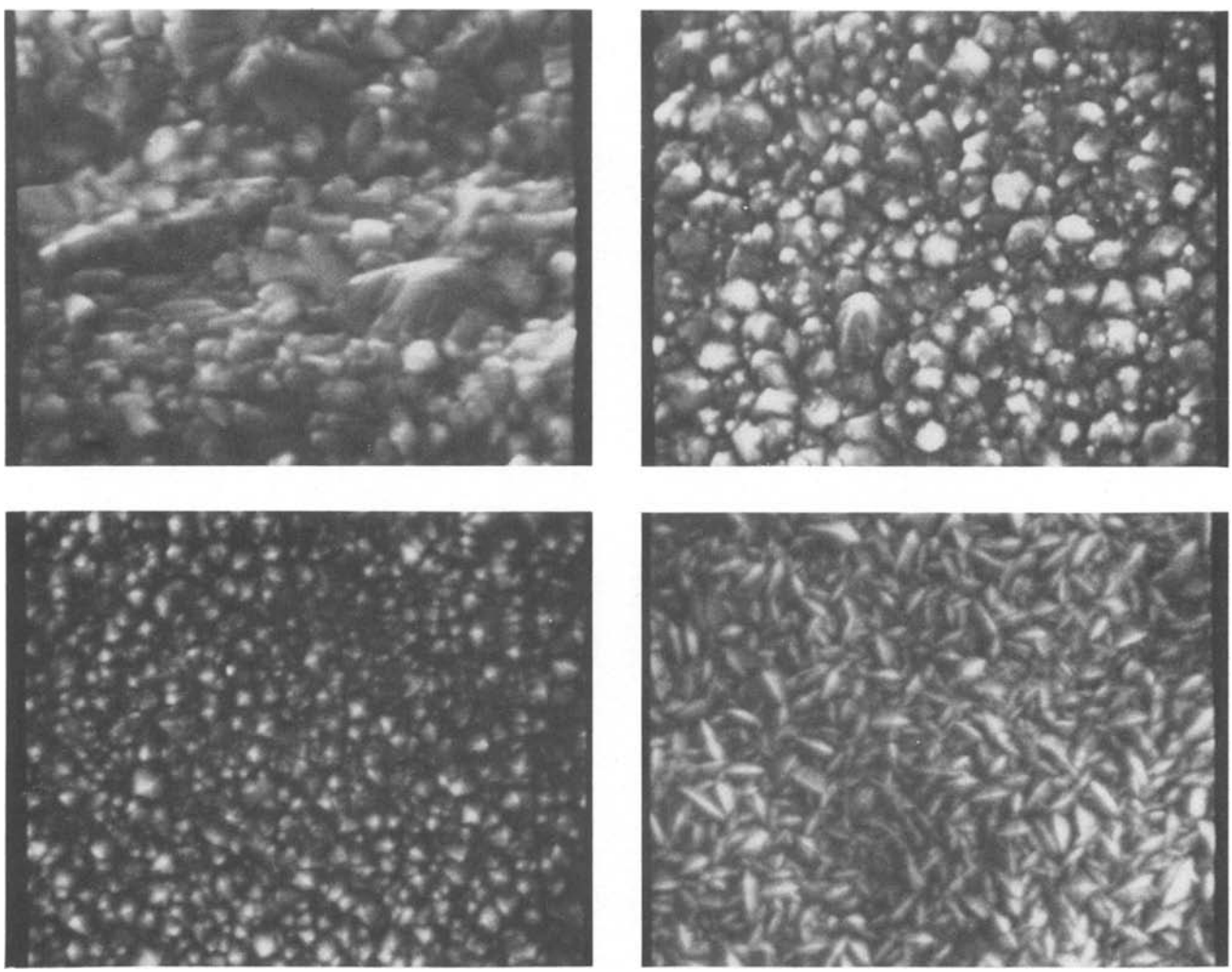

Fig. 4. Scanning electron micrographs (8000×) taken from a brass mesh electroplated with nickel: (a, top left) plated with $I_+ = 0.5$A where I_+ is the cathodic (deposition) current, $t_+ = 1$ sec where t_+ is the flowing time of the cathodic current, $I_- = 0$ where I_- is anodic (dissolution) current, and $t_- = 0$ where t_- is the flowing time of the anodic current; (b, top right) $I_+ = 0.7$A, $t_+ = 0.75$ sec, $I_- = 0.1$A, $t_- = 0.25$ sec; (c, bottom left) $I_+ = 1$A, $t_+ = 0.5$ sec, $I_- = 0$, $t_- = 0.5$ sec; (d, bottom right) $I_+ = 0.7$A, $t_+ = 0.56$ sec, $I_- = 0.7$A, $t_- = 0.144$ sec.

Table I. Deposition parameters

Sample	I_+ (A)	I_- (A)	t_+ (sec)	t_- (sec)	Deposit thickness μm	I_{DC} (A)	ρ/ρ_0	$\Delta Q_{AC}/Q_{DC}$
a	0.5	0	1	0	6.6	0.5	1	0
b	0.7	0.4	0.817	0.18	4.3	0.5	1.53	0.32
c	0.7	0.7	0.856	0.14	3.3	0.5	2	0.34
d	0.7	1	0.88	0.12	3.8	0.5	1.73	0.36

4(c), and 4(d) show platings obtained under periodically reversed step current conditions. They are seen to have a very smooth appearance. The sample shown in Fig. 4(b) was plated using a constant positive current superimposed on a pulsed square wave with deposition and dissolution periods. There is a significant improvement in structure coherency. The dissolution of metal and the periodic relaxation of the diffusion fields prevent the development of phenomena that appear under d-c conditions of electrolysis. The sample shown in Fig. 4(c) was plated using a constant positive current superimposed on a pulsed square wave resulting in a net positive pulsed current on the cathode. The microstructure obtained is similar to the one shown in Fig. 4(b), except that the diameter of the growth feature is smaller. The deposit shown in Fig. 4(d) was obtained with a pulsed current where the negative amplitude was larger than the positive one, but the deposition period was longer than the dissolution period, resulting in the same total positive charge as in the deposits shown in Fig. 4(a), 4(b), and 4(c). The deposit is dense and coherent, and the microstructure may be called worm-like. The result indicates that the dissolution current density determines the microstructure when it is larger than the deposition current density.

Other deposits with deposition parameters shown in Table I were investigated by optical microscopy and photographs were taken from representative samples. Cross-sectional views of the nickel-plated brass meshes are shown in Fig. 5(a)-(d). Figure 5(a) shows the polished cross section of a nickel-plated brass wire obtained by applying a constant plating current. Figures 5(b)-(d) show micrographs of films deposited under PRS plating conditions. The plating parameters are presented in Table I together with the results obtained under various plating conditions, (a), (b), (c), and (d), characterized by dissolution and deposition, current amplitudes, and pulse widths. The other parameters shown are: the measured deposited layer thickness, which has a clear minimum value, the deposit layer density under PRS conditions, ρ, normalized with respect to the value found under d-c plating conditions, ρ_0, the constant term of the Fourier series expansion of the plating current I_{DC}, and the ratio of the alternating charge in one cycle ΔQ_{AC}, defined as $(I_+ - I_{DC})t_+ =$

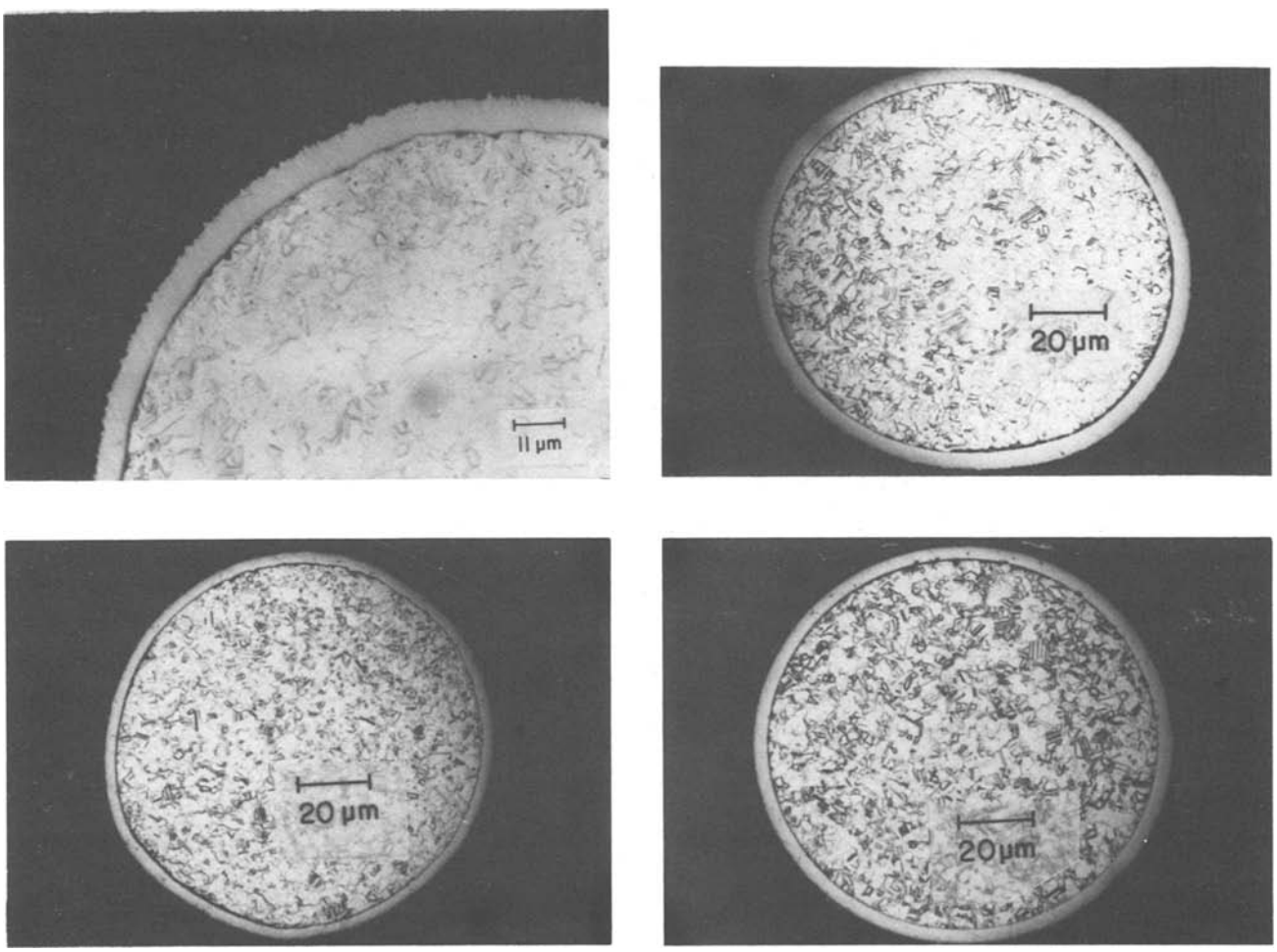

Fig. 5. Optical micrographs of cross-sectional views of nickel-plated brass meshes. (a, top left) D-C plating conditions: $I_+ = 0.5$(A); $I_- = 0$, $t_+ = 1$ sec, $t_- = 0$. Micrographs of films deposited under a-c plating conditions: (b, top right) $I_+ = 0.7$A, $I_- = 0$, $t_+ = 0.817$ sec, $t_- = 0.18$ sec; (c, bottom left) $I_+ = 0.7$A, $I_- = 0.04$A, $t_+ = 0.856$ sec, $t_- = 0.14$ sec; (d, bottom right) $I_+ = 0.7$A, $I_- = 0.7$A, $t_+ = 0.88$ sec, $t_- = 0.12$ sec.

$(I_- + I_{DC})t_-$, to the deposited charge Q_{DC} in one cycle defined as $I_{DC}(t_+ + t_-)$.

The deposited layer density under PRS conditions, ρ, normalized with respect to the value under d-c plating conditions, ρ_o, was then plotted as a function of the following parameters: ratio of dissolution and deposition currents, I_-/I_+ shown in Fig. 6(a), dissolution and deposition pulse widths, t_-/t_+, shown in Fig. 6(b), and $\Delta Q_{AC}/Q_{DC}$ shown in Fig. 6(c). We observe that the PRS plated deposits display a more even thickness than the d-c plating deposit.

A deposited mass of 0.0801g was obtained for the d-c plating. For the PRS plating, the smallest deposited mass was 0.0738g. The difference between them is less than 10%. The lower cathode efficiency for PRS plating is due to the charging and discharging of the double layer.

Discussion

This paper shows how periodically reversed step currents affect the microstructure and porosity of electroplated nickel. In order to compare various deposition conditions, the total current was maintained constant while the sample was rotated for averaging the total electric field. In d-c plating, portions of the metal deposit grow faster than the rest of the deposit due to local electric field inhomogeneities, which result in a nonuniform surface. The asymmetrical pulsed electrolysis corrects this problem by deplating metal preferentially at points of highest potential gradient and replenishing the depleted layer of ions facing the electrodes. During the subsequent pulse, metal is uniformly deposited over the whole growth front.

It is believed that the anodic pulses, in addition to removing protrusions on the surface, may also act to remove precursory defective solid material. The periodic regression of the solid interface removes species blocking the interface along with the solid material, thus yielding, adsorption-free, crystalline interface for further growth. Such a mechanism may avoid secondary nucleation and results in much larger grains. Other defects may similarly be avoided (3). We, however, observe that the dissolution in nickel plating using a Watts solution is not absolutely necessary since we obtain very similar results with plating using a positive square wave with no dissolution current [Fig. 4(c)] and with plating using a dissolution current (Fig. 4(b)].

A direct consequence of the charging and discharging of the double layer, with the same total deposited charge, should be a larger deposited mass for d-c plating than for PRS plating, but we observe the difference to be smaller than 10% for the plating conditions shown in Table I.

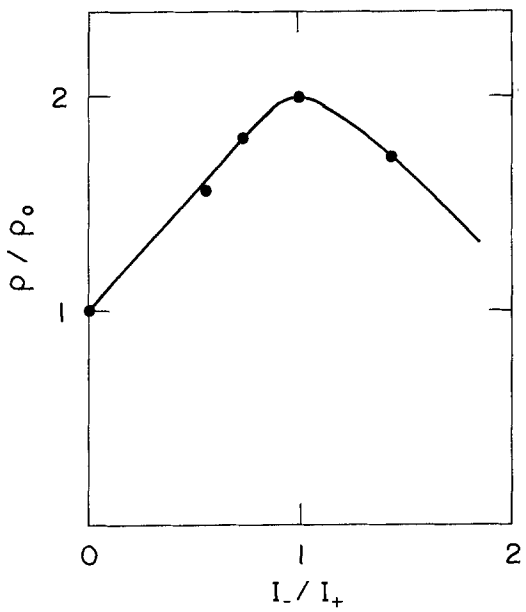

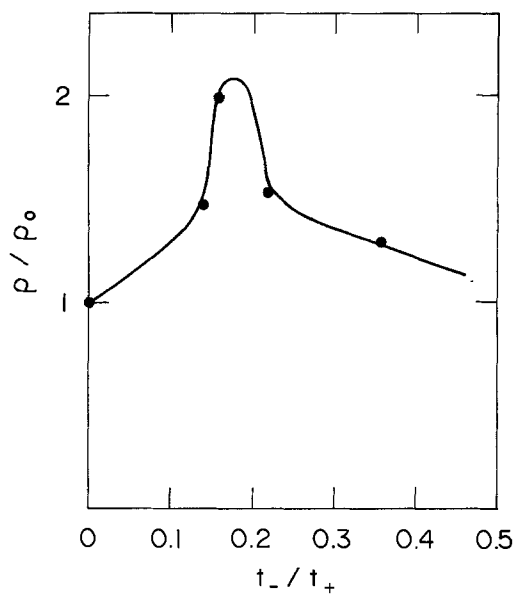

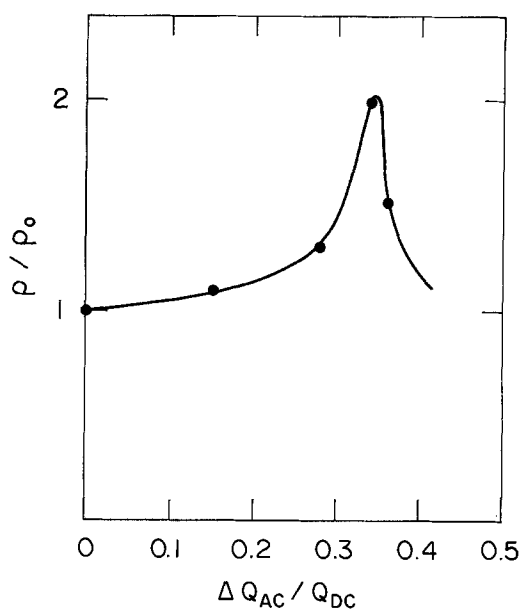

Fig. 6. Normalized deposited film density ρ/ρ_o plot vs. the following periodically reversed step current parameters: (a, above left) ratio of dissolution and deposition current amplitudes; (b, above right) ratio of dissolution and deposition pulsewidths; (c, left) ratio of the alternating charge ΔQ_{AC} in one cycle defined as $(I_+ - I_{DC})t_+ = (I_- + I_{DC})t_-$ and the deposited charge in one cycle defined as $I_{DC}(t_+ + t_-)$.

Figures 4(b)-(d) show that the features resulting from columnar growth of the nickel deposits become more oriented and smaller in diameter as the rate of plating is increased. This different morphology results in deposits with different filling factors or porosity; consequently, the density of the deposit is changed, as shown in the cross-section optical micrographs [Fig. 5(a)-(d)].

A d-c plated sample [Fig. 5(a)] shows a dendritic growth up to several microns on the top of an underlying coherent layer of thick nickel. The PRS plating led to densification as shown in Fig. 5(b)-(d). These results are presented in Fig. 6, which shows the normalized deposited film density ρ/ρ_0 as a function of periodically reversed step current parameters. Figure 6(a) shows a plot of ρ/ρ_0 as a function of ratio of the dissolution and deposition currents. The maximum of ρ/ρ_0 is obtained for $I_-/I_+ \cong 1$. Figure 6(b) shows a plot of ρ/ρ_0 as a function of the ratio of pulse widths t_- and t_+. Vene and Nikolayeva (11) claim that the most important characteristic of a reversing current is the ratio t_+/t_-, irrespective of the overall current density and that the best results are obtained at $t_+/t_- = 7$. At higher ratios, they claim the effect of reversing the current rapidly decreases, while at a lower ratio, the current efficiency is considerably reduced and the porosity of the deposit is increased. We observe that the best deposit (higher density) is obtained for $t_+/t_- = 5.9$, which is close to the value given in Ref. (11). However, we have found that this value is a strong function of plating bath conditions, such as pH, temperature, and concentration, so that the observed agreement with previous reports is merely coincidental.

Figure 6(c) shows a plot of the normalized deposit density ρ/ρ_0 as a function of $\Delta Q_{AC}/Q_{DC}$. The maximum of ρ/ρ_0 is obtained for $\Delta Q_{AC}/Q_{DC} = 0.34$. This result shows that a plating current with dissolution and deposition periods should be used in order to further improve the density of the deposited layer.

From the above evidences it is reasonable to conclude that the periodically reversed step current parameters t_-/t_+, I_-/I_+, $\Delta Q_{AC}/Q_{DC}$ determine the deposit density. The observed density maximum [see Fig. 5(a) to 6(c)] in nickel film deposits is explained by the size of growth features, as shown in Fig. 3 and Fig. 4(a)-(d).

Conclusions

This paper shows that the deposition of nickel and subsequent dissolution, due to periodically reversed step currents, produce more dense, coherent, and smooth deposits.

The effects of the pulse plating variables were not comprehensively investigated. Several trends, however, were clearly observed. It was found that the important parameters for periodic reverse current plating are t_-/t_+, $\Delta Q_{AC}/Q_{DC}$ and I_+/I_-, and not just t_-/t_+ as suggested in Ref. (11). Optimum values of these parameters corresponding to the highest deposit density were found for the described plating conditions.

Cathodic currents as high as 150 mA were used successfully. High current induces nucleation and thus produces finer grains and uniform growth features.

Chemical dissolution is not necessary in order to obtain a good uniformity in the microstructure. It is enough to use a pulsed current. The anodic current will also control the deposit structure when its amplitude is higher than the cathodic current.

Asymmetric periodically reversed step galvanostatic plating is a single method of controlling the growth morphology which may be of considerable practical importance since mechanical properties as well as electrocatalytic properties depend on morphology, in such practical applications as water electrolysis.

Acknowledgment

This research was supported by the Fundação de Amparo à Pesquisa do Estado de São Paulo (FAPESP).

Manuscript submitted June 24, 1981; revised manuscript received Aug. 2, 1982.

Any discussion of this paper will appear in a Discussion Section to be published in the December 1983 JOURNAL. All discussions for the December 1983 Discussion Section should be submitted by Aug. 1, 1983.

Publication costs of this article were assisted by UNICAMP.

REFERENCES

1. G. W. Jernstedt, *Proc. Am. Electroplating Soc.*, **36**, 63 (1949).
2. G. W. Dini, *Metal Finish*, **61** (7), 52 (1963).
3. M. Ceresa, in "Electroplating Engineering Handbook," 3rd ed., A. K. Grahan, Editor, Van Nostrand-Reinhold, New York (1971).
4. G. T. Bakhralov, Sb. Nauchn. Tr. MITCMIZ im. Kalinina, p. 222, Metalurgiz dar (1950).
5. G. W. Gernsted, *Steel*, **120**, 100 (1947); *ibid.*, **120**, 134 (1947); *Steel Processing*, **33**, 479 (1947); *ibid.*, **33**, 498 (1947).
6. G. W. Gernsted, *Plating*, **35**, 708 (1948).
7. U.S. Pat. 2,470,755, 24/V (1949).
8. French Pat. 932,039, 10/III (1948).
9. A. R. Despic and K. I. Popov, in "Modern Aspects of Electrochemistry," Vol. 7, B. E. Conway and J. O'M. Bockris, Editors, p. 199, Plenum, New York (1972).
10. W. A. Wesley and E. J. Roehl, *Trans. Electrochem. Soc.*, **86**, 419 (1944).
11. Yu. Ya Vene and S. A. Nikolayeva, *Zh. Fiz. Khim.*, **39**, 811 (1955).

A Cyclic Voltammetric Study of Pd-Sn Colloidal Catalysts for Electroless Deposition

Jean Horkans*

IBM Corporation, Thomas J. Watson Research Center, Yorktown Heights, New York 10598

ABSTRACT

A cyclic voltammetric method is described that allows the evaluation of catalysts for electroless deposition. Information about the chemical state and activity of the catalytic layers can be inferred from the measurements. Differences are illustrated between Pd deposited on Cu through electrochemical exchange, a two-step procedure using $SnCl_2$ and $PdCl_2$, and a one-step activation with a Pd-Sn colloid. The method is sensitive to small differences between colloids of similar structure. It has been used to investigate the effect of varying solution composition during synthesis of Pd-Sn colloids. XPS and electron microprobe analysis have supported the conclusions of the electrochemical measurements.

Catalysts for electroless plating on nonconducting materials are important as more than simple initiators of the plating reaction; they can also determine the quality of the resulting deposit, its adhesion to the substrate, the coverage, etc. It is thus essential to understand and to be able to characterize these catalysts. A reliable means of evaluating their catalytic activity would be very useful.

Electroless deposition on nonconductors is usually initiated by first depositing Pd in the form of a mixed Pd-Sn activator that adheres to the dielectric surface. Typical Pd-Sn activators are described in some representative patents (1-3). The literature contains conflicting claims about the nature of these catalytic materials, but the work of Cohen and West (4, 5), Cohen and Meek (6), and Matijevic *et al.* (7) has convincingly established that they are colloids and not solution complexes. These authors (4-7) summarize the earlier literature and the controversies about the structure of the Pd-Sn catalysts.

Cohen and West (5) postulate the following model of the Pd-Sn colloids on the basis of Mössbauer spectroscopic studies of these materials. When acid solutions of $SnCl_2$ and $PdCl_2$ are mixed, a complex between Sn(II) and Pd(II) is first formed. Subsequently, the reduction of the Pd(II) to Pd(0) occurs within the complex, forming a nucleus for the growth of the colloid. The core of the colloid is a metallic alloy of Pd and Sn. This core is surrounded by a stabilizing layer of Sn(II) as Cl^- and OH^- complexes. Formation of the stabilizing Sn(II) stops the growth of the colloid and determines the particle size.

Cohen and West (5) do not speculate on the mechanism for the formation of the alloy at the center of the colloid. The crucial question is how the tin is reduced to the metallic state. It is likely that this occurs through the underpotential deposition of tin on the growing Pd nuclei. There is little information in the literature concerning UPD of tin on Pd. A prediction of the strength of underpotential interactions can be made (8, 9), however, from the difference between the electronic work functions of the substrate metal (Pd) and the adsorbate (Sn). Trasatti's tabulated work function values (10) show that $\Delta\Phi$ for Pd and Sn is on the same order as $\Delta\Phi$ for systems that show marked UPD (*e.g.*, Tl and Au). Thus UPD of Sn on Pd is likely to occur and can explain the presence of metallic Sn in a Pd-Sn alloy at the colloid core.

Colloidal Pd-Sn activators are generally used in conjunction with accelerators, which remove tin from activated surfaces and expose the catalytic Pd at the colloid core. Meek (11) has used Rutherford backscattering to study activated surfaces and to investigate how the Pd/Sn ratio changes after acceleration and after the early stages of electroless Cu deposition. Similar information was obtained by Grunwald *et al.* (12) using Auger spectroscopy.

The processes of activation and acceleration have also been investigated by Osaka *et al.* (13, 14), who used x-ray diffraction, surface analytical techniques, and electrochemical methods in their study of Pd-Sn colloids. One of the electrochemical measurements involved adsorbing the catalyst on an Au electrode, then determining the coverage of Pd and tin on the Au by a subsequent anodic voltage sweep in 1M HCl solution. The Pd coverage determined by this method correlates with the activity of the Pd-Sn mixed colloids, as evaluated by monitoring the potential of an activated Cu wire during electroless Ni plating.

Activation of surfaces with Pd-Sn colloids has now largely replaced the two-step procedure of sensitization in $SnCl_2$ followed by activation in $PdCl_2$. In assessing a technique for evaluating activated surfaces, however, it is useful to compare the one- and two-step procedures. The two-step procedures have been reviewed by Goldie (15).

Deposition of good catalytic Pd layers in the two-step procedure requires that a nonconducting surface first be covered with Sn(II). It is known (16, 17) that the presence of some Sn(IV) in the $SnCl_2$ solution can improve the performance of the $SnCl_2$ sensitizer. Cohen *et al.* (18, 19) have used Mössbauer spectroscopy to study tin sensitizing solutions. They propose a model of a tin colloid nucleated by Sn(IV) and mediated by Sn(II). They point out (19), however, that the formation of the colloid can depend on the way the $SnCl_2$ is prepared (*i.e.*, the order of the mixing of chemicals). Controlled colloid formation is attained by suspending the $SnCl_2 \cdot 2H_2O$ in H_2O, then adding HCl. If the $SnCl_2 \cdot 2H_2O$ is first dissolved in concentrated HCl, then diluted, a true solution may result.

The present paper describes a cyclic voltammetric method for studying surfaces activated by one-step and two-step procedures. Used in conjunction with XPS and electron microprobe measurements, the technique gives information about the structure of the colloids. It can also be used for a quick and simple estimate of catalytic activity.

Experimental

Copper test electrodes were used for most of the measurements, but Au and other metals could also be employed. The electrodes consisted of 2000Å of Cu evaporated over a 200Å Nb adhesion layer (20) on Corning 0211 glass. Although nonconducting surfaces could not be studied by the electrochemical technique, they were used as substrates for electron microprobe analysis, as explained below.

Each electrode was cleaned just before use by sequential immersions of a minute or two in ~10% solutions of NaOH and H_2SO_4. After thorough rinsing, the Cu surface was submitted to the activation procedure being studied, then once again thoroughly rinsed. The

* Electrochemical Society Active Member.

Key words: activation, catalysis, electroless, printed circuits.

activated electrode was then mounted in a glass and Kel-F cell, described elsewhere (21), and the cyclic voltammetry was studied in 0.01M $HClO_4$. The electrolyte was deaerated with bubbling N_2 before measurement; the bubbler was raised above the solution surface during the measurement itself.

The instrument used for XPS analysis was a Hewlett-Packard 5950B x-ray photoemission spectrometer that has a crystal monochromator on the x-ray source, yielding 1486.6 eV aluminum Kα x-rays. X-ray photoemission spectra were obtained by cutting the prepared samples to size and inserting them into the instrument. No particular precautions were taken to protect the samples from air.

A wide binding energy range was first scanned to identify the surface species; subsequently, narrow energy windows were scanned for each element present. The Sn 3d, oxygen 1s, and Pd 3d binding energies were monitored, as was the Cu Auger peak. Since the binding energy shift for the Sn(II) and Sn(IV) were about the same with respect to the metal, they were not resolved. The Cu Auger signal could be used as a monitor of the surface coverage by the Pd-Sn colloid within the sampling depth (~30Å).

The electron microprobe technique is a method developed by Reuter (22). The detection sensitivity for Pd and Sn is approximately 0.1 monolayer. The relative accuracy is at best ±10% and can be worse depending on the counting statistics. The relative precision is a function of the statistics and for thicker films is on the order of ±2% at the 95% confidence level. The data were taken on an Applied Research Lab Scanning Electron Microprobe Quantometer. The characteristic x-ray transitions used were Pd Lα and Sn Lα, which were monitored simultaneously using wavelength dispersion spectroscopy. Nonconducting samples were coated with approximately 100Å of Al to prevent charging during analysis.

The concentrated suspension of the Pd-Sn colloid is synthesized similarly to those described in the patents of Zeblisky (3). The catalyst is prepared from this concentrate by dilution with NaCl solution. [Zeblisky (3) claims that catalysts prepared according to these patents are true solutions. Such catalysts were included in the investigation of Matijevic *et al.* (7), however, and were shown to be colloidal.]

In order to assess the effects of the Sn/Pd ratio, the total palladium concentration, and the HCl concentration in the catalyst, we have also prepared some colloids varying these factors. The colloids were synthesized in both concentrated and dilute forms. Although we had anticipated that a dilute preparation would lead to more uniform and controlled formation of the colloid, in practice the colloids prepared already dilute did not give better performance than those prepared as concentrates.

The activity of catalysts was also evaluated by monitoring the open-circuit potential of an activated surface during the initial moments of electroless Cu plating. The electroless Cu solution used contains EDTA as complexant and formaldehyde as reducing agent (23). It is operated at 78°C, and air is bubbled to prevent the formation of metallic Cu in the bulk of the solution. The reference electrode was separated from the main solution compartment by a Luggin capillary and was maintained at room temperature. Care was taken to ensure that the measured potential-time dependence was characteristic of the activated surface and not of the electroless Cu bath. The solution was heated before the addition of the HCHO. Fresh solutions were used for each series of measurements; the solutions were used for no longer than an hour; and the reproducibility was checked several times during the course of the measurement. Nonetheless, irreproducibility was a problem, as is further discussed below.

The reference electrode in all measurements was the mercury sulfate electrode (MSE), Hg/Hg_2SO_4, sat. K_2SO_4.

Results and Discussion

The cyclic voltammetry of clean evaporated Cu in 0.01M $HClO_4$ is shown in Fig. 1. In this potential range, the main reactions are the dissolution of Cu at potentials more positive than ~ −0.4V in the anodic sweep and the reduction of the Cu(II) species thus formed in the subsequent cathodic sweep.

The curve in Fig. 2 is obtained using a Cu electrode that had been immersed 15 sec in a sensitizing solution containing 56 g/liter of $SnCl_2 \cdot 2H_2O$ and enough

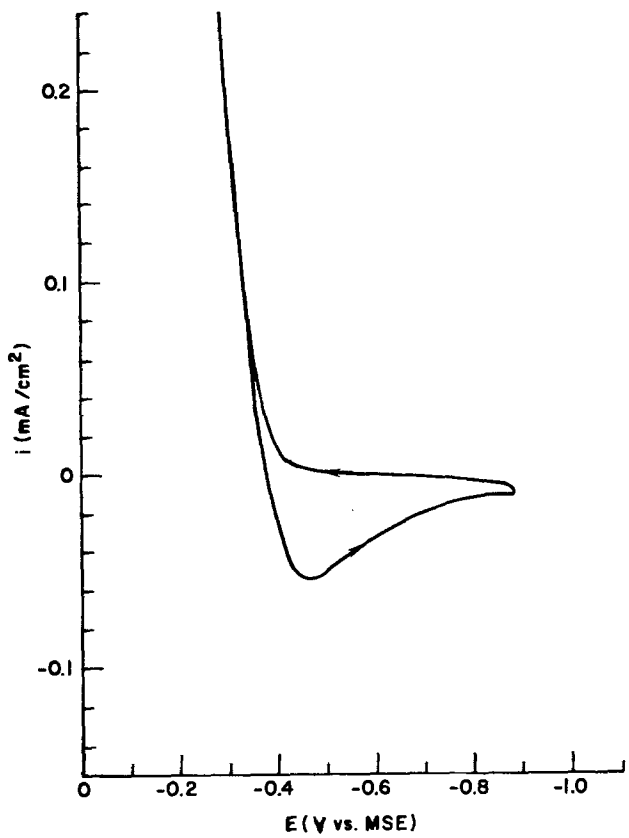

Fig. 1. Cyclic voltammetry of a clean Cu surface in 0.01M $HClO_4$. Sweep speed is 20 mV/sec.

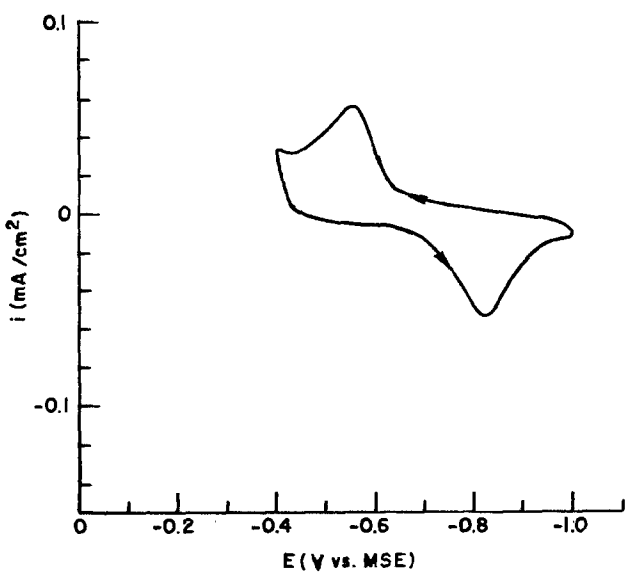

Fig. 2. Cyclic voltammetry in 0.01M $HClO_4$ of a Cu electrode that had been immersed in $SnCl_2$ solution. Sweep speed is 20 mV/sec.

HCl to give a pH of 0.5. The system is characterized by a pair of peaks centered at ~ −0.69V *vs.* MSE (*i.e.*, ~ −0.05V *vs.* NHE). The integrated charges under the anodic and cathodic peaks of Fig. 2 are approximately equal. Some measurements have shown a larger charge under the cathodic peak; the worst discrepancy observed was ~15%.

The tin-containing layer on the Cu surface is fairly stable, but it is slowly removed on continued cycling, as evidenced by the decrease in the magnitude of the current peaks. After 15 sweeps, the integrated charge under the peaks typically decreases by ~15%. The initial sweep is quite reproducible, however, for samples receiving the same sensitization.

It is difficult to assign unequivocally the observed pair of peaks to a given electrochemical process. We can repeatedly oxidize and reduce the tin species that have been deposited on the Cu electrode and most of which remain there during potential cycling. Is the oxidation reduction reaction

$$Sn(II) + 2e^- \leftrightarrow Sn(0)$$

$$Sn(IV) + 4e^- \leftrightarrow Sn(0)$$

or

$$Sn(IV) + 2e^- \leftrightarrow Sn(II)?$$

Pourbaix (24) considers potential-pH diagrams for Sn for which the oxides are in either the hydrated or unhydrated state. A colloidal preparation of the $SnCl_2$ (19) makes it likely that the hydrated oxides are the more relevant to the present experiment.

At pH 2, the Pourbaix diagram predicts that Sn dissolves as Sn^{2+} at ~ −0.35V *vs.* NHE when $[Sn^{2+}] = 10^{-6}$M; the reversible potential for the reaction

$$Sn^{2+} + 4H_2O \leftrightarrow Sn(OH)_4 + 4H^+ + 2e^-$$

is shown as ~0.05V. These potentials are either side of the potential of ~ −0.05V *vs.* NHE about which the peaks of Fig. 2 are centered. The repeatability of the voltammetry curve on continued cycling, however, implies that major amounts of tin are not removed from the surface as readily soluble Sn^{2+} species. In light of this fact, it seems most reasonable to assume that the anodic peak in Fig. 2 is due to oxidation of adsorbed tin species to $Sn(OH)_4$ (or a related Sn(IV) salt) and that the cathodic peak is due to the reduction of this compound to $Sn(OH)_2$ (or a related Sn(II) salt).

The charge under either the anodic or the cathodic peak can be used to estimate the tin coverage on the "sensitized" metal surface. No information is available about the original oxidation state of the tin as it was deposited on the Cu. In the example of Fig. 2, the integrated charge is 470 $\mu C/cm^2$ (~0.3 $\mu g/cm^2$ of tin, assuming a two-electron reaction).

The same amount of tin is deposited from $SnCl_2$ solutions on Au test electrodes, on which the peak potentials and charges under the peaks are the same as on Cu. Since the cyclic voltammetry is virtually the same on "sensitized" Cu and Au electrodes, UPD phenomena do not appear to be playing a role in this potential region.

The electrochemically determined coverages have been compared to electron microprobe analyses of the same surfaces. The two methods always agree in the relative amounts of tin coverage, but the electrochemical technique gives a significantly lower tin determination than electron microprobe. The electrochemical measurements are quite sensitive to small changes in surface coverage, but at these low coverages the microprobe analyses have a precision of only ±20-30%. Thus, small differences in sensitization solutions are easily detected by the electrochemical, but not by the electron microprobe, analysis. Nonetheless, the electrochemically determined tin coverage is ~50% of that determined by electron microprobe. It is possible that this low apparent tin coverage is a consequence of the colloid structure. The tin is adsorbed in clumps, and part of the colloidal particle may not be in direct contact with the electrode. Only that portion of the tin in contact with the electrode surface will contribute to the total electrochemical charge, but the microprobe analysis detects all of the tin.

The most important experimental variable determining tin coverage was found to be the method of preparation of the $SnCl_2$ solution. Cohen and West (19) point out that the order of the mixing of the chemicals in preparing an $SnCl_2$ sensitizer can determine whether a colloid or a true solution results. The present study shows that sensitization with colloidal $SnCl_2$ gives a higher surface coverage of tin than sensitization with a true solution of the same nominal composition. Changes in $SnCl_2$ concentration, acidity, and immersion time resulted in much smaller variations in coverage than did changes in the colloidal nature of the $SnCl_2$.

Electron microprobe analyses showed that the tin coverage on epoxy board was the same as on Cu. This observation also rules out UPD as contributing to the adsorption of tin on Cu or Au.

The potential sweeps of "sensitized" Au electrodes that Osaka *et al.* (13) have published were obtained under different conditions from ours. Only the anodic sweep was recorded; the electrolyte was 1M HCl; and the potential range of the measurement was more positive than the potential range of our study. Whereas we observe only one oxidation peak attributable to oxidation of tin species, they observe two. The more cathodic of these (~0.14V *vs.* NHE) they assign to desorption or oxidation of Sn(0) formed by UPD of tin on Au; the more anodic peak (~0.41V *vs.* NHE) is assumed to be due to

$$Sn(II) \rightarrow Sn(IV) + 2e^-$$

The differences between the two studies cannot be completely resolved without further experimentation. The observation of a single peak in the present study may be due to conversion of all tin species to hydroxides or oxides when the surface is transferred to the 0.01M $HClO_4$ solution. The strongly acidic Cl^- solution in which Osaka *et al.* obtained their data (13) should facilitate dissolution of tin species (25) and may prevent the formation of such oxides.

Figure 3 shows the cyclic voltammetry in 0.01M $HClO_4$ of a Cu film electrode that had been immersed 15 sec in a 0.1 g/liter $PdCl_2$ solution of pH 2.0 (pH adjusted with HCl). This treatment results in deposition of Pd by an exchange mechanism. Electron microprobe analysis has shown that the Pd coverage on this sample is 0.5 ± 0.1 $\mu g/cm^2$. A hydrogen sorption current is observed in the cathodic sweep for Pd-

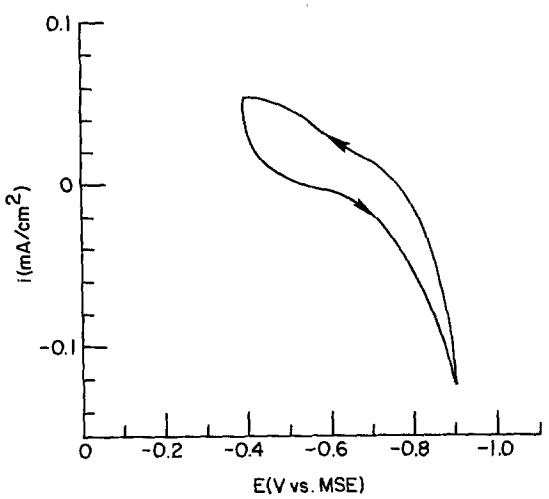

Fig. 3. Cyclic voltammetry in 0.01M $HClO_4$ of a Cu electrode that had been immersed in $PdCl_2$ solution. Sweep speed is 20 mV/sec.

covered Cu where none is observed for clean Cu. The reverse sweep shows anodic currents due to desorption of the hydrogen. The process is quite irreversible, presumably due to the small size of the Pd crystallites. It is known (26) that the grain size can have a large effect on the hydrogen sorption processes in Pd.

The potential at which the hydrogen sorption process begins is a reliable qualitative measure of the amount of Pd on the surface: the less negative the potential at which the cathodic current appears, the more Pd is on the surface. It is difficult to quantify the method, however, since H_2 evolution is also thermodynamically possible over part of the potential range in which the sorption reaction occurs.

A somewhat different behavior is observed for Cu surfaces after two-step activations. In Fig. 4 is shown the cyclic voltammetry in 0.01M $HClO_4$ of a Cu surface after a 15 sec immersion in an $SnCl_2$ solution containing 30 g/liter of $SnCl_2 \cdot 2H_2O$, 10 ml/liter of 12M HCl followed by a 15 sec immersion in a $PdCl_2$ solution with 0.1 g/liter of $PdCl_2$, pH 2.0. Electron microprobe analysis of the surface showed 0.8 ± 0.1 $\mu g/cm^2$ of Pd and 0.6 ± 0.1 $\mu g/cm^2$ of tin. The cyclic voltammetry in 0.01M $HClO_4$ of a clean Pd foil is also shown for comparison. The Pd deposited on the Cu surface by the two-step activation requires a substantially more negative potential than bulk Pd for hydrogen sorption. The two-step procedure deposited on the Cu nearly twice as much Pd as the equivalent immersion in $PdCl_2$ with no tin sensitization. Hydrogen sorption is more reversible in Pd deposited by the two-step procedure than in Pd deposited by exchange. This is perhaps due to the greater amount of Pd deposited by the two-step procedure, but it may also be related to differences in morphology in the Pd deposited by the two processes.

There is no clear tin contribution of the cyclic voltammetry of Fig. 4, even though the tin coverage is comparable to that of the tin-only sample of Fig. 2. To some extent, the currents due to tin may be masked by those due to Pd. Another contributing factor may be the manner in which the tin species contact the electrode. It may be that, after the $PdCl_2$ immersion, the tin tends to be clumped and not in intimate contact with the electrode surface; such a hypothesis requires further substantiation.

The cyclic voltammetry of a Cu surface covered by an activating layer of a Pd-Sn colloid is shown in Fig. 5. The Cu was immersed in the colloidal solution for 5 min prior to being examined in the 0.01M $HClO_4$ solution. Activation using these conditions typically results in ~1 $\mu g/cm^2$ of Pd and 2-5 $\mu g/cm^2$ of tin on a Cu surface. The currents in Fig. 5 can be divided into those due to the Pd-Sn alloy at the colloid core and those due to the stabilizing stannous layer surrounding the core. The anodic peak at ~ −0.55V *vs.* MSE and the cathodic shoulder at ~ −0.8V occur at the same potentials as the pair of peaks observed on Cu immersed only in $SnCl_2$ (Fig. 2). These peaks are due to the oxidation and reduction of the stabilizing tin layer. The Pd-Sn alloy at the colloid core contributes a cathodic hydrogen sorption current, which partially overlaps the Sn(IV) reduction peak, and a peak at ~ −0.75V due to desorption of hydrogen.

Coverage by the colloid markedly reduces the Cu dissolution current. The extent of depression of the Cu dissolution current can be taken as an indication of the unformity of the surface coverage. Uniform coverage is not necessarily associated with good catalytic activity, however, since the inhibition of Cu dissolution can be caused by tin species.

The charge due to oxidation and reduction of the tin salts on the surface was found to correlate poorly with the tin coverage determined by electron microprobe. Only the ionic stabilizing tin contributes to this pair of peaks; the alloying tin in the colloid core does not. It is also possible that a portion of the ionic tin is not in electrical contact with the electrode surface and cannot be oxidized and reduced. Electron microprobe shows that the one-step activation deposits more tin than the two-step activation.

Hydrogen sorption into the Pd-Sn core is seen to occur less readily than into Pd deposited by a two-step activation. In other words, the cathodic hydrogen sorption currents and the anodic desorption peak occur at more negative potentials for the one-step activation of Fig. 5 than for the two-step activation of

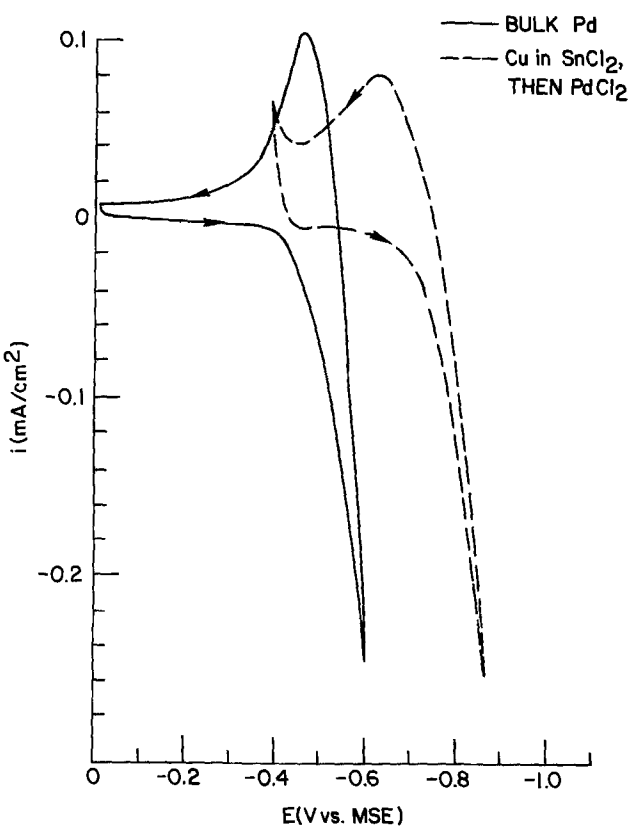

Fig. 4. Cyclic voltammetry in 0.01M $HClO_4$ of clean Pd metal (———) and of Cu after sequential immersions in $SnCl_2$ and $PdCl_2$ solutions (— — —). Sweep speed is 20 mV/sec.

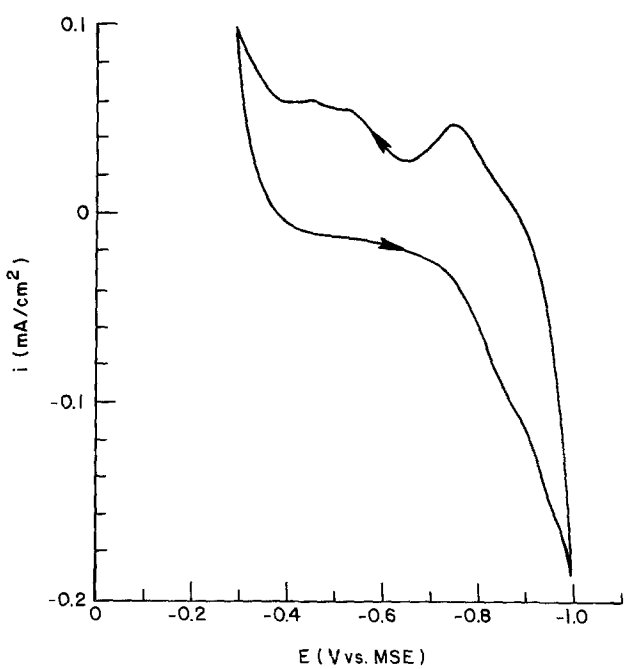

Fig. 5. Cyclic voltammetry in 0.01M $HClO_4$ of a Cu electrode that had been immersed in a Pd-Sn mixed colloid solution. Sweep speed is 20 mV/sec.

Fig. 4. The alloying of Pd with Sn in the colloid core and the presence of ionic tin in the stabilizing layer undoubtedly account for the larger energy required for hydrogen sorption in the colloid.

The size of the desorption peak at ~ −0.75V can be used to estimate the catalytic activity of the colloid. The peak height does not correlate well with Pd coverage of the Cu; the observed magnitude of the peak can vary extensively for samples that are shown by microprobe analyses to have similar Pd coverages. The peak height is instead related to the structure of the catalyst. A small peak is observed under conditions of high tin coverage; that is, a very thick stabilizing tin layer results in a small hydrogen desorption peak. The thick tin layer can isolate the Pd in the core from the electrode surface, and it will not be detected electrochemically. Since a thick tin layer can also isolate the Pd from reactants in solution, a small hydrogen desorption peak is associated with low catalytic activity.

Electron microprobe results show that the Pd-Sn colloids give a significantly higher coverage on Cu than on the surface of epoxy board.

Behavior characteristic of a poor catalyst is shown in Fig. 6. The colloid was prepared with half the HCl concentration of the colloid studied in Fig. 5 and was known to have inferior catalytic activity. The peak at −0.75V is much smaller for the less active catalyst. The lower acid concentration is insufficient to maintain stannic species in solution (25), and the stabilizing layer grows very thick, burying the Pd catalyst. In such cases, the Cu dissolution current is usually small, since the Cu is also uniformly covered by tin species.

Changes in the curve will occur on continued cycling, as shown in Fig. 7. Repeated cycling removes some of the tin from the surface. As the colloid core is thus exposed, the currents due to hydrogen sorption in Pd increase in magnitude. Because we want to assess the activity of the catalyst as it is deposited on the surface, only the first and second sweep are recorded in practice. Care is taken that all samples are handled identically.

Comparison of Fig. 3, 4, and 5 shows that this technique gives information about the state of the Pd catalyst on the surface. In this, it differs from the technique of Osaka *et al.* (13) that gives a quantitative determination of the surface coverage of tin and Pd but does not differentiate between Pd deposited by various methods. The present method is sensitive

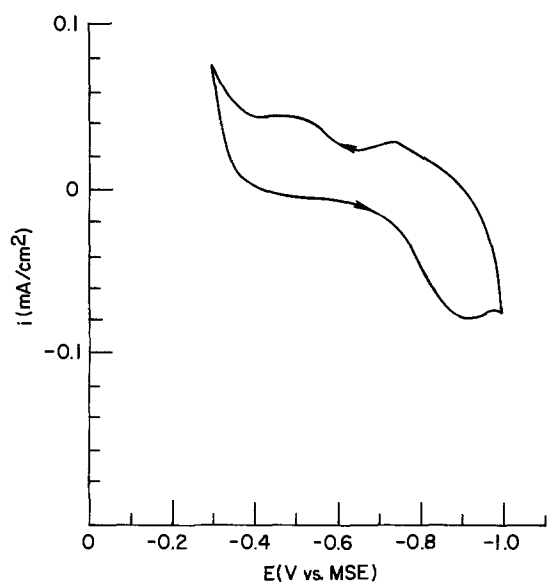

Fig. 6. The cyclic voltammetry in 0.01M $HClO_4$ of a Cu electrode activated with a Pd-Sn colloid known to have inferior catalytic activity.

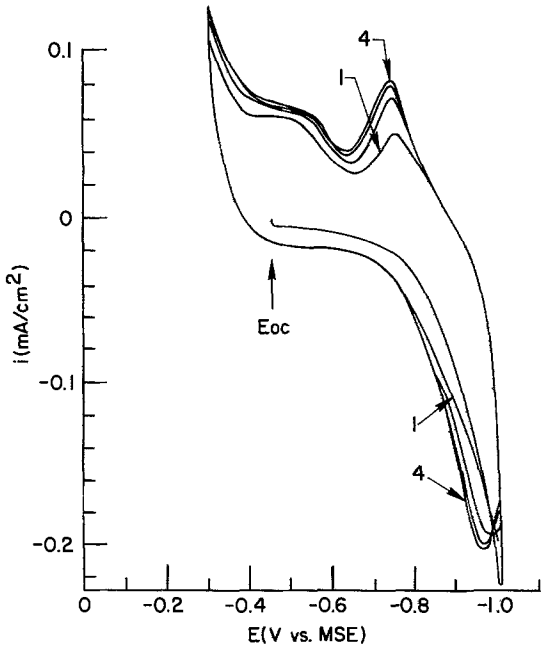

Fig. 7. Changes that occur upon repeated cycling. Same conditions as Fig. 5.

to changes in colloid structure; it can differentiate between catalysts that may give similar Pd coverages but that may vary in activity because the growth or aging of the colloid differed.

Examination of activated Cu surfaces using XPS has corroborated the conclusions of the electrochemical studies. Typical results are given in Fig. 8. Three evaporated Cu films were activated by immersion in Pd-Sn colloids. Although both catalysts A and B nominally had the same composition as the catalyst of Fig. 5, colloid A had been found electrochemically to be less active than colloid B. The peaks in Fig. 8 are assigned as follows: the 570 eV peak is a Cu Auger peak; the 530 eV peak is due to oxygen; the doublet at ~490 eV is due to tin; the small doublet at ~330 eV is due to Pd.

Comparison of the top and bottom curves in Fig. 8 shows differences between the colloids entirely consistent with the conclusions of the electrochemical investigation. For the worse catalyst, the main signals are due to tin and oxygen. The Cu Auger signal is indistinct, and there is no significant Pd signal. It is known from electron microprobe that the Pd cover-

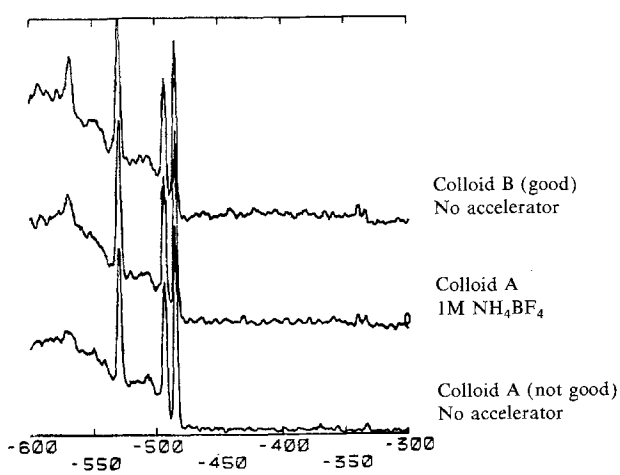

Fig. 8. XPS spectra of three activated Cu surfaces. Top: activation using a catalyst shown electrochemically to have good catalytic behavior; bottom: activation using a catalyst shown electrochemically to have bad catalytic behavior; center: same as bottom catalyst, but followed by NH_4BF_4 accelerator.

ages are 0.6 ± 0.1 $\mu g/cm^2$ for colloid A and 1.0 ± 0.1 $\mu g/cm^2$ for colloid B and that tin coverages are 2.0 ± 0.3 $\mu g/cm^2$ for A and 1.9 ± 0.1 $\mu g/cm^2$ for B. (In other words, microprobe does not show major differences between the colloids.) Yet XPS shows that the Pd of colloid A is buried by a layer of tin salts at least 30Å thick (the sampling depth).

The tin salts can be removed by an accelerating solution, such as 1M NH_4BF_4. The effect of such an accelerator is shown in the middle spectrum of Fig. 8. A strong tin signal remains even after the acceleration step, but the Cu and Pd signals are much more pronounced. The XPS spectrum of catalyst A after acceleration is similar to that of catalyst B with no acceleration.

We have used cyclic voltammetry to examine the effect of varying solution composition during synthesis of the colloid. It was found that colloids with the same Sn/Pd ratio gave identical results even though the absolute values of the tin and palladium concentrations varied by a factor of two. Increasing the palladium concentration with all other variables held constant led to degradation in the catalytic activity as estimated from the cyclic voltammetry. The effect of reducing the acid concentration has already been discussed. These results are quite consistent with Cohen and West's (5) model of colloid formation and growth: the most uniform growth occurs with a high Sn/Pd ratio.

The cyclic voltammetric estimate of catalytic activity was compared to estimates based on the potential-time dependence of activated Cu surfaces during the initial moments of electroless Cu plating. Clean Cu will initiate the electroless Cu reaction without a Pd catalyst. Plating begins as soon as a Cu surface is immersed in an electroless Cu bath; that is, the initiation time is too short for convenient measurement using an X-t recorder. Copper that has been immersed in Pd-Sn mixed colloids is less active than clean Cu; it shows a measurable initiation time before the steady-state plating potential is reached. The length of this initiation time is used to evaluate the activity of the colloid.

Figure 9 shows the potential-time dependence for Cu wires that had been "activated" by two different colloid formulations. The curve showing a very short initiation time before reaching the steady-state potential was obtained for the colloid formulation represented in Fig. 5, shown by cyclic voltammetry to have readily accessible catalytic Pd. The other curve, which shows a delay of several seconds before the steady-state plating potential is reached, was obtained using a colloid prepared with half the $SnCl_2$ concentration of the first. This colloid had shown unpromising behavior in a cyclic voltammetric analysis.

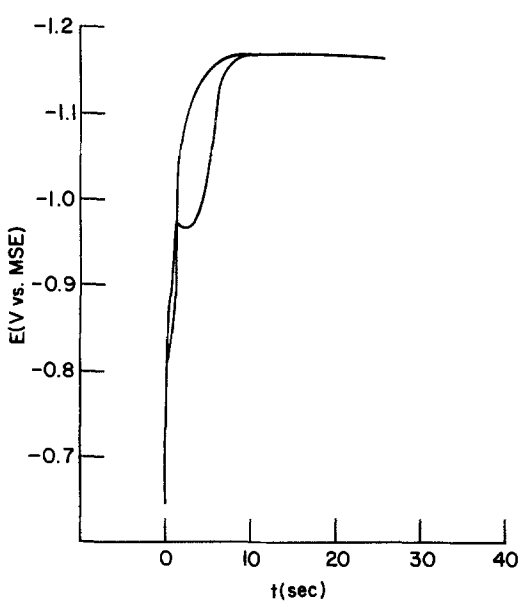

Fig. 9. Potential-time measurements during electroless Cu plating of Cu wires activated using a good sample of the Pd-Sn colloid and using a sample prepared with half the $SnCl_2$ concentration. The latter requires longer to reach the steady-state potential.

Cyclic voltammetry and potential-time measurements gave generally good agreement in evaluating the relative activities of catalysts. The cyclic voltammetric evaluation, however, was considerably more reproducible than the potential-time measurement. Using the latter method, measurement-to-measurement variations for the same colloid could be as large as sample-to-sample variations for different colloids. Electrode materials other than Cu gave equally irreproducible results.

Some of the irreproducibility of the potential-time measurements may be inherent in the electroless deposition process; evaporation of formaldehyde causes a constant drift in the steady-state plating potential. This explanation does not entirely account for our results, however. Osaka and co-workers (27) also monitored electrode potential in evaluating catalysts. They report good reproducibility when the activator was used in conjunction with an accelerator; otherwise, they also observe irreproducibility. These irreproducibilities when using unaccelerated colloidal activators probably arise from slow breakdown and removal of the stannous layer covering the Pd nuclei.

An additional factor in the present work is that we are measuring small differences in colloids of similar structure. Because of its reproducibility and sensitivity, the cyclic voltammetric method is well suited for measuring these small differences.

Conclusions

A cyclic voltammetric method has been described that allows a straightforward evaluation of the activity of catalysts for electroless deposition. Activated Cu surfaces are studied in 0.01M $HClO_4$ solution. The present technique differs from an earlier linear sweep method (3) in that it gives information about the chemical state of the catalyst on the activated surface, rather than simple quantitative information about the amount of catalyst deposited. The differences are illustrated between Pd layers deposited on Cu by exchange, by a two-step procedure using $SnCl_2$ and $PdCl_2$, and by a one-step procedure using a Pd-Sn mixed colloid.

These three activation procedures deposit Pd with quite different electrochemical behavior. The amount of Pd deposited by electrochemical exchange with Cu can be estimated from the potential at which hydrogen sorption begins. Unless it is very thick, Pd deposited in this way shows highly irreversible hydrogen sorption. The two-step procedure deposits more Pd than a simple exchange with the same immersion time in $PdCl_2$. Hydrogen sorption in this Pd is more reversible than in the exchange deposit, but still requires a substantially more negative potential than hydrogen sorption in bulk Pd.

The cyclic voltammetry of surfaces activated with Pd-Sn colloids is more complex than either of the above cases. The stannous layer that serves to stabilize the colloid contributes a pair of peaks due to the $Sn(IV) + 2e^- \leftrightarrow Sn(II)$ couple. The integrated charge does not correlate with the tin coverage because the metallic tin in the colloid core does not contribute to the current and because some of the ionic tin may not be in direct contact with the electrode surface. The hydrogen sorption in the Pd-Sn colloid core requires a more negative potential than the hydrogen sorption in the Pd deposited by a two-step procedure. The magnitude of the hydrogen desorption peak gives a good estimate of the catalytic activity.

The method can be used for day-to-day monitoring of catalysts. Differences between catalysts of the same nominal composition are readily detected. The electrochemical method has been used in conjunction with XPS and electron microprobe analyses to show that thick tin layers can build up around the active colloid core, thus decreasing the catalytic activity. The small differences between similar colloids are readily detected using the present technique; the method of monitoring the electrode potential of activated (but not accelerated) surfaces is too irreproducible to allow the detection of these small differences.

The technique has been used to evaluate the effect of changing the solution composition during preparation of the alloys. It is the Sn/Pd ratio that most strongly determines activity. This finding is in agreement with current models of colloid growth (5), which postulate the most uniform growth for a high Sn/Pd ratio. The HCl concentration is also important; a high HCl concentration is necessary to maintain Sn(IV) in solution.

Acknowledgments

The author is deeply grateful to R. W. Johnson and J. D. Kuptsis for expert support in the XPS and EMP analyses. P. Hesleitner of Clarkson College participated in some aspects of this work during summer employment at IBM. The author also thanks K. Ho, Z. Kovac, V. Markovich, L. T. Romankiw, and B. Stoeber for their contributions.

Manuscript submitted May 26, 1982; revised manuscript received Aug. 30, 1982. This was Paper 316 presented at the Denver, Colorado, Meeting of the Society, Oct. 11-16, 1981.

Any discussion of this paper will appear in a Discussion Section to be published in the December 1983 JOURNAL. All discussions for the December 1983 Discussion Section should be submitted by Aug. 1, 1983.

Publication costs of this article were assisted by IBM Corporation.

REFERENCES

1. C. R. Shipley, Jr., U.S. Pat. 3,011,920 (1961).
2. E. D. D'Ottavio, U.S. Pat. 3,532,518 (1970) and 3,650,913 (1972).
3. R. J. Zeblisky, U.S. Pat. 3,672,938 (1972) and 3,672,671 (1972).
4. R. L. Cohen and K. W. West, *Chem. Phys. Lett.*, **16**, 128 (1972).
5. R. L. Cohen and K. W. West, *This Journal*, **120**, 502 (1973).
6. R. L. Cohen and R. L. Meek, *J. Colloid. Interfac. Sci.*, **55**, 156 (1976).
7. E. Matijevic, A. M. Poskanzer, and P. Zuman, *Plating*, **62**, 958 (1975).
8. D. M. Kolb in "Advances in Electrochemistry and Electrochemical Engineering," Vol. 11, H. Gerischer and C. Tobias, Editors, p. 125, Wiley-Interscience, New York (1978).
9. S. Trasatti, *Z. Phys. Chem., N.F.*, **98**, 75 (1975).
10. S. Trasatti, *J. Electroanal. Chem. Interfacial Electrochem.*, **33**, 351 (1971).
11. R. L. Meek, *This Journal*, **122**, 1177 (1975).
12. J. J. Grunwald, S. Gottesfeld, and D. Laser, *Plating*, **68**, 71 (Oct. 1981).
13. T. Osaka, H. Takematsu, and K. Nihei, *This Journal*, **127**, 1021 (1980).
14. T. Osaka, H. Nagasaka, and F. Goto, *ibid.*, **127**, 2343 (1980).
15. W. Goldie, "Metallic Coating of Plastics," Vol. I, Electrochemical Publications Ltd., Middlesex (1968).
16. N. Feldstein, J. A. Weiner, and G. L. Schnable, *This Journal*, **119**, 1486 (1972).
17. N. Feldstein and J. A. Weiner, *ibid.*, **120**, 475 (1973).
18. R. L. Cohen, J. F. D'Amico, and K. W. West, *ibid.*, **118**, 2042 (1971).
19. R. L. Cohen and K. W. West, *ibid.*, **119**, 433 (1972).
20. R. Adzic, J. Horkans, B. D. Cahan, and E. Yeager, *ibid.*, **120**, 1219 (1973).
21. J. Horkans and L. T. Romankiw, *ibid.*, **124**, 1499 (1977)).
22. W. Reuter, in "Proceedings of the Sixth International Conference on X-ray Optics and Microanalysis," G. Shinoda, K. Kohra, and T. Ichinokawa, Editors, University of Tokyo Press (1972).
23. R. E. Acosta and L. T. Romankiw, Abstract 277, The Electrochemical Society Meeting, Altanta, Georgia, Oct. 9-14, 1977.
24. M. Pourbaix, "Atlas of Electrochemical Equilibria," p. 479, Pergamon, Oxford (1966).
25. J. Kragten, "Atlas of Metal-Ligand Equilibria in Aqueous Solution," pp. 613, 623, Halsted, New York (1978).
26. J. Horkans, *J. Electroanal. Chem. Interfacial Electrochem.*, **106**, 245 (1980).
27. T. Osaka, H. Nagasaka, and F. Goto, *This Journal*, **128**, 1686 (1981).

$Ni(OH)_2$-Impregnated Anodes for Alkaline Water Electrolysis

D. E. Hall

Inco Alloy Products Company Research Center, Sterling Forest, Suffern, New York 10901

ABSTRACT

Porous nickel-coated oxygen evolution anodes were impregnated with nickel hydroxide by electrochemical precipitation methods. A one-step process produced superior $Ni(OH)_2$ deposit morphology and control over the $Ni(OH)_2$ loading. The quantity of $Ni(OH)_2$ deposited was a linear function of the charge passed during electrochemical precipitation. Oxygen evolution overpotentials in 30 weight percent KOH at 80°C were about 45-60 mV lower on $Ni(OH)_2$-catalyzed anodes than on similar uncatalyzed anodes. The maximum overpotential reduction was obtained at low $Ni(OH)_2$ loadings. An overpotential increase at higher loadings was caused by plugging of the coating surface pores by $Ni(OH)_2$, leading to a decrease in effective surface area.

Nickel and its alloys have been and remain the materials of choice for alkaline electrolysis anodes. Nickel is highly corrosion resistant under anodic polarization in alkaline electrolytes and is relatively inexpensive. The oxygen evolution overpotential on nickel, while too high to be fully satisfactory, is nevertheless lower than on other nonprecious metals.

Efforts to improve the efficiencies of nickel anodes have focused on raising their effective surface areas (1, 2) as well as applying electrocatalysts to their surfaces (3). More fundamental studies have investigated the oxygen evolution reaction mechanism (4) and the nature of the surface on which the reaction takes place (5). The latter work established that nickel oxyhydroxide is the preferred electrocatalytic species for oxygen evolution. Nickel oxyhydroxide forms

* Electrochemical Society Active Member.
Key words: catalysis, electrode.

when nickel hydroxide is electrochemically oxidized to the +3 valence state. Appleby and co-workers recently demonstrated that oxygen evolution overpotentials were considerably lower on porous sintered nickel when it was impregnated with nickel hydroxide (6). It is likely that nickel hydroxide impregnation produces more of the preferred electrocatalyst nickel oxyhydroxide than is generated anodically on a metallic nickel surface.

The nickel hydroxide impregnation process has been examined thoroughly as a means of loading active mass into battery electrodes. The requirements for oxygen evolution anodes are not necessarily the same, because the reasons for using $Ni(OH)_2$ are considerably different. The intent in making the battery electrode is to load the maximum practical amount of nickel hydroxide into the electrode voids, while a high surface area catalyst coating is desired on the water electrolysis anode. No systematic study of the optimum impregnation method or electrocatalyst loading and morphology has appeared in the literature. However, the fundamental and applied results cited above would seem to warrant such work.

The present paper reports on such a study with nickel hydroxide-impregnated, porous nickel-coated electrodes. The properties of the unimpregnated electrodes were described in a recent publication (1).

Experimental

Preparation of high surface area nickel-coated electrodes.—High surface area nickel-coated electrodes in sheet form were prepared as described elsewhere (1, 7) using INCO[1] Type 123 nickel powder as the coating material. Polysilicate-based paint containing the nickel powder was spread onto steel sheets using a drawbar. Anode screens were prepared from 20 × 20 mesh (wires per inch) mild steel screen with 0.036 cm wire diameter. The screen, in the uncoated state, had a weight per unit area of 0.138 ± 0.0007 g/cm^2. The screen samples, each measuring about 2.7 × 5.2 cm, were dipcoated. The coated sheets and screens were then sintered in a dissociated ammonia atmosphere for 10 min at 870°C.

The coating weights per square centimeter of anode screen (average ~65 mg/cm^2) were determined by weight difference. On this basis, the anode screens were divided into three sets; within a given set, the variation in the quantity of sintered nickel coating per unit area from one electrode to another was less than ±5% from the set average. The total variation in coating weight per unit area from the thinnest to the thickest coating in the three sets was less than 25%. Earlier work (1) showed that this variation produced negligible differences in the oxygen evolution overpotentials of uncatalyzed anodes.

$Ni(OH)_2$ impregnation.—Two nickel hydroxide impregnation methods were used. The first, referred to in this paper as method A, was outlined by Salkind and Falk (8), and was used only with sheet-type electrodes. In this method, the electrodes were first soaked in an electrolyte solution containing 250 g/liter of nickel as the nitrate salt and 1% by volume of nitric acid. The temperature of the soak solution was 50°C; the soak time was not critical. The electrodes were lifted from the soaking tank and excess electrolyte was drained from their surfaces. They were then immediately immersed in a 20 weight percent (w/o) KOH solution at 70°C and cathodically polarized for 20 min at a current density of 80 mA/cm^2 to electrochemically precipitate $Ni(OH)_2$ within the coating pores. The electrodes were then washed thoroughly for 1-4 hr with deionized water at 60°-80°C and oven dried at 80°C. To increase the $Ni(OH)_2$ loading, the entire sequence was repeated as many as four times. Catalyst loading was determined by weight gain.

[1] Trademark of the Inco family of companies.

Impregnation method B generally followed the process described by McHenry (9). In preliminary experiments, electrodes were first cathodically cleaned in 30 w/o KOH at 50°C, a step recommended for impregnating porous nickel battery plaques. However, subsequent experiments indicated that this pretreatment step was unnecessary, and it was eliminated. The nickel-coated sheet electrodes were immersed in aqueous nickel nitrate solution at 50°C and allowed to soak for 1-2 min while the electrolyte was stirred. Stirring was then discontinued and the electrodes were cathodically polarized to precipitate $Ni(OH)_2$. The $Ni(NO_3)_2$ concentration was 0.2M, and the cathode current density was 7 mA/cm^2. Cathodization times were varied, producing different $Ni(OH)_2$ loadings which were determined by weight gain. These times varied from 2 to 25 min. The electrodes were then water rinsed and dried.

Anode screens were impregnated using method B only. Screens were soaked for 1 min in the electrolyte before cathodic current was applied. Two oversize nickel counterelectrodes were used, one on each side of the screen and plane parallel to it. A cathodic current density of 12 mA/cm^2, based on the geometric dimensions of the screens, was used to precipitate $Ni(OH)_2$. This current density was calculated by multiplying that used for sheet electrodes (7 mA/cm^2) by a 1.7 area correction factor relating the actual surface area of the screen to its geometric area.

Impregnation of the anode screens in each set was carried out by successively increasing the period of time that current was applied. Weight gains showing the $Ni(OH)_2$ loading obtained per square centimeter of geometric area were determined by weight difference measurements for sets 1 and 2. The morphologies of $Ni(OH)_2$ deposits in the anode screen coatings, and their variation with $Ni(OH)_2$ loading, were investigated by scanning electron microscopy.

Electrochemical tests.—The impregnated anodes were tested in 30 w/o KOH at 80°C. All testing was performed galvanostatically, with electrodes operated at a current density of 200 mA/cm^2 for about 6 hr. Experimental overpotential measurements were made *vs.* a commercial SCE reference electrode connected to the cell through a Luggin probe. Data were further corrected for the effects of resistive components of the measured potential using a computer method originally developed by LeRoy *et al.* (10). Coefficients of determination for the linearized, *IR*-free data were high, *i.e.*, greater than or equal to 0.997 for 80% of the anodes tested. After testing, several catalyzed anodes were thoroughly washed with water, dried, and examined by scanning electron microscopy to determine if structural degradation had been caused by the electrochemical test.

Results and Discussion

Impregnation method A.—The oxygen evolution overpotentials of porous nickel-coated sheet anodes were reduced significantly by $Ni(OH)_2$ impregnation. However, some difficulties with the impregnation process were identified. The morphology of the $Ni(OH)_2$ impregnated using method A was not completely satisfactory. A uniform distribution of catalyst throughout the porous coating without surface pore blockage was desired; pore blockage interferes with electrolyte penetration and gas evolution. However, some buildup of $Ni(OH)_2$ on at least part of the face of the porous coating was usually observed even at low loadings. On some electrodes, this was extensive enough to be visible as a dense green layer over parts of the electrode surface. It was concluded that surface buildup of precipitated $Ni(OH)_2$ was more of a problem with the porous electrode coatings impregnated in the present work than with porous nickel battery plaques because the coating was less porous and only accessible from one side. In areas where surface buildup was not ob-

served, method A produced a uniform, fluffy catalyst distribution.

Nickel hydroxide loading could not be easily controlled through changes in process variables. In successive impregnation cycles, it was not possible to predict the $Ni(OH)_2$ pickup accurately. The initial electrode soak in the acidic $Ni(NO_3)_2$ solution with no applied potential produced slight but noticeable corrosion of the steel substrates, as shown by stains on the impregnated electrodes. It was possible to minimize this problem by using short soak times, as only a slight reduction in oxygen evolution overpotential was obtained by extending the soak time beyond 3 min.

Despite these difficulties, overpotential reductions of 30-55 mV at a current density of 200 mA/cm^2 were produced by method A nickel hydroxide impregnation. An experiment which investigated the overpotential reduction as a function of the number of impregnation cycles showed that there was little or no benefit in increasing the $Ni(OH)_2$ loading from 2.3 to 5.3 mg/cm^2. As discussed in more detail in the next section, this indicates that the higher loadings produced plugged coating pores or excessive surface buildup, thus blocking portions of the electrode from participating in the electrode reaction.

Impregnation method B.—In 1967, McHenry (9) described an electrochemical precipitation process for impregnating porous nickel battery electrodes in which a porous electrode is cathodized at constant current density in a nickel nitrate electrolyte. A local pH rise within the coating pores causes $Ni(OH)_2$ to precipitate from the nickel nitrate solution. This method was found to have several advantages for impregnating high surface area nickel electrode coatings. In method A, the amount of nickel precipitated as $Ni(OH)_2$ was limited to what had been carried within the coating pores from the soak solution. In the one-step process of method B, however, nickel ions continued to diffuse into the coating until the pores were uniformly plugged, permitting a considerable range of $Ni(OH)_2$ loadings with only one cycle. Thus, process time and the number of operations required were minimized. The surface buildup of $Ni(OH)_2$ which occurred with method A was eliminated by proper selection of impregnation conditions. Because the electrodes were held at a cathodic potential during most of their exposure to the acidic nitrate solution, and there were fewer exposures of moist electrodes to air than in method A, substrate corrosion was reduced. In practice, there was no rust staining.

McHenry's results indicated that it should be possible to control the $Ni(OH)_2$ loading accurately by regulating the total charge passed during the impregnation process. In the present work, the $Ni(OH)_2$ loading increased linearly with the charge passed until saturation loading was reached, as shown in Fig. 1 for several series of impregnations from 0.2M $Ni(NO_3)_2$ solution. The dashed line is a linear regression (correlation coefficient 0.980) for the sheet anode data points. The linear regression (correlation coefficient 0.998) of the screen anode data is shown as a solid line. For both sheet and screen anodes, Fig. 1 shows that passage of 1C of charge produced an $Ni(OH)_2$ loading of about 0.7 mg, indicating nearly constant charge requirements from one electrode form to another.

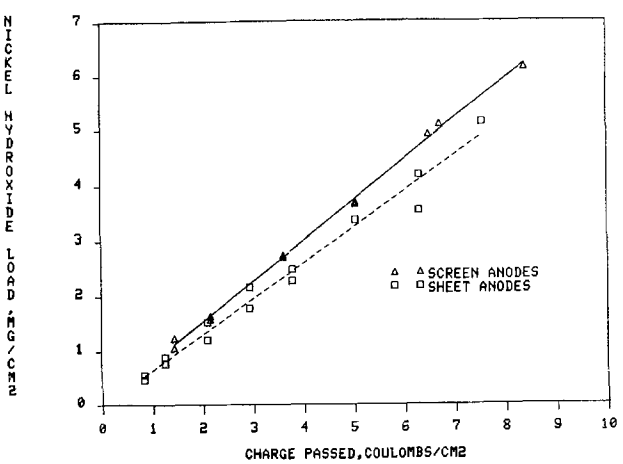

Fig. 1. $Ni(OH)_2$ loading vs. total charge passed for sheet and screen anodes impregnated in 0.2M $Ni(NO_3)_2$.

Scanning electron micrographs of the $Ni(OH)_2$ deposits produced by method B showed that they were compact rather than open-structured or dendritic. The morphology of the underlying sintered nickel was preserved, as shown in Fig. 2a. With higher catalyst loadings, the $Ni(OH)_2$ deposit began to plug the nickel coating pores, as seen in Fig. 2b, and the deposit displayed a cracked, "mud flats" appearance. This progression in deposit morphology with increasing $Ni(OH)_2$ loading was always observed at both sheet and screen anodes. However, the onset of plugged pores and cracked deposits did not always occur at the same loading. For example, with screen anodes, this occurred at lower loadings in set 2 than in set 1.

When the $Ni(OH)_2$-impregnated sheet anodes of Fig. 1 were operated, their overpotentials were considerably lower than those obtained with similar non-impregnated anodes. The overpotential for oxygen evolution decreased rapidly at low $Ni(OH)_2$ loadings (0 to 1.5 mg/cm^2) and then remained nearly constant

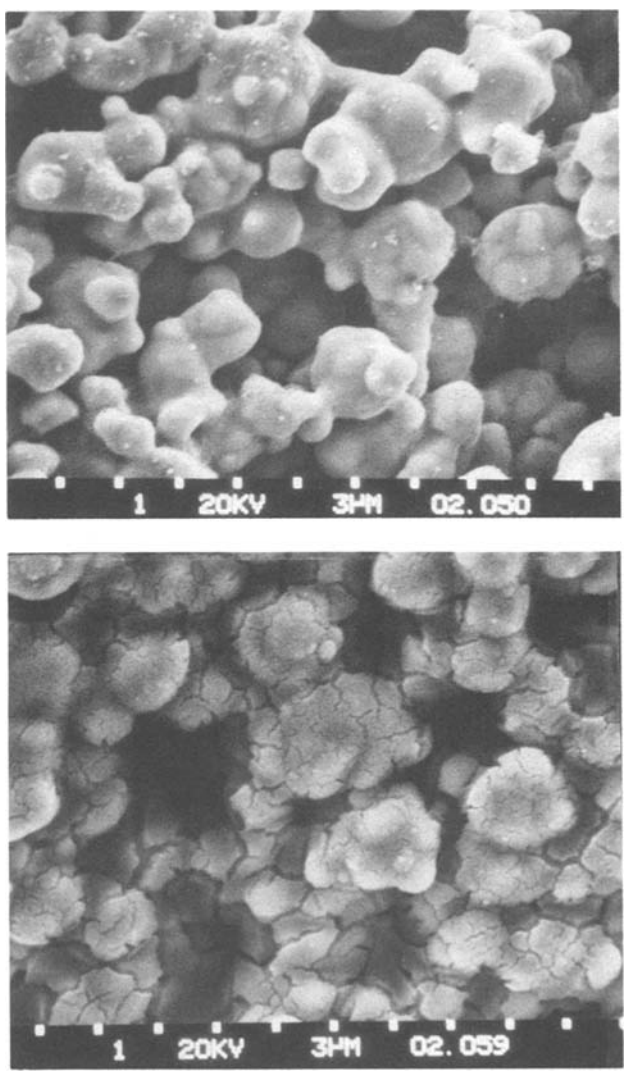

Fig. 2. Scanning electron micrographs of $Ni(OH)_2$ deposits on screen anodes, 3000×. (a) Set 1, 180 sec impregnation, $Ni(OH)_2$ loading = 1.6 mg/cm^2. (b) Set 1, 700 sec impregnation, $Ni(OH)_2$ loading = 6.1 mg/cm^2.

up to 5 mg/cm^2, the maximum load studied. At that loading, the overpotential reduction was about 60 mV at a current density of 200 mA/cm^2.

The majority of the overpotential decrease at the $Ni(OH)_2$-impregnated sheet anodes was caused by a decrease in Tafel slope rather than an increase in exchange current density. The Tafel slopes of the catalyzed sheet anodes were 23-30 mV/decade, with most in the range 23-27 mV/decade. The slopes of the uncatalyzed anodes, in agreement with earlier results (1), were 33-34 mV/decade. The exchange current densities for the uncatalyzed anodes were $\sim 1 \times 10^{-8}$ A/cm^2. This value for the present anodes, sintered at 870°C, was slightly lower than that reported earlier for similar anodes sintered at 760°C, where more of the surface area of the nickel powder was retained after sintering (1). In comparison, the $Ni(OH)_2$-impregnated sheet anodes had i_o values ranging from 5.7×10^{-9} to 5.2×10^{-8} A/cm^2, *i.e.*, both above and below the i_o value for the uncatalyzed anodes. In order for the observed 60 mV overpotential decrease to have been a surface area effect, a surface area increase of 66 times would have been necessary for anodes with a 33 mV/decade Tafel slope. However, this is not supported by the exchange current density data. In addition, no evidence of a large increase in surface area was detected by scanning electron microscopy, as discussed earlier.

The results with $Ni(OH)_2$-catalyzed anode screens were similar to those for anode sheets in several respects. As shown in Fig. 3, the anode overpotential showed a sharp initial drop at low $Ni(OH)_2$ loadings. This was followed by a range of $Ni(OH)_2$ loadings (about 2-4 mg/cm^2) in which the overpotential was relatively constant. The $Ni(OH)_2$ loadings for set 3, which were not measured, were assumed to follow the change *vs.* loading line for screen anodes in Fig. 1.

At higher $Ni(OH)_2$ loadings, anode overpotentials again rose. A reasonable explanation for this behavior is that pore plugging by the $Ni(OH)_2$ deposits hindered the interior surface of the coatings, which are known to participate in the oxygen evolution reaction (1), from serving as reaction sites. This explanation is consistent with the anode overpotential rise at lower $Ni(OH)_2$ loadings in set 2 than in set 1, because scanning electron micrographs showed that the onset of pore plugging also occurred at lower loadings in set 2.

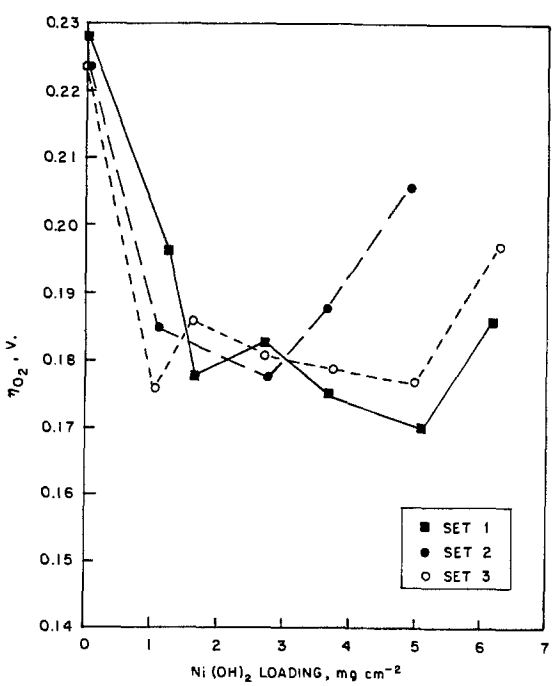

Fig. 3. Overpotentials for oxygen evolution at $Ni(OH)_2$-catalyzed screen anodes, for various catalyst loadings. Optimum results (*i.e.*, lowest overpotentials) are generally obtained at about 1-4 mg/cm^{-2} $Ni(OH)_2$ loading. Anode current density = 200 mA/cm^{-2} based on geometric area.

The conclusion drawn from the data for sheet anodes, *i.e.*, that the observed overpotential decrease at $Ni(OH)_2$-impregnated anodes is not merely a surface area effect, is substantiated by the screen anode data. Tafel slopes for uncatalyzed screen anodes were 34 mV/decade, while catalyzed screen anodes had Tafel slopes in the range 23-29 mV/decade. The exchange current densities for uncatalyzed screen anodes were $4\text{-}6 \times 10^{-8}$ A/cm^2 (geometric). Corresponding i_o values for the catalyzed screen anodes fell within or below this range. The exchange current density for the most heavily impregnated anode in set 2 (Fig. 3) was significantly lower (4.2×10^{-10} A/cm^2) than all others. This is further confirmation for the pore plugging effect discussed above.

The porous nickel coatings in the present work were about 50% dense. Using a coating weight of 65 mg/cm^2, the approximate average of the three anode screen sets, complete packing of the coating pores would produce an $Ni(OH)_2$ loading of 30 mg/cm^2. However, plugging of coating surface pores with $Ni(OH)_2$ occurred at considerably lower loadings, about 6 mg/cm^2 or 20% of the theoretical maximum value. This indicates that the coating interior received a much lighter loading than the surface, even using a low current density (7 mA/cm^2) for impregnation. The relatively low porosity ($\sim$50%) and small pore size of the anode coatings limit the diffusion of Ni^{+2} into the coatings. Using porosity and thickness specifications reported by McHenry (9) for the porous nickel plaques, a maximum theoretical $Ni(OH)_2$ loading of about 250 mg/cm^2 was calculated for those electrodes. However, saturation loading (*i.e.*, passing further charge produced little or no weight gain) occurred at a loading of about 80 mg/cm^2, or roughly 30% of the theoretical maximum. The higher percentage loading was due to the greater porosity and average pore size of the nickel plaques, compared to the porous nickel-coated electrodes of the present study, and to the fact that two faces rather than one were exposed to the impregnation electrolyte.

Differences in the behavior of the two types of electrodes as a function of $Ni(OH)_2$ loading were evident. The capacities of the impregnated battery plaques increased until saturation loading was reached. In addition, $Ni(OH)_2$ deposited in the initial phase of impregnation was less efficient than that deposited subsequently. In the present work, however, as Fig. 3 shows, the opposite behavior was found. The first 2 mg/cm^2 of $Ni(OH)_2$, about 6% of the theoretical maximum, produced almost all of the improvement in the electrocatalytic activity of the porous nickel-coated screen anodes.

The anodes from set 1 were examined by scanning electron microscopy at the conclusion of electrochemical tests. There was no evidence of degradation of the $Ni(OH)_2$ catalyst deposits or of the porous nickel coatings themselves.

Acknowledgments

Nickel hydroxide impregnations and electrochemical measurements were carried out by A. M. Rapun and E. M. Witheford. High surface area nickel electrodes were prepared by G. Hawks. Their assistance is gratefully acknowledged.

Manuscript submitted Nov. 9, 1981; revised manuscript received *ca.* Aug. 23, 1982.

Any discussion of this paper will appear in a Discussion Section to be published in the December 1983 JOURNAL. All discussions for the December 1983 Discussion Section should be submitted by Aug. 1, 1983.

Publication costs of this article were assisted by INCO Research and Development Center, Incorporated.

REFERENCES

1. D. E. Hall, *This Journal*, **128**, 740 (1981).
2. G. E. Stoner and P. J. Moran, in "Industrial Water Electrolysis," S. Srinivasan, F. J. Salzano, and A. R. Landgrebe, Editors, p. 169, The Electrochemical Society Softbound Proceedings Series, Princeton, NJ (1978).
3. A. C. C. Tseung, S. Jasem, and M. N. Mahmood, in "Industrial Water Electrolysis," S. Srinivasan, F. J. Salzano, and A. R. Landgrebe, Editors, p. 461, The Electrochemical Society Softbound Proceedings Series, Princeton, NJ (1978).
4. G. Bronsel and J. Reby, *Electrochim. Acta*, **25**, 973 (1980).
5. P. W. T. Lu and S. Srinivasan, *This Journal*, **125**, 1416 (1978).
6. A. J. Appleby, G. Crepy, and J. Jacquelin, *Int. J. Hydrogen Energy*, **3**, 21 (1978).
7. D. E. Hall, *This Journal*, **129**, 310 (1982).
8. A. J. Salkind and U. Falk, "Alkaline Storage Batteries," John Wiley & Sons, Inc., New York (1969).
9. E. J. McHenry, *Electrochem. Technol.*, **5**, 275 (1967).
10. R. L. LeRoy, M. B. I. Janjua, R. Renaud, and U. Leuenberger, *This Journal*, **126**, 1674 (1979).

Ceramic $SrTiO_3$ Photoanodes: Enhancement of Photoactivity Through Donor Doping

B. Odekirk and J. S. Blakemore*

Oregon Graduate Center, Beaverton, Oregon 97006

ABSTRACT

Results are reported for the photoactivity of lanthanum-doped, strongly reduced $SrTiO_3$ in microcrystalline ceramic form. Photoanodes of $La_xSr_{1-x}TiO_3$ (with x up to 0.01) were used in photoelectrochemical cells with simulated AM2 solar illumination, and aqueous electrolytes of various pH. The photoresponse was highest for strongly basic electrolytes, and 1M NaOH was used for subsequent experiments. Samples with heavy doping and strong reduction (heated at 1325 K with $P_{O_2} \leq 10^{-18}$ atm, and quenched) showed good photoactivity without external bias. Impurity band formation for $x \geq 0.003$ provides an extension of the spectral response to longer wavelengths, and improves the quantum efficiency. Weakly doped samples ($x \leq 0.002$) show a modest photo-oxidation after operation in a PEC cell for several hours, but this feature is absent for larger doping. No significant photodecomposition effects were seen after operation at AM2 illumination for up to 50 hr.

$SrTiO_3$ has received a great deal of attention in the past few years as being the first of the wide bandgap semiconductors to be shown to successfully photodissociate water without any external biasing and without decomposing (1). Since then a number of studies have appeared on the performance of single crystal $SrTiO_3$ (made n-type semiconducting by donor doping and/or reduction) in a photoelectrochemical cell (2-9).

Thus, gases produced during cell operation have been collected and analyzed (2-4), and shown to be O_2 (formed at the photoanode) and H_2 (at the cathode). The ratios of H_2 to O_2 conformed to the desired chemical reaction, and the quantities collected agreed with the current densities produced, indicating electrode stability (2). High density photocurrents of up to 5 A/cm^2 produced by irradiation with the 351, 364 nm lines of an argon ion laser (380 W/cm^2) indicated that single crystal $SrTiO_3$ is stable to decomposition, and that the cell rate-limiting step is illumination intensity (5). Use with p-type semiconductor photocathodes in bipolar illuminated cells has produced efficiency to sunlight of 0.18% (with p-CdTe) and 0.67% (with p-GaP) (7).

$SrTiO_3$ is of particular interest not only because of its stability, but also because it requires no biasing potential to assist the process. The biasing requirement of a particular material is determined by the flatband potential, V_{fb} (*i.e.*, the position of the conduction band edge, E_c, when there is no band bending in the semiconductor). V_{fb} for $SrTiO_3$ has been measured in a number of different ways, including by standard capacitance measurements (4), by differential stress measurements (10), and by rectified alternating photocurrent voltammetry (11). These measurements indicate that in 1M NaOH, $V_{fb} \approx -1.2$V (*vs.* SCE) and that it changes with pH in the expected manner (-60 mV/pH). It is generally known that n-TiO_2, while also useful as a stable photoanode in the photodissociation of water, requires anodic biasing of about 0.2V to initiate the process (12); and since it has been shown that V_{fb} for TiO_2 is about 0.3 to 0.4V more positive than that of $SrTiO_3$ (4), it is apparent that $SrTiO_3$ acts as a good demarcation between those materials that will require biasing to assist photolysis and those that will not.

The energy level of the O_2/OH^- redox agent in a photoelectrochemical cell (PEC) lies at 1.23 eV below the system Fermi level (*i.e.*, the H_2/H^+ level), which in turn is very near the conduction bandedge of the semiconductor. Since the bandgap of single crystal $SrTiO_3$ is $E_g = 3.21$ eV (considered to be indirect, with a direct transition at 3.78 eV) (13), the photogenerated minority carriers must find a way to communicate with the appropriate redox level without the possibility of isoenergetic charge transfer to the valence band. This has generally been attributed to the action of surface states.

LCAO and Green's function calculation techniques, applied to the predominant $pd\pi$ interaction by Wolfram (14, 15), indicate that the two-dimensional character of the $SrTiO_3$ conduction band will trap impurity-related surface states in the bandgap. Powell and Spicer (16) subsequently deduced from UVPS analysis that midgap surface states on the $SrTiO_3$ (001) face, if existent, would have a density less than 10^{13} cm^{-2}. On the other hand, Henrich *et al.* (17) (also using UVPS techniques) found for vacuum-fractured surfaces, a surface state density $\sim 5 \times 10^{13}$ cm^{-2}, at an energy some 1.7 eV above the valence bandedge E_v. This was attributed by Henrich *et al.* to extrinsic states composed of Ti^{3+}-O_V complexes, because of the effect of O_2 exposure in decreasing the peak height. States were also found near $E_v + 2.2$ eV, associated with step sites on the fracture plane.

Using a variety of analytical techniques (LEED, AES, EELS, UVPS), Lo and Somorjai (18) also reported midgap surface states on $SrTiO_3$, near $E_v +$

* Electrochemical Society Active Member.
Key words: photoelectrochemistry, semiconductor electrode, $SrTiO_3$, impurity doping, spectral response.

1.6 eV. They attributed these to Ti^{3+} ions. Using a vibrating capacitance probe for surface photovoltage measurements, Mavroides and Kolesar (19) found a strong dependence of the $SrTiO_3$ work function on the incident light frequency, caused presumably by filling and emptying of surface states within the gap.

Henrich *et al.* (20, 21) have also reported on the effects of O_2 adsorption on disordered surfaces of crystalline $SrTiO_3$. It has been shown (22) that orbital overlap of oxygen adsorbants can result in a broad surface band, some 3 eV wide.

The statements and citations of the preceding paragraphs were made to emphasize that midgap surface states do appear in a number of guises on $SrTiO_3$ surfaces, and that the effectiveness of $SrTiO_3$ as a photoanode material depends critically on the role such states can play. Thus the condition of the crystal surface, how this was formed, and the defect chemistry of the underlying lattice, all influence the photoactivity. We thus suggest that a (controllably) disordered surface may well be superior to an ordered one for photoelectrochemical purposes, provided this can be created reproducibly, and that it is stable. The suitability of microcrystalline ceramic $SrTiO_3$ as a photoanode material thus merits careful examination: on the one hand since this can be much less costly than the single crystals used for the above-cited work, and also because this could well be more effective than the same mass of monocrystal in providing useful surface states.

Goodenough *et al.* (23) have briefly reported the improved spectral response of ceramic $SrTi_{1-x}Cr_xO_{3-y}$, as compared with the action spectrum for undoped $SrTiO_3$ (also in polycrystalline form). They demonstrated an extension of the optical activity to around 550 nm, and attributed this to electron tunneling under high anodic bias from the O^{2-} ($2p^6$) valence band to a localized hole on a Cr^{4+} ion. This interesting result is, however, too slow to prevent trapping of conduction band electrons by the Cr^{4+} ions, and hence decays rapidly except with high anodic bias.

The results in the present paper concern $SrTiO_3$ in microcrystalline ceramic form as influenced by lanthanum doping, and with preparation, high temperature equilibration reduction (24, 25) and quenching (26) so as to establish a known thermodynamic condition for the interior of each crystallite. We find this material to be stable, and to be photochemically active.

Experimental

Ceramic samples used in this work were prepared by a liquid mix technique (24, 25) that permitted impurity stabilization to 10 ppm. Powder samples were pressed into disks, 1 cm diam, and some 0.1 cm thick, and sintered in air at 1625 K for 12 hr. The particle size was determined from SEM analysis to be about 0.5 μm, with a density 95% of that for single crystal material. The sintered disks were then equilibrated at a chosen P_{O_2} (from a flowing CO_2/CO or H_2/CO_2 gas mixture) for a period of 8-15 hr at 1325 K, and quenched in the ambient gas.

Of the $La_xSr_{1-x}TiO_3$ compositions that can be prepared in the above manner, we have on occasion studied samples with x as large as 0.05. That corresponds to [La] $\approx 9 \times 10^{20}$ cm^{-3}. However, all the results reported herein relate to the doping range $0 \leq x \leq 0.01$.

For each reduced and quenched ceramic disk, ohmic contact was made to the back by rubbing with $In_{0.995}Ga_{0.005}$ alloy. Indium solder was then used to attach a tinned copper wire to this back surface, which was then coated with du Pont conducting silver paste. We have found contacts so prepared to be ohmic, of low resistance, and with no detectable aging effects at room temperature for periods on the scale of a year.

The photoanode disk was then sealed with epoxy resin to the lower open end of a U-shaped glass tube, so that only the untreated front face was exposed to the electrolyte; the rear contact wire being protected inside the U-tube.

For the cathode of the PEC cell, we have used a Pt wire helix (of surface area ~0.3 cm^2) or Pt foil of area ~6 cm^2. Samples were at first tested in electrolytes ranging in pH from 2 to 14; with acid solutions made from HCl and deionized water, and basic solutions from NaOH. As it became clear that strongly basic solutions worked best, almost all subsequent experiments were done with 1M NaOH. In all cases reported herein, the photoanode was tested in a one compartment cell exposed to the atmosphere. Thus, operation was photovoltaic for low bias.

Irradiation for PEC cell operation was provided by an Oriel 300W solar simulator filtered to AM2. The (almost) short-circuit photocurrent was monitored from the voltage across a 100Ω resistor, and continuously plotted with a Hewlett-Packard 7100B strip chart recorder. External bias, when applied, came from a Hewlett-Packard 6248A d-c power supply, while electrolyte pH was measured with a VWR digital pH meter.

The spectral response of a ceramic photoanode was determined by recording the PEC cell photocurrent (as described above) with chopped monochromatic light and phase-sensitive detection. Irradiation for this experiment came from the combination of a 75W xenon lamp source, Jarrell-Ash Mark X monochromator, and Rofin variable speed chopper. The monochromator resolution was usually set for ~3 nm. The photocurrent output at the chopping frequency (in the range 50-800 Hz) was detected with a PAR 113/5101 preamplifier/lock-in detector combination; coaxial cable was used for contacts to both PEC cell electrodes to obviate extraneous pickup. Spectral response curves, such as those to be presented shortly in Fig. 3, were derived from X-Y recorder traces, using the signal from the monochromator spectral drive to control the abscissa scale.

Results and Discussion

Figure 1 shows 300 K data of photocurrent density J *vs.* any applied bias V, for microcrystalline ceramic $La_xSr_{1-x}TiO_3$ photoanodes in aqueous electrolytes of various pH. Each of the photoanodes for Fig. 1 had been strongly reduced ($P_{O_2} = 10^{-20}$ atm at 1325 K) and quenched.

The trend shown in parts (A) and (B) of Fig. 1, that photoactivity is most pronounced for a high pH electrolyte in both undoped $SrTiO_3$ and 1% La-doped material, was found also to be the case for other doping strengths. Accordingly, almost all subsequent PEC cell tests have used a 1M NaOH electrolyte.

The two parts of Fig. 1 have very different ordinate scales, so that part (B) could show the large photocurrent resulting from external bias to a PEC cell with a strongly basic electrolyte, and a strongly doped, strongly reduced photoanode. This should not obscure the experimental observation of zero-bias photocurrent densities of from 2.5 to 95 μA/cm^2 for variously prepared photoanodes and electrolytes under AM2 illumination.

All photoanode materials reported on here were reduced by a 1325 K equilibration under conditions in the range $10^{-20} \leq P_{O_2} \leq 10^{-16}$ atm prior to quenching. Parts (A) and (B) of Fig. 2 illustrate the dependence of the illuminated J-V characteristic (in 1M NaOH electrolyte) on lanthanum doping strength for these two extremes of the reduction condition. For the strongest reduction, $P_{O_2} = 10^{-20}$ atm, Fig. 2(A) shows a monotonic increase of photoactivity with doping. This contrasts with the situation in Fig. 2(B), for less severe reduction ($P_{O_2} = 10^{-16}$ atm).

That contrast is not incongruous, since the defect chemistry of quenched $La_xSr_{1-x}TiO_3$ has been shown (26, 27) to change form within the reduction range

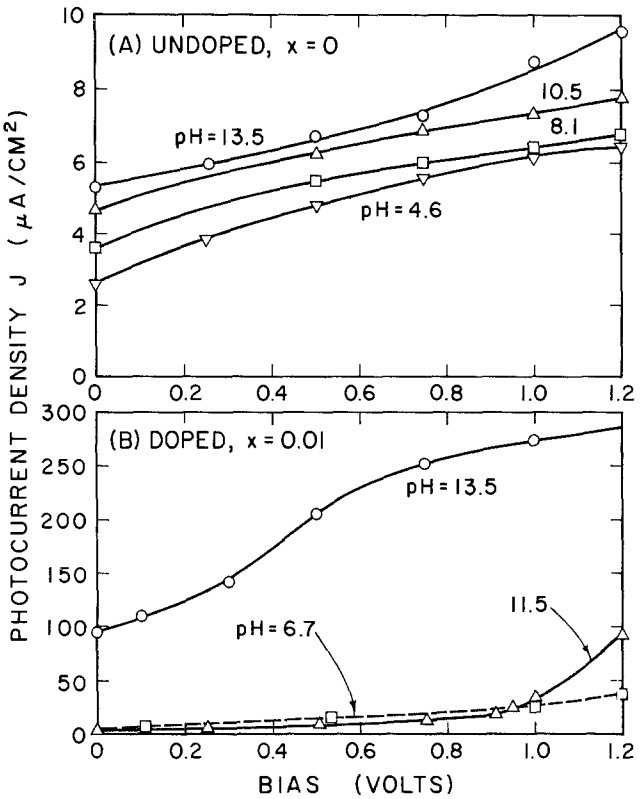

Fig. 1. Photocurrent density J ($\mu A/cm^2$) vs. applied bias (if any) for PEC cells using ceramic photoanodes, and aqueous electrolytes of various pH. For all cases shown here, the photoanode material was reduced at $P_{O_2} = 10^{-20}$ atm. (A) For $SrTiO_3$ that was not deliberately doped. (B) For $La_xSr_{1-x}TiO_3$ with $x = 0.01$. Results for other values of the dopant index x were similar to these data. The illumination intensity and spectral distribution was AM2.

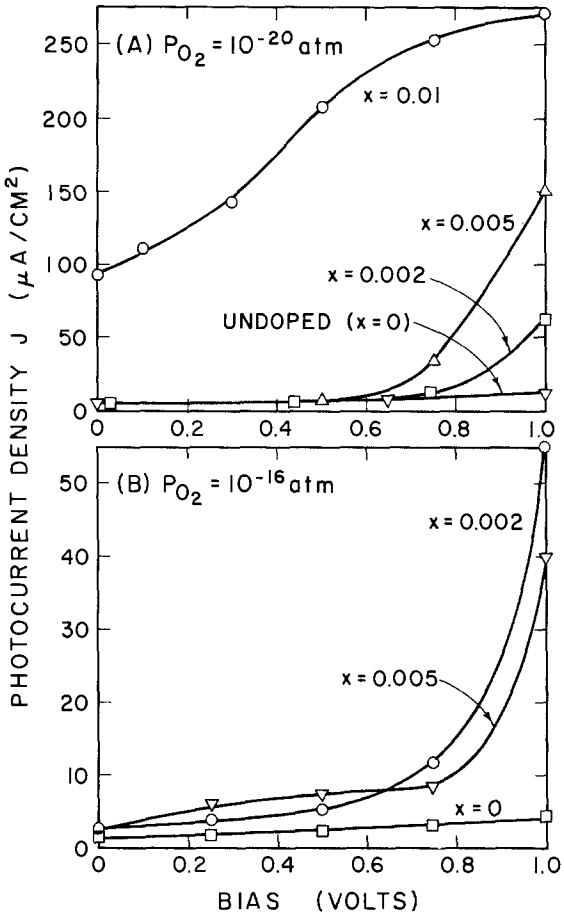

Fig. 2. Photocurrent density vs. bias for variously prepared ceramic $La_xSr_{1-x}TiO_3$ photoanodes, in PEC cells with a 1M NaOH strongly basic electrolyte. (A) J-V plots for undoped $SrTiO_3$, and for $x = 0.002$, 0.005, and 0.010; all material reduced at $P_{O_2} = 10^{-20}$ atm. (B) Plots for undoped $SrTiO_3$, and for $x = 0.002$ and 0.005; material reduced at $P_{O_2} = 10^{-16}$ atm.

$10^{-20} \leq P_{O_2} \leq 10^{-16}$ atm. At the upper end of that P_{O_2} range, the lattice contains excess oxygen, has Sr vacancies in the perovskite cells, and parts of SrO planes interleaving those perovskite units (28). For more severe reduction, the oxygen content is forced back to stoichiometry, lanthanum incorporation promotes $Ti^{IV} \rightarrow Ti^{III}$ (controlled-valency mechanism), and an extra electron from donor doping can become available for conduction. High temperature (27) and low temperature (26) conductivity measurements indicate that this requires $P_{O_2} \leq 10^{-18}$ atm for the 1325 K equilibration.

Figure 3 shows spectral response scans for four of the many $La_xSr_{1-x}TiO_2$ photoanodes studied, recorded in a working PEC cell. These show quantum efficiency η (response per incident photon) *vs.* λ, with the logarithmic ordinate scale a relative one. The vertical separations of the four curves have been reduced, but are in the correct order: thus curve (A) is for a weakly responsive anode (undoped $SrTiO_3$), while samples with $x = 0.005$ or 0.01 as in curves (C) and (D) showed a larger responsivity, as well as an extended spectral response.

The dark conductivity of $La_xSr_{1-x}TiO_3$ through the temperature range $10 \leq T \leq 500$ K was found to be maximized for $x \approx 0.002$ (26). This was attributed to the formation of a donor impurity band, with significant overlap occurring with the conduction band for $x \approx 0.003$. [The dark conductivity continued to decrease until $x \approx 0.005$, and thereafter increased slowly with further doping (26).] That interpretation of dark conductivity data is supported by the change of spectral response with doping illustrated by the various curves of Fig. 3.

Thus curve (A) shows the characteristic spectral response of undoped $SrTiO_3$ that has been sufficiently reduced to provide enough dark conductivity in the bulk for facilitation of the measurement. The quantum efficiency η falls off rapidly for $h\nu < 3.5$ eV ($\lambda > 355$ nm), as the actual "edge" of intrinsic transitions is approached.

Koffyberg *et al.* (13) and Dwight and Wold (29) have both analyzed comparable data for the rapid fall-off of responsivity with decreasing $h\nu$ for monocrystal $SrTiO_3$, using a (quite) simplified form of the expression (30) appropriate for an indirect (phonon-aided) transition. Thus if one assumes that $\eta \approx (A/h\nu)(h\nu - E_g)^2$, then E_g is obtained as the intercept in a plot of $(\eta h\nu)^{1/2}$ *vs.* $h\nu$. In this way, Koffyberg *et al.* deduced $E_g = 3.21$ eV, and Dwight and Wold reported $E_g = 3.2$ eV ($\lambda_g \simeq 388$ nm). A similar value is obtainable with the comparable plot for the undoped ceramic sample of curve (A). The shorter wavelength features of curve (A) [*i.e.*, the decrease of slope at 355 nm (3.5 eV), and the maximum near 310 nm (4.0 eV)] both correspond to those features as seen by Dwight and Wold (29) for undoped single crystal material.

Several differences are apparent between curves (A) and (B). It is important to keep in perspective those arising from lanthanum doping ($x = 0.002$), ones influenced by the oxygen defect chemistry [$P_{O_2} = 10^{-16}$ atm for the samples of both curves (A) and (B)], and those influenced by other variables: mean crystallite size, and the granule surface characteristics. Thus, compared with curve (A), one can say of curve (B) that: (*i*) The overall responsivity is larger for all wavelengths. (*ii*) The quantum efficiency changes more between 310 and 355 nm. (*iii*) The "edge" region for $\lambda > 355$ nm is less steep, and extrapolates to an E_g some 0.1 eV smaller.

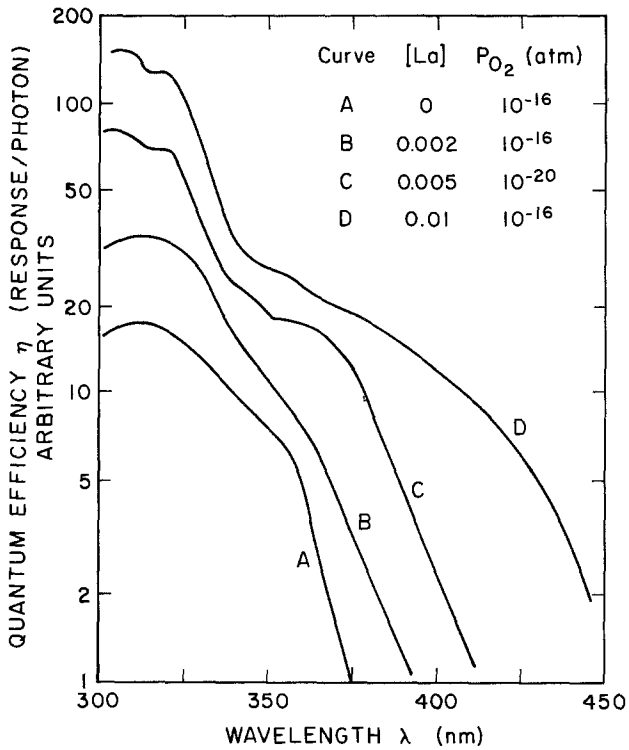

Fig. 3. Semilogarithmic spectral response plots for four representative $La_xSr_{1-x}TiO_3$ microcrystalline photoanodes, as identified above for dopant index x, and for reduction state. All were measured in 1M NaOH. The ordinate scale is the quantum efficiency η, i.e., the response per incident photon, expressed in arbitrary units. To make the figure more compact, the curves have been moved closer together than their actual responsivities would have placed them. Thus, at λ = 350 μm, the sample of curve D had η some 25 times larger than for the undoped sample of curve A.

That small evidence of gap reduction is greatly amplified by the spectral curves for samples (C) and (D), with their stronger lanthanum doping, and is consistent with electrical conductivity data (26) concerning the formation of an impurity band, which merges with the conduction band and provides a low energy tail to that band.

Thus curve (C), compared with curve (B), shows a distinct extension of the long wavelength response, with a perceptible structure at the spectral location ($h\nu \simeq 3.37$ eV, $\lambda \simeq 368$ nm) where Dwight and Wold (29) had speculated about one of the indirect thresholds. For longer wavelengths, the quantum efficiency of curve (C) has an exponential slope similar to that in curve (B). However, the more heavily doped sample of curve (D) ($x = 0.01$) shows a large extension of the long-wave response, still detectable at 440 nm (2.2 eV).

One may note also that separate maxima near 310 nm (4.0 eV) and 320 nm (3.9 eV) are apparent for both curves (C) and (D) of Fig. 3, as indeed they were for other strongly doped photoanodes we have measured. Koffyberg *et al.* (13) and Dwight and Wold (29), both inferred a direct gap for $SrTiO_3$ between 3.7 and 3.8 eV, and one can expect the optical absorption coefficient α to exceed 10^4 cm^{-1} for shorter wavelengths. One might expect some maximization of the quantum efficiency for a ceramic sample when the optical penetration depth α^{-1} is comparable with the average particle radius (~0.2 μm), provided that minority carriers can have a diffusion length at least this large, even for strong doping.

In order to maximize the useful photoactivity of a material, it is desirable to minimize the optical bandgap, while at the same time allowing efficient separation of charge carriers within the depletion region. This is controlled by V_{fb} of the material, in the solution to be used. It is also important that the dark bulk conductivity be large enough not to detract from the expectation of a high quantum efficiency. As pointed out in the introduction, there must additionally be a mechanism by which photogenerated holes can communicate with the appropriate species in the electrolyte. This is presumably accomplished via surface states with energies in the semiconductor bandgap.

As has been shown (26), the conductivity itself is maximized by moderate doping ([La] ≃ 0.002), and the room temperature conductivity is some ten times smaller for $x = 0.01$. On the other hand, extension of the spectral response is accomplished by lanthanum doping up to 1%. These competing effects are best reconciled by use of heavy doping and quenching from a fully reduced state, since reduction assists σ_{300} for a given [La] until exhaustion is reached. We have confirmed this with the performance of $La_{0.01}Sr_{0.99}TiO_3$ reduced at $P_{O_2} = 10^{-20}$ atm, as epitomized by the curves in Fig. 1(B) and 2(A).

Before leaving the spectral response curves of Fig. 3, and the indications therein of (*i*) impurity banding, (*ii*) reduction of the photon energy threshold, and (*iii*) increase of the overall responsivity with doping, a further comment on the experimental techniques is appropriate. The interpretations were based on a-c photoconductivity measurements, as a matter of convenience in data acquisition. However, d-c photocurrents were observed for $h\nu < E_i$ with the more strongly doped samples. Indeed, the d-c response was used in calibrating the X-Y plotter for the subsequent a-c scans.

Figures 4 and 5, and Table I, address the question of electrode stability. This is a question which appears important enough even with single crystal electrodes of some semiconductors, and can be expected to be of extreme importance in deciding on the viability of an electrode in microcrystalline form. Figure 4 shows the dark electrical conductance (expressed as the equivalent bulk electrical conductivity in ohm^{-1} cm^{-1} for fully densified homogeneous material) for $La_{0.002}Sr_{0.998}TiO_3$ that had been quenched from $P_{O_2} = 10^{-20}$ atm equilibration. The conductivity was mea-

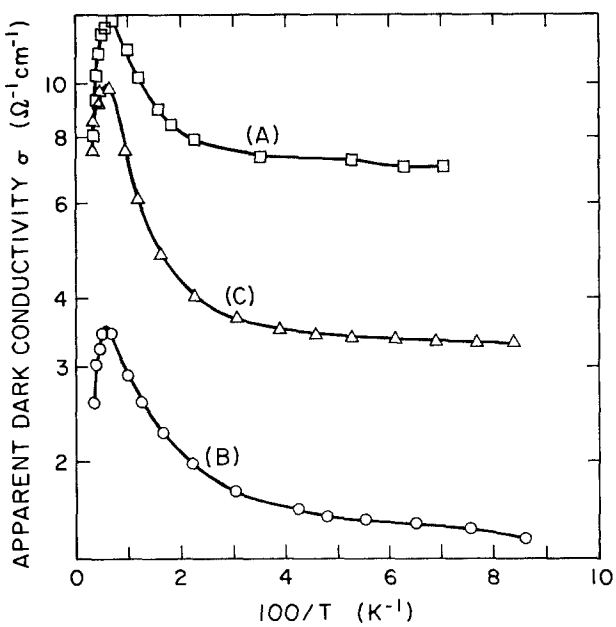

Fig. 4. Electrical conductance (measured in a back surface van der Pauw arrangement, and expressed as equivalent to bulk conductivity σ for homogeneous material) vs. 100/T, for microcrystalline $La_xSr_{1-x}TiO_3$ samples ($x = 0.002$) reduced at $P_{O_2} = 10^{-20}$ atm. (A) The material as first prepared, reduced, and quenched. (B) Material similarly prepared, measured after operation in a PEC cell with a 1M NaOH electrolyte and AM2 illumination for 13.6 hr. (C) The sample of curve (B), after a rereduction at 1325 K with $P_{O_2} = 10^{-20}$ atm.

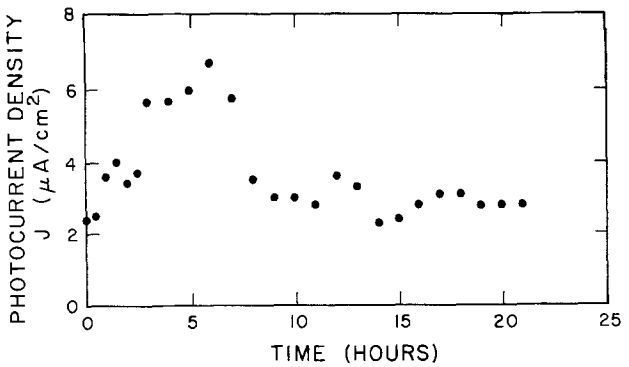

Fig. 5. Photocurrent density J ($\mu A/cm^2$) vs. time of illumination at AM2 spectrum and intensity, in a PEC cell with a 1M NaOH electrolyte. The sample here is microcrystalline undoped $SrTiO_3$, partially reduced in $P_{O_2} = 10^{-16}$ atm prior to quenching. For most of the other (doped) photoanodes studied in the same way, the responsivity was (of course) larger, but the fractional change of J with time was smaller.

sured using a four corner van der Pauw probe to the unexposed (back) surface of the photoanode, done to avoid surface effects.

Curve (A) in Fig. 4 shows $\log(\sigma)$ *vs.* $100/T$ over the range 10-300 K for this material as quenched. Curve (B) shows the conductance (similarly expressed as equivalent conductivity) for a similarly prepared sample that was then operated in a PEC cell for 13.6 hr, using 1M NaOH electrolyte and AM2 illumination. It will be seen that this operation in a PEC cell has lowered the conductance, by a factor of some 3:1 for the higher temperatures, and by nearly 5:1 for low temperatures. Curve (C) is for the same sample as in curve (B), but after a second high temperature equilibration/reduction/quench sequence. Note that the room temperature conductivity has been restored essentially to the original value, though this is not so for low temperatures.

The tests illustrated in Fig. 4 are not perfectly quantitative, since all three curves could not be obtained with the identical sample. Moreover, sample cleaning after PEC cell use (30 min ultrasonic bath in 37% HCl, and running deionized water rinse) may not have removed all of the indium and silver contact material. Subsequent reduction at 1325 K could then have allowed in-diffusion of these impurities, where they would serve as acceptors, and reduce especially the low temperature conductivity. Thus the most interesting aspect of Fig. 4 is that, despite that source of potential contamination, re-reduction did restore the room temperature conductivity to almost its original value.

Thus electrode photo-oxidation may be occurring to some extent, but as a reversible process. Similar tests done with more strongly doped $La_xSr_{1-x}TiO_3$ anodes showed an interesting reversal of the trend. Table I gives values for the apparent σ_{300} of six representative doped samples, before and after PEC cell operation.

Table I. A comparison of 300 K conductance (expressed as apparent bulk conductivity) for samples before and after use as a photoanode in a PEC cell

Material preparation			Apparent bulk conductivity σ_{300} (Ω^{-1} cm^{-1})		
La doping x	Reduction P_{O_2} (atm)	Time in PEC cell (hr)	Before	After	Comments
0.002	10^{-18}	12.3	6.0	1.8	Different samples
0.002	10^{-20}	13.6	8.5	2.6	Different samples
0.005	10^{-18}	27.6	0.56	0.48	Identical samples
0.005	10^{-20}	49.1	0.66	0.50	Identical samples
0.01	10^{-18}	28.4	0.64	0.73	Different samples
0.01	10^{-20}	20.8	1.3	1.7	Different samples

Note that samples doped with $x = 0.005$ show a quite small drop in conductance after operation in a cell, while samples doped with $x = 0.01$ actually show a small conductance increase. This suggests that photo-oxidation may occur only for weakly doped material, and may be precluded for [La] ≥ 0.005. That is indeed fortuitous, in the light of our finding that strong doping is advantageous for optimizing the quantum efficiency and the spectral response.

Figure 5 plots photocurrent *vs.* time for a ceramic photoanode. These data happen to be for undoped $SrTiO_3$ reduced in $P_{O_2} = 10^{-16}$ atm; one of our less responsive samples. The figure shows that zero-bias photocurrent for AM2 illumination tends to rise to a maximum after some 4-6 hr, followed by a fairly rapid decline to a steady level. No further change in performance was observed out to 22 hr of operation.

Various other photoanodes have been monitored for periods of 12-50 hr of simulated solar illumination; showing only modest changes in photoactivity, mostly less prominent than those in Fig. 5. Visual and microscopic examination showed no apparent changes, supporting an interpretation that $SrTiO_3$ and $La_xSr_{1-x}TiO_3$ in reduced ceramic form are stable to photodecomposition in 1M NaOH.

Conclusions

The performance of ceramic $SrTiO_3$ photoanodes, modified by both donor doping and reduction, has been investigated for use in the photodissociation of water. The monitoring of photocurrents (produced in the photovoltaic mode) as a function of materials defect chemistry, in conjunction with measurements of electrical conductivity (26) and of spectral response, provide the following conclusions: (*i*) These materials function best in a high *p*H environment, as do $SrTiO_3$ monocrystals (3, 4, 9). (*ii*) Lanthanum doping promotes formation of an impurity band for [La] $\geq$ 0.002, and the spectral response confirms expectations from dark conductivity (26) that the conduction and impurity bands are fully merged with a substantial band tail by the time [La] $\approx$ 0.01. (*iii*) As a result of (*ii*), and the fact that conductivity increases with reduction until complete reduction ($P_{O_2} \leq 10^{-18}$ atm) is attained, optimal photoanode performance requires strong lanthanum doping and strong reduction prior to quenching. (*iv*) No significant photocomposition effects were seen as a result of operation in a PEC cell at AM2 illumination for periods of up to 50 hr. (*v*) Modest photo-oxidation appears to occur for samples with [La] $\leq$ 0.002, but not with stronger lanthanum doping. (*vi*) Ceramic $La_xSr_{1-x}TiO_3$, doped with $x \approx$ 0.01, and fully reduced (high temperature equilibration at $P_{O_2} \approx 10^{-20}$ atm prior to quench), shows a vigorous photoactivity in 1M NaOH, without any external bias requirement. It is assisted in this regard by an amply adequate dark conductivity, by the effect of impurity band tailing below the conduction band in reducing the optical bandgap, and evidently by the presence of a substantial density of midgap surface states.

Of more significance than any of the above noted individual and specific conclusions, is the demonstration that studies of photosensitive materials in microcrystalline form can yield a great deal of useful information, with a considerable savings of time and cost. While the response of ceramic $SrTiO_3$-based materials is apt to be orders of magnitude smaller than for their single crystal counterparts, it is nevertheless adequate for analytical study. The implications of this are clear: families of materials (particularly oxides) that are either unavailable or too costly in monocrystalline form, can often be created and brought into a specified thermodynamic condition in the laboratory, at minimal expense. Results obtained with such microcrystalline samples can then provide enough information to indicate the areas of maximum priority for any (narrower range) single crystal investigations.

Acknowledgments

It is a pleasure to acknowledge support of this research, in part by a grant from the Gas Research Institute, with additional support from Tektronix, Incorporated. We also wish to thank N. G. Eror and U. Balachandran for the microcrystalline materials used in this study, and for many valuable discussions.

Manuscript submitted Jan. 22, 1982; revised manuscript received *ca.* Aug. 6, 1982.

Any discussion of this paper will appear in a Discussion Section to be published in the December 1983 JOURNAL. All discussions for the December 1983 Discussion Section should be submitted by Aug. 1, 1983.

Publication costs of this article were assisted by the Oregon Graduate Center.

REFERENCES

1. J. G. Mavroides, D. I. Tchernev, J. A. Kafalas, and D. F. Kolesar, *Mater. Res. Bull.*, **10**, 1023 (1975).
2. M. S. Wrighton, A. B. Ellis, P. T. Wolczanski, D. L. Morse, H. B. Abrahamson, and D. S. Ginley, *J. Am. Chem. Soc.*, **98**, 2774 (1976).
3. J. G. Mavroides, J. A. Kafalas, and D. F. Kolesar, *Appl. Phys. Lett.*, **28**, 241 (1976).
4. T. Watanabe, A. Fujishima, and K. Honda, *Bull. Chem. Soc. Jpn.*, **49**, 355 (1976).
5. A. B. Bocarsly, J. M. Bolts, P. G. Cummins, and M. S. Wrighton, *Appl. Phys. Lett.*, **31**, 568 (1977).
6. H. H. Kung, H. S. Jarrett, A. W. Sleight, and A. Ferretti, *J. Appl. Phys.*, **48**, 2463 (1977).
7. K. Ohashi, J. McCann, and J. O'M. Bockris, *Nature*, **266**, 610 (1977).
8. A. K. Ghosh and H. P. Maruska, *This Journal*, **124**, 1516 (1977).
9. M. A. Butler, M. Abramovich, F. Decker, and J. F. Juliao, *ibid.*, **128**, 200 (1981).
10. L. J. Handley and A. J. Bard, *ibid.*, **127**, 338 (1980).
11. J. F. McCann and J. Pezy, *ibid.*, **128**, 1735 (1981).
12. M. S. Wrighton, D. S. Ginley, P. T. Wolczanski, A. B. Ellis, D. L. Morse, and A. Linz, *Proc. Nat. Acad. Sci. USA*, **72**, 1518 (1975).
13. F. P. Koffyberg, K. Dwight, and A. Wold, *Solid State Commun.*, **30**, 433 (1979).
14. T. Wolfram, *Phys. Rev. Lett.*, **29**, 1383 (1972).
15. S. Ellialtioglu and T. Wolfram, *Phys. Rev. B*, **18**, 4509 (1978).
16. R. A. Powell and W. E. Spicer, *ibid.*, **13**, 2601 (1976).
17. V. E. Henrich, G. Dresselhaus, and H. J. Zeiger, *ibid.*, **17**, 4908 (1978).
18. W. J. Lo and G. A. Somorjai, *ibid.*, **17**, 4942 (1978).
19. J. G. Mavroides and D. F. Kolesar, *J. Vac. Sci. Technol.*, **15**, 538 (1978).
20. V. E. Henrich, G. Dresselhaus, and H. J. Zeiger, *Solid State Commun.*, **24**, 623 (1977).
21. V. E. Henrich, G. Dresselhaus, and H. J. Zeiger, *J. Vac. Sci. Technol.*, **15**, 534 (1977).
22. M. Tomkiewicz, *Surf. Sci.*, **101**, 286 (1980).
23. J. G. Goodenough, A. Hammett, M. P. Dare-Edwards, G. Campet, and R. D. Wright, *ibid.*, **101**, 531 (1980).
24. N. G. Eror and D. M. Smyth, in "Chemistry of Extended Defects in Non-Metallic Solids," L. Eyring and M. O'Keefe, Editors, p. 62, North-Holland, Amsterdam (1970).
25. U. Balachandran and N. G. Eror, *Comm. Am. Ceram. Soc.*, **64**, C-75 (1981).
26. B. Odekirk, U. Balachandran, N. G. Eror, and J. S. Blakemore, *Mater. Res. Bull.*, **17**, 199 (1982).
27. N. G. Eror and U. Balachandran, *J. Solid State Chem.*, **40**, 85 (1981).
28. S. N. Ruddlesden and P. Popper, *Acta Cryst.*, **11**, 54 (1958).
29. K. Dwight and A. Wold, in "Photoeffects at Semiconductor-Electrolyte Interfaces," A. J. Nozik, Editor, p. 207, (Amer. Chem. Soc., Washington, DC, 1981).
30. J. I. Pankove, "Optical Processes in Semiconductors," Dover Publications, Inc., New York (1975).

Photoelectrolysis of Water under Visible Light with Doped $SrTiO_3$ Electrodes

Michio Matsumura, Masahiro Hiramoto, and Hiroshi Tsubomura

Department of Chemistry, Faculty of Engineering Science, Osaka University, Toyonaka, Osaka 560, Japan

ABSTRACT

Various pieces of sintered strontium titanate doped with metal oxides were used as photoanodes in aqueous solutions. Some of them (having Ru, V, Cr, Ce, Co, Rh) caused photocurrents with light in the visible region. The production of oxygen at the semiconductor electrode and hydrogen at the counterelectrode was confirmed. For the electrode doped with RuO_2, the quantum efficiency of the photocurrents with the visible light (400-500 nm) reached *ca.* 2% under anodic polarization. Based on these results and the reflection and electroluminescence spectra of the sinter, it is concluded that the photocurrent arises from an electronic transition from a dopant level to the conduction band, the former lying a little above the valence band.

The photoelectrochemical phenomena of semiconductor electrodes have been attracting attention in recent years in view of solar energy conversion. The feasibility of hydrogen production from water or of other chemical storage process is the most interesting point of these electrochemical solar cells. Some oxide semiconductors, *e.g.*, TiO_2 (1), $SrTiO_3$ (2, 3), $BaTiO_3$ (4), SnO_2 (5), etc. (6) are known to decompose water in photoelectrochemical cells. Unfortunately, their bandgaps are so large (> 3.0 eV) that they can absorb light only in the ultraviolet region. The theoretical limit of the sunlight engineering efficiency for the semiconductor with a bandgap of 3.0 eV is only 7%. The practical efficiency is much lower. Therefore, it is very important to develop electrode materials having smaller bandgaps.

Key words: semiconductor electrode, photoelectrochemical cell, hydrogen production, electroluminescence.

Scaife (7) pointed out that, for oxide semiconductors with their valence bands formed by the 2 p orbitals of oxygen atoms, the bandgaps should be higher than 2.94 eV in order that they can decompose water. Semiconductors with their valence bands formed by the d orbitals of the metal ions may be devoid of such restriction. In fact, Cr-doped TiO_2 (8) and $SrTiO_3$ (9) and some other similar systems (10-14) have been reported to show photoresponse to visible light. In this paper, we report the photoelectrochemical behavior of $SrTiO_3$ sintered electrodes doped with various metal oxides. $SrTiO_3$ has a flatband potential most suitable for the decomposition of water.

Experimental

The $SrTiO_3$ sintered electrodes doped with metal oxides were synthesized by the following procedure. $SrTiO_3$ powder, 99.9% pure, from Fuji Titanium Indus-

try Company, Limited, was mixed with reagent grade metal oxide in an agate mortar. The mixture was pressed into disks 1 cm in diameter and sintered at 1400°C for 2 hr. The two faces of the sintered disks were polished with alumina powder 1 μm in particle size and were heated in a stream of hydrogen at 900°-1200°C for 1 hr so as to gain electrical conductivity. The optimal temperature depended on the kind of the added metal oxide. The ohmic contact with a copper wire was taken by indium evaporated on the sinter surface. Single crystals of $SrTiO_3$ from Nakazumi Crystal Company, Limited were also used as electrodes.

The electrochemical measurements were made in most cases under potentiostatic condition using a Hokutodenko HA 101 potentiostat with a saturated calomel electrode (SCE) as a reference electrode. A platinum plate was used as a counterelectrode. Measurements were made in 1M (mol dm^{-3}) NaOH, 0.5M K_2SO_4, borate buffer (*p*H 8.8), and acetate buffer (*p*H 4.6) solutions. The electrodes were illuminated with a 500W high pressure Hg lamp or a 500W Xe lamp, both from Ushio Electric Incorporated combined with a grating monochromator from Japan Jarrel-Ash Company.

The reflection spectra of the sinters were measured with a Shimadzu UV-360 spectrophotometer equipped with an integrating sphere. The electroluminescence from the electrodes was measured under cathodic polarization in aqueous solutions of 0.5M $Na_2S_2O_8$ and 0.2M NaOH using a grating monochromator (Jobin Yvon, H-20) and a Hamamatsu TV, R-712 photomultiplier.

Results

The undoped $SrTiO_3$ sintered electrodes showed almost the same quantum efficiency, action spectra, and onset potential of the photocurrent as those of the single crystal electrodes. This suggests that the mobility of the electric carriers and the photoabsorptivity of $SrTiO_3$ in the polycrystalline structure of the sinter do not differ much from those of the single crystal.

The $SrTiO_3$ electrodes doped with RuO_2, V_2O_5, Cr_2O_3, Ce_2O_3, CoO, and Rh_2O_3 showed photoresponse to the visible light, while undoped $SrTiO_3$ and those doped with other metal oxides, ZnO, Al_2O_3, etc., showed photocurrent only with u.v. light as indicated in Table I. The action spectra of the photocurrents for the electrodes either undoped or doped with the oxides in the former group are shown in Fig. 1. Most of the results shown in Table I and those described later were obtained by the electrodes containing dopants from 0.01 to 0.05 weight percent (w/o). When they were doped more lightly, the photocurrents due to visible light were smaller. When they were doped more heavily, the photocurrents became smaller in the whole wavelength region from u.v. to visible.

The quantum efficiency of the photocurrent, *i.e.*, the number of flowing electrons per incident photon, can be calculated from the results of Fig. 1 and the intensity of the incident monochromatic light. The quantum efficiency of the electrode doped with RuO_2 is 1-2% over the wavelength region from 400 to 500 nm as shown in Fig. 2.

The undoped $SrTiO_3$ sinter is colorless before the reduction by hydrogen. After the reduction, it turned gray presumably by the formation of oxygen vacancies.

Table I. Classification of dopants with respect to the sensitizing effect on the photocurrents of the $SrTiO_3$ sintered electrodes at wavelengths longer than 400 nm

1. Those showing sensitizing effect:
   RuO_2, V_2O_5, Cr_2O_3, Ce_2O_3, CoO, Rh_2O_3
2. Those showing weak effect:
   Fe_2O_3, La_2O_3
3. Those showing very little or no effect:
   Al_2O_3, SiO_2, TiO_2, MnO_2, NiO, CuO, ZnO, Ga_2O_3, SrO, Nb_2O_5, MoO_3, PdO, SnO_2, Ta_2O_5, WO_3, Tl_2O, PbO_2, Bi_2O_3

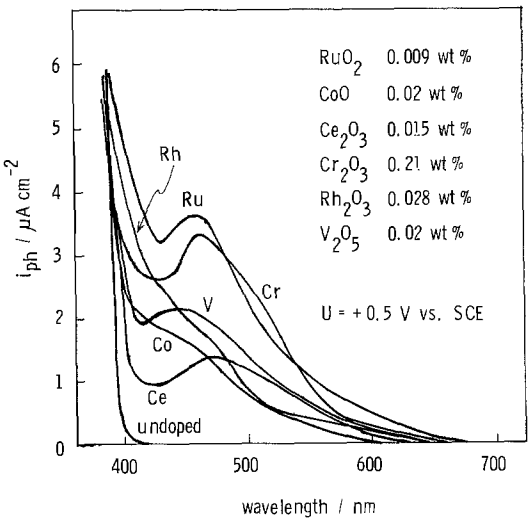

Fig. 1. Action spectra of the photocurrents for the $SrTiO_3$ electrodes doped with metal oxides in aqueous solutions of *p*H 4.6 under the potential of 0.5V *vs.* SCE.

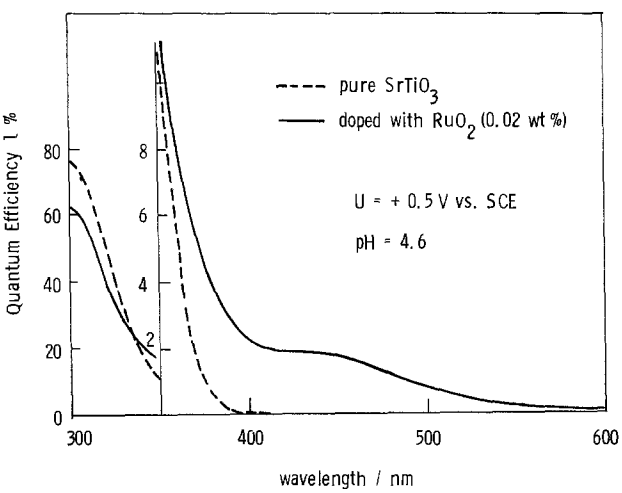

Fig. 2. The quantum efficiency of the photocurrent for the undoped and RuO_2-doped (0.02 w/o) $SrTiO_3$ electrodes in aqueous solutions of *p*H 4.6 under 0.5V *vs.* SCE.

On the other hand, the doped sinters showing photoresponse in the visible region are colored before the reduction. The reflection spectra of the doped sinters which caused photocurrents in the visible region have absorption bands in the visible region as shown in Fig. 3. Even after the reduction, the absorption bands due to the dopants persist in the same wavelength region, though they become diffuse. It can be seen from Fig. 1 and 3 that the absorption spectra of the sinters are not all in good parallelism with the action spectra of the photocurrents. Though the electrodes doped with Cr_2O_3 or Rh_2O_3 have strong absorption at around 600 nm, they have no photocurrent response in this region. Similarly, some colored electrodes such as CuO-doped electrode have no photocurrent response in the visible region. It is expected from these results that the photocurrents in the visible region are caused by the transitions from dopant levels to the conduction band. This is discussed later in more detail.

When the electrodes doped with RuO_2, V_2O_5, Cr_2O_3, Ce_2O_3, CoO, and Rh_2O_3 were irradiated in the visible region by use of a 500W Hg lamp and a cutoff glass filter ($\lambda < 430$ nm) dipped in a water jacket, photocurrents higher than 1 mA cm^{-2} flowed under anodic polarization, and bubbles appeared on the electrode surfaces irrespective of the *p*H of the solutions from 4.6 to 14. The photocurrent flowed continuously as shown

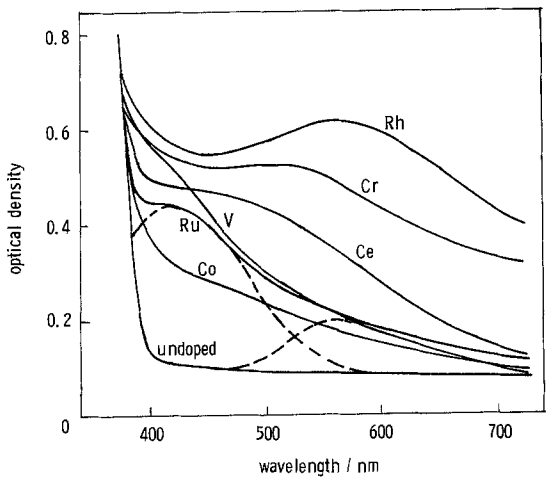

Fig. 3. The reflection spectra of $SrTiO_3$ sintered disks before the reduction by hydrogen. The broken lines show possible division into two components of the spectrum for the RuO_2-doped sinter.

in Fig. 4. The total electrical quantity carried through by the illumination reached 40C. The bubbles formed by illuminating the RuO_2-doped electrode biased at +0.9V with respect to the counterelectrode in a cell containing a platinum counterelectrode and an aqueous solution of K_2SO_4 were collected and analyzed by a quadrupole mass spectrometer. The mol ratio found was $H_2:O_2:N_2 = 2:1:0.2$. It is substantiated from this result that water is decomposed by visible light into hydrogen and oxygen. No corrosion of the semiconductor electrode was observed.

The *i-V* curve of the undoped sintered electrode observed under irradiation in the u.v. region was nearly the same as that of the single crystal electrode (Fig. 5a). The photocurrent rises at *ca.* −0.65V (*vs.* SCE), which is 0.15V more negative than the potential of the hydrogen electrode in an aqueous solution of *p*H 4.6. On the other hand, the photocurrents for the doped electrodes starts and reaches saturation at more anodic potentials. For example, the *i-V* curves for the Ru-doped electrode observed under illumination with an Hg lamp are shown in Fig. 5b and c. In this case, the short-circuit current density was 50 and 19 $\mu A\ cm^{-2}$, respectively, by illumination from an Hg lamp and from the same lamp with a u.v. cutoff filter. The current densities were much lower than that observed for the undoped electrodes illuminated by the same lamp without a filter. These low current densities are probably due to the generation of the electron-hole recombination centers produced by the doping. The electrodes doped with other dopants showed short-circuit

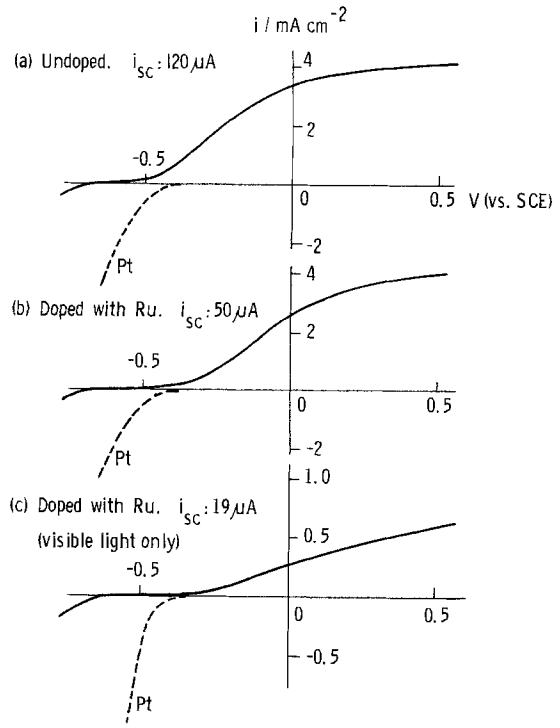

Fig. 5. The *i-V* curves for the undoped $SrTiO_3$ sintered electrode (a), and for that doped with RuO_2 (0.02 w/o) (b) and (c), obtained in aqueous solutions of *p*H 4.6. The electrode was illuminated by a 500W Hg lamp in the case of (a) and (b), and by the same light source equipped with a cutoff filter ($\lambda < 430$ nm) in the case of (c). i_{sc} means short-circuit photocurrent. Broken lines indicate the current for a platinum electrode.

photocurrents nearly equal to or lower than that of the RuO_2-doped electrode.

Discussion

The appearance of photocurrents in doped $SrTiO_3$ sintered electrodes with less-than-bandgap excitation can be explained by the formation of localized levels in the bandgap as shown in Fig. 6. The electronic transition from such levels to the conduction band produces free electrons and trapped holes. The trapped holes are expected to move toward the surface by hopping through the localized levels and decompose water to oxygen and protons.

It is found from the *i-V* curves (Fig. 5) that the anodic photocurrent rises up much more slowly with increasing anodic polarization in the case of the less-than-bandgap excitation than in the case of the bandgap excitation. As the density of the dopant in the electrode is very low, the photoabsorption by the

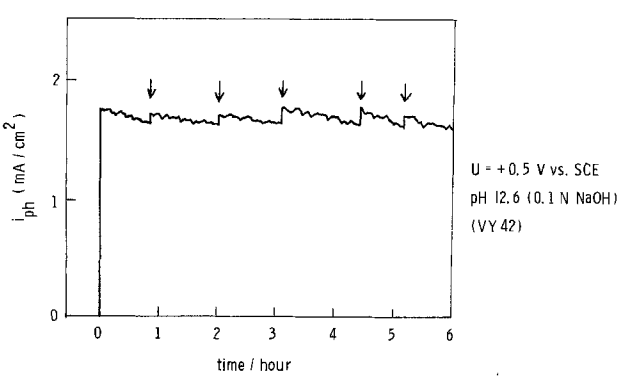

Fig. 4. The photocurrent *vs.* time for the 0.02 w/o RuO_2-doped electrode in aqueous solutions of *p*H 12.6 under 0.5V *vs.* SCE. The arrows indicate the time when the bubbles formed on the glass filter in the water jacket are removed.

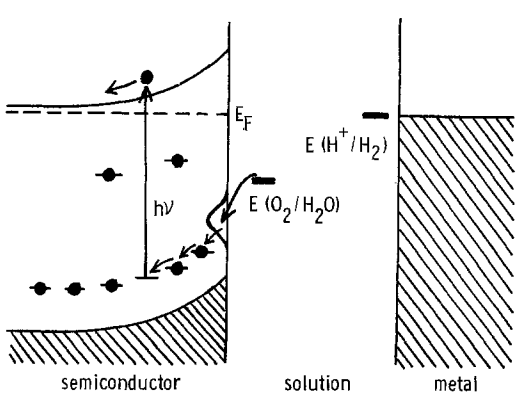

Fig. 6. A model for the generation of the photocurrent by the irradiation of less-than-bandgap light in the < doped $SrTiO_3$/ solution/metal > cell system.

dopant is usually weak. By increasing the anodic polarization, the thickness of the space charge layer is increased and the dopant absorption in this layer will increase. This should enhance the photocurrent. The slow rising of i-V curve for less-than-bandgap excitation can thus be understood.

As to the origin of the localized levels in the bandgap, there may be two possibilities: (*i*) the impurity levels due to doped metal ions, *i.e.*, the d orbitals of the metal ions, and (*ii*) the defect of the lattice introduced by the doping treatment. Maruska *et al.* (8) have proposed that the photocurrent of the Cr-doped TiO_2 caused by visible light is due to the former mechanism. We also conclude that the former mechanism is appropriate for the photocurrents observed in the doped $SrTiO_3$ electrodes by reason that the action spectra of the photocurrents for the electrodes doped with various metals differ one after another as shown in Fig. 1, showing that the various dopant levels are responsible for the photocurrents.

The above-mentioned results are consistent with the model (Fig. 6) in which the oxidation reactions are assumed to proceed through surface states [or surface-trapped holes (15)]. In this model, only those dopants with energy levels existing below the surface states are capable of transporting holes to the solution via the surface states. This mechanism is supported by the results of Fig. 7, where the response of the photocurrent of the Ru-doped $SrTiO_3$ electrode measured at several wavelengths are shown. Steady photocurrents are observed by excitation at wavelengths shorter than 500 nm, whereas decaying photocurrents were observed by excitation at longer wavelengths. The decaying photocurrents are attributable to those from dopant levels existing at energy levels higher than the surface states, where the holes produced in the bandgap are not transported to the surface levels and thus are unable to cause steady photocurrents.

Based on this model, the reflection spectrum of the Ru-doped $SrTiO_3$ can be explained by assuming that it consists of two components as shown qualitatively by broken lines in Fig. 3. The bands at wavelengths longer than 500 nm are attributable to the levels lying above the surface state. Only the other band is therefore relevant to the photocurrent. Similar interpretation can be made for the electrodes doped with other dopants.

In an attempt to further elucidate the dopant levels and the surface state, the electroluminescence spectra arising from the cathodically polarized electrodes were measured in alkaline $Na_2S_2O_8$ solutions. Typical results are shown in Fig. 8. The electrode of $SrTiO_3$ single crystal showed nearly the same spectra as that of the undoped sintered electrode. These spectra are assigned to a transition from the conduction band to the

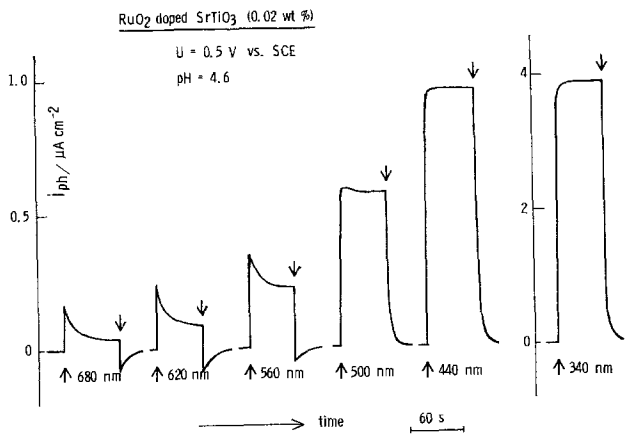

Fig. 7. The change of the photocurrents *vs.* time observed at several wavelengths in aqueous solutions of *p*H 4.6 at 0.5V *vs.* SCE.

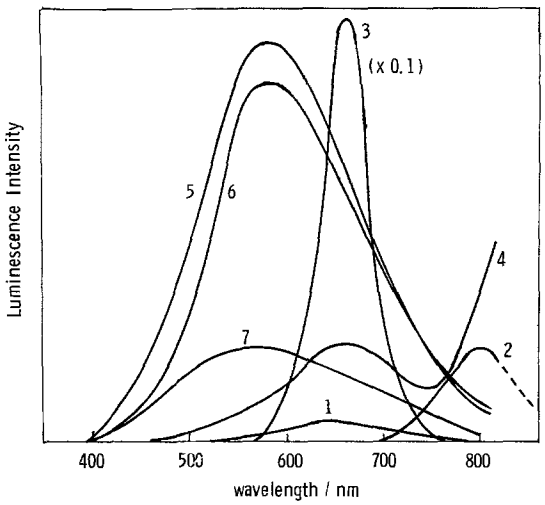

Fig. 8. The electroluminescence of the doped $SrTiO_3$ sintered electrodes observed in aqueous solutions of 0.5M $Na_2S_2O_8$ and 0.2M NaOH under −4.0V *vs.* SCE. 1, undoped. 2, 0.1 w/o Cr_2O_3. 3, 0.03 w/o PdO. 4, 0.01 w/o SiO_2. 5, 0.015 w/o Ce_2O_3. 6, 0.05 w/o RuO_2. 7, 0.02 w/o V_2O_5.

surface state (15), emptied by the $SO_4^{\cdot-}$ radical ion (16). From the peak wavelength of the electroluminescence of the undoped electrode, the energy level of the surface state on the $SrTiO_3$ electrode is estimated to lie at 1.9 eV below the conduction band.

The electroluminescence spectra of the doped electrodes can be classified into the following three groups:

1. Those which are almost the same as that of the undoped electrode; observed in the electrodes doped with ZnO, Al_2O_3, Ta_2O_5, etc., which show no photocurrent and absorption bands in the visible region. It is asserted that the metal ions of this group have no energy levels in the bandgap, or, alternatively do not penetrate into the lattice of $SrTiO_3$.
2. Those having very intense and narrow luminescence bands; found in the Cr_2O_3- and PdO-doped electrodes. These luminescence bands can be assigned to the transitions between the energy levels of the doped ions themselves, viz., $^2E \rightarrow {}^4A_2$ transition of Cr^{3+} ion (17) in the case of Cr-doped $SrTiO_3$.
3. Those with a broad band at wavelengths shorter than that of the undoped electrode; found in the electrodes doped with Ru, V, and Ce, showing photoresponse in the visible region. The luminescence of the third group is expected to be due to the electronic transition from the conduction band to the vacant dopant levels. From the wavelength of the luminescence, the differences of the energy levels of the doped ions from the conduction band can be estimated. They indicate that the dopant levels of this group lie deeper than the surface states.

These results of the electroluminescence are consistent with the mechanism of the photocurrent shown in Fig. 6, where the photogenerated trapped holes in the bandgap deeper than the surface states can cause photocurrents.

Manuscript submitted May 20, 1981; revised manuscript received July 13, 1982.

Any discussion of this paper will appear in a Discussion Section to be published in the December 1983 JOURNAL. All discussions for the December 1983 Discussion Section should be submitted by Aug. 1, 1983.

Publication costs of this article were assisted by Osaka University.

REFERENCES

1. A. Fujishima and K. Honda, *Nature*, **238**, 38 (1972).
2. T. Watanabe, A. Fujishima, and K. Honda, *Bull. Chem. Soc. Jpn.*, **49**, 355 (1976).
3. M. S. Wrighton, A. B. Ellis, P. T. Wolczanski, D. L.

Morse, H. B. Abrahamson, and D. S. Ginley, *J. Am. Chem. Soc.*, **98**, 2774 (1976).
4. J. H. Kennedy and K. W. Frese, *This Journal*, **123**, 1683 (1976).
5. H. Kim and H. A. Laitinen, *ibid.*, **122**, 53 (1975).
6. H. P. Maruska and A. K. Ghosh, *Solar Energy*, **20**, 443 (1977).
7. D. E. Scaife, *ibid.*, **25**, 41 (1980).
8. A. K. Ghosh and H. P. Maruska, *This Journal*, **124**, 1516 (1977).
9. H. P. Maruska and A. K. Ghosh, *Solar Energy Mater.*, **1**, 237 (1979).
10. J. Augustinski, J. Hinden, and C. Stalder, *This Journal*, **124**, 1063 (1977).
11. G. Campet, M. P. Dare-Edwards, A. Hammett, and J. B. Goodenough, *Nouv. J. Chim.*, **4**, 501 (1980).
12. Y. Matsumoto, J. Kurimoto, Y. Amagasaki, and E. Sato, *This Journal*, **127**, 2148 (1980).
13. R. D. Rauh, J. M. Buzby, T. F. Reise, and S. A. Alkaitis, *J. Phys. Chem.*, **83**, 2221 (1979).
14. J. Claverie, J. Verniolle, G. Campet, J. P. Doumerc, and P. Hagenmuller, *Mater. Res. Bull.*, **16**, 1019 (1981).
15. Y. Nakato, A. Tsumura, and H. Tsubomura, *This Journal*, **127**, 1502 (1980); *Chem. Lett.*, **1981**, 127, 383; "Photoeffects at Semiconductor-Electrolyte Interfaces," Am. Chem. Soc. Symposium Series, No. 146 (1981).
16. B. Pettinger, H.-R. Schöppel, and H. Gerischer, *Ber. Bunsenges. Phys. Chem.*, **80**, 849 (1976).
17. S. E. Stokowski and A. L. Schawlow, *Phys. Rev.*, **178**, 457 (1969).

Photoelectrochemical Processes In Bismuth Germanium Oxide, $Bi_{12}GeO_{20}$ Single Crystals

K. Kochev, K. Tzvetkova, and M. Gospodinov

Central Laboratory for Solar Energy and New Energy Sources, Institute for Solid State Physics, and Bulgarian Academy of Sciences, Sofia, Bulgaria

ABSTRACT

The basic photoelectrochemical behavior of reduced $Bi_{12}GeO_{20}$ single crystals has been investigated for the first time. Photoinduced current as a function of applied voltage as well as the spectral distribution of the photoresponse were measured. Photosensitivity up to 0.5 μm in the visible range of the spectrum has been observed. The approximate value of the flatband potential was determined from the linear Mott-Schottky relation and it occurred to be $U_{FB} \approx -0.68$V *vs.* SCE. No apparent electrode degradation under anodic polarization has been observed. The role of hydrogen reduction process is discussed.

In recent years an ever increasing interest has been demonstrated toward photoelectrochemical processes at the semiconductor-electrolyte interface, which may be applicable for direct solar energy conversion into chemical or electrical energy. Many semiconductor materials were investigated as photosensitive electrodes (1, 2), but no suitable one that is stable in the electrolyte and has a good absorbance for sunlight has been found until now. Generally the semiconductors that are stable in the electrolyte, such as TiO_2, $SrTiO_3$ and others, have large bandgaps ($E_g \sim$ 3-3.5 eV). As a result they have essentially zero solar absorptivity. Hence, they are ineffective in systems for solar energy conversion (maximum reported conversion efficiency with sunlight is 1%). In our opinion promising materials for electrodes are some complex oxides, $Bi_{12}GeO_{20}$, $Bi_{12}SiO_{20}$ and others, which having large bandgaps nevertheless are sensitive in the visible range of the solar spectrum (3). In this paper for the first time are reported some photoelectrochemical properties of $Bi_{12}GeO_{20}$ (BGO) single crystals. These crystals have photoconductivity and optical activity and have been used so far in electro-optical devices and as a material for volume holographic storage of information (4, 5).

Experimental

Single crystals of BGO crystallize in the cubic phase body-centered lattice and have bandgap $E_g = 3.25$ eV (3). Our crystals were grown by the Czochralski method (6-8) from the Bi_2O_3 and GeO_2 melt. All semiconductor samples were cut perpendicular to the growth axis into 500 μm slices. The crystals were polished with diamond abrasive and then etched for 15 sec in concentrated HCl. Such prepared samples have resistivity of $10^{11}\ \Omega \cdot$ cm. To decrease the material resistance, the single crystals were reduced in hydrogen atmosphere at 500°-600°C for 1 hr. As a result of this treatment, the samples were reduced uniformly in the whole volume, and their resistance fell down to $\sim 10\Omega$. After the reduction process the initial yellow color of the crystals changed to dark gray. The In-Ga eutectic was used to provide the wafers with an ohmic contact.

The electrochemical measurements have been performed in usual two compartment cell. The 5*N* NaOH electrolyte was prepared from reagent grade chemicals and distilled water. As a reference electrode a saturated calomel electrode was used and platinum as counterelectrode. The light source was either 100W xenon high pressure lamp or tungsten lamp. The light intensity of the illumination was ~ 200 mW/cm^2. The direction of the light beam was normal to the (100). The spectral response measurements were carried out employing interference filters and the results were normalized to constant light intensity. The space charge capacity measurements were carried out with a Solartron 1174 Frequency Response Analyzer.

Results

A typical current-potential curve with sweep rate of 200 mV/min, for a reduced sample of $Bi_{12}GeO_{20}$, is shown in Fig. 1. During anodic polarization a small dark current is observed. Illumination of the semiconductor electrode results in significant anodic photocurrent which is typical for n-type semiconductor electrode. In this potential range the photocurrent is associated with oxygen evolution. During cathodic polarization a high cathodic current is observed when the voltage is below the threshold of $U = -0.6$ to -0.7V *vs.* SCE. It was noticed that after the flow of large cathodic current of more than 300 μA/cm^2, the anodic current increases significantly in the potential range of -0.5 to 0V *vs.* SCE both in dark and under illumination. Unreduced BGO samples had negligible anodic and cathodic current and didn't show any photosensitivity.

The spectral response of the photocurrent measured at 0.5V *vs.* SCE for reduced BGO single crystal is

Key words: photoelectrochemical cell, visible light photoresponse, flatband potential, hydrogen reduction.

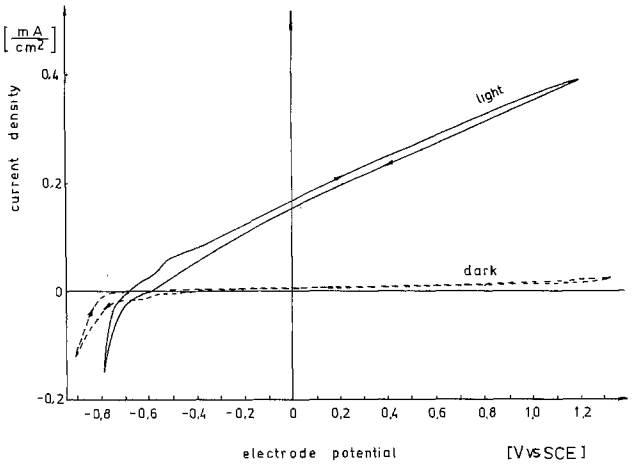

Fig. 1. Current-potential curves of BGO crystal in 5*N* NaOH, sweep rate 200 mV/min.

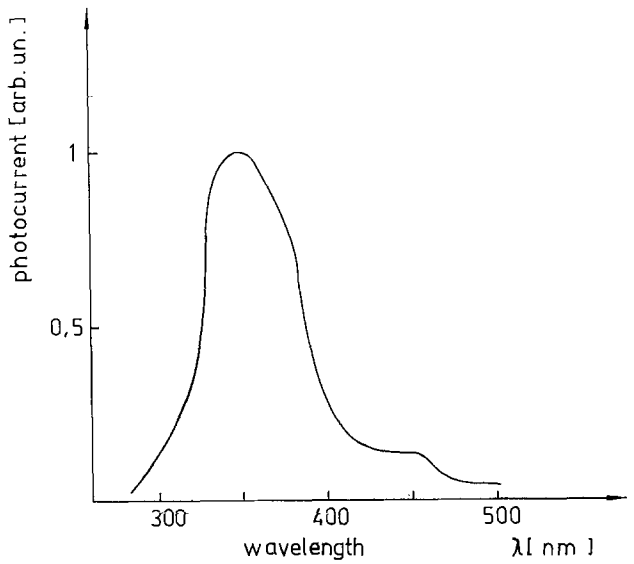

Fig. 2. Spectral distribution of the anodic photocurrent at V_E = +0.5V *vs.* SCE for BGO crystal in 5*N* NaOH.

shown in Fig. 2. The maximum of photosensitivity lies between 330-380 nm which corresponds to the intrinsic absorbance of this material (9). In the visible range a photosensitivity was observed up to 500 nm.

The differential capacitance, measured in 5*N* NaOH, of the reduced samples as a function of applied potential is shown in Fig. 3. The frequencies 10-20 kHz in our measurements were selected in such a way so that the dominant measured capacitance was a result of the space charge layer. The flatband potential determined from C-V measurements is $U_{FB} \approx -0.7$V *vs.* SCE. As can be seen from the curve in Fig. 3 two parts with different slopes can be distinguished, from which donor density can be obtained, resulting in $N_d = 4.8 \cdot 10^{17}$ cm^{-3} and $N_d = 1.24 \cdot 10^{18}$ cm^{-3} for $\epsilon = 38$ (10).

The stability of the semiconductor electrodes in basic electrolyte was investigated. After five hours illumination, no apparent changes in the photocurrent were noticed, and no changes in the surface were visible under microscopic examination.

Discussion

As can be seen from current-voltage characteristics the reduced wafers of BGO show typical electrochemical properties of n-type semiconductor. It can be assumed that during thermal treatment in the reduction atmosphere, oxygen vacancies are created which lead to changes in stoichiometry. This is supported by the fact that a thermal treatment for a short time in oxy-

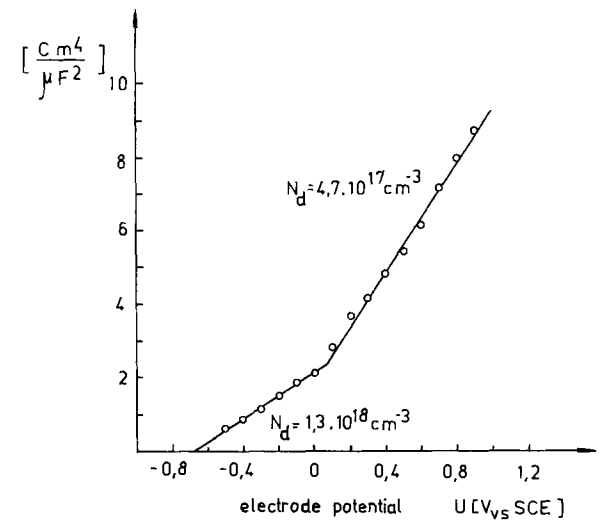

Fig. 3. Mott-Schottky plot of BGO crystal immersed in 5*N* NaOH for 10 kHz.

gen atmosphere of the already reduced samples leads to complete restoration of their primary electrical and optical properties. Some attempts were made for reduction of the BGO crystals in argon atmosphere. They showed that crystal properties change negligibly with respect to the changes that could be observed after reduction in hydrogen atmosphere. It is possible that during the reduction process hydrogen is introduced in the crystal creating shallow donor levels. At room temperature they are completely ionized which leads to considerable increase of conductivity. As can be seen from Fig. 3 the Mott-Schottky plot is described by two curves. In our opinion regions of different slopes (Fig. 3) may represent a change of donor concentration as a function of distance. We assume that the breaking of Bi-O bonds during heat treatment in a reducing atmosphere is responsible for the existence of the donor levels (11).

The observed photosensitivity in the visible range of 400-500 nm is considered to be due to Ge vacancies (3), which appear during the growth of BGO crystals. As far as the application of these crystals for photoelectrolysis of water is concerned, the relative position of the energy bands at the semiconductor surface is of significant importance. Since the flatband potential of these crystals is more positive than the H^+/H_2 potential, it is impossible to use them in photoelectrolysis without applying an external voltage. However one cannot rule out the use of this material with appropriate redox system in self regenerating solar cells.

Acknowledgments

The authors would like to express their gratitude to Professor Kanev for his helpful discussions and to Dr. Dimitrov for his kindness in performing the C-V measurements.

Manuscript submitted April 27, 1982; revised manuscript received *ca.* Aug. 5, 1982.

Any discussion of this paper will appear in a Discussion Section to be published in the December 1983 JOURNAL. All discussions for the December 1983 Discussion Section should be submitted by Aug. 1, 1983.

REFERENCES

1. R. Memming, *Electrochim. Acta*, **25**, 77 (1980).
2. L. A. Harris and R. H. Wilson, *Ann Rev. Mater. Sci.*, **8**, 99 (1978).
3. S. L. Hou, R. B. Lauer, and R. E. Aldrich, *J. Appl. Phys.*, **44**, 2652 (1973).
4. A. T. Klipko, P. E. Kotliar, E. S. Negevenko, V. I. Feldbush, and V. S. Shiabanov, *Autometria*, **4**, 34 (1976).

5. J. P. Huiguard and F. Micheron, *Appl. Phys. Lett.*, **29**, 591 (1976).
6. A. A. Ballman, *J. Cryst. Growth*, **1**, 37 (1967).
7. A. I. Safonov, S. A. Baryshev, G. I. Nikiforova, G. N. Antonov, and S. A. Fedulov, *Kristallografiya* **14**, 152 (1969).
8. Yu. S. Kuz'minov, M. G. Lifshits, and V. D. Sal'nikov, *ibid.*, **14**, 363 (1969)
9. G. G. Douglass and R. N. Zitter, *J. Appl. Phys.*, **39**, 2133 (1968).
10. A. J. Slobodnik, Jr. and J. C. Sethares, *ibid.*, **43**, 247 (1972).
11. O. A. Gudaev, V. A. Detinenko, and V. K. Malinovsky, *Fiz. Tverd. Tela.*, **23**, 195 (1981.)

Diffusivity in Zinc Chloride-Potassium Chloride Electrolyte

D. Loftus, J. Roberts, R. Weaver,*[1] S. Leach,* and L. Nanis*[2]

SRI International, Menlo Park, California 94025

ABSTRACT

Integral and differential salt diffusivities have been measured by the capillary method for electrolytes of interest to mass transfer of zinc in the zinc-chlorine hydrate battery. No dependence of diffusivity on the concentration of $ZnCl_2$ was found over the range 0.4-1.6M $ZnCl_2$ in 3.5M KCl. The average diffusivity was 0.88×10^{-5} cm^2 sec^{-1} at 26.5°C and 1.49×10^{-5} cm^2 sec^{-1} at 47.5°C.

Diffusivity is an important transport parameter in concentrated electrolyte mixtures of practical interest. In proposed load leveling batteries with flowing electrolyte, large changes in ion concentration may occur as, for example, during the charging cycle in a zinc-chlorine hydrate or zinc-bromine cell. Typically, electrolytes for these systems require high concentrations of zinc halide to sustain a large loading on the zinc electrode without total depletion of zinc ion during charge and also large concentrations of indifferent salts to improve conductivity and energy efficiency. The diffusivity is needed for application of mass transport correlations for optimization of battery performance such as prediction of the diffusion-limited current density for zinc deposition during charging of a zinc-chlorine cell.

In general, the electrolyte composition varies from 3M $ZnCl_2$ + 3M KCl to 0.5M $ZnCl_2$ + 3M KCl during the charge cycle in the zinc-chlorine hydrate cell. Agnew and Paterson (1) confirmed that $ZnCl_2$-H_2O solutions are self-complexing since the zinc transference number becomes negative at concentrations greater than 1.9M $ZnCl_2$. Zinc chloro-aquo complexes such as $ZnCl_4^=$, $ZnCl_3^-$ may exist depending on the chloride-to-zinc ion ratio during the charge-discharge cycle of the zinc-chlorine hydrate cell, thus influencing the diffusivity and transport behavior. Accordingly, the present study was undertaken to determine whether diffusivity depends on concentration in the $ZnCl_2$-KCl-H_2O system.

Experimental Details

The capillary method was selected for the experiment because of its simplicity for measurement of both the integral and differential salt diffusivity and was determined on the basis of zinc ion concentration changes. The capillary method has been described in detail (2-4) and is reviewed here only briefly.

The diffusivity measurement is started by placing a closed-end capillary initially filled with concentrated solution in a large volume of dilute solution. The concentrated solution is permitted to diffuse out of the open-ended mouth of the capillary into the surrounding dilute volume for a specified period of time. Analysis of the zinc ion concentration in the capillary yields the average concentration remaining after a predetermined time has elapsed. From a mathematical analysis of the diffusion profile within the capillary, the average concentration is known as a function of the dimensionless parameter Dt/L^2 where D is the diffusivity (cm^2 sec^{-1}), t is the time (sec), and L is the capillary length (cm).

For one-dimensional diffusion within the capillary, the concentration profile at any time is obtained by solution of the diffusion equation, Eq. [1] with the boundary conditions of zero flux at the closed end of the capillary, Eq. [2], and zero concentration at the open mouth ($x = L$) of the capillary, given by Eq. [3]. For differential measurements, the concentration parameter is considered to be with respect to the external reservoir concentration as background, as defind in Eq. [4].

$$\frac{\partial^2 c}{\partial x^2} - \frac{1}{D}\frac{\partial c}{\partial t} = 0 \qquad [1]$$

$$\frac{\partial c}{\partial x} = 0; \quad x = 0 \qquad [2]$$

$$C = 0 \quad x = L \qquad [3]$$

The experimental establishment of the boundary condition at the mouth of the capillary to match the mathematical requirements of Eq. [3] has been the subject of several studies. Stirring in the external reservoir for this purpose has introduced errors in the measured diffusivity by convecting diffusant out of the capillary. The average concentration in the capillary becomes less than that corresponding to diffusion only, and an erroneously large apparent diffusivity is measured.

When the external solution is not stirred, the requirement of Eq. [3] is relaxed and diffusion out of the capillary is, in theory, continued by diffusion into a quiescent external volume. Such a diffusion situation has been analyzed (5) to show that Eq. [4] and [5] provide a diffusivity value which is only a few percent too large when the mathematical treatment based on stirring (Eq. [3]) is used, even when there is no actual stirring, provided the capillary is depleted to about 60% of the original concentration. However, it has been shown (2) that natural convection is induced by the difference in solution density at the mouth of the capillary compared with the less dense external solution. The downward streaming natural convection is linked to a flow of solution across the mouth of the capillary that acts as virtual stirring. In the present study, there was no external stirring. However, the average capillary concentration was fitted to the mathematical results for stirring, obtained from the solution to Eq. [1], [2], and [3]. The convective flow induced by density

* Electrochemical Society Active Member.
[1] Present address: Electric Power Research Institute, Palo Alto, California 94306.
[2] Present address: Consultant, Electrochemical Engineering, Palo Alto, California 94036.
Key words: zinc-chlorine battery, diffusivity, capillary.

gradients at the capillary mouth and by thermal gradients in the external volume were considered sufficient to meet the requirements of Eq. [3].

Capillary lengths were from 2 to 4 cm and were chosen so that at 26.5°C, a cross check would be provided by fitting Eq. [5] to a depletion level less than 50% remaining of the initial concentration ($\Phi < 0.5$) for the 2 cm capillary, whereas Eq. [4] would be a best fit for the 4 cm capillary. Typically, the 2 cm capillary would be depleted to 45% of the initial concentration remaining in 30 hr, during which time the 4 cm capillary was depleted to 72% of the original concentration. Diffusion times of about 7 hr at 26.5°C and 4 hr at 47.5°C were sufficient to deplete the 2 cm capillary to 75% of the initial concentration. The capillaries had internal diameters of about 2 mm, giving approximately 60-100 μliter of solution for analysis. At the conclusion of an experimental run, the capillary contents were washed into 10 ml flasks and diluted with distilled water. The zinc concentration in the aliquots from these samples was evaluated by atomic absorption spectrometry and polarography. Standard solutions for calibration were prepared by dissolution of a known weight of pure zinc (99.999% Zn) in HCl.

At least five determinations of diffusivity were made for each $ZnCl_2$ concentration at 26.5° and 47.5°C. Temperature was controlled to ±0.5°C in an air bath. Unwanted stirring at the start of each experiment was avoided by covering the mouth of the filled capillary with a thin microscope cover glass. After the reservoir solution was filled to a level above the capillary mouth, the cover glass was slowly removed with a smooth sideways motion to initiate diffusion. Termination of the diffusion experiment is accomplished with a reverse procedure. The cover glass is replaced and the reservoir drained. Separate experiments with strongly colored $KMnO_4$ solutions were used to verify that there was minimal disturbance of the liquid caused by the sideways motion of the thin cover glass.

Results

The integral salt diffusivity may be obtained from the analysis of the residual concentration of zinc in the capillary, measurement of the length of the capillary, and the time of diffusion. For the measurement of the differential diffusivity, the zinc concentration in the reservoir is required in addition. Solution of Eq. [1] with Eq. [2] and [3] as boundary conditions can be accomplished by the method of separation of variables and also by Laplace transform techniques. Each method yields a series solution for which the first term is entirely adequate over a wide range of residual concentration. From the Laplace transform methods, an accurate result valid for $0.5 < \Phi < 1$ is

$$\Phi = \frac{C_{ave}(t) - C_{res}}{C_{init} - C_{res}} = 1 - \frac{2}{\pi^{1/2}} \frac{(Dt)^{1/2}}{L} \qquad [4]$$

From the separation of variables method, for $0 < \Phi < 0.5$

$$\Phi = \frac{8}{\pi^2} \exp\left[\frac{-\pi^2 Dt}{4L^2}\right] \qquad [5]$$

where $C_{ave}(t)$ is the average concentration remaining after time t, C_{init} is the initial constant concentration in the capillary, C_{res} is the concentration of diffusant in the large volume of the reservoir external to the capillary, L is the capillary length, and D is the diffusivity.

Integral diffusivity results are summarized in Table I together with the apparent activation energies for the temperature interval 26.5°-47.5°C. The reservoir solution initially contained no $ZnCl_2$ and was of sufficient volume so that the amount that diffused out of the capillary made a negligible contribution.

For all integral diffusion runs, the reservoir solution was 3.65M KCl.

Table I. Integral salt diffusivities of $ZnCl_2$-KCl solutions diffusing into 3.65M KCl

Initial capillary concentration, (M)		Diffusivity ($cm^2\ sec^{-1} \times 10^5$)		Activation energy (kcal/mol)
KCl	$ZnCl_2$	26.5°C	47.5°C	
3.48	0.40	0.82 ± 0.06	1.53 ± 0.16	5.6 ± 1.6
3.44	0.81	0.87 ± 0.05	1.55 ± 0.10	5.2 ± 1.0
3.35	1.21	0.94 ± 0.04	1.40 ± 0.21	3.6 ± 1.8
3.25	1.62	0.88 ± 0.03	1.46 ± 0.12	4.6 ± 1.1

Differential diffusivity results are shown in Table II in which the associated KCl concentrations are the same as those listed in Table I.

Discussion

From the results shown in Tables I and II, it may be seen that, at 26.5°C, both the integral and differential salt diffusivities are essentially constant over the range of concentrations studied, within the confidence limits (95%) obtained. Since the integral salt diffusivity at 47.5°C is essentially constant, it is reasonable to consider the differential diffusivity to be constant also. The diffusivity results are useful in predicting limiting electrochemical rates and electrode kinetic behavior in the zinc-chlorine battery system. Kim and Jorne (6) report a value of 0.89×10^{-5} $cm^2\ sec^{-1}$ for the diffusion coefficient of zinc ion in 0.05M $ZnCl_2$-1.0M KCl at 25°C, in good agreement with the present results. However, the rotating disk method used by Kim and Jorne is limited to solutions that are relatively dilute in electroactive species. This limitation also applies to the polarographic method for obtaining diffusion coefficients. At higher concentrations, both the rotating disk and the polarographic method require large currents to achieve the limiting current density condition. A further problem occurs when the overpotential for the simultaneous evolution of hydrogen masks the concentration polarization wave. The current efficiency for the metal ion reduction step must also be determined to properly apply the equations relating current and concentration to diffusivity. The capillary method offers no such problems. In addition, it is not necessary to know the viscosity of the solution or its temperature dependence in order to apply the capillary method at temperatures of interest in contrast with the rotating disk method. Further advantages of the capillary method are the ability to obtain differential diffusivities (as presently shown) and the diffusivities of nonelectroactive species.

Additional transport parameter information such as transference number and conductance are required to use the present diffusivity data for modeling the distribution of complex ions in the KCl-$ZnCl_2$ electrolyte. Raman spectroscopic data will also be useful for this purpose. The effective activation energies listed in Table I are centered around 5 kcal/mol, in agreement with values found typically for ion diffusivity in aqueous electrolytes (7).

Agnew and Paterson (1) confirmed that $ZnCl_2$-H_2O electrolytes exhibit self-complexing on the basis of transference number measurements. For diffusivity

Table II. Differential salt diffusivities* of $ZnCl_2$-KCl at 26.5°C

Reservoir concentration (M) of $ZnCl_2$	Initial capillary concentration (M) of $ZnCl_2$			
	0.40	0.81	1.21	1.62
0	0.82 ± 0.06	0.87 ± 0.05	0.94 ± 0.04	0.88 ± 0.03
0.40		0.89 ± 0.10	0.98 ± 0.08	1.01 ± 0.15
0.81			1.02 ± 0.13	0.94 ± 0.05
1.21				0.88 ± 0.08

* $D \times 10^5$ ($cm^2\ sec^{-1}$).

measurements, they used an interferometric method to follow concentration as a function of distance and time. However, the interferometric method is more readily applied to solutions of a single salt rather than to mixed electrolytes. Their experimental salt diffusion coefficient for 0.05M $ZnCl_2$ at 25°C is 1.048×10^{-5} cm^2 sec^{-1}. For dilute $ZnCl_2$ concentrations in mixtures of $ZnCl_2$ and KCl in water, the KCl-H_2O electrolyte may be considered as the solvent for $ZnCl_2$. The Einstein-Stokes relation or Walden's rule may be used to provide an estimate of the diffusivity of $ZnCl_2$, with the proviso that the size of the single diffusing species is unchanged. The product of solution viscosity and salt diffusivity should be constant at constant temperature, as indicated in Eq. [6]

$$\eta_{H_2O} D_{ZnCl_2} = \eta_{H_2O + KCl} D_{ZnCl_2 + KCl} \quad [6]$$

The product of salt diffusivity for 0.05M $ZnCl_2$ and the viscosity (η) of water at 25°C (0.8903 centipoise) may be used in Eq. [6] to estimate the diffusivity for a KCl solution. For 1M KCl, the recent viscosity determinations of Kestin *et al.* (8) may be used. The contribution of the $ZnCl_2$ to the density is ignored in computing molality for use in the Kestin correlation. At 25°C, the viscosity of 1M KCl is computed to be 0.904 centipoise, in agreement with the value 0.898 centipoise determined by Roffel and van de Graaf (9). From Eq. [6], a diffusivity of 1.03×10^{-5} cm^2 sec^{-1} is predicted, in contrast with the experimental value of 0.89×10^{-5} cm^2 sec^{-1} obtained by Kim and Jorne (6) for effective diffusivity and the value 0.82×10^{-5} cm^2 sec^{-1} obtained for 0.40M $ZnCl_2$, the most dilute concentration used in the present study. Increased solvation of zinc ions or enhanced formation of zinc chloro-complex ions may account for the smaller than predicted salt diffusivities in $ZnCl_2$-KCl aqueous electrolytes.

Summary

The capillary method has been used to determine the integral salt diffusivity of $ZnCl_2$, based on Zn analysis in $ZnCl_2$-KCl aqueous mixtures at 25.6° and 47.5°C and the differential diffusivity at 26.5°C. No dependence on concentration from 0.4 to 1.6M $ZnCl_2$ (in approximately 3.5M KCl) was found for the diffusivity, which has an average value of 0.88×10^{-5} cm^2 sec^{-1} at 26.5°C and 1.49×10^{-5} cm^2 sec^{-1} at 47.5°C.

Acknowledgment

This work was performed under contract RP 370-2, Electric Power Research Institute. The authors gratefully acknowledge the interest and encouragement of William Spindler, EPRI project manager.

Manuscript submitted Dec. 11, 1981; revised manuscript received *ca.* June 21, 1982.

Any discussion of this paper will appear in a Discussion Section to be published in the December 1983 JOURNAL. All discussions for the December 1983 Discussion Section should be submitted by Aug. 1, 1983.

Publication costs of this article were assisted by SRI International.

REFERENCES

1. A. Agnew and R. Paterson, *Faraday Trans. I*, **74**, 2896 (1978).
2. C. Y. Luk, L. Nanis, and M. Litt, *Ind. Eng. Chem. Fundam.*, **14**, 92 (1975).
3. L. Nanis, S. R. Richards, and J. O'M. Bockris, *Rev. Sci. Instrum.*, **36**, 673 (1975).
4. L. Nanis, M. Litt, and J. Chen, *This Journal*, **120**, 509 (1973).
5. L. Nanis and C. M. Ablow, Abs. 424, p. 699, The Electrochemical Society Extended Abstracts, Vol. 82-1, Montreal, Canada, May 9-14, 1982.
6. J. T. Kim and J. Jorne, *This Journal*, **127**, 8 (1980).
7. C. J. D. Fell and H. P. Hutchison, *J. Chem. Eng. Data*, **16**, 427 (1971).
8. C. E. Grimes, J. Kestin, and H. E. Khalifa, *ibid.*, **24**, 121 (1979).
9. B. Roffel and J. J. van de Graaf, *ibid.*, **22**, 300 (1977).

Water Absorption and Donnan Equilibria of Perfluoro Ionomer Membranes for the Chlor-Alkali Process

K. Kimoto*

Asahi Chemical Industry Company, Limited, 1-2, Yurakucho 1-chome, Chiyoda-ku, Tokyo, Japan

ABSTRACT

The water absorption and Donnan equilibria of perfluoro ionomer membranes for chlor-alkali production were thermodynamically analyzed, utilizing an elastic matrix model. To relate these equilibria, two single parameter model equations were developed that express effective fixed ion concentration and swelling pressure. The empirical parameters α and β were chosen to give the best fits to the observed water absorption data by Nelder and Mead's modified simplex method of optimization. The value of α, which is related to ion pair formation and strong association in the ion cluster in the membrane, was in the range of 0.09-0.12 and was fairly uniform among the four membranes investigated. From the calculated value, it was concluded that the degree of ion pair formation increases sharply when the hydration number of sodium ion decreases below 4 and that it is higher for carboxylic acid membrane than for sulfonic acid membrane, increasing with the equivalent weight (*EW*) of the membrane and the external concentration. The parameter β, expressing the resistance of the polymer matrix against swelling, ranged from 0.14 to 0.55 and was larger for the carboxylic acid membrane than the sulfonic acid membrane. It was larger for the membrane with shorter and less bulky pendant structure to which the ion-exchange group is connected. Conversely, it was found to be smaller for the pretreated membrane which exhibits a greater rate of swelling. Calculated swelling pressure was in the expected range, and sorbed electrolyte concentration agreed quite well with the observed value. The factors to be considered in membrane design and use in the chlor-alkali process are discussed on the basis of these results.

The first commercial application of the ion-exchange membrane chlor-alkali process utilized perfluorosulfonic acid membrane, which has excellent chemical durability in cell environments (1). This membrane, however, exhibits relatively low current efficiency in concentrated caustic soda, due to its high water content. Various membranes containing weaker acid groups, such as those of carboxylic acid (2-7) and sulfonamide (8), have been developed in attempts to

* Electrochemical Society Active Member.
Key words: ion-exchange membrane, water equilibria, chlor-alkali.

overcome this difficulty and research for this purpose continues highly active.

In this paper, a semi-empirical model is proposed as a basis for understanding and predicting the membrane characteristics and for the design and use of the membranes.

Water absorption and Donnan equilibria are the most important factors in predicting the performance of the ion-exchange membrane. Water absorption data (9-11) and an empirical equation with three parameters (9, 11) have been reported for perfluoro ionomer membranes, as have results for computer simulation of water absorption based on a statistical dynamics approach utilizing an ion cluster model with four empirical parameters (12, 13). No quantitative data have yet been reported on Donnan equilibrium, although qualitative comments have been made (14). However, none of these reports have provided a sufficient basis for prediction of membrane performance in concentrated caustic soda, because they do not meet the need for simultaneous consideration of both water absorption and Donnan equilibria.

Thermodynamic models of elastic matrices have been employed in many studies on ion-exchange membranes consisting of hydrocarbon polymers (15-17). With the aid of an optimization technique, this orthodox approach was also adopted here in order to relate the water absorption and the Donnan equilibria of perfluoro ionomer membranes. Two single parameter equations expressing effective fixed ion concentration and swelling pressure were introduced, and a set of model equations was developed to describe the system. The empirical parameters α and β were chosen to give the best fits to the observed water absorption data, by Nelder and Mead's modified simplex method (18). Calculations were made for two perfluorosulfonic acid membranes (PSA-1, PSA-2) and two perfluorocarboxylic acid membranes (PCA-1, PCA-2). Water absorption data were measured for PSA-1 and PCA-1 and were obtained from the literature for PSA-2 (9) and PCA-2 (10). Discussion centers on the essential factors in designing and using the membranes, with consideration of the obtained parameter values as well as of osmotic coefficient, activity coefficient, swelling pressure, effective fixed ion concentration, and sorbed electrolyte concentration in terms of the formation of ion clusters and ion pairs in the membrane.

Theoretical

Donnan equilibrium is generally expressed by Eq. [1] for the ion-exchange membrane in equilibrium with an aqueous solution of a strong electrolyte AB, one mol of which dissociates into one equivalent of the cation A and one of the anion B (19)

$$RT \ln \left[\left(\frac{a_A}{\bar{a}_A} \right) \left(\frac{a_B}{\bar{a}_B} \right) \right] = \pi V_{AB} \qquad [1]$$

where a_i, $\bar{a}_i$ = activity of ion i in the solution and in the membrane, respectively; π = swelling pressure (atm); V_{AB} = partial molar volume of the electrolyte AB (1 mol^{-1}); R = gas constant (1 atm mol^{-1} deg^{-1}); and T = absolute temperature (K).

For an electrolyte of NaOH, Eq. [2] was obtained

$$\frac{m_{Na} m_{OH} \gamma_{NaOH}^2}{\bar{m}_{Na} \bar{m}_{OH} \bar{\gamma}_{NaOH}^2} = \exp \left(\frac{\pi V_{NaOH}}{RT} \right) \qquad [2]$$

where m_i, $\bar{m}_i$ = molality of ion in the solution and in the membrane, respectively (mol/kg-H_2O); and γ_{NaOH}, $\bar{\gamma}_{NaOH}$ = mean activity coefficient of NaOH in the solution and in the membrane, respectively.

For a cation exchange membrane, Eq. [3] expresses the electroneutrality condition

$$\bar{m}_{Na} = \bar{m}_R + \bar{m}_{OH} \qquad [3]$$

where $\bar{m}_R$ = total fixed ion molality in the membrane (mol/kg-H_2O).

Equation [4] can be obtained by substitution of Eq. [3] into Eq. [2]

$$\bar{m}_{OH}(\bar{m}_R + \bar{m}_{OH}) = m_{Na} m_{OH} \left(\frac{\gamma_{NaOH}}{\bar{\gamma}_{NaOH}} \right)^2 \exp \left(- \frac{\pi V_{NaOH}}{RT} \right) \qquad [4]$$

Y is defined by Eq. [5] employing m_{NaOH} (mol/kg-H_2O), the molality of the external solution

$$Y = m_{Na} m_{OH} \left(\frac{\gamma_{NaOH}}{\bar{\gamma}_{NaOH}} \right)^2 \exp \left(- \frac{\pi V_{NaOH}}{RT} \right) = m_{NaOH}^2 \left(\frac{\gamma_{NaOH}}{\bar{\gamma}_{NaOH}} \right)^2 \exp \left(- \frac{\pi V_{NaOH}}{RT} \right) \qquad [5]$$

From Eq. [4] and [5], it follows that $\bar{m}_{OH}$ and $\bar{m}_{Na}$ can be expressed as follows

$$\bar{m}_{OH} = (1/2)(\sqrt{\bar{m}_R^2 + 4Y} - \bar{m}_R) \qquad [6]$$

$$\bar{m}_{Na} = (1/2)(\sqrt{\bar{m}_R^2 + 4Y} + \bar{m}_R) \qquad [7]$$

On the other hand, water absorption equilibrium can be expressed by Eq. [8] (19)

$$\pi V_w = - RT \ln \frac{\bar{a}_w}{a_w} \qquad [8]$$

where V_w = partial molar volume of water (liter mol^{-1}); and a_w, $\bar{a}_w$ = activity of water in the solution and in the membrane, respectively.

$\bar{a}_w$ in Eq. [8] is related to the osmotic coefficient $\bar{\phi}$ through Eq. [9] (19)

$$-\ln \bar{a}_w = \frac{\bar{\phi} \Sigma \bar{m}_i M_w}{1000} \qquad [9]$$

where $\bar{\phi}$ = osmotic coefficient of the electrolyte in the membrane; $\Sigma \bar{m}_i$ = total molality of all mobile ions in the membrane (mol/kg-H_2O); and M_w = molecular weight of water (g mol^{-1}).

Equation [10] is obtained by substituting Eq. [9] into [8]

$$\frac{\pi V_w}{RT} - \frac{\bar{\phi} \Sigma \bar{m}_i M_w}{1000} = \ln a_w \qquad [10]$$

The set of Eq. [5], [6], [7], and [10] describes the water absorption and Donnan equilibria of the cation exchange membrane which is in equilibrium with a caustic soda aqueous solution. As Helfferich pointed out (19), however, theoretical calculations are impossible for $\bar{\gamma}_{NaOH}$, $\bar{\phi}$, $\bar{a}_w$, and π, thus preventing the analysis from proceeding further.

Empirical model Eq. [11] and [16] are therefore introduced in connection with the total fixed ion concentration $\bar{m}_R$ and the swelling pressure π, based on the following considerations.

1. Sorbed electrolyte in the membrane forms a mixed solution with the salt of fixed ion-exchange groups. Attempts to calculate the mean activity coefficient of the electrolyte in these systems by application of Harned's rule, which was originally derived for free aqueous mixed solutions, have not been highly successful (16, 19). On the other hand, spectral studies have shown that ion-exchange groups, sodium ions, and associated water molecules form hydrophilic ion clusters, while the fluorocarbon backbone constitutes a hydrophobic region in the perfluoro ionomer membranes (12-14). Furthermore, marked ion pair formation occurs when the hydration number of sodium ion decreases below 4, as revealed by NMR study (20). The contribution of the fixed ion-exchange

groups to $\bar{\gamma}_{NaOH}$ is therefore quite complicated and is greatly reduced from that which would be indicated by the value of $\bar{m}_R$. Here, we define the effective fixed ion concentration $\bar{m}_R^*$ (mole/kg-H_2O) by Eq. [11], to express the influence of ion pair formation and strong association in the ion cluster, and assume that $\bar{\gamma}_{NaOH}$ can be calculated as if caustic soda solution in a concentration of $\bar{m}_R^* + \bar{m}_{OH}$ exitsts in the membrane

$$\bar{m}_R^* = \frac{\bar{m}_R}{1 + \alpha \bar{m}_R} \quad [11]$$

where α = an empirical parameter.

In Eq. [11], $\bar{m}_R^*$ decreases with increase of α. This corresponds to a decrease in the contribution of fixed ion-exchange groups to $\bar{\gamma}_{NaOH}$, which is caused by ion pair formation or strong association in the ion cluster. Polynomial Eq. [12] for γ_{NaOH} was developed by least squares, from data on the mean activity coefficient of caustic soda aqueous solutions given in Robinson and Stokes' table (21).

$$\gamma_{NaOH} = -0.835814 \times 10^{-5} m_{NaOH}^5 + 0.346129 \times 10^{-3} m_{NaOH}^4 - 0.304021 \times 10^{-2} m_{NaOH}^3 + 0.404923 \times 10^{-1} m_{NaOH}^2 - 0.105001 m_{NaOH} + 0.763891 \quad [12]$$

To calculate $\bar{\gamma}_{NaOH}$, m_{NaOH} will be substituted by $\bar{m}_R^* + \bar{m}_{OH}$ as shown in Eq. [13]

$$\bar{m}_R^* + \bar{m}_{OH} \rightarrow m_{NaOH} \quad [13]$$

Equation [12] reproduces Robinson and Stokes' data fairly well in the range from 0 to 22 (mol/kg-H_2O) as shown in Fig. 1. This covers a sufficient range of concentrations, as calculations show the maximum value of $\bar{m}_R^* + \bar{m}_{OH}$ to be 17 (mol/kg-H_2O).

2. Gregor *et al.* calculated the osmotic coefficient of the salt of fixed ion-exchange group from water absorption data on H-form sulfonated polystyrene resin and toluene sulfonic acid in an atmosphere of varying humidity and concluded that the number of ions produced upon dissociation is one for sulfonated polystyrene resin and 2 for toluene sulfonic acid (15). Gluekauf reported similar results for polystyrene sulfonates (17). It has been concluded that under these conditions the fixed ion-exchange groups have a negligible effect on the osmotic coefficient of the electrolyte in the membrane. However, it is not clear how these results can be applied to perfluoro ionomer membranes when they are utilized in the concentrated alkali of the chlor-alkali process, as they were obtained for systems containing no sorbed electrolyte. We therefore calculated the osmotic coefficient $\bar{\phi}$ in the same manner as $\bar{\gamma}_{NaOH}$, by assuming that caustic soda exists in the membrane in the concentration of $\bar{m}_R^* + \bar{m}_{OH}$. Polynomial Eq. [14] was developed by least squares to reproduce Robinson and Stokes' data (21), as shown in Fig. 2

$$\bar{\phi} = 0.886714 \times 10^{-7} (\bar{m}_R^* + \bar{m}_{OH})^5 + 0.108135 \times 10^{-4} (\bar{m}_R^* + \bar{m}_{OH})^4 - 0.96884 \times 10^{-3} (\bar{m}_R^* + \bar{m}_{OH})^3 + 0.188595 \times 10^{-1} (\bar{m}_R^* + \bar{m}_{OH})^2 + 0.215761 \times 10^{-2} (\bar{m}_R^* + \bar{m}_{OH}) + 0.94022 \quad [14]$$

The total concentration of mobile ions in the membrane is therefore expressed by Eq. [15]

$$\Sigma \bar{m}_i = 2(\bar{m}_R^* + \bar{m}_{OH}) \quad [15]$$

3. Swelling pressure π, resulting from the contracting force of the elastic matrix, increases with the strength of the polymer matrix and the degree of matrix expansion. In the polystyrene-divinyl benzene resin, swelling pressure increases linearly with the content of divinyl benzene utilized for cross-linking (15, 17, 22) and with the equivalent volume of the resin, which increases with the water activity of the atmosphere (17, 22). Perfluoro ionomer membranes are prepared by copolymerizing tetrafluoroethylene (TFE) and perfluoro vinyl ether with ion-exchange group or its precursor (PVEX), the structures of which are shown below (23)

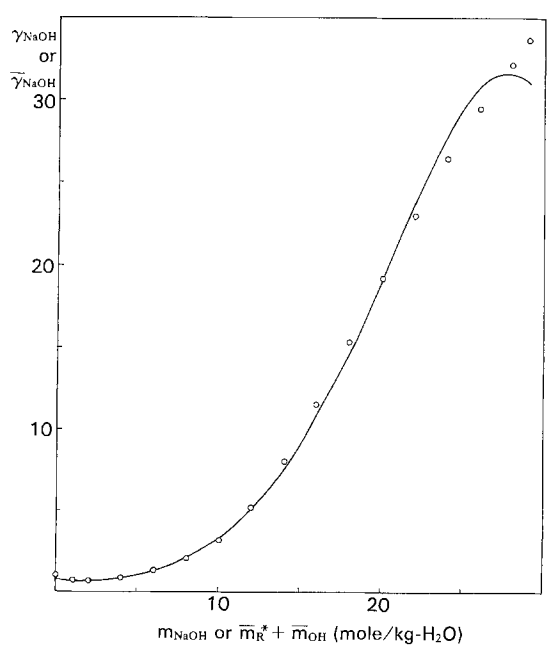

Fig. 1. Mean activity coefficients of NaOH aqueous solution. ——, Calculated by Eq. [12] or [13]; ○, Robinson and Stokes (21).

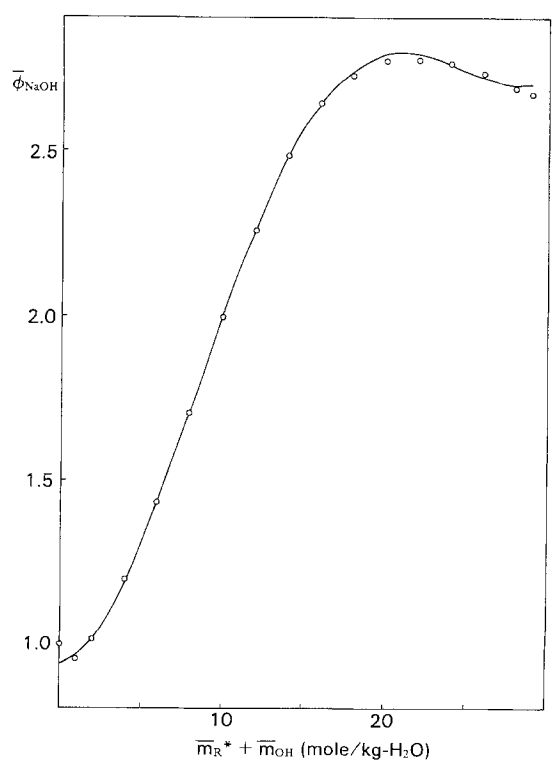

Fig. 2. Osmotic coefficients of NaOH aqueous solution. ——, Calculated by Eq. [14]; ○, Robinson and Stokes (21).

TFE: $CF_2 = CF_2$

PVEX: $CF_2 = CFO\,(CF_2\underset{\displaystyle CF_3}{\underset{|}{C}}FO)_p(CF_2)_qX$

where X = ion-exchange group or its precursor; and $p = 0 - 1$, $q = 1 - 12$.

Although no cross-linking agent is generally utilized, the polymer backbone based on TFE forms a partially crystallized hydrophobic region, which can be considered to function as a quasi cross-linked point (4, 6, 23). It is therefore reasonable to postulate that the swelling pressure tends to vary proportionally to the TFE content. Gluekauf's data seem to show the swelling pressure varies proportionally to $a_w \sim a_w^3$ of the atmosphere for polystyrene sulfonates (17). If in this light the swelling pressure is assumed to vary with the second power of the water activity of the external solution, a_w^2, the following model equation is obtained, in which the parameter β is an expression of the resistance of the polymer matrix against swelling

$$\pi = \beta(EW - MWo)a_w^2 \qquad [16]$$

where β = empirical parameter; EW = equivalent weight of the membrane (g-dry polymer/equivalent); and MWo = molecular weight of PVEX monomer with the ion-exchange group in H-form (g mol^{-1}). A comparison of this equation and a similar equation with a water activity exponent of one is presented in the Discussion section.

By definition, the total fixed ion concentration $\bar{m}_R$ is related to the water content of the membrane through Eq. [17]

$$\bar{m}_R = \frac{1000}{EW \times W} \qquad [17]$$

where W = water content of the membrane (g-H_2O/g-dry polymer).

The value of α and β can be chosen to give the best fits to the observed water absorption data obtained as a function of EW and m_{NaOH} utilizing a set of these equations. For this purpose, water activity a_w is read from the curve of Robinson and Stokes' data (24) in Fig. 3, or calculated by Eq. [18]

$$\begin{aligned} a_w = {} & -0.94963 \times 10^{-10}\, m_{NaOH}{}^6 - 0.455318 \times 10^{-6} m_{NaOH}{}^5 \\ & + 0.196235 \times 10^{-4}\, m_{NaOH}{}^4 - 0.123436 \times 10^{-3}\, m_{NaOH}{}^3 \\ & - 0.237131 \times 10^{-2}\, m_{NaOH}{}^2 - 0.299838 \times 10^{-1}\, m_{NaOH} \\ & + 1.0 \end{aligned} \qquad [18]$$

The optimum value of α and β can be calculated by the following algorithm:

(a) Assume certain values of α and β.

(b) Calculate $\bar{m}_R$, $\bar{m}_R{}^*$, γ_{NaOH}, and π with Eq. [17], [11], [12], and [16].

(c) Assume a certain value of $\bar{m}_{OH}$.

(d) Calculate $\bar{\gamma}_{NaOH}$ and Y with Eq. [13] and [5], and then obtain $\bar{m}_{OH}{}^{calc}$ with Eq. [6].

(e) Repeat steps (c) and (d), until $\bar{m}_{OH}{}^{calc}$ converges to $\bar{m}_{OH}$.

(f) Calculate $\bar{m}_{Na}$, $\bar{\phi}$, and $\Sigma\bar{m}_i$ with Eq. [7], [14], and [15].

(g) Calculate $a_w{}^{calc}$ with the following equation, which is derived from Eq. [10]

$$a_w{}^{calc} = \exp\left(\frac{\pi V_w}{RT} - \frac{\bar{\phi}\Sigma\bar{m}_i M_w}{1000}\right) \qquad [19]$$

(h) For all data, the summation of squares of errors is calculated with Eq. [20] and minimized by adjusting α and β

$$\Sigma E^2 = \Sigma(a_w - a_w{}^{calc})^2 \qquad [20]$$

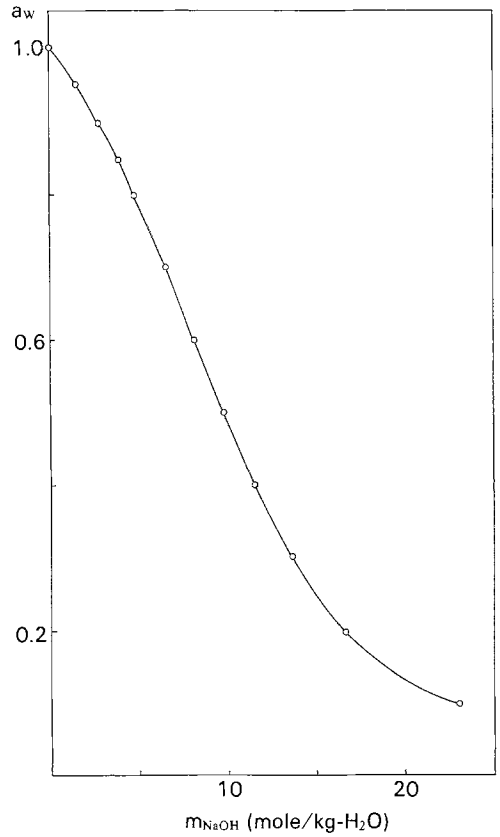

Fig. 3. Activity of water in NaOH aqueous solution. ——, Calculated by Eq. [18]; ○, Robinson and Stokes (24).

The convergence of $\bar{m}_{OH}$ was performed by a secant method. For optimization, Nelder and Mead's modified simplex method (18) was employed. Though it is also possible to adopt $\Sigma E^2 = \Sigma(W - W^{calc})^2$ as the function to be minimized, the convergence of W necessary to the algorithm for all sets of α and β was difficult to achieve and required a very long computation time. The aforementioned algorithm, with W as input data and a_w as an observed value, was adopted for this reason.

The following value is used for V_w in the calculation

$$V_w = 0.018 \quad (\text{liter mol}^{-1})$$

The partial molar volume of NaOH, V_{NaOH}, is expressed by Eq. [21] as a function of the molarity C (mol liter^{-1}) for relatively dilute aqueous solutions (25)

$$V_{NaOH} = -6.7 + 4.18\sqrt{C} \qquad [21]$$

On the other hand, Eq. [1] was derived on the assumption that V_{NaOH} does not vary with the concentration (19). Furthermore, the applicability of Eq. [21] is not clear, because sodium hydroxide forms a mixed solution with the salt of fixed ion group in the membrane, the molality of which is 4-60 (mol/kg-H_2O). In this study, V_{NaOH} was set at 0.015 (liter mol^{-1}), as the partial molar volume is generally in the range of 0.015-0.040 (liter mol^{-1}) for most electrolytes (19), and the results were compared with those obtained with values of 0.010 and 0.030 (liter mol^{-1}).

Experimental

Membrane samples were perfluorosulfonic acid membranes (PSA-1) with EW of 1000, 1200, 1350, and 1600 and perfluorocarboxylic acid membranes (PCA-1) with EW of 1014, 1114, 1264, and 1514. The chemical structures of the membranes are as follows:

$$-(-CF_2CF_2-)_x-(-CF_2\underset{\displaystyle CF_3}{\underset{|}{C}}F-)_y-$$
$$\qquad\qquad\qquad\qquad\quad |$$
$$\qquad\qquad\qquad\qquad\quad O\,CF_2\,CFO\,CF_2\,CF_2\,SO_3H$$

$$-(-CF_2CF_2-)_x-(-CF_2\underset{\underset{O\ CF_2\ CFO\ CF_2\ CO_2\ H}{|}}{\overset{\overset{CF_3}{|}}{CF}}-)_y-$$

A sample in Na form was equilibrated in water and caustic soda solutions at 90°C for 16 hr after boiling in hot water for 1 hr. The surfaces were wiped with filter paper, and the sample was then weighed to obtain W_1. The sample was next dried at 50°C for 16 hr in vacuum and then at room temperature for 40 hr in a desiccator and then weighed to obtain W_2. Sample equilibrated in caustic soda solution was washed in water for 2 days to remove attached and absorbed sodium hydroxide, dried in the above manner, and then weighed to obtain W_3. The water content was, respectively, calculated as $(W_1 - W_2)/W_2$ and $(W_1 - W_2)/W_3$.

The concentration of sorbed sodium hydroxide $\bar{m}_{OH}$ was obtained for the membrane PSA-1 with $EW = 1200$ and the membrane PCA-1 with $EW = 1114$ by measuring the weight (W_2), eluting the sorbed sodium hydroxide by immersion in water at room temperature, titrating with 0.1N HCl, and then dividing the equivalent of sorbed electrolyte by the water content.

Results and Discussion

The computer program was written in BASIC and took 17 min to find the optimum values of α and β with 16 sets of input data, and about 4 min after compiling. The convergence was stable when the initial values of α_0 and β_0 were (0.01, 0.01), (1, 1), and (4, 4).

Computational results are shown in Tables I to V. The results do not change when V_{NaOH} is varied from 0.010 to 0.030 (liter mol^{-1}), as indicated in Table I, which means that the swelling pressure π is deter-

Table I. Calculated parameters[a]

Membrane	Structure of PVEX monomer	MW_o	α	β	Coefficient of correlation	Standard deviation	ΣE^2
PSA-1	$CF_2{=}CFOCF_2\underset{\underset{CF_3}{\vert}}{CF}OCF_2CF_2SO_3H$	444	0.0924	0.274	0.998	0.0132	2.26×10^{-3}
PSA-1[b]	As above	444	0.0887	0.278	0.998	0.0145	2.72×10^{-3}
PSA-1[c]	As above	444	0.0937	0.272	0.998	0.0128	2.14×10^{-3}
PCA-1	$CF_2{=}CFOCF_2\underset{\underset{CF_3}{\vert}}{CF}OCF_2CO_2H$	358	0.0968	0.346	0.996	0.0218	6.16×10^{-3}
PSA-2[d]	$CF_2{=}CFOCF_2\underset{\underset{CF_3}{\vert}}{CF}OCF_2CF_2SO_3H$	444	0.1157	0.144	0.999	0.0074	4.93×10^{-4}
PCA-2[e]	$CF_2{=}CFOCF_2CF_2CF_2CO_2H$[f]	292	0.0907	0.542	0.999	0.0093	4.33×10^{-4}

[a] $\alpha_0 = \beta_0 = 1$, and $V_{NaOH} = 0.015$ (liter mol^{-1}) except for [b] and [c].
[b] $V_{NaOH} = 0.030$ (liter mol^{-1}).
[c] $V_{NaOH} = 0.010$ (liter mol^{-1}).
[d] Water absorption data taken from Ref. (9).
[e] Water absorption data taken from Ref. (10).
[f] Estimated from Ref. (4 and 10).

Table II. Calculated results for PSA-1

Observed values					Calculated values								
EW	m_{NaOH}	a_w	W	$\bar{m}_{OH}$	a_w^{calc}	$\bar{a}_w$	γ_{NaOH}	$\bar{\gamma}_{NaOH}$	$\bar{\phi}$	π	$\bar{m}_R$	$\bar{m}_R^*$	$\bar{m}_{OH}$
1100	0	1	0.217	—	1.01	0.888	0.764	0.759	1.09	180	4.19	3.02	0
1100	5.1	0.783	0.139	—	0.794	0.732	1.08	1.32	1.44	110	6.54	4.08	1.94
1100	8.2	0.595	0.109	—	0.590	0.563	2.20	2.51	1.82	63.6	8.34	4.71	4.04
1100	10.7	0.445	0.097	—	0.436	0.425	3.92	4.28	2.14	35.6	9.37	5.02	6.08
1200	0	1	0.172	0	1.02	0.873	0.764	0.792	1.12	207	4.84	3.35	0
1200	5.1	0.783	0.109	1.8	0.795	0.725	1.08	1.35	1.46	127	7.64	4.48	1.66
1200	8.2	0.595	0.086	4.0	0.592	0.561	2.20	2.52	1.83	73.3	9.69	5.11	3.67
1200	10.7	0.445	0.076	5.5	0.438	0.425	3.92	4.27	2.14	41.0	11.0	5.45	5.65
1350	0	1	0.093	—	0.975	0.812	0.764	0.977	1.26	248	7.96	4.59	0
1350	5.1	0.783	0.073	—	0.792	0.708	1.08	1.44	1.49	152	10.2	5.24	1.18
1350	8.2	0.595	0.060	—	0.594	0.557	2.20	2.55	1.84	87.8	12.3	5.78	3.08
1350	10.7	0.445	0.050	—	0.442	0.426	3.92	4.24	2.14	49.1	14.8	6.25	4.82
1600	0	1	0.062	—	0.982	0.778	0.764	1.11	1.34	317	10.1	5.22	0
1600	5.1	0.783	0.050	—	0.799	0.693	1.08	1.53	1.53	194	12.5	5.80	0.866
1600	8.2	0.595	0.038	—	0.599	0.551	2.20	2.59	1.85	112	16.4	6.53	2.41
1600	10.7	0.445	0.027	—	0.451	0.430	3.92	4.17	2.13	62.7	23.1	7.38	3.62

Table III. Calculated results for PCA-1

Observed values					Calculated values								
EW	m_{NaOH}	a_w	W	$\bar{m}_{OH}$	a_w^{calc}	$\bar{a}_w$	γ_{NaOH}	$\bar{\gamma}_{NaOH}$	$\bar{\phi}$	π	$\bar{m}_R$	$\bar{m}_R^*$	$\bar{m}_{OH}$
1014	0	1	0.184	—	1.02	0.865	0.764	0.813	1.14	227	5.36	3.53	0
1014	5.1	0.783	0.130	—	0.807	0.729	1.08	1.33	1.45	139	7.59	4.37	1.70
1014	8.2	0.595	0.105	—	0.600	0.565	2.20	2.49	1.82	80.4	9.39	4.92	3.80
1014	10.7	0.445	0.090	—	0.442	0.428	3.92	4.23	2.14	45.0	11.0	5.32	5.73
1114	0	1	0.140	0	1.02	0.845	0.764	0.871	1.19	262	6.42	3.96	0
1114	5.1	0.783	0.100	2.1	0.811	0.721	1.08	1.38	1.47	161	8.98	4.80	1.41
1114	8.2	0.595	0.072	3.9	0.601	0.561	2.20	2.51	1.83	92.7	12.5	5.65	3.13
1114	10.7	0.445	0.052	3.6	0.446	0.430	3.92	4.14	2.13	51.9	17.3	6.46	4.56
1264	0	1	0.077	—	0.985	0.782	0.764	1.09	1.33	314	10.3	5.15	0
1264	5.1	0.783	0.056	—	0.794	0.690	1.08	1.55	1.54	192	14.1	5.96	0.757
1264	8.2	0.595	0.040	—	0.601	0.554	2.20	2.56	1.84	111	19.8	6.78	2.12
1264	10.7	0.445	0.028	—	0.459	0.439	3.92	4.03	2.11	62.1	28.3	7.56	3.30
1514	0	1	0.042	—	0.966	0.719	0.764	1.39	1.47	400	15.7	6.23	0
1514	5.1	0.783	0.025	—	0.755	0.630	1.08	1.95	1.67	245	26.4	7.42	0.259
1514	8.2	0.595	0.017	—	0.597	0.538	2.20	2.74	1.88	142	38.9	8.16	1.00
1514	10.7	0.445	0.010	—	0.478	0.451	3.92	3.80	2.08	79.3	66.1	8.93	1.71

Table IV. Calculated results for PSA-2

Observed values				Calculated values								
EW	m_{NaOH}	a_w	W	a_w^{calc}	$\bar{a}_w$	γ_{NaOH}	$\bar{\gamma}_{NaOH}$	$\bar{\phi}$	π	$\bar{m}_R$	$\bar{m}_R^*$	$\bar{m}_{OH}$
1000	0	1	0.530	1.00	0.947	0.764	0.689	0.985	80.1	1.89	1.55	0
1000	5.1	0.783	0.400	0.791	0.763	1.08	1.18	1.37	49.1	2.5	1.94	3.55
1000	8.2	0.595	0.350	0.593	0.580	2.20	2.35	1.78	28.4	2.86	2.15	6.33
1000	10.7	0.445	0.300	0.438	0.433	3.92	4.14	2.12	15.9	3.33	2.41	8.55
1200	0	1	0.270	0.996	0.919	0.764	0.708	1.03	109	3.09	2.27	0
1200	5.1	0.783	0.200	0.792	0.754	1.08	1.22	1.39	66.8	4.17	2.81	2.83
1200	8.2	0.595	0.180	0.591	0.574	2.20	2.37	1.80	38.6	4.63	3.02	5.56
1200	10.7	0.445	0.160	0.438	0.432	3.92	4.16	2.13	21.6	5.21	3.25	7.73
1400	0	1	0.170	0.992	0.896	0.764	0.743	1.08	138	4.20	2.83	0
1400	5.1	0.783	0.120	0.794	0.746	1.08	1.25	1.41	84.4	5.95	3.53	2.26
1400	8.2	0.595	0.100	0.595	0.574	2.20	2.40	1.80	48.7	7.14	3.91	4.67
1400	10.7	0.445	0.090	0.441	0.432	3.92	4.14	2.13	27.3	7.94	4.14	6.84

Table V. Calculated results for PCA-2

Observed values				Calculated values								
EW	m_{NaOH}	a_w	W	a_w^{calc}	$\bar{a}_w$	γ_{NaOH}	$\bar{\gamma}_{NaOH}$	$\bar{\phi}$	π	$\bar{m}_R$	$\bar{m}_R^*$	$\bar{m}_{OH}$
699	3.9	0.843	0.160	0.845	0.753	0.862	1.22	1.39	157	8.94	4.94	0.716
699	6.2	0.720	0.126	0.712	0.655	1.38	1.76	1.61	114	11.4	5.60	1.69
699	10.7	0.445	0.084	0.440	0.426	3.92	4.26	2.14	43.7	17.0	6.69	4.39
699	16.7	0.200	0.055	0.208	0.207	12.2	11.7	2.66	8.83	26.0	7.75	8.69
813	3.9	0.843	0.112	0.849	0.733	0.862	1.32	1.44	201	11.0	5.50	0.501
813	6.2	0.720	0.084	0.714	0.641	1.38	1.86	1.65	146	14.6	6.29	1.22
813	10.7	0.445	0.055	0.448	0.428	3.92	4.22	2.14	55.9	22.4	7.39	3.66
813	16.7	0.200	0.039	0.214	0.212	12.2	11.4	2.65	11.3	31.5	8.17	8.07

mined substantially by Eq. [8] and is largely unaffected by Eq. [1].

The values a_w^{calc} and a_w agree quite well, with correlation coefficients of 0.995 or higher. The calculated swelling pressure π ranges from 9 to 400 (atm), in close correspondence with the values for membrane of polystyrene-divinyl benzene resin (15, 17, 19, 22). Agreement between the calculated and observed values for the concentration of sorbed electrolyte $\bar{m}_{OH}$ is quite satisfactory for PSA-1 and fairly good for PCA-1 in view of the experimental difficulty in handling concentrated caustic soda.

For PSA-1, calculation was also performed with a_w held to the first power in Eq. [16]. Obtained values were $\alpha = 0.0697$, $\beta = 0.304$, and $\Sigma E^2 = 6.21 \times 10^{-3}$, much less favorable than when the equation was applied with a_w in Eq. [16] raised to the second power.

In Fig. 4, calculated $\bar{m}_R^*$ is plotted against $\bar{m}_R$. As α is fairly constant among the four membranes, all data fall on a smooth curve which shows a rapid saturation with the increase of $\bar{m}_R$. Although $\bar{m}_R$ itself does not contribute directly to $\bar{\gamma}_{NaOH}$ or $\bar{\phi}$, as noted in the theoretical discussion, these results indicate that the effective fixed ion concentration $\bar{m}_R^*$ is decreased by ion pair formation or strong association in the ion cluster as $\bar{m}_R$ increases. To show this more clearly, the ratio of $\bar{m}_R^*/\bar{m}_R$ was plotted against the hydration number of sodium ion, which is calculated as $55.6/(\bar{m}_R + \bar{m}_{OH})$, as shown in Fig. 5 and 6. The value of $\bar{m}_R^*/\bar{m}_R$ decreases sharply when the hydration number falls off below 4 for the membranes PSA-1, PCA-1, and PCA-2, which corresponds to the rapid increase in ion pair formation in the same region, which is revealed by NMR study (20). These results indicate that the ion pair formation is greater for perfluorocarboxylic acid than for perfluorosulfonic acid membrane, and also greater for higher EW and concentrations of caustic soda. The membrane PSA-2 shows much less tendency for ion pair formation than PSA-1, even though the two have the same chemical structure, as

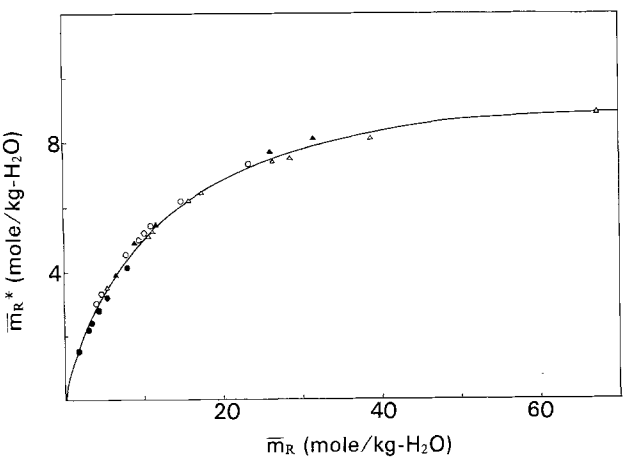

Fig. 4. Calculated effective fixed ion concentration vs. total fixed ion concentration. ○, PSA-1; △, PCA-1; ●, PSA-2; ▲, PCA-2.

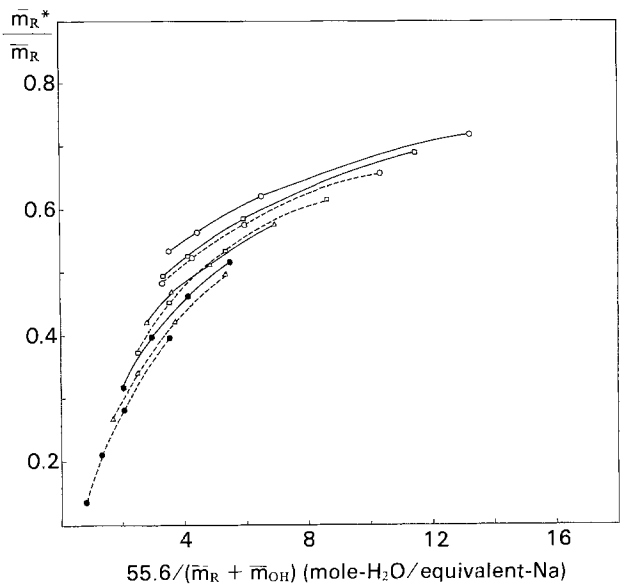

Fig. 5. The ratio $\bar{m}_R^*/\bar{m}_R$ vs. the hydration number of sodium ion. ——, PSA-1; -------, PCA-1; ○, EW = 1100 or 1014; □, EW = 1200 or 1114; △, EW = 1350 or 1264; ●, EW = 1600 or 1514.

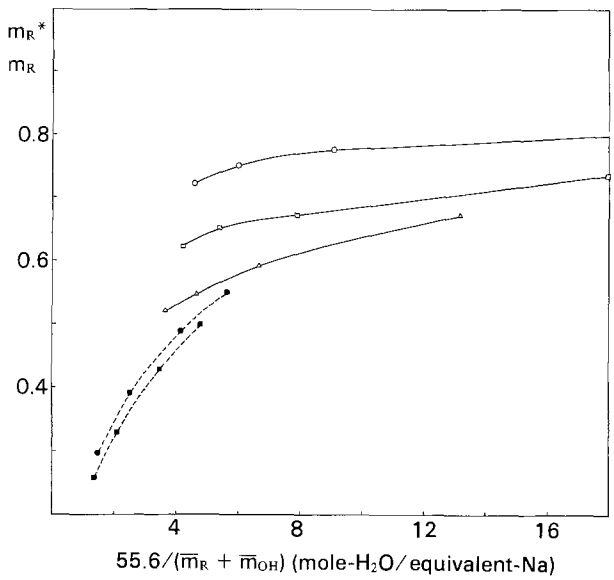

Fig. 6. The ratio $\bar{m}_R^*/\bar{m}_R$ vs. the hydration number of sodium ion. ——, PSA-2; -------, PCA-2; ○, EW = 1000; □, EW = 1200; △, EW = 1400; ●, EW = 699; ■, EW = 813.

shown in Table I. This is probably caused by the swelling of the PSA-2 membrane prior to the measurement, due to boiling in hot water with H-form (9, 26), which expands the distance between the fixed ion groups. This would also explain why the value of α is slightly higher for PSA-2 than for the other three membranes.

The swelling pressure π is plotted against the external concentration as shown in Fig. 7 and 8. The slope of the curve is larger with higher values of β and EW, as indicated by Eq. [16]. Perfluorocarboxylic acid membrane has less tendency to swell than perfluorosulfonic acid membrane, as indicated by comparison of the values of β for PCA-1 and PSA-1. Among the perfluorocarboxylic acid membranes, the value of β is much larger for PCA-2 than for PCA-1. This is probably due to the shorter, less bulky pendant structure of PCA-2, which is indicated in Table I, and the resulting denser polymer matrix with higher resistance

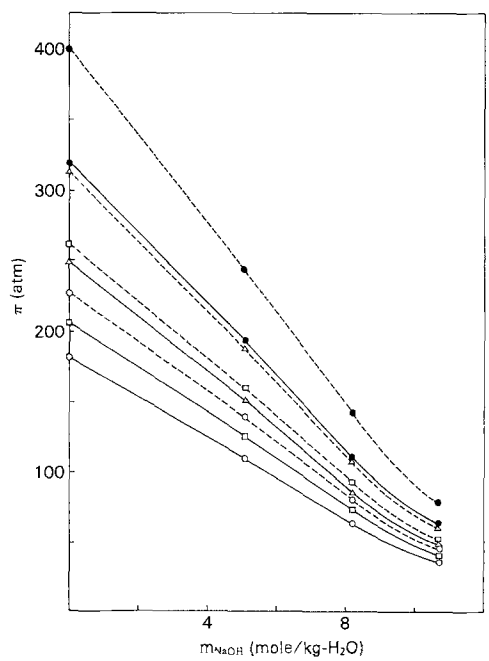

Fig. 7. Calculated swelling pressure vs. m_{NaOH}. ——, PSA-1; -------, PCA-1; ○, EW = 1100 or 1014; □, EW = 1200 or 1114; △, EW = 1350 or 1264; ●, EW = 1600 or 1514.

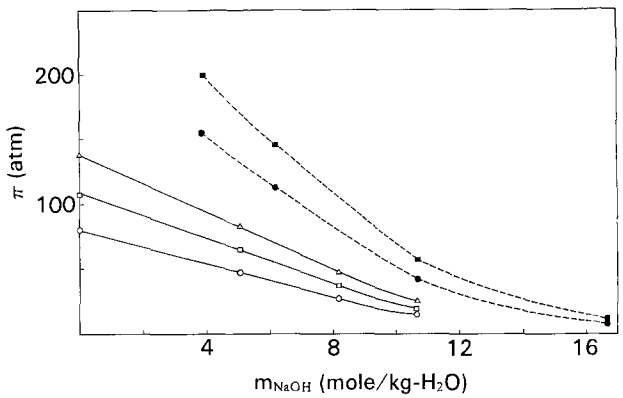

Fig. 8. Calculated swelling pressure vs. m_{NaOH}. ——, PSA-2; -------, PCA-2; ○, EW = 1000; □, EW = 1200; △, EW = 1400; ●, EW = 699; ■, EW = 813.

against swelling. For perfluorosulfonic acid membrane also, the pendent structure is a key factor in designing the membrane (6, 23). The value of β is lower for PSA-2 than for PSA-1. This is attributable to the increased swelling and weakened interaction of ion-exchange groups caused by the pretreatment process (9). Munn reports the strong dependence of water content of perfluorosulfonic acid membrane on the pretreatment procedures (26).

Current efficiency is generally known to increase as the concentration of sorbed electrolyte decreases. $\bar{m}_{OH}$ is lower at higher EW and greater TFE content as indicated in Tables II-V. This corresponds to the general tendency for the perfluorosulfonic acid membrane with higher EW to exhibit higher current efficiency (14). $\bar{m}_{OH}$ is also lower for membranes with greater values of β, as shown in Fig. 9, where $\bar{m}_{OH}$ is plotted for membranes PSA-1, PCA-1, and PSA-2 of similar TFE content and for membrane PCA-2 of lower TFE content. The value of β is highest for PCA-2, and results in a low $\bar{m}_{OH}$ despite an EW of 813 which corresponds to its low TFE content. For comparison, a plot of the results calculated from data reported for polystyrene sulfonate in an aqueous sodium chloride solution is also included in the figure (27). The relative position of the curve is reasonable when considering its higher water content than PSA-2.

In Fig. 10, $\bar{m}_{OH}$ is plotted against EW with m_{NaOH} held at 10.7 (mol/kg-H_2O) for all four membranes. With its high β value, membrane PCA-2 with EW of 699 to 813 yields $\bar{m}_{OH}$ values equal to those for membrane PCA-1 with EW of 1120-1220 and membrane PSA-1 with EW of 1450-1590. This clearly indicates that the optimum range of EW should be lower for membrane

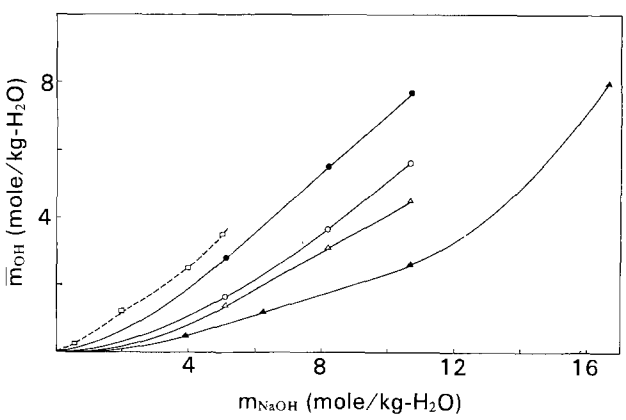

Fig. 9. Calculated sorbed electrolyte concentration vs. m_{NaOH}. ○, PSA-1 (EW = 1200); △, PCA-1 (EW = 1114); ●, PSA-2 (EW = 1200); ▲, PCA-2 (EW = 813); □, polystyrene sulfonate (EW = 900) (27).

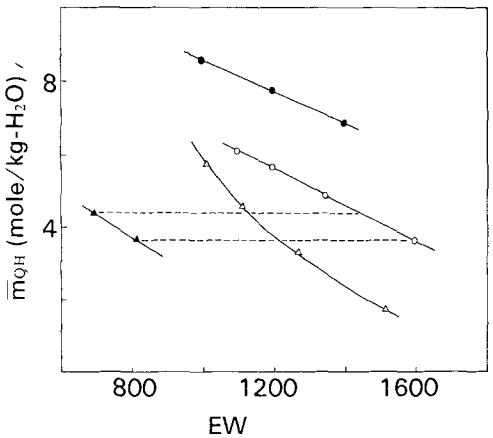

Fig. 10. Calculated sorbed electrolyte concentration *vs.* EW at m_{NaOH} = 10.7 (mol/kg-H_2O). ○, PSA-1; △, PCA-1; ●, PSA-2; ▲, PCA-2.

with higher β, which is in accord with our experience. As the model indicates higher $\bar{m}_{OH}$ values for membrane PSA-2 than for PSA-1, it also predicts lower current efficiency. This is in agreement with Munn's report of a decrease in the current efficiency of the perfluorosulfonic acid membrane after it is subjected to pretreatment which induces swelling (26).

In Eq. [15], Na^+-OH^- ion pair formation in the membrane phase is not considered, as $\bar{m}_R$ is generally much larger than $\bar{m}_{OH}$ under conditions strongly favoring ion pair formation, and also because α, by its nature as an empirical parameter, incorporates the effect of any Na^+-OH^- ion pairing which actually does occur.

In conclusion, the model developed here provides a theoretical basis for the design and use of membrane for the chlor-alkali process. It will be extended to other systems and also be utilized in analysis of membrane transport properties.

Acknowledgment

The author expresses his thanks to Asahi Chemical Industry Company, Limited for permission to publish this paper.

Manuscript submitted Nov. 11, 1982; revised manuscript received *ca.* Sept. 20, 1982.

Any discussion of this paper will appear in a Discussion Section to be published in the December 1983 JOURNAL. All discussions for the December 1983 Discussion Section should be submitted by Aug. 1, 1983.

Publication costs of this article were assisted by Asahi Chemical Industry Company, Limited.

REFERENCES

1. M. Seko, Paper presented at Centennial Meeting of American Chemical Society, New York, April 4-9, 1976.
2. M. Seko (to Asahi Chemical Ind. Co., Ltd.), U.K. Pat. 1,497,748 (1978).
3. M. Seko (to Asahi Chemical Ind. Co., Ltd.), U.K. Pat. 1,497,749 (1978).
4. H. Ukihashi, CHEMTECH 1980 (February), 118.
5. M. Seko, Y. Yamakoshi, H. Miyauchi, M. Fukumoto, K. Kimoto, I. Watanabe, T. Hane, and S. Tsushima, (to Asahi Chemical Ind. Co., Ltd.), U.S. Pat. 4,151,053 (1979).
6. K. Kimoto, H. Miyauchi, J. Ohmura, M. Ebisawa, and T. Hane (to Asahi Chemical Ind. Co., Ltd.), U.S. Pat. 4,329,434 (1982), U.S. Pat. 4,329,435 (1982).
7. C. J. Molnar, E. H. Price, and P. R. Resnick (to E. I. du Pont de Nemours and Co.), U.S. Pat. 4,176,215 (1979).
8. W. G. Grot (to E. I. du Pont de Nemours and Co.), U.S. Pat. 3,969,285 (1976).
9. W. G. F. Grot, G. E. Munn, and P. N. Walmsley, Paper 154 presented at the Houston, Texas, Meeting of the Society, May 7-11, 1972.
10. H. Ukihashi, O. Shiragami, Y. Oda, and T. Asawa, in Proceeding of the 3rd Meeting of Japan Soda Association 5, Kyoto, Japan, Nov. 1979.
11. M. Seko, Paper 417 presented at the Minneapolis, Minnesota, Meeting of the Society, May 10-15, 1981.
12. A. J. Hopfinger, K. A. Mauritz, and C. J. Hora, Paper 439 presented at the Atlanta, Georgia, Meeting of the Society, Oct. 9-14, 1977.
13. K. A. Mauritz, C. J. Hora, and A. J. Hopfinger, in "Ions in Polymers," A. Eisenberg, Editor, Chap. 8, ACS Advances in Chemistry Series, No. 187, American Chemical Society, Washington, D.C. (1980).
14. T. D. Gierke Paper 438 presented at the Atlanta, Georgia, Meeting of the Society, Oct. 9-14, 1977.
15. H. P. Gregor, B. R. Sundheim, K. M. Held, and M. H. Waxman, *J. Colloid Sci.*, **7**, 511 (1952).
16. J. F. Duncan, *Proc. R. Soc. London, Ser. A*, **214**, 344 (1952).
17. E. Gluekauf, *ibid.*, **214**, 207 (1955).
18. J. A. Nelder and R. Mead, *Computer J.*, **7**, 308 (1965).
19. F. Helfferich, "Ion Exchange," Chap. 5, McGraw-Hill, New York (1962).
20. R. A. Komoroski and K. A. Mauritz, *J. Am. Chem. Soc.*, **100**, 7487 (1978).
21. R. A. Robinson and R. H. Stokes, *Trans. Faraday Soc.*, **45**, 612 (1949).
22. G. E. Boyd and B. A. Soldano, *Z. Electrochem.*, **57**, 162 (1953).
23. M. Seko, S. Ogawa, and K. Kimoto, in "Perfluorinated Ionomer Membranes," American Chemical Society, Washington, D.C., ACS Symposium Series 180 (1982).
24. R. A. Robinson and R. H. Stokes, "Electrolyte Solutions," Butterworths Scientific Publications, London (1959).
25. F. T. Gucker, Jr., *Chem. Rev.*, **13**, 111 (1933).
26. G. E. Munn, Paper 436 presented at the Atlanta, Georgia, Meeting of the Society, Oct. 9-14, 1977.
27. Y. Oda and T. Yawataya, *Bull. Chem. Soc. Jpn.*, **29**, 673 (1956).

Design And Performance Of A Modular, Multi-Purpose Electrochemical Reactor

L. Carlsson, B. Sandegren, and D. Simonsson

Swedish National Development Company, Box 34, S-184 00 Åkersberga, Sweden

M. Rihovsky

Department of Chemical Technology, Royal Institute of Technology, S-100 44 Stockholm, Sweden

ABSTRACT

A new multipurpose electrochemical reactor, based on the plate and frame principle, has been developed for use in both laboratory research and industrial production. Among its advantages, this ElectroSynCell (ESC) exhibits good mass transfer characteristics due to efficient turbulent promoters. Experimental studies of limiting currents have shown that the specially designed grid promoter gives a more than threefold increase in mass transfer rates. The possible application in small-scale chlor-alkali processes has also been investigated. Cost estimates based on the reported experimental results show that the ESC is competitive in this field.

In the development of new electrochemical processes, the scale up of laboratory reactors to commercial production units costs a lot of time and money, and is often not well planned for in the design of the laboratory experiments. A new monopolar membrane cell system has therefore been developed for use in both laboratory and pilot plant evaluations, as well as in the commercial production of chemicals. The design is based upon the plate and frame principle (Fig. 1).

The electrodes are mounted in injection molded frames made of polymer material, and these are stacked with membranes in between (if needed) to form modules of the desired size. The projected electrode area of such a module can be chosen in the range of 0.04-1.04 m^2. The design objectives and the details of the cell design have recently been discussed elsewhere (1).

In many presumptive applications of the ElectroSynCell the optimal current density corresponds to a mass transfer limited process. In order to achieve high mass transfer rates, the turbulence promoter is a vital part of the design. The effects of various types of turbulence promoters in the ESC have therefore been investigated experimentally. As one of the objectives of this paper the results of these experiments will be reported.

The ESC has earlier been tested with good results for the production of glyoxylic acid from oxalic acid and the oxidation of Ce^{3+} to Ce^{4+} (1). An expanding market for small-scale chlor-alkali processes can be expected in the near future. The membrane process fits very well for this purpose. The performance of an ESC for this application has been investigated. The second objective of this paper is thus to report the results of these studies.

Mass Transfer Studies

Experimental.—The enhancement of mass transfer to the electrodes by means of turbulence promoters was studied in an ESC with only one anode chamber and one cathode chamber, both equipped with nickel electrodes. The dimensions of the electrodes were 148 × 297 mm and the distance between the electrodes was 9 mm. The cross-sectional area for the electrolyte flow was 12 × 154 mm, including the space behind the electrodes.

The experimental apparatus is shown in Fig. 2. The electrolyte was stored in a vessel at room temperature (20°C) and was recycled through the ESC by means of a centrifugal pump. The flow rate was measured with a calibrated rotameter and the pressure drop over the cell with a U-tube with water. The cathode potential was measured *vs.* an Hg/HgO reference electrode.

The electrolyte was an equimolar solution of $K_3Fe(CN)_6$, and $K_4Fe(CN)_6$ in 1.0*M* KOH. The electrode reactions were thus the reduction of ferricyanide at the cathode with its reoxidation at the anode. Before each experimental run, the electrodes were cleaned by the evolution of hydrogen and oxygen, respectively, in a strong alkaline solution.

In order to determine mass transfer rates, limiting currents were measured at different recycle flow rates of the electrolyte and for the following different types of turbulence promoters: (*i*) cylindrical rods of plexiglass with diam of 5 and 7 mm, respectively. These were placed between the electrodes in the middle of the flow channel, perpendicularly to the direction of the electrolyte flow. (*ii*) a specially designed plastic grid with triangular threads of polypropylene. The grid is attached to the electrodes and is supplied with flow distributors at the inlet and the outlet (see Fig. 3).

In addition, the use of electrodes of expanded nickel instead of flat electrodes was studied. The mesh size was 10 × 5 mm. Preliminary experiments showed no

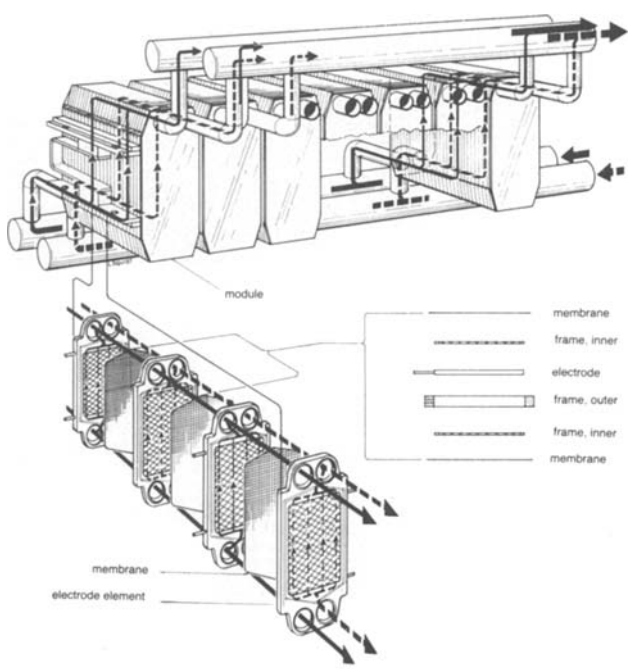

Fig. 1. Principal design of the ElectroSynCell. The figure shows a seven-module unit.

Key words: membrane, cell, mass transfer, electrolysis.

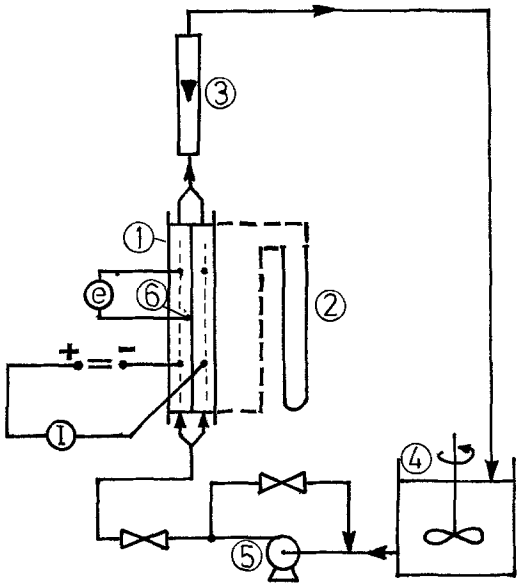

Fig. 2. Experimental apparatus used in the mass transfer studies. 1, ESC; 2, U-tube manometer; 3, rotameter; 4, reservoir; 5, centrifugal pump; 6, reference electrode with capillary.

effect of an ion exchange membrane upon the limiting current. All experiments were therefore performed without membrane.

Results.—The limiting current plateau was very distinct up to a concentration of 3.0 mM (see Fig. 4). This concentration was therefore chosen as a standard in the experimental plan. The limiting current measured as a function of $Fe(CN)_6^{3-}$ concentration at a flow rate of 3.0 liters/min gives a good linear dependence (Fig. 5). The straight line in Fig. 5 does not pass through the origin, because of the reduction of dissolved oxygen. In the experimental design with high recycle flow rates, it was difficult to deaerate the electrolyte. Instead, the measurements of limiting current were corrected by subtracting the current at zero concentration.

The experiments with cylindrical promoters started with a search for the optimal distance between the rods. With 10, 20, 30, and 40 mm distances, respectively, the maximum limiting current was obtained for the distance of 20 mm for both diam of the rods. The results of the experiments using this distance are shown in Fig. 6. This figure also shows the results for the SU-grid as well as the results for flat and expanded metal electrodes without any turbulence promoters. The straight lines in Fig. 6 are least square fits of $\log(I_{lim})$ *vs.* $\log q$ with correlation coefficients varying between 0.996 and 0.999. The figure also shows the results expressed in dimensionless quantities as Sh *vs.* Re. The straight lines then represent correlations of the form

$$Sh = a\,Re^{x}Sc^{1/3} \qquad [1]$$

Here, Re is defined with respect to an equivalent diam

$$D_e = 2bh/(b + h),$$

$$Re = uD_e/\nu \qquad [2]$$

The average mass transfer coefficient used in the evaluation of the Sherwood number can be calculated from the limiting current

$$k = \frac{I_{lim}s_i}{AnFc_b} \qquad [3]$$

The estimated values of a and x in Eq. [2] are summarized in Table I for the various promoters. Figure 6 shows that the specially designed grid was the most

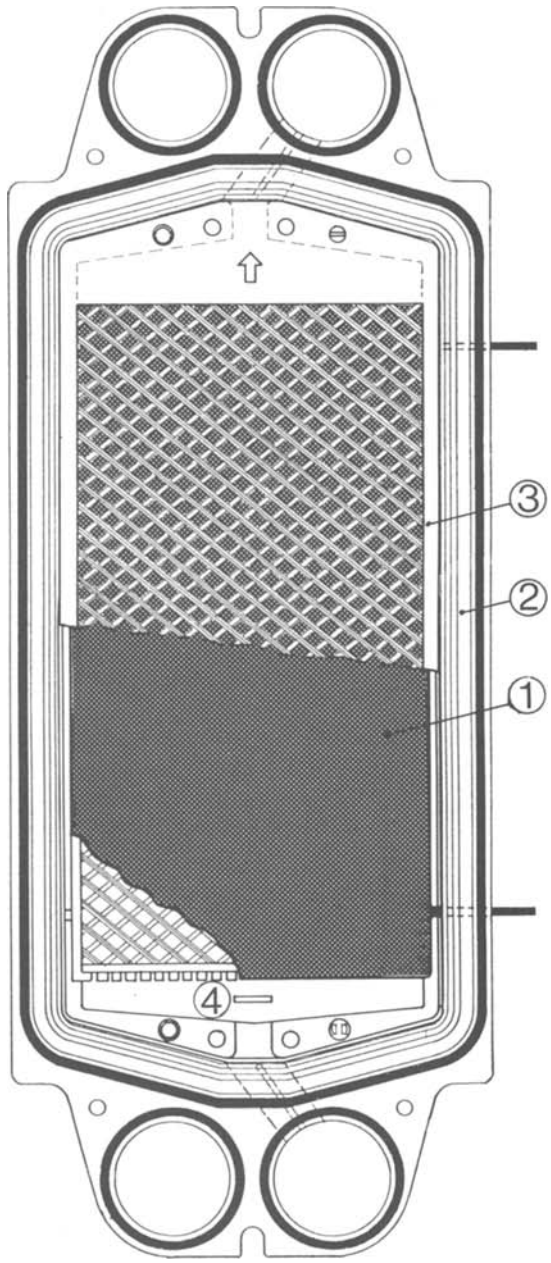

Fig. 3. Single electrode compartment with: 1, electrode; 2, frame; 3, grid; 4, flow distributor.

effective turbulence promoter among those investigated.

In Fig. 7 the enhancement of mass transfer to the electrodes due to turbulence promoters is plotted as a function of flow rate. In the experiments, the grid promoter gave between three and six times higher mass transfer rates than flat electrodes alone. It is also interesting to note that without turbulence promoters the electrode of expanded metal gave almost twice as high mass transfer rates as a flat electrode, in spite of its smaller effective area. This could be explained by

Table I. Correlation of mass transfer data for ESC with various types of promoter. $70 < Re < 800$, $Sc = 1572$, $\nu = 1{,}065 \cdot 10^{-6}$ m²/sec

Electrode	Promoter	Sh(Re)
Flat	Without	$0.39\,Re^{0.63}\,Sc^{1/3}$
	Cylinders d = 5 mm	$0.38\,Re^{0.71}\,Sc^{1/3}$
	Cylinders d = 7 mm	$0.98\,Re^{0.62}\,Sc^{1/3}$
	SU-grid	$5.57\,Re^{0.40}\,Sc^{1/3}$
Expanded metal	Without	$0.82\,Re^{0.61}\,Sc^{1/3}$
	SU-grid	$2.15\,Re^{0.54}\,Sc^{1/3}$

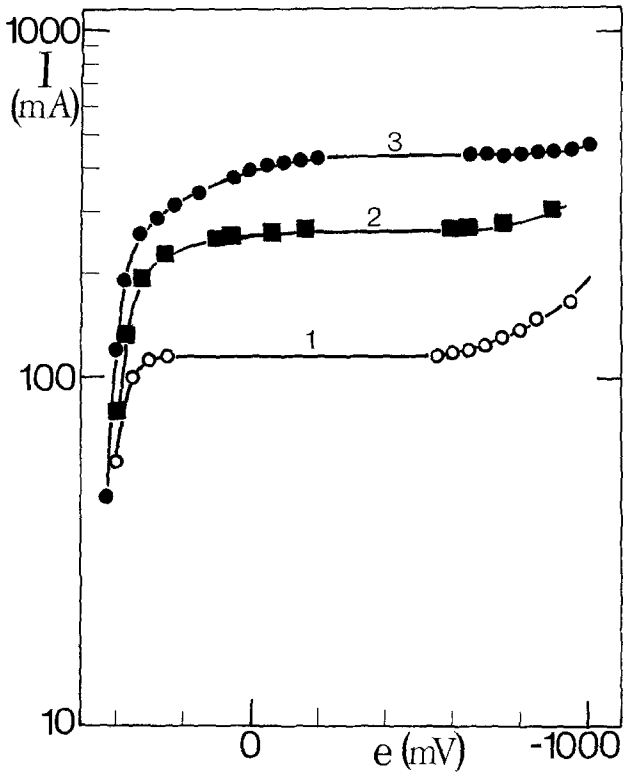

Fig. 4. Limiting currents for different turbulence promoters. 1, Without promoter; 2, cylinders d = 7 mm; 3, SU-grid flat electrodes, ferricyanide concentration = 3.0 mM, flow rate = 3.4 liters/min.

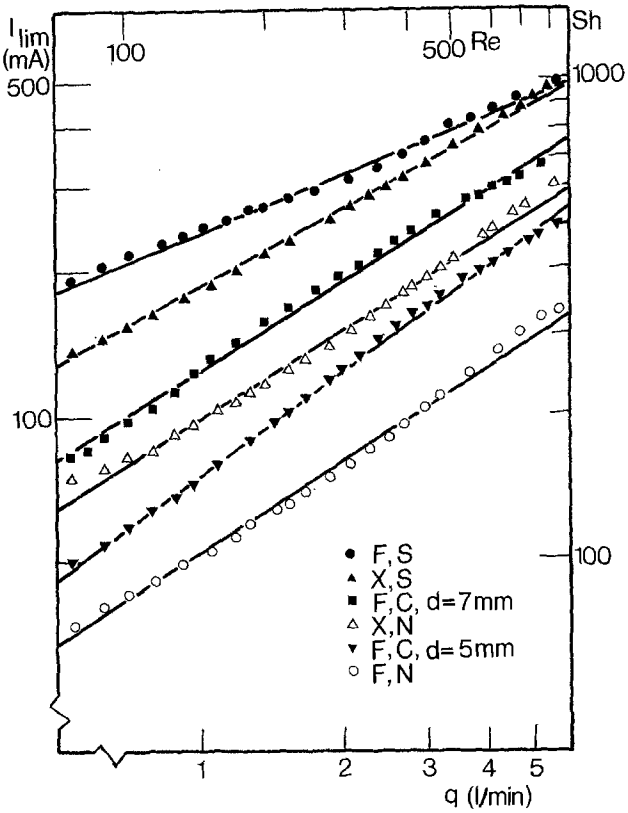

Fig. 6. Limiting current as a function of flow rate and Sh vs. Re for different turbulence promoters. Data for flat electrode (F) and expanded metal electrode (X). S = SU-grid, C = cylinders, N = no promoter.

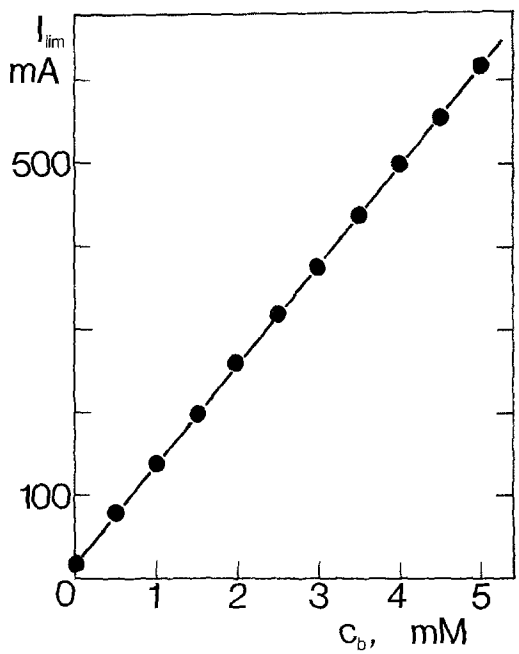

Fig. 5. Limiting current as a function of the ferricyanide concentration in the bulk. SU-grid, flow rate = 3.0 liters/min.

the fact that the expanded metal electrode itself acts as a turbulence promoter. With grid promoters, on the other hand, the flat electrode with its higher surface area gives a higher limiting current.

A comparison with literature data (2) shows that our measured mass transfer coefficients are about 1.3-3 times higher. This may be due to the special geometric design or the effect of the flow distributor. The results for empty channel are in fairly good agreement with literature data for the entrance region of a cell.

Application in Small Scale Chlor-alkali Processes

Experimental.—The experimental apparatus is shown in Fig. 8. The frames in the cell were in this case made of PVDF to insure thermal and chemical resistance. The anode was a DSA 107. Steel, graphite, and nickel were used as cathode materials in different runs. The best results were obtained with nickel cathodes. NAFION 390 and 901 were used as membranes respectively. Although there are no mass transfer limitations in the chlor-alkali electrolysis, the plastic grids were used to hold the membrane in its correct position. In technical applications of the ESC for chlor-alkali production, the grids could be omitted to avoid their shielding effect on the current.

Especially the NAFION 901 requires an ultrapure brine. The variation of the cell voltage with time when using an unpurified brine can be seen in Fig. 9. The tests with NAFION 901 were carried out continuously and purification of the brine was evidently necessary. The brine was therefore passed through an ion exchange column with Amberlite IRC-718. On the other hand, the tests with NAFION 390 were carried out batchwise with recycled flow and therefore no ion exchange was necessary.

Both the anolyte and catholyte were recycled through their respective electrode chambers. The residence time was about 1 sec. Distilled water was fed to and caustic was taken out from the catholyte flow into a vessel where also the hydrogen was vented off. Purified brine was in a similar way supplied to and drained from the anolyte flow in a vessel where the chlorine was vented off. For the purification of the raw brine it has to be slightly alkaline (pH = 8-10) and warm (60°-70°C), and was therefore heated in the chlorine venting vessel. To simplify the experimental setup, and since the ion-exchanger resin does not stand free chlorine, water was evaporated from the anolyte recycling system keeping the salt contents high.

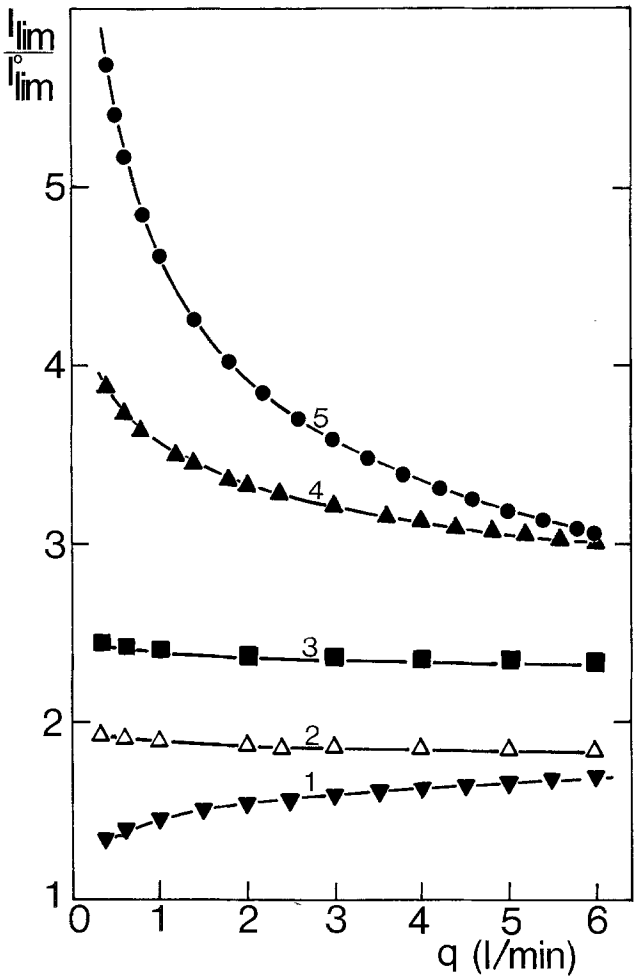

Fig. 7. Enhancement factor due to the effect of different turbulence promoters. The symbols are the same as in Fig. 6.

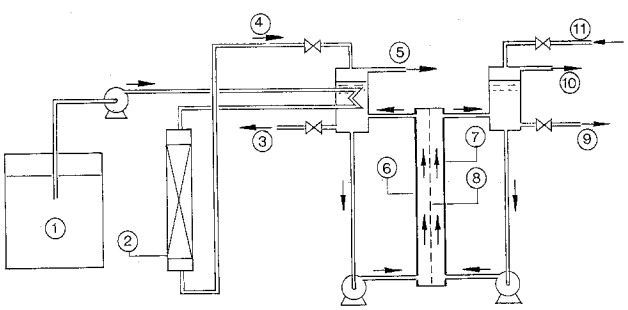

Fig. 8. Experimental setup. 1, Brine storage; 2, ion exchanger; 3, brine outlet; 4, brine inlet; 5, chlorine outlet; 6, anode; 7, cathode; 8, membrane; 9, caustic outlet; 10, hydrogen outlet; 11, water inlet.

Results.—Cell voltage and current efficiency are important factors as they determine the energy consumption. The cell voltage is affected by the choice of electrodes and membrane. In Fig. 10 cell voltage *vs.* current density for the two membranes are shown. At 3.0 kA/m² the cell voltage could be as low as 3.6V when NAFION 390 is used. The measured value at 3.0 kA/m² when NAFION 901 was used is somewhat higher, about 4.0V, but planar nickel was then used instead of porous. NAFION 901 also seems to be more sensitive to alkaline earth metal impurities. In the tests of NAFION 901 these impurities were kept at a level of 250 ppb.

The current efficiency was strongly dependent on the caustic strength produced. However, there are principal differences between NAFION 390 and 901. When using the 390 the current efficiency decreased

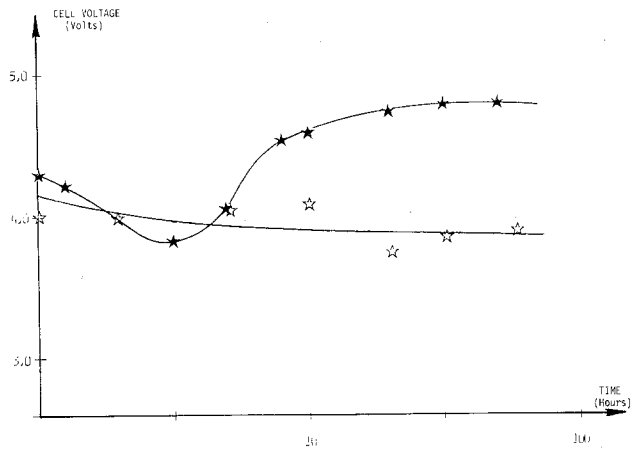

Fig. 9. Cell voltage *vs.* time. (☆) Purified brine, (★) unpurified brine.

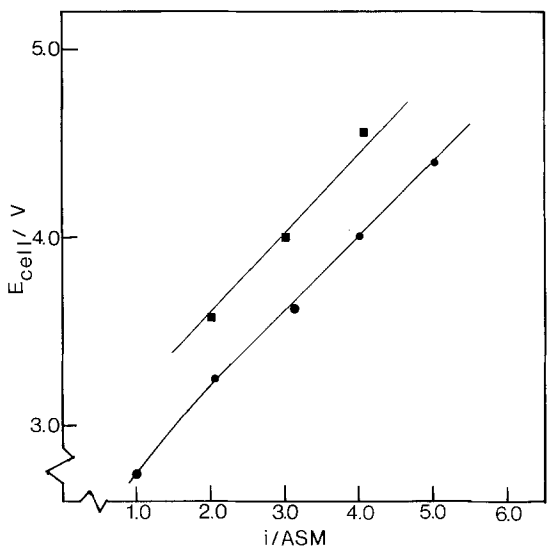

Fig. 10. Cell voltage for various membranes. (■) NAFION 901, 70°C, caustic strength 10M. (●) Nafion 390, 60°C, caustic strength 3M.

Table II. Comparison of data for the SU ElectroSynCell

	SU ElectroSynCell with NAFION 390						NAFION 901		Hooker MX	Diamond DM-14	Asahi chemical	Asahi glass
Current density (kA/cm²)	2.0		3.0		4.0		2.0	3.0	3.0	3.1	4.0	2.0
Cell voltage (V)	3.2		3.6		4.0		3.6	4.0	n.a.	3.9	3.75	3.7
Temperature (°C)	60		60		60		70	70	n.a.	n.a.	n.a.	n.a.
Caustic conc. (w/o)	10	20	10	20	10	20	30	30	17-30	28	22	35
Power consumption d-c kW-hr/MT NaOH	2520	2820	2840	3170	3150	3530	2540	2820	2800	2950	2703	2610
Power cost $/MT NaOH	101	113	114	127	126	141	102	119	—	—	—	—

n.a. = not available.

with increasing strength of the caustic. Caustic with a strength of 10% can be produced with 90% current efficiency, but at a strength of 20% is only about 75%. This is in good agreement with data presented in (3). On the other hand, when using the 901, current efficiency reaches a peak at about 35% caustic. At 30% caustic the current efficiency is over 90%. Data obtained are presented in Table II. This table also gives a comparison with data for other commercial cells (3).

Very little chloride diffused over the membrane and sealing gaskets. Under proper conditions just about 100 ppm chloride was measured in the caustic.

Conclusions

The results of these investigations show that the ESC fits into the small-scale chlor-alkali application area. Suitable production volumes should range from 150 kg Cl_2/day (1 module) up to 5-10 tons Cl_2/day (50 modules).

Since the capital cost is a comparatively large part of the total production cost, the total economics favor a high current density. The highest accepted level for the membrane and current collectors is 5 kA/m^2 with the ESC. The production costs are clearly competitive in small-scale production.

Manuscript submitted June 30, 1982; revised manuscript received Sept. 2, 1982. This was Paper 393 presented at the Montreal, Que., Canada, Meeting of the Society, May 9-14, 1982.

Any discussion of this paper will appear in a Discussion Section to be published in the December 1983 JOURNAL. All discussions for the December 1983 Discussion Section should be submitted by Aug. 1, 1983.

Publication costs of this article were assisted by the Swedish National Development Company.

LIST OF SYMBOLS

a	dimensionless coefficient in Eq. [1]
A	electrode area, m^2
b	cell width, m
c_b	bulk concentration of $K_3Fe(CN)_6$, kmol/m^3
d	diameter of cylindrical promoter
D	diffusion coefficient of $Fe(CN)_6^{3-}$, m^2/sec
D_e	equivalent diameter of the cell $= 2\,bh/(b+h)$, m
F	Faraday's constant, 96.5×10^6 As/kmol
h	distance between electrodes, m
I	current, A
I_{lim}	limiting current, A
I^o_{lim}	limiting current for cell without promoter, A
k	average mass transfer coefficient over the electrode, m/sec
n	number of electrons transferred in the electrode reaction
q	flow rate, liters/min
Re	Reynolds number, see Eq. [2]
s_i	stochiometric coefficient in Eq. [3]
Sh	Sherwood number, kD_e/D
Sc	Schmidt number, ν/D
u	liquid velocity, m/sec
x	parameter in Eq. [1]
ν	kinematic viscosity, m^2/sec

REFERENCES

1. L. Carlsson, H. Holmberg, B. Johansson, and A. Nilsson in "Technique of Electroorganic Synthesis," Part III, N. L. Weinberg and B. V. Tilak, Editors, J. Wiley & Sons, New York (1982).
2. A. Storck and D. Hutin, *Electrochim. Acta*, **26**, 127 (1981).
3. D. L. Caldwell in "Comprehensive Treatise of Electrochemistry, Vol. 2: Electrochemical Processing," p. 153, Plenum Press, New York (1981).

Electrochemically Modified Electrodes

Poly(2-Methyl-8-Quinolinol) and Poly(8-Quinolinol) Complexing Films Obtained by Electropolymerizing Substituted Phenols: Their Voltammetric and Electrical Properties in Relation to Their Geometric Structure

Minh-Chau Pham, Jacques-Emile Dubois,* and Pierre-Camille Lacaze

Institut de Topologie et de Dynamique des Systèmes de l'Université Paris VII, associé au C.N.R.S., 75005 Paris, France

ABSTRACT

Poly(2-methyl-8-quinolinol) and poly(8-quinolinol) films strongly adherent to metal electrodes are obtained by electrochemical oxidation of phenol derivatives. Cu(II) and Co(II) ions can be coordinated by these polymer ligands. The structures of the complexed films are analyzed by XPS and infrared spectroscopy: their electrical and electrochemical properties depend on the complex geometry. Only the equivalent of *ca.* a fifth of the layer of cationic sites at the metal-film interface takes part in the redox process for the cobalt complex, whereas the equivalent of *ca.* a dozen layers are involved for the copper complex.

There are many recent studies on modifying electrode surfaces by coating them with metal complexed films to obtain new electrocatalytic properties (1-6). As shown herein, it is possible to elaborate polymer films by extending our recently developed techniques for the electropolymerization of phenols to hydroxyquinoline derivatives (7, 8). The resulting films are very adherent to metal surfaces, very stable in various electrolytic media, and have good metal-binding properties, *viz.* with Cu(II) and Co(II) ions. The distinct electrochemical and electrical behavior of these films after complexation of these ions can be ascribed to the differences in the geometry of the metal complexes formed by coordination of these ions with ligands from the polymer films.

* Electrochemical Society Active Member.

Key words: polymer film formation, metal complexes, XPS analysis.

Experimental

Reagents.—The quinolinol derivatives studied were commercial products: 2-methyl-8-quinolinol (Baker, laboratory grade) and 8-hydroxyquinoline (Koch-Light Laboratories). The copper (II) chloride ($CuCl_2$, $2H_2O$) and cobalt (II) chloride ($CoCl_2$, $6H_2O$) were from Prolabo (R.P. Normapur). CF_3COOH, CF_3COONa, and $NaClO_4$ were Aldrich products. $LiClO_4$ was from Fluka. MeOH was a Merck p.a. product. Deionized water was twice distilled in a quartz apparatus.

Electrochemical apparatus.—Electrochemical experiments were performed using a PAR potentiostat (Model 173) connected to a PAR programmer (Model 175). The electrodes were bulk metals (Fe, Cu, Pt, Ni, C), or thin layer Pt, deposited on glass plates by sputtering according to a previously described process (9).

Film identification.—Multiple-reflection infrared spectroscopy and x-ray photoelectron spectroscopy (XPS) were used to identify the films formed on the electrodes. The infrared spectra were recorded on a Wilks device (Wilks Scientific Corporation, Model 9) mounted on a Perkin-Elmer 225 spectrophotometer. The XPS spectra were recorded on a AEI-ES 200 spectrometer with an FRR adaptation and a magnesium anode.

The Pt|polymer film|Au capacitors and the conductivity measurements were realized according to a previously described process (10). Thin layer platinum electrodes (300 nm) were deposited by sputtering (Balzers Model Sputron II). The Au counter electrode (60 nm) was deposited on the polymer film by thermal evaporation (Joule effect) in a vacuum at 10^{-7} Torr (Balzers Model BA 350).

Results

Polymer Film Formation by Oxidizing 8-Quinolinol or 2-Methyl-8-Quinolinol

We recently showed that the electrochemical oxidation of 2-methyl-8-quinolinol leads to the formation of polymer films on Pt, Fe, and Cu electrodes (11). Analogous results have now been obtained by electrochemically oxidizing 8-quinolinol (0.1M) in 0.3M NaOH-MeOH with electrodes such as Fe, Cu, C, and Pt (Fig. 1). After six successive potential sweep cycles between 0 and 1.4V (SCE) a very adherent homogeneous film with a thickness of *ca.* 60 nm forms on the electrode surface.

XPS analysis confirms the formation of a polymer film with the characteristics of polyphenylene oxide-type films. The following signals are detected: a C_{1s} signal at 286.6 eV corresponding to the C—O—C binding energy blended with the C—N bond (12), a C_{1s} signal at 285 eV corresponding to the aromatic C—C bonds (13) blended with the carbon reference (13), an O_{1s} signal at 532 eV corresponding to the C—O—C binding energy of the polymer, and an N_{1s} signal at 398.9 eV ascribed to the C—N bonds (14).

As in the case of the films of the polyphenylene oxide type (7), multiple-reflection infrared spectroscopy shows that, after oxidation, these films no longer display an absorption band around 3200 cm^{-1} corresponding to the OH monomer, while they do display a very intense band at around 1235 cm^{-1} that can be ascribed to the C—O—C bond of the polymer. The absence in these spectra of an absorption band ascribable to C=O groups at around 1700 cm^{-1} confirms the exclusive formation of C—O—C polyoxide bonds.

Metal Complexes Formed by Coordination of Cu(II) or Co(II) Ions with Ligands from Polymer Films

The formation of complexes between Cu(II) or Co(II) ions and poly(2-methyl-8-quinolinol) (polymer A) or poly(8-quinolinol) (polymer B) films requires different treatments.

For instance, although a polymer film need only be immersed for 15 min in a 10^{-1}M aqueous solution of $CuCl_2$ in order for complexation between Cu(II) ions and polymer A to occur, this method does not work with a polymer B film. Likewise, this method does not result in the formation of complexes between Co(II) ions and polymer A or B films.

For complexation with Co(II) ions, an organic medium is required. Thus, after dissolving 10^{-1}M $CoCl_2$ in DMF and bringing this solution to boiling point, a polymer B film immersed therein for 15 min forms a complex with the Co(II) ions. However, this technique cannot be used with polymer A films which dissolve in boiling DMF.

After complexation, polymer A-Cu(II)) film is rinsed in distilled water by ultrasonic agitation and then air-dried.

For polymer B-Co(II) film, the complexation reaction is done in DMF medium, the sample is therefore first rinsed in DMF by ultrasonic agitation to eliminate $CoCl_2$ traces. After that the cobalt-complex film is rinsed in methanol by ultrasonic agitation to eliminate DMF traces. It is finally air-dried before using in XPS analysis or electrochemical experiments.

XPS analysis of a polymer A-Cu(II) complex.—XPS analysis of a polymer A film before and after the treatment with $CuCl_2$ (Fig. 2a and b) indicates that the treatment indeed results in the formation of a complex between Cu(II) ions and the polymer A film.

The untreated polymer A film emits four XPS signals (Fig. 2a): an O_{1s} signal at 532.2 eV corresponding to the C—O—C binding energy in the polymer, an N_{1s} signal at 398.8 eV ascribed to the C—N bonds, a C_{1s} signal at 286.6 eV corresponding to the C—O—C binding energy blended with the C—N bond, and a C_{1s}

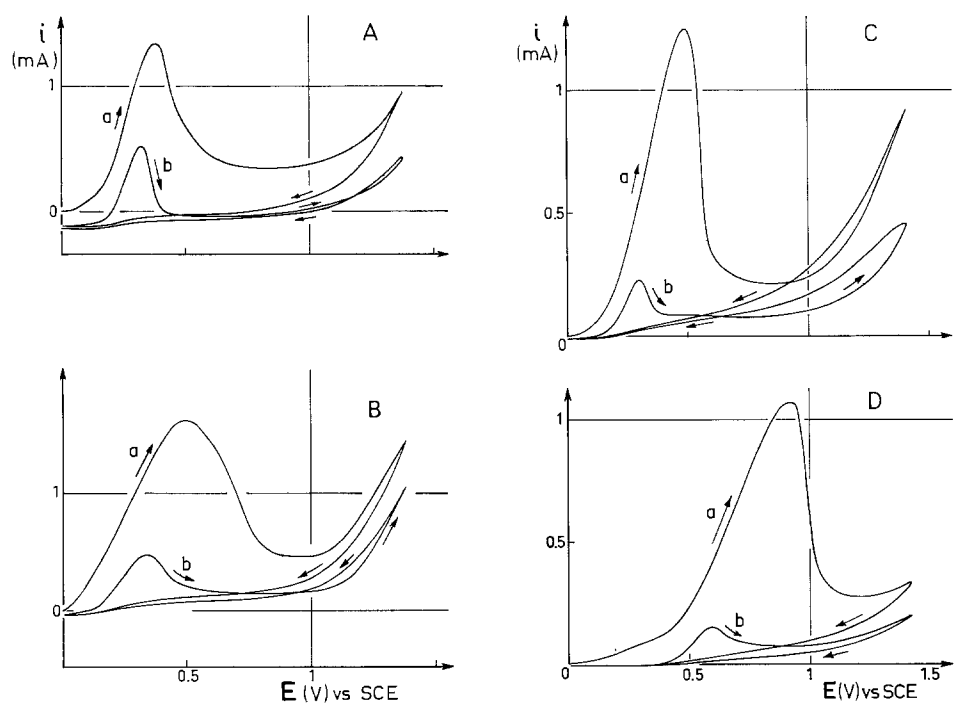

Fig. 1. *i-E* curve recorded during oxidation of 8-quinolinol on different electrodes: (A) Pt, (B) carbon, (C) Cu, (D) Fe; (sweep speed, 50 mV · sec^{-1}; medium, 0.1M 8-quinolinol, 0.3M NaOH-MeOH). (a) First sweep, (b) second sweep.

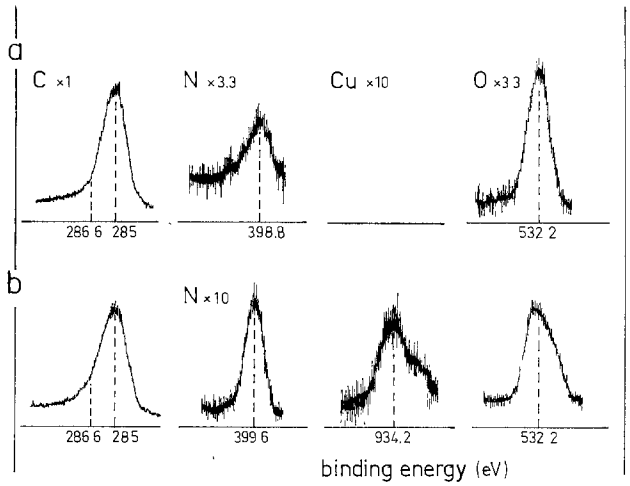

Fig. 2. XPS spectra of (a) poly(2-methyl-8-quinolinol) film, (b) same film after treatment with $CuCl_2$.

signal at 285 eV due to the aromatic C-C bonds blended with the carbon reference.

After the treatment with $CuCl_2$ (Fig. 2b), there is another signal at 934.2 eV characteristic of $Cu_{2p3/2}$(II) (15, 16) and a broadening of the O_{1s} band. This broadening could be indicative of two unresolved bands, one of which might be due to C—O—C bonds in interaction with Cu(II) ions. The N_{1s} signal formerly at 398.8 eV has shifted to 399.6 eV, thereby indicating the involvement of nitrogen atoms in the coordination of the Cu(II) ions with ligands from the polymer A film. Unlike the XPS spectrum of the polymer B-Co(II) complex described hereafter (Fig. 3), that of the treated polymer A film displays no second O_{1s} signal ascribable to ion complexation with H_2O molecules; this indicates that Cu(II) ions form a complex only with the N and O ligands of polymer A.

XPS analysis of a polymer B-Co(II) complex.—The XPS spectra of a polymer B film before and after the treatment with $CoCl_2$ (Fig. 3a and b) show that: the N_{1s} signal from the nitrogen binding energy increases from 398.9 eV to 400.1 eV (indicating thereby that the partial charge from the N atoms increases, in accordance with actual coordination between Co(II) ions and N); the $Co_{2p3/2}$ signal from the Co binding energy drops from 781.7 eV in $CoCl_2$, $6H_2O$ to 779.6 eV in the film (thereby indicating a decrease in the partial charge of the Co atom); instead of the single O_{1s} signal at 532 eV, there are two O_{1s} signals, at 532 eV (broader than the initial one) and at 529.4 eV.

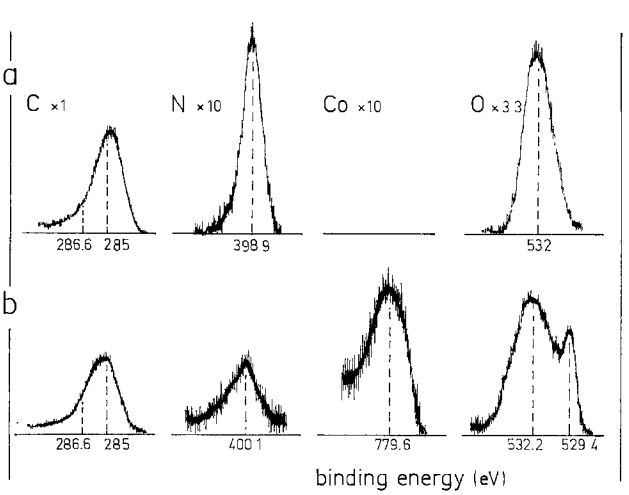

Fig. 3. XPS spectra of (a) poly(8-quinolinol) film, (b) same film after treatment with $CoCl_2$.

As in the case for the polymer A-Cu(II) complex, the broader O_{1s} signal at 532 eV can be ascribed to coordination between Co(II) ions and the C—O—C bonds of the polymer. As for the O_{1s} signal at 529.4 eV, which is not observed for the polymer A-Cu(II) complex, it seems likely that this might arise from interaction between H_2O molecules and Co(II) ions. It should be noted that XPS analysis of $CoCl_2$, $6H_2O$ also reveals an O_{1s} signal at 532.2 eV emitted mostly by the contamination oxygen, and a weaker O_{1s} signal at 531 eV. The H_2O-Co(II) interaction could account for the signal at 531 eV.

Cyclic voltammetry also indicates that the water molecules act as ligands with the Co(II) ions. When a Pt electrode with a polymer B-Co(II) coating is subjected for several hours to repeated potential scan cycles between 0 and 0.4V (SCE) in NaOH-H_2O, the polymer B-Co(II) complex is a reversible redox system. XPS analysis of the resulting film shows that when the cobalt signal diminishes by a factor of 10, the O_{1s} signal at 529.4 eV becomes very weak, whereas the O_{1s} signal at 532 eV remains constant.

Measuring the intensity of the XPS signals emitted by the various elements while taking into account the sensitivity of each (17) gives the following approximate formula of the polymer B-Co(II) complex: $C_{18}O_5N_{1.6}Co_1Cl_{0.16}$. This calculation, based on the atomic percentage of the elements in the XPS spectra, corroborates that, at the most, two moieties of the polymer take part in the complexation of a Co(II) ion.

The overall information points to a penta- or hexacoordinate structure for the polymer B-Co(II) complex in which the O and N ligands of two moieties of the polymer form a complex with a Co(II) ion, and the fifth or fifth and sixth ligands of the structure are water molecules.

Multiple-reflection infrared spectroscopy of polymer B films before and after treatment with $CoCl_2$ confirms the formation of a complex, as detected by XPS.

The infrared spectrum of polymer B-Co(II) films displays two intense absorption bands at 580 and 660 cm^{-1} which, by comparison with observations of Co(II)-pyridine complexes in solution reported in the literature, can be ascribed to an O-Co(II) and an N-Co(II) bond, respectively. Indeed, the infrared absorption band at 605 cm^{-1} of pyridine in solution shifts to a much higher frequency after complexation of the metal ions (18, 19). This shift compares with that of polymer B from 630 to 660 cm^{-1} after complexation with Co(II) ions. Like the absorption band at 565 cm^{-1} for oxygenated bis-salicylaldehyde-ethylenediimine-Co(II) complexes, the intense band at 580 cm^{-1} for the polymer B-Co(II) complex can be ascribed to the O-Co(II) bond (18).

Voltammetric Properties of Polymer A-Cu(II) and Polymer B-Co(II) Films

The behavior of the complexed film-Pt system was studied by cyclic voltammetry in an aqueous medium with different electrolytes.

Polymer A-Cu(II) films were studied in 0.2M CF_3COONa with the *p*H adjusted to 4 by CF_3COOH and in 0.2M $NaClO_4$ or $LiClO_4$ with the *p*H adjusted to 4 by $HClO_4$. In each case, a "forming" phenomenon is observed, corresponding to a progressive increase of the peak current with the number of potential cycles. After about ten potential sweep cycles between 0.0 and 0.8V (SCE), the peak current stabilizes (Fig. 4a). The peak current then varies linearly with the scan rate. Integration of the voltammograms shows the approximate concentration of redox centers in the complex to be 4×10^{-9} mol cm^{-2} (11).

The voltammogram in Fig. 4b, obtained in 0.2M $LiClO_4$-$HClO_4$ (*p*H 4), shows an oxidation and a reduction peak for the polymer A-Cu(II)/polymer A-Cu(I) couple at +0.51 and +0.36V (SCE), respectively.

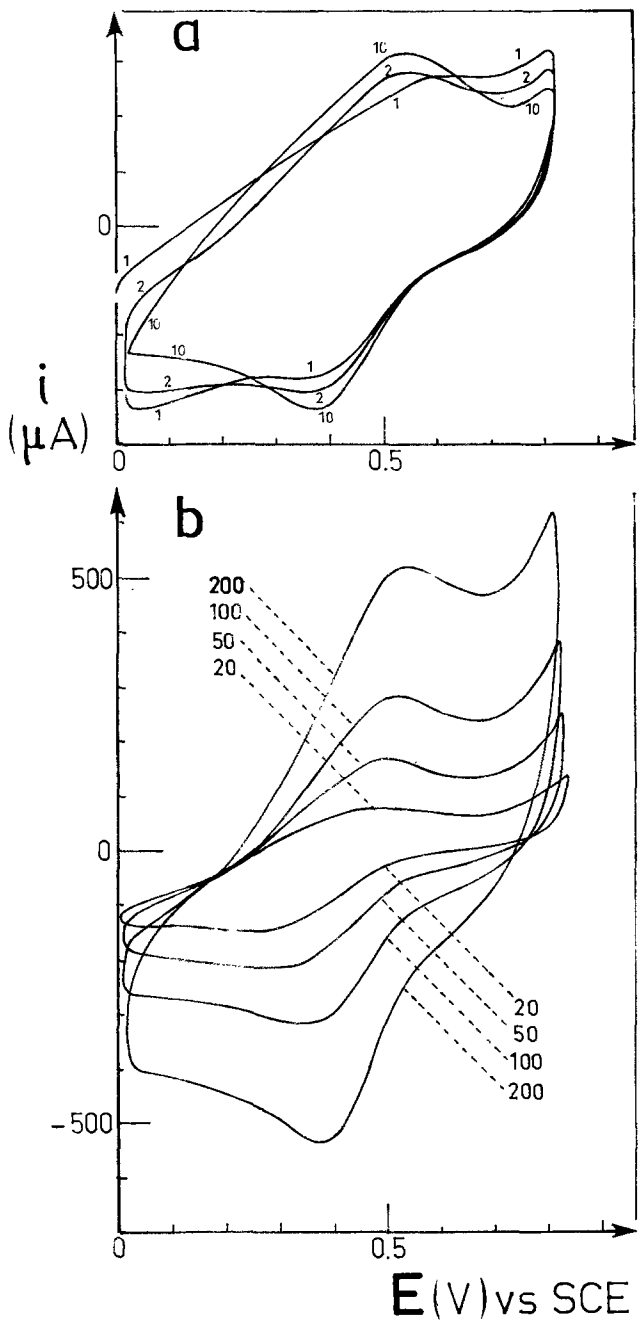

Fig. 4. (a) Cyclic voltammograms recorded with a Pt electrode coated with poly(2-methyl-8-quinolinol)-Cu(II) film: successive sweeps from 1st to 10th; (medium, 0.2M $LiClO_4$ adjusted to pH 4 with $HClO_4$; scan rate, 200 mV · sec^{-1}). (b) Voltammograms recorded at different scan rates with a polymer A-Cu(II) coated electrode. The scan rate (mV · sec^{-1}) is indicated for each curve; electrode surface, 2.5 cm^2.

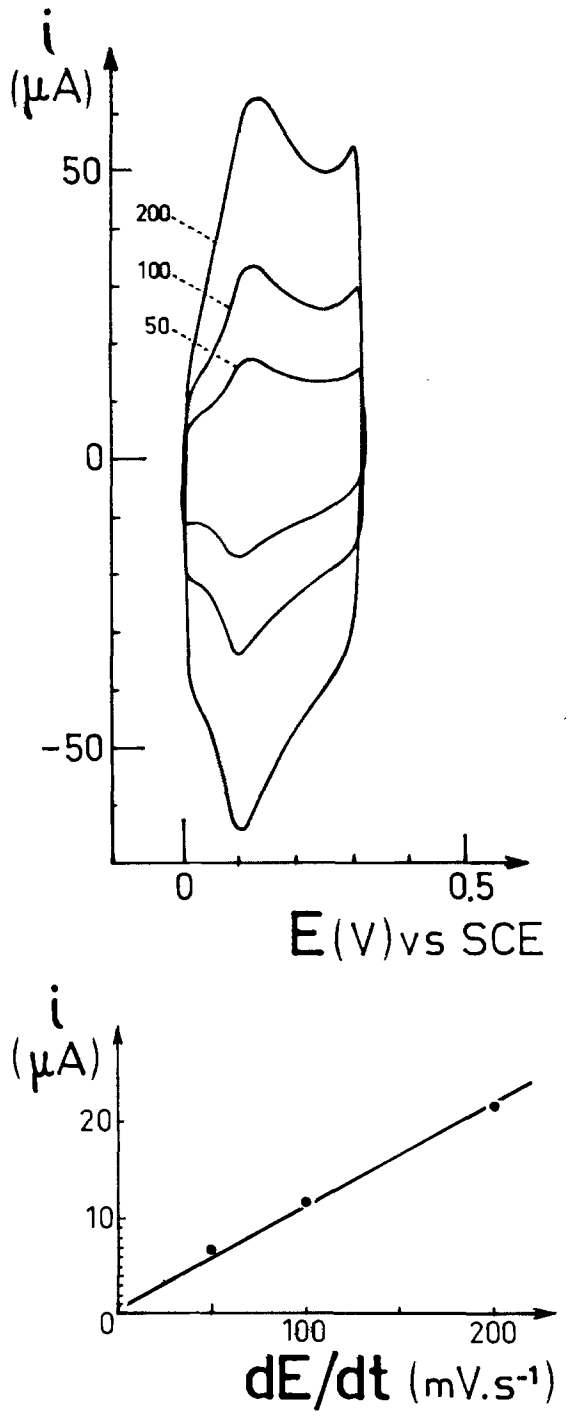

Fig. 5. Cyclic voltammograms recorded with a Pt electrode coated with poly(8-quinolinol)-Co(II) film. The scan rate is indicated for each curve (medium, 0.1M NaOH-H_2O; electrode surface, 2.5 cm^2).

Unlike the voltammograms of the film with a copper complex, that of a polymer B-Co(II) coated Pt electrode in 0.1M NaOH-H_2O indicates a reversible redox system. Indeed, in this case, "forming" occurs in a different way. The polymer B-Co(II)/polymer B-Co(III) redox system is perfectly well-defined provided there is a first potential cycle between 0 and 1.5V (SCE). As for the second sweep between 0 and 0.4V, the voltammogram is characteristic of a reversible redox system corresponding to the polymer B-Co(II)/polymer B-Co(III) couple at 0.12V (SCE). The peak currents are proportional to the scan rates (Fig. 5) and the width of the peak at half-height is 90 mV.

The polymer B-Co(II) film is very stable when immersed in water or organic solvents. When subjected to successive cyclic voltammetry scans between 0 and 0.3V at 200 mV sec^{-1}, the $Co_{2p3/2}$ signal detected by XPS diminishes by *ca.* 60% after 3 hr.

Integration of the current peaks shows that about 6×10^{-11} mol cm^{-2} of the cationic sites participate in the redox process. An approximate calculation achieved by considering the size of the moieties of the polymer (0.27 nm^2/molecule) yields a theoretical concentration of 6×10^{-10} mol cm^{-2}. Assuming that all the ligands of the polymer take part in the complexation, the maximum concentration of cationic sites would be *ca.* 3×10^{-10} mol cm^{-2} (two polymer moieties would form a complex with one cation according to the proposed structures). Thus one can estimate that for the polymer B-Co(II) complex, the equivalent of *ca.* a fifth of the layer in the vicinity of the electrode participates in the redox process, whereas for the polymer A-Cu(II) complex the equivalent of

ca. a dozen layers are involved. This would explain why $\Delta E_p = (E_{pa} - E_{po})$ is nil for the polymer B-Co(II)/polymer B-Co(III) couple and 150 mV for the polymer A-Cu(II)/polymer A-Cu(I) couple (11). This difference in behavior should probably be sought in the structure of the complexes. As shown previously, the cobalt in the polymer B-Co(II) complex can coordinate with five or six ligands of the polymer and water molecules, whereas the copper ion in the polymer A-Cu(II) complex can coordinate with four ligands of the polymer. In this tetracoordinate structure, the distances between the Cu(II) ions are more enhancing to the electron transfer between redox centers than in the complex with cobalt. The electron transfer within the polymer A-Cu(II) coating is probably electron hopping conduction, whereas within the polymer B-Co(II) coating probably only the cationic sites at the metal-film interface participate in the redox process. This interpretation is in keeping with the fact that the voltammograms of two electrodes coated with polymer-cobalt films of unequal thickness (60 and 10 nm) are identical ($\Delta E_p = 0$) and have the same current peak intensity.

Electrical Properties of Polymer A-Cu(II) and Polymer B-Co(II) Films

Dry state measurements of the conductivity of the Pt|film|Au capacitors also corroborate the results obtained by cyclic voltammetry.

For the polymer A-Cu(II) film, the concentration of Cu(II) can be made to vary. Like the variation in peak currents (Fig. 6a), the conductivity is highly dependent on Cu(II) concentration (Fig. 6b). With concentrations between 10^{-3} and 10^{-2}M of $CuCl_2$ solutions used to treat the polymer A films, the conductivity, like the peak current, is noticeably constant. In the 5×10^{-2}-10^{-1}M range, the conductivity increases abruptly from 5×10^{-10} to 5×10^{-7} Ω^{-1} cm^{-1}; likewise, the cathodic peak current increases from 18 to 230 μA cm^{-2}. For $CuCl_2$ solutions in concentrations greater than 10^{-1}M, the conductivity remains practically constant at 5×10^{-7} Ω^{-1} cm^{-1} and the cathodic peak current also stays at the maximum 230 μA cm^{-2}. These variations in current and conductivity show that the treatment with Cu(II) can lead to the fixation of a sufficiently high concentration of redox centers so that the charge transfer could occur within the thickness of the polymer A-Cu(II) film.

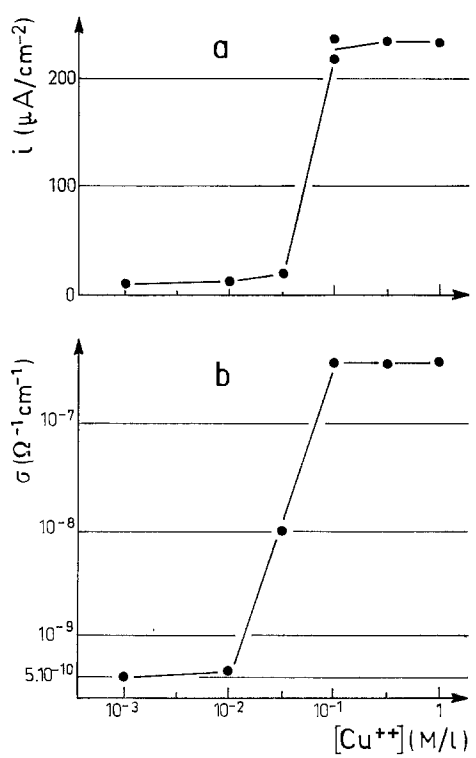

Fig. 6 (a). Peak current variation for a polymer A-Cu (II) coated electrode with $CuCl_2$ concentration of the solutions used in the treatment of the polymer films. (b) Conductivity variation of polymer A-Cu (II) film (in dry state) with $CuCl_2$ concentration in the treatment solutions.

For the polymer B-Co(II) film, the treatment of the polymer B film with $CoCl_2$ does not allow for variation of the Co(II) concentration in the film. The conductivity of the complexed film is ca. 10^{-10} Ω^{-1} cm^{-1}, which is identical to that of the untreated polymer B film. It is noteworthy that this value is the same as that of the polymer A-Cu(II) film with a low Cu(II) concentration.

Conclusion

Films with stable complexes formed by coordination of Cu(II) or Co(II) ions with ligands from quinolinol polymers have been obtained by chemically treating electrochemically obtained polymers. The structure of the poly(2-methyl-8-quinolinol)-Cu(II) complex seems to be tetracoordinate, whereas that of the poly(8-quinolinol)-Co(II) complex seems to be penta- or hexacoordinate. Indeed, the electrochemical behavior actually observed for these complexes would be appropriate for such structures. The more compact tetracoordinate structure enhances electron transfer by electron hopping conduction between redox centers, whereas with the penta- and hexacoordinate structures only the cationic sites at the metal-film interface take part in the redox process.

The results reported here indicate that aside from applications in analytic and electrocatalytic fields, films with metal ion complexes can provide fundamental insight into the electron transfer mechanism in polymer carriers. In view of these goals we are extending our research on stable metal ion complexes formed by the coordination of these ions with polymer ligands.

Manuscript submitted March 1, 1982; revised manuscript received ca. June 15, 1982. This was Paper 624 presented at the Montreal, Quebec, Canada, Meeting of the Society, May 9-14, 1982.

Any discussion of this paper will appear in a Discussion Section to be published in the December 1983 JOURNAL. All discussions for the December 1983 Discussion Section should be submitted by Aug. 1, 1983.

REFERENCES

1. (a) J. Zagal, R. K. Sen, and E. Yeager, *J. Electroanal. Chem. Interfacial Electrochem.*, **83**, 207 (1977); (b) J. Zagal, C. Fierro, and R. Rozas, *ibid.*, **119**, 403 (1981).
2. (a) R. Nowak, F. A. Schultz, M. Umana, H. Abruna, and R. W. Murray, *ibid.*, **94**, 219 (1978); (b) R. D. Rocklin and R. W. Murray, *ibid.*, **100**, 271 (1979).
3. (a) N. Oyama and F. C. Anson, *J. Am. Chem. Soc.*, **101**, 739 (1979); (b) N. Oyama and F. C. Anson, *This Journal*, **127**, 640 (1980); (c) J. P. Collman, P. Denisevich, Y. Konai, M. Marrocco, C. Koval, and F. Anson, *J. Am. Chem. Soc.*, **102**, 6027 (1980).
4. J. M. Calvert and T. J. Meyer, *Inorg. Chem.*, **20**, 27 (1981) and references cited therein.
5. C. M. Elliott and C. A. Marrese, *J. Electroanal. Chem. Interfacial Electrochem.*, **119**, 395 (1981).
6. (a) H. Behret, H. Binder, G. Sandstede, and G. G. Scherer, *ibid.*, **117**, 29 (1981); (b) H. Behret, G. Sandstede, G. G. Scherer, and H. G. Schomann, *ibid.*, **117**, 339 (1981).
7. F. Bruno, M. C. Pham, and J. E. Dubois, *Electrochim. Acta*, **22**, 451 (1977).
8. (a) M. C. Pham, P. C. Lacaze, and J. E. Dubois, *J. Electroanal. Chem. Interfacial Electrochem.*, **86**, 147 (1978); (b) M. C. Pham, P. C. Lacaze, and J. E. Dubois, *ibid.*, **99**, 331 (1979); (c) M. C. Pham, P. C. Lacaze, and J. E. Dubois, *ibid.*, **117**, 233 (1981).
9. G. Tourillon, J. E. Dubois, and P. C. Lacaze, *J. Chim. Phys.*, **74**, 685 (1977).

10. J. E. Dubois, P. C. Lacaze, and G. Tourillon, *Thin Solid Films*, **65**, 83 (1980).
11. M. C. Pham, G. Tourillon, P. C. Lacaze, and J. E. Dubois, *J. Electroanal. Chem. Interfacial Electrochem.*, **111**, 385 (1980).
12. U. Gelius, P. F. Haden, J. Hedman, B. J. Lindberg, R. Manne, R. Nordberg, C. Nordling, and K. Siegbahn, *Physica Scripta*, **2**, 70 (1970).
13. J. P. Contour and G. Mouvier, *J. Electron. Spectrosc.*, **7**, 85 (1975).
14. R. Nordberg, R. G. Albridge, T. Bergmark, U. Ericson, J. Hedman, C. Nordling, K. Siegbahn, and B. J. Lindberg, *Ark. Kem.*, **18**, 257 (1967).
15. D. Briggs, "Heyden Handbook of X-Ray and Ultraviolet Photoelectron Spectroscopy," London (1978).
16. R. R. Gagne, J. L. Allison, C. A. Koval, W. S. Mialki, T. J. Smith, and R. A. Walton, *J.Am. Chem. Soc.*, **102**, 1905 (1980).
17. B. Barbaray, Third Cycle Thesis, Universite Paris 7 (1977).
18. D. M. Adams, "Metal Ligands and Related Vibrations," p. 284, Edward Arnold Publishers, London (1967).
19. R. J. H. Clark and C. S. Williams, *Inorg. Chem.*, **4**, 350 (1965).

Photoelectrochemical Properties of Polycrystalline TiO_2 Thin Film Electrodes on Quartz Substrates

S.-E. Lindquist,* B. Finnström, and L. Tegnér*

Institute of Physical Chemistry, University of Uppsala, S-751 21 Uppsala, Sweden

ABSTRACT

Thin film electrodes of TiO_2 have been prepared by vapor deposition of Ti on a quartz substrate followed by partial oxidation to leave a thin Ti layer as back-side contact. The electrodes were characterized for their photoelectrochemical activities both on illumination through the electrolyte and through the substrate (back-side illumination). The transparent substrate made it possible to record the action spectrum for back-side illumination down to 250 nm. Simple theory has been used to estimate bandgap, flatband potential, and doping density. Observed bandshifts in the action spectra due to changes in doping density and electrode potential have been shown to be in accordance with theory.

During the last decade much interest has been devoted to TiO_2 as a semiconducting photoanode in photoelectrochemical cells with the aim of finding a material suitable for the production of hydrogen from water using light as the energy source. Studies have been performed on single crystals of rutile structure (1-7) and on polycrystalline material either as a sintered powder (7-9) or as thin layers of TiO_2 films (10-22). Experiments to extend the photoresponse into the visible region by doping have also been reported (6-13).

Thin film electrodes of TiO_2 have been prepared by chemical vapor deposition (CVD) and radio-frequency sputtering (16-22). Möllers *et al.* (19) sprayed titanium acetylacetone onto a hot substrate of titanium sheet metal or glass plates covered with a conducting SnO_2 layer. Fleischauer and Allen (22) prepared photosensitive anodes by radio-frequency sputtering of TiO_2 onto a glass plate coated with a thin layer of Sn-doped In_2O_3.

In the present work, thin film electrodes of TiO_2 have been prepared from vapor-deposited titanium on quartz-glass substrates. The titanium films were treated in pure oxygen at elevated temperatures in the range 400°-650°C.

No special transparent back-side contact layer was used. Instead a very thin film of Ti was left after the oxidation which allowed investigation of the spectral response even for "back-side" illumination down to 250 nm. This extension of the spectral range made feasible a more complete analysis of the action spectra of the TiO_2 thin film electrodes.

Theory

Since thin film semiconducting electrodes on transparent substrates can be illuminated from either side the following assignations are made: EE, light incident upon the electrolyte-electrode interface and SE, light incident upon the substrate-electrode interface.

Light incident upon the electrolyte-electrode interface (EE).—Elaborated models, taking surface recombination, reaction kinetics at the interface, recombination in the space charge region, etc. into account, have been worked out (23-28). As a limiting case at high transfer velocity (27) most of these models reduce to the well-known Gärtner-Butler expression (29, 30). To unify the description of the experimental data we have chosen to reduce the number of adjustable parameters and present our results in terms of this simple model. Deviation and reasons for deviation from the theoretical model are discussed further on.

The quantum efficiency ϕ_{EE} is, according to the Gärtner-Butler model expressed by

$$\phi_{EE} = 1 - \frac{1}{1 + \alpha L_p} \exp(-\alpha w) \qquad [1]$$

where α is the optical absorption coefficient, L_p the diffusion length of the minority carrier (holes in the case of an n-doped semiconductor), and w the depletion layer width given by

$$w = \left(\frac{2\epsilon\epsilon_0}{eN_D}\right)^{1/2} (U - U_{FB})^{1/2} = w_0 (U - U_{FB})^{1/2} \qquad [2]$$

Here the band bending is expressed by the difference between the electrode potential U and the flatband potential U_{FB}, ϵ is the relative dielectric constant, ϵ_0 is the permittivity of free space, N_D is the donor concentration, and e the elementary charge.

For small values of α the exponential factor in Eq. [1] can be expanded in a Taylor series and one obtains after simplification

$$\frac{1}{\phi_{EE}} = \frac{1}{L_p + w}\left(\frac{1}{\alpha} + L_p\right) \qquad [3]$$

As shown by Butler (30), Eq. [1] can be combined with (31)

* Electrochemical Society Active Member.
Key words: photoelectrolysis, polycrystalline, semiconductor, thin film, tunneling.

$$\alpha = A\frac{(h\nu - E_g)^{n/2}}{h\nu} \qquad [4]$$

which assuming $\alpha L_p << 1$ gives

$$(-h\nu \ln|1 - \phi_{EE}|)^{n/2} = S_n(h\nu - E_g) \qquad [5]$$

In Eq. [4] and [5] A is a constant and E_g the bandgap energy, ν the freqency of light, h Planck's constant, and $S_n = (Aw)^{2/n}$. The value of n depends on whether the optical transition is direct ($n = 1$) or indirect ($n = 4$). In the case of an indirect transition and after insertion of Eq. [2] one obtains

$$S_4^4 = (A \cdot w_o)^2(U - U_{FB}) \qquad [6]$$

Light incident upon the substrate-electrode interface (SE).—For the case of back-side illumination the following expression (32) applies

$$\phi_{SE} = \frac{1}{1 - \alpha L_p}\exp[-\alpha(d - w)] - \exp[-\alpha d] \qquad [7]$$

where d is the thickness of the semiconductor.

By differentiating Eq. [7] (assuming $\alpha L_p << 1$) the extreme values of ϕ_{SE} can be found:

1. Maxima or minima are found for $d\alpha/d\lambda = 0$, that is for all extreme values of the absorption coefficient.
2. Maxima appear in ϕ_{SE} when

$$w/d = 1 - \exp(-\alpha_{max}{}^* w) \qquad 0 < w/d < 1 \qquad [8]$$

is satisfied. Here $\alpha_{max}{}^*$ denotes the absorption coefficient at the wavelength where ϕ_{SE} has a maximum value. If $\alpha L_p << 1$ a comparison of Eq. [1] and [8] shows that

$$w/d = \phi_{EE} \qquad [9]$$

at this wavelength. Consequently if d can be determined independently, a combination of results of measurements made for the two cases of illumination EE and SE gives information about the depletion layer width.

Rearranging Eq. [8] to $\ln|1 - w/d| = -\alpha_{max}{}^* w$ and expanding the left-hand side in a Taylor series (two terms) gives after insertion of Eq. [2]

$$\alpha_{max}{}^* = -\frac{w_o}{d^2}(U - U_{FB})^{1/2} + \frac{1}{d} \qquad [10]$$

As can be seen from Eq. [10] the value of $\alpha_{max}{}^*$ is dependent on w_o, the film thickness d and the band bending $U - U_{FB}$. Thus if α changes monotonically in a wavelength interval, one expects a shift in the position of the maximum $\phi_{SE}{}^{max}$ of the quantum efficiency if any of the parameters is changed. If, *e.g.*, $d\alpha/d\lambda < 0$ the shift of $\phi_{SE}{}^{max}$ will be toward shorter wavelengths when U is increased. In the limit of very small ratios w/d, $\alpha_{max}{}^*$ will be given by

$$\alpha_{max}{}^* = \frac{1}{d} \qquad [11]$$

Materials

Titanium, Ti(Tec) technical quality contains, according to the producer, traces of O (0.07%), Fe (0.03%), N (0.007%), and C (0.002%).

Titanium, Ti (Pure), Kock-Light van Arkel (99.9%).

Chromium, Highways (99.998%).

Aluminum, technical quality.

Na_2SO_4, Anhyd, CP Baker's Analyzed.

For etching a solution of 20% hydrofluoric acid, 30% nitric acid, and 50% deionized water was used (15).

Oxygen, 2.8 AGA Special Gas.

Apparatus

The instrumental arrangement is shown in Fig. 1. The light source was a 450W xenon lamp (Osram XBO). Its output passed through a 40 mm water filter into a high intensity grating monochromator (Schoeffel GM252) with a grating blazed at 240 nm and with 1180 groves/mm and an analogous readout for scanning. The image of the exit slit was focused onto the surface of the working electrode (WE) of the photoelectrolysis cell. To eliminate the effect of stray light passing through the monochromator, a Schott filter UG5 was used when measurements were performed at wavelengths shorter than 350 nm. A cutoff filter (Schott GG15) was used when action spectra were registered in the wavelength region above 400 nm.

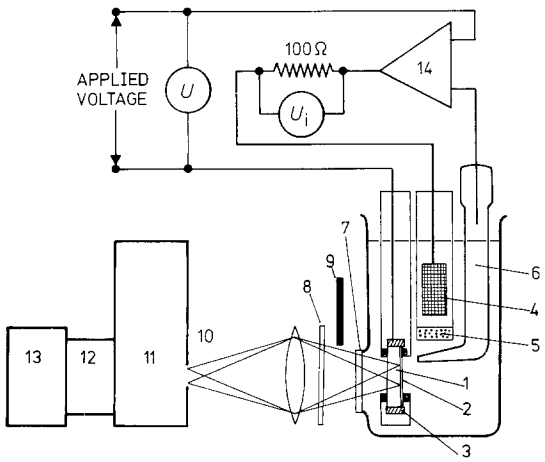

Fig. 1. Photoelectrolysis apparatus with side view of cell. 1, O-ring sealed quartz glass substrate; 2, TiO_2 thin film anode (WE); 3, Mercury contact; 4, Pt electrode (CE); 5, glass filter; 6, saturated calomel electrode (SCE); 7, optically flat quartz window; 8, optical filter; 9, shutter; 10, exit slit of monochromator; 11, high intensity monochromator; 12, water filter; 13, 450W xenon lamp; 14, operational amplifier.

The light entered the cell (see Fig. 1) through an optically flat fused quartz (Suprasil) window. The circular quartz substrate ($\phi = 20$ mm) with the thin film working electrode was mounted in a plexiglass holder exposing the central film area (~ 1.8 cm^2) to the electrolyte. Ohmic contact was made at the periphery of the film with mercury. The edge of the substrate and the mercury was sealed from contact with the electrolyte by Viton O-rings. The holder could be turned through 180° so that the light beam could enter the electrode film from either side.

The cell was equipped with a platinum net counter-electrode (CE) (area ~ 3 cm^2) separated from the reference electrode (RE) and WE by a glass filter (No. 1). A calibrated saturated calomel electrode (SCE) (0.242 ± 0.001V) served as the RE. The light intensity was measured in the position of the WE with an optical power meter (Photodyne, Model 44XL with a silicon photodiode Model 450 AS radiometric sensor head. Calibration accuracy ± 10%, reproducibility ± 0.5%). The potential U of the working electrode relative to SCE was controlled by a potentiostat. The photocurrent between the WE and CE was measured as a potential drop U_i over a 100Ω external resistance. The potentials were displayed on two Keithley microvolt digital multimeters Model 177 or fed to a Hewlett Packard Model 7044A X-Y recorder. All current-potential curves were registered (usually point by point) from negative to positive potentials.

Absorbance and reflectance spectra were recorded on a Zeiss DMR 10 spectrophotometer (range 200-800 nm) and on a Beckman DK 2A spectrophotometer (range 400-2500 nm). The reflectance measurements were performed with a specially constructed reflection assembly.

The TiO_2 electrode surfaces were analyzed by using an x-ray powder diffractometer (Philips PW 1050), while powder scratched from the surface of the electrodes was examined in an x-ray powder diffraction Guinier-Hägg focusing type. In both cases monochromatic $CuK\alpha_1$ radiation was employed.

Preparations

In the case of titanium films on quartz plates the metals were evaporated in vacuum (at ~ 1 mPa) from point sources (hair pin filaments) on electrically heated tungsten wires and condensed onto the substrate. Typical condensation rates were ~ 20 nm min^{-1}. The substrates were pretreated in the etching solution (see Materials) for ~ 10 sec and rinsed with deionized water before being placed in the vacuum chamber. In the case of simultaneous evaporation of Al (or Cr) and Ti, the relative composition of the film was controlled by a rotating disk with a slit between the sources and the substrate and by their relative distance. In these experiments Ti (Pure) was used. No attempt was made to keep a constant evaporation rate. To get as homogeneous a composition as possible, the amount on each point source was matched and only partly evaporated. The metal films produced were smooth and bright and showed almost neutral spectra (see Fig. 2).

The thermal oxidation of the Ti films and Ti metal plates was carried out as follows: the preparations were placed in an evacuated quartz tube at a pressure < 10 mPa and introduced into a preheated oven. After 12-15 min when temperature equilibrium had been established, oxygen was introduced. After a predetermined time the oxygen was pumped off and the evacuated tube was removed from the oven. The temperature was measured with a Pt/Pt, Rh (10%) thermocouple close to the sample(s). The gradient along the largest sample (20 mm) was less than 2° at 408°C, which was the temperature most frequently used. Typical oxygen pressure was 13.3 kPa. No systematic investigation of the TiO_2 film depth as a function of temperature and oxidation time was made. Single observations, however, were in agreement with those reported by Hass (33).

The thickness of the TiO_2 films was determined from the interference fringes of the reflection spectra recorded in the range 400-2500 nm. In the calculation of the film thickness, the refractive index of TiO_2 (rutile) given by Hass (33) was used.

From experiments on a great number of preparations (*ca.* 40), only data from a few but typical are presented in detail. Table I summarizes some essential properties of the TiO_2 films and conditions of their fabrication.

Characterization of the TiO_2 Thin Film Electrodes

According to Hass (33) TiO_2 layers prepared by oxidation of pure titanium films at 400°-450°C in air are of rutile structure. The present x-ray analysis of the thin films produced around 400°C gave no information about the crystal structure, probably due to the small crystal sizes. Samples treated at 650°C gave typical TiO_2 rutile lines. Transmission electron microscopy (TEM) pictures of self-supporting thin films indicate an increasing crystal size with time of oxidation.

Table I. Some essential parameters for the TiO_2 electrodes used in the present work. Common parameters for all electrodes are oxidation temperature 408°C and oxygen pressure 13.3 kPa (100 mm Hg). The final film thickness (when all Ti in the film has been converted to TiO_2) is estimated from the interference pattern of the reflection spectra. Refractive index from Hass (33) was used in the calculations.

Preparation No.	Material	Substrate	Oxidation time (hr)	Final film thickness of TiO_2 (nm)	Remarks
1a	Ti (Tec)	Quartz	1+1+3+16	4_3	Last 21 hr at 505°C
1b	Ti (Tec)	Quartz	1+1+3+16 +21	16_8	Last 21 hr at 505°C
2a	Ti (Tec)	Quartz	3	5_8	Back-side contact of Al
2b	Ti (Tec)	Quartz	3	5_3	Back-side contact of Al
3a	Ti (pure)	Quartz	2		
3b	Ti (pure)	Quartz	2		Cr doped
3c	Ti (pure)	Quartz	2		Al doped

Results and Discussion

Absorption and action spectra.—Curves showing absorption and photoresponse spectra at six different oxidation times for two Ti(Tec) thin films (Preparation 1a and 1b) on the same quartz substrate are presented in Fig. 2 and 3, respectively. Figure 2 shows how the almost neutral spectrum of titanium gradually disappears and how an absorption band corresponding to TiO_2 builds up in the wavelength region below 400 nm. Interference fringes in the transparent region ($\lambda >$ 400 nm) of TiO_2 can be observed for the fully oxidized films. Note in Fig. 2 (Preparation 1a) the slight difference between curve 5 which shows a spectrum of an electrode with good photoresponse (see Fig. 3) and curve 21 which shows the spectrum of a completely oxidized Ti film with no photoresponse. The absorption coefficient α was estimated from three fully oxidized TiO_2 films of the following thicknesses: 43, 150, and 168 nm. Curve c in Fig. 4 is fitted to the experimental points (mean values) and extended to 400 nm by application of Eq. [4]. $\alpha = 1.0 \cdot 10^7$ m^{-1} at λ = 335 nm

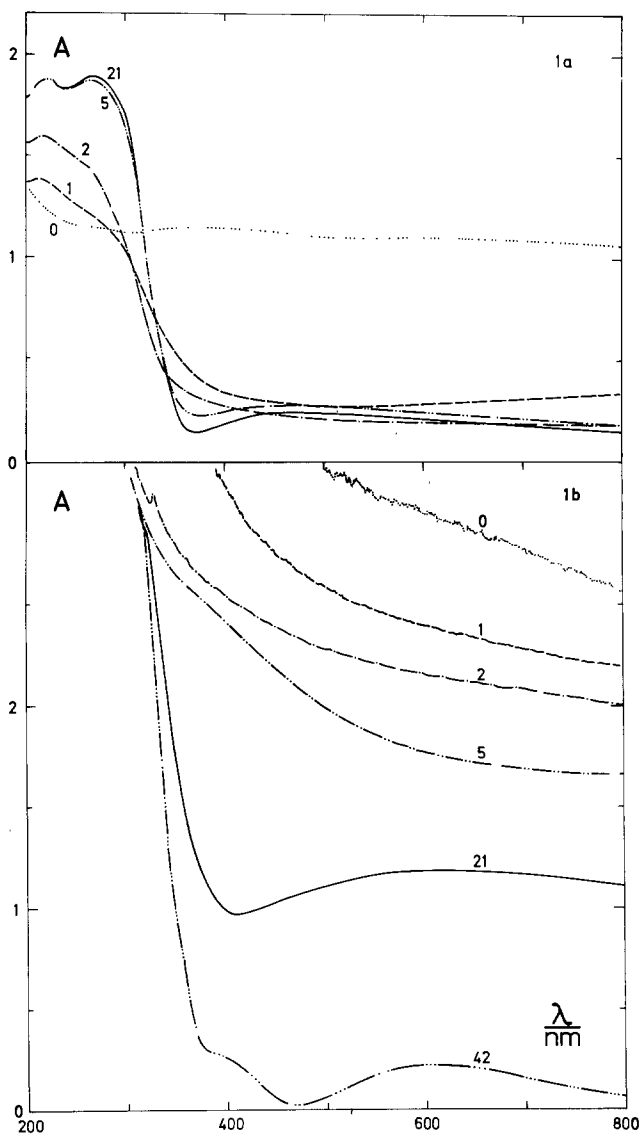

Fig. 2. Absorbance, *A*, of two thin films 1a and 1b on the same quartz substrate cumulatively oxidized in oxygen at 408°C and 100 mm Hg (13.3 kPa). Reference: quartz plate. The numbers on each curve show oxidation time in hours. For film 1b the last 21 hr of oxidation took place at 505°C. Final thicknesses of the films were $d_{1a} = 4_3$ nm and $d_{1b} = 16_8$ nm.

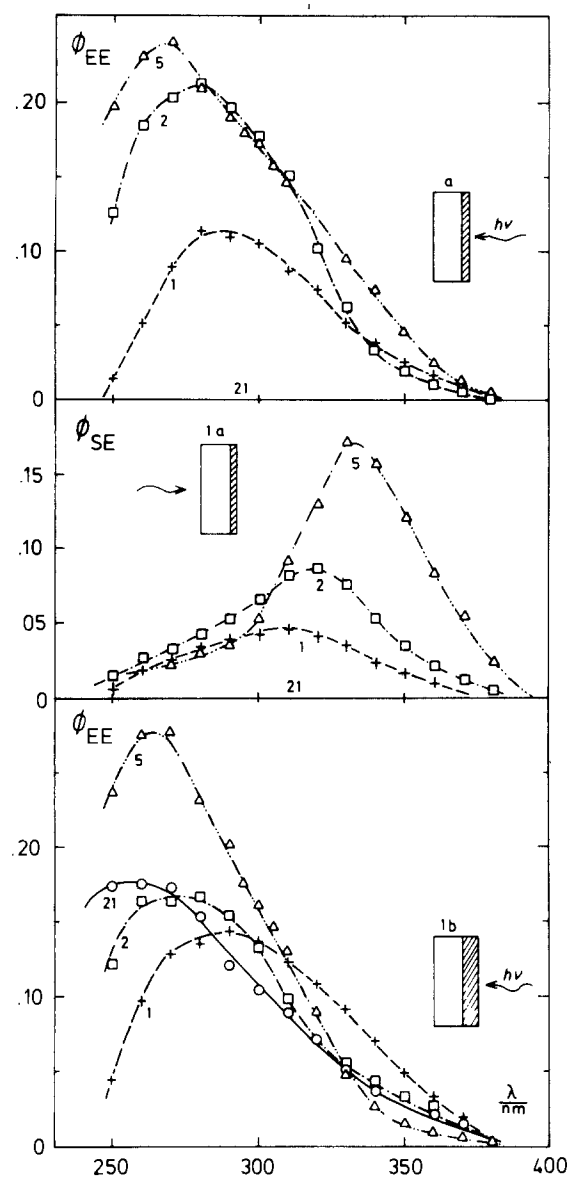

Fig. 3. Action spectra for the films 1a and 1b recorded with a bandwidth (FWHM) of 6.7 nm. The incidence of light is evident from the small sketch in each figure. The oxidation times (in hours) are indicated by the numbers on each curve. The potential of WE vs. SCE was kept constant at 1.00V.

and $E_g = 4.89 \cdot 10^{-19}$ J (3.05 eV) were used to adjust the calculated part of the curve to the experimental data. A value $A = 5.5 \cdot 10^{26}$ m^{-1} J^{-1} was thus obtained.

Parameters influencing the photoresponse of the TiO_2 thin film electrodes.—The properties of the TiO_2 films formed in the oxidation process depend on a number of parameters such as the nature of the underlying substrate, the initial Ti film thickness, the concentration and nature of impurities, the oxidation atmosphere, the temperature, and time in the oxidizing environment.

The TiO_2 films produced showed photoresponse directly after the oxidation period. No subsequent treatment in a reducing atmosphere was made. For some of the very thin films (< 50 nm) the photoresponse diminished when oxygen was bubbled through the electrolyte and when they were subjected to long time measurement series.[1]

Impurity doping.—Figure 5 shows that the TiO_2 electrodes made from thin films of Ti (Pure) on quartz

[1] Aging effects in defect-doped semiconducting electrodes have been reported [cf. Butler (34) for references].

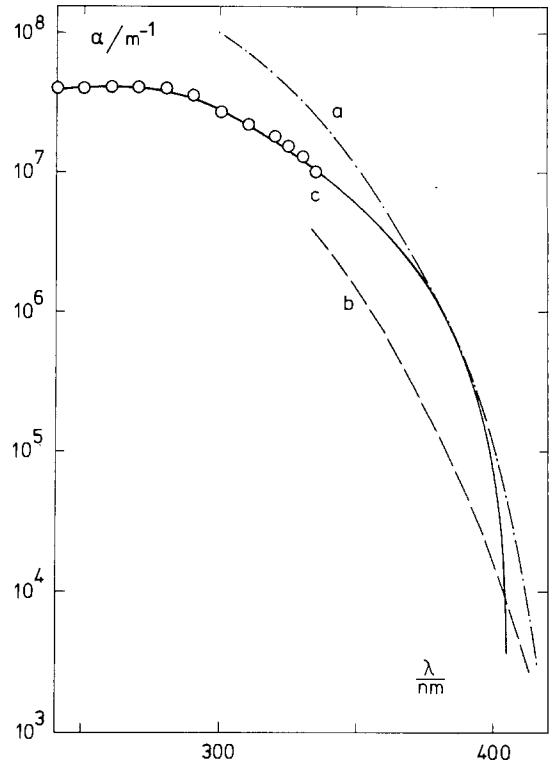

Fig. 4. The absorption coefficient of TiO_2 as a function of wavelength. Curve c has been fitted to experimental data [O] and extended to 400 nm, as described in the text. Curves a and b from Ref. (35) and (19).

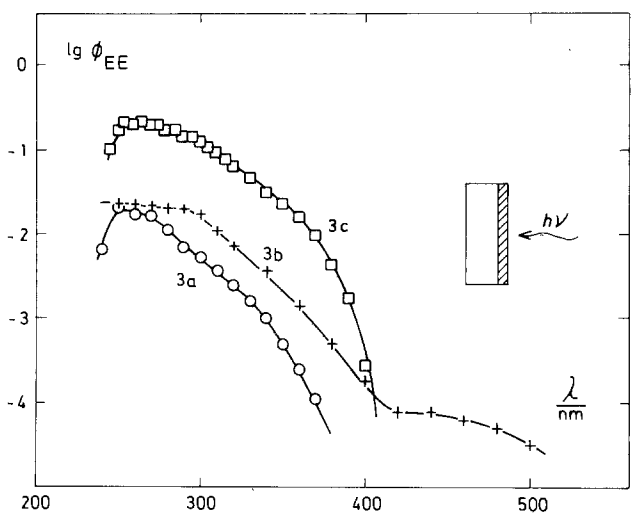

Fig. 5. Action spectra of thin film TiO_2 electrodes oxidized in pure oxygen for 2 hr at 408°C and 100 mm Hg (13.3 kPa). 3a, no doping; 3b, Cr-doped; and 3c, Al-doped. Light incident upon the electrolyte-electrode interface (EE).

substrates have a much lower photoresponse than such electrodes doped with Al or Cr. Similarly, TiO_2 films made from TiO_2 (Tec), containing Fe, gave good quantum efficiencies in the range 250-400 nm. These results are in agreement with the observations of Ghosh and Maruska (6) on single crystals of TiO_2 of rutile structure and with the results of Augustynski *et al.* (14) on polycrystalline mixed oxides of TiO_2-Al_2O_3. Thin films doped with Cr showed the same spectral broadening toward the visible region as has previously been reported (6, 7, 9, 11-13).

Bandshifts in the action spectra upon increased oxidation.—By varying only the oxidation period, some

general trends in the development of the TiO_2 films can be distinguished. As the oxidation proceeds the grain size and film depth (33) increase while the number of oxygen vacancies (or donor sites) in the TiO_2 lattice decrease, which (at a given working electrode potential) results in an extension of the depletion layer. Figure 3 shows the action spectra of Preparations 1a and 1b registered with the WE fixed at 1V *vs.* SCE. Both films were formed on the same quartz disk and oxidized at 408°C at the time intervals shown in Table I. The distinctive features of the spectra in case of EE (light incident on the TiO_2/electrolyte interface) upon increased oxidation are: (*i*) an increased quantum efficiency in the short wavelength region and (*ii*) a shift of the maximum toward shorter wavelength.

With reference to the general trends in the development of the TiO_2 films given above one can expect very narrow barriers (*vide infra*, Table II) in the initial steps of oxidation. Tunneling of the electrons from the interior of the semiconductor to the surface is a probable process and it should be most significant for electrons photoexcited to the conduction band in the immediate vicinity of the TiO_2 surface. As oxidation proceeds the barrier region is broadened. The increase in quantum efficiency (see Fig. 3) will thus be most pronounced in the short wavelength region (250-280 nm) where the TiO_2 absorption coefficient is largest.

If the TiO_2 films are very thin, electron-hole pairs generated in the barrier region at the Ti/TiO_2 interface may also contribute to the photocurrent. The anomalous behavior of the action spectra in the long wavelength region ($\lambda > 330$ nm), especially the high quantum efficiency at short oxidation times, may be attributed to such a "double barrier." Application of the Gärtner-Butler model for very thin films is thus not suitable.

With longer oxidation periods the maximum ϕ_{SE}^{max} is displaced toward longer wavelengths, while at the same time the overall quantum efficiency is increased (Fig. 3). These changes can qualitatively be explained as follows: as oxidation proceeds, thicker layers are formed and the almost wavelength independent absorption in the Ti back-side contact is replaced by the strongly wavelength dependent absorption in TiO_2. With an increased TiO_2 film depth the ratio w/d will also decrease and Eq. [11] will apply. As ϕ_{SE}^{max} appears in a wavelength region where $d\alpha/d\lambda < 0$, a red shift will be observed.

The observed band shifts in the action spectra of the thin films, both in the case of EE and SE, contrast with the results of Möllers *et al.* (19). Using the CVD technique they produced somewhat thicker TiO_2 electrodes (100-1000 nm) than the films used in the present work. A conducting layer of SnO_2 served as the back-side contact in their samples. In the case of EE they observed a red shift with increasing film thickness and in the case of SE reported that "the highest yield in photocurrent is obtained if the electron-hole pair is created near the back-side contact" since "the spectral distribution of the photocurrent is independent of the thickness of the TiO_2-layer and its maximum occurs in the shorter wavelength range." Preliminary measurements made at our laboratory on thick (50-3000 nm) TiO_2 layers produced by thermal oxidation of Ti-plates give (in the case of EE) results in good agreement with those of Möllers *et al.* Estimated depletion layer widths in these preparations are, however, much larger (10-150 nm, at a working electrode potential of 1V *vs.* SCE) than in Preparations 1a and 1b. Such wide barriers make tunneling of photoexcited electrons through the barrier insignificant.

Onset voltage.—As can be seen from Fig. 6 the "apparent onset voltage" for thin film electrodes made from Ti (Tec) are shifted to higher potentials with increasing oxidation time. There is no significant difference in the onset voltage of the ϕ *vs.* U curves[2] for a film continuously oxidized for 5 hr, compared to a film oxidized for 5 hr at various time intervals (such as 1a and 1b) if the conditions are otherwise the same. An Al-doped Ti (Pure)-thin film (Preparation 3c) oxidized at 408°C for 2 hr gave, however, a much lower onset voltage (− 0.3V *vs.* SCE, pH = 5.7) (*vide infra*, Fig. 11).

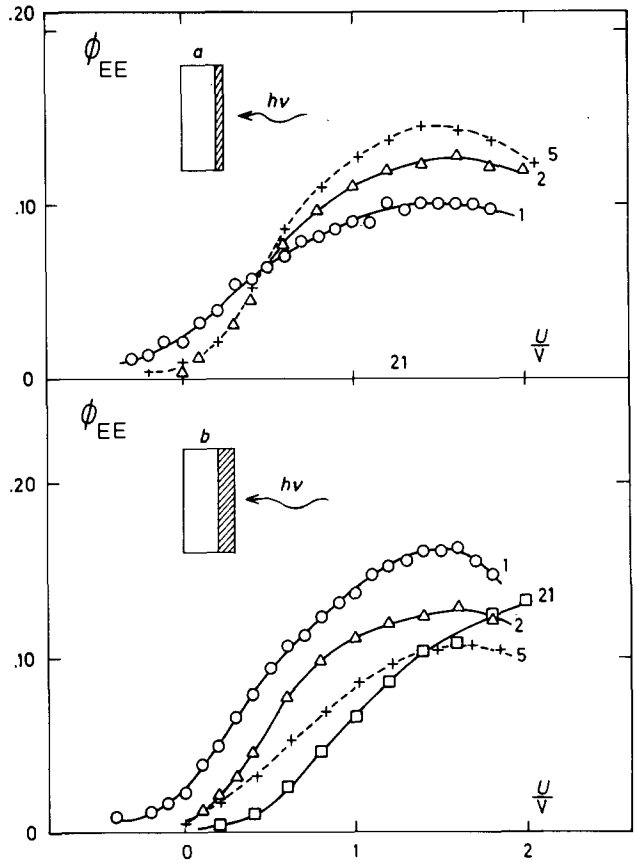

Fig. 6. The quantum efficiency ϕ at a constant wavelength of 320 nm as a function of the potential U (vs. SCE) of the working electrode. The measurements were made on the same thin films 1a and 1b as represented in Fig. 2 and 3. Electrolyte 0.2M Na_2SO_4, pH = 5.7. The numbers on each curve denote oxidation times in hours (pure oxygen, 13.3 kPa) at 408°C.

The same results of Al-doping have earlier been obtained by Ghosh and Maruska (6) who also give a brief discussion in which they try to explain the effect.

Determination of w and E_g.—The calculations are demonstrated on measurements made on two TiO_2 (Tec)-thin films, Preparations 2a and 2b on the same quartz substrate. The films were identical (see Table I) with the exception that 2b was furnished with a thin back-side contact of aluminum. The Ti films were oxidized to near full transparency in the visible region of the spectrum.

Figure 7 shows quantum efficiencies of Preparations 2a and 2b represented in accordance with Eq. [5]. A least squares fit of the straight line to the experimental points for $\lambda > 330$ nm gives a bandgap of $4.9_1 \cdot 10^{-19}$ J (3.06 eV). From the slope $S = (Aw)^{1/2}$, a depletion layer width, w, of 8 nm was estimated using the value $A = 5.6 \cdot 10^{26}$ m^{-1} J^{-1} as calculated from Eq. [4] by the insertion of $E_g = 3.06$ eV and $\alpha = 1.0 \cdot 10^7$ m^{-1} at $\lambda = 335$ nm derived from Fig. 4.

Band shifts in the action spectra due to variations in working electrode potential.—Equation [10] predicts

[2] It should be mentioned that the quantum efficiencies given in the present work have not been corrected for reflection losses at the interfaces electrolyte/TiO_2 (case EE) and at the interfaces quartz/Ti and Ti/TiO_2 in the case of SE.

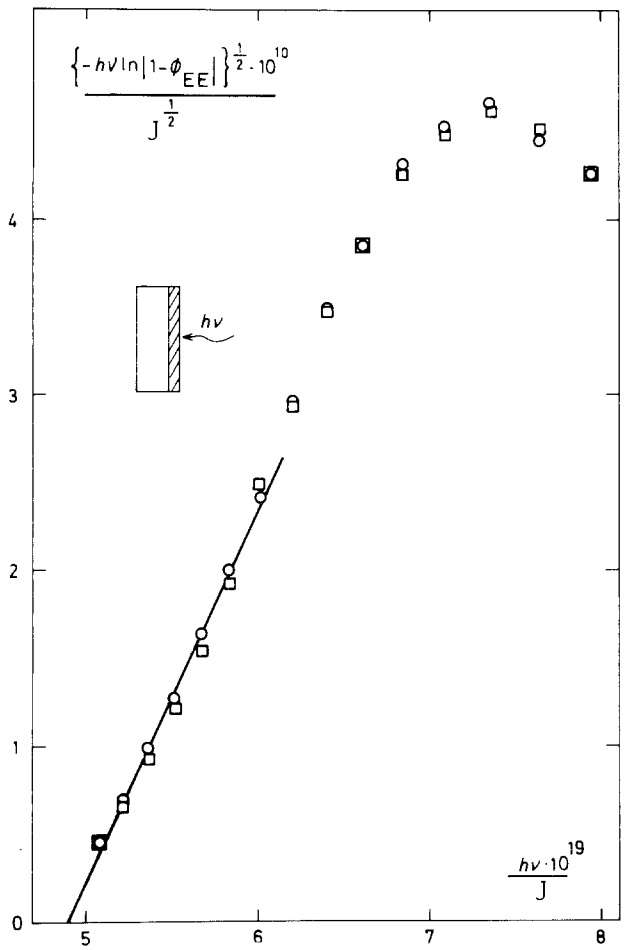

Fig. 7. Preparation 2a and 2b. Data represented in a plot based on Eq. [5]. For $\lambda > 330$ nm a least squares fit of a straight line to the experimental points (□ with ○ without back-side contact of aluminum) indicates an indirect optical transition corresponding to a bandgap of $4.9_1 \cdot 10^{-19}$J (3.06 eV). The slope gives a depletion layer width of 7.7 nm U(vs. SCE) = 1.00V.

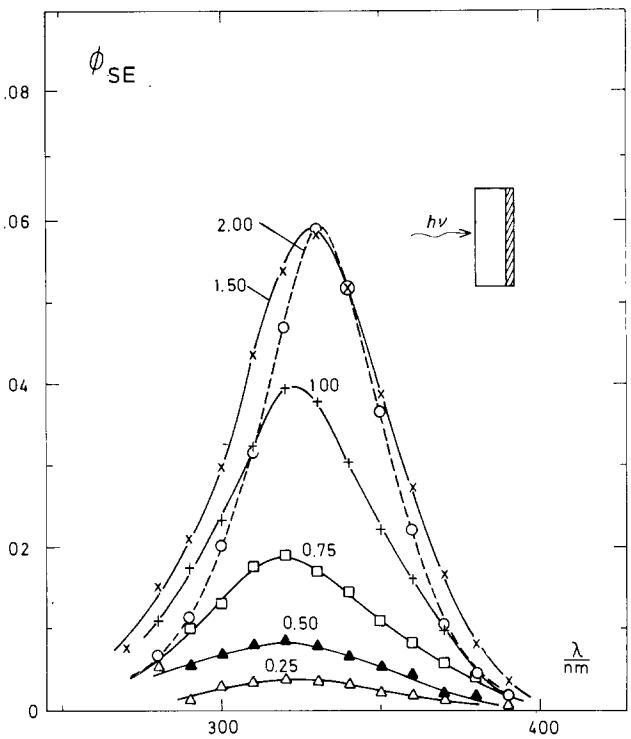

Fig. 8. The quantum efficiency, ϕ, as a function of wavelength at six different potentials U (vs. SCE) of a thin film (Preparation 2a) TiO_2 electrode illuminated from the substrate side (SE). Electrolyte 0.2M Na_2SO_4, pH = 5.7. NB: the red shift of the maximum with increasing U.

that, for a given film illuminated from the substrate side (case SE), α_{max}* should decrease with increasing values of U. A set of experiments was performed on the two thin films of TiO_2 (Tec) Preparations 2a and 2b as mentioned above.

Figure 8 shows the quantum efficiency as a function of wavelength in the case of back-side illumination for film 2a in a series of measurements in which U (vs. SCE) was varied. The predicted shift of the maximum point with increased value of U is confirmed (See Theory after Eq. [10]). The shift is minor indicating that the ratio w/d is small, and that Eq. [10] is closely approximated by Eq. [11]. Precise quantitative information in accordance with Eq. [10] cannot be expected from the experiment. A value of d can, however, be calculated from Eq. [11]. Taking $\alpha = 1.8 \cdot 10^7$ m^{-1} (Fig. 4), corresponding to the maximum point for the lowest curve $U = 0.25$V at $\lambda = 320$ nm (Fig. 8), gives $d = 5_6$ nm which is close to $d = 5_3$ as estimated from interference fringes in the reflection spectrum on the same film.

Figure 9 shows experimental points of ϕ vs. λ for EE and SE illumination together with theoretical curves calculated from Eq. [1] and [7] using the values of $w = 7.5$ nm, $L_p = 0$, and $d = 70$ nm. The value of w is seen to be in good agreement with the value obtained from Fig. 7 as given above. The value of d, however, is somewhat large compared to $d = 5_3$ nm estimated from the interference fringes in reflection measurements for the fully oxidized film and $d = 5_6$ nm obtained from the position of the maximum point ϕ_{SE} vs. λ curve (see above). The discrepancy can at least

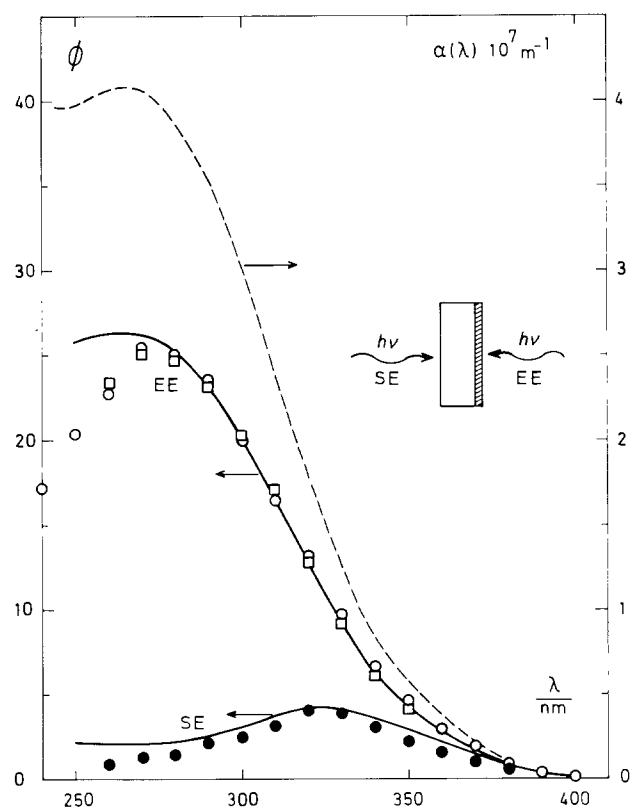

Fig. 9. Preparation 2a and 2b. The measured (□, ○, ●) and calculated (solid lines) quantum efficiency spectra depicted together with the absorption coefficient spectrum (dashed line) of TiO_2. Light incident upon the substrate-TiO_2 interface (SE) ● and upon the electrolyte-TiO_2 interface (EE) with □ and without ○ back contact of Al. Calculated curves are based on Eq. [1] and [7] with $d = 70$ nm, $w = 7.5$ nm, $L_p = 0$ nm. U (vs. SCE) = 1.00V.

partly be explained by the reflection and absorption losses at the back-side contact in the case of SE. These losses do not affect the position of the maximum ϕ_{SE}^{max} to any great extent as they are relatively independent of wavelength.

With the values given above for w (8 and 7.5 nm) and d (7_0, 5_3, and 5_6 nm) the ratio w/d falls in the range 0.11-0.14. Equation [9] predicts $w/d = \phi_{EE}$ at the wavelength of ϕ_{SE}^{max}. From Fig. 9 it can be seen that at this point $\phi_{EE} \simeq 0.13$. Although not conclusive, the good agreement between the results supports the validity of the derived Eq. [5], [7], and [9].

Determination of U_{FB} and w_o from action spectra measurements.—A systematic investigation of the quantum efficiency as a function of the wavelength and the potential U (*vs.* SCE) will, in addition to the bandgap energy E_g, also give the "depletion layer width constant" w_o and the flatband potential U_{FB} provided the conditions for the derivation of the Gärtner-Butler expression Eq. [1] are met and that Eq. [4] is valid. The method based on Eq. [5] and [6] is here applied for the TiO_2 (pure) film doped with Al (Preparation 3c) (Fig. 10 and 11). Table II summarizes some calculated data for Preparation 3c (least squares fitted). In the calculation of N_D a value $\epsilon = 120$ (3, 19) has been used. It can be concluded (see Fig. 10) that the bandgap corresponding to the indirect transition is, within experimental error, independent of the potential of the working electrode. Extrapolated flatband potentials determined from graphs based on Eq. [6] (Fig. 11) are in good agreement with those estimated from plots of ϕ_{EE} *vs.* U keeping λ constant.

If the data used in Fig. 10 are plotted in accordance with Eq. [3], $L_p + w$ can be determined from the slope of the curve (Fig. 12). The values of L_p which can

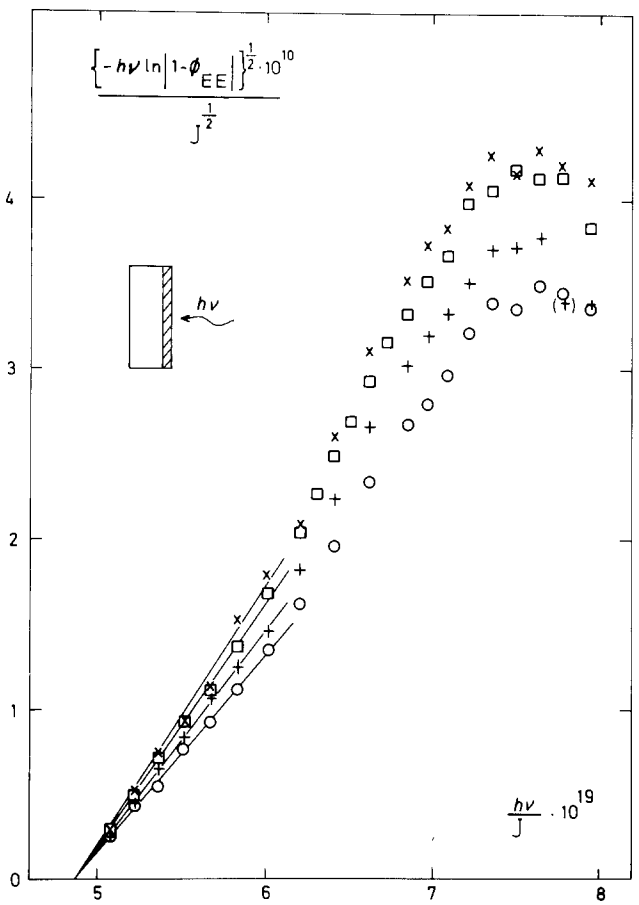

Fig. 10. The photoresponse of Al-doped TiO_2 (Preparation 3c) represented in accordance with Eq. [5]. The intercepts with the abscissa give the bandgap of the indirect transition. Mean value of $E_g = 4.89 \cdot 10^{-19}$J (3.05 ± 0.02 eV). ○, 0.25V; +, 0.50V; □, 1.00V; ×, 1.6V vs. SCE.

Table II. Some fundamental properties of Preparation No. 2 and 3c. U_{FB} is given in volt *vs.* SCE at pH = 5.7

Preparation No.	E_g (eV)	U_{FB} (V)	w_o (nm $V^{1/2}$)	N_D (m^{-3})
2	3.06 ± 0.02	—	8	$2 \cdot 10^{26}$
3c	3.05 ± 0.02	−0.3	3, 2	$1 \cdot 10^{27}$

Table III. Comparison of w values calculated from w_o and U_{FB} values of Table II, and $w + L_p$ determined according to Eq. [3]

Preparation No. 3c	U (*vs.* SCE) (V)	0.25	0.50	1.00	1.60
	w (nm)	2.3	2.8	3.6	4.4
	$w + L_p$ (nm)	2.8	3.5	4.1	4.7

be calculated from the intersection with the α^{-1} axis are of low significance because of the uncertainties introduced by the long extrapolations. In Table III, $L_p + w$ values, estimated for Preparation 3c can be compared with w values calculated (according to Eq. [2]) from the resulting w_o and U_{FB} values of a plot according to Eq. [6] (see Fig. 11).

Comments on calculated values of w, w_o, U_{FB}, and E_g.—Equations [4] and [5] are only valid for $h\nu$ close to E_g (31), *i.e.*, for 330-400 nm. As here, the absorption coefficient increases with decreasing wavelength, a larger part of the light incident on the surface of the electrode (EE) is absorbed deeper in the depletion layer than for wavelength < 330 nm. Therefore, for excitation in the above-mentioned interval, tunneling of electrons to the surface is less probable. Increased oxidation as discussed above also counteracts tunneling. For this reason and to avoid too thin films, in which the barrier at the Ti/TiO_2 interface has an influence on the photoresponse, estimations of w, w_o, U_{FB}, and E_g have only been demonstrated on somewhat thicker TiO_2 films, produced by oxidation in 2 hr or more at 408°C giving film thicknesses $d \lesssim 35$ nm (33). Resulting bandgap energies (Table II) are in good

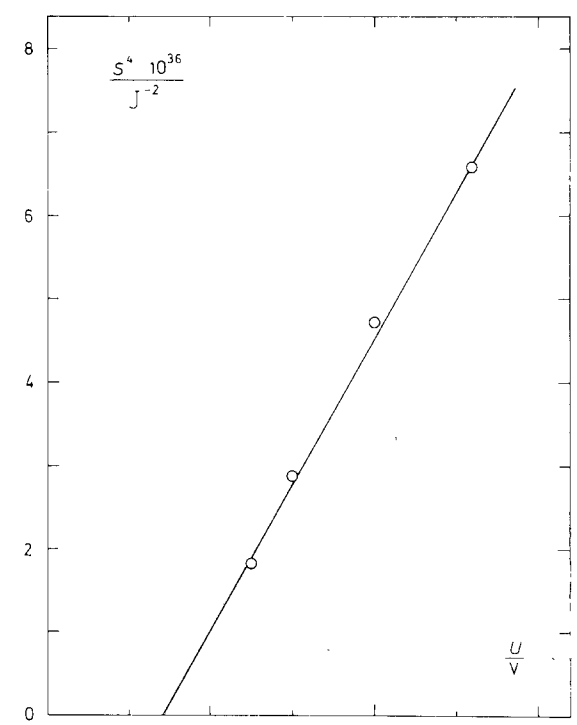

Fig. 11. S-values from Fig. 10 plotted in accordance with Eq. [6]. Extrapolated value of $U_{FB} = -0.30$V *vs.* SCE. $w_o = 3.2$ nm (giving $N_D = 1 \cdot 10^{27} m^{-3}$) determined from the slope. pH = 5.7.

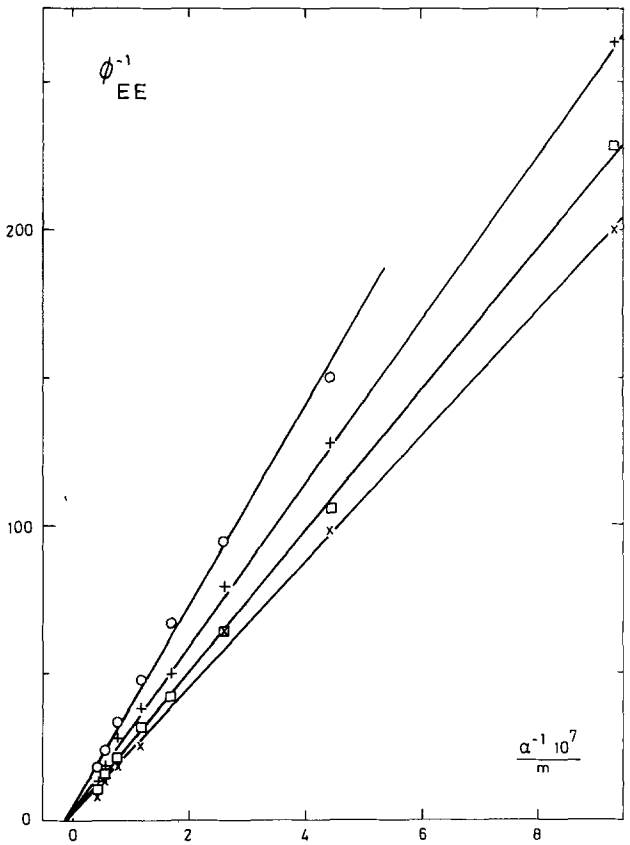

Fig. 12. Same data as in Fig. 10 plotted in accordance with Eq. [3]. $L_p + w$ values calculated from the straight lines are collected in Table III.

agreement with values found in the literature (36). The flatband potential of the Al(impurity)-doped sample 3c also agrees with the results of other workers (14).

Conclusions

In the present work it has been shown that the action spectra of thin film TiO_2 electrodes on quartz can be described by a simple theory both in the case of illumination through the electrolyte and through the back-side contact. Band shifts in the action spectra due to changes in film thickness and electrode potential have been explained qualitatively in terms of the theory. The adopted model does not account for tunneling and recombination processes. Estimated depletion layer widths are for this reason probably too small. It has also been shown that back-side illumination (case SE) can give complementary information about polycrystalline thin film electrodes. Thus w/d (Eq. [8] and [9]) and d (Eq. [10] and [11]) can be estimated from the action spectra if the absorption coefficient is known.

The produced TiO_2 thin films have a high donor concentration which results in small depletion layer constants (w_o). The hole diffusion length L_p is small compared to w_o in the studied film. Thus the efficiency is mainly governed by the depletion layer width. Tunneling of photoexcited electrons through the barrier is significant in very thin films, especially in the short wavelength region, where the absorption coefficient is large. Increased oxidation counteracts the tunneling. Impurity doping with Cr extends the photosensitivity into the visible region. Al-doped electrodes were more "well behaved" than electrodes made from a technical quality of titanium [Ti (Tec)], which showed a shift of the flatband potential to higher potentials with increasing oxidation time.

Acknowledgments

The authors wish to express their thanks to Mrs. M. Eklöf who has performed most of the photoelectrochemical measurements in the present work and to Mr. G. Karlsson for his assistance with the Ti-film preparations. Thanks also to Dr. B. Karlsson at the Institute of Technology, Uppsala, for helpful discussions and the assistance in the optical measurements and to Dr. J.-O. Carlsson and his colleagues at the Institute of Chemistry, Uppsala, for their collaboration in the x-ray analysis. We are also indebted to Dr. A. Mård for many stimulating discussions. This work was partly supported by the National Swedish Board for Energy Source Development (NE).

Manuscript submitted Jan. 25, 1982; revised manuscript received Sept. 17, 1982.

Any discussion of this paper will appear in a Discussion Section to be published in the December 1983 JOURNAL. All discussions for the December 1983 Discussion Section should be submitted by Aug. 1, 1983.

REFERENCES

1. A. Fujishima and K. Honda, *Nature*, **238**, 37 (1972).
2. A. Fujishima, K. Kohayakawa, and K. Honda, *Bull. Chem. Soc. Jpn.*, **48**, 1041 (1975).
3. J. F. Julião, F. Decker, and M. Abramovich, *This Journal*, **127**, 2264 (1980).
4. J. F. Julião, F. Decker, R. Brenzikofer, and M. Abramovich, *ibid.*, **127**, 2067 (1980).
5. T. Ohnishi, Y. Nakato, and H. Tsubomura, *Ber. Bunsenges. Phys. Chem.*, **79**, 523 (1975).
6. A. K. Ghosh and H. P. Maruska, *This Journal*, **124**, 1516 (1977).
7. J. Gautron, P. Lemasson, and J. F. Marucco, *Faraday Disc.*, **70**, 81 (1980).
8. Ya. L. Kogan and A. M. Vakulenko, *Solar Energy Mater.*, **3**, 357 (1980).
9. R. D. Rauh, J. M. Buzby, T. F. Reise, and S. A. Alkaitis, *J. Phys. Chem.*, **83**, 2221 (1979).
10. V. Guruswamy, P. Keillor, G. L. Campbell, and J. O'M. Bockris, *Solar Energy Mater.*, **4**, 11 (1980).
11. Y. Matsumoto, J. Kurimoto, Y. Amagasaki, and E. Sato, *This Journal*, **127**, 2148 (1980).
12. Y. Matsumoto, J. Kurimoto, T. Shimizu, and E. Sato, *ibid.*, **128**, 1040 (1981).
13. A. Monnier and J. Augustynski, *ibid.*, **127**, 1576 (1980).
14. J. Augustynski, J. Hinden, and Chs. Stalder, *ibid.*, **124**, 1063 (1977).
15. K. Yasawa, H. Kamogawa, and H. Morisaki, *Int. J. Hydrogen Energy*, **4**, 205 (1979).
16. K. L. Hardee and A. J. Bard, *This Journal*, **122**, 739 (1975).
17. S. N. Frank and A. J. Bard, *J. Am. Chem. Soc.*, **99**, 4667 (1977).
18. R. Schumacher, R. H. Wilson, and L. A. Harris, *This Journal*, **127**, 96 (1980).
19. F. Möllers, H. J. Tolle, and R. Memming, *ibid.*, **121**, 1160 (1974).
20. M. Takeuchi, H. Nagasaka, and S. Okazaki, in Proceedings of 3rd World Hydrogen Energy Conf., Tokyo, 1980, p. 581.
21. M. Tomkiewicz and J. M. Woodall, *This Journal*, **124**, 1436 (1977).
22. P. D. Fleischauer and J. K. Allen, *J. Phys. Chem.*, **82**, 432 (1978).
23. R. H. Wilson, *J. Appl. Phys.*, **48**, 4292 (1977).
24. H. Reiss, *This Journal*, **125**, 937 (1978).
25. J. O'M. Bockris and K. Uosaki, *ibid.*, **125**, 223 (1978).
26. J. Reichman, *Appl. Phys. Lett.*, **36** (7), 574 (1980).
27. F. El Guibaly, K. Colbow, and B. L. Funt, *J. Appl. Phys.*, **52**, 3480 (1981).
28. F. El Guibaly and K. Colbow, *Can. J. Phys.*, **59**, 1682 (1981).
29. W. W. Gärtner, *Phys. Rev.*, **116**, 84 (1959).
30. M. A. Butler, *J. Appl. Phys.*, **48**, 1914 (1977).
31. E. J. Johnson, in "Semiconductors and Semimetals," Vol. 3, R. K. Willardson and A. C. Beers, Editors, Chap. 6, Academic Press, New York (1967).
32. A. Mård, Private communication.
33. G. Hass, *Vacuum II*, 329 (1952).
34. M. A. Butler, *This Journal*, **126**, 338 (1979).
35. D. M. Eagles, Jr., *Phys. Chem. Solids*, **25**, 1243 (1964).
36. D. C. Cronemeyer, *Phys. Rev.*, **87**, 876 (1952).

Characterization of the Interface Energetics for N-Type Cadmium Selenide/Nonaqueous Electrolyte Junctions

A. Aruchamy,* James A. Bruce,† Shinichi Tanaka, and Mark S. Wrighton*

Department of Chemistry, Massachusetts Institute of Technology, Cambridge, Massachusetts 02139

ABSTRACT

Single crystal, n-type CdSe photoanodes have been studied in 0.1*M* [*n*-Bu_4N]ClO_4/CH_3CN solutions containing low concentrations of fast, outer-sphere, one electron redox reagents. A number of redox couples were studied spanning a wide range of redox potentials, $E^{\circ\prime}$. We find that reversible electrochemical response is seen at both dark and illuminated (632.8 nm light) n-CdSe for couples with $E^{\circ\prime}$ more negative than −1.2V *vs.* SCE, *e.g.*, $Ru(bpy)_3^{2+/+/0/-}$. For couples with $E^{\circ\prime}$ positive of −1.2V *vs.* SCE we find that CdSe is blocking to the oxidation of the reduced form of the redox couple in the dark, but illumination results in its oxidation. The photoanodic current peak in a cyclic voltammogram occurs more negative than at a Pt electrode, the difference between these values is the photovoltage, E_V, taken to approximate the barrier height, E_B. For $E^{\circ\prime}$ between −1.2 and −0.1V *vs.* SCE, E_V increases as $E^{\circ\prime}$ increases in a nearly ideal manner. Thus, E_B increases nearly linearly as $E^{\circ\prime}$ moves positive of the flatband potential, E_{FB}, of −1.2V *vs.* SCE. For $E^{\circ\prime}$ more positive than −0.1V *vs.* SCE E_V is constant, independent of $E^{\circ\prime}$. The effect of a number of different etches on the interface energetics of CdSe was investigated, since it was previously determined that an oxidizing or reducing etch would yield quite different results for n-CdTe. For CdSe, however, the different etches do not give significantly different results with respect to E_B *vs.* $E^{\circ\prime}$, despite large variation in surface composition deduced from Auger and XPS spectra. The highest E_V obtained is ~0.8V using $Fe(C_5Me_5)_2^{+/0}$ and more positive redox couples. In general, with respect to E_B *vs.* $E^{\circ\prime}$, n-type CdSe more closely mimics the behavior of CdS than CdTe, despite the fact that the bandgap of CdSe (E_g = 1.7 eV) is closer to that of CdTe (E_g = 1.4 eV) than to CdS (E_g = 2.4 eV).

Results from this laboratory have been reported for the interface energetics of n-type CdS (E_g = 2.4 eV) and CdTe (E_g = 1.4 eV) photoanodes (1, 2). CdS was found to nearly fit the ideal model (1, 3, 4) of a semiconductor/liquid electrolyte interface that follows from the considerations for an ideal semiconductor/metal interface (4). Reversible electrochemical response was obtained in the dark for couples with redox potentials, $E^{\circ\prime}$, more negative than the conduction bandedge, E_{CB}, Scheme I. For couples with $E^{\circ\prime}$ positive of E_{CB} and negative of the onset of decomposition current the open-circuit photovoltage, E_V, was found to vary linearly with $E^{\circ\prime}$ as predicted by Eq. [1], where E_{FB} is the electrochemical potential of the semiconductor, E_f, when

$$E_V \approx E_B = |E^{\circ\prime} - E_{FB}| \qquad [1]$$

there is no band bending, and E_B is the barrier height, $|E_{CB} - E^{\circ\prime}|$. The ideal model leads to the expectation that only couples having $E^{\circ\prime}$ more positive than the conduction bandedge, E_{CB}, would have output photovoltage. Couples near the top of the valence band, E_{VB}, would have the highest photovoltage. In the ideal model we assume that E_{VB} and E_{CB} remain fixed relative to a reference for $E^{\circ\prime}$ no more than E_g positive of E_{CB}, and thus changes in $E^{\circ\prime}$ will result in changes in E_V (1-4).

With respect to E_B *vs.* $E^{\circ\prime}$, CdTe was found to behave quite differently depending on whether it was etched with an etch containing oxidizing or reducing agents (2). For CdTe etched with an oxidizing etch nonideal behavior is obtained. The open-circuit photovoltage does not obey Eq. [1], but instead E_V is constant at ~0.5V regardless of the $E^{\circ\prime}$ of the couple used. Couples with $E^{\circ\prime}$ from −2.0 to +0.7V *vs.* SCE were studied spanning a potential range larger than the separation of E_{CB} and E_{VB}. N-type CdTe was concluded to be Fermi level pinned (5). This refers to a situation in which a semiconductor is measured to have a constant barrier height, E_B, independent of the contacting medium over a wide range of redox potentials. This is analogous to the behavior obtained for some semiconductor/metal (Schottky barrier) interfaces, where the work function of the metal should determine the barrier height for an ideal semiconductor (4, 6). But for a number of semiconductor/metal interfaces E_B is essentially independent of the work function of the metal over a wide range of work functions (6). This is referred to as Fermi level pinning for a semiconductor/metal interface and is analogous to an $E^{\circ\prime}$ independent E_B for a semiconductor/electrolyte interface. In the ideal model the bandedges, E_{CB} and E_{VB}, remain fixed relative to a reference as redox couple potential is varied, whereas with Fermi level pinning E_B is fixed, the bandedges move, and the potential changes occur across the Helmholtz layer, not across the semiconductor. When carrier inversion occurs the E_V can be independent of $E^{\circ\prime}$ (7, 8) but inversion occurs only when the band bending is $> \frac{1}{2} E_g$ at charge transfer equilibrium. For CdTe (2) the band bending is 0.5V, and for TiO_2 (9) and $SrTiO_3$ (9) the band bending is also $< \frac{1}{2} E_g$. In such cases the $E^{\circ\prime}$ independent E_V is attributable to surface states (5, 9).

Interestingly, for CdTe etched with a reducing etch the behavior obtained is nearly ideal (2). Thus, the reducing etch presumably removes oxidized material which causes Fermi level pinning. The emphasis of this study has been to measure the effects of different etches on the electrochemical behavior of CdSe, in particular to determine whether Fermi level pinning occurs and whether it can be induced or removed with an oxidizing or reducing etch. For CdSe E_g = 1.7 eV placing it between CdTe and CdS in terms of E_g. In addition the nature of the oxidized material formed

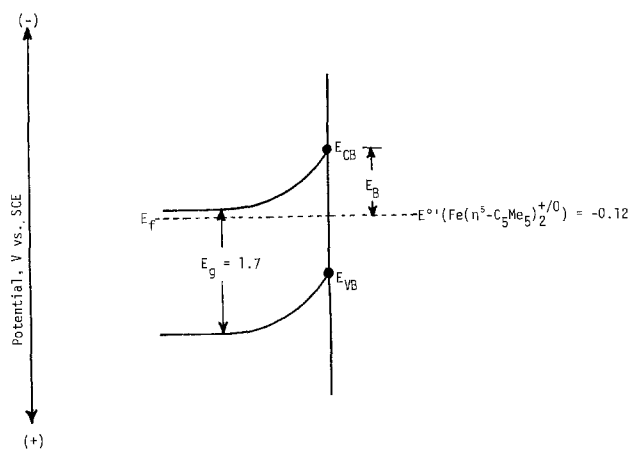

Scheme 1. Representation of the interface energetics for n-CdSe in contact with a redox couple in an electrolyte solution.

* Electrochemical Society Active Member.
† Electrochemical Society Student Member.
Key words: photoelectrochemistry, surface etching, barrier height.

on the surface of each of these three semiconductors when etched with an oxidizing etch is quite different. S is an insulator, Se a semiconductor, and Te is a very small bandgap semiconductor. Thus, whether Fermi level pinning occurs may depend on the material formed on the surface by an oxidizing etch, and the distribution, density, and nature of surface states associated with it. These properties should be quite different for S, Se (or SeO_x, Se_x^{2-}), and Te (or TeO_x, Te_x^{2-}), and we do find rather different behavior from CdS, CdSe, and CdTe photoanodes.

The solid-state data for CdX/metal (Schottky barrier) interfaces show different behavior for X = S, Se, and Te. For CdS, E_B is shown to vary from 0 to 0.85V as the work function of the metal varies, while for CdTe E_B is almost constant varying from ~0.6 to ~0.8V for a range of work functions spanning ~2V (6, 10). For CdSe E_B also appears constant for the metals used, however, the range of work functions for the metals used was not as large as for CdS/metal or CdTe/metal interfaces (6). Thus, it is possible that E_B might decrease and drop to zero for metals with smaller work functions. We now report our results for CdSe/liquid electrolyte interfaces that show behavior with respect to E_B *vs.* $E^{\circ\prime}$ that is very similar to CdS, despite the significantly smaller bandgap of CdSe.

Experimental

Electrode fabrication.—Oriented single crystals of n-CdSe, (001) plane exposed, ~0.9 Ω-cm, were obtained from Cleveland Crystals, Incorporated, Cleveland, Ohio. The crystals were polished first with 20 μm alumina and then with 10 μm alumina on a polishing glass. The crystals were finished with 0.3 μm alumina on a polishing cloth (Politex Supreme PS, Gros Corporation, Stamford, Connecticut), fixed onto the glass. Ohmic contact was made to the CdSe by rubbing Ga-In eutectic onto the back of the crystal. A Cu wire was attached using Ag epoxy. The Cu wire was encased in a 4 mm Pyrex tube and all surfaces but the exposed front surface of CdSe were sealed with ordinary epoxy. The exposed surface of the CdSe (typically 3 × 3 mm in dimensions) was the (001) face. Just prior to use all electrodes were etched and cleaned as described below.

CdSe etching procedures.—The CdSe pretreating etch was one of the following: (*i*) 5% Br_2/MeOH for 30 sec at 25°C followed by rinsing with MeOH, (*ii*) 4g $K_2Cr_2O_7$, 10 ml conc HNO_3, and 20 ml H_2O for 30 sec at 25°C followed by rinsing with distilled H_2O, (*iii*) an acid etch consisting of conc HNO_3/conc H_2SO_4/glacial acetic acid/conc HCl (30/20/10/0.1 by volume) for 8 sec at the mixing temperature followed by a rinse with conc H_2SO_4 for 15 sec at 25°C followed by rinsing with distilled H_2O, or (*iv*) the reducing pretreatment which involved first the oxidizing etch (*i*) or (*ii*) followed by immersion into a boiling solution of 2.5*M* NaOH and 0.6*M* Na_2SO_4 for 3 min. The electrode was then liberally rinsed with distilled H_2O.

Chemicals.—Spectrograde CH_3CN was freshly distilled from P_2O_5 prior to use. The [*n*-Bu_4N]ClO_4 from Southwestern Analytical Chemicals was vacuum dried at 70°C for 24 hr prior to use, and $NaClO_4$ was obtained from commercial sources and used without further purification. Triply distilled H_2O was used for solvent in aqueous electrolyte systems. All chemicals used for etching were reagent grade except for $Na_2S_2O_4$ which was purified (low in iron).

Redox reagents were generally obtained from commercial sources; TMPD was purified by sublimation; $Fe(\eta^5\text{-}C_5H_5)_2$ was used as received. Other redox couples are those used and purified in this laboratory previously (1, 2). Abbreviations for redox couples are MV^{2+} ≡ N,N′-dimethyl-4,4-bipyridinium and TMPD ≡ N,N,N′,N′-tetramethyl-*p*-phenylenediamine. The $E^{\circ\prime}$ values are from cyclic voltammograms at Pt or Hg electrodes. The $E^{\circ\prime}$ value was taken to be the average position of the anodic and cathodic peaks in the cyclic voltammogram.

Electrochemical equipment and general procedures.—Electrolyte solutions were CH_3CN/0.1*M* [*n*-Bu_4N]ClO_4. The nonaqueous electrolyte solution was passed through anhydrous, neutral Al_2O_3 just prior to use to insure dryness. All electrochemistry was carried out under a positive pressure of pure Ar.

Cyclic voltammograms were obtained using a PAR Model 173 potentiostat driven by a PAR Model 175 programmer. Data were recorded on a Houston Instruments X-Y recorder. The electrochemical cell was a single-compartment cell consisting of a working electrode of n-CdSe, Pt, or Hg, a Pt counterelectrode, and a reference electrode. A 0.1*M* $AgNO_3$/Ag/0.1*M* [*n*-Bu_4N]ClO_4/CH_3CN reference (+0.35V *vs.* SCE) was used as the reference electrode. All E_B determinations are from cyclic voltammograms at 100 mV/sec.

For cyclic voltammograms redox reagents were added to solution at ~1 m*M* concentration in all cases. The photoelectrodes were illuminated using a beam expanded He-Ne laser from Coherent Radiation, providing ~50 mW/cm² at 632.8 nm. This is sufficient light intensity to insure that photocurrent for ~1 m*M* solutions of redox reagent is limited by diffusion, not excitation rate (light intensity).

XPS and Auger studies.—Auger spectra were obtained on a Physical Electronics Model 590A scanning Auger spectrophotometer. A 5 keV electron beam with a beam current of 0.1-1 μA was used as the excitation source. The samples were mounted by attaching the Cu wire lead to the sample holder to insure electrical grounding. A Physical Electronics Model 04-303 differential ion gun was used to produce a 2 keV Ar^+ ion beam for sputtering. The pressure was maintained at ~3 × 10^{-8} Torr in the main vacuum chamber and 1.5 × 10^{-4} Torr of Ar in the ionization chamber, while sputtering.

X-ray photoelectron spectra (XPS) were obtained on a Physical Electronics Model 548 spectrometer with a magnesium anode. The broad scans (0-1000 eV) were recorded with a pass energy of 100 eV and the narrow scans with a pass energy of 25 eV. The peak energies of the Cd and Te peaks were referenced to the C 1s binding energy (284.6 eV) to correct for charging. Samples were mounted as above and sputtering was done with a 5 keV Ar^+ beam, after introducing Ar into the vacuum chamber to bring the pressure to ~7 × 10^{-5} Torr. Elements detected by Auger and XPS were identified by reference to data previously reported using these techniques (11, 12).

Results

The barrier height, E_B, is taken to be equal to the maximum photovoltage, E_V, obtained from the n-CdSe anode. At least, E_V gives a good, reproducible value, though E_V underestimates E_B by at least 0.1V owing to the difference in E_{CB} and E_{FB}, cf. Scheme I. Cyclic voltammetry of various redox couples at Pt and dark and illuminated n-CdSe has been examined in quiet solutions of CH_3CN/0.1*M* [*n*-Bu_4N]ClO_4 to measure E_V. Low concentrations of redox reagents were used (~1 m*M*), to make sure that currents observed are not limited by light intensity, and redox couples having fast kinetics were used to insure that the data reflect properties associated with variation in $E^{\circ\prime}$ and the semiconductor energetics. Further, the choice of redox couples has been restricted to fast one-electron, outer-sphere reagents to minimize complications from adsorption such as I^- on $MoSe_2$ (13) and S^{2-} on CdS (14). The photovoltage, $E_V \approx E_B$, is obtained by comparing the position of the peak of photoanodic current for a given redox couple at n-CdSe, $E_{PA,\,CdSe}$, with the peak of anodic current, $E_{PA,\,Pt}$ at a reversible Pt electrode, Eq. [2]

$$E_B \approx E_V = |E_{PA,\,CdSe} - E_{PA,\,Pt}| \quad [2]$$

The anodic current peak is the approximate potential at which there is a 1/1 ratio of the oxidized and reduced form of the redox couple near the surface of the electrode. Thus, E_V is the extent to which the anodic peak on illuminated n-CdSe is more negative than at a Pt electrode. With high enough light intensity this is the maximum photovoltage. Equation [2] then gives E_B to within 100 mV. There are five classes for electrochemical behavior of fast, one-electron, redox couples at n-type semiconductor electrodes (15). These are as follows:

Class I: $E^{\circ\prime}$ is sufficiently negative that reversible behavior is observed at the semiconductor; $E^{\circ\prime}$ is more negative than E_{CB} and there is no photoeffect.

Class II: $E^{\circ\prime}$ is near E_{CB} but slightly positive of it so that dark oxidation is observed but rate is poor and is improved by irradiation with a small negative shift of the anodic current peak.

Class III: There is no dark oxidation of the reduced form of the couple; E_B depends on $E^{\circ\prime}$ such that E_B is proportional to $|E^{\circ\prime} - E_{FB}|$ for $E^{\circ\prime}$ between E_{FB} and E_{VB}.

Class IV: There is no dark oxidation of the reduced form of the couple but E_B is independent of $E^{\circ\prime}$.

Class V: Redox couples have $E^{\circ\prime}$ sufficiently negative or positive that the decomposition current for the electrode is too great to allow study of the redox couple.

We have used this classification scheme in this characterization of the behavior of CdSe electrodes in CH_3CN solutions. A number of etches have been used to pretreat and/or clean the surface. Among these are oxidizing etches ($K_2Cr_2O_7/HNO_3$, Br_2/CH_3OH), and a reducing etch ($Na_2S_2O_4$/NaOH). We found previously with CdTe that these oxidizing and reducing etches give the different results mentioned above (2).

Table I summarizes the data for determination of E_B for n-CdSe. Variation in E_B for independently prepared samples is < 100 mV for a given redox couple. Table I and Fig. 1 show that the $Ru(bpy)_3^{2+/+/0/-}$ couples all give reversible behavior in the light or in the dark at n-CdSe. Thus, according to the ideal model, E_{FB} must be more positive than -1.3V *vs.* SCE. Since some photovoltage is observed for the $MV^{+/0}$ couple ($\sim$260 mV) E_{FB} is placed at ~ -1.2V. A larger photovoltage is observed for $MV^{2+/+}$ ($\sim$350 mV), however, two, one-electron photoanodic peaks are still discernible corresponding to $MV^0 \rightarrow MV^+$ and $MV^+ \rightarrow MV^{2+}$. For a completely ideal case only one, two-electron wave would be observed, since both $E^{\circ\prime}(MV^{2+/+})$ and $E^{\circ\prime}(MV^{+/0})$ are positive of E_{FB}. Thus, when MV^0 can be oxidized MV^+ should also be able to be oxidized.

Table I. Cyclic voltammetry data for various redox couples at Pt and illuminated n-type CdSe

Couple	$E^{\circ\prime}$[a]	E_{PA} at Pt[b]	E_{PA} at n-CdSe[c]	Class[d]
$TMPD^{2+/1+}$	+0.72	+0.72	+0.12	IV
$(biferrocene)^{2+/1+}$	+0.5	+0.52	−0.24	IV
$Fe(\eta^5\text{-}C_5H_5)_2^{1+/0}$	+0.43	+0.43	−0.34	IV
$(biferrocene)^{1+/0}$	+0.28	+0.31	−0.57	IV
$TMPD^{1+/0}$	+0.10	+0.14	−0.42	IV
$Fe(\eta^5\text{-}C_5Me_5)_2^{1+/0}$	−0.12	−0.07	−0.87	III
$MV^{2+/1+}$	−0.45	−0.41	−0.76	III
$MV^{1+/0}$	−0.85	−0.82	−1.08	III
$Ru(bpy)_3^{2+/1+}$	−1.3	−1.26	−1.26	I
$Ru(bpy)_3^{1+/0}$	−1.49	−1.45	−1.45	I
$Ru(bpy)_3^{0/-1}$	−1.73	−1.69	−1.69	I

[a] Formal potential, *V vs.* SCE in CH_3CN/0.1*M* [*n*-Bu_4N]ClO_4.
[b] Potential, *V vs.* SCE, of anodic peak in a cyclic voltammogram at a scan rate of 100 mV/sec using a Pt (smooth) working electrode in CH_3CN/0.1*M* [*n*-Bu_4N]ClO_4.
[c] Potential, *V vs.* SCE, of photoanodic peak in a cyclic voltammogram at a scan rate of 100 mV/sec using illuminated (632.8 nm) n-CdSe working electrode in CH_3CN|0.1*M* [*n*-Bu_4N]ClO_4. These are typical data for freshly etched electrode surfaces using the Br_2/CH_3OH etch.
[d] Class I, II, III, IV, and V behavior is given in the text.

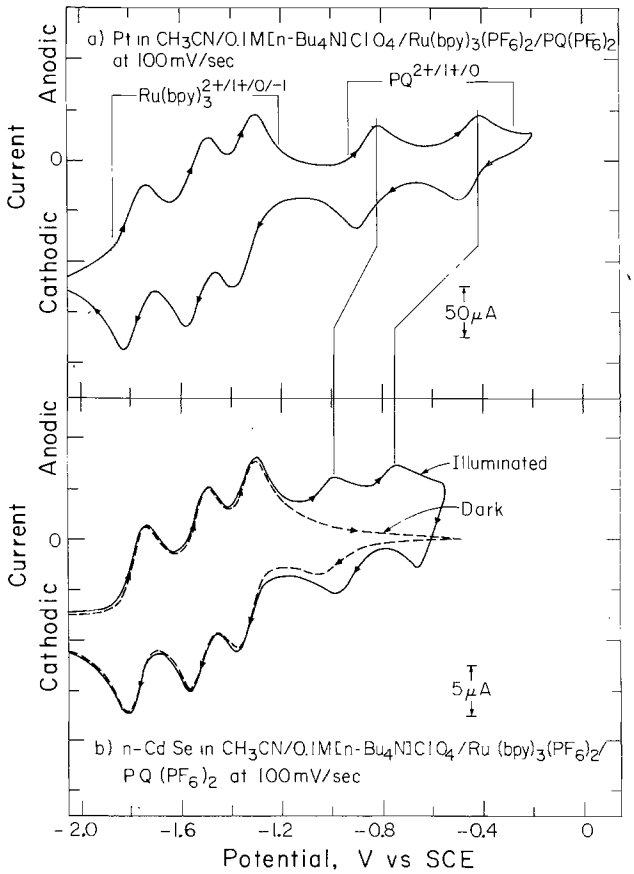

Fig. 1. Comparison of cyclic voltammetry at Pt (a) and at illuminated (———), 632.8 nm, ~50 mW/cm^2) and dark (-----) n-CdSe (b) in the presence of ~1 mM N,N'-dimethyl-4,4-bipyridinium, PQ^{2+}, and ~1 mM $(Ru(bpy)_3)^{2+}$ in CH_3CN/0.1M [*n*-Bu_4N]ClO_4. For these scans the initial potential is −2.2V *vs.* SCE; consequently, the scan in the dark shows nearly no reducible PQ^{2+}, since no PQ^{2+} is made in the dark positive sweep owing to the position of E_{FB}.

The separation of the two photoanodic waves is less than at Pt, and the fact that two waves are discernible is probably associated with interface states which facilitate back electron transfer (5, 15). In the dark no current at all is seen for the $MV^{2+/+}$ couple as expected for a couple positive of E_{FB}. Figure 2 shows cyclic voltammograms for $Fe(\eta^5\text{-}C_5Me_5)_2^{+/0}$ at Pt and illuminated n-CdSe showing an $E_V = \sim 0.8$V. Scheme I represents the interface energetics in this case. The waves for $Fe(\eta^5\text{-}C_5Me_5)_2^{+/0}$ are somewhat broader on CdSe than on Pt. However, the peak current is still proportional to (scan rate)$^{1/2}$, as expected for a diffusion-limited oxidation process. The data for couples with more positive $E^{\circ\prime}$ ($TMPD^{2+/+/0}$ and $Fe(C_5Me_5)_2^{+/0}$) seem to indicate that the photovoltage reaches ~800 mV for $E^{\circ\prime} \approx -0.2$V *vs.* SCE then levels off and is independent of $E^{\circ\prime}$. This is indicative of Class IV behavior positive of −0.20V *vs.* SCE and could mean that the maximum ideal photovoltage is not obtained due to photoanodic decomposition processes. Photoanodic corrosion of CdSe is known to occur, Eq. [3] (16)

$$CdSe + 2h^+ \rightarrow Cd^{2+} + Se \quad [3]$$

The data from Fig. 1 and 2 and Table I were taken on the first several scans after etching the electrode in Br_2/CH_3OH, since some surface changes occur after repeated scanning. Couples having $E^{\circ\prime}$ more positive than +0.7V *vs.* SCE cannot be examined, owing to severe photoanodic corrosion of the n-CdSe. Thus, couples with $E^{\circ\prime}$ more positive than +0.7V *vs.* SCE

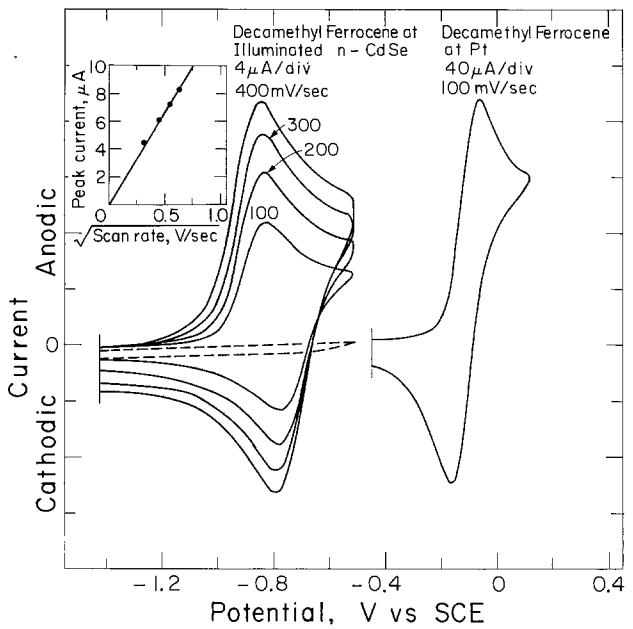

Fig. 2. Cyclic voltammetry for ~1 mM $Fe(\eta^5\text{-}C_5Me_5)_2$ at illuminated n-CdSe (pretreated with Br_2/MeOH etch) in CH_3CN/0.1M $[n\text{-}Bu_4N]ClO_4$ and at Pt. Different current scales are due to different electrode areas. The dashed curve is for n-CdSe in the dark. Inset shows the scan rate dependence for the photoanodic current peak at n-CdSe. In all cases the initial potential is the negative potential limit.

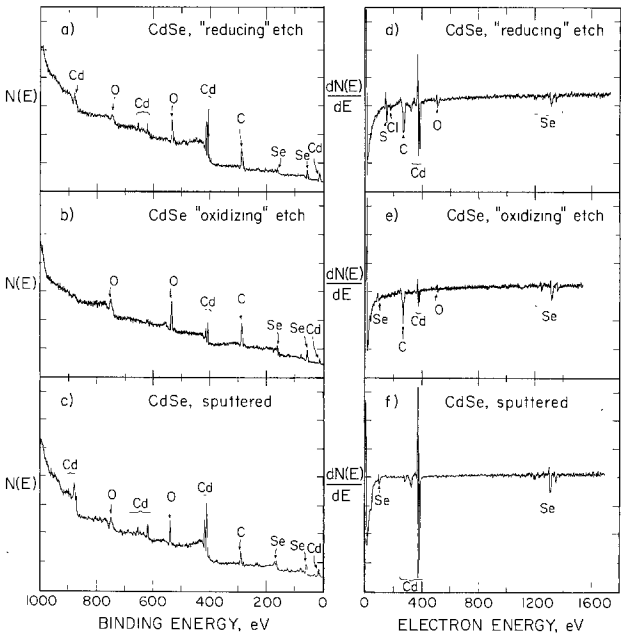

Fig. 3. Comparison of XPS (left) and Auger spectra (right) for n-CdSe pretreated with a reducing etch ($NaOH/Na_2S_2O_4$), an oxidizing acid etch (HNO_3/H_2SO_4/HOAc/HCl), and sputtered with Ar^+ in the spectrometer until no changes in relative signals occurred.

are assigned to Class V in CH_3CN/0.1M $[n\text{-}Bu_4N]ClO_4$. Indeed, it appears that E_B declines somewhat for the more positive redox couples and we attribute this to decomposition of the surface to yield a film of Se on the surface. Generally, couples negative of ~0.0V *vs.* SCE will give a constant E_B for many scans when the electrode potential is not taken more than 100 mV more positive than the photoanodic peak. For the more positive couples photoanodic corrosion leads to lower photovoltage even after < 5 scans.

Etches other than Br_2/CH_3OH have been used to pretreat the electrode surface, but the best cyclic voltammograms, in terms of peak width and separation of the anodic and cathodic peaks, were obtained using a Br_2/CH_3OH etch. Other etches used are listed in the Experimental, and include both oxidizing ($K_2Cr_2O_7/HNO_3$) and reducing etches ($Na_2S_2O_4$/NaOH). Auger spectroscopy and x-ray photoelectron spectroscopy (XPS) have been used to examine etched n-CdSe electrodes and to determine whether differences in the quality of electrochemical behavior using different etches could be correlated to surface stoichiometry. Auger and XPS spectra of oxidized, reduced, and sputtered n-CdSe surfaces do reveal large differences in the ratio of Cd/Se as shown in Fig. 3. Using either Br_2/CH_3OH or $K_2Cr_2O_7/HNO_3$ as the oxidizing etch gives similar spectra to the ones shown in the middle. Table II gives the Cd/Se signal ratios obtained by Auger spectroscopy for n-CdSe electrodes etched with a variety of etchants. There is considerable variation in the values obtained using a given etch, thus the values given are only approximate. However, it can be easily seen that the ratio of Cd/Se is significantly lower for electrodes etched using an oxidizing etch than for electrodes etched with a reducing etch or Ar^+ sputter. The HCl etch gives a similar ratio to that for a sample etched with a reducing etch. The ratios obtained are essentially independent of whether the Cd or Se face was exposed, when any etch was used except the HCl etch. Using the HCl etch the average value obtained for the Cd/Se ratio was somewhat higher (~40%) for the Se face than for the Cd face. The range of values obtained for each face was fairly large, and the ranges of values for the two faces do overlap each other. This result may be due to differences in topography of the two surfaces. The HCl etch produces a smooth mirrored finish on the Cd face and a dull surface consisting of microscopic 6-sided pyramids on the Se face. Since the escape depth (and thus sampling depth) for the Cd (376 eV) and Se (1315 eV) electrons are significantly different (17), changes in topography could change the ratio of Cd/Se detected. All other etches produced smooth finishes.

In spite of the large differences in Cd/Se ratios obtained for different etches there appears to be no correlation between the electrochemical data and the surface analytical results. Poor electrochemical behavior is obtained using etches that produce low as well as high Cd/Se ratios. It is evident from the Auger data that the oxidizing etches leave a surface rich in Se. However, this does not cause Fermi level pinning over the entire potential range found for n-CdTe etched with an oxidizing etch (2).

Discussion

Despite rather large surface composition changes from different etches, Table II, the behavior of n-CdSe with respect to E_B *vs.* $E^{\circ\prime}$ of a contacting redox couple is independent of the etch. In particular, Class I behavior is exhibited by $Ru(bpy)_3^{2+/1+/0/1-}$ at all n-CdSe surfaces. This result stands in contrast to that for n-CdTe for the same solvent/electrolyte/redox

Table II. Auger data for n-CdSe electrodes after various pretreatments

Surface pretreatment[a]	Cd/Se ratio[b]
Conc HCl	5 ± 1
Br_2/CH_3OH	1 ± 0.5
$Na_2S_2O_4$/NaOH	6 ± 1
HNO_3/H_2SO_4/HOAc/HCl	1 ± 0.5
$K_2Cr_2O_7/HNO_3$	1 ± 0.5
Ar^+ sputtered	7.5 ± 0.5

[a] Etches used and Ar^+ sputtering conditions are described in the Experimental.
[b] Ratio of the peak-to-peak heights of the Cd (376 eV) and Se (1315 eV) Auger signals, uncorrected for elemental sensitivity.

couple where an oxidizing etch gives Class IV behavior and a reducing etch gives Class I behavior (2). In fact, the behavior of n-CdSe closely resembles that for n-CdS (1) in that there is an ~1.0V range of $E^{\circ\prime}$'s where E_B *vs.* $E^{\circ\prime}$ is nearly ideal, Table III. For n-CdSe, though, the region more positive than −0.2V *vs.* SCE gives no greater E_B out to the most positive $E^{\circ\prime}$. In the same region, n-CdS is likewise clearly nonideal, but experimental data showing E_B to be completely independent of $E^{\circ\prime}$ are not available owing to photoanodic corrosion for the very positive $E^{\circ\prime}$'s. As noted above, it is possible for photoanodic decomposition to account for a lowering of photovoltage, and E_B values for the most positive redox couple are likely lower for this reason. But for both n-CdS and n-CdSe the $Ru(bpy)_3^{2+/1+/0/1-}$ couples are Class I, independent of surface pretreatment.

Further, both n-CdS and n-CdSe give an E_B *vs.* $E^{\circ\prime}$ that is nearly ideal (Class II, III behavior) until some positive $E^{\circ\prime}$ beyond which Class IV behavior is found. For n-CdSe the E_V associated with Class IV behavior is ~0.8V, showing that the surface is not strongly inverted where E_B is independent of $E^{\circ\prime}$. Similarly, the E_V associated with Class IV behavior at n-CdS is ~0.9V, less than ½ E_g. The behavior of n-CdS and n-CdSe appears to be similar to that for n-TiO_2 (9) and n-$SrTiO_3$ (9) where there is a region below E_{CB} that is essentially free of surface states. But below E_{CB} the surface state density becomes sufficiently great that for some sufficiently positive $E^{\circ\prime}$ (~ −0.2V *vs.* SCE for n-CdSe) some potential drop occurs across the semiconductor, E_B, and any additional drop occurs across the Helmholtz layer, as shown in Scheme II for CdSe. It is noteworthy that CdSe gives an E_B about as large as for CdS, despite its 0.7 eV smaller E_g. The ratio E_B/E_g is even larger for reduced n-CdTe (2).

At the oxidized surface of n-CdTe all redox couples exhibit Class IV behavior with $E_B \approx 0.5$V (2). This is consistent with an overlayer of material on the n-CdTe that behaves as a metal with a work function that gives an E_B of 0.6V (5). For such a situation the E_V measured by cyclic voltammetry would be independent of $E^{\circ\prime}$, since the electrode would behave as a buried Schottky barrier. We proposed that the oxidized overlayer is a Te-rich layer, removable by reduction with $S_2O_4^{2-}$ (2). While a Te overlayer could serve as a metal to form a Schottky barrier on CdTe, the oxidation of CdSe does not lead to a surface layer having such properties.

Table III. Comparison of barrier heights at n-CdSe/metal or liquid electrolyte interfaces

Metal (ϕ, V)[a]	Barrier height, E_V, (eV)[b]	Redox couple ($E^{\circ\prime}$, V *vs.* SCE)[c]	Barrier height, E_B (eV[c] ± 0.1V)
Pt (5.30)	0.37	$TMPD^{2+/1+}$ (0.7)	0.6
Au (4.75)	0.49	$(Biferrocene)^{2+/1+}$ (0.5)	0.76
Cu (4.53)	0.33	$Fe(\eta^5\text{-}C_5H_5)_2^{1+/0}$ (0.43)	0.77
Ag (4.40)	0.43	$(Biferrocene)^{1+/0}$ (0.28)	0.88
		$TMPD^{1+/0}$ (0.10)	0.56
		$Fe(\eta^5\text{-}C_5Me_5)_2^{1+/0}$ (−0.12)	0.80
		$MV^{2+/1+}$ (−0.45)	0.35
		$MV^{1+/0}$ (−0.85)	0.26
		$Ru(bpy)_3^{2+/1+}$ (−1.3)	"Ohmic"
		$Ru(bpy)_3^{1+/0}$ (−1.49)	"Ohmic"
		$Ru(bpy)_3^{0/-1}$ (−1.73)	"Ohmic"

[a] Data for work functions of metals are from Ref. (10a).
[b] Data for n-CdSe/metal barrier heights are from Ref. (6).
[c] This work. Barrier height, E_B, is taken as the difference in photoanodic current peak at CdSe and at Pt, Table I, in the cyclic voltammogram at 100 mV/sec scan rate. "Ohmic" refers to a situation where E_B is 0.0 and essentially reversible electrochemistry is observed. These data are ±0.10 eV and are culled from a variety of measurements of the sort represented in Fig. 1 and 2 and Table I.

The use of cyclic voltammetry to measure the interface energetics of semiconductor/liquid electrolyte interfaces is a technique that could lead to significant errors. Such a problem has been suggested in a recent study of p-GaAs (18). In the present case there appears to be good internal consistency, and the E_{FB} for CdSe determined here in CH_3CN is similar to that in H_2O in the absence of specifically adsorbed species such as S^{2-} (14). Further, while there may be an error of ~100 mV, the value of E_{FB} is rather well defined by the fact that it is located between $E^{\circ\prime}(Ru(bpy)_3^{2+/+})$ and $E^{\circ\prime}(MV^{+/0})$ because the Ru system exhibits Class I behavior and the $MV^{+/0}$ is in Class III.

Data for metal/CdSe Schottky barrier systems are sparse (6), but the E_B determinations seem to give small E_B values compared to those from the liquid junction systems, Table III. The E_B data from the liquid junctions suggest that better Schottky barriers could possibly be made with CdSe by exploring a wider range of barrier formation conditions. However, it should be emphasized that any metal/semiconductor contact will result in greater interface chemistry than is associated with the interaction with an outer-sphere redox couple such as $Fe(\eta^5\text{-}C_5Me_5)_2^{+/0}$. The metal/semiconductor interface energetics will likely vary in

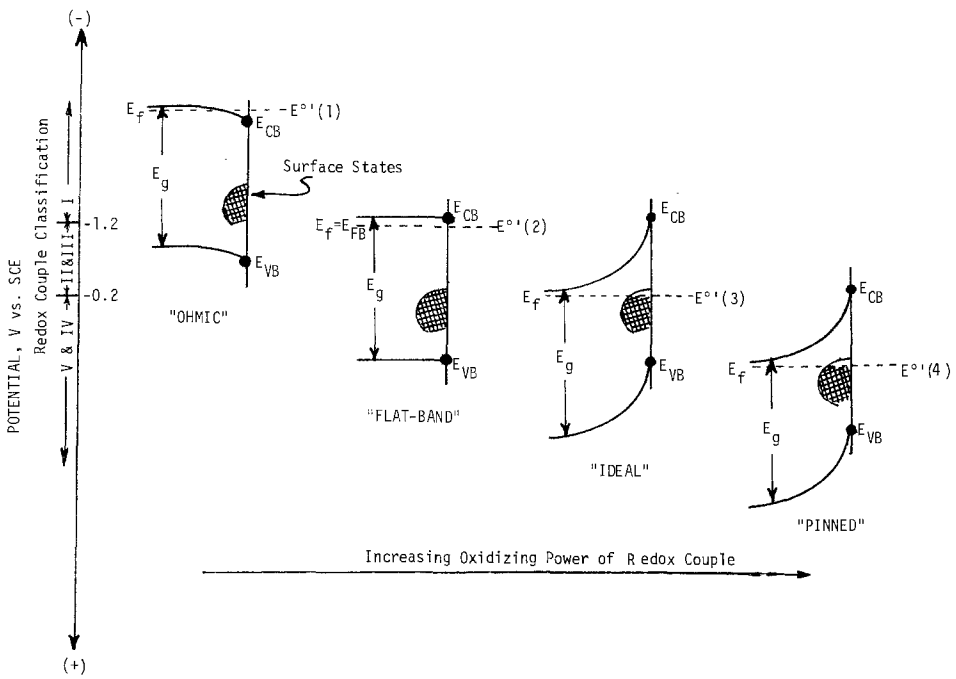

Scheme II. Interface energetics for n-CdSe as a function of the $E^{\circ\prime}$ of the contacting redox couple. For $E^{\circ\prime}$ more negative than E_{FB} = −1.2V *vs.* SCE the redox couple makes an "ohmic" contact whereas couples between E_{FB} and −0.2V *vs.* SCE nearly "ideal" variation in E_B obtains. For $E^{\circ\prime}$ more positive than −0.2V *vs.* SCE the density of surface states is sufficiently high that additional potential drop across the interface occurs in the Helmholtz layer and not in the space charge layer of the n-CdSe and E_B is effectively fixed. Redox couples beyond +0.7V *vs.* SCE give corrosion.

ways that depend on the chemistry that occurs as well as on variations in work functions (19). The analogous complication in electrochemistry is the finding that different redox couples, having the same $E^{\circ\prime}$'s but differing chemistry give different E_B's at a given semiconductor/solvent/electrolyte interface. For example, in the same aqueous electrolyte where E_{redox} of $Fe(CN)_6^{3-/4-}$ and I_3^-/I^- can be the same, a different E_V would be obtained for n-MoS_2 and related metal dichalcogenides for these two couples (15). The I_3^-/I^- system gives a significantly larger E_V owing to its strong adsorption to the surface (15). Manipulating and exploiting metal/semiconductor or liquid/semiconductor interfaces depends on controlling the interface chemistry.

Acknowledgments

We thank the Office of Naval Research for partial support of this research. A.A. acknowledges support as a predoctoral fellow of the Indo-American Fellowships Programme, 1979-1980 and S.T. acknowledges partial support of his research activities as a Fellow at the M.I.T. Center for Advanced Engineering Studies while on leave from the Toyobo Company Limited, Japan.

Manuscript submitted May 26, 1982; revised manuscript received Aug. 23, 1982.

Any discussion of this paper will appear in a Discussion Section to be published in the December 1983 JOURNAL. All discussions for the December 1983 Discussion Section should be submitted by Aug. 1, 1983.

Publication costs of this article were assisted by Massachusetts Institute of Technology.

REFERENCES

1. A. Aruchamy and M. S. Wrighton, *J. Phys. Chem.*, **84**, 2848 (1980).
2. S. Tanaka, J. A. Bruce, and M. S. Wrighton, *J. Phys. Chem.*, **85**, 3778 (1981).
3. H. Gerischer, *J. Electroanal. Chem. Interfacial Electrochem.*, **58**, 263 (1975).
4. W. Schottky, *Z. Phys.*, **118**, 539 (1942).
5. A. J. Bard, A. B. Bocarsly, F.-R. Fan, E. G. Walton, and M. S. Wrighton, *J. Am. Chem. Soc.*, **102**, 3671 (1980).
6. (a) T. C. McGill, *J. Vac. Sci. Technol.*, **11**, 935 (1974); (b) C. A. Mead and W. G. Spitzer, *Phys. Rev.*, **134**, A713 (1964); (c) C. A. Mead, *Solid State Electron.*, **9**, 1023 (1966).
7. J. A. Turner, J. Manassen, and A. J. Nozik, *Appl. Phys. Lett.*, **37**, 488 (1980).
8. W. Kautek and H. Gerischer, *Ber. Bunsenges. Phys. Chem.*, **84**, 645 (1980).
9. M. S. Lin, N. Hung, and M. S. Wrighton, *J. Electroanal. Chem. Interfacial Electrochem.*, **135**, 122 (1982).
10. J. P. Ponpon and P. Siffert, *Rev. Phys. Appl.*, **12**, 427 (1977).
11. L. E. Davis, N. C. MacDonald, P. W. Palmberg, G. E. Riach, and G. E. Weber, "Handbook of Auger Electron Spectroscopy," 2nd ed., Perkin-Elmer Corp., Eden Prairie, MN (1976).
12. C. D. Wagner, W. M. Riggs, L. E. Davis, J. F. Moulder, and G. E. Muilenberg "Handbook of X-Ray Photoelectron Spectroscopy," Perkin-Elmer Corp., Eden Prairie, MN (1979).
13. J. Gobrecht, H. Tributsch, and H. Gerischer, *This Journal*, **125**, 2085 (1978).
14. (a) A. B. Ellis, S. W. Kaiser, J. M. Bolts, and M. S. Wrighton, *J. Am. Chem. Soc.*, **99**, 2839 (1977); (b) H. Minoura, T. Watanabe, T. Oki, and M. Tsuiki, *Jpn. J. Appl. Phys.*, **16**, 865 (1977); (c) H. Minoura, M. Tsuiki, and T. Oki, *Ber. Bunsenges. Phys. Chem.*, **81**, 588 (1977); (d) D. S. Ginley and M. A. Butler, *This Journal*, **125**, 1968 (1978).
15. L. F. Schneemeyer and M. S. Wrighton, *J. Am. Chem. Soc.*, **102**, 6964 (1980); *ibid.*, **101**, 6496 (1979).
16. A. B. Ellis, S. W. Kaiser, and M. S. Wrighton, *ibid.*, **98**, 1635 (1976).
17. I. Lindau and W. E. Spicer, *J. Electron Spectrosc. Relat. Phenom.*, **3**, 409 (1974).
18. J. J. Kelly and R. Memming, *This Journal*, **129**, 730 (1982).
19. J. L. Freeouf and J. M. Woodall, *Appl. Phys. Lett.*, **39**, 727 (1981) and references therein.

A Mechanistic Study of Oxygen Evolution on Li-Doped Co_3O_4

P. Rasiyah* and A. C. C. Tseung*

Department of Chemistry, The City University, Northampton Square EC1, England

ABSTRACT

Oxygen evolution studies were carried out on preanodized Teflon-bonded Co_3O_4 and Li-doped Co_3O_4 electrodes in KOH medium. The oxygen evolution performance was found to increase with increase in Li doping. The results suggest the Co^{3+} ions are the major active sites for oxygen evolution. Steady-state current-potential measurements gave a Tafel slope of ~60 mV per decade on all the oxides. This Tafel parameter was confirmed by potentiostatic transient measurement. A mechanistic sequence for oxygen evolution

$$T + OH^- \rightarrow TOH + e$$
$$TOH + OH^- \rightarrow TO^- + H_2O$$

$$TO^- + M \rightarrow T\begin{matrix}O\\/\quad\backslash\\\quad\quad M\end{matrix} + e$$

$$2T\begin{matrix}O\\/\quad\backslash\\\quad\quad M\end{matrix} \rightarrow 2T + 2M + O_2$$

has been put forward where T is trivalent cobalt and M is divalent or trivalent cobalt. The proton abstraction step is rate determining. This is supported by experimental reaction order parameters. These studies enabled the development of an efficient oxygen evolution electrocatalyst. Teflon bonded, preanodized, 10 a/o Li-doped Co_3O_4 electrode was found to be 1.52V *vs.* the dynamic hydrogen electrode (DHE) at a current density of 1A cm^{-2} in 5*N* KOH in 70°C. Laboratory durability tests carried out on these electrodes under practical conditions showed good stability of structure and performance for 5800 h.

Hydrogen has recently attracted considerable interest as a secondary energy vector (1, 2). Various methods have been proposed for the large scale production of hydrogen fuel, of which water electrolysis remains the simplest and most economical method. Further research leading to improvements in water electrolysis may lower the cost of electrolytically produced hydrogen fuel so that it will be competitive with other fuels. One main drawback in the energy economics of alkaline water electrolysis is the high overvoltage of the oxygen evolving anode. In the recent past many workers have developed electrocatalyst based on transition metal oxides such as MnO_2 (4), $Li_xNi_{1-x}O$ (5), $NiCo_2O_4$ (5, 6), $NiLa_2O_4$ (7), and Co_3O_4 (8) having potential use as practical oxygen evolving anodes for alkaline water electrolysis. The use of metal anodes is not feasible due to its tendency to form a nonconducting oxide film, causing its oxygen evolution performance to deteriorate with time. This is specially true for nickel anodes (9), whose oxygen evolution potential is found to increase by 10^{-4}V every hour after 300 hr of oxygen evolution. On similar reasoning it will be important for bulk oxides to have fairly good electrical conductivity to give a stable oxygen evolution performance on a long term basis.

In a recent investigation (10) we suggested that the initial oxygen evolution currents on $NiCo_2O_4$ having a Tafel slope of 40 mV per decade to be due to active trivalent cation sites and higher current having a Tafel slope of 120 mV per decade was attributed to divalent Ni and Co ions being active. The cation distribution (11) of the mixed spinel $NiCo_2O_4$ obtained by freeze drying is shown to be $Co_{0.9}^{2+}Co_{0.1}^{3+}(Ni_{0.9}^{3+}Ni_{0.1}^{3+}Co^{3+})\ O_{3.2}^{2-}O_{0.8}^{-}$, where cations inside the parenthesis are in octahedral environment and those outside are in tetrahedral environment. Accordingly 40% of the cations are trivalent, of which 92% are Co^{3+}. Therefore, if the postulation that the presence of Co^{3+} in an oxide system having lower oxygen evolution potential is correct, then an oxide containing a high concentration of Co^{3+} should be a good oxygen evolving anode.

This paper reports the oxygen evolution studies obtained by steady-state galvanostatic technique on Co_3O_4 with different levels of Li doping, in KOH medium. From the trends shown in these experiments and by the analysis of Tafel and reaction order parameters, a reaction mechanism has been put forward. The oxygen evolution performance of the Li doped oxides at 70°C have also been determined. A major problem encountered in studying gas evolving electrodes is the blockage of the electrochemically active surface area by gas bubbles. The amount of blockage will vary with current density. This problem is further enhanced in porous electrodes (14), where the bubbles formed within the pores will push the electrolyte out of the pores, thus significantly reducing the amount of surface available for electrochemical reaction. Therefore, to confirm that the Tafel parameter obtained by the steady-state technique is solely due to activation polarization, and is free of (*i*) the above mentioned complication caused by oxygen bubbles and (*ii*) concentration polarization which is associated with porous electrodes, the Tafel slope was also obtained by potentiostatic transient technique (15, 16).

The Choice of Cobalt Oxide Systems

Co has three well-defined oxides (12), CoO (cubic), Co_2O_3 (hexagonal) and Co_3O_4 (normal spinel). The cation distribution (13) in Co_3O_4 is $Co^{2+}[Co_2^{3+}]\ O_4^{2-}$ where all the Co^{2+} are in tetrahedral environment and all Co^{3+} are in octahedral environment. The electrical resistivities of CoO and Co_2O_3 are $> 10^5$ Ω-cm and the electrical resistivity of Co_3O_4 is 4×10^3 Ω-cm. However, it is possible to lower the electrical resistivity of CoO and Co_3O_4 by incorporating Li into the lattice. The Co^{3+} concentration could be increased ideally from 0 to 33% of total cations in CoO (*i.e.*, $Li_x^+\ Co_{1-2x}^{2+}\ Co_x^{3+}O^{2-}$) and from 67 to 83% in Co_3O_4 (*i.e.*, $Li_x^+\ Co_{1-2x}^{2+}\ Co_x^{3+}\ [Co_2^{3+}]\ O_4^{2-}$). Thus the Li-doped Co_3O_4 system was chosen for this study. A further advantage of studying the spinel system compared to the CoO is that the former requires rela-

* Electrochemical Society Active Member.

Key words: oxygen evolution, Li-doped cobalt oxide, potentiostatic transient study.

tively low sintering temperatures for spinel formation whereas the CoO phase is formed only above 950°C.

Experimental

Electrocatalyst preparation and electrode fabrication: Co_3O_4 containing 0, 4, 7, and 10 a/o of Li were prepared by freeze drying (17) a solution containing appropriate amounts of Li and Co nitrate (ANALAR) that will give 10g of product in 150 cm^3 of water. The dried mixed nitrate solution was vacuum decomposed at 300°C and subsequently heat-treated at 600°C for 10 hr to obtain the Li-doped spinel. Teflon-bonded electrodes of the four polycrystalline powders were prepared by mixing the powder, Teflon dispersion, and methanol, and painting the resulting slurry on 100 mesh nickel screen. The electrodes were dried at 100°C for 1 hr and cured at 300°C for 1 hr. The electrocatalyst to Teflon ratio was 10/3 (W/W) in all cases.

Electrochemical evaluation.—The Teflon-bonded electrodes were preanodized at 1 Acm^{-2} in 5N KOH at 70°C for approximately 200 hr in each case. This treatment reduced the oxygen bubble size considerably. A three compartment glass cell was used for this study. A 6 × 8 cm^2 nickel mesh was used as a evolution V-*i* measurements were obtained on the (DHE) was used as the reference electrode. The electrolyte was prepared by dissolving ANALAR KOH in doubly distilled deionized water. A Chemical Electronics potentiostat (Mode TR40-3A) was used in the galvanostatic mode to obtain the steady state V-*i* measurements, and the interruptor technique (18) was used to measure the ohmic drop between the Luggin capillary and the working electrode. The oxygen evolution V-*i* measurements were obtained on the preanodized Teflon-bonded electrodes of the four oxides (electrocatalyst loading ~10 mg cm^{-2}) in 5N KOH at 25°C. The V-*i* measurements on 10 a/o Li-doped Co_3O_4 oxide electrode was also obtained in 0.4, 0.6, 1.0, and 1.5N KOH at 25°C. The DHE was calibrated against the RHE in the five KOH solutions at 25°C. The oxygen evolution performance was also measured at 70°C in 5 mol dm^{-3} KOH on the Li-doped Co_3O_4 electrodes (electrocatalyst loading ~23 mg cm^{-2}). The potentiostatic transient studies (15, 16) for oxygen evolution were carried out on preanodized Teflon-bonded 10 a/o Li-doped Co_3O_4 electrode in 5*N* KOH at 25°C. Single potential jump inputs were applied to the electrode under study from 1.5V in steps of 50 mV(until the transient oxygen evolution current is ~1A cm^{-2}) by means of a Wenking potentiostat in conjunction with a Chemical Electronics (Type 01) pulse generator. The transient current response was measured against time across a 1Ω resistor in series with the cell and stored in a transient recorder (Data Laboratory DL 901) and the stored response was obtained on an *X-Y-t* recorder (Bryans 29000, A4). The transient current was read only after the double layer charging had been completed. The double layer time was determined experimentally to be 200 μsec, by pulsing from 0.8 to 0.9V in 5*N* KOH purged with N_2. The potential range 0.8-0.9V was chosen to obtain the double layer charging time because at this range there were no faradaic currents. This was indicated by cyclic voltammetry. The transient potential was corrected for *iR* by the interruptor technique.

Results and Discussion

The room temperature electrical resistivities of the four powders were measured using a Teflon dye (17), and are given in Table I. The BET specific surface areas of the powders were found to be ~8 m^2 g^{-1}. X-ray powder diffraction analysis confirmed spinel phase formation in all four powders. The incorporation of Li into the lattice was confirmed by chemical analysis.

Table I. Resistivity and oxygen evolution performance of Li-doped Co_3O_4 (21)

Li (a/o)	Resistivity (Ω-cm)	O_2 evolution performance (V)*
0	10^4	1.69
4	10	1.56
7	1	1.535
10	1	1.52

* 5 mol dm^{-3} KOH, 70°C, 1A cm^{-2}.

Figure 1 gives the V-i plot for oxygen evolution on the four Co_3O_4 electrodes at 25°C in 5*N* KOH. A point to note is that the oxygen evolution potential decreases with Li doping. Two reasons could be attributed for this trend: (*i*) an increase in electrical conductivity with Li doping (see Table I); and (*ii*) an increase in the Co^{3+} ions with Li doping. A consideration based solely on increased electrical conductivity will not explain the trend, especially the difference in performance of the 7 and 10 a/o Li-doped Co_3O_4, both having an electrical resistivity of 1 Ω-cm. However, if all the Li^+ enters the tetrahedral sites, the cationic percentage of Co^{3+} ion in this spinel will be 70, 69, 68, and 67 for 10, 7, 4, and 0 a/o doping. This trend is more in accordance with the oxygen evolution trends. The tetrahedral site preference of the Li^+ ion in Co_3O_4 spinel lattice can at present only be justified by (*i*) the ionization potential (3) of Co^{3+} (53 eV) being greater than that of Co^{2+} (33.5 eV), and (*ii*) Co_2O_3 being resistant to Li doping. The resistivity of Co_2O_3 (10^6 Ω-cm) was not lowered when sintered with 10 a/o Li^+ in the form of LiOH, at 600°C in N_2 for 10 hr. Therefore, the increased electrical conductivity of the Li-doped Co_3O_4 is attributed to an electron hopping process in the Co^{2+} and Co^{3+} ions in the tetrahedral sites of the lattice.

Figure 2 gives the V-log i relationship for oxygen evolution on preanodized 10 a/o Li-doped Co_3O_4 obtained by potentiostatic pulse technique in 5*N* KOH at 25°C showing a Tafel region of slope 64 mV per decade up to a current density of 1A cm^{-2} (~1.7V).

The Tafel slopes for the evolution of oxygen on all four oxide systems obtained by the steady-state technique (Fig. 1) are ~60 mV per decade up to a current density of ~0.05A cm^{-2}, thus indicating that the steady-state slopes of 60 mV per decade to be activation controlled. Figure 3 gives the V-i plots for evolution of oxygen on the 10 a/o Li-doped Co_3O_4 electrode in KOH concentrations of 0.4, 0.6, 1.0, and 1.5 mol dm^{-3} KOH at 25°C. The experimental reaction parameters $(2V/\partial \log C_{OH^-})_{i,T}$ and $(\partial \log i/\partial \log C_{OH^-})_{V,T}$ for the oxygen evolution were obtained

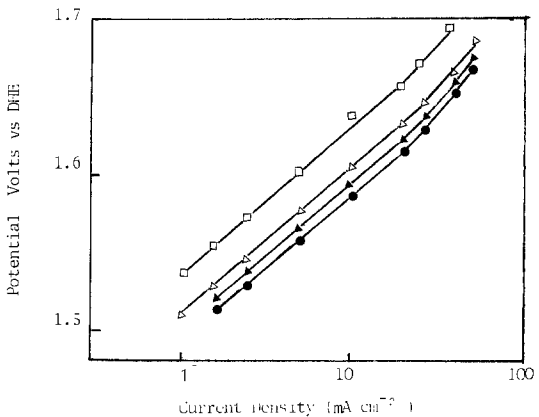

Fig. 1. Oxygen evolution on preanodized, Teflon-bonded Co_3O_4 doped with 0 (□), 4 (△), 7 (▲), and 10 (●) a/o Li at 25°C in 5*N* KOH.

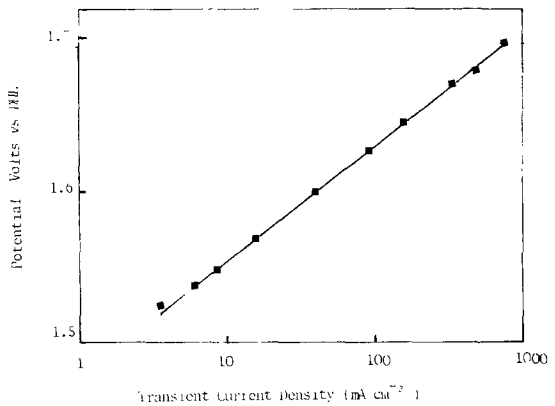

Fig. 2. Oxygen evolution on preanodized, Teflon-bonded 10 a/o Li-doped Co_3O_4 at 25°C in 5*N* KOH obtained by potentiostatic pulse technique.

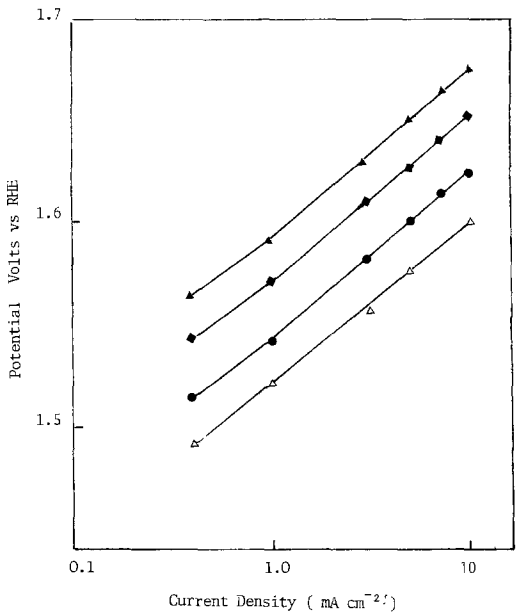

Fig. 3. Oxygen evolution on preanodized, Teflon-bonded 10 a/o Li-doped Co_3O_4 at 25°C in KOH electrolyte of concentration 0.4 (▲), 0.6 (■), 1.0 (●), and 1.5 (△) mol dm^{-3}.

as shown in Fig. 4 and 5, and are −0.117V and 1.76, respectively.

Coulometric studies carried out on $NiCo_2O_4$ (19) indicated $M^{2+} \rightarrow M^{3+} \rightarrow M^{4+}$ transitions, where M is nickel or cobalt. Thus cobalt in the spinel lattice will attain a maximum oxidation state of +4 at a potential of 1.45V before decomposing to give oxygen. Controlled potential coulometry carried out on Li-doped Co_3O_4 showed similar behavior and these results will be published at a later date.

The first mechanistic step during oxygen evolution on a Co^{3+} ion site (T) in the anode, in alkali medium, will form the tetravalent oxidation state

$$T + OH^- \rightarrow TOH + e \qquad [1]$$

the next step should necessarily be the chemical proton abstraction step

$$TOH + OH^- \rightarrow TO^- + H_2O \qquad [2]$$

It is to be noted that mechanistic steps such as

$$TOH + OH^- \rightarrow T(OH)_2 + e \qquad [3]$$

or

$$TOH + OH^- \rightarrow TO + H_2O + e \qquad [4]$$

are not possible since these will form a Co^{5+} state. Therefore, the reaction cannot proceed via the Krasilshchikov mechanism (20), *i.e.*, steps [1], [2], [4] and

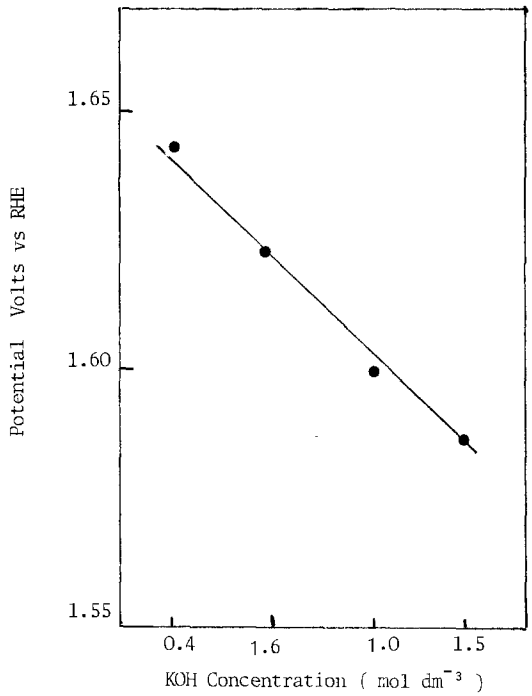

Fig. 4. Effect of KOH concentration on the oxygen evolution potential of a 10 a/o Li-doped Co_3O_4 Teflon-bonded electrode at a current density of 5 mA cm^{-2}, at 25°C.

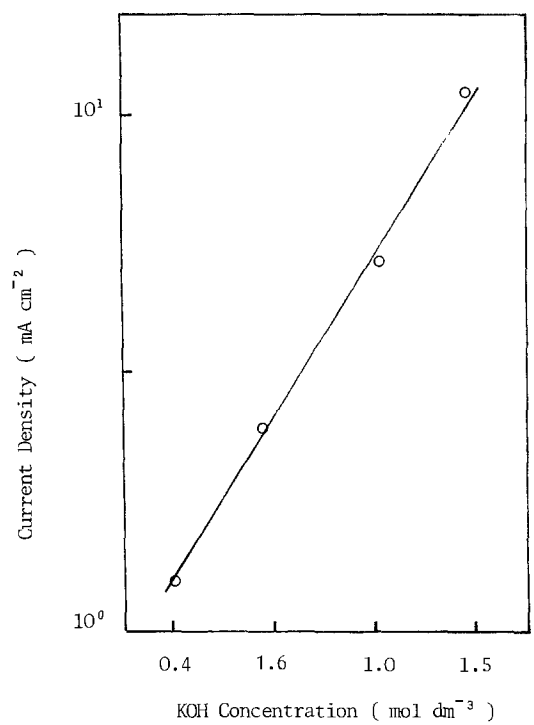

Fig. 5. KOH concentration dependence of current density on 10 a/o Li-doped Co_3O_4 at an oxygen evolution potential of 0.75V, at 25°C.

$$2TO \rightarrow 2T + O_2 \qquad [5]$$

For the reaction to proceed to evolve oxygen, the tetravalent TO^- species (19) should react with a divalent cobalt ion (M) to form a bridge compound, *i.e.*

$$TO^- + M \rightarrow T\overset{O}{\diagdown\diagup}M + e \qquad [6]$$

and the oxygen evolution will take place by

$$2T\overset{O}{\diagup\diagdown}M \rightarrow 2T + 2M + O_2 \qquad [7]$$

The rate-determining step (RDS) is step [2] at low coverage conditions. Accordingly, the rate equation that will govern oxygen evolution is

$$i = nFKC_{OH^-}{}^2 \exp\frac{VF}{RT}$$

where K is constant, C_{OH^-} is the activity of OH^- and n, F, R, V and T have the usual meanings.

The experimental Tafel slope and the reaction order parameters are in reasonable agreement with the theoretically predicted values from the rate equation. This is shown in Table II. The divalent cobalt ion does not interfere with the above discussed kinetics, since (*i*) it is M in the bridged compound formed after the RDS, (*ii*) it forms a trivalent species and takes part in step [2], and (*iii*) even if it attains a tetravalent state, it is isolated and cannot evolve oxygen.

The oxygen evolution potential of Co_3O_4 and the three Li-doped oxides at a current density of 1A cm^{-2} in 5*N* KOH at 70°C are shown in Table I. This indicates that the performance is remarkable, the 10 a/o Li-doped Co_3O_4 electrode gave 1A cm^{-2} at a potential of 1.52V *vs.* the DHE.

Long term durability tests (21) carried out on Teflon-bonded 10 a/o Li-doped Co_3O_4, at 1A cm^{-2}, 85°C in 45% KOH showed good stability of performance. After 5800 hr of continuous running, the performance of Li-doped Co_3O_4 electrode was found to increase by only ~60 mV. Furthermore, chemical Li analysis carried out on a electrode after 5800 hr of running indicated no change in the Li content of the electrocatalyst, compared to its original Li level.

Conclusions

The oxygen evolution performance of a preanodized Teflon-bonded electrode made of 10 a/o Li-doped Co_3O_4, is remarkable, being 1.52V *vs.* the DHE at a current density of 1A cm^{-2} at 70°C in 5*N* KOH. This performance is attributed to Co^{3+} active sites in the oxide. The mechanism of oxygen evolution is similar to the Krasilshchikov mechanism. However, due to the restriction of electron transition on the Co^{3+} active site, the formation of a bridged compound is postulated before oxygen is evolved.

Table II. Kinetic parameters for oxygen evolution on 10 a/o Li-doped Co_3O_4

Kinetic parameter	Theoretical	Experimental
$(\partial V/\partial \log i)_{C_{OH^-},T}$	2.303 (*RT*/*F*) = 59 mV	60 mV
$(\partial \log i/\partial \log C_{OH^-})_{V,T}$	2	1.76
$(\partial V/\partial \log C_{OH^-})_{i,T}$	2.303 (−2 *RT*/*F*) = −118 mV	−117 mV

Acknowledgment

This study was supported by the U.K. Science Research Council.

Manuscript submitted May 26, 1982; revised manuscript received Aug. 12, 1982. This was Paper 529 presented at the Minneapolis, Minnesota, Meeting of the Society, May 10-15, 1981.

Any discussion of this paper will appear in a Discussion Section to be published in the December 1983 JOURNAL. All discussions for the December 1983 Discussion Section should be submitted by Aug. 1, 1983.

REFERENCES

1. W. E. Winsche, E. C. Hoffman, and F. J. Salzano, *Science*, **180**, 1325 (1973).
2. T. N. Viziroglu and W. Seifritz, Editors, "Hydrogen Energy Systems," Proceedings of the 2nd World Hydrogen Energy Conference, International Association of Hydrogen Energy (1978).
3. M. C. Ball and A. H. Norbiery, "Physical Data for Inorganic Chemists," p. 40, Longman Group Ltd., (1974).
4. H. Tamura, C. Iwakura, and M. Morita, *Kagaku*, **33**, 407 (1978).
5. A. C. C. Tseung, S. Jasem, and M. N. Mahmood, in "Hydrogen Energy Systems," Vol. 1, T. N. Viziroglu and W. Seifritz, Editors, pp. 214-225, Pergamon Press, Elmsford, NY (1978).
6. A. C. C. Tseung and S. Jasem, *Electrochim. Acta*, **22**, 31 (1977).
7. G. Fiori, C. Mandelli, C. M. Mari, and P. V. Scolari, in "Hydrogen Energy Systems," Vol. I, T. N. Viziroglu and W. Seifritz, Editors, p. 193, Pergamon Press, Elmsford, N.Y (1978).
8. S. Trasatti, in the International Society of Electrochemistry, 31st Meeting Proceedings, E. Vecchi, Editor, p. 115 (1980).
9. H. Vandenbore and R. Leysen, in the International Society of Electrochemistry, 31st Meeting Proceedings, E. Vecchi, Editor, p. 319 (1980).
10. P. Rasiyah and A. C. C. Tseung, Paper 530 presented at The Electrochemical Society Meeting, Minneapolis, Minnesota, May 10-15, 1981.
11. W. J. King and A. C. C. Tseung, *Electrochim. Acta*, **19**, 492 (1974).
12. J. W. Mellor, "A Comprehensive Treatise on Inorganic and Theoretical Chemistry," Vol. XIV, p. 558, Longmans, Green and Company (1957).
13. B. Cossec, *J. Inorg. Nucl. Chem.*, **8**, 483 (1958).
14. A. C. C. Tseung and P. Vassie, *Electrochim. Acta*, **21**, 315 (1976).
15. B. S. Hobbs, P. R. Vassie, and A. C. C. Tseung, in "Electrochemical Engineering Symposium," Vol. I, p. 1.123, Institute of Chemical Engineers, J. D. Thornton, Editor (1971).
16. S. M. Jasem and A. C. C. Tseung, *This Journal*, **126**, 1353 (1978).
17. A. C. C. Tseung and H. L. Bevan, *J. Mater. Sci.*, **5**, 604 (1970).
18. K. R. Williams, "An Introduction to Fuel Cells," p. 58, Elsevier, New York (1966).
19. P. Rasiyah, A. C. C. Tseung, and D. B. Hibbert, *This Journal*, **129**, 1724 (1982).
20. A. I. Krasilshchikov, *Zh. Fiz. Khim.*, **37**, 531 (1963).
21. A. C. C. Tseung, P. Rasiyah, and D. B. Hibbert, Provisional British Patent Application No. 804483, 1980.

The Nickel Metal Catalyzed Decomposition of Aqueous Hypophosphite Solutions

James H. Marshall

Bell Laboratories, Murray Hill, New Jersey 07974

ABSTRACT

Hot aqueous hypophosphite ($H_2PO_2^{-1}$) solutions are exhaustively decomposed to orthophosphite (HPO_3^{-2}) in the presence of etched Ni wire according to the rate law $d[H_2PO_2^{-1}]/dt = -k_o[H_2PO_2^{-1}]x$ (catalyst area). The activation energy is about 2.6 kcal/mol and the rate increases 4-fold with pH in the range $3 \leq pH \leq 7$. Ni catalyzes the isotopic exchange between $H_2PO_2^{-1}$ and D_2O as well as the decomposition. When $[HPO_3^{-2}] \geq 0.15M$ at the start of reaction, the catalyst is completely passivated with respect to the decomposition but not with respect to the isotopic exchange. The H_2:HD:D_2 volume ratio of the evolved gas is about 5:6:7. A mechanism for the decomposition is discussed and related to "electroless" plating.

In spite of numerous investigations into the chemistry of "electroless" plating (1), experimental results relevant to the primal catalyzed hypophosphite decomposition

$$H_2PO_2^{-1} + H_2O \xrightarrow[\Delta]{Ni} HPO_3^{-2} + H_2\uparrow + H^{+1} \qquad [1]$$

are few. Although $H_2PO_2^{-1}$ is distinguished by a standard redox potential of -0.50V (2), reactions with most oxidizing agents are very slow, especially at 25° and neutral pH. This lack of reactivity is generally ascribed to very small concentrations of a "3-centered" intermediate (3-5) which $H_2PO_2^{-1}$ must rearrange prior to its oxidation.

The electrochemical oxidation of $H_2PO_2^{-1}$ is also slow and occurs at appreciable rates only at elevated temperature on Ni and Pd surfaces (6). At room temperature only O_2 is evolved from an Ni anode, and $H_2PO_2^{-1}$ is not electrochemically oxidized on Pt even at elevated temperature.

Similarities between the behavior of the standard hydrogen electrode and that of Ni electrodes immersed in hot $H_2PO_2^{-1}$ solutions suggested that Ni electrodes are saturated with hydrogen (7). At room temperature and neutral pH, the rate of isotope exchange between $H_2PO_2^{-1}$ ($D_2PO_2^{-1}$) or HPO_3^{-2} (DPO_3^{-2}) and D_2O (H_2O) is negligible (8-12), but at room temperature and $pH \leq 2$ the rate of exchange for $H_2PO_2^{-1}$ is comparable to the rate of decomposition conducted at 100° and neutral pH (13, 14).

Reaction [1] is negligible in the absence of catalyst at 100° and does not take place without H_2O (15). The decomposition rate at 100° is 1.2 mM/hr · cm² for $[H_2PO_2^{-1}] = 0.25M$ (Fig. 2). In the presence of 3 mM Ni^{+2}, but under otherwise comparable conditions, $H_2PO_2^{-1}$ is consumed at 3.2 mM/hr · cm² (16). During "electroless" plating ($[Ni^{+2}] = 0.1M$) $H_2PO_2^{-1}$ is consumed at 5 mM/hr · cm² (15).

When $H_2PO_2^{-1}$ and D_2O or $D_2PO_2^{-1}$ and H_2O are decomposed at pH's between 3 and 5 over finely divided Ni, approximately equal amounts of the hydrogen isotopes are present in the evolved gas (17-19). During Ni plating the gas is heavily enriched in the hypophosphite isotope while this isotope is not detected in the water (17, 20, 21).

Difficulties in preparing a reproducible Ni surface exhibiting a sustainable and useful level of activity have been a major hindrance to obtaining definitive mechanistic data. This problem was noted in Ref. (16 and 22). Catalyst sensitivity may be more noticeable under conditions for reaction [1] which do not provide continued renewal of the catalyst surface as "electroless" plating does. Certain anions and cations (16, 22, 23), as well as O_2 (24), have been shown to inhibit catalyst activity. Because of these results and our own experiences we wish to emphasize that the use of quality reagents and the elimination of O_2 may be especially important for achieving reproducible experimental results for reaction [1].

Due to the sketchiness of previously reported experimental procedures, the degree to which difficulties with catalyst preparation persist is unclear although mention of them was made in a recent review (1). Subsequently the possibility of obtaining reliable kinetic data for reaction [1] was demonstrated (25). It is apparent that reported experiments with reaction [1] have frequently, if not invariably, utilized freshly prepared Ni in a finely divided form. To what degree these catalysts maintain their activity is not reported, but their surface areas are difficult to estimate and Ni^{+2} (which enhances the rate of reaction [1]) may have been present. In contrast to the above reports we have determined that a useful catalyst surface is easily obtained by an acid etch of bulk Ni and that such a surface sustains its activity until the complete conversion of $H_2PO_2^{-1}$ to HPO_3^{-2}, a process requiring over 48 hr for most of our experiments.

Key words: hydrogen, isotopes, electroless, exchange, plating.

Experimental

Preparation of Ni catalysts.—30.5 cm lengths of 0.63 mm diam Ni wire (Alfa Inorganics) were loosely wound into coils about 0.5 cm in diameter and 2.5 cm long. Immediately before placement in the hot $H_2PO_2^{-1}$ solution, 2 coils were washed with acetone, washed with deionized H_2O (Millipore Super-Q), etched for 5.0 min in 25 mliters of 70% HNO_3,[1] and thoroughly rinsed in deionized H_2O. Two coils were used for most experiments. For kinetic calculations we assume the area of each coil equals its geometric area prior to etching (6.03 cm²). Coils were weighed before and after each experiment to confirm that the etch had reduced their weight by the usual 11%. The ±10% scatter in data can be accounted for by etching variations.

Preparation of solutions.—Solutions were prepared daily from analytical grade chemicals and deionized H_2O. They were refluxed under argon for 15 min prior to addition of the Ni coils. The pH was adjusted at room temperature to ±0.05 pH units with sodium citrate/citric acid buffer. The pH changes during some experiments exceeded 1 pH unit, but most of this change occurred in the first hour of the experiment

[1] The primary reason for utilizing the HNO_3 etch was the ease with which reproducible results could be obtained. Other etch procedures are effective in producing an Ni surface capable of sustaining the decomposition of $H_2PO_2^{-1}$. For example, if the coils are etched in concentrated HCl followed by an etch in 1:1 volumes of 98% H_2SO_4 and 70% HNO_3 the decomposition rate was approximately 10 times greater than that observed for coils etched by 70% HNO_3 alone. The faster decomposition rate is comparable to or exceeds most of the reported decomposition rates observed during "electroless" Ni plating. Only the HNO_3 etch was tested with respect to reproducibility. The sensitivity of the HNO_3 etched catalyst is illustrated by the fact that a final rinse in acetone followed by drying in a stream of N_2 completely passivates it with respect to the decomposition.

and we have relied only on data obtained after 1 hr. For runs requiring D_2O (Aldrich 99.8 atom percent D), $NaH_2PO_2 \cdot H_2O$ was dried overnight at 105° and $Na_3C_6H_5O_7 \cdot 2H_2O$ at 150°, while citric acid was not employed. Sodium orthophosphite was prepared from H_2O solutions of NaOH and H_3PO_3 followed by crystallization from H_2O/methanol.

Experimental runs.—Solutions were decomposed under argon/hydrogen with mild refluxing. Stirring had a negligible effect and was not employed. The amount of decomposed $H_2PO_2^{-1}$ was determined by measuring the volume of evolved hydrogen. (Hydrogen volumes refer to dry gas at STP.) The volumetric results were confirmed by measurement of the H^1 NMR signal height ratio of $H_2PO_2^{-1}$ to HPO_3^{-2} with a spectrometer operating at 60 MHz. Between *p*H's of 4 and 8 the H^1 NMR linewidths of $H_2PO_2^{-1}$ and HPO_3^{-2} are nearly equal. Results from the two methods agreed to within 2%. Based on the result that $\Delta[H_2PO_2^{-1}] = -\Delta[H_2]$ and in order to avoid confusion in the reading of graphs only "$[H_2PO_2^{-1}]$" labels are employed even though the primary method of determining $[H_2PO_2^{-1}]$ was by measuring hydrogen volumes. Fifty milliliters of solution were placed in a 100 mliters round bottom flask topped with a reflux condenser and attached to a gas collector. For NMR measurements 0.5 mliter of solution was removed at appropriate intervals. Runs were frequently continued to 25% decomposition (*ca.* 7 hr) to insure that the reaction was proceeding regularly.

Results and Discussion

The H^1 NMR intensity of HPO_3^{-2} in a thoroughly decomposed $H_2PO_2^{-1}$ solution is half the intensity of $H_2PO_2^{-1}$ in the unreacted blank showing that HPO_3^{-2} accounts for all the $H_2PO_2^{-1}$ decomposed. (The amount of PO_4^{-3} generated, if any, does not exceed the NMR measurement error of 2-3%.) Figure 1 is a plot of data from a typical Ni catalyzed decomposition. The slope of the curve at $t = 1$ hr, $(d[H_2PO_2^{-1}]/dt)_1$, was selected as the point best representing the kinetics. The use of slopes at points where $t < 40$ min introduced substantial scatter in the analysis. These discrepancies are probably due to slight variations in manipulative procedures with the catalyst that affect the time required for the catalyst surface to reach a steady state.

Figures 2, 3, and 4 illustrate the $-(d[H_2PO_2^{-1}]/dt)_1$ dependence on $[H_2PO_2^{-1}]_1$, catalyst area, and pH_1, respectively. Measurement of $(d[H_2PO_2^{-1}]/dt)_1$ for solutions to which sodium orthophosphite was

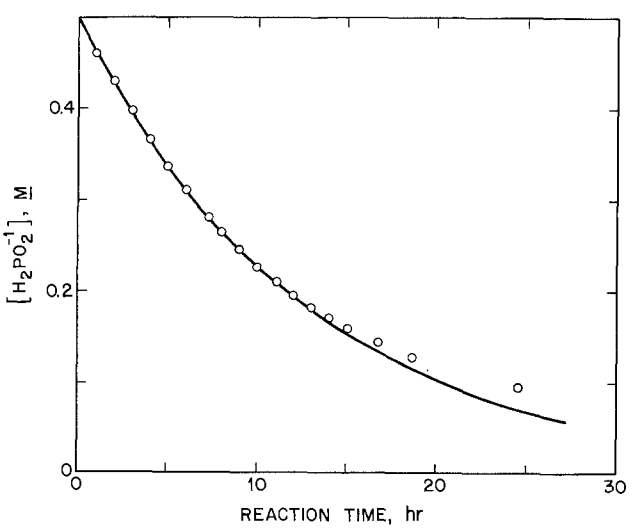

Fig. 1. $[H_2PO_2^{-1}]$ as a function of reaction time. Solid line represents exponential decay. Conditions: $pH_0 = 6.1$ (total citrate = 1.0M); $pH_{25} = 5.9$; catalyst area = 24 cm².

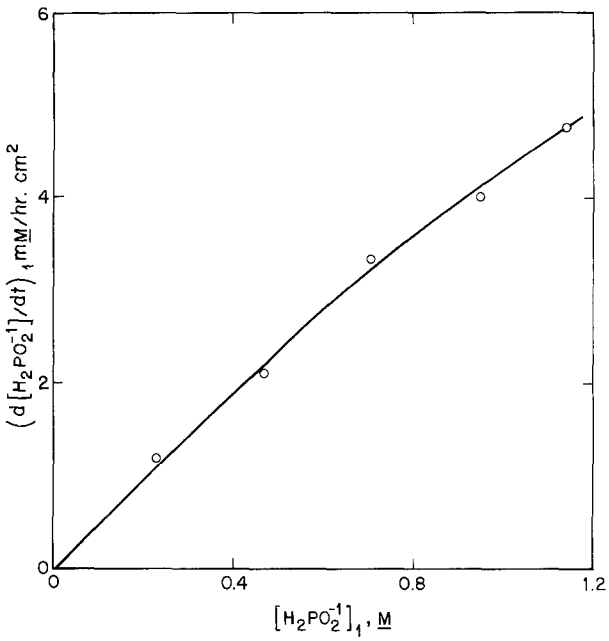

Fig. 2. Rate of decomposition after 1 hr of reaction as a function of $[H_2PO_2^{-1}]$. Conditions: $pH_0 = 8.1$ (total citrate = 0.34M); $pH_1 \approx 6.5$; catalyst area = 12 cm².

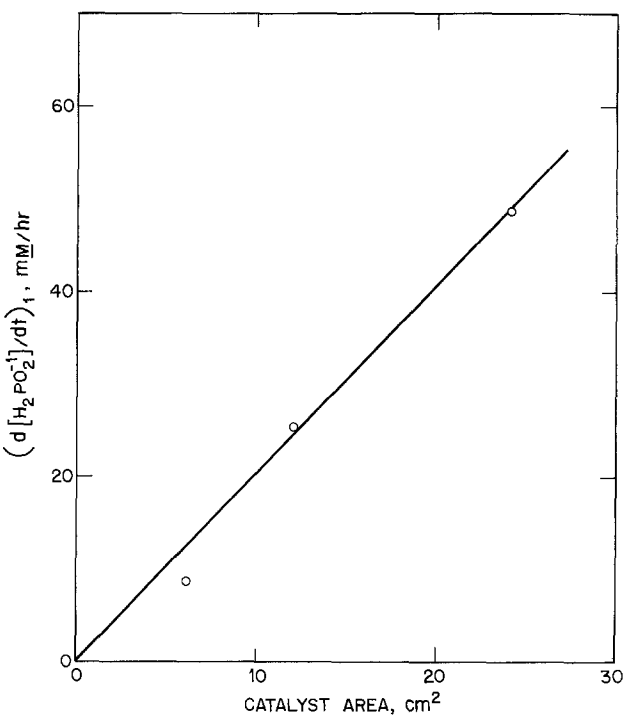

Fig. 3. Rate of decomposition after 1 hr of reaction as a function of catalyst area. Conditions: $[H_2PO_2^{-1}]_0 = 0.4M$; $pH_0 = 8.1$ (total citrate = 0.34M); $pH_1 \approx 6.5$.

added prior to the start of decomposition indicated that for $[HPO_3^{-2}]_0 \geq 0.15M$, the catalyst is completely passivated. This contrasts with the fact that solutions in Fig. 1 ($[HPO_3^{-2}]_0 = 0$) totally decompose to HPO_3^{-2} in about 60 hr ($[HPO_3^{-2}]_{60} = 0.5M$), showing no dependence on $[HPO_3^{-2}]$. These results suggest that during the initial stages of decomposition when $[HPO_3^{-2}] < 0.15M$ the catalyst undergoes a fast (with respect to decomposition) conditioning reaction which desensitizes it to higher $[HPO_3^{-2}]$.

In its linear region, Fig. 2 yields a rate constant, $k_0 = 4.7 \times 10^{-3}$/hr · cm². Leveling for $[H_2PO_2^{-1}]_0 > 0.8M$ probably results from the larger decrease in *p*H during the 1 hr of decomposition for the more concentrated solutions.

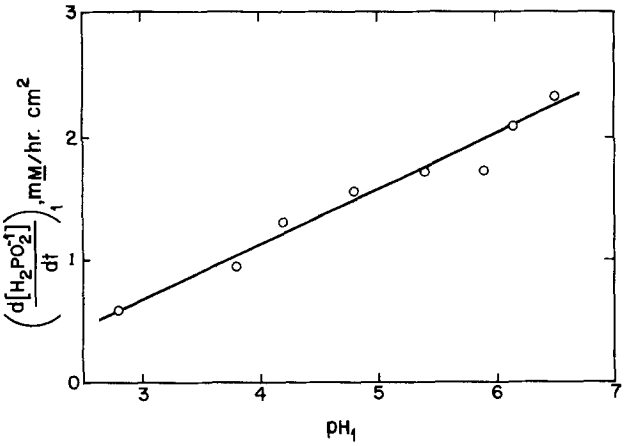

Fig. 4. Rate of decomposition after 1 hr of reaction as a function of pH. Conditions: $[H_2PO_2^{-1}]_0 = 0.5M$; total citrate $= 0.34M$; catalyst area $= 12$ cm^2.

Figure 3 confirms a previous experiment (26) which suggested that the rate of reaction [1] is directly proportional to catalyst area. The slope yields a rate constant of 4.3×10^{-3}/hr · cm^2 which is close to the value of k_0 above.

Figure 4 illustrates that an increase in $[H^+]$ of 10^4 decreases the decomposition rate by a factor of 4. This small effect of pH on the decomposition rate suggests that it stems from changes in the electrochemical potential of the catalyst (7, 25) imposed by the half-cell reaction

$$\tfrac{1}{2}\, H_2 \rightleftarrows H^{+1} + e^{-1}$$

In fact this result suggests that the decomposition rate is independent of $[H^+]$. The rate of decomposition is also nearly independent of citrate concentration although data for low citrate concentrations are difficult to analyze due to inadequate buffering.

Measuring $(d[H_2PO_2^{-1}]/dt)_i$ at 100°, 93°, and 69° yielded an activation energy of about 2.6 kcal/mol. Such a small value reflects the effectiveness of the catalyst in lowering the energy required to initiate the decomposition. A large entropy component seems apparent and lends credence to the "3-centered" intermediate concept (3-5) proposed for the homogeneous phase reactions of $H_2PO_2^{-1}$ as well as for its Ni catalyzed decomposition. For example

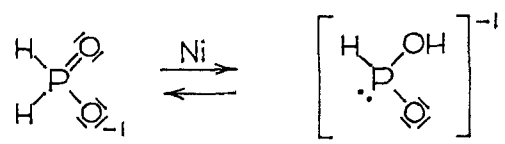

Mass spectrographic analyses[2] of the gases evolved during the decomposition of $H_2PO_2^{-1}$ in D_2O are shown in Table I. In all cases the H:D ratio is about 1:1. Experiments I-IV suggest that the H_2:HD:D_2 ratio is about 5:6:7 at pH ≅ 5 and favors D_2 at higher pH. Experiment V was run at $[H_2PO_2^{-1}]_0 = 3M$ without buffer, and the catalyst was not activated by our usual procedure. V was included in spite of the variant procedure employed to illustrate the factor of 2 difference in the amounts of H_2 and D_2 detected even though the H:D ratio is not too far removed from 1:1 and the amount of HD detected lies between that of H_2 and D_2 as in IV.

[2] The mass spectrographic analyses were performed by F. Gollob and Associates, Berkeley Heights, NJ.

Table I. Composition of gas evolved during decomposition of $H_2PO_2^{-1}$ in D_2O

Expt. No.	%D	%H_2	%HD	%D_2
I[a]	42	NR[c]	NR	NR
II[a]	44	NR	NR	NR
III[a]	48	NR	NR	NR
IV[b]	55	28.0	34.1	37.9
V[b]	62	22.5	30.9	46.6

[a] From Ref. (17).
[b] This work.
[c] NR = Not reported.

Exposure of catalytic metals to equal amounts of H_2 and D_2 results in equal surface coverages of H·* and D·*. Simple recombination statistics demand H_2:HD:D_2 ratios of 1:2:1 at equilibrium (27). Although the chemical system we are investigating is more complex than the gas phase catalytic equilibrium, reasonable mechanistic options for the decomposition of $H_2PO_2^{-1}$ in D_2O including the one we propose (see below) dictate equal steady-state coverages of H·* and D·*. The 5:6:7 ratio we observe appears feasible if the steady state is a nonequilibrium mixture of H·* and D·*. Such a steady state could arise if $H_2PO_2^{-1}$ decomposes at specific catalytic sites. This would result in a localized deposit of H·* and a surface "concentration" gradient (of H·* with respect to D·*) if surface diffusion were slow.

The rate of decomposition of $H_2PO_2^{-1}$ in H_2O or D_2O is nearly the same within experimental error. However when $H_2PO_2^{-1}$ is decomposed in D_2O, the number of mols of HPO_3^{-2} detected (by NMR) represents less than half the hypophosphite (by gas volume) decomposed. Only for reaction times less than 1 hr does the amount of HPO_3^{-2} detected appear to approach the amount of hypophosphite decomposed. After a few hours of reaction, NMR satellites attributable to $HDPO_2^{-1}$ make up an increasingly greater portion of the NMR detectable hypophosphite. When the catalyst is passivated with added HPO_3^{-2}, the rate at which these satellites grow increases with passivation.

Under no conditions was there evidence that HPO_3^{-2} undergoes isotopic exchange. If the catalyst is passivated (using HPO_3^{-2}) so that NMR detects no change in $[HPO_3^{-2}]$ during 24 hr of reflux, NMR indicates that $[H_2PO_2^{-1}]$ and $[HDPO_2^{-1}]$ approach zero in the same period. After 7 hr of reflux no exchange between $H_2PO_2^{-1}$ and D_2O was detected in the absence of catalyst. Therefore Ni appears to catalyze both the decomposition of $H_2PO_2^{-1}$ and its isotopic exchange with D_2O, and only HPO_3^{-2} results from the decomposition of $H_2PO_2^{-1}$ in D_2O while DPO_3^{-2} results from the decomposition of $HDPO_2^{-1}$ or of $D_2PO_2^{-1}$ in D_2O. The decomposition rate is comparable to the exchange rate.

In summary our results indicate that the decomposition stoichiometry corresponds to

$$H_2PO_2^{-1} + D_2O \rightarrow HPO_3^{-2} + H\cdot + D\cdot + D^+$$

The mechanism we propose is

$$H_2PO_2^{-1} \underset{k_{-1}}{\overset{k_1}{\rightleftarrows}} H_2PO_2^{-1*} \qquad [2]$$

$$H_2PO_2^{-1*} \underset{k_{-2}}{\overset{k_2}{\rightleftarrows}} HPO_2H^{-1*} \qquad [3]$$

$$HPO_2H^{-1*} + D_2O \xrightarrow{k_3} HPO_3^{-2} + H\cdot{}^* + e^{*-} + 2D^{+1} \qquad [4]$$

$$D_2O + e^{-*} \xrightarrow{k_4} D^{*}\cdot + OD^{-1} \qquad [5]$$

$$H^{*}\cdot + D^{*}\cdot \rightarrow H_2, HD, D_2 \qquad [6]$$

where the asterisk indicates a catalyst adsorbed species.

Reactions [4] and [5] are the key reactions. Reaction [4] is rate determining and represents the de-

composition of the rearranged $H_2PO_2^{-1}$ to HPO_3^{-2}, $H^{\cdot}$, and e^-, with D_2O serving only as the supplier of O^{-2} rather than as an electron acceptor. D_2O is not reduced until step [5] and only half the reducing capacity of the $H_2PO_2^{-1}$ (½ of $2e^{-1}$) is available due to the irreversibility of [5]. Steps [4] and [5] impose an H:D ratio of 1:1 on the evolved gases. They are also consistent with the observation that the evolved gases are enriched in the hypophosphite isotope when Ni^{+2} and water are competing oxidizing agents (17), and with reports that the number of mols of $H_2PO_2^{-1}$ oxidized are at least twice those of Ni^{+2} reduced (1). The irreversibility of [5] implies that $H^{\cdot *}$, once deposited on the catalyst as in [4], does not revert to H^+ (in solution) and e^{*-}. Steps [2] and [3] provide the catalyst adsorbed intermediate (HPO_2H^{-1*}) for either the isotopic exchange or the decomposition.

A 1:1:1 H_2:HD:D_2 ratio follows from a simple model involving $H^{\cdot *}$ formation at a linear source. In the steady state a linear concentration gradient will occur (28) with $[H^{\cdot *}] \propto (1 - x)$, where $0 \leq x \leq 1$ measures the distance on the crystalline surface from the source. For full monolayer coverage, $[D^{\cdot *}] \propto x$ and

$$\frac{d[H_2]}{dt} \propto \frac{1}{2}\int_0^1 (1-x)^2\,dx = \frac{1}{6}$$

$$\frac{d[HD]}{dt} \propto 1\int_0^1 x(1-x)\,dx = \frac{1}{6}$$

Our experimental result of 5:6:7 is then explicable on the basis of the catalyzed isotopic exchange.

Reactions [2]-[6] yield the kinetic expression

$$-\frac{d[H_2PO_2^{-1}]}{dt} = \frac{k_1k_2k_3[H_2PO_2^{-1}][H_2O][Ni^*]}{k_{-1}k_{-2} + k_3[H_2O](k_{-1} + k_2)}$$

where [Ni*] equals the concentration of unoccupied catalytic centers. For Langmuir kinetics

$$[Ni^*] + [H_2PO_2^{-1}Ni^*] + [HPO_2H^{-1}Ni^*] = [Ni_s]$$

In terms of coverage parameters

$$\theta_{Ni} + \theta_{H_2PO_2} + \theta_{HPO_2H} = 1$$

the kinetic expression becomes

$$-\frac{d[H_2PO_2^{-1}]}{dt} = \frac{k_1k_2k_3[H_2PO_2^{-1}][H_2O][Ni_s]}{k_{-1}k_{-2} + k_3[H_2O](k_{-1} + k_2)} \times (1 - \theta_{H_2PO_2} - \theta_{HPO_2H})$$

Solving for $\theta_{H_2PO_2}$ and θ_{HPO_2H} yields

$$-\frac{d[H_2PO_2^{-1}]}{dt} = \frac{k_1k_2k_3[H_2PO_2^{-1}][H_2O][Ni_s]}{k_1[H_2PO_2^{-1}](k_2 + k_{-2} + k_3[H_2O]) + k_{-1}k_{-2} + k_3[H_2O](k_{-1} + k_2)}$$

The exponential hypophosphite decay found experimentally for $t \geq 1$ hr indicates that

$$k_1[H_2PO_2^{-1}](k_2 + k_{-2} + k_3[H_2O]) << k_{-1}k_{-2} + k_3[H_2O](k_{-1} + k_2)$$

and therefore

$$-\frac{d[H_2PO_2^{-1}]}{dt} \cong \frac{k_1k_2k_3[H_2PO_2^{-1}][H_2O][Ni_s]}{k_{-1}k_{-2} + k_3[H_2O](k_{-1} + k_2)}$$

Combining the constants and assuming Ni_s is proportional to catalyst area, A

$$-\frac{d[H_2PO_2^{-1}]}{dt} = k_0A[H_2PO_2^{-1}]$$

A plot of $\ln [H_2PO_2^{-1}]_0/[H_2PO_2^{-1}]_t$ *vs.* t for the data of Fig. 1 yields $k_0 = 3.3 \times 10^{-3}$/hr · cm². This compares favorably with the value $k_0 = 4.7 \times 10^{-3}$/hr · cm², obtained from Fig. 2 and with the value, $k_0 = 4.3 \times 10^{-3}$/hr · cm², obtained from Fig. 3.

We suggest that the phosphorus (P) in "electroless" Ni deposits results from the occlusion of one or more of the P-containing species (followed by its reduction) (1, 29). If the mechanism for the "codeposition" of P is distinct from the mechanism for the catalytic decomposition of $H_2PO_2^{-1}$ and "electroless" plating, then except for possible complexation equilibria of Ni^{+2} with citrate anions and $H_2PO_2^{-1}$, the only addition to [2]-[6] needed to encompass "electroless" plating is

$$Ni^{+2} + 2e^{*-} \rightarrow Ni^0 \qquad [7]$$

Manuscript submitted Jan. 14, 1982; revised manuscript received Aug. 13, 1982.

Any discussion of this paper will appear in a Discussion Section to be published in the December 1983 JOURNAL. All discussions for the December 1983 Discussion Section should be submitted by Aug. 1, 1983.

Publication costs of this article were assisted by Bell Laboratories.

REFERENCES

1. P. Cavallotti and G. Salvago, *Electrochim. Metall.*, **3**, 239 (1968) and references therein.
2. W. M. Latimer, "Oxidation Potentials," 2nd ed., p. 109, Prentice Hall, Englewood Cliffs, NJ (1952).
3. A. W. Frank, *Chem. Rev.*, **61**, 389 (1961).
4. A. D. Mitchell, *J. Chem. Soc.*, **117**, 1322 (1920); *ibid.*, **120**, 1266 (1921); *ibid.*, **121**, 1624 (1922); *ibid.*, **132**, 629 (1923).
5. J. R. van Wazer, "Phosphorus and its Compounds," Vol. I, pp. 355-367, Interscience, New York (1958).
6. A. Hickling and D. Johnson, *J. Electroanal. Chem. Interfacial Electrochem.*, **13**, 100 (1967).
7. K. M. Gorbunova and A. A. Nikiforova, *Zashch. Met.*, **1**, 63 (1965).
8. G. C. Roper, T. E. Haas, and H. D. Gillman, *Inorg. Chem.*, **9**, 1049 (1970).
9. R. B. Martin, *J. Am. Chem. Soc.*, **81**, 1574 (1959).
10. A. I. Brodski and L. V. Sulima, *Dokl. Akad. Nauk SSSR*, **85**, 1277 (1952).
11. H. Erlenmeyer, W. Schoenauer, and G. Schwarzenbach, *Helv. Chim. Acta*, **20**, 726 (1937).
12. H. Erlenmeyer and H. Gartner, *ibid.*, **17**, 970 (1934).
13. A. Fratiello and E. W. Anderson, *J. Am. Chem. Soc.*, **85**, 519 (1963).
14. W. A. Jenkins and D. M. Yost, *J. Inorg. Nucl. Chem.*, **11**, 297 (1959).
15. G. Gutzeit, *Plating*, **46**, 1158 (1959).
16. G. Gutzeit, *ibid.*, **46**, 1275 (1959).
17. A. A. Sutyagina, K. M. Gorbunova, and M. P. Glazunov, *Dokl. Akad. Nauk SSSR*, **147**, 1133 (1962).
18. W. Franke and J. Monch, *Ann. Chim.*, **550**, 1 (1942).
19. H. Weiland and A. Wingler, *ibid.*, **434**, 198 (1923).
20. A. A. Sutyagina, K. M. Gorbunova, and M. P. Glazunov, *Zh. Fiz. Khim.*, **37**, 2214 (1963).
21. A. A. Sutyagina, K. M. Gorbunova, and M. P. Glazunov, *ibid.*, **37**, 2022 (1963).
22. A. Brenner and G. Riddell, *Nat'l. Bur. Stds. Res. J.*, **39**, 385 (1947).
23. N. Feldstein and P. R. Amodio, *This Journal*, **117**, 1110 (1970).
24. C. Gabrielli and F. Raulin, *J. Appl. Electrochem.*, **1**, 167 (1971).
25. G. A. Sadakov and Z. K. Slepenkova, *Electrokhimiya*, **9**, 1111 (1973).
26. G. Gutzeit, *Plating*, **46**, 1377 (1959).
27. C. C. Bond, "Catalysis by Metals," pp. 149-181, Academic Press, New York (1962).
28. A. J. Bard and L. R. Faulkner, "Electrochemical Methods," pp. 32-34, John Wiley & Sons, Inc., New York (1980).
29. A. Brenner, "Electrodeposition of Alloys," Vol. II, pp. 457-483, Academic Press, New York (1963).

Chronopotentiometry of One- and Two-Ion Transport at Immiscible Liquid Interfaces: Tests of Theory

Owen R. Melroy, William E. Bronner, and Richard P. Buck*

Department of Chemistry, The University of North Carolina, Chapel Hill, North Carolina 27514

ABSTRACT

Experimental verification for theoretical behavior of ion crossings at a water/nitrobenzene interface is given. This includes study of migration-dependent single ion transport, as well as diffusion-controlled simultaneous and successive two-ion transport. Chronopotentiograms have been obtained for tetra-n-alkylammonium salts from methyl through heptyl and for tetrabutylammonium ion in supporting electrolytes CsCl through LiCl. These are discussed in terms of partitioning effects, interfering ions, limited potential windows, and free energies of ion transfer. Problems in obtaining "true" transition times and associated transfer coefficients for various ammonium ions are also discussed.

Liquid/Liquid Interface Studies

Separation of bulk and interfacial kinetic properties for two-interface membrane systems is not theoretically possible in all situations. Consequently, detailed analyses of potential, field, and concentration profiles at single interfaces, such as aqueous electrolyte/synthetic ion exchanger and aqueous electrolyte/immiscible organic electrolyte must be achieved by other methods. The obvious choice is use of thick phases such that electrodes can be placed within the phases on each side of the single interface under study. This option is not generally available for biological membranes, many polymer films, and synthetic ion exchange membranes. Use of immiscible liquid/liquid interface systems that mimic properties of related microscopic membranes seems to open possibilities for determination of processes and electrochemical conditions at single interfaces. In 1902, Nernst and Riesenfeld (1) began a study of ion crossings at immiscible liquid/liquid interfaces in the absence of supporting electrolytes. Only in the last 10 years has this topic been pursued in a fundamental way. Frumkin's last work (2-8) renewed interest, and research began anew in a few laboratories around the world: Gavach (Montpelier) (9-20), Koryta (Prague) (21-26), Senda (Koyoto) (27-28), and Buck (Chapel Hill) (29-32).

Structure of the double layer, (charge, potential, field) at immiscible liquid electrolyte interfaces is a controversial topic, and the solution is essential to correct interpretation of ion-crossing kinetics. For single partitioned salt systems, ($NR_4^+X^-$) at water-nitrobenzene interfaces, for example, single-ion free energies in each phase determine equilibrium space charge and, in part, control potential differences, (p.ds.). For non-equilibrium applied p.ds. and currents, the overpotential may be entirely accounted for in space charge perturbations, or as p.ds. in compact layers in each phase, or as combinations of both. We have previously published analyses of chronopotentiometric potential-time curves for these various assumptions (29, 30). Log analytical plots are now available for interpreting p.d. dependences on time for the various cases including a compact layer whose order and capacitance depend on charge. The one- and two-ion transport problems at constant current have been treated for a variety of kinetic conditions, including reversible cases, with and without additional supporting electrolyte in each phase (29, 30).

In addition to double layer charge distribution, the surface excesses of solvents and possible motion of the interface during current flow must be considered. Desolvation during ion transport can, in principle, create nonuniform solvent excesses that dilute transporting and nontransporting (supporting) electrolytes with creation of spurious *IR* drops and the appearance of irreversibility.

Experimental methods for studying rates of ion transport across immiscible interfaces are timely for four reasons: (*i*) kinetic barriers (*e.g.*, dependences on activities, interfacial p.ds., and temperature) for ion crossings need measurement to determine relationships that suggest rate-determining processes; (*ii*) rates of interfacial ion crossings are presumed to reflect local structures such as potential and concentrations in diffuse and compact layers at the interface. These structures are not presently known for liquid/liquid interfaces; (*iii*) secondary processes such as involvement of homogeneous reactions during interfacial processes (*e.g.*, rates of interfacial reactions between aqueous ions and oil-soluble translocators) may become directly measurable or calculable using transport theory of coupled processes; and (*iv*) processes at liquid/liquid interfaces may resemble processes between electrolytes and cell or tissue components.

In this paper we present systematic experimental data on one- and two-ion transfers in supporting electrolytes. The results are interpreted on the assumption that overpotentials occur mostly across compact layers. Experimental evidence for this assumption has already been published (30). Systematic effects of supporting electrolyte components and concentrations are explored.

Experimental

Cell design.—Cell designs derive from classical U-tube experiments. Our best design is shown in Fig. 1. The cell is constructed of Pyrex and consists of three compartments. The left compartment contains a Kontes O-ring Teflon valve which is opened for degassing and stirring with N_2. The nitrogen line is connected to the open side arm. A capillary tube connects the left to the central compartment, so as to produce small bubbles when stirring the solution. The right compartment contains a second Teflon valve for adjusting the level of the interface. The central compartment is the working area of the cell. This contains the four electrodes, a piece of Teflon tubing, and a Teflon stopcock. The latter is opened to allow stirring with the electrodes in place. There are two identical electrode housings (glass) each containing a reference and working electrode. A housing has two concentric tubes, the center serving to sheathe the electrode leads from one another. A copper wire passing through the center tube is solder-connected to the reference wire. Another between the glass tubes is soldered to the working coil. All the electrodes are platinum. The housings are connected to the central compartment by O-ring joints and held in place by joint clamps, assuring reproducible positioning. The compartment is narrowed in the interface region, giving a cross-sectional area of 0.32 cm^2 inside the Teflon tubing.

* Electrochemical Society Active Member.

Key words: kinetics, potential window, ion crossing, migration, transition time.

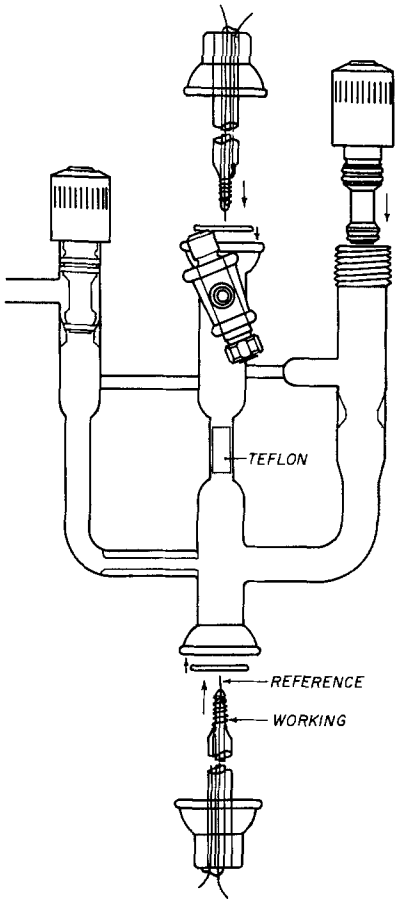

Fig. 1. Cell for liquid/liquid transport studies

Chemicals.—Fisher reagent grade nitrobenzene, the organic solvent, was first dried over Linde 3A molecular sieve and passed through an activated alumina column. The nitrobenzene was then repeatedly washed with 0.1M sodium carbonate, followed by washing with copious amounts of deionized water. The water-saturated nitrobenzene was stored in a dark bottle. The electrolyte for the organic phase was the tetraphenylborate salt of the tetraalkylammonium ion (TAATPB) to be studied. This salt was prepared by dissolving Aldrich Gold Label sodium tetraphenylborate (NaTPB) in a 50/50 water/acetone solution and mixing with an equal molar quantity of Kodak tetraalkylammonium bromide (TAABr) dissolved in the same solvent pair. The precipitate was suction filtered through a glass frit, redissolved in reagent grade acetone, and reprecipitated by the slow addition of an equal volume of water. After filtering, the precipitate was vacuum dried at 60°C for 24 hr and then stored in a desiccator. Aqueous supporting electrolyte solutions were prepared from Mallinckrodt LiCl, NaCl, NaBr, NaI, $NaClO_4$, KCl, and alpha RbCl and CsCl. Kodak TAAX salts were used for the transporting ion without further purification.

Summary of Galvanostatic Theory for One- and Two-Ion (Same or Opposite Sign) Transfer

In 1902 Nernst and Riesenfeld (1) treated the problem of single salt transport under constant current across an immiscible liquid/liquid interface. They considered the reversibly partitioned case (KI_3 at water/phenol) in the absence of supporting electrolyte. Their solutions for concentration-distance and concentration-time profiles predate the better known work of Sand on the closely related topic of solid electrodes. Their initial transport equation is

$$I(t_+ - \bar{t}_+)/\mathbf{F} = \left[-D\frac{\partial c}{\partial x} + \bar{D}\frac{\partial \bar{c}}{\partial x} \right]_{x=0}$$

in which transference numbers (t_+ and $\bar{t}_-$ for positive aqueous and organic phase ions) and salt diffusion coefficients (D, $\bar{D}$, c, and $\bar{c}$ aqueous and organic, respectively) appear. This equation does not apply in the presence of supporting electrolytes, but other appropriate equations can be found. However, transport of ions across immiscible liquid-electrolyte interfaces differs in several significant ways from electrolyte-metal interface processes. Diffusion-migration via the Nernst-Planck equation must be considered on both sides of an interface. Interfacial transport of ions of opposite sign must be accounted for with consideration of salt partition equilibria. Partition equilibria lead to nonlinear boundary conditions that preclude use of linear transform methods for the general transport equation solutions. Linearization conditions can be found. These factors cause a somewhat wider range of behavior, even for reversible systems, than is observed for electrolyte-metal examples. Coupling of ionic motion in partition-controlled cases causes a great difference between transport of a single salt component in the absence or presence of a supporting, nonpartitioning, inert electrolyte in one or both phases. Absence of inert salt can render a single salt system with a well-defined transition time to be completely ohmic, with no transition time at all. This difference is more than a prolonging of transition times by migration. There is a fundamental change in the shapes of concentration-distance profiles caused by inert salts for systems that involve migration and partitioning.

For reversible and irreversible single ion transport in the presence of excess, inert, nonpartitioning electrolytes, depletion concentration polarization on the side of the exiting ion determines the transition time. Since ion fluxes are continuous across the interface, concentration profile slopes have the same sign in each phase. Accumulation of the transporting ion occurs on the entering side. For a reversibly partitioned salt in supporting electrolyte, ions of both sign carry current across the interface. For all of the cases computed, as a consequence of the limited accessible potential range, depletion concentration polarization occurs on both sides of an interface in a coordinated way.

A further unusual effect in the absence of supporting electrolyte is electrosorption, identified by Blank (33). For a single reversible salt, mass transport with partitioning produces accumulation or depletion of salt in the diffusion layer, depending on current direction and relative ion transference numbers in the two phases.

The procedure for the solution of the linear problems uses semi-infinite boundary conditions and Laplace transformation methods for the arrangement:

Aqueous solution	Organic solution
Concentration c_i	Concentration $\bar{c}_i$
Diffusion coefficient D_i	Diffusion coefficient $\bar{D}_i$
Increasing negative x	Increasing x

$x = 0$

Fick's second law is obeyed in all cases with proper definition of salt diffusion coefficient. The latter eliminates the field term in the Nernst-Planck equation. Positive currents are positive charges moving in the positive x-direction. Concentrations in the organic phase, and the corresponding transport parameters have super bars. The basic Nernst-Planck equation is

$$J_i = -D_i\frac{\partial c_i}{\partial x} - \frac{z_i D_i \mathbf{F}}{RT}\frac{\partial \phi}{\partial x}c_i$$

In supporting electrolytes the second term can be omitted, and equations for both ions combined with electroneutrality of fluxes (equality of partial currents) gives

$$J_i = -D\frac{\partial c_i}{\partial x} + z_i t_i \frac{I}{\mathbf{F}}$$

with $D = 2D_+D_-/(D_+ + D_-)$, the "salt" diffusion coefficient. The transference numbers are bulk values: $t_i = D_i/(D_i + D_j)$ for aqueous ions and $\bar{t}_i = \bar{D}_i/(\bar{D}_i + \bar{D}_j)$ for organic ions. Boundary conditions for all ion transfers are continuity of fluxes at $x = 0$, and for salt (two ion) transfers

$$K^2 = \frac{\bar{c}_+\bar{c}_-}{c_+c_-} \quad \text{at} \quad x = 0$$

is obeyed by surface concentrations. In addition, $c_i = c_i^0$ at $x = -\infty$ and $\bar{c}_i = \bar{c}_i^0$ at $x = \infty$.

Methods for solution are straightforward. Only the use of boundary conditions differs from case to case. From Fick's second law, for supported cases

$$\mathcal{L}c_i = c_i^0/s + A_i \exp\left[(s/D_i)^{1/2}\, x\right]$$

$$\mathcal{L}\bar{c}_i = \bar{c}_i^0/s + B_i \exp\left[-(s/\bar{D}_i)^{1/2}\, x\right]$$

For the unsupported conditions, replace D_i by D, and $\bar{D}_i$ by D. For two-ion transport cases there will be two A unknowns and two B unknowns to be established from other boundary conditions. Here s is the transform variable.

The following cases have been studied by analytical and by numerical methods.

Case I: Single ion of charge +1 reversibly transferred from aqueous to organic phases (or the reverse) in supported electrolyte.

Case II: Single ion of charge +1 reversibly transferred from aqueous to organic phases in the absence of supporting electrolyte.

Case III: Two ions of charge +1 and −1, respectively, reversibly transferred from aqueous-organic phases in the presence of supporting electrolyte.

Case IV: Two ions of charge +1 and −1, respectively, reversibly transferred from aqueous-organic phases in the absence of supporting electrolyte.

Case V: Single ion of charge +1 reversibly transferred from aqueous to organic (or the reverse) in aqueous supporting electrolyte, but not organic-phase supporting electrolyte.

Case VI: Two ions of charge +1 and −1, respectively, reversibly transferred from aqueous-organic phases with aqueous supporting electrolyte, but no organic-phase supporting electrolyte.

Digital simulations were used to evaluate numerically the nonlinear problems, Cases III and VI.

Concentration-distance-time profiles.—For the simplest classical case of one cation moving from aqueous to organic phase (left to right), typical depletion and accumulation regions are seen in Fig. 2. These results are essentially the same as those described by Delahay (34). When the supporting electrolyte is removed, as in Case II, the results are similar for the single ion cases. Transition times, discussed below, are significantly different.

In Fig. 3, the transport of two ions of opposite charge in supporting electrolyte (Case III) is illustrated. For positive current, depletion of aqueous cations and organic anions occur simultaneously. The transition time occurs when both surface concentrations reach zero. The concentration profiles for Case III are similar to Cases I and II, in the sense that cation depletion and accumulation occur in aqueous and organic phases, respectively, while simultaneous anion depletion and accumulation happen in the organic and aqueous phases, respectively.

Conversely, in Case IV, the most interesting result for a single salt without supporting electrolyte, is shown in Fig. 4. The response depends on all diffusion coefficients, current, concentrations, and partition coefficients. For example, here the current is positive and $K = 1$; consequently surface concentrations are equal initially, and profiles show simultaneous depletion or

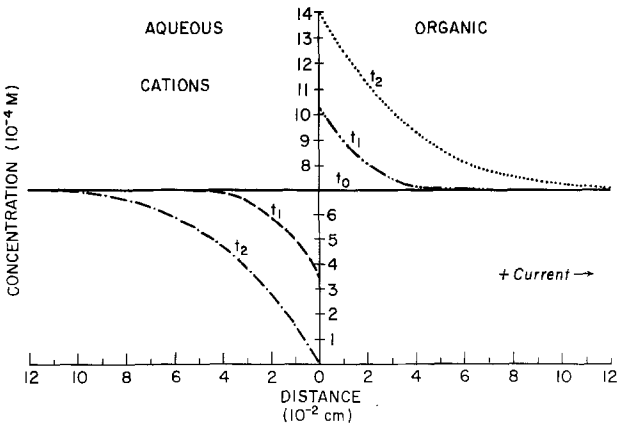

Fig. 2. Concentration-distance-time profiles for one univalent cation moving reversibly from aqueous to organic with inert, blocked supporting electrolyte. $K = 1$, $I = 1 \times 10^{-4}$ A/cm².

Ion	Charge	D_{aq}	D_{org}	c_{aq}	$\bar{c}_{org}$
Rev. cation	1	0.3	0.75	1×10^{-3}	1×10^{-3}
Inert	1	0.3	0.3	1	1
Inert	−1	0.3	0.3	1.001	1.001

$t_0 = 0$; $t_1 = 30$; $t_2 = 48.2 = \tau$.

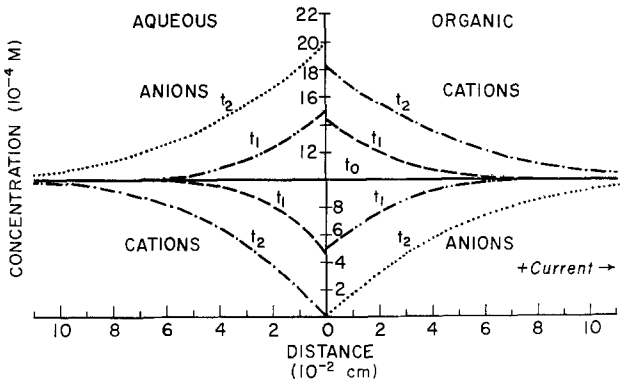

Fig. 3. Concentration-distance-time profiles for two, univalent, reversible ions moving: cation aqueous to organic; anions moving organic to aqueous with supporting, inert, blocked electrolyte. $K = 1$, $I = 1 \times 10^{-4}$ A/cm².

Ion	Charge	D_{aq}	D_{org}	c_{aq}	c_{org}
Rev. cation	1	0.3	0.3	1×10^{-3}	1×10^{-3}
Rev. anion	−1	0.3	0.3	1×10^{-3}	1×10^{-3}
Inert	1	0.3	0.3	1	1
Inert	−1	0.3	0.3	1	1

$t_0 = 0$; $t_1 = 30$; $t_2 = 78.1 = \tau$.

accumulation in both phases. Depletion occurs (for positive current) when $\bar{t}_+ < t_+$.

Irreversible transport of one and two ions has been treated theoretically for the same cases. Rate constants can be expressed in several ways depending on whether rates are computed in the space charge region or in the bulk, and for unit activity or for equilibrium activities (30). In terms of the potential-independent "chemical" rate constants $\vec{k}_c$ and $\overleftarrow{k}_c$, individual ion fluxes can be written

$$J_\pm = \vec{k}_{c\pm}\,(\mathrm{FC})\; a(\mathrm{bulk}) \exp\left[\mp \alpha z f \Delta\phi\right]$$

$$- \overleftarrow{k}_{c\pm}\,(\mathrm{FC})\; \bar{a}(\mathrm{bulk}) \exp\left[\pm (1-\alpha) z f \Delta\phi\right]$$

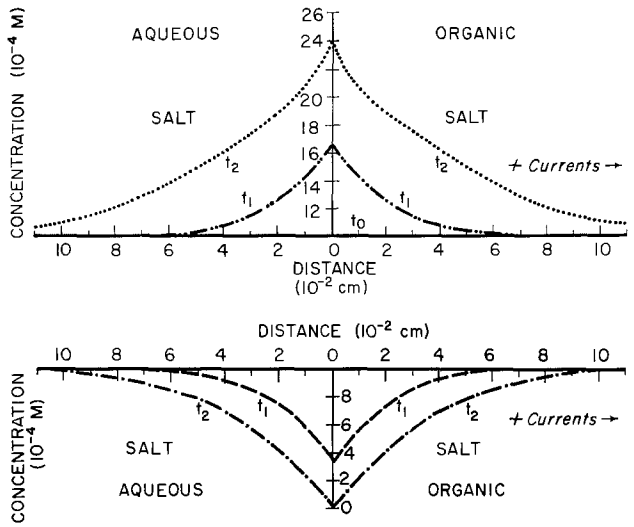

Fig. 4. Concentration-distance-time profiles for two, univalent, reversible ions moving as in Fig. 3. No supporting electrolyte. $K = 1$, $I = 1 \times 10^{-4}$ A/cm².

Ion	Charge	D_{aq}	D_{org}	c_{aq}	$\bar{c}_{org}$
(a, top) Electrosorption					
Rev. cation	1	0.3	0.75	1×10^{-3}	1×10^{-3}
Rev. anion	−1	0.075	0.4	1×10^{-3}	1×10^{-3}
$t_0 = 0$; $t_1 = 50$; $t_2 = 192 = \tau$.					
(b, bottom) Electrodesorption					
Rev. cation	1	0.075	0.3	1×10^{-3}	1×10^{-3}
Rev. anion	−1	0.4	0.075	1×10^{-3}	1×10^{-3}
$t_0 = 0$; $t_1 = 50$; $t_2 = 94.5$.					

with $\Delta\phi = \bar{\phi} - \phi$, FC = the Frumkin Correction = $[\exp\{(\alpha - 1)zf(\phi_2 - \phi) + zf(\phi - \bar{\phi}_2)\}]$ derived previously (30), for ion transfers at doubly diffused interfaces. The simplification in terms of bulk concentrations gave approximate formal expressions for fluxes

$$J_{\pm} = k_{f\pm}\, c \exp[\mp \alpha zf\Delta\phi] - k_{b\pm}\, \bar{c} \exp[\pm(1 - \alpha)zf\Delta\phi]$$

Signs apply to mobile positive and negative ions.

The principal results of the theory using digital simulation are hypothetical chronopotentiograms and log analytical plots. The characteristic behavior from distinguishable two-wave, kinetically limited cases to merged, undistinguishable, single-wave behavior has been illustrated. When both ions are slow ($10^{-11} < k_f < 10^{-2}$ cm/sec), but one of the ions has a forward rate constant four orders of magnitude or more larger than the other, two distinct waves are predicted. As k_f for each ion approaches a common value, a single, totally irreversible wave is found. Merging of two waves into an unusual single-transition time chronopotentiogram is the intermediate result. Merging of two irreversible waves into a single, reversible wave can also occur when the rate constants are allowed to increase.

Log analytical plots of separated waves give expected irreversible slopes, $RT/\alpha F$. Sub-Nernstian curvature at times near the transition time is characteristic of interference by a second transporting ion of the same or opposite charge.

Results

Aqueous ionic strength effects.—In solutions of low ionic strength, both diffusion and migration play important roles in the determination of chronopotentiometric transition times (τ). The effects have been extensively studied by Morris and Lingane for redox processes at metal surfaces (35-36). It has also been proposed that similar variations of τ with ionic strength should be observed (29) for single ion transport across a liquid/liquid interface. The results should depend only on the ionic strength of the liquid from which the ion is existing. Migration becomes most important when the concentration of supporting electrolyte is equal to or less than the concentration of the transporting ion. Experimental verification of this is shown in Fig. 5 for the transport of tetrabutylammonium (TBA^+) from water to nitrobenzene at various concentrations of aqueous NaCl. Qualitative agreement between the theory (29) and experimental observation of the dependence of the transition time on supporting electrolyte is very good.

The transition time for a univalent ion in supporting electrolyte is given by the Sand equation

$$\tau^{1/2} = \frac{c_+ \mathbf{F} (D_+)^{1/2}}{2I}$$

For a univalent ion with no supporting electrolyte, the transition time is (30)

$$\tau^{1/2} = \frac{c_+ \mathbf{F}[2(D_+ + D_-)(D_+\pi/D_-)]^{1/2}}{2I}$$

The relationship between the transition times can be expressed as

$$\tau_{unsupp} = \frac{2(D_+ + D_-)}{D_-} \tau_{supp}$$

where D_+ and D_- are the diffusion coefficients of the transporting ion and its anion, respectively, in the phase from which the cation exists. The diffusion coefficient for TBA^+ can be calculated from its transition time in supported electrolyte. The value obtained is 6.2×10^{-6} cm²/sec. The tabulated value for Cl^- is 2.03×10^{-5} cm²/sec (37). From these, theory predicts a transition time of 40 sec for the totally unsupported system, in good agreement with the observed value of 38 sec.

Anticipated equilibrium potential "window" for two salt systems: MX, MY.—For a typical two-phase, water/nitrobenzene system containing equilibrated salts MX and MY, some MX and MY will be found in

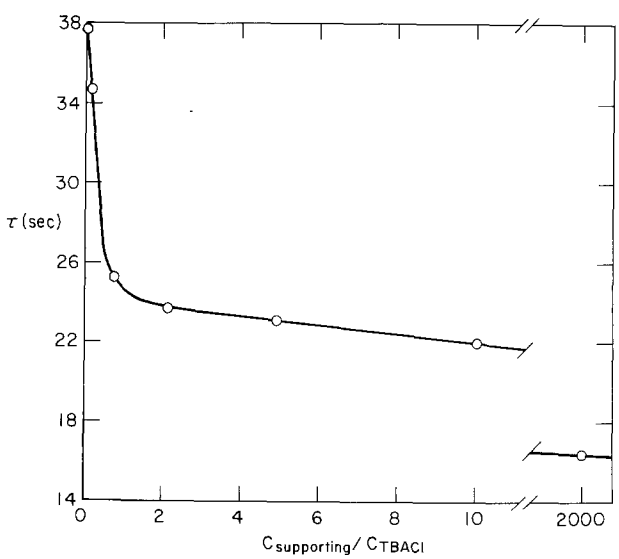

Fig. 5. Variation of transition time vs. concentration of supporting electrolyte (LiCl). Aqueous solution of TBACl 5.7×10^{-4}M; nitrobenzene solution TBATPB 2×10^{-2}M; current density: 47 μA/cm².

each phase. The concentrations in each depend on the salt partition coefficients K^M/K^X and K^M/K^Y. When M^+ is a short chain tetraalkylammonium ion TAA^+ and $X = Cl^-$, while Y = tetraphenylborate (TPB^-), MX is predominately in water while TAATPB is predominately in nitrobenzene. This result, determined experimentally, can now be predicted from tabulated values (Table I) of K_i or G(trans. $w \rightarrow 0$) (25, 38). For this example we have chosen $K_Y >> K_X$ and from the relation $\Delta G = -RT \ln K_i$, the transfer free energy for X is more positive than the value for Y.

The interfacial p.d. for an entirely equilibrated system containing constant $MY = 10^{-2}F$ in nitrobenzene with variable added formality of MX, can be calculated. For illustration, consider a system with $K_Y = 10^6$, $K_M = 10^2$, and $K_X = 10^{-2}$. The interfacial p.d. $\Delta\phi = \bar{\phi} - \phi$ is shown in Fig. 6. The potential "window" is determined by the p.ds. for excess MX (point A) and pure MY (point E). The limiting p.d. at point A is given by

$$\Delta\phi = \frac{1}{2f} \ln \left[\frac{K_M \gamma_M \bar{\gamma}_X}{\bar{K}_X \bar{\gamma}_M \gamma_X} \right] = -118 \text{ mV at } 25°C$$

while at point E

$$\Delta\phi = \frac{1}{2f} \ln \left[\frac{K_M \gamma_M \bar{\gamma}_Y}{\bar{K}_Y \bar{\gamma}_M \gamma_Y} \right] = -118 \text{ mV at } 25°C$$

(Activity coefficient values have been assumed to be unity.) At point A, Donnan Exclusion by Y is violated, while at infinite dilution of MX the interfacial p.d. is determined by extraction equilibrium of MY at point E.

In the midrange of the figure, point C, the response approaches Nernstian behavior. In the transition regions, points B and D, the p.d. equations are quadratic (31). The potential window depends on the ratios K_M/K_X and K_M/K_Y. The response along the activity axis depends on the extraction coefficient products $K_M K_X$ and $K_M K_Y$.

Effects of aqueous alkali cations on the potential window.—There is very little freedom in choice of acceptable aqueous supporting electrolytes for general ion transport studies. The tendency for support cations to carry current, in addition to the cation being studied, is related to the free energy of transfer for the co-cation. The most hydrophilic co-cations are required to obtain the best negative-going potential limit. The limited potential range is illustrated by comparing the chronopotentiograms of TBA^+ transport from water to nitrobenzene using various aqueous alkali chloride solutions, Fig. 7. The ultimate negative potential limit is determined by TPB^- transport. The TBATPB electrolyte gives a range of about 375 mV for observation of the TBA^+ chronopotentiogram. This accessible range, required for sharp breaks with easily determined τ values, is attainable with LiCl, and NaCl is also acceptable. Clearly, Cs^+, Rb^+, and K^+ are unacceptable as supporting electrolyte cations in many transport studies.

Table I. Standard Gibbs energies of transfer from water to nitrobenzene, single ion partition coefficients (nitrobenzene over water), and the standard electrical potential difference, ϕ_n-ϕ_w (38)

Ion	$\Delta G^\circ_{tr}{}^{w \rightarrow n}$ (kJ/mol)	$k_{n/w}$	$\Delta\phi^{n \rightarrow w}$ (V)
Li^+	38.2	2.10×10^{-7}	−0.395
Na^+	34.2	1.04×10^{-6}	−0.354
K^+	23.4	8.12×10^{-5}	−0.242
Rb^+	19.4	4.01×10^{-4}	−0.201
Cs^+	15.4	2.05×10^{-3}	−0.159
TMA^+	3.4	0.256	−0.035
TEA^+	−5.7	9.94	0.059
TPA^+	−15.5	5.06×10^{2}	0.160
TBA^+	−24.0	1.55×10^{4}	0.248
TPB^-	−35.9	1.94×10^{6}	−0.372
I^-	18.8	5.06×10^{-4}	0.195
Br^-	28.4	1.03×10^{-5}	0.295
Cl^-	31.4	3.34×10^{-6}	0.324

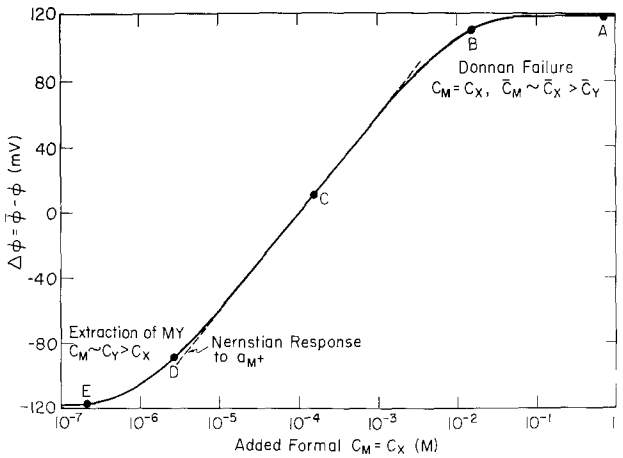

Fig. 6. An example of the potential "window." Computation for two salts: MX mainly water soluble and MY mainly oil soluble. Formal concentration of MY = 10^{-2}; single-ion partition coefficients $K_Y = 10^6$, $K_M = 10^2$, and $K_X = 10^{-2}$. The computed potential window is 336 mV. c_M and c_X and added concentrations, e.g., formal concentrations.

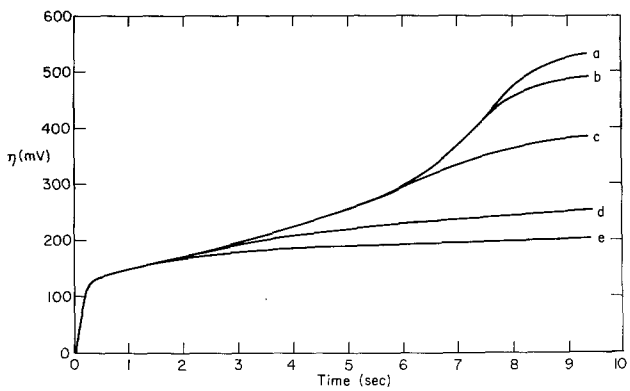

Fig. 7. Overvoltage-time curves for aqueous solution of TBACl 8×10^{-4}M; nitrobenzene solution of current density: 59 μA/cm^2. Curve a, 0.1M LiCl; b, 0.1M NaCl; c, 0.1M KCl; d, 0.1M RbCl; and e, 0.1M CsCl.

As the small potential window for observing ion crossings via chronopotentiometry is diminished, transition regions are spread out and τ values are more difficult to determine. The source of this effect is current distribution (between the ion under study and other electrolyte components) at times near the transition time, *i.e.*, the cation of the aqueous supporting electrolyte (or the anion of the organic supporting electrolyte) carries part of the current. This distribution is apparent when the potential is plotted against $-\ln [1 - (t/\tau)^{1/2}]$. Figure 8 shows these plots for the chronopotentiograms in Fig. 7. As more current is carried by the supporting electrolyte at long times, the log analysis plots show a marked sub-Nernstian deviation from linearity. This deviation becomes greater as the interference increases. Although it is not illustrated here, the effect of varying the anion of the organic supporting electrolyte (in this case TPB^-) is equivalent to changing the cation of the aqueous supporting electrolyte.

While not as important as the partitioning of current at long times, another cause of sub-Nernstian deviation in the log analysis plots is the limited solubility of most TAATPB salts in nitrobenzene (particularly for the low molecular weight TAA^+'s). The result is a breakdown of the assumption that the surface concentration of the transported ion on the entrance side is approximately constant, a requirement needed to ob-

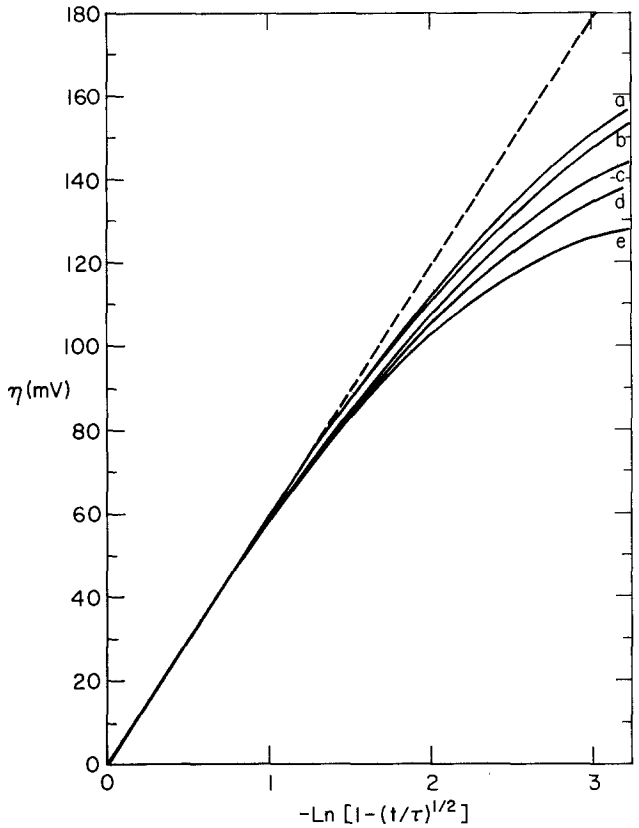

Fig. 8. Log analysis plots of curves in Fig. 7

tain linear log analysis plots. This result has previously been described in detail (29).

Aqueous anion effects.—There are two effects of anions on observed chronopotentiometric transition times of the TAA^+ cation. These arise from relative anion hydrophobicities. First, the inert salt in the aqueous phase can partition into the organic phase. This results in transportable anions, *e.g.*, I^- from NaI, ClO_4^- from $NaClO_4$, etc., that can be carried back into the aqueous phase as TAA^+ moves under positive current. Second, the salt TAAX can partition into the organic phase. The effect on chronopotentiograms is one of altering the transition time, but not creation of a second wave. If only transport of TAA^+ is desired, the aqueous supporting electrolyte needs to be LiF, LiCl, NaF, or NaCl.

Typically, partitioning causes transport by both TAA^+ and X^-. The result may be a longer or a shorter transition time depending on D_+ *vs.* D_-. When all of the TAA^+ is extracted into the organic phase, all current is carried by X^-. If excess X^- is in the organic phase, as in the case of TAAI in NaI, the transition time will be increased over that of TAA^+ alone. For supporting electrolytes containing oil-soluble anions such as I^- and ClO_4^-, the dominant factor is the solubility of TAAX in nitrobenzene. As shown in Fig. 9, when NaI or $NaClO_4$ is used as the supporting electrolyte, all of the TBA^+ has partitioned into the nitrobenzene as TBAX. When current is passed, only I^- is transported from the nitrobenzene to water (or ClO_4^- if $NaClO_4$ is used). The change in the initial potential required to pass current (TBA^+ *vs.* I^- *vs.* ClO_4^-) provides a key to the transporting ion and reflects the relative solubility of the transporting ion in the two phases. Standard Gibbs free energies of transfer from water to nitrobenzene and standard electrical potential differences between these phases have been calculated and reported for several ions (25, 38).

The complicated intermediate case arises when a slightly oil-soluble anion is used as the supporting electrolyte. An example is Br^- that partitions (as

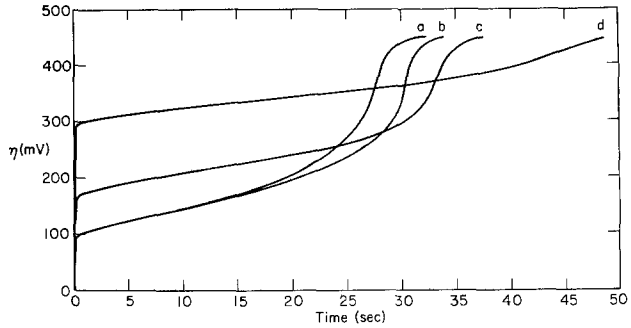

Fig. 9. Overvoltage-time curves for aqueous solutions of TBACl 1×10^{-3}M; organic solutions of TBATPB 2×10^{-2}M; current density 62.5 $\mu A/cm^2$. Curve a, 0.1M NaCl; b, 0.1M NaBr; c, 0.1M NaI; and d, 0.1M $NaClO_4$.

TAABr) into the nitrobenzene and increases the net concentration of transporting ions. The resulting increase in the transition time is shown in Fig. 9. Since the concentration of supporting electrolyte is two to three orders of magnitude larger than the concentration of the ion to be studied, the salt partition coefficient of the supporting electrolyte does not need to be very large to yield prolonged transition times.

Examples of two-ion transport.—When the forward rate constants of two ions differ by one order of magnitude or less, only one wave is predicted. This behavior is seen in the co-transport of TBA^+ and I^-. Simultaneous transport of two oppositely charged ions can be achieved through the use of mixed supporting electrolytes. For example, Fig. 10 shows the chronopotentiograms for a 9×10^{-4} solution of TBACl with combinations of NaCl and NaI used as the aqueous supporting electrolyte. For relatively small amounts (0.04M) of NaI in the supporting electrolyte, the transport involves both TBA^+ from water to nitrobenzene and I^- from nitrobenzene to water. Since the potentials at which the two ions transport are close, only one wave is observed in the chronopotentiogram. At higher concentrations of NaI, all current is carried by I^-.

Two-ion transport can also result in the appearance of two separate waves. An example of this effect for two ions of opposite charge is the transport of tetraethylammonium$^+$ (TEA^+) from water to nitrobenzene and I^- from nitrobenzene to water, Fig. 11a. Similar potential-time transients are obtained for the crossing of TBA^+ and TEA^+ from water to nitrobenzene shown in Fig. 11b. In supported electrolyte solutions, simultaneous crossing of two oppositely charged ions is virtually indistinguishable from the transport of two ions of the same charge.

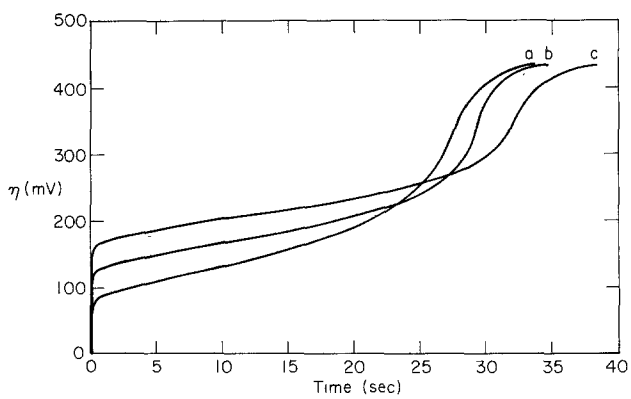

Fig. 10. Simultaneous two-ion transport; aqueous solution 9×10^{-4}M TBACl; organic solution 2×10^{-2}M TBATPB; current density 59 $\mu A/cm^2$. Curve a, 0.1M NaCl; b, 0.1M NaCl + 1.4×10^{-2}M NaI; and c, 0.1M NaCl + 0.1M NaI.

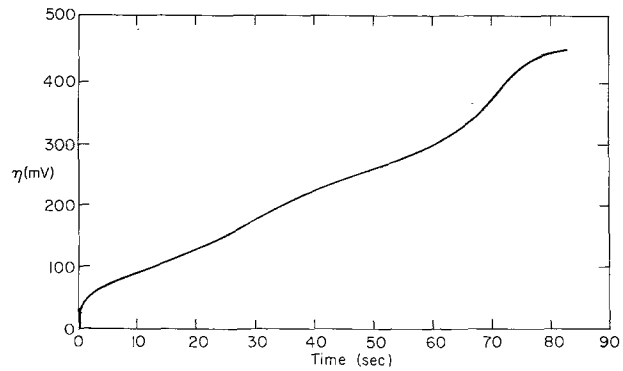

(a) Aqueous solution of 2.8 × 10^{-4}M TEACl and 0.1M LiCl; organic solution of tetraheptylammonium iodide 6.6 × 10^{-4}M and 7.0 × 10^{-3}M tetraheptylammonium tetraphenylborate; current density 59 μA/cm². First process I^-(org) → I^-(aq). Second process TEA^+(aq) → TEA^+(org).

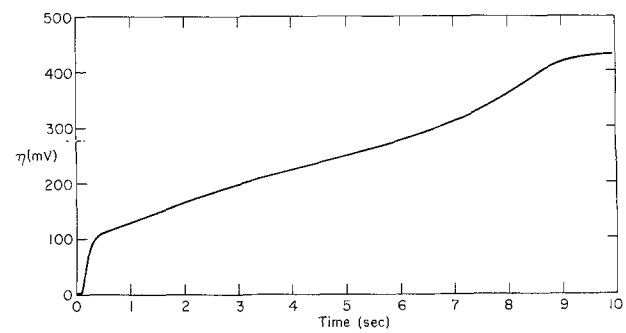

(b) Aqueous solution of 4.8 × 10^{-4}M TBACl, 2.6 × 10^{-4}M TEACl, and 0.1M LiCl; organic solution of 2 × 10^{-2}M TBATPB; current density 125 μA/cm².

Fig. 11. Two-step ion transport.

Comparison of various cation crossings.—Representative chronopotentiograms for the transport of several TAACl's are shown in Fig. 12. As expected, as the TAA^+ becomes less oil soluble, a more negative potential must initially be applied to pass current. In the case of tetramethylammonium ion (TMA^+), the potential difference between the transport of TMA^+ and that of TPB^- is too small to provide an accurate transition time. Even with a clear break in the potential-time transient, accurate determination of the transition time can be difficult. We have used the Kuwana method in which the transition times are determined by extending tangential lines from the two inflection points on the chronopotentiogram. τ is taken to be the time between the beginning of current flow and the intersection point of the two lines. Unfortunately, onset of transport by a second ion (TBP^- in this example) affects the slope of one tangent, thereby altering the point of intersection and changing the apparent τ. As the potential window diminishes, measured transition times become shorter. This effect is, unfortunately, not noticeable for various solutions having different concentrations of the same transporting ion and supporting electrolyte, and it is not affected by current densities. Apparently constant $i\tau^{1/2}/c$ values are obtained for a given salt system, but these reproducible values cannot be considered accurate.

A method of curve superposition at short times improves accuracy for a given transporting ion. Comparison of transition times for solutions containing different aqueous supporting electrolytes (same anion, different cations in Fig. 7) shows the variation of τ values. Using these uncorrected transition time values would result in logarithmic plots each with different initial slope and inaccurate determination of transfer coefficients. Figure 8 shows the logarithmic plots after correction of τ values for second ion transport.

A more difficult problem is determination of τ for different transporting ions as in Fig. 11. The interference of TPB^- transport during simultaneous cation transport for the less oil-soluble ammonium ions distorts the shapes of the potential-time profiles and shortens the measured transition times. Superposition is not a viable process and variation of alpha with alkyl chain length is difficult to measure. Transfer coefficients for a few TAA^+'s have been reported (10), but these values seem much too low. Accurate measurement of these quantities is fundamental to the understanding of the barrier at the liquid/liquid interface.

Distortion of chronopotentiogram shape is greater when TAA^+ ions larger than tetrabutyl are studied. Figure 13 shows the results for the transport of tetrapentylammonium ions. The shape of this transient clearly shows adsorption of the cation at the interface. Evaluation of rate constants and transfer coefficients may not be possible using conventional data treatment.

Conclusion

Small potential windows and relatively low solubility of presently available organic supporting electrolytes restrict the number of ions whose behavior at a liquid/liquid interface can be studied. The tendency for large ions to adsorb at these interfaces creates further difficulties in the analysis of kinetic parameters. Two-ion successive or simultaneous co-transport is expected to be a frequent occurrence, a phenomenon that must be recognized if the chronopotentiograms are to be correctly interpreted. The limited potential window makes accurate determination of transition times much more difficult than for redox processes at a metal/liquid interface. Until this problem can be re-

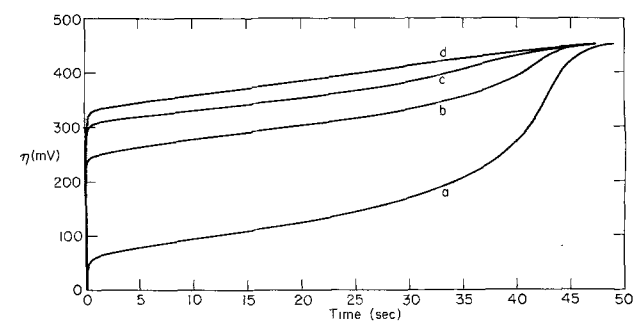

Fig. 12. Overvoltage-time profiles for various TAA^+ ions from water to nitrobenzene. Aqueous solution 0.1M LiCl, organic solution 2 × 10^{-2}M TAATPB; current density 62.5 μA/cm². Curve a, 1 × 10^{-3}M TBACl; b, 1 × 10^{-3}M tetrapropylammonium chloride; c, 1 × 10^{-3}M tetraethylammonium chloride; and d, 1 × 10^{-3}M tetramethylammonium chloride.

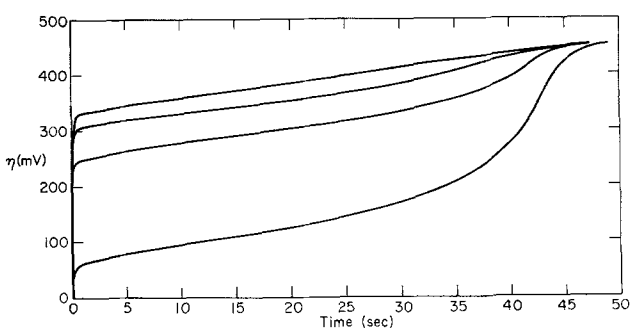

Fig. 13. Overvoltage-time profiles for tetrapentylammonium$^+$ from water to nitrobenzene. Aqueous solution 0.1M NaF and 2.5 × 10^{-4}M tetrapentylammonium fluoride; organic solution 2 × 10^{-2}M tetrapentylammonium tetraphenylborote; current density 78 μA/cm².

solved, it is unlikely that meaningful kinetic parameters can be obtained.

Manuscript submitted April 12, 1982; revised manuscript received Aug. 10, 1982. This was paper 635 presented at the Montreal, Quebec, Canada, Meeting of the Society, May 9-14, 1982.

Any discussion of this paper will appear in a Discussion Section to be published in the December 1983 JOURNAL. All discussions for the December 1983 Discussion Section should be submitted by Aug. 1, 1983.

Publication costs of this article were assisted by the University of North Carolina.

REFERENCES

1. W. Nernst and E. H. Riesenfeld, *Ann. Phys.*, **8**, 600 (1902).
2. L. I. Boguslavsky, A. N. Frumkin, and M. T. Gugeshashvili, *Bioelectrochem. Bioenerg.*, **1**, 337 (1976).
3. M. A. Manvelyan, G. L. Neugodova, and L. I. Boguslavsky, *Elektrokhimiya*, **12**, 310 (1976).
4. A. N. Frumkin, L. I. Boguslavsky, and M. A. Manvelyan, *ibid.*, **12**, 723 (1976).
5. L. I. Boguslavsky, A. N. Frumkin, and M. I. Gugeshashvili, *ibid.*, **12**, 799 (1976).
6. M. A. Manvelyan, G. L. Neugodova, and L. I. Boguslavsky, *ibid.*, **12**, 1145 (1976).
7. M. A. Manvelyan and L. I. Boguslavsky, *ibid.*, **12**, 1541 (1976).
8. M. A. Manvelyan and L. I. Boguslavsky, *ibid.*, **12**, 1636 (1976).
9. C. Gavach, P. Seta, and F. Henry, *Bioelectrochem. Bioenerg.*, **1**, 329 (1974).
10. C. Gavach, B. d'Epenoux, and F. Henry, *J. Electroanal. Chem. Interfacial Electrochem.*, **64**, 107 (1975).
11. B. d'Epenoux, P. Seta, G. Amblard, and C. Gavach, *ibid.*, **99**, 77 (1979).
12. C. Gavach, T. Mlodnicka, and J. Guastalla, *C.R. Acad. Sci. (Paris), Ser. C*, **266**, 1196 (1968).
13. C. Gavach and B. d'Epenoux, *ibid.*, **272**, 872 (1971).
14. C. Gavach and F. Henry, *ibid.*, **274**, 1545 (1972).
15. C. Gavach, *J. Chim. Phys. Physiochim. Biol.*, **70**, 1478 (1973).
16. C. Gavach, F. Henry, and R. Sandeaux, *C.R. Acad. Sci. (Paris), Ser. C*, **278**, 491 (1974).
17. C. Gavach and F. Henry, *J. Electroanal. Chem. Interfacial Electrochem.*, **54**, 361 (1974).
18. C. Gavach and B. d'Epenoux, *ibid.*, **55**, 59 (1975).
19. C. Gavach, P. Seta, and B. d'Epenoux, *ibid.*, **83**, 225 (1977).
20. M. Gros, S. Gromb, and C. Gavach, *ibid.*, **89**, 29 (1978).
21. J. Koryta, P. Vanysek, and M. Brezina, *ibid.*, **67**, 263 (1976); **75**, 211 (1977).
22. J. Koryta, P. Vanysek, M. W. Khalil, V. Maracek, Z. Samec, and M. Brezina, in "Ion-Selective Electrodes," E. Pungor and I. Buzas, Editors, pp. 441-444, Akademiai Kiado, Budapest (1978).
23. J. Koryta, *Electrochim. Acta*, **24**, 293 (1979).
24. J. Koryta, in "Ion Selective Electrodes, 3," Symposium, Oct. 13-15, 1980, E. Pungor, Editor, pp. 53-72, Akademiai Kiado, Budapest (1981).
25. J. Koryta and P. Vanysek, in "Advances in Electrochemistry and Electrochemical Engineering," Vol. 12, H. Gerischer and C. Tobias, Editors, p. 113, John Wiley & Sons, Inc., New York (1981).
26. D. Homolka, L. Q. Hung, A. Hofmanova, M. W. Khalil, J. Koryta, V. Maracek, Z. Samec, S. K. Sen, P. Vanysek, J. Weber, M. Brezina, M. Janda, and I. Stibor, *Anal. Chem.*, **52**, 1606 (1980).
27. M. Senda and T. Kakutani, *Hyomen*, **18**, 535 (1980).
28. M. Senda, T. Kakutani, and T. Osakai, *Denki Kagaku*, **49**, 322 (1981).
29. O. R. Melroy and R. P. Buck, *J. Electroanal. Chem. Interfacial Electrochem.*, In press.
30. O. R. Melroy, R. P. Buck, F. S. Stover, and H. C. Hughes, *ibid.*, **121**, 93 (1981).
31. O. R. Melroy and R. P. Buck, *ibid.*, In press.
32. O. R. Melroy, W. E. Bronner, and R. P. Buck, *Chem. Biomed., Environ. Instrum.*, **12** (2), 77 (1982).
33. M. Blank, *J. Colloid Interface Sci.*, **22**, 51 (1966).
34. P. Delahay, "Newer Instrumental Methods in Electrochemistry," p. 181, John Wiley & Sons, Inc., New York (1954).
35. M. D. Morris and J. J. Lingane, *J. Electroanal. Chem. Interfacial Electrochem.*, **6**, 300 (1963).
36. M. D. Morris, *ibid.*, **8**, 1 (1964).
37. I. M. Koltoff and J. J. Lingane, "Polarography," Vol. 1, p. 52, Interscience Publishers, New York (1952).
38. L. Q. Hung, *J. Electroanal. Chem. Interfacial Electrochem.*, **115**, 159 (1980).

Applications of Porous Flow-Through Electrodes

I. An Experimental Study on the Hydrogen Evolution Reaction on Packed Bed Electrodes

B. G. Ateya*,[1] and E. S. Arafat

Department of Chemistry, Faculty of Science, Cairo University, Cairo, Egypt

ABSTRACT

This work was aimed to test the possibility of using porous (packed bed) flow-through electrodes for generating hydrogen electrolytically. It has been shown that this electrode system can be used for this purpose. The system chosen for study was copper electrodes in H_2SO_4 media. Measurements were obtained over a range of variables, *e.g.*, particle size, flow rate, and electrode material and thickness. Over the tested range of variables, variations in the electrolyte flow rate did not affect the current-polarization relations. On the other hand, the electrolyte concentration was found to affect the current-polarization relations. This behavior has been accounted for. It was concluded that concentration polarization is negligible, and the polarization behavior of the electrode is controlled by activation polarization, and by the ohmic potential drop in the pore electrolyte. The effect of electroplated Ag and Pt on the current-polarization relations has been evaluated and explained.

The electrolysis of water has long been the means of obtaining pure hydrogen. At the present time, there is a recurrent interest in hydrogen as a medium for energy storage and transport. A good deal of the literature pertaining to this subject is available in several chapters, books, and symposia proceedings (1-5). An electrolysis cell consists of two electrodes separated by an ion-permeable membrane while an aqueous basic solution circulates between them. The design and construction of industrial water electrolyzers has received considerable attention. Nevertheless, conventional electrolyzers operate with essentially primitive electrodes, being usually in the form of steel plates coated with a thin layer of nickel. It is recognized that the major part of power consumption in water electrolyzers is used to overcome the various types of polarizations, *e.g.*, activation and ohmic polarizations. Consequently,

* Electrochemical Society Active Member.
[1] Present address: Faculty of Science, University of the United Arab Emirates, Al-Ain, Abu Dhabi.

a large decrease in the activation polarization and/or in the ohmic potential drop would constitute a significant improvement in the power consumption of this process.

The electrode reactions of water electrolysis, namely, hydrogen and oxygen evolution, are very slow on all but the noble metals, *e.g.*, Pt, Ir, Pd, . . ., etc. The use of such materials is excluded for obvious reasons. Since the rate of an electrochemical reaction increases with the surface area of the electrode, it is possible to increase the reaction rate considerably, at the same level of polarization, by using porous (three-dimensional) electrodes. These electrodes possess very large true (internal), compared to apparent (external), surface areas. The specific surface area of a porous electrode (area/unit volume) may be several powers of 10 depending on the structural properties of the electrode material.

Porous electrodes working on liquid reactants may be classified according to the predominant mode of mass transfer into flooded diffusion electrodes, where the reactant ions are transferred to the interior of the electrode by diffusion, and flow-through electrodes, where the reactants are transferred by forced convection (mass flow) through the electrode. A flooded diffusion electrode does not perform particularly well for gas evolution reactions since the evolved gas displaces the electrolyte away from the internal surface of the electrode (6). Eventually, only the external surface of the electrode remains available for the reaction, and the porous electrode behaves much like a planar electrode. This problem can be eliminated by using flow-through electrodes. As a result of the continuous flow of electrolyte, the resulting gas bubbles are swept away. In fact, electrolyte circulation was found to have a significant effect in lowering the ohmic potential drop, due to gas bubbles in a conventional vertical cell with planar electrodes (7).

In this paper, we present the preliminary experimental results obtained on the current-polarization relations of the hydrogen evolution reaction (HER) at a porous flow-through electrode from a sulfide acid solution. The electrode material was copper particles. These particles were subsequently electroplated *in situ* with either Ag or Pt. The effects of these noble metals on the current-polarization relations were measured and explained.

Experimental

Steady-state current-potential relations were measured for HER in H_2SO_4 at various concentrations and flow rates. The details of the cell have been reported elsewhere (8). Figure 1. shows a schematic of the arrangement of the porous electrode, counterelectrode, and the respective directions of current and electrolyte flow. A constant electrolyte flow speed was maintained using a simple flow system with a constant pressure head. The electrodes were in the form of packed cylindrical beds 2 cm in diameter and 2.1 cm long composed of copper particles. Some electrodes were made of spherical particles about 0.03 cm average diam (specific surface area as measured by liquid permeability is $S = 130$ cm^2/cm^3), and others were made of wirelets 0.2-0.3 cm long and 0.04 cm in diam ($S = 175$ cm^2/cm^3). The porosity for both was 0.47. Copper particles were used for reasons of cost and availability, and H_2SO_4 to ensure that the electrode surface was oxide-free. In principle, any good conducting material can be used for preparing the porous electrode.

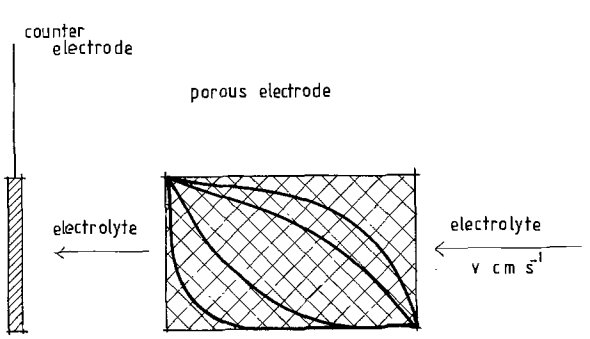

Fig. 1. Schematic of the arrangement of electrode and electrolyte flow. Curves 1-4 represent distribution of reaction rate for increasing electrolyte conductivity (for 1-4) see text.

One of the electrodes (spherical particles) was subsequently electroplated with silver *in situ* using a dilute solution of silver cyanide complex, while the other was similarly coated with platinum from a dilute solution of hexachloroplatinic acid.

Measurements were taken galvanostatically at 25° ± 2°C. The direction of electrolyte flow was opposite to that of the current. The packed bed electrode was held in a vertical position. The electrolyte entered through the lower end and exited through the upper end which faced the counterelectrode. The potential was measured at both ends using Hg/Hg_2SO_4 reference electrodes with fine Luggin capillaries. We report below only the polarization at the exit side, because it is the value of practical interest (after correcting for the ohmic potential drop external to the electrode). The polarization was defined from the thermodynamic equilibrium potential, and was corrected for the liquid junction potential between the electrolyte solutions inside and outside the tip of the Luggin capillary.

Results and Discussion

Effects of electrolyte concentration and flow rate.— The effect of acid concentration on the current-polarization relations, at various flow rates, is shown in Fig. 2-4 for Cu electrodes and Ag- and Pt-coated electrodes, respectively. The results on Cu show considerably more random scatter than those on Pt and Ag. This may be attributed to possible differences in the mechanism of

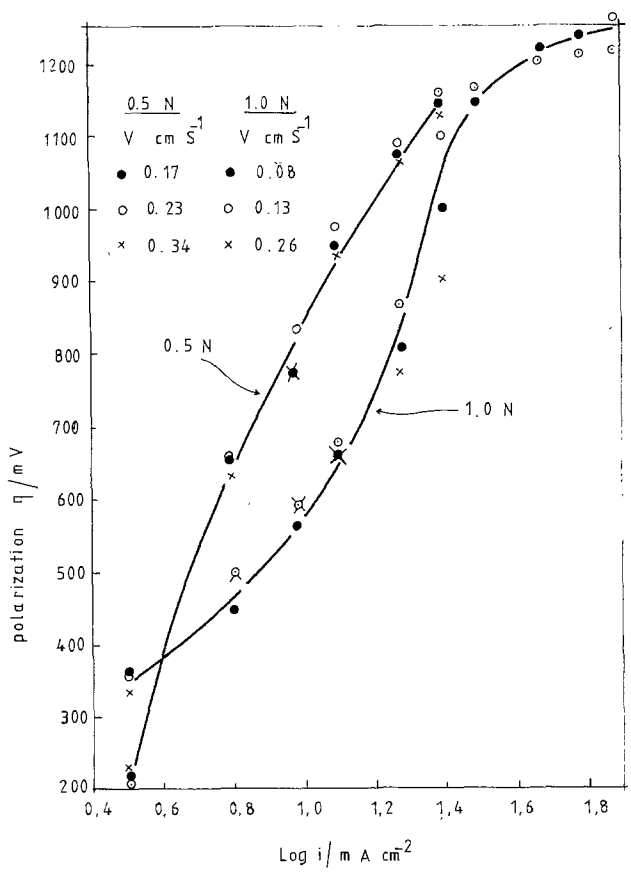

Fig. 2. Effect of the sulfuric acid concentration on the current-polarization relations for the HER on Cu electrodes.

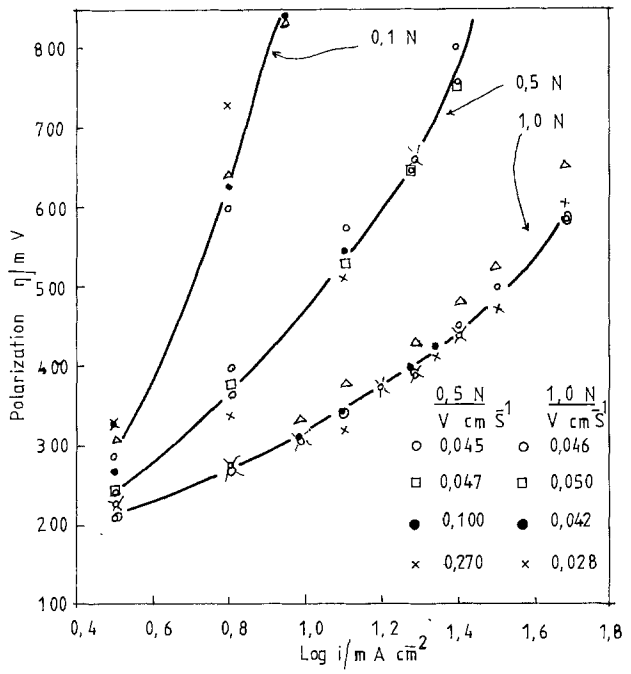

Fig. 3. Effect of the sulfuric acid concentration on the current-polarization relations for the HER on Ag-coated Cu electrodes.

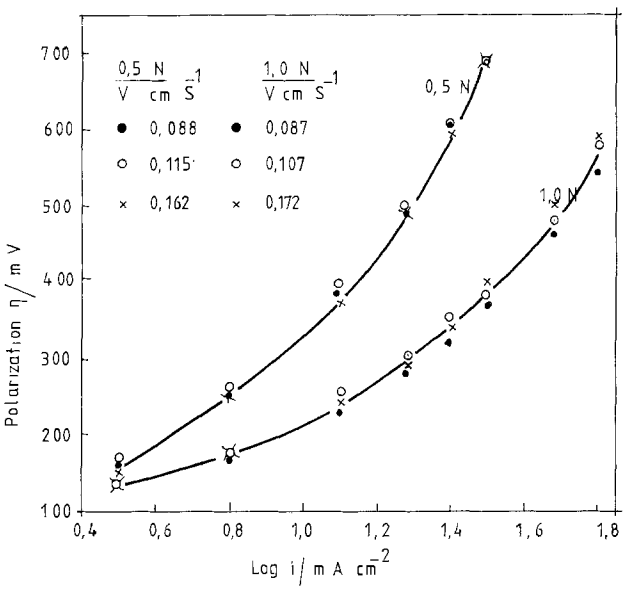

Fig. 4. Effect of the sulfuric acid concentration on the current-polarization relations for the HER on Pt-coated Cu electrodes.

bubble growth and release on the different metal surfaces. An increase of electrolyte concentration causes a decrease in polarization at a certain current for either Cu, Ag, or Pt. At this level of acid concentration, the conductivity increases with concentration. This decrease in polarization may be due to one or more of the following reasons: (*i*). Decrease of the magnitude of concentration polarization. (*ii*). Decrease of the ohmic potential drop in the pore electrolyte as a result of the increase of its conductivity. The latter is necessarily accompanied by a more uniform distribution of the reaction within the porous electrode (see Fig. 1). In less conductive electrolytes, and due to the difficulty of ion transport, most of the reaction is localized in a thin reaction zone near the end of the electrode (9, 10). Consequently, the current travels only a shorter distance in a more resistive medium. Under this condition, a large part of the internal surface of the electrode is not participating in supporting the reaction. (*iii*). Decrease of the activation polarization. This is a consequence of the increase in the surface area participating in the reaction, as a result of the more uniform distribution of the reaction inside the pores (see above).

It appears that concentration polarization is not a possible cause of the observed effect, since, as discussed below, the hydrogen ion concentration is not significantly depleted upon passage of the electrolyte through the electrode.

The results of Fig. 2-4 also show that the flow speed of the electrolyte, over the tested range, has no effect on the current-polarization relations for Cu, Ag, and Pt. This can only be true if there is no significant decrease in the hydrogen ion concentration inside the electrode, and, hence, no significant concentration polarization. This conclusion can be supported by the following argument. In a porous flow-through electrode, the current density (per unit of cross-sectional area) is given by

$$i = nFv\,(R_i - R_o)$$

$$= nFvR_i\,(1 - R_o/R_i)$$

where i is the current density, F is the Faraday constant, v is the electrolyte flow speed, and R_i and R_o are the inlet and the outlet reactant concentrations. For most of the results reported here, $v \leq 0.05$ cm sec^{-1}, $R_i \geq 0.5N$, and $i \leq 200$ mA cm^{-2}. Therefore, $(R_i - R_o)/R_i \leq 10\%$, and concentration variations inside the porous electrode are negligible. Hence, it is concluded that the polarization (power) loss of the electrode, under the present experimental conditions, is caused by both activation polarization and ohmic potential drop in the pore electrolyte.

The concentration effect, shown in Fig. 2-4, does not continue much above 1*N* H_2SO_4. Thus, it was found that the current-polarization relations in 1-3*N* H_2SO_4 solutions are virtually the same, as shown in Fig. 5a-c for Cu, Ag, and Pt surfaces. This becomes more surprising in view of the fact that the specific conductance of 0.5, 1, and 3*N* sulfuric acid solutions are about 0.1, 0.2, and 0.5 Ω^{-1} cm^{-1}, respectively. Thus, whereas about a twofold increase of conductance (from 0.5 to 1*N*) brings about a 200 mV decrease in polarization (at a current of 20 mA cm^{-2}), a greater increase (from 1*N*

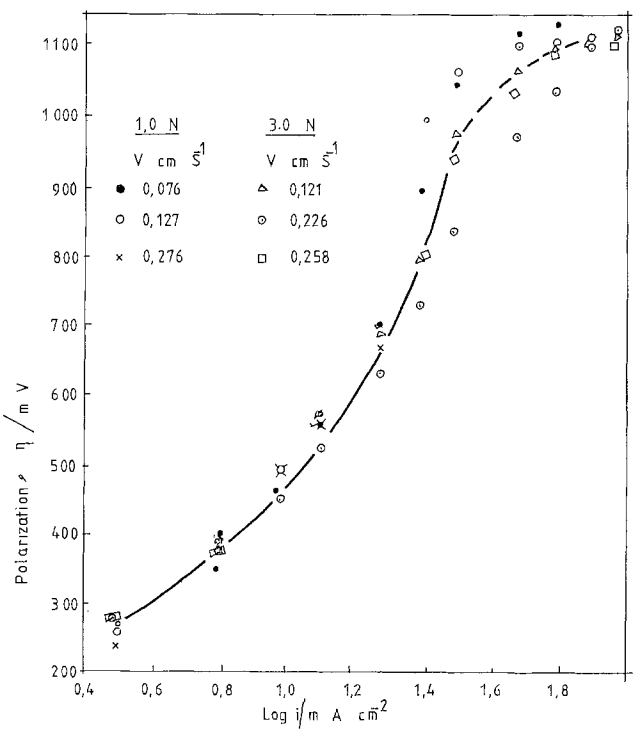

Fig. 5a. Comparison of the current-polarization relations for the HER on Cu electrodes in 1 and 3*N* H_2SO_4.

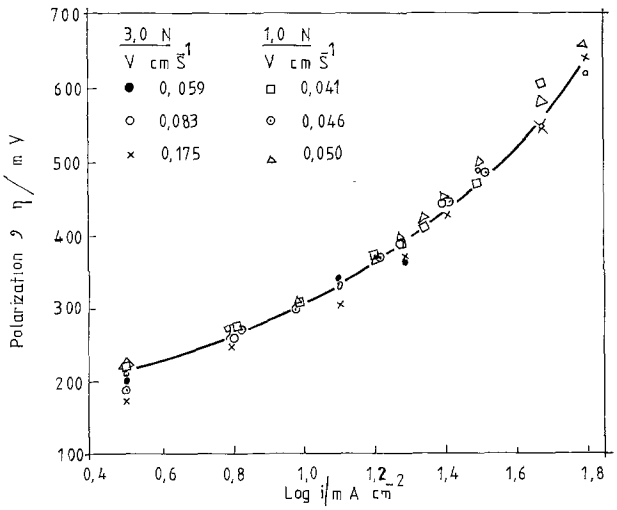

Fig. 5b. Comparison of the current-polarization relations for the HER on Ag-coated electrodes in 1 and 3*N* H_2SO_4.

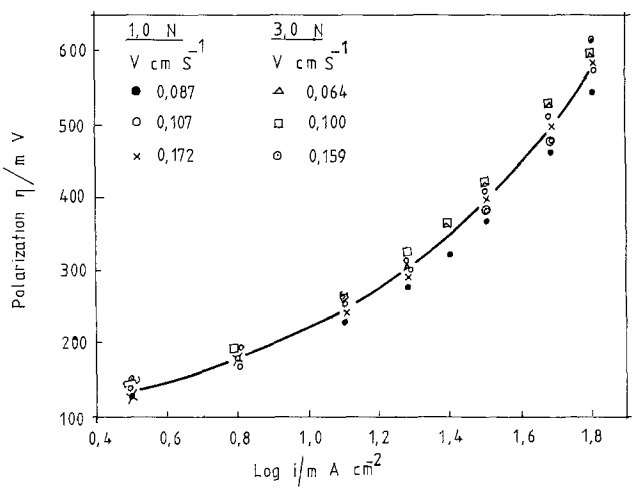

Fig. 5c. Comparison of the current-polarization relations for the HER on Pt-coated electrodes in 1 and 3*N* H_2SO_4.

to 3*N*) hardly causes any decrease in polarization. This phenomenon may result from the interplay of some interrelated, and possibly opposing factors, resulting from resistance variations. Thus, as the resistance of the electrolyte increases, most of the reaction is localized in a narrow region near the (exit) end of the electrode (see above). Since the surface area of this reaction zone is less than that of the entire electrode, a corresponding increase in activation polarization is necessary if the electrode is to support the same current output. On the other hand, most of the current travels only a short distance albeit in a more resistive medium. Under some conditions, this might result in a decrease of the overall ohmic potential drop in the pore electrolyte. There is an obvious optimization problem which needs to be dealt with, but it appears that above 1*N* H_2SO_4 the two effects balance each other. The situation is admittedly more complex because of the profuse hydrogen evolution taking place inside the pores which generates vigorous convection. The gas bubbles are likely to change the electrolyte resistance, current distribution, and to insulate some of the internal area of the electrode from the electrolyte. These effects may also be current-dependent in view of the findings (11, 12) that the size and velocity of the hydrogen gas bubbles evolved on planar electrodes and their hydrodynamic effects depend on the current. A more quantitative explanation of this concentration effect necessarily requires the development of an adequate model. Work in this direction is underway.

Effect of electrodeposited Ag and Pt.—Figures 6a-c show the effect of electroplated Ag and Pt on the current-polarization relations for hydrogen evolution from 0.5, 1, and 3*N* H_2SO_4, respectively. The results are presented for various flow speeds at each acid concentration. The general trend of the results is quite clear regardless of the acid concentration of flow rate. Thus, at the same polarization, the Pt-coated surface sup-

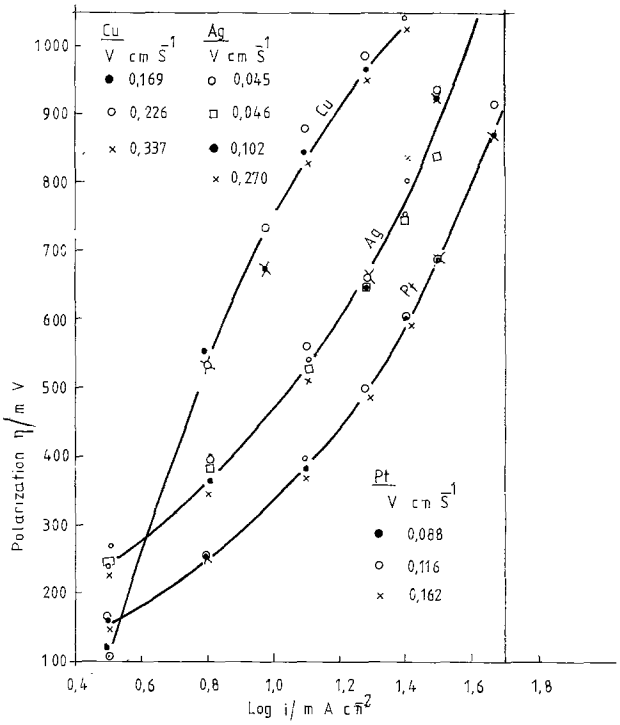

Fig. 6a. Effect of electroplated Ag and Pt on the current-polarization relations of the HER in 0.5*N* H_2SO_4.

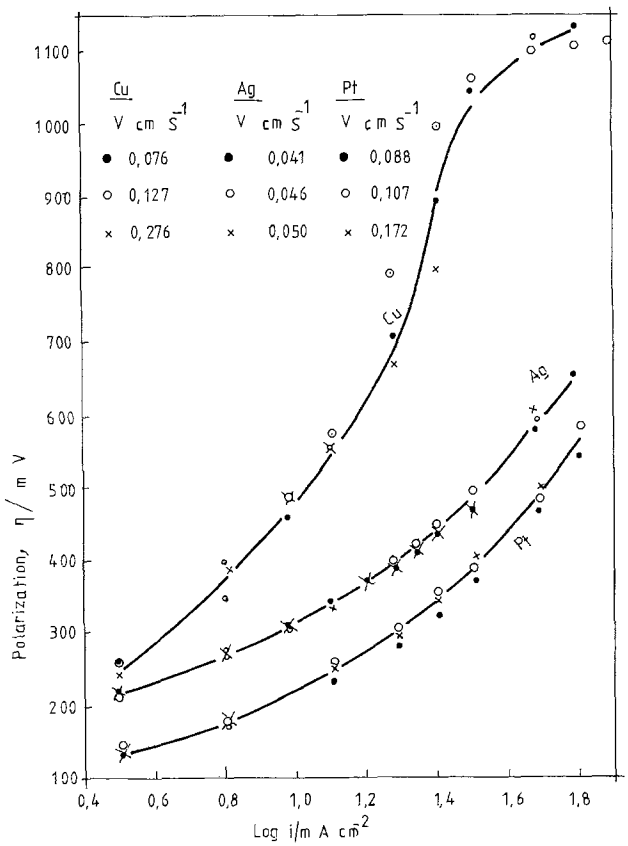

Fig. 6b. Effect of electroplated Ag and Pt on the current-polarization of the HER in 1*N* H_2SO_4.

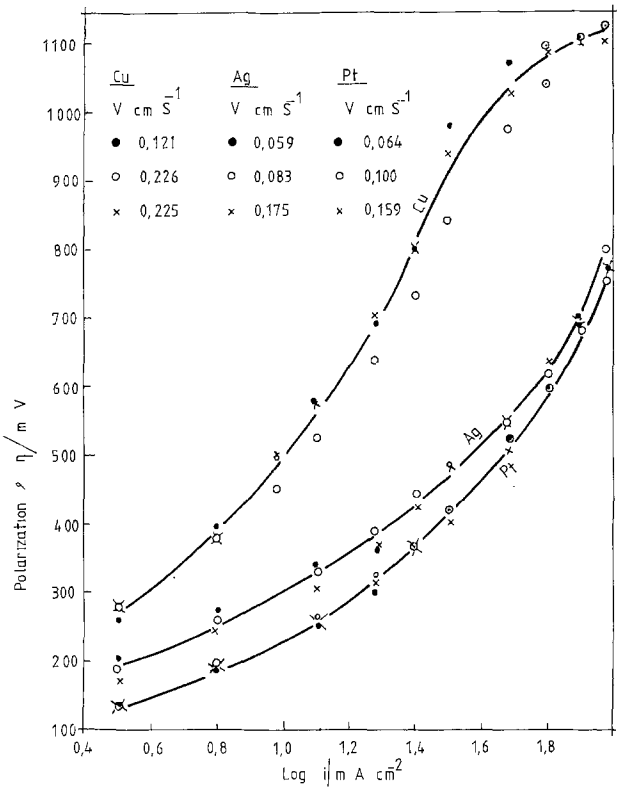

Fig. 6c. Effect of electroplated Ag and Pt on the current-polarization relations of HER in 3N H_2SO_4.

ports more current than the Ag-coated surface, which in turn supports more current than the copper electrode surface. This effect of the electroplated metals (Ag and Pt) can be explained on the basis of their better catalytic activity towards the HER, which is in the order of Pt > Ag > Cu. This sequence has been amply confirmed on planar electrodes (13).

Conclusions

The main objective of this work was to test whether porous flow-through electrodes can be used for water electrolysis. It has been proven that such an electrode can be used for the HER. There is no reason to preclude the use of a similar electrode with a suitable packing material for the oxygen evolution reaction. Assuming the electrolyte flow rate is constant and there is a convenient outlet for the gas, the electrode would operate steadily.

The choice of sulfuric acid was dictated by the use of a less noble (oxidation prone) packing material, *i.e.*, copper particles. This, in turn, was used because of cost and availability. It is recognized that the activation polarization for the HER on Cu is rather high, and sulfuric acid is corrosive. Nevertheless, the results prove the validity of the system for this purpose.

Furthermore, we have shown that the electrolyte flow rate does not significantly affect the current-polarization relations under the present conditions. A better-designed system would involve a much thinner electrode made of much finer particles of either a noble metal or a good quality graphite. The electrolyte should preferably be alkaline, in order to avoid corrosion problems. Work in this direction is in progress and will be reported later.

There now exist in the literature (14) several mathematical models which describe the behavior of porous flow-through electrodes. However, most of these models treat electrode reactions with soluble reactants and products. Neimark *et al.* (15) have used simple models of pore structure and gas streams to calculate the gas content of porous electrodes operating on gas evolving reactions. The evolution of gas within the porous electrode admittedly complicates the problem further, since gas bubbles, even at the conventional planar electrodes, increase the electrolyte resistance, change the potential and current distributions, and cause other related hydrodynamic effects, see Ref. (7, 11, 12, 16-18). We are now developing a model which simulates the dynamic character of this process, and includes the effect of the generated gas bubbles on the current-polarization relations. This will also be reported later, along with a comparison with the experimental results.

Manuscript submitted Jan. 19, 1982; revised manuscript received Aug. 23, 1982.

Any discussion of this paper will appear in a Discussion Section to be published in the December 1983 JOURNAL. All discussions for the December 1983 Discussion Section should be submitted by Aug. 1, 1983.

REFERENCES

1. "Hydrogen Energy," T. Nejat Veziroglu, Editor, Plenum, New York (1975).
2. J. O'M. Bockris, "Energy: the Solar Hydrogen Alternative," John Wiley and Sons, New York (1975).
3. C. L. Mantell, "Electrochemical Engineering," 4th ed., p. 308, McGraw-Hill, New York (1960).
4. "Industrial Water Electrolysis," S. Srinivasan, F. J. Salzano, and A. R. Landgrebe, Editors, The Electrochemical Society Softbound Proceedings Series, Princeton, NJ (1978).
5. B. V. Tilak, in "Comprehensive Treatise of Electrochemistry," Vol. 2, "Electrochemical Processing," J. O'M. Bockris, B. E. Conway, E. Yeager, and R. White, Editors, Plenum, New York (1978).
6. A. C. C. Tseung and P. R. Vassie, *Electrochim. Acta*, **12**, 31 (1976).
7. F. Hine and K. Murakami, *This Journal*, **127**, 292 (1980).
8. B. G. Ateya, E. S. Arafat, and S. Kafafi, *J. Appl. Electrochem.*, **7**, 107 (1977).
9. R. Alkire and B. Gracon, *This Journal*, **122**, 1594 (1975).
10. B. G. Ateya and L. G. Austin, *ibid.*, **124**, 83, 1540 (1977).
11. L. J. Janssen and J. B. Hoogland, *Electrochim. Acta*, **15**, 1013 (1970).
12. I. Rousar and V. Cezner, *ibid.*, **20**, 289 (1975); *ibid.*, **20**, 295 (1975).
13. H. Kita, in "Electrode Processes," E. Yeager, H. Hoffman, and E. Eisenman, Editors, p. 79, The Electrochemical Society Softbound Proceedings Series, New York (1967).
14. J. Newman and W. Tiedeman, in "Advances in Electrochemistry and Electrochemical Engineering," H. Gerischer and C. Tobias, Editors, Vol. 11, John Wiley and Sons, New York (1978).
15. A. V. Neimark, L. M. Pis'men, and L. I. Kheifets, *Soviet Electrochem.*, **11**, 580 (1975); *ibid.*, **11**, 1208 (1975).
16. F. Hine, M. Yasuda, R. Nakamura, and T. Noda, *This Journal*, **122**, 1185 (1975).
17. P. J. Sides and C. W. Tobias, *ibid.*, **127**, 288 (1980).
18. G. Kreysa and H. J. Külps, *ibid.*, **128**, 979 (1981).

Semiconductor Electrodes

XLVII. A-C Impedance Technique for Evaluating Surface State Properties of n-$MoTe_2$ in Acetonitrile Solutions Containing Various Redox Couples

G. Nagasubramanian, Bob L. Wheeler, G. A. Hope,*[,1] and Allen J. Bard*

Department of Chemistry, University of Texas at Austin, Austin, Texas 78712

ABSTRACT

Measurement of the in-phase (0°) and quadrature (90°) components of a small (12 mV) a-c signal at frequencies of 1-5000 Hz imposed on the d-c potential allows the determination of the a-c equivalent circuit. Study of the a-c impedance as a function of potential and frequency permits the determination of the properties of the semiconductor/solution interface. Results of measurements on n-$MoTe_2$ in MeCN containing various redox couples spanning a wide range of redox potentials are reported. The advantages of the in-phase (0°) component for extracting properties of surface states are discussed. In the region 0.3-0.5V negative of the valence bandedge, the total surface-state density is *ca.* 10^{10} cm^{-2}. The adsorption in the I^-/I_3^- system on the n-$MoTe_2$ surface in aqueous and acetonitrile solvents are compared.

Surface states, due to the abrupt discontinuity at a clean surface, were first postulated by Tamm (1) and a rigorous analysis of a more general model was given by Shockley (2). The abrupt discontinuity of the ordered crystal lattice at the surface results in dangling or unsaturated bonds, producing surface energy levels different from those in the bulk material. Interface states produced by impurities incorporated at the surface, *e.g.*, by specific adsorption of solution species or by formation of corrosion products at the semiconductor electrode surface, also can produce localized energy levels in the bandgap of the semiconductor electrode. These energy levels in the forbidden gap can serve as reservoirs of charge at the semiconductor surface. The position of the Fermi level at the surface determines whether these energy levels are filled or vacant. The determination of the energy and density of interface states as well as the time constant associated with the exchange of charge carriers with the bulk and the capture cross section is important in understanding the behavior of semiconductors in contact with a metal or with a solution.

Indeed, the relative independence of the Schottky barrier heights of low bandgap semiconductors in contact with metals of widely differing work functions was explained by Bardeen (3) and others (4, 5) in terms of pinning of the Fermi level at the surface by a high density of surface states. A similar phenomenon has been observed in photoelectrochemical (PEC) cells where low bandgap semiconductors such as Si (6, 7), CdTe (8), and GaAs (9) exhibit a nearly constant photovoltage in contact with solutions containing a number of redox couples whose redox potentials span a potential regime much wider than the E_g of the semiconductor. Such behavior can also be explained by pinning of the Fermi level by interface states (10). Interface states can be studied by a number of optical and electrical methods. Several techniques have been developed for the measurement of interface-state properties in solid-state devices. These include measurements of (*i*) the isothermal dielectric relaxation current (IDRC) (11); (*ii*) the thermal dielectric relaxation current (TDRC) (12); (*iii*) the low frequency capacitance-voltage behavior (13); and (*iv*) the a-c conductance (14). However, the liquid electrolyte in PEC systems precludes the application of the first two methods, since meaningful results can be obtained only over a wide range of temperatures which is restricted by the liquid range of the solvent. The quasi-static low frequency capacitance technique and the a-c conductance method do not suffer this limitation, and capacitance measurements have been frequently employed to study the semiconductor/liquid interface (15, 16). However, the capacitance technique is of limited value in studying interface states. For example, in the case of metal-oxide-semiconductor (MOS) devices the capacitance method for the determination of surface-state properties is said to suffer from the following limitations (14a): (*i*) The variation in the capacitance values required to find the surface capacitance, even when the frequency is increased by one order of magnitude, is very small; this leads to errors in calculating the density of surface states and their time constants. (*ii*) The surface-state capacitance has to be extracted from a combination of the space charge layer, surface state, and the oxide layer capacitances. Since the oxide layer capacitance is in series with the semiconductor capacitance, it determines the maximum semiconductor capacitance that can be measured. This means that surface states located near the middle of the gap cannot be identified without greatly decreasing the thickness of the oxide layer, which in turn permits tunneling of charge carriers. The picture may be further complicated by the inversion layer capacitance.

The parallel equivalent conductance (G_p) (the in-phase component of the total admittance corrected for the space charge resistance) is more useful in characterizing interface states since one can measure directly the properties related to the capture and emission rates of charge carriers by surface states. Further, it is useful in extracting data when the surface-state density is as low as 10^9-10^{11} cm^{-2} eV^{-1} (14a). In addition, G_p can be used to determine the values for capture probability. Even in those cases where the quadrature signal gives a frequency independent capacitance-voltage plot, the location of surface states and their time constants can be determined from the in-phase component. If the time constant for the surface states is independent of potential, the in-phase component is related to the surface-state capacitance by the following equation (see Appendix)

$$G_p/\omega = \frac{C_{ss}\omega\tau}{(1 + \omega^2\tau^2)} \qquad [1]$$

where C_{ss} is the surface-state capacitance, ω is the angular frequency of the applied a-c signal, and τ is the time constant associated with carrier exchange. From the relevant equivalent circuits for the interface given in Fig. 1a, it is clear that the conductance does not contain C_D, the depletion layer capacitance, but depends only on the surface-state branch of the equivalent circuit. A plot of G_p/ω at a given potential will have a maximum value at a particular frequency; the reciprocal of that frequency yields a weighted average of the time constant associated with the surface states, when $\omega\tau = 1$. This leads to a maximum value in C_{ss}

* Electrochemical Society Active Member.
[1] Permanent address: School of Science, Griffith University, North Brisbane, Queensland 4111, Australia.
Key words: impedance, semiconductor, surfaces.

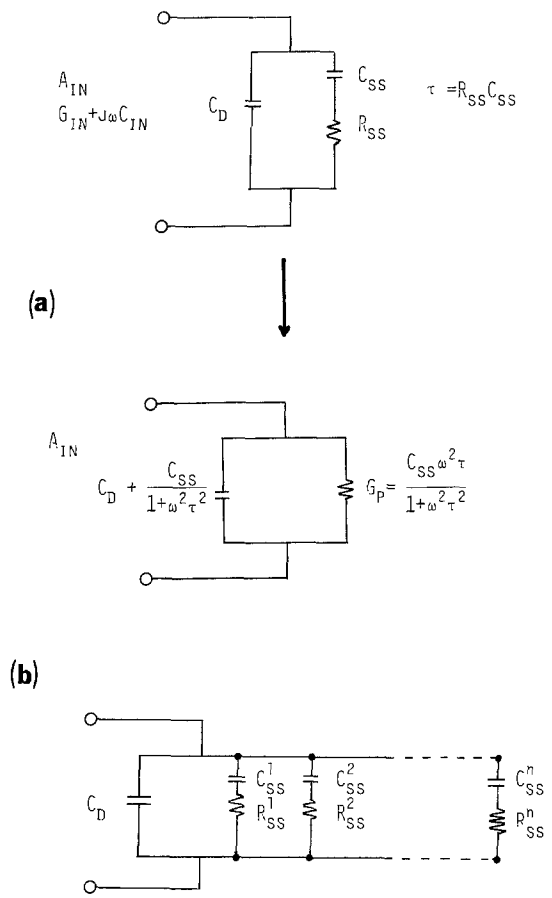

Fig. 1. (a) Equivalent circuit for "single-level" time constant surface states in parallel to the depletion layer capacitance in MOS devices. (b) Equivalent circuit for "multi-level" time constant surface states in parallel to the depletion layer capacitance in MOS devices. Key: C_D, depletion layer capacitance; C_{ss}, surface-state capacitance; R_{ss}, surface-state resistance; G_p, equivalent parallel conductance of the surface states.

equal to $2G_p/\omega$. Hence, the capacitance associated with the surface states can be readily calculated. The density of surface states at a given energy, N_{ss} (in units of eV^{-1} cm^{-2}), can easily be obtained from G_p, since

$$N_{ss} = 2G_p\tau/e \qquad [2]$$

(where e is the electronic charge). The value of τ, assumed to be independent of potential, is taken as that corresponding to the peak value in a plot of G_p/ω *vs.* ω.

There have not been many reports on the use of the a-c conductance technique in studies of electrolyte/semiconductor PEC systems (17, 18). Barabash and Cobbold (17) reported some preliminary investigations on the dependence of interface-state properties of electrolyte/SiO_2/Si structures on *p*H. Essentially the results parallel those observed for MOS devices and confirm the validity of a-c conductance technique for evaluating interface-state properties of semiconductor/liquid junctions. DuBow and Rajeshwar (18) have reported a systematic study of the admittance characteristics of the n-GaAs/$AlCl_3$-butylpyridinium chloride room temperature molten salt interface and demonstrated that the equivalent parallel conductance is more sensitive to interface-state properties than the parallel equivalent capacitance, although both fundamentally contain identical information about the surface-state properties.

We report below the results of a-c impedance technique studies of n-$MoTe_2$ in MeCN, 0.1*M* tetra-n-butylammonium perchlorate (TBAP) containing a number of redox couples with widely differing redox potentials. $MoTe_2$ is a layered compound whose properties as a semiconductor electrode were first studied by Tributsch and co-workers (19). More recent studies of PEC cells with $MoTe_2$ are described by Abruna *et al.* (20).

Experimental

Crystal growth.—The α-$MoTe_2$ crystals were grown by halogen vapor transport from $MoTe_2$ powder (Great Western Inorganics, Golden, Colorado, 99.9%.) Either Br_2 (70 mg) or $TeCl_4$ (100 mg) was used as a transporting agent for every 5g of $MoTe_2$. These were introduced into a quartz tube (length 19 cm, diameter 18 mm), evacuated to better than 5×10^{-5} Torr, and sealed. Samples using bromine transport were held at liquid nitrogen temperature during evacuation. The sealed tube, with the powder evenly distributed along the length of the tube, was introduced into a horizontal split tube furnace (Hevi-Duty Electric Company, Watertown, Wisconsin; length, 18 in., diameter 1¼ in.) and held at a maximum temperature of 875°C. The temperature decreased to around 800°C at the ends of the sample and increased crystal growth could be noticed in these regions. Favorable conditions for crystal growth were ensured when the tube was cooled by convection of air through the split tube furnace, with the majority of the crystals growing on the wall above the original charge. After the transport had proceeded sufficiently, the tube was removed from the furnace and a suitable section was held under running water to condense the vapor phase. The rest of the tube could then be cooled without heavy contamination of the crystals with the transport agent.

Samples transported with bromine required 2-3 days to produce large crystals (~ 50 mm^2), whereas $TeCl_4$ could transport good crystals in approximately 18 hr. In both cases, an increased concentration of transport agent increased the growth rate; conditions for growth of the best crystals are those given above. Crystals occurred in clusters, away from the side of the tube in the form of platelets of up to 1 cm^2 in area. Some crystals exhibited hexagonal growth spirals and many were twinned. However, a significant fraction had one flat crystal surface, and a few grew as flawless hexagonal plates from one corner. Electron microprobe analysis could not detect the presence of halogens in the transported crystals or any variation in composition between crystals.

Electrodes.—Single crystals of α-$MoTe_2$ were selected from the clusters of crystals and cut with a razor blade to the desired dimensions. The face $\perp$ C axis was peeled off with adhesive tape and back-ohmic contacts were made with Ga/In alloy. A copper wire lead for electrical contact was attached to the back-side with silver conductive paint (Allied Product Corporation, New Haven, Connecticut) and was subsequently covered with 5 min epoxy. The assembly was mounted into 7 mm diam glass tubing and held in position with silicone rubber sealant (Dow Corning Corporation, Midland, Michigan) which also served as an effective seal against the seepage of electrolyte solution to the rear of the semiconductor. The exposed area of the electrode was about 0.05 cm^2. The surface of the electrode was treated prior to use with 6*M* HCl for 5-10 sec and then rinsed thoroughly with distilled water and dried.

The solvent, acetonitrile (MeCN), was purified and stored as described elsewhere (21). All chemicals, employed after purification or in the purest form commercially available, were dried under vacuum before use. A check of the purity of all chemicals used was performed by cyclic voltammetry at a Pt disk electrode (0.02 cm^2) at the beginning of each experiment. Polarographic grade tetra-n-butylammonium perchlorate (TBAP), which was twice recrystallized from acetone-ether and dried under a vacuum of $< 10^{-5}$ Torr for two days, was used as the supporting electrolyte at 0.1*M* concentration.

A three-compartment electrochemical cell was used. A large area (> 40 cm²) Pt gauze counterelectrode immersed in the same compartment as the working electrode was used in impedance measurements. A Pt gauze, separated from the main compartment by a medium porosity glass frit was used as the counterelectrode for coulometric bulk electrolysis. The reference electrode was an aqueous saturated calomel electrode (SCE) with a saturated KCl agar plug, immersed directly in the main compartment. All potentials, unless stated otherwise, are reported *vs.* this SCE.

A Princeton Applied Research (PAR) Model 173 potentiostat and a PAR Model 175 universal programmer, equipped with a Houston Instruments (Austin, Texas) Model 2000 X-Y recorder were used to obtain cyclic voltammograms. For impedance measurements, a Soltec (Sun Valley, California) Model 6432 X-Y_1Y_2 recorder was employed. The lock-in amplifier technique, which yields the in-phase (0°) and out-of-phase (90°) components of a sine wave superimposed onto a linear potential ramp was employed. The a-c signal (12 mV peak-to-peak) at different frequencies was provided by an external signal generator, a Hewlett-Packard (Palo Alto, California) Model 200CD wide range oscillator. Components of the total impedance were obtained with a PAR Model 5204 lock-in amplifier. All solutions were prepared and sealed in a helium-filled Vacuum Atmosphere Corporation (Hawthorne, California) glove box.

Results

Capacitance-voltage plots.—The two important parameters, the flatband potential (V_{FB}) and doping density are usually deduced from Mott-Schottky (MS) plots. Such MS plots for n-$MoTe_2$ in MeCN containing 0.1*M* TBAP alone are given in Fig. 2 for frequencies in the range 200 Hz-7 kHz. Although there is a very small dispersion in the slope, the V_{FB} for all plots is located at −0.3V *vs.* SCE. If the dielectric constant of n-$MoTe_2$ is taken as that of n-$MoSe_2$ (22), the donor density (N_D) is calculated to be about 2×10^{17} cm^{-3}. The difference (ΔE_F) between the conduction bandedge (CB) and the Fermi level (E_F) can be calculated from the Fermi-Dirac equation (23). With the reduced mass for the electron taken as the rest mass (22), ΔE_F is ~ 0.1 eV, so that the conduction bandedge lies at −0.4V. With an $MoTe_2$ bandgap 1.1 eV (24), the valence bandedge is at 0.7V *vs.* SCE. The band positions and the formal potentials of the redox couples employed in this study are given in Fig. 3.

Conductivity.—The value of the conductivity has been computed from the equation $\sigma = ne\mu$, where σ is the conductivity (Ω^{-1} cm^{-1}), n is the charge carrier density (cm^{-3}), e is the electronic charge (1.6×10^{-19}C), and μ is the mobility (cm^2/V sec). A value of $\mu = 20$ is taken from the literature (25). With $n = 2 \times 10^{17}$ cm^{-3}, the resistivity ($1/\sigma$) is found to be 1.56Ω cm. This is in good agreement with previous values reported (26) for single crystal n-$MoTe_2$.

Impedance measurements.—The properties of the interface were primarily deduced from a-c impedance measurements. The impedance of the semiconductor/electrolyte interface was measured as a function of both the electrode potential and frequency (or angular frequency, ω). The frequency range studied was 50 Hz-7 kHz. Typical plots of G_p *vs.* V and C *vs.* V are shown in Fig. 4 for n-$MoTe_2$ in MeCN containing 0.1*M* TBAP alone. Figure 5 shows similar plots in the presence of various redox couples. As described previously, a plot of G_p/ω *vs.* f can be employed to determine the time constant of surface states. Such a plot is given in Fig. 6a for MeCN, 0.1*M* TBAP at 0.3V *vs.* SCE. Plots of G_p *vs.* V and C *vs.* V in MeCN in the presence of I^- (as TBAI) and both I^- and I_3^- are shown in Fig. 7 and 8, respectively. For comparison, plots of n-$MoTe_2$ in aqueous solutions containing I^- and I^-/I_3^- are given in Fig. 9.

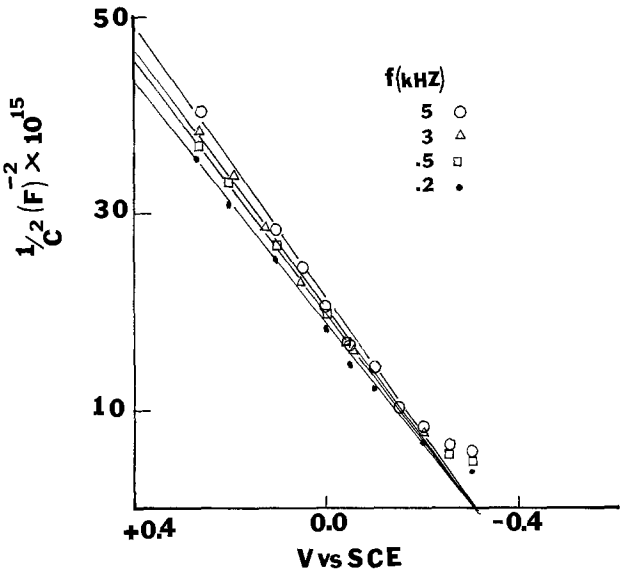

Fig. 2. Mott-Schottky (MS) plots of n-$MoTe_2$ in MeCN containing 0.1M TBAP alone, at different frequencies.

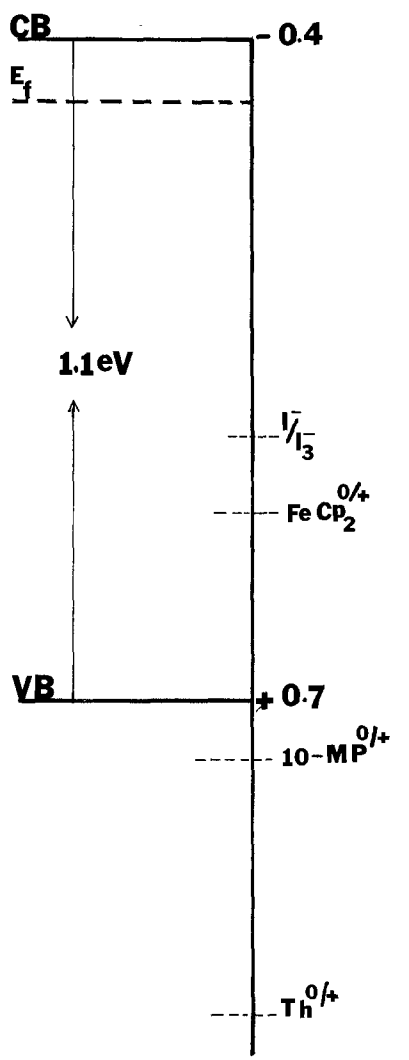

Fig. 3. Position of bandedges of n-$MoTe_2$ in MeCN containing 0.1M TBAP. CB, conduction bandedge; VB, valence bandedge; E_F, Fermi level; I, iodine; $FeCp_2$, ferrocene; 10-MP, 10-methylphenothiazine; Th, thianthrene.

Discussion

The presence of surface states can cause frequency dependent slopes and flatband potentials (V_{FB}) in MS plots, and the absence of surface states is sometimes assumed when one obtains frequency independent MS plots. Although n-$MoTe_2$ shows frequency independent MS plots, the in-phase component provides evidence for surface states. The in-phase component of the total impedance has been shown to deal directly with rates of emission and capture of carriers from surface states to either the bandedges or the bulk traps (14a). Consider Fig. 4, where the G_p *vs.* V and C *vs.* V plots are given for n-$MoTe_2$ in MeCN containing 0.1*M* TBAP alone. The C-V plots are frequency independent; however, the plot of G_p *vs.* V shows a hump near +0.3V whose magnitude is frequency dependent. The G_p values in the depletion region vary with frequency by nearly two orders of magnitude while the overall capacitance values change only marginally in the same frequency regime. This observation, that the equivalent parallel conductance is more sensitive to the presence of surface states than the quadrature component for semiconductor/liquid junctions, parallels that observed in MOS devices (17). Nicollian and Goetzberger (14a) observed that for $Si/SiO_2/M$ the capacitance increased by only 14% while the in-phase component varied by one order of magnitude for the same frequency domain. Several authors have shown that the surface states located in a particular potential regime may be composed of surface states with different time constants (27). The equivalent circuit for this condition is shown in Fig. 1b, where several different R_i-C_i elements are connected in parallel with the space charge layer capacitance. For simplicity, however, we assume that the surface states in n-$MoTe_2$ can be represented by a single time constant and the equivalent circuit is shown in Fig. 1a. The plot of G_p/ω *vs.* f for a given potential exhibits a peak at a particular frequency characteristic of the time constant of the surface state (Fig. 6a). The peak value occurs at 3000 Hz, corresponding to a time constant $\omega^{-1} = (2\pi f)^{-1} = 5 \times 10^{-5}$ sec. This time constant probably represents a weighted average of time constants associated with surface states near 0.3V. The increase in G_p/ω at low frequencies suggests that a faradaic component also contributes to the measured total conductance at these frequencies (18). If the 50 μsec time constant is taken to represent that associated with surface states at n-$MoTe_2$, the density of surface states (N_{ss}) can be calculated from Eq. [2]. Figure 6b is a typical plot of N_{ss} (cm^{-2} eV^{-1}) for the n-$MoTe_2$ electrode in MeCN, 0.1*M* TBAP solution containing $FeCp_2^{0/+}$ over the potential range +0.4 to +0.1V *vs.* SCE, where a peak in the G_p *vs.* V plot occurs. The surface-state density in this potential range varies between 5×10^{10} and 3×10^{11} cm^{-2} eV^{-1}. The time constant indicates that these surface states are fast surface states (28). Integration of N_{ss} with potential over this region (0.2-0.4V) yields a total surface density, N_{ss}', of *ca.* 10^{10} cm^{-2}. Note that this density of surface states is not sufficient for Fermi level pinning to occur (10). This is demonstrated for a 10-methylphenothiazine (10-$MP^{0/+}$) solution (Fig. 5c) whose

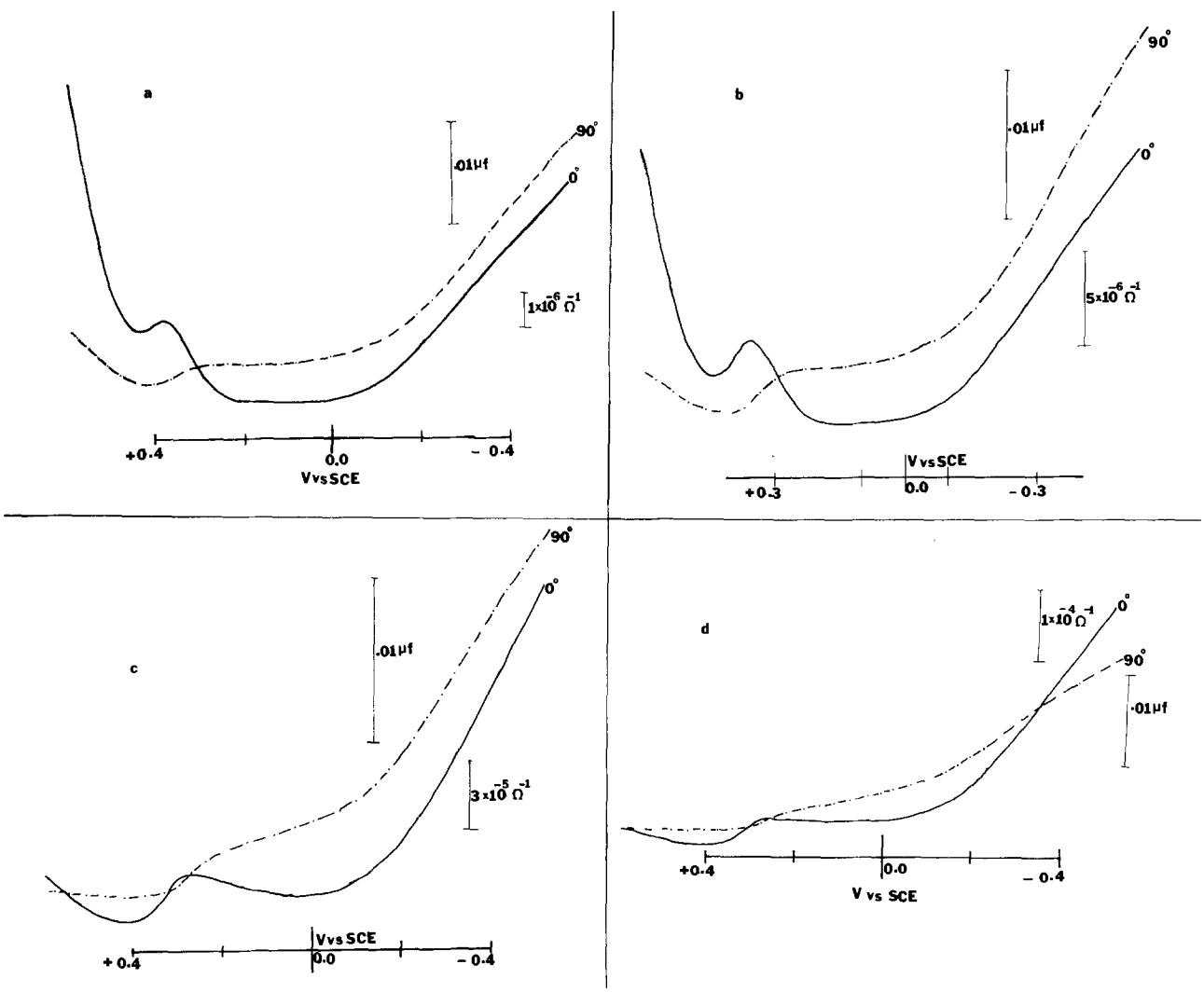

Fig. 4. Parallel equivalent conductance (G_p) (0° component) and capacitance (C) (90° component) *vs.* V for n-$MoTe_2$ in MeCN containing 0.1*M* TBAP. Frequency (f) = (a) 200 Hz; (b) 500 Hz; (c) 3000 Hz; (d) 5000 Hz.

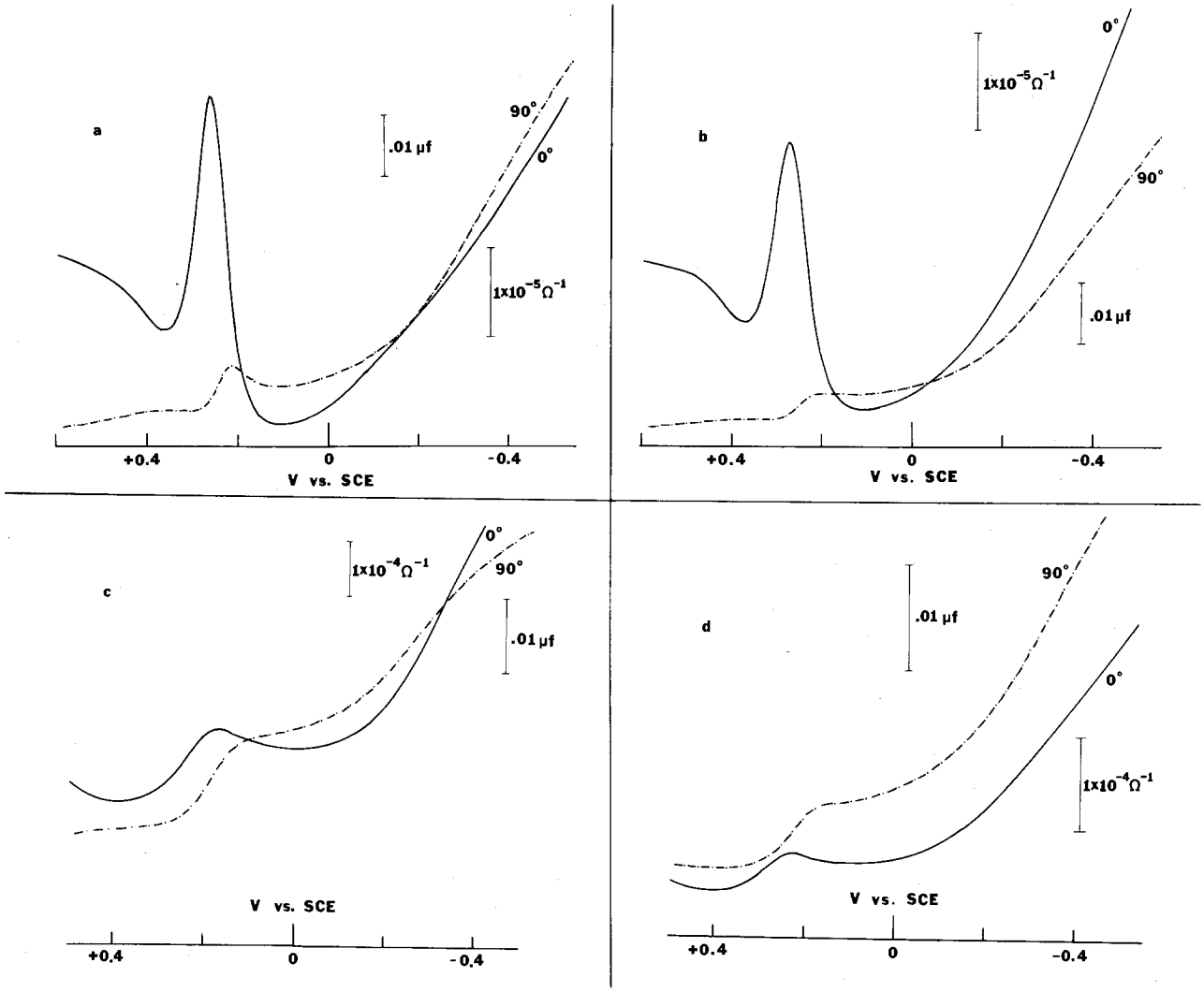

Fig. 5. G_p and C vs. V for n-$MoTe_2$ in MeCN, 0.1M TBAP solution containing (a) 10 mM $FeCp_2$ and 1.2 mM $FeCp_2^+$; $f = 200$ Hz. (b) 10 mM $FeCp_2$; $f = 500$ Hz. (c) 10 mM 10-MP and 1 mM 10-MP^+; $f = 2000$ Hz. (d) 8 mM Th°; $f = 2000$ Hz.

V_{redox} is located +0.1V positive of the VB of n-$MoTe_2$. In the presence of 10-$MP^{0/+}$, the G_p *vs.* V and C *vs.* V curves are essentially the same as those obtained with blank solution, indicating no change in V_{FB}. Addition of other redox couples, such as thianthrene ($Th^{0/+}$) and $FeCp_2^{0/+}$, also produced no apparent shift in V_{FB}. This lack of change in V_{FB} for n-$MoTe_2$ in the presence of both forms of the redox couple parallels the behavior found for other layered compounds (29). These results can be contrasted to those of other elemental and compound semiconductors where a monotonic shift of V_{FB} with V_{redox} in the presence of both forms of the couple in MeCN solution was found (30). This behavior of the layered compounds suggests that surface states are not important in establishing the equilibrium properties of the interface and that specific adsorption of electroactive species on the electrode surface does not occur. Note that the a-c impedance mea-

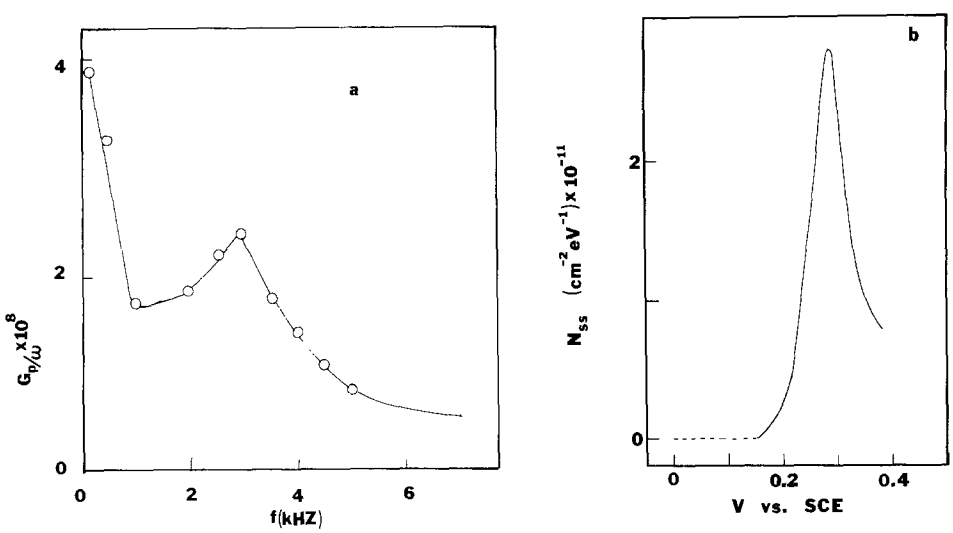

Fig. 6. (a) G_p/ω (in sec/Ω cm^2) *vs.* f for n-$MoTe_2$ in MeCN, 0.1M TBAP solution. Potential: +0.3V vs. SCE. (b) N_{ss} *vs.* V for n-$MoTe_2$ in MeCN, 0.1M TBAP containing $FeCp_2^{0/+}$.

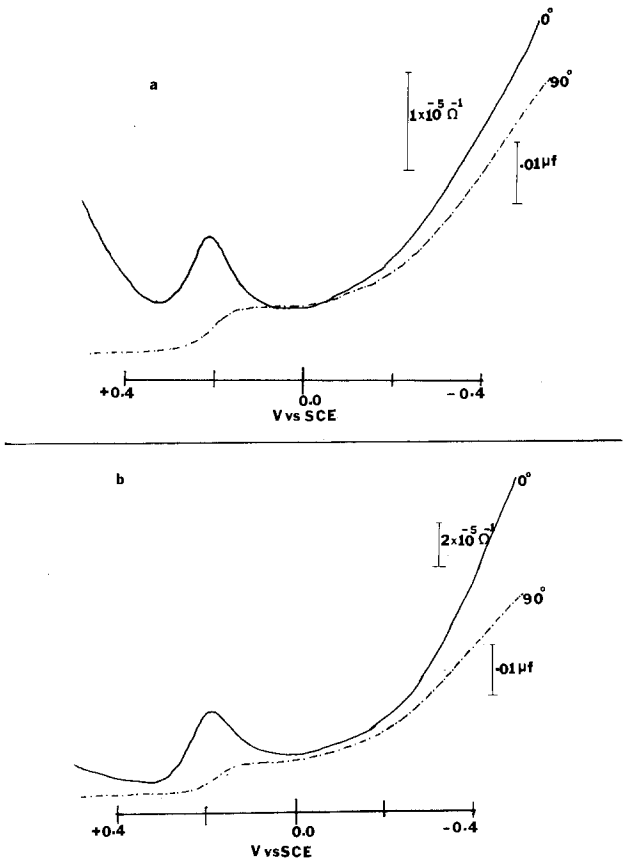

Fig. 7. G_p and C vs. V for n-$MoTe_2$ in MeCN, 0.1 TBAP solution containing 10 mM I^-. (a) $f = 500$ Hz. (b) $f = 2000$ Hz.

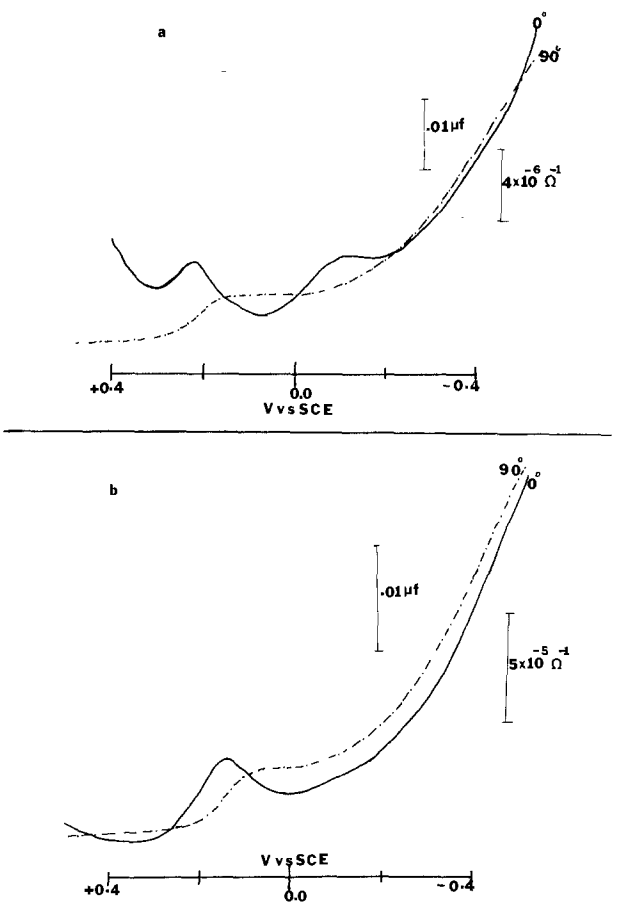

Fig. 8. G_p and C vs. V for n-$MoTe_2$ in MeCN/0.1 TBAP solution containing 10 mM I^- and 1.2 mM I_3^-. (a) $f = 200$ Hz. (b) $f = 2000$ Hz.

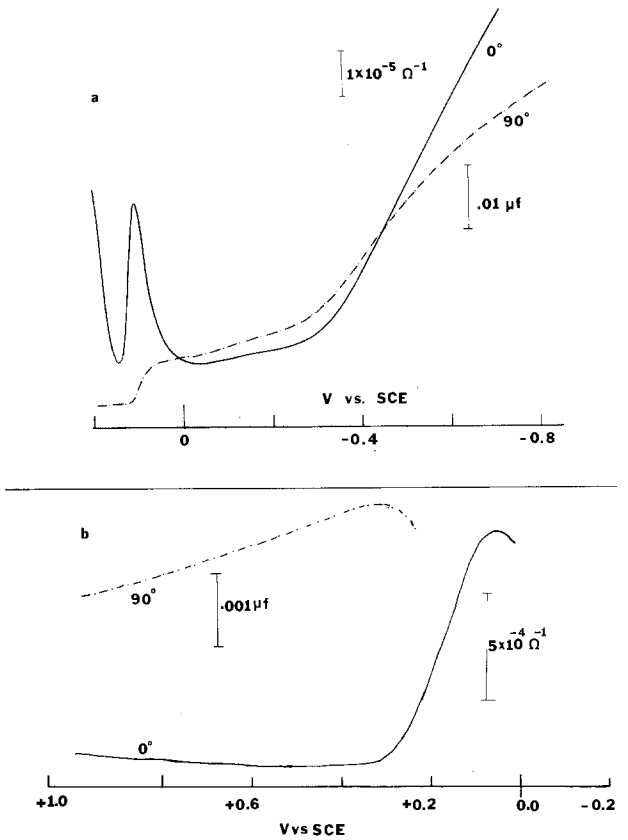

Fig. 9. (a) G_p and C vs. V for n-$MoTe_2$ in aqueous solution containing 1M KI. $f = 2000$ Hz. (b) G_p and C vs. V for n-$MoTe_2$ in aqueous solution 1M KI/0.1M I_2. $f = 2000$ Hz.

surements carried out in the presence of I^- and I^-/I_3^- (Fig. 7 and 8) [iodine has been shown to be specifically chemisorbed on electrode surfaces (31)] indicates no change in the G_p *vs.* V and C *vs.* V plots except for a small hump around -0.1V *vs.* SCE at low frequencies in MeCN. This suggests that in MeCN, I^- and I_3^- are not specifically adsorbed on layered compounds. However, impedance measurements in aqueous solution in the presence of both I^- and I^-/I_3^-, shown in Fig. 9a and b, demonstrate that while there is no effect with I^- alone, the presence of I_3^- shifts V_{FB} to more positive values and completely eliminates the humps attributed to the surface states. Kautek and Gerischer (32) reached a similar conclusion for $MoSe_2$ in aqueous solutions in the presence of I^-/I_3^-.

Conclusions

The a-c impedance of the semiconductor/liquid interface parallels that for MOS devices. The in-phase component is more sensitive to surface-state properties than the quadrature component. For n-$MoTe_2$ in MeCN, the total surface-state density was about 10^{10} cm^{-2}, which is too small for Fermi level pinning to occur. The single-level time constant was estimated as 5×10^{-5} sec, which falls in the domain of fast surface states. The behavior of n-$MoTe_2$ parallels that of other layered compounds in MeCN. While adsorption of I_3^- in MeCN solutions was not found, shifts of V_{FB} in aqueous I_3^- solutions suggests interaction of this species with the electrode surface under these conditions.

Acknowledgments

The support of this research by the National Science Foundation (CHE8000682) and the Solar Energy Research Institute is gratefully acknowledged.

Manuscript submitted April 26, 1982; revised manuscript received *ca.* Sept. 13, 1982.

Any discussion of this paper will appear in a Discussion Section to be published in the December 1983

JOURNAL. All discussions for the December 1983 Discussion Section should be submitted by Aug. 1, 1983.

Publication costs of this article were assisted by the University of Texas at Austin.

APPENDIX

The overall equivalent circuit for the semiconductor/solution/metal counterelectrode cell is given in Fig. A-1(a).

Since the counterelectrode area is about 500 times larger than that of the semiconductor electrode, the contribution of the $C_{counter}$ and $R_{counter}$ to the overall cell impedance can be neglected. Because the electrolyte concentration is fairly high and the bulk resistance of the electrode is small, the contribution of C_H and C_{diff} should be small. The equivalent circuit then reduces to that shown in Fig. A-1(b). Finally, since dark faradaic currents are not observed, R_F should be very high. Since it is in parallel to R_{ss}, the R_F term can be neglected. Then the equivalent circuit of the semiconductor/liquid junction in the dark reduces to Fig. 1(a). Analysis of the admittance of this circuit, A_p, where

$$A_p = G_p + j\omega C_p \qquad [A\text{-}1]$$

yields the following expressions for the conductance, G_p (in-phase component) and capacitance, C_p (quadrature component)

$$G_p = \frac{(\omega C_{ss})^2 R_{ss}}{1 + (\omega R_{ss} C_{ss})^2} = \frac{\omega^2 C_{ss} \tau}{1 + (\omega\tau)^2} \qquad [A\text{-}2]$$

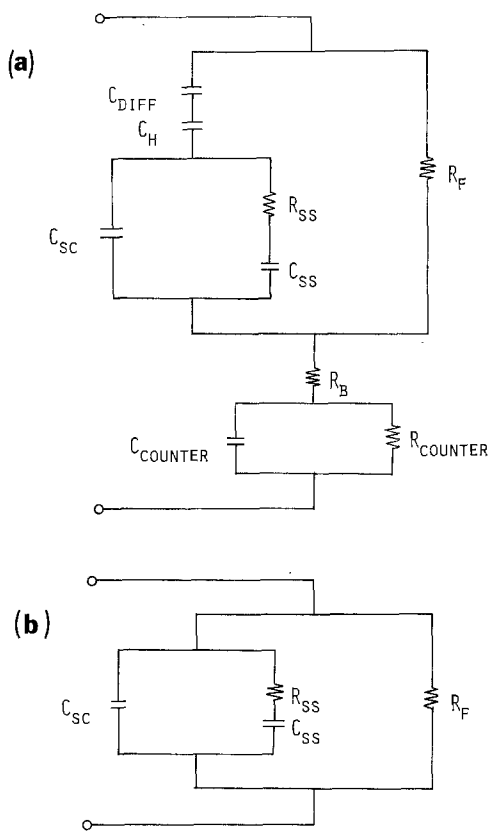

Fig. A-1. Equivalent circuit for the semiconductor/solution/metal counterelectrode cell. $C_{counter}$, capacitance associated with counterelectrode/liquid junction; C_{diff}, diffuse layer capacitance; C_H, Helmholtz layer capacitance; C_{sc}, space charge layer capacitance; C_{ss}, surface-state capacitance; R_B, resistance associated with bulk resistance of the electrode and solution resistance; $R_{counter}$, any resistance associated with interface between counterelectrode and solution; R_F, resistance due to faradaic impedance; R_{ss}, resistance arising from the presence of surface states.

$$C_p = C_{sc} + \frac{C_{ss}}{1 + (\omega R_{ss} C_{ss})^2} = C_{sc} + \frac{C_{ss}}{1 + (\omega\tau)^2} \qquad [A\text{-}3]$$

where $\tau = R_{ss}C_{ss}$.

REFERENCES

1. T. Tamm, *Phys. Z. Sowjetunion*, **1**, 733 (1932).
2. W. Shockley, *Phys. Rev.*, **56**, 317 (1939).
3. J. Bardeen, *ibid.*, **71**, 717 (1947).
4. C. A. Mead and W. G. Spitzer, *Phys. Rev. A*, **134**, 713 (1964).
5. W. G. Spitzer and C. A. Mead, *J. Appl. Phys.*, **34**, 3061 (1963).
6. (a) R. E. Malpas, K. Itaya, and A. J. Bard, *J. Am. Chem. Soc.*, **101**, 2535 (1979); (b) J. N. Chazalviel and T. B. Truong, *J. Electroanal. Chem. Interfacial Electrochem.*, **114**, 299 (1980).
7. A. B. Bocarsly, D. C. Bookbinder, R. N. Dominey, N. S. Lewis, and M. S. Wrighton, *J. Am. Chem. Soc.*, **102**, 3683 (1980).
8. A. Aruchamy and M. S. Wrighton, *J. Phys. Chem.*, **84**, 2848 (1980).
9. F.-R. Fan and A. J. Bard, *J. Am. Chem. Soc.*, **102**, 3677 (1980).
10. A. J. Bard, A. B. Bocarsly, F.-R. Fan, E. G. Walton, and M. S. Wrighton, *ibid.*, **102**, 3671 (1980).
11. (a) J. G. Simmons and L. S. Wei, *Solid-State Electron.*, **17**, 117 (1974); (b) H. A. Mar and J. G. Simmons, *ibid.*, **17**, 131 (1974).
12. J. G. Simmons and G. W. Taylor, *ibid.*, **17**, 125 (1974).
13. G. Declerck, R. Vanoverstraeten, and G. Broux, *ibid.*, **16**, 1451 (1973).
14. (a) E. H. Nicollian and A. Goetzberger, *Bell Syst. Tech. J.*, **46**, 1055 (1967); (b) H. Deuling, E. Klausmann, and A. Goetzberger, *Solid-State Electron.*, **15**, 559 (1972).
15. K. Kobayashi, Y. Aikawa, and M. Sukigara, *Chem. Lett.*, 679 (1981).
16. P. Janietz, R. Weiche, J. Westfahl, R. Landsberg, and R. Dehmlow, *J. Electroanal. Chem. Interfacial Electrochem.*, **106**, 23 (1980).
17. P. R. Barabash and R. S. C. Cobbold, *IEEE Trans. Electron Devices*, **ed-29**, 102 (1982).
18. J. DuBow and K. Rajeshwar, Final Report, Oct. 1981, submitted to SERI Division, Golden, CO.
19. H. Tributsch, H. Gerischer, C. Clemen, and E. Bucher, *Ber. Bunsenges. Phys. Chem.*, **83**, 655 (1979).
20. H. D. Abruna, G. A. Hope, and A. J. Bard, *This Journal*, **129**, 2224 (1982).
21. G. Nagasubramanian and A. J. Bard, *ibid.*, **128**, 1055 (1981).
22. W. T. Hicks, *ibid.*, **111**, 1058 (1964).
23. G. Nagasubramanian, A. S. Gioda, and A. J. Bard, *ibid.*, **128**, 2158 (1981).
24. A. Lepetit, *J. Phys.*, **26**, 175 (1965).
25. (a) J. A. Wilson and A. D. Yoffe, *Advan. Phys.*, **18**, 193 (1969); (b) A. D. Yoffe, in "Annual Review of Material Science," Vol. 3, R. A. Huggins, Editor, p. 147, Annual Review, Palo Alto (1973).
26. (a) S. Kabashima, *J. Phys. Soc. Jpn.*, **21**, 945 (1966); (b) M. B. Vellinga, R. deJonge, and C. Hass, *J. Solid State Chem.*, **2**, 299 (1970).
27. A. Goetzberger and S. M. Sze, *Appl. Solid State Sci.*, **1**, 153 (1969).
28. A. Goetzberger and S. M. Sze, *ibid.*, **1**, 154 (1969).
29. G. Nagasubramanian, Bob Lee Wheeler, F.-R. Fan, and A. J. Bard, in "Photoelectrochemistry: Fundamental Processes and Measurement Techniques," W. L. Wallace, A. J. Nozik, S. K. Deb, and R. H. Wilson, Editors, Vol. 82-3, pp. 372-380, The Electrochemical Society Softbound Proceedings Series, Pennington, NJ (1982).
30. G. Nagasubramanian, Bob Lee Wheeler, F.-R. Fan, and A. J. Bard, *This Journal*, **129**, 1742 (1982).
31. W. W. Harvey, W. J. LaFleur, and H. C. Gatos, *ibid.*, **102**, 155 (1962) and references therein.
32. W. Kautek and H. Gerischer, *Electrochim. Acta*, **26**, 1771 (1981).

Open-Circuit Photopotentials at Doped α-Fe_2O_3 Electrodes in Aqueous Solution

Ruth Shinar and John H. Kennedy*

Department of Chemistry, University of California, Santa Barbara, California 93106

ABSTRACT

The influence of redox couples in aqueous solution on the interface energetics of chemically and thermally doped polycrystalline α-Fe_2O_3 photoanodes has been investigated. Experiments were carried out at several pH values. Results are compared to those obtained from a single crystal electrode. It is shown that the potential of the semiconductor under illumination shifts toward positive values when the energy level of the redox couple in solution is increased. The role that grain boundaries in the sintered electrodes may play, the effect of pH and the redox couple concentration are discussed.

Photovoltage measurements aimed at studying the interfacial energetics at the semiconductor/liquid junction using a variety of redox couples in aqueous (1-6) and nonaqueous (7-9) solutions have been studied previously. Several models, adopted from models describing the semiconductor-metal interface, have been used to describe the experimental results (10).

The ideal model assumes that the bandedges, V_{cb} and V_{vb}, are fixed. According to the model the maximum open-circuit photovoltage, $V_{oc(max)}$, is given by

$$V_{oc(max)} = V_{FB} - V_{redox} \quad [1]$$

where V_{redox} is the redox potential of the couple and V_{FB} is the flatband potential of the semiconductor.

Thus, if the species in solution do not interact with the semiconductor surface (10), changes in V_{redox} will result in identical changes in the photovoltage. However, for n-type semiconductors no photovoltage is expected for V_{redox} more negative than V_{cb}. For V_{redox} more positive than V_{vb} the photoeffects are also expected to be minimal (10). Such an ideal behavior was observed for a CdS electrode in aqueous solution (1). However, changes in V_{FB} will occur whenever specific adsorption or surface reactions take place (10).

For several semiconductors in solution (2, 6-8, 10 and references therein) it was observed that $V_{oc(max)}$ is practically constant over a wide range of V_{redox} values. In addition, redox couples with V_{redox} situated outside the bandgap gave rise to a photovoltage (9, 10 and references therein). The model describing this behavior assumes pinning of the Fermi level in the semiconductor due to a high density of surface states around a certain potential.

Studies dealing with the semiconductor/liquid junction were carried out mainly on nonoxide semiconductors (1-10) and the Fermi level pinning model was usually employed, in accordance with results obtained at the semiconductor/metal interfaces (6-8, 10 and references therein) for similar materials. However, fewer studies have been carried out on oxide semiconductors in contact with solution.

In this work we have studied the energetics of the α-Fe_2O_3/liquid junction in the presence of several redox couples. An α-Fe_2O_3 semiconductor electrode interacts with H^+ and OH^- ions and thus its flatband potential is pH dependent (11) similar to other semiconductors (12 and references therein). This interaction must be considered as well as the effect caused by other couples in solution. Therefore, whenever it was possible, experiments were carried out at several pH values for each couple. The possible effect of the electrode preparation procedure (*i.e.*, the existence of grain boundaries) and the concentration of the redox couple were also considered.

* Electrochemical Society Active Member.

Key words: grain boundaries, redox couples, pH.

Experimental

Polycrystalline, thermally and chemically doped α-Fe_2O_3 electrodes were prepared as described earlier (13). The dopants used in this study were mainly 0.5 atomic percent (a/o) Nb_2O_5, 0.05 a/o V_2O_5, 0.005 a/o FeO, and 0.004 a/o HfO_2. However the behavior of many other chemically doped electrodes was checked and found to be qualitatively the same. The thermally doped electrodes were prepared by reduction in an He atmosphere as described earlier (13), or by sintering α-Fe_2O_3 containing 1% (mol percent) Al_4C_3. Single crystal α-Fe_2O_3 electrodes were prepared from Atomergic Chemicals Corporation platelets. These platelets were reduced at ~1000°C in an He atmosphere to improve conductivity. Electrical contact was made with silver epoxy for both single crystal and sintered samples.

The electrodes were about 1 cm^2 area and their resistances, measured at 1 kHz with a conductivity bridge, were 10-1000Ω.

Open-circuit photopotentials were measured in an electrochemical cell containing the semiconductor electrode, a Pt electrode, and a saturated calomel electrode (SCE). The redox potential of the couple in solution was measured as an equilibrium potential using the Pt electrode *vs.* SCE, and the open-circuit photopotential was measured *vs.* the Pt electrode. The potentials of α-Fe_2O_3 electrodes were also measured in the dark *vs.* the Pt electrode.

The light source was a 150W Xe lamp used with an infrared filter. The light intensity was measured with an EG & G Model 450-1 radiometer/photometer. Lamp intensity at the electrode surface was about 380 mW/cm^2. Neutral density filters were used to reduce light intensity to a desired value.

Measurements were carried out over a wide pH range (4*N* H_2SO_4 to 4*N* NaOH) without an additional redox couple and at several pH values (pH = 0, 4.5, 8.5, and 11.5) in the presence of redox couples. Flatband potentials, $V_{FB}°$, have been measured previously in solutions containing no added redox couple at several pH values using capacitance measurements (11) and also by using chopped illumination (11).

The following redox couples were used: S_2^{2-}/S^{2-} prepared by adding sulfur to a solution of sodium sulfide at basic pH values; 0.1M $Na_2S_2O_3$ containing a small amount of the oxidized form, $S_4O_6^{2-}$; 10^{-4}-0.1M $Fe(CN)_6^{3-/4-}$, ~5 · 10^{-5}-3 · 10^{-3}M I_2/0.1M I^-; ~10^{-3}M IO_3^-/0.1M I^-; 0.05M $Fe^{3+/2+}$ (perchlorate); ~5 · 10^{-5}-10^{+3}M Br_2/0.01-0.1M Br^-; and 10^{-3}-1M $Ce^{4+/3+}$. All materials were obtained from Mallinckrodt except for Alfa Products $Fe(ClO_4)_2 \cdot 6H_2O$, $Fe(ClO_4)_3 \cdot 9H_2O$, and $Ce(NO_3)_3 \cdot 6H_2O$ and MC & B $(NH_4)_2\,Ce(NO_3)_6$. Iodine and bromine were generated in solution by means of a constant current source. The pH of the solutions was regulated by addition of H_2O_4 and NaOH.

Measuremenets under illumination were usually taken at low concentrations of the redox couples to avoid light absorption by highly colored solutions. In addition, the electrodes were kept as close as possible to the cell's window. However, measurements in the dark were also carried out at relatively high concentrations. We did not use all the redox couples over the whole *p*H range since their stability is generally confined to a limited *p*H range.

Results

Open-circuit photopotentials of polycrystalline, doped α-Fe_2O_3 electrodes, in the presence of several redox couples and at several *p*H values were measured as a function of light intensity. Typical results are shown in Fig. 1. It can be seen that the photopotentials reached a saturation value at the highest light intensity employed (~380 mW/cm²). This qualitative behavior was observed for all dopants and reduction methods used in the preparation of the electrodes, and in the presence of all redox couples and electrolytes used.

Semilogarithmic plots of the photopotential as a function of light intensity (ln I_L) are shown in Fig. 2. The lowest light intensity used was 0.21 mW/cm². Usually, the slopes of the lines were in the range of 25-28 mV, however, somewhat larger slopes were obtained for Br_2/Br^- and $Fe(CN)_6^{3-/4-}$ (~38 and ~43 mV, respectively).

The open-circuit photopotential as a function of the actual redox potential of the solution for an He-treated sintered electrode is shown in Fig. 3. It should be noted that the measured redox potentials for some couples differed from the thermodynamic, reversible values. Measurements were taken at *p*H = 0, 4.5, 8.5, and 11.5. As can be seen from this figure, the open-circuit photopotential changed gradually with V_{redox}. However, the curve deviated from the ideal straight line of unity slope expected when the bandedges are fixed. Similar values of open-circuit photopotentials were observed for different electrodes showing similar properties and photoactivity, including a single crystal electrode.

The potential of the semiconductor was also measured in the dark. Results for several electrodes, including a single crystal, are presented in Table I. The potential in the dark was measured at different concentrations of the reduced and oxidized forms of the redox couples and at several *p*H values. In addition

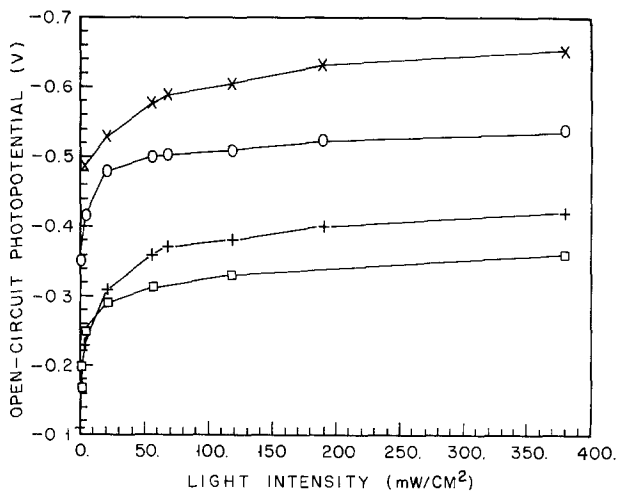

Fig. 1. Open-circuit photovoltage as a function of light intensity for doped α-Fe_2O_3 electrodes. (a) ×: 0.05 a/o V_2O_5 in Br_2/Br^-, *p*H = 6.4; V_{redox} = 0.79. (b) ○: 0.05 a/o V_2O_5 in I_2/I^-, *p*H = 9.0; V_{redox} = 0.24. (c) +: He-treated in $Fe(CN)_6^{3-/4-}$, *p*H = 6.5; V_{redox} = 0.13. (d) □: 0.5 a/o Nb_2O_5 in I_2/I^-, *p*H = 4.1; V_{redox} = 0.23.

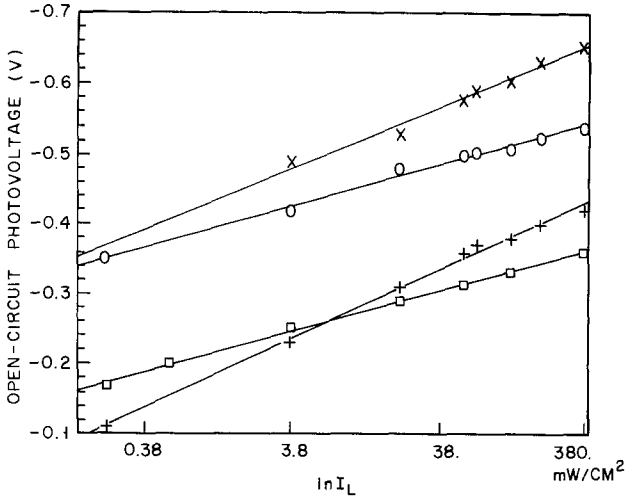

Fig. 2. Open-circuit photovoltage as a function of light intensity. (a) ×: 0.05 a/o V_2O_5 in Br_2/Br^-, *p*H = 6.4; V_{redox} = 0.79, slope = 37.7 mV. (b) ○: 0.05 a/o V_2O_5 in I_2/I^-, *p*H = 9.0; V_{redox} = 0.24, slope = 25.6 mV. (c) +: He-treated in $Fe(CN)_6^{3-/4-}$, *p*H = 6.5; V_{redox} = 0.13, slope = 42.6 mV. (d) □: 0.5 a/o Nb_2O_5 in I_2/I^-, *p*H = 4.1; V_{redox} = 0.23, slope = 25.0 mV.

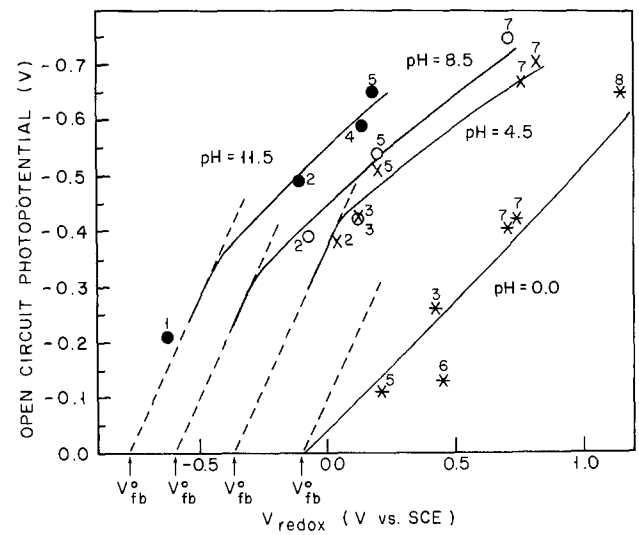

Fig. 3. Open-circuit photopotential as a function of the actual redox potential at *p*H = 0, 4.5, 8.5, and 11.5 for a sintered He-treated electrode. 1, S_2^{2-}/S^{2-}; 2, $S_4O_6^{2-}/S_2O_3^{2-}$; 3, $Fe(CN)_6^{3-/4-}$; 4, IO_3^-/I^-; 5, I_2/I^-; 6, $Fe^{3+/2+}$; 7, Br_2/Br^-; 8, $Ce^{4+/3+}$. Broken lines are of slope one, starting at the flatband potentials measured in the absence of an added redox couple, using chopped light.

for sake of comparison, Table I includes open-circuit photopotentials for the various electrodes.

The open-circuit photovoltage in electrolytes such as NaOH, H_2SO_4, or Na_2SO_4 was independent of the *p*H as expected from the ideal model. A value of about −0.4V *vs.* Pt was measured for an He-treated electrode. The potential of the semiconductor under illumination *vs.* SCE, V_1 (though different from the flatband potential, $V_{FB}°$, measured from capacitance values or by using pulsed illumination in the absence of an added redox couple) also shifted to more positive values at ~60 mV/*p*H as the *p*H was decreased. However, a potential difference between the sintered semiconductor electrode and Pt electrode was observed under dark conditions. The dark potential *vs.* SCE was also *p*H dependent but increased ~45 mV/*p*H as the *p*H decreased. A stable value was obtained only after soaking the electrodes for about 24 hr in the solution. The potential at the single crystal electrode in the dark was essentially zero in basic and neutral solu-

Table I. Potential measurements at α-Fe_2O_3 electrodes

Dopant	Solution	V_{redox} V_{Pt} vs. SCE	V_d $V_{Fe_2O_3}$ (dark) vs. V_{Pt}	V_{oc} $V_{Fe_2O_3}$ (light) vs. V_{Pt}
0.05 a/o V_2O_5	0.1M $Fe(CN)_6^{3-/4-}$ pH = 4.5	0.13	0.00	−0.41
0.05 a/o V_2O_5	10^{-3}M $Fe(CN)_6^{3-/4-}$ pH = 4.5	0.13	−0.02	−0.42
0.05 a/o V_2O_5	~2 · 10^{-5}M $Fe(CN)_6^{3-/4-}$ pH = 4.5	0.14	−0.09	—
He-treated	~5 · 10^{-5}M I_2/0.1M KI pH = 4.5	0.20	−0.20	−0.51
Single crystal	~5 · 10^{-5}M I_2/0.1M KI pH = 4.5	0.20	−0.03	−0.43
He-treated	~3 · 10^{-3}M I_2/0.1M KI pH = 4.5	0.26	−0.03	−0.54
He-treated	5 · 10^{-5}M Br_2/0.1M Br^- pH = 4.5	0.76	−0.47	−0.67
He-treated	10^{-3}M Br_2/10^{-1}M Br^- pH = 4.5	0.83	−0.17	−0.67
Single crystal	10^{-3}M Br_2/10^{2}-M Br^- pH = 4.5	0.83	−0.14	−0.63
He-treated	10^{-2}M $Ce^{4+/3+}$ in 1F H_2SO_4	1.15	−0.25	—
He-treated	10^{-3}M $Ce^{4+/3+}$ in 1F H_2SO_4	1.13	−0.35	−0.65
0.5 a/o Nb_2O_5	0.1N H_2SO_4, 1M Na_2SO_4		−0.24	−0.37
He-treated	0.1N H_2SO_4, 1M Na_2SO_4		−0.24	−0.37
Single crystal	0.1N H_2SO_4, 1M Na_2SO_4		−0.21	−0.40
He-treated	10^{-3}M $Fe(CN)_6^{3-/4-}$ pH = 8.5	0.12	−0.02	−0.37
0.002 a/o HfO_2	10^{-3}M $Fe(CN)_6^{3-/4-}$ pH = 8.5	0.12	−0.04	−0.36
He-treated	~0.05M $Fe^{3+/2+}$ 1M $HClO_4$	0.45	−0.01	−0.13
He-treated	0.1M $Na_2S_2O_3$ pH ~ 8.5	−0.07	−0.02	−0.39
He-treated	0.1M $Na_2S_2O_3$ pH ~ 11.5	−0.11	+0.01	−0.49
He-treated	S^{2-}/S_2^- pH ~ 11.5	−0.62	+0.03	−0.21
0.5 a/o Nb_2O_5	10^{-3}M IO_3^-/~0.1M I^- pH ~ 13	0.16	−0.03	−0.59

tions; however, in acidic solutions the potential in the dark was always negative *vs.* the platinum electrode. Surface treatment on the sintered electrode, mechanical polishing and chemical etching in dilute or concentrated acids, did not change this behavior.

Figure 4 shows an energetic scheme for an almost ideal situation of the α-Fe_2O_3 semiconductor/liquid junction in the presence of (a) 3 · 10^{-3}M I_2/0.1M I^- and (b) 10^{-3}M $Fe(CN)_6^{3-/4-}$ at pH = 4.5. The flatband potential, $V_{FB}°$, and the O_2/H_2O energy level are also indicated. A different situation, markedly deviating from the ideal behavior, is presented in Fig. 5 for (a) 5 · 10^{-5}M I_2/0.1M I^- solution at pH = 10.9 and (b) 10^{-3}M $Ce^{4+/3+}$ in 1M H_2SO_4. The flatband potentials at pH = 0 and 10.9 in the absence of added redox couples, the corresponding O_2/H_2O energy levels, and the decomposition level of Fe_2O_3 (14), $E_D{}^0$, are also indicated.

The open-circuit dark and photopotentials in 1M NaOH were measured before and after soaking a 0.005 a/o FeO-doped α-Fe_2O_3 electrode in I_2/I^- solution, at a neutral pH, for 10 days. No appreciable change was observed, although the short-circuit photocurrent was considerably higher, similar to previously published results (15).

Discussion

From the plateau values in Fig. 1 it is clear that the open-circuit photopotential reaches a near-maximum at the highest light intensity employed. However it is still possible that h^+-e^- recombination processes may prevent achieving even higher values, and indeed, it appears that $V_{FB}°$ [the flatband potential measured in a solution containing no added redox couple (11)] was never quite reached. Similar values of open-circuit photopotentials were obtained for sintered and single crystal electrodes. It should be noted that essentially the differences between single crystal and sintered electrodes were observed in the dark. Thus, recombination at grain boundaries in the sintered electrodes was not a main source for losses. It should also be noted that surface treatment on the sintered electrodes did not improve the situation. As can be seen from Fig. 4 and 5 the electrodes' potentials under illumination were always positive to $V_{FB}°$ but were equal to the turn-on voltages, V_o* (the voltage of the photocurrent onset). This positive deviation may be due to recombination processes or to changes in V_{FB} induced by the redox couples, as is discussed later.

A slope of ~25 mV in $V_{oc(max)}$ *vs.* ln I_L plot is expected according to a simplistic model (4 and references therein) and indeed a slope of ~25 mV has been observed in several cases (4, 13). However, higher values have been reported for CdS and CdSe (3) and for $MoSe_2$ and WSe_2 used in solutions con-

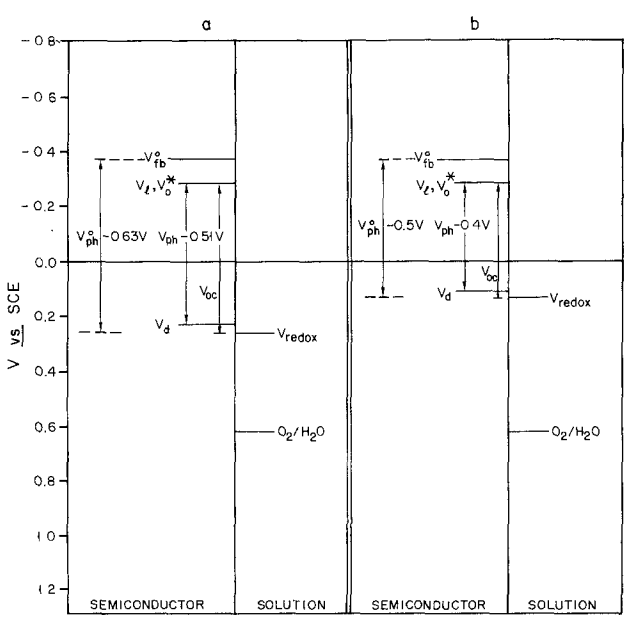

Fig. 4. An energetic scheme of the semiconductor/liquid junction for two systems approaching the ideal behavior. (a) In 3 · 10^{-3}M I_2/0.1M I^- and (b) in 10^{-3}M $Fe(CN)_6^{3-/4-}$ at pH = 4.5. V_d = electrode's potential in the dark, V_l = electrode's potential under illumination, V_o* = turn-on voltage, $V_{ph}°$ = theoretical photopotential, and V_{ph} = observed photovoltage ($V_l - V_d$).

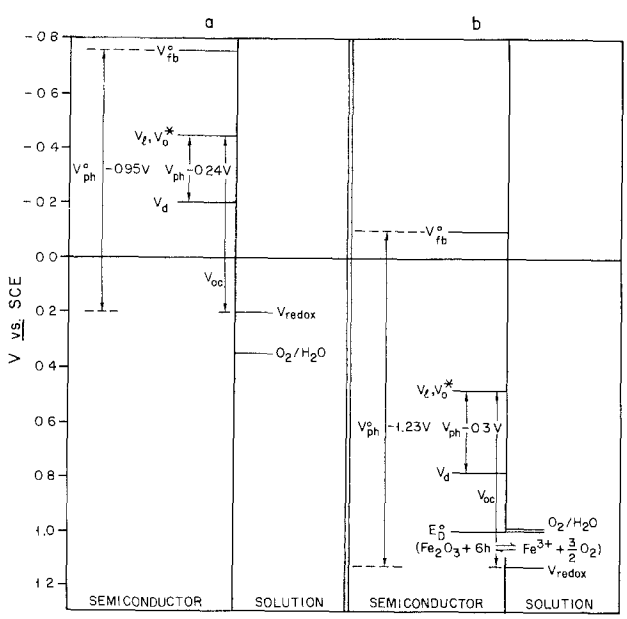

Fig. 5. An energetic scheme of the semiconductor/liquid junction for two systems exhibiting marked deviation from the behavior predicted by the ideal model. (a) In 5 · 10^{-5}M I_2/0.1M I^- at pH = 10.9 and (b) in 10^{-3}M $Ce^{4+/3+}$ in 1M H_2SO_4. V_d = electrode's potential in the dark, V_l = electrode's potential under illumination, V_o* = turn-on potential, $E_D°$ = decomposition potential for Fe_2O_3, $V_{ph}°$ = theoretical photopotential, and V_{ph} = observed photovoltage ($V_l - V_d$).

taining I_2/I^- and several other redox couples (4). In our work a slope of ~25 mV was usually observed. However, somewhat higher slopes were obtained for Br_2/Br^- and $Fe(CN)_6^{3-/4-}$ as can be seen in Fig. 2. Values near 25 mV probably indicate that specific interactions between the couples used and α-Fe_2O_3 which affect the carrier distribution in the space charge layer do not exist (4). Even surface adsorption of I_2/I^- that was confirmed earlier (15) and caused photocurrent enhancement did not affect recombination centers according to these photopotential results.

Since the flatband potential of α-Fe_2O_3 is *p*H dependent (11, 12 and references therein) the effect of different redox couples was studied at constant *p*H values. Results for several couples at four *p*H values are shown in Fig. 3. It can be seen that neither the ideal model (that predicts a straight line of slope 1 when $V_{oc(max)}$ is plotted *vs.* V_{redox}) nor the Fermi level pinning model (that predicts a constant output voltage over a wide range of V_{redox}) is applicable to the Fe_2O_3 system. An increase in $V_{oc(max)}$ magnitude as V_{redox} increased was observed but as can be seen in Fig. 3, all the curves deviated from the straight line of slope 1 starting at $V_{FB}°$.

A possible explanation for this deviation is a corrosion reaction of the electrode in contact with a redox couple in the dark (4). If corrosion were the only reason for the behavior then the electrode's potential *vs.* Pt in the dark should also differ from zero. Potentials of the electrodes in the dark in the presence of various redox couples were measured and the results are summarized in Table I. It can be seen that for the $Fe(CN)_6^{3-/4-}$ couple the potential of the semiconductor against the Pt electrode was practically zero down to concentrations $<10^{-3}$M. For the I_2/I^- couple this dark potential was nearly zero for a single crystal in a solution containing 5×10^{-5}M I_2/0.1M I^- and for a sintered electrode in 3×10^{-3}M I_2/0.1M I^- at *p*H = 4.5. Thus, the deviation from a straight line of unity slope occurred even for cases of zero dark potential. From this it may be concluded that corrosion in the dark was not the only reason for the experimental results shown in Fig. 3. This conclusion was confirmed by checking the stability of the electrodes in these solutions for long periods in the dark or under illumination in open- or short-circuit conditions. No change in the electrodes' performance was observed.

Differences between single crystal and sintered electrodes shown in Table I suggest that preparation conditions play a role in establishing dark potentials. It is possible that the dark potentials originate from grain boundaries and other defects (16) in the sintered samples. The dark potential may be a steady-state value arising from charge exchange between the semiconductor and some other donor/acceptor level in addition to the redox couple level through levels due to flaws or grain boundaries. It should be remembered that the O_2/H_2O couple was always present and might have contributed to the observed values. If more than one level is involved in the charge transfer processes in the dark (a mixed potential), an increase of the concentration of the redox couple may increase the rate of its charge exchange with the semiconductor and thus change the dark potential. Indeed, dark potentials approached zero at relatively high concentrations of several redox couples, as can be seen from Table I. It should be noted that the potentials measured in the dark in the presence of the redox couples were reproducible, whereas values measured in the absence of an added redox couple depended on the time the electrodes were exposed to the solution and on previous use in the presence of other couples.

In highly acidic solutions and in solutions containing Br_2/Br^- and $Ce^{4+/3+}$ couples (V_{redox} ~0.8 and 1.1V *vs.* SCE, respectively) the dark potentials were never zero as shown in Fig. 5 for $Ce^{4+/3+}$ even at the single crystal electrode. However, their values were somewhat reduced as the concentrations of the redox couples were increased. In highly acidic solutions corrosion of the electrode under open-circuit conditions occurred. It was especially noted in the presence of $Ce^{4+/3+}$. This is in accordance with the decomposition energy level, $E_D°$ (14) of α-Fe_2O_3 as indicated in Fig. 5b. Therefore, corrosion does play a role with some redox couples.

Returning to the previous question concerning deviation from the theory shown in Fig. 3 we note that Tributsch (4) observed a similar trend in the open-circuit photopotential with V_{redox} for $MoSe_2$ and WSe_2. Because of the gradual change of $V_{oc(max)}$ with V_{redox} he ruled out the possibility of a specific chemical interaction between the electrode and the solution and concluded that the results indicated that charge extraction from the electrode took place. It is possible that in our case, as for $MoSe_2$ and WSe_2 (4), experimental results can be explained by a shift of the flatband potential to positive values as V_{redox} is increased. Such a shift may be a result of several situations. First, the reduced form, Fe^{2+}, in a doped α-Fe_2O_3 electrode may be partially oxidized by a redox couple resulting in a change in the surface charge. Such a process should affect the photoactivity of the electrode while in this electrolyte because of the shift in flatband potential. If the effect is irreversible a permanent change in photoactivity will result. A change in an electrode's performance was observed only after experiments at *p*H = 0 and mainly after using $Ce^{4+/3+}$, as mentioned before. A second more likely mechanism is the existence of surface states (in single crystal or sintered electrodes). The charge of the surface states on an electrode's surface could vary with V_{redox} (1, 5) and thus cause a change in the flatband potential.

In Fig. 4 an energetic scheme for an almost ideal situation is presented. The potential of the electrode in the dark *vs.* SCE is close to V_{redox} and the potential under illumination differs from $V_{FB}°$ by <100 mV. On the other hand, Fig. 5 presents two situations far from ideal. No equilibrium exists between the redox couple and the semiconductor, and the potential of the semiconductor electrode under illumination is significantly more positive than $V_{FB}°$. Differences between the situations presented in Fig. 4 and 5 include the following effects: (*i*) V_d, the dark potential, differs from V_{redox} for low concentrations of iodine but not at high concentrations; (*ii*) V_l, the potential under illumination, differs from $V_{FB}°$ at the same *p*H and this difference is pronounced the higher the *p*H for the I_2/I^- couple; (*iii*) for $Ce^{4+/3+}$ corrosion in the dark takes place, and (*iv*) the observed open-circuit photopotentials shown in Fig. 3, which are lower than predicted by the simple theory, may be caused by a positive shift in V_{FB} with increasing V_{redox}.

Summary

The behavior of α-Fe_2O_3 in acid-base solution is in accordance with the ideal model that assumes fixed bandedges. However, $V_{FB}°$ was never achieved, probably due to h^+-e^- recombination processes. The differences in the dark potential between single crystal and sintered electrodes, suggest that grain boundaries play an important role in producing this dark potential.

In the presence of redox couples in aqueous solution the ideal model cannot explain all the experimental results. The $V_{oc(max)}$ *vs.* V_{redox} curves (Fig. 3) may result from a change in V_{FB} with V_{redox} due to surface states. However, the density of surfaces states on an α-Fe_2O_3 surface is apparently not high enough to cause complete Fermi level pinning which would result in an output voltage that is constant over a wide range of V_{redox} values.

Decomposition and/or oxidation ($Fe^{2+} \rightarrow Fe^{3+}$) probably take place in acidic solutions and at high, positive V_{redox} values under open-circuit conditions.

Equilibration with some couples in the dark occurred only when relatively high concentrations of the oxidized forms were used.

Acknowledgment

This work is supported by the Division of Chemical Sciences, Office of Basic Energy Sciences, Department of Energy.

Manuscript submitted May 10, 1982; revised manuscript received ca. July 15, 1982.

Any discussion of this paper will appear in a Discussion Section to be published in the December 1983 JOURNAL. All discussions for the December 1983 Discussion Section should be submitted by Aug. 1, 1983.

Publication costs of this article were assisted by the University of California.

REFERENCES

1. J. Gobrecht and H. Gerischer, *Solar Energy Mater.*, **2**, 131 (1979).
2. F.-R. Fan and A. J. Bard, *J. Am. Chem. Soc.*, **102**, 3677 (1980).
3. H. Gerischer, *J. Electroanal. Chem. Interfacial Electrochem.*, **58**, 263 (1975).
4. H. Tributsch, *Solar Energy Mater.*, **1**, 257 (1979).
5. H. Tributsch, H. Gerischer, C. Clemen, and E. Bucher, *Ber. Bunsenges. Phys. Chem.*, **83**, 655 (1979).
6. A. B. Bocarsly, D. C. Bookbinder, R. N. Dominey, N. S. Lewis, and M. S. Wrighton, *J. Am. Chem. Soc.*, **102**, 3683 (1980).
7. A. Aruchami and M. S. Wrighton, *J. Phys. Chem.*, **84**, 2848 (1980).
8. J.-N. Chazalviel and T. B. Truong, *J. Electroanal. Chem. Interfacial Electrochem.*, **114**, 299 (1980).
9. P. A. Kohl and A. J. Bard, *This Journal*, **126**, 59 (1979).
10. A. J. Bard, A. B. Bocarsly, F.-R. Fan, E. G. Walton, and M. S. Wrighton, *J. Am. Chem. Soc.*, **102**, 3671 (1980).
11. J. H. Kennedy and K. W. Frese, Jr., *This Journal*, **125**, 723 (1978).
12. H. Gerischer, in "Physical Chemistry," Vol. IXA, H. Eyring, D. Henderson, and W. Jost, Editors, Chap. 5, Academic Press, New York (1970).
13. R. Shinar and J. H. Kennedy, *Solar Energy Mater.*, To be published.
14. A. J. Bard and M. S. Wrighton, *This Journal*, **124**, 1706 (1977).
15. J. H. Kennedy, R. Shinar, and J. P. Ziegler, *ibid.*, **127**, 2307 (1980).
16. S. R. Morrison, "Electrochemistry at Semiconductor and Oxidized Metal Electrodes," Plenum Press, New York (1980).

Electrochemical and Spectroscopic Studies of Metal Hexacyanometalate Films

I. Cupric Hexacyanoferrate

Lorraine M. Siperko and Theodore Kuwana*

Department of Chemistry, The Ohio State University, Columbus, Ohio 43210

ABSTRACT

A method for the electrodeposition of thin films of cupric hexacyanoferrate (CuHCF) on glassy carbon and tin oxide electrodes has been devised. At low scan rates, in 0.5M K_2SO_4, these films exhibit nearly ideal cyclic voltammetric current-potential waves with a peak potential of +0.69V *vs.* SCE on glassy carbon. Similar to the Prussian blue films described by Neff (1, 2), Itaya (3), and others (4), potassium ion is transported into the film during reduction. XPS and visible spectroscopy indicate that the redox involves the ferric and ferrous states of the hexacyanoferrate and not Cu(+2/+1). The electrochemical properties as a function of potassium ion concentration and film thickness have been determined primarily from cyclic voltammetric studies, and evidence for electronic conduction through the film has been observed. Optical properties of the films were determined using CuHCF deposited on tin oxide substrates. Supporting description of the electrochemical properties of the film has been obtained by a-c impedance measurements. The CuHCF film behavior is consistent with a model previously reported for Prussian blue films.

Our interest in the fabrication and subsequent electrochemical and spectroscopic study of metal hexacyanometalate films deposited on conducting substrates has been stimulated by the reports of Neff (1) and Ellis, Eckhoff, and Neff (2) on the iron hexacyanoferrate film of Prussian blue (PB). They observed that the PB film could be electrochemically reduced to Everitt's salt (ES) or oxidized to Berlin green (BG) and that these redox processes gave well-defined cyclic voltammetric waves. Because marked color changes were associated with the redox processes, it was proposed that such films could be used for electrochromic devices. Thin films of PB have now been deposited by chemical (1, 2), galvanostatic (3), potentiostatic (5), and other electrochemical methods (4). The impetus for considering other metal hexacyanometalate films such as the copper hexacyanoferrate film reported herein has been provided by Neff's work (1, 2). Also, we have been intrigued by the prospects of using such films as mediators to catalyze electron transfer reactions (6, 7).

To date, we have been able to form electroactive films of metal hexacyanoferrates, hexacyanoruthenates, and hexacyanocobaltates on conducting substrates. Our present discussion is restricted to the thin films of copper hexacyanoferrate (CuHCF). The bulk properties of CuHCF, a PB analog, have been well studied and documented. Infrared, visible and ultraviolet spectroscopic (8-10), and x-ray crystallographic (11) data as well as physical properties of stability, solubility, and ion permeability (12) have been tabulated.

Stable films of CuHCF on glassy carbon surfaces, for example, that can withstand repeated redox cycling seem to be formed only through a specific electrochemical sequence. The film deposition procedure is discussed in addition to the electrochemical and spectroscopic characterization of these films by cyclic voltammetry (CV), a-c impedance, x-ray photoelectron spectroscopy (XPS), Fourier transform infrared

* Electrochemical Society Active Member.
Key words: films, electrode, spectra, conduction.

(FTIR), external reflectance (FTIR-ER), and photoacoustic spectroscopy (FTIR-PAS).

Experimental

Reagent grade (ACS) cupric nitrate, cupric sulfate (Fisher Scientific Company), potassium ferrocyanide (Matheson, Coleman and Bell Company), potassium perchlorate (J. T. Baker Chemical Company), and potassium sulfate (Mallinkrodt, Incorporated) were used without further purification. Water was triply distilled with the final distillation made from an alkaline permanganate solution in an all-glass still.

The glassy carbon electrodes (GC-20 grade, Tokai Electrode Manufacturing Company, Tokyo, Japan) were circular disks with a geometric area of 0.61 cm^2 which were polished to a mirror-like finish on an optical flat using 1.0, 0.3, and 0.05μ alumina (Buehler Limited). After polishing, the electrodes were cleaned in an ultrasonic bath with a 1:1 water-methanol mixture, and then cleaned with triply distilled water. Substrates of doped tin oxide on glass (PPG Glass Company, Pittsburgh, Pennsylvania) were used as optically transparent electrodes (OTE's) for spectroelectrochemical studies. These electrodes were pretreated by washing with dilute acid and base solutions followed by ultrasonic cleaning as described for the glassy carbon (GC) electrodes.

A glass electrochemical cell with a volume of 25 ml was constructed for use with the GC electrodes. The GC disk was placed in a vertical position by insertion into an ACE adaptor with threaded fitting. Electrical contact was made by the placement of a brass screw against a thin copper sheet placed at the back of the GC disk away from the solution side and held in place by the adaptor bushing. A BAS (BioAnalytical Systems, Incorporated, West Lafayette, Indiana) saturated calomel electrode (SCE) with a Luggin capillary adaptor-tip served as the reference electrode. The capillary tip was placed *ca.* 1 mm from the surface of the working electrode. The auxiliary electrode was a shielded Pt wire that was separated from the main compartment by a fritted disk. Standard tapered joints sealed to the cell allowed for the placement of the reference and auxiliary electrodes and the tubings used for degassing purposes. The configuration for the spectroelectrochemical cell has been previously described (13).

Electrochemical experiments were performed using a PAR Model 174A/175 Polarographic Analyzer/Universal Programmer (Princeton Applied Research Corporation, Princeton, New Jersey) and data were recorded on a Houston Model 2000 X-Y recorder (Houston Instrument Company, Houston, Texas). The coulombic charge consumed by the film in any redox process was calculated from the integration of the CV current-potential (i-E) curve.

Faradaic impedance measurements were made using a Solartron Frequency Response Analyzer Model 1174 (Solartron Electronics Group, Limited, Furnborough, England) coupled to a Wenking potentiostat (Brinkmann Instruments, Incorporated, Westbury, New York) with data acquisition and control by an Apple II microcomputer (Apple Company, Cupertino, California). A sinusoidal modulation of 10 mV peak-to-peak was added to the d-c bias voltage, and the frequency range studied was between 0.2 and 10^5 Hz. The electrochemical cell used for the impedance measurement was the same as that used for the CV work except that a large Pt gauze served as the auxiliary electrode and was placed in the main solution compartment with the working electrode.

Visible spectral data were obtained using a previously described scanning spectrometer under computer data acquisition and control (14). Infrared external reflectance and photoacoustic spectroscopic data were obtained using a modified (15) Nicolet FTIR spectrometer (Nicolet Instrument Company, Madison, Wisconsin).

A Cambridge S4-10 Scanning Electron Microscope (EG & G Ortec, Oak Ridge, Tennessee) was used to examine the surface topography. Energy Dispersive X-ray Analysis (EDAX) was performed for elemental analysis using an ORTEC multichannel Analyzer Model 6200 which was attached to the Cambridge unit.

A PHI Model 548 ESCA/Auger Spectrometer (Physical Electronics, Incorporated, Eden Prairie, Minnesota) with sample introduction system and computer controlled data acquisition (16, 17) and smoothing (18, 19) was used for the XPS studies. XPS spectra were obtained with the analyzer chamber operating at a base pressure of less than 10^{-9} Torr of pressure with the x-ray source (magnesium anode) operating at a voltage of 10 kV and a current of 40 mA. Low resolution spectra were taken with the spectrometer pass energy set at 100 eV and high resolution, signal-averaged spectra were obtained at 25 eV pass energy. The spectrometer was calibrated assuming the gold $4f_{7/2}$ peak to be at 83.8 eV.

Procedure for Film Deposition

The GC electrodes were initially CV scanned between the potentials of +0.40 and +0.05V for several cycles in an aqueous solution of *ca.* 4×10^{-3}M cupric nitrate in 0.05M $KClO_4$. The i-E "background" was devoid of any current assignable to redox reactions such as copper deposition or background oxidation. Copper was then deposited on the electrode by stepping the potential from +0.03 to −0.50V, and subsequently removed (stripped) by linearly scanning the potential from −0.50 to +0.50V. The deposition and removal sequence was repeated until a reproducible i-E curve was obtained during the stripping procedure. The CuHCF film was formed by stepping the electrode potential in the presence of cupric ion from +0.03 to −0.50V and after waiting for a period between 3 and 10 sec, an aliquot of $K_4Fe(CN)_6$ solution was injected into the cell. The final ferrocyanide concentration in the cell was *ca.* 4×10^{-3}M. Thicker films could be formed by lengthening the delay time prior to the ferrocyanide injection. Within a few seconds after the addition of ferrocyanide, the current decayed to zero. The cell was then disconnected from the potentiostat and the electrode was removed and washed thoroughly with distilled water. It was used immediately or stored in a desiccator.

Results and Discussion

PB analogs of the general composition $(M_1^A)_k[M_2^B(CN)_m]_l \cdot xH_2O$, where M_1 and M_2 are either identical or dissimilar metals; A and B are the valences of M_1 and M_2, respectively, and k, m, and l indicate the stoichiometry of the complex; are formed by mixing solutions of $M_2^B(CN)_6^{n-}$ with an appropriate salt of M_1^A (20, 21). If M_1 and M_2 are transition metals, the possibility of forming a wide variety of compounds exists due to the ability to change not only the metal ions, but also their valences. When the ferrocyanide solution is injected into the electrochemical cell, a red-brown ferrocyanide sol is immediately formed. After a short time, the current of the working electrode falls to zero indicating complexation of the Cu^{2+} ion. The actual mechanism of the film formation has not been elucidated but the codeposition of copper is important in the formation of stable films. Films formed by a galvanostatic or potentiostatic method from solutions of cupric ion and ferricyanide ion showed noticeable deterioration within a few CV scans. Films formed by the codeposition procedure, however, are able to withstand CV cycling on the order of 10^3 in K_2SO_4. It is noted that the lifetime is highly dependent on several factors, including film thickness, electrolyte, scan rate, and the potential range scanned. The codeposited films are also able to

be stored for periods of up to six weeks in dry state with no apparent change in the cyclic voltammetric behavior. It is believed that the codeposition procedure provides a fresh copper surface to which the film adheres. For example, it has been shown that cyanide and cyanide compounds strongly adhere to copper surfaces (22). When the compound is immobilized on the electrode surface, it is able to undergo oxidation and reduction in the presence of potassium ions.

Cyclic Voltammetry

If a CuHCF film in 0.5M K_2SO_4 is CV scanned between the potentials of −0.20 and +0.95V, two redox couples appear. There is a well-defined reversible couple that is characteristic of an adsorbed species appearing with a peak potential of *ca.* +0.69V. Another couple at more negative potential is observed with the cathodic peak at *ca.* 0.00V and the anodic peak at *ca.* +0.35V. This latter broad, ill-defined CV wave probably involves the reduction of cupric ion in the CuHCF film. Because of the irreversible nature of the wave at more negative potentials, the data reported herein deal with the reversible-appearing CV wave at +0.69V. Figure 1 shows a typical steady-state i-E curve for a CuHCF film cycled in 0.5M K_2SO_4 at a sweep rate of 0.002 V/sec between the potentials of +0.50 and +0.90V. Steady-state i-E waves occurred after one complete CV cycle; *i.e.*, there is no break-in period. The ratio of the anodic to cathodic charge obtained from the integrated i-E curve for all the films observed is 1.00 (±0.03). In Fig. 1, the cathodic (E_{pc}) and anodic (E_{pa}) peak potentials are at +0.690 (±0.007) V *vs.* SCE and the peak widths at half-height are 0.12 and 0.11V, respectively. From the viewpoint of ideal behavior, the peak-to-peak separation should be zero at all sweep rates and the peak width should be 0.0906/n V (*i.e.*, 3.53 $RT/n\mathbf{F}$) with the anodic and cathodic i-E curves being mirror images of each other (23). From the corresponding data in Table I, it can be seen that the peak-to-peak separations for sweep rates of less than 0.005 V/sec are zero, indicating that the rates of charge transfer and counterion transport are fast compared to the scan rates and that the film behavior approaches ideality (24). The slightly broader than ideal peak width may be caused by: (*i*) repulsive interactions between ions in the lattice, (*ii*) differences in spatial distribution of redox centers, and (*iii*) distribution of species with different E° values (25).

The relationship that describes the peak current for a thin film of a monolayer or less with an idealized behavior (23) is given by Eq. [1]

$$i_p = (n^2\mathbf{F}^2/4RT)\nu A\Gamma^* \qquad [1]$$

where $A\Gamma^*$ is the number of mols of electroactive surface species, ν is the sweep rate, and the other symbols have their usual meaning. The peak current for the film in Fig. 1 was found to be linear with scan rate up to *ca.* 0.10 V/sec. As noted in Table I, the film behavior

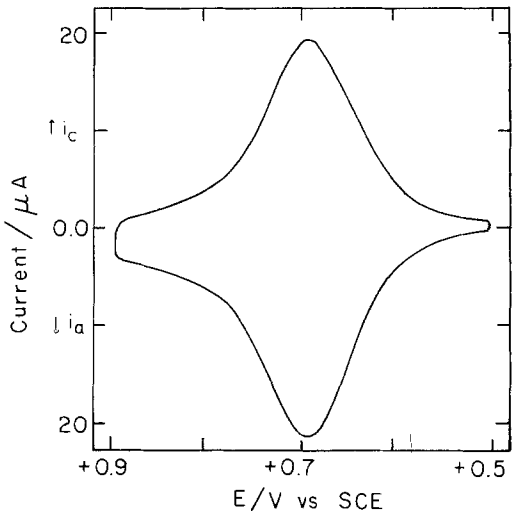

Fig. 1. Cyclic voltammetric curve of a CuHCF film on GC. Electrolyte: 0.5M K_2SO_4. Sweep rate: 0.002 V/sec. Charge: *ca.* 2.8 mC/cm². $E_{pa} = E_{pc} = +0.69$V *vs.* SCE. $E_{pa,1/2} = 0.11$V. $E_{pc,1/2} = 0.12$V.

in KCl is similar to that observed in K_2SO_4 but with narrower peak widths and with peaks appearing at slightly more positive potentials at low scan rates. The film in Fig. 1 consumed *ca.* 2.8 mC/cm² of charge which corresponds to a thickness of *ca.* 500Å. The thickness of the film, d, may be estimated from the ratio of the actual number of unit cells present on the electrode surface to the theoretical number necessary to form one molecular layer, for example

$$d = (C/n\mathbf{F}A)(l^3N_o/4) \qquad [2]$$

where C is the value of the integrated charge in coulombs, l is the length of the unit cell (10.0Å) (26), $\mathbf{F}$ is the Faraday constant, A is the area of the electrode, and N_o is Avogadro's number. It is assumed that the redox reaction involves one electron change per each iron and that all the HCF in the film are electroactive. Thus the value of 4 appears in the equation since there are 4 effective iron atoms in an unit cell. SEM topographical studies of films on glassy carbon have shown that the surface of a CuHCF modified electrode is fairly smooth with no exposed substrate; therefore it was assumed that the film thickness was uniform.

For each of the electrolyte conditions listed in Table I, there is a scan rate region above which the i_{pc} and i_{pa} become linear with the square root of scan rate. We are assuming that the ion transport rate of K^+, to-and-from or through the film, is responsible for this square root dependence. The deviation from linearity of peak currents with the sweep rate also occurs earlier as the film thickness increases, and the observed "tailing" of the current at high sweep rates is attributed to such kinetic effects (27). However, the

Table I. Peak widths and peak potentials for CuHCF films on GC

Sweep rate ν/V sec⁻¹	0.5M K_2SO_4[a]				1M KCl[b]				1M KCl + 10% EtOH[c]			
	E_{pa}/V	E_{pc}/V	$\Delta E_{pa,1/2}$/V	$\Delta E_{pc,1/2}$/V	E_{pa}/V	E_{pc}/V	$\Delta E_{pa,1/2}$/V	$\Delta E_{pc,1/2}$/V	E_{pa}/V	E_{pc}/V	$\Delta E_{pa,1/2}$/V	$\Delta E_{pc,1/2}$/V
0.001	+0.690	+0.690	0.110	0.122	+0.710	+0.705	0.094	0.109	+0.712	+0.712	0.091	0.097
0.002	0.690	0.690	0.110	0.122	0.710	0.705	0.100	0.103	0.712	0.710	0.091	0.097
0.005	0.690	0.685	0.110	0.122	0.710	0.702	0.100	0.106	0.715	0.707	0.094	0.097
0.010	0.692	0.685	0.110	0.126	0.710	0.697	0.100	0.108	0.720	0.705	0.088	0.094
0.020	0.697	0.682	0.114	0.124	0.715	0.692	0.100	0.113	0.727	0.700	0.100	0.103
0.050	0.705	0.680	0.114	0.126	0.730	0.680	0.109	0.125	0.742	0.680	0.106	0.119
0.100	0.745	0.665	0.128	0.134	0.760	0.660	0.128	0.134	0.760	0.660	0.128	0.128

[a] Peak current linear with sweep rate up to 0.100V sec⁻¹.
[b] Peak current linear with sweep rate up to 0.050V sec⁻¹.
[c] Peak current linear with sweep rate up to 0.010V sec⁻¹, linear with square root of sweep rate from 0.010 to 0.100V sec⁻¹. $\Delta E_{p,1/2}$ is the width of the peak at half-height.

influence of pure resistance on the shape of the *i-E* wave cannot be dismissed (28).

It has been noted that potassium ion is important in the redox chemistry of CuHCF films, as in PB, due to its ability to fit within the zeolite cage. The diameter of the zeolitic channel has been determined to be 3.2Å (26) and the effective diameter of the hydrated K^+ ion is 2.4Å (29). It would be expected, therefore, that a larger cation would interfere with the incorporation of K^+. Figure 2 illustrates the effect of Na^+, a cation with an effective hydrated diameter of *ca.* 3.6Å (29), on the CV behavior of a film with a charge of *ca.* 4.2 mC/cm² at a scan rate of 0.002 V/sec. As the mol ratio of Na^+ increases and K^+ decreases, the i_{pc} and i_{pa} values and consequently the Q_c and Q_a values also correspondingly decrease. The E_{pc} and E_{pa} also shift to less positive values. In Fig. 3 the logarithm of the K^+ concentration is plotted as a function of the midpoint potential $[(E_{pc} + E_{pa})/2]$. A linear plot is observed indicative of the film behavior being Nernstian in potassium ion, in accord with the results found by Ellis, Eckhoff, and Neff (2) for PB films. The slope of the plot is 77 mV per decade change in the K^+ concentration rather than the ideal 60 mV Nernstian slope. The reason for this small deviation from ideality is presently unexplained. However, the

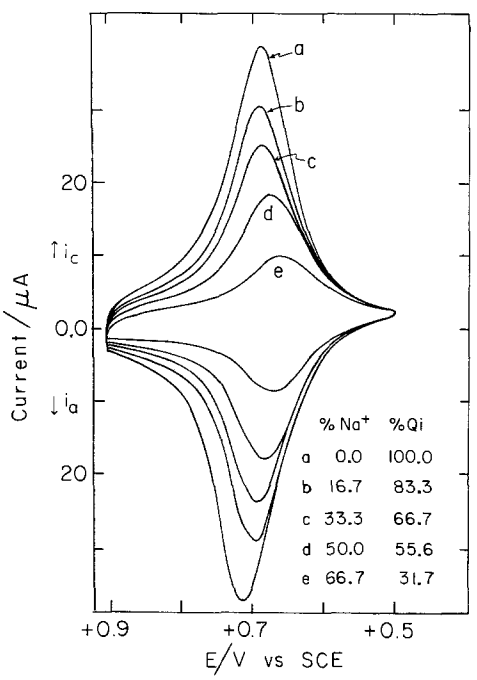

Fig. 2. Cyclic voltammetric curves of a CuHCF film on GC in solutions containing varying amounts of sodium and potassium ions. Total concentration of cation is 1.0M, anion is sulfate. Sweep rate: 0.002 V/sec. Initial charge, Q_i: *ca.* 4.1 mC/cm².

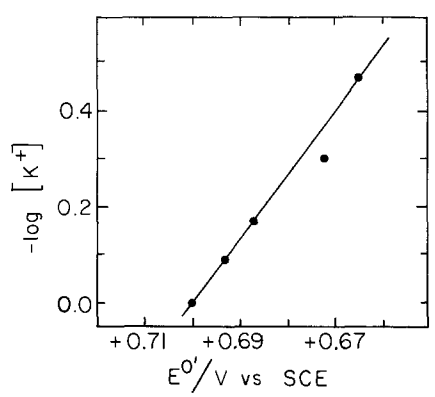

Fig. 3. Plot of −log of potassium ion concentration vs. $(E_{pa} + E_{pc})/2$. Taken from data in Fig. 2.

unexpected and striking result is the linear relationship found between the integrated charge, Q_c or Q_a, of the *i-E* waves on the mol ratio of Na^+ or K^+ as seen in Fig. 4. Obviously, the CuHCF film has preferential selectivity to K^+ with respect to Na^+. On the other hand, the concentration of K^+ in the solutions at all the mol ratios used is more than sufficient to satisfy the amount needed to maintain charge neutrality for the electrolyzed films. The inhibition to the charge transfer process by the presence of the Na^+ suggests a "blocking" mechanism at the film-solution interface. Irrespective of the mechanism which may be governing the amount of film being electrolyzed, the interesting aspect is the dependence of the faradaic charge on the mol ratio of sodium ion with respect to potassium ion.

If an aqueous solution of 1M KCl which is 10% ethanol by volume is used as a solvent, the peak current is linear with scan rate up to only 0.010 V/sec and then becomes linear with the square root of scan rate after *ca.* 0.010 V/sec which is considerably earlier than for solutions without ethanol. In addition the presence of alcohol causes a decrease in the peak width as may be seen from the data in Table I. The role of alcohol in narrowing the peak widths is probably due to the same phenomenon as observed for bulk CuHCF. In the bulk species, alcohols tend to alter the membrane permeability, and in some instances the presence of alcohols allows species not usually permeable to pass readily because of alterations of the pore size (11); *i.e.* swelling of the membrane. For the films at high sweep rates, the addition of alcohol results in a pronounced tailing of the *i-E* wave, indicating that there is insufficient time for the reaction to occur inside the film (27). This is what would be expected if the addition of alcohol resulted in film swelling and would correspond to a behavior that would be expected of a thicker film.

If alcohol is added to the solution containing Na^+, the inhibition effect is less pronounced. Also, lithium ion, with an effective diameter of 4.7Å (29), has little effect on the *i-E* waves at the same mol ratios as previously used for sodium to potassium ion. At an Li^+ concentration of 1M, however, the *i-E* wave is considerably broadened and the charge is reduced. Transferring this film from the Li^+ solution to one containing 1M K^+ and CV cycling virtually restored completely the original *i-E* wave obtained in a potassium ion medium. This is in contrast to a film exposed to sodium ion where the film electroactivity cannot be restored. It appears that the reversibility of the film to different cations depends both on the type and size of the cation.

Preliminary studies of the use of CuHCF films as electron transfer mediators indicate that these films are

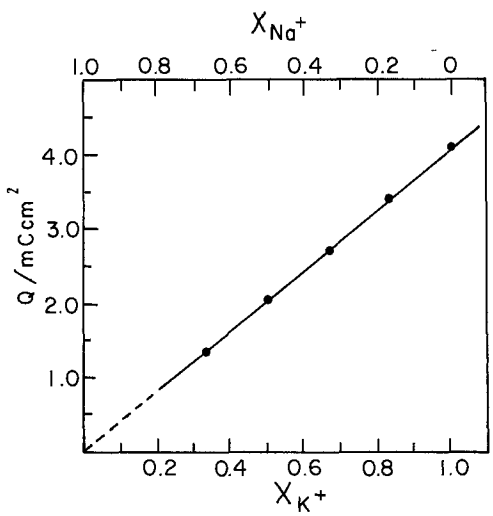

Fig. 4. Plot of charge vs. mol fraction of cation. Taken from data in Fig. 2.

able to electrolyze solution species (*e.g.*, ferri-/ferrocyanide, ascorbic acid) over a wide range of potentials in the presence of potassium ion. The *i-E* wave in these instances is a composite of the wave for CuHCF and the solution species. Hence, the redox wave of the solution species is clearly observed, suggesting that the film behaves essentially as an electronic conductor. A plausible mechanism is "electron-hopping" between metal atoms in the film as bridged by the cyanides. Such a mechanism has been suggested by Neff (2) and Itaya (6) for PB films. Additional studies are currently underway to evaluate more fully the extent and mechanism of charge coupling with solution species.

The CV *i-E* waves of CuHCF deposited on a tin oxide OTE are much broader than those on glassy carbon and are characteristic of irreversibility. The peak-to-peak separation of the E_{pc} and E_{pa} ranges from 0.03 to more than 0.30V at scan rates of 0.002-0.050 V/sec, respectively. In addition to the large peak width, the foot of the wave is extended and the integrated charge decreases as the scan rate increases. This is in contrast with the film behavior at a GC electrode where the values of Q_c or Q_a were independent of scan rate over a wide range. The CuHCF films on tin oxide were useful, however, for obtaining optical absorption spectra of the oxidized and reduced forms of the films as is discussed later.

A-C Impedance Measurements

Since the CV behavior of a CuHCF modified electrode in the presence of alcohol as well as preliminary cation studies gave evidence for membrane porosity, the possibility of applying an a-c impedance method to evaluate electrochemical parameters of the film appeared attractive. This method has been used in the study of porous electrodes (30-32) and PB films (5). Among the advantages offered by the a-c method is the ability to obtain values of the double layer capacitance and the activation resistance in the same measurement. A detailed discussion of analysis of a-c impedance data is available (33).

Figure 5 shows the impedance plane plot (imaginary component, Z'' *vs.* real component, Z') for a CuHCF film in contact with 0.5M K_2SO_4. The intercept of the semicircle at high frequencies with the real axis (Z') yields a value for the ohmic resistance (R_Ω) of 1.6 Ω/cm^2 which represents the value of the solution resistance. The necessity of placing the radius of the semicircle below the real axis is due to the complexity of the system; *i.e.*, a simple model does not suffice and a transmission line model is more appropriate (30, 32). In this model, the activation resistance, R_a, is found to be 42.4Ω. Since the data were taken at $E_{d.c.} = E^{\circ\prime}$, the exchange current density may be calculated from the equation (34)

$$R_a = RT/n\mathbf{F}i_o \quad [3]$$

where R_a is the activation resistance in ohm; i_o is the exchange current density, and the other symbols have their usual meaning. The value of i_o was found to be 0.61×10^{-3}A or normalized to the geometric area of the electrode, *ca.* 1×10^{-3} A/cm². The magnitude of this rate is indicative of a fast electron transfer reaction.

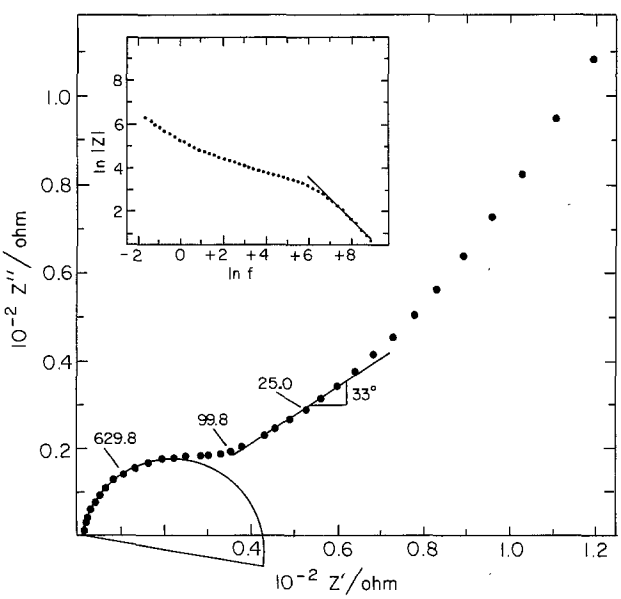

Fig. 5. Impedance plane plot (partial) for CuHCF film on GC in contact with 0.5M K_2SO_4. $E_{d.c.} = E^{\circ\prime}$. $R_\Omega = 1.6$ Ω/cm², $i_o = 1$ mA/cm². Inset: Bode plot of impedance data. Double layer capacitance: 100 μF/cm⁻². Adsorption pseudocapacitance: 13.4 mF/cm².

The inset to Fig. 5 is a Bode plot, or a plot of ln $|Z|$ *vs.* ln f, where f is the frequency and $|Z|$ is defined as

$$|Z| = (Z'^2 + Z''^2)^{1/2} \quad [4]$$

When Z' is corrected for ohmic resistance, the double layer capacitance may be found from the Bode plot. In the high frequency region the slope of the line tends toward a value of −1 (−1.020 in Fig. 5) and the double layer capacitance, C_{dl}, may be obtained from the value of $|Z|$ where this line intersects the point at which ln f is equal to zero (*i.e.*, $f = 1$). The value of C_{dl} equal to 100 μF/cm² is obtained. Also, in the low frequency region, the points approach a slope of −1, and a similar analysis gives an approximate value of 13.4 mF/cm². This region of the Bode plot corresponds to the low frequency portion of the impedance plot where the slope of the line rises sharply indicating an adsorption pseudocapacitance associated with highly adsorbed species. High values of the adsorption pseudocapacitance have also been observed for porous gold and nickel electrodes (35), as well as for PB (5). In the frequency range between 79.2 and 12.5 Hz, the slope of the impedance plot is 33° indicating that the behavior of the CuHCF film is similar to that of porous electrodes (31, 35). It has been shown that when the rate of heterogeneous electron transfer processes is diffusion limited by the membrane pore size, in theory the impedance plane plot will be a straight line with a slope equal to π/8. The more occluded the pore, the more the impedance exhibits a pseudo transfer resistance (32), *i.e.*, the line will bend in the high frequency region and will assume a semicircular shape. If the impedance behavior of a CuHCF film is examined at potentials far removed from $E^{\circ\prime}$, for example at $E_{d.c.} = +0.50$ or 0.90V, it is found that the behavior is essentially capacitive in nature. Extensive a-c impedance studies including an evaluation of the effects of alcohol are currently underway.

Spectroscopic Results

The utility of tin oxide OTE's for obtaining visible absorption spectra was noted earlier. Figure 6 shows the background corrected spectra of a CuHCF film on tin oxide in contact with 0.5M K_2SO_4. It is noted that similar spectra are observed in 1.0M KCl. Trace a is a spectrum of the reduced film obtained by applying a potential of +0.35V *vs.* SCE. The broad band at *ca.* 490 nm is associated with the iron to copper charge transfer in cupric ferrocyanide. Trace b is the corresponding spectrum of the oxidized film obtained by applying a potential of +1.05V *vs.* SCE. The band at *ca.* 420 nm is attributed to the cyanide to iron charge transfer band for the ferricyanide species. Both bands are shifted from those reported for the bulk species, which are only in fair agreement with calculated values (10). The change in the optical spectra with the applied potential indicates that the redox process involves a change in the oxidation state of the iron in

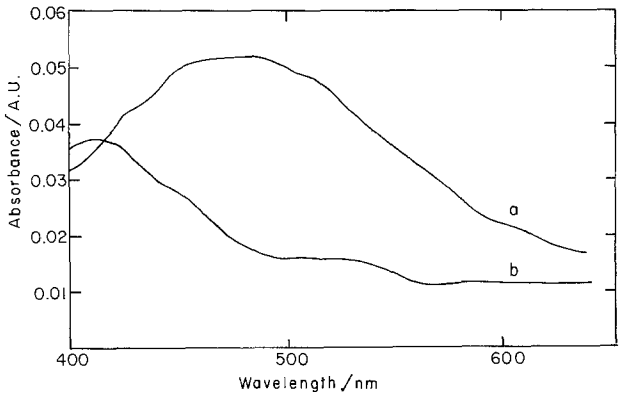

Fig. 6. Background corrected absorbance spectra for CuHCF film on SnO_2 in contact with 0.5M K_2SO_4. Trace a: reduced form. E_{appl} = +0.35V vs. SCE. Trace b: oxidized form. E_{appl} = +1.05V vs. SCE.

ferri- and ferrocyanide. The corresponding change in the optical spectra with the change in oxidation state of iron is corroborated by bulk CuHCF experiments. That is, when one mixes cupric ion with an equimolar amount of ferrocyanide, a red-brown cupric ferrocyanide sol results. However, the mixing of cupric ion with an equimolar amount of ferricyanide produces a yellow sol. The average value of the molar absorptivity of CuHCF calculated from the experimental absorbance at *ca.* 490 nm is on the order of 2×10^3 liter/mol cm. This value is approximately 1/3 that for the charge transfer band in PB films (3). One of the reasons for the low value of the molar absorptivity may be the effect of nonhomogeneity which would result in a nonuniform path length. Nonhomogeneity would also contribute to the peak broadening observed in the CV behavior of the films on tin oxide substrates.

Hysteresis effects are observed in the absorbance *vs.* time profiles obtained by stepping the potential between +0.35 and +1.05V *vs.* SCE and monitoring the absorbance at 490 nm. It was necessary to apply a considerable overpotential to completely reduce or oxidize the CuHCF, due to the less reversible behavior of the film on the tin oxide surface. Upon oxidation, the absorbance decreases linearly with time before attaining the minimum value of the fully oxidized film. Upon reduction, the absorbance correspondingly increases, but in a nonlinear manner, as the maximum value is approached for a fully reduced film. The time to achieve a fully oxidized or reduced film required *ca.* 5 sec for the overpotentials used.

The use of XPS for the study of mixed valence compounds (MVC's) has been reported in the literature (36, 37). Recently our laboratory and others (6) have applied XPS to study thin films of PB and CuHCF in order to define the surface composition.

When a cupric salt is added to an alkali salt of $Fe(CN)_6^{4-}$, a cupric ferrocyanide complex which incorporates nonstoichiometric amounts of the alkali ion (12), is formed. However, it has been shown that for a given set of conditions, the amount of alkali metal is constant, but the molecule is probably very complex and may consist of a definite number of molecules of the pure metallic ferrocyanide with one or more molecules of the double salt (21).

When cupric sulfate and potassium ferrocyanide are mixed together in a potassium perchlorate solution, the precipitated CuHCF is contaminated by electrolyte species. High resolution XPS spectrum of the washed and dried sample shows considerable amounts of elemental potassium, as listed in Table II. Survey XPS of the sample also revealed the presence of sulfur and chlorine. Similarly, the surface of a freshly prepared CuHCF film on a carbon electrode, after washing and drying, indicated incorporation of potassium in the film as well as traces of other "impurities" from the solution electrolyte. However, when a CuHCF film is redox cycled between the potentials of +0.50 and +0.90V *vs.* SCE by CV, the reduced film contains potassium ion whereas the oxidized film does not. No sulfur is observed in the spectra of either of the cycled films. As noted in Table II, the K/Fe elemental ratios as calculated from the integrated XPS high resolution band, after cross-section correction, are 1.9 ± 0.7 and less than 0.2 for the reduced and oxidized films, respectively. EDAX, which has a much greater surface penetration depth than XPS, confirmed the results. Thus, the difference in the potassium content, as determined by XPS, is not a reflection of alteration of the sample surface by the wash/dry procedure of the films prior to introduction into the XPS chamber.

The surface elemental ratios of N/Fe and Cu/Fe do not vary appreciably from bulk to electrode samples. It appears that electrochemically prepared samples have no appreciable nitrate contamination, since no additional peak at *ca.* 6 eV higher binding energy from the cyanide N 1s peak (38) is observed. The nonstoichiometric Cu/Fe and K/Fe ratios indicate the formation of complex species or variations in the surface composition with respect to the bulk. However, a significant amount of potassium is consistently detected in the reduced film, whereas in the oxidized CuHCF, at most only trace amounts are observed.

High resolution spectra of the copper 2p region for all samples reveal "shake-up peaks," additional peaks at a higher binding energy than the main peaks. These are characteristic of the copper +2 oxidation state (39) and their presence in both the oxidized and reduced films indicate that no change occurs in the copper oxidation state. The full widths at half-maximum (FWHM) are large (*ca.* 2.4 eV) but comparable for both forms.

High resolution spectrum of the iron $2p_{3/2}$ region reveals a peak for the reduced film to be symmetrical with a FWHM of *ca.* 1.5 eV. This same band for the oxidized film, however, is broad and unsymmetrical with a FWHM of *ca.* 2.7 eV. The broader peak for the oxidized film is consistent with the trend observed for potassium ferri- and ferrocyanide and for ferrocene modified electrodes (37, 40). The very broad asym-

Table II. XPS peak[1] positions and atomic ratios[2]

Sample	Fe $2p_{3/2}$	Cu $2p_{3/2}$	N 1s	K $2p_{3/2}$	C 1s*	N/Fe	K/Fe	Cu/Fe
Powder[3]	712.4	937.7	401.4	297.5	288.4	10.0 ± 0.9	10.1 ± 3.2	1.8 ± 0.3
Fresh electrode[4]	712.2	937.7	401.5	296.5	288.2	9.6 ± 0.6	3.2 ± 0.4	3.1 ± 0.5
Oxidized[5]	**	938.7	401.4		288.0	10.0 ± 0.7	0.0 to trace	1.8 ± 0.6
Reduced[6]	712.4	939.4	401.7	297.5	288.7	9.5 ± 0.6	1.9 ± 0.7	2.2 ± 0.4

[1] Experimental, uncorrected (±0.5 eV).
[2] Normalized to photoelectron cross-sections. C 1s = 1.00.
[3] Precipitated from cupric sulfate and potassium ferrocyanide in perchlorate media.
[4] Film prepared as described in procedure, not electrochemically cycled.
[5] Electrochemically cycled in 0.5M K_2SO_4 between +0.500 and +0.900V *vs.* SCE, then open-circuited at +0.900V.
[6] Electrochemically cycled in 0.5M K_2SO_4 between +0.500 and +0.900V *vs.* SCE, then open-circuited at +0.500V.
* C 1s (from Ref. 37) for the cyanide carbon PB, 286.1; $K_4Fe(CN)_6$, 286.4; $K_3Fe(CN)_6$, 286.3.
** Refer to discussion.

metric shape of the peak makes determination of the peak position difficult, but qualitatively useful. It is felt that the change in the shape and width of the iron peak is associated with a change in oxidation state. The narrow, symmetric peak is observed for the ferrocyanide species, and the broad, asymmetric peak is observed for the ferricyanide species. The unusual breadth of the peak for the oxidized films is not associated with residual ferrocyanide, and this assumption is substantiated by infrared data.

Both the reflectance and photoacoustic spectra of oxidized films on GC substrates place the cyanide band at 2090 wave numbers (cm^{-1}). This is in close agreement with Ayers *et al.* (8) who place the CN stretch of a bulk cupric ferricyanide sample in KBr at 2100 cm^{-1}. No additional peak at 2060 cm^{-1}, indicative of cupric ferrocyanide (8), was observed in the oxidized films.

The change in the XPS spectra of the iron $2p_{3/2}$ region, substantiated by the infrared spectra, establishes the redox couple as the ferri-ferrocyanide couple. The detection of significant amounts of potassium in the reduced form, as well as the cyclic voltammetric behavior, infer a potassium ion dependence. The reaction can thus be formally represented by the following equation

$$Cu_3^{+2}[Fe(CN)_6^{3-}]_2 + 2K^+ + 2e = K_2Cu_3^{+2}[Fe(CN)_6^{4-}]_2 \quad [5]$$

where the role of potassium ion is its incorporation within the zeolitic cage to maintain charge neutrality during reduction.

Summary

The values of the ohmic resistance and the exchange current for a typical film in 0.5M K_2SO_4 indicate that the barrier to electron transfer through the CuHCF film is very low. Thus, the film behavior is similar to a conductor whereby different solution species undergo oxidation/reduction reactions governed by their redox potentials and independently of the film redox reaction. This is in contrast to immobilized polymer redox mediators that control the potential at which charge can be transported through the polymer film to solution species. The change in the optical properties of these metal hexacyanoferrates, such as Prussian blue and copper hexacyanoferrate, and related mixed metal valent compounds that can be stabilized as films, make these films potentially valuable for electrochromic devices. We also envision several other interesting applications. Further details of the physical and electrochemical properties of the PB and CuHCF films as well as those fabricated from other transition elements will be reported in the near future.

Acknowledgment

Financial support from the National Science Foundation and Koppers Company, Incorporated is greatly appreciated. The suggestion by S. Holter regarding the possibility of forming various mixed metal valent films is hereby acknowledged. Discussions with V. Neff regarding Prussian blue films and the assistance of M. Porter in making FTIR measurements are appreciated. Access to the Solartron instrument in the Department of Metallurgical Engineering was made possible by D. MacDonald.

Manuscript submitted May 19, 1982; revised manuscript received Sept. 3, 1982.

Any discussion of this paper will appear in a Discussion Section to be published in the December 1983 JOURNAL. All discussions for the December 1983 Discussion Section should be submitted by Aug. 1, 1983.

Publication costs of this article were assisted by The Ohio State University.

REFERENCES

1. V. D. Neff, *This Journal*, **125**, 886 (1978).
2. D. Ellis, M. Eckhoff, and V. D. Neff, *J. Phys. Chem.*, **85**, 1225 (1981).
3. K. Itaya, H. Akahoshi, and S. Toshima, *This Journal*, **129**, 1498 (1982).
4. H. Kellawi and D. R. Rosseinsky, *J. Electroanal. Chem. Interfacial Electrochem.*, **131**, 373 (1982).
5. A. C. Ramamurthy, T. Kuwana, and D. D. MacDonald, In preparation.
6. K. Itaya, Private communication.
7. L. M. Siperko and T. Kuwana, In preparation.
8. J. B. Ayers and W. H. Waggoner, *J. Inorg. Nucl. Chem.*, **33**, 721 (1971).
9. Surendra Nath Ghosh, *Inorg. Nucl. Chem.*, **36**, 2465 (1974).
10. P. S. Braterman, *J. Chem. Soc. (A)*, 1471 (1966).
11. J. F. Keggin and F. D. Miles, *Nature*, 577 (1936).
12. H. B. Weiser, "Inorganic Colloid Chemistry," Chap. 18, Baunworth Press, Bridgeport (1938).
13. F. M. Hawkridge and T. Kuwana, *Anal. Chem.*, **45**, 1021 (1973).
14. J. W. Strojek, G. A. Gruver, and T. Kuwana, *ibid.*, **41**, 487 (1969).
15. M. D. Porter, D. H. Karweik, and T. Kuwana, In preparation.
16. C. W. Miller and T. Kuwana, Paper presented at the 3rd Symposium on Applied Surface Analysis, June 3-5, 1981.
17. C. W. Miller, D. H. Karweik, and T. Kuwana, *Anal. Chem.*, **53**, 2319 (1981).
18. A. Savitzky and M. F. E. Golay, *ibid.*, **36**, 1627 (1964).
19. J. Steiner, Y. Termonia, and J. Deltour, *ibid.*, **44**, 1900 (1972).
20. A. Ludi and H. U. Gudel, *Structure and Bonding*, **14**, 1 (1973).
21. H. E. Williams, "Cyanogen Compounds," p. 167, Edward Arnold and Co., London (1948).
22. R. E. Benner, K. U. von Raben, R. Dornhaus, and R. K. Chang, *Surf. Sci.*, **102**, 7 (1981).
23. A. J. Bard and L. R. Faulkner, "Electrochemical Methods," Chap. 12, John Wiley & Sons, New York (1980).
24. E. Laviron and J. Roullier, *J. Electroanal. Chem. Interfacial Electrochem.*, **115**, 65 (1980).
25. P. J. Peerce and A. J. Bard, *ibid.*, **114**, 89 (1980).
26. G. B. Seifer, *Russ. J. Inorg. Chem.*, **7**, 621 (1962).
27. E. Laviron, L. Roullier, and C. Degrand, *J. Electroanal. Chem. Interfacial Electrochem.*, **112**, 11 (1980).
28. V. D. Neff, Personal communication.
29. E. A. Moelwyn-Hughes, "Physical Chemistry," p. 589, MacMillan Co., New York (1951).
30. R. de Levie, "Advances in Electrochemistry and Electrochemical Engineering," Vol. 6, P. Delahay, Editor, p. 329, Interscience, New York (1969).
31. H. Keiser, K. D. Beccu, and M. A. Gutjhar, *Electrochim. Acta*, **21**, 539 (1976),
32. R. Buck, *J. Electroanal. Chem. Interfacial Electrochem.*, **18**, 381 (1968).
33. F. Mansfeld, *Nat'l. Assn. Corrosion Eng.*, **36**, 539 (1981).
34. A. J. Bard and L. R. Faulkner, in "Electrochemical Methods," Chap. 9, John Wiley & Sons, New York (1980).
35. J-P. Candy, P. Foilloux, M. Keddam, and H. Takenouti, *Electrochim. Acta*, **26**, 1029 (1981).
36. B. M. Chadwick and A. G. Sharpe, *Inorg. Chem. Radiochem.*, **8**, 83 (1966).
37. G. K. Wertheim and A. Rosencwaig, *J. Chem. Phys.*, **54**, 3235 (1971).
38. T. A. Carlson, "Photoelectron and Auger Spectroscopy," Appendix 3, Plenum Press, New York (1975).
39. D. C. Frost, A. Ishitani, and C. A. McDowell, *Molec. Phys.*, **24** (4), 861 (1972).
40. M. Umana, D. R. Rolison, R. Nowak, P. Daum, and R. W. Murray, *Surf. Sci.*, **101**, 295 (1980).

Technical Notes

Anodic Dissolution of Copper in Concentrated LiCl Solution at *p*H Between 3 and 7

Louis Brossard*

Quebec-Hydro Research Institute (IREQ), Materials Division, Varennes, Québec, Canada J0L 2P0

Interest in the anodic dissolution of copper in acidic chlorinated solutions has come about as the result of the wide use of such solutions particularly for the electropolishing and electrochemical machining of copper, and the dominant role played by Cl^- ions in the copper corrosion process (1-12). The determining step in the active dissolution of copper in the presence of Cl^- is generally attributed to the diffusion of an ionic species in the liquid phase, such as Cu^+, Cu^{++}, $CuCl_2^-$, $CuCl_3^-$, and Cl^-, according to the concentrations under study (1-12).

Recently, Moreau (2) proposed a dissolution mechanism based on the theory of absorbed intermediate species. This model provides a consistent explanation for the behavior of copper while the copper dissolution rate, calculated according to this model, is in accordance with experimental results for concentrated HCl solutions. However, comparison between the calculated values and experimental results has been limited to a simple activity in chloride ions, namely, 1 mol/liter for currents below 0.08 mA/cm^2. Kozin and co-workers (3), on the other hand, who studied the dissolution of copper in acidic aqueous solutions with 1-4M LiCl, suggest that copper dissolves according to the mechanism $Cu \rightarrow Cu^+ + 1e$ and that the dissolution rate is determined by the diffusion of Cu^+ from the electrode to the solution.

The aim of the work presented here is to pursue the study of the active dissolution of copper in slightly acidic or quasi neutral aqueous solutions with a high LiCl concentration.

Experimental

Cell and accessories.—Conventional electrochemical cells were used with a copper working electrode, a platinized platinum counterelectrode, and saturated calomel reference electrode. The solution in contact with the counterelectrode was separated from the parent solution by a sintered glass; whereas, the reference electrode was immersed in the upper section of the Luggin capillary tube, the end of which was only 1 mm from the surface of the copper electrode.

The copper electrode (Ventron Corporation, 99.99%) consisted of a vertical 0.64 mm diameter wire or of a horizontal 0.95 cm diameter disk, which gave a sample surface area of 0.5 and 0.71 cm^2, respectively. The samples were not exposed to heat-treatment prior to the experiments, and triple-distilled water was used to prepare the solutions.

Test procedure.—After 6 hr of argon bubbling, the working electrode was immersed in the solution. The solutions were either slightly acidic or quasi-neutral, with a *p*H ranging from 3 to 7. and contained between 0.2 and 10M of dissolved LiCl. When necessary, a potassium phtalate-based buffer was used to stabilize the *p*H.

Using Shoesmith *et al.*'s copper polishing method (13), the sample was buffed with silicon carbide paper then polished with a 1μ alumina paste. It was subsequently rinsed with alcohol, acetone, and finally distilled water before being immersed in the solution.

Experimental techniques.—The cell polarization curves were obtained by standard techniques. A Tacussel G-STP2C generator connected to a Wenking potentiostat served to vary the voltage applied to the copper electrode either linearly with time or in steps. An electronic coulometer measured the quantities of electricity in the oxidation stage.

In order to determine the influence of stirring on the copper dissolution current, a constant voltage was applied to the copper electrode and ω was varied stepwise from 100 to 9 rps, keeping it constant for 1 min at each value. The electrode was polished between each experiment.

The chloride activity $|Cl^-|$ was calculated from Davies' formula as modified by Robinson, and by Guggenheim, and Bates (14) taking account of the values for the mean activity coefficient available in the literature for dissolved LiCl (15). Moreau (2) adopted a similar approach to determine $|Cl^-|$ in solutions with a high HCl concentration.

The dissolution valency was determined by applying a constant voltage to the copper and measuring the electric charge involved during copper active dissolution. The amount of copper dissolved was obtained by weight loss measurement. Once it had been ensured that there were no corrosion products on the surface of the electrode. Faraday's law was applied giving the dissolution valency (2, 16). Unless otherwise noted, all electrode potential values are given with respect to an SCE as reference.

Experimental Results and Discussion

Copper electrode behavior.—The formation of a corrosion product, CuCl, on a stationary electrode surface was observed only at applied potentials very close to the reversible potential for the reaction $Cu + Cl^- \rightarrow CuCl + e$. Similar observations have been done in concentrated HCl solutions (17). So, the electrode surface should be considered free of corrosion product during its dissolution in the potential range considered here.

The main characteristics of the behavior of the copper electrode are: (*i*) The relation $E - \log_{10} i$ is linear with a slope close to 60 mV/decade (Fig. 1) at a fixed ω and Cl^- concentration. (*ii*) The $i - \omega^{1/2}$ relations are linear and the ordinate at the origin passes very close to zero (Fig. 2) at a fixed applied potential and Cl^- concentration. (*iii*) The relations $E - \log_{10} (i\omega^{1/2})$ are linear with a slope equal or very close to 60 mV/decade (Fig. 3) at a given Cl^- concentration.

* Electrochemical Society Active Member.

Key words: corrosion, anodic dissolution, copper dissolution kinetics.

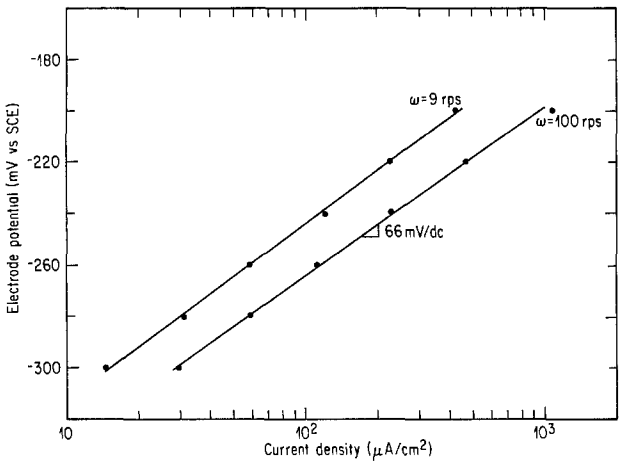

Fig. 1. Anodic polarization curves on a copper disk electrode LiCl: 1M, $\nu = 0.5$ mV/sec.

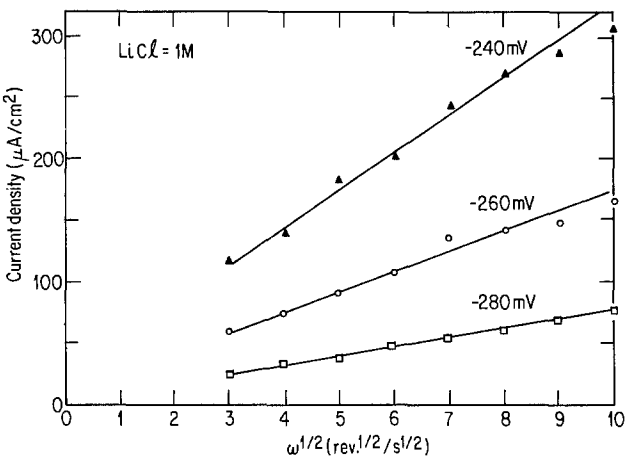

Fig. 2. Dependence of the rotation speed of the electrode on the anodic current density at 3 potentials values. □, 280 mV (/SCE); ○, 260 mV; △, 240 mV; LiCl; 1M. Electrode potentials are in the zone where the relationship $E_I - \log_{10} I$ is linear (Fig. 1).

(*iv*) The dissolution valency is close to 1, as it was observed by Kinoshita *et al.* (16) for the active dissolution of copper in concentrated LiCl solutions.

Proposed dissolution mechanisms.—Copper that dissolves in aqueous solutions with high concentration in Cl^- shows a marked tendency to be associated with chloride (1-10), $CuCl_2^-$ and $CuCl_3^=$ being the most probable complexes in the range of concentration considered. In addition, the relations $i - \omega^{1/2}$ given in Fig. 2 suggest that the anodic dissolution of copper is diffusion controlled. When the $CuCl_2^-$ species is considered, the reactions of importance are

$$Cu + 2Cl^- = (CuCl_2^-)_i + e \qquad [1]$$

and

$$(CuCl_2^-)_i \rightarrow (CuCl_2^-)_s \text{ rds} \qquad [2]$$

where the subscripts i and s refer to concentrations at the copper-solution interface and the bulk solution, respectively. The rate-determining-step [2] is the diffusion transport of $CuCl_2^-$ from the interface to the bulk solution. Step [1], the oxidation of copper to $CuCl_2^-$, is assumed to be in equilibrium for which the Nernst equation

$$E = E^\circ + \frac{RT}{\mathbf{F}} \ln \frac{(CuCl_2^-)_i}{(Cl^-)^2} \qquad [3]$$

is applicable and from which $(CuCl_2^-)_i$ is obtained

$$(CuCl_2^-)_i = (Cl^-)^2 \exp \frac{\mathbf{F}(E - E^\circ)}{RT} \qquad [4]$$

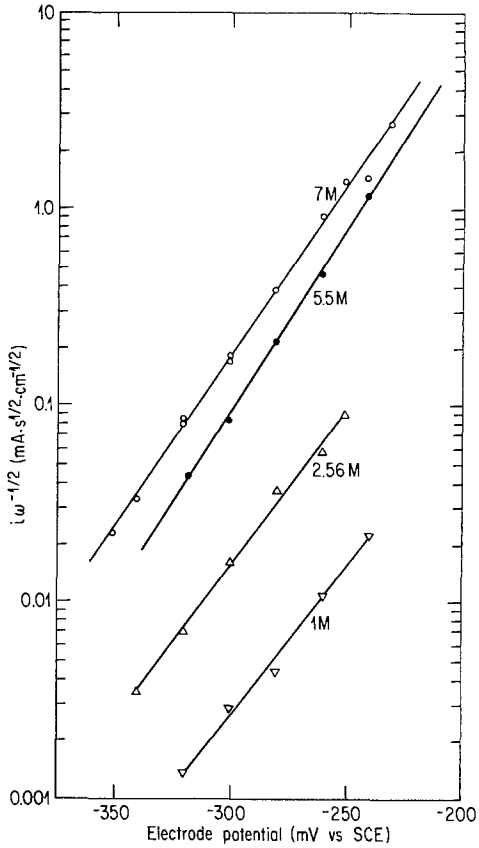

Fig. 3. $i\omega^{-1/2}$ vs. applied potential at different LiCl concentrations.

Substituting $(CuCl_2^-)_i$ into the rate determining diffusion transport equation (Fick's first law)

$$i = \frac{\mathbf{Z}\mathbf{F}D(CuCl_2^-)_i}{\delta} \qquad [5]$$

leads to the rate expression

$$i = \frac{\mathbf{Z}\mathbf{F}D}{\delta}(Cl^-)^2 \exp \frac{\mathbf{F}(E - E^\circ)}{RT} \qquad [6]$$

δ is given by (18)

$$\delta = 1.61\, D_{CuCl_2}^{-1/3} \nu^{1/6} \omega^{-1/2} \qquad [7]$$

The substitution of δ in Eq. [6] gives

$$I = 0.62\, \mathbf{Z}\mathbf{F}\nu^{1/6} D_{CuCl_2}^{-2/3} \omega^{1/2} |Cl^-|^2 \exp \frac{\mathbf{F}(E - E^\circ)}{RT} \qquad [8]$$

In Eq. [8], Z, the charge on the species undergoing mass transport ($CuCl_2^-$), is 1; ν is the kinematic viscosity which was determined experimentally; $D_{CuCl_2^-}$ is the diffusion coefficient for $CuCl_2^-$; ω is the rotating speed in radians per seconds; $|Cl^-|$, the activity of Cl^-, is substituted to Cl^- concentration. E° may be deduced from thermodynamic values (19).

The derivatives of Eq. [8] are

$$(\partial E/\partial \log i)_{298\text{ K},\,|Cl^-|} = 59 \text{ mV/decade (Fig. 1)} \qquad [8a]$$

$$\left(\frac{\partial i}{\partial \omega^{1/2}}\right)_{Cl^-,\,E} = \text{CONSTANT (Fig. 2)} \qquad [8b]$$

$$\left[\frac{\partial E}{\partial \log\left(\frac{\partial I}{\partial \omega^{1/2}}\right)}\right]_{E,\,298\text{ K}} = 59 \text{ mV/decade (Fig. 3)} \qquad [8c]$$

They correspond to characteristics (*i*), (*ii*), and (*iii*) found for the dissolution of copper. The diffusion co-

Table I. Experimental values of diffusion coefficient[a]

Cl^- (M)	−300 mV_{SCE}	−275 mV_{SCE}	−250 mV_{SCE}
1	2.6×10^{-5} cm^2/sec	2.7×10^{-5} cm^2/sec	2.0×10^{-5} cm^2/sec
1.83	1.8	1.9	2.2
2.56	2.2	2.1	2.0
3.54			1.7
4	1.9	1.8	1.9
5.5	0.88	1.1	1.3
7	0.5	0.6	0.6

[a] D was calculated from Eq. [8] and the experimental values of I-$\omega^{1/2}$ slopes.

Table II. Influence of pH on anodic current[a] at three potentials

pH	−200 mV (/SCE)	−150 mV	−100 mV
3	0.11[b]	0.62	3.2
4	0.06	0.35	1.9
5	0.09	0.50	2.9
5.8	0.09	0.50	3.0
5.9	0.08	0.49	3.1
6.3	0.07	0.36	2.0

[a] These values are derived from cyclic voltammetric curves $E - \log_{10}I$ with $\nu = 0.4$ mV/sec and LiCl = 0.71M.
[b] In mA/cm^2.

efficient calculated from the experimental values of current are given in Table I for different values of Cl^- concentration and applied potentials.

The values of D are 0.5×10^{-5} cm^2/sec at 7M LiCl to be $2.0\text{-}2.6 \times 10^{-5}$ cm^2/sec at 1M LiCl. D values given in the literature vary from 0.6×10^{-5} cm^2/sec beyond 4M in Cl^- (20) to 1.6×10^{-5} cm^2/sec at around 1M (21). The slight difference observed between the calculated D values and those given in the literature may be attributed to the fact that Cl^- ion activities used in Eq. [8] are approximates and D_{CuCl_2} available in the literature are for dissolved NaCl or $CuCl_2$ only.

It should also be pointed out that H^+ or OH^- ions are not involved in the dissolution process. Consequently, the pH of the solution is expected to have no influence on the rate of dissolution. The experimental results confirmed that the influence of pH is marginal (Table II).

Conclusions

The anodic current process is under diffusion control of an ionic species in the solution. The dissolution current observed, over a wide range of Cl^- concentrations in slightly acidic solutions, is in agreement with the current values calculated from a two-step reaction where the limiting step is the diffusion of $CuCl_2^-$ from the electrode surface to the bulk. The main characteristics of the anodic dissolution of copper, namely, the linearity of the $E - \log_{10}(i\omega^{-1/2})$ relationship with a slope close to 59 mV/decade, and the linearity of the $i - \omega^{1/2}$ relations are in agreement with the dissolution process considered here. In accordance with this model, the dissolution current is independent of the pH and the dissolution valency is close to 1.

Acknowledgments

The author extends his grateful thanks to Dr. G. Bélanger of IREQ for useful discussions and to J. Hardy who is carrying out most of the tests.

Manuscript submitted April 13, 1982; revised manuscript received June 28, 1982.

Any discussion of this paper will appear in a Discussion Section to be published in the December 1983 JOURNAL. All discussions for the December 1983 Discussion Section should be submitted by Aug. 1, 1983.

Publication costs of this article were assisted by Hydro-Quebec Research Institute (IREQ).

REFERENCES

1. M. Braun and K. Nobe, *This Journal*, **126**, 1666 (1979).
2. A. Moreau, *Electrochim. Acta*, **26**, 497 (1981).
3. L. F. Kozin, K. K. Lepesov, and S. N. Naguigin, *Izv. Akad. Nauk Kaz. SSR Ser. Khim.*, **6**, 28 (1980).
4. L. F. Kozin, K. K. Leposov, and S. N. Naguigin, *ibid.*, **4**, 11 (1980).
5. H. Lal and H. R. Thirsk, *J. Chem. Soc.*, 2638 (1953).
6. A. L. Bacarella and J. C. Griess, *This Journal*, **120**, 459 (1973).
7. T. Hurlen, *Acta Chem. Scand.*, **15**, 1231 (1961).
8. R. S. Cooper and J. H. Bartlett, *This Journal*, **20**, 109 (1958).
9. F. M. Al-Kharafi and Y. A. El-Tantawy, *ibid.*, **128**, 73 (1981).
10. R. K. Astakova and B. S. Krasikov *Zh. Prikl. Khim.*, **44**, 363 (1972).
11. C. H. Bonfiglio, H. C. Albaya, and O. A. Cobo, *Corros. Sci.*, **13**, 717 (1973).
12. L. Kiss, J. Farkas, and A. Korosi, *Magy Kem. Foly*, **77**, 35 (1971).
13. D. W. Shoesmith and W. Lee, *Electrochim. Acta*, **22**, 1411 (1977).
14. "Lange's Handbook of Chemistry," 11th ed., pp. 5-6, McGraw-Hill Book Co., New York (1973).
15. R. A. Robinson and R. H. Stokes, "Electrolyte Solutions," pp. 491, 504, Butterworth Scientific Publications, London (1959).
16. K. Kinoshita, D. Landolt, R. H. Muller, and C. W. Tobias, *This Journal*, **117**, 1246 (1970).
17. M. Turner and P. A. Brook, *Corros. Sci.*, **13**, 973 (1973).
18. V. G. Levich, "Physicochemical Hydrodynamics," Prentice Hall, Englewood Cliffs, NJ (1962).
19. N. Vanmuylder, N. De Zoubov, and M. Pourbaix, Cebelcor Rapp. Tech. No. 101, Brussels, July 1962.
20. A. Rizenkamps and E. Beltovska, *Elektrokhimiya*, **11**, 374 (1975).
21. I. A. Semenov, V. F. Lazare, V. Anda, and I. Levin, *Sov. Electrochim.*, **11**, 1013 (1975).

The Equilibrium Constant for the Reaction $H_2S + 3H_2O + (Li_{0.66}K_{0.34})_2CO_3 \leftrightarrows 4H_2 + CO_2 + (Li_{0.66}K_{0.34})_2SO_4$ at Elevated Temperature

S. W. Smith* and S. M. Kapelner

United Technologies Corporation, Power Systems Division, South Windsor, Connecticut 06074

The presence of trace levels of H_2S in the fuel stream of a molten carbonate fuel cell causes a cell performance loss (1-3), which depends on the bulk gas composition fuel utilization, and the H_2S level. One of the possible causes for this performance loss is the reaction of the H_2S with the electrolyte according to

$$M_2CO_3 + H_2S + 3H_2O = M_2SO_4 + CO_2 + 4H_2$$

* Electrochemical Society Active Member.

Such conversion of the electrolyte would cause a Nernst potential loss at the anode due to a reduction in carbonate ion activity in addition to other possible effects, *i.e.*, changes in electrolyte conductivity, wetting angle, viscosity, etc.

A previous study (2) concluded that major electrolyte conversion would occur for most operating conditions and fuels. The rate would, of course, be determined by the rate of H_2S input, the electrolyte volume, and the scrubbing effectiveness of the cell. Because of some doubt that these experimental results were actually obtained at equilibrium, the measurements have been repeated using a modified technique where equilibrium can be obtained in a short time and approached from both sides.

Experimental

The technique used to determine the equilibrium constant consisted of the passing of various fuel gases containing H_2S over a thin layer of electrolyte, and determining the composition of the electrolyte at equilibrium.

A schematic diagram of the apparatus used is shown in Fig. 1. The electrolyte was contained in a 100 cm^3 crucible of 80 Au-20 Pd alloy (PALAU). The amount of electrolyte normally used was 2-4 cm^3 which gave a thin layer of melt in the bottom of the container and, thus, short equilibration times. The cup had a gold foil cap with a central hole through which the gas inlet tube extended. The gas left the cup around the inlet tube and under the foil at the rim, then exited from the containment vessel through an air condenser to remove water, followed by a sampling port for inserting a Kitagawa tube for H_2S determination.

A small Ni tube was inserted down the center of the gas inlet tube to a point just above the melt. Samples removed from this tube were analyzed in a gas chromatograph to determine the CO and CO_2 levels. Since the melt gas was a mixture of H_2 and CO_2 saturated to the desired dew point, water-gas shifting of this gas occurred within the test apparatus. This analysis enabled the degree of shifting to be determined.

A Chromel-Alumel thermocouple inserted through the containment vessel cover touched the outside of the crucible. H_2S was added to the inlet H_2 stream by means of a Dynacal tubular type permeation device. This stream was mixed with a wet CO_2 stream just prior to entering the vessel. The salts used were of reagent grade. The gases were of "high purity," and the flow rate was measured by bubble meter. Weighing was done on a single pan balance to ±0.1 mg.

Each experiment was started by adding a mixture of dry salts to the crucible to give the desired sulfate/carbonate ratio at a constant Li/K ratio of 1.63. The gas composition was adjusted to approximately that expected to be in equilibrium with the melt, and the system allowed to equilibrate for about 20 hr. The inlet and effluent H_2S levels were then measured, and the gas composition altered stepwise until the two levels were equal. In some experiments, the equilibrium was approached from both sides with respect to gas composition, and in one case, with respect to temperature.

After equilibrium had been attained, the system was cooled rapidly by removing the pot from the furnace. The solid was removed and analyzed for Li, K, CO_3^{-2}, and SO_4^{-2}. The Li and K were determined by atomic absorption, the CO_3^{-2} by a gravimetric method, and the SO_4^{-2} by ion chromatography.

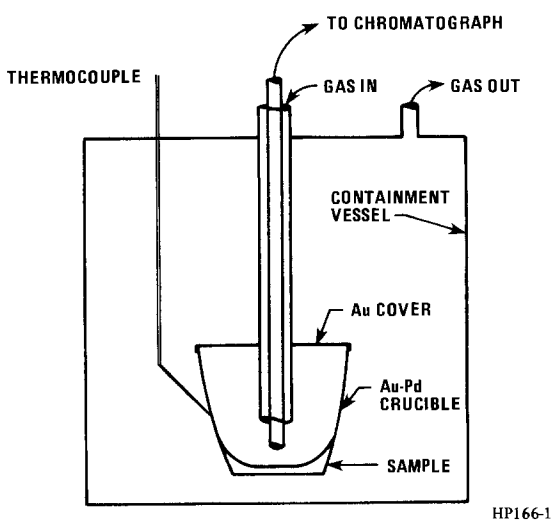

Fig. 1. Apparatus used for determining equilibrium fuel gases

Results and Discussion

Measurements were made at three ratios of CO_3^{-2}/SO_4^{-2} and at three temperatures. The results are given in Table I where X_i is the mol fraction of i and K is the equilibrium constant for the reaction above.

The gas compositions for each of these experiments is given in Table II.

These results are markedly different from those presented previously (2), except for one previous result, which was obtained at conditions where sulfate levels in the range of the present study were found. The other experiments had low H_2S concentrations, where the values found for SO_4^{-2} were only at the 10-100 ppm level. Spuriously high SO_4^{-2} contents were apparently found as a consequence of the initial sulfur contained in the reagent grade salts used, 2000 ppm for Li_2CO_3 and 40 ppm for K_2CO_3, and the design of the experimental apparatus. The melt was contained in a small Ni cup with an L/D ratio larger than one, making the process of sulfur removal from the melt a slow one, and equilibrium was apparently not reached. These results are also in reasonable agreement with those reported in (1) runs CS 8-10, which were closely approaching equilibrium.

Table I. Variation of the equilibrium constant K with temperature

Run No.	Temp. °F	$X_{SO_4^{-2}}/X_{CO_3^{-2}}$	X_{Li}*	X_K*	K (atm)
1	1096	0.25	0.67	0.33	0.498
2	1200	0.24	0.71	0.29	0.043
3	1200	0.25	0.66	0.34	0.045
4	1200	0.83	0.69	0.31	0.0124
5	1200	1.83	0.64	0.36	0.092
6	1306	0.25	0.66	0.34	0.0024

* Post test data—initial values were $X_{Li} = 0.62$, $X_K = 0.38$.

Table II. Gas compositions for the experiments of Table I.

Run No.	Pi (atm)				
	H_2	CO_2	H_2O	CO	$H_2S \times 10^6$
1	0.065	0.550	0.385	0.0002	80
2	0.036	0.571	0.393	0.0003	82
3	0.036	0.571	0.393	0.0003	84
4	0.020	0.421	0.558	0.0000	32
5	0.033	0.483	0.484	0.0002	102
6	0.027	0.380	0.594	0.0004	94

Table III. Free energy of formation, ΔF° for several temperatures and compositions

Temp., °F	m/o CO_3^{-2}	ΔF° (M_2SO_4) kcal mol^{-1}
1096	80	−283.1
1200	35	−273.7
1200	55	−270.0
1200	80	−272.3
1306	80	−260.4

These data alter the expected effects of sulfate formation on the molten carbonate cell somewhat. The maximum sulfate concentration at equilibrium will not be sufficient to cause significant anode Nernst concentration potential loss. However, the electrolyte will not act as a large sump for H_2S, and thus, the H_2S pressure in the cell, for any given H_2S input, will be larger than previously thought. This may increase other sulfur-related performance losses.

Using these data and the literature values for the thermodynamic properties which are known (2), the free energy of formation, ΔF°, for (0.66 Li_2SO_4 — 0.34 K_2SO_4), can be calculated. These results are presented in Table III.

From the slope of a plot of ln K *vs.* $1/T$, the enthalpy change in the reaction can be determined. From the data for 80 m/o carbonate at 1200°F, the value is −76.8 kcal/mol.

Acknowledgments

The present study was undertaken with support of the U.S. Department of Energy. Their permission to publish the results is gratefully acknowledged. The authors would like to thank Dr. John P. Ackerman for his interest and support.

Manuscript submitted Sept. 15, 1981; revised manuscript received March 29, 1982.

Any discussion of this paper will appear in a Discussion Section to be published in the December 1983 JOURNAL. All discussions for the December 1983 Discussion Section should be submitted by Aug. 1, 1983.

Publication costs of this article were assisted by United Technologies Corporation.

REFERENCES

1. IGT Project 8984, Final Report, Vol. 1, 77 (Sept. 1977).
2. UTC, "Advanced Fuel Cell Technology," EPRI, September 1978, Molten Carbonate Fuel Cell Seminar, Oak Ridge National Laboratory, Oct. 1978.
3. D. Townley, J. Winnick, and H. S. Huang, *This Journal*, **127**, 1104 (1980).

JOURNAL OF THE ELECTROCHEMICAL SOCIETY

SOLID-STATE SCIENCE AND TECHNOLOGY

FEBRUARY 1983

Modeling of High Field Ionic Conduction in Anodic Oxide Films

L. Young* and D. J. Smith*

Electrical Engineering Department, University of British Columbia, Vancouver, British Columbia, Canada V6T 1W5

ABSTRACT

Experimental data for the stepped current and open-circuit transient methods were fitted to one form of the modeling equations given by Dignam. A good representation of the data was obtained except that extreme linearity was found for $\log J_2$ *vs.* E data for the peak field in stepped current experiments where some degree of nonlinearity was expected. Another question involves the role of electrolyte incorporation in causing the observed curvature of steady-state $\log J$ *vs.* E plots. It is shown that if a model is preferred in which the history effects are due to structural changes in the glassy oxide rather than to the special current-driven polarization model of Dignam, then one can obtain equations equivalent to Dignam's by writing the activation energy for ionic transport as a function of a parameter describing the structural condition of the oxide, except that some relations between parameters which follow naturally from Dignam's model do not then appear.

The study of the growth of anodic oxide films gives a unique means of investigating ionic conduction at high fields (10^6-10^7 Vcm^{-1}), and the very reproducible and precise data which are obtained clash very effectively with the classical models for ionic conductors. The purpose of the present paper is to test some new data, which we have recently reported, against a model due to Dignam and to test whether a model can be developed in which history effects are due to structural changes in the oxide rather than the special polarization process proposed by Dignam.

We start by briefly outlining what we consider to be the key problems which have to be dealt with by any set of equations which are proposed to predict the ionic current density for all experimental situations, whether these equations are purely empirical or are based on some specific physical model.

If the classical equation for ionic conduction at high fields applied

$$J = J_0 \exp - [(W - qaE)/kT] \qquad [1]$$

in which ions of charge q are supposed to hop over energy barriers W lowered with assistance from an electric field E by an amount qaE, where a is the distance from minimum to maximum potential energy, then $kT\ \partial \log J/\partial E$ should be a constant. In practice, for steady-state conditions for tantalum (1), this quantity for different fields and temperatures is fitted by $q(\alpha - 2\beta E)$, *i.e.*, it is linear in E. Plots of $\log J$ *vs.* E are curved instead of being linear as predicted by Eq. [1]. This seemed to be explained if the activation energy was considered to be nonlinear in E in Taylor series fashion, through some secondary effect such as quadratic electrostriction (which would affect W by a term proportional to E^2). However, the ionic current is history dependent, that is, it depends not just on the instantaneous field but on the history of fields which have been applied. If the field is rapidly swept through a range of values, starting from steady-state conditions which are obtained (supposedly) by holding E constant at some value E_0 for sufficient time, then the ionic current at each E should correspond to its value with whatever causes the history effects frozen at its condition for the initial steady-state value E_0. For this situation it was found (2) (and our recent data (3, 4) confirm this with increased accuracy) that $kT\ \partial \log J/\partial E$ for different E_0 and T is again linear in E_0, as for the steady-state case. However, no definite curvature of $\log J$ *vs.* E where E is the swept field (as opposed to E_0, the initial field) has ever been observed in stepped field experiments. If, therefore, the $kT\ \partial \log J/\partial E$ dependence or E is taken as due to nonlinear dependence of activation energies on E, a combination of activation energies for steady state, a single one referring to the hopping process for stepped fields, one has an anomaly of sorts, which we will discuss later.

When a high constant field is applied to a film whose history makes it exhibit a low latent ionic conduction, the current builds up with time slowly at first and then more rapidly (2). One of us suggested that this was because the buildup of current was current-controlled due to some kind of momentum transfer process involving moving ions. For the initial stages of buildup it was found that $\partial J/\partial t \propto J^2$. If one assumes the "transient" to be due to the buildup in the concentration N of some kind of lattice defect involved in ionic transport (5), then the required buildup towards a steady state in which N is exponentially dependent on the steady-state field could be obtained by writing $\partial N/\partial t = CNJ\ (\gamma E/kT - \ln N)$.

Structural Change Model

Anodic oxide films have usually been considered to be glassy in nature. Because of this, as Vermilyea (6) has stressed, their structure is to be expected to be quite variable. This is borne out by recent structural studies. In the case of films on tantalum, the structure is probably made up of variable length, irregularly linked, and bent chains of pentagonal bipyramids with tantalum atoms in the middle and oxygen at the apexes (7, 8). We have argued in a previous paper (5) that such a structure would appear to have ample possibilities of showing history effects of the kind observed. These history effects might be conveniently described in terms of variations in the concentrations of mobile species or variations in activation energies. The extent of the variation of the ionic current which is produced by a given field in the oxide is so large that, to attribute it entirely to a variation in the concentration of

* Electrochemical Society Active Member.

some mobile species could be questionable. It is interesting to take a general approach to this by assuming that the structure of the oxide is characterized by some parameter S, the nature of which need not be specified. It is easy to extend this to have more than one parameter (S_1, S_2, etc.). The activation energy for ionic transport is then a function of S as well as E. In a MacLaurin expansion (with E and S small)

$$W(S,E) = W(0,0) + \frac{\partial W}{\partial E}E + \frac{\partial W}{\partial S}S + \frac{1}{2}\frac{\partial^2 W}{\partial E^2}E^2 + \frac{1}{2}\frac{\partial^2 W}{\partial S^2}S^2 + \frac{\partial^2 W}{\partial E \partial S}ES$$

$$\equiv W_o + a\,E + b\,S + c\,E^2 + d\,S^2 + e\,ES$$

The ionic current density is then at all times given by

$$J = J_o \exp - \left(\frac{W(S,E)}{kT}\right)$$

It is clear that S varies sluggishly with change of E. To obtain the desired initial experimental law $\partial J/\partial t \propto J^2$ and the following saturation for steady-state conditions, we can construct an equation for the rate of change of S

$$\frac{\partial S}{\partial t} = BJ(fE - S)$$

Here we have assumed a linear dependence of S on E in the steady state. This would correspond to the simplest linearization approach for the variation of W. The dependence on J implies that each moving ion catalyzes the adjustment of the structure as it sweeps out a volume determined by some area of influence attached to the ion. The form of the equation for the rate of change of S is, of course, determined teleologically. However, any mathematical modeling of such structural changes must, it seems to us, be somewhat empirical and based on plausibly constructing a set of equations which fit the experimental data.

Current Driven Polarization Model

A set of equations which in varying forms have been applied by Dignam and collaborators to a developing model will now be considered. Dignam originally proposed these equations for conduction in an electrically neutral film (9), but later modified them to describe rate control by the oxide/electrolyte interface (10, 11). Neglecting many subtleties, for which the original papers should be consulted, the basic physical content from which the equations are derived is that ionic conduction is driven by an effective or cavity field E_d, which involves contributions from the polarization (dipole moment per unit volume), in which κ_1 is a relative permittivity corresponding to polarization which follows the field rapidly, κ_d is a parameter relating to details not important here, and P_j are components of polarization which are supposed to have a Debye type of time dependence, except that the relaxation times τ_j are inversely proportional to the ionic current density

$$\frac{dP_j}{dt} = \frac{1}{\tau_j}(\epsilon_o \chi_j E - P_j)$$

where $1/\tau_j = B_j J$. Usually only one or two terms P_j have been invoked. The basic physical idea was that the motion of the ions sweeps out a volume in which the approach to an equilibrium polarization is expedited. This idea is indeed plausible, but we would be happier with the concept if the change induced by ionic motion was in the structure of the films, since there is no precedent for a dielectric polarization process of the kind envisaged. At fields low enough for no growth to be occurring, the dielectric behavior corresponds to a wide range of relaxation times approximating the distribution $f(\tau) = 1/\tau$ for $\tau_1 < \tau < \tau_2$, such that $\tan \delta = \epsilon_2/\epsilon_1$ is roughly constant (12). There is no evidence for one or two discrete processes.

In order to complete the model, Dignam has to assume that the activation energy for ionic transport is nonlinear in the effective field

$$J = J_o \exp\{-(W - \alpha E_d + \beta E_d^2)/kT\} \qquad [2]$$

If this assumption is not made, then the field dependence of $kT\partial \log J/\partial E$ both for steady state and stepped field is not accounted for.

In the steady state each P_j has come to its equilibrium value $P_j = \epsilon_o \chi_j E$ so that $\kappa_d E_d = (\kappa_1 + \Sigma \chi_j)E = \kappa_S E$, say where κ_S a static permittivity (which is, however, very different from the value measured at fields where no ionic current flows). Thus in the steady state

$$J = J_o \exp(-\{W - \alpha(\kappa_S/\kappa_D)E + \beta(\kappa_S/\kappa_D)^2 E^2\}/kT)$$

Comparing coefficients with the relation proposed by one of us to fit experimental data (1): $J = J_o \exp(-\{W - 5q\alpha_{SS}E + 5q\beta_{SS}E^2\}/kT)$

$$5q\alpha_{SS} = \alpha(\kappa_S/\kappa_D)$$

$$5q\beta_{SS} = \beta(\kappa_S/\kappa_D)$$

In the above J is the ionic conduction current density. The external current per unit of oxide area is

$$J_{ex} = J + \epsilon_o \kappa_1 \frac{dE}{dt} + \sum_j \frac{dP_j}{dt}$$

In the stepped field experiment the film is grown under a steady-state field E_S and the electric field is then stepped to some new value E. The value of the polarizations P_j remain at their initial values corresponding to E_S (*i.e.* $P_i = \epsilon_o \chi_i E_S$) so that $E_d = (\kappa_1/\kappa_D)(E + (\kappa_S - \kappa_1/\kappa_1)E_S)$, and hence J is given by the usual Eq. [2] with E_d given this value. Hence

$$kTd \ln J/dE = \alpha\kappa_1/\kappa_D - 2\beta(\kappa_1/\kappa_D)(\kappa_S/\kappa_D)E_S + 2\beta(\kappa_1/\kappa_D)^2 \Delta E$$

where $\Delta E \equiv E - E_S$ or, for $\Delta E \to 0$, an initial value is obtained

$$kTd \ln J/dE = \alpha(\kappa_1/\kappa_D) - 2\beta(\kappa_1/\kappa_D)(\kappa_S/\kappa_D)E_S$$

Comparing coefficients with the empirical relation reported by one of us (2)

$$kTd \ln J/dE = 5q\alpha_{SF} - 10q\beta_{SF}E_S$$

gives

$$5q\alpha_{SF} = \alpha(\kappa_1/\kappa_D)$$

and

$$5q\beta_{SF} = \beta(\kappa_1/\kappa_D)(\kappa_S/\kappa_D)$$

The numerical values of the various parameters which we have used are listed in Table I.

Comparison of the Structural and Current Driven Polarization Models

The equations for these models, taking only one S_j parameter and only one P_j parameter, are essentially identical as regards predicting the ionic current density. A change of P should be observed as an external current in Dignam's model whereas no explicit relation of this kind has been made for S. If, for example,

Table I. Values of parameters

Parameter	Value	Reference
J_o	$10^{12.24}$ A/m^2	
W	2.185 eV	1
α_{SS}	0.6995 nm	
β_{SS}	0.335 nm/MVmm^{-1}	
α_{SF}	0.223 nm	
β_{SF}	0.106 nm/MVmm^{-1}	2
κ_1	27.6	19

variations in S made a difference in thickness, some effect of this kind might be observed. However, as discussed previously (5), the evidence for any direct observation of such effects is questionable. However, the experimental value of the ratio α_{SS}/β_{SS} was noted by Dignam (13) to equal those for α_{SF}/β_{SF} both for Ta and Al. This was taken as not accidental. This equality follows from Dignam's model because in the expression for $W - \alpha E_d + \beta E_d^2$, E_d is a linear combination of E and P. In the equations derived by writing W as a general function $W(E, S)$ the equality is not implied. If the equality is not accidental, then it tells one something about how E and S enter W.

Comparison with Experiment

We now test the applicability of these equations to new experimental data which we have reported in two recent papers, involving firstly stepped current experiments (3) in which the field in the oxide is followed after a step in the external current, and secondly so-called open-circuit transient data (4), which is the time evolution of the field when the specimen is open circuited after being at steady state, *i.e.*, the oxide capacitor is self-discharged by ionic conduction, or if, one wishes, a special case of stepped current in which the second current is zero.

In both cases the equations were numerically integrated using a UBC Computer Centre 4th order Runge-Kutta routine with error correction. The accuracy was checked by comparison of single and double precision versions.

Stepped Current Experiment

Figure 1 shows stepped current $E(Q)$ data recorded at 1°C with $J_1 = 0.08$ A/m^2 and current ratios $J_2/J_1 = 4$, 16, and 64. $E(Q)$ data calculated by numerical integration are also plotted in the figure. The values of x_i and B_i, given in Table II, are the same as reported by Goad and Dignam (14) from an analysis of Dewald's stepped current transient data (15). We note

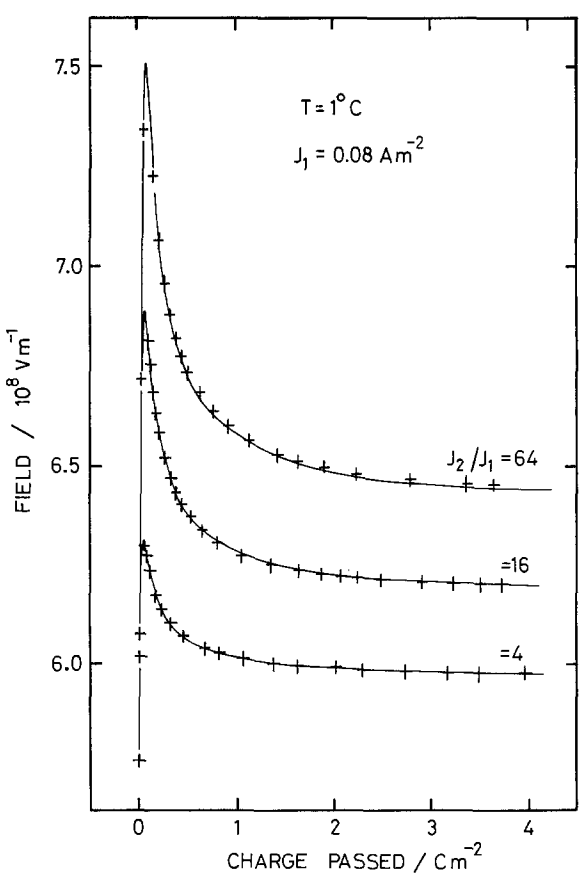

Fig. 1. Experimental (+) and computed stepped current transients for the same J_1 but different current ratios J_1/J_2.

Table II. Parameter values used in fitting stepped current transient $J(E)$ data

Parameter	Value
x_2	36
x_3	16.4
B_2	0.657 m^2/C
B_3	4.34 m^2/C

that Goad and Dignam obtained their values of x_i and B_i by a method of analysis different from the one used here. The experimental and calculated data are in close agreement everywhere except near the peak field. Similar agreement between experiment and theory was obtained at other values of J_1 and temperature. The temperature independence of x_i and B_i is consistent with data obtained with the constant field transients method (16).

Other values of x_i and B_i were tried, but the fit to the data could not be improved significantly. In particular, if only one polarization term was used, no combination of x_2 and B_2 could be found which gave as good a fit to the data as when two terms were used.

Figure 2 shows J_2 plotted against the peak field E_p for stepped current transients recorded at 25°C with $J_1 = 0.08$ A/m^2 and 3.0 A/m^2. The calculated $J_2(E_p)$ relations (using the parameter values in Table II) are also plotted for these formation currents. The computed log $J_2(E_p)$ relations are clearly nonlinear whereas the experimental data, as discussed in the second paper of this series (3), are best represented by a linear relation. This is most apparent with the data for $J_1 = 0.08$ A/m^2, since the data extend over a very large range of fields. It seems improbable that a relaxation process would so exactly compensate the predicted nonlinearity. Some of the difference may also be due to experimental errors.

The curvature of the experimental and computed log $J_2 - E_p$ data for $J_1 = 0.08$ A/m^2 in Fig. 2 are compared in Fig. 3. The slope d log J/dE of the experimental data was approximated by taking first divided differences between adjacent data points. Apart from scatter in the data, the slope of the experimental data is constant. The slope of the computed curve, however, decreases at a constant rate. The rate of change of this slope is almost independent of J_1 and temperature. Introducing a third slow polarization term did not eliminate the curvature of the computed curve.

Open-Circuit Transient

Figure 4 shows $E(t)$ data for an open-circuit transient recorded at 25°C with an initial steady-state current $J_1 = 0.33$ A/m^2. Only every third data point is plotted. The $E(t)$ relation calculated with the same parameter values as for the stepped current transient (Table II) is plotted as curve A in the figure. The experimental and computed data are in relatively close

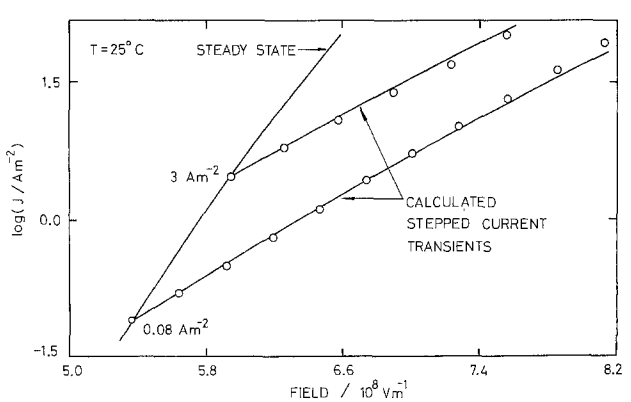

Fig. 2. Experimental and computed stepped current data showing J_2 plotted against the peak field E_p.

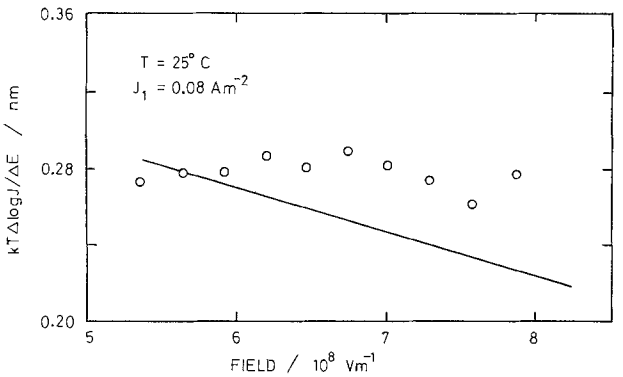

Fig. 3. The slope of the J_2-E_p data in Fig. 2, calculated by divided differences. The diagonal line is the slope predicted by Dignam's equations.

agreement during the initial stages of the transient, but diverge with increasing time, the experimental data falling off more rapidly with time than the computed data. The faster rate of decrease of the experimental data indicates a larger ionic current than predicted with the values of x_i and B_i in Table II. With the values of B_2 and B_3 taken as correct, the values of x_2 and x_3 were "corrected" to obtain a better fit to the data. Curve B in Fig. 4 was obtained with $x_2 = 45$ and $x_3 = 30$. For this combination of x_i and B_i, the experimental and computed data are in close agreement over the entire range of data plotted in the figure.

The $E(t)$ data were also fitted using only one slow polarization term. Taking $B_2 = 0.657$ m²/C (as above), the computed curve with $x_2 = 62.5$ gave as good a fit visually to the data as with two terms.

As shown in Fig. 5, the open-circuit transient $E(t)$ recorded at other initial steady-state current densities and temperatures were in close agreement with the computed data. The computed curves were obtained using the values of x_i and B_i given in Table III(a). The temperature independence of B_2 and B_3 is consistent with the analysis of the stepped current transient data in the previous section.

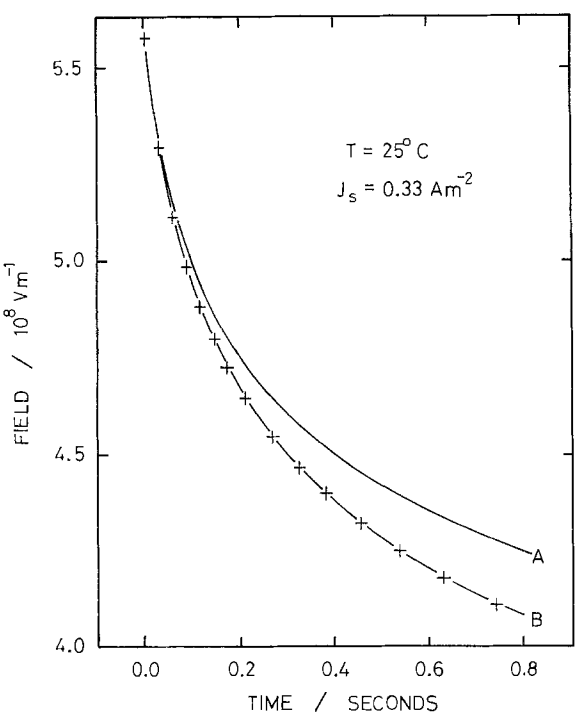

Fig. 4. Experimental (+) and computed $E(t)$ data for an open-circuit self-discharge. Curve A was calculated using the same parameter values as used to fit the stepped current data. Curve B was calculated using a different set of values to fit the experiment data.

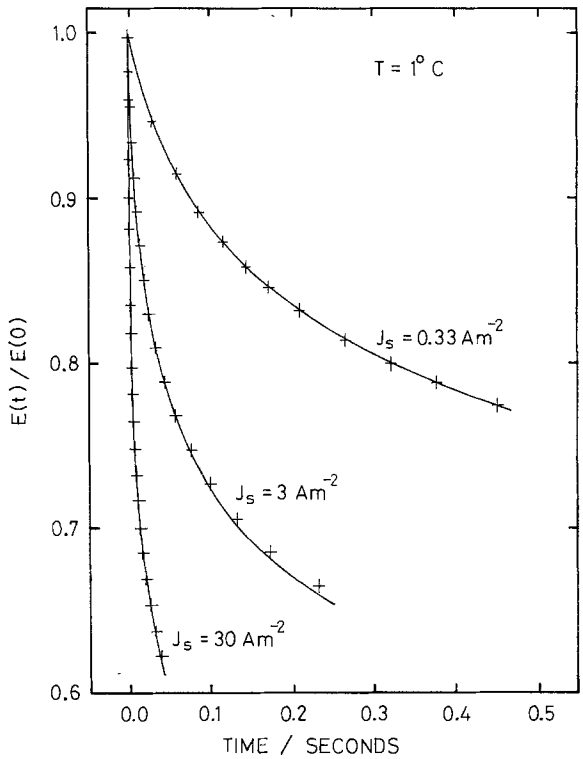

Fig. 5. $E(t)$ data for 3 open-circuit transients. The solid lines were computed using the same parameter values as for curve B in Fig. 4.

Figure 6 shows typical open-circuit transient $J(E)$ data calculated by numerical differentiation of experimental $E(t)$ data, assuming ϵ = constant. The initial current densities are 0.33, 3.0, and 30 A/m². Only some of the experimental data are plotted so as to avoid cluttering the graph. The solid line drawn through the data points for each transient is the $J(E)$ relation predicted by the equation for the ideal stepped field transient. The close agreement between experimental and computed data shows that the open-circuit transient is an excellent approximation to the stepped field transient. The $J(E)$ data calculated for the open-circuit transients with the parameter values given in Table III also agreed with the experimental data, as expected from the agreement with the $E(t)$ data in Fig. 4 and 5.

Discussion

One problem is the remarkable linearity of log J *vs.* peak field for the stepped current data. If these are taken as approximating rapidly swept field conditions, the predicted nonlinearity seems quite detectable. The anomaly is, however, arguable. It could be dismissed as a cancellation of the curvature by appreciable relaxation towards steady-state conditions. The problem that the values for parameters selected to give the best fit to one type of experiment give appreciable error for others is to be expected. Regarded as no more than empirical equations, which can be used to represent the data for all conditions, the equations are re-

Table III. Values of parameters χ_i and B_i used in fitting the open-circuit transient data

Parameter	Value (a)	Value (b)
χ_2	45	62.5
χ_3	30	0
B_2	0.657	0.657 m²/C
B_3	4.34	0 m²/C

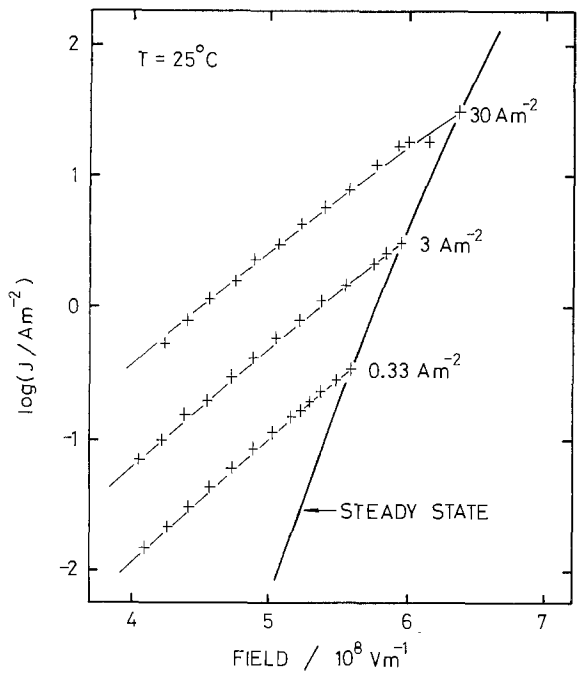

Fig. 6. *J(E)* data calculated by numerical differentiation of the self-discharge data, assuming ϵ = constant. The lines drawn through the data points are the *J(E)* relations calculated for the ideal stepped field transients.

markably effective. However, the data are for one particular dilute electrolyte solution only. It is known that the curvature of the steady-state log J *vs.* E line increases as the concentration of H_2SO_4 is increased (12). The curvature is also larger for dilute phosphoric acid. Dell'Oca and Young (17) attempted to explain this curvature on the basis that the films consist of two layers, an inner part due to oxygen ion transport and an outer part due to metal ion transport. The latter picks up electrolyte species during its growth. There is evidence that the electrolyte species may be mobile during subsequent growth. The field appears to be higher for the lower permittivity outer film. The curvature was attributed to the observed variation of transport number with field (18). It is difficult to explain this away. If true it seems to destroy the whole basis of the explanations for the behavior of $kTd \log J/dE$ for swept field and transient field conditions. However, the behavior of this quantity is so precise and simple that it would seem probable that it has some simple basis. We have not been able to construct a detailed theory based on the two layer nature of the films. Dignam has expressed the view that this duplex nature of the film does not matter for the solution used. It is certainly true that, unlike films grown in phosphoric acid, ellipsometry shows no signs of a duplex nature for films grown in the present solution (19). However, the original tracer studies showed some sulfate to be incorporated (20).

A further question is whether the success of the equations implies the validity of Dignam's model. The model has changed from bulk control to surface control, and doubtless in other respects, but the features which are essential are (*i*) the special polarization process, (*ii*) the validity of an effective field, and (*iii*) the quadratic dependence of activation energy on this field. As regards the history effects we prefer a model based on structural changes. However, as we have seen, making the activation energy a function of a structural parameter as well as E does not produce the relation between the α's and β's which the polarization model predicts.

Acknowledgment

This work was supported by the Natural Sciences and Engineering Research Council of Canada.

Manuscript submitted June 2, 1982.

Any discussion of this paper will appear in a Discussion Section to be published in the December 1983 JOURNAL. All discussions for the December 1983 Discussion Section should be submitted by Aug. 1, 1983.

Publication costs of this article were assisted by The University of British Columbia.

REFERENCES

1. L. Young, *Proc. R. Soc. London, Ser. A*, **258,** 496 (1960).
2. L. Young, *ibid.*, **263,** 395 (1961).
3. D. J. Smith and L. Young, *This Journal*, **129,** 2513 (1982).
4. D. J. Smith and L. Young, *ibid.*, **129,** 2518 (1982).
5. L. Young and D. J. Smith, *ibid.*, **126,** 765 (1979).
6. D. Vermilyea, "Advances in Electrochemistry and Electrochemical Engineering," Vol. 3, Interscience, New York (1963).
7. R. S. Roth and N. C. Stephenson, "Chemistry of Extended Defects in Solids," North-Holland Publishing Co., Amsterdam (1976).
8. N. C. Stephenson and R. S. Roth, *Acta Crystallogr. Sect. B*, **27,** 1037 (1971).
9. M. J. Dignam, *This Journal*, **112,** 792 (1965).
10. D. F. Taylor and M. J. Dignam, *ibid.*, **120,** 1299 (1973).
11. M. J. Dignam, in "Oxide and Oxide Films," Vol. 1, J. W. Diggle, Editor, p. 91, M. Dekker, New York (1972).
12. L. Young, "Anodic Oxide Films," Academic Press, London and New York (1961).
13. M. J. Dignam, *This Journal*, **112,** 792 (1965).
14. D. G. W. Goad and M. J. Dignam, *Can. J. Chem.*, **50,** 3259 (1972).
15. J. F. Dewald, *J. Phys. Chem. Solids*, **2,** 55 (1957).
16. W. D. Cornish, M.A.Sc. Thesis, The University of British Columbia, British Columbia, Canada (1972).
17. C. J. Dell'Oca and L. Young, *This Journal*, **117,** 1548 (1970).
18. J. P. S. Pringle, as quoted by C. J. Dell'Oca, D. L. Pulfrey, and L. Young, in "Physics of Thin Films," Vol. 6, Academic Press, London and New York (1971).
19. D. J. Smith and L. Young, Paper 5 presented at The Electrochemical Society Meeting, Minneapolis, Minnesota, May 10-15, 1981.
20. J. J. Randall, W. J. Bernard, and R. R. Wilkinson, *Electrochim. Acta*, **10,** 183 (1965).

On the Reaction Mechanism of GaAs MOCVD

J. Nishizawa* and T. Kurabayashi

Research Institute of Electrical Communication, Tohoku University, Sendai 980, Japan

ABSTRACT

In this paper, the reaction mechanisms of GaAs metalorganic chemical vapor deposition (MOCVD) have been investigated using infrared absorption spectroscopy. The growth of GaAs from Ga $(CH_3)_3$ and AsH_3 under H_2 gas atmosphere in a hot wall reactor was studied. The compositions of gases which are sampled through a quartz capillary are observed by infrared spectroscopy. Infrared spectra of $(Ga(CH_3)_3 + H_2)$, $(AsH_3 + H_2)$, and $(Ga(CH_3)_3 + AsH_3 + H_2)$ systems were measured in the range from room temperature to 930°C. In the $(Ga(CH_3)_3 + AsH_3 + H_2)$ system, a new absorption peak at 2080 cm^{-1} which exists in neither the $(Ga(CH_3)_3 + H_2)$ nor the $(AsH_3 + H_2)$ system is observed. In the $(AsH_3 + H_2)$ system, when $Ga(CH_3)_3$ is added into the reacting gas, the concentration of AsH_3 decreases drastically. The decomposition of AsH_3 is affected strongly by the addition of $Ga(CH_3)_3$.

In our laboratory, since 1961, the reaction mechanisms of silicon chemical vapor deposition (1-4) and plasma etching (5) have been investigated using infrared absorption spectroscopy and photochemical reactions. Infrared spectroscopy, *in situ* observation, and indirect sampling measurements have given information about the reaction mechanism of these processes. Complete understanding of the reaction mechanisms and the establishment of *in situ* monitoring of every process seem very important for obtaining better devices. In the case of emission spectroscopy, the sorts of existing atoms can be identified; however, sorts of molecules that we want to know most can be identified by the use of infrared spectroscopy.

There are two methods for infrared spectroscopy measurements (3); they are sampling and direct (*in situ*) observation methods. In the sampling method, the spectrum of gas sampled through a quartz capillary from the reactor is measured. This method has an advantage of quantitative analysis at the sampling position and a simple system for optical measurements. However, since the gas is cooled for the sampling time, we cannot obtain exact information about the hot reactants in the reactor. In the direct (*in situ*) spectroscopy, the infrared beam penetrates the high temperature gas. This has the disadvantage that the absorption spectrum is averaged along the light beam and it is difficult to determine the spatial distribution of the gaseous species and their quantitative concentrations because of the nonuniform distribution of the temperature.

The crystal growth of II-VI and III-V compounds by MOCVD (6) has been investigated actively. The growth of GaAs is comparable with halogen transport systems, and device fabrication has been accomplished. Nevertheless, the reaction mechanism is not yet clarified, and only a few reports have been published (7, 8).

In this paper the reaction mechanisms of GaAs grown by MOCVD from trimethylgallium (TMG) and AsH_3 is reported. Here the reactants in the hot wall reactor were measured by infrared absorption spectroscopy of gas sampled through a quartz capillary (sampling method). In another paper, we will report the data of infrared spectroscopy by direct observation in a hot furnace.

Experimental Procedure

Figure 1 shows a schematic diagram of the atmospheric pressure MOCVD system and the measurement system. As a gallium source, liquid trimethylgallium (TMG) is kept at a constant temperature (0°C). As an arsenic source, 1% AsH_3 in pure H_2 is used. A quartz horizontal reactor is used, and it is heated by a resistance furnace. Because the furnace heats up the quartz tube, susceptor, and gas, the gas temperature is nearly equal to the measured temperature at the susceptor. The temperature of the furnace is constant around the sampling position. The length of the constant temperature zone is about 10 cm. The inner diameter of the quartz tube is 32 mm. The reactants were sampled through a quartz capillary to the infrared gas cell in which the spectra of the gases were measured. The sampling flow rate in the capillary is 140 cm^3/min. The sampling position and temperature measurement are shown in Fig. 2. The sampling position is in the flat temperature region, and it is expected that the temperature and the reactant distribution in radial direction of the quartz tube hardly changes. The length of the gas cell is 10 cm and the inner diameter is 3 cm. TMG and AsH_3 are measured by the infrared spec-

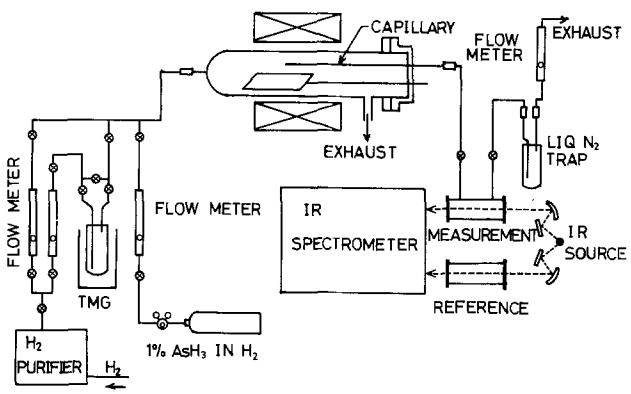

Fig. 1. Schematic diagram of atmospheric pressure MOCVD system.

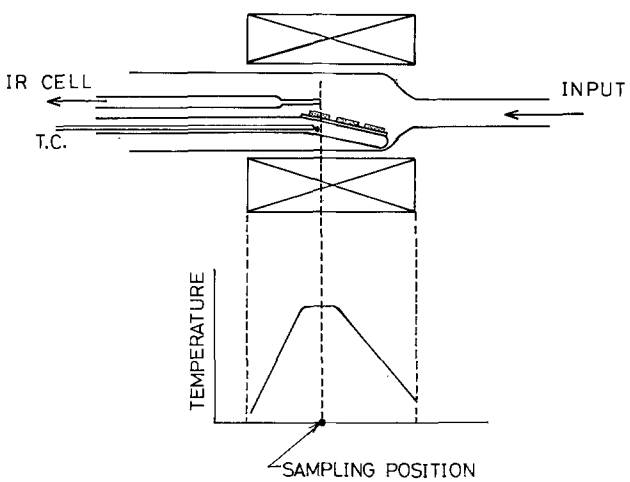

Fig. 2. Schematic diagram of sampling position and temperature measurement.

* Electrochemical Society Active Member.

Key words: MOCVD, infrared spectroscopy, reaction mechanism.

trometer distinguishably at the 50-100 ppm level without any special arrangements.

Results and Discussion

(TMG + H_2) system.—The infrared absorption spectrum of the (TMG + H_2) system was measured at various temperatures. The spectra are shown in Fig. 3a, b. In Fig. 3a, the absorption peaks of TMG in H_2 at room temperature are given. When the temperature is about 400°C, CH_4, which has peaks at 3014 and 1304 cm^{-1}, was detected. Above 580°C, the percent transmissions of CH_4 peaks saturated, and the TMG spectrum disappeared. Here, TMG is measured distinguishably about 100 ppm in our infrared spectrometer. At high temperature (930°C), peaks at 946 and 729 cm^{-1} were observed in addition to those at 3014 and 1304 cm^{-1}.

From this result, we think that the C—H bonds of CH_4 decompose, and C_2H_4 (946 cm^{-1}) and other hydrocarbons (729 cm^{-1}) are composed. The decomposition of TMG *vs.* temperature is shown in Fig. 4. TMG decomposed drastically from 500° to 550°C, and when the gas was heated up above 580°C, TMG decomposed completely. From these results the next reaction is suggested

$$Ga(CH_3)_3 + \frac{3}{2} H_2 \rightarrow Ga + 3CH_4$$

(AsH_3 + H_2) system.—In the measurements of the (AsH_3 + H_2) system, the decomposition of AsH_3 was critical in the range of 650°-710°C as shown in Fig. 5. The pyrolitic reaction of (AsH_3 + H_2) follows

$$AsH_3 \rightarrow \frac{1}{4} As_4 + \frac{3}{2} H_2$$

Infrared absorption peaks of AsH_3 were observed at 2122, 2112, 1002, and 906 cm^{-1}. Above 750°C, these peaks vanished and the spectrum coincided with the base line completely, most of AsH_3 decomposed at this temperature.

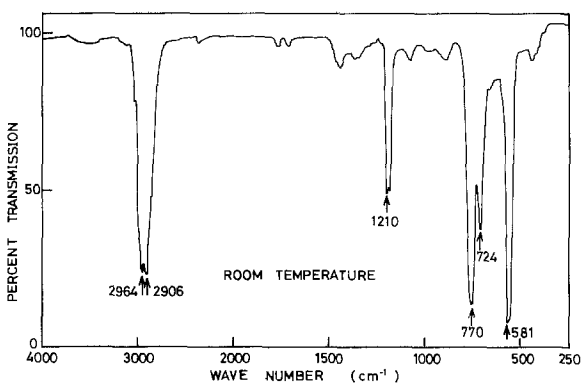

Fig. 3a. Infrared absorption spectrum of TMG at room temperature. Concentration of TMG is 1.54% in H_2.

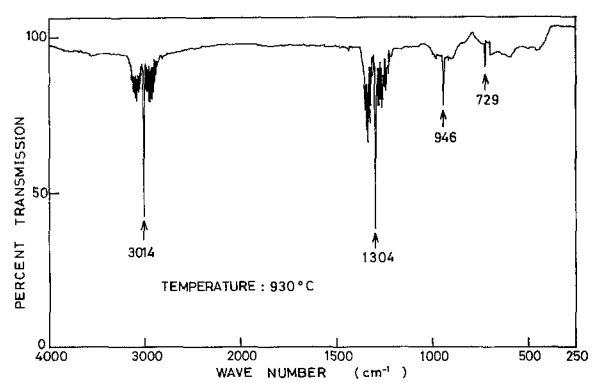

Fig. 3b. At 930°C, TMG decomposes completely, CH_4 and other material are detected.

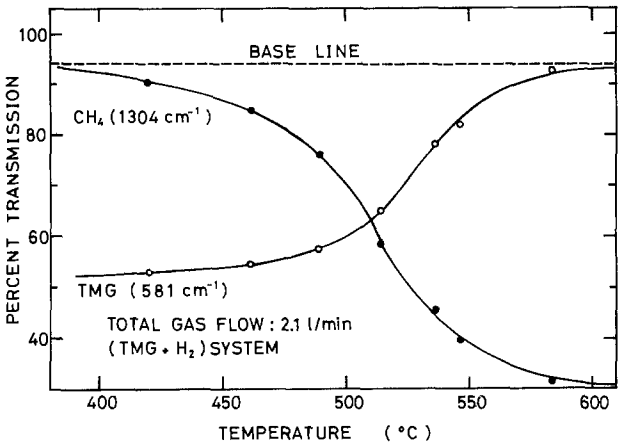

Fig. 4. TMG decomposition *vs.* temperature. Concentration of TMG in input gas is 4400 ppm.

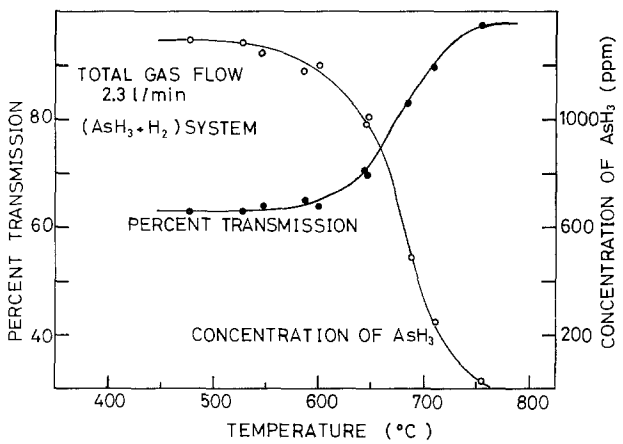

Fig. 5. AsH_3 decomposition *vs.* temperature. Concentration of AsH_3 in input gas is 1340 ppm.

(TMG + AsH_3 + H_2) system.—In the measurements of the (TMG + AsH_3 + H_2) system, the spectrum differed from that expected from (TMG + H_2) and (AsH_3 + H_2) spectra separately. The spectrum was not equal to a superposition of (TMG + H_2) and (AsH_3 + H_2) spectra in the measured range of 400°-560°C. The result is that the concentration of CH_4 increases, TMG and AsH_3 decrease, and a new absorption peak is observed at 2080 cm^{-1} in the (TMG + AsH_3 + H_2) system, comparing with (TMG + H_2) and (AsH_3 + H_2) systems, as shown in Fig. 6a-c. For example, in the (TMG + H_2) system, the percent transmission of the peak at 581 cm^{-1} is 74%, but in the (TMG + AsH_3 + H_2) system the value is 83%. Furthermore, the CH_4 peak at 1304 cm^{-1} changes from 82 to 70%. As for AsH_3, the percent transmission at 2122 cm^{-1} changes from 37% in the (AsH_3 + H_2) system to 45% in the (TMG + AsH_3 + H_2) system. The infrared absorption peak at 2080 cm^{-1} did not exist for either the (TMG + H_2) or the (AsH_3 + H_2) spectra.

From Lambert-Beer's law, the intensity of the infrared absorption is proportional to the concentration of the material. The result of the absorbability at 2080 cm^{-1} *vs.* input AsH_3 concentration is shown in Fig. 7. The absorbability D is defined as

$$D = \log \frac{T_a}{T_b} = abc$$

T_b is the percent transmission of the peak at 2080 cm^{-1}. T_a is the percent transmission of AsH_3 at 2080 cm^{-1}, as shown in Fig. 8, a is the absorption coefficient of the 2080 cm^{-1} peak (unknown), b is the length of gas cell (10 cm), and c is the concentration of this

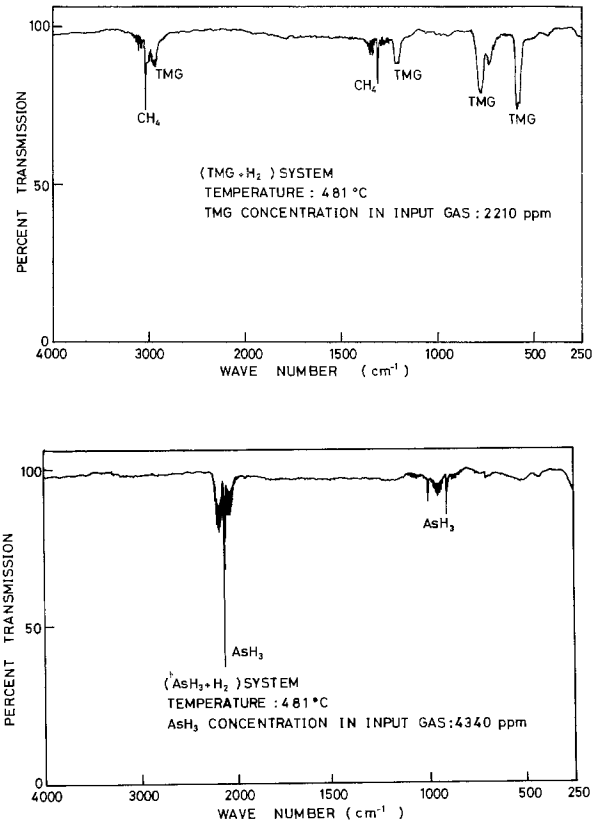

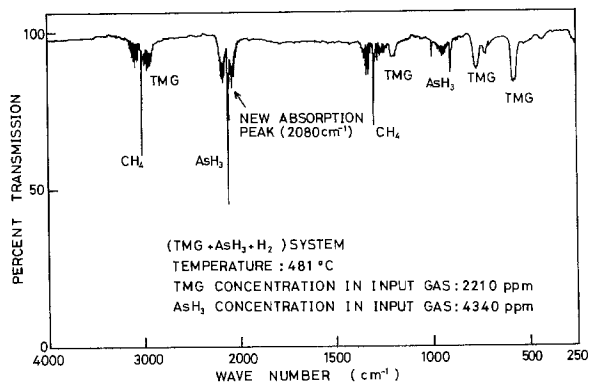

Fig. 6. Comparing the (TMG + AsH_3 + H_2) system with the (TMG + H_2) and the (AsH_3 + H_2) systems. Total gas flow is 2.2 liters/m.

material (unknown). D can be measured from $D = \log T_b/T_a$; D is proportional to the concentration from $D = abc$, as here ab is constant. Therefore, we estimated the peak by D. The result is that by increasing the AsH_3 concentration in input gas, the absorbability

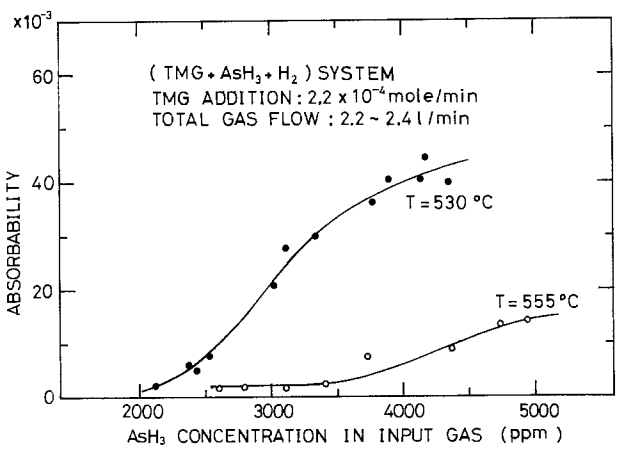

Fig. 7. Dependence of 2080 cm^{-1} peak on AsH_3 concentration in input gas.

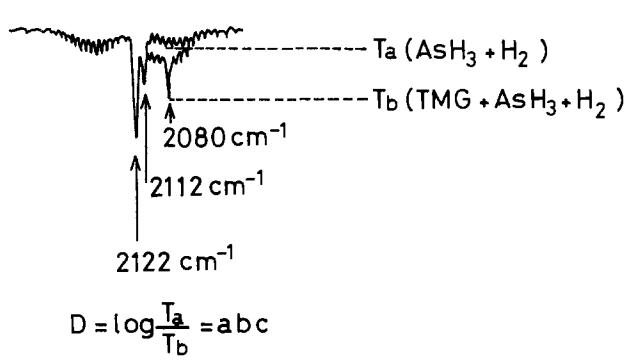

Fig. 8. Absorbability D of 2080 cm^{-1} peak is obtained by measuring T_a and T_b.

D at 2080 cm^{-1} increases, on the condition that the TMG concentration is constant.

Furthermore, observing the peak at 2080 cm^{-1}, stopping TMG supply, this peak disappeared completely and only AsH_3 was observed. From the dependence of this peak on TMG addition, we think that the new material is composed of TMG and AsH_3. The absorbability at 2080 cm^{-1} *vs.* temperature is measured as shown in Fig. 9. It seems that the composition is actively in the range of 510°-530°C. The spectrum at this temperature is shown in Fig. 10. The peak at 2080 cm^{-1} is clearly distinguished. We think this material suggests an intermediate formation in the reaction, but we have not yet identified the material.

Decomposition of AsH_3 in the (AsH_3 + H_2) and the (TMG + AsH_3 + H_2) systems.—In the measurements of the (TMG + AsH_3 + H_2) system, the spectrum is not superposition of the (TMG + H_2) and the (AsH_3 + H_2) spectra as shown in Fig. 6. Quantity of decomposed AsH_3 is different between the (AsH_3 + H_2) and the (TMG + AsH_3 + H_2) systems. We think TMG addition is the cause of this effect. The result of detected AsH_3 concentration *vs.* AsH_3 concentration in input gas

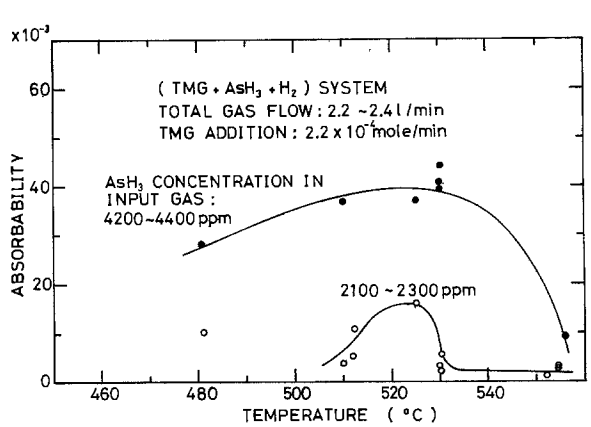

Fig. 9. Absorbability D of 2080 cm^{-1} peak depends on temperature.

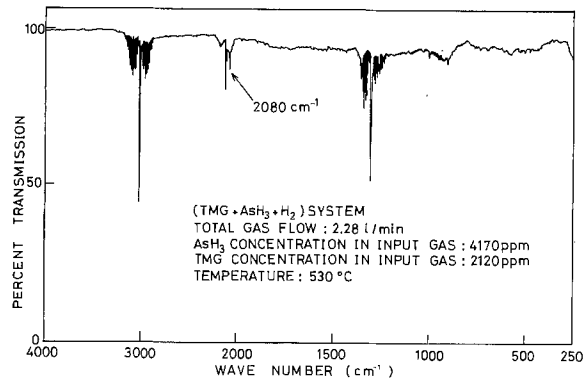

Fig. 10. Spectrum of the (TMG + AsH_3 + H_2) system

in these systems is shown in Fig. 11. In the (TMG + AsH_3 + H_2) system (○), the decomposition of AsH_3 is promoted compared with the (AsH_3 + H_2) system (●). Namely, the decomposition of AsH_3 is promoted by TMG addition. When the concentration of AsH_3 in input gas was lower than 2400 ppm in the (TMG + AsH_3 + H_2) system (○), AsH_3 decomposed perfectly. When the concentration of AsH_3 was higher than 3000 ppm, the graph runs parallel to the one of (AsH_3 + H_2) system (●).

We think that the decomposition of AsH_3 in the (TMG + AsH_3 + H_2) system is promoted by forming GaAs at the vapor phase and by GaAs or Ga particles in the hot wall reactor. The reason is that by the formation of GaAs, As, and Ga species are consumed, therefore, partial pressures of As_4 and Ga species reduce and decompositions of AsH_3 and TMG are promoted. The other possibility is that Ga or metalorganic radicals formed by TMG affect the decomposition of AsH_3. The effect of surface reactions on GaAs wafers will be estimated by bringing GaAs wafers into the reactor. However, when there are wafers on the susceptor, the difference in AsH_3 concentrations was not measurable compared to reactions occurring without wafers on the susceptor. But in the decomposition experiments, GaAs and Ga were deposited on the reactor wall, and this deposited area is much larger than that of the wafers, making it possible to detect the effect of GaAs or Ga on the decomposition of AsH_3.

We think that deposited GaAs or Ga particles near the sampling position affect the reaction of AsH_3. In the (AsH_3 + H_2) system, the concentration of AsH_3 with GaAs (●) and without GaAs (▲) in the reactor is clearly different as shown in Fig. 11. The decomposition of AsH_3 is largely promoted by GaAs or Ga in the hot region. Furthermore, we carried out another experiment as follows. First of all, after the quartz tube is cleaned, only AsH_3 + H_2 mixed gas is introduced in the reactor, then only the peaks of AsH_3 are detected. At this time, detected AsH_3 concentration was 2120 ppm. Second, TMG was added (2.2×10^{-4} mol/min) for 6 min. Now, AsH_3 concentration was below 50 ppm. Next, stopping the addition of TMG, the detected AsH_3 concentration is 490 ppm. The result of this experiment is shown in Fig. 12. The last concentration level did not recover to the first level again. The difference between the last and the first level is the effect of deposited GaAs or Ga particles by TMG addition. Furthermore, to estimate the effect of GaAs or Ga in the reactor, the following experiments were carried out. After cleaning of the reactor, AsH_3 concentration was measured in AsH_3 + H_2 mixed gas at 530°C. At this time, total TMG addition is zero. Next, after AsH_3 was purged out completely by hydrogen, TMG + H_2 mixed gas was introduced into the reactor at 530°C, and Ga was deposited about 20 cm length in the direction of gas stream around the center of the furnace. TMG gas was purged out by hydrogen, now, AsH_3 + H_2 mixed gas was introduced, and the AsH_3 concentration was measured. These procedures were done over and over again; the concentrations of AsH_3 were measured in relation to the total TMG addition. The results are shown in Fig. 13. Concentration of AsH_3 which is calculated from percent transmission of AsH_3 at 2122 cm^{-1} peak decreases exponentially, as the total TMG addition increases. In this figure, saturation of AsH_3 concentration may correspond to saturation of surface concentration of Ga particles in hot region. It is suggested that the concentration of Ga particles affects the decomposition of AsH_3. At this time, Ga particles may turn to GaAs partially. But, this effect of GaAs or Ga does not vary in spite of the

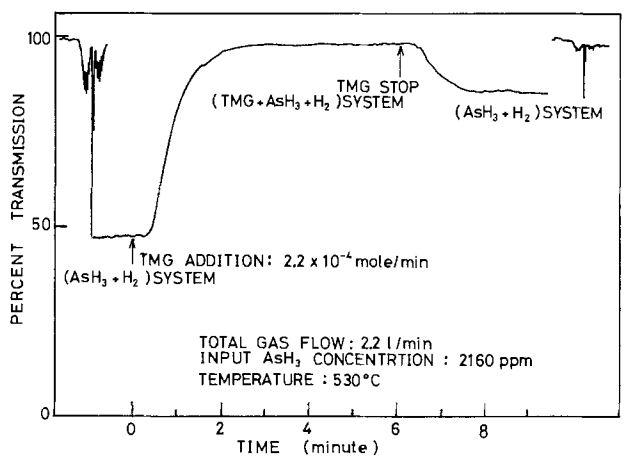

Fig. 12. TMG is added for 6 min. Wave number was fixed at 2122 cm^{-1} and time was scanned. Before 0 min, GaAs did not deposit on the reactor wall.

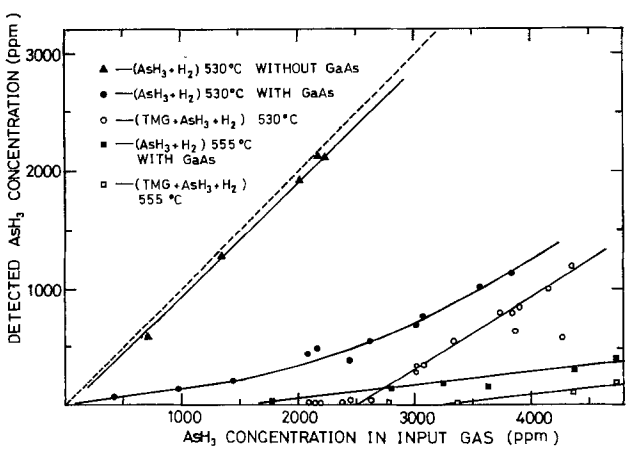

Fig. 11. AsH_3 concentration depends on TMG addition and GaAs existence. Broken line indicates AsH_3 concentration in input gas.

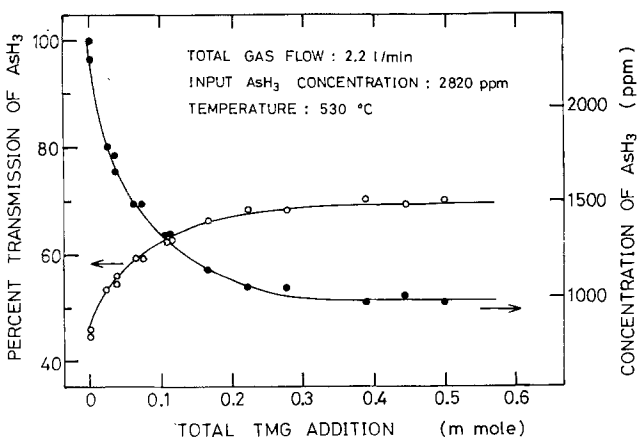

Fig. 13. AsH_3 decomposition depends on the amount of Ga in the hot region.

amount of AsH_3 which is introduced in the reactor. It seems that GaAs or Ga catalyze the decomposition of AsH_3.

Conclusion

(TMG + H_2), (AsH_3 + H_2), and (TMG + AsH_3 + H_2) systems were measured to obtain information about the reaction mechanisms. In the (TMG + H_2) system, TMG decomposes drastically in the range of 500° ~ 550°C, and above 580°C only CH_4 was detected. But at high temperature (930°C), peaks at 946 and 729 cm^{-1} were observed. We think that C_2H_4 and other hydrocarbons are composed. This phenomenon may relate to carbon contamination in MOCVD.

In the (AsH_3 + H_2) system, AsH_3 decomposes drastically in the range of 650°-710°C. In the (TMG + AsH_3 + H_2) system, we could observe the new infrared absorption peak at 2080 cm^{-1}; this may be intermediate formation in the reaction. But we have not yet identified the material. This material may be composed actively in the range of 510°-530°C.

Decomposition of AsH_3 was affected sensitively by TMG addition. We think that forming of GaAs or some kinds of radicals formed by TMG are the cause of this effect. In the (AsH_3 + H_2) system, the quantity of AsH_3 decomposition is affected by deposited GaAs or Ga particles on the reactor wall. We think that this phenomenon is caused by the catalysis of AsH_3 decomposition by GaAs or Ga particles. In the (TMG + AsH_3 + H_2) system, this effect is expected for the decomposition of AsH_3 as well as TMG addition. After writing this paper, it has been observed that a lot of GaAs wafers on the susceptor promote the decomposition of AsH_3. In another paper, we will report these data. To identify the reaction mechanisms of MOCVD growth, many more *in situ* experiments are necessary.

Manuscript submitted April 27, 1982; revised manuscript received July 29, 1982.

Any discussion of this paper will appear in a Discussion Section to be published in the December 1983 JOURNAL. All discussions for the December 1983 Discussion Section should be submitted by Aug. 1, 1983.

Publication costs of this article were assisted by Tohoku University.

REFERENCES

1. M. Kumagawa, H. Sunami, T. Terasaki, and J. Nishizawa, *Jpn. J. Appl. Phys.*, **7**, 1322 (1968).
2. M. Kumagawa, H. Sunami, and J. Nishizawa, *This Journal*, **117**, 907 (1970).
3. J. Nishizawa and H. Nihira, *J. Cryst. Growth*, **45**, 82 (1978).
4. J. Nishizawa and M. Saito, *ibid.*, **52**, 213 (1981).
5. J. Nishizawa and N. Hayasaka, Paper 124 presented at The Electrochemical Society Meeting, St. Louis, Missouri, May 11-16, 1980.
6. H. M. Manasevit and W. I. Simpson, *This Journal*, **116**, 1725 (1969).
7. M. R. Leys and H. Veenvliet, *J. Cryst. Growth*, **55**, 145 (1981).
8. A. Zaouk, E. Salvetat, J. Sakaya, F. Mauly, and G. Constant, *J. Cryst. Growth*, **55**, 135 (1981).

The Low-Energy-Electron (LEE) Excitation of SnO_2:Eu Powder Phosphor; Fundamental Characteristics

T. Matsuoka,* T. Tohda, and T. Nitta*

Matsushita Electric Industrial Company Limited, Material Research Laboratory, 1006 Kadoma, Osaka, Japan

ABSTRACT

The physicochemical properties and fundamental luminescent characteristics of SnO_2:Eu powder were examined for use as low-energy-electron (LEE) excitation phosphor. Solubility limit of Eu into SnO_2 was 0.05-0.06 a/o and smaller mean diameter, higher resistivity (order of 10^6 Ω · cm), and more intensive diffused reflectance were observed with increased Eu addition. Although the same emission spectra by f-f transition of Eu ($^5D_0$-$^7F_1$ strongest peaks) were observed in u.v., high and low-energy-electron excitation, broad intrinsic emission from SnO_2 matrix, which coexist with the f-f transition emission, was different for each excitation method. In LEE excitation, the maximum intensity wavelength of the intrinsic emission was longer than in high-energy-electron excitation. The intrinsic emission was not observed at room temperature in u.v. excitation. Excitation spectrum with a peak at 300 nm was attributed to matrix excitation, *i.e.*, electron hole generation. Optimal addition of 0.1 a/o Eu for brightness, 5.9 msec decay (1/10), and an efficiency of 2 lm/W at 9 ~ 10 V were observed under LEE excitation. Efficiency increased with lower voltage and current excitation due to sublinearities of brightness-voltage and current dependences.

Recently, new LEE excitation phosphors, in addition to ZnO:Zn emitting bluish-green color have been intensively developed in response to a strong demand for flat panel display devices such as graphic, character, and TV displays, and for instrument panels in the automobile and output level meters in audio equipment (1-6).

These display devices have more and more tended toward multicolor, so three primary colors of LEE excitation phosphors, especially red color, are imperative.

We have successfully developed a new powder phosphor SnO_2:Eu emitting reddish orange color by LEE excitation (7). Subsequently, we investigated fundamental properties and preparation methods of SnO_2:Eu powder phosphor for practical use. Although luminescent characteristics of single crystal SnO_2:Eu excited at high-electron-energy were examined by Crabtree (8-11), the fundamental physicochemical and luminescent characteristics of SnO_2:Eu powder phosphor have not yet been examined. Since surface electrical resistivity of SnO_2 has been reported to be extremely different from that of bulk (12), some of the powder characteristics of wide surface areas were expected to be different from those of the single crystal. This paper is arranged in two parts. The first part outlines the physicochemical properties. The second part describes the luminescent characteristics of the powder phosphor.

* Electrochemical Society Active Member.
Key words: inorganic, cathodoluminescence.

Experimental Procedures

Powder preparation.—The prior art powder phosphor was prepared by rapidly pouring $SnCl_2 \cdot 2H_2O$ and $EuCl_3$ alcohol solution into $(NH_4)_2C_2O_4 \cdot H_2O$ aqueous solution to make an oxalate coprecipitate, and then, firing the precipitate into an oxidizing atmosphere at 1300°C for 2 hr (7). The improved procedure is as

follows. High purity $SnCl_2 \cdot 2H_2O$ and $EuCl_3$ aqueous solution was poured slowly at a rate of 4.8 cm^3/min into $(NH_4)_2C_2O_4 \cdot H_2O$ aqueous solution at temperatures of 70°-80°C to make a single crystal-like oxalate coprecipitate. The precipitate contained no segregation. The oxalate coprecipitate containing 1 atom percent (a/o) Eu showed slight shift of x-ray peaks to longer d-values, which was not observed in the prior procedure.

The oxalate coprecipitate was then fired at 850°C for 3-5 hr in a vitreous quartz boat in air atmosphere without the powder spouting phenomenon, observed in the prior art. In this stage, the powder emitted reddish-orange luminescence, although the oxalate prepared by the prior procedure did not show luminescence under 850°C firing.

This fact suggests more intimate mixing of Sn and Eu ions than in the previous procedure. After slight mixing in mortar, the powder was fired at 1350°C for 2-3 hr in a loosely covered alumina crucible. Further additives for the SnO_2:Eu phosphor were introduced after heat-treatment of the oxalate at 850°C. Sb, Nb, Ta, V, and F, which are considered to form donors in SnO_2, showed a strong killer effect. This effect is probably due to Auger quenching, observed in ZnS:Mn phosphor (13). Furthermore, even Ti, Ge, and Ce, which are thought to dissolve into the SnO_2 lattice without making any defects, were also found to have a killer effect. It was found that the SnO_2:Eu phosphor required a crystal lattice as pure as possible. Among the fluxes examined, MgF_2, $Li_2B_4O_7$, CeF_3, and $ZnF_2 \cdot 4H_2O$ exhibited a strong particle growth effect and a simultaneously strong killer effect, both of which were considered mainly due to the fluoride ion. Fluxes without a killer effect have not been found to date. Therefore, the physicochemical and luminescent properties of SnO_2:Eu phosphor described hereafter were examined in the state of no additives.

Measurements of physiocochemical properties.—In each preparation step, SEM was used to examine the diameter and shape of the powder. Chemical phase and Eu solubility limit were examined by x-ray powder diffraction and line analysis of XMA. Mean diameter of the powder was measured as a mean specific surface diameter using an N_2 gas adsorption method and shape factor of 6.

Electrical resistivity was measured using an SnO_2:Eu ceramic prepared as follows. The powder, after thermal decomposition of the oxalate coprecipitate, was pressed at 800 kg/cm^2 into a disk of 16 mm diam using PVA as a binder. The disk was embedded in the same composition, SnO_2:Eu powder, in an alumina crucible, and sintered at 1350°C for 2 hr in air. The sintered disk showed an apparent density of 53-60% of theoretical. The disk had In-Ga electrodes attached to it, and electrical resistivity was measured by Wheatstone bridge in a dark vacuum chamber. Diffuse reflectance spectra were measured using a spectrophotometer and an MgO ceramic as a standard of 100% reflectance.

Measurements of luminescent characteristics.—In LEE excitation, brightness-Eu addition, and brightness-voltage, current dependences were measured using the demountable apparatus shown in Fig. 1.

The powder phosphor was coated on an alumina substrate attached to an Ag-Pd electrode at a rate of 15 mg/cm^2 with no binder. Five substrates at most were mounted on a turntable in a vacuum chamber able to attain 5×10^{-7} Torr. A hot wire cathode and mesh grid were fixed just below the viewing port, and the sample substrates were set just below the mesh and cathode in sequence, by rotating the turntable to excite the phosphors under the same conditions. The excitation voltage was changed by applying different voltages between the hot cathode and Ag-Pd electrode (anode), and current was controlled by voltage of the mesh grid.

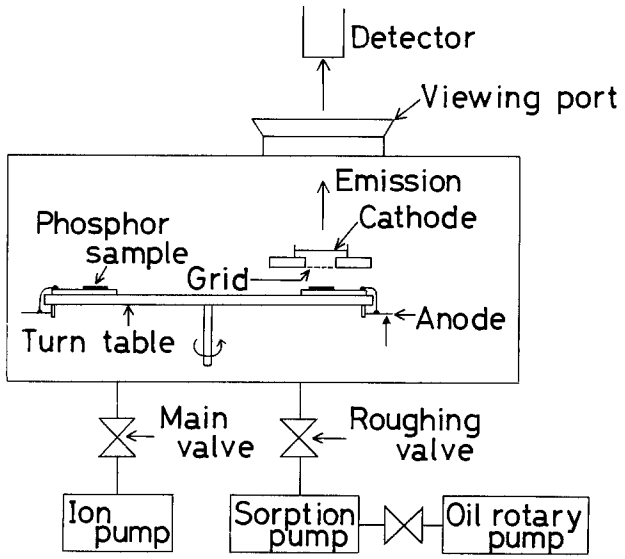

Fig. 1. Demountable measurement apparatus of luminescence for LEE excitation.

The emission spectrum, brightness-temperature dependence, decay characteristic, and efficiency were measured by constructing plate-like vacuum fluorescent tubes which were completely the same in principle as in Fig. 1.

In those tubes, the phosphor was coated on the anode composed of carbon and low melting point glass, at a rate of about 6 mg/cm^2 by screen printing method. The tubes were evacuated (at 350°C) and sealed, then the Ba-Al getter was operated. The temperature dependence of brightness was measured by controlling the temperature of the tube itself. The emission spectrum, decay, and efficiency were measured at room temperature. Under high-energy-electron excitation, the emission spectrum, brightness-Eu addition dependence, and decay characteristic were measured in the demountable electron bombardment equipment. The phosphor layer in a thickness of 3 mm in a copper cell was excited by high-energy-electrons at a current density of 0.05 μA/cm^2.

The excitation spectrum was measured using a deuterium discharge tube as a light source, and emissions with wave length greater than 550 nm were monitored.

A cryostat was used to examine the glow curves. The phosphor was coated (3 mg/cm^2) on a copper plate, cooled by liquid nitrogen, excited at 254 nm u.v., and then heated at a rate of 16°C/min. To detect the glow emission, a 590 nm interference filter was used for $^5D_0$-$^7D_1$ emission of Eu and no filter was used for the intrinsic emission of pure SnO_2.

The same cryostat, as in the glow curve measurement, was used for measurement of emission intensity-temperature dependence in 254 nm u.v. excitation, where a 590 nm interference filter for $^5D_0$-$^7D_1$ emission of Eu, and a 512 nm interference filter for the intrinsic emission of pure SnO_2 were used.

Results and Discussion

Characterization of powder.—The resultant crystalline phases were similar to those previously reported (7). Further refined x-ray powder diffraction and line analyses of XMA showed that the compositions with $\geqq$0.1 a/o Eu consisted of the SnO_2 phase and the $Eu_2Sn_2O_7$ phase. No change in lattice constants was observed within experimental error.

The particle size of the system SnO_2:Eu was affected by added Eu, as shown in Fig. 2. The particle size is considerably reduced in the addition region 0.01-0.06 a/o Eu. Above 0.06 a/o, the particle size hardly changes with the addition. This behavior coincides with a solubility limit of Eu into the SnO_2, as also discussed later. Therefore, the reduced particle size may be due to

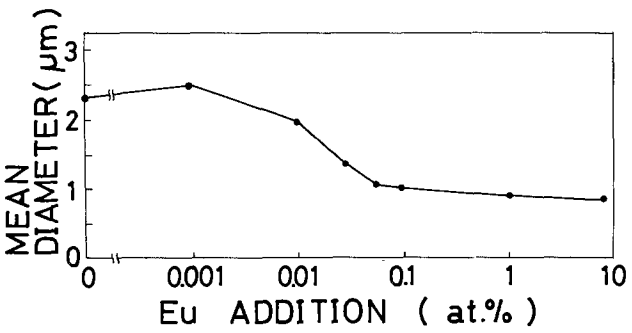

Fig. 2. Dependence of mean particle size of SnO_2:Eu powder on Eu addition.

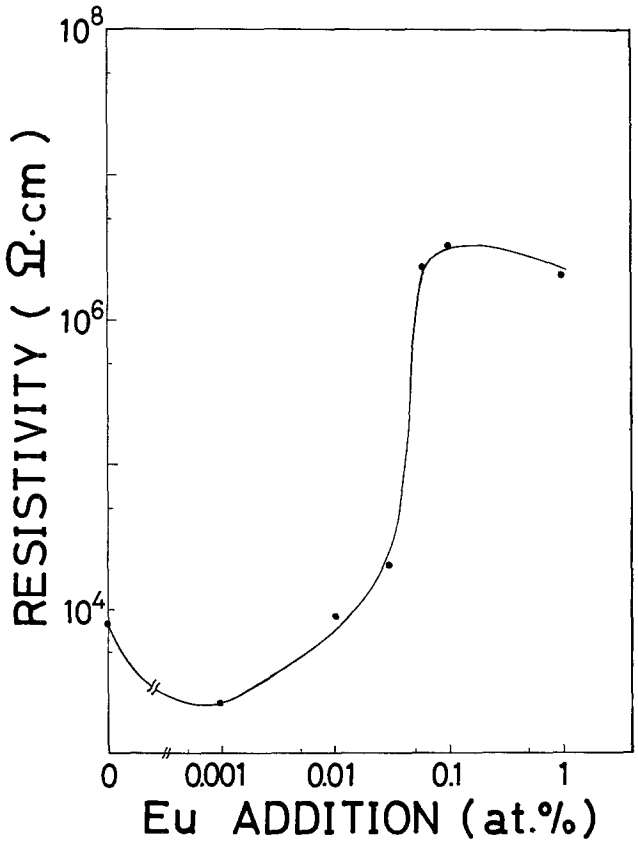

Fig. 3. Dependence of resistivities of SnO_2:Eu ceramics on Eu addition.

formation of $Eu_2Sn_2O_7$ at the surface of SnO_2 particles at an initial stage of Eu diffusion.

The resistivity of the SnO_2:Eu increased with addition of Eu, as shown in Fig. 3. This fact indicates that Eu acts as an acceptor for n-type semiconductor SnO_2. From the results, it was confirmed that the solubility limit of Eu into SnO_2 was 0.05-0.06 a/o. The resistivity was about 3×10^6 Ωcm at most. Hence, conduction electrons were not compensated for completely by doping.

The conduction mechanism can be explained in terms of the controlled-valence theory as follows. Nearly pure SnO_2 exhibits nonstoichiometry (14-17)

$$O_O \rightleftarrows V_O^{\cdot\cdot} + 2e^- + 1/2\,O_2(g) \quad [1]$$

$$K_O = [V_O^{\cdot\cdot}]\,[e^-]^2\,Po_2^{1/2} \quad [2]$$

or

$$Sn_{Sn}^{4+} \rightleftarrows Sn_i^{\cdot\cdot\cdot\cdot} + 4e^- + O_2(g) \quad [3]$$

$$K_i = [Sn_i^{\cdot\cdot\cdot\cdot}]\,[e^-]^4\,Po_2 \quad [4]$$

By the doping of Eu^{3+}

$$Eu_2O_3 + 1/2\,O_2(g) + 2e^- \rightleftarrows 2Eu_{Sn}' + 2SnO_2 \quad [5]$$

Decrease of electron concentration, resulting from incorporation of Eu^{3+}, is responsible for increased resistivity of SnO_2:Eu. Furthermore, assuming K_O and K_i constant, $[V_O^{\cdot\cdot}]$ and $[Sn_i^{\cdot\cdot\cdot\cdot}]$ must increase by moving the equilibria equations [1] and [3] to the right. Therefore, incorporation of Eu^{3+} should increase ionized lattice defects such as oxygen vacancy (the first ionized level 0.03 eV, and the second ionized level 0.15 eV) (17).

The diffused reflectance spectra of the SnO_2:Eu are shown in Fig. 4 (right side). The SnO_2:Eu powder with higher Eu addition exhibited higher reflectance at <500 nm, and the body color became more whitish. The rapid decrease at 380-310 nm may be due to the fundamental absorption of the SnO_2 itself, which is related to the bandgap (3.54 eV at room temperature (18). That rapid decrease is also considered due to charge transfer absorption by Eu^{3+}—O^{--} bonds, but we concluded this possibility should be rejected because of an excitation spectrum described later. Weak absorption was observed at 400-420 nm (2.9-3.1 eV) and tends to reduce with addition of Eu. Houston and Kohnke proposed an energy level scheme for SnO_2 (19, 20). The energy level consists of several trap levels such as 0.21, 0.52, and 0.62 eV. Since the energy at weak absorption of the SnO_2:Eu is not different from pure SnO_2, weak absorption may be explained by electron transitions relating to the trap levels described above and valence band.

The trap concentration and electron density at each trap level should be naturally different from those of pure SnO_2, because of introduction of the Eu ion acting as acceptor.

Luminescent Characteristics

Emission spectra.—The prior art f-f transition spectrum at 10 kV high-energy-electron (7) was observed at both 18V LEE and 365 nm u.v. excitation in the present examination.

High sensitivity measurements under LEE excitation (Fig. 5) revealed green emission peaks from $^5D_1$ level with very low intensities, which are due to the $^5D_1$-$^5D_0$ relaxation process (1750 cm^{-1}). A relatively high maximum phonon energy 750 cm^{-1} of the SnO_2 (21) is thought to make the relaxation probability high.

The relative intensity of $^5D_1$ peaks to $^5D_0$-$^7F_1$ emission in 0.001 a/o Eu was higher than that in 0.1 a/o Eu as observed in other Eu-doped phosphors. The intrinsic emission of the SnO_2 matrix was found not to be completely suppressed by added Eu. The SnO_2:Eu with smaller added Eu showed stronger intrinsic emission. This is also confirmed by a change of color point as described in Fig. 5. The maximum intensity of intrinsic emission excited at 10 kV was observed at about 490 nm. On the other hand, the intensity of intrinsic emission excited at 18 V LEE increased monotonically toward higher wavelengths. Therefore, the emission excited at 10 kV seems more yellowish to the naked eye than the LEE emission. The intrinsic emission at

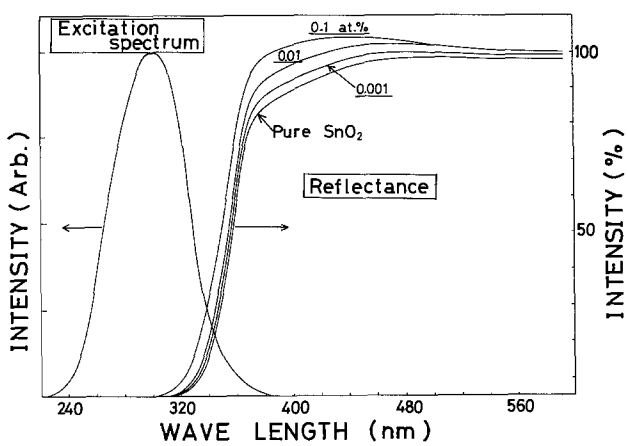

Fig. 4. Diffused reflectance spectra and excitation spectrum of SnO_2:Eu powder phosphors.

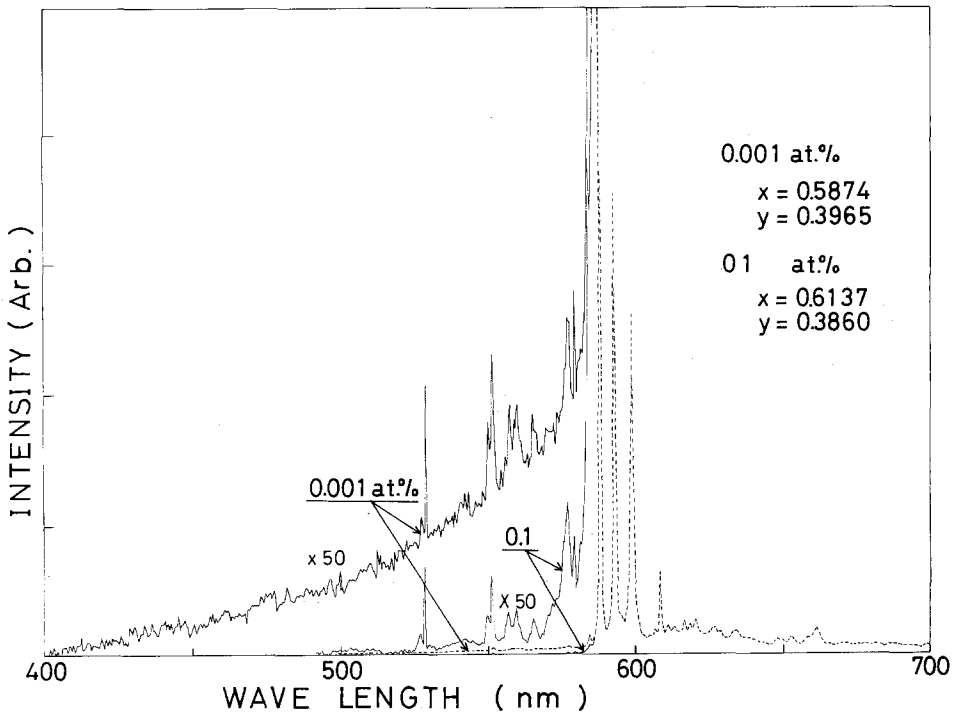

Fig. 5. LEE emission spectra of SnO_2:Eu (0.001 and 0.1 a/o) powder phosphors.

u.v. excitation was completely quenched at room temperature, but observed at low temperatures.

Brightness-Eu addition.—The dependence of brightness on added Eu was examined over a wide range of 10 kV to 20V. The currents are 0.05 $\mu A/cm^2$ and 0.4 mA/cm^2 at 2.5-10 kV and 20-100V excitations, respectively. The results are shown in Fig. 6. The brightness is normalized at 1 a/o Eu addition. An amount of added Eu at maximum brightness changed with the excitation voltage 10 kV (1 a/o Eu) and 20-100V (0.1 a/o Eu). SnO_2:Eu (0.1 a/o) virtually contains the soluble limit of Eu^{3+} ion. The highest concentration of Eu in the SnO_2 lattice without any segregation of the $Eu_2Sn_2O_7$ is preferred for LEE excitation of SnO_2:Eu.

Effects of different resistivity of the phosphor (shown in Fig. 3) on brightness should be considered in LEE excitation. Assuming an effective phosphor layer thickness of 22 μm (15 mg/cm^2), voltage drop through the phosphor layer was simply calculated to be 0.88V using a current 0.4 mA/cm^2 and a resistivity of $10^6\ \Omega \cdot cm$. Therefore, the effect of resistivity was considered negligible. The intrinsic low resistivity of 10^4-$10^6\ \Omega \cdot cm$ is generally preferable for LEE excitation. Therefore, the SnO_2:Eu system can be understood to show no charge-up phenomena even at 20V excitation.

Brightness-voltage, current.—The dependence of brightness on voltage is shown in Fig. 7. The relationship is expressed by $B \propto V^{0.33}$ at 0.3 mA/cm^2 and $B \propto V^{0.29}$ at 3 mA/cm^2, being different from $B \propto V^1$ at >5 kV excitation in prior art (7). The brightness also depends sublinearly on current density (Fig. 8); $B \propto I^{0.59}$ at 20V, $B \propto I^{0.50}$ at 40V, and $V \propto I^{0.44}$ at 70V. The sublinearities are promoted at both high current density and high voltage side, which may be attributed to the low soluble limit of Eu^{3+} ion into SnO_2 and an effect of surface defects.

Decay.—The decay characteristic of SnO_2:Eu under high-energy-electron-excitation (10 kV, $\approx$0.05 $\mu A/cm^2$, 12.5 msec pulse) is shown in Fig. 9. The decay curve consisted of the intrinsic matrix and Eu^{3+} emissions. The intrinsic emission has a very short decay time of 5 μsec(1/e), 8 μsec(1/10).

On the contrary, the decay time of Eu^{3+} red emission is only 4.1 msec(1/e), 13-14 msec(1/10); almost the same for SnO_2:Eu with different Eu additions. Influence of increased lattice defects, such as ionized oxy-

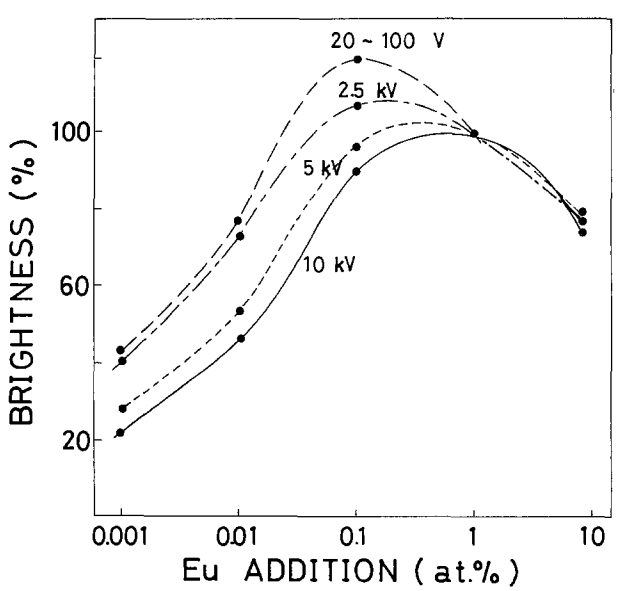

Fig. 6. Dependence of brightness of SnO_2:Eu phosphor on Eu addition in high and LEE excitations.

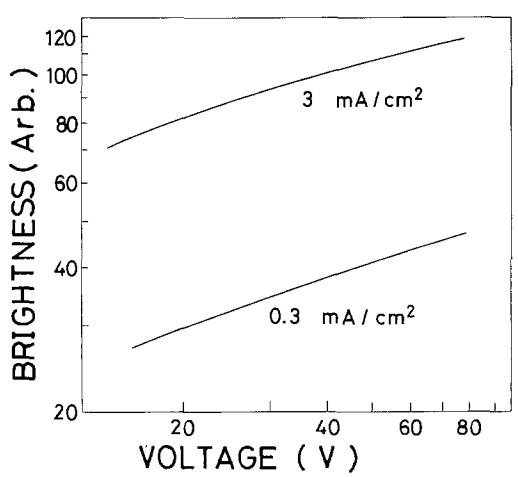

Fig. 7. Dependence of brightness on voltage in LEE excitation of SnO_2:0.1 a/o Eu (current parameter).

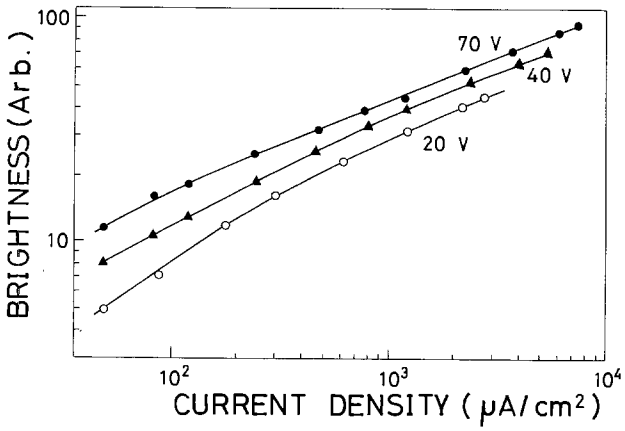

Fig. 8. Dependence of brightness on current density in LEE excitation of SnO_2:0.1 a/o Eu (voltage parameter).

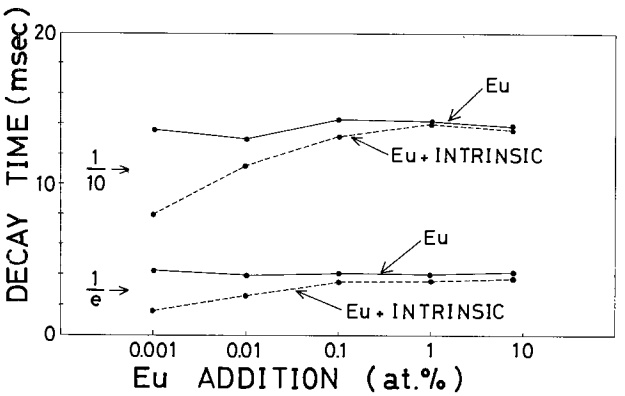

Fig. 9. Decay times of SnO_2:Eu phosphors in high-energy-electron excitation.

gen vacancy by Eu incorporation, was not found. But decay times of the overall emission (intrinsic + Eu^{3+} red emissions) become shorter in phosphors with smaller Eu additions, because of the lower ratio of Eu^{3+} emission intensity to that of intrinsic emission. The decay curve of the Eu^{3+} red emission was found to follow the e^{-t} relation, and to be a mixture of spontaneous afterglow and metastable afterglow.

On the other hand, a different decay characteristic was observed in LEE excitation. The decay and build-up time excited at 70V, 30 msec pulse were examined using fluorescent vacuum tubes. A decay time of 5.9 msec(1/10) and build-up time 1.5 msec (90%) were observed. The decay time under LEE excitation was found to be about half that under high-energy-electron excitation. This difference is probably related to the geometrical structure of the fluorescent vacuum tube. In fact, with other tube dimensions in prior art (7) a 10-11 msec decay was observed under LEE excitation.

Excitation spectrum.—The excitation spectrum of the SnO_2:Eu(1 a/o) powder phosphor is shown in Fig. 4 (left side). A band spectrum with a peak at 300 nm (4.1 eV) was observed. The excitation energy absorption mechanism can be explained on the basis of the excitation spectrum, and the ionic field strength of the SnO_2 matrix. The absorption bands of phosphors at u.v. excitation are usually classified into four cases: (*i*) f-d transition, (*ii*) charge transfer, (*iii*) fundamental absorption, and (*iv*) sensitizer.

The excitation spectrum in Fig. 4 can be apparently explained by the fundamental absorption of the SnO_2 matrix. However, superposition of the matrix fundamental and charge transfer absorption should be taken into consideration. Representative phosphors such as Y_2O_3:Eu and Y_2O_2S:Eu exhibit charge transfer bands at 270 and 310 nm, respectively. The charge transfer bands with lower electron potential energy of O^{2-} ion in the matrix tend to shift toward shorter wavelengths. Therefore, the ionic field strength of the matrix was considered a good criterion for estimating the charge transfer band energy.

Dietzel (22) calculated the ionic field strengths of the various oxides, using the following equation

$$\text{F.S.} = Z/a^2$$

Z = valence of cation

a = average interionic distance

According to the calculated results, SnO_2 has a stronger ionic field strength than Y_2O_3. This implies that SnO_2:Eu has a charge transfer band at shorter wavelength than Y_2O_3:Eu (270 nm). Therefore, we attributed the excitation spectrum of SnO_2:Eu at 300 nm to the matrix fundamental excitation, not to charge transfer.

Temperature dependence.—The temperature dependence of SnO_2:Eu phosphor emission excited by 254 nm u.v. is shown in Fig. 10. The intensity is normalized at 20°C to be 100%. As shown in the figure, the temperature dependence of the photoluminescence shows almost the same trend independent of Eu addition. Two peaks at about −20° to 10°C (highest emission intensity) and −90° to −80°C were observed.

The peak at the −20° to 10°C shifts to higher temperatures with increase of Eu addition. The emissions of SnO_2:Eu with any Eu addition are almost quenched at 120°C. The temperature dependence of intrinsic emission in pure SnO_2 was also examined (Fig. 10).

Intrinsic emission shows a strong decrease at about −190° to −140°C and is completely quenched at −20°C. However, intrinsic emission can be observed at room temperature in high energy and LEE excitation although only the longer wavelength region appears under LEE, especially in SnO_2:Eu with the small Eu additions as described before. The temperature dependence of brightness under LEE excitation (30V) was also examined for SnO_2:Eu with 1 a/o Eu addition (Fig. 10).

A temperature dependence curve similar to that of photoluminescence was observed with a peak at about 0°C. But temperature quenching is smaller in the high temperature region 0-100°C than for photoluminescence. The temperature dependences of SnO_2:Eu show temperature-sensitive characteristics. This might be due to the relatively high maximum phonon energy 750 cm^{-1} of SnO_2 (21).

Glow curve.—The glow curves of pure SnO_2 (the intrinsic emission) and SnO_2:Eu phosphors (0.001 and 0.1 a/o Eu) were measured. The results are shown in

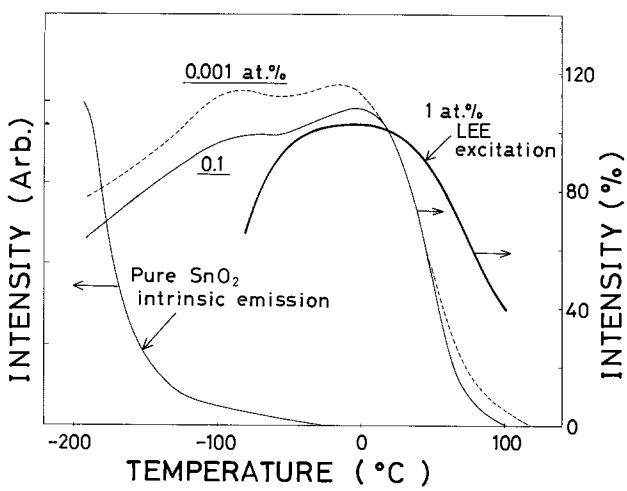

Fig. 10. Dependences of emission intensity on temperature excited at 254 nm u.v. ($^5D_0$-$^7F_1$ emission of Eu^{3+} and pure SnO_2 intrinsic emission), and temperature dependence of brightness for SnO_2:1 a/o Eu phosphor in LEE excitation (30V).

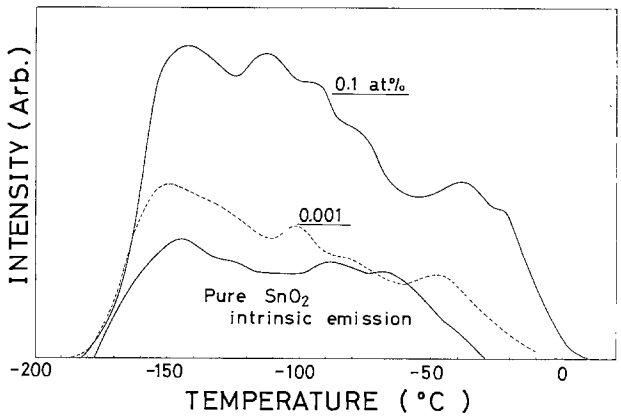

Fig. 11. Glow curves of pure SnO_2 (intrinsic emission) and SnO_2: Eu phosphors ($^5D_0$-$^7F_1$ emission).

Fig. 11. As shown in Fig. 11, the peak at about −150° to −130°C does not change with Eu additions. But new peaks at about −120° to −90°C and −40° to −20°C appear by adding Eu. The glow curves are composed of superposition of several peaks, and it is difficult to be quantitatively exact. Our results were found to be different from those of the single crystal examined by Crabtree (9) as described in the following. In the pure SnO_2, Crabtree observed fairly sharp single peak at 147 K (−126°C, E = 0.19 eV) in single crystal heat-treated in an alumina environment; we further observed broad peaks extending to higher temperatures up to −30°C.

According to the Crabtree examination, a glow peak at −63°C, which appears when heat-treating in a silica environment, was attributed to Si impurity. Since we used an alumina crucible for heat-treatment at 1350°C, the broad glow peaks extending to −30°C were considered due to not the impurity, but surface trap levels characterized by powder form. On the other hand, the glow curves of Eu-doped SnO_2 are also different for powder and single crystal (Crabtree). Although the same glow peaks at about −150° to −130°C, and −40° to −20°C were observed in both single crystal and powder, several glow peaks were furthermore observed in the temperature region of −120° to −70°C between the two peaks described above. Since no glow peaks were observed at −100° to −80°C by Crabtree, the above results may be attributed to a characteristic of the powder with large surface area because of well-known large differences of characteristics between surface and bulk such as electrical resistivity (12).

It is estimated that the glow peak at about −140°C in both the pure and Eu-added SnO_2 is due to a doubly ionized oxidized vacancy. The origin of the newly appearing glow peaks at about −30°C by the Eu incorporation are not clear. These trap levels have no influence on decay time of Eu emission as described above.

Luminescent efficiency.—The efficiencies under LEE excitation were examined using fluorescent vacuum tubes. The efficiencies 2 lm/W (9 ~ 10V, 1.9 ~ 2.0 mA/cm^2), 1 lm/W (18 ~ 19V, 3.2 mA/cm^2), and 0.5 lm/W (32V, 5.0 mA/cm^2) were obtained under LEE d-c excitation. Higher efficiencies are observed at lower voltages and current densities. We attribute this fact to the sublinearities of the brightness-voltage, current density dependences described before. The higher efficiencies above 2 lm/W can be obtained in the voltage region lower than 10V. When a lumen equivalent of ≈480 lm/W (calculated from 595 nm) is applied, then an efficiency of 0.42 w/w/o is obtained.

Summary

The solubility limit of Eu ion into SnO_2 was found to be 0.05-0.06 a/o. The excess Eu forms $Eu_2Sn_2O_7$ phase with relatively small particles.

The mean diameter of the phosphor decreases rapidly at 0.01-0.06 a/o Eu and hardly changes above 0.06 a/o coinciding with the solubility limit of Eu.

The electrical resistance of the SnO_2:Eu can be explained by considering the acceptor action of Eu ion and its solubility limit. The resistivity increases up to 0.06 a/o Eu addition (Eu solubility limit), and then saturates at an order of 10^6 Ω · cm.

In the diffused reflectance spectra, absorption by charge transfer could not be observed and only fundamental matrix absorption was observed. The reflectance increases with the addition of Eu.

In emission spectra, the same spectra were obtained in the high and low-energy-electron and u.v. excitations. The very weak emission from $^5D_1$ level was further detected in the green emission region. The intrinsic emission from matrix SnO_2 was found not to be suppressed completely by Eu addition except for u.v. excitation at room temperature. The intrinsic emission spectra changed according to the electron energy of excitation. Under LEE excitation, longer wavelength emission appears.

An excitation spectrum having a peak at 300 nm was observed. The spectrum was ascribed to matrix fundamental excitation mechanism, not to charge transfer.

The brightest phosphors were obtained at 0.1 a/o Eu for the low energy electron excitation (<100V), and at 1 a/o Eu for 10 kV electron excitation. The SnO_2:Eu phosphor was found to show strong sublinearities in brightness *vs.* voltage and current density.

The decay curves are composed of the superposition of the intrinsic emission from SnO_2 matrix and Eu^{3+} red emission. The intrinsic emission has very short decay time of 8 μsec (1/10). On the other hand, Eu^{3+} red emission has a long decay time of 13-14 msec (1/10) at 10 kV. The decay curve of the Eu^{3+} red emission follows an e^{-t} relation, and is a mixture of spontaneous afterglow and metastable afterglow. Under LEE excitation, 5.9 msec (1/10) decay time was obtained. This value was considered to change according to the dimensions of the tubes used.

The emission of the SnO_2:Eu phosphor shows a relatively strong temperature dependence. At higher temperatures than 100°C, emission by u.v. is almost quenched, but the emission by LEE keeps >40% of the brightness at 20°C.

Different glow curves from those of Crabtree (single crystal) were obtained for both pure SnO_2 intrinsic emission and Eu^{3+} red emission. Several peaks were further observed in the temperature region between the two main peaks observed by Crabtree in SnO_2:Eu single crystal. These peaks were considered due to surface trap levels in the powder.

The efficiencies under LEE excitation were higher in lower voltage and current density excitations. Efficiency of 2 lm/W (≈0.42%) at 9-10V, 1.9 ~ 2.0 mA/cm^2 was obtained.

Acknowledgments

We would like to thank T. Fukuda and K. Morimoto (Futabe Corporation, Mobara, Chiba, Japan) for valuable discussion and support of the research.

Manuscript submitted Feb. 8, 1982; revised manuscript received Oct. 9, 1982.

Any discussion of this paper will appear in a Discussion Section to be published in the December 1983 JOURNAL. All discussions for the December 1983 Discussion Section should be submitted by Aug. 1, 1983.

Publication costs of this article were assisted by Matsushita Electric Industrial Company, Limited.

REFERENCES

1. M. Hiraki, A. Kagami, T. Hase, K. Narita, and Y. Mimura, *J. Lumin.*, **12/13**, 941 (1976).
2. S. Oda and H. Kukimoto, *IEEE Trans.*, **ed-24**, 956 (1977).
3. S. Oda, K. Akagi, H. Kukimoto, and T. Nakayama, *J. Lumin.*, **16**, 323 (1978).

4. K. Akagi, H. Kukimoto, and T. Nakayama, *ibid.*, **17,** 237 (1978).
5. H. Kukimoto, S. Oda, and T. Nakayama, *ibid.*, **18/19,** 365 (1979).
6. *Nikkei Electronics (in Japanese)*, **10,** 74 (1980).
7. T. Matsuoka, Y. Kasahara, M. Tsuchiya, T. Nitta, and S. Hayakawa, *This Journal*, **125,** 102 (1978).
8. D. F. Crabtree, *J. Phys. D: Appl. Phys.*, **7,** L17 (1974).
9. D. F. Crabtree, *ibid.*, **8,** 107 (1975).
10. D. F. Crabtree, *Phys. Status Solidi A*, **38,** 217 (1976).
11. D. F. Crabtree, *J. Phys. D: Appl. Phys.*, **11,** 1543 (1978).
12. M. Nagasawa and S. Shionoya, *Jpn. J. Appl. Phys.*, **10,** 727 (1971).
13. N. T. Gordon and J. W. Allen, *Solid State Commun.*, **37,** 441 (1981).
14. R. E. Aitchison, *Aust. J. Appl. Sci.*, **5,** 10 (1954).
15. J. A. Marley and T. C. MacAvoy, *J. Appl. Phys.*, **32,** 2504 (1961).
16. M. Nagasawa, S. Shionoya, and S. Makishima, *Jpn. J. Appl. Phys.*, **4,** 195 (1965).
17. S. Samson and C. G. Fonstad, *J. Appl. Phys.*, **44,** 4618 (1973).
18. E. E. Kohnke, *J. Phys. Chem. Solids*, **23,** 1557 (1962).
19. J. E. Houston and E. E. Kohnke, *J. Appl. Phys.*, **36,** 3931 (1965).
20. J. E. Houston and E. E. Kohnke, *ibid.*, **37,** 3083 (1966).
21. H. J. Van Daal, *ibid.*, **39,** 4467 (1968).
22. A. Dietzel, *Z. Electrochem.*, **48,** 9 (1943).

Kinetics of the Cubic → Hexagonal Transformation of Cadmium Sulfide

Koichi Matsumoto and Katsuki Takagi

Research Institute of Electronics, Shizuoka University, Johoku, Hamamatsu 432, Japan

and Shoji Kaneko

Department of Industrial Chemistry, Faculty of Engineering, Shizuoka University, Johoku, Hamamatsu 432, Japan

ABSTRACT

The kinetics of cubic→hexagonal transformation of CdS conforms to a second-order rate equation with an activation energy of *ca.* 67 kcal/mol. The transformation is enhanced by the addition of NaCl of 0.001-0.1 weight ratio with little change of the activation energy. The role of the NaCl added is considered to reside, in that NaCl makes the movement and rearrangement of atoms in CdS easy as a flux, and that the contact points of CdS particles with NaCl provide the starting points of the further phase transformation. The mechanism of this transformation is presumed to be a linear growth process where the cubic-hexagonal interface moves progressively along the [111] direction of the cubic form.

Cadmium sulfide (CdS) has been utilized as a yellow pigment and as an excellent material for photoconductors, phosphors, etc. This compound is well known to have two crystal structures, the zinc-blende and wurtzite types (1). Since there is a significant difference between the bandgaps or the fundamental absorption edges of each type, their photoconductive, luminescent properties and color also differ from each other. These properties are affected by the degree of crystallization, the stacking faults, the lattice defects, etc.

For zinc sulfide (ZnS), an isomorph of CdS, it is known that zinc blende (cubic form) is stable below 1020°C, and wurtzite (hexagonal form) above that temperature. The phase transformation of ZnS has been investigated by a number of workers as follows: the influence of additives (2-5); the influence of atmospheres (6, 7); the transformation induced with the aid of mechanical stress (8); the transformation behaviors of the solid solutions (Zn,Cd)S (9, 10).

On the other hand, only a few facts are known about the phase transformation of CdS. No established transformation temperature has been reported so far, although it is empirically known that this compound transforms completely to hexagonal around 600°C, through the heat-treatment used in a dry process without oxidation for the preparation of a photoconducting material. The lack of detailed knowledge appears to be attributed to the facts that the behavior of the phase transformation depends largely on the starting material and the treatment method, and that the reverse hexagonal → cubic transformation is not known up to now. Rittner *et al.* (11) reported that in ammonium sulfide solution of high concentration, the phase transformation occurred even at room temperature. Ahlburg *et al.* (12) also showed that the hexagonal form was stable above 20°C in ammonium hydrogen sulfide solution of high concentration, and that in a hydrothermal treatment, cubic seeds for single crystal growth of CdS transformed to hexagonal at relatively low temperatures (120°-250°C).

Key words: inorganic, crystallography, phase transformation.

Besides the above studies, other investigations with regard to the phase transformation are: the influence of the conditions of precipitation on the crystal form of CdS (13), the effect of grinding (14), and both the effects of grinding and afterheating with those to the body-color change (15).

The present authors have found under hydrothermal conditions that the phase transformation of CdS proceeded at appreciably low temperatures; that it also proceeded more rapidly in CdS of poorly crystalline state; and that hydrothermally treated CdS showed a high reflectance of visible rays, implying a low content of lattice defects (16).

In the present study the kinetics of the phase transformation of CdS has been studied with the addition of NaCl, which is usually used as a flux for the preparation of photoconducting or luminescent materials; and the role of NaCl on the phase transformation has been discussed.

Experimental

Cadmium sulfide powder of luminescence grade (Dai Nippon Painting Company, Limited) and NaCl of G. R. (Wako Pure Chemical Industries, Limited) were used. CdS was carefully mixed with NaCl at various weight ratios in an alumina ball mill with ethyl alcohol. The mixture was then evacuated ($\sim 10^{-2}$ Torr) to dryness at about 100°C in half a day, ball-milled again for about an hour, and stored in a desiccator with silica gel. Several grams of the mixed powders were heat-treated in an evacuated, dry-nitrogen-filled silica tube.

A horizontal electric furnace with SiC heating element controlled by an electronic temperature controller was used. It took a few minutes for the temperature to be restored to a prescribed value, after placing the silica tube in the furnace. Temperature fluctuation was within 2°C. After the heat-treatment the silica tube was taken out from the furnace and cooled by an electric fan to room temperature within a few minutes. The samples were still loose and powdery without any sintering.

X-ray diffraction measurements on the powders were carried out by using a Rigaku Geigerflex x-ray diffractometer with Ni-filtered CuKα radiation. Hexagonal content, H, of CdS was calculated by means of Eq. [1] proposed by Short *et al.* (17).

$$H = \frac{1.96R}{0.96R + 1} \qquad [1]$$

where R is the ratio of two integrated intensities measured in the ranges $2\theta = 46.75°$-$48.75°$ and $2\theta = 42.75°$-$44.75°$, respectively.

Results and Discussion

Since CdS and NaCl were mixed by using a ball mill, the phase transformation of CdS might possibly be affected simply by a mechanochemical effect (14, 15). To ascertain this question, CdS powder alone was ball-milled for various intervals of 0-60 min and then was heated at 600°C for 30 min. Since there was no significant change in the hexagonal content with the milling time, the mechanochemical effect of ball-milling on the phase transformation was considered to be negligible under the present experimental conditions.

Figure 1 shows the temperature ranges in which the phase transformation of CdS occurred for 100 min of the heating time without and with added NaCl. The temperature at which the hexagonal content, H, became 50% was about 530°C in the case of CdS alone, and it was lowered to about 500°C in CdS added with NaCl of 0.001 weight ratio, and to about 390°C of 0.01 or more.

The H's in CdS without and with NaCl added of 0.001 weight ratio are shown in Fig. 2 as a function of heating time at various temperatures; the phase transformation was accelerated by means of the addition of NaCl. These data were found to be compatible with a special case of the treatment given by Avrami (18) and formulated in a second-order rate equation at sufficiently large t by Czanderna *et al.* (19), which takes the form

$$\frac{1}{1 - H} = 1 + \sigma G N_g t \qquad [2]$$

where σ is a shape factor, G is the linear growth rate of the new phase, N_g is the initial density of nuclei, and t is the heating time. As shown in Fig. 3, a plot of $1/(1 - H)$ *vs.* t will give a slope equal to the composite quantity $\sigma G N_g$ which is taken to be the formal rate

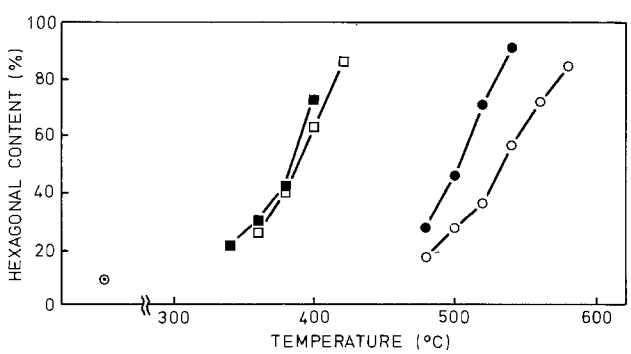

Fig. 1. Effect of the addition of NaCl of various ratios on the cubic→hexagonal transformation of CdS heated for 100 min: ○, null; ●, 0.001; □, 0.01; ■, 0.1; ⊙, starting, as-received material.

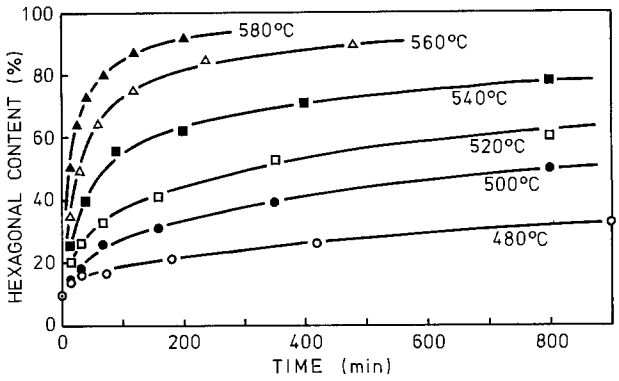

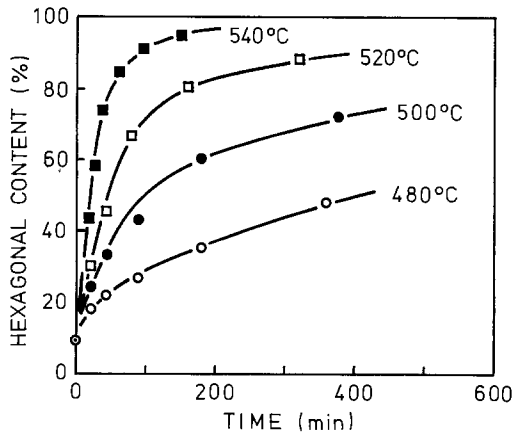

Fig. 2. Time dependence of hexagonal content in CdS at various temperatures: (a), CdS; (b), CdS with NaCl of 0.001 weight ratio.

constant k. The intercepts were not always in unity, because the as-received CdS powder already contained 9.8% H, and little time was taken for the temperature to rise or fall, as a sample was inserted into or pulled out of the furnace.

One of the several assumptions in the application of this rate equation to the phase transformation was that the growth of the new phase was linear. Gashurov *et al.* (4) showed by a kinetic study that the hexagonal → cubic transformation of ZnS proceeded by a linear growth process, where the hexagonal-cubic interface moved along the c-axis of the hexagonal form. Subsequently, Bansagi *et al.* (6) confirmed this finding in ZnS heat-treated in vacuo and in sulfur vapor. This phase transformation could crystallographically be represented by changing the stacking sequence of the common close-packed layers, the (111) plane of the cubic form and the (00 · 1) plane of the hexagonal form, at the interface through the rotational displacements of atoms within the layers (3). It seems reasonable then to presume that the mechanism of the cubic → hexagonal transformation of CdS also is similarly a linear growth process, where the cubic-hexagonal interface moves progressively along the [111] direction of the cubic form.

The activation energy was calculated from the standard Arrhenius plots; the logarithm of the formal rate constant, k, *vs.* the reciprocal temperature, $1/T(K)$, as shown in Fig. 4. The activation energies of 66.8, 77.6, 57.9, and 62.3 kcal/mol for NaCl of 0, 0.001, 0.01, and 0.1 weight ratios, respectively, show no substantial differences.

Thus, the phase transformation of CdS was markedly enhanced by the addition of NaCl. The role of NaCl appears to be to enlarge the frequency factor without significant change of the activation energy. The effect described above appeared even when the ratio was only 0.001, gradually increased with an increase in the ratio up to 0.01, and was saturated at the larger ratio than that. This behavior appears to be analogous to the effect of CuO addition on the anatase-rutile trans-

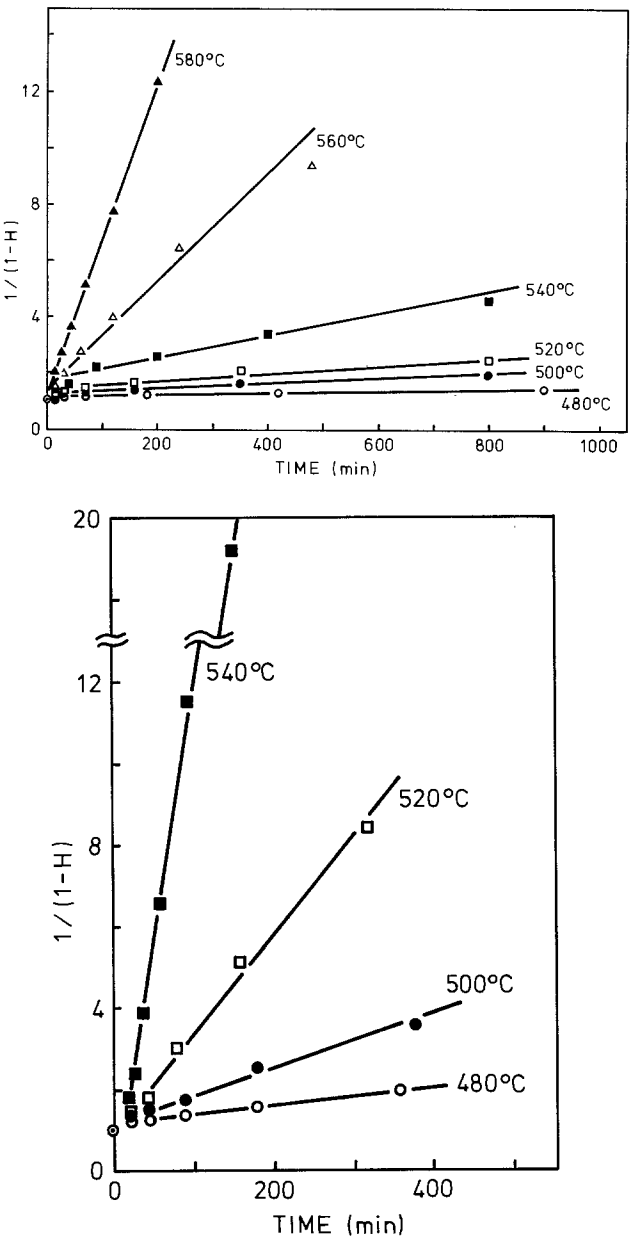

Fig. 3. Plots of $1/(1 - H)$ vs. time at various temperatures: (a), CdS; (b), CdS with NaCl of 0.001 weight ratio.

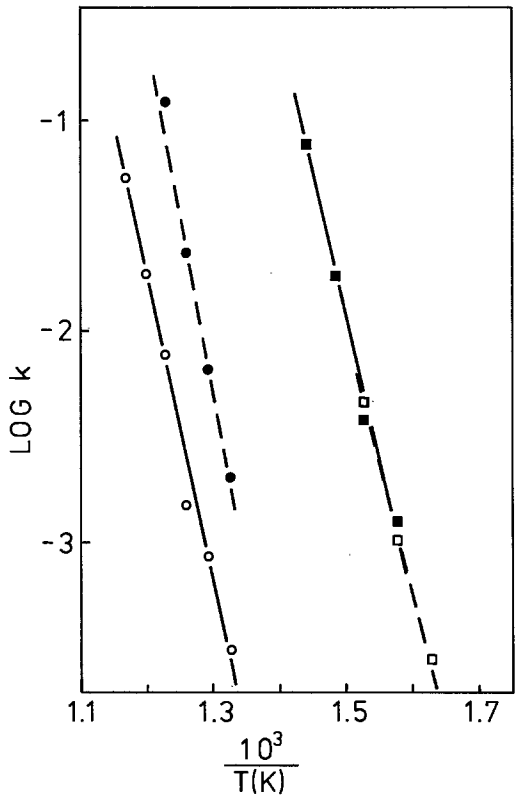

Fig. 4. Standard Arrhenius plots for the phase transformation of CdS mixed with NaCl; weight ratios of NaCl: ○, null; ●, 0.001; □, 0.01; ■, 0.1.

formation by Shannon *et al.* (20); 1% CuO would completely cover the available TiO_2 surface as a monomolecular layer of the oxide and its promotion effect on the phase transformation was saturated above this content. It is therefore suggested that the contact points of CdS particles with NaCl provide the starting points of the further phase transformation of CdS.

The question also arises whether the phase transformation might be influenced by means of an intermediate or catalytic compound, such as in the case of GeO_2, where lithium or potassium germanate formed by the reaction of Li_2CO_3 or KCl as additives, respectively (21). In the present study, such a compound was not observed in any x-ray diffraction pattern; no solid-state reaction occurred between CdS and NaCl even if the equimolar mixture was heated up to 800°C in N_2. Although the phase diagram in the system CdS-NaCl is not known thus far, it is speculated that NaCl, whose melting point is not so high (800.4°C), serves as a flux to enhance the movement and rearrangement of atoms in CdS, but a more detailed analysis must await further work.

Summary

The kinetic study of the cubic → hexagonal transformation of commercially available CdS was carried out with NaCl additions. The phase transformation, to which a second-order rate equation was applicable with an activation energy of *ca.* 67 kcal/mol, was effectively enhanced by the addition of NaCl of 0.001-0.1 weight ratio without substantial change of the activation energy.

An interpretation of the mechanism is that the phase transformation proceeds through a linear growth process where the cubic-hexagonal interface moves progressively along the [111] direction of the cubic form being common to the [00 · 1] direction of the hexagonal form. NaCl serves as a flux to enhance the movement and rearrangement of atoms in CdS. The contact points of CdS particles with NaCl provide the starting points of the phase transformation.

Manuscript submitted June 15, 1982; revised manuscript received Oct. 1, 1982.

Any discussion of this paper will appear in a Discussion Section to be published in the December 1983 JOURNAL. All discussions for the December 1983 Discussion Section should be submitted by Aug. 1, 1983.

Publication costs of this article were assisted by Shizuoka University.

REFERENCES

1. A. F. Wells, "Structural Inorganic Chemistry," 4th ed., p. 606, Oxford University Press, London (1975).
2. J. Nickerson, P. Goldberg, and D. H. Baird, *This Journal*, **110**, 1228 (1963).
3. H. Gobrecht, H. Nelkowski, J. W. Baars, and G. Brandt, Proceedings Int. Conf. Luminescence 1966, p. 1086 (1968).
4. G. Gashurov and E. Banks, *This Journal*, **114**, 1143 (1967).
5. K. Takagi and Y. Onoda, *Bull. Res. Inst. Electron. Shizuoka Univ.*, **2**, 89 (1967).
6. T. Bansagi, E. A. Secco, O. K. Srivastava, and R. R. Martin, *Can. J. Chem.*, **46**, 2881 (1968).
7. M. Sakaguchi, M. Ohta, M. Satoh, and T. Hira-

bayashi, *This Journal*, **124**, 550 (1977).
8. M. Farkas-Jahnke and P. Gacs, *Krist. Tech.*, **14**, 1475 (1979).
9. M. J. Kozielski, *J. Cryst. Growth*, **30**, 86 (1975).
10. M. Satoh and M. Sakaguchi, *Denki Kagaku*, **47**, 544 (1979).
11. E. S. Rittner and J. H. Schulman, *J. Phys. Chem.*, **47**, 537 (1943).
12. H. Ahlburg and R. Caines, *ibid.*, **66**, 185 (1962).
13. R. Sato and H. Itoh, *Jpn. J. Appl. Phys.*, **3**, 626 (1964).
14. K. Hashimoto and Y. Toda, *Kogyo Kagaku Zasshi*, **71**, 1402 (1968).
15. M. Tsunashima, K. Mohri, K. Tsutsumi, and H. Takahashi, *ibid.*, **74**, 1733 (1971).
16. S. Kaneko, K. Matsumoto, T. Sugiyama, and F. Imoto, Abstracts Int. Symp. Hydrothermal Reactions, No. 68, Yokohama, Japan (1982).
17. M. A. Short and E. G. Steward, *Am. Mineral.*, **44**, 189 (1959).
18. M. Avrami, *J. Chem. Phys.*, **8**, 212 (1940).
19. A. W. Czanderna, C. N. R. Rao, and J. M. Honig, *Trans. Faraday Soc.*, **54**, 1069 (1958).
20. R. D. Shannon and J. A. Pask, *J. Am. Ceram. Soc.*, **48**, 391 (1965).
21. Y. Kotera and M. Yonemura, *ibid.*, **52**, 210 (1969).

Phosphor Deterioration in Fluorescent Lamps

Willi Lehmann

Westinghouse Research and Development Center, Pittsburgh, Pennsylvania 15235

ABSTRACT

The well-known deterioration of phosphors in fluorescent lamps consists essentially of two parts, a short-time degradation over roughly one hour possibly due to color center formation, and a long-time effect extending over thousands of hours explained by a slow build-up of a disordered and non-luminescent layer on the phosphor particles. Such layer has been observed on deteriorated zinc silicate, it is very thin. Its optical absorption is the main reason of decreasing lamp brightness. Mercury buried in, but not absorbed on, the dead layer may contribute to the optical absorption. The brightness-time function of the long-time degradation is $B/B_0 = \exp(-\sqrt{t/\tau})$ with τ as a time constant. This model agrees well with observations. Conclusions are drawn concerning the stability of phosphors in lamps and its dependence on some parameters.

The slow but steady deterioration of phosphors in fluorescent lamps has been the object of some speculations and controversy in the past. Several possible models have been proposed. (*i*) Absorption of mercury (or, possibly, mercury oxide) on the phosphor particle surfaces (1-6). Involvement of mercury certainly does occur at least in some cases. However, Burns and Kastner (7) studied the deterioration of halophosphate phosphors in lamps using radioactive mercury as tracer but could not find a quantitative correlation between mercury absorption and decreasing phosphor brightness. Also, degradation has been reported in cases where the phosphor did not come into contact with any mercury (8-13). These latter observations were confirmed in our laboratory on many different phosphors tested in lamps containing only argon (no mercury) which, in every case, gave degradations at least comparable to that observed in presence of mercury. Clearly, mercury absorption cannot be the main cause of phosphor deterioration in fluorescent lamps. (*ii*) Formation of color centers by the ultraviolet radiation in the lamp. Color centers have been fairly extensively investigated in halophosphate phosphors (10-14) and, at least for this phosphor type, have been considered to be a major cause of deterioration. It has also been shown that color centers in halophosphate phosphors are created by the 185 nm but bleached again by the 254 nm radiation of the Hg-discharge (11-13). How far that applies also to other phosphors is still unknown. (*iii*) Structural changes in the phosphor material caused by exposure to ion bombardment of the gas discharge. Some undefined change on the surface of zinc silicate particles in lamps had been reported by Harrison (6) already in 1960. In later years, ion bombardment has only occasionally been mentioned, but not seriously investigated, in connection with phosphor in lamps, apparently because it is not clear where the necessary energetic ions should come from. Only two very recent papers consider the possibility again. Tada *et al.* reported an amorphous surface layer on zinc silicate after deterioration in a 300V rf discharge in argon and, with various other phosphors, a correlation between the rapid deterioration in such rf discharge and the much slower one in regular fluorescent lamps (15). Lehmann *et al.* limited the work to $Na_3Ce_{0.65}Tb_{0.35}(PO_4)_2$ and report a nonluminescent and apparently heavily damaged surface layer to grow on the particles during aging in a demountable lamp (16). (*iv*) Oxidation or reduction of activator ions, or of the phosphor host material itself, to a nonluminescent state by action of energetic light quanta (mainly 185 nm u.v.) (8, 9). The oxidation of Mn^{2+} to Mn^{3+} may be an example. This effect has been criticized, however, (17) and the effect has not been studied in detail. (*v*) Some dependence of phosphor deterioration on the kind of lamp glass has been reported implying an interaction between phosphor and glass substrate (18). As an explanation, Na^+ ions might diffuse out of the glass and onto the phosphor particles where they could act as seeds for mercury adsorption. This possibility cannot be completely ignored and might warrant further investigation but, with our present knowledge, there is no reason to expect it to be a major cause of phosphor deterioration. (*vi*) Electrode effects. Material may be removed from the electrodes by sputtering, or already during activation of the electrodes, and be deposited onto the phosphor particles causing optical absorption of exciting ultraviolet and/or visible emission light. Alternatively, electrode material on the phosphor particles might act as seed for subsequent absorption of mercury. In either case, the effect must be restricted to the ends of the lamp and be insignificant in the middle.

Given this abundance of possibilities one might expect the complete deterioration of a phosphor in a lamp to be a superposition of several effects, each one acting to a degree depending on the circumstances. This view is expressed by Butler and co-workers (18), who describe the lamp brightness as a function of time, t, by a sum of three terms each one of the form $A_i [1 - \exp(-a_i t)]$ where A_i, a_i are constants. The equation implies three different deterioration mechanisms but does not permit identification. Also, since the accuracy with which experimental deterioration dependences can be measured is not too good, their comparisons with an equation containing six arbitrarily adjustable constants appears to be open to question.

We observed a surprisingly good fit of experimental lamp phosphor degradations to a very much simpler formula

$$B/B_0 = \exp(-\sqrt{t/\tau}) \quad [1]$$

where t is the time and B/B_0 the brightness ratio with B_0 as the zero-hour brightness. The only arbitrary parameter in this equation is the time constant, τ, denoting the time necessary to let the brightness, B, decrease to $\exp(-1) \approx 37\%$ of the original.

Equation [1] had originally been derived under the assumption of ion bombardment damage as the most important mechanism of phosphor degradation. This assumption may not strictly be correct; its applicability is discussed in the Discussion and Conclusion Section. The following section describes some experiments designed to shed more light onto the problem of phosphor deterioration in fluorescent lamps.

Some Experiments

Damage caused by low-energy ions.—Very thin and uniform (quasi-monoparticle) layers of various phosphors were coated onto metal plates with an organic binder which, subsequently, was burned out in air at 400°-500°C. The particles of the phosphors in these screens were directly in contact with the metal substrates. The screens were tested about 2 cm under a coated tungsten filament serving as electron emitter (Fig. 1). The electrons from the filament were accelerated by an alternating (10 Hz) voltage and, in vacuum, caused about 1 cm^2 area of the phosphor layer to light up in cathodoluminescence. That required a screen voltage of several 100V for insulating phosphors. Severe space charge effects occurred in the phosphor layers at lower voltages. Only ZnO (P-24) was enough electrically conducting to permit uniform and visible cathodoluminescence down to about 20V. In vacuum, of course, the current consisted entirely of electrons and was measurable only during the half-cycles when the filament was negative. Phosphor exposures for 1 hr with about 10^{-4}A did not cause a detectable deterioration.

The situation became different with the admission of about 10^{-4} Torr of argon. The current now had equal magnitudes in both directions (*i.e.*, no rectification) and, fairly obviously, consisted largely of argon ions during the half-cycles when the filament was positive. The energy of singly charged ions could not have been more than the applied screen voltage. A contribution of doubly, or higher, charged ions is believed to be negligible. The phosphor screens were so exposed to a beam of about 10^{-4}A consisting alternatingly of electrons and ions. All observed phosphor deterioration is believed to be caused by ions, not by electrons. Little or no disturbing space charge effects were observed on the phosphor layers, down to about 25V, because of mutual neutralization of adsorbed electrons and ions.

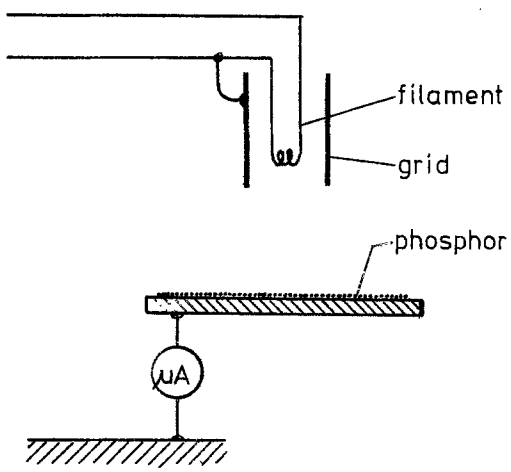

Fig. 1. Experimental setup used to bombard phosphor layers with low-voltage electrons and ions. Applied voltage: variable ac of 10 Hz. Filament: 2V ac of 60 Hz.

Deterioration of the phosphor layers exposed to this mixed electron-ion current was quite severe and easily visible already during the first few minutes of bombardment. All phosphor layers also became slightly discolored to a degree, and of a color, depending on the phosphor. Deterioration data were obtained by measuring the brightness of photoluminescence of the screen under excitation by 254 nm u.v. before and after 1 hr bombardment. Some results are given in Table I. Although this brief experiment was too simple to permit more quantitative conclusions, it does confirm that phosphors can be damaged by ions of fairly low energies.

Tests in a demountable fluorescent lamp.—The construction of this lamp is described elsewhere (16). The phosphor samples to be tested were coated on small glass pieces with an organic binder which, subsequently, was burned out by lehring in air at 400°-500°C. The atmosphere in the lamp consisted of slowly flowing argon (99.995% pure, from a tank) which could be loaded with mercury from a drop of mercury at the "upstream" end of the lamp. Electric power was applied from a current-limited transformer. Limitation of the current to 18 mA caused a potential of about 400V between the two ends of the lamp. When Hg was present in the lamp, the phosphor brightnesses were about comparable to those in a regular fluorescent lamp. Most tests were limited to 20 hr. Obtained maintenances were reproducible to about ± 1%. Some data obtained with typical lamp phosphors are given in Table II.

This demountable lamp was used to test zinc silicate under various conditions. Results are summarized in Table III. Zinc silicate phosphor deteriorates in plain argon even stronger than in Ar + Hg, indicating that, at least for this phosphor, mercury adsorption cannot be a dominant factor. This confirms earlier reports (8-13) on zinc silicate and other phosphors. Some

Table I. Results of 1 hr bombardment with electrons plus ions, ~10^{-4} A/cm^2

Phosphor	Emission color	Screen voltage	Maintenance (%)	Discoloration
Zn_2SiO_4:Mn	green	25V	94	brownish
Zn_2SiO_4:Mn	green	50	87	brownish
Zn_2SiO_4:Mn	green	100	75	brownish
Zn_2SiO_4 (no Mn)	dead	110	—	grayish
ZnO (P-24)	blue-green	110	88	brown-gray
$MgAl_2O_4$:Mn	green	110	—	very little
$CaBaAl_{24}O_{38}$:Ce,Mn	green	110	92	brownish

Table II. Maintenances of some lamp phosphors tested in demountable lamp, 20 hr in Ar + Hg

	%
Cool-white halophosphate	93
$Sr_5(PO_4)_3$:Eu^{2+}	97
Y_2O_3:Eu^{3+}	94
Zn_2SiO_4:Mn^{2+}	85

Table III. Maintenance of zinc silicate under various conditions (demountable lamp, 20 hr)

Samples covered	Atmosphere	Maintenance %
no	Ar + Hg	85
no	Ar	52
quartz glass	Ar + Hg	100
MgF_2-glass	Ar + Hg	100
Y_2O_3 (evap.)	Ar + Hg	95

samples were tested, not openly exposed to the gas discharge but loosely covered with thin and optically clear slices, either of quartz glass or of hot-pressed MgF_2. These samples, although excited in the lamp to brightnesses comparable to those of the uncovered ones, did not measurably deteriorate within 20 hr, indicating that ultraviolet radiation in the lamp cannot be a factor either. In still another experiment, some samples were coated (after lehring) with about 0.17 μm of clear Y_2O_3 applied by vacuum evaporation. When interpreting the result of the life test in the lamp, one should keep in mind that deposition by vacuum evaporation is a highly directional process; only the front surfaces of the phosphor particles can be expected to be covered. By contrast, the gas discharge in the lamp is very diffuse and can reach also parts of particles not covered by Y_2O_3. The consequence is a limited protection, the maintenance is improved but not to 100%. The extrapolation appears to be warranted to expect a near-100% protection if the Y_2O_3 would have coated all particles from all sides, in perfect agreement with the results on samples covered with quartz glass or with MgF_2 mentioned above.

Test by cathodoluminescence.—The buildup of a dead surface layer during deterioration of zinc silicate in a lamp could be confirmed by measuring the cathodoluminescence. Two glass pieces were coated with zinc silicate using an organic binder and lehred at ~ 500°C in air. One sample was then aged in the gas discharge (Ar + Hg) of the demountable lamp until the emission brightness had deteriorated to 67.5% of the original, the other sample was not aged and served as control. Both samples were then excited, side by side, by electrons in vacuum to cathodoluminescence using beam voltages of 2-10 kV. The ratios of the emission brightnesses aged/unaged were multiplied with the used beam voltages and the results plotted as function of the beam voltage (Fig. 2). The points are very closely on a straight line intersecting the abscissa at a "dead voltage" of about 150V which, from the known relationship between dead voltage and layer thickness (19), translates to a dead layer thickness of 5-10Å. This is a dead layer present on the aged but not on the unaged phosphor, and the only way it could have come from is the exposure of the aged sample to the discharge in the lamp.

It might be surprising that such a thin surface layer on the phosphor particles could have a noticeable effect on the emission brightness. However, all it requires is an optical absorptivity for the exciting u.v. of some 10^6 cm^{-1}, well within the range of normal materials. It is also in line with the known protection due to the addition of a little Sb_2O_3 to fluorescent lamp phosphors. Sb_2O_3 is slightly volatile at lamp lehring temperatures (~600°C) and, after lehring, apparently surrounds (to some degree at least) all phosphor particles with thin layers. If one assumes uniformly coated particles in the 1-10 μm size range, the customarily added 0.1-0.2% of Sb_2O_3 ends up in layers about 2-20Å thick, the same order as that observed above.

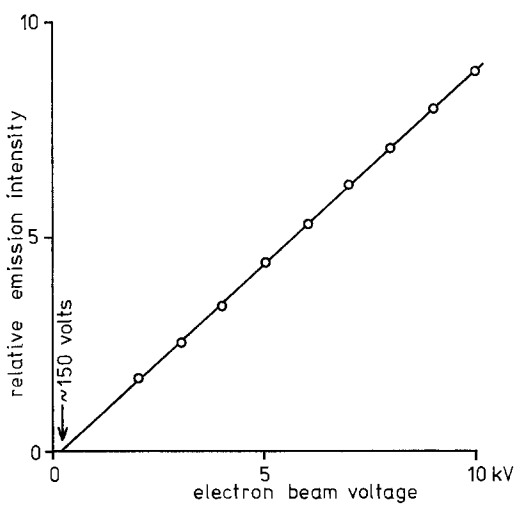

Fig. 2. Cathodoluminescence of a sample of zinc silicate aged in the demountable fluorescent lamp to 67.5% of the original, compared to that of fresh zinc silicate. The ratio between the readings on these two samples is multiplied by the number of kV used to accelerate the electron beam and the result is plotted as ordinate. The "dead voltage" of about 150V indicates a dead layer about 5-10Å thick on the particles of the aged sample.

Theoretical Considerations

The experimental results described above point to ion bombardment damage, or a related effect, as a cause of phosphor deterioration in fluorescent lamps. The question may be considered what possibly could be expected if ion bombardment damage would be the only responsible mechanism.

Damage of phosphors by high-energy ions is well known. Streck, in 1939, studied the effect of α-rays (= He^{2+} ions) on phosphors (19), and Berthold, in 1957, the damage caused by H_2^+ ions (20). Much recent research relevant to ion beam damage of crystals (although not necessarily phosphors) can be found in various publications dealing with ion implantation or with radiation from other sources (21-23). The general observation is that the ion beam causes gross lattice disorder. Crystal atoms are displaced from their original positions to other, more or less irregular, sites; the crystal becomes increasingly amorphous. If the crystal is a phosphor, this approach to the amorphous state effectively kills all luminescence. That all is well established.

Gas ions in a fluorescent lamp have much lower energies. They cannot possibly penetrate into the crystal lattice but can affect only the crystal surfaces. As an approximation, the writer considers the model schematically shown in Fig. 3. Lattice atoms are assumed to be knocked from their original positions to others which are not necessarily regular lattice sites. This type of damage restricted to the surface is known (23) and the required minimum energies can be estimated. For zinc silicate, for instance, they are about 20-25 eV.[1] Incidentally, that is also the energy range from which sputtering occurs (24). The writer assumes a disordered surface layer slowly to build up in this way, and considers the process to be essentially a diffusion of a lattice disorder into the crystal with the diffusion energy supplied by the gas discharge.

If this view is correct, then, as in any other diffusion, the thicknesses, s, of the disordered top layer can be expected to grow proportional to the square root of the time, t, and intensity, I, of the gas discharge in the lamp

$$s = c\sqrt{t\,I} \qquad [2]$$

[1] Estimate supplied by one of the reviewers of this paper, based on Ref. (23).

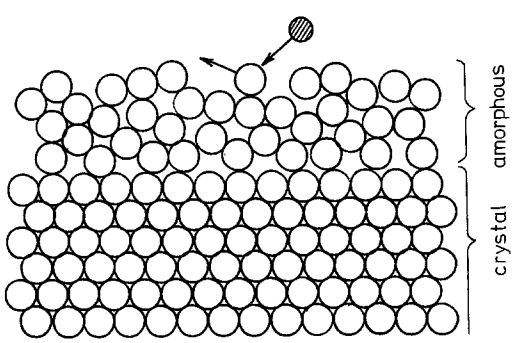

Fig. 3. Creation of an amorphous surface layer on a crystal by ion bombardment (schema).

where c is a constant describing the stability of the phosphor against damage by bombardment. This layer is nonluminescent but optically absorbs lights, mainly the exciting u.v. If its optical absorption constant is α, the emission brightness, B, of the phosphor must be

$$B = B_0 \exp(-\alpha s)$$
$$= B_0 \exp(-\alpha c\sqrt{t\,I}) \quad [3]$$

The intensity, I, of the gas discharge in a lamp normally does not significantly change with time so that the three constants in [3] can be combined to

$$\tau = 1/(\alpha^2 c^2 I) \quad [4]$$

which immediately leads to Eq. [1].

The shape of the curve described by Eq. [1] is shown in Fig. 4. The curve declines most rapidly in the beginning in accord with what one intuitively would expect, since a top layer already on the phosphor protects the healthy phosphor underneath against further damage (the better the thicker the top layer is). It is also in accord with what actually is observed during deterioration of lamps.

Comparison With Observations

The deterioration formula of Eq. [1] has been checked against various experimental data by plotting log B as function of the square root of the time, t. If Eq. [1] is valid, all points should be on a straight line. Results are shown in Fig. 5-10.

Figure 5 corresponds to the maintenance of ordinary Zn_2SiO_4:Mn observed during a run in a demountable fluorescent lamp in our laboratory. Technical reasons did not allow this test to be extended to times beyond about 45 hr.

Figure 6 shows data from routine maintenance tests on Westinghouse 40W lamps containing halophosphate phosphor. Every point represents the average over some 100-200 individual lamps tested during one of the years 1974-1978. Although only three readings per

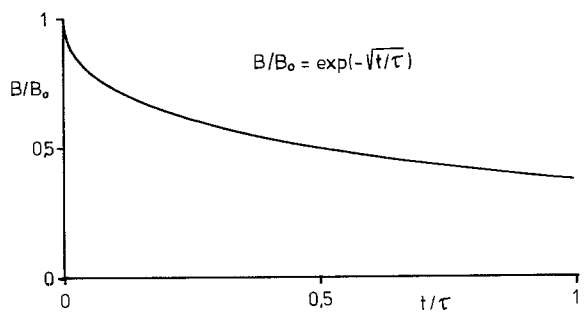

Fig. 4. Deterioration curve according to Eq. [1]

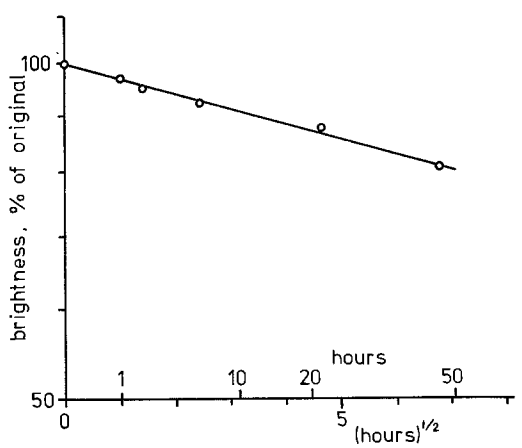

Fig. 5. Average maintenance of three samples of Zn_2SiO_4:Mn tested in this laboratory in the demountable fluorescent lamp.

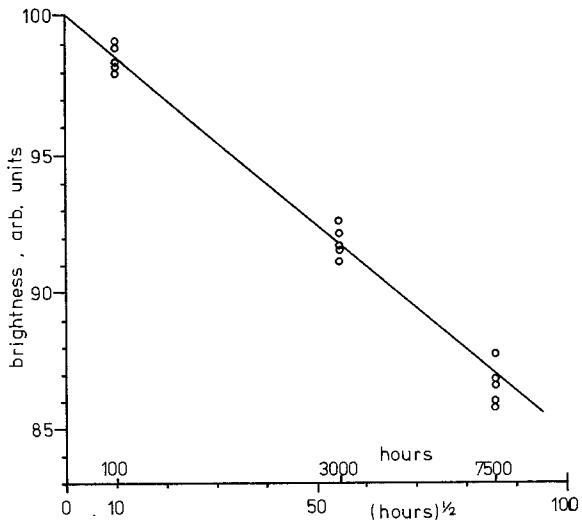

Fig. 6. Maintenances of Westinghouse 40W fluorescent lamps containing halophosphate phosphor. Each point represents a year with an average of more than 100 lamps.

lamp (100, 3000, and 7500 hr) were available, the approach to a straight line is evident.

Figures 7 and 8 correspond to experimental 40W lamps made by GE and containing either Zn_2SiO_4:Mn (Fig. 7) or $CaSiO_3$:Pb,Mn. (Fig. 8). The brightness data are taken from a table in a paper published in 1956 (7).

Figures 9 and 10 show data of 40W Sylvania lamps made back in 1948 when (Zn, Be)SiO_4:Mn was still commonly used. The data are taken as well as could be done, from figures in a 1949 publication (5). Figure 9 corresponds to production lamps, Fig. 10 apparently to experimental lamps.,

Considerable experimental scatter seems to be unavoidable in measuring lamp maintenances. For this reason, every point in Fig. 5-10 corresponds to not one, but to averages over many lamps. Some scatter still remains. However, the approach to straight lines in the figures is very obvious.

In routine maintenance tests of fluorescent lamps, the "zero-hour" brightness reading usually is done not immediately after the lamp is turned on, but after a short burn-in time. This time was about 1/2 to 1 hr for the data of Fig. 6, and is believed to be in the same order for Fig. 7-10. The question arises, what

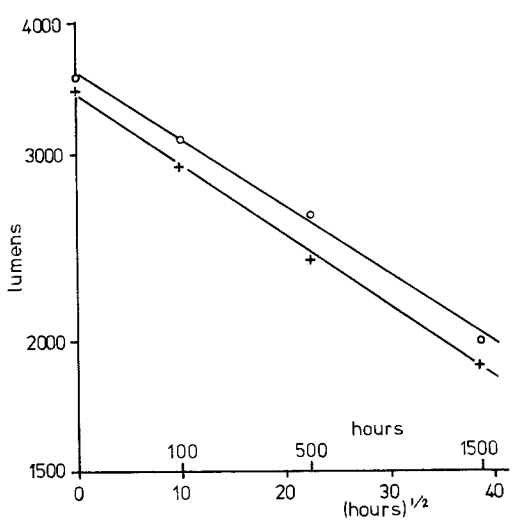

Fig. 7. Average maintenances of two sets (8 lamps each) of experimental 40W fluorescent lamps made by GE. The lamps contain two different samples of Zn_2SiO_4:Mn. Data from Ref. (7).

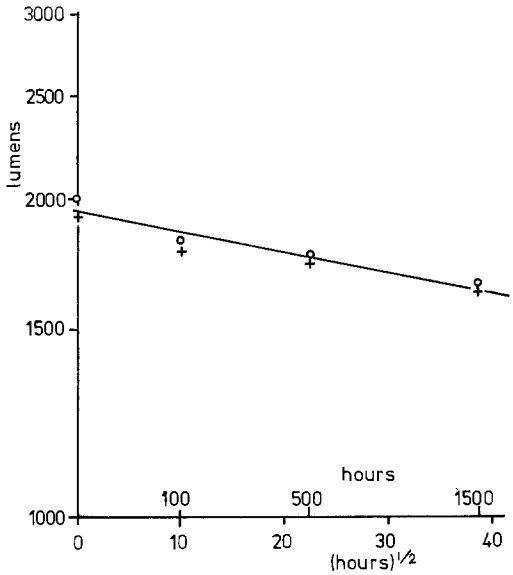

Fig. 8. Average maintenances of two sets (8 lamps each) of experimental 40W fluorescent lamps made by GE. The lamps contain two different samples of $CaSiO_3$:Pb,Mn. Data from Ref. (7).

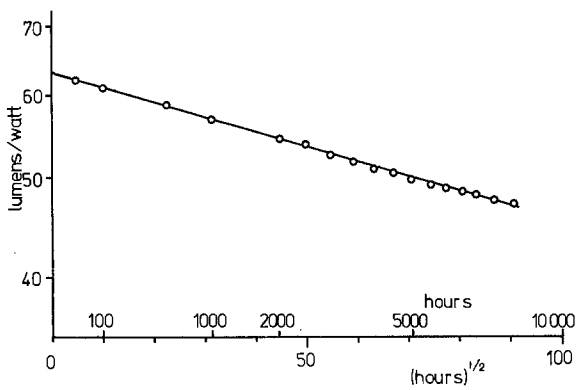

Fig. 9. Average maintenances of 20 40W fluorescent lamps made by Sylvania. The lamps contain a blend of 88% $(Zn,Be)_2SiO_4$:Mn and 12% $MgWO_4$. Replotted from a diagram in Ref. (5).

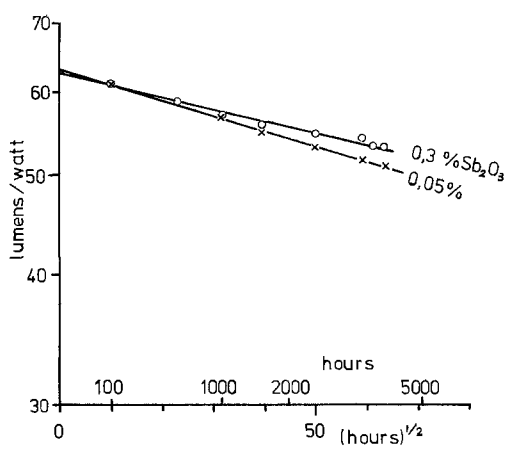

Fig. 10. Average maintenances of 40W fluorescent lamps made by Sylvania. The lamps contain a blend of 88% $(Zn,Be)_2SiO_4$:Mn and 12% $MgWO_4$. Two groups of lamps with different amounts of Sb_2O_3 added to the phosphor blends. Replotted from a diagram in Ref. (5).

happens during the very first time when the lamps are turned on?

The only published measurements covering also the first few minutes appear to be those by Vrenken *et al.* (25). Data were taken from a figure of that paper, as well as could be done, and replotted in Fig. 11. All points in Fig. 11 are on straight lines for times in excess of about 1 hr indicating Eq. [1] to be valid, and pointing to buildup of a dead surface layer as the dominant mechanism of long-time deterioration. The writer believes the additional deterioration during the first hour of operation to be caused by color center formation. This effect appears to come to an equilibrium between formation (by 185 nm u.v.) and bleaching (by 254 nm u.v.) within about 1 hr. Accepting this explanation, it appears from Fig. 11 that an addition of small amounts of cadmium to a halophosphate phosphor reduces the intensity of color center formation, but has little or no effect on the buildup of a dead surface layer.

Discussion and Final Conclusions

The observations and results described above point to the slow buildup of a nonluminescent but light absorbing surface layer on the phosphor particles, as the dominant mechanism of long-time phosphor degradation in fluorescent lamps. The layer is nonluminescent because its crystal structure is heavily damaged, perhaps approaching or reaching the amorphous state. Such damage can, in principle, be created by gas ions if their energy exceeds some threshold. This threshold is in the 20-25 eV range for zinc silicate and can be expected to be not too different in other lamp phosphors. The question is whether there are gas ions of that energy in a fluorescent lamp.

The mean energy of ions in the positive column of the gas discharge is little over $3/2\ kT$ ($\approx$ 0.04 eV), which certainly is too small to cause any damage. The mean energy of free electrons is higher, probably several eV, but the mass of an electron is too low to cause much havoc on the phosphor surface. A radial "sheath potential" of 10-15V near the lamp walls (26) caused by the very different mobilities of electrons and ions can accelerate ions towards the phosphor, and might at least partially be responsible, but is still on the low side. Several discrete energies are available, *e.g.*, light quanta of the ultraviolet radiation of 254 nm (= 4.9 eV), of 185 nm (= 6.7 eV), and several very weak lines going to more than 10 eV. Further energies are from the neutralization of Hg^+ (10.4 eV) and Ar^+ (15.7 eV) which both are liberated primarily in contact with a solid surface, *e.g.*, the phosphor. The overall situation is very complex but it seems that neither of the above energies reaches the threshold.

One might argue that a gas ion hitting the phosphor surface may have the combined energy of the sheath potential and of its neutralization. That would amount to about 20-25 eV for Hg^+ and to about 25-30 eV for Ar^+, and these energies appear to be high enough to cause atom displacement by collision on the phosphor surface. These and other details are still open for investigation.

Independent of details, the model of ion bombardment, or a related effect, building up a damaged and nonluminescent surface layer on the phosphor par-

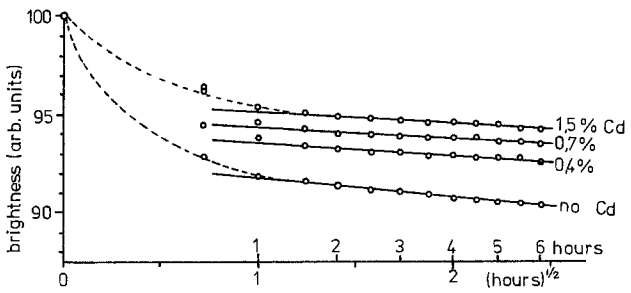

Fig. 11. Short-time maintenance of 40W fluorescent lamps containing halophosphate phosphor with different amounts of added cadmium. Replotted from a diagram in Ref. (25).

ticles permits the following conclusions. (*i*) The damaged surface layer is very thin, probably below 100Å even after strong deterioration of the phosphor. The layer grows in thickness proportional to (time)$^{1/2}$. (*ii*) Mercury simply adsorbed on top of the damaged layer is not likely involved. At least, there is no visible reason why such adsorption should lead to a deterioration-time dependence described by Eq. [1]. However, mercury buried in the dead layer may very well be involved. It simply contributes to the optical adsorption constant, α, in Eq. [3] but leaves the shape of the deterioration function [1] unchanged. It is at least conceivable also that the amount of mercury buried in the layer depends on the phosphor material. This point may warrant further study. (*iii*) Even without any contribution of buried mercury, the dead top layer has also an optical absorption on its own. That is particularly so for Zn_2SiO_4 because it contains so much u.v.-absorbing ZnO, and that may be a reason of its well-known relatively poor maintenance in fluorescent lamps. The same is the case for any other phosphor absorbing exciting u.v. directly into the host lattice. Optical absorption caused by impurities generally is much weaker and may largely disappear when the crystal becomes amorphous. It appears that phosphors with impurity absorption can, in principle, be expected to be more stable than otherwise comparable phosphors with host crystal absorption. That seems to be in agreement with general experience. (*iv*) The stability with which a phosphor resists damage by bombardment is a function of the binding energy between atoms of the material; the higher this energy the more stable the phosphor. This binding energy also determines the stability against thermal disruption; the higher the energy the higher the melting temperature. Consequently, phosphors whose host materials have the highest melting points likely are those which have the best maintenance in lamps. Examples are Y_2O_3 and various aluminates. Again, this is in general agreement with experience. (*v*) An oxidation of Mn^{2+} to Mn^{3+} in Mn-activated phosphors, a reduction of V^{5+} to V^{3+} in vanadate phosphors, or any similar oxidation or reduction observed during deterioration of a phosphor in a lamp can easily be understood for quasi-free atoms or ions kicked about the surfaces of the phosphor particles by primary energy quanta but not so easily for atoms deeper in the healthy lattice. From this point of view, oxidations and reductions are not the cause of deterioration but a consequence of the damage and the buildup of a dead layer on the phosphor particles. (*vi*) Color center formation appears to be a separate effect independent of bombardment damage. The tendency to form color centers must depend on the phosphor material. Zinc silicate shows little indication of it and halophosphates, where color centers are well known, apparently come rapidly to a near equilibrium between formation and bleaching (Fig. 11). The possibility exists that color center formation is not a major cause of long-time deterioration of any phosphor in fluorescent lamps. (*vii*) A barrier between gas discharge and phosphor, optically transparent for exciting ultraviolet but not for gas ions, should considerably improve long-time phosphor maintenance in fluorescent lamps. This barrier needs to be only very thin, about 100Å or less should already be effective, provided only that it is at least as stable against ion bombardment as the phosphor to be protected. This idea has already been anticipated in a recent patent (27) but, to our knowledge, is not yet used in practice.

Acknowledgment

The writer is indebted to Dr. F. M. Ryan of this laboratory for stimulating discussions and to one of the reviewers of this paper for supplying data on the displacement threshold of surface atoms on zinc silicate.

Manuscript submitted Feb. 2, 1982; revised manuscript received *ca.* Sept. 15, 1982.

Any discussion of this paper will appear in a Discussion Section to be published in the December 1983 JOURNAL. All discussions for the December 1983 Discussion Section should be submitted by Aug. 1, 1983.

Publication costs of this article were assisted by Westinghouse Research and Development Center.

REFERENCES

1. H. C. Froelich, *Trans. Electrochem. Soc.*, **87**, 429 (1945).
2. H. C. Froelich, *J. Appl. Phys.*, **17**, 537 (1946).
3. E. F. Lowry, W. S. Frolock, and G. A. Meyers, *Ill. Eng.*, **41**, 859 (1946).
4. E. F. Lowry, *ibid.*, **43**, 141 (1948).
5. E. F. Lowry, *Trans. Electrochem. Soc.*, **95**, 242 (1949).
6. D. Harrison, *This Journal*, **107**, 210 (1960).
7. G. Burns and J. Kastner, *ibid.*, **103**, 447 (1956).
8. G. Meister and R. Nagy, *J. Opt. Soc. Am.*, **36**, 696 (1946).
9. G. Kressin, *Techn. Wiss. Abh. Osram-Ges.*, **7**, 235 (1958).
10. L. Suchow, *This Journal*, **108**, 847 (1961).
11. J. H. Singleton and L. Suchow, *ibid.*, **110**, 36 (1963).
12. E. F. Apple, *ibid.*, **110**, 374 (1963).
13. R. W. Warren, F. M. Ryan, R. H. Hopkins, and J. van Broekhoven, *ibid.*, **122**, 752 (1975).
14. J. M. Flaherty, *ibid.*, **128**, 131 (1981).
15. O. Tada, K. Tominada, T. Kondo, and K. Ichinomiya, Paper 499 presented at The Electrochemical Society Meeting, Montreal, Canada, May 9-14, 1982.
16. W. Lehmann, F. M. Ryan, A. S. Manocha, and W. McAllister, Paper 500 presented at the Electrochemical Society Meeting, Montreal, Canada, May 9-14, 1982. To be published.
17. H. C. Froelich, *J. Opt. Soc. Am.*, **37**, 308 (1947).
18. K. H. Butler, "Fluorescent Lamp Phosphors," p. 71, Pennsylvania University Press, State College, PA (1980).
19. E. Streck, *Ann. Phys.*, **34**, 96 (1939).
20. W. Berthold, *Vac. Techn.*, **6**, 130 (1957).
21. G. T. Bauer, *This Journal*, **123**, 79 (1976).
22. L. W. Hobbs, *J. Am. Ceram. Soc.*, **62**, 267 (1979).
23. B. T. Kelly, "Irradiation Damage to Solids," p. 2, Pergamon Press, England (1966).
24. R. V. Stuart and G. K. Wehner, *J. Appl. Phys.*, **33**, 2345 (1962).
25. L. E. Vrenken, J. H. de Vette, and R. W. v.d. Wolf, *Ill. Eng.*, **59**, 59 (1964).
26. F. M. Ryan, *J. Lumin.*, **24/25**, 827 (1981).
27. M. Denko, Jpn. Pat. 55-137 661 (1980).

Preparation and Cathodoluminescence of CaS:Ce and $Ca_{1-x}Sr_xS$:Ce Phosphors

F. Okamoto[1] and K. Kato[1]

RCA Research Laboratories, Incorporated, 971-2 Zushi-machi, Machida City, Tokyo 194-02, Japan

ABSTRACT

Efficient CaS:Ce phosphors consisting of well-grown crystallites have been prepared by heating calcium carbonate containing an appropriate amount of cerium with sulfurizing flux. The flux consists of either elemental sulfur plus carbonates, or thiosulfates of alkali metals. Because of good crystallinity and large particle size, the phosphors prepared by the flux method are relatively stable against atmospheric carbon dioxide and water, yet have luminescence efficiency comparable to the best CaS:Ce prepared by the H_2S method. The emission spectrum of the flux-grown CaS:Ce phosphors is similar to that of the CaS:Ce prepared by the H_2S method, but shifted to shorter wavelengths by about 10-15 nm. $Ca_{1-x}Sr_xS$:Ce phosphors have also been prepared by the flux method. With the increase of the mol fraction of SrS, the lattice parameter increased linearly, and the emission spectrum shifted toward shorter wavelengths.

Alkaline earth sulfides have been known to be excellent and versatile phosphor hosts. A large number of different activators produce phosphors having different emission colors ranging from the near ultraviolet to the deep red (1-5). Calcium sulfide activated by trivalent cerium has been known as an excellent green-emitting phosphor (2). The cathodoluminescence efficiency and emission color are comparable to those of the best green-emitting ZnS-type phosphors. Furthermore, CaS:Ce phosphor shows much less brightness saturation at high beam currents (2). In recent years, cathode-ray phosphors are desired for operation at higher currents to get higher brightness, especially for applications in projection TV. The CaS:Ce phosphor is one attractive candidate for such application because of its small current saturation.

The alkaline earth sulfides are usually prepared by the sulfurization of the corresponding oxides or carbonates with hydrogen sulfide or carbon disulfide. These sulfides are also prepared by reducing the corresponding sulfates with hydrogen or carbon, or by reacting the corresponding oxides or carbonates with sulfur. Lehmann and Ryan (1, 2) prepared CaS:Ce phosphors by a two-step reaction; unactivated CaS was prepared by firing $CaSO_4$ in an atmosphere of H_2 and H_2S. Then the CaS mixed with Ce_2S_3, NH_4Cl, and sulfur was fired in argon atmosphere at 1200°C for 2 hr. Vij and Mathur (6, 7) prepared CaS:Ce phosphors by reducing $CaSO_4$ containing cerous nitrate [$Ce(NO_3)_3 \cdot 6H_2O$] with carbon in the presence of a large amount of Na_2SO_4 flux at 900°C for 2 hr. In this process the reduction of $CaSO_4$ to CaS, and the activation of CaS with Ce, were achieved in a single firing process at relatively low temperatures.

Lehmann, Vij, and Mathur (8) compared the CaS:Ce phosphors prepared at Lehmann's laboratory (2) with those prepared by Vij and Mathur (6, 7). They found that the latter phosphor consists of well-developed particles about 10 μm in size, having somewhat higher stability in a water slurry, but the luminescence efficiency is only approximately 30-40% of the former phosphor.

In this paper, we report new flux compositions to prepare CaS:Ce and $Ca_{1-x}Sr_xS$:Ce phosphors. The phosphors prepared by this method have good crystallinity, large particle size, and high luminescence efficiency. The results are compared with those of phosphors prepared by the other methods.

Experimental

X-ray diffraction.—Lattice parameters were determined by x-ray powder diffraction using a JEOL (Type JDX-7D) x-ray diffractometer with Ni-filtered CuK_α radiation. Sodium chloride was used as an internal standard.

Cathodoluminescence measurements.—Cathodoluminescence spectra were measured on powder samples packed into shallow stainless steel pans. Twelve samples were mounted on a rotating sample holder of a demountable cathode-ray tube. A focused electron beam was magnetically deflected to produce a raster of the desired size. The incident beam was normal to the sample face and the luminescence was observed from the bombarded side at an angle of 30° to the incident beam. The phosphors were typically excited by 8 kV electrons at approximately 0.1 $\mu A/cm^2$ current density at room temperature. Luminescence spectra were measured with a Nikon P-250 monochromator and an HTV-R376 photomultiplier. The spectral response of the monochromator and photomultiplier was calibrated with an EG&G Model 595 Standard Tungsten-Halogen Lamp.

Results and Discussions

Preparation.—The sulfurizing flux method is widely used for preparing rare earth oxysulfide phosphors (9-11). However, apparently no one has attempted to apply the sulfurizing flux method to prepare CaS, probably due to the *a priori* assumption that CaS cannot withstand hot water washing of the fluxed products because CaS is known to dissolve in water by decomposition. We found that the same flux method is applicable to prepare high quality CaS phosphors. The flux can be removed by washing with cold water without deteriorating the CaS in any appreciable amount. The CaS prepared by the flux method consisted of well-developed and nonaggregated particles. The particle sizes were much larger than those prepared by the nonflux method. It seems that good crystallinity and large particle size enhance chemical stability against water reducing the rate of dissolution. The lower dissolution rate allows the flux method to be used to prepare CaS.

Starting compositions.—All chemicals except sulfur were of reagent grade. The sulfur was of 99.999% purity. Calcium and strontium compounds used were either oxides, hydroxides, carbonates, or oxalates of calcium and strontium. The sulfurizing flux used was a mixture of sulfur and either sodium carbonate, potassium carbonate, or their combinations. The carbonates may be substituted up to 50 mol percent by lithium carbonate. Sodium or potassium thiosulfate was also used as a sulfurizing flux. To prepare phosphors, a source of activator is included in the starting mixture. Any elements known to be activators for CaS and SrS can be used. We have successfully tested activation with Ce, Eu, Mn, Sb, and Pb. For cerium activation, trivalent cerium compounds such as sulfate

[1] Present address: Corning Research, Incorporated, 971-2 Zushi-machi, Machida City, Tokyo 194-02, Japan.

Key words: inorganic, luminescence, synthesis, cathode-ray, current saturation, flux, calcium sulfide, strontium sulfide, cerium.

$[Ce_2(SO_4)_3 \cdot 8H_2O]$, nitrate $[Ce(NO_3)_3 \cdot 6H_2O]$, chloride $(CeCl_3 \cdot 7H_2O)$, or sulfide (Ce_2S_3) were used. The change in anions had no effect on the material and luminescence properties. The nominal concentration of cerium is expressed by the mol ratio to one mol of phosphor host (CaS or $Ca_{1-x}Sr_xS$) before firing. For example, $CaS:Ce_{0.001}$ means that the phosphor was prepared from a starting mixture containing one mol of $CaCO_3$ and 0.001 mol of cerium. The actual concentration of cerium in the produced phosphor has not been chemically analyzed.

The CaS:Ce phosphors cited in this paper were prepared from starting compositions consisting of $CaCO_3$, Na_2CO_3, sulfur, and $Ce_2(SO_4)_3 \cdot 8H_2O$. To prepare $Ca_{1-x}Sr_xS$:Ce, $CaCO_3$ was proportionally substituted by $SrCO_3$. The amount of Na_2CO_3 and sulfur was not critical to the particle size and the luminescence efficiency, but excess sulfur was always required for good reproducibility of results. The mol ratio of $CaCO_3$, Na_2CO_3 (anhydrous), and sulfur was usually 1:1:3 or 1:1:4. The concentration range of cerium studied was from 10^{-4} to 10^{-2} mol per one mol of $CaCO_3$.

Procedure.—The starting compositions were intimately mixed by ball milling. For uniform mixing of an extremely small amount of activator, slurry mixing was used. The mixture was placed in a covered alumina crucible. When high temperature and long heating were used, the crucible was put in a large alumina crucible, and the space between the two crucibles was filled with carbon to avoid oxidation of the reactants and products. The crucible with its contents was placed in a resistance-heated furnace with lid under ordinary atmospheres, and heated to about 800°-1200°C for 0.2 to 72 hr. It was then cooled to room temperature. During heating, sulfides and polysulfides of alkali metal are formed in the mixture and these dissolve substantially all of the calcium compounds and the activator source. During the cooling step, particles of the desired sulfide crystallize in the molten mass, which then solidifies. The solidified mass was crushed to a fine powder and then the flux was removed by dissolving and washing with cold deionized water. After rinsing with ethyl alcohol, the product was dried at 100°C.

CaS:Ce.—As mentioned previously, the CaS prepared by the sulfurizing flux method consisted of well-crystallized, independent particles. Figure 1 shows photographs of CaS:Ce phosphor particles prepared using the flux mixture of Na_2CO_3 and sulfur at different reaction temperatures and times. Particle size ranges from a few microns to submillimeters depending upon the reaction temperature and time. The higher the temperature and the longer the time, the larger the particle size. Table I gives the approximate particle size obtained at different firing conditions. The phosphors prepared by the flux method had a smaller dissolution rate in water than those prepared by nonflux method, as confirmed by the time variation of the pH and the conductance of the water containing dispersed phosphor particles. The good crystallinity and the large particle size (small surface-to-volume ratio) seems to enhance the stability against water. Particle growth was much slower

Table I. Particle size of $CaS:Ce_{0.001}$ prepared using the flux mixture of Na_2CO_3 and sulfur at different firing conditions

Reaction temp (°C)	Reaction time (hr)	Max. size (μm)	Average size (μm)
900	6	10	5
900	72	37	26
1000	4	20	12
1000	12	23	14
1100	4	30	23
1100	72	120	70

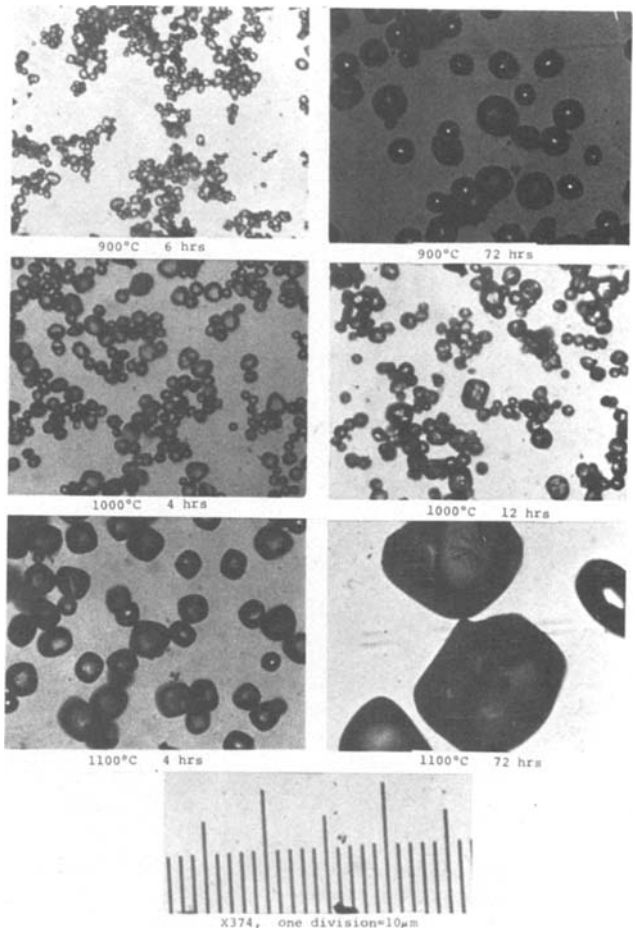

Fig. 1. Photomicrographs of particles of $CaS:Ce_{0.001}$ prepared using the flux mixture of Na_2CO_3 and sulfur at different firing conditions. (Observed under Nikon differential interference microscope.)

for the flux combination of K_2CO_3 and sulfur than for the combination Na_2CO_3 and sulfur.

The yield of CaS:Ce was studied for different batch sizes between 14 and 170g of the starting mixture. We found that yields were in the range 85-95% of the theoretical yield independent of batch size. The main losses in the yield are caused by fused mass stuck to the crucible wall, and by the washing away of small particles in the process of removing the fluxes by decantation. The unactivated CaS appeared as a slightly discolored white powder. It had the NaCl type of structure with the lattice parameter $a = 5.696$A (13). The body color of the cerium-activated CaS changes from light brown through a light yellowish green to light yellow as the cerium concentration increases from 10^{-4} to 10^{-2} mols.

$Ca_{1-x}Sr_xS$:Ce.—The sulfurizing flux method is also applicable to the preparation of SrS by replacing $CaCO_3$ with $SrCO_3$ in the starting mixture. Because SrS decomposes in contact with water much more easily than CaS, the flux was first washed with the minimum amount of cold deionized water, then with a large quantity of ethyl alcohol.

Solid solutions, $Ca_{1-x}Sr_xS:Ce_{0.001}$ ($x = 0$-1), were also prepared by the reaction at 1100°C for 4 hr. Increasing the strontium fraction causes the body color to change from yellowish green to light bluish green. The crystal structure was NaCl-type in the whole range of x, and the lattice parameter increased linearly with the mol fraction of SrS as shown in Fig. 2. This result indicates that the solid solution obeys Vegard's law, and also suggests that the flux method produces the solid solution having the same mol fraction as added to the starting mixture. Chemical stability

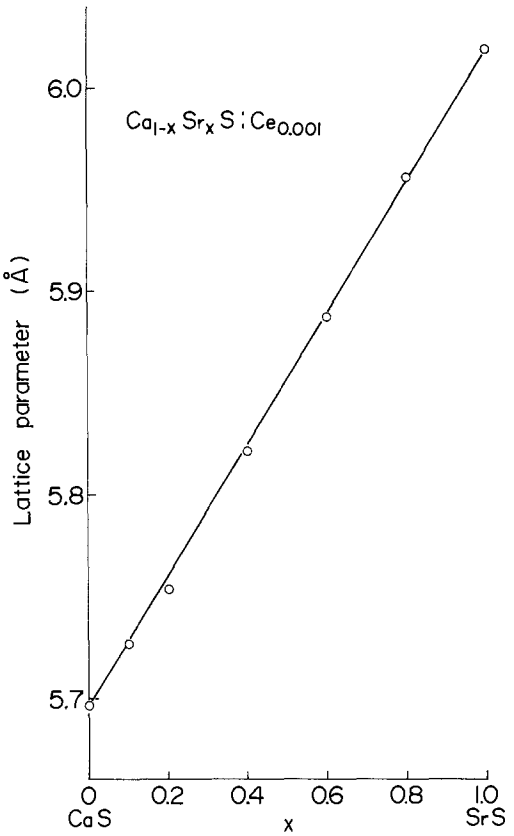

Fig. 2. Lattice parameters of $Ca_{1-x}Sr_xS:Ce_{0.001}$ as a function of the mol fraction of SrS.

against water decreases with increasing strontium content.

Other alkaline earth sulfides such as MgS and BaS could not be prepared by the sulfurizing flux method because these sulfides are very easily attacked by water.

Cathodoluminescence

Cathodoluminescence spectrum and efficiency.—Figure 3 shows that the cathodoluminescence spectra of CaS:$Ce_{0.001}$ prepared by the sulfurizing flux method,

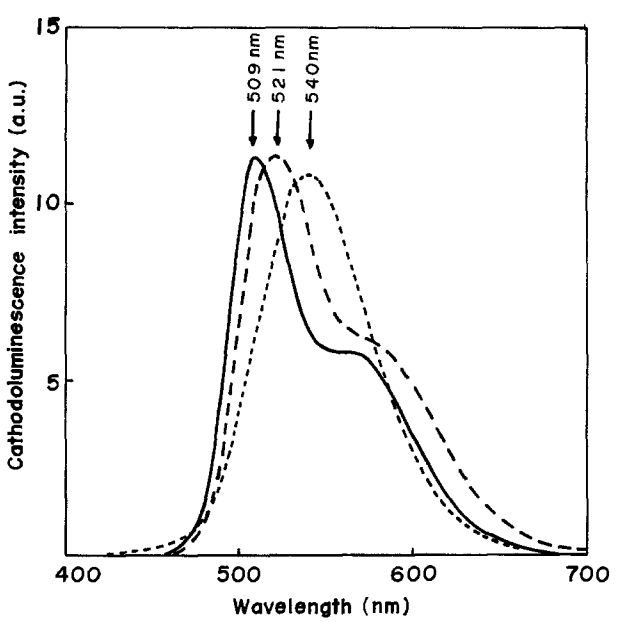

Fig. 3. Cathodoluminescence spectra of CaS:$Ce_{0.001}$ (———), CaS:Ce (Lancaster) (---), and (Zn,Cd)S:Cu,Al (.....), measured at 8 kV and 2 $\mu A/cm^2$.

CaS:Ce [2] prepared by the non-flux method, and (Zn, Cd)S:Cu,Al.[2] They all had comparable peak intensities. However, the emission band of CaS:$Ce_{0.001}$ was narrower and was more shifted toward shorter wavelengths further away from the eye sensitivity maximum than the others. These two factors account for the lower visual efficiency of CaS:$Ce_{0.001}$. The emission color was visibly different; green for CaS:$Ce_{0.001}$ and yellowish green for CaS:Ce (Lancaster) and (Zn,Cd)S:Cu,Al. Table II summarizes the cathodoluminescence characteristics of these three phosphors measured at 8 kV and 2 $\mu A/cm^2$.

The luminescence efficiency depended on beam current. Figure 4 shows that the efficiency of (Zn,Cd)S:Cu,Al drops markedly as current density increases, whereas the efficiency drops are small for the CaS:Ce phosphors. Because the beam was applied continuously (not pulsed), the measured results include both current saturation and heat effects.

Comparison of the sulfurizing flux method with the flux-reduction method.—For comparison, we also prepared CaS:Ce by the flux-reduction method described in Ref. (6, 7), that is, by reducing $CaSO_4$ containing cerium activator with carbon in the presence of a large amount of Na_2SO_4 flux. The CaS:Ce prepared by this method consisted of well-developed large particles, and the emission peaks were shifted to shorter wavelengths similar to our phosphors prepared by the sulfurizing flux method. However, the luminescence efficiency was always much lower. Because carbon powder and a carbon crucible were used in the reaction, the carbon stoichiometry was very difficult to control. If an insufficient amount of carbon was used, the reduction was incomplete, but if too much was used, excess carbon remained in the product. Unreacted $CaSO_4$ or excess carbon was difficult to remove from the fluxed product. This seems to be one of the reasons for the low luminescence efficiency of the phosphor prepared by the flux-reduction method. On the other hand, our sulfurizing flux method uses an excess amount of sulfur and Na_2CO_3, and the fluxes such as sodium sulfide and polysulfides formed at high temperature are easily removed by water washing because these fluxes are very soluble in water.

Effect of sodium ions on Ce^{3+} luminescence in CaS:Ce.—Lehmann (8) pointed out that the emission peak of the CaS:Ce prepared by the flux-reduction method (6, 7) is shifted to shorter wavelengths than that of the CaS:Ce prepared by the nonflux method (1, 2). We found almost exactly the same peak shifts in our CaS:Ce phosphors prepared by the sulfurizing flux method. This result suggests that the peak shifts are

[2] Both phosphors were furnished by RCA Picture Tube Division, Lancaster, Pennsylvania. The CaS:Ce was prepared by reacting $CaCO_3$ containing 1000 ppm cerium with H_2S at 1200°C for 2 hr, followed by cooling in nitrogen atmosphere. The phosphor consisted of aggregated small particles of a few microns in size. In the following, the phosphor is designated as CaS:Ce (Lancaster). (Zn,Cd)S:Cu,Al was the standard phosphor for color TV application.

Table II. Cathodoluminescence characteristics of CaS:$Ce_{0.001}$,CaS:Ce (Lancaster), and (Zn,Cd)S:Cu,Al, measured at 8 kV and 2 $\mu A/cm^2$

Phosphor	CaS:$Ce_{0.001}$	CaS:Ce (Lancaster)	(Zn,Cd)S:Cu,Al
Peak position (nm)	509	521	540
Relative peak intensity	103.8	105.1	100.0
Relative energy efficiency	100.3	114.5	100.0
Relative visual efficiency	87.0	103.1	100.0
Color coordinates:			
x	0.318	0.356	0.333
y	0.582	0.583	0.602

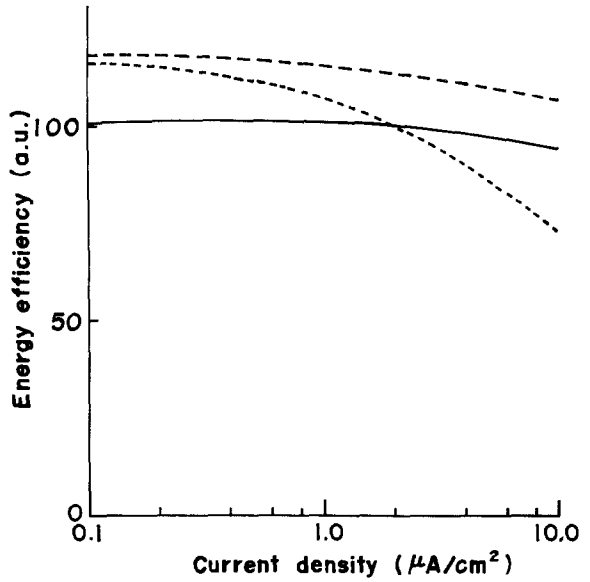

Fig. 4. Energy efficiency as a function of current density for $CaS:Ce_{0.001}$ (———), CaS:Ce (Lancaster) (---), and (Zn,Cd)S: Cu,Al (.....), measured at 8 kV.

caused by sodium ions incorporated into the CaS:Ce because, in both methods, a large amount of sodium compound is used as a flux component. In fact, in the CaS:Ce phosphors prepared by the sulfurizing flux method, 0.06-0.08 weight percent (w/o) of sodium was detected by atomic absorption spectrophotometry, whereas the CaS:Ce (Lancaster) contained only 0.004 w/o of sodium.

To confirm the effect of sodium ions on the peak shift, CaS:Ce phosphors were prepared using the starting compositions with or without sodium by the nonflux method, that is, by sulfurization with carbon disulfide vapor carried by nitrogen gas flow at 850°C for 5 hr. The emission spectra of the phosphors thus prepared were compared with each other. The results are given in Table III, which shows that the emission peak of the phosphors prepared in the presence of sodium was shifted to shorter wavelengths from those of the other phosphors. From this result, it is clear that the peak shift is due to the incorporation of sodium into CaS-lattice, and not due to the difference in cerium concentration or to the other unknown impurities which might be introduced from fluxes. This is further supported by the fact that our CaS:Ce was prepared using fluxes different from Vij's (6, 7), but both showed a very similar peak shift. CaS:Ce prepared using K_2CO_3 (with or without Li_2CO_3) as a flux component also showed the peak shift similar to that found for CaS:Ce prepared using Na_2CO_3-flux. From these results, we conclude that the peak shift is caused by the incorporation of alkali metal ions into the CaS-lattice as a charge compensator for trivalent cerium ions.

In the case of $CaS:Eu^{2+}$, the peak position of the emission spectrum was not affected by the presence of alkali metal ions (12). This is probably due to the fact that divalent Eu ions do not need charge compensation in the CaS-lattice.

Effect of chloride ions on Ce^{3+} luminescence in CaS:Ce.—The good results we obtained with luminescence efficiency in CaS:Ce tend to refute Lehmann's statement (2) that the presence of halogenide ions is essential to strong emission. To explore this further, we prepared CaS:Ce by the sulfurizing flux method using a starting mixture containing a large amount of NaCl or NH_4Cl. We did not find any efficiency improvement. In general, our negative results on the effect of chloride ions on luminescence properties tend to agree with the observation by Vij and Mathur (8). However, it may be that the effect of chloride ions is overwhelmed by the large quantity of sodium ions in the CaS phosphors prepared by the flux methods.

Dependence of luminescence characteristics on Ce-concentration.—The emission spectrum shifted to longer wavelengths as the cerium concentration increased from 10^{-4} to 10^{-2} mol. Efficient phosphors were obtained for CaS containing about 10^{-3} mol of cerium. Table IV gives the peak position of the main emission band and also the x,y-coordinates of the cathodoluminescence.

$Ca_{1-x}Sr_xS:Ce_{0.001}$ (x = 0 to 1).—The emission spectrum consisted of main and minor peaks similar to that of CaS:Ce as shown in Fig. 5. As the mol fraction of strontium increased, the emission peak shifted toward shorter wavelengths. Accordingly, the emission color changed from yellowish green to bluish green. Luminescence efficiency decreased with increasing strontium fraction. The peak wavelength shifted linearly with the mol fraction of SrS as shown in Fig. 6. Table V gives the lattice parameter, the peak position of the main emission band, and the x,y-coordinates of the cathodoluminescence. The x,y-coordinates of $Ca_{1-x}Sr_xS:Ce_{0.001}$ and the other green phosphors of interest are plotted in Fig. 7.

Summary and Conclusions

We have shown that the sulfurizing flux method widely used to prepare rare earth oxysulfides is applicable to the preparation of CaS, SrS, and their solid solutions. If an activator source is added to the starting mixture, the corresponding phosphor is obtained

Table III. Cathodoluminescence characteristics of $CaS:Ce_{0.001}$ prepared by nonflux method using different starting compositions

Starting composition: $CaCO_3$ + $0.001Ce_2(SO_4)_3 \cdot 8H_2O$	Phosphor phase	Peak position (nm)	Color coordinates x	Color coordinates y
+ $0.05Na_2CO_3$	CaS:Ce,Na	508	0.296	0.578
+ 0.05NaCl	CaS:Ce,Na,Cl	508	0.303	0.577
+ (None)	CaS:Ce	517	0.342	0.581
+ $0.1NH_4Cl$	CaS:Ce,Cl	521	0.356	0.578
—	CaS:Ce (Lancaster)	521	0.354	0.587

Table IV. Dependence of cathodoluminescence characteristics of $CaS:Ce_x$ on cerium concentration

Ce-concentration x	Peak position (nm)	Color coordinates x	Color coordinates y
1.0×10^{-4}	504	0.288	0.558
5.0×10^{-4}	506	0.294	0.571
7.5×10^{-4}	506	0.299	0.573
1.0×10^{-3}	507	0.303	0.574
2.5×10^{-3}	509	0.322	0.579
5.0×10^{-3}	512	0.350	0.571
1.0×10^{-2}	516	0.376	0.564

Table V. Dependence of lattice parameter and cathodoluminescence characteristics of $Ca_{1-x}Sr_xS:Ce_{0.001}$ on the mol fraction of SrS

Composition x	Lattice parameter (A)	Peak position (nm)	Color coordinates x	Color coordinates y
0	5.696 (5.6948*)	508	0.317	0.579
0.2	5.754	504	0.299	0.566
0.4	5.822	501	0.279	0.551
0.6	5.887	494	0.249	0.522
0.8	5.956	488	0.217	0.477
1.0	6.018 (6.020**)	483	0.198	0.435

* From Ref. (13).
** From Ref. (14).

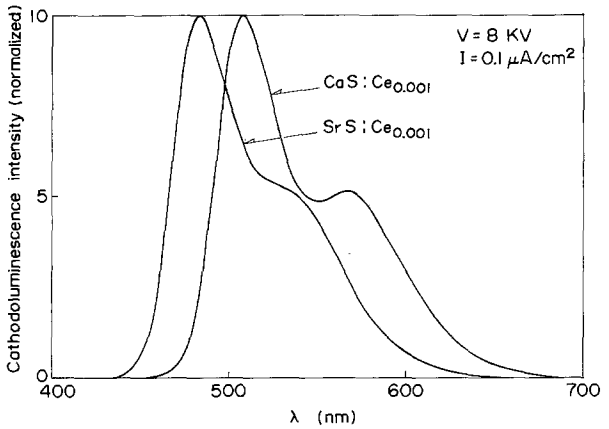

Fig. 5. Cathodoluminescence spectra of CaS:$Ce_{0.001}$ and SrS:$Ce_{0.001}$.

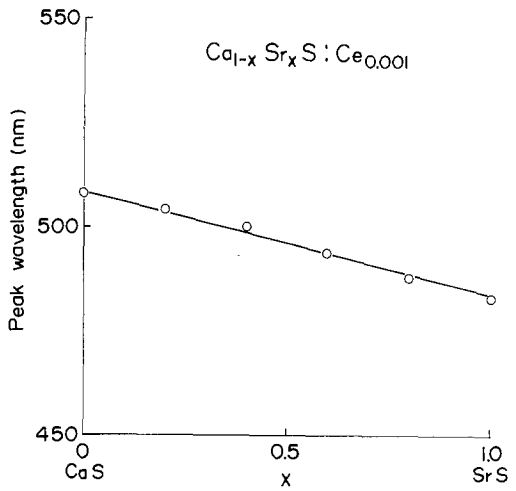

Fig. 6. Peak wavelength of the main emission band of $Ca_{1-x}Sr_xS$:$Ce_{0.001}$ as a function of the mol fraction of SrS.

in a single firing process. Sulfides prepared by the flux method consist of well-crystallized and nonaggregated particles. The higher the reaction temperature, and the longer the reaction time, the larger the particle size. We have obtained CaS particles ranging in size from a few microns to a fraction of a millimeter. Because of good crystallinity and large particle size, the phosphors prepared by the flux method are relatively stable against atmospheric carbon dioxide and water. This made it possible, at the final stage of the flux method, to wash away the flux without deteriorating the CaS phosphor particles to any appreciable extent. The flux method uses a moderately low temperature (900°-1100°C) without any reactive gas, and is practical for a large quantity production. Another advantage is the easy control of crystallite size by reaction temperature and time. The yield of CaS:Ce was 85-95% of theoretical.

The CaS:Ce phosphors prepared by our flux method had high luminescence efficiencies comparable to those prepared by the H_2S method. The emission spectrum of the flux-grown CaS:Ce phosphors was similar to that of the CaS:Ce prepared by the H_2S method, but shifed to shorter wavelengths by about 10-15 nm. Cause for the shift is possibly due to sodium or the other alkali metal ions introduced into the CaS lattice from the flux. Increasing Ce-concentration shifted the emission bands toward longer wavelengths. Phosphor containing about 10^{-3} mol of cerium had the highest luminescence efficiency. Chloride ions had no effect on the emission properties of the flux-grown CaS:Ce. With increasing mol fraction of SrS, the lattice parameter of $Ca_{1-x}Sr_xS$:Ce increased linearly, and the emission spectrum shifted toward shorter wavelengths.

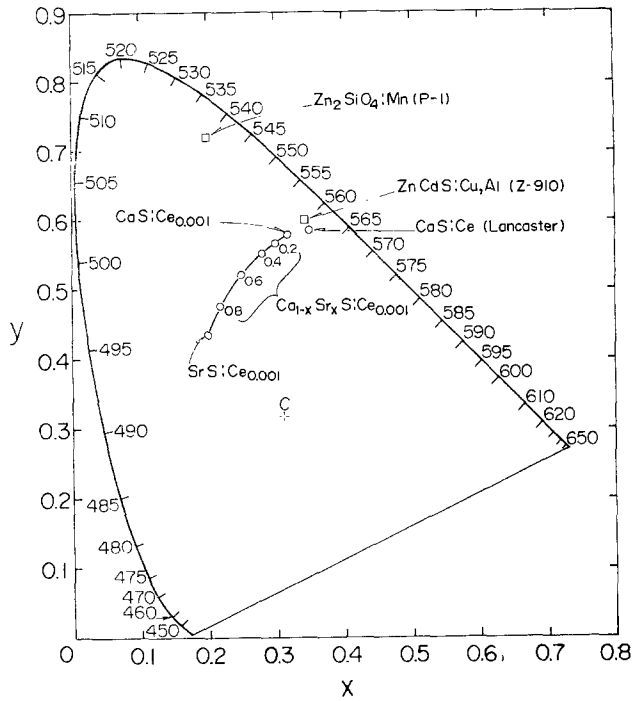

Fig. 7. X,y-coordinates of the cathodoluminescence of $Ca_{1-x}Sr_xS$:$Ce_{0.001}$ and other green phosphors of interest.

The sulfurizing flux method is also applicable to the preparation of CaS and SrS phosphors activated with elements other than trivalent cerium. Other alkaline earth sulfides such as MgS and BaS could not be prepared by the flux method because they were very easily attacked by water.

Acknowledgments

The authors wish to thank E. O. Johnson for his stimulating discussions and continuing encouragement during the course of this work, and K. Ametani for his valuable advice and chemical analysis of the phosphors. Thanks are also due to T. Oka for his assistance in the cathodoluminescence measurements, and to Y. Okada for setting up the demountable cathode-ray tube system. The authors are indebted to M. R. Royce and D. Shaffer of the RCA Picture Tube Division, Lancaster, Pennsylvania, for providing us with samples of their CaS:Ce and (Zn,Cd)S:Cu,Al.

Manuscript submitted April 14, 1982; revised manuscript received *ca.* Sept. 14, 1982.

Any discussion of this paper will appear in a Discussion Section to be published in the December 1983 JOURNAL. All discussions for the December 1983 Discussion Section should be submitted by Aug. 1, 1983.

Publication costs of this article were assisted by RCA Research Laboratories, Incorporated.

REFERENCES

1. W. Lehmann, *This Journal*, **117**, 1389 (1970).
2. W. Lehmann and F. M. Ryan, *ibid.*, **118**, 477 (1971).
3. W. Lehmann, *ibid.*, **118**, 1164 (1971).
4. W. Lehmann and F. M. Ryan, *ibid.*, **119**, 275 (1972).
5. W. Lehmann, *J. Lumin.*, **5**, 87 (1972).
6. D. R. Vij and V. K. Mathur, *This Journal*, **122**, 310 (1975).
7. D. R. Vij, V. K. Mathur, Virendra Shanker, and P. K. Ghosh, *J. Phys. D: Appl. Phys.*, **9**, 1509 (1976).
8. W. Lehmann, D. R. Vij, and V. K. Mathur, *This Journal* (Discussion Section), **122**, 1743 (1975).
9. M. R. Royce, U.S. Pat. 3,418,246 (1968).
10. P. N. Yocom, U.S. Pat. 3,418,247 (1968).

11. M. R. Royce and P. N. Yocom, U.S. Pat. 3,502,590 (1970).
12. K. Kato and F. Okamoto, To be published in *Jpn. J. Appl. Phys.*, **22**, 76 (1983).
13. H. E. Swanson, N. T. Gilfrich, and M. I. Cook, NBS Circular 539, **7**, 15 (1957).
14. H. E. Swanson, N. T. Gilfrich, and M. I. Cook, *ibid.*, **7**, 52 (1957).

Long-Term Persistency of X-Ray Intensifying Phosphor Screens

P. De Maayer* and R. Bollen*

Agfa-Gevaert N. V., R and D Laboratories, Mortsel, Belgium

ABSTRACT

Two methods are presented to measure the photographic effect of long-term persistency in x-ray intensifying screens. The influence of afterglow on the sensitometric characteristics of screen-film systems has been studied, respectively, as a function of time and of excitation radiation level. Data accumulated for most current and potential x-ray phosphors prove that a certain persistency level may be tolerated without any risk of ghost images.

The overall performance profile of x-ray intensifying screens depends on a number of phosphor characteristics. Luminescence brightness under x-ray excitation and resolution, or signal modulation transfer are functions of the intrinsic optical properties of the phosphor material, and of the binder system used in screening the phosphor. Conversion efficiency, noise equivalent x-ray absorption, position of the K-edge of the primary absorbing element of the luminescent compound, as well as its specific weight have their bearing on the signal-to-noise ratio and the overall image quality.

When optimizing the diagnostic image quality of screen-film systems for medical and industrial radiography, or when "screening" or evaluating potential candidate materials for this application, other "lesser" properties may be decisive for the choice of either concept or material, or both. One of these material characteristics is afterglow or persistency.

We have studied the photographic effect of long-term persistency (afterglow with relaxation times longer than 1-5 min) both as a function of radiation excitation level and as a function of time after excitation. The methods used and the values generated may be of direct interest to screen-film manufacturers, as they allow for direct assessment of the possible adverse effects of persistency on diagnostic x-ray imaging.

Experimental and Evaluation Procedure

A pair of screens is made from the phosphor to be evaluated by using standard doctor blade dispersion coating techniques. The exact nature of binders and solvents used is not relevant to the method, nor are the pigment-binder ratios and coating thicknesses.

In our studies, the binder system consisted of a mixture of an acrylic resin and a cellulose ester. A multisolvent combination, comprising butanone, methylglycol, and ethylacetate was used, while the incorporation of dispersing agents and plasticizers is known to those skilled in the art of screen making. A pigment-binder weight ratio 8/1 was chosen, irrespective of phosphor density or specific weight. The pigment-binder layers were coated to an average phosphor coating weight of 45 mg/cm². Screens currently on the market span a thickness range of 30 to 60 mg/cm².

Method I: Afterglow vs. Time

The measurement of long-term persistency proceeds as follows:

(*i*) Persistency registration: Part of the screens is exposed to a high, uniform x-ray dose, E_{exc}, measured directly by means of an Ionex 2500/3 dosemeter. Unfiltered, 80 kVp, large focus tungsten radiation is used from a standard Philips tube. After 1 min, the screens are brought in close contact with the two sides of regular double coated x-ray film in a vacuum sealed, light tight plastic bag. This so-called Vacumat bag obviates the need for any particular cassette and ensures ideal screen-film contact. For blue and/or u.v. emitting phosphors Agfa-Gevaert Curix RP1 film is used, green sensitized Eastman Kodak Ortho G film for green-emitting phosphors. The screens are left in contact with these films for varying times.

(*ii*) Sensitometric exposure: Before processing the film, a further series of exposures is made at right angles to the first excitation exposure. Small focus, 80 kVp, tungsten radiation is used, filtered by an Ansi Ph 2.43 standard test object for chest radiography. By varying the x-ray tube *vs.* screen-film system distance a sensitometric step wedge is created with exposure increments of $\Delta \log E = 0.10$ on both pre-exposed and nonexposed parts of the films. After development, we can now generate the respective sensitometric diagrams D *vs.* $\log E$, where D is the transmission density of the processed film.

(*iii*) Determination of equivalent persistency dose $E_{per\text{-}eq}$: As is shown in Fig. 1. for any given reference dose E_{ref} used for sensitometric exposure, the density increase resulting from persistency can be determined. A dose $E_{per\text{-}eq}$ needed to cause an equivalent density increase in the nonexcited area can be defined, and

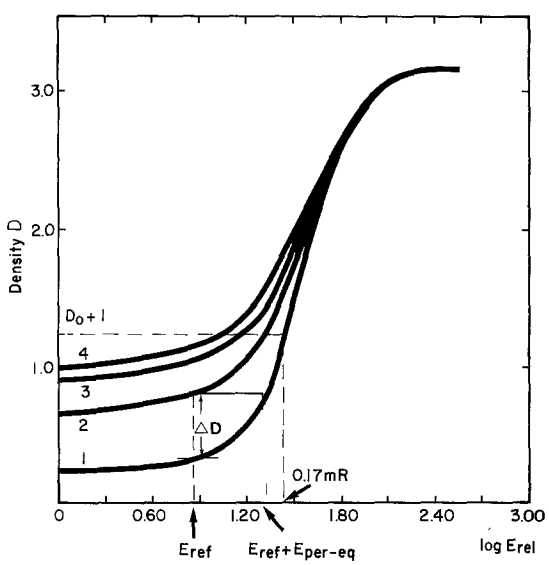

Fig. 1. Sensitometric curves for the nonexcited screen area, 1, and after 5 min, 2, 30 min, 3, and 24 hr, 4, persistency registration at the pre-excited screen area for the MR 400/Curix RP1 combination (Method I).

* Electrochemical Society Active Member.
Key words: coatings, x-ray, luminescence.

will be a function of E_{ref}. The most stringent condition for the phosphor occurs at $E_{ref} = 0$, as the extrapolated value of $E_{per\text{-}eq}$ will be largest at this point and perceptibility of density variations, caused by afterglow, greatest in the range of lowest density. On the sensitometric curves, the equivalent persistency dose may be deduced directly from the dose needed to obtain a density increase in the nonexcited area equal to the fog level of the curves, including the effect of persistency.

(*iv*) Definition of persistency ratio (*PR*): Long-term persistency in x-ray phosphors may best be characterized by the persistency ratio $PR = E_{exc}/E_{per\text{-}eq}$ at $E_{ref} = 0$. Since the exposure scale is logarithmic, the logarithm of *PR* is actually the most practical measure of the eventual photographic effect of afterglow on the radiographic image.

Method II: Afterglow vs. Excitation Radiation Level

This second evaluation method roughly follows the outline of the previously described procedure. It differs mainly in the construction of sensitometric curves for screen areas receiving different amounts of excitation exposure, and after having given persistency ample time to register on the silver halide medium (72 hr). The exact values of these pre-exposure energies will depend on the magnitude of the persistency effect, but typically exposures are given from 0 to 20 Röntgen with increments of 5R.

The values *Y*, seen in Fig. 2. directly correlate to persistency and, actually, define the extra exposure to be given to the nonexcited screen area (curve 1) in order to cause an equivalent photographic effect. By a simple mathematical derivation, we find

$$\log (\text{antilog } Y - 1) = \log (E_{per\text{-}eq}/E_1)$$

where E_1 is the dose needed to obtain a density of 1.0 above fog level, and is a function of screen-film system sensitivity; $E_{per\text{-}eq}$ is an equivalent dose indicating the effect of persistency for a particular excitation level (Fig. 2). In Fig. 3, log $(E_{per\text{-}eq}/E_1)$ is plotted as a function of excitation dose. From this plot we deduce the dose A yielding sufficient afterglow, to cause a density 1.0 above fog, *i.e.*, $E_{per\text{-}eq}$ equals E_1.

In this second method, we define afterglow by the ratio A/E_1. Again, the logarithmic value will be of more direct relevance to the potential disturbance of the radiographic image.

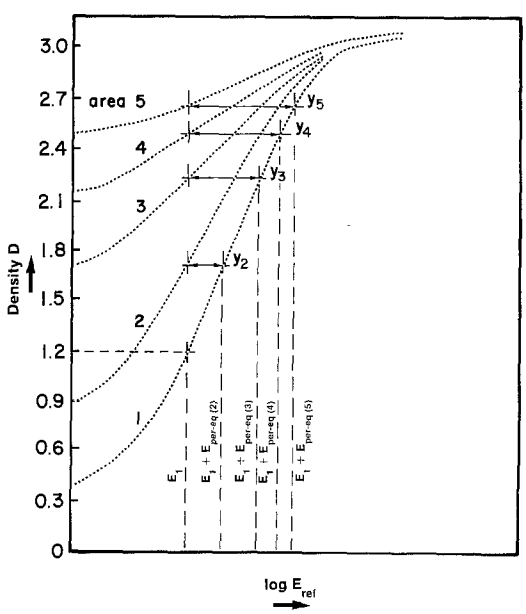

Fig. 2. Sensitometric curves for the MR 400/Curix RP1 screen-film system for the nonexcited area, 1, and after 72 hr persistency registration of screen areas which received a pre-excitation exposure of 5, 10, 15, and 20 Röntgen (curves 2-5) (Method II).

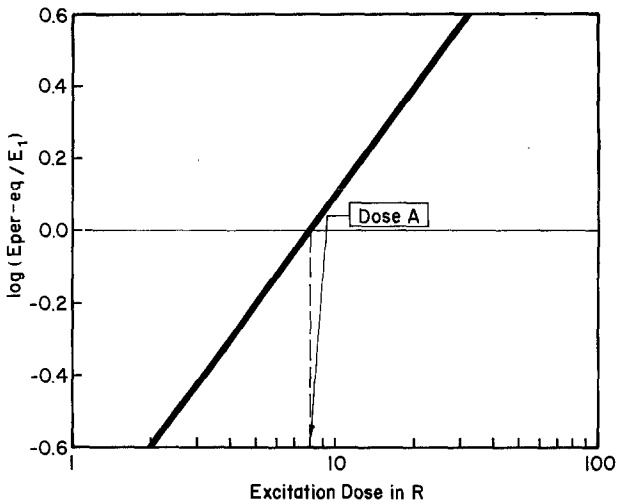

Fig. 3. Plot of log $(E_{per\text{-}eq}/E_1)$ as a function of excitation dose E_{exc}. Dose A yields sufficient persistency to cause a transmission density increase of 1.0 above fog level of the processed x-ray film.

Results

Long-term persistency of MR 400 screens as a function of time.—The first evaluation procedure was applied to Agfa-Gevaert MR 400 screens in combination with Curix RP1 film. These screens, based on LaOBr: Tb^{3+} phosphor, were given a pre-exposure of 8R. After contact with the films for 5 min, 30 min, and 24 hr, these were given a sensitometric exposure and processed. The results are shown in Table I and Fig. 1. A dose of 0.17 mR was required in the nonexcited area in order to obtain an optical film transmission density of 1.0 above fog level. Figure 4 indicates how, in this particular case, the afterglow becomes negligible after approximately 60 min.

Afterglow as a function of exposure energy level.—The results of our investigation of a number of rare-earth x-ray phosphors as well as of $CaWO_4$, their "classical" counterpart, is summarized in Table II. For some phosphors, several lots from the same supplier have been evaluated indicating their reproducibility. Figures 2 and 3 are typical results for the LaOBr: Tb^{3+} used in our MR 400 screens. From Fig. 3, we note the linear increase in persistency with excitation level over the complete excitation range studied.

Discussion

The question we have to answer is whether or not the levels of persistency measured for x-ray phosphors will be of consequence to image quality through the generation of ghost images. As can be seen from Fig. 4, the afterglow decay times of the screens are generally long compared to the time between successive exposures. With modern fast film-changers working up to 8 exposures per sec, a cumulative effect takes place and eventually problems may occur. In industrial applications, the effect may be primarily caused by the extremely high doses that are sometimes used.

Table I. Long-term persistency of MR 400 screens as a function of time

Time of contact (min)	$E_{per\text{-}eq}$[a] × 10^{-8}R	$E_{exc}/E_{per\text{-}eq}$[b]	log $(E_{exc}/E_{per\text{-}eq})$
5	0.11	72,700	4.84
30	0.14	57,100	4.76
1440 (24 hr)	0.15	53,300	4.73

[a] For $E_{ref} = 0$.
[b] $E_{exc} = 8$ R.

Table II. Long-term persistency of various x-ray phosphors

Phosphor type	Lot specification	E_{exc}/E_{per-eq}	log (E_{exc}/E_{per-eq})
LaOBr:Tb^{3+} (high brightness)	Lot I	9.7×10^4	4.99
	Lot II	6.7×10^4	4.83
	Lot III	4.5×10^4	4.65
LaOBr:Tb^{3+} (fine-grained)	Lot I	1.9×10^4	4.34
(low brightness)	Lot II	2.2×10^4	4.28
LaOBr:Tb,Yb (killed, low conversion efficiency)		None ($>10^5$)	5.0
LaOBr:Tm^{3+}		None	
$Y_2O_2S:Tb^{3+}$	Several suppliers	None	
$CaWO_4$	Several suppliers	None	
$Gd_2O_2S:Tb^{3+}$	Several suppliers	None	
$Y_2O_3:Gd^{3+}$		2.8×10^4	4.45
BaFCl:Eu^{2+}	Supplier A: lot I	1.2×10^3	3.08
	lot II	2.2×10^3	3.34
	lot III	3.3×10^4	4.52
	Supplier B: lot I	8.3×10^4	4.92
	lot II	3.9×10^4	4.59
	Supplier C	None	
	Supplier D	None	

In order to determine our maximum tolerable persistency, we have to go back to the sensitometric curve of the screen-film system (Fig. 5). We have chosen a relative exposure energy scale, since the exact position of the sensitometric curve will depend on the actual system sensitivity. The persistency values resulting from our evaluation do not depend on system sensitivity; however, the effect on image quality does, as this is a direct function of the position of the sensitometric curve.

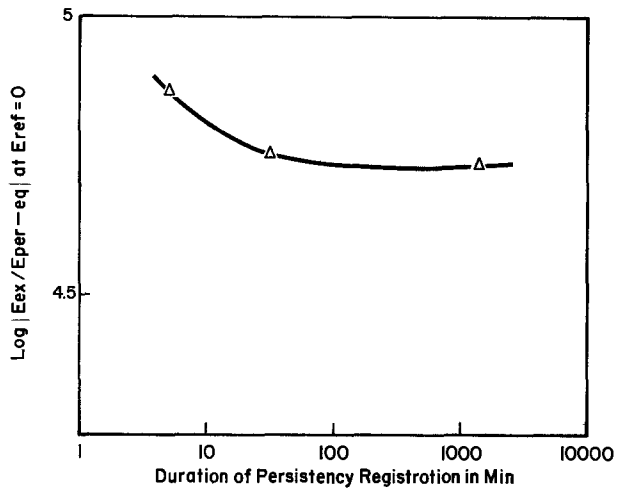

Fig. 4. Log of the persistency ratio E_{exc}/E_{per-eq} as a function of time. Clearly in the case of the LaOBr:Tb^{3+}, phosphor used in the MR 400 screen persistency is virtually completed after approximately 60 min.

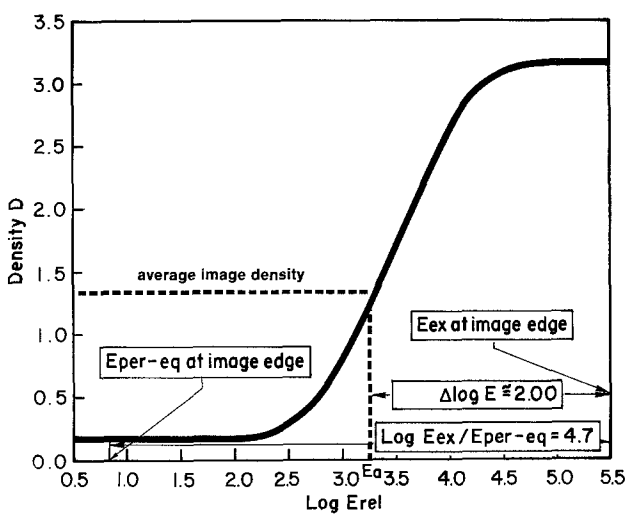

Fig. 5. Possible adverse photographic effects of persistency will occur if the position of E_{per-eq} is shifted into the low density foot of the sensitometric curve. The negligible effect for a single lateral lumbo-sacral exposure with an MR 400/Curix RP1 screen-film combination is illustrated in this graph.

In medical applications, the average density in the radiographic image area will be 1.3 and, depending on the patient, the total exposure latitude, in case of a lateral lumbo-sacral exposure, may be in the order of $\Delta \log E = 2.0$. For the typical example of our MR400/Curix RP1 system, the persistency dose can be seen to be unimportant, the density increase resulting from afterglow being smaller than the fogging level of the film. However, when taking several radiographs in fast sequence, E_{exc}, at the image edge, will shift to larger values. A similar shift of the sensitometric curve to the left occurs when a higher sensitivity film is used immediately after a low sensitivity one. The situation will become even more critical in the case of the extremely high doses, which are common practice in industrial radiography (100R and more for screen-film systems).

Taking all this and an additional safety factor into account, a maximum tolerable persistency level of log (E_{exc}/E_{per-eq}) = 4.0 may be chosen. We conclude from our results, therefore, that most x-ray phosphors on the market to-date present no problem with regard to persistency. Only for the BaFCl:Eu^{2+} of one particular supplier did we find an unacceptable level of persistency. A word of caution seems therefore appropriate.

Concluding Remarks

Due to its reciprocity, silver halide film is particularly suited as an integrator for the registration of afterglow. The methods we described in this paper offer the possibility of a direct insight in eventual image quality problems arising from long-term persistency. Method I has the advantage of giving a more critical value, but it is more tedious and requires the use of several x-ray films. The second method, yielding a good approximate value, is, therefore, preferred as a standard technique for the evaluation of afterglow of x-ray phosphors in our labs.

Manuscript submitted July 20, 1982; revised manuscript received July 22, 1982. This was Paper 488 presented at the Montreal, Canada, Meeting of the Society, May 9-14, 1982.

Any discussion of this paper will appear in a Discussion Section to be published in the December 1983 JOURNAL. All discussions for the December 1983 Discussion Section should be submitted by Aug. 1, 1983.

Publication costs of this article were assisted by Agfa-Gevaert N.V.

Mechanism of Glass Darkening by a Low Pressure Mercury Discharge

B. J. Mulder and S. van Heusden

Philips' Research Laboratories, Eindhoven, The Netherlands

ABSTRACT

A study was made of the darkening of sodium and potassium silicate glasses by a low pressure mercury discharge, using electron spectroscopy, Rutherford backscattering, and transmission electron microscopy. Initial changes in glass exposed to a mercury discharge are twofold: *(i)* mercury from the discharge penetrates very rapidly into the glass to depths of the order of 1 nm. *(ii)* Alkali ions migrate more slowly away from the surface in a photoelectric field that is caused mainly by trapping of photoelectrons. However, mercury entering the glass does not replace alkali ions. Rather, the mercury penetrates into voids in the glass network that are sufficiently close to the surface. From this "surface reservoir" mercury migrates slowly deeper into the glass. This migration is slower in mixed than in single alkali glasses. We assume that mercury migrates as ions in a photoelectric field, assisted by photoelectrons. Ultimately the mercury ions are reduced by photoelectrons to atoms that agglomerate into droplets of metallic mercury reponsible for glass darkening. A mercury discharge provides not only *(i)* mercury ions and (excited) atoms entering the glass and *(ii)* photons, creating a photoelectric field in the glass. The discharge also provides *(iii)* low energy electrons flooding the glass. The latter greatly enhance the strength of the photoelectric field in the glass by recombination with photoholes in the glass near the surface. As regards the effect on the darkening of the glass composition, not only the overall composition is considered (*e.g.*, conductivity, molar volume, shear modulus), but also superficial changes in the composition.

It is well known that a low pressure mercury discharge operated in a soda lime glass envelope will gradually darken the envelope unless the latter is coated with a fluorescent powder or otherwise protected (1-4). This darkening is associated with the intense bombardment of the glass by photons, mercury ions and electrons, and the associated recombination energy of the ions (10.4 eV). For a 1 in. fluorescent tube geometry the photon flux is about 10^{17} photons of 4.9 eV and 10^{16} photons of 6.7 eV per cm^2 per sec. For the ions and electrons the flux is about 10^{14} (5). An interpretation of long standing for the darkening, that is well known from the patent literature [see examples in Ref. (2)], is as follows. Sodium ions from the glass migrate to the inner surface of the envelope. Here they are neutralized by the incoming electrons from the discharge and the resulting sodium atoms serve as nuclei for the condensation of minute droplets of mercury on the surface of the glass. These give the glass its dark appearance. This view is tempting, since it is well known that the inner surface of the envelope acquires a negative potential of about 8V with respect to the discharge. The existence of this potential difference can easily be demonstrated by painting a conductive coating on the outer wall of the envelope and connecting it via an electrometer with one of the electrodes of an a-c operated discharge tube. A spontaneous d-c current of about 1 nA cm^{-2} is then seen to flow through the glass corresponding to the transport of sodium ions from the outer to the inner wall. When this current is enhanced with an external d-c voltage the glass soon turns a grayish dark color, caused by minute droplets of sodium amalgam on the inner wall of the glass (1, 2). This effect has long been mistaken for the cause of the spontaneous darkening of soda lime glass exposed to a mercury discharge. In an earlier paper (3) we showed the true nature of the spontaneous darkening. It has nothing to do with the condensation of mercury on the surface of the glass but is caused by mercury forming minute droplets inside the glass network. In the following the earlier results are discussed in more detail and expanded. We show that one can distinguish at least three stages in the penetration of mercury into the glass: (*i*) a very rapid penetration into the outermost region of the glass, (*ii*) a much slower migration of mercury to depths of about 30 nm, and (*iii*) the formation of droplets of metallic mercury inside the glass. We also discuss some of the underlying mechanisms of the darkening as well as some properties of the discharge and the glass that affect the rate of the darkening.

Key words: mixed alkali effect, ESCA, RBS, transmittance, photoelectric effect.

Effects of a Mercury Discharge on Sodium Silicate Glass (ESCA)

Early changes in sodium silicate glass exposed to a low pressure mercury discharge have been studied with photoelectron spectroscopy (ESCA). The information depth of this technique is determined by the mean free path of photo or Auger electrons ejected from various (core) levels by the exciting monochromatic roentgen radiation (Al Kα; energy 1487 eV). Average reported values (6) of this free path vary from roughly 2 nm for sodium-1s electrons (kinetic energy 410 eV) to 4 nm for the silicon-2p peak (photoelectron energy 1380 eV). Since the escape angle of the detected photoelectrons is about 42 degrees the effective attenuation depth is correspondingly smaller. On the average it amounts to a depth of 3-7 layers of SiO_4-subunits in the glass.

Since fresh glass surfaces are very rapidly modified by reactions with water and carbon dioxide from the surrounding air (7), we took precautions to minimize this glass corrosion. Part of our studies were made on fractured surfaces of glass rods broken inside an attachment to the ESCA apparatus (vacuum 10^{-6} Pa). From here samples could be transferred within minutes to the ESCA chamber (vacuum 10^{-8} Pa) to be analyzed.

To study the effects of a discharge on a sample, it could be transferred from the ESCA chamber, without exposure to air, via the compartment where the glass rod had been broken, into a third compartment consisting of a pumped glass tube provided with a gas inlet and two electrodes, in which a discharge could be operated. During exposures samples were positioned on an insulated support, with the fractured surface flush with the inner surface of the discharge tube (Fig. 1). Our technique for handling and transfer of samples between evacuated compartments has been described elsewhere (8).

The lower curve in Fig. 2 represents a typical ESCA spectrum measured on the fractured surface of a rod of sodium silicate glass containing 20 mol percent (m/o) of sodium oxide. The rod was broken in the vacuum of the ESCA apparatus and analyzed immediately afterward. Peaks characterizing the elements of the glass are marked accordingly. The subscript A designates an Auger peak. The background, increasing at lower kinetic energies, is caused by "secondary" electrons, that is, electrons that have suffered one or more collisions on their way out of the glass,

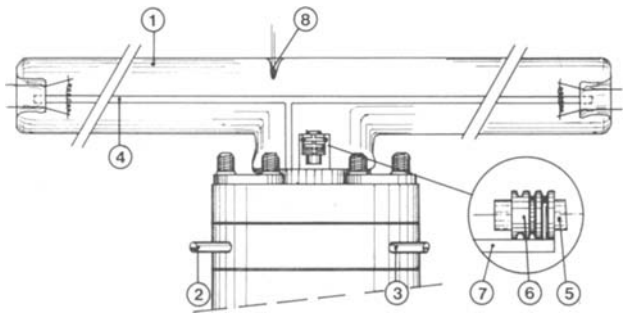

Fig. 1. Discharge tube, 1, diameter about 1 in., attached to ESCA apparatus via straight-through valve (not shown), with gas inlet, 2, and pump outlet, 3. Most of the gas streams through a T-tube, 4, inside the discharge tube to the tube ends. The sample, 5, has the form of a glass rod, which rests in its holder, 6, on an insulated support, 7. As a measure of the temperature of the sample we used the temperature reading obtained from a thin thermocouple, 8, making thermal contact with a thin walled "finger" through a droplet of mercury.

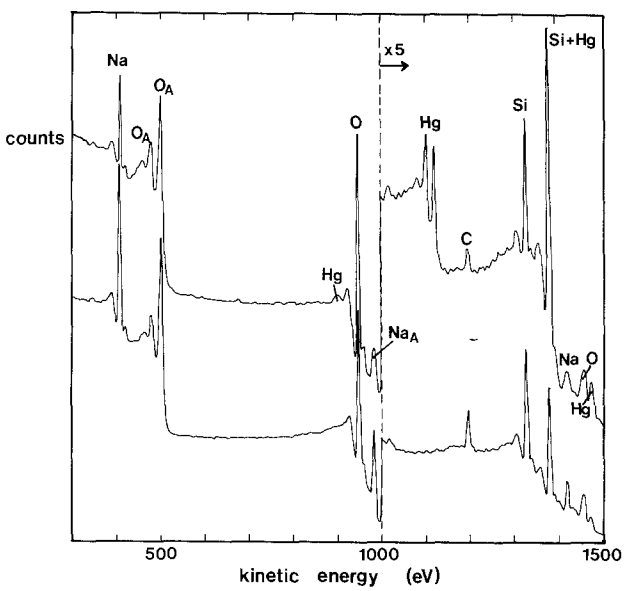

Fig. 2. ESCA spectra of sodium silicate glass with 20 m/o Na_2O, broken inside the vacuum of the ESCA apparatus and analyzed before (lower curve) and after exposure (upper curve) to a normal mercury discharge during 1 hr.

thereby losing their information value. Secondary peaks to the left of major peaks represent photoelectrons that have lost a well-determined amount of energy by producing a plasmon in the glass. Small peaks to the right of photoelectron (but not Auger) peaks are excited by the weak AlKβ component of the exciting roentgen radiation. In addition to the elements that constitute the glass, carbon is seen in the spectrum, presumably stemming from carbon dioxide picked up by the glass surface from the residual gas. Using literature data (9) on the cross sections of the sodium 1s, oxygen 1s, and silicon 2p peak the Na:O:Si ratio works out as 0.25:2:1, which should be compared with the expected ratios of 0.5:2.2:1. A partial explanation of the low observed sodium intensity may be screening of sodium by the rather large amount of carbon (dioxide) selectively bound by sodium at the surface of the glass. The total carbon concentration is estimated to be 1.6×10^{15} cm^{-2}. This is far too low to account for the low apparent sodium concentration. Cross sections for ESCA have limited accuracy (9), but even so it seems that the sodium concentration is lower at the surface than in the bulk of the glass.

A second spectrum taken on the same sample gave an identical picture, showing that ESCA is a relatively mild technique, inducing no changes in the surface composition of glass samples. In particular, no changes were induced in the surface concentration of the very mobile sodium ions. This is in contrast with techniques where glass samples are bombarded with charged particles (electrons in Auger electron spectroscopy or ions in secondary ion mass spectroscopy). The carbon peak did not change, either, showing that no further carbon dioxide was picked up and that no carbonaceous fragments of residual gas accumulated on the surface, as is often seen in Auger spectroscopy.

After being analyzed in its virgin state the sample was transferred to the discharge tube attached to the ESCA apparatus, exposed to a mercury discharge of normal intensity (a-c current density of 80 mA cm^{-2}), and returned to the ESCA chamber for further analysis. The spectrum recorded after an exposure of about 1 hr is represented by the upper curve in Fig. 2. Mercury peaks are clearly in evidence in the spectrum after exposure. In the low resolution wide scan spectra of Fig. 2, the largest mercury (unresolved, double 4f) peak coincides with the (unresolvable, double) silicon-2p peak.

What is the amount of mercury as seen with ESCA? One can make two extreme assumptions. First, one can assume that the mercury is uniformly distributed over the information depth of ESCA (< 10 nm). In that case standard cross sections can be used and the mercury concentration is found to correspond to one mercury atom for about 20 SiO_4 units, or 10^{14} mercury ions per cm^2 and per nm thickness of the glass. The opposite assumption is that the mercury is concentrated so close to the surface that attenuation of the mercury photoelectrons by the glass matrix can be neglected. When it is further assumed that the mean free path of these electrons is 4 nm (uncorrected for the escape angle of the photoelectrons) the surface concentration works out to be about 2.4×10^{14} cm^{-2}. In the following it will become apparent that this second assumption is nearer the truth.

Assuming for the moment that the mercury seen with ESCA is very close to the surface, the next question to ask is whether it is present as a compound, most probably mercury oxide, adsorbed on the surface, or rather inside the glass. A first clue seems to be that the silicon-2s peak (1330 eV) is not smaller, but in fact somewhat larger in the spectrum after exposure than in the original spectrum. This is not only found after brief exposures, but also after exposures of hundreds of hours. The presence of mercury compounds on the surface of the glass would, of course, tend to reduce the intensity of the silicon peaks. The amount of mercury seen with ESCA is too small, however, to cause serious screening of the glass. Unambiguous evidence that all the mercury is indeed inside the glass is discussed later. The mercury seen with ESCA is apparently firmly lodged inside the glass, since the mercury peaks were stable in the vacuum of the ESCA apparatus under exposure to the roentgen source: taking successive spectra on the same exposed sample produced no changes in the mercury peaks.

A second important effect of the mercury discharge is the marked decrease of the sodium peak. A glass surface with less sodium will have a reduced affinity for carbon dioxide. It is not unexpected, therefore, to find that the decrease in sodium is accompanied by a decrease of the carbon peak, even though the sample was passed from the discharge tube to the ESCA chamber via the compartment where the rod had originally been broken and where carbon dioxide was originally picked up. The disappearance of sodium from the surface of the glass is a second factor, that, together with desorption of carbon dioxide, tends to enhance the intensity of the silicon peak after exposure to the discharge.

A typical behavior of the height of various peaks in the ESCA spectrum is shown as a function of the log-

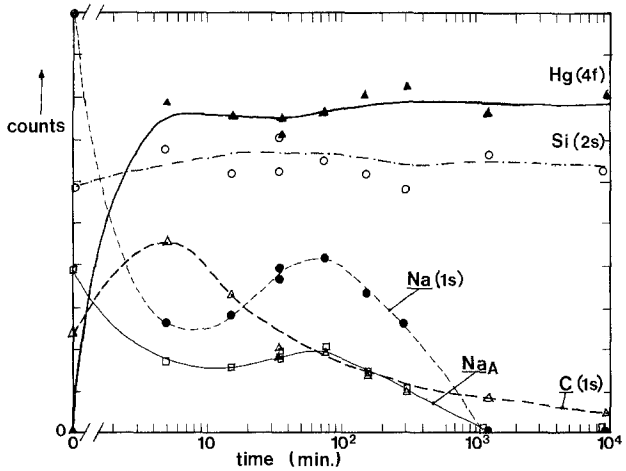

Fig. 3. Area of selected ESCA peaks measured on sodium silicate glass as a function of the logarithm of the accumulated time of exposure to a normal mercury discharge.

arithm of the exposure time in Fig. 3. It is seen that the mercury peak is completely saturated within 5 min exposure to the discharge. Sodium and carbon disappear in about 1000 min and silicon remains approximately constant.

Comparison of Single and Mixed Alkali Glasses (ESCA)

Considering Fig. 2 and 3 one might be tempted to conclude that the mercury penetrating the glass essentially substitutes the sodium ions that are seen to disappear from the surface. This is not, however, the case. To show this we discuss results obtained with ESCA for three types of glass: sodium silicate, potassium silicate, and a mixed sodium-potassium silicate glass (1:1), each with 20 m/o alkali oxide and, in addition, 10 m/o calcium oxide. Rods of these three glasses were broken in a stream of dry argon and, without exposure to air, placed side by side in a discharge tube attached to the ESCA apparatus (an earlier version, accessible via a UHV flange). The tube was sealed, pumped, and ignited. After 36 hr exposure to a normal mercury discharge the samples were transported through vacuum into the ESCA chamber and analyzed. For comparison we also give the data obtained on a second sample of the mixed sodium-potassium glass, but this time broken in the vacuum of the ESCA apparatus and analyzed without exposure to a discharge. Table I gives the amounts of sodium, potassium, silicon, and mercury found in the four samples. It is seen that the amount of mercury is twice as high in the potassium-containing glasses as in the sodium silicate glass. The mercury concentrations have been calculated neglecting attenuation of the mercury photoelectrons by the glass matrix. Sodium, potassium, and silicon concentrations are given in terms of ions cm^{-3}, normalized to Si = 100 in the potassium-containing glasses, in each of which the same silicon (2s) intensity was measured. The numbers between brackets give the relative concentrations calculated from the bulk composition of the glass, again assuming Si = 100. It is seen that sodium has almost completely disappeared from the surface of the sodium silicate glass. In contrast, the alkali ions are present in high concentrations at the surface

Table I. Concentrations of sodium, potassium, silicon, and mercury in silicate glasses measured with ESCA

Alkali (m/o)		Sodium	Potassium	Silicon	Mercury
Na_2O	K_2O	(Relative concentrations)			(10^{14} cm^{-2})
20	—	0.3 (57)	—	127	1.9
—	20	—	78 (57)	100	4.2
10	10	13 (29)	32 (29)	100	4.2
10	10	6 (29)	22 (29)	100	—

of the exposed potassium-containing glasses. Comparing the exposed and the unexposed mixed glass both sodium and potassium are seen to have in fact increased as a result of exposure to the mercury discharge. In the exposed glasses the potassium is higher even than the bulk concentration. The higher silicon signal in the sodium glass agrees with the higher relative concentration of silicon, caused by the disappearance of the sodium.

We are led to the conclusion that, although mercury penetrates inside the glass network, it does not do so by substituting for alkali ions. To study the distribution of mercury and to obtain unambiguous quantitative information, we turned to the technique of Rutherford backscattering.

Comparison of Single and Mixed Alkali Glasses (RBS)

Rutherford backscattering (RBS) is a suitable technique for studying mercury in glass. Since mercury has a higher atomic weight than all the elements normally present in soda lime glass, the impinging (2 MeV helium) ions colliding with mercury nuclei loose less energy than those scattered by the atoms of the glass matrix. Therefore mercury gives rise to a well-resolved, isolated peak at a higher kinetic energy than the remainder of the spectrum. The number of scattered ions gives accurate information about the total amount of mercury in the glass, while the width of the peak shows the distribution of the mercury with a resolution of about 7 nm (information depth 1 μm). To avoid electrostatic charging, all samples studied with RBS were coated with 20-30 nm of carbon. An illustration of an RBS spectrum is given in Fig. 4, taken on a fractured surface of a rod of a mixed alkali glass exposed to a normal mercury discharge for 1500 hr. Carbon is present on the surface and mercury is also concentrated relatively close to the surface. These elements give rise, therefore, to peaks, whereas the constituents of the glass give rise to plateaus, each starting at a characteristic energy. Mercury is seen to be concentrated at a depth of about 30 nm below the surface of the glass. The total amount of mercury in this particular sample is about 10^{16} cm^{-2}.

We begin with some results of experiments with siggle and mixed alkali glasses that can be compared with the ESCA results obtained on similar glasses and discussed earlier. Rods of a sodium, a potassium, and a mixed sodium-potassium glass were broken and short lengths of the rods were introduced into a discharge tube in a stream of dry argon. The rods were placed

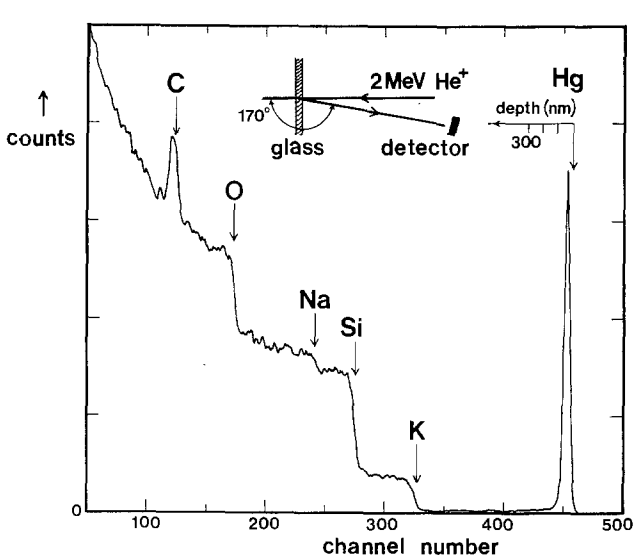

Fig. 4. Rutherford backscattering spectrum taken on a sample of a mixed alkali glass (fracture surface of a rod) after 1500 hr exposure to a normal mercury discharge. Surface positions are indicated for various elements.

in the tube side by side, perpendicular to the tube axis. The tube was sealed and processed without delay. The alkali content of all three glasses was 17 m/o. Minor constituents were barium, aluminum, and boron. Table II gives the sodium and potassium contents of the glasses and the amounts and penetration depths of mercury found in these glasses after exposure to a normal mercury discharge (80 mA cm^{-2}) during 50 hr (two sets of samples exposed in separate discharge tubes) and after 500 hr exposure.

An important conclusion can be drawn from a comparison of the amounts of mercury in the two sets of glasses exposed during 50 hr, as given in Table II. One of the two sets was washed, before being analyzed, with a 10% solution of acetic acid in methanol. This is a very good solvent for various mercury compounds, especially mercury oxide. The fact that washing with the acid solution had no effect on the amount of mercury found in the glass is strong evidence that all the mercury is inside the glass network, and not adsorbed on the surface of the glass.

A comparison of Tables I and II shows a striking difference between the results of ESCA and RBS. In the ESCA experiment about twice as much mercury is found at the surface of the potassium-containing glasses as in the sodium silicate glass (after 36 hr exposure), whereas with RBS the total amount of mercury is about half as large in the mixed glass as it is in the single alkali glasses (after 50 hr exposure). With RBS all the mercury is found to be located within 7 nm of the surface. These results are clearly incompatible when it is assumed that the mercury is uniformly distributed over this depth. Given the different information depths of ESCA and RBS, the obvious conclusion is that much of the mercury is present in a shallow surface reservoir with a depth of the order of 1 nm. Mercury in this surface reservoir contributes strongly to ESCA (effective mean free path of photoelectrons about 3 nm). This surface reservoir is rapidly filled (Fig. 3) with a concentration that is relatively high and higher in the potassium-containing glasses than in the sodium silicate glass (ESCA). From the surface reservoir mercury slowly migrates deeper into the glass. The rate of this migration seems to correlate with the mobility of the alkali ions in the glass. It is relatively high in the single alkali glasses and lower in the mixed glass (Table II). A major difference between single and mixed alkali glasses is, of course, in the mobility of the alkali ions, which is two to three orders of magnitude smaller in mixed glasses. In the mixed glasses, where most of the mercury is still in the surface reservoir the two techniques should yield about the same results. This is indeed seen to be the case: 4.2×10^{14} cm^{-2} is found with ESCA (minimum concentration calculated on the assumption that all mercury is concentrated right at the surface), while RBS gives 5.1×10^{14} cm^{-2}. The difference between the mercury contents of single and mixed glasses is even larger after an exposure of 500 hr (see Table II). Whereas the amount has doubled or quadrupled in the single alkali glasses, that in the mixed glass has increased by only 50%. It is clear, then, that we are dealing with two consecutive processes: rapid filling of a surface reservoir and slow migration of mercury, presumably as mercury ions, from the reservoir deeper into the glass.

Table II. Mercury content in silicate glasses measured with RBS

Alkali (m/o)		Mercury content in 10^{14} cm^{-2} and (between brackets) maximum penetration depth in nm		
Na_2O	K_2O	After 50 hr	After 50 hr*	After 500 hr
17	0	10.7 (7 ± 3)	9.5	16.4 (30)
0	17	11.1 (<4)	11.3	42.8 (20)
9.5	7.5	5.1 (<4)	4.2	7.43 (7 ± 3)

* Washed with 10% acetic acid in methanol before analysis.

A Photoelectric Effect in Glass

One of the driving forces operative in the migration of mercury and sodium ions from the surface deeper into the glass seems to be a photoelectric field. Evidence for a photoelectric field in glass was obtained when glass was exposed to radiation from a pure argon discharge (80 mA cm^{-2}). In these experiments glass rods were broken in the vacuum of the ESCA apparatus and irradiated in the discharge tube attached to the ESCA apparatus. Before igniting the discharge the discharge tube and the sample inside it were preheated with hot air to the temperature that is also reached by samples inside the tube during normal operation of the discharge (about 60°C). In this manner heating-up effects were largely eliminated. After irradiation the sample was transported "internally," without exposure to air, to the ESCA chamber and analyzed. It was then transported back to the discharge tube for further irradiation. The solid line curves in Fig. 5 show the relative decrease of the sodium 1s and sodium Auger peaks for a sodium silicate glass (single alkali, with 17 m/o sodium oxide), while the dashed curves give the corresponding decrease of sodium 1s and potassium 2s peaks for a mixed alkali glass (9.5 m/o sodium and 7.5 m/o potassium oxide).

The curves give the relative peak area as a function of the square root of the accumulated exposure time. The composition of the glasses corresponds to that mentioned in Table II. From the disappearance of the sodium Auger peak (marked Na_A in Fig. 5) it can be concluded that 90% of the sodium had disappeared from the topmost 2 nm of the glass within 6 min. Sodium and potassium are seen to disappear much more slowly from the surface of the mixed alkali glass. The rate at which alkali ions disappear from the surface of irradiated glass apparently correlates with the mobility of the ions in the glass. This suggests that their disappearance is caused by an electric field generated by the radiation from the discharge in the surface region of the glass, where the radiation is absorbed (10, 11). This local photon-generated field runs counter to, and overrules the plasma-generated field due to the recombination of ions and electrons at surfaces exposed to the discharge. This suggests that the disappearance of sodium from the surface of sodium silicate glass exposed to a mercury discharge, as illustrated in Fig. 3, is also caused by a (much weaker) photoelectric field in the glass. The same cause would be responsible for the (slow) migration of mercury ions from the surface reservoir deeper into the glass. The lower strength of the photoelectric field in glass irradiated with a mercury discharge is understandable given the lower energy of the mercury photons (4.7

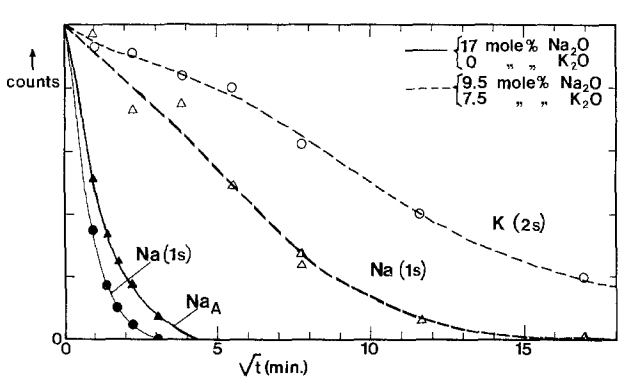

Fig. 5. Decrease of the area of sodium ESCA peaks measured on sodium silicate glass (solid line curves) and of sodium and potassium peaks for a mixed alkali glass (dashed line curves) vs. the square root of the accumulated time of exposure to an argon discharge (3 Torr, 80 mA cm^{-2}).

and 6.9 eV *vs.* 11.7 eV for argon), the lower flux of high energy 6.9 eV mercury photons entering the glass and the much larger penetration depth of the mercury photons. The latter can be inferred from the absorption spectrum measured on a 1.6 μm film of (mixed alkali) glass measured up to 7.5 eV (Fig. 6).

Penetration of Mercury into the "Surface Reservoir"

The photoelectric effect in glass will become weaker when the flux of photons entering the glass is decreased. This flux can be decreased by decreasing the discharge current. The following experiment, designed to study the effect of the discharge current density on the influx of mercury, gave some intriguing clues as to the mechanism of this influx. Small portions of one and the same 1 in. discharge tube made of soda lime glass were exposed sequentially, varying the discharge current. This was possible by moving a glass cylinder, having an open window of about 2 × 2 cm^2, inside the discharge tube (Fig. 7).

Each time the cylinder is moved 2 cm to the left a fresh portion of the wall is exposed, while screening the regions previously exposed through the window. The envelope was made of glass that had suffered relatively little corrosion by ambient air, since the tube had been taken hot from the production line and had been stored in dry argon until it was made into a discharge tube. Before exposures were started the tube was operated for several days to clean up as much as possible adsorbed and residual gases. The temperature of the exposed part of the tube wall was controlled by water circulating through a thermostat and was kept at 70°C. The amounts of mercury found with RBS exposure of 1 hr are plotted *vs.* the current density in Fig. 8.

It can be seen that the amount of mercury penetrating into the glass is perfectly constant for current densities from 5 μA cm^{-2} to about 5 mA cm^{-2}. For larger currents there is a slow increase, a threefold increase

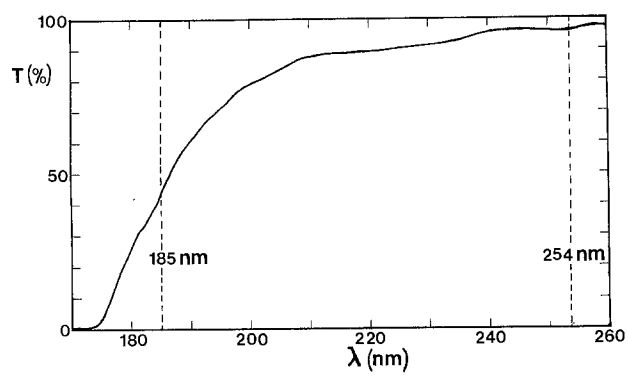

Fig. 6. Transmission of a 1.6 μm thick film of the mixed alkali glass of Table II.

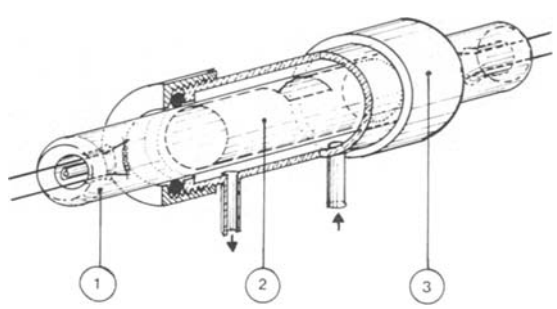

Fig. 7. Discharge tube, 1, with cylindrical glass screen, 2, inside the tube. By shifting the cylinder a selected region of the tube can be exposed through an open 2 × 2 cm^2 window in the cylinder, while screening previously exposed regions. The temperature of the exposed region is controlled through water circulating through a jacket, 3, and a thermostat.

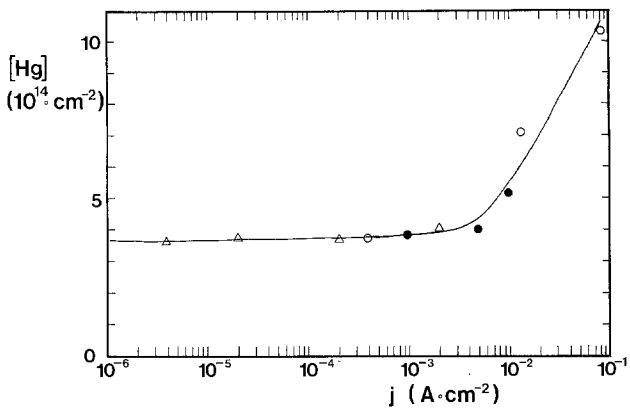

Fig. 8. Effect of discharge current on mercury take up. Total amounts of mercury in different regions of the wall of a discharge tube made of soda lime glass and exposed during 1 hr to a mercury discharge are plotted *vs.* the current density of the discharge. Different regions of the wall were exposed sequentially using the cylindrical screen of the preceding figure.

being observed when the current density has reached 80 mA cm^{-2}. No mercury was found in parts of the wall that had been permanently protected by the cylinder. This experiment shows the influx of mercury to be independent of the flux of mercury ions arriving from the discharge at the surface, when the discharge current is sufficiently low. Since the photon flux is also proportional to the discharge current it can be further concluded that the rapid initial influx of mercury is not limited by the photon flux reaching the glass from the discharge.

The influx at low currents was independent of the temperature of the glass wall. The same amounts of mercury were found whether the water circulating around the tube wall was kept at 50°, 70°, or 90°C.

What is the limiting factor for the influx of mercury at low discharge currents? We suggest that it is the limited number of voids in the glass that are sufficiently large and sufficiently close to the surface to be accessible to mercury atoms or ions arriving at the surface with a limited energy (excitation, recombination and/or kinetic energy). Since this energy is at most of the order of 10 eV the accessible voids could hardly be located at depths much in excess of 1 nm. The mechanism by which mercury penetrates into the glass network needs further consideration. We return to this point later.

Diffusion *vs.* Migration in an Electric Field

The slow increase of the influx of mercury with increasing current for current densities above 5 mA cm^{-2} (Fig. 8) may reflect the onset of the photoelectric effect. Such an effect would not be operative at low current densities, however. Still, the total amount of mercury in the glass increases with time, also at low current densities, long after the surface reservoir has been filled. In experiments with a discharge tube with cylindrical screen (Fig. 7) the amount of mercury found with RBS in the tube wall increased approximately as the square root of the exposure time, for exposures of up to 12 hr. This type of time dependence suggests that we might be observing, in the absence of a photoelectric field, a diffusion process. A square root dependence on time has also been found for the amount of mercury in glass protected by a coating of fluorescent powder (12). After a diffusion process one expects to find a distribution profile characteristic of a diffusion process. The wall of a discharge tube is not, however, a promising sample in which to look for a diffusion profile. For all our precautions the glass would have been corroded to some extent, and this would imply an inhomogeneity in depth. A simple setup, where the initial homogeneity of the sample ex-

posed to the discharge seems assured, is illustrated in Fig. 9.

Here glass rods about 150 mm long and with a circular scratch in the middle, are placed in a discharge tube with borosilicate ends sealed to a central metal bellows. To begin with an argon discharge was run for several days to clean up and desorb residual gases. A mercury capsule was then opened and the discharge was operated for another day. Finally the rods were broken by bending the bellows and the half-rods slid into the side tubes, so that the fractured surfaces were flush with the discharge wall. The samples were then exposed during 1 month to a low current discharge at an ambient temperature of 80°C. The tube was opened and the fractured surfaces studied with RBS. In none of the samples studied was evidence found for a diffusion profile. Either all the mercury was concentrated at 7 ± 3 nm below the surface (the resolution of the technique is about 7 nm) or there was a concentration at a slightly larger depth of not more than 20 nm below the surface. The penetration of the mercury is not, therefore, a passive diffusion process, even in the absence of a photoelectric field. We seem to be observing, in all cases, a process of migration in an electric field.

Further evidence that mercury migrates as mercury ions was obtained when rods of single and mixed alkali glasses were broken inside the "flexible" discharge tube. After an exposure of 1 hr to a low current discharge at 70°C, ten times more mercury was found in the single alkali than in the mixed glass. In glasses with compositions as specified in Table I these amounts were, in terms of 10^{14} ions cm^{-2}, 10 for the potassium glass, 9 for the sodium glass, and 1 for the mixed glass.

To obtain some idea of the strength of the local fields responsible for the migration of mercury ions in the glass, we studied the effect on the migration of an external potential applied between the plasma and the outer discharge wall. The experiment was made with a "fresh" tube of soda lime glass (wall thickness 0.8 mm), in which a low current a-c discharge was maintained. Five equally spaced, cylindrical, silver electrodes were painted on the tube wall, four of which were maintained at negative potentials of 2000, 1500, 1000, and 500V, respectively, with respect to the earthed electrode of the discharge. The fifth silver electrode floated electrically, with an earthed guard ring between it and the neighboring −500V electrode. The amounts of mercury found after 8 hr operation are plotted *vs.* voltage in Fig. 10 for ambient temperatures of 20° and 50°C.

As before, the amount of mercury is almost independent of temperature in the absence of an applied field. However, there is a pronounced effect of temperature in the presence of an applied field. At 2000V 170 mercury has entered the glass in 8 hr (in terms of 10^{14} ions cm^{-2}). During the same period the "spontaneous" influx (in the absence of an applied voltage) is about 10. This indicates that the spontaneous electromigration takes place in an electric field that is about 16 times smaller than the applied field of 2000V over 0.8 mm glass or, say, a field of 1000 V/cm.

A striking illustration of the concepts of a surface reservoir and subsequent migration in an electric field can be seen in Fig. 11.

Here we give RBS spectra measured on fragments of the soda lime glass discharge tube after exposure during 8 hr to a low current mercury discharge at an ambient temperature of 50°C. The dotted line spectrum was measured on glass exposed in the absence of an applied field and the solid line spectrum for −2000V applied between the discharge and the outer tube wall. In the high voltage spectrum one sees two accumulations of mercury: one at the very surface (the reservoir) and a second one just above the interface between sodium-depleted and normal glass. The sodium depletion is clearly evident in the spectrum, as is a small accumulation of potassium, between the bulk glass and the mercury pile up. This indicates that the mobility of potassium ions is intermediate between those of sodium and mercury ions.

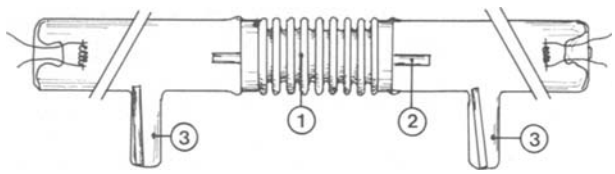

Fig. 9. Discharge tube with metal bellows, 1. After cleanup of residual gases one or more prescratched rods, 2, are broken by bending the bellows. The half-rods are slid into the side tubes, 3, with their fractured surface flush with the tube wall.

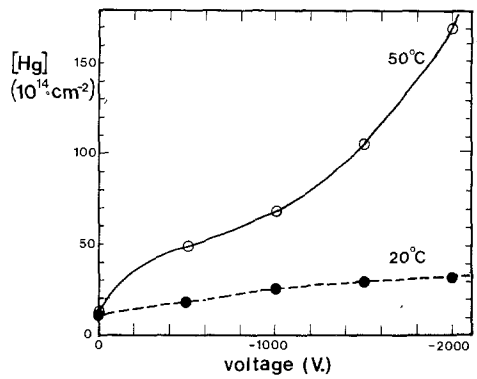

Fig. 10. Effect of d-c applied field on mercury take up. Total mercury in the wall of a discharge tube made of soda lime glass and exposed to a low current discharge (5 mA cm^{-2}) during 8 hr at a temperature of 50°C is plotted *vs.* the d-c potential difference applied between the discharge and different portions of the outer wall of the tube.

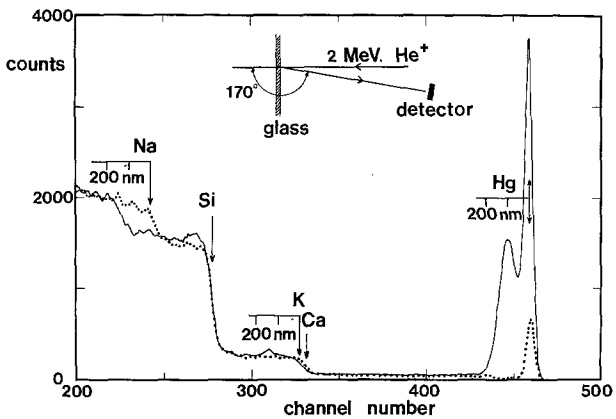

Fig. 11. RBS spectra of soda lime glass exposed to a low current mercury discharge during 8 hr and at 50°C. Solid line curve, in the presence of an applied field of −2000V; dotted curve, without applied field. In the solid line spectrum two mercury peaks are seen, one forming the surface reservoir and a second showing a pileup of mercury just above the interface between normal and sodium-depleted glass.

Darkening: Effect of High Energy Photons

So far we have been concerned with the initial stages of the penetration of mercury into glass. In these stages the glass remains perfectly transparent. This can be inferred from Fig. 12 that gives the optical density (at 560 nm) of soda lime glass darkened to various degrees plotted against the amount of mercury in the glass determined with Rutherford backscattering.

The relationship between the absorbance and the amount of mercury is seen to be linear, but the straight line fitting the data does not pass through the origin.

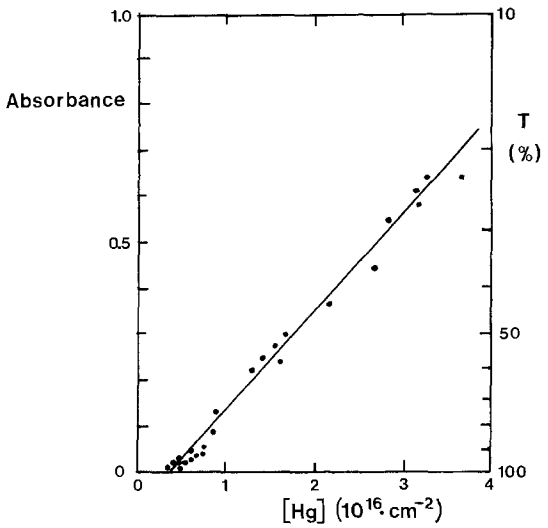

Fig. 12. Absorbance of soda lime glass at 5600 nm vs. the total amount of mercury in the glass (RBS). Mercury in glass does not absorb at visible wavelengths below a critical concentration.

The glass begins to turn dark only when the mercury concentration is higher than a critical concentration of about 3×10^{15} cm^{-2}. Below this concentration the mercury is apparently present in an invisible form, primarily as mercury ions. Beyond this concentration darkening sets in.

In an earlier paper (3) we showed glass darkening to be caused by the growth of very small droplets of metallic mercury inside the glass matrix. The presence of mercury droplets inside darkened glass was revealed by transmission electron microscopy. Figure 13 gives an example of an electron micrograph showing a galaxy of tiny mercury droplets in a matrix of soda lime glass.

The sample was a thin glass film darkened inside a mercury discharge tube and thinned down further by ion milling. The mercury is evidently inside the glass, since the droplets did not disappear in the vacuum of the electron microscope, although occasionally a black dot was seen to boil off by the heat of the electron beam. ESCA spectra taken on strongly darkened glass yielded a silicon-2s signal of the same magnitude as that obtained on fresh glass, showing the glass network to extend to the very surface also in darkened glass. RBS performed on samples of darkened glass showed mercury to be concentrated at depths of typically 30-40 nm.

The theory of the optical properties of finely dispersed metals has been given by Mie (13). One result is that the optical density of the metal is proportional to the total amount of the metal in the particles, in agreement with Fig. 12.

What is the mechanism by which droplets of metallic mercury are formed from mercury ions? It seems that the primary process is photoreduction of mercury ions. This follows from experiments where the energy of the photons from the discharge was increased without changing other external parameters (discharge current, wall temperature, type of glass). The photon energy was increased by creating a cold spot in a discharge tube. Mercury will condense on the cold spot, its vapor pressure decreases and the lower the pressure the more the color of the discharge turns into that of a pure argon discharge. Increasing the proportion of energetic argon radiation in this manner had a dramatic effect on the rate of darkening, as illustrated in Fig. 14.

The curves in this figure represent the darkening of adjoining regions of one and the same discharge tube, made of soda lime glass. The different parts were exposed to the discharge (80 mA cm^{-2} in all cases) by moving an open-ended inner tube sliding in the discharge tube. A cold spot was created behind one of the electrodes mounted on extended supports. The part of the wall being exposed was held at 70°C by water circulating through a thermostat, as in Fig. 7, and the darkening of the newly exposed region was continuously monitored by recording the intensity of the 365 nm radiation from the discharge. The parameters in Fig. 14 give the temperature of the cold spot and the associated intensity of the argon radiation as measured in the near ultraviolet. The rate of darkening is seen to increase enormously with increasing intensity of the argon radiation, down to cold-spot temperatures of 10°-15°C. Further cooling did not result in a further increase in the rate of darkening.

The general shape of the darkening curves in Fig. 14 is the same, apart from different time scales. Also where flat curves are seen in Fig. 14 (cold spot temperatures of 25°C and above) similarly shaped darkening curves are obtained after much longer exposures. Comparing the absorbances in Fig. 12 and 14 it can be concluded that there is an induction period of at least 4 hr during which the mercury content increases to a few times 10^{15} cm^{-2}, followed by a sudden influx of up to 3×10^{15} cm^{-2} hr^{-1}. The latent period can be interpreted as a period in which nuclei of metallic mercury are formed. These act as sinks for mercury ions during the subsequent period of rapid influx. Increasing the intensity of the argon radiation

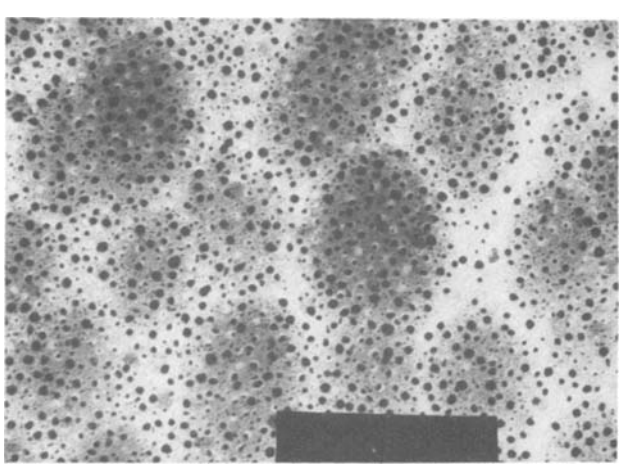

Fig. 13. Electron micrograph of mercury droplets in a matrix of soda lime glass. Bar length designates 0.1 μm.

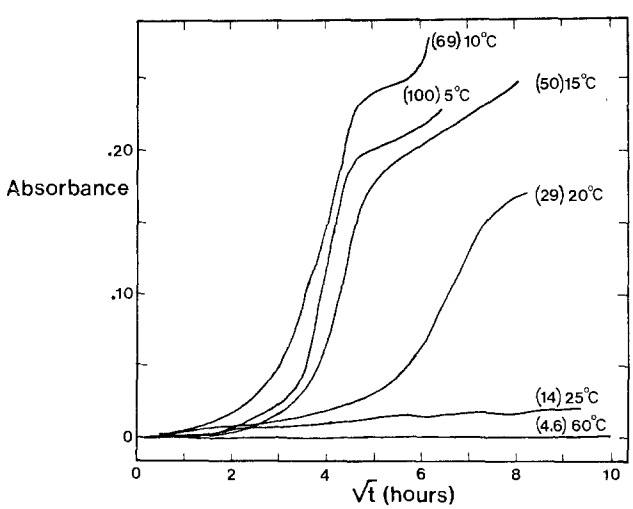

Fig. 14. Effect of cold-spot temperature on the increase of the absorbance of a soda lime glass discharge tube during operation of a mercury discharge (80 mA cm^{-2}, wall temperature 60°C). The curves are marked by the cold spot temperatures and the associated intensities of the argon radiation in arbitrary units.

enhances both the nucleation and the growth of mercury droplets.

Argon radiation with its shorter wavelength compared to mercury radiation will produce a steeper gradient and a higher concentration of charge carriers at the surface of the glass. The steeper gradient will result in a higher photoelectric field strength in the glass, resulting in a higher transport rate of mercury ions. The higher concentration of photoelectrons will cause a more rapid photoreduction of mercury ions.

The reason for the saturation of the darkening rate for cold-spot temperatures below 10°-15°C (the argon intensity doubles between 15° and 5°!) is not so obvious. The darkening is certainly not rate limited by the flux of mercury ions and atoms arriving from the discharge at the glass surface. This follows immediately from the very steep rise of the "5°C curve." A possibility to be considered is saturation of the photoelectric field strength, limiting the transport of mercury ions from the surface to the nearest droplet. Saturation will occur when all electron traps are filled, even the shallower ones.

Darkening: Effects of Glass Structure

Finally we mention the role of the glass matrix in the darkening process. The ease with which mercury nuclei can be accommodated in the network will depend on the details of the structure and composition of the glass. The growth of relatively large droplets (up to 20 nm in diameter in Fig. 13) is even more demanding, given the modest size of the voids normally present in glass. An example of a compositional effect on the rate at which mercury accumulates in glass is given in Table III.

In this table we compare again a sodium and a potassium silicate glass and some mixed glasses, all with the same total alkali content of 17 m/o. Short rods of these glasses, with one fresh, fractured surface, were placed in a normal mercury discharge with the fractured surface perpendicular to the axis of the discharge. After 500 hr exposure the tube was opened and the amount of mercury in the fractured surfaces determined with RBS (see table). Other data given in the table are the water content of the glasses, the electrical resistance at the temperature of the experiment (60°C) extrapolated from data at 250° and 350°C and, finally, the calculated shear moduli. The latter is the mechanical parameter important for the growth of particles of a foreign substance (mercury droplets) inside a given matrix (glass) (14). Comparing glasses 1 and 2, it is seen that the pure potassium glass contains far more mercury than the pure sodium glass, although the latter has a much lower electrical resistance. The same applies to the mixed alkali glasses 3 and 4. These have a much higher resistance, not very different for the two glasses, and an accordingly lower mercury content, but the highest content is found in the glass with the larger potassium concentration. Potassium glasses not only offer more space to mercury ions on account of their larger molar volume. Another difference between potassium and sodium glasses is in the shear moduli (see table), facilitating the growth of mercury droplets in potassium glasses. Glasses 4-6 are identical and demonstrate the reproducibility of the procedure. Glass No. 7 is identical to items 4-6, except that its water content is extremely low. The low water content seems to lead to a low rate of mercury take up, since only half as much mercury is found in the dry glass as in glasses 4-6, that are otherwise identical. One well-known role of water (OH-groups) in glass is that of electron trap (18). This would be important for the strength of the photoelectric field discussed earlier, explaining the relatively low rate of mercury take up by dry glasses.

Table III. Mercury content in silicate glasses

Glass No.	Alkali (m/o) Na_2O	Alkali (m/o) K_2O	Water content (ppm)	Mercury content (10^{14} cm^{-2})	Resistivity log (Ω · cm)	Shear modulus
1	17	0	4.4	16.4	10.7	22.1
2	0	17	2.1	42.8	12.4	21.2
3	7.5	9.5	2.6	12.6	14.9	21.6
4	9.5	7.5	2.9	7.4	14.5	21.7
5	9.5	7.5	6.1	7.6	14.5	21.7
6	9.5	7.5	5.8	7.8	14.5	21.7
7	9.5	7.5	0.4	4.6	14.5	21.7

A final example of an effect of glass structure on the rate of darkening is illustrated by darkening curves given in Fig. 15, that were measured on a mercury discharge tube made of soda lime glass with a locally modified composition of the glass. The composition of the glass had been locally modified at the inner wall by passing a d-c current through the wall of the tube, while an a-c mercury discharge was running, using electrodes of silver paint on the outer wall. After 1, 2, ..., 8 hr electrolysis, creating a sodium-depleted region of increasing depth at the inner wall, the silver electrodes were removed. At this point the underlying glass was still perfectly clear. When the discharge was now continued the "electrolyzed" regions of the glass darkened very rapidly, the more so, the deeper the depletion layer (the parameter of the curves in Fig. 15 is the depletion depth calculated from the charge transported and confirmed by RBS data). It is not clear just how the depleted glass is restructured. At any rate one would not expect problems with electroneutrality (photoconduction) and indeed no polarization effects were observed, when the electrolysis was interrupted. The point to be stressed here is the enormous effect on the darkening rate of the softening of the glass network that results from the removal of sodium ions from the surface region, where the mercury droplets are formed.

Summary and Discussion

In the darkening of silicate glasses by a low pressure mercury discharge at least three stages can be distinguished: (*i*) a very rapid influx of mercury into a surface layer of the glass with a thickness of the order of 1 nm, (*ii*) a much slower migration of mercury from the surface reservoir deeper into the glass, and (*iii*) a photoreduction of mercury ions and agglomeration of mercury atoms to droplets of metallic mercury absorbing visible light.

(*i*) During the rapid initial influx of mercury into the glass the mercury does not substitute for alkali ions (Table I). The mercury is firmly lodged in the glass: it is not removed when the glass is washed with acetic acid, nor does it disappear in the ultrahigh vacuum of the ESCA apparatus, not even under irradiation with

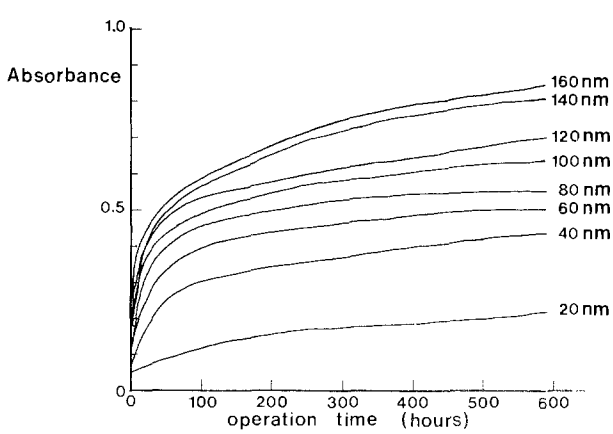

Fig. 15. Development of the optical density at 500 nm of "electrolyzed" regions of a soda lime glass discharge tube during subsequent exposure to a normal mercury discharge. The parameters denote the calculated sodium depletion depths (confirmed by RBS measurements).

the ESCA roentgen source. It seems, then, that the mercury penetrates in the small voids that are commonly present in glass [compare the density of quartz crystals (2.65) and that of fused quartz (2.2 g cm^{-3})]. The voids at the surface are rapidly filled (Fig. 3) and the amount of mercury at the surface, as seen with ESCA, seems to be determined essentially by the number of accessible voids.

It is worth mentioning in this connection that we found mercury also in the surface region of fused quartz, after this had been exposed to a mercury discharge. The amount found at the surface of quartz was comparable to that found in soda lime glass (ESCA). It is also understandable in this picture that more mercury is found at the surface of potassium silicate glasses (single alkali or mixed) than in sodium silicate glasses, given the larger molar volume and consequently larger proportion of sizable voids in the potassium glasses (15). More work will be needed to establish the precise valency of the mercury in the voids at the surface of the glass.

Since thermal mercury atoms do not enter the glass, what is the source of energy allowing the mercury to enter the glass from a discharge? The mercury ions arriving from the plasma through the "sheath" between plasma and wall at the surface of the glass have a kinetic energy of about 1 eV (16). This seems rather low for penetrating into the glass. A more serious problem is that the surface reservoir is filled within 1 hr at current densities of the discharge that are so low that the total number of mercury ions arriving from the plasma at the surface in this period (about 10^{13} cm^{-2}) is an order of magnitude less than the amount of mercury penetrating the glass (Fig. 8). There is, of course, one energetic species that is not in short supply, not even at the lowest currents used in Fig. 8, viz., mercury atoms excited at the surface, or so close to the surface that they can reach the wall before de-excitation. De-excitation at the wall produces a local thermal spike that apparently allows the mercury to enter the glass. Mercury ions, acquiring a (larger) recombination energy will *a fortiori* be able to enter. The relatively low energy of the mercury ions or atoms entering the glass implies that the depth of the "surface reservoir" could not be much in excess of 1 nm.

(*ii*) From the rapidly filled surface reservoir ionic mercury migrates slowly deeper into the glass. One of the driving forces is a photoelectric field generated by absorption of ultraviolet radiation close to the surface (185 nm radiation from mercury and, to an extent depending on the vapor pressure of the mercury, 115 nm radiation from argon). This photoelectric field, often called Dember field, arises when absorption of light causes a gradient in the density of charge carriers. The strength of the field depends on different mobilities of photoelectrons and photoholes. An electric field will also arise when one type of carriers is preferentially trapped in the glass (17). Since electrons are generally more mobile than (photo)holes and are, moreover, preferentially trapped in glass, the general trend is that mobile mercury ions are pulled in the direction of decreasing light intensity. Important electron traps in glass are water molecules (OH-groups) (18) that are present in the bulk of soda lime glass in concentrations of, typically, 3 ppm. Water concentrations at the surface of glass that has been exposed to the atmosphere can be considerably higher. When glass is exposed to a vacuum, water molecules tend to diffuse out of the near-surface region of the glass, especially under irradiation with ultraviolet light (19). In that case a water gradient will develop, which would enhance the trap-determined photoelectric field. This photoelectric field runs counter to, and apparently overrules, the macroscopic field across the tube wall that tends to drive positive ions from the outer to the inner wall. Superposition of the two fields will produce a potential minimum at some small distance from the surface. The position of this minimum can be inferred from the depth at which mercury ultimately accumulates: generally at 30-40 nm below the surface.

Mercury migrates from the "surface reservoir" deeper into the glass also at very low discharge currents. In this case the existence of a photoelectric effect seems unlikely, however. We are nevertheless dealing with migration of mercury ions, not atoms. A clear indication for the migration of ions is the pronounced mixed alkali effect at low discharge currents. Could we be observing, then, passive diffusion of mercury ions? This seems not to be the case. Long-term exposures of clean fractured surfaces to a low current discharge resulted in concentration of mercury generally at depth of 4-10 nm and sometimes as deep as about 20 nm. This type of profile cannot arise in a diffusion process and points to migration of ions in an electric field. Could it be that some of the low energy electrons flooding the glass penetrate sufficiently deep into the glass, get trapped, and set up a local "plasma-generated" field analogous to the photoelectric field? Mean free paths of very low energy electrons can be considerable: the largest value reported in Ref. (6) is 100 nm at 1 eV for a number of elemental solids. Values of 10 nm are commonly quoted for inorganic solids at 10 eV.

At high discharge currents one cannot rule out the possibility that the migration of mercury is to some extent photon assisted. A fleeting existence as mercury atoms would lower coulomb barriers and facilitate the migration. That mercury ions easily pick up photoelectrons is evident, because they are ultimately reduced by photoelectrons and form droplets of metallic mercury. An indication of photon-assisted migration is that the mixed alkali effect is much less pronounced at high discharge currents than at low currents! Barriers to ionic migration existing in mixed glasses are apparently relaxed in the presence of high concentrations of photoelectrons. It would be difficult, however, to disentangle photon-assisted migration and migration in a photoelectric field.

(*iii*) Before the nucleation and growth of metallic droplets the mercury exists in the glass as mercury ions that do not absorb light. A second form of "invisible" mercury that has to be considered, however, is that of droplets of molecular mercury of a subcritical size, bound by Van der Waals forces similar to those binding mercury dimers (20).

The nucleation and growth of mercury droplets is vastly enhanced when the proportion of argon radiation from the discharge is increased by lowering the mercury vapor pressure. There is, however, a limit to the darkening rate that may well be set by saturation of the trap-determined photoelectric field that occurs when all available electron traps are filled, even the shallower ones.

If the "surface reservoir" can be filled by excited mercury atoms and if mercury ions migrate from this reservoir in a photoelectric field and are ultimately reduced by photoelectrons, what, then, is the role of the plasma in the process of glass darkening? Will glass darken also in the absence of a plasma and in the presence of mercury vapor and ultraviolet light? The answer is that it will not or hardly at all. This was found when part of the wall of a discharge tube of soda lime glass was screened by a quartz glass cylinder, with 50% transmission for 185 nm radiation, inside the tube. However, ultraviolet photons in combination with mercury vapor were able to darken soda lime glass after it had been modified by "electrolysis," removing sodium ions from the glass near the inner wall. Thus modified, soda lime glass is exceptionally prone to darkening, apparently on account of its relatively open structure (compare with Fig. 15). The darkening of

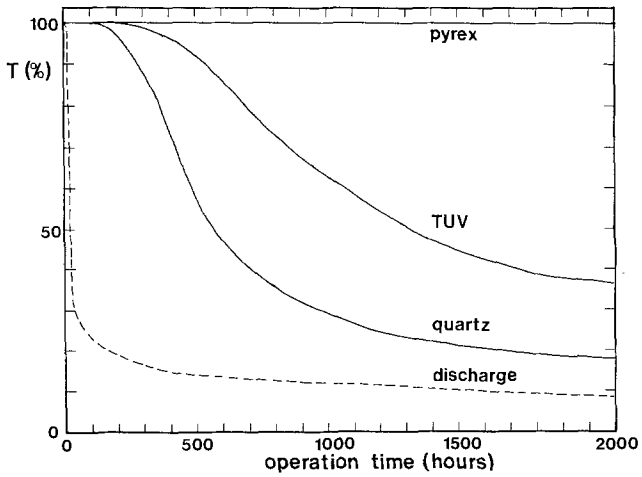

Fig. 16. Darkening of different sections of a discharge tube of soda lime glass after "electrolysis" of the glass with a d-c current. The dashed curve gives the darkening of a tube section exposed to the plasma, while the solid curves were measured on sections screened from the plasma. One section was totally screened from energetic ultraviolet light (curve marked "Pyrex"), another section was irradiated with 254 nm only ("TUV"), and a third was irradiated with both 254 and 185 nm radiation ("quartz").

"electrolyzed" glass screened by various optical filters is shown in Fig. 16.

Sections of a discharge tube of soda lime glass were electrolyzed by passing a d-c current through the tube wall while an a-c mercury discharge was running. As mentioned above this treatment leaves the glass perfectly transparent. The amount of mercury at the end of the "electrolysis" was 7×10^{15} cm^{-2}, which would normally cause a slight darkening (compare with Fig. 12). No darkening is expected, however, when this amount of mercury is distributed over a much greater depth than it normally is (compare with the profiles in Fig. 11). Cylinders of different kinds of glass inside the tube were now shifted to screen the electrolyzed regions and normal operation of the a-c discharge was resumed. The curves in Fig. 16 show that the tube section screened by glass opaque to ultraviolet light did not darken at all, the tube section seeing 254 nm radiation darkened appreciably and the section exposed to both 254 and 185 nm radiation darkened rapidly. The very rapid darkening of unscreened, electrolyzed glass is given by the dashed curve.

The fact that normal soda lime glass requires exposure to a full plasma for appreciable darkening and the large effect of the plasma on the darkening of "electrolyzed" soda lime glass (compare curves marked "quartz" and "discharge" in Fig. 16) show that the plasma contributes an essential factor to the darkening process, in addition to ultraviolet light and (excited) mercury atoms. This contribution is not in the form of mercury ions, since the influx of mercury is not a limiting factor (compare with Fig. 8). Having eliminated mercury and photons, this leaves only low energy electrons from the plasma flooding the glass wall. Low energy electrons can penetrate from the plasma into the glass and recombine with photon-excited holes. As a result the stationary concentration of photoelectrons trapped in electron traps (for example, OH-groups) will be much higher in the presence of the full discharge, with a concomitant increase in the strength of the photoelectric field. In the absence of a plasma this field is too weak to cause darkening of normal soda lime glass, but strong enough to cause rapid darkening of "electrolyzed" glass.

Finally, we sum up some examples of effects of properties of the glass matrix on the darkening rate. The darkening will obviously depend on the overall composition of the glass. Potassium glass darkens more rapidly than sodium glass, because it is roomier and softer mechanically. In mixed-alkali glasses the migration of mercury ions is impeded. The rate of darkening can also be affected by minor components of the glass. Thus water molecules (OH-groups) can act as electron traps increasing the strength of the photoelectric field, and, possibly, also as nucleation sites for mercury droplets. Finally, the darkening rate can be influenced by local changes in the composition of the glass, for instance, where glass has been softened by "electrolysis," removing sodium ions from the network.

Acknowledgments

RBS data were obtained and interpreted by Dr. Y. Tamminga. The TEM picture was taken by Mr. H. B. Haanstra. Various glasses were prepared by Mr. W. van Pelt. Part of the experiments were carried out by Mrs. N. van Weert and Mr. T. Rietveld. The drawings are by Mr. I. van Dommelen. The manuscript was critically read by Dr. Q. H. F. Vrehen. We had many stimulating discussions with Dr. B. Bölger and also with Dr. J. Dieleman.

Manuscript submitted May 17, 1982; revised manuscript received Aug. 23, 1982. This was Paper 502 presented at the Montreal, Quebec, Canada, Meeting of the Society, May 9-14, 1982.

Any discussion of this paper will appear in a Discussion Section to be published in the December 1983 JOURNAL. All discussions for the December 1983 Discussion Section should be submitted by Aug. 1, 1983.

Publication costs of this article were assisted by Philips Research Laboratories.

REFERENCES

1. U. Kümmel, *Appl. Phys.*, **7**, 93 (1975).
2. S. van Heusden and B. J. Mulder, *ibid.*, **23**, 355 (1980).
3. B. J. Mulder and S. van Heusden, *Phys. Status Solidi A*, **63**, 137 (1981).
4. S. van Heusden and B. J. Mulder, Abstract 502, p. 819, The Electrochemical Society Extended Abstracts, Montreal, Quebec, Canada, May 9-14, 1982.
5. L. Vriens, R. A. Keyser, and F. A. Ligthart, *J. Appl. Phys.*, **7**, 3807 (1978).
6. M. P. Seah and W. A. Dench, *Surf. Interface Anal.*, **1**, 2 (1979).
7. L. L. Hench, *J. Non-Cryst. Solids*, **19**, 27 (1975).
8. B. J. Mulder, *J. Phys. E.*, **12**, 908 (1979).
9. C. D. Wagner *et al.*, "Handbook of X-ray Photoelectron Spectroscopy," Perkin Elmer, Minnesota (1978).
10. S. M. Ryvkin, "Photoelectric Effects in Semiconductors," Consultants Bureau, New York (1964).
11. S. R. Goldman, K. Kalikstein, and B. Kramer, *J. Appl. Phys.*, **49**, 2849 (1978).
12. E. R. Kreidler, Abstract 217, p. 560, The Electrochemical Society Extended Abstracts, St. Louis, Missouri, May 11-16, 1980.
13. G. Mie, *Ann. Phys.*, **25**, 377 (1908).
14. J. Frenkel, "Kinetic Theory of Solids," p. 10, Oxford University Press, London (1946).
15. H. Scholze, "Glas—Natur, Struktur und Eigenschaften," Springer, Berlin (1977).
16. H. G. Lergon and U. G. Muller, *Z. Naturforsch.*, 1093 (1977).
17. Y. Moreau, C. Manificier, and H. K. Henisch, *Solid-State Electron.*, **24**, 883 (1981).
18. E. H. Nicollian, C. N. Berglund *et al.*, *J. Appl. Phys.*, **42**, 5654 (1971).
19. J. Bonk, Private communication.
20. A. R. Miedema and J. W. Dorleyn, *Philos. Mag.*, **43**, 251 (1981).

Composition and Structure Control by Source Gas Ratio in LPCVD SiN_x

Takahiro Makino

Nippon Telegraph and Telephone Public Corporation, Musashino Electrical Communication Laboratory, Musashino-shi, Tokyo 180, Japan

ABSTRACT

The effect of the ammonia(NH_3)-to-dichlorsilane(SiH_2Cl_2)ratio, R, on film composition and structure have been investigated using He backscattering, infrared absorption, ellipsometry, and electron spin resonance. Films were deposited at 770°C with an R ranging from 0.1 to 10 at reduced pressure in hot wall reactor. The composition of film with $R=10$ was found to be nearly stoichiometric, whereas silicon-rich films were obtained when R decreased. To be silicon-rich, nitrogen atoms should be coordinated with less than three silicon atoms as a result of the formation of N-H or N-N bonds. However, in the present work, the concentration of N-H bonds was so small that nitrogen-rich film was not obtained. The refractive index on the SiN_x was deduced to be a bonding-density-weighted linear combination of $n_{Si_3N_4}$ and n_{Si}. An ESR signal with a g-value of 2.003 was found for silicon-rich films, and was associated with silicon dangling bonds. Annealing at 1100°C caused complete effusion of hydrogen atoms, but a slight increase in ESR spin density. This indicated that formation of Si-N bonding or valence alternation pairs during the annealing was responsible for rather small ESR spin density.

CVD (chemically vapor deposited) silicon nitride has been widely used for oxidation and diffusion masks (1-3), dielectric layers, and nonvolatile MNOS memory elements in LSI's (4, 5). Because of the interest in this material, several attempts have been made to use differing methods to obtain silicon nitride films, including through pyrolysis of SiH_4-NH_3 (1, 4, 6-10), $SiCl_4$-NH_3 (11), or $SiBr_4$-NH_3 (12) gases in an atmospheric pressure cold wall reactor. In addition to its hydrogen content and stress, the electrical properties of this material, its refractive index, and etch rate in HF acid have been extensively studied. Nevertheless, only a small amount of information about defects in silicon nitride has come to light, and the relationship between defects and film structure remains similarly unknown.

In recent years, there has been a growing interest in a new LPCVD (low pressure chemical vapor deposition) method (13, 14), owing mainly to the excellent uniformity of film thickness and composition, and high through-put of wafers that results from it. It is reported that SiH_4-NH_3 pyrolysis under a variety of flows and pressures provides wafer thickness uniformities worse than ±20%, while the use of SiH_2Cl_2 achieves excellent wafer uniformity without requiring any quartz modifications (13). As with atmospheric CVD silicon nitride, the refractive index and etch rate in HF acid of LPCVD silicon nitride have been examined under various deposition conditions (13, 14). However, the physical properties of LPCVD silicon nitride are not well known. Film composition and defects have not been investigated, either.

The purpose of this study was to characterize LPCVD silicon nitride, including its physical properties, film composition, and defects. This was done through analysis of the silicon nitride by means of He RBS (Rutherford backscattering), ellipsometry, infrared (IR) absorption and ESR (electron spin resonance). On the basis of these results, film structure is discussed in relation to its defects.

Experimental

Sample preparation.—Silicon nitride films were prepared by pyrolytic reaction between gaseous SiH_2Cl_2 and NH_3 in a resistance-heated conventional hot wall reactor at reduced pressure (13, 14). Total gas flow rates for the SiH_2Cl_2 and NH_3 were maintained at 220 cm^3/min, and total pressure was kept constant at about 0.4 ± 0.04 Torr with an automatically controlled butterfly valve. In order to change film properties, the gas flow ratio NH_3/SiH_2Cl_2 ($\equiv R$) was changed from 0.1 to 10. Immediately after cleaning in an H_2O_2-H_2SO_4 mixture and subsequent dipping in dilute HF acid, the substrates were placed vertically on a fused silica boat, and positioned in the level temperature zone (770°C) of the reactor. On loading the boat into the reactor, it was evacuated to 10^{-3} Torr and then nitrogen gas was introduced during the substrates warm-up period, during which a pressure of 0.4 Torr was maintained. Silicon nitride films were deposited to a thickness of 2000-2500Å on both sides of the substrates.

Key words: backscattering, ESR, infrared absorption.

Silicon substrates used were (111) oriented n-type single crystal wafers of a 100-200 Ωcm resistivity, mechanically and chemically polished. For ESR and RBS measurements, ordinary 0.3 mm thick substrates were used. For IR absorption measurements, 1 mm thick substrates polished on both sides were used so as to avoid any optical interference.

The film thickness and refractive index were measured by an ellipsometer (Rudolph Research Auto EL-I) equipped with an He-Ne laser light source (λ = 6328Å). A complex index of 3.858-0.018i for the silicon substrate was adopted (15, 16). No correction was performed for the possible 10-20Å native oxide between the silicon nitride film and silicon substrate. Since the film thickness was confirmed by Talysurf measurement, the measured refractive index seems correct, at least for the thick films, despite ignoring the native oxide.

RBS measurements.—RBS measurement of 2 MeV ^4He ions was utilized to determine the film composition, such as the silicon and nitrogen concentrations, and the atomic ratio N/Si. Figure 1 shows a typical spectrum for RBS measurements. The atomic ratio N/Si ($\equiv X$) was determined with a yield ratio of Si in SiN_x to pure Si. Pure silicon yield was estimated by interpolation of Si yield between the substrate and polycrystalline silicon deposited on SiN_x prior to RBS measurement. The stopping power of SiN_x was calculated according to Bragg's rule with Si and solid-phase N stopping power (17). Density and atomic concentrations were quotients of the surface density and atomic concentration (measured by RBS) divided by film thickness (measured by ellipsometer), assuming uniform density and atomic concentrations throughout the films. A detailed description of the analysis will be given elsewhere (18).

IR absorption measurements.—Hydrogen atoms, which were expected to be introduced in the SiN_x films as decomposition products from SiH_2Cl_2 and NH_3, were detected with IR absorption. A typical IR absorption spectrum is shown in Fig. 2. The bands at 2190 cm^{-1} and 3310 cm^{-1} are ascribed to Si-H and NH vibrations, respectively (8).

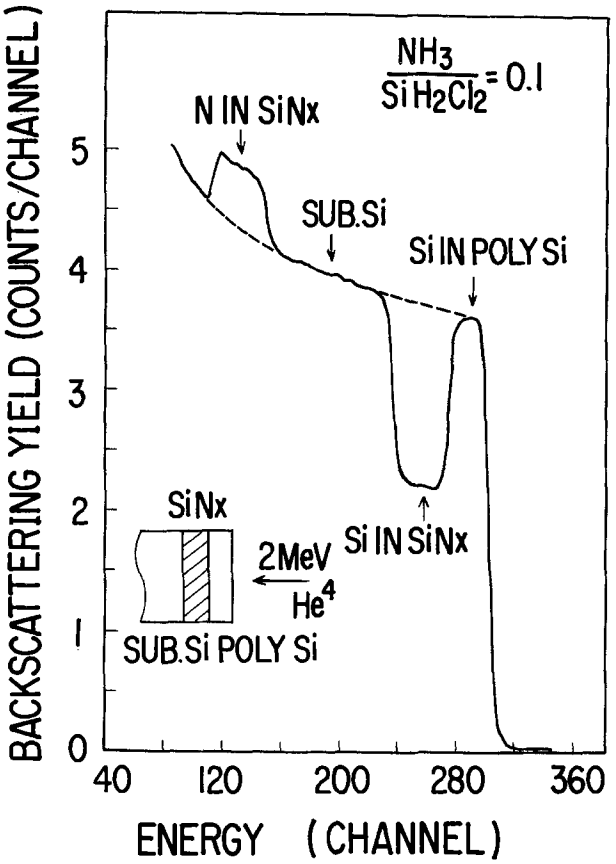

Fig. 1. Random spectrum of He ions backscattered from the substrate-SiN_x-poly Si structure.

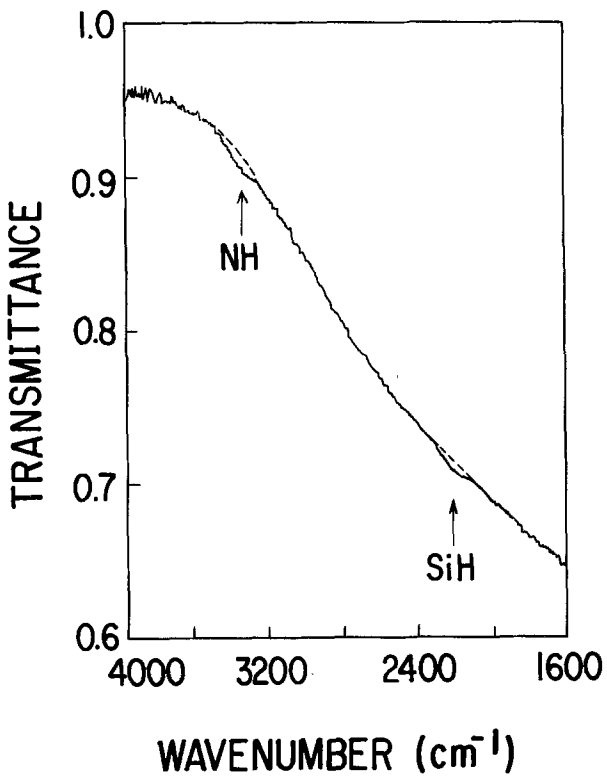

Fig. 2. Infrared transmittance spectrum of $SiN_{1.28}$

ESR measurements.—ESR was measured at room temperature using an X-band spectrometer with a field modulation frequency of 100 kHz and a modulation field of 2G. Care was taken to avoid power saturation which causes incorrect absorption intensity. Specimens were cut into thin rectangular plates 50 × 3 × 0.3 mm. The measured g-value and line width were calibrated with Mn^{++} in MgO. The number of spins was estimated from $N_S \propto IW_H^2$ (19). Here, N_S is the total number of spins that contribute to a signal with a peak-to-peak height I and width W, which was calibrated with standard sample containing a known number of spins.

Figure 3 shows the derivative ESR absorption curves of as-deposited silicon nitride with NH_3/SiH_2Cl_2 = 0.1 and 10. The observed signal has a nearly gaussian shape, with a g-value of 2.003 and line width (peak-to-peak width) of 9.9G. The signal does not show any g-factor anisotropy; the same g-value was obtained regardless of sample orientation in the magnetic field. No other signals were observed for the magnetic field ranging from 3150-3550G, which corresponds to a g-factor of 1.9-2.14.

Structure and Properties of SiN_x

Film composition.—RBS measurements were made in order to determine the atomic ratio, atomic concentration, and density of deposited SiN_x films. The results are summarized in Fig. 4 as a function of the NH_3/SiH_2Cl_2 gas ratio ($\equiv R$). With decreasing R, the silicon concentration, N_{Si}, increases slightly from 3.75 to 3.95 × 10^{22} cm^{-3}, while the N_N decreases from 4.9 to 4.2 × 10^{22} cm^{-3}. At the highest R (R = 10), the composition of the film is found to be nearly stoichiometric (N_N/N_{Si} = 1.31), whereas it becomes silicon-rich with decreasing R. Namely nitrogen-rich film was not obtained despite the fact that the NH_3 flow rate was ten times as large as that of SiH_2Cl_2, though silicon-rich films can be easily obtained as long as gas ratio R is at least less than 1. These results are discussed in the following section.

Refractive index and etching rate.—Since film composition affects the properties of silicon nitride films, the refractive index and etch rate in 49% HF solution were measured (Fig. 5). At the highest R, the refrac-

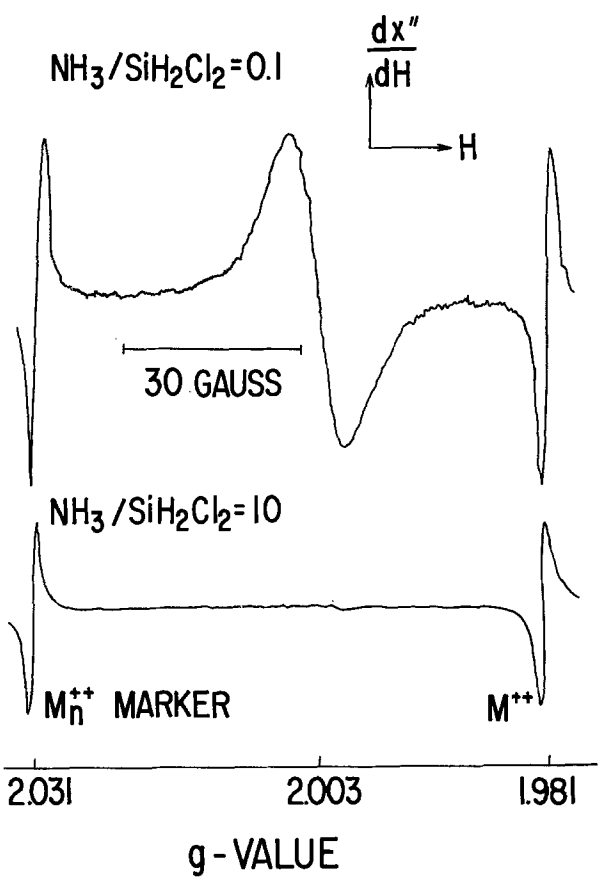

Fig. 3. ESR absorption derivative curves of as-deposited SiN_x

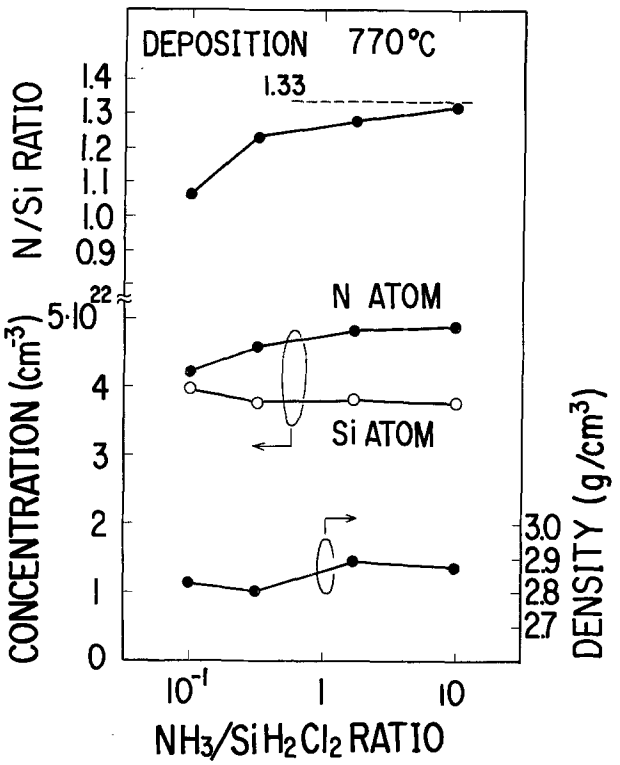

Fig. 4. Si and N concentration, N/Si ratio, and density of SiN_x as a function of the NH_3/SiH_2Cl_2 ratio.

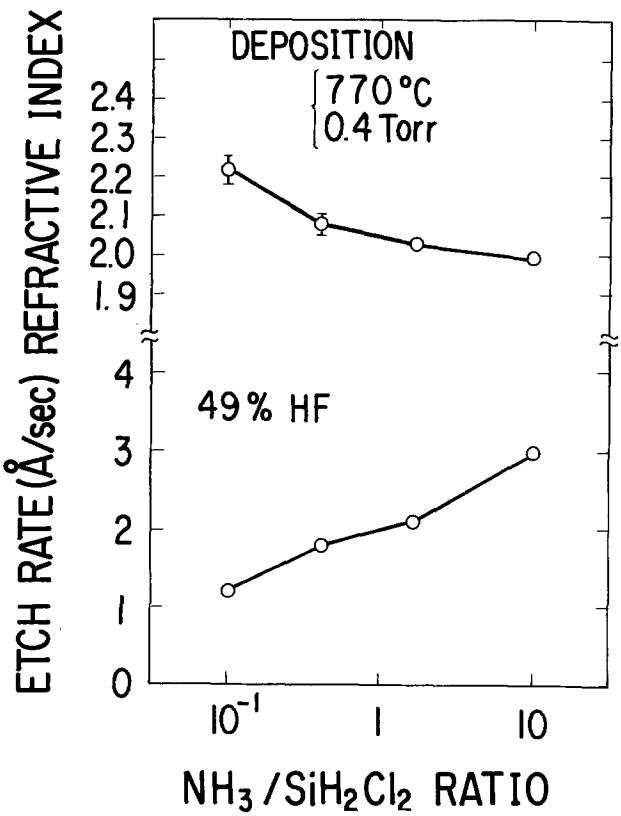

Fig. 5. Refractive index and etch rate as a function of the NH_3/SiH_2Cl_2 ratio.

tive index is 1.987, which is the value of Si_3N_4 (20). With decreasing R, the refractive index increases, and the etch rate decreases. This is presumably because the composition of the films gradually becomes silicon-rich.

Figure 6 shows the relationship between the film atomic ratio and the refractive index, both for the present SiH_2Cl_2-NH_3 system at 770°C and for the

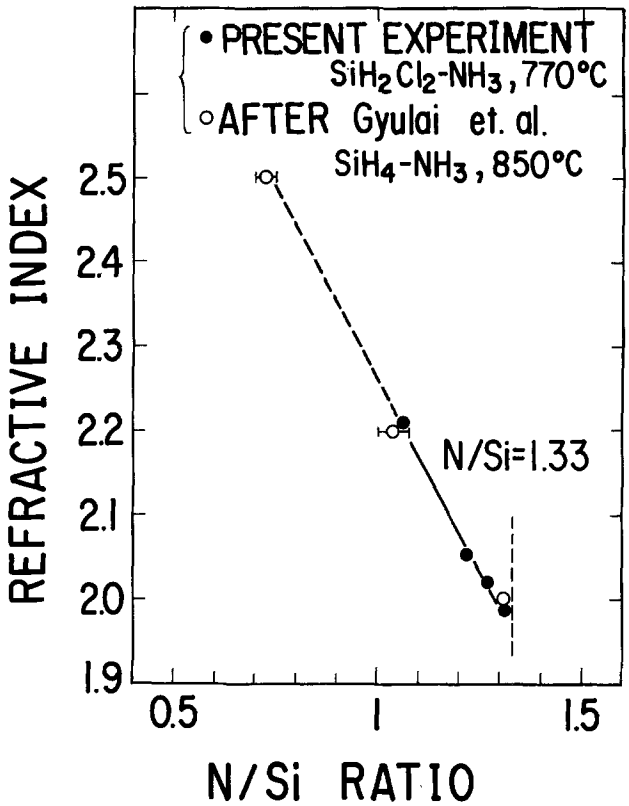

Fig. 6. Optical density for peaks of the NH and SiH bands as a function of the NH_3/SiH_2Cl_2 ratio.

SiH_4-NH_3 system at 850°C (20). The two results are in good agreement with each other, suggesting that the relationship between the atomic ratio and refractive index is independent of deposition conditions. This relationship will be theoretically discussed in the following section. Figure 6 can be used to determine the N/Si ratio from the value of the refractive index, which is easily measured.

Hydrogen content.—Hydrogen atoms were not intentionally added, but were introduced as decomposition products from the SiH_2Cl_2 and NH_3 source gases. The optical density log (Io/I) for the Si-H and N-H absorption peaks is plotted in Fig. 7 as a function of R. The N-H absorption increases with increasing R, while Si-H is only slightly dependent on R.

Stein and Wegener (8) calibrated the optical density of the N-H bond to bond density on hydrogen-implanted silicon nitride samples as

$$\text{bond density} = \frac{2.3\ [\text{optical density}]}{[8 \times 10^{-20}(\text{cm}^2)]\,[\text{film thickness}]}$$

Consequently, an optical density of 1×10^{-3} gives a 6.5×10^{20} cm^{-3} bond density. However, Stein's relation seems to overestimate the bond density because the ion-implanted hydrogen atoms may not all form bonds with silicon or nitrogen atoms.

After annealing in a nitrogen atmosphere at 1100°C, both Si-H and N-H bond absorption are completely lost, as was previously reported for silicon nitride films prepared by a reaction of SiH_4 and NH_3 (8, 9).

ESR measurements.—Since ESR is an effective tool for studying paramagnetic defects and impurities in solids, many reports have been published concerning defects in SiO_2 and Si-SiO_2 as measured by ESR (21, 22). However, less is known about Si_3N_4 or SiN_x films.

Figure 3 shows typical ESR absorption curves. The ESR signal was observed only for silicon-rich SiN film (R = 0.1 film), and disappeared for stoichiometric Si_3N_4 film (R = 10 film). This suggests that the observed ESR center exists at an Si dangling bond

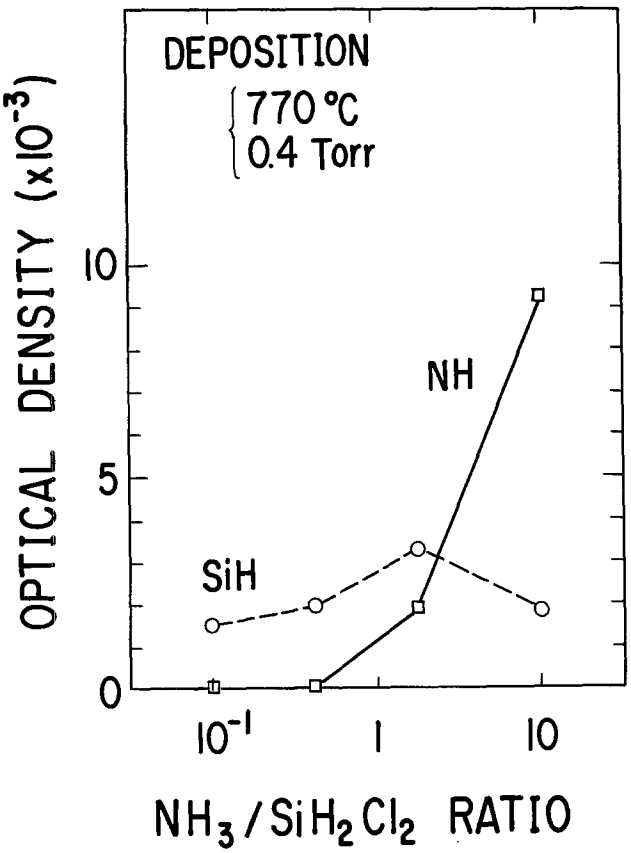

Fig. 7. Relationship between refractive index and N/Si ratio of SiN_x.

(trivalent Si having one unpaired electron). Figure 8 summarizes the dependence of spin density on NH_3/SiH_2Cl_2 gas ratio, both before and after annealing at 1100°C. After the annealing, spin density increased exclusive of the stoichiometric Si_3N_4 case ($R \equiv 10$). It is noted that the observed spin density is far smaller than the Si-H or N-H bond concentration.

In order to determine the distribution of the ESR center in the film, ESR measurements were performed after successive film etchings in HF solution. Signal intensity is almost proportional to film thickness, as is shown in Fig. 9. Therefore it is thought that the ESR center is distributed almost uniformly in the film. In other words, the signal is closely involved with the film's bulk property, and not its surface.

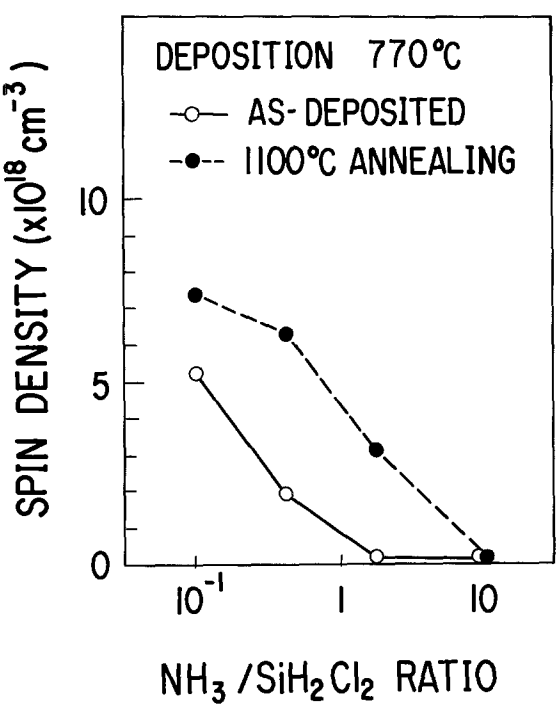

Fig. 8. ESR spin density of as-deposited and 1100°C annealed SiN_x as a function of the NH_3/SiH_2Cl_2 ratio.

Discussion

Nitrogen-rich silicon nitride.—In ideal stoichiometric silicon nitride (Si_3N_4) (23), the silicon atom is coordinated by four nearest-neighbor nitrogen atoms in a distorted tetrahedral arrangement. The nitrogen atoms are threefold coordinated by silicon atoms in a nearly planar trigonal arrangement.

Here, let us consider the composition of silicon nitride that contains hydrogen atoms. To be nitrogen-rich, it is clear that the nitrogen atoms should be coordinated by less than three silicon atoms as a result of the formation of N-H and/or N-N bonds. If half of the nitrogen atom has one N-H bond, $Si_{2.5}N_4H_2$ (N/Si = 1.6) film will be obtained. In other words, an N-H bond concentration of about 2.4×10^{22} cm^{-3} (cf. Fig. 4) yields N/Si = 1.6 film. Similarly silicon-rich film can be deposited by the formation of Si-H and/or Si-Si bonds.

Nitrogen-rich silicon nitride film was not obtained even with a high NH_3/SiH_2Cl_2 gas ratio of 10, whereas silicon-rich film was easily deposited as long as R was small. A similar result was reported for the pyrolysis system of SiH_4 and NH_3 in an atmospheric pressure cold wall reactor (20). In that case the film composition was stoichiometric despite the fact that the NH_3/SiH_4 gas ratio was 100. Accordingly it is concluded that by the CVD method the N-N or N-H bond concentration was too small to yield nitrogen-rich film. This can be confirmed by the following reasons. The N-N bond formation is prevented by the fact that sp^2 hybrid orbitals of nitrogen atoms arranged in a planar trigonal arrangement are not favorable for the formation of three-dimensional material. The small N-H bond concentration is due to the deposition method of CVD, which involves thermal decomposition of gaseous SiH_2Cl_2 (SiH_4) and NH_3 requiring reduction of hydrogen in principle. It is noted that a smaller hydrogen

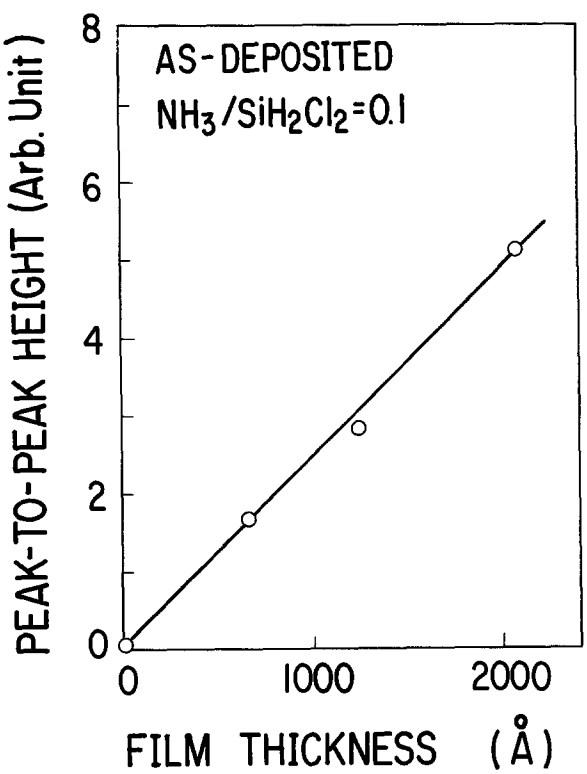

Fig. 9. Distribution of the ESR signal through the film

atom concentration is introduced than expected with use of Stein's calibration factor, because through it (an assumption of 5.9×10^{21} NH and 1.3×10^{21} SiH bond concentration) $Si_{2.92}N_4H_{0.59}$ film, *i.e.*, N/Si = 1.38, is derived. On the contrary, Si-Si bonding is readily formed as in the case of amorphous silicon. Therefore silicon-rich film can be obtained without a large amount of Si-H formation.

In contrast with CVD method, Yoshimi *et al.* reported that nitrogen-rich film is obtainable by means of glow-discharge method under low temperature of 130°C (24). Composition of the nitrogen-rich film is $Si_{2.5}N_4H_{3.3}$, corresponding to 33 a/o hydrogen content (24). This result indicates that nitrogen-rich films should contain a large amount of hydrogen atoms. According to the principle to be nitrogen-rich as mentioned before, it is thought that the hydrogen atoms form bonds with nitrogen. A large amount of the hydrogen is attributed to the deposition method with rf plasma to provide some of the activation energy needed for the reaction between SiH_4 and NH_3 or N_2. In conclusion, nitrogen-rich film is obtained only with glow-discharge method as a result of a large amount of N-H bond formation.

Atomic ratio refractive index relationship.—The relation of the atomic ratio, N/Si ($\equiv x$), to the refractive index, n (x), is a simple one as is shown in Fig. 6. It is deduced as follows.

Assuming that n (x) of the silicon-rich film is a bonding-density-weighted linear combination of $N_{Si_3N_4}$ and N_{Si}, the simple n (x) expression

$$n(x) = \frac{N_{Si\text{-}N} n_{Si_3N_4} + N_{Si\text{-}Si} N_{Si}}{N_{Si\text{-}N} + N_{Si\text{-}Si}}$$

can be obtained. Here the contribution of small amounts of $N_{N\text{-}H}$ and $N_{Si\text{-}H}$ is ignored. Bonding density ratio is given by the atomic ratio

$$\frac{N_{Si\text{-}N}}{N_{Si\text{-}Si}} = \frac{3N_N}{2\left(N_{Si} - \frac{3}{4}N_N\right)} = \frac{3x}{2\left(1 - \frac{3}{4}x\right)}$$

In this way, the n (x) to x relation is obtained as

$$n(x) = \frac{n_{Si} + \frac{3}{4}x \quad (2n_{Si_3N_4} - n_{Si})}{1 + \frac{3}{4}x}$$

This relation agrees well with the experimental results, when $N_{Si} = 3.85$ (16) and $N_{Si_3N_4} = 1.98$ are chosen.

Origin of ESR signal.—Silicon dangling bonds have one lone pair electron and are accordingly paramagnetic. In thermally oxidized silicon, the ESR signal (g-value 2.000-2.010) has been confirmed to originate from the silicon dangling bonds perpendicular to the (111) Si-SiO_2 interface, where silicon-rich silicon dioxide exists (21, 22). In CVD SiO_2, an ESR signal with a g-value of 2.003 and a line width of 6G was observed (25). The ESR signal in CVD SiO_2 is probably the same one observed in thermally oxidized silicon. Therefore, the present ESR signal of silicon-rich silicon nitride is thought of as belonging to silicon dangling bonds.

As shown in Fig. 8, ESR signals increase with annealing. In annealing at 1100°C, hydrogen is freed from Si-H and N-H bonds, and leaves additional silicon and nitrogen dangling bonds. However, it seems that the increase in ESR spin density after the annealing is smaller than the number of Si-H bonds, although Stein's relation overestimates Si-H bond number.

This discrepancy comes from the fact that silicon and nitrogen dangling bonds form new Si-N or Si-Si bonds, or new valence alternation pairs (VAP). Spinless defects are formed via the exothermic reaction of silicon dangling bonds: $2Si_3^{\circ} \rightarrow Si_3^{+} + Si_3^{-}$ (26). Here the positively charged Si_3^{+} atom has three sp^2 bonding orbitals, and the negatively charged Si_3^{-} has three p bonding orbitals, both orbitals being occupied with three electrons. Therefore, Si_3^{+} and Si_3^{-} are spinless defects. The concept of VAP occurring in silicon nitride was proposed to explain the characteristics of MNOS memory devices (27). In this conceptualization, one of the lone pair electrons of the threefold coordinated nitrogen is transferred to a nitrogen atom that has a dangling bond, and a silicon atom that has a dangling bond forms a new Si-N bond. This results in a spinless Si-N_4^{+} bond and N_2^{-}, out of a pair of silicon and nitrogen dangling bonds (27). In any case, whether through the formation of new Si-N, Si-Si bonds or VAP, these reactions reduce the concentration of unpaired electrons. By assuming these rearrangements, the experimental results can be well explained. Spin density does not increase with annealing at 1100°C for silicon nitride when $R = 10$. In $R = 10$ film, the number of silicon dangling bonds is supposed to be smaller than that of nitrogen. Therefore silicon dangling bond forms bonds with nitrogen so readily that the spin density does not increase.

It is noted that $R = 10$ silicon nitride annealed at 1100°C contained a large number of nitrogen dangling bonds even after formation of Si-N bonds or VAP. This is supposedly due to the fact that the amount of N-H is larger than that of Si-H. However, an ESR signal corresponding to a nitrogen dangling bond was not observed. This fact can be attributed to valence alternation of the nitrogen dangling bonds, *e.g.*, $2N_2^{\circ} \rightarrow N_2^{+} + N_2^{-}$, or to weakly bonded N-N. To confirm this valence alternation, further studies are required.

Acknowledgment

The author wishes to thank K. Kajiyama and H. Ikawa for their stimulating discussions and continuous encouragement. The technical assistance of S. Ohyama is also gratefully acknowledged. The author would like to thank S. Maeyama for backscattering measurements.

Manuscript submitted July 16, 1981; revised manuscript received *ca.* Aug. 15, 1982.

Any discussion of this paper will appear in a Discussion Section to be published in the December 1983 JOURNAL. All discussions for the December 1983 Discussion Section should be submitted by Aug. 1, 1983.

Publication costs of this article were assisted by Musashino Telegraph and Telephone Public Corporation.

REFERENCES

1. I. Franz and W. Langheinrich, *Solid-State Electron.*, **12**, 955 (1969).
2. J. V. Dalton and J. Drobek, *This Journal*, **115**, 865 (1968).
3. E. Bassous, H. N. Yu, and V. Maniscalco, *ibid.*, **123**, 1729 (1976).
4. C. T. Naber and G. C. Lockwood, in "Semiconductor Silicon," H. R. Huff and R. P. Burgess, Editors, p. 401, The Electrochemical Society Softbound Proceedings Series, Princeton, N.J. (1973).
5. H. A. Mar and J. G. Simmons, *IEEE Trans. Ed-24*, **5**, 540 (1977),
6. J. M. Andrews, B. G. Jackson, and W. G. Polite, *J. Appl. Phys.*, **51**, 495 (1980).
7. J. R. Yeargan and H. L. Taylor, *This Journal*, **115**, 273 (1968).
8. H. J. Stein and H. A. R. Wegener, *ibid.*, **124**, 908 (1977).
9. H. J. Stein, *J. Electron. Mater.*, **5**, 161 (1976).
10. V. Y. Doo. D. R. Kerr, and D. R. Nichols, *This Journal*, **115**, 61 (1968).
11. M. J. Grieco, F. L. Worthing, and B. Schwartz, *ibid.*, **115**, 525 (1968).
12. J. A. Aboaf, *ibid.*, **116**, 1736 (1969).
13. R. S. Roster, *Solid State Technol.*, 63 (April, 1977).

14. W. A. Brown and T. I. Kamins, *ibid.*, July, 51 (1979).
15. W. C. Dash and R. Newman, *Phys. Rev.*, **99**, 1151 (1955).
16. Y. J. Meulen and N. C. Hien, *J. Opt. Soc. Am.*, **64**, 804 (1974).
17. J. F. Ziegler and W. K. Chu, *J. Appl. Phys.*, **47**, 2239 (1976).
18. S. Maeyama and K. Kajiyama, *Jpn J. Appl. Phys.* Submitted.
19. M. H. Brodsky and R. S. Title, *Phys. Rev. Lett.*, **23**, 581 (1969).
20. J. Gyulai, O. Meyer, and J. W. Meyer, *Appl. Phys. Lett.*, **16**, 232 (1970).
21. P. J. Caplan and E. H. Poindexter, *J. Appl. Phys.*, **50**, 5847 (1979).
22. Y. Nishi, *Jpn. J. Appl. Phys.*, **10**, 52 (1971).
23. M. V. Coleman and D. J. D. Thomas, *Phys. Status Solidi*, **25**, 241 (1968).
24. T. Yoshimi, H. Sakai, and K. Tanaka, *This Journal*, **127**, 1853 (1980).
25. M. Maeda, Private communication.
26. D. Adler, *Phys. Rev. Lett.*, **41**, 1755 (1978).
27. C. T. Kirk, Jr., *J. Appl. Phys.*, **50**, 4190 (1979).

Partial Purification of Metallurgical Silicon by Acid Extraction

T. L. Chu and Shirley S. Chu

Southern Methodist University, Dallas, Texas 75275

ABSTRACT

Metallurgical grade silicon may be purified by the acid extraction technique because of the segregation of impurities at grain boundaries during the solidification of the melt in the manufacturing process. The partial purification of pulverized metallurgical silicon by refluxing with acids has been investigated in detail using aqua regia, hydrochloric acid, and an equivolume mixture of sulfuric acid and nitric acid. Aqua regia is most effective, and the extent of removal of metallic impurities under atmospheric pressure has been determined as a function of the duration of refluxing. Although more than 80% of metallic impurities can be removed, the dissolution of impurities is a slow process. The rate of dissolution may be increased many folds by carrying out the aqua regia extraction in a closed system at high temperatures under pressure.

Semiconductor grade silicon is manufactured from the metallurgical grade silicon through the formation, purification, and thermal reduction of trichlorosilane. Because of the high cost of this process, several direct purification techniques have received renewed interest recently as low cost means for the partial purification of metallurgical grade silicon for solar cell purposes. They include the treatment of pulverized metallurgical silicon with acids to dissolve the impurities (1, 2), the gettering of impurities from molten metallurgical silicon with fused silicates (2, 3), and the treatment of molten metallurgical silicon with gaseous reagents to selectively remove impurities (4, 5).

The acid extraction technique, being a low temperature process is more economical compared with other approaches. The acid extraction technique is based on the large difference in solubilities of many metals in liquid silicon and in solid silicon. Metallic impurities such as iron, aluminum, copper, gold, nickel, titanium, etc., are highly soluble in molten silicon; however, their solubilities in solid silicon are relatively low. For example, the solubilities of iron, copper, and aluminum in silicon at 850°C are approximately 2×10^{15}, 7×10^{16}, and 10^{19} cm^{-3}, respectively, and are lower at lower temperatures (6). Thus, during the solidification of molten metallurgical silicon in the manufacturing process, a major portion of the low-solubility impurities should precipitate at grain boundaries or at interstitial positions. When the cast metallurgical silicon blocks are pulverized, the breakage occurs mostly at grain boundaries. The small grains, 1 mm for example, are either single crystalline or are aggregates of several single crystals. Therefore, a major portion of the metallic impurities are concentrated at the surface of the grains, and prolonged treatment of pulverized metallurgical silicon with acids should be effective in removing these impurities as well as the impurities at grain boundaries. The treatment of pulverized metallurgical silicon with aqua regia, sulfuric acid, hydrofluoric acid, etc., has been claimed to produce silicon suitable for microwave diodes (1). It has also been reported that over 90% of all impurities except boron, copper, and phosphorus can be removed from metallurgical silicon by etching with hydrochloric acid, aqua regia, and hydrofluoric acid for 12 hr at 75°C (2). The effectiveness of this technique depends on the particle size of metallurgical silicon, the chemical reactivity of the acid, and the temperature and duration of treatment. In this work, the purification of metallurgical grade silicon by acid extraction has been studied in detail, and the experimental procedures and results are summarized below.

Relative Effectiveness of the Acids

Metallurgical grade silicon used in this work was purchased from the Ferroalloys Division of the Union Carbide Corporation. It contains about 0.35% (weight) iron and 0.15% aluminum as the major impurities. Three types of acids were used for the extraction process: hydrochloric acid, aqua regia, and an equivolume mixture of sulfuric acid and nitric acid. To determine the relative effectiveness of the acids, 1.5 kg of pulverized metallurgical silicon was refluxed with 2.5 liters of the acid for 100 hr, and the acid was replaced and the refluxing process repeated. The iron content in the successive extracts and in the resulting silicon was used as the criterion for the effectiveness of the acid.

The concentration of iron was determined spectrophotometrically using the complex formed by the ferrous ion and 1,10-phenanthroline, $C_{12}N_2H_8$ (7). Ferric ions can be reduced to the ferrous state by using hydroxylamine hydrochloride. The complex formed is an octahedrally coordinated ferrous ion and three molecules of 1,10-phenanthroline. Its optical absorption band peaks at about 510 nm. At low concentrations, the intensity of this peak is directly proportional to the concentration of iron in solution when an excess of the complex agent is present. For example, an aqueous solution with an iron concentration of 0.10 ppm at a thickness of 1 cm shows a transmittance of 95.5% at 510 nm. Thus this technique is suitable for the quantitative determination of iron at very low concentrations. To determine the concentration of iron in silicon, a weighed quantity of the specimen was dissolved in an ammonium fluoride-nitric acid mixture (20g NH_4F in 100 ml 70% HNO_3); ammonium fluoride was used instead of hydrofluoric acid because of the presence of a relatively high concentration of iron in hydrofluoric acid, about 17 μg/ml. The solution was neutralized with ammonia to a pH of 2-2.5, followed by the addi-

tion of 5 ml of a 10% solution of hydroxylamine hydrochloride to reduce the ferric ions to the ferrous state, and 15 ml of 0.3% solution of 1,10-phenanthroline to form the complex (this amount is four times the stoichiometric amount required to complex all the iron in a 5 ppm solution). However, no color develops until the pH of the solution is increased to 6.5, and the pH of the solution is the most important factor determining the reliability and reproducibility of this spectrophotometric technique. The solution was then diluted to a known volume, and its absorbance was measured at 510 nm.

A series of acid-extraction experiments were carried out. The results indicate that aqua regia is most effective while hydrochloric acid is least effective for the removal of iron from metallurgical silicon. Figure 1 shows the iron concentration in four successive aqua regia and sulfuric acid-nitric acid extracts; the iron concentration in hydrochloric acid extracts is considerably lower and is not shown here. In all cases, the first extract contained the highest concentration of iron, and the iron concentration decreased rapidly with further extractions. Since the reaction between iron and the acids are known to be rapid at the boiling point of the acids, the observed results suggest that the dissolution of iron from the surface of metallurgical silicon takes place readily, while the dissolution of iron from the grain boundaries is a slow process. After four extractions with aqua regia, the concentration of iron in silicon is reduced to 0.03-0.04%.

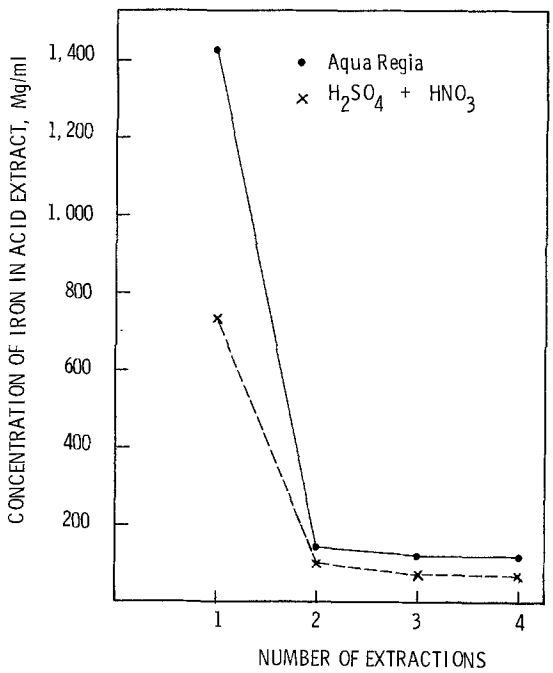

Fig. 1. Concentration of iron in solution (mg/l) after successive extractions of pulverized metallurgical silicon with acids.

Aqua Regia Extraction Under Atmospheric Pressure

The purification of metallurgical silicon by refluxing with aqua regia under atmospheric pressure was further studied to determine the extent of removal of other impurities. About 1.5 kg of metallurgical silicon and 2.5 liters of aqua regia were refluxed for a prescribed time period, 24 or 100 hr. The aqua regia was replaced, and the refluxing continued for the same duration. This process was repeated two more times, and the total time of aqua regia treatment was 96 or 400 hr. The impurity contents in the successive aqua regia extracts were analyzed by atomic absorption and spectrophotometric techniques, and the results of 4 successive 24 hr and 100 hr refluxing experiments are summarized in Table I. The dissolution of iron is considered first. The major portion of extractable iron is removed by the first acid treatment, and the longer duration of refluxing is more effective. During the first extraction, about 2.15g of iron was removed from 1.5 kg of metallurgical silicon after 24 hr of refluxing, and 3.75g of iron was removed after 100 hr of refluxing. The total amounts of iron removed after 4-100 hr and 4-24 hr of extraction are 4.38 and 3.05g, respectively. Since the starting material contains about 0.35% or 5.25g iron, more than 80% of the iron was removed by 4-100 hr refluxing with aqua regia. These results are in qualitative agreement with the iron concentration in the starting material and in the acid-treated metallurgical silicon described later. The dissolution of aluminum, copper, manganese, vanadium, and titanium takes place more readily than that of iron, as indicated by the concentration of these impurities in the successive extracts; more than 90% of the extractable impurities are dissolved after 100 hr of refluxing with aqua regia.

It should be noted that the impurity concentrations in the second extract after 24 hr refluxing are higher than those after 100 hr refluxing, due to the higher impurity content in metallurgical silicon after the first 24 hr refluxing. The total amount of each impurity removed after the four refluxing periods increases with increasing duration of refluxing, and the use of 100 hr refluxings is more effective. However, not all impurities which can be dissolved by aqua regia have been removed by the four 100 hr refluxing. The presence of an appreciable concentration of iron and nickel in the fourth extract indicates that further extraction would be useful.

The concentration of major impurities in metallurgical silicon after four 100 hr refluxing with aqua regia was analyzed by atomic absorption and spectrophotometric techniques. The average concentrations determined by at least three analyses are shown in Table II. The removal of aluminum and iron from metallurgical silicon is far from complete, due mainly to the inability of acids to dissolve impurities precipitated within the grains. Their concentrations can be reduced to 100-150 ppm by gettering with phosphorus pentoxide at 1100°C. However, this procedure is tedious, and silicon becomes heavily doped with phosphorus.

Metallurgical silicon purified by aqua regia extraction was unidirectionally solidified on graphite to yield large grain polycrystalline silicon sheets. The resulting material is p-type with a room temperature resistivity of 0.04-0.06 Ω-cm. The minority carrier diffusion length in the recrystallized metallurgical silicon, measured by the surface photovoltage method (8), is 3-5 μm. Large grain polycrystalline ingots prepared by the unidirectional solidification of aqua regia treated metallurgical

Table I. Concentration of metallic impurities (mg/liter) in successive aqua regia extracts after refluxing with metallurgical silicon for various durations

Duration of refluxing (hr)	First extract		Second extract		Third extract		Fourth extract		Total	
	24	100	24	100	24	100	24	100	96	400
Aluminum	470	670	25.4	14.2	2.1	4.1	0.80	3.1	498	691
Iron	860	1,430	136	135	120	76	102	112	1,218	1,753
Copper	10.2	13.8	0.53	0.31	0.31	0.33	0.25	0.24	11.3	14.7
Manganese	169	250	11.4	10.7	8.6	3.9	3.0	2.7	192	267
Nickel	5.0	35.6	12.3	10.6	14.5	11.7	11.4	11.2	43.2	69.1
Vanadium	0.9	3.1	0.2	0.3	0.1	0.2	0.1	0.1	1.3	3.7
Titanium	7.6	16.7	1.1	1.1	0.4	0.7	0.4	0.5	9.5	19

Table II. Concentration of major impurities (ppm by weight) in as-received and purified metallurgical silicon

Element	Metallurgical silicon	Purified metallurgical silicon
Al	1450	320
Cu	35	15
Fe	3450	350
Mn	200	20
Ni	80	25
Ti	N.D.	N.D.
V	N.D.	N.D.
Zr	N.D.	N.D.

silicon in a graphite container exhibit similar properties. Large area (30 cm^2) solar cells have been prepared by depositing a silicon layer containing an n^+p junction on unidirectionally solidified acid-treated metallurgical silicon, and AM1 efficiencies higher than 9% have been obtained (9).

Aqua Regia Extraction under High Pressures

One major disadvantage of the purification of metallurgical silicon by refluxing with aqua regia is the low rate of dissolution of metallic impurities. The low dissolution rate is due at least to two factors: the gradual depletion of acids in solution and the low reaction temperature. Commercial grade nitric acid and hydrochloric acid contain about 68% (weight) HNO_3 and 38% (weight) HCl, respectively. During the refluxing process, the boiling point of the solution is about 86°C initially, and the reaction between nitric acid and hydrochloric acid yields nitrogen dioxide and chlorine which escape from the solution. Hydrogen chloride also vaporizes from the solution until its concentration is reduced to about 20% (weight), when the concentration of hydrochloric acid in solution remains constant (constant boiling hydrochloric acid) and the boiling point of the solution is increased to about 110°C. Thus, the rate of reaction between aqua regia and impurities in metallurgical silicon decreases with time due to the depletion of acids in the solution. Since the dissolution of metallic impurities in constant boiling hydrochloric acid is known to be slower than that in aqua regia, the aqua regia must be replaced periodically. The temperature of the refluxing process at atmospheric pressure is limited by the boiling point of the acid, about 110°C for the constant boiling hydrochloric acid. Thus, the dissolution rate of metallic impurities can be increased by increasing the temperature of the reaction mixture and by maintaining the acid concentration at a high level. This can be achieved by carrying out the aqua regia treatment in a closed system at high temperatures under pressure. Since the activation energy of the dissolution reaction is on the order of 1 eV, the reaction rate approximately doubles for each 10°C increase in temperature. The vapor pressure of the acid mixture increases exponentially with temperature. It is estimated that the boiling point of the acid mixture can be increased from about 86°C at atmospheric pressure to 200°C at approximately 10 atm. Thus, by carrying out the aqua regia treatment in a closed system, the reaction rate can be increased more than 50 times as compared with the atmospheric process. Further, since the acid concentration remains essentially constant, the increase in reaction rate will be more pronounced. This high pressure process is more readily scaled up than the atmospheric process, and the acid mixture can be better utilized because of no evaporation loss.

Because of the corrosive nature of the acids, no commercial autoclave is suitable for this purpose. Teflon, being chemically inert and stable at temperature up to 250°C, is best suited as the container for the aqua regia treatment of metallurgical silicon in a closed system. To withstand the high pressure encountered in the process, a close fit metal vessel was used to enclose the Teflon container, and the temperature outside the Teflon container was monitored continuously. The important process parameters in the closed system process are the temperature (pressure) and duration of the treatment. Many experiments were carried out using 1.5 kg of metallurgical silicon and 2 liters of aqua regia at 200°C for various durations, and the concentrations of iron in the resulting silicon analyzed by the spectrophotometric technique. It has been found that 60 hr of treatment at 200°C yields about the same results as four 100 hr periods of refluxing under atmospheric pressure. The concentration of iron is in the range of 200-250 ppm, and the results of spectrophotometric determinations were confirmed by atomic absorption analysis. The concentrations of aluminum and copper determined by the atomic absorption technique are 190-200 and 4-5 ppm, respectively. Thus, the use of aqua regia extraction in a closed system increases the reaction rate significantly, and considerably less acid is required.

Conclusions

The treatment of pulverized metallurgical silicon with boiling acids is an economic technique to dissolve a major portion of the metallic impurities precipitated at grain boundaries. Among the three types of acids investigated, their effectiveness decreases in the order: aqua regia > equivolume mixture of nitric acid and sulfuric acid > hydrochloric acid. However, the dissolution of impurities is a slow process, and the rate of dissolution may be increased significantly by using high temperatures and pressures in a closed system.

Acknowledgments

The authors wish to thank Messrs. Roshdy Abderrassoul, Ching L. Lin, and Richard M. Davis for their assistance in experimental work.

This work was supported by the Solar Energy Research Institute.

Manuscript received June 22, 1982.

Any discussion of this paper will appear in a Discussion Section to be published in the December 1983 JOURNAL. All discussions for the December 1983 Discussion Section should be submitted by Aug. 1, 1983.

Publication costs of this article were assisted by Southern Methodist University.

REFERENCES

1. W. Voos, U. S. Patent 2,972,521 (1961).
2. L. P. Hunt, V. D. Dosaj, J. R. McCormick, and L. D. Crossman, in Record of the 12th IEEE Photovoltaic Specialists Conference, p. 125, Nov. 1976.
3. C. J. Brockbank, U. S. Patent 1,180,968 (1916).
4. E. Enk and J. Nickl, German Patent 1,098,931, C. A., **56**, 5633 (1960).
5. T. L. Chu, G. A. van der Leeden, and H. I. Yoo, *This Journal*, **125**, 661 (1978).
6. F. A. Trumbore, *Bell Syst. Tech. J.*, **39**, 205 (1960).
7. L. G. Saywell and B. B. Cunningham, *Ind. Eng. Chem., Anal. Ed.*, **9**, 67 (1937).
8. ASTM F391-78, 1978 Annual Book of ASTM Standards, ASTM, p. 776, Philadelphia, PA (1978).
9. T. L. Chu, Shirley S. Chu, L. L. Kazmerski, Ray Whitney, C. L. Lin, and R. M. Davis, *Sol. Cells*, **5**, 29 (1981).

Oxidation Resistance Characteristics of Silicon Thermal Nitride Films

Ching-Yuan Wu and Chwan-Wen King

Institute of Electronics, National Chiao-Tung University, Hsin-Chu, Taiwan, China

and Ming-Kwang Lee,* Chin-Tang Chen, and Chin-Tay Shih

IC Developement Center, Electronics Research and Service Organization, Industrial Technology Research Institute, Hsin-Chu, Taiwan, China

ABSTRACT

The oxidation resistance characteristics of silicon thermal nitride films are studied theoretically and experimentally. A four-layer model for the oxidation resistance kinetics has been developed in general, and the oxidation resistance time has been defined and used to evaluate the oxidation resistance of high structure density films on silicon in oxygen ambient. The thermal silicon nitride films prepared by nitridizing the silicon surface in ammonia ambient have been used to justify the developed oxidation resistance model, and reasonable agreement between the developed model and the oxidation resistance characteristics of the fabricated thermal silicon nitride films have been obtained. Based on the developed model, the diffusivity and diffusion length of the oxidant species in the thermal silicon nitride films have been deduced and their activation energies are estimated to be −2.091 and −0.672 eV, respectively.

Silicon nitride has been an important material in the fabrication of high performance integrated circuits and devices due to its higher structure density which exhibits strong oxidation resistance and barrier against diffusion of impurities (1-3). Recently, several investigators (4-6) have reported that higher structure density films can be prepared by directly nitridizing the silicon surface in ammonia gas or nitrogen. Some important applications of the as-grown thermal nitride films in MOSFET (7) and electrically alterable ROM (8) have also been reported.

The major difference between the thermal nitridation and the thermal oxidation is that the as-grown thermal nitride films have higher structure density, so "self-limiting" growth can easily occur for the thermal nitridation of the silicon surface in nitrogen or ammonia ambient. The growth kinetics of the as-grown thermal nitride film in ammonia or nitrogen gas has been proposed by us (9). It has been shown that the self-limiting growth of the thermal silicon nitridation in ammonia or nitrogen gas is mainly due to the fact that the characteristic diffusion length of the nitridant species in the as-grown thermal nitride film is much smaller than the thickness of the as-grown films. The characteristic diffusion length of the nitridant species has been estimated to be smaller than 10Å for nitridation temperatures below 1200°C.

In this paper an oxidation resistance model for the silicon thermal nitride films in oxygen ambient is developed to interpret the oxidation resistance characteristics observed from the silicon thermal nitride films oxidized in dry O_2 ambient. A characteristic time which is called the oxidation resistance time is defined and used to evaluate the structure density of the as-grown silicon thermal nitride films. Based on comparisons between the developed model and the oxidation resistance characteristics of the as-grown silicon thermal nitride films, the diffusivity and diffusion length of the oxidant species in the as-grown silicon thermal nitride films are deduced. It has been shown that the diffusivity of the oxidant species in the as-grown silicon thermal nitride films is much smaller than that of the oxidant species in the as-grown silicon dioxide and the diffusion length of the oxidant species in the as-grown silicon thermal nitride films is smaller than 12Å for dry O_2 oxidation below 1154°C.

Theoretical Model

For a high structure density film grown on a silicon surface, the transport of the oxidant species across this film can be represented by Fig. 1, in which this film can be a CVD Si_3N_4 or silicon thermal nitride. According to Fig. 1, there are four basic steps for the oxidation kinetics: (*i*) the oxidant species must be transported from the bulk of the oxygen ambient to the interface between the film and the bulk gas; (*ii*) some oxidant species may diffuse across the film and reach the interface between the film and the silicon dioxide. During this process, some oxidant species may react with silicon nitride film and then transform the silicon nitride film into silicon dioxide or oxynitride film; however, these transformed films are of lower structure density and are assumed to be transparent to the oxidant species; (*iii*) the oxidant species must transport across the previously as-grown silicon dioxide and reach the silicon surface; (*iv*) the oxidant species then react with silicon. Note that the four basic processes described above form the generalized oxidation resistance model, which can be used to describe some important special cases. For example, in the case of thick silicon nitride film, the oxidant species may not transport across the whole silicon nitride film, then $X_2 = 0$ and $C_{in} = 0$, so the oxidation processes are limited at the surface of the silicon nitride film. Moreover, this model may also be used to describe the chemical resistance properties of the silicon nitride film or others. According to the oxidation processes described above, the oxidant flux in each region can be separately described as follows:

(*i*) In region (I), the oxidant flux can be expressed by the conventional form for the thermal oxidation, which can be written as (10)

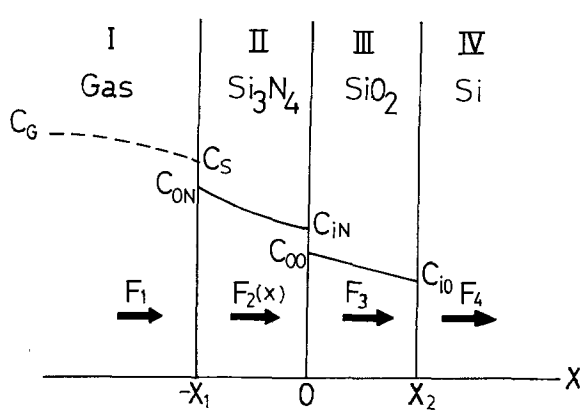

Fig. 1. Schematic diagram of the oxidation resistance model

* Electrochemical Society Active Member.

$$F_1 = h\,(C^* - C_{on}) \qquad [1]$$

where C^* is the concentration of the oxidant species, which is in equilibrium with the partial pressure in the bulk of the oxygen gas P_G; C_{on} is the concentration of the oxidant species at the outer surface of the silicon nitride, which is proportional to the partial pressure of the oxidant species right next to the silicon nitride surface P_s, *i.e.*, $C_{on} = HP_s$, where H is the Henry law constant.

(*ii*) In region (II), the oxidant flux can be assumed to be a diffusive flux and is written as

$$F_2(X) = -D_{on}\frac{dC_o(x)}{dx} \qquad [2]$$

where D_{on} is the diffusivity of the oxidant species in the silicon nitride layer. As described before, the oxidant species does react with silicon nitride and form silicon dioxide or oxynitride film at the outer surface of the silicon nitride film. However, this oxidized film has lower structure density and can be assumed to be transparent to the oxidant species. If the oxidant species across the silicon nitride film are characterized by a lifetime τ_{on}, then the diffusion equation for the oxidant species across the silicon nitride film can be written as

$$\frac{d^2C_o(X)}{dX^2} - \frac{C_o(X)}{L_{on}^2} = 0 \qquad [3]$$

where $L_{on} = (D_{on}\tau_{on})^{1/2}$ is the diffusion length of the oxidant species in the silicon nitride film.

Solving Eq. [3] by using the boundary conditions $C_o(-X_1) = C_{on}$ and $C_o(o) = C_{in}$ we obtain

$$C_o(X) = \frac{C_{in}\sinh\left(\frac{X+X_1}{L_{on}}\right) - C_{on}\sinh\left(\frac{X}{L_{on}}\right)}{\sinh\left(\frac{X_1}{L_{on}}\right)} \qquad [4]$$

The diffusive flux in region (II) can then be written as

$$F_2(X) = -D_{on}\frac{dC_o(X)}{dX} = \left(\frac{D_{on}}{L_{on}}\right)\left\{\frac{C_{on}\cosh\left(\frac{X}{L_{on}}\right) - C_{in}\cosh\left(\frac{X+X_1}{L_{on}}\right)}{\sinh\left(\frac{X_1}{L_{on}}\right)}\right\} \qquad [5]$$

(*iii*) In region (III), the as-grown silicon dioxide layer has lower structure density, the diffusion length of the oxidant species in the oxide layer can be assumed to be much larger than the oxide thickness, then the flux of the oxidant species can be expressed by

$$F_3 = D_{oo}\frac{C_{oo} - C_{io}}{X_2} = \text{Constant} \qquad [6]$$

where D_{oo} is the diffusivity of the oxidant species in the oxide layer; X_2 is the thickness of the as-grown silicon dioxide; C_{oo} is the concentration of the oxidant species at the outer surface of the as-grown silicon dioxide; C_{io} is the concentration of the oxidant at the silicon surface.

(*iv*) In region (IV), the rate of the oxidation at the silicon surface can be expressed by the conventional form for the thermal oxidation, which can be expressed by

$$F_4 = K_{so}C_{io} \qquad [7]$$

where K_{so} is the chemical surface-reaction rate constant for the thermal oxidation.

Using the continuous conditions for the flux at each boundary, *i.e.*, $F_2(-X_1) = F_1$, $F_2(0) = F_3 = F_4$, and letting $C_{oo} = mC_{in}$ with m the solubility ratio of the oxidant species between these two regions, we obtain

$$C_{on} = hC^*\left\{\frac{D_{on}}{L_{on}}\coth\left(\frac{X_1}{L_{on}}\right) + h - \frac{D_{on}^2}{L_{on}}(1 + k_{so}X_2/D_{oo})\,\text{csch}\left(\frac{X_1}{L_{on}}\right)\times\left[mk_{so}L_{on}\sinh\left(\frac{X_1}{L_{on}}\right) + \left(1 + \frac{k_{so}X_2}{D_{oo}}\right)D_{on}\cosh\left(\frac{X_1}{L_{on}}\right)\right]^{-1}\right\}^{-1} \qquad [8]$$

$$C_{in} = C_{on}\left[\cosh\left(\frac{X_1}{L_{on}}\right) + \frac{mk_{so}L_{on}\sinh\left(\frac{X_1}{L_{on}}\right)}{D_{on}\left(1 + \frac{k_{so}X_2}{D_{oo}}\right)}\right]^{-1} \qquad [9]$$

If the number per unit volume of the oxidant species needed to replace nitrogen radicals in silicon nitride is N_1 and the number per unit volume of the oxidant species incorporated into a unit volume of oxide is N_2, then we obtain

$$-N_1\frac{dX_1}{dt} = \Delta F = F_2(-X_1) - F_2(0) = \left(\frac{D_{on}}{L_{on}}\right)\left\{\frac{(C_{on} - C_{in})\left[\cosh\left(\frac{X_1}{L_{on}}\right) - 1\right]}{\sinh\left(\frac{X_1}{L_{on}}\right)}\right\} \qquad [10]$$

$$N_2\frac{dX_2}{dt} = k_{so}C_{io} = \frac{k_{so}mC_{in}}{1 + \frac{k_{so}X_2}{D_{oo}}} \qquad [11]$$

Putting Eq. [8] and [9] into Eq. [10] and [11] we obtain two simultaneous first order differential equations which can be solved by using a computer. However, if the silicon nitride film is thicker than the diffusion length of the oxidant species, *i.e.*, $X_1 >> L_{on}$, then $F_3 = F_4 = 0$. In this case, Eq. [8] and [9] can be simplified to be

$$C_{in} = 0 \qquad \text{for } X_1 >> L_{on} \qquad [12]$$

$$C_{on} = \frac{hC^*}{h + \frac{D_{on}}{L_{on}}} = \text{Constant} \qquad [13]$$

and Eq. [10] and [11] can also be expressed as

$$-N_1\frac{dX_1}{dt} = \frac{hC^*}{1 + \frac{hL_{on}}{D_{on}}} = \text{Constant} \qquad \text{for } X_1 >> L_{on} \qquad [14]$$

$$N_2\frac{dX_2}{dt} = 0 \qquad [15]$$

From Eq. [14] and [15] it is clearly seen that the oxidation rate of the silicon nitride is a constant and that of the silicon surface is zero if the thickness of the silicon nitride film is much larger than the diffusion length of the oxidant species in the silicon nitride. The oxidation resistance time of the silicon nitride can be defined as the time that the thickness of the residual nitride film approaches to half of the diffusion

length L_{on}. This definition will cause the hyperbolic terms in Eq. [8] and [9] to have greater changes so that the oxidation rate increases very rapidly. Based on this definition, the oxidation resistance time t_{or} can be expressed as

$$t_{or} = \frac{X_1 - \frac{L_{on}}{2}}{\left|\frac{dX_1}{dt}\right|} = \frac{\left(X_1 - \frac{L_{on}}{2}\right) N_1}{hC^*} \left(1 + \frac{hL_{on}}{D_{on}}\right) \quad [16]$$

From Eq. [16] it is shown that the oxidation resistance time is linearly dependent on the thickness of the silicon nitride film for $X_1 >> L_{on}/2$. Note that there are a total of nine variables in two simultaneous differential equations as shown in Eq. [8]-[11]; some of them can be chosen from the pure oxidation of silicon and the others can be deduced from the experimental curves of the oxidation resistance experiments, which will be discussed later.

Experimental Results and Theoretical Comparisons

Silicon p-type wafers of <100> orientation and the resistivity of 10 Ω-cm were used as the starting materials. After standard cleaning processes, the wafers were dipped into buffered HF acid for 1 min in order to remove the native oxide on the silicon surface and then were rinsed in deionized water for 10 min. After drying using a nitrogen gun, the cleaned wafers were then put into the quartz tube prepurged with nitrogen. Hydrogen gas was then used to replace the nitrogen gas in order to remove the residual native oxide on the silicon surface. After several minutes of hydrogen gas flow, the ammonia gas was introduced into the reactor tube for thermal nitridation and the hydrogen gas was then turned off. The thickness of the as-grown silicon thermal nitride films was measured by ellipsometer (Rudolph 436-200E). The growth rate of the as-grown thermal nitride films at different nitridation temperature has been discussed in detail (9), and will not be repeated here. However, it has been shown that the "self-limiting" growth of the as-grown thermal nitride films is mainly due to the fact that the characteristic diffusion length of the nitridant radicals in the as-grown thermal nitride films is always smaller than 10Å for nitridation temperatures below 1200°C, and the activation energy of the characteristic diffusion length is measured to be about 0.181 eV. The structure density of the as-grown thermal nitride films has been tested by the chemical resistance method, which shows similar properties to those of silicon nitride. The oxidation resistance studies of the as-grown silicon thermal nitride films are another test for structure density. In this paper, the as-grown silicon thermal nitride films were oxidized in dry O_2 ambient at three temperatures, 1000°, 1050°, and 1154°C. The thickness of the oxidized silicon thermal nitride films was measured by ellipsometer.

Figure 2 shows the characteristic curves of the fabricated silicon thermal nitride in 1000°C dry O_2 ambient, in which the solid curves are calculated by the developed model and the parameters used are cited in Table I. It is clearly seen that general agreement between the experimental measurements and the theoretical calculations has been obtained although some experimental data are slightly out of the theoretical curves. From Fig. 2, it is shown that thicker thermal nitride films do give stronger oxidation resistance, and longer nitridation time does give higher structure density for the silicon thermal nitride film, which, in turn, shows stronger oxidation resistance. Similarly, Fig. 3 and 4 show the oxidation resistance characteristics of some silicon thermal nitride films oxidized in dry oxygen for the oxidation temperatures of 1050° and 1154°C, respectively, in which the parameters used

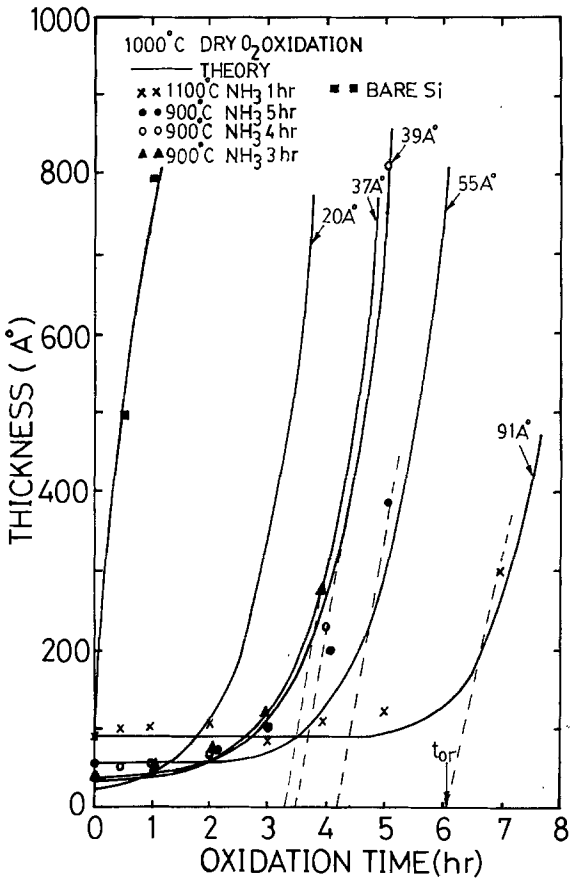

Fig. 2. Oxidation resistance characteristics of thermal nitride films oxidized in 1000°C dry O_2 ambient. Solid lines represent theoretical calculations; *, ●, ○, ▲, ■ represent experimental data.

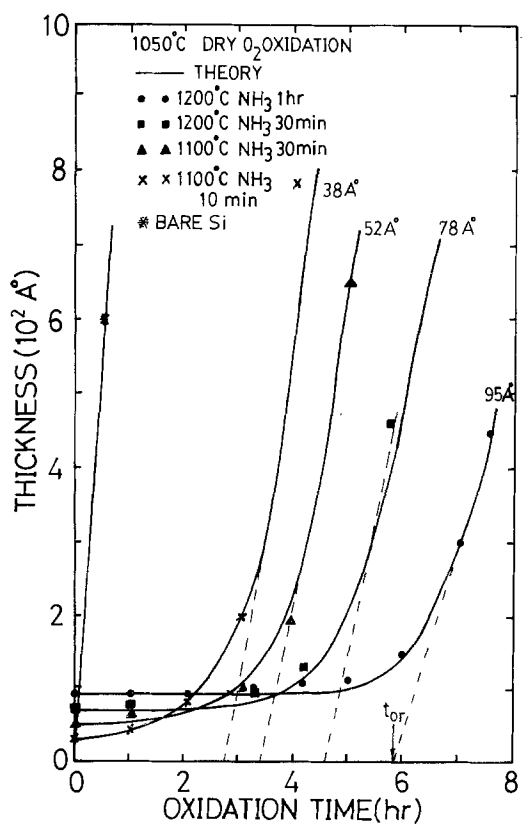

Fig. 3. Oxidation resistance characteristics of thermal nitride films oxidized in 1050°C dry O_2 ambient. Solid lines represent theoretical calculations; ●, ×, △, ■, * represent experimental data.

Table I. Parameters used for theoretical calculations

Parameters oxidation temp,	D_{on} (μm^2/hr)	L_{on} (Å)	D_{oo} (μm^2/hr)	h (μm/hr)	k_s (μm/hr)
1000°C	0.12	6.2	2.11×10^3	1.39×10^6	3.6×10^4
1050°C	0.20	8	3.135×10^3	10^6	3.6×10^4
1154°C	0.98	12	1.023×10^4	9.217×10^5	3.6×10^4

$N_1 = 6.674 \times 10^{22}/cm^3$, $N_2 = 2.2 \times 10^{22}/cm^3$, $m = 12$, $C^* = 5.47 \times 10^{17}/cm^3$.

in the theoretical calculations are also cited in Table I. Again, general agreement between the experimental measurement and the theoretical calculations has been obtained, and the oxidation resistance properties of the as-grown silicon thermal nitride films with respect to the film thickness and nitridation temperature are similar to those discussed for the silicon thermal nitride films oxidized at 1000°C.

If the diffusion lengths of the oxygen species in the silicon thermal nitride films as cited in Table I are plotted as a function of the inverse temperature, the straight line using the least square fitting is shown in Fig. 5, which gives the activation energy of −0.672 eV for the diffusion length of the oxygen species in the silicon thermal nitride films. It is shown that the diffusion length of the oxygen species in the silicon thermal nitride films is smaller than 12Å when the oxidation temperature in dry oxygen is below 1154°C, which is the major reason that the as-grown silicon thermal nitride films have stronger oxidation resistance when the thickness of the as-grown thermal nitride films is larger than the diffusion length of the oxygen species. Note that the diffusion length of the oxygen species in the silicon thermal oxide is much longer than that in the silicon thermal nitride films, which is mainly due to the fact that the silicon thermal oxide films are less dense in structure when compared to that of the as-grown silicon thermal nitride films. Similarly, the diffusivity of the oxygen species in the silicon thermal nitride films as a function of the inverse temperature is shown in Fig. 6, the

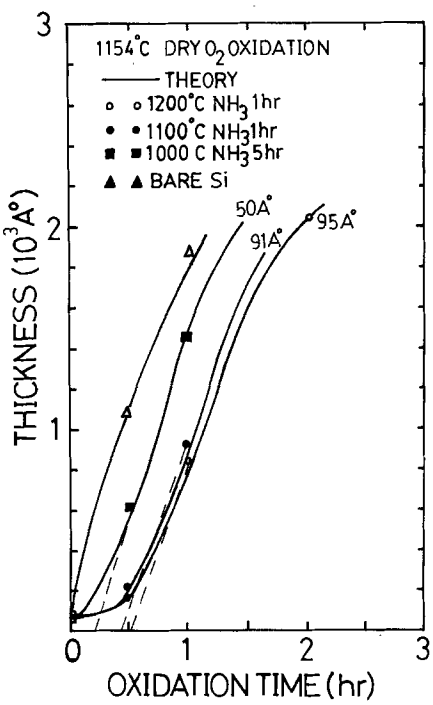

Fig. 4. Oxidation resistance characteristics of thermal nitride films oxidized in 1154°C dry O_2 ambient. Solid lines represent theoretical calculations; ●, ○, ■, ▲ represent experimental data.

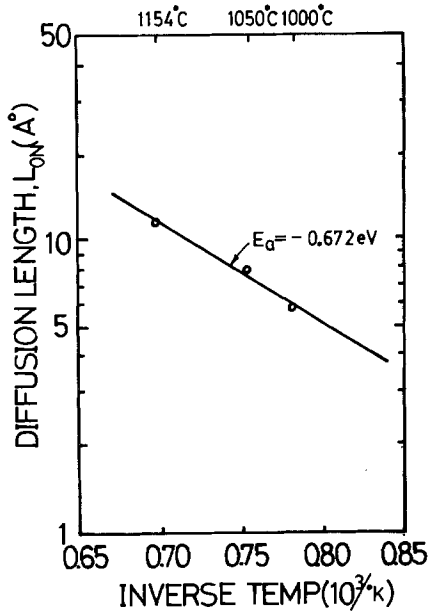

Fig. 5. Diffusion length of oxygen species in thermal nitride film as a function of inverse temperature.

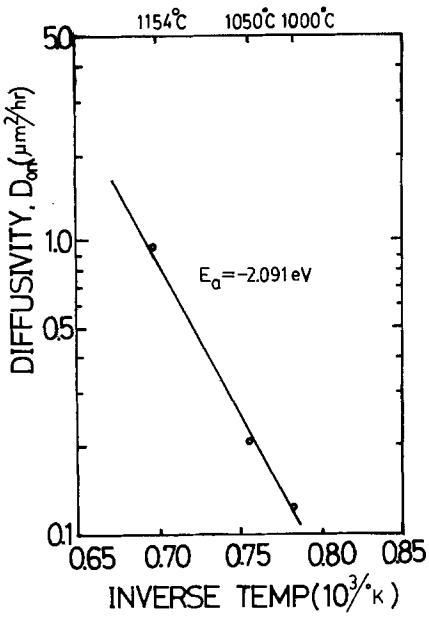

Fig. 6. Diffusivity of oxygen species in thermal nitride films as a function of inverse temperature.

straight line using the least squares method is plotted, which gives the activation energy of −2.091 eV. From this plot, it is shown that the diffusivity of the oxygen species in the as-grown silicon thermal nitride films is much smaller than that of the oxygen species in the silicon thermal oxide. However, the activation energy of the diffusivity for the oxygen species in the as-grown silicon thermal nitride films is larger than that of the oxygen species in the as-grown thermal oxide films. This shows that the oxidation resistance of the as-grown silicon thermal nitride films becomes poor at higher oxidation temperature, which is mainly due to larger diffusion length and diffusivity of the oxygen species in the as-grown nitride films as the oxidation temperature is increased. In the last, the oxidation resistance time as a function of nitride thickness deduced from the extrapolation of the oxidation characteristics of Fig. 2-4 is plotted in Fig. 7. It is shown that the oxidation resistance time is linearly dependent on the thickness of the silicon thermal nitride film, which is

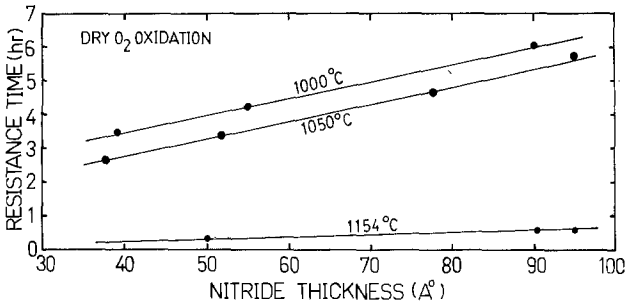

Fig. 7. Oxidation resistance time as a function of thermal nitride film thickness.

in agreement with the prediction of Eq. [16] for $X_1 >> L_{on}/2$.

Conclusions

This paper has developed an oxidation resistance model for the silicon thermal nitride films oxidized in dry oxygen ambient. The developed model has been formulated by using four-layer transport for the silicon thermal nitride films oxidized in oxygen ambient, in which the transport of the oxygen species across the silicon thermal nitride films has been characterized by a diffusion length. It has been shown that the developed model is in agreement with the experimental measurements. Moreover, based on comparisons between the developed model and the experimental data, the diffusivity and diffusion length of the oxygen species in the silicon thermal nitride films have been deduced and their activation energies are +0.672 and +2.091 eV, respectively. The most interesting result obtained is that the diffusion length of the oxygen species in the as-grown silicon thermal nitride films is smaller than 12Å for oxidation temperature below 1154°C in dry oxygen ambient. In addition, an analytic oxidation resistance time is defined and shown to be proportional to the thickness of the as-grown thermal nitride films when the diffusion length of the oxygen species is much smaller than the thickness of the as-grown silicon thermal nitride films, which is in agreement with the experimental data.

Acknowledgment

The authors would like to express their sincere thanks to the Electronics Research and Service Organization, Industrial Technology Research Institute (ITRI) for grant support and stimulations.

Manuscript received April 23, 1982.

Any discussion of this paper will appear in a Discussion Section to be published in the December 1983 JOURNAL. All discussions for the December 1983 Discussion Section should be submitted by Aug. 1, 1983.

Publication costs of this article were assisted by the National Chiao-Tung University.

REFERENCES

1. F. K. Heumann, D. M. Brown, and E. Mets, *This Journal*, **115**, 331 (1968).
2. S. M. Hu, *ibid.*, **113**, 693 (1966).
3. R. G. Frieser, *ibid.*, **115**, 1092 (1968).
4. S. P. Murarka, C. C. Chang, and A. C. Adams, *ibid.*, **126**, 996 (1979).
5. T. Ito, S. Hijiya, T. Nozaki, H. Arakawa, M. Shinoda, and Y. Fukukawa, *ibid.*, **125**, 3, 448 (1978).
6. T. Ito, T. Nozaki, and H. Ishikawa, *ibid.*, **127**, 2053 (1980).
7. T. Ito, T. Nozaki, H. Arakawa, and M. Shinoda, *Appl. Phys. Lett.*, **32**, 330 (1978).
8. S. Hijiya, T. Ito, T. Nakamura, N. Toyokura, and H. Ishikawa, IEDM Digest of Tech. Papers, 590 (1980).
9. C. Y. Wu, C. W. King, M. K. Lee, and C. T. Chen, *This Journal*, **129**, 1559 (1982).
10. A. S. Grove, "Physics and Technology of Semiconductor Devices," Chap. 3, John Wiley & Sons, New York (1967).

Physiochemical Effects of Heating Gold Thin Films on Gallium Arsenide

Siu Leung

Department of Electrical Engineering and Center for the Joining of Materials, Carnegie-Mellon University, Pittsburgh, Pennsylvania 15213

L. K. Wong

School of Pharmacy, University of Pittsburgh, Pittsburgh, Pennsylvania 15261

D. D. L. Chung

Department of Metallurgical Engineering and Materials Science and Center for the Joining of Materials, Carnegie-Mellon University, Pittsburgh, Pennsylvania 15213

and A. G. Milnes

Department of Electrical Engineering and Center for the Joining of Materials, Carnegie-Mellon University, Pittsburgh, Pennsylvania 15213

ABSTRACT

The physiochemical effects of heating gold thin films on GaAs, namely, the arsenic evolution, gold-to-silver color transition, and microstructural changes, were investigated by *in situ* mass spectrometric evolved gas analysis and scanning electron microscopy. The gold-to-silver color transition was found to occur after a small amount of arsenic evolution. The transition temperature increased with increasing air pressure and gold film thickness. The relative quantities of arsenic species evolved followed the order $As_4 > As_2 > As > As_3$. We observed a new microstructure consisting of interconnected irregularly shaped protrusions which appeared after a small amount of arsenic evolution and changed to the previously reported microstructure of aligned rectangular protrusions near the completion of the arsenic evolution.

Gold has been used extensively as a contact metal for Schottky barrier diodes, Gunn diodes, IMPATT diodes, and as an ohmic contact metal for GaAs power microwave FET's and devices. The reliability and performance of the devices at high temperatures are of technological concern.

Various physiochemical effects of heating gold thin films on GaAs have been reported. They include ar-

senic evolution (1-3), the gold-to-silver color transition (4), and microstructural changes (2, 4-11). This paper describes the correlation among these physiochemical effects. Furthermore, we report the first observation of the pressure dependence of the gold-to-silver color transition. The effect of the ambient atmosphere (vacuum, nitrogen, or air) on the physiochemical changes is also presented. The arsenic evolution was studied by *in situ* mass spectrometric evolved gas analysis (EGA), which showed that the relative quantities of arsenic species evolved were in the order $As_4 > As_2 > As > As_3$. The color transition was monitored visually; the microstructural changes were observed by scanning electron microscopy (SEM); chemical analysis was performed by x-ray spectroscopy and scanning Auger electron spectroscopy.

Experimental Techniques

The GaAs substrates were p-type, Zn-doped, with a dopant concentration of 2.5×10^{18} cm^{-3} for the (100) wafers and 2.0×10^{18} cm^{-3} for the (111) wafers. The polished wafers were cleaned by trichloroethylene, acetone, and ethyl alcohol, etched in H_2O_2-H_2SO_4-H_2O solution for 2 min and then were soaked in HCl-H_2O solution for 5 min. After rinsing in deionized water, the wafers were coated with gold by electron beam evaporation at a pressure of 10^{-6} Torr. The thickness of the gold film was measured by an interference microscope.

Heat-treatment was done either in vacuum (10^{-6} Torr) inside the bell jar of a vacuum system or on a hot stage in air or flowing nitrogen. The sample temperature was measured by an iron-constantan thermocouple. Heating in vacuum was achieved by a furnace with a small thermal mass placed inside an evacuated bell jar; the temperature of the furnace was controlled by a TECCO temperature programmer. EGA was performed *in situ* with a Finnigan 3200 mass spectrometer, which had a specially designed sample probe controlled by a temperature programmer to an accuracy of ±5°C. The ionization potential of the mass spectrometer was 70 eV. SEM was performed *ex situ* by using a JEOL JSM 35 scanning electron microscope with a KEVEX energy dispersion x-ray attachment. For elemental depth profile analysis, a Physical Electronics scanning Auger system with an electron beam spot size of 0.1 μm was used.

Correlation of the Physiochemical Effects

The Au/GaAs samples were heated to various temperatures at an average heating rate of ~30°C/min for EGA studies. Then the samples were allowed to cool to room temperature, removed from the mass spectrometer, and their color and microstructure observed. Figure 1 shows the results obtained on four 690Å Au/(100)GaAs samples which were separately heated in the mass spectrometer at $\sim 5 \times 10^{-7}$ Torr to 225°, 255°, 273°, and 400°C. These temperatures were on both sides of the peak temperature for arsenic evolution, *i.e.*, 269°C, as indicated in Fig. 1 (a). The sample heated to 225°C did not exhibit arsenic evolution; its color remained gold and it showed little microstructural change. [See Fig. 1(b)]. In spite of little microstructural change, small rectangular protrusions were faintly visible underneath a film of unreacted gold. The sample heated to 255°C underwent a small amount of arsenic evolution; its color turned silver, and it exhibited a dramatically different microstructure consisting mainly of the interconnected, irregularly shaped protrusion shown in Fig. 1(c). The sample heated to 273°C had almost completed arsenic evolution; its color turned silver and it exhibited a microstructure consisting mainly of aligned rectangular protrusions. [See Fig. 1(d).] The sample heated to 400°C completed the arsenic evolution; its color turned silver and it exhibited a microstructure [Fig. 1(e)] quite similar to that of Fig. 1(d). Fig. 1(d) and (e) are similar to those reported by previous workers (2, 7-11).

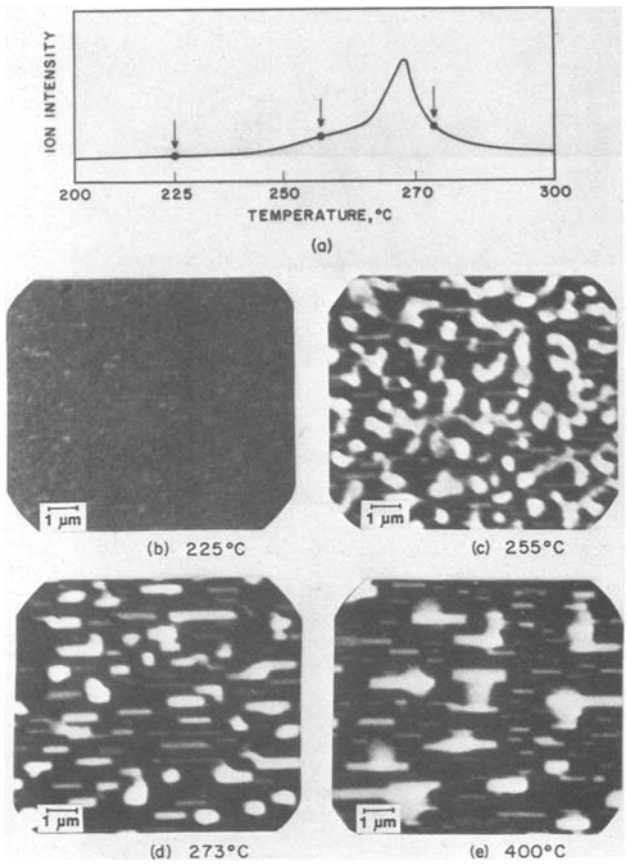

Fig. 1. EGA and SEM results on 690Å Au/(100) GaAs. (a) EGA As^+ ion temperature profile at $\sim 5 \times 10^{-7}$ Torr. (b) SEM micrograph of sample heated to 225°C during EGA [arrow in (a)]. (c) SEM micrograph of sample heated to 255°C during EGA [arrow in (a)]. (d) SEM micrograph of sample heated to 273°C during EGA [arrow in (a)]. (e) SEM micrograph of sample heated to 400°C during EGA [not indicated in (a)].

We have thus found that (*i*) little microstructural change occurred before arsenic evolution, (*ii*) a new microstructure consisting of interconnected irregularly shaped protrusions appeared after a small amount of arsenic evolution, (*iii*) the previously reported microstructure consisting of aligned rectangular protrusions appeared after the arsenic evolution was near completion, (*iv*) little additional microstructural change occurred upon further heating after the completion of arsenic evolution, (*v*) the gold-to-silver color transition occurred after a small amount of arsenic evolution; (*vi*) the silver color was not affected by further arsenic evolution or further microstructural change. Thus, the completion of arsenic evolution signifies the attainment of equilibrium, which is characterized by the microstructure in Fig. 1(e) and the silver color.

The detailed characteristics of arsenic evolution, color transition, and microstructural change were found to depend on the gold film thickness and the ambient pressure. These dependences are given below for each physiochemical effect.

Arsenic Evolution

Figure 2 shows the effect of film thickness on the peak temperature for arsenic evolution. Two Au/(100)GaAs samples with film thicknesses of 200 and 2100Å were used. The heating was done at 25°C/min in the mass spectrometer at $\sim 5 \times 10^{-6}$ Torr. The peak temperature was observed at 305°C for the 200Å sample, and at 358°C for the 2100Å sample. The increase in the peak temperature with increasing film thickness was more significant than that reported by Kinsborn *et al.* (2), probably partly due to the higher heating rates used in this work. The effect of heating rate is described later in this section.

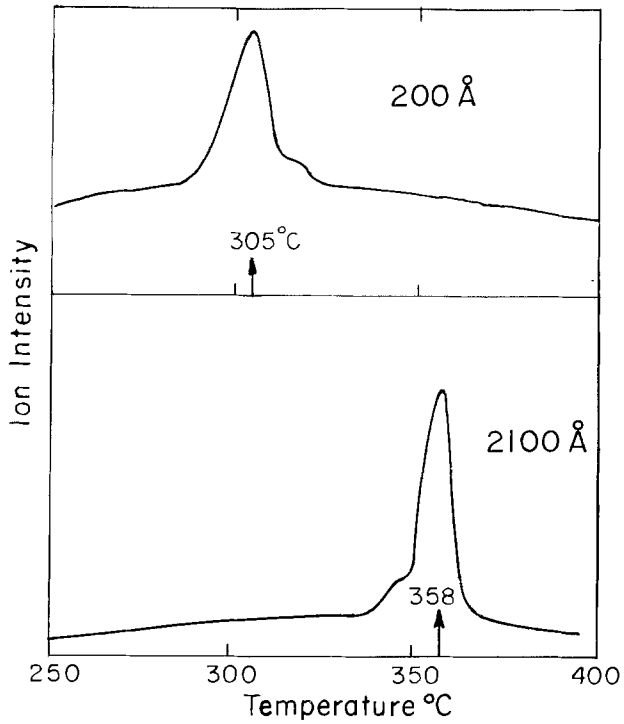

Fig. 2. EGA As^+ ion temperature profiles of 200Å Au/(100) GaAs and 2100Å Au/(100) GaAs at ~5 × 10^{-6} Torr.

In addition to As^+ ions (shown in Fig. 2), ions of As_2^+, As_3^+, and As_4^+ were simultaneously observed. Except for the difference in intensity, all four arsenic species were observed at the same temperatures, with the same shape in the plot of ion intensity *vs.* temperature. For this reason, such plots for ions other than As^+ are not shown here. No Ga evolution was detected.

The relative quantities of the four arsenic species were found to follow an order which was consistently

$$As_4 > As_2 > As > As_3$$

for film thicknesses larger than 1000Å. For smaller film thicknesses, the ordering did not follow a consistent pattern from sample to sample.

The dependence of arsenic evolution on the heating rate was also explored. Figure 3 shows the plots of the As^+ ion intensity against the temperature for 1000Å Au/(100) GaAs heated at 25°C/min and 100°C/min in the mass spectrometer at ~5 × 10^{-6} Torr. The width of the peak was found to decrease with increasing heating rate. The difference in peak temperature for the two heating rates in Fig. 3 was due to a systematic error of temperature measurement.

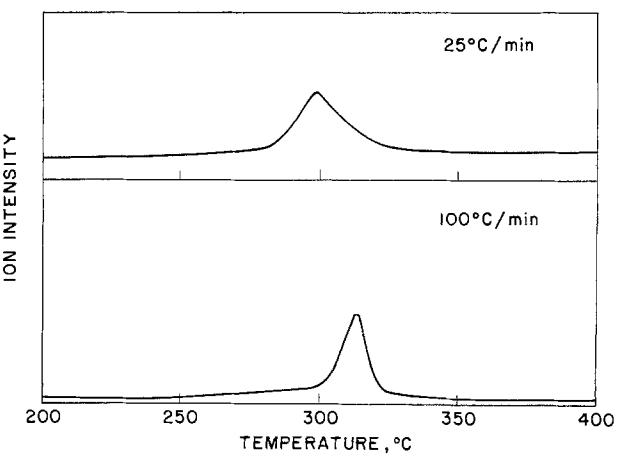

Fig. 3. EGA As^+ ion temperature profiles of 1000Å Au/(100) GaAs at ~5 × 10^{-6} Torr and heating rates of 25°C/min and 100°C/min.

Comparison of the peak arsenic evolution temperatures of Fig. 1 (~5 × 10^{-7} Torr) and Fig. 2 (~5 × 10^{-6} Torr) suggests that the peak temperature decreases with decreasing air pressure. The pressure dependence was investigated systematically by observing the gold-to-silver color transition, as given in the next section.

Similar *in situ* mass spectrometric study on Pd/(100)GaAs led to the detection of As, As_2, As_3, As_4, and PdGa. At a heating rate of 100°C/min, the peak arsenic evolution was observed at around 380C.

Gold-to-Silver Color Transition

Figure 4 shows the variation of the gold-to-silver color transition temperature (T) with the hydrostatic air pressure (P) ranging from 10^{-6} Torr to 1 atm. The transition temperature at each pressure was determined visually by heating a number of samples separately to different temperatures and noting the temperature which resulted in a color between gold and silver. The heating was carried out at a rate of 100°C/min and the temperature was then held constant at the maximum for 5 min. After that, the heater was turned off and the sample was allowed to cool to room temperature. The temperature range through which the color change took place was ~20°C wide. Because of the high heating rate used, the transition temperatures given in Fig. 4 are not equilibrium transition temperatures. However, Fig. 4 clearly shows that the color transition temperature increased with increasing pressure.

Also shown in Fig. 4 is the variation of the color transition temperature with the gold film thickness. Thicknesses of 200, 690, and 2750Å were employed. For each pressure, the transition temperature increased with increasing film thickness.

In a plot of log P against $1/T$, the data points for each film thickness fell roughly on a straight line, having a negative slope. The magnitude of the slope appeared to increase with increasing film thickness. This suggests the similarity of the transition with the vaporization of arsenic liquid, for which the magnitude of the slope gives the heat of vaporization. This

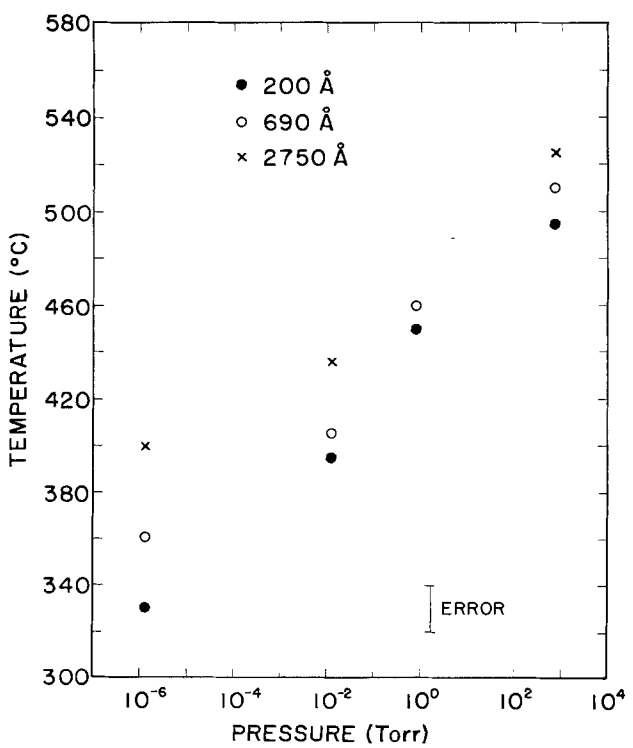

Fig. 4. Variation of the gold-to-silver color transition temperature with the hydrostatic air pressure for Au/(100) GaAs of three different Au film thicknesses.

In addition to studying the color transition in air, this transition was observed in nitrogen at 1 atm, where the transition temperature was 530°C for 1000Å film thickness. This value is close to the value of 525°C determined in air at 1 atm for the same film thickness. Thus, the pressure dependence in nitrogen is probably similar to that in air (Fig. 4), implying that oxidation, if any, does not affect the pressure dependence.

Microstructural Changes

To study the process of formation of the new microstructure, namely, the interconnected irregularly shaped protrusions [Fig. 1(c)], three 200Å Au/(100) GaAs samples were separately heated in a vacuum of $\sim 10^{-6}$ Torr to 295°, 310°, and 336°C at a heating rate of 100°C/min. The samples were then held at the respective maximum temperatures for 25 min. After this, the furnace was turned off and the samples were allowed to cool to room temperature at a cooling rate of ~70°C/min. In contrast to Fig. 1, a small film thickness was used in order to reveal the microstructural changes at the interface. Figure 5 shows SEM micrographs of these samples after heating. After the 295°C heat-treatment, Au-rich rectangular protrusions were observed below a thin gold film. After the 310°C heat-treatment, the breaking up of the thin gold film was observed. After the 336°C heat-treatment, the gold film balled up and was replaced by irregularly shaped globules which bridged the rectangular protrusions. The thicker the gold film, the higher was the temperature needed for obtaining the microstructure shown in Fig. 5(c). Because of the limited heating time, the microstructure transition temperatures given above are not equilibrium transition temperatures.

Elemental analysis of various parts of the microstructure of Fig. 5(c) was performed by selected area x-ray spectroscopy. Figure 6 shows x-ray spectra obtained at (a) the dark region, (b) the rectangular bright region, and (c) the large irregular bright region. The dark regions were found to be primarily GaAs, with a small amount of gold; the bright rectangular regions were relatively rich in gold; the large bright irregular regions were very rich in gold. In support of the results of x-ray spectroscopy are results of scanning Auger spectroscopy. Shown in Fig. 7 are elemental concentration profiles of 1000Å Au/(100) GaAs before and after heating. The heating was carried out in vacuum ($\sim 10^{-6}$ Torr) from 25° to 400°C at 100°C/min. The profiles after heating shown in Fig. 7 were obtained at an Au-rich globule. Figure 7 indicates that interdiffusion had occurred at room temperature and that heating increased the extent of interdiffusion. The sputtering rate of gold was ~128 Å/min in obtaining the Auger concentration profiles.

A similar microstructural study was carried out with (111) GaAs. Figure 8 shows SEM micrographs of 200 and 800Å Au/(111) GaAs after heating in vacuum ($\sim 10^{-6}$ Torr) from 25° to 400°C at 100°C/min. Triangular Au-rich protrusions were observed in the 200Å sample [Fig. 8(a)]. The triangular shape was less clear for thicker gold films, *i.e.*, the 800Å sample [Fig. 8(b)]. Elemental concentration profiles obtained by scanning Auger spectroscopy after heating are shown in Fig. 9 for the 800Å sample at an Au-rich globule and off the globules. At the surface, a 50Å thick region rich in oxygen and gallium was observed, probably due to an oxide of Ga at the surface. Figure 9 shows the occurrence of interdiffusion. The region off the Au-rich globules was not pure GaAs but contained a small amount of gold.

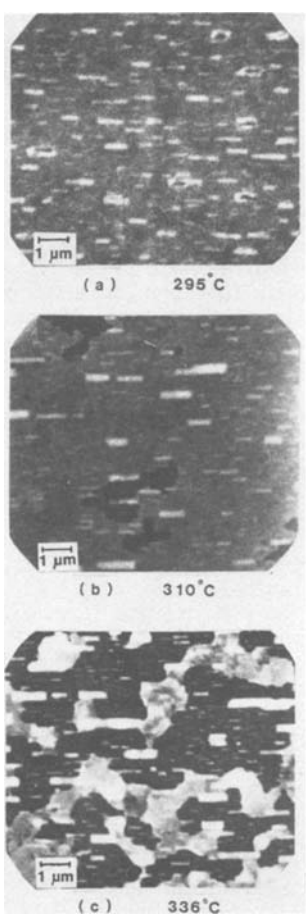

Fig. 5. SEM micrographs of three 200Å Au/(100) GaAs samples which were separately heated in vacuum to (a) 295°C, (b) 310°C, and (c) 336°C.

Relationship of Microstructural Changes with Etching of GaAs

To investigate the relationship of the microstructural changes with the structure of the GaAs substrate, the surface morphology of chemically etched GaAs was compared with that of heated Au/GaAs.

Figure 10(a) and (b) show SEM micrographs at two different magnifications of the (100) GaAs surface which had been etched for 6 min by the Sirtl etch, a solution of 33 weight percent (w/o) CrO_3 and 46 w/o HF. The micrograph of higher magnification [Fig. 10(b)] clearly shows that the etching produced rectangular hillocks. The sides of the rectangular etch hillocks were aligned along the [110] and [1$\bar{1}$0] directions. This alignment is similar to that of the rectangular Au-rich protrusions observed in heated Au/(100) GaAs [Fig. 1(d)]. Figure 10(c) and (d) show SEM micrographs of (111) GaAs which had been etched in a similar manner. Hexagonal (almost triangular) etch hillocks were observed, in contrast to the rectangular etch hillocks observed on the (100) surface. These hillocks were similar to the triangular (almost hexagonal) Au-rich protrusions observed in heated Au/(111) GaAs [Fig. 8(a)].

It was observed by Olsen *et al.* (12) that the rectangular etch hillocks of (100) GaAs were aligned in such a way that the directions of alignment on the two sides of a wafer were perpendicular to each other. Moreover they suggested that the formation of such etch hillocks was due to the different etching rates for the (111) As and (111) Ga planes of GaAs. Figure 11 shows the SEM micrographs of an Au/(100) GaAs/Au sample (*i.e.* GaAs with a 200Å gold film on each side) after heating. The alignment direction of the rectangular Au-rich protrusions on one side [Fig. 11(a)] was found to be perpendicular to that on the other side [Fig. 11(b)]. This directional behavior is similar to that of the rectangular etch hillocks.

The strong similarity between the etched GaAs surface and the heated Au/GaAs suggests that the rectangular or triangular Au-rich protrusions and the etch hillocks have similar origins, as suggested by

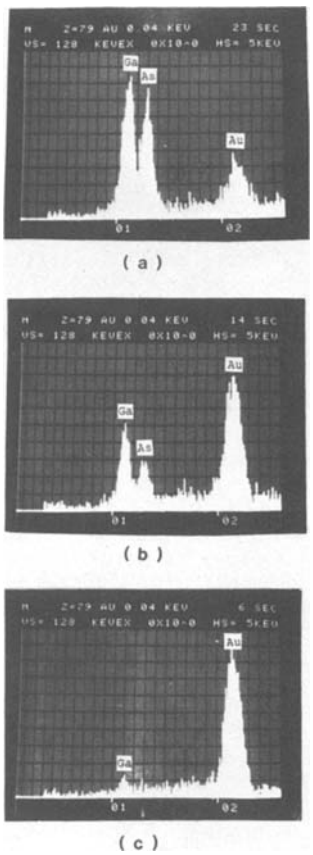

Fig. 6. X-ray spectra obtained at various parts of the microstructure of Fig. 5(c): (a) the dark region, (b) the rectangular bright region, and (c) the large irregular bright region.

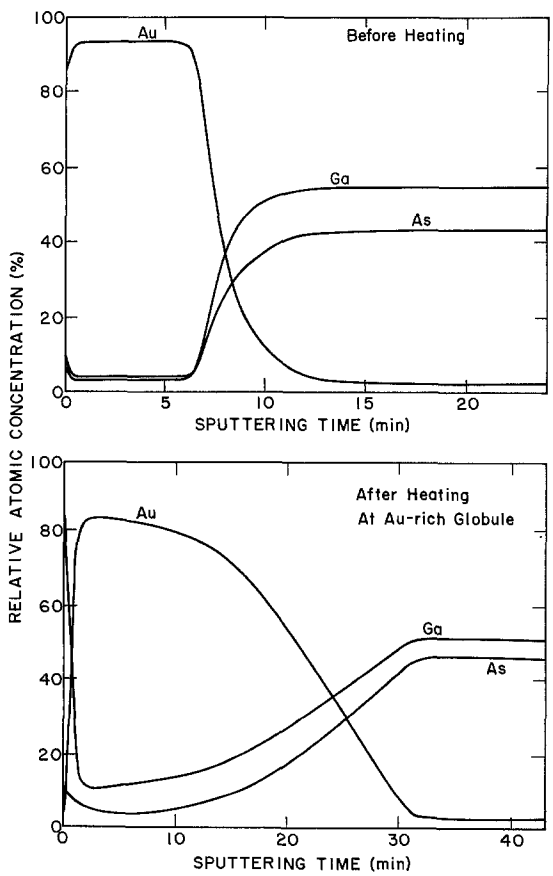

Fig. 7. SAM elemental concentration profiles perpendicular to the Au-GaAs interface for 1000Å Au/(100) GaAs before and after heating.

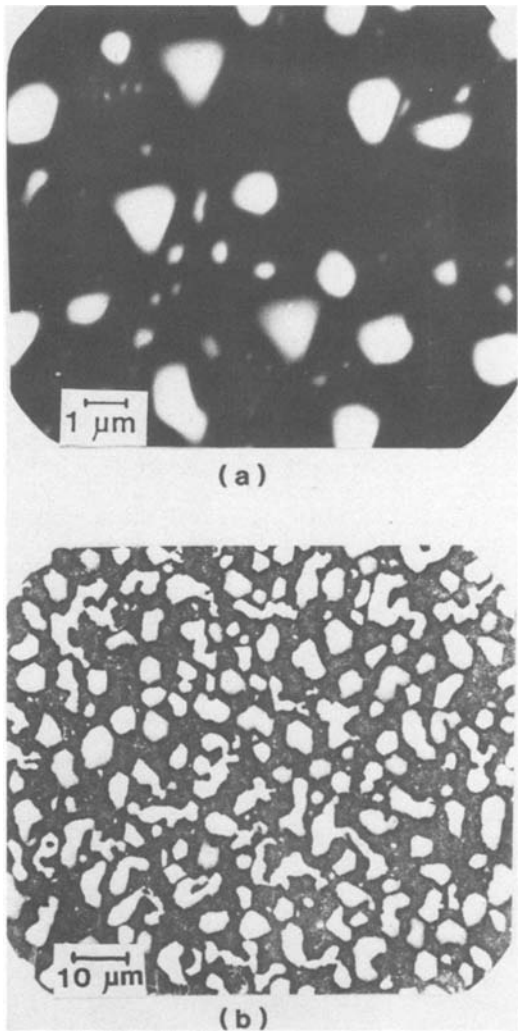

Fig. 8. SEM micrographs of Au/(111) GaAs after heating for Au film thicknesses (a) 200Å, and (b) 800Å. Note that (a) and (b) have different scales.

Kumar (8). The reaction between Au and GaAs may be considered as the chemical etching of GaAs by Au. Since Au "removes" Ga more effectively than As, we may consider Au as a preferential etchant. Vozmilova *et al.* (13) showed that different etchants have different relative etching rates on the (111) As and (111) Ga planes of GaAs. Therefore, the aspect ratio of the rectangular etch hillocks obtained by using the Sirtl etch is not necessarily similar to those of the hillocks obtained by other etchants.

Discussion

The pressure dependence of the gold-to-silver color transition temperature was observed for the first time. The transition temperature increased with increasing air pressure ranging from 10^{-6} Torr to 1 atm. Similar pressure dependence was observed for the arsenic evolution temperature in the pressure range from $\sim 5 \times 10^{-7}$ to $\sim 5 \times 10^{-6}$ Torr. This dependence is attributed to the arsenic evolution process, which accompanies the color transition. The transition temperature of 480°-515°C observed by Miller (4) for heating in H_2 (1 atm) agrees with the value for heating in air (1 atm) determined in this work.

The arsenic evolution phenomenon was studied by *in situ* mass spectrometric evolved gas analysis. In addition to As and As_2, which were observed by previous workers (1-3), As_3 and As_4 were observed. Furthermore, the abundance of the four arsenic species was found to be in the order $As_4 > As_2 > As > As_3$

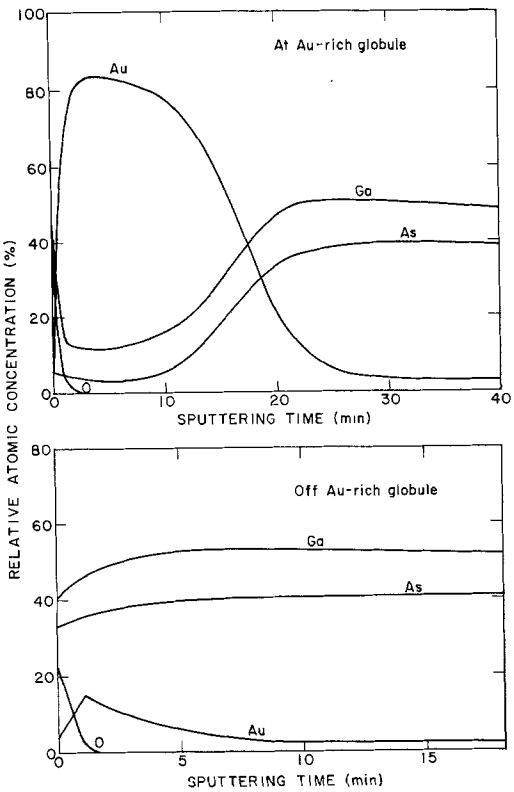

Fig. 9. SAM elemental concentration profiles perpendicular to the Au-GaAs interface for 800Å Au/(111) GaAs after heating (a) at an Au-rich globule, (b) off the Au-rich globules.

for gold film thicknesses larger than 1000Å. For thinner gold films, no consistent ordering was observed. On the other hand, the abundance of the arsenic species evolved is in the order $As_4 > As_2 > As$ for As metal at 700°C and is in the order $As_2 > As_4 > As$ for GaAs at 900°-1250°C (14). The resemblance of the ordering between Au/GaAs and As metal suggests similarity between these two arsenic evolution processes. The presence of As_3 from our Au/GaAs samples is probably due to the high sensitivity of our gas detection technique. It is not clear if the formation of arsenic molecules occurs at the surface or in the Au film. The

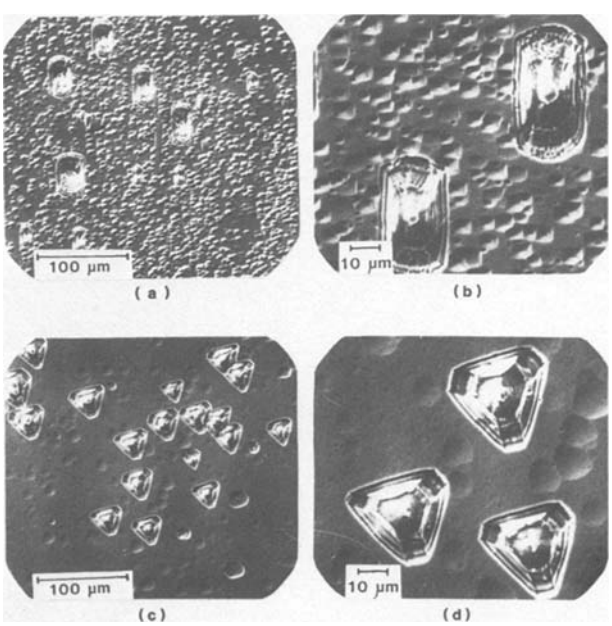

Fig. 10. SEM micrographs of GaAs (without gold) after etching. (a) and (b): (100) GaAs at two different magnifications, (c) and (d): (111) GaAs at two different magnifications.

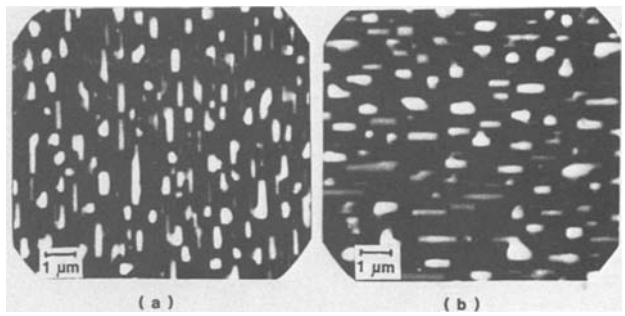

Fig. 11. SEM micrographs of the two sides of an Au/(100) GaAs/Au sample after heating.

widening of the arsenic evolution peak with decreasing heating rate (Fig. 3) is probably because a higher heating rate provides less time for equilibration and results in a larger arsenic concentration gradient.

The rectangular protrusions observed by SEM on Au/(100) GaAs after heating were also noted by previous workers by SEM (2, 9-11) or TEM (7, 8). The triangular protrusions which we found by SEM on Au/(111) GaAs after heating were observed by Kumar (8) by TEM. The elemental analysis results obtained here are in agreement with previous analyses of Au/GaAs using selected area electron diffraction (7) and x-ray spectroscopy (11), and of Au:Ge/GaAs using scanning Auger spectroscopy (9). The fact that interdiffusion occurred in Au/GaAs at room temperature is in agreement with the Auger electron spectroscopy results of Hiraki *et al.* (15).

The new microstructure of irregular and interconnected protrusions reported here [Fig. 1(c)] is an intermediate state which occurs prior to the formation of the large aligned rectangular protrusions [Fig. 1(d)] in Au/(100) GaAs. It should be noted that small aligned rectangular protrusions coexist with the large irregular protrusions and are formed prior to the formation of the large irregular protrusions. A small amount of arsenic evolution accompanies the formation of the large irregular protrusions. In contrast, negligible arsenic evolution accompanies the formation of the small rectangular protrusions, which can be faintly seen under the gold film in Fig. 1(b). To reach the final state represented by the large aligned rectangular protrusions [Fig. 1(d)], the arsenic evolution process needs to be close to completion. Once this final state has been reached, further heating causes little additional microstructural change [Fig. 1(e)]. Although the new microstructure reported here is an intermediate state, it can be obtained as a stable room temperature structure by careful control of the heating conditions. It is of technological interest to investigate the electrical characteristics of this intermediate state.

The process of the microstructural changes was followed *ex situ* by SEM examination of 200Å Au/(100) GaAs. As shown in Fig. 5, the process appears to involve (*i*) formation of small rectangular protrusions at the interface underneath a thin unreacted Au film, (*ii*) breaking up of the gold film, and (*iii*) balling up of the gold film to form irregularly shaped protrusions.

The silver color is characteristic of both the intermediate state [Fig. 1(c)] and the final state [Fig. 1(d)], whereas the gold color is maintained after the small interfacial microstructural change which occurs prior to arsenic evolution [Fig. 1(b)]. The origin of the silver color is not clear, although it might be due to the color of the Au-Ga compound(s) (16).

The arsenic evolution temperature, the color transition temperature, and the microstructural change temperature were all found to increase with increasing gold film thickness. This common characteristic is a

further indication of the close relationship among these three physiochemical effects.

Acknowledgments

Support from the Materials Research Laboratory Section, Division of Materials Research, National Science Foundation under Grant No. DMR 76-81561 A01 is acknowledged. The authors greatly appreciate the assistance of Dr. Lynn Rathbun of the National Research and Resource Facility for Submicron Structures at Cornell University in performing the scanning Auger electron spectroscopy. They also thank Professor Xian-Fu Zeng of Carnegie-Mellon University for stimulating discussion.

Manuscript submitted March 30, 1982; revised manuscript received Sept. 9, 1982.

Any discussion of this paper will appear in a Discussion Section to be published in the December 1983 JOURNAL. All discussions for the December 1983 Discussion Section should be submitted by Aug. 1, 1983.

Publication costs of this article were assisted by Carnegie-Mellon University.

REFERENCES

1. T. Sebestyen, M. Menyhard, and D. Szigethy, *Electron. Lett.*, **12**, 96 (1976).
2. E. Kinsbron, P. F. Gallagher, and A. T. English, *Solid-State Electron.*, **22**, 517 (1979).
3. D. D. L. Chung and L. K. Wong, Proc. 10th Conf. of North American Thermal Analysis Society, pp. 149-151, Boston (1980).
4. D. C. Miller, *This Journal*, **127**, 468 (1980).
5. H. Gyulai, J. W. Mayer, V. Rodriquez, A. Y. C. Yu, and H. J. Gopen, *J. Appl. Phys.*, **42**, 3578 (1971).
6. C. J. Todd, G. W. B. Ashwell, J. D. Speight, and R. Heckingbottom, in "Metal-semiconductor Contacts," p. 171, The Institute of Physics Conf. Ser. No. 22, London (1974).
7. T. J. Magee and J. Peng, *Phys. Status Solidi A*, **32**, 695 (1975).
8. K. Kumar, *Jpn. J. Appl. Phys.*, **18**, 713 (1979).
9. A. Christou, *Solid-State Electron.*, **22**, 141 (1979).
10. J. M. Vanderberg and E. Kinsbron, *Thin Solid Films*, **65**, 259 (1980).
11. X.-F. Zeng and D. D. L. Chung, *ibid.*, **93**, 207 (1982).
12. G. H. Olsen, M. S. Abrahams, and T. J. Zamerowski, *This Journal*, **121**, 1650 (1974).
13. L. N. Vozmilova and V. T. Maslennikova, *Inorg. Mat.*, **8**, 1147 (1972).
14. F. E. Roberts, *Phys. Status Solidi*, **22**, 373 (1967).
15. A. Hiraki, S. Kim, W. Kammura, and M. Iwami, *Surf. Sci.*, **86**, 706 (1979).
16. V. Simic and Z. Marinkovic, *Thin Solid Films*, **34**, 179 (1976).

Incorporation of a Resistivity-Dependent Contact Radius in an Accurate Integration Algorithm for Spreading Resistance Calculations

R. Piessens

Department of Computer Sciences, Catholic University of Leuven, Leuven, Belgium

and W. B. Vandervorst and H. E. Maes[1]

Department of Electrical Engineering - E.S.A.T., Catholic University of Leuven, Leuven, Belgium

ABSTRACT

An integration technique is described which allows the rapid calculation of the correction factor introduced by Schumann and Gardner for spreading resistance calculations. The time required to calculate one point is typically 0.03 sec on a VAX-11/780 minicomputer, the accuracy being better than 0.1%. The technique can be easily implemented for using a resistivity-dependent contact radius. Model spreading resistance data are used to illustrate the efficiency of the integration technique.

Two-probe spreading resistance measurements are widely used for determining doping profiles in semiconducts (1-4). The conversion of the measured resistance profile to a resistivity profile has been the subject of a number of publications during the last decade (1, 2, 5-16). One conversion scheme which is very attractive with respect to speed and computation time is the local slope approximation proposed by Dickey (5). This method, however, is not very accurate in some cases, and the computed resistivities can differ from the correct solution by as much as 25% as was shown by Albers (6). Another powerful scheme is based on the multilayer approach of Schumann and Gardner (7, 8). The solution of this approach is given by

$$R = \frac{\rho_n}{2a} CF \qquad [1]$$

where R is the resistance measured on the nth-layer with resistivity ρ_n, a is the contact radius, and CF accounts for the influence of the resistivities of the underlying layers and is given by

$$CF = \frac{4}{\pi}\int_0^\infty [1 + 2\theta(t)]\left\{\frac{J_1(at)}{at} - \frac{J_0(st)}{2}\right\}\frac{\sin(at)}{t}\,dt \qquad [2]$$

In this formula a is the separation between the probes, J_0 and J_1 are the Bessel functions of zero and first order, respectively, and $\theta(t)$ is a function which is determined by the resistivity profile of the sample. The

[1] H. E. Maes is a research leader of the Belgian National Science Foundation (NFWO).

Key words: spreading resistance, multilayer analysis, impurity profiles.

derivation of Eq. [2] was based on the assumption of a variable current density distribution under the probe contact. An alternative approach is to assume a uniform current density distribution (17). The correction factor is then given by (20)

$$CF = \frac{8}{\pi}\int_0^\infty [1 + 2\theta(t)] \left\{ \frac{J_1(at)}{at} - \frac{J_0(st)}{2} \right\} \frac{J_1(at)}{t} dt \quad [3]$$

The validity of both formulations was investigated by Leong *et al.* in a series of papers (18-22). From their work we may state that (*i*) in case of a layer on top of a conducting substrate (perfectly conducting or of finite conductivity) the uniform density distribution is preferable as long as the thickness of the layer is less than 0.3 times the contact radius; (*ii*) in case of an insulating substrate the choice of the distribution is not relevant since the resistance is almost entirely determined by the lateral flow of the current and not by the distribution under the contacts; (*iii*) the results differ at most by 8% from each other. It should be remarked here that since the contact radius is of the order of 1-4 μm (2), the uniform distribution is more suited for submicron profiles (0.3-1.2 μm deep) while the variable distribution complies more for the deeper profiles.

We decided to use the variable current density distribution by realizing that most of the submicron profiles to be profiled, are formed by a junction (*i.e.*, emitter region of a bipolar transistor, the drain and source contacts of MOS transistors) which corresponds to an insulating boundary where the distribution does not matter, and that for the deeper profiles the variable density distribution is the best approximation. Finally it should also be mentioned that the use of the variable current density distribution allows obtaining a rather simple expression for the integral of Eq. [2] where for Eq. [3] such an expression is not available.

The use of Eq. [1] was originally limited by two problems. First of all in order to determine $\theta(t)$ one had to invert a $(2N \times 2N)$ matrix which becomes an enormous task for a large number of layers N. This problem could be circumvented by different authors by using a power-law interpolation (9), a reduction technique of the $(2N \times 2N)$ matrix inversion to the solution of N (2×2) matrices (10), or finally by the widely used recurrence relation of Choo *et al.* (11). The second problem arises from the integral in Eq. [2] or Eq. [3] which contains strongly oscillating functions. As shown by Lee (12) standard integration techniques would require an extremely large number of evaluations of the integrand in order to obtain a reasonable accuracy. Choo *et al.* (13) solved this problem by splitting the integral into three pieces and using an adaptive Simpson rule for each of them. Using 150 integrand evaluations they obtain an accuracy better than 2% (14). However as pointed out in recent papers (6, 14) the accuracy of the integration is extremely important in the conversion procedure. We have found that the inaccuracy should be less than 0.1% in order to calculate the resistivities with an inaccuracy of less than 1% (14).

Requiring an accuracy of 0.1% on the integration does not mean that the final calculated values of a real profile will be accurate within 1%. It only guarantees that Eq. [1] is solved within 1% and that the calculated resistivities do not have an error, which may be quite large (14), simply due to the limited integration accuracy (6).

In addition to the integration error there are still other factors influencing the accuracy, such as calibration errors and bevel rounding effects which become the limiting factors when Eq. [1] is solved accurately.

With these conclusions in mind one can conclude that the use of this technique is inadequate. In a later publication, Choo *et al.* (15) proposed an integration procedure based on a 33-point Gauss-Laguerre formula which is about 6-8 times faster than the Simpson integration. Unfortunately the inaccuracy with this formula is as high as 5%, which can cause serious errors (14). Following the approach of Choo *et al.* (15), a modified formula for Eq. [2] has been derived (14) which can be integrated by a 150-points Gauss-Laguerre formula with an accuracy of 0.15%.

Another technique based on the use of pre-stored partial integrals as proposed by D'Avanzo *et al.* (1, 2), also attains an inaccuracy less than 0.1% using 70 evaluations of the integrand and 210 calculations of coefficients. The calculations of the partial integrals are performed using the Romberg method and are very slow but need to be done only once.

In a recent paper Berkowitz *et al.* (16) proposed an integration technique based upon an approximation of the part of the integrand in Eq. [2] containing the Bessel functions. This technique requires only 22 evaluations of $\theta(t)$ but reaches an accuracy of not better than 1%.

It should be emphasized that all the methods mentioned above make use of the fact that, if the effective contact radius does not change with resistivity, the Bessel functions need to be calculated only once and can be stored in the computer. The assumption that the effective contact radius is independent of resistivity is however not entirely justified as can be concluded from the calibration curves of resistance *vs.* resistivity (1, 2, 9, 23-26). Usually a relation of the form

$$R = A\rho^B \quad [4]$$

is found with a B value between 0.8-1.2 and A varying from 900 to 6000 depending on impurity type, crystal orientation, and surface preparation (2, 25). A number of contact models have been proposed which more or less describe the dependence of the contact radius on resistivity (27-30). [For a detailed discussion on contact models see Ref. (30)]. Kramer and Van Ruyven (31) proposed a model with a constant contact radius and a resistivity dependent barrier term $K(\rho)$. This term is defined as

$$K(\rho) = 1 + \frac{R_B}{R_S}$$

with R_B = the barrier resistance and R_S = the spreading resistance $\rho/2a$.

It is clear that $K(\rho)$ should always be greater than one. However when assuming a constant radius a, Kramer and Van Ruyven found values less than one for very high and very low resistivities. Measurements by other investigators, mentioned in Ref. (31), also indicate values of K less than one. As Kramer and Van Ruyven (31) pointed out, this invalidates the assumption of a constant contact radius.

Strong evidence for the resistivity-dependent contact radius can also be found in the work of Ehrstein *et al.* (32). They calculated the resistivity profile using different conversion algorithms with constant and with varying contact radius and compared the results with SIMS and C-V measurements. They found that when using a variable contact radius the best agreement with the experiments can be obtained. Hence, incorporation of a resistivity-dependent contact radius into Eq. [1] seems to be necessary (30). An attempt in this direction was made by Yeh (33), who performed the double iteration on resistivity and contact radius using the slow matrix-inversion technique for determining $\theta(t)$. Morris *et al.* (34) also use a resistivity-dependent contact radius in their program SRPROF for epitaxial layers. The usefulness and the accuracy of this program however are very limited. Due to the simplicity of the equations in the local slope approximation of Dickey (5), this can be easily implemented when using a continuously changing contact radius (30, 32). Unfortunately this approach is not universally applicable with

sufficient accuracy, as can be deduced from model data calculations (6).

Looking at the Schumann and Gardner approach the problem becomes very tedious due to the complex integral function. Use of a resistivity-dependent contact radius is impossible with the method of D'Avanzo (1, 2) since the partial integrals have to be recalculated for each value of a. An intermediate solution, although very inefficient with respect to computer storage, would be to calculate the integrals for a number of values of a. For any arbitrary value of a an interpolation technique could then be used. This technique, however, will probably lack accuracy and speed.

In principle, the 150-points Gauss-Laguerre formula (14) is suited for incorporating a variation of a. However, changing the value of a means that one can no longer store the values of the Bessel functions as is usually done (13-15), but that one has to recalculate the Bessel function of the first order in each iteration on a. Using the normalized equation by replacing ta by x (15) does not solve the problem, since when doing so, the normalized probe spacing $d = s/a$ and $\theta(t/a)$ would now be a function of a. This then would require the recalculation of the Bessel function of zero order and the recalculation of the recurrence relation describing $\theta(t/a)$. This results in considerable long computation times.

The same problem exists for the integration technique of Berkowitz *et al.* (16). The original version was described for the normalized form of Eq. [2] with ta replaced by x. Their integration technique uses fixed values of x where the integrand is evaluated. This means, however, that $\theta(t/a)$ has to be recalculated each time a different value of a is used. This implies that the recurrence relation has to be applied for all the underlying layers each time a is changed. This results in long computation times.

Using the actual form of Eq. [2] with ta instead of x does not eliminate the problem since Berkowitz *et al.* (16) determine the points where the integrand is evaluated in terms of the normalized probe spacing and the zeros of the Bessel function of first order. Changing a would mean that the position of the zeros changes and hence necessitates evaluating the integrand at other points. This again requires the recalculation of $\theta(t)$.

With regard to the shortcomings of the above-mentioned techniques, we developed a new integration technique keeping in mind the following two requirements: first, the accuracy should be better than 0.1%, and second, the technique should be suited for incorporating a resistivity-dependent contact radius. It will be shown in the following sections that the developed method satisfies both requirements since accuracies better than 0.1% are obtained and since the Bessel functions are no longer evaluated due to the fact that the integral is computed analytically.

Description of the Integration

The correction factor of Eq. [2] can be written in the following form (11)

$$CF = \frac{4}{\pi}\int_0^\infty \left(\frac{1 - k(t)e^{-pt}}{1 + k(t)e^{-pt}}\right)\phi(t)\,dt \qquad [5]$$

where

$$\phi(t) = \left[\frac{J_1(at)}{at^2} - \frac{J_0(st)}{2t}\right]\sin at$$

$p = 2 \times d$ with d the thickness of one layer, $a =$ the contact radius, $s =$ the separation between the probes, $t =$ the integration variable, and $k(t)$ is given the recurrence relation of Choo (11). Equation [5] can be written as

$$CF = (4I_1 - 8I_2)/\pi \qquad [6]$$

where

$$I_1 = \int_0^\infty \phi(t)\,dt \qquad [7]$$

and

$$I_2 = \int_0^\infty G(t)\phi(t)\,dt \qquad [8]$$

where

$$G(t) = \frac{k(t)e^{-pt}}{1 + k(t)e^{-pt}} \qquad [9]$$

I_1 can be calculated analytically to give

$$I_1 = \frac{\pi}{4} - \frac{1}{2}\arcsin\left(\frac{a}{s}\right) \qquad [10]$$

For the computation of I_2, $G(t)$ is approximated by a sum of exponentials

$$G(t) \simeq e^{-pt}\sum_{l=0}^{M} c_l e^{-lqt} \quad 0 \leq t \leq \infty \qquad [11]$$

where q is a free parameter. The choice of q, M, and the computation of the coefficients c_l will be discussed later. When substituting Eq. [11] into Eq. [8] we obtain

$$I_2 \simeq \sum_{l=0}^{M} c_l \int_0^\infty e^{-(lq+p)t}\phi(t)\,dt \qquad [12]$$

The integral on the right-hand side of Eq. [12] can be evaluated analytically (35) using the expression

$$\int_0^\infty e^{-dt}\phi(t)\,at = \frac{1}{2}\left\{R\sqrt{1 + \left(\frac{\alpha}{a}\right)^2}\right.$$
$$\sin(\theta + \psi) - \left(1 + \left(\frac{\alpha}{a}\right)^2\right)\sin 2\theta$$
$$+ \arctan\left[\frac{R\sin\psi + \sqrt{1 + \left(\frac{\alpha}{a}\right)^2}\sin\theta}{R\cos\psi + \sqrt{1 + \left(\frac{\alpha}{a}\right)^2}\cos\theta}\right]$$
$$\left. - \arcsin\frac{2a}{\nu_1 + \nu_2}\right\} \qquad [13]$$

where

$$\theta = \arctan\frac{a}{\alpha}$$

$$R = \sqrt[4]{\left(\frac{\alpha}{a}\right)^4 + 4\left(\frac{\alpha}{a}\right)^2}$$

$$\psi = \frac{1}{2}\arctan\frac{2a}{\alpha}$$

$$\nu_1 = \sqrt{\alpha^2 + (s + a)^2}$$

$$\nu_2 = \sqrt{\alpha^2 + (s - a)^2}$$

We now consider the construction of the approximation of $G(t)$, *i.e.*, Eq. [11]. Substituting $e^{-qt} = u$, we have for $e^{pt} \cdot G(t)$ in Eq. [9] and [11]

$$\frac{k\left(-\frac{1}{q}\ln(u)\right)}{1 + k\left(-\frac{1}{q}\ln(u)\right)u^{p/q}} \simeq \sum_{l=0}^{M} c_l u^l \quad \text{for } 0 \leq u \leq 1 \qquad [14]$$

The construction of the polynomial approximation in Eq. [14] is a standard problem in numerical analysis and several computer programs are available, but of course, the efficiency of the method and the accuracy of the final result depend on the approximation method used. The following technique, based on a Chebyshev

polynomial approximation (36), has provided excellent results. Using a very efficient Fast Fourier Transform technique (37), the coefficients b_l are computed in the approximation

$$\frac{uk\left(-\frac{1}{q}\ln(u)\right)}{1+k\left(-\frac{1}{q}\ln(u)\right)u^{p/q}} \simeq \sum_{l=0}^{12} b_l T^*_l(u) \quad [15]$$

where $T^*_l(u)$ is the shifted Chebyshev polynomial of the first kind and degree l. It is well known that fast FFT-algorithms can be developed for some special cases (38). The use of 12 or 24 polynomials in Eq. [15] presents such a case (38). We tried 12 as well as 24 polynomials in Eq. [15]. From the calculations it turned out that the coefficients b_l ($l > 12$) were so small that they did not bring any change in the calculated result. Only in case of an insulating substrate neither 12 nor 24 polynomials were able to approximate the integrand accurately. This special case shall be treated further.

The accuracy of the fit can be deduced from the fact that the coefficients b_l form a decreasing row with b_l for the largest values of l, being very small (typically less than 10^{-4}). A small value of b_l means that the approximation is no longer improved by an additional Chebyshev polynomial. The parameter q must be chosen so that the Chebyshev series expansion in Eq. [15] is rapidly convergent. From an extensive set of calculations we found $q = 0.2 \times 10^{-6}$ to be an appropriate value. It must be emphasized that the choice of q was not critical in order to obtain the required accuracy. After expanding $T^*_l(u)$ in terms of u^j ($0 \leq j \leq l$) using standard formulas, dividing both sides of Eq. [15] by u and neglecting the term in $1/u$, the approximation of Eq. [14] is obtained. Neglecting the term in $1/u$ does not introduce any serious error since the coefficient corresponding to this term is very small, usually less than 10^{-15}. It should be noted that the approximation requires only 12 evaluations of the function $k(t)$ for the computation of the 13 coefficients. Hence this is approximately one evaluation of $k(t)$ for each b_l.

When the resistance of the substrate is very high, $G(t)$ becomes very large in the neighborhood of $t = 0$. In the case of a perfectly insulating substrate $G(t)$ even has a singularity at $t = 0$. In this case it is impossible to approximate $G(t)$ by a sum of exponentials (Eq. [11]). The method described above is then modified as follows. Instead of trying to approximate $G(t)$ in $(0, \infty)$ by a sum of exponentials, we only approximate $G(t)$ in the interval (L, ∞) by Eq. [11], where L is a positive real number. By an appropriate choice of L, the singularity of $G(t)$ is eliminated and the approximation is quite accurate.

The sum of exponentials represents now a function $G^*(t)$ which is almost identical to $G(t)$ for t larger than L but differs from $G(t)$ for t smaller than L. This is illustrated in Fig. 1.

$G^*(t)$ can now be described, similarly to Eq. [11], as

$$G^*(t) \simeq e^{-pt} \sum_{l=0}^{M} c_l e^{-lqt} \quad [16]$$

The function $G(t)$ can then be written as

$$G(t) = [G(t) - G^*(t)] + G^*(t)$$

$$= [G(t) - e^{-pt} \sum_{l=0}^{M} c_l e^{-lqt}] + e^{-pt} \sum_{l=0}^{M} c_l e^{-lqt} \quad [17]$$

The integral I_2 (Eq. [8]) can be expressed as the sum of integrals I_{2A} and I_{2B}

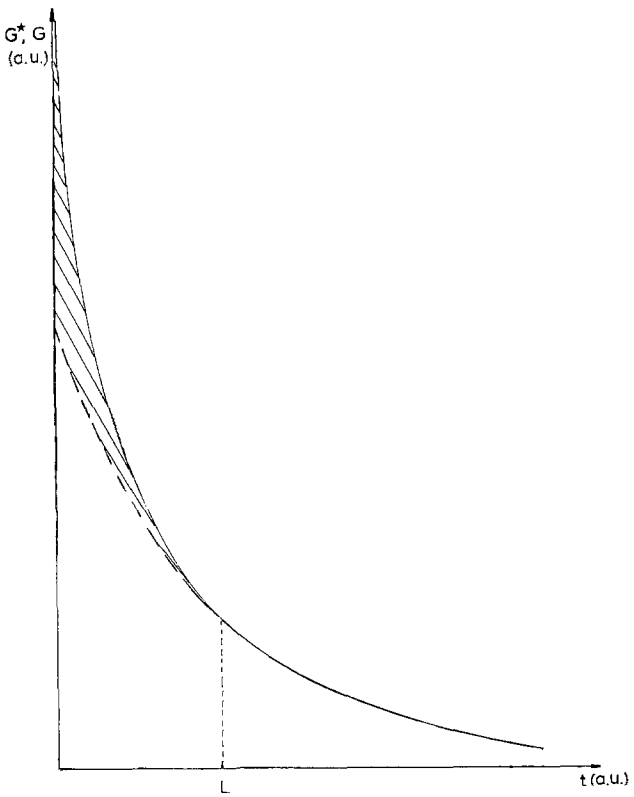

Fig. 1. The function G(t), solid line, and the approximation $G^*(t)$, dashed line, as function of the integration variable t for a layer on top of an insulating substrate. For $t > L$ $G^*(t)$ coincides with $G(t)$. The shaded part represents the integrand which is used for the computation of Eq. [19].

$$I_2 = \int_0^\infty G(t)\phi(t)\,dt$$

$$= I_{2A} + I_{2B} \quad [18]$$

where

$$I_{2A} = \int_0^\infty [G(t) - G^*(t)]\phi(t)\,dt$$

and

$$I_{2B} = \int_0^\infty G^*(t)\phi(t)\,dt$$

$$= \sum_{l=0}^{M} c_l \int_0^\infty e^{-(lq+p)t}\phi(t)\,dt$$

I_{2B} can be calculated using the analytical expression (Eq. [13]) for the integral. Since $G(t) = G^*(t)$ for $t > L$, I_{2A} reduces to

$$I_{2A} = \int_0^L [G(t) - (G^*(t)]\phi(t)\,dt$$

$$= \int_0^L [G(t) - e^{-pt} \sum_{l=0}^{M} c_l e^{-lqt}]\phi(t)\,dt \quad [19]$$

The integrand between brackets of I_{2A} corresponds to the shaded area of Fig. 1. I_{2A} can be computed using a standard integration procedure because the singularity or peaked behavior of $G(t)$ is smoothed out by the presence of the factor $\phi(t)$. The difficulty of the numerical integration depends on the value of the probe spacing s. If s is large the integrand is strongly oscillating. For this integration we use an integration formula of high precision, *i.e.*, a high order Gauss-Kronrod rule (40). A lower bound on L is imposed by the requirement that the singularity of $G(t)$ has to be removed sufficiently to allow an accurate approximation with exponentials. An upper bound is given by the fact that far too large values of L, the numerical

integrator cannot adequately perform the integration of the oscillating functions over the large interval with 87 evaluations. A suitable value of L was found to be 0.35×10^6 which was derived from a large number of integrations with different values of L and comparing the results with the exact values obtained from a numerical integration program (14).

The value of 0.35×10^6 is very reasonable since when multiplied with α (1-4 μm), one obtains values between 0.35 and 1.4 for ta. As illustrated in the work of Choo *et al.* (41), at these values of ta the singularity in the integrand has already disappeared. For the numerical integration one can see that as the probe spacing varies from 30 to 500 μm, there are approximately 3 or 50 zeros of J_0 included in the integration interval. As has been shown in the work of Piessens *et al.* (37), the numerical integrator is accurate for oscillating functions as long as the number of oscillations is less than or roughly equal to the number of function evaluations used in the integrator. Since we allow a maximum of 87 evaluations, the integrations will be accurate for probe spacings less than 500 μm. Limiting the value of s to 500 μm is a conservative restriction in view of the trend to smaller probe spacings (our setup now has a spacing of 57 μm).

Results and Discussion

As mentioned in the previous section we calculated the profiles of Choo (15) with the above-described techniques with an accuracy of at least 0.1% on the correction factor. The profiles with a perfectly conducting or a homogeneous substrate could be calculated using only 12 evaluations of $k(t)$.

For the case of the insulating substrate the use of Eq. [16] was required. This required in addition to the 12 evaluations of $k(t)$, 23 or 87 evaluations of the integrand depending on whether a normalized probe spacing of 30 or 500 was used, respectively. The time required to perform the calculations with this new technique varies from 3/4 to 5/4 of the time required when using the 150-point Gauss-Laguerre formula which uses storage of the Bessel function values. A typical value for computing all the spreading resistance values of a profile subdivided into 300 layers using an inverse program (6), is 10 sec on a VAX-11/780 minicomputer. In order to decide whether Eq. [12] or Eq. [16] should be used during routine calculations, the convergence of the Chebyshev coefficients is tested. It was found during our calculations, including simulations of Gaussian profiles, that as long as b_{12} is less than 9×10^{-3} Eq. [12] can be used. This was tested by calculating the correction factor for the top layer for a set of profiles using Eq. [12] and Eq. [16]. As long as b_1 was less than 9×10^{-3} the results using both equations agreed within 0.1%. Convergence of this Chebyshev coefficient means that the algorithm is capable of approximating the integrand factor with sufficient accuracy.

The above-mentioned results were obtained using a constant contact radius. The use of a resistivity dependent contact radius presents no problem for this algorithm. The coefficients of the Chebyshev polynomials are determined independent to the contact radius and are only influenced by the resistivity profile since they represent an approximation to $G(t)$ where $k(t)$ is depending only on the resistivities of the underlying layers. The radius a enters only in Eq. [13] which is easily calculated.

D'Avanzo *et al.* (1, 2) determine their constant radius from Eq. [4] by the following relation at $\rho = 1$ Ω-cm

$$\frac{\rho}{2a} = A\rho^B \qquad [20]$$

In order to demonstrate the versatility of the algorithm, we used Eq. [20] for each value of ρ to establish a relationship between ρ and a. Generation of spreading resistance values for a model resistivity profile required the same time as when using a constant radius. Recalculating the resistivity profiles, again, with using Eq. [20], only required 1.5-2 times more than with a constant radius. A typical value for calculating a 300-layer profile is 55 sec as compared to 30 sec for the constant radius version. The increase in time is explained by the fact that one has to perform two or three more iterations in order to arrive at the correct values of ρ and a. One should realize that we are dealing now with a set of two nonlinear equations, *i.e.*, Eq. [1] and Eq. [20], with two unknowns. The double iteration is performed as follows. Starting with a value of ρ, estimated from the already calculated values of the underlying layers, the corresponding value of a is calculated using Eq. [20]. The correction factor, Eq. [2], is then calculated using these values. The convergence of Eq. [1] is then checked and if not, a new estimate of ρ is made and the iteration is restarted. Usually convergence is reached after 5-6 iterations. The use of two nonlinear equations however, presents a special problem since the solution now is no longer unique. This is illustrated in Fig. 2. By using an inverse program we calculated the spreading resistance values for a Gaussian profile ($R_p = 0.17$ μm, $\Delta R_p = 0.054$ μm) on top of a homogeneous substrate with $\rho = 126$ Ω-cm. The structure was assumed to be 1 μm deep, the probe spacing being equal to 30 μm. The structure was subdivided into 300 layers with layer 300 being the substrate. Arriving at layer 122 during the recalculation of the resistivity profiles, we calculated ρ and CF (ρ, a) for different values of a such that Eq. [1] was satisfied. The solid line in Fig. 2 shows the obtained combinations $\{\rho, a\}$. Using Eq. [20] we also determined the variation of the contact radius a as a function of ρ ($A = 5000$, $B = 0.9$). As indicated on Fig. 2 there are two combinations $\{\rho, a\}$. which satisfy both Eq. [1] and Eq. [20]. The exact combination $\{\rho_e, a_e\}$ is one of them. During a large number of simulations the following technique was found to always lead to the exact solution $\{\rho_e, a_e\}$. Before starting the iteration in one layer, a cubic spline extrapolation of the profile is made using the previous corrected points. In the second layer the extrapolation is determined on the basis of the spreading resistance value with regard to that of the first layer. If the resistance of the second layer is higher, the extrapolated resistivity is also taken higher than the last one and vice versa. (A similar extrapolation is used by D'Avanzo (2) for determining a first guess in the resistivity iteration.) The iteration is then forced to proceed into the direction indicated by the extrapolated resistivity. The resistivities of previous layers are also indicated on Fig. 2 by the arrows followed by

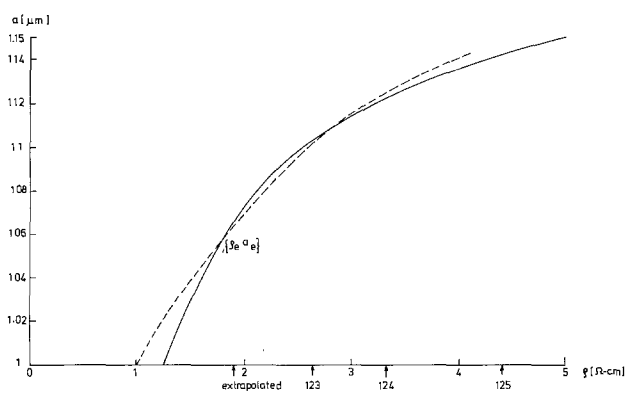

Fig. 2. The dashed line gives the contact radius a as determined from Eq. [16] with $A = 5000$, $B = 0.9$. The solid line gives every pair $\{\rho,a\}$ which satisfies Eq. [1] for layer 122 of a Gaussian profile. For details see text. Also indicated are by the arrows followed by the number of the layers, the resistivities of the previous layers. $\{\rho_e,a_e\}$ correspond to the exact solution.

the number of the layer. Also indicated is the extrapolated resistivity for the layer 122. The success of this technique can be explained by the fact that it forces the algorithm to maintain the continuity of the resistivity profile which physically is very reasonable. It should be mentioned that if one uses the wrong solution $\{\rho, a\}$ in one layer, sometimes differing only 15% of the exact one, the program always breaks down in the next layer. This means that if the program finds a solution for the profile, one can be reassured that it also is the correct one.

Using the model resistance data, calculated with a resistivity dependent contact radius, for an exponentially varying profile ($\rho(z) = 0.5 \exp(-2z)$, 0.5 μm deep, $\rho_{substrate} = 1.356$ Ω-cm, $A = 5000$, $B = 0.9$), we recalculated the profile with both a resistivity-dependent contact radius and a constant radius. For this last case a was determined from Eq. [20] at $\rho = 1$ Ω-cm and found to be 1 μm. The resultant profiles are shown in Fig. 3. The solid line shows the profile calculated with the radius continuously varying from 1.031 μm for the substrate layer to 0.933 μm for the topmost layer. The radius is indicated by the dash-dotted line in Fig. 3. The profile differs from the original one by less than 0.2%. The dashed line shows the profile calculated with constant radius which differs by as much as 17% from the exact solution as can be expected. By this simulation we intend to show that if there is a dependence of the radius on resistivity and this would be neglected, serious errors can be introduced in the calculations. It is clear that the next step will be to investigate whether there is a dependence of the radius on the resistivity by comparing a real profile measured with different techniques and calculated with and without variation of the contact radius, similar to the work of Ehrstein *et al.* (32).

Finally it should be mentioned that in some cases it was impossible to recalculate the entire profile because at a certain point during the calculations a deviation from the exact profile was found, which increased almost exponentially as successive layers were computed. Increasing the accuracy of the calculations could only retard the problem a few points. As we found from a detailed investigation, this deviation is not due to an error in the calculation of the integral neither, to the choice of the wrong pair $\{\rho, a\}$ in the iteration. We suspect that it is caused by instabilities (42) introduced by the correction algorithm, which incorporates a recurrence relation into an inversion problem. Evidence in this direction is given by the fact that when using double precision variables throughout all the calculations in the program, the problem was solved in one case while in another case it was delayed a number of layers. Also the observation of Lee (12) that the calculations of a resistivity profile amplifies the noise on the spreading resistance data, points in the same direction. This problem is however still under investigation.

Conclusion

We have presented a new integration technique[2] for determining the correction factor of Schumann and Gardner. This technique allows a very fast (less than 0.03 sec/point) and accurate (better than 0.1%) evaluation of the integral. It is also very well suited for using a resistivity-dependent contact radius in the calculations. This has been demonstrated using model data and Eq. [20] for establishing a relation between a and ρ. The problems involved have been discussed. It should be mentioned that although we used Eq. [20] to determine a, this is not restrictive. One could, instead of using a log-log fit for the calibration data, use a table of the measured values and interpolate at intermediate points. We have pointed out that it is possible to use a variable contact radius with this integration technique in case a means for determining the resistivity-dependence of the contact radius is available. Using this integration technique we are now investigating how this resistivity dependence can be determined from measurements on a known profile.

[2] The program PROFA incorporating this technique for spreading resistance analysis is available from the authors (W. Vandervorst and H. Maes) on request.

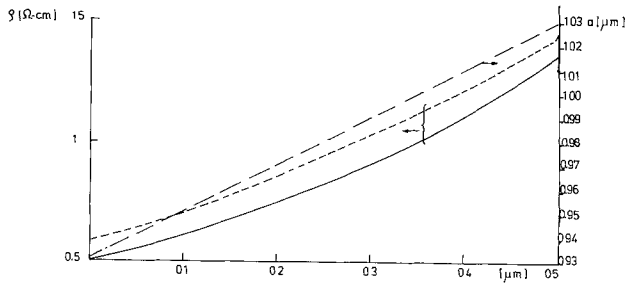

Fig. 3. Comparison between the profile calculated with a resistivity-dependent contact radius (solid line) and with a constant radius (dashed line). Also indicated is the variation of a (dash-dotted line) for the first case.

Manuscript submitted Nov. 10, 1981; revised manuscript received July 24, 1982.

Any discussion of this paper will appear in a Discussion Section to be published in the December 1983 JOURNAL. All discussions for the December 1983 Discussion Section should be submitted by Aug. 1, 1983.

REFERENCES

1. D. C. D'Avanzo, R. D. Rung, A. Gat, and R. W. Dutton, *This Journal*, **125,** 1170 (1978).
2. D. C. D'Avanzo, R. D. Rung, and R. W. Dutton, Stanford Electronics Laboratories, Technical Report No. 5013-2 (February 1977).
3. D. A. Antoniadis, A. M. Lin, and R. W. Dutton, *Appl. Phys. Lett.*, **33,** 1033 (1978).
4. A. M. Lin, D. A. Antoniadis, and R. W. Dutton, *This Journal*, **128,** 1131 (1981).
5. D. H. Dickey and J. R. Ehrstein, NBS Special Publication 400-48 (1979).
6. J. Albers, *Solid-State Electron.*, **23,** 1197 (1980).
7. P. A. Schumann and E. E. Gardner, *This Journal*, **116,** 87 (1969).
8. P. A. Schumann and E. E. Gardner, *Solid-State Electron.*, **12,** 371 (1969).
9. S. M. Hu, *ibid.*, **15,** 809 (1972).
10. Y. Iida, H. Abe, and M. Kondo, *This Journal*, **124,** 1118 (1977).
11. S. C. Choo, M. S. Leong, and K. L. Kuan, *Solid-State Electron.*, **19,** 561 (1976).
12. G. A. Lee, NBS Special Publication No. 400-10, 75 (1974).
13. S. C. Choo, M. S. Leong, H. L. Hong, L. Li, and T. S. Tan, *Solid-State Electron.*, **20,** 839 (1977).
14. W. B. Vandervorst and H. E. Maes, *ibid.*, **24,** 851 (1981).
15. S. C. Choo, M. S. Leong, H. L. Hong, L. Li, and L. S. Tan, *ibid.*, **21,** 769 (1978).
16. H. L. Berkowitz and R. A. Lux, *This Journal*, **128,** 1137 (1981).
17. P. J. Severin, NBS Special Publication No. 400-10, 27 (1974).
18. M. S. Leong, S. C. Choo, and K. H. Tay, *Solid-State Electron.*, **19,** 397 (1976).
19. M. S. Leong, S. C. Choo, and C. C. Wang, *ibid.*, **20,** 255 (1977).
20. M. S. Leong, S. C. Choo, and L. S. Tan, *ibid.*, **21,** 933 (1978).
21. M. S. Leong, S. C. Choo, and L. S. Tan, *ibid.*, **22,** 527 (1979).
22. S. C. Choo, M. S. Leong, and L. S. Tan, *ibid.*, **24,** 557 (1981).
23. A. Mayer and S. Schwartzman, NBS Special Publication No. 400-10, 123 (1974).
24. G. A. Gruber and R. F. Pfeifer, *ibid.*, 209.
25. W. B. Vandervorst and H. E. Maes, Internal ESAT-report (1979).
26. J. R. Ehrstein, in "Semiconductor Silicon 1977," H. R. Huff and E. Sirtl, Editors, p. 377, The Electrochemical Society Softbound Proceedings Series, Princeton, NJ (1977).

27. W. A. Keenan, P. A. Schumann, A. M. Tong, and R. P. Philips, in "Ohmic Contacts to Semiconductors," B. Schwartz, Editor, p. 263, The Electrochemical Society Softbound Proceedings Series, Princeton, NJ (1969).
28. A. M. Tong and M. Poponiak, IBM Technical Report 22-407 (1967).
29. S. J. Fonash, NBS Special Publication No. 400-10, 17 (1975).
30. J. R. Ehrstein, in "Non-Destructive Characterization of Semiconductor Materials," Zemel, Editor, Chap. 1, NATO-Advanced Institute, Plenum Press, (1978).
31. P. Kramer and L. J. Van Ruyven, *Solid-State Electron.*, **15**, 757 (1972).
32. J. R. Ehrstein, J. A. Albers, R. G. Wilson, and J. Comas, Paper 496 presented at The Electrochemical Society Meeting, St. Louis, Missouri, May 11-16, 1980.
33. T. H. Yeh, NBS Special Publication No. 337, 111 (1970).
34. B. L. Morris and P. H. Langer, NBS Special Publication No. 400-10, 63 (1974).
35. A. D. Wheelan, Tables of Summable Series and Integrals Involving Bessel Functions, Holden-Day (1968).
36. L. Fox and I. B. Parker, "Chebyshev Polynomials in Numerical Analysis," Oxford University Press (1968).
37. R. Piessens, E. De Doncker, C. W. Uberhuber, and D. Kahaner, In preparation.
38. W. M. Gentleman, *Comm. Assoc. Comp. Mag.*, **15**, 337, 343 (1972).
39. G. P. Tolstov, in "Fourier Series," Prentice Hall, Englewood Cliffs, N.J. (1962).
40. P. J. Davis and P. Rabinowitz, "Methods of Numerical Integration," Academic Press, New York (1975).
41. S. C. Choo, M. S. Leong, M. L. Hong, Ling Li, and L. S. Tan, *Solid-State Electron.*, **20**, 839 (1977).
42. J. Oliver, *Numerische Mathematik*, **11**, 323 (1967).

Practical Considerations in the Implementation of Same-Level Mixed Lithography

T. D. Berker*

Sperry Research Center, Sudbury, Massachusetts 01776

ABSTRACT

Some practical considerations involved in the use of same-level mixed lithography are discussed. This new process involves e-beam exposure of the fine features of a pattern and optical exposure of the large features onto the same resist layer, followed by a single-development step. With the use of a diazo-type resist, either positive or negative e-beam images can be obtained so that suitable selection of the photomask tone allows complete flexibility in the choice of polarity of the composite pattern. In the positive-polarity mode, patterning of a 0.5 μm AZ-2415 film typically requires an electron dose of 50 μC/cm^2 and an optical dose of 80 mJ/cm^2, with a 70 sec development time in a 1:3.5 mixture of AZ-2401:H_2O. A negative-polarity mode patterning of a 0.5 μm AZ-2415 film typically requires an electron dose of 60 μC/cm^2 and an optical dose of 300 mJ/cm^2, with a 15 sec development in the same 1:3.5 mixture of AZ-2401:H_2O. In each polarity mode, a close examination is made of the "joint" region where the e-beam-exposed area meets the optically exposed area. Patterning of an MOS device using this same-level mixed lithography process in the negative polarity mode is described. Gate lengths as small as 0.6 μm have been defined and anisotropically plasma etched into doped polysilicon. This new technique combines high resolution with high throughput on the same level while maintaining a simple process with only one coating, one development, and one transfer step.

Electron-beam lithography (EBL) is an excellent method for defining small geometries in complex semiconductor devices. However, this high resolution is accompanied by an increase in the time required to serially expose the pattern. In order to make use of the high-resolution patterning capability of EBL without totally sacrificing the higher throughput of photolithography, the exposure of an integrated circuit is sometimes done by combining optical and e-beam methods. In this "mixed lithography" approach, EBL is usually restricted to just those levels which contain critically small features while photolithography is used exclusively on the remaining levels. It frequently happens, however, that the e-beam levels also contain large geometries which do not require high-resolution patterning; serially exposing these areas can lead to excessively long writing times. Furthermore, because different resist systems are generally used for the e-beam and optical exposures, processing is needlessly complicated.

In order to solve these deficiencies in conventional mixed lithography processing, we have recently developed a new approach. This same-level mixed lithography (SLML) process (1) utilizes EBL and photolithography on the same level and in the same resist layer followed by a single-development step.

* Electrochemical Society Active Member.
Key words: polymers, integrated circuits, masking.

Same-Level Mixed Lithography

The same-level mixed lithography process is shown in Fig. 1. The small geometries on any given level of an integrated circuit pattern are exposed using an electron beam, while the large geometries of the same level are defined using optical lithography. The two exposures are followed by a single development step which yields the complete pattern of the entire level. The imaging is done in commonly used diazo-type positive photoresists such as Shipley's AZ resists, which are sensitive to both electrons and photons. An attractive feature of these resists is that they can be processed to form either positive or negative images. The use of these resists with SLML, therefore, makes possible a very flexible lithographic process, capable of high resolution and acceptable throughput.

Water plays a key role in the imaging process in diazo-type photoresists (2). Irradiation of the resist in the presence of water converts the photoactive (diazo) compound (PAC) to a carboxylic acid, and substantially enhances the solubility of the resist in a basic developer solution. Positive resist behavior results. In a water-free environment (*e.g.*, vacuum), optical or electron exposure converts the PAC to an ester, which diminishes the subsequent development rate of the resist in the basic developer. The important point here is that the chemistry of these two processes is domi-

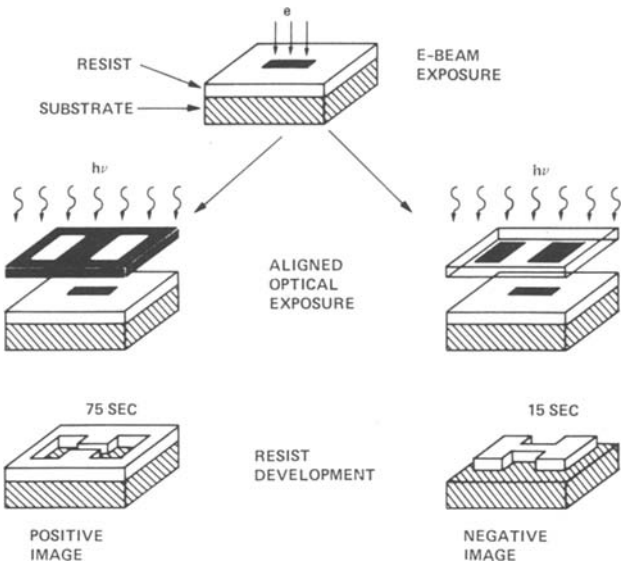

Fig. 1. Same-level mixed lithography (SLML). The left-hand path uses a dark-field photomask and a long development time, which results in an overall positive image. The right-hand path uses a light-field photomask and a short development time, which results in an overall negative image.

nated by the availability of water during exposure and not by the radiant sources.

Electron exposure in a vacuum causes not only the conversion of the PAC to an ester, which can lead to negative behavior, but also scission reactions in the Novalac resinous base of the resist, which can lead to positive behavior (3). Diazo-type resists can therefore be processed either as positive or negative electron resists by controlling the development rate of the background areas (those regions not exposed to electrons) relative to the electron-exposed areas. Negative resist structures can be formed by exposure of the pattern with an electron beam in vacuum, followed by a flood optical exposure in air, to change the background into a highly soluble state (4, 5). A short development time (typically 15 sec) is used, so that the negative nature of the electron-exposed areas is preserved while the background is developed away. In the absence of a flood exposure in air, the background areas develop very slowly and a longer development time (typically 60 sec) causes the electron-induced scission reactions to dominate, resulting in a positive image. It is the relative development rate of the background and the electron-exposed area, as well as the total development time, that determines the tone of the image.

The flexibility of SLML hinges upon the fact that diazo-type resists can be used as either positive or negative electron resists. Shaw and Hatzakis (6) first characterized the positive electron behavior of several positive photoresists. Their results showed that the AZ-type resists have moderate sensitivity, high resolution, and high etch resistance. The use of AZ-1350 as a negative electron resist was reported by Oldham and Hieke (4) and Mochiji *et al.* (15). They found that the sensitivity, resolution, and etch resistance of negative AZ-1350 are similar to those of positive AZ-1350. Berker and Casey (7) recently characterized the negative electron resist behavior of AZ-2415. They investigated the effect of electron dose, optical dose, and development time on the resist profiles. These studies have shown that diazo-type resists make excellent negative electron resists with moderate sensitivity, submicron resolution, and high dry etch resistance. Furthermore, unlike conventional negative resists, they do not swell during development and exhibit no vacuum curing effect.

Positive-Polarity Exposure Mode

When a diazo-type resist is processed in a positive-polarity dual-exposure mode (Fig. 1), the resist acts as a positive electron resist and a positive photoresist. The small features of the pattern are defined with an electron beam. The large features are then optically exposed using a darkfield photomask so that the background areas receive no radiation. During development, the background develops very slowly, while the large optically exposed areas are removed rapidly. The development time is made long enough for the e-beam exposed areas, which develop more slowly due to conversion of some PAC's to esters, to be removed, and a positive composite image is obtained.

Except for the overlap areas of the pattern, each region of resist receives only one type of radiation. In the region of the overlap, exposures "add" and, under certain conditions, this can lead to a slight widening of the e-beam generated line at the "joint" region where the electron-exposed area meets the optically exposed area. Figure 2(a) shows an SEM micrograph of a developed resist pattern in a Shipley Microposit 3000 film of 1.2 μm initial thickness on doped polysilicon. E-beam generated 0.7 μm lines are connected to a large optically generated pad. The electron dose was 80 μC/cm^2 with an acceleration voltage of 20 keV. The optical exposure was done with a 4:1 projection aligner and the integrated dose was 56 mJ/cm^2. The development time was 75 sec in Microposit 300 developer.

Figure 2(b) is an enlargement of the joint region and shows clearly the standing waves on the optically exposed resist walls. The e-beam defined area is

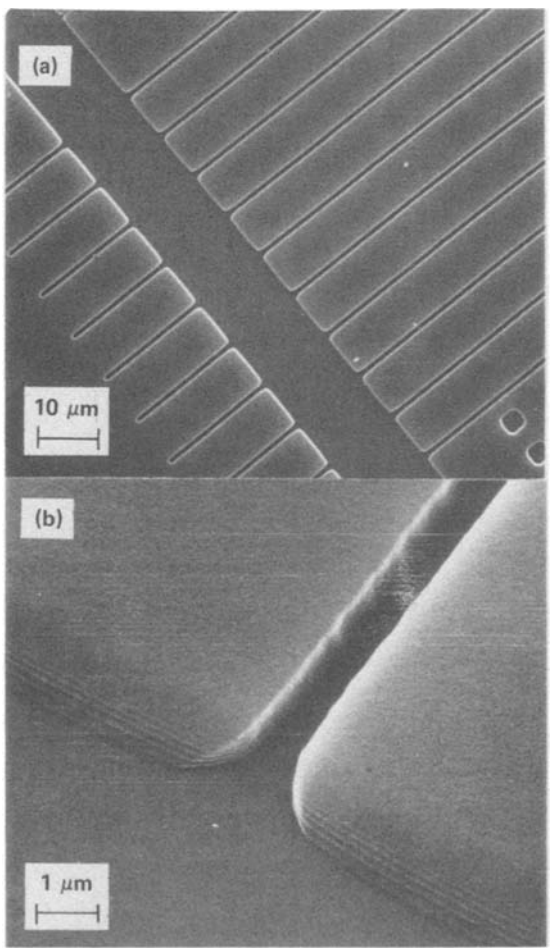

Fig. 2(a). Positive-polarity SLML resist image in a Shipley Microposit 3000 film of 1.2 μm initial thickness. (b) An enlargement of the 0.7 μm e-beam generated line joining large optically generated pad. The electron dose was 80 μC/cm^2, optical dose was 56 mJ/cm^2, and development was for 75 sec in Microposit 300 developer.

undercut and there are no standing waves. The optical exposure is not completely attenuated at the photomask edge, and a small amount of radiation is absorbed along the perimeters of the masked areas. This causes a slight broadening of 0.1 μm of the e-beam generated line at the joint region, with the standing wave pattern extending around the corner.

Negative-Polarity Exposure Mode

When a diazo-type resist is processed in a negative-polarity dual-exposure mode (Fig. 1), the resist acts as a negative electron resist and a positive photoresist. The small features of the pattern are defined with an electron beam. The large features are now exposed using a light-field photomask with a high optical dose, so that the background is changed into a highly soluble state. The background is removed very rapidly during a short development, which preserves both the e-beam exposed areas and the optically masked pads.

Figure 3 shows an SEM micrograph of a developed resist pattern in an AZ-2415 film of 0.5 μm initial thickness. E-beam generated 0.4 μm lines are connected to large optically generated pads. The electron dose was 50 μC/cm², the optical dose was 222 mJ/cm², and development was for 12 sec in a 1:3.5 mixture of AZ-2401:H_2O. The electron exposures have continued into the pad area. A standing wave pattern shows clearly on the optically exposed resist walls.

The electron-exposed areas also receive optical radiation. As explained earlier, the mechanisms involved in the negative electron generated behavior and the positive optically generated behavior are different, and the exposures do not "add." However, diffraction at the mask-pattern edge can lead to a variation in optical dose which affects the e-beam defined linewidth at the overlap region (7). Figure 4 shows the effect of optical dose on the developed linewidth of AZ-2415 at several electron doses. The initial film thickness was 0.5 μm and the development time was 15 sec in a 1:3.5 mixture of AZ-2401:H_2O. The nominal written linewidth was 1 μm. As the optical dose increases above the minimum value, which causes complete development of the background areas (170 mJ/cm²), the linewidth decreases rapidly, then saturates at an optical dose of approximately 300 mJ/cm².

If a pattern is exposed at an optical dose below the saturation value, any diffraction at the photomask edge will result in linewidth variations of the e-beam defined areas. Figure 5(a) is a schematic of the pattern and Fig. 5(b) is an SEM

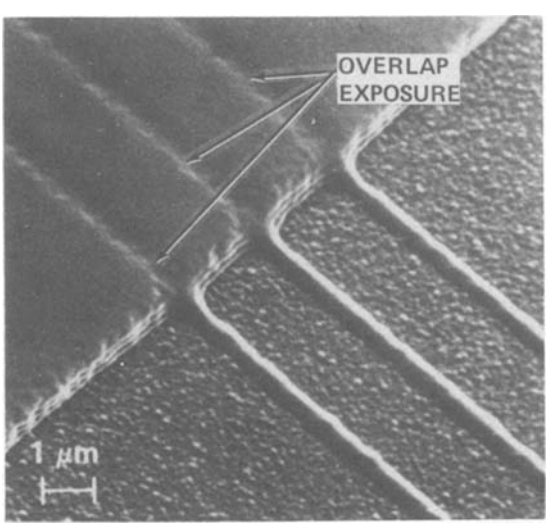

Fig. 3. Negative-polarity SLML resist image in an AZ-2415 film of 0.5 μm initial thickness. The 0.4 μm e-beam generated lines continue into the optically generated pad. The electron dose was 50 μC/cm²; optical dose was 222 mJ/cm²; and development was for 12 sec in a 1:3.5 mixture of AZ-2401:H_2O.

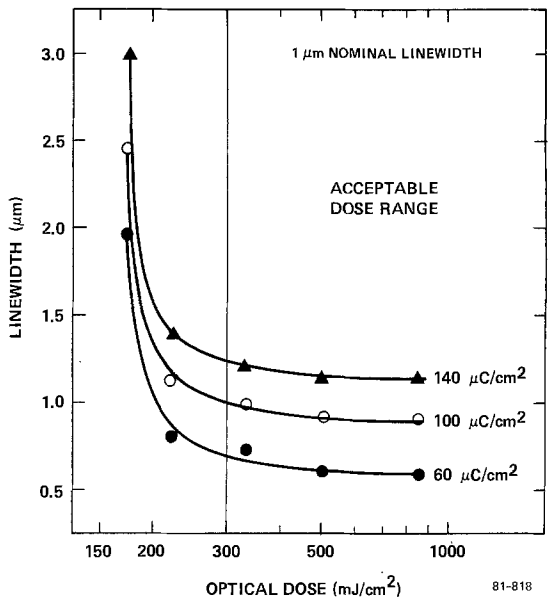

Fig. 4. Negative AZ-2415 developed linewidth vs. optical dose for a nominal 1 μm line. The linewidth saturates at approximately 300 mJ/cm², independent of electron dose.

micrograph of an etched polysilicon structure after resist removal. Figure 6 shows a properly exposed pattern. There is no linewidth variation and the electron-defined gate connects smoothly to the optically defined pad.

Device Patterning

An MOS device with a submicron gate was patterned using same-level mixed lithography. The gate level was defined using the negative-polarity exposure mode (Fig. 1) in 0.5 μm of AZ-2415 and anisotropic plasma

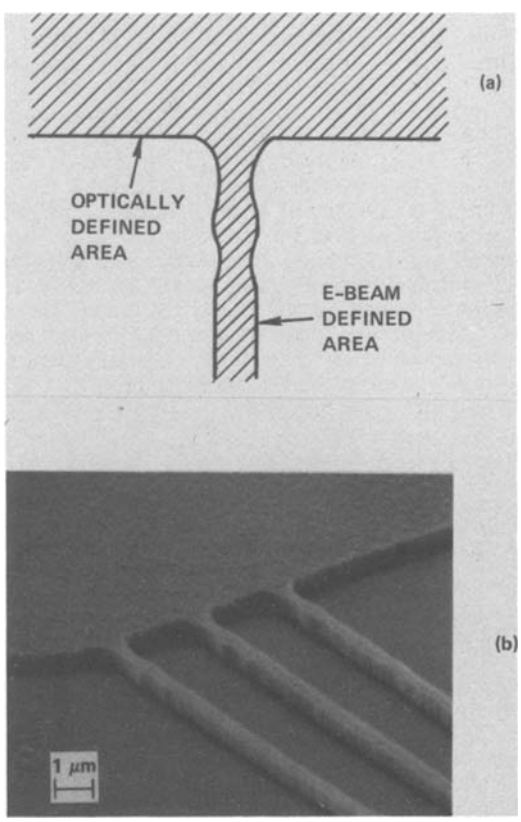

Fig. 5. (a) Schematic and (b) SEM micrograph of a polysilicon structure patterned using negative polarity SLML. Diffraction at the photomask edge has caused a variation of linewidth in the e-beam defined areas.

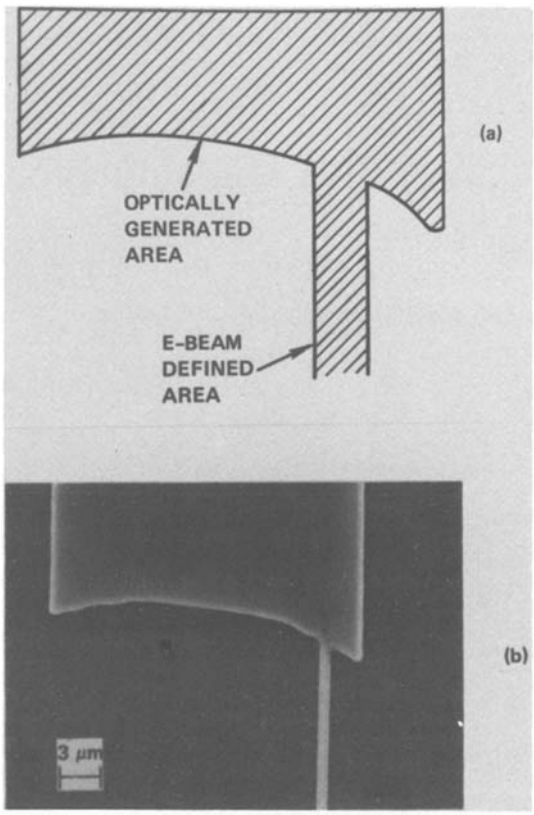

Fig. 6. (a) Schematic and (b) SEM micrograph of a resist-covered polysilicon structure patterned using negative-polarity SLML. Proper optical exposure has resulted in an e-beam defined gate which has a constant linewidth as it joins the optically generated pad.

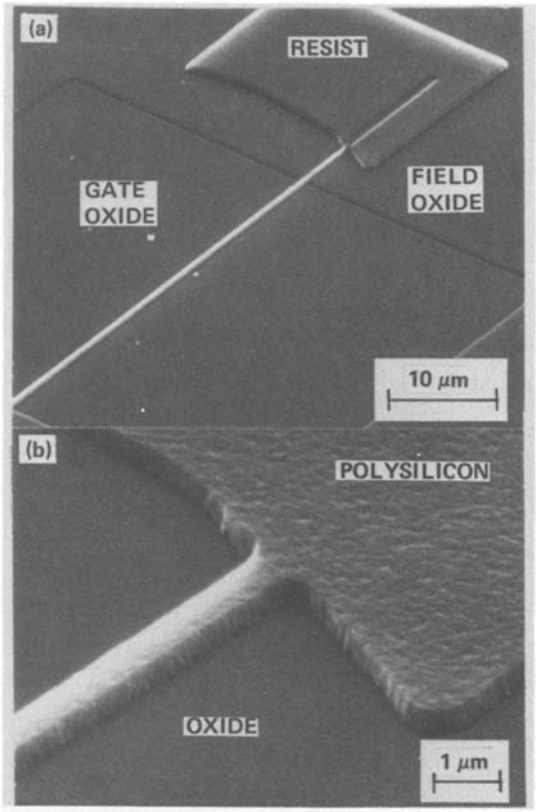

Fig. 7. (a) SEM micrograph of a plasma-etched polysilicon gate defined by negative-polarity SLML prior to resist removal. (b) An enlargement of the joint area after resist removal.

etching of the underlying 5000Å of doped polysilicon. An electron dose of 80 μC/cm^2, an optical dose of 300 mJ/cm^2, and a development time of 15 sec was used. The developed gate length was 0.7 μm and there was no measurable loss of linewidth during plasma etching. Figure 7(a) is an SEM micrograph of the plasma-etched structure prior to resist removal. Figure 7(b) shows the connection between the e-beam defined gate and the optically defined pad after resist removal.

As in conventional mixed lithography, alignment to any previous patterned levels is done using e-beam registration marks. The photomask is then aligned to the present and previous levels using optical alignment marks. Any desired overlapping of the e-beam areas and optically masked areas is provided for in the design of the patterns. As can be seen in Fig. 7(a), the e-beam defined gate extends well into the optically defined pad.

Conclusion

We have examined here the use of a new lithographic process that uses both e-beam and optical exposure of a single resist layer. Same-level mixed lithography makes use of the high-resolution patterning capability of EBL while preserving much of the throughput of photolithography. This simple process uses only one coating, one development, and one transfer step. Furthermore, diazo resists hold up well under the dry etching processes which are necessary for the faithful transfer of very high resolution patterns. The ability to create both positive and negative images from one commonly used photoresist makes this an extremely flexible process that is fully compatible with existing semiconductor processing.

Same-level mixed lithography was developed, in part, to address the throughput problem of EBL. There can be a significant time savings when using SLML instead of EBL; however, the exact savings depends upon the particular pattern being exposed. The time saved by not exposing the large geometries by serial exposure with the electron beam must be offset by the time spent by an extra alignment and flood exposure. The time savings and throughput increase are therefore maximized in a full-wafer optical exposure system and somewhat reduced in a wafer-stepped system. To date, we have only used SLML to fabricate discrete devices. We are now initiating a quantitative analysis of the throughput considerations of SLML through the use of specialized patterns and more complicated circuit designs.

Acknowledgments

The author wishes to thank D. D. Casey and J. A. Donahue for many helpful discussions. The aid of S. Bernacki, who coordinated the fabrication of the submicron MOS device, is gratefully acknowledged.

Manuscript submitted June 25, 1982; revised manuscript received Sept. 21, 1982. This was Paper 286 presented at the Montreal, Canada, Meeting of the Society, May 9-14, 1982.

Any discussion of this paper will appear in a Discussion Section to be published in the December 1983 JOURNAL. All discussions for the December 1983 Discussion Section should be submitted by Aug. 1, 1983.

Publication costs of this article were assisted by the Sperry Research Center.

REFERENCES

1. T. D. Berker and S. E. Bernacki, *IEEE Electron Dev. Lett.*, **edl-2**, 281 (1981).
2. J. Pacansky and S. R. Lyerla, *IBM J. Res. Dev.*, **23**, 42 (1979).
3. H. Hiraoka and A. R. Gutierrez, *This Journal*, **126**, 860 (1979).
4. W. G. Oldham and E. Hieke, *IEEE Electron. Dev.*

Lett., **edl-1**, 217 (1980).
5. K. Mochiji, Y. Maruyama, F. Murai, S. Okazaki, Y. Takeda, and S. Asai, *Jpn. J. Appl. Phys.*, **20**, Suppl. 20-1, 63 (1981).
6. J. M. Shaw and M. Hatzakis, *IEEE Trans. Electron Dev.*, **ed-25**, 425 (1978).
7. T. D. Berker and D. D. Casey, *ibid.*, **ed-29**, 524 (1982).

A Three-Layer Resist System for Deep U.V. and RIE Microlithography on Nonplanar Surfaces

E. Bassous,*[1] L. M. Ephrath,* G. Pepper, and D. J. Mikalsen

IBM, Thomas J. Watson Research Center, Yorktown Heights, New York 10598

ABSTRACT

The three-layer resist system AZ1350J/Si/PMMA was used to define high-resolution patterns on nonplanar surfaces with topographical features typically encountered in the fabrication of VLSI circuits. The substrate was coated successively with a thick layer of polymethyl methacrylate (PMMA) for planarization, a thin layer of amorphous silicon for masking, and a thin AZ1350J resist layer in which the optical or electron beam exposed pattern was defined. Transfer of the resist image pattern into the amorphous silicon film was performed anisotropically by reactive ion etching (RIE) in a CF_4 plasma. The pattern in the Si layer was then replicated in the underlying PMMA layer either by blanket deep u.v. exposure (200-300 nm) and solvent development or by *in situ* RIE in an O_2 plasma. Both patterning techniques were comparable in defining submicrometer features in PMMA films 1-3 μm thick with good linewidth control and high aspect ratio over steps 1 μm high. Experimental details are described and the complexity of deep u.v. and RIE patterning techniques are discussed with particular emphasis on the planarizing characteristics of PMMA.

High-resolution submicrometer resist patterns for VLSI applications are often difficult to generate on nonplanar surfaces due primarily to the nonuniform thickness of the resist layer covering topographical structures. Good linewidth control with high resolution requires, ideally, a uniform resist film less than 1 μm thick on a perfectly planar surface. Good step coverage and large height-to-width aspect ratio over 1 μm high topography demand, however, the use of a resist layer substantially thicker than 1 μm (1).

To overcome the conflicting requirements imposed on the resist film thickness, multilayer resist systems have been developed which separate the imaging and step-coverage functions in different layers. Sensitivity of the imaging process and definition of resist patterns could thus be enhanced independently, without sacrificing step coverage or aspect ratio (1-33). In two-layer systems (4-18), a thick resist film is first applied over the surface to cover vertical features and to planarize its topography. The thick layer is then overcoated with a thin resist film in which the image pattern is defined. The small thickness of the top imaging layer, and its relatively large distance from the substrate surface, enhance the resolution of patterns obtained by optical and electron beam exposure. This is due to a reduction of diffraction effects in the optical case and a decrease of electron scattering effects in the latter. Transfer of the top image pattern to the underlying thick layer has been accomplished by the use of solvents (7-9), selective developers (10, 34, 35), deep u.v. exposure and development (4, 15-18), and by dry etching in an oxygen plasma (11-14, 19-29).

One of the drawbacks of two-layer resist systems is the nonuniform mixing which sometimes occurs at the interface between the layers, resulting in processing difficulties and poor pattern definition. To minimize this effect, and to improve processing selectivity, three-layer resist systems have been introduced which incorporate a barrier film sandwiched between the two resist layers (17-32). The barrier film prevents mixing between the top and bottom layers, and thus, permits a wider choice of resist materials and pattern transfer techniques. The increased processing flexibility serves to enhance imaging sensitivity, and to achieve better control of pattern geometry. The pattern transfer processes in two-layer and three-layer resist systems are similar and their selectivity determines how faithfully the exposed image is replicated.

This study was undertaken to explore the feasibility and processing complexity associated with the use of a silicon barrier layer in a three-layer system for patterning submicrometer features over 1 μm topography employing wet and dry processes. The imaging layer used was AZ1350J, and the planarizing layer was polymethyl methacrylate (PMMA). Silicon was selected as the barrier material (23, 25, 26) in the AZ1350J/Si/PMMA three-layer system because of its compatibility with Si integrated circuit fabrication processes, its very low etch rate in an oxygen plasma, and its opacity in the deep u.v. region of the spectrum (200-300 nm). Amorphous Si barrier layers with smooth uniform surfaces are readily deposited as doped or undoped films on resist surfaces (36-38). The use of doped Si films is advantageous in electron beam exposures because an electrically conducting layer is less subject to surface charging, and thus, misregistration associated with this effect is significantly reduced (25).

The pattern in AZ1350J resist was defined by either optical or electron beam exposure, and then replicated in the Si film by RIE. Amorphous Si films were obtained by plasma CVD of silane or by electron-gun evaporation of silicon (38). Pattern transfer to the PMMA planarizing layer was accomplished either by blanket deep u.v. exposure and solvent development or by *in situ* RIE in an oxygen plasma. Processing details will first be described, followed by a discussion of the experimental results.

Experimental Procedure

High-resolution test patterns in the AZ/Si/PMMA system were defined on 57 mm diameter Si wafers patterned with surface steps 1 μm high. The steps were repetitive grating structures of different size, defined photolithographically in an SiO_2 film 1 μm thick. The stepped surface was first coated with a layer of PMMA 1.5-3 μm thick followed by a thin silicon film ~100 nm thick and finally a film of AZ1350J photoresist ~0.5 μm thick to serve as the top imaging layer.

The high-resolution line/space test pattern which ranged from 0.5 to 5 μm was defined in the AZ imaging

* Electrochemical Society Active Member.
[1] Present address: IBM Corporation, White Plains, NY 10604.
Key words: multilayer lithography, submicron lithography, trilevel resist, planarization, topography.

layer perpendicular to the underlying grating structures. Exposures were performed either with a direct write Vector Scan electron beam system (39) or with a 5× step-and-repeat optical projection printer (40). The exposed and developed image pattern in the AZ resist layer was replicated in the sandwiched Si film by RIE in a CF_4 plasma (41). Transfer of the Si pattern to the underlying PMMA layer was performed either by flood exposure to deep u.v. radiation (200-260 nm) followed by development of the image pattern in organic solvents, or by *in situ* RIE in an oxygen plasma (11-14, 19-29). A typical process sequence is outlined below and is illustrated schematically in Fig. 1. Typical patterns of PMMA resist lines crossing over SiO_2 steps are shown in Fig. 2.

Process sequence.—Spin-coat HMDS. Spin-coat 1 μm PMMA. (Dupont Elvacite 2041, 10% by weight in 2-methoxyethyl ether). Bake 15 min at 85°C. Repeat, spin-coat 1 μm PMMA. Bake 1 hr at 160°C. Deposit amorphous Si 30-200 nm by plasma CVD of SiH_4 or by electron gun evaporation of Si. Bake 1 hr at 100°C in air. Spin-coat HMDS. Spin-coat 0.45 μm AZ1350J using 2 AZ1350J:1 AZ thinner. Bake 15 min at 85°C. Expose test pattern either by (*i*) electron beam at 30 $\mu C/cm^2$, 20 keV, or (*ii*) on a 5× optical projection printer at 15 mJ/cm^2 using 405 nm monochromatic radiation. Develop image in AZ developer, then bake 30 min at 100°C. RIE Si in CF_4. RIE patterning: (*i*) *In situ* RIE PMMA in O_2 plasma, and (*ii*) dip etch 5-10 sec in buffered HF to clean off residues. Deep u.v. patterning: (*i*) flood expose to deep u.v. at 0.5-1 J/cm^2, and (*ii*) develop image in either chlorobenzene or methyl isobutyl ketone (MIBK).

Resist films.—Although resist films other than PMMA were used for planarization, PMMA was selected for

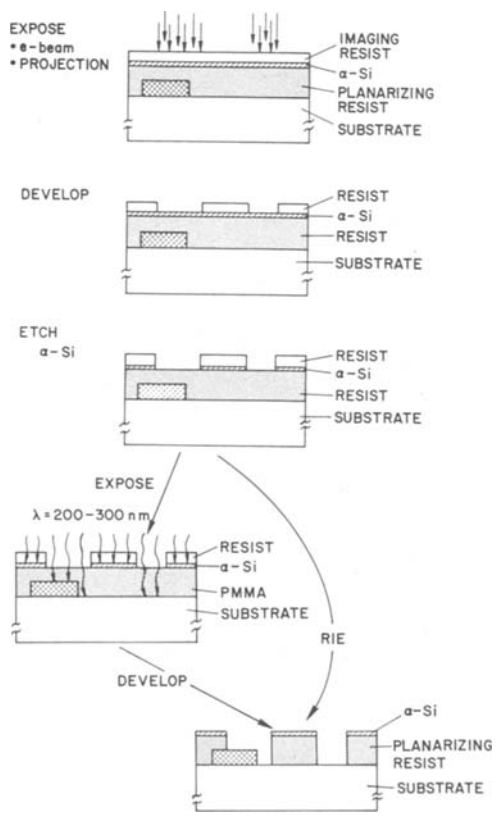

Fig. 1. Deep u.v. and RIE processes for patterning over topography using the three-layer resist system AZ1350J/Si/PMMA. The electron beam or optically exposed pattern is generated in the thin top AZ layer, and then replicated in the sandwiched amorphous silicon film by RIE in CF_4. The Si pattern is transferred to the thick bottom PMMA planarizing layer by deep u.v. exposure and solvent development or by RIE in oxygen.

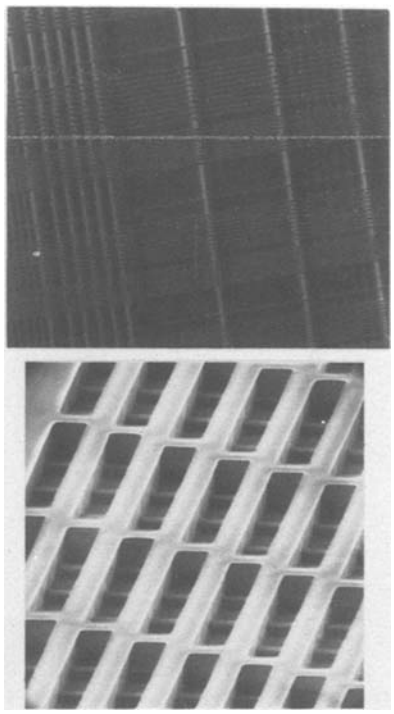

Fig. 2. Typical high resolution line/space test patterns in the three-layer system AZ/Si/PMMA defined over 1 μm high grating structures etched in an SiO_2 film. Top: Optical micrograph of part of the test pattern showing line/space features ranging between 0.5-5 μm. Bottom: SEM of equal line/space features 3 μm wide in 3 μm thick PMMA generated by RIE in oxygen.

detailed study because of its deep u.v. sensitivity (42) and its high etching rate in an O_2 plasma. PMMA films >1 μm thick were obtained by applying multiple coatings in order to avoid cracking, and to promote better planarization of the substrate surface as discussed below. Adhesion of PMMA to Si and SiO_2 surfaces was enhanced by prior coating with the adhesion promoter hexamethyl disilazane (HMDS). However, the use of HMDS was essential to ensure adequate adhesion of AZ1350J photoresist to the Si surface.

Despite its low sensitivity, AZ1350J resist was selected as an imaging layer because it offered the convenience of both optical and electron beam sensitivity. The initial thickness of AZ1350J resist was reduced by ~0.1 μm after development to a final nominal thickness of 0.4 μm. The latter was quite adequate to mask the underlying Si layer in a CF_4 plasma during the pattern transfer process.

Silicon films.—Plasma CVD silicon films were deposited in the plasma reactor illustrated in Fig. 3 using a mixture of SiH_4 and He at 4 and 65 mTorr partial pressures, respectively. The wafers were placed on the 125 mm diameter lower electrode, and after pumping to a pressure of 5×10^{-7} Torr, the deposition was performed at 50°C substrate temperature, at a rate of 15 nm/min using a power density of 0.6 W/cm^2. Films deposited under these conditions were hydrogenated amorphous silicon containing as much as 30% H_2 (43-46). Films obtained by electron gun evaporation of pure silicon on substrates maintained at or slightly above room temperature were functionally indistinguishable from CVD Si films.

Thin films obtained by plasma CVD of silane and electron gun evaporation of silicon were particularly well suited for lithographic processing because the films were clear, smooth, and amorphous. The optimum thickness for most patterning applications was 90 ± 20 nm although patterns were defined in films 30-200 nm thick. Silicon films were transparent in the visible spectrum as shown in Fig. 4, but more importantly,

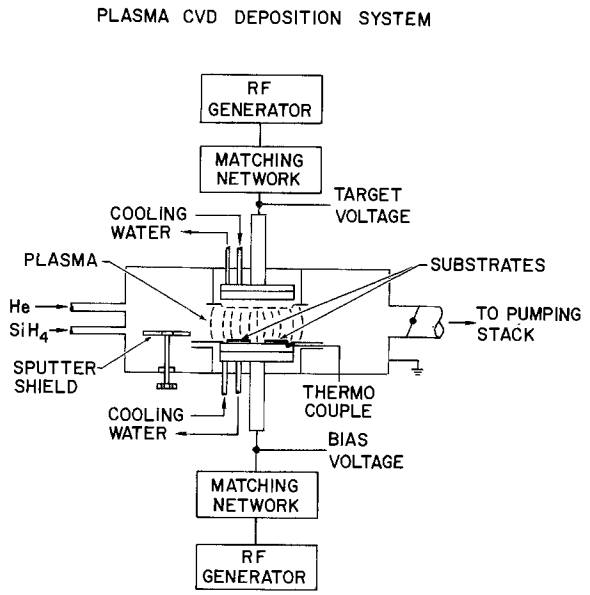

Fig. 3. Sketch of plasma CVD system for the deposition of hydrogenated amorphous silicon films from a silane/helium mixture. The 14 cm diameter electrodes 6 cm apart operated at 13.56 MHz. Typical conditions: SiH_4 4 mTorr, He 65 mTorr, upper electrode 850V, lower (substrate) electrode 0V, power 0.6 W/cm^2, deposition rate 15 nm/min.

they were totally opaque in the deep u.v. region below 300 nm. The films were excellent blocking layers for deep u.v. pattern transfer applications as suggested by the PCM techniques discussed by Lin (1, 4, 16-18).

Pattern replication.—Transfer of the image pattern from the top AZ layer to the Si film was performed by RIE in a diode reactor with a perforated grounded aluminum catcher plate positioned between the electrodes to minimize backscattering of sputtered aluminum (47). The system was first pumped down to 10^{-6} Torr, and Si was then etched in CF_4 at 2.5 mTorr pressure, 0.25 W/cm^2 rf power density at 13.56 MHz. Using endpoint laser detection (48) and 50% overetching beyond end point ensured complete and uniform removal of the Si layer.

Etching of the underlying PMMA or polymer layer was performed in an oxygen plasma at 20 mTorr pressure and 0.06 W/cm^2 rf power density. Overetching varied between 50 and 100% depending on the topography present and the maximum thickness of resist. The etch rates of the 3 layers viz., Si, AZ1350J, and PMMA in CF_4 were 40, 50, and 70 nm/min, respectively, while in O_2 the etch rates of the same films were 0, 35, and 70 nm/min, respectively. Replication of the AZ image pattern in an Si film 100 nm thick resulted in an AZ film loss of 200 nm, while replication into a PMMA layer $\leq$1 μm resulted in the total loss of the AZ film.

Transfer of the Si image pattern to the PMMA layer was also performed by flood exposure to deep u.v. radiation, followed by development in either chlorobenzene or MIBK at room temperature. A 1 kW Hg-Xe deep u.v. source manufactured by Hanovia was used to expose individual wafers in air. The exposure time varied between 2-10 min depending on the sensitivity and thickness of the planarizing resist as well as on the composition of the developing solvent. To obtain the same dissolution rate of PMMA, the deep u.v. exposure necessary for MIBK development was approximately twice that required for chlorobenzene.

Results and Discussion

High-resolution line/space features over 1 μm topography were defined in the three-layer system AZ/Si/PMMA using RIE and deep u.v. patterning techniques. The minimum dimension defined in PMMA layers 1-3 μm thick was 0.5 μm using electron beam exposure of the top AZ layer. Optical exposure on a 5$\times$ step-and-repeat projection system using 405 nm monochromatic radiation produced minimum line/space features of 1 μm. Figure 5 shows 1 μm and 0.75 μm line/space features defined in the Si layer, and replicated in 2 μm thick PMMA by deep u.v. exposure, and development in chlorobenzene. Similar test patterns 1 μm/0.5 μm

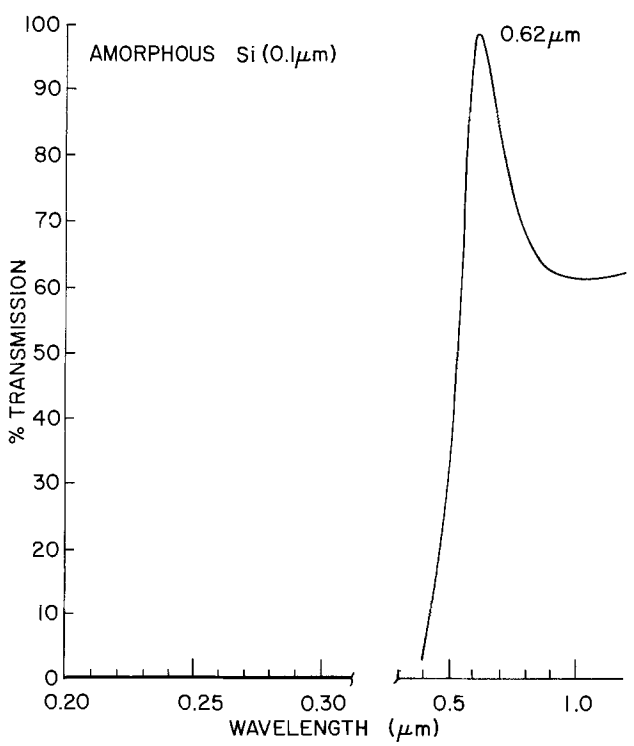

Fig. 4. Transmission spectrum of a 100 nm thick film of hydrogenated amorphous silicon deposited by plasma CVD of a silane/helium mixture on a quartz (suprasil) substrate. The film is transparent in the visible region with a peak at 620 nm and is totally opaque below 400 nm. Similar spectra are exhibited by films as thin as 20 nm including those obtained by electron-gun evaporation.

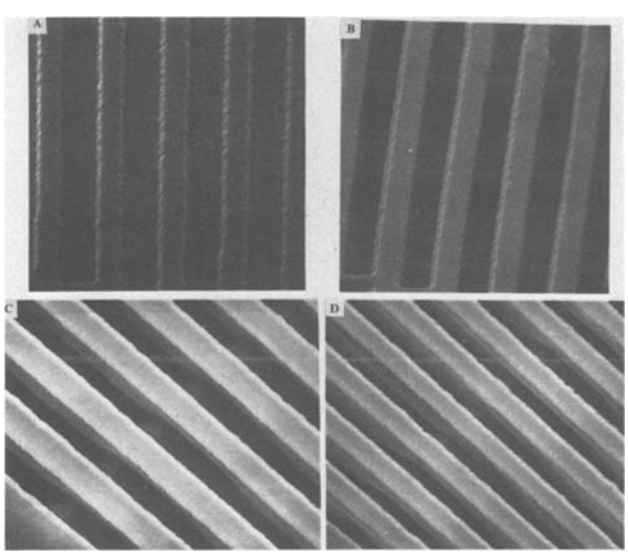

Fig. 5. SEM micrographs of high resolution line/space test patterns defined in the AZ/Si/PMMA system over 1 μm high topography. A: Equal 1 μm line/space features in AZ1350J and Si obtained by electron beam exposure followed by RIE etching of Si. B: Same pattern after deep u.v. exposure and development of PMMA 2 μm thick. C: Same as B showing vertical sidewalls of PMMA crossing over an oxide step 1 μm high. D: Equal 0.75 μm line/space features similar to C.

and 1 μm/1 μm were obtained by RIE of PMMA in an oxygen plasma as shown in Fig. 6.

The RIE and deep u.v. patterning techniques were equally capable of generating uniform resist features with good linewidth control, quasi-vertical sidewalls, and high aspect ratio over 1 μm topography as illustrated in Fig. 2, 5, and 6. Such patterns are highly desirable for subtractive and additive processes in VLSI fabrication. The differences between the RIE and deep u.v. patterning techniques were mainly determined by the characteristics of the planarizing layer as discussed below.

RIE patterning.—RIE processing was more tolerant of variations in thickness and composition of the planarizing layer by virtue of the anisotropy of RIE, and the high etch rate of organic resist materials relative to Si in an oxygen plasma. Radiation sensitivity of the planarizing layer was also not a requirement in RIE processing. The selection of useful organic coatings was, therefore, wider, and the processing flexibility, for example with respect to high-temperature baking and thermal cycling, was greater than deep u.v. processing.

Undesirable resist residues, which appeared on surfaces after etching by RIE, were removed by a cleaning procedure such as dip-etching in dilute HF solution. Figure 7 illustrates the effectiveness of the HF dip-etching technique in cleaning off all traces of residues from RIE-patterned surfaces. Where exposure to HF was incompatible with the materials on the wafer surface, alternate cleaning procedures were used in conjunction with modified RIE conditions. Potential contamination from metals sputtered from the substrate holder and radiation damage from energetic photons could be drawbacks in some applications, but their effects could be eliminated or minimized by adjusting RIE conditions (47).

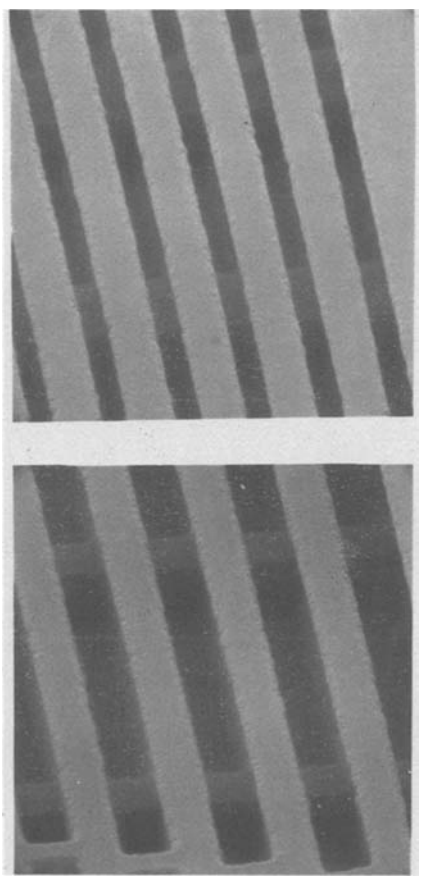

Fig. 6. SEM micrographs of line/space patterns defined in the AZ/Si/PMMA three-layer system over 0.8 μm high topography. Top: Line/space pattern 1 μm/0.5 μm obtained by RIE of PMMA 2.5 μm thick. Bottom: Similar pattern with line/space features 1 μm/1 μm. Decrease in linewidth is less than 0.1 μm.

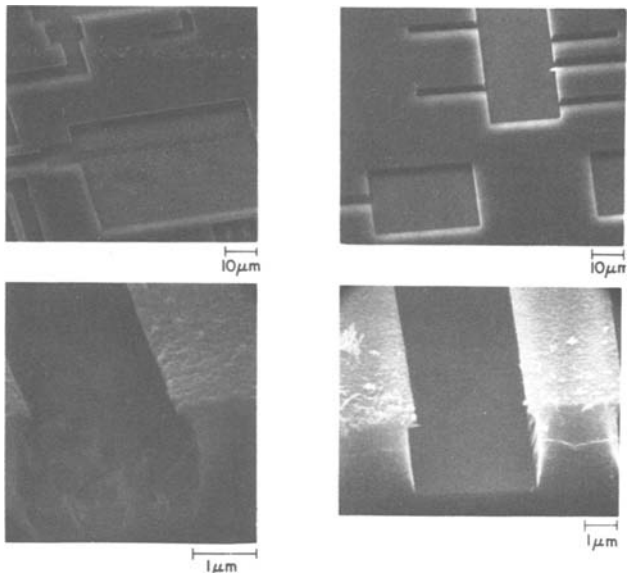

Fig. 7. SEM micrographs of patterns defined in a PMMA film 2 μm thick by RIE in oxygen. Resist residues on etched surfaces were cleaned off by dip etching in buffered HF for 10-15 sec. A,C: After RIE. B,D: After cleaning.

Deep u.v. patterning.—In deep u.v. patterning, resist residues seldom appeared after solvent development of adequately exposed PMMA. Residues tended to appear when the overall PMMA thickness was excessive, or the thickness variation over steps was large. This could be attributed to the strong attenuation of the deep u.v. intensity in thick layers, resulting from the strong absorption of PMMA in the spectral region between 200-260 nm (42). As the solubility of PMMA was a strong function of the energy absorbed, the attenuation from top to bottom of thick PMMA layers resulted in a corresponding decrease in development rate. This phenomenon influenced residue-formation, as well as the cross-sectional profile and aspect ratio of resist features. Where PMMA thickness variations due to topography were large, development in chlorobenzene resulted in better linewidth control than undiluted MIBK. Development in chlorobenzene could also be used to retain the top imaging resist film, and generate a three-layer structure which is potentially useful in lift-off applications (49-51). Similar structures could also be generated by RIE using a top imaging resist film which is stable in an oxygen plasma.

An advantage of the deep u.v. patterning process was its relative insensitivity to pinholes or cracks in the barrier layer when the top imaging film was intact and opaque in the deep u.v. In the absence of the Si barrier layer, a film of AZ1350J photoresist 0.3 μm thick is sufficient to block deep u.v. radiation from exposing the PMMA layer (4). Despite the infinite solubility of exposed PMMA relative to silicon, the maximum useful thickness of PMMA was limited to 3 μm due to the severe attenuation of the deep u.v. intensity, and the tendency of thicker layers to crack after baking or pattern development.

Film integrity.—Successful patterning of the AZ/Si/PMMA system required careful optimization of the film thicknesses and the experimental conditions which affected the integrity of the 3 layers. In particular, the stress, the adhesion, and defect levels in one layer affected directly the integrity of the two other layers during processing. The film characteristics and the processing tolerances varied with the horizontal and vertical geometry of the underlying topography.

Hydrogenated amorphous Si films deposited by plasma CVD often formed blisters (Fig. 8) on poorly planarized PMMA surfaces. Such blister formation was presumably due to excessive stress induced in the Si film by the underlying topography. Silicon films deposited at room temperature by electron gun evaporation were more susceptible to loss of adhesion than plasma CVD Si films. The evaporated films were more specular and uniform, resulting in better defined patterns. The etching and deep u.v. blocking characteristics of evaporated and CVD films were identical.

Poorly adhering and highly stressed silicon films often cracked and peeled after the imaging layer was patterned. Deposition above room temperature and annealing of the films prior to the application of the top imaging layer alleviated this problem. Similar behavior was observed with evaporated films of Al and Ti used as barrier layers between PMMA and AZ1350J.

The thickness of the top imaging resist layer and the baking conditions also influenced the integrity of the silicon barrier layer. Resist films ≤0.5 μm thick baked at about 100°C were readily processed over a wide range of PMMA and Si film thicknesses. Good step coverage and adequate planarization were essential to obtain a uniformly thick imaging layer. Inadequate planarization resulted in variations in thickness of the imaging layer with corresponding variations in linewidth and profile geometry. Multiple reflections at the resist-silicon interface also contribute to linewidth variations in the case of optically exposed patterns. The effect is clearly illustrated in Fig. 9 which shows the systematic variation in linewidth of 5 parallel resist lines nominally 2 μm wide crossing over 2 raised oxide steps 1 μm thick and 2 μm wide.

Planarization.—Due to the importance of the planarizing function of PMMA, an empirical evaluation of the coating characteristics of a variety of films was made using single and multiple coatings on stepped surfaces. Oxidized wafers, with sets of periodic line/space structures 2.5-25 μm wide, were coated by conventional resist spinning and baking methods. The undulations of the resist surface profile conforming to the substrate topography were scanned with a mechanical stylus to determine the planarization or leveling accomplished by a coating layer.

The curves in Fig. 10 show the peak-to-valley amplitude of the resist surface profile covering surface steps 0.8 μm high. The degree of planarization, represented by the amplitude, varied with the molecular weight of PMMA, the thickness and number of PMMA layers, the line/space dimensions of the substrate topography, and their periodicity or pitch. As the average molecular weight of PMMA decreased, the amplitude of the surface undulations decreased indicating enhanced planarization. This effect is illustrated in Fig. 10(a) with three PMMA compositions of average molecular weight 500,000, 150,000, and 33,000. The films were nominally 2 μm thick coated on sets of parallel steps 5 μm wide and varying pitch.

The expected improvement in planarization with increasing PMMA thickness is illustrated in Fig. 10(b) for the same sets of steps 5 μm wide and 0.8 μm high. The amplitude of the surface undulations also progressively decreased as the number of PMMA layers increased. It is interesting to note that better planar-

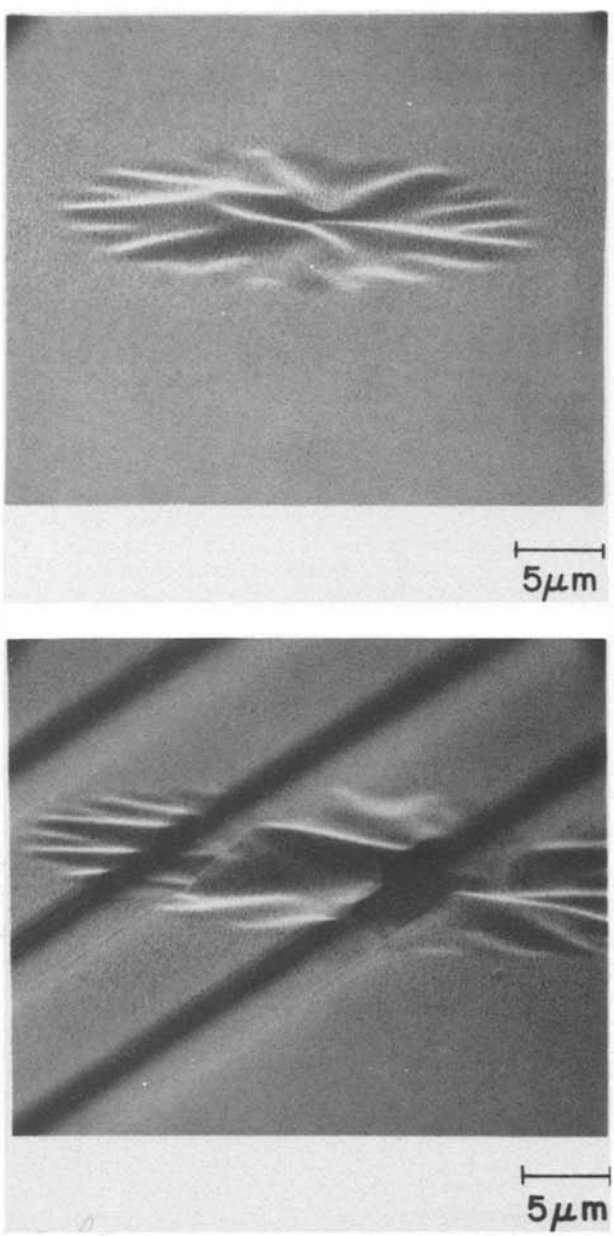

Fig. 8. Hydrogenated amorphous silicon films 100 nm thick deposited on PMMA at room temperature. Blisters indicative of compressive stress in the film are randomly distributed on the surface. Top: Single blister after film deposition. Bottom: Appearance of blister after patterning.

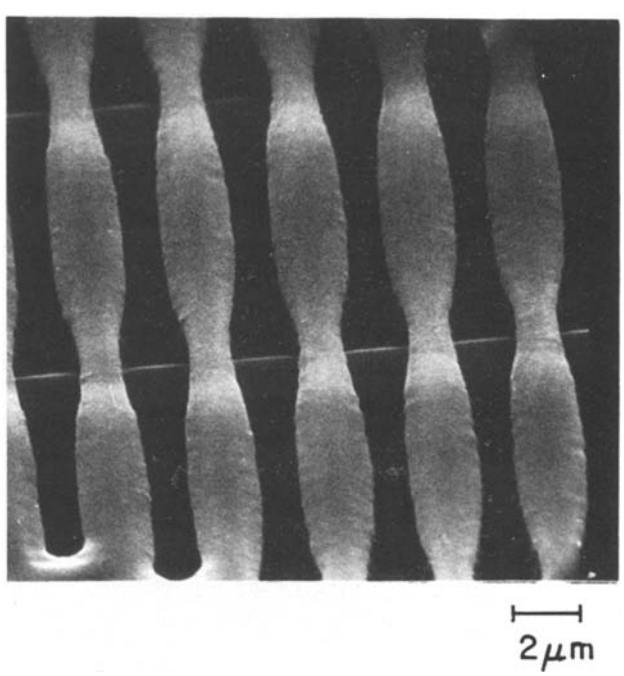

Fig. 9. Linewidth variation of PMMA resist lines that run from top to bottom of the micrograph traversing two 1 μm high SiO_2 steps. Narrowing of the resist lines occurs at the top of the steps where the resist is thinnest.

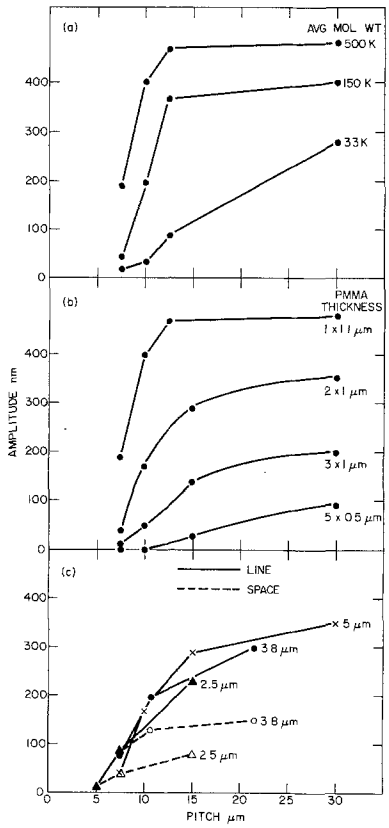

Fig. 10. Planarization of 0.8 μm high steps with PMMA films of various thickness. The steps consisted of repetitive grating structures 2.5-25 μm wide. The amplitude representing the vertical distance between the maxima and minima of the undulations of the PMMA surface profile is plotted against the pitch, *i.e.*, width of step or gap. (a) Amplitude decreases, *i.e.*, planarization improves as the average molecular weight decreases from 500,000 to 150,000 to 33,000. The PMMA films were 2 μm thick covering steps 5 μm wide; (b) Amplitude decreases as the thickness of PMMA is increased by succesive coat-and-bake cycles. From the top down: 1 layer 1.1 μm, 2 layers 1 μm each, 3 layers 1 μm each, and 5 layers 0.5 μm each. Despite the lower overall thickness, 5 × 0.5 μm layers planarize more effectively than 3 × 1 μm layers. PMMA 2041 (avg. MW = 500,000), covered steps 5 μm wide; (c) Amplitude increases or planarization degrades as the pitch increases for steps 2.5, 3.8, and 5 μm wide, and for gaps 2.5 and 3.8 μm wide. PMMA 2041 was 2 μm thick and covered steps 0.8 μm high.

ization was achieved with five 0.5 μm layers than with three 1 μm layers. A PMMA film nominally 2.5 μm thick was thus more effective than a 3 μm film to planarize the same substrate topography. This result suggests that multiple thin coatings could be applied to planarize severe topography withcut unduly increasing the overall resist thickness.

Planarization also improved as the horizontal dimensions of line/space patterns and their periodicity decreased as shown in Fig. 10(c). For a given line/space pattern between 2.5-5 μm, the amplitude of the surface undulations increased as the pitch increased. Isolated lines were thus more difficult to planarize than closely spaced lines or isolated spaces. This observation suggests that nonfunctional topographical steps deliberately introduced in the vicinity of critical surface regions would promote better planarization and consequently achieve better control of pattern dimensions. Similar effects on the planarization of metal patterns with thin polyimide films have been reported by Rothman (52).

The planarization experiments, though limited, lead to the conclusion that step coverage cannot be predicted from step height and resist thickness only. Important factors which also affect the planarization of topography include the horizontal geometry and periodicity of surface structures, as well as the molecular weight of the resist and its mode of application.

Patterning by deep u.v. and RIE was also accomplished in a variety of three-layer systems using high-sensitivity imaging resists, Ti and Al barrier layers, and Novolak-based planarizing photoresists baked at elevated temperature. The processing complexity was essentially similar to AZ/Si/PMMA, and their lithographic performance was comparable.

Conclusions

Deep u.v. and RIE patterning of submicrometer features over 1 μm topography were achieved in the three-layer system AZ1350J/Si/PMMA. The patterns in PMMA 1-3 μm thick exhibited uniform linewidth and high aspect ratio which are desirable attributes for VLSI applications. The two patterning methods were comparable in processing complexity, and were equally sensitive to defect levels in the three layers. Adequate planarization of topography, and optimization of the adhesion and stress in the Si layer were essential requirements for both processes. Planarization of topography was strongly influenced by the horizontal geometry and periodicity of surface structures, as well as by the resist composition and its mode of application. Deep u.v. patterning was performed by conventional wet processing methods which are adaptable to large-scale fabrication. New positive and negative deep u.v. resists (53-61) offer the potential for deep u.v. patterning of both imaging and planarizing layers in the same three-layer system. RIE patterning allowed a wider selection of imaging and planarizing resist materials as well as a greater latitude in processing. RIE was more readily adaptable to all-dry processing, and was particularly useful in the generation of resist patterns with vertical sidewalls and large aspect ratio over extreme topography.

Acknowledgments

We wish to thank R. C. Guarnieri and J. J. Cuomo for supporting the plasma CVD work, and S. Krongelb, J. Harper, R. S. Bennett, and J. L. Speidell for their cooperation in the RIE experiments. We also thank J. V. Powers for the electron beam exposures, C. Lapadula for the 5× optical exposures, and E. J. Petrillo, C. J. Lucchese, S. B. Brodsky, and D. L. Quinlan for expert technical assistance. We gratefully acknowledge the many helpful discussions with M. Hatzakis, J. M. Shaw, and L. B. Rothman, and the support of B. J. Lin throughout this work.

Manuscript submitted July 30, 1982; revised manuscript received Sept. 30, 1982.

Any discussion of this paper will appear in a Discussion Section to be published in the December 1983 JOURNAL. All discussions for the December 1983 Discussion Section should be submitted by Aug. 1, 1983.

Publication costs of this article were assisted by IBM T. J. Watson Research Center.

REFERENCES

1. "Fine Line Lithography," R. Newman, Editor, North-Holland Publishing Co., Amsterdam (1980).
2. W. Moreau and C. H. Ting, U.S. Pat. 3,934,057 (1976).
3. C. M. Horwitz, *Appl. Phys. Lett.*, **32**, 803 (1978).
4. B. J. Lin, *SPIE Proc.*, **174**, 114 (1979).
5. T. H. P. Chang, U.S. Pat. 4,165,395 (1979).
6. M. Hatzakis, D. Hofer, and T. H. P. Chang, *J. Vac. Sci. Technol.*, **16**, 1631 (1979).
7. M. Hatzakis, *ibid.*, **16**, 1984 (1979).
8. J. R. Kitcher, *ibid.*, **16**, 2030 (1979).
9. W. D. Grobman, H. E. Luhn, T. P. Donohue, A. J. Speth, A. Wilson, M. Hatzakis, and T. H. P. Chang, *IEEE Trans. Electron Dev.*, **ed-26**, 360 (1980).
10. C. Li and J. Richards, in *Proc. IEDM*, p. 1112, Washington, D.C. (1980).

11. K. L. Tai, W. R. Sinclair, R. G. Vadimsky, J. M. Moran, and M. J. Rand, *J. Vac. Sci. Technol.*, **16,** 1977 (1979).
12. J. M. Moran and D. Maydan, *ibid.*, **16,** 1620 (1979).
13. K. L. Tai, R. G. Vadimsky, C. T. Kemmerer, J. S. Wagner, V. E. Lamberti, and A. G. Timko, *ibid.*, **17,** 1169 (1980).
14. M. Sato and K. Kawabuchi, *ibid.*, **19,** 1329 (1981).
15. B. F. Griffing, P. D. Johnson, and J. F. Norton, Semiconductor Microlithography VI, 275, 136 (1981).
16. B. J. Lin, *This Journal*, **127,** 202 (1980).
17. B. J. Lin and T. H. P. Chang, *J. Vac. Sci. Technol.*, **16,** 1669 (1979).
18. B. J. Lin, E. Bassous, V. W. Chao, and K. E. Petrillo, *ibid.*, **19,** 1313 (1981).
19. J. R. Havas, J. Franco, and H. A. Levine, U.S. Pat. 3,873,361 (1975).
20. J. R. Havas, J. Franco, and L. Rompala, U.S. Pat. 4,004,004 (1977).
21. J. R. Havas and G. Paal, U.S. Pat. 4,202,914 (1980).
22. J. S. Logan, G. C. Schwartz, and L. B. Zielinsky, *IBM Tech. Discl. Bull.*, **20,** 1024 (1977).
23. E. C. Fredericks, G. C. Schwartz, and L. B. Zielinski, *ibid.*, **20,** 989 (1977).
24. D. Maydan, *J. Vac. Sci. Technol.*, **17,** 1164 (1980).
25. R. K. Watts, W. Fichtner, E. N. Fuls, L. R. Thibault, and R. L. Johnston, in *Proc. IEDM*, Washington, D.C. (1980).
26. J. B. Kriger, P. Rissman, and M. S. Chang, *J. Vac. Sci. Technol.*, **19,** 1320 (1981).
27. S. P. Lyman, J. L. Jackel, and P. L. Liu, *ibid.*, **19,** 1325 (1981).
28. D. M. Tennant, L. D. Jackel, R. E. Howard, E. L. Hu, P. Grabbe, R. J. Capik, and B. S. Schneider, *ibid.*, **19,** 1304 (1981).
29. M. M. O'Toole, E. D. Liu, and M. S. Chang, Semiconductor Microlithography VI, Vol. 275, 128, SPIE, Washington, D.C. (1981).
30. J. H. Bruning, *J. Vac. Sci. Technol.*, **17,** 1147 (1980).
31. M. J. Bowden, *Solid State Technol.*, **24** (6), 73 (1981).
32. M. Hatzakis, *ibid.*, **24** (8), 74 (1981).
33. B. F. Griffing, *J. Vac. Sci. Technol.*, **19,** 1423 (1981).
34. K. Grebe, I. Ames, and A. Ginzberg, *ibid.*, **11,** 458 (1974).
35. G. J. Dolan, *Appl. Phys. Lett.*, **31,** 337 (1977).
36. W. E. Spear, P. G. Le Comber, S. Kinmond, and M. H. Brodsky, *ibid.*, **28,** 105 (1976).
37. W. E. Spear and P. G. Le Comber, *Philos. Mag.*, **33,** 935 (1976).
38. J. R. Hollahan and R. S. Rosler, "Thin Film Processes," J. L. Vossen and W. Kern, Editors, Academic Press, New York (1978).
39. T. H. P. Chang, A. D. Wilson, A. J. Speth, and C. H. Ting, Proceedings of the Symposium on "Electron and Ion Beam Science and Technology, Seventh International Conference," R. Bakish, Editor, p. 392, The Electrochemical Society Softbound Proceedings Series, Princeton, N.J. (1976).
40. J. S. Wilczynski *J. Vac. Sci. Technol.*, **16,** 1929 (1979).
41. C. M. Melliar-Smith and C. J. Mogab, "Thin Film Processes," J. L. Vossen and W. Kern, Editors, Academic Press, New York (1978).
42. B. J. Lin, *J. Vac. Sci. Technol.*, **12,** 1317 (1975).
43. M. H. Brodsky, M. A. Frisch, J. F. Ziegler, and W. A. Lanford, *Appl. Phys. Lett.*, **30,** 561 (1977).
44. M. H. Brodsky, M. Cardona, and J. J. Cuomo, *Phys. Rev. B*, **16,** 3556 (1977).
45. "Amorphous Semiconductors," M. H. Brodsky, Editor, Springer-Verlag, New York (1977).
46. J. I. Pankove and D. E. Carlson, *Appl. Phys. Lett.*, **30,** 561 (1977).
47. L. M. Ephrath, *This Journal*, **129,** 62C (1982).
48. K. Sugawara, T. Yashimi, H. Okuyama, and T. Shirasu *ibid.*, **121,** 1233 (1974).
49. M. Hatzakis, *ibid.*, **116,** 1033 (1969).
50. M. Hatzakis, U.S. Pat. 4,024,293 (1977).
51. M. Hatzakis, B. J. Canavello, and J. M. Shaw, *IBM J. Res. Dev.*, **24,** 452 (1980).
52. L. B. Rothman, *This Journal*, **127,** 2216 (1980).
53. P. van Pelt, Semiconductor Microlithography VI, Vol. 275, 150, SPIE, Washington, D.C. (1981).
54. R. L. Hartless and E. A. Chandross, *J. Vac. Sci. Technol.*, **19,** 1333 (1981).
55. Y. Mimura, T. Ohkubo, T. Takeuchi, and K. Sekikawa, *Jpn. J. Appl. Phys.*, **17,** 541 (1978).
56. Y. Yamashita, K. Ogura, M. Kunishi, R. Kawazu, S. Ohno, and Y. Mizokami, *J. Vac. Sci. Technol.*, **16,** 2026 (1979).
57. C. W. Wilkins, Jr., E. Reichmanis, and E. A. Chandross, *This Journal*, **127,** 2510 (1980).
58. M. Tsuda, T. Tsumori, Y. Nakamura, H. Nagata, A. Yokota, H. Nakane, T. Tsumori, Y. Nakane, and T. Mifune, *Photogr. Sci. Eng.*, **23,** 290 (1979).
59. S. Imamura, *This Journal*, **126,** 1628 (1979).
60. T. Iwayanagi, T. Kohashi, S. Nonogaki, T. Matsuzawa, K. Douta, and H. Yanazawa, *IEEE Trans. Electron Dev.*, **ed-28,** 1306 (1981).
61. E. Gipstein, A. C. Ouano, and T. Tompkins, *This Journal*, **129,** 201 (1982).

Short Time Annealing

T. O. Sedgwick*

IBM Corporation, T. J. Watson Research Center, Yorktown Heights, New York 10598

ABSTRACT

Short time annealing has recently become of interest in silicon processing as a technique to activate ion implanted dopants, remove defects, and regrow amorphized silicon, with minimal diffusion of the dopant atoms. Short time annealing is carried out using a variety of energy sources ranging from arc lamps and resistance heaters with heating times of a few tens of seconds, to laser, electron, and ion sources with heating times of a few milliseconds down to nanoseconds. The annealing processes are grouped according to the time durations of the anneal and with reference to the thermal response time of the silicon. These are designated as adiabatic for $< 10^{-6}$ sec; thermal flux for 10^{-6}-10^{-2} sec, and isothermal for $> 10^{-2}$ sec. Processes in the adiabatic regime result in surface melting, regrowth of silicon free of extended defects, and complete dopant activation. However, the dopant diffuses throughout the melt zone. In the thermal flux and isothermal annealing regimes the dopant can be activated, and amorphous silicon regrown epitaxially with little dopant diffusion. In the limited results reported to date, the complete removal of extended defects has not been achieved. Further investigation may yield new results in extended defect removal.

Short time annealing (STA) encompasses a wide range of processing techniques that can thermally process materials over an extremely wide range of times, 10^{-8}-10^{2} sec, all short compared to standard annealing. This paper deals with the application of STA techniques in silicon technology particularly to activate, regrow, and remove damage in ion implanted junctions. The scaling down of device dimensions, which is a continuing trend and an integral part of VLSI device design, requires shallower junctions, higher doping levels, and reduced defect density. The inadequacy of standard furnace annealing to achieve

* Electrochemical Society Active Member.
Key words: silicon, ion implant.

these goals has motivated the search for new processes that, in addition to the above, will hopefully have advantages in minimizing the overall thermal cycle and process power consumption while simultaneously increasing wafer throughput.

In this paper, first, the basic processes important in annealing of ion implant damage, *i.e.*, dopant activation, crystal regrowth, diffusion, and both point and extended defect removal, are discussed in the time-temperature regime made available by these new processes. Second, evaluations of material quality, processing compatibility, and device results from the extensive studies using pulsed and CW lasers, electron beams, and the more recent efforts to use 1-100 sec isothermal annealing techniques are made. Finally, an attempt is made to perceive trends, point out areas left unexplored, and make some comment on possible future promise and directions.

Other reviews and articles have dealt with this subject and with processing compatibility considerations (1), other potential processing areas for STA processes, such as material reflow (2), silicon on insulators (3), laser-induced diffusion (4, 5), laser cleaning of semiconductor surfaces (6), and annealing of other semiconductors (7).

Annealing Time, Silicon Thermal Response, STA Apparatus, and Geometry Factors

Short time annealing (STA) techniques vary over a wide range in the mode of energy transfer from source to sample. They include visible and infrared laser light, incoherent light, electron and ion beams, and black body radiation from a resistance heater. The absorption depth of the radiation depends on doping, crystallinity, and wavelength but except for the CO_2 laser with 10.2 μm radiation, which penetrates Si deeply, the visible wavelengths as well as electrons at 10-30 keV are all absorbed within 0.01-2 μm of the surface and are converted to heat in a time short compared to the processes indicated in Fig. 1.

The most important difference between these heat sources is the time scale in which the energy is delivered and how it compares with the thermal response time, t, of silicon where

$$t = s^2 k^{-1}$$

where s is the thermal diffusion length or the sample dimension and k is the thermal diffusivity (8). k varies between 0.8 cm^2/sec at 25°C and 0.1 at 1400°C. For $k = 0.2$ cm^2/sec and $s = 10$ μm, *i.e.*, the extended junction region, $t_j \cong 5 \times 10^{-6}$ sec but for the wafer thickness $s = 375$ μm and $t_w \cong 7 \times 10^{-3}$ sec. Figure 2a shows graphically that for pulsed energy sources where the energy is absorbed in the surface region and where the pulse is short, <100 nsec, compared to the thermal response time, the system behaves adiabatically. The temperature rise is extremely rapid and the sample melts. The melt depth depends only on the energy density. After the pulse the melt cools, resolidifies, and the heat is removed by thermal spreading into the bulk in a few hundred nanoseconds.

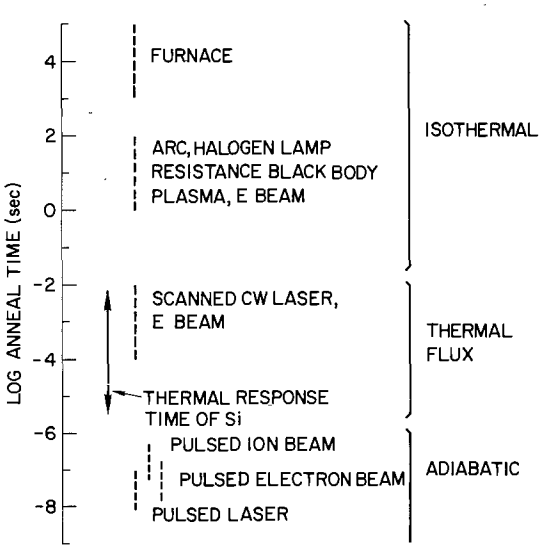

Fig. 1. Schematic showing time duration of various short time annealing (STA) processes.

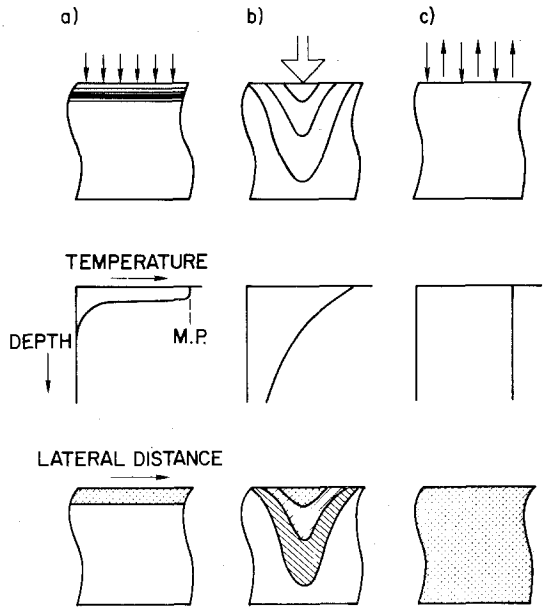

Fig. 2. Schematic showing spatial temperature distribution in STA processes: (a) adiabatic, (b) thermal flux, and (c) isothermal. Top diagrams show isothermal lines. Midde diagrams show temperature-depth profiles. Bottom diagrams show lateral temperature distributions.

In the thermal flux regime a point (or line) source with input diameter (or width) small compared to the wafer thickness is raster scanned over a larger area. The dwell time is typically in the range 10^{-4}-10^{-2} sec, which is long compared to the thermal response time of the 10 μm deep surface region, but is comparable to the thermal response time of the Si wafer thickness. In this case the temperature of the heated region is a function of beam power/beam diameter ratio, the scan rate, and the temperature of the heat sink at the wafer back. For implant damage removal, CW scanning is operated at a power level below the melting point. Both the adiabatic and the thermal flux techniques result in intense heating of only the surface. In principle, this could have an advantage in avoiding the heating of buried layers. Similarly, the use of small area beams could facilitate localized lateral processing. However, to date, this has not been shown to be advantageous. In fact, the disadvantages of localized thermal stress, scan overlap problems as well as wafer throughput considerations, where a whole wafer must be scanned, greatly limit the general use of such techniques. These concerns have strongly influenced the search for more desirable "line" and "area" sources, Fig. 3.

The third regime of STA processing, isothermal, 1-100 sec, exploits all the advantages of line or area energy sources while at the same time minimizing thermal gradients. In this time regime, the anneal time is clearly longer than the thermal response time of the silicon wafer, Fig. 2c. In addition, a faster wafer throughput compared to scanned beams is obviously attainable and the energy sources themselves are much more energy efficient than pulsed or scanned lasers.

Annealing Processes in Ion Implanted Silicon

In forming shallow junctions, 500-1500Å deep, for VLSI technology, there is a demanding list of criteria

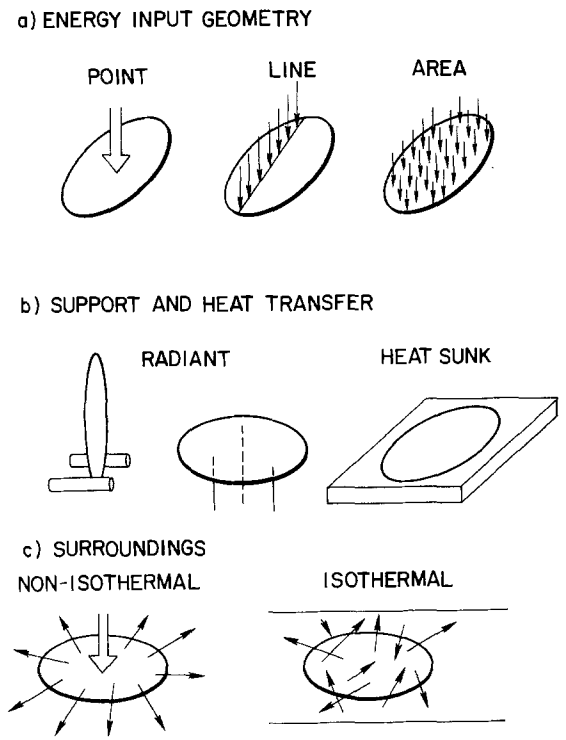

Fig. 3. Schematic showing various important physical aspects of STA annealing apparatus.

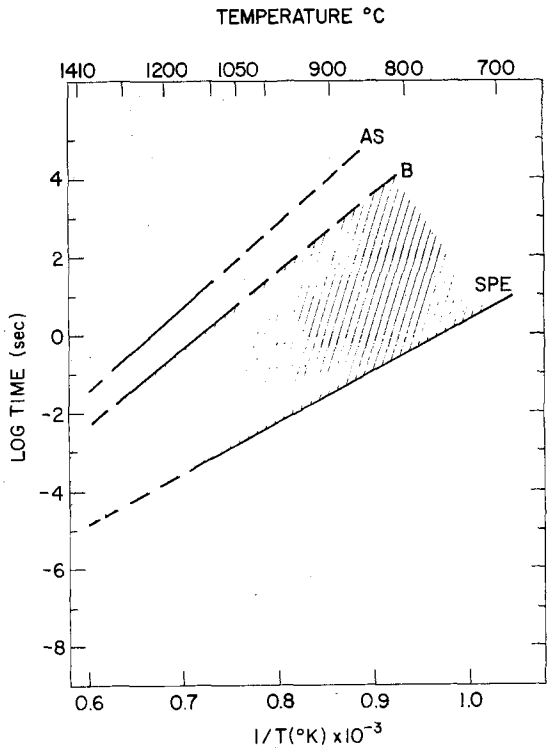

Fig. 4. Reciprocal temperature plot showing time required for B and As diffusion to 500Å and solid phase epitaxial (SPE) growth of 1000Å layer (see text).

which must simultaneously be satisfied in any anneal process. They are: (*i*) regrow epitaxially the ion implanted amorphized layer, (*ii*) activate dopant substitutionally to achieve full conductivity, (*iii*) severely limit extent of dopant diffusion to ≤500Å, (*iv*) remove or avoid formation of point and cluster defects below implant region to maintain mobility and suppress recombination-generation centers to reduce junction leakage, and (*v*) remove or avoid formation of extended defects, dislocations, loops, or slip to prevent diffusion pipes, precipitates, and junction shorting.

For shallow junctions these criteria, particularly item (*v*), are much harder to attain than for deeper, *e.g.*, 4000Å, junctions for two interacting reasons. In deep junctions the furnace anneal time of an hour or more at 1000°C or higher allows dopant diffusion of several thousand angstroms and it also allows removal of some of the extended defects. However, the key factor is that the junction has moved beyond the region of extended defects deeper into the crystal so that those defects remaining no longer penetrate the junction depletion region. In shallow junction annealing the available time-temperature cycle is less, hence fewer defects are removed, and because of the limited diffusion, item (*iii*), the effect of extended defects remaining is greater because of their location within the space charge region. The presence of "knock on oxygen" when the implant is done through a screen oxide additionally complicates this process.

In adiabatic annealing, only to be considered very briefly here, the melting and epitaxial regrowth are found to satisfy items (*i*), (*ii*), and (*v*) extremely well and item (*iv*) only incompletely provided the melt depth is deep enough, which, in most cases, must be well beyond the implant region (see below). However, the melting gives rise to very fast diffusion in the liquid phase that results in dopant motion essentially equal to melt depth (9). For shallow junctions reproducible melt depths of 500-1500Å may be very difficult to achieve.

In order to discuss quantitatively the time-temperature space available for shallow junction annealing consider Fig. 4 and 5. Figure 4 shows a plot of the time required for solid phase epitaxial (SPE) regrowth of 1000Å of amorphous silicon (10). Clearly, time-temperature processing above this curve is required to assure complete regrowth. The curves for B and As diffusion are also displayed, which show the maximum time allowed for junction motion, Δx_j of 500Å or less. [This is calculated using $\Delta x_j \cong 5\sqrt{D\Delta t}$. The factor 5 is appropriate for Gaussian law diffusion. A complementary error function law diffusion would give 10% less distance. D is the diffusion coefficient (5) and t the time, and, finally, the ratio of doping used at the peak concentration to the concentration at the junction is 2×10^{-3}.] For the sake of simplicity, neither concentration (11) nor radiation (12) enhanced diffusion effects are included in Fig. 4 which would, if included, tend to move the curves downward and hence shorten the time allowed at a given temperature. Thus the desirable parameter space defined by items (*i*) and (*iii*) for STA lies below the B and As diffusion curves and above the SPE curve (shaded area).

Figure 5 shows a similar time-temperature plot showing the rates of removal of various defects. The lower three curves show removal rates for some typical defect pairs vacancy-phosphorus (V-P), vacancy-oxygen (V-O) (13), and divacancy (V-V) (14) extrapolated from low temperature measurements. Since these pair defects and probably many others in the catch-all group of item (*iv*) anneal out in times short compared to SPE growth, Fig. 4, they are not a problem. It is clear, however, that some nonextended defects will not be annealed out in such short times.

The most difficult to remove defects are dislocations, item (*v*) which seem to form from clusters of point defects in the early stages of a conventional anneal but may be reduced in number by prolonged annealing. In order to obtain a measure of their removal rates, the following calculations and extrapolations have been made from literature results on Si(100) surfaces. Curve I is the time it would take to shrink a stacking fault, originally formed during oxidation, by 1000Å by annealing in nitrogen (15). Curves II are the calculated times for removal in nitrogen of 700-

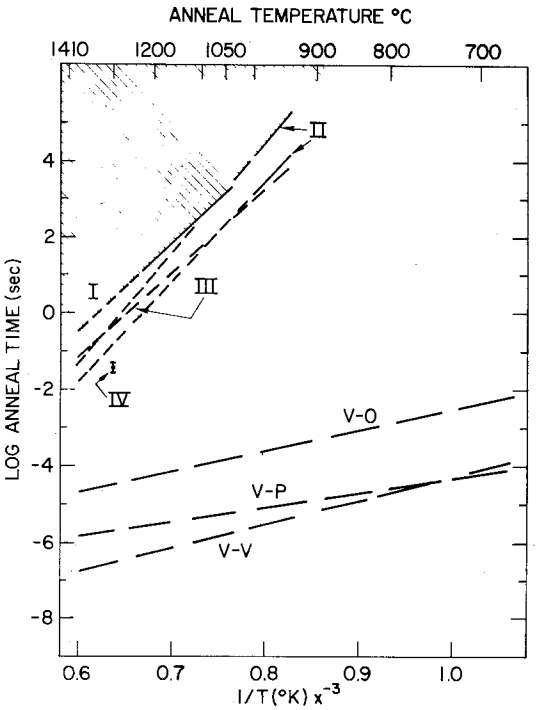

Fig. 5. Reciprocal temperature plot showing time required to remove various point defects (lower curves) and extrapolated time to remove extended defects (upper curves) (see text).

1500Å diam interstitial loops observed in a boron implant (16). Curve III is the calculated and extrapolated time to anneal out in vacuum loops of up to several thousand angstroms in diameter observed in a boron implant (17). The temperature dependence was calculated from the temperature dependence of the silicon self-diffusion coefficient. Point IV is the observed time-calculated temperature condition for complete removal of observed 200-400Å loops in As ion implanted Si using a CW Nd:YAG laser (18). The time-temperature parameter space for removal of these defects lies above (shaded area) these curves.

An overlay of Fig. 5 on Fig. 4 reveals that there is no region in time-temperature space where diffusion is ≤500Å and where the extended defects will be removed. Although this comparison dampens any hope of finding an adequate annealing process for shallow junction, there are a number of comments that should be made that in some sense define the area for future research. First, the higher activation energy for defect removal as compared to dopant diffusion implies that the most favorable region for defect removal lies at the highest temperature. Second, the extended defect removal curves of Fig. 5 at high temperatures are extrapolations. The defects observed in these cases were all first formed and then removed under standard annealing conditions. It is at least conceivable that STA for times of 10^{-3}-100 sec and at high temperatures will yield new results on defect formation and removal. Third, as a hint in that direction we note the dramatic disappearance of oxidation induced stacking faults at 1175°-1250°C reported by Hu (19). Fourth we note the removal of loops by CW laser annealing at high power by Ishida *et al.* (18) even though in this latter case slip was introduced into the sample. In addition, the observation by Baumgart *et al.* (20) that no loops were formed and good electron beam induced conductance (EBIC) collection efficiency was observed at the center of CW laser scans, points to the fact that under some conditions and in localized regions thermal flux annealing can result in silicon free of extended defects. It will be discussed in detail below that significant reduction in the thermal stress conditions in CW laser annealing can be made that may greatly diminish the defect formation observed along the edges of the scans (20, 21).

Finally, it is worth mentioning that control of the conditions of the ion implantation itself, particularly as regards the avoidance of surface contamination or avoidance of a screen oxide as well as the use of low temperature implantation can potentially reduce the number of defects in junctions after annealing.

Thermal Stress and Dislocation Generation

Spatial thermal gradients and the associated induced stress will, when larger than the critical yield stress, cause dislocation formation and motion during annealing, the most obvious of which is slip. Since slip is often seen in material CW laser annealed at relatively high powers, there is a significant reason to find line or area radiation sources which more easily avoid this problem.

The evolving 1-100 sec isothermal STA techniques utilize rapid heating and cooling rates of the wafer as a whole. These rates of 10^{2}°-10^{3}°C/sec are very modest compared to pulsed laser heating rates of 10^{10}°C/sec (22) and CW laser heating rates of 10^{6}°C/sec. One of the reasons that slip is not observed over a wider range of annealing conditions in CW laser annealing is likely because the critical yield stress increases with the strain rate that must be very large in pulsed or scanned CW laser annealing. Even in 1-100 sec isothermal STA annealing, it will be difficult to totally avoid spatial gradients. Relevant is Fig. 6, which shows the occurrence of wafer warpage and slip generation for vertically stacked wafers that were quickly pulled from a conventional annealing furnace at the indicated temperature into air and allowed to cool by radiation and convection (23). The maximum ΔT from the wafer center to edge reached after a few seconds for a pull at 1000°C is about 175°C. Note that all the wafers pulled under these conditions warped. Also, the dependence of warpage on precipitated oxygen content is strong. This data should make clear the need for careful design of annealing apparatus in the 1-100 sec isothermal region. Since the critical yield stress decreases with increasing temperature, this concern becomes even more critical at the likely anneal temperatures of 1050°-1200°C in STA. As in all semiconductor processing, the use of wafers free of dislocation sources such as edge cracks and chips will be also very important.

Adiabatic Annealing

Pulsed laser.—Pulsed laser annealing studies usually employ a Q switched ruby or Nd:YAG laser. The large diameter beam several millimeters to 1 cm, of the ruby laser makes it easy to anneal and analyze single shot samples and this laser could conceivably be used in a single shot per chip fabrication mode. Cullis *et al.* (24) have reported a beam homogenizer which greatly improves the uniformity of the beam. Very large areas are obtained by rapid pulsing and scanning with the inevitably necessary but undesirable overlap problems. In this adiabatic process pulses 10-100 nsec long and with energies of about 1 J/cm² will melt the silicon surface. The temperature of the bulk wafer is not controlled. To achieve good single crystal regrowth it is necessary to melt in depth at least to the amorphous-crystalline interface (25).

The dramatic discovery that by using pulsed laser annealing the regrown silicon was in fact totally free of external defects (26) was a tremendous boost to the STA approach. It was, however, also shown that in order to get good electrical junction properties the melt must proceed well below the original amorphous-crystalline interface (27-29). Wang *et al.* (27) have shown, for instance, that for a 8×10^{15}/cm² implant of 90 keV As with a mean range of about 650Å, it was necessary to melt to a depth of about 7000Å in order to remove damage and produce good low leakage, 2×10^{-8} A/cm², mesa diodes.

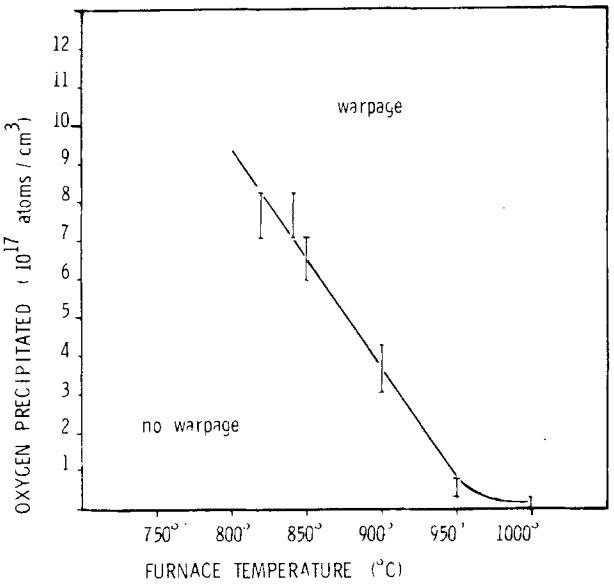

Fig. 6. Wafer warpage as a function of "pull" temperature and precipitated oxygen concentration [after Leroy and Plougonven (23)].

Perhaps the most serious side effect of pulsed laser annealing is the formation of ripples (vertical undulations) in bare silicon or SiO_2 coated silicon areas (30). There are several explanations for this effect, but it appears to be partially avoidable by the use of Al, polycrystalline Si, or phosphosilicate glass masks (22, 31-33) which have been employed in the fabrication of diodes (31-33) and transistors (32, 33). Diodes were made by P or As implantation with a dose of 10^{15}-10^{16}/cm^2 followed by pulse laser annealing and finally followed by a 415°C forming gas anneal or a 600°C N_2 anneal. The post laser annealing step (34-36) greatly reduces the reverse leakage giving values of 10^{-9}-10^{-8} A/cm^2 at 1-2V and seems to some extent to avoid the necessity of very deep melting to remove defects menioned earlier. In the few cases where transistors have been made, the results were only partially successful (33, 37).

Pulsed e-beam.—Electron beams in general have important advantages, at least in principle, compared to laser beams for STA. The beam energy and hence the depth of electron penetration may be selected from a few keV to several hundred keV. 20 keV electrons penetrate about 2 μm (38). Electrons at 125-150 keV should be avoided since they can cause displacement damage (39). Current is also variable, although current and voltage are not always independently variable. E-beams penetrate many materials including polycrystalline Si, crystalline Si, and SiO_2 with about the same absorption and to the same depth for a given energy. At the same time interference effects due to the reflecting and antireflecting properties of SiO_2 of various thicknesses encountered with laser annealing are totally avoided.

There is currently available commercial pulsed e-beam equipment which is being evaluated for low cost solar cell impurity dopant activation and silicon regrowth. In this equipment (40) electron pulses of 10-100 keV for 20-200 μsec yield an energy of 0.5-10 J/cm^2. Pulses at a repetition rate of 0.5 Hz can be achieved and the beam diameter can be as large as 10 cm.

Pulsed e-beam processing like pulsed laser processing occurs in the adiabatic regime with the resultant melt formation and silicon regrowth from the melt. Similarly, dislocation-free silicon has been observed (41). Inada *et al.* (42) have shown by anodic sectioning 100% dopant activation, a relatively flat phosphorous concentration profile at 1.5-2 $\times$ 10^{20}/cm^3 which implies melting and a mobility of 60 cm^2/Vsec down to about 0.3 μm depth of an e-beam pulse annealed phosphorous implanted sample. The sample was implanted with a 5 $\times$ 10^{15}/cm^2 dose of 120 keV phosphorous and was annealed with a single 60 nsec pulse of 20 keV electrons. The mobility was increased to 80 cm^2/Vsec upon post e-beam annealing from 500° to 700°C for 20 min in inert gas. Kamins *et al.* (43) have prepared diodes by implanting 1 $\times$ 10^{16}/cm^2 As ions with an energy of 185 keV through 1000Å gate oxide as in conventional MOS integrated circuit fabrication. The diodes were pulse e-beam annealed with a 4 cm diam beam with ±5% lateral power uniformity. This was followed by a final anneal at 450°C in a hydrogen ambient. The test diodes had leakages of 1 $\times$ 10^{-8} A/cm^2 with a square root dependence on reverse voltage implying uniform generation-recombination in the space charge region and hence no important localized defects. On the other hand, the diode leakage was quite variable across the beam diameter indicating a high sensitivity to beam nonuniformities. In addition, melting of the surface under the oxide was observed to cause ripples as is often observed in pulsed laser annealing.

Ion beam annealing.—Hodgson *et al.* (44) have reported the use of a pulsed ion beam source to produce ions *e.g.*, Ba^+, Ar^+, Li^+, B^+ for simultaneous ion implantation and melt annealing. Ion pulses of 50-400 nsec and energies of 150-350 keV with typical doses of 10^{13} ions/cm^2 have been investigated. Although the technique is only in the early stages of exploration, it has already been found that Si layers can be melted and regrown epitaxially as indicated by Rutherford backscattering spectroscopy.

To date, full activation of dopants has not been reported nor have electrical properties been discussed. Initial defect studies show the layers to contain extended defects (45). This technique which couples annealing with implantation is restrictive, the ability to achieve shallow junctions when melting is required is uncertain, and the disadvantages of melting, diffusion, and likely ripple formation make this technique not promising for practical STA processes.

Thermal Flux Annealing

CW laser annealing.—Argon ion, Nd:YAG, and to a much lesser extent CO_2 lasers have been used in CW laser STA studies. Most CW lasers can be quite stable and the argon laser power is stable to within 1%. For the argon laser, a spot size of 20-150 μm diam, a scan speed of 1-10 cm/sec, and an overlap between scans of 5-95% includes most experimental conditions. The substrate temperature is a significant process parameter and studies using samples held between room temperature and 500°C are reported. Successful annealing takes place within a small "power window" where low power levels do not result in complete SPE (see Fig. 4) and high power levels result in slip formation in addition to annealing. At sufficiently high power the Si melts. Typically the "power window" for implantation damage annealing would be centered at about 75% of the power needed to melt. Depending somewhat on parameters, the power/beam diameter ratio (W/μm) found to melt silicon is 0.20-0.22.

The early result (46-49) in CW laser annealing that greatly stimulated interest was the discovery that dopants could be fully activated and amorphous silicon epitaxially regrown in the solid state with minimal, <200Å for B (50) and <50Å for As (48, 49), dopant redistribution. In addition, the surface was smooth, showed no signs of roughening or ripple formation due to melting, and optically, at least, showed no evidence of the scan overlapping which is necessary to cover large areas. Early reports of material free of defects were overly optimistic and there is no doubt the early results with pulsed laser annealing in eliminating de-

fects were extrapolated inadvertently to include the CW case.

Recent extensive studies of both extended and electrically active defects by transmission electron microscopy (TEM) (18, 20, 21), deep level transient spectroscopy (DLTS) (51-53), luminescent efficiency (54, 55), EBIC collection efficiency (20, 21, 56, 57), and in diode formation (58, 59) all give greater detail to the nature and distribution of both extended and point defects in CW laser annealed Si and suggest some approaches to avoid them. It is apparent from the luminescence, DLTS, and diode measurements that there is a rather narrow range in laser power for optimal electrical properties and implied low defect density. EBIC and TEM studies also reveal the dramatic change in properties across (orthogonal to scan direction) a typical scan where the center region of the scan yields high efficiency electron collection in an EBIC picture and few if any extended defects (18, 21, 56). At the edges of the scan, however, are tangled networks of dislocations and an extremely low EBIC collection efficiency. With an unusually broad laser beam, 500 μm, Ishida *et al.* (18) were able to remove extended defects, but only at laser powers so high that slip was introduced into the sample.

It is clear that considerable improvement can still be made in CW laser annealing. Close examination of the literature shows that the detailed experimental conditions used are very important. In all cases the "best" low defect, high electrical quality results were obtained with either a wide beam (18), high beam overlap (55, 57-59) up to even 95%, tuning to optimum power level (18, 55, 58), use of high substrate temperature (18, 53, 57-60) at least 250°C and up to 500°C, or some combination of these conditions and including a post laser anneal in forming gas. Annealing with a CO_2 laser, which because of its low absorption coefficient tends to heat the silicon very deeply and hence with lower spatial thermal gradients, also was capable of yielding layers without extended defects (21). All these conditions indicate a fairly narrow laser "power window" for optimum properties and also point to the need to minimize thermal gradients to even out the wafer exposure so that all parts of the sample have equivalent or near-equivalent thermal experience. Still higher substrate temperatures above 500°C as well as faster scan rates may have significant advantages since the critical yield stress increases with the strain rate.

Under near optimal conditions (58) shallow p^+n and n^+p diodes were made using ion implantation of 10^{13}-10^{14}/cm^2 of 20 keV B or 10^{14}/cm^2 of 50 keV As into 1700Å thick oxide defined areas followed by argon laser annealing in a forming gas atmosphere at 500°C. Low reverse leakage values of 10^{-9}-10^{-8} A/cm^2 at 65 and 30V breakdown for the p^+n and n^+p devices, respectively, were obtained. These compared very closely to reverse leakage values for furnace annealed diodes. Sandow (59) also reports that diodes formed by a 4×10^{15}/cm^2 dose 35 keV As implantation through 3200Å thick SiO_2 openings and argon laser annealed at 350°C substrate temperature resulted in leakages of only 10^{-8} A/cm^2 at 10V. In addition, N and P channel MOSFET's have been made (60) by argon laser annealing at 300°-350°C substrate temperature which displayed reduced ring oscillator delays and source-drain leakages of $1\text{-}3 \times 10^{-11}$ A/μm of channel length. The laser irradiation was carried out with a polycrystalline Si gate in place and an oxide coating on the source and drain regions. In each of the above cases, the oxide thickness was designed to be appropriately reflecting or antireflecting to achieve the desired anneal. In no case was it reported that the oxide rippled or was damaged during the process.

CW e-beam annealing.—Much less extensive than pulsed or CW laser annealing studies are investigations of CW e-beam annealed silicon. In spite of the potential advantages of e-beam annealing (see above), the scarcity of scanning e-beam apparatus may be limiting such studies. To date most experiments have been carried out with scanning point sources, but swept line sources (61-63) are now becoming available. A point source e-beam is raster scanned similar to CW laser scanning where the sample at least starts at room temperature and in some cases has been deliberately heat sunk. Typical beam parameters are 10-30 keV, 15-150 μA, 5-500 μm beam diameter, and scan rates in the 1-10 cm/sec range.

To first order the results with CW e-beam annealing are the same as those for CW laser annealing. The amorphous silicon is regrown epitaxially, the dopants are activated and do not diffuse much. At least in the early work (64, 65), extended defects and a high resistance layer (66) were observed in the region of the implant after annealing.

Recent work using EBIC and DLTS indicate that CW e-beam annealed silicon has fewer defects (31, 57) than similarly CW laser annealed silicon. These studies and others show that there is a somewhat wider "power window" in e-beam scanning for optimum luminescent efficiency. The optimum overlapping of the raster scan can be more easily arranged to give high and uniform EBIC electron collection efficiency (57). The differences could be due to different thermal profiles caused by the different shape and depth of energy deposition of the two techniques or to some other unidentified intrinsic difference. However, the fact that samples in the vacuum environment of an e-beam apparatus may rise in temperature during annealing unless deliberately heat sunk, could play a role in these results (see below). In any event, the use of higher substrate temperatures is a promising way to minimize thermal gradients and reduce thermally induced damage and may lead to interesting results. No diode or transistor fabrication results are known at this time (see below).

Isothermal Annealing

Incoherent light annealing.—The newest and currently the most actively investigated area of STA and probably the most promising approach uses a variety of incoherent light sources to heat the sample for 1-100 sec. Typically the silicon is brought to, say, 1100°C in a few seconds, allowed to "soak" at 1100°C for 2-10 sec, then cooled. Light sources are high power halogen lamps (67-69), arc lamps (63, 70-72), radiating resistance heaters (73, 74), and even a CO_2 laser (obviously coherent) (75). In order to get sufficient power into a sample and to evenly distribute the radiant energy, multiple halogen lamps are necessary in combination with reflectors. A new arc lamp (72) with very high power, 125 kW, in a tube 11 mm diam $\times$ 210 mm long can yield 60 W/cm^2 over a 5×6 in. area. Most such lamp systems thermally isolate the wafer on an insulating substrate holder or simply allow it to stand in air or an inert gas (Fig. 3). Cooling occurs by radiation. An even simpler arrangement uses the wafer horizontally placed on a resistance heated graphite slab where heating and cooling is directly dependent on the temperature of the graphite slab (73). A technique whereby wafers are placed at a distance from the radiating graphite heater has also been investigated (74).

There are several obvious advantages of these techniques. They use area sources, or swept line sources (63, 70) and use incoherent light so that interference effects observed in the coherent light exposures are avoided. Depending on design it is possible to assure that the wafer will not be in contact with another hot surface or in fact it may be the only hot object in the annealing cavity, thus greatly reducing the possibility of contamination. Finally, all such sources are intrinsically cheaper in initial cost and are powerwise more efficient, 50-100%, as compared to lasers or e-beams.

Compared to furnaces they are high loss systems, but the exposure is for seconds instead of hours.

Results to date show that the common dopants B, P, As, and Sb can all be activated substitutionally after a few seconds at 1050°-1200°C. Reported dopant profiles show that As (69, 70) redistribution can be held to <100Å and B (74, 67) to <1000Å. However, at high concentrations near or above the solubility limit at the peak of the implant, these relatively long anneal times, seconds, can lead to less than 100% substitution for both As and Sb probably because precipitation occurs more rapidly than diffusion (68, 69). Reported carrier mobility values are comparable to bulk values, but few diode measurements are available. An exception is the study of the n^+p diodes made by Fulks *et al.* (74) by implanting $1 \times 10^{16}/cm^2$ As ions at 185 keV and annealing for 10 sec in a resistance radiant heater. The estimated wafer temperature was 950°-1000°C. Excellent low leakage values of 7×10^{-10} A/cm² at 5V were obtained uniformly over a 3 in. wafer. This compares very favorably to leakage values of 5×10^{-10} A/cm² for furnace annealed controls after an anneal at 1000°C for 30 min.

Detailed studies of damage by TEM and other studies are presumably forthcoming. One DLTS study indicates the presence of Fe contamination in material annealed by a halogen lamp (69).

E-beam annealing.—Plasma annealing.—Plasma sources for annealing of ion implant damage are only just beginning to be studied (76, 77). The first report describes the use of an abnormal discharge in neon in a long tube at 30-160 mTorr using a current of 5-80 mA and a voltage of 3-10 keV. In this apparatus the cold cathode emits electrons that are accelerated in the cathode dark space and increase their number by avalanching. When they reach the negative glow they have an energy about half of the anode-cathode potential drop. A magnetic lens may be placed beyond the anode to give a wide range of power densities on the sample, 0.2-170 W/cm², placed still farther down the tube. Annealing of 150 keV BF_2^+ implant doses of 5×10^{14}-$2 \times 10^{15}/cm^2$ for 15 sec at an apparent temperature of 660°C resulted in complete activation and epitaxial regrowth. Differential sheet ρ measurements on sectioned samples show complete activation and no measurable diffusion, but the presence of deep damage located deeper than the ion implantation peak (77) is observed.

E-beam annealing.—The first actual report of isothermal, 1-100 sec STA annealing employed an e-beam (78, 79). In this case a rapidly raster scanned or randomly interlaced e-beam was used to heat a thermally floating silicon chip of a few millimeters on a side to an unknown annealing temperature for 5-10 sec. Recently, this technique has been modified to include a second beam for spot or line scanning (80) on top of the chip while the first beam heats the chip as a whole from the bottom.

More recently, a similar approach has been reported (81). In this case a very large diameter beam, 0.25 in. diam at 5.2 keV and 52 mA was slowly rastered at 0.13 in./sec across a wafer where the pyrometrically measured temperature of 850°C was observed to hold for 3-4 sec. Each area was annealed only once. 50 keV B atoms implanted with a dose of $10^{14}/cm^2$ showed an activation of only 75% perhaps because of precipitations, see above, and a maximum diffusion of 500Å. Diodes were subsequently annealed in forming gas at 450°C and showed leakages of 4×10^{-9} A/cm² at 5V. Diodes had a $V^{1/2}$ dependence of leakage on reverse voltage indicating uniform junctions free of defects to a depth of 4 or 5 μm. No ripples or damage to the oxide were observed.

Summary and Conclusions

A wide variety of annealing techniques are being used to anneal ion implanted silicon junctions. These techniques, which use pulsed and CW lasers and e-beams ion beams, plasmas, incoherent light sources, and black body radiant heaters, may be called short time annealing (STA) processes. They differ significantly from conventional annealing by delivering energy to the work piece in very short times, 10^{-8}-10^2 sec, compared to furnace annealing.

VLSI devices require shallower junctions, higher doping levels, and lower defect densities than in previous generations of devices. Successful junction annealing requires that dopant activation, silicon epitaxial regrowth, point defect removal, and extended defect removal all take place in a time-temperature exposure that does not result in significant dopant diffusion.

The first group of STA techniques, which includes pulsed laser, e-beam, and ion beams, all deliver energy to the silicon in times short, *i.e.*, 10-100 nsec, compared to the thermal response time of the silicon wafer. All result in surface melting in essentially an adiabatic process. This melting and subsequent epitaxial regrowth yields silicon layers totally free of extended defects and is the only annealing process currently available that does so. On the other hand, the combination of surface melting, fast dopant diffusion in the liquid phase, and particularly the formation of ripples on bare silicon or oxide-coated silicon surfaces is undesirable for microstructure fabrication. Ripple formation can be suppressed by an additional masking step. The reproducibility and uniformity of large area e-beams have not been demonstrated. For these reasons, adiabatic STA involving melting is not promising for shallow junction formation for VLSI.

In other STA processes where the silicon regrows by solid-state epitaxy, the most difficult requirement to achieve is the removal of extended defects. In fact, extrapolation of furnace annealing data of extended defect removal rates to the short times and high temperatures of STA indicates that such defects cannot be completely removed. However, it is possible that at these relatively high temperatures experiments will yield new results not predicted by extrapolation of furnace annealing data.

The second group of STA techniques heat the silicon for times of 10^{-4}-10^{-2} sec, comparable to the thermal response time of the silicon work piece. These are called thermal flux processes and include raster scanned point (or line) CW laser and e-beam energy sources. With thermal flux annealing, dopant diffusion is minimal, but both point and extended defects that are largely removed at the center of a line scan are not removed and in fact are introduced at the edges of a line scan under high thermal stress conditions. It appears possible that considerable optimization in CW scanning, including power level, scan speed, scan overlap, and especially substrate temperature, will reduce thermal stress and could yield significantly better results than obtained so far. Since thermal flux processing occurs at the highest temperatures short of melting, it would seem that the chance of obtaining new results on extended defect removal would be best at high temperature and in the 10^{-4}-1 sec time region. It would be highly desirable in future work to actually measure the temperature of the workpiece in what is fundamentally a thermal process (82) in order to meaningfully characterize a given experiment. As disadvantages, we note that interference effects due to oxide thickness and laser (but not e-beam) energy coupling may be restrictive for device design and could require an additional masking step. Raster scanned energy point sources will necessarily introduce localized thermal stress into a silicon wafer and will result in lower wafer throughput than techniques employing large area radiation sources.

Isothermal annealing in the 1-100 sec time range is currently the most actively investigated area in STA. Incoherent light from halogen or arc lamps, electrons;

from e-beams or plasmas, or infrared radiation from black body resistance heaters are all being used. In most cases, the whole wafer is heated. This greatly reduces localized thermal stresses. Early results show partial dopant activation and limited dopant diffusion. Extended defect removal studies are not yet available. Of all STA techniques, isothermal annealing could have the highest wafer throughput and would seem to be easily adaptable to manufacturing. The lowest leakage diodes to date, 7×10^{-10} A/cm^2 at 5V, have been made by a black body radiant isothermal process (74).

In order to demonstrate the quality of ion implanted silicon after annealing by any process, a number of electrical and materials evaluations should be made. TEM micrographs should be taken to reveal any extended defects. The extent of dopant activation must be determined. Dopant concentration profiles should be obtained before and after annealing to show any dopant motion. To reveal damage deep beneath the implantation which is electrically active, conductivity and Hall measurements on samples sectioned as a function of thickness would be desirable. Diode reverse leakage as a function of voltage out to breakdown gives a good indication of junction quality and some measure of minority carrier lifetime. Diode leakage on realistic structures with other thin films in place and as a function of position over the whole wafer seem necessary. The effect of the annealing on oxide integrity must also be ascertained.

Until the above range of information is available we must consider all the proposed STA processes as exploratory.

Acknowledgments

I would like to thank S. Mader, A. Michel, T. Y. Tan, and D. Smith for helpful discussions.

Manuscript submitted June 18, 1982; revised manuscript received Aug. 30, 1982.

Any discussion of this paper will appear in a Discussion Section to be published in the December 1983 JOURNAL. All discussions for the December 1983 Discussion Section should be submitted by Aug. 1, 1983.

Publication costs of this article were assisted by IBM Corporation.

REFERENCES

1. C. Hill, in "Laser and Electron-Beam Solid Interactions and Materials Processing," J. F. Gibbons, L. D. Hess, and T. W. Sigmon, Editors, Vol. 1, p. 361, Proceedings of the 1980 Materials Research Soc. Conf. in Boston, Elsevier, North-Holland (1981).
2. L. D. Hess, S. A. Kokorowski, G. L. Olson, and G. Yaron, in "Laser and Electron-Beam Solid Interactions and Materials Processing," J. F. Gibbons, L. D. Hess, and T. W. Sigmon, Editors, Vol. 1, p. 307, Proceedings of the 1980 Materials Research Conf. in Boston, Elsevier, North-Holland (1981).
3. J. C. C. Fan, B-Y. Tsaur, and M. W. Geis, in "Laser and Electron Beam Interaction with Solids," B. R. Appleton and G. K. Celler, Editors, Vol. 4, p. 751, Proceedings of the 1981 Materials Research Soc. Conf. in Boston, Elsevier, North-Holland (1982).
4. J. M. Fairfield and G. H. Schwuttke, *Solid State Electron.*, **11,** 1175 (1968).
5. S. Matsumoto, J. F. Gibbons, V. Deline, and C. A. Evans, Jr., *Appl. Phys. Lett.*, **37,** 821 (1980).
6. D. M. Zehner, C. W. White, and G. W. Ownby, *ibid.*, **36,** 56 (1980).
7. J. S. Williams and H. B. Harrison, in "Laser and Electron-Beam Solid Interactions and Materials Processing," J. F. Gibbons, L. D. Hess, and T. W. Sigmon, Editors, Vol. 1, p. 209, Proceedings of the 1980 Materials Research Soc. Conf. in Boston, Elsevier, North-Holland (1981).
8. R. A. Ghez and R. A. Laff, *J. Appl. Phys.*, **46,** 2103 (1975).
9. J. C. Wang, R. F. Wood, C. W. White, B. A. Appleton, P. P. Pronko, S. R. Wilson, and W. H. Christie, in "Laser-Solid Interactions and Laser Processing-1978," S. D. Ferris, H. J. Leamy, and J. M. Poate, Editors, p. 123, Proceedings of the 1978 Materials Research Soc. Conf. in Boston, American Institute of Physics (1979).
10. J. A. Roth, S. A. Kokorowski, G. L. Olson, and L. D. Hess, in "Laser and Electron Beam Interaction with Solids," B. R. Appleton and G. K. Celler, Editors, Vol. 4, p. 169, Proceedings of the 1981 Materials Research Soc. Conf. in Boston, Elsevier, North-Holland (1982).
11. S. M. Hu and S. Schmidt, *J. Appl. Phys.*, **39,** 4272 (1968); A. F. W. Willoughby, *J. Phys. D. Appl. Phys.*, **10,** 455 (1977).
12. W. K. Hofker, Philips Res. Suppl. No. 8, p. 69 (1975).
13. L. C. Kimerling and J. L. Benton, in "Laser and Electron Beam Annealing of Materials," C. W. White and P. S. Peercy, Editors, p. 385, Proceedings of the 1979 Materials Research Soc. Conf. in Boston, Academic Press (1980).
14. H. J. Stein, J. A. Knapp, and P. S. Peercy, in "Laser and Electron Beam Interaction with Solids," B. R. Appleton and G. K. Celler, Editors, Vol. 4, p. 319, Proceedings of the 1981 Materials Research Soc. Conf. in Boston, Elsevier, North-Holland (1982).
15. Y. Sugita, H. Shinizu, A. Yoshinaka, and T. Aoshima, *J. Vac. Sci. Technol.*, **14,** 44 (1977).
16. W-K. Wu and J. Washburn, *J. Appl. Phys.*, **48,** 3747 (1977).
17. J. A. Lambert and P. S. Dobson, *Philos. Mag. A*, **44,** 1031 (1981).
18. K. Ishida, H. Okabayashi, and M. Yoshida, *Appl. Phys. Lett.*, **37,** 175 (1980).
19. S. M. Hu, *J. Appl. Phys.*, **45,** 1567 (1974).
20. H. Baumgart, F. Phillip, and H. J. Leamy, in "Laser and Electron Beam Interaction with Solids," B. R. Appleton and G. K. Celler, Editors, Vol. 4, p. 355, Proceedings of the 1981 Materials Research Soc. Conf. in Boston, Elsevier, North-Holland (1982).; H. Baumgart, O. Hildebrand, F. Phillip, and G. A. Rozgonyi, Inst. Phys. Conf. Ser. No. 60, Section 2; paper presented at Microstructure Semiconductor Materials Conference, Oxford, 1981, p. 127.
21. G. A. Rozgonyi, H. Baumgart, and F. Phillip, in "Laser and Electron-Beam Solid Interaction and Materials Processing," J. F. Gibbons, L. D. Hess, and T. W. Sigmon, Editors, Vol. 1, p. 193, Proceedings of the 1980 Materials Research Soc. Conf. in Boston, Elsevier, North-Holland (1981).
22. C. Hill, in "Laser and Electron Beam Processing of Electronic Materials," C. L. Anderson, G. K. Celler, and G. A. Rozgonyi, Editors, p. 26, The Electrochemical Society Softbound Proceedings Series, Princeton, N.J. (1980).
23. B. Leroy and C. Plouganven, *This Journal*, **127,** 961 (1980).
24. A. G. Cullis, H. C. Webber, and P. Bailey, *J. Phys. E. Sci. Instrum.*, **12,** 688 (1979).
25. A. G. Cullis, H. C. Webber, and N. G. Chew, *Appl. Phys. Lett.*, **36,** 547 (1980).
26. C. W. White, J. Narayan, and R. T. Young, in "Laser-Solid Interactions and Laser Processing-1978," S. D. Ferris, H. J. Leamy, and J. M. Poate, Editors, p. 275, Proceedings of the 1978 Materials Research Soc. Conf. in Boston, American Institute of Physics (1979).
27. K. L. Wang, Y. S. Liu, C. G. Kirkpatrick, and G. E. Possin, in "Laser-Solid Interactions and Laser Processing-1978," S. D. Ferris, H. J. Leamy, and J. M. Poate, Editors, p. 569, Proceedings of the 1978 Materials Research Soc. Conf. in Boston, American Institute of Physics (1979).
28. A. Bhattacharyya, V. Iyer, B. G. Streetman, J. E. Baker, and P. Williams, *IEEE Trans. Comp. Hybr. Manuf. Technol.*, **chmt-4,** 425 (1981).
29. H. Itoh, H. Tamura, M. Miyao, T. Warabisako, K. Itoh, and Y. Sasaki, *Jpn. J. Appl. Phys.*, **19,** Suppl. 19-2, 55 (1980).
30. C. Hill and D. J. Godfrey, *J. Phys.*, Colloque C4, Supplément No. 5, **41,** C4-79 (1980).
31. H. Boraffka, E. F. Krimmel, M. Lindner, and H. Runge, in "Laser and Electron Beam Interaction with Solids," B. R. Appleton and G. K. Celler, Editors, Presented at the 1981 Materials Research

Soc. Conf. in Boston.
32. M. Koyanagi, H. Tamura, M. Miyao, N. Hashimoto, and T. Tokuyama, *Appl. Phys. Lett.*, **35**, 621 (1979).
33. N. Natsuaki, T. Miyazaki, M. Ohkura, T. Nakamura, M. Tamura, and T. Tokuyama, in "Laser and Electron-Beam Solid Interactions and Materials Processing," J. F. Gibbons, L. D. Hess, and T. W. Sigmon, Editors, Vol. 1, p. 375, Proceedings of the 1980 Materials Research Soc. Conf. in Boston, Elsevier, North-Holland (1981).
34. J. L. Benton, C. J. Doherty, S. D. Ferris, D. L. Flamm, L. C. Kimerling, and H. J. Leamy, *Appl. Phys. Lett.*, **36**, 670 (1980).
35. M. S. Skolnick, A. G. Cullis, and H. C. Webber, *ibid.*, **38** 464 (1981).
36. A. Mesli, J. C. Muller, and P. Siffert, Submitted to *Appl. Phys. Lett.* (1982).
37. T. E. Seidel, L. C. Parrillo, and T. G. Melone, in "Semiconductor Characterization Techniques," P. A. Barnes and G. A. Rozgonyi, Editors, p. 517, The Electrochemical Society Softbound Proceedings Series, Princeton, N.J. (1978).
38. A. R. Kirkpatrick, J. A. Minnucci, and A. C. Greenwald, *IEEE Trans. Electron Devices*, **ed-24**, 429 (1977).
39. D. S. Billington, Editor, "Radiation Damage in Solids," Academic Press (1962).
40. R. G. Little and A. C. Greenwald, *IEEE Trans. Nuclear Sci.*, **ns-28**, 1751 (1981).
41. A. C. Greenwald, A. R. Kirkpatrick, R. G. Little, and J. A. Minnucci, *J. Appl. Phys.*, **50**, 783 (1979).
42. T. Inada, T. Sugiyama, N. Okano, and Y. Ishikawa, *Electron Lett.*, **16** (2), 54 (1980).
43. T. I. Kamins and P. H. Rose, *J. Appl. Phys.*, **50**, 1308 (1979).
44. R. T. Hodgson, J. E. E. Baglin, R. Pal, J. M. Neri, and D. A. Hammer, *Appl. Phys. Lett.*, **37**, 187 (1980).
45. S. Mader and W.-K. Chu, Private communication.
46. A. G. Klimenko, E. A. Klimenka, and V. I. Donin, *Sov. J. Quantum Electron*, **5**, 1289 (1976).
47. G. A. Kachurin, E. V. Nidaev, A. V. Khodyachikh, and L. A. Kovaleva, *Sov. Phys. Semicond.*, **10**, 1128 (1976).
48. A. Gat, J. F. Gibbons, T. J. Magee, J. Peng, V. R. Deline, P. Williams, and C. A. Evans, Jr., *Appl. Phys. Lett.*, **32**, 276 (1978).
49. J. S. Williams, W. L. Brown, H. J. Leamy, J. M. Poate, J. W. Rodgers, D. Rousseau, G. A. Rozgonyi, J. A. Shelnutt, and T. T. Sheng, *ibid.*, **33**, 542 (1978).
50. T. O. Sedgwick and R. Johnson, Unpublished results.
51. N. M. Johnson, D. L. Bartelink, M. D. Moyer, J. F. Gibbons, A. Lietoila, K. N. Ratnakumar, and J. L. Regolini, in "Laser and Electron Beam Annealing of Materials," C. W. White and P. S. Peercy, Editors, p. 423, Proceedings of the 1979 Materials Research Soc. Conf. in Boston, Elsevier, North-Holland (1980).
52. A. Chantre, M. Kechouane, and D. Bois, in "Laser and Electron-Beam Solid Interactions and Materials Processing," B. R. Appleton and G. K. Celler, Editors, Vol. 4, p. 325, Proceedings of the 1981 Materials Research Soc. Conf. in Boston, Elsevier, North-Holland (1982).
53. N. H. Sheng and J. L. Merz, in "Laser and Electron-Beam Solid Interactions and Materials Processing," B. R. Appleton and G. K. Celler, Editors, Vol. 4, p. 313, Proceedings of the 1981 Materials Research Soc. Conf. in Boston, Elsevier, North-Holland (1982).
54. R. A. Street, N. M. Johnson, and A. Lietoila, in "Laser and Electron Beam Annealing of Materials," C. W. White and P. S. Peercy, Editors, p. 435, Proceedings of the 1979 Materials Research Soc. Conf. in Boston, Elsevier, North-Holland (1980).
55. M. Mizuta, N. H. Sheng, and J. L. Merz, *Appl. Phys. Lett.*, **38**, 453 (1981).
56. J. P. Gonchond, G. A. Rozgonyi, and D. Bois, in "Laser and Electron-Beam Solid Interactions and Materials Processing," B. R. Appleton and G. K. Celler, Editors, Vol. 4, p. 189, Proceedings of the 1981 Materials Research Soc. Conf. in Boston, Elsevier, North-Holland (1982).
57. M. Mizuta, N-H. Sheng, and J. L. Merz, *J. Appl. Phys.*, **52**, 6437 (1981); W. H. Sheng, M. Mizuta, and J. L. Merz, in "Laser and Electron-Beam Solid Interactions and Materials Processing," J. F. Gibbons, L. D. Hess, and T. W. Sigmon, Editors, Vol. 1, p. 155, Proceedings of the 1980 Materials Research Soc. Conf. in Boston, Elsevier, North-Holland (1981).
58. T. O. Sedgwick, P. M. Solomon, and H. J. Vollmer, in "Laser and Electron-Beam Solid Interactions and Materials Processing," J. F. Gibbons, L. D. Hess, and T. W. Sigmon, Editors, Vol. 1, p. 337, Proceedings of the 1980 Materials Research Soc. Conf. in Boston, Elsevier, North-Holland (1981).
59. P. M. Sandow, in "Laser and Electron Beam Processing of Electronic Materials," C. L. Anderson, G. K. Celler, and G. A. Rozgonyi, Editors, p. 187, The Electrochemical Society Softbound Proceedings Series, Princeton, N.J. (1980).
60. L. D. Hess, S. A. Kokorowski, G. L. Olson, Y. M. Chi, A. Gupta, and J. B. Valdez, in "Laser and Electron Beam Interaction with Solids," B. R. Appleton and G. K. Celler, Editors, Vol. 4, p. 633, Proceedings of the 1981 Materials Research Soc. Conf. in Boston, Elsevier, North-Holland (1982).
61. T. Yu, K. J. Soda, and B. G. Streetman, *J. Appl. Phys.*, **51**, 4399 (1980).
62. J. A. Knapp and S. T. Picraux, *ibid.*, **53**, 1492 (1982).
63. J. F. Gibbons, Private communication.
64. J. L. Regolini, J. F. Gibbons, T. W. Sigmon, R. F. W. Pease, T. J. Magee, and J. Perry, *Appl. Phys. Lett.*, **34**, 410 (1979).
65. G. G. Bentini, R. Galloni, and R. Nipoti, *ibid.*, **36**, 661 (1980).
66. K. N. Ratnakumar, R. F. W. Pease, D. J. Bartelink, N. M. Johnson, and J. D. Meindl, *ibid.*, **35**, 463 (1979).
67. K. Nishiyama, A. Arai, and N. Watanabe, *Jpn. J. Appl. Phys.*, **19**, L563 (1980).
68. H. B. Harrison, M. Grigg, K. T. Short, J. S. Williams, and A. Zylewicz, in "Laser and Electron Beam Interaction with Solids," B. R. Appleton and G. K. Celler, Editors, Vol. 4, p. 771, Proceedings of the 1981 Materials Research Soc. Conf. in Boston, Elsevier, North-Holland (1982).
69. J. L. Benton, G. K. Celler, D. C. Jacobson, L. C. Kimerling, D. J. Lischner, G. L. Miller, and McD. Robinson, in "Laser and Electron Beam Interaction with Solids," B. R. Appleton and G. K. Celler, Editors, Vol. 4, p. 765, Proceedings of the 1981 Materials Research Soc. Conf. in Boston, Elsevier, North-Holland (1982); S. Shatas and A. Gat, Abstract B-2 presented at the Electronic Materials Conference, June 23-25, 1982 at Fort Collins, Colorado.
70. A. Gat, *IEEE Electron Device Lett.*, **edl-2** (4), 85 (1981).
71. R. A. Powell, T. O. Yep, and R. T. Fulks, *Appl. Phys. Lett.*, **39**, 150 (1981).
72. Nova Rapid Optical Processor, Eaton Corp., Beverly, MA.
73. B-Y. Tsaur, J. P. Donnelly, J. C. C. Fan, and M. W. Geis, *Appl. Phys. Lett.*, **39**, 93 (1981).
74. R. T. Fulk, C. J. Russo, P. R. Hanley, and T. I. Kamins, *ibid.*, **39**, 604 (1981).
75. M. Miyao, K. Ohyu, and T. Tokuyama, *ibid.*, **35**, 228 (1979).
76. N. J. Ianno, J. T. Verdeyen, S. S. Chan, and B. G. Streetman, *ibid.*, **39**, 622 (1981).
77. C. B. Fleddermann, N. J. Ianno, J. T. Verdeyen, and B. G. Streetman, in "Laser and Electron Beam Interaction with Solids," B. R. Appleton and G. K. Celler, Editors, Vol. 4, p. 795, Proceedings of the 1981 Materials Research Soc. Conf. in Boston, Elsevier, North-Holland (1982).
78. R. A. McMahon, H. Ahmed, J. D. Speight, and R. M. Dobson, *Electron Lett.*, **15**, 433 (1979).
79. R. A. McMahon and H. Ahmed, *ibid.*, **15**, 45 (1979).
80. R. A. McMahon, J. R. Davis, and H. Ahmed, in "Laser and Electron Beam Interaction with Solids," B. R. Appleton and G. K. Celler, Editors, Vol. 4, p. 783, Proceedings of the 1981 Materials Research Soc. Conf. in Boston, Elsevier, North-Holland (1982).
81. T. O. Yep, R. T. Fulks, and R. A. Powell, *Appl.*

Phys. Lett., **38**, 162 (1981).
82. T. O. Sedgwick, in "Laser and Electron-Beam Solid Interactions and Materials Processing," J. F. Gibbons, L. D. Hess, and T. W. Sigmon, Editors, Vol. 1, p. 147, Proceedings of the 1980 Materials Research Soc. Conf. in Boston, Elsevier, North-Holland (1981); T. O. Sedgwick, *Appl. Phys. Lett.*, **39**, 254 (1981).

Initial Results of a High Throughput MBE System for Device Fabrication

J. C. M. Hwang, T. M. Brennan, and A. Y. Cho

Bell Laboratories, Murray Hill, New Jersey 07974

ABSTRACT

A custom-designed MBE system has been used for device fabrication with high throughput. Up to six, 2 in. diameter substrates can be prepared and loaded into the system at once. The growth cycle for a GaAs FET structure is typically 2-3 hr. As many as 200 FET wafers with a total of more than 300 μm epitaxial layers can be grown between source replenishments. With continuous azimuthal rotation of the substrate, extreme uniformity in doping and thickness was achieved. The surfaces of the epitaxial layers were highly specular. The irregularly shaped defects commonly associated with the gallium spitting problem were eliminated. The remaining surface defects were oval-shaped with a density $< 10^4$ cm^{-2}. Silicon nitride was used to protect the back side of the substrate from indium attack during growth. Doping concentrations from 2×10^{14} cm^{-3} to 2×10^{18} cm^{-3} were obtained using Sn as dopant. Highest Hall mobilities measured were 7,600 cm^2/Vsec at 300 K and 67,000 cm^2/Vsec at 77 K. State-of-the-art FET's were fabricated from materials grown by using this system.

Molecular beam epitaxy (MBE) is a powerful materials preparation technique because of its superb control over doping and thickness. It has many important applications in the growth of compound semiconductors for high speed and optoelectronic devices, such as the high electron mobility transistor (1) and the double-heterostructure laser (2). However, for MBE to become a viable technique for large scale device fabrication, a system which can reproducibly grow very pure and uniform layers with high throughput is required. Such a system was custom designed in collaboration with Varian engineers (3) and has been used to generate some very encouraging results within a year since it was installed.

In this paper, we will briefly describe the system hardware and then how it was used to achieve high throughput and extremely uniform growth without sacrificing the quality of the material. Some preliminary results of devices fabricated from materials grown by this system will also be presented.

System Description

The MBE system consists of three ultra high vacuum chambers: a loading chamber, an analysis chamber, and a growth chamber. The chambers are independently pumped and are connected to one another through gate valves. The substrates are moved between the chambers using magnetically coupled transfer rods. The loading chamber and the analysis chamber each have six substrate holders, whereas the growth chamber has only one. The analysis chamber is equipped with a scanning Auger electron spectrometer and extra ports for future addition of other analytical instruments such as secondary ion mass spectrometer, etc.

The details of the growth chamber are shown schematically in Fig. 1. This chamber incorporates many important features, such as a substrate holder capable of continuous azimuthal rotation, an auxiliary port above the substrate holder for a cold finger or a mechanical mask, viewpoints which allow one to look down to the bottom of the source crucibles, two 10 kW electron guns for evaporation of refractory metals, and a viewport/gas inlet at normal incidence to the substrate. A microcomputer, which controls the source temperatures and shutters as well as substrate temperature and motion, is also included. These features make the system flexible for either research or production application.

Throughput

The following are important factors for high throughput of epitaxial materials: large size substrate, multiple wafer loading, short growth cycle, and large capacity source. These factors will be discussed in sequence.

The substrate size has been standardized to 50 mm diameter circular wafers. The use of standardized substrates helped to streamline not only substrate preparation before growth, but also device processing after growth. Larger substrates up to 4 in. diameter can be accommodated by simple modification of the substrate holders.

Specially designed quartz jigs and wafer spinner are used for multiple substrate preparation. The wafers are usually boiled in solvents and etched in acids in a batch of six. At the last step, each wafer is rinsed in deionized water to grow a controlled surface oxide layer then spun dry. The wafers are then mounted on the substrate blocks and loaded into the MBE system together. Immediately before growth is initiated on each wafer, it is heated to a high temperature to desorb

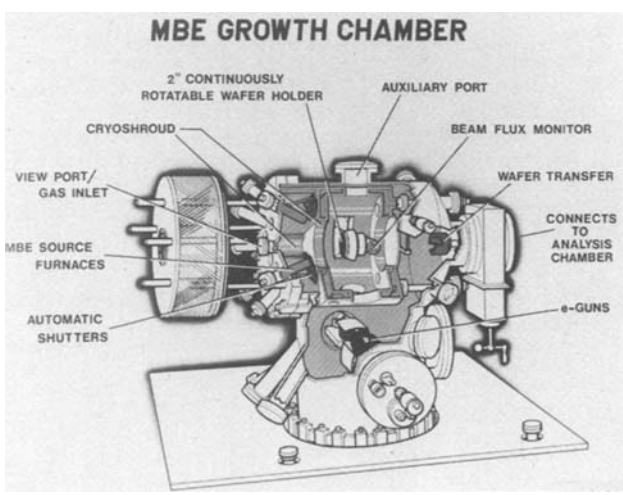

Fig. 1. Schematics showing the details of the growth chamber

[1] Present address: General Electric Electronics Laboratory, Syracuse, New York 13221.

the oxide so that growth commences on an atomically clean surface. The temperatures at which the oxide desorbs as determined by reflection high energy electron diffraction (RHEED) observations from a number of wafers prepared in the same batch are listed in Table I. The tight distribution of the oxide desorption temperatures indicated that the substrate preparation was reproducible from wafer to wafer, and that multiple substrate preparation for MBE is feasible. After oxide desorption the substrate temperature is fixed at approximately 600°C for growth.

A GaAs field effect transistor (FET) structure typically consists of 1-2 μm of epitaxial material. At a growth rate of 1 μm/hr, actual growth of an FET wafer takes 1-2 hr. Transfer of the substrate, heating up and cooling down the substrate, etc., take approximately 1 hr in total. Therefore, the cycle time of each wafer is typically 2-3 hr. Thus, we have been able to prepare and grow six FET wafers each day. It is conceivable that a higher growth rate may shorten the cycle time. Eventually, the finite preparation time involved in each cycle will become the limiting factor.

The incorporation of vacuum loadlocks in the system design makes it possible to operate the system continuously and vent the growth chamber only when the source materials are depleted. The group V elements are usually the first to be depleted. Using a 40 cm^3 capacity As source, we have grown epitaxial layers with a total thickness greater than 150 μm. Therefore, with two As sources installed in the system, a total of 200 FET wafers can be grown between source replenishments.

Uniformity

For high yield device processing, we need wafers that are not only uniform in doping and thickness, but also smooth on both sides. By using the rotatable substrate holder, we have obtained extreme uniformity in doping and thickness. Figure 2 shows the doping concentration as a function of depth as measured by the Miller (4) profiler from a GaAs layer grown while the substrate was rotated at 4 rpm and doped periodically with Sn. Five doping profiles were measured on different spots of the wafer. The spread in the peak heights of the doping profiles indicated that the variation in doping was within ±1%. Whereas the spread in the periodicity of the doping profiles indicated that the variation in thickness was within ±0.5%. Similar uniformity results have been previously reported (5).

Next we will discuss uniform surface morphology. There are usually two types of morphological defects present on the surface of the MBE grown layers. One type of defect, irregularly shaped, is attributed to "gallium spitting" (6). The other type is oval-shaped and its origin is not well understood (7).

As an example, Fig. 3a shows a scanning electron microscope (SEM) image of an irregularly shaped defect. X-ray analysis confirmed that it was Ga-rich compared to the surrounding area (Fig. 3b). In order to understand the effect of Ga source on defect density, we have compared Ga sources of different configurations side by side in the same system. We found that filling the Ga crucible to its capacity or keeping the lip hotter than the rest of the crucible had little effect on the defect density. However, we could reproducibly eliminate the irregularly shaped defects by a long (72 hr) bake out of the entire growth chamber at approximately 200°C. Our observations suggest that the "spitting" is probably related to the presence of an impurity layer on the surface of the Ga source due to the reaction between molten Ga and the residual gases (*e.g.*, H_2O) in the vacuum chamber. The bake out reduces the partial pressure of the residual gases thereby inverting the direction of the reaction and eliminating the impurity layer.

After the "gallium spitting" problem was eliminated only the oval defects remained on the surface. Figure 4a is an optical micrograph taken under Normaski contrast condition which shows that the oval defect density was typically $<10^4$ cm^{-2} on an FET wafer. The

Table I. Oxide desorption temperatures of substrate wafers prepared in the same batch

Wafer	Oxide desorption temperature (°C)
J-6290	633
J-6300	630
J-7010	630
J-7060	631
J-7070	630
J-7310	640

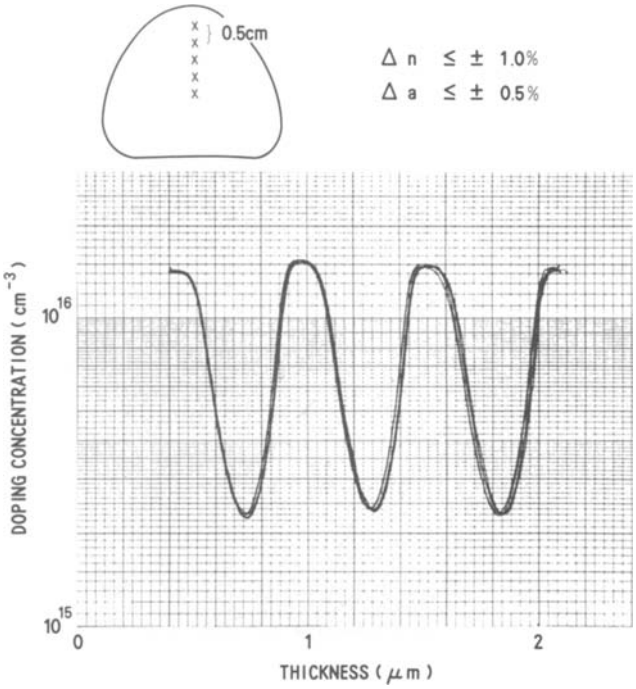

Fig. 2. Doping concentration as a function of depth from the surface of a GaAs layer grown with the substrate rotated at 4 rpm and doped periodically with Sn. Five traces were measured on different spots of the wafer as indicated.

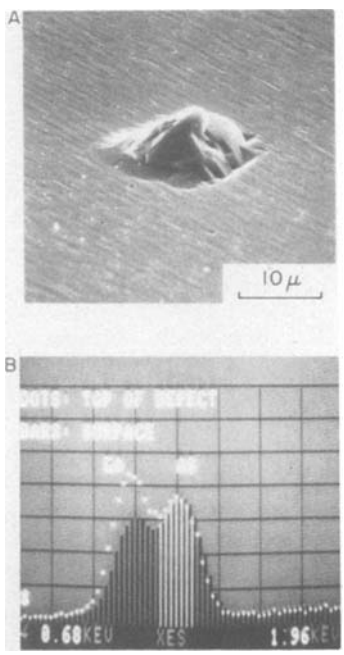

Fig. 3. (a) SEM picture of an irregularly shaped defect. (b) X-ray analysis of the defect (dotted line) showing that it is Ga-rich compared to the surrounding area (bar graph).

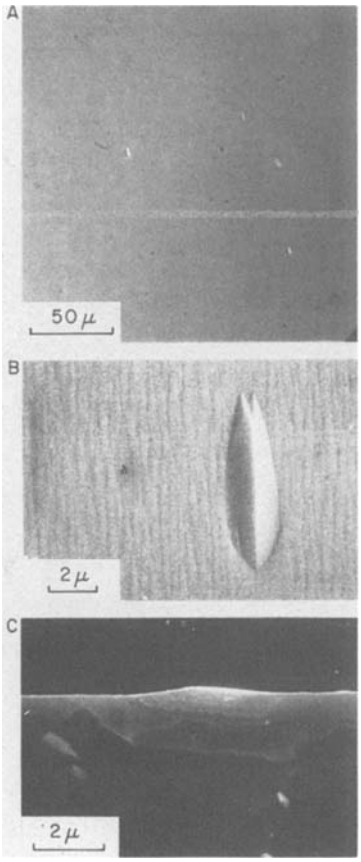

Fig. 4. (a) Normaski optical micrograph showing typical density of oval defects. (b) SEM micrograph showing details of an oval defect. (c) SEM micrograph of the cross section of an oval defect showing that its ridge is approximately 0.2 μm high.

oval defect is typically 10 μm long and 2 μm wide, with its long axis parallel to [1$\bar{1}$0] on a (001) substrate (Fig. 4b). Its ridge is approximately 0.2 μm high (Fig. 4c). Presently, there is evidence indicating that at least some of these defects are related to the threading dislocations originated from the substrate (8). Although we have found no adverse effect of the oval defects on discrete devices, they may present a problem for integrated circuits.

The indium, which is used to mount the substrate onto its heater block, usually reacts with the GaAs substrate during MBE growth. When the indium is etched off after growth, the back side of the epitaxial wafer becomes very rough. This in turn causes severe processing difficulties in vacuum handling, mask alignment, etc. We have used plasma-deposited silicon nitride on the back side of the wafer to protect it from the indium attack (9). Figure 5b shows that the back side of the GaAs substrate in this case was much smoother than in the case without silicon nitride protection (Fig. 5a). However, a few pits were still present probably due to pinholes in the silicon nitride. This made it difficult to chemically thin the substrate during the final processing steps, if it is necessary to reduce the thermal impedance of the devices. Further improvements are obviously in order.

Mobility

It is important that the quality of the materials grown is not sacrificed in the attempt to achieve high throughput. Figure 6 shows the preliminary results of the 77 and 300 K electron mobilities in 3 μm thick GaAs layers doped with different concentrations of Sn. The solid curves indicate the theoretical values calculated by Rode and Knight (10) for the case of zero compensation. The experimental data followed the same trend as the theoretical curves with the compensation ratio

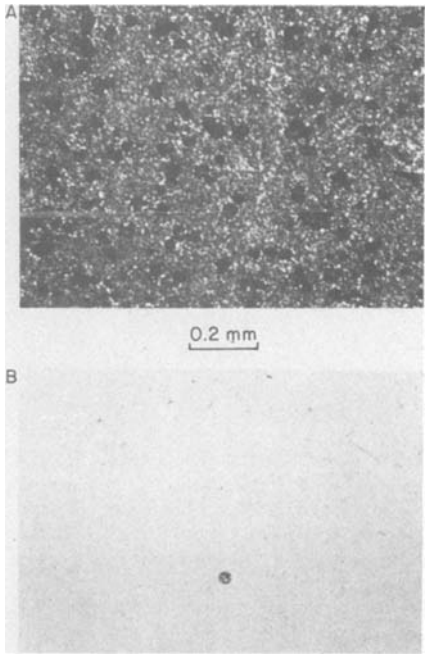

Fig. 5. Optical micrographs comparing the back-side morphology of GaAs wafers (a) without and (b) with silicon nitride protection during MBE growth.

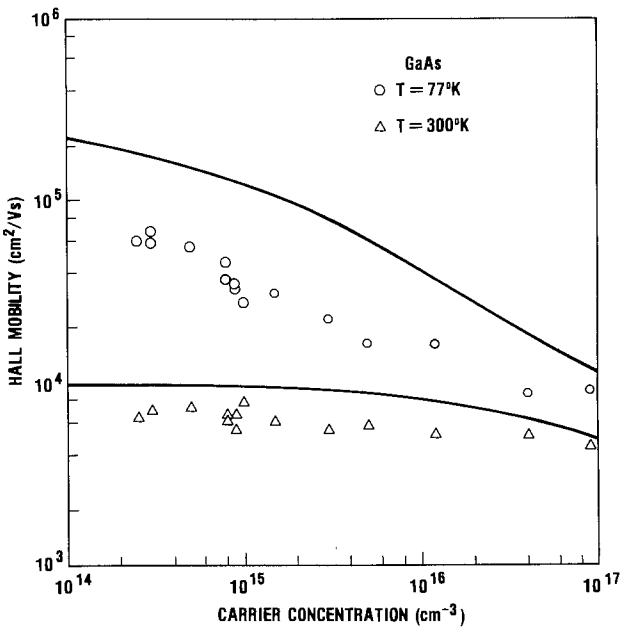

Fig. 6. 77 and 300 K electron mobilities in GaAs layers doped with Sn. The solid curves indicate theoretical values for the case of zero compensation.

(N_A/N_D) varying from 0.3 to 0.7. These results are comparable to the previously reported values for MBE-grown Sn-doped GaAs layers of comparable thickness (11).

Device Results

To illustrate the device quality of the MBE materials, power and low noise FET wafers were grown according to previously developed specifications based on wafers grown by chemical vapor deposition (CVD) (12, 13). Throughout the device processing sequence, the MBE wafers exhibited the same characteristics as state-of-the-art CVD wafers.

As an example, Fig. 7 shows the drain characteristics of a typical power FET processed from an MBE wafer. The total gate width was 1 mm and the gate length was 1.5 μm. The channel thickness was approximately 0.5

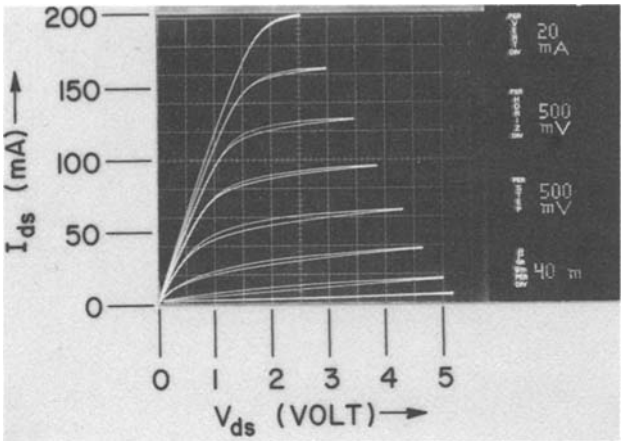

Fig. 7. Drain characteristics of a typical power FET processed from the MBE material. Total gate width = 1 mm. Gate length = 1.5 μm. Channel doping = 9 × 10^{16} cm^{-3}. Channel thickness ≃ 0.5μ.

μm with doping equal to 9 × 10^{16} cm^{-3}. The transistor showed an 80 ms/mm transconductance which is typical for devices of this type. RF measurements (14) confirmed that these MBE FET's were state-of-the-art microwave devices.

Summary

The feasibility of MBE as a materials preparation technique for large scale device fabrication has been studied using a specially designed system. The following capabilities have been demonstrated:

1. Six 2 in. diameter standard-sized wafers can be simultaneously prepared and loaded.
2. A typical GaAs FET structure can be grown within a 2-3 hr cycle.
3. A total of more than 300 μm epitaxial layers can be grown between source replenishments.
4. Extreme uniformity over a 2 in. wafer was achieved with doping variation less than ±1% and thickness variation less than ±0.5%.
5. Surface defect density was reduced to less than 10^4 cm^{-2}.
6. GaAs with high purity was obtainable as evidenced by mobility measurements.
7. State-of-the-art FET's were obtained from materials grown by this high throughput system.

Acknowledgment

We are grateful to J. V. DiLorenzo for his initial stimulation and continuous encouragement. We wish to thank V. G. Keramidas for his support and many constructive comments. We also appreciate the technical assistance provided by F. Ermanis, P. Cullen, A. Dori, and S. Cullins.

Manuscript submitted July 26, 1982; revised manuscript received Oct. 6, 1982.

Any discussion of this paper will appear in a Discussion Section to be published in the December 1983 JOURNAL. All discussions for the December 1983 Discussion Section should be submitted by Aug. 1, 1983.

Publication costs of this article were assisted by Bell Laboratories.

REFERENCES

1. T. Mimura, S. Hiyamizu, T. Fujii, and K. Nanbu, *Jpn. J. Appl. Phys.*, **19**, L225 (1980).
2. W. T. Tsang, *Appl. Phys. Lett.*, **36**, 11 (1980).
3. J. C. M. Hwang, J. V. DiLorenzo, P. E. Luscher, and W. S. Knodle, *Solid State Technol.*, **25**, 166 (1982).
4. G. L. Miller, *IEEE Trans.*, **ED-19**, 1103 (1972).
5. A. Y. Cho and K. Y. Cheng, *Appl. Phys. Lett.*, **38**, 360 (1981).
6. C. E. C. Wood, L. Rathbun, H. Ohno, and D. DeSimone, *J. Cryst. Growth*, **51**, 299 (1981).
7. Y. G. Chai and R. Chow, *Appl. Phys. Lett.*, **38**, 796 (1981).
8. J. C. M. Hwang and P. Cullen, Unpublished.
9. P. A. Garbinski, J. C. M. Hwang, and C. L. Allyn, Unpublished.
10. D. L. Rode and S. Knight, *Phys. Rev. B*, **3**, 2534 (1971).
11. H. Morkoc and A. Y. Cho, *J. Appl. Phys.*, **50**, 6413 (1979).
12. B. S. Hewitt, H. M. Cox, H. Fukui, J. V. DiLorenzo, W. O. Schlosser, and D. E. Iglesias, *Inst. Phys. Conf. Ser.*, **33a**, 246 (1977).
13. W. C. Niehaus, H. M. Cox, B. S. Hewitt, S. H. Wemple, J. V. DiLorenzo, W. O. Schlosser, and F. M. Magalhaes, *ibid.*, **33b**, 271 (1977).
14. J. C. M. Hwang, P. G. Flahive, and S. H. Wemple, *IEEE Electron Device Lett.*, **edl-3**, 320 (1982).

Electromigration Induced Shallow Junction Leakage with Al/Poly-Si Metallization

S. Vaidya,* A. K. Sinha,* and J. M. Andrews*

Bell Laboratories, Murray Hill, New Jersey 07974

ABSTRACT

It is generally accepted that one way to prevent junction spiking during the 450°C/H_2 anneal at shallow junction contacts, is to use a composite metallization of Al over n^+ poly-Si. We observe that while such a composite can prevent thermally induced Al/Si interpenetration, the devices are still susceptible to failure by junction leakage at positively biased windows, resulting from the electromigration of Si into the overlying metal. The process involves a localized diffusion of poly-Si into Al, followed by the transport of Si across the metal-semiconductor interface. The lifetimes exhibit a strong dependence on current, varying as I^{-N}, where $N \approx 10$, indicative of steep temperature gradients in vicinity of the contacts. However, if the contact window current is scaled down in accordance with the established criterion for electromigration in the interconnect (~ 10^5 Acm^{-2}), our results indicate that Al/poly-Si contacts to shallow junctions will remain electromigration resistant despite a decrease in window dimensions.

The phenomenon of electromigration in thin film Al has been extensively investigated in the past. However, most of the reported work deals with the formation of hillocks and open circuits either in the interconnects themselves or at metal-semiconductor contacts (1, 2). Relatively little effort has been expended in characterizing the effect of current flow through contact windows on the underlying junction itself. With Al contacts, joule heating in the windows could accelerate Si

* Electrochemical Society Active Member.

dissolution into Al, producing crystallographic etch pits in the substrate and, ultimately, shorted junctions (3). Alternatively, the electromigration of Si into the overlying metal at positively biased windows could also lead to the formation of Al-spikes in the contact region. Black (4) has suggested that, whereas at low temperatures, device-electromigration failures are caused by open circuits in the Al runners, at $T > 210°C$ they occur predominantly by the electromigration of Si from the substrate into the overlying Al and the development of shunted junctions. More recent results (5) have also pointed out that "burned contacts" are the predominant cause for failure in 3500Å deep junction devices.

With the progressive scaling in device dimensions, such nonuniform Al/Si interaction at contacts could pose a serious threat to device reliability. As a consequence, various approaches are currently being explored to minimize this phenomenon. Among these, a two-layer metallization consisting of Al over doped, CVD poly-Si appears to be a particularly attractive alternative, since the poly-Si layer is sufficient to satisfy solubility requirements in Al at elevated temperatures while simultaneously compensating for Al-thinning at steps (6). Moreover, this structure can easily retrofit into the current silicon integrated-circuit process line (7). However, this paper demonstrates that, although the poly-Si layer successfully inhibits junction penetration during the contact anneal, as well as resulting from localized joule heating, the devices are still susceptible to the transport of Si from the substrate into the overlying metal at positively biased contacts by momentum exchange with the conducting electrons. Si electromigration continues, until a pit filled with Al grows to short the underlying junctions. This failure mechanism may, therefore, appear to define an inherent limitation to the adequacy of Al/poly-Si in maintaining contact integrity. However, if the contact window current, assumed equal to the interconnect current, is scaled down with the design rule on the basis of the established criterion for electromigration in the latter ($\sim 10^5$ Acm^{-2}), results indicate that Al/poly-Si contacts to shallow junctions will remain electromigration resistant despite a reduction in window size from 6 to 2 μm.

Experimental Details

The test structures were fabricated using a specially designed mask set (8). P-type <100> Si wafers of 6-8 Ω cm material were oxidized in a dry-HCl ambient at 1000°C, followed by steam at 950°C, to a total oxide thickness of 3500Å. Windows were opened in the oxide by reactive-ion etching (9) (RIE), and the wafers implanted with 7×10^{15} As$^+$ ions/cm^2 accelerated to 30 keV. The implanted regions were reoxidized at 950°C for 10 min in steam to grow a 1200Å layer of SiO_2. This heat-treatment served simultaneously to activate and drive in the As to a depth of ~1000Å below the oxide, forming n^+/p junctions, of sheet resistance $R_s \sim 80$ Ω/□, in selected areas. Such a shallow junction depth (x_j) was deliberately chosen to characterize the worst case situation with real devices, since 1000Å approaches the current lower limit on junction depths, which can be reproducibly fabricated using conventional methods of ion-implantation and furnace annealing. Windows, nominally 2, 4, and 6 μm square, were subsequently etched in the regrown oxide over the junctions. A 0.25 μm layer of CVD poly-Si was then deposited and phosphorus diffused at 900°C for 60 min to yield a sheet resistance of 70 Ω/□. Such a heat-treatment was not expected to increase the junction depth by $\gtrsim$ 200Å in the contact regions. Finally, a 0.7 μm Al-0.5% Cu layer was evaporated onto the wafers, maintained at 250°C during the deposition from an inductively heated source. Contacts and interconnections were defined in the Al/poly-Si metallization by RIE in a ($BCl_3 + Cl_2$) gas mixture (7). The runners were 5 μm wide for structures with 2 and 4 μm windows, and 7 μm wide for those with 6 μm windows. An Al-contact was deposited on the back side, and the wafers were given a 450°C/30 min H_2 anneal prior to aging. Avalanche breakdown for these diodes occurred at ~40V; junction leakage (I_R) at a 10V reverse bias was in the 10^{-9}A range. Such a high reverse bias current may be due to the absence of gettering or a "chanstop" implant, without which, impurities and/or surface inversion will give rise to an additional contribution to junction leakage. (This I_R, however, is negligible in the context of this study.) A plan-view and cross section of a typical junction tester are illustrated in Fig. 1.

Accelerated aging was conducted at average window current densities ($J_{\square}$) of 8×10^4 to 7×10^5 Acm^2, and at various temperatures (T) in the range of 135°-190°C. At higher temperatures or currents, either the lifetime was too short to be measurable, or else the reverse bias exceeded the junction avalanche breakdown. The test structure for each window size consisted of 7 interconnected n^+-tubs (Fig. 1) powered from a constant current source, in order to simulate multiple contacts in real circuits. Failure was defined as the time taken to produce an irreversible junction leakage of $\cong$ 50 μA at 10V reverse bias (RT). Once failed, the devices were examined by scanning electron microscopy (SEM) to identify the failure modes. Eight to ten lifetime measurements in each case were used to obtain the mean time to failure (MTF), and the standard deviation (σ) of the distribution. The activation energy for failure was extracted from the MTF's at different temperatures to support the physical evidence of failure mechanism presented in the scanning electron micrographs. Furthermore, an interrelationship between lifetime and contact window current (I) was established by measuring the MTF for each window size, at different current levels.

Results

Figure 2 illustrates typical plots of increase in junction leakage (I_R) with time for a nominally 2×2 μm window and a 4×4 μm window, respectively. Each data point was taken by interrupting the test, cooling the wafer to room temperature, and measuring leakage. It is clear that I_R remains fairly low almost up to failure, and then increases several orders of magnitude in a relatively short time interval. Above 2-300 μA, this increase in I_R is accompanied by a sharp decline in voltage required to maintain the preset current, or equivalently, a marked decrease in the total effective string resistance from its initial value. Comparing the plots for different window sizes, it is evident

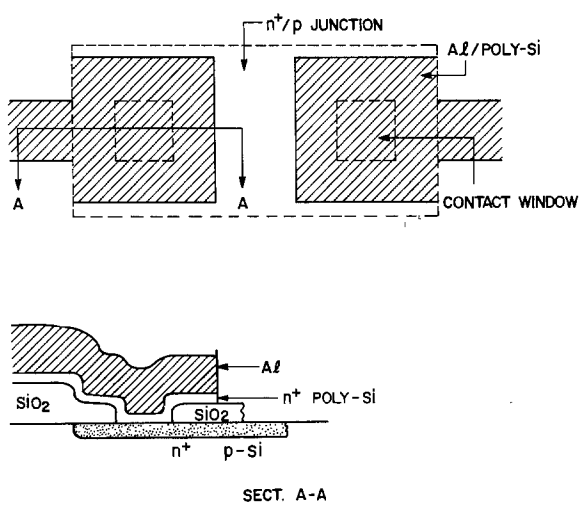

Fig. 1. Typical device used for contact electromigration studies. Each test structure consists of 7 interconnected junctions.

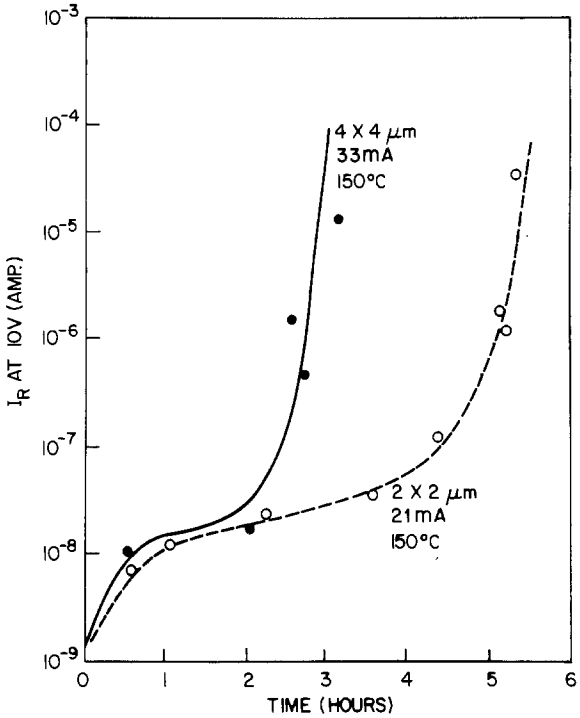

Fig. 2. Reverse bias junction leakage (I_R) at room temperature vs. aging time for 2 and 4 μm windows. The respective aging temperatures and window currents are specified.

that smaller windows can withstand substantially higher $J_{\square}$'s prior to failure.

The MTF for strings of different window sizes as a function of wafer temperature are shown in Fig. 3. The lifetimes fitted a lognormal distribution with σ's ranging between 0.5-1.0. The right ordinate axis has been scaled such that a line through ⊕ parallel to the experimental data points directly measures the activation energy (Q) for failure. It is obvious that the thermal activation for failure is independent of window size and ranges between 0.85-1.0 eV. The MTF's corresponding to varying window current levels, at a fixed test temperature, are shown in Fig. 4. For both the 2 μm and the 6 μm window-strings, it is clear that the lifetimes exhibit a strong dependence on current, varying in accordance with $(I)^{-10\pm1}$.

In order to rationalize these observations, the test devices were examined both optically and by SEM at various stages during the aging process. The results are illustrated in Fig. 5 and 6. Figure 5a depicts a typical positively biased 2 μm window in a multiple-junction string which has been aged to failure and is character-

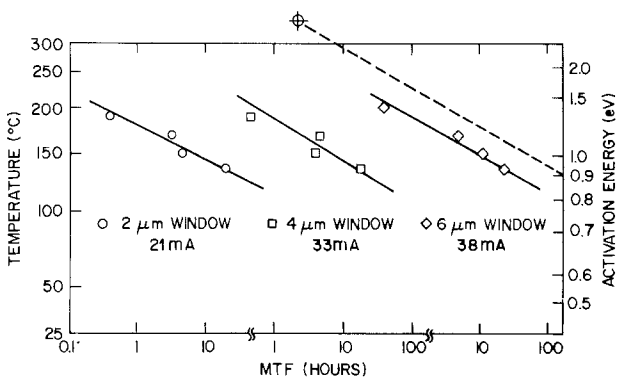

Fig. 3. MTF for the 2, 4, and 6 μm windows at different test temperatures. Respective window currents are listed on the plot. A line through ⊕ parallel to the data points intersects the right-hand axis to directly yield the activation energy for failure.

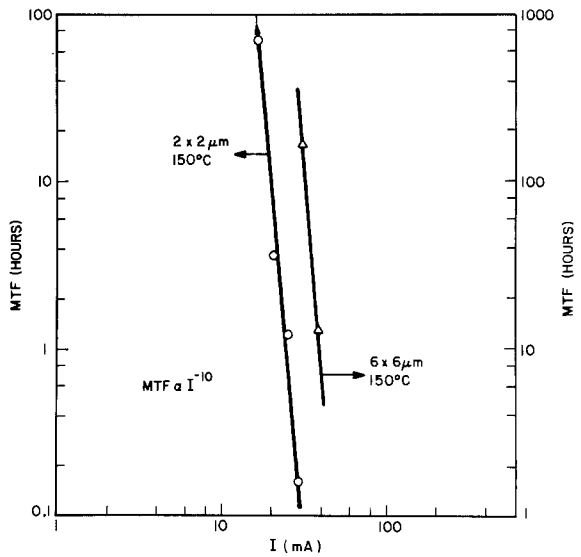

Fig. 4. Log-log plot of MTF vs. window current, for the 2 and 6 μm window-strings, at a constant substrate temperature of 150°C. The slope of the straight lines ≃ 10.

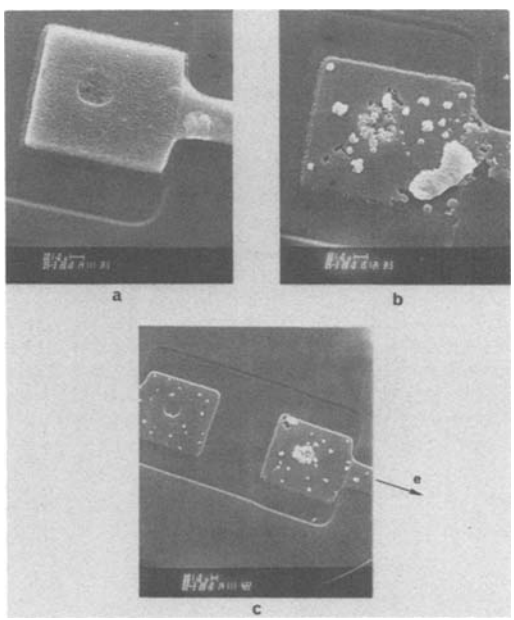

Fig. 5. Scanning electron micrographs depicting typical failures at 2 μm windows; (a) and (b) illustrate the same, positively biased window, as-failed and after Al etch; (c) illustrates a complete junction with both positive and negative contacts, exhibiting a reverse leakage of 200 μA at 10V. While the negative window is intact, the positive window has developed a large density of Si precipitates.

ized by a reverse leakage of 600 μA at 10V. Besides some evidence of void growth in the Al over the contact window, there is no other indication of contact deterioration or any subsurface interaction. However, upon preferentially etching away the Al (Fig. 5b), a large density of precipitates is exposed over the entire window area. Preceding the increase in junction leakage, the poly-Si starts to become porous over the periphery of the positive contact with a higher density of pores at the inner contact edge. This is followed by the appearance of one or more particles in the window, of the kind depicted in Fig. 5b, and coincides with the increase in I_R to the μA range (Fig. 2). In contrast, the negatively biased window (Fig. 5c) appears completely undisturbed by current flow. Auger analysis (10) of the particles observed on the surface after the Al etch indicates their composition to be Si. Isolated

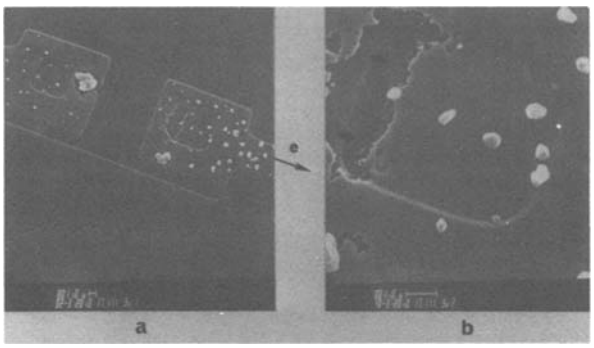

Fig. 6. Scanning electron micrographs of a failed junction with 6 μm windows, exhibiting a reverse bias leakage of 100 μA at 10V. Only the positive window is damaged, with the development of a poly-Si denuded zone containing crystallographic etch pits, as identified in (b).

large precipitates (away from the contacts), observed in both Fig. 5b and c, appear to be generated by the dissolution of poly-Si into Al during the 450°C hydrogen sinter and its reprecipitation (11). They are, therefore, extraneous to this study.

Such a polarity effect in contact degradation, with the negative window remaining intact and the positive window exhibiting extensive metal-substrate interaction, is observed for all window sizes. However, the distribution of poly-Si underneath the Al is considerably different in the positively biased 4 and 6 μm windows (Fig. 6). In these, the passage of current causes a gradual disappearance of poly-Si from the leading/inner edge of the positive contacts. This Si-denuded zone continues to widen into a crescent shape, covering 1/3-1/4 the window area, as illustrated in Fig. 6. Up to this stage, there is no detectable increase in junction leakage above the initial value of $\leq$1 nA (Fig. 2). Further aging results in the formation of crystallographic etch pits in the substrate within this denuded area, as illustrated in Fig. 6b. As these pits, filled with Al, grow to pierce the n^+/p junction interface, the reverse leakage begins to register an increase, until the depletion layer is fully penetrated and the device "fails." Subsequent aging causes the voltage across the strings to collapse (for all window sizes), with a simultaneous increase in junction leakage to the mA range. Viewed optically, devices in this state reveal a metallic (high reflectivity) filament bridging the positive and negative contacts.

A more comprehensive study describing the different stages in contact degradation, together with the effect of eliminating the poly-Si layer or varying the junction depth, will be the subject of a subsequent publication (12). This article will be restricted to the mechanism for junction leakage at positively biased windows, the kinetics of the process, as well as, the effect of varying window size, and finally, the impact of this failure made on shallow junction device reliability.

Discussion

Prior to electrical aging, a preferential Al etch confirmed that both the positive and the negative windows were covered with a uniform layer of poly-Si. Since the contacts are ohmic, the joule-heating produced in the contact, as well as the metal, should be independent of the direction of current flow. However, the deterioration of positive contacts only suggests a superimposed electron current contribution at the positively biased metal-semiconductor interface. Moreover, the asymmetrical nature of damage, especially in the case of the larger windows, indicates a size dependent nonuniformity in current distribution. In this section, a rationale for such an increasing asymmetry in contact degradation with increasing contact size will be developed first. This will be followed by the derivation of an interrelationship between lifetime, contact window current, and contact dimensions. This relationship will subsequently be utilized to predict the influence of a scaling in window size on device performance.

For horizontal current flow in Si, several analytical models have been developed to describe the current distribution at metal-semiconductor contacts (13, 14). On the basis of these, it is generally accepted that the current density $J(x)$ in the windows is nonuniform, decreasing with increasing distance x from the leading contact edge ($x = 0$). Berger (13), for example, has attributed this vertical current crowding to the difference between the semiconductor sheet resistance and the interface contact resistance, and used the equations of the transmission line to describe its magnitude. For different values of a parameter αd, where

$$\alpha = \sqrt{\frac{(\text{Si sheet resistance, } R_s)}{(\text{contact resistivity, } \rho_c)}}$$

and d is the lateral dimension of the window, collinear with x, his model predicts varying current density profiles as illustrated in Fig. 7. Although these calculations do not correct for horizontal current crowding or a finite junction depth, they are nevertheless useful in analyzing our results. If we assume $\rho_c \simeq 2 \times 10^{-6}$ Ω cm^2, as suggested by measurements on similarly fabricated wafers (15), αd in the present testers would increase from 1.2 for the 2 μm windows to 2.5 and 3.6 for the 4 and 6 μm windows, respectively. According to Fig. 7, this increase in αd will be manifested in greater current crowding in the larger windows.

An increase in inhomogeneity in current distribution with increasing window size is verified by Fig. 5 and 6 which depict the poly-Si coverage in the positively biased windows prior to pit formation and junction spiking. An electron current from the substrate into the metallization will create a diffusion flux of poly-Si into the overlying Al. The extent of Si transported from each point over the contact will be proportional to the corresponding $J(x)$ at that point. Thus, the de-

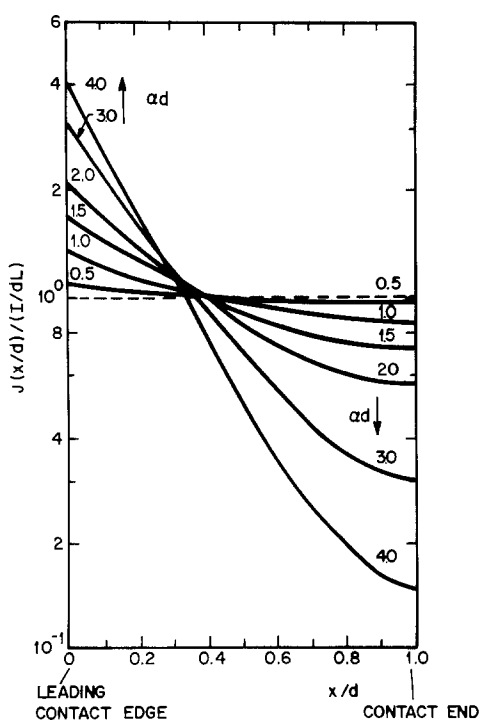

Fig. 7. Current density $J(x)$ distribution along a rectangular dxL contact for horizontal current flow with αd as a parameter (13). I is the total current through the window. The variable x and dimension d are measured parallel to, and L, perpendicular to the current. In the present testers, $d \simeq L = 2$, 4, or 6 μm and, assuming $\rho_c = 2 \times 10^{-6}$ Ωcm^2, $\alpha = 6.3 \times 10^3$ cm^{-1}.

pletion of poly-Si will essentially replicate the initial current distribution in the contact. Such nonuniform poly-Si electromigration will be further enhanced by the corresponding nonuniform joule heating in the window. Although the diffusion of poly-Si into Al is expected to be at least partially compensated by electromigration of Si from the substrate into poly-Si, this latter must evidently proceed much more slowly. The electromigrating Si will be carried downstream by the current until it equilibrates with the surroundings and precipitates out. The observation of a higher density of Si particles over the positive contact pad in comparison to the negative (Fig. 6a) supports the above argument. Once the poly-Si is removed from over the window, albeit locally, the Al can directly communicate with the substrate in this region. Thus, further current flow will transport Si from the substrate into the metal, until a pit filled with Al grows to shunt the underlying junction. Examples of such etch pits are identified in Fig. 6b. This mechanism for failure is corroborated by the measured 0.9 eV activation energy (Fig. 3), which corresponds to grain boundary diffusion of Si in thin film Al, and has been recently verified for thermally induced pit growth at Al/Si contacts (16). The lack of poly-Si edge displacement and the symmetrical deterioration of the 2 μm windows is consistent with much less current crowding (see Fig. 7) in these in comparison to larger geometries. However, even a localized substitution of poly-Si by Al in the window area will be sufficient to provide a high conductivity path for funneling the current and creating subsurface pits. Hence, varying the contact dimensions merely alters the current distribution in the contacts, and in turn the window morphology, without affecting the failure mechanism.

Figure 4 demonstrates an $\sim I^{-10}$ proportionality of lifetime on window current for both the small and the large contacts. Similar large exponents on current density have been observed in electromigration lifetime tests on conductors at high current levels ($\geqslant 10^6$ Acm^{-2}) (17), and ascribed to excessive joule heating and consequent large thermal gradients in the runners. In the present test structure, high temperatures will be generated as the current passes from the semiconductor into the metal. Furthermore, current crowding in the windows will enforce an additional temperature gradient in the contact region. Thus, under the synergistic influence of a nonuniform current, as well as temperature profile, such an exaggerated dependence of MTF on I, as depicted in Fig. 4, is not implausible. It may be argued that a process activated by excessive heating in the contacts should be independent of substrate temperature within the prescribed range of test conditions. However, beyond the confines of the window, the current will fan out into the Al, with a precipitous decline in temperature to the ambient state. This latter will, therefore, control the diffusion kinetics of Si in Al and, in turn, the rate of subsurface pitting and failure.

The appearance of a negatively biased window (Fig. 5 and 6) remains unchanged upon aging. This confirms that the poly-Si layer protects the substrate from any thermally generated Al-substrate interaction, such as observed on devices metallized with plain Al (16). Furthermore, despite identical current crowding effects at both contacts, there is no evidence of any damage or even of Al deposition in the negative window resulting from electromigration in the runner. This latter suggests that within the specified range of test conditions, electromigration in the interconnect is much slower than that occurring at the positive contact interface. The absence of damage in the negative window confirms that the positive contact degradation is a consequence of electromigration rather than of joule heating.

Figures 2 and 3 appear to suggest that smaller windows can carry higher $J_{\square}$'s prior to failure. However, since the current profiles within the windows vary with window size, it is inaccurate to compare their resistance to electromigration on the basis of the average current per unit area or even per unit length of the leading contact edge. On the basis of Fig. 3, the median lifetimes for the three window sizes are comparable for the current levels specified in the figure. This suggests that the effective $J(x)$ contributing to failure must be similar for the three cases. The above hypothesis can be verified by developing a mathematical relationship between lifetime, window current, and contact dimensions. From the results presented in Fig. 4

$$\mathrm{MFT} \propto \left[\frac{I}{w^{0.6}}\right]^{-10} \qquad [1]$$

at a constant test temperature. Thus, instead of an areal current density, an edge current density, or even the maximum value of $J(x)$ calculated from Berger's model (13), the lifetime depends upon an effective current density J_e defined by $[I/w^{0.6}]$. The magnitudes of J_e for the 2, 4, and 6 μm windows, corresponding to the currents listed in Fig. 3, are 13.7, 13.9, and 13.0, respectively, which corroborates the similarities in their MTF's.

With a scale down in device geometry, the failure times will decrease in accordance with Eq. [1] for a constant current flow through the contacts. It may, therefore, appear as if this mechanism will present an inherent limitation to Al/poly-Si metallization for smaller contact geometries. However, if I_{runner} ($= I_{\text{contact}}$) is scaled with design rule according to the established criterion for electromigration, *viz.*, keeping its current density constant at 10^5 Acm^{-2}, I_{contact} will no longer be constant, but instead, vary as

$$I_{\text{contact}} = 0.7\ (w + 2)\ \text{mA} \qquad [2]$$

for 0.7 μm thick Al films, where w represents the edge of a square window and 2 arises from including a 1 μm metal border around the window. Thus I_{contact} will decrease from 5.6 mA, for the 6 μm windows, to 2.8 mA only, in the case of the 2 μm windows. This corresponds to a $<5\%$ change in J_e upon decreasing window dimensions from 6 to 2 μm. From Eq. [1] and the measured MTF's (Fig. 4), the lifetimes at specified design currents (Eq. [2]) can be computed. These are 3.7×10^9 and 3.1×10^9 hr at 150°C, for the 6 and 2 μm windows, respectively. These time scales are significantly longer than those predicted for the development of an open circuit in the runners (18) or for other failure modes operating in a device. Hence, contact electromigration does not represent a potential reliability hazard for Al/poly-Si contacts to shallow junctions, despite a progressive scaling in contact dimensions.

Conclusions

The electromigration behavior of shallow junction (1000Å) devices metallized with Al/poly-Si has been investigated. Results indicate that (*i*) although such a two-layer metallization protects the structures from thermally induced substrate shorts, the devices are prone to junction leakage by Si-electromigration at the positively biased windows; (*ii*) the failure times exhibit a thermal activation of $\sim$0.9 eV and a strong dependence on window current given by $I^{-10\pm1}$; (*iii*) decreasing the window size reduces the extent of current crowding in the windows; (*iv*) however, for a constant runner current density of 10^5 Acm^{-2}, Al/poly-Si contacts remain electromigration resistant, in spite of a reduction in window dimensions from 6 to 2 μm.

Acknowledgments

The authors are indebted to MOS Lab II for fabrication of the test structures, to Cynthia Sarday for electrical measurements, and to E. N. Fuls, W. T. Lynch, and H. Levinstein for many valuable discussions.

Manuscript received Feb. 24, 1982. This was Paper 228 presented at the Montreal, Canada, Meeting of the Society, May 9-14, 1982.

Any discussion of this paper will appear in a Discussion Section to be published in the December 1983 JOURNAL. All discussions for the December 1983 Discussion Section should be submitted by Aug. 1, 1983.

Publication costs of this article were assisted by Bell Laboratories.

REFERENCES

1. "Thin Films—Interdiffusion and Reactions," J. M. Poate, K. N. Tu, and J. W. Mayer, Editors, p. 243, Wiley-Interscience Publ., New York (1978).
2. G. S. Prokop and R. R. Joseph, *J. Appl. Phys.*, **43**, 2595 (1972).
3. G. S. Prokop, C. Y. Ting, and R. R. Joseph, Proc. IEEE Rel. Phys. Symp., p. 121 (1970).
4. James R. Black, *ibid.*, p. 233 (1978).
5. P. B. Ghate, *ibid.*, p. 243 (1981).
6. J. T. Clemens and K. M. Locke, Bell Labs Internal Memorandum (Sept. 1978).
7. W. E. Willenbrock, Jr., *ibid.*, (Oct. 1980).
8. J. M. Andrews, Manuscript in preparation.
9. D. N. K. Wang, D. Maydan, and H. J. Levinstein, *Solid-State Technol.*, 122 (Aug. 1980).
10. C. C. Chang, Personal communication.
11. K. Nakamura, M.-A. Nicolet, J. W. Mayer, R. J. Blattner, and C. A. Evans, Jr., *J. Appl. Phys.*, **46**, 4678 (1975).
12. S. Vaidya, To be published.
13. H. H. Berger, *Solid-State Electron.*, **15**, 145 (1972).
14. Chung-Yu Ting and Charles Y. Chen, *Solid-State Electron.*, **14**, 433 (1971).
15. E. N. Fuls and D. Boullin, Personal communication.
16. S. Vaidya, *J. Electron. Mater.*, **10**, 337 (1981).
17. R. A. Sigsbee, *J. Appl. Phys.*, **44**, 2533 (1973).
18. S. Vaidya, D. B. Fraser, and A. K. Sinha, Proc. 18th Int. Rel. Phys. Symp., p. 165 (1980).

On the Kinetics of the Thermal Oxidation of Silicon

IV. The Two-Layer Film Approximation

William A. Tiller

Department of Materials Science and Engineering, Stanford University, Stanford, California 94305

ABSTRACT

An analysis has been made of the oxidation rate for a film that contains an interface blocking layer with different transport properties than the bulk oxide. The results reproduce the Deal-Grove (11) formalism, satisfy the Doremus requirement (12), the Tiller requirement (2), the Taft-Cordes results (6), and the van der Meulen experiment (13). The temperature and oxygen pressure results for thin oxides may be quantitatively matched by the two-layer film model. The present analysis restricts itself to neutral species.

In Part I of this series (1), it was shown that the free energy, ΔG_x, released by the reaction of Si and O_2 is consumed via three main processes: (*i*) oxygen transport through SiO_2, ΔG_S, (*ii*) atomic reaction to form the SiO_2 species, ΔG_K, and (*iii*) storage of energy in the form of strain and defects, ΔG_E. Since the molecular valence of SiO_2 is so much larger than that for Si, very large ΔG_E are possible and pathways for the system to reduce ΔG_E become first-order considerations. Clearly, the transformation occurring at the Si/SiO_2 interface will be to a structure that uniquely reduces the strain energy associated with the volume change, and two mechanisms have been proposed to do this: (*i*) the preferred SiO_2 structure, crystalline or amorphous, requires the generation of appreciable silicon interstitials, Si_I, at the interface which partition between the Si and the SiO_2 (2, 3) and (*ii*) a significant portion of the volume difference between the Si and SiO_2 may be accommodated by an array of disclinations or dislocations lying parallel to the Si/SiO_2 interface (4) (see Fig. 1). The growth of the oxide involves climb of these dislocations plus the nucleation of new ones at the edge of the sample. Since this dislocation climb is most likely to require the movement of Si_I in the SiO_2, we may assume that both mechanisms operate simultaneously and cooperatively.

As discussed in Part III (3), because of the Si_I, the region of the SiO_2 close to the interface is more dense than regions in the bulk SiO_2 because viscous flow and vacancy diffusion relieve the bulk oxide. The silica stoichiometry and structure in the near interface region changes due to the internal oxidation of these Si_I. Because of the associated swelling stresses, this oxide becomes vitreous (3). Qualitative plots of the swelling stresses, σ_s, and of the interstitial channel volume, v_{ch}, through this region are given in Fig. 2. Thus, this interface region out to the distance δ, where σ_s begins to exceed the silica flow stress, σ_f, becomes a blocking layer for oxygen transport and we may consider a two-layer film approximation wherein oxygen transport is normal in the region $x \geq \delta$ and is much reduced in the region $0 \leq x < \delta$ (4, 5). Because the internally oxidized SiO_x fragments that have not progressed to

Key words: semiconductor processing, silicon dioxide, thin oxides, pressure dependence, field dependence, new model formulation.

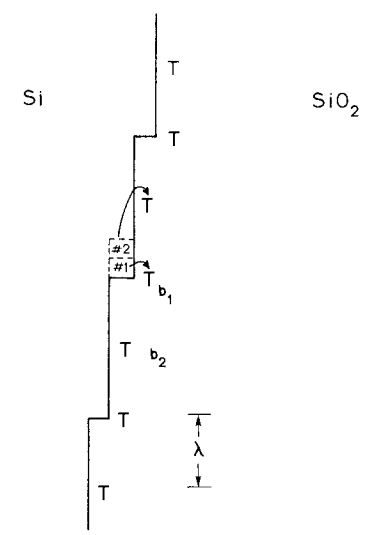

Fig. 1. Interface ledges between Si and SiO_2 for a ledge density factor of 2 between Si and SiO_2. The dislocations at the kink positions have Burger's vector $b_1 = a_{SiO_2} - a_{Si}$, while those between the kink positions have Burger's vector $b_2 = a_{SiO_2}$ (a = molecular spacing).

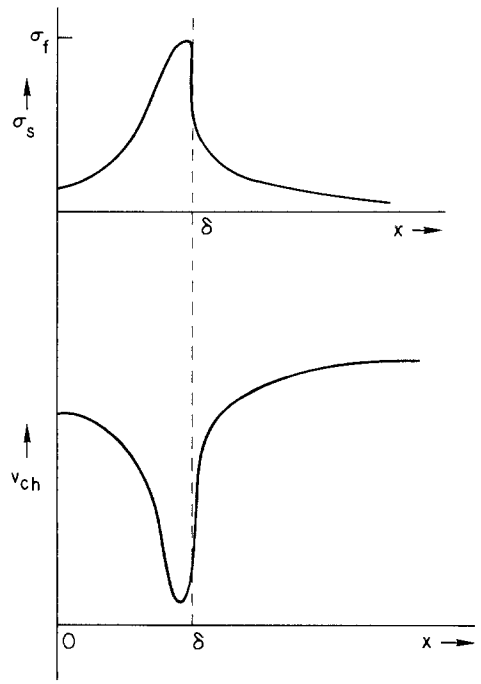

Fig. 2. Schematic plot of swelling stress σ_s, and interstitial channel volume, v_{ch}, as a function of position ahead of the interface relative to the blocking layer thickness, δ.

the SiO_4 state are thought to be the origin of fixed oxide charge (3) (perhaps in association with vacancies at bridging oxygen sites), the blocking layer will have a voltage difference, ΔV_δ, across it which impedes the motion of negatively charged species to the interface.

This two-layer film approximation is consistent with the findings of Taft and Cordes (6) and others (7). They found that an optical layer ~ 6Å thick with an index of refraction of 2.8 at $\lambda = 5461$Å was required between (111) silicon and its thermal oxide in order to fit their ellipsometric data. Oxides grown at lower temperatures require a thicker layer of intermediate optical material than oxides grown at higher temperatures. They suggested that their interlayer contains two extra layers of Si atoms (2×10^{15} Si atoms/cm^2) producing an SiO_x stoichiometry with $x \sim 1.2$. Ion backscattering studies also find excess Si in an interface transition layer between Si and SiO_2 (8, 9). From an earlier study (10), Taft found, using a single layer film approximation, that the average index of refraction increased with decrease of oxidation temperature and was larger for the <100> than for the <111> substrate orientation. This orientation difference disappeared for oxidation temperatures $\gtrsim$ 1100°C. From this, one might conclude that $\delta_{(100)} > \delta_{(111)}$ for a given temperature.

The purpose of the present paper is to analyze the two-layer film approximation for the oxidation of Si to see if it can account for the experimental data better than can the single layer film model proposed by Deal and Grove (11). The general data constraints that we attempted to satisfy were:

1. The Deal-Grove (11) mathematical formalism of linear and parabolic growth domains must result.
2. The Doremus result (12) that the parabolic rate constant, B, must be proportional to P_{O_2} and have the activation energy for O_2 diffusion in bulk silica.
3. The Tiller conclusion (2) that a much larger ΔG_s is needed for oxygen diffusion than that predicted by the single layer film model.
4. The van der Meulen findings (13) that, for thin oxides, the linear rate constant exhibits (*i*) a pressure dependence, at constant T, that varies between ~0.5 and ~1.0 and (*ii*) a temperature dependence, at 1 atm pressure, that cannot be fitted by a single activation energy. It will be shown that all of these constraints plus others can be satisfied by the two-layer film approximation. The present analysis is restricted to neutral species for simplicity. The case of both neutral plus ionized species will be treated in the next paper of this series.

Analysis

We shall begin by considering the following approximations: (*i*) single layer, single diffusing species, (*ii*) two-layer, single diffusing species, same species in each layer, (*iii*) two-layer, single species, different species in each layer, and (*iv*) two-layer, multiple species diffusing in each layer. The mathematical formalism for each will be developed to see if they match the Deal-Grove (DG) formalism (11), that is a good fit to the main body of experimental data. By single or multiple species, is meant major oxidant species. After finding those cases that match the DG formalism, we shall proceed with the assessment of the other data constraints.

(*i*) *Single layer, single species.*—This is the case leading to the DG treatment (11) which is pictorially illustrated in Fig. 3a. The mathematical results are

$$X_o^2 + A X_o = B(t + \tau) \quad [1]$$

$$A = 2 D_{\text{eff}}\left(\frac{1}{k_i} + \frac{1}{h}\right) \quad [2]$$

$$B = 2 D_{\text{eff}} C^*/N_1 \quad [3]$$

$$B/A = \frac{k_i h}{k_i + h}\left(\frac{C^*}{N_1}\right) \quad [4]$$

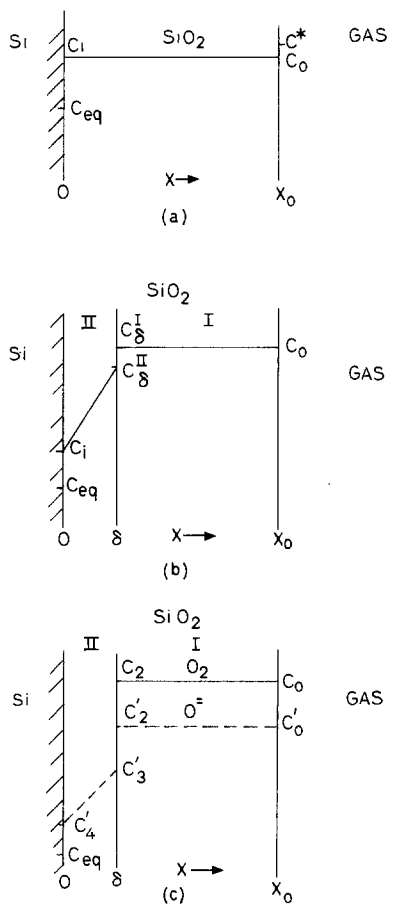

Fig. 3. Plot of oxidant concentration vs. distance in the bulk oxide (region I), plus oxidant concentration in the blocking (region II): (a) single layer film, single species approximation, (b) two-layer film, single species, same species approximation, (c) two-layer film, single species, different species.

and

$$\tau = (X_i^2 + AX_i)/B \quad [5]$$

Here, X_o is the oxide film thickness, t is time, D_{eff} is the effective diffusion coefficient of the oxidant species through the film, C^* is the solubility of the oxidant in the film at the gas/film interface, N_1 is the number of O_2/cm^3 in SiO_2, k_i and h are the reaction coefficients at the Si/SiO_2 and SiO_2/gas interfaces respectively, B is the parabolic rate constant, and B/A is the linear rate constant while X_i is some initial film thickness that has a higher oxidation velocity than given by the linear rate regime.

(*ii*) *Two-layer, single species, same species.*—The concentration profile for this case is illustrated in Fig. 3b where we have assumed that a partition coefficient for the oxidant, $k^* = C_\delta^{II}/C_\delta^{I}$, exists between the "average" blocking layer density and the bulk oxide density. The procedure followed was the same as that used by DG so that, in terms of oxidant fluxes, we have

$$F_1 = F_2 = F_3 = F_4 = F \quad [6]$$

where

$$F_1 = h(C^* - C_o) \quad [7]$$

$$F_2 = D_I W_I \frac{(C_o - C_\delta^I)}{x_o - \delta} \quad [8]$$

$$F_3 = D_{II} W_{II} \frac{(k^* C_\delta^I - C_i)}{\delta} \quad [9]$$

$$F_4 = k_i C_i \quad [10]$$

and W_I and W_{II} are the diffusivity enhancement factors due to all types of fields (14), *i.e.*, for the i species of a multiple diffusing species system

$$W^i = (1 - t_i) \frac{\partial \ln a^*_i}{\partial \ln C^*_i} - \sum_{j \neq i, e^-, e^+} t_j \frac{Z_i \partial \ln a^*_j}{Z_j \partial \ln C^*_j} \quad [11]$$

In Eq. [11], a = activity, * refers to neutral species, Z = valence, and t_i is the transference number for species i. In Eq. [8] and [9], D refers to the tracer diffusion coefficient.

The oxidation velocity, dX_o/dt, is given by

$$\frac{dX_o}{dt} = \frac{F}{N_1} \quad [12]$$

and, by insertion of Eq. [6]-[10], we obtain

$$\frac{dX_o}{dt} = \frac{C^*/N_1}{\frac{\delta}{k^* D_{II} W_{II}} + \frac{1}{k^* k_i} + \frac{1}{h} + \frac{(x_o - \delta)}{D_I W_I}} \quad [13]$$

On integration, this leads to

$$(X_o - \delta)^2 + A(X_o - \delta) = Bt \quad [14]$$

$$A = 2D_I W_I \left[\frac{1}{h} + \frac{1}{k_i k^*} + \frac{\delta}{k^* D_{II} W_{II}} \right] \quad [15]$$

$$B = 2 D_I W_I C^*/N_1 \quad [16]$$

since $X_o = \delta$ at $t = 0$, and time is only considered to start after the blocking layer has been built up.

We note briefly that the DG formalism is obtained for this case, that the parabolic rate constant is unchanged, and that transport through the blocking layer enters the linear rate constant.

(*iii*) *Two-layer, single species, different species.*—The concentration profiles for this case are given in Fig. 3(c) where a specific example of O as the diffusing species in layer II has been used only for illustration. For this case, the results are identical to case (*ii*), except for A which is now given by

$$A = 2 D_I W_I \left[\frac{1}{h} + \frac{1}{\tilde{k} k_i} + \frac{\delta}{\tilde{k} D'_{II} W'_{II}} \right] \quad [17]$$

where the prime refers to the species in region II and where $\tilde{k}$ is given by

$$O_2 \leftrightarrows 2\,O; \quad K_2 = [O]^2/[O_2] \quad [18]$$

$$k'^* = C_\delta^{II}/C'^{I}_\delta \quad [19]$$

and

$$\tilde{k} = C'^{II}_\delta/C'^{I}_\delta = k'^* C'^{II}_\delta/C^{II}_\delta = k'^* K_2^{1/2}/[O_2]_\delta^{1/2} \quad [20]$$

When equilibrium does not hold for Eq. [18] and supersaturation (SS) of the O_2 species prevails, we replace K_2 by $K_2 \exp(\Delta G_{ss}/RT)$. This value of $\tilde{k}$ may have a different P_{O_2} dependence depending upon the particular species diffusing through region II. Again, we see that the DG formalism holds.

(*iv*) *Two-layer, multiple species, same species.*—For this case, Eq. [12b] becomes

$$\frac{d(X_o - \delta)}{dt} = \sum_j \frac{m_j C_j^*/N_1}{\left[\frac{1}{h_j} + \frac{1}{k_{ij} k_j^*} + \frac{\delta}{k_j^* D_{IIj} W_{IIj}} + \frac{(X_o - \delta)}{D_{Ij} W_{Ij}} \right]} \quad [21]$$

where $m_j = 1$ for O_2 species and $m_j = \frac{1}{2}$ for all O species. The j species to be considered are O_2, O, etc. Clearly, the solution of this differential equation will not lead to a result like Eq. [1] or Eq. [13]. Thus, we can conclude that multiple major oxidant species diffusion is not consistent with the experimental data.

From the foregoing, we may conclude: (*i*) that oxidation occurs primarily via the diffusion of only one constituent in each layer (even though several may be present), (*ii*) that the parabolic rate constant, B, is determined by $D_I W_I \approx D_I$ so that O_2 diffusion in layer I would provide the proper activation energy and pressure dependency, (*iii*) that diffusion through layer II enters the linear rate constant B/A, and (*iv*) that most of the driving force, ΔG_s, is consumed in layer II. The latter conclusion is fortified by Fig. 3(b) and 3(c) where we find that

$$\Delta G_s = -RT \ln [\gamma_4^{O_2} C_4^{O_2}/\gamma_1^{O_2} C_1^{O_2}] \quad [22a]$$

where $C_1^{O_2}$ is the concentration of O_2 in the oxide at the oxide/gas interface and $C_4^{O_2}$ is the equilibrium concentration of O_2 for the particular concentration C'^{O}_4 of the species O at the Si/SiO_2 interface. This assumes equilibrium existing at the I/II interface for both the partitioning of O species and for the O_2/O reaction. If these equilibria are not maintained, we find that

$$\begin{aligned}\Delta G_s = & -RT \left\{ \ln \left[\frac{\gamma_2^{O_2} C_2^{O_2}}{\gamma_1^{O_2} C_1^{O_2}} \right] + \ln \left[\frac{\gamma_2^{O} C_2^{O}}{\gamma_2^{O}(eq) C_2^{O}(eq)} \right] \right. \\ & \left. + \ln \left[\frac{\gamma_3^{O} C_3^{O}}{\gamma_3^{O}(eq) C_3^{O}(eq)} \right] + \ln \left[\frac{\gamma_4^{O} C_4^{O}}{\gamma_3^{O} C_3^{O}} \right] \right\} \\ = & -RT \left\{ \ln \left[\frac{\gamma_2^{O_2} C_2^{O_2}}{\gamma_1^{O_2} C_1^{O_2}} \right] + \ln \left[\frac{\gamma_2^{O} C_2^{O}}{\gamma_2^{O}(eq) C_2^{O}(eq)} \right] \right. \\ & \left. + \ln \left[\frac{\gamma_4^{O} C_4^{O}}{\gamma_3^{O}(eq) C_3^{O}(eq)} \right] \right\} \end{aligned} \quad [22b]$$

where $\gamma_4^{O_2}$ is the activity coefficient for O_2 at location 4 in Fig. 3c. This result would also hold for a different

species in layer II with $C_4^{O_2}$ being the concentration of O_2 in equilibrium with the concentration of C'^{O}_4 of species O. Since the ratio C_4/C_1 is so much larger than the ratio C_2/C_1, the ΔG_s value for the two-layer film model is much larger than that for the single layer film model.

Discussion

In the last section, we saw that the two-layer film model is able to account for the constraints (*i*)-(*iv*) listed in the introduction. Before we address constraint (*v*), let us note that Eq. [13] does not include the parameter τ. This is because the steady state was assumed to begin at the point in time when the blocking layer of thickness δ had been formed, *i.e.*, $t = 0$ at $X_o = \delta$. The length of time that is required for the transient conditions to create the blocking layer and the magnitude of δ are not considerations that can be dealt with at the present level of modeling. They must be assumed as "given" in the study. If τ' is considered as the time needed to reach this steady-state condition and t' is the time from the beginning of oxidation, then $t = t' - \tau'$. For thick oxides, $X_o \gtrsim 500$Å, Eq. [13] becomes

$$\frac{X_o^2}{B} + \frac{X_o}{B/A} = t' - \tau' \qquad [23]$$

which is the DG result (11). For thin oxides, $50\text{Å} \lesssim X_o \lesssim 500\text{Å}$, we can expect to find

$$\frac{X_o^2}{B} + \frac{X_o}{B/A} = t' - \left(\tau' - \frac{\delta}{B/A} - \frac{2\delta X_o}{B}\right) = t' - \tau''(X_o) \qquad [24]$$

where $\tau''(X_o)$ is a function of X_o, decreasing as X_o increases. For the case of very thin oxides where $X_o \lesssim \delta$, it is preferable to use

$$\frac{(X_o - \delta)^2}{B} + \frac{(X_o - \delta)}{B/A} = t' - \tau' \qquad [25]$$

so that two parameters, δ and τ', need to be selected to place the experimental data in this simple form. From a numerical point of view, if $\delta \sim 6$Å at 1000°C, $\tau = 0.35$ hr in Eq. [23], $\delta/(B/A) \sim 0.01$ hr and $2\delta X_o/B \lesssim 0.1\ X_o$ hr with X_o in μm. Thus, the effect is very small for this choice of δ and $\tau'' \approx \tau'$. However, if δ is an order of magnitude larger, then the effect becomes significant. Although the region of SiO_x nonstoichiometry may be ~ 6Å at the interface, the region of enhanced density and reduced channel volume, v_{ch}, could indeed be ~ 50Å because three events are involved in forming the blocking layer: (*i*) the internal oxidation of the Si_I to the SiO_2 state, (*ii*) the eventual presence of two bridging oxygen vacancies in the adjacent network containing the internal fragment so that it can truly become a part of the network, and (*iii*) the relaxation of the network to form the proper ring size (6-membered rings).

If we wish to characterize the thin film data using the thick film parameters, B, B/A, and τ' then, for $X_o \gtrsim 300$Å, Eq. [25] yields

$$\frac{X_o^2}{B} + \frac{X_o}{(B/A)'} = t' - \tau' \qquad [26a]$$

where

$$(B/A)' = (B/A)\frac{1}{\left(1 - \frac{\delta}{X_o}\right)} = \frac{B}{A}\left(1 + \frac{\delta}{X_o} - \frac{1}{2}\left(\frac{\delta}{X_o}\right)^2 + \cdots\right) \qquad [26b]$$

Thus, the thin film effects can be looked at phenomenologically as a departure from the thick film results. No change in B and τ' is needed to describe the thin film results provided that the $(B/A)'$ parameterization is used.

To illustrate the point made following Eq. [21] that the diffusion of multiple major oxidant species do not lead to an equation of the form exhibited by Eq. [1] and Eq. [13], let us consider the case of two oxidant species 1 and 2 in each layer. From Eq. [21], we have

$$\frac{d(X_o - \delta)}{dt} = \sum_j \frac{m_j B_j}{2(X_o - \delta) + A_j} \qquad [27a]$$

$$\approx \frac{m_1 B_1}{2(X_o - \delta) + A_1} + \frac{m_2 B_2}{2(X_o - \delta) + A_2} \qquad [27b]$$

$$= \frac{B_1}{2(X_o - \delta) + A_1}\left\{ m_1 + \frac{m_2(B_2/B_1)}{\left[\frac{2(X_o - \delta) + A_2}{2(X_o - \delta) + A_1}\right]}\right\} \qquad [27c]$$

Rearranging and integrating, this leads to

$$\frac{(X_o - \delta)^2}{B_1} + \frac{(X_o - \delta)}{B_1/A_1} = m_1 t + m_2(B_2/B_1)\int\left[\frac{2(X_o - \delta) + A_1}{2(X_o - \delta) + A_2}\right]dt \qquad [28]$$

Only for the case of very thin oxides, where $2(X_o - \delta) << A_1 \sim A_2$, or for very thick oxides, where $2(X_o - \delta) >> A_1 \sim A_2$, will Eq. [28] lead to the same form as Eq. [1] and [13]. In between these two limits, a different behavior is evidenced. Increasingly $X_o - \delta$ from very small values, we find the second term on the right of Eq. [28] to be given by

$$m_2\frac{B_2}{B_1 B_2}\int [2(X_o - \delta) + A_1]\left[1 - \frac{2(X_o - \delta)}{A_2} + \frac{(X_o - \delta)^2}{A_2^2} - \cdots\right]dt \qquad [29a]$$

and, for $(X_o - \delta) \approx \beta t$, this becomes

$$\frac{m_2 B_2}{B_1 A_2}\left\{A_1 t + \beta\left(1 - \frac{A_1}{A_2}\right)t^2 + \frac{2\beta^2}{3A_2}\left(\frac{A_1}{A_2} - 2\right)t^3 + \cdots\right\} \qquad [29b]$$

The inclusion of Eq. [29b] for the second term on the right of Eq. [28] illustrates that, for small times but not very small times, the linear growth region does not obtain. Only at very small times does Eq. [28] with Eq. [29b] conform to the DG formalism.

The van der Meulen constraint.—In our evaluation of Eq. [13], an important issue is the pressure dependence of the rate constants. The most obvious conclusion is that the pressure dependence of the parabolic rate constant, B, in Eq. [15] is given by the pressure dependence of C^* provided W_I is independent of pressure (which it should be to first order). This is the same as the DG result (11).

The pressure dependence of the linear rate constant, B/A, is not so easily assessed. If we neglect $1/h$ with respect to the other two terms in Eq. [14], in accordance with DG, then we obtain the form

$$B/A = a(T)\ P_{O_2}{}^n/[1 + b(T)P_{O_2}{}^q] \qquad [30a]$$

$$a(T)P_{O_2}{}^n = k_i k^* C^*/N_1 \qquad [30b]$$

$$b(T)P_{O_2}{}^q = \delta\, k_i/D_{II}W_{II} \qquad [30c]$$

with n and q as parameters that may be functions of T. We know that C^* has a linear P_{O_2} dependence, but

we do not know the pressure dependence of k_i, k^*, or $\delta/D_{II}W_{II}$. Fortunately, the data of van der Meulen (13), on the kinetics of formation of ultrathin oxide layers on silicon, provides us with a testing ground for the different factors in Eq. [30].

Van der Meulen (13) found that a plot of $\log B/A$ *vs.* $\log P_{O_2}$ gave a linear relationship for a single temperature and wafer orientation with the slope increasing toward unity as T increases ($T_{max} = 1000°C$) and with the slope decreasing towards ½ as T decreases ($T_{min} = 700°C$). The latter pressure limit is consistent with the observation of Law (15) who observed, close to room temperature, an exponential growth rate in the 1-2 monolayer region with a square root dependence on P_{O_2} in the 10^{-4}-10^{-2} Torr range. It was also found by van der Meulen (13) that (*i*) a plot of B/A *vs.* $1/T$ did not lead to a straight line with a single activation energy and (*ii*) $d \ln (B/A)/d \ln P_{O_2}$ was greater for the (111) than for the (100) orientation at a given T just as $(B/A)_{(111)} > (B/A)_{(100)}$ for a given P_{O_2}. Let us see if Eq. [30] can account for the observations.

From Eq. [30], we note that there will be at least two activation energies involved in a B/A *vs.* $1/T$ plot, one from each of $a(T)$ and $b(T)$. We note also that, if $b(T)$ is large w.r.t. unity at high temperatures and small w.r.t. unity at low temperatures, we can have (*i*) a P_{O_2} dependence at high temperatures given by $n - q$ and (*ii*) a P_{O_2} dependence at low temperatures given by n. Thus, if the P_{O_2} dependence of k_i is $-$ ½, then n = ½, which would be consistent with Law's data (15), and $n - q = 1$ provided $\delta/D_{II}W_{II}$ and k^* have no pressure dependence at high T. If $\delta/D_{II}W_{II}$ has a pressure dependence that changes with T, because of thermal relaxation processes in the blocking layer, the q will definitely be temperature dependent and the slope of $d \log (B/A)/d \log P_{O_2}$ will change with temperature, *i.e.*

$$\frac{d \log (B/A)}{d \log P_{O_2}} = n - \frac{q\, b(T) P_{O_2}^{q}}{1 + b(T) P_{O_2}^{q}} \qquad [31]$$

We can see qualitatively from Eq. [31] that, even for q = constant, a temperature dependence is found for the slope. We see also that the slope, at fixed T, is not completely independent of P_{O_2} as suggested by the data of van der Meulen (13). However, for $b(T)P_{O_2}^{q} >> 1$, Eq. [31] can be expanded to give

$$\frac{d \log (B/A)}{d \log P_{O_2}} = n - q + \frac{q}{b(T)} P_{O_2}^{q} + \cdots \qquad [32]$$

and the pressure dependence enters only as a small correction term. This small degree of curvature may not have been noticed in the data.

A quantitative fit of Eq. [30] and [31] to the van der Meulen temperature and pressure data has been made for the (111) orientation with a good match being given by

$$a(T) = 10^{10} \exp (-45.5/RT) \qquad [33a]$$

$$b(T) = 350 \exp (-10.2/RT) \qquad [33b]$$

$$n = 0.5 \qquad [33c]$$

and

$$q \approx -0.5 \exp (-1.35/RT) \qquad [33d]$$

The expression for q in Eq. [33d] is a forced fit to an exponential function whereas it actually exhibits an S-shape as shown in Fig. 4. There is insufficient data to fully assess the (100) orientation case; however, the following give a good representation of the existing data

$$a(T) = 7.4 \times 10^{9} \exp (-45.5/RT) \qquad [34a]$$

$$b(T) = 260 \exp (-10.2/RT) \qquad [34b]$$

and

$$n = 0.5 \qquad [34c]$$

$$q \approx -0.5 \exp (-2.55/RT) \qquad [34d]$$

whereas, the more appropriate description of $q(100)$ is also given in Fig. 4.

From the foregoing, we see that the two-layer film approximation also satisfies all the constraints of the van der Meulen results (13). Matching these results leads to the interesting conclusion that the pressure dependence of k_i is $P_{O_2}^{-1/2}$. This will require a very specific mechanism for the interface reaction and will be treated in the next paper of this series. Because of this specific dependence of k_i, we note that the pressure dependence of $\delta/D_{II}W_{II}$ is $q + ½$ which goes to zero at high temperatures. This is exactly as expected for a relaxation process that is controlled by viscous flow at high temperatures.

Before concluding this section it should be noted that a characteristic signature of the two-layer film model is the one illustrated in Fig. 5. A plot of oxidation velocity, V, as a function of $1/T$, for fixed oxide thickness, $X_o - \delta$, exhibits a concave upwards plot with the curve straightening out as $X_o - \delta$ increases in magnitude. This conclusion follows directly from Eq. [12b]. The data of van der Meulen (13), for B/A at P_{O_2} = 1 atm, represents the case for $X_o - \delta = 0$.

The most likely neutral oxygen species to diffuse through the blocking layer is O so that this model would have some characteristics similar to the model proposed by Blanc (16). However, in the present model, one need only be concerned about the dissociation reaction of O_2 into 2 O at the outer edge of the blocking layer, $x = \delta$, rather than at all x. This greatly simplifies the mathematical treatment. Since the main purpose of this paper was to introduce and evaluate the blocking layer concept, there is little point in discussing the relative merits of Blanc's contribution (16) *vs.* the present contribution because the present work is incomplete in that it ignores the effects of ionized oxygen species, O^+, O^-, O^{++}, $O^=$, etc. These ionized oxygen species are thought to be an important contribution to the overall oxidation process even in the case of zero applied field.

The blocking layer concept is an important concept to be included in the ultimate, general model, of silicon oxidation; however, it is only one factor and others are still needed to complete the picture. This paper has been restricted to a discussion of the blocking layer concept primarily to emphasize the need for breaking with a single layer film model.

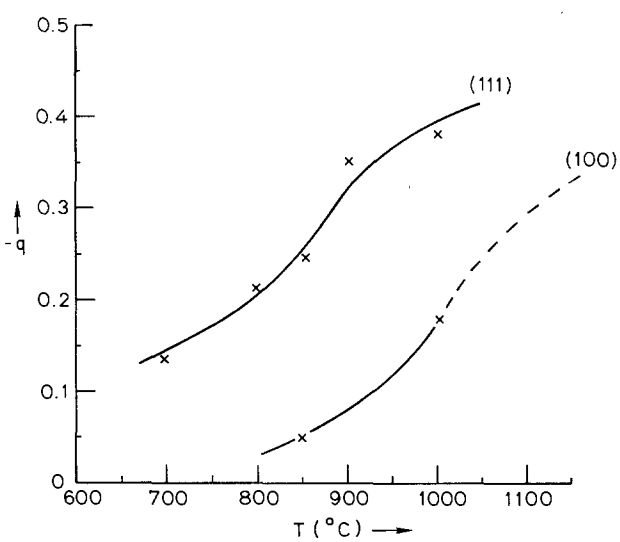

Fig. 4. Plot of oxygen pressure exponent, $q(T)$, as a function of temperature for (111) and (100) orientations needed to fit the van der Meulen data (15) via. Eq. [30] and [31], respectively.

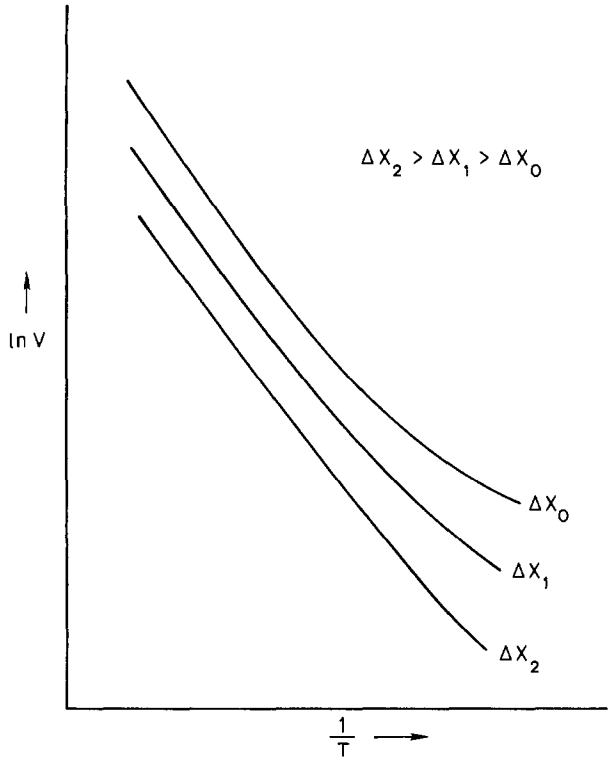

Fig. 5. Qualitative plot of ln$V$ vs. $1/T$ to illustrate the upward curvature and its increase in magnitude as $\Delta X = X_0 - \delta$ decreases in magnitude.

Conclusions

The two-layer film model, in its phenomenological form, has been studied with respect to a wide range of experimental data and general theoretical expectations for the oxidation process and found to fully satisfy the wide range of constraints. This model gives a much better fit with the broad range of data than the original single layer film model of Deal and Grove (11).

Acknowledgments

Discussion with John Hirth, Bruce Deal, Jim Plummer, Hisham Massoud, and Doug Modlin are gratefully acknowledged. This work was supported by the Defense Advanced Research Project Agency under Contract No. DAAB07-77-C-2684.

Manuscript submitted Sept. 10, 1981; revised manuscript received July 29, 1982.

Any discussion of this paper will appear in a Discussion Section to be published in the December 1983 JOURNAL. All discussions for the December 1983 Discussion Section should be submitted by Aug. 1, 1983.

Publication costs of this article were assisted by Stanford University.

REFERENCES

1. W. A. Tiller, *This Journal*, **127**, 619 (1980).
2. W. A. Tiller, *ibid.*, **127**, 625 (1980).
3. W. A. Tiller, *ibid.*, **128**, 689 (1981).
4. J. P. Hirth and H. Ehrenreich, DARPA LaJolla Conference on Thermal Oxidation, July 1980.
5. G. J. Yurek, R. P. Rapp, and J. P. Hirth, *Oxidation of Metals*, **8**, 265 (1974).
6. E. A. Taft and L. Cordes, *This Journal*, **126**, 131 (1979).
7. M. E. Pedinoff, D. C. Mayer, O. M. Stafsudd, and G. Dun, Paper 311 presented at The Electrochemical Society Meeting, Hollywood, Florida, Oct. 5-10, 1980.
8. T. W. Sigmon, W. K. Chu, E. Lugujjo, and J. W. Mayer, *Appl. Phys. Lett.*, **24**, 105 (1974).
9. W. L. Harrington, R. E. Honig, A. M. Goodman, and R. Williams, *ibid.*, **27**, 644 (1975).
10. E. A. Taft, *This Journal*, **125**, 968 (1978).
11. B. E. Deal and A. S. Grove, *J. Appl. Phys.*, **36**, 3770 (1965).
12. R. H. Doremus, *J. Chem. Phys.*, **80**, 1773 (1976).
13. Y. T. van der Meulen, *This Journal*, **119**, 530 (1972).
14. W. Weppner and R. A. Huggins, *ibid.*, **124**, 1569 (1979).
15. J. T. Law, *J. Phys. Chem. Solids*, **4**, 91 (1958).
16. J. Blanc, *Appl. Phys. Lett.*, **33**(5), 424 (1978).

Electrochemical Studies of Dopant Redoxing and Diffusion at the Pt, O_2 | CaF_2 Interface

Schiao F. Chou[1] and Robert A. Rapp*

Department of Metallurgical Engineering, The Ohio State University, Columbus, Ohio 43210

ABSTRACT

The transport of mass and charge across the Pt, O_2| CaF_2 interface has been studied by a-c complex impedance (admittance) measurements as a function of the oxygen pressure in the gas phase. In very pure argon, the interface is blocking to reactions; with increasing oxygen content in the gas phase, redox reactions become possible and the circuit exhibits a Warburg impedance corresponding to a diffusion mechanism in CaF_2. D-C measurements of the CaF_2 conductivity with reversible oxygen electrodes and Tubandt-type titration experiments support the existence of oxygen redoxing and conduction in CaF_2. The use of a CaF_2 electrolyte to measure differences in oxygen chemical potentials in a galvanic cell is clarified.

The CaF_2 solid electrolyte has been used to measure the free energies of formation of borides (1), phosphides (2), carbides (3), sulfides (4), and silicates (5). In each case, the electrodes were chosen to define specific fluorine activities indirectly. Galvanic cell measurements of the following oxygen concentration cell have also been previously reported (6, 7)

$$Ni + NiO \mid CaF_2 \mid Cu + Cu_2O \qquad [I]$$

The emf values of this cell at various temperatures are in good agreement with well-known Gibbs energy of formation data for nickel oxide and cuprous oxide.

Ramanarayanan, Narula, and Worrell (7) proposed a model to explain the behavior of cell I, which involved assumptions that the CaF_2 electrolyte/electrode interface was saturated with CaO, but that fluorine ions were involved in both the electrode reactions and in conduction in the electrolyte. The present authors (6) interpreted the behavior of cell I as an oxygen con-

* Electrochemical Society Active Member.
[1] Present address: Babcock and Wilcox Research Laboratory, Alliance, Ohio 44601.
Key words: solid electrolyte, CaF_2, oxygen doping, a-c impedance.

centration cell as evidence that the oxygen (an impurity) ion is involved in both the electrode reaction and in conduction in CaF_2, and the presence of a CaO precipitate in CaF_2 is not necessary.

A Tubandt-type oxygen titration experiment also demonstrated significant transference of oxygen ions in CaF_2 (6). The bulk electrical conductivity of a CaF_2 single crystal increases irreversibly upon heating in oxygen because of the following doping reaction (8)

$$\tfrac{1}{2}\,O_2 + 2F_F^x \rightarrow F_2 + O_F' + V_F^{\cdot} \qquad [1]$$

where F_F^x, O_F', and $V_F^{\cdot}$ are a normal sited fluorine ion, an oxygen ion substituted on a fluorine lattice site, and an anion vacancy, respectively. Considering the low oxygen activities at the Ni + NiO and Cu + Cu_2O electrodes and the much higher stability of CaF_2 compared to that of CaO, the CaO precipitates reported in previous work (9) were probably formed during the cooling process. Even upon heating a CaF_2 single crystal in 1 atm oxygen for 20 hr at 850°C, the CaF_2 exhibits only a thin oxidized surface layer with cloudy appearance; the bulk of the electrolyte remains clear and no CaO precipitate is detected by x-ray diffraction.

The a-c impedance analysis can separate the elements of interfacial and bulk electrochemical phenomena upon the interpretation of an electrical equivalent circuit. A circuit containing frequency-independent R and C components generally produces semicircular figures in an admittance or impedance complex plane. If the system has frequency-dependent R and C components (a distributed time constant), the center of the semicircle is below the real axis. The $\omega^{-1/2}$ dependent Warburg impedance, corresponding to an infinite R-C combination in series with a bulk resistance, produces ideally a quarter circular arc in the admittance diagram (9) and a straight line with 45° slope in the impedance diagram (10). The Warburg impedance generally corresponds to a slow field-free diffusion process in the electrolyte in the presence of a supporting electrolyte (11). This condition may correspond to the discharge of a foreign charge carrier or an electronic species at an electrode which is blocking to the native charge carrier. The diffusion of electrochemically generated atoms in the electrode (12), a porous electrode (13), and small inhomogeneities in the electrolyte (14) (such as pores, crevices, rough surface, or a precipitate in the electrolyte) may also produce Warburg impedance. The ideal Warburg impedance is expressed as (10)

$$Z = (1 - J)K\omega^{-1/2} \qquad [2]$$

where K is the Warburg parameter, ω is the angular frequency, and j is $\sqrt{-1}$.

In the present paper, electrical conduction in the CaF_2 electrolyte and the characteristics of the electrode/CaF_2 electrolyte reaction in an oxygen atmosphere were investigated by a-c impedance and d-c polarization and titration experiments. More generally, this investigation represents a study of the redox reaction for a dopant and dopant impurity conduction in the CaF_2 solid electrolyte.

Experimental Materials and Procedures

The CaF_2 electrolytes were Harshaw optically pure, randomly oriented, single crystals of 12.7 mm diam and different thicknesses. In the galvanic cell and titration experiments, the Cu + Cu_2O, Ni + NiO, and nickel electrodes were 12.7 mm diam × 3.0 mm thick powder pellets sintered in oxygen-purged Ar (O.P. Ar) with $P_{O_2} \sim 10^{-15}$ atm, at 900°C; commercial argon with $P_{O_2} \sim 10^{-4}$ atm was further cleaned and purged of oxygen by flowing through Drierite, Ascarite, Cu turnings at 500°C, and Ti sponge at 750°C. Oxygen activities were measured separately by a ZrO_2(CaO) solid electrolyte oxygen probe with a Cu + Cu_2O reference electrode.

The elements of galvanic cell (I) were positioned and held in a closed-end ceramic mullite tube by spring pressure. Nickel wires used as electrical leads were spark-welded to platinum foils contacting the electrode. Voltages for cell I were measured over a temperature range from 820° to 1040°C. The following Tubandt-type cells were used at 850°, 962°, and 986°C

$$Cu + Cu_2O \mid CaF_2 \mid Ni \qquad [IIa]$$

$$Ni + NiO \mid CaF_2 \mid Ni \qquad [IIb]$$

where the Cu + Cu_2O and Ni + NiO electrodes were used as oxygen source electrodes. The cell current was maintained at 200 to 300 μA, such that the voltage across the cell (less than 1400 mV) was far below the CaF_2 decomposition potential.

A Wayne-Kerr a-c conductivity bridge, a General Radio tuned amplifier, and a Hewlett-Packard oscillator were used to determine the total circuit conductance (R^{-1}) and capacitance C simultaneously over a frequency range from 20 Hz to 20 kHz. The impedance and admittance of cell III were studied (without any d-c bias) in argon and oxygen atmospheres at different temperatures

$$Pt \mid CaF_2 \mid Pt \qquad [III]$$

The electrodes were nonporous platinum foils pressed against the CaF_2 crystal. The signal amplitude was maintained at 5 to 50 mV. The results were not sensitive to the a-c amplitude. A lump circuit with known resistances and capacitance was used to assure the proper functioning of the instrumentation. The complex admittance Y was easily obtained as

$$Y = R^{-1} + j\omega C \qquad [3]$$

The impedance was calculated through the following transformation equations (2)

$$\tan\theta = R\,C\,\omega \qquad [4]$$

$$Z = R\cos^2\theta - jR\sin\theta\cos\theta \qquad [5]$$

where θ is the phase angle.

D-C polarization measurements were conducted with the following cell IV

O.P. Ar, Pt 1	CaF_2	porous Pt paint 2	ZrO_2 (CaO)	Cu^+ Cu_2O 3	Pt

[IV]

With this cell, the local oxygen activity in the thin porous Pt electrode 2 was established by the application of a voltage between electrodes 2 and 3, $E_{2\text{-}3}$

$$P_{O_2}(2) = P_{O_2}(3)\exp(E_{2\text{-}3}/RT) \qquad [6]$$

Then d-c current-time measurements between electrodes 1 and 2 were made as a function of the voltage $E_{2\text{-}3}$, *i.e.*, the oxygen activity of electrode 2.

Results and Discussion

Galvanic cell measurements.—Figure 1 shows the emf values of cell I measured in the temperature range 820°-1040°C. The solid line described by Eq. [7] results from a ZrO_2(CaO) electrolyte cell with the same electrodes (15)

$$E(\text{mV}) = 346 - 7.16 \times 10^{-2}\,T \qquad [7]$$

Then the measurements of the cell I voltage are in good agreement with the existing equilibrium data (15) for oxide stabilities and the work of Ramanarayanan *et al.* (7).

Titration experiments.—For cells IIa and b, green films were formed at the interface of the Ni anode with the CaF_2 electrolyte in all three titration experiments

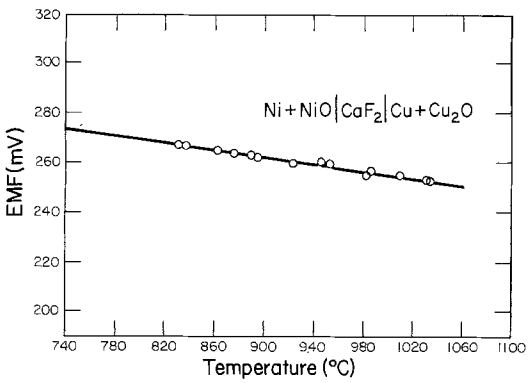

Fig. 1. EMF values for cell I as a function of temperature. Solid line corresponds to values calculated from well-known thermodynamic data (16).

at 850°, 962°, and 986°C for periods of four to five days. These green films were all identified as NiO by x-ray diffraction. Other exposed surfaces of the nickel electrodes were bright and free from oxidation in the oxygen-purged argon atmosphere.

In the two runs at 962° and 986°C the current and the titration time were recorded. The green NiO films adherent to the CaF_2 at the Ni/CaF_2 interfaces were dissolved in a boiling 1*N* HCl solution, and the nickel amounts were determined by atomic absorption analysis. The calculated (minimum) oxygen transference numbers were 0.31 and 0.20 for the 962° and 986°C runs, respectively. Some further NiO left on the nickel electrode could not be separated successfully. The results do not exclude that considerable fluorine ions were also involved in the current passage, especially for short times. But these results from the titration experiments do prove that oxygen enters the CaF_2 electrolyte at the oxygen source electrode surface through one of the following electrochemical reduction steps

$$M_xO + V_{F}^{\cdot} + 2e' \rightarrow O_F' + xM \quad [8a]$$

$$\tfrac{1}{2}\,O_2 + V_{F}^{\cdot} + 2e' \rightarrow O_F' \quad [8b]$$

where M represents either Cu or Ni. Under the influence of the applied field, the oxygen ions migrate across the CaF_2 electrolyte via a countercurrent of fluorine vacancies and react with the nickel electrode to form NiO. Considering the similar ionic radii of oxygen and fluorine ions, 1.36Å and 1.33Å (16), respectively, and their identical electronic structure, it is not surprising that oxygen ions migrate readily over fluorine vacancies.

A-C admittance analysis in Ar.—The complex admittance diagram of cell III in O.P. argon ($P_{O_2} \sim 10^{-15}$ atm), or in commercial argon ($P_{O_2} \sim 10^{-4}$ atm), shows the semicircular figure, Fig. 2, with its center located slightly below the real axis. The semicircle intersects the real axis at σ_{ct} (charge transfer conductance) on the low frequency side and σ_b (bulk conductance) on the high frequency side. Figure 3 gives a magnified view of the low frequency data. Similar a-c admittance plots were obtained at various temperatures in O.P. argon for cells with different electrolyte thickness, 0.079 cm and 0.638 cm, respectively. For instance, the ratios of σ_b values are 7.1:1 at 850°C, 8.3:1 at 767°C, and 8.4:1 at 692°C, while the ratio of the electrolyte thicknesses was 8.1:1. According to this correlation, the σ_b value is identified as the bulk conductance, *i.e.*, for blocking Pt electrodes, the conductance of fluorine over vacancies in CaF_2. Because the σ_{ct} intercept value of Fig. 3 was independent of the electrolyte thickness, σ_{ct} represents the extremely low charge transfer conductance of the two CaF_2|Pt interfaces. The equivalent circuit is shown in Fig. 4a

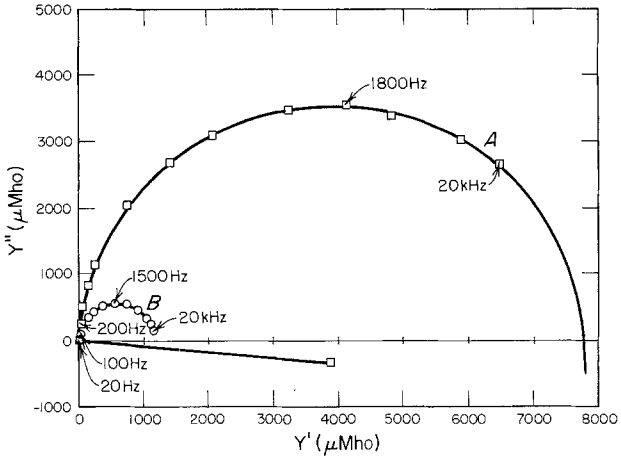

Fig. 2. Complex admittance plots for cell III, Pt|CaF_2|Pt, in O.P. argon at 850°C. Curves A and B for 0.079 and 0.638 cm thick CaF_2 electrolytes, respectively.

where C_{dl} is the double-layer capacitance. Because the σ_b value is higher than σ_{ct} by 2 to 3 orders of magnitude, cell III in Ar involves practically blocking electrodes (ideally polarized electrodes). According to Eq. [10], the double-layer capacitances at different temperatures were calculated from the frequency at the maximum of the semicircle in the admittance diagram and are listed in Table Ia.

$$R_bC_{dl}\omega_{max} = 1 \quad [9]$$

The double-layer capacitances are 2 to 3 orders of magnitude lower than those from some other solid elec-

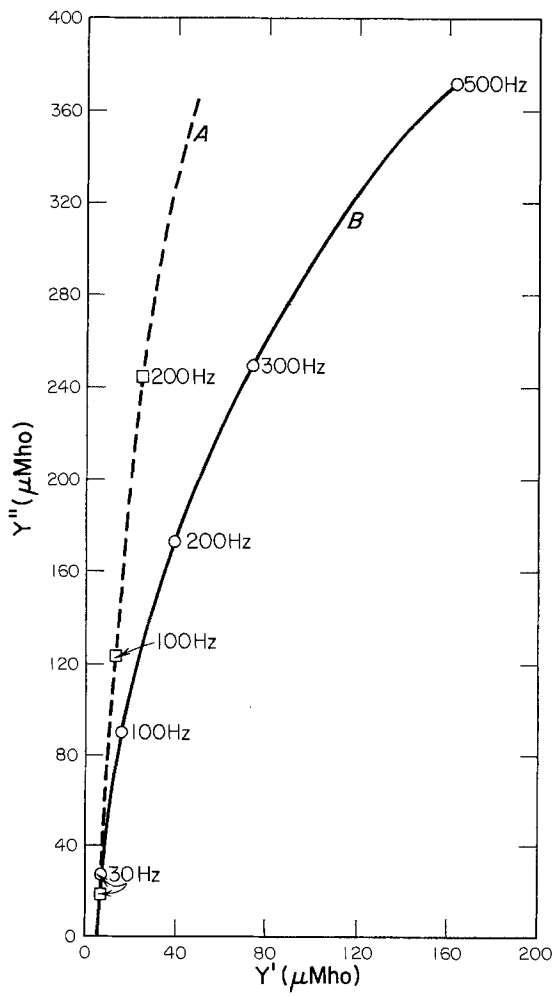

Fig. 3. Complex admittance plots for cell III, Pt|CaF_2|Pt, in O.P. argon at 850°C, enlarged low frequency portion of Fig. 3.

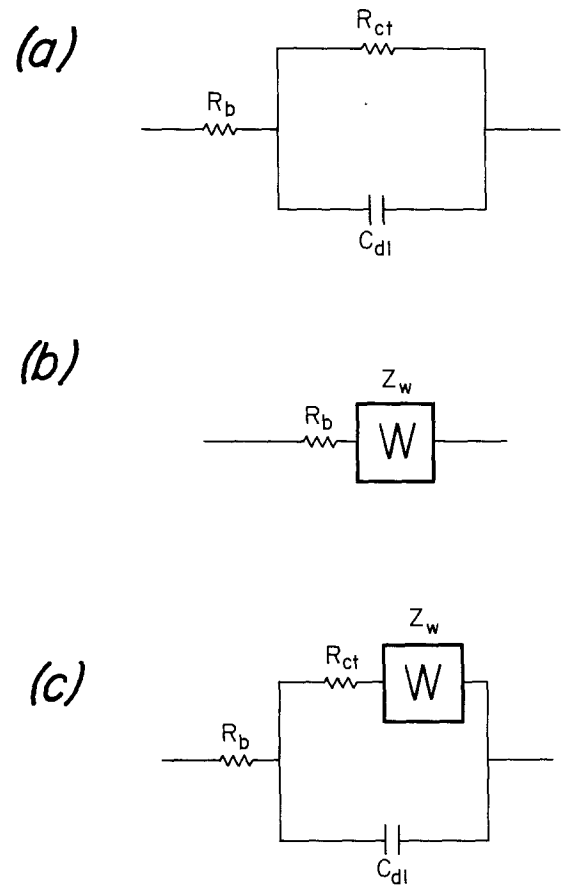

Fig. 4. Equivalent circuits for interpretation of a-c impedance measurements for cell III: a.) ideally blocking electrode in O.P. argon, b.) non-blocking electrode, c.) Randle's circuit.

trolyte systems (9, 17, 18) probably because the Pt electrodes were not tightly bonded to the electrolyte so that gas gaps existed at the electrode/electrolyte interface. Miliotis and Yoon (9) interpreted the dielectric relaxation of NaCl and KCl in terms of air gaps in the electrolyte-electrode contacts. Also, Bert *et al.* (20) demonstrated that the small temperature-dependent capacitance of 0.2-0.5 μF/cm^2 in the cell Ag/AgCl/C might be caused by the air gaps at the interface. At low temperatures, a second rise in the admittance plot at high frequencies corresponds to the dielectric relaxation in the electrolyte probably associated with defect complexes (21).

The a-c admittance of cell III preheated in 1 atm of oxygen at 888°C for 3 days was also measured in O.P. argon at various temperatures. The admittance figures are similar to those of virgin electrolyte in O.P. argon and commercial argon. The σ_b values are shown in Fig. 5 and C_{dl} values are listed in Table Ib. These double-layer capacitances are close to those from other solid electrolyte systems and independent of temperature. The C_{dl} values for CaF_2 annealed in O_2 increased significantly, probably because the cell experienced

Table I. Values of double-layer capacitances for one interface of cell III, Pt|CaF_2|Pt; a) in O.P. argon, $P_{O_2} \sim 10^{-15}$ atm, at different temperatures; b) preheated in pure O_2, measured in O.P. argon

a. Temperature, °C	C_{dl}, μF/cm^2	b. Temperature, °C	C_{dl}, μF/cm^2
413	1.2×10^{-3}	567	11
474	3.5×10^{-3}	620	17
617	2.2×10^{-2}	678	19
675	1.9×10^{-2}	734	19
692	8.5×10^{-2}	791	19
767	1.2×10^{-1}	835	15
850	8.5×10^{-2}	887	15

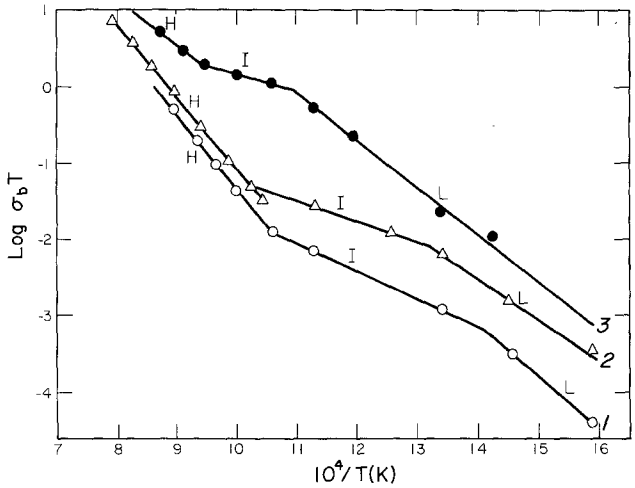

Fig. 5. Log $\sigma_b T$ *vs.* $1/T$(K) for cell III, Pt|CaF_2|Pt; (1) in O.P. argon, $P_{O_2} = 10^{-15}$ atm; (2) in commercial argon, $P_{O_2} = 10^{-4}$ atm; (3) in O.P. argon for CaF_2 preheated in oxygen at 888°C.

prolonged heating at high temperature and high d-c currents, such that the gas gaps at the interfaces were collapsed. The CaF_2 pretreated in oxygen exhibited the highest σ_b, and the σ_b value in commercial argon ($P_{O_2} \sim 10^{-4}$ atm) is higher than that in O.P. argon ($P_{O_2} \sim 10^{-15}$ atm). Each plot of log $\sigma_b T$ *vs.* $1/T$ in Fig. 5 has three domains, *L*, *I*, and *H*. The intrinsic anti-Frenkel defects dominate in domain *H* at high temperatures. The activation energy of conduction is

$$E_H = \frac{E_f}{2} + E_m \qquad [10]$$

where E_f and E_m are the enthalpy of formation for the intrinsic anti-Frenkel defects, and the activation energy for the mobility of the anion vacancy, respectively. The extrinsic defects created by the oxygen dopant must dominate in domain I at intermediate temperatures. For CaF_2 preheated in oxygen or in the commercial argon $P_{O_2} \sim 10^{-4}$ atm, the concentration of anion vacancies equals that of the oxygen dopant; the conduction activation energy must equal the activation energy for vacancy migration, E_m. At low temperatures, domain *L*, oxygen dopant should be associated with an anion vacancy to form a neutral complex

$$V_F^{\cdot} + O_F' \rightarrow (V_F^{\cdot} O_F')^x \qquad [11]$$

The activation energy for electrical conduction in this domain is

$$E_L = \frac{E_{diss}}{2} + E_m \qquad [12]$$

where E_{diss} is the standard enthalpy for the dissociation of the complex. In O.P. argon, $P_{O_2} \sim 10^{-15}$ atm, the complex could arise either from residual oxygen originally present in the crystal or from other impurities. The E_L, E_I, E_H, E_m, E_f, and E_{diss} values from this study are in good agreement with the results of other researchers, as shown in Table II.

Figure 6 shows for three different temperatures that the charge transfer conductance σ_{ct} in commercial argon ($P_{O_2} \sim 10^{-4}$ atm) is higher than that in O.P. argon ($P_{O_2} \sim 10^{-15}$ atm) by a factor of approximately 15. Obviously, in the presence of oxygen at a Pt electrode, redox reactions become possible and oxygen ions enter or leave the CaF_2 crystal according to Eq. [8b]. This electron transfer reaction should involve the following steps: (*i*) diffusion of oxygen molecules into the gas gaps at the Pt/CaF_2 interface, (*ii*) adsorption of molecular oxygen on the surface of the Pt electrode, (*iii*) dissociation of oxygen molecules on the Pt electrodes, (*iv*) diffusion of oxygen atoms on the Pt to the Pt/CaF_2 interface, (*v*) electrochemical reduction to

Table II. Values of the activation energies for the intrinsic, extrinsic, and association regions; formation energy of anti-Frenkel defects, activation energy for the mobility, and dissociation energy for defect complexes

Atmosphere	E_H, kcal/mol	E_M, kcal/mol	E_L, kcal/mol	E_m, kcal/mol	E_f, kcal/mol	E_{diss}, kcal/mol		
CO-CO_2	46.1				59.0			Levitskii *et al.* (8)
Ar	46.1	14.5	30.0	14.5	62.3	30.0		
Oxygen	48.4	14.8	30.0	14.8	66.9	30.0		
Neon	44.3	12.7	22.8	12.7	62.3	20.3		Bollmann *et al.* (22)
O.P. Ar, $P_{O_2} \sim 10^{-15}$ atm	44.5	16.0	31.4	16.0	57.0	30.9	Virgin	
Commercial Ar, $P_{O_2} \sim 10^{-4}$ atm	42.4	12.6	23.2	12.6	59.6	21.2	CaF_2	This work
O.P. Ar, $P_{O_2} \sim 10^{-15}$ atm		12.3	26.4	12.3		28.2	CaF_2 preheated in O_2	

form oxygen ions at the Pt/CaF_2 interface

$$O + 2e^- \rightarrow O^{2-} \quad [13]$$

(*vi*) incorporation of oxygen ions into the CaF_2 lattice

$$O^{2-} + V_F^{\cdot} \rightarrow O_F' \quad [14]$$

The values for C_{dl} in Table Ia indicate that the Pt foil electrode of cell III contained gas pockets.

It is known that platinum is covered with a tightly bound monolayer of oxygen atoms even at low oxygen pressure and high temperature, and that oxygen molecules are weakly adsorbed on this monolayer (23, 24). Then heating Pt in O.P. argon should not destroy the adsorbed monolayer of atomic oxygen. In O.P. argon $P_{O_2} \sim 10^{-15}$ atm, the concentration of oxygen molecules adsorbed on top of the monolayer is believed to be insignificant; most of the adsorbed oxygen is in the form of atoms strongly bound to the platinum surface. Therefore, for the electrode reaction in a virtually oxygen-free gas, the first three steps are not considered important to the mechanism. The small alternating current only involves a small fraction of the atomic oxygen in the monolayer in the redox reaction. According to the resistance for the charge transfer step, the amount of charge carried by the Faradaic current across the interface in one cycle in O.P. argon at 900°C corresponds to only about 10^{-4} of the total oxygen atoms in a monolayer. Since the concentration of tightly bonded atomic oxygen is rather insensitive to the oxygen pressure in the atmosphere, the σ_{ct} value increased only by a factor of 15 when the oxygen pressure increased from 10^{-15} to 10^{-4} atm. As will be indicated later, the σ_{ct} value increases rapidly in the oxygen pressure range from 10^{-4} atm to 1 atm; therefore, the corresponding mechanism for the redox reaction in oxygen-containing gases also involves the first three steps previously suggested. Figure 7 shows a plot of log σ_{ct} *vs.* $1/T$ for both O.P. and commercial argon. The activation energy in O.P. argon is 24.4 kcal/mol corresponding to the steps (*v*) and (*vi*) (redox and incorporation reactions). Presumably the activation energy is much less for surface diffusion (25). In commercial argon the activation energy is 30.2 kcal/mol, corresponding to a mechanism involving also the first three mechanistic steps of molecular arrival and dissociation. Thus, for argon containing oxygen, the concentration of adsorbed oxygen atoms near triple points also exhibits a small temperature dependence, probably through the dissociation step.

Impedance analysis in oxygen.—Figure 8 shows the complex impedance diagram of cell III (electrolyte thickness 3.2 mm) for (a) O.P. argon, (b) oxygen, and (c) vacuum at 888°C. In O.P. argon the curve represents a blocking electrode, curve A. In oxygen (curve B), the curve is a straight line of 48° slope between 200 and 20 kHz. The plots of Z' and Z'', the real and imaginary parts of the impedance, *vs.* $\omega^{-1/2}$ are two straight lines with slopes of 2.64×10^3 and 2.80×10^3 $\Omega sec^{-1/2}$, respectively; the line from the Z'' *vs.* $\omega^{-1/2}$ plot passes through the origin. The average of these slopes is the Warburg parameter, so that the total impedance is

$$Z(\Omega) = 50 + 2.72 \times 10^3 (1 - j)\, \omega^{-1/2} \quad [15]$$

When the oxygen pressure is reduced by evacuation (or by replacing oxygen with argon), the curve rises

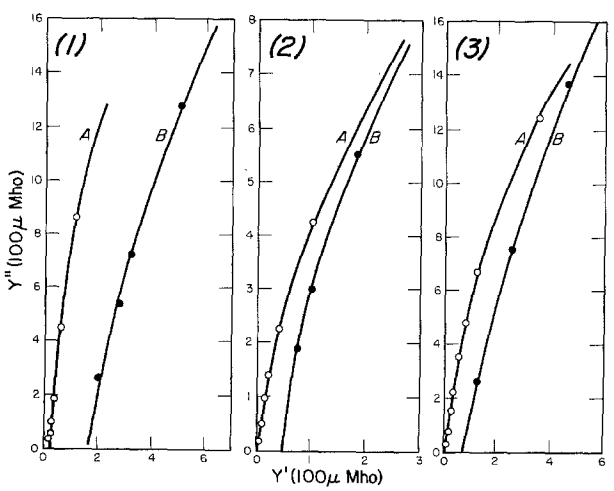

Fig. 6. Partial complex admittance plots for low frequency region for cell III, Pt|CaF_2|Pt; *A*) in O.P. argon, $P_{O_2} = 10^{-15}$ atm; *B*) in commercial argon, $P_{O_2} = 10^{-4}$ atm: (1) at 900°C; (2) at 800°C; (3) at 850°C.

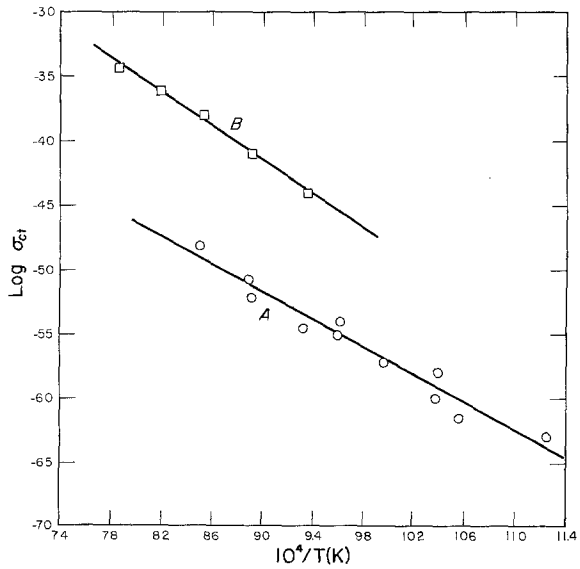

Fig. 7. Log σ_{ct} *vs.* $1/T$(K) for cell III, *A*) in O.P. argon, $P_{O_2} = 10^{-15}$ atm; *B*) in commercial argon, $P_{O_2} = 10^{-4}$ atm.

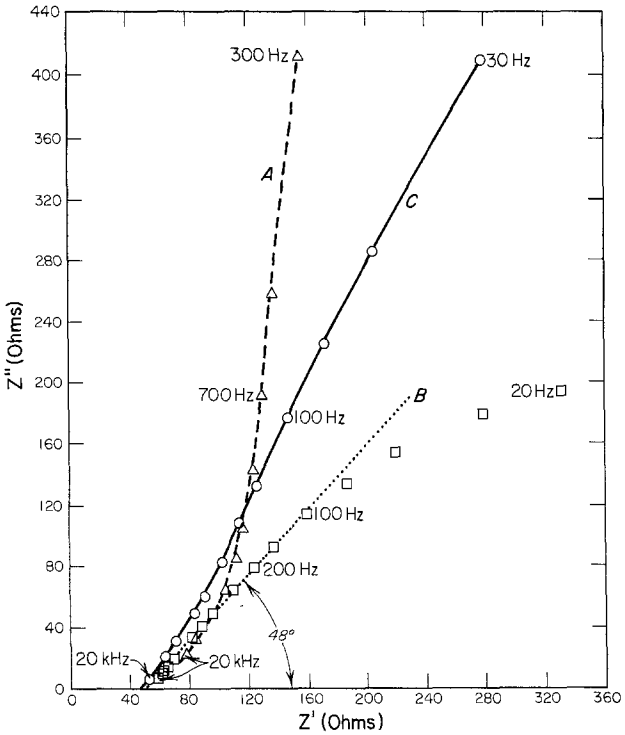

Fig. 8. Complex impedance diagrams for cell Pt|CaF_2|Pt at 888°C, curve A, in O.P. argon; curve B, in oxygen, curve C, in vacuum.

rapidly again, curve C in Fig. 8, and the electrodes become rather blocking.

After cooling the same cell to 773°C, the impedance figure is close to a 45° slope line between 20 and 20 kHz. The slopes of Z' and Z'', *vs.* $\omega^{-1/2}$ plots are 5.96×10^3 and 6.00×10^3 $\Omega sec^{-1/2}$, so that the total impedance is

$$Z(\Omega) = 1.5 \times 10^2 + 6.0 \times 10^3 (1 - j)\, \omega^{-1/2} \quad [16]$$

The intercept on the high frequency end in the impedance diagram (50Ω at 888°C and 150Ω at 773°C) is in good agreement with the bulk resistance of the CaF_2 electrolyte preheated in 1 atm oxygen and measured in O.P. argon, Fig. 5. The impedance of cell III with a 0.8 mm thick electrolyte was also studied in pure oxygen at 773°C. The real part of the impedance obtained from the high frequency intercept (35Ω) is in good proportion to that of the earlier cell according to their electrolyte thicknesses. Cell III transforms from a blocking electrode in Ar of Fig. 4a to a nonblocking electrode with Warburg impedance in oxygen, as described in Fig. 4b. The total impedance for cell III in oxygen is described by

$$Z = R_b + K(1 - j)\omega^{-1/2} \quad [17]$$

where the Warburg parameter K is a function of the concentration and diffusivity of a diffusing species generated at the electrode (26). In oxygen, the interface resistance R_{ct} for the electrode reaction is much less than the bulk resistance of the electrolyte. Compared to the interface resistance in O.P. argon and commercial argon, Fig. 6, the interface resistance is decreased drastically in oxygen. The Warburg impedance may be attributed to the relatively slow diffusion of oxygen ions compared to the fast electrode reaction. Fluorine vacancies act as a supporting electrolyte to shield the oxygen ions from the external electrical field, as oxygen ions diffuse over fluorine vacancies in the CaF_2 lattice according to their concentration gradient. The rate-determining step in the oxidation of CaF_2 is also the diffusion of oxygen ions in CaF_2 (27).

The following reaction could increase the electronic conductivity of CaF_2

$$\tfrac{1}{2} O_2 + V_F^{\cdot} \rightarrow O_F' + 2h^{\cdot} \quad [18]$$

where $h^{\cdot}$ is a positive hole. The diffusion of positive holes in CaF_2 could also contribute to the existence of the Warburg impedance (under the condition that reaction [18] is reversible, since the Warburg impedance disappeared when oxygen was removed). The true Warburg impedance and interface resistance for each interface are one-half of the values in Eq. [17], because the cell had two identical interfaces. At 880°C, the 45° slope line curved down toward the real axis in the impedance diagram, because at lower frequencies the a-c diffusion layer becomes comparable with the thickness of the electrolyte (26).

Cell III re-established the characteristics of a blocking electrode when the oxygen pressure is reduced. The transformation from a nonblocking electrode to a blocking electrode is a slow process, since the oxygen adsorbed at the electrode/electrolyte interface in the gas gaps is still available in the electrode reaction. The ideal blocking electrode was observed when the cell stayed in O.P. argon for 2-3 days.

The complex impedance diagram of cell III in oxygen with 3.2 mm thick electrolyte shows two relaxation mechanisms at 675°C, Fig. 9. The equivalent circuit is the well-known Randle circuit, Fig. 4. At high frequencies the relaxation corresponds to the double layer polarization, while at low frequencies a Warburg impedance arises from a diffusion mechanism in CaF_2. The Randle circuit requires (9)

$$R_{ct} + R_b - 2K^2C_{dl} = 470\Omega \quad [19]$$

$$R_{ct} \cdot f_m \cdot 2\pi C_{dl} = 1 \quad [20]$$

where C_{dl} and K are the effective double layer capacitance and Warburg parameter for the two identical interfaces, and f_m, corresponding to the maximum dispersion frequency for the double layer, is taken to be 3000 Hz. The best curve fitting gives $R_b = 280\Omega$, $R_{ct} = 235\Omega$, and $C_{dl} = 0.23$ μF. The normalized double layer capacitance is 0.36 μF/cm² for each interface. For cell III with a 0.8 mm thick electrolyte, the similar analysis gives $C_{dl} = 0.66$ μF, $R_{ct} = 96\Omega$, and $R_b = 80\Omega$. The ratio of the bulk resistances for two cells is 3.5 which is reasonably close to the ratio of two electrolyte thicknesses, 4.0. The bulk conductivity obtained is in good agreement with that of the CaF_2 electrolyte preheated in oxygen, Line 3 in Fig. 5. The differences in R_{ct} and C_{dl} for the two cells are attributed to the different degree of contact between the electrode and electrolyte.

Admittance analysis of cell III in oxygen.—Figure 10 shows the influence of oxygen on the complex admittance plot of cell III at 798°C. For measurements in argon, the complex plot is a slightly tilted semicircle

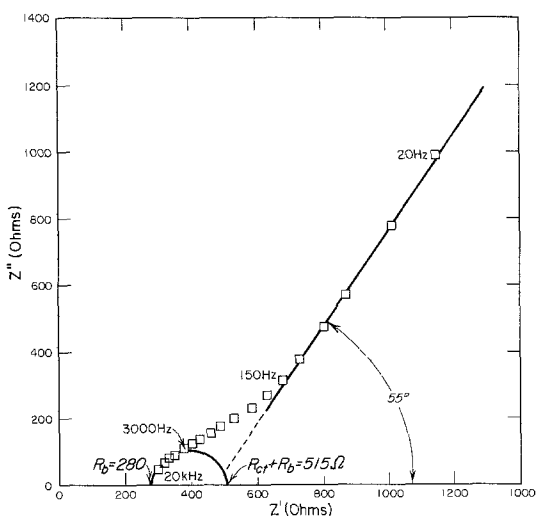

Fig. 9. Complex impedance diagram for cell III Pt|CaF_2|Pt, 0.32 cm thick CaF_2 in oxygen at 675°C.

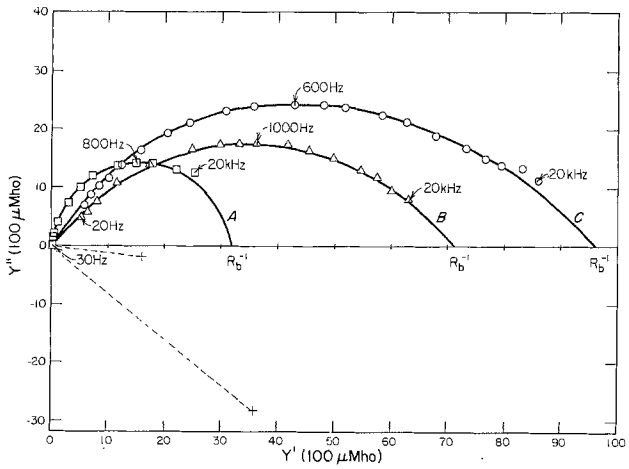

Fig. 10. Complex admittance plots for cell III, Pt\|CaF_2\|Pt, at 798°C, *A*) in O.P. argon; *B*) in oxygen after 33 hr; *C*) in oxygen after 43 hr.

with a depressed angle of 6°, curve A, corresponding to a blocking electrode. Upon introducing oxygen into the system, the semicircle expands and the center moves further below the real axis. Curves B and C are admittance plots after the cell was exposed in oxygen for 33 and 43 hr, respectively. At 888°C, the admittance plot in oxygen shows an approximate quarter circular arc with a depressed angle of 45°. After evacuating and exposing in O.P. argon for two days, the cell reestablished the blocking electrodes. In oxygen the admittance plot at 773°C is an exact quarter circular arc with a depressed angle of 45°, which is expected according to Fig. 4b.

Results and discussion of d-c analysis.—In support of the a-c measurements, a 50 mV d-c voltage was applied across cell III with a CaF_2 electrolyte preheated in oxygen at 888°C for 72 hr. Then the current variation with time at the same temperature was recorded. Compared to the d-c current in O.P. Ar, the d-c current in oxygen was higher by a factor of 80 at $t = 0$ and a factor of 50 at $t = 26$ sec. This result supports the previous conclusion that Pt electrodes on CaF_2 exposed to O_2 support a redox reaction.

The cell III was polarized with 50 mV in oxygen and then discharged by shorting the leads. Plots of the discharge current *vs.* $t^{-1/2}$ for many temperatures were linear, again, indicating a diffusion mechanism in CaF_2.

In cell IV, the oxygen potential at electrode 2 was monitored by applying various d-c voltages, −100, 100, 200, 300, 400, 500, and 700 mV to electrode 2 with respect to the reference electrode Cu + Cu_2O. The oxygen partial pressure in electrode 2 is related to the applied voltage, *E*, by Eq. [6]. A d-c voltage of 150 mV was applied to electrode 1 with respect to electrode 2 with electrode 1 at positive polarity; Fig. 11 shows the plot of the corresponding d-c current *vs.* time for various electrical potentials on electrode 2 at 897°C. The higher d-c current through CaF_2 for higher oxygen pressure at electrode 2 is attributed to the conduction of the oxygen ion or an electronic species in CaF_2.

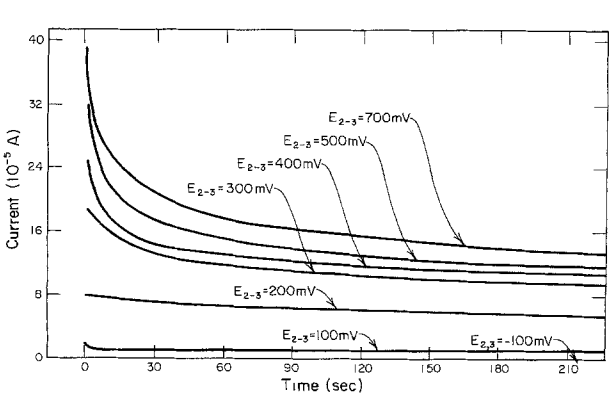

Fig. 11. Current *vs.* time for cell IV at 897°C

The Warburg impedance is not attributed to the microheterogeneities such as microcrevices, rough surface, and/or CaO precipitates. These factors cannot explain the presence and disappearance of Warburg impedance in response to the changes in oxygen pressure. The permeability of oxygen in Pt is extremely low (28). Since the d-c current in cell III increased significantly and instantaneously when changing the surrounding atmosphere from argon to oxygen, oxygen must have reached the electrode/electrolyte interface through the gas gaps rather than by diffusing in the electrode. The diffusion of oxygen in the Pt electrode is then not considered to be the cause of the Warburg impedance.

Oxygen Concentration Cell with CaF_2 Solid Electrolyte

The following equations describe the equilibrium conditions at the two interfaces of cell I according to Eq. [8b]

$$\eta_{V_F^{\cdot\cdot}}(R) + \tfrac{1}{2}\mu_{O_2}(R) + 2\eta_e(R) = \eta_{O_F'}(R) \quad [21a]$$

$$\eta_{V_F^{\cdot\cdot}}(L) + \tfrac{1}{2}\mu_{O_2}(L) + 2\eta_e(L) = \eta_{O_F'}(L) \quad [21b]$$

where $\eta_{V_F^{\cdot\cdot}}$, $\eta_{O_F'}$ η_e represent the electrochemical potentials of the fluorine vacancy, oxygen dopant, and electron, *R* represents the Cu + Cu_2O (right-hand) electrode, *L* represents the Ni + NiO (left-hand) electrode, and μ_{O_2} is the chemical potential of oxygen. Subtracting Eq. [21b] from Eq. [21a] gives

$$\eta_{V_F^{\cdot\cdot}}(R) - \eta_{V_F^{\cdot\cdot}}(L) + \tfrac{1}{2}[\mu_{O_2}(R) - \mu_{O_2}(L)] + 2[\eta_e(R) - \eta_e(L)] = \eta_{O_F'}(R) - \eta_{O_F'}(L) \quad [22]$$

When galvanic cell I reaches equilibrium during an open-circuit emf measurement, the electrochemical potential $\eta_{V_F^{\cdot\cdot}}$ of the fluorine vacancy, which is the most mobile defect in pure CaF_2 crystal, is constant throughout the electrolyte. The d-c titration experiment proves that the oxygen ion is quite mobile over fluorine vacancies, $t_0 \geq 0.31$. Therefore, the electrochemical potential of $\eta_{O_F'}$, is also constant in the equilibrium state, so that

$$\eta_{V_F^{\cdot\cdot}}(R) = \eta_{V_F^{\cdot\cdot}}(L) \quad [23a]$$

and

$$\eta_{O_F'}(R) = \eta_{O_F'}(L) \quad [23b]$$

Then the electrochemical potentials of electrons at the two electrodes can be expressed as

$$\eta_e(R) = \mu_e(R) - \mathbf{F}\phi(R) \quad [24a]$$

$$\eta_e(L) = \mu_e(L) - \mathbf{F}\phi(L) \quad [24b]$$

Also, the chemical potential of electrons is the same when both electrodes are connected to platinum or other identical leads

$$\mu_e(R) = \mu_e(L) \quad [25]$$

Then Eq. [22] can be simplified as

$$\mu_{O_2}(R) - \mu_{O_2}(L) = 4\mathbf{F}[\phi(R) - \phi(L)] = 4\mathbf{F}E \quad [26]$$

The emf values obtained from cell I confirm Eq. [26].

Acknowledgment

This research was sponsored by the DOE Materials Science Program, Division of Physical Research under Contract E(11-1)-2671. The authors appreciate the help and advice of S. N. S. Reddy and W. C. Fang.

Manuscript submitted March 5, 1982; revised manuscript received Oct. 4, 1982.

Any discussion of this paper will appear in a Discussion Section to be published in the December 1983 JOURNAL. All discussions for the December 1983 Discussion Section should be submitted by Aug. 1, 1983.

Publication costs of this article were assisted by the Ohio State University.

REFERENCES

1. S. Aronson and A. Auskern, *Thermodynamics*, **1**, 165 (IAEA, Vienna, 1965).
2. S. Aronson and K. A. Gingerich, Paper 6-RS-66 presented at 68th Meeting of American Ceramic Society, 1966.
3. S. Aronson, "Compounds of Interest in Nuclear Reactor Technology, **10**, 247 (Boulder, Colorado, AIME, 1964).
4. T. A. Ramanarayanan and W. L. Worrell, *This Journal*, **127**, 1717 (1980).
5. R. Benz and C. Wagner, *J. Phys. Chem.*, **65**, 1308 (1961).
6. S. F. Chou and R. A. Rapp, in "High Temperature Metal Halide Chemistry," D. L. Hildenbrand and D. D. Cubicciotti, Editors, pp. 392-400, The Electrochemical Society Softbound Proceedings Series, Princeton, N.J. (1978).
7. T. A. Ramanarayanan, M. L. Narula, and W. L. Worrell, *This Journal*, **126**, 1360 (1979).
8. V. A. Levitskii, A. Hammou, M. Duclot, and C. Deportes, *J. Chim. Phys.*, **73**, 305 (1976).
9. J. E. Bauerle, *J. Phys. Chem. Solids*, **30**, 657 (1969).
10. M. Rehbach and J. H. Sluyters, *Recueil Trav. Chim.*, **79**, 1092 (1960).
11. D. C. Grahame, *This Journal*, **99**, 370C (1952).
12. R. D. Armstrong, T. Dickinson, and P. M. Willis, *Electroanal. Chem.*, **48**, 47 (1973).
13. R. DeLevie, in "Advances in Electrochemistry and Electrochemical Engineering," P. Delahay, Editor, p. 358, Wiley Publ., New York (1967).
14. J. Bruinink and G. H. J. Broers, *Electroanal. Chem.*, **33**, 1713 (1972).
15. R. A. Rapp and D. A. Shores, in "Technical Metal Research, IV, part 2," R. A. Rapp, Editor, p. 159, Wiley Publ., New York (1970).
16. Y. D. Tretyakov and A. R. Kaul, in "Physics of Electrolytes," J. Haldik, Editor, Academic Press, London (1972).
17. E. Schouler, M. Kleitz, and C. Deportes, *J. Chim. Phys.*, **70**, 923 (1974).
18. D. O. Raleigh, *This Journal*, **121**, 632 (1974).
19. D. Miliotis and D. N. Yoon, *J. Phys. Chem. Solids*, **30**, 1241 (1969).
20. J. Bert, J. L. Picot, and J. Dupuy, *Phys. Status Solidi A*, **19**, 119 (1973).
21. R. G. Breckenridge, *J. Chem. Phys.*, **16**, 959 (1948).
22. W. Bollmann, P. Gorlich, W. Hank, and H. Mothes, *Phys. Stat. Sol. (a)*, **2**, 157 (1970).
23. I. Langmuir, *Trans. Faraday Soc.*, **17**, 621 (1922).
24. G. C. Fryburg and H. M. Petrus, *This Journal*, **108**, 498 (1961).
25. D. O. Hayward and B. M. W. Trapnell, in "Chemisorption," Chap. 9, Butterworth, Washington (1964).
26. M. Sluyters-Rehbach and J. H. Sluyters, in "Electroanalytical Chemistry," A. J. Bard, Editor, Vol. IV, 1 (1970).
27. K. Muto and K. Awazu, *J. Phys. Chem. Solids*, **29**, 1269 (1968).
28. F. J. Norton, *J. Appl. Physics*, **29**, 1122 (1958).

Chemical Bath Deposition of Thin Film Cadmium Selenide for Photoelectrochemical Cells

R. A. Boudreau and R. D. Rauh*

EIC Laboratories, Incorporated, Newton, Massachusetts 02158

ABSTRACT

Chemical bath deposition provides an attractive, low cost method of producing cadmium chalcogenide thin films. Intimate contact between the bath solution and the substrate material permits uniform deposition on substrates of complex geometry, presently difficult with spray pyrolysis, vacuum evaporation, or electrodeposition techniques. For CdSe, rigorous control of deposition conditions promotes the formation of a hexagonal, specularly reflecting deposit rather than a less desirable sphalerite (cubic) powdery deposit. Scanning electron microscopy reveals a small grained layered plate morphology similar to that produced by the evaporation method. Specularly reflecting CdSe films can be formed over large area substrates at a thickness optimal for their use as photoelectrochemical cells (PEC). Employing polysulfide as the redox couple, conversion efficiencies as high as 6.8% have been achieved in our laboratory for these films using a tungsten-halogen white light source.

Cadmium selenide has shown great promise as a semiconductor material for photoelectrochemical solar cells (PEC's) (1, 2). In aqueous polysulfide electrolytes, solar conversion efficiencies of 8.4% (3) and 6.5% (4) have been reported for single crystal and vacuum evaporated thin film CdSe, respectively. CdSe thin films for PEC's have also been prepared by spray pyrolysis (5) and electrodeposition (6). In a recent communication (7), we demonstrated that PEC devices could be fabricated with CdSe films derived from a chemical bath method. Pursuing further refinements of the deposition process, we have found that this method produces CdSe films yielding cell efficiencies comparable to any of the other methods, but that careful control of plating conditions were necessary for achieving reproducibility of morphology and photovoltaic properties. Compared to the other methods, the bath process is uniquely suited for depositing a uniform film over large substrates of complex geometry, as might be found in production scaled solar panels. The substrate need not be conductive, have a high melting point, or be combustion resistant. Film formation is truly a deposition of CdSe rather than a co-deposition of separate elements. Chemical bath deposition (CBD) is a low technology process, requiring no high vacuum, high power supply, or expensive equipment.

The chemical bath method has been used in the past to make polycrystalline films of PbSe (8, 9). ZnSe (10), CdSe (9), and CdS (11). In each case, thin film formation proceeds simultaneously with the precipitation of the respective chalcogenide. The precipitation is controlled by slowly generating ions that are in equilibrium with a chalcogenide precursor and a cation complexing agent, usually NH_3. The reactions are highly dependent on temperature and complexing agent concentrations. For the case of cadmium chalcogenides, the following reactions apply

$$Cd(NH_3)_4^{2+} \rightleftarrows Cd^{2+} + 4NH_3 \qquad [1]$$

* Electrochemical Society Active Member.
Key words: solar, photovoltaic, liquid junction, polysulfide.

$$(AX) + OH^- \rightleftarrows A' + HX^- \quad [2]$$

$$HX^- + OH^- \rightleftarrows H_2O + X \quad [3]$$

For CdSe, the compound AX is either sodium selenosulfite (Na_2SeSO_3) or selenourea. The symbol A' represents the oxidized counterpart to AX', while X represents the appropriate chalcogen. Reactions [1] and [3] provide for slow generation of reacting ions. Ammonia complexation prevents the precipitation of excess $Cd(OH)_2$ in the alkaline media.

The CdSe CBD process, as originally engineered by Kainthla and co-workers (9), was not addressed at the reproducible preparation of efficient photoelectrochemical films. Attempts to use the process directly in photoelectrode fabrication lead to several problems including: (*i*) the deposition of films having a terminal thickness too low for efficient solar collection, (*ii*) the deposition of weakly photoactive, poorly structured films, and (*iii*) the uncontrolled evolution of NH_3 during deposition, making conditions difficult to reproduce. The work described below addresses these problems, further refining CBD as a process for producing large area CdSe semiconducting films which yield efficient photoelectrochemical devices.

Experimental Procedures

All chemicals were reagent grade. Titanium and stainless steel substrates were prepared by abrading with emory cloth and cleaning with chromic acid. Indium tin oxide (Nesatron) conductive glass substrates ($\rho = 8\ \Omega/\square$) were prepared by cleaning in dilute HCl. CdSe film thickness was determined by weighing, using the literature density and the geometric area of the deposit. Photoelectrochemical evaluation of the films was carried out in an aqueous polysulfide electrolyte (1M NaOH, 1M Na_2S, 1M S).

All current-voltage measurements were made using a Wenking LT 73 potentiostat coupled with a ramp function generator and X-Y plotter. Counterelectrodes consisted of CoS coated Ni screen or CuS coated brass (12). Solar radiation was simulated with a 100W tungsten halogen lamp employing a KG2 Melles Griot infrared filter. Half-cell electrochemical potentials were determined *vs.* a platinum wire reference. Full cell measurements were made by connecting the high performance counterelectrode to both the counter and reference inputs of the potentiostat. Light intensities were calibrated and measured using an EG&G Model 450-1 Radiometer.

CdSe deposition.—The deposition bath was prepared by mixing 30 ml of 0.13M Na_2SeSO_3 reagent, 1.0 ml of 7M NH_4OH, and 3.0 ml of 0.5M $Cd(CH_3COO)_2$ in that order. The sodium selenosulfite reagent was freshly prepared by filtering a 500 ml solution containing 95g of Na_2SO_3 and 5g of finely powdered amorphous black Se that had been stirred for several hours at exactly 65°C under nitrogen bubbling to dissolve the selenium. The excess Na_2SO_3 enhanced the Se dissolution rate, and had little discernible effect on the resulting films. After mixing, the deposition bath turned yellow in color, probably indicating the onset of colloidal CdSe precipitation.

The abraded and cleaned substrates to be used for CdSe deposition were soaked at ~50°C in a suspension of $Cd(OH)_2$ for 5 min and lightly rinsed in distilled water just before use. The substrates were added, and the bath solution was heated rapidly in a stoppered glass container with a 90°C constant temperature bath. While heating, the deposition bath developed a red CdSe precipitate. Occasionally, the bath was swirled to prevent the precipitate from adhering to the substrate. By placing the substrate in the bath so that the desired face of the substrate pointed downward, precipitate adherence was minimized. After 30-60 min of deposition, the CdSe film appeared as a transparent red coating on surfaces exposed to the bath. The substrates were then removed from the bath, rinsed with distilled water, and heat-treated for 15 min at 500°C.

Following the heat-treatment, which improved film adherence, the substrates were treated again with $Cd(OH)_2$ suspension, rinsed, and plated again. No intervening heat-treatments were necessary for subsequent depositions to sustain film adherence. After the final deposition, a final heat-treatment of 550°C for 30 min in air was used to activate the films. Air was a necessary ingredient for the heat-treatment, and higher heat-treatment temperatures resulted in excessive film vaporization and damage while lower temperatures resulted in incomplete film restructuring and lower photoresponse. The heat-treatments converted the reddish films to a dark gray color. Following the final annealing, the CdSe films were etched for 20 sec in 9M HCl at room temperature and rinsed. A post etch treatment to reduce dark current losses consisted of dipping the electrode in 1M $ZnCl_2$ (13), allowing the zinc solution to dry on the electrode, and then rinsing with distilled water.

The ammonia concentration and reagent freshness were critical to good film formation. If a yellow color did not form in the solution prior to heating, the ammonia concentration was too high, but if excessive white $Cd(OH)_2$ precipitated, the concentration was too low.

CBD process optimization.—The procedure of Kainthla and co-workers (9) for bath deposition of CdSe was carried out in an open vessel and employed a large excess of NH_4OH. This excess gives rise to an induction period for CdSe precipitation, while enough NH_3 evaporates from the hot bath to allow the release of some Cd^{+2} ions. No deposit forms if the vessel is sealed.

Using the published procedure (9), the resulting films were, in our hands, of irreproducible morphology, which may be related to an uncontrolled NH_3 effusion rate. The deposits were sometimes specular and sometimes powdery in nature. On glass substrates, the as-deposited specular films appeared clear red or orange in transmitted light and shiny dark brown in reflected light. In contrast, the powdery films appear translucent pink in transmitted light and light brown in reflected light. After annealing, the mechanically softer powdery deposits appeared flat black and etched rapidly in HCl, while the specular films possessed a metallic sheen and etched slowly. The electron micrograph in Fig. 1A shows that the specular deposits are large grained and exhibit widely spaced cracks. The electron micrograph of a powder deposit, Fig. 1B, reveals smaller grains and smaller cracks.

In order to remove the NH_3 effusion step and bath contact with the open atmosphere, further experiments were conducted in sealed tubes. The bath composition was held constant except for the NH_4OH concentration, which was varied from 2M to below 0.1M. The deposit began to appear at ~1.5M NH_4OH, gradually thickening as the NH_4OH concentration was lowered. At the higher NH_4OH concentrations, the powdery morphology was observed. Only below ~0.3M NH_4OH did the desired transparent red deposits occur in these sealed tubes. Our modified procedure employs 0.2M NH_4OH, at which concentration a small amount of $Cd(OH)_2$ precipitate forms at room temperature.

Even with the optimized bath composition, substrates that were not thoroughly cleaned often developed inhomogeneous mixed powder and specular deposits. Homogeneous specular deposits, with microscopic structure similar to Fig. 1A, could be enhanced by pretreating the substrates with a paste of $Cd(OH)_2$. It has been suggested by Kainthla and co-workers (9) that $Cd(OH)_2$ provides nucleation sites for CdSe, and promotes the formation of hexagonal over the thermodynamically less favorable cubic crystal structure.

Adapting the process for producing films of thickness $>1\text{-}2\mu$ is, of course, critical to photovoltaic application. It was found that by carrying out the deposition in

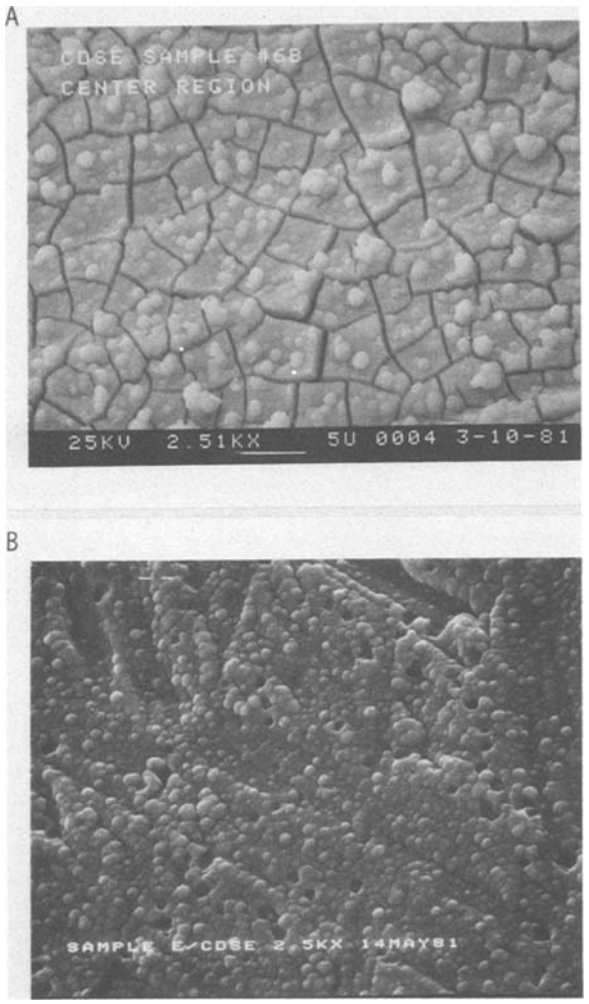

Fig. 1. Scanning electron micrographs of chemically deposited CdSe. Sample annealed at 500°C for 15 min in air. Magnification, 2500×. A) Specularly reflecting deposit; B) powdery deposit.

sealed tubes at 90°C with a stoichiometric excess of Na_2SeSO_3, an optimized average growth rate of ~0.02 μ/min could be achieved without adversely affecting the specular morphology. Under these conditions, the bath becomes depleted of active reagents in ~20 min due to competing homogeneous CdSe precipitation. Thus, the deposit could, in principle, be continually thickened by periodically renewing the reagents. Figure 2 shows how the thickness of the CBD film develops with successive depositions, with intervening anneals. The heat-treatments are most important in the early depositions, as they not only improve film adherence, but also photovoltaic activity.

CdSe photoelectrochemical cells.—Employed as a photoelectrode in polysulfide, half-cell characteristics for 1 cm² CdSe films were measured as a function of deposit thickness. Figure 3 shows that for films on titanium substrates at 67 mW/cm² insolation, solar conversion efficiency increases linearly with thickness up to a thickness of 2.5 microns. The output voltages were typically 0.1V higher than voltages observed for films prepared by other techniques, although voltages were highly dependent on film morphology (see below). Deposits on stainless steel displayed open-circuit voltages ~0.1V lower than comparable films on titanium, primarily as a result of increased cathodic dark current. Deposits on stainless steel and titanium showed little difference in their short-circuit photocurrents. The best films to date, possessing an area of 1 cm², displayed a conversion efficiency of 6.8% at 50 mW/cm² insolation on titanium at room temperature.

Figure 4 shows half-cell characteristics for a typical 1 cm² electrode as a function of light intensity. The

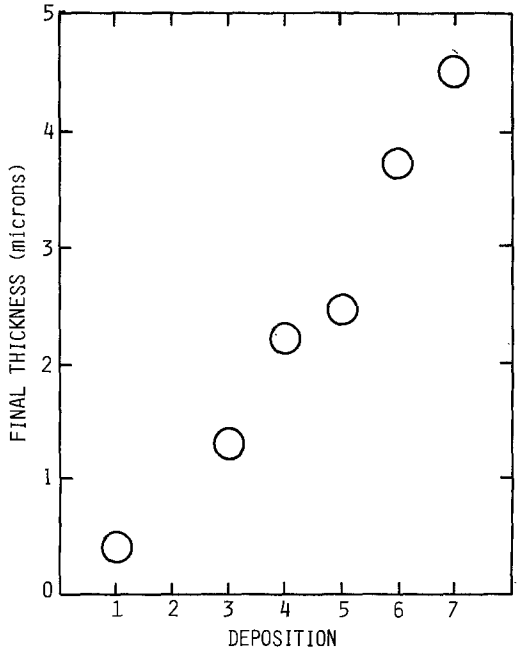

Fig. 2. Thickness of CBD CdSe film following successive depositions with intervening heat-treatments at 500°C.

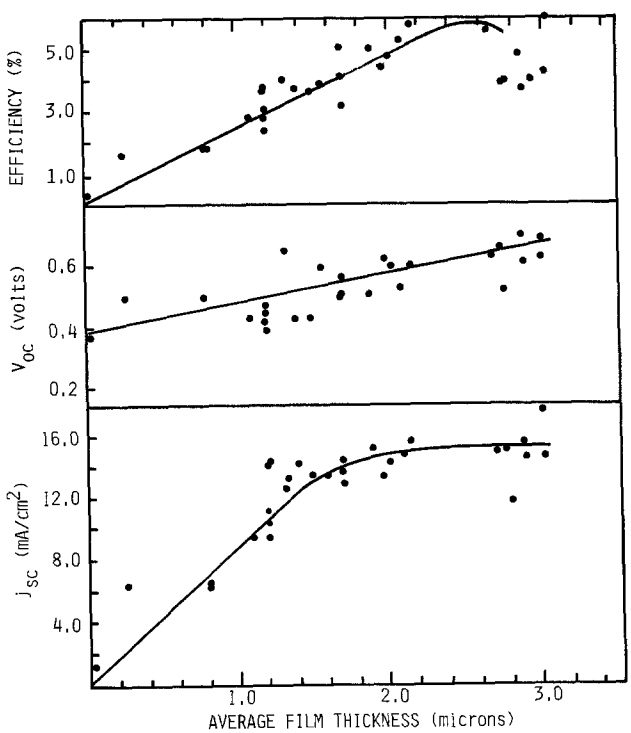

Fig. 3. Effect of film thickness on photoelectrochemical cell characteristics of chemical bath deposited CdSe on Ti. Test conditions: 67 mW/cm² tungsten-iodide lamp with KG-2 filter, unstirred aqueous polysulfide (1M NaOH, 1M Na_2S, 1M S), room temperature.

efficiency increased as the light intensity was reduced until a point was reached where the cathodic dark current proportionately contributed a large influence. Concentration polarization or a limiting dissolution rate of anodically formed neutral sulfur decreased the photoanode efficiency at high light intensities.

Deposit structure and morphology were critical to the performance of these films. The powdery films display very high cathodic dark currents and consequently low solar conversion efficiencies. One typically observed a dark current of ~5 mA/cm² for powdery deposits as compared to ~1 mA/cm² for specular deposits at −0.4V *vs.* Pt/redox. The difference may arise

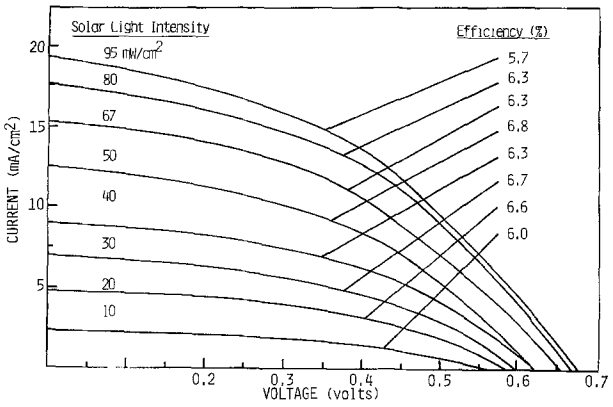

Fig. 4. Half-cell current-voltage characteristics for a 1 cm² CBD CdSe deposit on Ti as a function of light intensity. Test conditions: tungsten-iodide lamp with KG-2 filter, unstirred aqueous polysulfide, room temperature.

from the film defects or differences in surface area. The observed dark current losses represent a catalyzed reduction of polysulfide by the CdSe deposit. The reduction is represented by

$$2e^- + S_2^{2-} \rightleftarrows 2S^{2-}$$

The catalysis mechanism is presumably similar to that operating at the surface of the CoS and CuS counterelectrodes when the current if flowing in the normal direction for generating power (13). When bare Ti substrates were measured in place of the photoelectrodes, there was only about 0.1 mA/cm² of dark current. The poor catalytic behavior of bare Ti probably explains why we observe essentially no detrimental effects arising from the presence of pinholes on Ti. The PEC is thus more "forgiving" to the effects of pinholes than would a solid-state photovoltaic device.

The use of conducting glass substrates enabled the construction of chemically deposited backwall PEC's. These PEC's operated by illuminating the semiconductor through the transparent substrate material rather than from the top. Backwall PEC's possess the advantage of allowing the use of stabilizing opaque electrolytes such as polysulfide/selenide and permits the counterelectrode to be placed very close to the semiconductor electrolyte interface. The CdSe backwall cells of 4 cm² area and ~1.5μ film thickness produced 8 mA/cm² short-circuit current and an open-circuit voltage of ~0.4V *vs.* Pt/redox under 67 mW/cm² insolation with polysulfide electrolyte. The beneficial acid etch and zinc treatments were not employed as they tended to shear the deposits from the very smooth conductive glass.

The CBD method is useful for homogeneously coating large area electrodes with irregular surfaces, as might be found in practical photoelectrochemical cell designs. Preliminary measurements on CBD CdSe/polysulfide cells possessing photoelectrodes of 100 cm² area resulted in measured efficiencies that were about half those found for 1 cm² electrodes. Losses appear to relate to restricted ion flow to some segments of these large electrodes, and to the impedance of electrode structure itself. The design and scaling of practical photoelectrochemical cells will be a subject of a future publication.

Summary

The procedure of Kainthla and co-workers (9) for the chemical bath deposition of CdSe has been modified to produce high efficiency photoanodes for photoelectrochemical solar cells. These modifications include: (*i*) operation at a lower NH_4OH concentration in a sealed cell, to improve morphological reproducibility; (*ii*) employing a $Cd(OH)_2$ substrate coating, to promote specular deposits of hexagonal crystal structure; (*iii*) depositing at a higher temperature and with excess Na_2SeSO_3, to improve the deposition rate; and (*iv*) layering successive deposits to achieve practical film thicknesses. Using the modified procedures, CdSe films on Ti substrates may be routinely produced which yield >6% solar conversion efficiencies in photoelectrochemical cells with a polysulfide electrolyte.

Acknowledgment

This work was supported by the Solar Energy Research Institute under subcontract to the Department of Energy.

Manuscript submitted April 26, 1982; revised manuscript received *ca.* July 23, 1982. This was Paper 533 presented at the Denver, Colorado, Meeting of the Society, Oct. 11-16, 1981.

Any discussion of this paper will appear in a Discussion Section to be published in the December 1983 JOURNAL. All discussions for the December 1983 Discussion Section should be submitted by Aug. 1, 1983.

REFERENCES

1. M. A. Butler and D. S. Ginley, *J. Mater. Sci.*, **15,** 1 (1980).
2. A. Heller, *Acc. Chem. Res.*, **14,** 5 (1981).
3. A. Heller, K. C. Chang, and B. Miller, *This Journal*, **124,** 697 (1977).
4. M. Russak, J. Reichman, and J. DeCarlo, Paper 488 presented at The Electrochemical Society Meeting, Denver, Colorado, Oct. 11-16, 1981.
5. C. Liu and J. H. Wang, *Appl. Phys. Lett.*, **36,** 852 (1980).
6. G. Hodes, J. Manassen, and D. Cahen, *Nature* (London), **261,** 403 (1976); M. Tomkiewicz, I. Ling, and W. S. Parsons, *This Journal*, **129,** 2016 (1982); R. A. Boudreau and R. D. Rauh, *Solar Energy Materials*, **7,** 385 (1982).
7. D. R. Pratt, M. E. Langmuir, R. A. Boudreau, and R. D. Rauh, *This Journal*, **128,** 1627 (1981).
8. R. A. Zingaro and D. O. Skovlin, *ibid.*, **111,** 42 (1964).
9. R. C. Kainthla, D. K. Pandya, and K. L. Chopra, *ibid.*, **127,** 277 (1980).
10. G. A. Kitaev and T. P. Sokolova, *Russ. J. Inorg. Chem.*, **15,** 176 (1970).
11. I. Kaur, D. K. Pandya, and K. L. Chopra, *This Journal*, **127,** 943 (1980).
12. G. Hodes, J. Manassen, and D. Cahen, *ibid.*, **127,** 544 (1980).
13. G. Hodes, D. Cahen, J. Manassen, and M. David, *ibid.*, **127,** 2252 (1980).

Surface and Redox Reactions at GaAs in Various Electrolytes

S. Menezes* and B. Miller*

Bell Laboratories, Murray Hill, New Jersey 07974

ABSTRACT

The behavior of n- and p-GaAs at open circuit and under controlled potential in various redox electrolytes has been investigated by rotating ring-disk electrode voltammetry and hydrodynamically modulated disk techniques. These methods established the reactions at the GaAs surfaces to be one or more of the following: oxidation or reduction of solution species, corrosion of GaAs by charge injection from an oxidant, photoanodic corrosion of GaAs, cathodic protection of GaAs against dissolution, and the participation of surface film products on GaAs in altering the possible reaction paths. In six redox systems in acid and base where surface films do not form, the reaction path at both n- and p-GaAs can be well correlated with the relative position of solution redox potential and the bandedges of GaAs at the given *p*H per Gerischer theory. At intermediate *p*H, when film formation at the GaAs interface is a competitive path, further surface oxidation is suppressed and hole transfer to a soluble reductant (Fe^{+2}-EDTA) occurs efficiently, although not expected from potential level alone. In the case of GaAs, however, film thickness cannot be well enough controlled, either over time or potential range, to be suitable for the demands of photoelectrochemical cells.

Understanding the processes of substrate corrosion and charge transfer to redox species at the semiconductor-electrolyte interface is vital to the application of such junctions, whether they act as the photoactive element in a light-stimulated electrochemical cell or are being deliberately etched to a pattern. The partial and externally imposed currents accounting for these reactions at the semiconductor are made more complex in appearance than those at metals because of the rectifying nature of the semiconductor-liquid interface and its sensitivity to generation of carriers in the semiconductor by light.

The dissolution of n-type semiconductors tends to be suppressed in the dark, both under open-circuit (o-c) and impressed potential, because of the deficiency of hole current attributable to the existence of a forbidden gap. Mass transfer (MT) controlled corrosion, however, can occur even at o.c. by appropriate oxidizing agents through charge injection into the semiconductor producing a partial anodic corrosion current (1) or by equivalent chemical steps (2). The o-c behavior is of particular importance since it determines the chemical stability of the semiconductor in the medium. In regenerative photoelectrochemical cells based on n-type semiconductor liquid junctions under illumination, it is required that the desired electrochemical reaction proceed in the reverse direction to that of the hole injection described above. Holes are generated by light absorption in the solid and are accepted by reducing agents in solution. Electrons then flow toward the back ohmic contact and cell counterelectrode to produce an external current through a load.

Both the experimental demonstration of redox charge injection resulting in substrate corrosion and the theory for its origin in a charge transfer involving the overlap of energy levels in the semiconductor with available states of the solution redox pair were given sometime ago by Gerischer (1). Experiments in the case of GaAs determined the partial currents at the semiconductor interface through the integral procedure of post-solution analysis after allowing sample corrosion under controlled conditions (3, 4). The assignment of valence or conduction band participation in the charge injection process with different redox couples was made by comparison of light and dark current-voltage characteristics (1).

Related systematic studies of the charge transfer reactions at a semiconductor substrate with measurement techniques capable of real-time information such as the rotating ring-disk electrode (RRDE) began only more recently (5). Subsequent studies have been mainly oriented to monitoring the competition under illumination between the processes of photocorrosion and hole transfer to reducing agents. We have applied rotating disk electrode (RDE) and RRDE methodology in several forms, including that of sinusoidal hydrodynamic modulation (SHM) (7), to systematic studies of semiconductor o-c stability to oxidants, analogous to those done with metals (6) to yield partial currents. These experiments yield real-time analytical information combined with an understanding of the sensitivity of the systems to surface concentrations of reactive species.

In the course of such photoelectrochemical work in this laboratory we have accumulated diverse data on GaAs relating to o-c dark corrosion and the relative position of redox potentials and bandedges. These measurements have been made on n- and p-substrates to compare the influence of both the common chemical properties of the material and different charge type on the protection of the photoconverting surface against dissolution.

In prior electrochemical studies on GaAs some redox pairs such as $Fe(CN)_6^{-3/-4}$ have been cited both as dark corrodents and photo hole acceptors (3, 8), an apparent incompatibility only partially resolved by such considerations as bandedge shifts with *p*H. Dominant here is the function of surface filming in kinetically directing the competition of substrate and solution species reacting at the photoelectrodes (9, 10). For information on this point we have also studied GaAs in media in which surface oxide films are a competitive anodic path.

Experimental

n-GaAs (Si doped to 2×10^{17} cm^{-3}) and p-GaAs (Cd doped to 2×10^{16} cm^{-3}) crystals cut to expose (111) faces were fabricated into RDE's and RRDE's after ohmic back contacts were applied. Ring electrodes were platinum. The electrodes were normally etched in 1:1 H_2SO_4:30% H_2O_2 prior to runs.

Electrolytes were prepared with reagent grade chemicals and triply distilled water. A nitrogen atmosphere was maintained for all cell runs. The electrode faces were illuminated by a 100W tungsten-halogen lamp in conventional electrochemical cells through the addition of bottom optical flat windows. Carbon rod counterelectrodes were used with saturated calomel electrodes as reference. Voltammetric instrumentation for the RRDE experiments and signal processing electronics for SHM methods have been described before (11, 12).

Nominal RRDE dimensions were 0.47, 0.52, and 0.63 cm for the disk (same for RDE's) and inner and outer ring diameters, respectively. The collection efficiency, *N*, for this geometry is 0.33 (13). To obtain the unshielded ring current, i_r^o, (defined as that attributable to oxidant or reductant flux in the absence of disk

* Electrochemical Society Active Member.

Key words: ring-disk electrode voltammetry, modulated disk techniques, oxidation, corrosion.

reactions) where the disk was reactive, a lacquer coating was applied to the disk.

Results and Discussion

RRDE Monitoring of Corrosion

The ring electrode monitors the flux of either product (collection) or of reactant (shielding) due to redox reactions at the disk. In the case of zero net disk current (deliberate o.c. or the region in which the near equivalent results from diode blocking), the ring can still detect changes in the flux of redox species originating from the partial anodic and cathodic disk current components. Under the zero applied current condition, the partial currents must algebraically cancel, $i_{anodic} + i_{cathodic} = 0$ at the disk. The soluble products from GaAs itself [Ga(III) and As(III) species] were generally not found to interfere with these measurements and are thus not further mentioned here. The possible control of disk reactions by MT of the redox reagents was investigated by observing appropriate ring current changes with rotation speed, ω.

n-GaAs behavior was examined in the following redox electrolytes.

$Fe(CN)_6^{-3/-4}$, pH 14.—The Pt ring current-potential curves with the open-circuited disk, either exposed (i_r^e) or lacquered (i_r^o), are shown in Fig. 1. The ring limiting current regions correspond to $Fe(CN)_6^{-4}$ oxidation (+ sign) at 0.4V and $Fe(CN)_6^{-3}$ reduction (− sign) at 0.0V *vs.* SCE. The $i_r^o(+)$ and $i_r^e(+)$, and $i_r^o(-)$ and $i_r^e(-)$ nomenclatures are followed for the various redox systems in the subsequent figures. The respective differences between the i_r^e and i_r^o traces at the two monitoring potentials represent the consumption of $Fe(CN)_6^{-3}$ and formation of $Fe(CN)_6^{-4}$ from the oxidation of the exposed disk. Further measurements at constant ring potentials, not shown here, verify that $i_r^o(+)$, $i_r^o(-)$, $i_r^e(+)$, and $i_r^e(-)$ are all linear with $\omega^{1/2}$. In the absence of bulk $Fe(CN)_6^{-4}$, $i_r^o(+)$ is zero. For given rotation speeds at these limiting currents, the data show $[i_r^o(-) - i_r^e(-)] = [i_r^o(+) - i_r^e(+)]$. These differences are also found equal to the product of N and the disk limiting current for $Fe(CN)_6^{-3}$ reduction. The latter is either separately determined at a metal electrode, or from Fig. 2.

The more general experiment is the controlled disk potential scan shown in Fig. 2, with the ring detecting $Fe(CN)_6^{-4}$ and $Fe(CN)_6^{-3}$ limiting currents, as defined above. Three disk situations are considered; i_d^o (no current flow, disk lacquered), and i_d^e (dark) and i_d^e ($h\nu$) corresponding, respectively, to exposed disk

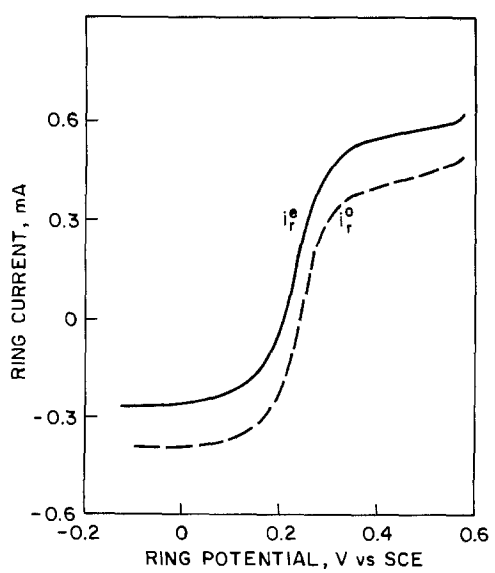

Fig. 1. Ring potential (E_r) scans at 10 mV/sec. Pt ring currents with n-GaAs disk lacquered, i_r^o, or exposed, i_r^e, to 5 mM $Fe(CN)_6^{-4}$ + 5 mM $Fe(CN)_6^{-3}$ + 1M KOH. ω = 1600 rpm.

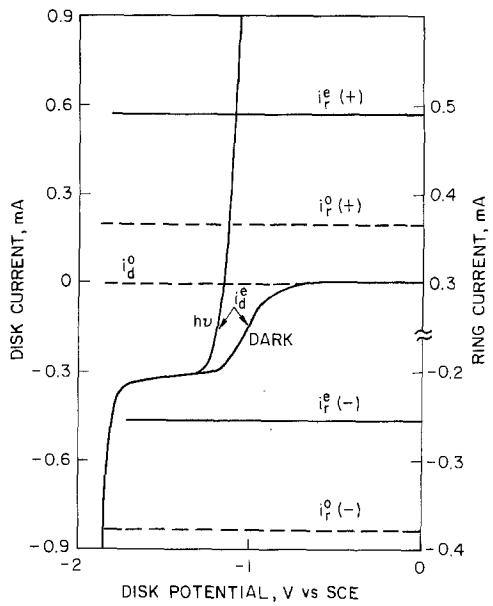

Fig. 2. Disk potential (E_d) scans at 10 mV/sec in 5 mM $Fe(CN)_6^{-4}$ + 5 mM $Fe(CN)_6^{-3}$ + 1M KOH with n-GaAs disk lacquered, i_d^o (zero current line), or exposed, i_d^e, indicated on plot as to in light ($h\nu$) or dark. Corresponding ring traces, $i_r^o(+)$ and $i_r^e(+)$ at $E_r(+)$ = 0.4V; $i_r^o(-)$ and $i_r^e(-)$ at $E_r(-)$ = 0V. ω = 1600 rpm. Both i_r^e traces same in light and dark.

in the dark and light. The ring current responses for exposed disk scans in the dark or light are found identical and thus are given only by the single traces $i_r^e(+)$ and $i_r^e(-)$. At potentials positive of the reduction wave at the disk, $i_r^e(+)$ and $i_r^e(-)$ do not revert to the unshielded levels $i_r^o(+)$ and $i_r^o(-)$, as would be observed at an all noble metal RRDE under parallel conditions, but continue to detect $Fe(CN)_6^{-3}$ reduction by the disk at an unchanged level. Thus the dark cathodic current component at o.c. must be compensated by an equal anodic current component.

Illumination results in a negative shift of the potential and an anodic photocurrent controlled by light flux. None of this is recognized by the ring processes which remain unchanged from dark to light. An MT limited disk reduction of $Fe(CN)_6^{-3}$ must still proceed even when the disk is photocorroding. This reduction current, detected by the ring, has still to be compensated by an equivalent anodic current resulting from hole injection. Both of these components algebraically cancel in the externally measured disk photocurrent which is light-flux limited. Thus the net disk current observed positive of the o-c potential (−1.15V) is the sum of partial currents of the coupled cathodic reduction-anodic oxidation hole injection process (adding to zero) and that attributable to electron-hole pair generation by photon absorption. No part of the anodic current can be going to $Fe(CN)_6^{-4}$ oxidation since it would be observed as a ring flux change. Thus the holes injected by the $Fe(CN)_6^{-3}$ and by light excitation must both lead to the dissolution of the GaAs surface.

$Ce^{+4/+3}$, pH 0.—The behavior of n-GaAs in this redox system in acid solution is not shown because it is identical in all respects to that seen in the corresponding experiments of Fig. 1 and 2, except only that the potential scale shifts positive by nearly a volt from that observed in $Fe(CN)_6^{-3/-4}$, pH 14 electrolyte.

$Fe^{+3/+2}$, pH 0.—In this system the behavior of GaAs is different from that above and is shown in Fig. 3 for an experiment carried out as that in Fig. 2. The disk current traces, i_d^e (dark) and i_d^e ($h\nu$), are, however, not in essence different from those of Fig. 2, except that due to a lower illumination level, anodic

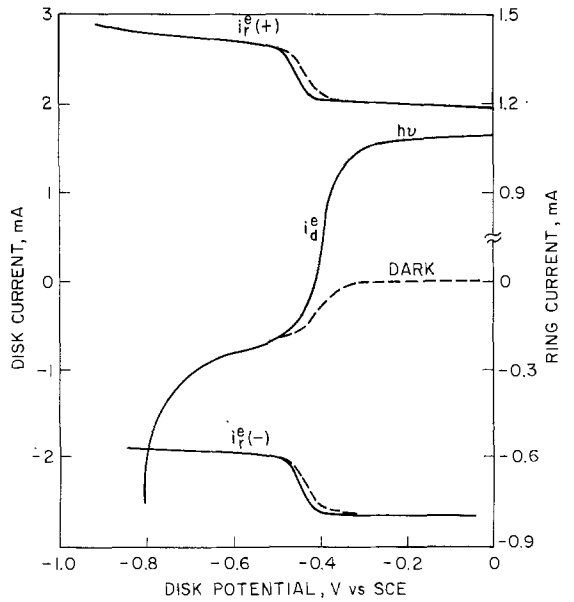

Fig. 3. Potential scans as in Fig. 2 at n-GaAs disk exposed (i_d^e) to 5 mM Fe^{+2} + 5 mM Fe^{+3} + 1M H_2SO_4 in light and dark. Ring traces, $i_r^e(+)$ at $E_r(+) = 1.0V$ and $i_r^e(-)$ at $E_r(-) = -0.2V$.

dissolution current is light limited at positive potentials. The ring curves $i_r^e(+)$ and $i_r^e(-)$, at E_r of 1.0 and −0.3V *vs.* SCE, respectively, monitor the fluxes of Fe^{+2} and Fe^{+3}, but in contrast to Fig. 2, $i_r^e(+)$ and $i_r^e(-)$ are not constant throughout. In the region for which i_d is zero or anodic in Fig. 3, these traces coincide with those of the constant values of i_r^o (not indicated) measured with a lacquered disk. The difference between the two plateau levels within each ring trace is in agreement with N times the i_d^e limiting cathodic current in the −0.6V *vs.* SCE region. From these observations it may be concluded for the dark case that Fe^{+2} is produced only by external current, *i.e.*, hole injection by Fe^{+3} is minimal and corrosion of n-GaAs at o.c. is correspondingly low.

The photocurrent, i_d^e ($h\nu$) does not generate a change in ring response over that in the dark case. Thus Fe^{+2} is not photo-oxidized at n-GaAs in this medium and the photogenerated holes are all involved in n-GaAs dissolution, within ring detectability limits.

$Fe(CN)_6^{-3/-4}$, pH 0.—RRDE curves in this system were analogous to those shown in Fig. 3, noting also that the redox potentials of the two electrolytes are essentially identical. There is a clear operational difference, however, in that the reduction wave could only be observed at a freshly etched disk and disappeared on cycling. A probable explanation is that the small amount of external anodic disk current in the blockage direction, or the anodic component of charge injection at levels not detectable to ring electrode accuracy, forms a film, insoluble in acids, which inhibits reduction of $Fe(CN)_6^{-3}$ at the potentials observed at a clean surface. The addition of $Fe(CN)_6^{-4}$ to Ga^{+3} dissolved in 1M H_2SO_4 produces a green precipitate (which dissolves in alkaline solution). Except for the effects attributed to the electrode filming by a specific anion effect, the conclusions relating to only a low level of o-c corrosion would be identical to those of the Fe^{+3}-pH 0 case.

I^-I_2, pH 0.—For this redox system with a potential less than 200 mV negative of the acid $Fe^{+3/+2}$ and $Fe(CN)_6^{-3/-4}$ couples, the characteristics found for n-GaAs disk electrodes resembled those of Fig. 3.

p-GaAs.—The above combinations of redox systems and RRDE experiments were repeated with p-GaAs as a disk electrode. Two representative situations were encountered, as in the case of n-GaAs.

$Fe(CN)_6^{-3/-4}$, pH 14.—Ring shielding and collection experiments with p-GaAs, which may be directly compared to those in Fig. 2 with n-GaAs, are shown in Fig. 4. The p-type semiconductor crystal used in these experiments was much more resistive in the dark than the n-GaAs analog. The apparent resistance decreased on illumination but the slopes and definition of the *E-i* characteristics were lower than with the n-type material and result in a widening of the potential scale. Nevertheless, the flux changes identified by the ring were as seen in Fig. 2; constant values for $i_r^e(+$ and $-)$ and $i_r^o(+$ and $-)$ across the potential scan, independent of illumination level. Cathodic current for $Fe(CN)_6^{-3}$ reduction at the disk is low in the dark (blocking direction for p-type electrodes) and increases to an MT-controlled level on sufficient illumination. The forward or anodic dissolution curve is steepened considerably by the photoconductive, rather than the photovoltaic, effect of light.

The lack of effect on ring current when the illuminated disk is passing a net cathodic current implies that dissolution of p-GaAs is suppressed in the light [$Fe(CN)_6^{-3}$ is reduced by external current] and occurs in the dark (hole injection). The ring monitors an MT-controlled reduction of $Fe(CN)_6^{-3}$ at the disk in all cases so that the sum of these two modes of $Fe(CN)_6^{-3}$ reduction is a constant. Positive of o-c potential dissolution processes at the p-type disk are independent of illumination except for varying potential sensitivity traceable mainly to the aforementioned resistive effects. The conclusions are thus parallel to those observed at illuminated n-GaAs, including no evidence of $Fe(CN)_6^{-4}$ oxidation detectable in the ring traces.

$Fe^{+3/+2}$, pH 0.—The p-GaAs disk current curve $i_d(h\nu)$ and ring responses shown in Fig. 5 display the same overall characteristics as the n-type analogy in Fig. 3. The ring currents are consistent with cathodic reduction of Fe^{+3} at the illuminated disk and no oxidation of Fe^{+2} at the disk for any case. The ring currents remain the same throughout the disk scan in the dark when the reduction of Fe^{+3} attributable to photocathodic current is blocked. The ring currents for disk potentials positive of 0V *vs.* SCE are at the same level seen when the disk is lacquered.

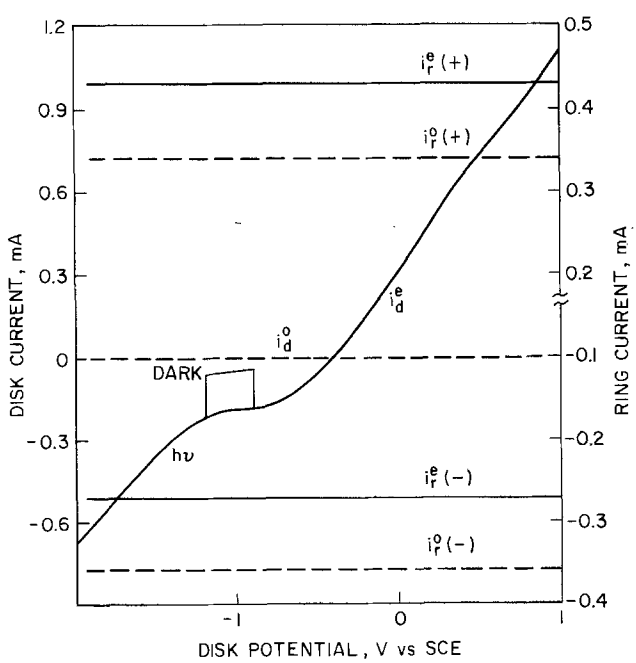

Fig. 4. Experiment of Fig. 2 at p-GaAs RRDE

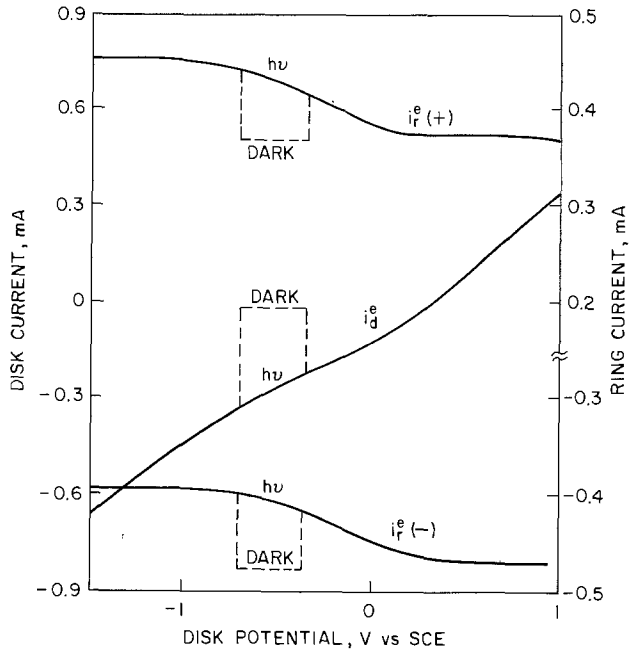

Fig. 5. Experiment of Fig. 3 at p-GaAs RRDE. Dashed lines represent changes in ring and disk currents when light is intercepted.

p-GaAs behavior in the other redox systems falls into one of the two categories shown in Fig. 4 and 5, keeping the same grouping as found for n-GaAs.

SHM Application

The sensitivity of GaAs reactions to MT of redox reagents was also investigated by means of the response of the disk current to SHM. The results for the semiconductor are compared to those for the superficially analogous case of an Fe disk in an Fe^{+3}/H^+ solution to relate charge injection processes to classical metal (14) behavior.

The response of n-GaAs to SHM in alkaline $Fe(CN)_6^{-3}$ for dark and light conditions is shown in Fig. 6. Only the reduction of $Fe(CN)_6^{-3}$ by external current, in either light or dark, produces the theoretical SHM current plateau with $\Delta i = (\Delta\omega^{1/2}/\omega^{1/2})i_d$ relation for an MT limited disk current. Neither the reduction of supporting electrolyte (H_2 evolution) at < -1.7V nor the semiconductor light-stimulated oxidation have any dependence on MT. Although the ring currents in the previous figures show the partial currents to be totally MT controlled in the blocking region (E_d positive of -0.8V *vs.* SCE), the internal cancellation of cell current implicit in the hole injection process eliminates the MT effect on the disk response. This situation corresponds to essentialy galvanostatic control (thus no SHM output), even though the external potential is apparently being experimentally regulated. This situation has been elsewhere elaborated upon in the context of photoelectrochemical cells (15).

The SHM experiment in Fig. 7 parallels the corresponding curves in Fig. 6. Reduction of Fe^{+3} by external current at the semiconductor is the only MT sensitive process occurring. Disk data alone do not discriminate between the two contrasting situations given by Fig. 2-3 and Fig. 4-5 pairs for n- and p-materials, respectively. Ring monitoring of mass flux chemical changes is necessary to distinguish the different behaviors of each charge type.

The behavior of an Fe disk in an Fe^{+3}-acid solution (16), as shown in Fig. 8, is an analog of the Fig. 2 and 4 semiconductor/oxidant situations. SHM and conventional current response to Fe dissolution in acid is first examined in the region of o-c potential with no Fe^{+3} present. The SHM response is nil over the entire region from H_2 evolution at the disk, $H^+ + e \rightarrow H_2$, to an-

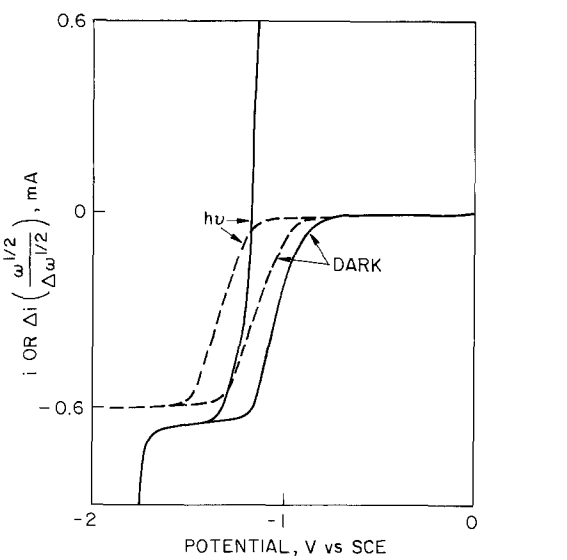

Fig. 6. Average disk current (solid lines) and modulated component normalized to average disk current level (dashed lines) at n-GaAs in 10 mM $Fe(CN)_6^{-3}$ + 1M KOH. ω = 1600 rpm, $\Delta\omega^{1/2}$ = 2 rpm$^{1/2}$, and modulation frequency = 2 Hz.

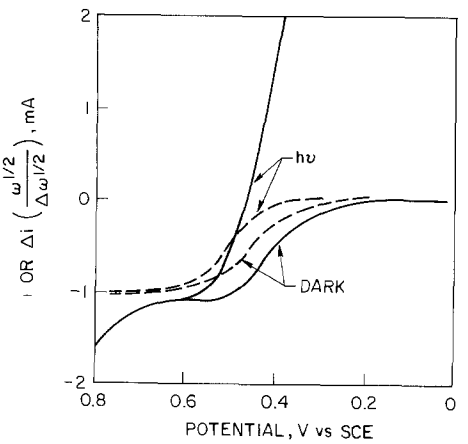

Fig. 7. SHM experiment of Fig. 6 but in 10 mM Fe^{+3} + 1M H_2SO_4.

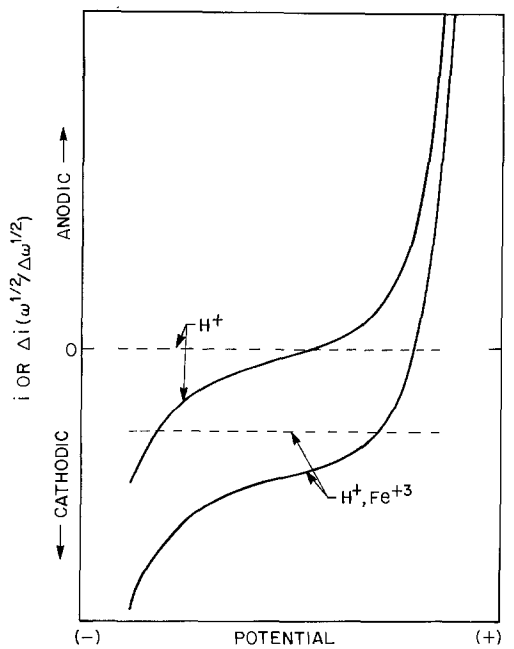

Fig. 8. SHM experiment as in Fig. 6 at Fe disk in 1M H_2SO_4 or 2 mM Fe^{+3} + 1M H_2SO_4, as indicated on traces. ω = 3600 rpm, $\Delta\omega^{1/2}$ = 3 rpm$^{1/2}$, and modulation frequency = 3 Hz.

odic disk dissolution, $Fe \rightarrow Fe(II) + 2e$. Fe anodic dissolution is kinetically irreversible (Tafel), dependent only on potential and not at all on the surface concentration of Fe^{+2} in this region of free (no film) dissolution. The H^+ reduction by external current has no ω dependence (nil SHM current) because of both the high H^+ concentration and the irreversibility of the process (7 and references therein).

When Fe^{+3} is present the conventional trace in Fig. 8 shows the MT controlled reduction of Fe^{+3}, $Fe^{+3} + e \rightarrow Fe^{+2}$, added to the other two processes above. The SHM trace, however, responds throughout the range of the scan at the theoretical level to the MT controlled Fe^{+3} reduction (seen in the total disk current cathodic step), even when the net disk current is distinctly anodic. (The o-c potential is about a volt negative of the $Fe^{+3} + e = Fe^{+2}$ potential.) Most important for discussion per the GaAs experiments is the fact, that, in contrast to the semiconductor case (Fig. 6), modulated current response to the partial cathodic current for the reduction of Fe^{+3} continues unchanged during metal dissolution.

For the metal case the partial anodic and cathodic components have independent characteristics as a function of potential (14) and the net disk current will vary with speed because of its cathodic, MT controlled component. In the case of the semiconductor the process of charge injection dissolution is a coupled one. The partial anodic dissolution current cannot flow in the dark at any given potential without the exactly compensating partial cathodic current of Fe^{+3} reduction. Thus the sensitivity to SHM vanishes because of the complete coupling of the partial currents and their algebraic cancelation. Yet, as seen clearly from the ring data, o-c corrosion rates are proportional to $\omega^{1/2}$ as expected for MT control.

Thus, for the semiconductor, an SHM current response in the regions of active substrate dissolution, but zero external current, will not exist, in contradistinction to the superficially similar case of a corroding metal under MT controlled oxidant reaction. Ring currents which monitor the actual mass loss will respond to rotation speed variation in both instances. SHM response may occur at the semiconductor under applied potential when the external current is both in the forward direction of the diode (cathodic at n-type) and sensitive to surface concentrations of some electroactive species, as in Fig. 6 and 7. Anodic dissolution of the semiconductor by photon stimulated processes does not have an SHM response for the same kinetic reasons (irreversibility) as in the Fe case.

Influence of Interfacial Films

The RRDE results in the various *p*H 0 and 14 solutions above showed no detectable efficiency for oxidation of the reducing member of any of the redox couples investigated with either n- or p-GaAs, in the dark or light. Between these two extremes of *p*H, varying degrees of efficiency for hole transfer to $Fe(CN)_6^{-4}$ (8) and Fe(II) EDTA (9) have been reported. Since the Fe(II)-EDTA couple is more stable with time than $Fe(CN)_6^{-4}$, particularly in white light (17), we have investigated the potential and time dependence of these processes at the n-GaAs RRDE in different buffered solutions of EDTA.

The traces in Fig. 9 show the effects of successive additions of EDTA and $Fe^{+3/+2}$ redox couple on the voltammetry of an illuminated n-GaAs disk in *p*H ~ 0 solution. $i_d(1)$ represents the photodissolution current in 1M $HClO_4$ alone, finally limited only by light level. $i_d(2)$ shows the effect of saturating the solution with EDTA which is to produce a passive transition (peak) in the anodic current. On addition of 0.1M Fe^{+2} containing a much lower concentration of Fe^{+3} from air contact, trace $i_d(3)$ shows a cathodic Fe^{+3} reduction wave and an anodic photocurrent similar to that seen in the case of Fig. 3. The corresponding ring curve,

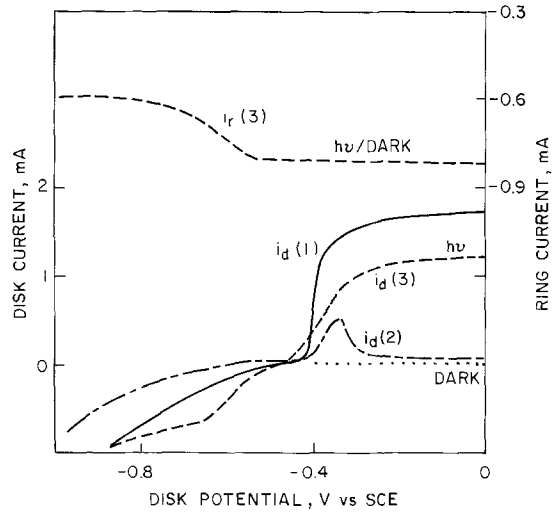

Fig. 9. Disk potential scans at illuminated n-GaAs RRDE at *p*H ~ 0. $i_d(1)$ in 1M $HClO_4$; $i_d(2)$ in saturated EDTA + 1M $HClO_4$; $i_d(3)$ in 0.1M total $Fe^{+3/+2}$ + saturated EDTA + 1M $HClO_4$ with $i_r(3)$ at $E_r = -0.2V$. Effect of light blocking shown on $i_d(3)$ trace. Plateau levels for $i_r(3)$ same in light and dark. Scan rate = 10 mV/sec. Rotation speed = 1600 rpm.

$i_r(3)$, monitoring Fe^{+3} flux, detects the Fe^{+3} reduction but no evidence of Fe^{+2} oxidation by the disk as $i_r(3)$ traces are identical in the dark (no anodic disk current) and light.

The same series of experiments available at higher EDTA concentration in a *p*H 2 buffer are shown in Fig. 10. The disk curves are roughly similar in shape but ring response (collection of Fe^{+3}) definitely increases from dark to illuminated conditions, indicating proportionate photo-oxidation of Fe^{+2} by the disk. The collection efficiency for this process is, however, lower than that observed for the cathodic disk reaction which is close to theory. Thus the anodic disk process at *p*H 2 involves both surface and solution reactions.

Figure 11 shows that GaAs passivates in *p*H 5 buffer, curve $i_d(1)$, in the absence of EDTA, and gives even lower currents again with EDTA, curve $i_d(2)$. In the presence of the redox couple, however, the collection efficiencies for both photo-oxidation of Fe^{+2} and dark reduction of Fe^{+3} are identical and close to theory. But, as seen in the scan to more positive potentials (or indeed by holding the potential constant in the region of initial Fe^{+2} oxidation currents), both $i_d(3)$ and $i_r(3)$ decline to the dark level. GaAs is stabilized against

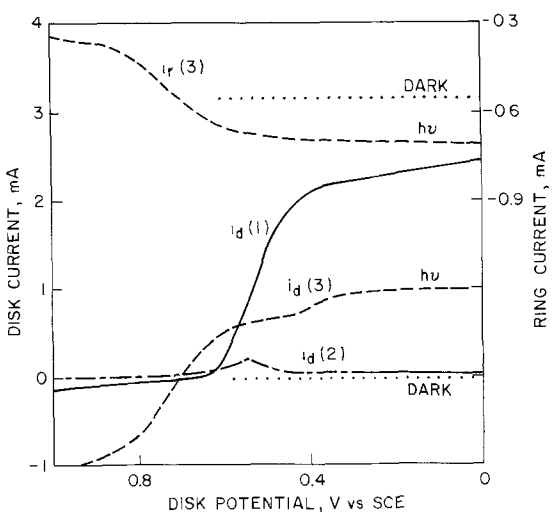

Fig. 10. Experiment of Fig. 9 but with 0.1M EDTA + 0.5M Na_2SO_4 + 0.5M $NaHSO_4$ *p*H 2 buffer replacing 1M $HClO_4$ + saturated EDTA.

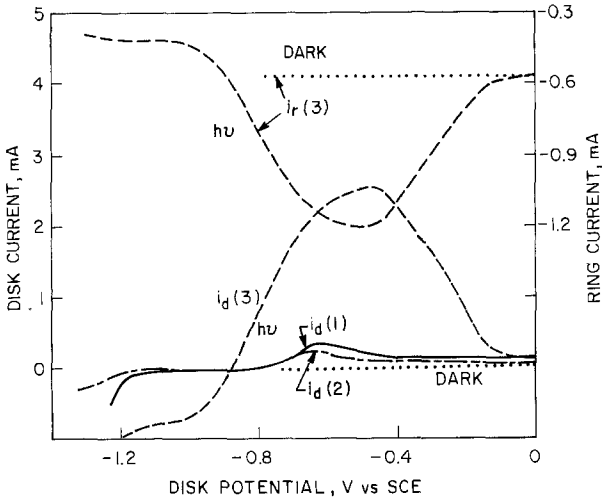

Fig. 11. Experiment of Fig. 10 at pH 5, in 0.5M HOAc + 0.5M NaOAc. $E_r(3) = -0.5V$.

photocorrosion to a low level in this solution by the formation of a passive, protective film, initially thin enough to sustain a redox reaction. The film thickens as a function of time or potential and eventually inhibits both corrosion and redox reactions.

As pH increased the trend to achieving a nearly theoretical, if transitory, collection efficiency tends to reverse and N decreases to the negligible level exhibited in Fig. 9, in very alkaline solutions. This trend is shown in Fig. 12 in the plot of the maximum normalized collection efficiency of the photo-oxidation of Fe(II)-EDTA as a function of pH. This plot is in general agreement with the trend of results shown by Frese *et al.* (9) for Fe(EDTA) or citrate complexes and the earlier work of Memming (8) with $Fe(CN)_6^{-4}$. These methods involved chopped light schemes and/or initially cleaned surfaces to obtain maximal response at the ring. The scans here and the decay with time clearly indicate that n-GaAs in these media could not likely be the basis of steady-state regenerative cells. Our earlier work, comparing porous displacement plated gold with nearly homogenous electrodeposits on n-GaAs surfaces in pH 5 $Fe(CN)_6^{-4}$, indicates (17, 18) that protection (19) in this manner is not permanent either and that growth of oxide films will eventually inhibit current transfer. We conclude that in the intermediate pH region, the GaAs surface is modified by the formation of an insoluble film that, when sufficiently thin, can support efficient photo-oxidation of the reduced solution species. Slow thickening of the film will quench charge transfer through it to low rates. In strong acids and bases alone, films do not normally play a role since the anodic reactions of GaAs yield soluble products and solution oxidation reaction

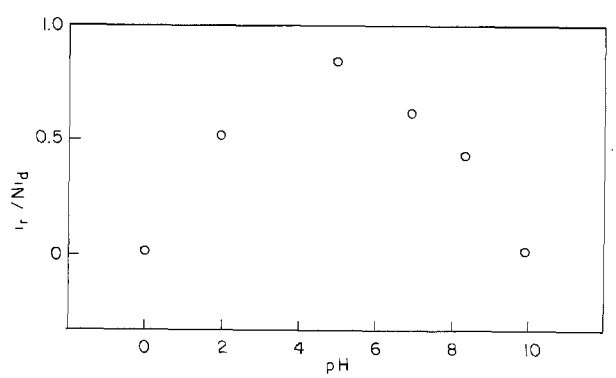

Fig. 12. Plot of normalized collection efficiency for n-GaAs RRDE as a function of solution pH. N measured as the ratio of the differences between light and dark values of $i_r(3)$ and $i_d(3)$ near the plateau of ring collection for scans as in Fig. 9-11.

cannot compete for holes with the substrate dissolution reaction. The tendency to film formation is strongly accentuated by the reaction of Ga^{+3} products with EDTA under the conditions shown. (Note this is parallel to the behavior described above for $Fe(CN)_6^{-4/-3}$ in acid solution where an insoluble product could be expected.) The nature of the film formed in the presence of a complexing agent of $K = 10^{20}$ formation constant, as for (soluble) Ga-EDTA, is not known from this work, only its voltammetric consequences.

Conclusions

Voltammetry at the GaAs interface and the underlying chemistry can be analyzed in terms of the following possible reactions: (*i*) reduction of an oxidant, (*ii*) oxidation of a reductant, (*iii*) surface passivation, (*iv*) substrate dissolution by external current, and (*v*) substrate dissolution by hole injection from an oxidant. These reactions may be coupled or consecutive. From the various systems surveyed by the RRDE four categories emerge, each characterized by a specific combination of reactions (*i*) to (*v*). They are discussed with reference to Fig. 13 where the redox couples are placed with respect to the conduction and valence bandedges of GaAs at the respective pH values for which they were examined here. The results for Se^{-2}/Se_x^{-2} are cited from a previous RRDE and SHM study by us (20).

A. In redox electrolytes with potential sufficiently negative of the valence band and adequate kinetics, the redox reactions (*i* and *ii*) can compete against GaAs corrosion reactions (*iii-v*). This category is exemplified by the Se^{-2}/Se_x^{-2} redox couple. The n-GaAs junction with that electrolyte is the basis of an efficient regenerative solar cell (21).

B. In the Fe(II)-EDTA, pH 5 system redox reactions (*i* and *ii*) are concurrent with film formation (*iii*).

C. In this group of redox couples located positive of midgap, anodic dissolution (*iv*) at potentials positive of o.c. is observed. The oxidant can undergo reduction (*ii*) at GaAs at potentials negative of o.c.

D. With these redox couples lying at potentials positive of valence band, corrosion predominates at potentials both positive of o.c. (*iv*) and at o.c. (*v*). Oxidant reduction by external current (*i*) occurs at n-GaAs and illuminated p-GaAs at potentials negative of o.c., where both are stable as long as sufficient cathodic protection is maintained.

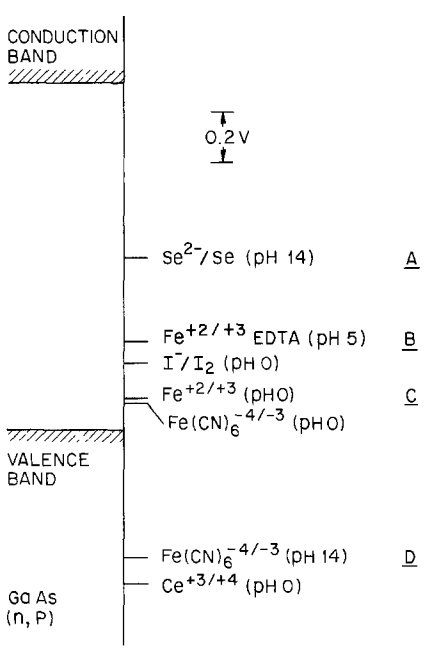

Fig. 13. Redox potentials correlated to the levels of the GaAs bandedges for the respective pH values of the given redox couple.

The interfacial chemistry at both conduction types of the semiconductor in the various electrolytes is consistently similar, as expected. Observed differences arise from the photon-generated flux of minority carriers and the accompanying increased photoconductivity. Photo-oxidation has always to compete with corrosion at an n-type crystal, whereas photoreduction at a p-type crystal can shield its surface against degradation, even in category D-type situations. These results on n- and p-substrates illustrate both the overriding influence of the common chemical properties and the recognized advantages of constructing photoelectrochemical cells with photocathodes. In these cases the possible photocathodic corrosion of GaAs (to Ga^0 + AsH_3) does not seem a significant factor in the presence of any of the oxidants.

The energy band diagram in Fig. 13 provides a useful reference frame from which the search for a given semiconductor-electrolyte pair for solar cell application can be started. It is, however, not always possible to foresee category B from Fig. 13. Interposition of a film distinguishes the type B junction from type C with which it overlaps. The practicality of type B junctions depends on the optimization of the interfacial layer thickness and the nature of the products. In spite of the fact that the circumstances can be adjusted to achieve close to 100% current efficiency for a given photo-oxidation on a film, in the GaAs systems it appears from our results that this situation will be extremely difficult to sustain effectively against passivation over a period of time.

Manuscript submitted June 15, 1982; revised manuscript received ca. Sept. 7, 1982. This was Paper 486 presented at the Denver, Colorado, Meeting of the Society, Oct. 11-16, 1981.

Any discussion of this paper will appear in a Discussion Section to be published in the December 1983 JOURNAL. All discussions for the December 1983 Discussion Section should be submitted by Aug. 1, 1983.

Publication costs of this article were assisted by Bell Laboratories.

REFERENCES

1. H. Gerischer, in "Advances in Electrochemistry and Electrochemical Engineering," Vol. 1, P. Delahay and C. W. Tobias, Editors, p. 139, Interscience, New York (1961).
2. H. Gerischer and W. Mindt, *Electrochim. Acta*, **13**, 1329 (1968).
3. H. Gerischer, *Ber. Bunsenges. Phys. Chem.*, **69**, 578 (1965).
4. H. Gerischer and I. Mattes, *Z. Phys. Chem.*, **49**, 112 (1966).
5. A. Fujishima, E. Sugiyama, and K. Honda, *Bull. Chem. Soc. Jpn.*, **44**, 304 (1971).
6. B. Miller and M. I. Bellavance, *This Journal*, **119**, 1510 (1972).
7. S. Bruckenstein and B. Miller, *Acc. Chem. Res.*, **10**, 54 (1977).
8. R. Memming, *This Journal*, **125**, 117 (1978).
9. K. W. Frese, Jr., M. J. Madou, and S. R. Morrison, *J. Phys. Chem.*, **84**, 3172 (1980).
10. M. J. Madou, K. W. Frese, Jr., and S. R. Morrison, *This Journal*, **127**, 987 (1980).
11. B. Miller, *ibid.*, **116**, 1117 (1969).
12. B. Miller and S. Bruckenstein, *Anal. Chem.*, **46**, 2026 (1974).
13. W. J. Albery and S. Bruckenstein, *Trans. Faraday Soc.*, **62**, 1920 (1966).
14. C. Wagner and W. Traud, *Z. Elektrochem.*, **44**, 391 (1938).
15. S. Bruckenstein and B. Miller, *This Journal*, **129**, 2029 (1982).
16. B. Miller and M. I. Bellavance, Unpublished data.
17. S. Menezes, A. Heller, and B. Miller, *This Journal*, **127**, 1268 (1980).
18. S. Menezes and B. Miller, Unpublished data.
19. K. W. Frese, Jr., M. J. Madou, and S. R. Morrison, *This Journal*, **128**, 1939 (1981).
20. B. Miller, S. Menezes, and A. Heller, *ibid.*, **126**, 1483 (1979).
21. K. C. Chang, A. Heller, B. Schwartz, S. Menezes, and B. Miller, *Science*, **196**, 1097 (1977).

Technical Note

Hydrocarbon-Oxygen Mixture as a Resist Etching Gas with Highly Anisotropic Etching Feature

H. Namatsu, Y. Ozaki, and K. Hirata

Nippon Telegraph and Telephone Public Corporation, Musashino Electrical Communication Laboratory, Musashino-shi, Tokyo, 180 Japan

Multilevel resist schemes are a promising approach for providing high resolution patterns on stepped and highly reflective substrate surfaces, such as are typically encountered in LSI fabrication processes (1-2). In the multilevel process, the pattern formed on a top resist is transferred to a thick bottom resist with or without an inorganic, intermediate, masking layer. The bottom resist is usually patterned by reactive ion etching (RIE) in pure oxygen plasma. To obtain fine patterns with submicron accuracy, it is necessary to realize anisotropic etching of the thick bottom resist. The authors have already reported that the undercutting decreases markedly with etching performed at low oxygen pressure, and a low substrate temperature (3). This paper describes a novel anisotropic resist etching approach using hydrocarbon-oxygen mixtures as an etching gas. With this approach, substrate cooling is not necessary.

Key words: resists, etching, polymerization.

Experimental

Samples were prepared as follows. A 1.3 μm thick photoresist AZ-1370 layer was spun on a silicon wafer. It was baked at 200°C for 1 hr in a nitrogen atmosphere. Then, an SiO_2 intermediate layer was deposited by an ion beam sputtering technique to a 0.4 μm thickness. A 0.5 μm thick photoresist AZ-1350 layer was

used as a top resist. After patterning the top resist, the SiO_2 was reactive ion-etched in $CF_4 + H_2$ plasma (4). Etching of the bottom resist was accomplished in a conventional RIE apparatus. The sample was set on a 465 mm diameter carbon electrode, which was connected to a 13.56 MHz rf generator. The distance between the carbon electrode and counterelectrode was 65 mm. The temperature rise during etching was at least 100°C.

Hydrocarbons employed in the present experiments were methane (CH_4), ethane (C_2H_6), ethene (C_2H_4), and ethyne (C_2H_2). The rf power density, total gas flow rate, and pressure were kept at 0.06 W/cm², 15 sccm, and 3.3 Pa, respectively.

Results

Figure 1 shows the dependence of undercutting on gas composition. Undercutting (A) is normalized to etching depth (B). Etching depth was kept at 60-70% of initial thickness. As is seen, the A/B ratio value was above 0.1 in pure oxygen plasma. It decreased gradually as the hydrocarbon fraction increased, except in the case of methane, where A/B was reduced by only a factor of 2 at a 40% hydrocarbon content. Methane mixing was not efficient in reducing the undercutting.

Figure 2 shows the dependence of the vertical etching rate on the gas composition. Hydrocarbon addition caused the etching rate to decrease linearly. This can be understood as the result of an oxygen content decrease in the mixed gas of a fixed flow rate, the consumption of the active oxygen radical(O) due to the following oxidation reaction in the plasma $C_xH_y + (O) \rightarrow CO_2, H_2O$, and the possible formation of a polymerized film on the etched resist surface, as is discussed below.

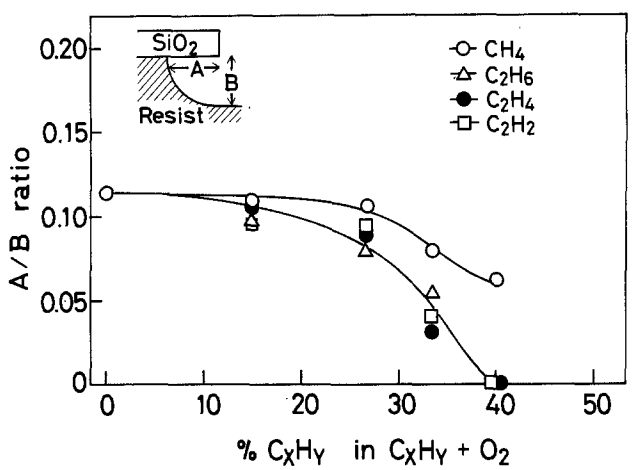

Fig. 1. Undercutting as a function of hydrocarbon content in hydrocarbon-oxygen mixtures.

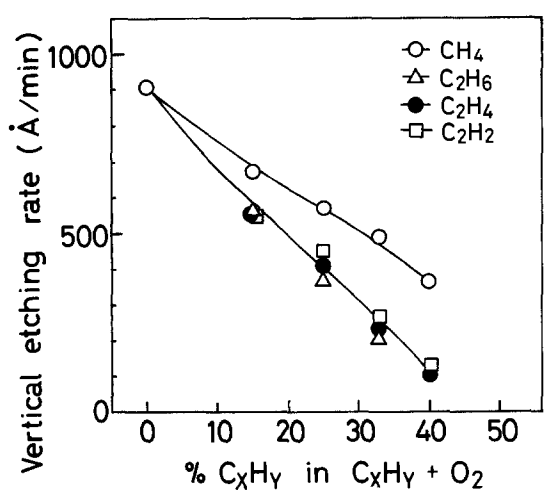

Fig. 2. Vertical etching rate as a function of hydrocarbon content in hydrocarbon-oxygen mixture.

The relationship between etching time and undercutting is shown in Fig. 3. The etching gas was 33% ethene/67% oxygen. Etching time was normalized to the time when resist was just removed completely. In an oxygen plasma, the undercutting increases linearly with increased etching time. In an ethene-oxygen plasma, on the other hand, undercutting does not increase at all. Rather, it decreases and disappears under prolonged over-etching. This indicates that the use of a hydrocarbon-oxygen plasma is extremely suitable for the providing of accurate anisotropic submicron multilayer resist patterns.

The reason for the hydrocarbon mixing effect on the reduction of undercutting was examined next. First, a resist pattern with about 0.2 μm undercutting under an SiO_2 mask was prepared in oxygen plasma. Figure 4(a) shows an SEM photograph of the resist pattern thus formed. Next, the pattern was etched in a 33% ethene/67% oxygen plasma. Figures 4(b) and (c) show SEM photographs of the patterns etched for 45 and 90 min, respectively. Films were observed at these patterns' sidewalls. The film thickness increased as the etching time increased. These films seemed to be plasma polymerized films synthesized by the ethene-oxygen plasma process. The unique etching behavior shown in Fig. 3 can easily be understood from the results shown in this figure.

Similar experiments were performed on a silicon substrate. First, the silicon pattern was formed with an undercutting under an SiO_2 mask. The pattern was then exposed to 33% ethene/67% oxygen plasma. No plasma polymerized film was observed on the silicon sidewall. This was differing from the case for the resist sidewall. Such a result indicates that the plasma polymerized film formed tends to be deposited on the organic underlayer surface.

Figures 5(a) and (b), respectively, show patterns after 60% removal of the bottom layer, and with 50% overetching using a 33% ethene/67% oxygen plasma. As can be seen in Fig. 5(a), plasma polymerized film was also observed as splotchy patches on the flat etched organic surface. However, this film was removed by prolonged overetching, and remains only at the sidewall, as can be seen in Fig. 5(b).

These results are interpreted as follows. On a flat etched surface, the etching rate is faster than the polymerization rate, because ions having large kinetic energy enhance the etching reaction, perhaps by sputtering the plasma polymerized film. On a sidewall, on the other hand, incidence of high energy ions is prevented by the SiO_2 mask. Consequently, the polymerization rate becomes faster than the etching rate (5-7).

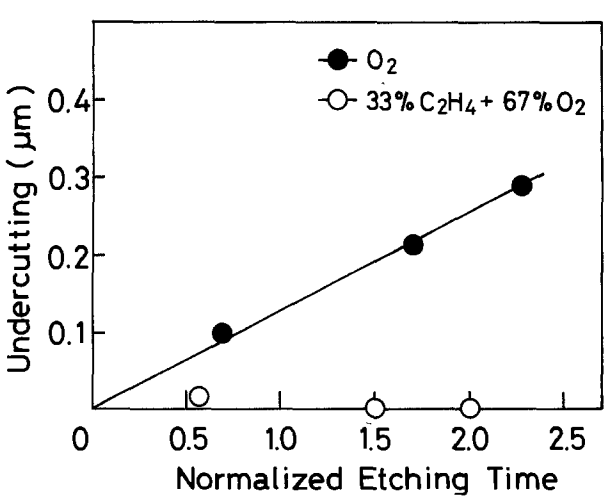

Fig. 3. Undercutting as a function of normalized etching time

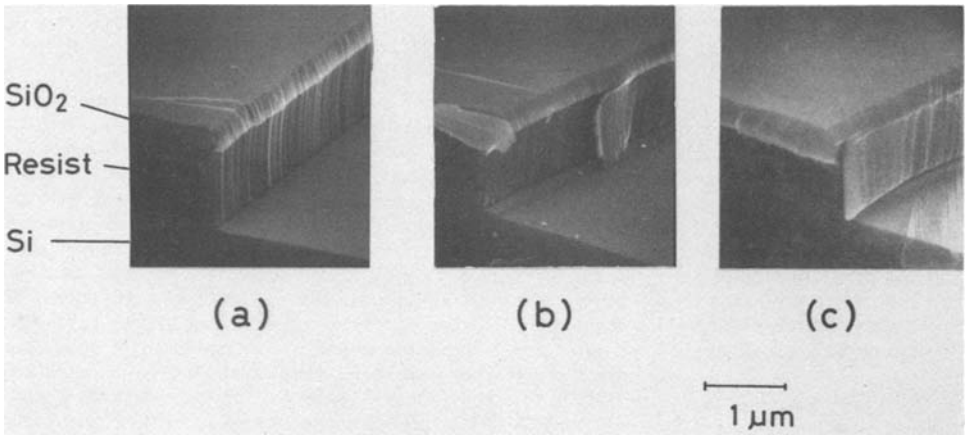

Fig. 4. SEM photographs of resist patterns with 0.4 μm thick SiO_2 mask (a) before etching, (b) after etching for 45 min, and (c) after etching for 90 min in a 33% ethene/67% oxygen plasma.

Similar experiments were performed on ethane and ethyne, and essentially the same results as those shown in Fig. 3-5 were obtained. Methane provided inferior results, probably because of its slow methane polymerization rate (8).

Conclusions

Based on these results, it is concluded that the use of hydrocarbon-oxygen plasma is very effective in achieving a steep profiled resist pattern showing no undercutting during multilevel RIE processing. This appears to be due to the fact that the hydrocarbon forms a polymerized film at the resist pattern sidewall.

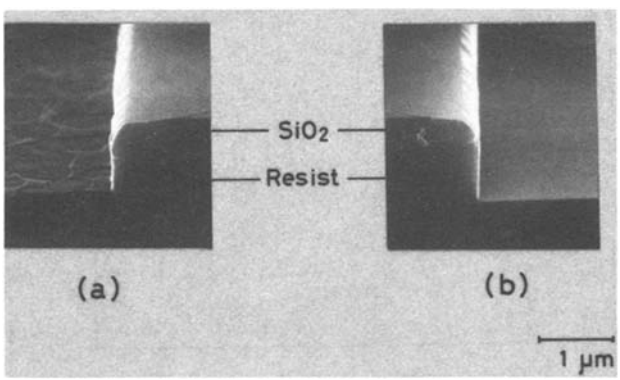

Fig. 5. SEM photographs of patterns after (a) 60% removal, and (b) 50% overetching. A 33 ethene/67% oxygen plasma was employed.

Acknowledgments

The authors wish to thank H. Mukai, M. Kondo, and T. Kitayama for their encouragement. They are also grateful to the staff of the Patterning Technology Section at the Musashino Electrical Communication Laboratory for useful discussions and comments.

Manuscript submitted May 3, 1982; revised manuscript received Aug. 27, 1982.

Any discussion of this paper will appear in a Discussion Section to be published in the December 1983 JOURNAL. All discussions for the December 1983 Discussion Section should be submitted by Aug. 1, 1983.

Publication costs of this article were assisted by Nippon Telegraph and Telephone Public Corporation.

REFERENCES

1. J. M. Moran and D. Maydon, *J. Vac. Sci. Technol.*, **16**, 1620 (1979).
2. K. L. Tai, W. R. Sinclair, R. G. Vadimsky, J. M. Moran, and M. J. Rand, *ibid.*, **16**, 1977 (1979).
3. H. Namatsu, Y. Ozaki, and K. Hirata, *ibid.*, To be published.
4. L. M. Ephrath, *This Journal*, **126**, 1419 (1979).
5. C. J. Mogab and H. J. Levinstein, *J. Vac. Sci. Technol.*, **17**, 721 (1980).
6. R. H. Bruce, G. Malafsky, A. R. Reinburg, and W. W. Yao, Tech. Digest, p. 578, Int. Electron Devices Meeting, Dec. 7-9, Washington, D.C., IEEE, New York (1981).
7. R. H. Bruce and G. Malafsky, Abstract 288, p. 703, The Electrochemical Society Extended Abstracts, Vol. 81-2, Denver, Colorado, Oct. 12-16, 1981.
8. H. Kobayashi, A. T. Bell, and M. Shen, *Macromolecules*, **7**, 277 (1974).

JOURNAL OF THE ELECTROCHEMICAL SOCIETY

ACCELERATED

—BRIEF COMMUNICATIONS—

FEBRUARY 1983

Porous Perovskite Electrode as Molten Carbonate Cathode

Kevin Scott,* M. P. Kang,* and Jack Winnick

Georgia Institute of Technology, Atlanta, Georgia 30332

The standard cathode in molten carbonate fuel cells is porous NiO, formed from sintered Ni powder, reinforced with Ni screen and oxidized in-situ. Long-term degradation and economic considerations have stimulated the search for alternative materials.

The perovskite-type compounds $Ln_{1-x}M_xM'O_3$(Ln = lanthanoid element, M = alkaline earth element, M' = transition metal element) have been shown (1) to be satisfactory in both polarization characteristics and stability under working conditions as oxygen electrode materials. We have tested the performance of a partially sintered $La_{0.8}Sr_{0.2}CoO_3$ electrode in a molten carbonate CO_2 concentrator cell. The perovskite powder was prepared by decomposing the metal acetates and oxidizing in air. This powder was then mixed with methylcellulose to form a mixture approximately 95% by weight perovskite. This was then cold-pressed at 10,000 psia and sintered in air for 4 hours at 1150°C to form a 1.5 mm thick disc conductive at 25°C and with good mechanical strength.

Figure 1 shows an electron micrograph of the final electrode material. For comparison, a section of a NiO electrode is shown in Figure 2. The NiO electrode was prepared by using a section of Ni electrode material supplied by Gould, Inc. It was not pre-lithiated and was oxidized in-situ. BET specific surface analysis indicated 0.9± 0.1 m^2/g for the perovskite and 0.5± 0.1 m^2/g for the NiO.

The perovskite discs were used as both electrodes in a simple cell with 7.92 cm^2 superficial electrode area as shown by Winnick (3,4). The electrolyte tile, donated by General Electric Corporation, was of the 62/38 Li-K carbonate eutectic hot-pressed with 45 weight percent $LiAlO_2$. The reference electrode, as shown by ref. 4, was a gold flag bathed in 30% CO_2, 70% air.

All polarizations were run at 600°C with two cathode gas compositions: 0.5% CO_2 in air and 1.0% CO_2 in air. These are gas compositions appropriate to tests of the molten carbonate CO_2 concentrator for application to manned spacecraft (2,3,4). The anode was swept with nitrogen at 80 cc/min.

The IR-free polarizations are shown in Figures 3 and 4. The data are compared with those taken under identical conditions with NiO electrodes. The NiO and perovskite data at each gas composition were combined, first in the low polarization region to estimate the exchange current density, i_o (superficial area basis):

$$i_o = \frac{di}{d\eta}\,\frac{RT}{2F}$$

Linear regression produced i_o values of 32 ma/cm^2 and 21 ma/cm^2 at 0.5 and 1.0% CO_2 on a superficial area basis. The exchange currents, based on the BET areas, are shown in Table 1.

Table 1: Exchange Current Densities, $ma/cm^2 x10^3$

	Perovskite	Nickel Oxide
0.5% CO_2	11. ± 4.	21. ± 8.
1.0% CO_2	6. ± 2.	15. ± 7.

The values for the NiO are approximately an order of magnitude lower than those found recently by Kunz (5). However, while the surface areas compare well, that study was performed at 650°C with 67% CO_2 and 33% O_2.

The intermediate-range data were fit with the Butler-Volmer equation in the Allen-Hickling form:

$$\ln i/[\exp(2F\eta/RT)-1] = \ln i_o - \alpha\eta F/RT$$

with i_o set with the low-polarization values. The transfer coefficients, α, obtained from linear regression were 0.59 and 0.73 for the

*Electrochemical Society Active Member.

0.5 and 1.0% CO_2 data as shown in Figure 5. The scatter in the data precludes any conclusion other than that they are consistent with an α of 0.6, as found earlier in a more comprehensive study using NiO. The difference in exchange current densities between the 0.5 and 1.0% CO_2 gases is also not considered significant.

At high current densities at higher gas flow rates mass transfer effects become appreciable. Here, in Figure 4, the perovskite cathode is seen to be somewhat inferior to the NiO. We presume this to be due to mass transfer resistance in our crudely-formed material.

Figure 3 shows that at the lower gas flow rate 100% CO_2 utilization is obtained at a much lower current density, 21 ma/cm^2. At these lower current densities, the mass transfer characteristics of the perovskite electrode appear equivalent to those of the NiO.

The most significant finding is the correspondence between the perovskite and NiO kinetic performance. Other features equally important for commercial electrode materials e.g., life, cost, were beyond the scope of this preliminary study. However, our results indicate perovskite materials are attractive candidates for such further assessment.

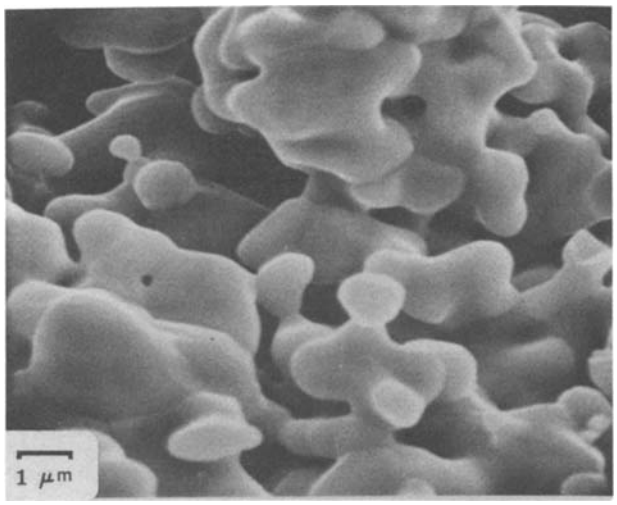

Fig. 1. Scanning electron micrograph of perovskite electrode.

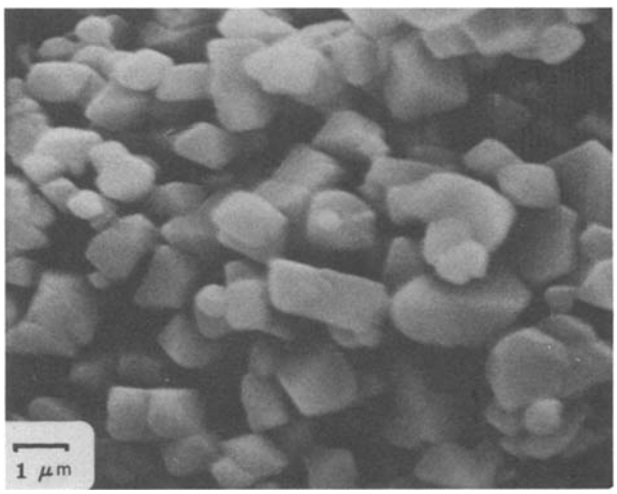

Fig. 2. Scanning electron micrograph of NiO electrode.

References

1. T. Kudo, H. Obayashi, M. Yoshida, J. Electrochem. Soc., 124, 321 (1977).

2. J. Winnick, et al., I.E.C. Proc. Des. Dev., 13, 59 (1974).

3. J. Winnick, H. Toghiani and P. Quattrone, AIChE J., 28, 103 (1982).

4. J. Winnick and Philip N. Ross, Jr., J. Electrochem. Soc., 128, 991 (1981).

Manuscript submitted Aug. 12, 1982; revised manuscript received Oct. 25, 1982.

Publication costs of this article were assisted by Georgia Institute of Technology.

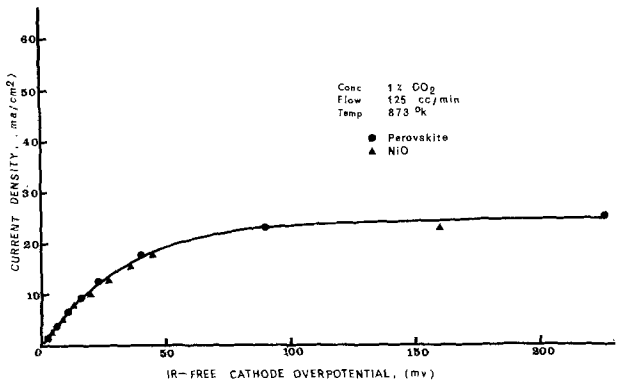

Fig. 3. I.R.-free polarizations with 1% CO_2 in air.

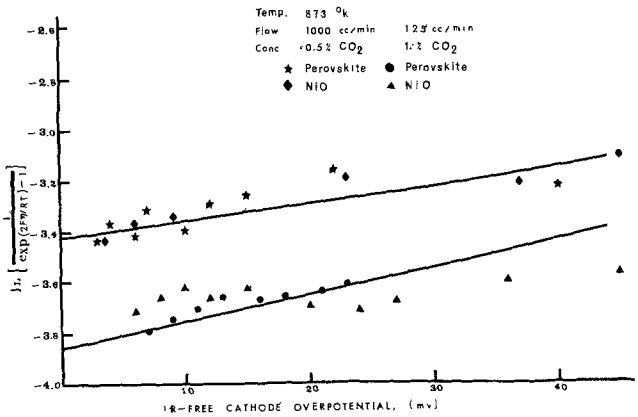

Fig. 5. Allen-Hickling plot for determination of transfer coefficients.

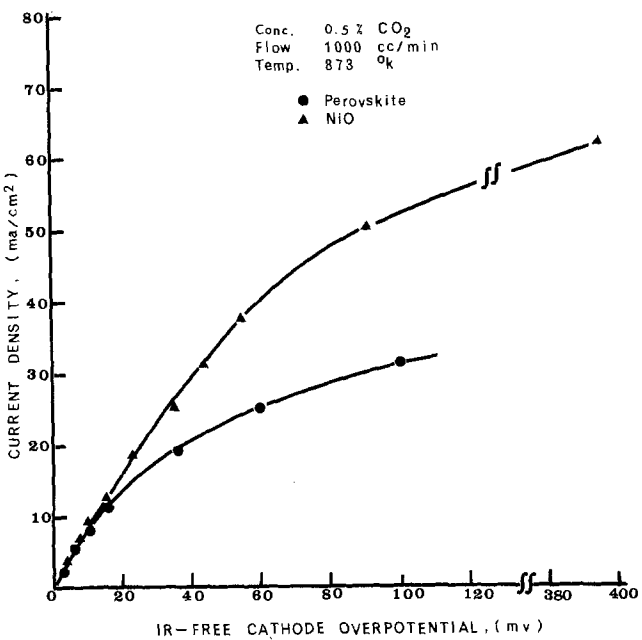

Fig. 4. I.R.-free polarizations with 0.5% CO_2 in air.

Thermodynamic Considerations in the Crystal Growth of Yttrium Oxide by the Chemical Transport Reaction

Koichi Matsumoto, Tsuneaki Kawanishi, and Katsuki Takagi

Research Institute of Electronics, Shizuoka University, Johoku, Hamamatsu 432, Japan

and Shoji Kaneko

Department of Industrial Chemistry, Faculty of Engineering, Shizuoka University, Johoku, Hamamatsu 432, Japan

A chemical transport method which has been used as a kind of crystal growth techniques is applicable even to nonvolatile or dissociative compounds, because they react with transporting agents (mainly halogens or halides) changing to volatile substances. Also, it can be employed to advantage for the reason of a simple apparatus and procedure. However, the chemical transport of oxides where the equilibrium relevant to the transport reaction is apt to lie far away in either side of the system is often difficult. In such a case the chemical transport may be carried out if any reductant is used together with a halogen or a halide and then the equilibrium condition becomes adequate (1).

Yttrium oxide (Y_2O_3) has been used as receptacles of Na lamps, and as phosphors for color tubes and luminescent lamps with high color rendering. Its application to infrared-visible converters or to laser matrix has also been investigated (2,3). The crystal growth of Y_2O_3 has mostly been carried out by means of a fusion method (4). A largely complicated apparatus is required in the method, as the melting point of the compound is so high (2440°C). Hence we attempted the crystal growth of Y_2O_3 by the chemical transport method. Small needle crystals of Y_2O_3 were grown at relatively low temperatures by using simultaneously bromine and carbon monoxide as transporting agents, on which thermodynamic considerations were performed in detail.

EXPERIMENTAL

The chemical transport was carried out by heating a fused silica ampoule of ∿12 mm in inner diameter and ∿190 mm in length (∿20 cm^3 volume) containing Y_2O_3 powder (Dai Nippon Painting Co., Ltd., luminescence pure) in an electric furnace with two separated zones. Bromine as a transporting agent was filled in the ampoule by slow heating of frozen bromine after evacuation. Carbon monoxide as a reductant was introduced to the ampoule by heating of a mixture of calcium carbonate and zinc at 750°C.

Key words: yttrium oxide, crystal growth, chemical transport method, thermodynamics.

RESULTS AND DISCUSSION

The chemical transport of Y_2O_3 was attempted by using bromine as a transporting agent first. In this case the equilibrium relevant to the reaction is assumed to be Eq. [1].

$$Y_2O_3(s) + 3Br_2(g) \rightleftarrows 2YBr_3(g) + 3/2\,O_2(g) \quad [1]$$

In practice, however, any reaction did not occur.

Thermodynamic data required to discuss this situation are listed in Table I. The values given in ref. (3) were adopted for $Y_2O_3(s)$, $Br_2(g)$, and $O_2(g)$. The values of $YBr_3(g)$ which were not found in any reference were estimated as follows. For the standard enthalpy of formation of $YBr_3(s)$, the arithmetic mean value -193 kcal/mol between -239.0 kcal/mol of $YCl_3(s)$ and -149.4 kcal/mol of $YI_3(s)$ (6) was adopted. According to the estimation methods described in ref. (5) with various values of YBr_3 (melting point 904°C, enthalpy of fusion 9 kcal/mol, boiling point 1470°C, and enthalpy of evaporation 44 kcal/mol) (7), -126 kcal/mol was obtained as the standard enthalpy of formation $\Delta\bar{H}^\circ_{f_{298}}$ of $YBr_3(g)$, 86.3 cal/K·mol as the standard entropy $\bar{S}^\circ_{f_{298}}$ for the molecular weight 329, and 18 cal/K·mol as the heat capacity $\bar{C}_p$ due to the case of nonlinear gaseous molecule of four atoms. The standard free energy change from left to right

Table I. Thermodynamic data relevant to the chemical transport of Y_2O_3

	$\Delta\bar{H}^\circ_{f\,298}$ (kcal/mol)	$\bar{S}^\circ_{298}$ (cal/K·mol)	$\bar{C}_p$ (cal/K·mol)
Y_2O_3(s)	-455.4±1.5	23.7±0.1	$29.60+1.20\times10^{-3}T-4.78\times10^{5}T^{-2}$
Br_2(g)	7.39±0.03	58.64±0.05	$8.93+0.11\times10^{-3}T-0.31\times10^{5}T^{-2}$
YBr_3(g)	-126*	86.3*	18*
O_2(g)	0	49.0±0.01	$7.16+1.0\times10^{-3}T-0.40\times10^{5}T^{-2}$
CO(g)	-26.42±0.05	47.22±0.01	$6.79+0.98\times10^{-3}T-0.11\times10^{5}T^{-2}$
CO_2(g)	-94.05±0.03	51.07±0.01	$10.55+2.16\times10^{-3}T-2.04\times10^{5}T^{-2}$

* Estimated by the procedure described in the text.

in the reaction [1] is given by means of Eq. [2] which was determined by using these values.

$$\Delta G^\circ_T[1] = 184000 + 23.0T\log T - 114T \quad [2]$$

The temperature dependence of the equilibrium constant ($K[1]=\exp\{-\Delta G^\circ_T[1]/RT\}$) is shown by curve [1] in Fig. 1. Under the present conditions logK takes large negative value, and it is therefore presumed that the reaction scarecely occurs. The experimental results agreed well with this presumption.

For the optimum transport logK should be near zero, or the extreme value must be avoided. This can be done, for instance, if one choose carbon monoxide as a reductant jointly with bromine. Then the equilibrium relevant to the transport reaction is assumed to be Eq. [3].

$$Y_2O_3(s) + 3Br_2(g) + 3CO(g) \rightleftarrows 2YBr_3(g) + 3CO_2(g) \quad [3]$$

The additional data necessary to the thermodynamic discussion are also given in Table I. The standard free energy change from left to right in the reaction [3] is given by means of Eq. [4].

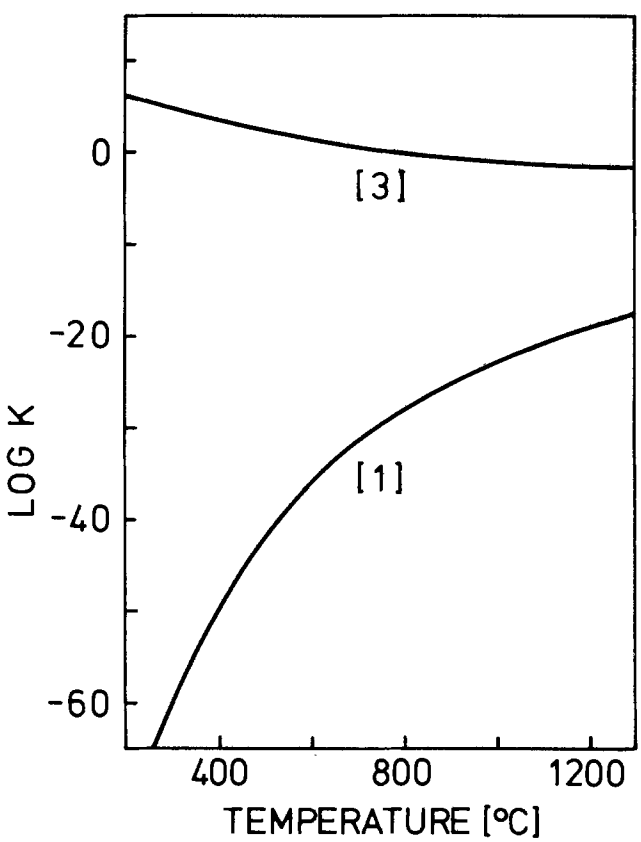

Fig. 1. Temperature dependence of the equilibrium constant in the following equations: [1] $Y_2O_3(s)+3Br_2(g) \rightleftarrows 2YBr_3(g)+3/2\,O_2(g)$ and [3] $Y_2O_3(s)+3Br_2(g)+3CO(g) \rightleftarrows 2YBr_3(g)+3CO_2(g)$.

$\Delta G^{\circ}_{T}[3] = -19600 + 16.1T\log T - 31.4T$ [4]

The temperature dependence of the equilibrium constant K[3] is shown by curve [3] in Fig. 1. The equilibrium condition is now considered to be optimum for the small absolute value of K[3], although the transport rate is presumed to be low on account of the small temperature dependence.

An experiment based on these considerations caused the transport of Y_2O_3 to occur, and then small needle crystals were obtained (Fig. 2). The conditions were as follows: bromine 3 atm, CO 3 atm (at 1130°C); source zone 1160°C, growth zone 1100°C; 13 days.

It is summarized that the crystal growth of Y_2O_3 by the chemical transport method was unsuccessful by using bromine alone as a transporting agent, but was successful by using simultaneously bromine and carbon monoxide, being in agreement with the thermodynamic considerations.

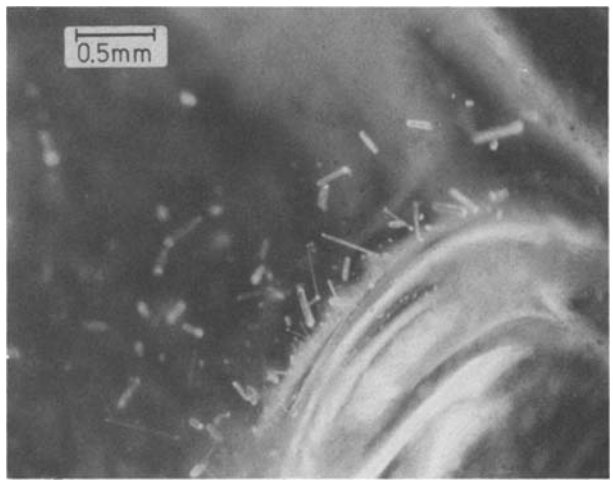

Fig. 2. Needle crystals grown.

REFERENCES

1. K. Matsumoto, S. Kaneko, and K. Takagi, J. Cryst. Growth, 40, 291 (1977).
2. C. Greskovich and J. P. Chernoch, J. Appl. Phys., 45, 4495 (1974).
3. H. Tsuiki, T. Masumoto, K. Kitazawa, and K. Fueki, Jpn. J. Appl. Phys., 21, 1017 (1982).
4. H. Tsuiki, K. Kitazawa, T. Masumoto, K. Shiroki, and K. Fueki, J. Cryst. Growth, 49, 71 (1980).
5. O. Kubaschewski and C. B. Alcock, "Metallurgical Thermochemistry, 5th Edition," Pergamon, Oxford (1979).
6. "NBS Technical Note 270-5," U.S. Government Printing Office, Washington, D.C. (1971).
7. "Comprehensive Inorganic Chemistry, Vol. 3," J. C. Bailar, Jr. et al., Editors, Pergamon, Oxford (1973).

Manuscript received Sept. 24, 1982.

Publication costs of this article were assisted by Shizuoka University.

JOURNAL OF THE ELECTROCHEMICAL SOCIETY

ELECTROCHEMICAL SCIENCE
— AND TECHNOLOGY —

MARCH
1983

Ion Clustering and Proton Transport in Nafion Membranes and Its Applications as Solid Polymer Electrolyte

Richard S. Yeo*

Pinnacle Research Institute, Cupertino, California 95014

ABSTRACT

The concentrations of fixed ion in Nafion® membranes have been calculated based on both the homogeneous model and the ion cluster model while the concentrations of co-ion were calculated from the Donnan expression. The experimental results on the concentrations of co-ion reveal that the ions in this material do form clusters and the membrane also exhibits a strong Donnan exclusion effect. The ionic mobilities obtained from the conductivity and diffusivity studies are in fairly good agreement. Strong acidity coupled with high proton mobility in this membrane provide an important solid polymer electrolyte for a variety of electrochemical applications. The impact of polymer morphology on cell performance is also discussed.

Interest in perfluorosulfonic acid (Nafion®) has increased considerably in recent years (1-23) and it has been an important subject in many recent scientific meetings (24-30) because of its industrial importance, especially in electrolytic processes. Because of their excellent chemical stability and high conductivity, Nafion membranes find applications in chlor-alkali cells (10), water electrolyzers (4, 12, 13), hydrogen-air fuel cells (12), hydrogen-halogen cells (2, 3), zinc-bromine cells (11), and Donnan dialyzers (19).

Nafion belongs to a class of materials known as ion-containing polymers (31). Although a significant number of studies have been undertaken on the ion-containing polymers to date, the state and structure of the ion aggregation, and the modifications which occur on hydration are generally not known quantitatively, even though they may have major importance. The reasons for the lack of understanding of the microstructure of ion-containing polymers lie in their complexity. One series of studies (1, 15, 32-36) postulates the existence of sizable regions, of dimensions of *ca.* 50Å, in which the ions are clustered (37), the most direct evidence coming from small angle x-ray scattering. Another group (38-40) suggests that the ions are dispersed throughout the sample in a very low state of aggregation, *i.e.*, either as ion pairs or ion quartets. The evidence in support of these small ionic groups was derived from dynamic mechanical data (38), nuclear magnetic resonance data (39), and viscosity measurements (40).

Ion cluster phenomena in Nafion were first indicated by Yeo and Eisenberg based on small angle x-ray scattering and thermo-rheological data (1). Many recent studies (5, 7, 9, 14-17) have also arrived at the same conclusion that the ions are clustered. This ion cluster morphology of Nafion accounts for its many unusual properties, such as thermo-rheological complexity (1), dual cohesive energy densities (5), and percolative ion transport (14).

Extensive studies have been made on the transport of the alkali ions (9, 10, 14), especially the sodium ion, in Nafion membranes because of their wide application in the chlor-alkali industry. In contrast, there have been few studies on transport properties of Nafion in acidic electrolytes (2, 3, 7, 11).

In this study an attempt is made to bridge the gap between the basic polymer science concerning the microstructure of this perfluorinated ionomer and the electrochemical criteria determining the performance characteristics of this polymer for various electrochemical applications. This research is aimed at investigating the role the ion clustering of the polymer plays in cell performance. The results of this study may provide some direction for the future development of high performance membrane cells in industrial electrolytic or separation processes. Finally, this paper serves the purpose of demonstrating the use of a "simple" electrolyte sorption technique in investigating the mysterious ion clustering phenomena in ionomers.

Experimental

Membrane materials.—Measurements were made on Nafion membranes, obtained from du Pont, that had an equivalent weight of 1200 and a thickness of 0.025 cm. Equivalent weight (*EW*) is defined as the weight of acid polymer that will neutralize one equivalent of base. *EW* is equal to the reciprocal of ion exchange capacity (IEC). The received material absorbs *ca.* 17 weight percent (w/o) water when immersed in water. These samples are assigned as normal (N) form. The water uptake of the material increases to *ca.* 30 w/o when boiled in water for more than 30 min and these samples are denoted as expanded (E) form. The membrane will continue to hold that same amount of water at room temperature, unless the effect is destroyed by drying at elevated temperatures (22).

Electrolyte concentration in membranes.—The equilibrium electrolyte content of the membrane was determined by a method previously described (3). Also, the membrane, on reaching equilibrium in the electrolyte, was removed, surface dried, and then thoroughly leached with water. The extract was titrated for acid content. The concentration of co-ion in the membrane was calculated from the electrolyte content and the amount of acid leached out of the membrane.

Electrolyte diffusion in membranes.—A dry film sample was immersed in the electrolyte in a constant-

* Electrochemical Society Active Member.
Key words: electrolyte, polymers, separators, transport.

temperature bath. After a certain time period, the sample was removed from the electrolyte, surface dried, and the weight gain (M_t) was determined. The same sample was then replaced in the bath at the same temperature for a second time period, and the weight was redetermined. The procedure was repeated until there was no further weight gain; the total weight gain is referred to as the equilibrium sorption M_∞. All the weighing procedures were done in less than 10 sec.

Membrane conductivity.—The membrane conductivities were measured in a Teflon cell described elsewhere (7). The electrodes were bonded onto the membrane surface by a hot pressing method. The electrodes were connected to an a-c bridge (Gen Rad 1658 RLC Digibridge). Measurements were made at 1 kHz.

Results and Discussion

The sulfonic acid groups of Nafion membranes are highly ionized in water. The proton of these groups is a mobile, replaceable ion (so-called counterion) while the sulfonate group is fixed into or retained by the polymeric matrix (so-called fixed ion). The anions, with charge similar to the fixed ions, are called co-ions.

Concentration of fixed ion.—Homogeneous model.—If one assumes low, or no, ion aggregation in the membrane, then the membrane is regarded as a microscopically homogeneous medium. The amount of ionic groups is given by IEC whereas the volume that the ionic groups represent is equal to the whole volume of the wet membrane, V_0. V_0 can be estimated from the weight and the density of the wet membrane. The concentration of fixed ion (in term of mol/liter) can be given by

$$\bar{C}_f = 1000 \times \frac{\text{IEC}}{V_0} = \frac{1000}{EW} \times d_0 \qquad [1]$$

where d_0 is the density of the wet membrane, which can either be estimated from the expression given elsewhere (23) or by direct measurements.

Ion cluster model.—In this model, two basic types of ionic aggregates are postulated (37): small aggregates consisting of a few ion pairs termed multiplets and larger aggregates termed ion clusters. The structure of Nafion membrane can be broadly described as that of a microphase-separated system in which a matrix of low ion content (due to multiplets) is interspersed with ion-rich domains (ion clusters). Part of the water contained within the membrane is associated with the sulfonic acid groups; part interacts with the organic matrix (17, 18, 20); while still another part forms water clusters (16). Roche *et al.* (16) has proposed a two-phase model in which the ion clusters are considered as a hydrophilic phase whereas the organic matrix is the hydrophobic phase.

The amount of ionic groups within the hydrophilic phase (ion clusters) is equal to IEC $\times$ f_i where f_i is the fraction of ionic groups in the ion clusters. The volume of the ion cluster is given by $V_w \times f_w$ where V_w is the volume of electrolyte absorbed by the membrane and f_w is the fraction of electrolyte in the ion clusters. V_w can be calculated from the electrolyte uptake of the membrane.

If one assumes that the concentration of fixed ion in the hydrophilic phase can represent that of the whole membrane, that concentration can be given by

$$\bar{C}_f = 1000 \times \frac{\text{IEC}\, f_i}{V_w f_w} = \frac{1000 d_e}{EW\, f_e} \times \left(\frac{f_i}{f_w}\right) \qquad [2]$$

where f_e and d_e are the weight fraction and density of the electrolyte absorbed by the membrane, respectively.

Although the structure of Nafion membrane has been characterized, the evaluation of f_i and f_w values seems quite difficult because of the limitation of available research tools. In addition, these values change with the prehistory of the membrane and the environment the membrane encounters. Roche *et al.* (16) have made a rough estimation of f_i and f_w for Nafion-Na by using a small angle neutron scattering technique. They found that f_i and f_w are >40% and >76%, respectively, for N-form samples whereas the values are >60% and >84%, respectively, for E-form samples. Falk also estimates that about three quarters of the water is in the ion cluster based on infrared data (18). Therefore, the value of f_i probably varies between 0.4 and 1.0 whereas the value of f_w varies in the range of 0.76-1.0. Accordingly, the ratio of f_i/f_w varies between 0.4 and 1.32. It is very likely that $f_i/f_w \approx 1$ because of the hydrophilic nature of the ionic groups. Since no perfectly satisfactory values of f_i and f_w can be used, it is assumed that $f_i/f_w = 1$ for the sake of simplicity in calculation. The error in this assumption, to a reasonable approximation, may be mitigated by the experimental error in determining the value of f_e. Moreover, Gierke (15) has assumed that both f_i and f_w are equal to 1 in the estimation of the size of ion clusters.

The water uptake of Nafion for various *EW* has been reported previously (22). Figure 1 shows the calculated concentration of fixed ions for Nafion of various *EW* in equilibrium with water. For the case of no ion aggregation, the concentration of fixed ion decreases with increasing *EW* due to less ionic groups present in the sample while V_0 varies very little with *EW*. In contrast to the homogeneous model, the concentration of fixed ion increases with *EW* if the ion clustering concept is adopted, because V_w is far smaller than V_0. Thus, the decrease of ionic groups with increasing *EW* is less significant in comparison with the decrease of V_w, which in turn is related to the water uptake. Another important feature is that membrane pretreatment has a strong effect on the concentration of fixed ion, especially in the case of ion clustering. The concentration of fixed ions is higher for N-form samples than for E-form samples since water uptake increases by boiling the sample in water. It is expected that the concentration of fixed ion could further increase by drying the membrane at elevated temperatures prior to the soaking in water (3).

It is important to note that the material should exhibit a very strong acidic behavior in water when ion clustering occurs. As can be seen from Fig. 1, the concentration of fixed ion for Nafion of 1200 *EW* in E-form is equivalent to 13 w/o sulfuric acid and it is in good agreement with the value of 10 w/o sulfuric acid reported by LaConti *et al.* (41). Recently, an apparent $pK_a < 1$ for Nafion of 1150 *EW* has been observed, suggesting a strong acidic behavior in this material (10).

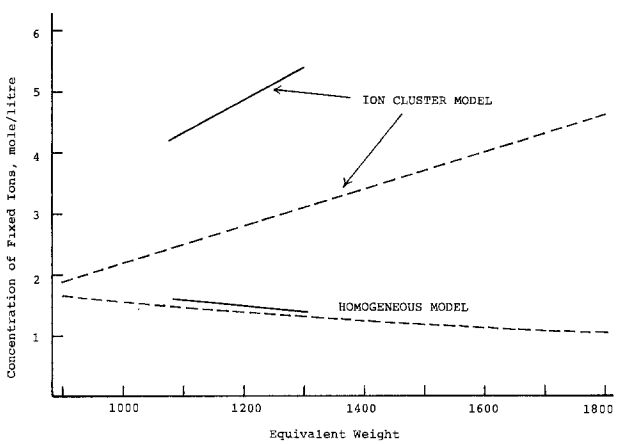

Fig. 1. Calculated concentration of fixed ion for Nafion of various *EW* in equilibrium with water at 25°C. —— N-form, --- E-form.

The electrolyte uptake of Nafion in various electrolytes has been reported previously (3, 22, 42). Figure 2 shows the dependence of concentration of fixed ion on HCl concentration for Nafion of 1200 *EW*. As ion clustering occurs the concentration of fixed ion increases drastically with electrolyte concentration.

Concentration of co-ions.—The equilibrium of this ion exchange membrane with a uni-univalent salt in a solution of concentration C is given by the Donnan expression

$$C^2 = \bar{C}_n(\bar{C}_n + \bar{C}_f)\,(\bar{\gamma}/\gamma)^2 \qquad [3]$$

where $\bar{C}_f$ and $\bar{C}_n$ are the concentrations of fixed ion and co-ion, respectively. γ and $\bar{\gamma}$ are the activity coefficients in the external and membrane phase, respectively.

Figure 3 indicates a plot of $\bar{C}_n$ *vs.* C for N-form Nafion in HCl electrolyte. The solid curves are calculated by Eq. [3] based on $\bar{C}_f$ given in Fig. 2 and on the basis that the activity coefficient ratio in Eq. [3] is unity. For estimation of co-ion concentration, this assumption seems useful as the agreement with the experimental data is reasonable. Besides, the same assumption has also been employed successfully in many membrane systems which differ considerably in structure (43, 44). The dashed line is for the case in which there is no Donnan exclusion effect for the membrane ($\bar{C}_f = 0$). A similar plot for E-form Nafion in HBr electrolyte is given in Fig. 4.

The data strongly support the suggestion that Nafion possesses ion-cluster morphology and is not a homogeneous medium. Furthermore, the materials exhibit a Donnan exclusion effect, which decreases significantly when the material is boiled, primarily due to the lower concentration of fixed ion, resulting from dilution by absorbed water. An extremely high Donnan exclusion effect in Nafion has also been found for the case of NaOH electrolyte (45).

Conductivity of hydrated membrane.—Figure 5 represents the membrane conductivity of Nafion in water as a function of water content (in terms of H_2O/SO_3^-).

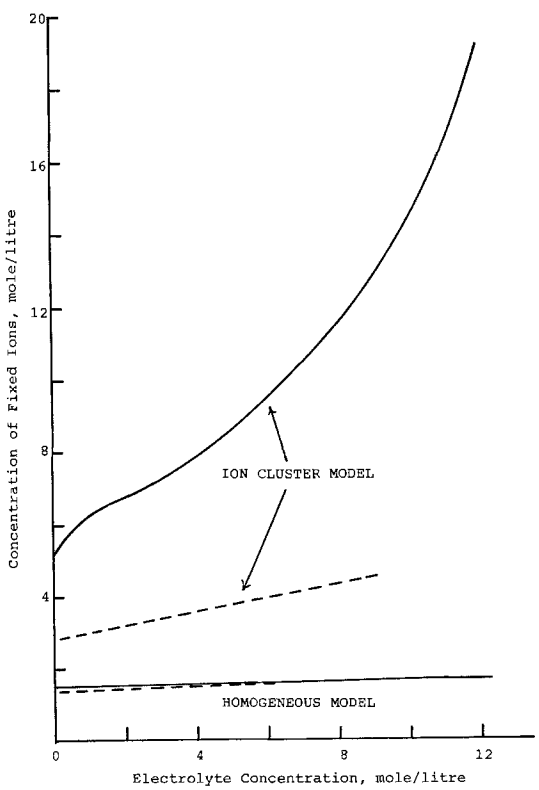

Fig. 2. Calculated concentration of fixed ion for Nafion of 1200 *EW* in various HCl electrolyte at 25°C. —— N-form, --- E-form.

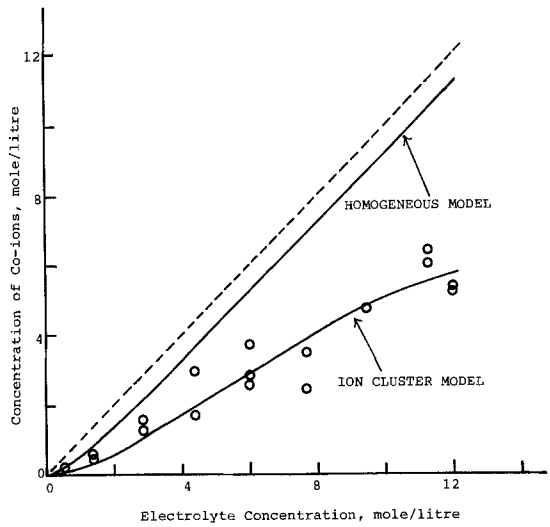

Fig. 3. Concentration of co-ion for N-form Nafion of 1200 *EW* in equilibrium with various HCl electrolytes at 25°C. Dashed curve, no Donnan effect; solid curves, calculated from Eq. [3].

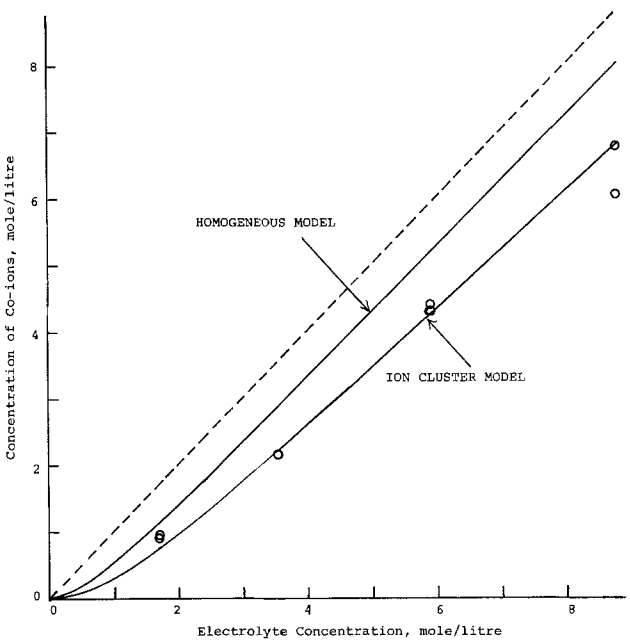

Fig. 4. Concentration of co-ion for E-form Nafion of 1200 *EW* in equilibrium with various HBr electrolytes at 25°C. Dashed curve, no Donnan effect; solid curves, calculated from Eq. [3].

Due to the strong acidity of the sulfonic acid groups (as shown by the dashed curve), the membrane is highly conductive to protons. The solid curve is calculated from the following equation

$$\kappa = A\kappa_e\,(1 - \theta)^{1.5} \qquad [4]$$

where θ is the volume fraction of polymer and κ_e is considered as the conductivity of sulfuric acid with concentration equal to that of the sulfonic acid group of the ion-clustered membrane. The pre-exponential factor $A = 0.54$ is observed. This factor could be ascribed to both the physical shape of the conductivity cell as well as the deviations from the assumption made on κ_e.

It has been reported (2, 3) that the conductivity of Nafion in concentrated acid electrolytes is one order of magnitude smaller than the electrolyte conductivity. However, the membrane conductivity is higher than the electrolyte conductivity in the case of very dilute electrolytes or nonaqueous solvents (7, 46) because the intrinsic conductivity (42) of the membrane becomes important.

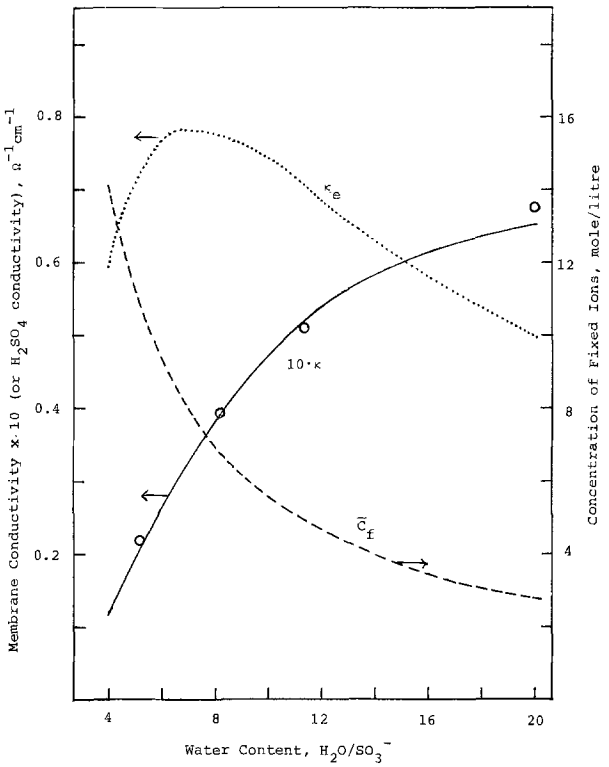

Fig. 5. Membrane conductivity of Nafion 1200 *EW* with various water content at 25°C. Solid curve, calculated from Eq. [4]; dashed curve, concentration of fixed ions as a function of water content; dotted curve, the conductivity of sulfuric acid with concentration equal to $\bar{C}_f$.

Hsu *et al.* (14) reported that the membrane conductivity of Nafion in alkaline electrolyte exhibits ion percolative behavior and can be given by

$$\kappa = \kappa_e (1 - \theta - \phi)^{1.5} \quad [5]$$

where ϕ is the threshold volume fraction of the aqueous phase and κ_e is the electrolyte conductivity. There is an (ionic) insulator-to-conductor transition in Nafion around ϕ. Based on the percolation theory, ϕ is 0.15 whereas the experimental value of 0.10 for Nafion in NaOH electrolyte is observed.

In order to explore the relationship between the membrane conductivity and the volume fraction of the polymer phase, the conductivity results on other systems are of interest. The conductivity of composite materials can be related to the volume fraction of nonconducting particles by the following equation

$$\kappa = \kappa_e (1 - \theta)^n \quad [6]$$

where n is an empirical exponent, which Archie (47) found to be applicable to unconsolidated sand ($n = 1.3$) and sandstones ($n = 1.8$-2.0).

Equation [6] becomes the well-known Bruggemann equation (48) if $n = 1.5$. Tobias *et al.* (49) have shown that the Bruggemann equation can be used to describe the conductivity of random dispersions of spherical insulators with a large size range of spheres, such as occurs in gas-electrolyte emulsions. More recently, Hino *et al.* (50) have reported that the superficial conductivity of the NaOH solution containing gas bubbles also agreed well with the Bruggemann equation.

There is a strong similarity between these different systems. The relationship between the conductivity and the volume fraction of nonconducting media can be very well described by different forms of the Bruggemann equation.

The Bruggemann equation was derived with the assumption that the nonconducting particles are spherically shaped. It is generally not applicable, particularly not if the particles are greatly elongated or when they contain cavities.

The conductivity of membranes with various water content and at various temperatures has been measured. Figure 6 shows a plot of log κ *vs.* $1/T$. The behavior is of the Arrhenius type, the activation energy for conduction is 2.25 kcal/mol, smaller than that for the case of HCl electrolytes (2).

Sorption of HCl by Nafion membrane.—For short times, the amount of electrolyte M_t absorbed by the polymer film in time t is given by the following equation (51)

$$\frac{M_t}{M_\infty} = 4\left(\frac{Dt}{l^2}\right)^{1/2}\left[\frac{1}{\pi^{1/2}} + 2\sum_{n=0}^{\infty}(-1)^n \text{ierfc}\frac{nl}{2(Dt)^{1/2}}\right] \quad [7]$$

where D is the diffusion coefficient, l is the thickness of the sheet, n is a positive integer, and ierfc $X = (1/\pi^{1/2}) \exp(-X^2) - X$ erfc X, where erfc X is $1 -$ erf X, erf being the error function.

Figure 7 shows the typical sorption curves for various HCl concentrations. The linearity of the plots below $M_t/M_\infty = 0.5$ suggests that the diffusion is Fickian and that a constant diffusion coefficient is operative. The values of D were calculated from the initial slope of the plots, *i.e.*, by setting tthe second term in the bracket equal to zero (52, 53).

Figure 8 shows a plot of log D as a function of HCl concentration. It is clear that the diffusion of HCl electrolyte in Nafion is fast. For dilute electrolytes, it is one order of magnitude smaller than the self-diffusion of HCl.

Ion mobility in Nafion membrane.—Ion mobility can generally be calculated from conductivity and diffusivity data. The results of these calculations are summarized in Table I. The conductivity test measures the sum of proton mobility and co-ion (OH^- and Cl^-) mobility. On the other hand, the ion mobility obtained from the diffusivity study is ascribed to the "combined" mobilities of the HCl molecules and water molecules. It is largely attributed to the co-ion mobility as the proton mobility is relatively high. Furthermore, the results in Fig. 3 indicate that the Donnan effect of the membrane could make the mobility of HCl in the membrane slower than that for the water molecule. The diffusion coefficient obtained from the sorption method can be considered only as an "apparent" value because of these complications. It is thus meaningless to estimate the transport numbers

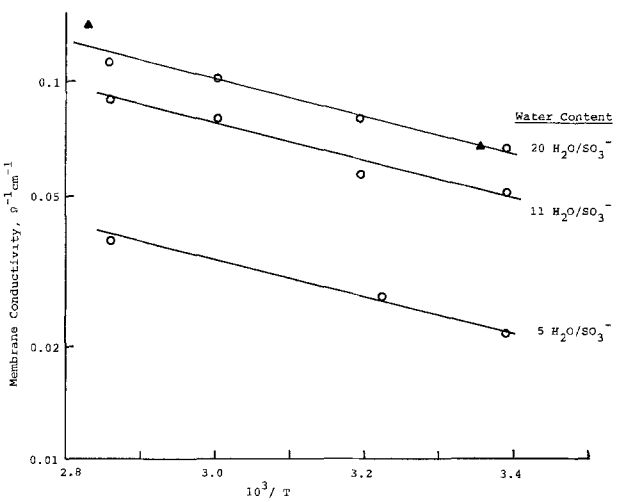

Fig. 6. Arrhenius plots for membrane conductivity of Nafion with various water contents. (○) This study; (▲) Ref. (41).

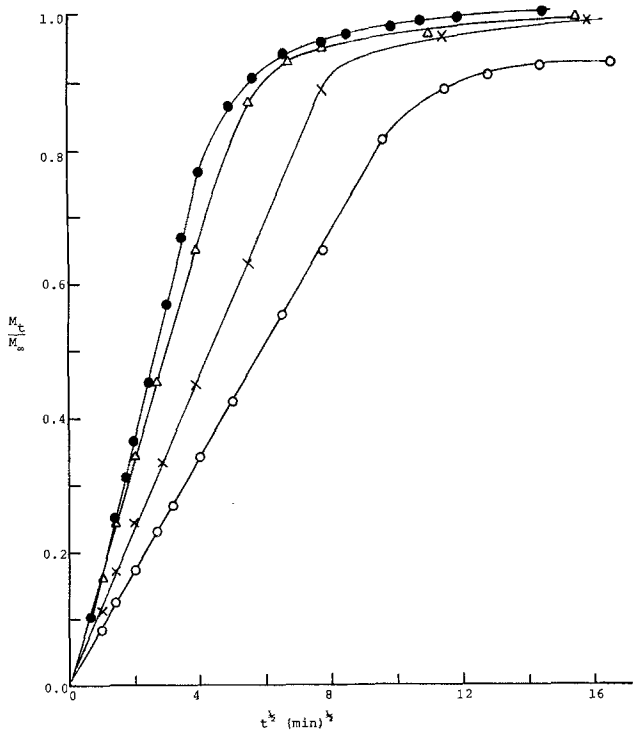

Fig. 7. Plot of M_t/M_∞ vs. $\sqrt{t}$ for Nafion of 1200 *EW*. (•) H_2O, (△) 10% HCl, (×) 20% HCl, (○) 25% HCl.

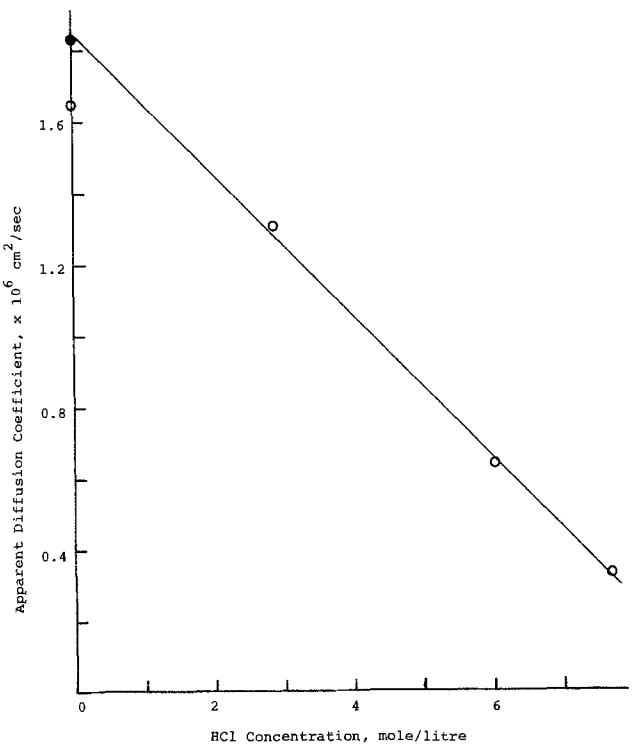

Fig. 8. Apparent diffusion coefficient of HCl electrolyte in Nafion of 1200 *EW* as a function of HCl concentration at 25°C. (○) This study, (•) Ref. (1).

of various ions in the membrane by combining the two sets of mobility data despite that they are in the same order of magnitude and follow the same trend with electrolyte concentrations.

Applications of Nafion as solid polymer electrolyte.— High ion mobility, together with strong acidity and hydrophilicity, makes this membrane a good "electrolyte" for many electrochemical applications. This perfluoro sulfonic acid polymer has recently been shown to have potential for use as a solid "superacid" catalyst for many electro-organic syntheses (54) as well as a semisolid proton conductor in WO_3-based electrochromic displays (55). The concept of using an ion exchange membrane as "electrolyte" in fuel cells was introduced by Grubb (56) in the early sixties.

Table I. Ion mobilities calculated from conductivity and diffusivity data

Electrolyte concentration (w/o HCl)	κ (Ω^{-1} cm^{-1})	$\bar{C}_f$ (mol/liter)	$U_\kappa \times 10^{5a}$ (cm^2 V^{-1} sec^{-1})	$D \times 10^6$ (cm^2 sec^{-1})	$U_D \times 10^{6b}$ (cm^2 V^{-1} sec^{-1})
0	0.051	5.21	10.1	1.66	6.53
10	0.06	7.13	8.72	1.31	5.15
20	0.028	9.40	3.09	0.64	2.52
25	0.016	11.21	1.48	0.33	1.30

[a] U_κ: ion mobility calculated from conductivity data.
[b] U_D: ion mobility calculated from diffusivity data.

The beauty of using Nafion membranes in electrochemical cells can be witnessed by the uniqueness of the solid polymer electrolyte (SPE) cells, which are being developed at various industrial laboratories (12, 57). The catalytic particles are bonded to the membrane that also serves as both the cell separator and the sole "electrolyte." Although deionized water is the only fluid circulated through the SPE water electrolyzer, the environment that the electrodes encounter is highly acidic. The sulfonic acid groups at the membrane surfaces produce an acidity equal to 20 w/o sulfuric acid. Because of this acidic media, acid resistant noble metals or their oxides are used as anode materials (13, 58) while platinum serves as the cathode material.

The relationship between the morphology and properties of the permselective membrane and its implication to the electrochemical application is rather complicated (59). It is desirable for the membrane to have the ion cluster morphology such that the concentration of fixed ion is higher, which, in turn, yields a higher Donnan effect. Consequently, a better current efficiency in electrochemical cells can be realized. This is particularly true for chlor-alkali cells, hydrogen-bromine cells, and zinc bromine cells. However, this ion cluster morphology may introduce poor conductivity as ion percolation occurs at low volume fraction of aqueous phase. On the other hand, the homogeneous morphology is desirable if one requires good conductivity while sacrificing current efficiency. Of course, it is essential that the membrane is macroscopically homogeneous, free of pinhole and defects, such that an even current distribution across the cell can occur.

The current efficiency of a cell utilizing a Nafion membrane can be facilitated by the ion-clustering effect of the membrane. Also, the conductivity of this membrane is rather high because of its fast ion transport properties. In most cell operating conditions, the percolation effect in Nafion disappears as the volume fraction of the aqueous phase is in excess of the threshold value. For the case of alkaline solutions, a volume fraction of more than 0.1 is required (14). For the case of acid electrolytes, it is likely there is no percolation effect in the proton transport since the threshold volume fraction is almost zero, as indicated by Eq. [4]. These results strongly suggest that Nafion can provide good current efficiency and voltaic efficiency in electrochemical applications. Of course, for chlor-alkali cells, the carboxylic analogue, such as Nafion 900 series (60) and Flemion (61), etc., are better than conventional Nafion as regards to the current efficiency.

Acknowledgment

The author is grateful to Dr. K. C. Tsai and Dr. J. Lee Morris of Pinnacle Research Institute for helpful discussions.

Manuscript submitted July 12, 1982; revised manuscript received Sept. 16, 1982.

Any discussion of this paper will appear in a Discussion Section to be published in the December 1983 JOURNAL. All discussions for the December 1983 Discussion Section should be submitted by Aug. 1, 1983.

REFERENCES

1. R. S. Yeo and A. Eisenberg, *J. Appl. Polym. Sci.*, **21,** 875 (1977).
2. R. S. Yeo and J. McBreen, *This Journal*, **126,** 1682 (1979).
3. R. S. Yeo and D-T. Chin, *ibid.*, **127,** 549 (1980).
4. R. S. Yeo, J. McBreen, G. Kissel, F. Kulesa, and S. Srinivasan, *J. Appl. Electrochem.*, **10,** 741 (1980).
5. R. S. Yeo, *Polymer*, **21,** 432 (1980).
6. R. S. Yeo, S. F. Chan, and J. Lee, *J. Membrane Sci.*, **9,** 273 (1981).
7. R. S. Yeo, in "Ion Exchange: Transport and Interfacial Properties," R. S. Yeo and R. P. Buck, Editors, pp. 235-248, The Electrochemical Society Softbound Proceedings Series, Pennington, NJ (1981).
8. R. S. Yeo and H. L. Yeager, in "Modern Aspects of Electrochemistry," J. O'M. Bockris, B. E. Conway, and R. E. White, Editors, Plenum Press, New York, In press.
9. H. L. Yeager, Z. Twardowski, and L. M. Clarke, *This Journal*, **129,** 324 (1982).
10. Z. Twardowski, H. L. Yeager, and B. O'Dell, *ibid.*, **129,** 328 (1982).
11. F. G. Will, *ibid.*, **126,** 36 (1979).
12. R. S. Yeo, in "Perfluorinated Ionomer Membranes," A. Eisenberg and H. L. Yeager, Editors, p. 453, American Chemical Society Symposium Series (1982).
13. J. L. Weininger and R. R. Russell, *This Journal*, **125,** 1482 (1978).
14. W. Y. Hsu, J. R. Barkley, and P. Meakin, *Macromolecules*, **13,** 198 (1980).
15. T. D. Gierke, G. E. Munn, and F. C. Wilson, *J. Polym. Sci., Polym. Phys. Ed.*, **19,** 1687 (1981).
16. E. J. Roche, M. Pineri, and R. Duplessix, *ibid.*, **20,** 107 (1982).
17. C. Heitner-Wirguin *et al.*, *Polymer*, **21,** 1327 (1980).
18. M. Falk, *Can. J. Chem.*, **58,** 1495 (1980).
19. P. K. Ng and D. D. Snyder, *This Journal*, **128,** 1714 (1981).
20. N. Sivashinsky and G. B. Tanny, *J. Appl. Polym. Sci.*, **26,** 2625 (1981).
21. K. Erdmann and A. Narebska, *Bull. Acad. Polon. Sci.*, **27,** 589 (1979).
22. W. G. F. Grot, G. E. Munn, and P. N. Walmsley, Paper 154 presented at the Electrochemical Society Meeting, Houston, Texas, May 7-11, 1972.
23. T. Takamatsu and A. Eisenberg, *J. Appl. Polym. Sci.*, **24,** 2221 (1979).
24. Symposium on "Perfluorocarbon Ion Exchange Membranes," The Electrochemical Society Meeting, Atlanta, Georgia, Oct. 9-14, 1977.
25. A. Eisenberg, Editor, "Ions in Polymers," American Chemical Society Symposium Series (1979).
26. R. S. Yeo and R. P. Buck, Editors, "Ion Exchange: Transport and Interfacial Properties," The Electrochemical Society Softbound Proceedings Series, Pennington, NJ (1981).
27. Workshop on Structure and Properties of Solid Ion-containing Polymers, M. Pineri, Chairman, Villard de Lans, France, June 1981.
28. Symposium on Electrochemical Membrane Technology, R. S. Yeo and H. L. Yeager, Chairmen, American Institute of Chemical Engineers Meeting, Orlando, Florida, February 1982.
29. A. Eisenberg and H. L. Yeager, Editors, "Perfluorinated Ionomer Membranes," American Chemical Society Symposium Series (1982).
30. R. S. Yeo, D-T. Chin, and T. Katan, Editors, "Transport Processes in Electrochemical Systems," The Electrochemical Society Softbound Proceedings Series, Pennington, NJ (1982).
31. A. Eisenberg and M. King, "Ion-containing Polymers," Academic Press, New York (1977).
32. T. C. Ward and A. V. Tobolsky, *J. Appl. Polym. Sci.*, **11,** 2403 (1967).
33. A. Eisenberg and M. Navratil, *J. Polym. Sci.*, **B10,** 537 (1972).
34. E. J. Roche, R. S. Stein, T. P. Russell, and W. J. MacKnight, *J. Polym. Sci., Polym. Phys. Ed.*, **18,** 1497 (1980).
35. C. L. Marx, D. F. Caulfield, and S. L. Cooper, *Macromolecules*, **6,** 3 (1973).
36. R. Longworth and D. J. Vaughan, *Nature (London)*, **2,** 85 (1968).
37. A. Eisenberg, *Macromolecules*, **3,** 147 (1970).
38. E. P. Otocka and T. K. Kwei, *ibid.*, **1,** 401 (1968).
39. E. P. Otocka and D. D. Davis, *ibid.*, **2,** 437 (1969).
40. E. P. Otocka, M. Y. Hellman, and L. L. Blyler, *J. Appl. Phys.*, **40,** 4221 (1969).
41. A. B. LaConti, A. R. Fragala, and J. R. Boyack, in "Electrode Materials and Processes for Energy Conversion and Storage," J. D. E. McIntyre, S. Srinivasan, and F. G. Will, Editors, p. 354, The Electrochemical Society Softbound Proceedings Series, Princeton, NJ (1977).
42. R. S. Yeo, in "Transport Processes in Electrochemical Systems," R. S. Yeo, T. Katan, and D-T. Chin, Editors, pp. 178-204, The Electrochemical Society Softbound Proceedings Series, Pennington, NJ (1982).
43. T. R. E. Kressman, P. A. Stanbridge, F. L. Tye, and A. G. Wilson, *Trans. Faraday Soc.*, **59,** 2133 (1963).
44. T. R. E. Kressman, P. A. Stanbridge, and F. L. Tye, *ibid.*, **59,** 2139 (1963).
45. R. S. Yeo, Unpublished data.
46. R. S. Yeo, in "Perfluorinated Ionomer Membranes," A. Eisenberg and H. L. Yeager, Editors, p. 65, American Chemical Society Symposium Series (1982).
47. G. E. Archie, *Trans. AIME*, **146,** 54 (1942).
48. D. A. G. Bruggemann, *Ann. Phys.*, **24,** 636 (1935).
49. R. E. De La Rue and C. W. Tobias, *This Journal*, **106,** 827 (1959).
50. F. Hino and K. Murakami, *ibid.*, **127,** 292 (1980).
51. J. Crank and G. S. Park, in "Diffusion in Polymers," J. Crank and G. S. Park, Editors, p. 16, Academic Press, New York (1968).
52. G. S. Park, in "Diffusion in Polymers," J. Crank and G. S. Park, Editors, p. 141, Academic Press, New York (1968).
53. G. J. van Amerongen, *Rubber Chem. Technol.*, **37,** 1065 (1964).
54. G. A. Olah, J. Kaspi, and J. Bakala, *J. Org. Chem.*, **42,** 4187 (1977).
55. J. P. Randin, *This Journal*, **129,** 1215 (1982).
56. W. T. Grubb, *ibid.*, **106,** 275 (1959).
57. A. B. LaConti, E. N. Balko, T. G. Coker, and A. G. Fragala, in "Ion Exchange," R. S. Yeo and R. P. Buck, Editors, p. 318, The Electrochemical Society Softbound Proceedings Series, Pennington, NJ (1981).
58. R. S. Yeo, J. Orehotsky, W. Visscher, and S. Srinivasan, *This Journal*, 128, 1900 (1981).
59. R. S. Yeo, in "Ion Exchange," R. S. Yeo and R. P. Buck, Editors, p. 311, The Electrochemical Society Softbound Proceedings Series, Pennington, NJ (1981).
60. H. L. Yeager, J. D. Malinsky, and R. L. Dotson, in "Transport Processes in Electrochemical Systems," R. S. Yeo, T. Katan, and D-T. Chin, Editors, pp. 215-222, The Electrochemical Society Softbound Proceedings Series, Pennington, NJ (1982).
61. M. Suhara and Y. Oda, in "Transport Processes in Electrochemical Systems," R. S. Yeo, T. Katan, and D-T. Chin, Editors, pp. 223-234, The Electrochemical Society Softbound Proceedings Series, Pennington, NJ (1982).

A Zinc Paste Primary Battery

Raymond Jasinski,* Robert McCarron,*,[1] and George Brilmyer*,[2]

Occidental Research Corporation, Irvine, California 92713

ABSTRACT

Zinc metal pastes can be electrolytically discharged in a concentrated caustic electrolyte. The ease with which a paste can be pumped is determined by the relative ratios of liquid, zinc, and a smaller particle size phase such as ZnO. These ratios are not arbitrary but are predictable via a model based on the packing of spherical particles. The depth of discharge is limited in part by the original liquid content of the paste.

Zinc/air batteries could, in principle, be used to power electric vehicles. One scheme for enhancing the practical performance of this battery system has been to separate energy density factors from power density factors. This can be accomplished by employing the active negative plate material in the form of a zinc slurry (1, 2) to be circulated from a reservoir through the negative electrode compartment. In this manner, the battery per se, *i.e.*, the current collectors, membranes, leads, frames, etc., are sized for the maximum required power. Only the zinc paste storage reservoir is sized for the required vehicle range. Obviously, the zinc loading per unit volume of fluid should be as high as possible for maximum range. State-of-the-art slurries contain nominally 0.27g of usable zinc per milliliter of slurry.

An extension of this fuel cell-battery concept is to use the active material as a pumpable paste rather than as a slurry (3). Much higher loadings of zinc were reported, *e.g.*, 1.9 g/ml, as well as, high zinc discharge efficiencies, *e.g.*, 85% depth of discharge for 1.6g of active zinc per milliliter of paste. The solid zinc was kept in suspension with Teflon particles; gelling agents were not needed (3).

In this paper, we discuss preliminary experiments on formulating and characterizing pumpable zinc/zinc oxide pastes in the context of a primary zinc/oxygen battery. A "paste" is defined here as a thick viscous mass of solid, uniformly and semipermanently dispersed in a liquid phase.

Not all mixtures of Zn, ZnO, and electrolyte are pumpable. First, we discuss the physical basis for predicting those solid/liquid mixtures that are pumpable pastes. Then, we show that this model has a basis in fact, and that the pastes so formed are indeed electroactive.

Experimental

The zinc dust, obtained from Mallinkrodt, had a mean particle size of 7 microns. Zinc oxide, also obtained from Mallinkrodt, had a mean particle size of 0.3 microns. This was determined from SEM photographs, since agglomeration effects caused sedimentation experiments to overestimate the particle size (0.75 microns). "Fluoroglide" Teflon powder and du Pont 15162 Teflon had average particle sizes of 0.4 microns. All zinc metal-KOH pastes were prepared and handled in a glove box under a nitrogen atmosphere. The silicate-containing pastes (nominally 1M SiO_2) were easier to handle, in that air oxidation appeared to be slower. The ratio "vol. ZnO/100g Zn" was particularly convenient for preparing and identifying pastes, and the data herein is, therefore, presented according to this ratio.

Viscosity measurements were made with a Brookfield viscometer and a "flow apparatus." The flow system, using gas pressure to force paste from a reservoir through the sample tube, was particularly well suited for characterizing paste flow through tubing, bends, and constrictions.

The electromechanical functions of the plate-and-frame cell were first established with static zinc paste mixtures painted into the grooves of the negative plate. The flow patterns of paste were first established with ZnO/KOH mixtures. A plexiglass cover was placed over the current collector so that stagnant areas would be visible; air bubbles were helpful in following paste flow.

The electrochemical capacity of the pastes ("depth of discharge") was the total number of coulombs passed to 70% of open-circuit voltage. The 5 × 5 mm negative electrode channels machined from steel blocks were gold plated to reduce ohmic resistance. The paste was delivered at typically 20 ml/min, into a plenum, through the channels, down the face of the current collector, and was collected at an exit plenum. The positive current collector used 2 × 2 mm silver plated channels with commercial platinum-on-carbon oxygen cathodes (Giner Incorporated, Waltham, Massachusetts). Electrode active area was 100 cm^2.

The anode compartment was separated from the cathode by a Celgard microporous polypropylene separator. Electrolyte was continuously circulated with a peristaltic pump through the cathode compartment. Flow through the membrane was minimal. A double junction reference electrode (SCE) was placed in the cathode compartment.

The equipment used for the paste discharge and polarization studies was of conventional design. A d-c power supply (Hewlett-Packard Model 6267B) was used to operate the zinc paste/oxygen battery under constant current conditions. The applied current was measured with a Keithley Model 179-20A digital voltamp meter. Cell voltages were monitored with a high impedance Keithley digital electrometer and displayed on a Linear Instruments/Strip Chart recorder. A slight positive pressure (nominally 2 in. of H_2O) was maintained across the oxygen cathodes. The electrolyte reservoir was continuously purged with nitrogen. Potential measurements were also made with an interruputer bridge of conventional design, at an interruption frequency of 1000 Hz.

Results

Mixtures of zinc powder and water, or caustic, could not be readily pumped through Tygon, glass, or Teflon-lined glass tubing by either peristaltic or piston pumps. Mixtures of zinc, caustic, and Teflon prepared according to the recipe of Ref. (3) were paste-like initially, but quickly separated into a Teflon phase and a zinc/caustic phase, and could not be pumped. However, mixtures of zinc plus zinc oxide in water and in caustic could be pumped, but only if the proper combination of ingredients was used. The following model, based on paint technology (4), was developed to predict those combinations of fluid, zinc, and zinc oxide which would be pumpable with a peristaltic pump. Commercial metallic zinc paints used for corrosion

* Electrochemical Society Active Member.
[1] Present address: Maintex Incorporated, El Monte, California 91734.
[2] Present address: Johnson Controls, Milwaukee, Wisconsin 53201.

Key words: mixing spherical particles, paste rheology, zinc slurries, critical pigment volume composition.

protection are made with pigments of 80% zinc and 20% zinc oxide.

The basis of the model is that the solid portion of the paste must consist of particles with significantly differing particle diameters, so that the small particles fill the voids between the large particles. Consider mixtures of noninteracting large and small spherical particles. (Photomicrographs indicated that the zinc and zinc oxide particles as received were substantially spherical in shape.) These are five different types, or stages, of mixing spherical particles with differing sizes: (*i*) dense random packing of the large spheres, (*ii*) dense random packing of the large spheres with some interstitial space filled with small spheres, (*iii*) dense random packing of large spheres with maximum filling of interstitial space by dense random packed small spheres, (*iv*) large spheres in a matrix of dense random packed small spheres, and (*v*) dense random packed small spheres. The equations relating the void volume of these mixtures (Q) to the packing fraction of the pure powders (ϕ) are listed in Table I and are derived in the Appendix. For present purposes, the void volume is taken to be that of the electrolyte fluid. The (V) terms are the volumes of the solids only (exclusive of void space). ϕ_A and ϕ_B are measured according to standard techniques (4). Equations [4] and [5] are indeed identical. Q_C can also be expressed by the same equation (see Appendix 1).

The equations of Table I were combined with these data to develop the plot in Fig. 1. The data are plotted out in terms of liquid-to-(solid + liquid) volume ratio *vs.* ZnO to Zn ratio (vol. ZnO/100g Zn).

Mixtures below the solid line have insufficient liquid to completely fill the void space. The circles indicate specific mixtures of zinc, zinc oxide, and water used to establish that these pastes were not pumpable. The "critical pigment volume composition" is the standard term to describe paint mixtures on the line.

The minimum in the curve is a unique ZnO/Zn ratio for given values ϕ_A and ϕ_B. The maximum amount of ZnO fills the interstices of the random close packed zinc, without disturbing the packing of the zinc. The remaining void space is filled with the maximum amount of fluid, again without disturbing the packing of the zinc particles. Increasing either the ZnO or liquid content must force some of the zinc particles apart, increasing the ohmic resistance of the paste. Increasing the liquid content did decrease paste viscosity so that the mixtures were more readily pumped. Mixtures with ZnO/Zn ratios lower than the curve minimum were difficult to pump, and had the appearance of wet gray sand. Mixtures above the dashed line in Fig. 1 were poorly dispersed, in that free-standing electrolyte was visible. With 12*N* KOH and 10*N* NaOH, the upper limit ratio was about 6.

The squares in Fig. 1 represent pumpable zinc pastes with zinc metal loadings of 1.5-2.8 g/ml of paste. These pastes were pseudoplastic; the viscosity decreased with time of mixing and rate of mixing. Figure 2 shows a plot of paste viscosity *vs.* zinc metal loading, in 12M KOH with a constant weight ratio of 0.45 for ZnO to Zn. The viscosity numbers are steady-state readings off the Brookfield viscometer at a constant rotation rate of 30 rpm.

Stable pumpable pastes were also formed with TiO_2 and zinc metal powder. These pastes followed the same model as the zinc oxide pastes (Fig. 1), adjusted for

Table I. Relationships of void volume to packing fractions

1. Dense random packing large spheres	$Q_A = V_A\left(\frac{1}{\phi_A} - 1\right)$
2. Some interstitial small spheres	$Q_B = V_A\left(\frac{1}{\phi_A} - 1\right) - V_B$
3. Maximum filling of interstices	$Q_C = (1 - \phi_B)\left(\frac{1}{\phi_A} - 1\right)V_A$
4. Large sphere in small sphere matrix	$Q_D = V_B\left(\frac{1}{\phi_B} - 1\right)$
5. Dense random packing of small spheres	$Q_E = V_B\left(\frac{1}{\phi_B} - 1\right)$

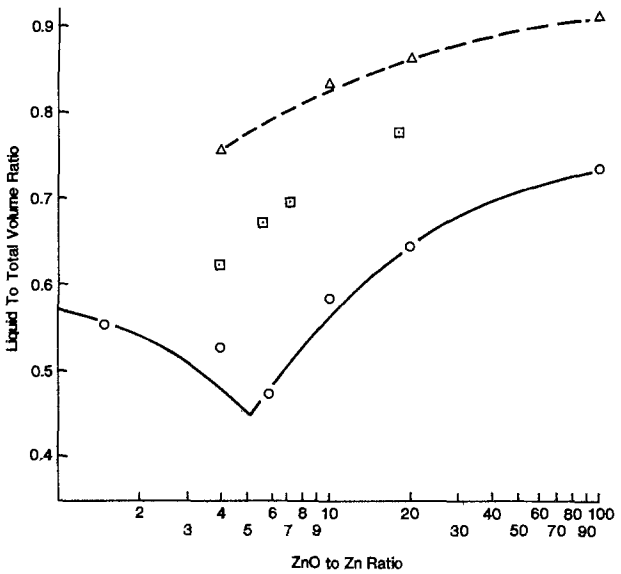

Fig. 1. Plotted are the ratio, liquid volume-to-total paste volume *vs.* volume ZnO(ml)/100g zinc powder forming the paste. Compared are the predictions of the packing model (the curved solid line) with experiment (the data points). The solid line represents the calculated CPVC. The dashed line represents the experimental ratio at which clear fluid separates from the paste. The points represented by squares are readily pumpable.

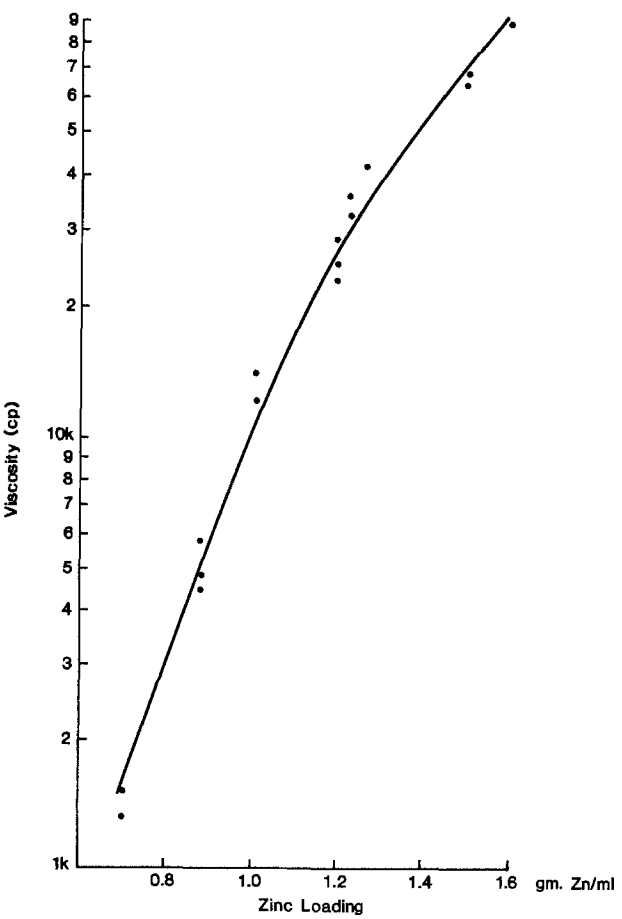

Fig. 2. Viscosity (kcp) readings of a Brookfield viscometer at a constant 30 rpm are plotted for pastes, *vs.* their zinc loading (g Zn/ml). The fluid phase was 12M KOH. The weight ratio ZnO/Zn was 0.45.

the different packing fraction of the particular titanium dioxide used.

Stable pastes could be formed with carbon and zinc, but only if the trace metal content of the carbon was low enough to maintain a low rate of hydrogen evolution. Otherwise, the mix would froth rapidly. Shown in Table II are the hydrogen evolution rates for a variety of zinc/carbon pastes. Considerable frothing was observed with the XC 72 and vitreous carbon materials but not with the Ultra F. Successful pastes were constructed with Ultra carbons. The packing fractions of these carbons were not determined.

Surfactants were tested as a means of decreasing paste viscosity. Fluorosurfactants did decrease viscosity but they invariably resulted in separation of the liquid and solid phases, especially under pressure. Including sodium silicate with the paste mixture significantly decreased viscosity. Silicates are used for this purpose in commercial zinc paint formulations. At high head pressure, liquid separation was again observed. Shown in Table III are Brookfield viscosity data at 30 rpm for zinc/ZnO/OH^- pastes with and without silicate present (1M SiO_2). Different electrolytes and concentrations were used than those for the data of Fig. 2. However, since the relative viscosity of 10M NaOH (16.8) is higher than the relative viscosity of 20M KOH (6.5), it is clear that sodium silicate does decrease paste viscosity.

The pastes made, according to the model of Fig. 1, are electroactive even well away from the CPVC line. Shown in Fig. 3 are the IR free zinc electrode potentials as a function of current density for 2 pastes. These rate data and the following capacity data were carried out with the "static" test cell. The ZnO/Zn mix (x points) had a liquid/solid ratio of 0.98, for a ZnO/Zn ratio (as defined for Fig. 1) of 28. The zinc/carbon mixture had a liquid/solid ratio of 3.4. Zinc/ZnO/KOH, silicate pastes gave similar performance data.

In all electrolytes, the discharge product was initially a blue-colored solid. Microscopic observation of this material indicated zinc metal coated by a waxy gelatinous mass which we presumed to be zinc hydroxide A white translucent material coating a gray mass will give the illusion of a blue-colored solid.

While the initial current/voltage profiles were essentially independent of paste composition and electrode configuration, paste capacity was significantly dependent upon these factors. It is to be expected from Ohm's law considerations that narrow channels, as well as the presence of an inert conductor (carbon) within the mix, would increase utilization of the zinc component. Indeed, this was the case. Shown in Table IV, as a function of channel depth, are discharge capacities for zinc pastes containing zinc oxide and carbon. The data shown are for equal weight ratios of zinc to carbon and to zinc oxide. Since the graphite is 2.5 times less dense

Table II. H_2 evolution rate from zinc-carbon pastes (2.9g carbon + 11g Zn + 11g KOH)

Carbon	Rate (ml/min)
None	0.006 ± 0.003
Vitreous carbon	1.45
Cabot XC 72	0.66
Ultra F	0.014

Table III. Effect of silicate on paste viscosity

Zinc loading (g/ml)	Paste viscosity (10^{+3} cp) 12M KOH	Silicate* + 10M NaOH
0.84	6.2	1.8
1.01	12	4.3
1.2	26	8.0

* Nominally 1M as SiO_2.

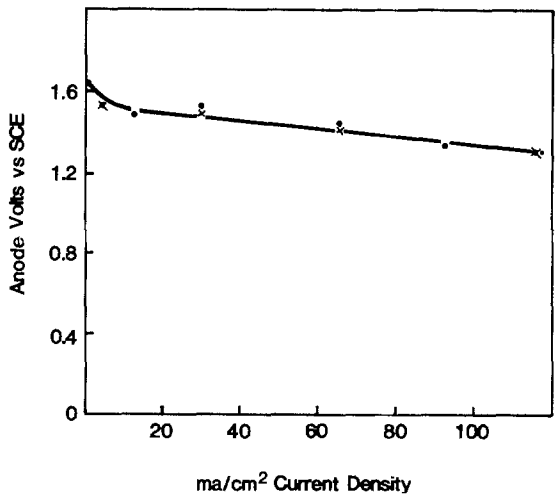

Fig. 3. Shown are the initial internal resistance-free potentials for the zinc electrode (SCE) vs. current density (mA/cm^2) for two pastes ZnO/Zn (×) and graphite/Zn (°).

than ZnO, the volume content of the conducting phase is much larger. At equal volume ratios, the depth of discharge of the 2.8g Zn/ml paste was 26% with graphite and 9% with ZnO (5 × 5 mm channels).

A preliminary study was made of pumping paste through an electrochemical cell. The major considerations in system design were to avoid constrictions and to avoid stagnant zones. With the appropriate cell design, we were able to sustain a current density of 10 mA/cm^2 at 1.1V (including internal resistance losses) pumping a Zn/ZnO/silicate-caustic paste for 18 hr over a 3 day period. In this case, the cell electrolyte was immobilized and not circulated; the pumping was deliberately semicontinuous to simulate on/off operation, and nominally 2% of the paste capacity was discharged. Eventual deterioration of the cell was due to oxygen electrode poisoning.

Half-cell measurements indicated a fall off in cell voltage above 50 mA/cm^2 due primarily to the effects at the oxygen electrode. Rotating disk studies confirmed an increase in platinum oxygen electrode overvoltage due to dissolved silicate.

Discussion

It is indeed possible to formulate metal/electrolyte pastes that are stable with time, pumpable, have high metal loadings, and are also electroactive. The ratios of the components within such pastes are not arbitrary, but approximate values calculated from a model based on the following precept. It is necessary that there be two solid particle size distributions within the paste, and sufficient smaller particles so that they at least completely pack within the spaces between the larger particles. The required ratio of fine particles to large particles is then readily determined by simple measurements of the packing density of the individual solids. This concept is classic to preparing metal paints (4).

We have shown herein that electroactive pastes can be formulated according to this model from binary mixtures of zinc dust, with ZnO, or TiO_2 powders. Satisfactory (as defined above) graphite/zinc pastes could also be formed. Presumably, finely divided zinc could

Table IV. Depth of discharge vs. channel size (at 10mA/cm^2)

Paste (gram Zn/ml)	Channel size	Depth of discharge (%)
2.48 + ZnO	5 × 5 mm	9.4
	1.5 × 1.5 mm	35
1.05 + graphite	5 × 5 mm	40
	1.5 × 1.5 mm	49

have been substituted for the oxides. The smaller particle size component, in principal, need not be a different chemical than the larger particle size material. This particular variant on the concept was not tested.

These pastes were pumpable but had high viscosities. The addition of surfactants lowered the viscosities, but also had an adverse effect on the flow characteristics at high head pressures. The flow patterns chosen for the pastes must avoid stagnant regions, such as found at abrupt constrictions. Pumping through glass tubes and bends was possible; pumping through Teflon-lined tubing required a lower pressure. It is to be expected that the half-cell potentials governing the rate at which electrical charge can be exchanged between the paste and current collector will be influenced by particle-particle contact (metal/oxide ratio) and the particle-collector contact. Indeed, the depth of discharge (to a preselected cutoff voltage) was found to increase by using more narrow channels surrounding the paste. Pastes containing conductive graphite rather than insulating ZnO gave higher depths-of-discharge.

In principle, this model can also predict the maximum depth of discharge for the electroactive paste. The half-cell reactions, the packing density of the discharge product(s), and the packing density of the partially discharged starting material (here Zn) must be known. Rigorous values for these parameters are not available for the zinc/oxygen system. Nevertheless, an approximate depth of discharge can be calculated. Assuming the cell reaction to be

$$Zn + \tfrac{1}{2}\,O_2 + H_2O = Zn(OH)_2$$

and assuming zinc particles are replaced by zinc hydroxide particles of the same packing density as the ZnO used to make the paste, the maximum capacity for the 2.48 g/ml paste described above is 20%. This is 0.5g active zinc per milliliter of paste. The 2.48g Zn/ml paste discharged to 35% had no fluid properties. The 9% depth of discharge material (originally 2.43g Zn/ml) had a solid crust, coating a paste-like material. It is inferred that the approximation is not totally unreasonable. Thus, this 2.48g Zn paste could have a capacity significantly higher than zinc/caustic slurries (0.28 g/ml).

Manuscript submitted July 22, 1982; revised manuscript received Sept. 28, 1982.

Any discussion of this paper will appear in a Discussion Section to be published in the December 1983 JOURNAL. All discussions for the December 1983 Discussion Section should be submitted by Aug. 1, 1983.

Publication costs of this article were assisted by Occidental Research Corporation.

APPENDIX

Derivation of Table I

1. Define the packing fraction as $\phi_A = V_A/V_T$ and $\phi_B = V_B/V_T$. V_A, V_B are the volumes of the particulate substances, exclusive of the void volume. These can be calculated from the density and the weight of the particles. V_T is the total volume actually occupied by the powder. In this discussion (A) represents the large particles, and (B) represents the smaller particles.

2. Thus, $V_{void} = V_T - V_A$, and $V_{void} = V_T(1 - \phi_A)$. Here, V_{void} is the space occupied by the liquid, *i.e.*, Q_A. Hence, $Q_A = (V_A/\phi_A)(1 - \phi_A) = V_A(1/\phi_A - 1)$.

3. The most dense packing occurs when V_{void} is V_T for the smaller particles. Thus, with V_{void} defined as above

$$V_B = \phi_B\, V_{void}$$

The volume of liquid Q_C is, by definition

$$Q_C = V_{void} - V_B$$

$$Q_C = V_{void}(1 - \phi_B) = V_T(1 - \phi_A)(1 - \phi_B)$$

$$V_T = V_A/\phi_A$$

$$Q_C = V_A\left(\frac{1}{\phi_A} - 1\right)(1 - \phi_B)$$

Q_C can also be expressed in terms of ϕ_B and V_B as follows

$$V_B = \phi_B\, V_{void}$$

$$Q_C = \frac{V_B}{\phi_B}(1 - \phi_B) = V_B\left(\frac{1}{\phi_B} - 1\right)$$

This relationship deserves some explanation. Q_C is the volume of liquid to be added. All the space among the large particles that can be occupied by smaller particles is occupied by smaller particles. The void space left over is that associated with the smaller particles only. The total volume of spheres plus liquid is now larger because of the larger particles, but the liquid volume is the same as with the smaller particles alone. For the same reason Q_D lacks a contribution from V_A.

REFERENCES

1. A. J. Appleby and M. Jacquier, *J. Power Sources*, **1**, 17 (1976).
2. H. Baba, SAE Tech. Paper 71-02-37 (1971).
3. B. Warszawski, U.S. Pat. 4,172,924 (1979).
4. T. Patton, "Paint Flow and Pigment Dispersion," John Wiley & Sons, New York (1979).

Incorporation of Chloride Ion in Passive Oxide Films on Nickel

B. MacDougall,* D. F. Mitchell, G. I. Sproule, and M. J. Graham

National Research Council of Canada, Division of Chemistry, Ottawa, Ontario, Canada K1A 0R9

ABSTRACT

Auger electron spectroscopy and secondary ion mass spectrometry, in conjunction with ion sputtering, have been used to demonstrate that chloride is incorporated in anodic oxide films formed on nickel in Cl^--containing, pH 4.0 Na_2SO_4 solutions. X-ray photoelectron spectroscopy indicates that this chloride is present as Cl^-. Cl^- is found in the first two layers of the four layers of the oxide, with the amount in the second layer being about twice that in the outermost layer. The extent of Cl^- incorporation is dependent on the $[Cl^-]$ in solution, electrode pretreatment (whether electropolished or cathodically reduced), and the potential and time of anodization. The amount of Cl^- in the oxide can thus be carefully controlled and varied. Cl^- incorporation does not occur when electropolished nickel is cathodically reduced in a 1.0M Cl^- solution and then air-exposed; anodic polarization in the passive potential region is necessary to fix Cl^- in the oxide lattice. Cl^- is incorporated when passive oxide films are formed in non-Cl^- solutions and then exposed to Cl^--containing electrolytes with an applied anodic potential. This incorporation is most probably associated with local breakdown-repair events at defects in the film as the rate of incorporation decreases with increasing perfection of the oxide.

It is well known that aggressive anions like Cl^- cause pitting of metals such as nickel, iron, and the stainless steels. The rapid metal dissolution associated with pitting appears to be due to the ability of the Cl^- to interfere with formation of the passive oxide film at localized surface sites. The importance of the oxide film in pit initiation and propagation is recognized and some of the pitting work in the literature has been specifically concerned with the influence of Cl^- on the nature of passive oxide films (1-13). In this previous work, there has been considerable disagreement as to whether Cl^- is incorporated in the oxide film prior to pitting. Ellipsometric studies on both iron and stainless steel suggest that incorporation of Cl^- is an integral part of the pitting process and may even determine the induction time for pitting (3-5). On the other hand, analyses (using UHV surface analytical techniques) of passive films formed in Cl^- solutions, both before and after pit initiation, appear to indicate that Cl^- is only adsorbed on the oxide surface, no detectable Cl^- being found in the oxide film (7-13). The present paper employs both Auger electron spectroscopy (AES) and secondary ion mass spectrometry (SIMS) to establish that Cl^- is incorporated in passive oxide films on nickel. The influence of the $[Cl^-]$ in solution, potential and time of anodization, and electrode pretreatment on the extent of incorporation is studied.

Experimental

Polycrystalline nickel specimens, 1 × 2.5 cm, were prepared as described previously (14). Potentials are referred to the saturated calomel reference electrode. Experiments were conducted at 25°C in a deaerated solution of 0.15*N* Na_2SO_4 at pH 4.0. In one series, nickel samples electropolished (EP) in 57 volume percent sulfuric acid were cathodically reduced (CR) at 20 $\mu A\ cm^{-2}$ and then were passivated in solutions of various $[Cl^-]$ using the potential step technique. The same solution was used for both CR of the prior oxide and the anodic passivation treatment. In a second series of experiments, electropolished nickel was immersed directly in the electrolyte with the anodic potential applied, *i.e.*, with no CR of the prior oxide. In a third series, nickel samples were passivated in non-Cl^- solutions and then transferred to Cl^--containing solutions for further anodic polarization. In all cases, samples were extensively flushed with doubly distilled water after the anodic treatment to ensure that all of the Cl^--containing electrolyte was removed from the surface. They were then dried with compressed air before installing in a Physical Electronics Incorporated Model 590 System for analysis by AES, SIMS, and x-ray photoelectron spectroscopy (XPS). Xenon ion sputtering at 0.5 kV was used to obtain both Auger and SIMS depth profiles through the oxide films (15-17), and the Auger sputter profiles were evaluated to give a layer-by-layer composition using the quantitative approach previously described (18).

* Electrochemical Society Active Member.
Key words: corrosion, passivity, surfaces.

Results and Discussion

AES and SIMS analyses of oxide films.—Figure 1 shows Auger spectra of EP nickel electrodes passivated at 0.3V for 15 sec in pH 4.0 Na_2SO_4 solutions of various $[Cl^-]$, both with and without CR of the prior oxide. Principal Auger electron signals associated with chlorine, carbon, oxygen, and nickel are indicated; of particular interest is the Cl signal at 181 eV. While little or no Cl is evident for the sample passivated in the Cl^--free solution, *i.e.*, Fig. 1(a), the samples treated in Cl^--containing solutions show a distinct Cl Auger signal. XPS spectra showed that the chlorine is present as Cl^- rather than as an oxychloride such as ClO_3^- and ClO_4^-. The Auger signals in Fig. 1 indicate homogeneous atomic concentrations of Cl^- of 1.0

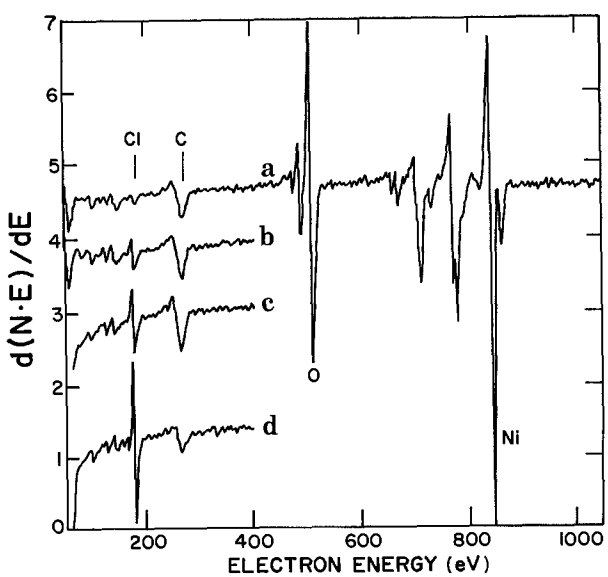

Fig. 1. Auger electron spectra of electropolished (EP) nickel passivated, either with or without cathodic reduction (CR) of the prior film, at 0.3V for 15 sec in pH 4.0 $NaSO_4$ solutions with different $[Cl^-]$. (a) CR and passivation in a solution with $[Cl^-] = 0$; (b) no CR and $[Cl^-] = 1.0M$; (c) CR and $[Cl^-] = 0.1M$; (d) CR and $[Cl^-] = 1.0M$. Above ~400 eV, spectrum (a) is typical of the other three spectra. (Electron beam 5 keV with a current ~0.3 μA; modulation 4 eV peak-to-peak.)

atomic percent (a/o) in Fig. 1(b), 1.8 a/o in (c), and 4.4 a/o in (d); the oxygen signal corresponds to ~30 a/o in each case and this represents an average oxide thickness of ~9Å, *i.e.*, the usual value for the passive film on nickel (14, 16, 17). The homogeneous atomic percent of Cl^- is defined as the concentration present if the chloride was uniformly distributed within the analysis volume.

While the Auger analyses indicate the presence of Cl^- in the surface regions of nickel passivated in Cl^--containing solutions (most of the signal comes from the top 15Å), they do not indicate how the Cl^- is distributed through the oxide. In fact, different concentrations of Cl^- within the analysis volume could give the same homogeneous atomic concentration simply by being distributed differently throughout the ~4 layers of nickel oxide. This situation arises because the contribution of any species to its overall measured Auger signal decreases exponentially with increasing distance from the outer surface. A layer-by-layer distribution of Cl^- can, however, be determined when the Auger analysis is performed in conjunction with ion beam sputtering (18).

An Auger sputter profile for a nickel oxide film with a homogeneous atomic concentration of Cl^- of 4.4% is shown in Fig. 2. The peak-to-peak (P/P) signal heights are plotted (cf. Fig. 1) for the various species through the film. The carbon signal falls off rapidly with most disappearing before the equivalent of one oxide layer has been sputtered, indicating that the carbon is an adsorbed surface contaminant. On the other hand, the Cl^- signal initially increases and then falls off slowly as the oxide is removed. While the initial increase is at least partly due to the removal of the carbon contamination which absorbs some of the Cl^- signal, it appears that Cl^- is incorporated or buried in the film rather than simply adsorbed on the surface. The Auger sputter profile in Fig. 2 quantitatively analyzed on a layer-by-layer basis (18) gives the elemental compositions listed in Table I. While the Cl^- is concentrated in the outer layers of the oxide, the increase from 6 a/o in the outermost layer to ~14 a/o in the second layer suggests that the Cl^- is incorporated in the oxide lattice. These calculated concentrations best fit the experimental profiles of Fig. 2; noticeable differences between calculated and experimental values occur if some of the Cl^- of layer 2 is put into layer 3. It should be further noted that the depth distribution given in Table I is independent of the total amount of Cl^- incorporated in the oxide. Also, similar layer-by-layer analysis of

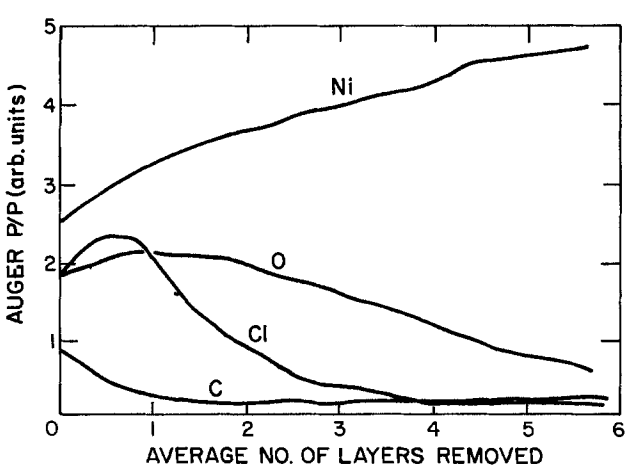

Fig. 2. Auger peak-to-peak (P/P) sputter profiles of various species in a nickel oxide film formed at 0.3V in 1.0M Cl^- solution. (Film corresponds to spectrum (d) in Fig. 1 and has a homogeneous Cl^- concentration of 4.4 a/o.) Sputter rate using 0.5 kV xenon is 0.6 layer min^{-1}; 1 layer ≃ 2Å of NiO. (Each profile drawn through ~60 data points.)

Table I. Layer-by-layer composition (18) of the oxide formed by anodizing cathodically reduced (CR) nickel at 0.3V for 15 sec in pH 4.0 Na_2SO_4 + 1.0M Cl^- solution. Electron neutrality is maintained in each layer. (1 layer ≡ 1.6 × 10^{15} atoms cm^{-2} ≃ 2Å NiO).

Layer	Atomic composition (%)			
	Ni	O	Cl	C
1	0.37	0.34	0.06	0.24
2	0.47	0.40	0.14	0.00
3	0.50	0.50	0.00	0.00
4	0.50	0.50	0.00	0.00

the oxide film on Fe-26Cr electropolished in $HClO_4$/CH_3COOH shows that substantial amounts of Cl^- are also incorporated in the outer 6 layers of the ~10 layers of oxide (18).

The anodic oxide films formed with various [Cl^-] were also analyzed by SIMS which has a very high sensitivity for Cl^- detection; the sputter profiles for films corresponding to (a), (b) and (d) in Fig. 1, are shown in Fig. 3. The curve shown for oxygen is representative of the O^- SIMS profile in each case. The SIMS profiles also indicate that Cl^- is incorporated in the oxide, the maximum Cl^- SIMS signal occurring after ~1 layer has been removed. The passive film gives only a very small Cl^- signal as anticipated for a film formed in a non-Cl^- solution. This Cl^- is thought to be due to system contamination and like C is on the sample surface. The film formed in 1.0M Cl^- solution after CR of the prior oxide gives a substantially higher maximum Cl^- signal than the film formed without CR, in agreement with the Auger analysis in Fig. 1. Indeed, the maximum SIMS signal for Cl^- may be correlated with the homogeneous atomic percent concentration of Cl^- determined by AES over a wide range of incorporated Cl^- levels. This is shown in Fig. 4 and Table II for samples prepared at different potentials and with different [Cl^-] in solution.

As indicated by the data in Table II, the Auger analysis is not reliable below a Cl^- level of ~0.5 a/o, but SIMS can detect very small amounts of Cl^- in

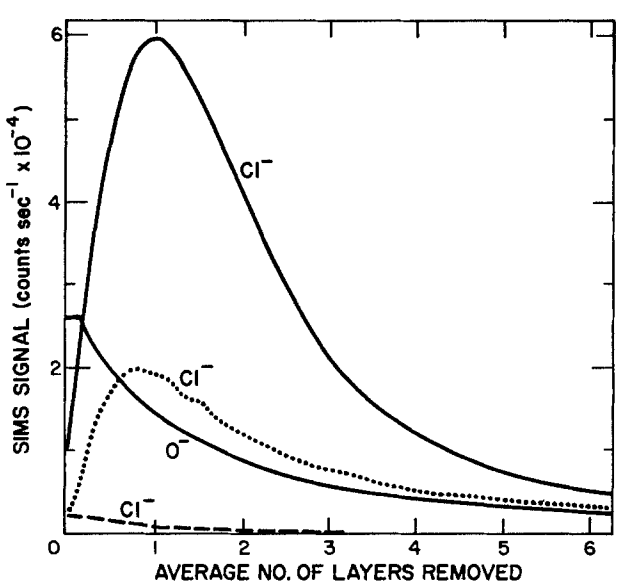

Fig. 3. SIMS Cl^- (mass 35) sputter profiles of electropolished (EP) nickel, passivated either with or without cathodic reduction (CR) of the prior film, at 0.3V for 15 sec in pH 4.0 Na_2SO_4 solutions with different [Cl^-]. (i) CR and passivation in a solution with [Cl^-] = 0 (---); (ii) no CR and [Cl^-] = 1.0M (•••); (iii) CR and [Cl^-] = 1.0M (——). Also shown is a representative sputter profile for O^- (mass 16). Sputter rate using 0.5 kV xenon is 0.6 layer min^{-1}; 1 layer ≃ 2Å of NiO. (Each profile drawn through ~60 data points.)

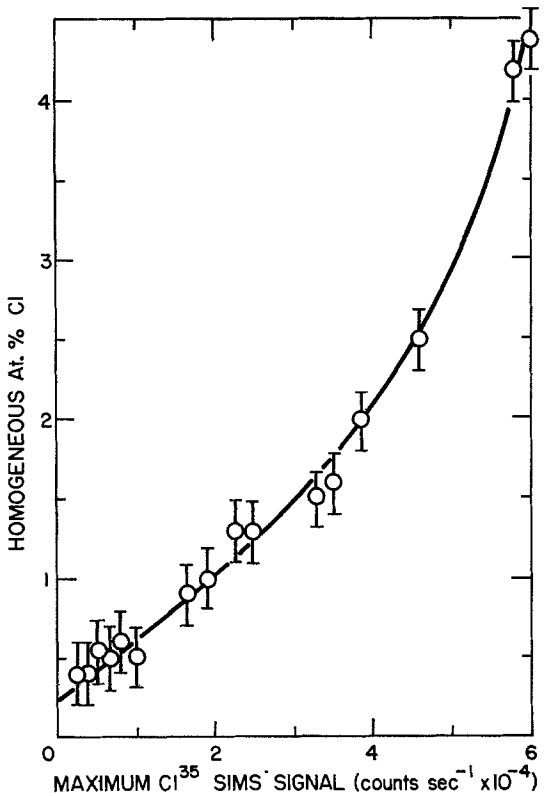

Fig. 4. Correlation between the homogeneous atomic percent concentration of Cl^- determined by AES and the maximum SIMS signal for Cl^- obtained during sputtering of anodic oxide films containing various incorporated Cl^- concentrations. (Error bars represent a 95% confidence level determined from five measurements.)

the oxide film. As the Cl^- level increases above ~5 a/o, the SIMS signal (Fig. 4) becomes less sensitive to changes in $[Cl^-]$ so that at these higher concentrations AES is the preferred method of analysis. At intermediate Cl^- levels both SIMS and Auger can be effectively used to study Cl^- incorporation into anodic oxide films on nickel.

Factors influencing the extent of Cl^- incorporation. —Figure 5 shows the influence of bulk $[Cl^-]$ in pH 4.0 Na_2SO_4 solution on the amount of Cl^- in the anodic oxide film formed at 0V. This amount increases logarithmically with increasing bulk $[Cl^-]$. Figure 6 shows the influence of anodic potential on the extent of Cl^- incorporation in solutions containing 0.1 and 1.0M Cl^-. The amount of Cl^- in the film increases with potential, the data generating an S-shaped profile

Table II. Comparison of SIMS and Auger signals for Cl^- in oxide films formed on nickel after different electrochemical treatments in pH 4.0 Na_2SO_4 solutions with various $[Cl^-]$ (EP, electropolished; CR, cathodically reduced). The SIMS signal quoted is the maximum obtained during sputter etching by 0.5 kV Xe ions.

Treatment		Counts (Cl-) by SIMS (±10%)	Homogeneous a/o Cl- by Auger (±0.2%)
Anodized in Cl-free solution		2,000	0.4
EP + CR in 0.1M Cl- + air exposure		2,800	0.4
EP + CR in 1.0M Cl- + air exposure		3,500	0.4
CR and anodized at 0V in:	0.025M Cl-	7,800	0.6
	0.1M Cl-	16,000	0.9
	1.0M Cl-	37,000	1.8
CR and anodized in 1.0M Cl- at:	−0.3V	8,400	0.6
	0V	37,000	1.8
	0.3V	60,000	4.4
Anodized at 0.2V in 0.1M Cl- after:	CR	33,600	1.5
	No CR	10,000	0.5
Anodized at 0.3V in 1.0M Cl- after:	CR	60,000	4.4
	No CR	19,000	1.0

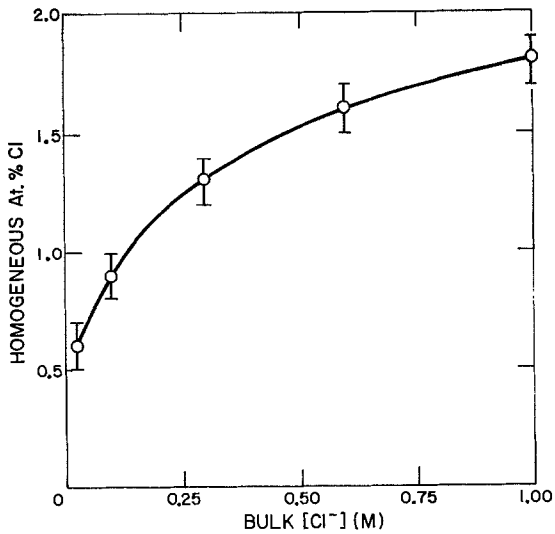

Fig. 5. Dependence of amount of Cl^- in oxide film, determined by AES, on bulk $[Cl^-]$ in pH 4.0 Na_2SO_4 solutions. In each case, electropolished nickel was cathodically reduced (CR) to remove the prior oxide film; the potential was then stepped to 0V and held there for 15 sec. (Error bars for the 95% confidence level are smaller than in Fig. 4 and 6 since all samples were analyzed during same machine loading.)

often found for adsorption isotherms [cf. Ref. (19)]. (Experiments cannot be performed beyond 0.5V with 1.0M Cl^- since pitting starts almost immediately under these conditions.) The results in Fig. 5 and 6 indicate that the amount of Cl^- incorporated in the passive oxide film on nickel can be controlled and varied through the bulk $[Cl^-]$ in solution and the anodic potential.

To check the influence of time of anodization on the amount of incorporated Cl^-, samples were prepared at 0V (in both 0.1 and 1.0M Cl^-) for 3 sec, 60

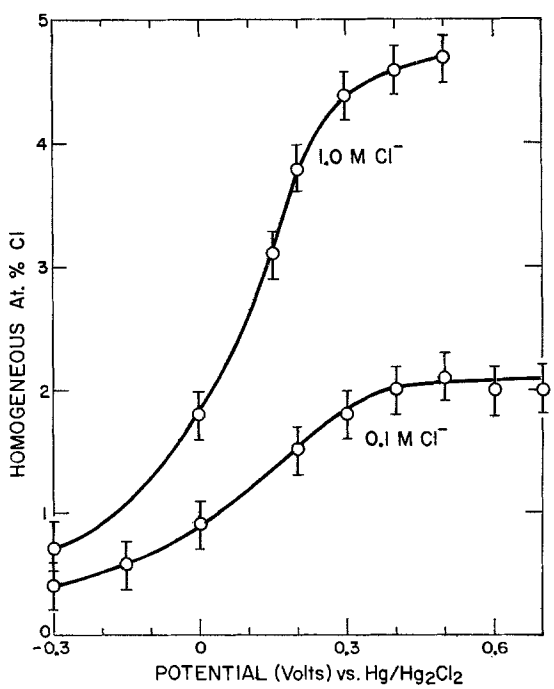

Fig. 6. Dependence of amount of Cl^- in the oxide film, determined by AES, on anodizing potential in pH 4.0 Na_2SO_4 solutions containing 0.1M Cl^- and 1.0M Cl^-. Electropolished nickel was cathodically reduced (CR); the potential was then stepped to the desired value and held there for 15 sec. At potentials above 0.4V with 0.1M Cl^- and 0.3V with 1.0M Cl^-, the holding time was only 3 sec since pitting began at longer times. (Error bars represent a 95% confidence level determined from five measurements.)

sec, and 1 hr and then analyzed for Cl^- by AES. The amount of incorporated Cl^- was independent of anodizing time at each solution [Cl^-], indicating that Cl^- incorporates rapidly. This is not surprising since most of the Cl^- should incorporate while the film is forming and most of the oxide forms during the first few seconds after the potential is stepped into the passive region (14, 20). Thus, the extent of Cl^- incorporation determined at higher potentials (>0.4V), using shorter anodization times to avoid pitting, can be compared with the data obtained at lower potentials where somewhat longer anodizing times are used (cf. Fig. 6).

To determine the extent of Cl^- incorporation in the absence of an applied anodic potential, electropolished electrodes were immersed in 0.1 and 1.0M Cl^- pH 4.0 Na_2SO_4 solutions, the prior oxide was cathodically reduced and the electrodes were then exposed to the air, immediately flushed with doubly distilled water, and dried. The results of the Cl^- analysis indicate that very little Cl^- is incorporated in the oxide in the absence of an anodizing potential (Table II). While an oxide is formed immediately on the oxide-free nickel surface upon exposure to the air, Cl^- in the electrolyte remaining on the surface is not substantially incorporated into the film.[1] This indicates that most of the Cl^- present in the film is fixed in the film during the passivation treatment and is not due to the specimen either being cathodically reduced in the Cl^- solution or being briefly in contact with the Cl^--containing electrolyte after removal from the cell prior to washing. Table II also shows that the extent of Cl^- incorporation is substantially decreased if the prior oxide on the electropolished electrode is not cathodically reduced before the anodic passivation (see also Fig. 1). The increase in oxide film thickness upon passivation of electropolished samples is only ~30% (17), and the small amount of Cl^- that is incorporated in the oxide may be associated with this increase in film thickness.

Finally, the kinetics of Cl^- incorporation into passive oxide films were studied by initially preparing the oxide in a Cl^--free solution followed by polarization for different times in a Cl^--containing solution. The results obtained with a 10 min prior passivation at 0.2V and subsequent polarization at this potential for different times in 1.0M Cl^- are shown in Table III. The amount of incorporated Cl^- increases with time of polarization in 1.0M Cl^- solution and eventually approaches the value expected if the film had been prepared in the 1.0M Cl^- solution (cf. Fig. 6). The results can be explained in terms of the "defect model" of the passive oxide film and the breakdown-repair events that occur at local sites within the film (13, 17, 20-22). When the film is polarized in Cl^- solution, local breakdown of the oxide (by, *e.g.*, chemical dissolution) is followed by its reformation, and thus Cl^- is locally incorporated into the film. Breakdown-repair events occur at random on the surface and, if the time period is sufficiently long, all of the surface will experience these events and the level of incorporated Cl^- will eventually reach a steady value appropriate for that solution [Cl^-] and anodic potential. The rate of increase of incorporated Cl^- is not constant with time because the oxide film perfects with time of anodization, even in a Cl^--containing solution. This means that there are fewer defects to break down and thereby lead to Cl^- incorporation in the film. The kinetics of Cl^- incorporation are also highly dependent on the defect state of the prior oxide since this determines the frequency of breakdown-repair events. The rate of incorporation is understandably higher with the electropolished film (Table III) since this oxide is more defective than the anodic film formed after 10 min at 0.2V. On the other hand, a highly perfect passive film like that formed by a 50 hr anodization at 0.2V has few defects and consequently, as seen in Table III, the rate of Cl^- incorporation is low.

Local incorporation of Cl^- into passive oxide films may be important in the initiation of pitting on previously passive metal surfaces and more work along these lines is underway. It should be noted, however, that while the present work shows that considerable Cl^- can be incorporated into the oxide lattice, this does not mean that such incorporation is a necessary precursor to pit initiation.

[1] The same result is obtained if the flushing of the Cl-containing electrolyte from the sample with doubly distilled water is delayed for ~5 sec after air exposure.

Table III. Extent of Cl^- incorporation (as determined by AES) into preformed Cl^--free oxide films as a function of time of exposure to 1.0M Cl^- pH Na_2SO_4 solutions at 0.2V (EP, electropolished).

Prior treatment	Time of exposure to 1.0M Cl- at 0.2V	Homogeneous a/o Cl- (±0.2%)
Anodized at 0.2V for 10 min	60 sec	0.5
Anodized at 0.2V for 10 min	10 min	0.8
Anodized at 0.2V for 10 min	24 hr	2.7
Anodized at 0.2V for 50 hr	24 hr	0.6
EP	15 sec	1.0
EP	10 min	2.1

Manuscript submitted May 10, 1982; revised manuscript received Sept. 2, 1982.

Any discussion of this paper will appear in a Discussion Section to be published in the December 1983 JOURNAL. All discussions for the December 1983 Discussion Section should be submitted by Aug. 1, 1983.

Publication costs of this article were assisted by the National Research Council of Canada.

REFERENCES

1. M. E. Curley-Fiorino and G. M. Schmid, *Corros. Sci.*, **20**, 313 (1980).
2. G. Okamoto and T. Shibata, in "Passivity of Metals," R. P. Frankenthal and J. Kruger, Editors, p. 646, The Electrochemical Society Inc., Princeton, NJ (1979).
3. J. R. Ambrose and J. Kruger, in "Proceedings of Fourth International Congress on Metal Corrosion, Amsterdam, 1969," p. 698, NACE, Houston (1972).
4. S. Matsuda, K. Sugimoto, and Y. Sawada, in "Passivity of Metals," R. P. Frankenthal and J. Kruger, Editors, p. 699, The Electrochemical Society, Inc., Princeton, NJ (1979).
5. C. L. McBee and J. Kruger, in "Proceedings of U.R. Evans International Conference on Localized Corrosion, 1971," p. 252, NACE, Houston (1974).
6. T. P. Hoar, D. C. Mears, and G. P. Rothwell, *Corros. Sci.*, **5**, 279 (1965).
7. Z. Szklarska-Smialowska, H. Veifhaus, and M. Janik-Czachor, *ibid.*, **16**, 649 (1976).
8. M. Janik-Czachor, A. Szummer, and Z. Szklarska-Smialowska, *ibid.*, **15**, 775 (1975).
9. M. Janik-Czachor, *Werkst. Korros.*, **30**, 225 (1979).
10. M. Janik-Czachor, *Corrosion*, **35**, 360 (1979).
11. M. da Cunha Belo, B. Rondot, F. Pons, and J. P. Langeron, *This Journal*, **124**, 1317 (1977).
12. A. E. Yaniv, J. B. Lumsden, and R. W. Staehle, in "Passivity and its Breakdown on Iron and Iron Base Alloys," R. W. Staehle and H. Okada, Editors, p. 72, NACE, Houston (1976).
13. B. MacDougall, *This Journal*, **126**, 919 (1979).
14. B. MacDougall and M. Cohen, *ibid.*, **121**, 1152 (1974).
15. D. F. Mitchell, G. I. Sproule, and M. J. Graham, *J. Vac. Sci. Technol.*, **18**, 690 (1981).
16. B. MacDougall, D. F. Mitchell, and M. J. Graham, *This Journal*, **127**, 1248 (1980).
17. B. MacDougall, D. F. Mitchell, and M. J. Graham, *Corrosion*, **38**, 85 (1982).

18. D. F. Mitchell, *Appl. Surf. Sci.*, **9**, 131 (1981).
19. G. Horanyi, J. Solt, and F. Nagy, *J. Electroanal. Chem. Interfacial Electrochem.*, **31**, 95 (1971).
20. B. MacDougall, D. F. Mitchell, and M. J. Graham, *Israel J. Chem.*, **18**, 125 (1979).
21. B. MacDougall and M. Cohen, *This Journal*, **124**, 1185 (1977).
22. B. MacDougall, *ibid.*, **125**, 1183 (1978).

Experimental Determination of the Passive-Active Transition for Iron in 1M Sulfuric Acid

Philip P. Russell* and John Newman**

Department of Chemical Engineering, University of California, Berkeley, California 94720

ABSTRACT

Current-voltage curves from three iron rotating disks are obtained using a polarization device which permits determination of the transition region between the active and passive states. Diameters of the three electrodes are 0.494, 0.298, and 0.0986 cm, respectively. Results from the smallest electrode have the least amount of ohmic distortion. Trends in the data, which are observed as the electrode size is decreased, form the basis for the conclusions that are drawn from this work. Analysis of these trends indicates that the active-passive transition is characterized by a nearly vertical line on a current *vs.* potential plot. The Z-shaped nature of the current-voltage curves, reported by Epelboin *et al.*, is entirely due to ohmic potential drop in the solution. Analysis of the data, within the framework of a mathematical model presented by Law and Newman, indicates that the average current density on the active portion of the disk increases as the size of the active area decreases during the passivation process.

Passivation of iron in sulfuric acid was first observed by Flade (1). More recently, it has been shown that polarization curves for iron rotating disk electrodes, obtained with a potentiostat, in 1M sulfuric acid have displayed a hysteresis loop that obscured the current-voltage behavior of the active-passive transition. Epelboin *et al.* (2) have shown how this obscured current-voltage behavior can be traced in a stable manner using a polarization device known as a Negative Impedance Converter. Because of their characteristic shape, current-voltage curves obtained with this device were termed Z-shaped curves. Law and Newman (3) developed a mathematical model describing the passivation process. This model qualitatively duplicated the Z-shaped passivation curves that were experimentally obtained by Epelboin *et al.* The model indicates that the Z-shape is due entirely to ohmic potential drop. The resistance between the disk and the counterelectrode increases as the active area of the electrode decreases during the passivation process, resulting in a complication of the analysis.

The purpose of this paper is to present and analyze a series of experimentally determined passivation curves, each having a different amount of distortion due to ohmic potential drop. Results of this analysis indicate that the underlying assumptions in Law and Newman's mathematical model are correct. Specifically, the important assumption that the local passivation behavior of iron can be represented by a vertical transition on a current density *vs.* $(V - \Phi_0)$ plot is verified. Here, V is the electrode potential and Φ_0 is the potential in the solution just outside the electric double layer.

Three rotating disk electrodes, each having a different diameter, were used in this study. The smallest of these electrodes passed the least amount of total current; therefore, it rendered results that had the least amount of ohmic distortion. Conclusions were drawn from trends in the experimental results that were observed as the degree of ohmic distortion was reduced.

The active area of the disk decreases as the disk goes from the active to the passive state. The mathematical model of Law and Newman (3) indicates that the average current density on the active portion of the electrode should increase as the active area decreases. Using optical microscopy to determine the active area, Epelboin *et al.* (2) reported the opposite phenomenon; current density on the active area decreased as the active area decreased. Analysis of our experimental results, in a manner similar to that developed by Law and Newman, indicates that the average current density on the active area of the electrode increases as the active area decreases during the passivation process.

The principles governing a polarization device that provides a load line with a positive slope have been presented by Epelboin *et al.* The reasons why such a device must be used for polarization control of a passivating system are briefly reviewed.

Assume the I *vs.* $(V - \Phi_{RE})$ characteristics of an electrochemical system that undergoes passivation can be represented as in Fig. 1. If a polarization device with a vertical load line, such as a potentiostat, is used to polarize this cell, the curve a-b-c-d-e will be obtained for a positive voltage sweep. For a negative voltage sweep, the curve e-d-f-b-a is obtained. Curve c-f, which is of interest, is obscured within the hysteresis loop. The special polarization device produces a positive sloping load line, represented by L. This allows determination of a stable data point at (V^*, I^*). Adjustment of the potential, E, and the slope of line L allows determination of the curve c-f. A polarization device with this capability was used to

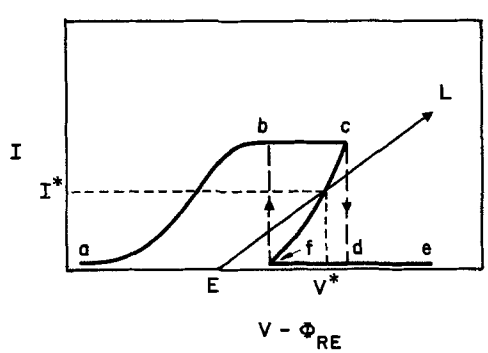

Fig. 1. Current vs. $(V - \Phi_{RE})$ characteristics for a passivating electrochemical system.

* Electrochemical Society Student Member.
** Electrochemical Society Active Member.
Key words: rotating disk electrode, ohmic potential drop, voltammetry.

study the three different sized iron rotating disk electrodes in the active-passive transition region.

Experimental

The rotating disk electrodes were the cross sections of different diameter iron rods (Johnson-Matthey, Puratronic). Three electrodes, each with a different diameter, were used in this work. Table I gives the radius and the cross-sectional area of each electrode. The electrodes were embedded in an insulating cylinder that was 1.95 cm in diameter. The insulating cylinder was composed of a 6:5 mix of Shell Epon 826 epoxy resin and Versamid 140 polyamid hardener.

Electrode surface preparation was carried out on a polishing wheel obtained from Buehler, Limited. Initially, 600 grit silicon dioxide abrasive paper was used on the wheel. This step rendered a matte finish on the iron surface. Next, a polishing cloth was used with 9, 3, and 1 micron diamond pastes. The electrodes were then carefully rinsed in distilled water. Initial surface preparation with abrasives finer than 1 micron was not necessary because the surface of the electrode was rapidly dissolved during the experiments.

The glass cell that was used is shown schematically in Fig. 2. Separate compartments were provided for both the reference electrode and the counterelectrode. Each compartment had two connections to the central portion of the cell. The upper connection had an inner diameter of approximately 0.6 cm and contained a porous glass frit. The lower connection was an open glass tube with an inner diameter of approximately 1 cm.

Nitrogen (Liquid Carbonic, "High Pure") was bubbled through the 1M sulfuric acid electrolyte for at least 1 hr before the experiments were begun. Nitrogen bubbling was continued during the experiments. The cell was placed in a constant temperature bath that was controlled to 25.0° ± 0.5°C. Polarization of the cell was controlled with a potentiostat (Stonehart Model BC 1200) that had auxiliary circuitry providing a load line with a positive slope.

Two different types of experiments were carried out. The first type, which is referred to as potentiodynamic sweeps, were runs where the load line of the potentiostat was vertical. The potential of the disk was varied from −1.0 to 0.6V with respect to a mercury-mercurous sulfate reference electrode. Slow sweep rates of 20-40 mV/sec were used. The sweep generator was a Princeton Applied Research, Model 175, Universal Programmer. Current-voltage plots were recorded on a Hewlett-Packard, Model 7047A, X-Y Recorder. Transients associated with the active-passive and passive-active transitions exceeded the time response capabilities of the X-Y recorder. These transients were accurately monitored with a Nicolet Instrument Corporation, Model 206, Digital Storage Oscilloscope.

The second type of experiment incorporated the use of the potentiostat circuitry that provided a positive sloping load line. By choosing a base potential, E, which was usually −0.27V with respect to the mercury-mercurous sulfate reference electrode, the Z-shaped part of the polarization curve (c-f) could be traced out by decreasing the slope of the load line.

A schematic diagram of the experimental apparatus is given in Fig. 3. All runs were made at a disk rotation speed of 1600 rpm (167.6 rad/sec).

Table I. Values of the radius and the cross-sectional area for each electrode

Electrode	Radius r_o (cm)	Cross-sectional area (cm²)
A	0.247	0.1917
B	0.149	0.06984
C	0.0493	0.00763

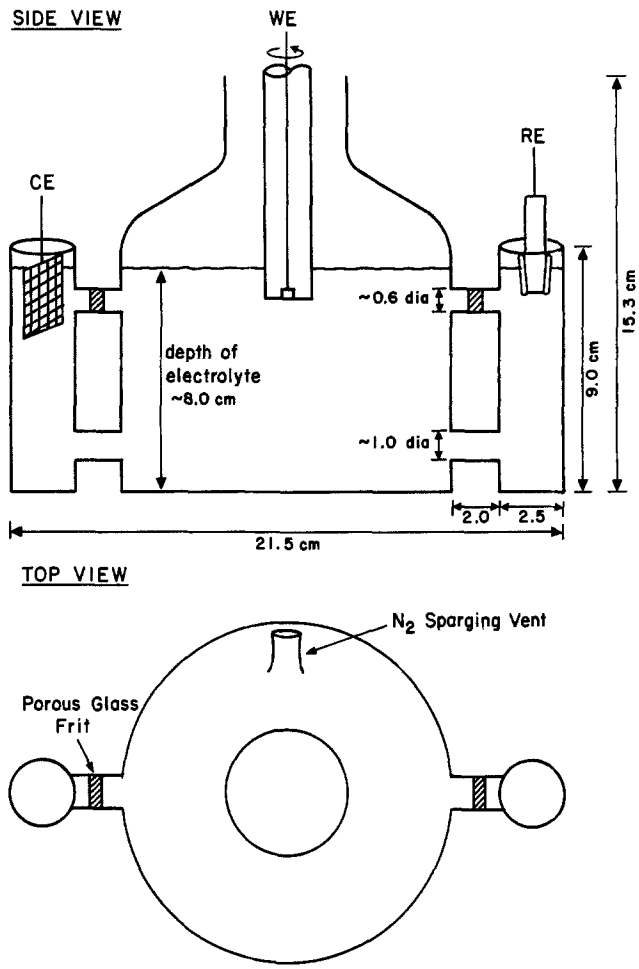

Fig. 2. Schematic diagram of the experimental cell. All dimensions are given in centimeters and are approximate. The electrodes are indicated in their usual operating positions: WE, working electrode; RE, reference electrode; and CE, counterelectrode.

Two different purities of the 1M sulfuric acid electrolyte were used. One solution was prepared using Mallinckrodt Sulfuric Acid, "Analytical Reagent," and distilled water. The second solution, which was composed of J. T. Baker Sulfuric Acid-Ultrex and purified water having a specific resistance of 17 MΩ-cm, was much lower in contaminants than the first solution. There was no apparent change in the results due to the difference in these solutions.

Results and Discussion

Figure 4, which is taken from Epelboin *et al.*, shows a hysteresis loop in the current-voltage curve observed when a potentiostat (vertical load line) is

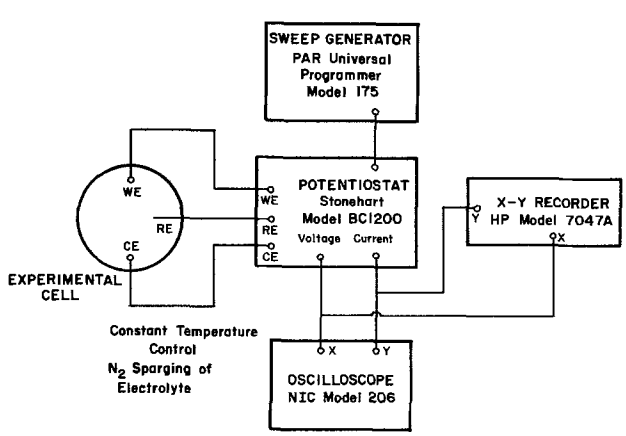

Fig. 3. Schematic diagram of the experimental apparatus

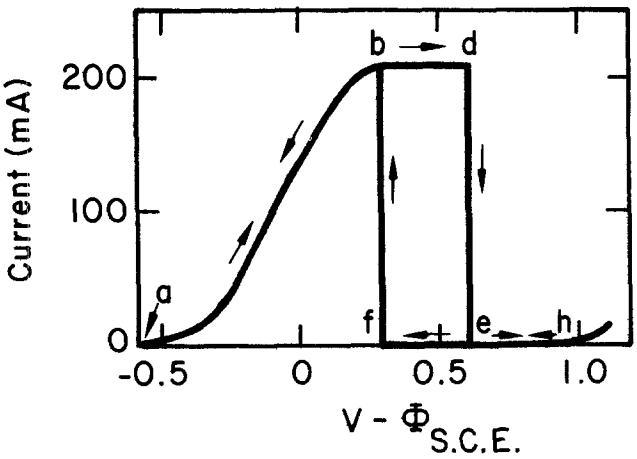

Fig. 4. Current-voltage curve for a 5 mm diam iron disk in 1M sulfuric acid, rotating at 750 rpm, taken from Epelboin *et al.*

used to polarize a 5 mm iron disk in 1M sulfuric acid at 750 rpm. A saturated calomel reference electrode was used in their work.

The total current is reduced when an electrode with smaller cross-sectional area is used. A reduction in current will cause the ohmic potential drop in solution to decrease, even though the resistance increases. This should result in a decrease of the width of the hysteresis loop. Figure 5 shows potentiodynamic sweep results for the three different sized electrodes. The current is reported as the average current density, $\bar{i} = I/\pi r_0^2$, where r_0 for each electrode is given in Table I. As expected, electrode C has the narrowest hysteresis loop because it passed less current than either electrode A or electrode B. The width of the hysteresis loop for electrode B is narrower than for electrode A for the same reason.

A limiting current plateau was observed on all of these runs. Epelboin *et al.* observed the same phenomenon in their experiments. A limiting current density of 1350 mA/cm^2 was observed for electrodes A and B. The limiting current density for electrode C was 8% lower than that for the larger electrodes. A possible explanation for the lower current density on electrode C could involve disruption of the known disk hydrodynamics. As the electrodes dissolve they recede up into the insulating disk. As this recess becomes deeper we would expect an increased resistance to mass transfer. This effect will be the greatest for electrode C because the ratio of depth of recess to r_0 will be the largest for this electrode.

For electrodes B and C we see an overshoot above the limiting current that is observed only on the potential sweep in the positive direction. This current overshoot has been previously observed and is considered to be an experimental artifact due to the finite voltage sweep rate (2). As evidence of this, consider the curve for electrode C in Fig. 5. If the positive sweep is stopped at point *s*, the current will fall to the limiting value at point *t*. The current will remain there so long as the potential is held at V_t. As further evidence, the current followed the curve through point *t* on the negative sweep. Similar phenomena were observed for electrode B; however, the negative sweep is not included in Fig. 5 to minimize confusion. This overshoot was not observed with electrode A because the sweep rate was only 20 mV/sec as compared to 40 mV/sec for the other two electrodes.

An unexpected feature of this plot is the difference in potentials at which the passive-active transitions occur for the three electrodes. For electrodes A, B, and C the transition occurred at $V - \Phi_{Hg/Hg_2SO_4} = -0.170$, -0.185, and -0.192V, respectively. Epelboin *et al.* (4) obtained a value of $V - \Phi_{Hg/Hg_2SO_4} = -0.17$ for a 5 mm diam disk, which is in precise agreement with our results for electrode A. The dependence of this potential on electrode size indicates that the change from passive to active states does not occur precisely at the Flade potential, but instead at a slightly more positive potential. A definition of the Flade potential is best delayed until the results obtained using the positive sloping load line have been discussed.

The determination of the current-voltage behavior of a passivating system requires the use of a polarization device having a load line with a positive slope. The positive feedback circuit on the Stonehart potentiostat provided this capability. Figure 6 presents these experimental results; again, the current is expressed in terms of the average current density based on the cross-sectional area of each electrode. The most important feature of Fig. 6 is the shape of the curves during the transition between the active state and the passive state. The Z-shape for electrode A is most prominent. However, the transition for electrode C is more closely characterized by a vertical line. The curve for electrode C has less ohmic distortion than the curves for either electrodes A or B.

From the progressive changes observed in these three curves, it is concluded that, in the limit of zero electrode size, both the active-passive and passive-active transitions are characterized by a nearly vertical line on an I *vs.* $(V - \Phi_{RE})$ plot. The voltage at which this transition would occur is the Flade potential. The determination of this potential and the generation of the dotted portions of the curves in Fig. 6 are discussed later in this section. Some difficulties associated with ohmic compensation and a discussion of some of the other features of Fig. 6 are now taken up.

Attempting to compensate for the ohmic resistance in solution by subtracting IR_Ω, using a constant R_Ω, is not valid for the passivation process. As the disk passivates, the active area decreases. This leads to a

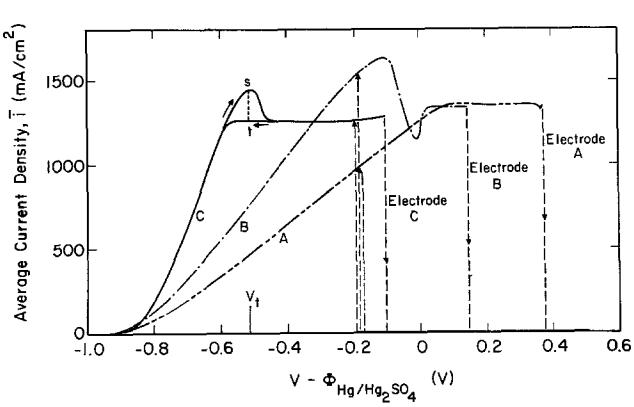

Fig. 5. Potentiodynamic sweep results. Note the different potentials at which the passive-active transition occurs for the three electrodes.

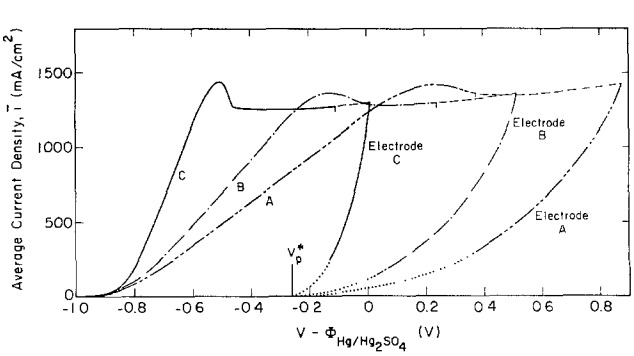

Fig. 6. Current-voltage curves for the three electrodes obtained using a polarization device having a load line with a positive slope. Electrode C has signifcantly less ohmic distortion than the two other electrodes. Anodic sweep rates: electrode A, 20 mV/sec; electrode B, 40 mV/sec; electrode C, 30 mV/sec.

continuous increase in the ohmic resistance. This can be seen more clearly by recalling the formula for the ohmic resistance between the edge of the active portion of the disk and a hemispherical counterelectrode located at infinity given by Law and Newman

$$R_\Omega = \frac{\epsilon}{4\kappa r_p} \quad [1]$$

where ϵ is a number which varies from 1 for a primary current distribution to $8/\pi^2$ for a uniform current distribution. Interpreted physically, ϵ is the ohmic potential drop to the edge of the disk at the given current distribution divided by the potential drop to the edge of the disk which would exist for a primary current distribution, assuming I and r_p are constant. Therefore, ϵ can be thought of as a dimensionless ohmic potential drop, scaled by the primary current distribution case. The passivation radius, r_p, is defined in the following way. For $r > r_p$, the disk is passivated; for $r < r_p$, the disk is active.

In Fig. 6, the dashed portions of the limiting current curves represent an unstable region in which the current could not be controlled. In certain potential ranges of this unstable region the current oscillated in a sustained manner. The average value of these oscillations is represented by the dashed line. This effect is different from the rather slow fluctuations which were described by Epelboin *et al.* in the same region of the curve.

The current overshoot above the limiting current is again seen for the positive voltage sweep. The cause and associated phenomena are the same as for the curves which were obtained under potentiodynamic control.

The determination of the Flade potential, which will be denoted as V_p^*, is now made. The basic procedure involves fitting the current-voltage data to a theoretically based equation. The extrapolation of this equation to the point of zero current will then yield the Flade potential.

Extrapolation of the Z-shaped curve.—The dotted portions of the curves in Fig. 6 could not be obtained with our polarization device because the minimum load line slope that the potentiostat could provide had been reached. The dotted portions of the curves were extrapolated from a least squares curve fit (5) through the data.

To begin, the following equation is recalled from Law and Newman

$$V - \Phi_{RE} = V_p^* + \frac{\epsilon\sqrt{\pi I i_{avg}^*}}{4\kappa} - \Phi_{RE} \quad [2]$$

This equation describes the current-voltage behavior during the passivation process. The Flade potential, V_p^*, is the point at which the local current density, i, goes to zero. It is presumed that the Flade potential prevails at the edge of the active portion of the disk. When the Flade potential reaches the center of the disk the entire surface is passive, and the total current falls to zero. It is important to understand the difference between $\bar{i}$ and i_{avg}^*. The average current density, $\bar{i}$, is defined as the total current divided by the cross-sectional area of the electrode, $\bar{i} = I/\pi r_o^2$. The quantity i_{avg}^* is the total current divided by the active area of the electrode, $i_{avg}^* = I/\pi r_p^2$. Equation [2] can be rearranged to give

$$I = b(V - V_p^*)^2 \quad [3]$$

where

$$b = \left(\frac{4\kappa}{\epsilon}\right)^2 \frac{1}{\pi i_{avg}^*} \quad [4]$$

If ϵ and i_{avg}^* are constants, then a plot of I *vs.* $(V - V_p^*)^2$ should be a straight line passing through the origin. Table II is a representative set of I *vs.* V data from the three electrodes. The electrode from which each data point was taken is noted. Extensive work with the data indicated that a plot of I *vs.* $(V - V_p^*)^2$ would not be linear for any reasonable value of V_p^*. This indicated that the quantity $(\epsilon^2 i_{avg}^*)$ was varying as the passivation process occurred. In order to account for these variations the data were fit with the following equation

$$I = a_0 + a_1(V - V_p^*)^2 + a_2(V - V_p^*)^4 \quad [5]$$

The current must be zero when $V = V_p^*$ because the disk becomes fully passivated at that point; therefore, $a_0 = 0$.

The computer program which determined V_p^* worked in the following way. An initial value of V_p^* was provided. A least squares curve fit program then generated values of a_0, a_1, and a_2 that were based on the 18 data points in Table II. If a_0 was not equal to zero, then a new value of V_p^* was determined, and the least squares program recalculated a_0, a_1, and a_2. This process was repeated until a_0 was sufficiently close to zero. The final values obtained for a_0, a_1, a_2, and V_p^* are shown in Table III. Figure 7 is a plot of the current against $(V - V_p^*)^2$, where $V_p^* = -0.26168$V. The computer generated curve (Eq. [5]) is shown as the solid line for comparison with the data.

The value of the passive-active transition potential depends on the passive film stability. A smaller disk electrode has smaller potential and concentration fluctuations over its surface. If such fluctuations lead to breakdown of the film, then it is reasonable to expect that the passive film will remain stable at a more negative potential on a smaller electrode.

In the potentiodynamic sweep experiments, the passive-active transition potential becomes more negative as the electrode size decreases. The result from the curve fit procedure is equivalent to obtaining the passive-active transition from a potentiodynamic sweep experiment for an electrode of infinitesimal area.

This explains the range of transition potentials varying from a calculated value of −0.2168V for an infinitesimally small electrode to an observed value of −0.17V for the largest electrode.

The dotted portions of the curves in Fig. 6 were obtained in the following way. From a given value of $(V - V_p^*)^2$, Eq. [5] estimates the total current, I.

Table II. Values of the current at various potentials for the three electrodes

Electrode	Potential ($V - \Phi_{RE}$) (V)	Current (mA)
C	−0.125	1.78
C	−0.100	2.61
C	−0.075	3.59
C	−0.050	4.80
C	−0.025	6.20
C	0.000	7.95
B	0.040	10.5
B	0.100	14.5
B	0.200	24.0
B	0.300	38.0
A	0.370	56.0
B	0.400	57.0
A	0.400	62.0
B	0.450	69.0
A	0.500	90.0
A	0.600	125
A	0.650	143
A	0.700	164

Table III. Values of the parameters in Eq. [5] determined by the least squares fit

Variable	Dimension	Least squares result
V_p^*	V	−0.26168
a_0	mA	0.00040397
a_1	mA/V²	99.737
a_2	mA/V⁴	86.525

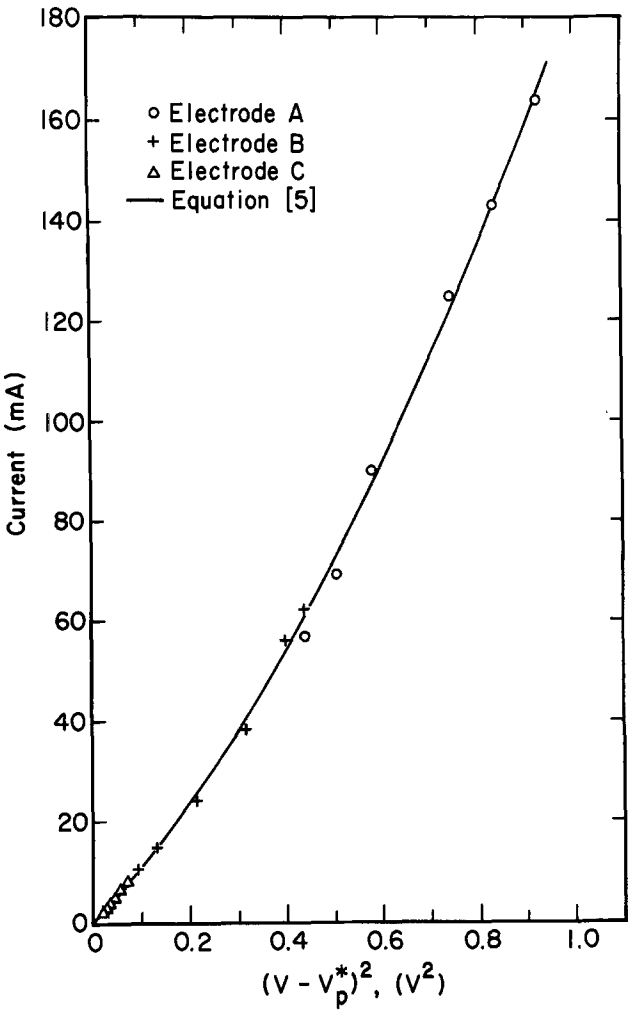

Fig. 7. Experimental values of I plotted against $(V - V_p^*)^2$. Equation [5] is shown as the solid line for comparison with the data.

This value was divided by the appropriate cross-sectional areas (see Table I) to obtain the corresponding average current densities for each electrode. This procedure was used to extrapolate from the point of zero current at $V = V_p^*$ up to the first data point for each electrode.

Determination of i_{avg}^*.—We now determine the variations in i_{avg}^* as the electrode passivates. This is accomplished within the framework of the model presented by Law and Newman. The curvature in Fig .7 indicates that ϵ and or i_{avg}^* are changing during passivation. Equations [3] and [4] can be combined to give

$$\epsilon^2 i_{avg}^* = \left(\frac{4\kappa}{\pi}\right)^2 \frac{(V - V_p^*)^2}{I} \qquad [6]$$

At this point, Eq. [5] indicates how I varies with $(V - V_p^*)$; therefore, i_{avg}^* could be determined from Eq. [6] if the dependence of ϵ on $(V - V_p^*)$ was also known. Previous results obtained for a nonpassivating disk electrode by Newman (6) indicate the complexity of this dependence. We now apply these results on the active portion of the electrode to calculate how ϵ depends on $(V - V_p^*)$. This procedure is now developed.

In general, the current distribution will depend on the parameters J, δ, α_a, and α_c. For the passivation problem

$$J = \frac{i_0 r_p n\mathbf{F}}{RT\kappa} \qquad [7]$$

Law and Newman give a value of 9.1×10^{-5} A/cm^2 for the exchange current density when the ferrous ion concentration is 4.0 mol/liter. Hurlen (7) indicates that the dependence of the exchange current density on hydroxide and ferrous ion concentrations is

$$\log (i_0)\,[\text{A/cm}^2] = 3.58 - \text{pOH} - \text{pFe} \qquad [8]$$

Because only small amounts of iron were dissolved during the experiments, the ferrous ion concentration can be considered negligible. Equation [8] indicates that the exchange current density was very small for our experimental conditions. From this reasoning, it was concluded that the approximation $J = 0$ was valid in the analysis of this work.

The second parameter is given by

$$\delta = \frac{\alpha_a \mathbf{F} r_p i_{avg}^*}{RT\kappa} \qquad [9]$$

In 1M sulfuric acid κ is 0.40 $(\Omega\text{-cm})^{-1}$ at 25°C (8), and α_a is 1.0 for the anodic dissolution process (3). The dependence of $(i/i_{avg}^*)|_{r=0}$, the current density at the center of the disk divided by i_{avg}^*, on δ is illustrated in Fig. 8. Focusing attention on the curve for $J = 0$, we see that as $\delta \to \infty$, $(i/i_{avg}^*)|_{r=0}$ approaches a value of 0.5 and a primary current distribution is obtained. Under these conditions $\epsilon = 1.0$.

At the other extreme when $\delta \to 0$, a uniform current distribution is obtained. For this case $(i/i_{avg}^*)|_{r=0}$ has a value of 1.0. Under these conditions $\epsilon = 8/\pi^2$.

With the relationship

$$I = i_{avg}^* \pi r_p^2 \qquad [10]$$

it is possible to eliminate r_p from Eq. [9] and obtain

$$\delta = \frac{\alpha_a \mathbf{F}}{RT\kappa} \sqrt{\frac{i_{avg}^* I}{\pi}} \qquad [11]$$

Substitution of Eq. [2] into Eq. [11] gives

$$\delta = \frac{4\alpha_a \mathbf{F}}{\epsilon\pi RT} (V - V_p) \qquad [12]$$

Equation [11] can be rearranged to give

$$i_{avg}^* = \delta^2 \left(\frac{RT\kappa}{\alpha_a \mathbf{F}}\right)^2 \frac{\pi}{I} \qquad [13]$$

In order to evaluate δ from Eq. [12] we must once again face the problem of determining how ϵ varies with $(V - V_p^*)$. A computer program describing the secondary current distribution on a disk electrode, developed by Newman (6), was available to calculate ϵ and δ for given values of J and the potential. Results from this program are given in Fig. 9. This plot indicates how ϵ varies with the parameter $\alpha_a \mathbf{F}(V - V_p^*)/RT$, when $J = 0.1$. The program could be rerun with $J = 0$; however, the change in results would be insignificant, as can be seen from Fig. 8.

The remaining steps in the determination of i_{avg}^* as a function of r_p were as follows. First, a value of $(V - V_p^*)$ was selected. With $\alpha_a = 1.0$ (3), a value

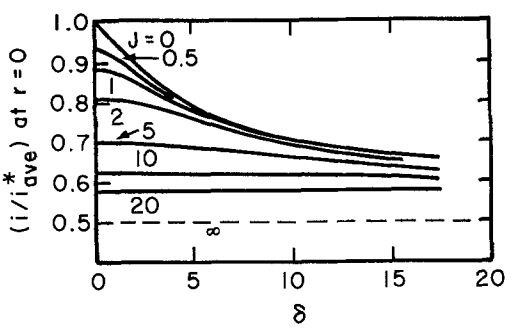

Fig. 8. Current density at the center of the disk as a function of δ.

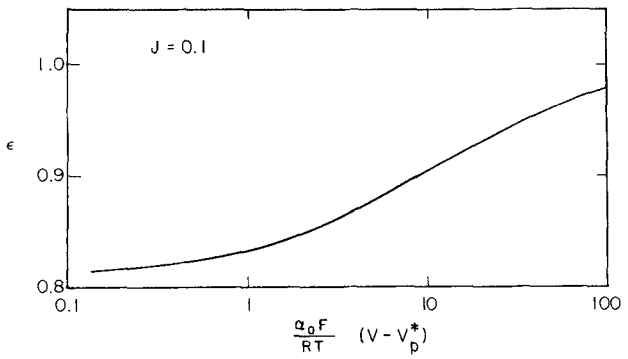

Fig. 9. Plot of ϵ vs. the parameter $\alpha_a F/RT(V - V_p^*)$ from Newman.

of ϵ was obtained from Fig. 9. The parameter δ was then determined from Eq. [12]. The total current, I, at the given value of $(V - V_p^*)$ was given by Eq. [5]; ultimately, i_{avg}^* was obtained from Eq. [13]. These results are presented in Table IV. The first two columns were taken directly from the computer program used to generate values plotted in Fig. 9. The values of δ and i_{avg}^* were computed according to the method outlined above. The radial point of passivation, r_p, was obtained from Eq. [10], using the known values of I and i_{avg}^*.

The calculations used to determine δ, i_{avg}^*, and r_p were repeated for the extreme cases of a primary and a uniform current distribution. For a primary distribution, ϵ is taken as 1, while for the uniform distribution, ϵ is taken as $8/\pi^2$ in the procedure outlined above. These results are shown as a plot of i_{avg}^* *vs.* r_p in Fig. 10. When the active portion of the disk was small, the calculated curve for i_{avg}^* approached the value corresponding to a uniform current distribution. As the active area increased, the calculated value of i_{avg}^* decreased rapidly and approached the primary distribution asymptotically.

For values of $r_p > 0.077$ mm, the calculations which generated the curves in Fig. 10 are based on the experimental data. For $r_p < 0.077$ mm the curves have been extrapolated. This region of extrapolation corresponds to the dotted portions of Fig. 6.

Table IV. Values of ϵ, δ, i_{avg}^*, and r_p at various potentials calculated from the experimental data

$\frac{\alpha_a F}{RT}(V - V_p^*)$	ϵ	δ	i_{avg}^* (A/cm²)	r_p (mm)	Source[a] of data	r_o (mm)
0.02752	0.811	0.04321	12.47	0.000357	Extrap.	—
0.05504	0.811	0.08653	12.45	0.000714	Extrap.	—
0.08703	0.812	0.1365	12.40	0.00113	Extrap.	—
0.1231	0.814	0.1925	12.33	0.00161	Extrap.	—
0.2752	0.820	0.4276	12.16	0.00361	Extrap.	—
0.3892	0.822	0.6029	12.09	0.00513	Extrap.	—
0.8703	0.831	1.334	11.83	0.0116	Extrap.	—
1.231	0.837	1.873	11.66	0.0165	Extrap.	—
1.741	0.844	2.626	11.45	0.0236	Extrap.	—
2.462	0.853	3.677	11.21	0.0337	Extrap.	—
3.015	0.860	4.466	11.00	0.0417	Extrap.	—
3.481	0.864	5.130	10.87	0.0485	Extrap.	—
3.892	0.868	5.713	10.76	0.0545	Extrap.	—
4.262	0.871	6.230	10.65	0.0601	Extrap.	—
4.768	0.875	6.938	10.54	0.0677	Extrap.	—
5.321	0.879	7.707	10.41	0.0761	C	0.493
6.294	0.886	9.045	10.18	0.0913	C	0.493
7.267	0.892	10.38	9.98	0.107	C	0.493
8.240	0.896	11.71	9.80	0.123	C	0.493
10.19	0.905	14.34	9.43	0.156	C	0.493
14.08	0.916	19.57	8.74	0.230	B	1.49
21.86	0.932	29.87	7.38	0.416	B	1.49
25.76	0.938	34.96	6.73	0.534	A	2.47
27.70	0.941	37.50	6.42	0.601	B	1.49
33.54	0.948	45.05	5.53	0.837	A	2.47
37.43	0.952	50.09	5.01	1.03	A	2.47
41.34	0.955	55.14	4.54	1.25	Extrap.	—

[a] The symbol "Extrap." indicates that this data point was obtained by an extrapolation of Eq. [5]. A capital letter identifies the electrode from which the given data point was obtained. For these cases, the corresponding electrode radius is given for comparison with r_p.

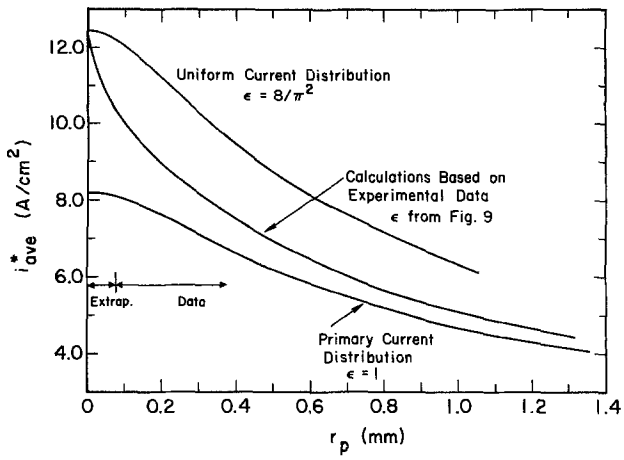

Fig. 10. Average current density on the active portion of the disk plotted against r_p.

The results obtained in this work are qualitatively similar to those presented by Law and Newman in their mathematical model describing the kinetically limited case. Both indicate that i_{avg}^* increases as the active electrode area decreases. As $r_p \to 0$ (complete passivation), the value of i_{avg}^* based on these experiments reaches a value of 12.44 A/cm², this compares with a value of 17.1 A/cm² estimated by Law and Newman. The qualitative agreement of these results was expected. The same model was used in both cases; however, the data bases were different.

The continuous increase in i_{avg}^* as r_p decreases can be explained in the following way. First, assume that the current density at $r = r_p$ is constant. For the experimental results obtained here, $i|_{r=r_p} = 12.44$ A/cm². For a large active area the primary current distribution is approached. Under these conditions $i|_{r=0} < i_{avg}^* << i|_{r=r_p}$, which is consistent with experimental observation. As the active area decreases and $r_p \to 0$, we approach a uniform current distribution, for which $i|_{r=0} \approx i_{avg}^* \approx i|_{r=r_p}$.

Law and Newman also calculated a value for the limiting current. Their calculations were based on a disk rotation speed of 4500 rpm. Since these experiments were carried out at 1600 rpm, it was necessary to correct for the difference in rotation speeds by using the Levich relationship (9)

$$I_{lim} = \beta\sqrt{\Omega} \qquad [14]$$

The adjusted value was 1.64 A/cm², which is to be compared with a value of about 1.35 A/cm² obtained in this work (see Fig. 5 and 6).

Conclusions

Experimental results obtained from three iron rotating disk electrodes indicate that the local passivation phenomenon can be represented as a nearly vertical line on a current *vs.* $(V - \Phi_o)$ plot. If it is assumed that the active portion of the electrode always has a disk configuration, then this work has shown that the Z-shaped polarization curve, obtained with a Negative Impedance Converter, is due only to ohmic potential drop in solution. This effect is complicated because the active area of the electrode decreases during the passivation process, resulting in a continuously increasing ohmic resistance to the disk. Analysis of the data obtained in these experiments, within the framework of the Law and Newman model, indicates the average current density on the active area of the electrode increases as the size of the active area decreases during passivation.

Recall that Epelboin *et al.* have observed the opposite phenomenon; current density on the active area decreased as the active area decreased. This difference can be explained if the local current density *vs.* poten-

tial behavior is assumed to be different, as explained in the following example.

Consider two cases: (*i*) the local current density monotonically increases as $V - \Phi_o$ increases toward V_p^* and (*ii*) the local current density monotonically decreases as $V - \Phi_o$ increases toward V_p^*. The value of i_{avg}^* is obtained by averaging the current density contributions over the values of $(V - \Phi_o)$ that exist on the active area. The variation in $(V - \Phi_o)$ from the center to the edge of the disk becomes smaller as the active area decreases. For case (*i*), a large active area implies that current densities considerably below $i|_{r=r_p}$ will be included in the average; for small active areas only current densities slightly below $i|_{r=r_p}$ will be included. The result is an increasing value of i_{avg}^* as r_p decreases. For case (*ii*), a large active area implies that current densities considerably above $i|_{r=r_p}$ will be included in i_{avg}^*; for small active areas only current densities slightly above $i|_{r=r_p}$ are included. The result is a decreasing value of i_{avg}^* as r_p decreases.

In this work we have measured $\epsilon^2 i_{avg}^*$ and calculated ϵ. This permits i_{avg}^* to be determined as a function of active area. This procedure indicates that i_{avg}^* increases as r_p decreases. Our results would have been stronger if i_{avg}^* itself had been experimentally measured, instead of relying on calculations. The apparent value of the current density at the point of passivation, $i|_{r=r_p}$, obtained from this study is 12.44 A/cm^2. Our local current density-potential relationship corresponds to case (*i*).

The result of Epelboin *et al.* corresponds to case (*ii*).

Further work is presently underway to determine the cause of the limiting current for the anodic dissolution of iron. Previous observation (2) has shown that the limiting current for this process obeys the Levich relation (9). In the unstable region of the limiting current curve it is observed that $i_{avg}^* > i_{lim}$ and $i|_{r=r_p} > i_{lim}$. We also see that $r_p < r_o$ for all data points listed in Table IV. This situation is unstable; the electrode may jump between states that have different active areas. This jumping explains the observed rapid current oscillations. Further study is needed to determine the triggering mechanism for the active-passive jumping.

The principal result of this work is Fig. 7. Having the active-passive transition data for the three electrodes fall on the same curve indicates that the passivated portion of the disk does not affect the active portion. This verified a major hypothesis in Law and Newman's model.

Acknowledgment

This work was supported by the Solar Energy Research Institute. The suggestions and comments of the reviewers are gratefully acknowledged.

Manuscript submitted April 30, 1982; revised manuscript received Sept. 5, 1982.

Any discussion of this paper will appear in a Discussion Section to be published in the December 1983 JOURNAL. All discussions for the December 1983 Discussion Section should be submitted by Aug. 1, 1983.

LIST OF SYMBOLS

a_0, a_1, a_2 constants in Eq. [5]
A electrode with diameter of 0.494 cm
B electrode with diameter of 0.298 cm
C electrode with diameter of 0.0986 cm
E base potential, Fig. 1, V
F Faraday's constant, 96,487 C/equiv.
i local current density, A/cm^2
i_0 exchange current density, A/cm^2
$\bar{i}$ average current density based on entire electrode area, A/cm^2
i_{avg}^* average current density based on active electrode area, A/cm^2
i_{lim} limiting current density, A/cm^2
I total current on the disk, mA
I_{lim} limiting current, A
J kinetic parameter, see Eq. [7]
L load line with positive slope, Fig. 1
r radial coordinate, cm
r_o radius of the electrode, cm
r_p radial point of passivation, cm
R universal gas constant, 8.3143 J/mol-K
R_Ω ohmic resistance in solution, Ω
T absolute temperature, K
V_p^* passivation potential, V
V disk potential, V

Greek letters

α_a anodic transfer coefficient
α_c cathodic transfer coefficient
β constant in Eq. [14], A-sec$^{1/2}$
δ kinetic parameter, Eq. [9]
ϵ current distribution parameter, Eq. [1]
κ bulk solution conductivity, $(\Omega\text{-cm})^{-1}$
π 3.14159
Φ_{Hg/Hg_2SO_4} potential of saturated mercurous sulfate reference electrode, V
Φ_o potential in solution just outside the electric double layer, V
Φ_{RE} reference electrode potential, V
Φ_{SCE} potential of saturated calomel electrode, V
Ω disk rotation speed, sec^{-1}

REFERENCES

1. Fr. Flade, *Z. Phys. Chem.*, **76**, 513 (1911).
2. I. Epelboin, C. Gabrielli, M. Keddam, J. C. Lestrade, and H. Takenouti, *This Journal*, **119**, 1632 (1972).
3. C. G. Law and J. Newman, *ibid.*, **126**, 2150 (1979).
4. I. Epelboin, C. Gabrielli, M. Keddam, and H. Takenouti, in "Comprehensive Treatise of Electrochemistry. Vol. 4: Electrochemical Materials Science," J. O'M. Bockris, B. E. Conway, E. Yeager, and R. E. White, Editors, pp. 151-192, Plenum Press, New York (1981).
5. R. Hornbeck, "Numerical Methods," pp. 122-125, Quantum Publishers, Inc., New York (1975).
6. J. Newman, *This Journal*, **113**, 1235 (1966).
7. T. Hurlen, *Acta Chem. Scand.*, **14**, 1533 (1960).
8. T. W. Chapman and J. Newman, "A Compilation of Selected Thermodynamic and Transport Properties of Binary Electrolytes in Aqueous Solution," UCRL-17767 (1968).
9. V. G. Levich, "Physicochemical Hydrodynamics," p. 70, Prentice-Hall, Inc., Englewood Cliffs, NJ (1962).

Laser-Enhanced Electroplating on Good Heat-Conducting Bulk Materials

H. K. Kuiken

Philips Research Laboratories, 5600 MD Eindhoven, The Netherlands

F. E. P. Mikkers

Philips Sub-components Development Center, Elcoma, Eindhoven, The Netherlands

and P. E. Wierenga

Philips Research Laboratories, 5600 MD Eindhoven, The Netherlands

ABSTRACT

Laser-enhanced electroplating on good heat-conducting bulk materials is not very effective, as laser-beam irradiation results in a limited temperature rise only. It is shown, both experimentally and theoretically, that the application of a thin layer of a relatively poor heat-conducting material may lead to a considerable local temperature increase. The dimensionless parameter determining this effect is given by the product of the ratio of the thermal conductivities of bulk and layer material and that of layer thickness to laser-spot diameter.

Laser-enhanced electroplating has been shown to be a promising technique for maskless selective plating (1, 2). By focusing a laser beam onto the surface of an optically absorbing substrate in a plating solution, the plating rate at the laser spot and in the area surrounding it can be increased significantly. For relatively low laser intensities the temperature of the solid-liquid interface in the irradiated area will remain below the boiling temperature of the solution. Under such circumstances the temperature dependence of the rate of the electrode reaction mainly determines the locally increased plating rates. At temperatures below the boiling point microconvection cannot significantly contribute to the enhanced plating phenomenon, as the Grashof numbers involved are far too small (3). With a heated area of 200 microns only, a maximum temperature difference of 80 K, a thermal expansion coefficient of 10^{-4} K^{-1}, and a kinematic viscosity of $4 \cdot 10^{-7}$ m^2/sec, the Grashof number will have the value 4. Thus, only a very modest contribution can be expected from ordinary convection.

At increasing intensity of the laser beam, the local temperature of the electrode surface will eventually exceed the boiling temperature of the liquid. In this case, "local boiling" occurs, *e.g.*, nuclei (cavities) at the heated spot on the electrode surface are activated to generate vapor bubbles periodically. These bubbles grow (at the side facing the electrode) and implode (at the opposite side facing the bulk liquid) simultaneously; *i.e.*, if the bulk liquid is at room temperature, the bubbles adhere to the electrode surface during their entire short lifetime (4). This bubble behavior causes very rapid oscillatory motions (and pressure waves) in the liquid adjacent to the electrode. Ultimately, the result of the periodical action of the bubbles is a considerable enhancement of the convective transport at the electrode surface up to an order of magnitude.

At sufficiently high laser power densities, a relatively large liquid region in the immediate vicinity of the electrode, and surrounding the heated spot, will be heated to temperatures considerably above the original bulk temperature. In this case tiny bubbles depart from the electrode, and bubble jets are ejected in a direction normal to the surface. It should be noted that local boiling differs from what is commonly known as "pool boiling." As the latter occurs in any tea kettle, it is the more familiar kind of boiling. Its main characteristic is that the bulk is first raised to the boiling temperature before actual boiling occurs at the heated surface. In that case bubbles are ejected almost right from the start of the boiling process.

Key words: boiling, electrodeposition, films, metals.

Bubble ejection leads to considerable stirring near the irradiated area and therefore to increased local transport of reactants toward the electrode. Moreover, forced convection causes a narrowing of the temperature profile in the irradiated area. This will yield a more selective plating and therefore a more discrete metal deposition.

Von Gutfeld *et al.* describe experiments in which various metals are deposited selectively on substrates (1, 2) consisting of thin metallic films on glass. If the layer thickness is very much smaller than the laser-spot diameter, laser-enhanced plating yields metal spots with sizes comparable to the size of the laser spot itself. Very discrete spots can be obtained with relatively low laser-power densities. However, for thicker films the radial heat flux through the film surface increases. This causes the plated spot to become larger and less discrete. Besides, more laser power is needed to reach the boiling point at the hot spot.

In electronics the application of laser-enhanced electroplating offers distinct advantages over other plating techniques, if it can be applied to selective metal deposition on bulk metals or metal alloys, especially for plating relatively expensive metals such as gold. We have carried out laser plating experiments with gold on nickel-iron and copper-zinc alloy substrates. On the nickel-iron substrates a continuous incident laser power of 4W (power density at laser spot of the order of 50 $kW \cdot cm^{-2}$) is found to be sufficient to cause local boiling and to deposit well-localized gold spots, *e.g.*, with a diameter of 400 μm and a height of 1 μm. The plated spot diameter increases as a function of time, mainly due to lateral heat diffusion through the gold deposit. The maximum deposition rate is of the order of 5 $\mu m \cdot sec^{-1}$.

However, the thermal conductivities of our copper-zinc substrates are about four times higher than the conductivity of nickel-iron. As a consequence, it is impossible to deposit discrete gold spots of the above-mentioned geometry on bare copper-zinc substrates with a continuous laser, even at a laser-power density as high as 250 $kW \cdot cm^{-2}$. It is true that discrete spots can be obtained by the application of very short light pulses from a pulsed laser (1), but the disadvantage

of such a method is the low duty cycle, which means that the effective deposition rate will decrease considerably. Indeed, growth will be minimal during the larger part of the cool-down period and in the initial stages of the power-on phase.

We have found that the problems with laser-enhanced plating on a good heat-conducting bulk metal can be solved by covering the substrate with a thin, optically absorbing, metallic layer of relatively low thermal conductivity. The relevant theory behind this result is described in this paper and illustrated by some experimental observations.

Temperature Calculation

If a good heat-conducting bulk substrate is irradiated by a laser beam, the temperature rise at the laser-impact area may be quite limited. In this section we show, using a simple mathematical model, that a considerable temperature rise can be achieved at the laser-heated spot when the substrate is covered with a thin film of a relatively poor heat-conducting material. In this model we avoid complicating factors, such as boiling heat transfer and lateral thermal conduction through the plated spot.

We are allowed to make these assumptions as we have a limited goal in mind. Indeed, we only wish to show that the thin film allows temperatures to be reached at which the enhanced plating effect can be observed. Below a given temperature there will be no boiling of the electrolyte and consequently heat transfer will occur mainly through conduction. If the thermal conductivity of the substrate material is considerably higher than that of the electrolyte, conductive and convective heat transfer toward the latter may be disregarded. As a result most of the dissipated laser power will be conducted into the substrate.

Let us consider a semi-infinite region bounded by an infinite plane surface (Fig. 1). We use Cartesian coordinates (x, y, z), denoting the bounding plane by $z = 0$. The semi-infinite region shall be that of positive z, and this region is occupied entirely by two heat-conducting materials of different thermal properties. The first material (thermal conductivity k_1) fills the layer denoted by $0 \leq z < \delta$, while the second (k_2) is to be found in $z > \delta$. The two materials are thought to have a perfect bond in the plane $z = \delta$ resulting in the absence of any additional thermal resistance.

The heat-conducting region described above is heated by a Gaussian laser beam which has its axis centered on the line $r = 0$, where $r = (x^2 + y^2)^{1/2}$. Assuming a negligible penetration depth for the absorbed laser power a continuous heat input at $z = 0$ is obtained

$$k_1 \frac{\partial T}{\partial z} = -\frac{Q}{\pi a^2} e^{-r^2/a^2} \qquad [1]$$

where T is the temperature and Q denotes the absorbed power of the laser. Clearly the parameter a is a measure of the width of the laser beam (63% of the laser power is expended in the interval $0 \leq r \leq a$).

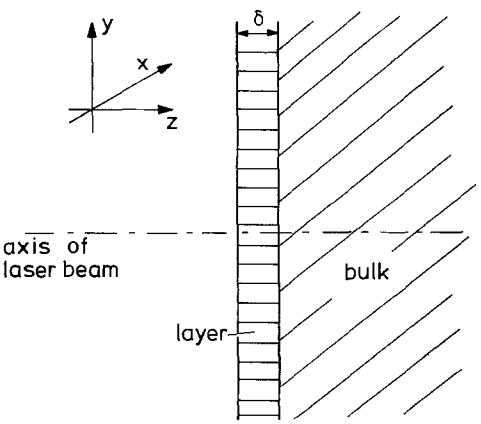

Fig. 1. Geometrical configuration

Transient effects may be neglected as the characteristic time $t_c = a^2/\kappa$ is much less than the time the laser is in operation, which is of the order of one second; κ is the thermal diffusivity of the bulk material. Since $a \sim 10^{-4}$m and $\kappa \sim 10^{-4}$ m$^2 \cdot$ sec^{-1}, we have $t_c \sim 10^{-4}$ sec, so that the investigations may be limited to the steady-state situation. We shall consider the Laplace equation

$$\nabla^2 \theta = 0 \qquad [2]$$

in the region $z \geq 0$, where θ denotes the temperature rise above the ambient level. At the interface $z = \delta$ the temperature and the heat flux ought to be continuous, which leads to the conditions

$$\theta|_{z=\delta-0} = \theta|_{z=\delta+0}, \quad k_1 \frac{\partial \theta}{\partial z}\bigg|_{z=\delta-0} = k_2 \frac{\partial \theta}{\partial z}\bigg|_{z=\delta+0} \qquad [3]$$

Finally

$$\theta \to 0 \text{ if } x^2 + y^2 + z^2 \to \infty \qquad [4]$$

The solution to the mathematical problem defined by the equations and boundary conditions given by Eq. [1]-[4] will be derived in the Appendix. In this section we concentrate on the final results. Although the general solution describes the temperature field in the complete domain, we are here only interested in the temperature distributions in the planes $z = 0$ and $z = \delta$. If the ratio of the thermal conductivities is denoted by

$$\gamma = k_2/k_1 \qquad [5]$$

and if it is assumed that

$$\gamma >> 1 \quad \text{and} \quad \delta/a << 1 \qquad [6]$$

we may derive the following approximate expression for the temperature in the plane $z = 0$

$$\frac{\pi a k_2}{Q}\theta(x,y,0) \sim \frac{\pi^{1/2}}{2} e^{-\frac{1}{2}r^2/a^2} I_0(\tfrac{1}{2} r^2/a^2) + \gamma \frac{\delta}{a} e^{-r^2/a^2} \qquad [7]$$

where I_0 is a modified Bessel function [Ref. (5), Chap. 9.6]. To the same level of approximation we have

$$\frac{\pi a k_2}{Q}\theta(x,y,\delta) = \frac{\pi^{1/2}}{2} e^{-\frac{1}{2}r^2/a^2} I_0(\tfrac{1}{2} r^2/a^2) \qquad [8]$$

where $\theta(x, y, \delta)$ is the temperature distribution in the plane $z = \delta$.

The conditions of [6] are actually in conformity with what we set out to investigate, namely, the influence of a thin layer of poor heat-conducting material on the temperature distribution in the laser-impact area. The second of the two conditions merely expresses that the laser beam is much wider than the layer is thick. It is Eq [7] that presents the answer to our question. Indeed, if the thickness of the layer tends to zero, the difference between [7] and [8] vanishes. This shows that Eq. [8] gives the temperature distribution at the outer surface in the absence of the poor heat-conducting skin. However, if the thickness of the layer increases, the importance of the second term on the right-hand side of [7] grows in relation to that of the first. Now a situation may arise where the second term is actually dominant, which is when the parameter

$$F = \gamma\delta/a > 1 \qquad [9]$$

Of course, in this model, the thickness of the poor heat conductor may not grow indefinitely, as the second condition of [6] would then be violated. In that case the layer itself would become a bulk material, so that it would no longer be justified to call it thin. However, it is perfectly obvious that values may be chosen for the parameters γ and δ/a that satisfy [6], but which yield a value of F in the range defined by [9]. This, then, leads to the temperature increase that we have

been trying to achieve by the application of the poor heat-conducting skin, which is the central theme of our paper.

It is interesting to note that the temperature in the good heat-conducting bulk is hardly affected by the presence of the layer. Indeed, the temperature in $z = \delta$, its bounding plane (Eq. [8]), is practically the same as that which would have existed in the absence of the skin.

In Fig. 2a the two terms on the right-hand side of Eq. [7] are shown separately. Clearly, the first term is represented by a much wider curve than the second. This can be attributed to the fact that the mathematical structures of the two terms are quite different. The second term reflects the power-input function of Eq. [1] with its typical rapid exponential decay. The first term, on the other hand, is a slowly decaying function. Using the asymptotic representation of the function I_0, valid for large values of the argument (5), we may find

$$\frac{\pi^{1/2}}{2} e^{-\frac{1}{2}r^2/a^2} I_0(\tfrac{1}{2} r^2/a^2) \sim \tfrac{1}{2} a/r \quad \text{if } r >> a \quad [10]$$

This suggests that spots plated on homogeneous substrates tend to be much wider than the laser spot itself (Eq. [1]). If [9] is satisfied we may expect a spot the width of which more or less reflects the lateral extent of the laser beam. Therefore, as a consequence of the enhanced temperature effect, the application of a thin film of poor heat-conducting material permits the plating of spots of limited size.

Unfortunately, should the material of the plated spots have a high thermal conductivity, the lateral spreading of injected heat through the spot tends to obscure this effect. Indeed, a high thermal conductivity results in elevated temperatures at the rim of the spot. Despite its low conductivity, the layer in the immediate neighborhood of the periphery will have a high temperature over a distance outside the spot which is of the order of δ. Since high temperatures at the outer surface of the film lead to increased plating rates, the spot will continue to grow until the temperature at its periphery drops below a critical value. The higher the conductivity of the plated material, the wider the spot will grow.

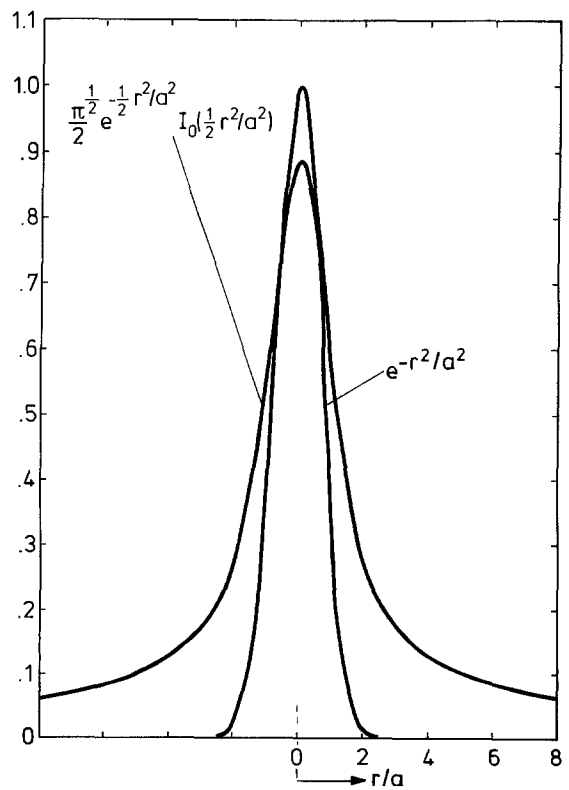

Fig. 2a. Comparison of the two functions appearing in Eq. [7]

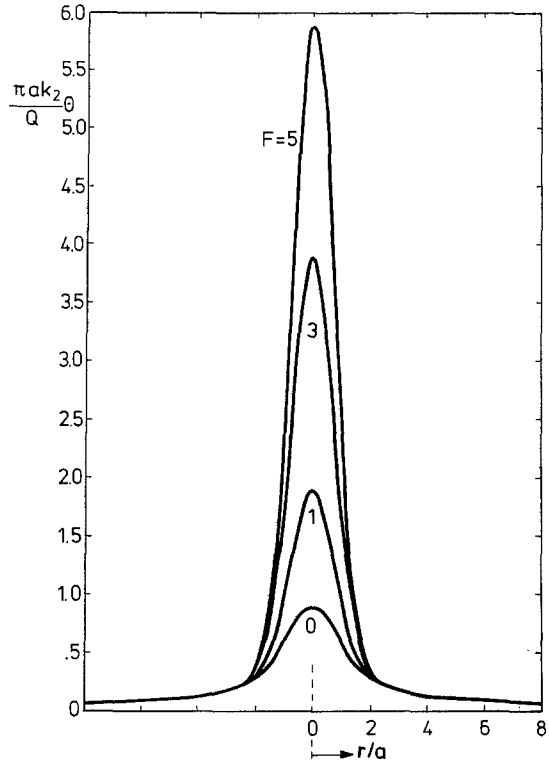

Fig. 2b. Temperature enhancement due to the presence of a layer of poor heat-conducting material.

Figure 2b presents the two terms of Fig. 2a, but now their effects are added up for various values of F. These graphs clearly indicate that the influence of the layer increases rapidly with F. Finally, from Fig. 3 one may obtain the temperature enhancement as a function of layer thickness at the center of the laser-impact area for various conductivity ratios.

Temperature distributions in laser-heated layered materials have been studied before, *e.g.*, in connection with laser welding (6), machining (7), and hole burning (8). It is difficult, however, to apply the general results obtained in these papers to the special case considered in our work. To obtain the temperature distributions ([A-8] and [A-9] of Appendix) a rederivation seemed justified.

Experimental

The experimental setup is shown in Fig. 4. The beam of a continuous argon-ion laser (Spectra Physics. Model 171; maximum output power 20W; wavelength region 450-510 nm) is focused onto the substrate sur-

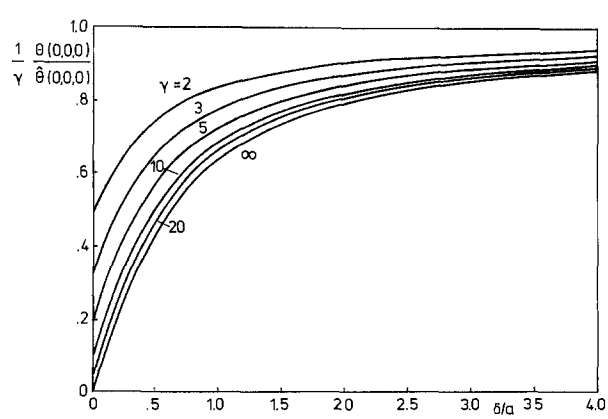

Fig. 3. Temperature enhancement as a function of layer thickness at the center of the laser-impact area for various conductivity ratios.

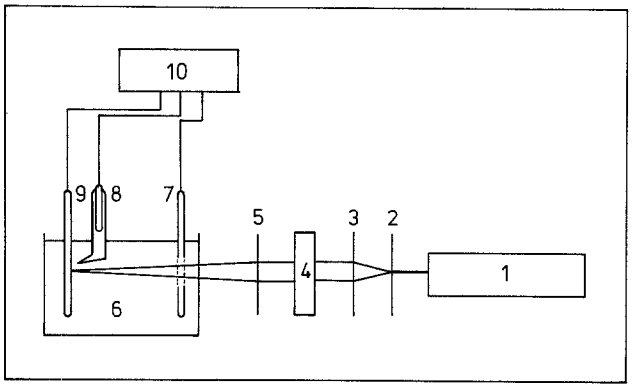

Fig. 4. Experimental set-up: 1, laser; 2-4, optical lenses; 5, photographic shutter; 6, electroplating cell; 7, anode; 8, reference electrode; 9, cathode; 10, potentiostat.

face by means of an optical lens system. A photographic shutter is applied to facilitate irradiation of the substrate during well-defined periods of time. The substrate is vertically mounted as the cathode in an electroplating cell. A saturated calomel electrode (SCE) is used as the reference electrode and a gold-plated titanium gauze functions as the anode. The electroplating voltage is set by a potentiostat.

The potential of the cathode with respect to the SCE is set at −800 mV. Our plating solution contains 100 g · dm^{-3} $KAu(CN)_2$ and 90 g · dm^{-3} citric acid. The pH of the solution is adjusted to 5.9 with KOH. Substrates of copper-zinc alloy (Tombak; 85% copper, 15% zinc), covered with nickel-phosphorous layers of variable thickness, are used for laser-enhanced electroplating. All experiments are carried out at ambient bath temperature.

Results and Discussion

The experimental results for Tombak substrates, covered with nickel-phosphorous layers of variable thickness, are shown in Fig. 5 and 6. The photographs were made through an optical microscope. For comparison, Fig. 6a shows the rather poor result for a substrate covered with a nickel layer. The explanation for this is that the thermal conductivity for nickel is almost 20 times higher than that for nickel-phosphorous. From Fig. 5 it appears that the critical layer thickness is about 4 μm. Inserting this value in Eq. [9], together with the thermal conductivities of Tombak ($k_2 \sim 160$ W · m^{-1} · K^{-1}) and nickel-phosphorous ($k_1 \sim 4$ W · m^{-1} · K^{-1}) and the laser-spot diameter of 50 μm, as used in the experiments, yields a value for the parameter F which is of the order of 3. This means that the temperature increase in the irradiated area of the surface is four times as high as for a substrate without a nickel-phosphorous layer. These two situations are shown in Fig. 5a and c, respectively. Well-localized gold spots of good quality are achieved for layer thicknesses above 4 μm with deposition rates on the order of 2 μm/sec.

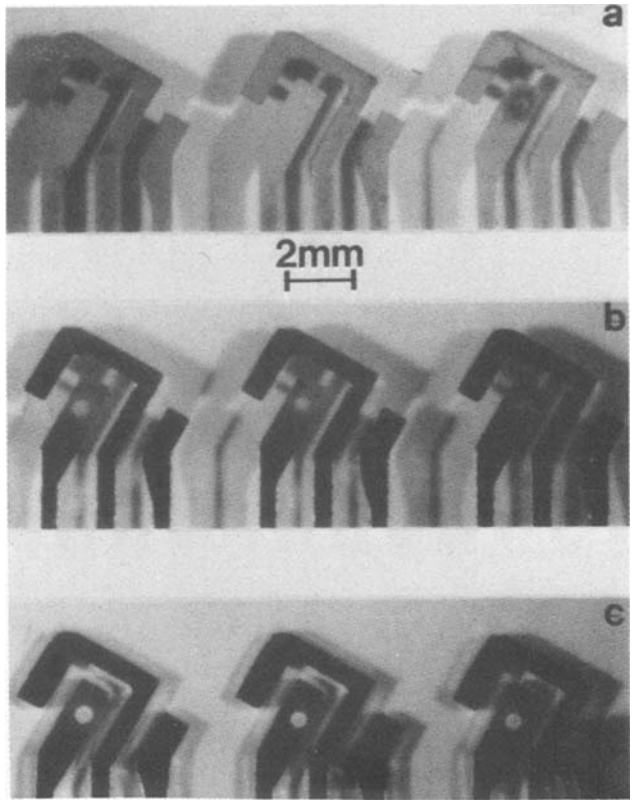

Fig. 6. The effect of a thermal film for laser-enhanced gold plating on Tombak; laser power 20W, irradiation time 2 sec. (a) 2 μm Ni; (b) 2 μm NiP; (c) 4 μm NiP.

The effect described above is very interesting from a physical point of view. The incident laser power will partly be absorbed and dissipated at the surface of the nickel-phosphorous layer. Most of this heat takes the shortest route through the poor heat conductor toward the region where the thermal conductivity is high. The influence of the thin layer on the temperature profile in the Tombak substrate is thus negligible. In the layer itself, however, a very definite and concentrated high temperature region is created. It is the combination of the poorly conducting film and the high conductivity bulk which is responsible for this effect. Should the substrate have consisted entirely of a poor heat conductor, the temperature concentration effect would have been absent.

Summarizing we may conclude that the selectivity and the plating rate of laser-enhanced electroplating on substrates that conduct heat well can be improved significantly by applying a thin film of a poor heat

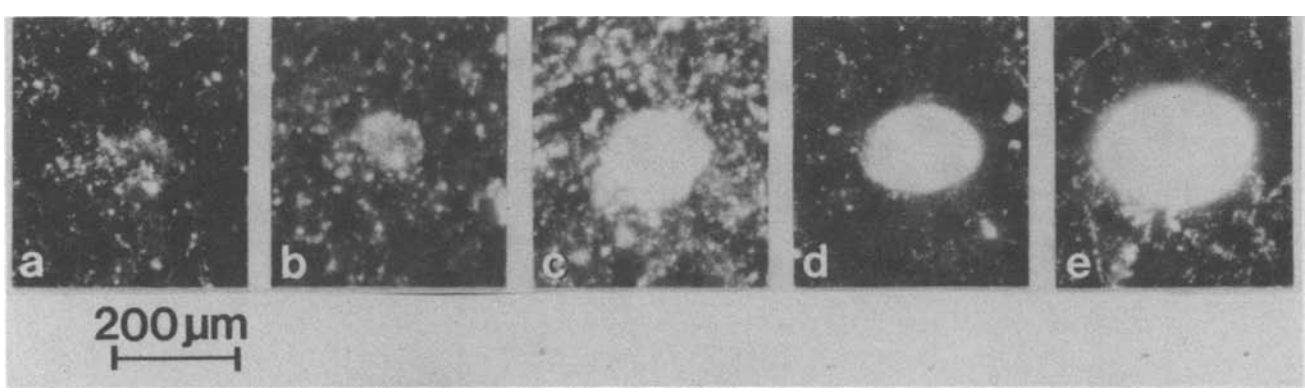

Fig. 5. The influence of the film thickness on the selectivity of laser-enhanced gold plating on Tombak; laser power 5W, irradiation time 32 sec. (a) NiP strike; (b) 1 μm NiP; (c) 4 μm NiP; (d) 8 μm NiP; (e) 16 μm NiP.

conductor on top of the substrate. In this way discrete metal spots can be obtained without the need of extremely high laser-power densities.

Acknowledgment

The authors wish to thank Dr. S. J. D. van Stralen of the University of Technology at Eindhoven for helpful advice on boiling phenomena.

Manuscript submitted May 11, 1982; revised manuscript received Sept. 27, 1982.

Any discussion of this paper will appear in a Discussion Section to be published in the December 1983 JOURNAL. All discussions for the December 1983 Discussion Section should be submitted by Aug. 1, 1983.

Publication costs of this article were assisted by Philips Research Laboratories.

APPENDIX

To solve the problem defined by Eq. [1]-[4], the double-Fourier transform

$$\bar{\theta}(\xi, \eta, z) = \int_{-\infty}^{\infty}\int e^{i(x\xi + y\eta)}\theta(x, y, z)\,dxdy \quad [A\text{-}1]$$

reduces the problem to

$$\frac{d^2\bar{\theta}}{dz^2} - (\xi^2 + \eta^2)\bar{\theta} = 0 \quad [A\text{-}2]$$

$$\frac{d\bar{\theta}}{dz} = -\frac{Q}{k_1}\exp\left[-\frac{a^2}{4}(\xi^2 + \eta^2)\right] \quad \text{if} \quad z = 0 \quad [A\text{-}3]$$

with three conditions that are similar to those of Eq. [3] and [4]; a simple calculation yields

$$\bar{\theta} = \frac{Q}{k_1\alpha}\cdot\frac{1 - Ne^{-2\alpha(\delta - z)}}{1 + Ne^{-2\alpha\delta}}\cdot\exp(-\alpha z - a^2\alpha^2/4) \quad \text{if} \quad 0 \leq z < \delta \quad [A\text{-}4]$$

and

$$\bar{\theta} = \frac{2Q}{(k_1 + k_2)\alpha}\cdot\frac{\exp(-\alpha z - a^2\alpha^2/4)}{1 + Ne^{-2\alpha\delta}} \quad \text{if} \quad z > \delta \quad [A\text{-}5]$$

with

$$\alpha = (\xi^2 + \eta^2)^{1/2} \quad \text{and} \quad N = \frac{k_2 - k_1}{k_2 + k_1} \quad [A\text{-}6]$$

Employing the inverse Fourier transform

$$\theta = \frac{1}{4\pi^2}\int_{-\infty}^{\infty}\int e^{-i(\xi x + \eta y)}\bar{\theta}(\xi, \eta, z)\,d\xi d\eta \quad [A\text{-}7]$$

using polar coordinates in the (ξ, η) plane we obtain finally

$$\theta(x, y, z) = \frac{Q}{2\pi a k_1}\int_0^{\infty} J_0\left(\frac{r}{a}\sigma\right)\frac{1 - Ne^{-2(\delta - z)\sigma/a}}{1 + Ne^{-2\delta\sigma/a}}\exp\left(-\frac{z}{a}\sigma - \frac{\sigma^2}{4}\right)d\sigma, \quad \text{if} \quad 0 \leq z < \delta \quad [A\text{-}8]$$

and

$$\theta(x, y, z) = \frac{Q}{\pi a(k_1 + k_2)}\int_0^{\infty} J_0\left(\frac{r}{a}\sigma\right)\frac{\exp\left(-\frac{z}{a}\sigma - \frac{\sigma^2}{4}\right)}{1 + Ne^{-2\delta\sigma/a}}d\sigma, \quad \text{if} \quad z > \delta \quad [A\text{-}9]$$

In deriving [A-8] and [A-9] we used the following relationship (3)

$$\int_0^{2\pi} e^{-i\sigma\cos\phi}\,d\phi = 2\pi J_0(\sigma) \quad [A\text{-}10]$$

The temperature distribution $\hat{\theta}$ that would have existed in the absence of the layer can be obtained from Eq. [A-9] by putting $\delta = 0$

$$\hat{\theta}(x, y, z) = \frac{Q}{2\pi a k_2}\int_0^{\infty} J_0\left(\frac{r}{a}\sigma\right)\exp(-z\sigma/a - \sigma^2/4)\,d\sigma \quad [A\text{-}11]$$

For convenience, it is assumed that the absorption coefficient of the bare substrate is equal to that of the substrate covered with a thin layer. This assumption does hardly influence experimental results, Q being determined by the optical properties of the plating material immediately after the initial plating step. We may now define the temperature-enhancement effect by considering the ratio

$$\frac{\theta(0, 0, 0)}{\hat{\theta}(0, 0, 0)} = \frac{\gamma}{\pi^{1/2}}\int_0^{\infty}\frac{1 - Ne^{-2\delta\sigma/a}}{1 + Ne^{-2\delta\sigma/a}}e^{-\sigma^2/4}\,d\sigma \quad [A\text{-}12]$$

Finally, it will be useful to know the temperature distributions in the planes $z = 0$ and $z = \delta$. In $z = 0$ we have

$$\frac{\pi a k_2}{Q}\theta(x, y, 0) = \tfrac{1}{2}\gamma\int_0^{\infty} J_0\left(\frac{r}{a}\sigma\right)\frac{1 - Ne^{-2\delta\sigma/a}}{1 + Ne^{-2\delta\sigma/a}}e^{-\sigma^2/4}\,d\sigma \quad [A\text{-}13]$$

When $\gamma >> 1$ and $\delta/a << 1$, we may simplify this expression as follows

$$\frac{\pi a k_2}{Q}\theta(x, y, 0) \sim \tfrac{1}{2}\gamma\int_0^{\infty} J_0\left(\frac{r}{a}\sigma\right)\left[\frac{1 - N}{1 + N} + \frac{4N}{(1 + N)^2}\frac{\delta\sigma}{a}\right]e^{-\sigma^2/4}\,d\sigma \sim \frac{\pi^{1/2}}{2}e^{-\frac{1}{2}r^2/a^2}I_0(\tfrac{1}{2}r^2/a^2) + \gamma\frac{\delta}{a}e^{-r^2/a^2} \quad [A\text{-}14]$$

A similar expression valid in the plane $z = \delta$ is given by Eq. [8]

REFERENCES

1. R. J. von Gutfeld, E. E. Tynan, R. L. Melcher, and S. E. Blum, *Appl. Phys. Lett.*, **35**, 651 (1979).
2. J. Cl. Puippe, R. E. Acosta, and R. J. von Gutfeld, *This Journal*, **128**, 2539 (1981).
3. S. Ostrach, in "Theory of Laminar Flows," F. K. Moore, Editor, Vol. IV of "High Speed Aerodynamics and Jet Propulsion," Princeton, NJ (1964).
4. S. van Stralen and R. Cole, "Boiling Phenomena," (see pp. 29, 200, and 691 on local boiling), Hemisphere Publishing Corp., McGraw-Hill (1979).
5. M. Abramowitz and I. A. Stegun, "Handbook of Mathematical Functions," Dover Publishers, New York (1965).
6. N. N. Rykalin, A. A. Uglov, and N. I. Makarov, *Sov. Phys. Dokl.*, **11**, 632 (1967).
7. K. Takamoto and S. Nakayama, *Rev. Electr. Comm. Labs.*, **21**, 647 (1973).
8. P. Kivits, R. de Bont, and P. Zalm, *Appl. Phys.*, **24**, 273 (1981).

Current Distribution during Electroplating Within a Tubular Electrode of High Ohmic Resistance

Mordechai Ben-Porat

Department of Chemical Engineering, Technion-Israel Institute of Technology, Haifa, Israel

Joseph Yahalom*

Department of Materials Engineering, Technion-Israel Institute of Technology, Haifa, Israel

and Eliezer Rubin

Department of Chemical Engineering, Technion-Israel Institute of Technology, Haifa, Israel

ABSTRACT

Current distributions during electroplating within a tubular electrode were studied. A theoretical model was developed taking into account the various factors influencing the current distribution: metal electrode resistance, electrolyte phase resistance, mass transfer resistance, charge transfer resistance, as well as geometrical parameters and the applied potential. The model enables the prediction of the relative importance of each of these factors in obtaining uniform current distribution inside the holes. Criteria for obtaining uniform metal thickness inside holes based on limiting values of four dimensionless parameters are presented and discussed.

Knowledge of the current distribution in various geometrical configurations in electrolytic cells is important both for the analysis of data obtained in electrochemical experiments and for the design and scale-up of useful plating tanks in the electroplating industry.

Tubular geometry has a particular importance in the printed circuit industry and the production of millimeter waveguides. For example, production of multilayer printed circuits requires careful electroplating of copper in holes drilled through boards in order to provide electrical connection between various circuit layers.

In millimeter waveguides complex forms that are basically cylindrical in shape are produced by electroplating on a die. In the case of a printed circuit the diameter and depth of the holes are in the order of magnitude of millimeters, whereas in the case of millimeter waveguides the dimensions may be much larger.

Knowledge of the parameters which influence the current distribution within tubular electrodes is important in finding the optimal plating condition in the electroplating processes. The current distribution depends on many factors such as cell and electrode geometry, electrolyte conductivity, electrode kinetics, mass transfer, and electrode resistance.

The mathematical analysis of the electrochemical system, and specifically the solution of the equations, are very complex.

Owing to the complexity of the problem of current distribution within electrolytic cells only relatively few specific cases for given geometries have been solved.

Newman (1) and Parrish and Newman (2) analyzed current distribution in laminar forced convection electrodes having various two-dimensional slots. Alkire and Mirarefi (3) analyzed current distribution within a tubular electrode under unidirectional flow. Newman (4) solved the probelm of current distribution on rotating disk electrode. However, none of these investigators considered the possible initial ohmic resistance of the metallic electrode. Alkire and Varjian (5) developed a mathematical model which simultaneously takes account of the concentration field and the potential field in both the electrode and electrolyte phases for a resistive wire electrode moving at a steady speed through an electrolysis cell. The transient behavior was treated by Alkire (6) for electrodeposition onto a metal strip of high ohmic resistance, and by Alkire and Tvarusko (7) for current distribution along high resistance wire electrode during unsteady-state diffusion. However, in these two studies a uniform primary current distribution was assumed to be formed along the electrode, and the electrolytic solution ohmic resistance was neglected.

In many electroplating processes such as those mentioned above, a thin metallic layer is first deposited chemically followed by electrochemical plating. In these cases, both initial ohmic resistance and mass transfer may be of considerable importance in current distribution.

The object of the present work was to study current distributions during electroplating within a tubular electrode taking into account both initial ohmic resistance and mass transfer effects.

Consideration was also given to a periodic fluctuation in the liquid flow fluid similar to those encountered in the plating through holes in printed circuit board fabrication.

Mathematically, the problem to be solved invokes coupling of the Laplace equation for the electrolyte solution, mass transfer equations and the electrode kinetics equation occurring near an electrode surface, together with a nonuniform electrode potential distribution due to the initial high ohmic resistance of the thin metal electrode. The latter introduces transient effects.

Mathematical Model

The electrochemical system under consideration is shown schematically in Fig. 1. An electrically insulated tube of length $2l$ and of radius r_0 is inserted in an electrolyte solution and positioned between two parallel counterelectrodes. The inside wall of the tube is initially plated with a thin metal layer of thickness a_0. This initial layer is obtained by chemical deposition prior to the onset of the electrochemical process.

The tube openings $z = 0$ and $z = 2l$ are cathodically connected to a power supply, while the parallel electrodes are connected anodically. The electric potential between the cathode and anode is kept constant. Therefore, it can be assumed that the potential difference between the electrical contact point at the tube openings ($z = 0$, $r = r_0$, and $z = 2l$, $r = r_0$) and the electrolytic solution near this point is also constant.

* Electrochemical Society Active Member.

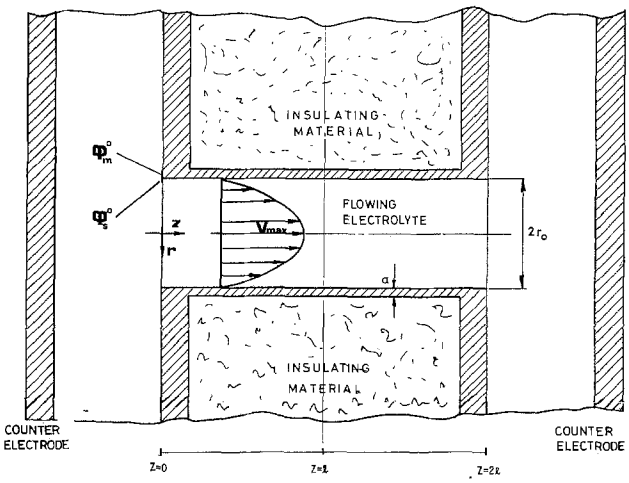

Fig. 1. Schematic diagram of the electrochemical system

The following simplifying assumptions are used:

I. Only one electrode reaction occurs and the reversible reaction rate has the form given by Eq. [1] in accordance with Butler-Volmer kinetics.

II. The electrical double layer and the mass transfer diffusion layer attain pseudo steady-state conditions relative to the rate of the electrode ohmic resistance changes.

III. The surface of the electrode remains smooth during the course of metal deposition. The electrode thickness change is small compared to the tube diameter, and therefore no significant geometric changes occur during the electrolysis.

IV. The reactive solution species are present in a dilute concentration. Therefore, because of the presence of a relatively high concentration of the supporting electrolyte, the effect of reactive species on the electric field is negligible.

V. The electrolyte flows through the tubular electrode in a fully developed laminar flow. Edge effects at the hole entrance are neglected.

VI. The dimensionless Péclet number, $2r_o\ \bar{v}_z/D$, is large. Therefore, the concentration differences in the electrolyte caused by the electrochemical reaction are confined to a very thin layer near the tube wall. Outside this layer the electrolytic solution is of uniform composition so that the potential distribution obeys the Laplace equation.

Assumption I requires further clarification and elaboration. 100% cathodic current efficiency is to be expected of a copper acid plating bath at the practical current densities, *e.g.*, Ref. (8). The local electrochemical reaction rate $j(z)$ proceeds at the tubular electrode wall ($r = r_o$) and is given by the Butler-Volmer expression

$$j(z) = i_o \left[\exp\left(\alpha_a \frac{nF}{RT}\eta_s\right) - \exp\left(-\alpha_c \frac{nF}{RT}\eta_s\right)\right] \quad [1]$$

The exchange current density i_o is related to the reactant cation concentration by an empirical expression

$$i_o(c = c_s) = \left(\frac{c_s}{c_b}\right)^{\gamma} i_o(c = c_b) \quad [2]$$

Since it is difficult to measure the local surface overpotential it is convenient to relate the reaction rate to the potential difference between metal and solution phase, thus including the concentration overpotential

$$\eta_T = (\phi_m - \phi_s) - E_{eq} = \eta_s + \eta_c \quad [3]$$

where the concentration overpotential is given by

$$\eta_c = \frac{RT}{nF} \ln \frac{c_s}{c_b} \quad [4]$$

Substitution of Eq. [2], [3], and [4] in [1] relates the reaction rate to the local surface concentration and potential difference

$$j(z) = i_o(c = c_s) \left[\left(\frac{c_s}{c_b}\right)^{\gamma-\alpha_a} \exp\left(\frac{\alpha_a nF}{RT}\eta_T\right) - \left(\frac{c_s}{c_b}\right)^{\gamma-\alpha_c} \exp\left(-\frac{\alpha_c nF}{RT}\eta_T\right)\right] \quad [5]$$

We may relate the potential difference between the metal and the solution to the applied potential

$$\phi_m - \phi_s = (\phi_m^\circ - \phi_s^\circ) + (\phi_m - \phi_m^\circ) - (\phi_s - \phi_s^\circ) \quad [6]$$

and by subtracting E_{eq} from both sides and rearranging

$$[(\phi_m^\circ - \phi_s^\circ) - E_{eq}] = (\phi_m^\circ - \phi_m) + \eta_s + \eta_c + (\phi_s - \phi_s^\circ) \quad [7]$$

The quantity on the left side of Eq. [7] is the applied potential between the electrode and the solution at the tube openings. This potential consists of four irreversible phenomena, namely, ohmic losses ($\eta_{\Omega m}$) in the electrode phase, surface (activity) overpotential (η_s), concentration overpotential (η_c), and ohmic losses ($\eta_{\Omega s}$) in the electrolyte phase.

Thus we see that the system may be conveniently divided into three regions: (*i*) the electrode phase, (*ii*) a thin diffusion layer near the electrode surface within which a concentration variation takes place, and (*iii*) the bulk solution, of uniform composition, which fills the tubular electrode.

The Bulk Region

The potential distribution in the bulk region obeys the Laplace equation. In cylindrical coordinates this is given by [9]

$$\frac{1}{r}\frac{\partial}{\partial r}\left(r\frac{\partial \phi_s}{\partial r}\right) + \frac{\partial^2 \phi_s}{\partial z^2} = 0 \quad [8]$$

With reference to Fig. 1, the boundary conditions are

$$\phi_s = f(r) \text{ for } z = 0 \text{ and } 0 \leq r \leq r_o$$

$$\phi_s = \phi_s^\circ \text{ for } z = 0 \text{ and } r = r_o \quad [9a]$$

$$\frac{\partial \phi_s}{\partial z} = 0 \text{ for } z = l \text{ and } 0 \leq r \leq r_o \quad [9b]$$

$$\frac{\partial \phi_s}{\partial r} = -\frac{j}{\kappa} \text{ for } r = r_o \text{ and } 0 \leq z < 2l \quad [9c]$$

The function $f(r)$ which describes the potential distribution at the tube openings ($z = 0$, $z = 2l$) should be found experimentally, however, we shall assume a uniform potential distribution, namely

$$f(r) = \phi_s^\circ \text{ for } z = 0 \text{ and } 0 < r < r_o$$

The Electrode Phase

Figure 2(a) describes schematically the metal layer on the tube wall. The current density is given by Ohm's law

$$i_m = -\sigma \frac{d\phi_m}{dz} \quad [10]$$

The current density in the metal phase varies with position owing to the electrode reaction. From a current balance on an element of length dz in the metal layer [Fig. 2(b)] a differential equation can be obtained describing the variation of the current density in the electrode phase

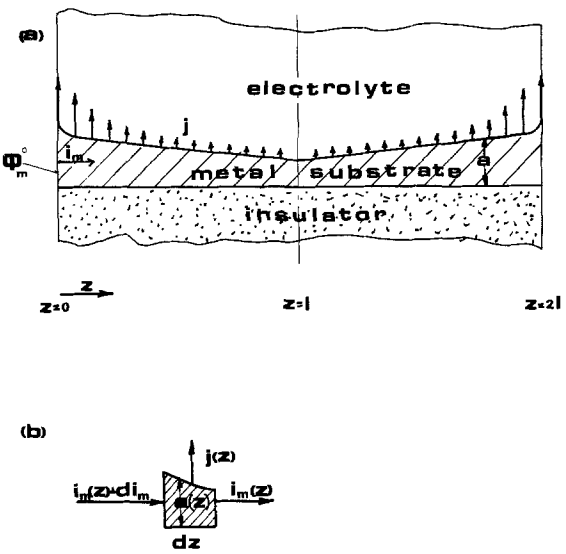

Fig. 2. (a) Schematic representation of the metal substrate on the tube wall. (b) Current balance on an element of length dz in the metal substrate.

$$\frac{d[i_m \cdot a]}{dz} = -j \qquad [11]$$

Substituting i_m from Eq. [10] in [11] gives a differential equation which describes the variation of the electrode potential

$$\frac{d}{dz}\left[a \cdot \frac{d\sigma_m}{dz}\right] = \frac{j}{\sigma} \qquad [12]$$

There are two boundary conditions

$$\phi_m = \phi_m^\circ \text{ at } z = 0 \text{ (and } z = 2l)$$

$$\frac{d\phi_m}{dz} = 0 \text{ at } z = l \qquad [13]$$

The local deposit thickness is obtained by integration of the local current density over the period of electrolysis

$$a(z,t) = a_o + \int_o^t \frac{M}{dn\mathbf{F}}|j|dt \qquad [14]$$

The Diffusion Layer

In accord with the assumption that the Péclet number is large, the steady-state equation of laminar convective diffusion in the tube is

$$v_s(r)\frac{\partial c}{\partial z} = D\left[\frac{\partial^2 c}{\partial r^2} + \frac{1}{r}\frac{\partial c}{\partial r}\right] \qquad [15]$$

The diffusion layer under this condition is very thin and the velocity distribution is approximately linear with distance from the wall; for small values of z provided that $(zD)/(2\bar{v}_z r_o^2) << 0.01$, Lévêque (9) recognized that there is a diffusion layer near the wall and derivatives with respect to r become large, thus the following approximations apply

$$\frac{1}{r}\frac{\partial c}{\partial r} << \frac{\partial^2 c}{\partial r^2} \qquad [16]$$

and

$$v_z = \frac{4\bar{v}_z}{r_o} y; \quad y << 1 \qquad [17]$$

where y is the distance from the tube wall

$$y = r_o\left(1 - \frac{r}{r_o}\right) \qquad [18]$$

By inserting these approximations in Eq. [15] one obtains

$$\frac{4\bar{v}_z}{r_o} y\frac{\partial c}{\partial z} = D\frac{\partial^2 c}{\partial y^2} \qquad [19]$$

At the limiting current condition the surface concentration of the solute is zero, and Eq. [19] can be solved using the similarity transformation

$$r_1 = y\left(\frac{4\bar{v}_z}{9zDr_o}\right)^{1/3} \qquad [20]$$

The concentration profile given by the solution of [19] is

$$\frac{c}{c_b} = \frac{1}{\Gamma(4/3)}\int_o^\eta e^{-\eta^3} d\eta \qquad [21]$$

The limiting current distribution is therefore

$$j_{lim} = n\mathbf{F}D\left.\frac{\partial c}{\partial y}\right|_{y=0} = \frac{n\mathbf{F}Dc_b}{\Gamma(4/3)}\left(\frac{4\bar{v}_z}{9Dr_o z}\right)^{1/3} \qquad [22]$$

In this electrochemical system the surface concentration of solute is not zero. Smyrl and Newman (10) solved Eq. [19] for currents below the limiting current. They obtained a relation between the surface concentration distribution and the current distribution by applying Duhamel's theorem to Eq. [22]

$$j = \frac{n\mathbf{F}D}{\Gamma(4/3)}\left(\frac{4\bar{v}_z}{9Dr_o}\right)^{1/3}\int_o^z \frac{dc_s(z')}{dz'}\cdot\frac{dz'}{(z-z')^{1/3}} \qquad [23]$$

Equation [23] gives the local electrochemical reaction rate.

The electrolyte velocity, $v(z)$, and therefore the local surface concentration, $c(z)$, are changing periodically due to the "side to side" tube motion caused by the cathode rod reciprocation agitation.

The theoretical prediction of the electrolyte velocity profile and the surface concentrations is exceedingly difficult under these circumstances. Edge-effects caused by the sharp-edged tube entrance, phase shift between the flow in the tube, and the cathode motion generated by the oscillating flow field are some of the considerations which indicate that fully developed laminar flow constitutes the conservative bound for the mixing in the mass diffusion layer at the tube surface [Engelmaier and Kessler (11)].

To avoid the mathematical difficulties we shall use an approximate value for the local surface concentration by defining the arithmetic mean of two surface concentration distributions: $\vec{c}_s(z)$ which would be if the electrolyte flows in the tube under fully developed laminar regime to one side and $\overleftarrow{c}_s(z)$ which would be if the electrolyte flows in the opposite direction, and assuming that the change in the electrode thickness during one cycle does not significantly affect the electrode potential.

This means, $\bar{c}_s(z)$, given by [24]

$$\bar{c}_s(z) = \frac{\vec{c}_s(z) + \overleftarrow{c}_s(z)}{2} \qquad [24]$$

gives an approximation to the effective local surface concentration.

Since the system is symmetrical around $z = l$ and if we assume that during one cycle the potential distribution, ϕ_m and ϕ_s do not change, one gets

$$\vec{c}_s(z) = \overleftarrow{c}_s(2l - z) \qquad [25]$$

and

$$\bar{c}_s(z) = \frac{\vec{c}_s(z) + \overleftarrow{c}_s(2l - z)}{2} \qquad [26]$$

The mean concentration calculated by Eq. [26] will be used in the subsequent analysis.

Dimensionless Equations

Complying with the assumptions of the model, the potential and the current distributions, as well as the concentration distribution inside the tubular electrode, may be determined from the solution of coupled differential Eq. [8] and [12], algebraic Eq. [5], and integral Eq. [14] and [23]. Before conducting the calculations, it is convenient to transform the equations into dimensionless form.

By introducing the following dimensionless variables

$$\zeta = \frac{z}{l} \qquad \rho = \frac{r}{l} \qquad \rho_o = \frac{r_o}{l}$$

$$\phi_m^* = \frac{nF}{RT}[\phi_m - \phi_m^\circ] \qquad \phi_s^* = \frac{nF}{RT}[\phi_s - \phi_s^\circ]$$

$$\phi_a^* = \frac{nF}{RT}[\phi_m^\circ - \phi_s^\circ - E_{eq}]$$

$$\eta_T^* = \frac{nF}{RT}\eta_T = \phi_m^* + \phi_s^* + \phi_a$$

$$c = \frac{\bar{c}_s}{c_b} \qquad a^* = \frac{a}{a_o} \qquad J = \frac{j}{i_{av}} \qquad [27]$$

where i_{av} is defined by [27]

$$i_{av} = \frac{\int_o^l j\,dz}{l} \qquad [28]$$

the number of independent system parameters is reduced to four independent dimensionless quantities

$$\xi_s = \frac{nF}{RT}\frac{l^2}{r_o}\cdot\frac{i_o}{\kappa}$$

$$\xi_m = \frac{nF}{RT}\frac{l^2}{a_o}\frac{i_o}{\sigma}$$

$$N = \frac{nF}{\Gamma(4/3)}\frac{Dc_b}{i_o}\left(\frac{4\bar{v}_z}{9Dr_o l}\right)^{1/3}$$

$$\beta = \frac{i_{av}}{i_o} \qquad [29]$$

The dimensionless equations which describe the model are

$$\frac{\partial^2\phi_s^*}{\partial\xi^2} + \frac{1}{\rho}\frac{\partial\phi_s^*}{\partial\rho} + \frac{\partial^2\phi_s^*}{\partial\rho^2} = 0 \qquad [30]$$

$$\phi_s^*(0,\rho) = f(\rho), \quad \phi_s^*(0,\rho_o) = 0$$

$$\frac{\partial\phi_s^*}{\partial\zeta}(1,\rho) = 0$$

$$\frac{\partial\phi_s}{\partial\rho}(\zeta,\rho_o) = \rho_o\xi_s\beta J \qquad [31]$$

$$\frac{d}{d\zeta}\left[a^*\frac{d\phi_m^*}{d\zeta}\right] = \xi_m\beta J \qquad [32]$$

$$\phi_m^*(0) = \frac{d\phi_m^*}{d\zeta}(1) = 0 \qquad [33]$$

$$J = \frac{1}{\beta}[c^{\gamma-\alpha_a}\exp(\alpha_a\eta_T^*) - c^{\gamma+\alpha_c}\exp(-\alpha_c\eta_T^*)] \qquad [34]$$

$$J = \frac{1}{\beta}N\int_o^\zeta \frac{dc(\zeta')}{d\zeta'}\frac{d\zeta'}{(\zeta-\zeta')^{1/3}} \qquad [35]$$

$$a^* = 1 + \int_o^t \frac{Mi_o}{dnFa_o}J\beta dt \qquad [36]$$

Boundary conditions [31] as well as Eq. [32] are nonlinear and therefore Eq. [30] and [32] cannot be solved analytically.

Method of Solution

The solution of the set of equations and boundary conditions which describe the model, Eq. [30]-[36], was carried out using an iterative procedure as described in Appendixes A and B.

The calculations were carried out on an IBM 370 digital computer at the Technion Computer Center.

Results presented in this work were determined with the use of 50 ξ_m increments in the axial direction in the interval $0 < \zeta < 1$ and time increment of

$$\Delta = \frac{1}{10}\frac{dnFa_o}{Mi_o}$$

For the range of parameters studied here, there was no appreciable improvement in the numerical results by the use of smaller steps. A run consists of calculations of metal and solution potential distribution for a particular set of parameter values, during the transient time of electroplating. The calculations were terminated when "practically" steady-state conditions were attained, that is, when ξ_m was below 0.001.

A typical run for one set of parameters was found to take approximately 30 sec on an IBM 360 computer when the program is compiled in FORTRAN X.

Results and Discussion

According to the model described here the applied potential drops over four resistances: metal (electrode) resistance, electrolyte resistance, charge transfer reaction resistance, and mass transfer resistance. The relative share of each is indicated by three dimensionless parameters

$$\xi_m = \frac{nF}{RT}\cdot\frac{l^2}{a_o}\cdot\frac{i_o}{\sigma}$$

This is proportional to the rate of the cathodic reaction rate divided by the metal conductivity

$$\xi_s = \frac{nF}{RT}\cdot\frac{l^2}{r_o}\cdot\frac{i_o}{\kappa}$$

which in turn is proportional to the rate of the cathodic reaction rate divided by the solution conductivity, and

$$N = \frac{nF}{\Gamma(4/3)}\frac{Dc_b}{i_o}\left(\frac{4\bar{v}_z}{9Dr_o l}\right)^{1/3}$$

indicating the ratio between rate of mass transfer to the cathode surface and the cathodic reaction rate. The value of the gamma function $\Gamma(4/3)$ is 0.893. An additional parameter defines the geometric configuration of the tubular electrode

$$\rho_o = \frac{r_o}{l}$$

Calculations based on the theoretical model have been conducted in order to predict several essential features of the tubular electrode of high ohmic resistance. All calculations have been conducted for cathodic deposition with use of symmetric transfer coefficient ($\alpha_a = \alpha_c = 0.5$) and $n = 2$.

The dimensionless parameters employed in the following analysis should permit the application of the results to a wide variety of actual systems (*e.g.*, the printed circuit industry).

First consider the four overpotentials which constitute the applied potential.

Figure 3 illustrates how these overpotentials vary with distance along a tubular electrode for one typical situation ($\xi_s = 0.1$, $\xi_m = 0.1$, $N = 100$, $\phi_a^* = -9$, and $\rho_o = 0.1$). Note that the sum of the four overpo-

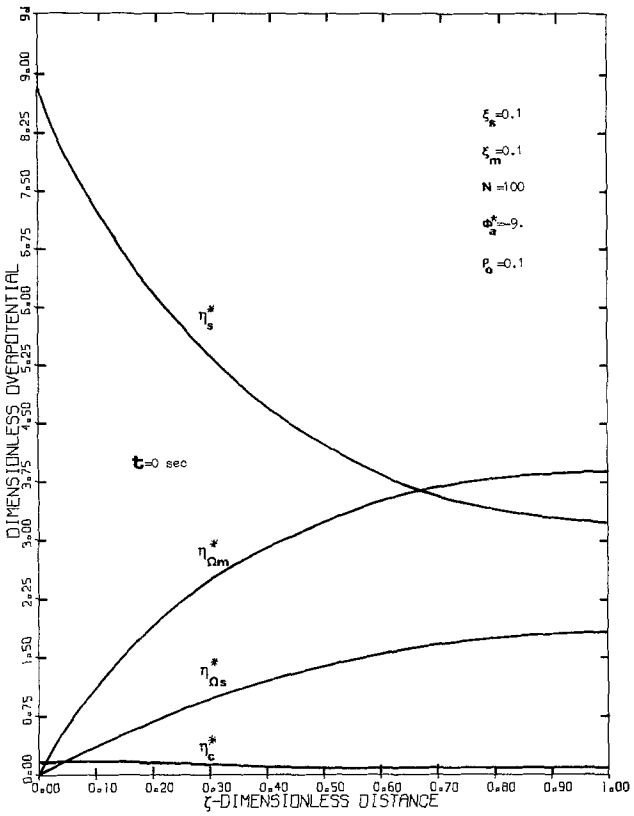

Fig. 3. Overpotential partition within a tubular electrode at the onset of electrodeposition.

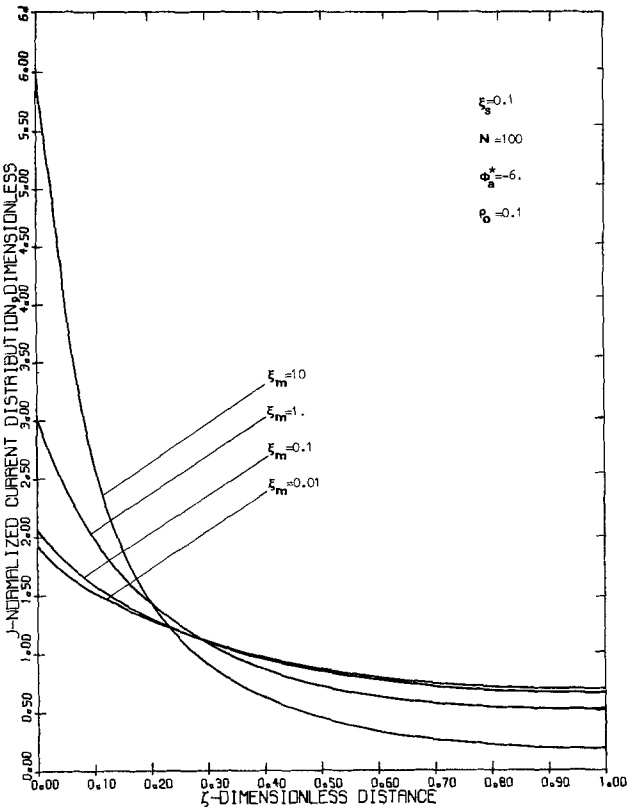

Fig. 4. Distribution of current density for different contributions of metal resistance, parameter ξ_m.

tentials is always a constant and equal to the applied potential.

Thus at the tubular electrode edge ($z = 0$), the only components of the applied potential are the charge transfer overpotential and the concentration overpotential (which is relatively small for this typical example). As we move inside the tube, the ohmic resistances of the metal and of the electrolyte, $\eta_{\Omega m}$ and $\eta_{\Omega s}$, respectively, act to consume an ever increasing proportion of the applied potential, decreasing the charge transfer overpotential. The variation of charge transfer overpotential along the tube length lead to a nonuniform current distribution Thus the local reaction rate is always the highest at the tube edge and decreases with distance inside the tube. The uniformity of the current distribution depends on the values of the parameters mentioned earlier.

Let us consider the influence of each of these parameters. Figure 4 illustrates the current density distribution dependence on parameter ξ_m.

If ξ_m is large, the ohmic loss in the metal is large and the current distribution is nonuniform; as the value of ξ_m decreases, the current distribution tends to be more uniform. When ξ_m is less than 0.01, the metal (electrode) resistance is negligible and the other overpotentials predominate. A similar behavior is described by Fig. 5 which shows the current density distribution dependence on the parameter ξ_s.

Again if ξ_s is large, there is a large ohmic loss, this time, in the electrolyte solution, and the current distribution is nonuniform. As the value of ξ_s decreases the current distribution becomes more uniform. At very low values of ξ_s (say, $\xi_s < 0.01$), the electrolyte ohmic resistance is very small and its value has no influence on the current distribution.

Let us now consider the influence of the third parameter, N. The current density distribution in the tubular electrode is shown in Fig. 6 for several values of N. For a large value of N the mass transfer resistance is small compared with charge transfer near the electrode.

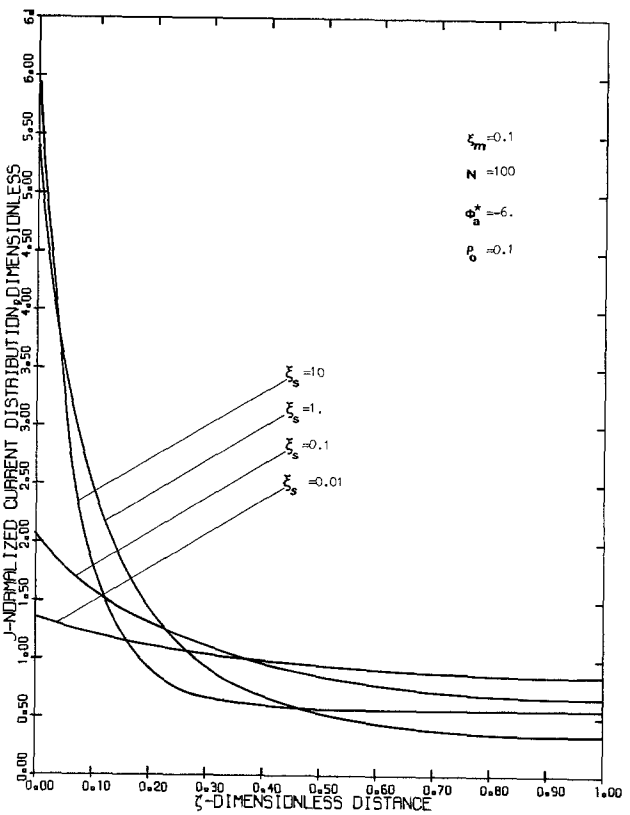

Fig. 5. Distribution of current density for different contributions of electrolyte resistance, parameter ξ_s.

Thus the current distribution depends merely on the charge transfer overpotential near the electrode (assuming that the electrolyte and metal ohmic resistance are small) and is relatively uniform. For small values of N, the mass transfer process tends to be rate limiting, the concentration overpotential predominates, and the current distribution is nonuniform.

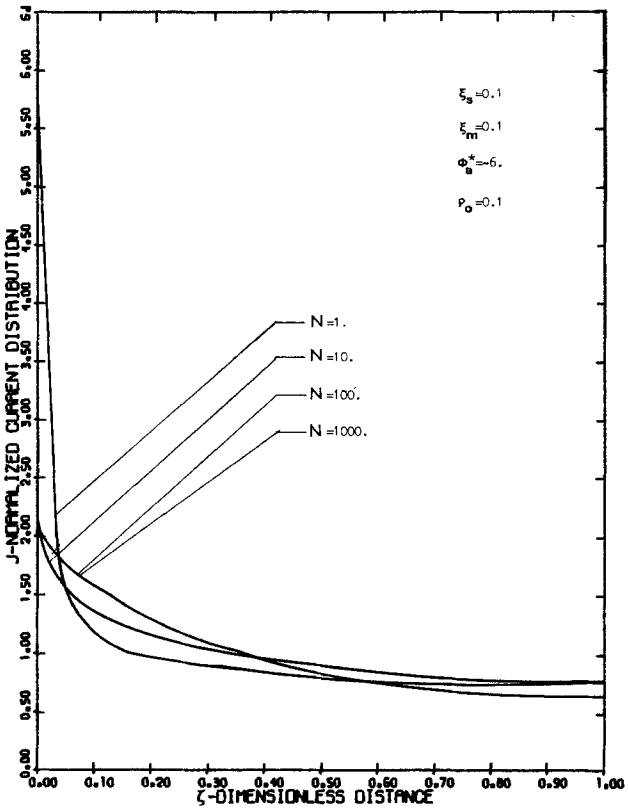

Fig. 6. Current density distribution for different mass transfer to charge transfer resistance ratios, parameter N.

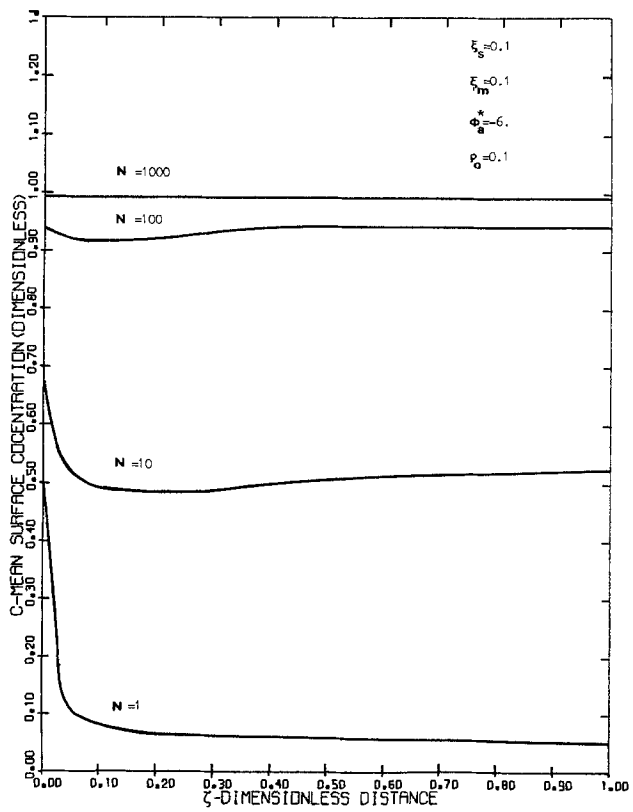

Fig. 7. Dependence of the mean surface concentration on the parameter N.

The concentration of reactive species near the tubular wall varies along the tube axis. Figure 7 illustrates the mean surface concentration dependence on parameter N. (The tube is placed between two counter-electrodes and is periodically moved to the left and to the right.)

When N has large values, mass transfer resistance is small and the surface concentration approaches that of the bulk. Note that surface concentration distribution is uniform. As N decreases the mass transfer resistance increases and lower surface concentrations are encountered. The surface concentration distribution tends to be nonuniform. For intermediate values of N at the tubular edge, the electrochemical reaction rate is high and also the reactive species is accessible; on the other hand, at the tube center the reactive species is less accessible but also the reaction rate is slower.

These phenomena cause the mean surface concentration to be higher at the tubular electrode edge and center than in intermediate points between them. They do not occur when N is small ($N < 1$) or large ($N > 100$).

The current density distribution varies with geometric configuration of the tubular electrode.

Figure 8 illustrates the effect of the geometric parameter ρ_0 on the current density distribution.

If ρ_0 is small, *i.e.*, the tube diameter is small compared to the tube length, ohmic resistances of the metal and the electrolyte are high (large values of ξ_m and ξ_s), the current distribution is very nonuniform. On the other hand, if ρ_0 is large, *i.e.*, the tube diameter is large compared to the tube length, the current distribution becomes uniform as on a flat electrode.

An important factor in the electroplating industry is the rate of plating which is proportional to the total current consumed by the electrochemical reaction. We refer here to the average current density which is obtained by integrating the local current density over the entire tubular electrode.

The dependence of the average current density β on the applied potential is illustrated in Fig. 9, for several values of parameter ξ_m.

For large values of ξ_m, most of the applied potential falls over an ohmic loss in the metal electrode, the charge transfer overpotential is small and therefore the electrochemical reaction rate which varies with charge transfer overpotential according to Eq. [1] is low and depends linearly on the applied potential. On

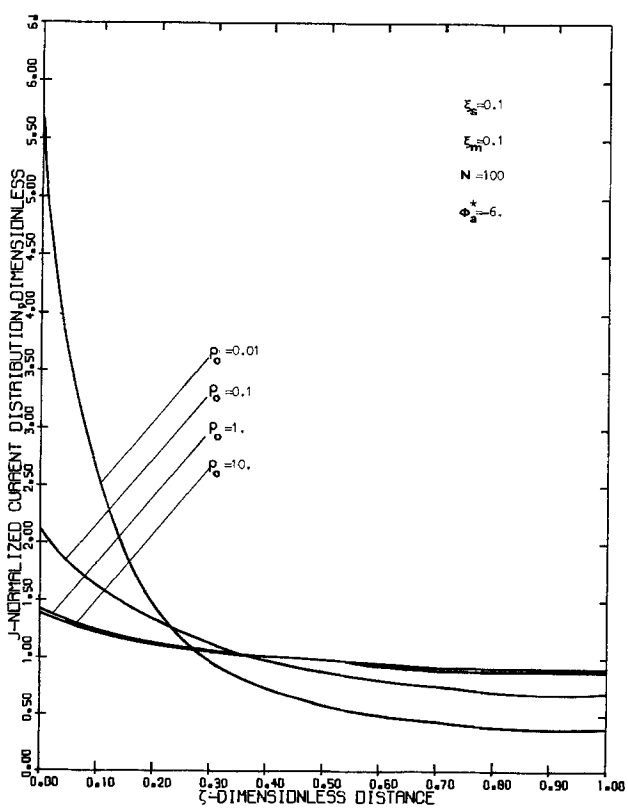

Fig. 8. Dependence of the current density distributions on the geometric parameter, ρ_0.

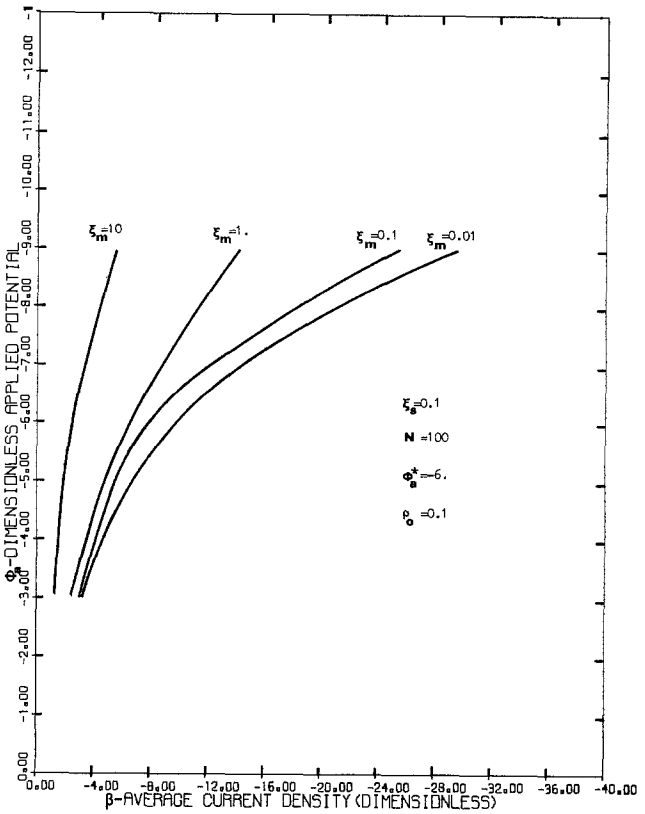

Fig. 9. Dependence of the average current density on applied potential for different metal resistance, parameter ξ_m.

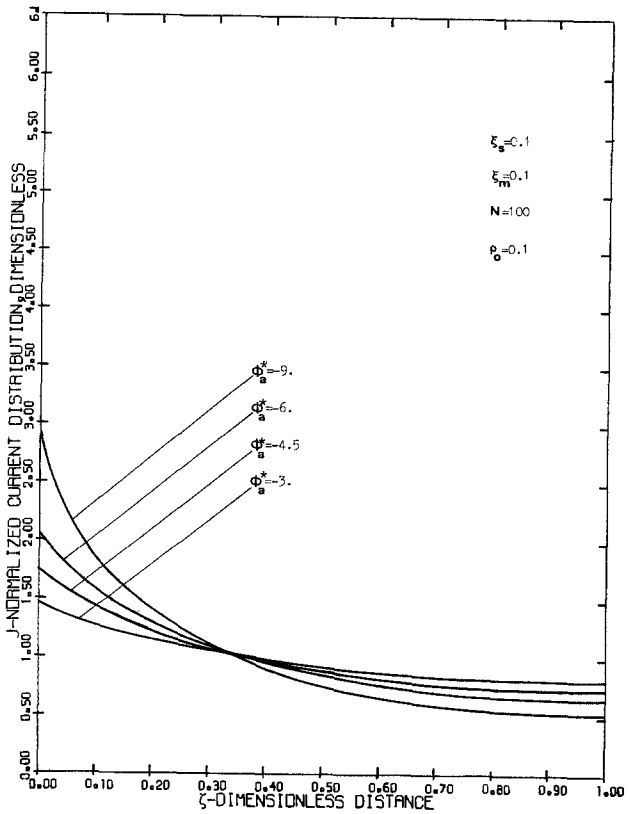

Fig. 10. Dependence of the current density distribution on the distance at different applied potentials ϕ_a^*.

the other hand, when ξ_m is small, the ohmic loss is negligible, the charge transfer overpotential dominates, and we obtain a Tafel-like (exponential) dependence of the reaction rate on the applied potential.

The applied potential also influences the current density distribution. An increase in the applied potential causes a more nonuniform current distribution within the tubular electrode. This phenomenon is shown in Fig. 10.

Finally, let us consider the transient behavior which occurs during the electroplating process (which causes thickening of the metal electrodes and lowers the ohmic resistance).

We turn back to the typical situation illustrated in Fig. 3 ($\xi_s = 0.1$, $\xi_m = 0.1$, $N = 100$, $\phi_a^* = 9$, $\rho_o = 0.1$): consider copper deposition from an acidified sulfate bath for which $M = 63.57$, $d = 8.9$ g/cm^3, $i_o = 10^{-3}$ A/cm^2, $a_o = 5 \times 10^{-5}$ cm (a typical electroless deposit thickness).

Figure 11 illustrates how the four overpotentials vary with distance along a tubular electrode after a long period of electroplating (in this situation after 2000 sec). ξ_m is small and thus the ohmic loss in the metal electrode is negligible, the charge transfer overpotential increases (by more than 50% at the tube center) and the electrochemical reaction is enhanced.

The electrolyte ohmic overpotential increases moderately (following an increase in the current density) while the concentration overpotential practically does not change, since for this typical example the mass transfer resistance is low ($N = 100$).

Variation of the current density distribution during electroplating is described in Fig. 12 for the same situation mentioned earlier but with $\xi_m = 1$.

The current distribution which is very nonuniform at the initial stage of the plating process becomes more uniform as the coating thickens and eventually attains the so-called "primary current distribution which is determined by the electrolyte properties (described by ξ_s) and the electrochemical cell geometry (ρ_o). For this typical example the mass transfer resistance is negligible.

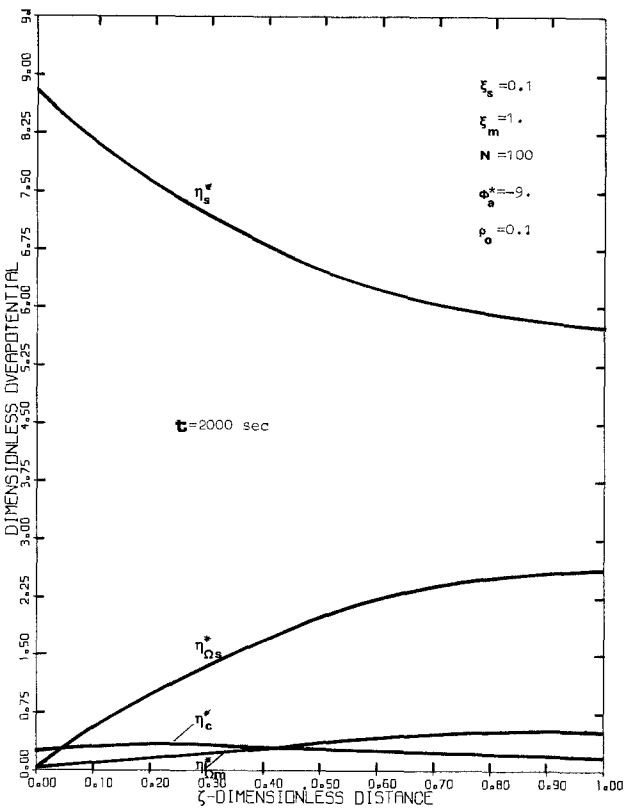

Fig. 11. Overpotential partition within a tubular electrode after a long period of time of electrodeposition.

Conclusions

A theoretical model has been developed which takes into account the various factors influencing the current distribution: metal electrode resistance, electrolyte phase resistance, mass transfer resistance, charge transfer resistance, as well as geometrical parameters

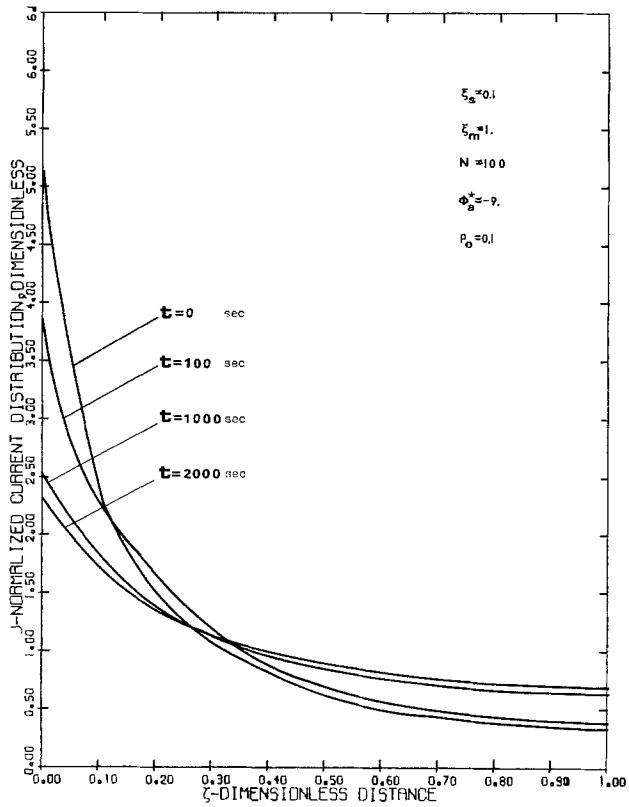

Fig. 12. Current density distribution during electroplating

and the applied potential. The model enables the prediction of the relative importance of each of the above-mentioned factors in obtaining uniform current distribution (*i.e.*, uniform metal thickness inside the holes).

It is shown that in order to obtain a uniform current distribution each one of the following dimensionless parameters:

ξ_m—proportional to the ratio of cathodic reaction rate to metal conductivity

ξ_s—proportional to the ratio of cathodic rate to solution conductivity

N—indicating the ratio between rate of mass transfer to the cathodic surface and the cathodic reaction rate

ϕ_a^*—dimensionless applied potential

should be in the following range: $\xi_m < 0.01$; $\xi_s < 0.01$, $N > 100$, $|\phi_a^*| < 3$. Also, it is desirable that the geometrical parameter ρ_o should be above 0.1. However, if this criteria for ρ_o cannot be met, it is possible to improve the current distribution by changing the other parameters as indicated below.

In industrial electroplating two effects are required: uniform metal thickness and high deposition rate. These two desired effects usually work in opposite directions when applied to planar surfaces. The present general model, through the above-mentioned dimensionless parameters, makes it possible to predict as well as to make the proper decision with respect to the optimal conditions for electroplating. The usual practical condition is that the geometrical factors, ρ_o, are given. ξ_m is dependent on the initial metal thickness and, after a short period of electroplating, its influence tends to become negligible. If the initial ξ_m is too large and it is not feasible to increase a_o during the metal deposition processes, the situation can be remedied by decreasing the initial applied potential (*i.e.*, decreasing ϕ_a^*). Once the value of a_o has increased enough due to thickening which occurs during electroplating process and ξ_m has reached a value below 0.01, the applied potential can be increased in order to speed up electroplating.

The value of ξ_s determines the primary current distribution. Small enough values of ξ_s can be achieved by increasing the electrolyte conductivity, *i.e.*, increasing κ.

Large enough values of N can be achieved by increasing the electrolyte flow velocity through the hole v_z, the metal ion concentration c_b, and the diffusion coefficient D. The latter can be obtained by increasing the temperature.

Manuscript submitted July 27, 1981; revised manuscript received July 1, 1982.

Any discussion of this paper will appear in a Discussion Section to be published in the December 1983 JOURNAL. All discussions for the December 1983 Discussion Section should be submitted by Aug. 1, 1983.

APPENDIX A

Iterative Solution of the Model Equations

(*i*) Make some initial guess of the potential distributions $\phi_s^*(\zeta, \rho_o)$ and $\phi_m^*(\zeta)$.

(*ii*) Calculate the concentration distribution $c(\zeta)$ (from Eq. [34] and [35].

(*iii*) Calculate $\phi_m^*(\zeta)$ by solving Eq. [32].

(*iv*) Calculate $\phi_s^*(\zeta, \rho_o)$ by solving Eq. [30].

(*v*) Using the calculated ϕ_m^* and ϕ_s^* return to iteration (*ii*) and repeat the sequence of operations until convergence is achieved.

(*vi*) Calculate the current density distribution $J(\xi)$ using the values of ϕ_s^*, ϕ_m^*, and C which were calculated previously. This is the initial current distribution through the hole (at $t = 0$).

(*vii*) Calculate the metal thickness which will be electrodeposited during a short time interval Δt at the calculated current density $J(\xi)$ (according to Eq. [36]).

(*viii*) Having the new metal thickness distribution repeat the sequence of calculations (*ii-vi*), this time the values are computed for Δt sec after the start of the electroplating. These values are used to calculate the metal deposit during the period of time of Δt sec from time Δt to $2\Delta t$.

(*ix*) The calculation is continued until the system arrives at a steady state and the change in the values of the variables from time t to $t + \Delta t$ is less than a small chosen value.

APPENDIX B

Mathematical Solution Details

By extracting J from Eq. [34] and [35], an algebraic-integral equation is obtained which may be evaluated by the method of Acrivos and Chambre (12), thus, for known values of ϕ_s^* and ϕ_m^* it is possible to calculate the concentration distribution inside the tube.

The potential distribution in the metal layer $\phi_m^*(\xi)$ is found by solving Eq. [32] and its boundary condition (given by Eq. [33]). This is a second-order, nonlinear equation which is solved numerically. The equation is linearized and then solved by using finite difference.

The potential distribution in the electrolyte solution ϕ_s^* is calculated from Eq. [30] and the set of boundary conditions given by Eq. [31].

The second-order partial differential equation with a nonlinear boundary condition is solved by a pseudo-analytical method. $\phi_s^*(\xi, \rho)$ is assumed to have a solution of the form

$$\phi_s^*(\zeta, \rho) = \frac{2}{\rho_o^2} \sum_{n=1}^{N} \frac{\sinh[\alpha_n(1-\xi)]}{\sinh(\alpha_n)} \frac{J_o(\alpha_n\rho)}{J_o^2(\alpha_n\rho_o)} \int_0^{\rho_o} \rho f(\rho) J_o(\alpha_n\rho)\, d\rho + \sum_{n=1}^{n=N} A_n \frac{1}{\lambda_n} \sin(\alpha_n\rho) \frac{I_0(\lambda_n\rho)}{I_1(\lambda_n\rho_o)}$$

where α_n, $n = 1$, and N are N roots of the equation

$$J_1(\alpha_n\rho_o) = 0$$

and λ_n are eigenvalues given by

$$\lambda_n = [2(m-1) + 1]\pi/2$$

The coefficients A_n, $n = 1$, and N were calculated numerically using Grey's algorithm (13) for nonlinear optimization.

LIST OF SYMBOLS

a metal electrode layer thickness, cm
a^* metal electrode layer thickness a/a_o, dimensionless
a_o initial metal electrode layer thickness, cm
c_b concentration of reactant in bulk electrolyte, gmol/cm^3
$\vec{c}_s$ reactant concentration at electrode surface when the electrolyte is moving to the right, gmol/cm^3
$\overleftarrow{c}_s$ reactant concentration at electrode surface when the electrolyte is moving to the left, gmol/cm^3
c mean reactant concentration at electrode surface, gmol/cm^3
C mean reactant concentration at electrode surface c/c_b, dimensionless
D diffusion coefficient, cm^2/sec
d density of electrode metal, g/cm^3
E_{eq} potential difference between electrode and electrolyte at equilibrium, V
$\mathbf{F}$ Faraday's constant, 96,500 C/g-equiv.
i_m current density in metal electrode, A/cm^2
i_{av} average current density (Eq. [28]), A/cm^2
i_o exchange current density, A/cm^2
j_{lim} local limiting current density, A/cm^2
j local reaction rate along electrode, A/cm^3
J local reaction rate along electrode, dimensionless
$2l$ tube length, cm
M atomic weight of electrode metal, g/g-atom
n number of electrons taking part in the electrode reaction, g-eq/mol
N ratio of mass transfer resistance to charge transfer resistance, $\frac{n\mathbf{F}}{\Gamma(4/3)}\frac{Dc_b}{i_o}\left(\frac{4\bar{v}_z}{9Dr_o l}\right)^{1/3}$, dimensionless
Pe Péclet number, $2r_o\bar{v}_z/D$, dimensionless
r special variable in radial direction, cm
r_o radius of tubular electrode, cm
R gas constant, 8.31 J/gmol K
Re Reynolds number, $2r_o v_z/\nu$, dimensionless
R_o radius of multilayer board hole, cm
Sc Schmidt number, ν/D, dimensionless
t time, sec
t_B multilayer board thickness, cm
T temperature, K
v_{max} electrolyte velocity along tube axis, cm/sec
v_z electrolyte velocity in z direction, cm/sec
y special variable normal to electrode surface, cm
z special variable parallel to the tube axis, cm
α_a anodic transfer coefficient in reaction rate expression, Eq. [1]
α_c cathodic transfer coefficient in reaction rate expression, Eq. [1]
β average current density, i_{av}/i_o, dimensionless
γ constant in Eq. [2], dimensionless
$\Gamma(4/3)$ gamma function of 4/3
ξ special variable in axial direction, dimensionless
η similarity transformation, $y(4v_z/9zDr_o)^{1/3}$, dimensionless
η_c concentration overpotential, V
η_c^* concentration overpotential, $(n\mathbf{F}/RT)\eta_c$, dimensionless
η_s charge transfer overpotential, V
η_s^* charge transfer overpotential, $(n\mathbf{F}/RT)\eta_s$, dimensionless
$\eta_{\Omega m}$ metal ohmic overpotential, V
$\eta_{\Omega m}^*$ metal ohmic overpotential, $(n\mathbf{F}/RT)\eta_{\Omega m}$, dimensionless
$\eta_{\Omega s}$ electrolyte ohmic overpotential, V
$\eta_{\Omega s}^*$ electrolyte ohmic overpotential, $(n\mathbf{F}/RT)\eta_{\Omega s}$, dimensionless
η_T total overpotential, V
η_T^* total overpotential, $(n\mathbf{F}/RT)\eta_T$, dimensionless
κ electrolyte conductivity, $(\Omega\text{-cm})^{-1}$
ν kinematic viscosity, cm^2/sec
ξ_m ratio of metal ohmic resistance to charge transfer resistance, $\frac{n\mathbf{F}}{RT}\frac{l^2}{a_o}\frac{i_o}{\sigma}$, dimensionless
ξ_s ratio of electrolyte ohmic resistance to charge transfer resistance, $\frac{n\mathbf{F}}{RT}\cdot\frac{l^2}{r_o}\frac{i_o}{\kappa}$, dimensionless
ϕ_a^* applied potential, dimensionless (Eq. [27])
ϕ_m potential in metal electrode, V
ϕ_{sm}° potential in the metal electrode at the tube entrance, V
ϕ^* potential in the metal electrode, $n\mathbf{F}/RT$ $(\phi_m - \phi_m^\circ)$, dimensionless
ϕ_s potential in the electrolyte (outside the diffusion layer), V
ϕ_s° potential in the electrolyte, at the tube entrance, V
ϕ_s^* potential in the electrolyte, $n\mathbf{F}/RT$ $(\phi_s - \phi_s^\circ)$, dimensionless
ρ special variable in radial direction, r/r_o, dimensionless
ρ_o geometric parameter, r_o/l, dimensionless
σ metal conductivity $(\Omega\text{-cm})^{-1}$

Subscripts

m pertains to metallic electrode phase
s pertains to electrolytic solution phase
r in r-direction
y in y-direction
z in z-direction

REFERENCES

1. J. Newman, *Int. J. Heat Mass Transfer*, **10**, 983 (1967).
2. W. R. Parrish and J. Newman, *This Journal*, **116**, 169 (1969); **117**, 43 (1970).
3. R. Alkire and A. A. Mirarefi, *ibid.*, **120**, 1507 (1973).
4. J. Newman, *ibid.*, **113**, 1235 (1966); **114**, 239 (1967).
5. R. Alkire and R. Varjian, *ibid.*, **124**, 388 (1977).
6. R. Alkire, *ibid.*, **118**, 1935 (1971).
7. R. Alkire and A. Tvarusko, *ibid.*, **119**, 340 (1972).
8. R. A. Lowenheim, "Modern Electroplating," 3rd ed., p. 185, John Wiley & Sons, Inc., New York (1974).
9. M. A. Lévêque, *Ann. Mines Memoires, Ser. 12, 13*, 201 (1928).
10. W. H. Smyrl and J. Newman, *This Journal*, **119**, 212 (1972).
11. W. Engelmaier and T. J. Kessler, *ibid.*, **125**, 36 (1978).
12. A. Acrivos and P. L. Chambré, *IEC*, **49**, 1025 (1957).
13. L. W. Cornwell, R. J. Pegis, A. K. Rigler, and T. P. Vogl, *J. Opt. Soc. Am.*, **63**, 576 (1973).

A Preparation of Perpendicular Magnetic Recording Media by an Electroless Plating Method

Tetsuya Osaka,* Naoki Kasai, and Ichiro Koiwa

Department of Applied Chemistry, Wasada University, Okubo Shinjuku-ku, Tokyo 160, Japan

and Fumio Goto and Yoji Suganuma

Nippon Electric Company Limited, Microelectronics Research Laboratories, Miyazaki, Takatsu-ku, Kawasaki 213, Japan

ABSTRACT

The perpendicularly oriented crystal structure conditions of electroless plated film for high density perpendicular recording media were investigated mainly by (002) plane rocking curves and cross sectional SEM observation. A highly oriented narrow dispersion of c-axis orientation normal to the surface plane was consequently obtained, and the columnar structure of hcp crystal with *ca.* 0.05 μm diam was confirmed. As a result of preparing disks A and B, which were chemically plated from an optimum bath and a more improved bath, respectively, the recording characteristics with a combination of ring head were obtained as recording densities of D_{50} = 18,500 FRPI for disk A and 25,000 FRPI for disk B, in spite of a relatively thick magnetic medium. The di-pulse waveforms, which are characterized with perpendicular recording, were observed at low bit recording density. It was indicated by the above results that the chemically plated Co alloy films are applicable as a perpendicular recording medium.

Perpendicular magnetic media for high density recording have been studied by many workers (1), since a proposal regarding its recording system by the Iwasaki school (2, 3). In a previous paper (4), the authors reported the development of electroless cobalt alloy plating bath for a perpendicular recording medium. The crystal structure for film plated from the electroless bath is reported in the present paper.

Recording and reproducing characteristics for a perpendicular Co-Cr flexible disk medium were first tried by using a single-pole head (3). The combination of a perpendicular medium with a ring head, which might be a first step toward practical use of a perpendicular recording system, was also reported by several workers (5, 6). This paper reports 8 in. diam disk media and their recording characteristics using a ring head.

Experimental

Plating conditions for Co alloy films and determining several properties for their films were the same as shown in a previous paper (4). The film cross section was observed by scanning electron microscopy. Two kinds of magnetic films for plated disks were prepared from electroless plating baths A and B, shown in Table I. Figure 1 demonstrates the disk structure, using a structure similar to that for 8 in. longitudinal high density recording plated disk (7) developed by Nippon Electric Company Limited. The magnetic films have a 5 μm plating for disk A or a 3 μm plating for disk B on a polished Ni-P substrate, which was chemically plated on an aluminum alloy plate. The SiO_2 (8) protective overcoat, 0.1 μm for disk A and 0.02 μm for disk B, was formed by heat-treatment at 200°C after being covered with tetrahydroxy silane alcohol solution by a spin-coat method. Disk and head properties for a read/write measurement are shown in Table II.

* Electrochemical Society Active Member.
Key words: electroless, ferromagnetism.

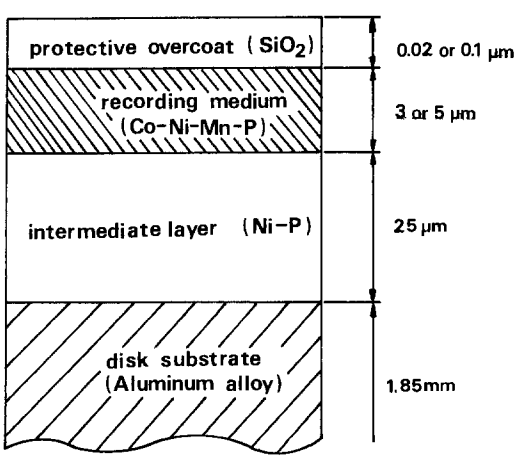

Fig. 1. Plated disk structure for perpendicular recording medium

Results and Discussion

Investigation on c-axis orientation normal to surface plane.—The effects of three factors in the bath (*i.e.*, $MnSO_4$ concentration, bath *p*H, and $NiSO_4$ concentration) on c-axis orientation were studied by rocking curves for the (002) plane. The $MnSO_4$ concentration effect on c-axis orientation is demonstrated in Fig. 2, where the $\Delta\theta_{50}$ value means the peak breadth at half-maximum intensity for (002) plane peak in rocking curve. The $\Delta\theta_{50}$ value represents the c-axis orientation

Table I. Electroless plating bath compositions and operating conditions

Chemicals	Bath A	Bath B
$NaH_2PO_2 \cdot H_2O$	0.20 M · l^{-1}	0.20 M · l^{-1}
$(NH_4)_2SO_4$	0.50	0.50
$CH_2(COONa)_2 \cdot H_2O$	0.50	0.50
$C_2H_5OH(COONa)_2$	0.05	0.05
$CoSO_4 \cdot 7H_2O$	0.025	0.035
$NiSO_4 \cdot 6H_2O$	0.01	0.01
$MnSO_4 \cdot 4 \sim 5H_2O$	0.04	0.04
Bath temperature	85°C	80°C
pH adjusted by NH_4OH	9.6	9.6

Table II. Disk and head characteristics

	Disk A	Disk B
Medium material	Co-Ni-Mn-P	Co-Ni-Mn-P
Medium thickness/μm	5.0	3.0
Coercivity, $Hc(\perp)$/Oe	1530	1040
Overcoat thickness/μm	0.10	0.02
Substrate material	Polished Ni-P on Al alloy	Polished Ni-P on Al alloy
Core material	Mn-Zn ferrite	Mn-Zn ferrite
Gap length/μm	1.0	0.5
Track width/μm	50	30
Flying height/μm	0.2 at 22 m/sec	0.1 at 7.89 m/sec

degree normal to the surface plane. In the 0 ~ 0.015M $MnSO_4$ range, the hexagonal crystal for plated films reaches an in-plane orientation. The c-axis orientation changes from in-plane to perpendicular form, with the increase in $MnSO_4$ concentration. From the 0.025M $MnSO_4$ point, the hexagonal crystal c-axis orients completely to the perpendicular. The $\Delta\theta_{50}$ value becomes minimum at 0.04M $MnSO_4$. This condition corresponds well to the x-ray diffraction patterns and magnetic properties shown in the previous paper (4). In Fig. 2, the results for two kinds of substrates, Cu and polished Ni-P, were plotted as a function of $MnSO_4$ concentration. The $\Delta\theta_{50}$ values for Ni-P substrate are always lower than those for Cu substrate. The substrate roughness effect on magnetic properties was previously discussed (9). It was concluded that the larger variation in surface roughness, obtained by an emery paper, for example, is too large to affect the magnetic properties. It was also concluded that the smaller variation, produced by such a crystallite grain size, greatly influences magnetic properties (9). The above fact may be due to the small difference in surface roughness produced by such a crystallite grain size (*cf.*, the mean surface roughness values for Cu and polished Ni-P are 0.1 and 0.015 μm, respectively). The most uniformly perpendicular-oriented condition for hcp crystals is obtained at the 0.04M $MnSO_4$ point, where $\Delta\theta_{50}$ reproducibly shows a minimum value of *ca.* 10°. This minimum value was always reproducibly obtained, but a more highly uniform structure, *ca.* 6°, was occasionally obtained. The plots in the figures do not show the best data indicating less than 10°. Instead, the plots show typical data reproducibly obtained. The $\Delta\theta_{50}$ value is very sensitive to surface roughness. Different values appear even in the case of a little difference, such as crystallite sizes in the order of, at least, less than 0.1 μm. Therefore, the surface flatness for such a little difference is also an important factor, which must be paid attention to in obtaining a more highly uniform c-axis orientation normal to the surface plane.

The bath *p*H effect on $\Delta\theta_{50}$ is shown in Fig. 3, where the $\Delta\theta_{50}$ value for Ni-P substrate is also always lower. There is a minimum $\Delta\theta_{50}$ value at bath *p*H 9.6 for Cu substrate. However, for Ni-P substrate, the $\Delta\theta_{50}$ values become the lower constant value for *ca.* 10.5° at the *p*H 9.4 ~ 9.8 range. The results for Cu substrate correspond well to those for x-ray diffraction patterns and magnetic properties described in a previous paper (4).

In order to get a perpendicular anisotropy it is also necessary to lower the saturation magnetization, *Ms*, for film as well as to make the c-axis orientation normal to the surface plane. An attempt was made to codeposit nickel into films for this purpose. The $NiSO_4$ concentration effect on $\Delta\theta_{50}$ was demonstrated in Fig. 4. When Cu substrate is used, the $\Delta\theta_{50}$ value gradually becomes larger with the increase in $NiSO_4$ concentration. For Ni-P substrate, the $\Delta\theta_{50}$ value gives a lower constant value, even with the increase in $NiSO_4$ concentration up to 0.01M $NiSO_4$ concentration. From that point on, it gradually becomes larger. Since the perpendicular orientation uniformity on the Ni-P substrate is retained up to 0.01M $NiSO_4$ concentration, as seen in Fig. 4, the $NiSO_4$ addition into the bath solution can be allowed up to 0.01M, in order to decrease *Ms* in the film.

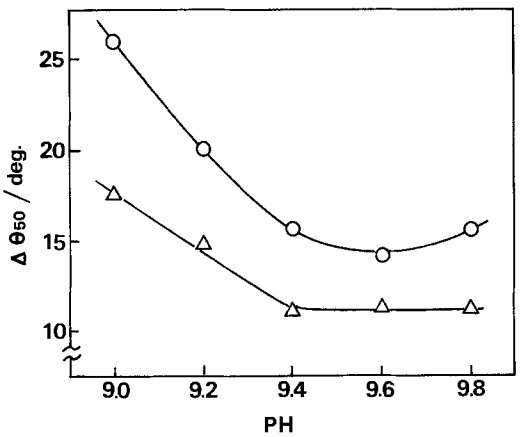

Fig. 3. Bath *p*H effect on $\Delta\theta_{50}$ for plated films. ○: Cu substrate, △: Ni-P substrate.

SEM observation on crystal structure for film plated under optimum conditions.—Figure 5 shows a typical cross section of Co alloy film plated under optimum plating condition shown in Table I-A. The most typical cross section micrograph is shown in Fig. 5(a), where the 11.6 μm thick cross section is shown inclined 60° from the substrate plane. In Fig. 5(a), the Co-Ni-Mn-P film cross section indicates a uniform columnar growth structure with *ca.* 0.2 μm diam in appearance, which is composed of pole-like crystals. Since the plated film surface gives fairly rough conditions, the surface was polished to mirror conditions when making disk B. In order to confirm columnar crystals in detail, a Co alloy film cross section containing part of the broken columnar crystals, produced during the cutting process, is demonstrated in Fig. 5(b). The arrow in Fig. 5(b) indicates the position revealed under magnification shown in Fig. 5(c). Since the columnar structures are composed of pole-like crystal with *ca.* 0.05 μm diam, as seen in Fig. 5(c), the apparent columnar structure with *ca.* 0.2 μm diam, shown in Fig. 5(a) or (b), is in a state of aggregation for column-like crystals with *ca.* 0.05 μm diam. Film made from such columnar crystals with *ca.* 0.05 μm diam is consid-

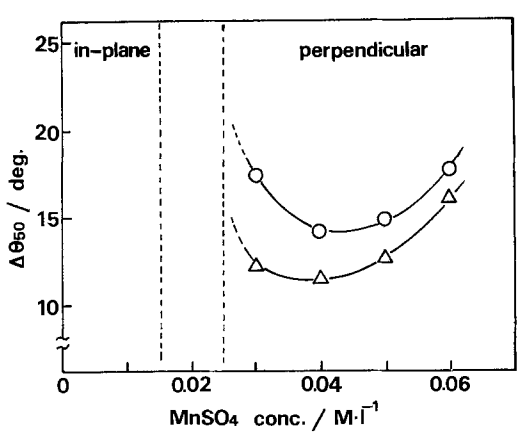

Fig. 2. $MnSO_4$ concentration effect on $\Delta\theta_{50}$ for plated films. ○: Cu substrate, △: Ni-P substrate.

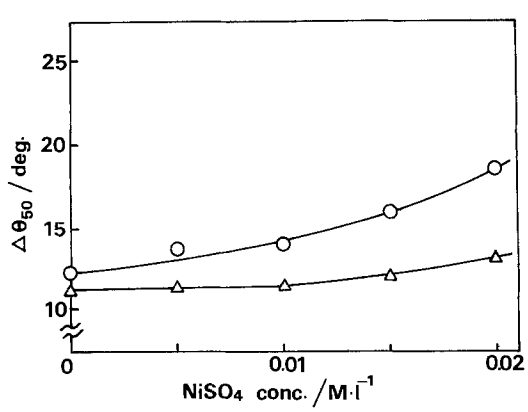

Fig. 4. $NiSO_4$ concentration effect on $\Delta\theta_{50}$ for plated films. ○: Cu substrate, △: Ni-P substrate.

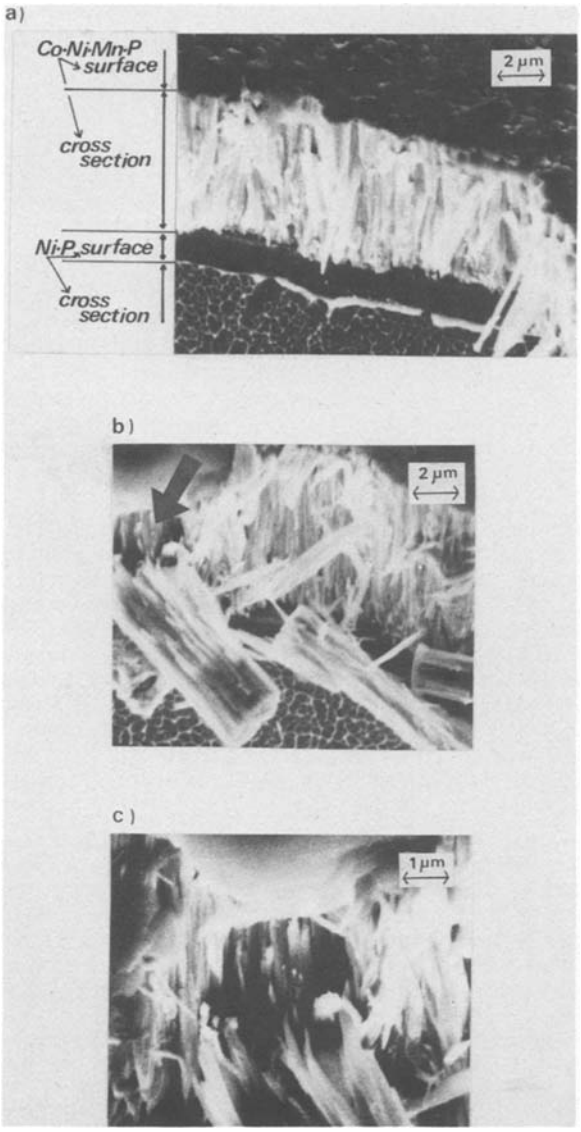

Fig. 5. Scanning electron micrographs showing a cross section of film plated under optimum condition listed in Table I-A using Ni-P substrate. (a): Typical cross section for plated film using Ni-P substrate (×5,000), (b) and (c): Other cross section parts of plated film containing broken columnar crystals, which are produced during cutting, [×5,000 for (b)] and [×10,000 for (c)]. The arrow shown in (b) indicates the part corresponding to the enlarged section shown in (c).

ered to be suitable for a high density perpendicular recording medium (*e.g.*, the 100,000 FRPI recording density corresponds to 0.25 μm length for one bit).

Magnetic disks preparation and their read/write properties.—Two kinds of 8 in. diam disks, A and B, were prepared from baths A and B shown in Table I. The composition and operation conditions for bath A for disk A were determined and reported in the previous paper (4). The conditions for bath B for disk B were improved for the higher density recording. The recording density naturally depends not only on disk properties, but also on read/write conditions, especially depending on gap length of ring head and head-medium spacing (5). Since the higher *Hc* for disk A has to be lowered, in order to be able to use a ring head with narrower gap length for establishing higher density recording, the bath B conditions were improved to obtain a lower *Hc* film than that plated from bath A. Improved bath B, with higher $CoSO_4$ concentration and lower bath temperature, makes it possible to combine ring head conditions for a narrower gap length. The protective overcoat for disk B is also made thinner, 0.02 μm, for lowering the head-medium spacing. The characteristics for disk media A and B and their read/write conditions are shown in Table II. The plated magnetic film polishing process was added only for disk B, using the head with lower spacing conditions.

Reproduced waveforms, low bit density (740 FRPI) and high bit density (23 KFRPI) for the read/write conditions in Table II-A, were shown in Fig. 6. Since an output voltage waveform at low bit density, in perpendicular magnetic recording using a ring head, is confirmed by the Iwasaki school (11) to show a dipulse shape, the dipulse waveforms shown in Fig. 6(b) is considered to be produced by the perpendicular recording results. It also supports the perpendicular recording performance wherein the waveforms at high bit density, 23 KFRPI, are produced by using the thicker magnetic medium, 5 μm thick, because such a high density recording is performed only in the case of very thin magnetic medium (less than *ca.* 0.1 μm) in the case of a longitudinal recording system.

Figure 7 demonstrates the recording characteristics for Co alloy magnetic disks A and B, which were measured under the disk and head conditions shown in Table II. The recording densities for D_{50}, which means the recording density at half the maximum output voltage value, are observed to be 18,500 FRPI for disk A and 25,000 FRPI for disk B, respectively.

The authors have studied the use of an electroless cobalt alloy magnetic medium for a perpendicular recording medium, considering that magnetic films showing incompletely perpendicular magnetic anisotropy can also be used for this medium, as well as when

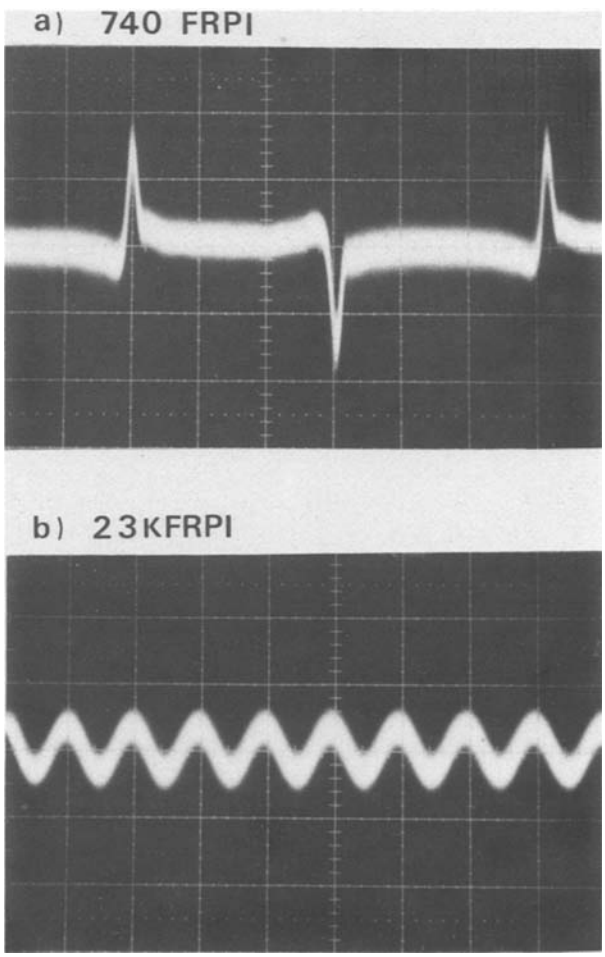

Fig. 6. Reproduced waveforms, (a) low density of 740 FRPI (b) high density of 23,000 FRPI. The disk and ring head are used with the condition shown in Table II-A.

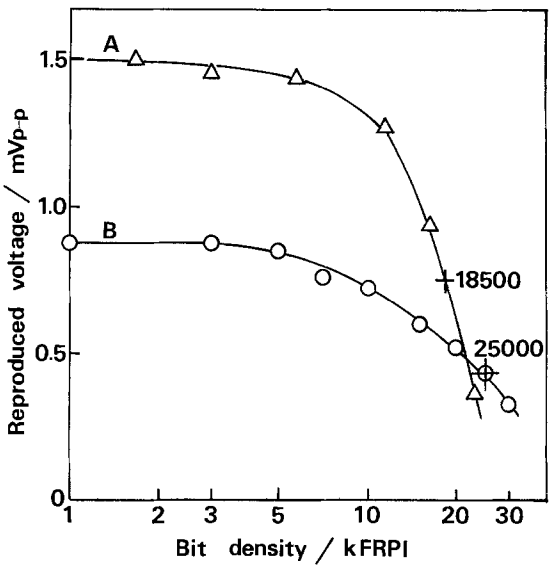

Fig. 7. Recording characteristics for Co alloy disks. A and B characters represent the data using disks A and B, respectively.

using complete perpendicular magnetic anisotropy media, such as an rf sputtered Co-Cr film. The possibility of a perpendicular recording medium is consequently confirmed by using disks A and B whose magnetic films do not show a complete perpendicular magnetic anisotropy (12), such as an rf sputtered film. Finally, it can be concluded that chemically plated Co alloy magnetic film is applicable as a high density perpendicular recording medium.

Acknowledgments

The authors would like to thank Professor Emeritus Dr. Tadashi Yoshida, Waseda University, and Dr. Takashi Furuoya, Dr. Daisaburo Shinoda, and Mr. Koichi Matsumi, Microelectronics Research Laboratories, Nippon Electric Company Limited, for their encouragement during the research. The authors also would like to thank Messrs. Hideo Tanaka, Masahiro Yanagisawa, and Morishige Aoyama for their assistance in read/write tests and in forming the protective overcoat.

Manuscript submitted May 20, 1982; revised manuscript received Nov. 12, 1982.

Any discussion of this paper will appear in a Discussion Section to be published in the December 1983 JOURNAL. All discussions for the December 1983 Discussion Section should be submitted by Aug. 1, 1983.

Publication costs of this article were assisted by Nippon Electric Company, Limited.

REFERENCES

1. *e.g.*, Proceedings of 1982 Sendai Symp. on Perpendicular Magnetic Recording, Research Institute of Electrical Commun., Tohoku University, Japan (1982).
2. S. Iwasaki and K. Takemura, *IEEE Trans. Magn.*, **mag-11**, 1173 (1975).
3. S. Iwasaki and Y. Nakamura, *ibid.*, **mag-13**, 1272 (1977).
4. T. Osaka, K. Kasai, I. Koiwa, and F. Goto, *This Journal*, In press.
5. T. Suzuki and S. Iwasaki, IECE Tech. Group Meeting of Magn. Rec., Japan, MR81-8 (1981).
6. K. Kobayashi and G. Ishida, *J. Appl. Phys.*, **52**, 2453 (1981).
7. M. Nagao, Y. Suganuma, H. Tanaka, M. Yanagisawa, and F. Goto, *IEEE Trans. Magn.*, **mag-15**, 1543 (1979).
8. M. Yanagisawa and F. Goto, Ann. Conf. in IECE, Japan, 1-189 (1980).
9. T. Osaka, H. Nagasaka, and F. Goto, *This Journal*, **128**, 1686 (1981).
10. T. Osaka, K. Kasai, I. Koiwa, F. Goto, and Y. Suganuma, The 65th Conf. of Metal Finishing Soc. of Japan, p. 136 (1982).
11. S. Iwasaki, *IEEE Trans. Magn.*, **mag-16**, 71 (1980); S. Iwasaki and M. Suzuki, Ann. Conf. in IECE Japan, 1-199 (1980).
12. F. Goto, T. Osaka, N. Kasai, I. Koiwa, H. Tanaka, M. Aoyama, and Y. Suganuma, Proc. of 1982 Sendai Symp. on Perpendicular Magn. Recording, Research Institute of Electrical Commun., Tohoku Univ., Japan (1982), p. 197.

Electric Field Enhanced Diffusion in Trans-$(CH)_x$

J. H. Kaufman, E. J. Mele, and A. J. Heeger

Department of Physics, University of Pennsylvania, Philadelphia, Pennsylvania 19104-3895

and R. Kaner* and A. G. MacDiarmid

Department of Chemistry, University of Pennsylvania, Philadelphia, Pennsylvania 19104

ABSTRACT

A theory is developed which shows how high power and high current densities can be generated by a $(CH)_x$ battery cell despite the slow diffusion and low conductivity characteristic of ionic motion in polyacetylene. The presence of a small driving potential (or a load) causes current to flow and generates a large electric field within the fibrils. This field dramatically increases the ion transport rate when the electronic screening length is comparable to or greater than the radius of a fibril.

Polyacetylene, $(CH)_x$, is the prototype example of a conducting polymer (1). Recent studies have demonstrated that after synthesis, $(CH)_x$ can be oxidized or reduced chemically (1, 2) or electrochemically (3) at room temperature. As a result of these controlled doping procedures, increases in electrical conductivity of over twelve orders of magnitude have been observed (4). Doping to high levels results in a semiconductor-metal transition (5-7), giving a whole new class of highly conducting "plastic" metals with a wide range of electronegativity. The partly oxidized material is relatively electronegative and exists as a stabilized polycarbonium ion, $(CH^{+y})_x$, in combination with the corresponding number of monovalent counterions, A^-, such that the overall composition is $(CH^{+y}A_y^-)_x$. Similarly, the partly reduced material is relatively electropositive and exists as a polycarbanion, $(CH^{-y})_x$, in combination with the corresponding number of monovalent countercations, M^+, such that the

* Electrochemical Society Active Member.

Key words: conducting polymer batteries $(CH)_x$, polyacetylene ionic diffusion.

overall composition is $(M_y^+CH^{-y})_x$. Since reversible electrochemical oxidation and reduction (*i.e.*, doping and "undoping") have been demonstrated, the possibility of using polyacetylene as an electrode in an electrochemical cell has been proposed (8-10). Indeed, in earlier experimental studies it has been demonstrated (8-10) that films of partly oxidized or reduced $(CH)_x$ can be used as the cathode and anode materials in lightweight rechargeable storage batteries.

Electron microscopy studies (11, 12) show that the as-grown $(CH)_x$ films consist of randomly oriented fibrils with typical fibril diameter ~200Å. The diameter can be reduced significantly with different polymerization conditions (13). The bulk density is about 0.4 g/cm^3 compared with 1.2 g/cm^3 as obtained by flotation techniques, indicating that the polymer fibrils fill only about 1/3 of the total volume, and that the effective surface area in contact with the electrolyte is quite high, ~60 m^2/g.

During the doping and undoping processes which accompany battery charge and discharge, the ions from the electrolyte must diffuse into and out of the $(CH)_x$ fibrils, *i.e.*, between the individual $(CH)_x$ polymer chains. However, since the solid-state ionic mobility in $(CH)_x$ is much smaller than the ionic mobility in the electrolyte, the short-circuit current and power density of an electrochemical cell might be expected to be limited by the slow diffusion of ions through the polyacetylene fibrils.

In fact, recent measurements (14) of free diffusion of Li^+ ions into $(CH)_x$ fibrils in electrochemical cells reveal diffusion constants of $D \simeq 4 \times 10^{-18}$ cm^2/sec. The diffusion of ClO_4^- during p-doping is of the same order of magnitude. On the same cells, however, high short-circuit currents and high power densities are obtained (8-10, 15). An explanation of this apparent contradiction is necessary, and it is the subject of this paper.

Summary of Experimental Results

A detailed description of the diffusion studies will be presented elsewhere (10, 14). We briefly summarize the experimental results here as background information for quantitative input into the calculations which follow and which are the principal point of this paper. A battery cell is constructed by pressing $(CH)_x$ film (~0.1 mm thickness by ~1 cm^2; ~3 mg) onto platinum mesh to act as the working electrode (9). Lithium metal embedded in nickel mesh (Delker Corporation) acts as the counterelectrode and is separated from the $(CH)_x$ by a kiln-dried piece of glass filter paper. A second (identical) lithium electrode is used as the reference electrode. Basic activated alumina serves as a scavenger for impurities. One molar $LiClO_4$/tetrahydrofuran is added as the electrolyte-solvent system for n-type doping of $(CH)_x$, while 1M $LiClO_4$/propylene carbonate is used for p-type doping. Prior to use, the $LiClO_4$ is melted under dynamic vacuum. Tetrahydrofuran (Fischer Scientific Company) is kept in sodium benzophenone, while propylene carbonate (Aldrich Chemical Company) is spin band distilled and stored over lithium chips. The cell is encased in rectangular glass and sealed under vacuum across platinum wires which are spot welded to the electrode. This construction yields stable cells with internal resistance which is typically about 100Ω.

Measurements of the diffusion time, τ_o, and the diffusion constant for Li^+ ions were made by monitoring the recovery of the open-circuit voltage (V_{oc}) after step potential changes in charging. In a typical experiment, the applied voltage was stepped by 0.1V and held at the new potential until the current fell (during about 20 min) to ~1/10 of its initial value. The power supply was then disconnected, and the open-circuit voltage was monitored by periodically connecting the cell to a high input impedance digital voltmeter. For example, at 3% doping, after an initial transient of about 1.5 hr, the open-circuit voltage approached its equilibrium value exponentially with a time constant τ_o of about 12 hr. Initial experiments yield a time constant of the same magnitude for p-doping (with ClO_4^-). During this time, no current was flowing; the change in V_{oc} occurs as the dopant ions freely diffuse into the fibrils in response to the concentration gradient imparted by the step change in applied voltage. Assuming cylindrical geometry for the $(CH)_x$ fibrils, the diffusion constant can be obtained from the exponential part of the curve (16)

$$D_o = r_o^2/((2.405)^2)\tau_o \quad [1]$$

where r_o is the radius of the $(CH)_x$ fibril, $r_o \simeq 100$Å. From this expression, a time constant of 12 hr corresponds to a diffusion constant $D_o \simeq 4 \times 10^{-18}$ cm^2/sec. On the same cells, short-circuit currents were typically as high as 100 mA/cm^2 of $(CH)_x$ film with maximum power densities, for $(CH(ClO_4)_y)_x$ *vs.* Li, of 30 kW/kg (excluding weight of electrolyte, current collectors, and container (10).

To further quantify the anomaly of high current and power densities in spite of small free diffusion rates, we use the measured free diffusion constants to estimate the internal resistance of the cell. The ionic conductivity is given by $\sigma_I = ne\mu$ where $\mu = eD/kT$ is the ionic mobility. For 1% doping, $n = 2 \times 10^{20}$ ions/cm^3; using $D_o = 10^{-18}$ cm^2/sec, one obtains for the ionic conductivity $\sigma_I = 10^{-15}$ Ω^{-1}-cm^{-1}. For a 1 cm^2 piece of $(CH)_x$ film, 0.01 cm in thickness, the effective surface area is $A_s = 2.5 \times 10^3$ cm^2. Using $R_I = \rho_I r_o/A_s$ to estimate the total resistance, we obtain $R_I = 4 \times 10^5\Omega$, three orders of magnitude greater than the value measured from the current (typically in the range 10-100 mA/cm^2) through a series of known load resistors.

Field Enhanced Diffusion in $(CH)_x$

The failure of this calculation stems from ignoring the effect of the electric field on the ionic transport. For example, after a voltage step, ΔV, current flows and an electric field exists; $E \sim \Delta V/r_o$ where r_o is the radius of a fibril. Taking $V = 0.5$V, and $r_o = 10^2$Å, $E = 5 \times 10^5$ V/cm. Such enormous electric fields will literally drive the ions into (or out of) the fibrils leading to significant enhancement of the net ion transport rate.

To understand this effect in more detail, we first consider the free diffusion equation describing mass transport due to a concentration gradient

$$\frac{\partial C_I}{\partial t} = -D_o \nabla^2 C_I \quad [2]$$

where C_I is the ion concentration, which will in general vary across the thickness of a fibril. This equation has been solved for the cylindrical geometry appropriate to polyacetylene fibrils (16). After a short transient, the time dependence of the concentration gradient becomes exponential, with time constant τ_o given by Eq. [1]. Under conditions of current flow, an electric field exists in the $(CH)_x$ fibrils, and a second term must be added to the first integral of the diffusion equation

$$\vec{J}_I = -D_o \vec{\nabla} C + \bar{\sigma}_I \vec{E}/e \quad [3]$$

where $\vec{J}_I$ is the ion current density in the $(CH)_x$ electrode, and $\bar{\sigma}_I$ is the average ionic conductivity in the absence of a field. Assuming that ion motion into (or out of) the fibril limits the kinetics, the local concentration of ions will differ from that of electrons while current is flowing, thereby, giving rise to the electric field term in Eq. [3]. Since this electric field can be screened by a redistribution of the electronic density, it will be important only under conditions when the electronic screening length transverse to the $(CH)_x$ chains is comparable to a fibril radius, ~50-100Å. This

will certainly be the case at low doping levels, *i.e.*, below the semiconductor-metal transition. Moreover, because of the highly anistropic electronic properties (implying a highly anisotropic effective mass), this condition should be satisfied well into the metallic regime. We note, however, that the existence of a significant electric field effect is directly related to the existence of the fibrillar morphology with fibril dimensions of the same magnitude as electronic screening lengths.

Differentiating Eq. [3] $(\vec{\nabla} \cdot \vec{J}_I)$ and using the continuity equation for the ion current $(\vec{\nabla} \cdot \vec{J}_I = \partial C_I/\partial t)$ and the Maxwell equation $[\vec{\nabla} \cdot \vec{E} = 4\pi e\ (C_I - C_e]$ leads to a "forced" transport equation

$$\frac{\partial C_I}{\partial t} = -D_o \nabla^2 C_I + 4\pi\bar{\sigma}_I (C_I - C_e) \qquad [4]$$

In the above, we have used the fact that the net charge density is $e(C_I - C_e)$ where e is the electronic charge, and C_I and C_e are the local concentrations of ions and electrons (or holes in the case of p-doping), respectively. Note that rigorously σ_I is proportional to C_I. In writing Eq. [4], we have linearized the equation by keeping only the leading term, *i.e.*, the dependence on $(C_I - C_e)$.

Under open-circuit conditions, no current flows and $C_I = C_e$. If the applied voltage differs from V_{oc}, or if the cell is placed under load, current flows from Ohm's law

$$\frac{V_{oc} - V_{ext}}{R_i} = evd \frac{\partial}{\partial t} (C_I - C_e) \qquad [5]$$

where V_{ext} is the external cell voltage (*i.e.*, the voltage at the polymer electrolyte interface), v is the volume of the $(CH)_x$ electrode, d is the number density of (CH) units, and R_i is the measured internal resistance of the cell. Although Eq. [5] applies to the sample as a whole, we can use it to calculate the local concentration within a fibril. This follows since the electrolyte is in contact with all the fibril surfaces. Moreover, even though electron injection into the $(CH)_x$ occurs only at the contact, the electronic resistivity is sufficiently small along the chain direction that all of the fibrils are at a common average electrical potential.

Assuming C_I and C_e have the same time dependence $(e^{-t/\tau})$, Eq. [4] can be linearized using Eq. [5] and the empirical relation[1] found for V_{oc} *vs.* Q for $(CH)_x$ (*vs.* Li)

$$V_{oc} \simeq A \pm bQ^\gamma = A \pm Bv^\gamma C_I^\gamma \qquad [6]$$

where A, B, and γ are fitting parameters. In Eq. [6], the + and − signs refer to p-type and n-type doping, respectively. From Eq. [4] and Eq. [5]

$$\frac{\partial C_I}{\partial t} = -D_o \nabla^2 C_I + 4\pi\sigma_I \left[\frac{\tau}{evdR_i} (V_{oc} - V_{ext}) \right] \qquad [7]$$

and from [6]

$$-D_o \nabla^2 C_I = -\frac{1}{\tau} - \left(\frac{4\pi\bar{\sigma}_I}{edR_i}\right) \tau \left[(A - V_{ext}) \left(\frac{B}{A - V_{oc}}\right)^{1/\gamma} - B \left(\frac{B}{A - V_{oc}}\right)^{1/\gamma - 1} \right] C_I \qquad [8]$$

With the above assumption of an exponential dependence for C_I, this equation has the form of the free diffusion equation (Eq. [2]) implying an effective decay rate given by

$$\frac{1}{\tau} = \frac{1}{\tau_o} + \left(\frac{4\pi\bar{\sigma}_I}{edR_i}\right) \tau \left[(A - V_{ext}) \left(\frac{B}{A - V_{oc}}\right)^{1/\gamma} - B \left(\frac{B}{A - V_{oc}}\right)^{1/\gamma - 1} \right] \qquad [9]$$

where $1/\tau_o$ is given by Eq. [1]. This expression is only valid for $\Delta V \equiv |V_{ext} - V_{oc}|$ small; for ΔV large, the change in V_{oc} over a time τ is too large, and the equation cannot be linearized.

Although Eq. [8] has the form of an effective diffusion equation, it should not be interpreted as implying an increase in the ionic conductivity. The entire analysis was carried out in the linear response regime, *i.e.*, σ_I was assumed to be field independent. The increased transport rate does not arise from an increase in σ_I, but from the internal electric field generated during current flow (see Eq. [3] and [4]). In obtaining Eq. [8] and [9], we assumed a simple exponential decay toward equilibrium for C_I. The true time dependence implied by simultaneous solution of Eq. [4], [5], and [6] in the cylindrical geometry appropriate to the $(CH)_x$ fibrils is more complex so that the result (Eq. [9]) is only approximate. We note, however, that the experimental results yield an exponential decay after an initial transient, suggesting that the assumption is reasonable. We have, furthermore, ignored any intrinsic dependence of D_o (and σ_I) on the dopant concentration. Therefore, Eq. [9] does not predict any fine structure arising from the dependence of τ_o on concentration.

Figures 1a and b show the dependence of τ on $V = |V_{ext} - V_{oc}|$ for different values of σ_I and V_{oc} (n-type doping) calculated from Eq. [9]. From the figures, it is evident that a small driving potential greatly reduces the ionic transport time. For example, at $V_{oc} = 1.7$V and $\sigma_I = 10^{-16}\ \Omega^{-1}$-cm^{-1}, an external potential $V_{ext} = 1.75$V decreases the diffusion time from 4×10^4 sec ($V_{ext} = V_{oc}$) to ~125 sec ($|V_{ext} - V_{oc}| = 0.05$V). The increase in ionic transport rate of $\sim 10^3$ indicated in Fig. 1a and b provides the explanation of the large values observed for short-circuit currents (and power density) in electrochemical cells using $(CH)_x$ electrodes.

When $V_{ext} = V_{oc}$, the potential dependent term vanishes, Eq. [10] becomes $\tau^{-1} = \tau_o^{-1}$, and the free diffusion behavior is recovered. We note that in absence of current flow, the electric field inside a fibril is zero (whether or not the doping is uniform). The sharp drop in τ due to small displacements from the equilibrium V_{oc} (resulting from current flow) is due directly to the unique morphology of polyacetylene and the large resulting potential gradients that occur within the fibrils.

Quantitative measurements of τ as a function of V are underway. Preliminary results are in order of

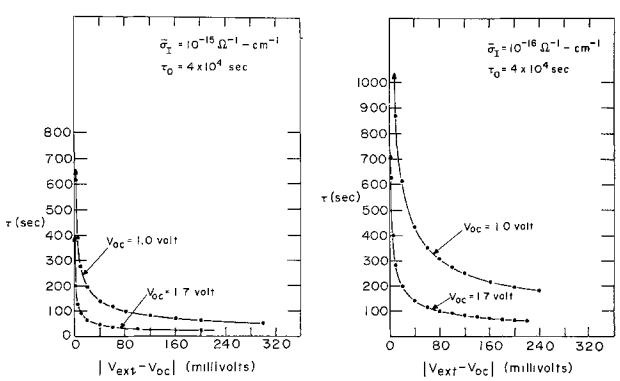

Fig. 1. τ *vs.* $|V_{ext} - V_{oc}|$ for $\sigma_I = 10^{-15}\Omega^{-1}$-cm^{-1} (Fig. 1a), and $\sigma_I = 10^{-16}\Omega^{-1}$-cm^{-1} (Fig. 1b). Curves corresponding to two values of V_{oc} are shown (1.0 and 1.7V). The internal resistance is taken to be 100Ω.

[1] Equation [6] provides an excellent empirical fit to the V *vs.* Q data for both p-type (Ref. 10) and n-type (Ref. 15) doping. Typical values (*e.g.*, for n-type) are $A = 1.9$V, $B = 0.75$, and $\gamma = 2/3$.

magnitude agreement with the behavior predicted above.

Conclusion

The theory developed in this paper shows how high power densities and current densities can be generated by a $(CH)_x$ battery cell despite the slow free diffusion and low conductivity characteristic of ionic motion in polyacetylene. The presence of a small driving potential (or a load) causes current to flow and generates a large electric field within the $(CH)_x$ fibrils. This field increases the effective ion transport rate by several orders of magnitude.

Other mechanisms may also contribute. For example, enhancement of diffusion can also arise from the change in electrochemical potential with concentration (17). Although this mechanism may play a role at the most dilute doping levels, it will not be important above about 0.5% where the V_{oc} *vs.* y curve is relatively flat (10). More rapid ionic diffusion might be expected in amorphous regions as compared to crystalline regions. However, this cannot explain the apparent contradiction (high measured short-circuit currents and slow measured free diffusion) outlined at the beginning of the paper. On the other hand, the electric field enhancement mechanism presented in this paper provides the explanation of the unusual result reported earlier (10) that one obtains higher Coulomb efficiency with a faster discharge. Under rapid discharge conditions, $V_{oc} - V_{ext}$ is large so that the field enhanced ion transport mechanism is most effective.

In conclusion, the fibrillar morphology of polyacetylene is critically important to the potential use of this polymer as a battery electrode in two ways: (*i*) the fibrils provide a microgrid such that ions from the electrolyte need to traverse distances no greater than about 100Å, and (*ii*) the small diameter of the fibrils provides an enhancement of the local electric field (during charging and discharging) which increases the ionic transport rate by several orders of magnitude over that obtained from free diffusion.

Acknowledgments

We thank Dr. K. Kaneto for many valuable discussions. This work was supported by DOE Advanced Energy Projects, DE-AC02-81ER10832.

Manuscript submitted July 29, 1982; revised manuscript received Oct. 6, 1982.

Any discussion of this paper will appear in a Discussion Section to be published in the December 1983 JOURNAL. All discussions for the December 1983 Discussion Section should be submitted by Aug. 1, 1983.

Publication costs of this article were assisted by the University of Pennsylvania.

REFERENCES

1. A. G. MacDiarmid and A. J. Heeger, in "The Physics and Chemistry of Low Dimensional Solids," L. Alcacer, Editor, p. 353, 393, Reidel, Dordecht (1980); S. Etemad, A. J. Heeger, and A. G. MacDiarmid, "Annual Reviews of Physical Chemistry," Vol. 33, p. 443, In press.
2. T.-C. Chung, A. Feldblum, A. J. Heeger, and A. G. MacDiarmid, *J. Chem. Phys.*, **74**, 5504 (1981).
3. P. J. Nigrey, A. G. MacDiarmid, and A. J. Heeger, *J. Chem. Soc. Chem. Commun.*, 594 (1979).
4. Y. W. Park, A. J. Heeger, M. A. Druy, and A. G. MacDiarmid, *J. Chem. Phys.*, **73**, 946 (1980).
5. C. K. Chiang, C. R. Fincher, Jr., Y. W. Park, A. J. Heeger, H. Shirakawa, E. J. Lowis, S. C. Gau, and A. G. MacDiarmid, *Phys. Rev. Lett.*, **39**, 1098 (1977).
6. D. Moses, A. Feldblum, E. Ehrenfreund, A. J. Heeger, T.-C. Chung, and A. G. MacDiarmid, *Phys. Rev. B*, **26**, 3361 (1982).
7. A. Feldblum, J. H. Kaufman, S. Etemad, A. J. Heeger, T.-C. Chung, and A. G. MacDiarmid, *ibid.*, **26**, 815 (1982).
8. D. MacInnes, Jr., M. A. Druy, P. J. Nigrey, D. P. Nairns, A. G. MacDiarmid, and A. J. Heeger, *J. Chem. Soc. Chem. Commun.*, 317 (1981).
9. P. J. Nigrey, D. MacInnes, Jr., D. P. Nairns, A. G. MacDiarmid, and A. J. Heeger, *This Journal*, **128**, 1651 (1981).
10. K. Kaneto, M. Maxfield, D. P. Nairns, A. G. MacDiarmid, and A. J. Heeger, *J. Chem. Soc. Faraday Trans.*, **78**, 3417 (1982).
11. T. Ito, H. Shirakawa, and S. Ikeda, *J. Polym. Sci.*, **13**, 1943 (1975); H. Shirakawa and S. Ikeda, *Synthetic Metals*, **1**, 175 (1979/80).
12. F. E. Karasz, J. C. W. Chien, R. Galkiewicz, G. E. Wnek, A. J. Heeger, and A. G. MacDiarmid, *Nature*, **282**, 286 (1979).
13. M. Aldissi, Ph.D. Thesis, Montpellier, France (1981).
14. R. Kaner, A. G. MacDiarmid, and A. J. Heeger, Paper 27 presented at The Electrochemical Society Meeting, Detroit, Michigan, October 17-21, 1982.
15. J. H. Kaufman, J. W. Kaufer, A. J. Heeger, R. Kaner, and A. G. MacDiarmid, *Phys. Rev. B*, Rapid Communications, **26**, 2327 (1982).
16. W. Jost, "Diffusion in Solids, Liquids and Gases," Academic Press, New York (1960).
17. W. Weppner and R. A. Huggins, *Ann. Rev. Mater. Sci.*, **8**, 269 (1981).

Studies of the Reduction of Oxygen on Gold in Molten Li_2CO_3-K_2CO_3 at 650°C

W. M. Vogel,* S. W. Smith,* and L. J. Bregoli

United Technologies Corporation, Power Systems Division, South Windsor, Connecticut 06074

ABSTRACT

Limiting currents obtained with rotating gold wire cathodes indicate that oxygen dissolves in Li, K carbonate melt predominantly as superoxide. The reduction of dissolved oxygen proceeds at polarizations only moderately larger than the diffusion overvoltage for the complete reduction of superoxide. The remaining polarization can be rationalized as mostly ionic concentration overvoltage. In some experiments, a second wave is observed which appears to be due to some cathodic process which does not involve oxygen.

A summary of previous work on the reduction of oxygen in molten carbonates has been given by Appleby and Nicholson (1). The same workers also studied the reaction in Li_2CO_3 on gold (1) and in the ternary Li, Na, K eutectic on gold and on silver (2, 3). Silver is a rather special case, presumably because of the large solubility of oxygen in this metal. The essential findings were that dissolved molecular O_2 can be neglected as primary (diffusing) species. The cath-

* Electrochemical Society Active Member.

odic current was stated to be due to successive reduction of peroxide and superoxide formed by chemical reaction of oxygen with the melt. The reaction was reported to be further complicated by the slow reaction of oxide ions with dissolved CO_2 to $CO_3^=$. The cation composition was of major importance for the kinetics of the reaction. The present work was undertaken to further elucidate the oxygen reduction mechanism with the binary melt 62 mol/percent (m/o) Li_2CO_3-38 m/o K_2CO_3 because of the importance of this electrolyte for molten carbonate fuel cells. Because of the indicated complex nature of the dissolved reactant, particular attention was paid to the control and selection of the O_2-CO_2 mixtures.

Separate studies of the oxygen solubilities (4) have quantified the findings of Appleby and Nicholson with regard to the nature of oxygen dissolved in this melt at 650°C. The total solubility should obey Eq. [1]

$$S = kP_{O_2} + 0.5\,K_1 P_{O_2}^{0.5}/P_{CO_2} + 0.75\,K_2 P_{O_2}^{0.75}/P_{CO_2}^{0.5}, \text{ equiv. mol } O_2/cm^3 \quad [1]$$

In Eq. [1], k is the Henry's law constant for molecular O_2, and K_1 and K_2 are equilibrium constants for the formation of peroxide and superoxide, respectively

$$K_1 \equiv (O_2^=)\,P_{CO_2}/P_{O_2}^{0.5}, \quad K_2 \equiv (O_2^-)\,P_{CO_2}^{0.5}/P_{O_2}^{0.75} \quad [2]$$

The solubility data was explained nearly equally well with

$$k_1 \sim 0, \quad K_1 \sim 3.2 \cdot 10^{-8} \text{ mol atm}^{0.5}/cm^3, \quad K_2 \sim 1.5 \cdot 10^{-7} \text{ mol}/cm^3 \text{ atm}^{0.25} \quad [3a]$$

or with

$$k \sim 0, \quad K_1 << K_2 \sim 2.5 \cdot 10^{-7}, \text{ mol}/cm^3 \text{ atm}^{0.25} \quad [3b]$$

These results indicate that superoxide is the reactive oxygen species in the melt under most conditions according to

$$(O_2^-)/(O_2^=) = \frac{K_2}{K_1}\,(P_{O_2}^{0.5}\,P_{CO_2})^{0.5} \geq 4.7\,(P_{O_2}^{0.5}\,P_{CO_2})^{0.5}, \text{ equiv./equiv.} \quad [4]$$

The present experiments were extended to very small reactant pressures in order to vary the ratio of reactants.

Experimental

The apparatus used is shown schematically in Fig. 1a. The electrolyte (approx. 300 cm^3) is contained in an alumina beaker (99.8% Al_2O_3), which is placed inside an Incoloy 800 container. A cover for the container carries all of the cell components and is sealed with a graphite gasket. The apparatus is heated in a crucible furnace controlled by a thermocouple between the container wall and the furnace elements; the temperature of the melt is measured by a thermocouple in an Al_2O_3 tube immersed in the melt.

The design of the working electrode is shown in Fig. 1b. It is rotated by a belt drive apparatus to a maximum capability of 10,000 rpm. Several electrode shapes were evaluated, with the one shown giving the most consistent results and used to take the data reported here. Because of the lack of strength of Au at operating temperature, it was necessary to use a relatively short electrode of large diameter (1 cm × 0.1 cm). Formation of a meniscus electrode inside the tube was prevented by choosing the wire and tube diameter such that a solid plug was formed which sealed the system.

The reference electrode and counterelectrode were both contained in Al_2O_3 tubes which communicate with the solution through a packed bed of crushed Al_2O_3 and a small slit cut in the side of the tube. The reference electrode consisted of a partially immersed gold-

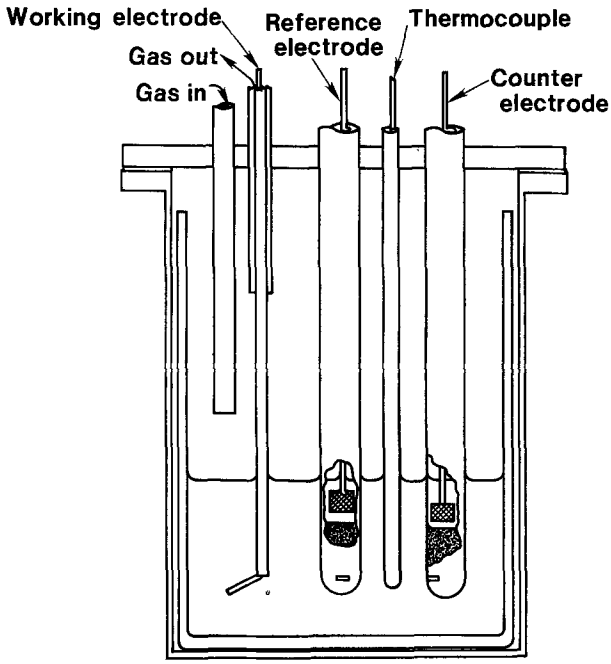

Fig. 1a. Schematic description of test apparatus

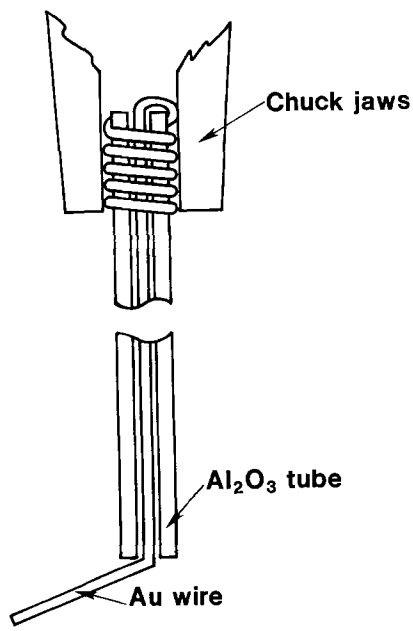

Fig. 1b. Details of electrode construction

wire under 1/3 atm O_2-2/3 atm CO_2. The furnace, rotator, and electrochemical cell were all attached to a common frame which made a solid connection from the working electrode to the rotator possible.

All experiments were conducted at 650°C in 62 m/o Li_2CO_3-38 m/o K_2CO_3. The salts used were reagent grade and were further purified to remove iron and sulfur. The iron was removed by treating the melt with O_2 to precipitate an insoluble oxide which was removed from the solid mass after freezing. The solids were crushed, remelted, and treated with H_2 for several days to remove sulfur. The gases were primarily of "high purity" grade, although several grades of CO_2 were evaluated to obtain minimum residual currents. Gas mixing was done with a Matheson Model 8249 mass flow controller.

The polarization data were taken at a sweep rate of 100 mV/min or with each point held for 5 min. These two techniques gave the same results. Higher rotation rates were not used because of the problem of keeping the wire shape constant.

Results and Discussion

The steady-state polarization curves show essentially two waves, the second one barely observable in some experiments, see Fig. 2. The first wave starts at the thermodynamic potential of the oxygen electrode and has a polarization not much larger than the concentration overvoltage for a two or three electron process

$$\eta_c = \frac{RT}{nF} \ln (1 - i/i_{lim}) \quad n = 2 \text{ or } 3 \qquad [5]$$

The limiting current of the first wave varied accurately with square root of rotational speed and is therefore diffusion controlled.

Values of limiting currents at 1600 rpm of the first wave are given in Table I. The currents in this wave are related to oxygen reduction since the wave disappears under oxygen-free CO_2 as is shown in Fig. 3.

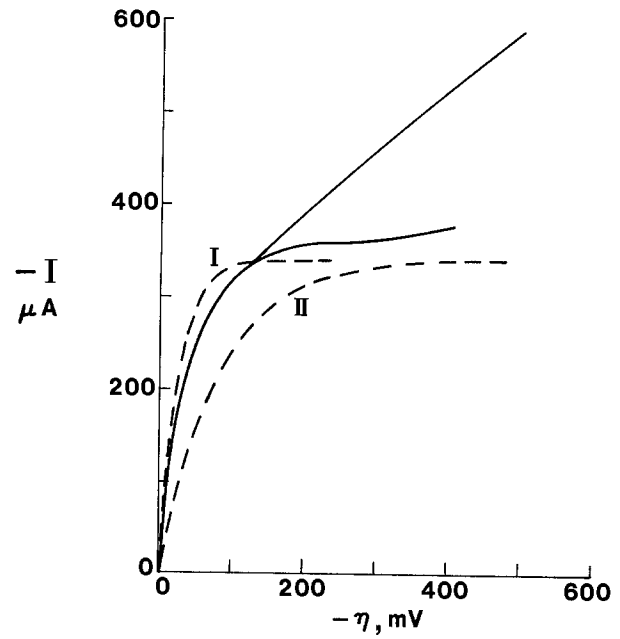

Fig. 2. Irreproducibility of second wave. Two experiments in supposedly similar melt batches. $P_{O_2} = 0.04$ atm, $P_{CO_2} = 0.0004$ atm, 400 rpm. Dashed lines: (I) calculated from Eq. [5] with $n = 3$, (II) with $n = 1$.

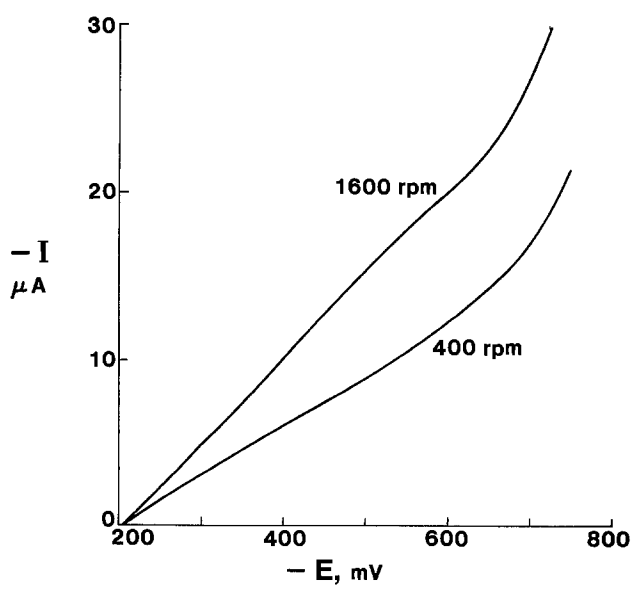

Fig. 3. Currents at $P_{CO_2} = 1$ atm, after best efforts to eliminate oxygen traces.

Table I. Limiting currents at 1600 rpm

P_{O_2} (atm)	P_{CO_2} (atm)	$-I_{lim}$ (1600 rpm)
0.64	0.0016	2290
0.64	0.0019	2030
0.33	0.67	80
0.296	0.098	106
0.16	0.0008	1260
0.16	0.0011	1070
0.16	0.0032	590
0.101	0.0016	615
0.0635	0.0008	750
0.074	0.098	48
0.04	0.0004	960
0.04	0.0007	670
0.04	0.0016	300
0.04	0.0032	200
0.04	0.0064	135
0.04	0.0256	68
0.04	0.1025	37
0.03	0.20	26
0.0076	0.01	40
0.0076	0.10	16
0.003	0.063	12

If the ocp for this case is assumed to be the equilibrium O_2 potential, the gas used would be calculated to contain about 5 ppm O_2. The corresponding oxygen concentration in the melt would be of the order $5 \cdot 10^{-11}$ mol O_2/cm^3 according to Eq. [1]. The data in Fig. 3 represent the best effort to eliminate all potential sources of trace oxygen from the counterelectrode, the reference electrode, and air leaks.

The limiting currents of the first wave could be due to the reduction of O_2^-, of $O_2^=$, or of both species simultaneously. In the latter case, a plot of the data in the table according to Eq. [6] should yield a straight line

$$I_{lim} P_{CO_2}/P_{O_2}^{0.5} = \text{const.} [K_1 \cdot D_{O_2^=} + K_2 D_{O_2^-} \cdot P_{O_2}^{0.25} P_{CO_2}^{0.5}] \qquad [6]$$

The plot is shown in Fig. 4. Not shown in the figure is the point for $P_{O_2} = 0.33$, $P_{CO_2} = 0.67$, which lies on the straight line at $P_{O_2}^{0.25} P_{CO_2}^{0.5} = 0.62$. From the slope and ordinate intercept of the line

$$K_2 \cdot D_{O_2^-} >> K_1 \cdot D_{O_2^=} \qquad [7]$$

This result indicates that superoxide is the predominant diffusing and electroactive species in the first wave. Equation [7] does not indicate if peroxide is present in the bulk melt in significant concentration, but is not reduced in the first wave.

The reduction of O_2^- appears to be complete in the first wave. If O_2^- were reduced to peroxide, it should be completely reduced at larger polarization in a second wave, and the latter should increase in proportion to the first wave. This has not been observed. Furthermore, the oxidant diffusion overvoltage due to partial reduction of O_2^- can be calculated from the observed limiting currents, using Eq. [5] with $n = 1$. An example is given in Fig. 2 as dashed line II. The calculated

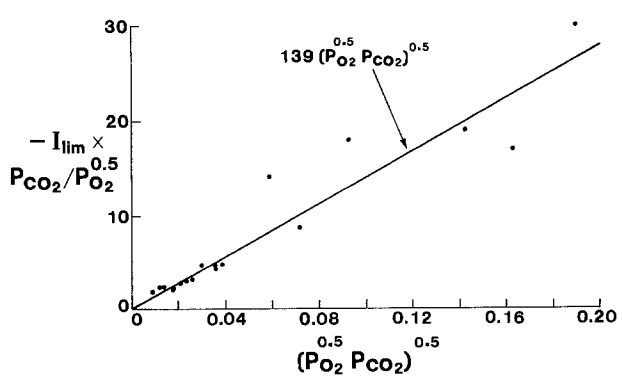

Fig. 4. Limiting currents at 1600 rpm, plotted assuming O_2^- and $O_2^=$ as diffusing species.

overvoltage is larger than the observed one, which makes no sense. Using the value $n = 3$ for complete reduction of O_2^- results in curve I in Fig. 2. Thus, the first wave is explained by essentially diffusion controlled and complete reduction of superoxide.

As has been mentioned, the resulting Eq. [7] leaves open the possibility that peroxide is present in the bulk melt, but that it is not reduced in the first wave. If this is true, $O_2^=$ should be reduced at larger polarization, *i.e.*, in a second wave. If P_{CO_2} is increased at constant P_{O_2}, the equilibrium concentrations of O_2^- and $O_2^=$ decrease, with the decrease in $(O_2^=)$ being more pronounced according to Eq. [4]. If the observed second wave were due to bulk peroxide reduction, it should decrease more than the first wave on such variation in gas composition. Results of relevant tests are shown in Fig. 5 for $P_{O_2} = 0.04$ atm. The first wave varies with $P_{CO_2}^{0.5}$, *i.e.*, with the superoxide concentration. The second wave should decrease with $P_{CO_2}^{-1}$, *i.e.*, by the factor 64 in the sequence $P_{CO_2} = 0.0016$ to 0.1024 atm. In actual fact, it remained approximately constant, indicating that the second wave does not represent the reduction of bulk peroxide. These results suggest that the second wave is not due to peroxide reduction, be it bulk peroxide or $O_2^=$ produced by partial reduction of O_2^- in the first wave.

The second wave in fact is very difficult to explain. It was found to be very irreproducible unless the same batch of the same age was used. It was essentially absent in some tests, but very pronounced in others as can be seen in Fig. 2. When observed, the second wave showed large polarization and no limiting current to potentials where CO_2 reduction commences. It is concluded that this wave is due to some other process not involving oxygen. This would also explain the results in Fig. 3 for extremely small O_2 and large CO_2 pressures.

Neglected in the discussion so far has been the very important role of CO_2 in the oxygen reduction. Owing to the small solubility of molecular CO_2, molten carbonate can be compared with a salt solution of small pH-buffer capacity. In such a solution, an H^+-consuming reaction such as the evolution of H_2 does not yield a cathodic H^+-limiting current. Rather, the polarization curve shows an inflection which corresponds to the change from the acidic to the alkaline hydrogen reaction (5). Similarly, CO_2-diffusion too slow to sustain the formation of carbonate should not result in a CO_2-limiting current, but in an inflection corresponding to the change from Eq. [8] to [9]

$$O_2^- + 2CO_2 + 3e^- = 2CO_3^= \quad [8]$$

$$O_2^- + 3e^- = 2O^= \quad [9]$$

Equations [8] and [9] are coupled by the acid/base reaction

$$O^= + CO_2 = CO_3^= \quad [10]$$

The combined oxidant and ionic diffusion overvoltage is derived by assuming equilibrium of Eq. [8]-[10]. The overvoltage is now

$$\eta_d = \frac{RT}{3F} \ln \frac{(O_2^-)}{(O_2^-)_o} \left[\frac{(O^=)_o}{(O^=)} \right]^2 = \frac{RT}{3F} \ln \frac{(O_2^-)}{(O_2^-)_o} \left[\frac{(CO_2)}{(CO_2)_o} \right]^2 \quad [11]$$

The index/suffix (o) indicates the values in the bulk melt. The ratio $(O_2^-)/(O_2^=)_o$ is calculated from the observed limiting current using Fick's law

$$\frac{(O_2^-)}{(O_2^-)_o} = 1 - \frac{i}{i_{lim}} \quad [12]$$

The ratios $(O^=)_o/(O^=)$ and $(CO_2)/(CO_2)_o$ are equal and are derived as follows. The current density is equal to the combined fluxes of $O^=$ and CO_2

$$i = \frac{1.5FD_{O^=}}{\delta} [(O^=)_o - (O^=)] + \frac{1.5FD_{CO_2}}{\delta} [(CO_2) - (CO_2)_o] \quad [13]$$

Introducing the following formal limiting currents

$$i_{O^=} = \frac{1.5FD_{O^=}}{\delta} (O^=)_o \quad [14]$$

$$i_{CO_2} = \frac{-1.5FD_{CO_2}}{\delta} (CO_2)_o \quad [15]$$

Equation [13] can be written in the form

$$i = i_{O^=} \left[1 - \frac{(O^=)}{(O^=)_o} \right] + i_{CO_2} \left[1 - \frac{(O^=)_o}{(O^=)} \right] \quad [16]$$

Equation [16] yields

$$2\frac{(O^=)}{(O^=)_o} = 1 + \frac{i_{CO_2}}{i_{O^=}} - \frac{i}{i_{O^=}} + \left[\left(1 + \frac{i_{CO_2}}{i_{O^=}} - \frac{i}{i_{O^=}} \right)^2 - 4\frac{i_{CO_2}}{i_{O^=}} \right]^{1/2} \quad [17]$$

The polarization curve for pure diffusion overvoltage can be calculated from Eq. [11] using Eq. [12] and [17] provided $i_{O^=}$ and i_{CO_2} are known. For certain combinations of the three limiting currents, single waves are calculated, for other values a double wave. All curves end in the O_2^- limiting current.

Such changes had been expected in the tests which produced the curves in Fig. 5. In these tests, the ratio of superoxide to CO_2 concentration in the melt varied from 170 (at 0.0004 atm CO_2) to 0.04 (at 0.1024 atm CO_2). These values were calculated with the value of Eq. [3b] for K_2, and the Henry's law constant of CO_2, $k = 10^{-5}$ mol/cm^3 atm (6, 7). Despite the very large range of the ratio $(O_2^-)/(CO_2)$, little change and certainly no inflection is seen in the shape of the curves in Fig. 5. The reason, presumably, is that changes in P_{CO_2} at constant P_{O_2} do not simply change i_{CO_2} and $i_{O^=}$ in opposite directions, but that the superoxide concentration also changes. Because of this, the transition from a single wave at low P_{CO_2} (Eq. [9]) to a single

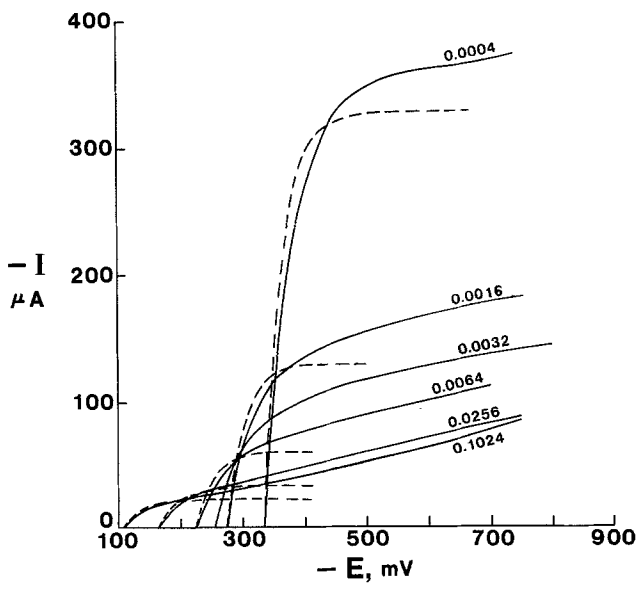

Fig. 5. Steady-state polarization curves at 400 rpm. $P_{O_2} = 0.04$ atm, P_{CO_2} as indicated. Dashed lines calculated from Eq. [5] with $n = 3$.

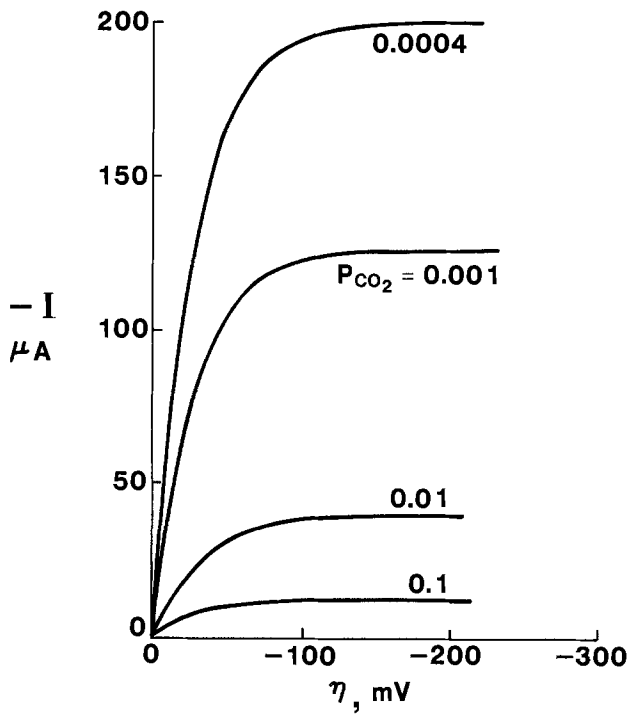

Fig. 6. Concentration overvoltage calculated from Eq. [11], [12], and [17] with $i_{CO_2} = 1500\ P_{CO_2}$, $i_{O^=} = 1.5/P_{CO_2}$, $i_{O_2^-} = 4/P_{CO_2}^{1/2}$ for $P_{O_2} = 0.04$ atm.

wave at large P_{CO_2} (Eq. [8]) may have occurred without a noticeable double wave at intermediate CO_2 pressures. This possibility is demonstrated in Fig. 6 which was calculated from Eq. [11], [12], and [17] with the following assumed values

$$F/\delta = 10^{13},\ \mu A\ sec/cm\ equiv.$$

$$D_{CO_2} k_{CO_2} = 10^{-10},\ mol/cm\ sec\ atm$$

$$K_2 \cdot D_{O_2^-} = 1.5 \times 10^{-12},\ mol/cm^3\ sec\ atm^{1/4}$$

$$K_B \cdot D_{O^=} = 10^{-13},\ mol\ atm/cm\ sec$$

where K_B is the equilibrium constant of Eq. [10]. The curves in Fig. 6 resemble the experimental ones in Fig. 5. No attempts at better fitting the latter were made because of the large number of unknown constants which have to be used. An experimentally determined value is available only for K_2 (Eq. [3]). Values for k_{CO_2} (6) and K_B (8) apply to ternary melts containing Li, Na, K-carbonate.

Conclusions

Oxygen dissolves in fused Li, K-carbonate (62 m/o Li) primarily as superoxide with some peroxide present at very small CO_2 pressures. Molecular O_2 is negligible in the melt. The dissolved oxygen is reduced completely on gold in a single wave. The polarization is moderately larger than the superoxide diffusion overvoltage. The difference appears to be mainly ionic concentration overvoltage for submerged electrodes.

Acknowledgments

The present study was supported by the Electric Power Research Institute under contract RP-1085-4. Dr. A. J. Appleby was the EPRI Project Manager for this contract; his suggestions and support are appreciated.

Manuscript submitted Aug. 3, 1981; revised manuscript received April 23, 1982.

Any discussion of this paper will appear in a Discussion Section to be published in the December 1983 JOURNAL. All discussions for the December 1983 Discussion Section should be submitted by Aug. 1, 1983.

Publication costs of this article were assisted by United Technologies Corporation.

REFERENCES

1. A. J. Appleby and S. B. Nicholson, *J. Electroanal. Chem.*, **53**, 105 (1974).
2. A. J. Appleby and S. B. Nicholson, *ibid.*, **83**, 309 (1977).
3. A. J. Appleby and S. B. Nicholson, *This Journal*, **127**, 759 (1980).
4. S. W. Smith, W. M. Vogel, and S. M. Kapelner, *ibid.*, In press.
5. See *e.g.*, K. Vetter, "Electrochemical Kinetics," Academic Press, New York (1967); E. Lange and H. Göhr, "Thermodyamische Electrochemie," p. 251, A. Huthig Verlag, Heidelberg (1962).
6. G. H. J. Broers, M. Schenke, and H. J. J. van Ballegoy, Ext. Abstr. No. II 77, 20th ISE Meeting, Druzhba, Bulgaria, Sept. 1977.
7. A. J. Appleby and C. van Drunen, *This Journal*, **127**, 1655 (1980).
8. N. Busson, S. Palous, J. Millet, and R. Buvet, *Electrochim. Acta*, **12**, 1609 (1967).

Structural and Compositional Characterization of Mixed CdS-CdSe Films Grown by Cathodic Electrodeposition

Andrzej S. Baranski, W. Ronald Fawcett,* Kazimierz Gatner, and Alex C. McDonald*

The Guelph-Waterloo Centre for Graduate Work in Chemistry, Department of Chemistry, University of Guelph, Guelph, Ontario, Canada N1G 2W1

and Jack R. MacDonald and Mats Selen

Department of Physics, University of Guelph, Guelph, Ontario, Canada N1G 2W1

ABSTRACT

Mixed CdS-CdSe films have been electrodeposited cathodically from DMSO solutions containing cadmium chloride, elemental sulfur and elemental selenium. The mixed films were characterized structurally using x-ray diffraction, scanning electron microscopy, and Rutherford backscattering spectrometry. The photoelectrochemical response of the CdS-CdSe material was studied in a photoelectrochemical cell with a sulfide-polysulfide electrolyte. It has been found that the composition and optical bandgap of the CdS-CdSe films can be varied by changing the composition of the deposition solution. However, the films with higher CdSe content are amorphous, and have a higher resistivity than pure CdS.

The cathodic electrodeposition of thin films of CdS and other metal chalcogenides on metal substrates from nonaqueous electrolyte solutions has been discussed previously (1, 2). This simple technique allows one to fabricate CdS films exhibiting a high degree of crystallinity and continuity, in a physical configuration suitable for direct incorporation into photovoltaic and photoelectrochemical cells (PEC). Since the bandgap of CdS is rather large (2.4 eV) for efficient utilization of incident solar radiation, it is desirable to examine composite CdS-CdSe materials with smaller bandgaps (1.7-2.4 eV).

There has been some interest in mixed n-type CdS-CdSe (3, 4) and CdSe (5) electrodes for incorporation into PEC's. The maximum theoretical efficiency of a PEC for illumination with light at the bandgap energy (6) can be expressed as

$$\eta = \frac{(V_{redox} - V_{FB})\mathbf{F}}{E_g} = \frac{V_{oc}\mathbf{F}}{E_g} \qquad [1]$$

where V_{redox} is the equilibrium potential of the redox couple in the electrolyte, V_{FB}, the flatband potential of the semiconductor in the electrolyte, V_{oc}, the open-circuit voltage, E_g, the bandgap of the semiconductor, and **F**, the Faraday. Both the maximum open-circuit voltage and the efficiency of the device are functions of V_{FB} and E_g. It has been shown that V_{FB} of CdX films can be shifted significantly in the cathodic direction in aqueous electrolytes containing S^{2-} (7), and that the degree of shift is a function of the composition of the mixed CdS-CdSe material (3, 4). Thus, the efficiency of such a solar device may be optimized by the manipulation of the composition of the semiconductor electrode, and hence V_{FB} and E_g. It has also been suggested that high efficiency PEC's could be obtained through the use of CdS-CdSe electrodes with a gradient composition as a function of depth (3). This gradient may allow a maximization of V_{oc} through an advantageous shift in V_{FB} achieved by altering the surface composition of the film, and a minimization of E_g on the basis of optimizing the composition of the bulk of the film.

It has been found that smooth coherent polycrystalline and amorphous films of CdS_xSe_y can be cathodically electrodeposited on metal substrates from a dimethylsulfoxide (DMSO) electrolyte solution containing cadmium chloride, elemental sulfur, and elemental selenium. The composition of the mixed semiconductor films may be altered, by varying the parameters controlling the electrodeposition of the films, and the concentration of Se in the electrolyte solution. The results of a characterization of the structural properties of the electrodeposited CdS_xSe_y films and measurements of E_g in aqueous electrolytes containing Na_2S and elemental S are presented in this paper.

* Electrochemical Society Active Member.

Key words: electrodeposition of semiconductors, CdS-CdSe films, semiconductor films.

Experimental

All CdS_xSe_y films were electrodeposited on smooth substrates of high purity Pt sputtered on glass. The preparation of the Pt substrate has been described elsewhere (2). The configuration of the cell and the procedure used for the electrolysis were identical to those described for the electrodeposition of the CdS films (1, 2). The electrolyte solution consisted of 0.055M $CdCl_2$, and 0.19M S with a varying concentration of Se in reagent grade DMSO. The temperature of the electrolyte solution was held constant by immersing the cell in an oil bath whose temperature was maintained at 110°C by a temperature controller/circulator.

The structural properties and composition of deposited SdS_xSe_y films were examined using electron microscopy, x-ray crystallography, Rutherford backscattering spectroscopy, and thickness measurements as described previously (2). Selected CdS_xSe_y films were incorporated into a photoelectrochemical cell, using a Pt counterelectrode and saturated calomel electrode reference. The aqueous electrolyte solution contained 1.0M NaOH, 1.0M Na_2S and 0.01M S. The cells were illuminated with a 1000W xenon lamp through a 7.0 cm H_2O infrared filter. All photocurrent outputs were corrected for the power against wavelength output of the lamp. For comparison purposes, the photoresponse for a CdSe film electrodeposited from an aqueous solution was also measured. In this case, the electrodeposition solution consisted of 2g $CdSO_4$, and ~1g H_2SeO_3 in 100 ml of 0.1M H_2SO_4 (9); the film was deposited at a current density of 15 mA cm^{-2} for 600 sec, the temperature of the bath being 60°C. It was annealed in argon for 1 hr at 400°C. No attempt was made to anneal films electrodeposited from DMSO because of problems with cracking.

Results and Discussion

The CdS_xSe_y films electrodeposited by the method described above appeared very smooth and uniform and exhibited extremely good adhesion to the Pt substrate. The color of the films was a function of the Se concentration in the electrolyte solution, ranging from the familiar yellow-gold of CdS for [Se] = 0 to a dark reddish-purple for films deposited from the solution saturated with Se (approximately 0.01M Se) at 110°C.

Electron micrographs of typical films grown from electrolyte solutions containing a range of Se concentrations are shown in Fig. 1. A transition from crystalline, highly cracked films (Fig. 1a) to smooth, glass-like films (Fig. 1d) was observed as the Se concentration in the electrolyte solution was increased from 0.0025M to saturation. This transition from a highly structured to an amorphous film upon incorporation of Se is also evident from the x-ray diffractometer pattern of the same series of films (Fig. 2a-2d). As the Se concentration was increased, the intense peak at $2\theta \simeq 32°$, which is attributed to CdS,[1] became less intense, until it disappeared for a film grown from a solution saturated with Se. The extraneous peaks at 36.5° and 38° are due to a limited degree of orientation of the underlying substrate Pt.

Plots of the voltage applied to the cell during deposition against the time of deposition are shown in Fig. 3. The increase in the slope of the V against t plots with

[1] Further x-ray analysis of the electrodeposited CdS films described in Ref. (2) has indicated that the CdS has a hexagonal structure. The intense peak in the x-ray pattern (see Fig. 2) at $2\theta \simeq 32°$ is due to secondary reflection from the 001 planes indicating that the crystallites are oriented with their c-axes perpendicular to the substrate.

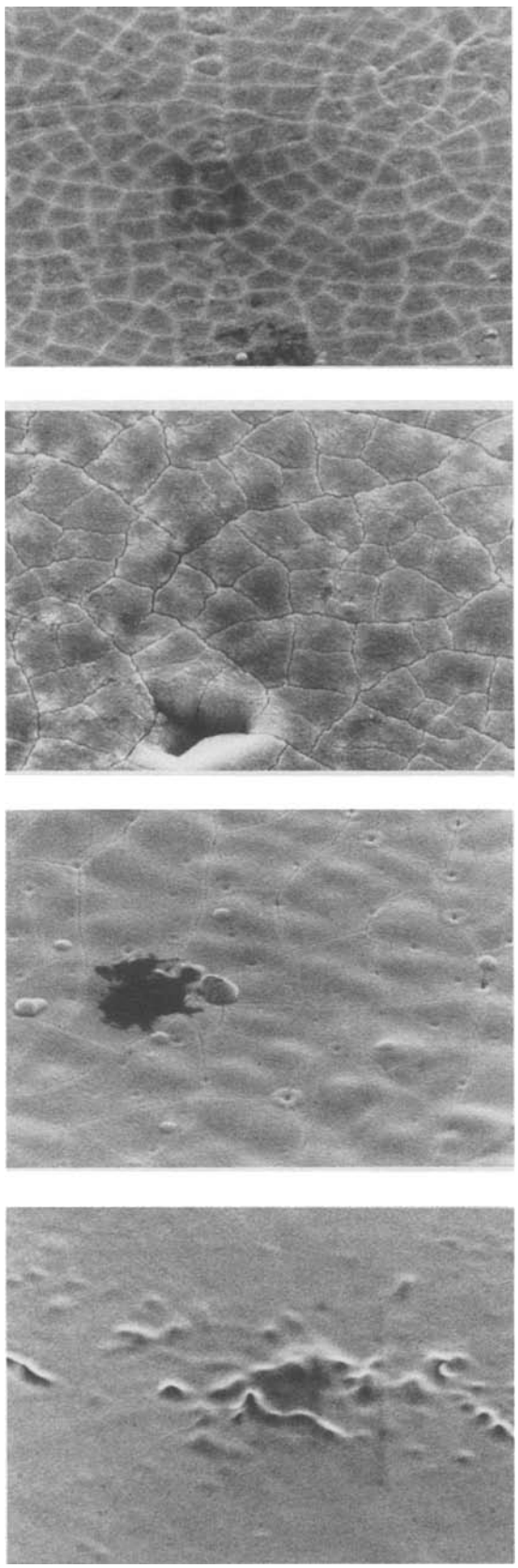

Fig. 1. Electron micrographs of CdS_xSe_y films deposited on Pt from DMSO electrolyte solutions containing 0.020M sulfur, 0.055M $CdCl_2$, and (a) 0.0025M Se (mag 5000×); (b) 0.0040M Se (mag 7900×); (c) 0.0050M Se (mag 5230×); (d) sat. Se at 110°C (mag 5340×).

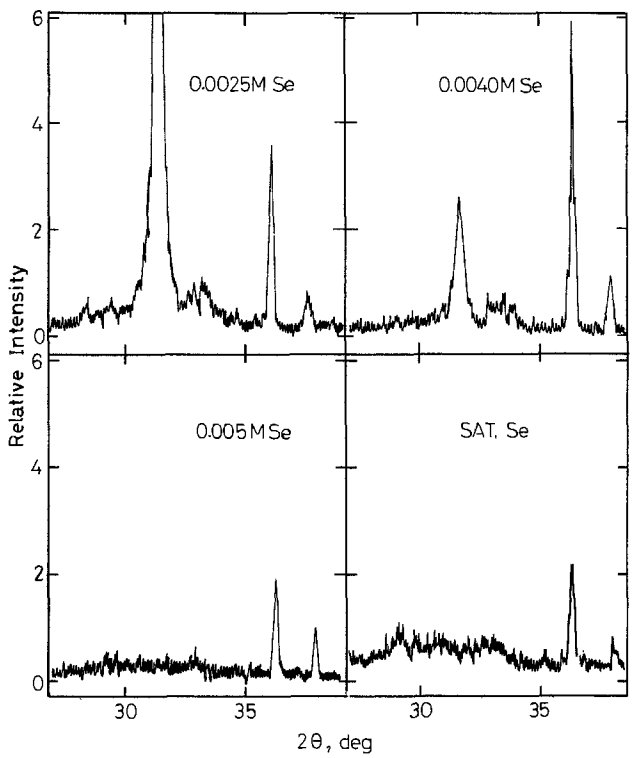

Fig. 2. X-ray diffractometer patterns of CdS_xSe_y films deposited on Pt from DMSO electrolyte solutions, containing various concentrations of Se as indicated (Co, K_α emission).

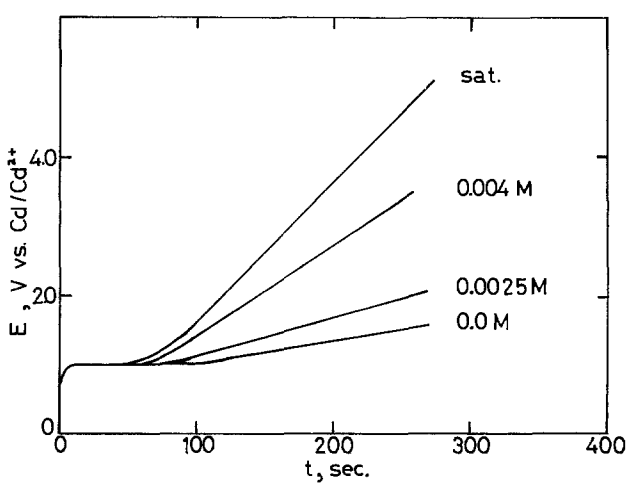

Fig. 3. Voltage against deposition time during deposition of CdS_xSe_y on Pt from electrolyte solutions, containing various concentrations of Se as indicated. The current density was 2.5 mA cm^{-2} and the temperature, 110°C.

increase in the Se concentration in the electrolyte indicates that the resistivity of the films also increases. This result is also consistent with the decrease in the degree of crystallinity of the CdS_xSe_y deposit with increasing Se concentration. Attempts to measure resistivities were not successful, due to the difficulty in making ohmic contacts to the thin films. The average film thickness as a function of applied current density during deposition and as a function of the time of deposition is shown in Fig. 4 for varying Se concentrations. The decrease in slope at both long deposition time and high current density with increasing Se concentration probably reflects a lower efficiency of deposition of CdS_xSe_y, with respect to that for CdS. These results suggest that the rate of film formation depends on the nature of the chalcogen involved.

A plot of the average CdS_xSe_y film thickness against the solution temperature during deposition for films grown from the electrolyte solution saturated with Se is shown in Fig. 5. The composition of the same series of films as determined by Rutherford backscattering spectrometry (8) is summarized in Table I (see also Fig. 6). The films grown at temperatures in the range from 350-390 K appeared to have the highest quality and uniformity, and exhibited good adhesion to the substrate. It is significant that the ratio of total chalcogen to cadmium in these films remains approximately constant and stoichiometric over this temperature range.

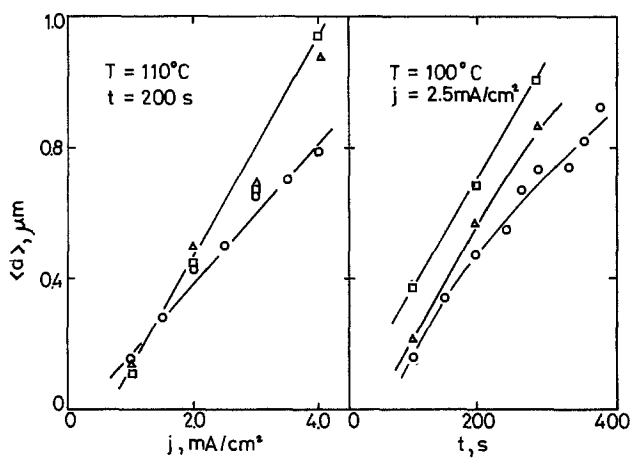

Fig. 4. Average thickness of CdS_xSe_y films deposited on Pt from electrolyte solutions containing 0.020M sulfur, 0.055M $CdCl_2$, and 0.0025M Se (□), 0.0040M Se (△), or sat. Se (○) at 110°C against current density, j. Deposition time and solution temperature were held constant as indicated.

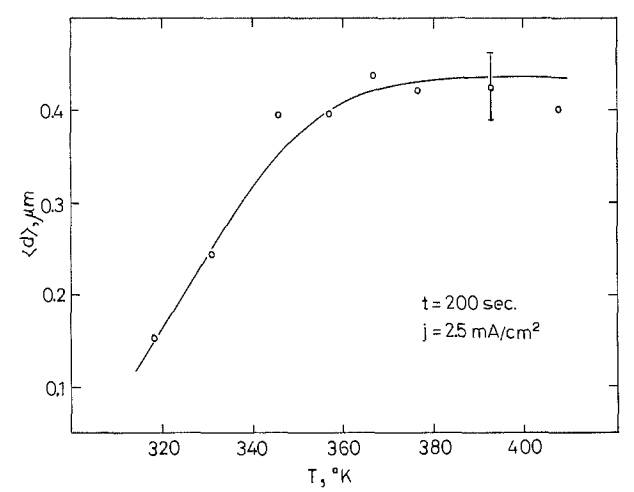

Fig. 5. Average thickness of CdS_xSe_y films deposited on Pt from electrolyte solutions containing 0.020M sulfur, 0.055M $CdCl_2$, and saturated with Se against solution temperature. Current density and deposition time were held constant as indicated.

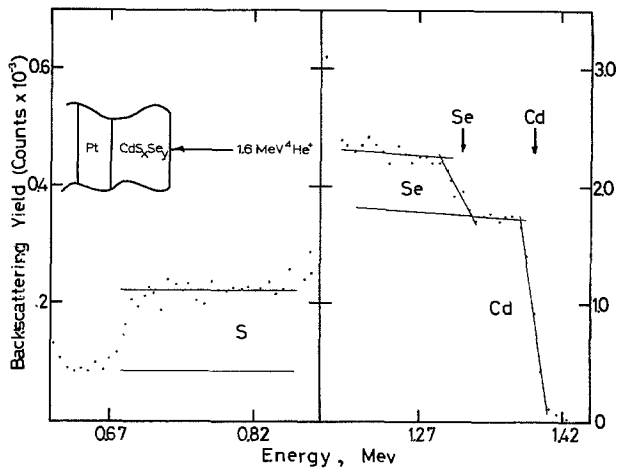

Fig. 6. Rutherford spectrum of backscattered α particles from a CdS_xSe_y film on Pt in the energy ranges 0.60-0.85 MeV and 1.15-1.43 MeV, corresponding to scattering from S and Se, Cd atoms respectively.

In Fig. 7, the S/Cd ratio is plotted against the Se/Cd ratio for a variety of CdS_xSe_y films grown from solutions with a range of Se content. Although there is considerable scatter in these results, there is a general trend of increasing Se/Cd ratio with decreasing S/Cd ratio. This result may indicate that the mechanisms by which the chalcogens, S and Se, are incorporated into the film are similar. A graph of the Se/Cd concentration ratio in the CdS_xSe_y films is plotted against Se content in the electrolyte solution in Fig. 8. It is apparent that the Se content of the semiconductor can be varied over a wide range by varying its concentration in the electrodeposition solution.

Typical plots of photoresponse against wavelength for selected electrodes in PEC's illuminated by the xenon lamp at 100 mW cm^{-2} are shown in Fig. 9. It was noted that films deposited from aqueous solution had a black porous appearance, as opposed to the

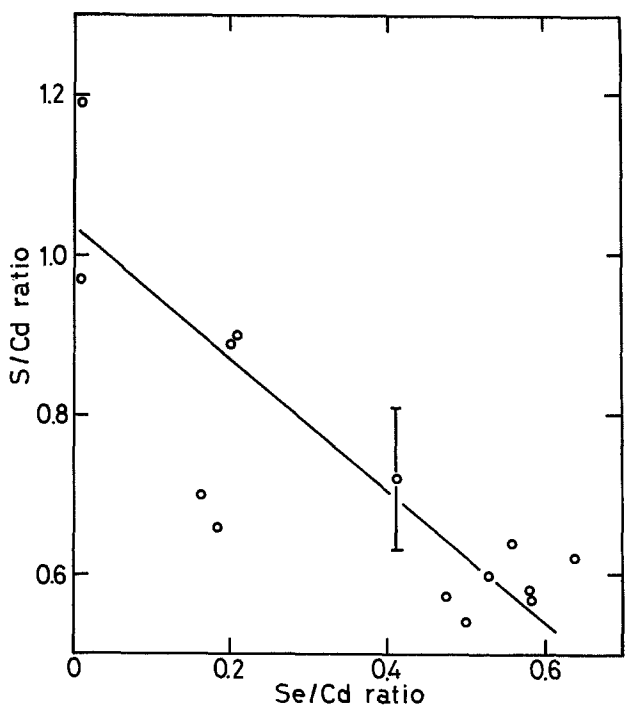

Fig. 7. S/Cd ratio against Se/Cd ratio for CdS_xSe_y films deposited on Pt, from electrolyte solutions containing various concentrations of Se, and at several current densities (from Rutherford backscattering spectrometry).

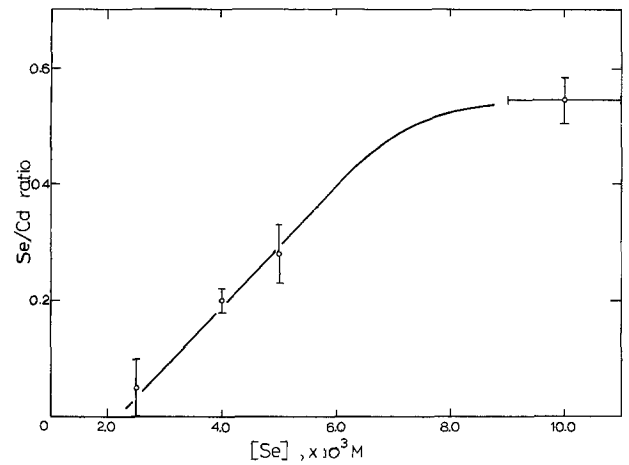

Fig. 8. Se/Cd ratio of CdS_xSe_y films deposited on Pt against Se concentration in electrolyte solution (from Rutherford backscattering spectrometry).

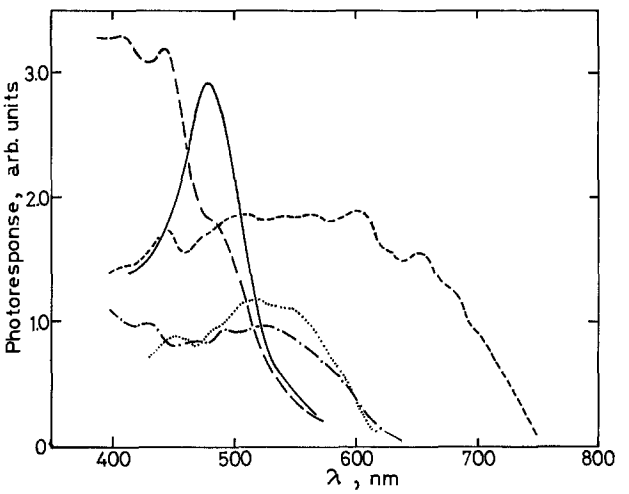

Fig. 9. Relative photoresponse of CdS_xSe_y electrodes in an aqueous solution containing 1.0M NaOH, 1.0M Na_2S, 0.01M S against wavelength of illuminating light: --- CdSe (deposited from aqueous solution), ... CdSe (deposited from DMSO solution saturated with Se at 110°C), — · — $CdS_{0.5}Se_{0.5}$, — — — — $CdS_{0.9}Se_{0.1}$, ——— CdS (deposited from DMSO solution).

smooth glassy appearance of CdSe films deposited from the nonaqueous bath. In recording the photoresponse curve for the sample grown from the aqueous medium, the wavelength was swept rapidly (1 nm sec^{-1}) to prevent any significant effect from surface degradation of the sample, due to S-Se exchange. Values of the bandgap, E_g, estimated from the onset of photoanodic current are summarized in Table II. The decrease in relative photoresponse with increasing Se content is probably due to the increasing resistivity of the films. The reason for the discrepancy between the estimate of E_g for CdSe deposited from DMSO (1.94 eV) and from aqueous solution (1.74 eV) is unclear, but it probably results from the great structural difference between the two materials. Moreover, the estimated bandgaps for all the CdS_xSe_y films are larger than expected on the basis of previously reported data for mixed films (4, 5). This result is probably due to the amorphous character of the electrodeposited material, and may also reflect some incorporated impurities, such as solvent molecules which may be trapped in the film during deposition.

The flatband potential, V_{FB} of the electrodeposited CdS films in the aqueous electrolyte used in the PEC, was determined to be −1.35V against a saturated calomel electrode on the basis of Mott-Schottky plots. Values of V_{FB} for the graded composition CdS_xSe_y material could not be determined precisely in the aqueous electrolyte. It is possible that H_2O interacts strongly with DMSO or its decomposition products incorporated in the films during deposition, thereby altering the adsorption characteristics of the system and making the determination of V_{FB} difficult. A slight negative shift in the onset potential of the PEC's from −1.2 to −1.3 *vs.* SCE was observed as the composition of the anode was changed from CdS_xSe_y to CdS. This shift may be due to a shift in V_{FB} to more negative values as the S content of the films is increased. As pointed out by Noufi *et al.* (3), a film of graded composition with high CdSe content in the bulk to achieve a low bandgap, and high CdS content at the surface to achieve a more negative flatband potential, would be more efficient according to Eq. [1]. The present electrodeposition technique would be ideally suited to the fabrication of such films.

In conclusion, the cathodically electrodeposited CdS_xSe_y films, despite their amorphous nature and high resistivity, are promising materials for incorporation into PEC devices. The films show excellent mechanical stability, and are photoconductive with a composition and bandgap which can be controlled by varying the Se content in the electrodeposition solution. The technique therefore lends itself well to the fabrication of composite electrodes.

Table I. Composition of CdS_xSe_y films as a function of deposition temperature*

T, K	[Se]/[Cd]	[S]/[Cd]	[Se + S]/[Cd]	[S]/[S + Se]
353	0.55	0.55	1.10	0.50
363	0.48	0.58	1.06	0.55
373	0.54	0.56	1.10	0.51
383	0.52	0.55	1.07	0.51

* The deposition solution contained 0.187M S and 0.055M $CdCl_2$, and was saturated with Se; the current density was 2.5 mA cm^{-2} and the growth time, 200 sec.

Table II. Variation in the estimated bandgap, E_g for Cd_xSe_y films in a PEC configuration as a function of film composition*

[Se], M	x	y	E_g, eV
0	1.0	0	2.34
0.0025	0.1	0.9	2.25
0.0040	0.2	0.8	2.25
0.0060	0.4	0.6	2.10
0.0080	0.5	0.5	2.00
Sat.	0.5	0.5	2.00
Sat. ([S] = 0)	0	1.0	1.94

* The deposition solution contained 0.187M S_8 and 0.055M $CdCl_2$; the current density was 2.5 mA cm^{-2}, growth time, 200 sec and temperature, 383 K. The electrolyte solution in the PEC contained 1.0M NaOH, 1.0M Na_2S, and 0.10M S.

Manuscript submitted June 1, 1982; revised manuscript received Sept. 30, 1982.

Any discussion of this paper will appear in a Discussion Section to be published in the December 1983 JOURNAL. All discussions for the December 1983 Discussion Section should be submitted by Aug. 1, 1983.

Publication costs of this article were assisted by the University of Guelph.

REFERENCES

1. A. S. Baranski and W. R. Fawcett, *This Journal*, **127**, 766 (1980).
2. A. S. Baranski, W. R. Fawcett, A. C. McDonald, R. M. de Nobriga, and J. R. MacDonald, *ibid.*, **128**, 963 (1981).
3. R. N. Noufi, P. A. Kohl, and A. J. Bard, *ibid.*, **125**, 375 (1978).
4. R. C. Kainthla, D. K. Pandya, and K. L. Chapra, *ibid.*, **129**, 99 (1982).

5. M. A. Russak, J. Reichman, H. Witzke, S. K. Deb, and S. N. Chen, *ibid.*, **127**, 725 (1980).
6. M. D. Archer, *J. Appl. Electrochem.*, **5**, 17 (1975).
7. T. Inoue, T. Wanatabe, A. Fujishima, and K. Honda, *Bull. Chem. Soc. Jpn.*, **52**, 1243 (1979).
8. W. K. Chu, J. W. Mayer, and M. A. Nicolet, "Backscattering Spectrometry," Academic Press, New York (1978).
9. G. Hodes, J. Manassen, and D. Cahan, *Nature*, **261**, 403 (1976).

Filtration Coefficient and Hydraulic Permeability of Nafion 125 Membranes in Metal Alkali Solutions

C. Fabiani, S. Scuppa, L. Bimbi, and M. De Francesco

E.N.E.A., Divisione Chimica, Laboratorio Chimica Fisica, CRE Casaccia, Rome, Italy

ABSTRACT

Membranes based on Nafion (trademark of E. I. du pont de Nemours & Company), a copolymer of tetrafluorethylene and a vinylsulfonic acid, have received to date a great deal of experimental work (1-6) because of their very interesting characteristics for use in electrolysis (7, 8), fuel cells (9), and batteries (10, 11). Experimental results on mechanical (2), structural (4), chemical (6, 10), and transport properties (5, 8) of Nafion membranes demonstrate that their peculiarity depends mainly on the ion sequestering structure (clusters) and swelling properties. The water content and salt up-take of the membrane exposed to electrolyte solutions are of fundamental importance for the membrane transport properties (7, 12). Among the transport coefficients, the hydraulic permeability and filtration coefficient have been less extensively studied despite the useful correlations which can be stated between them and the electroosmotic permeability, pore diameter, and solvation (13). In this paper experimental results on the hydraulic and filtration coefficients of Nafion 125, an homogeneous 5 mils thick membrane of 1200 equivalent weight, are presented. The dependence of these parameters on the applied pressure difference, salt concentration, and counterion nature is discussed.

Experimental

Membranes were activated according to the following procedure: equilibration in 0.1M HCl (~24 hr) and in boiling water (for 72 hr). Swelled membranes in the H^+ form are then equilibrated in the desired electrolyte solution until complete exchange is obtained. The hydraulic permeability (when membranes are exposed to pure water) and the filtration coefficient (when membranes are exposed to salt solutions) K_s, (both in $m^3\ N^{-1}\ sec^{-1}$ units), were determined, in a two chamber cell made of Perspex [a poly(methyl methacrylate)resin] and thermostated at 20° ± 0.5°C, by measuring the liquid meniscus displacement in a calibrated pipette (Δh) when a ΔP pressure difference is imposed between the two half-cells. The presence above and below the polymeric film of two rigid perforated stainless steel disks prevent the membrane from deforming. The two half-cells are filled with water or with identical solutions. The volume flow rate $\alpha = s\Delta h/t$ [with s (cm^2) the pipette cross section and t (sec) the experimental time interval] becomes a constant after some time, *i.e.*, a linear $s\Delta h$ *vs.* t plot is obtained. The hydraulic or filtration coefficient for a membrane of area A in cm^2 (we have assumed A = 7.08 cm^2, the geometrical membrane surface) is given by

$$K_s = (J_v/\Delta P) = (\Delta h/t)\,(s/A)/\Delta P = (\alpha/\Delta P)\,(1/A) \quad [1]$$

The independence of K_s on the applied pressure difference has been tested in the ΔP = 13.3-80.0 kPa range with all the examined NaCl solutions. Results for some of these solutions are reported in Fig. 1. The water permeability in any other system (*i.e.*, in the alkali hydroxide solutions) was measured at a fixed ΔP = 50.7 kPa value.

The filtration coefficient K_s is defined as

$$K_s = (J_v/\Delta P)_{\Delta E=0,\,\Delta C=0} \quad [2]$$

where E = electrical potential; C = concentration; J_v is the volume flow given by $J_v = \Sigma_i J_i V_i + J_w V_w$ (J_i and J_w are the fluxes of the ith species and water; V_i and V_w are partial molar volumes). Theoretically when a solution containing charged species is forced across a charged membrane, a streaming potential shows up. Therefore since $\Delta E \neq 0$, the experimental conditions of the K_s definition are not fulfilled. However, it has been demonstrated (14) that in charged membranes this contribution is less than 1% and therefore

$$(J_v/\Delta P)_{\Delta E=0,\,\Delta C=0} \cong (J_v/\Delta P)_{I=0,\,\Delta C=0} \quad [3]$$

(I = current density) and conditions $I = 0$, $\Delta C = 0$ correspond to our experimental arrangement.

It must be noted that the filtration coefficient represents also an hydraulic permeability (15) of the membrane exposed to salt solutions when the salt flow under an applied pressure is practically zero, *i.e.*

$$J_v = \Sigma_i J_i V_i + J_w V_w \cong J_w V_w \quad [4]$$

These conditions are obtained with highly charged and permselective membranes exposed to aqueous, nonconcentrated solutions (no salt up-take in the membrane phase and Donnan co-ion exclusion). In fact it is known (16) that Nafion 125 membranes are

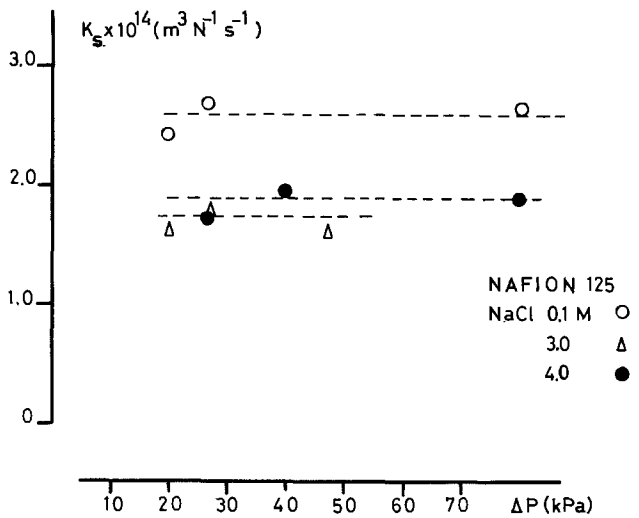

Fig. 1. Filtration coefficients, K_s, for Nafion 125 membranes in NaCl solutions at different concentrations as a function of the applied pressure difference ΔP (kPa).

Key words: applied pressure difference, salt concentration, counterion nature.

permselective in alkali chloride and hydroxide solutions for concentrations as high as 1-2M.

Results

The hydraulic and filtration coefficients, K_s, should depend on the water content of the membrane, w % (dry polymer), which is a function of the external solution concentration C (mols liter^{-1}). These effects are shown in Fig. 2 for Nafion 125 in NaCl solutions. The w % in the membrane phase was measured according to a procedure already reported (17). The pronounced decrease in K_s values above C = 1M corresponds to the observed drastic reduction in water content above this concentration (Fig. 2) which is also reflected in the decrease in cationic selectivity (t_{Na^+}, counterion transport number in NaCl solutions, decreases from C = 0.90 at 1M down to 0.72 at 4M) and electrical resistance (from 4.1 Ω-cm^2 in NaCl 1M to 2.0 Ω-cm^2 in NaCl 5.0M at 25°C) (18).

The water content and dependent membrane properties, such as the electrical resistance, depend on the counterion present in the external solution (18). This counterion dependence should also be expected in the filtration coefficient values. To show this effect the filtration coefficient in the alkali hydroxide series LiOH, NaOH, KOH, and CsOH has been measured at a fixed concentration 0.1M (Fig. 3). The K_s value still decreases as the membrane water content decreases. Moreover, as for other membrane transport properties dependent on the membrane solvation [for example the membrane resistance (7, 18)] a straight correlation between the filtration coefficient and the counterion hydration exists in Nafion membranes exposed to alkali hydroxide solutions. The correlation follows the series (Fig. 3)

$$M^+ (n_{hyd.}): \quad Li(4.25) > Na(2.9) > K(1.2) > Cs(0)$$

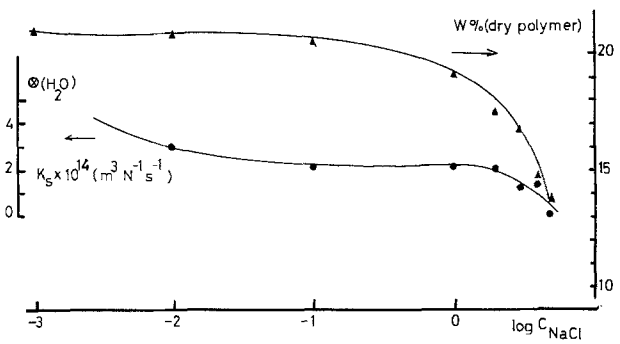

Fig. 2. Dependence of the filtration coefficient K_s and membrane water content, w % (referred to the dry polymer weight), on the salt concentration C for Nafion 125 membranes in NaCl solutions. The point x (H_2O) represents the membrane hydraulic permeability. All measurements were made at T = 20.0° ± 0.5°C.

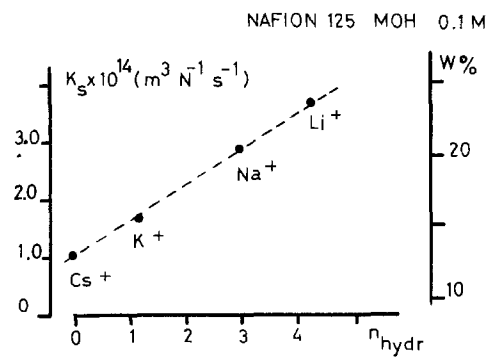

Fig. 3. Correlation between filtration coefficients and counterion hydration number, $n_{hyd.}$, for Nafion 125 membranes in alkali hydroxide 0.1M solutions at T = 20° ± 0.5°C. The membrane water content w % (referred to the dry polymer weight) is also shown.

Table I. Evaluation of the pore radius, r_p (Å) in Nafion 125 membranes by using Eq. [5]: with l = 0.013 cm and d = 47.3Å [from Ref. (20)]

Electrolyte (mols liter^{-1})		η(cP)*	$K_s \times 10^1$ (m^3 N^{-1} sec^{-1})	r_p (Å)
H_2O		1.002	5.33	7.89
NaCl	0.001	1.388	4.04	7.99
	0.010	1.424	3.17	7.57
	0.100	1.436	2.53	7.17
	1.00	1.589	2.48	7.31
	2.00	1.707	2.53	7.48
	3.00	1.974	1.79	7.12
	4.00	2.284	1.94	7.53
	5.00	2.609	0.97	6.55

* η(cP) in membrane has been calculated according to the method of Ref. (21).

[$n_{hyd.}$ are taken from Ref. (19)]. However, no difference in the filtration coefficients appears in electrolytes with a common counterion (Na^+) and different co-ions (Cl^-, OH^-) at a given concentration (0.1M). In fact K_s (NaCl 0.1M) = 2.53 × 10^{-1} and K_s (NaOH 0.1M) = 2.92 × 10^{-1} both in m^3 N^{-1} sec^{-1}.

Evaluation of membrane pore radius, r_p.— It seems interesting to evaluate the membrane pore radius from filtration coefficient data. Gierke (20) reports a pore diameter ($2r_p$) of 12Å (from water diffusion measurements) and 13Å (from hydraulic permeability data) for Nafion 120, a membrane which differs only in thickness (10 mils) from Nafion 125. These values were calculated by means of the equation (20)

$$r_p = (8/\pi l \eta K_s d^2)^{1/4} \qquad [5]$$

with l the membrane thickness (0.013 cm), K_s the hydraulic permeability, η the viscosity of the membrane interstitial solution, and d the Bragg distance between clusters in the Nafion structure. By means of Eq. [5] and the water permeabilities reported in Fig. 2 as K_s, the pore radius values for Nafion 125 in NaCl solutions in the concentration range 10^{-3}-5M have been obtained and are reported in Table I. These values do not seem to depend strongly on the membrane solvation as they change from 6.5 to 8.0Å. As compared with Gierke's data values reported in the table are very similar. In fact the two comparable quantities are 13Å (Gierke) and 2 × 7.9 = 16Å (from the K_s value reported in the table in the case of a membrane exposed to water).

From the above discussion we may conclude that the water permeability through Nafion 125 membranes depends on the membrane water content and on the electrolyte concentration. Moreover, a linear correlation between filtration coefficients and counterion hydration has been observed in the alkali hydroxide series. However, the membrane pore radius does not seem to depend on the membrane solvation.

Manuscript submitted March 15, 1982; revised manuscript received Oct. 7, 1982.

Any discussion of this paper will appear in a Discussion Section to be published in the December 1983 JOURNAL. All discussions for the December 1983 Discussion Section should be submitted by Aug. 1, 1983.

Publication costs of this article were assisted by CRE Casaccia.

LIST OF SYMBOLS

d	Bragg distance between clusters in Nafion structure (Å)
h	meniscus level in the cell capillary (cm)
l	membrane thickness (cm)
$n_{hyd.}$	counterion hydration number
r	membrane pore radius (Å)
s	capillary cross section (cm^2)
t	time (sec)
A	geometrical membrane area
C	concentration (mols liter^{-1})

J_v volume flow ($m^3 m^{-2} sec^{-1}$)
J_i, J_w fluxes of ith species and water, respectively, (mols $m^{-2} sec^{-1}$)
K_s hydraulic or filtration coefficient ($m^3 N^{-1} sec^{-1}$)
P pressure (Pa)
V_i, V_w partial molar volume of ith species and water, respectively, (cm^3)
w % water content (in weight) of the swelled membrane as referred to the dry polymer weight
α volume flow rate ($m^3 sec^{-1}$)
η viscosity of the membrane interstitial solution (cP)

REFERENCES

1. "Symposium on Fluorocarbon Ion Exchange Membranes," The Electrochemical Society Meeting, Atlanta, Georgia, Oct. 9-14, 1977.
2. A. Eisenberg and M. King, "Ion Containing Polymers," Polymer Physics, Vol. 2, R. S. Steiner, Editor, Chap. IV, pp. 162-169, Academic Press, New York (1978).
3. W. G. F. Grot, *Chem. Ind. Techn.*, **50**, 295 (1978).
4. R. S. Yeo and A. Eisenberg, *J. Appl. Polym. Sci.*, **21**, 875 (1977).
5. C. Heitner-Wirguins, in "Proceedings of the Symposium on Ion Exchange," R. S. Yeo and R. P. Buck, Editors, The Electrochemical Society Softbound Proceedings Series, Pennington, NJ (1981).
6. H. L. Yeager and B. Kipling, *J. Phys. Chem.*, **83**, 1653 (1979).
7. R. S. Yeo, J. McBreen, G. Kissel, F. Kulesa, and S. Srinivasan, *J. Appl. Electrochem.*, **10**, 741 (1980).
8. H. L. Yeager, B. Kipling, and R. L. Dotson, *This Journal*, **127**, 303 (1980).
9. R. S. Yeo, J. McBreen, A. C. C. Tseung, S. Srinivasan, and J. McElroy, *J. Appl. Electrochem.*, **10**, 393 (1980).
10. F. G. Will, *This Journal*, **126**, 36 (1979).
11. F. G. Will and H. S. Spacil, *J. Power Sources*, **5**, 173 (1980).
12. C. Fabiani, M. DeFrancesco, and L. Bimbi, Comitato Nazionale Energia Nucleare, Rome, Italy, Technical Report/Chemistry No. 10, (1979).
13. B. R. Breslau and I. F. Miller, *Ind. Eng. Chem. Fundam.*, **10**, 554 (1971).
14. Y. Kobatake, M. Yuasa, and F. Fujita, *J. Phys. Chem.*, **72**, 1752 (1968).
15. N. Lakshminarayanaiah, "Transport Phenomena in Membranes," Chap. 6, Academic Press, New York (1969).
16. B. Scuppa, L. Bimbi, M. DeFrancesco, and F. Croce, Comitato Nazionale Energia Nucleare, Rome, Italy, Technical Report/Chemistry No. 2 (1980).
17. C. Fabiani, B. Scuppa, M. DeFrancesco, and L. Bimbi, *ibid.*, No. 15 1981).
18. G. Scibona, C. Fabiani, and B. Scuppa, *J. Memb. Science*, To be published.
19. C. B. Monk, "Electrolytic Dissociation," Academic Press, New York (1961).
20. T. D. Gierke, Paper 438 presented at The Electrochemical Society Meeting, Atlanta, Georgia, Oct. 9-14, 1977.
21. B. R. Breslau and I. F. Miller, *J. Phys. Chem.*, **74**, 1056 (1970).

Cyclic Voltammetry in Solutions of Aluminum Bromide and KBr in Aromatic Hydrocarbons

II. The Behavior of Pb and Sn

M. Elam, E. Peled,* and E. Gileadi*

Institute of Chemistry, Tel Aviv University, Ramat Aviv, Israel

ABSTRACT

The electrochemical behavior of dilute solutions of $SnBr_2$ and $PbBr_2$ in a nonpolar solvent system consisting of solutions of 1.0M Al_2Br_6 and 0.80M KBr in ethylbenzene was studied. Cyclic voltammograms show well defined peaks for the deposition and dissolution of the divalent metal. Oxidation to the tetravalent state could not be detected in the available potential region. The diffusion coefficients were 1.1×10^{-6} cm^2/sec for lead and 2.7×10^{-6} cm^2/sec for tin. Lead ions inhibit the electrodeposition of aluminum while tin ions seem to have little or no effect. An overpotential associated with initial nucleation on a platinum electrode is observed for both metals and electrodeposition does not start until η reaches a value of about 30-40 mV. Formation of a thermodynamically unstable Al/Pb alloy at sufficiently cathodic potentials in solutions containing $PbBr_2$ is indicated.

In the first paper in this series (1) the surface processes taking place on three types of electrode materials (Pt, Au, and glassy carbon) were studied in solutions containing Al_2Br_6 and KBr in aromatic hydrocarbons (mostly ethylbenzene). On glassy carbon no surface phenomena were observed in the available potential region (*ca.* 1.4V in ethylbenzene) between aluminum deposition on the cathodic side and bromine evolution on the anodic side. When platinum is used as the working electrode in the same solvent, a clear anodic adsorption peak is observed, at about 1.0V *vs.* RAlE (reversible aluminum electrode in the same solution). Analysis of the peak (2-4) shows that it corresponds to the formation of a monovalent surface species, which was identified as adsorbed bromine atoms. Conductivity and transference number measurements in this system showed (5) that the ionic species existing in solution are rather complex, but a simple reaction corresponding to the transfer of a single electron per atom of bromine adsorbed on the surface can nevertheless be written (1).

The initial potential for bromine evolution was found to depend significantly on the solvent, ranging from 1.20V for mesitylene to 1.45V RAlE for benzene. Good correlation was observed (1) between this potential and the rate constant for halogenation of the solvent molecules.

The cyclic voltammograms on gold electrodes are more complex. The formation of several types of surface compounds such as $AuBr_3$, AuBr, and possibly $AuBr_4^-$ was assumed to account for the observed peaks.

In a subsequent paper (6) the behavior of iodide ions in the same type of solutions was studied, employing platinum working electrodes and a number of different solvents.

The half-wave potential for oxidation of iodide was found to be *ca.* 1.10V RAlE (compared to 2.20V RAlE in aqueous solutions). Perhaps the most striking result of these experiments is that iodine produced electrochemically (or introduced as such) can oxidize

* Electrochemical Society Active Member.

Key words: electrodeposition, overpotential, reversibility, nucleation.

bromide. The bromine liberated reacts with the solvent, shifting the equilibrium in the direction of further oxidation of bromide. This process can take place as a result of the relatively small difference in potential between iodine and bromine evolution (0.1V when mesitylene is employed as the solvent, compared to *ca.* 0.50V in aqueous solutions) and the fact that the solvent molecules act as scavengers for the bromine formed.

In the present work the behavior of $SnBr_2$ and $PbBr_2$ in solutions of Al_2Br_6 and KBr in ethylbenzene was studied. The standard reversible potentials, which are essentially equal for these two elements in aqueous solutions (1.54 and 1.53V RAlE for Pb and Sn, respectively) are different in the present solvent system (0.16 and 0.29V RAlE for Pb and Sn) and both are much closer to the reversible potential for aluminum deposition, as discussed elsewhere (1, 7, 8).

Experimental

The cell, electrodes, and electronic equipment employed for measurements of cyclic voltammograms were described in the first paper in this series (1). Potentiostatic transients were performed with a PAR Model 173 potentiostat and the currents were recorded on a Yokogawa Type 3077 X-Y-t recorder. All experiments were performed employing a Pt working electrode, unless otherwise specified.

All experiments were performed inside a glove box filled with pure argon (9, 10), in rigorously dried solutions of 1.0M Al_2Br_6 and 0.80M KBr in ethylbenzene. The methods of preparation of the solutions and the purification and drying of the compounds have been described elsewhere (1, 7, 9). Lead bromide (BDH, 98%) was dried by heating overnight at 250°C in vacuum. Stannous bromide (ROC/RIC, anhydrous 99.5%) was used without further purification. All potentials reported were measured against a reversible aluminum electrode in the same solution (RAlE).

Results and Discussion

Cyclic voltammograms for $SnBr_2$.—Typical cyclic voltammograms for a solution containing $SnBr_2$ are shown in Fig. 1 for two sweep rates. The reversible potential for tin in the same solution is 0.227V (11). The anodic peak corresponds to the oxidation of metallic Sn to Sn^{++} and has a characteristic shape corresponding to such processes, as is discussed below. A second anodic peak which would correspond to the oxidation of divalent to tetravalent tin could not be detected in the whole potential region up to bromine evolution.

The cathodic peak current $i_p(c)$ is proportional to the concentration of $SnBr_2$ up to a concentration of about 80 mM. At higher concentrations deviations occur. The same behavior was observed for $PbBr_2$ and is discussed below (cf. Fig. 5). The peak potential $E_p(c)$ changes by about 28 mV/decade for sweep rates ($v = dE/dt$) above 10 mV/sec as seen in Fig. 2. This behavior corresponds to an irreversible reaction with a Tafel slope of $2.3RT/F$ (12-14). On the other hand, $E_p(c)$ depends on the concentration of $SnBr_2$ (*ca.* 33 mV/decade) as shown in Fig. 3, as would be expected for a two-electron reversible process. The complexity of the reaction is further indicated by the fact that $i_p(c)$ is not proportional to $v^{1/2}$ and the coefficient $d \log i_p(c)/d \log v$ is about 0.36.

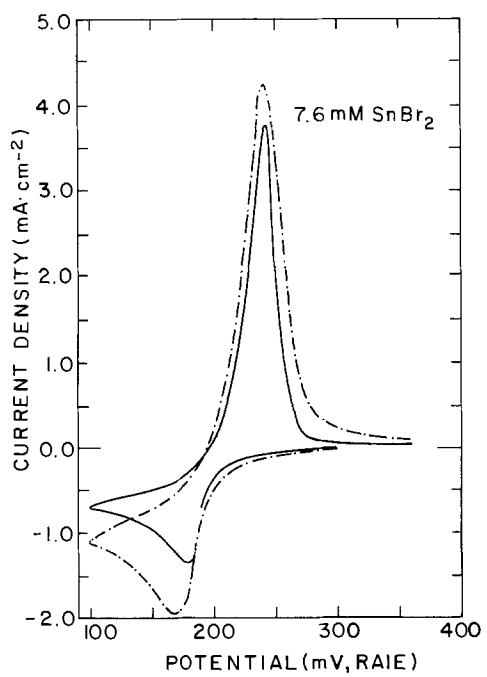

Fig. 1. Cyclic voltammogram of $SnBr_2$. Solid line: $v = 21$ mV/sec; broken line: $v = 55$ mV/sec.

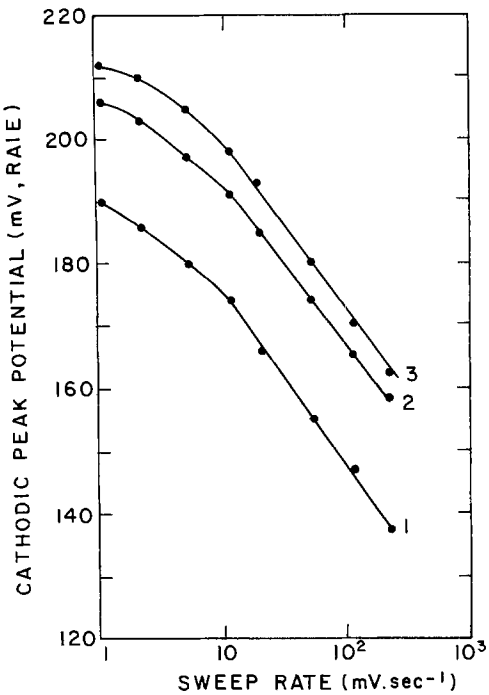

Fig. 2. Cathodic peak potential vs. log (v) for reduction of Sn^{++}. Concentration of $SnBr_2$: curve 1, 3.9; 2, 10.2; 3, 17.6 (mM).

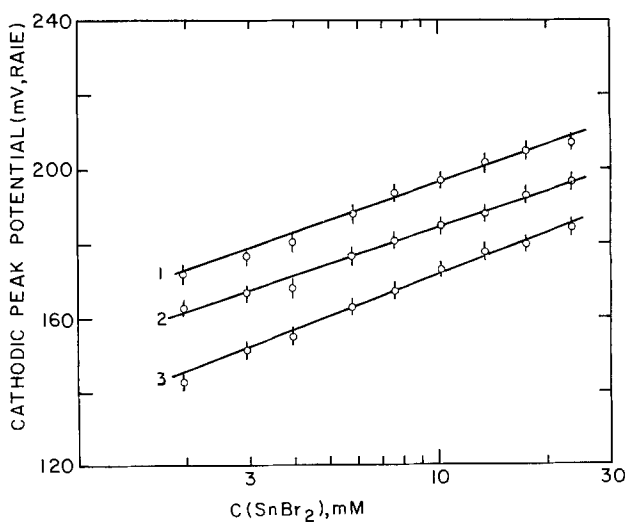

Fig. 3. Cathodic peak potential plotted as a function of log C ($SnBr_2$). Sweep rate: curve 1, 5.5; 2, 21; 3, 55 (mV/sec).

As the concentration of $SnBr_2$ was increased above 0.10M, the conductivity decreased significantly. Since $SnBr_2$ is not soluble in the pure aromatic solvent but dissolves well if aluminum bromide is added and, moreover, the conductivity of a solution of aluminum bromide in ethylbenzene is increased by several orders of magnitude on the addition of tin or lead bromide, it is reasonable to assume that these salts are complexed with aluminum bromide to form $[Sn(Al_2Br_7)_2]$, which is analogous to $[K(Al_2Br_7)]$ (5). Solution of 1.0M aluminum bromide and 0.80M KBr can accommodate no more than 0.10M tin or lead bromide before a significant change in the nature of the dissolved species must occur. This can account for the lower conductivity and also for the deviation from linearity of the $i_p(c)$ *vs.* $C(SnBr_2)$ relationship observed at higher concentrations. A similar deviation from linearity of the Nernst plots at high concentration of $SnBr_2$ and $PbBr_2$ was also observed (11).

Cyclic voltammetry for $PbBr_2$.—Two voltammograms taken in a solution containing $PbBr_2$ are shown in Fig. 4. The reversible potential for lead in this solution is 97 mV RAlE (11). Because of significant nucleation overpotential, the onset of lead deposition is delayed and the cathodic peak occurs at potentials negative to that of reversible aluminum. However, as a result of an inhibition effect, aluminum deposition does not commence in solutions containing Pb^{++} ions until much more negative potentials are reached.

The cathodic peak current is proportional to the concentration of $PbBr_2$ up to *ca.* 0.10M and then tends to level off, as seen in Fig. 5. As in solutions containing $SnBr_2$, this behavior is attributed to the fact that new types of species must be formed in solution above this concentration. These may allow deposition of the metal only at higher cathodic potentials and may have a smaller diffusion coefficient, which would explain the observed deviation from linearity in Fig. 5.

The cathodic peak potential shifts with concentration (implying reversibility) and with sweep rate (implying irreversibility) as in solutions containing Sn^{++} ions. The dependence of peak current on sweep rate is given by $(d \log i_p(c)/d \log v) = 0.41$, which deviates significantly from the value of 0.50 expected for a simple charge transfer process (12), indicating that a complex process takes place.

A second anodic peak, which would correspond to the oxidation of divalent to tetravalent lead, was not observed throughout the potential region up to bromine evolution.

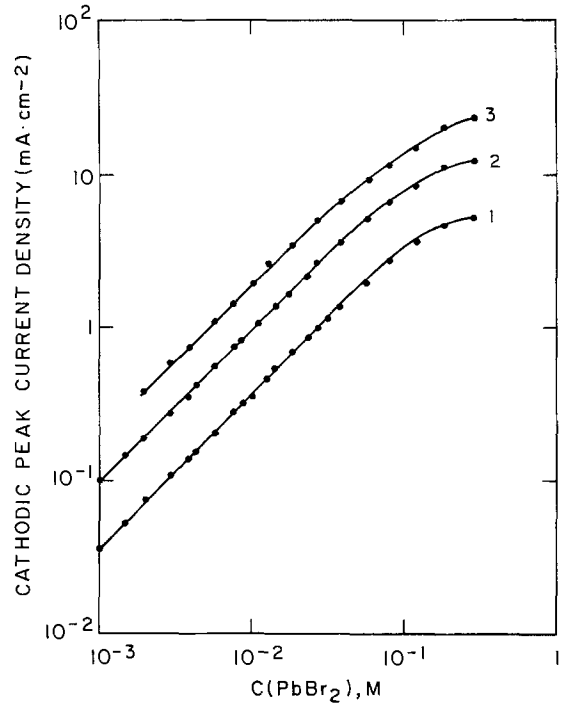

Fig. 5. Cathodic peak current density as a function of concentration of $PbBr_2$, on a log-log scale. Sweep rate: curve 1, 1.1; 2, 12; 3, 55 (mV/sec).

Aluminum deposition in the presence of $PbBr_2$.—In Fig. 6 three voltammograms, all started at +0.25V RAlE and taken under identical conditions, except for the extreme cathodic potential reached, are shown. The solid line, which ends at −50 mV RAlE (common to all three sweeps), is very similar to the voltammograms shown in Fig. 4. Aluminum deposition is completely inhibited by the presence of 2.0 mM $PbBr_2$ in solution. When the cathodic limit is extended to −70 mV RAlE, a nucleation loop, evidenced as a cathodic peak current during the anodic sweep, is clearly

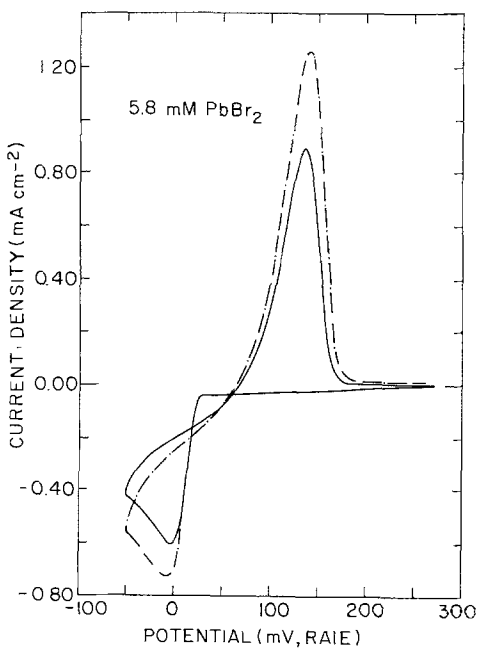

Fig. 4. Cyclic voltammogram of $PbBr_2$. Solid line: $v = 12$ mV/sec; broken line: $v = 21$ mV/sec.

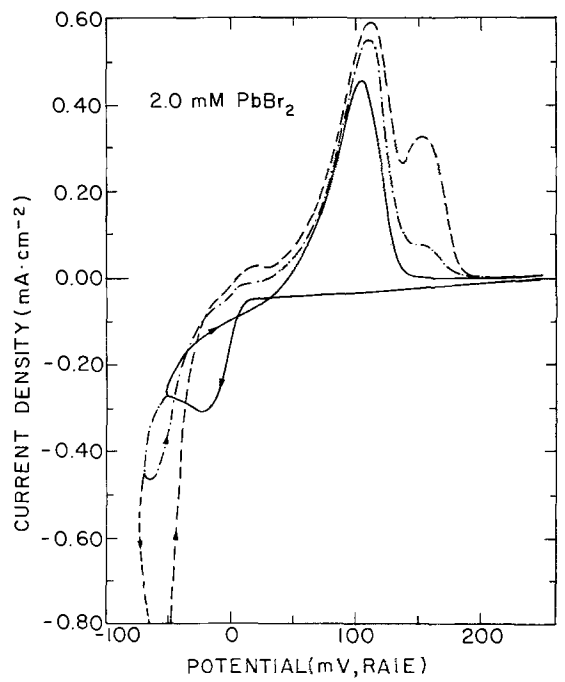

Fig. 6. Aluminum deposition and dissolution in the presence of $PbBr_2$. Sweep rate: 21 mV/sec.

seen. On the anodic branch, a small shoulder can be observed at the potential corresponding to the dissolution of aluminum (a few mV positive to zero). More significantly, a new anodic peak appears at a potential of *ca.* 0.15V, beyond the peak corresponding to the dissolution of lead. Extending the cathodic limit by a mere 5-75 mV causes a very large increase in the cathodic current, yet the aluminum dissolution peak at +10 mV stays very small. The new anodic peak at 0.15V increases fourfold while the main peak due to lead dissolution increases by less than 10%, showing that the new peak is to be associated with the dissolution of aluminum. Close examination of the voltammogram shows that, while the potential is swept anodically, lead deposition continues after aluminum deposition has stopped, so that most of the aluminum is buried under layers of lead and cannot be dissolved until most of the lead has been dissolved. The position of the dissolution peak at 0.15V probably indicates the formation of a Pb/Al alloy which dissolves anodically at a higher potential than lead itself. Although equilibrium phase diagrams show no Pb/Al alloy (15), it is well known (16-18) that supersaturation and formation of unstable phases can occur in electrodeposited alloys.

In Fig. 7 two voltammograms are shown, one in the presence of a low concentration of lead (0.5 mM $PbBr_2$) and the other in its absence.

With the sweep ending at −40 mV RAlE, cathodic deposition and anodic dissolution of aluminum are observed. The low concentration of $PbBr_2$ used clearly inhibits this process. The current loops formed in the cathodic region in Fig. 6 and 7 are characteristic of crystal growth requiring nucleation (19).

The inhibition effects discussed above were not observed in solutions containing $SnBr_2$ instead of $PbBr_2$.

Reversibility.—In metal deposition, the potential difference between the cathodic and anodic peaks cannot serve as a criterion for reversibility (20). The anodic peak depends on the amount of metal deposited in the previous cathodic sweep. This is demonstrated in Fig. 8 which shows that $i_p(a)$ increases and $E_p(a)$ moves to more positive potentials as the potential is swept to more cathodic values in the previous half-cycle, *i.e.*, as more metal is deposited.

When the dissolved metal ion is not stable in solution and must be complexed (as is the case in the present system), a diffusion limitation may be observed in the anodic peak as a result of depletion of the complexing agent near the electrode surface. Such behavior was observed for solutions containing $SnBr_2$ or $PbBr_2$, as seen in Fig. 9, where the function i/c is plotted *vs.* potential. A distinct broadening of the peak is observed at higher concentration on the descending part of the peak. The width of the peaks at half-height, $\Delta E_{1/2}$, is independent of concentration, while $\Delta E_{1/4}$ increased from 34 to 42 mV and further to 47 mV as the concentration of $SnBr_2$ is increased from 3.9 to 13.6 mM and further to 23.6 mM.

A convenient criterion for establishing reversibility in metal deposition is to examine the difference between the cathodic peak potential $E_p(c)$ and the value

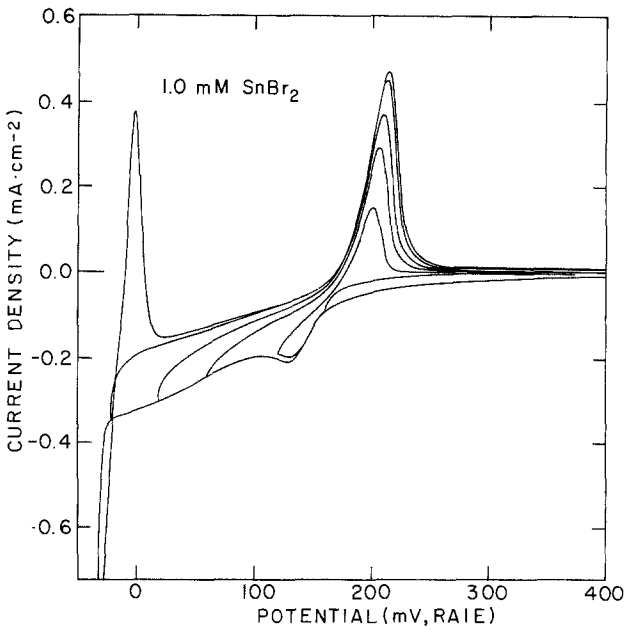

Fig. 8. The effect of the extreme cathodic potential reached on the anodic peak of Sn dissolution. Sweep rate: 12 mV/sec.

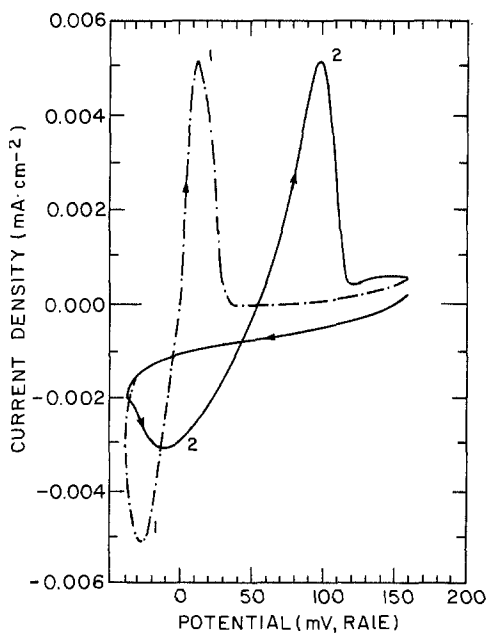

Fig. 7. The inhibiting effect of a low concentration of $PbBr_2$ on aluminum deposition. Broken line: no $PbBr_2$; solid line: 0.5 mM $PbBr_2$. Sweep rate: 1.1 mV/sec.

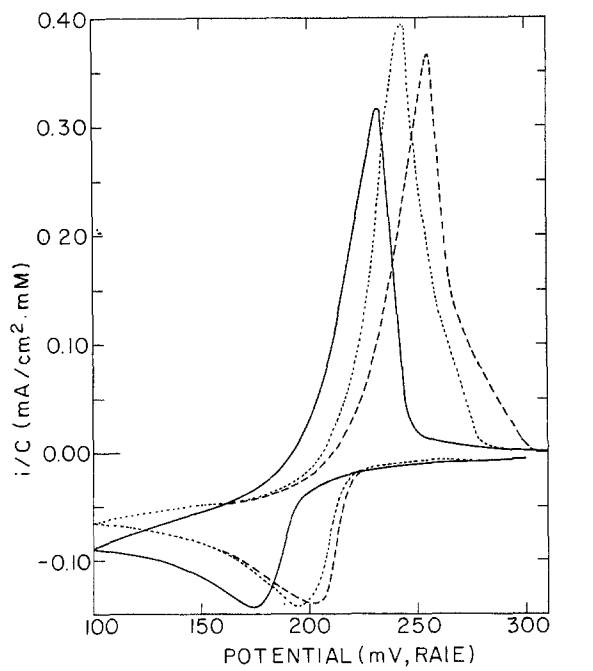

Fig. 9. Plots of the function i/C at constant $v = 12$ mV/sec for different concentrations of $SnBr_2$, showing broadening of the anodic dissolution peak due to diffusion-limitation at higher concentrations. Solid line: 3.9 mM; dotted line: 13.6 mM; broken line: 23.6 mM.

of the potential $E_{p/2}$ at $i = i_p(c)/2$. The difference

$$\Delta E = E_p - E_{p/2} \quad [1]$$

should be $-0.77RT/nF = -0.020/n$ V at 25°C for the reversible deposition of an insoluble substance (21). A value of $\Delta E = 10$ mV was observed in our experiments only for solutions of $PbBr_2$ at the lowest sweep rate tested (1.1 mV/sec). Assuming reversibility, one can estimate the diffusion coefficient from the relationship (22)

$$i_p(c) = 3.67 \times 10^5 n^{3/2} D^{1/2} C^\circ v^{1/2} \quad [2]$$

The value obtained for lead at 25°C is

$$D(Pb^{++}) = (1.1 \pm 0.1) \times 10^{-6} \text{ cm}^2/\text{sec}$$

This should be compared to values of 0.8×10^{-6} and 4.0×10^{-6} cm²/sec found for Hg^{++} in mesitylene and toluene, respectively, in somewhat more concentrated solutions (Al_2Br_6 1.15M; KBr 0.76M) (23).

The viscosity of solutions of Al_2Br_6 and KBr in different aromatic solvents was studied recently in our laboratory (24, 25). The results show that the value of $D(Hg^{++})$ in toluene quoted above was taken at nearly the same viscosity as in the present system, while in mesitylene the viscosity was *ca.* 80% higher. Thus the solvation radius of Pb^{++} calculated from the relationship

$$D = kT/6\pi r\eta \quad [3]$$

is comparable to that of Hg^{++} in mesitylene (5-6Å).

The value of the diffusion coefficient for Sn^{++} could not be determined accurately but was estimated to be

$$D(Sn^{++}) = (2.9 \pm 0.6) \times 10^{-6} \text{ cm}^2/\text{sec}$$

This estimate agrees well with a value of 2.7×10^{-6} obtained from potentiostatic transients, as is shown below.

The variation of $E_p(c)$ with concentration of either $PbBr_2$ or $SnBr_2$ would indicate reversible behavior, while the dependence of $E_p(c)$ on sweep rate shows lack of reversibility (22). At the same time, the plot of log $i_p(c)$ *vs.* log v is linear over three orders of magnitude of sweep rates (0.001-1.0 V/sec), but the slope deviates significantly from a value of 0.50 predicted for a simple charge-transfer reaction. Combining the above observations suggests that a preceding or following chemical step may be involved (12). This could be the decomposition or reforming of a complex ion of the type $[Pb(Al_2Br_7)]^+$ or $[Pb(Al_2Br_7)_3]^-$ or a surface process such as adatom formation or nucleation.

Nucleation.—The deposition of a metal on a foreign substrate is often controlled by the rate of nucleation (26-30). Figure 10 shows this type of behavior for both lead and tin. Curve No. 1 is taken in both cases on a Pt electrode freshly coated with the respective metal, while curve 2 is taken on a bare Pt electrode. Deposition of lead (or tin) on Pt does not start until a significant overpotential (*ca.* 30 mV) is reached. At this point the current rises very rapidly.

A different experiment depicting the same type of phenomenon is shown in Fig. 11, where current/time transients following a potential step from 0.30V RAlE to the values marked, are plotted. At the most cathodic potential (155 mV RAlE), the current decays in a regular manner with $t^{-1/2}$. At more anodic potentials, the current on the bare Pt electrode first decreases but as soon as a sufficient layer of Sn is formed, nucleating overpotential disappears and the current rises to the value it would have on a freshly deposited Sn electrode.

This behavior is further exemplified in Fig. 12, where the shapes of the transients obtained on Pt electrodes (broken lines) are compared to those obtained on freshly deposited tin electrodes. This type of behavior has been observed before for different

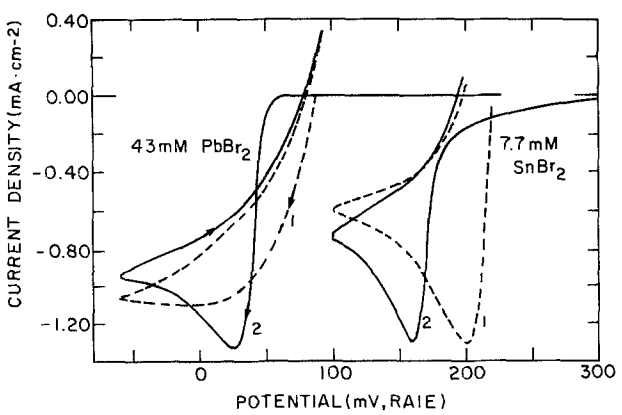

Fig. 10. Comparison of initial potential for deposition of Sn or Pb on Pt and on the respective metal. Curve 1, Pb deposited on Pb (or Sn on Sn); 2, Pb (or Sn) deposited on Pt. Sweep rate: 1.1 mV/sec for $PbBr_2$, 21 mV/sec for $SnBr_2$.

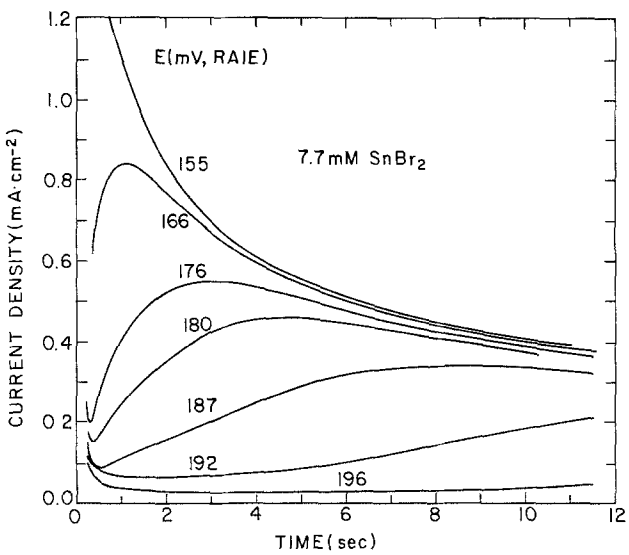

Fig. 11. Potentiostatic transients for deposition of Sn on Pt. Initial potential: +300 mV RAlE in all cases. Final potential as marked.

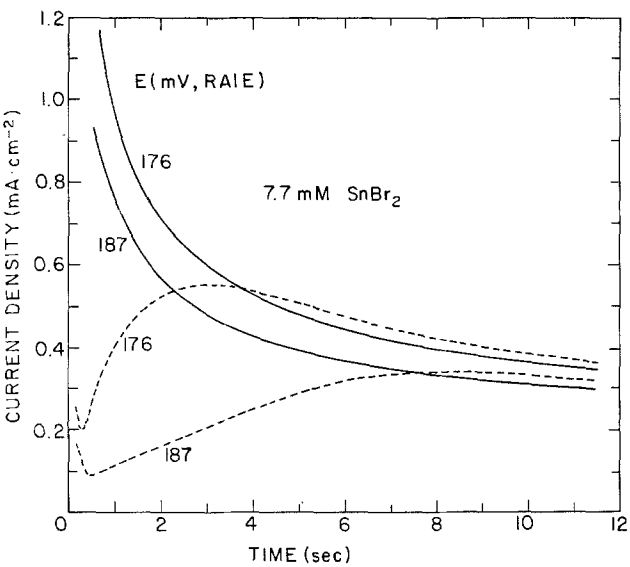

Fig. 12. Comparison of potentiostatic transients for deposition of Sn on Pt (broken line, same as in Fig. 11) and on Sn (solid line). In the latter the initial potential was the open-circuit reversible potential.

metals deposited from aqueous (26) solutions as well as from molten-salt systems (27-30) and has probably little to do with the nature of the solvent.

Replotting the uppermost curve in Fig. 11 as $1/i$ *vs.* $t^{1/2}$ yields a straight line. The diffusion coefficient of tin calculated from the slope is 2.7×10^{-6} cm^2/sec, in excellent agreement with the value of $(2.9 + 0.6) \times 10^{-6}$ cm^2/sec obtained above from cyclic voltammograms.

Conclusions

Lead and tin can be deposited from solutions of Al_2Br_6 and KBr in ethyl benzene and similar aromatic hydrocarbons. In the presence of lead, aluminum deposition is inhibited and does not occur until an overpotential of *ca.* −70 mV is reached.[1] Tin, which is deposited at a more anodic potential, does not exert a similar inhibition effect.

The anodic peak depends on the amount of metal deposited in the previous cathodic half-cycle and cannot be used to analyze the course of the reaction. When the potential is allowed to reach a sufficiently cathodic potential to deposit aluminum in the presence of lead, a second anodic peak appears, which can probably be associated with the formation of an Al/Pb alloy.

On platinum electrodes a nucleation process takes place and deposition of both Sn and Pb requires a threshold overpotential of *ca.* 30 mV for deposition to start. The diffusion coefficients of lead and tin were found to be 1.1×10^{-6} and 2.7×10^{-6} cm^2/sec, respectively, as compared to a value of 4.0×10^{-6} cm^2/sec for mercury in solutions of toluene of nearly the same viscosity (23-25).

Acknowledgments

Financial support by the "Foundation for Industrial-Applied Research at the Universities" of the Planning and Grants Committee of the Council for Higher Education is gratefully acknowledged.

Manuscript submitted June 7, 1982; revised manuscript received Sept. 20, 1982.

Any discussion of this paper will appear in a Discussion Section to be published in the December 1983 JOURNAL. All discussions for the December 1983 Discussion Section should be submitted by Aug. 1, 1983.

[1] The potential at which Al deposition starts moves to more negative values as the concentration of lead is increased. The value of −70 mV RAlE was observed for a concentration of 2.0 mM $PbBr_2$.

REFERENCES

1. M. Elam and E. Gileadi, *This Journal,* **126,** 1474 (1979).
2. S. Srinivasan and E. Gileadi, *Electrochim. Acta,* **11,** 321 (1966).
3. E. Gileadi and B. E. Conway, in "Modern Aspects of Electrochemistry," Vol. III, J. O'M. Bockris and B. E. Conway, Editors, Chap. 5, Butterworths, London (1964).
4. H. Angerstein-Kozlowska, J. Klinger, and B. E. Conway, *J. Electroanal. Chem. Interfacial Electrochem.,* **75,** 45 (1977).
5. A. Reger, E. Peled, and E. Gileadi, *J. Phys. Chem.,* **83,** 869, 874 (1979).
6. M. Elam and E. Gileadi, *This Journal,* **127,** 815 (1980).
7. E. Peled, A. Mitavski, A. Reger, and E. Gileadi, *J. Electroanal. Chem. Interfacial Electrochem.,* **75,** 677 (1977).
8. E. Gileadi, "Proceedings of 3rd Symposium on Electrode Processes," S. Bruckenstein, J. D. E. McIntyre, B. Miller, and E. Yeager, Editors, p. 366, Boston (1979).
9. A. Reger, E. Peled, and E. Gileadi, *This Journal,* **123,** 638 (1976).
10. S. Ziegel, E. Peled, and E. Gileadi, *Electrochim. Acta,* **23,** 363 (1978).
11. M. Elam, E. Peled, I. Bahatt, and E. Gileadi, In preparation.
12. R. S. Nicholson and I. Shain, *Anal. Chem.,* **36,** 706 (1964).
13. E. Gileadi, E. Kirowa-Eisner, and J. Penciner, "Interfacial Electrochemistry—An Experimental Approach," pp. 109-111, Addison-Wesley Publishing Co., Reading, MA (1975).
14. P. Delahay, "New Instrumental Methods in Electrochemistry," pp. 115-129, Interscience Publishers Inc., New York (1954).
15. M. Hansen and K. Anderko, in "Constitution of Binary Alloys," 2nd ed., p. 122, McGraw-Hill, New York (1958).
16. A. Brenner, in "Electrodeposition of Alloys," Vol. I, pp. 195-198, Academic Press, New York (1963).
17. K. M. Gorbunova and Yu. M. Polukarev, in "Electrodeposition of Metals and Alloys," N. E. Khomutov, Editor, p. 28, Israel Prog. Sci. Translations, Jerusalem (1969).
18. E. Raub, *Metalloberflache,* **7A,** 17 (1953).
19. J. N. Jovicevic, A. R. Despic, and D. M. Drazic, *Electrochim. Acta,* **22,** 577 (1971).
20. N. White and F. Lawson, *Electroanal. Chem.,* **26,** 113 (1970).
21. G. Mamantov, D. L. Manning, and D. M. Dale, *J. Electroanal. Chem. Interfacial Electrochem.,* **9,** 253 (1965).
22. T. Berzins and P. Delahay, *J. Am. Chem. Soc.,* **75,** 555 (1953).
23. E. Peled, A. Mitavski, and E. Gileadi, *Z. Phys. Chem.,* **98,** 111 (1975).
24. E. Peled, M. Brand, and E. Gileadi, *This Journal,* **128,** 1697 (1981).
25. E. Peled and E. Gileadi, in Proceedings of 1st International Symposium on Electrodeposition of Aluminum, G2, American Electroplaters Society, Boston, June 1981.
26. G. J. Hills, D. J. Shiffrin, and J. Thompson, *Electrochim. Acta,* **19,** 657 (1974).
27. B. Gilbert, G. Mamantov, and K. Fung, *Inorg. Chem.,* **14,** 1802 (1975).
28. P. Roland and G. Mamantov, *This Journal,* **123,** 1299 (1978).
29. C. L. Hussey, L. A. King, and J. K. Erbacher, *ibid.,* **125,** 50 (1978).
30. C. L. Hussey, L. A. King, and R. A. Carpio, *ibid.,* **126,** 1029 (1979).

Application of the "Swiss-Roll" Electrolysis Cell in Vitamin-C Production

P. M. Robertson*

Technisch Chemisches Labor, Swiss Federal Institute of Technology, 8092 Zurich, Switzerland

P. Berg and H. Reimann

F. Hoffmann-LaRoche Limited, Grenzach, Germany

and K. Schleich and P. Seiler

F. Hoffmann-LaRoche and Company Limited, 4002 Basel, Switzerland

ABSTRACT

The "Swiss-roll" cell was developed in 1973. This paper is concerned with the most important application of the cell; the oxidation of DAS to DAG, which is one of the steps in the synthesis of vitamin-C. For proprietary reasons the details of this work have not been divulged until now. Because of the differing factors involved, but more especially to give an insight into how the project developed, the material is presented in more or less chronological order.

Origin of the "Swiss-Roll" Design

The development of cell designs to make use of new materials took on a surge of activity in the 70's, mostly due to the impetus of the Southampton and Newcastle schools. An effort in this direction was needed since it was true to say that much of the resistance to organic electrosynthesis stems from the unsuitability of existing electrolysis cells or electrodes, mostly because of economics. The design of the "Swiss-roll" electrolysis cell came as a result of a consideration of electrode materials and also the electrode reaction rate. Up to that time, apart from a few isolated examples, the most commonly used electrode materials for anodes were platinum, graphite, or lead dioxide. These materials all have some disadvantages. Platinum is very expensive, graphite often undergoes severe erosion, and PbO_2 is also prone to stability problems. In contrast to many other materials they are all stable in acidic solutions. There are, however, many processes that can be carried out in alkaline solution, in which some very inexpensive metals are quite stable.

The Pourbaix diagrams for copper and nickel show that in the alkaline range and anodically polarized the oxides are the stable form present. These oxides are electronically conducting. In 1971 our attention was caught by the publication of Fleischmann *et al.* on the oxidation of alcohols and amines at nickel anodes in KOH (1). Although this was to be expected on the basis of early literature [Fichter (2)], it was seen as a confirmation that useful results could be obtained with inexpensive materials.

The oxidation of amines to nitriles, primary alcohols to acids, and secondary alcohols to ketones were all shown to give almost quantitative yields even before optimization of the oxidation conditions (Table I). The mechanism of the oxidation was proposed to go through a nickel (III) species which acts as a hydrogen abstractor

$$Ni(OH)_2 + OH^- \rightleftharpoons NiOOH + H_2O + e$$

$$NiOOH + R_1R_2CHOH \rightleftharpoons Ni(OH)_2 + R_1R_2\dot{C}OH$$

$$R_1R_2\dot{C}OH \xrightarrow{\text{further oxidation}} \begin{cases} \text{primary alcohol} \rightarrow \text{acid} \\ \text{secondary alcohol} \rightarrow \text{ketone} \end{cases}$$

The organic compound is thereby oxidized and the nickel (III) species reduced back to $Ni(OH)_2$ which at a suitable potential (~400 mV *vs.* Ag/AgCl) is immediately reoxidized to nickel (III). The nickel hydroxide is formed as a thin film on a nickel surface when placed in an alkaline solution. This film is stable as well as the oxidized form under normal conditions. Corrosion problems, however, occur with "obvious" agents such as chloride ions.

The oxidation rates measured by Fleischmann were found to lie well under the diffusion-controlled limit. The rate-controlling step was therefore the hydrogen atom abstraction. The oxidation currents for 0.1M substrates at polished nickel electrodes were well under 1 mA/cm^2.[1] This implies a factor of about 100 or more under the limiting current. This has very negative implications for a proposed industrial synthesis, since for operation at such a current density an excessively high electrode area would be needed (Table II). Despite the originally reported low oxidation rates, the oxidations with nickel anodes were regarded as important enough to warrant the development of a compact cell based on nickel sheet electrodes. The cell that

[1] Later work showed that the pretreatment of the anode allows significant higher current densities to be attained. Other factors that can increase the current are a higher substrate concentration and a higher temperature.

Table I. Percent current yield of products from the anodic oxidation of organic substrates at a nickel anode in 1M KOH

Substrate	Product*
n-Propylamine	Ethyl cyanide (84), propionaldehyde (11)
n-Butylamine	Propyl cyanide (85), n-butyraldehyde (6)
Ethanol	Acetic acid (98)
Propanol	Propionic acid (95)
Isopropanol	Acetone (90)

* Percent current yield in parentheses.

Table II. Anodic oxidation of alcohols

Substrate	Current for 0.1M substrate in 0.87M KOH at polished Ni (mA/cm^2)	Electrode area for production of 1 ton/day (m^2)
Methanol	0.24	29,100
Ethanol	0.34	14,300
n-Propanol	0.21	17,700
Isopropanol	0.08	46,500
Sec-butanol	0.07	43,100

* Electrochemical Society Active Member.

evolved was not far removed from the form of the nickel sheet received from the supplier, a roll. The electrochemical cell took the form of a rolled-up sandwich and thereby had a form very similar to that of the "Swiss-roll,'" the English name for the pastry shown in Fig. 1. (Incidentally, building instructions are widely available in books other than electrochemical ones!) The electrochemical equivalent of this structure is shown schematically in Fig. 2.

The main components of the "Swiss-roll" electrolysis cell are: two separator cloths, 1, which serve to electrically isolate the anode, 2, and cathode, 3, from each other and also to provide an electrolysis chamber. These layers are arranged as a sandwich, rolled up around an axis (often acting as a current feeder to one of the electrodes), and pressed into a cylindrical container with the necessary inlet and outlet for the electrolyte, which is pumped through. The main properties of the cell are a high specific electrode area, a very high mass transfer rate, constructional simplicity, and ease of scale-up. This then was the basic "Swiss-roll" cell as used in the laboratories at the ETH for the oxidation of organic substrates (3). At about the same time Williams and co-workers at du Pont had developed a very similar "Jelly-roll" cell (4). In future work (1975-1980) the components of the cell were studied in some detail and even new concepts in cell construction developed (5).

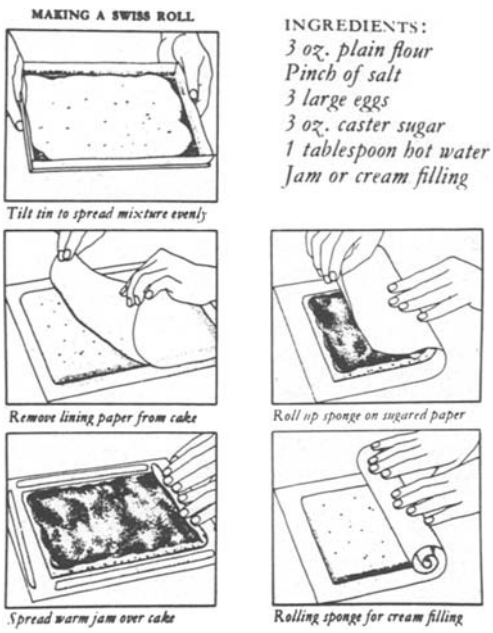

Fig. 1. The "original" "Swiss-roll" with "building" instructions!

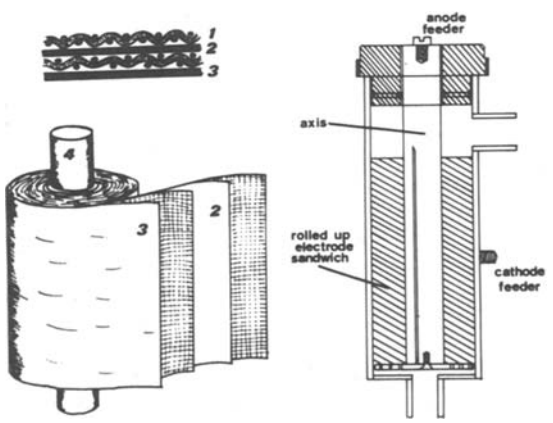

Fig. 2. The "Swiss-roll" electrolysis cell. The main components are: 1, separator net; 2, anode sheet; 3, cathode sheet.

As shown in Fig. 3 there are various components that can be incorporated into the "Swiss-roll" cell: sheet or net electrodes (6-8), turbulence promoting separator cloths (9), and "convection dampers" to reduce the extent of diffusion-controlled loss reactions at the counterelectrode (10, 11). So much for the developments that followed. Back in 1973 the "Swiss-roll" cell had merely been used to repeat the results of Fleischmann with alcohols and amines, which for industry were of little importance. The reaction that turned out to be the launching pad for the "Swiss-roll" cell was a step in the synthesis of vitamin-C.

Application of the "Swiss-Roll" Cell in Vitamin-C Synthesis

This industrial process is carried out on the scale of several 10,000 tons per year world-wide. It is a six step process (scheme 1). The first step, a hydrogenation, was carried out electrochemically between 1937 and 1948 (12) but is now superseded by a catalytic reaction. It was, however, the fourth step that was for us of interest. This is the oxidation of a primary alcohol to a carboxylic acid. The publication that turned our attention to it was that of Vertes *et al.* (13). They showed that high yields could be obtained by the direct electrolytic oxidation at nickel. Preliminary experiments with the "Swiss-roll" cell indeed confirmed the results of Vertes. A 95% material yield of diacetone-2-keto-L-gulonic acid (DAG) was obtained in an 11 batch oxidation of 10% diacetone-L-sorbose (DAS) in 1M KOH electrolyte.

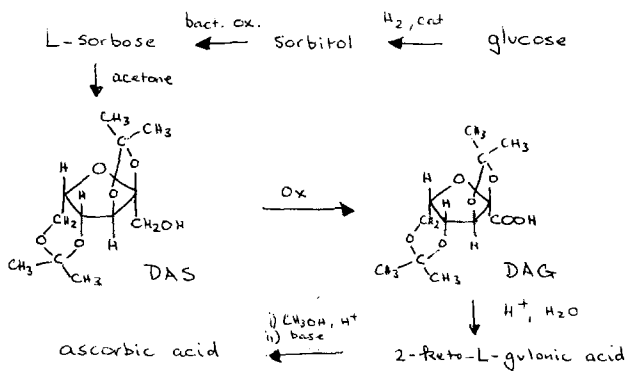

Scheme 1

The current industrial processes for the oxidation of DAS to DAG are a catalytic air oxidation or a sodium hypochlorite oxidation. Looking more closely at the sodium hypochlorite route in Fig. 4 it is obvious that it is similar to the direct electrolytic route in that an electrolysis step is involved as well as a nickel catalyst. The sodium hypochlorite oxidation may therefore be regarded as a very indirect electro-oxidation.

A comparison of both routes involving nickel would, at least in terms of the number of process steps in-

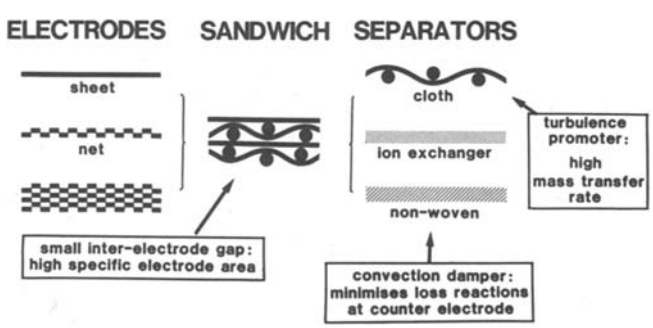

Fig. 3. Building blocks of the electrode sandwich

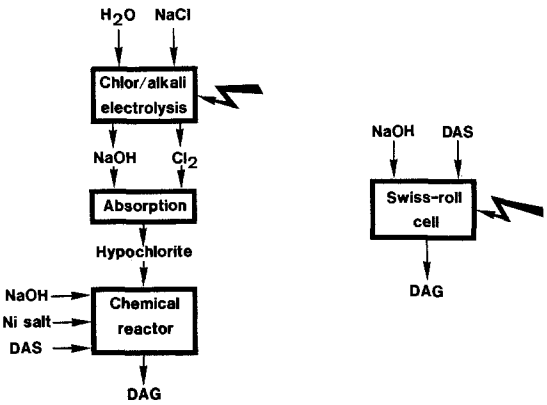

Fig. 4. Industrial routes for the oxidation of DAS to DAG. Left: hypochlorite oxidation with Ni catalyst; right: direct electro-oxidation at a nickel anode.

volved, appear to come out in favor of the direct electrochemical oxidation. At this stage of the work Hoffman-LaRoche showed an interest and thereafter carried out the bulk of the work on the direct electrolytic oxidation of DAS and the scale-up of the "Swiss-roll" cell to production size.

The work at the ETH concentrated on investigating various aspects of the behavior of nickel anodes and the mechanism of the oxidation of organic substrates at them. This served in most cases as confirmation of the results being obtained in Basel. For this work we were particularly fortunate in having a computerized instrument which allowed complex testing programs to be run (often simultaneously with 6 electrolysis cells). The main features of it are shown in Fig. 5. It is composed of a PAR polarograph which had been modified for remote control, an HP IEEE-interface and digital plotter and a Commodore PET "home" computer.

Questions of importance for the synthesis in Basel, such as "what is the best pH to oxidize at?," "what conditions lead to corrosion of the electrodes?," or "what are the factors having an influence on the activity of the electrodes?" were answered with the help of this equipment. The reinvestigation of the oxidation of organic compounds at nickel anodes in fact revealed some features that had not previously been reported.

Current/potential plots as a function of pH showed that the oxidation rate was not independent of pH as reported by Fleischmann, but a linear function of c_{OH^-} up to a critical c_{OH^-} beyond which the oxidation rate of the alcohol remained constant. In Fig. 6 the well-known features of the nickel electrode in alkaline solution are visible, namely, the oxidation of the $Ni(OH)_2$ to NiOOH at about 450 mV and its back reduction at 350 mV (here the computer was programmed so as to separate the forward and reverse scans, although they were obtained without any pause between). The linear dependence of the current on c_{OH^-}, its diffusion-controlled characteristic at lower c_{OH^-} values, and the formation of a steady-state oxidation peak beyond the diffusion-controlled region (kinetic control-hydrogen abstraction) came as a surprise (14).

The practical significance of these results was, in the first instance, to define the minimum OH^- concentration necessary to achieve the maximum limiting oxidation rate for a given DAS concentration. The results are summarized in Fig. 7, which shows the peak oxidation current as a function of c_{OH^-} for various DAS concentrations. The linear portion of the curve had more or less the same slope regardless of substrate or its concentration. Apparently in this region the oxidation is limited by the flux of OH^- to the electrode. These currents were diffusion-controlled as substantiated by rotating disk electrode experiments. The magnitude of the currents corresponded to those expected for a diffusion of the OH^-.

With regard to the oxidation rate, Vertes in his experiments prepared the nickel anodes by cathodic deposition of a nickel hydroxide layer from a solution of a nickel salt. By this means thick layers of hydroxide may be built up, which are apparently porous and offer a large active area for the oxidation of DAS to DAG. Much higher current densities may thereby be attained. We have also investigated this, in fact the data in the last two figures were obtained at "thick" nickel oxide electrodes.

Figure 8 compares electrodes that have been pretreated by varying amounts. Again the peak current for the oxidation of the organic substrate (in this case ethanol) is plotted as a function of c_{OH^-}. Longer deposition times give a thicker $Ni(OH)_2$ layer which is immediately obvious from the height of the peak for

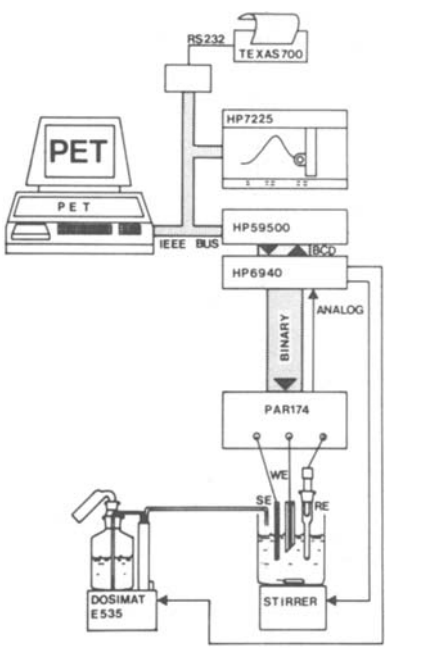

Fig. 5. Schematic of the computer-controlled instrumentation used for the study of the nickel anode behavior and the oxidation kinetics of DAS.

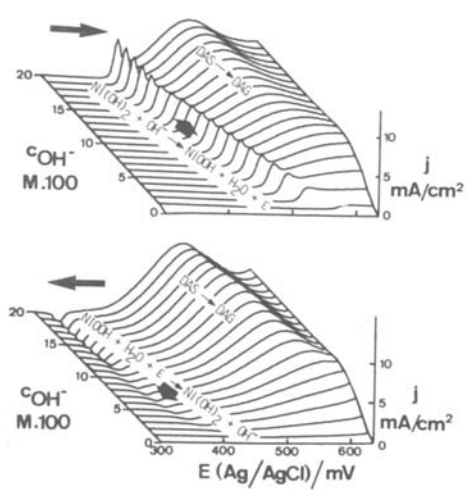

Fig. 6. Current potential sweep measurements for the oxidation of DAS at a nickel anode. Top: forward scan; bottom: backward scan (both at 5 mV/sec) at several different hydroxyl ion concentrations.

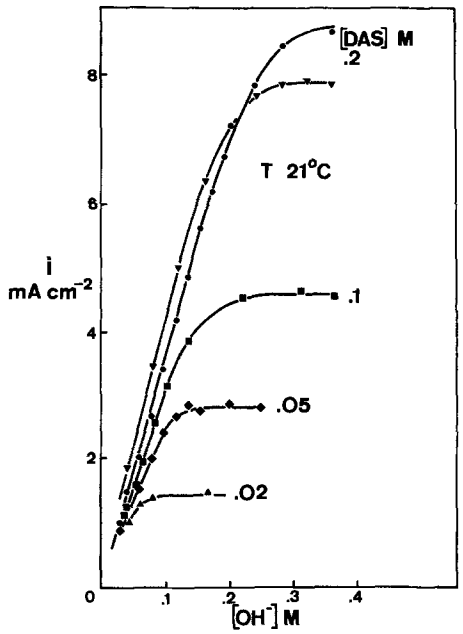

Fig. 7. Peak current for the oxidation of DAS on an etched nickel anode at various concentrations as a function of hydroxyl concentration.

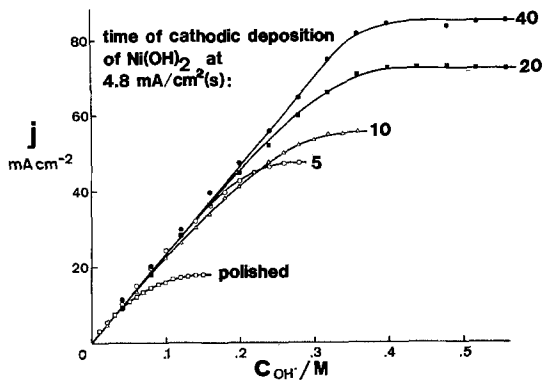

Fig. 8. Activity of a nickel oxide electrode as a function of the oxide layer thickness and hydroxyl concentration as manifest by the peak oxidation current for 0.17M EtOH. The following electrode pretreatments were employed: (a) polished; (b) 5 sec cathodic deposition of nickel at 4.8 mA/cm² from a 0.1M $Ni(NO_3)_2$ solution; (c) 10 sec; (d) 20 sec; (e) 40 sec.

the oxidation of Ni(II) to Ni(III) and from the increased activity for the oxidation of the organic substrate. Current increases of the order of about 10 (in comparison to the polished electrode) may be realized.

Scale-Up of the Process in Size and Time

In the meantime Roche had advanced to a somewhat larger synthesis setup with a "Swiss-roll" cell of area 3 m² and radial electrolyte flow. This equipment, which allowed continuous operation, is shown schematically in Fig. 9. The main features are: centrifugal pump, rotameter, mono-polar "Swiss-roll" cell, heat exchanger, electrolyte reservoir, and oxygen meter.

At first, batch experiments were carried out with a 12 liter charge of 10% DAS solution. About 500g of DAG could be prepared per hour. During the reaction only NaOH was added to maintain constant *p*H. In order to determine the behavior of the system over long periods of time, the first continuous experiment was planned. It was intended to run the experiment for 100 hr from Monday to Friday. The first phase of the experiment went very satisfactorily. After 5 hr a steady state was reached and all experimental parameters such as DAS, DAG, and NaOH concentration,

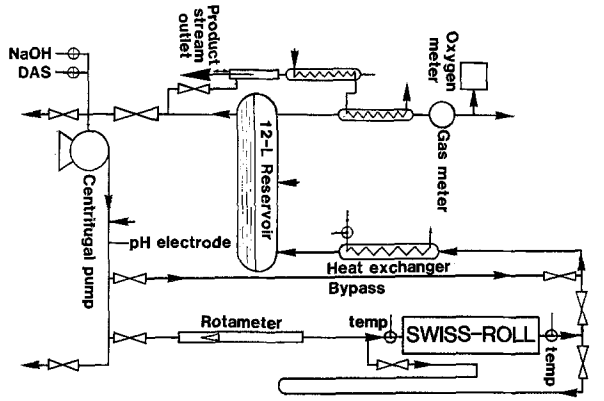

Fig. 9. Schematic diagram of flow system used for the batch and continuous oxidation of DAS with a "Swiss-roll" cell with anode area of 3 m².

current, cell potential, and oxygen content in the vent gas stayed constant. On the recorder hours and hours of straight lines were registered so that one almost had to fight against boredom. However, after 40 hr the anode became progressively deactivated, the degree of oxidation sank as well as the current and selectivity. The scale-up in time had encountered the first problems. The answer to this problem was luckily already at hand from previous work by Roche in Nutley and more recently published confirmation by Fioshin and co-workers who in the first half of the 70's were also working intensively on the electrolytic oxidation of DAS (15). The addition of catalytic amounts of a nickel salt effectively suppressed the deactivation. This phenomenon was studied at the ETH to define more precisely, using instrumental methods, the conditions leading to and the extent of the problem. These results confirmed those of Roche which were based more on the preparative experiments. The electrode activity was ascertained from current/potential curves obtained periodically during an electrolysis of DAS at 530 mV. The observations from the preparative experiments were confirmed (Fig. 10): the decrease of the peak height for DAS oxidation and the increased rate of oxygen production.

The addition of a small amount of nickel brought a stable activity to the nickel anode and, more strikingly, complete inhibition of oxygen evolution. The results shown in Fig. 11 are in the first 3 hr life of the electrode. The positive effect of the nickel salts was also confirmed over a 60 hr period (Fig. 12). Passivation would always set in if a nickel-free electrolyte was employed. In the diagram the results of such a test are also shown. After 60 hr successful

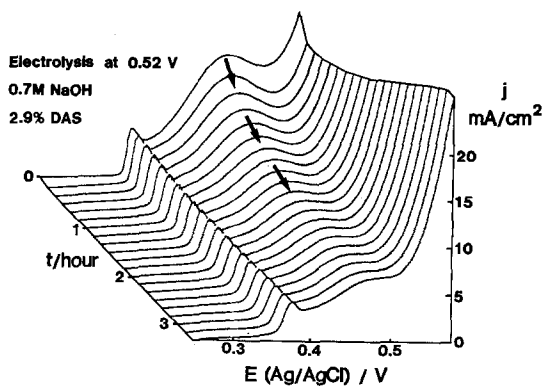

Fig. 10. Current/potential sweeps obtained during the electrolysis of DAS at 520 mV (vs. Ag/AgCl) as a function of electrolysis time. Note the decrease of DAS oxidation current and the increase (at end of scan) of the oxygen evolution.

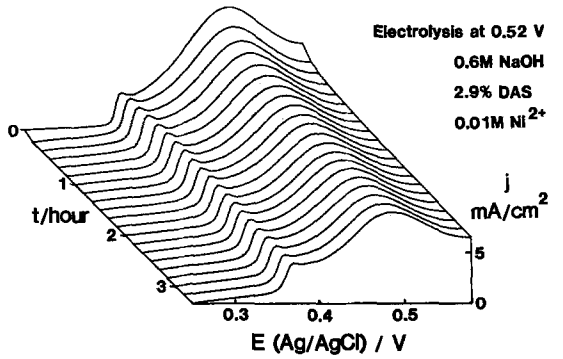

Fig. 11. As for Fig. 10 except that the electrolyte contains 10 mM nickel salt. The loss of electrode activity for the oxidation of DAS is not observed.

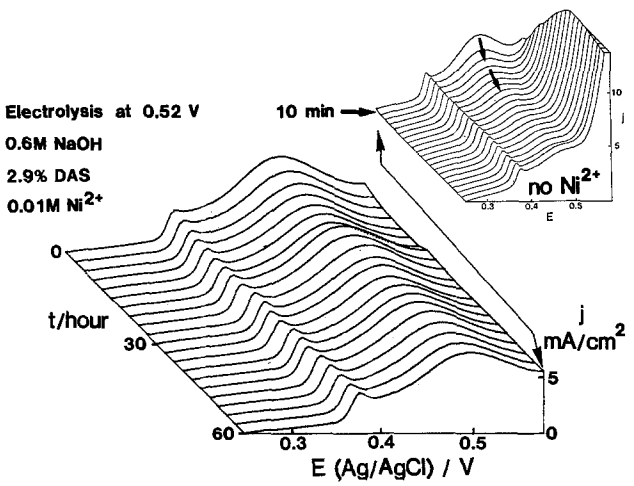

Fig. 12. As for Fig. 11 except over an extended electrolysis time of 60 hr. The insert figure shows the behavior of the 60 hr old electrode when the electrode is changed to no-nickel composition, the electrode deactivates.

operation in a nickel-containing electrolyte, the solution was changed to a nickel-free system and immediately the passivation, typified by a decrease of the DAS oxidation current and the onset of oxygen evolution, set in. A restoration of the original state proceeded only partly on addition of a nickel salt.

Because the solubility of nickel salts in such an alkaline solution is low it is to be expected that small amounts of nickel are sufficient to bring the beneficial effect. The activity of nickel anodes is expressed in Fig. 13 as the peak current for DAS oxidation normalized with respect to its initial value. It is plotted as a function of time for different values of the total nickel concentration. Already at 0.001M the problem of passivation is solved.

Interestingly the cation of the support electrolyte also influences the passivation behavior. In Fig. 14, which is similar to the previous, the effect of the cation of the support electrolyte (in the absence of a nickel salt) on the anode activity is shown. Potassium gives the least loss of activity, while a quaternary ammonium salt is the most serious offender.

All of the observations obtained here on the oxidation of DAS at nickel, of course, have implications on the reaction mechanism. It appears doubtful that the Ni(III) species is really the active species since the oxidation occurs in the range where Ni(III) is oxidized further, and cations are incorporated into the oxide film (perhaps explaining the sensitivity of the electrodes to cations and the observed passivation effects).

During this phase two complex questions had to be answered in Basel: (*i*) the process conditions for

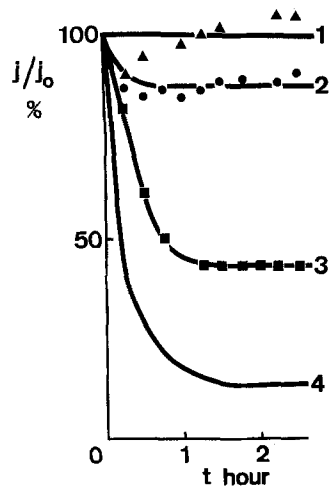

Fig. 13. Peak oxidation current normalized with respect to the initial value (new electrode) for the electro-oxidation of a 10% DAS solution in 0.1M NaOH as a function of time for different concentrations of nickel. 1, 1 mM; 2, 0.1 mM; 3, 0.01 mM; 4, 0.

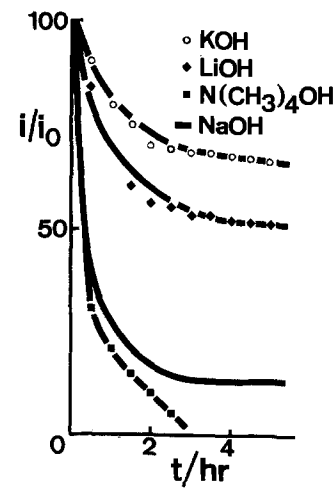

Fig. 14. Peak oxidation current normalized with respect to the initial value (new electrode) for the electro-oxidation of a 10% DAS solution in 0.1M NaOH as a function of time for different support electrolytes.

optimal operation (yield, current efficiency, energy consumption per kilo DAG, NaOH consumption as a function of the current density, temperature, NaOH concentration, pumping rate and so on, and (*ii*) the reaction conditions that led to a drop in yield! The latter seems to be a strange form of occupational therapy but, in fact, it was of considerable importance to define to the production engineers conditions that were to be avoided. The process, in fact, turned out to be extremely uncritical. In the continuous operating mode with recycling of the electrolyte a high conversion of DAS to DAG can only be realized with minimum electrode area when a cascade of reactors is operated in series. The next stage of the piloting was therefore to simulate a two-stage cascade of reactors. In this test the processed solution from a first pass in which a 90% conversion had been obtained was collected and then with conditions simulating a second stage re-electrolyzed to 99% conversion. The electrolysis conditions and the results obtained are given in Table III. In long-term experiments these conditions could be realized for several weeks.

Scale-Up to the Commercial Cell Size

The work in Basel was more or less complete. The development of the "Swiss-roll" cell and the process

Table III. Oxidation of DAS in mini-pilot plant

	Stage 1	Stage 2	Total
Current, A	120	18	
Cell potential, V	2.2	1.9	
NaOH conc, M	0.3	0.2	
Degree of oxidation, %	90	99	99
DAG production rate, kg/hr			0.26
Energy requirement, kW-hr/kg			1.2
Current efficiency, %			70
Isolated yield, %			93

for the oxidation of DAS was then transferred to Grenzach (the site of Roche Vitamin-C production in Europe). At first a "Swiss-roll" cell of anode area 30 m^2 was put into service (Fig. 15). The results obtained in the laboratory were reproduced or even bettered. The performance of bipolar "Swiss-roll" cells was also successful. The electrolytically produced DAG matched all production requirements and passed all quality controls. As a result a full scale unit was constructed, whereby through replication a production capacity of several thousand tons per year could be realized. The principles of the mini-pilot plant could be carried over to the large system with very little modification. The main features of the large plant were several bipolar "Swiss-roll" cells operating in a cascade at currents from 20 kA down in steps to 1 kA. Each "Swiss-roll" had several hundred m^2 anode area. One of these units is shown in Fig. 16. With this oxidation stage more than 2 tons of DAG could be produced daily. The cells have already been operating successfully for several thousand hours. A close investigation of the electrodes and the separator nets revealed that no corrosion had occurred.

Conclusions

The direct electrolytic oxidation has already been compared with the hypochlorite route. What can be said now that the process has been brought to the production stage? Although the production costs for the two routes do not greatly differ, the electrochemical route uses less electrical energy (mainly on account of the lower cell voltage of 2V in comparison to the 4V of a chlor/alkali electrolysis) and gives less NaCl-loaded waste water.

In terms of the criteria that are often used to point to profitable electrochemical routes, the DAS/DAG oxidation involves: (*i*) fewer processing steps, (*ii*) a product is produced on the anode and on the cathode (H_2 is used in the hydrogenation of the glucose), (*iii*) few scale-up difficulties were encountered, (*iv*) the stability of the electrodes was tolerable, (*v*) the electrolyte conductivity was high, (*vi*) DAS and DAG are very soluble in the electrolyte, (*vii*) there is no need for an expensive supporting electrolyte, and (*viii*) there was no special requirement for the feedstock and the product work-up was as for the conventional process.

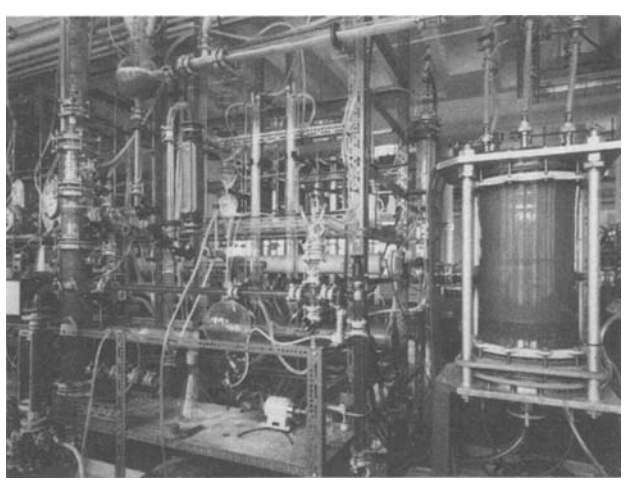

Fig. 15. Pilot-plant with 30 m^2 "Swiss-roll" electrolysis cell (left) for the continuous oxidation of DAS.

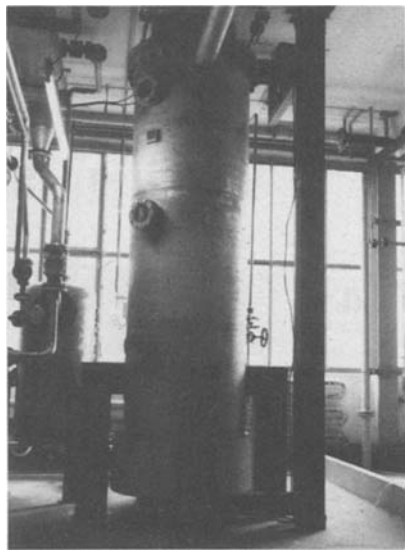

Fig. 16. One of the commercial size "Swiss-roll" cells used by Roche in a cascade of reactors for the production of 2 ton/day DAG.

Manuscript received July 16, 1982. This was Paper 586 presented at the Montreal, Quebec, Canada, Meeting of the Society, May 9-14, 1982.

Any discussion of this paper will appear in a Discussion Section to be published in the December 1983 JOURNAL. All discussions for the December 1983 Discussion Section should be submitted by Aug. 1, 1983.

Publication costs of this article were assisted by the Swiss Federal Institute of Technology.

REFERENCES

1. M. Fleischmann, K. Korinek, and D. Pletcher, *J. Electroanal. Chem. Interfacial Electrochem.*, **31,** 39 (1971).
2. F. Fichter, "Organische Elektrochemie," Steinkopff, Leipzig (1942).
3. P. M. Robertson, F. Schwager, and N. Ibl, *J. Electroanal. Chem. Interfacial Electrochem.*, **65,** 883 (1975); P. M. Robertson (Assignee: Roche) U.S. Pat. 4,040,938; P. M. Robertson (Assignee: Roche) U.S. Pat. 4,097,346.
4. J. M. Williams, U.S. Pat. 3,859,195 (to E. I. du Pont de Nemours).
5. P. M. Robertson, P. Cettou, D. Matic, F. Schwager, A. Storck, and N. Ibl, *AIChE Symposium Series No. 185,* **75,** 115 (1979).
6. P. Gallone, P. L. DeAnna, and P. L. Bonora, *Mater. Chem.*, **3,** 285 (1978).
7. A. Storck, P. M. Robertson, and N. Ibl, *Electrochim. Acta,* **24,** 373 (1978).
8. B. Scholder, ETH Dissertation, In preparation.
9. F. Schwager, P. M. Robertson, and N. Ibl, *Electrochim. Acta,* **25,** 1655 (1980).
10. D. Matic, P. M. Robertson, and N. Ibl, *ibid.*, **25,** 487 (1980).
11. P. M. Robertson, R. Oberlin, and N. Ibl, *ibid.*, **26,** 941 (1981).
12. C. L. Mantell, "Electro-organic Chemical Processing," Noyes Development Corp., Park Ridge, NJ, p. 147 (1968).
13. G. Horanyi, G. Vertes, and F. Nagy, *Acta Chim. Acad. Sci. Hung.*, **67,** 357 (1971).
14. P. M. Robertson, *Electrochim. Acta,* **22,** 411 (1977).
15. T. E. Mulina, I. A. Avrutskaya, M. Ya. Fioshin, and T. A. Malakhova, *Sov. Electrochem.*, **10,** 467 (1974); M. Ya. Fioshin, I. A. Avrutskaya, T. A. Malakhova, and T. E. Mulina, *ibid.*, **10,** 760 (1974); I. A. Avrutskaya, M. Ya. Fioshin, T. E. Mulina, and T. A. Arkhinova, *ibid.*, **12,** 1176 (1976).

Electrochemical Determination of Cation Radical Stabilities of Monomethylbenzo[a]pyrenes

Donald A. Tryk,* Su-Moon Park,* and Guido H. Daub

Department of Chemistry, University of New Mexico, Albuquerque, New Mexico 87131

ABSTRACT

All twelve monomethylbenzo[a]pyrenes were studied using cyclic voltammetry and single- and double-potential-step chronoamperometry at a platinum electrode in acetonitrile, in order to determine the kinetic stability of the cation radicals, and to obtain information on the decay reaction mechanisms. For most of the compounds there may be more than one mechanism operating in parallel, but single-potential-step chronoamperometric data were amenable to calculation of rate constants for the reaction of cation radical with water. With some exceptions, larger rate constants correlate with lower calculated localization energies. There are some parallels between the kinetic results and animal carcinogenicity data reported eleswhere.

Polycyclic aromatic hydrocarbons (PAH's) have long been studied with a view towards correlating physical properties and theoretical parameters with carcinogenicities. Examples of attempts at correlations of carcinogenicities with electrochemical properties can be found (1, 2). Ionization potentials and polarographic half-wave potentials (2, 3) yield fair correlations with carcinogenicities, and have led some to propose that cation radicals are involved as intermediates in carcinogenesis (4). More easily formed cation radicals should be more potent carcinogens. However, if there is a cellular oxidizing agent sufficiently strong to oxidize most PAH's, the next most important criterion should be the kinetic stability of the cation radical (5). This stability must fall within a certain range: too low a stability will not allow the species to reach a DNA molecule unchanged, whereas too high a stability will not allow it to react even after reaching a DNA molecule.

A theoretical measure of kinetic stability is the localization energy for the reaction of cation radical with nucleophile, a reaction in which charge becomes localized at a particular carbon in the PAH upon binding with the nucleophile. For most groups of related PAH's, a larger localization energy and consequently higher stability would mean greater carcinogenicity.

Caspary *et al.* (5) describe an experiment which measures such a kinetic stability, in which they determine the steady-state ESR signal of a frozen benzene solution containing iodine and PAH. The correlation is quite good for 14 compounds, with the exception of perylene, which probably falls into the too-stable category, and of dibenz[a,c]anthracene and dibenz[a,h]anthracene (discussed below).

An alternate method of determining cation radical stabilities is a transient electrochemical experiment, such as cyclic voltammetry or chronoamperometry (6). The advantages of such techniques are (*i*) that the potential can be controlled and (*ii*) that the cation radical decay mechanisms can be determined. Iodine activation is not a true test of radical stability because the yield of radicals varies with the redox potential of the compound in question. Dibenz[a,h]anthracene and dibenz[a,c]anthracene are relatively difficult to oxidize, and this fact may account for the low ESR signals observed (5). Both compounds are either mutagenic or carcinogenic, however (5, 7).

We have studied the monomethyl derivatives of benzo[a]pyrene (BaP) using cyclic voltammetry, and single- and double-potential-step chronoamperometry in order (*i*) to obtain information about the overall electron transfer/chemical reaction mechanisms. (*ii*) to obtain chemical reaction rate constants, (*iii*) to compare the latter with cation radical charge distributions and localization energies calculated using simple MO theory, and (*iv*) to compare all of these results with known carcinogenic properties. The numbering system for BaP is

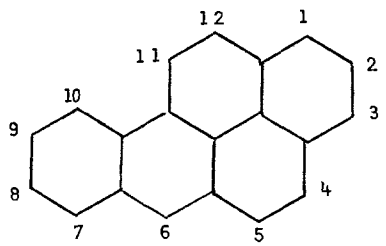

Experimental

Monomethylbenzo[a]pyrenes.—1-, 2-, 3-, 4-, 5-, 11-, and 12-methylbenzo[a]pyrenes (MeBaP's) were synthesized and purified by one of the authors (GHD) and co-workers (8-12). Syntheses for 3- and 5-MeBaP's have been reported (13-15). The remaining MeBaP's were obtained from the National Cancer Institute Chemical Repository and used as received. Syntheses have been reported (14, 16-19).

Reagents.—Eastman spectrograde acetonitrile was distilled on a high vacuum line three times from P_2O_5 and then stored under vacuum. The background water concentration has been estimated to be approximately 4 mmol on the basis of measured rate constants (k_1 in Eq. [1]) with standard additions of water. Polarographic grade tetrabutylammonium perchlorate (TBAP) from Southwestern Analytical Chemicals, Austin, Texas, was dried on a vacuum line overnight at 90°-100°C.

Preparation of electrochemical cell.—A three-electrode cell adapted for use on a vacuum line was used. The cell and its use have been described previously (20). The TBAP and MeBaP concentrations were 0.1M and approximately 0.5 mmol, respectively. The platinum working electrode (0.0228 cm^2) was polished with Fisher grade B gamma alumina (<0.1 μm particles), and placed in concentrated HNO_3 for 1 min. The reference electrode was an Ag wire pseudo reference, which was approximately +0.16V with respect to a saturated calomel electrode. Water was added to the cell while helium was flowing to minimize contact with air.

Electrochemical experiments.—Cyclic voltammetry (CV) and single- and double-step chronoamperometry (CA1 and CA2) were performed using a Princeton Applied Research Model 175 Universal Programmer and Model 173 galvanostat-potentiostat. For pulse widths less than 1 sec, a Tektronix Model 5115 storage oscilloscope was used and, for pulse widths of 1 sec or longer and for CV, a Houston Model 2000 X-Y recorder

* Electrochemical Society Active Member.

Key words: monomethylbenzo[a]pyrenes, cation radical, carcinogenicity, HMO calculation.

was used. For CA1 and CA2 experiments, the cell solution was manually stirred and then potentiostated at 0V for 10 sec prior to activation. At activation the potential was stepped to a value at which the concentration of electroactive material at the electrode surface would be reduced to zero, approximately 100 mV positive of the first oxidation CV peak. The first oxidation peak occurred at a potential at least 250 mV negative of the second oxidation peak, except in the case of BaP, where the separation was 200 mV. For CA2, the potential was then stepped after the nominal pulse width to a point at which the concentration of cation radical at the electrode surface would be reduced to zero, 100 mV negative of the re-reduction peak potential. *IR* compensation was not used; instead, current values were corrected by substracting background currents at various pulse widths, which were measured in a cell prepared without electroactive material and subjected to similar potentials. At 0.1 sec the correction was on the order of 10% of the total current. The n_{app} values were computed for the MeBaP's assuming that diffusion coefficients were the same as those reported by Jeftic and Adams for BaP (21).

MO calculations.—A standard Hückel MO program (22) was employed, in which an h value of -0.5 (inductive model) was used for the carbon at which a methyl group was attached (23). Charges were computed for the cation radicals by summing the squares of the AO coefficients, and localization energies were calculated by computing the difference in total binding energy between the cation radical and the conjugated system formed when the charge is localized at C-6. Both systems contain 19π electrons.

Results and Discussion

Electrochemical experiments.—In the presentation of results it will be helpful to refer to an anodic oxidation scheme for benzo[a]pyrene (BaP) itself based on the one developed by Jeftic and Adams (21). This scheme is in the form of a series of six electron transfer/chemical reaction (EC) steps. R refers to BaP without two of its hydrogen atoms. The groups represented without parentheses are attached at the 6-carbon, while the groups within parentheses can be attached at the 1-, 3-, or 12-carbons

$$E_1:\ R(H)H \overset{-e^-}{\rightleftharpoons} R(H)H^{\cdot+} \overset{H_2O,k_1}{\longrightarrow} R(H)HOH\cdot + H^+ \quad [1]$$

$$E_2:\ R(H)HOH\cdot \overset{-e^-}{\rightleftharpoons} R(H)HOH^+ \overset{k_2}{\rightarrow} R(H)OH + H^+ \quad [2]$$

$$E_3:\ R(H)OH \overset{-e^-}{\rightleftharpoons} R(H)OH\cdot^+ \overset{k_3}{\rightleftarrows} R(H)O\cdot + H^+ \quad [3]$$

$$E_4:\ R(H)O\cdot \overset{-e^-}{\rightleftharpoons} R(H)O^+ \overset{H_2O,k_4}{\longrightarrow} R(OH)OH + H^+ \quad [4]$$

$$E_5:\ R(OH)OH \overset{-e^-}{\rightleftharpoons} R(OH)OH\cdot^+ \overset{k_5}{\rightleftarrows} R(OH)O\cdot + H^+ \quad [5]$$

$$E_6:\ R(OH)O\cdot \overset{-e^-}{\rightleftharpoons} R(OH)O^+ \overset{k_6}{\rightleftarrows} R(O)O + H^+ \quad [6]$$

Thus the final product $R(O)O$ is a mixture of the BaP diones, 1,6-dione, 3,6-dione, and 6,12-dione. Also, some of the chemical steps may be reversible, especially [3], [5], and [6].

Reaction [1] is shown diagrammatically below, broken into elementary steps.

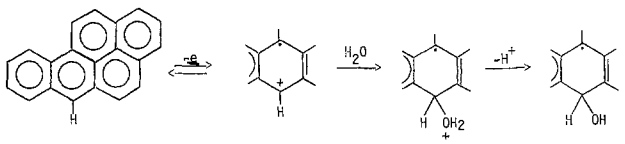

Cyclic voltammograms for BaP are shown in Fig. 1 before and after the addition of enough water to bring the concentration to 39.0 mmol. In this and other voltammetry shown, the initial positive potential scan is reversed after the cation radical is produced; the second scan is reversed after dication is produced at more positive potentials. In Fig. 1a, formation of cation radical is seen at +1.09V and formation of anion radical is seen at −2.09V, both *vs.* Ag. Two fused peaks corresponding to reduction of products with the main peak at +0.58V have been associated with the reduction of 6-oxo-BaP cation to its free radical (reaction [4]) and the reduction of 6-OH-BaP cation radical to 6-OH-BaP (reaction [3]) (21). After the addition of water (Fig. 1b) a peak corresponding to reduction of BaP dione appears at +0.27V (21).

Methylated BaP cation radicals are on the whole more stable than that of BaP, as can be seen in Fig. 2, showing CV of 3-MeBaP. Voltammograms for the other MeBaP's are fairly similar except for variations in peak shapes due to adsorption and kinetics. The most pronounced example of adsorption is 6-MeBaP, whose CV is shown in Fig. 3. Here the cation radical adsorbs, and its reduction is seen as a small spike when no water has been added. Note that the decay of cation radical gives rise to no clearly defined product peaks while the decay of dication gives rise to two clearly defined peaks. The second product peak, here seen at +0.23V, is much more pronounced than it was for any of the other compounds. This peak could again correspond to reduction of a dione. In support of this, there is a strong similarity between the CV for 6-MeBaP observed with added water (Fig. 3b) and that for BaP with added water (Fig. 1b).

CA2 current ratios ($R_i \equiv i_2\tau/i\tau$, where τ is the pulse width) are shown for representative MeBaP's in Fig. 4. It has been helpful to compare these results with

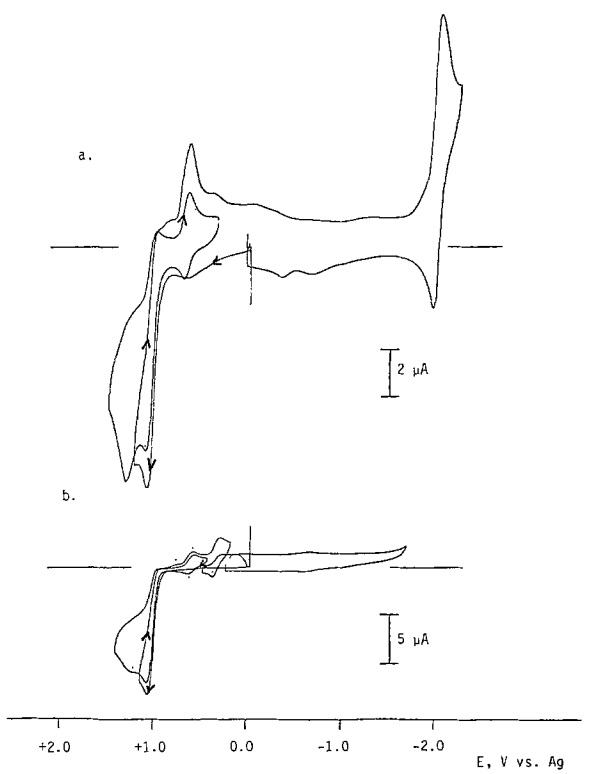

Fig. 1. CV of BaP (0.49 mmol) at 100 mV sec^{-1} in acetonitrile. The arrow marks indicate the potential scan corresponding to the cation radical generation. a. No H_2O added. b. 39.0 mmol H_2O.

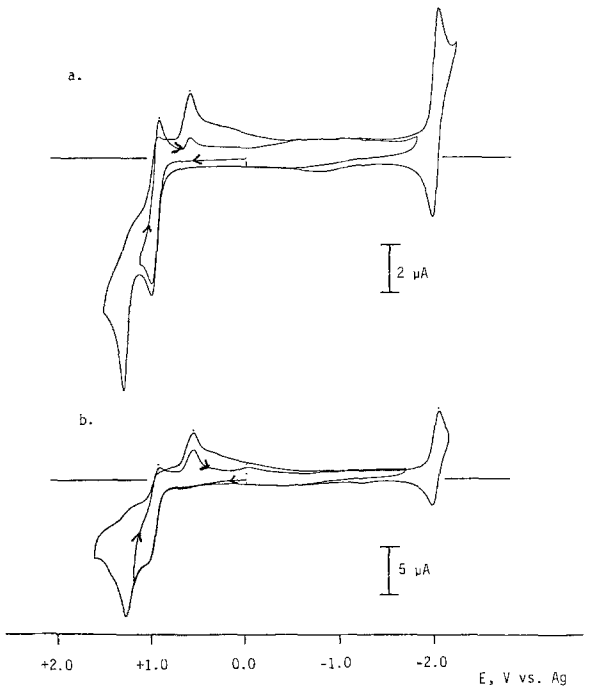

Fig. 2. CV of 3-MeBoP (0.46 mmol) at 100 mV sec^{-1} in acetonitrile. a. No H_2O added. b. 10.2 mmol H_2O.

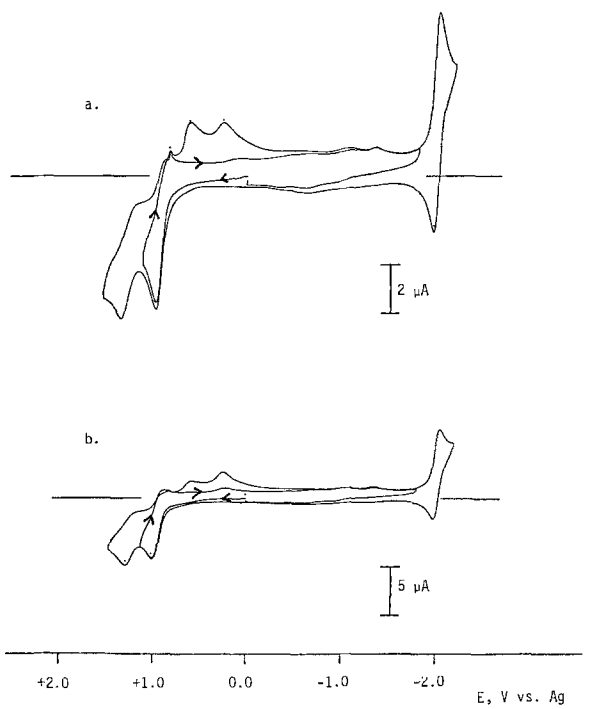

Fig. 3. CV of 6-MeBaP (0.49 mmol) at 100 mV sec^{-1} in acetonitrile. a. No H_2O added. b. 13.5 mmol H_2O.

the comprehensive set of digitally simulated working curves published by Hanafey *et al.* (24). The behavior of 11-MeBaP indicates that it has the most stable cation radical, and the curve approaches the first-order EC working curve shown for comparison at large τ values. However there are about ten other possible mechanisms which give similar working curves, including ECE, ECEC, and ECC mechanisms. All of these exhibit the approach at small τ values of R_i to the value of 0.293, which is predicted for a simple diffusion-controlled electron transfer uncomplicated by chemical reactions (25). The explanation for the fact that R_i is less than expected is that adsorption equilibrium is not being established at short times (26).

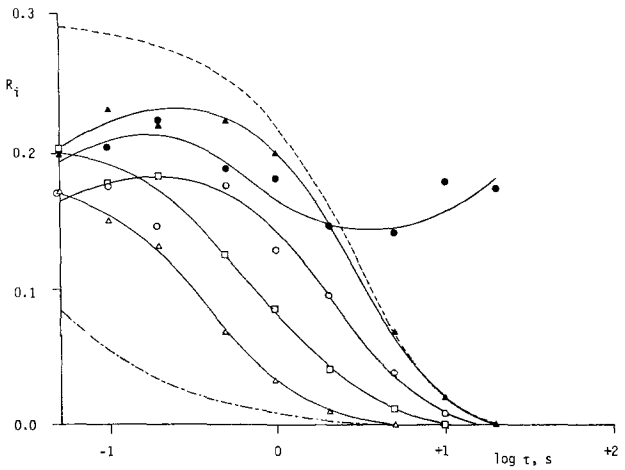

Fig. 4. CA2 current ratios as a function of pulse width for several MeBaP's in anhydrous acetonitrile. (○) 1-MeBaP; (△) 2-MeBaP; (□) 3-MeBaP; (●) 6-MeBaP; and (▲) 11-MeBaP. Points are averaged from two experimental values. All concentrations were approximately 0.5 mmol. Dashed line: first order EC working curve; dotted and dashed line: EC, radical-radical coupling working curve (37).

1-MeBaP has a somewhat stable cation radical according to its R_i *vs.* log τ behavior. Less stable are the cation radicals of 3-MeBaP and 2-MeBaP. 6-MeBaP exhibits unique behavior and is discussed below. All of the other MeBaP's not represented in Fig. 4 (4, 5, 7-10, and 12) exhibited plots intermediate between those of 2- and 3-MeBaP. As the stability of the cation radicals decreases, R_i seems to fall off more gradually, as in the case of 2-MeBaP. This kind of behavior is indicative of a second-order process for the decay of cation radicals. Hanafey *et al.* present working curves for five such possible mechanisms, all involving the coupling of two electrogenerated species (24). Two possible mechanisms which have relevance in the present case are (*i*) EC, radical-radical coupling and (*ii*) ECC, second-order disproportionation. The first possibility can be represented as follows

$$2R(H)H^{+\cdot} \rightarrow (H)R\text{—}R(H) + 2H^+ \qquad [7]$$

Here the coupling occurs at the 6-position, as has been documented for BaP (21). BaP, 8-MeBaP, and 11-MeBaP all experienced irreversible adsorption of product, which in the case of BaP has been found to be composed mainly of BaP dimer (21). A film coats the electrode as current is passed for extended periods. Thus for these compounds, reaction [7] is probably a significant pathway.

The second possibility can be represented as follows

$$2R(H)H^{+\cdot} \rightarrow R(H)H + R(H)H^{2+} \qquad [8]$$

$$R(H)H^{2+} + H_2O \rightarrow R(H)OH + 2H^+ \qquad [9]$$

Supporting evidence for this mechanism is the fact that when the potential is swept in the C-*V* to values at which dication can be formed (Fig. 1 and 2), there is more efficient production of products. Both mechanisms have virtually identical working curves (24), and the curve corresponding to reaction [7] is shown for comparison in Fig. 4.

For most of the MeBaP's the current ratio plots lie somewhere between the first-order EC-type and the second-order-type working curves. The reason is probably that reactions [1]-[6], [7], and [8]-[9] are occurring in parallel but in various proportions for the different MeBaP's.

After water was added to the level of about 10 mmol, the R_i plots for most of the compounds shifted to the left, indicating a lessening of cation radical stability.

Also, for all compounds except 1- and 11-MeBaP (and 6-MeBaP, to be discussed below) the second-order character of the plots increased. This phenomenon could be consistent with radical-radical coupling (reaction [7]) if one assumed that water, even while accelerating the decay of cation radical through reaction [1], was enhancing the adsorption of both parent compound and cation radical, and thus increasing the concentration of cation radicals near the electrode. The assumption is valid because the presence of 5.2 mmol water increased the surface excess of 1-MeBaP from 6.8×10^{-10} to 1.2×10^{-9} mol cm^{-2}, and that of 1-MeBaP cation radical from 2.1×10^{-10} to 4.6×10^{-10} mol cm^{-2}, as determined from chronocoulometric measurements. This phenomenon could also be consistent with disproportionation (reactions [8]-[9]) for the same reason. The R_i plot for 6-MeBaP (Fig. 4) shows values less than expected at the shorter pulse widths probably again due to adsorption of compound. As was seen with cyclic voltammetry, there is also adsorption of cation radical, which definitely accounts for the large R_i values at the longer pulse widths.

Representative results for single-potential-step chronoamperometric (CA1) experiments done without added water are presented in Fig. 5. All of the data are characterized by a monotonic increase in n_{app} as time proceeds. Results for the MeBaP's not presented in the figure are very similar in shape to those for 1- and 2-MeBaP. The plot for 6-MeBaP has been fit assuming $n_2 = 0.5$ and that for 11-MeB has been fit assuming $n_2 = 1$. Those compounds will be discussed in more detail below. At times shorter than 0.1 sec, all of the n_{app} values rise with decreasing time due to adsorption of compound at the electrode surface, as discussed above.

For simple ECE mechanism, n_{app}, the apparent number of electrons transferred should rise to a plateau value according to the number of electrons involved in the second electron transfer [6] based on the equation $n_{app} = n_1 + n_2 (1 - e^{-kt})$. Here n_1 and n_2 are the number of electrons transferred before and after the chemical step, and k is the rate constant for the chemical step. The lower portion of the experimental curves (Fig. 5a and b) can be fit reasonably well to the ECE working curve in which $n_1 = 1$ and $n_2 = 2$. Over the region where n_{app} is $2 \sim 3$ the curves start deviating due probably to the operation of further electron transfer steps. Finally at much longer times (<60 sec), the actual current reached a steady-state value in every case, and thus the n_{app} values began to increase steeply. It is probable that this phenomenon is due in part to a catalytic mechanism because the time at which steady state was reached depended on the compound. However, it is difficult to separate the contribution of steady-state currents brought on by radial diffusion and by natural convection from such a catalytic current.

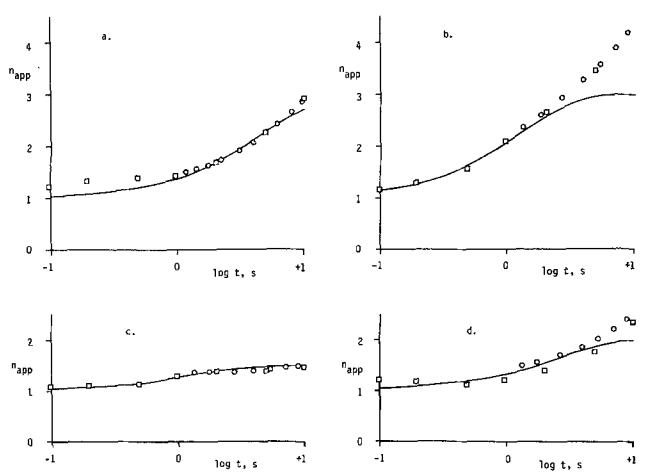

Fig. 5. CA1 n_{app} values as a function of time for (a) 1-MeBaP, (b) 2-MeBaP, (c) 6-MeBaP, and (d) 11-MeBaP in anhydrous acetonitrile. Concentrations were approximately 0.5 mmol. ECE working curves are shown which assume $n_1 = 1$ and (a) $n_2 = 2$, (b) $n_2 = 2$, (c) $n_2 = 0.5$, and (d) $n_2 = 1$. Squares and circles designate points obtained using an oscilloscope and an x-y recorder, respectively.

It has been shown using cyclic voltammetry and chronopotentiometry that several dimethylbenzo[a]-pyrenes exhibit catalytic or regenerative behavior in the presence of water (27). A possible mechanism would be

$$R(H)H^{+\cdot} + H_2O \rightarrow R(H)H + \text{products} \quad [10]$$

It appears that whatever mechanism is involved, it holds at long times for all of the compounds except for 6-MeBaP.

An ECE mechanism with $n_1 = 1$ and $n_2 = 2$ would be consistent with reactions [1]-[6] if k_2 were relatively large. Effectively then, reactions [2] and [3] would be combined

$$R(H)HOH\cdot \overset{-2e^-}{\rightleftharpoons} R(H)OH^{+\cdot} + H^+ \quad [11]$$

The resulting cation radical (derived from BaP) has been shown in our laboratory to be stable on the cyclic voltammetric time scale (100 mV sec^{-1} scan rate). Thus, the rate constant k_3 seems to be rather small. The product of reaction [3], the 6-oxo-BaP free radical, is also a stable species which can undergo further oxidation (reaction [4]) to form 6-oxo-BaP cation (21). Nucleophilic attack upon this cation by water (reaction [4]) is relatively slow, as seen by the fact that in the CV not much current is observed for reduction of further products, especially with the MeBaP's (Fig. 2). Thereafter the last two electron transfers seem to blend smoothly in the n_{app} *vs.* log t curves (Fig. 5b).

It is difficult simply by monitoring current to distinguish ECE from ECC-heterogeneous disproportionation, in which the electron transfer in reaction [2] is effected in solution by BaP cation radical, instead of at the electrode (24)

$$R(H)H^{+\cdot} + R(H)HOH\cdot \rightarrow R(H)H + R(H)HOH^+ \quad [12]$$

Parent compound is regenerated and thus this mechanism is similar to one-half-order regeneration (28). Amatore and Saveant (29) predict a distinguishing feature in the CA2 behavior between ECE and disproportionation, but it is not applicable here because of the existence of further chemical steps. ECEC and disproportionation can have very similar CA2 behavior (24). The CA1 behavior for the two mechanisms is also quite similar (30), and the calculation of k values should yield similar values in both cases.

It is also difficult in single-potential-step experiments to distinguish between ECE and ECC, second-order disproportionation (reactions [8] and [9]). Marcoux (31) predicts a slightly less steeply rising n_{app} *vs.* log t curve for the latter mechanism. However, the pronounced effect of a second-order mechanism which was seen in double-potential step experiments (Fig. 4) is not evident in the CA1 data (Fig. 5). Thus, the calculation of k values from CA1 data based on an initial ECE mechanism seems valid.

Rate constants for all compounds except for 6-MeBaP and 11-MeBaP have been determined by fitting the data to an ECE working curve in which $n_1 = 1$ and $n_2 = 2$; they are tabulated in Table I. For 6- and 11-MeBaP, values of n_2 of 0.5 and 1.0, respectively, were used for the calculation. The rate constants calculated, assuming $n_2 = 2$ will be controlled by both k_1 and k_2 and will be designated as k', although $k' \approx k_1$. The ranking of stabilities of cation radicals based on Table I generally follows the ranking based on CA2 results as well as that based on CA1 results with added water.

Table I. Pseudo-first order rate constants (sec^{-1}) for reaction of BaP and MeBaP cation radicals, based on CA1 data, assuming $n_1 = 1$

	k, sec^{-1}	n_2
BaP	1.12	2
1-MeBaP	0.21	2
2-MeBaP	0.76	2
3-MeBaP	0.63	2
4-MeBaP	0.32	2
5-MeBaP	0.71	2
6-MeBaP	0.72	0.5
7-MeBaP	0.36	2
8-MeBaP	0.60	2
9-MeBaP	0.20	2
10-MeBaP	0.26	2
11-MeBaP	0.37	1
12-MeBaP	0.32	2

The n_{app} values for 6-MeBaP plateau at around 1.5 electrons (Fig. 5c), indicating a different mechanism at work, as was hinted at by the CA2 results. Coupling of cation radicals is probably occurring as in reaction [6], but possibly through the methyl group. Interestingly, however, when the dication is produced in a CV experiment, highly efficient formation of a dione seems to occur (Fig. 3). This dione could be a 1,3 type.

In any case, 1-MeBaP has a rather reactive cation radical. In comparing rate constants in Table I, the fact that the decay rate for 6-MeBaP cation radical is second order in hydrocarbon makes it appear more stable than it actually is. Note that the concentration of hydrocarbon is about 0.5 mmol while the estimated concentration of background water is 4 mmol. Thus a comparison based on second-order rate constants would show this cation radical to be the most reactive.

The 11-MeBaP cation radical is the most stable, based on CV and CA2 data. The CA1 data points, if they are fit to an ECE working curve in which $n_1 = 1$ and $n_2 = 2$, also show a very low decay rate constant. However, the fit is better for $n_2 = 1$ (Fig. 5d), indicating that the k_2 value is small. Thus the calculated rate constant represents a true k_1 value.

Summarizing the mechanistic results for the MeBaP's there are several pathways which can operate in parallel: (*i*) ECEC...EC. (*ii*) ECC..., heterogeneous disproportionation. Here the successive electron transfers can be mediated by solution species, principally the cation radical. It is impossible at this point to determine the relative contributions of mechanisms [1] and [2], but calculated k values are virtually identical. (*iii*) EC, radical-radical dimerization. This pathway is important for the three compounds which undergo filming of the electrode, BaP, 8-MeBaP, and 11-MeBaP, as well as for 6-MeBaP. (*iv*) ECC..., second-order disproportionation. This pathway is important for all of the compounds except 1-MeBaP and 11-MeBaP, especially with added water. Mechanisms [3] and [4] affect the CA2 behavior much more than they affect the CA1 behavior. Therefore, k values can be calculated on the basis of mechanism [1] using CA1 data. (*v*) EC..., second-order regenerative. At long electrolysis times, this pathway predominates for all compounds except 6-MeBaP.

MO calculations.—HMO calculations give the result that the 6 carbon of the cation radical BaP and of the MeBaP's has the highest positive charge as well as the lowest localization energy. Thus it should be the most reactive, according to considerations of both the initial state in a potential energy diagram and of the activated complex with water. Values are given in Table II. For most of the MeBaP's there is an inverse relationship between charge and localization energy, except for 5- and 7-MeBaP. They have high charges but also high localization energies.

Table II. Charges and localization energies for MeBaP cation radicals

	q_r [$R(H)^{+\cdot}$][a]	ΔE_{loc}[b] in β units	r
BaP	0.1884	1.5893	6
1-MeBaP	0.1611	1.6479	6
2-MeBaP	0.1877	1.5914	6
3-MeBaP	0.1628	1.6417	6
4-MeBaP	0.1675	1.6271	6
5-MeBaP	0.1821	1.6361	6
6-MeBaP	0.4132	1.2416	6
6-MeBaP	0.0903	1.8681	1
7-MeBaP	0.1854	1.6349	6
8-MeBaP	0.1835	1.5917	6
9-MeBaP	0.1746	1.6217	6
10-MeBaP	0.1807	1.6057	6
11-MeBaP	0.1765	1.6098	6
12-MeBaP	0.1679	1.6343	6

[a] This quantity is the charge at the r position, where r is listed in the fourth column.
[b] This quantity is the localization energy or the energy difference between the cation radical and the cation radical plus water

$$\Delta E_{loc} = -\{E[R(H)HOH_2^{+\cdot}] - E[R(H)H^{+\cdot}]\}_r$$

β unit $\approx$ 18 kcal/mol.

Support for the concept of addition of water to the cation radical as a rate-determining step is given by a potential energy diagram (Fig. 6). HMO total binding energies were calculated for the species involved in reactions [1]-[3], in addition to the activated state itself, cation radical plus water. The fact that there is a plateau at the highest potential energy (lowest binding energy) is misleading however: the chemical transformations are occurring outside the conjugated system and thus do not affect the total energy.

If the logarithm of the rate constant k' is plotted against localization energy (Fig. 7), one sees a basic trend, but with several exceptions. 1-, 7-, 12-, 4-, 8-, and 2-MeBaP follow the expectation that lower localization energies are correlated with larger rate constants. The cation radicals of 5- and 7-MeBaP were predicted to have relatively large positive charges at the 6-carbon, but relatively high localization energies. The rate constant for 7-MeBaP seems to fit better with the localization energy, while that of 5-MeBaP fits better with the charge.

For 10- and 11-MeBaP there should be some steric hindrance between the methyl group and the neighboring hydrogen atom. By analogy with several meth-

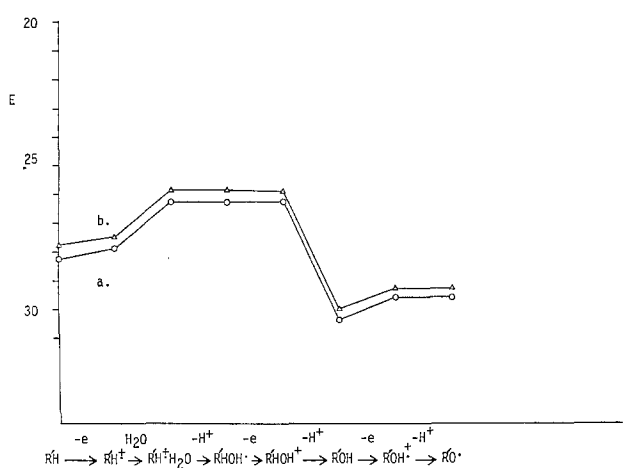

Fig. 6. Total HMO binding energies in β units for oxidation products and intermediates of BaP (○) and 1-MeBaP (△). *R'* refers to BaP or 1-MeBaP without a hydrogen atom at the 6 position.

ylbenz[a]anthracenes and methylchrysenes, there should also be a deviation from planarity for such compounds (32-34). Perhaps such an effect could explain the larger than expected stability of the cation radical if a thermodynamic argument were used: destabilization due to nonplanarity might affect the neutral molecule more unstable than the cation radical, leading to a lowered redox potential. Rough measurements using a saturated calomel reference electrode and correcting for following reactions indicate that 10- and 11-MeBaP do indeed have more negative potentials for oxidation. However, the apparent difference in k_2 value between 11-MeBaP and, say, 1-MeBaP remains to be explained. It implies something surprising, *i.e.*, that a dearomatized intermediate, $R(H)HOH^+$ in reaction [2], is stabilized for 11-MeBaP. Perhaps there is an interaction between the nonplanarity mentioned above and an enhanced resonance stabilization through a mechanism such as hyperconjugation.

Carcinogenicity.—Carcinogenicity data have been gathered from the literature and are given in Table III. Data in the lefthand column tend to support the theory of diolepoxide intermediacy (35), which would predict no activity for 7-, 8-, 9-, or 10-MeBaP, although the nonzero activities for 7- and 10-MeBaP suggest that there might be another mechanism at work (3). The lack of activity for 8- and 9-MeBaP is at complete variance with the theory of cation radical intermediacy, however.

Data in the righthand column of Table III for a limited group of MeBaP's show that methylation at some positions leads to enhanced carcinogenicity. This fact is consistent with the assumption that compounds with more stable cation radicals (within limits) should be more active. 2-MeBaP has greater radical stability than BaP, but has the lowest of the MeBaP's and also shows a slightly lower carcinogenic activity. 11-MeBaP has the highest cation radical stability and shows a slightly higher activity.

Even these very limited parallels should encourage further work along these lines, given the complex nature of the carcinogenic process. Since many biological testing systems may involve several simultaneous pathways, it may be useful to devise systems which involve only one pathway, such as that involving the cation radical. Such an approach is being taken by Cavalieri and co-workers (36, 37).

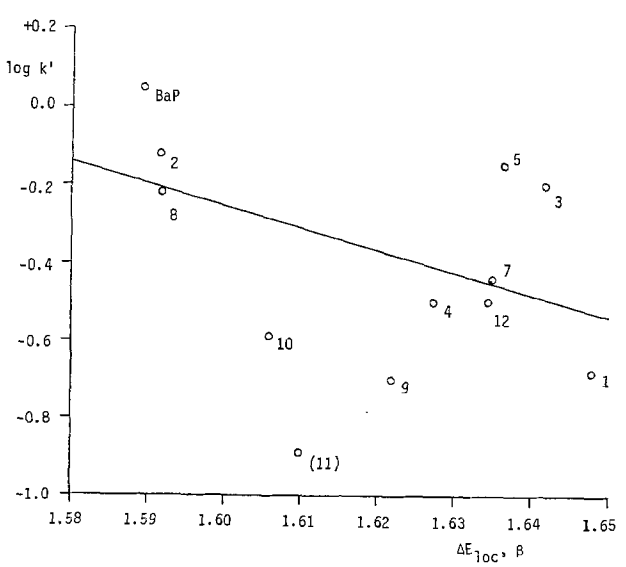

Fig. 7. Log of the ECE rate constant computed from CAI data (see Table I) vs. the localization energy for C-6 in β units. Log $k' = -0.89$ for 11-MeBaP assuming $n_2 = 2$ (see text). A least squares line is plotted based on all points except that for 11-MeBaP.

Table III. Carcinogenicities of MeBaP's

	No. of pulses (+)[a]	Iball index[b]
BaP	4	69
1-MeBaP	—	—
2-MeBaP	4	92
3-MeBaP	4	95
4-MeBaP	4	95
5-MeBaP	2	—
6-MeBaP	4	—
7-MeBaP	2	—
8-MeBaP	0	—
9-MeBaP	0	—
10-MeBaP[c]	1	—
11-MeBaP	4	103
12-MeBaP	4	97

[a] The number of pluses (+) is based on Badger's system (38). Data for 5- through 9-MeBaP are also from Badger. Data from Lacassagne *et al.* (39) for the remaining compounds were converted to this scale.

[b] The Iball (40)

$$\text{carcinogenicity index} = \frac{\%\ \text{tumors} \cdot 100}{\text{avg latency period in days}}$$

Indexes were computed using data from Lacassagne *et al.* (39).

[c] Data from Harvey (41) indicate that 10-MeBaP is less than 1/10 as potent as BaP, while that from Hecht *et al.* (33) indicates that it is roughly 1/2 as potent as BaP.

Acknowledgments

We would like to express our appreciation to Dr. J. N. Keith, NCI Chemical Repository, IIT Research Center, Chicago, for supplying samples of 6-, 7-, 8-, 9-, and 10-MeBaP. We would also like to acknowledge helpful discussions with Dr. Kenneth Wiberg, Yale University and with Dr. Tsutomu Ohzuku, Okayama University.

Manuscript submitted June 7, 1982; revised manuscript received ca. Oct. 10, 1982.

Any discussion of this paper will appear in a Discussion Section to be published in the December 1983 JOURNAL. All discussions for the December 1983 Discussion Section should be submitted by Aug. 1, 1983.

REFERENCES

1. A. C. Allison, M. E. Peover, and T. A. Gough, *Nature*, **197**, 764 (1963).
2. V. Podany, E. Rezabkova, and L. Bahna, *Neoplasma*, **25**, 57 (1978).
3. E. Cavalieri, R. Roth, C. Grandjean, J. Althoff, K. Patil, S. Liakus, and S. Marsh, *Chem.-Biol. Interactions*, **22**, 53 (1978).
4. M. Wilk, W. Bez, and J. Rochlitz, *Tetrahedron*, **22**, 2599 (1966).
5. W. Caspary, B. Cohen, S. Lesko, and P. O. P. Ts'o, *Biochem.*, **12**, 2649 (1973).
6. D. D. MacDonald, "Transient Techniques in Electrochemistry," Plenum Press, New York (1977).
7. J. McCann, E. Choi, E. Yamasaki, and B. N. Ames, *Proc. Nat. Acad. Sci. USA*, **72**, 5135 (1975).
8. J. L. Adelfang and G. H. Daub, *J. Am. Chem. Soc.*, **77**, 3297 (1955).
9. J. L. Adelfang and G. H. Daub, *ibid.*, **79**, 1751 (1957).
10. J. W. Patton and G. H. Daub, *ibid.*, **79**, 709 (1957).
11. J. L. Comp and G. H. Daub, *ibid.*, **80**, 6049 (1958).
12. C. Doyle, Jr. and G. H. Daub, *ibid.*, **80**, 5252 (1958).
13. J. M. L. Cameron, J. W. Cook, and R. Schoental, *J. Chem. Soc.*, 257 (1952).
14. L. F. Fieser and E. B. Hershberg, *J. Am. Chem. Soc.*, **60**, 2542 (1938).
15. R. S. Bodine and G. H. Daub, *J. Org. Chem.*, **44**, 4461 (1979).
16. L. F. Fieser and E. B. Hershberg, *J. Am. Chem.*

Soc., **60**, 1658 (1938).
17. L. F. Fieser and M. Fieser, *ibid.*, **57**, 782 (1935).
18. M. S. Newman and S. Kamer, *J. Org. Chem.*, **42**, 3284 (1977).
19. W. E. Bachmann and M. J. Carmack, *J. Am. Chem. Soc.*, **63**, 2494 (1941).
20. S.-M. Park, *This Journal*, **125**, 216 (1978).
21. L. Jeftic and R. N. Adams, *J. Am. Chem. Soc.*, **92**, 1332 (1970).
22. K. B. Wiberg, "Computer Programming for Chemists," pp. 215-225, W. A. Benjamin, New York (1965).
23. A. Streitwieser, Jr., "Molecular Orbital Theory for Organic Chemists," p. 135, John Wiley & Sons, New York (1961).
24. M. K. Hanafey, R. L. Scott, T. H. Ridgway, and C. N. Reilley, *Anal. Chem.*, **50**, 116 (1978) and supplementary material.
25. A. J. Bard and L. R. Faulkner, "Electrochemical Methods: Fundamentals and Applications," p. 182, John Wiley, New York (1980).
26. R. H. Wopshall and I. Shain, *Anal. Chem.*, **39**, 1514 (1967).
27. S.-M. Park, J. J. Michnovicz, and G. H. Daub, *Anal. Biochem.*, **90**, 374 (1978).
28. T. H. Ridgway, R. P. Van Duyne, and C. N. Reilley, *J. Electroanal. Chem.*, **67**, 1 (1976).
29. C. Amatore and J. M. Saveant, *ibid.*, **107**, 353 (1979).
30. C. Amatore and J. M. Saveant, *ibid.*, **102**, 21 (1979).
31. L. Marcoux, *J. Am. Chem. Soc.*, **93**, 537 (1971).
32. D. W. Jones and J. M. Sowden, *Cancer Biochem. Biophys.*, **4**, 43 (1979).
33. S. S. Hecht, N. Hirota, and D. Hoffman, *Cancer Lett.*, **5**, 179 (1978).
34. S. S. Hecht, M. Loy, R. Mazzarese, and D. Hoffman, *J. Med. Chem.*, **21**, 38 (1976).
35. D. M. Jerina, R. Lehr, M. Schaefer-Ridder, H. Yagi, J. M. Karle, D. R. Thakker, A. W. Wood, A. Y. H. Lu, D. Ryan, S. West, W. Levin, and A. H. Conney, in "Origins of Human Cancer," H. Hiatt, J. D. Watson, and I. Winsten, Editors, pp. 639-658, Cold Spring Harbor Laboratory, Cold Spring Harbor, NY (1977).
36. E. Cavalieri, E. Rogan, and R. Roth, in "Free Radicals and Cancer," R. Floyd, Editor, Marcel Dekker, New York (1982), In press.
37. E. Rogan, R. Roth, E. Cavalieri, P. Katomski, and J. Benderson, *Chem.-Biol. Interactions*, **22**, 35 (1978).
38. G. M. Badger, *Brit. J. Cancer*, **2**, 22 (1948).
39. A. Lacassagne, F. Zajdela, N. P. Buu-Hoi, O. Chalvet, and G. H. Daub, *Int. J. Cancer*, **3**, 238 (1968).
40. J. Iball, *Am. J. Cancer*, **35**, 188 (1939).
41. R. G. Harvey and F. B. Dunne, *Nature*, **273**, 566 (1978).

Crystallographic Anisotropies in Electrochemical Etching of Pt

R. Caracciolo and L. D. Schmidt

Department of Chemical Engineering and Materials Science, University of Minnesota, Minneapolis, Minnesota 55455

ABSTRACT

Single crystal microspheres of Pt are examined by scanning electron microscopy following electrochemical and chemical etching in chloride and cyanide solutions. In all cases, a single major crystal plane is formed which is not the close packed (111) plane. Rates of dissolution and facet formation also vary among planes and with etching conditions. The largest anisotropy occurs with aqua regia where initial attack is exclusively near (210) but only (110) facets are formed. The (111) and (100) planes are attacked in aqua regia only from their edges, but eventually these orientations are transformed completely into (110) facets. Electrochemical chloride etching with a-c potentials produces large smooth planes near (100), and the (111) plane is attacked readily to form (100) facets. Electrochemical cyanide etching produces the most rapid attack of the (111) orientation to produce facets of (110). Possible mechanisms for these processes and implications for preparation of Pt electrodes are discussed.

Platinum, the standard electrode in most electrochemical processes (1), derives its usefulness from its high reactivity in electrode reactions combined with inertness towards erosion and deactivation through solid compound formation. Because of these properties, Pt electrodes exhibit a reproducibility unequaled by any other electrode materials. On the other hand, Pt does erode electrochemically in some solutions, and faceting and recrystallization produce changes in properties with time. Platinum electrodes must be prepared and treated in a specified manner to obtain quantitative reproducibility.

Different crystal planes of Pt behave quite differently in adsorption and reactions. The variations in H_2 and O_2 evolution with crystallographic orientation have been particularly well documented (2-6). It has typically been assumed that polycrystalline wires or foils facet into the close packed (111) plane because this is the lowest free energy plane at the metal-vacuum interface. However, it is not obvious that this plane is most stable in electrolyte solutions because rates of surface dissolution and rearrangement processes influence which planes are formed.

Many years ago Gwathmy and co-workers (7, 8) introduced the use of polished single crystal spheres to study crystallographic anisotropies. They examined the thickness of oxide films on ~1 cm diam Cu spheres and also studied faceting produced by H_2 oxidation on Cu and Ni spheres. In this laboratory (9), smaller spheres of Pt have been used to study catalytic etching, the faceting which occurs in catalytic reactions of gases at high temperatures. We showed that the rates of etching and the stable planes depended strongly on crystallographic orientation. We also found that the stable plane is frequently not the (111), and that each reaction produces different morphologies. Single crystal spheres <1 mm in diameter are very easily prepared by melting of a wire in a torch, and these sizes are convenient for examination in the scanning electron microscope (SEM).

The objective of this research is to determine the role of crystallographic orientation in faceting of Pt in specimens which are free of grain boundaries and stresses, because both of these effects can compete with crystallographic anisotropies in influencing erosion processes.

There have been many studies of erosion of Pt electrodes (10-13). It is widely recognized that rates vary with crystal plane and conditions, and the mechanisms of etching have been discussed (10, 11). However, to our knowledge, the crystal plane dependence of rates of etching and stabilities have not yet been identified.

Experimental

The electrodes for these experiments were platinum single crystal microspheres, ~0.02 cm diam, prepared

by melting the ends of high purity (99.9+%) 0.006 cm Pt wires in a CH_4-O_2 torch as described previously (9). The surface of these spheres after solidification appears spherical and smooth except for flat (111) and smaller (100) facets. These planes are identified by their three- and four-fold symmetries, respectively. This is probably the high temperature equilibrium form in which the flat areas are orientations with minimum surface free energy which form cusps in a Wulff plot (9). The stereographic triangle, the "unit cell" of possible orientations on a curved surface, can be identified on a single crystal sphere by symmetry to give a complete characterization of the surface. Several spheres were spot welded to one larger wire so that a number of spheres could be treated and examined simultaneously.

Throughout this manuscript we shall use the notation (h, k, l) to designate the family of crystal planes with this Miller index. The same notation will be used for both the description of a crystal plane (smooth surface or orientation of facet planes), as well as for the nominal orientation of a surface. For example, the (111) orientation of the original sphere is in some cases etched into small (110) facets while the nominal orientation of the region can still be identified as (111).

For electrochemical etching, 2V a-c at 60 Hz was used with a Pt or carbon counterelectrode. Current density was maintained below 4 A/cm^2. The electrolyte for chloride etching was a solution of aqueous HCl, 20% by volume, with KCl added to saturation. For cyanide etching, the electrolyte was a mixture of 0.1M KCN and 0.1M KOH. Etching times varied from several minutes to several hours. Dissolution of Pt in cyanide solution was more rapid, resulting in the destruction of the electrode assembly in less than 10 min at this voltage. The reagent for chemical etching was boiling aqua regia. (HCl, HNO_3, H_2O in a 3-1-4 volume ratio). Etching times varied from 10 to 35 min.

The resulting surface morphologies were examined by SEM in either a Cambridge Instruments SEM or a JEOL JEM 100CX STEM with resolutions of 300 and 30Å, respectively. Some samples were also examined using a Perkin-Elmer Physical Electronics scanning electron microprobe (SAM) with a lateral resolution of 500Å. No nonmetallic impurities were present on the surfaces at levels up to 1%. The surfaces contained primarily C, O, N, and Cl, although no significant variations in composition between facets could be detected. Sputter depth profiling indicated that the spheres were pure Pt for depths > 10Å below the original surfaces.

Results

Chloride electrochemical etching.—Figure 1 shows spheres after etching in HCl/KCl under conditions just described. The original sphere transforms into a slightly deformed cube whose (100) facets bulge slightly and whose (111) corners remain flat. Figure 1a shows a complete sphere, while Fig. 1b, c, and d show another sphere at increasing magnifications.

The only stable planes are within 10° of (100), with this orientation being smooth except for a square of shallow curved pyramids at ~5° from (100). The region closer to (100) is again smooth, but a pointed cusp occurs exactly at the (100) poles.

The (111) is not smooth, but is completely broken into triangular etch pits which are between 0.1-3μ across. Examination of these facets shows that they are exclusively (100) planes.

The edges of the cube, with Miller indices (1, 1, x) with $0 < x < 1$, is constructed from the intersection of the large sharp smooth faces near (100). Thus, the (110) and its vicinals disappear completely. The only exception is a small flat facet on the edge near (331) which is visible in Fig. 1b and c.

We have examined ~50 spheres following 5 similar etching procedures, and all exhibited morphologies

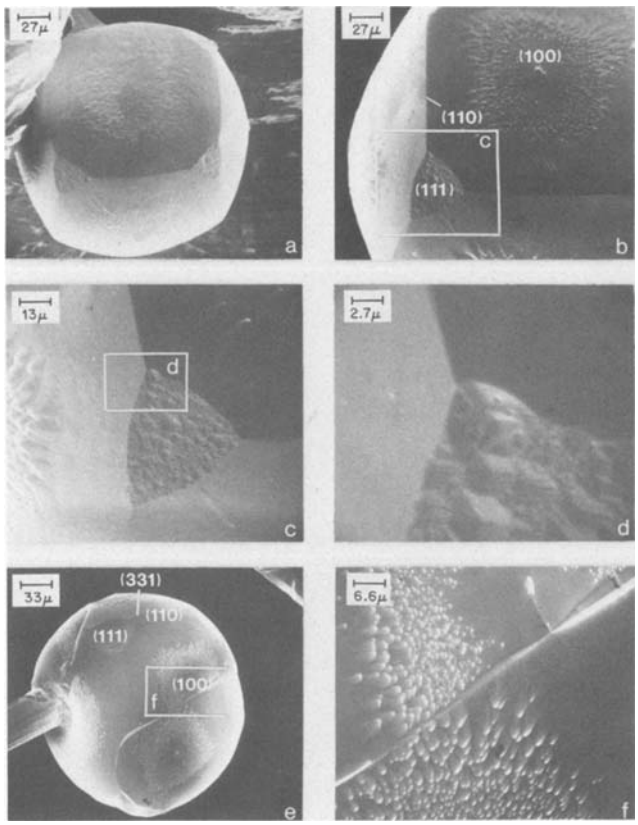

Fig. 1. Platinum spheres following electrochemical etching in aqueous chloride solution. Micrographs (a-d) show a single crystal sphere at increasing magnifications, while (e-f) show a sphere which contained a grain boundary.

essentially identical to those shown in Fig. 1, except for the extent of etching which varied somewhat among spheres.

Figures 1e and f show a sphere which illustrates etching at a grain boundary and earlier stages of etching than Fig. 1a-d. In this sphere, the edges have not yet become sharp, but the (100) and (111) regions can be identified by symmetry. Pyramids near (100) and etch pits on (111) are also observed to form after short times.

This sphere exhibits two grain boundaries which are formed on ~20% of spheres and are caused by nucleation of several crystals during solidification. These micrographs and others of spheres with grain boundaries show that no preferential etching occurs at grain boundaries. The boundary of Fig. 1f is between crystals which are near (100) as identified from cusps in each crystal. The walls of the grain boundary also appear to be near (100), and no evidence of extensive grain boundary grooving is noted.

Chloride chemical etching.—Figure 2 shows several Pt spheres after etching in boiling aqua regia. Extensive etching transforms the sphere into roughly a cubic shape, just as with chloride electrochemical etching. However, the morphology is quite different with the cube faces broken into microfacets of (110) planes.

Figure 2a shows the entire cube in nearly its final configuration. The corners of the cube are flat triangles, whose three-fold symmetry identifies them as (111) planes while the rest of the sphere is faceted. The corners are still smooth and unetched due to the progression of etching as will be explained below. Figures 2b and c show regions which include the (111) and (110) nominal orientations, respectively. One can determine the crystallographic orientation of the facets by examining the facets along the edge of the cube. These facets are parallel to the (110) nominal orienta-

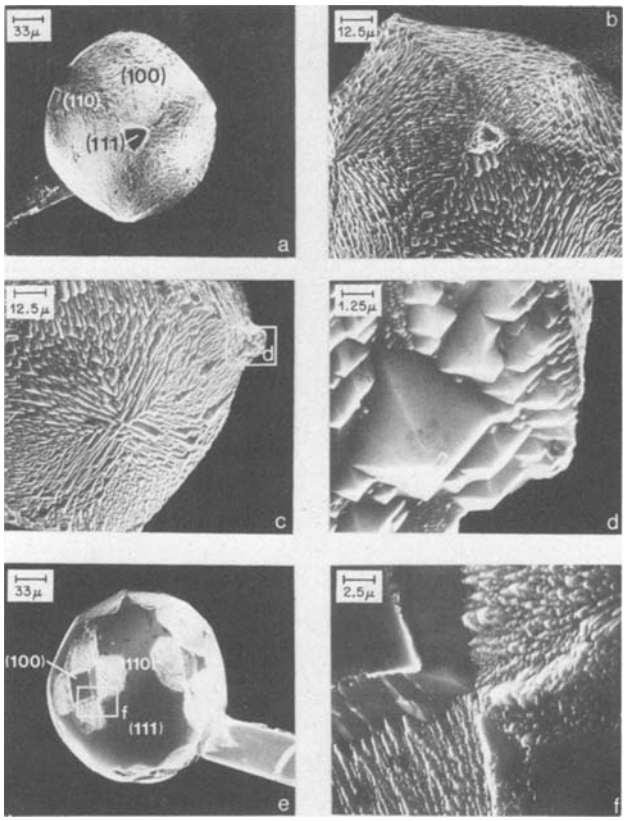

Fig. 2. Platinum spheres following chemical etching in aqua regia. Micrograph (a) shows the entire sphere while (b, c and d) show various regions of another sphere. Micrographs (e and f) show a sphere in initial stages of etching which shows that the (210) region is the first to be attacked.

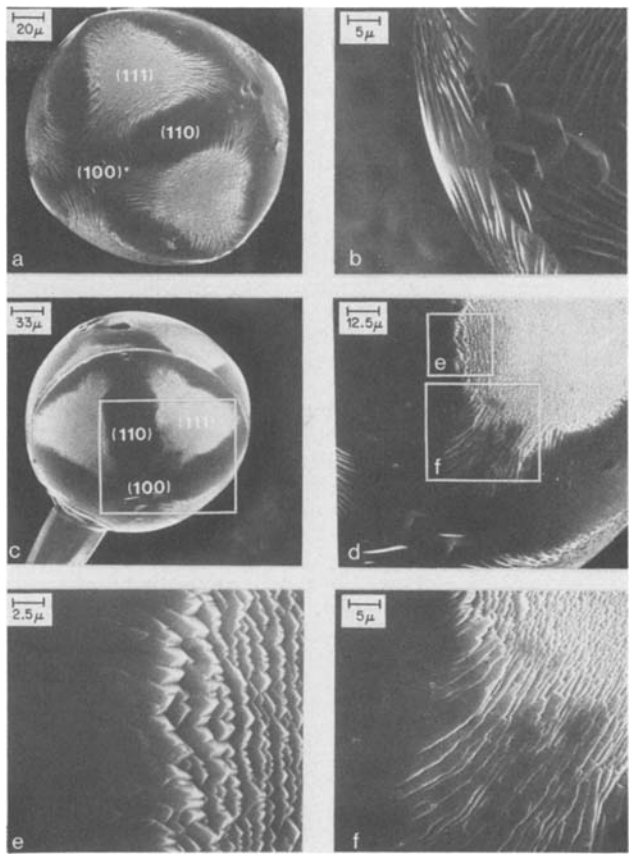

Fig. 3. Platinum spheres following electrochemical etching in aqueous cyanide solution. Micrographs (a and b) show one sphere while (c-f) show another sphere at increasing magnifications.

tion, and all facets on the rest of the sphere are parallel to them. Figure 2d is a high magnification of the corner of the cube on which is a small projection. Facets in this region are variable in size, but all facets have (110) orientation. At the end of the projection is the original (111) orientation which has shrunk and almost disappeared.

The progress of the dissolution process can be seen from Fig. 2e and f. Initial stages of attack show that chemical etching is more anisotropic than chloride electrochemical etching. The four-lobed depressions around the (100) poles indicate that etching initiates near the (210) regions and spreads until the entire sphere is eventually faceted. The wall around the (100) poles (upper left corner of Fig. 2f) is fairly large and smooth and consists of the relevant (110) planes. The original (110), (111), and (100) orientations are not attacked initially. These surfaces are only affected by the etching process as the "front," originating from the (210) orientation, spreads to finally envelop them from their edges. These edges are entirely (110) planes.

As noted previously, the (111) orientations at the corners of the cubes are resistant to the dissolution process. As a result, the sphere in its final configuration has projections at the corners (Fig. 3c and d), because as the sphere is dissolving and decreasing in size, the (111) planes are resistant to dissolution and do not disappear until they shrink to zero size.

In summary, faceting in aqua regia originates at the (210) orientation, spreads to envelope the (110), then the (100), and finally the (111). The final shape of the sphere is a cube covered with (110) facets which are 0.5-1μ across.

Electrochemical etching in cyanide solution.—Figure 3 shows micrographs of Pt spheres following a-c electrochemical etching in basic 0.1M KCN solution. It is found that platinum is removed more rapidly in this solution than in either aqua regia or electrolytic chloride solutions, since the support wires are etched away within several minutes. Examination of Fig. 3a and c shows that etching is most rapid near (111) and less on (110) and (100). The erosion of the (111) to produce nearly flat (but heavily faceted) regions causes the original sphere to transform into the shape of an octahedron with (100) at its corners and (110) at its edges. The (110) remains curved and smooth, while the (100) orientation becomes pointed but with large etch pits near the (100) pole.

The 0.5-2μ facets on the (111) region appear to consist exclusively of planes near (110). All walls in the sawtooth pattern at the right side of Fig. 3e and the triangular etch pits near the center (111) are exclusively (110) planes.

Towards (110), Fig. 3e, the facets disappear, and the surface is smooth with a large radius of curvature, showing that regions within ~10° of (110) are smoothly and uniformly etched.

Surrounding the (100) vertices at the corners of the octahedron are smooth partially faceted planes as shown in Fig. 3b. However, the angle between these nearly flat planes is not large enough to be (111) planes, and we estimate them to be approximately (211) or (311) planes. The vertices themselves are decorated with large (~5μ across), triangular etch pits which appear to have walls near (110).

Etching in other solutions.—Electrochemical etching in chloride or cyanide with d-c potentials produced no visible etching; after 1 hr with 2V applied, no etch patterns or sphere size reduction were evident with the spheres at either the anode or the cathode even though vigorous bubbling occurred.

Etching was attempted under similar experimental conditions using a-c and d-c potentials in 10% by volume sulfuric and phosphoric acid electrolytes. Although reconstruction or dissolution of platinum is re-

ported to occur (3, 14), no visible etching patterns could be detected after 1 hr.

Discussion

Etching is obviously a very complicated process, and our discussion will be limited to a survey of behavior, qualitative comments on the probable processes, and a summary of implications for Pt electrodes.

Table I summarizes these results for the three etching situations. After sufficient time, only a single plane exists on the sphere (two planes in cyanide). This is the "stable" plane, although it is not clear that it is the minimum free energy or equilibrium plane but merely the one which is formed under these etching conditions. The identification of the plane attacked most rapidly comes from noting which regions lose metal most rapidly. This may or may not be the crystallographic orientation which forms. The planes attacked most slowly are identified as those on which metal loss is least and which do not rapidly form facets. In aqua regia, the (111) and (100) planes are totally inert except for attack from their edges which eventually causes their complete disappearance.

The overall shape of the resultant single crystals is a result of the rapid erosion of (100) or (111) to form cubes and octahedra, respectively. It is evident that the shape does not necessarily correlate with the planes which form, because the regions attacked readily also facet except in the case of electrochemical chloride etching.

Crystallographic anisotropies involve: (*i*) relative rates of etching and (*ii*) relative stabilities of planes. In practice, these are intricately coupled because etching is a rate process in which the approach to equilibrium in various steps is unknown. The equilibrium configuration of a surface is determined by the surface free energy γ *vs.* crystallographic orientation. A crystalline solid may exhibit faces exposing one or more flat crystal planes, both flat and curved surfaces, or only curved surfaces, depending on the anisotropy in γ with orientation (15, 16). If γ exhibits cusps on a plot of γ *vs.* orientation (the Wulff plot), then those planes will exhibit flat faces while otherwise a range of orientations will be stable. Clean platinum exhibits large crystallographic anisotropies in γ with $\gamma_{(111)} < \gamma_{(100)} < \gamma_{(110)}$. A clean platinum crystal would form a cubo-octahedron exposing only (111) and (100) planes, and other orientation should form facets of these planes only.

However, with adsorbates, there is at present no way to predict the ordering of γ on different planes or the size of its anisotropies. If the stable planes observed in these experiments were controlled by equilibrium considerations, then the results imply that (100) or (110) and their vicinals have much lower γ than do other orientations including the close packed (111) plane.

Kinetics of dissolution and transport should be equally important in controlling morphologies and stabilities in an etching situation. It should also be noted that etching may involve both dissolution and deposition, particularly with a-c potentials. Thus, in some situations, material may be removed from some planes and deposited on adjacent facets, while in others, metal may be dissolved from all regions but at different rates. Calculations of concentration gradients parallel to the surface with reaction indicate that lateral transport in the boundary layer and by surface diffusion may be important (15).

Table I. Comparison of crystallographic anisotropies in etching

Etching method	Planes formed	Overall shape	Planes attacked most rapidly	Planes attacked most slowly
Aqua regia	(110)	Cube	(210) (100)†	(111)* (100)*
A-C Cl^- electrolysis	Near (100)	Cube	(100) (111)	(110)
A-C CN^- electrolysis	(110) Near (221)	Octahedron	(111)	(110)

* Inert except for attack from edges.
† The (100) plane is initially inert, but once attack from edges is complete, this region erodes more rapidly than any others.

Etching of a metal must involve formation of a soluble metal ion, and the inertness of Pt is associated with the instability and insolubility of most ions containing Pt. Chloroplatinate $PtCl_6^=$ and cyanoplatinate $Pt(CN)_4^=$ are the most stable aqueous ions of Pt, and these species are almost certainly formed in electrochemical and chemical etching as discussed by many authors (10-12). In any situation, dissolution involves oxidation of Pt at the surface to Pt^{+2} or Pt^{+4}, its complexing with Cl^- and CN^- at the surface, and the dissolution of the stable anion. In each solution, distinct processes should occur for each step.

Aqua regia.— Oxidation of Pt is probably by attack of Cl atoms generated in solution. A possible sequence of reactions is

$$Cl(sol'n) \rightarrow Cl(s)$$

$$4Cl(s) + Pt(s) \rightarrow PtCl_4(s)$$

$$PtCl_4(s) + 2Cl^- \rightarrow PtCl_6^=(sol'n)$$

although the oxidation states and complexes of Pt intermediates on the surfaces are of course unknown.

Etching in aqua regia exhibits the greatest crystallographic anisotropy with only the (210) orientation attacked initially to form (110) facets. The (111) and (100) planes are not attacked directly until facets of (110) have formed. This suggests that these planes either do not adsorb Cl atoms, that Cl is not capable of oxidizing Pt atoms, or that the complex does not dissolve. The hexagonal and square close packed planes of Pt are apparently inert toward direct attack. It is also possible that a monolayer or multilayer film such as oxide, carbide, or an impurity acts to passivate these planes.

Electrochemical chloride.—This process is probably similar to that in aqua regia, except now the Cl is deposited electrochemically at the surface

$$Cl^-(sol'n) \rightarrow Cl(s) + e^-$$

The electrochemical potential, thus, may induce Cl^- adsorption and Pt oxidation on planes where the Cl atom in solution will not react. The fact that a-c potentials are necessary for erosion has been suggested to arise from the necessity to remove adsorbed oxygen or oxide before Cl^- attack is possible (10-13). Evidence on the existence and nature of such oxides is not sufficient to decide this issue. An alternative is that, in the cathodic cycle, the adsorbed $PtCl_6^=$ species is desorbed into solution to allow attack of the underlying Pt metal. The etching rates also suggest that Pt metal may be redeposited on some crystals planes in Cl^- solutions.

Electrochemical cyanide.—Presumably, this process is similar to that in Cl^- except the anion involves Pt^{+2}. However, a different plane is formed, and dissolution is much more rapid in CN^- solution. Significant differences must, therefore, exist in the various steps leading to dissolution.

Summary

The most important conclusions from these experiments are that etching produces predominantly one crystal plane, that the plane formed is different for each situation, and that it is not the close packed (111) plane. Electrolytic treatment of polycrystalline Pt wires, foils, and single crystals is highly effective in transforming surfaces into these orientations. This transformation is much faster in a-c chloride and cyanide solutions than with d-c etching or in other electrolytes. However, our criterion is the formation of facets $\gtrsim$ 1000Å in size, shorter times, and milder con-

ditions may still readily produce microfacets. We suggest that the standard procedures prescribed for "cleaning" Pt surfaces are probably highly effective in forming facets of another crystallographic orientation. We know of no straightforward technique to detect formation of microfacets except by the chemistry they produce.

Adsorption studies on single crystal planes of Pt imply that the adsorption and reaction properties of each crystal plane are quite distinct. For CO (17), H_2 (18), and NO (19) on all of the major planes, results can be summarized as indicating much higher heats of adsorption and reactivities on those planes, exposing four-fold adsorption sites on (100) than the two- and three-fold sites on (110) and (111). The (111) and (110) planes exhibit similar behavior in most respects, and behavior on high index and stepped planes generally appears to be correlated with the existence of several types of sites. It is interesting to note that stepped planes, associated with curved surfaces near a high density orientation, do not appear to form in our experiments except for the (100) plane in chloride solution; this plane is itself highly reactive. Stepped planes are predicted to be highly unstable if the high density plane exhibits a cusp in its Wulff plot (15, 16).

While we have only attempted to offer qualitative explanations of the molecular processes responsible for these phenomena, detailed studies of these processes are obviously necessary to explain this behavior. Crystallographic anisotropies play a dominant (and unavoidable) role in all electrochemical processes. The use of additional analytical techniques and detailed modeling will be necessary to explain these situations and to exploit them to control processes at electrode surfaces.

Acknowledgments

This research was partially sponsored by the University of Minnesota Corrosion Center funded by the Department of Energy. Surface analysis was obtained through the Electron Microscopy Center and the Regional Instrumentation Facility for Surface Analysis.

Manuscript submitted April 12, 1982, revised manuscript received Sept. 20, 1982.

Any discussion of this paper will appear in a Discussion Section to be published in the December 1983 JOURNAL. All discussions for the December 1983 Discussion Section should be submitted by Aug. 1, 1983.

REFERENCES

1. Ronald Woods, in "Electroanalytical Chemistry," Vol. 9, p. 2, A. Bard, Editor, Marcel Dekker, New York (1976).
2. P. N. Ross, Jr., *This Journal*, **126**, 67 (1979).
3. K. Yamamoto, D. M. Kolb, R. Kotz, and G. Lehmpfuhl, *J. Electroanal. Chem.*, **96**, 233 (1979).
4. A. T. Hubbard, R. M. Ishikawa, and J. Katekaru, *ibid.*, **86**, 271 (1978).
5. L. D. Schmidt, in "Topics in Applied Physics," Vol. 4, p. 63, R. Gomer, Editor, Springer-Verlag, New York (1975).
6. E. Yeager, W. E. O'Grady, M. Y. C. Woo, and P. Hagans, *This Journal*, **125**, 348 (1978).
7. A. T. Gwathmey and A. F. Benton, *J. Chem. Phys.*, **8**, 431 (1940).
8. A. T. Gwathmey and R. E. Cunningham, *Adv. Catal.*, **10**, 57 (1948).
9. M. Flytzani-Stephanopoulos, S. Wong, and L. D. Schmidt, *J. Catal.*, **49**, 51 (1977).
10. J. Llopis and A. Sancho, *This Journal*, **108**, 720 (1961).
11. J. A. Bittles and E. L. Littauer, *Corros. Sci.*, **10**, 29 (1970).
12. M. Pourbaix, "Atlas of Electrochemical Equilibria in Aqueous Solutions," Pergamon Press, Oxford, New York (1966).
13. R. Juchniewicz, *Corros. Sci.*, **6**, 69 (1966).
14. P. Bindra, S. J. Clouser, and E. Yeager, *This Journal*, **126**, 1631 (1979).
15. M. Flytzani-Stephanopoulos and L. D. Schmidt, *Prog. Surf. Sci.*, **9**, 83 (1979).
16. C. Herring, *Phys. Rev.*, **82**, 87 (1951).
17. A. Crossley and D. A. King, *Surf. Sci.*, **95**, 131 (1980).
18. K. E. Lu and R. R. Rye, *ibid.*, **45**, 677 (1974).
19. R. J. Gorte, L. D. Schmidt, and J. L. Gland, *Surf. ibid.*, **109**, 367 (1981).

The Electroreduction of Carbon Dioxide and Formic Acid on Tin and Indium Electrodes

S. Kapusta* and N. Hackerman†

Chemistry Department, Rice University, Houston, Texas 77251

ABSTRACT

The electrochemical reduction of carbon dioxide and formic acid has been studied in aqueous solutions on tin and indium electrodes using a-c impedance and photoemission techniques. Carbon dioxide reduction to formic acid (or the formate ion) proceeds with high current efficiencies (about 95%) although the overall power efficiency is low due to the high overpotential of the reaction. The reaction mechanism on tin and indium is similar to that postulated on mercury cathodes (17). The reaction rates are higher than on mercury and are affected by adsorption of intermediates and kinetics complications due to side reactions. Reduction of formic acid was only observed on tin cathodes at low current densities. The poor efficiency of this reaction is related to the formation of organometallic complexes on the electrode surface that accelerate the rate of hydrogen evolution.

The cathodic reduction of carbon dioxide has attracted considerable attention in recent years, especially as an alternative to photosynthesis for the production of organic raw materials or fuels [Ref. (1-7) and references therein]. The main reaction product in aqueous solutions is formic acid (or the formate ion), with faradaic efficiencies of over 90% on metal electrodes. The reduction of formic acid is more difficult. The best electrocatalyst materials are metals with high hydrogen overpotential (lead, tin, indium) and low pzc (3, 7). This latter condition may be related to the adsorption and desorption of reaction intermediates.

In this paper we report on the reduction of both carbon dioxide and formic acid in aqueous solutions on tin and indium cathodes. Both a-c impedance and photoemission techniques have been used in addition

* Electrochemical Society Active Member.
† Electrochemical Society Honorary Member.
Key words: tin, indium, reduction, carbon dioxide, formic acid, photoemission.

to electrochemical measurements to determine the reaction kinetics and mechanism.

Experimental

All measurements were performed in a standard, three compartment, all-glass cell at 23° ± 0.2°C. The cell was fitted with a quartz window to allow illumination of the electrodes. Preparation of the electrodes has been described elsewhere (8). Solutions were made from analytical grade reagents and conductivity water (8) and were deaerated by continuous bubbling of purified nitrogen. Nitrous oxide was used as a standard to calibrate the photoemission currents (9). The concentration of carbon dioxide was altered by changing the ratio of N_2 to CO_2 in the gas flowing through the solution and was calculated from standard thermodynamic data (10). The partial currents of the CO_2 electroreduction were determined by subtracting the hydrogen evolution current measured in solutions saturated with nitrogen from the current measured in a CO_2/N_2 atmosphere. It was assumed that, as a first approximation, the partial currents of hydrogen deposition and CO_2 reduction were additive, *i.e.*, there is no catalytic acceleration or inhibition of the hydrogen evolution process in the presence of CO_2. The partial current of formic acid reduction was calculated from the charge consumed in methanol production during long-term electrolysis experiments, following the procedure described in Ref. (2).

The circuits and techniques used for electrochemical, photoelectrochemical, and impedance measurements were described earlier (8, 11). All results are referred to the geometrical electrode area (1 cm^2), although roughness factors of 2 for tin and 1.4 for indium were estimated from the capacitance results. All potentials are referred to the saturated calomel electrode (SCE).

Results and Discussion

Reduction of Carbon Dioxide

Electrochemical reduction.—The polarization curves of the electroreduction of CO_2 on tin and indium cathodes in a 0.95 KCl + 0.05 $NaHCO_3$ solution saturated with CO_2 are shown in Fig. 1, together with the results reported on mercury under similar conditions (7). The effect of concentration polarization has been eliminated using the values of $[i \cdot i_d/(i_d - i)]$ as ordinates, where i_d is the limiting diffusion current in unstirred solutions and i is the cathodic current measured at any potential E.

Two Tafel regions are observed in the case of tin. The first one, at potentials $E > -1.45$V, has a slope of 115 mV/decade and extends over approximately two orders of magnitude of current. The second region, at $-1.45\text{V} > E > -1.8$V, has a slope of 320 ± 20 mV. The partial current of the CO_2 reduction is difficult to estimate in this second region, since the hydrogen evolution currents are high and depend on both stirring and the buffer capability of the solution. In the case of indium, a single Tafel line, with a slope of 140 mV/decade, is observed over the entire potential range studied.

Within experimental accuracy, the partial CO_2 reduction current in the first Tafel region does not depend on solution pH, in the range 1-6.5. In the second region, the current tends to increase slightly with pH, although, as mentioned above, the experimental error is large at these large negative potentials. The partial current is also independent of solution composition, *i.e.*, similar results are obtained in carbonate, phosphate, acetate, and borate buffer solutions. Some experiments were performed using tetramethyl ammonium chloride instead of KCl as supporting electrolyte. In all cases, formate ions are the main product of the reaction. In fact, oxalate, mallate, or glycollate were not detected by careful analysis of the solution

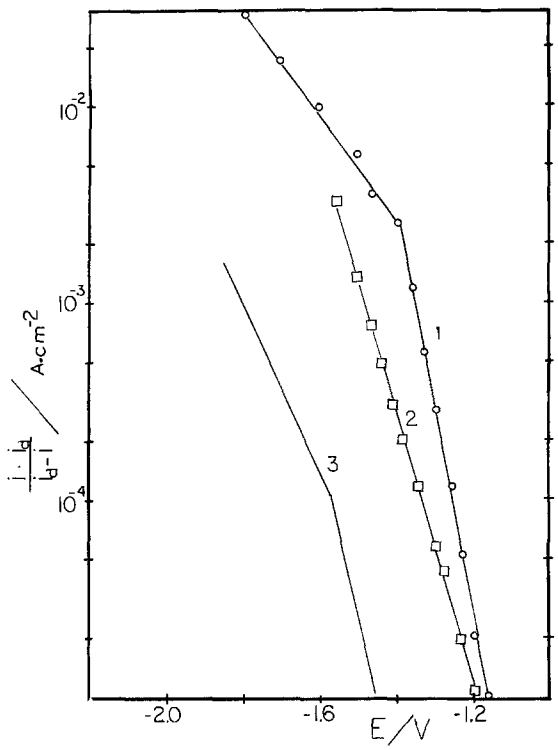

Fig. 1. Potentiostatic current, i (for Sn and Hg) or $[(i \cdot i_d)/(i_d - i)]$ (for In), *vs.* potential, E, polarization curves of the partial current of carbon dioxide reduction measured on tin (curve 1), indium (curve 2), and mercury (curve 3) electrodes in a 0.95 KCl + 0.05M $NaHCO_3$ solution saturated with CO_2 at 1 atm. Results for mercury taken from Ref. (7).

following the procedure described in Ref. (12). The reaction order with respect to CO_2 is 1 over the entire potential range. These results are in excellent agreement with previous reports (6, 13).

The CO_2 reduction process can be represented by two successive electron transfer reactions, preceded by an adsorption equilibrium

$$CO_{2\,aq} \rightleftharpoons CO_{2\,ads} \qquad [1]$$

$$CO_{2\,ads} + e^- \rightleftharpoons CO_2^-{}_{ads} \qquad [2]$$

and

$$CO_2^-{}_{ads} + AH + e^- \rightarrow HCO_2^- + A^- \qquad [3]$$

where AH is the proton donor and ads indicates an adsorbed species.

Both capacitance and potential decay measurements indicate that coverage of the electrode by adsorbed species is small (< 5%). Assuming Langmuir conditions, the Tafel slopes of ~120 mV/decade and the independence of the cathodic currents on pH indicate that step [2] is the rate-determining step (rds) of the reaction on both electrodes, at least at the more positive potentials. The change to a Tafel slope of ~340 mV/decade at more negative potentials ($E < -1.4$V) on tin cathodes can be taken as an indication of a change in the rds.

Extrapolating the Tafel lines measured at the more positive potentials in Fig. 1 to the reversible potential of the reaction under these experimental conditions (pH ~ 7), *i.e.*

$$CO_2 + H_2O + 2e^- \rightarrow HCO_2^- + HO^- \quad E_r = -0.76\text{V} \qquad [4]$$

the approximate values of the exchange current densities i_o for Hg = 5×10^{-11} A/cm^2, Sn = 1×10^{-9} A/cm^2, and In = 1×10^{-8} A/cm^2 can be calculated. Even though current efficiencies as high as 99% can be obtained, the overall power efficiency of the reduction process is low because of the low i_o (or high overvoltages) of the reactions involved.

Photoelectrochemical reduction.—Further information about these reactions can be obtained from photoemission experiments. The irradiation of a polarized metal surface in contact with aqueous electrolytes with light of a certain energy (wavelength) leads to the photoemission of electrons into the solution (9, 14). In the presence of an appropriate electron scavenger, capture of the photoemitted electrons results in generation of radical anions at or near the electrode surface. The measured photocurrent depends on the decay mechanism of these radicals: photocurrents can be observed only if they decay to electroinactive species either through dimerization or reduction at the electrode.

Figure 2 shows the potential dependence of the photocurrents measured on a tin electrode in a 0.95M KCl + 0.05M $NaHCO_3$ solution, saturated with N_2O and CO_2. In the first case a photocurrent i_p is observed at all potentials $E < -0.9$V. The shape of the i_p *vs.* E curve differs from that measured, *e.g.*, on mercury, since electrochemical reduction decreases the concentration of N_2O at the surface at high negative potentials (8). In the solutions containing CO_2 as electron scavenger, a photocurrent appears only at $E < -1.2$V. The ratio of the photocurrents, $i_p(CO_2)/i_p(N_2O)$, first increases with potential, but then remains constant for $-1.4 > E > -1.6$V. Once again, the decrease in $i_p(CO_2)$ at large negative potentials is due to the depletion of CO_2 by electrochemical reduction. Similar results were obtained on indium electrodes.

A parameter usually employed for analyzing the results of photoemission experiments is the stoichiometric number, ν. This number represents the total number of electrons transferred from the electrode for each successful act of photoelectron capture in solution. For instance, $\nu_{N_2O} = 2$. For any scavenger S, and using N_2O as calibration standard, the value of ν_S can be calculated from (15, 16)

$$\nu_S = \frac{2i_p(S)}{i_p(N_2O)}\left[\frac{k_{N_2O}\cdot C_{N_2O}}{k_S\cdot C_S}\right]^{1/2} \qquad [5]$$

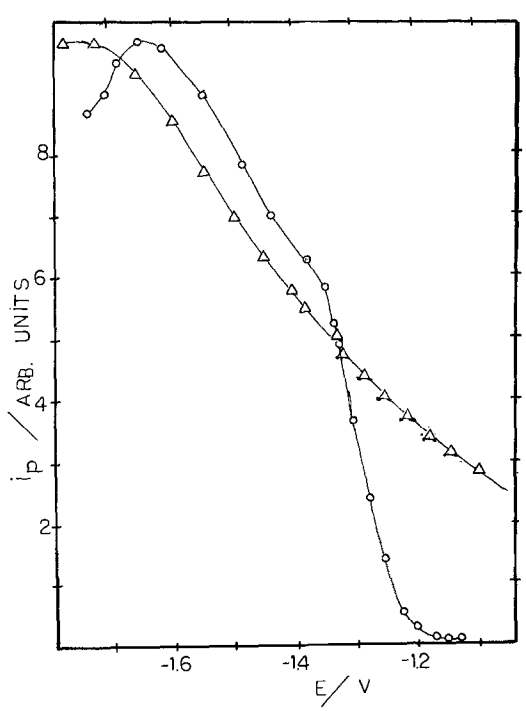

Fig. 2. Potential dependence of the photocurrent i_p measured on a tin electrode under periodic illumination. 0.95M KCl + 0.05M $NaHCO_3$ solution saturated with N_2O (△) or CO_2 (○). Chopping frequency 17 Hz. Wavelength = 410 nm. Light intensity ~10 mW/cm².

where k_S and k_{N_2O} are the rate constants for the homogeneous reaction of solvated electrons, e_{aq}, with S and N_2O, respectively, and C_S and C_{N_2O} are the corresponding concentrations. At potentials where the photocurrents are diffusion limited, the dependence of i_p on the concentration of scavenger, S, can be approximated by (9, 16)

$$i_p = i_e\delta\left[\frac{k_S\cdot C_S}{D_e}\right]^{1/2} \qquad [6]$$

where i_e is the total photoemission current, D_e is the diffusion coefficient of e_{aq}, and δ is a parameter that depends on the function used to describe the solvated electron redeposition. Therefore

$$\frac{i_p(CO_2)}{i_p(N_2O)} = \left[\frac{k_{CO_2}\cdot C_{CO_2}}{k_{N_2O}\cdot C_{N_2O}}\right]^{1/2} \qquad [7]$$

Figure 3 shows the dependence of the constant photocurrent ratio (see above) on the square root of the CO_2 concentration. From the slope of this line, the rate constant for the homogeneous reaction of hydrated electrons with CO_2 can be calculated. A value of $k_{CO_2} = 7 \times 10^9\ M^{-1}\ sec^{-1}$ is obtained, in excellent agreement with previous reports on Hg (15). This independence of the reaction rate on electrode material is typical of homogeneous reactions.

The following mechanism has been proposed to account for the photocurrents observed in CO_2 solutions (15)

$$CO_2 + e^-_{aq} \rightarrow CO_2^- \qquad [8]$$

followed by

$$CO_2^- + AH + e^-_M \rightarrow HCO_2^- + A^- \qquad [9]$$

and/or

$$CO_2^- \rightarrow CO_2 + e^-_M \qquad [10]$$

Here the subscripts aq and M indicate electrons that are hydrated in solution or in the metal, respectively. Some of these species may be adsorbed on the electrode surface (see below). This mechanism shows that a photocurrent will be observed only if the radical anion formed after capture of e_{aq} by CO_2, Eq. [8], is further reduced at the electron through step [9] ($\nu_{CO_2} = 2$). Otherwise, if the radical is re-oxidized through step [10], no photocurrent should appear ($\nu_{CO_2} = 0$). From the results in Fig. 2, we conclude that ν_{CO_2} goes from 0 to 2 over a narrow potential range (~150 mV).

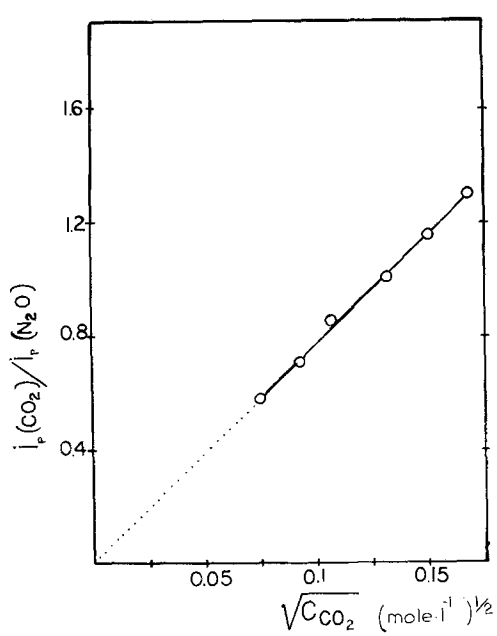

Fig. 3. Dependence of the ratio of the photocurrents, $i_p(CO_2)/i_p(N_2O)$, on the square root of the CO_2 concentration. Potential range −1.5 to −1.65V. Other conditions as in Fig. 2.

Considering Eq. [8]-[10], the steady-state photocurrent is given by (14, 15)

$$i_p = \frac{2i_o k_{o9} C_{AH} \exp[-\alpha f(E - E_{o9})]}{k_{o10} \exp[\beta \mathbf{F}(E - E_{o10})] + k_{o9} C_{AH} \exp[-\alpha f(E - E_{o9})]} \quad [11]$$

where i_o is the electron photoemission current after subtraction of the redeposition current of electrons that do not react with the CO_2 scavenger molecule, $f = \mathbf{F}/RT$, C_{AH} is the concentration of the proton donor AH, k_{o9} and k_{o10} are the rates of reactions [9] and [10], respectively, at the corresponding standard potentials E_{o8} and E_{o9}, and α and β are the charge transfer coefficients. The factor 2 in Eq. [11] represents the stoichiometric number for the total photoelectrochemical reduction of CO_2. From Eq. [11], the photocurrent goes to 0 at the more positive potentials ($E - E_{o10} >> 0$), and to $2i_o$ at more negative potentials ($E - E_{o9} << 0$).

Equation [11] can be rearranged to give

$$E = 1/f(\alpha + \beta)\{\ln[(2i_o/i_p) - 1] + \ln(k_9/k_{10}) + \ln C_{AH}\} \quad [12]$$

Here $k_9 = k_{o9} \exp(\alpha f E_{o9})$ and $k_{10} = k_{o10} \exp(-\beta f E_{o10})$.

The product of solvated electron capture by N_2O (*i.e.*, $HO^\cdot$) is completely reduced at potentials $E < -0.9$V. Therefore (14)

$$2i_o = i_p(N_2O) \times \left[\frac{k_{CO_2} \cdot C_{CO_2}}{k_{N_2O} \cdot C_{N_2O}}\right]^{1/2} \quad [13]$$

Figure 4 shows the results of plotting the experimental data obtained on tin and indium electrodes according to Eq. [12]. The value of $(2i_o/i_p - 1)$ gives the ratio between the rates of $CO_2^{-\cdot}$ reduction and oxidation according to Eq. [9] and [10], respectively. This ratio is equal to 1 at a potential $E^{\neq} = -1.35$V on tin, -1.25V on indium, and -1.5V on mercury (15). At more positive potentials, corresponding to the first Tafel region of the polarization curves of tin in Fig. 1, the oxidation rate of $CO_2^{-\cdot}$ is higher than its reduction rate. At potentials $E < -1.35$V, *i.e.*, in the second Tafel region in Fig. 1, the reduction of $CO_2^{-\cdot}$ predominates over its oxidation. From the slope of the lines in Fig. 4, the value $\alpha + \beta = 0.6$ for both tin and indium can be calculated. On mercury, on the other hand, this value is *ca.* 0.9. The values of $E^{\neq}$ are independent of pH above 5.5, indicating that water molecules act as proton donors. As expected from Eq. [11], $E^{\neq}$ are also independent of the CO_2 concentration.

The differences between the values of overpotential for CO_2 reduction on Hg and Sn in the dark ($\sim$0.25V) and under illumination ($\sim$0.15V) are almost equal. We can thus assume that the reaction mechanism on both metals is the same, as described by Eq. [1]-[3]. Step [2] is the rds at $E > -1.4$ (in the first Tafel region). At more negative potentials, step [3] determines the reaction rate. The small potential dependence of the current in this region may be due to a decrease in the surface concentration of $CO_2^{-\cdot}$ as the electrode potential is made more negative. As mentioned earlier, the partial current of CO_2 reduction increases slightly with pH in the second Tafel region, a result that is at variance with the postulated rds. This apparent contradiction arises from the assumption that the background current due to hydrogen ion reduction remains constant in solutions saturated with CO_2 or N_2. This assumption may not be valid in acid solutions (see below). The dependence of the reaction rate (and $E^{\neq}$) on the nature of the cathode indicates that the reaction intermediates are adsorbed on the surface. The surface coverage, however, is very small.

Some photoelectrochemical experiments were performed in 1M KCl solutions saturated with either N_2 or CO_2 and containing 1×10^{-3}, 2×10^{-3}, 5×10^{-3}, and 2×10^{-2}M HCl to adjust the solution pH. Since two electron scavengers, H^+ and CO_2, are present, the resulting photocurrents are determined by the electrochemical behavior of the primary products formed, H· atoms and $CO_2^{-\cdot}$ radicals. In a first approximation, we can neglect any secondary reactions between the radicals initially formed and the scavengers in solution. Thus, the photocurrent measured with two competing scavengers, A and B, is related to that produced by a single species by (9)

$$\frac{i_p(A + B)}{i_p(A)} = \frac{\nu_A k_A C_A + \nu_B k_B C_B}{\nu_A (k_A C_A)^{1/2} (k_A C_A + k_B C_B)^{1/2}} \quad [14]$$

Figure 5 shows some typical results obtained on tin electrodes in acid solutions saturated with N_2O, N_2,

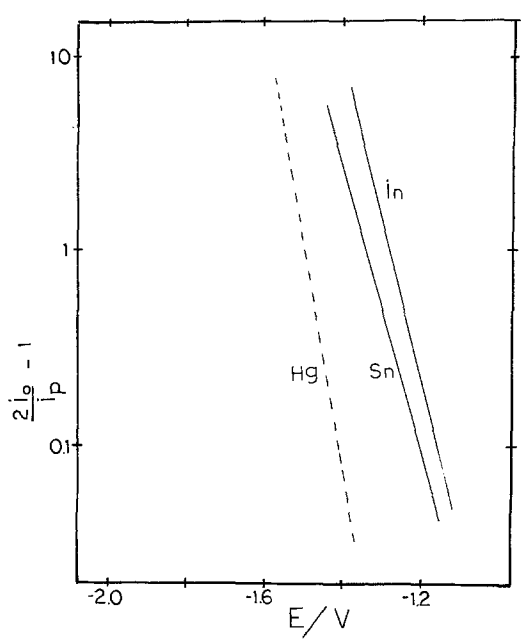

Fig. 4. Results of plotting the data from Fig. 2 according to Eq. [12]. Results for Hg taken from Ref. [15].

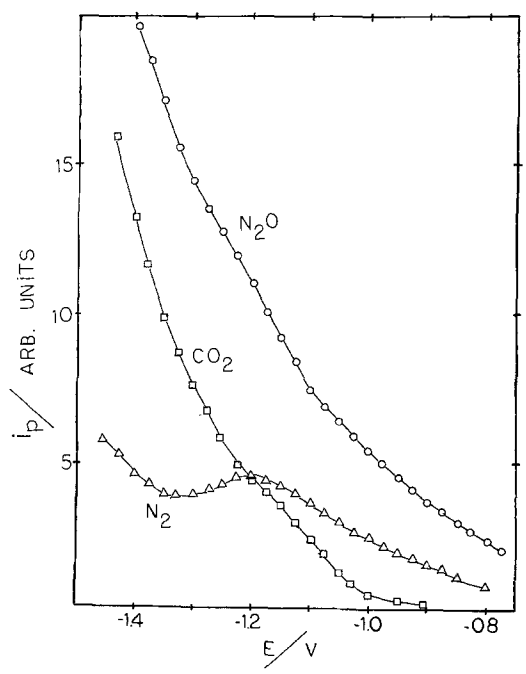

Fig. 5. Potential dependence of the photocurrents i_p measured on a tin electrode under periodic illumination in a 1M KCl + 0.001M HCl solution, pH = 3.0, saturated with N_2O (○), N_2 (△), and CO_2 (□). Other conditions as in Fig. 2.

and CO_2. A completely similar behavior was observed on indium cathodes. The constant ratio $i_p(H)/i_p(N_2O)$ at potentials $E > -1.2V$ indicates that oxidation of the H· atoms formed after the initial electron capture by H^+ does not occur within the potential range considered here. Thus, the photoelectrochemical reduction of H^+ can be described by

$$H^+ + e_{aq} \rightarrow H\cdot \quad [15]$$

$$H\cdot + H^+ + e_M^- \rightarrow H_2 \quad [16]$$

From the dependence of the photocurrent ratio on the hydrogen ion concentration, a value of $k_H = 1.3 \times 10^{10}\ M^{-1}\ sec^{-1}$ can be calculated, in good agreement with previous reports (9). The decrease in $i_p(H)$ at high negative potentials is caused by the depletion of H^+ ions due to their electrochemical reduction.

When the results obtained in the CO_2-saturated solution are analyzed using Eq. [14], negative values of ν_{CO_2} are calculated at $E > -1.1V$. The failure of this model to describe the behavior of acid CO_2 solutions arises from the assumption that there is no interaction between the radicals and the scavengers in solution. This interaction may be stated in terms of the reaction between a fraction of the H· atoms produced through Eq. [15] with CO_2 molecules in solution (15, 16)

$$H\cdot + CO_2 \rightleftharpoons COOH \quad [17]$$

or

$$H\cdot + CO_2 \rightleftharpoons CO_2^- + H^+ \quad [18]$$

If the COOH or CO_2^- radicals thus formed are oxidized there will be a net decrease in the photocurrent as compared with CO_2-free solutions. The ratio of photocurrents will then be given as (15, 16)

$$\frac{i_p(H^+ + CO_2)}{i_p(H^+)} = \frac{\nu_{CO_2}(k_{CO_2}C_{CO_2} + \delta Q_H k_H C_H) + \nu_H(1 - \delta Q_H)k_H C_H}{\nu_H(k_H C_H + k_{CO_2}C_{CO_2})^{1/2}(k_H C_H)^{1/2}} \quad [19]$$

where $Q_H = (k_H.C_{CO_2}/D_H)^{1/2}$, k_H. is the rate constant of the reaction of H· with CO_2, D_H is the diffusion coefficient of H·, and $\delta Q_H k_H C_H$ accounts for the reactivity of H· atoms toward CO_2. The parameter $(1 - \delta Q_H)$ can be calculated from the photocurrent ratio at potentials $E > -1.1V$ (15) and is equal to 0.7. Equation [19] can be used to determine the potential dependence of ν_{CO_2} in acid solutions. However, it is simpler to analyze the data in terms of an equation equivalent to Eq. [12], namely

$$\ln[(2/\nu_{CO_2}) - 1] = \ln(k_9/k_{10}) + f[E(1 - \alpha + \beta) - (1 - \alpha)E_{o9} - \beta E_o] - \ln C_H \quad [20]$$

where β and E_o are the transfer coefficient and standard potential of the reduction of CO_2^- radicals in acid solutions, *i.e.*

$$CO_2^- + H^+ + e_M^- \rightarrow HCO_2^- \quad [21]$$

or

$$CO_2^- + H^+ \rightarrow COOH$$
$$COOH + e_M^- \rightarrow HCO_2^- \quad [22]$$

Figure 6 shows the result of plotting the photocurrent data obtained on a tin electrode in acid solutions saturated with CO_2 according to Eq. [20]. Measurements at pH < 2 are difficult because the dark currents become high and the electrode surface is covered with hydrogen bubbles. An average value of $\alpha + \beta = 0.5$ can be calculated from the slope of the lines, as compared with 0.6 on mercury. As expected from Eq. [20], E_+ shifts toward more positive potentials with an increase in the hydrogen ion concentration. From the limited data available it is not possible to determine the pH at which the reaction mechanism changes from that described by Eq. [9]-[10] to that of Eq. [21]-[22].

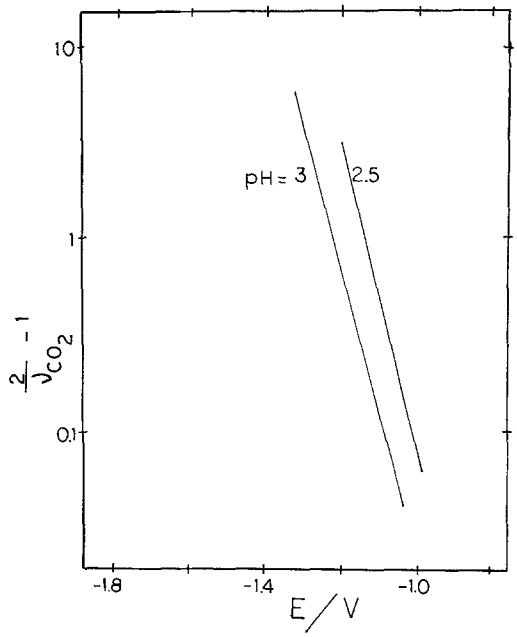

Fig. 6. Results of plotting the data from Fig. 5 according to Eq. [20].

Hydrogen atoms can also be formed during the electrochemical reduction of H^+ in the dark, *i.e.*, $H^+ + e_M^- \leftrightarrow H\cdot$. These atoms can then react with adsorbed CO_2 molecules, following a mechanism equivalent to Eq. [18]. The result of this process would be the "chemical" reduction of CO_2, with simultaneous elimination of H· atoms. For this reason, the partial current of hydrogen evolution may decrease in the presence of CO_2. The experimental procedure used to determine the partial CO_2 reduction current was based on the assumption that the hydrogen current remains constant in both N_2- and CO_2-saturated solutions. Therefore, coupling of the two reactions leads to erroneous conclusions regarding the pH dependence of the CO_2 reduction rate. A similar explanation was advanced in the case of mercury cathodes (15).

Reduction of Formic Acid

Electrochemical reduction.—The electrochemical reduction of formic acid on both tin and indium electrodes is a slow process. Solution analysis (2) revealed that methanol was the only detectable reaction product. During long-term electrolysis experiments (48 hr at currents between 1 and 50 μA), the highest current efficiency (~95%) was measured on tin cathodes in a 0.5M HCOOH + 0.5M HCOONa solution at $i \sim 5$ μA, corresponding to a potential $E = -0.95V$. The efficiency fell quickly at more negative potentials.

At constant potential ($-0.85V > E > -1.2V$) the current increased slowly with time due to an acceleration of the hydrogen evolution process. A similar behavior was observed during electrolysis of formaldehyde solutions (8) and ascribed to the formation of tin complexes on the surface that reduce the hydrogen overpotential. The low efficiencies for formic acid reduction can thus be attributed to the competition of the hydrogen evolution reaction.

Further information about the system can be obtained from electrode impedance measurements.

Photoelectrochemical reduction.—The primary product formed after capture of e_{aq} by HCOOH may decompose according to (15)

$$HCCOH^- \rightarrow HCOO^- + H\cdot \quad [23]$$

or

$$HCOOH^- \rightarrow HCO\cdot + HO^- \quad [24]$$

H· atoms may also react with the formate ion

$$H\cdot + HCOO^- \rightarrow H_2 + CO_2^{\cdot-} \quad [25]$$

The photoelectrochemical behavior of formic acid solutions should be similar to that of CO_2-saturated solutions, with the additional complication introduced by reaction [24]. This has been shown to be the case on mercury electrodes (15): the potential dependence of the photocurrent exhibited a prewave, due to the reduction of $CO_2^{\cdot-}$ radicals following Eq. [23] and [25] and a main wave due to the reduction of HCO· radicals. On tin and indium, on the other hand, a single wave is found. The ratio $i_p(HCOOH)/i_p(N_2O)$ is constant over the entire potential range considered, indicating that reduction of the HCO· radical is a diffusion-limited process. Figure 7 shows the HCOOH concentration dependence of this constant ratio, from which a value of $k_{HCOOH} = 1.4 \times 10^9$ M^{-1} sec^{-1} can be calculated. This value is one order of magnitude larger than the one reported by Gordon *et al.* (18), which seems too low, and similar to the one measured on mercury (15). From these results we conclude that the rds of HCOOH reduction on both tin and indium is the transfer of the first electron to the HCOOH molecule. The reaction mechanism involves HCO· radicals as an adsorbed intermediate. The differences observed with respect to mercury electrodes can be ascribed to the higher rate of H· and $CO_2^{\cdot-}$ reduction on these metals. It is also possible that the electrode surface has a significant influence on the way the initially formed radical decomposes, *i.e.*, the ratio of H· to HCO· produced.

Impedance measurements.—Impedance measurements have been extensively used in the study of electrochemical reactions [*e.g.*, Ref. (19) and references therein]. Figure 8 shows the frequency response of the impedance measured on a tin electrode in a 1M HCOOH + 0.1M HCOONa solution at pH = 3.5. Similar results were obtained on indium electrodes. The complex plane spectrum (CPS) shows a single loop within the frequency range 10 kHz-2 Hz that can be analyzed on the basis of a Randles equivalent circuit (19). It is then possible to calculate the double layer capacitance, C_{dl}, the charge transfer and electrolyte resistances, R_{ct} and R_e, and the Warburg impedance, R_w. Figure 9 shows the potential dependence of the electrode capacitance, C_s (series equivalent circuit), and C_{dl} obtained from the CPS analysis.

The low values of C_{dl} are usually taken as an indication of adsorption, in this case of HCOOH. Desorption of this species was not observed. The product

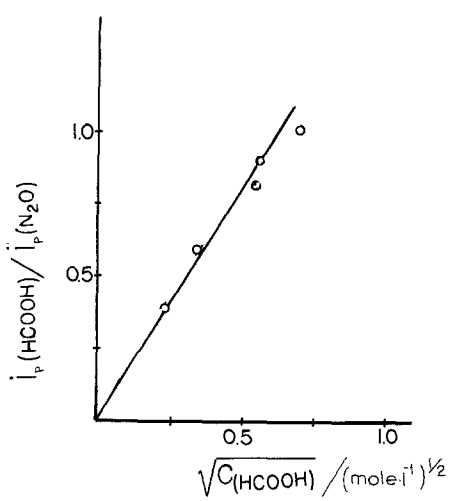

Fig. 7. Dependence of the photocurrent ratio $i_p(HCOOH)/i_p(N_2O)$ on the square root of the HCOOH concentration. Tin electrode. $E < -1.0V$.

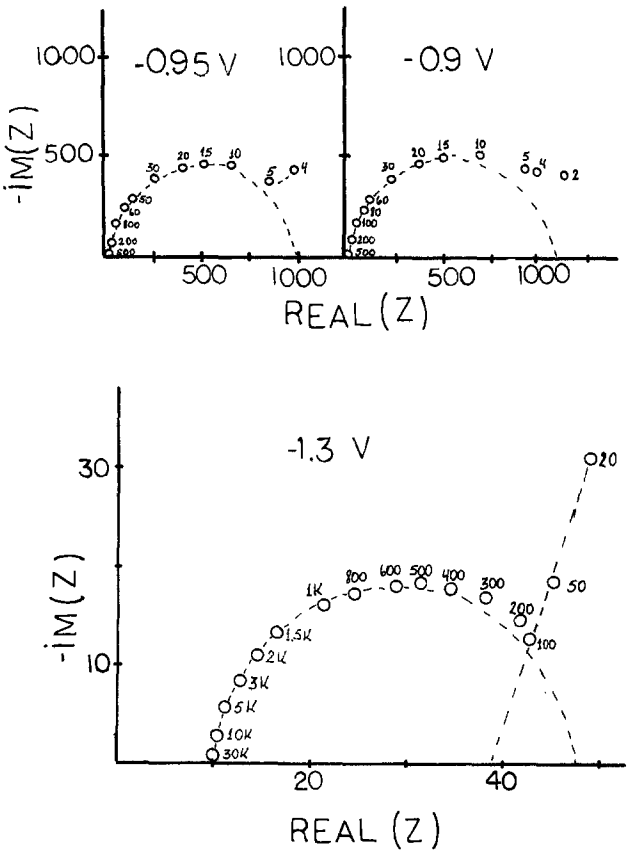

Fig. 8. Complex impedance Z = Real(Z) − j × Imaginary(Z) of a tin electrode measured in a 1M HCOOH + 0.1M HCOONa solution at the potentials indicated. Experimental points correspond to frequencies in Hz. Dotted lines show the best fitting to the results expected from a Randles equivalent circuit.

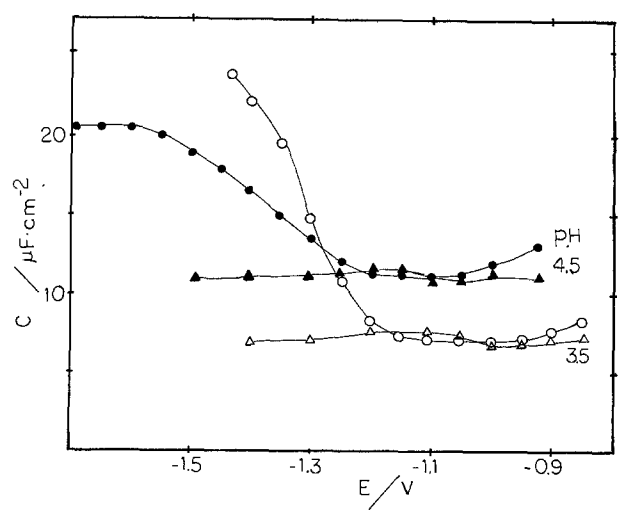

Fig. 9. Potential dependence of the series capacitance, C_s, measured at 1 kHz (○), and double layer capacitance, C_{dl}, determined from CPS (△), of a tin electrode in 1M HCOOH + 0.1M HCOONa, pH = 3.5 (open symbols) and 0.1M HCOOH + 1M HCOONa, pH = 4.5 (full symbols) solutions.

$R_{ct} \times i$ (where i is the cathodic current measured under potentiostatic conditions) is constant over the entire potential range here considered. Under these conditions it is not possible to separate the contribution of the HCOOH reduction reaction to the overall current. Future work will involve extending the low frequency limit below 1 Hz in order to observe slow processes, *e.g.*, desorption of HCOOH.

Acknowledgment

The financial support of the Robert A. Welch Foundation of Houston, Texas, is gratefully acknowledged.

Manuscript submitted May 20, 1982; revised manuscript received Oct. 18, 1982.

Any discussion of this paper will appear in a Discussion Section to be published in the December 1983 JOURNAL. All discussions for the December 1983 Discussion Section should be submitted by Aug. 1, 1983.

Publication costs of this article were assisted by Rice University.

REFERENCES

1. T. E. Teeter and P. Van Risselberghe, *J. Chem. Phys.*, **22**, 759 (1954).
2. F. H. Meller, Final Report (Phase II), Contract No. N00014-66-C0139, Office of Naval Research, Washington, DC (1968).
3. K. S. Udupa, G. S. Subramanian, and H. V. K. Udupa, *Electrochim. Acta*, **16**, 1593 (1971).
4. V. Kaiser and E. Heitz, *Ber. Bunsenges. Phys. Chem.*, **77**, 818 (1973).
5. J. Ryu, T. N. Andersen, and H. Eyring, *J. Phys. Chem.*, **76**, 3278 (1972).
6. A. V. Zakharyan, N. V. Osetrova, and Yu. B. Vasilev, *Sov. Electrochem.*, **13**, 1568 (1978).
7. P. G. Russell, N. Kovac, S. Srinivasan, and M. Steinberg, *This Journal*, **124**, 1329 (1977).
8. S. Kapusta and N. Hackerman, *J. Electroanal. Chem. Interfacial Electrochem.*, **138**, 295 (1982).
9. Yu. Ya. Gurevich, Yu. V. Pleskov, and Z. A. Rotenberg, "Photoelectrochemistry," Consultants Bureau, New York (1980).
10. "International Critical Tables," McGraw Hill, New York and London (1982).
11. S. M. Cai, C. Y. Liu, S. M. Wilhelm, and N. Hackerman, Abstract 697, p. 1115, The Electrochemical Society Extended Abstracts, Montreal, Quebec, Canada, May 9-14, 1982.
12. A. Bewick and G. P. Greener, *Tetrahedron Lett.*, **53**, 4623 (1969) **54**, 391 (1970).
13. A. V. Zakharyan, Z. A. Rotenberg, N. V. Osetrova, and Yu. B. Vasilev, *Sov. Electrochem.*, **14**, 1317 (1978).
14. Yu. V. Pleskov, Z. A. Rotenberg, V. V. Eletsky, and V. I. Lakomov, *Faraday Discuss. Chem. Soc.*, **56**, 52 (1974).
15. D. Schiffrin, *ibid.*, **56**, 75 (1974).
16. G. C. Barker, A. W. Gardner, and D. C. Sammon, *This Journal*, **113**, 1182 (1966).
17. W. Paik, T. N. Andersen, and H. Eyring, *Electrochim. Acta*, **14**, 1217 (1969).
18. S. Gordon, E. J. Hart, M. S. Matheson, J. Rabani, and K. J. Thomas, *Discuss. Faraday Soc.*, **36**, 193 (1963).
19. C. Gabrielli, "Identification of Electrochemical Processes by Frequency Response Analysis," Solartron Instrumentation Group, Irvine, CA (1980).

Polymer Films on Electrodes

XI. Electrochemical Behavior of Polymer Electrodes Produced by Incorporation of Tetrathiafulvalenium in a Polyelectrolyte (Nafion) Matrix

Timothy P. Henning* and Allen J. Bard**

Department of Chemistry, University of Texas, Austin, Texas 78712

ABSTRACT

The electrochemical behavior of the cation exchange polymer Nafion containing tetrathiafulvalenium (TTF^+) on a platinum substrate is described. The polymer electrode shows cyclic voltammetric behavior similar to that of solid films of TTF on platinum. In 1.0*M* KBr the oxidized form of the electroactive molecules in the polymer (TTF^+) forms nonstoichiometric complexes with Br^-. The peak potentials in cyclic voltammetry shift with changes in concentration of supporting electrolyte, temperature, and anion of the supporting electrolyte. Very narrow cyclic voltammetric waves are observed that result in part from attractive interactions between the electroactive molecules. The separation in peak potential of the reduction and oxidation waves is explained by formation of $TTFBr_{0.7}$ which stabilizes the oxidized form (TTF^+) and makes it harder to reduce. Peak potentials for the oxidation and reduction shift closer together as the scan rate is lowered, which is explained by a "square (reaction) scheme."

The electrochemistry of layers on electrode surfaces, both solids and polymers, has been investigated by many research groups. The cyclic voltammetric behavior of the surface-confined layers frequently deviates from the theoretical "thin film" behavior of a one-electron nernstian reaction at 25°C; *i.e.*, peak width at half-height ($\Delta E_{1/2}$) of 90.6 mV and no splitting between the anodic and cathodic peaks ($\Delta E_p = E_{pa} - E_{pc} = 0$) (1). Relatively few films show a $\Delta E_{1/2}$ significantly smaller than 90.6 mV (2). These narrow cyclic voltammetric (CV) waves were attributed to interactions among the electroactive molecules and phase formation in the layer. Large peak separations observed in cyclic voltammetry at fast scan rates (1 V/sec and larger) have been attributed to slow heterogeneous kinetics and resistance effects in the layer. Even at slow scan rates, where heterogeneous kinetics and resistance usually are not of importance, finite ΔE_p values have been observed. These have been explained by kinetic effects associated with phase formation (nucleation overpotential) (2d) and interconversion between different forms of the polymer-confined electroactive molecules with different standard potentials (3).

We recently described unusual CV behavior of a polymer electrode in which tetrathiafulvalenium ion (TTF^+) was incorporated into a layer of the perfluorinated sulfonate polymer, Nafion (NAF) (4). This polymer electrode exhibited narrow ($\Delta E_{1/2} < 20$ mV) CV waves and ΔE_p of $\sim$ 150 mV at intermediate scan rates (*e.g.*, 10 mV/sec). This is remarkably similar to the electrochemical behavior of solid films of TTF. In this paper we describe more detailed studies of the electrochemical behavior of the TTF/NAF polymer electrode, examining the effects of supporting electrolyte concentration, different supporting electrolytes, temperature, and different scan rates in cyclic voltammetry. We also obtained absorption spectra of the TTF polymer on SnO_2 transparent conducting electrodes, which yielded information about the nature of the electroactive TTF molecules in the polymer. In a related paper the behavior of solution redox species on the TTF polymer electrodes is described (5).

* Electrochemical Society Student Member.
** Electrochemical Society Active Member.
Key words: cyclic voltammetry, scan rate, chronoamperometric behavior.

Experimental

Materials.—TTF (Aldrich) was purified by several vacuum sublimations. TTFCl was synthesized by dissolving TTF in benzene and adding dropwise a benzene solution which was saturated with chlorine. The purple TTFCl precipitate was washed with ether and air dried. The supporting electrolytes were used as purchased. The 970 eq wt Nafion dissolved in ethanol was a gift from the E. I. du Pont de Nemours & Company.

Apparatus.—All electrochemical experiments employed a Princeton Applied Research (PAR) Model 175 universal programmer, Model 173 potentiostat, and Model 179 digital coulometer. Slow potential scans (< 1 mV/sec) were accomplished by introducing a voltage divider between the programmer and potentiostat. The working electrode used in all the electrochemical experiments was a Pt disk (area = 0.027 cm^2) embedded in a glass rod. A Pt mesh was used as a counterelectrode and a saturated calomel electrode (SCE) was used as a reference. Resistance compensation was used at all scan rates faster than 10 mV/sec by adjusting the amount of positive feedback just short of oscillation.

Procedure.—The electrodes were prepared by covering the Pt disk with 10 μliter of an EtOH solution of Nafion (2% by weight) and allowing the EtOH to evaporate. The dry thickness of the resulting films (typically 1 μm) was determined with a Sloan Dektak surface profile measuring system. The TTF^+ was incorporated into the Nafion film by immersing the electrode in an aqueous solution of ~ 1 m*M* TTFCl for 10 min. The electrode, denoted Pt/NAF,TTF^+, turned a golden color after immersion in the TTF^+ solution, indicating the incorporation of TTF^+. The average concentration of electroactive TTF in the electrode was typically about 0.3*M* as determined by the integrated charge under a steady-state CV wave.

Results

Cyclic voltammetry.—The behavior of a freshly formed Pt/NAF,TTF^+ electrode in aqueous 1.0*M* KBr is shown in Fig. 1. The first reduction scan of the electrode to TTF produced a broad cathodic wave. The oxidation of the electrode back to TTF^+ produced a sharp anodic wave which shifted toward less positive potentials with further cycling. The second reduction scan produced a sharp cathodic wave; this wave shifted very little in potential with further cycling. The Pt/NAF, TTF^+ electrode, which was originally golden in color, became colorless when the film was reduced in 1.0*M* KBr and then purple when the film was oxidized. After about 10 cycles the anodic wave attained a constant shape and peak potential. The integrated charge under the CV waves decreased for the first 4-5 cycles after which the integrated charge was about half that of the first reduction and then remained essentially constant. After about 2 hr the peak currents for the CV waves slowly decreased with continuous scanning and after about 12 hr the waves had disappeared.

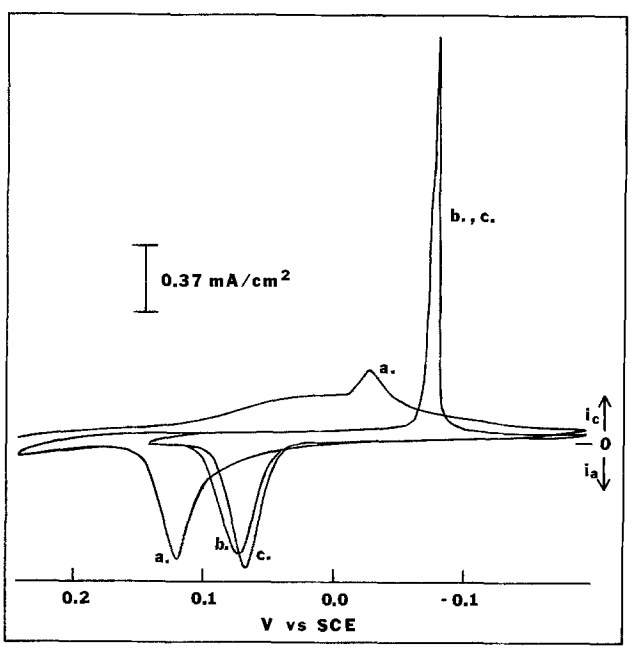

Fig. 1. Cyclic voltammogram of a Pt/NAF,TTF^+ electrode in 1*M* KBr at 10 mV/sec, (a) initial CV, first cycle; (b) third cycle; (c) fifth cycle. Integrated charge under the anodic wave, Q_t = 74 μC.

While the first CV reduction wave (Fig. 1) was a broad, drawn-out wave with a slowly decaying (diffusive) tail, which is characteristic of the CV waves seen for other electroactive molecules bound into Nafion polymer layers (6), the subsequent oxidation and reduction waves had shapes different from those previously seen in polymer electrodes. The purple color of the oxidized form of the electrode after the first and subsequent reductions has been ascribed to the formation of a $TTFBr_{0.7}$ complex, rather than the original golden material, where the TTF^+ ion is associated with the sulfonate group on the polymer. The stability of the freshly formed electrode was also very different from the electrochemically cycled electrode. When a freshly formed Pt/NAF,TTF^+ electrode was taken out of the aqueous TTFCl solution in which incorporation of TTF^+ took place, the golden-colored electrode could be immersed in water at open circuit for at least one week without any apparent effect on the subsequent electrochemistry of the polymer. If the electrode was immersed in 1.0*M* KBr, however, colored material diffused out of the polymer into the solution. Within a few minutes the amount of electroactive TTF^+ remaining in the polymer was greatly reduced over that which would have been found if the electrochemical cycling of the polymer had begun immediately. This experiment indicated that TTF^+ was indeed electrostatically bound into the Nafion polymer from the aqueous TTFCl solution and the stability of the polymer in water can be attributed to the absence of cations in solution capable of exchanging with the TTF^+ on the polymer sites. In 1.0*M* KBr, K^+ can replace TTF^+ on the polymer sites. Note, however, that after a few reduction or oxidation cycles, the electrode could be immersed at open circuit in 1*M* KBr in either the TTF^+ or TTF form with little loss of electroactive material over 1 hr. The difference in stability between the initially formed golden TTF^+ electrode and the electrochemically oxidized purple electrode in 1.0*M* KBr indicated that the electrochemically oxidized form of the polymer was very different from the initially formed material.

The steady-state cyclic voltammogram of a Pt/NAF, TTF^+ electrode is shown in Fig. 2a. For comparison, a cyclic voltammogram for a nernstian one-electron reaction showing thin layer behavior (7) with the same area under the waves is shown. This theoretical CV wave emphasizes both the unusual sharpness of the peaks and the nature of the peak separation at this scan rate. Also included in Fig. 2 is the CV of a solid film of TTF on a Pt electrode, denoted Pt/TTF. This film was formed by placing a drop of benzene containing dissolved TTF on a Pt electrode and allowing the benzene to evaporate. The similarities between the solid and polymer layers of TTF suggest that the TTF species in the polymer after cycling resembled the solid TTF and TTF^+-Br^- phases. However, while the Pt/NAF,TTF^+ electrode was reproducible and stable upon cycling for hours, the Pt/TTF electrode was less reproducible and became irreversibly oxidized in less than 1 hr of electrochemical cycling.

CV: effect of scan rate.—The CV behavior of a Pt/NAF,TTF^+ electrode was studied in 1*M* KBr for scan

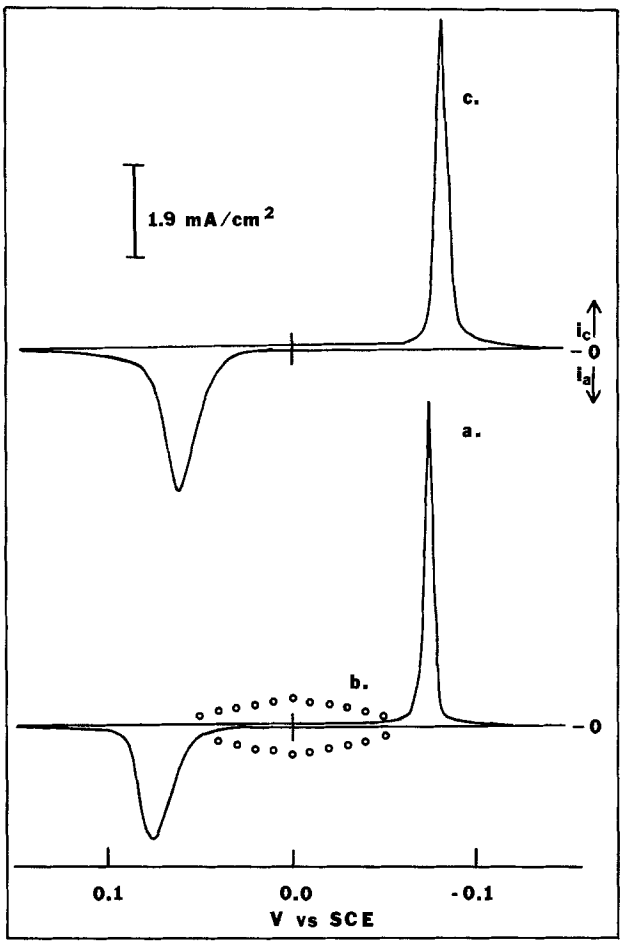

Fig. 2. Cyclic voltammogram at 10 mV/sec of (a) Pt/NAF, TTF^+ electrode in 1M KBr, $Q_t = 147$ μC; (b) ideal $1e^-$ thin layer electrode using Q_t as in (a) and an $E°$ of 0.0V; (c) Pt/TTF electrode (~800Å thickness) in 1M KBr.

rates (v) of 0.02-10 V/sec (Fig. 3-5). With increasing v, the peak potential of the anodic wave (E_{pa}) shifts toward more positive values and that of the cathodic wave (E_{pc}) toward more negative values (Fig. 6). In investigations at $v < 1$ mV/sec (Fig. 3), the electrode was scanned at 1 mV/sec until ~ 150 mV before the CV wave and then v was decreased to the desired value until the peak was traversed, then increased to 1 mV/sec again until the opposite peak was reached. Although both waves shifted with increasing v, the behavior of the anodic and cathodic waves with v was

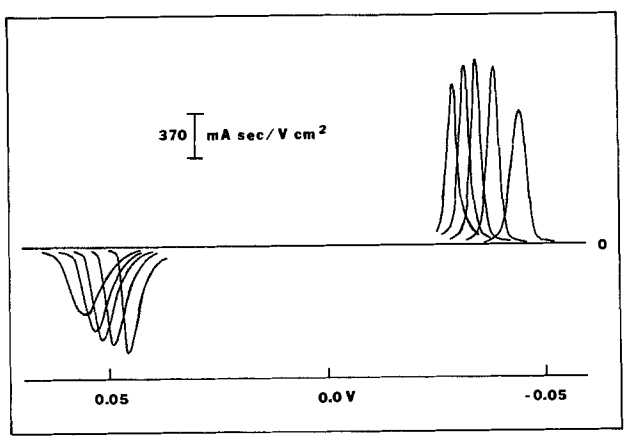

Fig. 3. Cyclic voltammogram (i_p/vA vs. E) of a Pt/NAF,TTF^+ electrode in 1M KBr at various sweep rates. The outside cathodic and anodic peaks correspond to a sweep rate of 0.5 mV/sec with subsequent anodic and cathodic peaks corresponding to sweep rates of 0.2, 0.1, 0.05, and 0.02 mV/sec. $Q_t = 152$ μC.

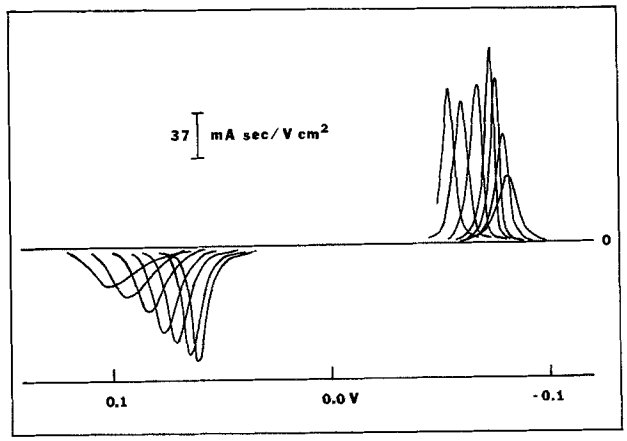

Fig. 4. Cyclic voltammogram (i_p/vA vs. E) of a Pt/NAF,TTF^+ electrode in 1M KBr at various sweep rates. The outside cathodic and anodic peaks correspond to a sweep rate of 100 mV/sec with subsequent anodic and cathodic peaks corresponding to sweep rates of 50, 20, 10, 5, 2, and 1 mV/sec. $Q_t = 44$ μC.

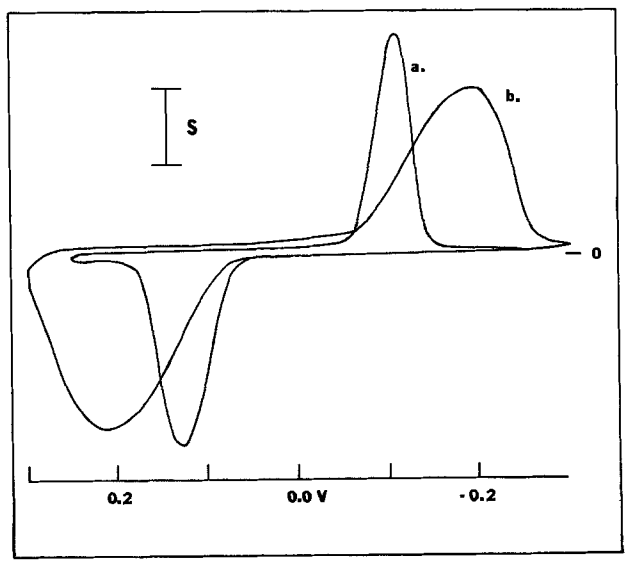

Fig. 5. Cyclic voltammogram of a Pt/NAF,TTF^+ electrode in 1M KBr at sweep rates of (a) 1 V/sec, $S = 14$ mA/cm², $Q_t = 55$ μC; (b) 10 V/sec, $S = 74$ mA/cm².

different. The anodic peak shifted out and became broader and i_{pa}/v decreased with increasing v. The cathodic peak shifted out but maintained roughly the same shape, and for $v < 50$ mV/sec, i_{pc}/v was nearly the same (Fig. 4). The integrated charges under the oxidation and reduction waves were within 5% of each other and constant for the range 1-10 V/sec. The integrated charge at $v < 1$ mV/sec was not measured, but the constant shape of the waves suggests that the charge was the same for all scan rates. The electrode deteriorated more rapidly at 10 V/sec than at slower scan rates, probably because of the large current density (0.16 A/cm²) being passed through the film at this v (Fig. 5).

The shape of the CV waves of Pt/NAF,TTF^+ electrodes varied slightly from electrode to electrode; the peak currents were directly influenced by the amount of TTF^+ incorporated into the polymer layer. The examples given in the figures represent typical behavior. Because the life of any single electrode was limited, the data represent the behavior from several different electrodes. The integrated charge under a steady-state wave in cyclic voltammetry is included with each figure to make comparisons between figures easier. The CV behavior for the Pt substrate was not unique. The CV waves of the NAF-TTF polymer on Au, pyrolytic

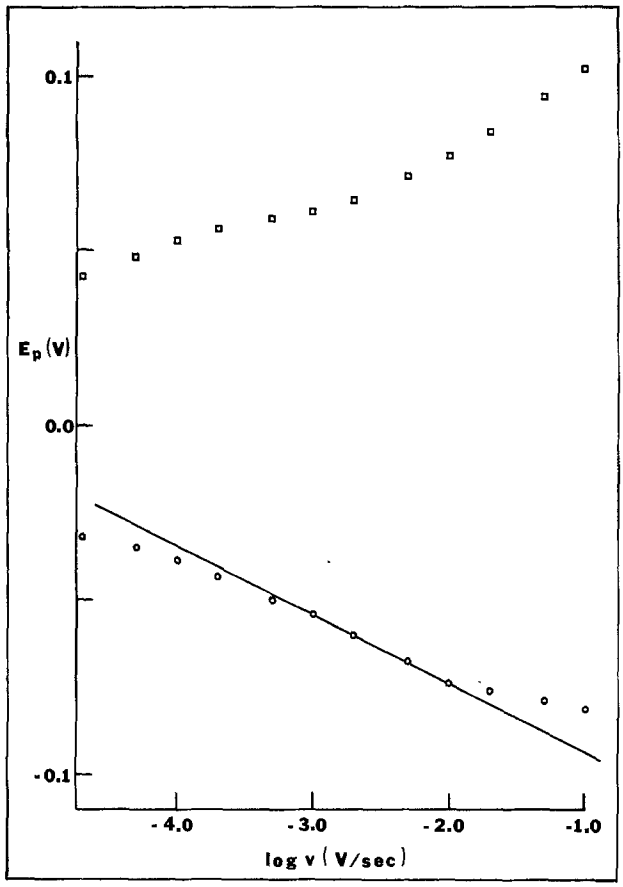

Fig. 6. Plot of E_{pc} (○) and E_{pa} (□) vs. log v. Same electrode as used in Fig. 4.

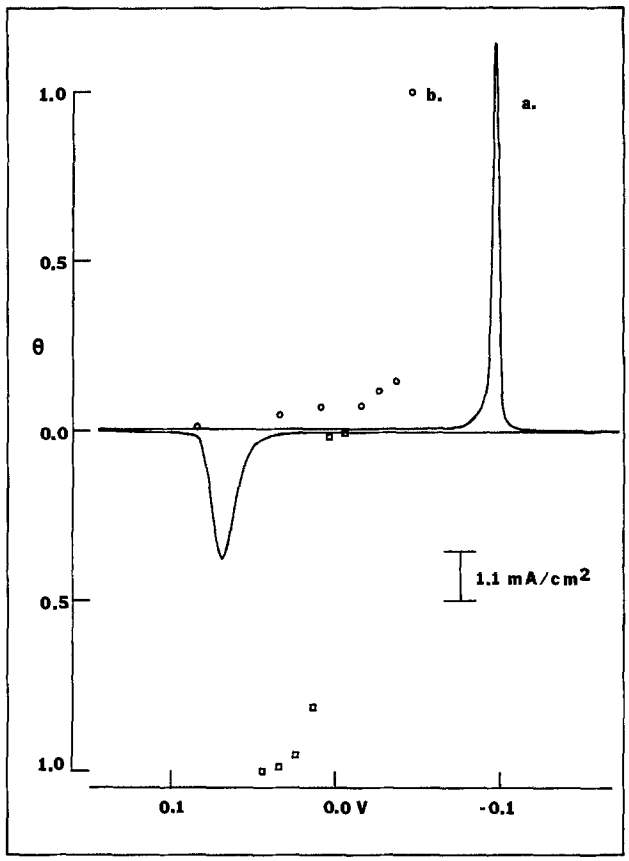

Fig. 7. (a) Cyclic voltammogram of a Pt/NAF,TTF$^+$ electrode in 1M KBr at 10 mV/sec, Q_t = 159 μC; (b) (circles and squares) electrochemical isotherm of the same electrode as shown in (a), showing total charge passed at given potential normalized to 159 μC.

graphite, optically transparent SnO_2-coated glass, and Ta substrates were very similar to that on a Pt substrate.

Equilibrium behavior.—To investigate whether the peaks would shift in and exhibit the same E_p value as equilibrium was approached, the potential was scanned to a given potential and held there until the current dropped below 1.5 nA (*i.e.*, 0.1 μC of charge per min). The ratio of the charge passed at a given potential to that needed for complete reduction or oxidation of the film, θ, as a function of E, is shown in Fig. 7. This CV isotherm taken at essentially an infinitesimal scan rate showed a sharp break in both the cathodic and anodic branches which occurred well before the peaks in the cyclic voltammogram at 10 mV/sec. If the time required for establishment of equilibrium was decreased by setting higher current limits, the effect on the isotherm was to shift the breaks in the isotherm to more negative and more positive potentials; this is the same effect as seen for the peak potentials in cyclic voltammetry with faster scan rates. The potential of the break was invariant with the amount of electroactive material reduced or oxidized in the layer during the break in the isotherm. If the potential was shifted to less negative potentials during the break in the cathodic isotherm the reaction immediately ceased. The cathodic isotherm had a long slow rise before the sharp break in the isotherm which possibly resulted from the existence of other forms of TTF$^+$, such as bound to the SO_3^- groups in the polymer.

CV: effect of scan reversal.—Reversal in the direction of a potential scan at different points along the CV wave was suggested by Conway *et al.* (8) to be a useful way of determining the effect of interactions among the molecules in the surface layer. The effect of scan reversal into both the oxidation and reduction waves of a Pt/NAF,TTF$^+$ electrode is shown in Fig. 8. The current after reversal of the scan was larger than that seen before the potential direction was reversed with this effect being more pronounced for the reduction wave. This effect is not usually seen with polymer or modified electrodes and points to strong positive (attractive) interactions among the oxidized molecules in the polymer with a smaller positive interaction among the reduced molecules. The potential of the reverse peak also showed a much larger shift for the reduction wave as compared to the oxidation wave.

CV: effect of supporting electrolyte concentration.—The concentration of supporting electrolyte was varied to determine the effect of changes in Br^- concentration on the cyclic voltammogram of a Pt/NAF,TTF$^+$ electrode. The results of varying the KBr concentration from 3.5 to 0.1*M* are shown in Fig. 9 for the same electrode. A plot of the shift in peak potential of both the cathodic and anodic waves *vs.* the log of the KBr concentrations for all concentrations investigated is shown in Fig. 10. The fact that the CV waves of the Pt/NAF,TTF$^+$ electrode responded to changes in the supporting electrolyte concentration was not surprising, because it has already been established that the oxidized form of the electrode involved formation of a TTF$^+$-Br^- complex. The shift in potential was close to the expected −59 mV per tenfold change in Br^- concentration. A significant deviation in the shape of the waves occurred at the lowest concentration, 0.1*M*. At this concentration each wave looked to be two waves, a broad diffusional looking wave with a sharper wave superimposed. Significantly, the color of the oxidized form of the wave at the lowest concentration was no longer purple but golden. The average molar concentration of electroactive TTF molecules in the polymer films, as was stated earlier, was typically 0.3*M*. The concentration of KBr present in the polymer after im-

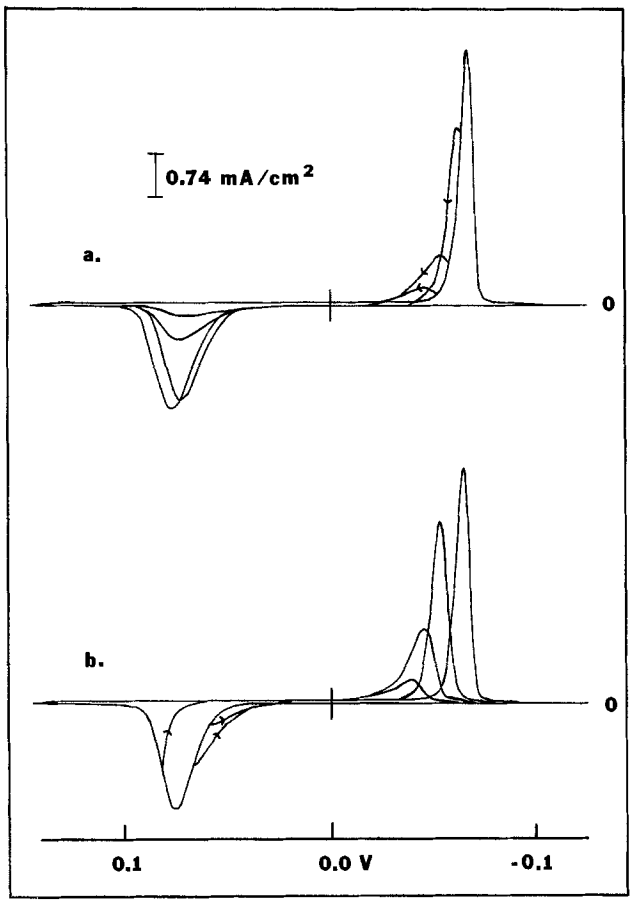

Fig. 8. Cyclic voltammogram of a Pt/NAF,TTF+ electrode in 1M KBr at 10 mV/sec with (a) scan reversal into the cathodic wave; and (b) scan reversal into the anodic wave; $Q_t = 90$ μC.

mersion in a KBr solution is unknown, but examination of the polymers coated on Pt in a scanning electron microscope using energy dispersive spectroscopy showed

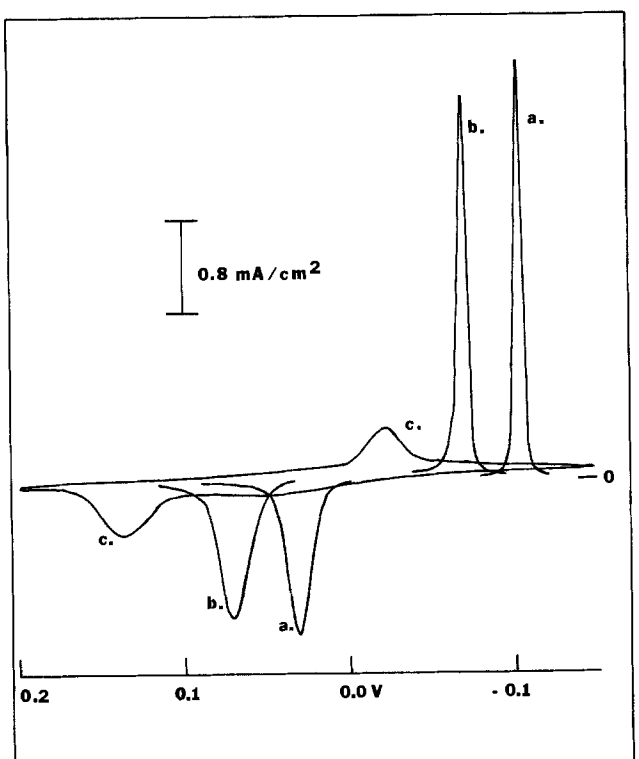

Fig. 9. Cyclic voltammogram of a Pt/NAF,TTF+ electrode at 10 mV/sec in (a) 3.48M KBr; (b) 1.0M KBr; $Q_t = 108$ μC; (c) 0.1M KBr.

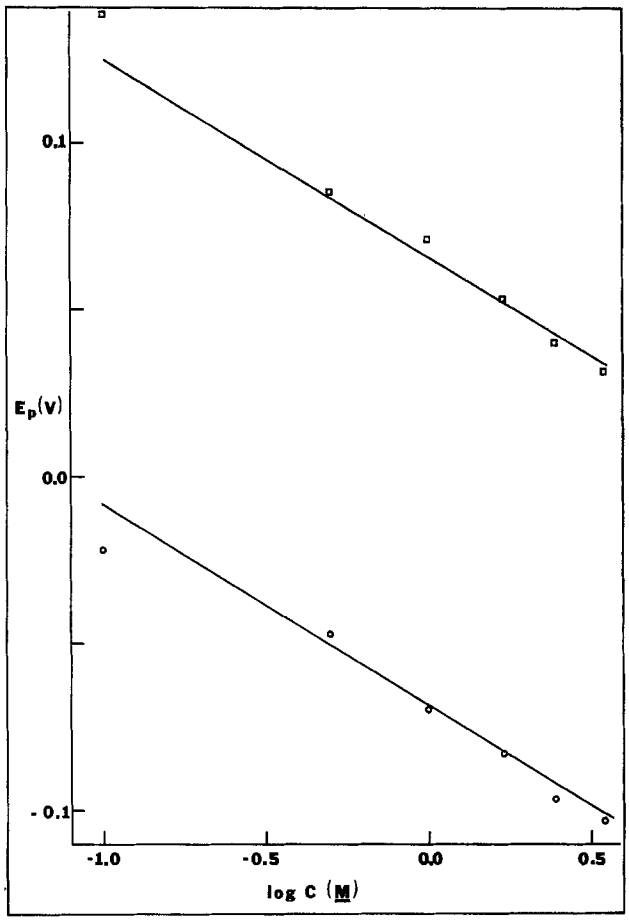

Fig. 10. Peak potential vs. log KBr concentration from the experiment shown in Fig. 9. Lines are drawn with a slope of —59 mV.

that after soaking in a KBr solution, Br was present in the polymer. Experiments using NaOH showed that after equilibration the Nafion achieved nearly the same concentration of NaOH as that present in solution (9). These facts suggested that the electrochemical process changed at the lowest concentration because of an excess in electroactive TTF over bromide ion present in the polymer.

CV: temperature effects.—The effect of varying the temperature on CV waves has been used to obtain information about the kinetics of reactions coupled to electron transfer reactions (10). Unusual temperature effects on the CV waves of TTF-TCNQ pressed pellet electrodes were previously observed (11). The temperature of the Pt/NAF,TTF+ electrode immersed in the solution was held at a given value by placing the electrochemical cell in a water bath. The SCE reference electrode remained at room temperature throughout the experiment with only the reference electrode tip in the solution. The CV waves of a Pt/NAF,TTF+ electrode were strongly temperature dependent as is shown in Fig. 11. Both the cathodic and anodic waves shifted closer together with increasing temperature. The reduction waves at the higher temperatures (36° and 55°C) were initially sharper than those at lower temperatures but within a few cycles broadened out to the shape shown in Fig. 11. The shift in peak potential with temperature was greater for the reduction wave as is shown in the plots of reduction and oxidation peak potentials *vs.* temperature (Fig. 12) which were linear over the temperature range studied.

CV: effect of different halide ions.—The halide ion in the supporting electrolyte was varied to determine the effect of the counterion on the CV waves of a Pt/NAF,TTF+ electrode (Fig. 13). The CV peaks shifted to more negative potentials in the order $Cl^- < Br^-$

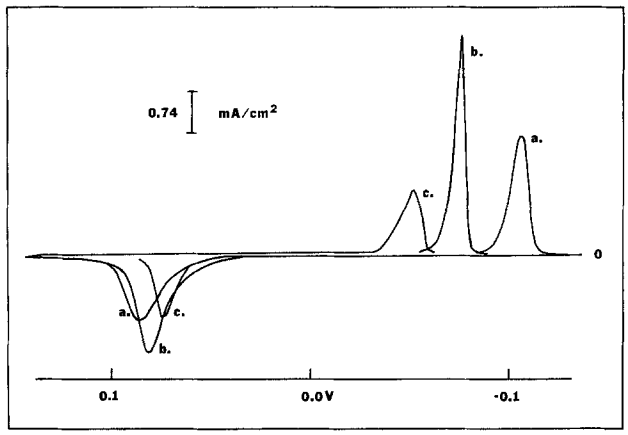

Fig. 11. Cyclic voltammogram of a Pt/NAF,TTF$^+$ electrode in 1*M* KBr at 10 mV/sec and at a temperature of (a) 1.5°C; (b) 21°C; Q_t = 97 μC; (c) 36°C.

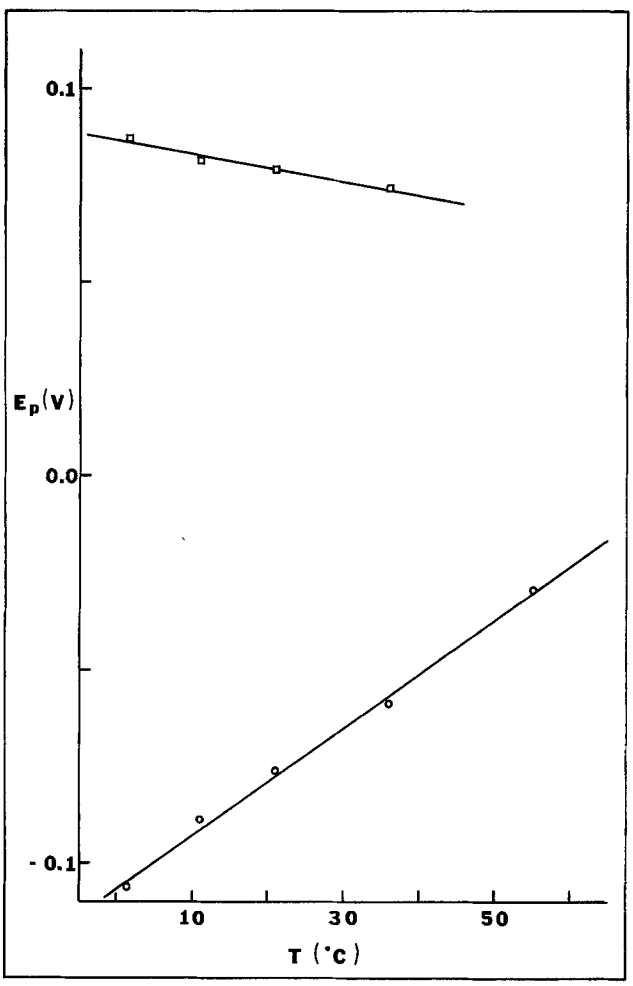

Fig. 12. Peak potential *vs.* temperature from the experiment shown in Fig. 11.

< I^- and the oxidized form of each electrode was purple. In KF the CV waves were broad and had a shape similar to that of other electroactive molecules observed in Nafion. The shape of the CV waves and the color of the oxidized form of the electrode, golden, in KF was identical to the electrode behavior observed using potassium acetate and potassium sulfate as supporting electrolytes. TTF$^+$ is known to form one-dimensional conducting complexes with Cl^-, Br^-, and I^-, but no conducting complexes have been reported using F^-, acetate, or sulfate. If the same electrode was used in different supporting electrolytes, the behavior was unaffected by the order in which the different solutions were investigated. No effect on the cyclic voltammogram of a Pt/NAF,TTF$^+$ electrode in a Br^- solution was seen when the cation of the supporting electrolyte was changed from potassium to sodium.

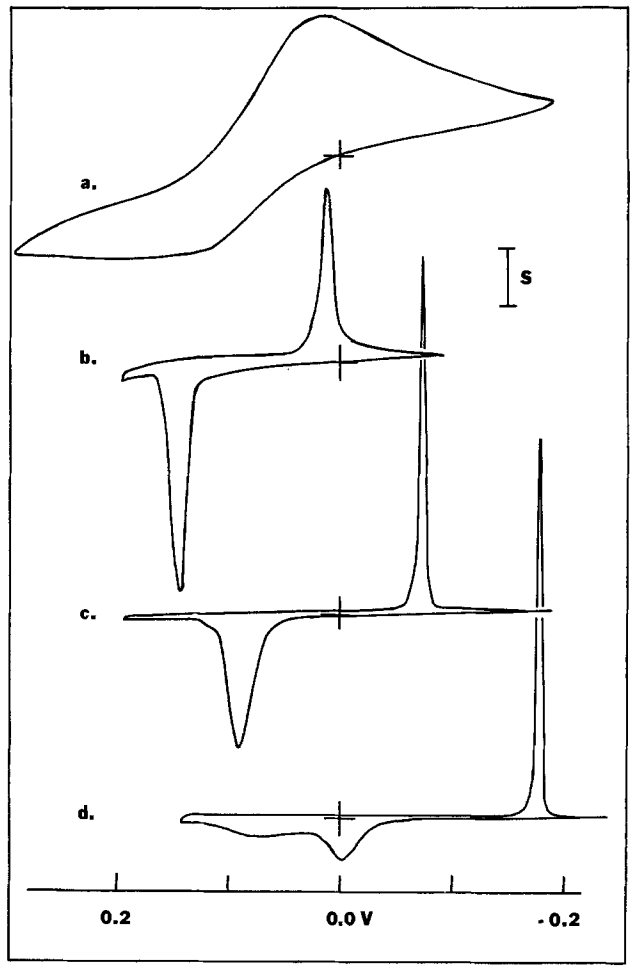

Fig. 13. Cyclic voltammogram of a Pt/NAF,TTF$^+$ electrode at 10 mV/sec in various supporting electrolytes: (a) 1*M* KF, S = 74 μA/cm^2; (b) 1*M* KCl, S = 740—(>40) μA/cm^2; (c) 1*M* KBr, S = 740 μA/cm^2, Q_t = 137 μC; (d) 1*M* KI, S = 740 μA/cm^2.

Chronoamperometric behavior.—Chronoamperometric methods can be useful in determining the apparent diffusion coefficient, D_{app}, of a species confined to a layer on an electrode surface. When D_{app} is measured using chronoamperometric methods, the value may be associated with a specific ion diffusion through the polymer, an electron hopping process, or both, depending on what process limits the current (12). A potential step (0-0.25V) was applied to a reduced Pt/NAF, TTF$^+$ electrode in a 1*M* KBr solution and the current-time (*i-t*) transient recorded. The plot of i *vs.* $t^{-1/2}$ (Fig. 14) shows a linear region with zero intercept (Cottrell region). The slope of the linear region yielded D_{app} of 8 × 10^{-7} cm^2/sec based on the Cottrell equation and assuming an average concentration of the electroactive TTF molecules uniformly distributed throughout the film and a one-electron process. Based on the thickness of the layer and D_{app}, the onset of deviations from Cottrell behavior which occur at longer times due to thin layer effects occurred at approximately the expected time. The current from the *i-t* trace for the reduction of the electrode using a potential step from 0.2 to −0.4V decayed rapidly after 2 msec, presumably showing the effect of reduction of the bulk of the TTF$^+$. The processes by which the electrode reduced and oxidized during a potential step were clearly different.

Spectroscopy.—Electrodes were formed on a transparent SnO_2 glass conducting substrate so that ab-

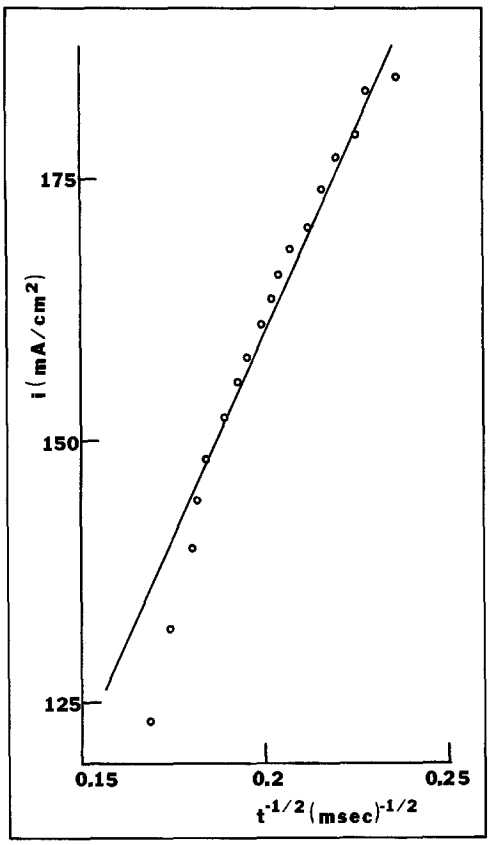

Fig. 14. Current vs. $t^{-1/2}$ for the oxidation of a Pt/NAF,TTF$^+$ electrode in 1M KBr. The potential was stepped from 0.0 to 0.25V.

sorption spectroscopy could be used to identify the form of the oxidized and reduced molecules in the polymer. The electrochemistry of the SnO_2/NAF,TTF$^+$ electrodes was similar to that of electrodes using Pt substrates. The vis-near infrared spectra of dry electrodes were recorded with a Cary 14 spectrophotometer for electrodes before electrochemical cycling and after electrochemical cycling with the electrode left in the reduced or oxidized forms (Fig. 15). The results from these spectra are shown in Table I along with results from previous studies of $TTFBr_{0.79}$ and TTFCl crystals (13). The spectrum of the electrode before electrochemical cycling was close to that of the dimer dication of TTF$^+$ as observed for TTFCl crystals (13). The peak at 790 nm (λ_{CT}) corresponds to an intermolecular electronic transition between the molecules of the dimer. The spectrum of the reduced form of the electrode did not show any peaks in the visible region; this corresponds to published spectra of TTF (13) where only an absorption peak in the u.v. was seen. The surface of the reduced form of the electrode

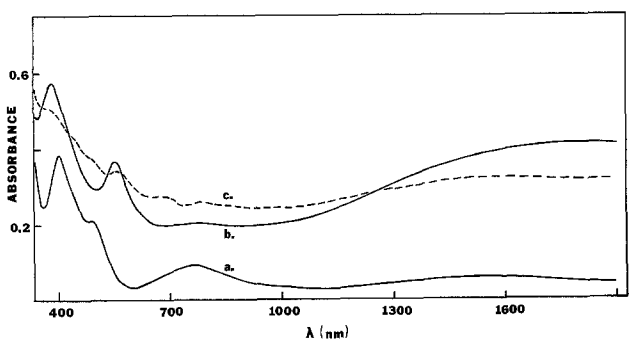

Fig. 15. Absorption spectrum of a dry glass-SnO_2/NAF,TTF$^+$ electrode (a) freshly formed; (b) after electrochemical cycling in 1M KBr, removed from solution in the oxidized state; (c) after electrochemical cycling in 1M KBr, removed from solution in the reduced state.

Table I. Absorption maxima of SnO_2/NAF,TTF$^+$ electrodes

	λ_{max} (nm)	λ_{sh} (nm)	λ_{CT} (nm)
Fresh SnO_2/NAF,TTF$^+$ electrode	400	490	760
TTFCl (dimer)*	380	530	790
Oxidized SnO_2/NAF,TTF$^+$ electrode	397	561	1890
$TTFBr_{0.79}$*	374	537	1970

* Absorption spectrum of powdered samples dispersed in KBr [from Ref. (13)].

was partially covered with the nonelectroactive crystals of $TTFBr_{0.7}$ (5), but the absence of any peaks in the spectra due to the nonelectroactive crystals means they contributed very little to the absorption spectrum. The spectrum of the electrode in the oxidized form also was similar to that for crystals of $TTFBr_{0.79}$, where the peak present in the near-infrared was shown to correspond to intermolecular electronic transitions along the conducting axis of the crystal. The presence of the near-infrared peak leads to the conclusion that the oxidized form of the electroactive molecules in the electrode was $TTFBr_{0.7\text{-}0.8}$.

Discussion

The electrochemical investigation of Pt/NAF,TTF$^+$ electrodes leads to the following model for the oxidation and reduction of the electroactive TTF molecules in the polymer layer. The consistency of the experimental results to this model is discussed below. Incorporation of TTF$^+$ into the Nafion layer produces a golden-colored film in which TTF$^+$ has no special structural arrangement and exists predominantly as TTF$^+$,$-SO_3^-$ pairs. However, upon several reduction and oxidation cycles, counterions from the electrolyte (*e.g.*, Br^- and K^+) are incorporated into the layer and the oxidized form of the layer is now purple and has an organized TTF$^+Br^-$ structure (probably in the conductive nonstoichiometric form, $TTFBr_{0.7}$). The overall redox reaction upon cycling can then be written as

$$TTFBr_{0.7} + 0.7e \rightleftharpoons TTF + 0.7Br^- \quad E^\circ_1 \qquad [1]$$

However, the structural changes that occur during these redox reactions cause the electrochemical behavior to deviate from that expected when all processes and elementary steps are rapid and reversible. Neutral TTF has a crystal structure in which the flat TTF molecules lie parallel to one another, forming stacks of TTF with each molecule assuming a staggered (st) configuration with respect to the one below it (14). The crystal structure of $TTFBr_{0.7}$ also involves stacks of TTF$^+$ molecules, but these assume an eclipsed (ec) position with respect to one another (13). The reduction of the film involves loss of Br^- and structural rearrangement of the molecules from the ec TTF$^+$ form to the st configuration of the neutral TTF molecules. The stabilization of the TTF$^+$ molecules by formation of the Br^- complex makes the complexed form of TTF$^+$ harder to reduce than the uncomplexed one. The reaction then occurs by a "square scheme" mechanism (3)

$$\begin{array}{ccc} TTFBr_{0.7}(ec) & + 0.7e - & TTF\ (ec) + 0.7Br^- \\ \uparrow k' & & \downarrow k \end{array} \qquad [2]$$

$$TTFBr_{0.7}(st) + 0.7e - \underline{TTF\ (st)} + 0.7Br^- \qquad [3]$$

(where the underlined forms are the stable ones). The E° for reaction [2] is more negative than E°_1 by an amount related to the energy difference between the ec and st forms of neutral TTF, and E° for reaction [3] is more positive than E°_1 by an amount related to the energy difference between the st and ec forms of the TTF$^+$ species. The different E°-values for oxidation and reduction result in the peak splitting shown in

the CV waves. However, the peaks do not occur at potentials governed by their respective E^{o}'s because the following irreversible reactions cause the peaks to shift in (toward E^{o}_1). This behavior is characteristic of reversible electron transfers followed by irreversible following reactions of solution species (an E_rC_i reaction) (1b, 15) and of surface monolayers (16). The extent of the shift in the CV peaks depends on the rate constants of the following reactions (k and k') and the scan rate (v) in a manner consistent with the behavior shown in Fig. 3 and 4. The rapidity and irreversibility of the structural rearrangements is shown by the rapid scan (v = 10 V/sec) experiments, where no reversal peaks corresponding to either reaction [2] or [3] are observed (Fig. 5). At essentially infinitesimal scan rates (Fig. 7), the behavior approaches that governed by the overall reaction, (Eq. [1]); the results suggest that $E^{o}_1 = 0.00 \pm 0.02$V *vs.* SCE.

The model is consistent with the 59 mV shift of both peaks per tenfold change in Br^- concentration (Fig. 10). The shifts in E^{o}_1 with supporting electrolyte anion (Fig. 13) point to stronger complexation of TTF^+ by I^- ($E^{o}_1 \sim -0.1$V *vs.* SCE) and weaker complexation by Cl^- ($E^{o}_1 \sim +0.05$V *vs.* SCE). Fluoride ion does not form a conductive complex, so the wave loses its thin-layer shape in a F^- medium and the structural reorganization effects are absent (Fig. 13a).

The quantitative electrochemical behavior and the detailed shapes of the waves depend on other factors, such as attractive interactions within the film which cause the extreme narrowness of the reduction peak. A digital simulation treatment of this system will be discussed elsewhere (17). However, thin layer E_rC_i behavior (16) probably is a reasonable approximation for both parts of the square scheme. The reaction of the Pt/NAF,TTF^+ electrode is considered to be thin layer at scan rates below 10 V/sec because the integrated charges under the CV waves are independent of v. The theory predicts that in the scan rate regime where the rate of the following reaction is much larger than the scan rate and the electron transfer is reversible (*i.e.*, where $(RT/n\mathbf{F})(k/v) > 10$), no peaks are observed for the unreacted form of the molecules and the variation in peak potential is described by Eq. [4] (16)

$$E_{pc} = E^{o} + (2.3RT/n\mathbf{F}) \log (RTk/n\mathbf{F}v) \qquad [4]$$

The plot of E_{pc} *vs.* log v for a Pt/NAF,TTF^+ electrode (Fig. 6) was linear over the intermediate range of scan rates ($\sim 10^{-4}$ to 10^{-2} V/sec). The slope of the line (−19.4 mV) is much smaller than that predicted by Eq. [4] for a one-electron transfer. The predicted value of $\Delta E_{1/2}$, the width at half-height, for a thin layer E_rC_i reaction is $66/n$ mV (16). The width of the anodic wave is ~20 mV but the cathodic wave is much narrower. The narrowness of the reduction wave can be explained by attractive interactions among the oxidized molecules in the polymer; these are also responsible for the unusual behavior found for scan reversal at different points into the cathodic wave, where the cathodic current increases on reversal (Fig. 8). This is explained as follows. The oxidized electrode is initially hard to reduce because the attractive interactions must be overcome; this causes the cathodic wave to be shifted to more negative potentials. As the electrode is partially reduced the retarding effect of the interactions is decreased because of the smaller concentration of oxidized molecules within the film, so the reduction rapidly accelerates, producing a narrow, tall reduction wave. This effect is less pronounced for the oxidation wave indicating that the attractive interactions among the reduced molecules are smaller than among the oxidized ones. Similarly, the $\Delta E_{1/2}$ of the oxidation wave is apparently less affected by attractive interactions than the reduction wave. If the E_rC_i model is valid for this system, the slope of the E_p *vs.* log v line suggests an n-value of 3 (*i.e.*, 3 electrons transferred per molecule). One can speculate that the critical lattice unit is $(TTF)_4Br_3$ and the overall reaction is

$$(TTF)_4Br_3 + 3e \rightleftharpoons (TTF)_4 + 3Br^- \qquad [5]$$

The deviations at high scan rates can be attributed to the onset of the significance of heterogeneous kinetics.

The effect of varying the temperature on the CV peak potentials of a Pt/NAF,TTF^+ electrode (Fig. 11) showed that the change in entropy (ΔS) for the reduction and oxidation processes were not of equal magnitude and, furthermore, did not have the same sign. This result can be explained by first assuming the cathodic and anodic processes are E_rC_i reactions in a thin layer, and then examining the temperature dependence of the peak potential for such a reaction (Eq. [4]). This is done by expressing E^{o} as a function of its enthalpic (ΔH^{o}) and entropic (ΔS^{o}) contributions and the rate constant, k, by the Arrhenius equation in terms of the activation enthalpic ($\Delta H^{\neq}$) and entropic ($\Delta S^{\neq}$) contributions. The result is Eq. [6] where h is Planck's constant and N_A is Avogadro's number. The sign is plus for a reduction and minus for an oxidation

$$n\mathbf{F}E_p = -\Delta H^{o} + T\Delta S^{o} \pm (T\Delta S^{\neq} - \Delta H^{\neq} + R \ln (RT^2/N_A n\mathbf{F}hv)) \qquad [6]$$

The derivative of Eq. [6] with respect to temperature is given by Eq. [7]

$$n\mathbf{F}\frac{dE_p}{dT} = \Delta S^{o} \pm (\Delta S^{\neq} + R \ln (R^2T^2/N_A n\mathbf{F}hv) + 2R) \qquad [7]$$

Over the experimental temperature range, dE/dT should be constant to within 2%. The experimental peaks shifted linearly with temperature (Fig. 12), with a cathodic peak slope of 1.44 mV/K, and an anodic peak slope of −0.34 mV/K. There are four terms in Eq. [7] which contribute to the slope, one of which, ΔS^{o}, has been extensively studied for solution redox species (18). The change in entropy for the reduction of a cation in solution is generally positive with dE/dT in the range 0.2-2.0 mV/K. The peak potentials of both the oxidation and reduction waves should shift to more positive potentials with increasing temperature as a result of the ΔS^{o} term. The other three terms in Eq. [7] result from the perturbation caused by the following reaction. While $\Delta S^{\neq}$ is unknown for the reaction, the other two terms can be estimated and yield ±2.79 mV/K for n = 1 (T = 298 K, v = 0.01 V/sec) and ±0.90 mV/K for n = 3 (T = 298 K, v = 0.01 V/sec) (+ for reduction, − for oxidation). The two terms cause a shift in the reduction wave to more positive potentials and the oxidation wave to more negative potentials with increasing temperature. The two calculated terms are in the same direction as the effect ΔS^{o} for the reduction peak, but are opposite to the ΔS^{o} term for the oxidation peak. This could explain why the cathodic process has a larger positive slope than the anodic process and why the anodic process has a slope with a sign opposite to that of the reduction process.

We do not believe that other explanations of the observed CV peak separations and narrow waves for Pt/NAF,TTF^+ electrodes are as reasonable. For example, resistance effects can cause peak separations in cyclic voltammetry (19), but a large resistance ($R >$ 0.1 MΩ) would be needed to cause the peak separations observed in the slow scan rate experiments, because of the small currents being passed. The cell resistance of a Pt/NAF,TTF^+ electrode in 1.0*M* KBr

was small (20Ω) as determined by observing the charging of the double layer in response to a potential step in a nonfaradaic region. A small heterogeneous electron transfer rate constant can produce peak splittings in cyclic voltammetry. However, the peak separation found at 0.02 mV/sec would yield (with $\alpha = ½$ and $n_a = 1$) a rate constant, k^o, of 2×10^{-8} cm/sec (20). This seems unreasonably small compared to other values reported for electroactive molecules in Nafion (6b, c). Attractive interactions between reduced and oxidized molecules will not normally produce CV peak splittings. Large attractive interactions that occur with the onset of phase transitions can produce CV peak splittings; however, the isotherm under those conditions would not have the shape found for Pt/NAF, TTF^+ electrodes.[1]

Conclusion

A freshly formed Pt/NAF,TTF^+ electrode contains TTF^+, probably as TTF_2^{2+}, electrostatically bound on the $-SO_3^-$ cation exchange sites of the polymer. After electrochemical cycling the electroactive molecules in the polymer form small domains of solid which show similar behavior to electrodes made from thin films of TTF. This aggregation occurs within the polymer film, where the reduced form of the electroactive molecules is neutral TTF and the oxidized form is $TTFBr_{0.7}$. The sharp, narrow CV waves for the oxidation of TTF and reduction of $TFBr_{0.7}$ are split by over 100 mV; this can be explained by structural transitions between the oxidized and reduced forms. The shape and hysteresis found on scan reversal demonstrates that attractive interactions which are greater for the oxidized form exist between the electroactive molecules.

Acknowledgment

The support of this research by the National Science Foundation (CHE 7903729) and the Robert A. Welch Foundation (F-079) is gratefully acknowledged.

Manuscript submitted April 26, 1982; revised manuscript received *ca.* Sept. 14, 1982.

Any discussion of this paper will appear in a Discussion Section to be published in the December 1983 JOURNAL. All discussions for the December 1983 Discussion Section should be submitted by Aug. 1, 1983.

Publication costs of this article were assisted by the University of Texas at Austin.

[1] For a detailed discussion of peak splittings in cyclic voltammetry resulting from phase transitions, see Ref. (2d and 8).

REFERENCES

1. (a) A. J. Bard and L. R. Faulkner, "Electrochemical Methods," p. 522, John Wiley & Sons, Inc., New York (1980); (b) A. J. Bard and L. R. Faulkner, "Electrochemical Methods," Chap. 11, John Wiley & Sons, Inc., New York (1980).
2. (a) P. Daum and R. Murray, *J. Electroanal. Chem. Interfacial Electrochem.*, **103,** 289 (1979); (b) F. B. Kaufman, A. H. Schroeder, E. M. Engler, S. R. Kramer, and J. Q. Chambers, *J. Am. Chem. Soc.*, **102,** 483 (1980); (c) D. Ellis, M. Eckhoff, and V. D. Neff, *J. Phys. Chem.*, **85,** 1225 (1981); (d) A. Bewick and B. Thomas, *J. Electroanal. Chem. Interfacial Electrochem.*, **85,** 329 (1977).
3. P. Peerce and A. J. Bard, *J. Electroanal. Chem. Interfacial Electrochem.*, **114,** 89 (1980).
4. T. P. Henning, H. S. White, and A. J. Bard, *J. Am. Chem. Soc.*, **103,** 3937 (1981).
5. T. P. Henning, H. S. White, and A. J. Bard, *ibid.*, **104,** 5862 (1982).
6. (a) I. Rubinstein and A. J. Bard, *J. Am. Chem. Soc.*, **102,** 6641 (1980); (b) I. Rubinstein and A. J. Bard, *ibid.*, **103,** 5007 (1981); (c) C. Martin, I. Rubinstein, and A. J. Bard, *ibid.*, **104,** 4812 (1982).
7. A. J. Bard and L. R. Faulkner, "Electrochemical Methods," p. 410, John Wiley & Sons, Inc., New York (1980).
8. (a) E. Laviron, *J. Electroanal. Chem. Interfacial Electrochem.*, **63,** 245 (1975); (b) H. Angerstein-Kozlowaska, J. Klinger, and B. E. Conway, *ibid.*, **75,** 45 (1977); (c) E. Laviron, *ibid.*, **122,** 37 (1981).
9. T. D. Gierke, Paper 438 presented at The Electrochemical Society Meeting, Atlanta, Georgia, Oct. 9-14, 1977.
10. R. P. Van Duyne and C. N. Reilley, *Anal. Chem.*, **44,** 153 (1972).
11. C. D. Jaeger, Ph.D. Dissertation, University of Texas at Austin, 1979.
12. (a) D. A. Buttry and F. C. Anson, *J. Electroanal. Chem. Interfacial Electrochem.*, **130,** 333 (1981); (b) H. S. White, J. Leddy, and A. J. Bard, *J. Am. Chem. Soc.*, **104,** 4811 (1982).
13. J. B. Torrance, B. A. Scott, B. Welber, F. B. Kaufman, and P. E. Seiden, *Phys. Rev. B,* **19,** 730 (1979).
14. W. F. Cooper, J. W. Edwards, F. Wudl, and P. Coppers, *Cryst. Struc. Commun.*, **3,** 23 (1974).
15. R. S. Nicholson and I. Shain, *Anal. Chem.*, **36,** 706 (1964).
16. (a) E. Laviron, *J. Electroanal. Chem. Interfacial Electrochem.*, **35,** 333 (1972); (b) E. Laviron, *ibid.*, **39,** 1 (1972).
17. T. P. Henning, Ph.D. Dissertation, University of Texas at Austin, 1982.
18. E. L. Yee, R. J. Cave, K. L. Guyer, P. D. Tyma, and M. J. Weaver, *J. Am. Chem. Soc.*, **101,** 1131 (1979).
19. R. S. Nicholson, *Anal. Chem.*, **37,** 1351 (1965).
20. A. J. Bard and L. R. Faulkner, "Electrochemical Methods," p. 412, John Wiley & Sons, Inc., New York (1980).

Different Aging Effects of Electrosorbed Oxygen Monolayers. The Polycrystalline Platinum/Molten Potassium Acid Sulfate Interface

M. E. Folquer, N. R. de Tacconi, and A. J. Arvía*

Instituto de Investigaciones Fisicoquímicas Teóricas y Aplicadas (INIFTA), Sucursal 4, C.C. 16, 1900 La Plata, Argentina

ABSTRACT

Molten $KHSO_4$ offers the possibility of studying the electrochemical process related to the electroadsorption and electrodesorption of the O-containing species on Pt, under a large concentration of ionic species and a low possibility of impurity interference. The potentiodynamic response of the corresponding interface with different complex potential/time perturbation functions, as well as the potential decay at open circuit, indicates the existence of at least three different aging effects of the O-electrosorbed species. Each aging effect can be related to a particular energetic configuration of the electrosorbed layer.

The electrochemical kinetics of the O-electroadsorption and O-electrodesorption in noble metal electrodes both in aqueous and in molten salt electrolyte is explained through a complex reaction pattern where various electron transfer and structural reactions related to aging effects of the O-electroadsorbed species, at the monolayer level are involved (1-6). Different configurations of the O-electroadsorbed species can be achieved through either short or long range term transformations involving as possible contributing processes, dehydration, *i.e.*, a change of interaction between the electroadsorbed species and surrounding water (7-9), surface reaccommodation of the O-containing layer (8, 9), restructuring of the metal substrate (12, 13), ionic specific adsorption (14), changes in the film stoichiometry related to possible disproportionation reactions occurring therein (2) and possible formation of peroxidic-type structures (15-17). This paper attempts to contribute to the understanding of the aging processes through the electrochemical behavior of the Pt/$KHSO_4$ (melt) interface, a system where the aging effect under open-circuit conditions was first determined (18).

Experimental

The experimental arrangement is similar to the one described in previous publications (18, 19). The working electrodes are made of polycrystalline Pt wires (spectroscopic quality) of apparent area in the 0.15-0.49 cm^2 range. The potential of the working electrode was measured against a reversible hydrogen electrode in molten $KHSO_4$ at 1 atm H_2 saturation. The smooth working electrode was cleaned in 1:1 H_2SO_4-HNO_3 mixture, and rinsed with triply distilled water. This procedure was repeated for each new experiment.

Molten AR (Merck) $KHSO_4$ was used as electrolyte. O_2 was carefully removed from the melt following the usual procedures. Runs were made at 245°C. Three different potential perturbation programs were used. Program A (Fig. 1) involves the potential sweep from $E_{s,c}$ to $E_{s,a}$ and backward until the null net current potential ($E_{i=0}$) is reached. At this potential the current is interrupted leaving the system under open circuit during the time τ_{oc}. After τ_{oc}, the open-circuit potential shifts to E_τ and immediately afterward the potential scan is continued to reach $E_{s,c}$. Program B (Fig. 2) involves a preset potential holding (for instance, at $E_{s,a}$) during the time τ_p. Program C (Fig. 3) corresponds to that already described to promote the potentiodynamic aging of the layer forming species (3). In this case $E'_{s,c}$ can be either more positive or more negative than the potential of the O-electrodesorption current peak (E_p). The nomenclature used in the present work to identify the different charges playing part in the potentiodynamic aging is the same as that already described in a recent publication (3).

* Electrochemical Society Active Member.

Key words: metal, electrode, voltammetry, chemisorption.

Results

Electroreduction profiles obtained with program A.—The electroreduction *E/I* displays obtained with program A (Fig. 1) when $\tau_{oc} = 1.5$ min start from a common potential ($E = 0.32$V). The electroreduction charge at any v remains constant and the first portions of the electroreduction profiles are coincident. At τ_{oc} larger than 10 min, the electroreduction charge decreases (18). For a constant electroreduction charge, the potential of the electroreduction peak at 50 mV/sec is shifted 25 mV more negative than the potential of the electroreduction peak recorded under comparable repetitive triangular potential sweeps (RTPS). The kinetic analysis of these profiles were already discussed in Ref. (18).

Electroreduction profiles run with program B.—The electroreduction *E/I* displays resulting after holding the potential at $E_{s,a}$ during a time τ_p ($0 < \tau_p < 30$ min) (Fig. 2) show a progressive increase in charge and a gradual shift of the potential of the electroreduction peak toward negative potentials as τ_p increases. The potential holding at $E_{s,a}$ involves the aging of the film and its subsequent growth beyond the monolayer thickness. In this case, a partial dissolution of the oxide film is probably also involved in the overall process occurring at $E_{s,a}$.

Electroreduction profiles after perturbation program C.—The intermediate repetitive triangular potential sweeps (IRTPS) in program C involve the periodical

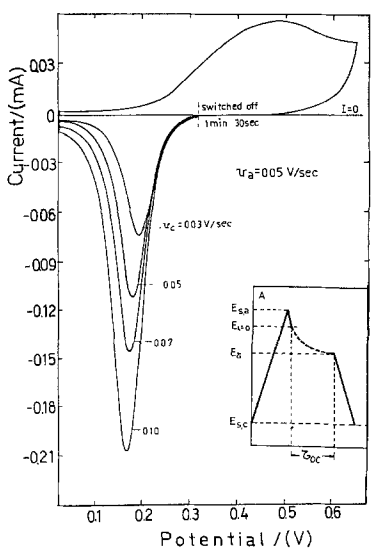

Fig. 1. Potentiodynamic *E/I* profiles run at a constant anodic potential sweep rate; $v_a = 0.05$ V/sec and at different cathodic potential sweeps; v_c after the current interruption at the null current potential. Apparent area = 0.49 cm^2.

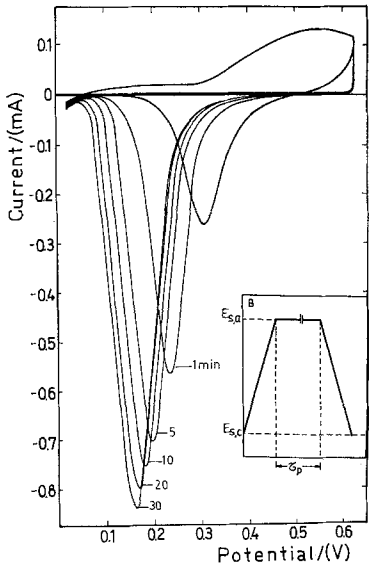

Fig. 2. Potentiodynamic *E/I* profiles run at 0.4 V/sec. Potentiostatic aging at $E_{s,a} = 0.62$V. Influence of τ_p, $\theta_i = 0.68$. Apparent area = 0.18 cm².

removal and rebuilding a fraction of the O-containing surface species initially produced. The electroreduction displays (Fig. 3) run at 0.4 V/sec IRTPS during a preset number of cycles depend quite remarkably on $E'_{s,c}$. The splitting of the electroreduction profile is only noticed when $E'_{s,c}$ is slightly more negative than E_p in the conventional RTPS display (3). The time required to attain a definite splitting in the electroreduction profile increases as $E'_{s,c}$ is increasingly more negative. The optimal splitting condition (OSC) corresponds to an $E'_{s,c}$ value involving the removal (θ_r) and rebuilding of about 70% of the initial O-containing surface species (θ_i) during the first IRTPS. Then, the potential difference of the two electroreduction peaks attained after $\tau_i = 4$ min is slightly larger than 0.1V.

When $E'_{s,c}$ is more positive than E_p (Fig. 4) and only 30-40% of the O-surface coverage is involved in the IRTPS, a single electrodesorption peak is observed afterward. The potential of the broad electroreduction peak becomes gradually more negative and simultaneously the cathodic charge increases accordingly with τ_i, exceeding that in the conventional RTPS profile when τ_i is greater than 10 sec. In this case, during the IRTPS most of the surface is covered by the O-species. The shift of the electroreduction peak potential after $\tau_i = 30$ min is *ca.* 0.20V (Fig .4).

When $E_{s,a}$ is such that only a fraction of the O-monolayer is formed, an increasing inhibition of the O-electroadsorption during the IRTPS is observed. This suggests a probable competition effect between

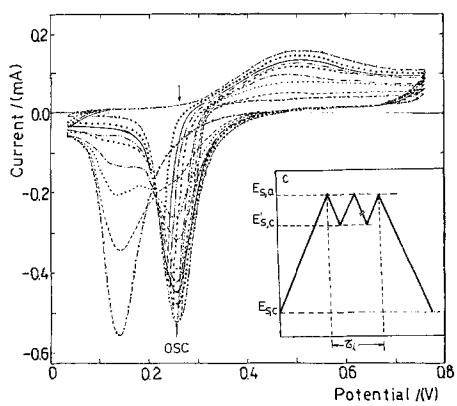

Fig. 3. Potentiodynamic *E/I* profiles run at 0.4 V/sec. IRTPS at 0.4 V/sec (100 cycles). Influence of $E'_{s,c}$. Apparent area = 0.18 cm².

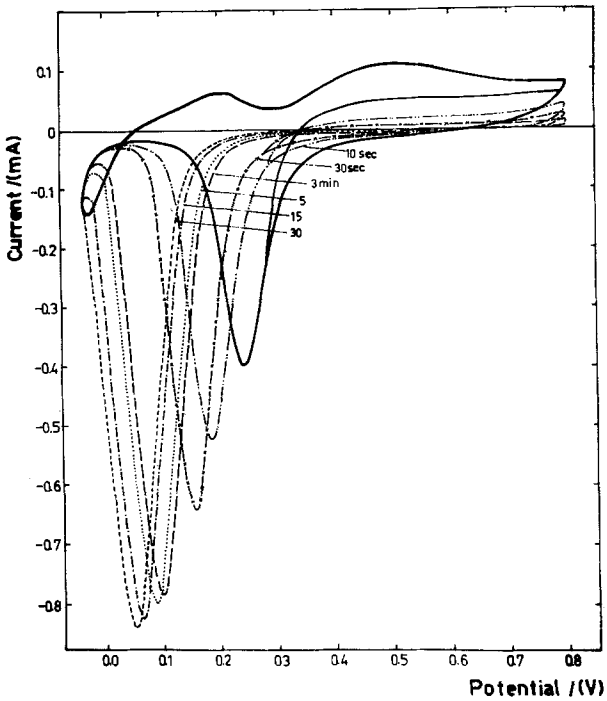

Fig. 4. Potentiodynamic *E/I* profiles run at 0.4 V/sec. IRTPS at 0.4 V/sec between $E'_{s,c} = 0.29$V, $E_{s,a} = 0.80$V. Influence of τ_i; ($\theta_r/\theta_i \approx 0.35$). Apparent area = 0.15 cm².

the restructuring of the O-containing species and the adsorption of anions on the available free metal sites (14).

Aging and film growth processes.—The charge of the O-containing species, Q_T, and the charge associated with aged O-species, Q_{ag}, increase proportionally to ln τ (Fig. 5). The potentiostatic O-layer growth fits a good linear Q_T *vs* ln τ relationship, whose slope increases with the initial amount of O-containing species at the metal surface. Otherwise, the accumulation of the

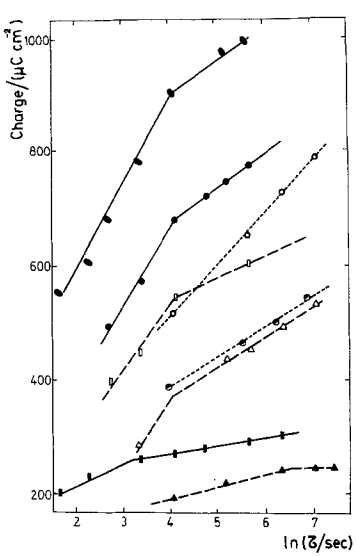

Fig. 5. Accumulated charge *vs.* ln τ plot for the potential perturbation programs B and C. ----- Potentiostatic aging, ——— potentiodynamic aging with $\theta_r/\theta_i < 0.5$, —·—·— potentiodynamic aging with $\theta_r/\theta_i > 0.5$, ○○○ Q_T *vs.* ln τ_p with $\theta_i = 0.68$ (potentiostatic aging), ◓◓◓ Q_T *vs.* ln τ_p with $\theta_i = 0.46$ (potentiostatic aging), ●●● Q_T *vs.* ln τ_i with $\theta_i = 1.2$ and IRTPS at 0.4 V/sec, ●●● Q_T *vs.* ln τ_i with $\theta_i = 0.98$ and IRTPS at 0.4 V/sec, ■■■ Q_T *vs.* ln τ_i with $\theta_i = 0.46$ and IRTPS at 0.4 V/sec, □□□ Q_{ag} *vs.* ln τ_i with $\theta_i = 0.61$ and IRTPS at 4 V/sec, △△△ Q_{ag} *vs.* ln τ_i with $\theta_i = 0.5$ and IRTPS at 0.4 V/sec, ▲▲▲ Q_T *vs.* ln τ_i with $\theta_i = 0.40$ and IRTPS at 0.4 V/sec.

O-containing species during the potentiodynamic aging also fits either a Q_T or Q_{ag} *vs.* ln τ_p plots but involving two linear regions. In the first region, at values of ln $\tau < 4$, the slope increases with θ_i and, at $\theta_i > 0.6$ approaches the slope of O-layer growing process under potentiostatic conditions. In the second region, at values of ln $\tau > 4$, the slope is lower than in the first region but increases on θ_i, for $\theta_i < 0.5$. It should be borne in mind that under potentiodynamic aging perturbation conditions, the smaller θ_i is, the smaller the average potential related to the IRTPS.

Runs using the potential perturbation program B (Fig. 2) at low values of v show the occurrence of two different processes when the potential is held at any $E_{s,a}$ lying within the range of the potential corresponding to the formation of the O-electroadsorbed monolayer and the equilibrium potential of the Pt/PtOH couple (1, 2). These processes can be related to the restructuring of the fraction of the O-monolayer initially formed and the competition between the O-electroadsorption and the anion adsorption for the sites available at the metal surface.

For the potentiodynamic aging at large values of v (high frequencies), a single O-electroreduction profile is recorded, its potential being shifted toward more negative values than that of the corresponding conventional RTPS profile. The potential shift (ΔE_p) is, however smaller than that observed when the splitting of the peak takes place. This suggests that at the largest frequency the reaccommodation of the O-species at the surface is to a large extent hindered, and as practically no free sites for the location of new species through the O-electroadsorption process become available.

For a constant percentage of the O-containing species removed and rebuilt in the IRTPS, ΔE_p increases as θ_i increases (Fig. 6) because as the amplitude of the IRTPS depends on θ_i, the time available to promote the restructuring of the surface species increases. Likewise, for a constant number of IRTPS cycles, ΔE_p increases as v increases, as in this case the formation of more stable O-containing species is assisted. On the other hand, when the electroreduction charge of the O-species involved in the IRTPS is lower than that corresponding to the OSC value, ΔE_p is sensitive to $E'_{s,c}$. But, when $E'_{s,c}$ is more cathodic than the OSC value, ΔE_p becomes independent of $E'_{s,c}$. The amount and degree of stabilized O-containing species decreases as the frequency of the IRTPS decreases.

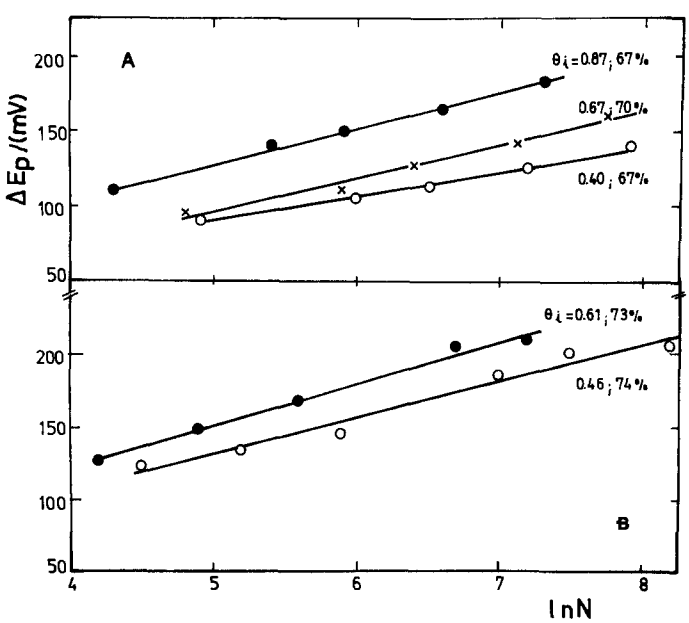

Fig. 6. ΔE_p *vs.* ln N (number of cycles) for different $E_{s,a}$ and $E'_{s,c}$. (a) $v = 0.4$ V/sec and (b) $v = 4$ V/sec.

Change of the open-circuit potential.—The decay of the open-circuit potential from $E_{s,a}$ was determined in the following different ways (Fig. 7); (*i*) after obtaining the stabilized *E/I* profile under RTPS, (*ii*) after the IRTPS during either 100 or 300 cycles, covering a potential range where 65% of the O-containing monolayer is initially removed and rebuilt, (*iii*) the same as (*ii*) but covering a potential range involving only 30% of the surface coverage, (*iv*) after holding the potential at $E_{s,a}$ during preset times which are the same as those used in (*iii*).

For case (*i*), (*iii*), and (*iv*) a single transition time was observed. The fastest potential decay corresponds to case (*i*). In case (*ii*) a complex potential decay is shown, where two relatively poorly defined transition times (at $E_r^{(1)}$ and $E'_r{}^{(1)}$, respectively) are apparently observed. In cases (*i*), (*iii*), and (*iv*) the potential decay plateau ($E_r^{(1)}$) is located between 0.30-0.35V. The final potential ($E_r^{(2)}$) which is the same for cases (*i*) to (*iv*), is located at 0.1V. The results from (*ii*) indicate the existence of at least two coupled reactions related to the potential decay. The time required to attain $E_r^{(2)}$ increases with the number of IRTPS.

Activation of the O_2 and H_2 evolution reactions.—Modifications in the electrolytic activity of the electrode surface is envisaged from the potentiodynamic *E/I* displays when the electrode is subjected to a combined potential perturbation program, covering the initial portions of both the H_2 and O_2 evolution reactions (Fig. 8) at $v = 0.3$ V/sec, adjusting later $E_{s,c}$ to a new $E'_{s,c}$ value to remove and rebuild about 90% of the O-containing species during each potential sweep at the same v and immediately afterward, applying an RTPS during 5-15 min at a greater v. Finally, the RTPS is again run in the $E'_{s,c}$ to $E_{s,a}$ range at the initial v.

Under these circumstances the O_2-evolution reaction is enhanced and the O-electroreduction charge is remarkably smaller than the one initially formed in the same potential range. A further potential cycling produces a gradual increase of the O-electroreduction peak, but the activity for the O_2 evolution reaction remains practically the same. At the final stage when $E'_{s,c}$ is changed to $E_{s,c}$, there is a remarkable electroreduction current at the low potential region. This perturbation procedure induces a drastic temporary activation of the electrode surface for both the H_2 and O_2 evolution potential ranges. On further cycling, the *E/I* profile approaches slowly that initially depicted under RTPS. The largest transient electrocatalytic activation of the O_2 evolution reaction is related to a set of optimal values ($E'_{s,c}$, f, and $E_{s,a}$) (Fig. 9).

Discussion

The application of each perturbation tehnique produces a definite shift of the O-electroreduction current peak toward the negative potential side which is interpreted in terms of aging of the O-electroformed

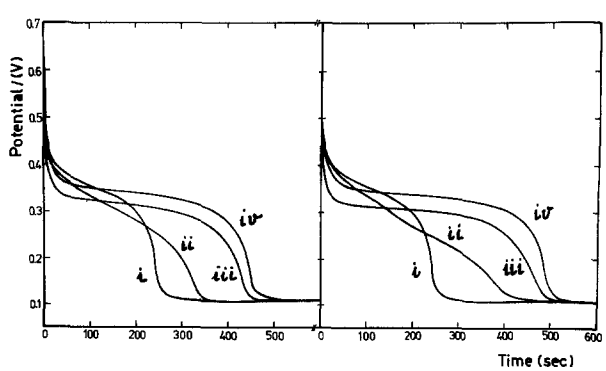

Fig. 7. Open-circuit potential decay curves. (a) IRTPS 100 cycles; (b) IRTPS 300 cycles. The identification of the curves is given in the text.

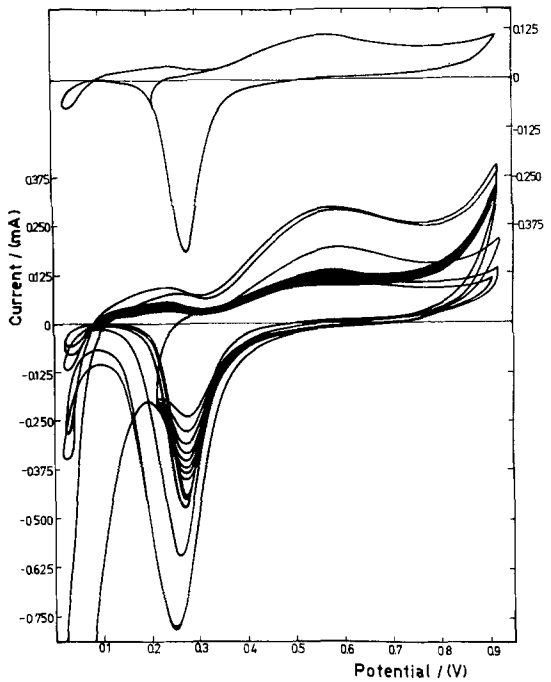

Fig. 8. Potentiodynamic *E/I* profile run at 0.3 V/sec. Initial RTPS, $E_{s,c} = 0.02$V and $E_{s,a} = 0.92$V. Afterward $E_{s,c}$ was changed to 0.22V, and v was increased to 26 V/sec and the IRTPS was maintained during 15 min. Immediately after the IRTPS was repeated at the same v initially used. After 10 cycles $E_{s,c}$ was extended again to 0.02V. The initial *E/I* profile is shown in the upper part of the figure. Apparent area = 0.18 cm^2.

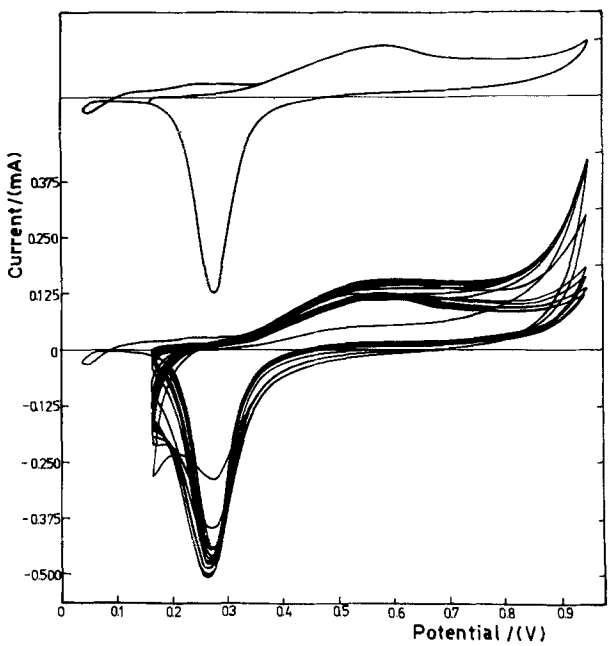

Fig. 9. Potentiodynamic *E/I* profile run at 0.3 V/sec with the same conditions described in Fig. 8, but the IRTPS was made at 115 V/sec during 4 min. Under these circumstances the largest increase in current at $E_{s,a}$ is obtained. Apparent area = 0.18 cm^2.

layer on platinum. In this case, however, the platinum electrode in $KHSO_4$ melt exhibits under perturbation programs B and C, an accumulation of charge larger than that found in 3.7M H_2SO_4 (3). A comparison of runs made for a constant number of potential sweeps (100 cycles) at 0.4 V/sec, is shown in Table I. The ΔE_p values resulting under perturbation programs B and C in any case are remarkably larger than

Table I. Potential shifts (ΔE_p) of the O-electroreduction current peak at 0.4 V/sec as compared to the peak potential of the stabilized *E/I* profile after 100 IRTPS cycles

θ_r/θ_i	IRTPS amplitude/ (V)	Splitting	ΔE_p/ (V)	Q_{ag} after IRTPS (mC/cm^2)	Perturbation program
—	—	No	0.025	—	A
~0	0.25	No	0.090	1.16	B
~0.35	0.52	No	0.150	1.03	C
~0.67	0.56	Yes	0.163	1.76×10^{-1}	C
~0.85	0.59	Yes	0.163	3.88×10^{-2}	C

those resulting from the O-electrodeposition profile after open-circuit aging (18). This shift is related to the overall energy change occurring at the surface after aging either because of rearrangement of the surface species or by accumulation of the O-containing species.

The ΔE_p obtained under open circuit is the same found for the aging of metal hydroxide multilayers in acid and alkaline electrolytes at room temperature (20). Its magnitude is close to that of hydrogen bonding energy. In these circumstances it appears that the energy does not depend on the type of film formed neither on the metal substrate. Hence, the main process under open-circuit aging, should be associated with either a dehydration of the O-containing layer or a structural change involving a shift of water through hydrogen bond breakage.

The electroreduction profile resulting after potentiodynamic perturbation program C exhibits two different behaviors depending whether the $E'_{s,c}$ during the IRTPS is more anodic or more cathodic than E_p in the conventional RTPS display. When $E'_{s,c}$ is more anodic than E_p, the accumulated charge increases exceeding the monolayer charge, and simultaneously, there is no splitting of the O-electroreduction peak, but a single peak progressively shifted to negative potentials. In this case, as $E'_{s,c}$ becomes more positive, the following features should be distinguished: (*i*) the decrease of the average area available for reaccommodation of the O-species during the IRTPS, as the average potential perturbing the interface during each cycling in the IRTPS becomes more positive; (*ii*) the greater possibility of producing higher oxidation states at the metal surface; (*iii*) the incorporation of anions either on or in the O-containing layer; (*iv*) the thickening of the film; (*v*) the possible dehydration of the film through electrochemical deprotonation. These contributions which are related to continuous and monotonous changes of the surface film properties should be magnified by both the high temperature and high ionic concentration in the molten electrolyte. Therefore, under these conditions no splitting of the O-electroreduction current peak should be expected.

As $E'_{s,c}$ approaches to $E_{s,a}$, the response of the *E/I* profile after the IRTPS tends to that obtained after holding the potential at $E_{s,a}$ for a certain time (program B). On the other hand, when $E'_{s,c}$ is more cathodic than E_p so that the charge playing part during the IRTPS is relatively large, the surface reaccommodation of the O-species becomes then possible as well as the simultaneous restructuring of the metal surface. Under these circumstances the Pt/$KHSO_4$ (melt) interface approaches the characteristics of the Pt/H_2SO_4 3.7M interface at 55°C, as previously discussed (3).

The ΔE_p corresponding to the potentiostatic and potentiodynamic aging for $E'_{s,c}$ not far from $E_{s,a}$ are nearly the same. The largest peak potential shifts are related to the more stable structure of the O-containing layer as well as to the thickening of the film. In this case, the stabilization of the film forming species could be assisted by anion adsorption. When the electrode potential in the melt is maintained at a value sufficiently positive during a relatively prolonged time,

then anion adsorption on the O-containing film would assist the stabilization of the O-containing film under a relatively strong electric field. The thickening of the film can then be conceived in terms of a place exchange mechanism assisted by the electrical field set up between the metal plane and the plane of anion adsorption. The O-containing layer should acquire a more compact structure because of the electrostriction effects produced through the adsorption of anions at the layer-electrolyte plane. Therefore, in this case the ΔE_p values may be considered a direct measure of the electrostriction effect.

The ΔE_p found for the potentiodynamic aging for $E'_{s,c}$ more cathodic than E_p implies a more remarkable change in the structure of the surface species. The main process has been assigned to a change in position of the O-species in relation to the metal lattice (3). This change also should imply a change in position of the atoms in the first metal plane and to a lesser extent in other metal planes in depth which may be comparable to the reorganization of the O-coverage in oxygen adsorption on Pt (10, 11). The overall process should include the participation of the solvent both as a constituent of the electrochemical interface and through its direct interaction with the O-containing film. The existence of the two surface species which are involved in this case is also revealed through the E/t curve at open circuit.

The existence of two well-defined O-species on Pt, depending on the aging conditions, is also clearly revealed through the Tafel plots (Fig. 10) of the initial portion of the electroreduction profiles shown in Fig. 4. A constant Tafel slope of about 1.5 times larger than the RT/F ratio is obtained for short aging times. Conversely, for aging times larger than 1 min a second constant Tafel slope results whose value is close to the RT/F ratio. Taking into account that the decrease in the Tafel slope follows the corresponding cathodic charge increase, the effect is justly the reverse of the effect predicted for this type of processes where any aging effects are disregarded (21).

The film growth process follows apparently the same form of rate law already established for anodic film growth on various metals (22), but the rate depends whether the growth occurs potentiostatically or it is produced potentiodynamically. For the latter, at $\theta_i < 0.4$, the low growth rate should be appreciably influenced by anion adsorption (14). The change of slope

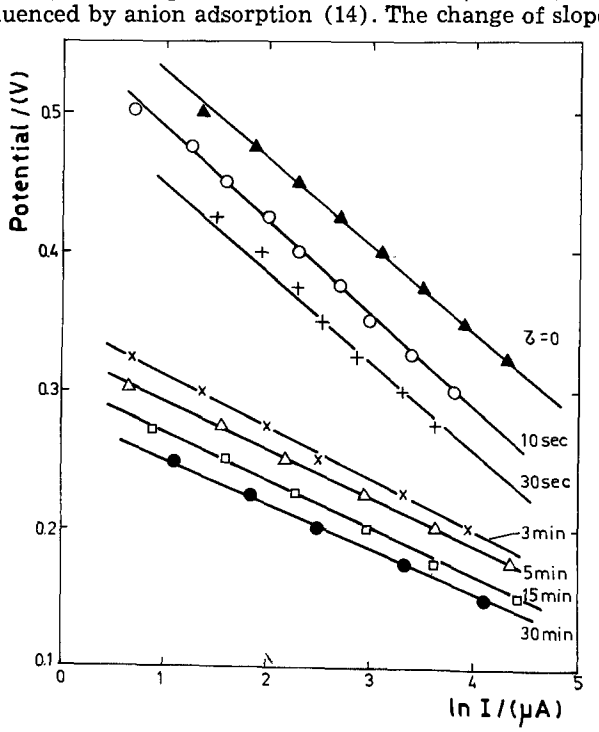

Fig. 10. Tafel plots obtained from the initial portion of the E/I cathodic profiles when $\theta_r/\theta_i \approx 0.35$. Data taken from Fig. 4.

in the Q_T *vs.* ln τ plots occurred at a τ value in the 30 sec $< \tau_t <$ 1 min range, and it is associated with the existence of at least two different O-containing species independently of the amount of O-containing species at the metal-solution interface.

The difference in the kinetics of film growth correlates with the $E/\ln I$ plots for the electroreduction of O-containing layer after different aging times (Fig. 10). In this case, the time range for the transition in the $E/\log I$ slope coincides with that related to the change of the slope in the $Q_T/\ln \tau$ plots.

The existence of different O-containing species is also deduced from the open-circuit potential decay. The different species involved in the potential decay process should be related to the values of the arrest potentials. The first arrest potential ($E_r^{(1)}$) obtained after the different aging conditions from the potential decay curves is practically the same, $E_r^{(1)} = 0.340 \pm 0.005$V while the final rest potential ($E_r^{(2)}$) is lower, $E_r^{(2)} = 0.110 \pm 0.005$V.

The contribution of each O-containing species during the electrochemical process associated with the potential decay at open circuit depends on the extent of the aging reached at the interface for the O-electroadsorbed species (Fig. 7).

Acknowledgment

INIFTA is sponsored by the Consejo Nacional de Investigaciones Científicas y Técnicas, the Universidad Nacional de La Plata, and the Comisión de Investigaciones Científicas (Provincia de Buenos Aires). This work was partially supported by the Regional Program for the Scientific and Technological Development of the Organization of American States.

Manuscript submitted July 30, 1981; revised manuscript received Oct. 11, 1982. This was Paper 504 presented at the Minneapolis, Minnesota, Meeting of the Society, May 10-15, 1981.

Any discussion of this paper will appear in a Discussion Section to be published in the December 1983 JOURNAL. All discussions for the December 1983 Discussion Section should be submitted by Aug. 1, 1983.

Publication costs of this article were assisted by Instituto de Investigaciones Fisicoquímicas Teóricas y Aplicadas (INIFTA).

REFERENCES

1. N. R. de Tacconi, J. O. Zerbino, and A. J. Arvía, *J. Electroanal. Chem.*, **79**, 287 (1977).
2. J. O. Zerbino, N. R. de Tacconi, A. J. Calandra, and A. J. Arvía, *This Journal*, **124**, 475 (1977).
3. M. E. Folquer, J. O. Zerbino, N. F. de Tacconi, and A. J. Arvía, *ibid.*, **126**, 592 (1979).
4. B. E. Conway and S. Gottesfeld, *J. Chem. Soc. Faraday Trans.*, **69**, 1090 (1973).
5. B. E. Conway, H. Angerstein-Kozlowska, F. C. Ho, J. Klinger, B. MacDougall, and S. Gottesfeld, *Discuss. Farad. Soc.*, **56**, 210 (1973).
6. A. J. Arvía, *Israel J. Chem.*, **18**, 89 (1979).
7. G. B. Fisher and B. A. Sexton, *Phys. Rev. Lett.*, **44**, 683 (1980).
8. B. A. Sexton, *Surf. Sci.*, **94**, 435 (1980).
9. G. B. Fisher and J. L. Gland, *ibid.*, **94**, 446 (1980).
10. S. K. Shi, J. M. White, and R. L. Hance, *J. Phys. Chem.*, **84**, 2441 (1980).
11. H. Niehus and G. Comsa, *Surf. Sci.*, **93**, L147 (1980).
12. M. Salmeron and G. A. Somorjai, *ibid.*, **91**, 373 (1970).
13. J. P. Biberian, *ibid.*, **97**, 257 (1980).
14. I. I. Labkovskaya, V. I. Luk'yanyacheva, and V. S. Bagotskii, *Elektrokhimiya*, **5**, 580 (1969).
15. S. Shibata, *Bull. Chem. Soc. Jpn.*, **38**, 1330 (1965).
16. A. Hickling and G. Vrojosek, *Trans. Faraday Soc.*, **57**, 123 (1951).
17. M. I. Florit. M. E. Martins, and A. J. Arvía, *J. Electroanal. Chem.*, **126**, 255 (1981).
18. N. R. de Tacconi, A. J. Calandra, and A. J. Arvía, *ibid.*, **51**, 25 (1974); **57**, 325 (1974).
19. J. O. Zerbino, N. R. de Tacconi, and A. J. Arvía, *This Journal*, **125**, 1266 (1978).

20. M. E. Martins, R. Córdova O., and A. J. Arvía, *Eleetrochim. Acta*, **25**, 453 (1980).
21. K. J. Vetter and J. W. Schultze, *J. Electroanal. Chem.*, **34**, 131 (1972); **34**, 141 (1972).
22. M. J. Dignan, in "Compressive Treatise of Electrochemistry," J. O'M. Bockris, E. B. Conway, E. Yeager, and R. E. White, Editors, Vol. 4, p. 247, Plenum Press New York (1981).

Technical Notes

A Lithium Electrode with a Zinc Substrate for Secondary Batteries

Yoshiharu Matsuda,* Masayuki Morita, and Hidenori Katsuma

Department of Industrial Chemistry, Faculty of Engineering, Yamaguchi University, Tokiwadai, Ube, Yamaguchi, Japan

The development of a lithium secondary battery using an organic electrolyte has been actively pursued in recent years (1, 2). An efficient Li electrode is required to realize such rechargeable batteries. Some Li negatives with metal substrates have been proposed in order to obtain good efficiency of charge-discharge cycling (3-9). Especially, it is worth noting that high coulombic efficiency was achieved by using an Al substrate, which forms an alloy with deposited Li during the period of the charging (8, 9). Previously, the authors pointed out the importance of the correlation between the alloy formation of the substrate metal and the charge-discharge efficiency on the substrate (10). Furthermore, it was found that Zn, as well as Al, is a promising substrate for secondary lithium electrodes (10). The present note shows the charge-discharge characteristics of the Li electrode with a Zn substrate in propylene carbonate (PC) solution containing lithium perchlorate ($LiClO_4$) or lithium tetrafluoroborate ($LiBF_4$). The results are briefly discussed by comparing the characteristics with those obtained on the Al substrate.

Experimental

The substrates used in this work were high purity (>99.9%) Zn and Al disks (12.5 diam, 0.5 mm thick). After having been polished with emery papers, these were thoroughly washed with acetone in an ultrasonic cleaner. The substrates were then fitted to Teflon holders; the effective surface area of the resulting substrate was 0.95 cm^2. The electrolyte was PC containing $LiClO_4$ or $LiBF_4$ (1 mol dm^{-3}). The solvent and the salts were purified and dehydrated by usual methods (11, 12). Water content of the solution was less than 80 mg · dm^{-3}. The charge-discharge characteristics were evaluated by half-cell tests. A platinum sheet having a large surface area was used as the counter-electrode. The reference electrode was a saturated calomel electrode (SCE), which was connected to the test electrode by a Luggin capillary filled with the organic solution being investigated. The charge-discharge test was carried out by a cycling procedure in which Li was charged at a constant current of 0.10 mA (0.11 mA/cm^2) for 1 hr followed by a discharge at the same current density until the electrode potential was −1.0V *vs.* SCE. The current-potential curves were measured after the fourth charge. These measurements were conducted under a dry N_2 atmosphere at 25°C.

Results and Discussion

Typical charge and discharge curves are shown in Fig. 1. In any case, the coulombic efficiency (ampere-hours discharged/ampere hours charged) tends to decrease slightly with cycling after the fourth discharge. The charge-discharge characteristics of the Zn substrate are almost similar to those of the Al substrate after several cycles, but the discharge potential of Li on Zn is a little lower than that on Al. This is because the potential of the alloy formation in the Li-Al system is more positive than that in the Li-Zn system (10, 13). On the Zn substrate, moreover, a little potential step is observed at the first stage of the discharge, which corresponds to the transition in the anodic dissolution from the metallic Li to the Li-Zn alloy. One of the advantages in the use of a Zn substrate is that the charge-discharge performance is little affected by a small amount of water in the electrolyte as compared with the case using an Al substrate (10). The cycling characteristics obtained in the $LiBF_4$ solution is almost the same as those in the $LiClO_4$ solution. From the viewpoint of solution stability (1), however, it would be preferable to use the $LiBF_4$ solution.

Figure 2 shows the polarization curves of the Li electrodes with Zn and Al substrates after the fourth charging. The polarization characteristics on the Al substrate in the $LiBF_4$ solution are almost equivalent to those in the $LiClO_4$ solution. On the Zn substrate, the potential in the $LiClO_4$ solution is generally more negative than that in the $LiBF_4$ solution, and the maximum current density in the former is also higher than that in the latter solution. Current shoulders, which resulted from the heterogeneous dissolution of the

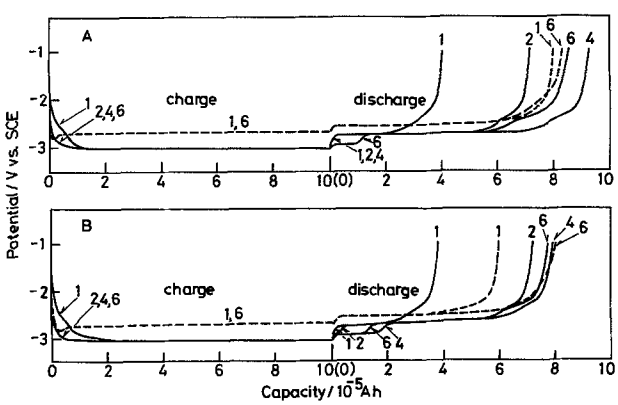

Fig. 1. Charge and discharge curves of Li negative electrodes with Zn and Al substrates, i = 0.10 mA (0.11 mA/cm^2), A: 1 mol dm^{-3} $LiClO_4$ in PC, B: 1 mol dm^{-3} $LiBF_4$ in PC, ———: Zn substrate, – – – –: Al substrate, (Figures on the lines denote cycling numbers).

* Electrochemical Society Active Member.

Key words: lithium cell, cycling, negative electrode, alloy formation.

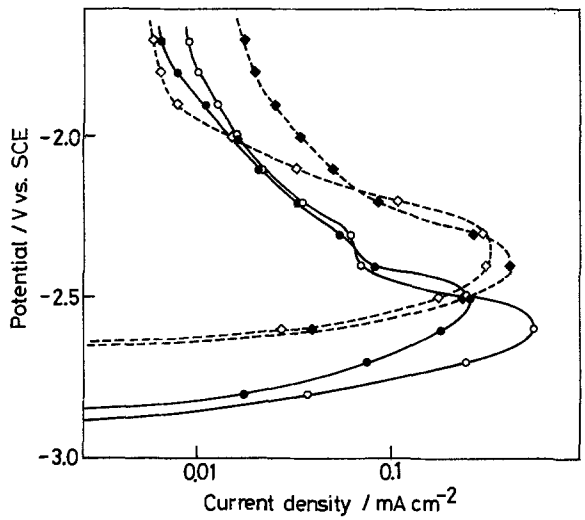

Fig. 2. Anodic polarization curves of Li electrodes with Zn and Al substrates, open symbols: 1 mol dm^{-3} $LiClO_4$ in PC, closed symbols: 1 mol dm^{-3} $LiBF_4$ in PC, ○, ●: Zn substrate, ◇, ◆: Al substrate.

alloy, are observed in both solutions at about −2.3V on the electrode with the Zn substrate while the anodic dissolution on the Al substrate seems to occur homogeneously. It is apparent from the current-potential curves that good discharge performances can be expected in the potential region from −2.7 to −2.4V at the Zn substrate. For both of the substrates, however, deep discharges should be avoided because of the lowering of the current density at more positive potentials.

The efficiency of the charge-discharge cycling on the Zn substrate, which alloys easily with deposited Li, is as high as that on the Al substrate. The present results hint on how to develop an efficient negative electrode for secondary lithium batteries. However, it is further necessary to examine the corrosion resistance of the substrates and the combination with other solvents, in connection with the durability of the cycling over a longer period of time.

Acknowledgment

The authors would like to acknowledge that this work was supported by the Grants in Aid for Scientific Research (No. 505577 and 56850187) by Japan Ministry of Education.

Manuscript submitted Feb. 16, 1982; revised manuscript received Oct. 19, 1982.

Any discussion of this paper will appear in a Discussion Section to be published in the December 1983 JOURNAL. All discussions for the December 1983 Discussion Section should be submitted by Aug. 1, 1983.

Publication costs of this article were assisted by Yamaguchi University.

REFERENCES

1. V. R. Koch, *J. Power Sources*, **6**, 357 (1981).
2. K. M. Abraham, *ibid.*, **7**, 1 (1982).
3. J. O. Besenhard and G. Eichinger, *J. Electroanal. Chem.*, **68**, 1 (1976).
4. F. W. Dampier and S. B. Brummer, *Electrochim. Acta*, **22**, 1339 (1977).
5. V. R. Koch and S. B. Brummer, *ibid.*, **23**, 55 (1978).
6. T. Takei, *J. Appl. Electrochem.*, **9**, 587 (1979).
7. V. R. Koch and J. H. Young, *Science*, **204**, 499 (1979).
8. I. Epelboin, M. Froment, M. Garreau, J. Thevenin, and D. Warin, *This Journal*, **127**, 2100 (1980).
9. Y. Takada, *Denki Kagaku*, **49**, 96 (1981).
10. Y. Matsuda, M. Morita, and H. Katsuma, *ibid.*, **49**, 537 (1981).
11. Y. Matsuda, Y. Ouchi, and H. Tamura, *J. Appl. Electrochem.*, **4**, 53 (1974).
12. Y. Matsuda, H. Nakashima, M. Morita, and Y. Takasu, *This Journal*, **128**, 2552 (1981).
13. A. N. Dey, *ibid.*, **118**, 1547 (1971).

Lithium Cycling in Polymethoxymethane Solvents

J. S. Foos* and J. McVeigh

EIC Laboratories, Incorporated, Newton, Massachusetts 02158

During the past few years, several Li battery electrolytes have been reported which allow the plating and stripping of Li in greater than 95% efficiency at 25°C. Newman reported the use of $LiClO_4$ in dioxolane in Li/TiS_2 cells (1). The cycling efficiency in these cells is very good, but unfortunately they are susceptible to detonation (2). Koch has reported the use of 2-methyltetrahydrofuran (2Me-THF) (3) and diethyl ether blends (4) as solvents for $LiAsF_6$ in Li half-cells. The conductivity of these electrolytes is low.

The solution of $LiAsF_6$ in dioxolane is an electrolyte with good conductivity but is reported to polymerize readily (5). Ring strain may contribute to the reactivity of dioxolane. It might be anticipated that the open-chain analogues of dioxolane might be less reactive. Dimethoxymethane (DMM) I and trimethoxymethane (TMM) II were investigated as solvents for possible use with $LiAsF_6$ in Li batteries

$CH_2(OMe)_2$ (I) $\quad$ $CH(OMe)_3$ (II)

We wish to report that these solvents produce conductive solutions with $LiAsF_6$, show good stability at 70°C, and cycle Li well in half-cell tests.

* Electrochemical Society Active Member.
Key words: electrolyte, organic, battery, conductance.

Experimental

The solvents, DMM and TMM (trimethyl orthoformate), were obtained from the Aldrich Chemical Company. Before use, the solvents were purified first by preliminary drying using $MgSO_4$ and /or molecular sieves (3 or 4A) for DMM; and molecular sieves (3 or 4A) only for TMM. Subsequently, they were distilled from Na benzophenone ketyl (6). Some difficulty was encountered in forming the blue ketyl in TMM. This was attributed to surface films on the Na which can be disrupted by placing the reaction flask in an ultrasonic bath.

The electrolytes for cycling and storage tests were prepared using $LiAsF_6$ (U.S. Steel, as-received) with cooling, using Cu shot previously cooled by Dry Ice. The solvents, if treated with alumina, were passed through a column of activated alumina (Woelm N-Super 1) and the first 10% discarded. Where applicable, pre-electrolyses were done by passing a current (1 mA/cm^2) between two Li metal electrodes (~30 cm^2) suspended in the electrolyte (100 ml) for ~16 hr.

Conductivities were obtained using dried distilled DMM and TMM. The conductivities were determined in conductivity cells with cell constants determined using aqueous KCl. An a-c conductivity bridge (YSI

Model 31) was used to measure the cell resistance. The conductivities were determined at, or corrected to, 25°C with a precision of ~5%. The storage tests were done in screw cap (Teflon-lined) glass vials. These were stored at 70°C.

The Li cycling was done in prismatic glass cells containing 15-20 ml electrolyte. This experiment, described previously (7), involves making a preplate of 4.5 C/cm² of Li on an Ni substrate (Ni shim) followed by stripping and then replating 1.1 C/cm² on the preplated Li. The average efficiency for cycle E, is calculated in Eq. [1]

$$E = \frac{Q_s - \frac{Q_{ex}}{n}}{Q_s} \quad [1]$$

where n is the number of apparent "100%" cycles, Q_s is the charge stripped (1.1 C/cm²), and Q_{ex} is the charge in the excess Li (3.4 C/cm²) at the start of the experiment.

Solution preparation and the electrochemical experiments themselves were conducted at room temperature under an Ar atmosphere in a Vacuum-Atmospheres Corporation dry box equipped with a Model HE-493 Dri-Train.

Results

Conductivity of electrolytes.—In order to minimize electrolyte IR drop, the electrolyte in a battery should show maximum conductivity. The solvents I and II give electrolytic solutions with greater conductivities than most other noncyclic ethers.

The conductivities of solutions of $LiAsF_6$ in ethers are generally high as compared to solutions of other salts such as $LiClO_4$, $LiBF_4$, etc. For instance, the maximum conductivity of $LiAsF_6$ in THF is 0.017 Ω^{-1} cm^{-1} (7) as compared to 0.006 and 0.004 for $LiClO_4$ (8) and $LiBF_4$ (9), respectively. The ethereal solutions of $LiAsF_6$ previously known to cycle Li with high efficiency, *i.e.*, 2Me-THF and DEE blends, have maximum specific conductivities in the 0.002-0.004 Ω^{-1} cm^{-1} range.

Conductivity *vs.* concentration profiles for $LiAsF_6$ in DMM and TMM are shown in Fig. 1. The conductivity profiles are typical for solutions of $LiAsF_6$ in ethers and show maximum conductivities of ~0.0065 Ω^{-1} cm^{-1} for DMM and ~0.008 Ω^{-1} cm^{-1} for TMM.

Lithium cycling in half-cells.—The plating and stripping of Li at 25°C is a rigorous test of electrolyte stability. Electrolytes were evaluated for half-cell cycling efficiency using electrolytes prepared using distilled solvent (D), distilled solvent treated with alumina (DA), and electrolytes that were additionally pre-electrolyzed (DP).

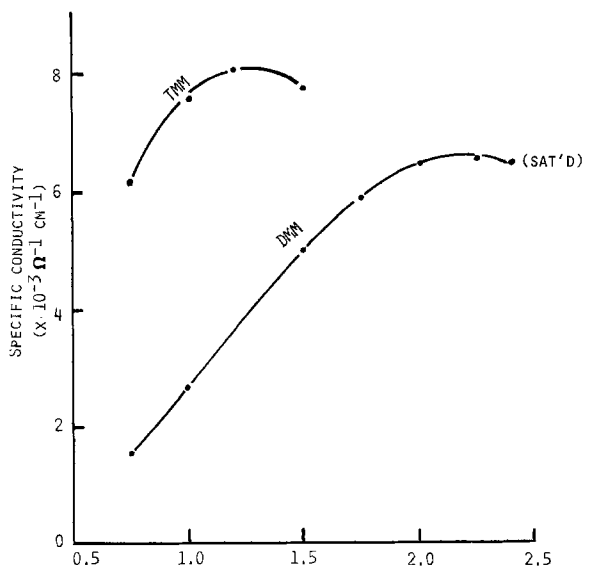

Fig. 1. Conductivity of $LiAsF_6$ solutions in DMM and TMM (25°C).

The freshly plated Li, generated during pre-electrolysis, should be especially reactive. It was hoped that this Li would react with impurities in the electrolyte giving insoluble reaction products and thereby purify the electrolyte. The results for DMM and TMM electrolytes are shown in Table I. This table shows representative cycling efficiencies which illustrate the effect of different purification on Li cycling. In these tests, both electrolytes show high cycling efficiency.

Electrolyte stability at 70°C.—The cycling test above allows the evaluation of room temperature stability of the electrolyte towards freshly plated Li over the period of the experiment, one or two days. An accelerated test for long term stability is the storage of electrolytes at 70°C in the presence and absence of Li. A solvent, 2Me-THF, which has proved useful in Li/TiS_2 cells shows excellent stability when stored with Li at 70°C (7).

Stability tests were conducted by storing samples of 1.5M $LiAsF_6$ in DMM and TMM in the presence and absence of Li at 70°C. The results are shown in Table II. The TMM appears more stable with no apparent reaction noted at 20 days at 70°C. These tests may be somewhat misleading. Although no reaction was observed visually, the TMM electrolyte stored at 70°C with Li subsequently failed completely to cycle Li. The DMM results were variable, with the results reported typical of several tests. Despite the apparent lack of stability in DMM electrolytes, the samples stored with Li retained moderate cycling ability.

Discussion

The conductivity of the electrolytes studied makes them interesting candidates for Li battery use. However, the stability of the electrolytes under actual cell conditions is of primary concern. This includes stability towards reduction by Li and to thermal decomposition in the bulk electrolyte. The half-cell cycling results indicate a relatively high degree of stability of electrolyte towards Li. However, this test is somewhat insensitive to electrolyte decomposition due to the large excess of electrolyte present. The variation of the cycling efficiency with purification appears to be reproducible. It is attributed to variations of the levels of impurities. What is not clear is the nature of the impurities and whether they improve half-cell and storage test behavior. It may be that the electrolyte containing only pure solvent and salt would give the best results. On

Table I. Half-cell cycling tests using DMM and TMM electrolytes

		%
1.5M $LiAsF_6$ in DMM	(D)	97.3
	(DA)	97.5
	(DP)	96.5
1.5M $LiAsF_6$ in TMM	(D)	93.2
	(DP)	95.1

Table II. Storage tests and cycling after storage using DMM and TMM electrolytes at 70°C

Solvent	With Li	Without Li
DMM (D)	Electrolyte clear with a small amount of Li corrosion at 10 days	Electrolyte clear >10 days then darkened rapidly
DMM (D)	Cycled after 10 days storage with Li → 87.5%	
DMM (DA)	Electrolyte clear with a small amount of Li corrosion, > 1 month	Electrolyte dark at 6 days
DMM (DA)	Cycled after 10 days storage with Li → 86.9	
TMM (D)	No reaction at 20 days	No reaction at 20 days
TMM (DP)	Cycled after 14 days with Li (no reaction) → 0%	

the other hand, perhaps small amounts of impurities may scavenge undesirable reactive intermediates. Differentiating between these possibilities is difficult.

In this work, electrolytes which were optimized in half-cell work were chosen for storage tests and cycling after storage. The DMM electrolytes (D and DA) gave similar cycling efficiencies before storage and similar, though decreased, efficiencies after storage. The electrolyte purified with alumina (DA) gave contradictory results in that it appeared more stable than the DMM (D) in the presence of Li and less stable in the absence of Li. The TMM electrolyte also gave contradictory results by showing no apparent reaction in stability tests and yet failing to cycle after storage.

The above observations illustrate the difficulty in evaluating electrolytes for Li batteries using half-cells and the appearance of storage tests. Further investigation of these electrolytes in Li/TiS_2 test cells as well as a more thorough chemical analysis of the storage tests is in progress.

Acknowledgment

We wish to acknowledge the support of the Office of Naval Research for this research.

Manuscript received Sept. 23, 1982. This was Paper 38 presented at the Detroit, Michigan, Meeting of the Society Oct. 17-21, 1982.

Any discussion of this paper will appear in a Discussion Section to be published in the December 1983 JOURNAL. All discussions for the December 1983 Discussion Section should be submitted by Aug. 1, 1983.

REFERENCES

1. G. H. Newman, in "Lithium Nonaqueous Battery Electrochemistry," E. B. Yeager, B. Schumm, Jr., G. Blomgren, D. R. Blankenship, V. Leger, and J. Akridge, Editors, p. 143, The Electrochemical Society Softbound Proceedings Series, Pennington, NJ (1980).
2. G. H. Newman, R. W. Francis, L. H. Gaines, and B. M. L. Rao, *This Journal*, **127**, 2025 (1980).
3. V. R. Koch and J. H. Young, *Science*, **204**, 499 (1979).
4. V. R. Koch, J. L. Goldman, C. J. Mattos, and M. Mulvaney, *This Journal*, **129**, 1 (1982).
5. P. G. Glugla, in "Power Sources for Biomedical Implantable Applications and Ambient Temperature Lithium Batteries," B. B. Owens and N. Margalit, Editors, p. 407, The Electrochemical Society Softbound Proceedings Series, Pennington, NJ (1980).
6. V. R. Koch, *This Journal*, **126**, 181 (1979).
7. J. L. Goldman, R. M. Mank, J. H. Young, and V. R. Koch, *ibid.*, **127**, 1461 (1980).
8. P. Jagodzinski and S. Petrucci, *J. Phys. Chem.*, **78**, 917 (1974).
9. S. D. James, *J. Chem. Eng. Data*, **23**, 313 (1978).

Electrodeposition of Calcium and Strontium Ions on Carbon Electrode

H. J. Huang

Department of Chemistry, National Sun Yat-Sen University, Kaohsiung, Taiwan 800, China

Electrodeposition is one of the versatile electrochemical techniques used in different fields for various purposes, *e.g.*, electroplating of Ag, Cd, Ni, and Cr for practical decorating and protection purpose, electrowinning and electrorefining of certain special metals for metallurgical purpose, electrogravimetry and coulometry for analytical purpose. But so far, the application of electrodeposition technique is limited to those electroactive species. In this experiment, the application of cathodic precipitation method for the deposition of certain electroinactive species (*i.e.*, the alkaline earth metal ions) was studied. Basically, instead of the electroinactive metal ion, an electroactive reagent can be reduced on electrode surface, and if the reduced species is subsequently able to form an insoluble compound with the inactive metal ion in solution, the inactive metal ion then becomes possible to be deposited on the electrode surface. The deposition processes can be expressed by following equations

$$R_{soln} + pe^- \rightleftharpoons R^{p-}{}_{elde} \quad [1]$$

$$M^{n+}{}_{soln} + qR^{p-}{}_{elde} \rightarrow MR_{q,elde} \quad [2]$$

Where $M^{n+}{}_{soln}$, R_{soln} are the inactive metal ion and the reducible reagent in solution, respectively, $R^{p-}{}_{elde}$ is the electrochemically generated species on electrode surface, $MR_{q,elde}$ is the insoluble metallic compound formed on electrode surface, and $q \cdot p = n$.

Experimental

The electrolysis was accomplished either potentiostatically or galvanostatically by PAR 173 Potentiostat/Galvanostat. The working electrode was prepared from spectroscopic carbon rod with a diameter of 0.78 cm (purchased from the National Carbon Company, division of Union Carbide and Carbon Corporation, New York, New York). A Tracor Northern NS-880 x-ray fluorescence (XRF) spectrometer was used for the determination of Ca^{2+} and Sr^{2+} deposition on carbon electrode. After polishing and cleaning, the electrode was inserted into a cylindric Teflon electrode holder which ensured a watertight fit and prevented seepage of electrolyte along the inner side of the cylinder.

Ammonium nitrate was used as the supporting electrolyte, and the ionic strength of the electrolytic solution was kept at 0.2. The *p*H of the solution was adjusted to 8.5 by the addition of NaOH solution. The polarization potential was set against a saturated calomel electrode (SEC). The electrodeposition was performed in stirred solutions at ambient temperature. On completion of each deposition, the carbon electrode with its holder was removed from the electrolytic solution with potential or current applied. The electrode holder was rinsed carefully with distilled-deionized water. After air drying, the carbon electrode with its holder was covered with a piece of KAPTON film (from SPEX Industries, Incorporated) and screwed onto a Teflon ring which has an outer dimension just fitted into the sample cell of the XRF spectrometer. Accumulated counting time used for collecting the XRF data was 500 sec. The data were obtained from the digitized spectra by a computer-assisted integration of the analytical peak. In order to eliminate the interference from absorbing gases and x-rays emitted by atmospheric argon, the XRF measurement of Ca^{2+} deposit was done in vacuum.

Results and Discussion

A simple system consisting of Ca^{2+} in aqueous solution was chosen for demonstration. The electrolytical solutions contained various concentrations of Ca^{2+} and fixed amount of supporting electrolyte. During electrolysis, the water molecule in solution (corresponds to R_{soln} in Eq. [1]) was decomposed to generate hydroxide ion OH^- (corresponds to $R^{p-}{}_{elde}$ in Eq. [1]) on

Key words: electroinactive, cathodic precipitation, diffusion control, dioxane.

carbon electrode. The electrochemical reaction proceeded on carbon electrode is

$$2H_2O + 2e^- \rightarrow H_{2,gas} + 2\,OH^- \quad [3]$$

Afer sufficient amount of OH^- has been generated, the Ca^{2+} started to react with the hydroxide ion and form the insoluble $Ca(OH)_2$ compound on electrode surface

$$Ca^{2+}{}_{soln} + 2\,OH^-{}_{elde} \rightarrow Ca(OH)_{2,elde} \quad [4]$$

The amount of Ca^{2+} deposited on electrode was determined by the XRF spectrometric method. The obtained XRF data were normalized and expressed as the number of counts per unit area (cm^2) of electrode surface per 500 sec of accumulated counting time. Due to the difficulty of reproducing exactly the same electrode surface, a 10% error was estimated for the variation of electrode surface area even if the same polishing procedures were followed.

Different from the conventional electrodeposition of metal ions, several steps are involved in the deposition processes of Ca^{2+} (Eq. [3], [4]) on electrode. They are (*i*) transport of the reducible reagent H_2O and the metal ion Ca^{2+} from solution bulk to electrode surface, (*ii*) transfer of electrons (preceding of electrochemical reaction), (*iii*) removal of the generated species OH^- from electrode surface to solution bulk, (*iv*) nucleation of insoluble compound $Ca(OH)_2$ on electrode surface or in the solution near electrode, and possibly, (*v*) diffusion of the insoluble compound from electrode to solution. After the beginning of electrolysis, the concentration of $OH^-{}_{elde}$ will increase rapidly, but no insoluble compound can be formed until the concentration of Ca^{2+} and OH^- is larger than certain supersaturation value. Whenever the solution is beyond the metastable supersaturation state, it is regarded as labile and is subjected to spontaneous deposition of the insoluble $Ca(OH)_2$ compound (1). After the initiation of nucleation, the insoluble compound $Ca(OH)_2$ will be formed spontaneously as long as the concentration product of (Ca^{2+}) and $(OH^-)^2$ is larger than the K_{sp} of $Ca(OH)_2$. During electrolysis if the applied potential or current density is large enough, Eq. [3] will proceed rapidly, and the reduced species OH^- is generated at a fast rate, therefore, the transport of H_2O or Ca^{2+} from solution bulk to electrode surface will dominate the whole deposition processes and become the rate-controlling step (for simplicity, the effect of the step (*iii*) and step (*v*) are assumed to be negligible). Since the concentration of the reducible species H_2O in solution is much larger than that of the metal ion Ca^{2+}, the diffusion of Ca^{2+} becomes the rate-determining step after the nucleation of the insoluble compound has been initiated.

For a diffusion controlled process, the rate of deposition and the total amount of deposit can be derived easily by following the same procedures as that of the conventional semi-infinite linear diffusion (2). The resulting equation describing the amount of insoluble compound $Ca(OH)_2$ formed on electrode surface $N_s(0, t)$ with electrolysis time, t is

$$N_s(0,t) = \frac{D_o A (C^\circ - C')t}{\delta} \quad [5]$$

for deposition in stirred solution. Where C° represents the Ca^{2+} concentration before electrolysis, C' represents the surface concentration of Ca^{2+} at time t, is equal to $K_{sp,Ca(OH)_2}/(OH)^2$, A is the geometric area of electrode, δ is the thickness of diffusion layer. Both C° and C' are in unit of mol cm^{-3}, while A is in cm^2, D_o is in $cm^2\,sec^{-1}$, t is in sec, δ is in cm, N_s is in mol.

According to Eq. [5], the amount of insoluble compound $Ca(OH)_2$ deposited on electrode surface is directly proportional to the concentration of Ca^{2+} in solution and to the electrolysis time t. The relationships between solution concentration (from 2.5×10^{-4} to 1.25×10^{-3}M) and the amount of Ca^{2+} deposit (electrolyzed at -1.6V for 30 min) are shown in Fig. 1. The intercepts obtained from extrapolation (as calculated by the linear regression method) is 0.28×10^{-4}M. This value is, therefore, equal to C' in Eq. [5] and represents the Ca^{2+} concentration on electrode surface during electrolysis. Since the deposition time used in this experiment is 30 min which is believed to be much longer than the possible induction period for nucleation of $Ca(OH)_2$ (3), the nucleation process would become unimportant and the diffusion process would thus dominate the whole deposition processes and become the rate-determining step. The dependence of the amount of Ca^{2+} deposit upon the time of electrolysis is shown in Fig. 2. The straight line obtained confirmed the existing linear relationship between the amount of deposit and the electrolysis time described by Eq. [5].

Since the formation of insoluble compound on electrode surface also depends on the magnitude of solubility product, the change of dielectric constant (also polarity) in electrolytic solution would affect the deposition processes. The influence of solvent on deposition efficiency was studied by adding an increasing amount of dioxane (from 10 to 50%) to

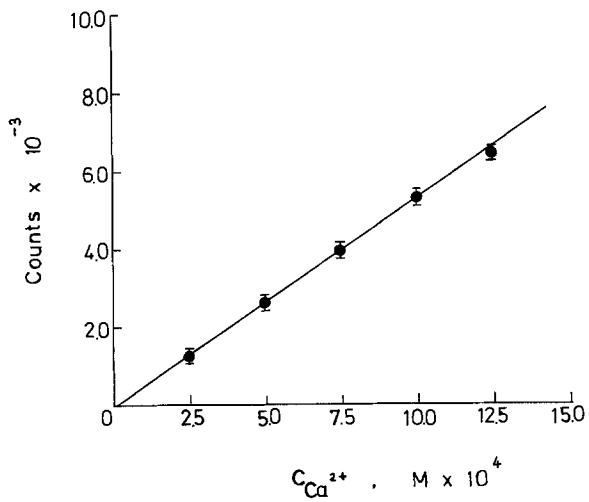

Fig. 1. Amount of Ca^{2+} deposit *vs.* Ca^{2+} concentration in solution. Electrodeposition was conducted potentiostatically at -1.6V for 30 min.

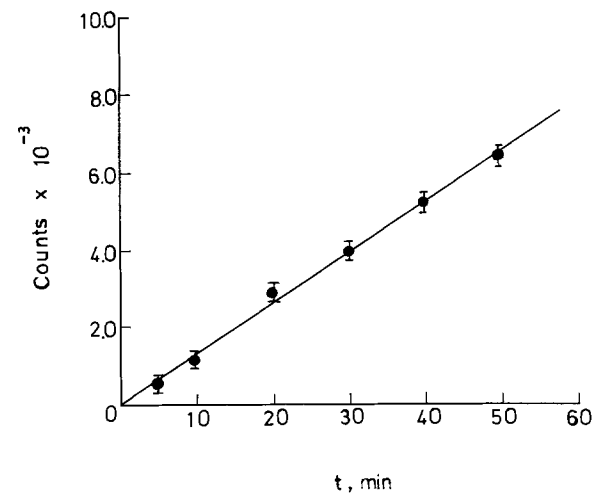

Fig. 2. Amount of Ca^{2+} deposit *vs.* electrolysis time. Electrodeposition was run potentiostatically at -1.6V with 7.5×10^{-4}M of Ca^{2+} in solution.

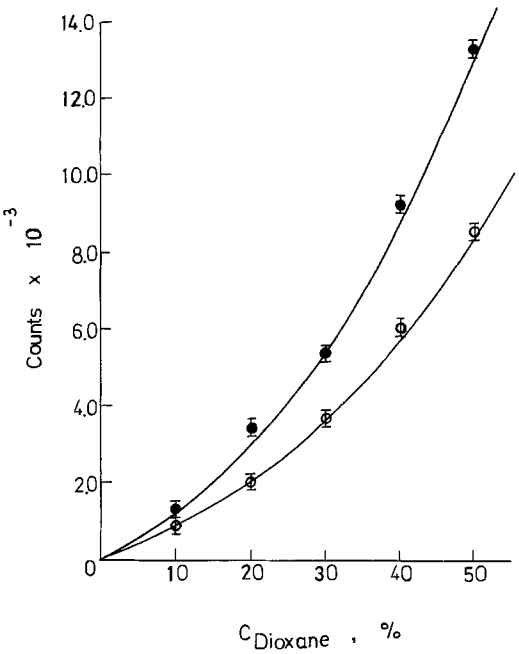

Fig. 3. Plots of the amount of Ca^{2+} (●) and Sr^{2+} (○) deposit vs. the dioxane concentration in solution. Solutions used contained 1.0×10^{-5}M of Ca^{2+} and 5.0×10^{-6}M of Sr^{2+}, respectively.

the aqueous electrolytic solution. Depositions were run galvanostatically with a current density of 1.0 A/cm^2 in vigorous stirring solution. Figure 3 shows the increment of the amount of Ca^{2+}, Sr^{2+} deposit in accordance with the change of dioxane concentration in solution. The relationships between the amount of Ca^{2+}, Sr^{2+} deposit and solution concentration, electrolysis time in dioxane solution were found to be similar to those shown in Fig. 1 and 2. Thus, the deposition processes in mixed solvent system follow the same behavior as that of aqueous. The deposition efficiency in 40% (arbitrarily selected) dioxane solution was found to increase approximately with an order of two in comparison with that of aqueous.

From the results of this investigation, deposition of other electroinactive species on appropriate substrate can be achieved easily if proper reagent (by Eq. [1]) has been chosen. Further exploration of this technique might lead to some useful applications. For example, thin films (with known quantity) of radioactive Sr^{2+} or Ba^{2+} (both are strong β-emitting species) ion can be prepared on suitable substrate and thus serve as a calibrated standard for radioactivity measurement. The possible simultaneous deposition of alkaline earth metal ion with other electroactive species might induce some interesting techniques for the deposition of binary metal oxides (or hydroxides), such as $SrTiO_3$, $BaTiO_3$ which are solar energy conversion related compound (4, 5). Also, the quantitative deposition of Ca^{2+}, Sr^{2+} on electrode can be used as a preconcentration step and, thus, might become a useful analytical procedure for trace analysis of these species.

Acknowledgment

The author wishes to thank UIRL in Hsinchu, Taiwan for the full support of this work.

Manuscript submitted March 18, 1982; revised manuscript received *ca.* Nov. 5, 1982.

Any discussion of this paper will appear in a Discussion Section to be published in the December 1983 JOURNAL. All discussions for the December 1983 Discussion Section should be submitted by Aug. 1, 1983.

Publication costs of this article were assisted by National Sun Yat-Sen University.

REFERENCES

1. H. A. Laitinen and W. E. Harris, "Chemical Analysis," 2nd ed., pp.142-149, McGraw-Hill Book Company, New York (1975).
2. P. Delahay, "New Instrumental Methods in Electrochemistry," p. 47, Interscience, New York (1954).
3. V. K. La Mer, *Ind. Eng. Chem.*, **44**, 1270 (1952).
4. M. S. Wrighton, A. B. Ellis, P. T. Wolczanski, D. L. Morse, H. B. Abrahamson, and D. C. Ginley, *J. Am. Chem. Soc.*, **98**, 2774 (1976).
5. R. D. Nasby and R. K. Quinn, *Mater. Res. Bull.*, **11**, 985 (1976).

Mechanism of Hole Injection on Ferric Oxide Photoelectrodes

Tamás Pajkossy

Hungarian Academy of Sciences, Central Research Institute for Physics, Budapest, H-1525, Hungary

It seems that ferric oxide is advantageous as a semiconductor photoelectrode for utilizing solar energy (1-10). Ferric oxide is an n-type semiconductor, its bandgap is reasonable for such purposes, it can be manufactured easily and cheaply, and it is reasonably stable. It does, however, suffer from the disadvantage of low quantum efficiency. The efficiency can be increased if the surface processes are understood, and it is known how to suppress surface recombination.

Recently, analysis of phototransients was used by Iwanski *et al.* to investigate processes taking place on illuminated ferric oxide electrodes (8). The results of similar experiments are presented here. Our aim was to determine whether hole injection at the interface proceeds directly from the valence band or via surface states. With this in mind, the photocurrent was measured on ferric oxide electrodes at constant electrode potential and slightly modulated illumination as a function of reducing agent concentration. The average value of the photocurrent was measured directly, and the current transients due to light modulation were recorded, using the signal averaging technique.

Key words: photoelectrochemistry, hole injection, ferric oxide, semiconductor.

Experimental

Ferric oxide electrodes made by thermal oxidation of iron specimens were used. The details of preparation and characterization of these electrodes are reported elsewhere (10). The electrodes behave similarly to those reported in Ref. (4 and 7); from the conventionally determined Mott-Schottky plots a donor density of 10^{18}/cm^3, and a flatband potential of around -0.35V *vs.* saturated calomel electrode (SCE) at pH 9.0 were evaluated. The long wavelength edge of the spectral response of the photocurrent was found to be around 610 nm, indicating that the bandgap of the semiconductor is about 2.1 eV. The overall oxide thickness was 0.15 mm.

The solutions were 0.2M borate buffers of pH 9.0 with different concentrations of KI (0-22 mM). These solutions were carefully deaerated before and during experiments by means of bubbling high purity nitrogen. The electrode potential was maintained at 0.2V *vs.* SCE, since at this potential only KI is oxidized under illumination (10).

The measurements were made using a standard three-electrode cell, whose overall resistance is around 30Ω, determined by extrapolation of high frequency impedance data. From the same impedance data the cell capacitance was also evaluated; it was found to be less than 1 μF, thus, the cell response time is less than 30 μsec. (The change in KI concentration of the solution had only a minor effect on the cell time constant.)

A medium speed potentiostat (AFKEL 415.5 μsec rise time) and a current amplifier of 30 μsec rise time range (Keithley 427) were applied. The electrode was steadily illuminated by a 150W tungsten lamp, fed from a d-c power supply, and by a smaller lamp (50W), whose light was interrupted by a rotating sector. This sector gave rectangular light pulses of 60 μsec rise time and about 5 msec duration every 30 msec. The light modulation depth was about 1%. (The use of white light may seem inexact in photoelectrochemical measurements; however, as our preliminary experiments revealed, the measured transients were of the same shape at any wavelength, they differed from each other only in height.)

It is seen from the above data that the time constants of the cell, electronics, and shutter are much smaller than 10 msec, this value being a characteristic decay time found in the experiments.

The current transients were recorded by means of an averaging transient digitizer (KFKI, Hungary). The number of the transients repeated and averaged was usually $2^{12} = 4096$.

Theory

As has been shown in detail elsewhere (10) the steady state photocurrent on ferric oxide at constant potential is highly influenced by the concentration of the reducing substances, *i.e.*, hole acceptors in the solution. The difference between the photocurrent and dark current, which we call excess photocurrent, j', depends on the concentration of reducing agent in the solution in steady state according to Eq. [1]

$$1/j_s' = (1/j_h)(1 + k_1/k_2 c_{red}) \qquad [1]$$

where j_h is the hole flux to the surface, and k_1 and k_2 are phenomenological rate coefficients for recombination and injection, respectively; j_s' is the steady-state excess photocurrent; and c_{red} is the concentration of the reducing agent at the interface.

Equation [1] was obtained taking into account the following (10): Photogenerated charges in the semiconductor space charge layer are separated by transport processes, the details of which are beyond our present scope. A hole flux reaches the surface of the semiconductor, where holes are either injected into the solution and react with a hole acceptor, or recombine with electrons in the semiconductor. At medium electrode potentials, holes react only with strongly reducing substances (*e.g.*, $[Fe(CN)_6]^{4-}$, I^-), not with water molecules. At these electrode potentials there is competition between hole injection and recombination; the competition between the different hole acceptors can be neglected. By means of Eq. [1], from the dependence of excess photocurrent on reducing agent concentration the hole flux and the ratio of the rate constants can be obtained.

A number of kinetic models can be formulated for steady state leading to Eq. [1] (11-14). The surface processes invclved in these models can be summarized as follows:

Hole injection proceeds either directly (model B) or via surface states (model A). Recombination is assumed to proceed via surface states only (15). These two alternative kinetic models are illustrated in Fig. 1. In order to be able to decide which of the two simplified models is more suitable for the illuminated ferric oxide electrode, rate equations are established and compared with light modulation experiments for both cases.

Let us suppose, for both cases, that hole current j_h arriving at the surface responds immediately to the change of illumination intensity, because the charge carrier transport in this semiconductor is considered to be very fast in comparison with surface processes. This can be supported by the results of photocurrent rise time calculations given in Ref. (13), being in the order of magnitude of 10^{-6}-10^{-3} sec. The characteristic decay time presented here, and ascribed to surface processes, is at least one order of magnitude longer.

On the other hand, the diffusion of hole acceptors in the liquid phase can also be considered to be very fast. This was elsewhere demonstrated (10) as a consequence of the measurements being carried out, using an illuminated rotating ferric oxide electrode.

Thus, the transport processes in both phases can be regarded as not to be rate determining and may be ignored, allowing our attention to be centered on the surface processes. The role of surface states in our models is to act as intermediate states of charge. Their physical and/or chemical nature is not known, and from the present point of view their nature is quite irrelevant.

Let us suppose for both models that the partial order for every reaction partner in the surface processes is one. A remark needs to be made concerning this assumption: The surface concentration of the hole acceptor in the liquid phase is considered to be proportional to the bulk concentration. In Ref. (10) it has been shown that the competition kinetics, expressed in the form of Eq. [1], holds only if the surface and bulk concentrations of the reducing substance are proportional to each other, *i.e.*, weak adsorption occurs.

In both models the measured excess photocurrent is the difference between the hole flux, j_h, and the electron flux due to recombination, j_r

$$j' = j_h - j_r \qquad [2]$$

In the following the rate equations are presented. We calculate the current response of suddenly increasing illumination for both models.

Model A (Fig. 1A)

Let the surface charge density of holes captured by surface states be denoted by p, then

$$dp/dt = + j_h - k_i c_{red}\, p - k_r n_e p \qquad [3]$$

where k_r is the rate coefficient of surface recombination, n_e the electron density at the interface, and k_i

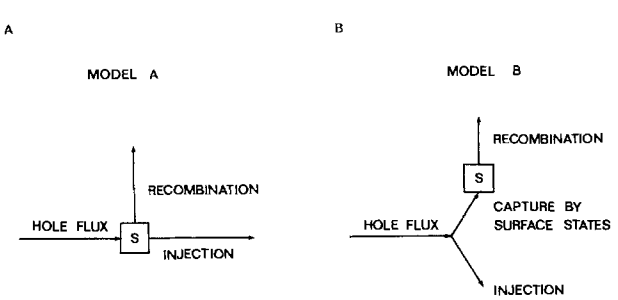

Fig. 1. Two possible kinetic schemes of surface reactions. Surface states are denoted by "S".

the rate coefficient of hole injection into the solution. Since both k_r and n_e are thought to be constant at constant electrode potential, $k_r n_e$ will be constant and denoted by k_r'. If, at $t = 0$, the light intensity is increased instantaneously from I to I + ΔI, then the hole flux, j_h, increases from $j_h°$ to $j_h° + \Delta j_h$. The latter change will be considered as an increase of step function form. In this case Eq. [3] has the form after rearrangement

$$dp/dt + (k_i c_{red} + k_r')p = j_h° + \Delta j_h \cdot u(t) = 0 \quad [4]$$

where $u(t)$ is the unit step function (16).

Since under steady illumination $dp/dt = 0$, the initial condition is given as the steady-state solution of Eq. [4], *i.e.*

$$p(t < 0) = j_h°/(k_i c_{red} + k_r') \quad [5]$$

Thus the solution to Eq. [4] equals

$$p(t) = (k_i c_{red} + k_r')^{-1} \cdot \{j_h° + \Delta j_h \cdot u(t) \cdot [1 - \exp(-(k_i c_{red} + k_r') \cdot t)]\} \quad [6]$$

The electron flux due to recombination, j_r', is equal to $k_r'p$, so for $t > 0$, j_A', the excess photocurrent from model A, using Eq. [2] and [6], is given as

$$j_A' = [k_i c_{red}/(k_i c_{red} + k_r')]\{j_h° + \Delta j_h(1 + (k_r'/k_i c_{red}) \cdot \exp[-(k_i c_{red} + k_r') \cdot t])\} \quad [7]$$

Model B (Fig. 1B)

For the analogous derivation we have to take it into account that only the $\xi = k_i c_{red}/(k_i c_{red} + k_a)$ fraction of the hole flux is injected into the solution, the remaining $(1 - \xi)$ fraction is captured by surface states. The phenomenological rate coefficient of capture is denoted by k_a. Generally the rate of hole capture by surface states is proportional to the occupancy of these states by electrons (15). In view of the small light perturbation applied, the occupancy can be regarded as constant, and therefore in the expression of ξ, it is incorporated into the phenomenological rate coefficient k_a. In this case for the surface charge density of holes, the following balance equation holds

$$dp/dt = j_h(1 - \xi) - k_r'p \quad [8]$$

Similarly to the derivation applied for model A, using illumination of the same step form, and taking initial condition for $t < 0$

$$p(t < 0) = (j_h/k_r')$$

one gets for the excess photocurrent from this model, j'_B, for $t > 0$

$$j' = \xi \cdot \{j_h° + \Delta j_h [1 + (1/\xi)(1 - \xi) \cdot \exp(-k_r' \cdot t)]\} \quad [9]$$

If the illumination of the electrode is modulated by small rectangular pulses, the photocurrent transients can be compared with Eq. [7] and [9]. Right at the start of the light pulses an immediate increase of photocurrent is expected. The increase for both models is the same, and equals Δj_h. Just after the photocurrent jump a decay portion is expected. The initial slope of the transients for model A is

$$dj_A'/dt \approx -j_h \cdot k_r' \quad [10]$$

which is seen to be independent of c_{red}.

For model B, however, one finds

$$dj_B'/dt \approx -j_h \cdot k_r' \cdot (1 - \xi) = -j_h \cdot k_r' \cdot k_a/(k_i c_{red} + k_a) \quad [11]$$

Introducing the notation

$$\tau = -(1/\Delta j_h)(dj'/dt)_{t \to 0} \quad [12]$$

one finds for model A the expression

$$\tau_A = 1/k_r' \quad [13]$$

whereas the same time constant for model B is

$$\tau_B = (1/k_r')(1 + k_i c_{red}/k_a) \quad [14]$$

If the modulation depth is very small, that is, $\Delta I << I$ hence $\Delta j_h << j_h°$, then the average value of j' under modulated illumination can be considered to be the same as that under constant illumination, that is, $\bar{j}' \approx j_s'$ so the average excess photocurrent for model A can be calculated as

$$1/\bar{j}_A' = (1/j_h°)(1 + k_r'/k_i c_{red}) \approx 1/j_s' \quad [15]$$

for model B, $\bar{j}'$ is given by

$$1/\bar{j}_B' = (1/j_h°)(1 + k_a/k_i c_{red}) \approx 1/j_s' \quad [16]$$

Both Eq. [15] and [16] are of the same form as Eq. [1]; but the physical meaning of the two former equations is more specified.

Results and Discussion

The transients in solutions containing different concentrations of KI can be seen in Fig. 2. The descending part of the transients depends on KI concentration. Consequently model A must be inadequate (cf. Eq. [10]).

The comparison between model B and experiments was as follows: Since the rise time of the transients is about 1 msec (not zero as in our oversimplified model), the initial slope of the descending part can be determined with limited accuracy only. However, the experimental values, according to Eq. [14], depend linearly on c_{red} (Fig. 3). From the slope and intercept of the τ *vs.* c_{red} plot, k_a/k_i can be determined. According to least squares fit $k_a/k_i = 23 \pm 6$ mM. As said above, k_a/k_i can be determined independently from the j_s' *vs.* c_{red} curve (Eq. [16]). From the steady-state measurement, $k_a/k_i = 36 \pm 1$ mM (Fig. 4). Given the simplifications of the model, these two values agree reasonably well.

Qualitatively, the same tendency of initial slopes was observed in the solutions of two other reducing substances, $K_4[Fe(CN)_6]$ and Na_2SO_3; the characteristic time of the decay of the transient, τ, significantly increased with their concentration in the solution,

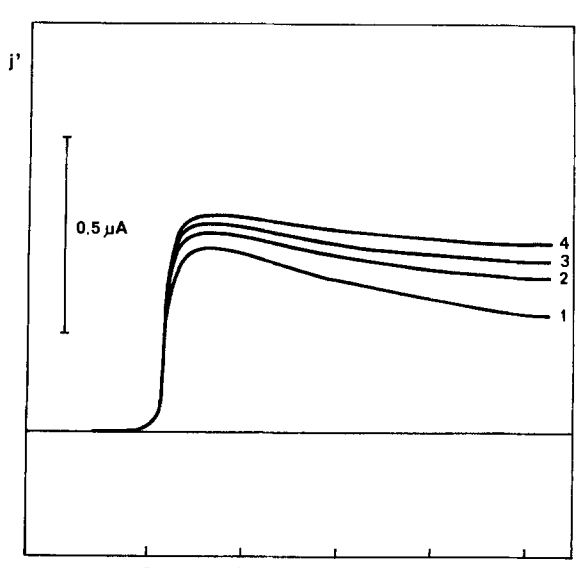

Fig. 2. Some representative current transients for different concentrations of KI in 0.2M borate buffer of pH 9.0 (1-0 mM, 2-9.5 mM, 3-16.3 mM, 4-18.2 mM). In each case the base lines are made to coincide.

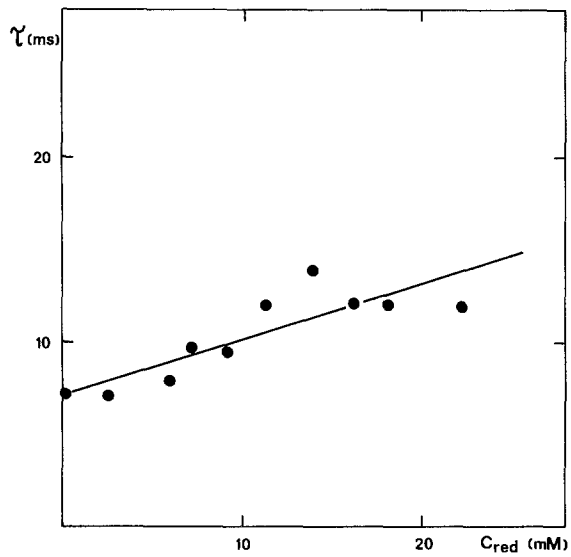

Fig. 3. Dependence of τ on c_{red}. The straight line is the least squares fit (cf. Eq. [14]).

indicating that model A is inappropriate also with these solutes.

Consequently, model B appears to be the more suitable for describing hole injection from ferric oxide, *i.e.*, holes are injected into the solution directly from the valence band, not via surface states.

This statement seems to be reasonable if we consider the energetics of the surface processes. The location of the valence bandedge of ferric oxide is 2.2 eV at pH 9.0 (17), the redox potential of the I^-/I_2 couple is 0.62 eV on the hydrogen scale. (The $E°_{redox}$ values for the two other redox systems, $[Fe(CN)_6]^{4-}/[Fe(CN)_6]^{3-}$ and SO_3^{2-}/SO_4^{2-} at pH 9.0, are 0.36 eV and −0.60 eV, respectively). Taking these data into consideration, hole injection from the valence band, since this process is highly exothermic, is energetically possible. It is not possible in view of there being insufficient data, however, to give any estimate of the phenomenological rate coefficients as they depend upon many factors: electrode potential, illumination intensity, nature of solute, etc. Our further work is aimed at the investigation of these dependences.

Acknowledgments

The author is indebted to Dr. R. Schiller and to Dr. L. Nyikos for stimulating discussions and help.

Manuscript submitted March 30, 1982; revised manuscript received Nov. 3, 1982.

Any discussion of this paper will appear in a Discussion Section to be published in the December 1983 JOURNAL. All discussions for the December 1983 Discussion Section should be submitted by Aug. 1, 1983.

Publication costs of this article were assisted by the Central Research Institute for Physics.

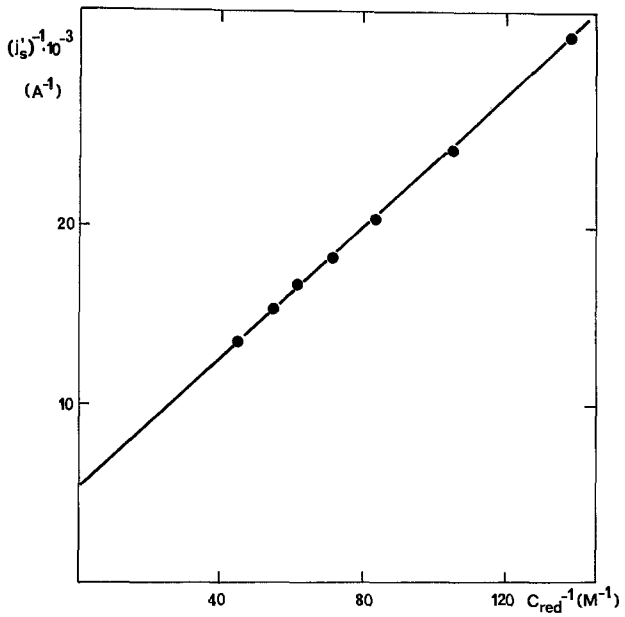

Fig. 4. Dependence of average excess photocurrent on c_{red}. The straight line is the least squares fit (cf. Eq. [16]).

REFERENCES

1. K. L. Hardee and A. J. Bard, *This Journal*, **124**, 215 (1977).
2. J. H. Kennedy and K. W. Frese, *ibid.*, **125**, 709 (1978).
3. L. R. Yeh and N. Hackerman, *ibid.*, **124**, 833 (1977).
4. S. M. Wilhelm, K. S. Yun, L. W. Ballanger, and N. Hackerman, *ibid.*, **126**, 419 (1979).
5. R. K. Quinn, R. D. Nasby, and R. J. Baughman, *Mater. Res. Bull.*, **11**, 1011 (1976).
6. A. F. Sammels and P. G. P. Ang, *This Journal*, **126**, 1831 (1979).
7. J. S. Curran and W. Gissler, *ibid.*, **126**, 56 (1979).
8. P. Iwanski, J. S. Curran, W. Gissler, and R. Memming, *ibid.*, **128**, 2128 (1981).
9. T. Pajkossy, I. Molnár, M. Pálfy, and R. Schiller, *Acta Chim. Acad. Sci. Hung.*, **101**, 93 (1979).
10. T. Pajkossy, *ibid.*, In press.
11. P. A. Kohl and A. J. Bard, *J. Am. Chem. Soc.*, **99**, 7531 (1977).
12. S. N. Frank and A. J. Bard, *ibid.*, **99**, 4667 (1977).
13. D. Laser, *This Journal*, **126**, 1011 (1979).
14. R. H. Wilson, in "Semiconductor Liquid Junction Solar Cells," A. Heller, Editor, pp. 67-83, The Electrochemical Society Softbound Proceedings Series, Princeton, NJ (1977).
15. V. A. Myamlin and Yu. V. Pleskov, "Electrochemistry of Semiconductors," Plenum Press, New York (1967).
16. Handbook of Mathematical Functions with Formulas, Graphs and Mathematical Tables, M. Abramowitz and I. A. Stegun, Editors, Dover Publications Inc., New York (1972).
17. S. R. Morrison, "Electrochemistry at Semiconductor and Oxidized Metal Electrodes," Plenum, New York-London (1980).

Reliable Glass-Polyethylene Dropping Mercury Electrode for Electrocapillary Measurements

M. Carlá and G. Aloisi

Universitá di Firenze–Istituto di Chimica Fisica, 50121 Firenze, Italy

The drop-time method is an attractive technique for interfacial tension measurements both because it is intrinsically simple and because it lends itself to automation.

Measurements are usually performed using drawn and internally siliconized glass capillaries. However, a high degree of training and skill is required to draw a good capillary. Moreover, measurements are unreliable in several electrolytic solutions, some of which are particularly useful for adsorption studies (say, HF, NaOH, diluted NaF (1, 2), etc.). Teflon tips joined to a glass capillary have been proposed for polarographic measurements (3, 4), but they are mechanically or electrically bored, and do not offer the geometrical regularity needed for accurate drop-time measurements; besides, they require a complex machines for construction. Polyethylene tips have been reported to give good results in drop-time measurements because of their accuracy, stability, and chemical inertness. However, following the construction procedure outlined in Ref. (2), we were unable to obtain fully satisfactory results.

In this communication, we describe in detail a very simple procedure for the construction of a composite glass-polyethylene dropping mercury electrode from readily available laboratory materials.

Capillary Construction

The polyethylene tip is drawn from a piece of 3 × 0.9 mm tube, about 8 cm long.[1] The tube is drawn by holding it in a vertical position under a 10g tension (applied through a silk wire to avoid tube bending), and by warming it locally at about 1/3 of its length with a flow of air heated to 200°C. As soon as the polyethylene tube reaches the softening temperature the air flow is removed, and the tube elongation is mechanically stopped at 3.5 cm. The polyethylene tube is allowed to cool before removing it, then it is frozen with liquid nitrogen together with a razor blade, and finally cut with the blade normal to its axis at its smallest cross section. The orifice which results has a very sharp and clean edge, with an internal diameter ranging from 200-300 μm.

The polyethylene tip is then joined, through an inox Swagelock (1/8-3/16) adapter with Teflon cones, to a standard glass capillary for polarography, whose internal diameter and length are chosen to provide the desired drop time. The electrode is connected to a mercury reservoir and filled, while keeping it in a vertical position with the tip upward. It is not necessary to connect the electrode to a vacuum system. If proper care is taken in cutting the polyethylene tube normal to its axis, the above procedure results in almost one working electrode for each attempt, with a limited scatter of characteristics.

Results

Several electrodes with drop times in the range from 10 to 20 sec were tested, and in all cases reproducibility in drop time of the order of 1 msec during a several hours' run was obtained. The instrument was calibrated against a Vos and Los electrocapillary curve for 0.1M KCl (5), the only available electrocapillary curve obtained entirely by an absolute method.

Key words: interfacial tension, drop time.

[1] We used the internal insulator of RG 58/U cable from Fabbrica Milanese Conduttori, Milano.

Electrocapillary curves for 0.1M $HClO_4$ and 1M KCl as measured with one of these electrodes are shown in Fig. 1 and 2. These figures also show that agreement with other authors' data (6, 7) is quite satisfactory, discrepancies being no greater than 0.6 dyne cm^{-1}. Data scatter between two different runs is better than 0.2 dyne cm^{-1} for any measured value.

One of these electrodes has been working for several months for adsorption measurements of aliphatic compounds from 0.1M NaOH solutions. As an example, Fig. 3 shows the electrocapillary curves of n-hexylamine solutions of different concentrations, as obtained by measuring three consecutive drop times for each applied potential at 25 mV intervals. The data are very regular even though no smoothing process was used. Even in these NaOH solutions, where the reproducibility attainable with conventional glass electrodes is

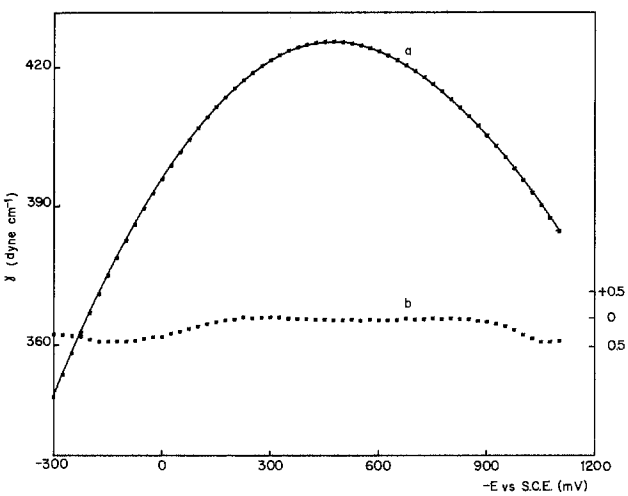

Fig. 1. Electrocapillary curve of 0.1M $HClO_4$: a) solid line: our data; squares: data from Ref. (6). b) Difference between the two sets of data.

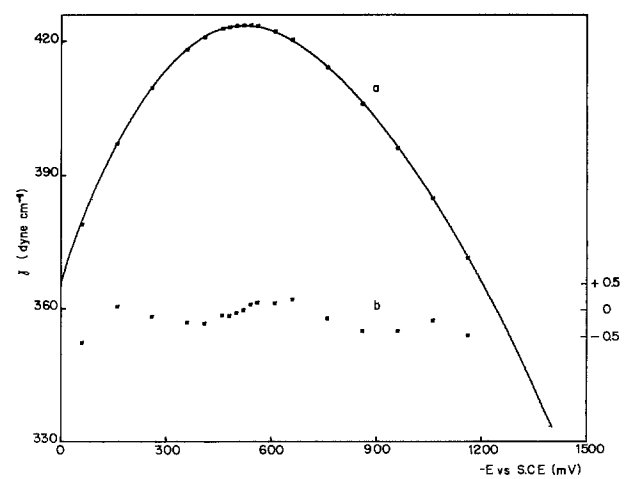

Fig. 2. Electrocapillary curve of 1M KCl: a) solid line: our data; squares: data from Ref. (7). b) Difference between the two sets of data.

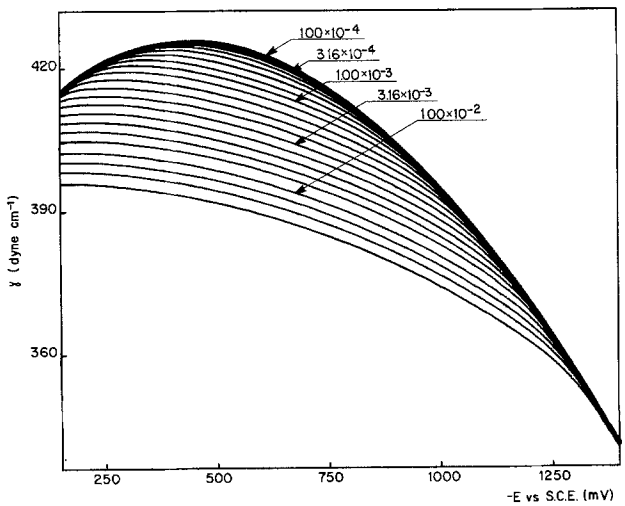

Fig. 3. Electrocapillary curves of N-hexylamine in 0.1M NaOH. Amine concentration ranges from 1.0 × 10^{-4}M to 2.0 × 10^{-2}M with 0.1 decimal logarithmic step.

very poor, a reproducibility of 0.2 dyne cm^{-1} was observed between different runs.

Acknowledgments

The authors thank Prof. S. Bordi and Prof. G. Papeschi for helpful discussions. Financial support of this work was granted by Menestro della Publica Intruzione.

Manuscript received Sept. 21, 1982.

Any discussion of this paper will appear in a Discussion Section to be published in the December 1983 JOURNAL. All discussions for the December 1983 Discussion Section should be submitted by Aug. 1, 1983.

Publication costs of this article were assisted by the Universita di Firenze.

REFERENCES

1. R. Payne, *J. Electroanal. Chem.*, **41**, 277 (1973).
2. L. Novotný, J. Kůta, and I. Smoler, *ibid.*, **88**, 161 (1978).
3. H. P. Raaen, *Anal. Chem.*, **34**, 1714 (1962).
4. A. M. Bond, T. A. O'Donnel, and A. B. Waugh, *J. Electroanal. Chem.*, **39**, 137 (1972).
5. H. Vos and J. M. Los, *J. Colloid Interface Sci.*, **74**, 360 (1980).
6. K. G. Baikerikar, J. Buckfelder, and R. S. Hansen, *J. Electroanal. Chem.*, **108**, 17 (1980).
7. R. G. Barradas and F. M. Kimmerle, *Can. J. Chem.*, **45**, 110 (1967).

Erratum

In the paper "Electron Traps in SiO_2 Grown in the Presence of Trichloroethylene" by A. B. Bhattacharyya and L. Manchanda which appeared on pp. 2772-2778 in the December 1982 JOURNAL, Vol. 129, No. 12, Fig. 9 should read as follows

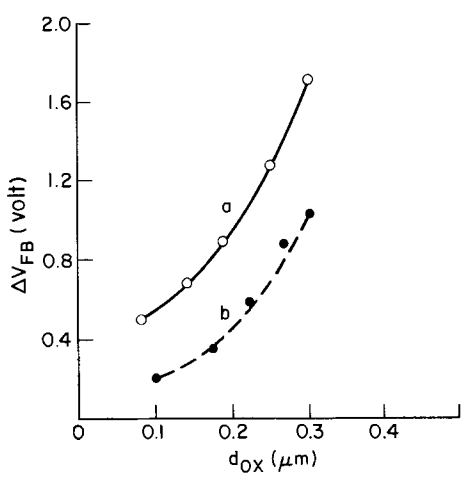

JOURNAL OF THE ELECTROCHEMICAL SOCIETY

SOLID-STATE SCIENCE AND TECHNOLOGY

MARCH 1983

Low Temperature Deposition of Silicon Nitride by Reactive Ion-Beam Sputtering

D. Bouchier, G. Gautherin, C. Schwebel, and A. Bosseboeuf

Institut d'Electronique Fondamentale, Bâtiment 220, Université Paris XI, 91405 Orsay-Cédex, France

and B. Agius* and S. Rigo

Groupe de Physique des Solides, E.N.S.-Université Paris VII, Tour 23, 2 Place Jussieu, 75221 Paris-Cédex, France

ABSTRACT

The deposition mechanism of reactive ion beam sputtered silicon nitride was studied. Using RBS analysis, the composition of Si_xN_y layers deposited at room temperature has been investigated as a function of different parameters. Irrespective of the nitrogen partial pressure, ranging from 10^{-4} to 0.2 Pa, the stoichiometry of the film depends only on the sputtering yield of silicon in the range 0.4-20 keV. Si_3N_4 layers can be obtained at low voltage, but only with a low deposition rate (typically 1 nm/min at our experimental conditions). In order to obtain Si_3N_4 films with higher deposition rates, we increased the nitridation of deposited silicon, either by introducing in the deposition chamber a highly reactive molecule such as NH_3, or by using electronic bombardment, which stimulates the adsorption of N_2 on the growing film.

Although the electrical characteristics of silicon oxide films and of their interface with silicon substrate are good enough to allow MIS silicon devices to be widely used, there are no commercially available MIS devices on GaAs or InP substrates. Direct oxidation of GaAs substrates can be performed by thermal oxidation (1), chemical anodization (2, 3), or plasma oxidation (4); however, up to now, these techniques led to a high value of interfacial trap density ($\simeq 10^{12}$ cm^{-2} eV^{-1}) and to various stoichiometries. Deposition of different dielectric layers has not given any significantly better results (5); following Wieder (6) this behavior seems to be inherent in using GaAs material. However, good MIS characteristics may be achieved when the natural oxide layer has been removed from the substrate before deposition of the dielectric layer, especially for pure Si_3N_4, as shown earlier by Bayraktaroglu (7). Another important use of Si_3N_4 is as an encapsulating layer: it has been shown that silicon nitride becomes an effective diffusion barrier for Ga atoms when its oxygen content is lower than 1% (8, 9).

Various nitride deposition techniques have been developed such as d-c and rf sputtering, ion plating, chemical vapor deposition (CVD), thermally initiated, catalyzed, or assisted by an rf plasma (10). The incongruent evaporation of Ga and As from GaAs at temperatures higher than 600°C (11) prohibits the use of thermally initiated CVD (at 900°-1100°C), while rf plasma deposition (at 200°-350°C) produces highly pure Si_3N_4 films (7, 8). Reactive d-c sputtering can be carried out at nearly room temperature and can lead to layers with suitable composition, but this method needs very careful handling (12). To avoid the complex phenomena arising from the presence of the plasma, which makes *in situ* characterizations more difficult, it is possible to use a variation of the basic sputtering method, ion beam sputtering, which was first proposed by Weissmantel (13).

In our case, reactive ion beam sputtering uses the interaction of a monoenergetic nitrogen ion-beam, generated in a separate duoplasmatron ion-source, with a silicon target situated in the deposition chamber which can be maintained at the required very low pressure ($< 10^{-2}$ Pa). Sputtered atoms are deposited on a substrate in front of the target. In this range of pressure, the mean free path is very large in comparison with the distance between the target and the substrate. We are concerned with the mechanisms of reactions occurring on the surfaces of the target, and of the growing film. A number of authors have shown that the bombardment of a silicon target by a nitrogen ion beam leads to the formation of a nitride layer at the surface of the target (14, 15).

The deposition mechanisms which may be considered to explain the composition of the nitride films are those we have previously discussed for ion-beam sputtered Nb-Ti thin films (16). The incorporation of nitrogen into the layer can occur according to three processes: (a) Nitrogen ions, after implantation into the target, are then sputtered, linked or not with silicon atoms, by subsequent ion bombardment. In the steady state, the sputtering yield of implanted nitrogen per impinging atomic ion is obviously equal to one, if the fraction of scattered ions can be neglected. Therefore, the corresponding ratio N/Si of the deposited layer should be in inverse ratio to the sputtering yield of silicon "S." For identical angular distributions and the same sticking coefficient on the deposition substrate for sputtered silicon and sputtered and/or reflected nitrogen species, the contribution of this process is equal to $1/S$. In any case, it is a function only of the ion energy. (b) Molecular nitrogen would be absorbed on the surface of the target and then sputtered as single or linked atoms towards the growing film. The contribution of this process depends on the nitrogen partial pressure and on the current density of ions which can produce two opposed effects such as ion stimulated desorption and a possible increase of the reactivity of adsorbed nitrogen with

* Electrochemical Society Active Member.
Key words: dielectric, films, stoichiometry, adsorption.

silicon. (c) Molecular nitrogen would be adsorbed on the thin film itself during its formation; this process contributes to the N/Si ratio, as a term proportional to the flow rate of nitrogen towards the growing film, and to the sticking coefficient of N_2 on it, for a given deposition rate of silicon.

The stoichiometry of the deposits is determined by the sum of the effects of these three mechanisms. The purpose of the present work is to evaluate each of their respective contributions. As our ion beam consists of both N^+ and N_2^+ ions, we first try to determine the contribution of each kind of ions during the stationary interaction of the beam with the silicon target. In a second part, we study the effect of the nitrogen partial pressure which was varied over a large range of pressure. Moreover, to try to evaluate the sticking coefficient of molecular nitrogen on the growing film, some deposits were made under a molecular beam bombardment of the substrate. In a third part, the effect of the ion-energy is shown and discussed. Finally, we propose two methods for obtaining stoichiometric silicon nitrides by increasing the nitridation of deposited silicon: (*i*) by introducing in the deposition chamber a highly reactive molecule such as NH_3, for example, and (*ii*) by using electronic bombardment (17) for dissociating or for exciting the molecular nitrogen.

Experimental Procedure

Deposition.—The experimental setup has been described elsewhere (16); however, some improvements have been included to make it suitable for this study (Fig. 1): (*i*) an electrostatic lens which allows us to lower the accelerating voltage down to 0.4 kV with a beam current up to 1.5 mA. (*ii*) a molecular beam generator made out of a multichannel nozzle with about 900 channels of 0.1 mm diam and 2.5 cm length. It provides on the substrate surface a molecular flow equivalent to a calculated (18) local pressure up to

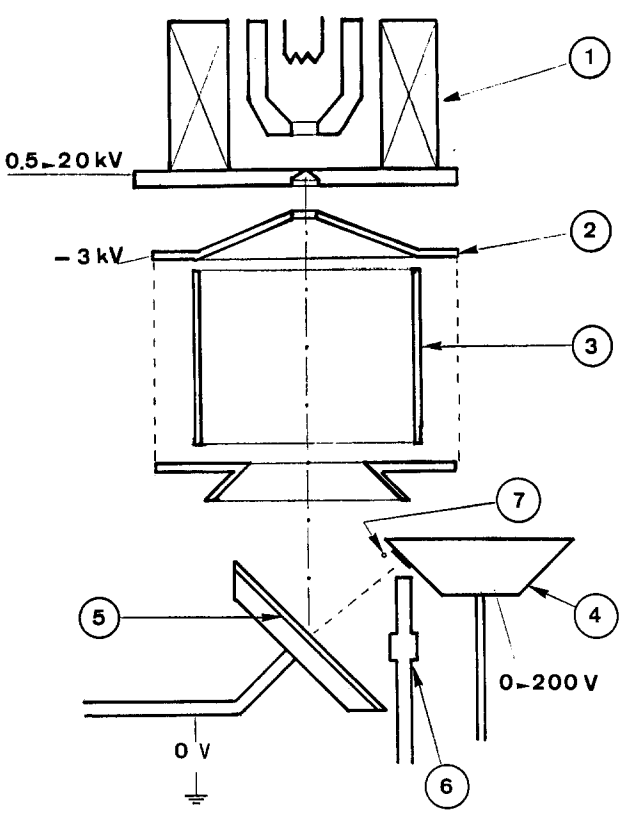

Fig. 1. Experimental setup used for silicon nitride deposition: 1. duoplasmatron ion source, 2. extractor, 3. electrostatic lens, 4. substrate-holder, 5. target, 6. molecular beam generator, 7. tungsten-rhenium filament.

0.2 Pa. A liquid He cryogenic pump with a pumping speed of 5000 l/sec for nitrogen gives a maximum isotropic pressure $P_I = 5 \times 10^{-3}$ Pa during the experiments with the molecular beam generator. (*iii*) a tungsten-rhenium ribbon which is positioned in front of the substrate. This simple electron gun delivers an electronic current up to 50 mA under an accelerating voltage of 150V. It may induce some tungsten incorporation in the deposit, but this does not change anything in the mechanisms we want to study.

High purity vitreous carbon substrates provided by Carbone Lorraine were used in order to obtain directly by MeV ^4He backscattering the composition of the deposits. These substrates were chemically cleaned by immersing them in trichloroethylene, ethanol, and acetone successively, rinsed in deionized water, and baked out at 160°C *in vacuo*. All the films described in this paper were deposited at room temperature.

During deposition, the isotropic pressure of N_2 can vary from 7×10^{-5} Pa to 5×10^{-3} Pa according to the different experiments. A gas analyzer gives a continuous monitoring of partial pressures: 2.4×10^{-3} Pa of N_2, 1.7×10^{-6} Pa of H_2O, and 5×10^{-7} Pa of CO_2 are typical values measured during a deposition process.

A separate apparatus was used to make N^+ or N_2^+ implanted silicon samples; it consisted of a duoplasmatron ion source and a magnetic mass separator. The energy of the ions can be varied from 4 to 10 keV, the current density on the sample being typically equal to 50 $\mu A/cm^2$.

Nuclear microanalysis.—The experiments were carried out on the 2 MeV Van der Graaf accelerator of the Groupe de Physique des Solides de l'E.N.S.

The composition and stoichiometry measurements by MeV $_2{}^4He$ backscattering have been described generally (19), and more accurately in the case of silicon nitride deposited on silicon and carbon substrates (12). The absolute determination of the numbers of atoms/cm^2 is made using a tantalum thin film standard (20).

The total amount of nitrogen N^+ or N_2^+ implanted in silicon samples has been determined by comparison with a standard (21), using the nuclear reaction $^{14}N(d, \alpha)^{12}C$ initiated by a deuteron beam with an energy of 1300 keV.

Results and Interpretation

Study of the implanted target.—During the ion bombardment of a solid, a steady state is reached when the surface of the solid has been etched further than the particle projected range R_p. The total amount of implanted atoms becomes constant, and their depth distribution in the target is stationary. If no diffusion occurs, the steady state implies that the sputtering yield of implanted atoms is equal to one atom per impinging atomic ion. Moreover, Biersack has calculated (22): (*i*) the total amount N_N of implanted nitrogen given by

$$N_N = \frac{q R_p}{v}$$

where q is the implantation rate (atoms cm^{-2} sec^{-1}) and v, the speed of surface erosion (nm sec^{-1} if R_p is expressed in nm). (*ii*) the maximum concentration, C_N, of implanted nitrogen, near the surface in our case, given by

$$C_N = \frac{q}{v}$$

If we neglect the reflected ions, this relationship may be expressed as $N/Si = n/S$ where S is the sputtering yield of silicon per molecular ion, constituted of n atoms (in our case, $n = 1$ or 2 for N^+ or N_2^+ respectively). We have to make some remarks about the dependence of N_N on the energy: N_N is propor-

tional to R_p and in inverse ratio to S. LSS theory (23) shows that R_p is nearly proportional to the energy E. Therefore, N_N would be linear with E in a range of energy where S is nearly constant: in our case, between 2 and 20 keV. This range has been determined using Sigmund's theory (24) for pure silicon sputtered by N^+ ions. We try now to use this argument in order to determine the effect of N_2^+ ions in comparison with that of N^+. A simple hypothesis which can be made about the behavior of N_2^+ as bombarding particle is that this ion with an energy E has its N—N bond broken when impinging on the surface of the solid, and can be then considered as two N^+ ions with the energy $E/2$. Therefore, the total amount of implanted nitrogen, in the steady state, would be lower by half for N_2^+ ions than that obtained for N^+ with the same energy.

Our experimental results seem to verify this hypothesis; some implantations at normal incidence have been made on (111) silicon targets with ion beam energies ranging from 4 to 10 keV, and with bombardment doses up to 10^{18} ions cm^{-2} of N_2^+ or N^+, respectively. Figure 2 shows that the implanted doses are nearly proportional to the accelerating voltage with slopes equal to 2.40×10^{16} atoms cm^{-2} keV^{-1} and 1.16×10^{16} atoms cm^{-2} keV^{-1} for N^+ and N_2^+, respectively.

The same experimental setup (25) permits us to measure the composition (N^+, N_2^+) of the ion beam delivered by the duoplasmatron source according to its discharge conditions. We were able to determine the values of the parameters, which give a composition of the ion beam stabilized at 80-90% of N_2^+. In the following text we call this value β. These experimental conditions were used to obtain the deposited films we study in this work.

Effect of nitrogen pressure.—Assuming the deposition conditions previously defined for Nb-Ti films (16) to be available for silicon-nitride film, we first tried to deposit Si_3N_4 films with an ion beam energy of 10-20 keV. Figure 3a shows the RBS spectrum obtained for a typical layer deposited on a carbon substrate with a beam energy of 10 keV at a nitrogen pressure $P_I = 10^{-4}$ Pa. The thickness of the deposit is about 65 nm. There is a slight oxygen peak near the surface, corresponding to about 10^{16} atoms cm^{-2}, the remainder being uniformly distributed. The analysis of this spectrum yields the following composition, expressed in atomic ratios: N/Si = 0.53 and O/Si ~ 0.01 in the depth of the film. Therefore, these deposition conditions lead to a film with an N/Si ratio much less than for stoichiometric nitride films (N/Si = 1.33 for Si_3N_4 films).

In order to evaluate the effect of molecular nitrogen, some deposits have been made with increasing pressures of N_2 ranging from $P_I = 10^{-4}$ Pa to $P_I = 7 \times 10^{-3}$ Pa. The results are presented in Table Ia: no significant increase of N/Si ratio can be noted in this range of pressure. Thus, a higher pressure is needed to determine the sticking coefficient of molecular nitrogen, but 7×10^{-3} Pa seems to be the maximum value compatible with a well-defined ion beam in our apparatus, because the scattering of ions by gas molecules becomes important at higher pressure. A molecular beam generator, in our case a multichannel nozzle, pointed at the surface of the film, allows us to avoid this difficulty. The flow rate of N_2 impinging on

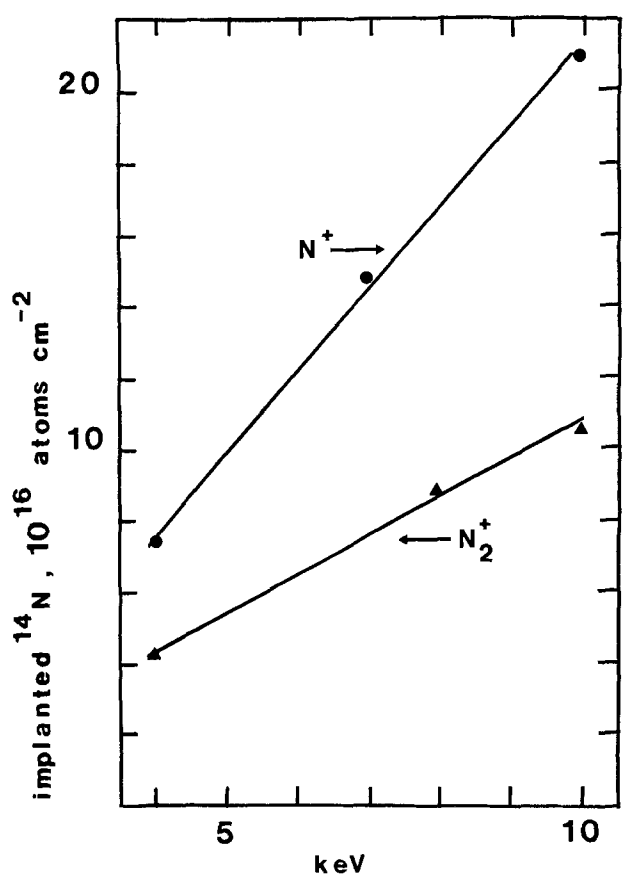

Fig. 2. Amount of nitrogen in (111) silicon target implanted with N^+ and N_2^+ beams expressed as a function of energy. Dose used: 10^{18} ions/cm^2.

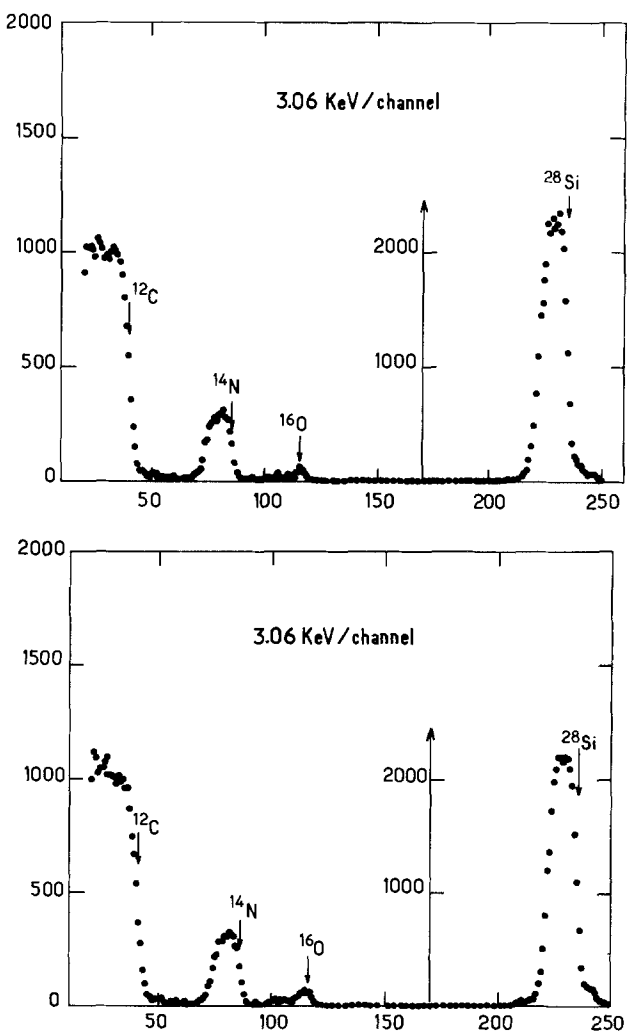

Fig. 3. Energy spectra of ^4He particles backscattered at 150° from a 1.8 MeV $^4He^+$ beam by Si_xN_y films deposited on carbon substrates: (a) $P_{N_2} = 10^{-4}$ Pa; (b) $p_{N_2} \sim 0.2$ Pa. Beam energy = 10 keV. Ion beam current 3 mA. Thickness of the deposits: ~65 nm.

Table I. Stoichiometry of nitride layers deposited at nearly constant deposition rate of silicon expressed as a function of

(a) the isotropic pressure of nitrogen P_I

P_I (10^{-4} Pa)	Ion-beam current (mA)	Deposition rate of silicon (10^{15} atoms cm^{-2} sec^{-1})	N/Si
1.0	6	1.0	0.49 ± 0.02
2.7	6	0.9	0.50 ± 0.02
13.3	6	1.0	0.51 ± 0.02
24.0	3	0.3	0.53 ± 0.02
70.0	6	0.7	0.48 ± 0.02

(b). The input pressure P_i in the molecular beam generator

Input pressure P_i (10^2 Pa)	Calculated local pressure (Pa)	Deposition rate of nitrogen (10^{15} atoms cm^{-2} sec^{-1})	Deposition rate of silicon (10^{15} atoms cm^{-2} sec^{-1})	N/Si
0	0.002	0.18	0.34	0.53 ± 0.02
1.6	0.02	0.18	0.32	0.57 ± 0.02
6.0	0.08	0.18	0.31	0.60 ± 0.02
13.4	0.18	0.20	0.34	0.59 ± 0.02
16.0	0.21	0.19	0.27	0.72 ± 0.02

the surface of the film has been calculated as a function of the dimensions of the channels and of the input pressure, P_i, according to numerical results (18) derived from Zugenmaier's theory.

The RBS spectrum shown on Fig. 3b corresponds to a layer deposited with a nitrogen molecular beam directed towards the film surface, the nitrogen beam being produced with an input pressure of 1300 Pa. The other deposition conditions are those described above for Fig. 3a. There is no difference between the two spectra: the amount of nitrogen is nearly the same, and furthermore, the oxygen peak in spectrum 3b corresponds to a small proportion of oxygen (~3%).

Table Ib shows the values of the deposition rates of nitrogen and silicon as a function of the input pressure P_i. No significant effect of nitrogen pressure is observed; however, if such an effect exists, the maximum increase of the nitrogen incorporation rate would be $\sim 2 \times 10^{13}$ atoms cm^{-2} sec^{-1} for a localized surface nitrogen pressure of $\sim 2 \times 10^{-1}$ Pa, corresponding to a sticking coefficient of N_2 on the growing film equal to $\sim 2 \times 10^{-5}$.

Other results (Fig. 4) obtained for a nitrogen partial pressure of 10^{-4} Pa and various ion beam intensities suggest that N/Si may be correlated to the deposition rate of silicon, N_{Si}. Figure 4 shows an increase of N/Si from 0.5 to 0.7 when N_{Si} decreases from 10×10^{14} to 1.6×10^{14} atoms cm^{-2} sec^{-1}; dividing N_{Si} by 6 induces much more effect than multiplying the pressure by 70. This can be explained by process (b). As we have shown that N/Si does not depend on the pressure from 10^{-4} to 10^{-2} Pa, the contribution of this process seems to be fixed only by the current density in this pressure range.

Effect of the beam energy.—We have assumed the stoichiometry of the nitride films to be determined by the sum of three contributions: the first (*i*) depends on the energy, the second (*ii*) is more difficult to evaluate but is certainly a function of the current density, and the third (*iii*) is proportional to the N_2 pressure. The latter has been found to be negligible and (*ii*) is of little influence. Study of the first one is the purpose of this section where we show the effect of the beam energy.

The RBS spectrum shown on Fig. 5 relates to a 70 nm thick nitride layer deposited with an accelerating voltage value of 500V, and a beam current of 1.5 mA. The N/Si ratio is found equal to 1.16, and the oxygen content in the depth of the layer does not exceed 2%.

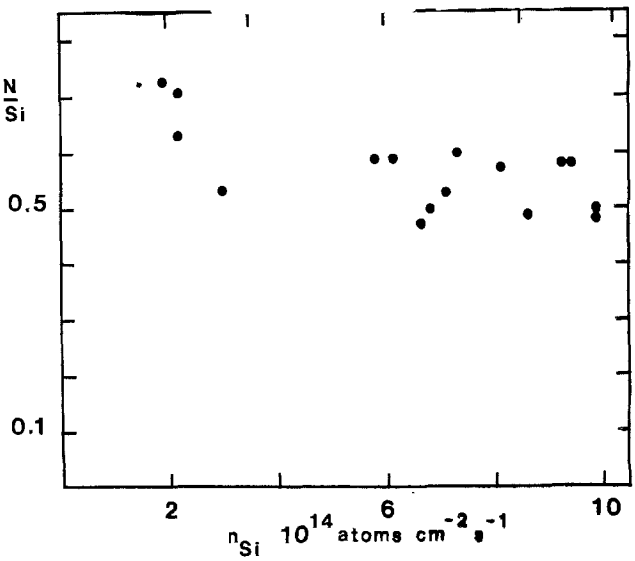

Fig. 4. Stoichiometry of Si_xN_y films expressed as a function of the deposition rate of Si. The nitrogen pressure is equal to 10^{-4} Pa. Ion beam energy = 10 keV. Current intensity varies from 1-6 mA.

Experiments have been made with ion beam energies ranging between 0.4 and 10 keV, and for two values of the beam intensity 1.5 and 0.75 mA. The focusing conditions have been adjusted to ensure the same divergence of the ion beam for each value of the current. For a given accelerating voltage, the average current densities could be roughly evaluated equal to 150 and 75 μA/cm^2 for 1.5 and 0.75 mA values, respectively. Figure 6 shows the normalized deposition yields of nitrogen and silicon N_{Si} (Fig. 6a), and N_N (Fig. 6b), respectively, and the N/Si ratio (Fig. 6c) expressed as a function of the accelerating voltage V. The N/Si ratio depends sharply on V in the range 0.4-1 kV, and for the lowest values the Si_3N_4 stoichiometry is nearly reached. The points corresponding to the lowest current density are slightly above the average curve. Above 5 kV, N/Si ratio is constant and equal to ~ 0.5. The value of N_{Si} increases linearly with log V up to 4-5 kV and becomes constant above this value, while N_N increases with V in a 0.4-0.9 keV range and then remains constant. In order to explain these results, we have to formulate the dependence of N_N and N_{Si} on the sputtering process itself: (*i*) assuming the sticking probability of silicon

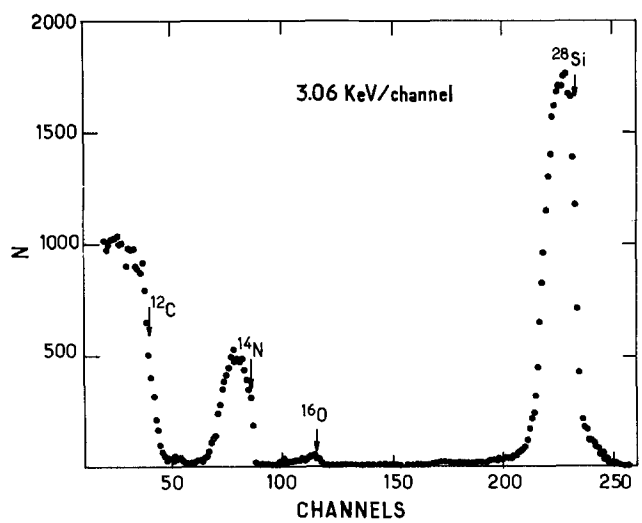

Fig. 5. ^{4}He backscattering spectrum for a 70 nm thick ion-beam sputtered silicon nitride film deposited with an ion beam energy of 500 eV at a current of 1.5 mA. The film observed here is slightly under stoichiometric.

to be equal to one, the deposition yield of the silicon by unity bombardment dose is given by

$$N_{Si} = K \cdot S \cdot I \cdot t \qquad [1\text{-a}]$$

where S is the sputtering yield of silicon, t the deposition time corresponding to the unity dose, I the beam intensity expressed in ions/sec, and K a geometrical coefficient. This formula summarizes the complete expression we have previously used (16)

$$N_{Si}/t = \int_s S \cdot j(x,y) \cdot \cos\theta/\pi \cdot \Omega(x,y)\,dxdy \qquad [1\text{-b}]$$

where s is the surface of the target, $j(x,y)$ the current density, $\cos\theta/\pi$ the proportion of sputtered atoms emitted in direction θ, measured from the normal to the surface, and $\Omega(x,y)$ is the solid angle under which the substrate is seen from point (x,y).

Assuming the ion beam has a gaussian spatial distribution of half-width δ, we can deduce the values of K as a function of δ [Eq. 1-b] and then evaluate S from the measurement of N_{Si} [Eq. 1-a]. The spot of the ion beam on the surface of the target gives a value of δ ranging from 2 to 3.5 cm; for instance, $S = 1$ atom/ion corresponds to $N_{Si} = 10.5 \times 10^{16}$ and 9×10^{16} atoms cm^{-2} $coulomb^{-1}$ for 2 and 3.5 cm, respectively. (*ii*) We have previously seen that an N_2^+ ion beam of energy E may be considered as an N^+ ion beam with the energy $E/2$ and a doubled current density. If the proportions of N^+ and N_2^+ in the ion beam are respectively α and β, S must be written as

$$S = \alpha S'(E) + 2\beta S'(E/2) \qquad [2]$$

where S' is the sputtering yield of Si by N^+ ion. The β value is in the range 0.8-0.9 (25). (*iii*) The sputtering yield of implanted nitrogen must be equal, in the steady state, to one atom/atomic ion if the fraction of reflected ions may be neglected; following the theoretical calculations of Bottiger (26), this fraction is equal to about 10% with our experimental conditions, a value which seems to be more likely at high energies (27). But, if the angular distribution of reflected ions is nearly the same as that of sputtered nitrogen the latter cannot be differentiated from the reflected species. So, N_N must be written as

$$N_N = a(\alpha + 2\beta)\, I \cdot t \cdot K \qquad [3\text{-a}]$$

where a is the sticking probability of sputtered nitrogen on the growing film. Assuming that sputtered nitrogen has the same angular distribution as sputtered silicon, we can use the same value of K for these various species. Considering our experimental value of β, [3-a] can be written

$$N_N \sim 2a \cdot I \cdot t \cdot K \qquad [3\text{-b}]$$

From Eq. [1-a] and [3-a], we obtain for N/Si ratio

$$\frac{N}{Si} = a(\alpha + 2\beta)/S \qquad [4\text{-a}]$$

If α can be neglected and if $S'(E/2) \simeq S'(E)$, Eq. [4-a] becomes

$$\frac{N}{Si} \simeq a/S'(E/2) \qquad [4\text{-b}]$$

Let us discuss the results of Fig. 6 using the above considerations. The first feature to examine is N_{Si} increasing with log V (Fig. 6-a). From this dependence and considering Eq. [1-a], we can deduce that S increases linearly with log V when V varies from 0.4 to about 5 kV. For higher values of V, S remains practically constant and equal to about 2. This kind of behavior is in good agreement with Sigmund's theory (24). Nevertheless, in the logarithmic domain, the variation of S with log V is two times larger than that

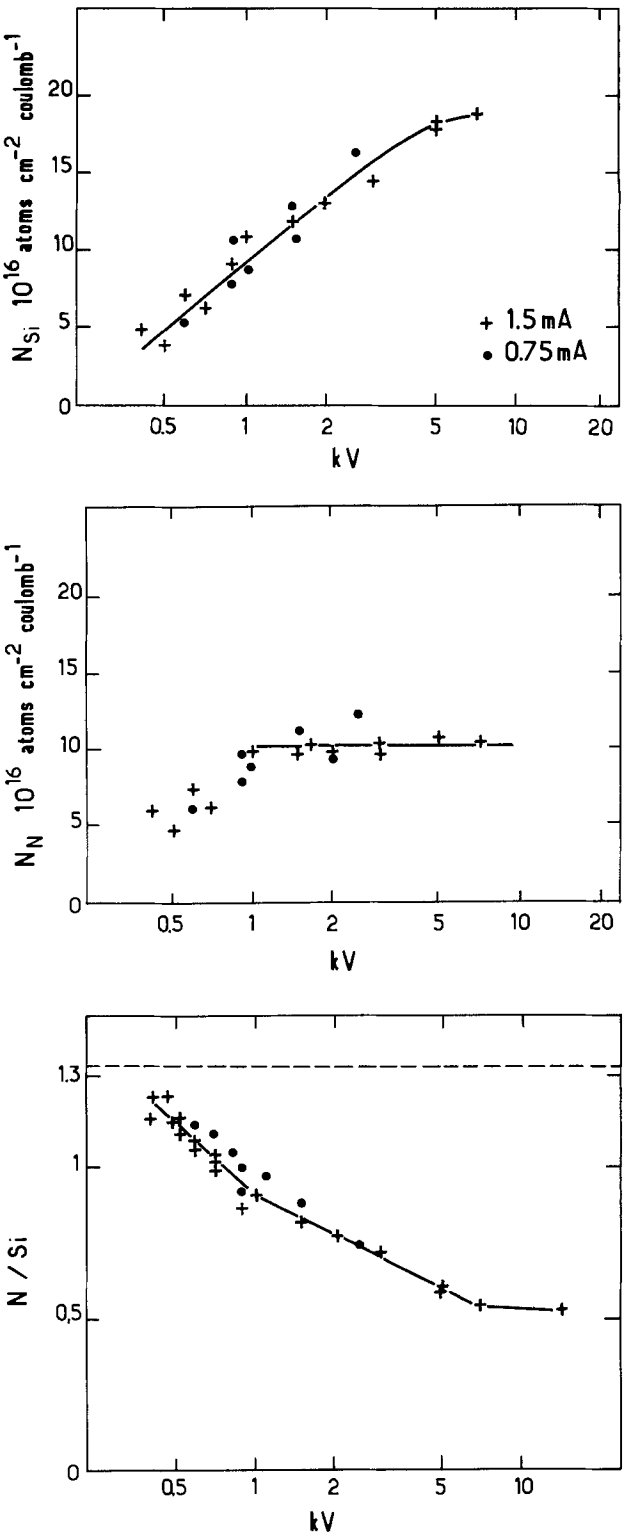

Fig. 6. Deposition yields of silicon N_{Si} (Fig. 6a), of nitrogen N_N (Fig. 6b) expressed in atoms cm^{-2} $coulomb^{-1}$, and the atomic ratio N/Si (Fig. 6c) as a function of the accelerating voltage V.

predicted by Sigmund. This unexplained result has already been reported in the case of a noble gas ion beam (24). If we took for the theoretical energy a value equal to half the experimental one, a satisfactory agreement would be obtained between the energy position of the maximum of S in the theoretical curve, and that of N_{Si} (*i.e.*, of S) in the experimental one. This is in agreement with the hypothesis we have made about the behavior of N_2^+ ions, which are the main component of the nitrogen beam. The theoretical value of the maximum of $S'(E/2)$ is found equal to 1.3, assuming a bond energy of 7.8 eV which is that of pure silicon, and con-

sidering a 45° angle of incidence. It appears that the experimental value of S maximum is in agreement with the theoretical one if $S \simeq 2S'(E/2)$.

Next, we shall discuss the variation of N_N with energy (Fig. 6-b). In the voltage range 1-10 kV and from Eq. [3-b], we deduce that a, sticking probability of sputtered nitrogen on the growing film, is equal to about 0.5. This is a large value in comparison with that of the sticking coefficient of molecular nitrogen, which has been estimated above to be lower than about 10^{-5}. This confirms that implanted nitrogen would be sputtered as atoms linked with silicon or as highly reactive single atoms. Let us note that the proportion of sputtered Si_xN_y clusters would depend on the density of damage induced by the impinging ions; consequently, the coefficient a is a function of the current density, and then varies with the focusing and the composition (N_2^+/N^+) of the ion beam.

Below 900V, N_N decreases with V. This can be explained by two processes: (i) the maximum concentration of nitrogen at the target surface is given by $N/Si = 2/S$ for N_2^+ impinging ions, if the fraction of reflected ions still may be neglected at low energy. (See section on study of the implanted target.) The surface of the target is then very over-stoichiometric when S is lower than 1, as is true in this range of energy (Fig. 6-a), and nitrogen in excess may be sputtered (or desorbed) as N_2 molecules with a low sticking probability. (ii) The fraction of reflected nitrogen ions increases with decreasing energy, as has been reported for inert gas (27) and nitrogen ions (17), and their angular distribution is very different than that of the sputtered species. In these conditions, an important part of emitted nitrogen does not reach the growing film.

For low values of V, giving nearly stoichiometric Si_3N_4 layers, the balance we can make for deposited silicon and incorporated nitrogen—~ 0.5 Si and ~ 0.6 N atoms for one N_2^+ ion—is in good agreement with the formal equation proposed by Weissmantel (13) for a sputtering yield of 0.48.

Deposition of stoichiometric Si_3N_4.—Stoichiometric nitride layers can be obtained in our apparatus with the required energy of the ions (Fig. 6), but with a very low deposition rate, typically 1 nm/min. In order to obtain Si_3N_4 films with higher deposition rates, we used two different methods. The first one consists of introducing a partial pressure of ammonia in the deposition chamber. This molecule being much more unstable that N_2 should be a more efficient nitriding agent. The sticking probability of N_2 has such a low value that the production of an intense molecular beam towards the growing film does not significantly change its stoichiometry (second section). The assumption that atomic nitrogen has a very different behavior suggests the second method, which consists of depositing a nitride layer with a significant flow rate of N_2 and a simultaneous electronic bombardment on the growing film. The following results were obtained:

Effect of a partial pressure of ammonia.—Typical results are presented in Fig. 7. They are for layers deposited with an ion beam of 6 keV energy and of 3 mA intensity, the partial pressure of ammonia $P(NH_3)$ being varied from 0 to 5 × 10^{-3} Pa. The N/Si ratio, N_N and N_{Si} are plotted *vs.* the pressure of NH_3. N/Si increases strongly with $P(NH_3)$ and reaches a saturation value greater than 1.33 for a pressure equal to 2 × 10^{-3} Pa. N_N also increases and reaches an asymptotic value, but at a lower pressure value (~ 3 × 10^{-4} Pa), while N_{Si} shows an unexpected decrease in the same range of pressure.

The behavior of N_N and N_{Si} cannot be entirely explained by process (c) (direct adsorption of NH_3 on the growing film) as this process cannot induce a decrease of N_{Si}. So we have to take into account the process (b)

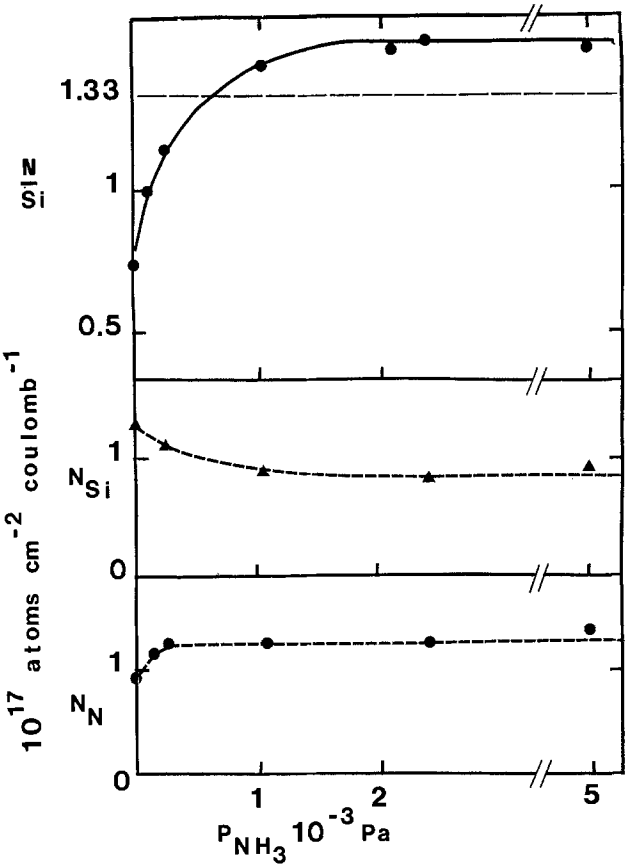

Fig. 7. Deposition yields of silicon and nitrogen and stoichiometry of ion-beam sputtered silicon nitride films deposited with an nitrogen ion-beam energy of 6 keV at a current of 3 mA expressed as a function of the partial pressure of ammonia.

which is related to the adsorption of NH_3 on the target: this adsorption should change the composition of the target surface and thus lower the sputtering yield of silicon. Moreover, over-stoichiometric nitride films were obtained for higher pressures of NH_3; nitrogen in excess may be incorporated as N-H radicals. We are studying this possible effect.

Effect of electron bombardment combined with N_2 molecular beam.—Layers were deposited with a beam of energy equal to 10 keV and of intensity equal to 3 mA. The input pressure in the molecular beam generator was maintained equal to 1600 Pa and the calculated value of the corresponding local pressure of N_2 was equal to 0.2 Pa (18). The intensity of the electronic bombardment ranged from 0 to 50 mA with 150V applied to the substrate. Figure 8 shows the N/Si ratio as a function of the electronic current: it increases and nearly reaches the Si_3N_4 stoichiometry for intensities higher than 30 mA. The oxygen content can be reduced to less than 3% (Fig. 3b) when great care has been taken for the gas entry system.

From the slope of this curve, at $I = 0$, and knowing the deposition rate of silicon, we obtain a value

$$\frac{dn_N}{dI} = 2.9 \times 10^{13} \text{ atoms cm}^{-2} \text{ sec}^{-1} \text{ mA}^{-1}$$

From this, we can deduce the increase of the sticking probability of N_2 with electronic bombardment

$$da/dI = 7 \times 10^{-5}/\text{mA}$$

To explain this increase we assume the following process: nitrogen molecules are adsorbed on the growing films and then are dissociated by the electronic bombardment; this atomic nitrogen is the reactant for nitridation of unbound silicon. We can also determine the

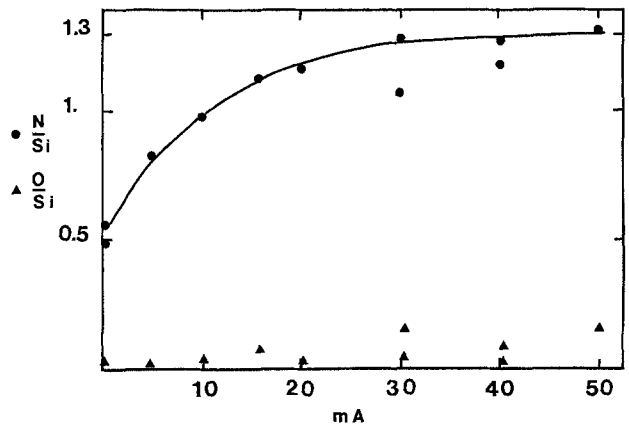

Fig. 8. N/Si ratio as a function of the electronic bombardment intensity corresponding to ion-beam sputtered silicon nitride films deposited under an N_2 molecular beam (local pressure: 0.2 Pa) with an ion-beam energy of 10 keV and a current intensity of 3 mA.

coverage density of adsorbed N_2, assuming the dissociation cross section to be the same for adsorbed and free molecules [about 2×10^{-16} cm^2 at 150 eV (28)]; we find a value of about 10^{13} atoms/cm^2, equivalent to one-hundredth of a monolayer.

Conclusion

This study allowed us to determine the respective contributions of different mechanisms which take place during the deposition of silicon nitrides by ion beam sputtering. It has been shown that: (*i*) The sticking probability of molecular nitrogen on the growing film is negligible (less than 2×10^{-5} in 10^{-4} to 0.2 Pa pressure range), (*ii*) The incorporation in the growing film of nitrogen sputtered and/or reflected from the target is independent of the ion beam energy in 1-10 keV range. The corresponding sticking probability is equal to 0.5. Moreover the contribution of the adsorbed molecular nitrogen on the target seems to be limited by the current density and independent of the pressure for values greater than 10^{-4} Pa. The N/Si ratio is fixed by the sputtering yield of silicon: it is equal to about 1 for 0.9 keV and decreases linearly with log E, from 1 to 0.5 in the 1-5 keV energy range, while the sputtering yield S varies from 1 to 2 atom/ion. Note that S must be reduced if we want to reach the Si_3N_4 stoichiometry; we have obtained 1.25 for the N/Si ratio at 0.4 keV, for $S = 0.5$ atom/ion. (*iii*) Stoichiometric silicon nitrides were obtained by increasing the sticking probability of molecular nitrogen on the growing film by using electronic bombardment; with our experimental conditions the corresponding increase is equal to about 10^{-4}/mA. Another possibility is to use NH_3 as a highly reactive molecule: nitrogen-rich nitride is obtained from P_{NH_3} greater than 10^{-3} Pa.

Acknowledgments

The authors wish to thank E. d'Artemare for his assistance with the experiments carried out on the Van de Graaf accelerator. This work was supported by the Centre National de la Recherche Scientifique (RCP 157) and Délégation Générale à la Recherche Scientifique et Technique.

Manuscript submitted Dec. 30, 1981; revised manuscript received Nov. 8, 1982. This was Paper 378 presented at the Denver, Colorado, Meeting of the Society, Oct. 11-16, 1981.

Any discussion of this paper will appear in a Discussion Section to be published in the December 1983 JOURNAL. All discussions for the December 1983 Discussion Section should be submitted by Aug. 1, 1983.

REFERENCES

1. Z. Shoita, N. Miyamoto, and J. I. Nishizawa, *This Journal*, **124**, 1405 (1977).
2. J. M. Poate, P. J. Silverman, and J. Yahalom, *J. Phys. Chem. Solids*, **34**, 1847 (1973).
3. C. Cohen, M. Croset, A. V. Drigo, and J. Siejka, Proc. of the Eighth International Vacuum Congress, Vol. I, F. Abeles, and M. Croset, Editors, p. 586, Sept. 1980, Cannes, France.
4. R. P. H. Chang, J. J. Coleman, A. J. Polak, L. C. Fellman, and C. C. Chang, *Appl. Phys. Lett.*, **34**, 237 (1979).
5. D. L. Lile and D. A. Collins, *Thin Solid Films*, **56**, 225 (1979).
6. Wieder, in *Inst. Phys. Conf.* **50**, 234 (1979).
7. B. Bayraktaroglu, W. M. Theis, and F. L. Schuermeyer, *ibid.*, **50**, 280 (1979).
8. K. V. Vaidyanathan, M. J. Helix, D. J. Volford, B. G. Streetman, R. J. Blattner, and C. A. Evans, *This Journal*, **124**, 178 (1977).
9. M. J. Helix, K. V. Vaidyanathan, B. G. Streetman, H. B. Dietrich, and P. K. Chatterjee, *Thin Solid Films*, **55**, 143 (1978).
10. C. E. Morosanu, *ibid.*, **65**, 171 (1980).
11. S. T. Picraux, in "Ion Implantation in Semiconductors and Other Materials," B. L. Crowder, Editor, Plenum Press, New York (1975).
12. S. Rigo, G. Amsel, and M. Croset, *J. Appl. Phys.*, **47**, 2810 (1976).
13. C. Weissmantel, *Thin Solid Films*, **32**, 11 (1976); H. J. Erler, G. Reisse, and C. Weissmantel, *ibid.*, **65**, 233 (1980).
14. T. Tsujide, M. Nojiri, and M. Kitagawa, *J. Appl. Phys.*, **51**, 3 (1980).
15. A. D. Yadav and M. C. Joshi, *Thin Solid Films*, **59**, 313 (1979).
16. D. Bouchier, G. Gautherin, B. Agius, and S. Rigo, *J. Appl. Phys.*, **49**, 12 (1978).
17. H. F. Winters, in "Topics in Current Chemistry," Vol. 94, S. Veprek and M. Venugopalan, Editors, New York (1980).
18. C. B. Lucas, *Vacuum*, **23**, 11 (1972).
19. W. K. Chu, J. N. Mayer, M. A. Nicolet, T. M. Buck, G. Amsel, and F. Eisen, *Thin Solid Films*, **17**, 1 (1973).
20. S. Rigo, C. Cohen, A. L'hoir, and E. Backelandt *Nucl. Instr. Methods*, **149**, 721 (1978). New York (1973).
21. G. Amsel and D. David, *Rev. Phys. Appl.*, **4**, 383 (1969).
22. J. P. Biersack, "Ion Surface Interaction Sputtering and Related Phenomena," Gordon and Breach, New York (1973).
23. J. Lindhard, M. Scharff, and M. E. Schiott, *Mater. Fys. Medd.*, **33**, 14 (1963).
24. P. Sigmund, *Phys. Rev.*, **184**, 2 (1969).
25. D. Bouchier, Ph.D. Thesis, Université Paris XI Orsay, France (1977).
26. J. Bottiger, J. A. Davies, P. Sigmund, and K. B. Winterbon, *Radiat. Eff.*, **11**, 69 (1971).
27. C. Carter, D. G. Armour, S. E. Donnely, D. C. Ingram, and K. P. Webb, *ibid.*, **53**, 143 (1980).
28. H. F. Winters, *J. Chem. Phys.*, **44**, 1472 (1966).

Sputter-Etching Planarization for Multilevel Metallization

H. Kotani, H. Yakushiji, and H. Harada

Computer Development Laboratories Limited, 4-1 Mizuhara, Itami, Hyogo 664, Japan

and K. Tsukamoto* and T. Nishioka

Mitsubishi Electric Corporation, LSI Research and Development Laboratory, 4-1 Mizuhara, Itami, Hyogo 664, Japan

ABSTRACT

A simple process of sputter-etching planarization was developed for multilevel metallization, which utilized an angular dependence of sputter yield. Silicon nitride and phosphosilicate glass as interlevel insulators were planarized to a slope angle of 45° by using rf sputter etching with an argon gas. The surface topology was well predicted by computer simulation. The sputter-etching planarization was successfully applied to three-level metallization, resulting in very high yields of interconnection continuity, interlevel insulation, and via holes.

Planar surfaces become increasingly important in LSI's, especially in multilevel interconnections for the demand of higher packing density. Since the existence of topographic steps extremely restricts minimum feature size, and reduces metallization yield and reliability, extensive works have been devoted to achieve planarization (1, 2, 3). Among them, it is a well-known technique to flow phosphosilicate glass (1), which cannot, however, be applied to aluminum-aluminum interconnections because of its higher temperatures required. Recently, other methods have been studied for low-temperature processing. For example, films covering stepped surfaces were coated with photoresist and then removed by either plasma etching (2) or ion beam etching (3) under the same etching rate for the film and the resist. Although this process provides very smooth surfaces, it was complicated and difficult to control the etching condition which depends on the film material.

Sputter etching is a commonly used technique to delineate fine patterns. A number of papers have reported on the change of surface profiles by ion bombardment (4-10). The etched profiles are mainly determined by an angular dependence of sputter yield, which results in sloping walls. It is the purpose of this paper to provide a simple process for planarization utilizing the angular dependence of sputter etching. The evolution of surface profiles of silicon nitride and phosphosilicate glass films is presented and compared with the results of a computer simulation. In order to evaluate the planarization effect, the technique is then applied to three-level metallization.

Computational Model

The basic mechanism of the sputter-etching planarization is based on the fact that the sputter-etching rate depends on the angle of ion incidence. Since substrates are normally bombarded by ions in an rf sputtering system, the etching rate is different at various locations on the surface due to its original topology, which results in a continuous modification of the profile. A computer simulation of the surface profile was performed in a similar manner which Lehmann reported as follows (10).

The variation of the sputter yield, as a function of the angle of incidence with respect to the surface normal, is written by the following analytical expression

$$S(\theta) = \alpha \cos\theta + \beta \cos^2\theta + \gamma \cos^4\theta \qquad [1]$$

where α, β, and γ are the constants given by the boundary conditions as

$$S(0°) = 1, \left.\frac{dS}{d\theta}\right|_{\theta = 45°} = 0, \text{ and } S(45°) = Sp \qquad [2]$$

Key words: multilevel metallization, planar metallization, surface coverage, sputtering.

This function $S(\theta)$ has a maximum of Sp at an angle $\theta = 45°$. Figure 1 plots these functions for $Sp = 3.3$ and 5.0.

The original profile is expressed by the curve as shown in Fig. 2, where D is the step height, and the corners at the step region are approximated by circles

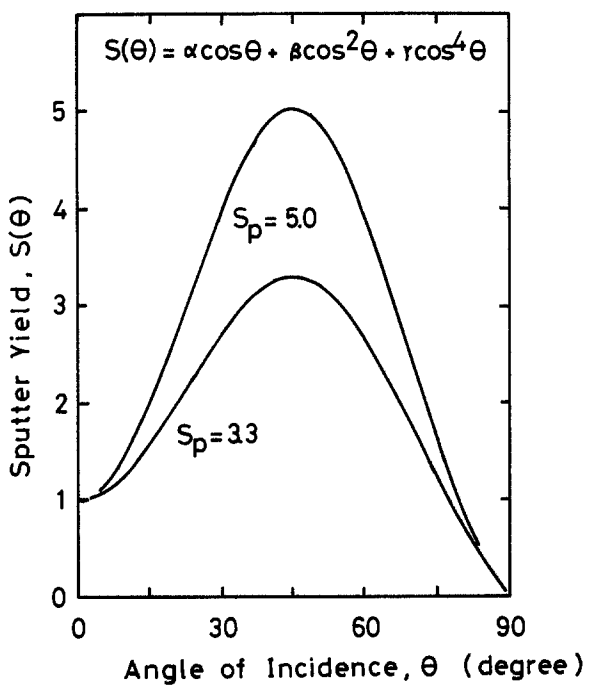

Fig. 1. Sputter yield as a function of angle of ion incidence for $Sp = 3.3$ and 5.0.

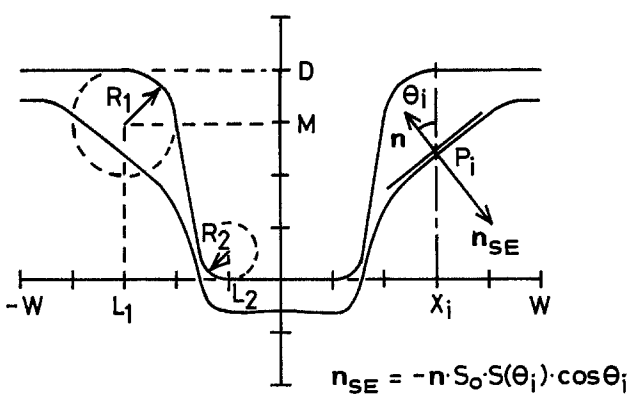

Fig. 2. Schematic illustration of evolution of surface profile due to sputter etching.

with radii R_1 at the top and R_2 at the bottom. These parameters, D, R_1, R_2, L_1, L_2, and M, are determined by tracing the original topology. The profile is approximated at all times by the same number of segments connecting a finite number of points P_i, where $i = 1, \ldots, 80$. As indicated in Fig. 2, the sputter etching causes the points P_i to move by the amount and the direction as

$$\mathbf{n}_{SE} = -\mathbf{n} \cdot S_0 \cdot S(\theta_i) \cdot \cos\theta_i \qquad [3]$$

where $\mathbf{n}$ is a unit vector of the surface normal and S_0 is the sputter yield for unit cycle when $\theta_i = 0°$. A new profile is then given by the shifted segments. In our simulations, the sputter-etched materials are assumed to be homogeneous and isotropic. Although the effect due to redeposition of sputtered materials might affect the etched profiles and become increasingly significant with decreasing feature size, the redeposition is a secondary effect, and is neglected in the present simulations. This point will be discussed later.

Experimental

Aluminum alloy films, Al-Si and Al-Si-Cu, were formed by d-c planar magnetron sputtering for interconnections. Silicon nitride films (P-SiN) and phosphosilicate glass films (LP-PSG) were utilized for interlevel insulators. P-SiN were deposited by a plasma CVD technique at 300°C, employing SiH_4 and NH_3 gases diluted with an inert gas. LP-PSG were deposited by a low pressure CVD technique at 430°C, using SiH_4, O_2, and PH_3 gases diluted with an inert gas. The via holes in P-SiN were opened by plasma etching employing a gas mixture of CF_4 and O_2, while those in LP-PSG by chemical wet etching using an HF solution. The surfaces were planarized by rf sputter etching using an Ar gas in the following conditions: a distance between parallel plate electrodes was 2.5 cm, an argon pressure was 1.7 Pa, and an rf power density was 0.5 W/cm^2. These conditions were mainly decided by the performance of the sputtering apparatus. The chosen argon pressure and the rf power density provided a stable rf plasma and uniform etching rates. The etching rates of Al, P-SiN, and LP-PSG were about 100, 70, and 60 A/min, respectively. During the sputter etching, the temperature of samples rose to above 200°C.

Results and Discussions

Figure 3 shows cross-sectional SEM pictures of as-deposited P-SiN, with a thickness of 1.47 μm covering 0.72 μm of patterned Al-Si, and those after sputter etching. It can be clearly seen that the facet with an angle of 45° develops and the surface is planarized. The etching rate of 67 A/min was obtained at the flat areas on metal lands.

The simulated profiles were then compared with the experimental ones as shown in Fig. 4, where we set $Sp = 3.3$ and $S_0 = 0.02$ μm, which corresponds to an etch time of 3 min. A fairly good agreement was obtained between the calculated and experimental results, which indicates that the analytical expression $S(\theta)$ employed is very similar to the actual sputter yield function. The only difference is observed at the bottom of the steps, where the actual etched depth is shallower than the calculated one. This would be attributed to redeposition of sputtered P-SiN, and was not observed when the width of the groove was larger than 5 μm. The effect of redeposition causes the limitation of ion etching, while it is advantageous for planarization because the step height decreases. In the case of the example shown in Fig. 4, the initial step height of 0.93 μm was reduced to 0.83 μm during sputter etching of 30 min by the redeposition effect.

Similar results were also obtained for LP-PSG. LP-PSG films exhibited poorer step coverage than P-SiN films, and the step angle made by the LP-PSG going over an Al step was larger than 90°, *i.e.*, a negative slope. Even if the slope angle was negative as in the

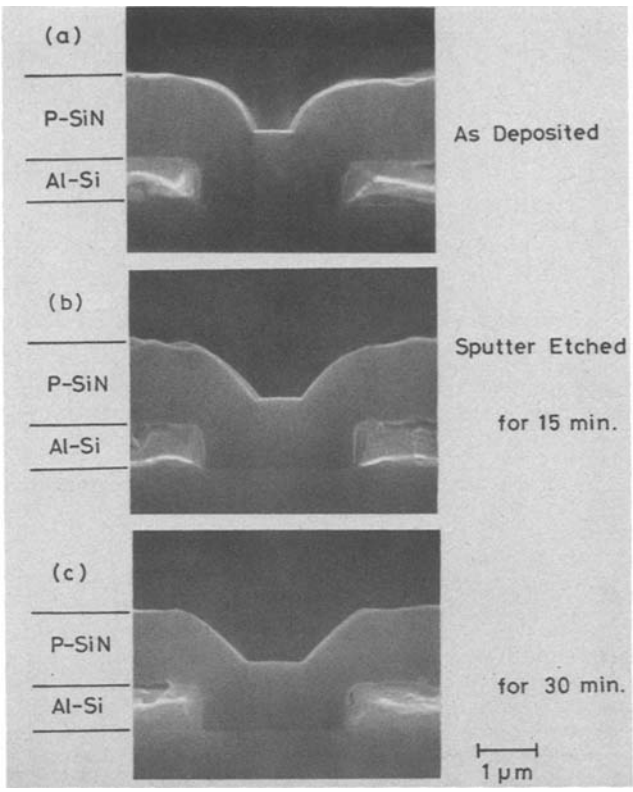

Fig. 3. Experimental evolution of profile for P-SiN covering patterned Al-Si steps. (a) Original profile. (b) After sputter etching for 15 min. (c) After sputter etching for 30 min.

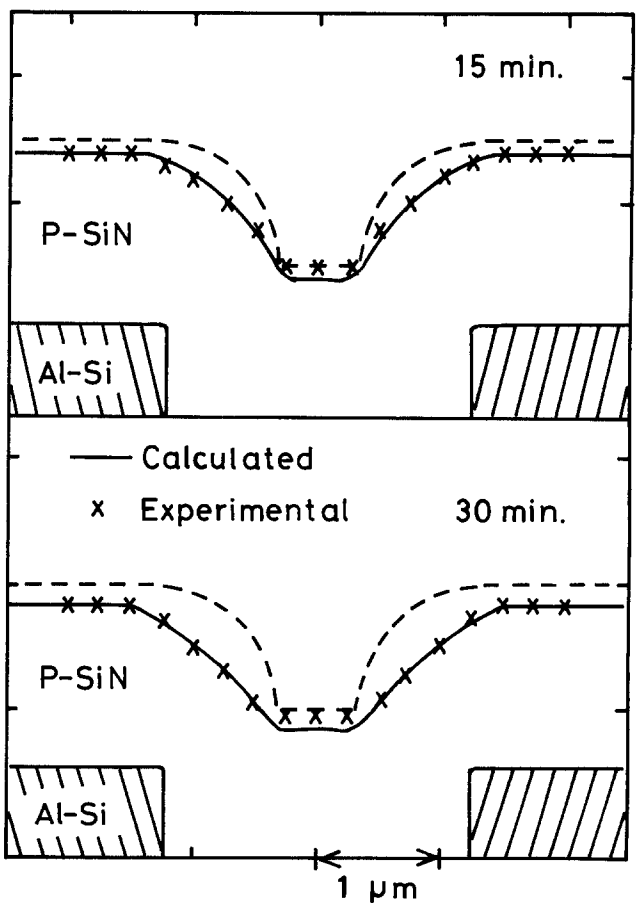

Fig. 4. Calculated evolution of profile corresponding to Fig. 3. Dotted line and X indicate original profile and experimental results on profile traces, respectively.

case of LP-PSG, sufficiently long etching time, say 60 min, resulted in a gentle slope with a step angle of 45°.

In order to evaluate the sputter-etching planarization, this technique was applied to three-level metallization. The process flow is summarized in Fig. 5. The deposition of sputtered Al films follows immediately after the sputter-etching process in the same apparatus, which leads to an additional advantage of a good step coverage of the metal, since the sputter etching causes the temperature rise of samples as mentioned above. Figure 6 shows a result of a test pattern of the three-level metal structure, where the coverage is relatively smooth due to the sputter-etching planarization. Figure 7 shows a cross-sectional SEM micrograph of a via hole between the first and second level metals. It can be seen that the sloped contour of the via sidewall provides a good step coverage of the second level conductor pattern. It also can be seen that the first level metal of about 0.3 μm is etched at the via by the planarization process.

The test chip was also used to determine crossover continuity yield, via hole yield and insulation yield. The structures and a typical set of results are listed in Table I, where the almost 100% yields have proved the usefulness of the planarization process. Although the size of the first via hole was 3 × 3 μm^2 and the contact resistance would be sensitive to the effect of redeposition, there was no difference observed between the contact resistances with and without the sputter-etching planarization. This is probably because the Al contact surface is sufficiently etched during the planarization process as mentioned above, so that the amount of the redeposited dielectrics onto the contact surface is negligible. The contact resistance of the second via hole, the size of which 10 × 10 μm^2, was not affected by the redeposition effect. The present sputter-etching planarization did not degrade the contact resistances of the via holes. Also the electrical characteristics of transistors were not affected by the sputter etching.

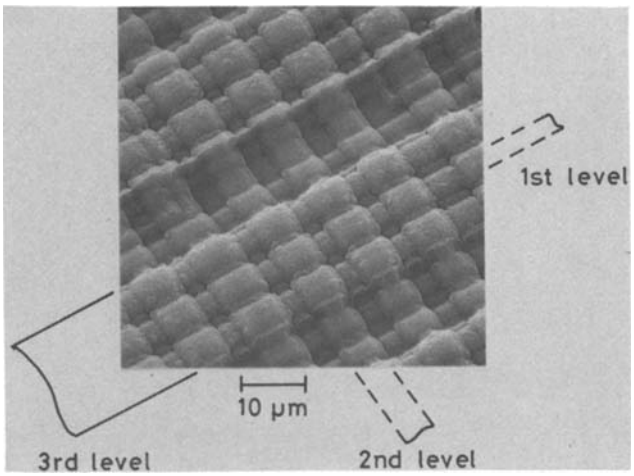

Fig. 6. 3rd-level metal coverage over 1st- and 2nd-level metals

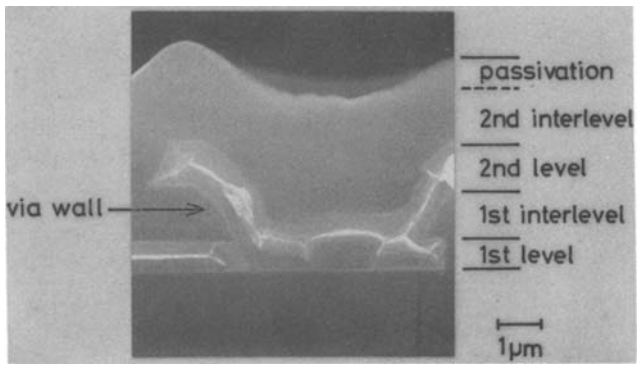

Fig. 7. 2nd-level metal coverage over via hole to 1st-level metal

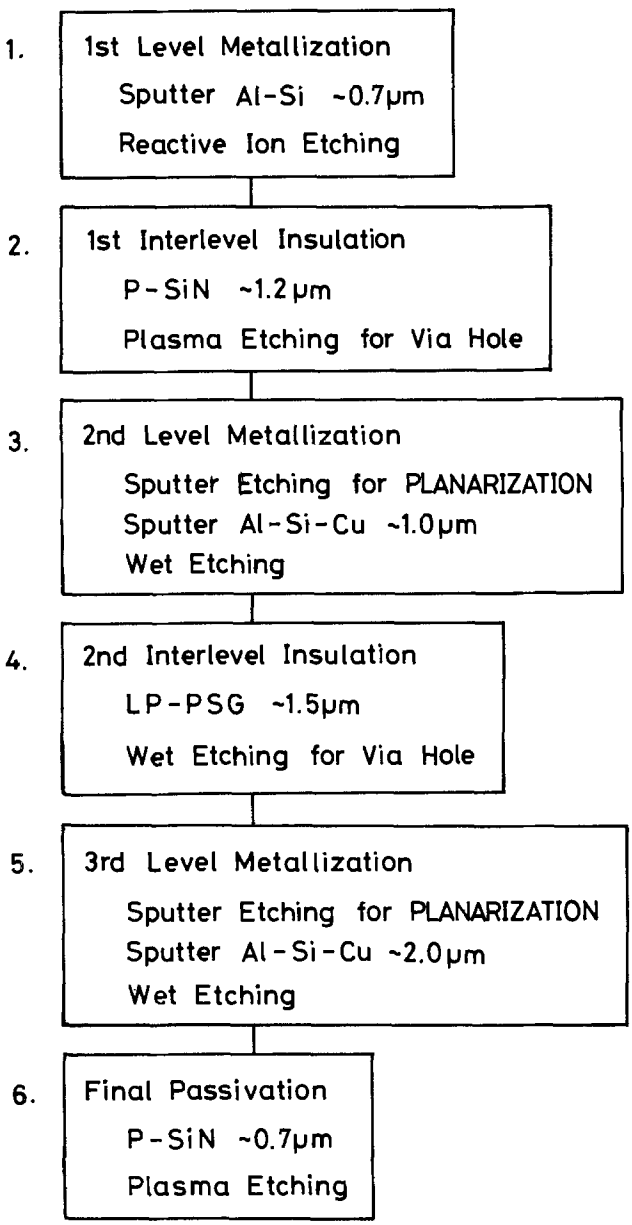

Fig. 5. Process flow and parameters for three-level metallization

Summary

The angular dependence of rf sputter etching was utilized to achieve planarization. The slope angle of 45° was obtained for P-SiN and LP-PSG as interlevel insulation films by sputter etching with an argon gas, an angle of which was determined by the angular variation of the sputter yield for the materials. Also the step height was slightly reduced, due to redeposition when the width of the groove was narrower than a few μm. The sputter-etching process has been successfully applied to three-level metallization, resulting in very high yields for interconnection continuity, interlevel insulation, and via holes. No effect on device characteristics was observed after the planarization process.

Although the slope angle obtained is relatively large, around 45°, due to the physical properties of the sputtered materials, the sputter-etching planarization for multilevel metallization appears to be of great advantage. It should be noted that the planarization process is extremely simple, and the subsequent metallization could be continuously carried out after the planar-

Table I. Structures of test patterns and resultant yields

Test	Structure			Average resistance (Ω)	Yield (%)
Metal integrity	Width (μm)	Space (μm)	Length (cm)		
1st level	3	3	15	2740	99
2nd level	5	4	10	847	99
3rd level	20	10	3	33.4	100
Interlevel insulation	Area (mm^2)				
1st to 2nd	1.8				99
2nd to 3rd	1.7				96
Via hole	Area (μm × μm)	Number			
1st to 2nd	3 × 3	1600		372*	97
2nd to 3rd	10 × 10	300		11.6*	100

* The resistance of Al interconnection is included.

ization in the same sputtering apparatus. The technique should be applicable to a wide variety of materials.

Acknowledgments

The authors would like to thank Dr. H. Oka, Dr. H. Nakata and Mr. T. Etoh for their helpful discussions and encouragements.

Manuscript submitted July 12, 1982; revised manuscript received Nov. 12, 1982.

Any discussion of this paper will appear in a Discussion Section to be published in the December 1983 JOURNAL. All discussions for the December 1983 Discussion Section should be submitted by Aug. 1, 1983.

Publication costs of this article were assisted by Computer Development Laboratories, Limited.

REFERENCES

1. W. E. Armstrong, *This Journal*, **121**, 307 (1974).
2. A. C. Adams, *Solid State Technol.*, **24**, 178 (1981).
3. L. F. Johnson, K. A. Ingersoll, and D. Kahng, *Appl. Phys. Lett.*, **40**, 636 (1982).
4. A. R. Bayly, *J. Mater. Sci.*, **7**, 404 (1972).
5. C. Catana, J. S. Colligon, and G. Carter, *ibid.*, **7**, 467 (1972).
6. D. J. Barber, F. C. Frank, M. Moss, J. W. Steeds, and I. S. Tsong, *ibid.*, **8**, 1030 (1973).
7. G. Carter, J. S. Colligon, and M. J. Nobes, *ibid.*, **8**, 1473 (1973).
8. T. Ishitani, M. Kato, and R. Shimiza, *ibid.*, **9**, 505 (1974).
9. J. P. Ducommun, M. Cantagrel, and M. Moulin, *ibid.*, **10**, 52 (1975).
10. H. W. Lehmann, L. Krausbauer, and R. Widmer, *J. Vac. Sci. Technol.*, **14**, 281 (1977).

Langmuir Probe Measurements on CHF_3 and CF_4 Plasmas: The Role of Ions in the Reactive Sputter Etching of SiO_2 and Si

Ch. Steinbrüchel

Laboratories RCA Limited, CH-8048 Zürich, Switzerland

ABSTRACT

Langmuir probe measurements on CHF_3, CF_4, CF_4-H_2, and CF_4-O_2 plasmas with concurrent etch rate measurements on SiO_2 and Si have been made in a reactive sputter etching system. At an rf power of 300W and a pressure of 15 mTorr, the ion density is typically 1.5×10^{10} cm^{-3}, the electron temperature 2 eV, the plasma potential 30 eV, and the ion energy (*i.e.*, the sheath potential) of the order of 500 eV. The dependence of these parameters on rf power, pressure, reactor geometry, and plasma gas composition is investigated, as well as the spatial uniformity of the plasma. For SiO_2, etch rates vary essentially in proportion to ion densities with all the different plasmas. For Si in CF_4-O_2 plasmas, the anisotropic part of the etch rate also parallels the ion density. From the measured ion densities the ion flux to the substrate is estimated. Thus, etch rates per ion can be determined, which turn out to be similar to those in reactive ion beam etching, although in reactive sputter etching ion energies are much smaller.

Dry processing is replacing more and more wet chemical methods in the fabrication of microelectronic devices, the reason being that dry methods allow for better dimensional control of structures to be formed in different materials.

For Si-based materials, dry processing occurs in a plasma of a reactive gas such as CF_4 or CHF_3. A large number of processes have been developed to etch a particular material selectively over another, with etching being preferably anisotropic at the same time (1). Yet information on the details of the chemical mechanisms underlying the various processes is still rather incomplete (1-3).

Key words: semiconductor, integrated circuits, discharge, sputtering.

The main difficulty in understanding dry etching processes at the molecular level stems from the fact that a reactive plasma is a complex mixture of interacting chemical species. Ions may remove material physically from the substrate, or they may react chemically with the substrate, or they may promote chemical reactions of the substrate with other gas phase species such as atoms and radicals. Not only is it difficult to measure the concentrations and reactivities of the various species, but the plasma composition also depends in a complicated manner on the external operating parameters.

Nevertheless, a coherent picture is beginning to emerge of the important qualitative aspects of dry etching, mostly from relating etch rate data to optical

(4-9) and mass-spectrometric measurements (8-14) on plasmas. The connection between the state of an etched surface and etching conditions has also been investigated (15, 16). For Si and SiO_2, the major characteristics of dry etching may be summarized very briefly from the literature as follows (1-3): A dry-etch process must yield only volatile products. In a fluorine-based plasma, F atoms are the main etchant for Si, but are probably less important for the etching of SiO_2. Selective etching of SiO_2 over Si requires a fluorine-deficient plasma. Anisotropic etching is related to the impact of ions on the substrate. Plasma conditions must be chosen such that no deposition of polymeric material on the substrate can occur.

It is the purpose of this paper to establish more clearly the role of ions in reactive sputter etching (36) [sometimes also called reactive ion etching (1)]. To this end we present Langmuir probe measurements of ion densities and electron temperatures in etching plasmas, and we relate these to concurrent etch rate measurements. Specifically, we study the etching of SiO_2 and Si in CHF_3, CF_4, CF_4-O_2, and CH_4-H_2 plasmas. In the process we are able to estimate plasma potentials, average ion energies, and ion fluxes onto the substrates. We discuss our results in relationship to previous work using other plasma-diagnostic techniques, and in relationship to recent results on reactive ion beam etching.

Langmuir Probe Plasma Diagnostics

A Langmuir probe is a simple well-known device (17) consisting of a small electrode in contact with the plasma. The basic measurement involves recording the current to the probe, I_p, as a function of the applied potential, V_p. Fom this type of measurement, information can be gained on the plasma ion density and electron temperature.

In spite of their simplicity, Langmuir probes have been used only rarely in connection with sputtering-type plasmas. This is due partly to experimental difficulties in obtaining reliable measurements (see section on experimental arrangement), and partly to problems in interpreting such measurements (see below). Langmuir probe experiments have been reported to map out the dark space in a discharge (18), to demonstrate the effect on the plasma potential of a positive electrode in contact with the plasma (19), and to determine ion densities and electron temperatures in an Ar discharge (20, 21). Langmuir probes were used also to compare qualitatively CF_4 and NF_3 discharges (22), to determine electron temperatures and estimate ion fluxes in plasma mixtures of He with other gases including F_2 (12), and to obtain electron densities in CF_4 plasmas (37).

Qualitatively it is straightforward to explain the current *vs.* potential characteristic of a Langmuir probe (21, 23, 24) (see also Fig. 1 and 2). At large negative potential, a sheath of positive ions forms around the probe such that only ions are collected, and electrons are repelled. In the transition region of small negative potential where the slope of the characteristic changes rapidly, the probe acts as an energy selector for electrons, and ions and electrons contribute in comparable measure to the probe current. At large positive potential the probe current consists only of electrons. The electron saturation current is much larger than the ion saturation current because of the higher mobility of electrons.

For the purpose of quantitative description it is easiest to deal with the electron current in the transition region (23, 24). There the probe reduces the electron density in its vicinity such that for a thermal electron distribution at a temperature T_e

$$I_e = eN_eA\,(kT_e/2\pi M_e)^{1/2} \exp X \qquad [1]$$

In [1] N_e is the electron density in the bulk plasma, A the probe area, M_e the electron mass and X a dimensionless potential defined as

$$X = e(V_p - V_s)/kT_e \qquad [2]$$

where V_p is the potential applied to the probe, and V_s is the local plasma potential. Thus, a plot of log I_e *vs.* V_p should give a straight line with a slope inversely proportional to T_e.

It is much more difficult to describe quantitatively the ion saturation region, at large negative V_p (23, 24). The difficulty arises because the positive ion sheath shields the probe only incompletely. A small but significant tail of the probe potential extends to large distances. At the same time, the ion density at the sheath edge is depressed somewhat with respect to the bulk of the plasma, and ions enter the sheath with a mean energy of about kT_e. Consequently, the simple Langmuir theory for ion collection assuming a sharp sheath edge (23) does not hold, and one must resort to elaborate numerical computation for obtaining the ion current as a function of the probe potential.

Comprehensive numerical results have been presented by Laframboise in a form useful to the experimenter (24, 25). First we note that a typical plasma in reactive sputter etching is collisionless: the mean free path for charged particle-neutral collisions is of the order of 1 cm, and thus much larger than the Debye length λ_D

$$\lambda_D = (kT_e/4\pi N_e e^2)^{1/2} \qquad [3]$$

which turns out to be of the order of 10^{-2} cm. Furthermore, the ions in the bulk plasma are close to room temperature (~0.1 eV), whereas T_e is typically a few eV. For such a plasma and a cylindrical probe of radius r_p, Laframboise represented the ion current I_i as

$$I_i = eN_iA\,(kT_e/2\pi M_i)^{1/2} i_i \qquad [4]$$

where N_i is the ion density in the bulk plasma, A the probe area, M_i the ion mass, and i_i a dimensionless current depending on r_p/λ_D and on the potential X, but only weakly on the ion temperature T_i. Moreover, from Laframboise's results, one can infer that as long as $r_p/\lambda_D \lesssim 3$ and $T_i/T_e << 1$

$$i_i^2 = 1.27(-X) \qquad [5]$$

to within about 3%. Thus, from [4] and [5], I_i^2 will be a linear function of the probe potential V_p with a slope determined by the ion density N_i

$$-\Delta(I_i^2)/\Delta V_p = 0.20e^3N_i^2A^2/M_i \qquad [6]$$

The plasma potential V_s can be deduced if one notes that at the floating potential X_f, electron and ion currents to the probe are equal (23, 24). Upon combining [1], [4], and [5], and assuming $N_i = N_e$, one finds that X_f must satisfy the equation

$$1.1\,(M_e/M_i)^{1/2}(-X_f)^{1/2} = \exp X_f \qquad [7]$$

Hence, X_f can be calculated as the solution of [7]. [For example $X_f = -4.8$ for a CHF_3 plasma and $X_f = -5.0$ for a CF_4 plasma.[1]] Then from [2] with $X = X_f$ (at $I_p = 0$)

$$V_s = V_p(I_p = 0) - kT_eX_f/e \qquad [8]$$

where $V_p(I_p = 0)$ is the potential applied to the probe at which the net probe current is zero. (It should be mentioned that in [8] a d-c shift, induced by the rf component of the potential between the probe and the plasma, is neglected [Ref. (37)]. This would imply a too negative $V_p(I_p = 0)$ as compared to X_f, and thus a somewhat too small V_s calculated from [8].)

Experimentally, one proceeds as follows: Having recorded an $I_p(V_p)$ curve, one determines first N_i from a plot of I_p^2 *vs.* V_p at large negative V_p, where $I_p = I_i$ (see Eq. [6]). Next, one extrapolates I_i into the transition region of $I_p(V_p)$ to obtain $I_e(V_p)$ as the difference

[1] We assume that CF_3^+ is the major ion in a CF_4 plasma, and CHF_2^+ in a CHF_3 plasma [see Ref. (3, 26)].

of I_p and I_i. A plot of log I_e *vs.* V_p will yield T_e (see [1]). The plasma potential V_s then follows from Eq. [7] and [8], together with the experimental value for $V_p(I_p = 0)$.[2]

Experimental Arrangement

The main components of our setup are a stainless-steel vacuum chamber pumped by a 1800 l/sec oil diffusion pump, and rf electronics by MRC, operating at 13.56 MHz, for maintaining a discharge in the chamber. The chamber is 42 cm in diam, and 24 cm in height, and acts as the grounded electrode for the discharge. The rf-driven electrode (or cathode) is made of copper, is watercooled, and covered by an SiO_2 plate, and is usually 38 cm in diam. It is also shielded at the edge by a dark space shield. The rf-induced d-c voltage is measured directly at the copper plate, via a low-pass filter. Several gases can be admitted independently to the chamber via flow controllers (Tylan FC-260). The pressure is measured by a baratron cell (MKS Type 170 M-6B). The pumping speed at the chamber can be varied with a home-built iris diaphragm.

Our Langmuir probe is similar in design to one by Eser *et al.* (21). It consists of a short piece of tungsten wire of 0.25 mm diam, soldered to a long piece of tungsten wire of 1 mm diam which, near the soldering joint, is sealed into a Pyrex tube of 5 mm diam. The thin probe wire is partially shielded by the glass tube, such that its length exposed to the plasma is 1 cm. The probe is connected via a tuned filter to a set of batteries with a voltage-dividing network, so that $I_p(V_p)$ characteristics can be recorded directly on an X-Y recorder, the reference electrode being the grounded vacuum chamber in contact with the plasma [cf. Ref. (21)].

In order to get reliable probe measurements, one needs to take certain short as well as long term precautions. First, if the probe is exposed to the plasma at floating potential, contamination can be noticed within a few minutes in a CHF_3 plasma, and within an hour even in an Ar plasma, since the probe characteristic becomes distorted in the transition region.[3] This is caused, presumably, either by material sputtered from the SiO_2 cathode (in Ar) or by polymers deposited from the plasma (in CHF_3). But if the probe is held at −180V between taking $I_p(V_p)$ traces, then ion bombardment is apparently sufficient to keep it clean, or at least in a reproducible condition, indefinitely in an Ar or O_2 plasma. In a CHF_3 plasma contamination still becomes noticeable after about an hour, but then the probe, at −180V, can be cleaned easily in an O_2 plasma. (A probe made out of a platinum wire turned out to be much more prone to contamination and more difficult to regenerate than the tungsten wire probe.) Unfortunately, the procedure for maintaining a clean probe has a side effect, in that the probe wire itself is being etched slowly. This brings about a noticeable decrease of the wire diameter over an extended period of time, thus affecting the effective probe area.

Effects of geometry on the discharge are investigated by comparing plasmas with cathodes of 38 and 15 cm diam. Also, the probe can be positioned either 4 or 12 cm above the center of the cathode, or it can be moved in a horizontal direction. (The cathode dark space in our experiments is typically 1-2 cm high.)

Samples to be etched are small (~1 cm^2) pieces of steam-grown SiO_2 or poly-Si ($\gamma = 0.05$) placed directly on the SiO_2 cathode plate. Etch rates are measured interferometrically using an He-Ne laser.

[2] Values for V_s thus obtained roughly agree with those using the point of electron current saturation, although that point is not too well defined (the "knee" in the $I_p(V_p)$ is not very pronounced, and the electron current does not really saturate). Also, in that region the probe draws enough current so as to get hot quickly and disturb the plasma.

[3] Similar contamination problems have been noted before [Ref. (18, 24)].

Results

In Fig. 1 to 3 we illustrate how to obtain ion densities N_i and electron temperatures T_e from recorded $I_p(V_p)$ curves. Figure 1 shows a set of representative $I_p(V_p)$ curves for a CHF_3 plasma at 11 mTorr pressure, and 14 sccm flow, with the probe close to the SiO_2-covered cathode (4 cm above the center). From these curves one can construct plots of I_p^2 *vs.* V_p (Fig. 2) and log I_e *vs.* V_p (Fig. 3) as described above. Clearly, the postulated straight-line relationships (cf. Eq. [1] and [6]) determining N_i and T_e are well obeyed. Also, one notes immediately the higher ion density and lower electron temperature at higher power.

On this basis, etching plasmas of several gases have been examined under various conditions. The results for CHF_3 etching SiO_2 are summarized in Fig. 4 to 7. At constant pressure and flow (Fig. 4), the etch rate R_e depends linearly on the rf power applied. The ion density N_i varies less strongly, being proportional to the square root of the power. Also, with decreasing power the electron temperature T_e increases markedly, whereas the ion energy E_i decreases mark-

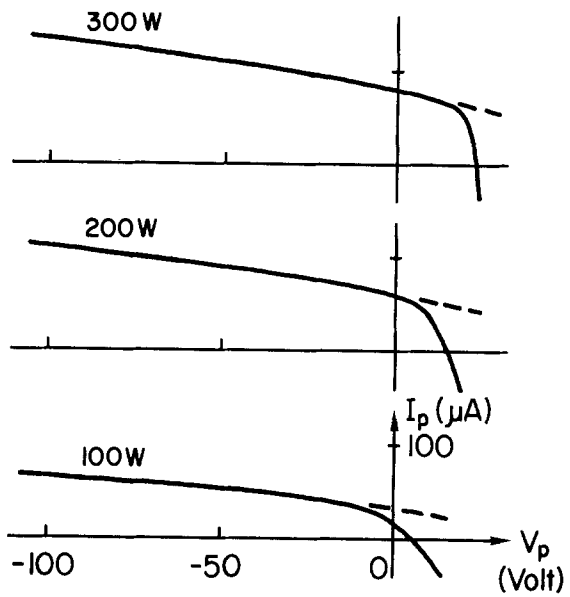

Fig. 1. Probe characteristics for CHF_3 at 11 mTorr and 14 sccm. Probe 4 cm above large cathode (see text). Dashed lines give extrapolated ion currents.

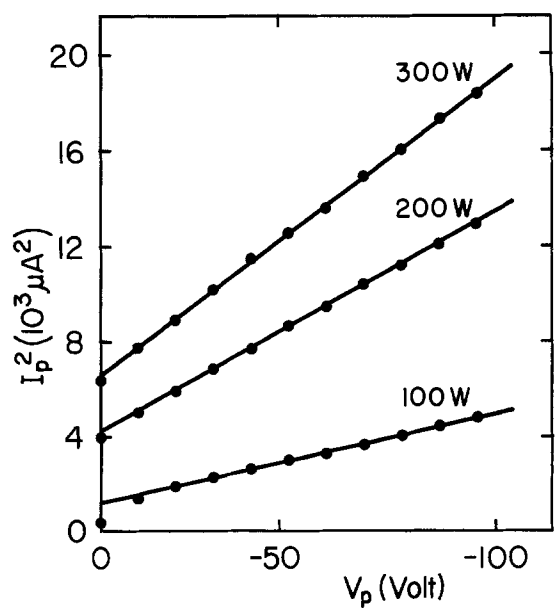

Fig. 2. Plots of I_p^2 *vs.* V_p from curves of Fig. 2

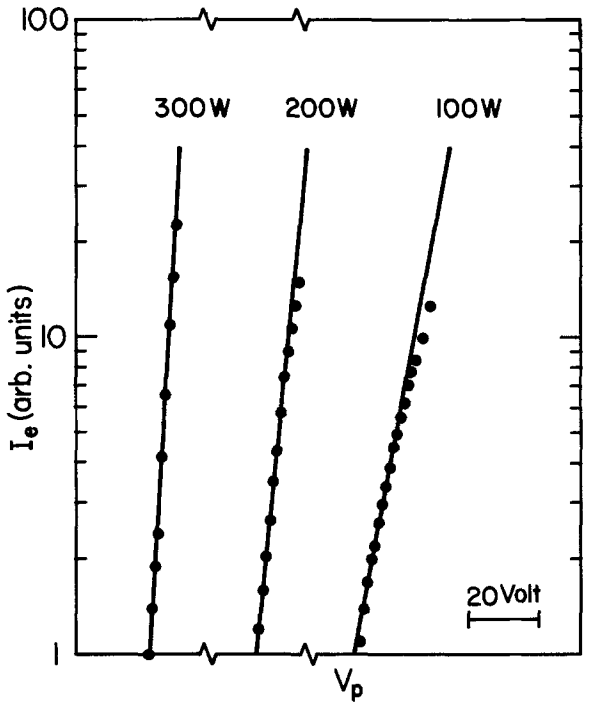

Fig. 3. Plots of log I_e (electron current) vs. V_p from curves of Fig. 1.

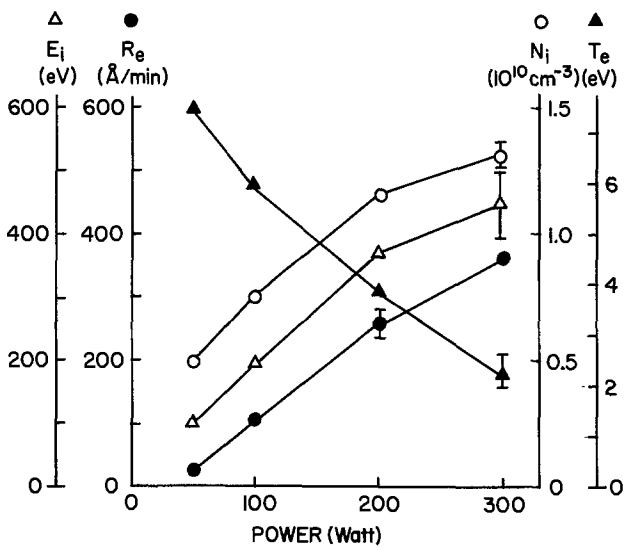

Fig. 4. Reactive sputter etching of SiO_2 in a CHF_3 plasma: plots of etch rate R_e, ion density N_i, electron temperature T_e, and ion energy E_i, vs. rf power. p = 10 mTorr, flow rate = 15 sccm. Probe 4 cm above large cathode.

edly. E_i is taken as the difference between the plasma potential V_s and the rf-induced d-c voltage at the cathode, V_{DC}. It is noteworthy that here, as well as in all other cases, variations in E_i are due mostly to changes in V_{DC}, V_s being quite constant. For the conditions of Fig. 4, V_s is about 30V, and V_{DC} varies between −400 and −70V, as the power varies from 300 to 50W. At constant power and flow but variable pressure, (Fig. 5), N_i, R_e, and E_i are fairly constant, whereas T_e increases strongly at lower pressure.

Certain geometrical aspects of the plasma are illustrated in Fig. 6 and 7. First, regarding the probe position, one consistently obtains somewhat higher values for N_i and T_e with the probe 4 cm rather than 12 cm above the center of the cathode (Fig. 6). Also, 4 cm from the edge of the cathode in the horizontal direction, N_i is typically 20% lower than in the center of the discharge. Figure 7 shows that for fixed external plasma parameters, R_e is considerably higher with the 15 cm than with the 38 cm diam cathode, even at a pressure where N_i is lower. Evidently, the major factor responsible for this difference is the ion energy which, in turn, is determined mostly by the induced d-c potential: For the small cathode $E_i \approx$ 1400V (V_{DC} = −1400V, V_s = 35V), and for the large cathode $E_i \approx$ 450V (V_{DC} = −400V, V_s = 30V), at 300W, regardless of the pressure. Interestingly, if with the small cathode the power is reduced (typically by a factor ~2.5) to the point where R_e is the same as with the large cathode, then N_i and E_i turn out to be very similar in the two cases.

Analogous results for a CF_4 plasma etching SiO_2 are displayed in Fig. 8 and 9. Overall, qualitative trends are very similar to those for a CHF_3 plasma.

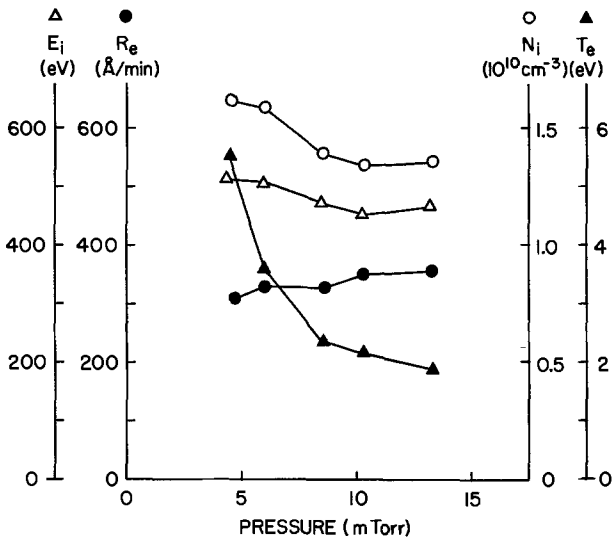

Fig. 5. Reactive sputter etching of SiO_2 in a CHF_3 plasma: plots of etch rate R_e, ion density N_i, electron temperature T_e, and ion energy E_i vs. pressure. RF power = 300W, flow rate = 15 sccm. Probe 4 cm above large cathode.

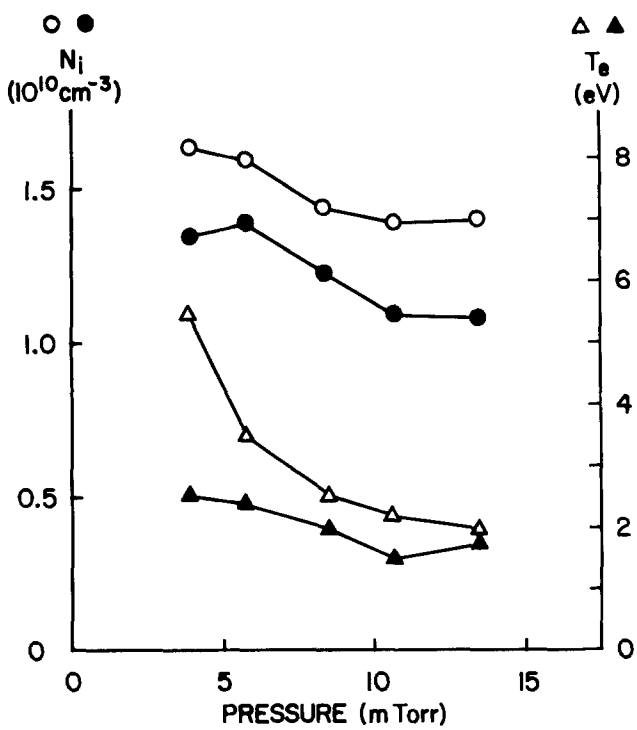

Fig. 6. Plots of ion density N_i and electron temperature T_e vs. pressure of CHF_3 with variable probe position. △, ○: probe 4 cm above large cathode; ▲, ●: probe 12 cm above large cathode. RF power = 300W, flow rate = 15 sccm.

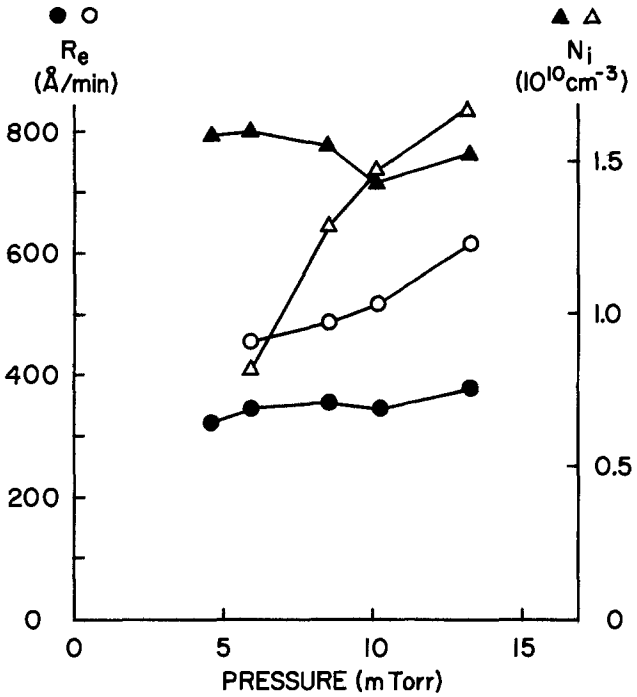

Fig. 7. Plots of ion density N_i and etch rate R_e of SiO_2 vs. pressure of CHF_3 with variable cathode size. ▲, ●: large cathode (38 cm diam); △, ○: small cathode (15 cm diam). RF power = 300W, flow rate = 15 sccm. Probe 4 cm above cathode.

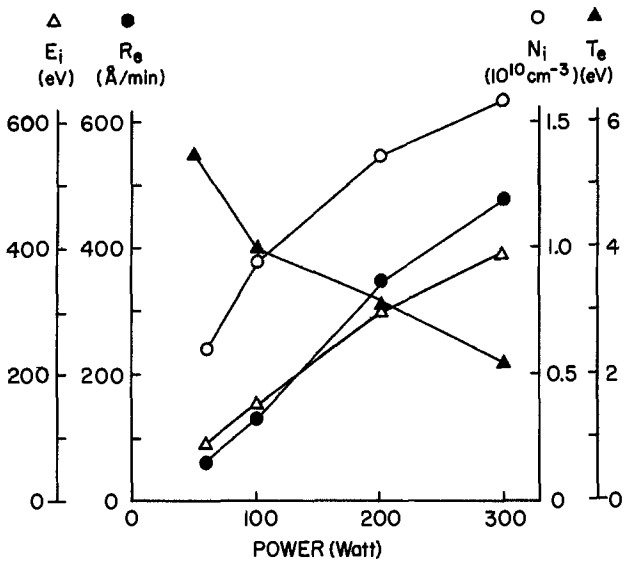

Fig. 8. Reactive sputter etching of SiO_2 in a CF_4 plasma: plots of etch rate R_e, ion density N_i, electron temperature T_e, and ion energy E_i, vs. rf power. p = 19 mTorr, flow rate = 19 sccm. Probe 4 cm above large cathode.

More specifically, with given external plasma parameters, R_e is about the same for the two gases, whereas N_i is slightly higher, and E_i slightly lower for CF_4 than for CHF_3. The effects in varying cathode size and probe position are the same as for CHF_3.

In Fig. 10-12 some mixtures of CF_4 with other gases are considered. In CF_4-H_2 mixtures, both N_i and R_e for SiO_2 decrease continuously with increasing H_2 content, whereas T_e is relatively constant (Fig. 10). On the other hand, in CF_4-O_2 mixtures N_i and R_e for SiO_2 exhibit a weak maximum at about 10% O_2 content, and T_e is increased markedly as soon as the plasma contains even a small amount of O_2 (Fig. 11). The etch rate for Si peaks much more sharply than that for SiO_2, but at about the same O_2 concentration (Fig. 12). Neither V_s nor E_i depend significantly on the gas com-

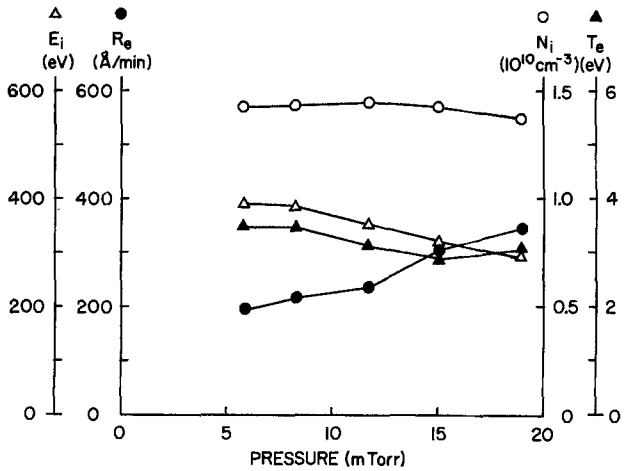

Fig. 9. Reactive sputter etching of SiO_2 in a CF_4 plasma: plots of etch rate R_e, ion density N_i, electron temperature T_e, and ion energy E_i vs. pressure. RF power = 200W, flow rate = 19 sccm. Probe 4 cm above large cathode.

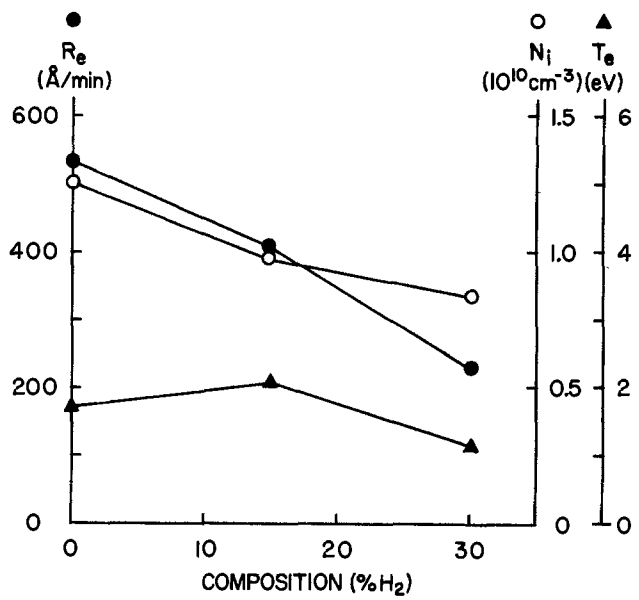

Fig. 10. Reactive sputter etching of SiO_2 in a CF_4-H_2 plasma: plots of etch rate R_e, ion density N_i, and electron temperature T_e vs. gas composition. RF power = 300W, p = 20 mTorr, flow rate = 24 sccm. Probe 12 cm above large cathode.

position. Our data on etch rates *vs.* composition agree with earlier work (8, 9, 27, 28).

Discussion

In the discussion of our work we wish first to address some practical issues related to obtaining reliable data. Second, we examine the properties of etching plasmas as they emerge from our results on the various microscopic plasma parameters. And third, we relate these parameters to etch rates, with a view on contributing to the ongoing discussion on etching mechanisms.

Experimental aspects.—Given a certain set of discharge parameters, the quantities best reproducible (*i.e.*, to within a few percent) are the ion density N_i and the etch rate R_e. Plots of I_p^2 *vs.* V_p determining N_i (Eq. [6]) indeed turn out to be accurately linear in the ion saturation region (cf. Fig. 2). A somewhat larger uncertainty is associated with the electron temperature T_e, a typical error being 10% for small values of T_e, less for larger values. Part of the reason for this is that T_e derives from the electron current I_e to the probe in the transition region (cf. Eq. [1]), where I_e is equal to the small difference $I_p - I_i$, and at the same time the probe is most sensitive to contamination (cf.

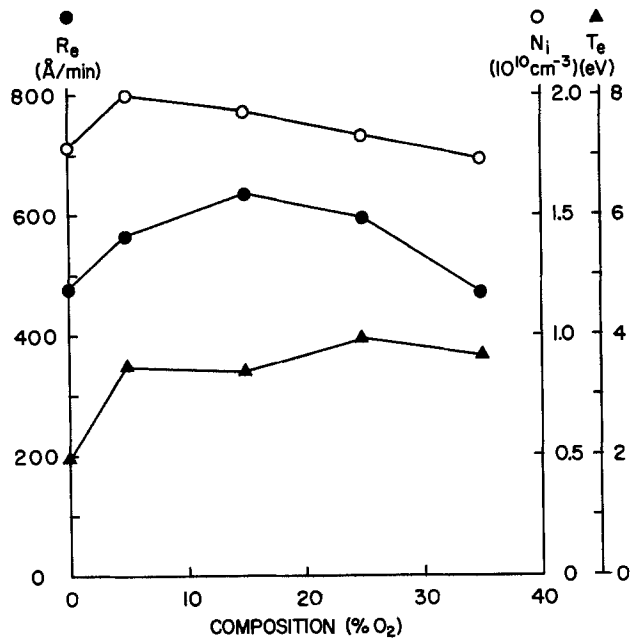

Fig. 11. Reactive sputter etching of SiO_2 in a CF_4-O_2 plasma: plots of etch rate R_e, ion density N_i, and electron temperature T_e vs. gas composition. RF power = 300W, p = 20 mTorr, flow rate = 20 sccm. Probe 4 cm above large cathode.

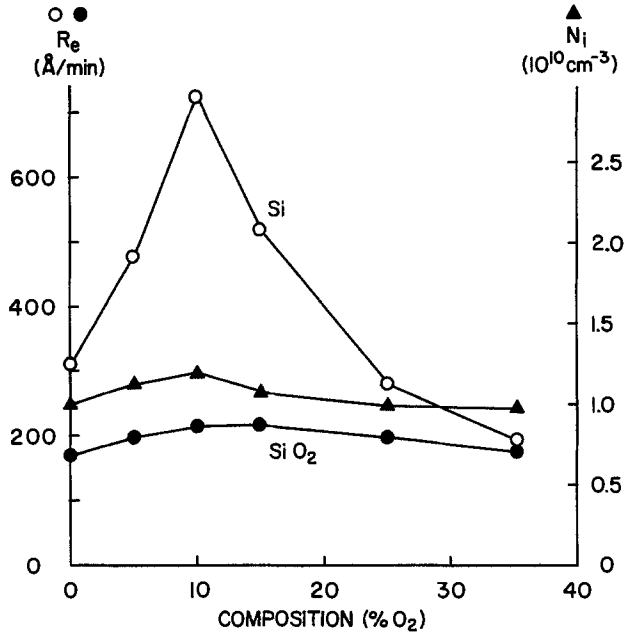

Fig. 12. Reactive sputter etching of SiO_2 and Si in a CF_4-O_2 plasma: plots of etch rates R_e and ion density N_i vs. gas composition. RF power = 100W, p = 20 mTorr, flow rate = 20 sccm. Probe 4 cm above large cathode.

Fig. 1). Nevertheless, log I_e usually is a linear function of V_p over at least a decade (cf. Fig. 3). The least reliable figures are those for the ion energy E_i, the reason being that E_i is largely a function of the induced d-c potential V_{DC} at the cathode, and the value of V_{DC} may vary appreciably on a day-to-day basis, depending on what gases have been used previously for etching, even though presputtering in O_2 is always done at the beginning of a run in order to clean the probe and the system. Furthermore, V_{DC} is measured at the copper cathode, whereas the sample is put on the SiO_2 plate on top of the copper cathode. However, the trends shown in the figures for the various quantities are observed consistently, and are thus believed to be representative of the plasma conditions investigated.

Plasma properties.—Our results show, as expected, that at a given pressure and flow, higher rf power leads to higher ion density N_i for both CHF_3 and CF_4 (Fig. 4 and 8). The highest values measured for N_i, around 1.5×10^{10} cm^{-3} at 300W, correspond to a degree of ionization of about 10^{-4}. Also, a high value for N_i always seems to go with a low value for T_e. This is somewhat contrary to expectations (1, 12), since ions are said to be produced by electrons from the high-energy tail of the distribution, and such electrons will be more numerous at higher T_e. The apparent contradiction may be resolved if one does not think in terms of a certain electron energy distribution giving rise to a certain ion density. Rather, one should see the plasma as maintaining a dynamic balance between electrons and ions, such that N_i, T_e, the sheath potential, as well as the cross sections and mean free paths for ionizing and other (inelastic or elastic) collisions, are all interdependent. Further insight into this contradiction might be gained from computational modeling, as described by Kushner (37).

With regard to the general validity of our analysis, we note that the plasma conditions investigated in our experiments typically range from $N_i = 1.5 \times 10^{10}$ cm^{-3}, $T_e = 2$ eV at high power (300W), to $N_i = 0.5 \times 10^{10}$ cm^{-3}, $T_e = 7$ eV at low power (50W). Thus the Debye length λ_D, Eq. [3], varies between 0.9×10^{-2} cm and 3×10^{-2} cm. and with the radius r_p of the probe wire equal to 0.0125 cm. one has $1.4 \geqq r_p/\lambda_D \geqq 0.4$. This means that the condition for I_i^2 to be proportional to X, $r_p/\lambda_D \lesssim 3$, is well fulfilled in all cases.

For fixed power and flow but variable pressure p, the ion density N_i, the plasma potential V_s, and the ion energy E_i are all fairly independent of p, whereas the electron temperature T_e tends to increase at lower p, particularly for CHF_3 (Fig. 5 and 9). Here again, a complicated interaction of various plasma processes manifests itself, in that a higher p does not necessarily produce a higher N_i (2) but, apparently, at lower p the increased mean free path of electrons, and thus the higher electron energy, compensate for the lower gas density as far as the creation of ions is concerned. It is worth noting that the behavior of T_e *vs.* p parallels the pressure-dependence of the excitation efficiency, as determined from optical emission measurements (5). Also, our values for the plasma potential V_s (~30V) are comparable to those observed in similar experiments at low p (~10 mTorr) (10, 12), but are much lower than values quoted for plasmas at higher p (>100 mTorr) (29).

In all experiments we have observed very little influence of the flow rate, at constant power and pressure, on the plasma parameters N_i, T_e, V_s, within a range of flow rates of 10-25 sccm.

Certain geometrical properties of the plasma can be inferred from the results obtained with different probe positions and different-sized cathodes. With the probe 12 cm away from the cathode, N_i and T_e are consistently lower than with the probe 4 cm from the cathode (Fig. 6). This slight inhomogeneity of the plasma can be explained if one notes that in the far position, the probe is certainly some distance into the negative glow, at which point electrons have undergone several more collisions than at the near position close to the dark space. If one moves the probe closer to the cathode yet, into the dark space, then a decrease of N_i becomes apparent.

The size of the cathode affects the plasma properties in subtle ways which cannot be explained easily. Whereas the plasma potential V_s is quite independent of cathode size, the induced d-c potential V_{DC} is considerably larger at the small cathode. However, the ratio of voltages at the powered and unpowered electrode varies much less strongly than the fourth power of the area ratio of the unpowered and powered electrode (29, 30). Also, with a small cathode, the ion density N_i changes roughly as the pressure p for both

CHF_3 (Fig. 7) and CF_4, but with the larger cathode, N_i is quite independent of p (Fig. 5-7, 9). Furthermore, we have seen evidence for an electron energy distribution corresponding to two different temperatures (~1 eV and ~4 eV) in a CF_4 plasma with the small cathode.

The most interesting features of CF_4-O_2 plasmas are a slight but clear maximum of N_i at around 10% O_2 content and a significant increase in T_e at even lower O_2 concentration (Fig. 11). At 35% O_2 N_i is still as high as in pure CF_4, and T_e is unchanged with respect to its value at 5% O_2 (Fig. 11). Thus, the addition of O_2 to CF_4 neither cools the electron distribution (5, 8), nor does it reduce the electron density if one assumes approximate charge neutrality (6). Furthermore, even at 35% O_2, the character of the plasma is still strongly determined by CF_4, in contrast to what was observed in the afterglow of a 2450 MHz discharge (13). (For a pure O_2 plasma at the conditions of Fig. 12 $N_i = 1.5 \times 10^{10}$ cm^{-3} and $T_e = 1.5$ eV.)

Etching mechanisms.—The importance of ions in many etching processes has, of course, been long recognized. In most instances, however, the evidence was indirect. For example, profiles etched in SiO_2 turned out to mirror the expected distribution of electric field lines in a reactor (31). Etching of Si and SiO_2 was typically faster and more anisotropic with the substrate on the driven, rather than on the grounded electrode (1, 10, 12), and was found also to depend on the coupling between the substrate and the electrode (32).

We believe that the present results establish, for the first time, a direct connection between ions in the plasma and etch rates for the case of SiO_2 etched in a CHF_3 or CF_4 plasma. The connection is simplest for CF_4-O_2 and CF_4-H_2 mixtures where, given no major variation of the relevant potentials, etch rates R_e and ion densities N_i (and thus ion fluxes) change proportionately (Fig. 10 and 12). The changes of R_e with rf power (Fig. 4 and 8) can also be understood via changes in N_i, if one allows for a slight dependence of R_e on the ion energy E_i (cf. also Fig. 7). For variable pressure p, the changes in R_e and N_i tend to be small although with opposite trends (Fig. 5 and 9), but one should keep in mind that varying p changes the spatial characteristics of the plasma (mean free paths, dark space height) so that the probe does not necessarily measure N_i at a uniform position relative to the dark space. As an aside, we note that the power density is not really relevant in characterizing an etching plasma, but the microscopic quantities N_i, T_e, and V_s are. Indeed we find that with the small cathode twice the power density is required to achieve the same R_e as with the large cathode, but conditions of equal R_e are always associated with very similar values for N_i, T_e, and V_s.

Of course, as one varies the composition of the plasma gas or other plasma parameters, additional changes in the plasma chemistry may occur. For example, it is well known (6-9, 11, 13) that adding O_2 to a CF_4 plasma will increase the F atom concentration but decrease the amount of CF and CF_2, whereas in CF_4-H_2 or CHF_3, just the opposite happens. Such changes seem to be of secondary importance, however, in light of the excellent correspondence between ion densities and etch rates of SiO_2.

The role of ions in the etching of Si is somewhat different as becomes evident from Fig. 12. The large increase in the etch rate with about 10% O_2 in CF_4 is not related to the ion density, but rather parallels the well-known increase in the concentration of F atoms (6, 8, 9). This additional etching is also essentially isotropic (9, 28). On the other hand, in pure CF_4 or at large O_2 concentration, the etching of Si has a considerable anisotropic component (9, 28, 32), and that again scales quite well with the ion density.

Since we can determine ion densities, plasma and sheath potentials, we are also able to estimate the ion flux to the substrate if we make a reasonable assumption about the ion velocity distribution at the probe position. Considering two extreme cases, we note that if the probe were sufficiently far away from the dark space, the distribution would be Maxwellian with temperature T_i (near room temperature). If the probe were at the edge of the sheath formed by the dark space, there would be a flux of ions with energy kT_e towards the cathode. Taking then typical conditions of $R_e = 140$Å /min and $N_i = 10^{10}$ cm^{-3} for CF_4 etching SiO_2 (Fig. 8), one finds that the ion fluxes to the substrate for the two velocity distributions are 0.012 mA/cm^2 and 0.29 mA/cm^2. Thus one obtains the following etch rates r_e per incoming ion in reactive sputter etching (RSE), which can be compared to values from ion beam experiments (RIBE)

SiO_2/CF_4	Ion energy (eV)	Etch rate r_e (atoms/ion)
RSE (100W, 20 mTorr)	120	$0.8 \leq r_e \leq 20$
RIBE: Ref. (33)	400	1.4
Ref. (34)	500	3

We note first that in our RSE experiments the probe is probably located near, but not at the dark space edge. Thus, r_e will probably be about 1, *i.e.* comparable to r_e in the RIBE mode. Also the values for r_e in RIBE are larger than expected for physical sputtering, the difference between the two figures probably being accounted for by variations in the ion beam composition, and in the flux of neutrals to the substrate.[4] From the above we conclude that etching of SiO_2, although induced by ions, is somewhat different in the two etching modes. In RIBE, etching results from the impact of ions on a surface whose state is also determined, to a considerable extent, by the ion beam, although neutral species participate significantly in the etching process. In RSE the etch rate per ion is of the same order as in RIBE, in spite of the ion energy being much lower. Because of the difference in pressure, in RSE neutral reactive species are present in abundance, essentially saturating the substrate surface, yet the overall etch rate is still determined largely by the ion flux to the substrate.

We also note the somewhat different selectivity for RSE and RIBE in etching Si over SiO_2 with CF_4. In RIBE the ratio of etch rates is typically 1:6 (33). In RSE, on the other hand, taking into account only the anisotropic (*i.e.* ion-induced) part of Si etching, the ratio of etch rates is about 2:1 (9, 28) (cf. also Fig. 12). For the etch rates r_e per incoming ion one finds

Si/CF_4	Ion energy (eV)	Etch rate r_e (atoms/ion)
RSE (100W, 20 mTorr)	120	$1.2 \leq r_e \leq 30$
RIBE: Ref. (15)	3000	1.5
(33)	1200	1.5
(35)	3000	1.7

Following arguments given above, we conclude that in the RIBE mode the etching of Si by CF_4 (*i.e.* CF_3^+) is mostly due to physical sputtering, whereas in the RSE mode the neutral species are responsible for etching, but etching is strongly ion-enhanced.

Summary

We have presented Langmuir probe measurements on low-pressure etching plasmas of CHF_3, CF_4, CF_4-H_2, and CF_4-O_2. Under conditions typical for reactive sputter etching, we find ion densities between 0.5×10^{10} cm^{-3} and 1.5×10^{10} cm^{-3}, and electron temperatures between 7 eV and 2 eV. We are also able to estimate plasma potentials, which turn out to be fairly low (~30 eV) and quite independent of the experimental conditions, as well as ion energies, which

[4] The ion composition of the beam depends on the ion source operating parameters, and different ions have different reactivities. Also, a dependence of the etch rate on pressure is observed [see Ref. (34)].

are 100-500 eV. For SiO_2 etch rates vary essentially in proportion to ion densities with all the different plasmas. In addition, there is evidence for a dependence of the etch rate on the ion energy. For Si in CF_4-O_2 plasmas of different composition, the anisotropic part of the etch rate also parallels the ion density. From an estimate of the ion flux to the substrate we are able to determine etch rates per ion in reactive sputter etching. These turn out to be comparable to, possibly even larger than, those in reactive ion beam etching, although in reactive sputter etching ion energies are much smaller.

Acknowledgments

I am grateful to H. W. Lehmann for suggesting this study, for useful discussions, and for a critical reading of the manuscript, and to K. Frick for technical assistance. I thank the referees for valuable comments.

Manuscript submitted Aug. 13, 1982; revised manuscript received Oct. 22, 1982. This was 361 RNP presented at the Detroit, Michigan, Meeting of the Society, Oct. 17-21, 1982.

Any discussion of this paper will appear in a Discussion Section to be published in the December 1983 JOURNAL. All discussions for the December 1983 Discussion Section should be submitted by Aug. 1, 1983.

Publication costs of this article were assisted by RCA Laboratories.

REFERENCES

1. L. M. Ephrath, *This Journal*, **129**, 62C (1982); C. J. Mogab, Inst. Phys. Conf. Series No. 53, 37 (1980).
2. J. W. Coburn and H. F. Winters, *J. Vac. Sci. Technol.*, **16**, 391 (1979).
3. J. Dieleman, Proc. Symp. Dry Processing, Tokyo, pp. I-1.1, October 26-27, 1981.
4. S. T. Griffin and J. T. Verdeyen, *IEEE Trans. Electron. Devices*, **ed-27**, 602 (1980).
5. J. W. Coburn and M. Chen, *J. Vac. Sci. Technol.*, **18**, 353 (1981).
6. R. d'Agostino, F. Cramarossa, S. De Benedictis, and G. Ferraro, *J. Appl. Phys.*, **52**, 1259 (1981).
7. M. M. Millard and E. Kay, *This Journal*, **129**, 160 (1982).
8. C. J. Mogab, A. C. Adams, and D. L. Flamm, *J. Appl. Phys.*, **49**, 3796 (1978).
9. M. Bolsen and D. Stephani, in Proc. Microcircuit Engineering 81, A. Oosenbrug, Editor, p. 467, Lausanne (Switzerland), September 28-30, 1981.
10. J. W. Coburn and E. Kay, *IBM J. Res. Develop.*, **23**, 33 (1979).
11. E. A. Truesdale and G. Smolinsky, *J. Appl. Phys.*, **50**, 6594 (1979).
12. M. J. Vasile, *ibid.*, **51**, 2503 and 2510 (1980).
13. C. I. M. Beenakker, J. H. J. van Dommelen, and R. P. J. van de Poll, *J. Appl. Phys.*, **52**, 480 (1981).
14. H. W. Lehmann, E. Heeb, and K. Frick, *Solid State Technol.*, **24**, 69 (1981).
15. J. W. Coburn, H. F. Winters, and T. J. Chuang, *J. Appl. Phys.*, **48**, 3532 (1977).
16. T. J. Chuang, *ibid.*, **51**, 2614 (1980).
17. I. Langmuir, in "Collected Works of Irving Langmuir," G. Suits, Editor, Vol. 4, Macmillan, New York (1961).
18. W. R. Larsen, C. W. Wilmsen, and P. W. Chan, *J. Appl. Phys.*, **44**, 2153 (1973).
19. H. Norstrom, R. Olaison, S. Berg, and L. P. Andersson, *This Journal*, **127**, 2680 (1980).
20. D. J. Ball, *J. Appl. Phys.*, **43**, 3047 (1972).
21. E. Eser, R. E. Ogilvie, and K. H. Taylor, *Thin Solid Films*, **68**, 381 (1980).
22. N. J. Ianno, K. E. Greenberg, and J. T. Verdeyen, *This Journal*, **128**, 2174 (1981).
23. F. F. Chen, in "Plasma Diagnostic Techniques," R. H. Huddlestone and S. L. Leonard, Editors, Chap. 4, Academic Press, New York (1965).
24. R. M. Clements, *J. Vac. Sci. Technol.*, **15**, 193 (1978).
25. J. G. Laframboise, Univ. of Toronto Inst. Aerospace Studies Rept. No. 100 (1966). (See also *Adv. Appl. Mech. Suppl.*, **3**, Vol. II, 1966).
26. S. G. Lias, J. R. Eyler, and P. Ausloos, *Int. J. Mass Spectrom. Ion Phys.*, **19**, 219 (1976).
27. L. M. Ephrath, *This Journal*, **126**, 1419 (1979).
28. J. Paraszczak and M. Hatzakis, *J. Vac. Sci. Technol.*, **19**, 1412 (1981).
29. J. L. Vossen, *This Journal*, **126**, 319 (1979).
30. H. R. Koenig and L. I. Maissel, *IBM J. Res. Develop.*, **14**, 276 (1970).
31. H. W. Lehmann and R. Widmer, *J. Vac. Sci. Technol.*, **15**, 319 (1978).
32. G. C. Schwartz, L. B. Rothman, and T. J. Schopen, *This Journal*, **126**, 464 (1979).
33. B. A. Heath, *ibid.*, **129**, 396 (1982).
34. T. M. Mayer and R. A. Barker, *ibid.*, **129**, 585 (1982).
35. S. Tachi, K. Mizake, and T. Tokuyama, Proc. Symp. Dry Processing, pp. I-3, 17, Tokyo, October 26-27, 1981.
36. N. Hosokawa, R. Matsuzaki, and T. Asamaki, *Jpn. J. Appl. Phys. Suppl.*, **2**, Pt. 1, 435 (1974).
37. M. J. Kushner, *J. Appl. Phys.*, **53**, 2923 and 2939 (1982).

A Laser Interferometer System to Monitor Dry Etching of Patterned Silicon

M. Sternheim and W. van Gelder*

Bell Laboratories, Murray Hill, New Jersey 07974 and Allentown, Pennsylvania 18103

and A. W. Hartman

National Bureau of Standards, Washington D.C. 20234

ABSTRACT

A laser interferometer system to monitor plasma etch rate, and to control etched depth of isolation areas in silicon for oxide isolated bipolar devices, is reported. The etching process is stopped as soon as the desired etched depth is achieved. The accuracy of the system is 4-6%, depending on the masking material. It is found that this method of laser interferometry can be particularly useful in process development for observations in real time of changes in etch rate.

Laser interferometers have been used in integrated circuit processing to monitor the etch rates of dielectric films in plasma etch processes (1, 2, 3). In particular the detection of the completion of the process, the so called end-point detection, is of high interest. This is because during an overetch period, undercutting may

* Electrochemical Society Active Member.
Key words: semiconductor, lasers, interferometry, etching.

occur as well as mask erosion, each causing undesirable loss of linewidth control. Also, etching through an underlying layer may occur as a result of poor selectivity between the etched film and the underlying layer.

In some processes, such as the planarization of phosphorous doped SiO_2 (4), and the etching of grooves or tubs in a silicon substrate, the etched material is not etched to completion. In these types of processes other methods of end-point detection, such as optical emission (5), mass spectroscopy (6), plasma impedance, and reactor pressure (7) cannot be used. But a laser interferometer can be used in these cases because it has the advantage of measuring the actual etched depth in real time.

In this paper we report the application of a laser interferometer system in monitoring the depth of plasma etched areas in a silicon substrate. The plasma etched regions are of the order of one micron deep, and are used as oxide isolation areas in "OXIL" bipolar device processing. The system monitors the etch rate by indicating at each moment in time how much "depth" has been etched. The plasma etching is stopped as soon as the required depth is reached.

Equipment and Experimental Setup

An interferometer that measures the distance between the etched surface and the unetched surface of a silicon wafer was chosen as the system to monitor the etched depth. A linearly polarized, 2 mW He-Ne laser was used as a light source with wavelength $\lambda = 6328$Å. (Shorter wavelength laser light sources would be desirable for higher fringe resolution, but are not as conveniently available.)

At first we built a two beam interferometer into a parallel-plate silicon plasma etcher. The principal of operation is shown in Fig. 1. This system is a simplified version of a double beam, double pass, step height polarization interferometer with one nanometer resolution, designed and built by Hartman (8). The laser light is split into two parallel beams (2 mm apart) by a beam splitter. The two beams pass through an optical window W in the top electrode and are then reflected from each side of a growing step in silicon. The reflected beams are brought together by the same beam splitter with a small offset, so that the reflected light can be collected by prism P and directed towards photocell F. The output of the photocell shows the normal interference response as a function of the growing step height d. With this system we have done real-time step height measurements in silicon using aluminum as a mask. The etching conditions were: pressure 0.4 Torr; power 1.5 kW 13.6 MHz, flow rate 100 ml/min CF_3Cl, electrode spacing 1 in., 22 in. diam, parallel plate plasma etching machine with a hole in the top electrode to admit the laser light. A typical fringe response curve is shown in Fig. 2. The agreement between the step height calculated from the interference fringes and the step height obtained by an "alpha" step profilometer was typically better than 2%.

But this system had some serious drawbacks. It requires large areas, approximately 2 × 2 mm, next to each other to reflect the two laser beams. Each laser beam is ~1 mm in diam and both beams have to be accurately positioned, so that one beam reflects from the masked (unetched) area and the other beam reflects from the unmasked (etched) area. This turned out to be a cumbersome and tedious procedure, which can be avoided by using a single beam system in which one beam is reflected from a closely spaced repeated number of steps in the silicon. This is basically reflection from a relief diffraction grating, where we only consider the central image reflection (or zero order diffraction). This single beam laser interferometer is similar to those described in (1) and (3), and was mounted on a parallel plate plasma reactor as well as in a reactive sputter etch (RSE) reactor. The principle of operation is shown in Fig. 3. A 2 mW linearly polarized He-Ne laser emits light into a polarizing beam splitter. With the polarization plane adjusted as shown almost all the light is reflected to the left. It passes a quarter wave retardation plate and an optional beam expander BE. The grating type sample is located in the plasma region behind an optical window. The reflected light is split into various diffraction angles, but we only collect the zero order reflected light. At 0° angle of incidence, the light passes back onto itself through the quarter wave plate. The plane of polarization is turned 90° as a result of double passage

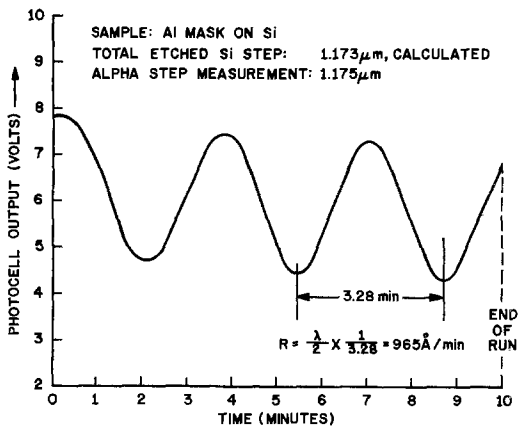

Fig. 2. Typical response curve with double beam interferometer

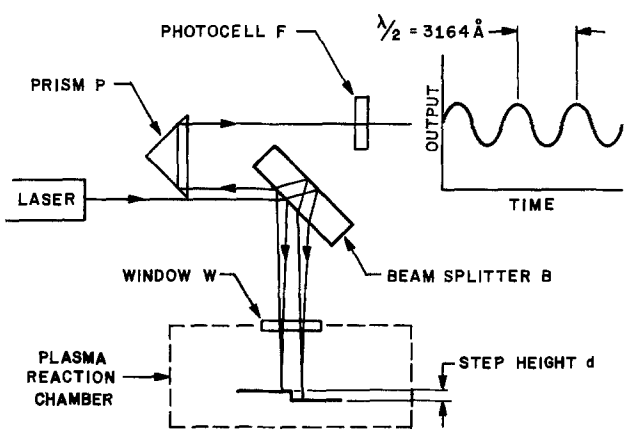

Fig. 1. Double beam laser step height interferometer

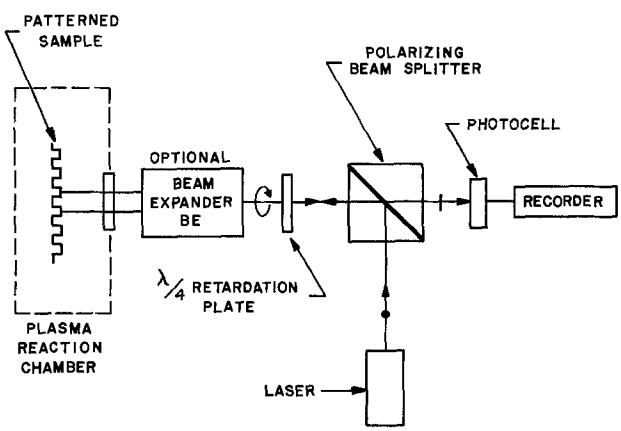

Fig. 3. Single beam grating step height interferometer

through the $\lambda/4$ plate, and the beam passes through the polarizing beam splitter into a photocell. The output of the photocell is recorded as a function of time. It appears that most integrated circuit patterns form a a grating during etching so that no extra test patterns are needed. For perpendicular illumination (0° angle of incidence), whenever the groove depth d satisfies the relation, $2d = \lambda/2, 3\lambda/2, 5\lambda/2, \ldots$, the reflected intensity of the central diffraction image will be at a minimum. On the other hand, when $2d = 0, \lambda, 2\lambda, \ldots$, the reflected light is at a maximum. During the etching process, the depth of the Si trenches increases and the light intensity in the zero order of the diffraction pattern changes periodically. In an ideal case where the etch mask itself has zero etch rate, the voltage output of the photocell will be sinusoidal. This happens when aluminum is used as a mask. In most practical cases, a dielectric film and/or a photoresist film is used as a masking material, which has itself a measurable etch rate. The output voltage of the detector in these cases is periodical but not purely sinusoidal. The period of the voltage waveform corresponds to a change of $d = \lambda/2$ in the depth of the etched trenches. A detailed treatment of a grating test pattern is given by Kleinknecht and Meier (3).

In order to make the system compatible with automatic process control, the voltage output signal $v(t)$ has to be processed. The signal must be smoothed and the time derivative calculated using a desk top computer. The zero crossings of the time derivative of the voltage function $v'(t)$ corresponds to the maxima and minima of the light intensity in the zero order of the diffraction pattern. The etched depth between two zero crossings of $v'(t)$ corresponds to $\lambda/4 = 1582$Å, and the average etch rate for a particular period can be calculated, knowing the period of $v'(t)$. The averaged etch rate per period can be integrated to calculate the total etched depth, and the process can be stopped when the preset depth is reached.

Experimental Results

The samples were silicon wafers patterned using 7000Å Al as a mask for experiments in a parallel plate plasma reactor, and using 4000Å SiO_2 as a mask for experiments in Reactive Sputter Etching (RSE) and other plasma reactors. The etched depth calculated from the etch rate was compared to Talystep or alphastep measurements. The etched area was reduced below 25% of the total area, without affecting the signal to noise ratio or the accuracy of determined depth. Figure 4 demonstrates the method for an Al mask on single crystal silicon in a plasma process. The etch conditions used were 100 ml/min CF_3Cl at 0.4 Torr and 1.5 kW; the average silicon etch rate was 1000 Å/min, and the aluminum was not etched. It is apparent from the voltage waveform that the optical properties of the surfaces are nearly constant during the process. The accuracy of the method in determining the etch rate is better than 4%. Figure 5 shows the results for an SiO_2 mask over silicon. The selectivity of the silicon etch rate over the SiO_2 etch rate was deliberately reduced to 5:1, and the accuracy was still better than 6%. The changes in the amplitude of the voltage signal correspond to beats because of the relative etch rates of the dielectric film and the silicon.

For an alignment free system a beam expander is used. An $\times 8$ expansion covers a full chip. There is no effect on the signal to noise ratio, or on the accuracy of the results when an expanded beam is used instead of the original beam size.

It was observed that when the selectivity of mask to substrate is further reduced to values approaching 1:1, the accuracy decreases fast and the method reaches its limit of usefulness.

Conclusions

A simple interferometric method to monitor the etch rate of patterned silicon layers was developed, to control the etched depth of isolation areas for bipolar technology. The accuracy of the method is better than 6%, even if the selectivity of silicon over the masking material is as low as 5:1. When the selectivity approaches a value as low as 1:1, the accuracy decreases

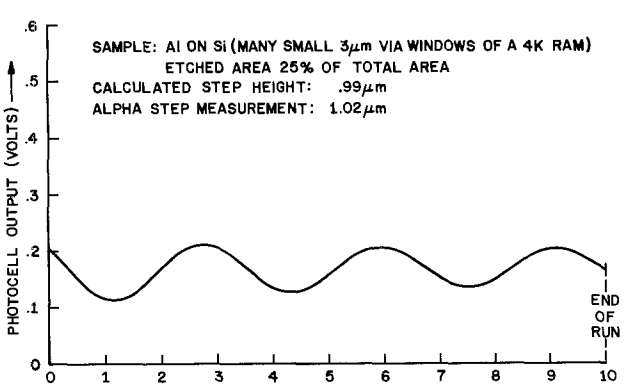

Fig. 4. Response from single beam grating interferometer

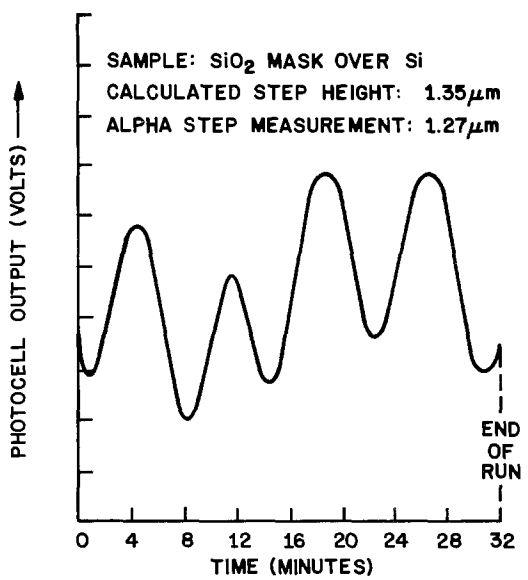

Fig. 5. Response from single beam grating interferometer

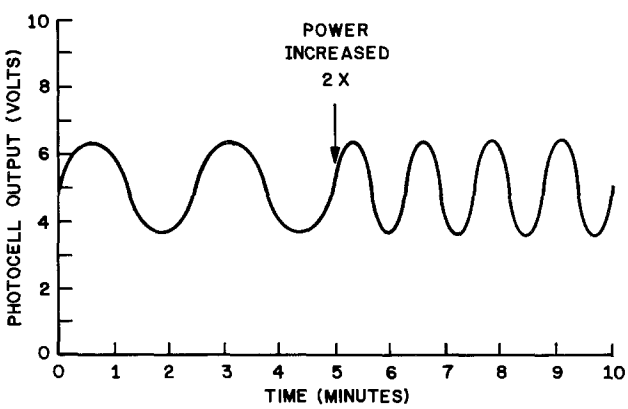

Fig. 6. Response curve showing real time result of power increase: etch rate increased ~2×.

and the method reaches its limit of usefulness. An accuracy of better than 4% is achieved for an infinite selectivity with the use of aluminum as a mask.

It was found that this method of laser interferometry can be particularly useful in process development. For instance, it can be observed in real time how etch rates change *in situ*, while process parameters such as pressure, power, and flow rate are changed (*e.g.*, Fig. 6).

The method is compatible with an automatic process control system. It can also be used to monitor the etch rates of patterned metals like Al. In order for the method to be reasonably accurate, the total etched depth has to be more than $\lambda/2$, where λ = laser wavelength. It should be noted that the interferometer system described herein is readily usable for the more conventional end-point detection of dielectric layers, where an optical grating is not needed (1, 2, 3, 9).

Acknowledgments

We would like to thank H. J. Levinstein, D. A. McGillis, and E. F. Labuda for their encouragement, M. Feldman, A. White, and S. D. Steenwyk for their helpful discussions, and A. C. Adams for correcting the manuscript.

Manuscript received June 1, 1982. This was Paper 294 presented at the Denver, Colorado, Meeting of the Society, Oct. 11-16, 1981.

Any discussion of this paper will appear in a Discussion Section to be published in the December 1983 JOURNAL. All discussions for the December 1983 Discussion Section should be submitted by Aug. 1, 1983.

Publication costs of this article were assisted by Bell Laboratories.

REFERENCES

1. J. A. Bondar, W. R. Case, and H. A. Clark, Abstract 303, p. 760, The Electrochemical Society Extended Abstracts, Seattle, Washington, May 21-26, 1978.
2. H. H. Busta, R. E. Lajos, and D. A. Kiewit, *Solid State Technol.*, **22**, 61 (1979).
3. H. P. Kleinknecht and H. Meier, *This Journal*, **125**, 798 (1978).
4. A. C. Adams, *ibid.*, **128**, 423 (1981).
5. R. G. Poulsen and G. M. Smith, in "Semiconductor Silicon 1977," H. R. Huff and E. Sirtl, Editors, p. 1058, The Electrochemical Society Softbound Proceedings Series, Princeton, NJ (1977).
6. G. B. Bunyard and B. A. Ruby, *Solid State Technol.*, **20**, 53 (1977).
7. M. L. Hitchman and V. Eichenberger, *J. Vac. Sci. Technol.*, **17**, 1378 (1980).
8. A. W. Hartman, *Opt. Eng.*, **15**, 180 (1976).
9. P. J. Marcoux and Pang Dow Foo, *Solid State Technol.*, **24**, 115 (1981).

Control of Silicon Dioxide Properties by RF Sputtering

M. K. Lee,* C. Y. Chang,* J. S. Tzeng, and Y. K. Su

Research Institute of Electronics and Electrical Engineering, National Cheng Kung University, Tainan, Taiwan, China

ABSTRACT

We have examined the effect of simultaneously sputtered Teflon on the properties of sputtered silicon dioxide films. C-V measurements show that positive ions in sputtered silicon dioxide can be compensated. It also shows that the compensation effect can be controlled by the negative voltage of bias sputtering during deposition.

Silicon dioxide films are extensively used in semiconductor device technology. They perform many functions such as surface passivation, impurity masking, active device dielectric, etc. SiO_2 films deposited by sputtering have many advantages over thermally grown films; for example, the former can be prepared at relatively low temperature. However, the resulting films show instability due to ionic contamination. Positive charges degrade SiO_2 films. The reduction of positive charges is an important factor in determining the quality of semiconductor devices. In this report, the effect of fluorine ions (1) sputtered into SiO_2 films to compensate positive charges was studied.

Experimental

An MRC SEM-8620 sputtering system was used for the deposition of SiO_2 films. It has a 1½ kW rf power generator, and provides the user with all rf sputtering functions, sputter-etching, and rf bias sputtering The space between target and substrate holder was adjusted to 5 cm in the experiments. The target, IC grade SiO_2, 6 in. in diam and 3/16 in. in thickness, was also supplied by MRC. It is water cooled via a cathode plate. The vacuum system consisted of an oil diffusion pump and a rotary pump. In an MRC 8620 sputtering system, the cathode head is insulated from its mounts by Pyrex glass. In a typical run, however, the Pyrex glass was substituted by Teflon ($CF_2 = CF_2$) in our experiments for comparison. High purity (5*N*) argon, purified by the inert gas purifier and filtered through millipore gas line filter (0.25 μm pore size), was fed into the chamber during deposition.

The silicon wafers are n-type <111> oriented, and have resistivities of 3-5 Ω-cm. Before being loaded onto the substrate holder, the silicon wafers were cleaned sequentially in TCE, ACE, H_2SO_4:H_2O_2 = 3:1, HF:H_2O = 1:10, then rinsed in deionized water.

The copper plating technique (2) was used for the pinhole test. MIS structure was adopted for the study of electrical properties of SiO_2 film. An aluminum (99.9%) electrode was evaporated over the oxide film through a metal mask. The thickness and area of Al films were 3000Å and 0.01 cm^2, respectively. For measurement of the breakdown strength, the polarity of Al electrode is positive. Capacitance was measured at 10 kHz with SANWA Type M1-316B capacitance meter.

Results and Discussion

In order to study the effects of Teflon simultaneously sputtered on the properties of SiO_2 film, three different sputtering processes were tried and compared. In process I, Teflon was used as insulator of the electrode. The initial pressure of the system was pumped down to less than 4×10^{-6} Torr. Prior to deposition, the target was presputtered under argon pressure of 5×10^{-3} Torr, then pumped down again to 4×10^{-6} Torr. The argon pressure was kept at 5×10^{-3} Torr during sputtering. The sputtering power was 300W.

In process II, Pyrex glass was used as insulator of the electrode. The substrates were sputter-etched at 400W under argon pressure of 3×10^{-3} Torr for about 1 μm. To minimize radiation damage, the rf power was de-

* Electrochemical Society Active Member.
Key words: sputtering, SiO_2, fluorine, doping.

Table I. Properties of sputtered SiO_2 films of three processes

Table I. Properties of films of three processes.

	Pinhole density ($1/cm^2$)	P etch rate (A/min.)	breakdown strength (V/cm)
Process I	26	132	3×10^6
Process II	18	140	7.5×10^6
Process III	12	128	1×10^7

creased toward the end in steps of 6 min at 50, 40, 15, and 10W (3). The other conditions were the same as that of process I.

In process III, bias sputtering was used. The Si substrate was negatively biased with bias voltage (4) of −40V for Teflon as insulator of electrode. The other conditions were the same as that of process II.

The quality of the SiO_2 films prepared from above three processes was examined by pinhole test, P etch rate (5), and breakdown strength. The results are summarized in Table I. Obviously, process III gives the best quality in all three measurements. The breakdown strength obtained is higher than those of previous reports. This may be due to the effect of F^- ion from the Teflon.

The C-V curves of MIS samples obtained from the above three processes are shown in Fig. 1. For Fig. 1b, Pyrex glass was used as insulator; the C-V curve is like that of a thermally oxidized one. The imbedded

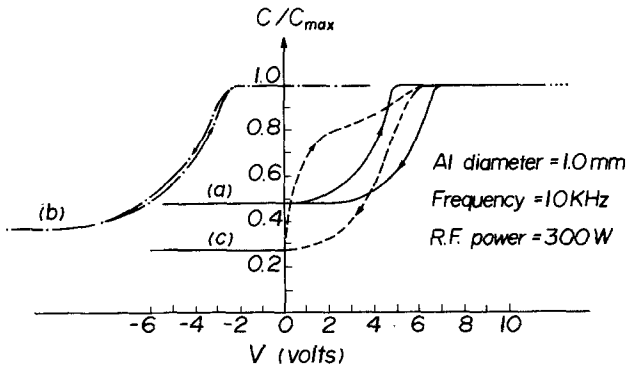

Fig. 1. (a) C-V curve for Teflon as insulator of electrode. SiO_2 film thickness is 1500Å. (b) C-V curve for Pyrex glass as insulator of electrode. SiO_2 film thickness is 1500Å. (c) C-V curve with bias voltage −40V for Teflon as insulator of electrode. SiO_2 film thickness is 1200Å.

charges are positive as usually reported (6). When Pyrex glass was substituted by Teflon, the C-V curve shifted toward the right as shown in Fig. 1a. It appears that negative charges are imbedded in the sputtered SiO_2 film, contrary to process II. It can be presumed that the negative charges were related to the Teflon. The negative charges might come from the F^- ions of Teflon, and the trapped F^- ions could compensate the effect of positive charges. If the Si substrate is negatively biased during bias sputtering, the negative bias voltage would retard the trapping of the negative charges. Figure 1c shows that the C-V curve shifted toward left with −40V bias voltage during bias sputtering. That is to say, the concentration of negative charges in SiO_2 film could be decreased by the negative bias voltage of the Si substrate during bias sputtering. This phenomenon could also prove the fact that the trapped charges are negatively charged. As to the sense of the hysteresis, Fig. 1a, c indicate charge exchange across the silicon dioxide-silicon interface. That is opposite to the sense of Fig. 1b. This phenomenon is usually referred to as Si injection (7). It could be associated with the trapped negative charges.

Conclusion

We conclude that if Teflon is simultaneously sputtered with the SiO_2 target, it can reduce positive charges in MOS device. The compensation effect could be related with the F^- ions.

Manuscript submitted April 4, 1981; revised manuscript received Nov. 2, 1982.

Any discussion of this paper will appear in a Discussion Section to be published in the December 1983 JOURNAL. All discussions for the December 1983 Discussion Section should be submitted by Aug. 1, 1983.

Publication costs of this article were assisted by Cheng Kung University.

REFERENCES

1. M. K. Lee, C. Y. Chang, and J. S. Tzeng, Paper 614 presented at The Electrochemical Society Meeting, Los Angeles, California, October 14-19, 1979.
2. W. J. Shannon, *RCA Rev.*, **31**, 431 (1970).
3. H. U. Schreiber and E. Fröschle, *This Journal*, **123**, 30 (1976).
4. J. S. Logan, *IBM J. Res. Develop.*, **14**, 172 (1970).
5. W. A. Pliskin and R. P. Gnall, *This Journal*, **111**, 872 (1964).
6. J. S. Logan, F. S. Maddocks, and P. D. Davidse, *IBM J. Res. Develop.*, **14**, 182 (1970).
7. S. M. Hu, D. R. Kerr, and L. V. Gregor, *Appl. Phys. Lett.*, **10**, 97 (1967).

Island Stage of InP Anodization

W. H. Makky and C. W. Wilmsen

Department of Electrical Engineering, Colorado State University, Fort Collins, Colorado 80523

ABSTRACT

The island growth of anodic oxides on InP has been studied with transmission electron microscopy. The islands appear smooth for all growth conditions tested in contrast to the rough edge anodic oxide islands of GaAs. Changing the *p*H, electrolyte, or illumination did not significantly change the island shape. The islands were often observed to form in closely spaced rows indicating a heterogeneous nucleation. Coalescence appeared to be caused by a rapid growth in the regions between the touching islands.

Recently we reported on a transmission electron microscope (TEM) study of the island growth of anodic oxides on GaAs (1). It was found that the islands on GaAs varied in size, had very rough and pitted edges, and had a distinct boundary between coalescing islands until the neck region was completely filled in. In this paper we briefly report on a similar TEM study of the anodic oxide islands of InP.

The growth and properties of anodic oxides on InP have been investigated by numerous authors (2-9)

who have reported the chemical composition, growth characteristics, and electrical properties of the oxides. The oxides appear to be a mixture of In_2O_3 and P_2O_5, with the ratio being dependent upon the electrolyte and electrolyte pH (6, 7). Based on the voltage *vs.* time curve during anodization it was previously suggested (5) that the oxide growth was initiated by a nucleation and island growth stage as is the case for the anodization of GaAs.

The present paper shows that the islands on InP differ from those on GaAs and that the island characteristics did not change for electrolyte pH equal to 2.7 and 7.0, the amount of illumination, the electrolyte, and rinsing with water or methanol.

Experimental Technique

The InP wafers were (100) undoped, n-type with carrier density of 4×10^{16} cm^{-3} from Crystal Communications, Incorporated. The samples were etched in 10% HCl for 10 min, rinsed with deionized (DI) water, and then blown dry with N_2. The surface was chemomechanically polished using 1% Br/methanol and a Pellon Pan-W polishing pad, rinsed thoroughly with methanol, then rinsed with acetone to remove the

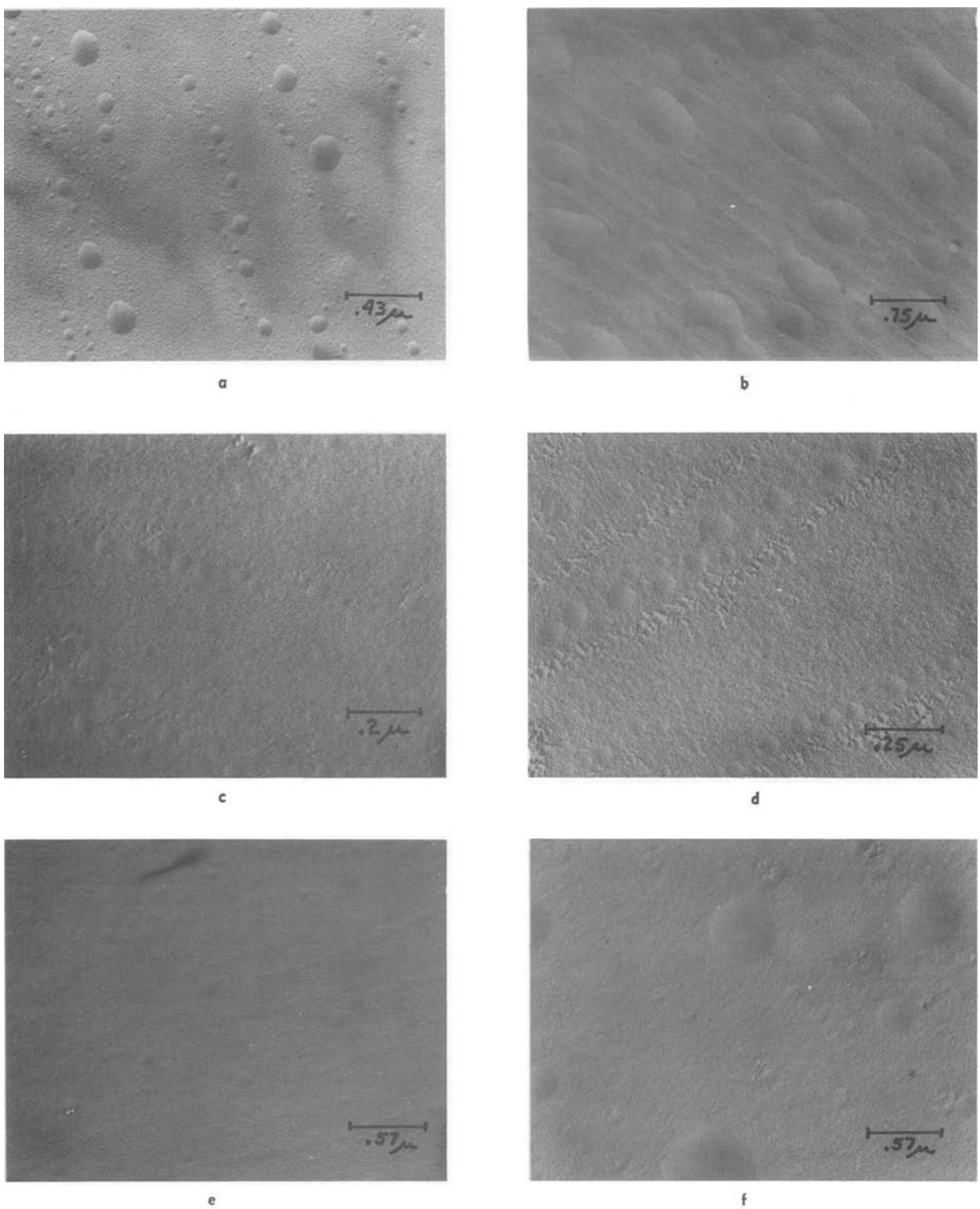

Fig. 1. Anodic oxide islands on InP formed with different growth conditions; (a) dipping in a tartaric acid electrolyte at a pH = 7, (b) growth in tartaric acid, pH = 7 with a strong light, (c) growth in phosphoric acid, pH = 2.7 with strong light, (d) same as (b) except in the dark, (e) same as (c) except in the dark, and (f) same as (b) except rinsed with methanol.

Crystal Bond, and blown dry with N_2. The surfaces of the bare substrates were replicated using a 4% collodion solution in amyl acetate. The collodion was left to dry at room temperature. The collodion replicas were then removed with the help of DI water vapor. The samples were then anodized with a constant current density of approximately 0.2 mA/cm^2. The anodization process was stopped before the passivation time was over, *i.e.*, somewhere during the "flat" portion of the voltage-*vs.*-time curve. Some samples were anodized in the dark while the others were anodized under a strong light. Electrolytes of a 3% phosphoric acid solution (*p*H = 2.7) mixed 1:1 with propylene glycol, and a 3% tartaric acid solution (pH = 7) mixed 1:6 with propylene glycol were used. The effect of rinsing the samples with methanol and DI water for a few seconds after anodization was examined. The surfaces of the anodized samples were replicated in the same way as discussed above.

The collodion replicas were then shadowed with Pt at an angle of 25° and coated with 200Å of carbon using a "Balzers 301 Evaporator." To eliminate possible variations in the shape of the TEM pictures of the sample before and after anodization due to the shadowing process, the collodion replicas of each sample before and after anodization were shadowed together. The Pt-C secondary replicas were obtained by placing the shadowed collodion replicas on SPI (400 mesh-3 mm) Cu TEM specimen grids and then digesting the collodion with amyl acetate.

Results

Nucleation and island growth.—The six photomicrographs of Fig. 1 illustrate the primary island structure of anodic oxides on InP. While the samples for Fig. 1 were prepared in different ways, each one has the same smooth, round islands which we believe to be the basic island shape. The smooth edged islands of the InP oxide are much different than the ragged and pitted edges of GaAs anodic oxide island shown in Fig. 2 and discussed in detail in a previous publication (1). The InP islands often (but not always) form rows $\approx$ 0.2-0.6μ apart. The lining up of the islands imply that there are lines of preferred nucleation sites which could be the result of mechanical damage due to sawing or polishing, steps on the surface, or doping striations. Saw damage is expected to be much more widely spaced and much larger in extent. Polishing scratches should have more random directions. Both sawing and polishing damage should be removed by deep polishing but this did not appear to be possible with these samples. Doping striations should not appear in low doped material such as was used in this investigation. Thus, surface steps appear to be the most likely cause of lines of preferred nucleation.

The islands shown in Fig. 1a were formed by dipping the InP in the electrolyte for 10 min without connecting any leads. The fact that the islands formed means that the contact potential between the InP and the electrolyte was sufficient to initiate the nucleation and growth process as we previously suggested for GaAs (5). There is a distribution of island sizes which suggests that the nucleation process occurs over a period of time. However, the islands' size of the other photomicrographs have a much smaller spread and most of the islands are approximately the same size on a given sample. This is different from GaAs anodic islands and may in part be due to the preferred nucleation sites on InP. The smallest island found on the sample of Fig. 1a had a diameter of $\approx$250Å and the largest was $\approx$5000Å.

The islands of Fig. 1b and c were grown under strong illumination while those of Fig. 1d and e were grown in the dark. The same basic island shape is observed for all growth conditions. The rough background (probably an oxide) seen in Fig. 1c cannot be attributed solely to the state of illumination since identical results were obtained with growth under strong light, Fig. 1d. We believe that the rough background seen in Fig. 1c and d is caused by a rough native oxide which sometimes grows on the InP and has occasionally been observed during the course of our work on thin plasma (10, 11), thermal (11), and anodic (12) oxides of InP, but the cause is not presently known.

The sample for Fig. 1f was grown under strong illumination and was rinsed with methanol instead of water as were the samples for Fig. 1a-e. It is seen that methanol rinsing produces the same type of smooth island as does a water rinse. The islands shown in Fig. 1f are randomly distributed and are all approximately the same size. The smaller dimpled "islands" seen in between the smooth islands were also observed with other growth conditions.

The approximate height of the islands was estimated by measurement of the shadow length and knowing the angle at which the samples were shadowed. The shadows on the InP replicas were not as distinct as those on GaAs (1), which reduces the accuracy of the measurement and prevents estimation of shadow length of the smaller islands. For the larger islands this method yields a height of $\approx$200Å, which is similar to that obtained on GaAs (1).

Coalescence.—Some coalescence is seen in the islands of Fig. 1b in which islands in the same line form elongated islands. Similar coalescence is seen in the islands of Fig. 3. The coalesced islands are all smooth with no distinct boundary between them, as is the case with GaAs (1). However, as with GaAs, the islands appear stationary with the neck regions filling in by a fast growth process due to electric field enhancement

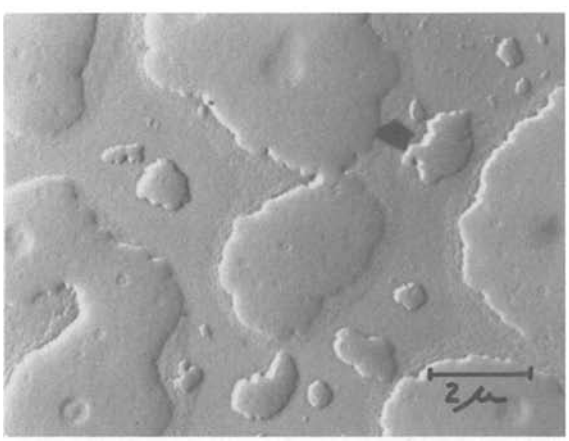

Fig. 2. Anodic oxide islands on GaAs grown in tartaric acid, pH = 7 with strong light.

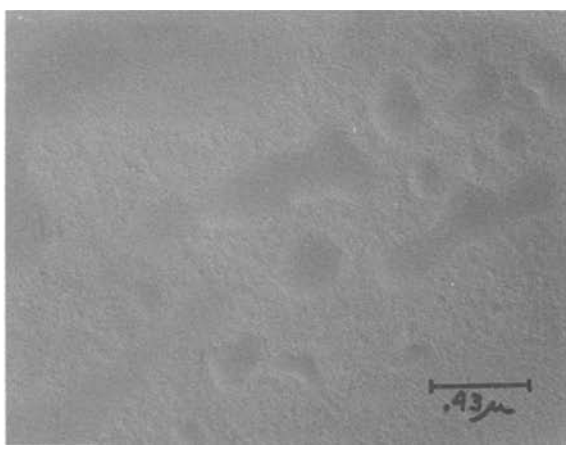

Fig. 3. Anodic oxide islands on InP showing coalescence. Growth in tartaric acid, pH = 7 in the dark.

in these regions. The elongated and irregular island shapes argue against a liquid-like coalescence due to surface migration of molecules as discussed previously for GaAs (1).

Summary

The TEM micrographs show that the anodic oxidation of InP is initiated by nucleation and island growth. In contrast to GaAs, the islands on InP are smooth without rough edges. However the islands on InP are approximately the same height and area as those observed on GaAs. The same basic island shape of the InP islands was observed for all growth conditions tested. Some variation from run to run was observed but this was not consistent and could not be attributed to the electrolyte, electrolyte pH, or intensity of illumination. It is believed that the observed variations were due to the quality of the substrate polish and not the changes in the growth conditions. On many of the samples, the islands were in rows separated by ≈ 0.2-0.6μ. These are thought to be due to surface steps which cause a heterogeneous nucleation.

The coalescence of the islands appeared to be caused by rapid growth in the neck region between the two touching islands similar to that observed for GaAs.

Acknowledgments

We wish to thank Kent Geib for his help with sample preparation and Dr. Morita for his assistance with the electron microscope. This work was supported by ARO.

Manuscript submitted June 15, 1982.

Any discussion of this paper will appear in a Discussion Section to be published in the December 1983 JOURNAL. All discussions for the December 1983 Discussion Section should be submitted by Aug. 1, 1983.

Publication costs of this article were assisted by the Colorado State University.

REFERENCES

1. W. H. Makky, F. Cabrera, K. M. Geib, and C. W. Wilmsen, *J. Vac. Sci Technol.*, **20**, 417 (1982).
2. D. L. Lile and D. A. Collins, *Appl. Phys. Lett.*, **28**, 554 (1976).
3. C. W. Wilmsen and R. W. Kee, *J. Vac. Sci. Technol.*, **14**, 953 (1977).
4. K. P. Pande and G. G. Roberts, *ibid.*, **16**, 1470 (1979).
5. K. M. Geib and C. W. Wilmsen, *ibid.*, **17**, 952 (1980).
6. D. H. Laughlin and C. W. Wilmsen, *Appl. Phys. Lett.*, **37**, 915 (1980).
7. D. A. Baglee, D. H. Laughlin, C. W. Wilmsen, and D. K. Ferry, "The Physics of MOS Insulators," G. Luscovsky, S. T. Pantelides, and F. L. Galeener, Editors, Pergamon, New York (1980).
8. A. A. Studna and G. J. Gualitieri, *Appl. Phys. Lett.*, **39**, 965 (1981).
9. A. Yamamoto and C. Uemura, *Electron. Lett.*, **18**, 63 (1982).
10. J. F. Wager, W. H. Makky, and C. W. Wilmsen, *Thin Solid Films*, **95**, 343 (1982).
11. J. F. Wager and C. W. Wilmsen, *J. Appl. Phys.*, To be published.
12. W. H. Makky, Unpublished.

The A-C Conductivity of Polycrystalline LISICON, $Li_{2+2x}Zn_{1-x}GeO_4$, and a Model for Intergranular Constriction Resistances

P. G. Bruce[1] and A. R. West

University of Aberdeen, Department of Chemistry, Meston Walk, Old Aberdeen AB9 2UE, Scotland

ABSTRACT

The a-c conductivity of a polycrystalline, Li^+ ion conducting solid electrolyte, LISICON, $Li_{2+2x}Zn_{1-x}GeO_4$, has been measured over the frequency range 10^{-3}-10^7 Hz and attention focused on the methods of data analysis. The data show intragranular (bulk) and grain boundary effects in which, for a given sample, both effects are characterized by a similar activation energy; a constriction resistance model for the latter is proposed based on air gaps existing in polycrystalline sinters of less than theoretical density. The data only crudely fit a Debye-like equivalent circuit, composed of frequency independent resistors and capacitors, but fit well an equivalent circuit that contains Jonscher elements, *i.e.*, frequency dependent admittances, in addition to normal R and C elements. Two such Jonscher elements are needed, one for the grain boundary and one for the intragranular contribution. With this circuit, departures from ideality in, *e.g.*, the complex impedance, admittance, and electric modulus planes are accounted for.

The a-c conductivity of solid electrolytes is generally analyzed in terms of equivalent circuits composed of frequency independent resistors and capacitors. Very often, however, the a-c response does not correspond to that predicted by simple, ideal circuits; for instance, semicircles in the complex impedance Z^* plane are often broadened and distorted into asymmetric arcs. Various attempts have been made to deal with this problem: empirical functions based on the Cole-Cole (1-3) or Cole-Davidson (4) expressions have been used to fit the experimental results; a distribution of hopping processes leading to a distribution of relaxation times has also been postulated (5). Such nonideal response is only observed in electrolytes with a high concentration of charge carriers. These are just the systems in which cooperative interactions are manifest.

A recent approach which is gaining increasing acceptance is based on Jonscher's "universal law of dielectric response" (6, 7), which, unlike the above approaches, can be derived from theories of cooperative migration (8-11). When this theory is applied to a-c conductivity, frequency dependent elements must be introduced into the equivalent circuit. This approach, utilizing one frequency dependent element, has been used by Jonscher (7, 12), Huggins and others (13-15) to model the a-c response of polycrystalline materials. We have shown (16) that the bulk a-c response of single crystal β-alumina can be treated in the same way, and that the observed large departures from Debye-like behavior can be fitted to a relatively simple equivalent circuit. In this paper, we discuss the application of Jonscher circuits to a polycrystalline Li^+ ion conducting electrolyte LISICON, and show how both the grain boundary and bulk regions may be satisfactorily described, extending previous approaches by utilizing

[1] Present address: Department of Inorganic Chemistry, University of Oxford, Oxford OX1 3QR, England.

two frequency dependent elements. We also show how the departures from Debye-like response are manifested in all four complex formalisms, the admittance (Y^*), impedance (Z^*), permittivity (ϵ^*), and modulus (M^*), which are interrelated (17)

$$Y^* = (Z^*)^{-1} = j\omega Co(M^*)^{-1} = j\omega Co\epsilon^* \quad [1]$$

where ω is the angular frequency, $2\pi f$, and Co is the vacuum capacitance of the conductivity cell.

In addition to the above-mentioned representation of grain boundary response, the origin of such grain boundaries in LISICON is discussed and a model for them presented.

Experimental

The synthesis of lithium zinc germanate phases and their analysis by x-ray diffraction has been discussed previously (18). Pellets for conductivity measurements were prepared by cold-pressing powders of the γ_{II}-type solid solutions at 45,000 psi, followed by sintering at temperatures between 1000° and 1100°C for 1-2 hr. A few pellets were covered with powder of the same composition to reduce lithia loss and sintered at 1200°C for 5-10 hr. Pellet densities were typically 75-80% of the theoretical values. In some cases, unsintered pellets were partially melted by heating in closed Pt envelopes for 10-15 min at temperatures above the solidus. No significant distortion of the pellets occurred. This gave densities ~ 85% of the theoretical value.

Gold electrodes were applied to opposite pellet faces, generally by vapor deposition. Care was taken to mask the edges of the pellet to prevent penetration of the gold onto the sides of the pellet. In other cases, gold electrodes were applied with Englehard paste, heated at 150°-500°C in successive steps to remove the organic solvent, decompose the organo-gold complex, and harden the metallic residue. In some instances, before the electrodes were applied, the pellet surfaces were polished with successively finer grades of silicon carbide paper, using ethanol as lubricant, and finally with a rotary polisher using 1 μm diamond paste. The internal microstructure and composition of some pellets were examined by scanning electron microscopy combined with microprobe analysis.

The conductivity jig took the form of a stainless steel G-clamp, Fig. 1. The cell was held between high purity silica glass disks and pressure maintained by a spring loaded plunger (evaporated electrodes). Connection was made to the measuring apparatus by inserting gold foil strips between each silica disk and cell face. Each gold foil strip was wrapped around a platinum wire mounted within a stainless steel cylinder, from which it was insulated by a concentric silica glass tube. Internal surfaces of the jig head were lined with an insulating material (pyrophyllite). The temperature was measured with a Chromel/Alumel thermocouple, the tip of which was maintained in close proximity to the cell for maximum accuracy. The jig was mounted in a silica glass tube, thus permitting measurements to be made in vacuum or different atmospheres. The entire assembly was clamped centrally inside a noninductively wound, horizontal tube furnace attached to a Eurotherm P.D.I. controller. Temperatures were controlled and measured to ±2°C.

Two terminal a-c measurements were conducted over the frequency range 10^{-3}-10^{7} Hz, using a combination of bridge and automated phase sensitive detection techniques. For the range 100 Hz-70 kHz, a Wayne Kerr B224 bridge was used with a Brookdeal 9472 signal source and 9654 null detector. The signal generator output was maintained at 25 mV rms throughout; however, the voltage output from the bridge depended on the particular admittance range selected. An accuracy, in the measured admittance values, of better than 3% was typically obtained.

For the range 70 kHz-7 MHz, a B602 rf bridge and combined source/detector unit, SR268L, were used although at the extremes of this frequency range, the experimental data points showed some scatter. The applied voltage was 25 mV rms. For the frequency range 10^{-3}-10^{4} Hz, a Schlumberger Solartron Frequency Response Analyzer (F.R.A.) Model 1170 was used. Normally 500 mV rms was applied across a standard resistance and the cell, which were connected in series; only a proportion of this applied voltage appeared across the cell therefore, and this proportion varied with frequency, since the cell impedance was frequency dependent.

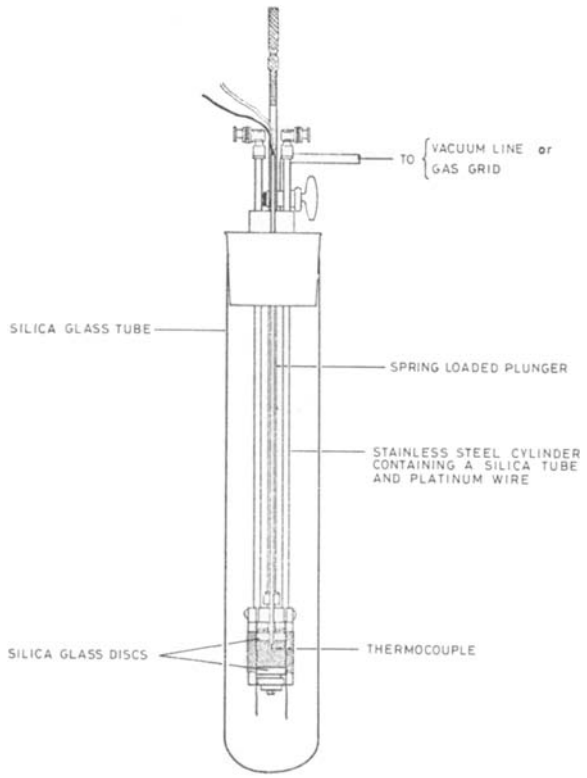

Fig. 1. A-C conductance jig

Generally, the matching and continuity of results from the F.R.A. and the two bridges was good.

Results

Impedance data—general comments.—Three typical sets of a-c data, in the form of complex impedance plane plots, are given in Fig. 2 for Au/LISICON/Au cells. The LISICON solid electrolyte composition was $Li_{2+2x}Zn_{1-x}GeO_4$: $x = 0.55$; similar behavior was observed for other x values. The data separate clearly into a high frequency region, which contains two semicircles, and a low frequency region, which contains a spike that was sometimes linear and sometimes curved. The spike was associated with the electrode-electrolyte interface since it was sensitive to polishing of the pellet surface prior to application of the electrodes. The high frequency region was assigned to the a-c response of the electrolyte itself, since it was independent of the magnitude of the applied electric field, at least up to 9.0V rms.

Within the high frequency region, Fig. 2, two slightly distorted semicircles are present, but their relative sizes are different in the three cases. The magnitude of the low frequency semicircle varied considerably from cell to cell and at the same temperature. In some cases it was the larger of the two (c) and in others it was the smaller (a, b). This indicates that the two semicircles had a different origin.

The high frequency semicircle, which passes through the origin, was associated with the intragranular or bulk response of the solid electrolyte. The intercept, R_g, on the Z' axis gives the resistance of the grains.

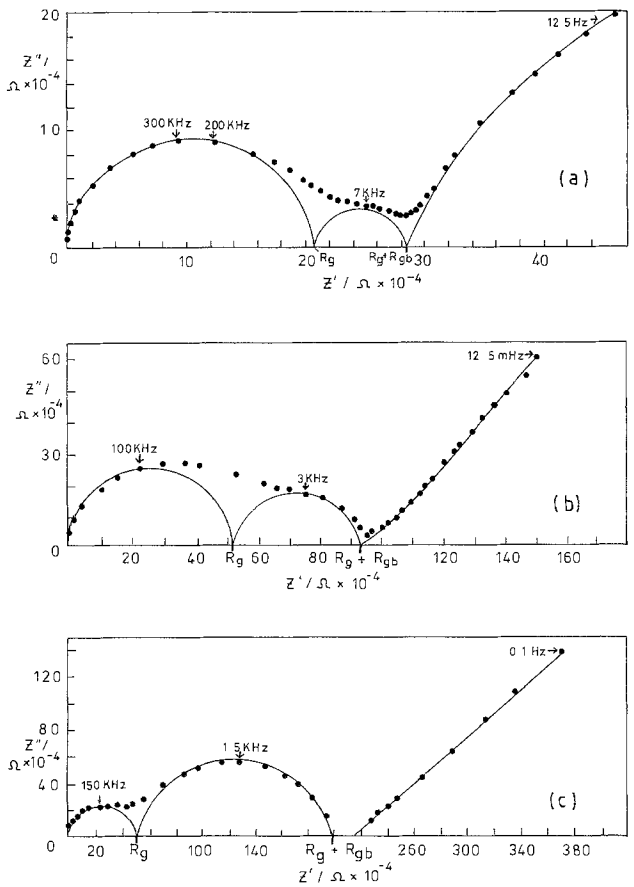

Fig. 2. Typical complex impedance plots for three Au/LISICON/Au cells, at 59°C: a) cell constant, $k = 0.55$ cm^{-1}; b) cell constant, $k = 0.47$ cm^{-1}; c) cell constant, $k = 0.64$ cm^{-1}.

For a given composition, x, and temperature, the value of R_g was the same, within a factor of 2-3, in all samples studied [large changes in R_g occurred on prolonged aging of samples, however (24): see later]. Using the relation $\omega RC = 1$, which holds at the maximum of an ideal semicircle, the capacitance of the high frequency semicircle was evaluated as ~1-2 pf cm^{-1}. This corresponds with that expected from the dielectric polarization of the crystals, assuming a typical bulk dielectric constant of ~5-25.

The second, low frequency semicircle is attributed to a grain boundary impedance in series with the intragranular impedance. The value of its capacitance, C_{gb}, calculated from the maximum of the second semicircle is in the range 10-400 pf cm^{-1} and represents charge polarization at the grain boundaries. These C_{gb} values are relatively small compared with grain boundary capacitances observed in solid electrolytes, such as Na β-alumina [800 pf cm^{-1} (Ref. 19) 21, nf cm^{-1} (Ref. 20)], and doped CeO_2 [50 nf cm^{-1} (Ref. 21)]. The magnitude of the grain boundary resistance, R_{gb}, varied from sample to sample at the same composition and was usually in the range $0.2\ R_g < R_{gb} < 8R_g$.

Although the magnitudes of R_g and R_{gb} were normally different, an important result is that, for a given sample, they appeared always to have the same activation energy, in contrast to the results of Bayard (22). Typical results are shown in Fig. 3 for a pellet in which both R_g and R_{gb} could be determined over a range of temperatures. The two sets of data fall on straight lines that are parallel within experimental error. Similarly, parallel sets of data were obtained: (*i*) for a variety of compositions, x; (*ii*) for samples that had undergone a phase transition to give one of various γ-derivative phases; (*iii*) for samples that had aged, *i.e.*, had undergone a marked decrease in conductivity on annealing (24).

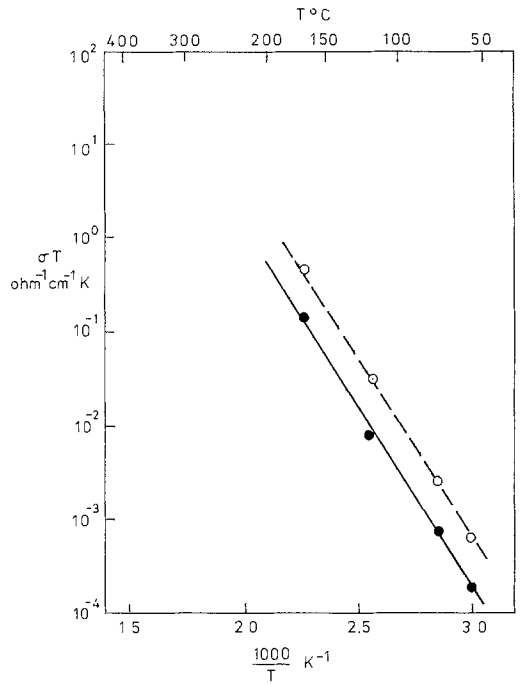

Fig. 3. Arrhenius plot of the intracrystalline conductivity ($1/R_g$)—⊙ and intercrystalline conductivity ($1/R_{gb}$)—● of an LISICON solid solution.

The similarity in the activation energies of R_g and R_{gb} indicates that charge migration in the intracrystalline and grain boundary regions occurred by the same process. In particular, the grain boundary effect is believed to be associated with a constriction of current pathways at the necks between crystals. A model for this is presented in the third section.

Various alternative explanations for the occurrence of more than one semicircle were considered but were rejected. These alternative explanations, with reasons for their rejection are as follows: (*i*) The presence of a surface layer on the electrolyte at the interface with the electrode, arising from, *e.g.*, surface attack (23) or electrochemical reactions. This layer would have a different structure and composition to the bulk, and probably, therefore, a different activation energy for conduction, in contrast to the results. (*ii*) If the crystal conductivity was markedly anisotropic, the presence of crystals in different orientations could possibly give rise to broadening of, or resolution into, two complex impedance semicircles. Again, however, it is likely that the two associated resistances would have different activation energies. (*iii*) Compositional variations between or within the crystallites (*i.e.*, a variation in x) could give rise to the appearance of more than one complex impedance semicircle. However, the activation energy for conduction in these LISICON solid solutions is very composition dependent (24), and any additional semicircles arising from compositional inhomogeneities should have different activation energy from the bulk. (*iv*) Dielectric relaxation may occur due to the formation of dipoles between, *e.g.*, substitutional and interstitial Li^+ ions. If this was the cause of the appearance of two semicircles, it can be shown that the dielectric relaxation time, which should be a fundamental property for each composition, in fact varied from sample to sample. This possibility is discounted, therefore. Details of the analysis and an equivalent circuit which may be used to represent a solid electrolyte that contains both free ions and dipoles, is given in the Appendix.

The intracrystalline (bulk) a-c response.—In the above analysis, it was assumed that the bulk properties could be approximated by a parallel combination

of a resistance and a capacitance. In fact, departures from this ideal behavior occurred, as shown in Fig. 4a, where data are presented as spectroscopic plots of M'' and Z'' against frequency. In the ideal case, the M'', Z'' peaks should be similar-shaped, Debye peaks ($\frac{1}{2}\Delta = 1.14$ decades) with their maxima occurring at the same frequency (17). In fact, the peak maxima occur at different frequencies in Fig. 4a, and the M'' peak is noticeably broadened on the high frequency side. The Z'' peak shows a spur on the low frequency side which is due to the onset of polarization associated with the grain boundary effect.

In order to analyze further these nonideal data, use is made of an equivalent circuit that contains a frequency dependent admittance, $Y^*(\omega)$, in parallel with the normal R and C elements, Fig. 5b. This circuit was also used to analyze data for single crystal beta alumina (16). The method of data analysis is as follows:

First, the impedance data are replotted in the admittance formalism, on logarithmic scales. This is done in Fig. 4b for one data set. The Y' plot shows two steps, or frequency independent plateaus, one below ~ 300 Hz and one between $\sim 10^4$ and 10^5 Hz, and a high frequency dispersion, above $\sim 10^5$ Hz. The low frequency plateau represents the overall electrolyte conductivity and after correction for the cell constant, is given by $(R_g + R_{gb})^{-1}$. The high frequency plateau represents the bulk, intracrystalline conductivity, $(R_g)^{-1}$. The Y'' plot shows an apparent plateau between 10^3 and 10^4 Hz, with a steep ramp at higher frequencies and another dispersion at lower frequencies. At this stage we are concerned with the bulk response only, which is given by the data above $\sim 10^4$ Hz.

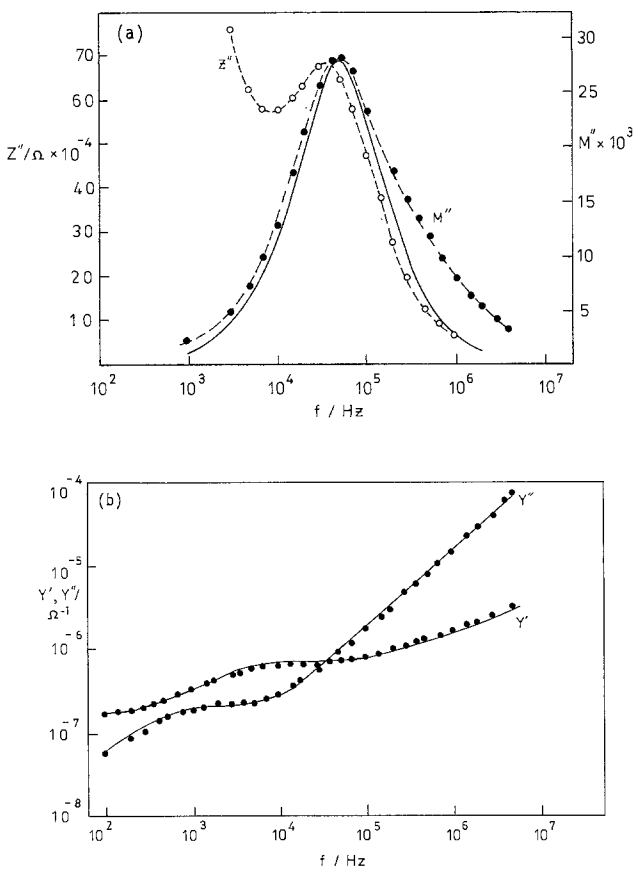

Fig. 4. (a) Z''-log f and M''-log f plots for an LISICON solid solution, $x = 0.55$, cell d, $k = 0.55$ cm^{-1}. The solid line represents an ideal Debye peak. Temperature: 39°C. (b) Log Y' and log Y''-log f plots of the data in (a). Solid circles are experimental points. Solid lines are calculated admittances.

The bulk admittance data, above $\sim 10^4$ Hz, can be represented by circuit (b), Fig. 5 whose complex admittance is

$$Y^* = R_g^{-1} + j\omega C_\infty + (A\omega^n + jB\omega^n) \quad [2]$$

The term in brackets is $Y^*(\omega)$, where A, B, and n are constants, $B = A\tan(n\pi/2)$ and $\omega = 2\pi f$: this describes the nonideal features of the response. Therefore

$$Y' = R_g^{-1} + A\omega^n, \quad Y'' = B\omega^n + \omega C_\infty \quad [3]$$

since

$$Y^* = Y' + jY'' \quad [4]$$

The equation for Y' contains two terms; R_g^{-1} is the value of the bulk conductivity and gives rise to the plateau in Y' between $\sim 10^4$-10^5 Hz; $A\omega^n$ represents the conductance ramp above $\sim 10^5$ Hz. The equation for Y'' also contains two terms; ωC_∞ gives the limiting slope of unity observed above $\sim 10^4$ Hz. The term $B\omega^n$ should give a low frequency slope of n, but below $\sim 10^4$ Hz, grain boundary phenomena influence the Y'' data and the region corresponding to $B\omega^n$ is not clearly distinguished. Values of the various parameters, extracted from Fig. 4b by curve fitting, are given in Table I. A test of the quality with which Eq. [2]

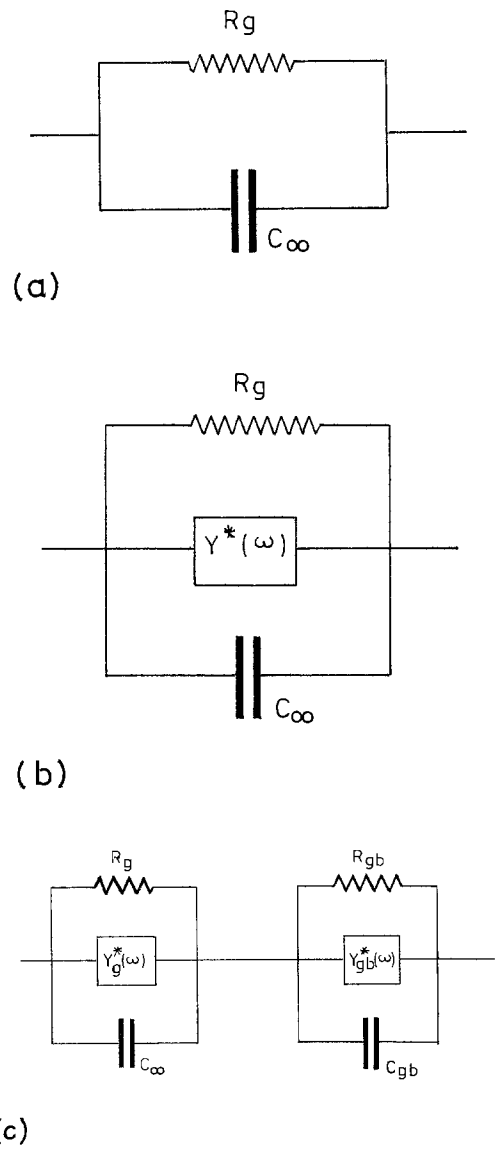

Fig. 5. Traditional (a) and new (b) equivalent circuits for the intracrystalline a-c response of a polycrystalline electrolyte. (c) Equivalent circuit for the entire a-c response of polycrystalline LISICON.

Table I. Equivalent circuit parameters extracted from Fig. 4b

	Bulk region	Grain boundary region
R^{-1}	3.9×10^{-7} ohm^{-1} cm^{-1}	1.2×10^{-7} ohm^{-1} cm^{-1}
A	4.3×10^{-11} ohm^{-1} cm^{-1} rad^{-n}	8.7×10^{-11} ohm^{-1} cm^{-1} rad^{-n}
B	5.9×10^{-11} ohm^{-1} cm^{-1} rad^{-n}	2.3×10^{-10} ohm^{-1} cm^{-1} rad^{-n}
n	0.60	0.77
C	1.3×10^{-12} F cm^{-1}	1.9×10^{-11} F cm^{-1}
k	0.55 cm^{-1}	0.55 cm^{-1}

models the experimental data is given by the closeness of the agreement between calculated and experimental admittance data. This is described in section below, in which the total admittance of the electrolyte, including both intragranular and grain boundary effects, is calculated and compared with the experimental results. The solid line in Fig. 4b represents calculated values and it can be seen that the agreement with the experimental data is good.

The complex admittance of circuit [Fig. 5(b)] may be converted into the three other complex formalisms using Eq. [1] and hence, the response of the equivalent circuit in all four formalisms may be calculated. The limiting high and low frequency expressions for each of the four formalisms are given in Table II. Equations [1] and [2] permit a better understanding of the different expressions of nonideality seen in the various formalisms and plots. For instance, the M'' peak, on a logarithmic scale, has a limiting slope of 1 at frequencies below the peak maximum, but a limiting slope of $n - 1$ $(0 < n < 1)$ at frequencies above the peak maximum. In contrast, the Z'' peak has limiting slopes of n and -1 at low and high frequencies, respectively, Table II. This accounts for the marked tendency, noted in various ionic conductors and Fig. 4a, for the M'' peak to be broader than the Z'' peak at frequencies above the peak maximum. Further, the simulations show that the maxima of the M'' and Z'' peaks are not coincident, but that the M'' spectrum always peaks at higher frequencies than the Z'' spectrum. The present results on LISICON show smaller departures from Debye response than observed in β-alumina (16). This may be because the mobile ion concentration in LISICON is considerably less than expected, in keeping with a model of ion trapping to be discussed elsewhere (25).

Grain boundary effects.—Polycrystalline LISICON sinters gave complex impedance plane plots that showed two semicircles, Fig. 2; the high frequency semicircle is attributed to the bulk response and the low frequency one to an intergranular or grain boundary effect. Since the resistances determined from the intercepts of the two semicircles on the Z' axis have similar activation energies in all samples studied, the origin of the low frequency semicircle is believed to be in the constriction of the current pathways at the necks which connect adjacent grains. These necks are clearly seen in a scanning electron micrograph, Fig. 6, and the porous nature of the sinter is also apparent. While, in some systems, an intergranular blocking phase of different composition to the bulk crystals may give rise to a constriction and a second semicircle in the a-c data (26), there is no evidence for such a second phase here: on extended exposure, Guinier x-ray powder diffraction photographs of powdered pellets, there was no evidence of a second phase. In addition, electron microprobe analysis of materials such as those shown in Fig. 6a, showed no difference in Zn,Ge content between the bulk and intergranular regions. It is believed, therefore, that the necks or intergranular regions are composed of material of the same composition and structure as the bulk of the crystals. In the following, a model is proposed to show how constriction of current pathways by the presence of air gaps between grains can lead to an extra semicircle in the complex impedance plane.

A schematic, idealized constriction between two grains is shown in Fig. 7a and a model equivalent circuit in Fig. 7b. The essential difference between grain and constriction regions lies in their relative cross-sectional area. It is assumed that there are no extra resistances at the contact points between grains, and that the crystal structure passes continuously from one grain to the next via the constricted region; it is also assumed that conduction is isotropic, and that differences in grain orientation do not affect the behavior. The grain and constriction resistances are set equal to R_1 and R_2 (the resistivities, ρ_1 and ρ_2, are equal, but the two regions have a different effective cell constant). The capacitances of the two regions are C_1 and C_2; C_1 corresponds to the bulk capacitance of the grains, C_2 represents the combination of the capacitance of the constriction region, C_c and the capacitance of the air gap, C_a. The Maxwell relaxation times, τ, of the grain and constriction regions are given, assuming simple geometries, by

$$\tau_1 = R_1C_1 = \rho\epsilon'e_o$$

$$\tau_2 = R_2C_2$$

where ϵ' is the bulk dielectric constant and e_o the permittivity of free space. But

$$C_2 = C_c + C_a$$

$$= \epsilon'\epsilon_o\frac{A_c}{l_c} + e_o\frac{(A_g - A_c)}{l_c}$$

where A_c, A_g, and l_c are defined in Fig. 7(a). Assuming that $A_g >> A_c$

$$C_2 = \epsilon'\epsilon_o\frac{A_c}{l_c} + \epsilon_o\frac{A_g}{l_c}$$

$$\therefore \tau_2 = \left(\rho\frac{l_c}{A_c}\right)\left(\epsilon'\epsilon_o\frac{A_c}{l_c} + \epsilon_o\frac{A_g}{l_c}\right)$$

Hence

$$\tau_2 = \tau_1 + \tau_1\frac{A_g}{A_c}\cdot\frac{l}{\epsilon'} \qquad [5]$$

As an order of magnitude calculation, if $\epsilon' = 10$ and $A_g = 90\ A_c$, then $\tau_2 = 10\tau_1$. In complex impedance plots, semicircle maxima occur when $\omega\tau = 1$, and therefore, two semicircles separated by one decade in frequency would be expected.

In order to try and modify the constriction resistances, some pellets were partially melted and their a-c conductivity measured. SEM photographs are shown in Fig. 6b, c for a pellet of composition $x = 0.55$, which was partially melted at ~ 1350°C and subsequently annealed at 1150°C for 1 hr. Electrodes were then applied and the a-c response of this cell determined. After conductivity measurements, the electrodes were removed, the pellet crushed to a fine powder, repelleted, and sintered at 1150°C for 1 hr; an SEM micrograph is given in Fig. 6d. The two pellets should differ only in their texture, therefore. It can be seen that the partially melted pellet, Fig. 6b, c, had a much larger average grain size than the reground

Table II. Limiting high and low frequency expressions calculated for the Jonscher circuit, Fig. 5(b)

	Y'	Y''	ϵ'	ϵ''	Z'	Z''	M'	M''
$\omega \to 0$	$1/R$	$B\omega^n$	$(B\omega^{n-1})/Co$	$1/\omega RCo$	R	$R^2B\omega^n$	$R^2CoB\omega^{n+1}$	$RCo\omega$
$\omega \to \infty$	$A\omega^n$	ωC_∞	C_∞/Co	$(A\omega^{n-1})/Co$	$(A\omega^{n-2})/C_\infty^2$	$1/\omega C_\infty$	Co/C_∞	$(CoA\omega^{n-1})/C_\infty^2$

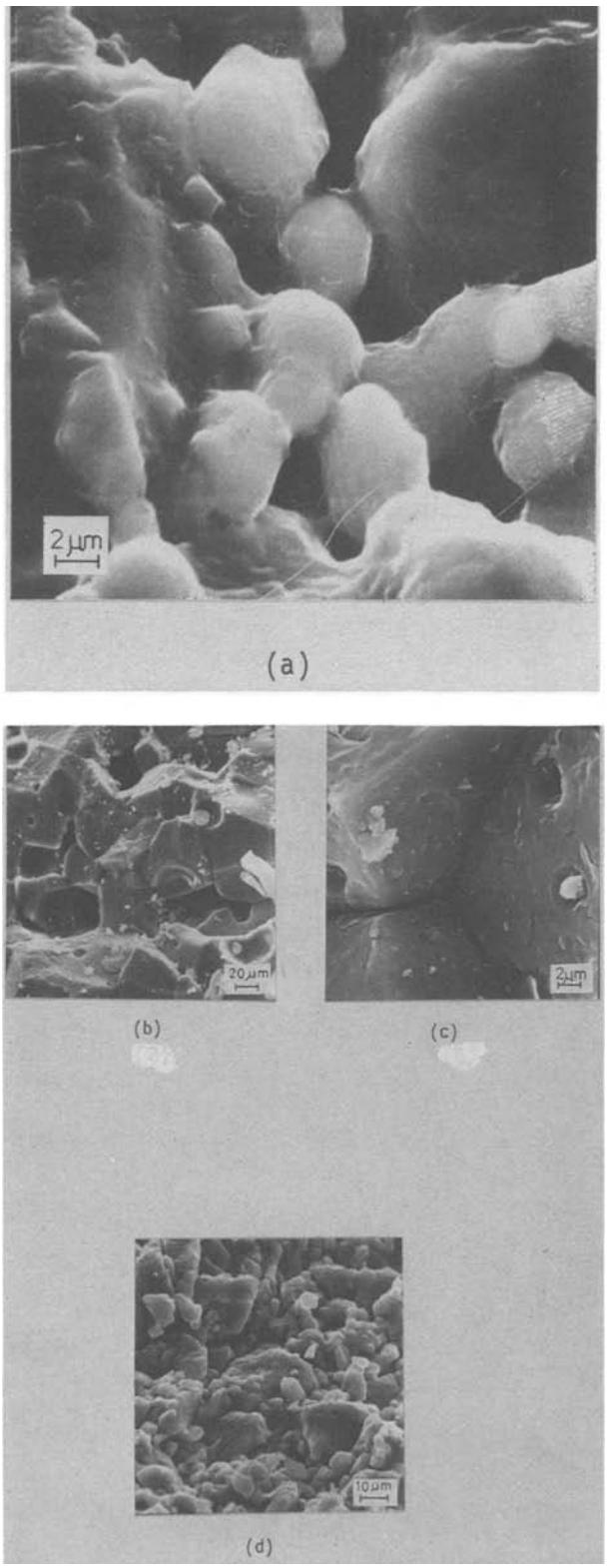

Fig. 6. Scanning electron micrographs of a) a sintered polycrystalline LISICON electrolyte, $x = 0.55$, fracture surface. b) and c) A partially melted electrolyte, $x = 0.55$, fracture surface. The micrograph (c) is a 10× magnification of the central region of (b). d) Sample (b, c) after grinding, repelleting, and sintering.

and sintered pellet, Fig. 6d. The partially melted pellet also had lower porosity, as confirmed by measurements of the densities of the two pellets: the partially melted electrolyte was 30% less porous than the reground sinter. The a-c response of the two pellets was markedly different, especially that part associated with the low frequency, grain boundary semicircle. In

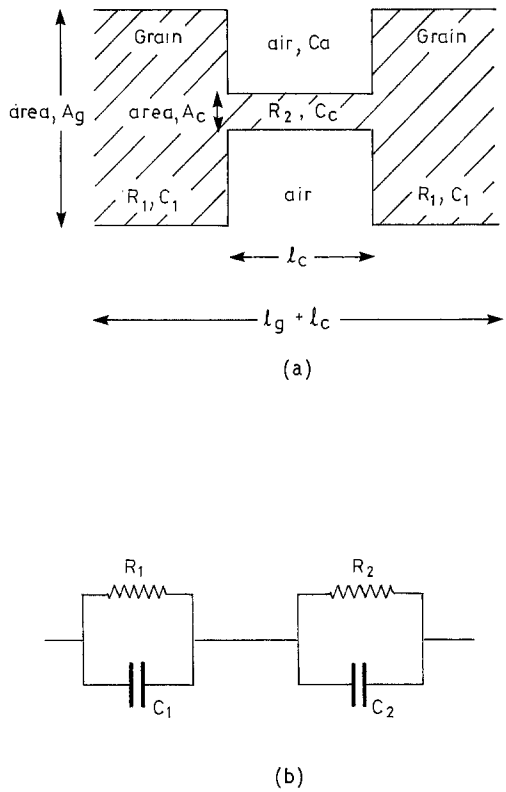

Fig. 7. (a) Schematic diagram of an intergranular constriction resistance. R_1—resistance of the grain region, R_2—resistance of the constriction region, C_1—capacitance of the grain region, C_c—capacitance of the constriction region, C_a—capacitance of the air gap, A_g—cross-sectional area of the grain region, A_c—cross-sectional area of the constriction region, l_g—length of the grain region, l_c—length of the constriction region. (b) The equivalent electrical representations. $C_2 = C_a + C_c$.

particular, C_2, the capacitance associated with the intergranular constriction was about ten times larger in the partially melted pellet than in the reground and sintered pellet. This is because the constriction resistances still exist but are now much thinner, Fig. 6c: the SEM micrographs show that in the partially melted sample, cracks run through some crystals and narrow gaps exist between grains.

It is concluded qualitatively that constriction resistances in porous sinters may be treated as separate *RC* elements in the equivalent circuit and, depending on the relative magnitudes of τ for the bulk and constriction regions, a separate or partly resolved second semicircle may be present in, *e.g.*, the complex impedance plane. The relative magnitudes of τ_g and τ_{gb} depend on the magnitude of the constriction capacitance C_a. This, in turn depends on: (*i*) the geometry, and (*ii*) the permittivity of the constriction region. For an air gap, ϵ' is approximately one tenth that expected for a second phase (which could also give rise to a constriction resistance). This contributes to the relatively low grain boundary capacitances observed here.

Quantification of the above model for constriction resistances is difficult because of the highly heterogeneous nature of polycrystalline sinters. However, account must also be taken of the nonideal response of the constriction region, in the same way that the bulk response is not Debye-like. In the next section, an analysis of the constriction region in terms of frequency dependent admittances is presented.

Analysis of grain boundary a-c data using a circuit containing a frequency dependent admittance.—It was shown in the section above that the intracrystalline response could be represented by an equivalent circuit, Fig. 5b, that incorporated a frequency dependent ad-

mittance. It is expected that a similar circuit may be of use in representing the constriction region. In order to analyze the data in this way, it was first necessary to subtract that component due to the intracrystalline response from the experimental data. Since the grain and constriction resistances are in series, this subtraction was made using corresponding impedance data

$$Z^*(gb) = Z^*(t) - Z^*(b) \quad [6]$$

where $Z^*(gb)$ is the residual impedance that is left after subtracting the intragranular impedance, $Z^*(b)$, calculated using the parameters given in Table I, from the total experimental impedance, $Z^*(t)$. Results are shown in Fig. 8b for $Z^*(gb)$, which was obtained by processing the data given in Fig. 8a. The $Z^*(gb)$ data fall on a distorted semicircle. These data were converted back into the Y^* formalism, replotted on logarithmic scales, Fig. 8c, and analyzed as described in the section above. The data again fit Eq. [2] but in this case, C_∞ is replaced by C_{gb}, and R_g by R_{gb}. In contrast to the intracrystalline response, C_{gb} is dominated by the expression $B\omega^n$ (Y'' data). The Y' data cover the frequency region over which both the terms R_{gb}^{-1} and $A\omega^n$ are significant. The values extracted from Fig. 8c are given in Table I.

Modeling the overall a-c response of LISICON polycrystalline electrolytes.—It has been shown that both the intragranular and constriction regions give an a-c response that may be described by an RC circuit containing an additional, frequency dependent admittance element. The total a-c response of the pellet may be represented by assuming that these two regions occur in series, with the equivalent circuit shown in Fig. 5c. Simulations based on this circuit are shown in Fig. 4b, 8a, d, and e for the parameters listed in Table I. The calculated response (solid curyes) agrees very well with the experimental data points within the limits of error inherent in the use of log-log plots to extract parameter values. It is particularly reassuring to note good agreement in all four formalisms, since each places a different emphasis

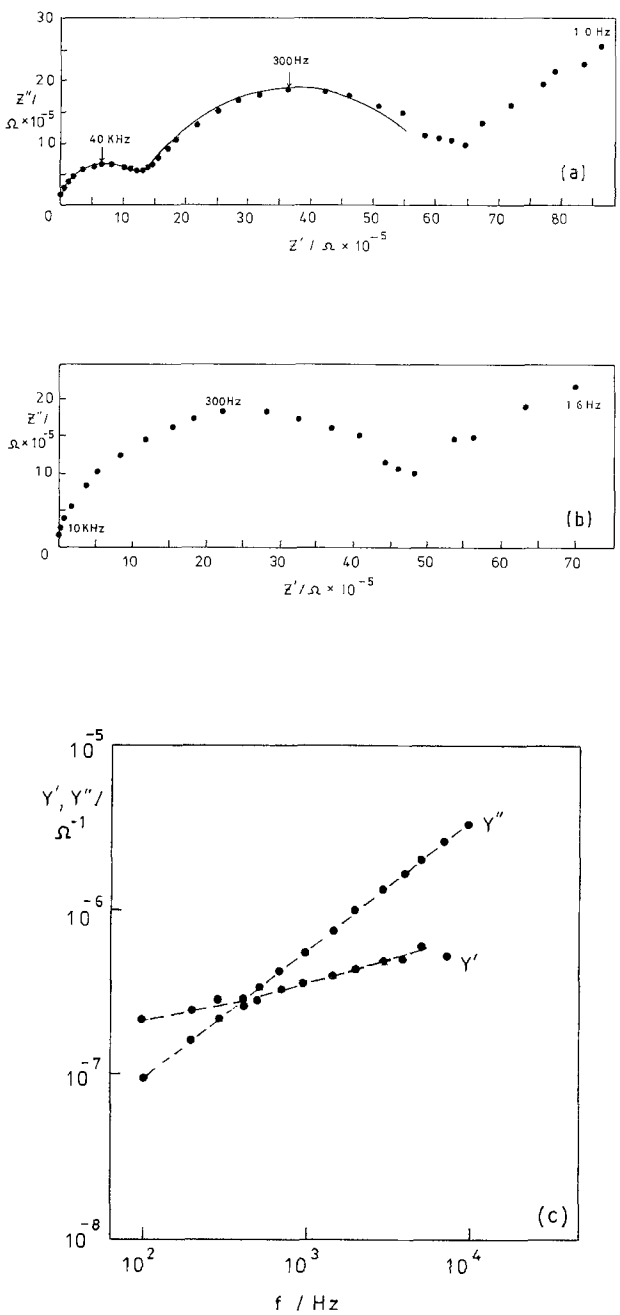

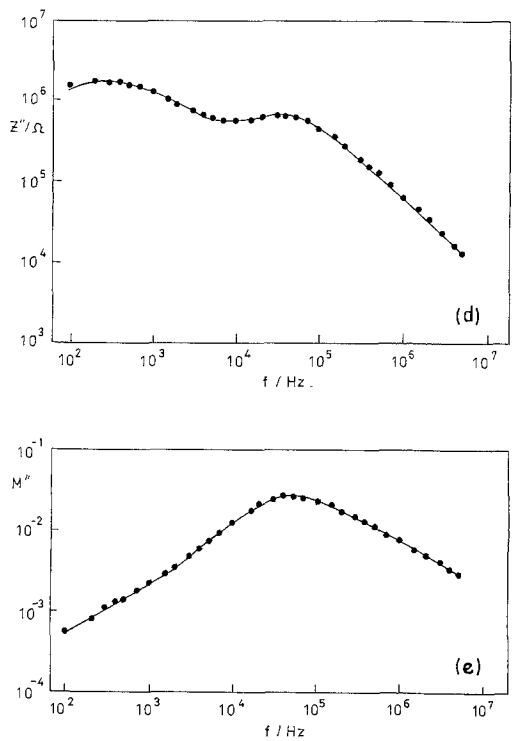

Fig. 8. (a) Complex plane plot of the total impedance, $Z^*(t)$, of cell d. The solid line represents the calculated total electrolyte impedance. (b) Complex plane plot of the grain boundary impedance, $Z^*(gb)$, of cell d, after subtracting the simulated intracrystalline impedance, $Z^*(b)$, from the total a-c response, $Z^*(t)$. At the lowest frequencies the data in (a) and (b) are significantly affected by the electrode impedance. (c) Log Y'-log f and log Y''-log f plots for the data in (b). Intra- and intercrystalline a-c response of cell d expressed as plots of: (d) log Z'' against log f for data in a), (e) log M'' against log f for data in a). In d) and e) solid circles represent experimental data and solid lines the calculated a-c response.

on the form of the a-c response. The use of a series circuit to model the total a-c response does not, of course, preclude the possibility of alternate parallel pathways. However, the current is likely to follow the parallel pathways of least impedance so that, to a first approximation, more than one parallel pathway need not be considered. The circuit then reduces to a series distribution of bulk and grain boundary elements.

The successful modeling of the overall electrolyte response, using circuit 5(c), is achieved without specifically taking into consideration any variation in the aspect ratio of crystal and neck geometries, which must inevitably be present in the pellets. It is possible that the difference in n between the two regions is related in some way to the considerable distribution in the geometries of the grain boundary regions. More work is clearly needed on different types of grain boundary in order to determine the factors that are important in controlling the a-c response.

The electrode-electrolyte interface.—Ideal blocking behavior at the electrode-electrolyte interface, which is signified by a limiting low frequency, vertical spike in the complex impedance plane, was not observed with the present materials. Instead, the electrode spike was inclined to the Z' axis at an angle of much less than 90° and, particularly at low frequencies, showed evidence of a downward curvature, Fig. 2a. A detailed study of the electrode-electrolyte response has not been made although some preliminary observations were made. The nonvertical nature of the spike was not associated simply with roughness of the electrolyte surface: although the spike was somewhat sensitive to polishing, a vertical spike was never obtained. It has been shown in other systems that a Jonscher expression, containing a frequency dependent admittance, may be used to model nonideal electrode-electrolyte response (12-14); it could probably also be relevant to the present, low frequency data.

APPENDIX

A Model for Dielectric Relaxation

Dielectric relaxation in solid electrolytes may occur if dipoles, formed by the pairing of ions, exist. In the LISICON solid solutions, dipoles may feasibly form by the pairing of substitutional and interstitial Li^+ ions, whch carry effective charges of -1 and $+1$, respectively. An equivalent circuit representation of a solid electrolyte that contains both mobile (*i.e.*, "free") ions and dipoles is given in Fig. 9. It is assumed that the dipole reorientation processes, represented by R_D and C_D, occur in parallel with the long range ionic motion, represented by R_g. The limiting, high frequency capacitance of the material is given by C_∞.

In the complex impedance plane, the circuit given in Fig. 9 would in principle give rise to two semicircles, due to the coupling of R_g, C_D and R_D, C_∞. The two semicircles can be resolved provided their time constants,

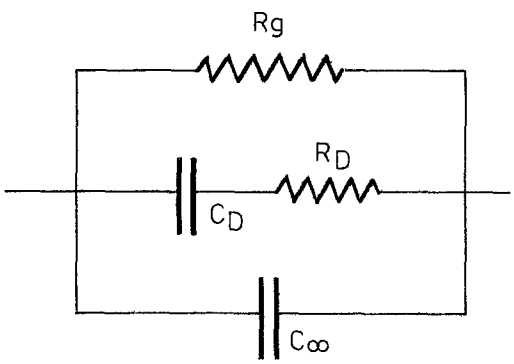

Fig. 9. Equivalent circuit for a solid electrolyte containing dipoles which give rise to dielectric relaxation. R_g—long range ionic migration, C_∞—high frequency polarization of the electrolyte, C_D, R_D—dipole reorientation process.

given by the magnitude of the products RC, are quite different and $R_D < R_g$. However, although these time constants may be defined for the complex impedance plane, the dielectric reorientation process has a different time constant τ_D, given by the product, R_DC_D. τ_D is a fundamental property of the reorientation process and should have an Arrhenius temperature dependence $\tau_D = \tau_0 \exp(E/kT)$, that is expressed in the temperature dependence of R_D. The dielectric relaxation process, which is represented by a series element, R_D and C_D, would not therefore be observed directly in the complex impedance plane, since semicircles arise from parallel R, C combinations. However, the relevant parameters may be extracted, R_D from the high frequency semicircles and C_D from the low frequency semicircle.

Acknowledgments

We thank SERC and Tioxide International Limited for a research studentship to PGB and SERC for a research grant to ARW. Dr. W. McHardy of the Macaulay Soil Research Institute, Aberdeen kindly provided facilities and assistance with the scanning electron microscopy. We thank Mr. A. Barclay for help with the design and fabrication of the conductivity jig.

Computing facilities were provided by the University of Aberdeen, Computing Centre.

Manuscript submitted Jan. 21, 1982; revised manuscript received Oct. 25, 1982.

Any discussion of this paper will appear in a Discussion Section to be published in the December 1983 JOURNAL. All discussions for the December 1983 Discussion Section should be submitted by Aug. 1, 1983.

REFERENCES

1. K. S. Cole and R. H. Cole, *J. Chem. Phys.*, **9**, 341 (1949).
2. D. Ravaine and J-L. Souquet, *J. de Chemie Physique*, **11**, 693 (1974).
3. E. Schouler, A. Hammou, and M. Kleitz, *Mater. Res. Bull.*, **71**, 693 (1976).
4. D. W. Davidson and R. H. Cole, *J. Chem. Phys.*, **18**, 1417 (1951).
5. I. M. Hodge, Unpublished work.
6. A. K. Jonscher, *Nature*, **267**, 673 (1977).
7. A. K. Jonscher, *J. Mater. Sci.*, **13**, 553 (1978).
8. K. L. Ngai, *Comments Solid State Phys.*, **9**, 127 (1979).
9. K. L. Ngai, A. K. Jonscher, and C. T. White, *Nature*, **277**, 185 (1979).
10. L. A. Dissado and R. M. Hill, *ibid.*, **279**, 685 (1979).
11. L. A. Dissado and R. M. Hill, *Philos. Mag.*, **B41**, 625 (1980).
12. A. K. Jonscher and J-M. Reau, *J. Mater. Sci.*, **13**, 563 (1978).
13. I. D. Raistrick, C. Ho, Y. W. Hu, and R. A. Huggins, *J. Electroanal. Chem.*, **77**, 319 (1977).
14. T. M. Gur, I. D. Raistrick, and R. A. Huggins, *Solid State Ionics*, **1**, 251 (1980).
15. I. D. Raistrick, C. Ho, and R. A. Huggins, *This Journal*, **123**, 1469 (1976).
16. P. G. Bruce, A. R. West, and D. P. Almond, *Solid State Ionics*, **7**, 57 (1982).
17. I. M. Hodge, M. D. Ingram, and A. R. West, *J. Electroanal. Chem.*, **74**, 125 (1976).
18. P. G. Bruce and A. R. West, *Mater. Res. Bull.*, **15**, 379 (1980).
19. E. Lilley and J. E. Strutt, *Phys. Status Solidi, A*, **54**, 629 (1979).
20. R. W. Powers and S. P. Mitoff, *This Journal*, **122**, 226 (1975).
21. D. Y. Wang and A. S. Nowick, *J. Solid State Chem.*, **35**, 325 (1980).
22. M. L. Bayard, in "Fast Ion Transport in Solids," P. Vashishta, J. N. Mundy, and G. K. Shenoy, Editors, North-Holland, Amsterdam (1979).
23. E. N. Boulos, A. V. Lesikar, and C. T. Moynihan, *J. Non-Cryst. Solids*, **45**, 419 (1981).
24. P. G. Bruce and A. R. West, *J. Solid State Chem.*, **44**, 354 (1982).
25. P. G. Bruce and A. R. West, In preparation.
26. J. E. Bauerle, *J. Phys. Chem. Solids*, **30**, 2657 (1969).

Lattice Parameter Changes in $Al_{0.39}Ga_{0.61}As$ Due to O, Ge, Si, and S Doping

W. R. Wagner, N. E. Schumaker,* J. L. Zilko, P. J. Anthony,* and V. Swaminathan

Bell Laboratories, Murray Hill, New Jersey 07974

ABSTRACT

The change in lattice parameter of epitaxial films of $Al_{0.39}Ga_{0.61}As$ was investigated as a function of growth solution doping. With the lattice constant of GaAs as the reference constant, it was found that the presence of either O_2 in the growth ambient or Ge in the growth solutions dilated the lattice. Growth solution doping with Si was found to initially dilate the lattice while further Si doping resulted in a lattice contraction. Sulfur doping contracted the lattice. It was found that the lattice dilation due to O_2 in the growth ambient principally resulted from a reduction in the background S contamination of the epitaxial films.

The purposeful addition of selected impurities is central to semiconductor materials technologies. The measurement of dopant incorporation into such materials is commonly limited to electrically active species since the measurement of total dopant incorporation is more difficult. Secondary ion mass spectroscopy (SIMS), radioisotope, and neutron activation techniques are the usual techniques used to monitor their incorporation. Insights into both dopant incorporation and dopant behavior can be provided by combining electrical measurements and less direct techniques such as precision lattice parameter measurements. The determination of dopant-induced or process-induced lattice parameter changes can provide a direct measurement of the effective size of an impurity or vacancy in the lattice. If the effective sizes are known, low impurity concentrations can be measured. Also, the defect chemistry of dopants can be investigated by measuring lattice parameter changes as a function of dopant incorporation. For instance, in GaAs, the incorporation of electrically active Te saturates at approximately 8×10^{18} free carriers/cm^3 (Ref. 1), but radiotracer techniques indicate that Te continues to be incorporated until at least 10^{20}/cm^3 (Ref. 2). When the effective Te distribution coefficient decreased, a relatively large lattice dilation was measured that increased directly with increased Te doping (3). This indicated the formation of strain centers such as high concentrations of interstitial defects or precipitates. Transmission electron microscopy revealed that these defects were nucleated by GaTe microprecipitates that were presumably the strain centers first detected with the x-ray lattice parameter measurement.

The lattice constant of GaAs has been measured often (4, 5). It is known as a function of the growth technology (5), *i.e.*, LPE, VPE, Bridgeman, and Czochralski, and as a function of doping (4, 5), and ranges from 5.65317 to 5.65333Å. On the other hand, only powder measurements of the lattice constant of AlAs exist (6, 7, 8), with $a = 5.6605 \pm 0.0005$Å. Also it has been shown that the lattice constant of $Al_xGa_{1-x}As$ alloys followed Veygard's law (6, 9, 10), such that

$$a_{(Al_xGa_{1-x}As)} = a_{(GaAs)} + x[a_{(AlAs)} - a_{(GaAs)}]$$

Lattice parameter measurements of $Al_xGa_{1-x}As$ alloys other than determinations of the lattice mismatch between a heteroepitaxial film and its substrate have not been made.

In this paper we report double-crystal x-ray diffractometric measurements of lattice parameter changes of LPE $Al_{0.39}Ga_{0.61}As$ films resulting from the addition of Si, Ge, and S to the growth solution and from the presence of O_2 in the growth ambient. Growth conditions resembled the multiple growth well, multiple layer growth environment used for manufacturing double heterostructure laser crystals. Selected contaminants were increased to identify their effects on a laser structure. This was deemed desirable because the reproducibility of the electrical characteristics of individual $Al_{0.4}Ga_{0.6}As$ films is excellent, while the electron transport properties of the same film grown from the same growth solution in a multiple growth well environment is not (11).

* Electrochemical Society Active Member.

Key words: double crystal x-ray diffractometry, thin films, liquid phase epitaxy, growth solution doping, lattice parameter, AlGaAs.

Fundamental Considerations

The underlying principle of the lattice parameter measurements is naturally Bragg's law

$$n\lambda = 2d \sin\theta$$

and its differential

$$\frac{\Delta d}{d} = \Delta\theta \cot\theta$$

where λ is the incident x-ray wavelength, d is the interplanar spacing of the diffracting planes, and θ is the angle of incidence of the x-rays. Implicit in the statement of Bragg's law is the assumption of a single incident x-ray wavelength and a single angle of incidence, *i.e.*, a plane wave. Real x-ray sources, however, generate polychromatic spherical waves. The double-crystal x-ray experimental arrangement (12) transforms this radiation into a good approximation to a plane wave such that the fundamental Darwin-Prins (12) linewidths can be closely realized. The incident radiation is first collimated, then diffracted from a highly perfect monochromator crystal. If the diffraction condition is arranged to be asymmetric, *i.e.*, the diffracting planes are not parallel to the surface, the divergence of the diffracted beam can easily be reduced by another factor of 10 (12)

$$b = \frac{\sin(\theta - L)}{\sin(\theta + L)}$$

where b is the asymmetry factor, θ is the Bragg angle, and L is the angle between the surface and the diffracting planes.

If a plane wave of x-rays is incident on a heterostructure consisting of an $Al_xGa_{1-x}As$ film on a GaAs substrate, the Bragg condition will be satisfied for two angles of incidence for every set of diffracting planes arising from the two different interplanar spacings. In practice, the sample is approximately aligned to the Bragg angle, then rotated slowly and precisely through both Bragg angles. The diffracted intensity is recorded as a function of rotation angle generating a "rocking" curve consisting of two peaks separated by an angle $\Delta\theta$ that defines the difference in interplanar spacing between the substrate and the epitaxial film.

The difference in interplanar spacing measured in this manner is a measurement of a stressed elastically deformed heterostructure. When a film of a different lattice constant is grown on a substrate, the resultant structure is stressed in such a way that the unit cell of the epitaxial film is tetragonally deformed (13, 14). Compared to the deformation of the epitaxial film the deformation of the substrate is negligible because (15)

$$\sigma_{sub} = -\frac{t_l}{t_{sub}}\sigma_l$$

where the ratio of epi-thickness t_l to substrate thickness t_s, t_l/t_s, is typically 1/50. In the epitaxial film, the planes parallel to the growth interface are constrained elastically to have the same interatomic spacings as the substrate. The lattice then deforms in the direction of growth. The relaxed lattice constant of the epitaxial film was derived by Hornstra and Bartels (16) and by Estop and Sauvage (6). For {100} growth interfaces

$$\frac{\Delta d}{d_{relax}} = 0.525\frac{\Delta d}{d_{stressed}}$$

This elasticity correction from the experimental values is indeed significant.

The tetragonal deformation of the unit cell is easily observed with x-ray diffractometry. Because of the deformation, lattice planes that are not parallel or perpendicular to the growth interface will not be parallel to corresponding planes in the epitaxial film. With a <511> diffraction condition and a (001) interface

$$\Delta\theta(\bar{1}15) \approx 2\Delta\theta(1\bar{1}5)$$

If a <511> diffraction condition is used to determine $\Delta a/a$, then the arithmetic mean of the two $\Delta\theta$ measurements (9) has to be used to compute $\Delta a/a$.

Experimental Arrangement

Double-crystal x-ray diffractometry.—The white Cu radiation (emitted by a 6 kW Rigaku rotating anode generator) is first collimated, then diffracted from a highly perfect Ge monochromator crystal. The monochromator had polished {111} faces and was aligned to the incident x-rays to excite the <511> reflection. This alignment corresponds to an asymmetry factor $b = 0.107$, indicating that the reflected beam will be roughly ten times wider than the incident beam while the angular dispersion is one-tenth its original value. A second slit was used to reduce the width of the reflected beam because samples were curved as a result of heteroepitaxial stresses and thereby dispersed the Bragg condition. Samples were aligned in a +-geometry to again excite the <511> reflection.

The possible Bragg reflections of a heterostructure wafer were examined by scanning a small angle near $\theta_B = 45.2°$ about an axis perpendicular to the x-ray beam. Specimens could be translated parallel to the {100} surface to examine the uniformity of alloy composition. The x-ray intensities reflected from the specimen wafer were measured with an LiF scintillation counter and plotted against the rocking angle in 0.25 sec/step increments.

Liquid phase epitaxy.—Great care was taken with the LPE growth of our specimens to insure that the reproducibility of the Al alloy compositions of the resultant epitaxial films was within ±0.25% Al. The basic LPE technique was patterned after Dawson's (17) source-seed-slider method. All LPE reactors were standardized to a common 780°C temperature with a single Pt-Pt 10% Rh thermocouple. The growth schedules were rigorously duplicated as were the basic compositions of the growth solutions. Several growths were made with varying amounts of Ge, Si, and S introduced into each melt and with a flowing growth ambient of pure He (<1 ppb O_2) or He containing 0.7 ppm O_2. In every growth, at least one melt composition of a previous experiment was duplicated as a check on reproducibility. With our growth technology, six different epitaxial films could be grown simultaneously on six different substrates. Twelve substrates from three adjacent wafers of the same Si doped ingot were used to assure a uniform substrate lattice constant. In all growth solutions used in this experiment, the Al content was 6.43 mg with a standard deviation of ±0.04 mg in an 8 ± 0.05g Ga growth solution. In the direction of the flowing ambient, the first growth solution remained undoped, the second contained 50 mg Ge as did the next four solutions. The third solution also contained 50 μg Si, the fourth 500 mg Si, the fifth 5 mg Si, and the sixth 50 mg Si, all in addition to the 50 mg Ge. A single layer of $Al_{0.39}Ga_{0.61}As$ approximately 3 μm thick was grown on every substrate. In all, three different epitaxy reactors supplied samples for this experiment.

Results

A pair of diffractometric plots of the <511> diffraction condition were obtained from every $Al_{0.39}Ga_{0.61}As$-GaAs heterostructure; one plot for the 29° angle of incidence (Fig. 1) and the other for the 61° angle of incidence (Fig. 1). From these, the relaxed ($\Delta a/a$) were computed. These values are plotted against the growth solution composition in Fig. 2 and listed in Table I. The addition of 0.7 ppm of O_2 to the growth ambient was found to uniformly dilate the lattice by 14 ± 4 ppm, as compared to films grown in the pure He ambient, regardless of the Ge or Si doping of the growth solution. Doping the growth solution with 0.6 atom percent (a/o) Ge was found to dilate the resultant $Al_{0.39}Ga_{0.61}As$ lattice compared to undoped films by 15 ± 4 ppm. Si doping to the level of 1.6×10^{-3} a/o was found to dilate the lattice by 3-10 (±4) ppm beyond the lattice constant of the Ge-doped films, while additional Si doping contracted the lattice by 13 ppm for each order of magnitude increase in the Si doping of the growth solution, a total decrease of 45 ppm between 1.6×10^{-3} to 1.6 a/o Si in the growth solution.

The incorporation of sulfur in the $Al_{0.39}Ga_{0.61}As$ lattice was found to result in a significant lattice contraction also. As little as 6.4×10^{-5} a/o S in the growth solution was found to contract the $Al_{0.39}Ga_{0.61}As$ lat-

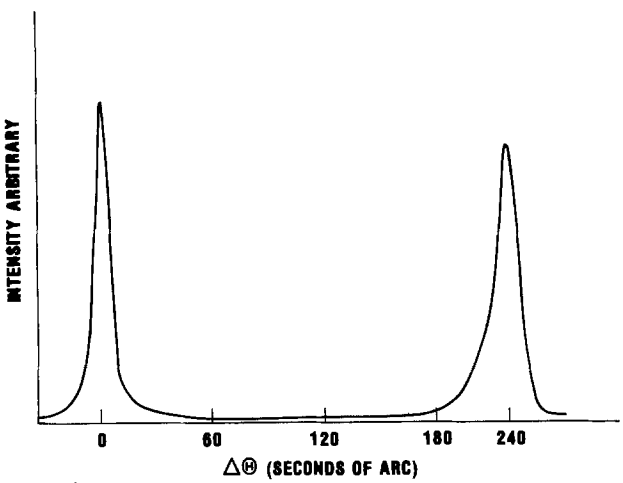

Fig. 1. Typical diffractometric plot of an $Al_{0.39}Ga_{0.61}As$ heteroepitaxial film on a GaAs substrate. The diffraction peak arising from the film is at the right.

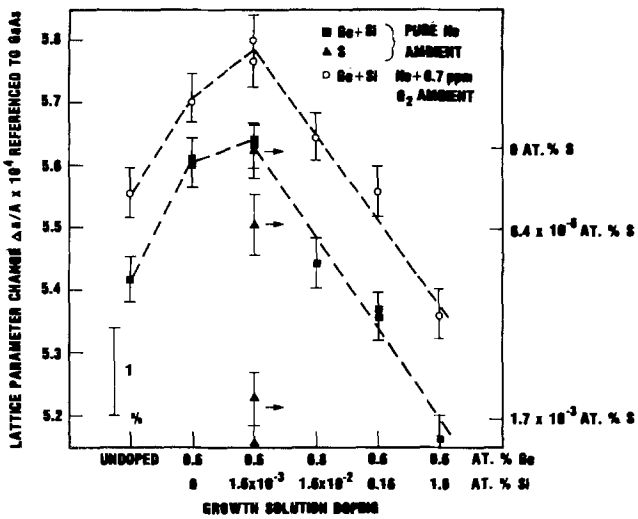

Fig. 2. Plot of the lattice changes $\Delta a/a$ as a function of growth solution doping and growth ambient.

tice by 14 ± 4 ppm from the Ge- and Si-doped level. Furthermore, 1.7×10^{-3} a/o S in the growth solution contracted the lattice by 44 ± 4 ppm. Separate samples reproducing earlier growths were found to have the same lattice constant well within the estimated limits of error of this experiment.

Discussion

Sources of error.—The measurement of dopant-induced lattice parameter changes on $Al_{0.4}Ga_{0.6}As$ films with double-crystal x-ray diffractometry requires two constants. The lattice parameter of the substrates used had to be uniform on the scale of the lattice parameter changes to be measured, and the Al content of the epitaxial films had to be reproducible and uniform to substantially better than 1%. The importance of reproducible Al concentrations is illustrated by the length of the 1% Al bar in Fig. 2. Lattice parameter fluctuations in melt-grown GaAs were studied extensively by Mullin *et al.* (5). Samples doped to 2×10^{18} free carriers/cm^3 with a variety of dopants ("Te and other dopants") as a group fluctuated by $\Delta a/a = \pm 4 \times 10^{-6}$. The subgroup of Si-doped samples was not separately identified, but it can be expected to fluctuate even less. Furthermore, the electrical characteristics of the substrates used for our study were quite homogeneous, 1.5×10^{18} free carriers/cm^3 and 2700 cm^2 V-sec mobilities at room temperature. Electrolytic etching of typical substrates indicated also that doping levels were homogeneous even on a small scale. It could, therefore, be presumed that the lattice parameter of the substrates used in this experiment was constant to 1 ppm. Included in this consideration were thermal expansion effects during the x-ray measurement. The thermal expansion coefficients of GaAs and AlAs lie between $5\text{-}6 \times 10^{-6}/(K^{-1})$ (17, 18). A 1°C temperature gradient in the 25 μm penetration depth of the x-ray beam is possible only for a 10°C temperature gradient in the entire sample. The thermal conductivity of the material (0.37 W/cm K) and the long equilibration time of each specimen indicate that even a 1°C temperature gradient in the sample was unlikely. Thermal expansion effects were then much less than 1 ppm.

A significant source of error consisted of the measurement of the angle $\Delta\theta$. This angle was generated with a differential micrometer, 100 divisions per 0.005 in., and 1.2 divisions per sec of arc. The repeatability of measurement was found to be ±1 div, *i.e.*, ±0.8 sec. The accuracy of the micrometer was found to be at least ± 0.001 $(\Delta l/l)$. Mechanical error should then be of the order of ±0.8 sec, corresponding to $\Delta a/a = \pm 3.8 \times 10^{-6}$ for the <511> reflection used. The accuracy in determining the center of mass of the diffraction peaks was substantially better. Rocking curves that did not result in two symmetric peaks of better than 10 sec half-maximum widths were repeated with better specimen alignments. The midchord peak construction (19) was used to determine the center of mass. For each diffraction peak, this determination was accurate to at least ±0.1 sec. The total error in $\Delta\theta$ was conservatively estimated to be ±1 sec of arc. The data, in fact, indicated a better degree of reproducibility. Repeated measurements of different areas of the same sample wafer at different times agreed to better than 1 sec of arc.

The reproducibility of the Al alloy compositions of the heteroepitaxial films was the most important consideration in assessing the validity of these results. An evaluation of this was, in fact, the secondary goal of this experiment. As already mentioned, considerable care was taken in the LPE growths to achieve reproducible growth conditions. Unfortunately, the determination of absolute Al compositions to the $x = \pm 0.001$ accuracy necessary to differentiate between alloy and doping effects appears impossible. Photoluminescence measurements of the completely undoped film and the equivalent film grown in the 1 ppm O_2 ambient indicated equivalent Al alloy compositions. Certainly, a $\Delta x = 0.03$ decrease in the alloy content of lightly and heavily Si-doped films did not occur. To an accuracy of $x = 0.01$, these measurements indicated that the Al compositions remained constant. The data listed in the

Table I. Data summary of growth solution doping, impurities, and lattice change

Wafer No.		Growth solution doping (a/o) x_e (Al)	x_e (Ge)	x_e (Si)	x_e (S)	Impurities in the solid ($\times 10^{-17}$/cm^3) Ge	Si	S	Lattice change measurements $(\Delta a/a) \times 10^4$ First	Second
426	—1	0.208	0.6	1.6	0.0	20*	500*	1*	5.16	
	—2	0.206	0.6	0.16	0.0	20*	50*	1*	5.36	5.37
	—3	0.204	0.6	0.016	0.0	20*	5*	1*	5.44	
	—4	0.209	0.6	0.0016	0.0	20*	0.5**	1**	5.64	5.63
	—5	0.207	0.6	0.0	0.0	20*	<0.1*	1*	5.61	5.60
	—6	0.208	0.0	0.0	0.0	<1*	<0.1*	1*	5.42	5.44
83	—1	0.208	0.6	1.6	0.0	20*	300*	0.3*	5.37	
	—2	0.209	0.6	0.16	0.0	20*	30*	0.3*	5.56	
	—3	0.206	0.6	0.016	0.0	20*	3*	0.3*	5.65	
	—4	0.208	0.6	0.0016	0.0	20*	0.3**	0.3**	5.80	5.77
	—5	0.209	0.6	0.0	0.0	20*	<0.1*	0.3*	5.71	
	—6	0.208	0.0	0.0	0.0	<1*	<0.1*	0.3*	5.55	
45	—3	0.208	0.6	0.0013	1.7×10^{-3}	20*	0.9**	300**	5.15	
46	—3	0.209	0.6	0.0013	1.7×10^{-3}	20*	1.2**	270**	5.23	5.20
	—6	0.209	0.6	0.0013	0.0	20*	0.5**	0.5**	5.64	5.62
48	—6	0.209	0.6	0.0013	6.4×10^{-5}	20*	0.4**	10**	5.48	5.52

* Estimated concentration.
** Concentration measured by SIMS.

table indicate an alloy reproducibility better than $\Delta x = 0.002$. Unquestionably, this data proves a satisfying degree of repeatability in our epitaxial growth technology. Two different LPE reactors on several occasions produced films with the same lattice constant from growth solutions of the same composition.

Without a precise determination of the Al alloy compositions of the epitaxial films, the data may be interpreted in two ways: either the distribution coefficient for Al in doped GaAs solutions changes systematically at low dopant concentrations, or the incorporation of impurities in $Al_{0.39}Ga_{0.61}As$ systematically changes the lattice constant. We support the latter view. It is difficult to accept that 0.7 ppm of O_2 in the growth ambient, the accepted background contamination of most LPE reactors, would increase the distribution coefficient of Al. This level is significantly below the solubility limit for oxygen in Ga; both Ga_2O_3 and GaO in Ga solutions are reduced in such an ambient. The level of oxygen in the growth solutions will be too small to result in any change in the distribution coefficient. Furthermore, a possible oxygen reaction with Al would tend to reduce the effective distribution coefficient. The same argument can be applied to the effects of S on the distribution coefficient of Al. It is not reasonable that 1.7×10^{-3} a/o S in the growth solution could reduce the Al concentration by $\Delta x = 0.03$. In fact, photoluminescence spectroscopy indicates that x changed by less than 0.01. In the case of Ge doping of $Al_xGa_{1-x}As$ films, an electron beam determination of Al compositions indicated a decrease in the Al distribution coefficient only for a/o Ge greater than 1% in the growth solution (20). Our result could be interpreted only in terms of an increase in the distribution coefficient. The Si doping of the growth solutions is more extensive, ranging from 1.6×10^{-3} to 1.6 a/o. While it is not inconceivable that 1.6 a/o Si in the growth solution might alter the Al distribution coefficient, the change must be less than $x = 0.01$, but then two and three orders of magnitude lower Si doping cannot be expected to have a significant effect.

The best argument for constant Al compositions and dopant-induced lattice changes lies in the self-consistent nature of the data as a set as shown in Fig. 2. The symmetry of the figure is a strong argument for the occurrence of dopant-induced lattice changes rather than changes in the Al distribution coefficient. Dilute dopants at concentrations of roughly one impurity atom per 1000 unit cells can be expected to behave as single strain centers with clearly differentiable effects for each dopant species. On the other hand, changes in the Al distribution coefficient with respect to the composition of the growth solutions can be expected to be interactive such that one species is predominant. A parallelism such as appears in this data where the effects of oxygen, Ge, Si, and S are clearly differentiated would be surprising.

The significance of the results.—The knowledge of the precise impurity concentration of the epitaxial films would be of great aid in the interpretation of the results. Hall measurements can give only an order of magnitude estimate of the total impurity concentration in this alloy because so many carriers enter the (L and X indirect) conduction bands. Actual impurity concentrations may be deduced from other data. There exists good evidence indicating that the distribution coefficient of Ge does not change in $Al_xGa_{1-x}As$ alloys at low doping levels (21). The observed lattice dilations due to Ge doping may then be compared to similar measurements in GaAs. According to Ketchow (22), our doping of 0.6 a/o Ge should be equivalent to 2×10^{18} free carriers/cm^3 (in GaAs). Two other lattice parameter measurements are known to us. Mullin *et al.* (5) measured $\Delta a/a = 1.5 \times 10^{-5}$ for 2×10^{18} free carriers/cm^3, Ge-doped, Bridgeman grown GaAs, also by x-ray techniques. Rode *et al.* (23) measured a dilation of $\Delta a/a = 4 \times 10^{-6}$ in a film doped to 4×10^{18} free carriers/cm^3 by curvature measurements of epitaxial bilayers. In this experiment, we measured a somewhat larger dilation of $\Delta a/a = 1.5 \times 10^{-5}$ in Ge-doped $Al_{0.39}Ga_{0.61}As$. There exists then a consensus that Ge-doping dilates both the GaAs and $Al_xGa_{1-x}As$ lattice, indicating again that Ge is incorporated into the As sublattice. However, the observed magnitude of this effect is at least one order of magnitude higher than can be calculated using Veygard's law and Pauling's covalent radii (5). Rode *et al.* (23) suggested that the principal source of this lattice dilation consisted of bond-breaking by free holes, but the lattice change calculated with his model is also significantly less than was observed here.

With Si doping, in addition to the "background" Ge doping, an initial slight lattice dilation was followed by a more severe contraction at higher growth solution doping. In four samples, the Si content of the epitaxial film was measured to be near 0.5×10^{17}/cm^3 by SIMS using a Cs^+ beam and negative ion spectroscopy, yielding an atomic distribution coefficient of 0.14, the published value (25) for an effective acceptor distribution coefficient for Si in GaAs is 8×10^{-2} at 800°C. If the assumption is made that the Si distribution coefficients for GaAs and $Al_xGa_{1-x}As$ are relatively insensitive to x, our data can be compared to the existing results of lattice changes in Si-doped GaAs. In Bridgeman-grown GaAs doped with Si to a level of 2×10^{18} free carriers/cm^3, a lattice contraction of approximately $\Delta a/a = 4 \times 10^{-6}$ was reported. This doping level would correspond to our growth solution doping of 0.16 a/o resulting in extrapolated Si levels of 5×10^{18}/cm^3 and 3×10^{18} free carriers/cm^3. The lattice change measured in this experiment was substantially greater than the reported value, namely, a contraction of $\Delta a/a = -2.5 \times 10^{-5}$. In view of the amphoteric nature of Si, this discrepancy is not surprising. During Bridgeman growth, Si is predominantly incorporated as a donor, while in LPE growth Si enters predominantly as an acceptor. The actual site distribution should be very complex, as is indicated by the great disparity between the estimated atomic and free-carrier distribution coefficient. These Si-doped films are certainly heavily compensated (26). For both Si and Ge doping in GaAs, it was suggested (26) that the incorporation of the impurity proceeds simultaneously with the incorporation of compensating centers that were presumed to be impurity-vacancy complexes. The lattice effects arising from these compensating centers cannot be identified at this time but they are certain to be a major cause of the discrepancy between measured and calculated lattice changes.

Qualitatively, the data suggest that the lattice dilation due to Ge doping should be principally an electronic effect while lattice changes due to the incorporation of Si will arise both from electronic effects and effects due to the smaller covalent radius of Si relative to Ge and As. The initial lattice dilation is probably an electronic effect akin to the bond breaking suggested by Rode (23). At higher doping levels, the electronic effects can be expected to diminish due to the increase in self-compensation (25). Then, covalent bond effects predominate to contract the lattice. With the simple model used by Mullin *et al.* (5), qualitative agreement with the measured lattice contraction is reached with the estimated 3×10^{18} free donors/cm^3 and 5×10^{19} atoms/cm^3 resulting from 0.16 a/o Si in the growth solution. Setting

$$N_a + N_d = N_a \text{ (Si on As sites)} + N_d \text{ (Si on Ga sites)} = 3.6 \times 10^{19}/\text{cm}^3$$

and

$$N_a - N_d = 3 \times 10^{18}/\text{cm}^3$$

a lattice contraction of $\Delta a/a = -9.5 \times 10^{-5}$ is cal-

culated and a contraction of $\Delta a/a = -4.5 \times 10^{-5}$ was measured.

The incorporation of S into the $Al_{0.39}Ga_{0.61}As$ lattice can be expected to contract the lattice solely on the basis of sulfur's small covalent radius, 14% smaller than that of As. SIMS measurements (24) of films grown from solutions containing 6.4×10^{-5} a/o S and 1.7×10^{-3} a/o S were found to contain 1×10^{18} and 3×10^{19} atoms S/cm^3, respectively. The corresponding lattice contractions were measured to be $\Delta a/a = -1.4 \times 10^{-5}$ and -4.5×10^{-5}. These results are at variance with the results of Mullin *et al.* (5) of Bridgeman-grown S-doped GaAs. At a presumed S level of 2×10^{18}/cm^3, a contraction of $\Delta a/a = -3.5 \times 10^{-6}$ was measured, and at a level of 4×10^{18}/cm^3, a dilation of $\Delta a/a = 7 \times 10^{-6}$ was measured. Their results are internally inconsistent and, thus, cannot be used as a reference standard.

The calculation of the expected sulfur concentration in the epitaxial films from our data based on covalent radii (5) results in a value of 5.2×10^{18}/cm^3 and 1.7×10^{19} impurities/cm^3 (as compared to the measured values of 1×10^{18}/cm^3 and 3×10^{19}/cm^3) for the two doping levels. As was the case with Si, at low doping levels the measured lattice change was too large to be explained with this simple model. At the higher doping levels, this model appears to hold up much better, but this is probably fortuitous. The unknown lattice effects of the high concentration of compensating centers (26) combined with the likely presence of structural defects (27, 28) should make the prediction of lattice changes at high doping levels a very difficult task.

Based on its very small covalent radius, the incorporation of oxygen in GaAs or $Al_{0.39}Ga_{0.61}As$ is expected to contract the lattice as sharply as sulfur. Indeed, in Bridgeman-grown O-doped GaAs, Mullin *et al.* (5) measured a contraction of $\Delta a/a = -1.2 \times 10^{-5}$ for only 1×10^{17} presumed oxygen doping. This contraction was more than one order of magnitude greater than could be expected based on covalent radii.

Quite different from their findings, our results clearly indicate a uniform lattice dilation, irrespective of growth solution doping, presumably the result of the presence of the intentional 0.7 ppm O_2 in the growth ambient. The observed lattice dilation is certainly not an ionic effect, but it could be an electronic effect if oxygen is thought to result in acceptor levels (29). But since oxygen has virtually the same covalent radius as sulfur, identical lattice effects should be expected. To explain this, the key findings resulted from SIMS. The expected increase in the background concentration of oxygen was not found. The oxygen content of all samples was found to be less than 3×10^{17}/cm^3, below the instrumental detection limit for the oxygen species. On the other hand, in the samples grown in an ambient of pure He plus 0.7 ppm O_2, the sulfur concentration decreased from 1×10^{17} to 3×10^{16}/cm^3. The observed lattice dilation could then be due in part to the decrease in the sulfur-based contraction and in part to the lattice dilation resulting in the increased concentration of free holes, *i.e.*, broken bonds arising from the decreased concentration of donors associated with sulfur (30). Reproducibly low film resistivities were achieved in the P-ternary layer ($Al_{0.4}Ga_{0.6}As$) of AlGaAs-GaAs laser heterostructures with the combination of O_2, Si, and Ge in the growth environment.

The incorporation of dopants into GaAs or $Al_xGa_{1-x}As$ is basically not understood. It seems fairly certain that high concentrations of compensating centers are formed readily (26), but it is not really known if they are impurity-vacancy complexes or interstitial clusters. The surprisingly large lattice dilations or contractions which were found here and by Mullin (5) indicate that simple substitutional incorporation, perhaps occasionally on the wrong sublattice, may not be the major mode of incorporation. Calculations based on simple electron bonding will be in error for the same reason. As long as the lattice effect of the compensating centers are unknown, computations based on covalent radii will be at best estimates.

Conclusion

With the demonstration that $Al_xGa_{1-x}As$ films could be reproducibly grown by LPE, lattice changes due to impurity incorporation have been measured. The observed lattice changes can be attributed to both electronic bonding effects and ion size effects, but the lack of the detailed knowledge of self-compensation effects makes it impossible at this time to reach more than a qualitative understanding of these changes.

Acknowledgments

The authors wish to thank D. Van Haren and S. M. Woelfer for their substantial assistance during this work.

Manuscript submitted May 27, 1981; revised manuscript received Sept. 23, 1981. This was 555 RNP presented at the Minneapolis, Minnesota, Meeting of the Society, May 10-15, 1981.

Any discussion of this paper will appear in a Discussion Section to be published in the December 1983 JOURNAL. All discussions for the December 1983 Discussion Section should be submitted by Aug. 1, 1983.

Publication costs of this article were assisted by Bell Laboratories.

REFERENCES

1. W. R. Wagner, *"Inst. Phys. Conf. Ser. #33b,"* L. F. Eastman, Editor, 65 (1977).
2. H. C. Casey, Jr. and M. B. Panish, *J. Cryst. Growth,* **13/14,** 818 (1972).
3. G. M. Kuznetsov, O. V. Pelevin, A. D. Barsukov, V. V. Olenin, and Savel'eva, *Jzv. Akad. Nowk. SSR Neorg. Mater.,* **9,** 759 (1973).
4. J. F. C. Baker, M. Hart, M. G. Halliwell, and R. Heckingbottom, *Solid State Electron.,* **19,** 331 (1976).
5. J. B. Mullin, B. W. Straughan, C. M. H. Driscoll, and A. F. W. Willoughby, *CRC Crit. Rev. Solid State Sci.,* 441 (Nov. 1975).
6. E. Estop, A. Izrael, and M. Saurage, *Acta Crystallogr.,* **A32,** 627 (1976).
7. M. Ettenberg and R. J. Paff, *J. Appl. Phys.,* **41,** 3926 (1970).
8. J. Whitaker, *Solid State Electron.,* **8,** 649 (1965).
9. W. J. Bartels and W. Nijman, *J. Cryst. Growth,* **44,** 518 (1978).
10. M. C. Rowland and D. A. Smith, *ibid.,* **38,** 143 (1976).
11. J. Zilko and P. J. Anthony, *This Journal,* **128,** 871 (1981).
12. R. W. James, "The Optical Principles of the Diffraction of X-Ray," Cornell U. Press, Ithaca, New York (1965).
13. M. C. Rowland and D. A. Smith, *J. Cryst. Growth,* **38,** 143 (1976).
14. C. Schiller, "Inst. Phys. Conf. Ser. #33a," C. Hilsum, Editor, p. 25 (1977).
15. F. K. Reinhart and R. A. Logan, *J. Appl. Phys.,* **44,** 3171 (1973).
16. J. Hornstra and W. J. Bartels, *J. Cryst. Growth,* **44,** 513 (1978).
17. L. Dawson, *ibid.,* **27,** 86 (1974).
18. E. D. Pierron, D. L. Parker, and J. B. McNeely, *J. Appl. Phys.,* **38,** 4669 (1967).
19. T. W. Baker, J. D. George, B. A. Bellamy, and R. Causer, *Nature,* **210,** 720 (1966).
20. H. T. Minden, R. Premo, and C. V. Collins, *J. Cryst. Growth,* **27,** 316 (1974).
21. A. J. Springthorpe, F. D. King, and A. Becke, *J. Electron. Mater.,* **4,** 101 (1975).
22. D. R. Ketchow, *This Journal,* **121,** 1237 (1974).
23. D. L. Rode, R. L. Brown, and M. A. Aframowitz, *J. Cryst. Growth,* **30,** 299 (1975).
24. Charles Evans and Associates, San Mateo, CA.

25. H. G. Hicks and P. D. Greene, "Inst. Phys. Conf. Ser. #9," 92 (1971).
26. C. M. Wolfe and G. E. Stillman, *Appl. Phys. Lett.*, **27**, 564 (1975).
27. H. Kressel, *J. Appl. Phys.*, **40**, 3587 (1969).
28. N. S. Belyaskaya, *Sov. Phys. Crystallography*, **17**, 129 (1972).
29. A. Fazzio, L. M. Brescansin, M. J. Caldas, and J. R. Leito, *J. Phys.*, **12**, L831 (1979).
30. P. J. Anthony, J. L. Zilko, V. Swaminathan, N. E. Schumaker, W. R. Wagner, and J. C. Norberg, *Appl. Phys. Lett.*, **38**, 434 (1981).

Deposition of GaAs Epitaxial Layers by Organometallic CVD

Temperature and Orientation Dependence

D. H. Reep* and S. K. Ghandhi*

Department of Electrical, Computer and Systems Engineering, Rensselaer Polytechnic Institute, Troy, New York 12181

ABSTRACT

Epitaxial layers of GaAs have been grown in an atmospheric organometallic CVD system, for a wide variety of gas phase reactant partial pressures and over a broad range of temperature (450°-1050°C). The growth rates for (100), (100) + 3° → <110>, (110), (111)Ga, and (111)As substrates are reported as functions of temperature and gas composition. Three distinct temperature dependent regions of growth are identified, corresponding to a mid-temperature mass transport limited range, a low-temperature kinetic controlled regime, and a high-temperature desorption limited region. The growth rate is studied as a function of the growth parameters and substrate orientation, and is related to the decomposition of the two reactants trimethylgallium and arsine. A model for the epitaxial growth of GaAs by the organometallic process is proposed, based on these findings.

The growth of thin epitaxial layers of GaAs, by the organometallic CVD technique, has received much attention recently. In particular, the use of such layers for optoelectronic (1, 2), microwave (3, 4), and high speed digital circuits (4) has given promising results. This technique has also produced layers approaching the purity and mobility of the best layers grown by the halide or hydride techniques, and has generated much interest due to its simplicity and flexibility.

Compared to the halide and hydride growth systems, little has been published in regard to the mechanisms of growth by the organometallic process. While it is considered to be a "simple" pyrolysis of trimethylgallium (TMG) and arsine, the growth of GaAs films by this technique certainly involves complex processes. This is, in part, due to the nature of the pyrolytic reaction, which occurs far from equilibrium and precludes reversal of the deposition reaction. Hence, there is no possibility of any "reordering" of the deposited GaAs film, in the sense of the reversible halide/hydride reactions, owing to the absence of an etching halogenic species in the deposition zone. This effect is most pronounced in terms of the resulting epitaxial layer morphology, as detailed in our earlier work (5).

In this paper, we report on the growth of GaAs epitaxial layers on a variety of substrate orientations [(100), (100) + 3° → <110>, (110), (111)Ga, and (111)As faces], and over a wide range of deposition temperatures and reactant partial pressures. We describe three distinct regions of growth: a mid-temperature mass transport limited region, a low temperature kinetically controlled growth regime, and a high temperature surface species desorption limited range. The dependence of the observed GaAs deposition rate on gas phase reactant partial pressures and substrate orientations is considered in conjunction with the activation energies of deposition that are associated with the three growth regions. A simple growth model is proposed, based on these observations.

Experimental Procedure

Epitaxial layers of GaAs were grown by the pyrolysis of arsine and TMG, using hydrogen as the carrier gas. Anhydrous hydrogen chloride was available for *in situ* etching of the GaAs substrates prior to epitaxial layer growth. The layers were deposited at temperatures ranging from 450° to 1050°C, with the input TMG partial pressure varying from 4.6-37 × 10^{-5} atm. Arsine flows were also varied over a wide range, corresponding to AsH_3/TMG ratios of 4.7-75 at the reactor inlet. The hydrogen carrier gas flow was fixed at 5 liters/min for all of the growth runs carried out for this study.

The single crystal semi-insulating GaAs substrate material that was used in this study was obtained from either Crystal Specialties, Incorporated, Monrovia, California or Cambridge Instruments, Incorporated, Monsey, New Jersey. The wafers were purchased lapped and chem-mechanically polished on one side, and were oriented (100), (100) + 3° → <110>, (110), or (111)As.

The (111)Ga substrates were prepared at our facility, by mechanically polishing the reverse side of (111)As wafers with successively finer grits, to a final 0.05 μm alumina (Buehler, Limited, Lake Bluff, Illinois) polish. After demounting from polishing slugs, the wafers were cleaned sequentially in baths of methanol, acetone, and trichloroethylene. A chemical polishing etch of 5 min duration, in a solution consisting of $1HNO_3$ (70%): $4H_3PO_4$ (85%) at 60°C, produced mirror-like, damage free (111)Ga surfaces (6).

The (100), misoriented (100), (110), and (111)As wafers were degreased as described earlier, and given a 1 min free etch in hot Caro's acid [$3H_2SO_4$ (97%): $1H_2O_2$ (30%): $1H_2O$, at 60°C], to remove any residual surface damage. This procedure gave mirror-like surfaces on all of these substrate orientations, and removed 15-25 μm from their surfaces.

The epitaxial reactor consisted of an atmospheric pressure, horizontal, rf heated, cold wall system as described earlier (7). Gases were delivered to the 50 mm ID quartz reaction chamber through 316 stainless steel or Monel tubing. The substrate temperature was monitored with a type R thermocouple (Pt/Pt-13% Rh), sheathed in quartz, and inserted into a well in the back of the graphite susceptor.

TMG (Alpha Products, Danvers, Massachusetts) vapor was introduced into the reactor by bubbling hydrogen through the liquid, which was held at 0°C in a stainless steel bubbler. An LED grade, 10% mixture of

* Electrochemical Society Active Member.
Key words: organometallic, OMVPE, OMCVD, epitaxy, gallium arsenide.

arsine in hydrogen (Air Products, Tamaqua, Pennsylvania), was used to provide AsH_3 in concentrations necessary for good epitaxial layer growth. A 1% mixture of electronic grade hydrogen chloride in hydrogen (Air Products, Tamaqua, Pennsylvania) was available for *in situ* etching of the substrate when required. Ultrapure hydrogen carrier gas was obtained by passing commercial grade hydrogen (Air Products, Tamaqua, Pennsylvania) through a Pd-Ag alloy purifier. In all cases, the reactants were mixed just prior to entry into the reaction chamber.

The substrates were loaded into the reactor immediately after chemical etching and microscopic inspection of their surfaces. The reactor was evacuated, and then purged with commercial grade argon (Air Products, Tamaqua, Pennsylvania), followed by hydrogen. After sufficient purging, the desired flows of hydrogen and arsine were set. For those experiments involving an *in situ* etch prior to growth, the susceptor was heated and allowed to stabilize at the etch temperature, typically 945°C. After a period of 5 min which was considered sufficient to remove any oxide on the GaAs surface left from the chemical free etch (8), the substrates were given an *in situ* etch of the type previously detailed (9). The susceptor temperature was then reset and allowed to stabilize at the growth temperature for 2 min prior to the commencement of TMG flow.

For experiments where no *in situ* etch was performed, the susceptor was heated to the growth temperature[1] and stabilized for 5 min, before the TMG flow was terminated, and the system maintained at the growth temperature for an additional 3 min. The susceptor was then allowed to cool in the AsH_3/H_2 atmosphere, followed by an argon purge after the temperature fell below 200°C.

The growth rate of the epitaxial layer was determined either by weight change, when no *in situ* etch was performed, or by cleaving and staining, followed by optical microscope inspection using Nomarski differential interference contrast. Scanning electron microscopy was employed to study the surface morphology.

The (100) + 3° → <110> orientation is often used in commercial practice. Consequently, an initial series of experiments were carried out with side-by-side growth on (100) and (100) + 3° → <110> oriented substrates for purposes of comparison. In all cases, these gave identical growth rates and morphology, which were dependent only on the growth parameters. Subsequently, the remaining experiments were conducted with simultaneous growth on (110), (111)Ga, and (111)As substrates, in addition to the (100) + 3° wafers, since they were more readily available for this study.

Results

All of the (100) layers (oriented as well as misoriented) showed good surface quality over a wide range of growth temperatures. Furthermore, the morphology was found to be essentially independent of the TMG or arsine flows for these samples as detailed earlier (5) for film growth at 700°C. However, layers grown on (110), (111)Ga, and (111)As faces showed a strong dependence of morphology on both the arsine and TMG flows. In the earlier study, it was also shown that for all growth conditions, the best morphology for these orientations was obtained with a gas phase AsH_3/TMG ratio at the reactor inlet in the 18-37 range. Consequently, the bulk of the growth rate data reported here will fall in this range as well.

The growth rate for the (100), (110), (111)Ga, and (111)As samples, plotted *vs.* reciprocal temperature, can be seen in Fig. 1 for inlet partial pressures of TMG equal to 1.8×10^{-4} atm and AsH_3 equal to 3.3×10^{-3} atm (AsH_3/TMG = 19). The apparent activation energies are shown for each orientation and for each of the three distinct growth regions. These are identified as a mid-temperature mass transport limited region, a low temperature kinetically controlled regime, and a high temperature desorption limited range.

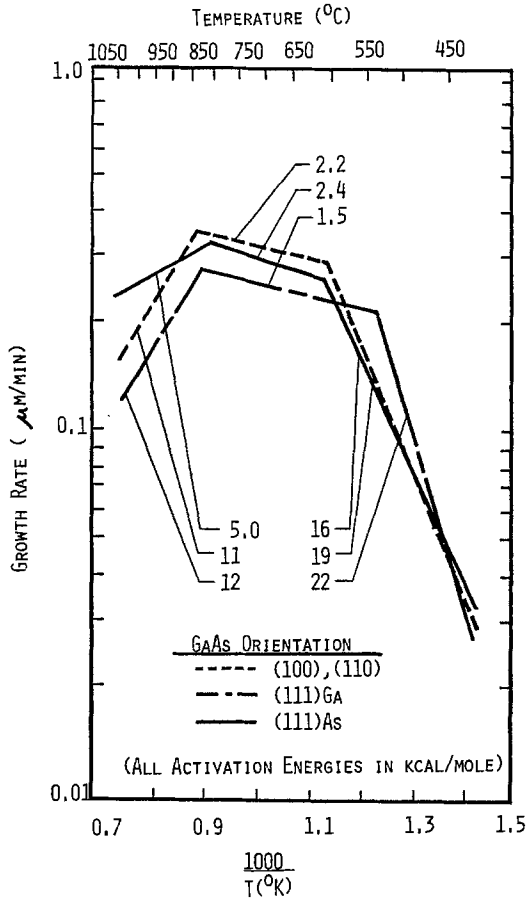

Fig. 1. Growth rate *vs.* reciprocal temperature for epitaxial layers on (100), (110), (111)Ga, and (111)As oriented GaAs substrates with $P_{TMG} = 1.8 \times 10^{-4}$ atm and $P_{AsH_3} = 3.3 \times 10^{-3}$ atm (AsH_3/TMG = 19).

Singling out one particular deposition temperature in each of the three growth regions, the effect of varying the TMG or AsH_3 partial pressures is seen in Fig. 2-4, as a function of substrate crystallographic orientation. Each of these regions will be considered separately, with the important features of each noted.

Mid-temperature, mass transport limited growth.— As seen from Fig. 1, the growth is weakly dependent on the deposition temperature between 600°-850°C. Here, the apparent activation energy ranges from 1.5 to 2.4 kcal/mol as is expected for diffusion controlled mass transport limited film growth (10). Additionally, the growth rate is relatively insensitive to the substrate orientation in this temperature region, with the maximum variation between the highest and lowest values shown being approximately 20%.

Figures 2a and b show the growth rate *vs.* P_{TMG} and P_{AsH_3}, respectively, at 700°C. Here, all substrate orientations used show the same linear variation in growth rate with P_{TMG}, and independence of growth rate (within the limits of experimental error) on P_{AsH_3}, as has been commonly reported in the literature (11-13). Moreover, in this mass transport limited regime, the nature of the growth mechanisms is masked since the growth rate is limited by the diffusion of the minority species in the gas stream to the growing crystal surface.

[1] A minimum of 700°C was used for the pregrowth heat-treatment, as this is just sufficient to rapidly remove any trace surface oxide (8). Thus, for those depositions performed below 700°C, the susceptor temperature was restabilized as appropriate following this deoxidation treatment.

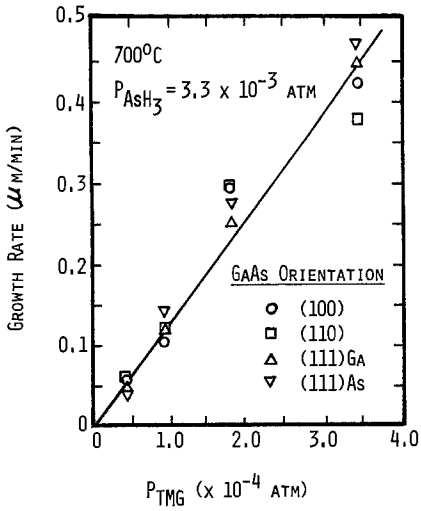

Fig. 2a. Growth rate vs. partial pressure of TMG for GaAs epitaxial layers at constant $P_{AsH_3} = 3.3 \times 10^{-3}$ atm and 700°C.

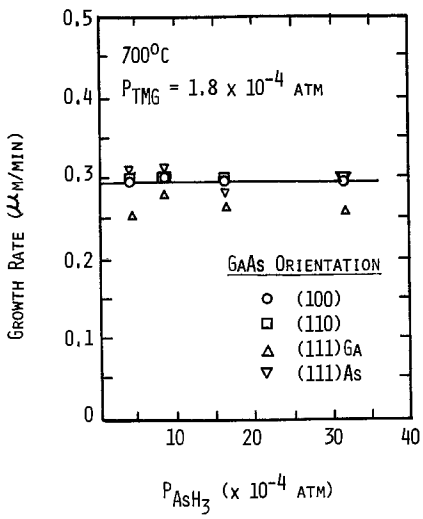

Fig. 2b. Growth rate vs. partial pressure of AsH_3 for GaAs epitaxial layers at constant $P_{TMG} = 1.8 \times 10^{-4}$ atm and 700°C.

Low temperature, kinetic controlled growth.—The deposition rate is kinetically limited at temperatures below approximately 600°C (550°C for the (111)Ga face), showing an overall activation energy for the deposition process ranging from 16 kcal/mol for the (111)As to 22 kcal/mol for the (111)Ga (Fig. 1). Figure 3a shows the effect of varying the TMG partial pressure while holding P_{AsH_3} constant at 500°C, while Fig. 3b shows the case for varying P_{AsH_3} at constant P_{TMG} again at 500°C. From these graphs, one can see that the (100), (110), and (111)As oriented layers all behave in a very similar manner, showing a slight sublinear variation of growth rate with P_{TMG} and weak dependence of the deposition on P_{AsH_3}. In contrast to this, the (111)Ga face shows strongly nonlinear behavior of the growth rate with P_{TMG}, and a significant dependence of growth rate on the magnitude of P_{AsH_3}.

High temperature, desorption limited growth.—For epitaxial deposition at temperatures greater than 850°C, the growth rate falls off with increasing temperature at a rate which is highly orientation sensitive (Fig. 1). The lowest fall off is seen for the (111)As face at 5 kcal/mol, whereas the (100), (110), and (111)Ga faces show a fall-off "activation energy" of 11-12 kcal/mol. The growth rate on the various orientations is also quite different, with growth on (111)As face being approximately 42% faster than the (111)Ga at 1000°C.

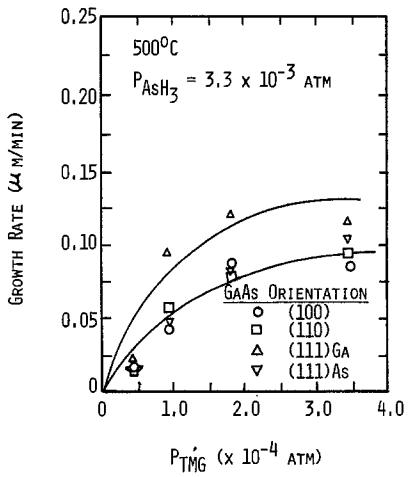

Fig. 3a. Growth rate vs. partial pressure of TMG for GaAs epitaxial layers at constant $P_{AsH_3} = 3.3 \times 10^{-3}$ atm and 500°C.

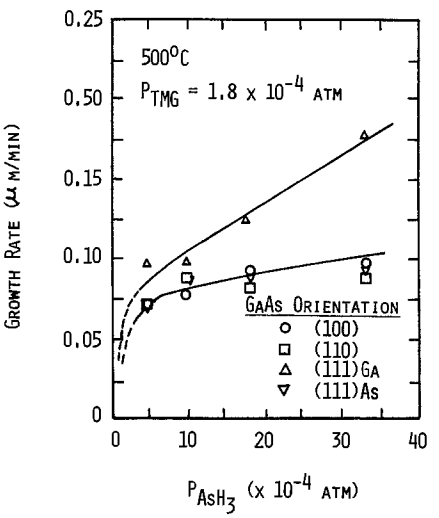

Fig. 3b. Growth rate vs. partial pressure of AsH_3 for GaAs epitaxial layers at constant $P_{TMG} = 1.8 \times 10^{-4}$ atm and 500°C.

Finally, Fig. 4a and b show the growth rate *vs.* P_{TMG} and P_{AsH_3}, respectively, at 1000°C. Here, the deposition rate was found to be linear with P_{TMG}, with growth being fastest on the (111)As face, and slowest for the (111)Ga orientation, with intermediate values for the (100) and (110) faces. The deposition rate was also found to be independent of P_{AsH_3} at this temperature, for fixed P_{TMG}, but varied with crystallographic orientation in the same order as above.

Discussion

This section interprets our experimental results in terms of classical growth mechanisms which have been described in the literature. For simplicity, reacting species are written as TMG and AsH_3. However, the actual surface species which lead to GaAs growth are considerably more complex in organometallic CVD. Although their nature is uncertain, some conjectures will be made based on the available studies of decomposition of the reactants.

In previous studies, the pyrolysis of TMG and AsH_3 has been modeled both with a Langmuir-Rideal mechanism (14) where gas phase gallium species react with surface adsorbed arsenic, and by a Langmuir-Hinshelwood mechanism (15) where TMG and AsH_3 adsorb on the surface prior to partial decomposition and reaction. These two heterogeneous reaction mechanisms should be distinguishable by the dependence of the growth rate on the partial pressures of TMG and AsH_3 in the gas phase.

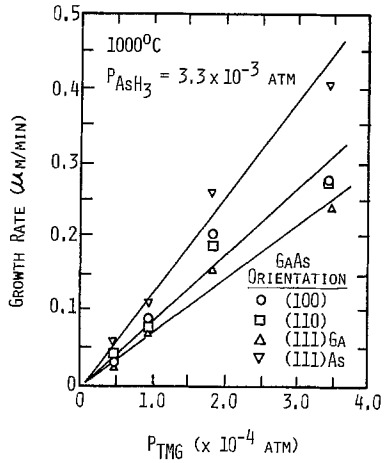

Fig. 4a. Growth rate vs. partial pressure of TMG for GaAs epitaxial layers at constant $P_{AsH_3} = 3.3 \times 10^{-3}$ atm and 1000°C.

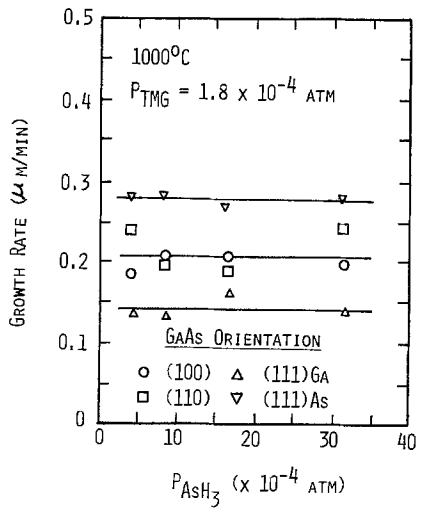

Fig. 4b. Growth rate vs. partial pressure of AsH_3 for GaAs epitaxial layers at constant $P_{TMG} = 1.8 \times 10^{-4}$ atm and 1000°C.

For the Langmuir-Rideal case, assuming AsH_3 is adsorbed prior to decomposition, the growth rate, R, is given by

$$R = K_1 \theta_{AsH_3} P_{TMG}$$

where K_1 is a rate constant, P_{TMG} is the gas phase TMG partial pressure, and θ_{AsH_3} is the surface coverage of arsine as predicted by the Langmuir adsorption isotherm (after (10))

$$\theta_{AsH_3} = \frac{\beta_{AsH_3} P_{AsH_3}}{1 + \beta_{AsH_3} P_{AsH_3}}$$

Here, P_{AsH_3} is the arsine gas phase partial pressure and β_{AsH_3} is the ratio of the rate constant for adsorption of arsine to the rate constant for desorption. If $\beta_{AsH_3} P_{AsH_3} >> 1$ due to strong arsine adsorption, then this equation reduces to

$$R = K_1 P_{TMG}$$

so that the predicted growth rate is linearly dependent on the partial pressure of TMG, and independent of the AsH_3 overpressure.

The Langmuir-Hinshelwood model for noncompetitive adsorption of TMG and AsH_3 [2] followed by surface reaction predicts that

$$R = K_2 \theta_{AsH_3} \theta_{TMG}$$

[2] Noncompetitive surface adsorption is expected, due to the strong Lewis acid-Lewis base interaction of AsH_3 with a Ga surface atom, or of an As surface atom with TMG. Thus, a two site adsorption mechanism is probable, as a result of this complexing of the reactants with the surface (16).

where the terms are analogous to those defined for the Langmuir-Rideal case, and

$$R = \frac{K_2 \beta_{AsH_3} \beta_{TMG} P_{AsH_3} P_{TMG}}{(1 + \beta_{AsH_3} P_{AsH_3})(1 + \beta_{TMG} P_{TMG})}$$

so that the predicted growth rate is sublinear in both TMG and AsH_3. This equation also assumes no hindering effect of desorption of reaction by-products such as CH_4 as has been experimentally verified (16).

Mid-temperature, mass transport limited region.— In the temperature range from 600°-850°C, the observed growth rate is linearly dependent on the TMG partial pressure and independent of the AsH_3 partial pressure. This is as expected for growth which is limited by diffusion of the less abundant species to the crystal surface. Moreover, the surface reactions proceed faster than this diffusion process, so that information on the growth rate gives little insight with respect to the mechanisms of reaction in this temperature range. Independence of growth rate on crystallographic orientation is also observed, since the surface dependent processes are effectively masked by the nature of the mass transport limited growth.

Low temperature, kinetically controlled growth.— Our results show that, over this temperature range, the growth of GaAs is sublinear with respect to both TMG and AsH_3 for all substrate orientations (Fig. 3a and b). Thus, the Langmuir-Hinshelwood model can be used to describe the growth process. Here, the adsorption of both arsenic and gallium species plays a role in this deposition. However, we propose that processes associated with arsenic adsorption dominate, since the growth rate on the (111)Ga face is higher than that on the (111)As face.

In this region, the measured activation energy for the deposition of GaAs on the (111)Ga face is 22 kcal/mol. Since this is very nearly the same as the energy measured for the heterogeneous decomposition of AsH_3 (23.2 kcal/mol, (17)) corresponding to rapid removal of the first H atom subsequent to adsorption, we postulate that the adsorption and rapid decomposition of arsine on the growing surface is the dominant process. Further, the lower value for the activation energy on the (111)As face (15 kcal/mol) suggests that the presence of the Ga-bearing reactant enhances the probability of chemisorption of AsH_2, probably as a result of coordination with these species. We expect this coordination to follow the gas phase partial pressure of the minority species (TMG), such that the decomposition remains a strong function of the minority reactant, as is verified by the experimental results of Fig. 3a.

The availability of many coordination sites for AsH_3 on the (111)Ga face should result in the growth being a function of the AsH_3 partial pressure, as seen in Fig. 3b. On the (111)As face, however, the growth should be relatively independent of the AsH_3 overpressure, since this surface provides an abundance of As atoms.

In the previous study (15), an activation energy of 13 kcal/mol was measured for the low temperature, surface catalyzed reaction of TMG and AsH_3, where no oriented single crystal substrate was present. A value of 13 ± 5 kcal/mol was reported previously (14), for the growth on (100)GaAs substrate material. Both of these values compare favorably with our results.

Thus, the growth of GaAs films at low temperatures is aided by the adsorption of both reactants leading to significant deposition even at low temperatures, where homogeneous AsH_3 decomposition cannot take place to any significant extent (18). Finally, comparison of the value for the third $GaCH_3$ bond dissociation energy (77.5 kcal/mol) (19) and the observed activation energy of GaAs deposition indicates that no gas phase reactions are expected to occur in this temperature range.

High temperature, desorption limited region.—In this region (>850°C), the growth rate falls off with in-

creasing temperature. This can be caused by gas phase depletion effects (which were not observed at the flow rates used in our experiments) or by increased desorption of reactant species. We note, however, that the growth rate varies linearly with P_{TMG} and is independent of the arsine overpressure to temperatures as high as 1050°C. This would indicate that the dominant factor controlling growth in the high temperature range is the desorption of the gallium species and not the arsenic species (14). Following this line of reasoning, we would expect the gallium species to be more strongly adsorbed on the (111)As face, resulting in a slower fall off with temperature than for the (111)Ga orientation. Moreover, we would expect the growth rate to be higher on the (111)As face due to the larger number of available gallium kink sites. Both of these observations were noted in our experiments (see Fig. 1 and 4).

Although desorption of the gallium species is the controlling factor, an important consideration is that growth takes place in an excess arsenic overpressure. Thus, the observed growth behavior may be explained by the Langmuir-Hinshelwood model (both species surface adsorb prior to reaction), where

$$\beta_{AsH_3} P_{AsH_3} >> 1 \text{ and } \beta_{TMG} P_{TMG} << 1$$

Under these conditions of relatively strong As adsorption, and increasing Ga-species desorption

$$R = K_2 P_{TMG}$$

as seen in our experimental results.

We have ruled out depletion reactions as a cause for the observed high temperature growth rate fall off for three reasons. First, we observed no gas phase reaction products either in the gas stream or on the reactor walls in the vicinity immediately preceding the hot susceptor, at the gas flows used in our work (total flow $\simeq$ 5 liters/min). Second, we observed no dependence of the fall off in growth rate on the AsH_3 partial pressure. This rules out gas phase TMG-AsH_3 coordination reactions of the type reported for the growth of GaInAs, where depletion of In from the gas phase increased monotonically with P_{AsH_3} (20). Third, the possibility of partial gas phase decomposition of TMG leading to polymers of the form $(GaCH_3)_n$ seems unlikely, since these polymers should react readily with AsH_3 at low temperatures (15, 16).

Nature of the surface species.—The form of the gallium and arsenic bearing species on the crystal surface has not yet been explicitly determined. However, several studies of the kinetics of TMG decomposition (19), the decomposition of arsine (17), the interaction of TMG with an arsenic film (21), and the surface interaction of TMG with AsH_3 (15, 16) can be used to gain some insight into their nature.

The study of the decomposition kinetics of TMG (19) gave dissociation activation energies of 59.5, 35.4, and 77.5 kcal/mol for the first, second, and third $GaCH_3$ bonds, respectively. For the temperature range of 400°-800°C, decomposition led to only formation of Ga-bearing polymers, presumably $(GaCH_3)_n$, in addition to CH_4, C_2H_6, and to a much smaller extent, several more complex hydrocarbons. Moreover, the rate constant for the dissociation of the first $GaCH_3$ bond was considerably higher than that of the second bond, even though its activation energy was higher. Thus, the rate limiter for the thermal decomposition of TMG is in all probability the breaking of the last $GaCH_3$ bond.

A study performed on the decomposition of AsH_3 (17) suggested that the rate limiter in this case is the removal of the first hydrogen atom or the energy for direct chemisorption onto the surface. Moreover, the chemisorption onto an As surface

$$AsH_3\ (g) \rightarrow AsH_2{}^* + H^*$$

(where the * denotes surface-adsorbed species) has been found to proceed with a relatively low activation energy of 23.2 kcal/mol, with subsequent hydrogen release being more rapid. In a later study (16), AsH_3 was found to decompose over GaAs at 172°C by a surface catalyzed reaction, lending support to the notion of its easy chemisorption followed by rapid decomposition.

A recent study detailing the homogeneous breakdown of AsH_3 using mass spectroscopy showed that the prevalent breakdown products are As and H_2 below 620°C, with As_2 and As_4 formation occurring only at higher temperatures (22). A study of the AsH_3 content of the gas stream of a cold wall organometallic CVD reactor near the end of the decomposition zone has also demonstrated significant amounts of undecomposed AsH_3 are present for a susceptor temperature of 700°C (23). This study provided additional evidence of enhanced AsH_3 breakdown in the presence of a GaAs substrate. Thus, at the growth temperatures commonly used for organometallic deposition of GaAs, the limited communication between the gas stream and hot susceptor at typical flow rates combined with the surface catalyzed breakdown of AsH_3 would suggest that the amount of As_2 and As_4 present will be less than that predicted by thermodynamics.

The interaction of TMG and AsH_3 enhances the breakdown of the Ga-bearing reactant. Support of this comes from the observation that heated mixtures of TMG and AsH_3 give products of the form $(CH_3)_{3-x}GaAsH_{3-y}$ which eventually evolve to GaAs by 420°C (15). Moreover, these partial decomposition products react with AsH_3 at temperatures as low as 364°C to give GaAs (16), and TMG breaks down in the presence of an arsenic-coated surface at temperatures in the vicinity of 285°C (21). In contrast, the decomposition of TMG to gallium in the absence of an As-bearing species has not been observed below 800°C (19).

Based on these observations, we propose that the most probable situation is that $GaCH_3$* and AsH* are the primary reactant species on the growing surface. Moreover, the abundance of hydrogen ($P_{H_2} \simeq 1$ atm) in our system should lead to a large surface population of AsH*, and promote dissociation of As_2 and As_4 species. The deposition reaction may follow

$$GaCH_3{}^* + AsH^* \rightarrow (CH_3Ga - AsH)^*$$

$$(CH_3Ga - AsH)^* \rightarrow GaAs_{(s)} + CH_{4(g)}$$

Thus, at growth temperatures above 420°C, the sequential demethylation of $(CH_3)_{3-x}GaAsH_{3-y}$ seems unlikely, in view of the probable surface catalyzed formation of CH_3Ga-AsH.

An alternate viewpoint is that $GaCH_3$* is chemisorbed on the surface and diffuses to a gallium kink site where it eventually forms GaAs. This process is enhanced by the presence of arsenic, so that this reaction most probably proceeds as follows

$$AsH^* \rightarrow As_{As} + H^*$$

$$GaCH_3{}^* + As_{As} + H^* \rightarrow GaAs_{(s)} + CH_{4(g)}$$

where As_{As} denotes arsenic on an arsenic lattice site. Finally, the reaction may be aided by the formation of C_2H_6, as detected both in the absence of AsH_3 (19) as well as in its presence (24). This would correspond to

$$2AsH^* \rightarrow 2As_{As} + H_{2(g)}$$

$$2GaCH_3{}^* + 2As_{As} \rightarrow 2GaAs_{(s)} + C_2H_{6(g)}$$

We note, however, that this situation is less probable than the previous, since TMG is the lesser reactant and much less abundant than hydrogen. Moreover, the excess of the As-species would suggest that interaction of the adsorbed Ga- and As-bearing reactants would occur faster than the Ga-species would find a lattice kink site. The distinction here is whether mobile Ga- and As-bearing reactants diffuse to their appropriate kink sites prior to decomposing, or whether these

species interact to form a mobile $(CH_3Ga\text{-}AsH)^*$ complex[3] which diffuses to the growing crystal step. Neither of these cases greatly alters the growth model, as both should fit a Langmuir-Hinshelwood type reaction and will be indistinguishable based on studies of the reactant input partial pressures and overall deposition process.

The gas phase complexing of AsH_3 with TMG has not been detected (15); however, the possibility of such a complex diffusing to the crystal surface and heterogeneously decomposing cannot be entirely ruled out.

In summary, therefore, the actual gas phase and surface reaction processes are quite complex. However, the primary result of these processes is the strong adsorption of $GaCH_3$* and AsH* on the surface of the gallium arsenide over the useful practical range of growth temperatures.

Conclusions

We conclude that the deposition of GaAs epitaxial layers by the pyrolysis of TMG and AsH_3 most probably occurs following a Langmuir-Hinshelwood type reaction. That is, both the gallium- and arsenic-bearing reactants are expected to adsorb on the growing crystal face prior to reaction. Furthermore, such a reaction is heterogeneous in nature, and no evidence of gas phase reactions was found even in the high temperature range.

Three distinct growth regions were identified as the deposition temperature was increased from 450°-1050°C. The low temperature kinetically controlled growth regime was characterized by an orientation dependent deposition rate and activation energy that suggest the chemisorption and subsequent decomposition of the As-bearing species is essential to the growth in that region. Furthermore, the deposition in this range was found to vary sublinearly with the gas phase partial pressures of both the Ga- and As-bearing reactants, as predicted by the Langmuir-Hinshelwood model. From approximately 600°-850°C, a mass transport limited growth region was observed. Here, the apparent activation energy for the deposition of GaAs epitaxial layers corresponded to growth which was limited by reactant diffusion through a stagnant boundary layer. Finally for temperatures above 850°C, a decrease in the layer growth rate with increasing temperature was noted. This was explained on the basis of $GaCH_3$ desorption, since even in that region, the growth was independent of the gas stream partial pressure of AsH_3. The substrate orientation dependence of the observed high temperature fall off in deposition rate was used to provide evidence of a lack of significant depletion effects for our reported flow conditions, and to give further support to the Langmuir-Hinshelwood growth model.

[3] This case is essentially analogous to that suggested to explain experimental results for the halide growth of GaAs, where AsGaCl is thought to be the mobile reactant responsible for deposition (25).

Acknowledgments

The authors wish to thank R. Reep and A. Hayner for manuscript preparation. This work was supported by the Solar Energy Research Institute, Golden, Colorado, under Contract No. XS-0-9002-4.

Manuscript submitted Sept. 3, 1982; revised manuscript received Oct. 22, 1982.

Any discussion of this paper will appear in a Discussion Section to be published in the December 1983 JOURNAL. All discussions for the December 1983 Discussion Section should be submitted by Aug. 1, 1983.

Publication costs of this article were assisted by Rensselaer Polytechnic Institute.

REFERENCES

1. R. R. Bradley, *J. Cryst. Growth*, **55**, 223 (1981).
2. J. P. André, P. Guittard, J. Hallais, and C. Piaget, *ibid.*, **55**, 235 (1981).
3. M. Bonnet, N. Visentin, G. Bessonneau, and J. P. Duchemin, *ibid.*, **55**, 246 (1981).
4. T. Nakanisi, T. Udagawa, A. Tanaka, and K. Kamei, *ibid.*, **55**, 255 (1981).
5. D. H. Reep and S. K. Ghandhi, *ibid.*, Submitted.
6. D. J. Stirland and B. W. Straughan, *Thin Solid Films*, **31**, 139 (1976).
7. K. P. Pande, D. H. Reep, S. K. Shastry, A. S. Weiner, J. M. Borrego, and S. K. Ghandhi, *IEEE Trans. Electron Devices*, **ed-27**, 635 (1980).
8. M. Otsubo, T. Oda, S. Mitsui, and H. Miki, *This Journal*, **124**, 1907 (1977).
9. R. Bhat, B. J. Baliga, and S. K. Ghandhi, *ibid.*, **122**, 1378 (1975).
10. D. W. Shaw, in "Crystal Growth," Vol. I, C. H. L. Goodman, Editor, p. 1, Plenum Press, New York (1974).
11. H. M. Manasevit and W. I. Simpson, *This Journal*, **116**, 1725 (1969).
12. A. L. Lin, V. Dao, and L. F. Donaghey, in "Chemical Vapor Deposition 1977," L. F. Donaghey, P. Rai-Choudhury, and R. N. Tauber, Editors, p. 264, The Electrochemical Society Softbound Proceedings Series, Princeton, NJ (1977).
13. S. J. Bass, *J. Cryst. Growth*, **31**, 172 (1975).
14. W. H. Petzke, V. Gottschalch, and E. Butter, *Krist. Tech.*, **9**, 763 (1974).
15. D. J. Schlyer and M. A. Ring, *This Journal*, **124**, 569 (1977).
16. D. J. Schlyer and M. A. Ring, *J. Organomet. Chem.*, **114**, 9 (1976).
17. K. Tamaru, *J. Phys. Chem.*, **59**, 777 (1955).
18. V. S. Ban, *This Journal*, **118**, 1473 (1971).
19. M. G. Jacko and S. J. W. Price, *Can. J. Chem.*, **41**, 1560 (1963).
20. J. S. Whiteley and S. K. Ghandhi, Submitted to *This Journal*.
21. D. J. Schlyer and M. A. Ring, *J. Organomet. Chem.*, **71**, C25 (1974).
22. A. R. Calawa, *Appl. Phys. Lett.*, **38**, 701 (1981).
23. M. R. Leys and H. Veenvliet, *J. Cryst. Growth*, **55**, 145 (1981).
24. N. N. Travkin, B. G. Gribov, C. P. Rumyantseva, I. G. Tonoyan, and E. N. Zorina, *J. Gen. Chem. USSR*, **45**, 316 (1975).
25. J. L. LaPorte, M. Cadoret, and R. Cadoret, *J. Cryst. Growth*, **50**, 663 (1980).

The Uranyl Ion, Fluorescent and Fluorine-Like: A Review

Christian K. Jørgensen

Département de Chimie Minérale, Analytique and Appliquée, Université de Genève, CH 1211 Geneva 4, Switzerland

and Renata Reisfeld

Enrique Berman Professor of Solar Energy, Department of Inorganic Chemistry, Hebrew University, Jerusalem, Israel

ABSTRACT

The uranyl ion has rather unique stereochemistry, and its ultraweak electron transfer bands are compared with other transition-group spectra. The 6 most recent MO calculations are shown to be inconclusive about the distribution of the many excited levels. The first excited state has very different chemical properties compared with the ground state, reacts with polarizable cations and anions, and shows a potent photochemistry of electron and of hydrogen atom abstraction. Its fluorescence (with much higher quantum yield in glasses than in aqueous solution) can be used for flat-plate concentrators of solar energy.

The fluorescence of uranyl compounds first studied by Brewster 1833 allowed Stokes to formulate his law (of photon energies lower or equal to the beginning of the first absorption band) in 1852 and played an incidental (but fate-changing) role in Becquerel's discovery of radioactivity in 1896. Contrary to absorption spectra approximately following Beer's law, the study of luminescence lacks notoriously a proportional (or even a monotonic) dependence of intensity on concentration, and in many cases, a tiny concentration of an "activator" (frequently of unknown constitution) provides the fluorescence. On the other hand, efficient energy transfer to quenchers, or concentration quenching due to cross-relaxation (1) may prevent the light emission. The first inorganic stoichiometric compound not needing a trace activator was a uranyl salt. This does not prevent that also uranium(VI) frequently acts as activator (1-6) in vitreous and crystalline solids.

The interpretation of excited states of luminescent species usually goes through a preliminary study of the absorption spectrum. In most of this century, there has been general agreement that the narrow absorption bands of trivalent lanthanides (of which the positions hardly depend on the ligating atoms) represent transitions to excited J-levels of a partly filled 4f shell (1), and in 1933, the same proposition was made for green $5f^2$ uranium(IV) compounds, which recently (7) could be compared with U^{+4}. This is so much more remarkable as the only gaseous M^{+3} of the 4f group with identified J-levels are Ce^{+3}, Pr^{+3}, and Yb^{+3}. On the other hand, the assignment of the (usually broader) absorption bands of d-group compounds only developed after 1954 (8, 9). The two main categories are "ligand field" transitions (9, 10) between approximately nonbonding and antibonding orbitals belonging to the partly filled d-shell, and electron transfer spectra (8, 11) of which the most common type involves one (or several) reducing ligands loosing one electron to empty or partly filled d-like orbitals centered on an oxidizing atom.

Since cerium(IV) is a closed-shell system isoelectronic with xenon, there was no doubt that the broad absorption bands in the near ultraviolet, providing the orange to yellow colors, are due to electron transfer, and the high wave-numbers for $4f \rightarrow 5d$ excitation (1) in cerium(III) and the detection (12, 13) of electron transfer bands in $4f^6$ europium(III), $4f^{13}$ ytterbium (III), $4f^5$ samarium(III), and $4f^{12}$ thulium(III) left no doubt that the electron goes to the 4f shell. In view of the ground states of U(V) and U(IV) belonging to $5f^1$ and $5f^2$, it was highly likely that the yellow colors of uranyl compounds are due to electron transfer to the empty 5f shell.

Key words: inorganic, solar, visible, quantum theory.

The crystal structures (14) frequently show a linear OUO^{+2} group, with the U-O distance as short as 1.7-1.8Å, to be compared with distances between 2.2 and 2.5Å to 6 or 5 oxygen or fluorine atoms in the equatorial plane. Like CO_2 and CO, the uranyl ion lacks proton affinity in solution, and the very slow ^{18}O exchange shows that tautomeric rearrangement to $U(OH)_4^{+2}$ does not occur. At this point, the chemistry of U(VI) is strikingly different from Cr(VI), Mo(VI), and W(VI) but shows some similarity (15) with *trans*-dioxo octahedral complexes of the diamagnetic (two electrons in a nonbonding xy-orbital) $4d^2$ ruthenium (VI), $5d^2$ rhenium (V), and $5d^2$ osmium(VI).

Seen from a spectroscopic point of view, it is surprising that the first electron transfer band of uranyl ions occurs already close to 20,000 cm^{-1} (2.5 eV) when compared with molybdate (43,200 cm^{-1}) and tungstate (50,300 cm^{-1}) of similar chemically oxidizing character. These tetroxo complexes (16, 17) also show unexpected trends compared with hexahalide complexes (11). Though the orange CrO_3X^- have their first electron transfer band earlier than the unsubstituted chromate, the wave number hardly depends on X = F, Cl, Br, or OH, and the usual treatment of optical electronegativities (9, 11) useful not only for halides, but also for many other ligands, is not as convincing for oxide (1, 18). It may be noted that the parameter 30,000 cm^{-1} (allowing x_{opt} for halides to have the Pauling values of the electronegativity x) most unexpectedly has shown up (19, 20) as the product of 3.7 eV and x_{opt} being roughly 1 eV lower than the lowest ionization energy I of gaseous halide molecules, and 0-1 eV higher than I of solid halides. The apparently excessive oxidizing character of U(VI) is also remarkable (6, 21) by comparison of UF_6 and WF_6.

It is very characteristic for uranyl complexes that they are highly anisotropic (22), the (much broader, and relatively more intense) electron transfer bands due to reducing ligands in the equatorial plane have wave numbers in much better agreement with x_{opt} determined from many other complexes. Thus, the fox-red color, of uranyl complexes of sulfur-containing ligands and of ferrocyanide, and orange $UO_2I_4^{-2}$, indicate x_{opt} of U(VI) as low as 1.8; whereas, x_{opt} = 3.1 for the two oxo ligands would provide x_{opt} = 2.4 for U(VI) to be compared with 1.8 (1.5, when corrected for spin-pairing energy) for U(IV) in UI_6^{-2} (22).

The anomalous low wave number of the electron transfer band due to the two ligands with exceptionally short U-O internuclear distances is not the only enigmatic aspect of the uranyl ion. The oscillator strength P (called f by many authors) is $4.32 \cdot 10^{-9}$ times the integrated area of the molar extinction coefficient as a function of the wave number, and is 7.2

$\cdot 10^{-5}$ for the whole blue and violet region between 20,000-25,000 cm^{-1} (23) now known to represent at least four electronic transitions as discussed below. This value is only one order of magnitude higher than for the narrow bands of trivalent lanthanides (1) and is much smaller than 10^{-3} characterizing parity-forbidden transitions (8) from even MO to d-like orbitals in hexahalide complexes, or 0.02-0.5 for corresponding parity-allowed transitions from odd MO.

In so far as the excitations are manifestly localized within the triatomic uranyl group, there is no longer any doubt that these ultraweak transitions are all parity-forbidden and, hence, go from π_u or σ_u orbitals formed mainly from oxygen 2p orbitals on a LCAO picture (6) to the empty 5f shell. There are certainly no parity-allowed transitions below 30,000 cm^{-1}; whereas, a rather indefinite background slope is raising at higher energies (2). It has been noted for a long time (23, 24) that the absorption spectrum consists of a roughly equidistant series of maxima with the distance around 700 cm^{-1}. The fluorescence emission spectrum typically shows 5-6 approximately equidistant peaks (one coinciding with the Stokes threshold at 20,600 cm^{-1} or 485 nm in the aqua ion) with a separation close to 850 cm^{-1}. This increased difference is interpreted as vibrational structure, the electronic ground state having a higher force constant than the excited state. The large Stokes shift indicates the equilibrium internuclear distances to be considerably elongated in the excited state.

However, it cannot be justified to speak about one excited state. It seems to be a numerical accident that the energy differences between several electronic states happen to be close to a multiple of the lower vibrational wave number, and still the intensity distribution and the variation of subsequent distances are perceptibly irregular. This situation was clarified by the careful study of $Cs_2UO_2Cl_4$ at liquid helium temperature by Denning, Snellgrove, and Woodwark (25) using isotopic ^{18}O substitution to shift the vibrational structure and identify 11 electronic origins between 20,096 and 27,758 cm^{-1}. It had previously been noted (24, 26) that the appropriate quantum number (besides even or odd parity) to use in the linear uranyl ion is Ω being O^+, O^-, or a positive integer (10, 27) having the same relation to J in spherical symmetry as Λ has to L. In particular, states with well-defined M_J have $\Omega = |M_J|$. The excited states of the uranyl ion are rather unique by combining strong effects of spin-orbit coupling ($^2F_{7/2}$ of $5f^1$ is situated (28) 7609 cm^{-1} above $^2F_{5/2}$ in gaseous U^{+5}, and the absorption spectrum of aqueous uranyl perchlorate (24) seems to repeat itself after 7900 cm^{-1} above the first origin) with almost coinciding energy of at least four 5f-like orbitals with symmetry types ϕ_u and δ_u. One corollary (26) is that it has no meaning to discuss whether the excited states (14) are triplet (S = 1) or singlet. The two MO of symmetry type π_u are expected to have the component $\omega = 3/2$ at slightly higher energy than $\omega = 1/2$. This separation is hardly due to spin-orbit coupling operating close to the oxygen nuclei, but could be a few thousand cm^{-1} by participation of the empty U7p or filled U6p in LCAO descriptions. The σ_u has exactly $\omega = 1/2$. Each of such two ω values provides 16 Ω values by transfer of an electron to the 5f shell. The lowest excited state (25) has selection rules in polarized light clearly indicating $\Omega = 1$. This can be interpreted as transfer of π_u ($\omega = 3/2$) to the lowest ($\Omega = 5/2$) component of $^2F_{5/2}$ representing about equal squared amplitude (24) of ϕ_u and δ_u. Another alternative is transfer of σ_u ($\omega = 1/2$) to the ($\Omega = 3/2$) component of $^2F_{5/2}$ expected (29, 30) to be some 2000 cm^{-1} above the ($\Omega = 5/2$) component. However, it is conceivable that the ligands in the equatorial plane destabilize ϕ_u to a slightly larger extent than δ_u. Denning *et al.* (25) assign six Ω values to the 11 origins found in $Cs_2UO_2Cl_4$, the tetragonal symmetry induced by the four equatorial chloride ligands splitting positive even Ω value by several hundred cm^{-1}. Denning prefers the second alternative, but this question is by far not resolved (6). It is beyond dispute that several (of at least 16) Ω values correspond to weak transitions hidden in the background.

One might have hoped that MO calculations might throw light on the problem whether σ_u or π_u is most readily excited. There have been several previous attempts (14), but Table I gives the predicted ionization energies I in eV (= 8065.48 cm^{-1}) of four relativistic calculations (31-34) at a high level of sophistication, and of one parameterized extended Hückel calculation (35). Wadt (36) is interested in the gaseous molecule ThO_2 (known to be bent at 122°), and Table I includes the results for linear ThO_2 with the distance $R = 1.92$Å and for the isoelectronic UO_2^{+2} assuming the short $R = 1.64$Å. Both Walch and Ellis (31) and Boring and Wood (33, 34) agree with the Denning hypothesis (that σ_u is the highest occupied MO), but in all three cases, even MO occur less than 1 eV below σ_u. This difficulty does not occur for Pyykkö and Lohr (35) nor for the ThO_2 calculation (36); whereas, the two other uranyl calculations (32, 36) have an even MO highest. The precision of these results does not seem better than 2 eV, making them inconclusive for the description of the electron transfer spectrum. It must be said in all fairness that the order of MO energies is more significant than the zero-point of energy. The neglect of a background Madelung potential for the uranyl cation has increased the four first lines of Table I by a contribution of the order 10 eV, but four calculations (on a comparable level of sophistication) of the neutral molecule UF_6 (33, 37-39) also scatter by several eV (6) though much better agreement exists about the order of MO energies, and the result that the highest occupied MO are the t_{1u} in contradistinction to t_{1g} in all other neutral hexafluorides and hexahalide anions. The dispersion of results for the uranyl ion in Table I is comparable to the effect of throwing dice.

A very interesting aspect of the calculations is that the squared amplitude of U5f character in the highest filled σ_u orbital is 0.87 by Pyykkö and Lohr (35), 0.59 by Boring and Wood (33), and in the results of Wadt (36) 0.57 for UO_2^{+2} (though here, σ_g is the highest MO), and 0.25 for linear ThO_2. A squared U5f amplitude well above ½ would mean that the visible absorption of uranyl compounds is not strictly speaking due to electron transfer, but to an electron jumping from a bonding to approximately nonbonding 5f-like orbitals, and also that the conditional oxidation state (9) of the ground state is U[IV]. This hypothesis has been further analyzed (40), and it is argued that if Denning's proposal of lower excitation energy of σ_u than of π_u is valid, it is rather due to "pushing from below" by the filled U6p orbitals having moderate I. The latter explanation is recognized in UF_6 (33, 38)

Table I. Calculated molecular orbital (MO) ionization energies in eV

Ref.	5f (ω = 3/2)	5f (ω = 5/2)	σ_u	π_u	π_g	σ_g
(31)	22.0	22.2	22.5	25.3	24.5	23.5
(32)	24.0	24.3	26.5	25.6	24.6	26.3
(33)	—	19.6*	23.1	23.6	23.5	24.9
(34)	19.38	19.52	23.0	23.3	23.2	24.6
(35)	—	—	10	12	13	13
(36), UO_2^{+2}	—	—	29.5	29.4	29.5	28.7
(36), linear ThO_2	—	—	8.8	10.7	11.9	12.3

* This value is obtained by correcting I = 19.09 eV reported for ϕ_u and δ_u by the spin-orbit stabilization 0.54 eV in gaseous U^{+5}.

where the squared U6p amplitude in the highest occupied MO (t_{1u}) is 0.09 and 0.07, and the large calculated spin-orbit coupling corresponds to about a-tenth U6p character (6). By the same token, Wadt (36) finds 0.09 in UO_2^{+2} and 0.15 Th6p character in linear ThO_2. Several authors (34, 36) point out that the U6p character increases strongly as a function of decreasing R. Hence, the high energy of σ_u is a specific effect of very short R.

This whole grid of rationalizations may have a weak point. All MO calculations tend to overestimate the extent of covalent bonding, when the d- or f-shell of a transition-group central atom has the same (or slightly higher) ionization energy I as the loosest bound orbitals of the ligands. A closer analysis (41-43) shows that this paradox has its root in the electron affinity of the partly filled shell (being much smaller than I in the case of small average radii) being the significant quantity to be compared with I of the ligands. It would seem that the calculations (33, 35, 36) predicting the squared amplitude of U5f in σ_u to be above ½ are influenced by the somewhat accidental coincidence of (predicted) I (U5f) and I (O2p). At this point, it should not be neglected that I (O2p) of solid oxides is known from photoelectron spectra (19, 20, 41) to fall in the interval 10-11 eV in most cases, and I (F2p) of solid fluorides usually between 12-13 eV.

The first excited state of the uranyl ion is notable both for its fluorescence and for its extensive photochemistry (2, 14, 44, 45). An excited state living for longer than some 10^{-9} sec looses its vibrational energy to the thermal reservoir of the surrounding condensed matter, and remains in the vibrational ground state (if the frequencies are much higher than kT) of the electronically excited state. Adamson (46, 47) calls such thermally equilibrated excited states "thexi" states. Frequently, their chemistry is highly different from the electronic ground state, corresponding to noble-metal central atoms with conspicuous chemical polarization (48). The excited state is simultaneously much more reducing and much more oxidizing than the ground state, by having its free energy increased by the Stokes threshold $h\nu$. Thus, the standard oxidation potential $E°$ for ionization $G \rightarrow G^+$ of the ground state is decreased to $(E° - h\nu)$ for the oxidation of the thexi state $T \rightarrow G^+$; $E_*°$ of the process $G^- \rightarrow G$ expressing the oxidizing character of G is increased to $(E_*° + h\nu)$ for $G^- \rightarrow T$. This argument is slightly modified by the Franck-Condon co-excitation of vibrations, but it is true within 1/10 eV that $E°$ for $UO_2^+ \rightarrow UO_2^{+2} = +0.06V$ (relative to the standard hydrogen electrode; it is (20, 48) +4.5V relative to vacuo) is increased by $h\nu = 2.56$ eV to close to +2.6V indicating an oxidizing character of the excited uranyl ion (in the following $*UO_2^{+2}$) almost as strong as of free fluorine. Seen from this point of view, one would have expected the photolysis of water to $2H_2 + O_2$ by visible light to have been much easier than it seems to be in practice (49, 50). It is also clear that the redox reactions of a thexi state during its lifetime are more determined by kinetic activation energy than by considerations of free energy.

Einstein proposed in 1917 a formula for the radiative half-life of an excited state (1, 6) being inversely proportional to the product $P(h\nu)^2$. The first ($\Omega = 1$) state of the uranyl ion has (at most) $P = 5 \cdot 10^{-6}$ corresponding to a mean lifetime (equal to 1.44 times the half-life for exponential decay) of 1.4 msec. Such lasting luminescence is known for several crystalline uranyl salts, and glasses; whereas, the lifetime is close to 10^{-6} sec for aqua ions (51, 52) though slightly dependent on pH and temperature. However, 0.67-15M phosphoric acid increases the lifetime to values between 0.2-0.02 msec, to be compared with 0.4 msec in phosphate glass of stoichiometry $NaPO_3$ (29, 51, 53). Since a single anion bound in the equatorial plane in many cases stretch the lifetime by a factor of 20-100, it cannot be argued that the nonradiative de-excitation by ephemeral hydrogen atom abstraction from water molecules (52) is prevented by lack of coordinated H_2O, but it may suggest that the H atom is abstracted close to one of the oxygen atoms in $*UO_2^{+2}$. If the ground state has a charge distribution (9) close to $z = +3$ on U and −0.5 on O, the thexi state may have almost neutral oxygen atoms. It would be comparable to O_2^+ if $z = +2$ for uranium in the ground state.

Many reducing anions quench the uranyl fluorescence (14, 51, 53) show the two main reactions induced by $*UO_2^{+2}$, electron, and (of greater versatility in organic molecules) hydrogen atom abstraction. Flash photolysis of uranyl solutions containing $Mn(OH_2)_6^{+2}$ produces purple manganese(III) aqua ions (54). Several other cations, usually with high chemical polarizability (48), quench, and it can be shown (55, 56) that $*UO_2^{+2}$ binds one silver(I), and one or two thallium(I) cations. The $5f^2$ system neptunium(V) NpO_2^+ reacts already in its ground state (57) with Al(III), Fe(III), In(III), Th(IV), and many other aqua ions, and it is possible (58) to isolate $ONpOM(OH_2)_5^{+4}$ with M = Cr and Rh. A comparable U(V) and Cr(III) adduct is formed (59) by reducing UO_2^{+2} with chromium(II) aqua ions. Both UO_2^+ and NpO_2^+ form adducts with UO_2^{+2} which were recently reviewed (6, 60). It is not surprising that $*UO_2^{+2}$ shows even more complicated behavior; Marcantonatos (52, 61) argues that exciplexes such as $*UO_2HUO_2^{+4}$ are formed, with the emission spectrum slightly different from $*UO_2^{+2}$. Oligomeric hydroxo-bridged complexes might form (6) at slightly higher pH.

The 10^{-8}M uranyl carbonate complexes present in sea water (and sometimes higher concentrations in rivers and lakes) are excited, on the average, every 10 min, when the sun stands in zenith. It is possible (15) that this catalyst (with rapid turn-over) photooxidizes otherwise nonbiodegradable organic compounds arriving in the ocean from the large Amazon and Zaíre rivers.

The fluorescence of uranyl glasses (62) and subsequent energy transfer (1, 63) to neodymium(III) and holmium(III) has been applied in flat-plate luminescent concentrators, trapping the radiation by a sequence of total reflections and, hence, diminishing the area of photovoltaic silicon on the rim of the plate an order of magnitude, relative to the plate area (64).

$*UO_2^{+2}$ is dark blue, having an intense broad band in the yellow (14). Among its other unusual physical properties is the Becquerel effect (65) of imperfectly understood differences between electrode potentials in illuminated and dark volumes of a uranyl solution. We have been speaking as if $*UO_2^{+2}$ is represented exclusively by the first excited state. Actually, it seems as if the previous reports about fluorescence originating in a second state have been reinterpreted as traps in cooled $Cs_2UO_2Br_4$ crystals (66) and as vibrational structure (67). Nevertheless, it is true (68) that all excited states start immediately to luminesce, with an integrated quantum yield which is the ratio between the observed and the (Einstein) radiative lifetime. The 48 Ω levels due to transfer of an electron from the odd MO to the 5f shell (they would split into 84 electronic origins in sufficiently low symmetry of the equatorial plane) must decay very rapidly to the ($\Omega = 1$) origin. If these levels have a radiative half-life of 1 msec, a higher level with the half-life 10^{-8} sec would have the quantum yield of 10^{-5}.

Besides the fascinating spectroscopic and photochemical properties, the inexpensive ^{238}U available as by-product from isotope separation may help the uranyl fluorescence contributing to utilization of solar energy (64, 69).

Acknowledgment

This work was made possible by the grant no. 2.841-080 from the Swiss National Science Foundation.

Manuscript received July 6, 1982. This was Paper 476 presented at the Montreal, Canada, Meeting of the Society, May 9-14, 1982.

Any discussion of this paper will appear in a Discussion Section to be published in the December 1983 JOURNAL. All discussions for the December 1983 Discussion Section should be submitted by Aug. 1, 1983.

Publication costs of this article were assisted by The University of Geneva.

REFERENCES

1. R. Reisfeld and C. K. Jørgensen, "Lasers and Excited States of Rare Earths," Springer-Verlag, Berlin (1977).
2. E. Rabinowitch and R. L. Belford, "Spectroscopy and Photochemistry of Uranyl Compounds," Pergamon Press, Oxford (1964).
3. G. Blasse, *This Journal*, **124**, 1280 (1977).
4. W. A. Runciman and E. Y. Wong, *J. Chem. Phys.*, **71**, 1838 (1979).
5. K. C. Bleijenberg, *Struct. Bonding*, **42**, 97 (1980).
6. C. K. Jørgensen and R. Reisfeld, *ibid.*, **50**, 121 (1982).
7. C. K. Jørgensen, *Chem. Phys. Lett.*, **87**, 320 (1982).
8. C. K. Jørgensen, *Adv. Chem. Phys.*, **5**, 33 (1963).
9. C. K. Jørgensen, "Oxidation Numbers and Oxidation States," Springer-Verlag, Berlin (1969).
10. C. K. Jørgensen, "Modern Aspects of Ligand Field Theory," North-Holland Publ. Co., Amsterdam (1971).
11. C. K. Jørgensen, *Prog. Inorg. Chem.*, **12**, 101 (1970).
12. C. K. Jørgensen, *Mol. Phys.*, **5**, 271 (1962).
13. J. L. Ryan and C. K. Jørgensen, *J. Phys. Chem.*, **70**, 2845 (1966).
14. H. D. Burrows and T. J. Kemp, *Chem. Soc. Rev. (London)*, **3**, 139 (1974).
15. C. K. Jørgensen, *Rev. Chim. Miner. (Paris)*, **14**, 127 (1977).
16. A. Müller, E. Diemann, and C. K. Jørgensen, *Struct. Bonding*, **14**, 23 (1973).
17. G. Blasse, *ibid.*, **42**, 1, (1980).
18. J. A. Duffy, *ibid.*, **32**, 147 (1977).
19. C. K. Jørgensen, *ibid.*, **24**, 1 (1975); **30**, 141 (1976).
20. C. K. Jørgensen, *Comments Inorg. Chem.*, **1**, 123 (1981).
21. R. McDiarmid, *J. Chem. Phys.*, **65**, 168 (1976).
22. J. L. Ryan and C. K. Jørgensen, *Mol. Phys.*, **7**, 17 (1963).
23. J. T. Bell and R. E. Biggers, *J. Mol. Spectrosc.*, **18**, 247 (1965).
24. C. K. Jørgensen, *Acta Chem. Scand.*, **11**, 166 (1957).
25. R. G. Denning, T. R. Snellgrove, and D. R. Woodwark, *Mol. Phys.*, **32**, 419 (1976); **37**, 1109 (1979).
26. C. K. Jørgensen and R. Reisfeld, *Chem. Phys. Lett.*, **35**, 441 (1975).
27. G. Herzberg, "Electronic Spectra and Electronic Structure of Polyatomic Molecules," Van Nostrand, Princeton (1966).
28. V. Kaufman and L. J. Radziemski, *J. Opt. Soc. Am.*, **66**, 599 (1976).
29. N. Lieblich-Sofer, R. Reisfeld, and C. K. Jørgensen, *Inorg. Chim. Acta*, **30**, 259 (1978).
30. C. K. Jørgensen, *J. Lumin.*, **18**, 63 (1979).
31. P. F. Walch and D. E. Ellis, *J. Chem. Phys.*, **65**, 2387 (1976).
32. C. Y. Yang, K. H. Johnson, and J. A. Horsley, *ibid.*, **68**, 1001 (1978).
33. M. Boring and J. H. Wood, *ibid.*, **71**, 392 (1979).
34. J. H. Wood, M. Boring, and S. B. Woodruff, *ibid.*, **74**, 5225 (1981).
35. P. Pyykkö and L. L. Lohr, *Inorg. Chem.*, **20**, 4405 (1981).
36. W. R. Wadt, *J. Am. Chem. Soc.*, **103**, 6053 (1981).
37. D. D. Koelling, D. E. Ellis, and R. J. Bartlett, *J. Chem. Phys.*, **65**, 3331 (1976).
38. P. J. Hay, W. R. Wadt, L. R. Kahn, R. C. Raffenetti, and D. C. Phillips, *ibid.*, **71**, 1767 (1979).
39. D. A. Case and C. Y. Yang, *ibid.*, **72**, 3443 (1980).
40. C. K. Jørgensen, *Chem. Phys. Lett.*, **89**, 455 (1982).
41. C. K. Jørgensen, *Chimia*, **27**, 203 (1973); **28**, 6 (1974).
42. C. K. Jørgensen, *Struct. Bonding*, **22**, 49 (1975).
43. R. Ferreira, *ibid.*, **31**, 1 (1976).
44. A. W. Adamson, W. L. Waltz, E. Zinato, D. W. Watts, P. D. Fleischauer, and R. D. Lindholm, *Chem. Rev.*, **68**, 541 (1968).
45. V. Balzani, F. Bolletta, M. T. Gandolfi, and M. Maestri, *Top. Curr. Chem.*, **75**, 1 (1978).
46. R. T. Walters and A. W. Adamson, *Acta Chem. Scand.*, **A33**, 53 (1979).
47. A. W. Adamson and A. R. Gutierrez, *J. Phys. Chem.*, **84**, 2492 (1980).
48. C. K. Jørgensen, *Top. Curr. Chem.*, **56**, 1 (1975).
49. J. Kiwi, K. Kalyanasundaram, and M. Grätzel, *Struct. Bonding*, **49**, 37 (1982).
50. H. Tributsch, *ibid.*, **49**, 127 (1982).
51. M. Moriyasu, Y. Yokoyama, and S. Ikeda, *J. Inorg. Nucl. Chem.*, **39**, 2199, 2205, and 2211 (1977).
52. M. D. Marcantonatos, *J. C. S. Faraday Trans. I*, **75**, 2273 (1979); **76**, 1093 (1980).
53. R. Matsushima, H. Fujimori, and S. Sakuraba, *ibid.*, **70**, 1702 (1974).
54. H. D. Burrows, S. J. Formosinho, M. da G. Miguel, and F. Pinto Coelho, *ibid.*, **72**, 163 (1976).
55. M. D. Marcantonatos and M. Deschaux, *Chem. Phys. Lett.*, **76**, 359 (1980); **80**, 327 (1981).
56. M. Deschaux and M. D. Marcantonatos, *J. Inorg. Nucl. Chem.*, **43**, 2915 (1981).
57. J. C. Sullivan, *J. Am. Chem. Soc.*, **84**, 4256 (1962).
58. R. K. Murmann and J. C. Sullivan, *Inorg. Chem.*, **6**, 892 (1967).
59. T. W. Newton and F. B. Baker, *ibid.*, **1**, 368 (1962).
60. B. Guillaume, G. M. Begun, and R. L. Hahn, *ibid.*, **21**, 1159 (1982).
61. M. Deschaux and M. D. Marcantonatos, *J. Inorg. Nucl. Chem.*, **43**, 361 (1981).
62. R. Reisfeld and S. Neuman, *Nature*, **274**, 144 (1978).
63. R. Reisfeld and Y. Kalisky, *ibid.*, **283**, 281 (1980).
64. R. Reisfeld and C. K. Jørgensen, *Struct. Bonding*, **49**, 1 (1982).
65. I. Lifschitz and S. B. Hooghoudt, *Z. Phys. Chem.*, **A146**, 145 (1930).
66. C. D. Flint and P. A. Tanner, *Inorg. Chem.*, **20**, 4405 (1981).
67. C. D. Flint, P. Sharma, and P. A. Tanner, *J. Phys. Chem.*, **86**, 1921 (1982).
68. C. D. Flint, *Chem. Brit.*, **14**, 223 (1978).
69. C. K. Jørgensen, in "Photochemical Conversion and Storage of Solar Energy," J. S. Connolly, Editor, p. 79, Academic Press, New York (1981).

Contact Angles Between III-V Melts and Several Substrates

U. König and W. Keck

AEG-TELEFUNKEN, Forschungsinstitut Ulm, D 7900 Ulm, Germany

ABSTRACT

The wetting behavior of several melts with different III-V compound semiconductors is studied. The characteristic parameter measured is the contact angle of a melt drop with a solid. It is evaluated by a geometrical measurement of the melt drop. The importance of clean surfaces of drop and solid is shown. Contact angles between 20° and 60° are found, depending on the type and composition of the melt and substrate. The temperature dependence amounts to about −4° per 100 K increase. In addition, the contact angle varies with the substrate orientation. The (100) orientated substrates are wetted better than (111) A orientated ones.

In liquid phase epitaxy (LPE) of a III-V compound semiconductor, a metallic melt is in contact with a solid substrate and a crucible, usually graphite. The wetting behavior of a III-V melt influences the carry-over of melt, and by this the epitaxial quality with respect to unintentionally grown layers [*e.g.*, (1)].

The quality of the wetting may also affect the crystalline perfection of an epitaxial layer along the melt meniscus due to surface tension (2). When removing the melt from the semiconductor, it moves by a "stick-slip" motion. This forms the well-known meniscus lines (3).

The representative parameter for wetting is the contact angle at the melt meniscus between the melt surface and the substrate surface covered by the melt [*e.g.*, (4)]. The better the wetting, the smaller the contact angle is. The literature data for Ga on GaAs with contact angles >90°, from Munir and co-workers (5, 6), do not agree with the phenomenological experience of capillary ascension at LPE of III-V compounds. When melt and substrate are brought into contact, one usually observes a creeping of the melt on the substrate under the melt chamber walls. Very recently, Small and Potemski (7) reported on smaller angles for GaAs and $Ga_{0.4}Al_{0.6}As$, when regarding a microscopical deformation of the solid around the periphery of the drop. We have evaluated contact angles in a macroscopical measure of melt and solid to find representative data for LPE. Several III-V compound systems and different substrate orientations have been studied in a hydrogen atmosphere.

Experimental

We have used a horizontal LPE apparatus, consisting of a movable heat pipe furnace, a quartz reaction tube, a Pd diffusion cell, and a crucible of high purity graphite with fixed melt chambers, and a sliding substrate holder. A side-wall of one melt chamber was omitted in order to directly observe the melt contact angles. During a 3 hr heat cleaning at 1145 K in purified hydrogen, the melt drop, of about 5 mm diam, lies on the graphite slider within the chamber of 24 × 24 mm^2 separated from the substrate. The substrate is protected by a graphite cover. The sliding mechanism allows us to roll the melt drop on the graphite slider so that its surface can be exposed to reducing hydrogen, even its incipient contact area. Only after the heat cleaning is the substrate rapidly moved under the melt drop. The drop spreads on the substrate surface without touching the chamber walls, and forms an equilibrium contact angle. For making a photograph, the furnace is moved partially away from the crucible. Moving of the melt and photographing did not last more than 10 sec in order to avoid a temperature decrease larger than 20 K (measured beneath the melt chamber with a thermocouple and deduced from the shiny drop surface free of crystallization). The photographs had to be corrected for the viewing angle to determine the contact angles.

In the case of a $Ga_{1-x}Al_xAs$ semiconductor which tends to form stable surface oxides, the wetting experiment takes place just after depositing an epitaxial $Ga_{1-x}Al_xAs$ layer under an appropriate melt in a separate chamber of the crucible. This may provide an oxide-free semiconductor surface when one brings the melt drop into contact with the solid.

The GaAs substrates are heavily Zn doped ($\approx 2 \cdot 10^{18}$ cm^{-3}). The doping level of the epitaxial layers $Ga_{0.35}Al_{0.65}As$ and $Ga_{0.96}In_{0.04}As$ are around $5 \cdot 10^{17}$ cm^{-3}.

To avoid the formation of a thermally stable oxide film on a drop containing Al, which would not allow representative wetting, a heat cleaning step at 750 K is introduced. This temperature is sufficient to liberate contaminations from the drop and low enough to prevent rapid Al oxidation (8).

The compositions of the melt drops are determined from their respective phase diagrams (9, 10). They correspond to a temperature a few degrees below our typical drop temperature. This avoids spontaneous crystallization within or on the melt drop, as well as, a severe melt back of the substrate. As a further preventive measure, the time period between the first contact of the drop with the substrate and the photograph is chosen as short as possible (see above).

Different cleaning precautions are used for the growth system and the components. The LPE reaction tube is heated under hydrogen flow for about 4 hr at 1150 K. The crucible is baked out in high vacuum for 8 hr at about 1400 K in a special reactor, followed by a gettering procedure for several hours at 1150 K with a hydrogen flow and with Ga filled melt chambers within the LPE system. The melts are composed of 6*N* metal components, wet chemically cleaned. All substrates are given a standard preepitaxial cleaning process.

Results and Discussion

The contact angles found for several III-V compound systems, *i.e.*, for (111) A orientated GaAs substrates, $Ga_{0.96}In_{0.04}As$ and $Ga_{0.35}Al_{0.65}As$ epitaxial layers with Ga, In, Ga-As, Ga-In-As, and Ga-Al-As, are listed in Table I. Because of the important influence of the wetting behavior with the crucible material during LPE, graphite is also regarded as a substrate. Contact angles above 140° are found (Table I). This angle depends on the graphite type and the machined surface roughness. Clean III-V semiconductors are better wetted by III-V liquids according to contact angles between 20° and 63°. Indium containing melts form the smallest contact angles with the GaAs and $Ga_{1-x}In_xAs$ substrates. For liquid compositions from $x_{As} = 0$ to $x_{As} = 3.16$ a/o, Table I, the contact angle is found to increase with the amount of the solute.

Special considerations are required for Al containing systems. An insufficiently heat cleaned Ga-Al-As melt forms no definite drop. In addition, a $Ga_{1-x}Al_xAs$ semiconductor will be poorly wetted (large contact

Key words: wetting, orientation dependence, gallium arsenide, liquid phase epitaxy.

Table I. Contact angles at 1125 K for several melt compositions with (111) A orientated III-V compound semiconductors and with two types of graphite, typically used in LPE

Substrate	Melt	Contact angle (°)
GaAs	Ga	28 ± 1
	In	20 ± 2
	Ga-As 3.16 a/o As	40 ± 2
	Ga-In-As 70 a/o In 11 a/o As	32 ± 2
	Ga-Al-As 0.8 a/o Al 1.29 a/o As	51 ± 1
$Ga_{0.96}In_{0.04}As$	Ga-In-As 70 a/o In 11 a/o As	34 ± 1
$Ga_{0.35}Al_{0.65}As$ oxidized		126 ± 4
$Ga_{0.35}Al_{0.65}As$ fresh	Ga-As 3.16 a/o As	53 ± 3
	Ga-Al-As 0.8 a/o Al 1.29 a/o As	63 ± 3
Graphite FE 49		140 ± 3
Graphite Poco	Ga-As 3.16 a/o As	153 ± 2

angle, see Table I), when the semiconductor is grown in a preceding LPE process, or well wetted (small contact angle, see Table I), when the $Ga_{1-x}Al_xAs$ layer is freshly deposited just before the wetting with the test drop. Apparently, there is a thermally stable oxide coating on the $Ga_{1-x}Al_xAs$ surface which prevents wetting.

The contact angles found at 1125 K, Table I, are for a typical LPE process temperature. For a wetting experiment with the Ga/GaAs (111) A-system at 570 K, we obtained a contact angle of 48° ± 2°. This indicates a contact angle decrease of about 3.6° for a 100 K increase.

The orientation dependence of the contact angle obtained for (111) A and (100) orientated GaAs and $Ga_{1-x}Al_xAs$ substrates is presented in Table II. The (100) orientated substrates are better wetted. This agrees with the observation of a stronger capillary ascension on (100) orientated substrates under melt chamber walls in an LPE-crucible. The contact angles seem to be independent of the orientations in the substrate surface, according to the circular contact areas of the drops.

Contrary to our low values <63° in hydrogen, and those <83° of Small and Potemski (7), contact angles around 110° were reported for a III-V system in high vacuum and inert gases (5, 6). The question is whether the different surrounding atmospheres can be responsible for such differences. Principally, a difference can be expected according to Young's law, which relates the contact angle with the surface tensions between

Table II. Dependence of the contact angle on the substrate orientation for two systems at 1125 K

Melt	Orientation	Substrate	Contact angle (°)
Ga-As 3.16 a/o As	(111) A	GaAs	40 ± 2
		$Ga_{0.35}Al_{0.65}As$	53 ± 3
	(100)	GaAs	35 ± 1
		$Ga_{0.35}Al_{0.65}As$	48 ± 3

solid-vapor (or vacuum), liquid-vapor (or vacuum), and solid-liquid [*e.g.*, (4)]. However, the surface tensions of the known liquid and solid elements (11, 12) and also of some compounds (13) are nearly unaffected by the ambient gas or vacuum. Presuming this for III-V compounds, too, the contact angles observed here and in (5, 6) should not differ so much. Even the lower temperatures (<752 K) of Ref. (5) cannot be responsible for this discrepancy, for we have found much lower angles also in this temperature range (see above). One should consider that, in Ref. (5, 6), melt and substrate were already brought into contact a few degrees above the melting point, where Ga oxides strongly affect the melt meniscus. The following heating up in vacuum is not sufficient to produce an oxide-free Ga drop like a reducing hydrogen atmosphere. Therefore, in Ref. (5, 6), the contact angle of the initial melt meniscus is given, which remains fixed on the substrate by oxides on the drop. In experiments with insufficiently cleaned Ga drops, we have obtained comparable large angles.

Conclusion

We have evaluated some quantitative dependences of the contact angle on the type of the III-V solid, on the type and composition of III-V melts, on the temperature, and on the substrate orientation. An estimation of contact angles by means of comparison with Young's law fails because of the poor knowledge of surface tension data for III-V components. Particularly, the solid-vapor and the solid-liquid surface tensions are very uncertain (14) or even unknown.

The carry-over of melts, undesirable during LPE, is probably due to the good wetting, particularly for In melts and (100) orientated III-V semiconductors. The knowledge of the contact angles will help to overcome these problems by adapting the crucible material and construction to the respective wetting behavior of the system melt/substrate.

Manuscript submitted July 20, 1982; revised manuscript received Oct. 7, 1982.

Any discussion of this paper will appear in a Discussion Section to be published in the December 1983 JOURNAL. All discussions for the December 1983 Discussion Section should be submitted by Aug. 1, 1983.

Publication costs of this article were assisted by AEG-TELEFUNKEN.

REFERENCES

1. M. B. Panish, S. Sumski, and I. Hayashi, *Met. Trans.*, **2**, 795 (1971).
2. M. B. Small, K. H. Bochem, and R. M. Potemski, *J. Cryst. Growth*, **39**, 216 (1977).
3. M. B. Small, A. E. Blakeslee, K. K. Shih, and R. M. Potemski, *ibid.*, **30**, 257 (1975).
4. H. Mykura, "Solid Surfaces and Interfaces," Routledge and Kegan Paul Ltd., London (1966).
5. B. E. Liebert and Z. A. Munir, *J. Cryst. Growth*, **118**, 368 (1971).
6. J. Y. Kashkooli, Z. A. Munir, and L. Williams, *J. Mater. Sci.*, **9**, 538 (1974).
7. M. B. Small and R. M. Potemski, Paper presented at SPIE Conference Semiconductor Growth Technology, Los Angeles, CA, Jan. 1982.
8. P. E. Blackburn and E. A. Gulbransen, *J. Mater. Sci.*, **107**, 944 (1960).
9. R. N. Holl, *ibid.*, **110**, 385 (1963).
10. T. Y. Wu and G. L. Pearson, *J. Phys. Chem. Solids*, **33**, 409 (1972).
11. G. Lang, "Handbook of Chemistry and Physics," 53rd ed., p. 15, CRC Press, Cleveland, OH (1972/73).
12. W. R. Tyson, *Can. Metal. Quarterly*, **14**, 307 (1975).
13. A. Bondi, *Chem. Rev.*, **52**, 417 (1953).
14. J. M. Blakely, "Introduction to the Properties of Crystal Surfaces," p. 116, Pergamon Press, Elmsford, NY (1973).

Effects of Ion Implantation on the Thermal Growth of Pt and NiPt Silicides

T. W. Orent,* C. I. Knudson, and J. A. Sartell

Honeywell Corporate Technology Center, Bloomington, Minnesota 55420

and S. Lee[1] and T. L. Brewer[2]

Honeywell Solid State Development Center, Plymouth, Minnesota 55441

ABSTRACT

The effects of low-dose ion implantation of inert gas ions, prior to thermal annealing on the interactions between Pt and NiPt thin films with various forms of silicon, have been investigated. Specimens were implanted with Kr^{2+} and then annealed along with unimplanted samples in the temperature range 350°-650°C. The extent of silicide formation and the phases formed were determined by Auger electron spectroscopy (AES), x-ray diffraction, and transmission electron microscopy (TEM). The unimplanted Pt films reacted to form complete layers of Pt_2Si which then continued to react to form highly textured layers of PtSi. However, in the implanted samples, no distinct Pt_2Si layers were observed, and the final PtSi phases were fine grained and polycrystalline. In the case of NiPt films, ion implantation inhibited the formation of the distinct Pt silicide layers found during the early stages of the reaction in unimplanted samples. The differences between implanted and unimplanted NiPt samples became progressively smaller with increasing annealing temperature. The final phase formed in both types of specimens was the ternary silicide, $Ni_xPt_{1-x}Si$.

Metal silicides are physically and chemically compatible with integrated circuit fabrication processing and are used currently as Schottky barriers, ohmic contacts and low-resistivity gates, and interconnects (1-4). There is interest in the use of silicides in VLSI devices since they can be processed to form self-aligning shallow contacts with fine-grained structures that are suitable for submicron patterning. There are several possible ways to adjust the Schottky-barrier heights of metal silicides in order to tailor them for a specific application, including ion implanting a thin p- or n-type layer at the interface between the metal and the silicon before forming the silicide (5, 6), by using parallel contacts (7), or by using two metals to form an alloyed silicide (8-10).

In the case of alloyed-silicide diodes, silicides formed by thermal annealing of platinum and nickel layers on silicon have received the most attention (8-10). Measured barrier heights on n-type silicon were between 0.66-0.87 eV, which are the values for NiSi and PtSi, respectively. There also appeared to be a correlation between the barrier height and the Pt content (8). While the system does appear to have highly desirable electrical characteristics, thermal annealing produced multilayer structures with nonuniform compositions (8, 10). This is a very undesirable characteristic since each diode has to be mechanically and electrically stable to further processing.

In order to form uniform stable alloy silicides, the nucleation processes and the growth kinetics must be modified in order to alter the composition, the uniformity, and the grain size. Nucleation is usually an activated process with an activation energy that is higher than that for subsequent growth of the new phase. As a result, while a highly energetic process must be used to initiate compound formation, a less energetic method can be employed to complete the growth. In the case of Pt silicides, Pt_2Si and PtSi have been the only two phases detected when thin films of Pt on Si have been thermally annealed (11). However, ion implantation of inert gas ions through the Pt into the Si prior to thermal annealing caused the formation of the metastable phase Pt_2Si_3 (12).

We investigated the structures formed when a combination of low-dose ion implantation followed by thermal annealing was used to form the silicides from double layers of nickel and platinum on various forms of silicon. The low ion dose should modify the nucleation process because of the resultant collision-cascade mixing and enhanced solid-state diffusion while producing minimal damage, and the subsequent thermal annealing should improve the thermal stability and reduce stresses in the silicide.

Experimental

Thin layers of Pt and Ni were sequentially deposited by rf sputtering at rates of 20Å/min onto several types of chemically cleaned and backsputtered substrates. Both n- and p-type Si(100), poly-Si, and SiO_2 were coated, and the substrate temperatures remained below 100°C during deposition. After deposition, some samples were ion implanted to a dose of 5×10^{14} cm^{-2} with 600 keV Kr^{2+} ions at room temperature. Krypton implantation into Au under these conditions would produce a broad profile peaked about 900Å below the surface (13). In order to insure that the ions penetrated into the substrate and caused the atomic mixing necessary for silicide formation (11, 12), the total metal thickness for the implanted specimens was kept less than 800Å.

Both implanted and unimplanted specimens were annealed in a tube furnace in flowing nitrogen at temperatures between 350° and 650°C for various times. The processed samples were analyzed by Auger electron spectroscopy (AES) to determine compositions as functions of depth, by x-ray and electron diffraction to determine the phases formed, and by transmission electron microscopy (TEM) to examine the microstructures of some of the Pt silicides. The wafers were not patterned to form diodes, and no electrical measurements were made.

Auger analysis showed the presence of carbon and oxygen on all surfaces and more oxygen present after annealing. Since the presence of impurities in the metal film has been shown to alter reaction rates and the phase growth sequence, the carbon and oxygen Auger peaks were monitored in all depth profiles; but, since these levels were less than 1 atomic percent (a/o) in both the as-deposited metals and the silicides, the traces were not included in the figures. No buildup of impurities was found at any interface in the as-depos-

* Electrochemical Society Active Member.
[1] Present address: Magnetic Peripherals, Incorporated, Bloomington, Minnesota 55435.
[2] Present address: Brewer Science, Rolla, Missouri 65401.
Key words: silicides, interdiffusion, ion implantation.

ited or annealed specimens. The peak Kr concentration was about 3×10^{19} cm^{-2} or about 0.05 a/o which was too low to be detected.

Results and Discussion

Pt/Si.—The as-deposited Pt layers had strong (111) textures. Texturing has been observed not only in thicker sputter-deposited Pt layers (14) but also in E-beam evaporated layers on Si(100) (15). Even though no interfacial mixing was apparent in AES depth profiles, selected-area electron diffraction data from a specimen thinned for TEM analysis did show the presence of both Pt_2Si and PtSi near the Pt/Si interface. When unimplanted samples were annealed at 350°C, Pt_2Si formed at the interface and grew rapidly consuming all of the Pt in a few minutes as shown in Fig. 1a (16-19). Continued annealing at 350° resulted in a slow conversion of the Pt_2Si to PtSi. The conversion rate was much faster at higher temperatures, but PtSi was still the final phase formed at temperatures up to 650°C.

Both silicides had uniform textures with grain sizes about 500Å, and both had sharp interfaces with the Si substrate. The systematic absence of lines in the x-ray diffraction data indicated that both silicides were highly oriented. The data for the PtSi were very similar to those of Joubert, Auvray, and Henry (14) who determined that their sample had a (101) texture. Other dominant orientations, such as (002) (20) or a mixture of (110) and (121) (15), have been reported also. The discrepancies have been attributed to different film thicknesses (20). There were no obvious differences in the sequence of phases formed, the rates of growth, or film morphology among the various types of substrates used, except for the SiO_2 where no reaction was observed at 350°C.

Auger depth profiles of the ion-implanted Pt/Si samples showed that the elements had been intermixed over a distance of several hundreds of angstroms. While no new phases could be detected in the x-ray diffraction pattern, high resolution AES spectra of the Si LVV region revealed the additional fine structure characteristics of Pt silicides (8, 21) throughout the mixed region. Thermal annealing at 350°C caused additional intermixing with the Pt to Si atomic ratio decreasing monotonically with depth (Fig. 1b).

The transmission x-ray diffraction patterns for unimplanted and implanted samples that had been annealed at 350°C for 10 min are shown in Fig. 2. The unimplanted sample (Fig. 2a) was Pt_2Si, and the discontinuous diffraction rings indicated that there was a preferred orientation for the grains. The implanted specimen (Fig. 2b) contained PtSi as well as Pt_2Si, and the grains were oriented randomly. This compound layer eventually formed a uniform layer of PtSi, but the rate of growth was much slower than that of thermally generated PtSi, and the grain size was much smaller. No macroscopic region of Pt_2Si was detected during growth.

Since ion implantation causes lattice damage as well as atomic mixing, a wafer was implanted with Kr^{2+} before Pt deposition in order to determine the relative importance of these effects for silicide growth. There were no differences in phase growth sequence, growth rate, or interface width between unimplanted samples and those implanted before metallization. As a result, the observed differences between unimplanted specimens and those implanted after metal deposition were due primarily to atomic mixing.

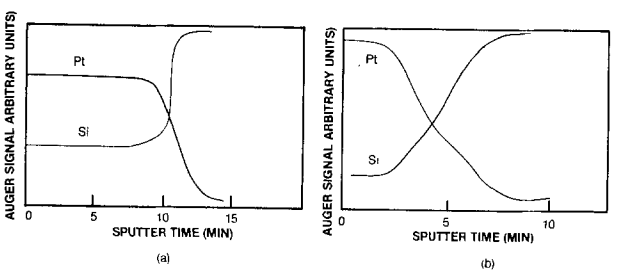

Fig. 1. Auger depth profiles (5 keV, 5 μA, 100 Å/min) of 500Å Pt/Si(100) after (a) annealing at 400°C for 10 min and (b) ion implantation (5×10^{14} cm^{-2} with 600 keV Kr^{2+}) followed by annealing at 350°C for 5 min.

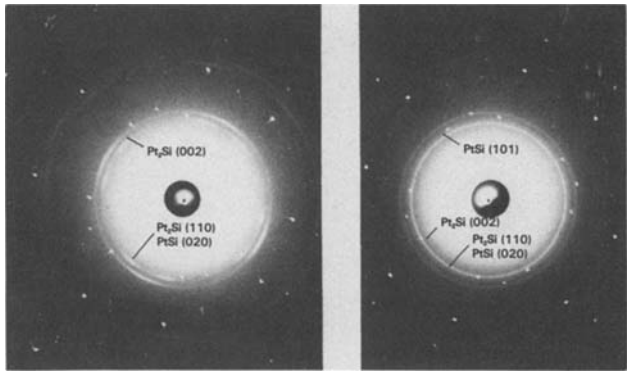

Fig. 2. Transmission x-ray diffraction patterns (Co radiation, 35 keV) of 500Å Pt/Si(100) samples annealed at 350°C for 10 min: (a) as deposited and (b) implanted with Kr^{2+} before annealing. Discontinuous diffraction rings indicate that the silicide film had a preferred orientation.

The results for the unimplanted Pt/Si samples are in good agreement with the fairly extensive literature on the thermal growth of Pt silicides from thin films deposited on Si (14-21). Both the reactions

$$2Pt + Si \rightarrow Pt_2Si \quad [1]$$

$$Pt_2Si + Si \rightarrow 2PtSi \quad [2]$$

are diffusion controlled with reproducible activation energies but with kinetics that were highly dependent upon impurity content (16-19). Rapid atomic diffusion at low temperatures can be strongly suppressed by the segregation of impurities along the fast diffusion paths. Very low levels of impurities decorating the silicide grain boundaries are the most probable cause for the large variation in observed Pt diffusivities (16, 17, 19). In fact, silicide growth can be inhibited completely by the formation of very thin layers of silicon oxides or nitrides (14, 19, 22, 23). The kinetics of Pt silicide formation are not yet established clearly, but several mechanisms have been proposed (2). The low temperature needed to initiate the reaction (19), the parabolic growth rate (16-19), and the radiotracer data that indicate that Pt is the dominant diffusing species (24) all favor a model in which interstitial diffusion of Pt into the Si is responsible for the release of Si atoms from the lattice.

Previous studies on the effects of ion implantation through Pt films on Si have shown that continued implantation resulted first in the formation of a complete layer of Pt_2Si followed by pure atomic mixing with no detectable silicide formation (11). The phase PtSi was not observed, and, in fact, it was shown to be unstable to ion bombardment (12). For low-dose ion implantation, both Pt_2Si and PtSi were observed after thermal annealing for a short time. In this case, microcrystallites of both phases were randomly generated throughout the intermixed region, and then the subsequent thermal growth produced a fine-grained, randomly oriented final phase of PtSi with no distinct intermediate layers ever being formed. The slow growth of the mixed phases indicated a reduced supply of reactant which prevented the predominant growth of Pt_2Si at the expense of PtSi. The reduced diffusion rate was similar to that observed for high levels of impurities (19); however, in this case, no excessive contamination was detected in the Pt film or at the Pt/Si interface.

The slower reaction rate was not due to the presence of Kr which is inert but rather to a change in the growth mechanism. Instead of the formation of a single phase along a uniform growth front, there was competitive growth of two Pt silicides from a large number of randomly distributed microcrystallites.

Ni/Pt/Si.—The presence of Ni over the Pt did not have any detectable effect on the initial Pt-Si interaction. Annealing an unimplanted sample at 350°C produced first a complete layer of Pt_2Si (25) via reaction [1]. No Ni/Pt interdiffusion was apparent in the AES depth profiles during this stage of growth. The next step was the formation of PtSi by reaction [2] at the Pt_2Si/Si interface. The growth rate of the PtSi was much slower than that observed in Pt/Si samples. The onset of PtSi formation was accompanied by the diffusion of Ni through the Pt silicides toward the Si substrate. Ni-rich layers were eventually formed at both the Pt_2Si/PtSi and PtSi/Si interfaces as seen in Fig. 3a.

Continued annealing produced the layered structure indicated by the spectrum shown in Fig. 3b. The presence of Pt silicides in these structures was confirmed by x-ray analysis, but no Ni silicides could be identified because the layers were so thin. The Ni to Si atomic ratio determined by AES suggested the formation of NiSi which is the end phase formed from Ni/Si couples at temperatures between 350°-750°C (26, 27).

Annealing at higher temperatures caused a reaction among the Ni remaining at the surface, the PtSi layer, and additional Si

$$Ni + PtSi + Si \rightarrow Ni_xPt_{1-x}Si \qquad [3]$$

The resultant $Ni_xPt_{1-x}Si$/NiSi layered structure has been observed previously (8, 10). Raising the annealing temperature even higher resulted in additional redistribution of the Pt and Ni to form a homogeneous layer of the ternary as shown in Fig. 3c. Concentration gradients were usually observed in the high temperature specimens with the Ni concentration highest near the substrate (22, 28). The x-ray diffraction data from several samples with different Ni to Pt atomic ratios correlated very well with the results reported for the proposed ternary silicide $Ni_xPt_{1-x}Si$ (25).

Ion implantation through a 400Å Ni/150Å Pt/Si sample (Fig. 4a) resulted in atomic mixing at both interfaces as shown in Fig. 4b. High-resolution Auger spectra again indicated silicide formation in the region near the Pt/Si interface. Annealing at 400°C for a short time (Fig. 5) did not produce the distinct Pt silicide layers that were evident in unimplanted samples annealed under the same conditions (Fig. 3a). Long-term annealing at 400°C eventually resulted in the formation of the layered $Ni_xPt_{1-x}Si$/NiSi structure. No uniform layers of Pt silicides were ever detected. Increasing the annealing temperature decreased the differences in annealing times needed to produce similar structures in the implanted and unimplanted specimens. The only detectable differences in the depth profiles were much longer Ni diffusion tails into the substrate in the implanted samples. It was not possible to ascertain if the Ni in the diffusion tail had reacted to form a silicide, because there is no fine structure in the Si LVV Auger peak for the Ni silicides and Ni diffusion into Si without silicide formation has been reported (29).

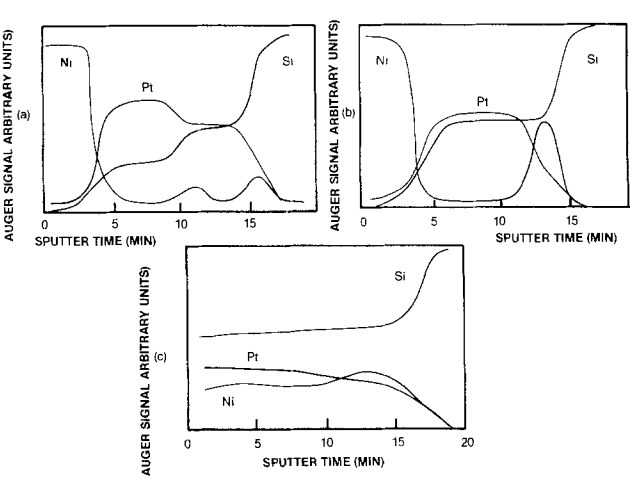

Fig. 3. Auger depth profiles of 400Å Ni/400Å Pt/Si(100) annealed for 30 min at (a) 350°C, (b) 400°C, and (c) 600°C.

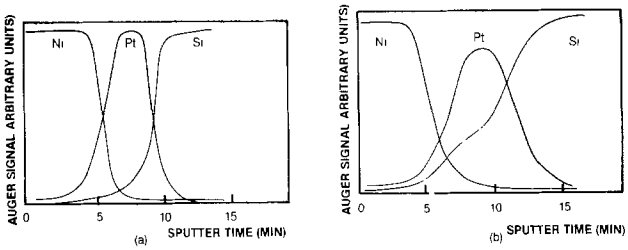

Fig. 4. Auger depth profiles of 400Å Ni/150Å Pt/Si(100) (a) as deposited and (b) after ion implantation with Kr^{2+}.

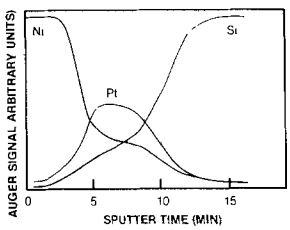

Fig. 5. Auger depth profile of an ion implanted sample of 400Å Ni/150Å Pt/Si(100) annealed at 400°C for 10 min.

The growth of silicides from Ni and Pt layers on Si will be described in terms of the relative interdiffusion coefficients, their temperature dependences, and the ability of some phases to act as diffusion barriers to some species. The initial stage in the thermal growth, *i.e.*, the formation of a complete layer of Pt_2Si below the Ni, occurred because of the rapid diffusion of Pt through Pt_2Si at temperatures as low as 200°C and because of the very slow interdiffusion of Pt and Ni at temperatures below 500°C (30).

Once all of the Pt had been converted to Pt_2Si, both Pt and Ni began to diffuse through that layer to form PtSi at the Pt_2Si/PtSi interface and NiSi between the PtSi and the substrate. This simultaneous diffusion resulted in different kinetics from those observed for either metal alone. The growth rate of PtSi was much slower than that observed in Pt/Si samples because the Ni in the grain boundaries probably interfered with the Pt diffusion. In the case of the Ni, no first phase of Ni_2Si (26, 2) was observed either because the Ni_2Si reacted very quickly to form NiSi or the Pt restricted the supply of Ni enough to alter the first phase formed. Implantation of nitrogen has been reported (23) to cause such an alteration in Ni silicide growth kinetics. The depth profile shown in Fig. 3a indicates that Ni diffuses faster through Pt_2Si than through PtSi. The relative growth rates of Pt_2Si and PtSi samples indicates that Pt also diffuses faster through Pt_2Si than PtSi.

Once the Pt_2Si had been completely converted to PtSi, no more Ni diffused into the substrate to form NiSi. In the thicker Pt samples, there was still a distinct layer of Ni at the outer surface along with some Ni in the PtSi (Fig. 3b). Since PtSi is clearly not a diffusion barrier to Ni, another phase must have begun to form at this point. A likely candidate is $Ni_xPt_{1-x}Si$ formed at the PtSi/NiSi interface by reaction [3].

The existence of this monosilicide as well as PdNi and PtPd ternary silicides has been proposed on the basis of x-ray data (25, 31). The additional Si could be supplied by either diffusion of Si atoms from the substrate through the NiSi or by the decomposition of NiSi at the PtSi/NiSi interface followed by Ni diffusion toward the substrate where it formed NiSi. These possibilities cannot be distinguished readily, and the slow reaction rate is consistent with both mechanisms.

These data indicate that the reaction of Si with Pt_2Si to form PtSi was favored over the reaction of Si with PtSi and Ni to form $Ni_xPt_{1-x}Si$, and that the formation of $Ni_xPt_{1-x}Si$ was favored subsequently over the reaction of the remaining outer layer of Ni with the PtSi to form NiSi and Pt. The ternary silicide continued to form until it consumed the Ni and PtSi layers resulting in a $Ni_xPt_{1-x}Si$/NiSi structure with some PtSi decorating the NiSi grains. This structure could be converted to a uniform layer of the ternary monosilicide by annealing above 500°C where Pt/Ni interdiffusion (23) and Si mobility (32) are known to be high. The gradients in the Ni and Pt concentrations would persist until complete interdiffusion of the monosilicide and the NiSi had occurred.

Electrical measurements have been made by others (8-10, 28) on layered structures with various Ni/Pt atomic ratios formed at temperatures below 500°C. The barrier heights were between 0.66-0.87 eV, which are the values for NiSi and PtSi, respectively; they appeared to vary smoothly with the Pt content. It has been suggested (25) that the amount and distribution of Pt (or a Pt silicide) among the NiSi grains controlled the barrier height. These data are in agreement with the previous observations. The reported stability of diodes annealed below 500°C may be related to the ability of the monosilicide to act as a diffusion barrier. The Pt distribution in the NiSi phase did not appear to change until the outer layers had been converted completely to the ternary monosilicide which is a slow process at temperatures below 500°C.

Comparison of Fig. 3a and 5 clearly show that ion implantation greatly reduced the amount of interdiffusion in Ni/Pt/Si samples during the initial stage of annealing. Analogous to the Pt/Si case, the most likely cause of the reduced silicide formation rate was the competitive growth of several phases that had been randomly nucleated as a result of the ion implantation. Even though Pt, Ni, and Si were intimately mixed at this stage and the Si Auger peak indicated the formation of a silicide, no detectable amount of the ternary silicide was formed. Continued annealing resulted in the eventual diffusion of Ni to the substrate where it formed NiSi.

Once an appreciable amount of NiSi had been formed, there were no differences between the implanted and unimplanted specimens with further annealing except for the deeper penetration of Ni into the substrate in the implanted samples. Berning and Levenson (29) proposed that, when Ni was deposited on defect-free Si, interdiffusion occurred without silicide formation. Comparison of the results for the implanted and unimplanted samples suggests the opposite conclusion. In the unimplanted samples, the near surface region of the Si substrate was first converted to PtSi; and then Ni diffused through that layer to form NiSi in the defect-free region and below the original surface. In the implanted samples, no distinct Pt layers were formed, and the Ni diffused into the damaged region where it not only formed some silicide but also continued to diffuse deep into the substrate.

Conclusions

Ion implantation of inert gas ions through Pt thin films into the Si resulted in the random nucleation of both Pt_2Si and PtSi and the subsequent formation of a layer containing both phases during thermal annealing instead of a layer of Pt_2Si. Continued annealing of an implanted specimen produced a final phase of PtSi that was fine-grained and randomly oriented instead of highly textured as found in unimplanted samples.

Unimplanted NiPt layers on Si formed multilayer structures when annealed at temperatures below 500°C. This nonuniformity may have resulted from the formation of a ternary silicide, $Ni_xPt_{1-x}Si$, which may be an effective diffusion barrier for Ni at low temperatures.

Ion implantation through NiPt thin films caused atomic mixing at both interfaces and inhibited the formation of distinct Pt silicide layers during thermal annealing at low temperatures possibly due to the random nucleation of several phases.

There were no major differences between implanted and unimplanted NiPt samples when they were annealed at high temperatures. The final phase formed in both types of specimens was the ternary silicide, $Ni_xPt_{1-x}Si$.

Note: G. Ottaviani *et al.* [*J. App. Phys.*, **53**, 4903 (1982)] observed the formation of NiSi at the metal/Si interface after annealing NiPt alloy films on Si(100) at low temperatures (300°-350°C).

Acknowledgments

The authors wish to thank D. W. Paananen and T. G. Gruchow for depositing the metal films, B. T. McClure and S. J. Tibbetts for doing the ion implantations, and A. D. Beck for helping with the Auger analysis.

Manuscript submitted Aug. 2, 1982; revised manuscript received Nov. 11, 1982. This was Paper 288 presented at the Minneapolis, Minnesota, Meeting of the Society, May 10-15, 1981.

Any discussion of this paper will appear in a Discussion Section to be published in the December 1983 JOURNAL. All discussions for the December 1983 Discussion Section should be submitted by Aug. 1, 1983.

Publication costs of this article were assisted by Honeywell, Incorporated.

REFERENCES

1. J. M. Andrews, *J. Vac. Sci. Technol.*, **11**, 972 (1974).
2. K. N. Tu and J. W. Mayer, in "Thin Films—Interdiffusion and Reactions," J. M. Poate, K. N. Tu, and J. W. Mayer, Editors, Chap. 10, Wiley, New York (1978).
3. F. Mohammadi, *Solid State Technol.*, **24**, 65 (1981).
4. A. K. Sinha, *J. Vac. Sci. Technol.*, **19**, 778 (1981).
5. J. M. Shannon, *Solid-State Electron.*, **19**, 537 (1976).
6. R. L. Thornton, *Electron. Lett.*, **17**, 485 (1981).
7. K. N. Tu, *J. Vac. Sci. Technol.*, **19**, 766 (1981).
8. S. Thomas and L. E. Terry, *J. Appl. Phys.*, **47**, 301 (1976).
9. L. E. Terry and J. Saltich, *Appl. Phys. Lett.*, **28**, 229 (1976).
10. A. Shepela, R. Phaneuf, and E. F. Kennedy, *J. Appl. Phys.*, **51**, 2928 (1980).
11. B. Y. Tsaur, Z. L. Liau, and J. W. Mayer, *Appl. Phys. Lett.*, **34**, 168 (1979).
12. B. Y. Tsaur, J. W. Mayer, and K. N. Tu, *J. Appl. Phys.*, **51**, 5326 (1980).
13. B. Smith, "Ion Implantation Range Data for Silicon and Germanium Device Technologies," Research Studies Press, Forest Grove, Oregon (1977).
14. P. Joubert, P. Auvray, and L. Henry, *Thin Solid Films*, **79**, 235 (1981).
15. H. B. Ghozlene, P. Beaufrere, and A. Authier, *J. Appl. Phys.*, **49**, 3998 (1978).
16. J. M. Poate and T. C. Tisone, *Appl. Phys. Lett.*, **24**, 391 (1974).
17. C. Canali, C. Catellani, M. Prodenziati, W. H. Wadin, and C. A. Evans, Jr., *Appl. Phys. Lett.*, **31**, 43 (1977).
18. C. Canali, F. Catellani, G. Ottaviani, and M. Prudenziati, *Appl. Phys. Lett.*, **33**, 187 (1978).
19. C. A. Crider, J. M. Poate, J. E. Rowe, and T. T. Sheng, *J. Appl. Phys.*, **52**, 2860 (1981).
20. J. Angilello, F. D'Heurle, S. Peterson, and A. Segmuller, *J. Vac. Sci. Technol.*, **17**, 471 (1980).

21. A. Roth and C. R. Crowell, *J. Vac. Sci. Technol.*, **15**, 1317 (1978).
22. R. J. Blattner, C. A. Evans, Jr., S. S. Lau, J. W. Mayer, and B. M. Ullrich, *This Journal*, **122**, 1732 (1975).
23. L. Wielunski, D. M. Scott, M. A. Nicolet, and H. von Seefeld, *Appl. Phys. Lett.*, **38**, 106 (1981).
24. R. Pretorius, A. P. Botha, and J. C. Lombaard, *Thin Solid Films*, **79**, 61 (1981).
25. T. G. Finstad, *ibid.*, **51**, 411 (1978).
26. K. N. Tu, E. I. Alessandrini, W. K. Chu, H. Krautle, and J. W. Mayer, *Jpn. J. Appl. Phys.*, Supple. **2-1**, 669 (1974).
27. D. J. Coe and E. H. Rhoderick, *J. Phys. D*, **9**, 965 (1976).
28. R. Pretorius, A. P. Botha, and J. C. Lombaard, *Thin Solid Films*, **79**, 61 (1981).
29. G. I. P. Berning and L. L. Levenson, *ibid.*, **55**, 473 (1978).
30. C. Chang and W. K. Chu, *J. Appl. Phys.*, **52**, 512 (1981).
31. T. G. Finstad and M. A. Nicolet, *ibid.*, **50**, 303 (1979).
32. R. Pretorious, J. O. Olowolafe, and J. W. Mayer, *Philos. Mag. A*, **37**, 327 (1978).

Compositional Depth Profile of a Native Oxide LPCVD MNOS Structure Using X-Ray Photoelectron Spectroscopy and Chemical Etching

J. A. Wurzbach[1] and F. J. Grunthaner

Jet Propulsion Laboratory, California Institute of Technology, Pasadena, California 91109

ABSTRACT

A compositional profile of a native oxide LPCVD MNOS structure has been obtained by x-ray photoelectron spectroscopy used in conjunction with a stopped-flow chemical etching procedure. A depth resolution of 5-10Å was achieved. Stoichiometric Si_3N_4 was found in the bulk with about 0.4 atomic percent (a/o) oxygen impurity. In contrast to profiles completed by other techniques, SiO_2 was found intact at the interface; complete conversion of oxide to oxynitride during LPCVD did not occur. The oxide/nitride interface is best described as sharp; the oxygen concentration drops by 80% in less than 8Å. There is also a diffuse oxynitride gradient extending into the film, but the oxygen concentration in this region is quite low. Evidence was also found for an 8Å layer containing excess bonds to silicon between the oxide and nitride layers. Possible charge trap structures that might limit device performance are discussed along with processing suggestions aimed at minimizing the formation of traps.

Studies of the composition and interfaces of silicon nitride on oxidized silicon have been driven by the wide application of these structures in electrically alterable, nonvolatile MNOS memory devices (1). Many of the electrical properties of these devices are related to the structure and composition of the nitride-oxide and oxide/silicon interfaces. Charge storage in MNOS structures involves modified Fowler-Nordheim tunneling across the thin oxide layer to traps at or beyond the nitride/oxide interface (2). Shifts in the logical voltage window have been related to states at the oxide/substrate interface (1). Endurance and retention problems (1) manifest themselves after repeated write/erase cycling moves charge across MNOS interfaces. It is, therefore, desirable to achieve an accurate understanding of the structure and composition of MNOS systems in the bulk region and particularly at the interfaces.

Numerous techniques have been applied to the characterization of silicon nitride and MNOS interfaces including: Auger electron spectroscopy (AES) (3-9), energy-loss spectroscopy (ELS) (10), spectroscopic ellipsometry (SE) (8, 11), Rutherford backscattering (RBS) (5c, 8, 12, 14), nuclear-reaction analysis (5c, 13, 15), secondary ion mass spectroscopy (SIMS) (9b), multiple internal reflection (MIR) (5c, 15, 16), and x-ray photoelectron spectroscopy (XPS) (17).

AES work has been done in conjunction with argon ion sputtering to obtain profiles of composition *vs.* depth. Early work (3) suggested an apparent width of 20-30Å FWHM, or 50Å 10/10%, for the interface between bulk silicon nitride and the silicon substrate of memory-type MNOS structures. These estimates were not corrected for the broadening effects of differential mean-free-paths and ion knock-on. More recent AES work (7, 8) also shows an apparent 20Å interface, but in recognition of sputter-broadening effects, 20Å is quoted only as an upper limit of interdiffusion and not as a defined width (8). Similar results were obtained by ELS (10).

All of this work has failed to show any evidence of interfacial SiO_2. This fact, together with the apparently broad interfaces seen by these techniques, has been interpreted in terms of complete conversion of SiO_2 to SiO_xN_y during nitride deposition (3, 10). However, Frenzel and Balk (9) have demonstrated that the broad interfaces observed by AES are experimental artifacts rather than the results of chemical reaction, diffusion, or nonuniform thickness. They show that sputtering induces surface roughness on the order of 20Å in SiO_2 (9a). In MNOS structures, they show that preferential sputtering (4, 9b) and bond cleavage lead to atomic mixing when sputtering across the interface of a double layer. Broadening due to these effects was calculated to be 45Å. Accordingly, an upper limit of 8 ± 4Å was placed on the actual width of the nitride/oxide interface (9b). These authors conclude that reliable information about interface structure can only be obtained by methods that do not require sputter profiling (9a).

SE has been shown to be an effective method of nondestructively detecting buried layers in thin films; however, the analysis of these layers must be inferred from least-square regression calculations. For example, SE data have identified an optically absorbing region between the oxide and nitride layers (11). This region has been modeled as a 12Å layer of amorphous silicon. However, the authors (11) caution that this model may not be quite realistic; they suggest only that the amorphous silicon dielectric function is a useful prototype for describing this region, and that this region must, therefore, contain Si-Si bonds. The oxy-

Key words: silicon nitride etching, charge trap structures, traps.

[1] Present address: General Dynamics Corporation, Pomona, California 91769.

gen analysis from SE refers to effective "SiO_2" volume fractions without implying an actual oxygen content.

RBS results have shown that bulk silicon nitride is stoichiometric (5c, 8, 12, 14), but the depth resolution (~ 40Å) was not adequate to quantify the oxide interface.

Thus, despite their technological importance, there has not been an unambiguous analysis of the composition and interfacial structure of MNOS systems. In this paper, we present the results of depth-profiling an MNOS structure by combining x-ray photoelectron spectroscopy (XPS) with a controlled stopped-flow chemical-etching procedure. XPS is sensitive to the structure of surface layers, while stopped-flow etching permits the controlled removal of overlying material on a scale of atomic layers (19), to expose new surface layers as a function of thickness. Therefore, with careful analysis of observed intensities at measured depths, this combination of techniques affords depth resolution between 5 and 10Å. Thus, direct observations can be made about the details of the composition and stoichiometry of the nitride/oxide/silicon interfaces and the transition to the bulk nitride in MNOS structures. The data show intact SiO_2 at the substrate interface and some evidence strongly suggestive of a thin layer containing excess bonds to silicon on top of the SiO_2. Although an oxynitride gradient is found to extend into the film from the oxide/nitride interface, the oxygen concentration is so low that the interface is still best described as sharp.

Experimental

Samples for the depth profile were prepared by LPCVD (750°C, 0.5 Torr, $NH_3/SiH_2Cl_2 = 9$) of silicon nitride onto crystalline silicon substrates (n-type, 4-8 Ω-cm, [100]) in a hot wall tube reactor. The final thickness was 483Å, measured ellipsometrically (6328Å, refractive index 1.99). The nitride was deposited directly onto the native oxide resulting from wet chemical processing of the substrate wafer. No thermal oxide was intentionally grown. The thickness of the native oxide has been estimated by ellipsometry to be 5-7Å. These dimensions correspond to a typical native oxide MNOS structure for memory applications.

Thin nitrides were prepared as control samples. Some were fabricated on native oxides, exactly as described above, to a nitride thickness of ~ 40Å. A second set was deposited over intentionally grown thermal oxides 22Å thick (steam, 700°C, 9.5 min). These 22Å oxides were then covered with ~ 20Å silicon nitride by LPCVD (800°C, $NH_3/SiH_2Cl_2 = 5$).

The etchant used is a modification of the patent by Loic (18). It consists of HF (48%), H_3PO_4 (85%), and ethanol (absolute) mixed in the ratio 15:10:60 by volume. Ethanol is used as a solvent instead of water because it films over silicon nitride more uniformly, it dries quickly, and it is relatively more inert. This etchant is nearly anhydrous; it contains about 9% water from the concentrated liquid acids, HF, and H_3PO_4.

A strictly anhydrous rinse was prepared by bubbling HCl gas through absolute ethanol. Sufficient HCl was dissolved in the ethanol to give an apparent "pH" of ~ 1.

Details of the stopped-flow etching procedure are described elsewere (19). In summary, the etchant is applied dropwise on a ⅜ in. square sample which is spinning at 12,000 rpm. The etch is done at room temperature in an inert N_2 ambient. Each etching step is followed by an ethanol/HCl rinse or a rinse with absolute ethanol, or both. The observed etch rate is 100-150Å nitride/ml. Many variables affect the etch rate. Some, such as temperature, are obvious; others which are related to the specific experimental geometry include: drop size (0.01-0.02 ml), dropping rate (~ 12 drops/min), rpm, and humidity in the N_2 ambient (ideally zero).

Uniformity of material removal was checked ellipsometrically and by C-V measurements. After etching ~ 300Å of the nitride, the remaining film thickness was found by ellipsometry to be uniform within ± 5Å at the center of the ⅜ in. square sample and within 10-15Å going from one corner to the opposite corner. Since the XPS experiment measures only a limited portion of the center of the sample, this uniformity was more than adequate. As an independent second check, mercury probe C-V measurements were performed. The results corroborated the ellipsometric findings of local uniformity and a slight thickness gradient across the sample diagonal.

Film thickness was measured ellipsometrically until about 60Å of the film remained. At that point, the Si2p signal from the substrate was detectable, and the film thickness could be determined from the ratio of the integrated Si2p signals from the nitride/oxide and substrate (20, 28).

The conversion of the nitride/oxide: substrate intensity ratio to a thickness requires a knowledge of the photoelectron mean-free-path λ through the overlying film material. Taylor *et al.* (21) have derived an estimate of λ_{Si2p} ~ 36Å in Si_3N_4. The data in this work are consistent with somewhat lower values ranging from the low to high twenties. Film thickness is the only calculated parameter which depends on λ_{Si2p}, the value of which is currently tentative. Therefore, to be technically correct, the thickness coordinate in figures relevant to the interface has been given in multiples of λ_{Si2p}. However, as an intuitive aid, a thickness scale is also given in angstroms, based on λ_{Si2p} selected at 30Å as a reasonable average of the available estimates. All other calculations are based on mean-free-path ratios, which can be calculated quite accurately (24) without any dependence on a specific choice of λ_{Si2p}.

To obtain accurate intensities for this study, it was necessary to account for residues left on the surface by the etching procedure. The dominant residues are surface reaction products of ethanol and ethyl fluoride, which form spontaneously at room temperature in acidic, alcoholic fluoride solutions. These species are tightly bound to the surface; in control experiments, temperatures exceeding 100°C failed to desorb them into the UHV environment. O1s from residual ethanol reaction products interfered with the O1s from impurities in the bulk nitride. It was possible to correct for this problem by estimating the magnitude of the ethanol contribution from a fit of the C1s spectrum. Additionally, a small peak was often observed 4 eV from the main N1s peak (see Fig. 1a). In control experiments, this feature disappeared after the sample was warmed to 50°C in vacuum; simultaneously, the F1s signal decreased by ~ 10%. These results are best interpreted as fluorine, probably in the form of HF, loosely bound to nitrogen lone pairs projecting from the surface. Therefore, we might use HF as a convenient marker for the fraction of surface nitrogen atoms with exposed lone pairs. The data in Fig. 1a, for example, suggest that HF is bound to the lone pairs of ~ 10% of the surface nitrogen atoms. Figure 2 shows that residual sodium, probably from trace amounts of sodium phosphate in the phosphoric acid, was effectively removed by a rinse with the anhydrous ethanol/HCl described above. Fewer sweeps were accumulated on the sample after the rinse than before, which resulted in a relatively higher noise level. After the data were scaled to the same number of sweeps, it was found that the sodium level had been reduced by at least an order of magnitude. A sodium 1s contribution equal to 10% of the original intensity would still be detectable despite the noise in the after-rinse spectrum. In a more sensitive test, the after-rinse data were smoothed by cross correlation with the initial sodium 1s signal. The result indicated a virtually complete elimination of sodium.

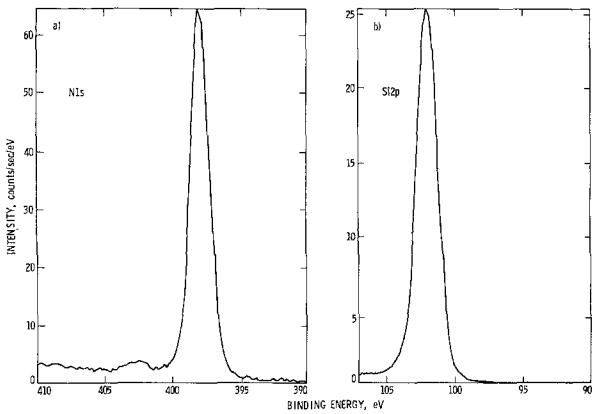

Fig. 1. (a) Nitrogen 1s spectrum from the bulk of the nitride film. These data show the most pronounced example of a peak shifted 4 eV to high binding energy, probably by HF loosely bound to surface nitrogen lone pairs. (b) Typical Si2p spectrum from the bulk of the nitride film.

Results and Discussion

Bulk film composition.—Typical N1s and Si2p lineshapes from the bulk nitride are shown in Fig. 1. The results (22) of a chemical depth profile are shown in Fig. 3. Integrated intensities corrected for relative photoemission cross sections (23), but not corrected for escape-depth differences (24), are shown in Fig. 3a. The N1s and Si2p signals correlate with one another, especially through the bulk region of the film from about 400 down to 75Å. Fluctuations of N1s and Si2p through this region are generally anticorrelated with the C1s intensity, which strongly suggests that the fluctuations are due to variations in a carbonaceous surface overlayer.

The data in Fig. 3a clearly show an oxynitride gradient extending from the surface into the bulk of the film. This familiar feature has already been well documented [Ref. (17, 3, 6, 8, 10, 11, 13, and 15)]. The O1s intensity drops off rapidly toward the bulk O1s value while the N1s intensity rises correspondingly. The width of the gradient at half-height can be estimated from the O1s data to be about 25Å, which is consistent with previous estimates of 6Å equivalent of SiO_2 (XPS on LPCVD nitride) (17), 8Å equivalent of SiO_2 (RBS on LPCVD nitride) (8), and ~30Å (AES on plasma nitride) (4). The O1s data points at 436 and 392Å suggest the possibility that the tail of the gradient may extend deeply, but at low concentration, into the bulk of the nitride film. If this deep penetration truly exists, it probably results from exposing the nitride film to the atmosphere while it is still hot from the furnace.

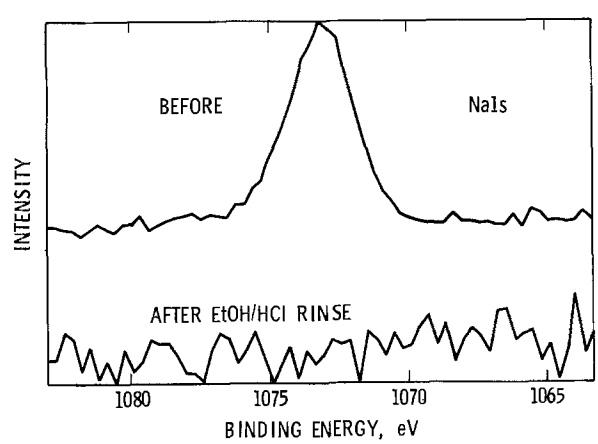

Fig. 2. Sodium 1s etchant residue was effectively removed by an anhydrous ethanol/HCl rinse. Fewer sweeps were accumulated in the lower spectrum, which resulted in a higher noise level relative to the upper spectrum. Smoothing of the lower spectrum by cross-correlation with the upper spectrum indicated the virtually complete removal of sodium.

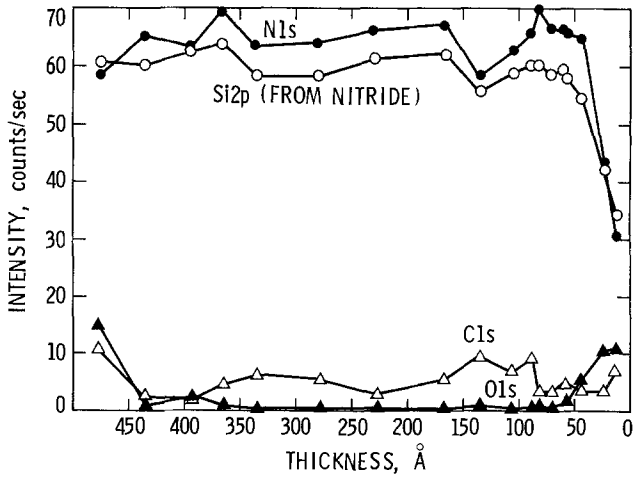

Fig. 3a. Intensities from a chemical depth profile of a nitride/native oxide/silicon structure. Intensities are corrected for cross sections, but not for escape-depth differences. Si2p refers to the contribution from silicon atoms in the silicon nitride film. Substrate was observed when the film was etched to less than 80Å; however, no Si2p intensity from the substrate is shown in the graph.

Within the bulk of the nitride film, the O1s intensity drops to a level indicative of 0.4 ± 0.2 atomic percent (a/o) oxygen. This level, and significantly higher levels, of oxygen incorporation within the bulk are also well documented in the literature (3, 5, 6, 8, 13), and it has been attributed to oxygen-containing impurities in the NH_3 stream by correlating oxygen intensity with with the NH_3/SiH_4 ratio (3, 6).

Using published procedures (24c, d), the integrated intensities in Fig. 3a were converted to the atomic ratio of nitrogen/silicon as a function of depth through the bulk. The integrated intensities of Fig. 3a were already corrected for relative photoionization cross section (23). Corrections for mean-free-path were made by taking $\lambda_{N1s}/\lambda_{Si2p} = (E_{N1s}/E_{Si2p})^{0.75}$ (24a, b, d), where λ is the mean-free-path and E is the photoelectron kinetic energy. This simple expression gave results which agreed within $< 1\%$ with the theoretical calculations of Penn (24c). These corrections are all based on a homogeneous film with a thickness much greater than the mean-free-path. Figure 3a shows that the composition of the film is rather uniform over hundreds of angstroms. Thus, the use of these corrections within the bulk seems justified. The results are replotted in Fig. 3b where the ordinate is now the atomic ratio of nitrogen/silicon corrected for cross section and mean-free-path.

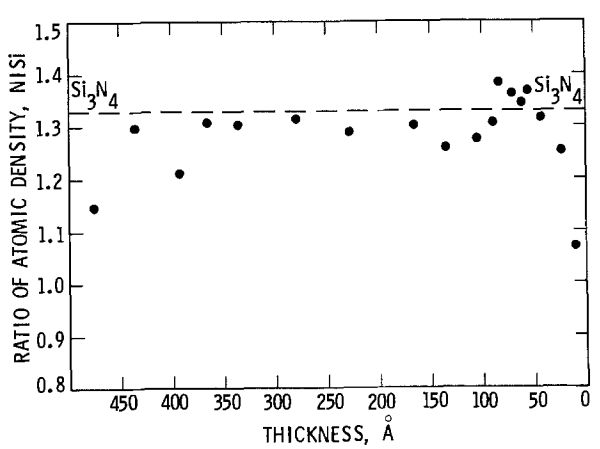

Fig. 3b. Atomic ratio of N/Si vs. depth, corrected for cross sections and mean-free-path. Dotted lines shows the ratio for Si_3N_4.

Figure 3b shows that the composition of the film is nearly stoichiometric Si_3N_4, in agreement with AES (6) and RBS analyses of CVD silicon nitride (5c, 8, 12). The average N/Si ratio through the bulk region is 1.31, compared to the stoichiometric ratio, 1.33. The agreement is good, and it lends confidence to the cross-section and mean-free-path corrections. The slight deviation below 1.33 may even suggest a small contribution from Si-Si bonding (12, 15a). Figure 3b also shows that the composition is more uniform than it would seem from Fig. 3a; the fluctuations in Fig. 3a are less significant when ratios are taken for Fig. 3b. The corrections leading to Fig. 3b are only valid within the bulk of the film. The compositional gradients at the interface require a more detailed treatment, which is given below.

Interfacial SiO_2.—It has generally been believed that nitridation converts the tunneling oxide of MNOS structures completely to a graded composition of oxynitride, with no SiO_2 surviving the nitridation process intact (3, 6, 10). We have observed a region of graded oxynitride in this work, but in addition, we have unambiguously identified SiO_2 at the substrate interface.

Figures 4a and b show, respectively, the N1s and Si2p regions after the final etch. These spectra represent a nitride + oxide film with a nominal thickness of 12Å, as determined by the ratio of nitride and oxide Si2p to substrate Si2p. The Si2p data show asymmetry at 103-105 eV, where SiO_2 contributes (25), and not the various forms of oxynitride (17). This asymmetry does not exist in the Si2p spectra of the bulk silicon nitride (Fig. 1b). It is possible to estimate the contribution of silicon nitride in Fig. 4b, subtract it, and analyze the region of asymmetry in detail. The result is in Fig. 4c, which shows the Si2p data of Fig. 4b with an overlay of a Si2p nitride signal from the bulk. The overlay has been scaled to represent the equivalent amount of nitride Si2p intensity corresponding to the nitride N1s intensity in Fig. 4a. Subtracting the overlay gives the result shown in Fig. 4d.

The small peak in Fig. 4d has the characteristics of an Si2p signal from amorphous SiO_2. The separation between the small peak and the substrate Si2p peak is 4.2 eV. Thin films of a-SiO_2 show a separation ranging from 3.9-4.3 eV (25b), depending on film thickness. The energy separation between the small Si2p peak and the corresponding O1s peak is 429.7 eV, which agrees exactly with the O1s-Si2p separation found for 1-2 monolayer films of a-SiO_2 [Fig. 2 in Ref. (25b)]. (O1s from residual ethanol does not interfere with the determination of this separation because it accounts for only 10% of the intensity in the O1s peak corresponding to Fig. 4d. It is only a minor perturbation in the spectra at the interface.) Finally, the atomic

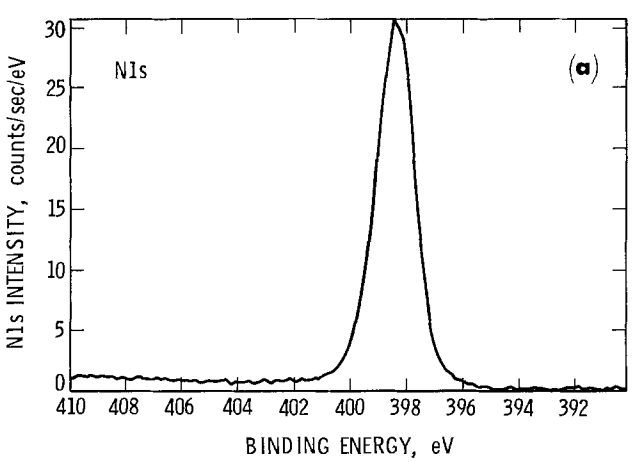

Fig. 4a. N1s signal from a nitride/oxide film with a nominal thickness of 12Å.

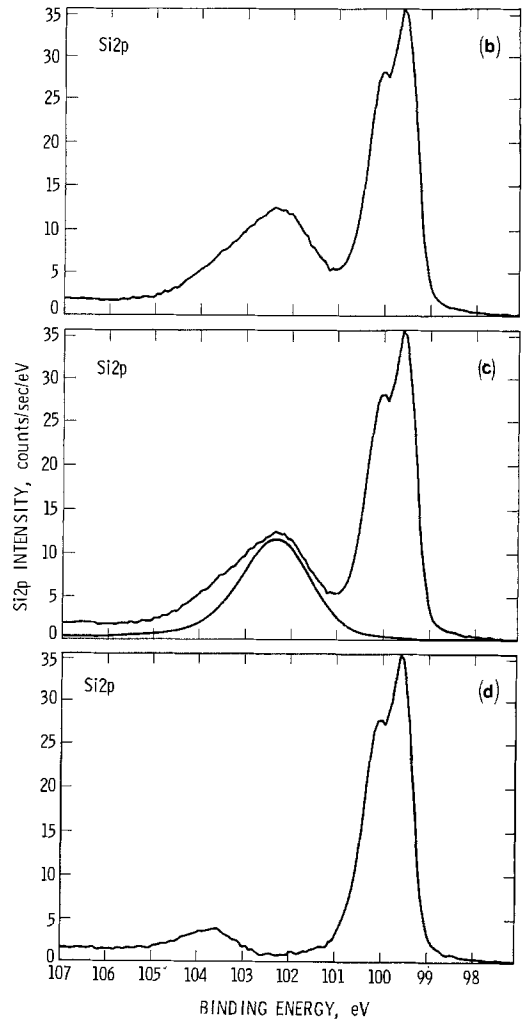

Fig. 4b. The corresponding Si2p signal from the same film as 4a. Fig. 4(c) 4b overlayed with an Si2p nitride spectrum from the bulk. Overlay has been scaled to represent that amount of nitride which would be necessary to account for the N1s intensity in 4a. Fig. 4(d) 4b minus the nitride contribution. Shows the interfacial SiO_2 contribution clearly.

ratio of O/Si for the 104 eV peak corrected for cross section and escape depth is 2.44, *i.e.*, SiO_2 with a small amount of oxygen available for some oxynitride formation and possibly SiOH species. Since this small peak in Fig. 4d appears where SiO_2 is expected, beyond the region where oxynitride is found (17), and since it shows the characteristics determined from pure a-SiO_2 films (25), it is clear that this peak represents SiO_2 still intact at the interface after nitridation. Taking the ratio of this SiO_2 peak to the substrate peak, it was found that this peak represents a thickness of a-SiO_2 equivalent to 4-5Å of SiO_2, approximately 0.8 monolayer. It is, therefore, likely that the SiO_2 layer is not continuous, and that nitrogen-containing species may extend all the way to the interface. The ratio of oxide to substrate intensities is independent of the thickness of an overlayer. Both intensities will be attenuated by the same factor after passing through the overlayer, and the ratio will remain unchanged. Therefore, the thickness of the interfacial SiO_2 layer, which is derived directly from the oxide to substrate ratio, can be determined more accurately than the depth resolution would ordinarily allow. There are, however, limits to the uniformity of the etching; consequently we allow for the possibility of a full monolayer of SiO_2, but certainly less than two monolayers.

The SiO_2 thickness observed here is then compared to estimates of a 15-20Å equivalent thickness of "SiO_2" in other nitride samples (11). First, it must be remem-

bered that the MNOS structure profiled in this work includes only a native oxide estimated by single wavelength ellipsometry to be approximately 5Å thick before the silicon wafer was placed in the reactor. A much stronger SiO_2 peak would be expected for a MNOS structure made with an intentionally grown thermal oxide. Second, the 15-20Å "SiO_2" estimate from SE results (11) is explained to be a virtual thickness which refers only to the silicon-oxygen content in a given nitride film, and not the identification of the specific chemical state of stoichiometric SiO_2. Finally, it is conceivable that the native oxide on this sample may have been partially etched at the start of LPCVD by chlorine-free radicals released from the pyrolysis of SiH_2Cl_2.

The existence of interfacial SiO_2 was strongly suggested by earlier experiments on specially prepared control samples (26). The samples were thin (20-40Å) layers of LPCVD silicon nitride on both native and thermally grown tunneling oxides. The deposited nitride films were intentionally made thinner than a few photoelectron mean-free-paths, so that XPS could be used to study the nitride/oxide and oxide/substrate interfaces simultaneously without the requirement of etching. The results are shown in Fig. 5, which compares the Si2p data for a 20Å nitride/22Å thermal oxide/silicon structure (Fig. 5a) with Si2p data from a 16Å film of thermal SiO_2 (Fig. 5b). A resolution enhancement algorithm based on maximum entropy spectral estimation has been applied to each set of data; this algorithm and its applications have been described in detail elsewhere (27). The results of the resolution enhancement are overlayered on the data in Fig. 5. Extensive work (25) has lead to a detailed understanding of the Si2p spectrum of SiO_2, such as the data in Fig. 5b. Three peaks are conspicuous near 104 eV in the resolution-enhanced SiO_2 spectrum in Fig. 5b. This triad is reproducibly found in all such enhanced SiO_2 spectra; it has been suggested (25) that these peaks reflect Si-O-Si bond angles of approximately 120, 144, and 160-180 degrees. The a-SiO_2 peaks in Fig. 5b are labeled with the bond angles which they represent. In the absence of gross interference, this triad can be taken as an identifying characteristic of a-SiO_2 in XPS Si2p data.

In the thin nitride/thermal oxide data of Fig. 5a, the energy regime where SiO_2 Si2p photoelectrons are found is chemically shifted beyond the region where the nitride and oxynitride Si2p contribute (17). Thus, the oxide region of the spectrum is relatively free of interference, and we can look for the a-SiO_2 triad in the resolution-enhanced spectrum as evidence of a-SiO_2 in the film. In the SiO_2 region of Fig. 5a, the resolution-enhanced data show a three-peak structure which closely corresponds to the triad in the SiO_2 model spectrum in Fig. 5b. This agreement was not built into either spectrum by any manipulation of the algorithm. Similar results on two other samples led us to conclude that a-SiO_2 was a component of these thin nitride control samples. Beyond the identification of a-SiO_2, the enhanced spectrum of Fig. 5a becomes difficult to interpret. Within the binding energy region of 101-102 eV, one expects a multiplicity of chemical states due to oxynitride, nitride, and hydrogen bonding. An extensive enhancement calculation would be required to resolve the diversity of subtly shifted chemical states in this region. Therefore, the peaks observed in this region of Fig. 5a are only representative of the possible contributions; these peaks cannot be assigned unambiguously. These complications were not present in the enhancement of SiO_2 data such as in Fig. 5b.

Interface composition.—The calculation of the N/Si atomic ratio in Fig. 3b was done assuming a thickness much greater than the mean-free-path with a uniform composition within the film. This reasoning was only valid in the bulk of the film; analysis of atomic ratios within a few mean-free-paths of the interface must account for the compositional gradients in this region. The method for calculating atomic ratios in this region is a straightforward adaptation of the calculation by Vasquez (28) on the SiO_2/Si interface.

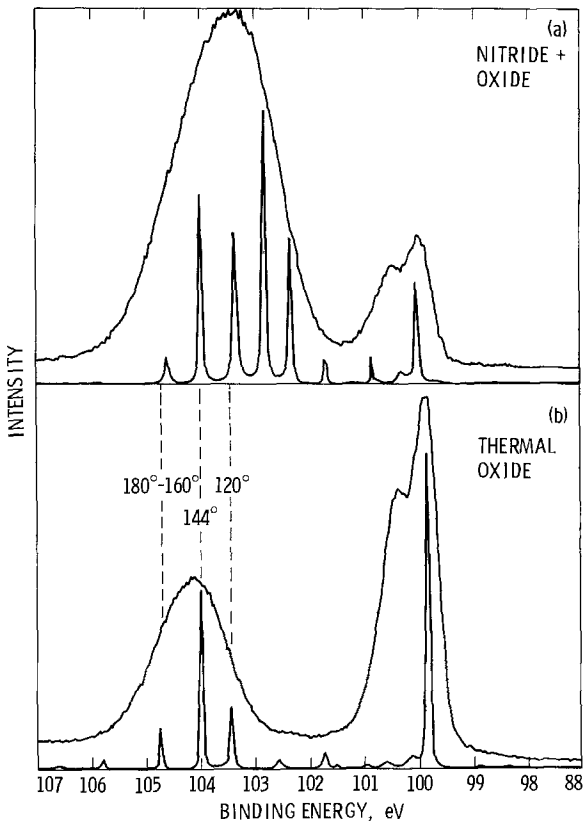

Fig. 5. (a) Si2p data from a 20Å LPCVD silicon nitride/22Å thermal oxide/silicon (100) structure. (b) Si2p data from a 16Å thermal oxide. Both data sets are shown with the results of resolution enhancement. [See Ref. (25 and 27).] The triad of oxide peaks is shown with each peak labeled according to the Si-O-Si bond angle which it represents (25, 27). Spectrum (a) has been shifted to align the 144° oxide peaks for clarity. It then appears that the substrate signals near 100 eV differ by 0.2 eV. This difference is within the errors of computation, doping differences, and surface potentials.

The region of variable composition is modeled as a stack of thin layers, with each layer having a uniform composition. The intensity (normalized with respect to relative cross section) from a stack of n layers, $I(n)/\sigma$ is related to the intensity from $n-1$ layers, $I(n-1)/\sigma$ by Eq. [1a]

$$\frac{I(n)}{\sigma} = \frac{I(n-1)}{\sigma} \exp(-d/\lambda \sin\theta) + I_x A T \rho \lambda \sin\theta [1 - \exp(-d/\lambda \sin\theta)] \quad [1a]$$

where I is the observed intensity of photoelectrons from a given orbital of a given atom, σ is the relative cross section for photoemission, ρ is the atomic density of the atom being measured, λ is the photoelectron mean-free-path, d is the thickness of one of the hypothetical layers, and $I_x A T \sin\theta$ are the instrument parameters representing x-ray intensity, sample area, spectrometer transmission, and photoelectron takeoff angle $\theta = 38.5°$. Equation [1a] can now be solved for ρ, the atomic density. If this procedure is followed for two components, *e.g.*, nitrogen and silicon, a ratio of atomic densities can be derived in which the instrumental parameters cancel to a close approximation

$$\frac{\rho_N}{\rho_{Si}} = \frac{[I(n)_{N1s} - I(n-1)_{N1s} \exp(-d/\lambda_{N1s} \sin\theta)]\,\sigma_{Si2p}\lambda_{Si2p}\,[1 - \exp(-d/\lambda_{Si2p} \sin\theta)]}{[I(n)_{Si2p} - I(n-1)_{Si2p} \exp(-d/\lambda_{Si2p} \sin\theta)]\,\sigma_{N1s}\lambda_{N1s}\,[1 - \exp(-d/\lambda_{N1s} \sin\theta)]} \quad [1b]$$

The intensities are measured, and ratios of cross section (23) and mean-free-paths (24) can be obtained to sufficient accuracy. The use of $\lambda_{Si2p} = 30$Å causes $<2\%$ error in the calculation of ρ_N/ρ_{Si}, because Eq. [1b] depends only weakly on the choice of λ_{Si2p}. Ratios of N/Si and O/Si were calculated, from which an N/O ratio could be derived. From these data, atomic fractions of O, N, and Si could be derived as a function of thickness, as shown in Fig. 6. These atomic fractions do not include a contribution from hydrogen, which cannot be directly measured by XPS.

The oxygen profile shown in Fig. 6 decreases rapidly at the interface, and the oxygen concentration drops to 20% of its initial value within a few angstroms, in general agreement with the conclusion reached independently by Frenzel and Balk (9). Over the next 16Å, the concentration decreases slightly and is approximately constant. After 24Å, the oxygen concentration declines until it merges with the bulk concentration of 0.4 ± 0.2 a/o. There is no apparent evidence of SiO_2 in this region; therefore, it is likely that the composition is best described in terms of a low concentration oxynitride gradient. Within 45Å, the oxygen level drops below 2 a/o; the bulk composition is reached at a thickness between 50-60Å. The amount of oxygen in this gradient is represented pictorially in Fig. 9.

The nitrogen profile is consistent with the oxygen results, showing the likelihood of nitrogen-containing species extending to the interface. The rest of the profile is consistent with the low concentration oxynitride gradient, which reaches nearly pure Si_3N_4 at ~45Å.

The silicon profile in Fig. 6 shows a conspicuous increase at a thickness of 4-8Å. To interpret this increase, we invoke the same bonding model described by Philipp (29) and Raider (17), that all silicon is bonded tetrahedrally by single bonds to other silicon, oxygen, and nitrogen (29), and that all oxynitride bonding occurs in the form of siloxane (Si-O-Si) and silazane (Si-N-Si) bridges (17). Within the context of this model, the total number of available silicon single bonds must equal the combined numbers of oxygen and nitrogen single bonds. In Fig. 7 we divide the number of available silicon single bonds (4× atomic fraction of Si) by the sum of oxygen and nitrogen single bonds (2× oxygen fraction + 3× nitrogen fraction). Where this fraction deviates from unity, we must consider some deviation from the simple oxynitride model, such as Si-Si or Si-H bonding. Figure 7 shows a layer of excess bonds to silicon about 8Å thick. The ratio in Fig. 7 peaks at 4-8Å, where there is found a clear excess of silicon bonds which cannot be accounted for by simple oxygen and nitrogen coordination. It seems that the excess exists on top of the native oxide layer.

Certain aspects of this observation are in qualitative agreement with results obtained by others (11). However, it is unlikely that this region contains any substantial amount of amorphous silicon. In the presence of oxygen and excess nitrogen at elevated temperatures, amorphous silicon would be unstable with respect to the formation of oxides and nitrides. Si-Si and Si-H bonding plus Si dangling bonds within an oxynitride framework are more plausible. Therefore, rather than speaking of excess silicon, we refer to this system in terms of excess bonds to silicon. Figure 7 indicates that as much as 90% of the silicon in the region of peak excess may have a bond not going to nitrogen or oxygen. A reasonable representation of this bonding arrangement is shown in Fig. 9.

It is important to emphasize that the excess bonds to silicon cannot be attributed to a spurious substrate silicon contribution due to nonuniform etching or some other artificial result. The substrate and nitride/oxide silicon form two distinct Si2p peaks resolved from one another. (See Fig. 4b.) Substrate Si2p appears at 99.5 eV; nitride/oxide Si2p appears at 102 eV. The substrate contribution was not included in taking Si2p intensities for the silicon profile.

While this evidence strongly suggests the existence of the excess bonds, full confirmation awaits the replication of these observations on other samples. The source of the excess also remains to be identified. Reaction products from etching are possible contributors. It is likely that etching leaves some surface silicon bonds hydrogenated after the elimination of nitrogen. The relative contribution of this surface layer becomes increasingly significant as the film thickness decreases; the apparent result would be a gradual increase in Si-H bonding as the etching approached the interface. However, the peak shown in Fig. 7 rises so sharply that one is led to also consider the LPCVD process as a source of the excess bonds to silicon. Perhaps the excess bonds hold clues about the mechanisms involved in the interaction of reactant gases with the native oxide during the initial stages of LPCVD.

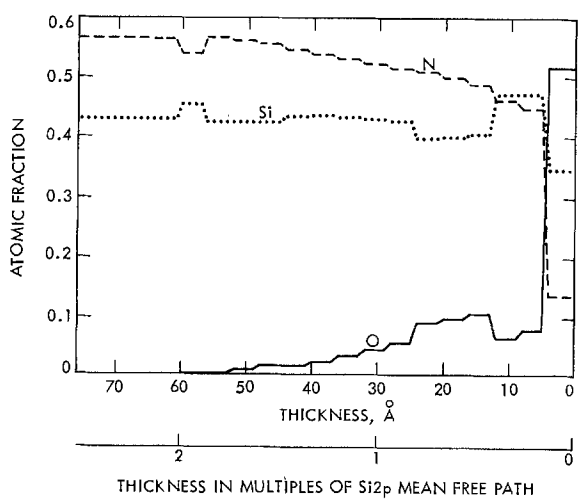

Fig. 6. Atomic fractions of oxygen, nitrogen, and silicon as a function of thickness. These atomic fractions do not include a contribution from hydrogen, which cannot be measured by XPS.

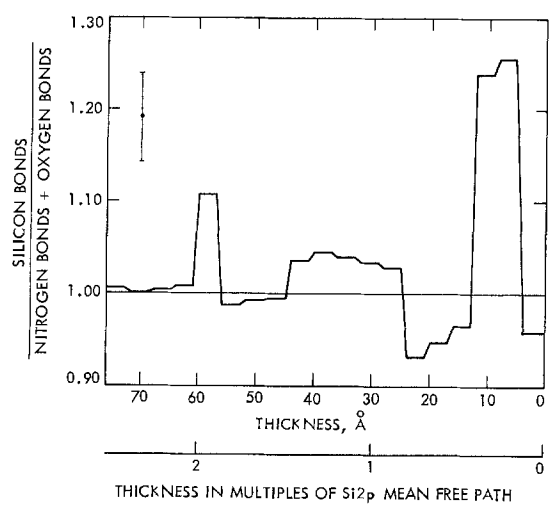

Fig. 7. Ratio of available silicon single bonds to the number of oxygen and nitrogen single bonds, vs. thickness. The excursion at 60Å represents the maximum limit of experimental error.

One possibility is the reduction of interfacial SiO_x and SiO_2 during the initial nitridation. This process was once used as a method of making silicon nitride according to the following reaction (30)

$$3SiO_2 + 6C + 2N_2 \xrightarrow[1200°\text{-}1500°C]{H_2} Si_3N_4 + 6CO \quad [2]$$

Many of the conditions of this reaction are satisfied by the system being considered here. Carbon is available as a contaminant found on the native oxide surface before deposition, and LPCVD conditions provide hydrogen and nitrogen species. Although reaction [2] could be run at 1200°C using oxide catalysts, the temperature still exceeds the LPCVD range of 750°C. However, the high temperature may only have been necessary to cleave the N_2 bond in reaction [2], and this step is not required in LPCVD using NH_3. Therefore, it is possible that, at lower LPCVD temperatures, a reaction would start, but not necessarily go to completion as in Eq. [2]. Instead, some mechanism similar to Eq. [2], and involving interfacial SiO_x, might govern a reaction which stops after consuming the carbon contaminant layer, and yields products of suboxides, subnitrides, and oxynitrides containing Si-Si and Si-H bonds.

Another possibility is a surge of SiH_2Cl_2 when the inlet valve is opened at the start of LPCVD. Other mechanisms are not as well defined. Nevertheless, under these conditions of deposition and etching, the data indicate the existence of one or two monolayers of oxynitride containing excess bonds to silicon on top of the native oxide.

Implications for Device Performance and Processing

Several features of the interfacial structure determined in this study may be significant in terms of MNOS endurance and retention effects. In particular, the region of excess bonds to silicon is likely to be chemically labile under electrical stress. A plausible bonding arrangement representative of this region is given schematically in Fig. 8. Two silicon atoms are connected to nitrogen and oxygen by single bonds. The silicons are also connected to one another through a single bond, which is one example of an excess bond to silicon not accounted for by nitrogen or oxygen. Other possibilities include Si-H and Si dangling bonds.

The Si-Si bond strength has been measured at various values ranging from 2-3 eV (31). Therefore, it is possible that during write/erase cycling, hot electrons (or holes) could cleave Si-Si bonds near the interface. Recombination is expected, unless the broken bond is stabilized chemically, or unless lattice relaxation pulls the silicon atoms too far apart to reestablish a bond, thus forming Si dangling bonds. Relief of lattice strain is, therefore, a central theme in this proposal. The strain concept has already been successful in providing a basis for understanding the formation of Si^{+3} sites at the SiO_2/Si interface (32); the Si dangling bond sites formed in Fig. 8 are analogous to the Si^{+3} formed in the SiO_2/Si system.

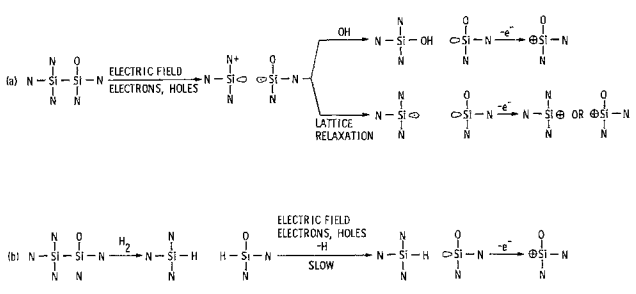

Fig. 8. Representation of Si—Si bond cleavage in an oxynitride structure to yield trapped positive charge at the interface after write/erase cycling.

During further write/erase cycling, electron impact may ionize the Si dangling bonds and leave a positive charge at the interface. The net effect observed electrically would be a shift in the logical voltage window. It is expected that, as an intrinsic result of the LPCVD process, some Si dangling bonds exist in the film even before write/erase cycling; they should behave the same way as the Si dangling bonds produced in Fig. 8.

Si-H bonds are also subject to cleavage and the formation of Si dangling bonds. It has, in fact, been shown that electron irradiation under a negative bias condition is capable of converting interfacial Si-H to Si^0 in native oxide MNOS structures; it is possible to interpret the Si^0 observed in this conversion as an Si dangling bond (35). Following hydrogen removal, an Si dangling bond is left to be ionized, again leaving a fixed charge at the interface.

In these terms, a mechanism can be proposed to explain recent experience in hydrogen annealing (34). In this case, Si-Si linkages would be converted to Si-H. No additional dangling bonds would be formed; those dangling bonds which exist intrinsically after LPCVD would also be converted to Si-H. There would be a substantial reduction in the number of Si dangling bonds remaining to be ionized by electron impact. Since the bond energies of Si-H and Si-Si are comparable (31), the cleavage of Si-Si bonds by H_2 is probably assisted by lattice strain. Thus, the hydrogen annealing process may also be interpreted as a strain relief mechanism. It is found that hydrogen annealing mitigates the endurance problem, but does not eliminate it. Therefore, we must propose that strained Si-Si bonds, which may exist before hydrogen annealing, cleave more readily than unstrained Si-H bonds after hydrogen annealing.

Si dangling bonds are not limited to a role as electron donors leading to interfacial positive charge. A singly occupied dangling orbital can also accept an electron. Therefore, dangling bonds are expected to be amphoteric, *i.e.*, having the ability to act as an electron acceptor as well as an electron donor. As electron acceptors, Si dangling bonds could receive electronic charge from the bulk and trap it near the interface, where it could tunnel out of the film. Thus, Si dangling bonds can function as "hopping" sites for electrons to leak back into the substrate, resulting in a loss of retention. Si dangling bonds resulting from the dehydrogenation of Si-H centers have been proposed as the cause of increased conductivity in thermally annealed silicon nitride films (37).

The silicon nitride, oxynitride, and oxide are also sources of dangling bonds and other amphoteric sites. Although Si-N and Si-O bonds are stronger than Si-Si and Si-H bonds, they are still subject to cleavage during electrical stress, particularly in the presence of a strained lattice. The cleavage of Si-O bonds in SiO_2 under electron bombardment has already been documented (32). The resulting Si^{+3} sites and nonbridging oxygen sites have been described in terms of being amphoteric, self-annealing charge traps. In silicon nitride, Si-N bond cleavage leading to amphoteric, annealable charge traps has also been proposed (36). The low-level oxynitride gradient extending into the film may, therefore, be a source of "hopping" sites for the dissipation of charge from the bulk back into the substrate.

The native oxide layer, which was found intact at the interface in this work, represents a system which has been shown to contain strained bonds and silicon suboxides (25, 32). Suboxides of silicon, especially Si^{+3}, have been found to be active as interface states (25, 32) which are capable of amphoteric charge trapping behavior. Si^{+3} has also been shown to disproportionate into Si^{+4} and Si^0 under electron irradiation (33); the Si^0 then becomes available for the formation of Si-Si and Si-H bonds, which have al-

ready been discussed in terms of charge trapping. These considerations are particularly relevant in the case of native oxide MNOS structures, because the conditions which exist at the interface during deposition (hydrogen, surface carbon, high temperature) would promote the reduction of the oxide to suboxides.

These results prompt the consideration of processing steps aimed at minimizing the formation of trap sites which limit device performance. The potential sources of traps implicated in this work include the excess bonds to silicon, lattice strain, intermediate oxidation states of silicon in the native oxide, and the oxynitride gradient extending into the film. This study suggests that excess bonds to silicon may be due to the interaction between the LPCVD reactant gases, surface carbon, and the native oxide; a momentarily high partial pressure of SiH_2Cl_2 may also contribute. Accordingly, control of surface carbon contamination and the elimination of an SiH_2Cl_2 pressure surge at the start of deposition might limit the formation of excess bonds to silicon.

Intermediate oxidation states, oxynitride, strained bonds, and excess bonds to silicon are all related to the native oxide. Therefore, it may also be desirable to eliminate the native oxide layer with an *in situ* HCl etch in the reactor tube. Pyrolysis of SiH_2Cl_2 probably contributes toward the removal of some native oxide; the brief addition of HCl to the gas stream immediately prior to SiH_2Cl_2 should complete the removal process.

Any or all of these processing changes may assist in producing more effective native oxide MNOS devices.

Conclusions

Stopped-flow chemical etching has been used in conjunction with XPS to obtain a detailed compositional profile of a native-oxide LPCVD MNOS structure. Numerous surface and bulk features were observed, including a surface oxynitride gradient and stoichiometric nitride in the bulk film. The bulk stoichiometry was essentially equal to the ideal Si_3N_4 with a 0.4 a/o oxygen impurity and possibly an observable contribution from Si-Si bonding.

The interfacial region has been revealed at a high level of detail and depth resolution. The essential features of the interface are summarized in Fig. 9. Some SiO_2 has been found intact at the interface after nitridation. The total amount present is approximately a monolayer, and probably about 0.8 monolayer. Therefore, it is likely that the SiO_2 is not continuous, and that nitrogen-containing species may reach all the way to the interface. This thin coverage is consistent with the fact that only a native oxide was present before nitridation.

On top of the native oxide, there is a layer containing excess bonds to silicon. The thickness of this region is about 8Å. The excess bonds do not imply a distinct phase of amorphous silicon. Instead, it is most likely that the excess bonds represent Si-Si and Si-H bonds plus Si dangling bonds in an oxynitride framework. These three possibilities cannot be distinguished easily because XPS cannot measure hydrogen directly. The mechanism of the formation of the excess bonds has not been confirmed. Etching by-products may account for some of the bonds, but the initial reaction of the LPCVD gases with the native oxide surface must also be involved. A reduction mechanism and an SiH_2Cl_2 surge are also proposed as possible explanations.

The oxide/nitride interface is characterized by both sharp and diffuse features. Within less than 8Å, the oxygen concentration drops off to one fifth of the initial concentration at the substrate interface. Thereafter, an oxynitride gradient does indeed exist. However, the amount of oxygen incorporation is quite modest, never exceeding 10 a/o, and dropping below 2 a/o within 45Å. At 50-60Å, the composition of the film is indistinguishable from the bulk within the detection limits of this technique. Thus, at least in this case of a native-oxide MNOS structure, the oxide/nitride interface is best described as being sharp with only a low concentration of oxygen extending into the LPCVD film.

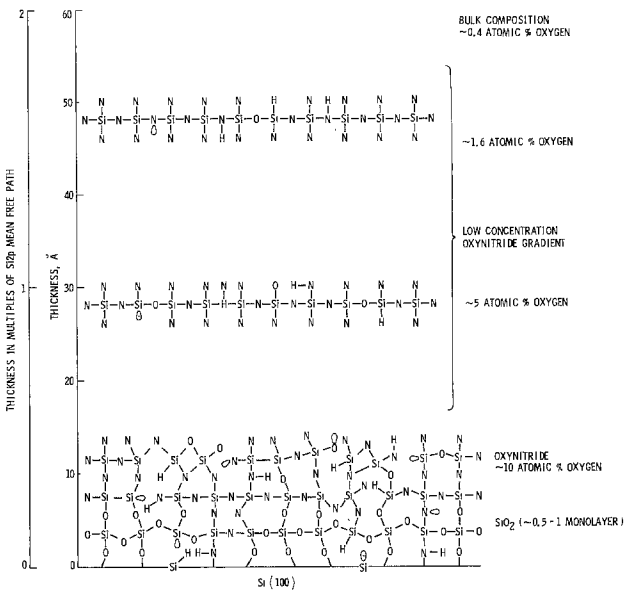

Fig. 9. Schematic diagram showing the essential features of a native-oxide LPCVD MNOS interface determined from this study. The bonding arrangement shown is one example of a geometry which would be consistent with the atomic fractions and chemical shifts observed in this work. Specific examples are given for excess bonds to silicon, strained bonds, and oxynitride. To maintain clarity in this 2-dimensional representation of a 3-dimensional situation, some of the bonds to nitrogen and oxygen have not been included. Also, for simplicity, strain is not shown explicitly in the oxynitride gradient, although it is believed to exist. The hydrogen bonds have been drawn from inference because hydrogen cannot be measured directly by the techniques used in this work.

Acknowledgments

LPCVD nitride samples were kindly provided with helpful discussion and explanation by J. R. Cricchi and F. L. Hampton of Westinghouse, M. C. Peckerar at the Naval Research Laboratory, and M. Beguwala and F. Erdmann of Rockwell International. J. Maserjian has also provided beneficial advice. The authors thank P. Chimiklis for assistance with the chemical etching, and C. Akers for help with data reduction. Thanks also to M. Brandenberg for manuscript preparation.

This work was supported by the U.S. Air Force, Rome Air Development Center, Deputy for Electronic Technology, Hanscom Air Force Base, and was monitored by Dr. P. Vail and Mr. H. DeAngelis. Instrument support was provided by the National Aeronautics and Space Administration under Contract NAS7-100. The work was performed at the Jet Propulsion Laboratory, California Institute of Technology.

Manuscript submitted Nov. 30, 1981; revised manuscript received April 12, 1982.

Any discussion of this paper will appear in a Discussion Section to be published in the December 1983 JOURNAL. All discussions for the December 1983 Discussion Section should be submitted by Aug. 1, 1983.

Publication costs of this article were assisted by the Californa Institute of Technology.

REFERENCES

1. P. Balk, in the "Proceedings of the 8th International Vacuum Congress," Vol. I, F. Abélès and M. Croset, Editors, p. 525, Cannes, France (1980).
2. (a) J. J. Chang, *IEEE Trans. Electron Devices*, **ed-24**, 511 (1977); (b) A. V. Ferris-Prabhu, *ibid.*, p. 524.
3. J. S. Johannessen, C. R. Helms, W. E. Spicer, and Y. E. Strausser, *IEEE Trans. Electron Devices*, **ed-24**, 547 (1977).
4. S. Thomas and R. J. Mattox, *This Journal*, **124**, 1942 (1977).
5. (a) P. H. Holloway, *Surf. Sci.*, **54**, 506 (1976); (b) P. H. Holloway and H. J. Stein, *This Journal*, **123**, 723 (1976); (c) H. J. Stein, S. T. Picraux, and P. H. Holloway, *IEEE Trans. Electron Devices*, **ed-25**, 1008 (1978).
6. V. J. Kapoor, R. S. Bailey, and S. R. Smith, *J. Vac. Sci. Technol.*, **18**, 305 (1981).
7. A. Van Oostrom, *Surf. Sci.*, **89**, 615 (1979).
8. F. H. P. M. Habraken, A. E. T. Kuiper, A. Van Oostrom, Y. Tamminga, and J. B. Theeten, To be published.
9. (a) H. Frenzel and P. Balk, in "The Physics of MOS Insulators," "Proceedings of the International Topical Conference, Raleigh, North Carolina," G. Luscovsky, S. T. Pantelides, and F. L. Galeener, Editors, p. 246, Pergamon Press, Inc., New York (1980); (b) H. Frenzel and P. Balk, in the "Proceedings of the 8th International Vacuum Congress," Vol. I, F. Abélès and M. Croset, Editors, p. 538, Cannes, France (1980).
10. R. Hezel and N. Lieske, in the "Proceedings of the Conference on Insulating Films and Semiconductors," Durham, 1979, Institute of Physics Conference Series No. 450, G. G. Roberts and M. J. Morant, Editors, p. 206.
11. J. B. Theeten, D. E. Aspnes, F. Simondet, M. Erman, and P. C. Mürau, To be published.
12. J. Gyulai, O. Meyer, J. W. Mayer, and V. Rodriguez, *J. Appl. Phys.*, **42**, 451 (1971).
13. S. Rigo, G. Amsel, and M. Croset, *J. Appl. Phys.*, **47**, 2800 (1976).
14. A. K. Sinha and E. Lugujjo, *Appl. Phys. Lett.*, **32**, 245 (1978).
15. (a) H. J. Stein and H. A. R. Wegener, *This Journal*, **124**, 908 (1977); (b) P. S. Peercy, H. J. Stein, B. L. Doyle and S. T. Picraux, *J. Electron. Mater.*, **8**, 11 (1979).
16. P. C. Mürau and B. Singer, in Proceedings of the International Electron Devices Meeting, Washington, D.C., 1978, p. 452.
17. S. I. Raider, R. Flitsch, J. A. Aboaf, and W. A. Pliskin, *This Journal*, **123**, 560 (1976).
18. H. Loic, "Method of Etching a Pattern in a Silicon Nitride Layer," U.S. Pat. 3,867,218 (1975); German Pat. 2,321,013 (1974); British Pat. 1,420,155 (1976).
19. F. J. Grunthaner, P. J. Grunthaner, C. Butler, R. P. Vasquez, and J. A. Wurzbach, Submitted to *This Journal*.
20. T. A. Carlson and G. E. McGuire, *J. Electron Spectrosc. Rela. Phenom.*, **1**, 161 (1972/1973).
21. J. A. Taylor, G. M. Lancaster, A. Ignatiev, and J. W. Rabalais, *J. Chem. Phys.*, **68**, 1776 (1978).
22. Preliminary results were presented at the Non-Volatile Semiconductor Memory Workshop, Vail, Colorado, August 1980.
23. J. H. Scofield, Lawrence-Livermore Laboratory Report No. UCRL-51326 (1973), and *J. Electron Spectrosc. Rela. Phenom.*, **8**, 129 (1976).
24. (a) C. J. Powell, *Surf. Sci.*, **44**, 29 (1974); (b) Handbook of X-Ray Photoelectron Spectroscopy, G. E. Muilenberg, Editor, p. 5, Perkin-Elmer Corp., Eden Prairie, Minnesota (1979); (c) D. R. Penn, *J. Electron Spectrosc. Rela. Phenom.*, **9**, 29 (1976); (d) C. D. Wagner, *Anal. Chem.*, **49**, 1282 (1977).
25. (a) F. J. Grunthaner and J. Maserjian, in "The Physics of SiO_2 and Its Interfaces," S. T. Pantelides, Editor, p. 389, Pergamon Press, Inc., New York (1978); (b) F. J. Grunthaner, P. J. Grunthaner, R. P. Vasquez, J. Maserjian, and A. Madhukar, *J. Vac. Sci. Technol.*, **16**, 1443 (1979); (c) R. N. Nucho and A. Madhukar, *Phys. Rev. B*, **21**, 1576 (1980); (d) F. J. Grunthaner, P. J. Grunthaner, R. P. Vasquez, B. F. Lewis, J. Maserjian, and A. Madhukar, *Phys Rev. Lett.*, **43**, 1683 (1979).
26. J. A. Wurzbach and F. J. Grunthaner, "Examination of Thin Silicon Nitride Layers on MNOS Tunneling Oxides by X-Ray Photoelectron Spectroscopy," Presented at the IEEE Semiconductor Interface Specialists Conference, New Orleans, 1979.
27. R. P. Vasquez, J. D. Klein, J. J. Barton, and F. J. Grunthaner, *J. Electron Spectrosc. Rela. Phenom.*, **23**, 63 (1981).
28. R. P. Vasquez and F. J. Grunthaner, *Surf. Sci.*, **99**, 681 (1980).
29. H. R. Philipp, *This Journal*, **120**, 295 (1973).
30. E. Friederich and L. Sittig, *Z. Anorg. Chem.*, **65**, 38 (1925).
31. E. Hengge, "Silicon Chemistry II, Topics in Current Chemistry," Vol. 51, p. 52, Springer-Verlag, New York (1974).
32. F. J. Grunthaner, B. F. Lewis, R. P. Vasquez, J. Maserjian, and A. Madhukar, in "The Physics of MOS Insulators," "Proceedings of the International Topical Conference, Raleigh, North Carolina, June 1980," G. Lucovsky, S. Pantelides, and F. Galeener, Editors, p. 290, Pergamon, New York (1980).
33. (a) J. A. Wurzbach, *ibid.*, p. 172; (b) P. J. Grunthaner, F. J. Grunthaner, and J. W. Mayer, *J. Vac. Sci. Technol.*, **17**, 924 (1980).
34. (a) F. L. Hampton and J. R. Cricchi, Private communication; (b) M. C. Peckerar and N. Bluzer, *IEEE Trans. on Nucl. Sci.*, **ns-27**, 1753 (1980).
35. (a) J. Wurzbach, F. Grunthaner, and J. Maserfian, Presented at the Semiconductor Interface Specialists Conference, Ft. Lauderdale, Fla., Dec. 1980. Manuscript in preparation; (b) F. Grunthaner, P. Grunthaner, R. Vasquez, J. Wurzbach, B. Lewis, and J. Maserjian, Presented at the same conference.
36. C. T. Kirk, Jr., *J. Appl. Phys.*, **50**, 4190 (1979).
37. H. J. Stein, *J. Electron. Mater.*, **5**, 161 (1976).

A Study of Impurities and Traps in Liquid Phase Epitaxial InP in Relation to Melt Prebaking

Jin K. Rhee and Pallab K. Bhattacharya

Department of Electrical and Computer Engineering, Oregon State University, Corvallis, Oregon 97331

ABSTRACT

Deep- and shallow-level defects in liquid phase epitaxial InP have been detected and characterized by transient capacitance, Hall transport, and photoluminescence measurements. The background impurity levels in the undoped crystals were varied by varying the period of prebaking of the In melt. A single deep electron trap with activation energy $\Delta E_T = 0.38 \pm 0.02$ eV is present dominantly with a concentration almost three orders lower than the background carrier concentration in the layers. From electron capture measurements, the electron capture cross section is found to obey the law $\sigma_n(T) = 4.78 + 10^{-15} \exp(-0.13/kT)$. The consistency of its concentration, irrespective of the purity of the crystal, and its removal after short-term heat-treatment leads us to believe that the trap is related to native defects. A hole trap with an activation energy of 0.22 eV was detected in some samples at low temperatures.

The fabrication of InP microwave and millimeter wave devices necessitates the growth of active layers of high purity. Liquid phase epitaxy (LPE) is a widely used technique for growing device quality InP. High-purity epitaxial InP and InP-based compounds are also being considered as an alternate host material for the fabrication of ion-implanted devices (1, 2). The presence of unintentional impurities in the melt, substrate, source materials, and growth ambient have plagued the growth of LPE InP with reproducible purity. It has now been recognized that Si and S are the two major background donor impurity species present in the In and InP used to form the growth solution, and C is the principal acceptor, originating from the graphite boat.

In addition to impurities giving rise to shallow donor and acceptor levels, there may also be present deep levels arising from impurities or grown-in and propagating native defects. There has not been any report of a detailed study of trap levels in LPE InP, except that of the presence of a 0.36 eV electron trap in such material by Nickel and Kuphal (3).

In this paper, we report the LPE growth of undoped single layers of InP which are suitable for a detailed study of traps. The layers were grown with varying periods of prebaking of the In melt in an ultrapure H_2 ambient. Prolonged prebaking of the melt is one of the most successful methods utilized to grow high-purity crystals (4, 5). Silicon present in the melt is converted to SiO_2 by minute traces (<0.1 ppm) of H_2O present in the H_2 ambient according to

$$Si(l) + 2H_2O(g) \rightleftarrows SiO_2(s) + 2H_2(g)$$

SiO_2 does not affect the purity of the crystal. Other techniques which are now being used to achieve high purity are: introduction of controlled amounts of H_2O in the growth ambient (6), use of epitaxial InP grown on dummy substrates as the source material (7), growth in a PH_3 atmosphere (8), and extended prebaking of the melt in high vacuum ($\sim 10^{-6}$ Torr) (9). The last method is claimed to be particularly effective for the removal of S. It has also been found that the intentional introduction of H_2O can lead to inferior surface morphology and the creation of O-related traps (9). The electrical and optical quality of the layers grown by us were evaluated from analysis of temperature dependent Hall-effect data and high-resolution photoluminescence (PL) spectra, respectively. We find that layers with reasonable purity ($n_{300\,K} = 4 \times 10^{15}$ cm^{-3}, $\mu_{77\,K} = 30{,}000$ cm^2/V · sec) can be grown with only 20 hr prebaking of the In melt in our growth system.

Detailed transient thermal emission and capture measurements were performed to determine the trap spectra in undoped LPE InP of reasonable purity. We find that the 0.36 eV electron trap reported by Nickel and Kuphal (3) is also dominant in our layers. We have studied the physicochemical origin of this trap by varying the growth conditions and by performing postgrowth annealing. An additional hole trap, located 0.22 eV above the valence band, was detected in some layers at low temperatures, but was not a dominant center. Our results lead us to conclude that the dominant electron trap in LPE InP is related to a native defect. Transitions involving acceptor impurities were detected in the low-temperature PL spectra.

Experimental

Liquid phase epitaxial growth of InP.—Single layers of LPE InP, 5-7 μm thick, were grown on nominally (100)-oriented InP:Fe substrates in a horizontal graphite sliding boat system. The reaction tube was made of suprasil quartz. The graphite boat was first heated at 1000°C for 4 hr under a vacuum of 2×10^{-7} Torr and then back-filled with He. The boat was then loaded in the reaction tube, and all the grooves were loaded with 99.9999% In (Johnson Matthey) and baked at 730°C for 72 hr under Pd-diffused H_2 flow. This purging step is crucial for the removal of residual impurities in the walls of the boat. The boat was cooled to room temperature and loaded with 4g In for the *in situ* melt-etch and 2.5g In for the growth melt which were then baked at 730°C for periods ranging from 10-70 hr. The system was again cooled and an appropriate amount of polycrystalline source InP ($\mu_{77\,K} = 75{,}000$ cm^2/V · sec) was added to the growth melt to form the growth solution. The time-temperature cycle for a typical epitaxial growth run is depicted in Fig. 1. The reaction tube was sealed and purged with purified H_2 for at least 2 hr (A to B). The In-InP solution was baked at 730°C for 10 hr (C to D). During this period, the solution was covered with a graphite cap to prevent evaporation of P atoms. At time E, the polished and cleaned substrate was loaded into the boat at room temperature. The growth system was again purged

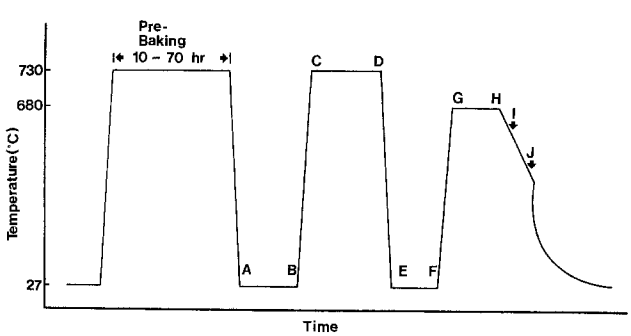

Fig. 1. Time-temperature cycle for a typical epitaxial growth run with ramp-cooling and *in situ* meltback etching.

with H_2 for 2 hr (E to F). The temperature was then raised to and held at 680°C for 30 min. During this time (G to H), the substrate was covered with a graphite cap to minimize loss of P from its surface. A ramp-cooling was then set in the programmer-controller, and the boat with its contents were cooled at 1°C/min. It is our experience that ramp-cooling gives better surface morphology than step-cooling for the growth of single InP layers. When the temperature of the growth melt reached 675°C (time I), *in situ* etching of the substrate was accomplished by sliding the pure In melt on top of the substrate for a few seconds. Epitaxial growth was then initiated by pulling the In-InP saturated melt on the substrate. Growth was terminated at time J by sliding the melt away from the grown epitaxial layer. The growth time varied typically from 15 to 20 min. Figure 2 depicts the surface morphology of a layer grown after 20 hr prebaking of the melt. The features are characteristic of LPE InP grown on (100)-oriented substrates and are similar to earlier reports (10).

Successful epitaxial growth largely depends on the availability of defect-free and clean substrates. A rigid procedure was followed to minimize the damage introduced into the substrate during substrate preparation and handling. The etch-pit density in the InP:Fe substrates, grown at Varian by the liquid encapsulation Czochralski technique, was less than 5×10^3 cm^{-2}. The surface morphology of the polished substrates were further improved by chemimechanical polishing with bromine methanol in stages. The final polish was achieved with a 0.5% solution. The polished substrate was degreased by boiling sequentially in high-purity trichloroethylene, acetone, and isopropyl alcohol (IPA). This was followed by a 30 sec etch in aqueous HCl (1:1) and a final rinse in IPA. The substrate was finally dried in IPA vapor and loaded in the growth cell. The same procedure was used to clean the polycrystalline InP source material. Indium for the melt was etched in aqueous HNO_3 (1:1) for 1 or 2 min immediately before each growth sequence.

The purity of the samples was greatly influenced by the ambient and flow rate of the purified H_2. It was ensured that the reaction tube was leak-proof to the extent that it could hold a vacuum of at least 10^{-5} Torr. A flow rate of ~15 liters/hr was maintained during epitaxial growth. The temperature profile along the entire length of the boat was uniform and was controllable within ±0.1°C.

Photoluminescence measurements.—Photoluminescence spectra of the LPE InP samples mounted in a strain-free manner were recorded at 4.2 K. Excitation was provided by the second harmonic (5300Å) line of a CW Nd:YAG laser. The focused beam at the sample surface had a diameter of ~0.1 mm, and the power absorbed by the sample was between 0.10 and 0.15W. The intensity of the light could be varied by neutral density filters. The luminescence was collected and analyzed by a double monochromator (SPEX 1402) with a resolution of 2Å or better.

Low temperature PL spectra of LPE InP have been recorded and analyzed by several authors (11-13). Their results were used as the basis for identification and comparison of our data. The main features in the PL spectra of our samples are observed in Fig. 3, where the bandedge luminescence of a layer grown after 10 hr prebaking of the melt is shown. The strong emission at 1.4168 eV is believed to arise from excitons bound to neutral donors (D°X) (11, 12). A shoulder to this peak on the high-energy side at 1.4184 eV has been identified as the free exciton-polaritron emission (11, 12). The peak at 1.38 eV, observed by several authors (13-15), is ascribed to band-to-acceptor (BA) and donor-to-acceptor (DA) transitions involving shallow acceptor impurities. It is recognized that C is the most dominant background acceptor impurity in LPE InP and peaks at 1.3803, and 1.3832 eV have been ascribed to DA and BA transitions involving C (13). No other acceptor species were detected in the layers. However, the peak at 1.38 eV, shown in Fig. 3, was the strongest observed in our samples and was undetectable in layers grown with longer prebaking intervals of the In melt. This strongly suggests that the peaks observed in our samples may not be due to C. It was also observed that in general the intensity of the free exciton peaks increased with increased durations of prebaking in the range 10-70 hr. Measurements at several points on the surface confirmed the spatial homogeneity of the layers.

Transport measurements.—The free-carrier concentration and Hall mobility in the undoped epitaxial layers were measured in the temperature range 77-300 K. Hall measurements were performed with a magnetic field of 0.5 Tesla and with the lowest possible current. The free-electron concentration at room temperature in the samples studied is listed in Table I.

The measured variation of the free-electron concentration (n_H) and the Hall mobility μ_H with temperature in a layer grown after 20 hr prebaking of the In melt are shown in Fig. 4. The data are representative of more than one sample grown under identical conditions. It might be noted that mobility at 77 K in our samples are lower than the highest values measured in undoped LPE InP (4, 9), but are still of the order of values claimed to be reasonably good (5).

The temperature dependence of the electron mobility in the different samples was analyzed by fitting the measured values with theoretically computed ones. These latter values were calculated by considering the mobilities limited by ionized-impurity, polar-optical phonon, piezoelectric, and deformation potential scattering. The temperature dependence of the carrier

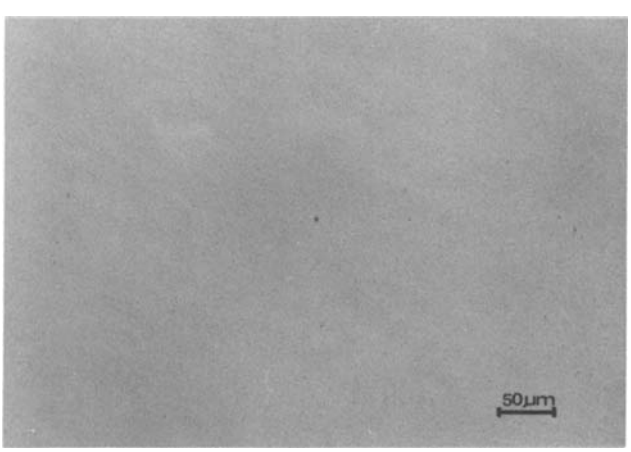

Fig. 2. Photomicrograph of an epitaxial layer grown on (100)-InP substrate after 20 hr melt prebaking.

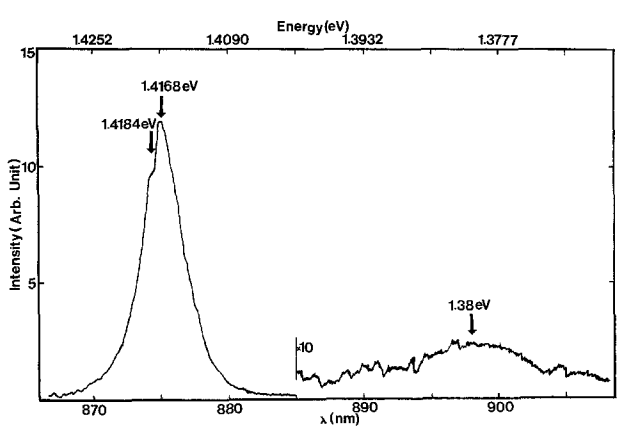

Fig. 3. Edge photoluminescence spectrum at 4 K of an epitaxial layer grown after 10 hr prebaking of the melt.

Table I. Variation of electrical properties and relative trap densities with duration of melt baking in LPE InP. The data indicate that the 0.38 eV trap concentration is almost independent of background doping

Melt baking time (hr)	n_H at 300 K ($\times 10^{15}$) (cm^{-3})	μ_H at 100 K ($cm^2/V \cdot sec$)	N_T/n ($\times 10^{-3}$)
10	14.0	11,041	0.6
20	4.5	26,331	1.9
30	4.3	21,128	1.9
40	6.1	14,972	0.7
50	1.6	6,601	4.1
60	9.5	14,008	0.6
70	10.0	16,761	0.8

concentration was fitted by taking charge-neutrality conditions into account. The continuous lines in Fig. 4 indicate the average fitting to the data. Values of $N_D = 5.3 \times 10^{15}$ cm^{-3} and $N_A = 8.0 \times 10^{14}$ cm^{-3} were obtained from the fits to the concentration and mobility data for this particular layer. It was observed that $(N_D - N_A)$ in the layers decreased, in general with longer prebaking of the melt. We believe that the values of N_A and N_D are representative of the concentrations of acceptors and Si and S as donors, respectively, in the LPE material. The low value of n_H in the sample grown after 50 hr melt-baking and the slight increase in its value in the samples grown after 60 and 70 hr melt-baking are attributed to additional impurity incorporation and compensation.

Trap measurements.—Transient capacitance measurements were performed with Schottky diodes made on the n-InP layers with Au dots and In-Sn ohmic contacts. In brief, the measurement procedure is as follows. The diode is normally reverse-biased in the quiescent state. Electron traps in a portion of the depletion region are filled by applying a majority-carrier pulse to the diode. The traps then thermally re-emit the captured electrons to the conduction band with a characteristic time constant dependent on temperature. Similarly, hole trap emission to the valence band can be observed after filling the traps with intrinsic photoexcitation. The resulting capacitance change is monitored by a 1 MHz capacitance bridge and recorded. The incremental capacitance change ΔC_0 due to trap-filling is a measure of the trap density N_T by virtue of the approximate relation

$$N_T = (N_D - N_A)^2 \Delta C_0 / C_\infty \quad [1]$$

where C_∞ is the quiescent reversed bias capacitance of the diode. Other expressions for calculating the trap density more accurately have been given by one of us (PKB) in earlier publications (16, 17). The thermal activation energy of the trap level ΔE_T, inclusive of the barrier to carrier capture, ΔE_B, is determined from the measured thermal emission rates by detailed balance considerations (16). The electrical field values in the depletion region should be kept at a low value to minimize the effects of field-enhanced trap emission. In our experiments, the quiescent bias was adjusted so that the electric field in the region of the depletion region, where trap capture and emission processes are operative, was less than 10^5 V/cm.

The thermal capture cross section of the trap can be estimated from the emission rate prefactor in the detailed balance equation (16), but a more accurate value can be obtained from direct measurements of electron capture rates. The capture cross section to electrons, σ_n, is related to the capture rate, c, by

$$c = \sigma_n v_{th} n \quad [2]$$

where v_{th} and n are, respectively, the thermal velocity and concentration of electrons in the conduction band.

The temperature dependence of the emission time constant for the only electron trap detected in all our layers is shown in Fig. 5. The activation energy obtained from a regression analysis of the data is $\Delta E_T = 0.38 \pm 0.02$ eV. An electron trap with $\Delta E_T = 0.36 \pm 0.005$ eV in the same temperature range was reported by Nickel and Kuphal (3). The temperature dependence of the capture cross section, σ_n, is also depicted in Fig. 5. The data can be fitted by the equation $\sigma_n(T) = \sigma_\infty \exp(-\Delta E_B/kT)$ and values of $\Delta E_B = 0.13 \pm 0.02$ eV and $\sigma_\infty = 4.78 \times 10^{-15}$ cm^2 are obtained. A value of $\sigma_\infty = 1.44 \times 10^{-15}$ cm^2 is obtained from the emission rate prefactor of the detailed balance equation (16).

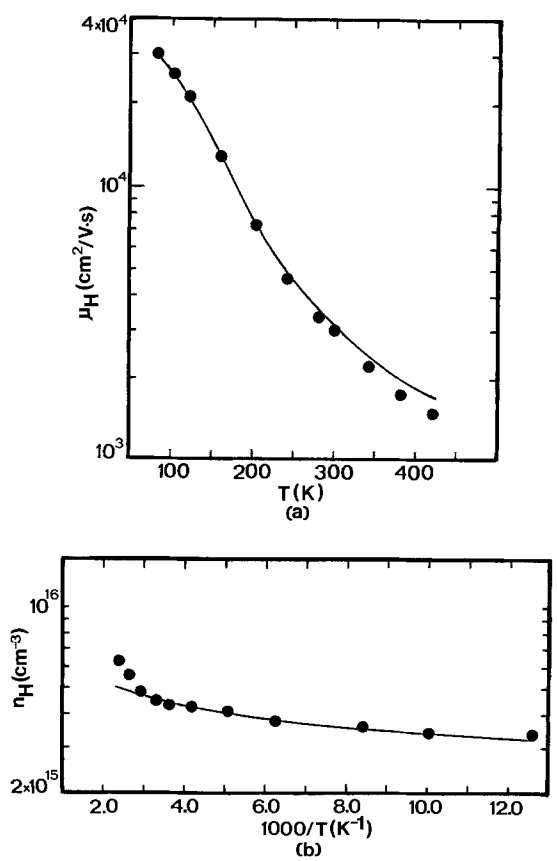

Fig. 4. Typical variation of the Hall mobility μ_H and Hall electron concentration n_H in undoped LPE InP. The solid lines are theoretical fits to the data.

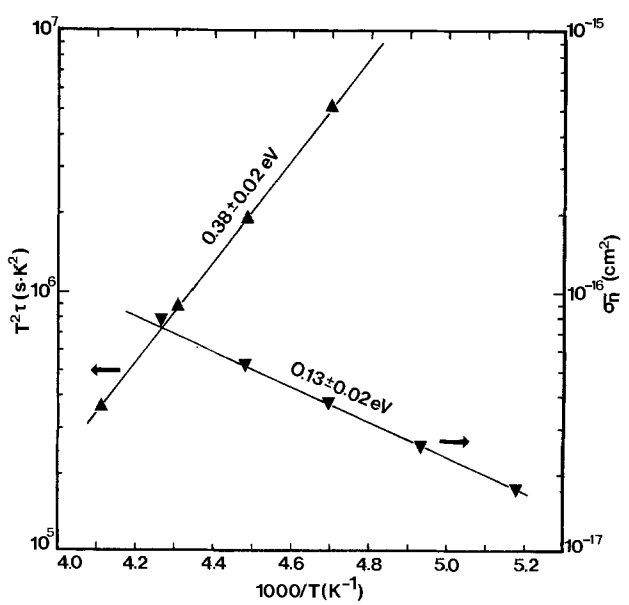

Fig. 5. Variation of the thermal emission time constant and thermal electron capture cross section of dominant traps in LPE InP. The slopes of the plots give the thermal activation energy and the barrier energy, respectively.

The ratio N_T/n in the different samples are listed in Table I. It is apparent that the absolute trap density is almost constant and thus independent of the baking period (purity) of the sample. A hole trap with $\Delta E_T = 0.22 \pm 0.01$ eV and $\sigma_\infty = 1.5 \times 10^{-23}$ cm^2 was observed in some layers in the temperature range 190-220 K. This center has not been detected before and more work on it is in progress in our laboratories.

Heat-treatment.—A few layers of as-grown InP were heat-treated in an LPE furnace under H_2-flow at 470°C for 15 min by placing the sample in the growth cell. The exposed surface morphology was severely degraded, and no device could be made without removal of this portion. By covering the sample with a piece of InP during the anneal, such degradation of the surface morphology could be avoided. It was observed that the 0.38 eV electron trap was removed at the surface. Considering a certain amount of P evaporation to be operative in our mode of heat-treatment the formation of, or an increase in, P-vacancies near the surface can be assumed. The possibilities of outdiffusion of impurities towards the surface or any indiffusion that might take place from spurious impurities from the surface cannot be ruled out.

Discussion

Our results clearly indicate that the 0.38 ± 0.02 eV electron trap is a dominant center in LPE InP. We have intentionally varied the purity of the crystals by varying the prebaking time of the growth melt. The concentration of the residual impurities, particularly S, Si, and C, are greatly altered and subsequently the background impurity concentrations in the crystals are also different. The trap concentration, however, remains almost invariant. This indicates that the center probably originates from native defects.

It is likely that in our mode of heat-treatment, with a proximity cap of InP, there is still a slight loss of P-atoms from the surface. In other words, the slight overpressure of P provided by the InP cap only helps to maintain the surface morphology, but does not enhance the P/In ratio at the surface. If this is true then the trap is related to an In site. Possibilities other than an isolated vacancy are an antisite defect P_{In}, in-site impurities, or V_{In}-impurity complexes. The possible source of some of these impurities have been mentioned in the previous section. However, if during the heat-treatment, there is enough overpressure of P, the trap could be related to P. These aspects are being studied by varying the conditions of heat-treatment.

The characteristics of the trap detected in our crystals is similar to those of the trap observed by Nickel and Kuphal (3), and we believe that they are the same centers. Our measurements have also revealed some of the electron capture properties of the trap. It is clear that the thermal capture cross-section for electrons is thermally activated with a barrier energy of 0.13 ± 0.02 eV. This value is about the same as for most dominant traps in GaAs and GaP (18). It is of interest to note that McAfee *et al.* (19) have reported an electron trap with an activation energy of 0.35 ± 0.03 eV (level E2) to be present in bulk LEC-grown InP. However, the temperature range in which level E2 was detected is much lower than the range in which the electron trap was detected in our samples.

Since the concentration of the 0.38 ± 0.02 eV electron trap is generally low, and it is detected at temperatures much lower than 300 K, it is expected that the performance of devices made from such layers will not be affected. And even if it did, our experiments show that defect-annealing can be achieved by a simple heat-treatment. In addition, LPE InP should prove to be a trap-free host material for ion-implantation.

Summary

We have grown high-purity undoped LPE InP with varying pregrowth conditions, which altered the purity of the layers. The electrical and optical properties of the layers were determined from temperature dependent Hall and low-temperature PL measurements. Detailed capacitance transient emission and capture measurements were performed on Au Schottky diodes made on the epitaxial layers. A single electron trap, with a thermal activation energy of 0.38 ± 0.02 eV has been consistently detected in all the crystals. Its capture cross section is thermally activated, with a barrier energy $\Delta E_B = 0.13 \pm 0.02$ eV and its concentration is $\sim 10^{12}$ cm^{-3} irrespective of the unintentional background doping. Short-term heat-treatment at 470°C anneals the trap completely in regions close to the surface of the layers. These facts point to the association of the traps with native defects.

Acknowledgments

The authors are grateful to T. Matsumoto for useful discussions and a critical reading of the manuscript and J. Staehli (Lausanne) for performing the photoluminescence measurements. The work was supported by the National Science Foundation under Grant ECS-8011917.

Note added in proof: Nakajima *et al.* [J. Crystal Growth, **59**, 572 (1982)] have recently reported that the intensity of the 1.38 eV PL peak decreases with baking, which agrees with our observations.

Manuscript submitted July 26, 1982; revised manuscript received Oct. 5, 1982.

Any discussion of this paper will appear in a Discussion Section to be published in the December 1983 JOURNAL. All discussions for the December 1983 Discussion Section should be submitted by Aug. 1, 1983.

Publication costs of this article were assisted by National Science Foundation.

REFERENCES

1. J. J. Berenz, F. B. Fank, and T. L. Hierl, *Electron. Lett.*, **14**, 683 (1978).
2. K. Tabatabaie-Alavi, A. N. M. M. Choudhury, N. J. Slater, and C. G. Fonstad, *Appl. Phys. Lett.*, **40**, 517 (1982).
3. H. Nickel and E. Kuphal, *Phys. Status Solidi A*, **65**, 583 (1981).
4. V. L. Wrick, K. T. Ip, and L. F. Eastman, *J. Electron Mater.*, **7**, 253 (1978).
5. E. Kuphal, *J. Cryst. Growth*, **54**, 117 (1981).
6. D. E. Holmes and G. S. Kamath, *ibid.*, **54**, 51 (1981).
7. L. F. Eastman, Presented at the NATO InP Workshop, June 1980.
8. M. G. Astles, F. G. H. Smith, and E. W. Williams, *This Journal*, **120**, 1750 (1973).
9. E. Kunphal and A. Pöcker, Presented at the Electronic Materials Conference, Fort Collins, June 1982.
10. T. Nishinaga, K. Pak, and S. Uchiyama, *J. Cryst. Growth*, **42**, 315 (1977).
11. A. M. White, P. J. Dean, L. L. Taylor, R. C. Clarke, D. J. Ashen, J. B. Mullin, and P. D. Green, *J. Phys.*, **C5**, 1727 (1972).
12. J. U. Fischbach, G. Benz, N. Stath, M. H. Pilkuhn, and K. W. Benz, *Solid-State Commun.*, **11**, 721 (1972).
13. K. Hess, N. Stath, and K. W. Benz, *This Journal*, **121**, 1208 (1974).
14. R. C. C. Leite, *Phys. Rev.*, **157**, 672 (1967).
15. U. Heim, *Solid-State Commun.*, **7**, 445 (1969).
16. P. K. Bhattacharya, J. W. Ku, S. J. T. Owen, C. B. Cooper, and R. L. Moon, *Appl. Phys. Lett.*, **36**, 304 (1980).
17. P. K. Bhattacharya, J. K. Rhee, S. J. T. Owen, J. G. Yu, K. K. Smith, and R. Y. Koyama, *J. Appl. Phys.*, **52**, 7224 (1981).
18. C. H. Henry and D. V. Lang, *Phys. Rev. B*, **15**, 989 (1977).
19. S. R. McAfee, F. Capasso, D. V. Lang, A. Hutchinson, and W. A. Bonner, *J. Appl. Phys.*, **52**, 6158 (1981).

Evaluation and Control of Resistivity in N^-/N^+ Epitaxial Depositions

J. L. Sachitano* and V. C. Kannan*[1]

Tektronix, Incorporated, Tektronix Laboratories, Beaverton, Oregon 97077

ABSTRACT

Autodoping from 0.001 Ω-cm arsenic-doped wafers interferes with the use of 10 Ω-cm P-type wafers for evaluating epi resistivities. A diffused layer is formed in the test wafers by arsenic atoms that evaporate from the N^+ wafers during the post-HCl bake prior to deposition. This layer leads to an erroneous four-point probe measurement of the epi-layer sheet resistance on the test wafer. A model is given that describes the formation of the diffused layer and its dependence upon the number of N^+ wafers. The model accounts for the epi resistivity as determined from the test water. A two-step epi procedure is described that allow the use of this type of test wafer for evaluating resistivities up to ≈30 Ω-cm.

A growing epi layer has many sources of dopants whose relative magnitudes influence the ability to control epi resistivity. The generally recognized sources are purposely introduced gas-phase dopants (inject), dopant evaporation from front and back sides of the substrates, solid-state diffusion of dopant from the substrate into the epi layer, and extraneous dopant evaporation from other surfaces such as the bell jar or susceptor. Extraneous sources can be ignored when the background resistivity can be controlled to greater than 100 Ω-cm by careful cleaning of the reactor surfaces and by proper treatment of the susceptor, such as etching and coating between runs. The contribution of solid-state diffusion (1, 2) is described by an erfc distribution with effects localized to the epi-substrate interface. Dopant evaporation from the front, back, and sides (3-8) of the substrate add to the inject dopant in the gas phase during the deposition cycle. Prior to the deposition, the substrate is at growth temperature with dopant evaporating and approaching a steady-state concentration in the stagnant layer above the substrate surface (9). When the deposition begins, the front surface is effectively sealed off and no longer contributes to the gas phase because the epi growth rate is greater than the dopant diffusion rate (1). However, in the case of antimony, surface adsorption and redistribution at the growing interface have been shown to occur (10). The back side may continue to contribute dopants throughout the deposition cycle. Various reports (3, 5, 7) demonstrate that sealing the back side, *e.g.*, with oxide (3), can reduce this contribution to autodoping. A comprehensive review (11) of autodoping in a horizontal epi reactor has considered the above effects in structures with buried layers (12).

We investigated the effect of autodoping on lightly doped P-type test wafers used to monitor the resistivity of high-resistivity arsine-doped $SiCl_4$ epi on N^+ arsenic-doped wafers in a vertical reactor. The extent of autodoping during the bake was correlated with the number of N^+ wafers, and the subsequent diffused layer is shown to dominate the test-wafer resistivity (4). A model that relates the surface area and concentration of the N^+ wafers to the diffused layer accounts for the measured resistivities. A two-step procedure, which reduces the front- and back-surface concentrations of the N^+ wafers before the test wafer is introduced, greatly reduces the autodoping and results in measured resistivity as high as 30 Ω-cm.

Experimental

The epi depositions ($SiCl_4$) were done in an Applied Materials AMV-800 vertical reactor. The test wafer was ≈10 Ω-cm, P type, <111>, and the run wafers were ≈0.001 Ω-cm, arsenic doped, <111>, and 2 in. in diam. The test wafer was actually quartered, and two chips were placed on the susceptor as shown in Fig. 1. (From here on, "P-type test wafer" means a quarter of a wafer.) The substrate placements for one-, four-, and eight-wafer runs are indicated. The epi sheet resistance was measured with a four-point probe, and junction depths were determined with a groove-and-stain technique using a sodium light source for interferometry. The spreading-resistance profiles were measured on an ASR-100 spreading-resistance probe.

A description of typical process conditions is given in Table I. To begin the procedure, the susceptor is etched with HCl, and a thick layer of polysilicon is coated onto it. An intrinsic run with only a test wafer is done to verify the background doping level of the system (typically 50-150 Ω-cm). The reactor is targeted for a specific resistivity in a test run using the above procedures to evaluate resistivity. After a satisfactory target run, N^+ wafers and test wafers are added to the reactor and a deposition using the doping conditions of the test run is done. The susceptor is etched and coated prior to subsequent depositions.

Results

Following these procedures, a series of depositions was done with differing numbers of wafers but with all other conditions held constant. The test run resistivity was 6.5 Ω-cm, and the results (Fig. 2) show that the test-wafer resistivity decreased as the number of N^+ wafers increased.

To aid in determining the cause of these effects, a scheme using three test wafers was introduced. The procedure, outlined in Table II, involves interrupting the process after the post-HCl bake. Test wafer 1 (TW1) is removed after the bake, TW2 remains and goes through the entire process, and TW3 is inserted after the bake and has only the epi deposition. A run using this procedure with four N^+ wafers was targeted for 5.1 Ω-cm. The results, summarized in Table III, indicate that the test wafer is affected before the epi deposition. An N-type layer is present after the bake, and the test wafer that has gone through the entire process shows a lower resistivity than the one that has only the epi deposition. A subsequent run substituted a 4 Ω-cm N-type test wafer in place of the usual 10 Ω-cm P type. This wafer was removed after the bake (*e.g.*, TW1), and a spreading-resistance profile (Fig. 3) shows a diffused layer at the surface.

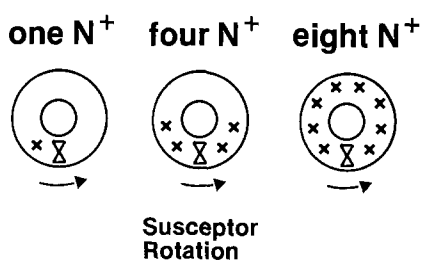

Fig. 1. Schematic representation of test-wafer (△) and run-wafer (×) placements on the susceptor.

* Electrochemical Society Active Member.
[1] Present address: Bell Laboratories, Allentown, Pennsylvania 18103.

Table I. Typical conditions for high-resistivity epi process on N⁺ substrates

Conditions \ Step	Warm Up	Etch	Bake	Dep $SiCl_4$
Time (min)	5	1	10	10
Temperature (°C)	23 - 1200	1200	1180	1180
H_2 (main)	38 ℓpm	38 ℓpm	38 ℓpm	38 ℓpm
$SiCl_4/SiH_4$	—	—	—	0.25 ℓpm
HCl	—	0.67 ℓpm	—	—
AsH_3 (source) ≈ 50 ppm in H_2	—	—	—	0.028 ℓpm
H_2 (diluent)	—	—	—	3.98 ℓpm
AsH_3 (inject)	—	—	—	0.021 ℓpm

Table II. Sequence to evaluate process effects on test-wafer resistivities

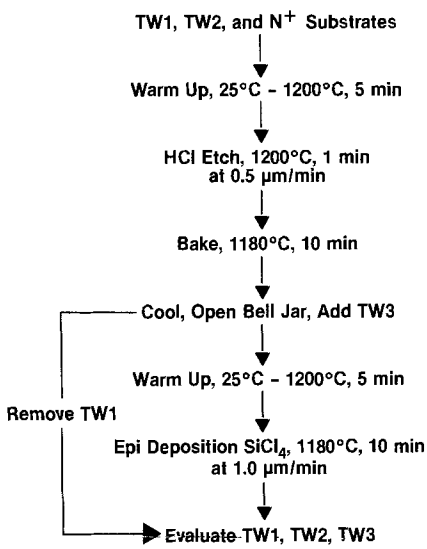

Table III. Test-wafer evaluation of epi process

Number of N⁺ Substrates	TW Resistivity (Ω-cm)		
	Warm Up to Bake (TW1)	Full Process (TW2)	Epi Only (TW3)
0	—	5.1	—
4	1.4	3.7	5.1

Model for Test-Wafer Resistivity

The essential features of the model are that arsenic evaporates from the N⁺ wafers and diffuses into the test wafer during the post-HCl bake, which results in an erfc distribution (dep) with a surface concentration that is dependent upon the number of N⁺ wafers present. This diffused layer then redistributes to a near-Gaussian profile during the epi deposition. The measured test-wafer conductance results from the sum of the conductances of the epi layer, the dep diffusion into the epi, and the dep diffusion into the substrate. The structure is shown schematically in Fig. 4.

Following Skelly and Adams (5), the amount of arsenic evaporating from the N⁺ wafer (13, 14) for the case of uniform initial dopant concentration C_0 and zero gas-phase concentration, is given by

$$\bar{C}(t) = 2C_0(Dt)^{1/2} \left\{ \frac{1}{(\pi)^{1/2}} - \frac{[1 - \exp(Z^2)\,\mathrm{erfc}(Z)]}{2Z} \right\} \quad [1]$$

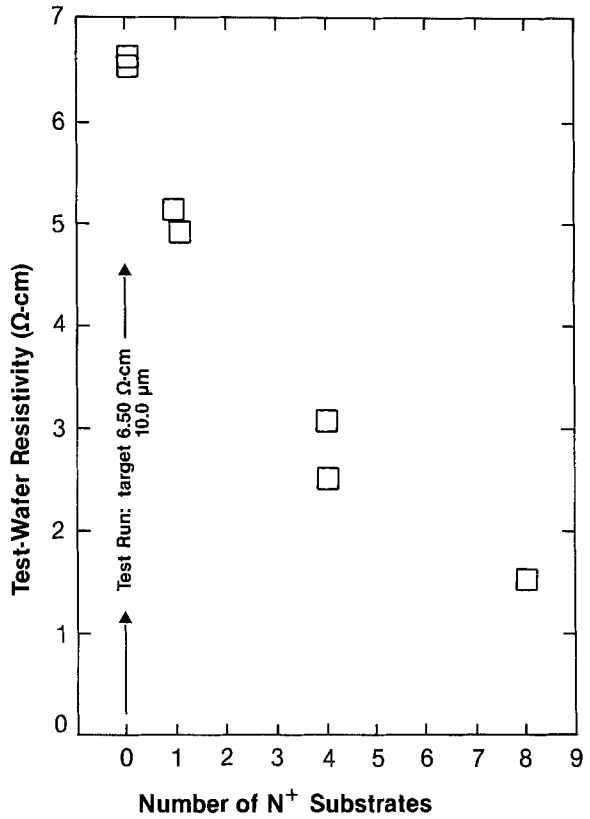

Fig. 2. Dependence of test-wafer resistivity on the number of N⁺ wafers in the epi run. Gas-flow settings, temperatures, and times were held constant for all data points. The epi targets were 6.5 Ω-cm and 10.0 μm.

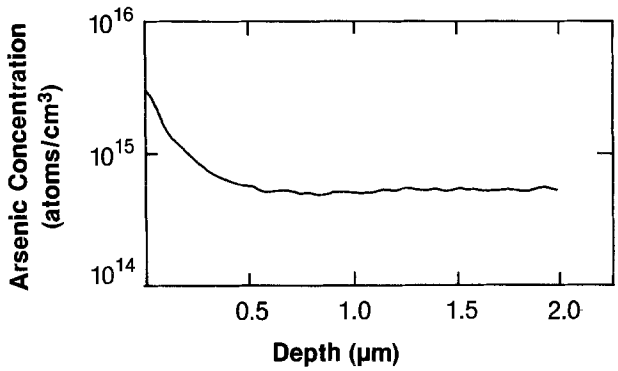

Fig. 3. Spreading-resistance profile of 4 Ω-cm N-type test wafer after post-HCl bake showing diffused layer at surface.

where $Z = Kt/(Dt)^{1/2}$. The arsenic diffusion coefficient is D, and the evaporation coefficient is K. In the following calculations, the diffusivity data of Masters and Fairfield (15) were used to calculate outdiffusion from the N⁺ substrates and the diffusion into the test wafer. Abe's (2) value of K at 1250°C, 7×10^{-9} cm sec^{-1}, was adjusted to 1200°C assuming that the temperature dependence of K is the same as that of D (16). Equation [1] gives the total number of evaporated atoms per unit surface area for a given time. In this way, the effect of varying the number of N⁺ substrates can be accounted for. Using this equation, the average rate of evaporation is just $\bar{C}(t)/t$.

The test-wafer surface concentration of arsenic during the bake can be calculated from Henry's law. If the maximum dopant concentration is $<10^{18}$ atoms/cm^3, then the activity coefficient of arsenic can be approximated to unity (17), and Henry's law becomes $C_0 = HP_{As}$, where H is Henry's law constant, P_{As} is the partial pressure of arsenic, and C_0 is the arsenic con-

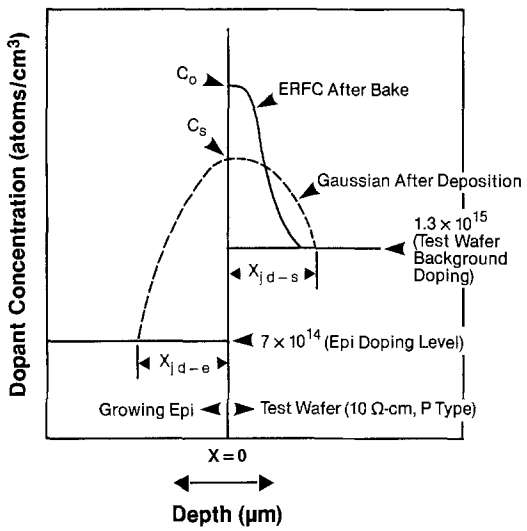

Fig. 4. Schematic illustration used for calculating test-wafer resistivity.

centration in the wafer. The arsenic partial pressure can be estimated from $P_{As} = R_{As}/R_{H_2}$, where R_{As} is the average rate of arsenic evaporation from Eq. [1], and R_{H_2} is the flow rate of hydrogen in the reactor. This estimation assumes complete mixing in the system, which gives the lowest estimate of P_{As}. Evaporation of arsenic occurs from both sides of the N^+ wafers, but the back side contribution is less effective because of transport limitations. This factor is estimated by assuming that the effective surface area of the back side is equal to 10% of the front. Henry's law constant was obtained from a plot, Fig. 5, of the partial pressure of arsine *vs.* the arsenic concentration in epi layers. This plot gives a value of $H = 3.2 \times 10^{24}$ atoms cm^{-3} atm^{-1} at 1200°C with a slope of 0.98. The resulting diffusion into the test wafer is described by

$$\frac{C(x,t)}{C_0} = \text{erfc}\,(y) - \exp\,(Z^2)\exp\,(yz)\,\text{erfc}\,(y+Z) \qquad [2]$$

where $y = x/2(Dt)^{1/2}$ and $Z = Kt/(Dt)^{1/2}$. This equation converges to a simple error function when $Kt > (Dt)^{1/2}$.

The predeposition cycle is divided into 3 time segments: warm up (5 min from room temperature to 1200°C), HCl etch (1 min), and bake (10 min). It is possible that some diffusion into the test wafer could occur before the HCl etch and remain after the etch. However, in our case, $(Et/Dt)^{1/2} \geq 12$, we have assumed that no diffusion remains after the etch, so only diffusion during the bake is considered.

Since the epi layer grows fast compared with the diffusivity of arsenic, the redistribution of the diffused layer can be treated as a thin source diffusing from two sides into an infinite body. This redistribution is analogous to a dep and drive in which the dep length $(D_1t_1)^{1/2}$ is small compared with the drive length $(D_2t_2)^{1/2}$, and the dep is then represented by a delta function. In the present case, $D_1t_1/D_2t_2 \approx 1$ and the distribution is better represented by solutions for the two-step diffusion (18). However, the assumption of a Gaussian distribution does not lead to an error greater than ≈25% in estimating conductance. This assumption was made to reduce the computational burden by using Irvin's curves (19). The resulting depth of diffusion into the wafer or into the epi layer is

$$x_j^2 = 4D_2t_2 \ln\left[\frac{C_0}{\pi C_B}\left(\frac{D_1t_1}{D_2t_2}\right)^{1/4}\right] \qquad [3]$$

where C_B is the appropriate background concentration. The conductance of the diffused layers can be estimated by using x_j calculated from Eq. [3]. The diffused-layers plus the epi-layer conductance then gives the total conductance $\sigma_T = \sigma_{d-s} + \sigma_{d-e} + \sigma_{epi}$. The resistivity is then $\rho \simeq x_j/\sigma_T$. In Eq. [1]-[3], we used $K = 1.63 \times 10^{-7}$ cm sec^{-1}, $D_{ex} = 5.078 \times 10^{-12}$ cm^2 sec^{-1}, $D_{in} = 2.59 \times 10^{-13}$ cm^2 sec^{-1} (1200°C), $D_{in} = 1.64 \times 10^{-13}$ cm^2 sec^{-1} (1180°C), and $C_0 = 1.92 \times 10^{17}$ atoms cm^{-3}, where D_{ex} is for N^+ wafers and D_{in} is for test wafers.

The results of these calculations are shown as the solid line in Fig. 6 superimposed on the experimental results of Fig. 2. Given the simplifications made in the model, it reasonably accounts for the observed results.

Modified Epi Process

In order to use a P-type test wafer in the presence of N^+ wafers, the diffused layer must be eliminated. The rate of arsenic evaporation is proportional to the surface concentration of the N^+ substrates (5). Reducing the front- and back-surface concentrations before the test wafer is put in place should reduce the extent of the diffused layer. A procedure for doing this, outlined in Table IV, involves sealing the back surfaces by transferring polysilicon from the susceptor to the back of the wafer (6) during the HCl etch and the short epi ($SiCl_4$) deposition. The front surface is also sealed by the short deposition. Spreading-resistance profiles, Fig. 7, of the front and back surfaces of an N^+ wafer after this treatment show several orders of magnitude reduction in surface concentrations.

The process is interrupted at this point; the test wafer is inserted, and the epi deposition follows. The short HCl etch included at this step is necessary in order to maintain good surface quality. Autodoping should now be reduced as a result of the low surface concentration of arsenic in the coated N^+ wafers. This reduction was verified by spreading-resistance profiles (Fig. 8) of intrinsic epi on ≈4 Ω-cm N-type test wafers

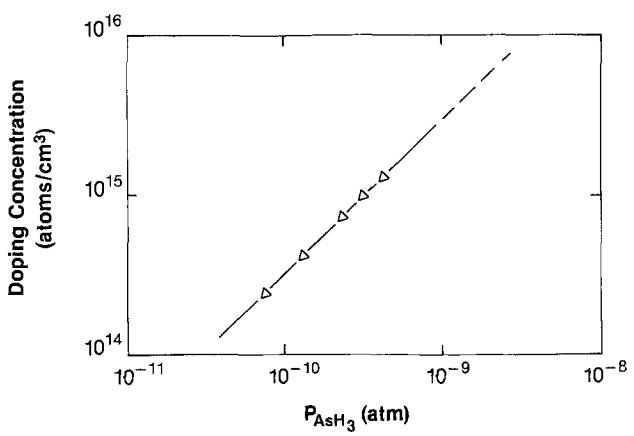

Fig. 5. Variation of doping concentration in the epi layer with arsine partial pressure for $SiCl_4$ epi.

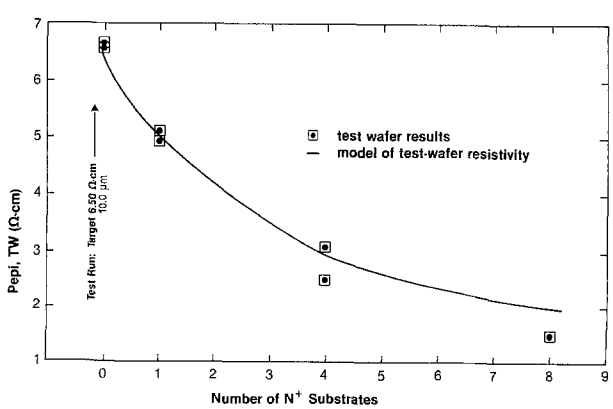

Fig. 6. Effect of number of N^+ substrates on test-wafer resistivity as predicted by the model (solid line).

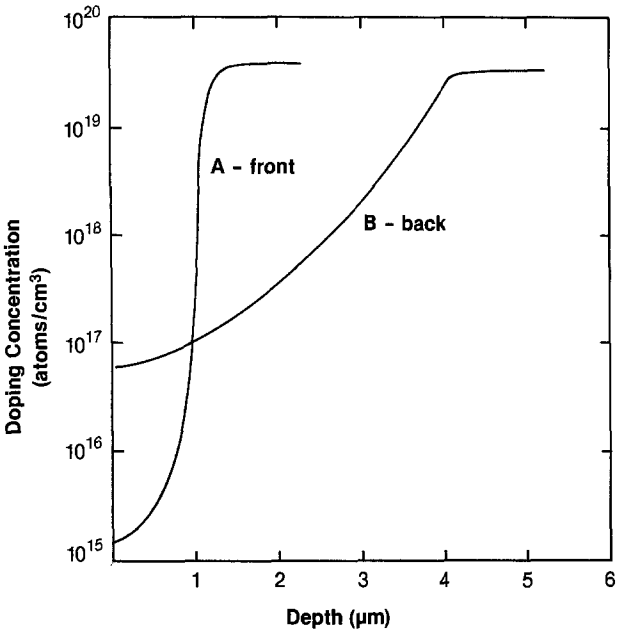

Fig. 7. (A) Front side concentration profile after a 1 min epi deposition, and (B) back side profile after HCl etch and 1 min epi deposition.

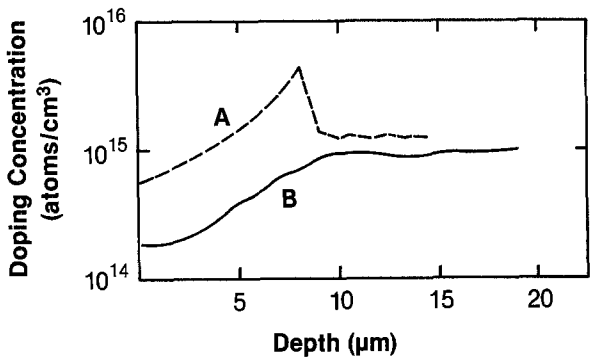

Fig. 8. Doping profiles of intrinsic epi layers obtained for (A) one-step and (B) two-step deposition processes. The test wafers were 4 Ω-cm, N type.

in the presence of seven N^+ wafers. The original single-step process clearly gives a diffused layer, but none is apparent in the modified two-step process.

In order to estimate the upper limit of resistivity obtainable with this process, the procedure was repeated using 10 Ω-cm P-type test wafers and intrinsic epi. The results of several runs with either 4 or 8 N^+ wafers are listed in Table V. Some residual autodoping effects are apparent since all results are less than the typical background resistivity (≥50 Ω-cm). A comparison of the results of 4 and 8 wafers also indicates a loading effect. These effects may have been reduced if the system had been cleaned and the susceptor etched and coated after the bell jar was opened.

Summary

The use of a 10 Ω-cm P-type test wafer to evaluate N^-/N^+ epi resistivities is inappropriate because of a diffused layer formed during the post-HCl bake. Arsenic out-diffusion and evaporation from the N^+ wafers is the source of the diffused layer, and the extent of the diffusion depends upon the number of N^+ wafers present. The diffused layer leads to erroneous resistivity evaluations. A model was given that relates the autodoping process and the resulting diffused layer to the observed resistivity evaluations. A two-step process in which the N^+ wafer surfaces are sealed before the test wafer is inserted has given 20-30 Ω-cm resistivity measurements.

Table IV. Sequence for the two-step process

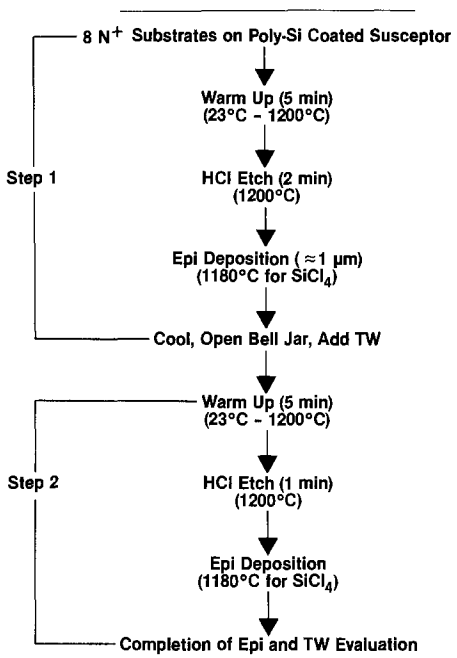

Table V. Test-wafer resistivities with intrinsic $SiCl_4$ epi using the two-step process

# Wafers	Resistivity (Ω-cm)	
	TW2 (complete)	TW3 (epi only)
4	5.7	27.3
4	5.1	32.4
8	2.7	20.3

Acknowledgments

The authors thank Mrs. I. Cady for assisting with the epi experiments and Mr. R. Osterman for the spreading-resistance measurements.

Manuscript submitted Jan. 28, 1980; revised manuscript received Sept. 20, 1982.

Any discussion of this paper will appear in a Discussion Section to be published in the December 1983 JOURNAL. All discussions for the December 1983 Discussion Section should be submitted by Aug. 1, 1983.

Publication costs of this article were assisted by Tektronix, Incorporated.

REFERENCES

1. S. D. Grove, A. Roder, and C. T. Sah, *J. Appl. Phys.*, **46**, 802 (1965).
2. T. Abe, Y. Nishi, K. Sato, and N. Oi, *Denki Kagaku*, **35**, 142 (1967).
3. B. A. Joyce, J. C. Weaver, and D. J. Maule, *This Journal*, **112**, 1100 (1965).
4. W. H. Shepard, *ibid.*, **115**, 652 (1968).
5. G. Skelly and A. C. Adams, *ibid.*, **120**, 116 (1973).
6. C. O. Bozler, *ibid.*, **122**, 1705 (1975).
7. P. H. Langer and J. I. Goldstein, *ibid.*, **124**, 591 (1977).
8. D. C. Gupta and R. Yee, *ibid.*, **116**, 1561 (1969).
9. T. Ishii, K. Takahashi, A. Kondo, and K. Shirahata, *ibid.*, **122**, 1523 (1975).
10. P. H. Langer and C. L. Paulnack, Abstract 295, p. 737, The Electrochemical Society Extended Abstracts, Vol. 78-1, Seattle, WA, May 21-26, 1978.
11. G. R. Srinivasan, *This Journal*, **127**, 1334 (1980).
12. G. R. Srinivasan, *ibid.*, **125**, 146 (1978).
13. F. M. Smits and R. C. Miller, *Phys. Rev.*, **104**, 1252 (1956).
14. R. N. Goshtagore, *Solid-State Electron.*, **15**, 1113 (1972).
15. B. J. Masters and J. M. Fairfield, *J. Appl. Phys.*, **40**,

2390 (1969).
16. K. Lehovec, K. Schoenic, and K. Zuleeg, *ibid.*, **28**, 420 (1957).
17. P. Rai-Choudhury and E. I. Salkovitz, *J. Cryst. Growth*, **1**, 361 (1970).
18. D. P. Kennedy and P. C. Murley, *Proc. IEEE*, **52**, 620 (1964).
19. J. C. Irvin, *Bell Syst. Tech. J.*, **41**, 387 (1962).

Some Illumination on the Mechanism of SiO_2 Etching in HF Solutions

Henry Nielsen and David Hackleman*

Hewlett-Packard Company, Corvallis, Oregon 97330

ABSTRACT

The etching of SiO_2 in aqueous buffered HF solutions can be impeded or stopped through the application of an electric field. In CMOS fabrication, very low levels of light can cause the effect. Parallel reaction paths are proposed for the dissolution process, coupled with the electric field's ability to stop or redirect the reaction at an intermediate step.

The dissolution of SiO_2 in HF solutions is a fundamental step in the fabrication of integrated circuits The overall chemical reaction involved is normally understood as

$$SiO_2 + 6HF \rightarrow 2H^+ + SiF_6^= + 2H_2O \quad [1]$$

Etch rates and etch profiles are controlled by buffering and/or diluting the HF solution (1, 2) and by doping or damaging the glass layer via thermal diffusions (2) or ion implantation (3). Based on the knowledge behind these techniques, etching the structure shown in Fig. 1 should occur isotropically, with only a modest decrease in the etch rate of the boron doped glass found over the p+ region when compared to the phosphorus doped material above the n+ area. A slight overetch on the p+ side of the hole may occur due to the differential in oxide thickness, but this would be a minor difficulty.

Under some conditions of high n+ and p+ doping concentrations, shallow junctions, and very low silicon surface defect densities, when the structure in Fig. 1 is etched in the yellow light present in most integrated circuit processing photomasking areas, it has been observed that the n+ side will not clear regardless of the overetch time. In some cases, a brightly colored layer is visible over the n+ oxide. This layer is insoluble in nonoxidizing HF solutions. On the other hand, if the etch is performed in absolute darkness, the oxide dissolves uniformly over both n+ and p+ silicon. This light sensitivity indicates possible photocharging of the junction structures. Experiments were set up to investigate the effect of an applied E-field on the etching of SiO_2 layers. The effect of varying the junction structure was also examined. Lastly, Auger and SEM analyses of the material remaining in actual contact hole etches on integrated circuits were performed.

Experimental

Wafers, with the structure shown in Fig. 1, with varying junction depths were etched in ambient light, 405 nm light, and total darkness. The wafers etched in darkness or 405 nm light produced no HF-insoluble layer. Wafers etched in the yellow ambient light generated the HF-insoluble layer. The junction depths ranged from 500 to 1000 nm. Changing the junction depth had no discernable influence on the etching behavior.

The effect of changing the overlap of the n+ and p+ junctions shown in Fig. 1 was examined using an alignment monitor test cell. The alignment monitor, shown in Fig. 2, consists of a series of p-well regions, each split into an n+ and a p+ diffusioin. The cross sections of these regions look similar to Fig. 1 except that the masks for the diffusions are drawn to give 0, ±1, ±2, and ±3 microns overlap of the n+ and p+ diffusions. (These values change somewhat in practice, due to thermal side-diffusion of the dopants during activation of the implants and also due to photomasking misalignments.) When these arrays are etched in ambient light, the oxide over both the n+ and p+ silicon is removed uniformly, provided the diffusions do not over-

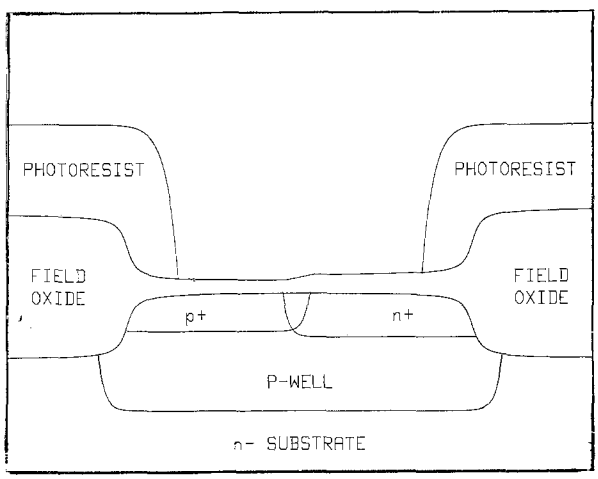

Fig. 1. Overlapped n+ and p+ diffusions in a CMOS p-well (vertical scale exaggerated for clarity). The oxide thickness over the n+ is 75 nm; over the p+, it is 50 nm.

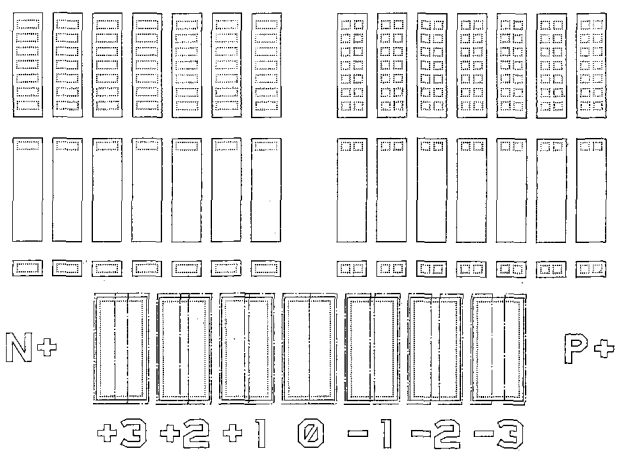

Fig. 2. N+/p+ diffusion overlap test structures. Solid lines designate islands; dotted lines are contacts; dot-dash lines are diffusions, as labeled. Diffusions are shown only on the bottom row for clarity; cross sections are similar to Fig. 1.

* Electrochemical Society Active Member.
Key words: glass, integrated circuits, photoelectricity, kinetics.

lap. If there is any overlap of the diffusions, the n+ oxide will not be removed. When an oxidant, such as oxalic acid, is added to the etchant, then diffusions that overlap only slightly will also clear uniformly in ambient light. When the same arrays are etched in total darkness with no oxidant in the etchant, the oxide is removed uniformly over both n+ and p+ silicon regardless of the diffusion overlap.

If the cross-sectional area of the hole being etched in the ambient light is small (10-40 μm^2), the n+ oxide appears highly colored. If the hole is larger (up to 1000 μm^2), a slight coloration may or may not be visible. In all cases, however, an insoluble film is present on the outer surface of the oxide, as shown in Fig. 3. The amount of coloration depends on the position of the hole with respect to the n+ diffusion and the amount of diffusion area attached to it. The pattern and degree of coloration are precisely that of the E-field that would exist if the n+ and p+ diffusions were being held at different potentials.

Samples were prepared for potentiostat experiments by growing 100 nm of oxide on n<100> silicon wafers, $\rho = 5\ \Omega$-cm, in a steam ambient. After a 1000°C, 30 min anneal in nitrogen, the wafers were diced and attached to IC lead frames. A wire was attached to the lead frame, and the samples were sealed in an electrically insulating plastic, leaving only the oxidized front surface exposed. The samples were then mounted on Plexiglas supports with epoxy.

The potentiostat samples were etched in a buffered HF solution (10.3M NH_4F, 1.2M HF) under an applied potential for 300 sec. The potential was maintained with respect to an Ag|AgF reference electrode using an EG&G Model 173 Potentiostat/Galvanostat. After the 300 sec etch, the residual oxide thickness measurements were obtained by using a Nanospec/AFT system. To obtain repeatable measurements, a 10 sec polysilicon etch (4) was necessary to remove the HF-insoluble layer. These results are shown in Fig. 4. Samples with no applied potential were found to etch completely in 180 sec, indicating an etch rate of 0.56 nm/sec. This etch rate did not change when the etchant was allowed to contact the back-side of the silicon substrate during the etch of samples with no applied potential.

The current required to maintain the applied potential on the samples was stable initially at approximately 5 nA. At 180 sec of etch time, the current rose sharply from the initial level to a second stable level which depended on the applied potential. This second current level is shown as a function of the applied potential in Fig. 5. The current seems to be limited by ionic transport between −1 and −2V, and surface limited at voltages more negative than this.

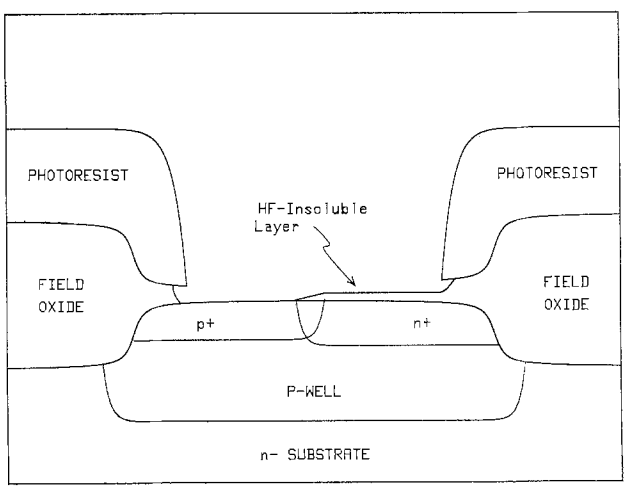

Fig. 3. Structure of Fig. 1 after etch in ambient yellow light

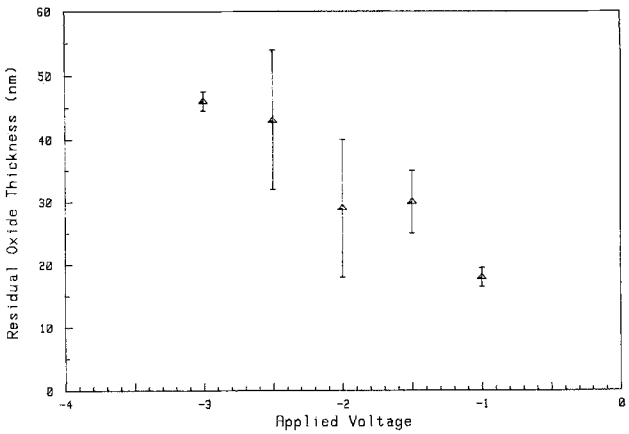

Fig. 4. Residual oxide thickness on potentiostat samples as a function of applied voltage.

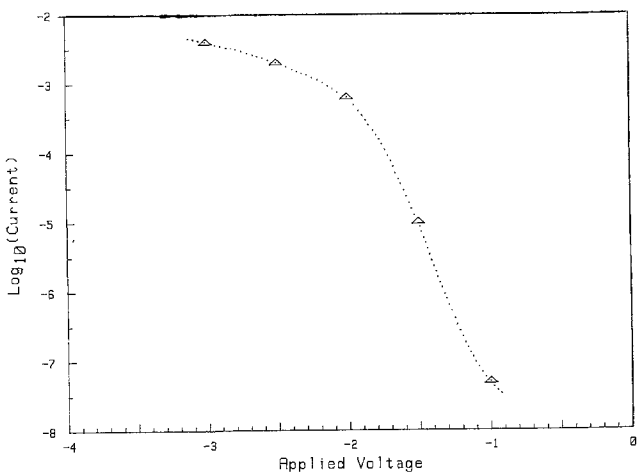

Fig. 5. Current required after 180 sec of etching to sustain a potentiostatic condition as a function of desired potential (Si with respect to AgF|Ag). Area of samples was constant at approximately 10 mm^2.

Auger and SEM analyses were performed on integrated circuit samples topologically similar to Fig. 6 directly after etching in ambient light. An overall line scan of the surface along line A of Fig. 6, after 5 nm of sputtering to remove contamination, is shown in Fig. 7. Note the sharp drop in the Si-O signal inside the contact hole even though the oxygen signal is not negligible over the n+ half of the contact. Figure 8 demonstrates the intermediate nature of the silicon peak found in the Pt 1 region (see Fig. 6). Pt 2 may be considered to represent an Si-Si bond, with Pt 3 an Si-O bond as in SiO_2. An Auger sputter profile of Pt 1, calibrated to SiO_2 yields a layer thickness of about 45 nm, in good agreement with the 40 ± 5 nm Nanospec readings obtained after removal of the HF-insoluble layer.

Discussion

The environmental lighting experiments show that the etch stopping effect occurs when photons with wavelengths longer than that of blue visible light are present. Changing the junction structure to allow a larger depletion region (more efficient photon absorption) enhances the effect, suggesting that the p+ and n+ diffusions are photocharged causing an electric field across the oxide. The potentiostat experiments, summarized in Fig. 4, show that an E-field across the oxide is capable of stopping the etch.

Referring to Fig. 1, note that the n+ oxide is thicker than the p+ oxide by about 15 nm. If both oxides etch at approximately the same rate, the p+ silicon will be in direct contact with the solution while 15 nm of ox-

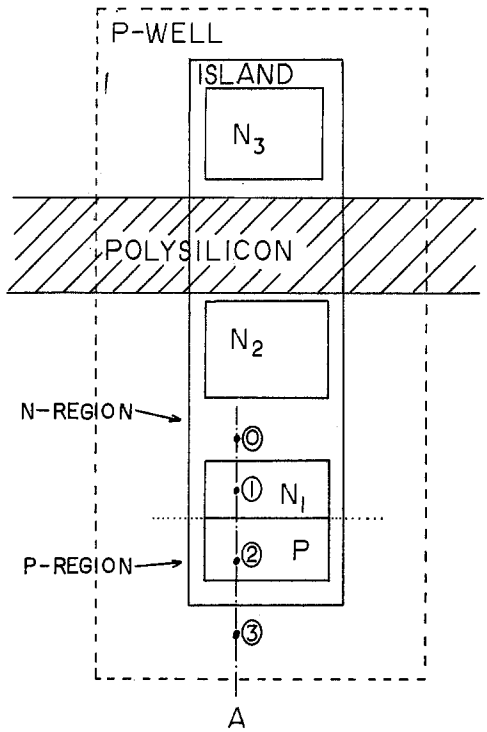

Fig. 6. Portion of CMOS IC used for Auger line scan and depth profiling. (Cross section similar to Fig. 1.) Under standard etching conditions, P clears; N1 does not clear; N2 may not clear; N3 does clear.

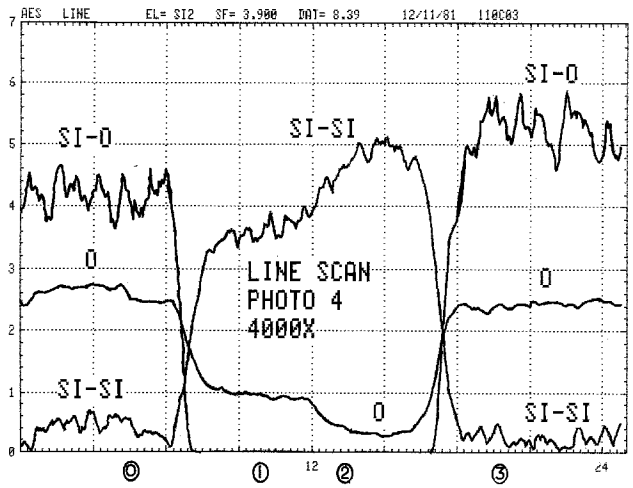

Fig. 7. Auger line scan along line A of Fig. 6

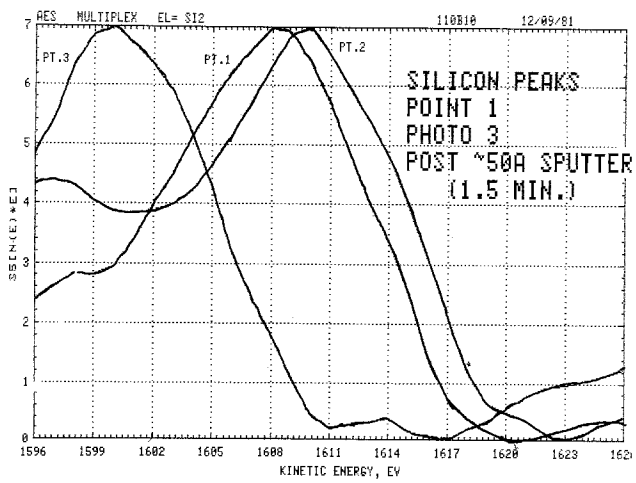

Fig. 8. Auger energy spectra from points 1, 2, and 3 of Fig. 6

ide remains over the n+ silicon. (The doping levels in the oxides are low enough that they do not affect the oxide etch rates). If there is a photoinduced potential difference between the p+ and n+ diffusions, a similar potential will appear across the n+ oxide when the p+ side clears. The E-field from the charged junctions may also impede the etching of the oxide over the n+ silicon before the p+ side clears. From Fig. 4, a potential difference of 0.5V is sufficient to stop the etching of SiO_2 at 10-15 nm. As long as this potential difference exists, no amount of overetch will clear the n+ oxide. The apparent thickness by Auger and Nanospec readings on actual contact holes of 40 nm are significantly greater than the 10-15 nm Nanospec readings on potentiostat samples from Fig. 4. The actual contact holes were etched for 150 sec while the potentiostat samples were etched for 300 sec. It is possible that the contact holes, if etched for 300 sec, would have oxide thicknesses nearer 15 nm. While this measurement was not made, it is known that no amount of overetch will completely clear the n+ side of the contact hole.

It is believed from the Auger analysis that the HF-insoluble layer formed on the outer surface of the oxide is a thin layer of partially reduced SiO_2 (SiO_x, where $x < 2$). Oxides such as this are believed to be insoluble in HF solutions unless an oxidant, such as HNO_3, is present (2). The observed films are soluble in HF/NHO_3 solutions. This identification of the insoluble layer is further supported by the results of the oxalic acid addition to the etchant. Slightly overlapped junctions, which have smaller depletion regions and subsequently smaller charging, clear uniformly in ambient light with oxalic acid in the etchant. The same junction structures do not clear in ambient light without the oxalic acid.

Mechanisms

The mechanism for SiO_2 dissolution in HF solutions is not known entirely. Bridging oxygen bonds are probably converted to silanol bonds which are then replaced by Si-F bonds, but the reactive species and mechanistic steps have not been isolated to our knowledge. The etch rate is not a strong function of the F^- concentration (5), but F^- may be indirectly involved in preventing the precipitation of silicon compounds from the solution. For solutions up to 10M in HF, this leaves HF_2^- and HF as the only appreciable fluoride species. Above 10M HF, more complicated H-F complexes have been implicated in the dissolution process (5).

For 1M ionic strength HF solutions, the etch rate is a linear function of the HF_2^- and HF molar concentrations (5)

$$\text{Etch rate (Å/sec)} = 9.66[HF_2^-] + 2.50[HF] - 0.14 \quad (23°C) \quad [2]$$

Equation [2] implies at least two parallel reaction paths where either reactive species can replace an Si-OH bond with an Si-F bond, as depicted in Fig. 9a. Silanol formation is not considered by this model. Silanol bond formation is most probably due to reaction of a bridging oxygen with H_2O or H^+, but the parallel reaction of HF with a bridging oxygen gives a silanol bond on one silicon and fluorinates the other (Fig. 9b). Thus, HF appears to have a dual function, reacting with either Si-OH bonds or bridging oxygens. Lowering the pH increases the HF concentration and probably enhances its action as a direct fluorinating agent.

The overall reaction given in Eq. [1] does not require either reduction or oxidation of silicon. However, the creation of the insoluble layer in all of the experiments performed suggests that the normal dissolution process involves steps that approach reduction of the

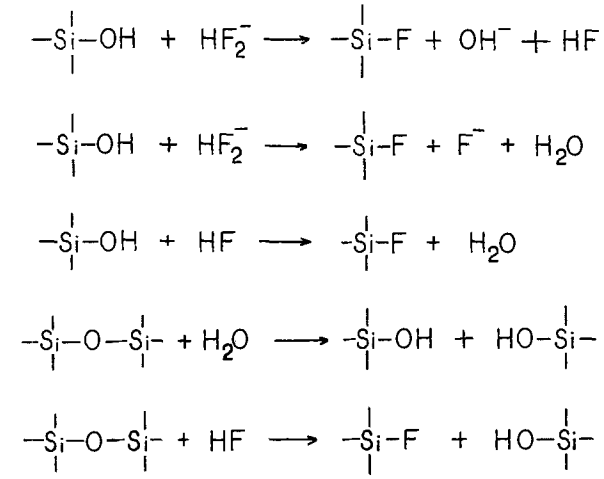

Fig. 9. (a, top) Reactions fluorinating silanol bonds by HF_2^- and HF. (b, bottom) Reactions creating silanols and silicon fluoride from bridging oxygen bonds in silicon dioxide.

SiO_2. The presence of an electric field then shifts the local chemical potential so that reduction is favored.

The dissolution of SiO_2 can be mechanistically modeled using only HF_2^- ions as in Fig. 10a. An alternative model using only HF is shown in Fig. 10b. Due to the similarity in the intermediate silicon structures, numerous combinations of the two distinct paths are possible, such as in Fig. 10c. The sum of all the possible combinations with the different rate constants for HF_2^- and HF at each step reduces to an expression for the etch rate of the form given in Eq. [2].

The insoluble layer formation can occur in the presence of an electric field from the initial steps of any

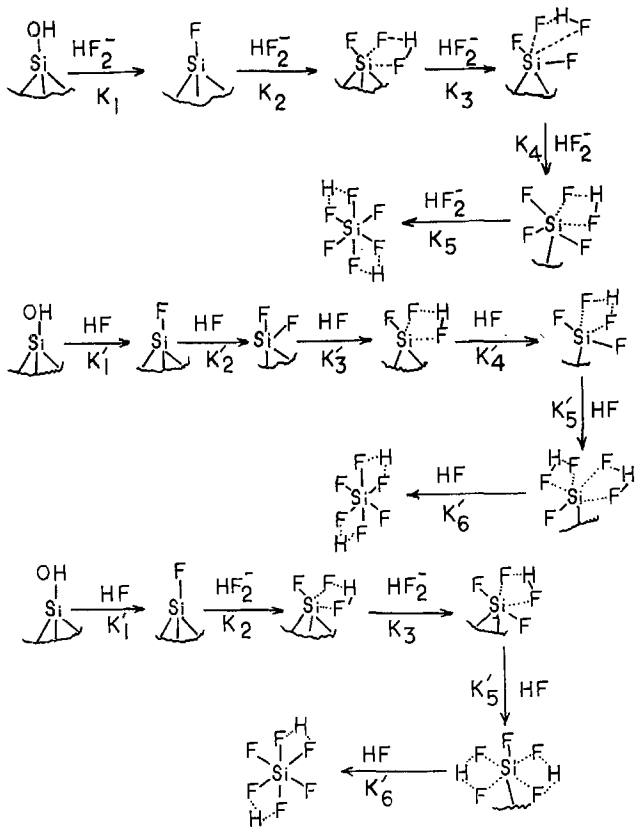

Fig. 10. (a, top) A dissolution model for SiO_2 employing only HF_2^-. (b, middle) A dissolution model for SiO_2 employing only HF. (c, bottom) A dissolution model for SiO_2 employing both HF and HF_2^-.

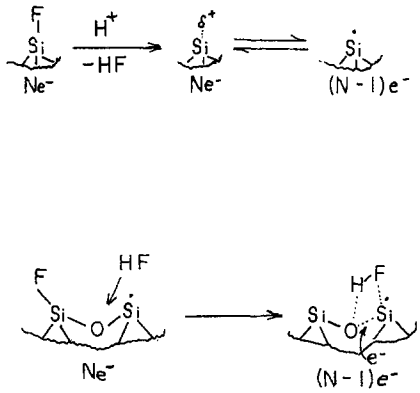

Fig. 11. (a, top) Reduction of a surface Si atom by H^+. (b, bottom) Formation of an Si—Si surface bond.

of the pathways shown in Fig. 10. Figure 11a shows the formation of a reduced Si surface atom, and Fig. 11b shows the formation of an Si-Si surface bond. The Auger energy scan of Fig. 8 suggests the surface region of the insoluble layer has bonds with an energy greater than a standard Si-Si but less than Si-O, which is consistent with the structure shown in Fig. 11b. Si-Si double bonds have been reported (6), but the expected energy in the Auger spectra would be closer to an Si-O bond than an Si-Si single bond. Also, the surface would need to reorganize substantially to allow silicon double bonds because one bridging oxygen would need to be removed from each of the participating silicons. This suggests the surface reduction as the more likely event. The reduction of the silicon surface below valence 4 could occur in a manner similar to the alleged behavior of silicon monoxide, a mixture of Si(O) and Si(IV). The only other explanation is that the silicon actually is in a reduced state, an unexpected, but nonexcludable possibility.

Conclusion

The dissolution of SiO_2 in HF solutions can be stopped by the application of an electric field across the SiO_2. The field strength required is small enough to be generated in shallow-junction CMOSC circuits through photon absorption. In some CMOS structures, it is possible to generate an HF-insoluble layer at the SiO_2|solution interface. This layer is most probably a film of partially reduced SiO and is soluble in HF/HNO_3 solutions.

Acknowledgments

The authors wish to thank Marzio Leban for useful discussions and help with the electrochemical system apparatus, and Ellen Tappon for SEM and Auger analysis.

Manuscript submitted Jan. 25, 1982; revised manuscript received Aug. 17, 1982.

Any discussion of this paper will appear in a Discussion Section to be published in the December 1983 JOURNAL. All discussions for the December 1983 Discussion Section should be submitted by Aug. 1, 1983.

Publication costs of this article were assisted by the Hewlett-Packard Company.

REFERENCES

1. G. Parisi, S. Haszko, and G. Rozgonyi, *This Journal*, **124**, 917 (1977).
2. W. Kern, in "Proc. Symp. Etching for Pattern Definitions," H. G. Hughes and M. J. Rand, Editors, pp. 1-18, The Electrochemical Society, Princeton, NJ (1976).
3. F. Schwettman, R. Dexter, and D. Cole, *This Journal*, **120**, 1566 (1973).

4. 200:80:1 by volume, Reagent grade HOAc:HNO_3:HF.
5. J. Judge, in "Proc. Symp. Etching for Pattern Definitions," H. G. Hughes and M. J. Rand, Editors, pp. 19-36, The Electrochemical Society, Princeton, NJ (1976).
6. R. West, M. Fink, and J. Michl, *Science*, **214**, 1343 (1981).

Amorphous Silicon Photovoltaic Modules

Y. Uchida, H. Sakai, N. Furusho, M. Nishiura, and H. Haruki

Fuji Electric Corporate Research and Development Limited, 2-2-1, Nagasaka, Yokosuka 240-01, Japan

ABSTRACT

In hydrogenated amorphous silicon solar cells of 100 cm^2, the conversion efficiency of more than 6% has been obtained for the cells with metal/n-i-p/ITO/glass and ITO/n-i-p/SS structures under AM1 (100 mW/cm^2) illumination. The module structure and encapsulating materials suitable for a-Si solar cell were investigated to make a low cost module. Typical output power under AM1 illumination is 16W for the module composed of 40 sheets of ITO/n-i-p/SS cells with 10×10 cm^2 area. The a-Si modules have been tested in various environments. The results show that the a-Si solar cells are highly resistive to high and low temperature, high humidity environments, and thermomechanical stress.

Hydrogenated amorphous silicon (a-Si:H) produced by glow discharge decomposition of silane has been shown to possess desirable properties for thin film solar cell (1). Because of the excellent photoconductive property and the high optical absorption coefficient of a-Si:H over the visible region of the solar spectrum, an efficient solar cell can be constructed with a 1 μm thick a-Si:H film. Amorphous silicon shows economical advantage in cell fabrication processes over conventional crystalline solar cells: lower growth temperature, capability of forming junction during the deposition process, and the easy production of large area cells.

Most of the previously reported discussions on the structure and performance of a-Si:H solar cell were concerned with small area cells (2). From a practical point of view, our efforts have been concentrated on the development of large area a-Si:H solar cell (3). We have developed a series of a-Si:H solar cells for consumer electronics like hand-held calculators, and put them on the market for the first time, in the summer of 1980 (4). For practical application of the cell to photovoltaic power generation, the cell performance under the sunlight must be further improved. In a-Si:H solar cells the conversion efficiency measured under the sunlight depends on the cell area, and decreases with increasing cell area (5). We have studied the causes of this cell area dependence of the cell performance, and have found that the conversion efficiency degradation is caused mainly by series resistance in the electrodes (6, 7). By employing these results, we have improved the performances of a-Si:H solar cells, prepared on stainless steel and glass substrates with an area of 100 cm^2, as a part of this work. Prior to applying the a-Si:H solar cell to practical power generation, the optimum module structure and encapsulating material must be developed to make a low cost module. The cell performance should be reasonably retained when the a-Si:H solar cell is assembled into a module. Furthermore, the module should stand for long-term use. We reported the module composed of 36 sheets of 7×7 cm^2 area a-Si:H solar cells, and a solar cell array which consisted of 108 pieces of the modules (4). These modules had the conventional glass/silicone/metal plate structure.

In this paper, we present a-Si photovoltaic modules with simpler structure. This paper also describes the environmental test results of the a-Si:H solar cells, encapsulating materials, and the photovoltaic modules.

Performance of Large-Area a-Si:H Solar Cell

The structures of a-Si:H solar cells discussed in this study include ITO/p-i-n/stainless steel (SS), ITO/n-i-p/SS, and metal/n-i-p/ITO/glass. The a-Si:H was prepared by glow discharge decomposition of silane in capacity coupled rf systems. The window-side a-Si:H layer is p-type in ITO/p-i-n/SS cell and n-type in ITO/n-i-p/SS cell. A 500Å thick phosphorous (or boron)-doped a-Si:H layer was deposited on an SS-substrate at first. Then 0.5 μm thick undoped a-Si:H layer and a 100Å thick boron (or phosphorous)-doped a-Si:H layer were successively deposited. Finally, a transparent conductive ITO film and metal grid electrodes were formed. In metal/n-i-p/ITO/glass cell, a 100Å thick boron-doped a-Si:H layer was deposited on a glass plate coated with a transparent conductive ITO film. Then 0.5 μm thick undoped and a 500Å thick phosphorous-doped a-Si:H layer were successively deposited. And finally metal film back-contact electrodes were formed. This type of solar cell was illuminated through glass-substrate. Since the excellent window-effect of a-SiC:H was reported by Tawada *et al.* for small-area cells (8), we have applied a-SiC:H film to a window-side layer in the large-area glass-substrate cell.

For practical application of the a-Si solar cell, enlargement of cell area without conversion efficiency degradation is required. However, the short-circuit current (*Jsc*) and the fill factor (*FF*) tend to decrease with increasing cell area. We proposed a method for analyzing the cell area dependence of *Jsc* and *FF* in the SS-substrate a-Si solar cell, and reported the results for a 7×7 cm^2 cell (6). By applying this technique, we have estimated degradation in the performance of the ITO/n-i-p/SS cell associated with the increase of cell area from 1.2 to 100 cm^2. The estimation has been done on a 100 cm^2 cell [Fig. 1(a)] in which the sheet resistance of ITO film is 50 $\Omega/\square$, and the grid electrodes are formed by 1.0 μm thick Ti-Ag layer of which resistivity is 2×10^{-6} Ω-cm. Table I summarizes the cell performances for the 1.2 and 100 cm^2 cells, and the factors influencing the cell area dependence of *Jsc* and *FF*. According to the results shown in Table I, half the decrease in *FF* associated with the increase in cell area from 1.2 to 100 cm^2 is caused by a series resistance, which consists of resistances of the grid electrodes and ITO. About 80, 10, and 10% of the decrease are caused by the power losses due to the series resistances in the stem and branch parts of grid electrodes, and the ITO film, respectively. About one third of *FF* degradation is caused by a contact resistance at the ITO and metal interface, and 10% is due to shunt resistance of the solar cell, which was measured as 40Ω from dark current-voltage characteristics. The rest (10%) is caused by an inhomogeneity of a-Si layer. Therefore, suppressing the series resistance offers an effective measure for improving *FF*.

Key words: amorphous semiconductor, solar cell, reliability.

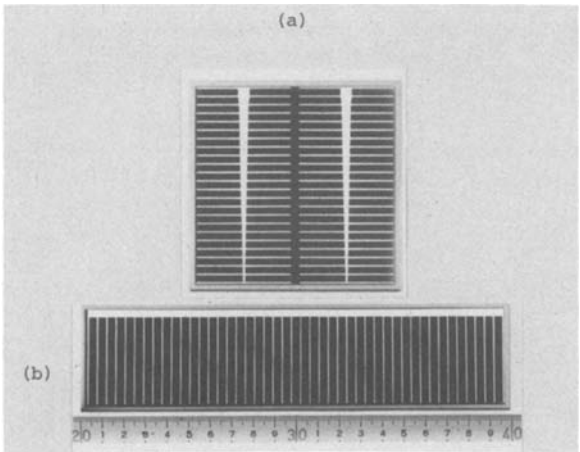

Fig. 1. Grid electrode configurations of two types SS-substrate solar cells with 100 cm² area.

Figure 2 shows *FF* in the 100 cm² cell as a function of grid electrode thickness calculated by considering a cell configuration shown in Fig. 1(a). By doubling the thickness of grid electrodes from 1 to 2 μm, we will be able to obtain 0.58 as the value of *FF* in type (a). However, Fig. 2 shows that the thickness of grid electrodes must be increased to over 10 μm in order to improve *FF* to more than 0.60. We designed and prepared another type of 100 cm² cell shown in Fig. 1(b).

For electrical interconnections of this type of cells, pieces of metal ribbons or wires can be soldered on any part of the stem without shadowing the active area of the cell, to make power loss in the stem part of grid electrodes negligible. In such cell, *FF* of 0.60 is expected.

The similar calcualtion was conducted in the design of a metal/n-i-p/ITO/glass cell in which unit cells formed on a glass-substrate are connected in series on the same substrate. The key parameters to determine the *FF* of such a cell include the length of a unit cell and the sheet resistances of ITO and metal electrodes. The power loss in ITO and metal electrodes is shown in Fig. 3. The power loss was calculated as a function of photogenerated current, with respect to the length *L* of the unit cell, indicated in the inset of Fig. 3. The sheet resistances of the metal and the ITO film were assumed to be 0.05 and 10 Ω/□, respectively. We found that the length of the unit cell should be limited within 15 mm to retain the *FF* degradation within 10% of the ideal *FF*, when the sheet resistance of a transparent conductive film is 10 Ω/□. The power loss decreases with decreasing *L*, while the active area of the solar cell decreases. To use more than 80% of the substrate area as an active area, *L* should be more than 7 mm. Two types of a-Si solar cells on glass-substrate shown in Fig. 4 were fabricated. In Fig. 4(a), 10 cells formed on a glass-substrate of 10 × 10 cm² were connected in series, and in Fig. 4(b), 6 cells formed on a glass-substrate of 11 × 12 cm² were connected in series.

Table I. Factors influencing the cell area dependence of short-circuit current (*Jsc*) and fill factor (*FF*) for ITO/n-i-p/SS solar cell

Cell area	FF	*Jsc* (mA/cm²)
1.2 cm²	0.659	11.2
100 cm²	0.549	10.6
Difference	0.110	0.6
Contribution to *FF* and *Jsc* lowering		
Shunt resistance	10%	
Series resistance	50%	
Inhomogeneity	10%	100%
Contact resistance	30%	

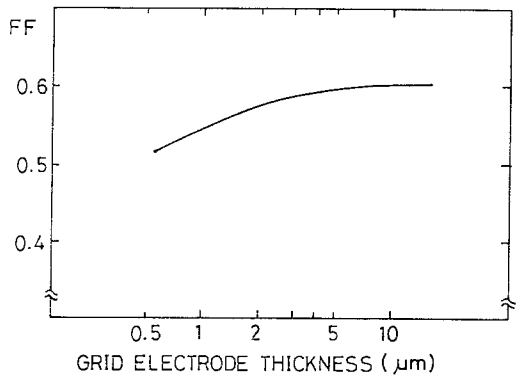

Fig. 2 Grid electrode thickness dependence of fill factor (*FF*) in a 100 cm² area cell [Fig. 1(a)]. In the calculation, the resistivity of the grid electrode is assumed to be 2 × 10^{-6} Ω-cm.

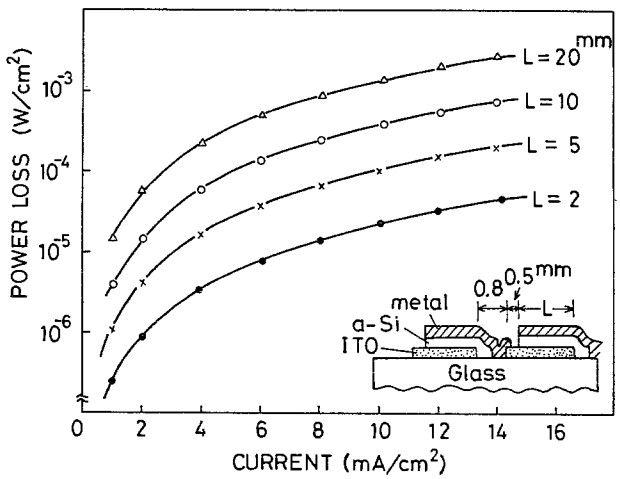

Fig. 3. Power loss *vs.* generated current with respect to the length of the unit cell (*L*) of a metal/n-i-p/ITO/glass cell.

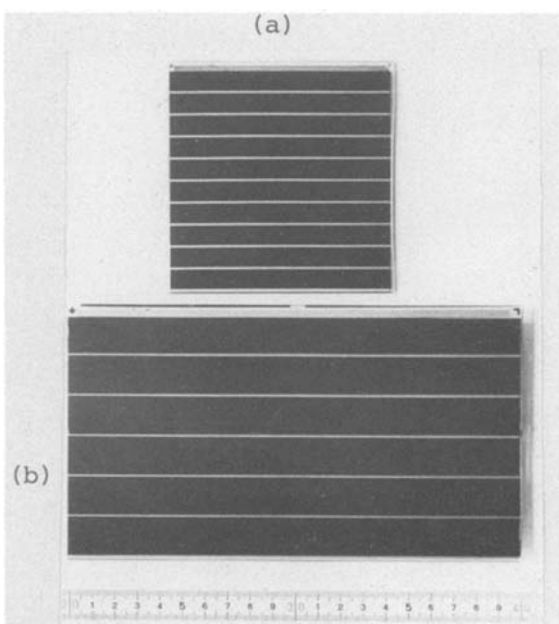

Fig. 4. Two types of glass-substrate cells: (a) 10 series connected cell with 10 × 10 cm² area, (b) 6 series connected cell with 11 × 20 cm² area.

Output characteristics of large area a-Si solar cells on SS- and glass-substrates are summarized in Table II. The *Jsc* and the conversion efficiency η in Table II

Table II. Output characteristics of large area solar cells under AM1 (100 mW/cm²) illumination

Cell structure	Cell area (cm²)	Voc (V)	Jsc (mA/cm²)	FF	η (%)
ITO/n-i-p/SS	10 × 10 (a)	0.88	11.4	0.58	5.8
	5 × 20 (b)	0.86	11.8	0.60	6.0
Metal/n-i-p/ITO/glass	10 × 10 (a)	8.5	12.3	0.59	6.2
	11 × 20 (b)	5.28	12.7	0.54	6.0

are active area values. The solar cell on SS-substrate shown in Fig. 1(a), in which the grid electrodes were 2 μm in thickness, gives the conversion efficiency of 5.8% and *FF* of 0.58. In the 5 × 20 cm² solar cell [(b) in Fig. 1], conversion efficiency of 6.0% was obtained. The *FF* for this cell was 0.60. These observed *FF*'s show fair agreement with the expected values proposed in the foregoing section.

The conversion efficiency of 6.2% was obtained in the a-Si solar cell formed on a 100 cm² glass-substrate [(a) in Fig. 4]. For larger solar cells, conversion efficiency of 6.0% has been obtained in an 11 × 20 cm² cell [(b) in Fig. 4]. The *FF* of the former cell is 0.59, and that of the latter cell is 0.54. This difference in *FF* between the 100 cm² cell ($L = 8$ mm) and the 11 × 20 cm² cell ($L = 15$ mm) is due to the difference in the unit cell length L as discussed above.

Photovoltaic Module for Power Application

The a-Si photovoltaic cells can be made on several kinds of substrate, such as metal, glass, and polymer film. Module structure should be chosen by considering the substrate used. We have conducted an investigation on module fabrication process for SS-substrate cells and glass-substrate cells.

For SS-substrate cells, semitempered soda-lime glass plate, silicone resin, and polyvinyl fluoride (PVF) film were used for a front cover, encapsulant, and a back cover, respectively. Figure 5 shows the module composed of 40 cells with 10 × 10 cm² area. These 40 cells were wired in 4 parallel strings of 10 cells wired in series.

When SS-substrate cells are assembled into a module, they show a definite advantage over other photovoltaic cells, because SS-substrate cells are resistive against mechanical shock, such as striking of hail or small stones. Another advantage is that positive and negative electrodes can be made on the same plane of substrate, as shown in Fig. 6. This cell structure makes wiring process easy. In order to make a low cost module, we will examine possibilities to replace the semitempered glass plate for a front cover by thin polymer film in the near future.

There is another possibility to make a low cost module with a glass-substrate cell. Since electrically separated unit cells are connected in series on a glass-substrate, high output voltage can be obtained from a glass-substrate cell. Moreover, the substrate glass plate may also play as the front cover of a module. Therefore, we proposed the "single substrate module," which is composed of a large area glass-substrate cell with resin coating and a metal or plastic frame, as schematically shown in Fig. 7(a). Figure 7(b) shows the prototype of the "single substrate module" with a 15 × 22 cm² glass-substrate cell.

We have tested applicabilities of various materials to front cover, encapsulant, and back cover. Table III shows the change in transparency of several candidate materials for encapsulant, under environmental test conditions. Two types of specimens, glass/polymer/glass(type 1), and PVB film/polymer/glass(type 2), were used for the test. After heat-treatment at 80°C for 500 hr, silicone resin, polyvinyl butyral (PVB), and ethylene vinylacetate copolymer (EVA) showed little change in transparancy, even when they were employed for the type 1 specimen. Under high humidity condition at 60°C, 95% RH for 500 hr, silicone resin and PVB showed little change in transparency when they were employed for the type 1 specimen. However, when the type 2 specimen was tested, PVB became opaque. In heat shock test (high temperature condition 80°C, 1 hr: low temperature condition −20°C, 1 hr: 10 cycles), unsaturated polyester resins showed severe change in their appearance, but the other materials shown in Table III showed no change. From the above

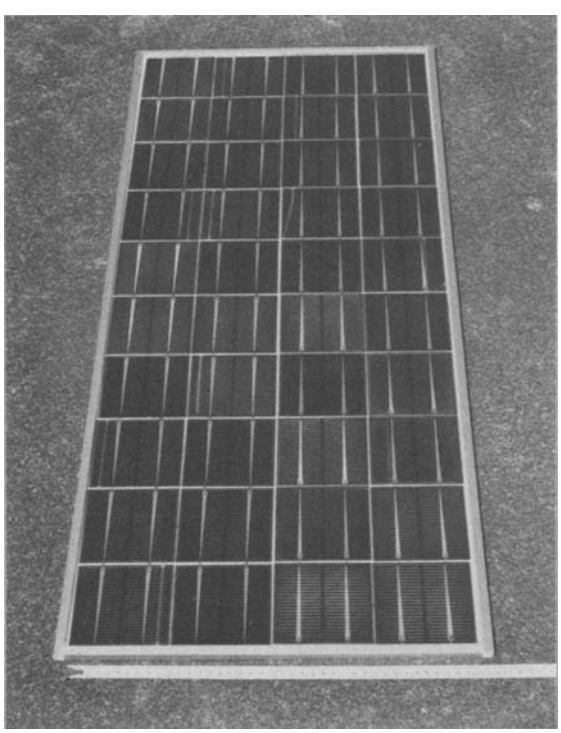

Fig. 5. a-Si photovoltaic module composed of 40 pieces of 10 × 10 cm² SS-substrate cells.

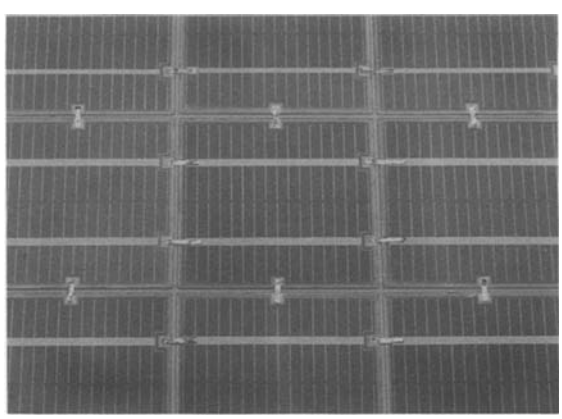

Fig. 6. SS-substrate cells connected with the same plane of each substrate.

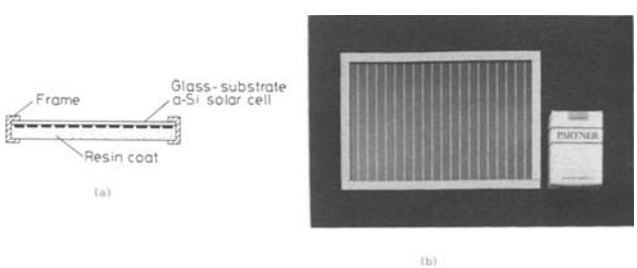

Fig. 7. Schematics of "single substrate module" (a) and the prototype with a 15 × 22 cm² glass-substrate cell (b).

Table III. Change in transparency of several materials under the environmental tests

Test condition	High temperature 80°C, 500 hr		High humidity 60°C, 95% RH, 500 hr	
Specimen construction	Type 1	Type 2	Type 1	Type 2
Silicone resin	96	94	97	97
PVB	100	95	100	80
EVA	98	98	—	—
Epoxy resin	94	85	91	89
Unsaturated polyester resin	87	80	90	90

results, it has been found that encapsulating materials are much affected by water vapor permeation, oxygen permeation, and mechanical stress in their life. Therefore, at selecting encapsulating materials, module structure should be considered at the same time.

To obtain maximum output power of photovoltaic module from incident solar energy, transparency of a front cover and reflection at a module surface are key parameters. As a front cover, semitempered soda-lime glass plate was found to be usable instead of semitempered low iron glass plate, which is generally used in single crystalline Si photovoltaic module, because the wavelength of the maximum sensitivity of a-Si photovoltaic cells lies near 550 nm, which is in the lowest optical loss region for soda-lime glass.

In order to reduce the reflection at the module surface, the wavelength dependence of surface reflectance was measured on an air/ITO/n-i-p/SS cell, and a glass/silicone resin/ITO/n-i-p/SS module. The wavelength for the minimum reflectance depends on ITO film thickness. The thickness which obtains the minimum reflectance at the wavelength of 550 nm is 750Å. Figure 8 shows reflectance of the cell and module when the thickness of ITO film is 750Å. The surface reflectance of the cell at 550 nm (curve a) is about 5%, and increases to 18% by impregnating a silicone resin between a semitempered glass plate cover and the cell (curve b). Thus, the conversion efficiency of SS-substrate cells decreases by about 10% when they are assembled into a module.

The output characteristics of the modules composed of 40 cells of 10 × 10 cm² have been measured with a large area solar simulator. Typical electric output power under AM1 (100 mW/cm²) illumination is 12 and 16W, for the modules using ITO/p-i-n/SS and ITO/n-i-p/SS cells, respectively. Figure 9 shows the typical output characteristics of the latter module.

Reliability of a-Si:H Solar Cell

An a-Si solar cell is composed of several layers with different thermal expansion coefficients, and also subjected to various temperatures in wiring, encapsulating, and servicing. Thermomechanical stress due to

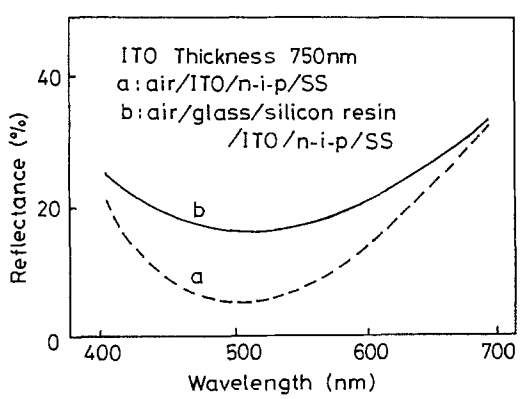

Fig. 8. Surface reflectance of SS-substrate cell (a) and module (b).

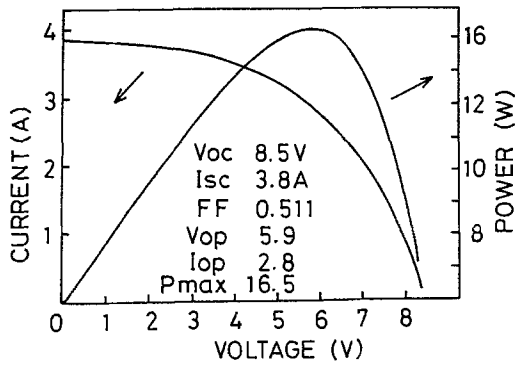

Fig. 9. Output characteristics of the module composed of 40 cells with 10 × 10 cm².

these temperature changes must affect the cell characteristics. To evaluate this effect, a heat cycle test was conducted on SS-substrate (0.5 mm thick) cells of 10 × 10 cm².

The cell performance before and after 10 heat cycles did not show any noticeable difference, as shown in Table IV. The cell appearance also showed no change under the usual test conditions. Only a bit of peeling-off in the a-Si:H film was observed after 10 cycles, under the unusually severe test condition (−200°C ↔ 200°C). In the bending test (center load up to 5 kg, two end supports), no crack and peeling-off in the a-Si film occurred, and the cells have retained their original performance.

Reliability tests for the modules composed of 36 sheets of ITO/p-i-n/SS cells with 7 × 7 cm² area were carried out under conditions listed in Table V. No change in the output characteristics and the appearance of modules was found, not only in the heat cycle test, but also in other tests listed in the Table.

A slight decrease in the conversion efficiency was found under continuous illumination of AM1 spectrum (100-1000 mW/cm²). Figure 10 shows the results under continuous illuminations of various light intensity. After 240 hr of illumination, the conversion efficiency

Table IV. Cell characteristics and appearance before and after heat cycle test for SS-substrate cells

Test condition	Cell characteristics: Initial	Cell characteristics: After 10 cycles	Appearance
100°C 30 min ↑ (1 min) −40°C 30 min	100	102	No change
200°C 30 min ↑ (1 min) −40°C 30 min	100	110	No change
200°C 30 min ↑ (1 min) −75°C 30 min	100	100	No change
200°C 30 min ↑ (1 min) −200°C 30 min	100	96	A bit of peeling

Table V. Reliability test conditions for the modules with glass/silicone/PVB film configuration

Tests	Present test level
Humidity cycling	80°C, 95% RH, −20°C, 10 cycles
Heat cycle	−20°C ↔ 80°C (50°C/hr), 50 cycles
Voltage loading	AC 2000V, 1 min
Cyclic pressure loading	Positive + 150 kg/m² + 300 kg/m², 2 sec interval, 1800 cycles Negative − 150 kg/m² − 300 kg/m², 2 sec interval, 1800 cycles
High humidity	70°C, 95% RH, 2000 hr
High temperature	80°C, 1000 hr
Cold temperature	−40°C, 1000 hr
Salt spray	5% NaCl solution, 35°C, 500 hr

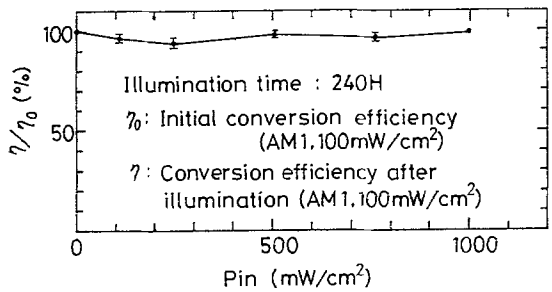

Fig. 10. Conversion efficiency of modules (ITO/p-i-n/SS) after 240 hr continuous illumination normalized by the initial value. The axis of abscissa is the incident power density of the continuous illumination.

of the module remained above 90% of the initial value η_0 under all the applied illuminances.

Conclusion

A considerable progress has been achieved in cell performances of large area a-Si:H solar cells. In the ITO/n-i-p/SS cell, the grid electrode configuration was designed by considering reduction of power loss, and consequently the conversion efficiency of 6.0% has been obtained for the 100 cm^2 cell. Intending to reduce the power loss and keep the active area of the cell above 80% of the substrate, we have fabricated 100 cm^2 cell in which 10 cells were connected in series, and obtained conversion efficiency of 6.2%.

The module structure for the a-Si solar cell was studied. By assembling 40 pieces of 100 cm^2 SS-substrate cells, we fabricated a-Si photovoltaic modules with glass/silicone/PVB film configuration. Typical output powers of the modules under AM1 illumination are 12 and 16W for ITO/p-i-n/SS and ITO/n-i-p/SS cells, respectively. We proposed the "single substrate module" and demonstrated the prototype with a 15 × 22 cm^2 glass-substrate cell.

The a-Si modules composed of SS-substrate cells have been tested under various conditions, including temperature, heat cycle, humidity, and bending load. The results show that the a-Si solar cells are highly resistive to high temperature, low temperature, high humidity environments, and thermomechanical stress. The remaining problem is the slight decrease in the conversion efficiency under continuous illumination of the sunlight.

Acknowledgment

The authors are grateful to Dr. A. Shimazaki, Dr. S. Fushimi, and Dr. H. Fujino for their helpful advice. This work was supported by the Agency of Industrial Science and Technology under the contract of the Sunshine Project.

Manuscript submitted June 17, 1982; revised manuscript received Oct. 15, 1982. This was Paper 44 presented at the Montreal, Que., Canada, Meeting of the Society, May 9-14, 1982.

Any discussion of this paper will appear in a Discussion Section to be published in the December 1983 JOURNAL. All discussions for the December 1983 Discussion Section should be submitted by Aug. 1, 1983.

Publication costs of this article were assisted by Fuji Electric Corporation.

REFERENCES

1. D. E. Carlson and C. R. Wronski, *Appl. Phys. Lett.*, **28**, 671 (1976).
2. D. E. Carlson, *Sol. Energy Mater.*, **3**, 503 (1980).
3. Y. Uchida, H. Sakai, and M. Nishiura, *Jpn. J. Appl. Phys.*, **20**, Suppl. 20-2, 191 (1981).
4. Y. Uchida, H. Sakai, T. Ichimura, M. Nishiura, and H. Haruki, *Fuji Electric Rev.*, **27**, 34 (1981).
5. Y. Uchida, H. Sakai, M. Nishiura, M. Miyagi, and K. Maruyama, Proc. 8th Int. Vacuum Congress, p. 699, Cannes, 1980.
6. Y. Uchida, H. Sakai, M. Nishiura, and H. Haruki, Conf. Rec. 15th IEEE Photovoltaic Specialists Conf., p. 922, Florida, 1981.
7. H. Haruki, Y. Uchida, H. Sakai, M. Nishiura, and M. Kamiyama, *Jpn. J. Appl. Phys.*, **21**, Suppl. 21-1, 283 (1982).
8. Y. Tawada, M. Kondo, H. Okamoto, and Y. Hamakawa, *J. Phys. (Paris)*, **42**, Suppl. 10, C4-471 (1981).

Technical Note

Incidence Angle Dependence of Planar Channeling in Boron Ion Implantation into Silicon

Masayasu Miyake, Masahiro Yoshizawa, and Hiroyuki Harada

Nippon Telegraph and Telephone Public Corporation, Musashino Electrical Communication Laboratory, Musashino, Tokyo, 180 Japan

Ion implantation has been widely used in LSI fabrication process due to its superiority in impurity concentration controllability and reproducibility. In order to achieve reproducible doping into single crystal silicon by the ion implantation, channeling effects must be avoided (1-4). For axial channeling, which is channeling along a low index axis, a number of reports have been published about depth profiles for channeled ions and the incidence angle dependence of the channeling (2-5). However, few such experimental reports have been published for planar channeling, which is channeling along a low index plane, in boron implantation into silicon. In order to avoid the channeling, it is important to reveal the channeling effect incidence angle dependence. In the present work, a new method for estimating the

Key words: pulsed MOS C-V technique, doping uniformity, critical angle.

channeling incidence angle dependence using C-V profiling technique was developed. Using this method, the incidence angle dependence of (110) planar channeling in boron implantation into silicon was studied.

CZ, p-type, 75 mm diam, <001> oriented silicon wafers with 30 ~ 50 Ω cm resistivity were used. Boron was implanted into the wafers at 40 ~ 150 keV energy and 1×10^{12} cm^{-2} dose. Figure 1 shows the relationship between the ion beam incidence direction and the wafer orientation. Tilt angle ψ is defined as the angle between the <001> axis and the ion beam direction to the center of the wafer as shown in Fig. 1. In order to avoid <001> axial channeling, boron implantations were accomplished at 8° misalignment from the <001> axis, *i.e.*, at $\psi = 8°$. A well-focused ion beam was scanned over a wafer using an electrostatic deflection system. The wafers have (110) orientation flat. Rotation angle θ is defined as the angle between the <1$\bar{1}$0> orientation and the horizontal plane, as shown in Fig. 1. Boron implantations were accomplished at $\theta = 0°$ so that planar channeling along the (110) plane might occur. The planar channeling ion beam incidence angle dependence was estimated from the variation in the implanted boron depth profiles in a wafer, since the ion beam incidence angles to the (110) plane vary in a wafer because of the ion beam electrostatic deflection system. The implanted boron depth profiles were measured by pulsed MOS C-V technique (6, 7) using the MOS diodes fabricated as follows. After boron ion implantation, the wafers were oxidized in dry O_2 ambient at 1000°C for 60 min to form 500Å thick gate oxide. Evaporating Al electrode, 0.5 × 0.5 mm square shaped MOS diodes were delineated by photolithography. MOS diodes were spaced 1.5 mm apart in a wafer.

Figure 2 shows boron depth profiles implanted at 150 keV energy measured by the pulsed MOS C-V technique for position A, which is the center of the wafer, and for position B, which is near the orientation flat. If the x-y orthogonal coordinate system is defined as shown in Fig. 2, position A is represented as (0 mm, 0 mm), and position B is represented as (0 mm, 24 mm). It can be seen that implanted boron penetrates deeper at the center of the wafer, A, than at the edge of the wafer, B, due to the planar channeling effect along the (110) plane. The profiles are not "as implanted" profiles, but are redistributed profiles due to diffusion, since the oxidation was performed at 1000°C for 60 min after implantation. Though the measured profiles are not "as implanted" profiles, the planar channeling effect can be estimated from the profiles, since the diffusion does not so seriously cause a redistribution (8). Penetration depth, R_{pe}, is defined as the depth where boron concentration is equal to 10^{16} cm^{-3}

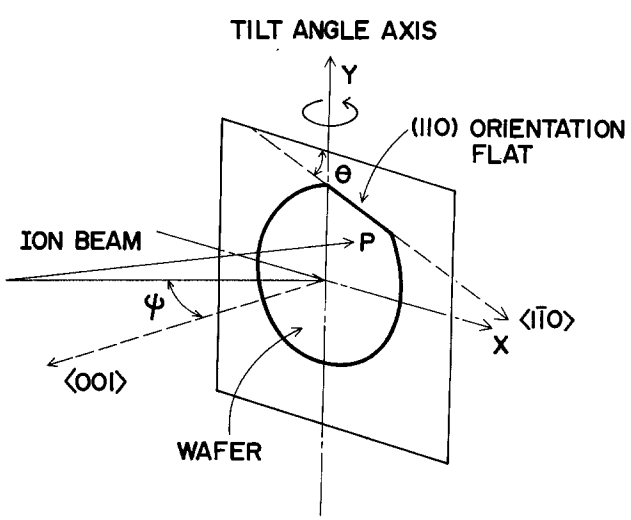

Fig. 1. Ion beam incidence direction and wafer orientation

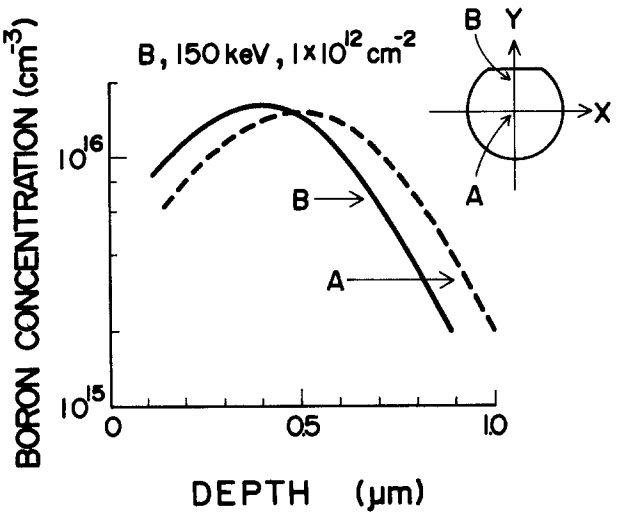

Fig. 2. Boron depth profiles measured by pulsed MOS C-V technique for position A, which is the center of the wafer, and position B, which is near the orientation flat.

(deeper one). The (110) planar channeling effect was estimated by measuring the penetration depth distribution in the wafer. Figure 3 shows the penetration depth dependence on the position along the y axis. As can be seen, the penetration depth has a maximum value of 7300Å at $y = -3$ mm. That is, the planar channeling along the (110) plane most remarkably occurred at $y = -3$ mm, which indicates that ion beam incidence direction was parallel to the (110) plane at $y = -3$ mm for the wafer. In Fig. 4, x direction dependence of the penetration depth is shown at $y = -3$ mm. As can be seen, the penetration depth does not vary with x direction, since ion beam incidence angle to the (110) plane is 0°, and does not vary with x direction at $y = -3$ mm. On the other hand, the ion beam incidence angle to the (110) plane varies with y direction. Angle ϕ between ion beam incidence direction and the (110) plane is represented as follows along the y axis

$$\phi = \tan^{-1}(y/l) - \tan^{-1}(y_0/l) \qquad [1]$$

where l is the distance from the electrostatic scanner to the wafer in the ion implanter (l is 100 cm in the present work), and y_0 is the position where the planar channeling most markedly occurs (y_0 is −3 mm in Fig. 3). Using Eq. [1] and the measured depth profile variation in the wafer, the channeling effect incidence

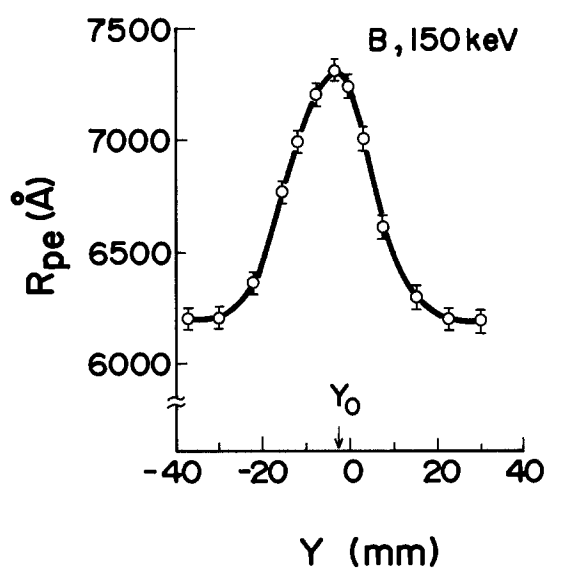

Fig. 3. Penetration depth dependence on the position along the y axis.

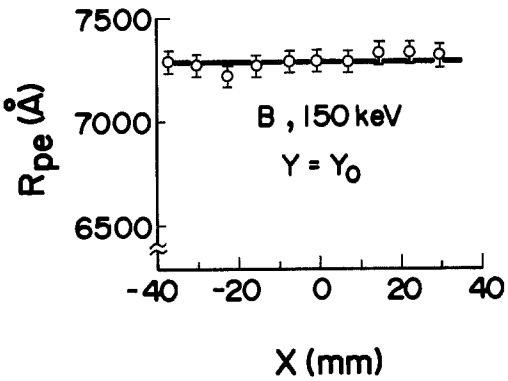

Fig. 4. Penetration depth dependence on the position along the x axis at y = −3 mm.

angle dependence can be estimated easily. The incidence angle dependence for the (110) planar channeling is shown in Fig. 5, which was deduced from the data shown in Fig. 3, using Eq. [1]. It can be seen that increase in the penetration depth due to the planar channeling is about 20%, and that the penetration depth decreases with increasing the incidence angle to the (110) plane. It can be also seen that the planar channeling does not occur for larger ϕ than 1.5°. It was confirmed that the projected range, R_p, agrees well with the LSS theory range for a larger ϕ than 1.5° (9). Cutoff angle, ϕ_{co}, is defined as the minimum angle that ensures a random equivalent implantation. The cutoff angle in the (110) planar channeling for 150 keV boron was estimated as 1.5°. Figure 6 shows boron ion energy dependence of the cutoff angle. It is seen that ϕ_{co} slightly decreases with increasing boron energy. The (110) planar channeling can be avoided by setting ϕ larger than about 2° for the boron energy range used for LSI fabrication. The dashed line in Fig. 6 represents the critical angle, ϕ_c, for (110) planar channeling calculated on the basis of the continuum potential model using screened Coulomb potential, which was described in Ref. (10). The critical angle is the maximum angle within which the continuum potential approximation holds. Slight channeling effect occurs even for $\phi > \phi_c$ (quasi-channeled case) (11). Therefore, the cutoff angle is considered to be slightly larger than the critical angle. It is seen from Fig. 6 that boron energy dependence of the cutoff angle obtained in the present work agrees well with boron energy dependence of the critical angle, and that the cutoff angle is slightly larger than the critical angle. The difference between

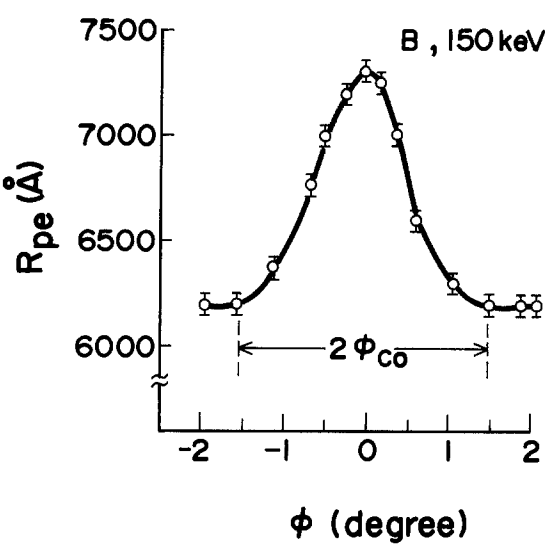

Fig. 5. Ion beam incidence angle dependence for (110) planar channeling.

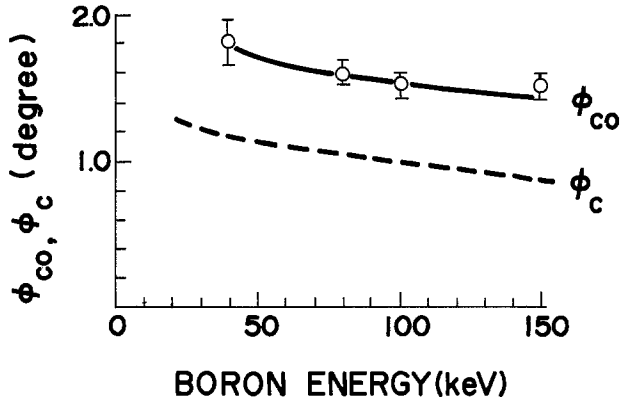

Fig. 6. Boron energy dependence of the cutoff angle for (110) planar channeling. Dashed line represents boron energy dependence of the calculated critical angle.

the cutoff angle and the critical angle probably arises from the above-mentioned quasi-channeling effect.

Next, we consider how the condition of $\phi > \phi_{co}$ can be achieved in a practical ion implantation. The incidence angle to the (110) plane, ϕ, for a point $P(x,y)$ in a wafer is represented as follows, referring to Fig. 1

$$\phi = \sin^{-1}\{|(x + 1\sin\psi)\sin\Theta + y\cos\Theta|/ \sqrt{(x + 1\sin\psi)^2 + y^2 + l^2\cos^2\psi}\} \quad [2]$$

The incidence angles in a 75 mm diam wafer were calculated using Eq. [2] for $\psi = 8°$ and various values of Θ. The calculated result indicated that the condition of $\phi > 2°$ can be achieved by setting Θ larger than 30° for any point in a 75 mm diam wafer. That is, uniform and reproducible implantation can be accomplished by setting $\psi = 8°$ and $\Theta = 30°$ for a 75 mm diam wafer. This result was also confirmed experimentally.

In summary, the incidence angle dependence of the (110) planar channeling was studied by measuring depth profile variation in a silicon wafer, into which boron was implanted using the ion implanter with an electrostatic scan system. The depth profile variation in the wafer was measured by the pulsed MOS C-V technique. The cutoff angle for 40 ~ 150 keV boron was estimated as 1.8 ~ 1.5°. It was found that the cutoff angle slightly decreases with increasing boron energy. Consequently, a random equivalent implantation, or uniform and reproducible implantation can be accomplished by setting ϕ larger than about 2° for boron energy range used for LSI fabrication. The condition of $\phi > 2°$ can be achieved by setting $\psi = 8°$ and $\Theta = 30°$ for a 75 mm diam wafer.

Acknowledgments

The authors express deep appreciation to Dr. H. Mukai, Dr. M. Kondo, and Dr. E. Arai for their advice and encouragement.

Manuscript submitted April 26, 1982; revised manuscript received Nov. 1, 1982.

Any discussion of this paper will appear in a Discussion Section to be published in the December 1983 JOURNAL. All discussions for the December 1983 Discussion Section should be submitted by Aug. 1, 1983.

Publication costs of this article were assisted by Nippon Telegraph and Telephone Public Corporation.

REFERENCES

1. F. H. Eisen, *Can. J. Phys.*, **46**, 561 (1968).
2. G. Dearnaley, J. H. Freeman, G. A. Gard, and M. A. Wilkins, *ibid.*, **46**, 587 (1968).
3. T. E. Seidel, in Second International Conference on Ion Implantation in Semiconductors, p. 47, Springer-Verlag, New York (1971).
4. V. G. K. Reddi and J. D. Sansbury, *J. Appl. Phys.*, **44**, 2951 (1973).
5. J. Comes and R. G. Wilson, *J. Appl. Phys.*, **51**, 3697 (1980).

6. W. van Gelder and E. H. Nicollian, *This Journal,* **118,** 138 (1971).
7. K. Ziegler, E. Klausmann, and S. Kar, *Solid-State Electron.,* **18,** 189 (1975).
8. M. Miyake and H. Harada, *This Journal,* **129,** 1097 (1982).
9. J. F. Gibbons, W. S. Johnson, and S. W. Mylroie, "Projected Range Statistics," 2nd ed., Dowden, Hutchinson and Ross, Inc., 1975, Distributed by Halsted Press.
10. D. V. Morgan and D. van Vliet, *Can. J. Phys.,* **46,** 503 (1968).
11. D. van Vliet, in "Channeling," Chap. 2, D. V. Morgan, Editor, John Wiley & Sons, London (1973).

JOURNAL OF THE ELECTROCHEMICAL SOCIETY

ACCELERATED

—BRIEF COMMUNICATIONS—

MARCH 1983

Phenomenological Model for Silicon Oxidation in Dry Oxygen in the Presence of HCl

A. I. Ellis,* K. M. Gardiner, and T. E. Cyr

Solid State Electronics Division, Honeywell Incorporated, Plymouth, Minnesota 55441

INTRODUCTION

Thermal oxidation of silicon to form a thin SiO_2 layer is one of the most important processes in VLSI and VHSIC technology. Presently, some commercially available, high performance MOS memory circuits use gate oxides as thin as 400 Å. There is a wide body of experimental evidence which indicates that such thin layers of SiO_2 are substantially different from thicker layers. These differences include growth kinetics, optical properties, breakdown characteristics, and physical structure. In spite of the pioneering studies of Deal and Grove [1] and several other authors [2-4], the growth of the first several hundred angstroms of oxide has not yet been quantitatively explained. In this paper we propose a conceptually simple modification of the Deal -Grove model based on the assumption that the oxygen atoms impacting the oxide surface have a definite probability of penetrating to a certain depth. Expressions useful for data analysis and simulation (SUPREM II and III) are given.

DRY OXIDATION MODEL

Blanc [3] proposed a simple model which explains well the anomalously high oxidation rate of thin oxide. This model assumes that although oxygen diffuses molecularly during the dry oxidation, the actual oxidant is atomic oxygen; this leads to a conceptually simple modification of the Deal-Grove model. Blanc's model was tested in both the thin and thick oxide regions and was found inadequate for the simulation of both oxide regimes. Therefore, here we suggest a semiempirical modification of the Deal-Grove formula. It was assumed after Deal and Grove, that the oxidation mechanism arises from the diffusion transport of oxidant through the growing amorphous SiO_2 layer followed by the reaction of Si with oxidant at the advancing interface. The equation of Deal and Grove which describes the change of oxide thickness, Z_{ox}, with the oxidation time, t, has the following form:

$$\frac{dZ_{ox}}{dt} = \frac{K_l K_p}{2K_l Z_{ox} + K_p} \qquad (1)$$

Here K_l and K_p are the linear and parabolic growth rates respectively. They are related to the linear and parabolic rate constants A and B by $A = K_p/K_l$ and $B = K_p$. We suggest that for thin oxides the linear growth rate K_l should be replaced by K_n, where

$$K_n = K_l\,(1 + Z_f \exp(-Z_{ox}/Z_l)) \qquad (2)$$

The new model parameters are: Z_f the growth acceleration factor, and Z_l the effective penetration depth. Their temperature dependences (for dry O_2) as determined by comparison to experimental data are:

$$Z_f = 39.965 - .08145 + 4.2552 \times 10^{-5}T^2 \qquad (3)$$

$$Z_l = 1/(692 - 1.3641T + 6.876 \times 10^{-4}T^2) \text{ (microns)} \qquad (4)$$

where T is in °C.

Integrating equation (1) one obtains the well known dependence (Grove's equation):

$$t = \frac{Z_{ox}^2}{K_p} + \frac{Z_{ox}}{K_l} \qquad (5)$$

This equation will take the following form if K_n is substituted for K_l in Eq (1):

---

* Electrochemical Society Active Member.

Key words: oxidation, growth, kinetics.

$$t = \frac{Z_{ox}^2}{K_p} + \frac{Z_{ox}}{K_l} + \frac{Z_l}{K_l} \ln \left[\frac{1 + Z_f e^{-Z_{ox}/Z_l}}{1 + Z_f} \right] \quad (6)$$

Equation (6) differs from equation (5) by an additional term which causes faster growth for thin oxides but is negligible for oxides 3 to 4 times thicker than Z_l.

The SUPREM II-05 program models the oxide growth by employing approximate empirical correction factors to the usual linear parabolic growth law. The model proposed here improves the predictive capabilities of SUPREM. In Fig.1 we compare the oxide growth rate dZ_{ox}/dt calculated from the Deal and Grove model with that predicted by the new model. Also shown is the growth rate which was used in the SUPREM II-05 program. Note the sharp discontinuity in the SUPREM II-05 curve. This is due to the attempt to fit the experimental data with a constant acceleration factor.

The analysis of the data [1,2,4,5] at 700, 780, 893, 980 and 1100°C further confirm the validity of the proposed model. Figure 2 shows the comparison of the theory with experimental data for oxidation in dry O_2 at 893°C. The dashed curve is the result of the SUPREM II-05 calculations and the solid curve shows that the new model provides a smooth transition from the accelerated to the linear growth regions while maintaining a good fit to experimental data for thick oxides. Such a good fit, over the entire oxide thickness range was not possible with Deal and Grove model.

Equation (10) was solved numerically for each of the A coefficients using least squares, and the following parametric equations were obtained

$$A_f = 69.79 + 0.150P - 0.13682T + 6.838 \times 10^{-5}T^2 + 5.18 \times 10^{-5}PT - 8.54 \times 10^{-3}P^2 \quad (11)$$

$$A_l = -12.20 - 0.198P + 3.221 \times 10^{-2}T - 1.871 \times 10^{-5}T^2 + 1.636 \times 10^{-4}PT - 1.92 \times 10^{-3}P^2 \quad (12)$$

$$A_p = -51.12 + 0.182P + 0.10414T - 5.143 \times 10^{-5}T^2 - 1.059 \times 10^{-4}PT + 2.55 \times 10^{-3}P^2 \quad (13)$$

where T is in °C.
Equations (3-5), (7-9), (11-13) were directly implemented into the SUPREM II program (Subroutine OXDEP) to account for the effect of chlorine in the dry O_2 oxidizing gas.

To verify our phenomenological model we have calculated the oxide thickness as a function of the oxidation time for dry O_2 oxidation of <100> silicon at 975°C and with 4% HCl. The calculation is compared with the measured values [12] in Figure 3. It is seen that our oxidation model agrees closely with the experimental data in both the linear and parabolic regimes. The dashed curve represents the calculations done assuming that there is no oxide present on the silicon surface at time t = 0. Usually however there is initially a thin layer of oxide present and this can easily be included in the calculations by using the DEPOSITION step in the SUPREM Input Data File before the OXIDATION steps are simulated. The full curve represents results of calculations for initial oxide thickness of 25 Å with a 9 minute push-in simulated prior to the high temperature oxidation. Incorporation of these two processing steps brings the theory into much closer agreement with the experimental data, especially in the thin oxide regime. The growth of the initial 25 Å of oxide can be easily associated with the standard R.C.A. cold clean process through which wafers went before high temperature oxidation.

CONCLUSION

The phenomenological model presented here should be useful for most (chlorine) oxidations of practical interest, within the range of conditions for which data is currently available. Better understanding of the mechanisms involved will be necessary, however, for complete predictive capability particularly outside the available data range.

ACKNOWLEDGMENT

The authors are indebted to J. S. T. Huang for comments and helpful suggestions. Special thanks are due to D. Suhl, S. Peck and G. Kirchner for supplying us with their experimental data and for helpful discussions.

REFERENCES

1. B.E. Deal and A.S. Grove, J. Appl. Phys., 36, 3770 (1965)
2. E.A. Irene and Y.J. Van der Meulen, J. Electrochem. Soc, 23, 1380 (1976)
3. J. Blanc, Appl. Phys. Lett. 33, 424 (1978)
4. E.A. Irene J. Electrochem. Soc. 125, 1708 (1978)
5. G. Wright, Private Communication
6. D.W. Hess and B.E. Deal, J. Electrochem. Soc. 124, 735 (1977)
7. B.E. Deal, J. Electrochem. Soc. 125, 576 (1978)
8. C. Hashimoto, S. Muramoto, N. Shiono, and O. Nakajima, J. Electrochem. Soc. 127, 129 (1980)
9. R.W. Dutton et. al. "Oxidation and Epitaxy", Tech. Report No. 5021-1, Stanford University, Stanford, California (1977)
10. J.R. Monkowski, J. Stach, and R.E. Tressler "A Model of Silicon Oxidation in Chlorine-Containing Ambients: Competition between two oxidants", IEEE Proc. Electron. Components Conf.,San Francisco, Calif., 61 (1980)
11. B.E. Deal, L.N. Lie and R.R. Razouk "Characterization of Silicon Oxidation in High Pressure Dry O_2", Technology Modeling Seminar, Stanford University, Stanford, California (1981)
12. G. Kirchner, S. Peck and D. Suhl, Private Communication
13. E.A. Irene, J. Electrochem. Soc., 121, 1631 (1974)

Manuscript submitted June 1, 1982; revised manuscript received Sept. 10, 1982.

Publication costs of this article were assisted by Honeywell Incorporated.

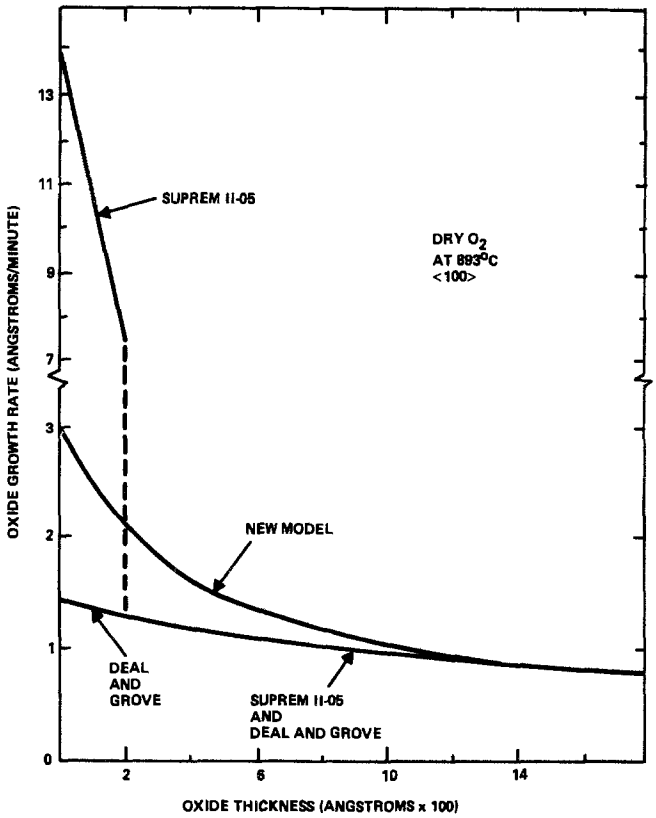

Fig. 1. Comparison of the predicted oxide growth rate for the new dry oxidation model with that of Deal and Grove and that used in SUPREM II-05.

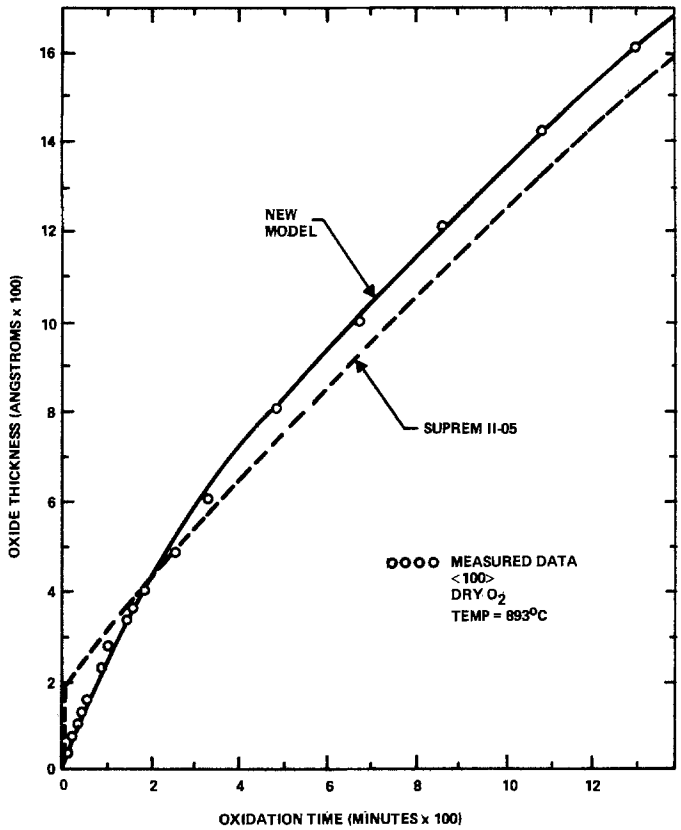

Fig. 2. Comparison of the theory with experimental data[1,2,4,5] for <100> silicon oxidation in dry O_2 at 893°C.

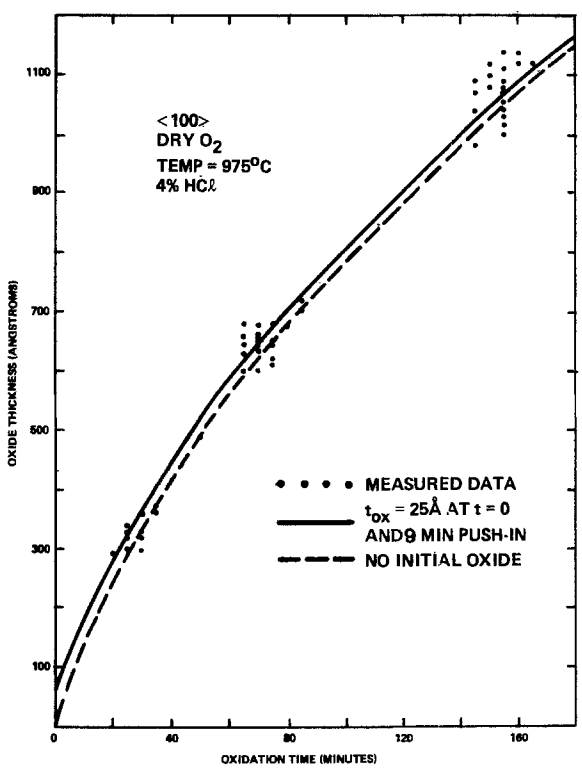

Fig. 3. Comparison of the theory with experimental data[12] for <100> silicon oxidation in dry O_2 with 4% HCl at 975°C. The dashed curve was calculated assuming that t_{ox} = 0 at t=0. The full curve represents results of calculations for initial oxide thickness of 25 Å with a 9 minute push-in simulated before the high temperature oxidation.

The Growth of Zn_3P_2 by Metalorganic Chemical Vapor Deposition

Judith Long

Bell Laboratories, Murray Hill, New Jersey 07974

INTRODUCTION

Recent studies resulting from the interest in developing new materials for low-cost photovoltaic devices have shown zinc phosphide (Zn_3P_2) to be a promising candidate for such applications. Amongst its advantages are a direct band gap of 1.5 eV and relatively cheap and abundant constituent elements. Previously, Zn_3P_2 for device applications has been grown principally by close space vapor transport (1,2). This paper reports the first growth of Zn_3P_2 by the method of metalorganic chemical vapor deposition. The metalorganic technique possesses the advantage that relatively low growth temperatures may be used in conjunction with the independent regulation of the Group II and Group V sources. Since the reactor contains only one hot zone, in the substrate region, the cold reactor walls do not interfere with the growth, which occurs only on the heated substrate. In addition, the apparatus may be easily scaled to accommodate large-area substrates.

EXPERIMENTAL

The growth apparatus, shown in Fig. 1, consisted of a vertical, water-cooled, quartz reactor tube, 50 mm in diameter, containing a molybdenum or silicon carbide coated graphite susceptor on which the substrate was mounted. The temperature was monitored by a thermocouple embedded in the susceptor and heating accomplished by means of an r.f. coil. The zinc source consisted of either of the two volatile metalorganic compounds diethylzinc or the considerably more volatile dimethylzinc (vapor pressures at 25°C = 16.0 torr and 369.1 torr respectively). These were contained in stainless steel bubblers held at room temperature. The metalorganic vapor was transported by passing a hydrogen gas stream through the bubbler. This was then mixed with a stream of phosphine gas in hydrogen, diluted with extra hydrogen and introduced into the reactor where decomposition of the reactants occurred at the heated substrate.

The effects of growth conditions, in particular, temperature, zinc source and P/Zn mole fraction ratio were examined in detail. Growth times were typically on the order of 30 minutes with a total gas flow of 3500 cm^3/min. The zinc mole fraction was generally kept at ~9 x 10^{-4}, whereas the phosphorus mole fraction was varied over the range 1 to 9 x 10^{-3}.

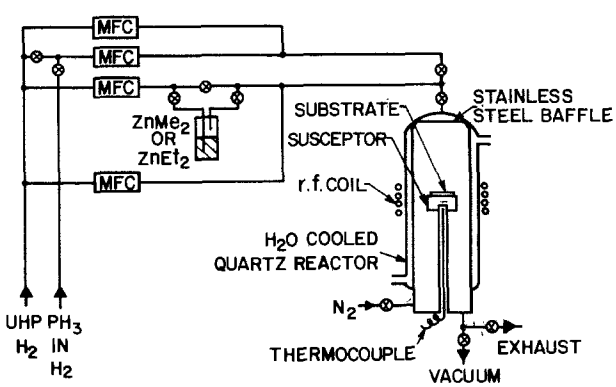

Fig. 1 Simplified schematic of the MOCVD apparatus.

Key descriptors: semiconductor, photovoltaic

RESULTS AND DISCUSSION

Initial growth studies employed $ZnEt_2$ as the zinc source and Carbone-Lorraine 5890-PT high-density graphite as the substrate. Although growth of Zn_3P_2 could be accomplished over the rather wide temperature range of 300 to 500°C, the layers were non-uniform and partially covered with a brown deposit. Positioning a stainless steel baffle, containing many small circular perforations, in the reactor tube, directly below the gas inlet greatly improved growth uniformity and eliminated the brown deposit, presumably as a result of more efficient mixing of the reactant gases.

Using $ZnEt_2$, and a P/Zn mole fraction ratio of 1.1:1 the Zn_3P_2 growth rate was examined as a function of temperature. As shown in Fig. 2, the growth rate was found to increase with increasing temperature, from a value of 3μm/hr at 300°C to one of 10μm/hr at 420°C, where it remained relatively constant over the next 70°. This dependence of the growth rate on temperature in the lower temperature range implies that kinetic control is in effect with the overall growth limited by some relatively slow surface process. For temperatures above 500°C the growth rate decreased rapidly, dropping to 3μm/hr at 550°C, suggesting that the reacting species may be re-evaporating off the substrate surface coupled with parasitic nucleation on the reactor walls.

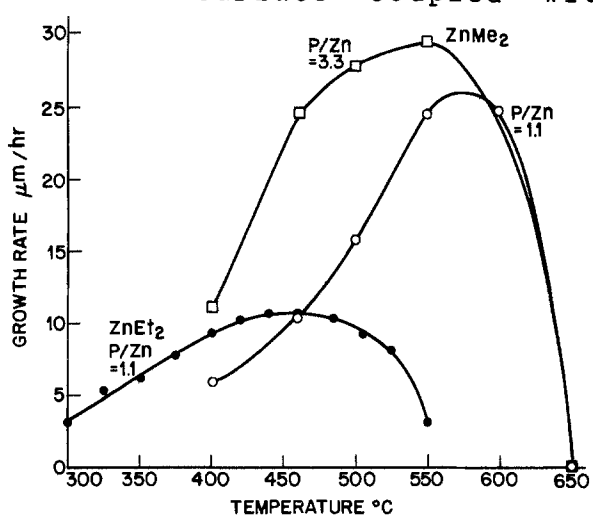

Fig. 2 Zn_3P_2 growth rate as a function of temperature.

Fig. 2 also shows the results obtained using $ZnMe_2$ as the zinc source with the same zinc mole fraction. Although the overall growth pattern was similar, with an initial growth rate increase with temperature followed by a rapid decrease, the highest rates were obtained in the 550 to 600°C range. This shift of the growth region to higher temperatures is in keeping with the higher decomposition temperature of $ZnMe_2$ compared with that of $ZnEt_2$ (3). A notable difference between the two sources was the value of the growth rate which reached a maximum of 25μm/hr with $ZnMe_2$ but only 10μm/hr using $ZnEt_2$. One possible explanation is that reaction at the substrate surface is less favorable for $ZnEt_2$ due to the greater steric bulk of the ethyl groups compared with the methyl. Parasitic nucleation on the reactor walls, which depletes the zinc source, may also be more of a problem for $ZnEt_2$, particularly since the growth occurs at lower temperatures.

Dependence of the growth rate on the P/Zn mole fraction ratio was also examined for the $ZnMe_2$ source. As shown in Figs. 2 and 3, the growth rate increased with increasing P/Zn ratio until a ratio of ~6:1 was reached. Above this value the rate became independent of the P/Zn ratio.

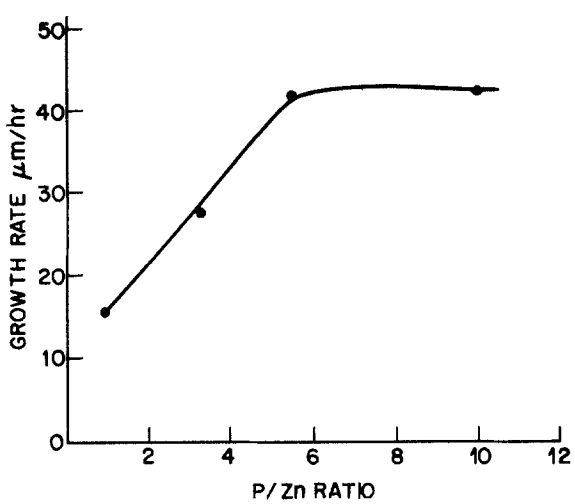

Fig. 3 Zn_3P_2 growth rate as a function of the P/Zn mole fraction ratio.

The Zn_3P_2 samples, however, were all found to exhibit p-type conductivity irrespective of the V/II ratio.

Fig. 4 shows the effect of varying the P/Zn ratio on the surface morphology. An increase in the ratio from 1:1 in a) to 10:1 in b) reduced the tendency for growth of isolated blocks of Zn_3P_2 crystals to occur at the surface. In addition, the grain size was found to be larger at the higher ratios, increasing from 2 to 3μm in a) to 5 to 10μm in b). A similar increase in grain size was also observed on increasing the substrate temperature from 400°C to 550°C.

Graphite was originally the substrate of choice because of its relatively low cost, in addition to several other desirable properties such as thermal stability and chemical inertness. However, despite the large variety of graphite types available, the high thermal expansion coefficient of Zn_3P_2 ($14 \times 10^{-6}\,°C^{-1}$) made it impossible to find one with a suitably closely-matched coefficient. As a result of this mismatch there was a problem with the occurrence of microcracks and pinholes in the Zn_3P_2 layers, which provide current leakage paths through the material. The cracks were particularly evident in the samples grown at higher temperatures. Previous workers have grown Zn_3P_2 successfully on mica and silicon steel substrates (4), both of which are compatible with the metalorganic technique. Thus, in order to improve the quality of the Zn_3P_2 layers we grew several samples on both mica and silicon steel. The growth conditions were essentially unchanged from those used with graphite substrates. The Zn_3P_2 layers were found to be highly resistive, those grown on mica having sheet resistances of 1 to 2×10^6 Ω/[]. Figure 5 shows SEM photographs of two samples grown on silicon steel, with P/Zn ratios of 1:1 in a) and 10:1 in b). No sign of microcracks was evident in these samples, nor in those grown on mica, and the improvement in surface morphology at higher P/Zn ratios was again observed.

CONCLUSIONS

The growth of undoped, polycrystalline Zn_3P_2 by the method of metal-organic chemical vapor deposition has been demonstrated for the first time and the growth characteristics determined as a function of growth conditions. The quality of the layers was observed to be highly dependent on the substrate material. The samples grown on graphite exhibited microcracks due to a mismatch of the thermal expansion coefficient of Zn_3P_2 with that of the graphite. This problem was eliminated by use of mica or silicon steel as the substrate.

ACKNOWLEDGEMENTS

The author would like to thank W. D. Johnston, Jr., H. J. Leamy and A. Heller for their help and encouragement and M. Bhushan for providing the silicon steel substrates.

REFERENCES

[1] A. Catalano, M. Bhushan, and N. Convers-Wyeth, Proceedings of the 14th. IEEE Photovoltaic Specialists Conference, San Diego, 1980, p. 641.

[2] M. P. Bendett and R. G. Hunsperger, J. Electron Mater., 10, 559 (1981).

[3] G. A. Razuvaev, R. F. Galiulina, and G. G. Petukhov, Zh. Obsh. Khim., 38, 3 (1968).

[4] M. Bhushan and A. Catalano, Proceedings of the 15th. IEEE Photovoltaic Specialists Conference, Orlando, 1981.

Manuscript received Oct. 19, 1982.

Publication costs of this article were assisted by Bell Laboratories.

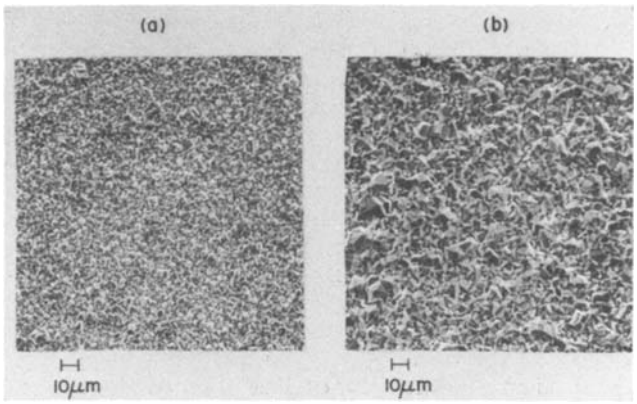

Fig. 4 SEM photographs of Zn_3P_2 growth on graphite a) P/Zn mole fraction ratio = 1:1, b) P/Zn = 10:1.

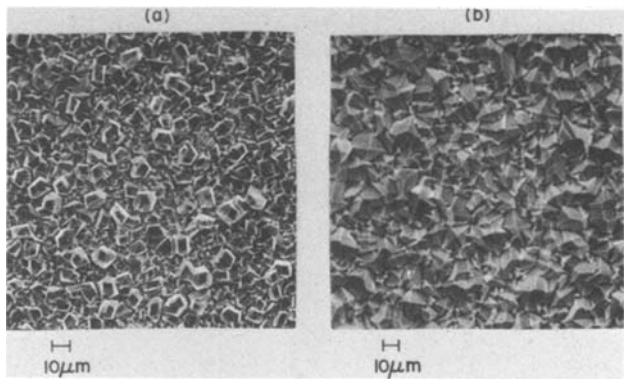

Fig. 5 SEM photographs of Zn_3P_2 grown on silicon steel a) P/Zn mole fraction ratio = 1:1, b) P/Zn = 10:1.

Metal Oxidation as a Heat Pump

Daniel Cubicciotti*

Electric Power Research Institute, Palo Alto, California 94303

The oxidation of a metal is generally an exothermic process, and the rate of heat release is slow enough in most cases that the detailed location of the site of heat evolution is not important. Heat transfer processes, under these conditions, are usually rapid enough to dissipate temperature gradients. Thus, other than being associated with the formation of oxide, the details of heat generation are not important in such situations.

During a rapid oxidation however, it is interesting to consider the detailed processes of heat generation. For example, rapid oxidation of Zircaloy by steam can occur during a nuclear reactor accident involving core dry out such as occurred at TMI-2, and the rate of heat generation from that oxidation can be larger than other heat sources such as radioactive decay. The locus of the heat generation can be important for calculating heat transfer rates and thus local, transient temperatures in a nuclear core during an accident.

The overall process of oxidation of a metal such as zirconium to form a coherent, protective oxide can be divided into three sets of reactions occurring in the following localized regions: (a) at the interface between the metal and the oxide layer, (b) transport of species through the oxide layer, and (c) at the interface between the oxide and the oxidizing gas.

For the oxidation of zirconium by steam, which is a case of interest in nuclear accidents, the reactions occuring in those locations can be represented as follows:

(A) $Zr\ (metal) = Zr^{+4}\ (oxide) + 4e\ (oxide)$

(B) $4e\ (in\ oxide\ at\ metal\ interface) = 4e\ (in\ oxide\ at\ gas\ interface)$

$O^{-2}\ (in\ oxide\ at\ gas\ interface) = O^{-2}\ (in\ oxide\ at\ metal\ interface)$

(C) $2H_2O\ (gas) + 4e\ (oxide) = O^{-2}\ (oxide) + 2H_2\ (gas).$

The heat effects associated with those reactions must be evaluated. The reactions in B have relatively small heats, which will be assumed equal to zero in the present treatment. To evaluate the heat associated with the reaction at A, the reaction will be represented as the sum of four reactions for which enthalpy changes can be evaluated:

(A1) $Zr\ (metal) = Zr\ (gas);\quad \Delta H(A1) = 143.7\ kcal$

(A2) $Zr\ (gas) = Zr^{+4}\ (gas) + 4e\ (gas);\quad \Delta H(A2) = 1783\ kcal$

(A3) $Zr^{+4}\ (gas) = Zr^{+4}\ (oxide);\quad \Delta H(A3) = -1320\ kcal$

(A4) $4e\ (gas) = 4e\ (oxide);\quad \Delta H(A4) = -287\ kcal$

The values quoted were obtained as follows: The value of $\Delta H(A1)$ was taken from Ref. 1. $\Delta H(A2)$ is the sum of the ionization potentials for the first four ionizations of gaseous zirconium, which is given in Ref. 2 as 1783 kcal. $\Delta H(A3)$ was assumed to be the negative of half of the lattice energy, that is, half of the enthalpy change for the reaction:

$$Zr^{+4}\ (gas) + O^{-2}\ (gas) = ZrO_2\ (solid);\quad \Delta H = -2640\ kcal$$

which was calculated from the enthalpy changes of the following reactions:

$Zr(s) = Zr(g);\quad \Delta H = 143.7\ kcal$ (Ref. 1)

$Zr(g) = Zr^{+4}(g) + 4e(g);\quad \Delta H = 1783\ kcal$ (Ref. 2)

Manuscript submitted Oct. 22, 1982; revised manuscript received Nov. 24, 1982.

Publication costs of this article were assisted by Electric Power Research Institute.

*Electrochemical Society Active Member,
Key words: metal oxidation, zirconium.

$1/2O_2(g) = O(g)$; $\Delta H = 59.2$ kcal (Ref. 3)

$O(g) + 2e(g) = O^{-2}(g)$;
$\Delta H = 166$ kcal (Ref. 4)

$\Delta H(A4)$ is equal to four times the negative of the work function of ZrO_2 which is given in Ref. (5) as 3.12 eV.

The sum of the enthalpy changes for reactions A1 to A4 is 320 kcal. This is, per mole of zirconium oxidized, 320 kcal of heat are absorbed at the metal-oxide interface (location A) for a constant pressure oxidation of one mole of zirconium.

At location C (the oxide gas interface), the enthalpy change is the sum of the following reactions:

(C1) $2\,H_2O\,(gas) + 4e\,(gas) = 2O^{-2}\,(gas) + H_2\,(gas)$;
$\Delta H\,(C1) = 566$ kcal

(C2) $2O^{-2}\,(gas) = 2O^{-2}\,(oxide)$;
$\Delta H(C2) = -1320$ kcal

(C3) $4e\,(oxide) = 4e\,(gas)$;
$\Delta H(C3) = 287$ kcal

For reaction C1, the enthalpy of formation of $H_2O(g)$ is -57.8 kcal (Ref. 1), and that of O^{-2} (g) is 225 kcal (Ref. 3 and 4). In reaction C2 the enthalpy change was assumed to be the negative of half of the lattice energy, and $\Delta H(C3)$ is four times the work function of ZrO_2.

The sum of the enthalpy changes for reactions C1 to C3 is -467 kcal per mole of zirconium oxidized. Thus, 467 kcal of heat are evolved at the metal-gas surface (location C) for a constant pressure oxidation of one mole of zirconium by steam.

Thus, at the metal-oxide interface 320 kcal of heat are absorbed due to the oxidation reaction and 467 kcal of heat are liberated at the oxide-gas surface when a mole of zirconium reacts with steam. That is, the oxidation process acts like a heat pump which transfers 320 kcal away from the metal-oxide surface and to the oxide-gas surface where it is evolved together with the net heat of reaction.

This rather surprising result means that during the rapid oxidation of zirconium, there should be a temperature gradient through the thickness of the oxide. The metal side should be cooler than the gas side of the oxide. If the zirconium were in a fast flowing stream of gas which could effectively remove the heat pumped through the oxide layer to the oxide-gas surface, then the substrate metal would be cooled by the oxidation process and the temperature of the metal would fall below its initial value.

It should be noted that there may be relatively large uncertainties in the values used for the reaction enthalpies. For instance the value used for the enthalpy of attachment of two electrons to an oxygen atom is the average of two indirectly obtained values that differ by 26 kcal. The work function of ZrO_2 in the literature has values that differ by 10 kcal and it enters as the fourfold product. Also the chemical states of the reactants are probably different from those assumed. For instance zirconium metal at the interface with oxide probably is a solution of the metal containing oxide. The oxide at the metal interface is probably substoichiometric in oxygen. Thus, the present treatment is only approximate. However, because the amounts of heat calculated to be transferred by the oxidation reaction are large, the conclusions are expected to be at least qualitatively correct.

The phenomenon can have some impact on the temperatures of the UO_2 in fuel rods during a nuclear power reactor accident. In such accidents, there is substantial gas flow past the Zircaloy cladding which is being oxidized, rapidly at times. Under those conditions, the above analysis would predict that the Zircaloy oxidation reaction should pump heat out of the fuel rods into the flowing gas stream.

Acknowledgment -- The author is indebted to Professor Leo Brewer, of the University of California, for helpful suggestions.

REFERENCES

1) O. Kubaschewski and C. B. Alcock, "Metallurgical Thermochemistry", Pergamon Press, NY, 1979.

2) C. Moore, "Ionization Potentials and Ionization Limits Derived from the Analyses of Optical Spectra", NSRDS-NBS34, U.S. Government Printing Office, Washington, D.C., 1970.

3) JANAF Thermochemical Tables, The Dow Chemical Company, Midland, Michigan, 1981.

4) P. J. Durrant and B. Durrant, "Advanced Inorganic Chemistry", p 356, Longmans Green & Company, London, 1962.

5) G. V. Samsonov, "The Oxide Handbook", 2nd Edition, Plenum Press, NY, 1982.

Activated Ir: An Electrode Suitable for Reversible Charge Injection in Saline Solution

L. S. Robblee,* J. L. Lefko, and S. B. Brummer*

EIC Laboratories, Incorporated, Newton, Massachusetts 02158

INTRODUCTION

Electrical stimulation of the nervous system with metal electrodes requires reversible charge injection processes to mediate the change in charge carriers at the metal/solution interface and to avoid the formation of toxic electrochemical reaction products (1). Reversible charge injection is possible either by a capacitive process, e.g., double layer charging, or by faradaic reactions involving species that remain bound to the electrode surface.

The multilayer oxide film that is formed on Ir by repetitive potential cycling may produce as much as a 100-fold increase in the charge capacity of the surface (2-4). The increased capacity of so-called "activated" Ir is the result of highly reversible H^+ or OH^- transfer reactions and valence transitions within the oxide layer (4-7). These reactions may provide an ideal mechanism for reversible charge injection providing they proceed reversibly in the in vivo saline environment and occur without excessive dissolution of the oxide. This paper describes the results of our initial evaluation of activated Ir for use as a stimulation electrode.

EXPERIMENTAL

Cyclic voltammetry was carried out with an Amel Model 551 potentiostat programmed with a Bromberg sweep generator, or a Bioanalytical Systems CV-1B voltammetry unit. Potentials were measured against a saturated calomel reference electrode and are reported vs. the reversible hydrogen electrode (RHE).

Iridium electrodes, 0.04 to 0.09 cm^2 geom., consisted of 0.05 cm diameter Ir wire (>99.9% Ir) sealed into Pyrex glass tubing. To obtain an oxide-free, deactivated surface, these electrodes were held for 5 to 10 minutes at 1.9V in 1M H_2SO_4 (3). Iridium microelectrodes, approximately 10^{-6} cm^2 geom., were supplied by M. Bak, National Institute of Neurological and Communicative Disorders and Stroke, NIH. These consisted of 25 μm Ir wire insulated with Parylene-C and having exposed tips of bare Ir 8 to 20 μm in length (8). Electrodes were activated by repetitive potential cycling at 100 mV sec^{-1} between 0.05V and 1.45V in 1M H_2SO_4, as described by others (4). Phosphate-buffered saline (PBS) was also investigated as an alternative electrolyte for activating Ir, particularly for use with the Parylene-insulated microelectrodes. The saline electrolyte contained 0.14M NaCl in 0.1M Na_2HPO_4/NaH_2PO_4 buffer, pH 7.4. In order to standardize our procedures, all electrodes activated for subsequent tests were cycled until the charge capacity in the oxide potential region, 0.4 to 1.4V, approximated 10 $mC \cdot cm^{-2}$.

Biphasic pulse tests and dissolution measurements of activated and deactivated Ir were carried out in 1 ml volume of PBS containing 0.02 wt% human serum albumin (PBS-protein) as described previously for Pt electrodes (9). Because of the low dissolution rates found for Ir, aliquots of pulse solution were analyzed only at the termination of the experiment and not at various time intervals as was done for Pt. Metal analysis was performed by flameless atomic absorption spectrometry. Analytical detection limits for Ir in PBS-protein were determined to be 0.03 to 0.06 μg/ml. Detection limits for Pt in the same solution were 0.01 to 0.02 μg/ml.

The charge limits for water electrolysis were determined with Ir microelectrodes. These were used "as received" or they were activated in PBS as described above. Monophasic, capacitively-coupled stimulation pulses (0.1 ms pulse width, 400 Hz) were applied to microelectrodes in PBS-protein while observing them at 100X magnification for gas bubble formation. The pulse waveform was monitored on an oscilloscope. The stimulation and monitoring circuits are described elsewhere (10). The pulse current

*Electrochemical Society Active Member

Key words: dissolution, microelectrode, electrochemistry of stimulation electrodes, electrical stimulation.

was increased very slowly until a gas bubble was observed to form at the electrode tip, at which time the current was decreased quickly to about one-half the gassing level. Pulsing was continued for several minutes after which the current was again slowly increased until bubble formation was observed. This procedure was repeated several times to evaluate the reproducibility of the determination. Both anodal and cathodal current pulses were evaluated.

RESULTS AND DISCUSSION

Activation of Ir.--Activation of Ir by repetitive cycling of the potential between 0.05V RHE and 1.45V RHE in PBS produced a progressive increase in charge capacity in the potential region above 0.4V RHE similar to what was observed in 1M H_2SO_4 (Fig. 1). In the saline electrolyte, the main anodic and cathodic current peaks occurred at slightly lower potentials and were less symmetrical about the current axis than in acid solution. However, when an electrode activated in PBS was placed in 1M H_2SO_4 for cyclic voltammetry, the resulting i vs. E curve was typical of Ir that had been activated in H_2SO_4 initially. The shift of peak potentials in the neutral saline is probably an effect due to electrolyte composition and pH (5) rather than due to differences in the oxide film itself. The buffered saline solution, therefore, should be an appropriate electrolyte for activating the type of Ir electrodes designed for in vivo use, such as the microelectrodes evaluated here.

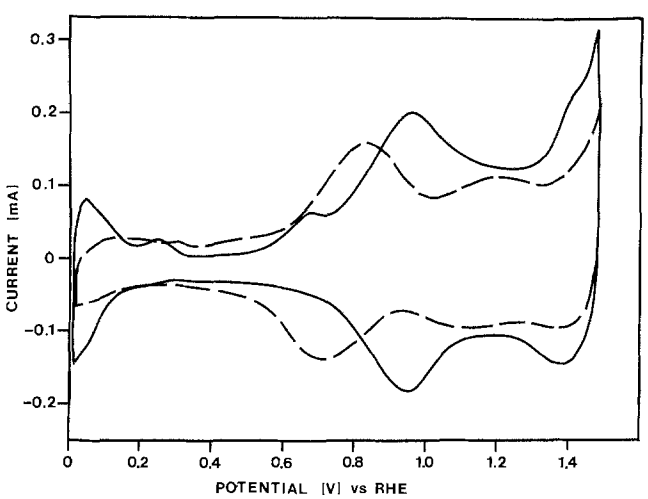

Fig. 1. Cyclic voltammetry curves for Ir after 60 min repetitive potential cycling in 1M H_2SO_4 (solid line) and PBS (dashed line). Scan rate: 100 mV sec^{-1}. Electrode area: 0.09 cm^2 geom. T = 25°C.

Dissolution Tests.--The results of comparative dissolution tests of Ir, Pt and Pt:30% Ir electrodes are shown in Table 1. No dissolution was detected for any of the activated Ir electrodes subjected to anodic-first (AF) biphasic pulses of varying current and charge densities. Deactivated Ir had a significantly greater dissolution than activated Ir with AF pulses of high current and charge density. However, with lower current and charge densities there was no detectable dissolution. Ir dissolution from the Pt:30% Ir alloy was higher than from 100% Ir; Pt dissolution from the alloy was comparable to that from 100% Pt. On the basis of dissolution behavior alone, activated Ir would seem to be the preferred metal for use as a stimulation electrode. The Pt:30% Ir alloy, which is frequently used in stimulation electrodes in place of pure Pt because of its greater mechanical strength, is at a disadvantage due to the likelihood of two metal dissolution products rather than just one.

Gassing Limits.--The evaluation of anodal and cathodal gassing limits for microelectrodes indicated that activation of the Ir surface extended the useful charge injection limits for anodal pulses as much as tenfold (Table 2). There was not as dramatic an effect on charge limits for cathodal pulses, consistent with the charge capacities seen in cyclic voltammograms. For instance, the cathodic charge between 0.7V and 0.0V on a cyclic voltammogram (the possible potential excursion experienced by an electrode during a cathodal pulse) is much less than the anodic charge between 0.7V and 1.45V (the possible potential excursion of an electrode during an anodal pulse).

CONCLUSIONS

Reversible charge injection requires that no new chemical species be produced in solution. With Pt, up to 400 $\mu C \cdot cm^{-2}$ of real area can be injected before the onset of water electrolysis, but a small amount of the injected charge is always lost to metal dissolution (9,11). The results of these initial studies of activated Ir indicate that the charge injection limits for water electrolysis might be increased by a factor of 10 or greater, and that little or no charge is lost to metal dissolution. We conclude that activated Ir is an exceptionally promising material for use as a stimulation electrode. The high capacity for reversible charge injection is of great advantage for applications such as intracortical stimulation of single neurons (12) where the small size of the stimulation electrode, $<10^{-6}$ cm^2 geom., may result in charge densities up to 10 $mC \cdot cm^{-2}$ geom. Moreover, the superior

corrosion resistance of activated Ir, compared to Pt or Pt:Ir alloy, will significantly extend the useful lifetime of a chronically implanted neural prosthesis.

ACKNOWLEDGMENT

The authors gratefully acknowledge the support of this work by the National Institute of Neurological and Communicative Disorders and Stroke, National Institutes of Health, under Contract N01-NS-9-2315.

REFERENCES

1. S. B. Brummer and M. J. Turner, IEEE Trans. Biomed. Eng., BME-24, 59 (1977).
2. D. A. J. Rand and R. Woods, Electroanal. Chem. Interfacial Electrochem., 55, 375 (1974).
3. D. N. Buckley and L. Burke, J. Chem. Soc., 71, 1447 (1975).
4. J. O. Zerbino, N. R. deTacconi, and A. J. Arvia, This Journal, 125, 1266 (1978).
5. S. Gottesfeld and J. D. E. McIntyre, This Journal, 126, 742 (1979).
6. G. Beni, C. E. Rice, and J. L. Shay, This Journal, 127, 1342 (1980).
7. W. C. Dautremont-Smith, Displays, 3, 67 (1982).
8. M. Salcman and M. J. Bak, Med. and Biol. Eng., 14, 42 (1976).
9. L. S. Robblee, J. Marston, J. McHardy, and S. B. Brummer, Biomaterials, 1, 135 (1980).
10. L. S. Robblee, E. M. Kelliher, M. E. Langmuir, H. Vartanian, and J. McHardy, J. Biomed. Mat. Research, in press.
11. S. B. Brummer and M. J. Turner, IEEE Trans. Biomed. Eng., BME-24, 440 (1977).
12. E. Schmidt and J. McIntosh, Exptl. Neurol., 63, 485 (1979).

TABLE 1. SUMMARY OF DISSOLUTION STUDIES OF Ir, Pt:30% Ir AND Pt ELECTRODES

Experimental Conditions: Continuous Charge-Balanced Biphasic Pulses; 50 Hz; PBS-Protein Pulse Solution

Electrode Type	Number of Tests	Current Density ($mA \cdot cm^{-2}$)	Charge Density ($\mu C \cdot cm^{-2}$)	Total Time (hr)	Aggregate Charge[1] (coul)	Ir Dissolution (μg)	Pt Dissolution (μg)
Activated Ir (0.04 to 0.09 cm^2 geom)	2	± 800	± 800	66 and 168	931 and 2080	N.D.[2]	
	2	± 400	± 100	48	35	N.D.	
	2	± 200	± 50	48	40	N.D.	
Deactivated Ir (0.04 to 0.09 cm^2 geom)	2	± 800	± 800	48	636	0.16 ± 0.04	
	1	± 800	± 800	24	297	0.46	
	2	± 400	± 100	48	35	N.D.	
	2	± 200	± 50	48	40	N.D.	
Pt:30% Ir (0.09 cm^2 geom)	4	± 800	± 800	48	648	1.85 ± 1.68	2.45 ± 2.24
Pt (0.06 cm^2 geom)	4	± 800	± 800	24	207		1.50 ± 0.16

[1]Charge per phase (anodic or cathodic) x total number of biphasic pulses.
[2]N.D. = None detected. With present analytical detection limits, this may be 0.06 μg or less.

TABLE 2. GASSING LIMITS FOR MICROELECTRODES

Experimental Conditions: Continuous Monophasic Capacitively-Coupled Pulses; 100 μsec Pulse Width; 400 Hz; PBS-Protein Pulse Solution

Electrode Type	Anodic Charge ($mC \cdot cm^{-2}$ geom)	Cathodic Charge ($mC \cdot cm^{-2}$ geom.)
Pt:30% Ir	1.2-1.3	5-5.3
∿3% x 10^{-6} cm^2 geom.	1.3-2.0	0.7-3.3
Ir, As Received	2.0-9.0	1.4
0.8-2 x 10^{-6} cm^2 geom.	1.0-7.0	1.9
Ir, Activated	31-40	3.0-4.0
0.8-1 x 10^{-6} cm^2 geom.	29-30	5.0

Manuscript submitted Sept. 13, 1982; revised manuscript received ca. Nov. 29, 1982.

Dinitrogen Electrochemical Reduction to Ammonia over Iron Cathode in Aqueous Medium

A. Sclafani, V. Augugliaro, and M. Schiavello

Istituto di Ingegneria Chimica, Università di Palermo, Palermo, Italy

The ammonia synthesis is one of the most important and best established catalytic industrial processes. Neverthless fundamental and applied research is still carried out on this subject with the objective of finding processes which can occur in milder conditions and in the more general field of dinitrogen fixation with the aim to discover new routes for transforming dinitrogen into ammonia.

In this latter field the attempts move along several paths. One tries to simulate the mechanism of biochemical processes carried out by dinitrogen fixing microbes, which operate at atmospheric pressure and room temperature. Indeed precise knowledge about the mechanism of operation of the nitrogenase enzyme will give in future substantial progress to this way. A second utilizes activating complexation of dinitrogen molecule with transition metals such as Ti, Ru, Os, Rh, Re, Mo, Co, etc. and subsequent reduction with very strong reducing compounds. Reviews on this matter have been reported by Kuchynka (1) and Venuto (2).

Recently a completely new route has been suggested by Schrauzer and Guth (3), which produced ammonia from water and dinitrogen on wet TiO_2 powder. Various photocatalysts have been used (4) and a correlation between semiconductors properties and the yield of ammonia has been found (5). Ammonia has been also obtained from dinitrogen and water vapour by heterogeneous photoassisted catalysis utilizing iron doped titanium oxides (6-9) and titanium exchanged zeolites (10, 11).

A method of electrolytic and chemical reduction of molecular dinitrogen has been presented by Van Tamelen and Akermark (12) and Van Tamelen and Seeley (13), which used the electrolytic cell as a chemical reducing agent. Dinitrogen fixation, at room temperature and atmospheric pressure, by a photoenhanced reduction process has been carried out in a photoelectrochemical cell containing a p-GaP cathode and an Al metal anode immersed in a nonaqueous electrolyte (14). An electrochemical reduction, catalyzed by the $Ti(OH)_3$ - Mo(III) system, has been performed by Gorodyskii et al. (15) on a mercury cathode in an alkaline methanol solution under mild conditions.

In this communication preliminary results of a study concerning the direct electrochemical reduction of dinitrogen over iron cathode, at atmospheric pressure and low temperatures, are reported. It must be outlined that at this stage of the research only the feasibility of dinitrogen reduction to ammonia has been studied by the use of an electrochemical cell with aqueous electrolyte at suitable values of cathodic potential.

EXPERIMENTAL

The experiments have been carried out in an electrochemical cell maintained at constant temperature by means of a thermostatic chamber. Three series of experiments at the temperatures of 25, 35 and 45 °C have been performed. An iron cathode with a surface area of 0.25 m^2 was utilized while the anode was a sheet of AISI 316 stainless steel. The electrolyte was a 6 N KOH aqueous solution and the cathodic compartment was separated from the anodic one by means of a porous polyethylene membrane.

Pure dinitrogen (99.99 % purity) was con-

Key words: dinitrogen electrochemical reduction, ammonia production, iron cathodes.

tinously fed to the cathodic compartment by means of properly positioned spargers so that the whole cathode was hit by the gas bubbles. Different values of the gas-solid interface have been obtained by using the following values of the gas flow rate: 1.1, 2.3, 3.7 and 8.3 cm^3/s. To decrease the dinitrogen concentration in the electrolytic solution, some runs have been performed by using dinitrogen-argon mixtures, 10 and 50 % in N_2, at the flow rate values previously reported.

The gas outlet contained the produced ammonia that was continuously stripped from the cell. The ammonia-dinitrogen mixture was bubbled in a 0.01 N HCl aqueous solution, which fixed all the ammonia. A standard colorimetric method (16), specific for ammonia and able to appreciate ten parts per billion, was used. Before starting the runs, the solutions have been carefully tested to check the total absence of ammonia.

The electrolytic process has been performed at potentiostatic conditions by using an Amel potentiostat mod. 551. The cathodic potential values, measured with reference to SCE, ranged from -920 to -1210 mV, for all the temperatures used. In order to calculate the values of faradic yield with respect to ammonia, the quantities of charge passed during the runs have been measured by an Amel integrator mod. 731. Each experiment lasted several hours; during the run, the ammonia fixing solution was replaced every two hours and tested. When the analysis of some consecutive samples gave the same figures, thus indicating steady state conditions in the cell, the run was stopped and the last figure was taken as indicative of the ammonia production.

RESULTS AND DISCUSSION

For the used temperatures the experimental results, obtained by feeding the cell by pure dinitrogen at a flow rate value of 2.3 cm^3/s, are reported in Fig. 1 as ammonia production, μmol/h, vs. cathodic potential, referred to SCE.

It has been found that, by varying gas flow rate and gas composition, the ammonia production, at equal temperature and cathodic potential, did not appreciably change. This behaviour suggests the following general considerations. The independence of ammonia production from the gas-solid interface indicates a transport of dinitrogen towards the cathodic surface which occurs through the liquid phase; moreover, the independence of ammonia production from dinitrogen concentration in the liquid phase suggests that the mass transfer resistances play a negligible, if any, role.

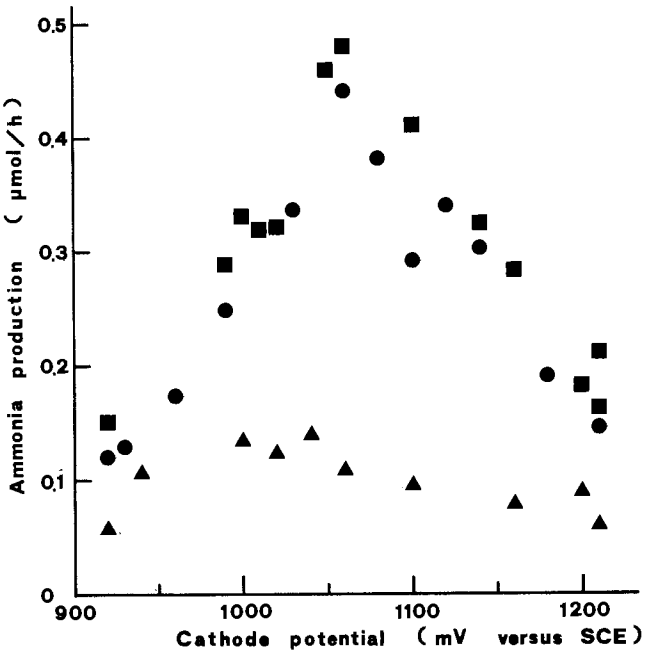

Fig. 1 - Experimental results of ammonia production per unit time vs. cathodic potential, referred to SCE, for the three temperatures used: ▲, 25 °C; ●, 35 °C; ■, 45 °C.

From the results reported in Fig. 1 the following considerations can be made:

a) ammonia is produced throughout the explored range of cathodic potential;
b) ammonia production is enhanced by increasing the temperature;
c) for each temperature ammonia production increases by increasing the cathodic potential; but, when the values of the cathodic potential are in the region of hydrogen discharge, ammonia production decreases.

For all the experiments performed at cathodic potential values below that of hydrogen discharge, the values of faradic yield, calculated with respect to ammonia, were of the order of magnitude of a percent. It has been also found that these values decreased by increasing the absolute value of cathodic potential as well as the gas flow rate, at equal temperature and potential. Indeed these very low values are explainable by considering that the relevant process that occurs in the cell consists in the redox process of iron ions (17, 18), as expected. Moreover, as the agitation of the electrolytic solution increases by increasing the gas flow rate, the transport rates of iron ions increase and therefore, being the ammonia production constant at equal temperature and potential, the faradic yield lowers.

Concluding, the feasibility of direct electrochemical reduction of molecular dinitrogen to ammonia, probably without the aid of activating complexes in the electrolytic solution, seems well proved. On the ground of all the previous considerations, one may hypothesize that the dissolved dinitrogen undergoes the following reaction:

$$N_{2(d)} + 3H_2O_{(l)} \rightarrow 2NH_{3(d)} + 1.5O_{2(g)} \cdot (E_{25^\circ C} = 1.14\ V)$$

The observed decrease of the ammonia production when the cathodic potential is in the region of hydrogen discharge, can be explained by the occurrence of a competitive adsorption between dinitrogen and hydrogen species on the cathodic surface.

REFERENCES

1. K. Kuchynka, Catal. Rev., 3, 111 (1969).
2. R. H. Fischer and P. B. Venuto, Bull. New Jersey Acad. Sci., 15, 1 (1970).
3. G. N. Schrauzer and T. D. Guth, J. Am. Chem. Soc., 99, 7188 (1977).
4. A. Fujishima, T. Inoue, S. Konishi, C. P. Weber, and K. Honda, The Annual Meeting of the Chemical Society of Japan, Nagoya, Japan, Oct. 17 1978.
5. H. Miyama, N. Fuji, and Y. Nagae, Chem. Phys. Letters, 74, 523 (1980).
6. V. Augugliaro, A. Lauricella, L. Rizzuti, M. Schiavello, and A. Sclafani, Int. J. Hydrogen Energy, 7, 845 (1982).
7. V. Augugliaro, F. D'Alba, L. Rizzuti, M. Schiavello, and A. Sclafani, Int. J. Hydrogen Energy, 7, 851 (1982).
8. M. Schiavello, L. Rizzuti, A. Sclafani, I. Majo, V. Augugliaro, and P. L. Yue, In T. N. Veziroglu, W. D. Van Vorst, J. H. Kelley (Eds.). Hydrogen Energy Progress IV, Pergamon Press, Oxford 1982, vol. 2 p. 821.
9. A. Brucato, I. Majo, A. Sclafani, and M. Schiavello, Proc. 4th Int. Conf. on Photochemical Conversion and Storage of Solar Energy, Jerusalem, August 8-13 1982, p. 116.
10. F. Khan, P. L. Yue, L. Rizzuti, V. Augugliaro, and M. Schiavello, J. C. S. Chem. Comm., 1050 (1981).
11. F. Khan, P. L. Yue, L. Rizzuti, V. Augugliaro, and A. Brucato, Ind. Eng. Chem. Prod. Res. Dev., submitted (1982).
12. E. E. Van Tamelen and B. Akermark, J. Am. Chem. Soc., 90, 4492 (1968).
13. E. E. Van Tamelen and D. A. Seeley, J. Am. Chem. Soc., 91, 5194 (1969).
14. C. R. Dickson and A. J. Nozik, J. Am. Chem. Soc., 100, 8007 (1978).
15. A. V. Gorodyskii, V. V. Danilin, O. N. Efimov, N. E. Nechaeva, and V. N. Tsarev, React. Kinet. Catal. Lett., 11, 337 (1979).
16. J. M. Henry, M. M. Cannon, and T. A. Winkelmann, "Clinical Chemistry: Principles and Techniques", Harper and Row, New York (1978).
17. L. Ojefors, This Journal, 123, 1691 (1976).
18. R. S. Schrebler Guzmàn, J. R. Vilche, and A. J. Arvìa, Electrochim. Acta, 24, 395 (1979).

Manuscript submitted July 20, 1982; revised manuscript received Nov. 10, 1982.

Publication costs of this article were assisted by the University of Palermo.

JOURNAL OF THE ELECTROCHEMICAL SOCIETY

ELECTROCHEMICAL SCIENCE
— AND TECHNOLOGY —

APRIL
1983

Interface Between Solid Electrode and Solid Electrolyte—A Study of the Li/LiI(Al_2O_3) Solid-Electrolyte System

T. R. Jow*,[1] and C. C. Liang*,[2]

Electrochem Industries Incorporated, Clarence, New York 14031

ABSTRACT

The interface contact between a solid electrode and a solid electrolyte during discharge was examined, using the Li/LiI(Al_2O_3)/PbI_2, Pb solid-state galvanic cell. Upon discharge, Li at the interface is oxidized to Li^+ which migrates through the electrolyte to the cathode. The departing Li^+ ions leave vacant sites at the Li anode surface. When the discharge rate exceeds the diffusion rate of Li to fill the vacant sites, the interface contact may be damaged resulting in a separation between the Li anode and the LiI(Al_2O_3) electrolyte. Based on the discharge time required for such a separation to occur, the Li diffusivity in the Li anode was determined to be $(5.6 \pm 0.9) \times 10^{-11}$ cm²/sec at ambient temperature (24° ± 2°C). In addition, from the results of anode polarization experiments, the exchange current density of Li/LiI(Al_2O_3) was determined to be 145 ± 25 μA/cm² at 24° ± 2°C.

In a solid-state galvanic cell, both the electrodes and the electrolyte are solid. The absence of any liquid component may cause difficulties in maintaining the interface contact between the solid electrode and the solid electrolyte during discharge. Assuming that the solid electrolyte, MX, is a cation conductor, the discharge process of an M/MX/cathode cell involves the oxidation of M atoms to M^+ ions at the M/MX interface. The M^+ ions migrate through the MX electrolyte to the cathode. The departing M^+ ions leave vacant sites at the M anode surface. Since the MX solid electrolyte is not a free-flowing liquid, the vacant sites must be filled by the diffusion of M atoms into the vacant sites or the vacancies into the metal and/or electrolyte to maintain the M/MX interface contact. However, in the event that the discharge rate is much higher than the diffusion rate of the M atoms, the demand for the metal atoms for anodic dissolution exceeds the supply by diffusion. As a result, more and more vacant sites will be generated on the metal surface at the M/MX interface and eventually coalesce into voids resulting in loss of interface contact.

This type of interface maintenance problem was noted by Raleigh (1) in his discussion of anodic dissolution mechanisms in solid-state systems. Liang (2, 3) observed experimentally, in his study of solid-state galvanic cells using an Li anode and LiI (Al_2O_3) electrolyte, that the Li anode was completely separated from the solid electrolyte after a short period of discharge at a relatively high current (500 μA/cm²) at room temperature.

Based on the physical model outlined above, the rate of void formation at the interface depends on the diffusion and anodization rates of the metal atoms. These processes may be described by Fick's second law

$$\frac{\partial C_M}{\partial t} = D\frac{\partial^2 C_M}{\partial x^2} \qquad [1]$$

where C_M is the concentration of metal atoms in the anode, D is the diffusion coefficient of metal atoms in the anode, and x is the distance of metal atoms from the interface where $x = 0$ (see Fig. 1). Initially, the concentration of metal atoms at the anode/electrolyte interface is C_o, *i.e.*

$$C_M = C_o, \qquad 0 \leq x \leq L, \qquad t = 0 \qquad [2]$$

Since a constant current is applied to the cell, a constant flow of ionized metal atoms migrate away from the metal surface, *i.e.*

$$-D\frac{\partial C_M}{\partial x} = \frac{I_o}{FA}, \qquad x = 0, \qquad t > 0 \qquad [3]$$

where I_o is the constant anodic current, A the anode/

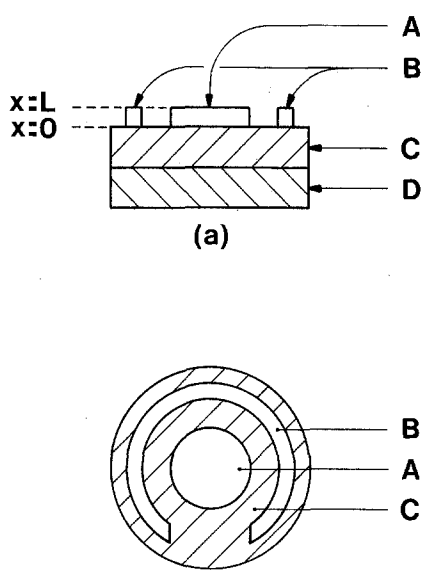

Fig. 1. Cell configuration: (a) side view, A—Li anode, B—Li reference electrode, C—Li^+ solid electrolyte, and D—cathode, and (b) top view.

* Electrochemical Society Active Member.
[1] Present address: Allied Corporation, Morristown, New Jersey 07960.
[2] Present address: OMNION, Incorporated, Clarence, New York 14031.
Key words: interfaces, diffusion, solid electrolyte, exchange current density.

electrolyte intersectional area, and **F** the Faraday constant. We assumed that no concentration gradient of metal atoms exists at the $x = L$ surface (Fig. 1a), *i.e.*

$$\frac{\partial C_M}{\partial x} = 0, \qquad x = L, \qquad t > 0 \qquad [4]$$

Accordingly, the solution of Eq. [1] with the conditions of Eq. [2]-[4] is as follows (4)

$$C_o - C_M(x,t) = \frac{2I_o t^{1/2}}{FAD^{1/2}} \sum_{n=0}^{\infty} \left[\text{ierfc} \frac{2(n+1)L - x}{2(Dt)^{1/2}} + \text{ierfc} \frac{2nL + x}{2(Dt)^{1/2}} \right] \qquad [5]$$

Assuming that at $t = t_o$, the concentration of the metal atoms at the interface approaches zero, *i.e.*

$$C_M(0, t_o) = 0, \qquad x = 0, \qquad t = t_o \qquad [6]$$

then Eq. [5] is reduced to

$$C_o = \frac{2}{F(\pi D)^{1/2}} \frac{I_o}{A} t_o^{1/2}, \qquad t_o << \frac{L^2}{D} \qquad [7]$$

Equation [7] can be rearranged to

$$\frac{I_o}{A} = j = \frac{C_o F}{2} (\pi D)^{1/2} t_o^{-1/2}, \qquad t_o << \frac{L^2}{D} \qquad [8]$$

Equations [7] and [8] are in fact the well-known Sand equation (5) for the transition time for depletion of an electroactive species at the electrode surface by a constant current in a liquid electrolyte. If one assumes that the time for a cell to discharge to zero volts corresponds to time t_o; *i.e.*, when the concentration of the metal atoms at the interface approaches zero, a linear relation between j and $t_o^{-1/2}$ is expected. The diffusivity of the metal atoms in the metal can be calculated from the slope of the linear relation.

In the present study, the solid anode/solid electrolyte interface was examined using the Li/LiI(Al_2O_3)/PbI_2, Pb solid-state galvanic cell, wherein the cathode served as a sink for the Li^+ ions. The experimental results obtained under constant current conditions were used to determine the diffusivity of Li in the Li anode in accordance with Fick's second law. In addition, the potential sweep technique was applied to determine the anode exchange current density at the Li/LiI(Al_2O_3) interface.

Experimental

Materials preparation.—The LiI(Al_2O_3) solid electrolyte was prepared according to the method used by Kuo *et al.* (6). LiI (Cerac 99.9%) was dried under vacuum while heated gradually from room temperature to 120°C and maintained at 120°C overnight. Alumina (Alcoa H151) was first dried under vacuum at 250°C and then treated with n-butyl lithium (Aldrich, 1.6M solution in hexane) using a ratio of about 2 cm^3 n-butyl lithium to one gram of alumina. The excess n-butyl lithium was washed using hexane. The dried LiI and the treated alumina were then mixed in a 1 to 1 mol ratio and compacted using a stainless steel die. The compact was then heat-treated at 500°C under vacuum for 2½ hr and quenched to room temperature. The quenched sample was pulverized into powder for use. The typical conductivity of the electrolyte thus prepared was 4.0 to 6.5 $\times 10^{-5}$ Ωcm^{-1}. The cathode powder was prepared by mixing PbI_2 (Alfa 98.5%), Pb (Alfa 99%, −200 mesh), and the electrolyte in an automatic grinder. Lithium foil (Foote Mineral) was scraped before use.

Cell fabrication.—The cell as shown in Fig. 1 was fabricated as follows: the electrolyte layer was prepressed at a pressure of 350 kg/cm^2 in a 1.3 cm diam stainless steel die. The cathode layer on one of the electrolyte surfaces was pressed at a pressure of 7000 kg/cm^2. The lithium anode with or without a lithium reference electrode was finally pressed onto the other surface of the electrolyte at a pressure of about 2500 kg/cm^2. With the help of a polyethylene disk having openings for Li, the Li anode and reference electrodes were arranged as shown in Fig. 1. The diameter of a typical Li anode was about 0.59 cm. The electrical leads from electrodes were pressed on the electrodes during each step of pressing.

Electrical measurements.—The cell potential and the polarization of the anode were both monitored using a Keithley 616 electrometer while constant current was applied using a Keithley 227 constant current source.

The anodic potential sweep experiment was carried out using a Princeton Applied Research Model 173 potentiostat/galvanostat, a Model 376 logarithmic current converter, a Model 175 universal programmer, and a Hewlett Packard Model 7044A X-Y recorder. A sweep rate of 1 mV/sec was used to approximate steady-state conditions. The current-potential curve obtained was digitalized and corrected for the IR drop across the electrolyte. The IR drop was obtained by the current interrupt method at low currents (typically 10-30 $\mu A/cm^2$).

All of the cell fabrication processes and electrical measurements were performed in argon-filled dry boxes (Vacuum Atmospheres) at 24° ± 2°C (ambient). The electrical leads of the cell were connected to various measuring instruments outside the dry box through proper feedthroughs.

Results and Discussion

The Li/LiI(Al_2O_3) interface contact.—The cell potential decreased sharply at the end of a constant current discharge (Fig. 2, 3a, and 4). This mode of cell failure was due to the loss of the interface contact between the anode and the electrolyte as indicated by the fact that after the cell voltage had reached zero volts or below, the anode had separated from the electrolyte and could be easily removed from the electrolyte surface using a pair of tweezers. The rapid change of voltage at the end of a constant current discharge may also correspond to charging of an air-gap capacitor created by the formation of voids. Indeed, in order to confirm that the loss of interface contact between the anode and the solid electrolyte

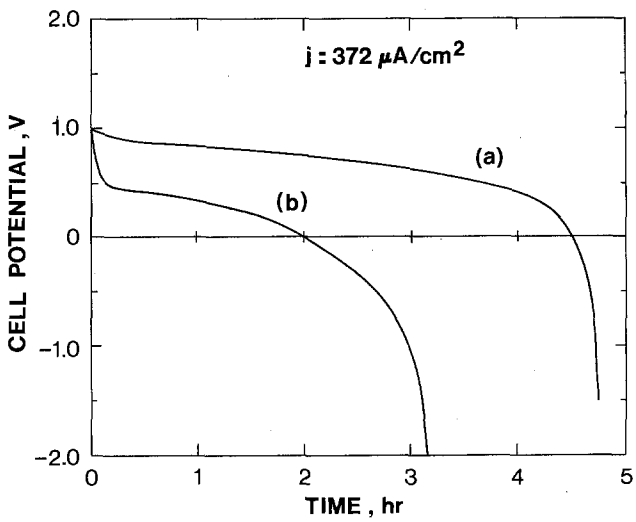

Fig. 2. Cell potential vs. time under a discharge current of 372 $\mu A/cm^2$ at ambient temperature. (a) Discharge curve of a fresh cell. (b) Discharge curve of the renewed cell (Li was pressed on the renewed electrolyte surface).

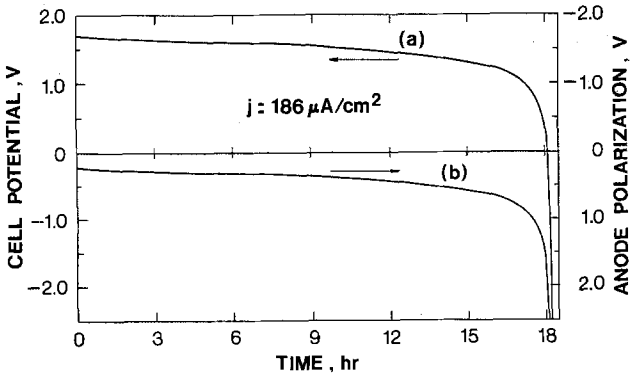

Fig. 3. Cell potential (a) and Li anode polarization potential (b) as a function of time under a discharge current of 186 $\mu A/cm^2$ at ambient temperature.

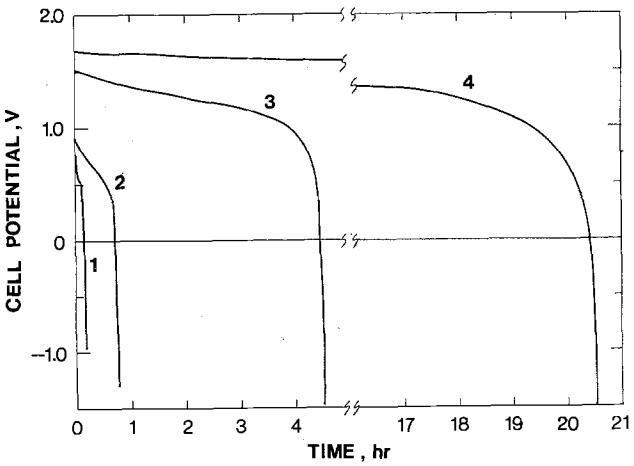

Fig. 4. Typical discharge curves of $Li/LiI(Al_2O_3)/PbI_2$, Pb, cells at 1, 1487; 2, 744; 3, 372; 4, 186 $\mu A/cm^2$ at ambient temperature.

was the principal cause for cell failure, the following experiments were conducted:

1. An $Li/LiI(Al_2O_3)/PbI_2$, Pb solid-state galvanic cell was discharged under a constant current of 372 $\mu A/cm^2$. After the cell had reached a potential below zero volts, the anode was removed and the electrolyte surface was scraped using an Exacto knife. A new disk of Li was pressed onto the electrolyte surface. It should be noted that the electrolyte/cathode pellet could not be reinserted into the steel die for pressing the new anode. Therefore, the new anode was pressed on the electrolyte surface without the constraint of the steel die. To avoid crushing the solid cell, the anode was pressed at 650 kg/cm^2 instead of the original fabricating pressure of 2500 kg/cm^2. Even under the reduced pressure, the periphery of the cell was cracked. In any event, the used cell with a new anode was discharged under the same 372 $\mu A/cm^2$ current and the discharge curve is shown in Fig. 2b. Although the cell potential was lower and the discharge time was shorter than the original, the fact that a used cell with an anode which was much less than ideal could be discharged, further indicated that the cathode was not responsible for the failure of the original cell. It should be noted that the initial discharge potential in Fig. 2 was somewhat lower than that shown by curve 3 in Fig. 4, though the discharge current of the two cells was 372 $\mu A/cm^2$. This discrepancy can be explained by the fact that the electrolyte thickness of the cell shown in Fig. 2 was greater than that of the cell shown by curve 3 in Fig. 4.

2. An Li reference electrode was incorporated in an $Li/LiI(Al_2O_3)/PbI_2$, Pb solid cell which was discharged under a constant current of 186 $\mu A/cm^2$. During discharge, both the cell potential and the anode polarization were monitored. As shown in Fig. 3, the cell potential followed the anode polarization during the entire course of the discharge. These results again showed that the cathode was not significantly polarized and that the cell failure was due to the interface contact between the solid anode and the solid electrolyte.

It should be noted, however, that under a high rate of discharge (*e.g.*, 1487 $\mu A/cm^2$) the anode was not completely separated from the electrolyte surface, though some portion of the contact surface did separate. The removal of the anode from the electrolyte, using a pair of tweezers, was more difficult than that experienced for cells discharged under lower currents. This may have been due to the fact that the current distribution was less uniform during the formation of voids at high current densities. As a result, the capacitative voltage buildup at the voids occurred more quickly, such that it canceled out the cell emf before complete interface separation had occurred.

Rate of discharge and diffusivity of Li.—Figure 4 shows discharge curves of the $Li/LiI(Al_2O_3)/PbI_2$, Pb solid-state galvanic cells under various constant currents. Indeed, according to the model of diffusion and anodization processes discussed previously, the rate of discharge, j, should be inversely proportional to the square root of discharge time before the failure of the interfacial contact, $t_o^{1/2}$. Figure 5 shows the plot of j *vs.* $t_o^{-1/2}$. A linear relation was indeed noted at low currents. The deviation from linearity at high currents may be attributed, at least in part, to the severe polarization at the anode as discussed previously.

The diffusivity of Li atoms in the Li anode was calculated from the slope of the j *vs.* $t_o^{-1/2}$ plot. A value of $(5.6 \pm 0.9) \times 10^{-11}$ cm^2/sec was obtained at 24° ± 2°C. This value of the Li diffusivity agreed well with the value of 8.1×10^{-11} cm^2/sec for Li self-diffusivity extrapolated from the results obtained by Lodding *et al.* (7) using tracer techniques.

Anodic exchange current density of $Li/LiI(Al_2O_3)$.—In order to investigate further the kinetic behavior of the $Li/LiI(Al_2O_3)$ interface, the Li anode was polarized using the potential sweep technique at a rate of 1 mV/sec. After correction for the IR drop, the current, j, *vs.* overpotential, η, was plotted and shown in Fig. 6. The j *vs.* η relation may be expressed in accordance with the Butler-Volmer equation (8)

$$j = j_o \{\exp[(1-\alpha)\mathbf{F}\eta/RT] - \exp[-\alpha\mathbf{F}\eta/RT]\} \quad [9]$$

where j_o is the exchange current density, α, the transference coefficient, and R, T, and $\mathbf{F}$ are the gas constant, temperature, and Faraday constant, respectively. At low polarization potentials, a linear relation between j and η may be approximated. Therefore

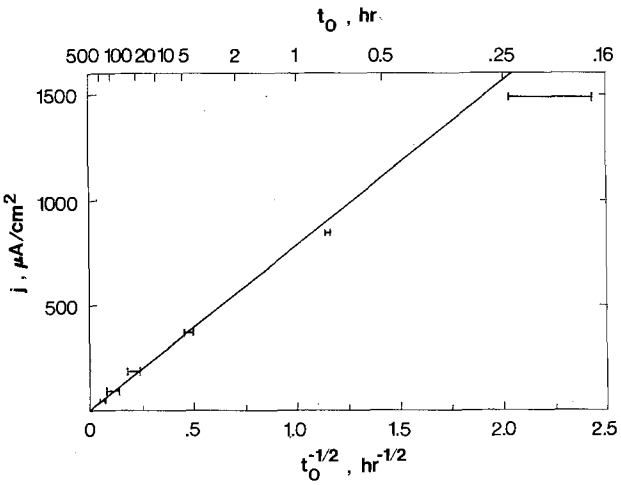

Fig. 5. Discharge current and discharge time relation (j *vs.* $t_o^{-1/2}$).

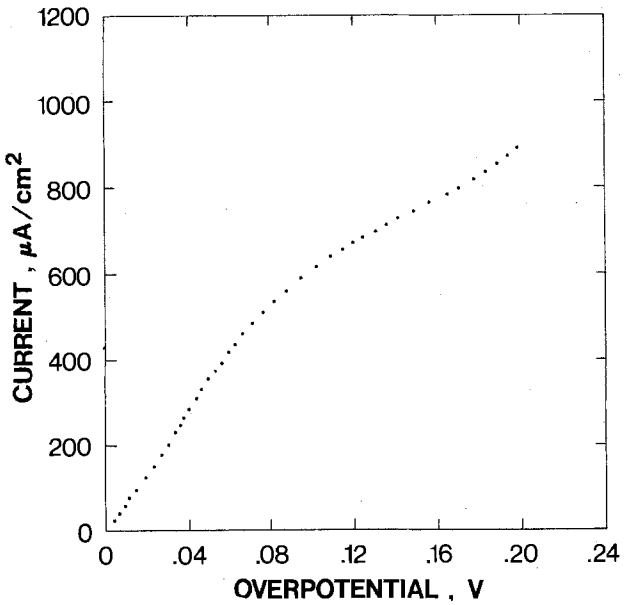

Fig. 6. Current-overpotential relation after correction for the electrolyte resistance. Sweep rate: 1 mV/sec.

$$j = j_o \frac{F\eta}{RT} \qquad [10]$$

Using the linear portion of the curve at low potentials in Fig. 6 and in accordance with Eq. [10], the exchange current density j_o at the Li/LiI(Al_2O_3) interface was found to be 145 ± 25 μA/cm² at room temperature. At higher potentials, the experimental j-η data (Fig. 6) did not follow the Butler-Volmer equation (Eq. [9]) due to the fact that a substantial change in Li concentration occurred at the interface during the potential sweep. Therefore, the steady state was not achieved at higher potentials. This is also evident from Fig. 7 which shows a reduced current for the same anode polarization potential at a subsequent sweep. On the other hand, at low potentials the change in Li concentration at the interface was not substantial. Consequently, the slow sweep could approximate the steady state well enough to obtain the exchange current density.

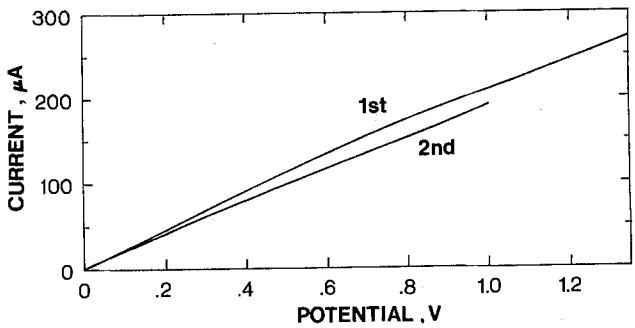

Fig. 7. Current-potential curves of the first and the second potential sweeps. No correction for the electrolyte resistance was made. Sweep rate: 1 mV/sec.

Manuscript submitted July 6, 1982; revised manuscript received Oct. 4, 1982.

Any discussion of this paper will appear in a Discussion Section to be published in the December 1983 JOURNAL. All discussions for the December 1983 Discussion Section should be submitted by Aug. 1, 1983.

Publication costs of this article were assisted by Electrochem Industries, Incorporated.

REFERENCES

1. D. O. Raleigh, "Electroanalytical Chemistry," Vol. VI, A. J. Bard, Editor, p. 87, Marcel Dekker, New York (1973).
2. C. C. Liang, "Fast Ion Transport in Solids—Solid State Batteries and Devices," W. van Gool, Editor, p. 19, North-Holland, Amsterdam (1973).
3. C. C. Liang, "Applications of Solid Electrolytes," T. Takahashi and A. Kozawa, Editors, p. 60, JEC Press, Cleveland, Ohio (1980).
4. H. S. Carslaw and J. C. Jaeger, "Conduction of Heat in Solids," p. 112, Oxford University Press, London (1959).
5. P. Delahay, "New Instrumental Methods in Electrochemistry," p. 184, Wiley-Interscience, New York (1954).
6. H. C. Kuo, J. R. Rea, G. S. Kelsey, and M. Kallianidis, *Proc. Power Sources Conf.*, **29**, 171 (1980).
7. A. Lodding, J. N. Mundy, and A. Ott, *Phys. Status Solidi*, **38**, 559 (1970).
8. A. J. Bard and L. R. Faulkner, "Electrochemical Methods: Fundamentals & Applications," p. 103, Wiley-Interscience, New York (1980).

The Electrochemistry of Molten Lithium Chlorate and Its Possible Use with Lithium in a Battery

Su-Chee Simon Wang*,[1] and Douglas N. Bennion*,[2]

Chemical Engineering Department, University of California, Los Angeles, California 90024

ABSTRACT

Lithium chlorate, $LiClO_3$, has reported melting points of 127.6° and 129°C. The specific conductance of molten lithium chlorate at 130°C is relatively high compared to common aqueous electrolytic solutions at room temperature. Therefore, lithium chlorate offers the chance to operate a new lithium battery system at a temperature between 130° and 150°C. It was found experimentally that lithium chlorate is stable in the potential range between 3.2 and 4.6V relative to an Li reference electrode. An Li-Cl_2 secondary battery system was observed to have an open-circuit potential of 3.97V, making an Li-Cl_2 secondary battery in molten lithium chlorate possible, in principle. A lithium-lithium chlorate primary battery system is also possible. Lithium negative electrode performance was found to be hindered by corrosion and possible runaway reactions with $LiClO_3$. Dendrite formation on charging was observed. The solubility of Li_2O and LiCl in $LiClO_3$ at 145°C is 7.5×10^{-5} and 1.78×10^{-3} mol/cm^3, respectively. The diffusion coefficients are 1.5×10^{-7} for Li_2O and 3.4×10^{-7} cm^2/sec for LiCl. Platinum appeared to be an inert positive electrode for chlorate, chlorine, or oxygen reactions for runs on the order of several hours. Nickel shows an active-passive behavior which is complex. Nickel appears suitable for use in a primary cell for the cathodic discharge of $LiClO_3$, but it does not appear suitable for a Cl_2 or O_2 electrode.

Lithium, with low equivalent weight and large negative electrochemical potential, is an attractive choice as a negative electrode for batteries of high specific energy and power density. Two types of nonaqueous lithium battery systems have been developed, ambient temperature and high temperature systems.

Compared to the ambient temperature systems, the high temperature systems have the advantage of higher power output capacity because of the higher conductivity and the faster electrode kinetics associated with molten salt electrolytes used in high temperature systems. However, disadvantages for high temperature systems are heating in the starting up stage and the material problems of sealing and separation. Looking for a molten salt electrolyte which works at a lower temperature, *e.g.*, below 200°C, might be one of the alternatives to solve the material problems. Lithium chlorate is one possible electrolyte for use in this temperature range since it has a reported melting point at about 128°C (1, 2). Therefore, lithium chlorate offers the chance to operate a new battery system at a temperature between 130° and 150°C. The specific conductance of molten lithium chlorate varies from 0.1150 $(\Omega\ \text{cm})^{-1}$ at 131.8°C to 0.1420 $(\Omega\ \text{cm})^{-1}$ at 143.01°C (3).

It is reported by Markowitz *et al.* (4) that after two days of heating at a temperature of 135°C under flowing argon, only 0.46% of the lithium chlorate was decomposed. The products were lithium chloride (0.06%) or lithium perchlorate (0.40%). It was also reported that a fast exothermic decomposition takes place at about 376°C. Lithium chlorate at about 140°C is believed to have good thermal stability.

In preliminary experiments, lithium could be successfully deposited and discharged reversibly from molten lithium chlorate on different inert negative electrode substrates including lithium, nickel, stainless steel, and platinum. All of these substrates are believed to be stable in molten lithium chlorate. However, the formation of a lithium-platinum alloy embrittled the platinum substrate.

The cathodic reaction occurring on the surface of an inert positive electrode during discharging is believed to be the reduction of lithium chlorate to lithium oxide and lithium chloride.

$$LiClO_3 + 6Li^+ + 6e^- \rightarrow LiCl + 3Li_2O \qquad [1]$$

$E^0 = 3.241$V (5, 6) (relative to Li ref. electrode)

The various anodic electrochemical reactions which are expected on the surface of a positive electrode during charging are

$$Li_2O \rightarrow 2Li^+ + \tfrac{1}{2}\,O_2 + 2e^- \qquad [2]$$

$E^0 = 2.903$V (6) relative to Li ref. electrode)

$$LiCl \rightarrow Li^+ + \tfrac{1}{2}\,Cl_2 + e^- \qquad [3]$$

$E^0 = 3.976$V (6) (relative to Li ref. electrode)

$$LiClO_3 \rightarrow Li^+ + 1/2\ Cl_2 + 3/2\ O_2 + e^- \qquad [4]$$

$E^0 = 4.6$V

(from experimental data, relative to Li ref. electrode)

In the present study inert materials which can be used as positive or negative electrodes in molten lithium chlorate were studied. The solution composition and the surface condition of the electrodes change as Li/$LiClO_3$ cells are discharged. Therefore, current-voltage curves were obtained after varying time periods of electrochemical discharge. Both Ni and Pt were used as the active surfaces for rotating disk electrodes to study the effects of the accumulation of discharge products, presumed to be Li_2O and LiCl, on the voltage-current sweeps as a function of time of discharge. The electrolyte was also analyzed at different charging and discharging states to investigate the possible occurrence of reactions [1], [2], [3], and [4] at inert positive electrodes. Gas, evolving from the positive electrode during charging, was collected and analyzed to complement the information obtained from liquid phase chemical analysis. The potential range, at which molten lithium chlorate is electrochemically stable, is discussed. The possibility of using lithium chlorate as the electrolyte in a primary and a secondary lithium battery is considered.

Experimental

Lithium chlorate used in all experiments was prepared as described by Campbell and Griffiths (7). A 1.0*M* solution of barium chlorate was heated to 85°C. Then a 1.0*M* solution of lithium sulfate was added slowly until equivalence was reached. The precipitated barium sulfate was removed by filtration. The lithium chlorate solution was evaporated slowly under 1 cm Hg pressure, the temperature being kept below 85°C, up to an approximate concentration of 90% lithium chlorate. The concentrated lithium chlorate solution

* Electrochemical Society Active Member.
[1] Present address: General Motors Research Laboratory, Warren, Michigan 48090.
[2] Present address: Chemical Engineering Department, Brigham Young University, Provo, Utah 84602.
Key words: molten salt, chlorine, lithium oxide, lithium chloride.

was then transferred into an argon atmosphere glove box and heated to 130°C under 50 μm Hg pressure for four weeks. Using this process the "dried" lithium chlorate melted between 126° and 128°C. According to the chlorate-water phase diagram proposed by Krauss *et al.* (8), a melting point of lithium chlorate between 126° and 128°C corresponds to a water content of less than 0.5%. Lithium chlorate is known to be extremely hygroscopic (8). As long as the water content in the lithium chlorate was 0.5% or less, no gross effects associated with water were observed. The 50 μm of Hg pressure in the drying chamber was mostly argon leaking into the flask. Thus, the partial pressure of water was some small fraction of the 50 μm total pressure at 130°C.

The polarization experiments were conducted using rotating disk electrodes. The electrochemical cell was a glass cylinder 1.9 cm in diameter and 3.8 cm high. Two glass tubes, 0.6 cm in diameter, were connected to the cylinder at the bottom to accommodate a lithium counterelectrode and a lithium reference electrode. Small sintered glass blocks 0.32 cm thick were embedded inside the 0.6 cm tubes to separate the main cylinder from the lithium counterelectrode and the reference electrode. Nickel and platinum rotating disk electrodes were used. The nickel electrode was made of 0.32 cm diameter rod, 4.71 cm long, held inside a Teflon sleeve 0.76 cm in diameter. The platinum rotating disk electrode was a wire, 0.13 cm in diameter, surrounded by a 0.76 cm diameter Teflon sleeve and supported from a 0.32 cm diameter aluminum rod.

The cell was placed on a hot plate inside a heavy aluminum tube, 0.64 cm wall thickness. The aluminum tube formed a cavity which was reasonably constant in temperature, ± 1°C. Temperature was measured using an iron-constantan thermocouple. Measurements were made at 145°C. About 6.5g of pure lithium chlorate was added into the main cylinder and melted. The two side arms were half filled with molten electrolyte. Two lithium ribbons, one inserted into the counterelectrode compartment and the other into the reference electrode compartment, were held in position by Teflon stoppers. The rotating disk electrode was dipped into the molten lithium chlorate in the main cylinder. The rotation rate was controlled by an adjustable speed motor and generally kept at 1000 rpm. Rotation rates of 1200, 1500, and 1800 rpm were used in a few cases.

All experiments were performed in an argon filled glove box, Model HE-243-2 DRI LAB, which was supplied by Vacuum Atmosphere Corporation. The impurity levels of oxygen and water were estimated by the life of a 25W light bulb tungsten filament in the glove box. The light burned for a month during the time of the experiments indicating, according to the operating manual of the dri-lab, that the oxygen plus water content was between 1 and 5 ppm. The temperature within the glove box was 29° ± 1°C.

A circuit consisting of a potentiostat and an ammeter for measuring the current was connected in series with the experimental cell. A digital voltmeter was connected between the rotating disk electrode and the lithium reference electrode for measuring potential. All of the polarization curves were obtained potentiostatically.

The chemical analysis for chloride ions and oxide ions suggested by Markowitz (5) was employed to investigate the production or consumption of lithium chloride and lithium oxide in electrochemical reactions occurring on the positive electrode of a lithium chlorate cell. Lithium chlorate electrolyte was sampled and dissolved in distilled water at various times during the polarization experiments. The oxide content was determined by titration to a phenophthalein end point with hydrochloric acid; the chloride content was determined gravimetrically as AgCl. The Ni content in the electrolyte was measured using a Perkin-Elmer Atomic Absorption Spectrometer.

Gas, often observed evolving from the positive electrode during charging, was collected and analyzed to add to the information obtained from liquid phase chemical analysis.

Results

In the first polarization experiments, 6.81g of fresh lithium chlorate were added to the main cylinder of the rotating disk cell. An Ni rotating disk, polished before using, was then dipped into the molten lithium chlorate electrolyte and left until the open-circuit potential reached a steady state. The anodic polarization curve in fresh lithium chlorate is shown in Fig. 1. Electrochemical reduction of the lithium chlorate was then carried out using an Ni plate 1 cm × 1 cm in the main cylinder and running current between the Ni plate and the Li counterelectrode. After 200, 600, and 1000 microequivalents were discharged, further anodic polarization curves were obtained on freshly polished Ni rotating disks. These curves are also shown in Fig. 1. After 1500 microequivalents were discharged from the lithium chlorate, three anodic polarization curves were run on an Ni rotating disk. The first one right after discharging, the second 2 hr later, and the third after 20 hr. The disk was polished before the first run and left standing in molten lithium chlorate afterwards. These three curves are shown in Fig. 2.

Comparing Fig. 1 and 2 shows that the first voltage plateau, at 3.0V, appeared in Fig. 1 after 1000 microequivalents were discharged. However, this plateau was partially or completely eliminated after the Ni rotating disk was left standing in molten lithium chlorate for 2-20 hr as shown in Fig. 2. It was also observed that the second plateau, at 3.6V for fresh

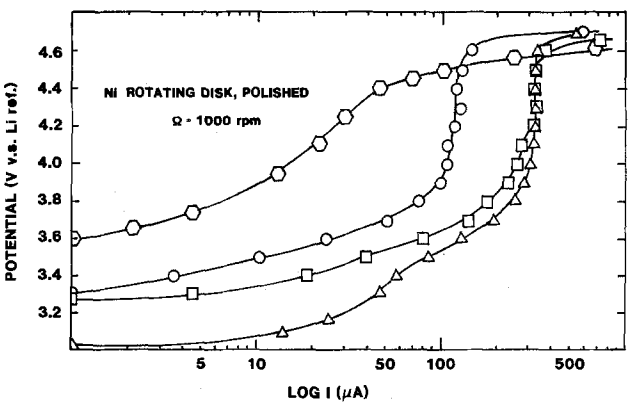

Fig. 1. Anodic polarization curves at different discharging stages, ○ fresh lithium chlorate, ○ after 200 microequivalents, □ 600 microequivalents, △ 1000 microequivalents discharged.

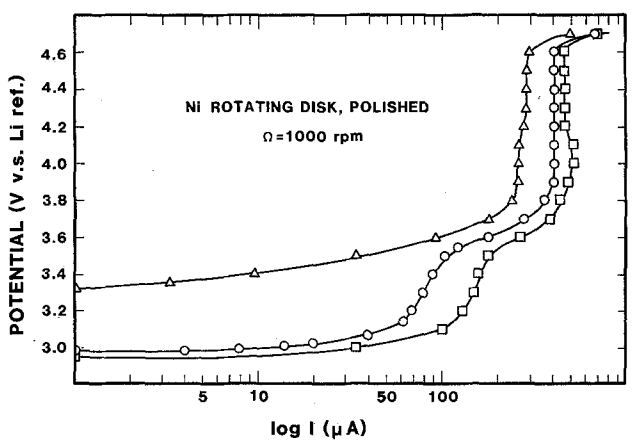

Fig. 2. Anodic polarization curves after 1500 microequivalents discharged □ right after discharging, ○ after 2 hr hot stand, and △ after 20 hr hot stand.

lithium chlorate or 3.3V for used lithium chlorate, extends further after discharging as shown in Fig. 1 and 2. The 4.7V plateau or the third plateau appeared at a lower potential when the lithium chlorate was fresh.

In the second set of experiments, 6.45g of fresh lithium chlorate was added to the electrochemical cell. Anodic polarization experiments were obtained using a polished Ni rotating disk at different rotating electrode speeds after 400 microequivalents were discharged from the electrolyte using an Ni plate 1 cm × 1 cm area. In Fig. 3, anodic polarization data, with Ω = 1000 rpm, 1200 rpm, 1500 rpm, and 1800 rpm, are shown. It was found that the limiting current observed between the second and the third plateaus obeyed the square root law of Levich's equation (9)

$$I_L = 0.62nFAD^{2/3}\nu^{-1/6}\Omega^{1/2}C \qquad [5]$$

The lithium chlorate electrolyte was then discharged further using the Ni plate. For 530, 630, and 704 microequivalents discharged, anodic polarization curves were obtained using a freshly polished Ni rotating disk. The limiting current observed in the anodic polarization experiments, shown in Fig. 4, reached a limiting value of 290 μA after 630 microequivalents were discharged.

Cathodic polarization curves were also obtained in the electrolyte after 704 microequivalents discharged. These curves, shown in Fig. 5, indicated that the cathodic current increases at higher rotating speeds. However, the increase is not proportional to the square root of rotation rate, indicating that the current is not completely or simply controlled by mass transfer.

In the following described experiments, a polished Pt disk was dipped into 6.91g of fresh lithium chlorate and rotated. The anodic polarization curve in fresh electrolyte is shown in Fig. 6. After 250 and 450 microequivalents were discharged from the electrolyte using an Ni plate, more anodic polarization experiments were run using a freshly polished Pt rotating disk at two different rotating speeds, 1000 rpm and 1800 rpm. The anodic current plateaus between 3.6 and 4.0V followed the square root law, indicating the limiting current is diffusion controlled.

Cathodic polarization curves on Pt in fresh lithium chlorate and after 450 microequivalents were discharged are shown in Fig. 7 and 8 at 1000 rpm and 1800 rpm. The cathodic current increased at the higher rotating speed but at less than $\sqrt{\Omega_1/\Omega_2}$ as was found using the Ni rotating disk. The cathodic current plateau decreased in magnitude with increased discharging.

The plateau between 4.0 and 4.6V for anodic polarization was studied at varying LiCl concentration. Vacuum dried LiCl was added to 8.32g of molten lithium chlorate stepwise. Anodic polarization curves were measured at different LiCl concentrations on a polished Pt rotating disk. At an analyzed LiCl concentration of 1.54 × 10^4 mol/cm^3, polarization experiments were conducted at rotating speeds of 1000 and 1800 rpm. Two limiting currents, 90 and 120 μA, respectively, were observed as shown in Fig. 9. At higher concentration, 1.57 × 10^{-3} mol/cm^3, the limiting current increased to 820 μA at 1000 rpm. When the lithium chlorate was saturated with LiCl, the limiting current increased to 1000 μA at 1000 rpm. A new voltage plateau near 4.8V was observed in all cases.

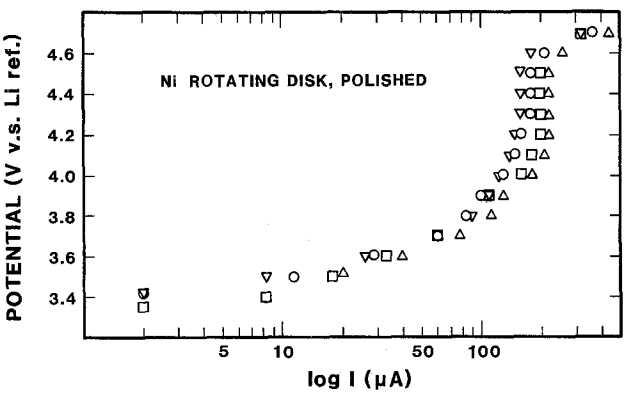

Fig. 3. Anodic polarization curves after 400 microequivalents discharged ▽Ω = 1000 rpm, ○Ω = 1200 rpm, □Ω = 1500 rpm, and △Ω = 1800 rpm.

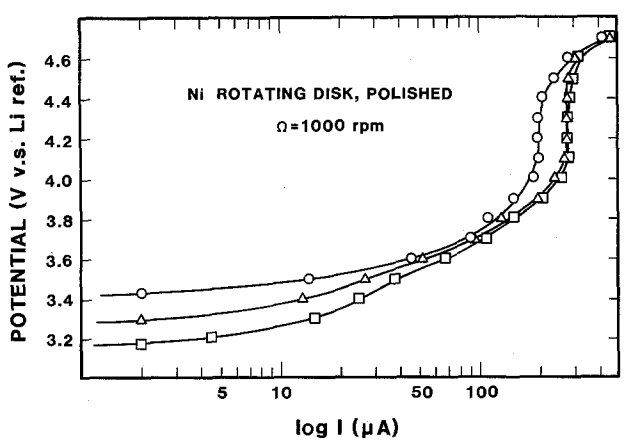

Fig. 4. Anodic polarization curves at different discharging stages, after ○ 530 microequivalents, □ 630 microequivalents, △ 704 microequivalents discharged.

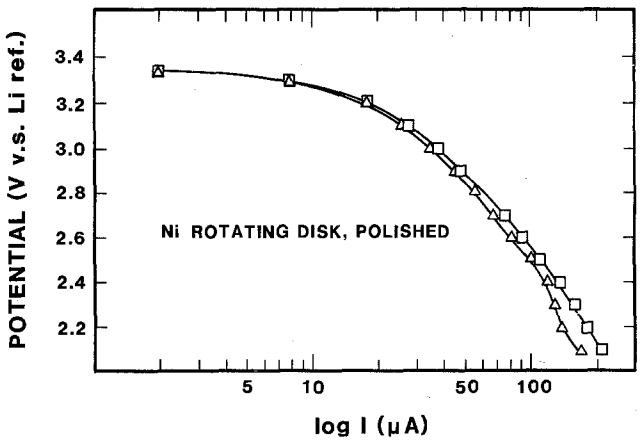

Fig. 5. Cathodic polarization curves after 704 microequivalents discharged, △Ω = 1000 rpm, □Ω = 1500 rpm.

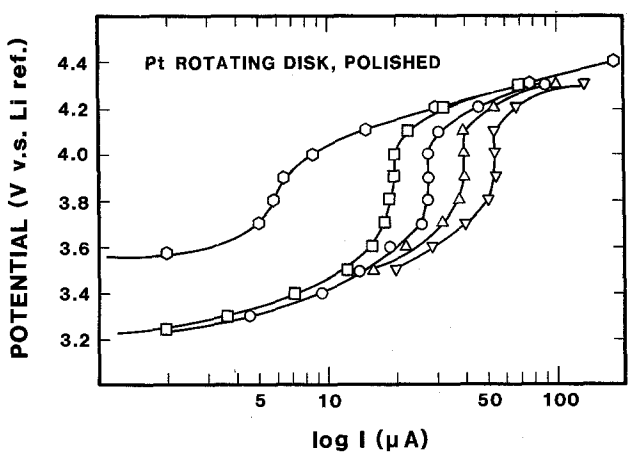

Fig. 6. Anodic polarization curves, ○ in fresh lithium chlorate Ω = 1000 rpm, □ after 250 microequivalents discharged Ω = 1000 rpm, ○ after 250 microequivalents discharged Ω = 1800 rpm, △ after 450 microequivalents discharged Ω = 1000 rpm, ▽ after 450 microequivalents discharged Ω = 1800 rpm.

Table I. Summarized results of chemical analysis after discharging using an Ni or a Pt electrode

Type of electrode	Ni	Ni	Pt
Amount of $LiClO_3$ in the positive compartment	5.01g	4.64g	5.31g
Amount of discharge	1200 microequivalents	2200 microequivalents	600 microequivalents
Amount of Li_2O created during discharging	477 μmol (953 microequivalents)*	922 μmol (1843 microequivalents)*	242 μmol (485 microequivalents)*
Amount of LiCl created during discharging	264 μmol (1590 microequivalents)*	500 μmol (3000 microequivalents)*	129 μmol (773 microequivalents)*

* Converted based on Eq. [1].

The involvement of Li_2O and LiCl in the electrochemical reactions on the positive electrode in lithium chlorate was explored by chemical analysis for LiCl and Li_2O (5). The lithium chlorate melt surrounding the positive electrode was sampled periodically while discharging at a voltage around 2.5V. Both nickel and platinum were used as the positive electrode material. The sampled electrolyte was then analyzed. The results are summarized in Table I. About 20% less Li_2O and 30% more LiCl than expected based on Eq. [1] were created during discharging of the electrolyte.

The experiments were continued by reversing the current and making the positive electrode compartment anodic. The charging current was occasionally adjusted to keep the potential between 3.0 and 3.8V. The electrolyte was sampled during charging and analyzed for Li_2O and LiCl. It was found that only Li_2O was consumed during charging, see Table II.

Gassing has been observed during charging between 3.0 and 3.8V on either Ni or Pt electrodes. The gas, collected from the positive compartment, was blown through an oxygen absorbent to analyze the oxygen content. The results are shown in Table III. Based on the results shown in Tables II and III, it is believed that the electrochemical reaction occurring on the positive electrode during charging between 3.0 and 3.8V is oxygen evolution from Li_2O as shown by Eq. [2].

When charging was carried out between 4.4 and 4.7V on an Ni positive electrode, the electrolytic solution became dark green in color. Chemical analysis of the electrolyte showed that Li_2O and LiCl were neither created nor consumed. However, after dissolving the cooled, solidified electrolyte and the dark green pre-

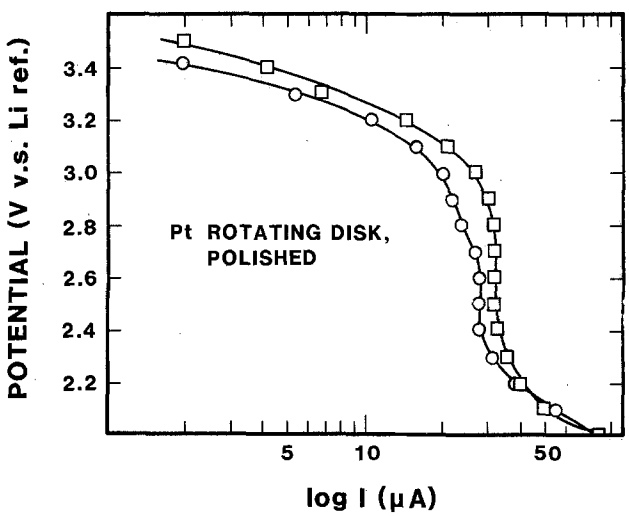

Fig. 7. Cathodic polarization curves in fresh lithium chlorate, ○Ω = 1000 rpm, □Ω = 1800 rpm.

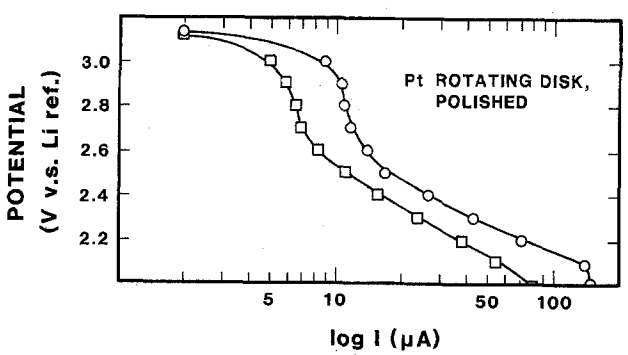

Fig. 8. Cathodic polarization curves after 450 microequivalents discharged, □Ω = 1000 rpm, ○Ω = 1800 rpm.

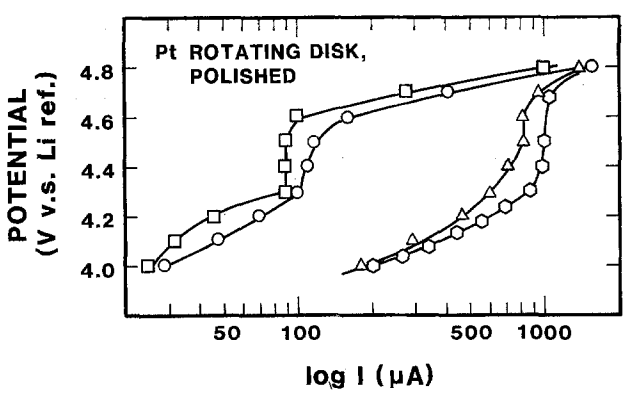

Fig. 9. Anodic polarization curves at different LiCl concentration, □ 1.542 × 10^{-4} mol/cm³, Ω = 1000 rpm, ○Ω = 1800 rpm, △ 1.574 × 10^{-3} mol/cm³, Ω = 1000 rpm, ○ saturated with LiCl Ω = 1000 rpm.

Table II. Summarized results of chemcal analysis after charging using an Ni or a Pt electrode below 3.8V

Type of electrode	Ni	Pt
Amount of $LiClO_3$ in the positive compartment	4.60g	5.19g
Amount of charge	500 microequivalents	437 microequivalents
Amount of Li_2O consumed during charging	204 μmol (407 microequivalents)*	174 μmol (348 microequivalents)*
Amount of LiCl consumed during charging	—	—

* Calculated based on Eq. [2].

Table III. The results of oxygen collection during charging between 3.0 and 3.8V

Testing electrode	Amount of charge (microequivalents)	Amount of gas collected (ml)	Oxygen content in the collected gas (ml)
Ni	200	1.6	1.2 (195 microequivalents)*
Pt	200	1.6	1.1 (179 microequivalents)*

* Converted based on Eq. [2].

cipitate in acid, nickel ions were found in the solution using an atomic absorption spectrometer.

When charging was carried out between 4.0 and 4.6V on a Pt positive electrode, it was found that both LiCl and Li_2O were consumed; see Table IV. However, during charging above 4.6V, LiCl is created as Li_2O is consumed on a Pt positive electrode.

During charging above 4.6V on a Pt positive electrode, gas was collected and analyzed for both Cl_2 and O_2. From the results shown in Table V, it was observed that the quantity of Cl_2 and O_2 evolved during anodic charging above 4.6V is roughly correlated by reaction [4]. However, deviations from the stoichiometry of Reaction [4] suggest that other reactions are also occurring.

Discussion

Based on the results summarized in Table I and after corrections are made for side processes, it can be concluded that the reaction occurring during cathodic discharge of $LiClO_3$ on Pt or Ni is reduction to form Li_2O and LiCl as shown in Eq. [1]. In line 4 of Table I, less Li_2O is reported than is theoretically predicted by applying Faraday's law to Eq. [1], that is, line 3 is greater than the values shown in parentheses in line 4. This result can be explained by the hypothesis that oxide ions were lost by transport through the sintered glass separator into the negative compartment or otherwise not sampled. Diffusion alone cannot account for the observed oxide deficiency of 115 to 246 microequivalents. However, a small amount of convection through the separator or precipitation of some Li_2O which was not representatively sampled can explain the lower values on line 4. More LiCl is reported on line 5 of Table I than is predicted by applying Faraday's law to Eq. [1], that is, the values in parentheses in line 5 of Table I are greater than the values shown in line 3. That discrepancy is explained by the slow decomposition of $LiClO_3$ to form additional LiCl plus O_2. For example, in the experiment in which 1125 microequivalents were discharged, 2.5 cm^3 oxygen (about 223 microequivalents) were collected. The actual excess shown of line 5 over line 3 of Table I column 2 is 390 microequivalents. The agreement is reasonable if the difficulty in capturing all of the oxygen is considered.

During charging between 3.0 and 3.8V, oxygen evolution from Li_2O occurs on an Ni or Pt positive electrode as shown by reaction [2]; see Table III. The transition between the second and the third plateau in the anodic polarization curves is due to the mass transfer controlled oxidation of Li_2O on the rotating disk, since the limiting current increases with increase in concentration of Li_2O and $\Omega^{1/2}$. The diffusion coefficient of Li_2O in molten lithium chlorate can be estimated using Levich's equation (9) (see Eq. [5]) where I_L is the limiting current; **F** is the Faraday constant; A is the disk area; D is the diffusion coefficient of Li_2O; ν is the kinematic viscosity of the electrolyte; Ω is the angular velocity of the disk; and C is the concentration of Li_2O. The n is equal to 2 in this case since two electrons are given up by each Li_2O molecule during its reduction. The ν can be calculated using the equation suggested by Campbell *et al.* (10) for pure lithium chlorate.

$$\nu(\text{cm}^2/\text{sec}) = \frac{1.979 \times 10^{-5}}{\rho} \cdot e^{7813/RT}$$

T between 128° and 170°C

$R = 1.987$ cal/g-mol · °K [6]

The densities of lithium chlorate, ρ, at various temperature are also reported by Campbell *et al.* (11). Accordingly, the diffusion coefficient of Li_2O in lithium chlorate at 145°C was evaluated from Fig. 6 with ν equal to 0.116 cm^2/sec. The diffusion coefficients of Li_2O as determined from various limiting current measurements and measured Li_2O concentrations are shown below.

$D = 1.40 \times 10^{-7}$ cm^2/sec for $I_L = 20$ μA,

$C_{Li_2O} = 3.221 \times 10^{-5}$ mol/cm^3

$D = 1.49 \times 10^{-7}$ cm^2/sec for $I_L = 28$ μA,

$C_{Li_2O} = 3.221 \times 10^{-5}$ mol/cm^3

$D = 1.50 \times 10^{-7}$ cm^2/sec for $I_L = 40$ μA,

$C_{Li_2O} = 6.135 \times 10^{-5}$ mol/cm^3

$D = 1.52 \times 10^{-7}$ cm^2/sec for $I_L = 54$ μA,

$C_{Li_2O} = 6.135 \times 10^{-5}$ mol/cm^3

The small value of the diffusion coefficient is attributed to the high viscosity of the molten salt compared to aqueous solutions, since the diffusion coefficient times viscosity is approximately a constant, *i.e.*, Waldon's rule. The fact that the limiting current is proportional to the Li_2O concentration to within experimental accuracy implies that the Li_2O is indeed the diffusion limiting species.

It is shown in Fig. 4 that the limiting current reaches a constant value of 290 μA, after 650 microequivalents were discharged. It is believed that this constant value is due to the concentration of Li_2O becoming saturated in the lithium chlorate. Therefore, the solubility of Li_2O in lithium chlorate can be evaluated from Eq. [5] to be 7.5×10^{-5} mol/cm^3 using an average diffusion coefficient of Li_2O of 1.48×10^{-7} cm^2/sec.

From Fig. 9, it can be observed that the length of the plateau between 4.0 and 4.6V on a Pt rotating disk is proportional to the concentration of LiCl in the electrolyte. Therefore, it is believed that chlorine evolution from LiCl electrolysis takes place on Pt during charging between 4.0 and 4.6V according to Eq. [3]. The limiting current, shown in Fig. 9, is apparently due to the mass transfer of LiCl to the Pt rotating disk. Accordingly, the diffusion coefficient of LiCl in the electrolyte can be estimated from Eq. [5]. At different LiCl concentrations and limiting currents, the diffusion coefficients have been calculated using the Levich equation as shown.

$D = 3.60 \times 10^{-7}$ cm^2/sec for $I_L = 90$ μA,

$C_{LiCl} = 1.542 \times 10^{-4}$ mol/cm^3

Table IV. Summarized results of chemical results after charging above 4.0V using a Pt positive electrode

Amount of $LiClO_3$ in the positive electrode	4.92g	5.47g
Amount of charge	600 microequivalents	600 microequivalents
Charging potential	4.0-4.6V	Above 4.6V
Amount of Li_2O consumed during charging	196 μmol	165 μmol
Amount of LiCl created or consumed during charging	91 μmol consumed	80 μmol created

Table V. The results of gas collection on Pt electrode during charging above 4.0V

No. of charging	Amount of charge (microequivalents)	Charging potential (V)	Charging current (mA)	Amount of Cl_2 evolved (microequivalents)*	Amount of oxygen evolved (microequivalents)**
1	150	4.72	15	111	514
2	150	4.72	15	132	611
3	150	4.72	15	133	579

* Converted based on Eq. [4].
** Based on 4 equivalents per mol.

$D = 3.56 \times 10^{-7}$ cm²/sec for $I_L = 110$ μA,

$C_{LiCl} = 1.542 \times 10^{-4}$ mol/cm³

$D = 3.04 \times 10^{-7}$ cm²/sec for $I_L = 820$ μA,

$C_{LiCl} = 1.574 \times 10^{-3}$ mol/cm³

The small value of these diffusion coefficients is again attributed to the high viscosity of molten salt compared to aqueous solution. The fact that the limiting current is approximately proportional to LiCl concentration supports the conclusion that LiCl is the limiting diffusion reactant during the third charging plateau.

The solubility of LiCl in lithium chlorate can be estimated from the limiting current in Fig. 9. When the electrolyte was saturated, a limiting current of 1000 μA was observed. Using the diffusion coefficient of LiCl in lithium chlorate, the solubility of LiCl in lithium chlorate is calculated to be 1.78×10^{-3} mol/cm³ at 145°C. The data in Table IV show that Li_2O was also consumed during charging between 4.0 and 4.6V at the Pt electrode. The following explanation is proposed. Since the observed charging potential of 3.4V is higher than oxygen evolution potential, oxygen evolution must be occurring at its limiting rate. In addition, the reaction between Li_2O and Cl_2 consumes Li_2O to reform LiCl

$$Li_2O + Cl_2 \rightarrow 2LiCl + \tfrac{1}{2} O_2 \qquad [7]$$

$$\Delta G = -49.5 \text{ kcal/mol} \qquad [6]$$

This also helps explain why the data in Table IV show less LiCl was consumed than expected based on Faraday's law as applied to reaction [3].

Operation at the 4.6V voltage plateau on a platinum electrode shows both chlorine and oxygen evolution occur as reported in Table V. For example, 3.8 cm³ or 153 μmol (611 microequivalents) of oxygen were collected in run number 2. If oxygen were evolved from Li_2O stoichiometrically, only 150 microequivalents (37.5 μmol) would be expected. Thus, there must be some other sources of oxygen. In addition, 132 microequivalents of chlorine were observed. The stoichiometry of reaction [4] roughly correlates with the observed data. However, according to reaction [4], 150 microequivalents of chlorine and 900 microequivalents of oxygen should have been produced. Although Eq. [4] comes reasonably close to explaining the results of Tables IV and V, there is insufficient chlorine, excess LiCl, and insufficient O_2 and Li_2O. Assuming that reaction [7] occurs to some extent qualitatively, explains the increased LiCl and decreased Li_2O. In addition, some current electrolyzing LiCl according to Eq. [3] raises the amount of chlorine compared to oxygen. The conclusion is that at the 4.6V plateau on platinum, the results reported in Tables IV and V can be quantitatively correlated, assuming that reaction [4] dominates while reactions [3] and [7] occur at moderate rates limited by mass transfer.

Chlorine evolution is not observed on Ni although a charging plateau appears around 4.6V for an Ni rotating disk. From chemical analysis, it is found that Ni is oxidized to NiO during charging above 4.6V.

The first charging plateau, observed on an Ni rotating disk in Fig. 2, appears at a potential close to the standard potential of the Ni electrode

$$Ni \rightleftarrows Ni^{+2} + 2e^-_{(2)}$$

$$E^\circ = 2.799\text{V} \quad \text{(relative to Li ref. electrode)} \qquad [8]$$

Therefore, it is believed that the first charging plateau is due to Ni dissolution and the third plateau is probably in the transpassive region. The mechanism of Ni passivation is described as follows.

As a polished Ni electrode is dipped into fresh molten lithium chlorate, a thin NiO film is believed to form on the surface of the Ni. The film reduces the active area for Ni dissolution and shifts Ni dissolution from curve i to ii as shown in Fig. 10. Then the mixed potential would be switched from (a), in Fig. 10, to (b) or (c). The points (b) and (c) are the intersections of curve (iv) for lithium chlorate reduction with curve (ii) for Ni dissolution and curve (vi) for oxygen evolution, respectively. A mixed potential at point (b) or (c) implies that Ni is passivated and the first charge plateau for nickel dissolution is no longer seen on the Ni rotating disk (see Fig. 1).

Lithium oxide and lithium chloride are formed in the molten lithium chlorate during discharge using Ni plates. As discharge goes on, Li_2O will start to precipitate on the electrode after the electrolyte is saturated with Li_2O. This Li_2O precipitate could reduce the active area for lithium chlorate reduction and move curve (iv) gradually toward curve (v). Finally, the cathodic curve (v) for lithium chlorate reduction will intersect the Ni dissolution curve (ii) in its active region, namely, point (d) in Fig. 10, and reactivate nickel dissolution.

When the nickel is reactivated, the first charging plateau appears again. As shown in Fig. 1, after 1000 microequivalents discharged from lithium chlorate, the first charging plateau was observed for a rotating disk.

The reactivated Ni is then reacting with molten lithium chlorate to form a more complete nickel oxide protective film. Eventually, the Ni will be passivated again, and the Ni dissolution curve is shifted to (iii) in Fig. 10. Since more Li_2O is present in the electrolyte after discharging the lithium chlorate, the oxygen evolution curve is also shifted from (vi) to (vii). Therefore, the mixed potential switches to the intersection of curve (ii) and (vii), *i.e.*, point (e) in Fig. 10. This could explain the disappearance of the first charging plateau after standing hot (see Fig. 2).

Pure lithium works to some extent as a reversible negative electrode. However, dendrites are a problem. This problem might be solved using a lithium alloy such as Li-Al (12). The corrosion reaction between Li and molten lithium chlorate is estimated to be

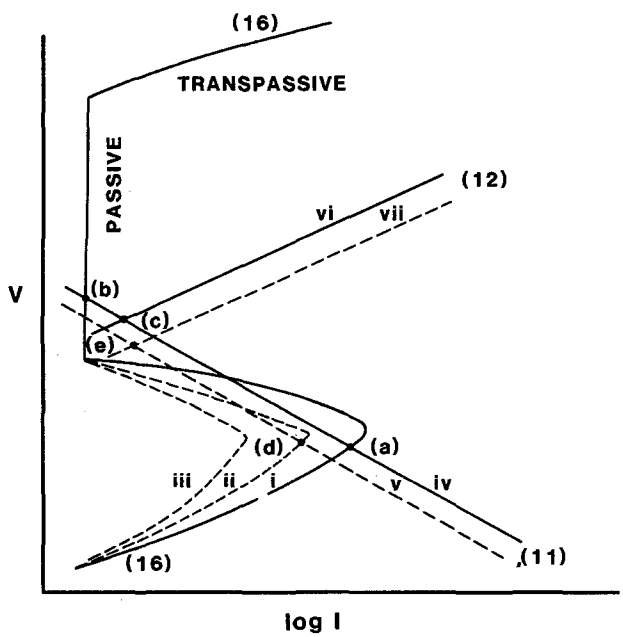

(11) $LiClO_3 + 6Li^+ + 6e^- \longrightarrow LiCl + 3Li_2O$

(12) $Li_2O \longrightarrow 2Li^+ + \frac{1}{2}O_2 + 2e^-$

(16) $Ni \longrightarrow Ni^{+2} + 2e^-$

Fig. 10. The change of mixed potential of Ni in molten lithium chlorate.

higher than 0.3 mA/cm² as Li_2O and LiCl are formed. No way to control this corrosion while the $LiClO_3$ is molten is now known. Therefore, if lithium chlorate is to be used as electrolyte in a lithium battery system, room temperature storage as a solid will be necessary to limit the corrosion reaction. The calorimetric data on lithium chlorate, given by Campbell *et. al.* (10), suggests that 5491 cal/mol is needed to raise the temperature of one mol of lithium chlorate from 25° to 145°C.

Conclusion

Based on the experimental results presented here, lithium chlorate is stable in the potential range between 3.2 and 4.6V. Above 4.6V, lithium chlorate will degrade to O_2, Cl_2, and Li^+. Below 3.2V, lithium chlorate will reduce to LiCl and Li_2O. Therefore, lithium chlorate can be used as the inert electrolyte of a lithium secondary battery only if the operating potential is between 3.2 and 4.6V. The Cl^-/Cl_2 half cell operates in this potential region on platinum.

An Li-$LiClO_3$ primary battery system is possible. With an energy density of 3898 W-hr/kg based on a discharge potential of 3.2V, the lithium chlorate primary battery is theoretically one of the highest specific energy primary batteries available. However, corrosion of Li by molten $LiClO_3$, the runaway or explosive interaction of Li plus $LiClO_3$, Li passivation by solid Li_2O and/or LiCl, and the catalytic decomposition of $LiClO_3$ to LiCl and O_2 are all serious problems that must be managed in order to realize a practical device.

Acknowledgment

This work has been supported by the United States Office of Naval Research.

Manuscript submitted Feb. 1, 1982; revised manuscript received *ca.* Oct. 18, 1982.

Any discussion of this paper will appear in a Discussion Section to be published in the December 1983 JOURNAL. All discussions for the December 1983 Discussion Section should be submitted by Aug. 1, 1983.

Publication costs of this article were assisted by Brigham Young University.

REFERENCES

1. CRC Handbook of Chemistry and Physics, R. C. Weast, Editor, The Chemical Rubber Company Press, Cleveland, OH (1972).
2. Lange's Handbook of Chemistry, 11th ed., J. A. Dean, Editor, p. 4, McGraw-Hill Book Co., New York (1973).
3. A. N. Campbell, E. M. Kartzmark, and D. F. Williams, *Can. J. Chem.*, **40**, 890 (1962).
4. M. M. Markowitz, D. A. Boryta, and H. Stewart, Jr., *J. Phys. Chem.*, **68**, 2282 (1964).
5. M. M. Markowitz, D. A. Boryta, and H. Stewart, Jr., *J. Chem. Eng. Data*, **9**, 576 (1964).
6. W. M. Latimer, "Oxidation Potential," 2nd edition, Prentice-Hall, Inc., New York (1952).
7. A. N. Campbell and J. E. Griffiths, *Can. J. Chem.*, **34**, 1647 (1956).
8. C. A. Krauss and W. M. Burgless, *J. Am. Chem. Soc.*, **49**, 1226 (1927).
9. V. G. Levich, "Physiochemical Hydrodynamics," pp. 286-297, Prentice-Hall, Inc., New Jersey (1962).
10. A. N. Campbell and M. K. Nagarajan, *Can. J. Chem.*, **42**, 1616 (1964).
11. A. N. Campbell and M. K. Nagarajan, *ibid.*, **42**, 1137 (1964).
12. D. H. Shen, M.S. Thesis, University of California, Los Angeles, CA (1979).

A Two-Step Anodization Process for Inhibition of the Oxygen Reduction Reaction on Iron

Henry Leidheiser, Jr.,* and Hidetaka Konno[1]

Department of Chemistry and Center for Surface and Coatings Research, Lehigh University, Bethlehem, Pennsylvania 18015

ABSTRACT

Anodization of iron by a two-step procedure, first in a borate solution, and second, in a borate solution containing 8-hydroxyquinoline, results in a surface which is inactive for the oxygen reduction reaction, and which has good corrosion resistance in chloride media. The anodized surface also exhibits good resistance to the disbondment of an organic coating under an applied cathodic potential. It is conjectured that the anodized surface consists of a very small amount of surface oxide, possibly a layer of a ferric complex of 8-hydroxyquinoline, and an outer layer of unreacted 8-hydroxyquinoline.

The cathodic half reaction during the corrosion of iron and steel in near neutral aqueous environments is the oxygen reduction reaction, $H_2O + \frac{1}{2} O_2 + 2e^- = 2\ OH^-$. Under many conditions this reaction is the rate-controlling step. Many methods are available for inhibiting the anodic half reaction but relatively few methods are available for inhibiting the oxygen reduction reaction. Previous work in this laboratory has shown that this reaction may be inhibited on zinc by doping the oxide on the surface with small amounts of cobalt or nickel (1, 2). It has also been shown that cathodic treatment of a chromated surface on zinc leads to a surface which has low activity for the oxygen reduction reaction (3).

We report herein a novel method for inhibition of the cathodic half reaction on iron. This method consists of anodizing iron in a borate buffer followed by a second anodization step in a solution containing an organic compound. This procedure leads to a surface which is inactive for the oxygen reduction reaction and which has a low rate of corrosion in a mildly corrosive medium.

Experimental Procedure

All measurements in this study were made on cold-rolled SAE 1010 steel panels, 0.5 mm thick, obtained from the Q-Panel Company. The as-received panels were cut in the form of a rectangle, 1 cm wide and 7.5 cm long, with an indentation at the waterline as shown in Fig. 1. They were immersed in the electrolyte to a depth such that the exposed area was 10 cm². Samples were used either in the electropolished condition or after abrasion with No. 240 emery paper. Electropolishing was carried out in a 4:1 mixture of glacial acetic acid and perchloric acid. All potentials described in the text are with reference to the saturated calomel electrode.

The steel was anodized in a vigorously stirred 0.15M sodium borate solution (*p*H 8.4) open to the air in a two-step process.

* Electrochemical Society Active Member.
[1] On leave from Hokkaido University, Sapporo, Japan.

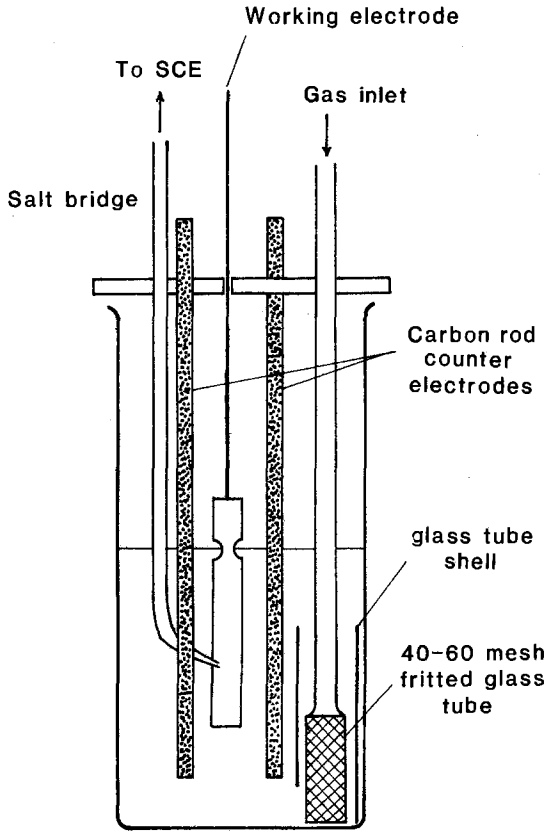

Fig. 1. Schematic diagram of cell used for electrochemical measurements.

Step I.—Anodization at a potential (E_{a_1}) between −0.4 and +2.2V in the borate solution for 2-10 min.

Step II.—Anodization at a potential (E_{a_2}) between +0.5 and +2.0V for 2-10 min in the borate buffer solution to which an organic compound was added.

Cathodic polarization curves and corrosion rate measurements were made in a 250 cm³ volume of 0.5M NaCl-0.15M borate at pH 7 in the cell shown in Fig. 1. The solution was aerated during the measurements by passing air through the solution at a rate of 600 cm³/min or was deaerated with purified argon gas. The measurements were performed using a Princeton Applied Research Model 350 Corrosion Measurement Console featuring microprocessors and a data storage system. Unless otherwise mentioned, polarization curves were determined using a scanning technique. Measurements were initiated after the sample had been exposed to the medium for 10 min and the scanning rate was 0.3 mV/sec. Cyclic voltammograms were obtained using a similar procedure with the exception that the scan rate was 1 mV/sec. Corrosion rates determined by the polarization resistance (R_p) method and corrosion potential measurements were made every 30 min during a 16 hr period. R_p values were obtained from the slope of the polarization curve in the potential range of ±5 mV from the corrosion potential.

Gravimetric measurements of the corrosion rate were made in 400 cm³ of solution maintained in a 600 cm³ beaker. Weighed specimens were immersed in either aerated or deaerated solutions for 4-16 hr and the loss in weight was determined. Corrosion products were removed from the specimen surface using a nylon test tube brush under running distilled water.

Impedance measurements were made by cementing a cylinder to the steel surface and using mercury as the counterelectrode. The means for making the measurements have been described previously (4).

Cathodic delamination tests were performed using the method previously described (5). Panels were coated with a commercial product (Rust-Oleum primer 7773 and Rust-Oleum topcoat 7791) using two primer coats and three topcoats to yield a coating of thickness 93 μm. A small defect was made in the coating and the specimen was made in the cathode while immersed in 0.5M NaCl solution open to the air. In all cases the cathode potential was potentiostatically maintained at −0.8V.

X-ray photoelectron spectroscopy measurements were made using a Physical Electronics Model 548 electron spectrometer. Samples were irradiated with the K_α radiation of magnesium in a vacuum of 2.5-4.5 × 10^{-7} Pa. The analyzer energy was set at 25 eV which yielded a resolution of 1.22 eV for the Au $4f_{7/2}$ peak for the full width at half maximum. In order to compensate for a small charging shift, the electron binding energy, E_B, was corrected by assigning a value of 285.0 eV to the aromatic carbon or hydrocarbon C 1s peak (6).

Experimental Results

During the earliest phases of this study, it was observed that the addition of several types of organic compounds to a borate anodizing bath caused a marked reduction in the current at a fixed potential. This observation suggested that the anodized procedure was leading to a steel surface with a lower activity. Determinations of the cathodic polarization curve, measurements of the corrosion rate, and general observations of the metal surface while it was exposed to a corrosive medium confirmed that the steel surface had been inactivated by the anodization treatment. As a first step in a study of this phenomenon, a survey was made of a large number of organic compounds that we felt might be suitable candidates for an intensive study. Table I summarizes the organic compounds that yielded positive results, the conditions of anodization, the effect on the current during anodization, the corrosion potential, the effect on the cathodic polarization curve, and the corrosion rate in a sodium chloride medium as determined by gravimetric measurements.

Table I. Results of an exploratory study of the effect of organic compounds on the electrochemical properties of steel during anodization

Organic compound	Conc. mol/l	i_a at E_{a_2} A/m²	Corrosion potential E_{corr} V *vs.* SCE	Effect on cathodic polarization curve i_c at −0.5V A/m²	i_c at −0.8V A/m²	Corrosion rate r_{ave} g/m² hr
N-benzoyl-N-phenyl-hydroxylamine	0.004	0.3	−0.434	0.22	1.68	0.48
Cupferron	0.01	1.3	−0.553	—	1.88	0.39
Diphenylguanidine	0.004	4.2	−0.448	0.22	1.42	0.23
8-Hydroxyquinoline	0.004	0.3	−0.422	0.02	1.01	0.10
1-Nitroso-2-naphthol	0.002	0.9	−0.463	0.24	1.70	0.25
Phenylthiourea	0.004	1.9	−0.454	0.03	2.15	0.34
Salicylamide	0.01	8.2	−0.425	0.26	1.12	0.21
Salicylanilide	0.002	2.8	−0.549	—	1.31	0.28
Blank	—	25	−0.389*	0.25*	2.03*	0.74

All samples anodized at E_{a_1} = 1.0V and E_{a_2} = 1.4V in a 0.15M borate solution (pH 8.4) for 10 min at each potential.
* Electropolished specimen.

The results summarized in Table I indicated that one of the more interesting and effective compounds was 8-hydroxyquinoline (HQ). The decision was then made to confine the work reported herein to observations with this compound. The optimum experimental conditions for maximum corrosion inhibition were determined by varying E_{a_1} in the borate solution and E_{a_2} in the borate-HQ solution at various pH values and for different anodizing times. The criterion used to identify the optimum condition was the degree of inhibition as determined by the cathodic polarization curve as measured in aerated 0.5M NaCl-0.15M borate solution. Optimum conditions were E_{a_1} = 0.9-1.8V in a borate solution, E_{a_2} = 1.0-1.7V in a 0.004M HQ-borate solution, pH 7-10, and anodizing time of 10 min at each potential. It was observed that a suitable value for E_{a_1} was in the transpassive region of the anodic polarization curve for steel in the borate buffer, and a suitable value for E_{a_2} was in the passive region of the anodic polarization curve for steel in the borate-HQ solution. See Fig. 2. At pH's lower than 7, a large number of small dark spots were formed on the surface during the anodization and a uniform layer was not obtained. At pH's higher than 10, the dissolution rate of the steel in Step I was greater than desired.

Typical cathodic polarization curves for HQ-treated and panels anodized in the absence of HQ (blank) are shown in Fig. 3 for electropolished specimens and in Fig. 4 for abraded specimens. Unless otherwise mentioned, experiments were carried out on specimens anodized at E_{a_1} = 1.0V, E_{a_2} = 1.4V, and pH 8.4. In the case of the abraded specimens the anodic oxide was reduced during the cathodic polarization but the oxide on the electropolished specimen was stable under mildly cathodic conditions. Under both sets of conditions the HQ-treated panels exhibited similar cathodic polarization characteristics. The cathodic current density for the HQ-treated panels was approximately 0.1 of that of the blank at −0.45V and approximately 0.5 of that of the blank at −0.8V. In order to obtain a clearer picture of the polarization characteristics in the vicinity of the corrosion potential, anodic and cathodic polarization curves are plotted for unanodized iron, anodized iron, and the HQ-treated iron in Fig. 5. It will be noted that the HQ-treated panels show substantial inhibition of the cathodic reaction and significant inhibition of the anodic reaction.

The two likely cathodic reactions on the anodized samples are (*i*) oxygen reduction and (*ii*) reduction of the oxide film on the surface. Both these reactions appear to be suppressed on the HQ-treated samples as shown by potentiostatic polarization at −0.8V and

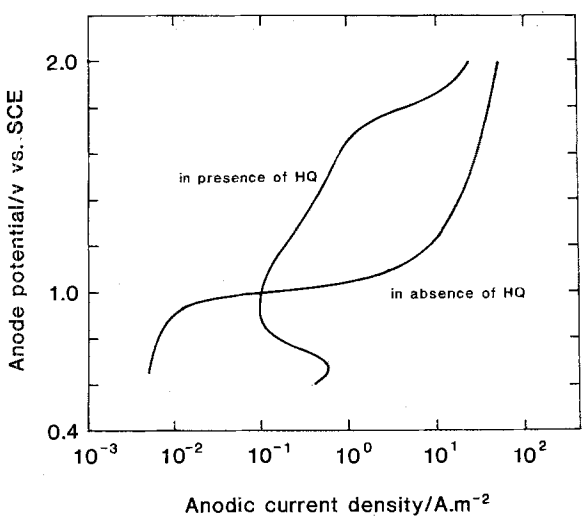

Fig. 2. Anodic polarization curves for steel as determined in 0.15M borate solution (pH 8.4) with and without 0.004M 8-hydroxyquinoline. Curves determined at a scan rate of 1 mV/sec.

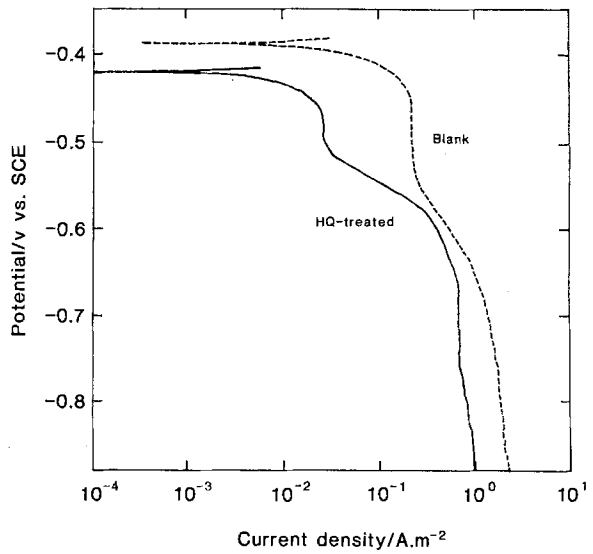

Fig. 3. Cathodic polarization curves for electropolished steel specimens in aerated 0.5M NaCl-0.15M borate solution. Both specimens were anodized in 0.15M borate solution, one in the presence of 8-hydroxyquinoline and the other in its absence.

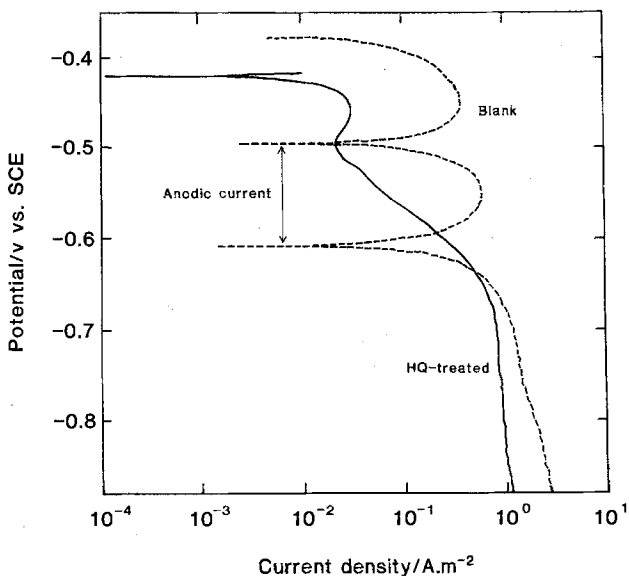

Fig. 4. Cathodic polarization curves for abraded steel specimens in aerated 0.5M NaCl-0.15M borate solution. Both specimens were anodized in 0.15M borate solution, one in the presence of 8-hydroxyquinoline and the other in its absence.

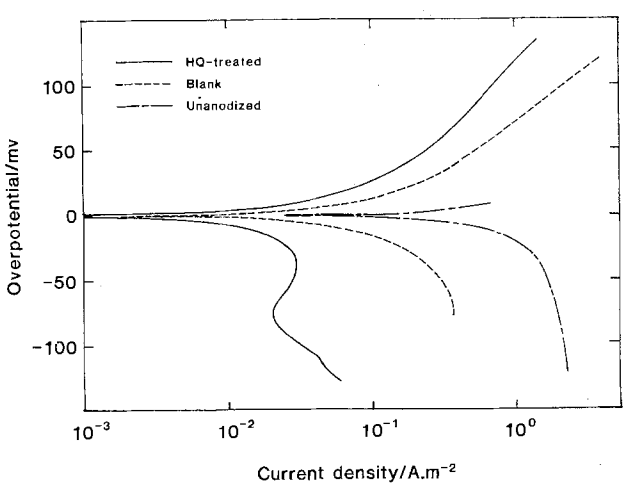

Fig. 5. Polarization behavior in the vicinity of the corrosion potential. The potential axis is normalized with respect to the corrosion potential.

cyclic voltammetry measurements. Potentiostatic polarization at −0.8V yielded a short-term, steady-state current value of approximately 0.9 A/m² for the HQ-treated panel and approximately 1.8 A/m² for the blank. These values became 0.73 A/m² and 1.87 A/m², respectively, after 1 hr. These latter values are assumed to represent the oxygen reduction current and are confirming evidence that the oxygen reduction reaction is inhibited on the HQ-treated sample.

Cyclic voltammograms for the HQ-treated sample (Fig. 6) demonstrated anodic and cathodic scans that were very similar in both directions, whereas the voltammogram for the blank (Fig. 7) suggested that reduction of the oxide occurred during the scan in the cathodic direction.

Cathodic polarization measurements in deaerated chloride-borate solution indicated that the hydrogen evolution reaction is also inhibited on the HQ-treated samples. Representative curves are shown in Fig. 8 in which it will be noted that the cathodic current density on the treated specimen is less than 1/3 that of the blank in the potential region between −0.8 and −1.1V.

Impedance measurements at 100, 1,000, and 10,000 Ω are summarized in Table II. It is noted from these data that the impedance of the HQ-treated sample is significantly greater than that of the blank.

The cathodic polarization curves and the anodic polarization curves suggested that the rate of corrosion of the HQ-treated panels would be significantly

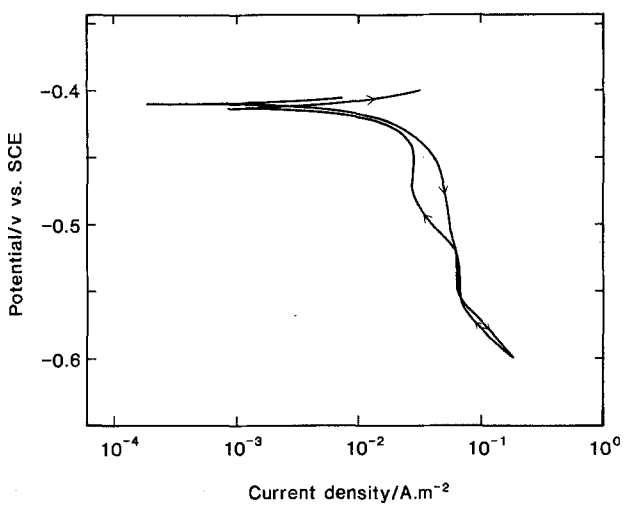

Fig. 6. Cyclic voltammogram in 0.5M NaCl-0.15M borate solution for a specimen anodized in the presence of 8-hydroxyquinoline.

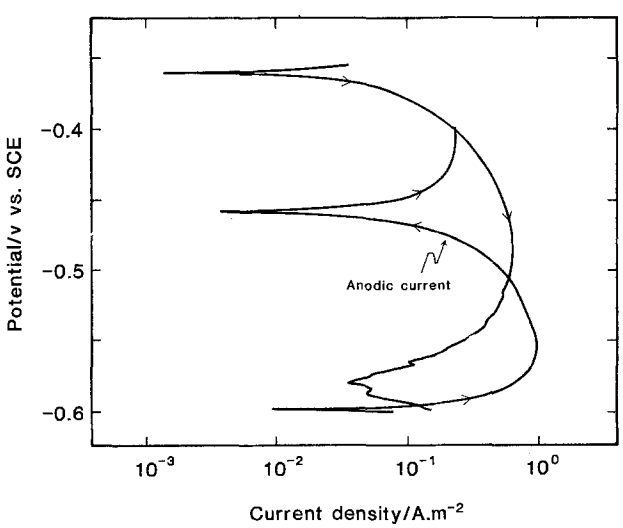

Fig. 7. Cyclic voltammogram in 0.5M NaCl-0.15M borate solution for an anodized specimen, a so-called blank.

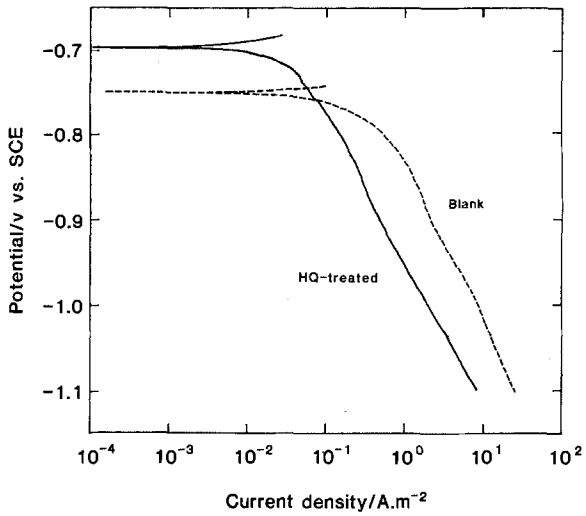

Fig. 8. Cathodic polarization curves for abraded steel specimens in deaerated 0.5M NaCl-0.15M borate solution. Both specimens were anodized in 0.15M borate solution, one in the presence of 8-hydroxyquinoline and the other in its absence.

less than that of an anodized blank. This conclusion was confirmed by polarization resistance, R_p, and gravimetric measurements. The variation of the R_p value with time is shown in Fig. 9 in the case of aerated chloride-borate solution, and in Fig. 10 in the case of deaerated chloride-borate buffer solution. In the aerated medium the R_p values were erratic during the first few hours and were occasionally very high. These values are probably of limited meaning because the polarization curve was not linear and the lack of linearity was maintained with change in scan rate or scan direction. The R_p for the HQ-treated panel in aerated media achieved a steady-state value of approximately 3300 Ω · cm² after 8 hr whereas the R_p for the blank was less than 1000 Ω · cm² after 2 hr. In deaerated solution the R_p value of the HQ-treated panel is higher than that for the blank over the entire time period, but the differences are much less than those observed in the aerated solution.

Gravimetric measurements are summarized in Table III. These results are in good support of the R_p measurements. The rates of corrosion of the anodized samples (blanks) were much greater in aerated solution than the HQ-treated samples, and were slightly greater during corrosion in deaerated solutions.

Figure 11 shows that the corrosion rates of both the blank and the HQ-treated material occur linearly with time, at least over the 16 hr period of the experiment.

Changes in the corrosion potential as a function of time of exposure to the chloride-borate medium are shown in Fig. 12 for the HQ-treated samples and the blanks under both aerated and deaerated conditions. The value of E_{corr} for the HQ-treated panel dropped abruptly after about 3 hr and achieved a steady-state value of −0.69V. This behavior as shown in Fig. 12 parallels the R_p behavior as shown in Fig. 9.

Cathodic delamination occurred much more slowly in the case of the HQ-treated samples as compared

Table II. Impedance measurements on HQ-treated and blank samples

Frequency (Hz)	Total impedance (Ω)		Calc. resistive component (Ω)	
	HQ-treated	Blank	HQ-treated	Blank
100	3.30	0.18	3.29	0.16
1,000	3.64	0.97	3.51	0.22
10,000	10.6	9.60	4.52	0.99

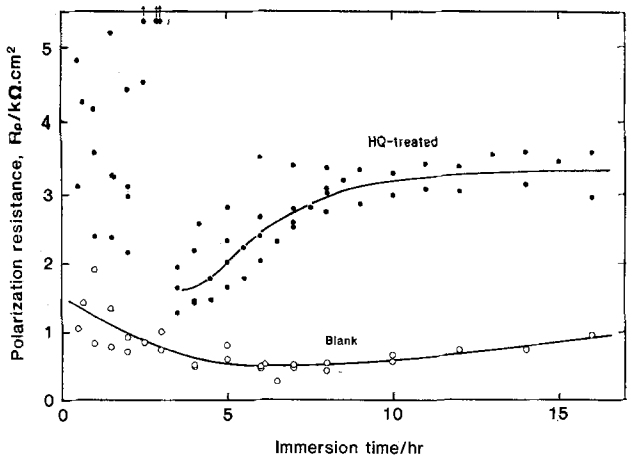

Fig. 9. Polarization resistance (R_p) values as a function of time in aerated 0.5M NaCl-0.15M borate solution. Both specimens were anodized in 0.15M borate solution, one in the presence of 8-hydroxyquinoline and the other in its absence.

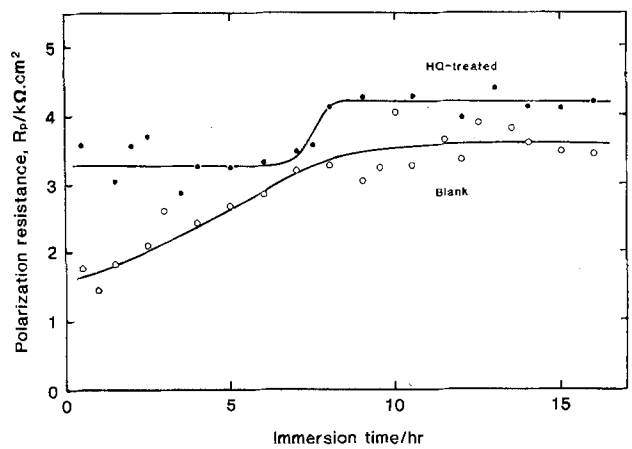

Fig. 10. Polarization resistance (R_p) values as a function of time in deaerated 0.5M NaCl-0.15M borate solution. Both specimens were anodized in 0.15M borate solution, one in the presence of 8-hydroxyquinoline and the other in its absence.

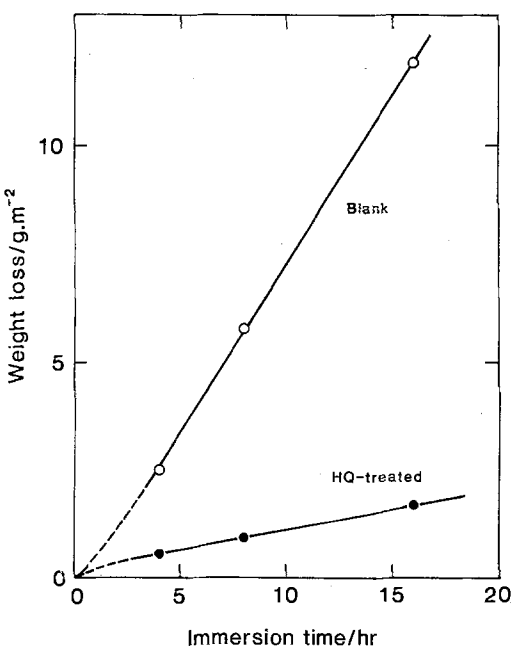

Fig. 11. Loss in weight as a function of time as determined gravimetrically. Both specimens were anodized in 0.15M borate solution, one in the presence of 8-hydroxyquinoline and the other in its absence.

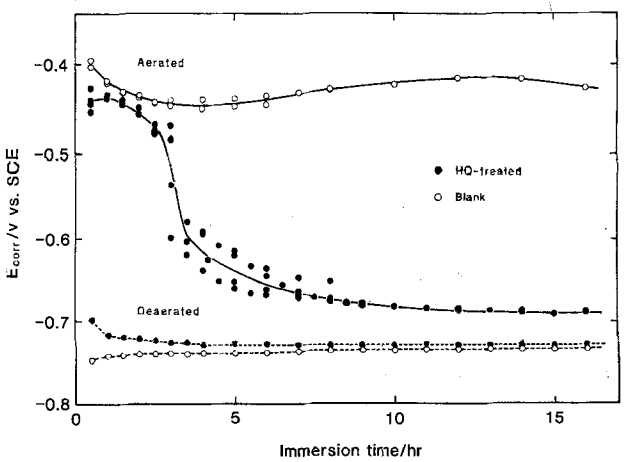

Fig. 12. Corrosion potential measurements as a function of time as measured in aerated and deaerated 0.5M NaCl-0.15M borate solution.

to the blank or abraded steel. The rate of delamination of the HQ-treated panels in 0.5M NaCl open to the air at a potential of −0.8V was 0.004 cm²/hr, whereas the abraded panels yielded values in the range of 0.015-0.023 cm²/hr. The rate of delamination of the blank was so high that no quantitative value was obtained.

XPS studies (Table IV) revealed that the surface of the HQ-treated specimen was covered with organic material which yielded a spectrum identical to the spectrum obtained from a sample of 8-hydroxyquinoline powder. The electron binding energy of the N 1s electron in the HQ-treated sample was identical to that obtained with the hydroxyquinoline powder,

Table III. Average corrosion rate during 16 hr period of immersion in 0.5M NaCl-0.15M borate (pH = 7)

Sample No.	Anodization conditions E_{a_1} (V)	E_{a_2} (V)	pH	Corrosion medium	Corrosion rate (g/m² · hr) HQ-treated	Blank
3, 4	1.0	1.4	8.4	Deaerated	0.060	0.094
1, 2	1.0	1.4	8.4	Aerated	0.10	0.74
5	1.0	1.4	7.0	Aerated	0.14	
6	1.0	1.4	10.0	Aerated	0.10	
7, 8	1.8	1.1	8.4	Aerated	0.14	0.95
9	—	1.4	8.4	Aerated	0.27	
10*, 11*	1.0	1.4	8.4	Aerated	0.22	0.99
12**	1.0	1.4	8.4	Aerated	0.18	
13		Abraded only		Aerated		0.91

Note: All specimens were abraded with No. 240 emery paper before anodizing.
* Heated at 200°C for 20 min after anodization.
** Dipped into methanol for 30 min after anodization.

Table IV. Results of XPS measurements for specimens and standard samples

Sample	Electron binding energy, E_B/eV C 1s	N 1s	O 1s	Fe $2p_{3/2}$
HQ-treated	285.0	399.5	533.1 max	Trace
			ca. 531 sh	
Blank	285.0	—	530.3 max	711.3
			ca. 532.5 sh	
HQ-treated and immersed*	285.0	399.0	530.2 max	711.3
	287.9		*ca.* 532 sh	
Electropolished steel	285.0	—	530.3 max	711.2
			ca. 532 sh	707.0
8-Hydroxyquinoline (HQ), powder	285.0	399.5	531.5	—
Fe(III)-8-hydroxyquinolate, powder	285.0	399.1	531.5	711.2

max = maximum, sh = shoulder.
* Specimen immersed in an aerated 0.5M NaCl-0.15M borate solution (pH 7.0) for 16 hr.

but was slightly different from the binding energy for a powder of the ferric complex of 8-hydroxyquinoline. Also, the Fe 2p peaks in the HQ-treated sample were very weak whereas they were strong in the ferric complex. After a 16 hr immersion in the aerated corrosion medium, the N 1s peak changed in value to that characteristic of the ferric complex. As judged from the intensities of C 1s and N 1s peaks, significant amounts of the organic compound remained on the surface after a 16 hr exposure to the corrosion medium. The data are consistent with the view that the outermost part of the surface layer of the HQ-treated sample consists of 8-hydroxyquinoline with very little chemical reaction to form the ferric complex.

Discussion

The experiments reported herein show conclusively that it is possible to inhibit the oxygen reduction reaction on steel using an organic compound. It is interesting to point out that under similar experimental conditions in which good inhibition was observed in this study on the HQ-treated panels, only insignificant corrosion inhibition was observed when 8-hydroxyquinoline was present in the corrosion medium and was absent during the anodization procedure. Weisstuch, Carter, and Nathan (8) observed corrosion inhibition of iron by 8-hydroxyquinoline in an aerated, simulated cooling water environment at pH 7, but they also observed the formation of an insoluble, nonadherent film. All the evidence generated to date indicates that anodization in the presence of 8-hydroxyquinoline is essential in order to obtain good corrosion inhibition. So far as we are aware a two-step anodization process, the second step of which is carried out in a medium to which an organic compound is added, is a novel method for developing a corrosion resistant surface on steel. It is our expectation that the procedure can be optimized to obtain metal surfaces with a high degree of corrosion resistance under service conditions.

The polarization curves shown in Fig. 3, 4, and 5 indicate that the HQ-treatment yields a surface which is less active for both the anodic and cathodic half reactions, although the effect is much greater on the cathodic half reaction. On the basis of the cathodic polarization curves in Fig. 3, it can be estimated that the corrosion rate of the blank should be approximately 9 times that of the HQ-treated material. The gravimetric measurements for samples 1 and 2 in Table III indicate that the rate is 7.4 times that of the HQ-treated material for corrosion measurements made over a 16 hr period. The two types of experiments. along with the R_p data in Fig. 9, conclusively show the large degree of corrosion inhibition which results from the anodization in solutions containing 8-hydroxyquinoline.

The mechanism by which this corrosion inhibition occurs is probably by the development at the iron surface of an organic layer, of unknown thickness at the present time, which impedes the flow of electrons which are a necessary reactant in the oxygen reduction reaction, $H_2O + \frac{1}{2} O_2 + 2e^- = 2 OH^-$. The data shown in Table II prove that the HQ-treated samples exhibit a much higher impedance than samples anodized in the absence of HQ. The data also suggest that the major contribution to the impedance is a resistive component, since over 96% of the impedance value can be attributed to the resistive component at measurement frequencies of 100 and 1000 Hz under the assumption that the equivalent circuit consists of a resistance and a capacitor in series.

The most interesting question raised by this study is "What is the chemical nature of the steel surface after the two-step anodization process?" This question is being addressed in studies now underway but the data already available allow certain conclusions to be drawn. The XPS studies summarized in Table IV show that the outer surface appears to be 8-hydroxyquinoline immediately after anodization, but that the outer surface approaches a form equivalent to a ferric complex of 8-hydroxyquinoline after exposure to the corrosive medium. It is impossible from the present data, and it could not be determined from spectra taken after sputtering, to ascertain whether the surface after anodization consists of an inner ferric complex of 8-hydroxyquinoline and an outer 8-hydroxyquinoline, or whether exposure to the corrosion medium caused the conversion of the 8-hydroxyquinoline to a ferric complex. It is well known that the ferric complex of 8-hydroxyquinoline is very insoluble.

The anodic film formed in borate solution is readily reduced as shown by the cathodic polarization curve in Fig. 4 and the voltammogram for the blank in Fig. 7, whereas there was minimal reduction in the case of the HQ-treated sample as shown in Fig. 6. These behaviors can be interpreted in either of two ways. First, the oxide present on the HQ-treated sample is reduced with great difficulty or, second, there is no appreciable amount of oxide on the HQ-treated sample. We are conjecturing at the present time, on the basis of very preliminary spectra obtained after sputtering, that the amount of surface oxide on the HQ-treated panel is very small. Infrared reflectance studies, laser Raman studies, and additional electrolytic reduction experiments must be performed before a definite conclusion can be reached.

It has been shown previously (7) in the case of galvanized steel that a surface treatment which leads to inhibition of the cathodic half reaction improves the performance of a coated metal in a cathodic delamination experiment. In the present studies the rate of cathodic delamination of an alkyd coating from the HQ-treated surface occurred at significantly lower rate than from either an abraded surface or one that had simply been anodized in the absence of 8-hydroxyquinoline. These data thus provide additional support for the concept that inhibition of a metal surface for the oxygen reduction reaction will increase the resistance of the metal to cathodic delamination. The procedure outlined in this paper holds promise for the development of a surface treatment method that will reduce the tendency of a coating to disbond from a metal either during corrosion or during cathodic treatment.

Acknowledgment

This work has been supported by the Office of Naval Research, to whom we are grateful.

Manuscript submitted Sept. 7, 1982; revised manuscript received *ca.* Nov. 17, 1982.

Any discussion of this paper will appear in a Discussion Section to be published in the December 1983 JOURNAL. All discussions for the December 1983 Discussion Section should be submitted by Aug. 1, 1983.

Publication costs of this article were assisted by Lehigh University.

REFERENCES

1. H. Leidheiser, Jr., and I. Suzuki, *This Journal*, **128**, 242 (1981).
2. H. Leidheiser, Jr., G. W. Simmons, S. Nagy, and S. Musić, *ibid.*, **129**, 1658 (1982).
3. H. Leidheiser, Jr., Y. Momose, and R. D. Granata, *Corrosion*, **38**, 178 (1982).
4. M. C. Hughes and J. M. Parks, "Corrosion Control by Organic Coatings," H. Leidheiser, Jr., Editor, p. 45, Natl. Assoc. Corrosion Engrs., Houston, Texas (1981).
5. H Leidheiser, Jr., and W. Wang, *J. Coatings Technol.*, **53**, No. 672, 77 (1981).
6. U. Gelius, P. F. Heden, J. Hedman, B. J. Lindberg,

R. Manne, R. Nordberg, C. Nordling, and K. Siegbahn, *Phys. Scr.*, **2**, 13 (1970).
7. H. Leidheiser, Jr., and W. Wang, "Corrosion Control by Organic Coatings," H. Leidheiser, Jr., Editor, p. 70, Natl. Assoc. Corrosion Engrs., Houston, Texas (1981).
8. A. Weisstuch, D. A. Carter, and C. C. Nathan, *Mater. Prot. Perform.*, **10**(4), 11 (1971).

Corrosion Study of a Carbon Steel in Neutral Chloride Solutions by Impedance Techniques

A. Bonnel and F. Dabosi

Equipe de Recherche Associée au CNRS, no 263 "Laboratoire de Métallurgie Physique," Ecole Nationale Supérieure de Chimie, 31077 Toulouse Cedex, France

C. Deslouis

Groupe de Recherche du CNRS, no 4 "Physique des Liquides et Electrochimie" Associé à l'Université Pierre et Marie Curie, 75230 Paris Cedex 05, France

M. Duprat

Equipe de Recherche Associée au CNRS, no 263 "Laboratoire de Métallurgie Physique," Ecole Nationale Supérieure de Chimie, 31077 Toulouse Cedex, France

and M. Keddam and B. Tribollet

Groupe de Recherche du CNRS, no 4 "Physique des Liquides et Electrochimie," Associé à l'Universitè Pierre et Marie Curie, 75230 Paris Cedex 05, France

ABSTRACT

The electrochemical behavior of a carbon steel in 3% NaCl solution has been investigated using a rotating disk electrode. Both steady-state (diffusional current *vs.* the disk angular velocity plots) and transient (frequency analysis of the electrohydrodynamical impedance) measurements which specifically sample mass transport phenomena, have been carried out. It is shown that oxygen transport takes place not only in the liquid phase but also through a porous layer of corrosion products. From electrochemical impedance measurements, it was found that at the corrosion potential the oxygen reduction reaction is under either diffusional or mixed (activation + diffusion) control depending on both the electrode rotation speed and on the hold time at the free corrosion potential. In addition, it was shown that the oxygen consumption occurs not only by electrochemical reduction but also by chemical oxidation of ferrous to ferric ions. Finally, because of the possible occurrence of mixed corrosion control, it is emphasized that the use of the polarization resistance in order to evaluate corrosion rates is not always valid.

In a previous study (1), steady-state electrochemical techniques (voltage-current curves and polarization resistance measurements) were used to study the corrosion of carbon steel in a stirred and aerated chloride solution (3% NaCl). It was concluded that the corrosion rate is controlled by the reduction of dissolved oxygen, and that the corrosion rate deduced from electrochemical techniques is in fair agreement with that obtained from an absolute measurement such as the determination of the amount of iron species in solution.

In the literature, many studies have been devoted to corrosion (and inhibition) in acidic media in order to measure the corrosion rate or to identify the elementary processes. However, relatively few studies have been carried out in neutral media (2), probably because of the formation of insoluble corrosion products which adhere to the metal surface (3a, b).

In this work, we aimed firstly to be more precise about the quantitative influence of mass transport in the corrosion process. This was achieved by the use of specific analytical methods, such as plotting of the diffusional component *vs.* the angular velocity of a disk electrode, and by the frequency analysis of the so-called EHD impedance (4).

Secondly, in order to separate the elementary anodic and cathodic contributions near to the corrosion potential, and, therefore, to get a better insight of the mechanism, we carried out electrochemical impedance measurements for various polarization conditions.

Key words: interface, disk electrode, porous films, activation-diffusion.

Experimental Conditions

The steel sample selected for the study is the N 80 type according to the API standards, and has the following composition by percent weight: C = 0.4; Mn = 1.38; P = 0.013; S = 0.024; Si = 0.19; Cu = 0.04; Ni = 0.03; Cr = 0.09; Mo = 0.19, and Fe to 100.

The working electrode consists of the cross section of a cylindrical rod of 1 cm^2 area, a thermoretractable sheath preventing the cylindrical area from making contact with the solution, the electrode surface being only the cross section. In order to avoid possible crevice conditions between the metal rod and the sheath induced by the successive polishings, the sheath was renewed after each run. The surface is polished with a silicon carbide emery cloth (grade 80), then rinsed with water, and finally dried in pulsed warm air after an ultrasonic washing in ethanol. This electrode is screwed into a conducting rotating shaft. The reference electrode is a saturated calomel electrode (SCE) and the auxiliary electrode is a platinum grid of large area. The corrosive medium is a 3% solution of NaCl (pro analysis grade) dissolved in bidistilled water. The current potential curves are plotted with either a galvanostatic or potentiostatic regulation (Tacussel).

The impedance measurements are performed by means of a frequency response analyzer (Schlumberger, Solartron 1174). The whole experimental set-up has been described in detail in Ref. (5) and in Ref. (4) concerning the specific mechanical features of the EHD impedance measurements.

Experimental Results

Current-Potential Curves

Prior to any experiment, the electrode is held at zero current for a given angular velocity Ω (rpm) of the disk till the corrosion potential is stabilized. The steady state occurs rather slowly and the current-potential curves are, therefore, plotted point by point in a quasi steady-state mode. As an example, two cathodic plots after a hold time at zero current of 30 min and 2 hr are displayed on Fig. 1. A shift of E_{corr} towards more cathodic potentials and a decrease of the diffusion current with an increasing hold time at zero current are concurrently observed.

From a detailed analysis of these curves (1), this diffusion plateau was ascribed to dissolved oxygen. Moreover, the variations of the limiting current density with the hold time have been explained by hindrance to diffusion due to the progressive deposit of corrosion products.

It has been verified that for anodic overpotentials, the current, even at some tens of $mA \cdot cm^{-2}$ is not dependent on the angular velocity of the disk (Fig. 2).

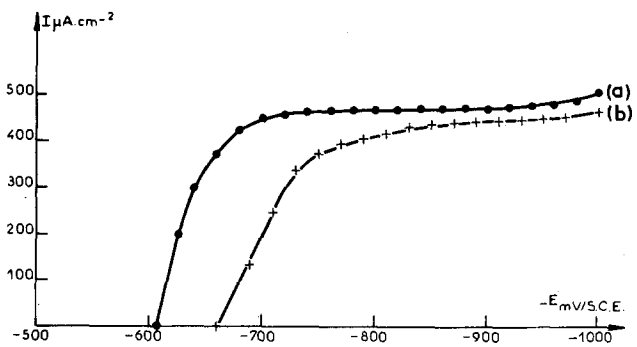

Fig. 1. Cathodic current-voltage curves obtained in potentiostatic mode at Ω = 1000 rpm. Hold time at E_{corr}: (a) 30 min, (b) 2 hr.

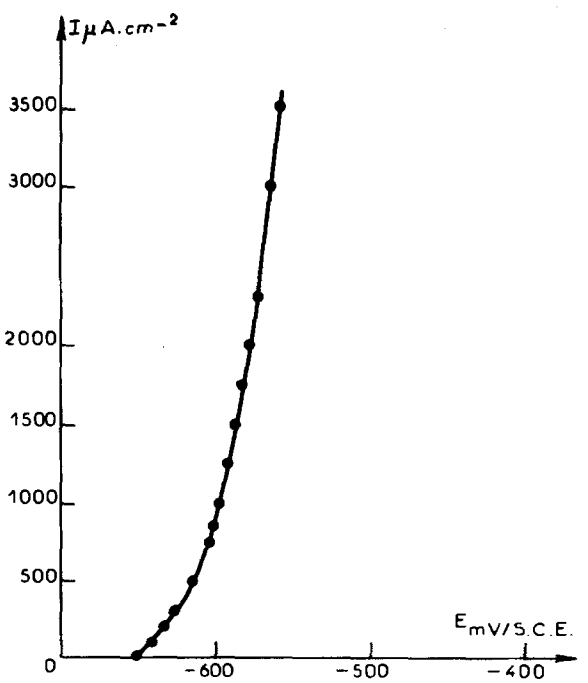

Fig. 2. Anodic current-voltage curve obtained in galvanostatic mode at Ω = 1000 rpm. Hold time at E_{corr}: 2 hr.

Cathodic Mass Transport Analysis

Steady-state measurements.—The elementary cathodic reaction may be written as

$$O_2 + 2H_2O + 4e^- \rightarrow 4\,OH^- \qquad [1]$$

For a short hold time at zero current (t = 30 min Fig. 1a), the limiting diffusion conditions of the cathodic wave are established from −650 mV/SCE; the shape of the current potential curve, between this potential and the corrosion potential, accounts for both the effect of the anodic elementary component and possibly that of mixed (diffusion-reaction) kinetics for reaction [1]. As a comparison, the limiting diffusion conditions of reaction [1] evolving on a platinum electrode in the same medium are established from 800 mV/SCE (Fig. 3). From the shape of the cathodic waves near to −700 mV/SCE, it can be inferred that the overpotential of reaction [1] is higher on platinum than on this carbon steel. Indeed, if one plots the cathodic current I_c as I_c/I_L *vs.* E(V/SCE), the wave obtained on Pt is shifted towards more cathodic potentials than that corresponding to carbon steel.

The variations of the diffusional component *vs.* Ω were measured, in potentiostatic regulation, for cathodic and anodic overpotentials, and for the corrosion potential. The results are reported in Fig. 4.

At the cathodic diffusion plateau (E_c = −914 mV/SCE) the diffusion current values (●) plotted as function of $\Omega^{1/2}$ fall on a straight line intersecting the origin of the axes. The experimental slope value is in agreement with that deduced from the Levich equa-

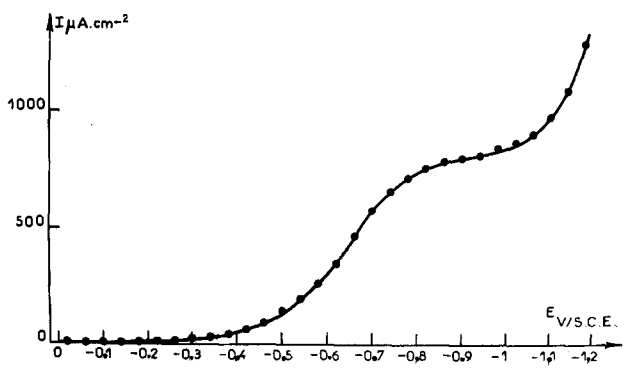

Fig. 3. Cathodic current-voltage curve obtained in potentiostatic mode at Ω = 1000 rpm on a Pt electrode; 3% NaCl solution.

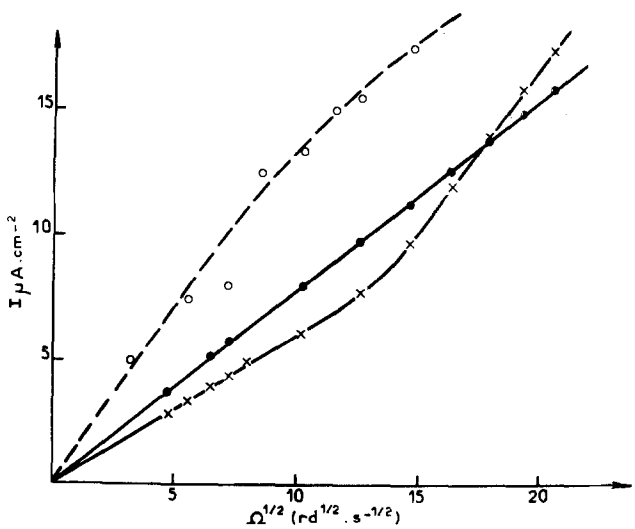

Fig. 4. Diffusion component of the current density vs. $\Omega^{1/2}$. ○: E corresponds to I_A = 250 $\mu A \cdot cm^{-2}$ at Ω = 1000 rpm. ●: E = −914 mV/SCE. ×: $E = E_{corr}$ (Ω = 1000 rpm). Actual diffusional components are obtained by multiplying the above value by: 4 (○), 20 (×), 100 (●).

tion (6)

$$I_L = 0.62nFc_\infty D^{2/3}\nu^{-1/6}\Omega^{1/2}A \qquad [2]$$

for the set of values at 20°C: $c_\infty = 2 \cdot 10^{-7}$ mol · cm^{-3}; $\nu = 10^{-2}$ cm^2 · sec^{-1}; $D = 1.74 \cdot 10^{-5}$ cm^2 · sec^{-1} [this value has been deduced from that measured at 25°C, $2 \cdot 10^{-5}$ cm^{-2} sec^{-1} (7)] where: n, the number of electrons transferred, is taken as 4, **F** is the Faraday, c_∞ the oxygen concentration in the bulk, ν the kinematic viscosity of the solution, D the molecular diffusion coefficient of oxygen, and A the electrode area (cm^2).

This result indicates that the whole electrode area is active in regard to the cathodic reaction.

At the corrosion potential (×) (Fig. 4), a linear plot through the origin is first observed up to 1500 rpm, but the slope is lower than that corresponding to Eq. [2]. Beyond 1500 rpm, a sharp increase of the current occurs, the data being fitted by a second linear plot whose extrapolation intersects the $\Omega^{1/2}$ axis at a positive abscissa. However, if the angular velocity is decreased, the current values lie again on a straight line going through the origin of the axes but with a higher slope than previously found between 0 and 1500 rpm. A fraction of the electrode area is then covered by a thick layer (1).

The bare portions of the disk are bounded by logarithmic spirals issued from the rotation axis which accounted for a hydrodynamic shearing of the layer formed during the hold time at zero current, under the flow action. Therefore, below 1500 rpm a low portion of the interface remains bare and gives rise to a dependence $I_d \alpha \Omega^{1/2}$, which can be expected for an active surface delimited by a convex contour on a rotating disk in laminar flow. Above 1500 rpm, the layer disruption becomes significant and, therefore, the increasing bare surface leads to a jump in the diffusion current.

After a hold time of 2 hr at an anodic current of 250 μA · cm^{-2} (Ω = 1000 rpm), the plot I_d *vs.* $\Omega^{1/2}$ (○) (Fig. 4) is curved. If the same data are replotted in the i^{-1}, $\Omega^{-1/2}$ coordinates, a straight line is found again, but it does not go through the origin of the axis (Fig. 5). Different causes are known to separately produce such an effect: (*i*) mixed kinetics, *i.e.*, electron transfer-mass transfer, for the cathodic reaction (6), (*ii*) the existence of a porous layer in which mass transport only depends on molecular diffusion, in addition to the convective diffusion transport in the liquid phase (8), and (*iii*) a partial blocking of the interface, *i.e.*, a decrease of the active area (9, 10).

Under the imposed hold time conditions, the metal is wholly covered by a colloidal layer of rust. It can be easily washed out under a water jet, and there remains an underlying black powdery layer. If one imposes then a cathodic polarization (E = −914 mV/SCE) on this surface, the measured diffusion current corresponds to that previously obtained on an active surface. The occurrence of a partial blocking of the interface must then be ruled out. This second layer can be also removed by an ultrasonic cleaning.

There only remains the role of a porous layer played by the colloidal layer, conceivably ferric hydroxide, in regard to oxygen diffusion. The mass transport of dissolved oxygen would proceed by both convective diffusion in the liquid phase (classical Nernst layer) and by molecular diffusion through the colloidal layer. Moreover, if one assumes a mixed kinetics control for the oxygen consumption, the total current resulting from the different series processes involved may be written as

$$I^{-1} = I_k^{-1} + I_{\Omega\to\infty}^{-1} + I_L^{-1} \qquad [3]$$

where I_k is the "kinetic current" of oxygen, *i.e.*, which would be measured at the corrosion potential on a bare surface in the absence of a mass transfer control. $I_{\Omega\to\infty}$ is the plateau current with the colloidal layer

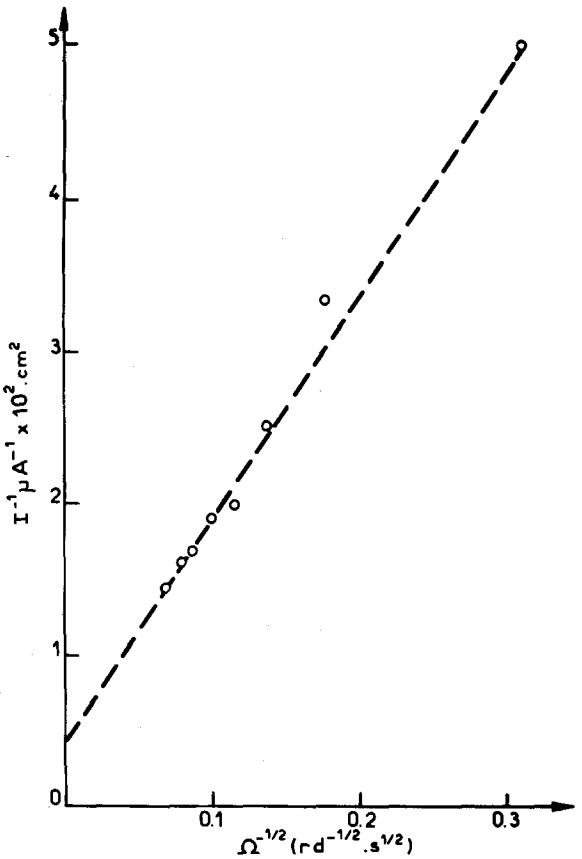

Fig. 5. Reciprocal values of the diffusional component *vs.* $\Omega^{-1/2}$ corresponding to the data (○) of Fig. 4.

for an infinite angular velocity. Given δ' and D', respectively, the thickness layer and the molecular oxygen diffusion coefficient in this layer, then

$$I_{\Omega\to\infty} = C_\infty D'/\delta' \qquad [3']$$

Finally I_L is given by Eq. [2]. Equation [3] provides then a linear relationship between I^{-1} and $\Omega^{-1/2}$, the slope of which must be identical to the reciprocal of that appearing in the Levich equation [Ref. (6)]. Now, the experimental slope value of 0.15 μA^{-1} rd$^{1/2}$ sec$^{-1/2}$ is at variance with the theoretical value of 0.0125. This discrepancy will be discussed later.

EHD impedance measurements.—The EHD impedance method which has been recently proposed for the study of electrode processes (11, 12) consists of frequency analysis of the current or potential response of the interface to a small sine wave modulation of the angular velocity. The quantities $\delta I/\delta\Omega|_V$ or $\delta V/\delta\Omega|_I$, according to whether a potentiostatic or galvanostatic regulation is used, have been predicted (4) in the case of a fast redox reaction occurring at the interface

$$\left.\frac{\delta I}{\delta\Omega}\right|_V = \frac{-3}{2\Omega_o}\exp(-0.26\,pj) \cdot \frac{c_\infty - c_o}{1.288}\,\frac{3^{1/3}}{\delta}\,\frac{K_1(s)}{Ai(s)}\,D\,\frac{Z_D}{Z} \qquad [4]$$

$$\left.\frac{\delta V}{\delta\Omega}\right|_I = \frac{-3}{2\Omega_o}\exp(-0.26\,pj) \frac{c_\infty - c_o}{1.288}\,\frac{K_1(s)}{Ai'(s)}\,R_T(k_f - k_b) \qquad [5]$$

Ω_o is the mean angular velocity and $p = \omega/\Omega_o$, where ω is the modulation frequency. $Ai(s)$ and $Ai'(s)$ are the Airy function of the first kind and its first derivative (4), respectively. $s = 1.57\,jp\,Sc^{1/3}$; $Sc = \nu/D$ is the

Schmidt number; $j^2 = -1$

$$K_1(s) = -\sum_{o}^{\infty} \frac{s^n}{n!} \int_o^{\infty} \frac{\delta^n A_i}{\delta \xi^n} \left[\xi^2 \exp\left(-\frac{\xi^3}{6}\right) + \xi^4 \rho_o(\xi) \exp\left(\frac{\xi^3}{6}\right) \right] d\xi$$

The definite integrals in the expression of $K_1(s)$ have been calculated in Ref. (9). Z_D is the diffusion impedance, R_T the charge transfer resistance, k_f and k_b the forward and backward rate constants of the redox reaction. Z is the overall impedance, *i.e.*, including the faradaic impedance Z_F the electrolyte resistance R_E and the double layer capacity C_D.

In the present case, the diffusional component is identical to the overall cathodic current, and it can be assumed that Eq. [4] and [5] established for a redox system only, are still valid.

A salient property of the ratio $\delta V/\delta\Omega$ is that for a given frequency modulation, its phase shift is constant whatever the polarization point is.

When the theoretical Eq. [5] is fitted to the experimental data, Sc may, therefore, be determined since p is given. The analysis of $\left.\frac{\delta I}{\delta \Omega}\right|_V$ (Eq. [4]) yields the same information for the region of diffusion plateau only and for frequency values in the mid range such that Z_D/Z tends towards unity.

As an example, the diagram displayed in Fig. 6 shows the variations of the reduced amplitude $A(p)/A(o)$ and the phase shift θ *vs.* p for the quantity $\left.\frac{\delta V}{\delta \Omega}\right|_I$, at $\Omega = 1000$ rpm and at the corrosion potential. The measurement is performed just after immersion of the electrode, which is, therefore, still free of corrosion products. The best fit of Eq. [5] to the experimental data is found for Sc = 615. This leads to an oxygen diffusion coefficient value of $1.63\ 10^{-5}$ cm^2 · sec^{-1} which is consistent with the steady-state measurements. Figure 7 shows the diagrams obtained under potentiostatic conditions at the oxygen diffusion plateau ($E = -914$ mV/SCE) and for different angular velocities Ω_o. At the velocity $\Omega_o = 200$ rpm, the same value of 615 as previously obtained is found for Sc. In fact, the relevant modulation frequencies ω are low and, therefore, $Z_D/Z \to 1$. For increasing Ω_o values, the adjusted Sc values increase. This may be ascribed to the fact that the condition $Z_D/Z \to 1$ is no longer fulfilled, mainly because of the presence of a large capacitance (1 mF · cm^{-2}) in the electrochemical impedance, as demonstrated later by the impedance measurements.

For an anodic current of 250 μA · cm^{-2} where the layer of corrosion products is homogeneous, the phase shift diagrams of the galvanostatic EHD impedance have the form depicted in Fig. 8. These diagrams, obtained at different Ω_o values cannot be reduced to a

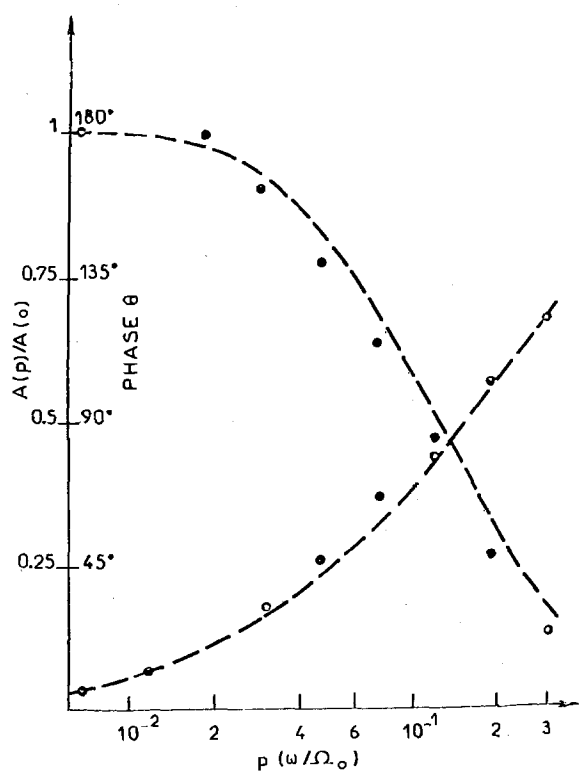

Fig. 6. Reduced amplitudes $A(p)/A(o)$ and phase lags θ of the EHD impedance obtained in galvanostatic mode at $\Omega_o = 1000$ rpm and at $I = 0$. The measurements are performed just after the electrode immersion in the solution.

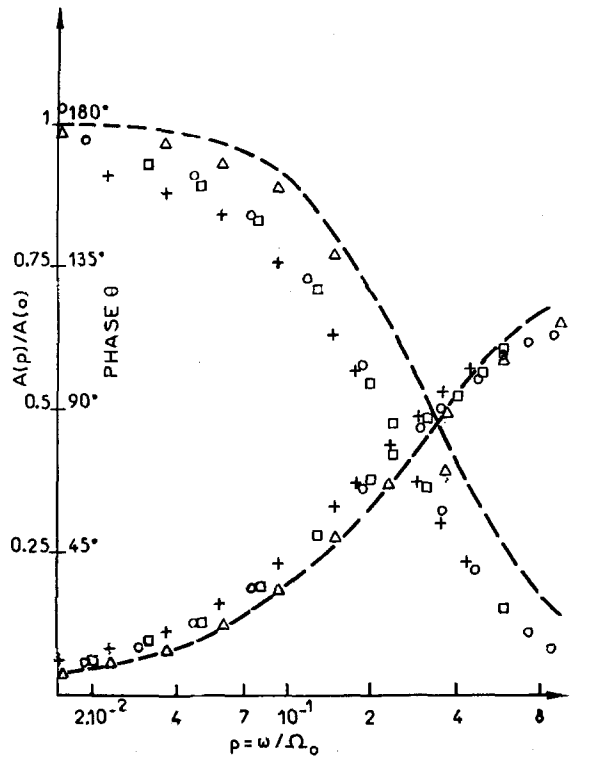

Fig. 7. Reduced amplitudes $A(p)/A(o)$ and phase lags θ of the EHD impedance obtained in potentiostatic mode ($E = -914$ mV/ECS) at $\Omega_o = 200$ rpm (○), 1000 rpm (+), 1500 rpm (△), 3000 rpm (□).

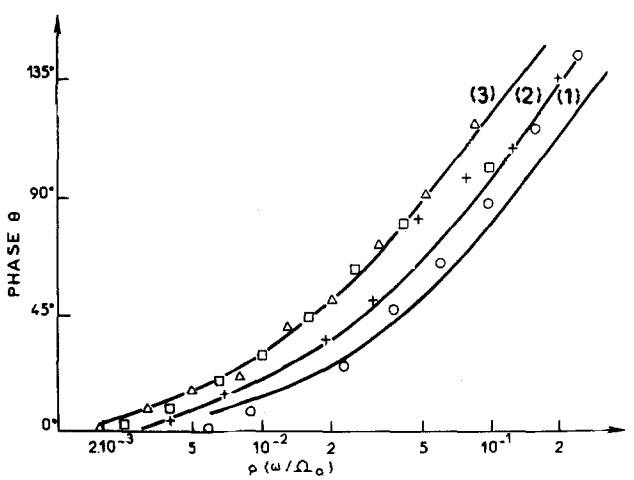

Fig. 8. Phase lags of the EHD impedance obtained in galvanostatic mode ($I_A = 250$ μA · cm^{-2}) at $\Omega_o = 200$ rpm (○), 1000 rpm (+), 1500 rpm (△), 3000 rpm (□).

single curve *vs.* p and lead to the adjusted *Sc* values of 1,500 (Ω_o = 200 rpm), 4,900 (Ω_o = 1,000 rpm), and 20,000 (Ω_o = 1,500 and 3,000 rpm). This behavior has been previously predicted when mass transfer control prevails not only in the liquid but also in a porous layer adherent to the interface (13).

It had then been demonstrated that the adjusted Sc number is linked to the true Sc number through the relation

$$Sc_{adj.}^{1/3} \sim Sc_{true}^{1/3} + k\frac{\delta'^2}{D'} \cdot \Omega$$

where δ' and D' have the same definition as above.

To sum up the EHD impedance measurements considered below give more information than the steady-state measurements about the role of the corrosion products layer concerning mass transfer.

Electrochemical impedance measurements.—As previously mentioned and unless otherwise indicated, the electrode has been held at zero current for 2 hr and at Ω_o = 1000 rpm. The electrochemical impedance has been measured in linear conditions (modulation signal amplitude of a few millivolts) at different points of the current potential curve, in galvanostatic or potentiostatic conditions. The Nyquist plots (R, $-jG$) are generally characterized by two capacitive loops which are more or less separated and which exhibit very low characteristic frequencies. In addition, it may be noted that the HF loop is not centered on the real axis. These points will be considered later in the discussion section.

The influence of different parameters on the impedance diagrams have been examined.

Effect of the angular velocity Ω_o.—An increase of Ω_o decreases the diameter of both loops as shown by the diagrams in Fig. 9, obtained in galvanostatic conditions. In contrast, impedance measurements performed in potentiostatic conditions (where obviously I = 0 for Ω = 1000 rpm) exhibit an HF loop whose amplitude and frequency dependence are not modified when Ω is varied (Fig. 10).

Effect of the oxygen concentration.—By keeping the angular velocity equal to 1000 rpm, the same experiment as before was carried out with two different bubblings, one with oxygen, the other with nitrogen (Fig. 11).

The oxygen concentration increase lowers the polarization resistance and plays the same role as the velocity increase at a fixed oxygen concentration.

Effect of the hold time at zero current.—Increasing the hold time at zero current before the impedance measurements leads to an expansion of both loops and, therefore, to an increase of the polarization resistance. In addition, a frequency shift of the LF loop towards lower values is observed (Fig. 12). In the same way the polarization resistance increases with the angular

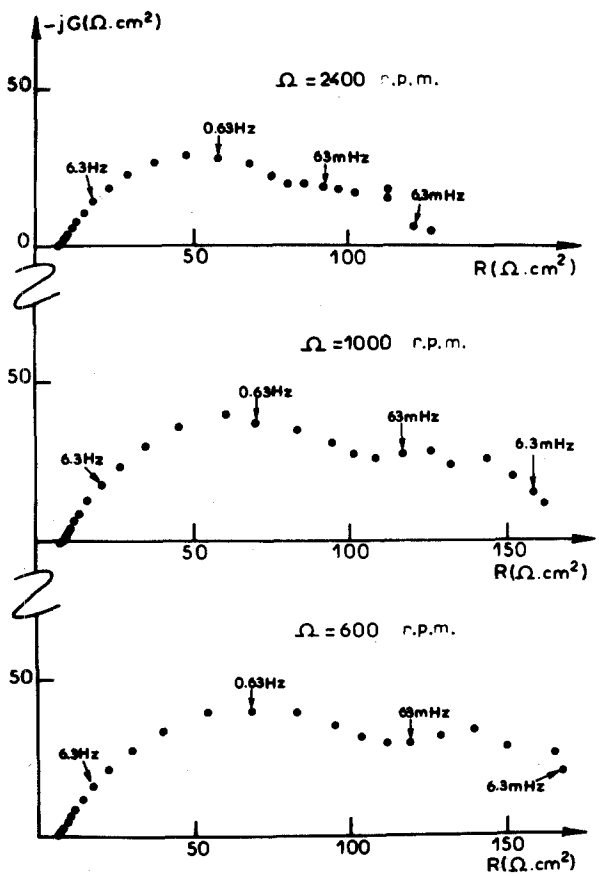

Fig. 9. Electrochemical impedance diagrams obtained in galvanostatic mode (I = 0) and at different rotation speeds.

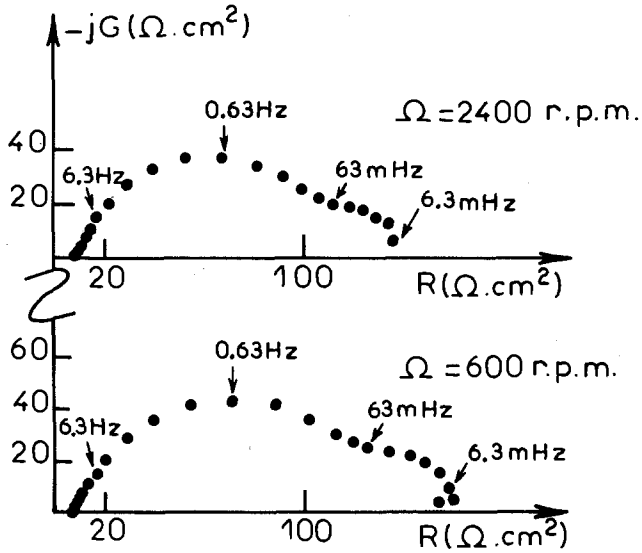

Fig. 10. Electrochemical impedance diagrams obtained in potentiostatic mode ($E = E_{corr}$ when I = 0 at Ω = 1000 rpm) at different rotation speeds.

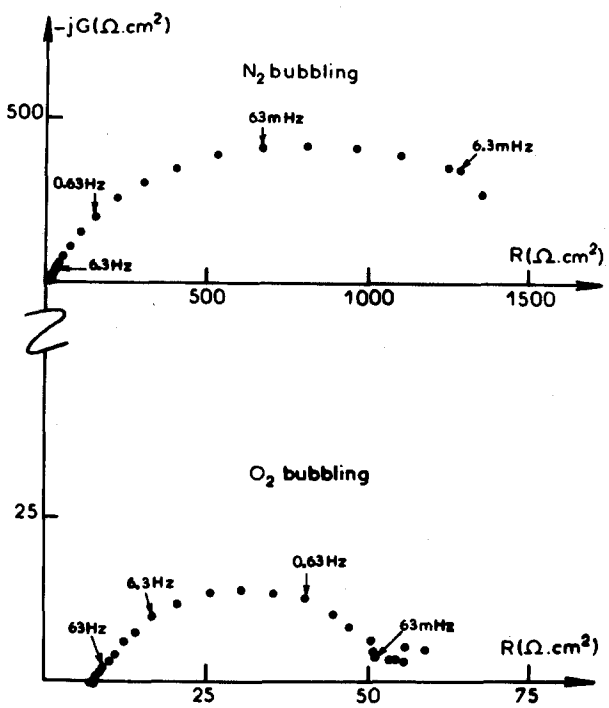

Fig. 11. Electrochemical impedance diagrams obtained in galvanostatic mode (I = 0) at Ω = 1000 rpm after a nitrogen (N_2) or oxygen (O_2) bubbling.

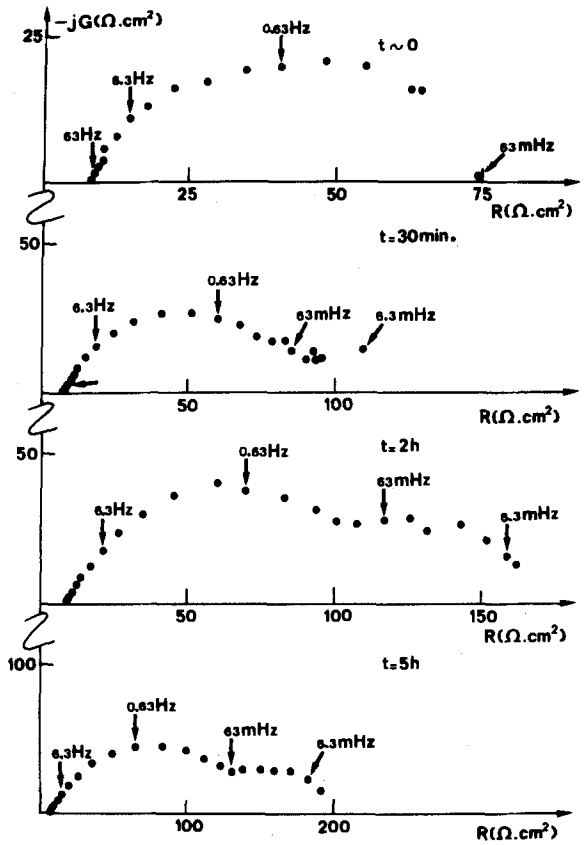

Fig. 12. Electrochemical impedance diagrams obtained at $I = 0$ after different hold times ($\Omega = 1000$ rpm).

velocity that has been imposed during the hold time at zero current for a given period of time.

Finally when the experiments are performed around the corrosion potential, two capacitive loops are still observed: (*i*) In the cathodic range, the LF loop dimension increases with overpotential (Fig. 3). (*ii*) In the anodic range, the dimensions of both loops decrease with overpotential.

Above an anodic current of 750 $\mu A \cdot cm^{-2}$, the LF loop vanishes and also no influence of the angular

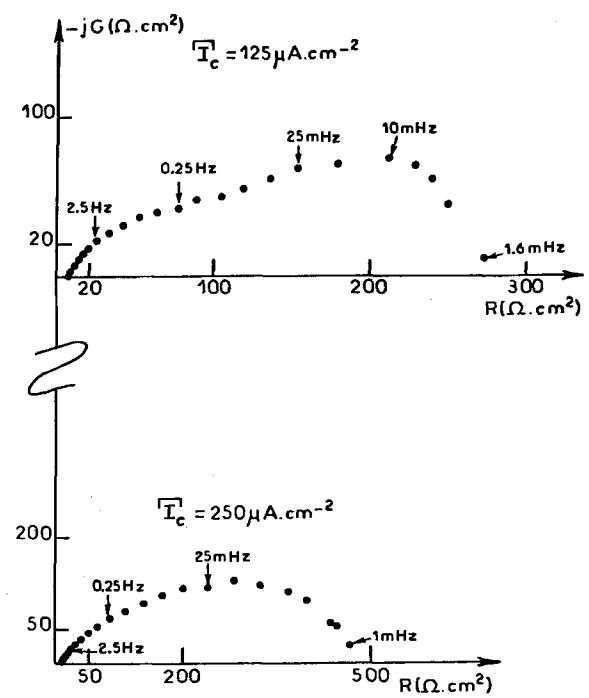

Fig. 13. Electrochemical impedance diagrams obtained in galvanostatic mode for two cathodic overpotentials ($\Omega = 1000$ rpm).

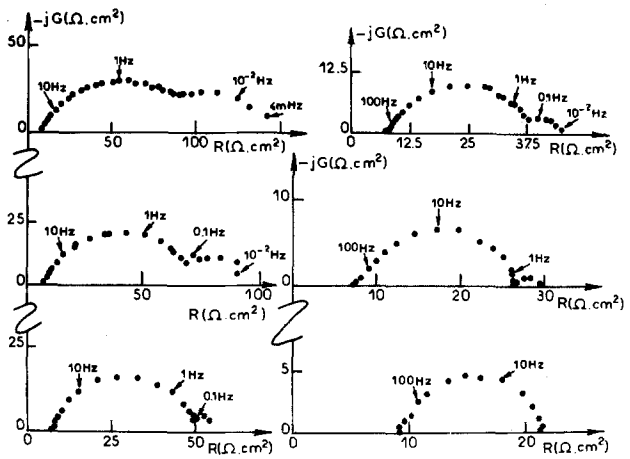

Fig. 14. Electrochemical impedance diagrams for anodic overpotentials ($\Omega = 1000$ rpm). Left column from top to bottom I_A = 125, 250, 500 $\mu A \cdot cm^{-2}$. Right column from top to bottom I_A = 750, 1500, 3000 $\mu A \cdot cm^{-2}$.

velocity is observed (Fig. 14) on the remaining HF loop. This behavior is qualitatively unchanged whatever the regulation, *i.e.*, galvanostatic or potentiostatic.

Discussion of the Results

To sum up, the examination of the electrochemical impedance diagrams near to the corrosion potential leads to the conclusion that the interface response contains two time constants which are more or less clearly separated.

HF loop.—The values of the HF loop diameter R_I, the characteristics frequency ω_c, the product $R_I I$, and the capacitance C are reported in Table I. The capacitance C has been roughly estimated since the HF loop is not centered on the real axis from the characteristic frequency ω_c of the high frequency loop by the relationship $C = (R_I \omega_c)^{-1}$. ω_c corresponds to the maximum value of the imaginary component, and R_I is the diameter of the HF loop.

The capacitance values C in Table I appear to be abnormally high since, being associated with the HF loop, C is likely to be considered as the double layer capacitance. The other fact previously mentioned is the frequency dispersion leading to a flattening of the HF loop. To tackle these problems, different hypotheses have been put forward independently or concurrently.

1. As to the high capacitance value: A faradaic capacitance relevant to the relaxation of an adsorbed intermediate which would interfere with the double layer capacitance (14).

2. As to the frequency dispersion: This behavior has often been observed with solid electrodes and is generally attributed to the surface heterogeneity caused by a distribution of the reaction rate with the location on the electrode surface. It has been shown for instance on Pt (14) that such a frequency distribution may happen, but the capacitance values (~100 $\mu F/cm^2$) are then of the same order of magnitude as that of a double layer.

However, a third cause, which is able to give rise simultaneously to effects 1 and 2 may originate from both the porous and conductive nature of the powdery

Table I. Parameter values deduced from the diagrams of Fig. 14.

I_A ($\mu A \cdot cm^{-2}$)	R_I ($\Omega \cdot cm^2$)	$\omega_c/2\pi$ (Hz)	$R_I I_A$ (mV)	C ($\mu F \cdot cm^{-2}$)
125	95 ± 3	1 ± 0.25	11.88 ± 0.38	1800 ± 500
250	66 ± 2	1.5 ± 0.25	16.50 ± 0.50	1664 ± 326
500	45 ± 2	3.2 ± 1	22.50 ± 1	1244 ± 438
750	33 ± 1	3.5 ± 1	24.75 ± 0.75	1515 ± 475
1500	19 ± 1	7.5 ± 1	28.50 ± 1.5	1148 ± 212
3000	11.5 ± 0.5	14 ± 1.5	34.50 ± 1.5	1007 ± 151

underlying deposit revealed after having washed out the colloidal outer layer as indicated in section "cathodic mass transport analysis."

In fact, the powdery structure of this layer is clearly substantiated by a scanning microscopic photograph (Fig. 15) of the interface after an anodic hold time prior to impedance measurements. In addition, an x-ray analysis indicates a significant content of Mn, possibly producing an electrical conductivity of this layer as suggested also by the steady mass transfer measurements. The resulting effect is, then, a large increase of the specific area in regard to the primary current distribution but, with such a structure, the effective area "seen" by the electric field depends on frequency and, therefore, is able to give rise to the frequency distribution and to the high C values at the same time (15).

In order to check the validity of the last hypothesis, we carried out the following procedure; the capacitance in parallel for a phosphate buffer having the same pH as the NaCl solution (pH = 6.20) has been measured. The measurement was first performed on the electrode surface just after a polishing. The capacitance was equal to 200 $\mu F \cdot cm^{-2}$.

Secondly, we imposed an anodic current of 1 mA $\cdot cm^{-2}$ during 2 hr in 3% NaCl so as to generate a thick corrosion products layer. The capacitance was, then, measured in the phosphate buffer with and without the colloidal layer and finally without the underlying layer (removed by an ultrasonic cleaning). The respective values were 1750, 500, and 200 $\mu F \cdot cm^{-2}$. The value of 500 $\mu F/cm^2$ is presumably underestimated since a part of the powdery layer is removed when the colloidal layer is washed out. The high C value must then be primarily ascribed to the existence of the inner corrosion products layer

LF loop.—By analogy with the diagrams corresponding to a redox process, controlled by diffusion (Randle's circuit), it would be tempting to ascribe the LF loop to a relaxation of mass transport. However, though an influence of hydrodynamic conditions can be detected on this loop, this influence is characterized neither by the usual shape of a diffusion impedance (16), nor by the relationship $\frac{\omega_c \delta^2}{D} \sim 2.5$ which links the characteristic frequency ω_c, the Nernst layer thickness δ, and the molecular diffusion coefficient D.

This may be explained by the fact that, on one hand, it has been previously established that mass transfer takes place not only in the fluid by convective diffusion, but also in the corrosion products layer by molecular diffusion.

On the other hand, due to the mixed nature of the corrosion potential the equivalent circuit reflecting the faradaic impedance variations with frequency must be considered as composed of the cathodic and anodic branches in parallel.

As to the cathodic process, the equivalent circuit is a combination of a resistance R_2 in series with a diffusion impedance Z_D, since it corresponds to a redox reaction partially controlled by mass transfer. For the sake of simplicity, the expression of Z_D resulting from the Nernst hypothesis will be chosen (11)

$$Z_D = R_D \frac{th\sqrt{j\omega\delta^2/D}}{\sqrt{j\omega\delta^2/D}}$$

From the analysis of the impedance diagrams recorded at an anodic current of the order of 1 mA $\cdot cm^2$, only one loop is observed. Therefore, the anodic branch can be represented by a resistance R_1 which is identical to R_I at high anodic overpotentials. This is confirmed in Table I by the product $R_I I$ which remains close to 30 mV above 750 $\mu A \cdot cm^2$, indicating a simultaneous transfer of the two electrons.

To sum up, the unsteady behavior of the interface can be satisfactorily represented by the equivalent circuit of Fig. 16. The relevant diagrams have been simulated for different sets of parameter values. As an example, four typical diagrams are reported in Fig. 17. They display similarities, as to the shape and the time constants associated with each loop, with the experimental diagrams, especially those obtained after different hold times (Fig. 12).

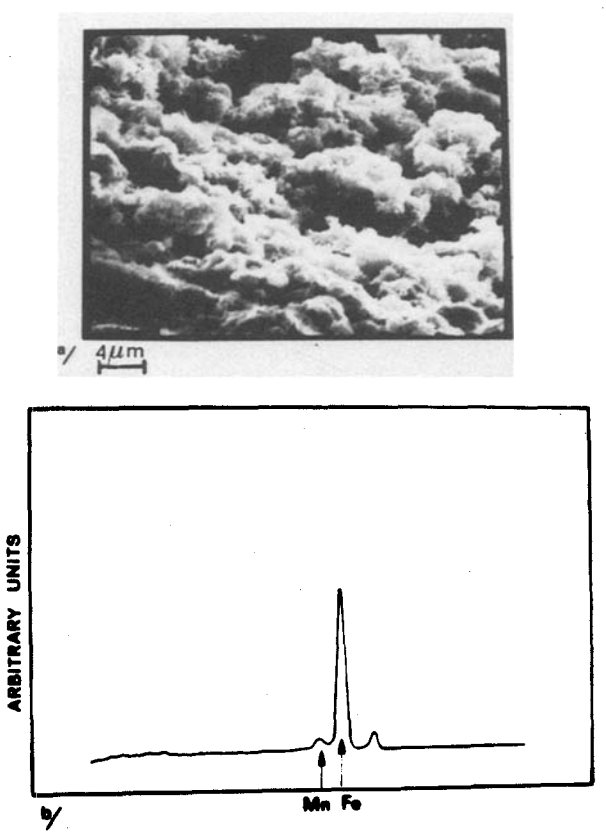

Fig. 15. (a) Interface aspect by scanning microscopy after an anodic hold time. (b) Energy dispersive x-ray analysis of the corrosion products layer.

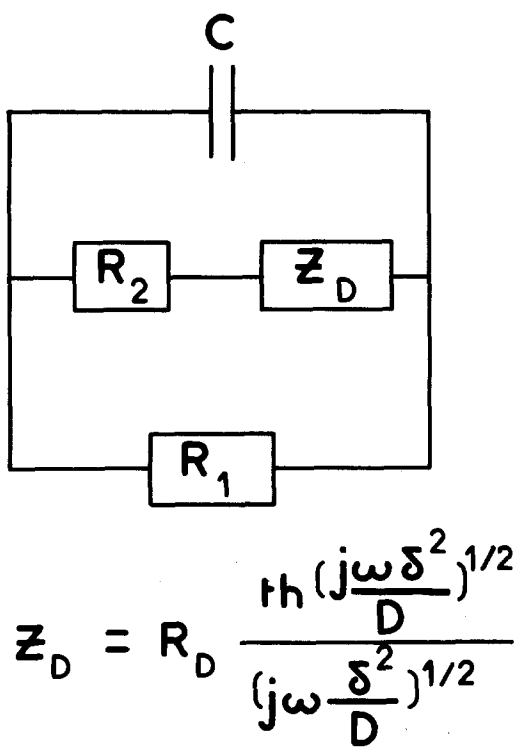

Fig. 16. Equivalent circuit of the interface carbon steel/3% NaCl solution, in the vicinity of the corrosion potential.

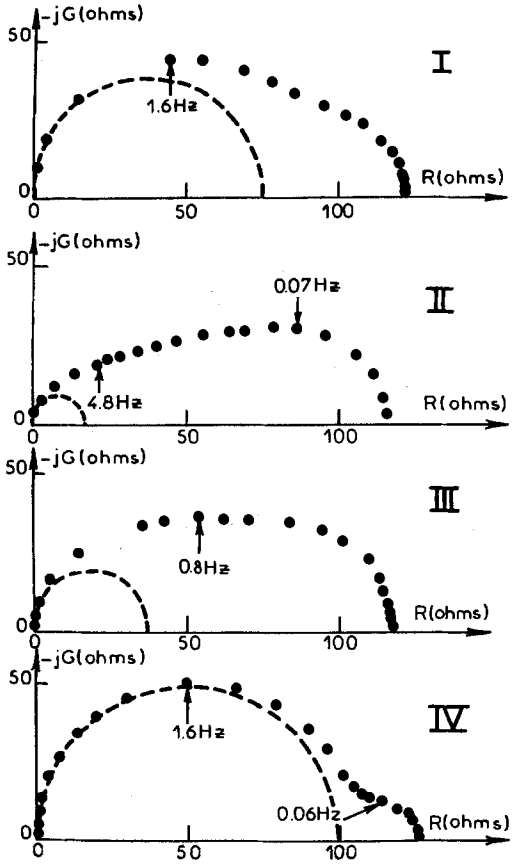

Fig. 17. Simulated electrochemical impedance diagrams according to the equivalent circuit of Fig. 16. $C = 1$ mF. *I*: $R_1 = 150\Omega$; $R_2 = 150\Omega$; $R_D = 500\Omega$; $\delta^2/D = 5$ sec. II: $R_1 = 150\Omega$; $R_2 = 20\Omega$; $R_D = 500\Omega$; $\delta^2/D = 20$ sec. III: $R_1 = 150\Omega$; $R_2 = 50\Omega$; $R_D = 500\Omega$; $\delta^2/D = 5$ sec. IV: $R_1 = 150\Omega$; $R_2 = 300\Omega$; $R_D = 500\Omega$; $\delta^2/D = 20$ sec.

According to the equivalent circuit, the diameter of the HF loop has the value $\frac{R_1R_2}{R_1 + R_2}$. This fact explains, therefore, why when using galvanostatic regulation, an effect of the angular velocity on the HF loop is observed though this loop does not explicitly depend on mass transport. In fact, when Ω is varied, a resulting potential shift of the interface is observed and, therefore, variations of R_1 and R_2 in the same direction. The ratio $\frac{R_1R_2}{R_1 + R_2}$ is, then, expected to be different as well as the characteristic frequency since C is supposed to be constant. Now, R_2 may be dependent on Ω even for a potentiostatic regulation when there is a mixed control kinetics since c_o^{ox} can increase up to c_∞ when Ω tends towards infinity and $R_{2\alpha}\frac{1}{c_o^{ox}}$. The experimental behavior mentioned above would, thus, substantiate the hypothesis expressed in Ref. (1) according to which the reduction reaction of oxygen at the corrosion potential would show mixed control (*i.e.*, electron transfer-mass transfer). In order to disentangle the elementary HF and LF loops so as to display their individual shapes, we simulated the diagrams with time constants differing by several orders of magnitude.

In Fig. 18, the simulated diagram shows a semicircular HF loop ascribed to the frequency response of the parallel association of C and $\frac{R_1R_2}{R_1 + R_2}$. In the LF range, the loop which is mainly due to the relaxation of the mass transfer process is strongly distorted with respect to the classical shape of a diffusion impedance simply because of the finite value of R_1 in parallel.

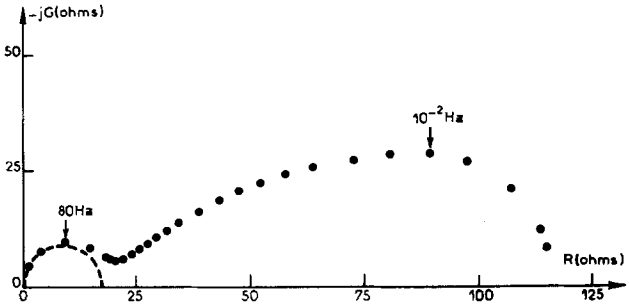

Fig. 18. Simulated electrochemical impedance diagram according to the equivalent circuit of Fig. 16. $C = 10^{-4}$F; $R_1 = 150\Omega$; $R_2 = 20\Omega$; $R_D = 500\Omega$; $\delta^2/D = 100$ sec.

As for the results of the mass transfer study, it has been shown that the oxygen diffusion is hindered by the existence of a porous layer. This effect must be attributed to the external colloidal layer of ferric hydroxide and not to the underlying oxide layer which is presumably an electronic conductor. However, as mentioned above, the disagreement observed on the slope (I^{-1}, $\Omega^{-1/2}$) in Fig. 5 after an anodic hold time cannot be explained by this interface model. Concurrently, the vanishing of the diffusional component at low anodic overpotentials is at variance with the broad potential range of mixed kinetics control observed for the same reduction wave on platinum. It must then be stated that an overconsumption of oxygen takes place in the vicinity of the interface. This process could be the oxidation of the Fe^{2+} ions generated in the dissolution. In fact, it is known that the Fe^{2+} ions cannot precipitate in our pH conditions (the pH of full precipitation is higher than 9). In constrast, the pH of full precipitation of Fe $(OH)_3$ is higher than 3.2, with a corresponding pK equal to 38. The Fe^{2+} ions at a neutral pH are highly reducing agents so that their oxidation to Fe^{3+} is fast. One part of the oxygen molecules close to the metal would, then, be consumed in the chemical oxidation of Fe^{2+}. This process would then be enhanced with the anodic current increase since a local increase in Fe^{2+} concentration would increase the O_2 consumption. The chemical oxidation of Fe^{2+} ions is obviously not a first-order chemical reaction, in which case one would find again the same slope for the straight line (I^{-1}, $\Omega^{-1/2}$) as that given by the Levich relationship. Qualitatively in our study, it can be assumed that the effective oxygen concentration c_∞ is lowered by a factor which is the more important as the anodic overpotential increases.

In conclusion, this work provided from both steady-state measurements and by the EHD impedance method a direct proof of the occurrence of mass transport through porous layers during the corrosion of a carbon steel in a neutral chloride medium.

In addition, it has been shown from a thorough analysis of the electrochemical impedance that the corrosion rate is controlled by the reduction of dissolved oxygen under mixed kinetics conditions, *i.e.*, mass transfer-electron transfer. In addition, the LF loop, which has been mainly assigned to mass transfer, includes as well the influence of the anodic process. It must be also emphasized that the measurement of only the polarization resistance in order to estimate the corrosion rate would lead to erroneous values for such a system which is typical of many practical corrosion problems.

Acknowledgment

This paper and the following constitute a part of M. Duprat's Thesis submitted to the University of Toulouse in July 1981.

Manuscript submitted Jan. 4, 1982; revised manuscript received *ca.* Nov. 30, 1982. This was Paper 140 presented at the Denver, Colorado, Meeting of the Society, Oct. 12-16, 1981.

Any discussion of this paper will appear in a Discussion Section to be published in the December 1983 JOURNAL. All discussions for the December 1983 Discussion Section should be submitted by Aug. 1, 1983.

Publication costs of this article were assisted by CNRS.

REFERENCES

1. M. Duprat, N. Bui, and F. Dabosi, *J. Appl. Electrochem.*, **8**, 455 (1978).
2. D. D. MacDonald, B. C. Syrett, and S. S. Wing, *Corrosion*, **34**, 289 (1978); *ibid.*, **35**, 367 (1979).
3. (a) R. D. Armstrong and A. C. Coates, *J. Electroanal. Chem.*, **50**, 303 (1974); (b) K. G. Boto and L. F. G. Williams, *This Journal*, **124**, 656 (1977).
4. C. Deslouis, C. Gabrielli, Ph. Sainte-Rose Fanchine, and B. Tribollet, *This Journal*, **129**, 107 (1982).
5. C. Gabrielli and M. Keddam, *Electrochim. Acta*, **19**, 355 (1974).
6. V. G. Levich, "Physicochemical Hydrodynamics," Prentice Hall, Englewood Cliffs, New Jersey (1962).
7. B. E. Conway, "Electrochima Data," Elsevier Publishing Company, Amsterdam (1952).
8. M. Delamare, I. Minh Chau Pham, P. C. Lacaze, and J. E. Dubois, *J. Electroanal. Chem.*, **108**, 1 (1980).
9. F. Scheller, S. Muller, R. Landsberg, *ibid.*, **19**, 187 (1968).
10. E. Levart, D. Schuhmann, O. Contamin, and M. Etman, *ibid.*, **70**, 117 (1976).
11. K. Tokuda and S. Bruckenstein, *This Journal*, **122**, 1316 (1975); *ibid.*, **126**, 431 (1979).
12. C. Deslouis, I. Epelboin, C. Gabrielli, and B. Tribollet, *J. Electroanal. Chem.*, **82**, 251 (1977).
13. Ph. Sainte-Rose Fanchine, 3rd Cycle Thesis, Paris (1980).
14. S. H. Glarum and J. H. Marshall, *This Journal*, **126**, 424 (1979).
15. J. P. Candy, P. Fouilloux, M. Keddam, and H. Takenouti, *Electrochim. Acta*, **28**, 1029 (1981).
16. C. Deslouis, I. Epelboin, M. Keddam, and J. C. Lestrade, *J. Electroanal. Chem.*, **28**, 57 (1970).

Corrosion Inhibition Study of a Carbon Steel in Neutral Chloride Solutions by Impedance Techniques

F. Dabosi

Equipe de Recherche Associée au CNRS, no 263 "Laboratoire de Métallurgie Physique," Ecole Nationale Supérieure de Chimie, 31077 Toulouse Cedex, France

C. Deslouis

Groupe de Recherche du CNRS, no 4 "Physique des Liquides et Electrochimie" Associé à l'Université Pierre et Marie Curie, 75230 Paris Cedex 05, France

M. Duprat

Equipe de Recherche Associée au CNRS, no 263 "Laboratoire de Métallurgie Physique," Ecole Nationale Supérieure de Chimie, 31077 Toulouse Cedex, France

and M. Keddam

Groupe de Recherche du CNRS, no 4 "Physique des Liquides et Electrochimie," Associé à l'Universitè Pierre et Marie Curie, 75230 Paris Cedex 05, France

ABSTRACT

The electrochemical behavior of a carbon steel in 3% NaCl solution containing 10^{-2}M of diamino-1,2-ethane has been investigated using a rotating disk electrode. Both steady-state (current-voltage curves for various disk rotation speeds) and transient (frequency analysis of the electrohydrodynamical and electrochemical impedances) measurements have been carried out. It was concluded that the oxygen reduction process at the corrosion potential was mainly controlled by charge transfer which is at variance with the uninhibited situation. Consequently, polarization resistance measurements can be used in this case to estimate corrosion rates. Regarding the mode of inhibition of diamino-1,2-ethane, the data are consistent with the chelation mechanism proposed for this type of bifunctional compound; it appears that the inhibitive action mainly affects the anodic reaction.

In previous works (1, 2), corrosion inhibition of a carbon steel in a 3% NaCl solution by aliphatic amino-alcohol and diamine type compounds has been studied by both weight loss measurements and steady-state electrochemical methods. The following conclusions have been drawn. (*i*) The inhibitive efficiency of these molecules is only partly due to their alkalinity; in addition they exhibit intrinsic inhibitive properties. (*ii*) Correlation between inhibitive efficiency and molecular structure suggested that the inhibitor stabilizes the ferrous hydroxide film formed on the metal surface at high pH values. A chelation mechanism is likely to take place between organic molecules and ferrous ions in the film or iron atoms at uncovered sites of the surface.

As illustrated in the first part of this series (3), impedance techniques have been shown to provide highly useful data regarding the corrosion mechanism of the interface studied in Ref. (1, 2) but in the absence of inhibitors. In the present paper, impedance techniques are applied to the corrosion inhibition study by diamino-1,2-ethane which appeared among the more efficient compounds investigated (2). The role of mass transport is analyzed both by means of steady-state current-voltage curves in the cathodic range at various rotation speeds of the disk and by electrohydrodynamical (EHD) impedance measurements. Electrochemical impedance measurements are also performed

Key words: interface, disk electrode, organic compound, kinetics.

under various polarization conditions in order to estimate the anodic and cathodic contributions to the corrosion kinetics in the presence of inhibitor.

It must be emphasized that these techniques have been extensively applied to the study of corrosion inhibition in acidic media but much less in neutral ones. Moreover, it seems that up to now EHD impedance has never been used in this field.

Experimental

The experimental procedure is similar to that adopted in the first part of this series. Previous to any steady-state or nonsteady-state measurement, the electrode is held for 2 hr at its free corrosion potential at a rotation speed of 1000 rpm. Since a concentration of 10^{-2}M of diamino-1,2-ethane in a 3% NaCl solution results in a *p*H value of 10.85 (2), a comparative test was performed by adjusting the *p*H to the same value as that of an inhibitor-free solution by means of a small addition of 0.5M NaOH. "Pro analysis" grade (Merck) diamino-1,2-ethane was used. All other experimental conditions are identical to those described in the first part of this series.

Results

Steady-state and EHD impedance.—Current-voltage curves.—The steady-state current-voltage curve in the cathodic range in a solution containing 10^{-2}M diamino-1,2-ethane at a rotation speed of 1000 rpm is shown in Fig. 1a. The dashed curve, c, corresponds to an inhibitor-free solution at its natural *p*H value of 6.20. A comparison of curves a and c already shows that the inhibitor gives rise to a shift of the corrosion potential in the anodic direction and to a possibly more marked region of mixed kinetic control of oxygen reduction. It is worth noting also that in contrast to the uninhibited solution the limiting current density is close to the value predicted by the Levich equation for a uniformly reactive surface (see first part of this series (3)). Curve b in Fig. 1 is obtained in the inhibitor-free NaCl solution, the *p*H of which was adjusted to 10.85 by means of 0.5M NaOH. From the view point of both corrosion potential and limiting current density, curve b is located between a and c.

Figure 2 shows the dependence of the cathodic current-voltage on the rotation speed of the disk. At potentials more cathodic than −900 mV/SCE, a limiting current density is observed obeying the Levich equation whereas the anodic current, as in absence of inhibitor, is nearly independent of the rotation speed (Fig. 3a). It must be emphasized that equating the corrosion current to the cathodic limiting current (Fig. 1) would lead to the conclusion that the addition of inhibitor increases the corrosion rate in contradiction to weight loss data (2). This surprising result can be explained by considering the relative position of the anodic curves shown in Fig. 3. Increasing the *p*H of the solution from 6.20 to 10.85 increases the overvoltage in the immediate vicinity of the corrosion potential; addition of inhibitor has a similar effect but more marked. Above approximatively 750 $\mu A \cdot cm^{-2}$, the anodic current density values in all cases scarcely change.

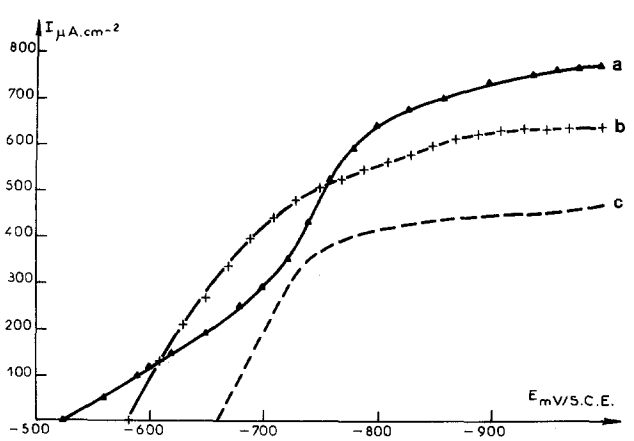

Fig. 1. Cathodic current-voltage curves (Ω = 1000 rpm) plotted in potentiostatic mode. (a) With diamino-1,2-ethane (10^{-2}M); *p*H = 10.85, (b) check sample; *p*H = 10.85 (adjusted by 0.5M NaOH), and (c) check sample; *p*H = 6.20.

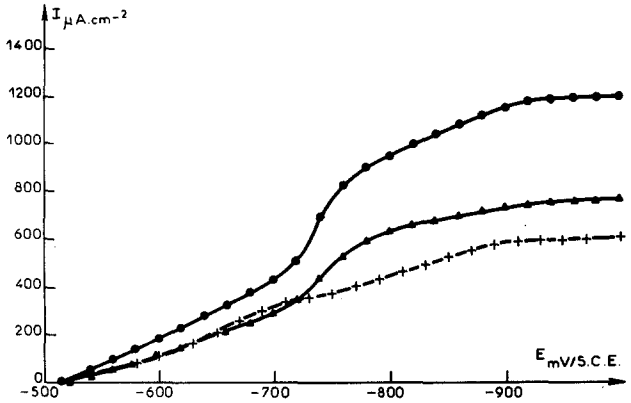

Fig. 2. Cathodic current-voltage curves (potentiostatic regulation) plotted at different rotation speeds and with diamino-1,2-ethane (10^{-2}M). Ω = 2400 rpm (●), 1000 rpm (▲), 600 rpm (+).

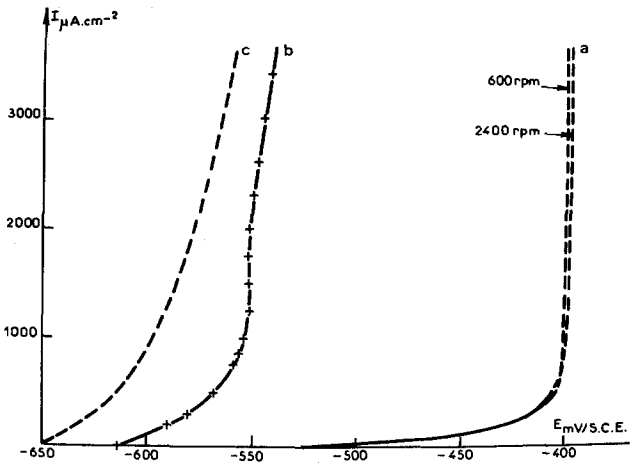

Fig. 3. Anodic current-voltage curves plotted in galvanostatic mode. (a) With diamino 1,2-ethane (10^{-2}M); *p*H = 10.85; Ω = 600 and 2400 rpm, (b) check sample; *p*H = 10.85 (adjusted by 0.5M NaOH); Ω = 1000 rpm, and (c) check sample; *p*H = 6.20; Ω = 1000 rpm.

EHD impedance.—Before any measurement, the electrode is allowed to corrode for 5 hr at its free corrosion potential. Figure 4 shows the phase lag θ as a function of dimensionless frequency p, relative to $\delta V/\delta\Omega|_I$ for various rotation speeds Ωo and polarization conditions. For comparison purposes the hachured region corresponds to the data obtained with an inhibitor concentration of $5 \cdot 10^{-3}$M ($600 < \Omega o < 3000$ rpm and $\bar{I} = 400$ and 800 μA).

In Fig. 5, the dimensionless modulus $A(p)/A(o)$ and the phase lag θ have been reported as functions of dimensionless frequency p, relative to $\delta I/\delta\Omega|_V$ at the half-wave potential ($E = -714$ mV/SCE) for various speeds Ωo.

The Schmidt numbers for the relevant Ωo values fitted from these data are, respectively, Sc = 1500 (Ωo = 200 rpm), 2500 (Ωo = 1000 rpm), 2750 (Ωo = 1500 rpm), and 3750 (Ωo = 3000 rpm).

Finally, EHD impedance diagrams for potentiostatic regulation in the cathodic range at a constant rotation speed are shown in Fig. 6. The fitted values of the Schmidt number corresponding to the different

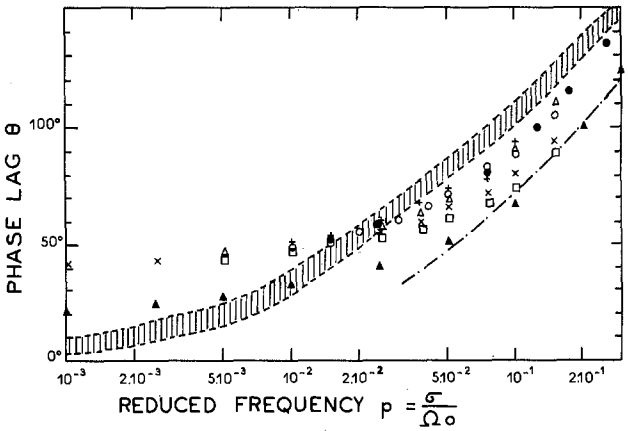

Fig. 4. Phase lag θ of the EHD impedance obtained in galvanostatic regulation. Ω = 240 rpm = (●) I = 300 μA, E = −700 mV/SCE; Ω = 600 rpm = (○) I = 300 μA, E = −684 mV/SCE; Ω = 1200 rpm = (+) I = 300 μA, E = −668 mV/SCE; (△) I = 600 μA, E = −764 mV/SCE; (×) I = 800 μA, E = −836 mV/SCE; (□) I = 900 μA, E = −930 mV/SCE; (▲) I = 1000 μA, E = −1050 mV/SCE.

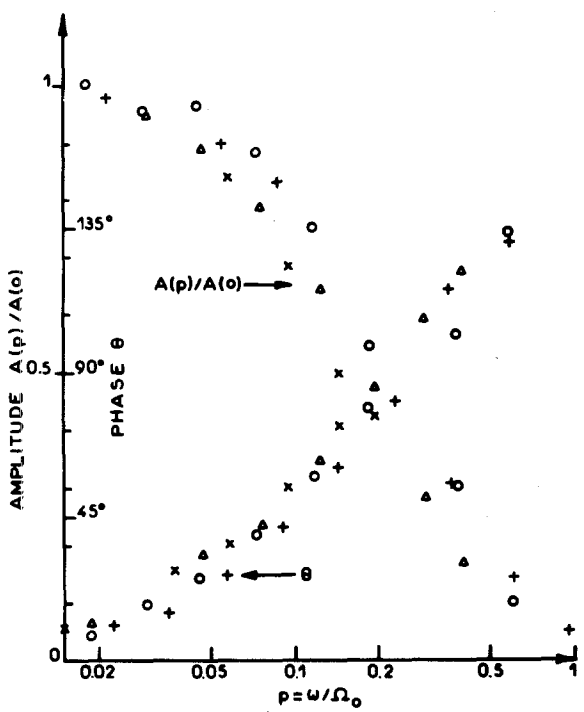

Fig. 5. Reduced amplitudes $A(p)/A(o)$ and phase lags θ of the EHD impedance obtained in potentiostatic regulation at E = −714 mV/SCE. Ω_0 = 200 rpm (+), 1000 rpm (○), 1500 rpm (△), 300 rpm (×).

polarization conditions in the inhibited solution are: 510 (E = −914 mV/SCE); 1500 (E = −714 mV/SCE) 3400 (E = E corr). These different behaviors will be discussed in the discussion section.

Electrochemical impedance.—The electrochemical impedance diagram obtained in galvanostatic regulation at zero d-c current and displayed in Fig. 7 is typical of the set of diagrams in the presence of diamino-1,2-ethane. By comparison with results from an uninhibited solution (3), it is observed that: (*i*) there only remains one capacitive loop with a very low characteristic frequency. In fact, the second loop, previously assigned to the molecular diffusion of oxygen through a porous layer built up by corrosion, has vanished; (*ii*) the polarization resistance is greatly increased. To examine the intrinsic influence of the inhibitor alkalinity (pH = 10.85), impedance measurements have been performed in the uninhibited

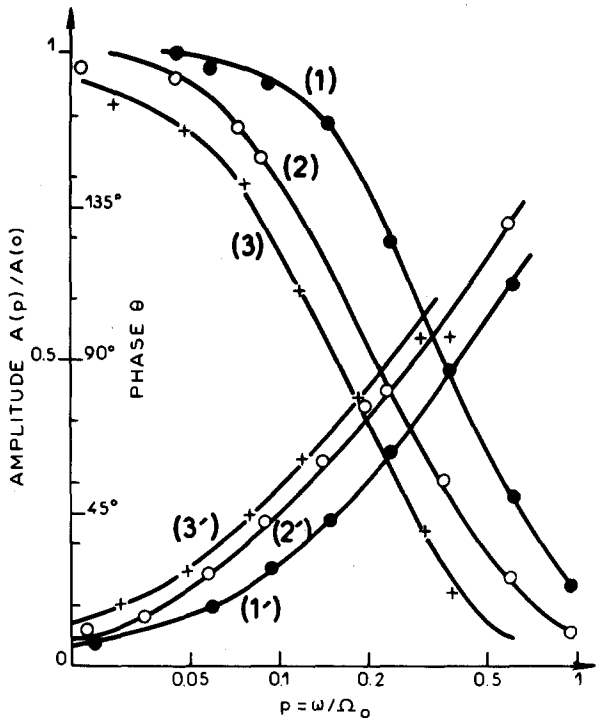

Fig. 6. Reduced amplitudes $A(p)/A(o)$ and phase lags θ of the EHD impedance obtained in potentiostatic regulation at Ω_0 = 200 rpm. E (mV/SCE) = −914 (1), −714 (2), E_{corr} (3).

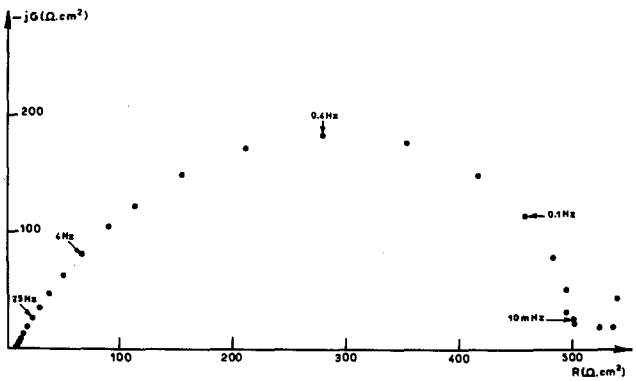

Fig. 7. Electrochemical impedance diagram corresponding to galvanostatic regulation at I = 0 and Ω = 1000 rpm after a hold time of 2 hr. Solution 3% NaCl + diamino-1,2-ethane (10^{-2}M); pH = 10.85.

medium but at the same pH adjusted by NaOH; the relevant diagram plotted in Fig. 8 presents the same form as that of Fig. 7 with an increasing characteristic frequency and a decreasing polarization resistance.

The diagrams plotted for potentiostatic regulation at the corrosion potential (E = E_{corr}) are not influenced by the rotation speed value as shown in Fig. 9; the same result holds at I = 0 in galvanostatic regulation.

In the cathodic potential range, one capacitive loop is observed, the dimension of which decreases with overpotential (Fig. 10) in step with the local slope of the current-voltage curves but which is at variance with the uninhibited situation. At low cathodic overpotentials (I_c = 125 $\mu A \cdot cm^{-2}$) the polarization resistance is found slightly higher only than without inhibitor. This rather surprising result with respect to the common use of R_p to evaluate the inhibiting effect will be considered in the discussion section.

In the anodic potential range, the capacitive loop becomes smaller as the overpotential increases (Fig. 11). Below 750 $\mu A \cdot cm^{-2}$, the capacitive loop diameter is higher than that measured in the absence of inhibitor. Above this current, no influence of the inhibitor on this diameter value is detected, in agree-

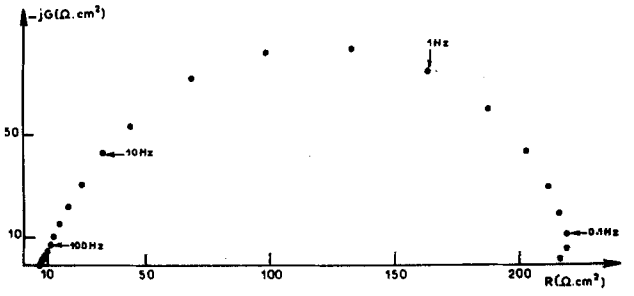

Fig. 8. Electrochemical impedance diagram corresponding to galvanostatic regulation at $I = 0$ and $\Omega = 1000$ rpm. Solution: 3% NaCl; pH = 10.85 (adjusted by 0.5M NaOH).

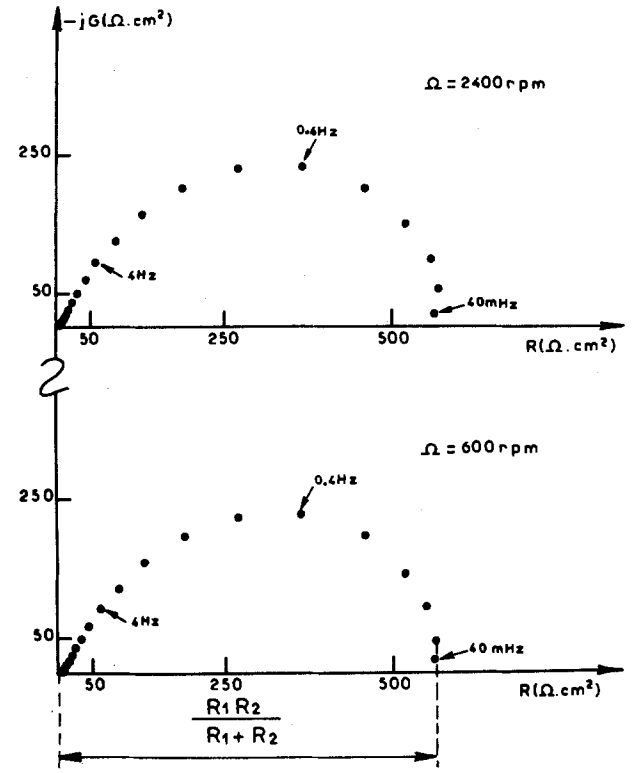

Fig. 9. Electrochemical impedance diagrams corresponding to potentiostatic regulation ($E = E_{corr}$) for two rotation speeds. Solution: 3% NaCl + diamino-1,2-ethane (10^{-2}M).

ment with the local slope of the current-voltage curves. However, a more pronounced flattening of the diagrams can be observed above 500 $\mu A \cdot cm^{-2}$. Concurrently, the average potential changes with time so that the diagrams cannot be obtained in pure steady-state conditions, and the resulting dispersion may be ascribed to an increase of the impedance elements with time.

Discussion

EHD impedance data.—Considering the case of a galvanostatic regulation (Fig. 4), the phase lag θ remains unexpectedly high when the frequency modulation tends toward zero. However, this limiting phase lag value at zero frequency is smaller at the most cathodic potential (curve ▲). Besides, the data obtained with an inhibitor concentration of $5 \cdot 10^{-3}$M (hachured region of Fig. 4) show that the low frequency limit is actually zero.

In contrast, the "high frequency" data ($p > 0.1$) fit the curve (—·—·—) adjusted with Sc = 550 when $E_c < -836$ mV/SCE, a value which was found for the oxygen reduction taking place on a wholly reactive electrode surface. At lower cathodic potentials, the adjusted Sc values increase. This trend is more conspicuous at an inhibitor concentration of $5 \cdot 10^{-3}$M.

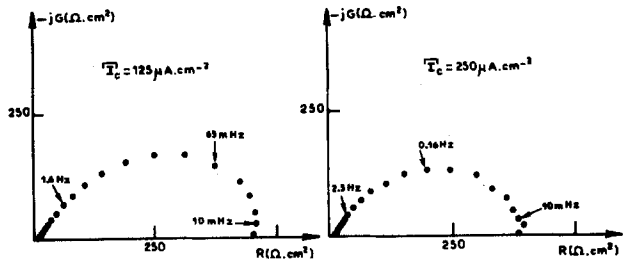

Fig. 10. Electrochemical impedance diagrams corresponding to galvanostatic regulation at two cathodic overpotentials and at $\Omega = 1000$ rpm. Solution: 3% NaCl + diamino-1,2-ethane (10^{-2}M).

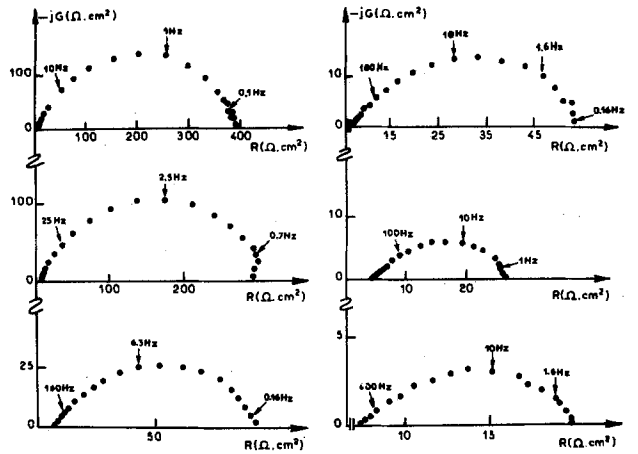

Fig. 11. Electrochemical impedance diagrams corresponding to galvanostatic regulation at different anodic overpotentials and at $\Omega = 1000$ rpm. Solution: 3% NaCl + diamino-1,2-ethane (10^{-2}M). Left column, from top to bottom: $I_A = 125, 250, 500$ $\mu A\ cm^{-2}$. Right column, from top to bottom: $I_A = 750, 1500, 3000$ $\mu A\ cm^{-2}$.

The analysis of these results led us to the hypothesis that the constant LF phase lag (~40°) whatever the rotation speed Ωo, arises from the coverage relaxation of the inhibitor with potential modulation, occurring with a galvanostatic regulation. It must be, furthermore, noticed that with a potentiostatic regulation (Fig. 5 and 6) the limiting LF phase lag is zero since in this latter case there is no potential modulation. The decrease of this limiting phase lag in galvanostatic regulation when $E_c \sim -1050$ mV/SCE (Fig. 4 curve (▲)) would then indicate a lower inhibitor adsorption when the cathodic overpotential increases. As previously mentioned, the Sc value (550) can also be interpreted by the fact that there is no meaningful "layer effect" caused by the accumulation of corrosion products.

On the contrary, when the overpotential is less cathodic than −764 mV/SCE, the increasing adjusted Sc values may be assigned as in Ref. (3) to the existence of a corrosion products layer. However, this layer appears to be much less hindering in regard to the molecular diffusion of oxygen when the inhibitor concentration is 10^{-2}M instead of $5 \cdot 10^{-3}$M since in the latter case the Sc values increase with Ωo. This effect is obviously more important in the absence of inhibitor (3).

It seems, therefore, difficult to unambiguously explain the EHD impedance diagrams in potentiostatic conditions either by the existence of a porous layer or by a mixed kinetics control of the oxygen reduction since there is no fair reducibility of the data in p coordinates neither when E_c nor Ωo are varied. However the p reducibility when keeping E_c constant at different Ωo values (Fig. 5) is much more satisfactory than the p reducibility when Ωo is kept constant and

V_c varied from V_{corr} to the diffusion plateau conditions (Fig. 6).

The prevailing electron-transfer control of the oxygen reduction is, therefore, likely to be the more appropriate explanation of the EHD impedance data in the vicinity of the corrosion potential. In addition, it must be emphasized that the potential or current responses to the velocity modulation at E_{corr} are very weak and needed to be measured with high gain amplifiers.

From the electrochemical impedance data, it appears that only one time constant remains in the vicinity of the corrosion potential; the low frequency loop, arising from the molecular diffusion of oxygen through the layer of corrosion products, has accordingly vanished. In addition, the impedance diagrams at the corrosion potential for either potentiostatic or galvanostatic conditions are not influenced by the rotation speed.

The values of the loop diameter R_I, the characteristic frequency ω_c as determined by the same procedure as in the first part of this series (3), the product $R_I I_A$, and the capacitance C are reported in Table I. It must be pointed out that these capacitance values are much lower than those reported without inhibitor (~ 2 mF $\cdot$ cm^{-2}) at low anodic overpotentials, but significantly higher than the value of 200 μF $\cdot$ cm^{-2} found on a surface practically free from corrosion products in a phosphate buffer solution (3). High capacitance values typical of uninhibited solutions are found again when the current density I_A reaches 3000 μA $\cdot$ cm^{-2}. This result, in agreement with the EHD impedance data, substantiates the presence of both dissolution products and inhibitor on the metallic surface. In fact, it seems difficult to conceive that even in the presence of a good inhibitor [94% efficiency has been measured at 10^{-2}M concentration of this compound (2)] the metal surface remains, strictly speaking, free from corrosion products after a 5 hr immersion time. However, the structure and composition of this film must be different from those observed in the absence of inhibitor, also because of the solution pH change due to the inhibitor (10.85 instead of 6.20).

Concerning the resistance R_I, which identifies itself here with the polarization resistance R_p, the salient feature is its nonmonotonous variation with the overpotential. Indeed, R_I decreases from the corrosion potential when both the cathodic or anodic overpotentials are increased. Such a behavior suggests that the kinetics of the elementary cathodic and anodic processes are mainly under electron transfer control; the value of the polarization resistance expressed in terms of the equivalent circuit elaborated in the first part of this series (3) is equal to the charge transfer resistance $\frac{R_1 R_2}{R_1 + R_2}$ (R_1 and R_2 are the charge transfer resistances, respectively, associated with the elementary anodic and cathodic processes). Since R_1 and R_2 are exponential functions which actually vary in opposite directions with potential, it is expected that the quantity $\frac{R_1 R_2}{R_1 + R_2}$ reaches a maximum value at or near to the corrosion potential. In this case only, a consistent relationship is found between the polarization resistance value and the observed corrosion rate in the presence of the inhibitor.

Finally, a better insight of the action mode of this type of inhibitor can be afforded by analyzing these different results. An inhibitor is usually classified as anodic, cathodic, or mixed according to the relevant corrosion potential shift. In the present case. such a criterion is meaningless because even in the absence of inhibitor a shift of E_{corr} is caused by the accumulation of corrosion products on the electrode. It is, therefore, necessary to examine the effect of the inhibitor on the whole current-voltage curve.

At high cathodic overpotentials, the interface behaves as a bare surface as demonstrated by both the current-voltage curves and the EHD impedance measurements; in particular, the Levich equation applies on the cathodic plateau (Fig. 2) which precludes any meaningful blocking process at the interface.

In contrast, in the cathodic range or near to the corrosion potential a strong effect is provided by diamino-1,2-ethane on the current-voltage curves and on the electrochemical impedance diagrams as well. The inhibiting action does not extend beyond 1 mA $\cdot$ cm^{-2} probably as a result of disruption of the protective layer.

Therefore, it must be inferred that the diamino-1,2-ethane and more generally this type of bifunctional compound having a chelation effect, can be essentially regarded as anodic inhibitors.

As mentioned previously, the diagrams of Fig. 7 and 8 exhibit the same features, and, hence, the electrochemical behavior of carbon steel in both solutions is presumably identical, though the pH increase alone does not provide such a protective effect as that due to diamino-1,2-ethane.

This conclusion is confirmed when considering the similar values of the product $R_I I_A$ found with and without inhibitor ($R_I I_A$ measurements performed without inhibitor at a pH of 10.85 lead also to an average value of 35 mV). The inhibitor action can, then, be clearly described as a drastic reduction of the active area of dissolution without modification of the anodic mechanism. The resulting highly localized distribution of d-c current on the anode can also provide an explanation for the unusually depressed semicircles shown in Fig. 11.

This analysis is consistent with previous assumptions regarding the inhibiting action of such a type of compound; the inhibitor is able to strengthen and fill in the "prepassive" layer of $Fe(OH)_2$ formed by the pH increase of the solution, as well as to directly make bonds with the atoms of the bare fraction of the metal.

Table I. Parameter values deduced from the diagrams of Fig. 10

I_A (μA $\cdot$ cm^{-2})	R_I ($\Omega \cdot$ cm^2)	$\omega_c/2\pi$ (Hz)	$R_I I_A$ (mV)	C (μF $\cdot$ cm^{-2})
125	390 ± 10	1.5 ± 0.1	48.75 ± 1.25	275 ± 25
250	310 ± 20	3.2 ± 0.5	77.5 ± 2.5	166 ± 36
500	85 ± 3	4.5 ± 0.5	42.5 ± 1.5	423 ± 61
750	49 ± 1	8 ± 1	35.75 ± 0.75	415 ± 60
1500	20.5 ± 0.5	12 ± 1	30.75 ± 0.75	655 ± 70
3000	11.5 ± 0.5	12 ± 1	33.5 ± 1.5	1170 ± 150

Conclusions

The following points can be emphasized: (*i*) by combining steady-state current-voltage curves at various rotation speeds of the disk and nonsteady-state techniques (electrochemical and electrohydrodynamical impedances); it has been established that at open-circuit corrosion potential the rate of oxygen reduction is mainly under charge transfer control; (*ii*) consequently, and in contrast to the noninhibited situation (3), polarization resistance measurements can be used to evaluate the corrosion rate; (*iii*) from a general viewpoint, the data are consistent with the chelation mechanism previously proposed for inhibition by this kind of organic compound; it is now clear that this inhibiting effect is mainly restricted to the anodic reaction; (*iv*) more quantitative conclusions can be expected from a numerical analysis of the data; this work is in progress.

Manuscript submitted Jan. 4, 1982; revised manuscript received *ca.* Nov. 30, 1982.

Any discussion of this paper will appear in a Discussion Section to be published in the December 1983

JOURNAL. All discussions for the December 1983 Discussion Section should be submitted by Aug. 1, 1983.

REFERENCES

1. M. Duprat, N. Bui, and F. Dabosi, *Corrosion*, **35**, 392 (1979).
2. M. Duprat and F. Dabosi, *ibid.*, **37**, 89 (1981).
3. A. Bonnel, F. Dabosi, C. Deslouis, M. Duprat, M. Keddam, and B. Tribollet, *This Journal*, **130**, 753 (1983).
4. C. Deslouis, C. Gabrielli, Ph. Sainte-Rose Fanchine, and B. Tribollet, *ibid.*, **129**, 107 (1982).

Blue Sputtered Iridium Oxide Films (Blue SIROF's)

Karam S. Kang* and J. L. Shay*

Bell Laboratories, Holmdel, New Jersey 07733

ABSTRACT

We report on the preparation and properties of "blue" sputtered iridium oxide films (blue SIROF) and compare their properties with those of previous "black" SIROF's as well as anodically grown iridium oxide films (AIROF's). Blue SIROF's are prepared by reactive d-c sputtering of iridium in argon/oxygen, 80/20 mixture, at deposition rates of about 200 Å/min onto substrates held at 238 K. The physical properties of blue SIROF show characteristics similar to AIROF's. In contrast to SIROF's previously deposited in pure oxygen onto substrates held at 289 K, the new films have an optical absorption spectrum which peaks at 610 nm. The cyclic voltammograms, the magnitude of the electronic conductivity change, and their density are closer to those of AIROF's than previous SIROF's. As electrochromic display electrodes, the blue SIROF's have an improved open-circuit bleached state and written-state memory, as well as an improved appearance.

Electrochromism in both AIROF's (1-6) and SIROF's (7-10) have been studied for their potential application in passive displays. The main attraction of the iridium oxide-aqueous electrolyte (0.5M H_2SO_4) system compared to other candidates, *e.g.*, WO_3, V_2O_5, MoO_3 for passive display technologies (11, 12), is in its rapid color-bleach cycle and its chemical stability in aqueous electrolyte. At room temperature, an AIROF, 170 nm thick, exhibits a reflectance contrast change, $\Delta R/R$, of 60% at 45° angle of incidence and wavelength of 546 nm in 40 msec, under an anodic potential of IV *vs.* saturated calomel electrode (SCE), in 0.5M H_2SO_4 (1). The ΔOD is 0.3 in normal-incidence double-pass for a charge density of 20 mC/cm^2. The fully bleached state is also obtained in 40 msec under cathodic potential of 0V *vs.* SCE.

For SIROF's on conducting semitransparent glass, complete bleaching and coloring occurs within 280-150 msec in response to higher potential limits from −0.25 to 1.05V *vs.* SCE, respectively (9). A ΔOD of 0.45 is obtained between the colored and bleached states, which is equivalent to 0.9 in a device configuration with a diffuse scatterer. If the response time is arbitrarily defined as the time during which the first 2/3 of the total ΔOD occurs, then the response times are comparable to those of AIROF. However, the fast response times are not obtained immediately on operation of a freshly deposited SIROF (900Å thick film), but only after the film has swelled by hydration. Film thickness change can be as much as 75% (10) of the freshly deposited SIROF. Freshly deposited SIROF suffers from a perceivable residual coloration which is not removed electrochemically (12). Preparation of improved SIROF's which can be electrochemically bleached to 100% has been reported (9). The initial coloration of the bleached state remains until the SIROF has been cycled a few times between −0.25 and 1.05V *vs.* SCE in 0.5M H_2SO_4.

The macroscopic and microscopic structure of AIROF is not replicated in SIROF's, mainly because each is prepared under different conditions. The AIROF is electrochemically grown in 0.5M H_2SO_4 by cycling, either the bulk iridium metal electrode between −0.25 and 1.25V *vs.* SCE, for which a typical growth rate is 75 Å/min (13), or iridium film evaporated on SnO_2 coated glass substrates (4). These films are porous, containing a high concentration of H_2O in the pores and bound in the lattice structure (3, 14). On the other hand, reactive SIROF's prepared on transparent conductors, either indium tin oxide (ITO) or SnO_2, in the absence of high concentrations of H_2O are not macroscopically porous (15). The fast electrochromism in an AIROF is attributed to its porosity (1, 3) and in a SIROF to its amorphous structure (15). Two different electrochromic coloring mechanisms have been proposed. One is based on cation extraction (1, 3) described by the reaction

$$Ir(OH)_3 - H^+ - e^- \underset{\text{bleach}}{\overset{\text{color}}{\rightleftharpoons}} IrO_2 \cdot H_2O \qquad [1]$$

and the second is based on anion insertion (5) described by the reaction

$$Ir(OH)_3 + OH^- - e^- \underset{\text{bleach}}{\overset{\text{color}}{\rightleftharpoons}} IrO_2 \cdot H_2O \qquad [2]$$

Irrespective of whether it is proton extraction, Eq. [1], or OH^- insertion, Eq. [2], the bleached state is $Ir(OH)_3$ and the colored state is $IrO_2 \cdot H_2O$.

We report here deposition conditions for preparing SIROF's having properties similar to AIROF's both optically, *i.e.*, blue in appearance, and electrically, *i.e.*, similar voltammograms. These "blue" SIROF's have a density intermediate between that of AIROF's and SIROF's. We show that the blue color results from a critical packing density of iridium oxide in bound water during preparation. As a consequence of this lower density, blue SIROF's can be fully bleached on the first cycle, in contrast to SIROF's which hydrate and become more completely bleached as they are cycled many times.

Experimental

Previously reported (7-10) SIROF's were prepared in a Cooke Model C-70-6-4B vacuum system, with downhill rf sputtering in 2 μm Hg oxygen pressure. The deposition rate at a power density of 0.7 W/cm^2 was 10 Å/min. We have prepared similar films by uphill d-c reactive sputtering from a 7.6 cm iridium target. A 0.015 in. thick iridium metal sheet is mounted on 5 mm thick stainless steel target backing with conducting epoxy bonding cement. The target backing is screwed onto a 2 in. diam water-cooled copper platform with thermal joint compound. A Pyrex glass dark space shield, 8.6 cm internal diam at the target, surrounds the copper platform and stands 3 mm above

* Electrochemical Society Active Member.

the iridium target. The iridium target was presputtered in 20 μm Hg oxygen pressure. At 1.6 kV, the high plasma current of 7 mA for target-shutter distance of 5.5 cm is due mainly to the secondary electrons. D-C sputtering onto a water-cooled substrate at 6.5 cm above the target was carried out in 20 μm Hg oxygen pressure, at 2 kV and 13 mA, and a deposition rate of 30 Å/min. SIROF's prepared by this method were also metallic and showed a featureless cyclic voltammogram in 0.5M H_2SO_4. The absorption spectrum was also featureless, the film being nearly black. Film adhesion and the absence of a background residual color in the bleached state were not consistently reproducible. The cause of poor adhesion was partially attributed to the changing conditions of the target. During the presputter, SIROF deposits accumulated on the rim of the iridium target shadowed by the dark space shield. These deposits are powdery and are incorporated into the film by sputtering and by electrostatic levitation in the plasma. Films could be easily wiped off on removal to the atmosphere or more frequently after cycling in 0.5M H_2SO_4. Film dissolution would be indicated by deposits appearing on the transparent conductor exposed in the electrolyte. The adhesion can be improved by presputtering at a higher pressure and power density than during the SIROF film deposition.

D-C sputtering of iridium oxide in argon/oxygen mixtures at high rates of deposition onto cooled substrates results in "blue" SIROF's. Substrates for blue SIROF deposition are mounted on a copper platform with water-cooling facility. A stainless steel sheet (with different size cutouts for varying substrate sizes) is used to hold the substrate all around the edges such that, (*i*) it is held evenly and tightly with thermally conducting paste against the cooling platform, and (*ii*) the copper is not exposed to the plasma, as it may be a source of contamination. A chamber pressure of 2×10^{-7} Torr is obtained before beginning the presputter. To avoid oil vapor backstreaming, liquid nitrogen is constantly maintained in the diffusion pump cold trap. The iridium target is presputtered in 40 μm Hg of high purity argon at 2.5 kV for 15 min. At this pressure and voltage setting, the plasma current is 8 mA. As the material deposited on the iridium target from the previous run is sputtered off, the plasma current reaches a steady value of 10 mA. The effective area of target cleaned is 90% of the total area.

The substrate is now cleaned *in situ* for 25 min using the Ion Tech B25W saddle field ion source (16-18) and B50 power supply operated at 5 kV/5.6 mA which gives an ion beam current of 140 μA in 1.6×10^{-4} Torr of Ar/O_2, 80/20 mixture. Following the substrate cleaning, the chamber pressure is raised to 33 μm Hg of Ar/O_2, and the substrate is cooled at 7°C/min by passing liquid nitrogen through the water-cooling coils. Simultaneously, a second presputter, in 33 μm Hg of Ar/O_2, 80/20 mixture is commenced at 2.5 kV and 6.5 mA. Presputter is maintained for 10 min while thermal equilibrium and substrate temperature of −35°C are obtained. Under these conditions, sputtering is from 75% of the target area. Exposing the substrate to the plasma results in a deposition rate of 200 Å/min. Film thickness and deposition rate are monitored on a water-cooled quartz crystal with an INFICON thickness and rate monitor Model XTM. Substrate temperature is held at −35° ± 3°C, measured on the front face of the substrate, by adjusting the rate of liquid nitrogen flow.

Immediately following the sputtering period, the chamber is evacuated and then refilled with 300 μm Hg of oxygen, during which time the substrate temperature decreases to −80°C. It is allowed to warm up to room temperature before letting the system up to nitrogen atmosphere.

We have observed that heating blue SIROF to 50°C in vacuum, which presumably drives off some water, results in films of similar optical chracteristics as SIROF. Film deposition under dry conditions obtained by prebaking the internal fixtures and the bell jar result in films which do not show blue color. Attempts to incorporate water by cooling the substrate to lower temperatures, such that more water adsorbs onto the substrate, produced lower density films of poor adhesion. Hence, the water vapor pressure in the system must be controlled within critical limits to reproducibly obtain adhering, blue SIROF's.

Blue SIROF Characterization and Discussion

Film thickness is checked using a stylus instrument, Talysurf Model 4, on a step defined by a photoresist pattern. The equilibrium emf *vs.* SCE of a freshly deposited blue SIROF on quartz substrates is 0.7V as determined using a potential probe[1] made from a half cell

$$|\text{NAFION, 0.5M } H_2SO_4|\text{SCE} \qquad [3]$$

The transmission and reflection spectra are taken on a Cary 14 double beam spectrometer from 0.3 μm to 1.7 μm. Cyclic voltammograms are taken in 0.5M H_2SO_4 at a scan rate of 10 mV/sec for films deposited on SnO_2-coated glass substrates.

Freshly deposited iridium oxide films are blue as shown by the absorption spectrum (Fig. 1) of a typical blue SIROF, deposited on a quartz substrate. The main features of the absorption are, (*i*) an absorption peak at 610 nm, (*ii*) lower absorption in the *IR*, decreasing with wavelength, (*iii*) a minimum in the visible at 465 nm which is in the middle of the blue range, and (*ii*) an intrinsic absorption edge at 400 nm. Figure 1 also shows the absorption of the same film after bleaching it in 0.5M H_2SO_4 with an optically flat disk of indium pressed in contact with the SIROF film and electrolyte. The shape of the absorption spectrum of blue SIROF is remarkably similar to that of AIROF (12).

Figure 2 compares the optical density of blue SIROF with SIROF and AIROF films of equivalent charge density. The SIROF spectrum is featureless with a constant and higher absorption in the *IR* compared to the blue SIROF or AIROF. The magnitude of the *IR* absorption is consistent with the electronic conductivities of all three types of films. SIROF has the highest electronic conductivity: 300 Ω^{-1} cm^{-1} in the colored state,

[1] Measurements with NAFION, 0.5M H_2SO_4, SCE probes have been confirmed with direct measurements in 0.5M H_2SO_4 *vs.* SCE. These probes have been constructed to measure the ionic conductivity in SIROF to be reported in a future publication.

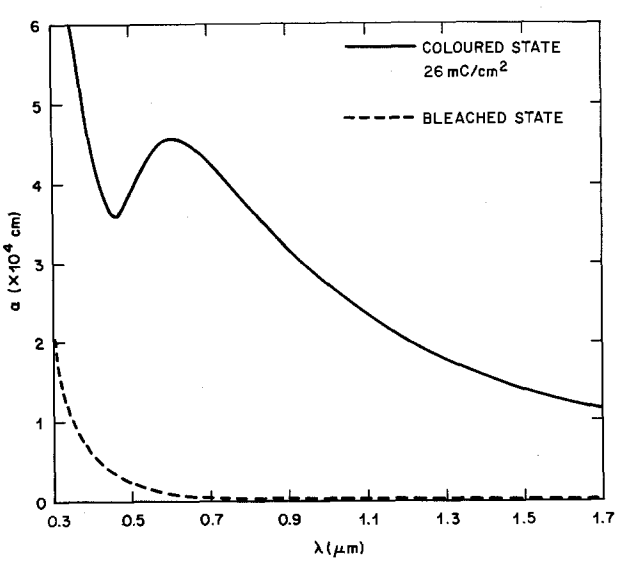

Fig. 1. Absorption spectra of colored and bleached "blue" SIROF deposited on a quartz substrate at 238 K in 80/20 argon/oxygen.

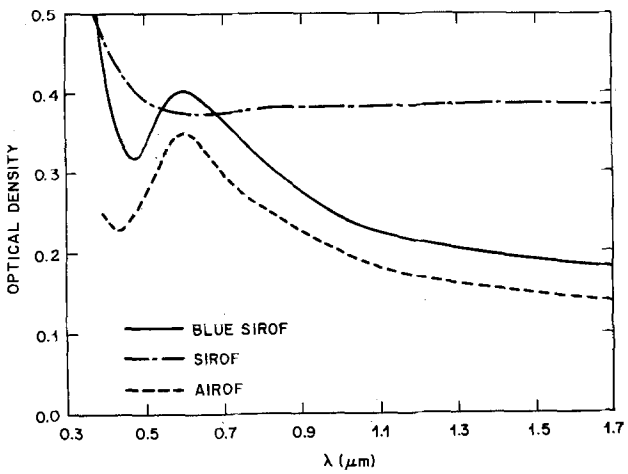

Fig. 2. Comparison of the optical absorption spectrum of "blue" SIROF in Fig. 1 with spectra previously reported for SIROF and AIROF, all at a coloration charge density of 26 mC/cm^2.

26 mC/cm^2, and 40 Ω^{-1} cm^{-1} in the bleached state. Blue SIROF has the lowest conductivity: 2.6×10^{-2} Ω^{-1} cm^{-1} in the colored state and 26 mC/cm^2 and 6×10^{-6} Ω^{-1} cm^{-1} in the bleached state. The d-c conductivity in blue SIROF changes by almost four orders of magnitude from its bleached to written (26 mC/cm^2) states, comparable to the a-c conductivity change of AIROF which ranges from 10^{-2} Ω^{-1} cm^{-1} (at ~0.4V *vs.* SCE) to 10^2 Ω^{-1} cm^{-1} at 1V *vs.* SCE (19).

Further similarity between AIROF and blue SIROF is shown in the cyclic voltammograms in Fig. 3. The cyclic voltammogram of a blue SiROF on SnO_2, taken at 10 mV/sec, has major peaks which coincide with those of AIROF's. The anodic peak is at 0.75V (*vs.* SCE), and the cathodic peak is at 0.7V *vs.* SCE, whereas the major peaks in SIROF's (9) occur at 0.44V *vs.* SCE, after hydration of the film has occurred. A small peak which at 0.42V for the blue SIROF is also present in the voltammogram of AIROF's at 0.3V. In blue SIROF, a bleached state of 98% is obtained at 0V *vs.* SCE on the first bleach cycle. No conditioning of the electrode is required as in SIROF.

Both AIROF, grown on SnO_2, and SIROF have a relatively short open-circuit bleach state memory in 0.5M H_2SO_4. Figure 4 and 5 show the change in optical density and open-circuit voltage *vs.* SCE for blue SIROF and SIROF, respectively, in both colored and bleached states. If we define memory as the time in which the transmission changes by 10%, *i.e.*, ΔOD of 0.046, then in blue SIROF the bleached state open-circuit memory is 8 hr (Fig. 4). This is three orders

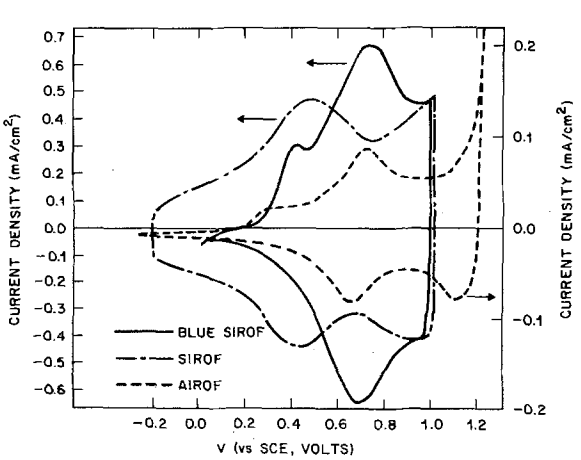

Fig. 3. Comparison of the voltammograms of "blue" SIROF on SnO_2, SIROF on ITO, and AIROF, all taken at a scan rate of 10 mV/sec in 0.5M H_2SO_4.

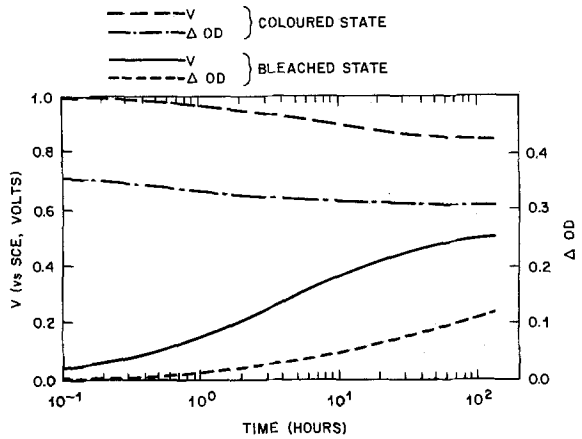

Fig. 4. Open-circuit memory (voltage and optical density) of blue SIROF in colored and bleached states in 0.5M H_2SO_4. In each case, the initial conditions had been held constant for 10 sec.

of magnitude better than 30 sec of open-circuit bleach state memory of SIROF (Fig. 5). Similarly, the open-circuit written-state memory is more than 100 hr compared to 1.5 hr in SIROF.

We tentatively postulate that the position of the major peak in the cyclic voltammogram is related to the degree of bound H_2O in the film during preparation which results in different packing densities. AIROF has the maximum water content in its structure during its preparation, and hence, a porous structure with the lowest density of 2 g/cm^3 (14). The density of a freshly deposited (20) SIROF is reported to be 10 g/cm^3 before swelling and 7.8 g/cm^3 after. These values measured on 3000Å thick film deposited at 12.5 Å/min are closer to the bulk density of IrO_2 (11.68 g/cm^3). The position of the peak current density in the cyclic voltammogram changes by approximately 0.3V towards higher potential *vs.* SCE as the film porosity increases from that of SIROF to AIROF.

Blue SIROF has been prepared with varying degrees of hydration. The optical and electrical properties are further reported elsewhere (21) for different density films. The resonance absorption peak is associated with small spherical particles (approximately 100Å diam) in a matrix of bound water. This system is a composite of a metal iridium oxide and a dielectric of water. The composite dielectric constant $\bar{\epsilon}$ for small spherical particles is given by the Maxwell-Garnett theory (22)

$$\frac{\bar{\epsilon} - \epsilon_2}{\epsilon - 2\epsilon_2} = f\left[\frac{\epsilon_1 - \epsilon_2}{\epsilon_1 + 2\epsilon_2}\right] \qquad [4]$$

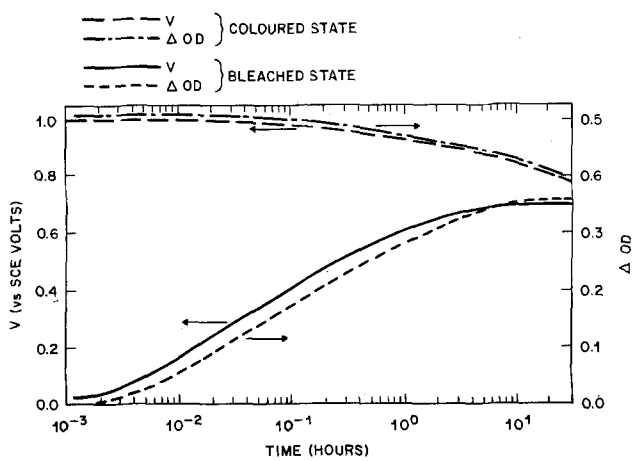

Fig. 5. Open-circuit memory (voltage and optical density) of "black" SIROF in colored and bleached states in 0.5M H_2SO_4. In each case, the initial conditions had been held constant for 10 sec.

where ϵ_1 is the dielectric constant of IrO_2, ϵ_2 is the dielectric constant of bound water, and f is the filling factor, *i.e.*, the fraction of volume occupied by IrO_2 particles. The average density $\bar{\rho}$ of the film is given by

$$\bar{\rho} = f\rho_1 + (1 - f)\rho_2 \quad [5]$$

where ρ_1 and ρ_2 are the densities of IrO_2 and H_2O, respectively. Taking the dielectric constant of metal to be given by

$$\epsilon = 1 - \frac{\omega_p^2}{\left(\omega^2 + \frac{i\omega}{t}\right)} \quad [6]$$

then, the resonance absorption peak is at

$$\omega_o = \omega_p \left[1 + \left(\frac{2 + f}{1 - f}\right)\epsilon_2 \right]^{-1/2} \quad [7]$$

where ω_p is the plasma resonance frequency (for IrO_2 $\hbar\omega_p = 5.39$ eV). The average density of blue SIROF reported here in Fig. 1 is 4 g/cm^3. Taking the density of water as 1 g/cm^3 and that of IrO_2 as 11.68 g/cm^3, we obtain a filling factor of 0.28. Substituting this value for f and for $\epsilon_2 = n_o^2 = 1.78$, the absorption peak predicted by Eq. [7] is at 5930Å. This is to be compared with the experimental value of 6100Å.

Based on the composite model for blue SIROF microstructure, it is now possible to understand the long electrochromic memory achieved by these films. The memory effect is basically dependent on the magnitude of the electronic and ionic mobilities. While it is difficult to give a magnitude of the ionic mobility, we can assume that it changes little between SIROF films and AIROF films on the basis that the electronic response times are the same. However, the electronic conductivity and, hence, the mobility has been considerably reduced by the low filling factor of 0.28 for blue SIROF compared with 0.84 for SIROF. In the absence of external fields applied to the electrode, equilibrium of ionic and electronic species is determined by their concentration gradients which exist for bleached and colored films with respect to the electrolyte pH. Both SIROF memory, Fig. 5, and blue SIROF memory, Fig. 4, approach an equilibrium potential of 0.65V *vs.* SCE, the rate of which we believe is determined by the electronic conductivity for a given filling factor, f.

Conclusions

We have shown that a fast deposition of iridium oxide in argon/oxygen on cold substrates results in "blue" SIROF's. These films are of a much lower density than the earlier "black" SIROF's deposited at lower rates in pure oxygen. The electronic conductivity change from the insulating bleached state to the semiconducting-metallic colored state is almost four orders of magnitude. The physical properties of blue SIROF approach those of AIROF more than the black SIROF.

As electrochromic display electrodes, the blue SIROF has an improved open-circuit memory in both the bleached and colored states. These films require no conditioning, *i.e.*, swelling, to produce the fast speed of response. The fully bleached state is also obtained in the first cycle. The existence of SIROF's in different packing densities of IrO_2 and H_2O and the discovery of the variation in their physical and chemical properties intermediate between those of SIROF and AIROF should greatly assist in identifying the electrochromic mechanism.

Manuscript submitted Nov. 4, 1981; revised manuscript received Nov. 4, 1982.

Any discussion of this paper will appear in a Discussion Section to be published in the December 1983 JOURNAL. All discussions for the December 1983 Discussion Section should be submitted by Aug. 1, 1983.

Publication costs of this article were assisted by Bell Laboratories.

REFERENCES

1. S. Gottesfeld, J. D. E. McIntyre, G. Beni, and J. L. Shay, *Appl. Phys. Lett.*, **33**, 208 (1978).
2. G. Beni and J. L. Shay, *ibid.*, **33**, 567 (1978).
3. S. Gottesfeld and J. D. E. McIntyre, *This Journal*, **126**, 742 (1979).
4. J. L. Shay, G. Beni, and L. M. Schiavone, *Appl. Phys. Lett.*, **33**, 942 (1978).
5. G. Beni, C. E. Rice, and J. L. Shay, *This Journal*, **127**, 1342 (1980).
6. J. D. E. McIntyre, W. F. Peck, Jr., and S. Nakahara, *ibid.*, **127**, 1264 (1980).
7. L. M. Schiavone, W. C. Dautremont-Smith, G. Beni, and J. L. Shay, *Appl. Phys. Lett.*, **35**, 823 (1979).
8. W. C. Dautremont-Smith, G. Beni, L. M. Schiavone, and J. L. Shay, *ibid.*, **35**, 565 (1979).
9. L. M. Schiavone, W. C. Dautremont-Smith, G. Beni, and J. L. Shay, *This Journal*, **128**, 1339 (1981).
10. S. Hackwood, W. C. Dautremont-Smith, G. Beni, L. M. Schiavone, and J. L. Shay, *ibid.*, **128**, 1212 (1981).
11. "Nonemissive Electrooptic Displays," A. R. Kmetz and F. K. Von Willisen, Editors, Plenum Press, New York (1976).
12. G. Beni and J. L. Shay, "Advances in Image Pick-Up and Display," Academic Press, Inc., New York (1982).
13. S. Gottesfeld and S. Srinivasan, *J. Electroanal. Chem.* **86**, 89 (1978).
14. J. D. E. McIntyre, W. F. Peck, Jr., and S. Nakahara, *This Journal*, **127**, 1264 (1980).
15. S. Hackwood, L. M. Schiavone, W. C. Dautremont-Smith, and G. Beni, Abstract 511, p. 1262, The Electrochemical Society Extended Abstracts, Vol. 81-1, Minneapolis, Minnesota, May 10-15, 1981.
16. J. Franks, *J. Vac. Sci. Technol.*, **16**, 181 (1979).
17. J. Franks and A. M. Ghander, *Vacuum*, **24**, 489 (1974).
18. J. Franks, P. R. Stuart, and R. B. Withers, *Thin Solid Films*, **60**, 231 (1979).
19. S. H. Glarum and J. H. Marshall, *This Journal*, **127**, 1467 (1980).
20. S. Hackwood, P. K. Gallagher, and G. Beni, *Solid State Ionics*, **4**, 355 (1981).
21. K. S. Kang and J. L. Shay, To be published.
22. J. C. Maxwell-Garnett, *Phil. Trans. R. Soc. London*, **203**, 385 (1904); *ibid.*, **205**, 237 (1906).

The CV Product of Etched Aluminum Anode Foil

H. J. de Wit and C. Crevecoeur

Philips Research Laboratories, Eindhoven, The Netherlands

ABSTRACT

This paper deals with the analysis of tunnel structures in etched aluminum foil for electrolytic capacitors. The dependence of the capacitance of such foil on anodization voltage and on frequency was measured. Electron microscopy data were also used. The product of series capacitance C_s and anodization voltage U_f shows a characteristic decrease with U_f. This behavior is first analyzed with the model in which it is attributed to the closing of tunnels during anodization. This model, however, leads to irremediable inconsistencies and has to be abandoned. It is proposed instead that the main cause of the decrease of $C_sU_f \sim U_f$ is the fact that the oxide layers of neighboring tunnels grow against each other during anodization. Results of anodization-stripping-anodization experiments are contrary to the former and in accordance with the latter model.

Aluminum foil to be used for low-voltage electrolytic capacitors is first electrolytically etched to increase its surface area. This treatment has the effect of forming tunnels in the metal which are tens of microns in length and a few tenths of microns in diameter. Subsequently the surface is covered with Al_2O_3 dielectric by anodic oxidation. The product of series capacitance C_s and anodization voltage U_f, which is constant for a plain specimen, decreases in the case of etched foil with increasing U_f. This is due to a decrease of the surface area of the dielectric and is ascribed (1, 2) to closing of tunnels when aluminum is replaced by aluminum oxide with a larger volume.

In this paper an attempt is made to quantify this picture, that is to say to construct a distribution of tunnels after etching which, upon anodization, reproduces the observed decrease of C_sU_f.

Within this "closing" model, C_sU_f gives information on the radii of tunnels only, since no distinction can be made between a large number of short tunnels and a small number of long tunnels closing at a certain stage. Information on the lengths of tunnels was obtained by measuring the frequency dependence of the capacitance of the foil. The dielectric is distributed on the surface of the tunnels and the different parts are connected by different electrolyte resistances with the outside of the foil. Figure 1 shows schematically a tunnel grown into the metal and covered with anodic oxide, with its equivalent circuit below. As discussed, *e.g.*, by Morley and Campbell (3), the tunnel behaves as a transmission line. Figure 2 shows the calculated frequency dependence of capacitance, resistance, and losses of such a transmission line. Its series capacitance is constant at low frequency but starts to decrease when the applied circular frequency becomes higher than $\omega_{char} = 1/(lc \cdot lr_s)$, where l is the length of the tunnel and c and r_s, respectively, the capacitance and resistance per unit length of the tunnel. ω_{char} is called the characteristic circular frequency of the transmission line. Therefore the measured decrease of the capacitance with frequency of the foil gives information on the lengths of tunnels.

Further information on the tunnel distribution was obtained from electron microscopy.

Experimental

Starting material.—Samples were taken from factory-produced low-voltage capacitor foil. 90 μm hard aluminum foil had been d-c etched in 20% NaCl and 1.5% Na_2SO_4 in water at 90°C, with a current density of 1.5 A/cm² to a weight loss of 8.5 mg/cm². For the present investigation 1 cm wide samples were punched from the etched unanodized foil.

Anodization.—Parts of the samples 5 cm long were anodized without any pretreatment in a solution of 17% ammonium pentaborate in ethylene glycol, at room temperature at a dV/dt of 0.04 V/sec to the desired voltage, which was then held constant until the current had decreased to below 1 mA/cm² (projected area). After the capacitance measurements a small part of each specimen was annealed for 15 min at 400°C in oxygen and reanodized in the same solution and with the same dV/dt, and the voltage V_p was measured at which a peak in the current occurs. From V_p the anodization voltage U_f was determined with the relation $U_f = 0.895\ V_p - 0.85$ (U_f and V_p in volts). See Ref (4).

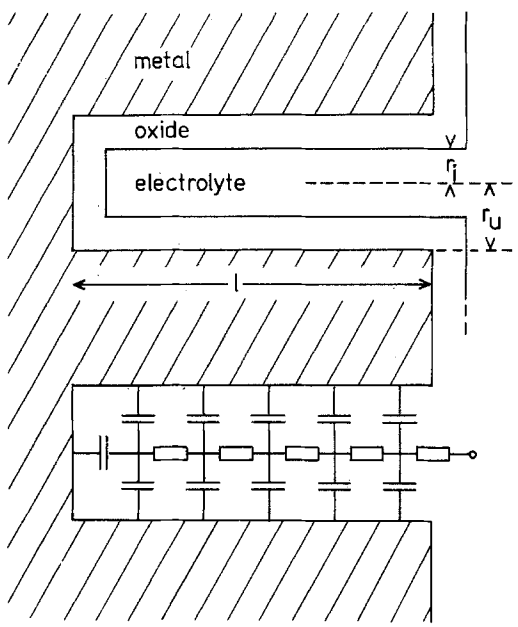

Fig. 1. Above: Tunnel grown in aluminum by etching, covered with oxide by anodization and filled with electrolyte. Below: Equivalent circuit.

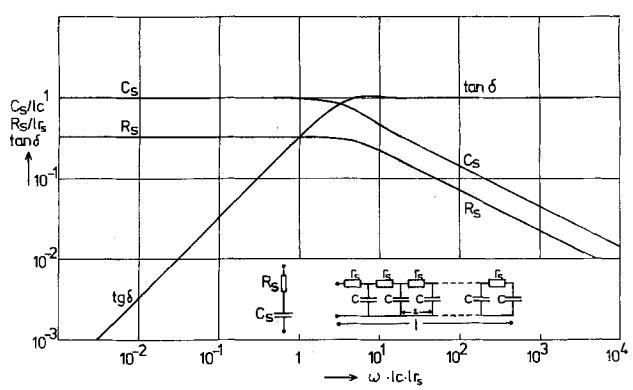

Fig. 2. Calculation of the series capacitance, series resistance, and losses of a transmission line representing a tunnel.

Key words: dielectrics, capacitor, impedance.

Capacitance measurements.—For the measurement of the capacitance the foil was clamped between two strips of platinized platinum with strips of capacitor paper in between. Prior to the measurement the non-anodized part of the specimen was covered with Technovit[1] in order to define the area to be measured. The capacitance was measured as a function of frequency in the solution of 17% ammonium pentaborate in glycol at room temperature. The measurements were not corrected for the capacitance of the Pt strips.

Figure 3 shows the capacitance *vs.* frequency for a sample anodized to 63V. The frequency dependence is more complex than the one calculated for the transmission line (Fig. 2). To characterize the experimental frequency dependence we differentiate it, and take the frequency at which the quantity[2] $\tan'\delta = -\pi/2 \cdot d \ln C_s/d \ln f$ has the value 0.2 as characteristic frequency f_{char}. In the measurement shown, it lies at 1.9 kHz. Note that f_{char} is an experimental quantity whereas ω_{char}, defined in the introduction, is a theoretical quantity. $\omega_{char}/2\pi \neq f_{char}$.

Electron microscopy.—For electron microscopy the aluminum metal was dissolved after anodization in a 10% Br-CH_3OH solution and the remaining oxide layers were investigated in a Philips EM 301 transmission electron microscope.

Results and Discussion

Experimental results.—The measurements presented in Fig. 4 form the starting point for the analysis presented in this section. This figure gives the value for C_sU_f and f_{char} obtained on samples anodized to different voltages. It shows the familiar decrease of C_sU_f with U_f. Simultaneously the characteristic frequency increases. It is noteworthy that for the experimental points $d^2f_{char}/dU_f^2 > 0$.

Closing of tunnels.—For an unetched sample C_sU_f is constant since $C_sU_f = (\epsilon_0\epsilon_r A/d) \cdot U_f = \epsilon_0\epsilon_r AE_{an}$ and the dielectric constant $\epsilon_0\epsilon_r$, the anodization field E_{an}, and the surface area A all remain constant during anodization. The decrease of C_sU_f for etched foil is ascribed (1, 2) to a decrease of the surface area during anodization and is explained with the model sketched in Fig. 5. It is supposed that the etching treatment leaves behind a number of separate tunnels with varying radii perpendicular to the surface of the foil. During anodization the metal is transformed into oxide. Since the volume of oxide is larger than the volume of metal it replaces, the inner surface of the tunnel grows inwardly. When the tunnel has been filled completely it no longer contributes to the capacitance. Figures 6 and 7 show examples of filled tunnels. Figure 5 is typical of a situation in which

[1] Technovit is a cold polymer manufactured by Kulzer GMBH.

[2] The reason for choosing this particular expression is the following: it can be shown that if the decrease of the capacitance is due exclusively to dielectric losses of the anodic oxide layer, with a loss angle δ_{ox} independent of frequency in a wide frequency range, then $\tan'\delta$ as defined here becomes equal to δ_{ox}.

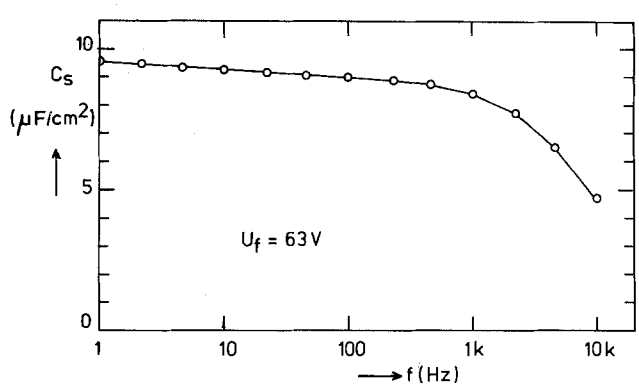

Fig. 3. Capacitance C_s as a function of frequency for foil anodized to 63V and measured in a solution of 17% ammonium pentaborate in glycol ($\rho \approx 1000\ \Omega$ cm).

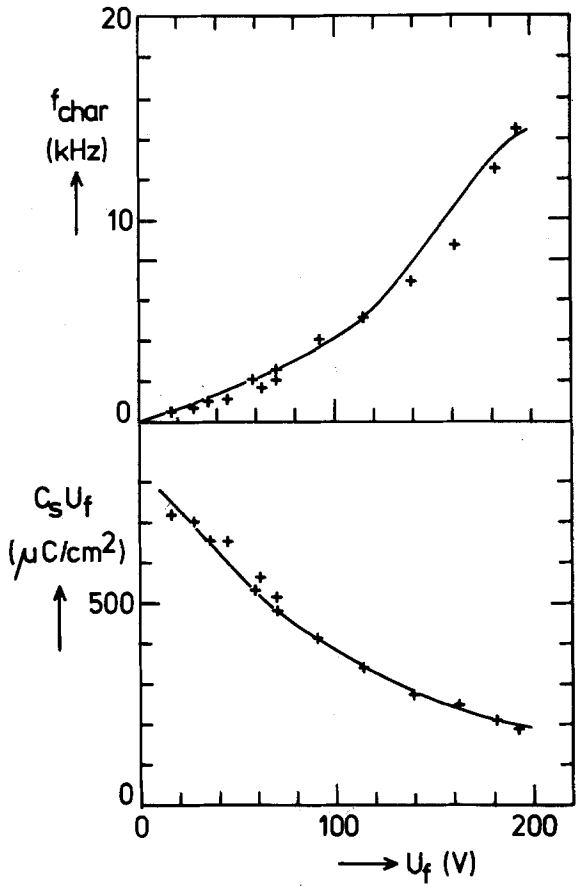

Fig. 4. C_sU_f and f_{char} as a function of the anodization voltage U_f for etched foil anodized in a solution of 17% ammonium pentaborate in glycol. The characteristic frequency is that frequency at which the quantity $\tan'\delta = -\pi/2 \dfrac{d \ln C_s}{d \ln f}$ has the value 0.2. The drawn lines are theoretical curves resulting from the model of the closing of tunnels during anodization.

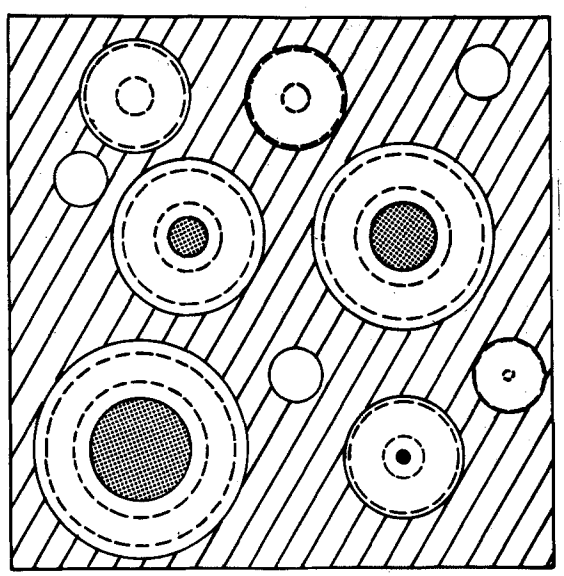

Fig. 5. Model of the closing of tunnels during anodization of etched foil. After etching, tunnels with different radii are present perpendicular to the aluminum surface which is drawn here. The broken lines indicate the oxide surface at U_f = 50V, the drawn lines indicate it at U_f = 100V. Between 50 and 100V a number of tunnels have become closed and no longer contribute to the capacitance at 100V. The heavily shaded areas indicate the electrolyte in those tunnels that are still open at 100V.

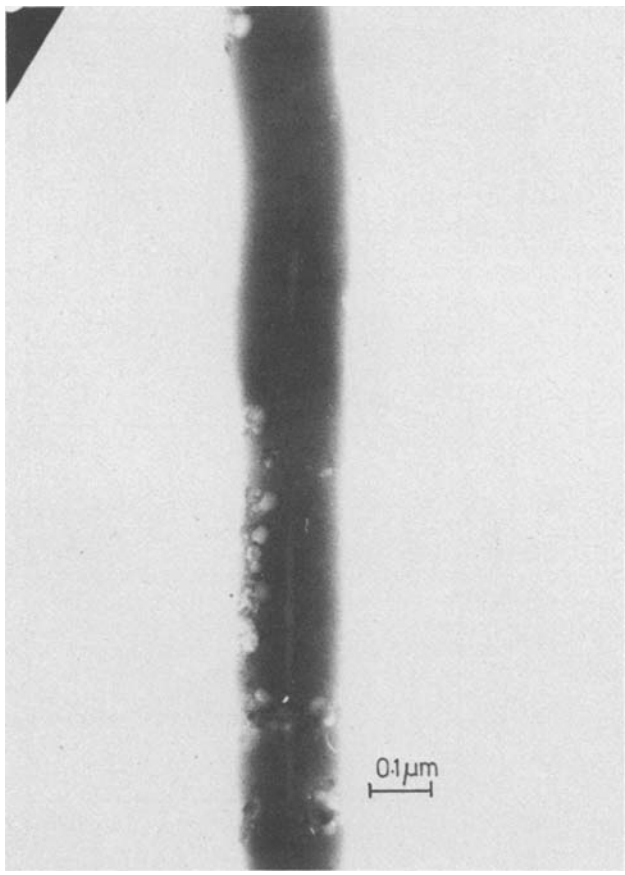

Fig. 6. Electron micrograph of a tunnel closed during anodization (only the oxide is shown after dissolution of the aluminum).

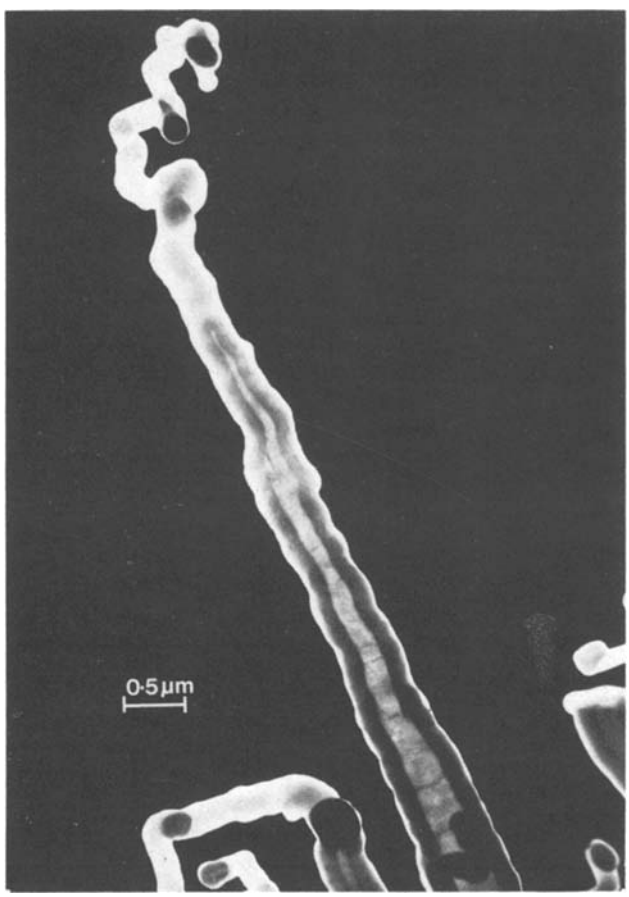

Fig. 7. Electron micrograph of a tunnel partially closed during anodization (dark field).

the anodization has been increased from 50V (broken lines) to 100V (solid lines). At 100V only the tunnels with a shaded center contribute to the capacitance. In this way the C_sU_f product gradually decreases with U_f. We have made a quantitative analysis of the data of Fig. 4 with the help of this model. The CU_f *vs.* U_f curve itself, interpreted with this model, gives information on the radii of the tunnels.

Qualitatively this runs as follows. If we anodize from voltage U_f to $U_f + dU_f$, the CU_f product decreases because a number of tunnels become closed by the increase of the oxide thickness. From the voltage U_f we know the oxide thickness and with the volume ratio of aluminum oxide to aluminum metal the original etching radius of these tunnels can be calculated. The decrease of the CU_f product at this voltage, then yields the total length of tunnels with that radius. Information about the lengths of tunnels is given by the characteristic frequencies. When the inner radius r_i and the outer radius r_u ($= r_i + d$) of the oxide have been determined from $CU_f \sim U_f$, then for a given electrolyte resistance, r_s and c are fixed, and $\omega_{char} = 1/(l^2 r_s c)$ only depends on l. Figure 8 gives the calculated oxide radii, $\omega_{char}/2\pi$ and CU_f values for a single tunnel with length 20 μm, radius after etching 0.148 μm, electrolyte resistance 1000 Ωcm, and relative dielectric permittivity 8.4. It is assumed that the oxide thickness is proportional to U_f, $d_{ox}/U_f = 12.05$ Å/V. The upper part shows the closing of the tunnel, r_i becomes zero at 200V. $\omega_{char}/2\pi$ shows a maximum, at low voltage it increases because the capacitance per unit length decreases, at high voltages it decreases as the electrolyte column becomes narrower and its resistance increases. The CU_f product remains high up to fairly high voltages and collapses close to the final voltage. The object of the analysis given in the present section now becomes to construct, starting from the known properties of a single tunnel, a distribution of

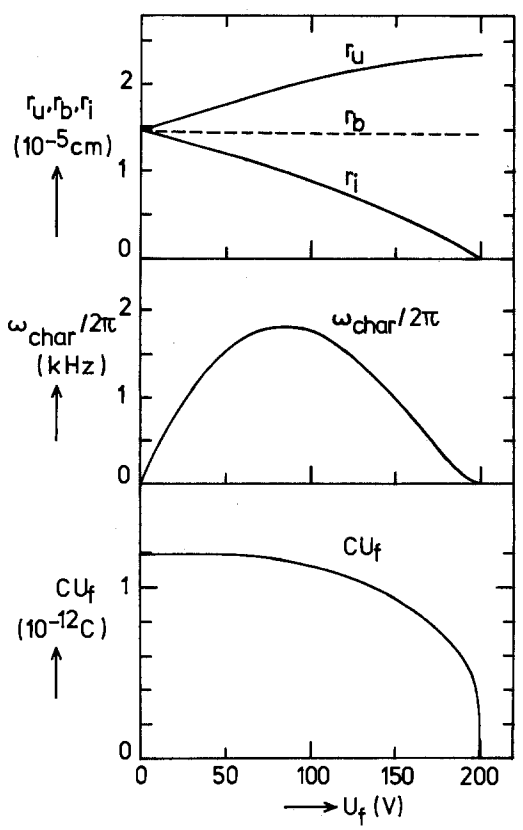

Fig. 8. Calculated values of the outer radius, r_u, the inner radius r_i, $\omega_{char}/2\pi$, and the CU_f product as a function of anodization voltage U_f for a tunnel which, after etching, had a radius r_b of 1.45×10^{-5} cm and a length of 20 μm. Electrolyte resistivity 1000 Ω cm. The tunnel closes at 200V.

tunnels with varying diameters and lengths which, on calculation, reproduces the measured dependencies of f_{char} and CU_f on U_f as plotted in Fig. 4. This task is performed in the Appendix along the lines sketched above.

One simplifying assumption has been made, *viz.*, that all the tunnels with one particular radius r_b have the same length $l(r_b)$, otherwise the calculations would become too voluminous. Apart from that, the calculation is straightforward.

Results.—The drawn lines in Fig. 4 have been calculated as explained above. The fit to the CU_f points is quite reasonable, the calculated characteristic frequencies deviate at high voltages. The accompanying tunnel distribution is shown in Fig. 9. $n(r_b)dr_b$ is the number of tunnels with etch radius between r_b and $r_b + dr_b$. It is shown in the Appendix that to a first approximation n is proportional to $-\frac{1}{U_f}\frac{dCU_f}{dU_f}$, and therefore it rises steeply at low voltages. The initial decrease of the tunnel length brings about the upward curvature of the characteristic frequencies at low voltages (remember that a tunnel with $r_b = 0.15$ μm closes at 200V).

Discrepancies.—Although the fit of theory with experiments in Fig. 4 is excellent, the resulting tunnel distribution leads to discrepancies, on the one hand, with the results of electron microscopy, on the other hand, with the electrical measurements themselves. The calculated distribution involves the presence of a large number of very narrow tunnels. The experimental distribution of the external radii of a low-voltage foil similar to the one investigated, anodized to 90V in a solution of 1.3% ammonium pentaborate and 1.5% adipic acid at 72°C, as determined from electron micrographs, is shown in Fig. 10. The wall thickness was experimentally determined to be $\approx$ 1000Å. The distribution shows a maximum when r_u is about 0.15 μm. These tunnels originally had an etch radius r_b of 0.1 μm. Tunnels with a much smaller r_b are not present in the distribution of Fig. 10. Narrow tunnels as predicted by Fig. 9 have been looked for specifically, but have hardly ever been found, the large number required is certainly not present. This could be due to (*i*) a low efficiency of anodization in this electrolyte and (*ii*) the dissolution of the thin pipes of anodic oxide during the preparation of the samples in the Br-methanol solution. Both these points were checked. It was found that the efficiency of anodization of this type of foil in adipic acid was better than 90%. Moreover the thickness of an amorphous anodic oxide layer (2420Å) prepared by anodization of high-voltage foil in apb-glycol and treated afterwards in the Br-methanol solution, corresponds reasonably well with the predicted wall thickness (2230Å).

A second discrepancy is found with the measurements of the impedance of the foil as a function of frequency. Up to now the decrease of the capacitance with frequency has been described with a single quantity, f_{char}, which was defined as that frequency at which the quantity $\tan\delta = -\pi/2\, d \ln C_s/d \ln f$ has the value 0.2. The pore lengths have been adjusted in such a way that the calculated and measured values of f_{char} coincide. However, if the complete experimental and calculated curves as a function of frequency are compared, a qualitative difference is found. As shown in Fig. 11, the experimental curve is much steeper than the calculated one.

This effect is also due to the narrow tunnels which are present in the calculated distribution. At a particular anodization voltage (see Fig. 5), some tunnels have been closed, others are about to be closed. The latter have a narrow hole, an electrolyte column with a high resistivity and therefore a low characteristic frequency (see Fig. 8). Still other tunnels are wide open and have a high characteristic frequency. Therefore this model predicts a wide range of characteristic frequencies, leading to a decrease of the capacitance in a wide frequency range (see Fig. 11). For the calculations we assumed that all tunnels of a particular

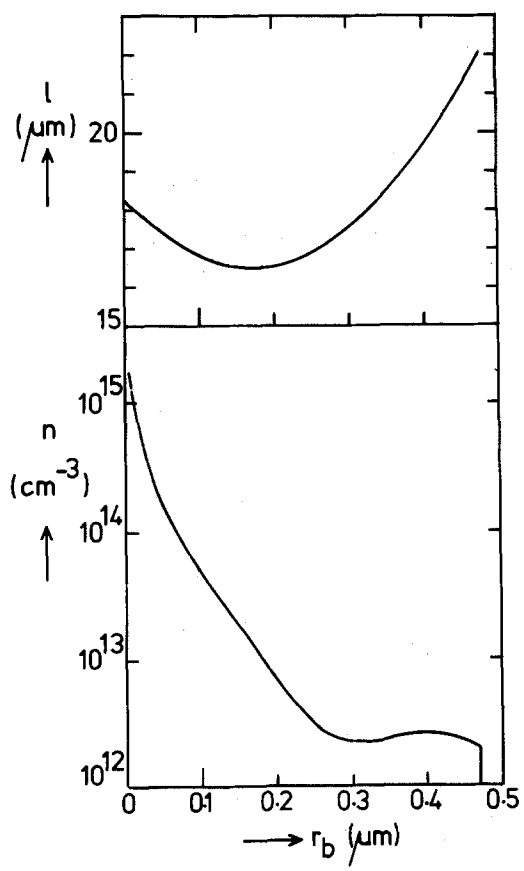

Fig. 9. Calculated tunnel distribution which yields the drawn lines for $C_sU_f \sim U_f$ and $f_{char} \sim U_f$ in Fig. 4. It was assumed for the calculation that all the tunnels with a particular r_b have the same length. $n(r_b)dr_b$ is the number of tunnels per unit area with radius between r_b and $r_b + dr_b$.

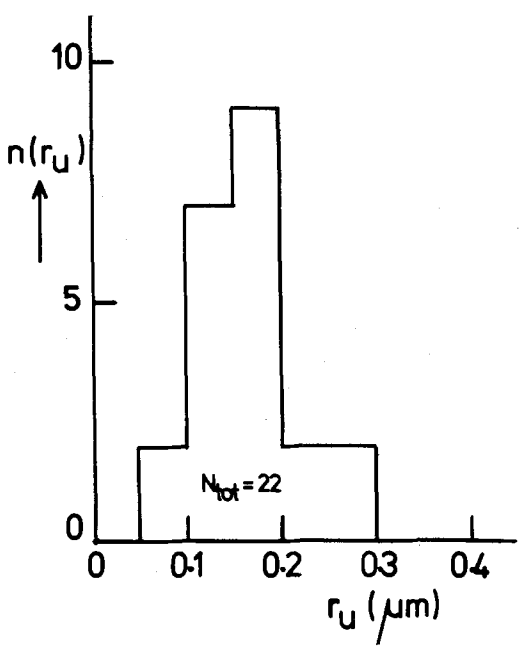

Fig. 10. Histogram of the outer radii of etched and anodized (90V) anode foil as determined from electron micrographs after dissolution of the aluminum metal.

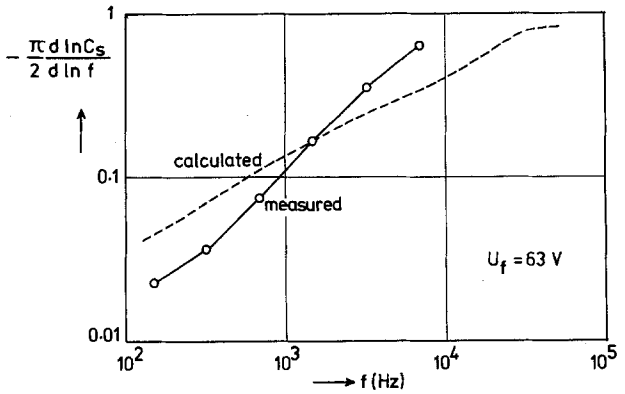

Fig. 11. Experimental and calculated curves of $\tan'\delta = -\frac{\pi}{2}\frac{d\ln C_s}{d\ln f}$ as a function of the frequency f for etched anode foil anodized to $U_f = 63$V.

r_b had the same length. If a distribution of lengths was assumed, this would lead to an even wider distribution of characteristic frequencies because we would then already have a distribution of characteristic frequencies at a single r_b. This would make the discrepancy even worse.

From both discrepancies we conclude that narrow tunnels are not present. Since in this model they are required to explain the decrease of C-$V \sim V$ we have to look for another explanation of this effect.

Growth of tunnels against each other.—The model used up to now is a special one, because it has been assumed that tunnels do not touch each other. During etching of the foil under investigation more than 30% of the aluminum had been removed. Nonoverlapping of tunnels in such a situation is improbable. If tunnels do touch at a certain stage and the anodization is continued, capacitance is lost because the area of the metal-oxide interface decreases. In the following we discuss a model in which the decrease of $CU_f \sim U_f$ is ascribed to this effect. The axes of cylinders perpendicular to the plane of the foil, all having the same radius, are assumed to be distributed randomly on the surface of the foil.

Figure 12 gives an example of such a distribution. It is typical of the case where a random arrangement of tunnels which close at 200V has been anodized from 50V (broken lines) to 100V (solid lines). The situation is equivalent to that of Fig. 5, in that the same increase of anodization gives about the same decrease of CU_f, but now this is due to the growth of cylinders against each other.

This already shows qualitatively that this model can also account for the decrease of $CU_f \sim U_f$. Moreover the discrepancies discussed above have been removed at one stroke. The model is made up of wide pores, so that narrow ones are not expected in the electron micrographs, and also the holes remain with a low electrolyte resistance, so that the wide distribution of characteristic frequencies which caused the slow increase of $\tan'\delta$ *vs.* f in Fig. 11 is not present.

Semiquantitative evaluation of the "random" model.—We have not made a complete quantitative evaluation of the random model. This would require, particularly for the calculation of the characteristic frequencies, more details of the spatial distribution of the tunnels than we have at present. Instead we treat a relatively simple case which shows some qualitative features. The case is the one shown in Fig. 12: a random distribution of cylinders with equal diameters and equal lengths l. The number of cylinders per unit area N is the only new variable introduced. The capacitance of such an arrangement is calculated following the theory of Avrami (5) on phase transformations, considering the etching and anodization processes as transformations of aluminum into nothing and anodic oxide, respectively. If the cylinders did not grow into each other during this transformation, the volume of transformed Al per unit total volume at a certain stage would be $N\pi r_u^2$, where N is the number of cylinders per cm^2 and r_u the outer radius. This hypothetical volume is called V_{ex}. Say that during a certain stage of the process this volume increases from V_{ex} to $V_{ex} + dV_{ex}$. If dV_{ex} is distributed randomly over already transformed and not yet transformed regions, the amount dV of Al per unit total volume that actually transforms is given by $dV = (1 - V) \cdot dV_{ex}$.

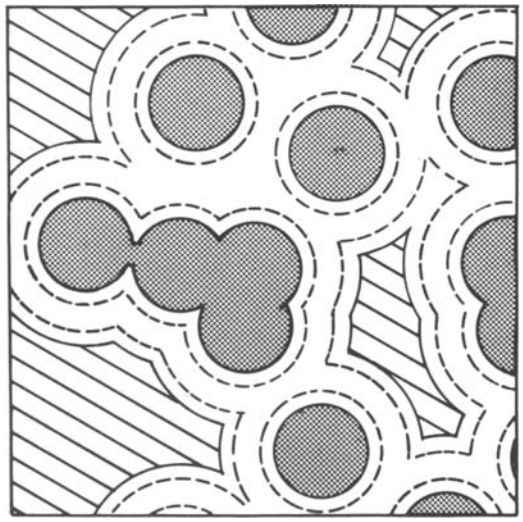

Fig. 12. Alternative model to explain the decrease of CU_f with U_f. After etching, the axes of tunnels that all have the same radius are randomly distributed on the aluminum surface. The broken lines indicate the oxide surfaces at $U_f = 50$V, the drawn lines indicate them at $U_f = 100$V. With increasing U_f the overlap of tunnels increases, leading to a decrease of the metal-oxide interface and a decrease of the CU_f product.

Integration gives $V = 1 - \exp(-V_{ex}) = 1 - \exp(-N\pi r_u^2)$. To calculate the capacitance, we need the surface area of the front between aluminum and aluminum oxide. If r_u increases by dr_u, the increase of the transformed volume is $dV = 2N\pi r_u dr_u \cdot \exp(-N\pi r_u^2)$ so that the area of the transformation front is equal to $2\pi N r_u \exp(-N\pi r_u^2)$. For a single cylinder the dielectric displacement at r_u is given by

$$D(r_u) = \epsilon_o \epsilon_r U_f / [r_u \ln (r_u/r_i)]$$

We assume that this is also the value of the dielectric displacement or surface charge density at the boundary Al-Al_2O_3 of the conglomerate of cylinders we are considering here. This quantity is multiplied by the surface area obtained above and so we obtain for CU_f per unit of volume

$$CU_f = [2\pi\epsilon_o\epsilon_r U_f/\ln (r_u/r_i)] \cdot N \cdot \exp(-N\pi r_u^2) \quad [1]$$

The volume of Al_2O_3 is 1.65 times the volume of Al it replaces. This gives

$$r_u = 0.606(U_f/E_{an}) + (r_b^2 - 0.2388(U_f/E_{an})^2)^{1/2}$$

A crude estimate of the characteristic frequency is obtained as follows. For a single tunnel ω_{char} is given by $\omega_{char} = 1/(l^2 c r_s)$. We assume that the same equation is valid for the complete distribution.

The capacitance per cm^2 per unit length is given by

$$C = [2\pi\epsilon_o\epsilon_r/\ln (r_u/r_i)] \cdot N \cdot \exp(-N\pi r_u^2)$$

The total area of the cross sections of electrolyte columns per unit area is obtained by substitution of r_i for r_u in [1], and the resistance per unit length of the complete distribution is $r_s = \rho/[1 - \exp(-N\pi r_i^2)]$.

In this way we obtain

$$\omega_{char} = \frac{\ln (r_u/r_i) r_i^2}{2l^2\rho\epsilon_0\epsilon_r} \cdot \frac{(1 - \exp(-N\pi r_i^2))}{N\pi r_i^2 \exp(-N\pi r_u^2)} \quad [2]$$

Here $[\ln (r_u/r_i) r_i^2]/2l^2\rho\epsilon_0\epsilon_r$ is the characteristic circular frequency of a single tunnel and it is indeed the limit of [2] for $N \to 0$ when cylinders do not overlap. In Fig. 13 calculations for CU_f/volume and f_{char} with Eq. [1] and [2] are presented.

The parameter g at the curves is the number N multiplied with πr_b^2. The figures also contain the experimental points of Fig. 4. They show that a relative decrease of $CU_f \sim U_f$ of the same order as the experimental one can be obtained with $g = 1$. The calculated CU_f product lies above the experimental points. This can be accommodated by assuming that the tunnel distribution is inhomogeneous on a larger scale: in some regions, "cauliflowers," the tunnel density is large, other parts have hardly been etched. The curve $g = 1$ is also not far from the experimental points for the characteristic frequency, but at high voltages it drops down rapidly. This is because we have assumed that the tunnels close at 200V, whereas the experimental points for CU_f clearly show that open tunnels also exist at 200V. This shows the need to introduce in this model too a distribution of tunnel diameters which makes a complete calculation very complex. The experimental points for the characteristic frequency in Fig. 4 and 13 form a concave curve, whereas the $f_{char} \sim U_f$ curve for a single tunnel is convex everywhere (see Fig. 8). In the calculated distribution of Fig. 9 this was accounted for rather artificially by an initial decrease of the tunnel length at increasing r_b. The calculated curves for $g = 1$ and even more for $g = 3$ show that the random model can account better for this behavior. It is due here to the fact that the decrease in capacitance is caused not only by the increase of the oxide thickness but also by the overgrowth of the oxide layers, whereas the resistance of electrolyte columns does not yet decrease appreciably. Altogether the model describes the experiments well.

Anodization-stripping (oxide removal)-anodization experiments.—In order to discriminate between the two models experimentally, samples of low-voltage foil were subjected to successive anodization and stripping treatments. Anodization occurred in 170 g/liter ammonium pentaborate in ethylene glycol, with dV/dt of 0.025 V/sec to 50.0V, after which the voltage was kept constant until the current had decreased to 1 mA/cm². Stripping occurred in a solution of 35 ml H_3PO_4 (85%) and 20g CrO_3 with water added to 1000 ml, at 95°C for 10 min.

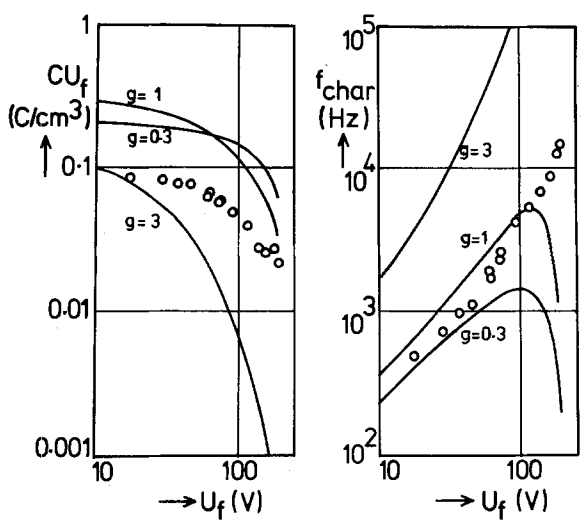

Fig. 13. Calculated values of CU_f and f_{char} as dependent on U_f for the random distribution of tunnels shown in Fig. 8, with length 40 μm and electrolyte resistivity 1000 Ω cm. The quantity g is the number of tunnels per unit area multiplied by r_b^2 where r_b is the etch radius of 1.45 × 10^{-5} cm. The circles are the experimental data of Fig. 4.

It is known that this treatment removes amorphous anodic aluminum oxide but does not attack aluminum. Specimens were either anodized, or anodized, stripped, and anodized, after which the capacitance was measured. The weight of the specimen was also measured after each step. The question is: What do both models predict for the capacitance after the second treatment relative to that after the first treatment?

In the first model (Fig. 5) the stripping solution is able at least to penetrate those holes that were also contacted by the measuring electrolyte and contributed to the capacitance. The oxide of these cylinders will be removed during stripping and holes will be left with a larger radius than the original etch radius. Therefore the capacitance after the second anodization will be larger than after the first anodization. In the second model (Fig. 12) the metal oxide surface after the first anodization is indicated by the broken line, after the second anodization it will lie near the solid line. The metal-oxide surface area thus decreases and the capacitance after the second anodization will be lower than after the first anodization.

In the experiment we found after the first anodization a capacitance of 9.9 μF/cm² which decreased to 8.4 μF/cm² after the second anodization. The weight measurements showed that more than 90% of the oxide formed was removed by the stripping treatment. This shows that the decrease of the C-V product is for the most part due to the overlapping of cylinders and not not to the closing of cylinders.[3]

Acknowledgments

Thanks are due to Ch. Wijenberg for performing a large number of the experiments, and to Mrs. G. v. Leeuwen for electron microscopy.

Manuscript submitted Aug. 16, 1982; revised manuscript received Oct. 20, 1982. This was Paper 96 presented at the Minneapolis, Minnesota, Meeting of the Society, May 10-15, 1981.

Any discussion of this paper will appear in a Discussion Section to be published in the December 1983 JOURNAL. All discussions for the December 1983 Discussion Section should be submitted by Aug. 1, 1983.

Publication costs of this article were assisted by Philips Research Laboratories.

APPENDIX

It is shown here how, with the tunnel-closing model, a tunnel distribution is derived from the experimental CU_f *vs.* U_f points and the measured characteristic frequencies. (*i*) First we assume that CU_f *vs.* U_f for a single tunnel is constant up to the voltage where the tunnel closes, and is given by its value at very low voltages $2\pi r_b\epsilon_0\epsilon_r U_f l(r_b)/d$, where r_b is the etch radius, $\epsilon_0\epsilon_r$ the dielectric constant, $l(r_b)$ the length of tunnels having radius r_b, and d is the oxide thickness. If the voltage increases from U_f to $U_f + dU_f$ the CU_f product decreases. We assume that this is due to the fact that $n(r_b)\, dr_b$ pores with original etch radius between r_b and $r_b + dr_b$ close at that U_f, and we have to know now the relation between r_b and U_f. The volume of Al_2O_3 is 1.65 times the volume of Al it replaces, which gives $d = 1.593\ r_b$ for the oxide thickness when the tunnel closes; d and U_f are related by the anodization field: $d = a_r U_f$ where

[3] At first sight one would expect the decrease of the C-V product in this experiment to be equal to the decrease of the C-V product between 50 and 100V of Fig. 4. The amount measured is distinctly less. It should be kept in mind however that the C-V product, for instance of a tunnel which closes at 200V, is appreciably lower at 100 than at 50V, as is shown in the lower part of Fig. 8. This causes the difference, and to that extent the decrease of the inner radius of the tunnel still plays a role in the new model.

$a_r = 1.2 \times 10^{-7}$ cm/V, so that $r_b = a_r/1.593 \cdot U_f$

The contribution to the U_f product from these $n(r_b)dr_b$ tunnels is

$$2\pi \epsilon_0\epsilon_r U_f r_b n(r_b) l(r_b) dr_b/d = -(dCU_f/dU_f) \cdot dU_f$$

This gives

$$n(r_b)\, l(r_b) = -\frac{(1.593)^2}{2\pi a_r \epsilon_0\epsilon_r} \frac{1}{U_f} \frac{dCU_f}{dU_f}$$

The experimental points of Fig. 4 can be fitted by

$$CU_f(U_f) = 870.8 + 6.691\, U_f + 0.2241 \times 10^{-1}\, U_f^2 - 0.3379\ 10^{-4}\, U_f^3 + 0.1831 \times 10^{-7}\, U_f^4$$

with CU_f in $\mu C/cm^2$ and U_f in volts. This gives as a first approximation

$$n(r_b)l(r_b) = 2.28 \times 10^6/r_b - 1.94 \times 10^{11} + 5.6 \times 10^{15}\, r_b - 5.157 \times 10^{19}\, r_b^2$$

(*ii*) An improvement on these values was obtained by calculating the values of the $CU_f(U_f)$ product with

$$CU_f = U_f \int dr_b \cdot [2\pi\epsilon_0\epsilon_r/\ln(r_u/r_i)] \cdot n(r_b)l(r_b)$$

and varying the constants until a better fit was obtained. This hardly changed the values of these constants. This completes the fit of $CU_f \sim U_f$. (*iii*) To obtain a fit with the experimental points for the characteristic frequencies, it was assumed that all the tunnels with one particular radius r_b have the same length $l(r_b)$, and that the dependence of l on r_b can be written as: $l(r_b) = l_o(1 + C_1 r_b + C_2 r_b^2)$, where l_o, C_1, and C_2 are constants. With these constants and the parameters obtained from the $CU_f \sim U_f$ fit, the tunnel distribution is completely described. It follows that we can make a complete calculation of the admittance G_f of the foil as a function of frequency

$$G_f = \int\int dl\, dr_b\, n(l, r_b)\, G_{tunnel}(r_b, l)$$

where G_{tunnel} is the complex admittance of a single tunnel with etch radius r_b and length l. Because of the assumption made above we have to integrate over only one variable, the radius r_b. After this we can calculate the value of $\tan'\delta = -\pi/2\ d \ln C_s/d \ln f$ and compare the frequency at which this quantity has the value 0.2, with the experimentally determined characteristic frequency. By variation of the constants l_o, C_1, and C_2 the fit of the upper half of Fig. 4 was obtained, resulting in the tunnel distribution of Fig. 9.

REFERENCES

1. J. H. Albella, A. Hormillos, J. M. Sanz, and J. M. Martinez-Duart, *This Journal*, **125**, 1950 (1978).
2. T. Matsuzaki and T. Yamazaki, *Fujitsu Sci. Tech. J.*, **16**(2), 49 (1980).
3. A. R. Morley and D. S. Campbell, *Radio Electron. Eng.*, **43**, 421 (1973).
4. C. Crevecoeur and H. J. de Wit, *This Journal*, **121**, 1465 (1974).
5. M. Avrami, *J. Chem. Phys.*, **7**, 1103 (1939); **8**, 212 (1940); **9**, 177 (1941).

The Kinetics of the Electrochemical Insertion of Lithium into Cubic Sodium Tungsten Bronzes

A. J. Mark, I. D. Raistrick,* and R. A. Huggins*

Department of Materials Science and Engineering, Stanford University, Stanford, California 94305

ABSTRACT

The kinetics of the electrochemical insertion of lithium into sodium tungsten bronzes, Na_xWO_3 ($0.4 \leq x \leq 0.7$) to form the mixed alkali bronzes, $Li_yNa_xWO_3$ ($0 < y < 0.5$, $x + y < 0.93$) have been studied, using transient techniques. The chemical diffusion coefficient of Li in single crystal samples was found to decrease with increasing lithium and sodium concentrations from initial values as high as 10^{-7} cm²/sec at room temperature. Above x values of about 0.7, insignificant quantities of lithium could be inserted into the structure. The trends in the diffusion coefficient are considered in terms of the structural and electronic properties of the tungsten bronzes.

The tungsten bronzes are wide range, vario-stoichiometric mixed valence oxides of formula M_xWO_3, where x varies between 0 and 1, and M is a metallic species (1, 2). Depending on the value of x, a variety of crystal structures are found which are composed of almost regular WO_6 octahedra, linked by corner-shared oxygens into three dimensional frameworks. In the case of sodium, for x values from 0.37 to 0.93, a single cubic defect perovskite phase exists. At somewhat lower x values (0.26-0.35), a more complex but related tetragonal structure containing 4- and 5-sided tunnels is found. For larger cations such as K^+, the cubic structure is not formed, but a hexagonal structure containing 6-sided tunnels parallel to the c axis exists. For all these phases, the alkali metal is essentially completely ionized and the electron donated to a π^* conduction band formed by overlap of Wt_{2g} and Op orbitals. The materials thus behave as completely degenerate semiconductors or metals and show very high electronic conductivities, metallic luster, and temperature independent paramagnetism. The bonding in these solids has been discussed by Goodenough (3).

Several studies have attempted to find evidence of ionic motion within these materials. Whittingham and Huggins (4) were able to use the tetragonal sodium bronze as a reversible electrode in solid-state cells. Steele (5) attempted to measure the thermodynamic and kinetic properties of cubic and tetragonal Na_xWO_3, using a solid-state galvanic cell. Although open-circuit emf values were in good agreement with values expected from calorimetric measurements of the enthalpies of formation (6), insignificant amounts of sodium could be added or removed from these structures at 300°C. The chemical diffusion coefficient of sodium in the cubic phase was estimated to be less than 10^{-15} cm²/sec at this temperature. Evidence of somewhat higher values at 100°C for the hexagonal potassium bronzes was found. Smith and Danielson (7) measured the diffusivity of sodium in $Na_{0.78}WO_3$ by effusion of sodium, and found a value of less than 10^{-11} cm²/sec at 1000 K.

Diffusion of Li and H in tungsten bronzes has been of interest in connection with WO_3-based electrochromic devices. The diffusion coefficient of H in amorphous WO_3 appears to be about 10^{-10} cm²/sec at room temperature (8), and that of lithium 1-2 orders of

* Electrochemical Society Active Member.
Key words: chemical diffusion, diffusion coefficient, perovskite, intercalation.

magnitude less (9). A recent study (10) made on thin polycrystalline films of the tetragonal and cubic lithium tungsten bronzes found values of 10^{-15} to 10^{-14} and approximately 10^{-13} cm^2/sec, respectively.

Recent work has suggested that much higher values for the diffusion coefficient of lithium in tungsten bronzes may be found if lithium is inserted into materials which already contain a larger alkali cation. Thus Cheng and Whittingham (11) have found that lithium may be inserted into hexagonal K_xWO_3 and $(NH_4)_xWO_3$ and tetragonal Na_xWO_3, either chemically, using n-butyl Li as the reducing agent, or electrochemically at ambient temperature from organic solvent-based electrolytes. The present authors (12) found that the chemical diffusion coefficient of lithium in single crystal samples of hexagonal K_xWO_3 was initially as high as 10^{-7} cm^2/sec, and preliminary results were also presented, indicating that Li could be inserted into cubic sodium tungsten bronzes, as long as the sodium content was less than about 0.7.

This latter result was unexpected, since the perovskite structure is rather close packed, and as mentioned above, the earlier results on lithium and sodium mobility in this structure had suggested slow diffusion. As part of an investigation into the thermodynamics (13) and kinetics of alkali metal insertion reactions into oxide electrode materials, a more detailed electrochemical study of the diffusion kinetics was therefore undertaken and those results are presented here.

Straumanis and Doctor (14) investigated phase relations in the $Li_yNa_xWO_3$ system on samples prepared at high temperature (850°-950°C). They found that a cubic phase containing both lithium and sodium existed at compositions close to the normal range of the cubic sodium bronze ($0.35 < x < 0.73$, $y < 0.3$) but that a two phase region containing pure Li_yWO_3 and $Li_yNa_xWO_3$ existed at compositions close to the normal range of the cubic lithium bronze ($0.11 < y < 0.51$, $x < 0.26$). In other words, lithium was found to be soluble in the cubic sodium bronze but sodium was insoluble in the cubic lithium bronze.

Spitsyn *et al.* (15) investigated the preparation of mixed Li-Na bronze crystals by electrolysis of molten tungstate-WO_3 mixtures. The only significant discrepancy between this work and that of Straumanis and Doctor was that the former claimed that sodium was soluble in cubic lithium bronze to produce compositions such as $Na_{0.05}Li_{0.33}WO_3$.

Sample Preparation and Characterization

Single crystal specimens of the sodium tungsten bronzes were produced by the electrolytic decomposition of molten mixtures of Na_2WO_4 and WO_3 in an alumina crucible (16). The electrolysis was performed at approximately 700°C under constant current conditions with platinum electrodes. Oxygen is evolved at the anode and crystal growth occurs on the cathode. The crystals were cleaned with a mild alkali solution and annealed *in vacuo* to eliminate compositional inhomogeneities.

Powder samples were prepared by solid-state reaction of Na_2WO_4, WO_3, and W in sealed quartz ampuls at about 700°C. Although diffusion coefficient measurements were made exclusively on single crystal samples, much of the thermodynamic data, discussed elsewhere (13), was gathered on sintered, polycrystalline electrodes.

In order to compare the materials produced by lithium insertion at ambient temperatures with the mixed bronzes prepared at high temperature by Straumanis and Doctor (14), a compound of composition $Li_{0.35}Na_{0.45}WO_3$ was made by solid-state reaction of Li_2WO_4, Na_2WO_4, WO_3, and W at 725°C. The sample was completely protected from reaction with the atmosphere at all times.

Three independent techniques: powder x-ray diffraction, thermogravimetric analysis (TGA), and chemical titration, were employed to determine the sodium stoichiometry of the tungsten bronze samples.

Brown and Banks (17) have shown that the lattice parameter, a_o, of the cubic phase of sodium tungsten bronze varies linearly with the sodium content according to the following equation

$$a_o = (3.7845 + 0.082x)\text{Å}$$

where x is the sodium composition parameter in Na_xWO_3. Lattice parameters were derived from high angle ($2\theta > 75°$) x-ray diffraction patterns using an internal standard. In addition, several samples were x-rayed after electrochemical lithium insertion. These samples were protected from reaction with the atmosphere.

Na_xWO_3 is easily oxidized at elevated temperatures in an air or oxygen atmosphere to WO_3 and sodium tungstates. The weight change due to the stoichiometric uptake of oxygen is related to the sodium content of the bronze. Oxidations were carried out at about 680°C.

In addition, the oxidation state of tungsten in the bronzes was determined by the method of Choain and Marion (18). This technique involved the quantitative oxidation of tungsten to the +6 oxidation state and the reduction of Ag(SCN) to Ag°. The silver was determined by Volhard's method. Assuming no deviations in oxygen stoichiometry, the sodium content of the bronze could then be determined from the average oxidation state of the tungsten in the bronze.

Electrochemical Measurements

Electrochemical measurements were carried out in a glove box with a helium atmosphere from which N_2, O_2, and H_2O were continuously removed.

Detailed kinetic measurements were carried out on single crystals of three different sodium concentrations ($x = 0.54$, 0.64, and 0.71). In addition, single crystals and powders of high sodium content ($x > 0.75$) were also examined electrochemically but, as will be seen later, almost no lithium could be inserted at room temperature.

Electrochemical cells of the following configuration were employed.

$$(-)\ \text{Li} \mid \text{LiAsF}_6\ (1\text{M in PC}) \mid \text{Li}_y\text{Na}_x\text{WO}_3\ (+)$$
$$\qquad\qquad\qquad\qquad\qquad\qquad\qquad\qquad\qquad\qquad \mid$$
$$\qquad\qquad\qquad\qquad\qquad\qquad\qquad\qquad\qquad\qquad \text{Li reference}$$

The solvent and the electrolyte solution were dried prior to use by agitation with lithium chips in the solvent and the solution for a period of approximately one week. The temperature of the cell was controlled between room temperature and 80°C.

Coulometric titration curves were generated by intermittently passing known quantities of charge through the above electrochemical cell and allowing the cell to re-equilibrate. The open-circuit voltage was then measured after each such compositional change. In order to remain within the stability range of the electrolyte, potential differences less than 1.65V or greater than 3.4V were not imposed on the cell. The change in the lithium composition was calculated from Faraday's law. The titration was repeated many times to generate the complete curve. Complete reversibility was demonstrated by removing lithium from the samples by reversing the direction of current flow.

At each composition at which a diffusion coefficient was measured on one of the single crystal samples ($x = 0.64$), the local slope of the coulometric titration curve was obtained as a function of temperature. This was necessary to properly analyze the temperature dependence of the diffusion coefficient.

Since cubic $Li_yNa_xWO_3$ is primarily an electronic conductor, the measured voltage of the cell is a direct measure of the lithium activity at the electrolyte-electrode interface. By perturbing the interface concentration of lithium in a controlled manner and by noting the time evolution of the system response, solutions of Fick's laws could be used to determine the chemical diffusion coefficient. Either of two transient measurement techniques, galvanostatic or potentiostatic, was employed to measure the chemical diffusion coefficient of lithium in bronze samples with two different concentrations of the immobile sodium species over ranges of concentration of the mobile lithium species and of temperature. Perturbations of the lithium concentration at the electrolyte-electrode interface were of such a small magnitude that the chemical diffusion coefficient and the molar volume could be assumed to be invariant during the measurement.

In the galvanostatic technique (19), a current step was imposed on previously equilibrated cells. The boundary conditions for solution of Fick's law were those of a constant flux of lithium ions across the electrolyte-electrode interface of a semi-infinite electrode. The voltage response $V(t)$, which represented the changing concentration of the lithium ions due to the flux of lithium ions through the interface, was then recorded and analyzed using the short time solution of Fick's law

$$V(t) = \frac{2V_m(dE/dy)I}{\mathbf{F}s}\left[\frac{t}{\pi D}\right]^{1/2} \quad \left(t << \frac{l^2}{D}\right) \quad [1]$$

where I, V_m, s, $\mathbf{F}$, l, (dE/dy), and D represent the imposed current, the molar volume, the surface area, Faraday's constant, the sample length, the local slope of the coulometric titration curve, and the chemical diffusion coefficient, respectively.

In the potentiostatic method (20) a voltage step was applied to the equilibrated electrochemical cell, altering the lithium activity at the electrolyte-electrode interface. The current response, $I(t)$, to this voltage change corresponded to the flux of lithium ions through the interface and was recorded and analyzed according to the following solution of Fick's law

$$I(t) = \frac{V\mathbf{F}s}{V_m(dE/dy)}\left[\frac{D}{\pi t}\right]^{1/2} \quad \left(t << \frac{l^2}{D}\right) \quad [2]$$

where V_m, l, t, and D represent the applied voltage, sample length, time, and chemical diffusion coefficient, respectively. The disadvantage of this technique compared to the current step method is that the voltage drop due to uncompensated resistance is not constant with time. The reference electrode must be carefully located near the bronze electrode to minimize such effects.

Results

In Table I, the results of the analysis performed on the single crystal bronze samples, using the techniques previously described, are presented. Good agreement between the results obtained from the various techniques was observed.

The x-ray powder diffraction experiments indicated that the lattice parameter decreased slightly on insertion of lithium into the sodium bronzes. Quantitative results are discussed elsewhere (13). The presence of low intensity superlattice lines on the lithium-containing samples necessitated indexing the powder patterns on a double cell of eight times the volume of the uninserted material.

Table I. Sodium content of single crystal samples as measured by several techniques

Lattice parameter	Thermogravimetric analysis	AgSCN reduction
0.64	0.61	0.64
0.54	0.53	—
0.71	—	0.72

In Fig. 1, the coulometric titration curve for three single crystal samples with $x = 0.54$, $x = 0.64$, and $x = 0.71$ are plotted. As may be seen, only very small quantities of lithium could be inserted into the bronze of highest sodium composition. This result was confirmed by measurements on single crystals and powders of several different compositions with sodium contents greater than $x = 0.7$. Detailed discussion of the thermodynamics of insertion is presented elsewhere (13); only the most important points are repeated here.

The dependence of lithium chemical potential on composition is well accounted for by three contributions. The first of these is the change in enthalpy of the free electron gas in the bronze conduction band as lithium is added to the bronzes. The second is the configurational entropy term, which arises from the distribution of the inserted lithium atoms over the vacant sites, and which gives the characteristic shape to the titration curves. The third contribution is a small, constant partial molar thermal entropy term. The entropy contributions were measured by observing the dependence of cell emf on temperature, and it was found that the lithium atoms were distributed randomly over $(1 - x)$ sites, where x is the atom ratio of sodium. For the single crystal sample, $Na_{0.71}WO_3$, only a small amount of lithium could be inserted; y had a maximum value of approximately 0.01. The chemical potential of lithium increased very rapidly with lithium content in this sample.

The chemical diffusion coefficients of lithium in the two single crystal specimens with $x = 0.54$ and 0.64 at $T = 300$ K are presented in Fig. 2 as a function of the lithium composition. A decrease in the chemical diffusion coefficient with an increase in the lithium composition parameter, y, was observed. Similarly, a decrease in the chemical diffusion coefficient with an increase in the sodium content for fixed values of y was noted. In the single crystal sample with $x = 0.71$, the chemical diffusion coefficient of lithium fell rapidly with the addition of lithium at low values of y, although initial values were similar to those measured on the materials of lower sodium content. Beyond approximately $y = 0.01$, the very rapid decrease in cell voltage with increase in y prevented further quantitative measurement of the diffusion coefficient.

The component diffusion coefficient (D_{Li}) is related to the chemical diffusion coefficient (D) by the following equation (19)

$$D = D_{Li}\frac{d\ln a_{Li}}{d\ln c_{Li}} = -D_{Li}\frac{\mathbf{F}}{RT}y\frac{dE}{dy} \quad [3]$$

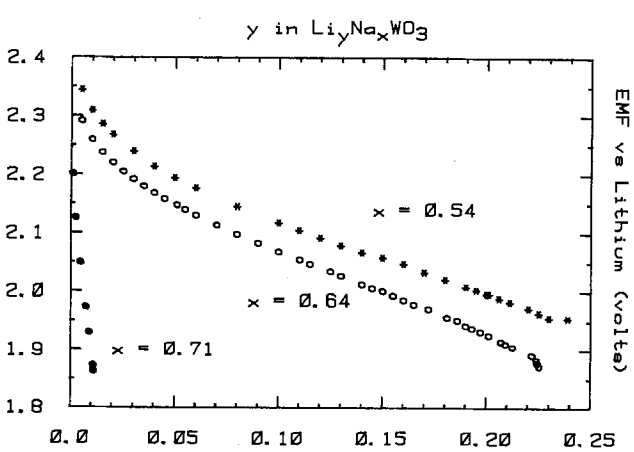

Fig. 1. Coulometric titration curves for the single crystal samples used in the diffusion coefficient measurements.

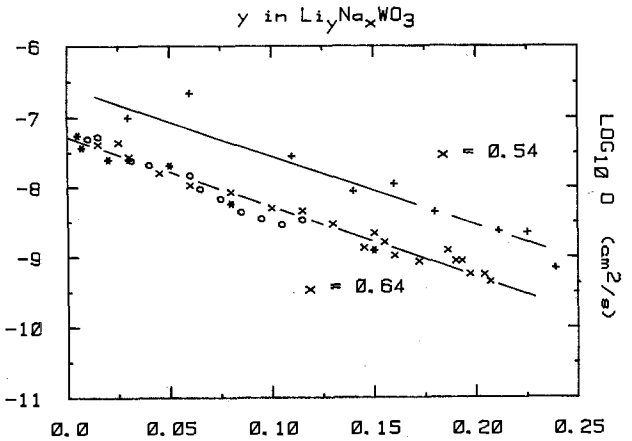

Fig. 2. Chemical diffusion coefficients at 300 K for $Li_yNa_{0.54}WO_3$ and $Li_yNa_{0.64}WO_3$. (Three sets of data, obtained on two different crystals are shown for $Li_yNa_{0.64}WO_3$.)

where $(d \ln a_{Li}/d \ln c_{Li})$ is the thermodynamic enhancement factor, which is calculated from (dE/dy), the local slope of the coulometric titration curve; R is the gas constant, and T the temperature. Chemical and component diffusion coefficients for the sample $Li_yNa_{0.64}WO_3$ are plotted in Fig. 3 as functions of the lithium composition at $T = 291$ K and $T = 350$ K. These curves show the same trends seen in Fig. 2.

Arrhenius plots of the component diffusion coefficients for a single crystal specimen of $Li_yNa_xWO_3$ $(x = 0.64)$ at several values of y are shown in Fig. 4. These plots appear to exhibit some curvature. The room temperature diffusion coefficients are a little lower than would be expected from an extrapolation of the high temperature results. Activation energies for diffusion for the same composition, which were derived from the higher temperature values for the component diffusion coefficients, are presented as a function of the lithium composition in Fig. 5. A general increase in the activation energy with increasing lithium content is observed, with the most rapid change occurring at low lithium contents.

The sodium ions in cubic sodium tungsten bronze are essentially immobile, and therefore it is assumed that the chemical diffusion coefficient is determined by the mobile lithium ions, rather than as a result of interdiffusion of these two ions. The cubic phase of sodium tungsten bronze is predominantly an electronic conductor and therefore the partial lithium ion conductivity is given by the following (19)

$$\sigma_{Li^+} = -\frac{\mathbf{F}D}{V_m}\left(\frac{dE}{dy}\right)^{-1} \qquad [4]$$

where D is the chemical diffusion coefficient, V_m is the molar volume, $\mathbf{F}$ is Faraday's constant, and (dE/dy) is the local slope of the coulometric titration curve. In Fig. 6, the partial lithium ion conductivity of $Li_yNa_xWO_3$ $(x = 0.64)$ is plotted as a function of the lithium composition parameter at $T = 291$ K and $T = 350$ K. This graph shows the increase in lithium ion conductivity with increase in temperature. Figure 7 is a plot of the lithium ion conductivity as a function of y for samples with sodium composition parameters $x = 0.64$ and $x = 0.54$, at room temperature. The variation of the lithium ion conductivity with the sodium composition for fixed values of y is evident in this plot.

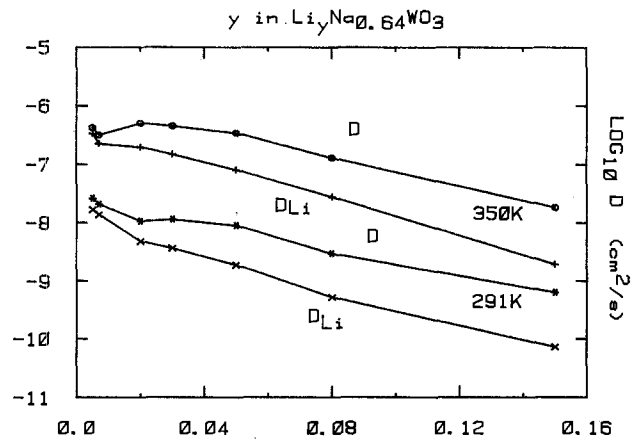

Fig. 3. Chemical (D) and component (D_{Li}) diffusion coefficients at 291 and 350 K for $Li_yNa_{0.64}WO_3$.

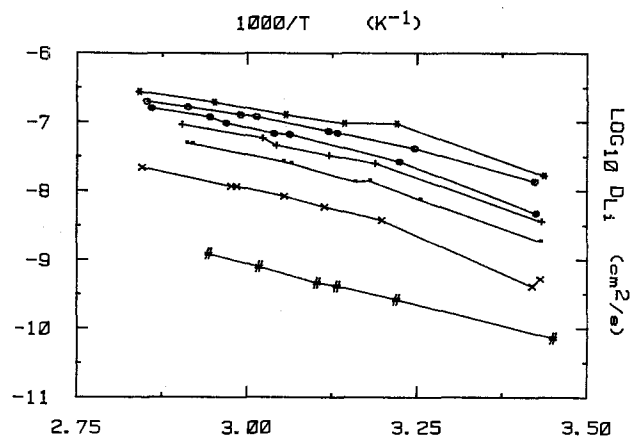

Fig. 4. Arrhenius plots of D_{Li} vs. T^{-1} for various lithium concentrations in $Li_yNa_{0.64}WO_3$. (* $y = 0.005$, ○ $y = 0.007$, ● $y = 0.020$, + $y = 0.030$, • $y = 0.050$, × $y = 0.080$, # $y = 0.150$.)

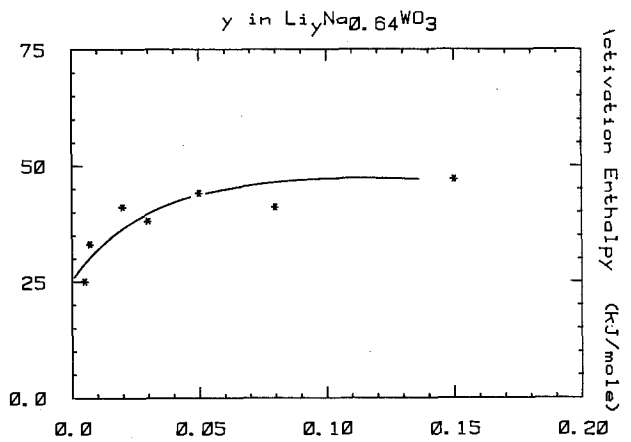

Fig. 5. Activation enthalpies for lithium diffusion in $Li_yNa_{0.64}WO_3$

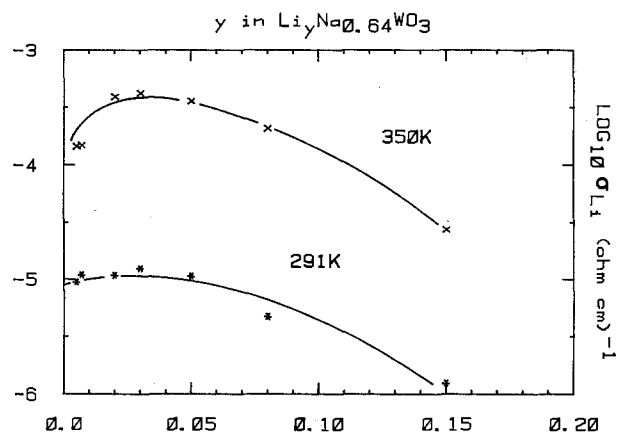

Fig. 6. Partial lithium ion conductivities at 291 and 350 K for $Li_yNa_{0.64}WO_3$.

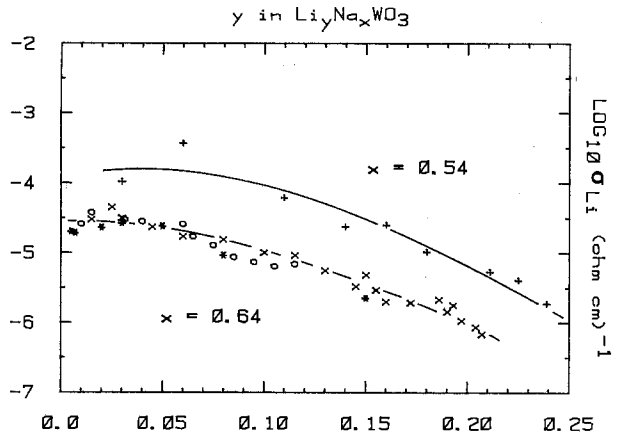

Fig. 7. Partial lithium ion conductivities at 300 K for $Li_yNa_{0.54}WO_3$ and $Li_yNa_{0.64}WO_3$. (Three sets of data, obtained on two different crystals are shown for $Li_yNa_{0.64}WO_3$.)

The powder sample of composition $Li_{0.35}Na_{0.45}WO_3$, prepared by high temperature solid-state techniques, was investigated briefly electrochemically. Lithium could be removed from this sample at room temperature at rates comparable to those found for the phases prepared at low temperatures, suggesting that at least some of the lithium in the high temperature material has a high diffusion coefficient.

Discussion

The data for the measured diffusion coefficients in $Li_yNa_xWO_3$ indicate relatively high values at these moderate temperatures. As mentioned earlier, the diffusion coefficients of both sodium in cubic Na_xWO_3 and lithium in Li_xWO_3 are very low.

In order to understand the relative magnitude of D_{Li} in these three systems it is necessary to examine the structures of these compounds in some detail.

All three compounds have the same defect perovskite structure, in which the alkali metal ions occupy sites at the center of a cube formed from 8 corner-shared WO_6 octahedra.

In recent years, however, it has become apparent that the true structures of the cubic bronzes are more complex than first thought, and that rotations of the almost rigid WO_6 octahedra lead to important deviations from the undistorted perovskite model. Wiseman and Dickens (21) performed a powder neutron diffraction study on several cubic bronzes: $Li_{0.36}WO_3$, $Na_{0.54}WO_3$, $Na_{0.73}WO_3$, and $La_{0.14}WO_3$, and found that, although the materials retained their cubic symmetry, rotation of the octahedra produced two kinds of sites for the inserted metals.

A more recent lattice parameter study (22) and a Raman study (23) of Na_xWO_3 ($0.6 < x < 1$) have identified four phases in this composition range. At temperatures above 400 K the materials have the undisturbed perovskite structure, with space group Pm3m. A second-order phase transition has also been seen at this temperature in specific heat measurements (24). Below this temperature three phases exist, which are related by successive tilts of the octahedra about each of the cubic axes. At room temperature the structure is tetragonal with space group I4/mmm (22). The difference between a_o and c_o, however, is only 0.15%. Wiseman and Dickens also found a slight tetragonal distortion in $Na_{0.73}WO_3$ (*ca.* approximately equal to 0.9992), but suggested the orthorhombic space group Immm. In the following discussion the crystallographic data due to Wiseman and Dickens are used.

If the slight tetragonal distortion is neglected, the two inequivalent sites in the room temperature structure are 2(a) and 6(b) in Im3 (21). The 6(b) sites are best described as 4-coordinated, the alkali metal is surrounded by a square arrangement of oxygens at a distance of 2.175Å in the case of $Li_{0.36}WO_3$, and 2.583Å in $Na_{0.55}WO_3$, whereas in the 12-coordinated sites the nearest oxygens are at 2.657 and 2.710Å, respectively, for the lithium and sodium compounds. The tilt of the octahedra depends very much on the radius of the inserted ion. It is about 14° for Li_xWO_3, 4° for Na_xWO_3, and 0° for La_xWO_3. The positions of the two kinds of sites in the crystallographic unit cell are shown in Fig. 8.

There are two kinds of diffusion pathways in the distorted structures: 6(b) → 6(b) and 2(a) → 6(b) → 2(a). A diffusing atom cannot move from one 2(a) site to another 2(a) site without passing through a 6(b) site. In fact, the aperture through which the diffusing atom must move is almost the same for both pathways. It is a triangular arrangement of oxygen atoms, with a passage of radius 0.229Å in Li_xWO_3, and 0.434Å in Na_xWO_3. The aperture is shown in Fig. 9. In the completely regular structure without the tilting of the octahedra, the size of this aperture would be 0.462 and 0.514Å for the lithium and sodium cases, respectively, assuming the same unit cell size. Thus, the distortion of the structure reduces the size of the critical aperture for diffusion. Assuming ionic radii of 0.56Å for Li^+ and 1.00Å for Na^+, it is clear that if they can be considered hard spheres, neither could pass through the pathway apertures in either Li_xWO_3 or Na_xWO_3, but that Li^+ is relatively close in size to the aperture in Na_xWO_3. This is a reasonable, although qualitative, explanation of the much larger diffusion

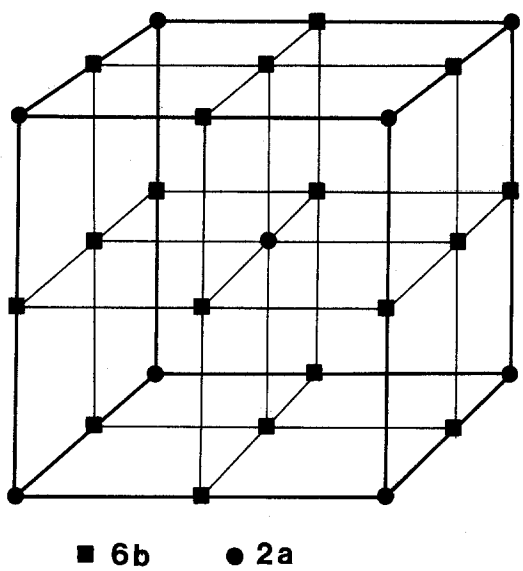

Fig. 8. Relative positions of the 2(a) and 6(b) sites of space group Im3 in the cubic tungsten bronzes.

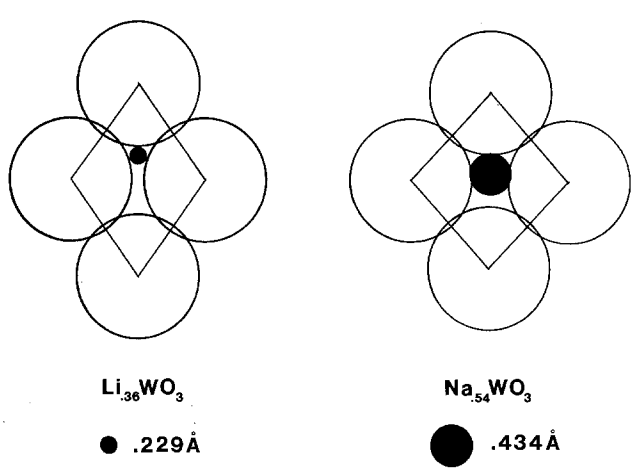

Fig. 9. The apertures through which a diffusing ion must move in $Li_{0.36}WO_3$ and $Na_{0.54}WO_3$.

coefficient of lithium in the mixed tungsten bronze containing sodium than in the pure lithium bronze.

The general trend in the self-diffusion coefficient shown in Fig. 3 is consistent with a noninteracting lattice gas model (25). In this model, it is assumed that there is no interaction between the diffusing atoms, except for short range repulsion, which prevents jumps into already occupied sites. A steady decrease in the diffusion coefficient with increasing lithium concentration is predicted, due to a decreasing probability of finding an unoccupied site next to an occupied one. Thus D_{Li} is proportional to the fractional number of vacant sites, assuming all sites have an equal probability of being occupied.

Such a model is consistent with other properties of the tungsten bronzes. The concentration of free electrons in these materials is very high (approximately 2×10^{22} cm^{-3}), and can be assumed to screen long range coulombic interactions between particles. Under these circumstances, only the relationship between the diameter of the particle and the dimensions of the surrounding lattice is important in determining the activation enthalpy for diffusion in a dilute system.

This model, however, predicts a concentration-independent activation enthalpy, and as seen in Fig. 5, this is evidently not the case. The activation enthalpy appears to increase quite rapidly at low concentrations of inserted lithium. This probably also accounts for the deviation of the partial ionic conductivity data, calculated by use of the Nernst-Einstein equation, from the parabolic dependence on lithium concentration expected from the noninteracting mobile ion model, shown in Fig. 6 and 7.

The explanation for this increase in activation enthalpy may lie in some local interaction between the lithium ions that is not screened by the free electron population, but it is more likely that it has a structural origin. As discussed above, the greater the tilting of the octahedra, the smaller the aperture through which the lithium must diffuse. The distortion in the cubic sodium tungsten bronzes is sufficiently small that x-ray reflections corresponding to a superlattice are not observed. In samples of low sodium content, intercalated by lithium, however, superlattice peaks are weakly visible, suggesting that the structure does distort as the lithium concentration increases. This distortion would presumably hinder diffusion, and thus increase the activation enthalpy for motion.

The last important observation to be accounted for is the dependence of D_{Li} on sodium concentration. As mentioned above, it is expected that the diffusion coefficient decreases as $(x + y)$ increases. Thus, high sodium bronzes should have lower diffusion coefficients, as observed in Fig. 2. What this model does not explain however, is the dramatic drop in lithium solubility and rapid decrease in diffusion coefficient at about $Na_{0.7}WO_3$. Only very small quantities of lithium could be inserted into powder samples of this composition.

If the sodium ions occupy the 2(a) and 6(b) sites randomly, then this observation is difficult to explain. If, however, the sodium ions were ordered on the 6(b) sites at around $x = 0.75$, then the lithium diffusion coefficient and solubility would fall rapidly as this value is approached, since all pathways would be blocked by the immobile Na^+ ions on 6(b) sites, and a direct 2(a) → 2(a) pathway is not possible. Although Na ordering at $x \approx 0.75$ was used by Atoji and Rundle (26) to account for the observation of a superlattice in a single crystal of $Na_{0.75}WO_3$ studied by neutron diffraction, their final agreement factors assuming the ordered structure were poor. In the powder neutron diffraction study of Wiseman and Dickens (21), evidence for Na ordering was not found, but agreement between observed and calculated intensities was very insensitive to the state of order of the sodium, so the possibility of ordering around 0.75 cannot be discounted. The recent Raman study of Flynn (23) also provides some indirect evidence supporting the hypothesis of sodium ordering at $x = 0.75$.

It is also noted that during electrolytic growth of single crystal bronzes, well-defined cubes are obtained when x is above about 0.7, but crystals grow with polyfaceted shapes at lower sodium concentrations. An explanation for this behavior has not been found, but Flynn (23) notes that crystals grown with this morphology apparently do not form the phases with slight tetragonal distortions between 300 and 400 K. In the present study, the crystals with x values of 0.54 and 0.64 grew in the polyfaceted form. Crystals with higher sodium compositions with the cubic morphology did not accommodate any lithium.

The stability of the cubic alkali bronzes towards air and water at room temperature is of kinetic origin, founded in the very slow diffusion of the alkali metal to the surface. It was observed in the present study that cubic $Li_yNa_xWO_3$ was very rapidly oxidized by air and/or moisture, although the products of this reaction have not been investigated. Straumanis and Doctor (14), on the other hand, reported that their mixed cubic Li-Na bronzes formed at higher temperatures were remarkably resistant to oxidation, and they were able to carry out x-ray diffraction studies, presumably in an air ambient. The implication of this is that the phases prepared at high temperature are somewhat different, at least in their kinetic properties, from the phases prepared at ambient temperature. In the ambient temperature phases, the sodium configuration is "frozen;" thus, any pathway which allows a lithium atom to diffuse into the structure is also available for out-diffusion on oxidation. In the high temperature phases, however, the sodiums are presumably mobile at the temperature of preparation, and thus will block out-diffusion of lithium when the phases are cooled to room temperature. This effect, however, will not be complete, since statistically there will still be some available diffusion paths. This is consistent with the electrochemical behavior of the material $Li_{0.35}Na_{0.45}WO_3$ prepared at high temperature, where it was found that some of the lithium could be removed rapidly. This would suggest that the high temperature phases are in fact unstable to atmospheric oxidation.

It is of interest to consider whether one of the main conclusions of this study, namely, that high lithium diffusion coefficients are due primarily to the presence of a larger, immobile cation, which effectively prevents distortions of the structure detrimental to rapid diffusion, is of more general validity. It seems likely that it is indeed so, especially in metallically conducting layer and framework structures, although other examples appear to be lacking at the present time.

Conclusions

The main findings of this study may be summarized as follows. (*i*) The chemical diffusion coefficient of lithium in the mixed cubic tungsten bronzes, $Li_yNa_xWO_3$, at ambient temperatures is very high, about 10^{-7} cm^2/sec for low y values, but decreases with increasing alkali metal content. Samples with $x \geq 0.7$ can accommodate very little lithium and the diffusion coefficient appears to fall rapidly with increase in lithium concentration. (*ii*) The diffusion coefficient of lithium measured in these phases is many orders of magnitude greater than the diffusion coefficient of either lithium in cubic Li_xWO_3 or of sodium in cubic Na_xWO_3. These differences are ascribed to the size of the aperture through which the alkali metal ion must move. The aperture size, which is controlled by the degree of tilting of the WO_6 octahedra, is of comparable size to the Li^+ radius in the $Li_yNa_xWO_3$, but much smaller than either the Li^+ radius in Li_xWO_3 or the Na^+ radius in Na_xWO_3. (*iii*)

As lithium is added to the bronzes of low sodium content, the degree of tilting of the octahedra increases, reducing the aperture size and increasing the activation enthalpy of motion. (*iv*) The sudden change in properties for sodium contents greater than about 0.7 is consistent with sodium ordering in the structure. (*v*) Mixed lithium-sodium bronze phases prepared at high temperature also contain mobile lithium ions, although no quantitative measurements on single crystals have yet been made.

Acknowledgment

This work was supported by the United States Department of Energy under Subcontract LBL 4503110.

Manuscript submitted Aug. 16, 1982; revised manuscript received *ca.* Nov. 24, 1982.

Any discussion of this paper will appear in a Discussion Section to be published in the December 1983 JOURNAL. All discussions for the December 1983 Discussion Section should be submitted by Aug. 1, 1983.

Publication costs of this article were assisted by Stanford University.

REFERENCES

1. P. G. Dickens and P. J. Wiseman, in "International Review of Science: Inorganic Chemistry," Series 2, Vol. 10, L. E. J. Roberts, Editor, p. 211, Butterworths, London (1975).
2. P. Hagenmuller, in "Pergamon Texts in Inorganic Chemistry," Vol. 1, p. 541, Pergamon Press, Oxford (1973).
3. J. B. Goodenough, *Bull. Soc. Chem.*, **4**, 1200 (1965).
4. M. S. Whittingham and R. A. Huggins, *J. Chem. Phys.*, **54**, 414 (1971).
5. B. C. H. Steele, in "Mass Transport Phenomena in Ceramics," A. R. Cooper and A. H. Heuer, Editors, p. 269, Plenum Press, New York (1975).
6. P. G. Dickens and D. J. Neild, *J. Chem. Soc. Dalton Trans.*, 1074 (1973).
7. J. F. Smith and G. C. Danielson, *J. Chem. Phys.*, **22**, 266 (1954).
8. B. Reichman, A. J. Bard, and D. Laser, *This Journal*, **127**, 647 (1980).
9. C. Ho, I. D. Raistrick, and R. A. Huggins, *ibid.*, **127**, 343 (1980).
10. M. Rivier, Ph.D. Dissertation, Stanford University, Palo Alto, CA (1981).
11. K. H. Cheng and M. S. Whittingham, *Solid State Ionics*, **1**, 151 (1980).
12. I. D. Raistrick, A. J. Mark, and R. A. Huggins, *ibid.*, **5**, 351 (1981).
13. A. J. Mark, I. D. Raistrick, and R. A. Huggins, To be published.
14. M. E. Straumanis and G. F. Doctor, *J. Am. Chem. Soc.*, **73**, 3492 (1951).
15. V. I. Spitsyn, T. I. Drobasheva, V. P. Zueva, and S. I. Uglich, *Russ. J. Inorg. Chem.*, **23**, 1807 (1978).
16. G. Hägg, *Nature*, **135**, 834 (1935); *Z. Phys. Chem.*, **B29**, 192 (1935).
17. B. W. Brown and E. Banks, *J. Am. Chem. Soc.*, **76**, 963 (1954).
18. C. Choain and F. Marion, *Bull. Soc. Chim. Fr.*, 212 (1963).
19. W. Weppner and R. A. Huggins, *This Journal*, **124**, 1509 (1977).
20. W. F. Chu, H. Rickert, and W. Weppner, in "Fast Ion Transport in Solids," W. van Gool, Editor, p. 181, N. Holland/Elsevier, Amsterdam (1973).
21. P. J. Wiseman and P. G. Dickens *J. Solid State Chem.*, **17**, 91 (1976).
22. R. Clarke, *Phys. Rev. Lett.*, **39**, 1550 (1977).
23. E. J. Flynn, *Phys. Rev. B*, **21**, 1105 (1980).
24. H. Inaba and K. Naito, *J. Solid State Chem.*, **15**, 283 (1975).
25. W. Dieterich, *Solid State Ionics*, **5**, 21 (1981).
26. M. Atoji and R. E. Rundle, *J. Chem. Phys.*, **32**, 627 (1960).

Electrochemical Nucleation and Growth of Silicon in Molten Fluorides

K. L. Carleton,* J. M. Olson,* and A. Kibbler

Solar Energy Research Institute, Golden, Colorado 80401

ABSTRACT

The electrochemical nucleation and growth of silicon on vitreous carbon and graphite are characterized. The anode is a copper:silicon alloy and the electrolyte is a molten solution of KF:LiF:K_2SiF_6 at 750°C. SEM examination of the initial stages of electrodeposition shows that the nucleation process is instantaneous and is followed by three dimensional growth. Because the nucleation is instantaneous, the initial nucleation density and the grain size of the deposited silicon can be controlled. Existing theoretical models for nucleation and their failure to model this system are also discussed.

The electrodeposition of metals from aqueous solutions and molten salts has been studied extensively. Particular interest in metal deposition on foreign substrates has led to nucleation studies (1-6) and the development of theoretical models to characterize the different nucleation and growth mechanisms.

This work characterizes the nucleation of silicon on carbon substrates in an electrochemical process for silicon purification. The silicon is electrorefined in a molten salt system and simultaneously electrodeposited on POCO® graphite substrates as thin sheets of polycrystalline material (7). One possible application of this process is to use the as-grown material as the active base in a photovoltaic cell. In this case, it is desirable to optimize the grain size of the deposited material through knowledge of the nucleation process. In this paper, empirical studies are described which provide a qualitative understanding of nucleation and, as a result, enable one to control the grain size of the electrodeposited material. Existing theoretical models for nucleation and their failure to model this system are also discussed.

* Electrochemical Society Active Member.

Key words: semiconductor, electrode, current, electrodeposition.

Background

Nucleation and growth processes in electrodeposition are characterized by three parameters (2, 3): the growing radially), or three dimensional (hemispherical time dependence of the nucleation process. There are three fundamental growth modes: the growth can be one dimensional (a planar surface growing normal to itself), two dimensional (such as cylindrical nuclei growing radially), or three dimensional (hemispherical or spherical nuclei). Independent from the growth mode is the limiting growth mechanism. This rate-determining step in the growth process can be either the interface kinetics (such as adatom surface diffusion or incorporation), charge transfer kinetics, or the mass transfer of metal ions to the electrode surface. Finally, there are two broad categories for the time dependence of

the nucleation process. If all the nuclei form at essentially the same time, nucleation is termed "instantaneous." If nucleation continues to occur over a period of time, it is considered progressive.

The important parameter in optimizing grain size of deposited material is the time dependence of the nucleation. If nucleation is progressive, nuclei will continually form and grow, making grain size difficult to control. However, if nucleation is instantaneous, grain size is easily optimized. The number of nuclei which form is a function of potential (2) and with constant current growth conditions, this potential is related to the current density. Because no nuclei form after the initial nucleation process in instantaneous nucleation, the initial current density controls the average nucleation density. The density of nuclei determines how soon the nuclei coalesce and therefore determines the ultimate grain size (4).

The growth mode and time dependence of the nucleation process are most easily determined from observations of the initial shape and size of the heterogeneous deposit. The size of each nucleus is proportional to the time since its formation. Therefore, if the nuclei are of random size, nucleation is progressive, whereas if the nuclei are of equivalent size, nucleation is instantaneous (2, 8).

Another method for determining the time dependence of nucleation is to compare the results of potential step experiments with theoretical models. Experimentally, a potential step is applied to a bare electrode and a current-time response is measured. In processes other than deposition, the current decreases with time. However, for electrodeposition, once nucleation has occurred, the current usually increases due to an increasing surface area and a change from planar to two- or three-dimensional diffusion. This rising current can be modeled as a function of time and as such can be used to determine the nature of the nucleation process.

Models have been developed for systems involving different combinations of the characteristic parameters for nucleation and growth processes. Earlier models resulted in simple current-time relations of the form

$$I = Kt^n \quad [1]$$

where K is a product of physical parameters (*e.g.*, nucleation density N_o, molecular weight of the deposited metal M, etc.) and n is generally some half integral number which is characteristic, but not unique, to the properties of the nucleation and growth process. For example, for the instantaneous nucleation and kinetics limited growth of three-dimensional nuclei, $n = 2$ (9).

These earlier models assume that only one process is rate controlling and that no overlap of nuclei occurs. More recent models (6) take into account the effects of overlap and ingestion of nucleation sites resulting in more complicated current-time relations. Alternatively, more than one mechanism may be rate controlling, such as the case of both kinetics and mass transfer control. In the following the potential step, current-time response for a mixed control, and instantaneous nucleation process are derived by equating the currents due to mass flux (10)

$$I = n\mathbf{F}AkC \exp(H^2t) \operatorname{erfc}(Ht^{1/2}) \quad [2]$$

and the current due to mass accumulation for hemispherical nuclei

$$I = (2\pi n\mathbf{F}r^2\rho/M)\frac{\partial r}{\partial t} \quad [3]$$

where $H = k/D^{1/2}$, k is the reaction rate constant, D and C are the diffusion coefficient and the concentration of the electrodepositing species, M and ρ are the molecular weight and density of the depositing metal, and the other terms have their usual meaning.

Integration of Eq. [3] yields an equation for r, the radius of the nucleus, as a function of time

$$r = (kCM/\rho)[\exp(H^2t) \operatorname{erfc}(Ht^{1/2})H^{-2} + 2t^{1/2}H^{-1}\pi^{-1/2}] \quad [4]$$

which can then be substituted back into I to give

$$I = (2\pi n\mathbf{F}k^3C^3AN_oM^2\rho^{-2})\{\alpha^3H^{-4} + 4t^{1/2}\alpha^2H^{-3}\pi^{-1/2} + 4t\alpha H^{-2}\pi^{-1}\} \quad [5]$$

where $\alpha = \exp(H^2t) \operatorname{erfc}(Ht^{1/2})$. This equation, along with those of the form of Eq. [1], is used to analyze potential step transients for this system.

Experimental

A vitreous carbon crucible containing the anode (silicon source) and the molten salt electrolyte is situated in a resistively heated furnace at 750°C (see Fig. 1). The anode is solidified *in situ* from a hypereutectic solution of semiconductor grade silicon [16 weight percent (w/o)] and copper (99.999%). The electrolyte is a mixture of KF:LiF:K_2SiF_6 [46 mol percent (m/o):46 m/o:8 m/o] where the K_2SiF_6 is formed by reacting SiF_4 with excess KF. The LiF and KF are Suprapur® grade.

The KF and LiF are dried *in situ* at pressures less than 10^{-5} Torr by slowly heating from 100°-300°C. This drying procedure effectively prevents the formation of hydrolysis products that have a detrimental effect on the morphology of the silicon electrodeposit. The molten salt is further purified by a pre-electrolysis step. A potential of 2V is applied to a graphite electrode (relative to the crucible) until the current is less than 1 mA/cm^2.

The silicon reference electrode is formed *in situ* by depositing silicon on a 3 mm vitreous carbon rod. This electrode is stable for 2-3 days. Alternatively, an oxide-free, single crystal silicon wafer may be used as a reference electrode. The working electrode is the rounded end of a 3 mm rod of either graphite or vitreous carbon with a geometric area of 0.3-0.4 cm^2.

The chronoamperometric data are recorded with a Nicolet digital storage oscilloscope. For curve fitting the oscilloscope is interfaced with a Hewlett Packard 9825 computer.

Results and Discussion

Figure 2 shows a scanning electron micrograph of silicon nuclei grown on vitreous carbon. The size and shape of the nuclei determine the time dependence of nucleation and growth mode for the system. The nu-

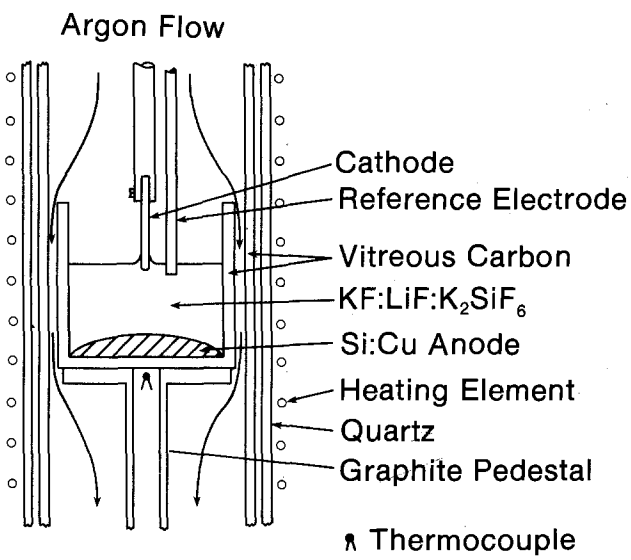

Fig. 1. Electrochemical cell for silicon deposition

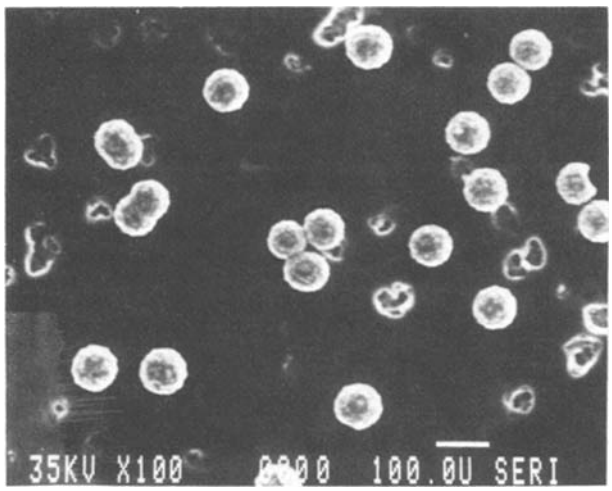

Fig. 2. Scanning electron micrograph of silicon nuclei electrodeposited at 15 mA/cm^2. Deposition was 10 C of material on 1.5 cm^2 vitreous carbon. Imperfections in the vitreous carbon surface also appear.

clei are hemispherical, indicating that the growth is three dimensional. The nuclei are also all of equal size. They must have formed at essentially the same time, implying that the nucleation process is instantaneous. This means the grain size of the deposited silicon can be controlled by the initial current density.

The importance of the initial current density in controlling the grain size is illustrated in Fig. 3. These SEM micrographs show two as-grown silicon surfaces. Although both were grown at the same final current density, the initial current-time profiles were different. The current for the deposit in Fig. 3a was stepped directly from zero to the final growth current density of 70 mA/cm^2. As a result, nucleation occurred at a high current density, the nucleation density was large, and the grain size was small. The current for the deposit in Fig. 3b was stepped from zero to an intermediate current density of 40 mA/cm^2 and then ramped up to the final current density of 70 mA/cm^2. In this case, a lower nucleation density was established by a lower current density, and the resulting grain size was larger. This means that, by controlling the initial current-time profile, the grain size of the material can be controlled independently of the final growth conditions. One problem can arise if the initial current density is too low. In this case, there are areas where the nuclei do not coalesce, leaving voids in the material. Therefore, there is a compromise between maximizing the grain size and ensuring complete surface coverage.

Having established that nucleation is instantaneous and that the grain size can be controlled, potential step experiments were done to try to apply nucleation theory in this system. A series of potential-step, current-response curves are shown in Fig. 4. [Note that the process occurs on a time scale of msec, not sec, as is often encountered (1-3).] The curves can be broken down into several characteristic regions. Initially the current is large as a result of double layer charging and decays exponentially. In the ideal case, this should be followed by a nucleation current which increases with time. However, in this system, the onset of nucleation is swamped by a large prenucleation current which decays slowly in a diffusion limited $t^{-1/2}$ manner. In order to incorporate this large prenucleation current into the theoretical models, linear sweep cyclic voltammograms were examined to determine its cause.

The cyclic voltammogram, shown in Fig. 5, has several key features (11). The inflection point at approximately 0V is the reversible potential for silicon reduction relative to the silicon reference electrode. The

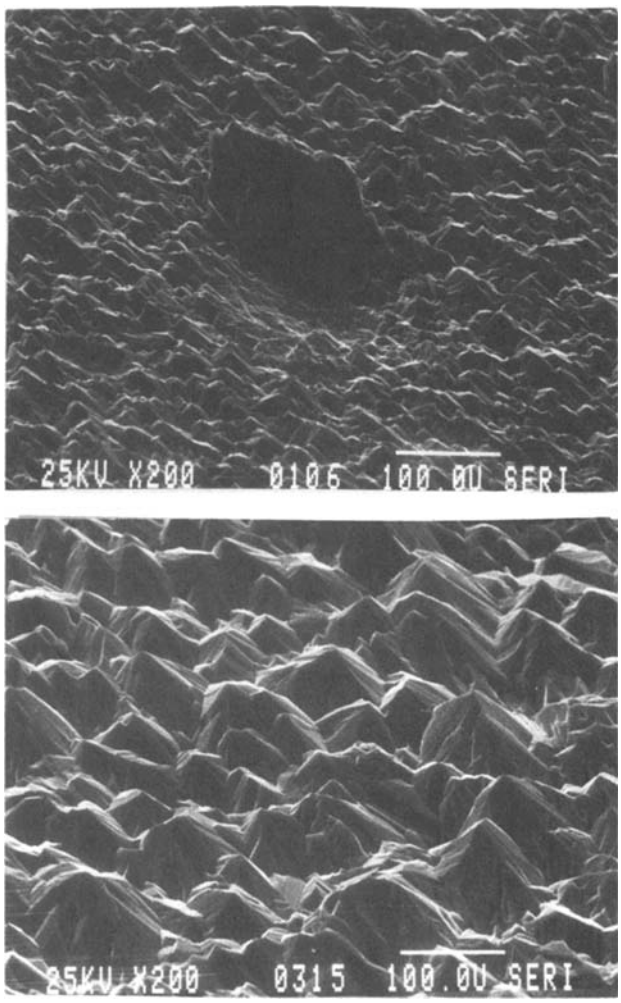

Fig. 3. Scanning electron micrographs of as-grown silicon deposits. Growth conditions: (a, top) current stepped to 70 mA/cm^2, (b, bottom) current stepped to 40 mA/cm^2 and then ramped to 70 mA/cm^2. Total coulombs in each case is approximately 300 C/cm^2.

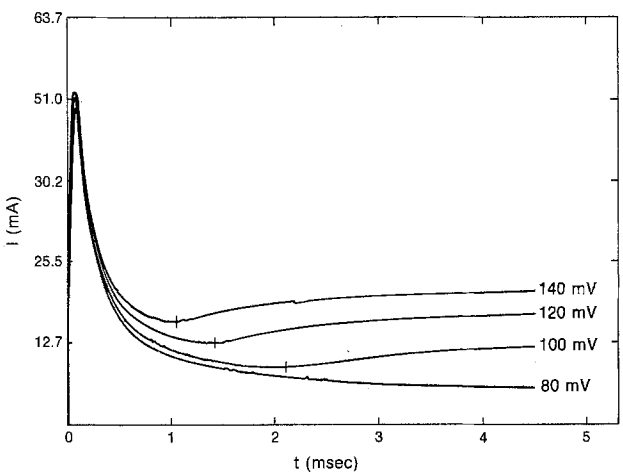

Fig. 4. Cathodic current transients for silicon electrodeposition on 0.3 cm^2 vitreous carbon. Steps are from +1V to the final cathodic step potentials shown.

onset of silicon deposition is slightly offset from this reversible potential by the nucleation threshold, indicating nucleation is the initial rate-limiting step in deposition. The cathodic excursion is due to silicon deposition. The surface increase loop implies that the area of the growth surface is increasing. The increasing surface area results in a larger current on the reverse scan than on the forward (cathodic) scan, and may be

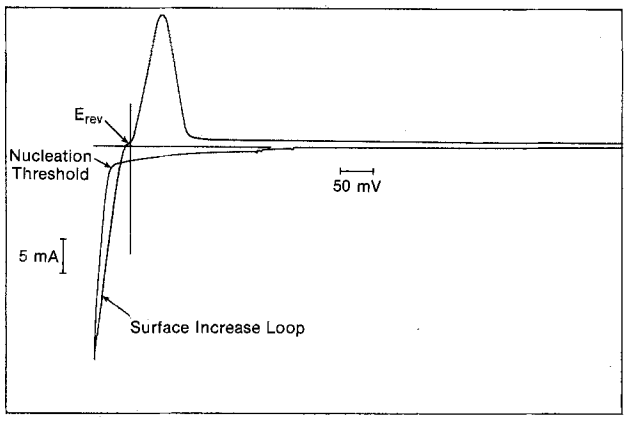

Fig. 5. Expanded cyclic voltammogram for silicon deposition on graphite vs. Si reference electrode with KF:LiF:K_2SiF_6 electrolyte, $T = 724°C$, scan rate = 50 mV/sec, and area = 0.4 cm^2. The cathodic limit, in this case, −50 mV, along with the scan rate determines the quantity of silicon deposited on the carbon electrode, which in turn is proportional to the height of the stripping peak anodic of the reversible potential. The anodic limit is +0.7V.

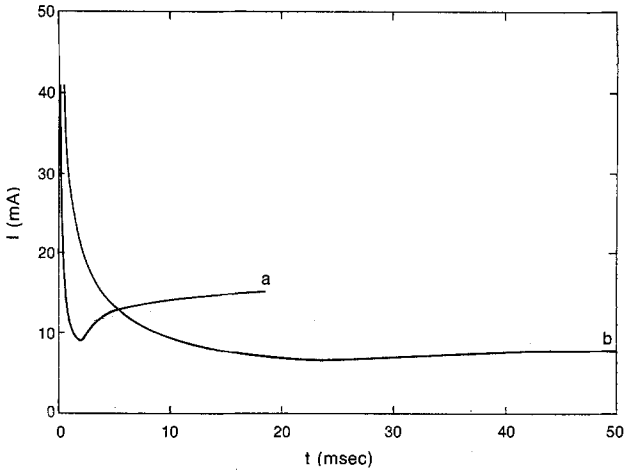

Fig. 6. Current time transients for (a) vitreous carbon and (b) graphite. Geometric areas are 0.3 cm^2 and potential steps are +1V to −100 mV.

due to either two-dimensional or three-dimensional growth. Anodic to the reversible potential, there is a small cathodic current which was correlated with the prenucleation current. There are several possible explanations for this current. For example, the cathodic current is associated with the underpotential deposition (UPD) of silicon on graphite. UPD is the adsorption of a monolayer of metal atoms onto a foreign substrate at potentials anodic of the reversible potential. There are two theoretical criteria to determine if UPD should occur. One involves the difference in lattice parameters of the substrate and depositing species. For differences in unit cell dimensions greater than 1.5Å, it has been shown that monolayer formation, and therefore UPD, does not occur (12). However, conclusions made by comparing unit cell dimensions for silicon on polycrystalline graphite are questionable since graphite is anisotropic. Other work has related UPD to differences in work function (13). The UPD shift is shown to be half the difference in work functions of the substrate and depositing species. Work function data for silicon and carbon are inconclusive due to the wide spread in reported results (14). If the mean values are used, UPD should occur at approximately 0.2V anodic of the reversible potential, which is approximately what is observed in cyclic voltammograms. However, the presence or absence of UPD is inconclusive at this time.

Another possibility for the prenucleation current is the reduction of impurities. In similar experiments in which silicon is purposely excluded from the system, *i.e.*, with KF, LiF, and Cu only, a large current results in response to a potential step. This current may be due to a change in oxidation state of a species such as copper, or it may be due to the presence of oxides since there is some correlation between this prenucleation current and the height of an oxidation peak at +2.0V. These processes are likely to occur with silicon also present in the system.

Because the causes of the prenucleation current could not be conclusively determined, two methods were used to treat the step response data. In one method the prenucleation current was assumed to drop to zero once nucleation occurred and the data were treated in a straightforward manner. In the other method, the prenucleation current was extrapolated and then subtracted from the total current. This residual current was treated as the nucleation and growth current. In neither method did the current fit any of the simple models (Eq. [1]).

It is surprising that this system does not follow a simple diffusion-controlled model. Most molten salt systems are diffusion controlled since at elevated temperatures, the temperature activated processes (such as charge transfer) are rapid (2). However, in this system, a diffusion-limited current has not been observed in cyclic voltammetry (within the limits of the apparatus). This suggests the mixed control model Eq. [5] might better describe the system; however, it did not. Using a model which accounts for nuclei overlap, again assuming mixed control (6), also failed to fit the data with meaningful parameters. This suggests there are several processes occurring simultaneously in this system which cannot be understood or deconvoluted by existing theories.

To explore the effects of the substrate material on the nucleation process, potential step experiments were done on graphite and vitreous carbon. Though both materials are made of carbon, they have different properties, as seen by comparing incubation times for silicon nucleation (Fig. 6). The incubation times on graphite were an order of magnitude larger than those on vitreous carbon. One possible reason is that vitreous carbon has a greater number of highly active sites for nucleation. At the same initial current density, grain sizes will be smaller on vitreous carbon than on graphite due to its lower resistance to nucleation. Other possible explanations can be formulated, but no supporting data or observations exist.

Conclusions

We have shown that the electrochemical nucleation of silicon on vitreous carbon or graphite in a molten fluoride is instantaneous and is followed by three-dimensional growth. Though the growth process cannot be completely characterized theoretically, the fact that nucleation is instantaneous enables the grain size of the as-grown silicon to be controlled, and its growth parameters and polycrystalline structure to be optimized.

Acknowledgments

Our thanks to Rick Matson for the SEM work and to C. Allman, B. Ayers, and A. Etheridge for their help in the preparation of this manuscript. We also acknowledge the support of DOE under Contract No. EG-77-C01-4042.

Manuscript submitted June 21, 1982; revised manuscript received Oct. 2. 1982. This was Paper 538 presented at the Denver, Colorado, Meeting of the Society, Oct. 11-16, 1981.

Any discussion of this paper will appear in a Discussion Section to be published in the December 1983 JOURNAL. All discussions for the December 1983 Discussion Section should be submitted by Aug. 1, 1983.

Publication costs of this article were assisted by the Solar Energy Research Institute.

REFERENCES

1. D. J. Astley, J. A. Harrison, and H. R. Thirsk, *Trans. Faraday Soc.*, **64**, 192 (1968).
2. G. J. Hills, D. J. Schiffrin, and J. Thompson, *Electrochim. Acta*, **19**, 657 (1974).
3. F. Palmisano, E. Desimoni, L. Sabbatini, and G. Torsi, *J. Appl. Electrochem.*, **9**, 517 (1979).
4. I. Morcos, *This Journal*, **122**, 50 (1975).
5. M. F. Bell and J. A. Harrison, *J. Electroanal. Chem.*, **41**, 15 (1973).
6. M. Y. Abyaneh, M. Fleischmann, and M. Labram, in "Electrocrystallization," R. Weil and R. G. Barrados, Editors, p. 1, The Electrochemical Society Softbound Proceedings Series, Pennington, NJ (1981).
7. J. M. Olson and K. L. Carleton, *This Journal*, **128**, 2698 (1981).
8. G. J. Hills, I. Montenegra, and B. Scharifker, *J. Appl. Electrochem.*, **10**, 807 (1980).
9. M. Fleischmann and H. R. Thirsk, in "Advances in Electrochemistry and Electrochemical Engineering," Vol. 3, P. Delahay and C. W. Tobias, Editors, Interscience, New York (1963).
10. A. J. Bard and L. R. Faulkner, "Electrochemical Methods," p. 166, Wiley, New York (1980).
11. A. R. Despic, in "Electrocrystallization," R. Weil and R. G. Barrados, Editors, p. 101, The Electrochemical Society Softbound Proceedings Series, Pennington, NJ (1981).
12. D. J. Astley, J. A. Harrison, and H. R. Thirsk, *J. Electroanal. Chem.*, **19**, 325 (1968).
13. D. M. Kolb, M. Przasnyski, and H. Gerischer, *ibid.*, **54**, 25 (1974).
14. "Handbook of Chemistry and Physics," 60th ed., R. C. Weast, Editor, p. E-82, CRC Press (1980).

Galvanostatic Pulse Plating of Copper and Copper (I) Halides from Acid Copper (II) Halide Solutions

C. W. Yeow and D. B. Hibbert*

Department of Chemistry, Bedford College, University of London, Egham Hill, Egham, Surrey, England

ABSTRACT

CuX (X = Cl or Br) is formed during the galvanostatic pulse plating of copper from acid solutions containing Cu^{2+} and X^-. The reaction $Cu^{2+} + Cu^\circ + 2X^- \rightarrow 2CuX$ occurs in the relaxation period of the pulse. Copper (I) chloride anodes for reserve seawater batteries may be made by this method. CuBr is oriented in the {220} plane when deposited on copper foil with the {200} plane uppermost. CuCl tends to dissolve in solutions containing Cl^- to give soluble copper (I) halides. Corrosion rates at pure copper were determined from the pulse-plating experiments.

Studies (1-3) of copper plating from acid baths by a variety of pulse methods have been made to improve efficiency and plate quality, especially in cathode geometries having small holes or pores (1). Different additives may also improve plate quality by complexing with ions in solution or by adsorption at the plating surface. This investigation was instituted to observe the effect of additives on pulse plating. Copper halides were chosen as model systems because of the availability of data and the body of previous work.

The corrosion of copper in solutions of copper(II) chloride has been studied by Hurlen (4, 5) who showed that layers of copper(I) chloride are formed which subsequently dissolve giving soluble species such as $CuCl_2^-$. The rate of copper(I) chloride formation is slow after an initial monolayer because of the need for solid-state movement of chloride ions to the underlying bulk copper. Numerous workers (4, 6-8) have studied the anodic behavior of copper in halide media. Copper dissolves to $CuCl_2^-$, $CuCl_3^{2-}$, and $CuCl_4^{3-}$ via films of CuCl.

Copper(I) chloride is used as an anode for reserve seawater batteries (9), which may be fabricated by mixing copper(I) chloride with an organic binder and graphite, or by dipping copper plates into molten copper(I) chloride (9). A method of manufacture by direct reaction at a copper electrode, as described in this paper, may provide electrodes which are more conducting, have a known discharge capacity, and ultimately be more economical.

Experimental

Materials

All materials were of Analar grade and used without further purification. Electrodes were 2 × 2 cm copper foil (BDH 99.999%) or 2 × 2 cm platinum foil (Johnson Matthey 99.99%) on which a thin layer of copper was plated from acid copper sulfate solution.

Methods

Corrosion of copper in solutions containing halide ions.—A clean copper foil was suspended from a balance (CI Electronics Microforce II) in a solution containing 1 mol dm^{-3} H_2SO_4, 0.34 mol dm^{-3} $CuSO_4$, and 0.1 or 0.34 mol dm^{-3} KCl or KBr. The solution was thermostated to 25°C (±0.5°C). During the experiment, the level of the solution was adjusted relative to the electrode to correct for the buoyancy of the electrode. The increase in weight of the foil was measured (±0.01 mg) with time. Similar experiments were attempted with solutions containing fluoride and iodide ions.

Pulse plating.—Copper was galvanostatically (300 mA) pulse plated from a series of electrolytes containing 1 mol dm^{-3} H_2SO_4, 0.1 to 0.34 mol dm^{-3} $CuSO_4$, and 0.05 to 0.34 mol dm^{-3} KCl or KBr. A single compartment cell was used with a copper or platinum foil anode. The potential of the working electrode was monitored by an oscilloscope against a saturated calomel reference electrode connected with the Luggin capillary by a salt bridge. The cell was continuously purged with nitrogen during all experiments, and thermostated to 25°C (±0.5°C). A train of square wave pulses was produced by a Chemical Electronics pulse generator (CE RB1) and the current controlled by a potentiostat (Thompson Associates 125) working in a galvanostatic mode. The range of pulse periods was 0.5-10 msec, and relaxation times of 10-1000 msec. For analysis of the deposited layer, plated platinum electrodes were used.

Analysis of plated layers.—Plated electrodes were washed with distilled water and dried in a nitrogen atmosphere to constant weight. For copper-plated

* Electrochemical Society Active Member.
Key words: pulse plating, battery anodes, corrosion.

platinum electrodes, the weight of the initial copper layer was subtracted from the total deposit weight. The total copper content was determined by atomic absorption spectroscopy of a solution obtained from dissolution of the deposit in nitric acid. Copper(I) halide was determined by cathodic coulometry in nitrogen-purged sulfuric acid at 25°C. A potentiostatic step, OCV to 0.1V (*vs.* SHE) for CuCl, and to −0.05V for CuBr, was applied to the copper(I) halide electrode and the current measured with time. The charge passed as CuX was cathodically reduced to copper and X^- (Eq. [1]) gave the amount of halide in the electrode

$$CuX + e \rightarrow Cu + X^- \qquad [1]$$

for X = Cl, E° = 0.137V; X = Br, E° = 0.033V. An x-ray diffraction pattern of the deposit was obtained by placing an electrode at the focal plane of a Phillips diffractometer. For comparison, the x-ray pattern of a copper foil was also recorded.

Results

Corrosion of copper in copper(II) halide solutions.—Figures 1 and 2 show the increase in weight of electrodes immersed in acid copper chloride and bromide solutions having 0.1 mol dm^{-3} and 0.34 mol dm^{-3} halide. It is seen that the corrosion rate for solutions containing bromide increases with increasing bromide concentration. In the case of chloride, the weight eventually decreases due to dissolution of CuCl giving soluble copper(I) chlorides, this effect being greater at higher concentrations. No action of solutions of F^- was noted. Solutions containing I^- and Cu^{2+} reacted extremely quickly giving CuI as a white precipitate which easily scaled from the foil.

Pulse Plating in Halide Solutions

Analysis of deposit.—For all conditions of plating, the weight of the deposit calculated from the total copper content and the amount of copper(I) halide agreed with the measured weight showing that the only species present in the deposit were Cu, and CuCl or CuBr. Table I contains x-ray data for a copper foil, and for foils coated with CuCl and CuBr. For the coated foils, a background pattern of the underlying copper was also observed.

Dependence of the formation of CuX on plating conditions.—Figure 3 shows the percentage of cop-

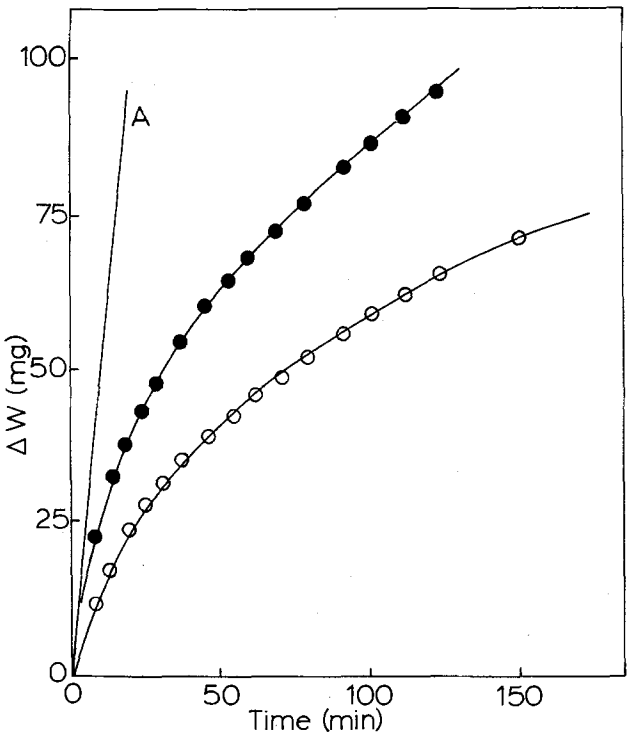

Fig. 2. Increase in weight (Δw) of an 8 cm^2 copper foil immersed in acid copper bromide solutions at 25°C. $CuSO_4$ = 0.34 mol dm^{-3}, H_2SO_4 = 1.76 mol dm^{-3}. ○: KBr = 0.1 mol dm^{-3}; ●: KBr = 0.34 mol dm^{-3}. Line A is the limiting corrosion rate calculated from Eq. [5].

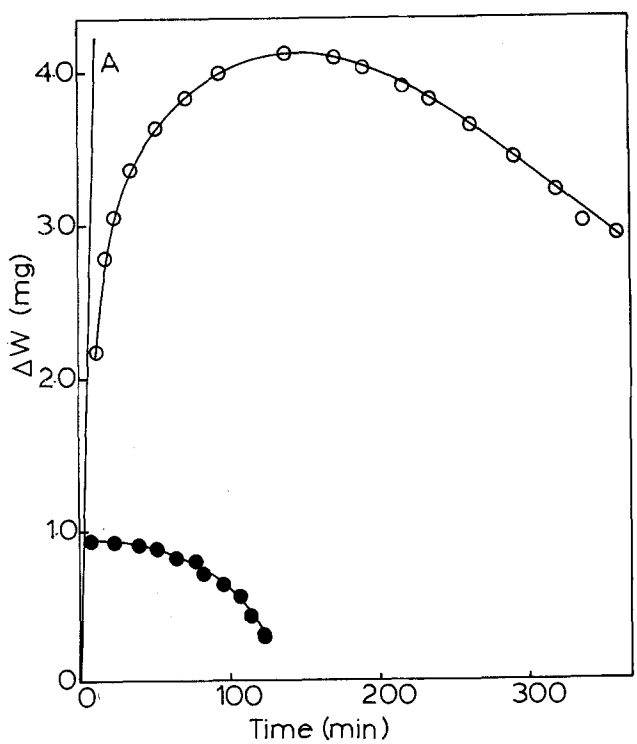

Fig. 1. Increase in weight (Δw) of a 8 cm^2 copper foil immersed in acid copper chloride solutions at 25°C. $CuSO_4$ = 0.34 mol dm^{-3}, H_2SO_4 = 1.76 mol dm^{-3}. ○ : KCl = 0.1 mol dm^{-3}; ●: KCl = 0.34 mol dm^{-3}. Line A is the limiting corrosion rate calculated from Eq. [5] and Fig. 6.

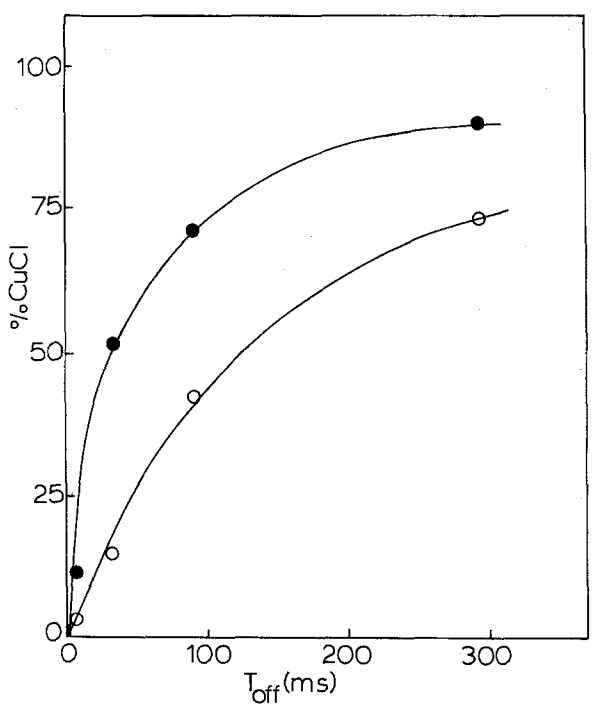

Fig. 3. Percentage of CuCl in the plated deposit as a function of relaxation time of the pulse, during pulse plating in acid copper chloride solution at 25°C. $CuSO_4$ = 0.34 mol dm^{-3}, H_2SO_4 = 1.76 mol dm^{-3}, KCl = 0.34 mol dm^{-3}. ●: Pulse length = 10 msec; ○: Pulse length = 2 msec.

Table I.

Cu						CuCl						CuBr					
d/A	I_{exp}	I_{th}	h	k	l	d/A	I_{exp}	I_{th}	h	k	l	d/A	I_{exp}	I_{th}	h	k	l
2.085	100	100	1	1	1	3.135	100	100	1	1	1	3.302	100	100	1	1	1
1.807	>800	46	2	0	0	2.722	4	8	2	0	0						
1.280	36	20	2	2	0	1.920	44	55	2	2	0	2.021	>800	60	2	2	0
1.090	21	17	3	1	1	1.633	23	30	3	1	1	1.722	50	35	3	1	1
						1.243	4	10	3	3	1	1.308	90	10	3	3	1

X-ray diffraction data for copper foil, and for copper foil coated by pulse-plated CuCl and CuBr. Theoretical intensities from Ref. (10).

per(I) chloride in the plate as a function of relaxation time at constant pulse length. For steady-state plating, no copper halides were found in the deposit. A similar plot is given for copper(I) bromide in Fig. 4 which shows the increase in percentage of CuBr with bromide concentration.

The effect of concentration of Cu^{2+} and Cl^- at constant pulse length and relaxation time was studied. The results are shown in Fig. 5.

Discussion

The reaction between copper and copper(II) halides.—In this study we have confirmed the corrosive action of halide ions in copper(II) solutions. The reaction to give copper(I) halide is

$$Cu + Cu^{2+} + 2X^- \rightarrow 2CuX \quad [2]$$

We have found that the order of reactivity of halides to Eq. [2] is $F^- < Cl^- < Br^- < I^-$. This is supported by thermodynamic data (13) which shows a similar increase in reduction potential for Eq. [2], E° = 0.401V, 0.607V, 1.045V for Cl^-, Br^-, and I^-, respectively. The reaction with chloride is complicated by dissolution of CuCl giving $CuCl_2^-$, $CuCl_3^{2-}$, and possibly $CuCl_4^{3-}$. This is seen from Fig. 1 where, on increasing the concentration of chloride, the increase in the weight of the foil is less by the reaction

$$CuX + X^- \rightarrow CuX_2^- \quad [3]$$

For X = Br, dissolution of CuBr is not so important. The equilibrium constant for Eq. [3] is 2.8×10^{-2} for X = Cl and 4.5×10^{-3} for X = Br (14). Conversion of $CuBr_2^-$ to further species is also less thermodynamically favorable (14).

For chloride and bromide solutions, therefore, the corrosion rate at a fresh copper surface is great, and it is this fact which is used in the pulse-plating experiments. During the pulse, approximately a monolayer of copper is formed which, during the relaxation time, reacts to give the copper(I) halide by Eq. [2]. Optimum production of CuX occurs when the relaxation time is sufficient to allow reaction of the monolayer of plated copper, but not so great as to allow dissolution of the halide layer.

The stoichiometry of the reaction forming CuCl and CuBr during pulse plating.—Noting that formation of CuX occurs only in the relaxation time of the pulse by corrosion of the newly plated copper, it is possible to obtain the stoichiometry of the reaction with respect to copper and halide ion and, thus, confirm that Eq. [2] is indeed of the reaction which produces CuX. Analysis of the layers formed gives the total copper content and the total weight of the deposit. The total charge passed is also known, and by coulometry of the reduction of CuX, the amount of CuX may be determined. Experiments have established that in steady-state plating under the same conditions, 100% current efficiency for

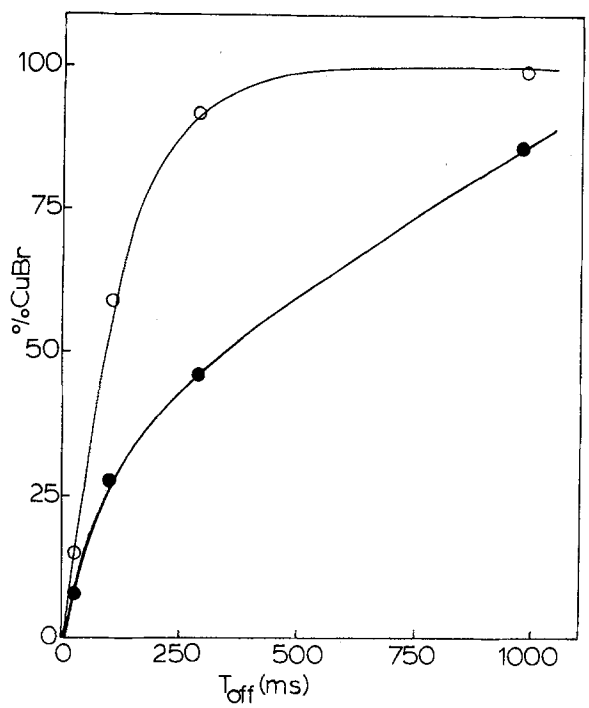

Fig. 4. Percentage of CuBr in the plated deposit as a function of relaxation time of the pulse, during pulse plating in acid copper chloride solution at 25°C. $CuSO_4$ = 0.34 mol dm^{-3}, H_2SO_4 = 1.76 mol dm^{-3}, pulse length = 30 msec. ○: KBr = 0.34 mol dm^{-3}; ●: KBr = 0.10 mol dm^{-3}.

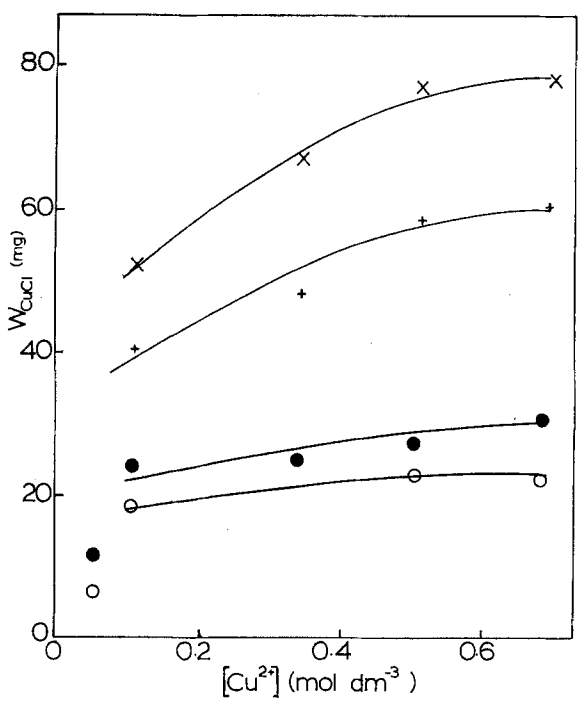

Fig. 5. Weight of CuCl deposited (W_{CuCl}) at different Cu^{2+} and Cl^- concentrations at 25°C. H_2SO_4 = 0.34 mol dm^{-3}, pulse length = 10 msec, relaxation time = 90 msec. Duration of plating = 103 min. ○: Cl^- = 0.05 mol dm^{-3}; ●: Cl^- = 0.10 mol dm^{-3}; +: Cl^- = 0.20 mol dm^{-3}; ×: Cl^- = 0.34 mol dm^{-3}.

plating copper is obtained. If the total charge passed during plating is Q coulombs, the copper deposited is $Q/2\mathbf{F}$ g atoms where $\mathbf{F}$ is the Faraday. If Q_2 coulombs are passed during reduction of CuX (molecular weight M_{CuX}), the amount of CuX formed is $Q_2/\mathbf{F}$ mol. Let a g atom of Cu° react with 1 g atom of X^- during the formation of CuX. Therefore, the amount of copper remaining after this reaction is $(Q/2\mathbf{F} - aQ_2/\mathbf{F})$ g atom. The total weight (W_T) of the deposit is, therefore

$$W_T = (Q/2\mathbf{F} - aQ_2/\mathbf{F}) \times 63.54 + M_{CuX} \times Q_2/\mathbf{F} \quad [4]$$

and thus, a may be found from the measured weight. Results during pulse plating in copper chloride gave $a = 0.51 \pm 0.03$ (from 12 experiments) and for copper bromide $a = 0.49 \pm 0.05$ (from 6 experiments). This treatment is, therefore, in agreement with a mechanism in which reaction occurs during the off time of the pulse according to Eq. [2].

Calculation of corrosion rates.—The rate of corrosion at a fresh copper surface may be determined from the formation of the copper(I) halide at different relaxation times. If conditions are chosen such that conversion to CuX is low, a constant corrosion rate may be assumed. Let n_{Cu} mol m^{-2} of copper be plated during the period of the pulse T_{on} sec, at a current density i A m^{-2}. Therefore

$$n_{Cu} = T_{on}i/2\mathbf{F} \quad [5]$$

At a corrosion rate of C mol sec^{-1} m^{-2} during the relaxation period, T_{off}, n_{CuX} mol m^{-2} are formed, *i.e.*, $n_{CuX} = CT_{off}$. Thus

$$n_{CuX}/n_{Cu} = C/(i/2\mathbf{F}) \times (T_{off}/T_{on}) \quad [6]$$

The ratio n_{CuX}/n_{Cu} calculated for a single pulse applies equally to any number of pulses. A plot of n_{CuX}/n_{Cu} against T_{off}/T_{on} should give, from its limiting slope at low relaxation times, a value for the corrosion rate C. Figure 6 shows such a plot for the corrosion of copper in 0.34 mol dm^{-3} $CuSO_4$ and 0.34 mol dm^{-3} KCl. The limiting corrosion rate is 1.10×10^{-4} mol m^{-2} sec^{-1}, which in terms of the increase in weight of a 8 cm^2 copper foil is 0.356 mg min^{-1}. This rate is drawn in Fig. 1 as line A. It is seen that the rate of corrosion by chloride stays close to the limiting value for several minutes until the effect of dissolution becomes important. A similar plot for corrosion in bromide solution gave $C = 9.30 \times 10^{-4}$ mol m^{-2} sec^{-1}, or 4.97 mg min^{-1} for an 8 cm^2 foil (line A in Fig. 2). Thus, for those metals which may be plated from solution, the pulse plating method may be used to give accurate values for corrosion rates at fresh metal surfaces.

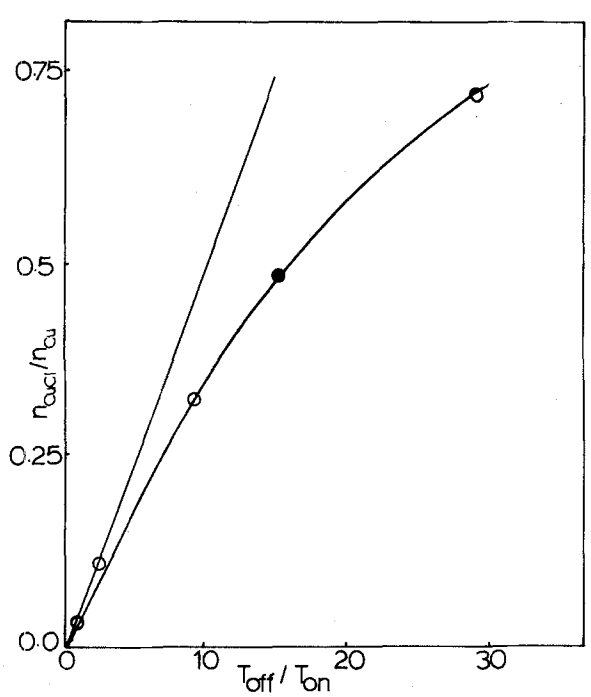

Fig. 6. Ratio of CuCl (n_{CuCl}/mol) formed in the relaxation time (T_{off}) to copper plated (n_{Cu}/mol) during the pulse (T_{on}), as a function of T_{off}/T_{on} at 25°C. $CuSO_4$ = 0.34 mol dm^{-3}, H_2SO_4 = 1.76 mol dm^{-3}, KCl = 0.34 mol dm^{-3}. ○: Pulse length = 10 msec; ●: Pulse length = 2 msec.

Reactions occurring during pulse plating.—The analysis of the processes above assumes that during the pulse copper alone is deposited by

$$Cu^{2+} + e \rightarrow Cu^+ \quad [7]$$

$$Cu^+ + e \rightarrow Cu \quad [8]$$

where Cu^{2+} and Cu^+ may be complexed by halide ion, and that the reaction in the relaxation time is given by Eq. [2]. The potential at the electrode during pulse plating (150-200 mV *vs.* SHE) allowed copper deposition to take place, but was not sufficient to result in reduction of the copper(I) halide via the reaction given by Eq. [1]. No evidence was found for the direct reduction of Cu^{2+} in the presence of halide ion

$$Cu^{2+} + X^- + e \rightarrow CuX \quad [9]$$

Orders of reaction with respect to Cu^{2+} and X^-.—The corrosion Eq. [2], which produces copper(I) halide, may be written as a pair of redox reactions of which Eq. [9] is the reduction, and

$$Cu + X^- \rightarrow CuX + e \quad [10]$$

If Eq. [10] is rate limiting, for a reaction at a monolayer of copper which does not involve diffusion, the reaction would be expected to be first order in halide and zero order in Cu^{2+}. Figure 5 shows that the production of CuCl is influenced more by chloride concentration than copper concentration, but that it is not possible to determine exact reaction orders. As Cu^{2+}, Cu^+, and Cl^- are complexed, a series of reactions involving $CuCl^+$, $CuCl_2$, $CuCl_3^-$, $CuCl_4^{2-}$, and $CuCl_2^-$, $CuCl_3^{2-}$, $CuCl_4^{3-}$ would need to be considered for a full analysis of the system.

Structure of the copper halide deposits.—The copper foil electrodes used in this work were oriented along

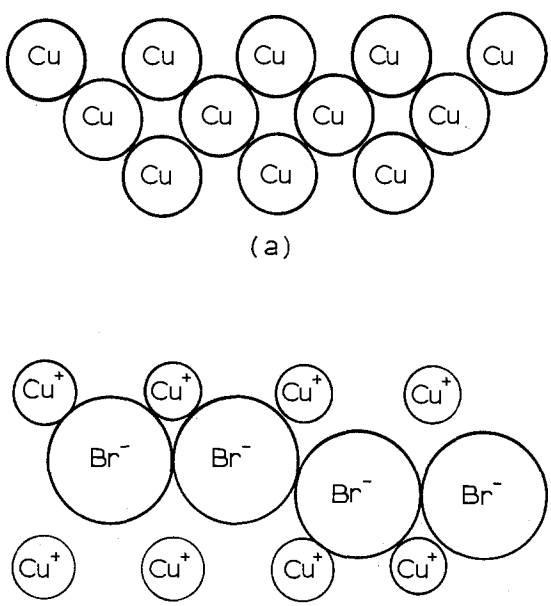

Fig. 7. (a) {200} plane of copper, (b) {220} plane of copper (I) bromide.

the {200} plane. From the x-ray results, copper bromide appears to have been deposited with the {220} plane uppermost. Copper crystallizes in a face-centered cubic arrangement with a unit cell length of 3.615Å (10). The {200} plane of copper is shown in Fig. 7a. Copper bromide exhibits a zinc blende structure in which copper is found in tetrahedral holes formed by bromide ions with $a = 5.691$Å (11). Figure 7b gives the {220} plane of CuBr in which the radius of Cu^+ and Br^- are 0.96 and 1.96Å, respectively (12). It is seen that the Cu-Cu distance in the x direction of the two planes is similar (3.6Å in copper and 3.9Å in copper(I) bromide), and thus, a CuBr lattice may be built up by the insertion of bromide ions with a limited relaxation of copper ions from the underlying lattice. Such an obvious orientation is not seen with CuCl, although geometrically the same considerations apply. Dissolution of CuCl as $CuCl_2^-$ may result in the reorganization of the CuCl layers.

The production of seawater battery anodes.—Pulse plating may be a useful method for the production of copper chloride anodes for reserve seawater batteries. Control of plating conditions can produce a nearly pure CuCl deposit of any required thickness and discharge capacity. A small amount of copper in the layer gives the anode conductivity which is an advantage for such electrodes.

Manuscript submitted Aug. 9, 1982; revised manuscript received Nov. 16, 1982.

Any discussion of this paper will appear in a Discussion Section to be published in the December 1983 JOURNAL. All discussions for the December 1983 Discussion Section should be submitted by Aug. 1, 1983.

REFERENCES

1. A. C. C. Tseung, H. K. Ng, and D. B. Hibbert, *This Journal*, **127**, 1034 (1980).
2. H. Y. Cheh, H. B. Linford, and C. C. Wan, *Plating and Surface Finishing*, **64**, 66 (1977).
3. K. I. Popov, D. N. Keca, S. I. Vidojkovic, B. J. Lazarevich, and V. B. Milojkovic, *J. Appl. Electrochem.*, **6**, 365 (1976).
4. T. Hurlen, *Acta. Chem. Scand.*, **15**, 1231 (1961).
5. T. Hurlen, *ibid.*, **15**, 1246 (1961).
6. C. H. Bonfiglio, H. C. Albaya, and O. A. Cobo, *Corros. Sci.*, **13**, 717 (1973).
7. M. Turner and P. A. Brook, *ibid.*, **13**, 973 (1973).
8. J. O'M. Bockris, B. T. Ruben, A. Despic, and B. Lovrcek, *Electrochim. Acta*, **17**, 973 (1972).
9. D. J. Doan, in "The Primary Battery," Vol. II, G. W. Heise and N. C. Cahoon, Editors, Wiley-Interscience, New York (1976).
10. Powder Diffraction File, J.C.P.D.S., Easton, Maryland (1972).
11. "Handbook of Chemistry and Physics," 53rd ed., Chemical Rubber Co., Ohio, F177 (1973).
12. G. Milazzo and S. Caroli, "Tables of Standard Electrode Potentials," Wiley-Interscience, New York (1978).
13. "Stability Constants," The Chemical Society special publication 17, London (1964).

A Study on Electroless Plating of Cobalt Alloy Films for Perpendicular Recording

Tetsuya Osaka,* Naoki Kasai, and Ichiro Koiwa

Department of Applied Chemistry, Waseda University, Okubo, Shinjuku-ku, Tokyo 160, Japan

and Fumio Goto

Nippon Electric Company Limited, Microelectronics Research Laboratories, Miyazaki, Takatsu-ku, Kawasaki 213, Japan

ABSTRACT

An electroless plating bath for the preparation of perpendicular recording media was developed. It was found that the hcp structure of Co-P is oriented normal to the film plane with the Mn codeposition into the films. First, an ammoniacal malonate-malate bath, containing $MnSO_4$, was selected. Nickel was codeposited into the films in order to decrease the saturation magnetization, Ms, since low Ms is necessary to decrease the demagnetizing field. Second, effects were investigated for three factors (*i.e.*, $MnSO_4$ concentration, bath pH, and $NiSO_4$ concentration) causing the c-axis perpendicular orientation of the film properties. Optimum plating conditions for perpendicular recording media were thus determined.

Since a perpendicular magnetic recording system suitable for high density recording was proposed by the Iwasaki school (1), much effort has been spent on developing that recording system. Co-Cr film prepared by an rf sputtering was first used by Iwasaki and Ouchi (2) for high density perpendicular recording with a combination of a single-pole and a ring head (3). Sputtered alloy films of Co-Cr-Rh (4), Co-Ru (5), or Ba ferrite (6), and vacuum evaporated alloy films of Co-Cr (7) and Co-Ni-P (8) were recently investigated as perpendicular recording media. However, these films were prepared in a high vacuum environment (*i.e.*, by a PVD method). Plated magnetic films, which have several advantages, such as mass production capability, good cost performance, and production easiness on a large scale, were studied by many workers. However, no plated film for perpendicular recording has been reported as yet.

It has been pointed out (1-3) that, in order to produce a perpendicular recording medium, the perpendicularly anisotropic magnetic field, Hk, should be larger than the demagnetizing field, $Hd = 4\pi Ms$ (Ms: saturation magnetization). A Co-Cr rf sputtered film is an ideal medium satisfying these conditions with the perpendicularly oriented c-axis of its hcp structure and with a low Ms due to Cr addition. In the case of perpendicular recording media, however, a relatively thick film can be used, since the medium thickness is almost independent of its potential perpendicular recording density. The condition, $Hk > 4\pi Ms$, is not always required for perpendicular recording media, because an actual demagnetizing field is smaller than $4\pi Ms$, which is the maximum demagnetizing field for thin films. Thus, a thick plated Co alloy film, whose

* Electrochemical Society Active Member.
Key words: electroless, ferromagnetism.

c-axis of cobalt crystal is uniformly oriented normal to the substrate plane, may be useful as a perpendicular recording medium (10).

This paper reports the development of an electroless plating bath for Co alloy films. Investigations have been made on electroless plated Co alloy films with a view toward developing a perpendicular recording medium.

Experimental

Electroless plating bath preparation and plating conditions for Co alloy films.—Electroless Co-Mn-P and Co-Ni-Mn-P films were plated from an ammoniacal malonate-malate plating bath. Bath $MnSO_4$ and $NiSO_4$ components were added to make the orientation of hcp structure normal to the substrate plane and to decrease *Ms* of films, respectively. A copper sheet was used as the substrate. At the optimum plating condition region, polished Ni-P film[1] was adopted as a substrate. Cobalt alloy films were plated after activation (HS-101, Hitachi Kasei Company Limited) only in the case of Cu substrate. Such a pretreatment was not used in the case of Ni-P substrate, and the optimum plating conditions were slightly different between Cu and polished Ni-P. The plating rate was calculated from weight change of deposits and the film thickness was controlled by plating time.

Determination of structural, compositional, and magnetic properties of plated films.—X-ray diffraction patterns and rocking curves for as-plated films were measured by an x-ray diffractometer, using an Fe target (RAD-IIA, Rigaku Denki Company Limited). Compositional contents of Co, Ni, Mn, and P in plated films were determined by an atomic absorption spectroscopy for Co, Ni, and Mn and by spectrophotometry using the molybdenum blue method for P. The magnetic properties of films were measured with a sensitive vibrating sample magnetometer (VSM-3, Toei Kogyo Company Limited). The hysteresis loops were measured parallel (//) and perpendicular ($\perp$) to the film surface with 10 kOe magnetic field.

Results and Discussion

Investigation on several complexing agents for plating bath.—A perpendicular orientation of plated Co structure c-axis has been discussed by several workers (11-14), but no paper on perpendicular recording application has been reported in the field of plated magnetic films.[2] It was pointed out (9, 10) that the codeposition of W into Co alloy film makes the c-axis perpendicular to the substrate plane, and that the codeposition of Mn also makes the c-axis perpendicularity more effective and the *Ms* value for the film lower. Thus, several complexing agents for electroless Co alloy plating bath containing $MnSO_4$ were first studied, regarding the basic four factors of plating rate, c-axis orientation, bath stability, and magnetic properties. Results are shown in Table I. Bath stability was judged from decomposition occurrence and precipitation presence. In the case of one complexing agent, the films plated from malonate and succinate baths, respectively, showed perpendicular c-axis orientation, but all the factors were not satisfied. Since the bath composed of mixed malonate-malate complexing agents gave good results in the case of mixed complexing agents, the following bath conditions were studied on the basis of the malonate-malate bath. Manganese sulfate concentration has the great effect on c-axis orientation for films. Bath pH and nickel sulfate concentration also greatly affect the c-axis orientation. Therefore, the three main factors in the bath were studied under the basic bath composition and operational conditions shown in Table II.

[1] Electroless plated Ni-P sheet containing 11 w/o phosphorus was used as a nonmagnetic film. Its surface was polished to a maximum roughness $R_{max} < 0.02$ μm.

[2] In the revising process, a paper on electroplated films concerned with perpendicular magnetic recording is reported (16).

Table I. Investigation of various complexing agents

Complexing agents	Plating rate	C-axis orientation	Bath stability	Magnetic properties
Citrate	Low	In-plane	○	—
Tartrate	Low	In-plane	○	—
Malonate	Medium	In-plane or perpendicular	×	○
Succinate	Medium	In-plane or perpendicular	△	△
Malate	Medium	In-plane	○	—
Malonate + gluconic acid	Low	Perpendicular	○	△
Malonate + succinate	Medium	Perpendicular	×	○
Malonate + malate	Medium	Perpendicular	○	○

○: excellent conditions, △: medium conditions, ×: worse conditions.

Table II. Basic bath composition and conditions for Co alloy films

Chemicals	Concentration/M liter^{-1}
$NaH_2PO_2 \cdot H_2O$	0.20
$(NH_4)_2SO_4$	0.50
$CH_2(COONa)_2 \cdot H_2O$	0.50
$C_2H_3OH(COONa)_2$	0.05
$CoSO_4 \cdot 7H_2O$	0.025
$NiSO_4 \cdot 6H_2O$	0.01
$MnSO_4 \cdot 4\text{-}5H_2O$	0.04

Bath temperature: 85°C, bath pH adjusted by NH_4OH: 9.6.

Effect of manganese sulfate concentration in the bath on film properties.—Typical x-ray diffraction patterns for Co-Ni-Mn-P films, plated from baths with various $MnSO_4$ concentrations, were shown in Fig. 1, where the film thickness was adjusted to 5 μm. The plated film with no addition of $MnSO_4$ shows only the (100) plane peak for hcp cobalt crystal. The diffraction peak for the (002) plane appears with the increase in $MnSO_4$ concentration. At 0.04M $MnSO_4$, a sharp large peak appears in the (002) plane, while the peak in the (100) plane disappears. The peak in the (002) plane means perpendicular orientation of hexagonal crystal. The diffracted x-ray intensity is mainly due to the orientation degree of crystallites, because the $\Delta\theta_{50}$ value in the Co(002) plane rocking curve, as seen in Fig. 7, becomes minimum at maximum x-ray intensity in the (002) plane. Thus, the $MnSO_4$ addition into the bath makes the c-axis orientation normal to the substrate surface, and the perpendicular orientation becomes maximum at 0.04M $MnSO_4$. $MnSO_4$ caused the plating rate to decrease with the increase in $MnSO_4$ concentration (*e.g.*, 6.0 mg cm^{-2} hr^{-1} at 0.04M $MnSO_4$).

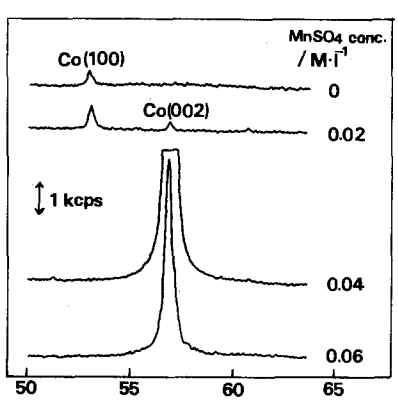

Fig. 1. X-ray diffraction patterns for films with various $MnSO_4$ concentrations using Cu substrate. Film thickness: 5 μm.

The film composition with various $MnSO_4$ concentrations was demonstrated in Fig. 2a. The Co, Ni, and P contents are almost independent of the $MnSO_4$ concentration (*i.e.*, Co $\simeq$ 70-80 w/o, Ni $\simeq$ 20-25 w/o, P $\simeq$ 3 w/o). The manganese is not mixed into the film until 0.02 $MnSO_4$. From that point, the Mn content gradually increases. The c-axis perpendicular orientation is clearly caused by the $MnSO_4$ addition into the bath, as seen in Fig. 1. However, the 0.04M $MnSO_4$ condition, which gives the highest perpendicular orientation for the hcp structure, does not necessarily correspond to that giving the maximum Mn content in the film.

Figure 3 demonstrates typical magnetic hysteresis loops under optimum condition measured in parallel (//) and perpendicular ($\perp$). The definition of an effective anisotropy magnetic field, Hk_{eff}, which represents the anisotropy magnetic field scale, estimated from the in-plane magnetization curve, is also shown in Fig. 3. The Hk_{eff} concept was proposed by the Iwasaki school. It is defined as the contact point between saturation magnetization value and the tangent line from zero point in the magnetization curve in a parallel magnetic field, as seen in Fig. 3. The $MnSO_4$ concentration effect on magnetic properties for plated films was shown in Fig. 2b and c. Two kinds of coercivity, $Hc(\perp)$ and $Hc(//)$, increase with increasing $MnSO_4$ concentration at the 0-0.04M $MnSO_4$ range. At the 0.04-0.05M $MnSO_4$ concentration range, very high maximum values of over 2 kOe for perpendicular ($\perp$) and over 1 kOe for parallel (//) coercivity were obtained. For such a high coercivity in the case of plated film, electroplated film was reported to give over 1 kOe under perpendicular orientation conditions (14). The difference between these two values also gives a maximum at 0.04-0.05M $MnSO_4$. Figure 2c demonstrates saturation magnetization, *Ms*, and effective anisotropy magnetic field, Hk_{eff}. The *Ms* value shows constant at 105-110 emu $\cdot$ g^{-1}, regardless of $MnSO_4$ concentration. The Hk_{eff} value also becomes maximum at 0.04M $MnSO_4$ concentration. The condition showing maximum Hk_{eff} and maximum $\Delta Hc = Hc(\perp)$-$Hc(//)$ coincides with that giving maximum diffracted x-ray intensity for the (002) plane, as shown in Fig. 1.

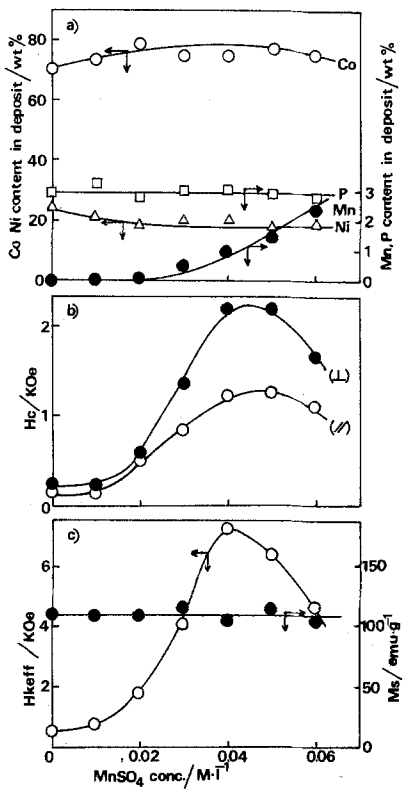

Fig. 2. $MnSO_4$ concentration effect on film composition and magnetic properties using Cu substrate. Saturation magnetization, Ms, is expressed with the value divided by film weight, emu $\cdot$ g^{-1}. Film thickness: 5 μm.

Bath pH effect on film properties.—The bath pH also greatly affects the perpendicular orientation of hcp structure in analogy with $MnSO_4$ concentration. Figure 4 represents the x-ray diffraction peak for the (002) plane on as-plated films with various bath pH values. Only the peak for the (002) plane is observed at the region between pH 9.0 and 9.8. Diffracted x-ray intensity for the (002) plane increases with the increase in pH value at the region between pH 9.0 and 9.6. It becomes maximum at pH = 9.6. The variation in x-ray intensity for the (002) plane is considered to be due to the crystallite orientation degree, similarly to the case for the $MnSO_4$ concentration effect. The bath is decomposed at the pH > 9.8 region. This might be due to the manganese hydroxide formation. At the pH < 9.0 region, no (002) plane peak appears and the inplane orientation of hexagonal crystal becomes predominant. Therefore, bath pH affects clearly the c-axis orientation, and pH = 9.6 may be the optimum condition for highly uniform orientation for the c-axis normal to the surface plane. The bath pH makes plating rate increase in the region between pH 9.0 and 9.8.

The compositional variation with various bath pH values was shown in Fig 5a. Though the Ni content becomes maximum at pH = 9.2, the Co or Ni content does not change so greatly with the bath pH factor. The phosphorus content shows a constant at the pH > 9.2 region. The manganese content is somewhat changed by pH variation and gives a maximum at pH = 9.4. However, the bath pH 9.4 does not coincide with the optimum condition for c-axis orientation.

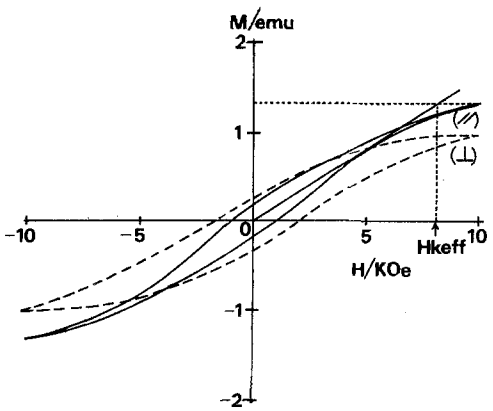

Fig. 3. Typical hysteresis loops for plated films, measured parallel (//) and perpendicular ($\perp$), using polished Ni-P substrate. Five μm film is plated under optimum conditions shown in Table II.

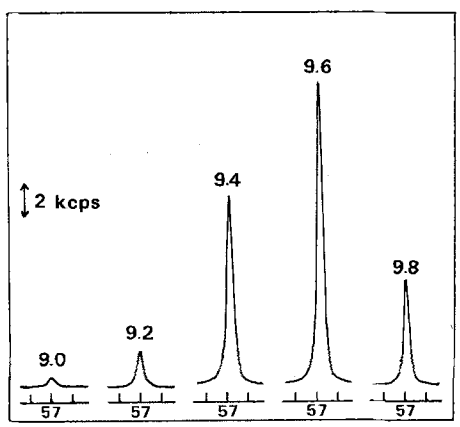

Fig. 4. X-ray diffraction patterns for films with various bath pH values using Cu substrates. Film thickness: 5 μm.

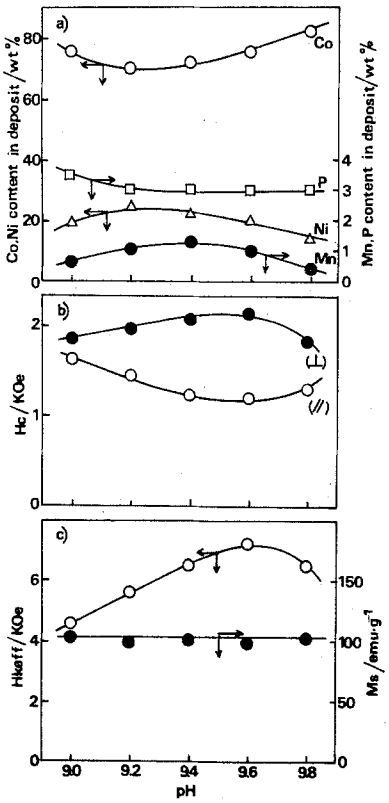

Fig. 5. Bath pH effect on film composition and magnetic properties using Cu substrate. Film thickness: 5 μm.

The bath pH effect on magnetic properties was shown in Fig. 5b and c. Coercivity $Hc(\perp)$ is always greater than that for Hc(//) in this experimental region. At pH = 9.6, the $Hc(\perp)$ and $Hc(//)$ values become maximum and minimum, respectively, and the difference between the values, ΔHc, also becomes maximum at this point. The Hk_{eff} value, which behaves in a similar manner to the $\Delta Hc = Hc(\perp) - Hc(//)$ value, also gives a maximum at pH = 9.6. The Ms value is constant with 105 emu · g^{-1}, regardless of bath pH variation. The condition giving maximum Hk_{eff} and maximum ΔHc is in good agreement with the condition showing maximum x-ray intensity for the (002) plane, as shown in Fig. 4.

Effect of nickel sulfate concentration in the bath on film properties.—Since the Ni saturation magnetization is almost equal to one-third of the Co value, Ni codeposition into the film is expected to decrease the saturation magnetization for Co alloy films. The Ms decrease for Co-Ni alloy is already shown by the Slater-Pauling curves (15). The compositional content of films with the increase in $NiSO_4$ concentration was demonstrated in Fig. 6a. Crystal states for Co alloy films change from hcp to fcc when the nickel content in the plated film becomes more than 30 w/o. The Ni or Co content increases or decreases, respectively, with the increase in $NiSO_4$ concentration. The manganese content is independent of the $NiSO_4$ concentration, while the phosphorus content becomes larger at a range greater than 0.013M $NiSO_4$. The plating rate is observed to increase with increasing $NiSO_4$ concentration.

Figures 6b and c represent the magnetic property dependence on $NiSO_4$ concentration. The coercivities for $Hc(\perp)$ and $Hc(//)$ are almost constant at the 0-0.01M $NiSO_4$ concentration range. They begin to decrease with the increase in $NiSO_4$ concentration at a more than 0.01M $NiSO_4$ range. The Ms value gradually decreases with the increase in $NiSO_4$ concentration, as expected previously. The Hk_{eff} value also starts to decrease relatively sharply from the 0.01M $NiSO_4$

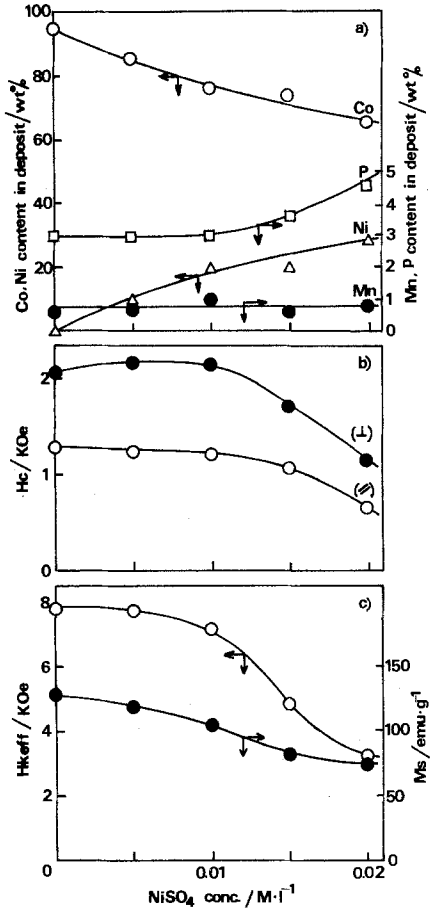

Fig. 6. $NiSO_4$ concentration effect on film composition and magnetic properties using Cu substrate. Film thickness: 5 μm.

point. Therefore, the optimum condition is considered to be 0.01M $NiSO_4$, at which the Ms value becomes somewhat lower without decreasing the Hk_{eff} value.

When the optimum plating conditions, as shown in Table II, which were determined by using Cu substrate, were applied to the polished Ni-P substrate, higher perpendicular orientation uniformity of c-axis was observed. A typical x-ray diffraction pattern for the best condition and its rocking curve for the (002) plane peak using Ni-P substrate were demonstrated in Fig. 7. In the optimum condition vicinity, the half-maximum intensity peak breadth for the rocking curve, $\Delta\theta_{50}$, became reproducible near ten degrees. The highest value, $\Delta\theta_{50}$, which was not so highly reproducible, became about six degrees.

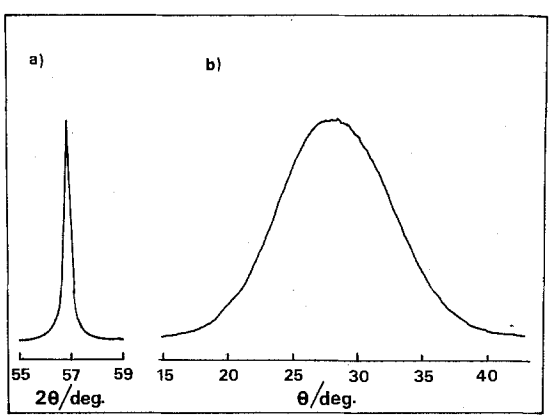

Fig. 7. X-ray diffraction pattern and rocking curve for Co(002) plane. Film was plated at optimum condition using polished Ni-P substrate. Film thickness: 5 μm.

In the present paper, the electroless ammoniacal malonate-malate plating bath was investigated for perpendicular recording media by changing three factors, manganese sulfate concentration, bath pH, and nickel sulfate concentration. Among the three factors, the manganese sulfate concentration plays the most effective role in making c-axis orientation normal to the substrate surface. The fact that manganese sulfate causes the c-axis perpendicular orientation may be concerned with the conditions for manganese complexing ions in the bath solution rather than for the Mn codeposition into the film, since the bath pH, which produces the variation in manganese complexing ion conditions, causes a large variation in perpendicular orientation of the c-axis, regardless of the same amount of codeposited Mn in films. Though the Mn codeposition into the films, of course, is considered to play an important role, the adsorption of manganese complexing ions at the interface might have a larger effect on the film crystal growth. The *Ms* decrease was performed by the Ni codeposition, but a large decrease was not established, because the increase in $NiSO_4$ concentration from the 0.01M point began to disturb the perpendicular orientation. Therefore, the study on a film which shows a lower *Ms* value should be continued. The recording and reproducing characteristics for a magnetic disk, plated from this basic electroless plating bath, will be reported in a future paper. (17).

Acknowledgments

The authors would like to thank Professor Emeritus Dr. Tadashi Yoshida, Waseda University, and Dr. Takashi Furuoya, Dr. Daisaburo Shinoda, Mr. Koichi Matsumi, and Mr. Yogi Suganuma, in the Microelectronics Research Laboratories, Nippon Electric Company, Limited, for their encouragement during the research.

Manuscript submitted May 20, 1982; revised manuscript received Nov. 12, 1982.

Any discussion of this paper will appear in a Discussion Section to be publisned in the December 1983 JOURNAL. All discussions for the December 1983 Discussion Section should be submitted by Aug. 1, 1983.

Publication costs of this article were assisted by Waseda University.

REFERENCES

1. S. Iwasaki and Y. Nakamura, *IEEE Trans. Magn.*, **mag-13,** 1272 (1977).
2. S. Iwasaki and K. Ouchi, *ibid.*, **mag-14,** 849 (1978).
3. S. Iwasaki, *ibid.*, **mag-16,** 71 (1980).
4. K. Kobayashi and G. Ishida, *J. Appl. Phys.*, **52,** 2453 (1981).
5. S. Hirono, Y. Maeda, and I. Hatakeyama, Ext. Abst. 5th Conf. on Magnetics of Magn. Soc. of Japan, p. 74 (1981).
6. M. Naoe, S. Hasunuma, Y. Hoshi, and S. Yamanaka, *IEEE Trans. Magn.*, **mag-17,** 3184 (1981).
7. R. Sugita, T. Kunieda, and F. Kobashi, *ibid.*, **mag-17,** 3172 (1981).
8. A. Otsubo, Y. Satao, and S. Shikama, IECE Tech. Group Meeting of Magn. Rec., Japan, MR81-4 (1981).
9. T. Osaka and N. Kasai, *Kinzoku Hyomen Gijutsu (J. Metal Finishing Soc. of Japan),* **32,** 309 (1981).
10. T. Osaka, F. Goto, N. Kasai, and Y. Suganuma, *Denki Kagaku (J. Electrochem. Soc. of Japan),* **49,** 792 (1981).
11. M. G. Miksic, R. Travieso, A. Arcus, and R. H. Wright, *This Journal,* **113,** 360 (1966).
12. J. R. Depew, *ibid.*, **120,** 1187 (1973).
13. M. Sato and Y. Hoshino, *Denki Kagaku,* **35,** 111 (1967).
14. J. S. Sollo and J. M. Carr, *This Journal,* **109,** 1040 (1962).
15. R. M. Bozorth, "Ferromagnetism," p. 441, D. Van Nostrand, New York (1951).
16. Tu Chen and P. Cavallotti, *Appl. Phys. Lett.,* **41,** 205 (1982).
17. T. Osaka, F. Goto, N. Kasai, I. Koiwa, and Y. Suganuma, *This Journal,* **130,** 568 (1983).

The Effect of Some Additives on Electroless Copper Deposition

Milan Paunovic* and Russ Arndt

Kollmorgen Corporation, PCK Technology Division, Melville, New York 11747

ABSTRACT

The effect of adenine, guanine, saccharin, and coumarin on electroless copper deposition has been studied by cyclic voltammetry and the weight gain method. It was found that guanine and adenine accelerate electroless copper deposition. Coumarin and saccharin have almost no effect on the deposition process. Differences in the effect of these two groups of additives have been correlated to differences in the electronic structure of molecules.

Additives present in an electroless plating solution can influence: (*i*) kinetics and mechanism of the crystal growth process, (*ii*) the bath passivation process, (*iii*) structure and morphology of the deposit, (*iv*) physical properties of metal deposit, and (*v*) purity of deposit (type and level of inclusions). The number of publications on the effect of additives on electroless copper deposition is relatively small (1-11).

This paper treats only two topics from this very complex research area. These topics are: (*i*) effect of additives on kinetics of partial processes composing electroless copper deposition and (*ii*) effect of additives on the anodic oxidation of copper in the alkaline solution. A study of effect of additives on kinetics of partial processes is important in order to understand the overall reaction of copper deposition. A study of effect of additives on the anodic oxidation of copper in the alkaline solution, in the absence of formaldehyde, is important in order to understand passivation phenomena in electroless copper deposition.

* Electrochemical Society Active Member.
Key words: adsorption, interfaces, electron, catalysis.

Experimental

Gravimetric experiments.—Experiments were carried out in a glass beaker placed in a constant temperature bath regulated at 25°C (± 0.5). Approximately 500 ml of the electroless copper solution was used with the stainless steel plate sample of 30 cm^2 area. The steel plate samples were activated in $PdCl_2$ prior to immersion into the plating solution in order to avoid effects of the variable induction time (13). During plating, argon was passed above the solution. After 30 min of deposition, the steel plate was taken out of the solution, dried, and the amount of the deposited copper was determined by weighing.

Electrochemical experiments.—The solutions were prepared with analytical grade reagents and deionized water. The electroless copper bath used for these

studies contained: 0.10M $CuSO_4$, 0.175M EDTA (ethylenediaminetetraacetic acid), 0.050M paraformaldehyde, 0.25M Na_2SO_4, and NaOH to give a pH of 12.50. Oxygen was removed by bubbling argon. Temperature was 25°C. Four additives were chosen: coumarin, saccharin, guanine, and adenine (Fig. 1). They were used in the amount of 1.5 mg/liter.

An all-glass, single compartment cell with three electrodes was used. The test electrode was a platinum wire, 0.359 cm^2 in area, and the auxiliary electrode a platinum sheet (2 cm^2 in area), both electroplated with copper. Plating was done in an acid copper solution (12) at 10 mA/cm^2. A saturated calomel electrode (SCE) was used as a reference electrode.

The voltammograms were obtained with a PAR (Princeton Applied Research, Princeton, NJ) Model 173 Potentiostat-Galvanostat and Model 175 Universal programmer. The current-potential (i-E) curves were recorded on a Houston Instruments (Austin, Texas) Model RE0074 recorder. The scan rate was 100 mV/sec.

Results

Rate of deposition determined gravimetrically.—The rates of electroless copper deposition, in the presence and the absence of additives, as determined using the weight gain method, are shown in Table I. It can be seen from this table that coumarin and saccharin do not affect the rate of copper deposition while guanine and adenine considerably increase it. In addition, saccharin and coumarin do not change the mixed potential, while adenine and guanine shift the mixed potential toward more negative values.

Cyclic voltammetry of the electroless copper bath.—Wide scan: −1.3 ↔ +0.20V vs. SCE.—The cyclic voltammogram of a copper electrode in the range from −1.3 (beginning of hydrogen evolution) to 0.20V *vs.* SCE (oxygen evolution) is shown in Fig. 2. Figure 2 shows that the cyclic voltammogram in this range has four distinct peaks, two anodic and two cathodic.

Cathodic (vs. E_{mp}) range.—The effects of additives on the cathodic peak in the range from the mixed potential, E_{mp} to 1.0V *vs.* SCE, are shown in Fig. 3. It can be seen from Fig. 3 that saccharin and coumarin do not change the current-potential relationship in this range while guanine and adenine produce a significant change. Adenine and guanine show an increase in the peak current when compared with the peak current in the absence of additives. The same additives show an increase in the rate of electroless deposition, Table I. Adenine shows a larger increase in the rate and in the peak current.

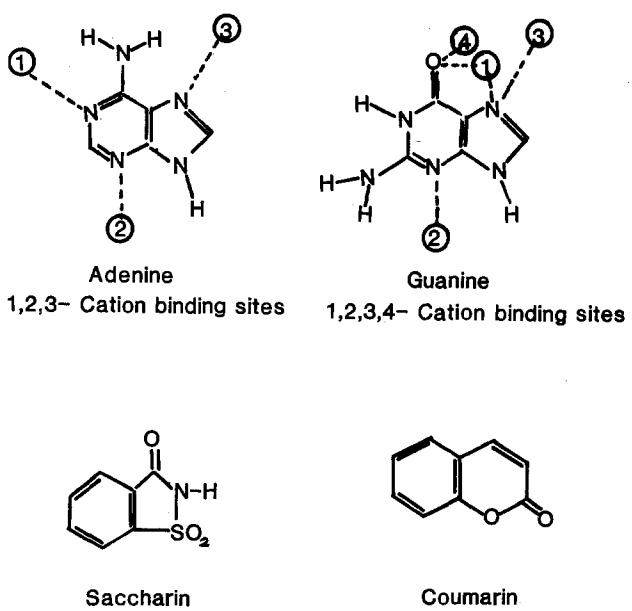

Fig. 1. Structure of additives used in this work

Table I. Effect of additives (1.5 mg/liter) on the rate of electroless copper deposition

Additive	Concentration (μM/liter)	E_{mp} (−mV *vs.* SCE)	Rate (mg/hr cm^2)
0	0.0	615	2.16
Coumarin	10.30	615	2.10
Saccharin	8.19	615	2.11
Guanine	9.93	650	2.76
Adenine	11.10	642	3.39

1 mg/hr $cm^2 \approx 1$ μm/hr

Anodic (vs. E_{mp}) range.—The effects of additives on the anodic peak in the potential range between the mixed potential E_{mp} and −0.30V *vs.* SCE are shown in Fig. 4 and 5. It can be seen that additives influence the i-E relationship for both forward and reverse directions of the sweep.

In the forward scan, between E_{mp} and −0.60V, there is an increase in current in the presence of adenine and guanine, and a decrease in current for sac-

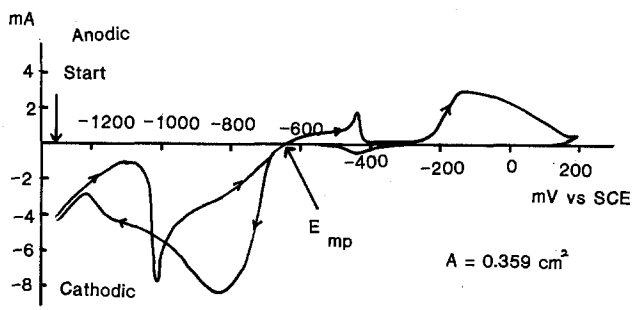

Fig. 2. Cyclic voltammogram of a copper electrode in electroless copper solution.

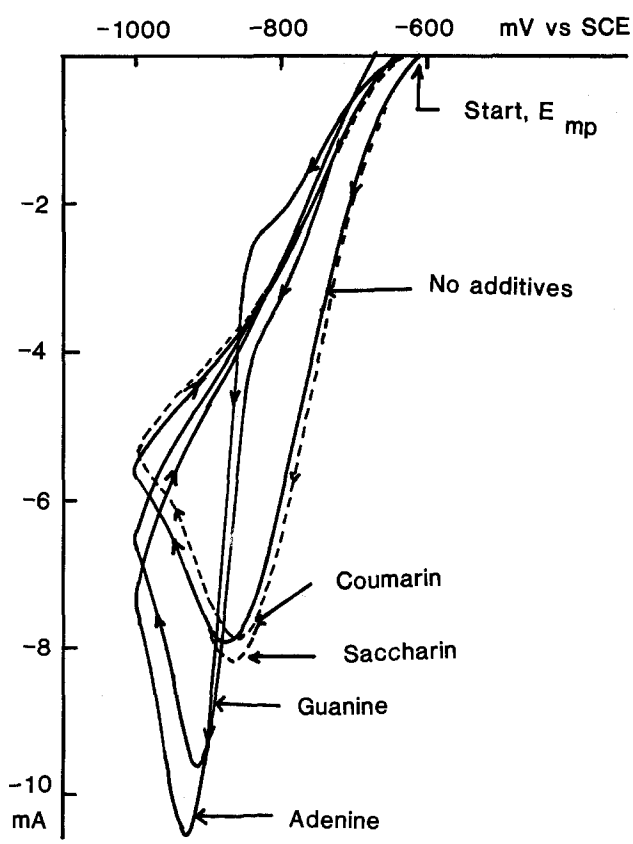

Fig. 3. Cyclic voltammograms of a copper electrode in electroless copper solution showing effects of additives on the reduction of Cu^{2+} ions.

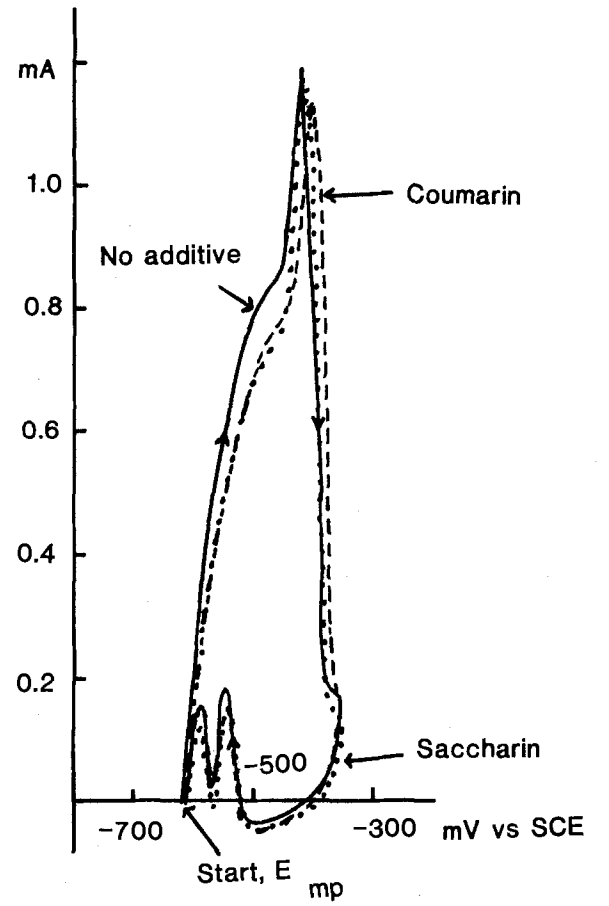

Fig. 4. Cyclic voltammograms of a copper electrode in electroless copper solution showing effects of coumarin and saccharin on the oxidation of formaldehyde.

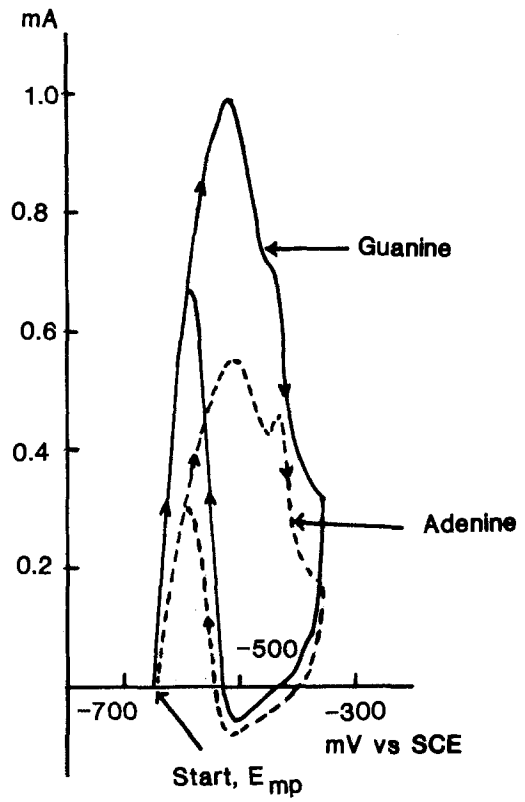

Fig. 5. Cyclic voltammograms of a copper electrode in electroless copper solution showing effects of adenine and guanine on the anodic oxidation of formaldehyde.

charin and coumarin. The increase in current (at a given potential) in the presence of adenine and guanine is related to the more negative E_{mp} in the presence of these additives. Also, the first peak potential which is associated with the oxidation of formaldehyde is more negative in the presence of guanine and adenine (−0.52V) than in the absence of additives or presence of saccharin and coumarin (−0.50V). The peak current at about −0.43V is due to the oxidation of the copper electrode. The peak current associated with the oxidation of formaldehyde is lower in the presence of saccharin, coumarin, and adenine, and higher in the presence of guanine.

All four additives are compared in Fig. 6. It can be seen that when the forward potential scan is started at −1.0V *vs.* SCE, adenine and guanine clearly show an increase in the current associated with the oxidation of formaldehyde. The peak current, at about −0.43V, associated with the oxidation of the copper electrode, is higher than that for the oxidation of formaldehyde when no additives are present, as well as when saccharin or coumarin are present (at the scan rate 100 mV/sec).

The most significant influence of additives is seen on the reverse scan. In the absence of additives as well as in the presence of coumarin and saccharin, the anodic peak due to the oxidation of formaldehyde, the reverse scan, is very small. In the presence of adenine and guanine, it is relatively large.

Effect of additives on the anodic behavior of copper in an alkaline solution.—Wide scan: −1.5 ↔ +0.20V vs. SCE.—The cyclic voltammogram for a single electrode (12) system Cu/Cu^{2+} in an alkaline solution (absence of formaldehyde) is shown in Fig. 7. A cyclic voltammogram for a copper electrode in an alkaline solution (absence of CH_2O and Cu^{2+}) is shown in Fig. 8. A comparison between Fig. 7 and 8 shows that

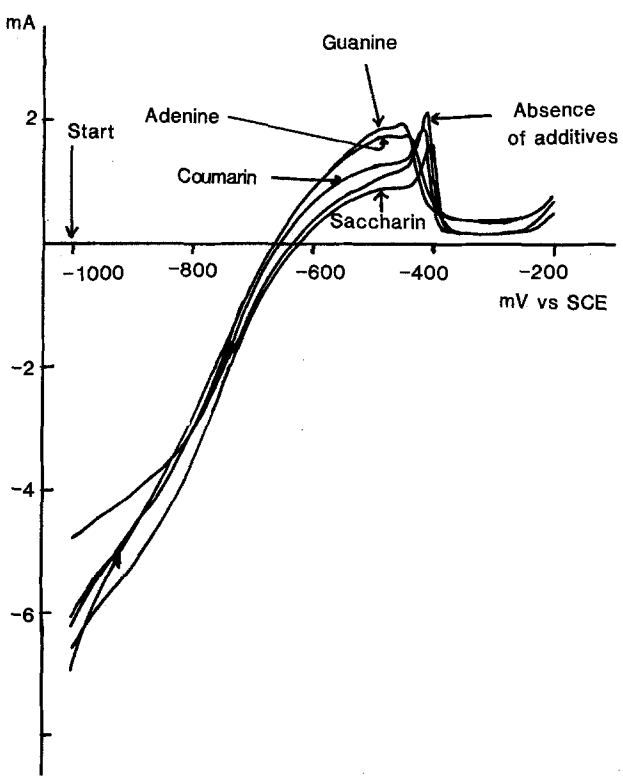

Fig. 6. Effects of additives on *i-E* relationships for a copper electrode in electroless copper solution.

the cathodic peak between −1.2 and −1.4V is due to the reduction of Cu(II)-complex ions since this peak appears only when Cu^{2+} ions are present. Two anodic peaks between −0.5 and 0.4V and two cathodic peaks between −0.3 and −0.9V are due to the oxidation and reduction of Cu electrode, respectively.

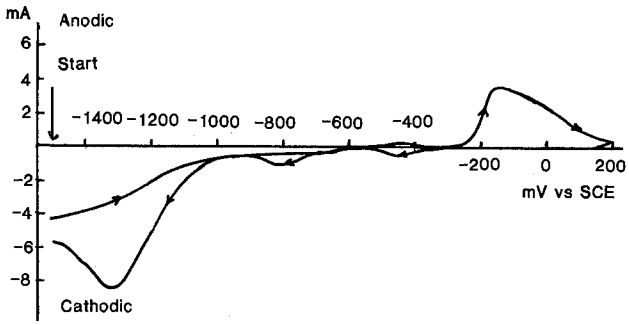

Fig. 7. Cyclic voltammogram for a copper electrode in 0.175M EDTA, 0.1M $CuSO_4$, 0.25M Na_2SO_4, and NaOH to pH 12.50. Presence of Cu^{2+} ions, absence of CH_2O.

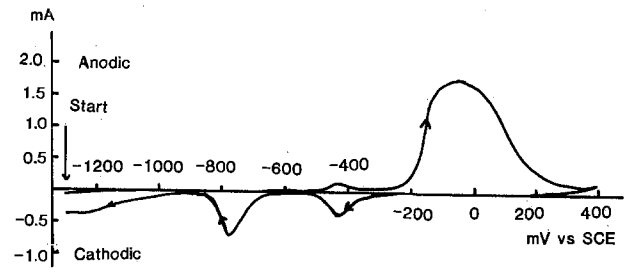

Fig. 8. Cyclic voltammogram for a copper electrode in 0.175M EDTA, 0.25M Na_2SO_4, and NaOH to pH 12.50. Absence of Cu^{2+} ions and CH_2O.

Scan between −1.0 and −0.2V.—The effects of additives on formation (−0.6 ↔ −0.3V) and reduction (−0.6 ↔ −1.0V) of the first oxide layer on the copper electrode are shown in Fig. 9 and 10. Scan reversal in this case is adjusted at the potential before formation of the upper layer of copper oxide. This range is of great importance for the interpretation of the effects of additives on bath passivation (14, 15) and copper brittleness (1, 16) associated with oxide formation.

Comparison between the detailed *i-E* profiles, shown in Fig. 9 and 10, and the wide scan *i-E* profiles shown in Fig. 7 and 8, shows one new important feature in the anodic range. This is a prewave with the peak at about −0.56V *vs.* SCE, which appears only in the absence of additives and in the presence of saccharin and coumarin (Fig. 9). The prewave is absent in the presence of guanine and adenine (Fig. 10).

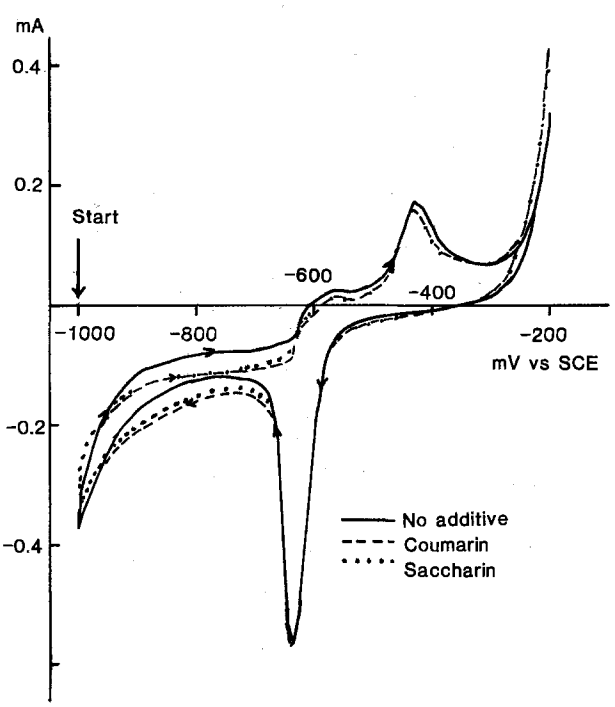

Fig. 9. Effect of coumarin and saccharin on the anodic behavior of copper in 0.175M EDTA, 0.1M $CuSO_4$, 0.25M Na_2SO_4, and NaOH to pH 12.50.

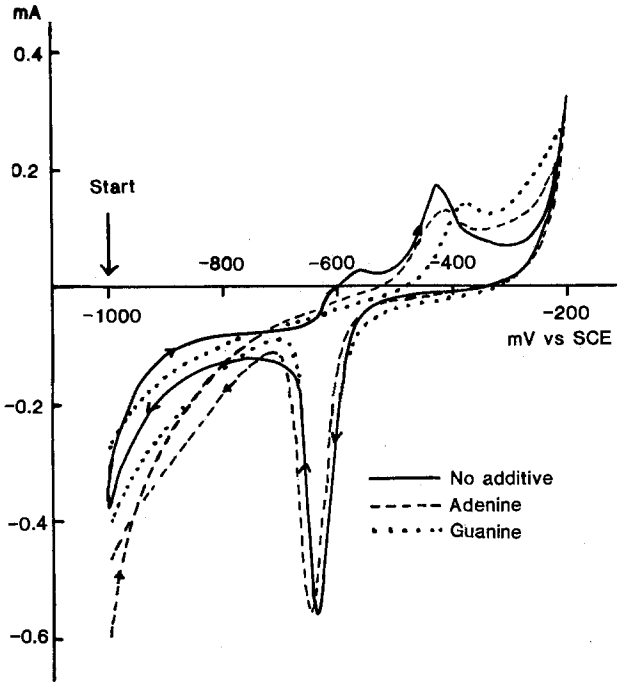

Fig. 10. Effect of adenine and guanine on the anodic behavior of copper in 0.15M EDTA, 0.1M $CuSO_4$, 0.25M Na_2SO_4, and NaOH to pH 12.50.

The reduction in the height of the peak current, in the range between −0.50 and −0.40V in Fig. 10, demonstrates that guanine and adenine suppress oxidation of copper. Saccharin and coumarin do not influence this process (Fig. 9).

Discussion

Effect of additives on the cathodic partial reaction.—The additive effect on the overall process of the electroless copper deposition is exhibited as a change in the mixed potential and the rate of deposition (Table I).

The effects of additives on the partial cathodic reaction are detected as a change of the peak current in a cyclic voltammogram (Fig. 3). Adenine and guanine show an increase in the deposition rate and in the peak current; adenine shows a larger increase in both. Saccharin and coumarin do not affect the rate of electroless copper deposition or the peak current associated with the cathodic partial reaction. Thus, additives used in this work belong to two different groups, as shown by their effects on the overall process and the partial cathodic process. The first group of additives, guanine and adenine, exhibits the accelerating effect, while the second group, saccharin and coumarin, does not.

A comparison of the molecular structures of the mentioned two groups of additives will be now made in order to gain some insight into the mechanism of the effects discussed above. All additives used in this work are fused rings and heterocyclic conjugated systems. Guanine and adenine are derivatives of purine and are made up of two heterocyclic rings: a pyrimidine and an imidazole ring (Fig. 1). Saccharin and coumarin are made up of one homocyclic ring, benzene ring, and one heterocyclic ring (Fig. 1). The heterocyclic ring contained in the coumarin molecule is pyran, and that in saccharin is isothiazol. These heterocyclic conjugated systems have multiple π bonds and binding sites for cations (17). These additives

can be adsorbed at the metallic substrate surfaces in a multiplicity of orientations (18-20) and thus introduce new electrostatic forces into the double layer of the copper-solution interphase (21-24). They can also form molecule-electrode charge-transfer complexes (21).

A basic difference between these two groups of additives is in the heteroatoms involved. Molecules of additives which show the accelerating effect have five nitrogen atoms, while those which do not show this effect have only one (saccharin) or no (coumarin) nitrogen atoms.

The nitrogen atoms in the accelerator molecules are bonded in two different manners, possessing unpaired electrons in different orbitals. In the first case discussed below (type 1 nitrogen) the nitrogen atoms contribute one unpaired p electron to the π bonding structure of the molecule, while in the second case (type 2 nitrogen), a lone pair of p electrons is donated to the molecular π bonding structure by each nitrogen atom. Type 1 nitrogen is sp^2 hybridized, and bonded to two other atoms (pyridine like), becoming a member of the conjugated ring. The nonhybridized nitrogen p_z orbital, which is free to π bind into the conjugated system, contains one nitrogen electron. Type 2 nitrogen is also sp^2 hybridized, but bonded to three other atoms (aniline like), and is not a member of, but a substituent on, the conjugated ring. The nonhybridized nitrogen p_z orbital, which contributes to the π bonding structure of the ring, contains two nitrogen electrons.

Guanine has two type 1 and three type 2 nitrogen atoms. These atoms contribute a total of eight π electrons to the π system of the ring. Adenine has three type 1 and two type 2 nitrogen atoms, which contribute a total of seven π electrons. On the basis of the above quantum mechanical analysis, we believe that major factors which are responsible for the accelerating effect of guanine and adenine are: (*i*) the charge density of the π electron system (25-27), and (*ii*) the exchange of electrons between electrode, π-adsorbed molecule, and the complexed Cu(II) ions in the solution (21).

Effect of additives on the anodic partial reaction.—It was shown that the effect of additives on the anodic oxidation of formaldehyde is exhibited in two ways. First, there is a change in the magnitude of the anodic peak due to the oxidation of formaldehyde in the forward direction scan (Fig. 6), then secondly, there is a change in the magnitude and the position (in the potential coordinate) of this peak in the reverse direction scan (Fig. 4, 5).

The accelerating effect of guanine and adenine could be explained, until additional experimental data are available, on the basis of the electrostatic interactions in the metal-solution interphase (22-24). New electrostatic forces can result in the decrease of adsorption of products or intermediates (*e.g.*, intermediates in the oxidation of formaldehyde) in the overall reaction of deposition. This decrease in adsorption of intermediates or products is equivalent to an increase in the available surface area. An increase in the surface area results in an increased peak current, transition time [Fig. 13 in Ref. (7)], and the rate of copper deposition. In this respect the accelerating effect of adenine and guanine is probably similar to that produced by other additives in other electrochemical reactions (22-24).

The very low anodic current for the oxidation of formaldehyde in the reverse scan, in the presence of saccharin and coumarin, indicates strong inhibition of formaldehyde oxidation. This inhibition is caused by the oxide formed at the electrode in the forward direction (peak at about −0.43V *vs.* SCE). In the presence of guanine and adenine relatively high anodic current for the oxidation of formaldehyde is observed in the reverse scan. This indicates less oxide formation and less electrode passivation in the forward scan. The ability of guanine and adenine to suppress oxide formation is of importance when passivation of electroless baths is a possibility.

Effect of additives on the anodic behavior of copper in the alkaline solution.—Anodic peaks in Fig. 7 are interpreted as follows (28-30): (*i*) prewave, the peak at −0.56V, is due to the free dissolution of copper to form Cu^+ and $Cu(OH)_n^{1-n}$; (*ii*) peak at −0.43V is due to the inhibited dissolution of Cu with formation of Cu_2O layer film; (*iii*) peak in the range between −0.15 and +0.15V is due to the oxidation of Cu_2O into CuO_2^{2-} and CuO.

The cathodic peak in the range from −0.40 to −0.60V is due to the reduction of CuO in the outer substrate layer into Cu_2O. The peak in the range from −0.70 to −0.90V is due to the reduction of Cu_2O and CuO, unreduced in the first range, into Cu (28-30).

Since guanine and adenine suppress the free and uninhibited dissolution of copper, they can prevent passivation of the copper substrate. It is known that passivation is accomplished by a shift of the mixed potential into the region where copper can anodically passivate (14). Formation of Cu^+ ions by the free oxidation of copper is related to the bulk instability of the electroless copper bath (31). Some have related the free oxidation of Cu^+ to the brittleness of the electroless copper deposit (1, 16).

Conclusions

Additives studied in this work, coumarin, saccharin, adenine, and guanine form two different groups as shown by their effects on the electroless deposition of copper. Adenine and guanine act as accelerators for partial reactions and the overall reaction of electroless copper deposition. They also suppress oxidation and passivation of metallic copper in an alkaline solution. On the other hand, coumarin and saccharin have almost no effect on the above processes.

Differences in the function of these two groups of additives are probably basically due to differences in the number of nitrogen atoms and the resulting differences in π electron density, loop current, and the exchange of electrons between electrode, π adsorbed molecule, and complexed Cu(II) ions in the solution.

Acknowledgment

The authors gratefully thank Dr. John Rie, PCK Technology, for valuable comments during the preparation of the manuscript.

Manuscript submitted Aug. 31, 1982; revised manuscript received Nov. 5, 1982.

Any discussion of this paper will appear in a Discussion Section to be published in the December 1983 JOURNAL. All discussions for the December 1983 Discussion Section should be submitted by Aug. 1, 1983.

Publication costs of this article were assisted by Kollmorgen Corporation.

REFERENCES

1. L. Schoenberg, *This Journal*, **119**, 1491 (1972).
2. H. Hirohata, M. Oita, and K. Honjo, *J. Met. Finish. Soc. Jpn.*, **21**, 485 (1970); **23**, 465 (1972).
3. T. L. Aycock, N. C. Huie, and G. Krauss, *Metall. Trans.*, **5**, 1215 (1974).
4. M. Paunovic, *This Journal*, **127**, 365 (1980).
5. M. Paunovic and C. Stack, in "Electrocrystallization," R. Weil and R. G. Barradas, Editors, p. 205, The Electrochemical Society Softbound Proceedings Series, Pennington, NJ (1981).
6. J. Duffy, M.S. Thesis, Saint Johns University, Jamaica, NY (1981).
7. M. Paunovic, C. Stack, J. Duffy, and R. Arndt, AES 1st Electroless Plating Symposium, March (1982).
8. M. Paunovic and R. Arndt, Abstract 321, p. 784, The Electrochemical Society Extended Abstracts, Denver, CO, Oct. 11-16, 1981.

9. A. Molenaar, J. Meerakker, and J. Boven, *Plating*, **61**, 649 (1974).
10. M. Saito and H. Houma, *Met. Surf. Technol. Jpn.*, **29**, 88 (1978); **29**, 190 (1978).
11. F. Nuzzi, *Plating and Surface Finishing*, In press.
12. M. Paunovic, *Plating*, **55**, 1161 (1968).
13. M. Paunovic, *This Journal*, **124**, 349 (1977).
14. Y. Okinaka, Abstract 269, p. 692, The Electrochemical Society Extended Abstracts, Las Vegas, NV, Oct. 17-22, 1976.
15. R. E. Acosta and L. T. Romankiw, Abstract 277, p. 736, The Electrochemical Society Extended Abstracts, Atlanta, GA Oct. 9-14, 1977.
16. H. Hirohata, M. Oita, and K. Honjo, *J. Met. Finish. Soc. Jpn.*, **21**, 550 (1970).
17. A. Pullman and A. M. Armruster, *Theor. Chim. Acta*, **44-46**, 249 (1977).
18. S. Sathyanarayan, *J. Electroanal. Chem.*, **50**, 195 (1974).
19. G. Dryhurst, "Electrochemistry of Biological Molecules," p. 275, Academic Press, New York (1979).
20. E. Dutkiewietz and A. Puacz, *J. Electroanal. Chem.*, **100**, 947 (1979).
21. A. B. Ershler, A. M. Foontikov, and I. M. Livinson, *ibid.*, **136**, 83 (1982).
22. H. Fischer, *ibid.*, **62**, 163 (1975).
23. H. Angerstein-Kozlowska, B. MacDougall, and B. E. Conway, *ibid.*, **39**, 287 (1972).
24. A. M. Baruzzi, V. Solis, and M. C. Giordano, *Electrochim. Acta*, **27**, 273 (1982).
25. M. J. S. Dewar and R. C. Dougherty, "The PMO Theory of Organic Chemistry," p. 109, Plenum Press, New York (1975).
26. A. Streitwieser, "Molecular Orbital Theory for Organic Chemists," p. 27, John Wiley & Sons, Inc., New York (1967).
27. R. E. Clapp, *Theor. Chim. Acta*, **61**, 105 (1982).
28. S. Fletcher, R. G. Barradas, and J. D. Porter, *This Journal*, **125**, 1960 (1978).
29. B. Miller, *ibid.*, **116**, 1675 (1969).
30. D. D. MacDonald, *ibid.*, **121**, 651 (1974).
31. R. M. Lukes, *Plating*, **51**, 1066 (1964).

A Modified Constriction Model for the Resistivity of a Bubble Curtain on a Gas Evolving Electrode

Oscar Lanzi and Robert F. Savinell*

Department of Chemical Engineering, The University of Akron, Akron, Ohio 44325

ABSTRACT

At gas evolving electrodes, the bubble curtain at the electrode surface contributes to the voltaic inefficiencies of the electrolyzer. Consequently, the structure of the bubble curtain and its effect on electrolyte resistivity is of practical importance. In order to predict the resistance of the bubble curtain several models have been suggested in the literature. Three-dimensional models provide an adequate prediction of the resistance of dilute bubble curtains with monolayer gas voidages less than 0.55. This paper proposes a two-dimensional constriction model of a dense bubble curtain which is modified to account for a three-dimensional dispersed phase within the monolayer. The resulting mathematical expression behaves properly in the limits of voidage and its prediction agrees well with the limited available data.

In chlor-alkali cells, water electrolysis, and other processes in which gases are produced in electrolytic cells, the bubbles that form as a result give rise to important engineering problems because they increase the total cell voltage. Factors contributing to this increase in voltage include: (*i*) At the electrode surface the bubbles are closely packed in a thin layer or "bubble curtain." The bubbles effectively screen the electrode, raise the effective current density, and thus increase the overpotential on the electrode. (*ii*) The crowded bubbles offer a high ohmic resistance at the electrode surface by severely restricting the current flow. (*iii*) Bubbles disperse into the bulk electrolyte and hence increase its resistance. If the bubbles accumulate, they greatly increase this resistance, so in practice they must be swept out by fluid flow.

Figure 1 depicts the distribution of bubbles in a cell with flat plate electrodes. Note that although the bubble curtain may be thin, it may increase the ohmic potential drop of the cell by several percent (1). This effect, *i.e.*, (*ii*) above, is the focus of this work. A model is proposed to relate the resistivity of the bubble curtain, relative to the resistivity of bubble-free electrolyte, to gas void fraction and contact angle.

Previous Work

The structure and behavior of the bubble curtain has been studied previously, particularly in connection with mass transfer studies (2-4), of which Vogt (5) gives an excellent summary. Landolt *et al.* (6) obtained an empirical bubble size distribution in turbulently flowing electrolyte and noted a wide range of bubble sizes.

Recently, Hine *et al.* (7) suggested that a bubble curtain, though it may be thin, can effect the total cell voltage. Vogt (1) derived a model for the overall ohmic potential drop in a gas evolving cell with vertical electrodes; he took into account the effect of the bubble curtain but did not examine it in detail. He did, however, estimate the thickness and relative resistivity of the curtain. DeJonge *et al.* (8) studied bubble effects in a cell, with a disk electrode and analyzed bubble curtain behavior. Sides and Tobias (9, 10) examined

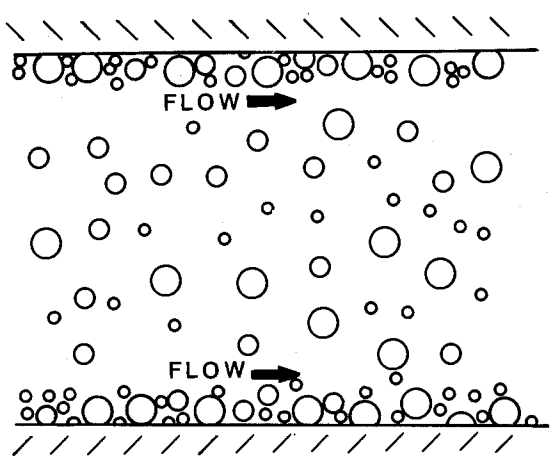

Fig. 1. Section of an electrolytic cell with gas evolving electrodes. The bubbles at the electrode surfaces are closely packed while those in the rest of the solution are more sparsely dispersed.

* Electrochemical Society Active Member.
Key words: transport, phases, cell, ohmic resistivity.

the effect of the bubble curtain and derived two models. These are the tangent-sphere model (9), in which the bubbles are taken to be noninteracting tangent spheres, and the constriction model (10), in which the bubbles are assumed to interact strongly, and current is uniformly distributed at any cross section parallel to the electrode, except for the area occupied by the bubbles (see Fig. 2). In the constriction model, the resistance was calculated for the simple case of monosized tangent spheres in a hexagonal array. Equation [1] describes the differential resistance but ignores the flow of current parallel to the electrode (which is caused by the need for current to get around the bubbles)

$$dR = dR_1 = dy/\kappa_1 \, (A_H - A_{B1}) \qquad [1]$$

Integration and division by $R_L = 2r_L/\kappa_L S$ gives

$$K = \frac{2}{\sqrt{\psi}} \tan^{-1} \frac{3\phi}{\sqrt{\psi}} \qquad [2]$$

where

$$\psi = 6\phi - 9\phi^2 \qquad [3]$$

Equations [2] and [3] represent the constriction model of Sides (10). Since this expression only applies in the monolayer, the maximum value of ϕ is $\pi/3\sqrt{3}$, *i.e.*, for hexagonally close-packed spheres. Although the original derivation was based on a hexagonal unit cell, the same result can be derived for a random distribution. We directed our attention to improving the predictions of the constriction model.

Theory

Equation [2], in itself, is not entirely satisfactory for a bubble curtain. It does not take into account the deformation of the current lines and hence the effective lengthening of these lines, or the fact that the current is not uniformly distributed over the cross section; these effects appear in the tangent-sphere model (9). The equation also assumes monosized spheres, which is a poor approximation.

However the constriction model is realistic enough so that the development may be extended. Experimental data of Glas and Westwater (11) suggest that the contact angle may be large enough to be significant, so the monosized spheres may be assumed to have a contact angle of θ with the electrode. It has been suggested (1, 2) that the large bubbles may entrap smaller bubbles, accounting for the multiple sizes of the bubbles in the curtain; thus the smaller bubbles may be considered as a three-dimensional dispersion in the spaces between the larger bubbles. A similar approach was taken by Meredith and Tobias (12) in developing their model for three-dimensional dispersions.

These modifications lead to the bubble curtain structure depicted in Fig. 3; note the greater complexity introduced by the modifications. The mathematics which describe the modified constriction model are now presented.

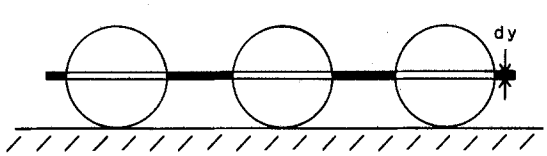

Fig. 2. The Sides' constriction model (10) of a densely packed bubble curtain. The current is uniformly distributed over the darkened area.

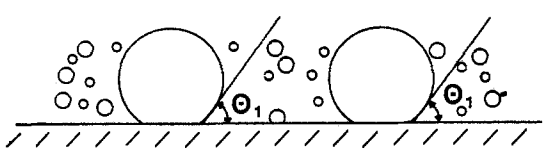

Fig. 3. The structure of the bubble curtain according to the modified constriction model.

The dispersion of small bubbles may be regarded as a continuum with conductivity κ_2. The resistance of the bubble curtain may be taken as

$$R = \int_{y=0}^{y=\delta} dR = \int_0^\delta \frac{dy}{\kappa_2 (S - N_1 A_{B1})} \qquad [4]$$

If the bubbles were absent the resistance would be

$$R_L = \frac{\delta}{\kappa_L S} \qquad [5]$$

From Eq. [4] and Eq. [5] we have

$$K = \frac{R}{R_L} = \left[\frac{S}{\delta} \int_0^\delta \frac{dy}{S - N_1 A_{B1}} \right] \left[\frac{\kappa_L}{\kappa_2} \right] = K_1 K_2 \qquad [6]$$

where

$$K_1 = \frac{S}{\delta} \int_0^\delta \frac{dy}{S - N_1 A_{B1}} \qquad [7a]$$

$\equiv$ resistivity factor due to monolayer and

$$K_2 = \frac{\kappa_L}{\kappa_2} \qquad [7b]$$

$\equiv$ resistivity factor due to the dispersion.

Substituting, $A_{B1} = \Pi(r_1^2 - (y - r_1 + \delta)^2)$ and $\delta = r_1(1 + \cos\theta_1)$ into Eq. [7a] and integrating gives

$$K_1 = \frac{S}{N_1 \Pi \delta} \cdot \frac{1}{\sqrt{S/N_1\Pi - r_1^2}} \left[\tan^{-1} \frac{r_1 \cos\theta_1}{\sqrt{S/N_1\pi - r_1^2}} + \tan^{-1} \frac{r_1}{\sqrt{S/N_1\pi - r_1^2}} \right] \qquad [8]$$

The volume fraction of gas in the monolayer is

$$\phi_1 = \frac{2N_1\pi r_1^2}{3S} (1 + \cos\theta_1) \left(1 - \frac{1}{2} \cos\theta_1 \right) \qquad [9]$$

which may be substituted into Eq. [8] to give

$$K_1 = \frac{2 - \cos\theta_1}{\sqrt{\psi_1}} \left[\tan^{-1} \frac{3\phi_1 \cos\theta_1}{\sqrt{\psi_1}} + \tan^{-1} \frac{3\phi_1}{\sqrt{\psi_1}} \right] \qquad [10]$$

where

$$\psi_1 = 6\phi_1(1 + \cos\theta_1) \left(1 - \frac{1}{2} \cos\theta_1 \right) - 9\phi_1^2 \qquad [11]$$

Equation [7b] may be expressed in terms of the dispersion void fraction ϕ_2

$$\phi_2 = \frac{\text{volume of bubbles in dispersion}}{\text{volume of curtain} - \text{volume of monolayer bubbles}}$$

Sides (10) recommends an equation given by Prager (13) for diffusion in a suspension of solid spheres in liquids, which may be considered analogous to conduction in a three-dimensional bubble dispersion and is written as

$$K_2 = 1/([1 - \phi_2]\,[1 - \phi_2/2]) \qquad [12]$$

This relation agrees quite well with data on dispersions (10). Combining Eq. [10], [12], and [6] gives our final expression

$$K = \left\{ \frac{2 - \cos\phi_1}{\sqrt{\psi_1}} \left[\tan^{-1} \frac{3\phi_1 \cos\theta_1}{\sqrt{\psi_1}} + \tan^{-1} \frac{3\phi_1}{\sqrt{\psi_1}} \right] \right\} \times \left\{ \frac{1}{(1 - \phi_2)(1 - \phi_2/2)} \right\} \qquad [13]$$

$$\psi_1 = 6\phi_1(1 + \cos\theta_1) \left(1 - \frac{1}{2} \cos\theta_1 \right) - 9\phi_1^2 \qquad [11]$$

where Eq. [11] is rewritten for completeness.

Discussion

Equations [13] and [11] represent the modification of the constriction model. This model introduces contact angle as a parameter in K_1. Table I is given to indicate the effect of contact angle on K_1. Note that the effect is secondary, which is fortunate since θ_1 is sensitive to surface properties of the electrode, bubble size, etc., and hence difficult to predict. Although contact angles do vary, in practice an average contact angle parameter θ_1, would be obtained through experimental measurement of monolayer voidage and surface coverage. The average contact angle could then be calculated by applying Eq. [9] with the experimentally measured monolayer surface coverage used instead on the quantity $N_1\pi r_1^2/S$. The modified constriction model introduces two voidage parameters. In practice, independent measurement of these two parameters may be accomplished by photographic techniques. A relationship between the two voidages, such as the one assumed by Meredith and Tobias (12), may exist.

Sides (10) experimented with hexagonal arrays of dielectric spheres placed tangent to an electrode. He used both monosized and two-sized distributions and obtained the experimental data in Table II. Also given in the table are the theoretical predicted values based on the original and modified constriction models, the Prager equation, and the Maxwell equation (14)

$$K = (1 + \phi/2)/(1 - \phi) \qquad [14]$$

This equation, a well-known three-dimensional model, fits the data remarkably well when $\phi_1 < 0.5$.

Table I. Effect of contact angle on monolayer resistivity, K_1

ϕ_1	$\theta_1 = 0°$	$\theta_1 = 22.5°$	$\theta_1 = 45°$	$\theta_1 = 67.5°$	$\theta_1 = 90°$
0.30	1.48	1.47	1.46	1.46	1.48
0.35	1.62	1.61	1.59	1.59	1.62
0.40	1.81	1.78	1.75	1.76	1.81
0.45	2.06	2.01	1.95	1.97	2.06
0.50	2.42	2.32	2.22	2.25	2.42
0.55	3.00	2.81	2.60	2.64	3.00
0.60	4.16	3.66	3.18	3.24	4.16
0.65	—	—	4.23	4.30	—
hcp*	4.34	4.46	4.85	5.31	4.34

* At hcp

$$\theta_1 = \frac{\pi}{3\sqrt{3}}(1 + \cos\theta_1)\left(1 - \frac{1}{2}\cos\theta_1\right)$$

The hcp value of θ_1 ranges from 0.6046 at $\theta_1 = 0°$ and 90° to 0.6802 at $\theta_1 = 60°$.

Table II. Comparison of original and modified constriction models, Maxwell's equation and Prager's equation with data from Ref. (10)

			Values of K for $\theta_1 = 0°$				
ϕ_1	ϕ_2	ϕ	Experimental	Constriction model	Modified constriction model	Maxwell equation	Prager equation
0.6046	0.0000	0.6046	4.640	4.339	4.339	3.294	3.625
0.6046	0.0478	0.6235	4.817	5.338	4.668	3.484	3.859
0.6046	0.0934	0.6415	5.176	7.216	5.020	3.684	4.107
0.5457	0.0000	0.5457	3.129	2.933	2.933	2.802	3.027
0.5457	0.0438	0.5656	3.258	3.264	3.136	2.953	3.210
0.5457	0.0856	0.5845	3.516	3.689	3.351	3.111	3.400
0.4897	0.0000	0.4897	2.453	2.332	2.332	2.439	2.595
0.4897	0.0411	0.5107	2.618	2.518	2.482	2.565	2.745
0.4897	0.0803	0.5307	2.791	2.738	2.641	2.696	2.900
0.4368	0.0000	0.4368	2.124	1.985	1.985	2.163	2.272
0.4368	0.0395	0.4591	2.223	2.113	2.108	2.273	2.400
0.4368	0.0771	0.4802	2.388	2.258	2.237	2.386	2.532
0.4368	0.1332	0.5118	2.806	2.528	2.453	2.572	2.753
0.2963	0.0000	0.2963	1.565	1.468	1.468	1.632	1.668
0.2963	0.0383	0.3232	1.660	1.541	1.556	1.717	1.762
0.2963	0.0749	0.3490	1.759	1.620	1.649	1.804	1.861
0.2963	0.1294	0.3874	1.971	1.746	1.803	1.948	2.025
0.1999	0.0000	0.1999	1.333	1.264	1.264	1.375	1.389
0.1999	0.0411	0.2327	1.423	1.326	1.347	1.455	1.475
0.1999	0.0802	0.2641	1.515	1.392	1.435	1.539	1.566
0.1999	0.1386	0.3108	1.675	1.507	1.578	1.676	1.718

The Maxwell equation predicts the data best in this voidage range because it underestimates the resistivity of a three-dimensional dispersion. Consequently in effect it corrects for the lower resistance offered by surface bubbles.[1]

At a monolayer voidage of ~0.55 the Prager equation predicts a resistivity of the bubble curtain which is about the same as predicted by the modified constriction model. This is shown in Fig. 4 as well as in Table II. However, at larger monolayer voidages the Prager equation predicts much lower resistivities because it does not account for a constriction effect. Also, at smaller monolayer voidages (< 0.5) the Prager equation predicts larger resistivities because it does not account for the lower resistance offered by a bubble tangent to a surface, as opposed to being in the bulk solution.

When $\phi_1 > 0.55$, the constriction and modified constriction models are needed because in this case the larger (monolayer) bubbles form a distinct layer on the electrode. Figure 4 graphically displays the results for one value of ϕ_1 in this range, *i.e.*, $\phi_1 = 0.6046$. Clearly the constriction model predicts a much too strong variation of K with ϕ_2. A major shortcoming of this model is that it fails to distinguish between monolayer and dispersion bubbles. It therefore fails when ϕ approaches or exceeds the value corresponding to monolayer close packing. For example, as ϕ approaches 2/3 the value of K predicted by the constriction model goes to infinity. In the modified constriction model K also approaches infinity as ϕ_1 approaches 2/3 for tangent spheres. In fact, for tangent hexagonally close-packed spheres in a monolayer, the limit on the monolayer voidage is $\pi/3\sqrt{3}$. However, in the modified constriction model, ϕ_2 is unrestricted and consequently ϕ can approach unity. Furthermore, the modified constriction model predicts K to approach infinity as ϕ approaches unity. This model generally underestimates the data by roughly 5%. This result is most likely caused by the fact that K_1 is underestimated by the theory, which does not account for the component of current flow parallel to the electrode or the nonuniformity of current distribution in any cross section parallel to the electrode. Another approximation in the modified model is that the dispersion may be treated as a continuum and therefore acts independently of the monolayer bubbles.

The discussion presented here is subject to the limitations of the experimental data. Specifically, the following should be noted: (*i*) There are only 21 data points in all. Of these only three are in the voidage ranges $\phi_1 > 0.55$, where three-dimensional equations fail to predict bubble layer conductivity. (*ii*) The experimental data are all taken with $\phi_2 < 0.14$; and for $\phi_1 > 0.5$ all the experimental data are taken with $\phi_2 < 0.10$. As a consequence the experimental data do not represent situations in which the dispersion is crowded with small bubbles. It is, however, apparent that the modified constriction model best correlates the data in the high voidage range. It may be considered suitable for extrapolation until more experimental data are obtained. (*iii*) Perhaps most important, the bubbles in the experiment were represented as dielectric spheres placed tangent to an electrode. Therefore, the effect of contact angle was not experimentally investigated, so that the theoretical dependence of K on θ_1 could not be analyzed.

Conclusions

The following conclusions may be made from this study: (*i*) Conductivity equations for three-dimensional dispersions are best for predicting the relative resistivity of a bubble curtain when the monolayer voidage is less than 0.55. (*ii*) When the monolayer

[1] The authors appreciate a reviewer's comment which pointed this fact out to us.

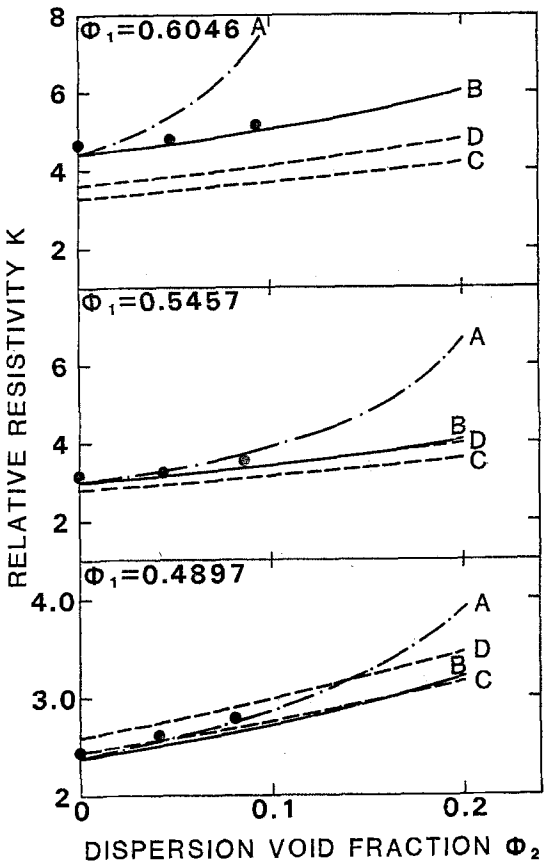

Fig. 4. Comparison of experimental data from Ref. (10) (closed circles) with theoretical predictions of bubble curtain resistivity at three monolayer voidages: Curves A—constriction model, curves B—modified constriction model, curves C—Maxwell equation, curves D—Prager equation.

voidage exceeds 0.55 the modified constriction model provides better results than the constriction model by distinguishing between monolayer and dispersion bubbles. The presence of a distinct monolayer in this voidage range is significant and causes three-dimensional equations to fail. (*iii*) Nothing definite can be said about contact angle effects due to the lack of experimental data, but the theory suggests this to be of secondary importance. Void fraction is the dominant variable. It may be worthwhile to verify this experimentally.

Acknowledgment

The authors are grateful for financial support for this work provided by The University of Akron Faculty Research (Projects) Committee.

Manuscript submitted Aug. 19, 1982; revised manuscript received *ca.* Nov. 10, 1982.

Any discussion of this paper will appear in a Discussion Section to be published in the December 1983 JOURNAL. All discussions for the December 1983 Discussion Section should be submitted by Aug. 1, 1983.

LIST OF SYMBOLS

A_{B1}	cross-sectional area of monolayer bubble
A_H	area of hexagonal unit cell
K	relative resistivity
N	number of bubbles on electrode surface
r_1	bubble radius in monolayer
R	resistance
S	total area of electrode surface
y	coordinate direction normal to electrode

Greek

δ	thickness of bubble curtain
κ	conductivity
θ	contact angle
ϕ	voidage; volume fraction of gas
ψ, ψ_1	parameter in Eq. [3] and [11]

Subscripts

L	bubble-free electrolyte
1	including monolayer only
2	including dispersion only
none	including all bubbles in curtain

REFERENCES

1. H. Vogt, *Electrochim. Acta*, **26**, 1311 (1981).
2. L. J. J. Janssen and S. J. D. Van Stralen, *ibid.*, **26**, 1011 (1981).
3. L. J. J. Janssen and E. Barendvecht, *ibid.*, **24**, 693 (1979).
4. L. J. J. Janssen, *ibid.*, **23**, 81 (1978).
5. H. Vogt, in "A Comprehensive Treatise on Electrochemistry," Vol. 6, E. Yeager, J. O'M. Bockris, B. Conway and S. Surangapai, Editors, Plenum, New York (1981).
6. D. Landolt, R. Acosta, R. H. Muller, and C. W. Tobias, *This Journal*, **117**, 839 (1970).
7. F. Hine and K. Murakami, *ibid.*, **127**, 292 (1980).
8. R. M. DeJonge, E. Barendrecht, L. J. J. Janssen, and S. J. D. Van Stralen, *Adv. Hydrogen Energy*, **2**(1), 195 (1981).
9. P. J. Sides and C. W. Tobias, *This Journal*, **127**, 288 (1980).
10. P. J. Sides, Ph.D. Thesis, University of California at Berkeley, Berkeley, CA (1981).
11. J. P. Glas and J. W. Westwater, *Int. J. Heat Mass Transfer*, **7**, 1427 (1964).
12. R. E. Meredith and C. W. Tobias, *This Journal*, **108**, 286 (1961).
13. S. Prager, *Physica*, **29**, 129 (1963).
14. J. C. Maxwell, "Treatise on Electricity and Magnetism," Vol. 1, 1st ed., p. 403, Clarendon Press, Oxford (1881).

Intermediates in the Electrochemical Reduction of Carbon Disulfide at a Mercury Cathode in Aprotic Solvents

Stanley Wawzonek,* Hsia-Fu Chang, Wayne Everett, and Michael Ryan*,[1]

Department of Chemistry, The University of Iowa, Iowa City, Iowa 52242

ABSTRACT

Cyclic voltammetric studies of the reduction of carbon disulfide at a HMDE in acetonitrile gave two irreversible reduction waves at −1.56V (SCE) and −2.2V (SCE), respectively. The data for the first wave suggested a reduction of carbon disulfide to an anion radical which dimerized utilizing the nucleophilic properties of the radical. The resulting species was reduced further to a dianion which is the basis for carbon monosulfide, trithiocarbonate, and tetrathiooxalate ions formed in large scale electrolyses. The second reduction led to extensive electrode filming and eventual insulation of the electrode. Large scale electrolysis at this potential gave a mercury complex. By-products isolated in the large scale reduction of carbon disulfide followed by methylation were 4-methylthio-1,3-dithiole-2-thione and 4,5-bis(methylthio)-2,2-dithiol-1,3-dithiole. GC-mass spectral studies indicated the presence of methyl dithioformate, dimethyl tetrathiooxalate, derivatives of this ester, species resulting from the interaction of the solvent acetonitrile and intermediates from the reduction of carbon disulfide, species from the interaction of sulfide ion with sulfur, and 4,5-bis(methylthio)-1,3-dithiole-2-one and dimethyl dithiocarbonate.

Two mechanisms have been proposed for the formation of 4,5-bis(methylthio-1,3-dithiole-2-thione (**1**), dimethyl trithiocarbonate (**2**) and carbon monosulfide in the electrochemical reduction and subsequent methylation of carbon disulfide in aprotic solvents containing tetraalkylammonium salts

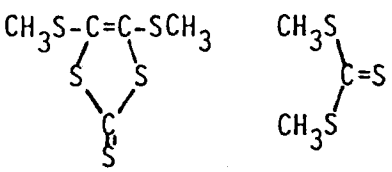

1 **2**

The first of these suggested the formation of an anion radical (**3**) by the addition of an electron to carbon disulfide followed by dimerization to the tetrathiooxalate ion (**4**). This intermediate (**4**) is considered

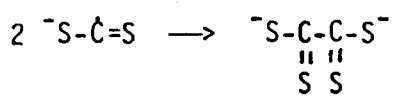

3 **4**

to react further with carbon disulfide and to form a product which on methylation would form (**1**) (1, 2).

Bontempelli and co-workers (3) on the basis of cyclic voltammetric studies of the reduction of carbon disulfide at a platinum electrode, coulometry, and isolation of carbon monosulfide, suggested the formation of trithiocarbonate ion and carbon monosulfide as products in the electrochemical reduction of carbon disulfide. A subsequent reaction of these two species was considered to give a product which on methylation formed (**1**).

In the present investigation, studies of the reduction of carbon disulfide in acetonitrile at a hanging mercury drop electrode and the nature of the by-products formed at a mercury cathode under various conditions have been carried out to obtain more information about the steps involved in the formation of (**1**) and (**2**).

Experimental

Physical methods.—Infrared spectra were determined using either a Perkin-Elmer Infracord or Beckman Acculab TMI Infrared Spectrophotometer. NMR spectra were obtained with either a Varian A60, Perkin-Elmer Model R12, or Joel JNM-FXPOQ FT nuclear magnetic resonance spectrophotometers. Carbon-13 NMR were determined with a Model 293 Bruker NMR. Mass spectra were measured using a Hewlett-Packard Model 5985A GC-MS system. The column employed was a 6 ft 3% OV101 coating on glass.

Electrochemical measurements were performed with a PAR Model 173 potentiostat/galvanostat and a PAR Model 175 universal programmer. The electrochemical cell used had a hanging mercury drop electrode (HMDE) (Metrohm AG Model 491) as the cathode and a platinum electrode as the anode. The reference electrode was a saturated calomel electrode. Studies were made in acetonitrile containing 0.2M tetrabutylammonium bromide and 0.001M and 0.005M of carbon disulfide, respectively. Purified nitrogen was used to purge the solution prior to electrochemical measurements.

Electrochemical reduction of carbon disulfide at a mercury cathode.—A reduction of carbon disulfide (18 ml) was carried out in dimethylformamide containing 0.5*M* tetrabutylammonium bromide (300 ml) at a mercury cathode at a constant potential of −2.06V (*vs.* Hg pool) using a PAR Model 371 Potentiostat. The anode was platinum and was placed in a porcelain cup with the same electrolyte. The initial current observed was 0.72A. After 7.5 hr approximately 21,600C had been utilized and the electrolysis was terminated. The resulting red solution upon removal of the dimethylformamide gave a red oil which was stirred with four 150 ml portions of distilled water which were discarded. The resulting red solid was stirred with four 100 ml portions of cold absolute ethanol, and the resulting ethanol extracts were filter. The resulting red solid (9.4g) (**5**) after recrystallization from absolute ethanol melted at 146.5-154° (dec); infrared (nujol) 3.50, 6.85, 7.15, 7.28, 8.5, 8.7, 9.05, 9.43, 9.7, 10.15, 11.1, 11.35, 12.45, and 13.5μ; NMR (D_8CCOCD_3) δ 0.89 (*t*, 3H, CH_3, J = 0.1 Hz), 1.15-2.18 (*m*, 4H, CH_2CH_2), 3.15-3.65 (*t*, 2H, CH_2N, J = 0.1 Hz).

Analysis calculated for $C_{38}H_{72}N_2S_{10}Hg$: C, 42.33; H, 6.73; N, 2.60. Found: C, 42.2; H, 6.49; N, 2.51.

Mass spectrum: *m/e* 310, 210, 202, 200, 185, 178, 143, 142, 122, 100, 90, 86, 76 (100).

C^{13}NMR (CD_3COCD_3) 206 (C = S); 136 (C = C); 59 (CH_2N); 32, 31, 30, 29.8, 29, 28, 27 ($CH_2CH_2CH_2N$); 24, 20, 14 (CH_3).

Methylation of mercuric complex (**5**).—A solution of the mercuric complex (**5**) (0.49g) in dimethylform-

* Electrochemical Society Active Member.

[1] Permanent address: Marquette University, Milwaukee, Wisconsin 53233.

Key words: cyclic voltammetry, hanging mercury drop electrode, mechanism.

amide was treated with methyl iodide (2 ml), and the resulting solution was stirred for 22 hr; the color changed in this period from a deep red to a red brown. The solution was poured into water (500 ml), and the resulting mixture was extracted with six 250 ml portions of petroleum ether (bp 60-68°). Concentration of the extracts to 10 ml gave brown needles which upon crystallization from the same solvent melted at 93°-96°C (lit. 100°-101.5°C); yield, 0.054g (27%). The infrared and mass spectra were identical to that of 4,5-bis(methylthio)-1,3-dithiole-2-thione **1**.

Reduction of carbon disulfide (18 ml) was carried out in an air-free solution of acetonitrile (400 ml) containing 0.5*M* tetrabutylammonium bromide in a similar fashion to that reported before. The resulting dark red solution upon removal of the acetonitrile gave a solid which was dissolved in dimethylformamide (150 ml) and treated with methyl iodide (8 ml) at room temperature for 24 hr; the resulting solution was then poured into water (600 ml). Extraction with hexane gave a black-brown solid which upon recrystallization from hexane gave 5.3g of bis(methylthio)-1,3-dithiole-2-thione (**1**) melting at 99°-100°C. Concentration of the hexane extract followed by purification on a thin layer preparative silica chromatographic plate using hexane gave dimethyl trithiocarbonate (**2**) (5% yield) and a mixture of (**1**) and 4-methylthio-1,3-dithiole-2-thione (**6**). Further chromatographic separation using carbon tetrachloride as an eluent gave an additional 0 7g of **1** or a total yield of 29%, and a 3% yield of 4-methylthio-1,3-dithiole-2-thione (**6**) melting at 58°-60° (lit. (1, 4) mp 71°). Mass spectral analysis of this sample indicated that it (**6**) was contaminated by a small amount of (**1**).

A small portion of the above hexane concentrate was examined by gc-mass spectrometry and found to contain the following additional compounds in approximately the yield indicated: 4,5-bis(methylthio)-1,3-dithiole-2-one (**22**) (0.6%); S-thio dimethyl disulfide (**19**) (0.07%); S,S-dithio dimethyl disulfide (**20**) (0.13%); dimethyl disulfide (0.08%); 2,4,5-tris(methylthio)-1,3-dithiole-2-acetylthiocarbonyl (**14**) (0.19%) *m/e* 360(12.3), 285(77.9), 238(13.2), 160(7.9), 135(18.1), 118(10.8), 103(34.0), 91(100), 88(44.5), 76(12.7), 75(12.5), 47(6.1), 45(8.2); tris(methylthio) acetyldithioethylene (**15**) (0.28%) *m/e* 272(19.6), 197(100), 150(33.1), 135(12.5), 118(85.9), 103(44.5), 91(71.7), 88(45.2), 75(20.9), 59(10.9), 47(17.5), 45(29.2); 4,4',5-tris(methylthio)-5'-acetylthio-2-spiro[5.5]-1,1,3',3'-dithiole (**16**) (0.04%) *m/e* 404(31.7), 329(77.7), 282(38.3), 250(69.7), 150(33.3), 135(28.4), 118(17.3), 103(58.4), 100(29.8), 91(100), 88(76.9), 75(24.7), 59(15.6), 47(9.5), 45(18.5); and dimethyl tetrathiooxalate (**13**) (0.07%).

The reduction of carbon disulfide was carried out in the presence of carbon dioxide using conditions given earlier. The carbon disulfide (25 ml) was introduced into the air-free acetonitrile solution by entrainment with carbon dioxide during the electrolysis. The dark red solution was separated from the mercury and treated with 26 ml of methyl iodide for 14 hr at room temperature. Removal of the acetonitrile by distillation gave a yellow distillate which upon examination by gc-mass spectroscopy contains dimethyl trithiocarbonate (**2**), methyl dithioformate (**7**), and dimethyl dithiocarbonate (**23**).

Extraction of the residue with six portions of 150 ml each of hexane followed by concentration of the combined extracts to 15 ml of hexane and separation by preparative tlc using hexane gave sulfur (2%) and dimethyl trithiocarbonate (**2**) (4.5%). Further elution with carbon tetrachloride gave 4,5-bis(methylthio)-1,3-dithiole-2-thione (**1**) (27%) and 4,5-bismethylthio)-1,3-dithiole-2,2-dithiol (**8**) (0.5%); mp 46°-48°. Infrared(nujol) 1415, 1320, 1210, 1065, 955, 840, 815, 780, 725 cm^{-1}; NMR($CDCl_3$) δ 5.29(s, 1H, SH), 2.76 (s, 3H, SCH_3); *m/e* 260(0.9), 169(40.7), 91(100), 77(7.7), 76(22.4), 59(4.6), 47(8.6), 45(14.8).

Analysis calculated for $C_5H_8S_6$: C, 22.80; H, 3.12. Found: C, 23.08; H, 3.07.

A small portion of the main hexane concentrate was examined by gc-mass spectrometry and found to contain the following additional compounds; their yields and fragmentation patterns in the mass spectrum are listed: methyl dithioformate (**7**) (0.07%) *m/e* 92(100), 77(23.1), 76(19.1), 47(9.2), 45(20.3); dimethyl dithiocarbonate (**23**) (0.01%) *m/e* 122(33.3), 94(100), 79(48.4), 75(58.1), 47(18.3), 45(16.1); dimethyl trisulfide (**21**) (0.02%) *m/e* 126(100), 111(17.3), 79(30.4), 64(7.6), 47(3.5), 45(6.1); methyl acetyl trithiocarbonate (**17**) (0.3%) *m/e* 166(100), 151(25.4), 104(57.8), 103(47.6), 91(28.2), 75(12.9), 45(7.9); 2,2,4-tris(thiomethyl)-5-thiol-1,3-dithiole (**12**) (0.7%) *m/e* 274(3.9), 227(21.5), 195(6.1), 180(6.4), 150(17.0), 135(16.4), 106(14.5), 103(22.4), 91(100), 76(33.6), 88(27.8), 77(9.1), 47(8.3), 45(22.7); methyl α-azirinedithioacetate (**18**) (3.4%) *m/e* 145(40), 98(100), 94(12.6), 58(9.4), 45(4.0); and 4-methylthio-1,3-dithiole-2-thione (**6**) (2%) *m/e* 180(100), 135(21.5), 104(38.0), 103(66.9), 91(27.3), 89(67.8), 88(14.0), 76(33.1), 59(19.0), 45(23.1).

Results

The cyclic voltammetric reduction of carbon disulfide at a HMDE in acetonitrile containing 0.2*M* tetrabutylammonium bromide occurred at $Ep = -1.56$V (SCE) with a second reduction at $Ep = -2.2$V (SCE). The second reduction led to extensive electrode filming and eventual insulation of the electrode (Fig. 1b). The first reduction wave had an inflection at −1.50V (Fig. 1a) for 1 mM carbon disulfide which indicated an overlap of two processes with approximately similar potentials. If only the first wave were scanned through, no anodic wave was seen. The reduction wave is quite sharp ($Epp/2$ values are about 46 mV), and the shift in the peak potential *EPc* shows only a weak dependence upon scan rate ($\Delta Ep/\Delta \log \nu = 15$ mV). The peak current function, $ipc/C\nu^{1/2}$, corresponds to an overall one electron process. For the 1 mM solutions a reversible adsorption wave at −1.03V was observed on the reverse scan and the second cathodic scan, but was absent in the initial cathodic scan. This

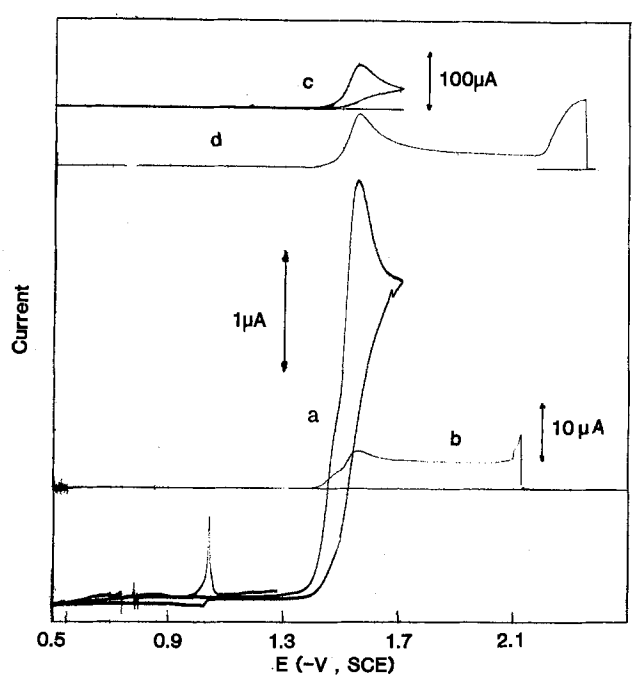

Fig. 1. Cyclic voltammograms for carbon disulfide in 0.2M tetrabutylammonium bromide in acetonitrile at a HMDE: (a) and (b) 0.001M CS_2 at 20 mV sec^{-1} at 25°C; (c) and (d) 0.005M CS_2 at 100 mV sec^{-1} at 25°C.

peak disappeared nearly completely for 5 mM solutions of carbon disulfide (Fig. 1c, d).

The electrolysis of carbon disulfide in dimethyl formamide at a mercury cathode at −2.06V (Hg pool) using 0.5*M* tetrabutylammonium bromide as the supporting electrolyte gave a solid which based on elemental analysis, spectral data, and conversion by methyl iodide into (1) is the mercuric complex (5)

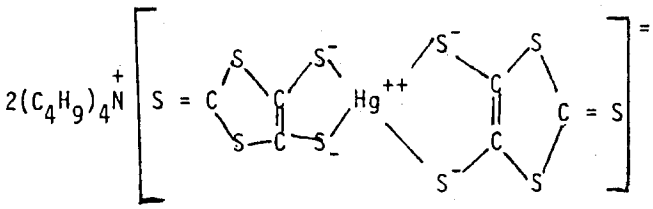

5

This complex may be responsible for the filming observed with the second reduction wave at the HMDE (Fig. 1a, d).

The products isolated or characterized by gc-mass spectral analysis from the reduction of carbon disulfide in acetonitrile alone or in the presence of carbon dioxide followed by methylation were numerous. Both types of reductions gave similar yields of the cyclic compound (1), dimethyl trithiocarbonate (2), and 4-methylthio-1,3-dithiole-2-thione (6). The last compound (6) has been isolated in the reduction of carbon disulfide using sodium amalgam (4) but has not been reported in electrolytic studies

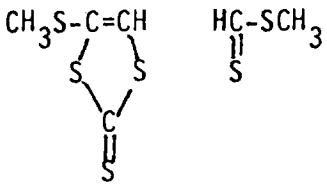

6 7

Methyl dithioformate (7) was only found and identified by gc-mass spectral studies in the reduction of carbon disulfide in the presence of carbon dioxide. This electrolysis also yielded 4,5-bis(methylthio)-2,2-dithiol-1,3-dithiole (8) and 2,2,4-tris(methylthio)-5-thiol-1,3-dithiole (12). The former structure was based on elemental analysis and nmr and mass spectral analysis. NMR analysis showed a singlet at δ 5.29 for the SH group and a singlet at δ 2.76 for the SCH_3

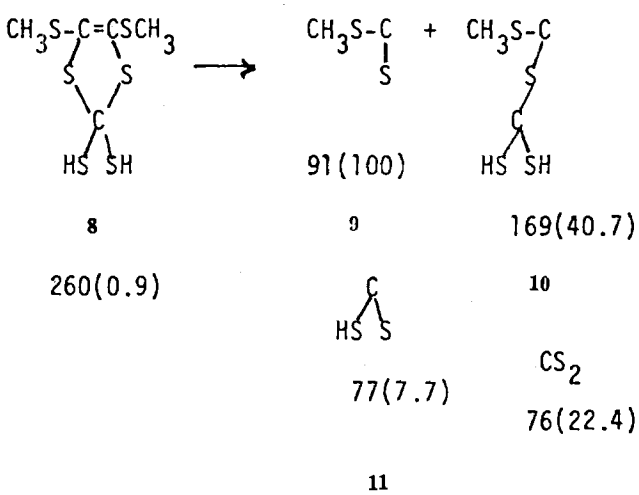

8 9 10

260(0.9) 91(100) 169(40.7)

77(7.7) 76(22.4)

11

The fragmentation pattern in the mass spectrum shown is in agreement with this structure.

Compound (12) was detected by gc-mass spectral analysis of the hexane extracts of the products in this electrolysis

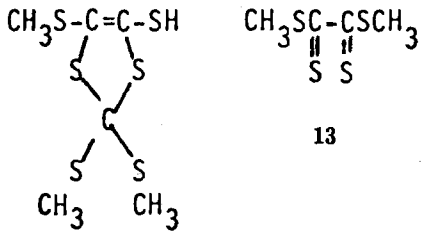

12 13

and had a parent ion peak of 91(100) similar to (8). A fragment with an *m/e* 106(14.5) would correspond to the $(CH_3S)_2C$ group.

Dimethyl tetrathiooxalate (13) was detected by gc-mass spectrometry in very small amounts (0.07%) in the reduction using acetonitrile alone. The reason for this low yield may be the utilization of the precursor of this ester, the tetrathiooxalate ion, in the formation of a number of the products identified by gc-mass spectrometry and listed (14-16) in the experimental. The complex behavior of this species has recently been demonstrated in the methylation of bis-tetraethylammonium tetrathiooxalate (5).

Other compounds listed in the latter may be formed by the interaction of the solvent, acetonitrile, with anion species from carbon disulfide (17, 18), and reactions between sulfide ions and sulfur (19-21). The oxygen derivatives (22), (23) listed were probably formed by the mercuric ion catalyzed hydrolysis of the corresponding sulfur compounds (1) and (2).

Discussion of Results

The voltammetric data obtained at the HMDE is consistent with an initial reduction of carbon disulfide to the anion radical (3) followed by a fast dimerization. The value of $\Delta Ep/\Delta \log \nu$ is in agreement with such a mechanism. The reversibility shown in the first step is solely based on the Nernstian behavior of the first reduction

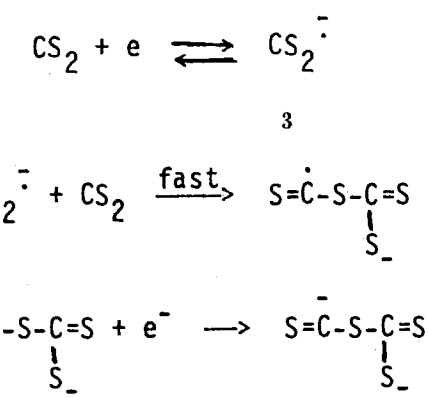

3 24

The second reaction is not fast enough to destroy this Nernstian behavior. The inflection in the wave for 1 mM carbon disulfide points to two reduction processes with rather similar reduction potentials. This break is absent for the reduction of 0.005M carbon disulfide.

The two step reduction wave observed for 1 mM carbon disulfide eliminates the possibility of the dimerization of the anion radical to the tetrathiooxalate ion suggested by Jeroschewski (6); such a mechanism would show only one wave.

The dimerization shown utilizes the nucleophilic addition of the anion radical (3) to carbon disulfide and forms a new radical which is reduced further to (24). This dianion (24) can dissociate into carbon monosulfide

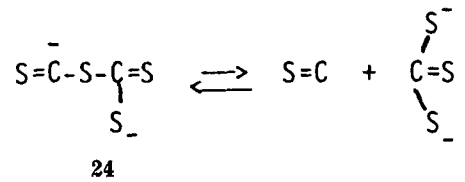

24

and trithiocarbonate ion; the reaction is considered to be reversible since Bontempelli (3) found that these species combined to form a product which on methylation gave (1).

The dianion (24) can react further with carbon disulfide and form a derivative of tetrathiooxalate (25)

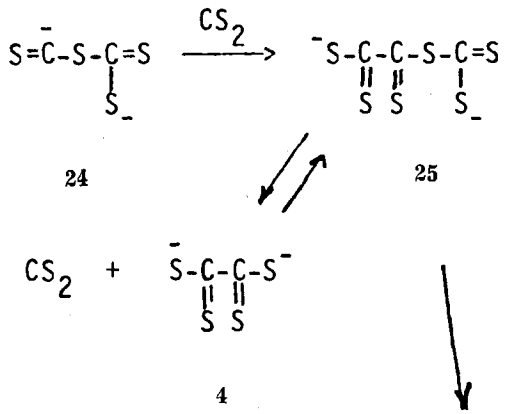

which could dissociate to carbon disulfide and tetrathiooxalate ion (4) or cyclize to (26). The last compound can lose sulfide ion and form (27). Reduction of (26) and (27) electrochemically or chemically with sulfide ion would lead to a precursor of (1), (8), and (12).

The rearrangement of (24) directly to tetrathiooxalate ion (4) cannot be eliminated in view of the work of

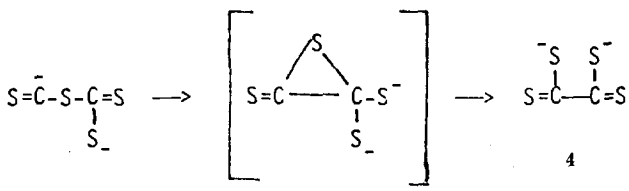

Bontempelli (3) and Chambers (2). This ion (4), which would be converted by carbon disulfide or carbon monosulfide into a precursor of (1), has been isolated as the insoluble tetraethylammonium and tetramethylammonium salts from the electrolysis of carbon disulfide in acetonitrile using either tetraethylammonium bromide or tetramethylammonium iodide as supporting electrolytes (6).

The detection of methyl dithioformate (7) in the large scale electrolysis mixture suggests a protonation of intermediate (24) followed by the loss of carbon disulfide and formation of dithioformate ion.

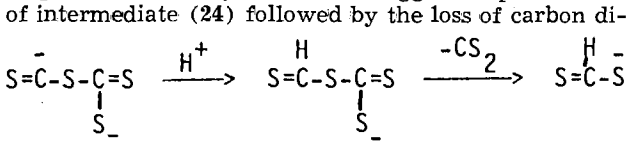

The formation of 4-methylthio-1,3-dithiole-2-thione (6) in small amounts could be explained by a reaction of (24) with carbon monosulfide followed by protonation

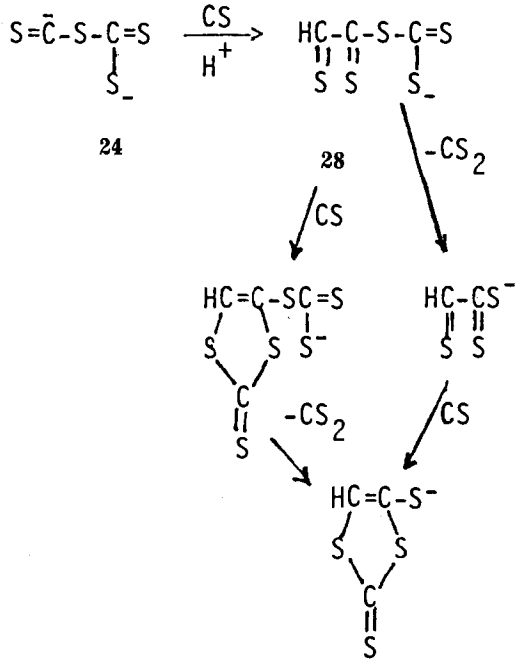

The intermediate (28) may lose carbon disulfide and form trithioglyoxylic acid or may be converted directly by carbon monosulfide or carbon disulfide to a precursor of (6). This precursor could also be formed by similar reactions with trithioglyoxylic acid.

The actual mode of formation of the mercuric complex (5) is not known. Metal complexes of this type have been prepared by treating the disodium salt of 4,5-dithiol-1,3-dithiole-2-thione with metallic and tetralkylammonium salts (7). In the present work complex (5) is apparently being formed by the oxidation of the mercury cathode by a species generated by the electrolysis. Since it is well known that mercury is oxidized by mercaptans and disulfides

$$RSH + Hg \rightarrow RSHg + e + H^+$$

$$(RS)_2 + Hg \rightarrow (RS)_2Hg$$

intermediate (27) could behave in a similar fashion and form complex (5) by the following reaction

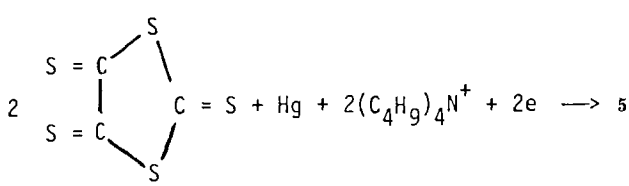

27

Acknowledgments

This paper is abstracted in part from the Ph.D. theses of Hsin-Fu Chang and Wayne Everett.

Manuscript submitted Nov. 3, 1982; revised manuscript received Dec. 13, 1982.

Any discussion of this paper will appear in a Discussion Section to be published in the December 1983 JOURNAL. All discussions for the December 1983 Discussion Section should be submitted by Aug. 1, 1983.

REFERENCES

1. S. Wawzonek and S. M. Heilmann, *J. Org. Chem.*, 39, 511 (1974).
2. J. C. Lodmell, W. C. Anderson, M. F. Hurley, and

J. Q. Chambers, *Anal. Chim. Acta*, **129**, 49 (1981).
3. G. Bontempelli, F. Magno, G.-A. Mazzocchin, and R. Seeber, *J. Electroanal. Chem.*, **63**, 231 (1975).
4. B. Fetkenheuer, H. Fetkenheuer, and H. Lecus, *Ber.*, **60B**, 2528 (1927).
5. P. Jeroschewski and P. Hansen, *Z. Chem.*, **22**, 223 (1982).
6. P. Jeroschewski, *ibid.*, **21**, 412 (1981).
7. G. Steimecke, R. Kirmse, and E. Hoyer, *ibid.*, **15**, 28 (1975).

Thermodynamic Aspects of Redox Reactions on Electrodes Coated with Thin, Ion Exchanging Polymer Films

Helga Braun, Winfried Storck, and Karl Doblhofer

Fritz-Haber-Institut der Max-Planck-Gesellschaft, D-1000 Berlin 33, Germany

ABSTRACT

Electrodes modified with various anion exchanging polymer films were investigated in contact with electrolytes containing the redox system $[Fe(CN)_6]^{3-/4-}$. With electrochemical techniques the concentrations of the redox ions in the polymer films were determined. A thermodynamic basis was derived on which the experimental data could be analyzed. Thus the work associated with the transfer of the redox ions from the solution into the ion exchanger could be obtained. These data are related to the selectivity of the investigated ion exchangers.

Depositing ion exchangers in the form of thin films on electrodes leads to drastic changes of the performance of the electrodes. This is mainly due to the selectivity properties of the ion exchangers. This means that the ratios of the concentrations of the oxidized and reduced form of a redox species in the film, C^M_{ox}/C^M_{red}, will usually differ significantly from the corresponding solution values, C^S_{ox}/C^S_{red}. Such parameters can be determined with the electrochemical methods cyclic voltammetry and chronoamperometry. The obtained data can be analyzed using standard thermodynamic concepts and give information characterizing the system. Thus, besides their electrochemical relevance, the film-covered electrodes can be used to get new insights into the ion exchange mechanisms, in particular, into the accumulation process of highly charged anions in anion exchange resins, which is little understood. For this reason anion exchangers derived from poly(4-vinylpyridine) and the redox system $Fe(CN)_6^{3-}/Fe(CN)_6^{4-}$ were chosen as the experimental system.

Experimental

Materials.—$K_3Fe(CN)_6$, $K_4Fe(CN)_6$, and CF_3COONa were used as reagent grade chemicals. Poly(4-vinylpyridine) was quaternized with the reagents summarized in Table I by the following procedure. Low molecular weight material and a red impurity were first extracted from the commercial poly(4-vinylpyridine) by stirring three times for 14 hr in 500 ml portions of acetonitrile. After washing twice with diethylether the polymer was dissolved in 125 ml of 6*N* HCl, diluted with an equal volume of water, filtered, and the clear solution poured dropwise into 2 liters of a stirred 1.5*N* NH_4OH solution. The off-white precipitate was isolated by suction, washed with water, and dried *in vacuo*; $[\eta] = 66.8\ cm^3\ g^{-1}$ (abs. ethanol, 298.2 K) which, according to Fuoss (1) corresponds to a mean molecular mass of 1.1×10^5. Approximately 5 mequiv. (referred to vinylpyridine) of the polymer were dissolved in 10 ml absolute methanol; a threefold molar amount of alkylbromide (reagent grade) was added. After degassing, this solution was heated in a sealed and evacuated tube for a minimum of 48 hr at 60°C (2). After filtering, the brownish solution was concentrated *in vacuo* and the residue extracted twice with boiling diethyl ether. The polymer was dissolved several times in methanol and reprecipitated in dry ether. The products (Q8-Q12, Table I) were colorless and quaternized to > 95%. In the case of p-toluenesulfonic acid methyl ester (Q1 in Table I) only 70 mol percent (m/o) of the alkylating agent were used yielding 50-60 m/o quaternization.

Products with an alkyl chain of C_8 or longer were water insoluble. They were applied to glassy carbon electrodes (SIGRI Elektrographit, Meitingen) (mounted in PTFE holders) with the spin-coating technique (3) from methanolic solution. The water soluble polymer Q1 was mixed with 1,3-bis(bromomethyl)-benzene in an amount corresponding to the number of free pyridyl groups in the polymer. A heat-treatment after application (60°C, 4 hr) caused a chemical crosslinking which rendered the films insoluble.

Apparatus and Procedures.—The thickness of the dry spin-cast films was determined from mechanical surface profile measurements using a Talystep, Taylor Hobson Step Profiler. A typical thickness of 200 nm on electrodes of 0.5 cm^2 surface area was used. The volumes of the unswollen films were used in the calculations of the approximate redox-ion concentration in the solvated ion exchange polymers.

Cyclic voltammograms were carried out in solution containing 2.5 mM $K_3[Fe(CN)_6]$, 2.5 mM $K_4[Fe(CN)_6]$, and 0.5M CF_3COONa. The accumulation of the redox system in the polymer films with long alkyl chains was followed by continuously cycling the potential between −0.4 and +0.4V *vs.* SCE until the peak current had reached a stable value.

Chronoamperometric current decay curves were recorded with a VUCO VK 22-2 transient recorder (2000 points). The data were evaluated with an LSI 11 computer (DEC) connected with the recorder via the IEC-Interface-Bus. Coated electrodes previously equilibrated in cyclic voltammetry experiments were trans-

Table I. Preparation of the poly(4-vinylpyridinum) salts

Starting material	Quaternizing agent	Product
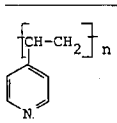	1. n-$C_{12}H_{25}Br$	Q12
	2. n-$C_{10}H_{21}Br$	Q10
	3. n-$C_8H_{17}Br$	Q8
	4. 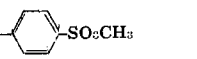 (+) → 55 m/o N—CH_3 then cross-linked with 1,3-bis(bromomethyl)-benzene	Q1

Key words: membrane, electrolyte, electrode, ion exchange, coatings.

ferred into solutions containing no redox system but the supporting electrolyte. In these inert solutions the chronoamperometric experiments were carried out. All measurements were conducted at ambient temperature (22° ± 2°C) in solutions freed of oxygen by bubbling with nitrogen. Potentials were measured and are reported with respect to a saturated calomel electrode, SCE.

Results

The $[Fe(CN)_6]^{3-/4-}$ anodic and cathodic cyclic voltammetry peaks obtained with the film-covered electrodes were found to be shifted systematically to more negative potentials compared with the uncoated electrode. Such potential shifts have been noticed previously by other authors (4, 5). The potential between the anodic and cathodic peak at which the positive and negative currents are equal (Fig. 1) will be designated as E_1. For the uncoated electrode E_1 corresponds to E^S, the open-circuit potential. As expected, identical open-circuit potentials were always measured with the coated and uncoated electrodes. For the generally used electrolyte (each 2.5 mM $[Fe(CN)_6]^{4-}$ and $[Fe(CN)_6]^{3-}$ in the presence of 0.5M CF_3COONa) this open-circuit potential was +0.190V (SCE). The negative potential shift, $E_1 - E^S$, increases with increasing chain length of the quaternizing agent (Table II). E_1 together with the open-circuit potential, E^S, can be used to analyze the system (see below).

Potential steps applied in the cathodic direction, starting at the equilibrium potential E^S, gave current decay curves as discussed in the literature (6) for thin film cells. By integrating these decay curves and using the volumes of the unswollen films, values of the concentration of $[Fe(CN)_6]^{3-}$ at the equilibrium potential, C^M_{ox}(equil.), could be determined. These values are included in Table II.

Discussion

The thermodynamic basis.—The investigated system is schematically shown in Fig. 2. For deriving the necessary equations it is, for simplification, assumed that the two metals Me and Me' are of the same inert material. In the following equations $\bar{\mu}_i$ symbolize electrochemical potentials of species i, as defined by Eq. [5]-[8]. The superscripts refer to the phase, in correspondence with Fig. 2. $^\circ\mu_i$ are the standard chemical potentials of species i; ϕ is the Galvani potential; a_i the activity, and γ_i the activity coefficient of species i. Z_i symbolizes the valence number of species i, whereby

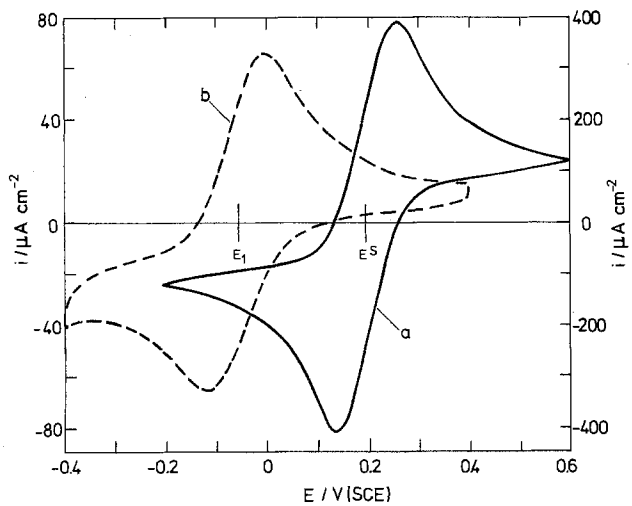

Fig. 1. Cyclic voltammograms obtained with a bare glassy carbon electrode (a) and a Q12 covered electrode (b). Film thickness 260 nm. Electrolyte: 2.5 mM $K_3Fe(CN)_6$, 2.5 mM $K_4Fe(CN)_6$, and 0.5M CF_3COONa. Scan rate 100 mV sec^{-1}. Curve b obtained after 30 min continuous cycling.

Table II. Experimental results obtained with each 2.5 mM $[Fe(CN_6)]^{4-}$, $[Fe(CN)_6]^{3-}$, and 0.5M CF_3COONa (for details see Fig. 1)

	E_1/V (SCE)	$E_1 - E^S$/V	C^M_{ox} (equil.)/ mol liter^{-1}
Q12	−0.055	−0.245	0.18
Q10	−0.04	−0.23	0.20
Q8	−0.025	−0.215	0.22
Q1	+0.07	−0.12	0.40
Uncovered GC 1	E^S +0.190	$E^S - E^\circ$ 0.073	C^S_{ox} 0.0025

$Z_{ox} - Z_{red} = 1$, according to Eq. [1]. R, T, and $\mathbf{F}$ have their usual significance.

For the redox reaction

$$ox + e^- = red \qquad [1]$$

the equilibrium conditions are given by (7-9)

$$\bar{\mu}^M_{ox} + \bar{\mu}^{Me}{}_{e^-} = \bar{\mu}^M_{red} \quad \text{at the interface Me/M} \qquad [2]$$

$$\bar{\mu}^S_{ox} + \bar{\mu}^{Me'}{}_{e^-} = \bar{\mu}^S_{red} \quad \text{at the interface Me'/S} \qquad [3]$$

$$\bar{\mu}^M_{ox} = \bar{\mu}^S_{ox}, \quad \bar{\mu}^M_{red} = \bar{\mu}^S_{red} \quad \text{at the interface M/S} \qquad [4]$$

with the electrochemical potentials
in phase Me

$$\bar{\mu}^{Me}{}_{e^-} = \mu^{Me}{}_{e^-} - \mathbf{F}\phi^{Me} \qquad [5]$$

in phase M

$$\bar{\mu}^M_i = \mu^M_i + Z_i \mathbf{F}\phi^M \qquad [6]$$

in phase S

$$\bar{\mu}^S_i = \mu^S_i + Z_i \mathbf{F}\phi^S \qquad [7]$$

in phase Me'

$$\bar{\mu}^{Me'}{}_{e^-} = \mu^{Me'}{}_{e^-} - \mathbf{F}\phi^{Me'} \qquad [8]$$

and the chemical potentials of the ions i (ox, red)

$$\mu_i = {}^\circ\mu_i + RT \ln a_i \qquad [9]$$

$$= {}^\circ\mu_i + RT \ln C_i + RT \ln \gamma_i \qquad [9a]$$

From the above equations the Galvani potential drops across the different interfaces are defined as

Me/M

$$\mathbf{F}(\phi^{Me} - \phi^M) = {}^\circ\mu^M_{ox} - {}^\circ\mu^M_{red} + RT \ln \frac{a^M_{ox}}{a^M_{red}} + \mu^{Me}{}_{e^-} \qquad [10]$$

M/S

$$\mathbf{F}(\phi^M - \phi^S) = \frac{1}{Z_{ox}}({}^\circ\mu^S_{ox} - {}^\circ\mu^M_{ox}) + \frac{RT}{Z_{ox}} \ln \frac{a^S_{ox}}{a^M_{ox}}$$

$$= \frac{1}{Z_{red}}({}^\circ\mu^S_{red} - {}^\circ\mu^M_{red}) + \frac{RT}{Z_{red}} \ln \frac{a^S_{red}}{a^M_{red}} \qquad [11]$$

S/Me'

$$\mathbf{F}(\phi^S - \phi^{Me'}) = -\left[{}^\circ\mu^S_{ox} - {}^\circ\mu^S_{red} + RT \ln \frac{a^S_{ox}}{a^S_{red}} + \mu^{Me'}{}_{e^-}\right] \qquad [12]$$

Adding Eq. [10] and [12] results in an expression for the potential drop at the interface M/S which is sometimes (10, 11) called the "Donnan potential"

$$\phi^M - \phi^S = \frac{1}{\mathbf{F}}({}^\circ\mu^M_{red} - {}^\circ\mu^S_{red}) - \frac{1}{\mathbf{F}}({}^\circ\mu^M_{ox} - {}^\circ\mu^S_{ox}) + \frac{RT}{\mathbf{F}} \ln \frac{a^S_{ox}\, a^M_{red}}{a^S_{red}\, a^M_{ox}} \qquad [13]$$

For the single ions this potential drop is defined by Eq. [11].

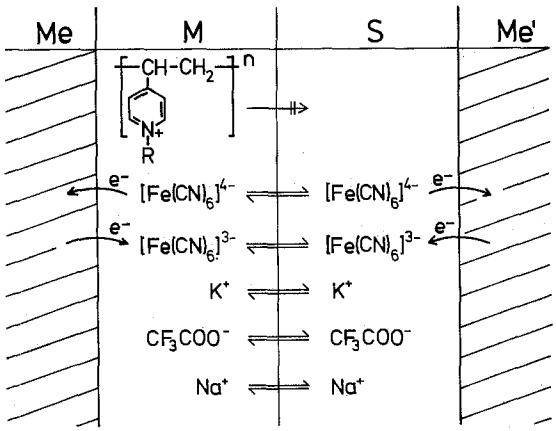

Fig. 2. Schematic representation of the investigated system. The electrode Me (= glassy carbon) is covered with the polymer film M. The film-covered electrode is in equilibrium with the aqueous solution phase S.

It is common practice in thermodynamic analyses of ion exchange equilibria to choose infinite dilution in both phases as a reference state (10-13). Then the standard free energy difference, ${}^{\circ}\mu^{M}_{i} - {}^{\circ}\mu^{S}_{i}$ (cf. Eq. [11] and [13]), is a measure of the chemical energy associated with the transfer of species i from the solution to the membrane phase at infinite dilution in each phase. We can define (12, 13)

$$ {}^{\circ}\mu^{M}_{i} - {}^{\circ}\mu^{S}_{i} = RT \ln k_i \qquad [14] $$

where k_i is the single ion extraction (partition) coefficient. Equation [13] can then be written

$$ \phi^{M} - \phi^{S} = \frac{RT}{F} \ln \frac{a^{S}_{ox}}{a^{S}_{red}} \cdot \frac{a^{M}_{red}}{a^{M}_{ox}} \frac{k_{ox}}{k_{red}} \qquad [15] $$

$$ = \frac{RT}{F} \ln \frac{C^{S}_{ox}\, C^{M}_{red}}{C^{S}_{red}\, C^{M}_{ox}} \cdot \frac{\gamma^{S}_{ox}\, \gamma^{M}_{red}}{\gamma^{S}_{red}\, \gamma^{M}_{ox}} \cdot \frac{k_{ox}}{k_{red}} \qquad [15a] $$

With Eq. [15]/[15a] salt partitioning is separated from activity coefficient effects. The membrane-activity coefficients have the usual property of going to unity at infinite dilution. In principle, it would be possible to calculate them; however, with the high charge (−3, −4) of the redox ions and the high ionic strength (up to approximately 10M) in our films, such calculations are unreliable with the available methods (14). Therefore calculations of γ^{M}_{i} were not attempted.

We can calculate the molar work associated with the transfer of ox and red from the solution to the membrane phase, W^{T}_{ox} and W^{T}_{red}

$$ W^{T}_{ox} = RT \ln \frac{\gamma^{M}_{ox}\, k_{ox}}{\gamma^{S}_{ox}} \qquad [16] $$

$$ W^{T}_{red} = RT \ln \frac{\gamma^{M}_{red}\, k_{red}}{\gamma^{S}_{red}} \qquad [17] $$

These works define the difference in specific chemical and electrical interaction energies which stabilize an ion in one phase, except for that part already accounted for in the Galvani potential terms (13). They are, of course, concentration dependent.

Among the ion exchanger materials used in this work the one containing the longest aliphatic chain as quaternizing substituent (Q12, Table I) has the stoichiometry $(C_{19}H_{34}NBr)_n$. With a specific mass of 1 gcm^{-3} one can calculate a (unswollen, unreacted) site concentration of 2.8 mol dm^{-3}, a relatively high value. The other polymers (Table I) have higher fixed site densities. Thus, in the reference state the water content of these hydrophilic films will be so high that (unlike the situation in, *e.g.*, liquid membranes) the extraction coefficient can realistically be assumed to be unity (13). The works of ion transfer, W^{T}_{ox} and W^{T}_{red} will thus solely be determined by the activity coefficients, and Eq. [15], [16], and [17] can be written

$$ \phi^{M} - \phi^{S} = \frac{RT}{F} \ln \frac{C^{S}_{ox}\, C^{M}_{red}}{C^{S}_{red}\, C^{M}_{ox}} \cdot \frac{\gamma^{S}_{ox}\, \gamma^{M}_{red}}{\gamma^{S}_{red}\, \gamma^{M}_{ox}} \qquad [15b] $$

$$ W^{T}_{ox} = RT \ln \frac{\gamma^{M}_{ox}}{\gamma^{S}_{ox}} \qquad [16a] $$

$$ W^{T}_{red} = RT \ln \frac{\gamma^{M}_{red}}{\gamma^{S}_{red}} \qquad [17a] $$

These equations are used as the basis of the following analysis.

The potential drop across the interface M/S, $\phi^{M} - \phi^{S}$, becomes high when the polymer film has a high concentration of fixed charges $\backslash\!\backslash\, N^{+}\!-\!R$ and the solution is a very dilute electrolyte. It becomes negligible when the concentration of ions in the solution is much higher than the concentration of fixed ions in the membrane M (10, 11).

One can, in principle, measure the two Galvani potential drops, $(\phi^{Me} - \phi^{M})$ and $(\phi^{S} - \phi^{Me'})$ against reference electrodes in the phases M and S, respectively. One obtains then the redox potentials E^{M} and E^{S}

$$ E^{M} = {}^{\circ}E + \frac{RT}{F} \ln \frac{C^{M}_{ox}}{C^{M}_{red}} \cdot \frac{\gamma^{M}_{ox}}{\gamma^{M}_{red}} \qquad [18] $$

$$ E^{S} = {}^{\circ}E + \frac{RT}{F} \ln \frac{C^{S}_{ox}}{C^{S}_{red}} \cdot \frac{\gamma^{S}_{ox}}{\gamma^{S}_{red}} \qquad [19] $$

${}^{\circ}E$ is the standard redox potential which is the same for both phases, when $k_{ox} = k_{red} = 1$. Experimentally, a direct measurement of E^{M} was not attempted with our system because of the difficulties connected with effectively inserting a reference electrode into the thin film. The difference

$$ E^{S} - E^{M} = \phi^{M} - \phi^{S} \qquad [20] $$

follows from Eq. [15b].

Thermodynamic analysis of the system with high concentration of background electrolyte.—As discussed above, with the high concentration of background electrolyte (0.5M CF_3COONa) the potential difference between the phases M and S (the Donnan potential) will be close to zero and we are justified in assuming

$$ \phi^{M} - \phi^{S} = 0 $$

With this assumption the above equations can be used to conduct a complete thermodynamic analysis of the system, based on the experimental data.

The ratio $\gamma^{M}_{ox}/\gamma^{M}_{red}$.—With $\phi^{M} - \phi^{S} = 0$ the potentials of the polymer-covered electrodes measured *vs.* a reference electrode in phase S, correspond to E^{M} values (Eq. [20]). Assuming that under the nonequilibrium condition of cyclic voltammetry near the electrode, C^{M}_{ox} at $E > 0.2$V equals C^{M}_{red} at $E < -0.3$V and with the charge transfer coefficient $\alpha = 0.5$ (15), the equilibrium potential on the E^{M}-scale corresponding to equal concentration of C^{M}_{ox} and C^{M}_{red} is defined as the potential at which the positive charge transfer current of the positive sweep is equal to the negative charge transfer current of the negative sweep. This value was estimated as indicated in Fig. 1 and designated as E_1. With E_1 and Eq. [18] one obtains

$$ RT \ln \frac{\gamma^{M}_{ox}}{\gamma^{M}_{red}} = F\,(E_1 - E^{\circ}) \qquad [21] $$

The ratios of activity coefficients in the matrix, $\gamma^{M}_{ox}/\gamma^{M}_{red}$ obtained for the different ion exchanging films are listed in Table III.

The work of transfer, WT_{ox} and WT_{red}.—The work of transfer was defined by Eq. [16] and [17]. To calculate it we note that, with $k_{ox} = k_{red} = 1$ and $\phi^{M} - \phi^{S} = 0$, Eq. [11] simplifies to

$$\frac{a^{S}_{ox}}{a^{M}_{ox}} = \frac{C^{S}_{ox}}{C^{M}_{ox}(\text{equil.})}\frac{\gamma^{S}_{ox}}{\gamma^{M}_{ox}} = 1 \qquad [22]$$

$$\frac{a^{S}_{red}}{a^{M}_{red}} = \frac{C^{S}_{red}}{C^{M}_{red}(\text{equil.})}\frac{\gamma^{S}_{red}}{\gamma^{M}_{red}} = 1 \qquad [23]$$

In these equations C^{S}_{ox} and C^{S}_{red} are given, and C^{M}_{ox}(equil.) was determined from the chronoamperometry experiments. Thus WT_{ox} values can be calculated using Eq. [16a] and [22]

$$WT_{ox} = RT \ln \frac{C^{S}_{ox}}{C^{M}_{ox}(\text{equil.})}$$

They are included in Table III.

The calculation of WT_{red} is less straightforward. This is due to the small equilibrium concentration of C^{M}_{red} which makes the chronoamperometric determination inaccurate. More reliable values could be obtained from the known values of E_1 and C^{M}_{ox}(equil.). Since we may assume that the ratio of activity coefficients in the matrix, $\gamma^{M}_{ox}/\gamma^{M}_{red}$, remains constant over the potential range E_1 to E^{S}, the concentration ratio $C^{M}_{ox}(\text{equil.})/C^{M}_{red}(\text{equil.})$ can be found from Eq. [18]

$$RT \ln \frac{C^{M}_{ox}(\text{equil.})}{C^{M}_{red}(\text{equil.})} = \mathbf{F}(E^{S} - E_1)$$

With the determined values of C^{M}_{red}(equil.) the WT_{red} values of Table III were calculated according to (cf. Eq. [17a] and [23]

$$WT_{red} = RT \ln \frac{C^{S}_{red}}{C^{M}_{red}(\text{equil.})}$$

Discussion of the obtained values (Table III).—The striking result of the above analysis (Table III) is borne out by the values of WT for the transfer of hexacyanoferrate (II/III) from the solution into the ion exchanger phase which could be obtained with the electrochemical techniques. Clearly, in the absence of a potential drop at the interface M/S the accumulation of hexacyanoferrate III (= ox) is favored by an associated negative energy change, while hexacyanoferrate II (= red) is repelled from the polymer phase. It is well known that such specific interactions are the origin of ion exchange selectivity (10).

Considering the aqueous phase, S, it is known that the equilibrium constant for ion pair formation with potassium is 225 liters mol^{-1} for $Fe(CN)_6^{4-}$ which is about ten times larger than the value for $[Fe(CN)_6]^{3-}$ (16). This equilibrium constant corresponds to a free energy change of −13 kJ/mol, associated with the ion pair formation. The values of WT_{red} in Table III can thus be understood as the energy of the dissociation process of the ion pair K^+ $Fe(CN)_6^{4-}$ which is required for the $Fe(CN)_6^{4-}$ ion to enter the ion exchanger. The variation of WT_{red} from Q12 to Q1 would thus suggest that Q12 contains nearly exclusively $Fe(CN)_6^{4-}$ while in the much better solvated Q1 the ion pair exists as in the solution.

The negative WT_{ox} values suggest ion pair formation of $Fe(CN)_6^{3-}$ with the pyridinium cations of the polymer matrix. The preference of R_4N^+ ions for $Fe(CN)_6^{3-}$ w.r.t. ionic association is well established (17-19). It was suggested by Gutmann and co-workers (20) to be the reason for negative shifts of the equilibrium potential of the $Fe(CN)_6^{3-/4-}$ couple observed upon addition of R_4N^+ in aqueous and nonaqueous electrolytes; an effect, which is rather similar to the phenomena discussed in this work. The stronger electron-pair donating properties of the CN-nitrogens in $Fe(CN)_6^{4-}$, compared with $Fe(CN)_6^{3-}$, were proposed to be the basic reason behind the effect (20). Thus, the relatively strong acceptor water in the coordination sphere can be replaced in the matrix by the acceptor ammonium ion to form the ion pair with $Fe(CN)_6^{3-}$. In the case of $Fe(CN)_6^{4-}$ stronger bonds with water hinder this ion pair formation.

Note that for the considered system $\phi^{M} - \phi^{S} = 0$, *i.e.*, there is no electrical work associated with the transfer of ox and red from the phase S into M. When, however, we reduce the concentration of background electrolyte, a positive Donnan potential will be established. According to Eq. [6] and [7] the transfer from S to M will then be associated with an electrical free energy change defined by $z_i\mathbf{F}(\phi^{M} - \phi^{S})$. Taking a realistic value of $\phi^{M} - \phi^{S}$, say 100 mV, we obtain $z_i\mathbf{F}(\phi^{M} - \phi^{S}) = -29$ kJ mol^{-1} for ox and −39 kJ mol^{-1} for red. Comparing these values with WT_{ox} and WT_{red} of Table III demonstrates that, in particular with highly charged ions, the energetic picture will easily be dominated by the electrical work terms. Indeed, experiments similar to the ones characterized in Fig. 1, but with decreasing concentration of background electrolyte, showed a decrease of $(E^{S} - E_1)$, with a value of nearly zero in the absence of CF_3COONa. Unfortunately, E_1 could only be measured *vs.* the reference electrode in the phase S, and values of $\phi^{M} - \phi^{S}$ were not determined (cf. Eq. [18]-[20]). Thus, these experiments could not be analyzed exactly. Still, the results strongly support the overall thermodynamic picture of the system derived above.

Table III. Results from the thermodynamic analyses of the film-covered electrodes in the electrolyte containing 2.5 mM $K_3[Fe(CN)_6]$, 2.5 mM $[Fe(CN)_6]$, and 0.5M CF_3COONa

	C^{M}_{ox} (equil.)/ C^{M}_{red} (equil.)	C^{M}_{red} (equil.)/ mol liter^{-1}	$\gamma^{M}_{ox}/\gamma^{M}_{red}$	WT_{ox}/kJ mol^{-1}	WT_{red}/kJ mol^{-1}
Q12	1.4×10^{4}	1.3×10^{-5}	1.2×10^{-3}	−10.6	+13.0
Q10	7.7×10^{3}	2.6×10^{-5}	2.2×10^{-3}	−10.9	+11.3
Q8	4.3×10^{3}	5.1×10^{-5}	4.0×10^{-3}	−11.1	+9.6
Q1	1.1×10^{2}	3.7×10^{-3}	1.6×10^{-1}	−12.6	−1.0

Acknowledgments

The authors thank Professor Gerischer for valuable discussions and continued support of this work. Helpful discussions with Professor Reich (Freie Universität Berlin) are also gratefully acknowledged.

Manuscript submitted Aug. 18, 1982; revised manuscript received Nov. 2, 1982. This was Paper 620 presented at the Montreal, Canada, Meeting of the Society, May 9-14, 1982.

Any discussion of this paper will appear in a Discussion Section to be published in the December 1983 JOURNAL. All discussions for the December 1983 Discussion Section should be submitted by Aug. 1, 1983.

REFERENCES

1. J. B. Berkowitz, M. Yamin, and R. M. Fuoss, *J. Polym. Sci.*, **28**, 69 (1958).
2. E. A. Boucher and C. C. Mollett, *J. Chem. Soc. Faraday Trans.*, **78**, 75 (1982).
3. F. B. Kaufmann, A. H. Schroeder, E. M. Engler, S. R. Kramer, and J. Q. Chambers, *J. Am. Chem. Soc.*, **102**, 483 (1980).
4. N. Oyama, T. Shimomura, K. Shigehara, and F. C. Anson, *J. Electroanal. Chem. Interfacial Electrochem.*, **112**, 271 (1980).
5. Kuo-Nan and R. W. Murray, *ibid.*, **131**, 37 (1982).
6. D. M. Oglesby, S. H. Omang, and C. N. Reilley, *Anal. Chem.*, **37**, 1312 (1965).
7. H. Gerischer, D. M. Kolb, and J. K. Sass, *Adv. Phys.*, **27**, 437 (1978).

8. R. P. Buck and V. R. Shephard, Jr., *Anal. Chem.*, **46**, 2097 (1974).
9. R. Parsons, in "Modern Aspects of Electrochemistry," Vol. 1, J. O'M. Bockris, Editor, pp. 103-179, Butterworth Publication Ltd., London (1974).
10. F. Helfferich, "Ion-Exchange," McGraw-Hill Book Co., Inc., New York (1962).
11. N. Lakshminarayanaiah, "Membrane Electrodes," Academic Press, New York (1976).
12. R. P. Buck, in "Ion Selective Electrodes in Analytical Chemistry," H. Freiser, Editor, pp. 1-141, Plenum Press, New York (1978).
13. R. P. Buck, F. S. Stover, and D. E. Mathis, *J. Electroanal. Chem. Interfacial Electrochem.*, **82**, 345 (1977).
14. R. A. Robinson and R. H. Stokes, "Electrolyte Solutions," pp. 239-253, Academic Press, New York (1955).
15. D. H. Angell and T. Dickinson, *Electroanal. Chem.*, **35**, 55 (1972).
16. A. G. Sharpe, "The Chemistry of Cyano Complexes of the Transition Metals," Academic Press, London (1976).
17. D. W. Larson and A. C. Wahl, *Inorg. Chem.*, **4**, 1281 (1965).
18. G. J. H. Hanania, D. H. Irvine, W. A. Eaton, and P. George, *J. Phys. Chem.*, **71**, 2022 (1967).
19. M. K. Basu and M. N. Das, *Inorg. Chem.*, **9**, 2781 (1970).
20. G. Gritzner, K. Danksagmüller, and V. Gutmann, *J. Electroanal. Chem. Interfacial Electrochem.*, **72**, 177 (1976).

On the Electrochemical Behavior of Iron Phthalocyanine Film Electrodes in Acid Solution

Carlos A. Melendres*

Argonne National Laboratory, Argonne, Illinois 60439

and Xikang Feng

Tianjin Institute of Power Sources, Tianjin, China

ABSTRACT

The electrochemical behavior of iron phthalocyanine (FePc) films, supported on gold and other metal substrates, was studied in 0.05M H_2SO_4 solution using cyclic voltammetry and rotating disk (with ring) electrode techniques. Reduction of oxygen on the electrodes was observed to be accompanied by the production of hydrogen peroxide. Previously reported "deactivation" of FePc films with repeated cycling was found to be associated with the adsorption of peroxide intermediates. Multiple redox waves on FePc in the region of −0.05 to −1.0V *vs.* Hg/Hg_2SO_4 have been assigned as due to hydrogen adsorbed on different surface sites.

Considerable research on using macrocyclic transition metal complexes as catalyst for the electrochemical reduction of oxygen have been undertaken recently (1-5). Iron phthalocyanine (FePc) and its derivatives appear to be one of the most potent catalysts for the oxygen reduction process (6-9). In a previous work (10), we reported on the electrochemical behavior of FePc films supported on glassy carbon substrates. Our results showed a deactivation of the FePc on repeated cycling. We also observed some voltammetric waves that we thought were due to FePc itself, but did not investigate these in detail. Recently, in the course of our laser Raman spectroelectrochemical investigations on FePc supported on various metal substrates, certain additional information became evident which we would like now to report in this communication. Cyclic voltammetry was used to characterize the electrochemical behavior of FePc films on Au, Pt, Ag, and Cu in 0.05M H_2SO_4; representative results with Au substrate will, however, be reported here. Rotating disk (with ring) electrode studies were undertaken to elucidate the deactivation phenomenon reported previously.

Experimental

Gold, platinum, silver, and copper electrodes were fabricated by spot-welding a 0.25 mm thick × 2.5 mm × 40 mm sheet of high purity (99.999%) metal to a lead wire of the same material. These were then polished with fine sandpaper, cleaned with acetone, thoroughly rinsed with triply distilled water, and dried in air. Gold and platinum ring disk electrodes were purchased from Pine Instrument Company, Grove City, Pennsylvania, which also supplied the RDE3 Double Potentiostat. FePc was purchased from Eastman Kodak Company, Rochester, New York. Sample purity was established by infrared, Mössbauer, and atomic emission spectroscopy together with a carbon, hydrogen, and nitrogen elemental analysis. As an additional precautionary measure, the material was resublimed under vacuum and used. Subsequently, we found no difference in the electrochemical behavior of the starting material and the resublimed sample, so that, henceforth, the FePc was used "as is." The FePc material was supported on the metal substrates in two ways: (*i*) the substrate was dipped in a solution of 0.25 weight percent (w/o) FePc in pyridine for 10 min with any excess solution being removed by shaking off the electrode, and (*ii*) a portion of the same solution was evaporated on the surface. In both cases, the electrode was subsequently washed with triply distilled water prior to use. The average thickness of FePc film was calculated from the amount of solution taken for evaporation. The 0.05M H_2SO_4 solution was prepared from high purity H_2SO_4 (ULTREX, J. T. Baker Chemical Company) and triply distilled water. It was saturated by bubbling commercial grade oxygen through; deaeration was done using He (grade AA) which was previously passed through molecular sieves at liquid nitrogen temperature. A three-compartment electrochemical cell was used for this study. A Princeton Applied Research Model 173 Potentiostat and a Model 179 Universal Programmer were used for cyclic voltammetry. All potentials were measured against Hg/Hg_2SO_4 and are reported here as such.

* Electrochemical Society Active Member.
Key words: iron phthalocyanine, cyclic voltammetry, rotating disk electrode.

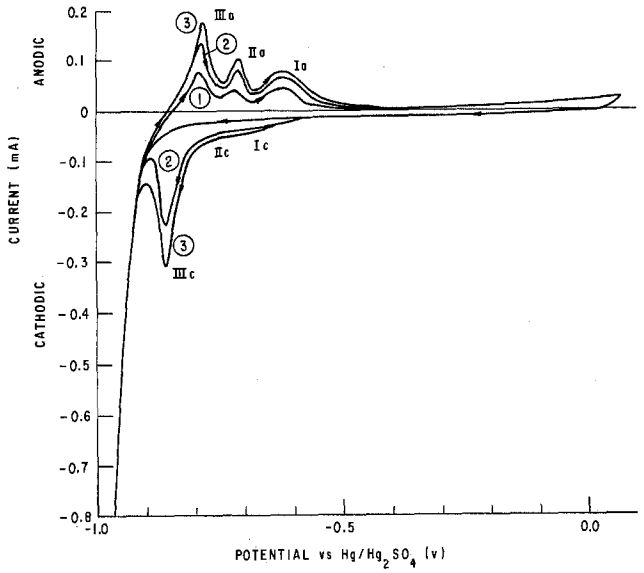

Fig. 1. Cyclic voltammograms on FePc film/Au electrode. He saturated 0.05M H_2SO_4 solution; scan rate = 20 mV/sec.

Cathodic behavior of FePc films supported on gold. —Figure 1 shows a cyclic voltammogram of an FePc film (~3000Å thick) on an Au substrate in 0.05M H_2SO_4 solution saturated with He. Three cathodic waves (I_c, II_c, and III_c) and three anodic waves (I_a, II_a, and III_a) are observed in the voltage range of −0.5 to −0.95V. The cathodic waves (I_c, II_c, and III_c) are hardly evident during the first cathodic scan. Both sets of anodic and cathodic waves appear only when the sweep potential is carried to the region of hydrogen evolution, *i.e.*, to −0.9V. As can be seen, the peaks are very symmetrical, characteristic of reactants confined to the electrode surface. The integrated charges under each peak are in the order of ~300 $\mu C/cm^2$ which correspond to less than 1 monolayer coverage. To further characterize the waves, the variation of peak current with scan rate was measured. Figure 2 shows that the peak currents are proportional to the scan rate for waves, I_a, II_a, III_a, and III_c. Furthermore, the peak potential remains roughly stationary with variation of scan rate. These evidences suggest that the electron transfer processes occurring involve species adsorbed on the FePc film (11). The same results

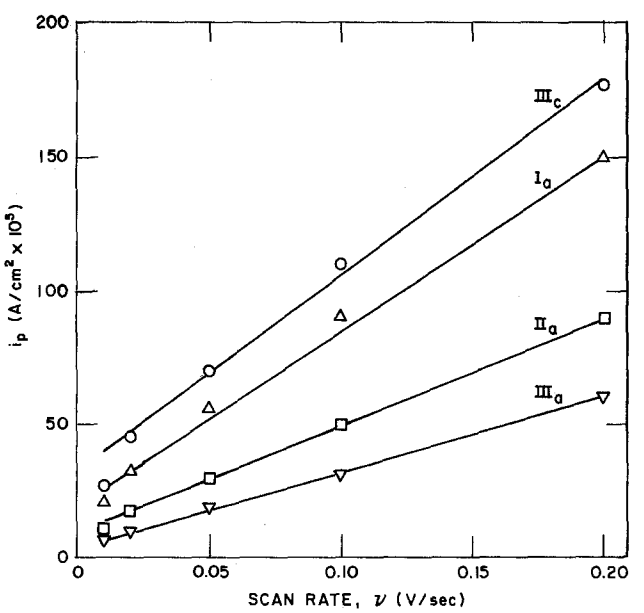

Fig. 2. Variation of peak current with scan rate for waves shown in Fig. 1.

have also been observed on FePc films on silver and copper substrates. The peak potentials of the respective waves are the same as that on FePc/Au system. This indicates that the electrochemical redox process is not related to the nature of substrate used. Our previous studies (10) also showed that the appearance of these waves is independent of the method of preparing the film, and, hence, we have ruled out the possibility that they are due to impurities or to an effect of pyridine on the FePc. To obtain an estimate of the number of electrons involved in the charge-transfer process associated with each wave, we assume that the following equation holds for each peak current, i_p, in the cyclic voltammogram ,*i.e.*

$$i_p = \frac{n^2F^2\Gamma\nu}{4RT} \qquad [1]$$

where Γ is the total surface concentration of the absorbed species in mol/cm², ν is the potential scan rate, and n is the number of electrons transferred per molecule. The value of Γ may be obtained from Q, the charge under the peak, *i.e.*, $\Gamma = Q/nF$. From the experimental values of Q and i_p, one obtains values of n for each process as $n_{III_c} = 1.2$, $n_{III_a} = 1.2$, $n_{II_a} = 1.3$, and $n_{I_a} = 0.94$.

These data provide an indication that one electron is involved in each of the redox processes, albeit approximate in view of the fact that the waves are not strictly reversible and our lack of knowledge of the type of adsorption isotherm involved in the process (11). Since in the region of potential where the waves occur, only hydrogen is oxidized and reduced, it is logical to conclude that the waves observed correspond to hydrogen adsorption and desorption on different surface sites of the FePc film. In this regard, it is worthwhile to point out the remarkable similarity of FePc to Pt which shows at least two different types of chemisorbed hydrogen. The waves appear to be more reversible on Pt than on FePc though.

As already mentioned, similar electrochemical behavior in the potential range of −0.50 to −0.95V to that for FePc-on-gold were found for FePc supported on silver, glassy carbon, and copper substrates. In our previous paper on carbon-supported FePc, we assumed that these waves were due to oxidation and reduction of FePc itself; our additional measurements here now allow a more rational interpretation of these waves to be made.

The electrochemical behavior of Au-supported FePc films in the presence of O_2 is illustrated in Fig. 3. It is evident that FePc films-on-gold promote O_2 reduction as exemplified by the shift of the O_2 reduction wave at −0.5V(II) on bare gold to about −0.05(I) on the FePc film. This well-defined wave is, however, observed only on the first scan, and its intensity is reduced gradually on subsequent cyclic scans. We have termed this phenomenon as "deactivation" (10). Some

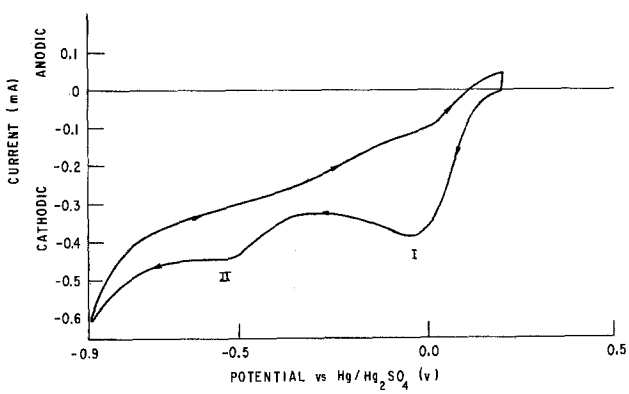

Fig. 3. Oxygen reduction on FePc film/Au electrode in 0.05M H_2SO_4 solution. Scan rate = 20 mV/sec.

of the intensity of the O_2 reduction wave can be recovered by leaving the electrode in solution at open circuit for more than 1 hr. We will discuss this phenomenon further in the next section. It is evident here, however, that the ability of FePc films to reduce O_2 is the same on Au substrates as on glassy carbon (10).

Rotating disk (with ring) electrode studies.—In order to elucidate the "deactivation" phenomenon of FePc films during continued scanning, studies were conducted using the rotating disk (with ring) electrode technique. It was first necessary to ascertain that the deactivation process is not due to a diffusional limitation in the transport of reactant or products at the electrode. To do this, the disk current for O_2 reduction was measured at various rotation rates at a given potential. Figure 4a shows the results obtained by holding the potential on an Au disk without FePc at −0.50V and rotating the disk at various angular frequencies (ω). The disk was kept at a particular rotation rate for 1 min before a current reading was made; the rotation rate was then stepped to the next higher value. As would be expected for a process limited by diffusion, the current for O_2 reduction on the pure Au electrode increases with rotation rate. The behavior of an FePc film on Au towards O_2 reduction is shown in Fig. 4b for comparison. The disk current falls off continually despite increasing rotational speed. Even if the rotation rate is held constant at a given potential, the current still decreases with time. Thus, the cause of current decrease during continued cycling of the FePc film electrode is not due to diffusional limitation in the transport of a solution species.

We speculated in our previous paper (10) that the observed deactivation phenomenon may be due, among other causes, to a limitation in the transport of charge carriers (*i.e.*, electrons) in the film. If this was so, the process should somehow depend on the thickness of the film used. We found, however, that near-monolayer films produced by adsorption of the FePc on the electrode from FePc/pyridine solutions exhibited "deactivation" to nearly the same extent as thick films. We now rule this possibility out.

Finally it is possible that the deactivation process may be due to adsorption of some species produced during the reduction of oxygen, *e.g.*, a peroxide intermediate. To test this, we measured the current on an Au ring concentric to the FePc-coated-Au disk. Figure 5 shows typical results with the ring potential set at +0.40V, a value designed to oxidize any peroxide that may be produced. Significant current was observed on the ring as the disk potential was scanned in the O_2-reduction region. Successive scans on the disk show the electrode deactivation and the consequent decrease in further production of peroxide. To ascertain

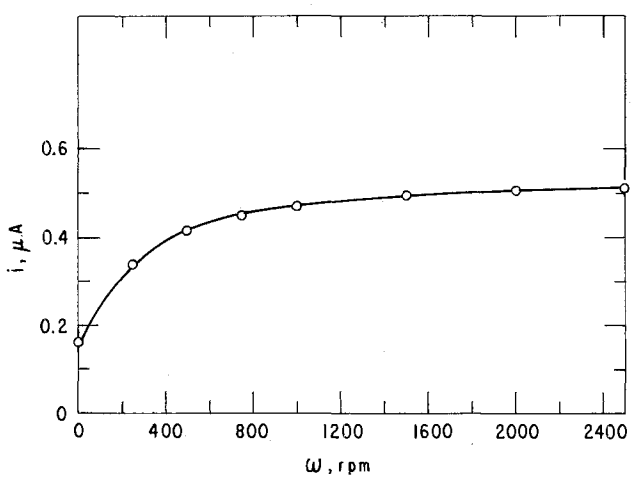

Fig. 4a. Variation of oxygen reduction current on Au disk electrode at −0.5V.

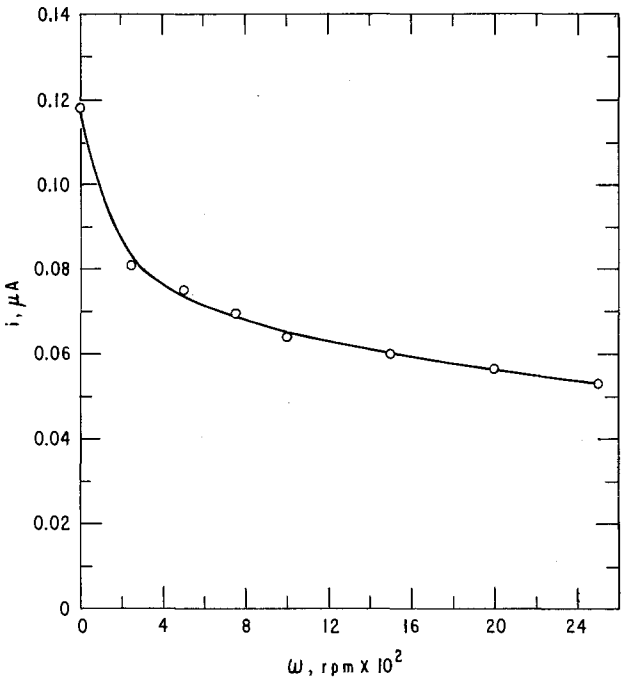

Fig. 4b. Oxygen reduction current on FePc film/Au disk electrode at −0.02V.

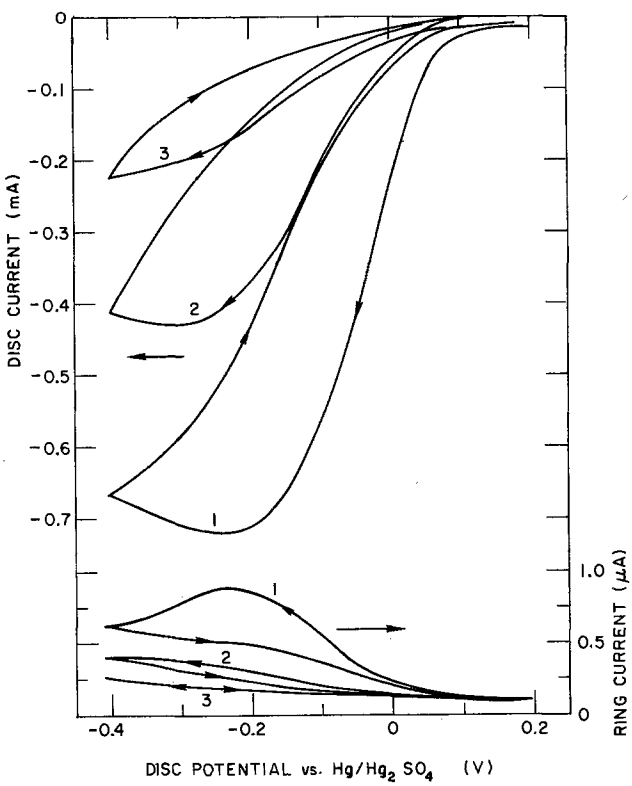

Fig. 5. Variation of disk and ring currents with disk potential during O_2 reduction. Ring potential set at +0.4V vs. Hg/Hg_2SO_4. Scan rate = 20 mV/sec; numbers indicate successive cyclic scan.

that the peroxide is truly produced on the FePc rather than on the bare Au surface, we conducted ring disk studies of O_2 reduction on pure Au. While peroxide is produced on the latter surface, this is generated at significantly more negative potentials than on the FePc.

The question next arises as to whether the deactivation is due to a loss in catalytic activity of the FePc film by attack of a peroxide intermediate with subsequent loss of the iron center or perhaps a loss in the number of active sites by adsorption of the peroxide

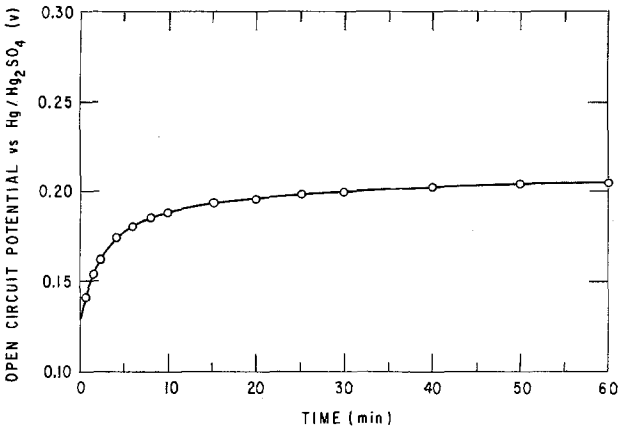

Fig. 6. Relaxation of open-circuit potential of FePc film/Au electrode.

intermediate. Further evidence for the latter comes from an observation of the relaxation of the open-circuit potential (OCV) of the electrode following a cyclic voltammetric sweep to the O_2-reduction region. Figure 6 shows a typical result, It is apparent that the OCV relaxes to its original value rather slowly. Following this return to OCV, the FePc is again active towards O_2 reduction. However, the activity is less than what it originally was. Thus, although the deactivation appears to be primarily due to the adsorption of a peroxide intermediate, some activity is also lost permanently by degradation of the catalyst, presumably through loss of the iron center.

Acknowledgments

One of the authors is grateful to the government of China for fellowship support during the course of this work. We thank Dr. F. A. Cafasso and Dr. V. A. Maroni for their continued interest and management of the program under which this investigation was undertaken. This work was carried out at Argonne National Laboratory under the auspices of the Materials Science Division of the Department of Energy's Office of Basic Energy Sciences.

Manuscript submitted May 27, 1982; revised manuscript received Oct. 20, 1982. This was Paper 539 presented at the Montreal, Canada, Meeting of the Society, May 9-14, 1982.

Any discussion of this paper will appear in a Discussion Section to be published in the December 1983 JOURNAL. All discussions for the December 1983 Discussion Section should be submitted by Aug. 1, 1983.

Publication costs of this article were assisted by Argonne National Laboratory.

REFERENCES

1. J. Zagal, P. Bindra, and E. Yeager, *This Journal*, **127**, 1506 (1980).
2. J. H. Zagal-Moya, Ph.D. Thesis, Case Western Reserve University, University Microfilms Publication No. 7816494 (1978).
3. G. McLendon and A. E. Martell, *Inorg. Chem.*, **16**, 1812 (1977).
4. H. Jahnke, M. Schonborn, and G. Zimmerman, *Top. Curr. Chem.*, **61**, 133 (1976).
5. J. Zagal, *J. Electroanal. Chem.*, **109**, 389 (1980).
6. A. Kozawa, V. E. Zilionis, and R. J. Brodd, *This Journal*, **117**, 1470 (1970).
7. A. Kozawa, V. E. Zilionis, and R. J. Brodd, *ibid.*, **117**, 1474 (1970).
8. J. Zagal, R. K. Sen, and E. Yeager, *J. Electroanal. Chem. Interfacial Electrochem.*, **83**, 207 (1977).
9. A. J. Appleby, J. Fleisch, and M. Savy, *J. Catal.*, **44**, 281 (1976).
10. C. A. Melendres and F. A. Cafasso, *This Journal*, **128**, 755 (1981).
11. S. Srinivasan and E. Gileadi, *Electrochim. Acta*, **11**, 321 (1966).

Error Analysis of the Coulostatic Technique and Comparison to Other D-C Relaxation Techniques for the Measurement of Kinetics of Electrode Reactions

Z. Nagy* and J. T. Arden[1]

Argonne National Laboratory, Chemical Engineering Division, Argonne, Illinois 60439

ABSTRACT

An error analysis of the coulostatic technique was carried out, including the charge impulse and current impulse relaxation modifications. The applicability of the coulostatic technique with graphical and computer curve-fitting data-evaluation methods was investigated for the determination of the exchange current density of electrode reactions. All random and systematic errors were taken into consideration. The results are presented in applicability diagrams in terms of two characteristic times of the electrode reaction: τ_c, the time constant of the double layer capacitance-reaction resistance system, and τ_d, the time constant of the diffusion impedance-reaction resistance system. The graphical method is limited to systems with $\tau_d/\tau_c > 100$ because of its complete neglect of the concentration changes occurring at the electrode surface during the potential relaxation. This method also neglects the concentration changes occurring during the charging pulse and, therefore, the field of applicability decreases with increasing pulse width. However, in practical terms, this does not limit the technique because at pulse width below 1 μsec (which is easily achievable) another effect, the dead time after the pulse, is the final limitation. A dead time of 0.1 μsec limits the technique to $\log \tau_c > -6.5$. The computer curve-fitting method increases the field of applicability of the coulostatic technique because it corrects for the concentration changes occurring during both the charging and discharging processes. This changes the diffusion limitation to $\tau_d/\tau_c > 0.2$, and eliminates the sensitivity to pulse width. In comparison to the single and double pulse galvanostatic techniques and the potential step technique, the coulostatic technique generally limits the determination of the exchange current density to slower reactions and/or larger concentrations. While the coulostatic technique is limited to $\log \tau_c > -6.5$, the other techniques can be used for orders of magnitude smaller τ_c as long as the uncompensated solution resistance is kept small. The coulostatic technique is, of course, totally insensitive to solution resistance. On the other hand, for slow reactions ($\log \tau_c > 1$) the coulostatic technique is more applicable because the others are limited by a large signal-to-noise ratio. For intermediate τ_c values, the fields of applicability of the techniques depend in a complicated fashion on all characteristic times of the electrode reaction (τ_c, τ_d, and τ_r), with the coulostatic technique being generally equal to or less applicable than the others.

The coulostatic technique is part of a group of d-c relaxation techniques frequently used for the determination of kinetics of electrode reactions. In these techniques, an electrode system is perturbed by an aperiodic signal, and the subsequent relaxation is used to gain information about the kinetics and mechanism of the reaction. In the coulostatic technique, the perturbation is the injection of charge into the double layer of an electrode, and the subsequent open-circuit potential relaxation of the electrode is recorded. In the original theory of the technique developed by Delahay (1) and Reinmuth (2), it was assumed that the charge injection is instantaneous, *i.e.*, the faradaic processes and, consequently, the concentration changes at the electrode surface were assumed to be negligible during the charging process. The charging was typically accomplished by discharging a capacitor through the measuring cell. This original version of the technique is often called the charge impulse relaxation technique. The current impulse relaxation technique was suggested by Weir and Enke (3) as a modified technique in which the charging signal is a short, constant-current pulse. For this case, a correction is possible for the faradaic processes occurring during the charging of the double layer, as was shown by Martin and Davis (4). One can consider the charge impulse technique an ideal limit of the current impulse technique as the pulse width approaches zero. This ideal limit can, of course, never be reached, but under some conditions, it can be sufficiently approximated. The exact shape of the charging pulse is immaterial, as long as either the charge impulse approximation can be used or a mathematical correction can be made for the faradaic process occurring during the pulse.

Several methods have been suggested for the determination of electrode kinetic parameters from the relaxation curve. These include: graphical extrapolation (1), numerical calculation (5), nomographic analysis (6), Laplace plane analysis (7, 8), and computer curve fitting (4, 9-11). Comparisons among the data-evaluation methods and comparisons of the coulostatic technique to other relaxation techniques have been published (4, 5, 10, 12), but the basis of these comparisons was not always the same. Consequently, a direct comparison among all relaxation techniques is difficult. Furthermore, no systematic comparison has been made previously between the charge impulse and current impulse techniques. Recently, a novel representation was suggested (13, 14) to describe unambiguously the limitations of relaxation techniques; this involves the definition of an applicability diagram in terms of characteristic times of the electrode reaction to be investigated. Detailed error analyses have been made already to determine the applicability diagrams for the current, potential, and voltage step techniques (13-16). It is desirable to extend the error analysis to the charge and current impulse techniques and to make a direct comparison of the applicability of all d-c relaxation techniques on the same basis.

Theory

The derivations of the basic equations of the charge and current impulse techniques are described in the literature. However, it is useful to recall the general assumptions which form the basis of the derivations. Consider a general redox reaction, $O + ne = R$, which can take place in any number of electrochemical and chemical elementary steps. It is assumed that one of these steps is rate determining and that none of the reaction intermediates are lost by diffusion into the bulk solution. The uniform flux of the reactant to the electrode surface, being equal to the flux of the product away from the electrode, is assumed to be completely supplied by semi-infinite, linear diffusion in the presence of excess supporting electrolyte. This flux is equivalent to the faradaic current density. A linear relation is assumed between the faradaic current density and the overpotential, limiting the experiment

* Electrochemical Society Active Member.
[1] Research participant from Glenville State College, Glenville, West Virginia 26351.
Key words: charge, transients, kinetics, computer, reliability.

to a few millivolts.[2] The double layer capacitance is assumed to be independent of potential and concentrations within the limits of the experiment. Adsorption and double layer effects are neglected. In the following error analysis, all these assumptions are considered completely fulfilled.

The form of the relaxation equation will depend on the shape of the charging pulse. The pulse shapes considered in this communication are shown in Fig. 1. Case a represents the ideal charge impulse approximation in which the time needed to charge the double layer is negligible. Case b represents the ideal current impulse technique in which the pulse generator has an infinitely short rise time. Case c represents a more realistic current pulse, a linearly rising and decaying pulse with finite rise times. The last case can also be used for any triangular pulse with $t_1 = t_2$. To a certain degree, all these cases are idealizations. One of the objectives of this error analysis is to determine the conditions under which these idealizations can be used without causing an unacceptable error in the determination of the exchange current density.

The simplest case is an ideal charge pulse (Fig. 1a) for which all diffusional effects are neglected; *i.e.*, the surface concentrations of the reactant and product are assumed to remain unchanged during charging and discharging of the double layer. This will result in an overpotential-time relation (1) of

$$\eta = \eta_o \exp(-i_o n\mathbf{F}t/\nu RTc) \quad [1]$$

where

$$\eta_o = q/c \quad [2]$$

From a plot of log η *vs.* t, the double layer capacitance can be determined from the intercept, and the exchange current density from the slope. For this graphical data evaluation, the relaxation should be measured at very short times to assure that the neglect of the diffusional effects is valid.

A correction can be made for the concentration changes occurring at the electrode surface during the discharge (1, 2). The potential relaxation following an ideal charge impulse (Fig. 1a) can be described as

$$\eta = \eta_o - \frac{i_o n\mathbf{F}\eta_o}{\nu RTc(b-a)}\left\{\frac{1}{a}[1-\exp(a^2t)\operatorname{erfc}(at^{1/2})] - \frac{1}{b}[1-\exp(b^2t)\operatorname{erfc}(bt^{1/2})]\right\} \quad [3]$$

where

$$a = \frac{i_o}{2\nu n\mathbf{F}}\left(\frac{1}{D_O^{1/2}C_O}+\frac{1}{D_R^{1/2}C_R}\right) + \left[\frac{i_o^2}{4\nu^2n^2\mathbf{F}^2}\left(\frac{1}{D_O^{1/2}C_O}+\frac{1}{D_R^{1/2}C_R}\right)^2 - \frac{i_o n\mathbf{F}}{\nu RTc}\right]^{1/2} \quad [4]$$

and b is the same as a except the expression in brackets is preceded by a minus sign. Equation [3] forms the basis of data evaluations by numerical calculations (5), nomograms (6), Laplace plane analysis (7, 8), and computer curve fitting (9-11).

A mathematical correction can also be made for the concentration changes occurring during the charging of the double layer, in addition to those occurring during the discharge. Thus, the potential relaxation following the pulse shown in Fig. 1b can be described by the equation derived by Matsuda *et al.* (19). (The original equation was derived for the galvanostatic double pulse technique, but it is also applicable for the current impulse relaxation technique if one sets the second pulse current to zero.) This equation is

[2] The limits of the linear i-η relation will be taken as 5 mV in this paper. There is some controversy in the literature about this point: Kooijman *et al.* (17) consider linearization to be allowed generally only for overpotentials less than 1 mV, while Kudirka and Enke (18) have shown by numerical calculations that, with the linearized relation, the coulostatic technique will give good results up to at least 25 mV.

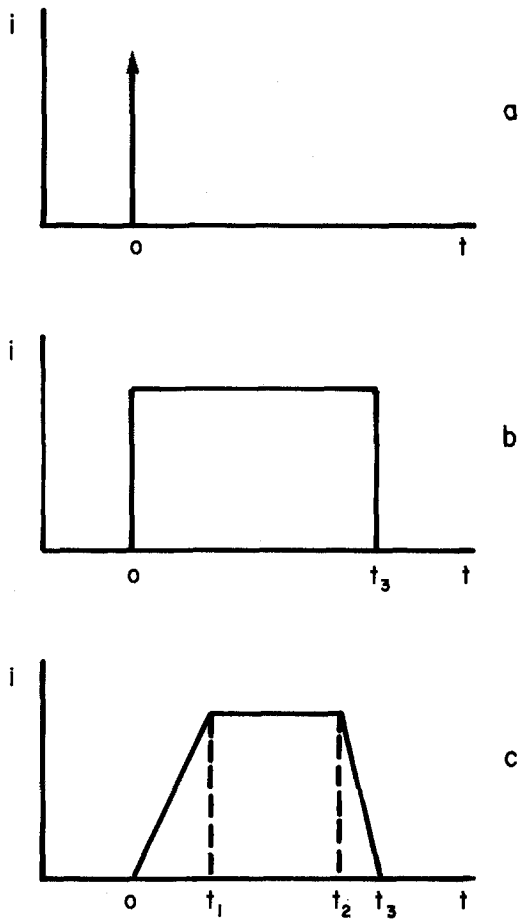

Fig. 1. Pulse shapes: a, idealized charge pulse; b, idealized current pulse; c, current pulse with finite rise times.

$$\eta = \frac{i}{c(b-a)}\left\{\frac{b}{a^2}[G_1(a,t)-G_1(a,t-t_3)] - \frac{a}{b^2}[G_1(b,t)-G_1(b,t-t_3)]\right\} \quad (\text{for } t>t_3) \quad [5]$$

where

$$G_1(x,y) = \exp(x^2y)\operatorname{erfc}(xy^{1/2}) + 2x(y/\pi)^{1/2} - 1 \quad [6]$$

The relaxation following the pulse of Fig. 1c can be expressed as (20)

$$\eta = \frac{i}{c}\left\{\frac{1}{t_1}[G_2(t)-G_2(t-t_1)] - \frac{1}{t_3-t_2}[G_2(t-t_2)-G_2(t-t_3)]\right\} \quad (\text{for } t>t_3) \quad [7]$$

where

$$G_2(y) = \frac{b}{a^4(b-a)}G_1(a,y) - \frac{a}{b^4(b-a)}G_1(b,y) + \frac{ab-(a+b)^2}{(ab)^2}y + \frac{4(a+b)}{3\sqrt{\pi}ab}y^{3/2} \quad [8]$$

Equations [5] and [7] form the basis of curve-fitting data evaluation (4).

The above equations are written for the classical electrochemical cell containing one working electrode. It was shown by Kooijman *et al.* (17) that the use of two identical working electrodes, one polarized anodically and the other cathodically, can extend considerably the magnitude of the linear current density-overpotential range. The above equations remain valid for a two-working-electrode cell if η is considered to be one half of the total measured overpotential. The

equations can also be extended to more complex reactions, as has been shown by Reller and Kirowa-Eisner (21).

The parameters which can be determined from the evaluation of the relaxation curves are: the ratio of the exchange current density to the stoichiometric number (i_o/ν), the double layer capacitance (c), and the diffusion parameter ($1/D_O^{1/2}C_O + 1/D_R^{1/2}C_R$). Since the technique is limited to the linear i-η range, only the i_o/ν ratio can be determined and not the exchange current density itself. For the sake of simplicity, the term "exchange current density" will refer to the i_o/ν ratio throughout this communication.

Error Analysis

The procedures used in the error analysis were similar to those published previously (13, 14) and will be described here only briefly. The error analysis consisted of essentially two steps: (*i*) synthetic data were generated with one of the basic relaxation equations, using a wide range of values for the electrode reaction parameters, and random errors were added to the data, then (*ii*) one of the data-evaluation methods was used to determine the exchange current density, double layer capacitance, and the diffusion parameter. The errors to be evaluated can be conveniently divided into systematic and random errors. The systematic errors are those caused by (*i*) the simplifications of the mathematical treatment (*e.g.*, the neglect of the pulse width or the concentration changes at the electrode surface during and after the pulse) and (*ii*) the selection of the measuring time. These errors were evaluated by (*i*) generating the synthetic data with an equation fully incorporating the given effect (*e.g.*, the pulse width) and evaluating the data with an equation neglecting it and (*ii*) by evaluating the data in different time regimes. The random errors include all measurement errors: charge, current, electrode area, potential, and time. These errors were considered at two levels: ±1.0% and ±0.1%. The errors of the first three parameters were introduced by assigning a value to the charge density or current density in the data evaluation that is different from the value used in the data generation. The error of the potential and time were combined in that of the potential, the value of which was rounded off after 2 or 3 significant figures. Thus, data sets were created with ±50 or ±5 μV error, corresponding to 1.0 or 0.1% of the maximum 5 mV overpotential.

The error analysis was carried out in terms of two characteristic times of the electrode reaction system: τ_c, the time constant of the reaction resistance-double layer capacitance system, and τ_d, the time constant of the reaction resistance-diffusion impedance system (14), as defined by

$$\tau_c = \frac{\nu RTc}{n\mathbf{F}i_o} \qquad [9]$$

and

$$\tau_d = \frac{\pi\nu^2 n^2 \mathbf{F}^2}{4i_o^2\left(\frac{1}{D_O^{1/2}C_O} + \frac{1}{D_R^{1/2}C_R}\right)^2} \qquad [10]$$

All the errors can be expressed as functions of these two time constants if η_o is kept constant. The situation is similar to that of the galvanostatic and potentiostatic techniques (13-16), except that in those cases a third time constant, τ_r, the time constant of the uncompensated solution resistance-double layer capacitance system, is also needed to fully define the errors. The results of the error analysis are presented graphically on an applicability diagram, a format discussed earlier (13, 14). On these diagrams, an area is defined in terms of log κ and log τ_c in such a way that if an electrode system falls within the borders of this area its exchange current density is measurable with an error less than ±20%.[3] In these diagrams, the rate constant parameter, $\kappa(= \sqrt{\pi/4\tau_d})$, is used instead of τ_d because the former can be directly related, under simplified conditions, to the first-order standard heterogeneous rate constant. If one assumes that $D_O = D_R = D$, $C_O = C_R$, and $\nu = 1$, then $\kappa = 2k_o/\sqrt{D}$; and for $D = 10^{-5}$ cm^2 sec^{-1}, $\kappa = 632k_o$.

Some general features of the applicability diagram are as follows. The main scales (log κ, log τ_c, and τ_r) are exact and valid for any combinations of the parameters they contain; under general conditions, only these scales can be used to define the position of an electrode system on the diagram. There are also three approximate, auxiliary scales shown (i_o, k_o, and C). These are convenient because they define a system with familiar parameters, but they are exact only under restricted conditions. The i_o scale assumes that $c = 20$ μF cm^{-2}, $T = 298$ K, and $n = \nu = 1$. The concentration scale further assumes that $D_O = D_R = 10^{-5}$ cm^2 sec^{-1} and $C = C_O = C_R$. All these restrictions apply to the k_o scale.

The errors will be a function, in addition to the time constants, of the measuring time regime. This, however, is under the control of the experimenter and the following time selection was made for this error analysis. The first data point was taken at t_3 + 0.1 μsec. The 0.1 μsec "dead time" is caused by experimental difficulties: an inductive spike at the end of the pulse and the following ringing caused by impedance mismatches make it impossible to obtain a meaningful potential measurement during this time. The end of the measuring time was set by the potential decay. The potential, which was set to 5 mV at time t_3 by appropriate selection of charging pulse, was allowed to decay to 1.0 ± 0.5 mV. It was considered that the signal-to-noise ratio will be unacceptably large below this overpotential. A minimum pulse length of 5 μsec was selected to allow sufficient time for data collection, and the maximum pulse length was set to 60 sec to avoid the development of convection in the solution (22). In every case, fifty data points were generated, evenly distributed during the measurement time. Other time regimes were also tested, but the above regime was found to result in the smallest overall error of the exchange current density.

Two data-evaluation methods were examined in detail: (*i*) the graphical method based on Eq. [1], for which the data were generated using Eq. [5] and (*ii*) curve-fitting methods based on Eq. [3], [5], and [7], for which data were generated using Eq. [5] and [7].

In the graphical data-evaluation method, the first ten of the fifty points were used to define the log η *vs.* t line; the intercept and slope were calculated using least squares fitting. The intercept was defined either at $t_o = 0$ or $t_o = t_3$. The double layer capacitance was calculated from the intercept, and this value was used to calculate the exchange current density from the slope. The double layer capacitance could also be determined from the initial slope of the η *vs.* t line, but, as has been shown by Kudirka *et al.* (10), the error of the exchange current density is smaller when the double layer capacitance is taken from the intercept, because of a cancellation of errors.

The curve-fitting evaluations were carried out using computer programs described previously (13). All fifty data points were used in the calculations; fitting with more than fifty points was not tried because earlier work indicated (13-15) that this will not appreciably increase the field of applicability. When fitting with Eq. [3], the zero time was set either to $t_o = 0$ or $t_o = t_3$. When fitting with Eq. [5], a correction could be made for the finite rise time of the pulse by determining the charge passed during the

[3] Applicability diagrams could also be defined for the measurement of the double layer capacitance and the diffusional parameter, but this error analysis was concentrated on the measurement of the exchange current density.

pulse and using a modified value of the current density ($i' = q/t_3$) in the data evaluation. All calculations were carried out on an IBM 370/195 computer; the computational time for the curve-fitting calculations ranged from a few seconds to a few tens of seconds.

Results

The applicability diagram for the measurement of the exchange current density with the graphical data evaluation, based on Eq. [1] and with $t_0 = t_3$, is shown in Fig. 2. The effects limiting the applicability of the method are different on each section of the diagram, and they are described below, proceeding clockwise from the upper left-hand corner. The limitation of the field of applicability at small τ_c values is caused by the neglect of the finite width of the charging pulse: the field of applicability increases as the pulse width decreases. When the pulse width becomes less than 10^{-6} sec, another limiting factor takes control: the 0.1 μsec dead time after the pulse. The κ limit of the applicability decreases continuously as τ_c increases because of the increased diffusional effects, which are completely neglected in this data evaluation method. The limit at large τ_c values is the result of the maximum 60 sec measuring time. Finally, the 10^{-2} mol cm^{-3} concentration limit is due to solubility limitations and the requirement of excess supporting electrolyte. The effect of increased measurement accuracy is indicated by the dotted lines in Fig. 2. Using $t_0 = 0$ in the data evaluation makes it much more sensitive to the pulse width, as shown by the solid lines in Fig. 3.

The curve-fitting data evaluation based on Eq. [3] resulted in the applicability diagram shown in Fig. 4, for $t_0 = t_3$. All the limiting effects are the same as those described for Fig. 2. When starting the time from $t_0 = 0$, the method is more sensitive to pulse width, as indicated by the dashed lines in Fig. 3. The synthetic data evaluated in Fig. 2-4 were generated with Eq. [5], using an idealized current pulse shape (Fig. 1b) which has a finite width but zero rise time, and the effect of the pulse width is indicated on the figures. Of course, all effects of the pulse width can be eliminated by using the curve-fitting procedure based on Eq. [5], thus resulting in a field of applicability identical to the maximum field shown on Fig. 4. To use the more realistic pulse shape of Fig. 1c, the data were generated with Eq. [7]. These data were

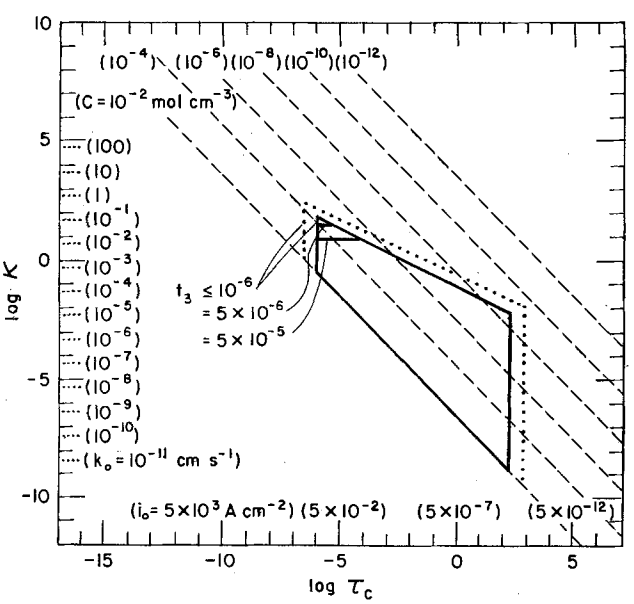

Fig. 2. Applicability diagram of the graphical data evaluation method based on Eq. [1]. The solid line marks the field of applicability for determining the exchange current density with a maximum error of ±20%, with a measurement accuracy of ±1%. The dotted line extends the field to the ±0.1% accuracy case.

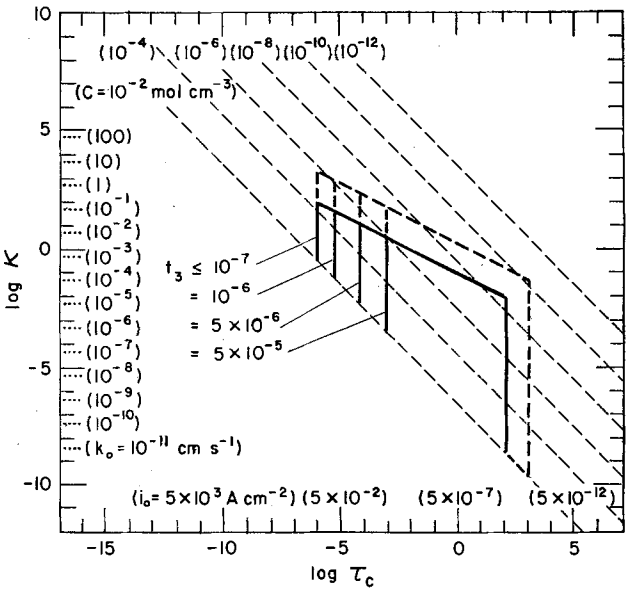

Fig. 3. Applicability diagram of the graphical data-evaluation method based on Eq. [1] (solid line) and the curve-fitting method based on Eq. [3] (dashed line), with $t_0 = 0$. Measurement accuracy: ±1%.

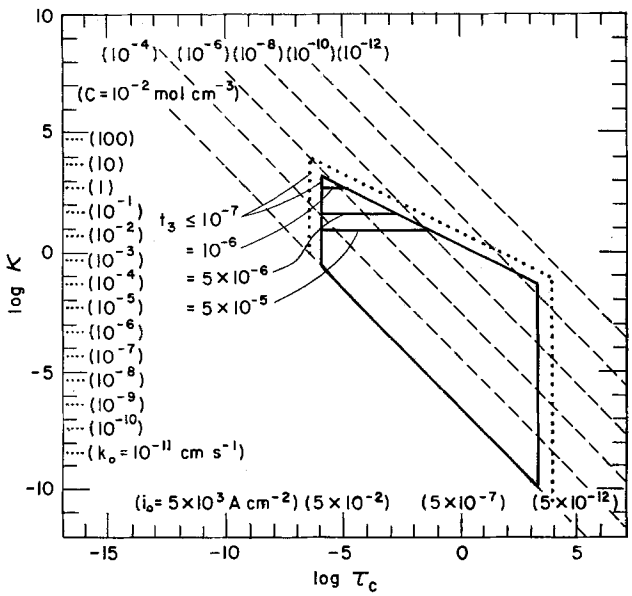

Fig. 4. Applicability diagram of the curve-fitting data-evaluation method based on Eq. [3]. Conditions same as for Fig. 2.

evaluated only with the curve-fitting procedures. Using the evaluation based in Eq. [7], one obtains the applicability diagram shown in Fig. 5. One can also evaluate the data generated using Eq. [7] with a curve-fitting based on Eq. [5] and make a correction for the finite rise time of the pulse by using the modified current density (i') in the data evaluation; this procedure resulted in a field of applicability only slightly smaller than that shown in Fig. 5.

For the curve-fitting evaluations, an initial guess is required to start the calculations. For Fig. 2-5, guess factors of ten were used for the exchange current density, the double layer capacitance, and the diffusion coefficients (the concentrations were assumed to be known exactly). Numerous tests were also made using higher guess factors for the exchange current density: it was found that the applicability diagrams will remain unchanged as long as this factor is not larger than 1000.

Applicability diagrams were not determined for the calculation of the double layer capacitance and the

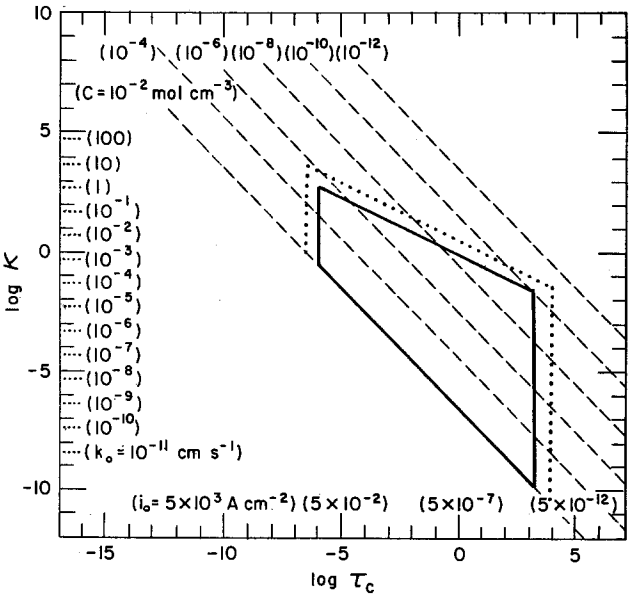

Fig. 5. Applicability diagram of the curve-fitting data-evaluation method based on Eq. [7]. Conditions same as for Fig. 2.

diffusion parameter, but the following observations were made. The fields of applicability for the calculation of the double layer capacitance completely overlap, and are larger than those of the exchange current density. This was the case for all data evaluation methods. On the other hand, the diffusion parameter can be calculated only with the curve-fitting methods and only for log $\kappa \geqq 1$. Under these conditions, its field of applicability is somewhat larger than that of the exchange current density.

Discussion

In the following paragraphs, a comparison will be made among the data evaluation methods of the charge and current impulse relaxation techniques, and the limiting effects will be discussed in comparison with the limitations of all other d-c relaxation techniques.

The neglect of the width of the charging pulse is a common limitation of the graphical data evaluation based on Eq. [1] and the curve-fitting evaluation based on Eq. [3]. As indicated in Fig. 2 and 4, the field of applicability decreases as the pulse width increases. However, from a practical standpoint, this does not limit the technique because pulses of 10^{-6} to 10^{-7} sec duration can be easily achieved with modern instrumentation. Another factor limits the applicability—the dead time at the end of the pulse when meaningful potential measurements cannot be made. The duration of the discharge process decreases with increasing reaction rate, and the technique cannot be used when most of the discharge occurs during the dead time. In this analysis a value of 0.1 μsec was used for the dead time; this or an even somewhat shorter value can be achieved by careful design of the cell and instrumentation (23-25). Therefore, it can be concluded that pulses shorter than 10^{-6} and 10^{-7} sec can be considered true charge pulses for the graphical and curve-fitting data evaluations, respectively. Of course, if the dead time is reduced by better instrumentation, this conclusion would be changed. The above remarks refer to the case when the time scale of the data evaluation starts at the end of the pulse ($t_0 = t_3$). Starting the time scale at $t_0 = 0$ will produce a much larger sensitivity to pulse width for both data evaluation methods (Fig. 3). This is understandable since in the derivation of Eq. [1] and [3] it was assumed that the discharge starts at the end of the pulse.

One advantage of the curve-fitting method over the graphical one is the ability to correct for the diffusional effects during the relaxation. This enlarges the field of applicability by about 1.5 log κ unit at any value of τ_c (compare Fig. 2 with Fig. 4). The decrease of the κ limit with increasing τ_c arises from the competition between the reaction resistance and the diffusion impedance for the control of the discharge curve. The limiting case is equivalent to $\tau_d/\tau_c \gtrsim 100$ and 0.2 for the graphical and curve-fitting methods, respectively. These limitations are in approximate agreement with the results of previous error analyses (3, 5, 11).[4] The curve-fitting method also extends the applicability field at large τ_c values, because it is able to extract the kinetic information from data with low kinetic content since it uses all data points of the experiment. At the large τ_c values, the limitation is caused by the fact that, for slow reactions, very little discharge occurs during the 60 sec maximum discharge time; this time limit was chosen to avoid convective effects in the solution adjacent to the electrode.

The curve-fitting evaluation method also gives one an opportunity to correct for the pulse width, that is, to account for the concentration changes at the electrode surface both during charge and discharge of the double layer. Equation [7] can be used as the basis of curve fitting, resulting in the complete elimination of the pulse-width effect (Fig. 5); however, this improvement occurs at the price of a slightly reduced field of applicability (with a loss of about 0.2 log κ unit at all τ_c values) due to the increased tendency of the curve fitting to give erroneous results as the complexity of the fitting equation increases. Using Eq. [5] as the basis of the curve fitting for data generated with pulses shown on Fig. 1c will result in a field of applicability smaller than that of Fig. 5. This error, which is introduced by the neglect of the rise times of the pulse in Eq. [5], can be shown to be nearly equal to the percent error in the charge and can be corrected for by using a modified value of the current (i'). This modification does not result in a larger field of applicability than shown on Fig. 5, but the principle can be used to allow curve fitting with nonideal pulses, as follows. Curve fitting can be carried out with an idealized pulse shape which describes the real pulse as closely as possible (*e.g.*, Eq. [7] with linearized rise and fall of the pulse). And, by measuring the actual charge passed during the real pulse (*e.g.*, nonlinear rise and fall), one can make a correction for the nonideality of the pulse by modifying the value of the current used in the evaluation.

All curve-fitting calculations require initial guesses of the parameters to be determined; however, they can be obtained easily. The guess for the exchange current density must be within a factor of 1000 of the true value; this can be obtained using the graphical evaluation method based on Eq. [1]. The other parameters must be known within a factor of ten, and the use of $c = 20$ μF cm^{-2} and $D = 10^{-5}$ cm^2 sec^{-1} will suffice in practically every case.

The effect of measurement accuracy is indicated on the applicability diagrams. The low accuracy ($\pm 1\%$) can be achieved with analog measuring equipment, while the high accuracy ($\pm 0.1\%$) can be approached using digital instrumentation. This higher accuracy will result in about a one-half order of magnitude gain in the κ limit because it allows a better correction for the diffusional effects.

As mentioned earlier, the time regime of the measurement also influences the error of the determination of the exchange current density. Early in the dis-

[4] Different criteria are used in these works, but it can be shown that they are approximately equivalent to the τ_d/τ_c ratio. Often, the ratio τ_c/τ_d' is used where τ_d' is the time constant of the double layer capacitance-diffusion impedance system; but $\tau_d' = \pi\tau_c^2/4\tau_d$ and, therefore, $\tau_c/\tau_d' \approx \tau_d/\tau_c$. Another ratio used is $(a + b)^2/ab$, which is also approximately equal to τ_d/τ_c because $(a + b) = \kappa = \sqrt{\pi/4\tau_d}$ and $ab = 1/\tau_c$.

charge, the reaction resistance is the controlling element, but the control will shift with time to the diffusional impedance as the concentration changes increase at the electrode surface. Therefore, the exchange current density should be determined from short time data when using the graphical data evaluation, which neglects the diffusion (1, 10, 12). The situation is different, however, for the curve-fitting data-evaluation methods. The transients were analyzed by several authors to establish the regions of maximum information content with respect to each parameter, and it was shown that the exchange current density is best calculated from the transient at around $t = \tau_c$ (5, 11), the double layer capacitance at $t \to 0$ (11), and the diffusional parameter at $t \to \infty$. Thus, to determine the best time regime for the calculation of the exchange current density, one needs an estimate of the exchange current density. This difficulty can be avoided by selecting a charge pulse that gives, at the beginning of the discharge, the maximum overpotential allowed by the linearization of the i-η relation, and by the following the discharge as long as practical (limited by the measurement error of the overpotential). If this is done, then one can be assured that all the information available from the given electrode system is contained in the transient. The curve-fitting method will then have all the information needed for the calculation of all three parameters, as long as the system is within the field of applicability. On the other hand, a different optimal time will exist if one does not need to determine all three parameters (5, 11). For example, a somewhat different type of curve-fitting procedure was suggested by Reller and Kirowa-Eisner (11): they proposed an iterative series of one-parameter curve fittings for the determination of the exchange current density and the double layer capacitance (assuming that the diffusion parameter is known), using different pulse lengths for each parameter to maximize the sensitivity of the measurements. This method was not fully examined in the present work. However, it was determined that, in order to take an advantage of the inherently lower error resulting from the use of fewer parameters, the effect of diffusion must be negligible or the diffusion parameter must be exactly known. The maximum permissible error of the diffusion parameter will depend on τ_c and τ_d; *e.g.*, for the case given by Reller and Kirowa-Eisner (Ref. 11, Table II; in our nomenclature: $\log \kappa = 2.9$, $\log \tau_c = -5.5$) the three-parameter curve-fitting will give better results unless the error of the diffusion parameter is less than 3%. Therefore, care must be exercised in fixing a parameter value, especially if it has a significant effect on the relaxation curve.

Some discussion of the charging pulse shape is in order. The practical shapes are limited, although in principle any shape can be used. This communication evaluates some of the most commonly applied shapes: the current pulse with finite rise and fall (the linearization of this rise and fall is a good approximation for modern pulse generators) and the triangular pulse. Another often used pulse shape is an exponentially decaying pulse generated by the discharge of a capacitor. This was not evaluated here, but the concentration change by the end of such a pulse would not be considerably different from that for a constant current pulse of the same duration and equal charge content; therefore, the results presented here will be approximately applicable for this case also. Of course, when the coulostatic approximation is correct, the shape of the pulse is immaterial, as has been pointed out previously (26).

In this communication, only two extreme cases were investigated: graphical data evaluation, which neglects concentration changes both during charge and discharge, and computer curve fitting, which has the capability to correct for both effects. Several other data evaluation methods, which will correct for the concentration changes at the electrode surface during the discharge but not during the charge, have been suggested (5-8). The applicability diagrams of these methods are expected to fall in between the two extreme cases investigated here and were, therefore, not evaluated.

In the comparison of the coulostatic techniques to other d-c relaxation techniques, only those data evaluation methods will be considered which result in the largest field of applicability for each technique. This is invariably a computer curve-fitting method, which extends the field of applicability to at least one order of magnitude faster reactions over the graphical data evaluation method.

A comparison of the coulostatic technique to the galvanostatic single pulse technique (14, 16) reveals them to be practically equivalent in the log τ_c range of 1 to -6.5 (Fig. 6). For smaller τ_c values only the galvanostatic technique is applicable, while for larger τ_c values only the coulostatic technique can be used. For fast reactions (small τ_c), the coulostatic technique is limited by the fast discharge of the double layer; this factor does not affect the galvanostatic technique, which therefore can be used for log $\tau_c < -6.5$. However, the galvanostatic technique is limited by the value of τ_r and has an advantage over the coulostatic technique only if $\tau_r < 10^{-7}$ sec, a value which can be achieved in practice (16). The coulostatic technique is, by its nature, unaffected by the value of τ_r.[5] For slow reactions (large τ_c), the galvanostatic technique is limited by the signal-to-noise ratio, while this ratio does not limit the coulostatic technique. Therefore, the coulostatic technique can be used for slower reactions than the galvanostatic technique, being finally limited by the slow discharge of the double layer and the maximum 60 sec measuring time. The diffusional limitations of the two techniques are approximately the same.

A comparison of the coulostatic technique to the galvanostatic double pulse technique (13, 16) results in similar conclusions (Fig. 7). At log $\tau_c < -6.5$, only the galvanostatic technique is usable for reasons given above; while at log $\tau_c > 1$ only the coulostatic technique is applicable because the galvanostatic double pulse technique is limited by the signal-to-noise ratio.

[5] At large τ_r values, a problem can arise if the measuring device goes into saturation during the charging pulse, but this can be avoided using appropriate instrumentation [*e.g.*, Ref. (27)].

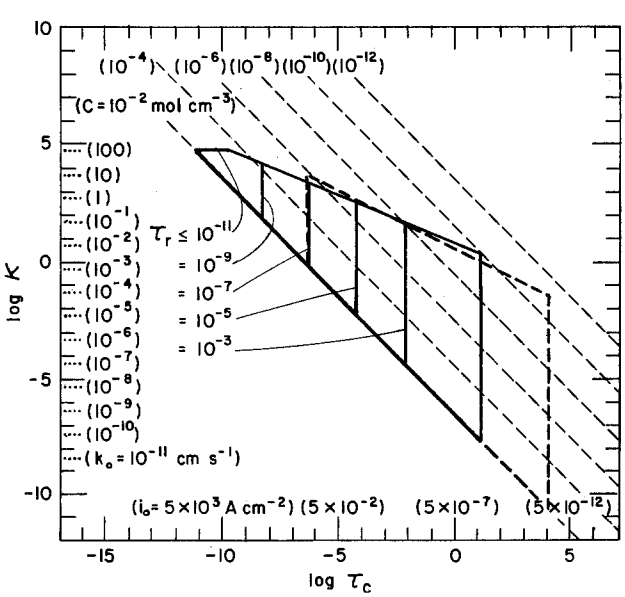

Fig. 6. Comparison of the coulostatic (dashed line) and the galvanostatic single pulse (solid line) techniques, using the best curve-fitting data-evaluation methods. Measurement accuracy: ±0.1%.

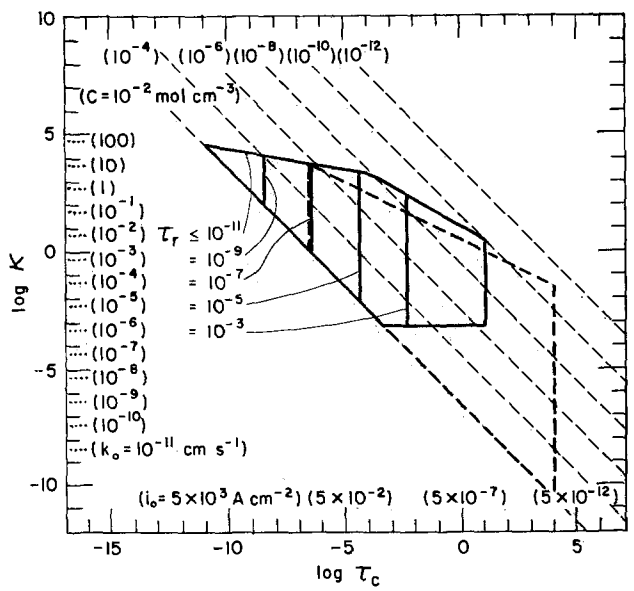

Fig. 7. Comparison of the coulostatic (dashed line) and the galvanostatic double pulse (solid line) techniques, using the best curve-fitting data-evaluation methods. Measurement accuracy: ±0.1%.

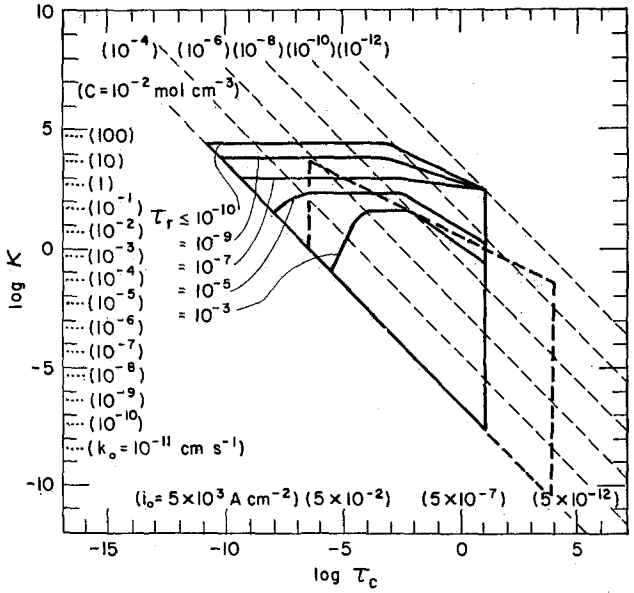

Fig. 8. Comparison of the coulostatic (dashed line) and the potential step (solid line) techniques, using the best curve-fitting data-evaluation methods. Measurement accuracy: ±0.1%.

However, their applicabilities are not identical for the intermediate τ_c range. At high κ values (large diffusional effect), the galvanostatic double pulse technique is applicable to electrode systems with at least one-half order of magnitude larger κ value, because this technique, due to the fast precharging of the double layer capacitance, is able to correct better for the diffusional effects. On the other hand, the galvanostatic double pulse technique is not applicable below a log κ value of −3, being limited by signal-to-noise ratio.

The comparison of the coulostatic technique to the potentiostatic technique (15) is more complicated, as shown in Fig. 8. Again, only the coulostatic technique is applicable at log $\tau_c > 1$, and only the potentiostatic one at log $\tau_c < -6.5$. In the intermediate range, the fields of applicability depend in a complicated fashion on τ_r, τ_c, and κ. One can generalize that the potentiostatic technique has the advantage if τ_r is small.

Conclusions

The graphical data-evaluation method of the coulostatic technique is severely limited by its complete neglect of the concentration changes occurring at the electrode surface during the potential relaxation. For the measurement of the exchange current density, this restricts the applicability of the method to $\tau_d/\tau_c > 100$, that is, to relatively slow reactions and/or large concentrations. The graphical method also neglects the concentration changes occurring during the charging pulse and, therefore, the field of applicability decreases with increasing pulse width. However, in practical terms, this does not limit the technique because at a pulse width below 1 μsec (which is easily achievable) another effect, the dead time after the pulse, is the final limitation. A dead time of 0.1 μsec limits the technique to log $\tau_c > -6.5$. At the other end of the scale, the method is limited to log $\tau_c \lesssim 3$ by the 60 sec limit on the measuring time.

The computer curve-fitting data-evaluation method considerably increases the field of applicability of the technique because it corrects for the concentration changes occurring during both the charging and discharging processes. This changes the diffusion limitation to $\tau_d/\tau_c > 0.2$ and eliminates the sensitivity to pulse width. In terms of κ, it enlarges the field of applicability by 1.5 log κ units, independently of the value of τ_c. That is, the computer curve fitting allows the measurement of two and a half order of magnitude faster reactions, at the same solution composition, than the graphical method. Furthermore, the curve-fitting method allows the calculation of the diffusion parameter from the same data as the exchange current density.

In comparison to the single and double pulse galvanostatic techniques and the potential step technique, the coulostatic technique generally limits the determination of the exchange current density to slower reactions and/or larger concentrations. While the coulostatic technique is limited to log $\tau_c > -6.5$, the other techniques can be used for orders of magnitude smaller τ_c as long as the uncompensated solution resistance is kept small. The coulostatic technique is, of course, totally insensitive to solution resistance. On the other hand, for slow reactions (log $\tau_c > 1$) the coulostatic technique is more applicable because the others are limited by a large signal-to-noise ratio. For intermediate τ_c values, the fields of applicability of the techniques depend in a complicated fashion on all characteristic times of the electrode reaction (τ_c, τ_d, and τ_r), with the coulostatic technique being generally equal to or less applicable than the others.

Acknowledgment

This work was performed under the auspices of the Division of Materials Science, Office of Basic Energy Sciences, U.S. Department of Energy.

Manuscript submitted June 22, 1982; revised manuscript received Nov. 5, 1982. This was Paper 601 presented at the Denver, Colorado, Meeting of the Society, Oct. 11-16, 1981.

Any discussion of this paper will appear in a Discussion Section to be published in the December 1983 JOURNAL. All discussions for the December 1983 Discussion Section should be submitted by Aug. 1, 1983.

Publication costs of this article were assisted by Argonne National Laboratory.

LIST OF SYMBOLS

a	defined by Eq. [4] (sec$^{-1/2}$)
b	defined by Eq. [4] (sec$^{-1/2}$)
c	capacity of the double layer (F cm^{-2})
C_j	concentration of species j in the bulk solution (mol cm^{-3})
D_j	diffusion coefficient of species j (cm^2 sec^{-1})
F	Faraday constant (C mol^{-1})
G_1	defined by Eq. [6]
G_2	defined by Eq. [8]

i current density (A cm^{-2})
i' modified current density, $= q/t_3$ (A cm^{-2})
i_o apparent exchange current density (A cm^{-2})
k_o apparent standard heterogeneous rate constant (cm sec^{-1}), $= i_o/n\mathbf{F}C_O^{(\alpha_a/n)}C_R^{(\alpha_c/n)}$, where α_a and α_c are the anodic and cathodic transfer coefficients
n total number of electrons transferred in the overall reaction
O (index) oxidant
q charge density (C cm^{-2})
R (index) reductant
R universal gas constant (J K^{-1} mol^{-1})
R_r reaction resistance, $= \nu RT/n\mathbf{F}i_o$ (Ω cm^2)
R_s uncompensated solution resistance between the working and reference electrodes (Ω cm^2)
t time (sec)
t_0 zero time for data evaluations (sec)
t_1 defined by Fig. 1 (sec)
t_2 defined by Fig. 1 (sec)
t_3 defined by Fig. 1 (sec)
T temperature (K)
η overpotential (V)
η_o overpotential at the beginning of discharge (V)
κ rate constant parameter, $= \sqrt{\pi/4\tau_d}$ (sec$^{-1/2}$)
ν stoichiometric number of the reaction mechanism
τ_c time constant of the double layer capacitance-reaction resistance system, $= cR_r$ (sec)
τ_d time constant of the diffusion impedance-reaction resistance system, $= \dfrac{\pi\nu^2n^2\mathbf{F}^2}{4i_o^2\left(\dfrac{1}{D_O^{1/2}C_O}+\dfrac{1}{D_R^{1/2}C_R}\right)^2}$ (sec)
τ_r time constant of the double layer capacitance-solution resistance system, $= cR_s$ (sec)

REFERENCES

1. P. Delahay, *J. Phys. Chem.*, **66**, 2204 (1962).
2. W. H. Reinmuth, *Anal. Chem.*, **34**, 1272 and 1446 (1962).
3. W. D. Weir and C. G. Enke, *J. Phys. Chem.*, **71**, 275 (1967).
4. R. F. Martin and D. G. Davis, in "Computers in Chemistry and Instrumentation," Vol. 2, J. S. Mattson, H. B. Mark, and H. C. MacDonald, Editors, Chap. 4, Marcel Dekker, New York (1972).
5. D. J. Kooijman and J. H. Sluyters, *Electrochim. Acta*, **12**, 1579 (1967).
6. D. J. Kooijman, *J. Electroanal. Chem. Interfacial Electrochem.*, **18**, 81 (1968).
7. H. P. van Leeuwen, D. J. Kooijman, M. Sluyters-Rehbach, and J. H. Sluyters, *ibid.*, **23**, 475 (1969).
8. A. A. Pilla, in "Computers in Chemistry and Instrumentation," Vol. 2, J. S. Mattson, H. B. Mark, and H. C. MacDonald, Editors, Chap. 6, Marcel Dekker, New York (1972).
9. D. J. Kooijman, *J. Electroanal. Chem. Interfacial Electrochem.*, **19**, 365 (1968).
10. J. M. Kudirka, P. H. Daum, and C. G. Enke, *Anal. Chem.*, **44**, 309 (1972).
11. H. Reller and E. Kirowa-Eisner, *This Journal*, **127**, 1725 (1980).
12. H. P. van Leeuwen, *Electrochim. Acta*, **23**, 207 (1978).
13. Z. Nagy, *This Journal*, **128**, 786 (1981).
14. Z. Nagy, *Electrochim. Acta*, **26**, 671 (1981).
15. Z. Nagy, *This Journal*, **129**, 1943 (1982).
16. Z. Nagy, *Electrochim. Acta*, In press.
17. D. J. Kooijman, M. Sluyters-Rehbach, and J. H. Sluyters, *Electrochim. Acta*, **11**, 1197 (1966).
18. J. M. Kudirka and C. G. Enke, *Anal. Chem.*, **44**, 614 (1972).
19. H. Matsuda, S. Oka, and P. Delahay, *J. Am. Chem. Soc.*, **81**, 5077 (1959).
20. Z. Nagy, *This Journal*, **125**, 1809 (1978).
21. H. Reller and E. Kirowa-Eisner, *J. Electroanal. Chem. Interfacial Electrochem.*, **103**, 335 (1979).
22. P. Delahay, "New Instrumental Methods in Electrochemistry," p. 46, Interscience, New York (1954).
23. E. Blomgren, D. Inman, and J. O'M. Bockris, *Rev. Sci. Instrum.*, **32**, 11 (1961).
24. A. D. Graves and D. Inman, in "Electromotive Force Measurements in High-temperature Systems," C. B. Alcock, Editor, p. 183, American Elsevier, New York (1968).
25. M. Kogoma, Y. Kanzaki, and S. Aoyagui, *Chem. Instrum.*, **7**, 193 (1976).
26. V. I. Chernenko, K. I. Litovchenko, Yu. E. Udovenko, and N. G. Krapivnyi, *Soviet Electrochem.*, **10**, 543 (1974).
27. D. R. Flinn, M. Rosen, and S. Schuldiner, *This Journal*, **117**, 79 (1970).

Analytic Expression of the Warburg Impedance for a Rotating Disk Electrode

Bernard Tribollet[1] and John Newman*

Department of Chemical Engineering, University of California, Berkeley, California 94720

ABSTRACT

In the presence of the convective flow pattern of the rotating disk, the classical Warburg impedance is modified, particularly at low frequencies. The transformation of Scherson permits the alternating current impedance problem to be related to the transient flux-step or concentration-step behavior of the same system. Here flux-step results are used to generate low and high frequency analytic expressions which overlap at intermediate frequencies.

Since Warburg (1) and Kruger (2), many authors (3-10) have given some analytic expression of the diffusion or convective Warburg impedance. Schuhmann (3) obtained an analysis based on a stagnant Nernst diffusion layer. Homsy and Newman (4) developed an asymptotic solution for the effect of convection at high frequencies, thereby providing correction to the Warburg result for a semi-infinite stagnant solution. Deslouis *et al.* (5-7) developed the method of Filinovskii and Kir'yanov (8), which, after an approximation, reduces the problem to the canonical equation for the Airy functions. Levart and Schuhmann (9) proposed a general method for evaluating the concentration impedance of a uniformly accessible rotating disk electrode; their solution is an exact solution, but it is necessary to use a computer in order to determine the real and imaginary parts of the impedance. Recently Scherson and Newman (10) showed how a Laplace transformation could make the problem identical to a transient concentration-step problem and thereby gave two series solutions corresponding, respectively, to the

* Electrochemical Society Active Member.
[1] Present address: Groupe de Recherche No. 4 du CNRS, "Physique des Liquids et Electrochimie," Associe a l'Universite Pierre et Marie Curie, 4 Place Jussieu 75230 Paris Cedex 05, France.

Key words: diffusion, convection, mass transfer, alternating current.

short-time series (11, 12) for the high frequencies and to the long-time series (13) for the low frequencies. This solution gave a very good accuracy only for the high frequencies. This problem was noticed by the authors (10) and discussed by Levart and Schuhmann (14).

In this paper we explain the difference between the low frequency solution of (10) and the exact solution, and we give an exact low-frequency solution valid for very large Schmidt numbers.

High-Frequency Solution

All analytic solutions (1-10) agree asymptotically with the expression of Warburg

$$-\frac{1}{\theta'_{HF}(0)} \xrightarrow[K\to\infty]{} -\frac{1}{\sqrt{jK}} \qquad [1]$$

Some differences may be observed if we consider different expansions for large values of a parameter; this problem had been discussed by Levart and Schuhmann (14, 15), and they show the interest in using the simplest expression for the same accuracy. In particular the high-frequency solution of Scherson and Newman (10) may be written in an easier form as

$$-\operatorname{Im}\left\{-\frac{1}{\theta'_{HF}(0)}\right\} = \frac{1}{\sqrt{2K}} - \frac{9}{32\sqrt{2K^{7/2}}} + 0(K^{-4}) \qquad [2]$$

$$\operatorname{Re}\left\{-\frac{1}{\theta'_{HF}(0)}\right\} = \frac{1}{\sqrt{2K}} + \frac{3}{4K^2} + \frac{9}{32\sqrt{2K^{7/2}}} + 0(K^{-4}) \qquad [3]$$

Equations [2] and [3] correspond exactly to the first terms of the development given by Levart and Schuhmann (14, 15) and are easy to use.

The approximate analytic method developed in (5-7) may be interesting for the high frequencies. The basis of this method is to neglect the fourth power of the dimensionless distance to the electrode, in comparison to the sum of the dimensionless distance to the electrode and of the dimensionless frequency. This method becomes valid when the frequency tends towards infinity. With the present notation

$$-\frac{1}{\theta'_{HF}(0)} = 0.6937\,\frac{A_i(0.4808jK)}{A_i'(0.4808jK)} \qquad [4]$$

By using the development of the Airy function (16) we obtain

$$-\operatorname{Im}\left\{-\frac{1}{\theta'_{HF}(0)}\right\} = \frac{1}{\sqrt{2K}} - \frac{63}{32\sqrt{2K^{7/2}}} + 0(K^{-5}) \qquad [5]$$

$$\operatorname{Re}\left\{-\frac{1}{\theta'_{HF}(0)}\right\} = \frac{1}{\sqrt{2K}} + \frac{3}{4K^2} + \frac{63}{32\sqrt{2K^{7/2}}} + 0(K^{-13/2}) \qquad [6]$$

The difference between the asymptotic solution [2], [3] and the approximate solution [5], [6] is only on the terms in $K^{-7/2}$; that explains, for the high frequencies, the good accuracy of the solution with the Airy functions.

Low-Frequency Solution

The exact analytic expression of the dimensionless diffusion or convective Warburg impedance given by Scherson and Newman (10) is

$$(-\theta_{LF}'(0))^{-1} = \left(\frac{1}{\Gamma(4/3)} + jK\sum_{n=0}^{\infty}\frac{B_n}{jK+\lambda_n}\right)^{-1} \qquad [7]$$

where B_n and λ_n are the coefficients and eigenvalues of the eigenvalue problem for a concentration step, respectively, and their values are given in (13). The expression [7] is applicable for low frequencies and corresponds to the long-time series (13). In real space, the short-time (11, 12) and the long-time series (13) overlap within a few tenths of a percent in a wide interval of time, a behavior not reproduced in the complex plane after a Laplace transformation [see Fig. 1, Ref. (10)].

In order to explain this difference of behavior, Fig. 1 shows, for two frequencies, the variation of the relative error in the real and imaginary parts of $-1/\theta_{LF}'(0)$ *vs.* n, the number of terms in the summation. For the two frequencies, the errors are significant and decrease slowly with n. In order to obtain an overlap for the two solutions [2], [3], and [7] it is necessary to use a very large number of terms in the sum.

The expression [7] is obtained in relation to the transient problem for a constant concentration at the interface. In fact, the expression of the diffusion or convective Warburg impedance may be obtained in relation to a transient problem with another boundary condition, in particular with a specified concentration gradient at the interface. Thus, the convective Warburg impedance may be obtained from the long-time series for a flux step (13) in a transient problem

$$-\frac{1}{\theta_{LF}'(0)} = \Gamma(4/3) - jK\sum_{n=0}^{\infty}\frac{B_n}{jK+\lambda_n} \qquad [8]$$

where, in this case, B_n and λ_n are the coefficients and eigenvalues of the eigenvalue problem, respectively, for a flux step, values being given in (13). (While referred to as long-time series, and correspondingly low-frequency series, these series are convergent for any time but converge very well for longer times. The corresponding impedance expressions might be expected to converge well for moderate to low frequencies.) From [8] the analytic expressions of the real and imaginary component may be easily written

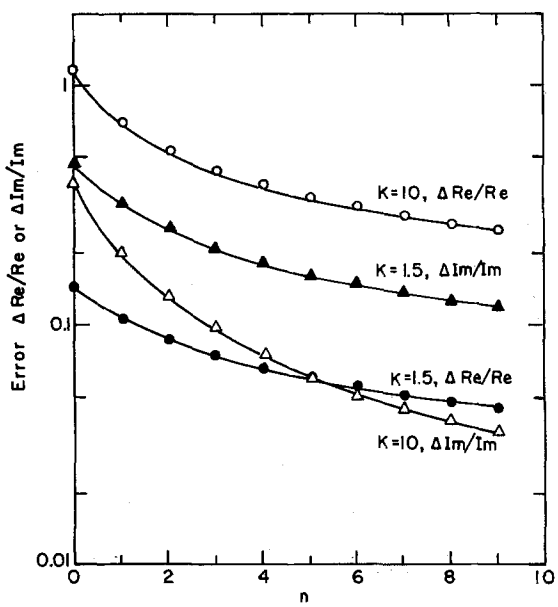

Fig. 1. Relative error in the real and imaginary parts of the convective Warburg impedance, when based on the concentration-step results according to the method of Scherson and Newman, as it depends on the numbers of terms used in the series expansion.

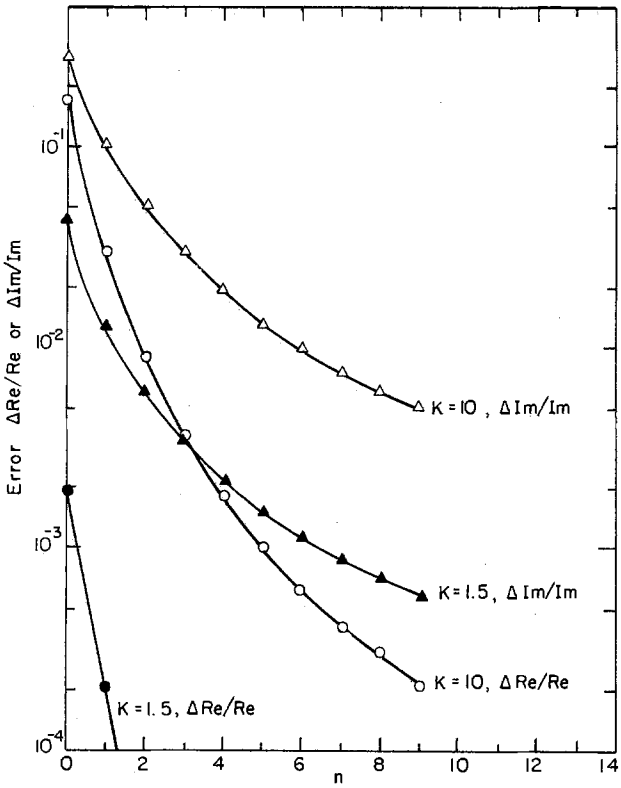

Fig. 2. Relative error in the real and imaginary parts of the convective Warburg impedance, when based on the transient flux-step results, as it depends on the number of terms used in the series expansion.

$$\mathrm{Re}\left\{\frac{-1}{\theta_{LF}'(0)}\right\} = \Gamma(4/3) - K^2 \sum_{n=0}^{\infty} \frac{B_n}{\lambda_n^2 + K^2} \qquad [9]$$

$$\mathrm{Im}\left\{-\frac{1}{\theta_{LF}'(0)}\right\} = -jK \sum_{n=0}^{\infty} \frac{B_n \lambda_n}{\lambda_n^2 + K^2} \qquad [10]$$

On Fig. 2 is plotted, for two particular frequencies, the variation of the relative error in the real and imaginary parts of $-1/\theta'_{LF}(0)$ *vs.* n, the number of terms in the summation. The error increases with the frequency, but it decreases with the number of terms faster than the error from [7]. The values of the real and imaginary components of the impedance are given

Table I. Comparison of low-frequency series solution based on the transient flux-step with the exact solution and with the asymptotic high-frequency result in Eq. [2] and [3].

K	Exact solution Real	Exact solution −Im	L.F. solution Real [9]	L.F. solution −Im [10]	H.F. solution Real [2]	H.F. solution −Im [3]
0.00	0.89298	0.00000	0.89298	0.00000		
0.01	0.89297	0.00266	0.89297	0.00266		
0.05	0.89293	0.01331	0.89273	0.01331		
0.1	0.89198	0.02659	0.89198	0.02658		
0.2	0.88899	0.05296	0.88901	0.05335		
0.5	0.86882	0.12850	0.86882	0.12845		
1.0	0.80575	0.23271	0.80575	0.23260		
1.5	0.72406	0.30195	0.72406	0.30178		
2.0	0.64160	0.33935	0.64160	0.33913	0.70508	0.48242
3.0	0.50637	0.35452	0.50638	0.35421	0.49583	0.40400
5.0	0.35556	0.31152	0.35558	0.31097	0.34694	0.31552
10.0	0.23143	0.22396	0.23147	0.22287	0.23117	0.22354
20.0	0.15998	0.15813	0.16016	0.15595	0.16000	0.15811
50.0	0.10030	0.10000	0.10125	0.09477	0.10030	0.10000
100.0	0.07071	0.07071	0.07428	0.06133	0.07071	0.07071

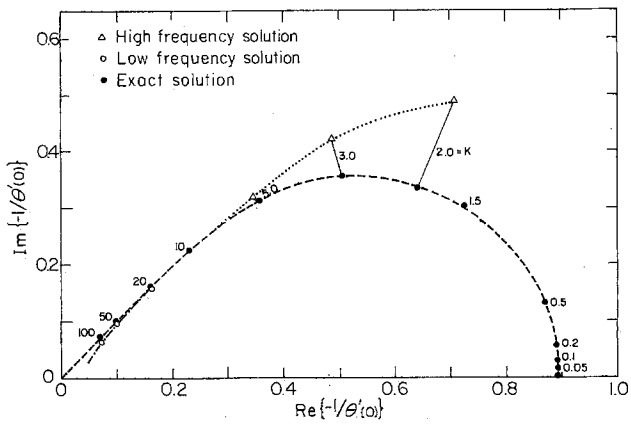

Fig. 3. Representation of the function $\{-1/\theta'(0)\}$ in the complex plane. Solid lines connect equal values of the dimensionless frequency K.

for $n = 9$ in Table I. For $K = 10$ the results from expressions [2], [3] and [9], [10] are very close, and the two solutions HF and LF overlap on a frequency range (Fig. 3) in good agreement with the results in the real space (13). The analytic expression of the dimensionless convective Warburg impedance may be [2], [3] for $K > 10$ and [9], [10] for $K < 10$. These expressions may be easily modified in order to use another dimensionless frequency, such as $pSc^{1/3}$.

Acknowledgment

This work was supported by the National Science Foundation through an Exchange Visitor Program with "Centre National de la Recherche Scientifique" No. G050252.

Manuscript submitted Oct. 11, 1982.

Any discussion of this paper will appear in a Discussion Section to be published in the December 1983 JOURNAL. All discussions for the December 1983 Discussion Section should be submitted by Aug. 1, 1983.

REFERENCES

1. E. Warburg, *Wied. Ann.*, **67**, 493 (1898).
2. F. Kruger, *Z. Phys. Chem.*, **45**, 1 (1903).
3. D. Schuhmann, *Compt. Rend.*, **262C**, 624 (1966).
4. R. V. Homsy and J. Newman, *This Journal*, **121**, 521 (1974).
5. C. Deslouis, These de Doctorat d'Etat No. AO11014, Paris (1975).
6. C. Deslouis and B. Tribollet, *Electrochim. Acta*, **23**, 935 (1978).
7. C. Deslouis, C. Gabrielli, and B. Tribollet, *This Journal*, To be published.
8. V. Yu Filinovskii and V. A. Kir'yanov, *Dokl. Akad. Nauk. SSSR*, **156**, 1412 (1964).
9. E. Levart and D. Schuhmann, *J. Electroanal. Chem. Interfacial Electrochem.*, **53**, 77 (1974).
10. D. A. Scherson and J. Newman, *This Journal*, **127**, 110 (1980).
11. V. S. Krylov and V. N. Babak, *Sov. Electrochem.*, **7**, 626 (1971).
12. J. R. Selman, Ph.D. Thesis, University of California, Berkeley, CA (1971).
13. K. Nisançioğlu and J. Newman, *J. Electroanal. Chem. Interfacial Electrochem.*, **50**, 23 (1974).
14. E. Levart and D. Schuhmann, *This Journal*, **127**, 2649 (1980).
15. E. Levart and D. Schuhmann, *ibid.*, **122**, 1082 (1975).
16. M. Abramowitz and I. A. Stegun, "Handbook of Mathematical Functions," p. 448, National Bureau of Standards, Washington, D.C. (1964).

XPS Studies of Oxygen Evolution on Ru and RuO_2 Anodes

R. Kötz, H. J. Lewerenz,*,[1] and S. Stucki

Brown Boveri Research Center, 5405 Baden, Switzerland

ABSTRACT

Anodic oxidation of Ru and RuO_2 electrodes in 1*N* H_2SO_4 has been investigated using x-ray photoelectron spectroscopy. During O_2 evolution on Ru a highly defective hydrated oxide film is formed as a result of corrosion. At a temperature of 310°C in vacuum this film decomposes to metallic ruthenium. The surface of RuO_2 anodes prepared by thermal decomposition of $RuCl_3$ contains some RuO_3, which is stable during anodic polarization. A reaction path for O_2 evolution and corrosion on Ru and RuO_2 anodes is proposed.

Oxygen evolution overpotentials of ruthenium and ruthenium dioxide based anodes are among the lowest ever observed (1). Therefore these materials have attracted much attention in recent years as prospective candidates for O_2-evolving anodes in hydrogen production by water electrolysis. The pure materials, however, suffer from a lack of stability. Ruthenium anodes corrode heavily during O_2 evolution, forming a black oxide on the surface that is not capable of preventing the underlying metal from further attack (2). The performance of the widely used ruthenium oxide coated titanium anode, prepared by thermal decomposition of $RuCl_3$ on titanium substrates, greatly depends on the preparation conditions (3). The catalytic properties of RuO_2-based anodes for chlorine and oxygen evolution have been investigated in a variety of experimental studies which were reviewed recently by Burke (4) and by Trasatti and O'Grady (5). RuO_2 single crystals have a rather low catalytic activity for O_2 evolution and seem to passivate (6). The immense difference in catalytic performance between Ru- and RuO_2-based anodes is far from being understood. Although the essential role of surface morphology is well accepted for RuO_2-based anodes, the nature of the active site and the mechanism of O_2 evolution in acid still remain questionable.

The expedience of the x-ray photoelectron spectroscopy (XPS) technique applied to electrochemical processes has been demonstrated by several authors investigating anodic oxidation (7), underpotential deposition (8), or specific adsorption (9). In the present study we have applied XPS in order to gain further information on the surface composition of Ru and RuO_2 anodes as a function of electrochemical treatment. Chemical shifts of the different ruthenium oxides, as determined by Kim and Winograd on commercially available powders (10), are the basis for our analysis.

Experimental

XPS measurements were performed in a Kratos ES 300 Electron Spectrometer using non-monochromatized AlK_α radiation. The instrumental resolution was 1.2 eV (FWHM of the Au $4f_{7/2}$ line), a value mainly determined by the width of the AlK_α line. Binding energies were determined using the Au $4f_{7/2}$ line as a reference with a binding energy of 84.0 eV. The base pressure in the sample chamber of the spectrometer was 1×10^{-10} Torr.

Ruthenium samples were prepared by arc melting or by sputtering onto a glass substrate. Before use, the arc-melted bulk Ru sample was polished mechanically with successively finer diamond paste until a mirror-like finish was achieved and then was rinsed thoroughly in distilled water. The two samples showed no significant difference in XPS spectra or cyclic voltammetry. At potentials more anodic than +1.3 V_{SCE}, however, only the bulk sample could be used because of substantial corrosion of the sputtered film with a thickness of 2000Å.

RuO_2 electrodes were prepared by thermal decomposition of $RuCl_3$ on an etched titanium substrate (3). A 0.1M $RuCl_3$ solution in 20% HCl was dried by heating and the residue was dissolved in 2-propanol. The solution was brushed onto the titanium substrate and dried by heating at 500°C. After deposition of several layers the electrode was annealed at 500°C for 1 hr.

Electrochemical treatment of the electrodes was performed in air-saturated 1*N* H_2SO_4 using the standard three-electrode potentiostatic arrangement. All potentials are quoted with respect to the saturated calomel electrode (SCE) which served as a reference electrode.

After an electrochemical experiment the electrodes were removed from the electrochemical cell under potential control, rinsed in distilled water, blown dry with nitrogen, and transferred to the electron spectrometer within 1 min. In order to provide equal starting conditions, the ruthenium metal electrodes were Ar-ion bombarded before any sequence of electrochemical experiments. This procedure could not be applied to the RuO_2 electrodes because of preferential sputtering of oxygen. These electrodes were used as received.

Sample transfer from the electrochemical cell to the spectrometer is a very critical step in any *ex situ* investigation of electrodes. It has been demonstrated, however, that noble metal electrodes (Au, Pt) are relatively insensitive to an aerobic transfer (11). The influence of the transfer on a metallic Ru sample was checked by removing a freshly sputtered Ru sample from the vacuum chamber, exposing it to air, and applying the above cleaning procedure (H_2O, N_2). No change in position of the Ru lines of the XPS spectrum could be detected.

Results and Discussion

XPS was used to study the influence of electrochemical treatment on the surface composition of ruthenium and ruthenium dioxide electrodes.

The ruthenium anode.—In Fig. 1, XPS spectra of an Ru electrode are shown for samples with three different treatments. For the sputtered sample with no oxygen on the surface, the position of the Ru $3d_{5/2}$ peak is in good agreement with published data (10). Exposure to 1*N* H_2SO_4 at 0.75V (SCE) does not shift the binding energies (E_B) of ruthenium. The intensity, however, is slightly reduced. In addition, an oxygen peak is observed at E_B = 530.6 eV. Upon anodizing the electrode at 1.5V, a bluish-black surface film is formed during oxygen evolution with simultaneous yellow coloring of the electrolyte. The change in surface composition of the Ru electrode is reflected in the XPS data by chemical shifts of the Ru lines and the O 1s peak. While the Ru 3d and Ru 3p lines shift to higher binding energies by 1.1 and 1.8 eV, respectively, the O 1s line shifts to lower binding energy with ΔE_B = −0.7 eV. In addition, a broadening of the Ru lines

* Electrochemical Society Active Member.
[1] Present address: Hahn Meitner Institut für Kernforschung, D-1000 Berlin 39, Germany.
Key words: electrode, ESCA, catalysis, corrosion.

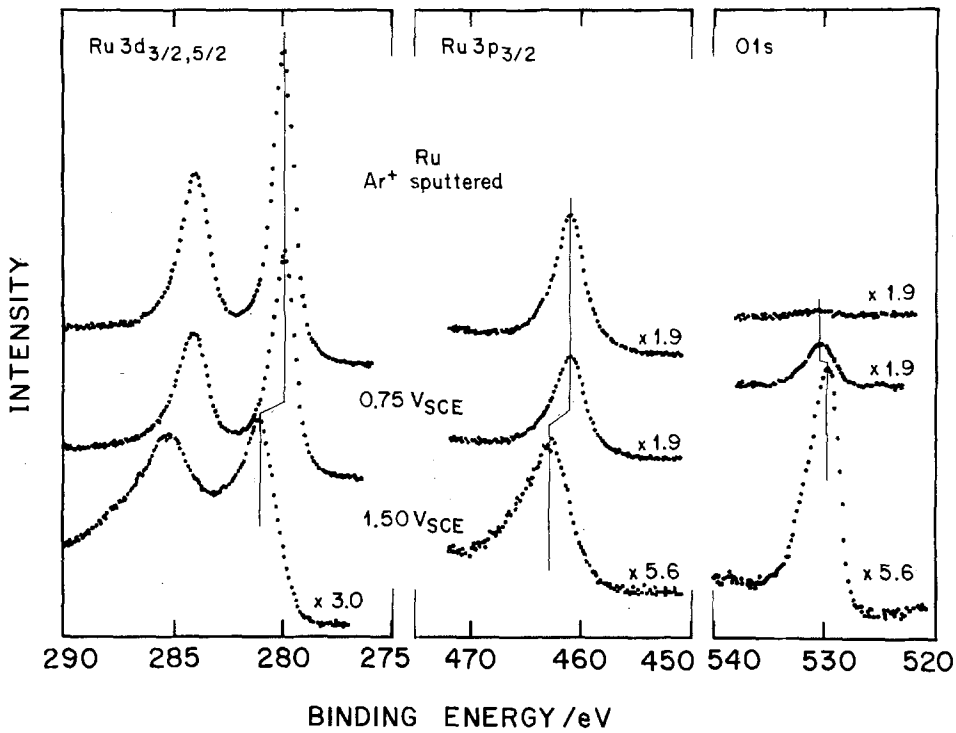

Fig. 1. X-ray photoelectron spectra of Ru $3d_{3/2,5/2}$, Ru $3p_{3/2}$, and O 1s levels of a bulk Ru electrode exposed to Ar^+ bombardment (4 keV, 30 min, 2.5 mA), 1N H_2SO_4 (15 min) at potentials of 0.75 and 1.5 V_{SCE}.

and a substantial increase of the oxygen peak is observed.

Upon varying the photoelectron emission angle, the surface is probed with different depth resolutions. Figure 2 shows the change in binding energy of the Ru $3d_{5/2}$ peak with emission angle for three electrode surface conditions. At 0V, no measurable dependence is found. The electrode polarized at 0.75V, however, shows a marked change in binding energy whereas at 1.5V the effect is negligible again.

At small emission angles, the detected photoelectrons originate mainly from the topmost surface layers, whereas the sampling depth is ~ 30Å for large emission angles. The lack of an angular dependence for 0.0V polarization indicates metallic Ru is independent of the sampling depth. At 0.75V, the more pronounced angular variation implies a thin surface layer of partially oxidized Ru. At 1.5V, the angular dependence is reduced again, due to the generation of a thick oxide layer.

In order to determine the potential dependence of the observed shifts in Fig. 1, the peak positions were analyzed for a sequence of exposures in the potential range between −0.2 and +2.0V. The results are plotted in Fig. 3a, b. For both lines, the chemical shift occurs within a narrow range. Above and below this potential, the peak positions are independent of the electrode polarization. The inflection points of the curves, however, are not identical; they occur at 1.25V for Ru $3d_{5/2}$ and at 1.15V for O 1s.

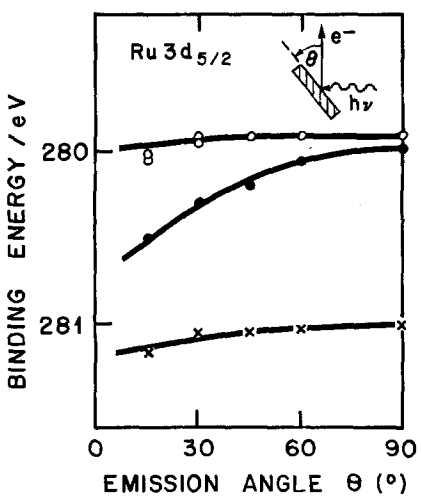

Fig. 2. Binding energy of the Ru $3d_{5/2}$ level as a function of electron emission angle for a bulk Ru electrode after polarization at 0.0 V_{SCE} (○○○), 0.75 V_{SCE} (●●●), and 1.5 V_{SCE} (×××). The emission angle is given with respect to the surface plane.

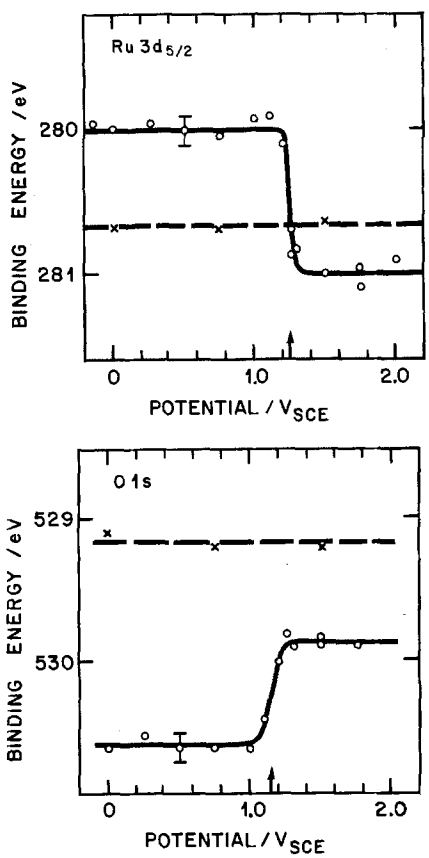

Fig. 3. Binding energies of (a) the Ru $3d_{5/2}$ level and (b) the O 1s level as a function of electrode potential for a bulk Ru electrode (———) and an RuO_2/Ti electrode (- - - -). Exposure to 1N H_2SO_4 for 15 min.

Below the inflection point, electrochemical treatment introduces an adsorbed oxygen species (Fig. 1, 0.75V; Fig. 2). The O 1s peak position correlates well with the value given by Wittrig *et al.* for dissociatively adsorbed water (12). This finding is also supported by cyclic voltammetry studies where the existence of a monolayer of oxygen is claimed from coulometric evidence (13). The slight decrease in peak intensity of the Ru lines is related to this adsorbate.

Above the inflection point, at 1.5V bias, the chemical shifts in the Ru lines and in the O 1s peak indicate the formation of a hydrated oxide phase. The stoichiometry of this phase appears to be somewhat different from the hydrated oxide powder, analyzed by Kim and Winograd (10). From binding energy assignments, the electrochemically generated hydrous oxide seems to have a stoichiometry between RuO_2 and pulverous hydrated oxide (see Table I). The increase of the O 1s peak height indicates a substantial thickness of the hydrous film.

The difference in inflection potential of the Ru and O lines observed in Fig. 3a, b may be due to consecutive steps in the formation of the hydrous oxide phase. The shift of the oxygen line, which occurs 100 mV more cathodic than the shift of Ru $3d_{5/2}$, may be associated with the transition from adsorbed OH to a thin oxide film.

At slightly increased anodic potential, site exchange between Ru and O might take place, leading to simultaneous oxide formation and corrosion evidenced by the shift of the Ru lines. The O 1s binding energy remains unaffected by this site exchange.

Figure 4 shows the effect of thermal treatment in the UHV chamber of the XPS spectrometer for a sample anodized at +1.5V. The Ru 3d lines shift from 281.0 eV at room temperature to 279.9 eV at 310°C. The line widths decrease with increasing temperature by a factor of ~2, whereas the peak heights increase substantially. A more complicated behavior is observed for the O 1s line. At room temperature the peak is located at 529.8 eV, shifts to higher binding energy (530.4 eV) upon heating to 120°C, and shifts back to 529.6 eV at 310°C; the peak height decreases accordingly.

From the shifts in Ru lines it is deduced that the temperature treatment leads to a largely oxide-free Ru surface. This is also evidenced by the decrease of the O 1s intensity. The O 1s binding energy at 310°C indicates the existence of residual oxide on the surface, possibly in island form.

The ruthenium dioxide anode.—Figure 5 shows the analogous experiment to Fig. 1 for titanium-supported RuO_2 electrodes prepared by thermal decomposition of $RuCl_3$ on Ti. Here, the only difference between samples as produced and those polarized to 0.75V and polarized to 1.5V is the occurrence of an additional maximum in the O 1s line at 531.7 eV which is removed upon exposure to the electrolyte. There is, however, still a shoulder detectable on the polarized

Table I. Binding energies (±0.1 eV) of Ru and RuO_2 electrodes

Electrode		Ru $3d_{5/2}$	Ru $3p_{3/2}$	O 1s	Assignment
Ru	Sputtered	279.9	461.1	—	Ru
	0.75V	279.9	461.1	530.6	Ru, OH ads.
	1.5V	281.0	462.7	529.8	RuO_2, $RuO_2 \cdot xH_2O$
	120C°C	280.8	—	530.5	Oxide decomposition,
Ru	230°C	280.3	—	530.4	H_2O loss
1.5V	310°C	279.8	—	529.8	Ru, RuO surface
RuO_2/Ti		280.7	462.2	529.2	RuO_2,
		282.4		530.7	RuO_2,
				(531.7)	(contamination)

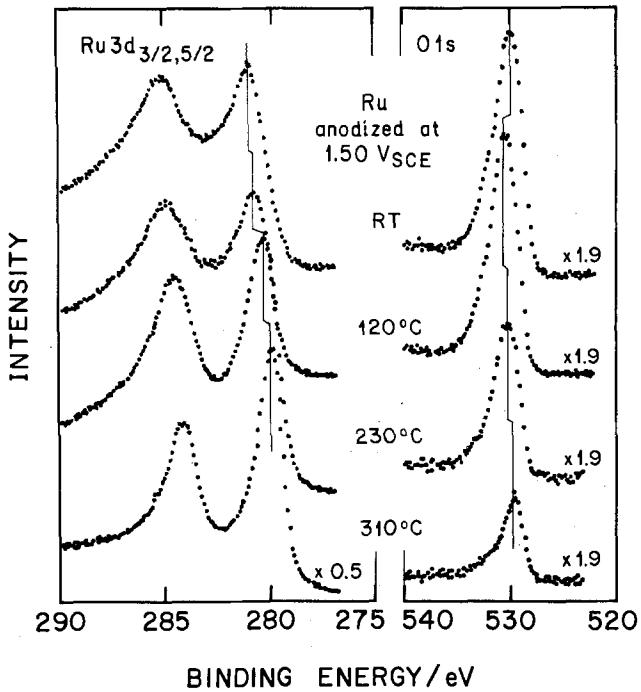

Fig. 4. X-ray photoelectron spectra of a bulk Ru electrode anodically oxidized at 1.5 V_{SCE} for 15 min for different temperatures.

samples, which is difficult to resolve because of the increasing intensity of the main O 1s peak.

The prevalent existence of RuO_2 is confirmed by the positions of the Ru $3d_{5/2}$ line at 280.7 eV and by the O 1s line at 529.2 eV (10). At a binding energy of 282.4 eV, an additional maximum occurs in the Ru 3d spectrum which is attributed to RuO_3 or another species with the same oxidation state. It appears that this compound is stable on the surface as no significant change in the corresponding XPS structure is observed with electrochemical treatment.

The influence of thermal treatment on RuO_2 anodes is shown in Fig. 6. The Ru $3d_{5/2}$ and $3d_{3/2}$ lines show no significant alteration up to a temperature of 230°C. At 310°C, both lines are shifted by ~0.5 eV to lower binding energies. In addition, the shoulder attributed to RuO_3 (282.4 eV) decreases continuously and disappears at 310°C. The temperature treatment results in a gradual decrease of the O 1s maximum without detectable chemical shift. An increasing asymmetry of the O 1s peak, however, is noticed with increasing temperatures, indicating a second oxygen species with a binding energy of ~531.7 eV. The origin of this shoulder appearing in Fig. 5 and 6 is not completely understood. On well-defined RuO_2 single crystal sur-

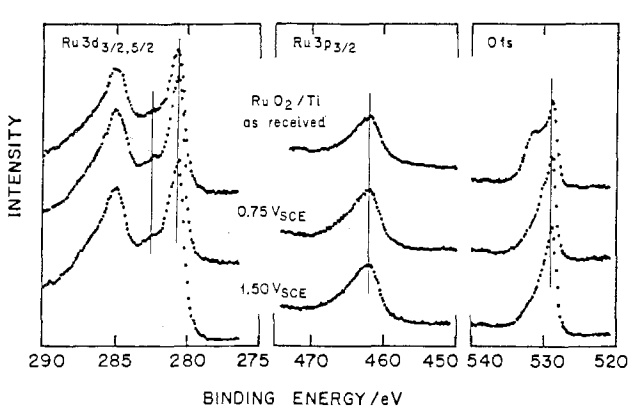

Fig. 5. X-ray photoelectron spectra of Ru $3d_{3/2,5/2}$, Ru $3p_{3/2}$, and O 1s level of an RuO_2/Ti electrode after preparation and after exposure to 1*N* H_2SO_4 electrolyte at 0.75 and 1.5 V_{SCE} for 15 min.

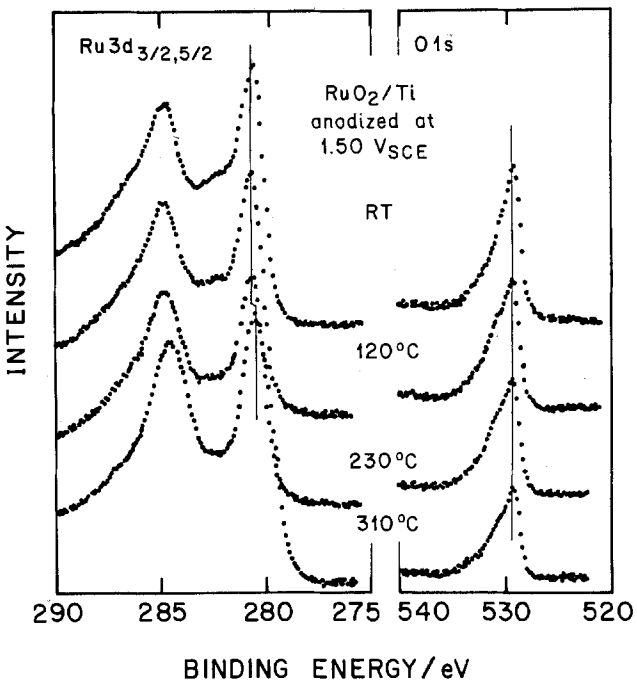

Fig. 6. X-ray photoelectron spectra of an RuO_2/Ti electrode after O_2 evolution at 1.5 V_{SCE} at different temperatures.

faces two oxygen species have been observed probably due to oxygen in different coordination sites (14).

Comparison of electrode behavior and interpretation. —The experimental data in Fig. 1 and 5 demonstrate that the behavior of Ru and RuO_2 anodes is distinctly different even in the potential range of oxygen evolution. In the case of Ru, a thick hydrous oxide deposit is formed during oxygen evolution and no evidence is found for the existence of a stable higher oxidized species. The simultaneous coloring of the electrolyte indicates the formation of RuO_4 or H_2RuO_5 as a corrosion product (4). On RuO_2, no influence of oxygen evolution on surface composition is detected. A persisting higher oxide in the six valent state [Ru(VI)], is present and stable up to 230°C (Fig. 6).

Basically, one would expect that upon oxidation of Ru toward oxygen evolution the same surface condition is reached as exists on an RuO_2 electrode. The different behavior must originate from the stability of intermediates on the two electrodes. Such an intermediate might be the Ru(VI) species detected on RuO_2 electrodes. We therefore assume that this species acts as substrate for oxygen evolution (15) and the corrosion reactions. In Fig. 7, we propose that both processes proceed via two-electron steps toward Ru(VIII). The relative stability of the intermediate Ru(VI) determines whether RuO_4 corrodes (either into the gas phase or into solution) or dissociates into oxygen and Ru(VI).

In principle, since RuO_2 also is not completely stable, both reactions will take place simultaneously with different rates. The corrosion of Ru electrodes is higher by orders of magnitude indicating a low stability of Ru(VI) on these surfaces, as is evidenced by the absence of a structure in Fig. 1 and 4. The instability of Ru(VI) on Ru can be understood by the mechanisms governing the oxidation of Ru electrodes. According to the Pourbaix diagram and the results of other investigators (16), oxidation of Ru in 1*N* H_2SO_4 starts at ~0.3V (SCE). Adsorbed oxide or hydroxide layers, formed in the potential range 0.3-0.8V, are reversibly reduced at about 0.1V (13). This adsorption layer is demonstrated in Fig. 1 (oxygen peak at 0.75V polarization) and Fig. 2 for the same electrode polarization. The peak shift of the O 1s line in Fig. 3b be-

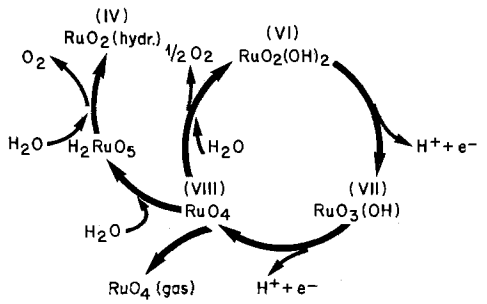

Fig. 7. Model for the oxygen evolution and corrosion on Ru and RuO_2 electrodes.

tween 1.1 and 1.2V indicates a transformation of the adsorbed oxygen layer. The absence of a corresponding peak shift of the Ru $3d_{5/2}$ line (Fig. 3a) is evidence that this transformation is not connected with a substantial increase in film thickness. We conclude that in analogy to investigations on Pt (17) a site exchange reaction takes place.

This view is supported by cyclic voltammetry experiments where an increasing irreversibility of the oxygen reduction peak is observed if the anodic sweep is extended to 1.1V and beyond (13). At a potential of 1.13V, oxygen evolution starts on this surface layer (2, 6, 13). Above 1.2V, after site exchange has taken place, the shift of the Ru $3d_{5/2}$ line in Fig. 3a demonstrates the growth of a thick hydrated oxide by redeposition of corroded Ru(VIII). We propose that similar surface species are formed on Ru and RuO_2. The difference in stability is due to different interactions of the formed intermediate with the respective substrate. For RuO_2, the intermediate matches the crystal structure and does not give rise to further attack. The same intermediate is easier to remove on Ru because bonding to the substrate with a different lattice geometry is weaker, thus giving rise to corrosion.

Acknowledgments

The authors would like to thank P. Brüesch for helpful discussions. The excellent technical assistance of W. Foditsch is gratefully acknowledged. This work was supported by the Nationale Energie Forschungs Fond.

Manuscript submitted May 26, 1982; revised manuscript received Oct. 21, 1982.

Any discussion of this paper will appear in a Discussion Section to be published in the December 1983 JOURNAL. All discussions for the December 1983 Discussion Section should be submitted by Aug. 1, 1983.

Publication costs of this article were assisted by BBC Brown, Boveri & Company Limited.

REFERENCES

1. S. Trasatti and G. Buzzanca, *J. Electroanal. Chem. Interfacial Electrochem.*, **29**, A1 (1971).
2. C. Iwakura, K. Hirao, and H. Tamura, *Electrochim. Acta*, **22**, 329 (1977).
3. G. Lodi, E. Sivieri, A. de Battisti, and S. Trasatti, *J. Appl. Electrochem.*, **8**, 135 (1978).
4. L. D. Burke, in "Electrodes of Conductive Metallic Oxides," S. Trasatti, Editor, p. 141, Elsevier Scientific Publishing Co., New York (1980).
5. S. Trasatti and W. E. O'Grady, in "Advances in Electrochemistry and Electrochemical Engineering," Vol. 12, H. Gerischer and C. W. Tobias, Editors, p. 177, Interscience, New York (1981).
6. S. Stucki and A. Menth, *Ber. Bunsenges. Phys. Chem.*, **84**, 1008 (1980).
7. P. M. A. Sherwood, *Surf. Sci.*, **101**, 619 (1980) and

references therein.
8. J. S. Hammond and N. Winograd, *J. Electroanal. Chem. Interfacial Electrochem.*, **80**, 123 (1977).
9. W. N. Hansen, D. M. Kolb, D. L. Rath, and R. Wille, *ibid.*, **110**, 369 (1980).
10. K. S. Kim and N. Winograd, *J. Catal.*, **35**, 66 (1974).
11. T. Dickinson, A. F. Povey, and P. M. A. Sherwood, *J. Chem. Soc., Faraday Trans. 2*, **71**, 298 (1975).
12. T. S. Wittrig, D. E. Ibbotson, and W. H. Weinberg, *Surf. Sci.*, **102**, 506 (1981).
13. M. Vukovic, H. Angerstein-Kozlowska, and B. E. Conway, *J. Appl. Electrochem.*, **12**, 193 (1982).
14. W. E. O'Grady, Private communication.
15. L. D. Burke and J. F. Healy, *J. Electroanal. Chem. Interfacial Electrochem.*, **124**, 327 (1981).
16. J. F. Llopis and I. M. Tordesillas, in "Encyclopedia of Electrochemistry of the Elements," Vol. 6, A. J. Bard, Editor, p. 277, Marcel Dekker, New York (1976).
17. B. E. Conway, in "Electrodes of Conductive Metallic Oxides," Part B, S. Trasatti, Editor, p. 433, Elsevier Scientific Publishing Co., New York (1981).

Inelastic Neutron Scattering and Transmission Electron Microscope Studies of Lead Dioxide

P. T. Moseley*

Materials Development Division, A.E.R.E. Harwell, Didcot, Oxon, OX110RA, England

J. L. Hutchison

Department of Metallurgy and Science of Materials, Oxford University, Oxford, England

C. J. Wright

Materials Physics, Division, A.E.R.E. Harwell, Didcot, Oxon, OX110RA, England

M. A. M. Bourke

Materials Development Division, A.E.R.E. Harwell, Didcot, Oxon, OX110RA, England

and R. I. Hill and V. S. Rainey

Materials Physics Division, A.E.R.E. Harwell, Didcot, Oxon, OX110RA, England

ABSTRACT

The complementary techniques of inelastic neutron scattering and high resolution transmission electron microscopy have been used to study different aspects of the constitution of several forms of lead dioxide. The neutron scattering techniques, which are particularly sensitive to the presence of hydrogenous species, indicate that lead dioxide can accommodate widely varying amounts of hydrogen. The vibration spectra, recorded after various dehydration procedures, do not show sharp characteristic vibrations consistent with hydroxyl groups similar to those known to be present in other hydrogen-containing oxides. They suggest that the temperature-induced changes observed are consistent with the presence of adsorbed water. There appears to be a relationship between the amount of hydrogen present in a sample of PbO_2, as measured by neutron transmission, and the proportion of reduced lead present (*i.e.*, other than Pb^{4+}) determined by chemical analysis. The electron microscopy has allowed the first direct imaging of the crystal structure of β-PbO_2. This form of lead dioxide, like α-PbO_2, is prone to coherent structure intergrowth but, unlike α-PbO_2, the range of defects present does not include planar faults.

Despite the antiquity of the concept of the lead acid battery a number of questions regarding its function remain unanswered. Two of these concern the structure of the active phase at the cathode (PbO_2). Not only is it unclear why this phase typically yields only 20 → 30% of its theoretical capacity, but it is also unclear why it has to be prepared by an electrochemical route. It has been reported (1, 2) that lead dioxide prepared by chemical routes is incapable of delivering electrochemical capacity, implying that the successful construction of a lead acid battery depends on the formation of the cathode material by electrochemical means. Further it has been suggested (3) that long-term degradation of battery capacity is related to the progressive conversion of the active lead dioxide into a form which resembles the chemically prepared product. These phenomena have not been adequately explained, and little is known of the difference between chemically and electrochemically prepared material.

* Electrochemical Society Active Member.
Key words: defects, cathode, crystallography, stoichiometry.

It has been proposed (3), on the basis of nuclear magnetic resonance measurements, that the active form of PbO_2 contains hydrogen which is related in some way to the electrochemical activity. However, it is not yet known what form this hydrogen takes, or where it is sited. A further theory (3, 4) offers the concept that electrochemical activity depends (inversely) on the degree of order in the crystals, and thermal decomposition studies (5) have led to the suggestion that positive plate active material contains an amorphous form of PbO_2 in addition to the two known crystalline polymorphs α (orthorhombic) and β tetragonal).

Questions relating to the possible presence of a hydrogen species in PbO_2 and to the form it might take in the active mass are conveniently investigated by thermal neutron scattering in view of the ratios of the scattering and absorption characteristics of the principal elements of interest (6). Until now neutrons have been used to study PbO_2 only by means of diffraction experiments (7, 8). In these, use has been made of the

similarity between the scattering lengths of lead and oxygen to derive a more precise model of the structure of β-PbO_2 than was achievable with x-rays. More recently (9) a neutron diffraction study has shown that the traditional view of lead dioxide as substantially oxygen deficient is probably incorrect and $Pb_{1-x}O_2$ is a better description. The presence of hydrogen in lead dioxide was deduced, in this experiment, from the level of the incoherent background scattering, but information concerning the whereabouts of the hydrogen was not obtained.

The present paper describes neutron transmission and inelastic scattering experiments. The former have been used to estimate the hydrogen content of PbO_2 samples, whereas the object of the latter was to identify whether local vibrational modes could be found which were characteristic of hydrogen bound in a specific manner to the PbO_2 lattice.

Specimens of α- and β-PbO_2 prepared by both chemical and electrochemical methods have been examined in addition to samples taken from commercial battery plates.

Recently (10) high resolution transmission electron microscopy (HRTEM) has been used to observe the crystal structure of chemically prepared α-PbO_2. It has demonstrated the presence of extensive defect structure which other, conventional, diffraction techniques had been unable to detect. The observation of defect structure in lead dioxide clearly has relevance for theories of electrochemical activity based on disorder. The present paper, in addition to the neutron scattering, takes the transmission electron microscope study on to an examination of other forms of PbO_2, which are arguably of more direct relevance for battery considerations than was the α-PbO_2 which was the subject of the earlier study.

Experimental

α- and β-PbO_2 were prepared by chemical routes as described previously (10). The two crystallographic modifications were also prepared by electrodeposition as anodic layers onto gold substrates following methods reported in the literature (11). For α-PbO_2 a 2N KOH solution saturated with lead monoxide was electrolyzed at 10 mA/cm^2 and for β-PbO_2 a solution which was 0.15M in both $Pb(NO_3)_2$ and nitric acid was electrolyzed at 100 mA/cm^2. The products were each removed from their gold substrates, ground, and checked for phase purity by x-ray powder diffraction using Cu$K\alpha$ radiation. Only peaks attributable to the major product phase were detected in each case. Calculations based on the breadth of the diffraction peaks indicated that the average crystallite size of the two products was of the order of 300Å.

The four materials together with two specimens taken from battery plates were analyzed for total lead content by a gravimetric method and for Pb^{IV} by iodometric titration. The results are given in Table I. Prior to the analyses, the laboratory-prepared samples were dried in warm flowing air. In this way it was expected that excess physisorbed water would be removed, but not that which could be essential to electrochemical activity. The two battery samples were dried by being left in air at room temperature. As pointed out previously (10), discrepancies between the values of Pb^{IV} and total lead might be explained on the basis of a hydrogen content and this possibility is discussed further below.

Crystals of the electrochemically prepared β-PbO_2 were distributed on a copper grid coated with a perforated carbon film for transmission electron microscopy.

Two types of neutron experiments were performed. In the first, the transmission of neutrons through compressed disks of PbO_2 samples provided a simple measurement of their total neutron cross sections. Before these measurements, the disks were heated at 120°C overnight in air to remove any weakly adsorbed water. In the second, the vibrational spectra of PbO_2 samples were recorded by time-of-flight and beryllium filter spectrometers on DIDO reactor at A.E.R.E. Harwell. The time-of-flight data were recorded at room temperature, whereas the beryllium filter spectra were recorded at 80 K.

Neutron Scattering

The neutron transmission, T, of a sample is related to its cross section via the relationship $T = \exp(-N\sigma t)$, where N is the number of scattering units per unit volume, σ is the unit total cross section, and t the sample thickness.

The masses per unit area of the samples used in the transmission experiments and the measured values of their neutron transmissions are given for an incident neutron wavelength of 10Å in Table II. From this data the cross section of each sample per mol of PbO_2 can be calculated. The cross sections, σ, appropriate to $\lambda = 10$Å are also recorded in the table. It is possible to compare these cross sections with that which would be expected for stoichiometric PbO_2. In the low temperature long wavelength limit, the total cross section, σ_{TOT}, where

$$\sigma_{TOT} = \sigma_{coherent} + \sigma_{incoherent} + \sigma_{absorption}$$

will reduce to the sum of the incoherent and absorption cross sections at wavelengths beyond the Bragg cutoff ($\lambda = 2d$ max) (12). This value is 7.66 and 7.0Å for α- and β-PbO_2, respectively. For PbO_2 at 10Å this limiting cross section is 1.4 ± 0.05 barns (13). The finding that for β-PbO_2 chemical $\sigma = 2.5$ barns suggests that inelasticity corrections to the limiting value of σ under our measurement conditions are small. The large cross sections determined by experiment for the other PbO_2 samples can only be accounted for if there is a substantial quantity of hydrogen present in the samples. We have estimated the molar quantity of water that each sample would have to incorporate to produce the measured cross sections and this is given in Table III. This calculation does not imply, however, that any hydrogen present in the PbO_2 is necessarily incorporated as water. The cross section used for the water was 245 barns/molecule (14). Since the cross section for hydrogen is so much greater than that for any other element, the discrepancy between the measured cross sections and those expected on the basis of the samples being pure PbO_2 can be accommodated with less disruption to the overall stoichiometry by including hydrogen, than would occur with any other element.

Table I. Analysis of lead dioxide (w/o), estimated errors 0.4 w/o

	Pb^{IV}*	Total Pb
α-PbO_2 (chemical)	72.2	86.6
β-PbO_2 (chemical)	85.6	85.5
α-PbO_2 (electrochemical)	80.5	84.7
β-PbO_2 (electrochemical)	82.0	84.6
β-PbO_2 (ex battery 1)	73.9	84.3
β-PbO_2 (ex battery 2)	75.8	83.3

* Stoichiometric PbO_2 requires 86.6 w/o Pb.

Table II. Transmission of neutrons through five samples of PbO_2

Sample	Mass/area (g/cm^2)	Transmission at 10A	σ (barns)	x in $PbO_{2-x}(H_2O)_x$
α-PbO_2 chemical	0.98	0.83	75	0.3
α-PbO_2 electrochemical	0.99	0.88	50	0.2
β-PbO_2 chemical	1.57	0.99	2.5	0.0
β-PbO_2 electrochemical	1.16	0.94	21	0.08
PbO_2 ex battery 1	2.34	0.88	22	0.08

Table III. Water contents of PbO_2 samples estimated from neutron transmission and chemical analysis data

	$xPbO_{2-x}(H_2O)_x$ estimated from neutron transmission	Total Pb-Pb^{IV} % difference
α-PbO_2 chemical	0.3	0.17
α-PbO_2 electrochemical	0.2	0.05
β-PbO_2 chemical	0.0	0.0
β-PbO_2 electrochemical	0.08	0.03
PbO_2 ex battery 1	0.08	0.12

There are other possible contributions to the cross section at wavelengths > 8Å, diffuse scattering being one example. The size of these contributions, however, will still be very much smaller than the quantities measured experimentally. Table III also shows the percentage difference between the analyses for total Pb and for Pb^{IV} and it will be seen that, in most cases, these correlate qualitatively with the values calculated for x in $PbO_{2-x}(H_2O)_x$ from the transmission experiment. The ratio of hydrogen to lead atoms for electrochemically prepared β-PbO_2 (0.16) is similar to that deduced for active β-PbO_2 (0.20) by Jorgenson *et al.* (9).

Measurements were made of the inelastic neutron scattering from PbO_2 samples in an attempt to identify scattering which might originate from adsorbed water or hydroxyl groups. It is possible to differentiate spectroscopically between those hydrogen atoms in single hydroxyl groups, as in $H_{0.34}MoO_3$ (15) and $H_{0.4}WO_3$ (16), those in coordinated and isolated water molecules, as in $H_{2.0}MoO_3$ (15), and those in adsorbed droplets of water as found in the pores of silicas (17).

The analysis of the measured scattering data was hindered by the lack of any previous experimental measurements of the vibrational spectrum of PbO_2, and in an effort to overcome this we recorded the inelastic scattering from the PbO_2 (ex battery 2) sample, after it had been subjected to heating *in vacuo* at 300°C. Thermal analysis data (5) indicate that at this temperature all the hydrogen will have been removed from the sample, with no attendant change in the PbO_2 stoichiometry. This was confirmed by our XRD data which did not reveal any PbO phase. Figure 1 compares the data measured with a beryllium filter spectrometer, at 80 K, between 150 and 1300 cm^{-1}, for two materials, dried in air at room temperature (ex battery 2 and ex battery 1), material (ex battery 1) heated *in vacuo* at 100°C, and material (ex battery 2) heated at 300°C *in vacuo*. It can be seen that there is a gradual reduction in scattering intensity as the drying procedure becomes more rigorous. There is a very pronounced change between spectra (a) and (b). In spectrum (a) the scattering shows peaks at 662 and 839 cm^{-1}, energies which resemble closely the energies previously observed for bulk ice at 646 and 831 cm^{-1} (17). The peaks in spectrum (b) at 642, 815, and 1081 cm^{-1} appear to persist in the spectra of the heated materials, but as the intensity of these bands declines, the relative intensity of the scattering at 476 cm^{-1} increases. It is assumed that spectrum (d) corresponds to the scattering from hydrogen-free PbO_2. Clearly the scattering from any ice remaining in the samples will reinforce the scattering from the PbO_2 at 642 and 815 cm^{-1}, and the observed changes in the scattering intensity on heating are all consistent with progressive loss of water nuclei. There is no evidence for any vibrations characteristic of isolated hydroxyl or $-OH_2$ groups, since all the features in spectra (b) and (c) are still to be found in spectrum (d). However they may be present, of course, in lower concentration than the water nuclei which have been removed by thermal treatment.

Comparisons of the low frequency time-of-flight spectra of α-PbO_2 (chemical), and β-PbO_2 (chemical),

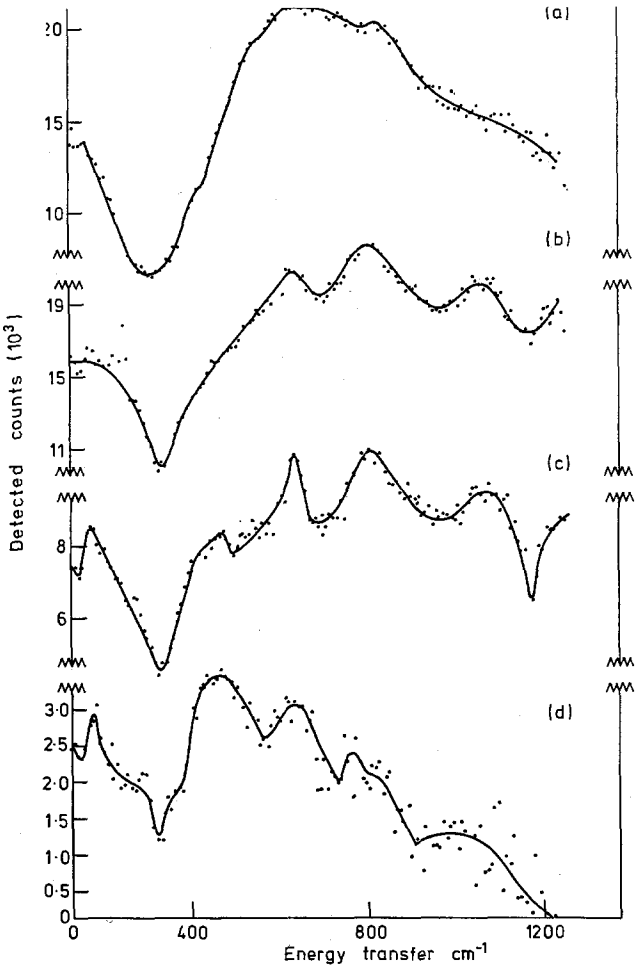

Fig. 1. Be filter spectra of PbO_2 specimens taken from battery plates: (a) material dried in air at room temperature ex battery 2, (b) material dried in air at room temperature ex battery 1, (c) material heated in vacuo at 100°C ex battery 1, (d) material heated in vacuo at 300°C ex battery 2.

which the transmission data showed to have the highest and lowest hydrogen contents, revealed very little difference between them. No local modes could be identified as originating from hydrogen-containing groups. In Fig. 2 the peaks with ~160 cm^{-1} and lower energies probably arise from the acoustic phonons of the PbO_2.

Electron Microscopy

Specimens of α-PbO_2 prepared electrochemically and β-PbO_2 prepared electrochemically and chemically have been examined in the present study.

Single crystal diffraction patterns of the electrochemically prepared β-PbO_2 (Fig. 3) are consistent with the rutile structure but contain some streaked intensity away from the maxima of the Bragg peaks, although not to the same extent demonstrated by chemically prepared α-PbO_2 (10).

High resolution images reveal the origins of those extraneous features. Figure 4 shows an area corresponding to the diffraction pattern shown in Fig. 3 [*i.e.*, with the $(01\bar{1})$ direction of the main crystal parallel to the beam]. Most of the crystal shows contrast consistent with an $01\bar{1}$ projection of the rutile structure but an area, marked A, is of a different projection or structure and another area, marked B, shows no contrast and is probably amorphous. Figure 5 shows another crystal which is predominantly composed of a rutile structure oriented on (011) but which has yet another structure or orientation (in areas marked A) coherently grown into the structure. In Fig. 6, we see that different orientations of the same structure can be grown into the parent (011) rutile crystal, as at

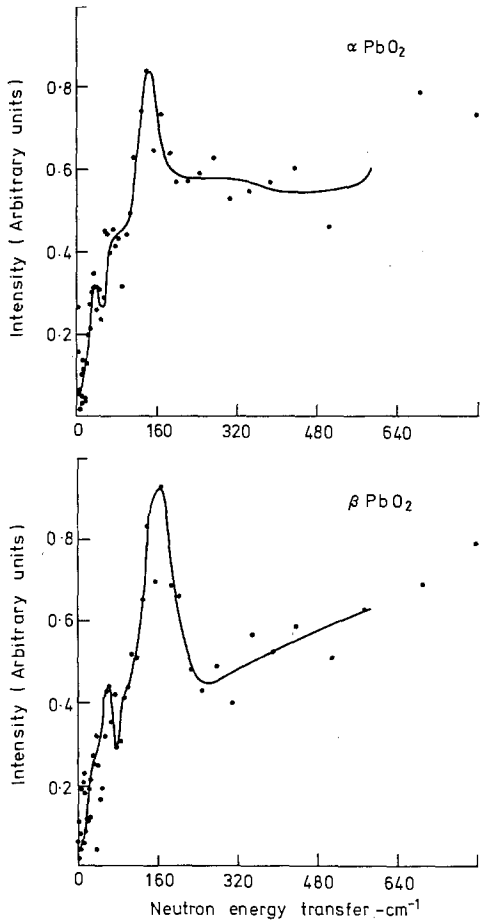

Fig. 2. Neutron scattering spectra recorded between 0 and 800 cm^{-1} for chemically prepared α- and β-PbO_2 (amplitude weighted densities of states).

B, and there are also areas, as at C, where the same structure [(011) rutile] is grown rotated by 90°. A similar situation in which different parts of the crystal are oriented identically with respect to one another is shown in Fig. 7 Here coherent twin boundaries, such as that arrowed, can be identified. The apparent absence of any crystallographic shear planes is consistent with the oxide being stoichiometric, although it does not, of course, represent a proof.

The types of coherent structural or orientational intergrowth shown in Fig. 4-7 appear to be typical of β-PbO_2. Chemically prepared β-PbO_2 crystals exhibit

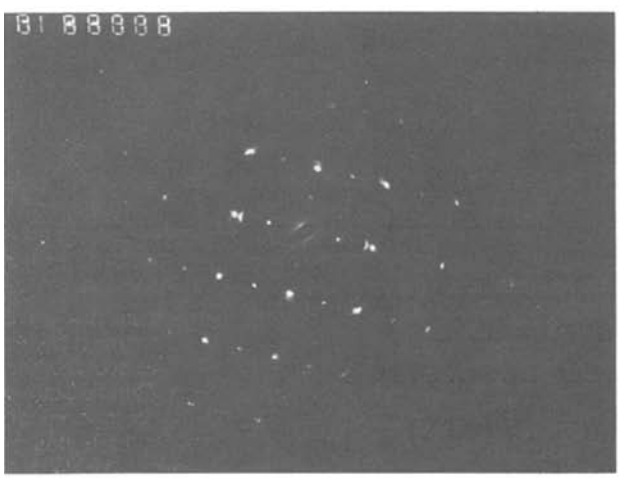

Fig. 3. Diffraction pattern from a crystal of β-PbO_2 (01$\bar{1}$) section with some streaking away from the intensity maxima of the Bragg reflections.

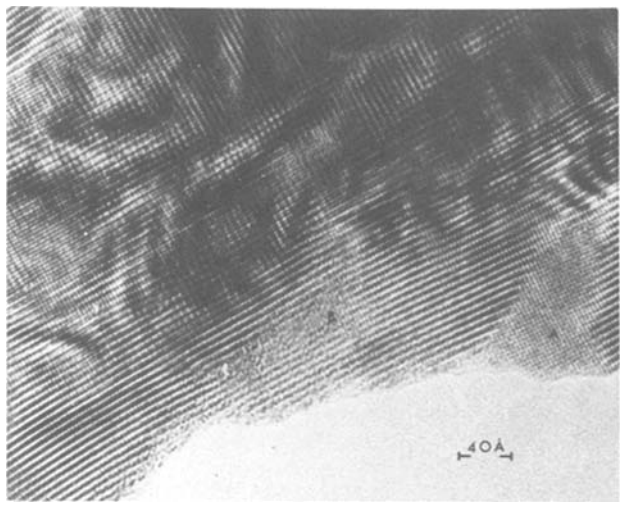

Fig. 4. High resolution image corresponding to the diffraction pattern shown in Fig. 3. Mainly shows contrast attributable to the (01$\bar{1}$) projection of the rutile structure, but there is also a second structure type or orientation at A and an amorphous area at B.

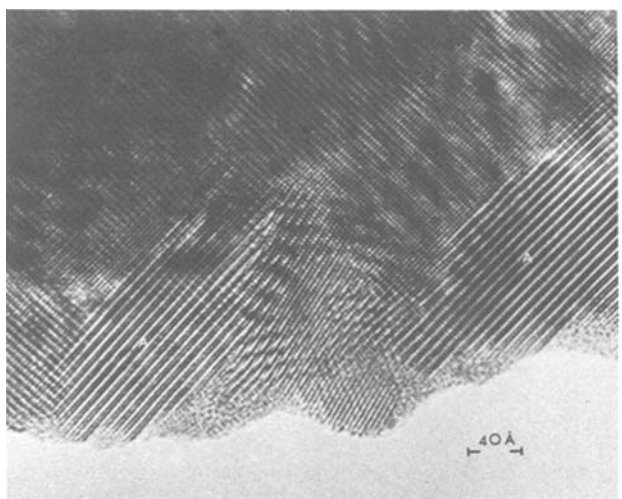

Fig. 5. A second crystal with mainly (01$\bar{1}$) rutile contrast, but a further structure or orientation type is coherently grown in at the two areas marked A.

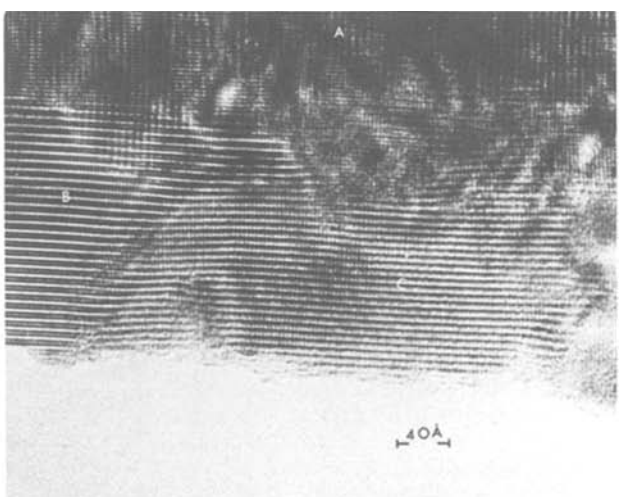

Fig. 6. Crystal with the (011) rutile contrast coherently grown together in two separate orientations (at A and C) also intergrown with a different structure or orientation type (at B).

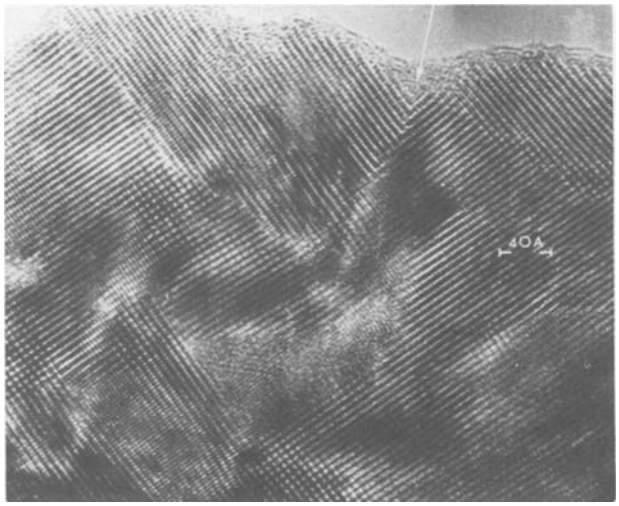

Fig. 7. Crystal with $(01\bar{1})$ rutile contrast in two separate orientations both parallel to the beam with a twin boundary marked.

similar substructure. These features do not appear to be caused by interaction with the electron beam since, when selected features were monitored over extended periods of electron irradiation, no changes were seen.

Crystals of electrochemically prepared α-PbO_2 yielded streaked diffraction patterns (Fig. 8) redolent of planar faulting like that exhibited by chemically prepared α-PbO_2 (10). No such faults were found in crystals of either form of β-PbO_2 and this would account for the different ways in which the two structure types responded to attempts at refinement with x-ray powder data (10).

Discussion

The neutron experiments in the present study appear to confirm the ability of PbO_2 to accommodate hydrogen and indicate that the majority of the hydrogen is present as water droplets either filling pores within the PbO_2, or adsorbed at the pore surfaces. The correlation between the quantity of hydrogen found from the neutron transmission measurements and the difference between the analysis figures for total Pb and for Pb^{IV} suggests a formulation of lead dioxide in which a reduced form of lead (probably Pb^{2+}) is present with total charge balance maintained by a component of this hydrogen. Thus we might write $Pb_{1-x/2}{}^{4+}Pb_{x/2}{}^{2+}H_x{}^{+}O_2$ and maintain the overall cation/oxygen ratio at 0.5. However the excess of hydrogen present in some of the specimens included in Table III, beyond that which could charge compensate for Pb^{2+}, and the absence of any observable inelastic scattering from hydroxyl groups indicate that the hydrogen in the water droplets is present in greater concentration than any cationic hydrogen even after heating at 120°C.

The electron microscopy has shown that the coherent intergrowth of crystals of PbO_2 in different orientations is just as characteristic of the β-form as it is of the chemically prepared α-form. These two materials differ in that the planar faults exhibited by the α-form are not found in the β-form and this may account for the different results of attempts to refine the two structures with x-ray powder data (10). The apparent absence of crystallographic shear planes in both cases is consistent with any departure from stoichiometry (*i.e.*, x in PbO_{2-x}) being very small.

The possibility that crystal faulting and structural intergrowth have some bearing on electrochemical capacity remains to be tested by a high resolution electron microscope study of a sample of PbO_2 which is known to lack electrochemical activity.

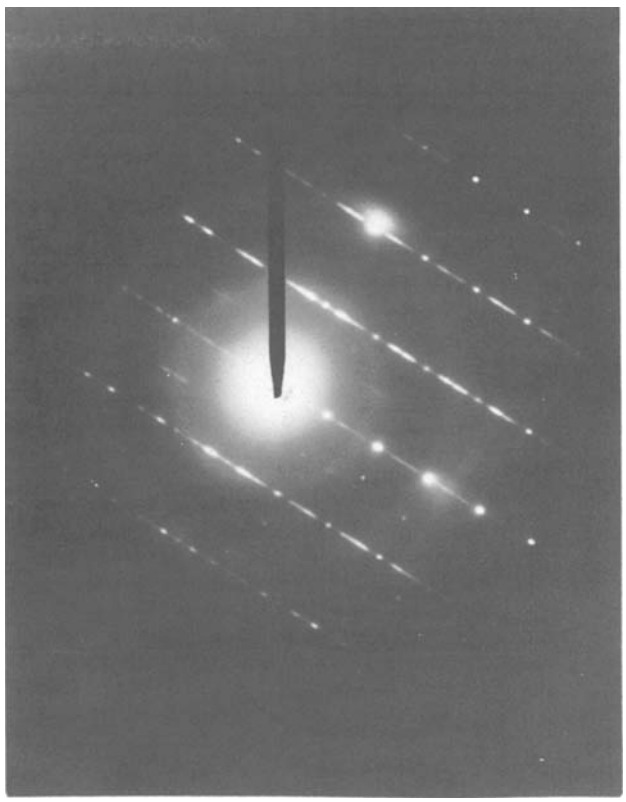

Fig. 8. Diffraction pattern of a crystal of electrochemically prepared α-PbO_2. The pattern represents the $(1\bar{1}0)$ section of the reciprocal lattice with streaking extending in the C* direction.

In future the neutron experiments can be used to test for a correlation between the presence of hydrogen and electrochemical capacity, to seek a connection between hydrogen content, crystal faulting, and surface areas, and to examine in further detail the manner in which hydrogen is accommodated.

Conclusions

High resolution transmission electron microscopy has been used to demonstrate that substantial and coherent structural intergrowth takes place in electrochemically prepared α- and β-PbO_2. Neutron scattering from a variety of specimens of lead dioxide confirms the ability of the material to accommodate hydrogen. Changes observed in the inelastic scattering from the PbO_2 after heat-treatment are consistent with a progressive loss of water droplets. There is no evidence for any characteristic vibrations associated with isolated hydroxyl or $-OH_2$ groups.

Acknowledgments

The authors gratefully acknowledge the assistance of Mr. T. J. Webber, who performed the chemical analyses, and helpful discussions with Dr. A. E. Hughes.

Manuscript submitted March 22, 1982; revised manuscript received ca. Oct. 15, 1982.

Any discussion of this paper will appear in a Discussion Section to be published in the December 1983 JOURNAL. All discussions for the December 1983 Discussion Section should be submitted by Aug. 1, 1983.

Publication costs of this article were assisted by A.E.R.E. Harwell.

REFERENCES

1. J. Perkins, *Mater. Sci. Eng.*, **28**, 169 (1977).
2. J. Brenet and P. Faber, *J. Power Sources*, **4**, 203 (1979).
3. S. M. Caulder, J. S. Murday, and A. C. Simon, *This Journal*, **120**, 1515 (1973).
4. A. C. Simon, S. M. Caulder, and J. T. Stemmle,

ibid., **122**, 1640 (1975).
5. S. M. Caulder and A. C. Simon, *ibid.*, **121**, 1546 (1974).
6. A. C. Simon and S. M. Caulder, in "The Electrochemistry of Lead," A. T. Kuhn, Editor, p. 43, Academic Press, New York (1979).
7. J. Leciejewicz and I. Padlo, *Naturwissenschaften*, **49**, 373 (1962).
8. P. D'Antonio and A. Santoro, *Acta Crystallogr., Sect. B*, **36**, 2394 (1980).
9. J. D. Jorgenson, R. Varma, F. J. Rotella, G. Cook, and N. P. Yao, Paper 604 presented at The Electrochemical Society Meeting, Denver, Colorado, Oct. 11-16, 1981.
10. P. T. Moseley, J. L. Hutchison, and M. A. M. Bourke, *This Journal*, **129**, 876 (1982).
11. F. Caldara, A. Delmastro, G. Fracchia, and M. Maja, *ibid.*, **127**, 1869 (1980).
12. G. E. Bacon, "Neutron Diffraction," 3rd ed., pp. 50-63, Oxford (1975).
13. D. I. Garber and R. R. Kinsey, "Neutron Cross Sections," 3rd ed., Brookhaven National Laboratory (1976).
14. R. May, K. Ibel, and J. Hass, *J. Appl. Crystallogr.*, Submitted.
15. P. G. Dickens, J. J. Birtill, and C. J. Wright, *J. Solid State Chem.*, **28**, 185 (1979).
16. C. J. Wright, *ibid.*, **20**, 89 (1977).
17. P. G. Hall, A. Pidduck, and C. J. Wright, *J. Colloid Interface Sci.*, **79**, 339 (1981).

Nickel Triphenylphosphine Electrodes

Raymond Jasinski*

Occidental Research Corporation, Irvine, California 92713

ABSTRACT

Electrodes can be formed from physical mixtures of carbon, nickel (o), and triphenylphosphinated/polystyrene beads. The immobilized Ni(PPh_3) complex exhibits electrochemistry similar to that of the electrolyte-soluble homogeneous catalyst and will also sustain a catalytic current for the cathodic reduction of chloroform. These physical mixture electrodes are longer lived than electrode surfaces modified with an adsorbed film of nickel-triphenylphosphinated polystyrene.

Chemically modified electrodes continue to be investigated as a means for doing electrocatalysis [*e.g.*, (1-3)]. Such electrodes must, of course, be electroactive as well as structurally durable, resistant to poisoning, and resistant to dissolution. To achieve these properties, we have developed a "physical mixture" electrode structure by combining a homogeneous electroactive catalyst (nickel triphenylphosphine) with a catalyst-insolubilizing agent [commercial polystyrenephenylphosphine beads (4), cross-lined 2% for insolubility]. These beads were mixed with an electronically conducting carbon paste to form the electrode. The questions addressed in this study were: (*i*) would the attached homogeneous catalyst resemble, chemically and electrochemically, its soluble, catalytic form and (*ii*) could charge be transferred into and out of the structure fast enough to mediate an electrocatalytic process?

The chemical catalytic properties of nickel triphenylphosphine have been investigated sporadically since 1948 (5). Some interesting potentialities have been discussed [*e.g.*, (6)] although commercial exploitation of these complexes has not yet been reported. Solid, air stable Ni(II) complexes of the stoichiometry $(PPh_3)_2NiX_2$ are found with X = Cl, Br, I, NO_3^-, NCS^-, but not F^-, NO_2^- (7). The solid PPh_3 compound with chloride and nickel is tetrahedral and paramagnetic. It is also possible to form nickel (II)/PPh_3 anions. Solid $[NEt_4]$ $[Ni(PPh_3)Br_3]$ has been precipitated from a solution containing an excess of bromide ion.

Complexes with PPh_3 also exist for monovalent nickel. Solid $(PPh_3)_3NiCl$ has been prepared and is paramagnetic (9, 10). Cryoscopic studies in benzene indicate some dissociation into $(PPh_3)_2NiX$ and no significant Ni-Ni interaction.

The solid, zero valent nickel-phosphine complex is $Ni(PPh_3)_4$. Cryoscopic studies, NMR, and absorption spectroscopy in benzene confirm the solution equilibrium: $Ni(PPh_3)_4 = Ni(PPh_3)_3 + PPh_3$, to yield coordinatively unsaturated Ni(O). The equilibrium constant was estimated as greater than 10, in that no association was found for 15 mM nickel in molar PPh_3. Such coordinative unsaturation is considered (12) a prerequisite for catalytic activities. There was no evidence for Ni-Ni interactions and no further dissociation to $Ni(PPh_3)_2$ (11).

Papers (13, 14) have recently appeared on the electrochemistry of Ni/PPh_3, *i.e.*, with $(PPh_3)_2NiCl_2$ in THF and AN, and with $Ni(ClO_4)_2$ + PPh_3 in acetonitrile. [Here $Ni(ClO_4)_2$ was prepared by anodization of metallic nickel in tetrabutylammonium perchlorate-acetonitrile solution (14).] In acetonitrile and in THF, with stoichiometric chloride and excess PPh_3, the major soluble nickel species was claimed to be $(PPh_3)_2NiCl_2$. Chloride ion, produced on cathodic reduction, was precipitated with lithium ion. With chloride scavenged from the system, Ni(II) was reduced in two distinct steps. The electrochemistry of Ni(II) in the absence of chloride ion, in AN, is again a two-step process, but with little (<50 mV) separation in half-wave potential; NMR studies of nickel (II) in solution indicated paramagnetic nickel; an octahedral configuration was claimed (14), with the composition $(PPh_3)_2Ni(AN)_4^{+2}$. However, the data is equally consistent with tetrahedral symmetry. It is likely that soluble Ni(II), in excess PPh_3, is still four coordinate with both solvent and PPh_3, having the composition $[(PPh_3)_2Ni(AN)_2^{+2}]$.

Experimental

The $(PPh_3)_2NiCl_2$ complex was prepared according to the method published in Ref. (15); elemental analysis gave the theoretical amount of nickel. $NiCl_2$DME was purchased from Alfa Chemical and used as received. $LiBF_4$ was purchased from Alfa Chemical Company; the tetrabutyl ammonium tetrafluoroborate was purchased from Southwestern Chemical Company, Austin, Texas.

To remove the residual water, the $LiBF_4$ was heated at 150°C under vacuum for 3 days, dissolved in the solvent mixture, and percolated down a column of 3A Molecular Sieves of twice the solvent volume. [Alumina powder reacts with the Ni(O)/TPP complex, which prevented use of the alumina drying procedure discussed in Ref. (16-18).] Oxygen was removed from the solution by purging with glove box argon. Tri-

* Electrochemical Society Active Member.
Key words: chemically modified electrodes, electrocatalysis, electroorganic synthesis.

phenylphosphine was purchased from Strem Chemical Company. This material contained at least one electroactive impurity which increased the residual Faradaic current to 10 $\mu A/cm^2$ at -800 mV. Subsequent electrolysis at -1400 mV, before addition of Ni(+2), decreased this "blank" to nondetectable levels.

The solubility of $NiCl_2$ in AN was less than 2 mM; no difficulty was experienced dissolving $(TPP)_2NiCl_2$ in 4 mM concentrations. Acetonitrile was purchased from Burdick & Jackson Company and from Mallinkrodt. The $TBABF_4$/AN electrolyte was dried by passage down an equal volume of neutral alumina. This technique removed peroxides and trace chloride ion; TEACl solutions treated similarly lost more than 90% solute to the alumina column. The effective cathodic limit of the SSE was nominally -2V on a glassy carbon electrode.

The electrochemical cell was of the conventional three-compartment design, with a coarse glass frit separating the counter and working electrode compartments and a Luggin capillary adjacent to the working electrode. Gold foil was used as the counter-electrode; a PAR/Brinkmann glassy carbon electrode (0.4 cm^2) was used as the working electrode. The reference electrode was a Beckman "Permaprobe," capacitively coupled to the electrolyte via a platinum wire (19, 20) to minimize electronic noise. Nominally 30 min were required for stabilization of the reference electrode. The Permaprobe avoided the possible leakage of water from an aqueous electrolyte reference electrode and was better poised than the low impedance silver wires commonly used as reference in nonaqueous electrolytes. The potential of the PP *vs.* an aqueous saturated calomel electrode was measured as +70 mV; two PP's gave potentials identical to within 5 mV.

The cell was operated within a Vacuum Atmospheres dry box. The measurements were made with a PAR Model 173 Potentiostat, Model 175 Universal programmer, Model 179 Coulometer, and a Hewlett-Packard 7045 X-Y Recorder. Weighings and solution preparation were also carried out within the dry box.

Controlled potential coulometry was done, under stirring, with a pyrolytic graphite electrode. The quantity of this charge that could be recovered by anodic oxidation was less than 100% due to chemical reactions of $Ni(PPh_3)_3$ with solution impurities. Since such chemical reactions yield Ni(II), "recovery" was determined by the amount of cathodic charge which could be delivered on the second electrolysis, *i.e.*, after the first anodic reoxidation.

Anodic stripping was used to detect adherent films of zero-valent nickel on the indicator electrode. Slow (20 mV/sec) cyclic sweeps were made from 0.0 mV to a selected cathodic potential, then to +600 mV and finally back to 0 mV. The solution was stirred throughout so that the observed anodic current would have to be due to adherent surface films. It was thus assumed that all nickel metal was adherent. The total cathodic and anodic charges passed were computed by integrating the cyclic voltammogram.

The catalytic polymer substrate was polystyrene (2% cross-linked) functionalized with 0.4 meq/g triphenylphosphine, purchased from Strem Chemical Company as 20-60 mesh "microspheres." These spheres were activated with Ni(II) as follows: the pale yellow beads were placed overnight in $NiCl_2$/ThF solution containing supporting electrolyte. The beads become olive green and were then washed with the solvent plus electrolyte. The beads remained green. Omission of the electrolyte resulted in beads that were electrochemically inactive, although still green in color. Subsequent equilibration with nickel-free electrolyte slowly resulted in electroactive material.

Films were also formed on polystyrene PPh_3, by a technique similar to that discussed in Ref. (21). The polymer beads [before adding Ni(II)], were first soaked with THF overnight and then removed. The residual solution containing some soluble polymer was dropped onto the surface of a glassy carbon electrode, and the solvent evaporated. An $NiCl_2$/THF solution was then dropped onto this surface to activate the polymer.

PVC was also used as a polymeric substrate for nickel/PPh_3. This material (obtained from Polyscience Corporation) was reacted with lithium diphenyl phosphide according to the procedure in Ref. (22). The product was then dissolved in THF and dropped onto an electrode surface. Electroactive nickel was also formed by reduction of $NiCl_2$-PPh_3 solution onto a polymer-coated surface.

The carbon paste electrode was purchased from Brinkmann. This "organic electrolyte" paste was stable in acetonitrile and propylene carbonate, but not in electrolytes containing THF, DME, or DMF. The background currents at potentials more negative than -1100 mV were excessive. No procedure was found which significantly diminished this current.

A vitreous carbon paste was prepared in-house with Apiezon grease, according to Ref. (23). This paste remained intact in PC, AN, HAc, EtOH, and DMF, but disintegrated in THF, DME, and CH_2Cl_2. The catalyst beads were much more adherent to the Apiezon paste than to the Brinkmann paste. This paste was used as a plug within a glass tube, backed with a pyrolytic graphite disk. It was also possible to form an electrode by spreading the paste across a metal screen; polystyrene beads were then pressed into the paste.

Results

Consider first the chemical speciation of divalent nickel in acetonitrile solutions containing chloride and triphenylphosphine and its effect on nickel electrochemistry. The variations in the optical spectra (Table I) are taken as evidence that chemical equilibria exist between nickel and two ligands. The identification of ionic species has been published (14, 24, 25). Variations in nickel electrochemistry were also found with variations in ligand concentration. In Fig. 1 are cyclic voltammograms taken for Ni(II) in $TBABF_4$, AN solutions free of chloride, with and without TPP present. The PPh_3 shifts the reduction process positive by nominally 350 mV; the process also appears to be more reversible. The anodic peak in the absence of PPh_3 is a stripping peak. Its potential depends on the quantity of nickel plated out during the cathodic sweep. The cathodic peak potential is sweep-rate dependent in the presence of PPh_3. The potential at 20 mV/sec is 120 mV more positive than at 200 mV/sec (Table II).

Stoichiometric $(PPh_3)_2Ni^{+2}$ shows two reduction waves while oxidation takes place in one broad wave. The addition of chloride ion in the atom ratio of 2Cl/1Ni [5 mM PPh_3, 0.6 mM Ni(II)] sharpened both reduction waves (Fig. 2). Both reduction peaks were then essentially sweep-rate independent. An excess of chloride (*vs.* Ni concentration) significantly altered the cyclic voltammogram (Fig. 2). However, now increasing chloride to 0.1M did not further alter the cyclic voltammogram. A broad oxidation wave at

Table I. Absorption spectra vs. solvent

Ligand ratio		Maxima (nm)
PPh_3/Ni	Cl/Ni	AN
0	0	580
24	0	495
0	2	570
		615
		670
0	100	655
		700
24	2	590
		640
12	12	625
		650
		700

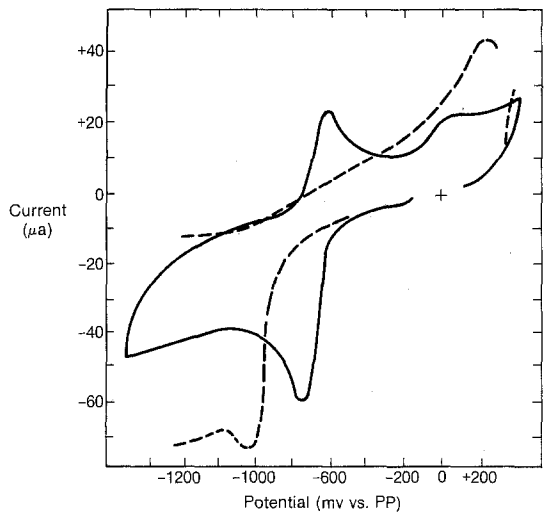

Fig. 1. The presence of PPh_3 ligand increases the Ni(II) reduction potential and the electrochemical reversibility. The electrolyte was 0.6 mM Ni(II) plus 0.1M $TBABF_4$, chloride free, in acetonitrile, without (- - - -) and with 4 mM PPh_3. The sweep rate was 200 mV/sec.

nominally +300 mV was present in all chloride solutions (not shown in Fig. 2).

Zinc and $NaBH_4$ are commonly used to prepare $Ni(PPh_3)_3$. The open-circuit potential in 0.1M $TBABF_4$/AN measured for a zinc strip was −650 mV. The ocp for platinum in a sodium borohydride solution was −930 mV (representing the positive potential limit for the effective reduction potential of BH_4^-). Obviously a number of ligand combinations exist (Table II) where zinc would not be effective as a reductant, which was confirmed by contacting the appropriate solutions with metallic zinc.

Controlled potential coulometry was used to identify the particular nickel valence states produced by the charge transfer process. Electrolysis of divalent $NiCl_2$/PPh_3 solution at −900 mV, with $TBABF_4$ and $LiBF_4$ as supporting electrolytes, yielded soluble red-brown solution, a decrease in reducible nickel, and an increase in oxidizable nickel. In Table III are listed the number of electrons transferred as a function of solute. Published coulometric data (14) indicated a two-electron reduction of Ni(II), yielding a red-brown precipitate in AN/$TBABF_4$/PPh_3 solution free of chloride. The solid rather than red-brown solution is due to a high PPh_3 and nickel concentration (11).

Nominally two electrons are transferred to Ni(II) at potentials more negative than −900 mV in all systems studied. The fractional electron change on electrolysis of $NiCl_2$/PPh_3/$TBABF_4$ at −500 mV, rather

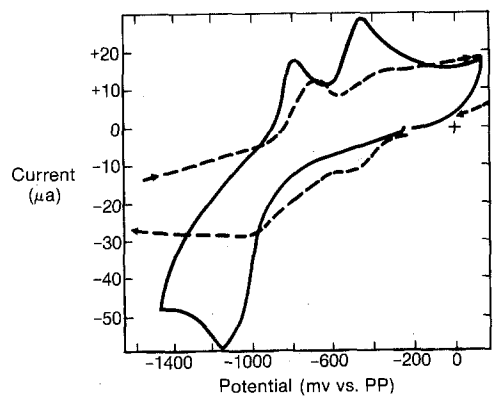

Fig. 2. The 200 mV/sec cyclic voltammogram of stoichiometric $(PPh_3)_2NiCl_2$ shows broad reduction and oxidation waves (- - - -). The addition of excess PPh_3 (14 mM) and excess chloride (8.4 mM) to 0.6 mM Ni(II) alters the redox behavior. The AN solution was 0.1M in $TBABF_4$.

Table II. Cyclic voltammetric parameters for nickel redox reactions (200 mV/sec on glassy carbon in $TBABF_4$/AN)

Solution composition			Cathodic (mV vs. PP)		Anodic	
PPh_3/Ni	Cl/Ni±*	ΣNi (mM)	$E_p/2$	ΔE**	E_p	ΔE**
0	0	1.4	−765	120	+560	—
7	0	0.6	−700	45	+80	10
0	10	1.4	−920	—	+120	—
7	2	0.6	−590 (−300)	0	+100	10
7	14	0.6	−970	30	−470	15
12	50	2	−970	30	−420	20

* ± atom ratio.
** 200 mV/sec vs. 20 mV/sec.

Table III. Controlled potential coulometry (AN + 2 mM $NiCl_2$ + 20 mM PPh_3)

Sequence	Parameter	Number of electrons $TBABF_4$	$LiBF_4$	TEACl
1	Cathodic reduction at −300 mV	0.40 ± 0.05	0.97	—
2	Anodic oxidation	0.24	0.90	—
3	Cathodic reduction at −900 mV	2.0	2.2	1.8
4	Anodic oxidation +200	1.9	1.7	1.3

than a single electron reduction, is a consequence of a shift in the reduction potential (Fig. 2) by the liberated chloride ions. In $LiBF_4$ solution, which yields insoluble LiCl on reduction of $(PPh_3)_2NiCl_2$, the −500 mV cathodic process consumes one electron. This half-reduced solution was colored pale yellow and was slightly turbid. In both solutions two electrons per nickel atom were transferred at −900 mV.

Also listed in the table are anodic "recovery" numbers, as defined in the Experimental section. The 95% recovery of Ni(O) in $TBABF_4$ may still have been due to chemical reaction and/or slow diffusion of solution out of the working electrode compartment. The 75% recovery for TEACl solution is not an experimental artifact. The cathodic/anodic cycle was repeated three times with 75% recovery each cycle. Furthermore, the cyclic voltammogram cathodic peak current decreased by 25% after each electrolysis cycle.

One possible product of the cathodic charge transfer process is nickel metal, part of which remains on the electrolysis electrode and part of which sinks to the bottom of the cell. Anodic stripping experiments were used to test for the possibility of an insoluble nickel film. No detectable nickel metal was found for $TBABF_4$ solutions with concentrations of PPh_3 equal to or above stoichiometry. For zero PPh_3 in $TBABF_4$, 66% of the input cathodic charge was recovered as nickel metal. In $LiBF_4$ electrolyte, some insoluble nickel was found at all PPh_3 levels.

Shown in Fig. 3 is a cyclic voltammogram for polystyrenephosphine beads, impregnated with nickel ions, and mixed in with carbon paste. The currents are much larger than for the millimolar Ni/PPh_3 solution but the cathodic pattern for the nickel beads resembles that for solutions of stoichiometric $(PPh_3)_2NiCl_2$ (Fig. 2). However, the only anodic current peak found for the nickel beads was at +300 mV. This peak shifted more positive as the cathodic wave became larger through repetitive cycling. The cyclic voltammogram was stable after five repetitive cycles. The results in $LiBF_4$ were similar to these, except that the sole anodic maximum was at nominally 0.0 mV, the potential for nickel metal oxidation in $LiBF_4$ solution.

This electrode was potentiostated at −1200 mV. When the current had decreased to 1 μA, sufficient chloroform was added to make the solution 0.07M. The

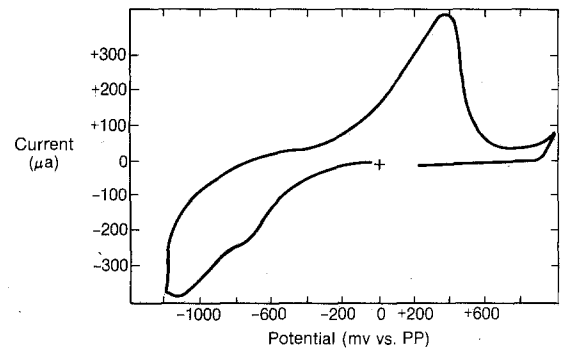

Fig. 3. The 200 mV/sec cyclic voltammogram for the nickel bead electrode shows high currents, cathodic behavior similar to stoichiometric $(PPh_3)_2NiCl_2$, and anodic behavior similar to nickel metal. Shown here is the third repetitive scan.

conversion observed was nominally 800 mols chloroform per mol Ni (Fig. 4). When the experiment was repeated in 0.04M chloroform/acetonitrile, with $LiBF_4$ as the supporting electrolyte, the current rose to a maximum of nominally 130 μA in 30 min and remained constant at that level for the following 8 hr, at which time the experiment was deliberately terminated. This particular electrode had been exposed to solution for a total of 24 hr to allow possible leaching of the divalent nickel out of the electrode structure.

It is presumed that the $HCCl_3$ is reduced to CH_2Cl_2 and H_3CCl by $Ni(PPh_3)_3$ in acetonitrile. No coupling products were present in acetonitrile, *e.g.*, 1,1,2 trichloroethane, while such products were found in tetrahydrofuran. Detailed product analysis was not done.

In the absence of nickel and the polystyrene-phosphine, the addition of chloroform generated less than 1 μA increase in current at -1200 mV. The electrocatalytic reduction of chloroform on nickel metal foil was much slower than on the zero valent triphenylphosphine complex. Similar results were obtained with electrodeposited nickel. For example, a glassy carbon electrode was potentiostated at -1200 mV in an $NiCl_2$ solution of $TBABF_4$ in acetonitrile. After the current decreased to 1 μA, chloroform was added to the 0.07M level and the current increased by only 5 μA, well below that of the beads.

Films made of polystyrene-triphenylphosphine and PVC-triphenylphosphine on glassy carbon also showed electrochemical activity after treatment with Ni^{+2} solution but were less adherent. In AN, a cathodic maximum was also found at -1400 mV and an anodic maximum at $+160$ mV. However, the peaks disappeared after a few repetitive cycles. Visual observation of the electrode showed little remaining polymer on the electrode surface.

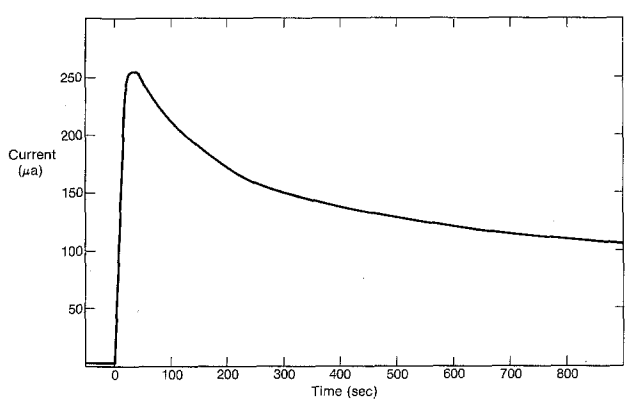

Fig. 4. The electrocatalytic reduction of 0.07M $CHCl_3$ in AN + 0.1M $TBABF_4$ is accomplished by the nickel bead electrode, potentiostated at -1200 mV vs. PP. Chloroform was added at time zero (after the background current had decayed to 5 μA).

Electrocatalysis was also found with the nickel polystyrenetriphenylphosphine beads, using chloromethylbenzoate as the organic substrate. The reaction was slow at room temperature, but showed a current increase of 70 μA at 50°C and at -600 mV applied potential.

Discussion

The speciation of Ni(II) in acetonitrile containing chloride and triphenylphosphine ligands is dependent on the relative ratios of nickel to the two ligands. The cyclic voltammetry is consistent with ligand-nickel interactions preceding and following charge transfer, *e.g.*, peak current shifts with sweep rate and the redox peak potentials are well separated. The reduction of $Ni(II)/PPh_3$ complexes appears to be a two-step process, *e.g.*, in the absence of Cl^-

$$Ni(PPh_3)_2^{+2} + e \rightarrow Ni(PPh_3)_2^{+} \rightarrow Ni(PPh_3)_2^{0}$$

followed by ligand addition to yield $Ni(PPh_3)_3$, the most stable form of Ni(0) (11). Since this material can be formed in high yields by electrolytic reduction, the initial product of charge transfer, $Ni(PPh_3)_2$, must be sufficiently long lived to await the arrival of the third PPh_3 ligand. Otherwise considerable nickel metal would have been formed. The fact that the final reduction product, $Ni(PPh_3)_3$, is not the direct product of charge transfer likely accounts for the electrochemical irreversibility of the charge transfer process.

The cyclic voltammetric peak potentials are not reliable indicators of the specific Ni(II) and Ni(0) speciation with PPh_3 and Cl^-. For example, the presence of PPh_3 in zero chloride solution shifts the reduction potential of Ni(II) nominally 300 mV positive of that for nickel metal deposition. The addition of excess chloride ion shifts the potential back to about that of nickel metal formation. Yet exhaustive electrolysis of the chloride solution still generates a red $Ni(PPh_3)_3$ solution rather than nickel metal. Anodization of $Ni(0)/PPh_3$ solutions usually generates a broad peak at nominally zero to $+300$ mV, *i.e.*, at the potential for reoxidation of nickel metal. However, stripping coulometry indicates little nickel metal. These two points, the finite lifetime of $Ni(PPh_3)_2$ and the nonspecie-specific cyclic voltammetry are also consistent with the behavior of Ni(II) in the phosphinated polystyrene beads.

The beads do absorb nickel (II) from solution (acetonitrile and tetrahydrofuran), implying the formation of $Ni(PPh_3)_x^{+2}$ entities. It is to be concluded that the internal phosphine groups are involved, rather than solely surface groups, since it was necessary to absorb solute into the beads to observe the electrochemistry. The cathodic cyclic voltammetric peaks are consistent with the formation of Ni/PPh_3 complexes, but with less than stoichiometric triphenylphosphine present. This stoichiometry is not unreasonable. The number of ligands involved in charging the beads with nickel should be nominally two per nickel (II) ion. However, the most stable $Ni(0)/PPh_3$ specie requires three ligands per nickel. That nickel $(0)/PPh_3$ complexes are formed at all is indicated by the electrocatalysis. The phosphine complexes catalyze the reduction of chloroform, while nickel metal does not. It is possible that some nickel $Ni(PPh_3)_3$ was formed by interaction of $Ni(PPh_3)_2$ molecules, with the concomitant formation of some nickel metal. However, given the finite lifetime of $Ni(PPh_3)_2$ species in solution, the following mechanism is also possible for chloroform reduction

$$Ni(PPh_3)_2 + CHCl_3 \rightarrow \text{adduct}$$

$$\rightarrow Ni(PPh_3)_2^{+2} + \text{product}$$

followed by

$$Ni(PPh_3)_2^{+2} + 2e \rightarrow Ni(PPh_3)_2$$

It is only required here that the rate of nickel-nickel

bond formation be slower than that of the reaction to form the Ni(0)/$CHCl_3$ adduct. Obviously considerable work would be required to unravel this question.

The chemistry of the bulk electrolyte does exert an effect on catalyst stability implying the inner phase of the bead does communicate with the bulk electrolyte. For example, chloride ion, formed by the cathodic reduction of chloroform, is soluble in $TBABF_4$ but not in $LiBF_4$-acetonitrile solution. Chloride ion is also capable of displacing phosphine ligands from divalent nickel complexes and eventually the nickel leaches out of the beads as a chloride complex. But this loss mechanism will not operate if Cl^- first precipitated out as LiCl. Thus the catalytic activity degrades with time in $TBABF_4$ but not in $LiBF_4$ solutions. (The quantity of nickel leached out of the beads was not measured.)

The main points of this study are the following:

1. Charge can be transferred into and out of 20-60 mesh, 0.4 meg/g polystyrene-phosphine beads containing divalent nickel ions.
2. The cathodic electrochemistry of nickel in these beads resembles that of nickel in PPh_3-containing solutions; the anodic electrochemistry does not. The stoichiometry of the reduced nickel PPh_3 complex in the beads is thus different than either nickel metal or $Ni(PPh_3)_3$.
3. These ligated nickel atoms can be used as mediators in charge transfer reactions, *i.e.*, as electrocatalysts.
4. The activities are persistent in organic solvents in the absence of nickel coordinating ligands.

It is presumed that these phenomena are not restricted to nickel, PPh_3, and the reduction of organic halides.

Manuscript submitted Sept. 2, 1982; revised manuscript received Nov. 12, 1982.

Any discussion of this paper will appear in a Discussion Section to be published in the December 1983 JOURNAL. All discussions for the December 1983 Discussion Section should be submitted by Aug. 1, 1983.

Publication costs of this article were assisted by Occidental Research Corporation.

REFERENCES

1. R. Murray, *Acc. Chem. Res.*, **13,** 135 (1980).
2. P. Peerce and A. Bard, *J. Electroanal. Chem. Interfacial Electrochem.*, **112,** 97 (1980).
3. N. Oyama and F. Anson, *This Journal*, **127,** 247 (1980).
4. C. Pittman, A. Hirar, C. Jones, R. Hanes, and Q. Ng, *Ann. N.Y. Acad. Sci.*, **295,** 15 (1977).
5. W. Reppe and W. Schwekenlick, *Justig Liebigs Anal. Chem.*, **560,** 104 (1948).
6. L. Cassar, S. Farrara, and M. Foã, *Adv. Chem. Ser.*, **132,** 252 (1974).
7. L. Venanzi, *J. Chem. Soc.*, 719 (1958).
8. F. Cotton, O. Faut, and D. Goodgame, *J. Am. Chem. Soc.*, **83,** 344 (1961).
9. M. Nilges, E. K. Barefield, R. L. Belfond, and P. H. Davis, *ibid.*, **99,** 755 (1977).
10. G. Heimbach, *Angew. Chem.*, Int. Ed., **3,** 648 (1964).
11. C. Tolman, W. Seidel, and L. Gossar, *J. Am. Chem. Soc.*, **96,** 53 (1974); *ibid.*, **94,** 266 (1972).
12. J. Coleman, *Trans. N.Y. Acad. Sci.*, **30,** 479 (1968).
13. M. Troupel, Y. Rollin, C. Cheviot, F. Pflueger, and J. Faubarque, *J. Chem. Res(s)*, 50 (1979).
14. G. Botempielli and F. Magno, *J. Electroanal. Chem. Interfacial Electrochem.*, **103,** 243 (1979).
15. M. Semmelhack, R. Stauffer, and T. Rogerson, *Tetrahedron Lett.*, **45,** 4519 (1973).
16. D. Burfield and R. Smothers, *J. Org. Chem.*, **43,** 3966 (1978).
17. O. Hammerich and V. Parker, *Electrochim. Acta*, **18,** 537 (1973).
18. T. Saji and A. Bard, *J. Am. Chem. Soc.*, **99,** 2235 (1977).
19. D. Garreau, I. Sageant, and S. K. Binh, *J. Electroanal. Chem. Interfacial Electrochem.*, **89,** 42 (1978).
20. C. Herrmann, G. Perrault, and A. Pilla, *Anal. Chem.*, **40,** 1173 (1968).
21. F. Kaufman and E. Engler, *J. Am. Chem. Soc.*, **101,** 547 (1979).
22. K. Allum, R. Hancock, I. Howell, R. Pitkethly, and P. Robinson, *J. Organomet. Chem.*, **87,** 189 (1975).
23. R. Nowak, C. Joyal, and D. Venezky, Paper 61 presented at The Electrochemical Society Meeting, St. Louis, Missouri, May 11-16, 1980.
24. F. Cotton and D. Goodgame, *J. Am. Chem. Soc.*, **82,** 2967 (1960).
25. L. Sillen and A. Martell, "Stability Constants of Metal Ion Complexes. Supplement No. 1," Special Publ. No. 25, The Chemical Society (1971).

Experimental Verification of the Space-Charge Model for Electrokinetics in Charged Microporous Membranes

G. B. Westermann-Clark[1] and J. L. Anderson

Department of Chemical Engineering, Carnegie-Mellon University, Pittsburgh, Pennsylvania 15213

ABSTRACT

A space-charge model for electrolyte transport in charged capillary pores was examined experimentally with aqueous solutions of alkali chlorides and $MgCl_2$ in track-etched mica membranes. The model combines the Gouy-Chapman view of the double layer with the Nernst-Planck and Navier-Stokes transport equations. The pores of experimental membranes were uniform capillaries with a well-characterized cross section. The pore sizes ranged from an order of magnitude smaller to an order of magnitude larger than the Debye screening lengths of solutions. Three independent quantities were measured: streaming potential, for which an applied pressure across the membrane is the driving force for transport; pore conductivity, for which an applied electrical potential is the driving force; and concentration potential, for which an electrolyte concentration difference is the driving force. Data follow the trends of model predictions but indicate that chloride ions affect the pore wall charge. For monovalent cations, the pore wall charge deduced from pore conductivity measurements yielded theoretical predictions for the streaming potential and for the concentration potential that agree quite well with the data. Such agreement was not obtained with Mg^{2+}, probably because these divalent cations adsorbed onto the negative pore wall. We conclude that, in the absence of strong interaction between the charged pore wall and free ions in solution, the model is quantitatively accurate for pores larger than 30Å in radius and for aqueous electrolyte concentrations of 0.1M or lower.

Coupling between electrical forces and mass transfer in charged porous media becomes important when the diffuse part of the double layer occupies an appreciable fraction of the pore volume. Stated another way, mass and charge transport mechanisms are interrelated when the Debye screening length (λ) is of the same order of magnitude as the smallest pore dimension. In the case of circular capillaries of radius a, this occurs when $a/\lambda < 10$. In aqueous solutions λ is usually less than 10^3Å, so microporous media ($a < 1$ μm) are susceptible to electrokinetic coupling; such media include ion-exchange and ultrafiltration membranes, porous separators in electrolytic cells, and porous electrodes.

There is considerable literature dealing with theoretical models for the effects of double layers on the transport of ions in long circular capillaries. The earliest and most complete publications are from Dresner (1) and from Osterle and co-workers (2-4), who assumed the Gouy-Chapman model for the double layer structure, the Nernst-Planck equation for ion fluxes, and a modified Navier-Stokes equation for viscous flow of solutions. Their analyses lead to definite integrals, involving the electrostatic potential profile, which must be evaluated to obtain the desired macroscopic transport coefficients for electrical, mechanical, and chemical (concentration) driving forces. Calculations for noncircular capillaries (5), using the same basic theory for fluid phase transport inside the pore, indicate that cross-sectional geometry is not important for ion-distribution dominated phenomena (such as conductance) but could be significant for viscous flow phenomena (such as electro-osmosis).

The basic theory of Osterle and Dresner is concerned only with the flux of mass and charge, given the pore wall electrostatic condition, and does not address the important question of charge-potential relationships at the pore wall.[2] By incorporating charge-potential relationships based on acid/base equilibria into the calculation of the double layer potential profile, Keesom *et al.* (6) and Koh (7) took the model a step further and obtained reasonably good fits to streaming potential data in large pores.

The paucity of experimental studies rigorous enough to test the theoretical models is explained by two experimental difficulties. First, most microporous membranes do not have the capillary structure assumed in the theory. Second, the solid matrix of a porous medium is usually a nonconductor, so neither the charge nor the potential of a pore can be measured for making *a priori* predictions from the theory. Thus, only qualitative comparisons between theory and experiment have been possible. Recent studies using track-etched mica membranes have overcome the pore geometry problem but still are hampered to some extent by uncertainty about the pore wall electrostatic condition (8). Bean (9) estimated the unknown wall charge by doing two independent electrokinetic experiments on a single membrane (conductance and streaming potential) and by then comparing the two measurements; his results are consistent with the theory of Osterle and Dresner. In an attempt to alter the wall charge, Frohlich *et al.* (10) attached acid functional groups onto the pore walls of mica membranes, but in the process may have changed the pore size by a substantial amount.

In this paper we present the results of experiments designed to test the quantitative accuracy of the "classical model" of electrokinetics in charged capillaries (1-4) with a/λ in the range 0.1-10.0, that is, with aqueous solutions of alkali chlorides and $MgCl_2$ in the concentration range 10^{-4}-10^{-1}M. The most important aspect of the experiments is the use of track-etched mica membranes whose pores were uniform capillaries in the range 34-265Å radius with pore lengths greater than 7 μm. The next section outlines the classical model and the mathematical strategy for computing the macroscopic parameters measured in experiments. Experimental techniques used to measure electrokinetic parameters are then described. The experimental results are presented in the context of evaluating the qualitative and quantitative features of the theory.

Model for Transport in Charged Capillaries

The porous membrane is considered to be a set of identical circular capillaries whose length l is infinitely greater than the radius a. Hence, the transport characteristics of the membrane are given by the behavior of a single pore, which forms the basis of the analysis. The immobile charge density at the pore wall (σ) is assumed to be uniform, which reduces the equations to a dependence on radial position (r) and axial position (x). Because $l/a \rightarrow \infty$, the dominant resistances to

[1] Present address: Department of Chemical Engineering, University of Florida, Gainesville, Florida 32611.

Key words: electrokinetic, transport, membrane, alkali chlorides.

[2] Gauss' electrostatic condition, relating the electric field to the charge density at the pore wall, is included in the theory (see Eq. [13]), but a physicochemical constraint is needed for the relationship between the pore wall charge and potential to close the model.

transport occur inside the pore; therefore, the pore contents just inside the pore at $x = 0$ and $x = l$ are at equilibrium with the bulk solutions just outside the pore at the respective ends. Boundary layer polarization effects are not considered here; if they exist then the term "bulk solution" refers to the solution at the membrane-bulk solution interface.

The bulk solution contains a single electrolyte which completely dissociates into ions with electrovalences Z_+ and Z_-, *i.e.*, the activity coefficient of the electrolyte is assumed to be unity at all concentrations. Ions resulting from solvent dissociation (H^+ and OH^-) are ignored since the concentration of these species is negligible compared to the electrolyte concentrations considered. The single ion diffusion coefficients (D_+ and D_-) are taken to be independent of electrolyte concentration and are assigned their infinitely dilute values, which are obtained from limiting equivalent conductances. Solution properties such as the dielectric constant (ϵ) and the coefficient of viscosity (η) are assumed to equal the bulk solution values.

The model outlined below follows the derivations by Dresner (1) and by Osterle and co-workers (2-4); we shall refer to it as the "classical theory." The basic equations are those of Poisson, Nernst-Planck, and Navier-Stokes (low Reynolds number form) along with conservation of mass and charge

$$\nabla^2\psi = -\frac{4\pi}{\epsilon}\rho_e \qquad [1]$$

$$\underline{N}_i = -D_i\left[\nabla C_i + \left(\frac{Z_i e}{kT}\right)C_i\nabla\psi\right] + C_i\underline{v} \qquad [2]$$

$$\underline{O} = \eta\nabla^2\underline{v} - \nabla p - \rho_e\nabla\psi \qquad [3]$$

$$\rho_e = e\,\Sigma\, Z_i C_i \qquad [4]$$

$$\nabla\cdot\underline{N}_i = 0 \qquad [5]$$

$$\nabla\cdot\underline{v} = 0 \qquad [6]$$

ψ is the electrostatic potential, $\underline{N}_i$ is the flux of ions of type i, and $\underline{v}$ is the mass-average velocity of the solution. The subscript i is + or − for a simple electrolyte. Equation [5] is the steady-state conservation equation for species i; the assumption of steady state inside the pore is valid provided that the time constant of the membrane (l^2/D_i) is much smaller than the time scale characterizing changes in the bulk solutions. The boundary conditions at the pore wall are

$$r = a: \quad v_r = 0, \quad v_x = 0 \qquad [7a]$$

$$(N_i)_r = 0 \qquad [7b]$$

In the limit $l/a \to \infty$, radial fluxes are negligible compared to axial fluxes and are taken to be zero

$$\text{all } r: \quad (N_i)_r = 0 \qquad [8a]$$

$$v_r = 0 \qquad [8b]$$

The total electrical potential is split into two parts

$$\psi(r,x) = \frac{kT}{e}\Psi(r,x) + V(x) \qquad [9]$$

where Ψ is dimensionless and will be identified with the electrostatic potential arising from the double layer, while V represents a potential whose difference can be measured across the bulk solutions on each side of the membrane. After [8] and [9] are substituted, the r-component of Eq. [2] can be integrated directly

$$C_i = n_i(x)\exp(-Z_i\Psi) \qquad [10]$$

The integration parameter $n_i(x)$ can be interpreted as the equivalent bulk concentration that would be at equilibrium with the solution in the pore cross section at axial position x. The ends of the pores are at equilibrium with the adjacent bulk solutions

$$C_i(r,0) = n_i(0)\exp[-Z_i\Psi(r,0)] = C_{ib}^{(I)}\exp[-Z_i\Psi(r,0)]$$

$$C_i(r,l) = n_i(l)\exp[-Z_i\Psi(r,l)] = C_{ib}^{(II)}\exp[-Z_i\Psi(r,l)] \qquad [11]$$

where $C_{ib}^{(I)}$ and $C_{ib}^{(II)}$ are the bulk solution concentrations of ion i. Defining $\hat{C}$ as Z_+C_{+b}, which is equal to $-Z_-C_{-b}$, we have

$$n_+(x) = \hat{C}(x)/Z_+$$

$$n_-(x) = -\hat{C}(x)/Z_- \qquad [12]$$

Substituting Eq. [4], [9], [10], and [12] into [1] we obtain

$$\frac{1}{\xi}\frac{\partial}{\partial\xi}\left(\xi\frac{\partial\Psi}{\partial\xi}\right) = \left(\frac{a}{\lambda}\right)^2\left[\frac{\exp(-Z_-\Psi) - \exp(-Z_+\Psi)}{2}\right]$$

$$\xi \equiv r/a$$

$$\xi = 0: \quad \frac{\partial\Psi}{\partial r} = 0 \qquad [13]$$

$$\xi = 1: \quad \frac{\partial\Psi}{\partial\xi} = S_o \equiv \left(\frac{4\pi e}{\epsilon kT}\right)a\sigma$$

The local Debye screening length λ depends on axial position x through $\hat{C}$

$$\lambda^2 = \frac{\epsilon kT}{8\pi e^2\hat{C}(x)} \qquad [14]$$

$\hat{C}$ is regarded as the equivalent bulk concentration that would be in equilibrium with the cross section in the pore at x. The dimensionless electrostatic potential Ψ depends explicitly on ξ with parameters a/λ and S_o, and derives its dependence on x from the fact that λ is a function of $\hat{C}(x)$. Given these parameters, Eq. [13] must in general be solved numerically for Ψ *vs.* ξ. Analytical solutions are possible when $|S_o| << 1$ (Debye-Huckel approximation) and when $|S_o| >> 1$ with $a/\lambda \leq 1$ (8).

The average pore flux is found by integrating the local flux over the pore cross section, for example

$$\langle(N_i)_x\rangle = \frac{2}{a^2}\int_0^a (N_i)_x\, r\,dr$$

We define the current density (I), the average electrolyte flux (J), and the average flow velocity (U) as

$$I = \langle Z_+(N_+)_x + Z_-(N_-)_x\rangle \qquad [15a]$$

$$U = \langle v_x\rangle \qquad [15b]$$

$$J = \langle(N_+)_x + (N_-)_x\rangle \qquad [15c]$$

These pore fluxes must be independent of x since the pore walls are impenetrable and transport is at steady state. By solving Eq. [3] and [6] for v_x and $p(r,x)$ using the equilibrium condition at each end of the pore to relate intrapore variables to bulk variables (see Eq. [11]), substituting the results into the x-component of Eq. [2], and then averaging the fluxes over the pore cross section according to [15], the following system of equations is obtained

$$I = L_{11}\frac{dV}{dx} + L_{12}\,kT\frac{d}{dx}\ln\hat{C} + L_{13}\frac{d\hat{P}}{dx} \qquad [16a]$$

$$J = L_{21}\frac{dV}{dx} + L_{22}\,kT\frac{d}{dx}\ln\hat{C} + L_{23}\frac{d\hat{P}}{dx} \qquad [16b]$$

$$U = L_{31}\frac{dV}{dx} + L_{32}\,kT\frac{d}{dx}\ln\hat{C} + L_{33}\frac{d\hat{P}}{dx} \qquad [16c]$$

$\hat{P}$ is the bulk-equivalent pressure which would be in mechanical equilibrium with the solution in the pore cross section at x. The coefficients L_{ij} are functions of definite integrals involving $\Psi(\xi; a/\lambda, S_0)$; formulas for the coefficients of interest in our experiments are given in the Appendix. Note that for Eq. [16] to follow Onsager's reciprocity theorem ($L_{ij} = L_{ji}$), the relative velocity between electrolyte and solvent would have to be substituted for the electrolyte flux J (3).

On first glance at the above equations one is tempted to assume that the coefficients L_{ij} are constants, but such is not the case. Since λ is a function of $\hat{C}(x)$, the L_{ij} are implicit functions of x, which causes some computational problems when different electrolyte concentrations exist in the bulk solutions on either side of the membrane. In this case Eq. [13] must be solved, given the electrolyte and the pore surface charge (S_0), for the range of a/λ from the low concentration side of the pore (smallest a/λ) to the high concentration side (largest a/λ). If this is done, all electrokinetic parameters can be evaluated by numerical integration (11).

Three electrokinetic parameters are considered here:

Pore conductivity

$$\kappa \equiv -\,l\left(\frac{I}{\Delta V}\right)_{\substack{\hat{}\\ \Delta C=0\\ \Delta\hat{P}=0}} = -\,L_{11} \qquad [17]$$

Streaming potential

$$\nu \equiv \left(\frac{\Delta V}{\Delta P}\right)_{\substack{\hat{}\\ \Delta C=0\\ I=0}} = -\,\frac{L_{13}}{L_{11}} \qquad [18]$$

Concentration potential

$$\omega \equiv \left(\frac{\Delta V}{(kT/e)\,\Delta\ln\hat{C}}\right)_{\substack{\hat{}\\ \Delta P=0\\ I=0}} \qquad [19]$$

$$= \frac{e}{\Delta\ln\hat{C}}\int_{\hat{C}^{(I)}}^{\hat{C}^{(II)}}\frac{L_{12}}{L_{11}}\,d(\ln\hat{C})$$

The direction of Δ is side II ($x = l$) minus side I ($x = 0$). Expressions for the L_{ij} are in the Appendix. For certain electrolytes (chlorides of lithium, potassium, sodium, and magnesium) in water at 25°C and for pore sizes corresponding to those of experimental membranes, we calculated the variation of κ, ν, and ω with $S_0 < 0$ and a/λ in the range 0.1-10.0. Certain limiting expressions can be used to estimate these electrokinetic parameters for small and large a/λ (5). For ω we selected the low concentration side ($C^{(I)}$) to specify a/λ and kept $\hat{C}^{(II)}/\hat{C}^{(I)} = \sqrt{10}$.

The discussion above outlines the classical theory. Important assumptions have already been noted: (*i*) uniform σ on the pore wall ["smear charge" assumption (12)]; (*ii*) $l/a \to \infty$; (*iii*) complete dissociation of the electrolyte; (*iv*) bulk solvent properties (ϵ, η); (*v*) immobile wall charge; and (*vi*) ion mobilities and diffusion coefficients which are independent of ion concentrations. Details of the mathematical manipulation of Eq. [1]-[6] can be found elsewhere (1-4, 11).

Experiments

The electrokinetic measurements were made with a diaphragm membrane cell (13) consisting of two Plexiglas® half-cells clamped firmly together with the membrane sealed between them with Viton® gaskets. Each 12 ml half-cell had several ports for introducing electrodes (silver wires coated with silver chloride) and for miniature Teflon® on-off valves used to fill and empty the cell. Teflon-coated magnets on internally mounted glass shafts were rotated by an external magnet, although only minimal stirring was needed to eliminate polarization effects at the membrane surface (membranes had pore area fractions less than 0.003%).

The membranes were made from thin ($\approx$ 7 μm) sheets of muscovite mica by the track-etch process (14). A circular disk of mica was weighed to determine its thickness. The central portion of the disk was irradiated by a collimated beam of fission fragments from a Cf^{252} source contained in a thick-walled glass desiccator. Pores were formed by etching the irradiated membrane in aqueous hydrofluoric acid. The important features of these membranes are that (*i*) the pores are uniform in size; (*ii*) the pores are parallel, cylindrical capillaries of rhombic (60°) cross section; and (*iii*) the number and size of the pores can be determined before performing the experiments of interest.

The pore length (l) was equal to the membrane thickness because the fission fragment beam was collimated. The number of pores in the irradiated area (n) was determined by covering the membrane with another mica disk during irradiation, and then etching the pores in the top disk to a large size, and counting their number density under a microscope. The pore radius (a), defined as the radius of a circle of equivalent area, was determined for each membrane by measuring the membrane resistance (R_m) as a function of electrolyte concentration, or equivalently, the bulk solution conductivity κ_b

$$a = \lim_{\kappa_b\to\infty}\left[\frac{(l/n\pi)}{R_m\kappa_b}\right]^{1/2} \qquad [20]$$

For even the smallest pores used (a = 34Å) the right side of Eq. [20] became independent of κ_b when the electrolyte concentration exceeded 1M.

All solutions were made with low conductivity water ($< 10^{-6}$ mho/cm) produced by feeding distilled water through a Milli-Q2 (Millipore Corporation) ion-exchange purifier. The electrolytes (KCl, LiCl, NaCl, and $MgCl_2$) were reagent grade. The silver electrodes were cleaned and recoated with AgCl whenever their resting bias exceeded 1 mV in 10^{-3}M electrolyte. Direct currents (< 1 μA) were passed through the membrane using a d-c current source (Keithley Model 225) attached to an outer pair of electrodes (see Fig. 1), while transmembrane potential differences were measured with a floating electrometer (Keithley Model 602) attached to an inner pair of electrodes.

The three electrokinetic parameters (κ, ν, ω) were measured as functions of electrolyte concentration for membranes having pore sizes of 34-265Å. To stabilize the charge on the pore wall, the bulk pH was kept between 9-10 by adding small amounts of KOH. All experiments were done at ambient temperature (25° ± 0.5°C). The pore conductivity was determined from the conductance of the membrane with $C^{(I)} = \hat{C}^{(II)}$ and $\hat{P}^{(I)} = \hat{P}^{(II)}$

$$\kappa = \frac{(l/n\pi a^2)}{R_m} \qquad [21]$$

To cancel electrode bias, the current direction was reversed in a square waveform (period > 5 sec). For currents varying by a factor of 30-100, the voltage-current proportionality (R_m) was excellent. The streaming potential was measured at near-zero current using an electrometer, with the direction of the applied pressure drop reversed periodically. The measured potential difference across the membrane showed excellent proportionality with the applied pressure.

Measuring the membrane concentration potential was more complicated than the other two measurements. The main difficulty was that the concentration difference between the two bulk solutions caused an electrode voltage shift independent of the membrane characteristics. To correct for this thermodynamic effect, the electrodes were assumed to be reversible only to the chloride ion

$$\Delta V = V_T + \frac{kT}{e} \ln (a_-^{(II)}/a_-^{(I)}) \qquad [22]$$

where a_- is the bulk solution activity of Cl^- and V_T is the measured voltage difference. Assuming that $a_-^{(II)}/a_-^{(I)} = \hat{C}^{(II)}/\hat{C}^{(I)}$ introduces only a small error (15, 16) because $\hat{C}^{(I)} \leq 0.1M$ and in all experiments $\hat{C}^{(II)}/\hat{C}^{(I)}$ was only $\sqrt{10}$.

Results and Discussion

Characteristics of the pore wall charge.—The pore walls in track-etched mica membranes are perpendicular to the basal (cleavage) plane. To study the pore wall charge we used streaming potential measurements on large pores ($a/\lambda > 30$). The wall charge (σ) was computed with the Helmholtz equation for the streaming potential and the "flat wall" relationship between the wall potential (Ψ_w) and charge (17, 18)

$$a/\lambda > 10: \quad \nu = \frac{\epsilon k T \Psi_w}{4\pi\eta e \kappa_b} \qquad [23a]$$

$$\sigma = \left[\frac{\epsilon k T \hat{C}}{2\pi}\right]^{1/2} \left[\frac{\exp(-Z_+\Psi_w) - 1}{Z_+} - \frac{\exp(-Z_-\Psi_w) - 1}{Z_-}\right]^{1/2} \qquad [23b]$$

We neglect Stern layer effects because the electrolyte concentration used in these large pore experiments was 10^{-2}M, for which $\lambda = 30$Å, an order of magnitude larger than the size of ions.

Figure 1 shows the results of wall charge determinations for a membrane with $a/\lambda > 60$ and pH > 8.5 at various times after etching. The charge was negative as expected (8), but required 48 hr to stabilize, much longer than expected. Since the ion diffusion time (l^2/D_i) was of order 0.1 sec, the long transient in σ must reflect kinetic limitations in the chemistry of the pore wall as it relaxes to some equilibrium state after etching. Because of this long transient in σ, freshly etched, small-pore membranes were allowed to equilibrate with 0.01M solutions for 2 days before electrokinetic experiments were started.

The pH dependence of σ for one membrane with $a/\lambda > 30$ (0.01M KCl) is plotted in Fig. 2. With this and other membranes we observed very little hysteresis in σ when the direction of the pH changes was reversed. Despite the 48 hr required after etching to reach a stable charge, less than 20 min were required to attain a new, stable charge when the pH was changed by adding HCl or M^+OH^-, where M^+ is the cation of the electrolyte (K^+, etc.). Titrations at other concentrations produced the same behavior as that shown in Fig. 3: a positive charge at pH < 4, zero charge at pH ≈ 4.5, and a pH-independent charge for pH 7-10. Note in Table I that the high pH charge is not the same for

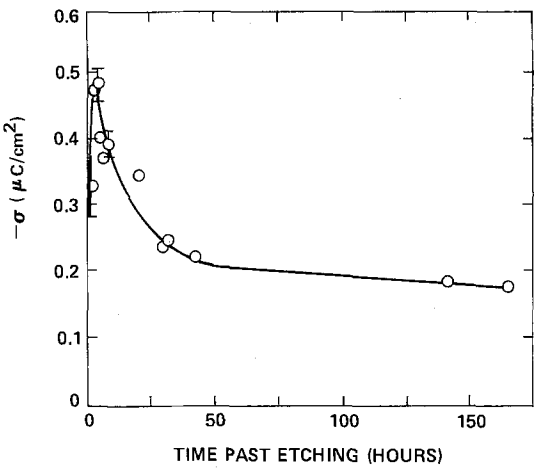

Fig. 1. Pore surface charge density vs. time past etching. The surface charge of this large-pore membrane was calculated from streaming potential measurements in 0.01M aqueous KCl with Eq. [23]. (a = 1880Å. pH ≧ 8.5.)

all membranes. These observations led us to perform subsequent electrokinetic measurements with pH in the range 9-10 to ensure a constant, stable wall charge with each membrane. Increases in the magnitude of σ with increases in $[Cl^-]$, shown in Table I, complicate the interpretation of data because they mean that σ is not constant as λ is changed.

We can only speculate about the origin of the pore wall charge in track-etched mica. The pH dependence of σ suggests that exposed silanol groups lose H^+, and the increase in $-\sigma$ with $[Cl^-]$ suggests that Cl^- adsorbs to the pore wall. In addition, cations (*e.g.*, K^+, Al^{3+}) may be extracted from the mica lattice, leaving negatively charged sites behind (19). However, all of these mechanisms would create a negative charge, and a source of positive charge must exist according to Fig. 3. The adsorption of cations from solution or the exchange of multivalent cations with ions in the mica lattice (*e.g.*, K^+) are but two possible sources of a positive wall charge. Adsorption and/or exchange of multivalent cationic impurities, the extent of which would depend on the history of the membrane, could explain the differences among membranes of the pH-independent value of σ. Because of the steps taken to purify the water, only small amounts of multivalent, cationic impurities should have been present. But as discussed later, the use of $MgCl_2$ as the primary electrolyte caused the normally negative wall charge to

Table I. Summary of pore wall charge density (σ) for large pores (a > 1000Å) as determined from streaming potentials in aqueous solutions (pH > 7) using Eq. [23]

Membrane	Electrolyte	σ (μC/cm^2)	pH	Days past etching
13MY9A	10^{-2}M KCl	−0.798 ± 0.020	7.0-7.9	<1
13MY9A	3×10^{-3}M KCl	−0.267 ± 0.004	7.3-9.7	1
13MY9A	10^{-3}M KCl	−0.098 ± 0.001	7.0-8.9	1
13MY9A	10^{-2}M KCl	−0.373 ± 0.021	7.1-9.8	2
13MY9A	10^{-2}M KCl	−0.460 ± 0.040	7.8-10.6	3
24AP0A	10^{-2}M KCl	−0.33	8.2	3
		−0.29	7.1	4
24AP0A	10^{-2}M NaCl	−0.31	9.4	4
		−0.26	8.4	5
		−0.21	9.1	6
		−0.18 ± 0.01	7.3-9.5	7
24AP0A	0.85×10^{-2}M LiCl	−0.18	9.6	7
		−0.16 ± 0.01	7.1-9.6	8
24AP0A	0.80×10^{-2}M $MgCl_2$	−0.14	9.4	8
		−0.11	9.3	9
		−0.11 ± 0.01	8.0-9.1	10

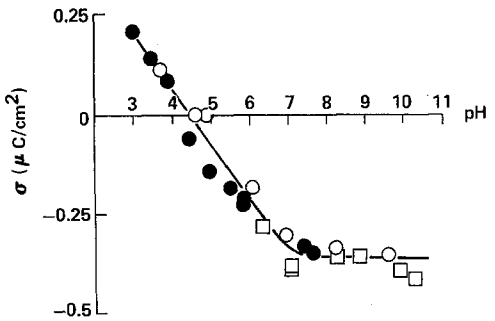

Fig. 2. Surface charge density vs. pH. The surface charge was calculated from streaming potential data in 0.01M aqueous KCl with Eq. [23]. (a = 1010Å. Squares: pH increased from 6.4 to 10.3; Open circles: pH 10.3 to 2.9; Closed circles: pH 2.9 to 7.6.)

become positive at sufficiently high $MgCl_2$ concentrations ($\approx$ 0.05M).

Although we are not certain of the precise origin of the pore wall charge, the large-pore studies helped us to plan and to interpret the small-pore experiments. To summarize the large-pore observations: (*i*) 48 hr were required after etching for the pore wall charge to stabilize, while after this period only minutes were required to reach a new, stable σ when the pH was changed; (*ii*) σ was nearly constant for each membrane in the pH range 7-10; and (*iii*) the pH-independent value of σ was negative for electrolytes with monovalent cations, and the magnitude of this negative charge increased with Cl^- concentration.

Pore fluid conductivity.—Experimental results are plotted in Fig. 3A-C for the pore fluid conductivity *vs.* a/λ for a membrane (a = 103Å) exposed to aqueous solutions of alkali chlorides. Each solid curve was computed from the classical theory and corresponds to a constant dimensionless wall charge (S_0), known to be negative from streaming potential measurements. Figures 4A and B show results for two other membranes in aqueous KCl. The superficial features of the data are the same regardless of pore size or cation. Pore size dependence is eliminated when the radius is scaled by the Debye screening length. For a given dimensionless wall charge the theoretical curves asymptotically approach a constant value as $a/\lambda \to 0$ because in this limit[3] the mean ion concentration in the pore fluid approaches $-2\sigma/ae$. The pore fluid conductivity exceeds the bulk phase conductivity because excess counterions (cations here) are needed to balance the charge on the pore wall; these excess counterions enhance the current-carrying ability of the pore fluid relative to that of the bulk fluid. The electrokinetic enhancement of the pore fluid conductivity is quite large when $a/\lambda < 1$; for example, with KCl in 103Å pores (Fig. 3C) the pore conductivity is 100 times larger than the bulk fluid conductivity when $a/\lambda \approx 0.2$.

In Fig. 3 and 4 the value of S_0 needed to make the theory agree with experiments increases as a/λ increases, or as Cl^- concentration increases. This trend is consistent with the streaming potential results for large-pore membranes discussed previously. Since σ is a free parameter, we fitted measurements of κ to the space-charge model (see Eq. [13] and [17], and the Appendix) to compute the pore wall charge for each membrane and electrolyte; the results are plotted in Fig. 5. These values of σ are used below to test the space-charge model as applied to the streaming potential and to the concentration potential. Compared with using streaming potential data or concentration potential data, the use of conductivity data to determine the only free parameter of the model is justified because the error in measuring κ was quite small ($\approx$ 1%), and κ is sensitive to σ when $a/\lambda \lesssim 3$ according to the theoretical model.

Streaming potential.—The streaming potential data for aqueous NaCl and LiCl are similar to the data for KCl in Fig. 6. The theoretical curves are interesting in that they cross at a/λ = 3-4. At large a/λ the Helmholtz relation Eq. [23a] applies, and hence the magnitude of ν increases with the magnitude of the wall charge; at small a/λ, however, $|\nu|$ increases as $|S_0|$ decreases. For aqueous alkali chlorides at high pH, all our streaming potential measurements in membranes with a = 34, 103, and 265Å indicate that the pore wall is negatively charged. The data follow the overall trend of theoretical predictions, but as observed with the pore conductivity, the magnitude of S_0 needed to reconcile theory and experiment increases with a/λ.

The magnitude of ν is quite sensitive to S_0 for $a/\lambda >> 1$, so in this range the streaming potential is a good measurement from which to determine the charge (or zeta potential) of the pore wall. However, the crossover of ν *vs.* a/λ in Fig. 6 has an important implication: ν is not even uniquely related to S_0 for $a/\lambda \approx$ 3-4, and below this a/λ, ν is not very sensitive to S_0. Thus, in the range of small a/λ, the pore fluid conductivity is preferred for estimating the magnitude of S_0; nevertheless, the polarity of the wall charge still must be ascertained from the streaming potential, even at small a/λ, since κ does not indicate the sign of S_0.

Figure 7 compares the measured streaming potentials with predictions from the space-charge model (see Eq. [13] and [18], and the Appendix) using σ values from Fig. 5. There are no adjustable parameters in this comparison, so the relatively good absolute agreement is solid evidence for the correctness of the theory. Not shown in Fig. 7 are the data for the membrane with 34Å radius pores; the measured potentials were so low, as predicted by the theory, that electronic noise was a problem.

Concentration potential.—If the pores of a membrane are neutral, or if the electrolyte solutions ($C^{(I)} \neq C^{(II)}$) outside the pores are concentrated ($\lambda << a$), a "diffusion" or "junction" potential is established (16), which for our system is

$$\omega_\infty = \lim_{S_0 \to 0} (\omega) = \lim_{a/\lambda \to \infty} (\omega) = \frac{D_- - D_+}{Z_+D_+ - Z_-D_-}$$

We assume that the ratio of ionic diffusivities (D_+/D_-) is the same for any a/λ. For infinitely dilute aqueous KCl at 25°C, D_+/D_- = 0.963 so ω_∞ = 0.019, which is negligibly small. For the other aqueous electrolytes (LiCl and NaCl) the value of ω_∞ is nonzero because the diffusion coefficients of Li^+ and Na^+ are substantially smaller than that of Cl^-. If electrolyte concentrations are low ($\lambda \geq a$), ions having an electrovalence whose sign is opposite to the sign of σ are virtually the only ions inside the membrane. In this case, the membrane acts like an electrode reversible to these ions (cations here) and the membrane potential approaches the Nernstian value, $(kT/e) \ln (\hat{C}^{(I)}/C^{(II)})$.

The theoretical relationship between ω and a/λ is therefore an S-shaped curve between -1 and ω_∞ as shown in Fig. 8A and B for aqueous KCl. In these graphs, λ is computed from the smaller of the two bulk electrolyte concentrations with $C^{(II)}/\hat{C}^{(I)}$ fixed at $\sqrt{10}$. Furthermore, the wall charge is assumed independent of electrolyte concentration in integrating the theoretical equations (Eq. [19]) across the membrane. While the data follow the S-shaped dependence on a/λ, Fig. 8B indicates that $|\sigma|$ increases with a/λ, as observed for the other electrokinetic measurements. The concentration potential data for aqueous LiCl and NaCl show the same S-shaped dependence on a/λ as the data for KCl except that ω_∞ is not zero.

[3] A bulk ion concentration of zero is never actually achieved since H^+ and OH^- must be accounted for.

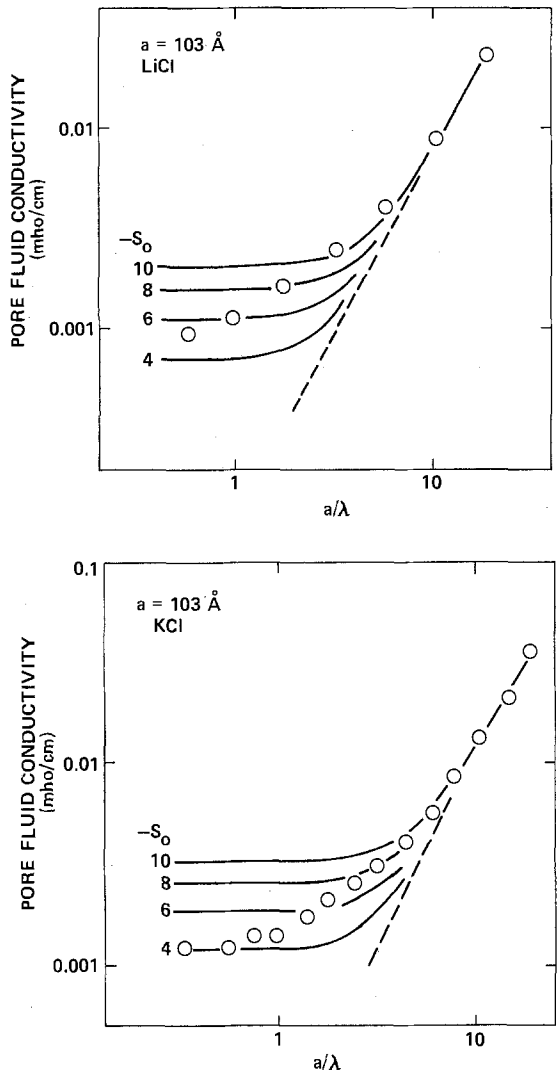

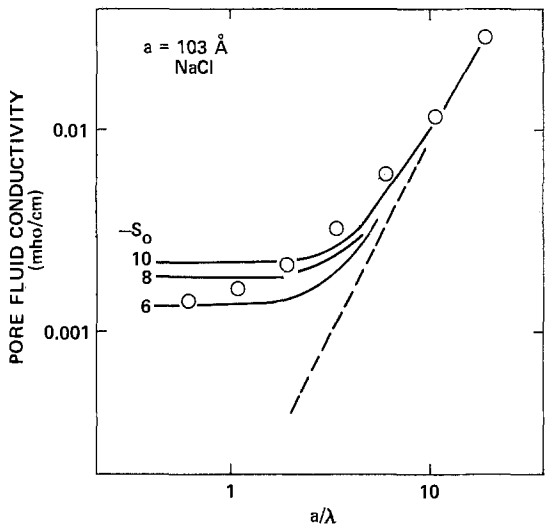

Fig. 3. Pore conductivity in aqueous alkali chlorides: (A, upper left) Aqueous LiCl. (B, upper right) NaCl. (C, lower left) KCl. The surface charge parameter S_o is negative. The theoretical predictions (solid curves) were made from Eq. [13], [17], and the expression for L_{11} in the Appendix. The broken curves are the bulk phase conductivities.

The space-charge model is tested again by using Fig. 5 to obtain σ for a given membrane and solution conditions (with the average electrolyte concentration used to determine the appropriate λ in Fig. 5), and predicting ω from Eq. [13] and [19] (see Appendix for L_{12} and L_{11}) without any adjustable parameters. Comparison of predictions and the data is made in Fig. 9, and the agreement is reasonably good, although not quite as good as for the streaming potential (see Fig. 7). An interesting aspect of Fig. 9 is that important changes in counterion selectivity, as evidenced by the departure from the Nernstian potential ($\omega = 1$), occur as a/λ passes through the range 1-3, even though the pore radius varies by a factor of ~8 for the data in Fig. 9.

Experiments with magnesium chloride.—Experiments with aqueous $MgCl_2$ were difficult to interpret because the streaming potential changed sign from negative to positive in going from low concentrations to high concentrations ($\gtrsim$ 0.05M) of $MgCl_2$ (see Fig. 10). This reversal of sign by ν implies that the sign of the pore wall charge became positive. However, the effect of high $MgCl_2$ concentrations was not permanent since ν reverted to within 1% of its negative value in more dilute $MgCl_2$ (0.01M) after the high concentration experiments. This suggests that Mg^{2+} reversibly adsorbs or exchanges with some component of the mica (*e.g.*, K^+), a result which is consistent with observations by Gaines (19) that Ca^{2+} reversibly exchanges with K^+ in muscovite mica.

Conclusions

Our experiments using microporous membranes having a well-defined capillary pore structure generally support the space-charge model of electrolyte transport developed by Osterle and Dresner for pores whose radius is comparable to the Debye screening length of the solution. This confirmation rests on the agreement between model predictions and data for the streaming potential (Fig. 7) and the concentration potential (Fig. 9) when the charge density on the pore wall is obtained from fitting data for the pore fluid conductivity to model predictions for the conductivity (Fig. 5). Additionally, the monovalent alkali cations (K^+, Na^+, Li^+) all seem to show nearly the same electrokinetic behavior, even in a quantitative sense. This conclusion does not lead to the assertion that all assumptions of the classical model are accurate, but rather that in some average way the model describes ion distribution and transport in charged pores, at least when the pores are 30Å in radius or larger, ionic strength is 0.1M or less, and the counterions (cations here) are monovalent. Bean (9) also reached this conclusion from more limited experiments with track-etched mica membranes. Based on conduction and electro-osmosis experiments with mica membranes, Koh and Anderson (8) concluded that the model is quantitatively deficient at small a/λ, especially at very large $|S_o|$ values which were obtained by adsorbing heparin to the pore wall. It is possible that the polymer (heparin) played a role in the disagreement, especially in the case of small pores. Furthermore, Koh and Anderson performed measurements of the two electrokinetic parameters on two different membranes which, although probably similar, may have differed in wall charge (see Fig. 5 here).

Our calculations of the three electrokinetic parameters show some interesting trends. When $a/\lambda \gtrsim 3$ the

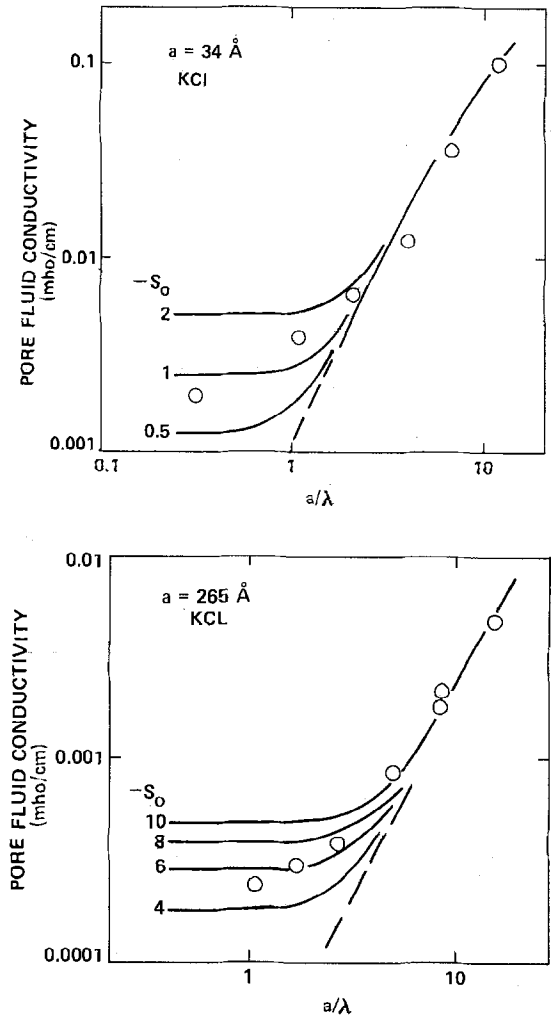

Fig. 4. Pore conductivity in aqueous KCl. The pore sizes were (A, top) 34Å and (B, bottom) 265Å. The solid curves are theoretical predictions; the broken curves are bulk phase conductivities.

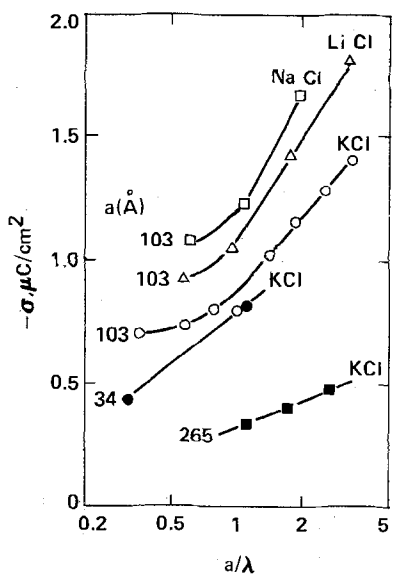

Fig. 5. Surface charge densities determined from pore conductivities. σ was determined in each case by fitting calculations from the space-charge model (Eq. [13] and [17] and Appendix) to pore fluid conductivity data.

pore fluid conductivity is sensitive to the pore wall charge density, but the sign of the charge cannot be deduced from this parameter. On the other hand, the streaming potential does allow determination of the

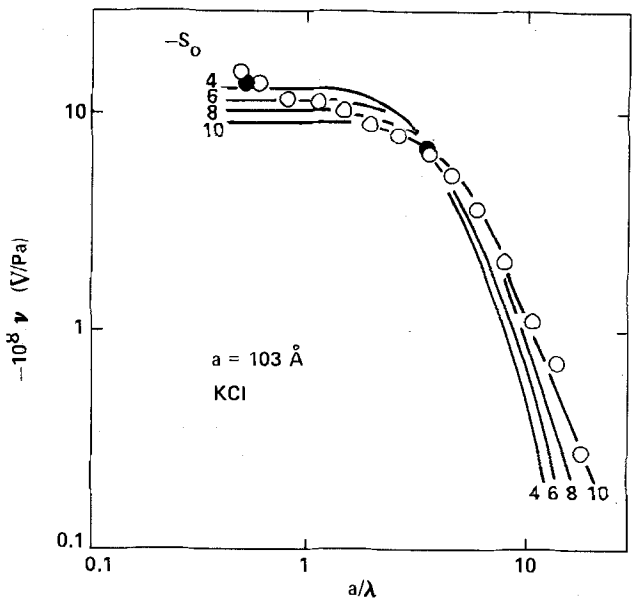

Fig. 6. Streaming potential in aqueous KCl. Note that the theoretical predictions (solid curves) made using Eq. [13] and [18] and the Appendix cross in the region $a/\lambda = 3$-4. The solid circles were taken more than 24 hr before the rest of the data to make sure that σ had stabilized.

sign of the wall charge but is somewhat insensitive to its magnitude when $a/\lambda \lesssim 3$. In fact, the magnitude of the streaming potential increases as the magnitude of the wall charge decreases in this range of a/λ. The concentration potential is sensitive to both the sign and the magnitude of the wall charge in the range $1 < a/\lambda < 5$.

Figure 5 indicates that the wall charge is not constant (nor is the potential) but depends instead on bulk electrolyte concentration, or equivalently λ. A most surprising result is that for the pore walls of muscovite mica a rather long time (48 hr) is required

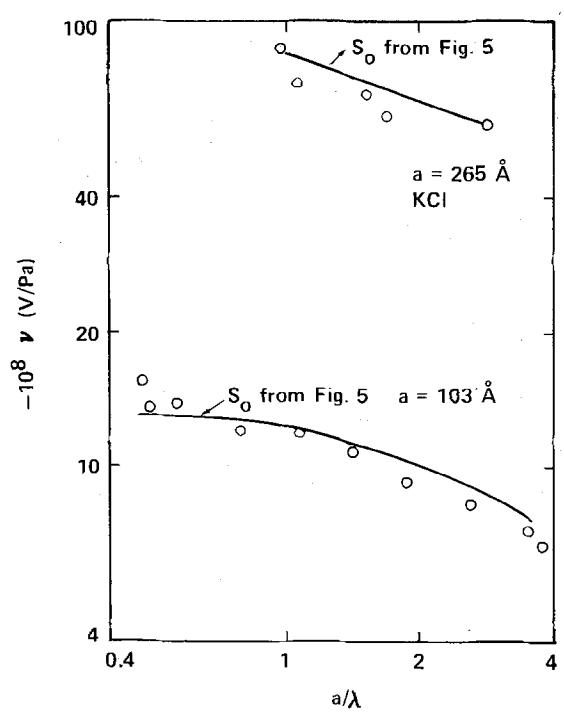

Fig. 7. Theoretical predictions vs. experiments for the streaming potential with KCl. The curves are predictions from the space-charge model using values of σ determined from Fig. 5 for each membrane at the particular a/λ values.

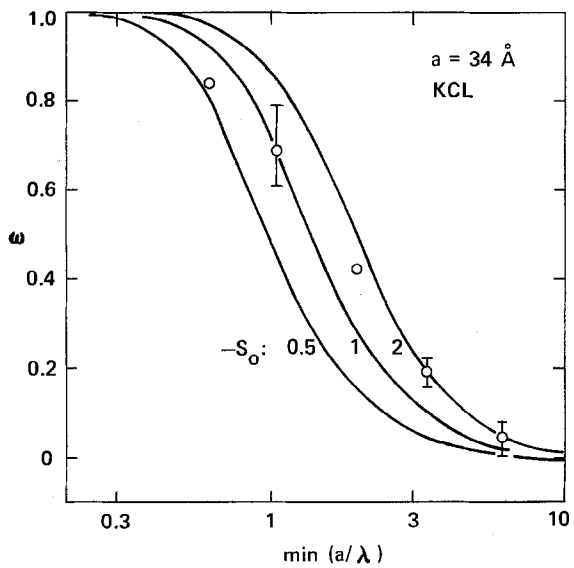

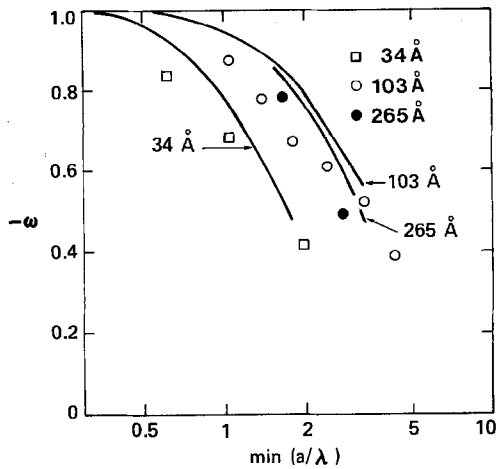

Fig. 9. Theoretical predictions vs. experiments for the concentration potential with KCl. The curves are predictions from the space-charge model using values of σ determined from Fig. 5 for each membrane at the particular a/λ values.

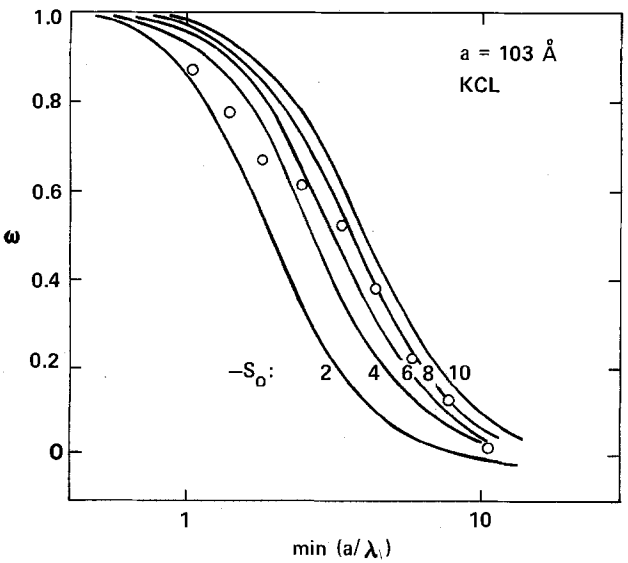

Fig. 8. Concentration potential in aqueous KCl. Values of λ refer to the low concentration side of the membrane. (A, top) $a = 34$Å, (B, bottom) 103Å. The solid curves are predictions from the space-charge model (Eq. [13] and [19] and the Appendix).

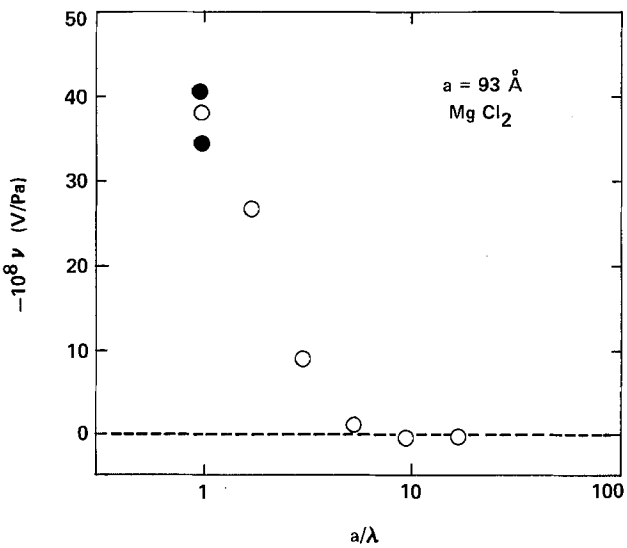

Fig. 10. Streaming potential vs. a/λ in aqueous $MgCl_2$. The streaming potential (ν) became positive as $[Mg^{2+}]$ went above $\approx$ 0.05M. (Closed circles: data taken more than 24 hr before other data.)

after etching the membrane with aqueous hydrofluoric acid to reach a stable charge; however, pH titration requires only minutes to reach a new stable charge and exhibits a reproducible point of zero charge ($\approx$4.5) and a stable region of constant charge ($7 < pH < 10$). The magnitude of the high pH charge varies among membranes, perhaps because of natural variations between different sheets of mica or because of multivalent cation impurities in solution. The charge at high pH is negative and increases in magnitude as the anion (Cl^-) concentration increases. Mg^{+2} reverses the sign of the wall charge even at high pH, implying that adsorption of this cation occurs.

Acknowledgments

We thank the National Science Foundation for supporting this work under grants ENG 78-06242 and CPE-8007524. We wish to thank J. F. Osterle for his helpful advice.

Manuscript submitted Aug. 31, 1981; revised manuscript received June 22, 1982. This was Paper 599 presented at the Electrochemical Society Meeting, Hollywood, Florida, Oct. 5-10, 1980.

Any discussion of this paper will appear in a Discussion Section to be published in the December 1983 JOURNAL. All discussions for the December 1983 Discussion Section should be submitted by Aug. 1, 1983.

APPENDIX

Listed below are the model coefficients L_{ij} in Eq. [17]-[19]

L_{11} [A-1]

L_{12} [A-2]

L_{13} [A-3]

L_{21} [A-4]

L_{22} [A-5]

It can be shown algebraically that by slightly altering the definition of the electrolyte flux J in Eq. [15c] the coefficients L_{ij} can be forced to equal L_{ji}, which should be true according to Onsager's reciprocity theorem (3, 11)

$$L_{11} = \frac{2e^2\hat{C}}{kT}\int_0^1 \xi[Z_-D_- \exp(-Z_-\Psi(\xi)) - Z_+D_+ \exp(-Z_+\Psi(\xi))]d\xi + \frac{\epsilon kT\hat{C}}{2\pi\eta}\int_0^1 \xi[\Psi(1) - \Psi(\xi)][\exp(-Z_+\Psi(\xi)) - \exp(-Z_-\Psi(\xi))]d\xi$$

$$L_{12} = \frac{2e\hat{C}}{kT}\int_0^1 \xi[D_- \exp(-Z_-\Psi(\xi)) - D_+ \exp(-Z_+\Psi(\xi))]d\xi + \frac{\epsilon kT\hat{C}}{2\pi\eta e}\left\{\int_0^1 \xi[\Psi(1) - \Psi(\xi)]\left[\frac{\exp(-Z_+\Psi(\xi))}{Z_+} - \frac{\exp(-Z_-\Psi(\xi))}{Z_-}\right]d\xi + \left[\frac{Z_+ - Z_-}{2Z_+Z_-}\right][\Psi(1) - \langle\Psi\rangle]\right\}$$

$$L_{13} = \frac{\epsilon kT}{4\pi\eta e}\left|\Psi(1) - 2\int_0^1 \Psi(\xi)\right|\xi d\xi$$

$$L_{21} = \frac{2e\hat{C}}{kT}\int_0^1 \xi[D_- \exp(-Z_-\Psi(\xi)) - D_+ \exp(-Z_+\Psi(\xi))]d\xi + \frac{\epsilon kT\hat{C}}{2\pi\eta e}\int_0^1 \xi[\Psi(1) - \Psi(\xi)]\left[\frac{\exp(-Z_+\Psi(\xi))}{Z_+} - \frac{\exp(-Z_-\Psi(\xi))}{Z_-}\right]d\xi$$

$$L_{22} = \frac{2\hat{C}}{\pi kT}\int_0^1 \xi\left[\frac{D_-\exp(-Z_-\Psi(\xi))}{Z_-} - \frac{D_+\exp(-Z_+\Psi(\xi))}{Z_+}\right]d\xi_3 + \frac{2\hat{C}^2a^2}{\eta}\int_0^1 \xi_3\left[\frac{\exp(-Z_-\Psi(\xi))}{Z_-} - \frac{\exp(-Z_+\Psi(\xi))}{Z_+}\right]d\xi_3\int_{\xi_3}^1 \frac{d\xi_2}{\xi_2}\int_0^{\xi_2}\xi_1\left[\frac{\exp(-Z_+\Psi(\xi_1)) - 1}{Z_+} - \frac{\exp(-Z_-\Psi(\xi_1)) - 1}{Z_-}\right]d\xi_1$$

LIST OF SYMBOLS

a	equivalent pore radius, m
$C_i(r,x)$	concentration of species i inside pore, mol/dm³
$\hat{C}(x)$	equivalent bulk concentration, mol/dm³
D_i	diffusion coefficient of i, m²/sec
e	magnitude of the charge on an electron, C
I	average current density, A/m²
J	average electrolyte flux, mol/m² sec
k	Boltzmann constant, J/K
l	pore length, m
L	transport coefficients, Eq. [16] and Appendix
$N_i(r,x)$	flux of i, mol/m² sec
$n_i(x)$	equivalent bulk concentration of i, mol/dm³
n	pore density in irradiated region of membrane, m⁻²
$\hat{P}(x)$	equivalent bulk pressure, Pa
$p(r,x)$	pressure inside pore, Pa
r	radial position, m
R_m	membrane resistance, Ω
S_o	dimensionless surface charge, Eq. [13]
T	temperature, K
U	average fluid velocity, m/sec
$V(x)$	electrical potential, V
$v(r,x)$	fluid velocity, m/sec
V_T	voltage measured in a concentration potential experiment, Eq. [22]
x	axial position, m
Z_i	electrovalence of i
ϵ	solvent dielectric constant
η	solvent viscosity, Pa sec
κ	specific conductivity of fluid in pore (Eq. [17]), mho/m
λ	Debye screening length (Eq. [14]), m
ν	streaming potential, V/Pa
ξ	dimensionless radial position, r/a
ρ_e	space charge density, C/m³
σ	surface charge density, esu/m² or μC/cm²
$\psi(r,x)$	electrostatic potential in pore, V
Ψ	dimensionless electrostatic potential arising from charged pore wall, $e\psi/kT$
ω	dimensionless concentration potential

REFERENCES

1. L. Dresner, *J. Phys. Chem.*, **67**, 1635 (1963).
2. F. A. Morrison, Jr. and J. F. Osterle, *J. Chem. Phys.*, **43**, 2111 (1965).
3. R. J. Gross and J. F. Osterle, *ibid.*, **49**, 228 (1968).
4. J. C. Fair and J. F. Osterle, *ibid.*, **54**, 3307 (1971).
5. J. L. Anderson and W. H. Koh, *J. Colloid Interface Sci.*, **59**, 149 (1977).
6. W. H. Keesom, R. L. Zelenka, and C. J. Radke, Paper presented at 71st Annual A.I.Ch.E. Meeting, Miami (1978).
7. W. H. Koh, *J. Colloid Interface Sci.*, **71**, 613 (1979).
8. W. H. Koh and J. L. Anderson, *A.I.Ch.E. J.*, **21**, 1176 (1975).
9. C. P. Bean, Paper presented at the International Conference on Colloids and Surfaces, San Juan, Puerto Rico, June 21-25, 1976.
10. H. P. Frohlich, B. Klump, and E. Woerman, *Z. Phys. Chem. (N.F.)*, **106**, 326 (1977).
11. G. B. Westermann-Clark, Ph.D. Thesis, Carnegie-Mellon University (1981).
12. A. N. Frumkin, *This Journal*, **107**, 461 (1960).
13. D. M. Malone and J. L. Anderson, *A.I.Ch.E. J.*, **23**, 177 (1977).
14. J. A. Quinn, J. L. Anderson, W. S. Ho, and W. J. Petzny, *Biophys. J.*, **12**, 990 (1972).
15. R. A. Robinson and R. H. Stokes, "Electrolyte Solutions," 2nd ed., Academic Press, New York (1959).
16. J. S. Newman, "Electrochemical Systems," Sections 30 and 43, Prentice-Hall, Englewood Cliffs, NJ (1973).
17. A. W. Adamson, "Physical Chemistry of Surfaces," 3rd ed., Chap. IV, John Wiley & Sons, Inc., New York (1976).
18. E. J. W. Verwey and J. Th. G. Overbeek, "Theory of the Stability of Lyophobic Colloids," Elsevier, New York (1948).
19. G. L. Gaines, Jr., *J. Phys. Chem.*, **61**, 1408 (1957); Also see G. L. Gaines, Jr. and C. P. Rutkowski, *J. Phys. Chem.*, **61**, 1439 (1957).

Photoelectrolysis of Water at α-Fe_2O_3 Electrodes in Acidic Solution

John H. Kennedy* and Menahem Anderman*

Department of Chemistry, University of California, Santa Barbara, California 93106

ABSTRACT

Photocurrent-potential curves at polycrystalline α-Fe_2O_3 electrodes in acidic solutions are reported to be similar to those found in basic solutions. Faradaic collection efficiency of 100% for photoelectrolyzed oxygen has been achieved in a closed cell configuration. Stable photocurrents has been demonstrated in various acidic media, and trace amounts of Fe(III) detected in the working solutions gave an indication of the dissolution rate. The stability of the α-Fe_2O_3 electrode is discussed and compared to other metal oxide photoanodes.

The photoassisted electrolysis of water at α-Fe_2O_3 photoanodes has been studied extensively in the last few years (1-11). Various types of electrodes have been fabricated and studied: chemical vapor deposited (CVD) films (1, 2), single crystals (3), sintered powders (5-11), and flame oxidized iron metal (4, 9). It was generally found that polycrystalline materials exhibited comparable photocurrents to the single crystal electrodes, and with the bandgap of only 2.2 eV, $\geq$20% of solar irradiation may be captured. While many nonoxide semiconductors are known with similar or lower bandgaps and possessing better solar absorption and higher photocurrent quantum yield characteristics [*e.g.*, CdSe (1.7 eV); $MoSe_2$ (1.5 eV); GaAs (1.4 eV) and others (12)] none of those materials resist corrosion during water photoelectrolysis.

Within the metal oxide semiconductors, it has been generally found that materials with wide bandgap are more stable. However, all materials with bandgap >3.0 eV are impractical for solar energy conversion because they absorb <4% of solar irradiation unless sensitized by a dye or other absorber. A number of oxide semiconductors with bandgap <3.0 were found as stable photoanodes for water photoelectrolysis, at least in some pH range (12). Iron oxide is one of the most important primarily because of its relatively low bandgap as an oxide semiconductor.

Though much work has been done on ferric oxide, hardly any report on its behavior in acidic solutions has been published after Hardee and Bard (1) reported dissolution of their CVD films at pH <4 even under open-circuit conditions. We report here the attainment of quite stable photocurrents resulting in 100 $\pm$ 5% of faradaic yield for oxygen obtained from α-Fe_2O_3 electrodes in acidic solutions, and a detailed study of the dissolution rate under open-circuit (dark) and short-circuit (light) conditions.

Experimental

Electrodes (~1 cm^2 area) were prepared from 99.999% α-Fe_2O_3 (Alfa Products) powder by mixing with various dopants, pressing, and sintering at 1300°-1360°C for 4-24 hr, followed by quenching to room temperature (10). Dopants used in this work were 0.02, 0.1, and 1 atomic percent (a/o) SiC, 1 a/o SiO_2, 0.05 a/o SnO_2, and 0.007 a/o GeO_2 (11). Densities ranged from 75% (visibly porous) to near 90% of theoretical density.

Ohmic contact was made by sputtering gold on the back surface and was tested for ohmic behavior with d-c probes. Then, a copper wire was attached to the contacting surface with Ag epoxy. The electrodes were mounted into an appropriate glass holder with epoxy resin. Resistances in solution measured at 1 kHz with a conductivity bridge varied from 20-200 Ω. A regular three-electrode arrangement was used with Pt foil as a counterelectrode and a saturated calomel electrode (SCE) as a reference electrode.

Experiments in which oxygen collection efficiency was measured were carried out in a specially constructed closed cell (Fig. 1). The working compartment had a 2 ml burette sealed on the top of a ~40 ml glass cell. The working electrode was mounted on the front of a male ground glass joint that was inserted into a female ground glass joint sealed to the sidewall of the 40 ml cell.

Current-potential curves were taken with a PAR 174A potentiometer or Pine Instrument RDE 3 potentiostat in conjunction with an X-Y recorder, at a scan rate of 5-10 mV/sec. The light source was a 150W Xe lamp, the light path included an infrared filter and quartz lens. The highest light intensity on the electrode surface was 700 mW/cm^2.

Iron(III) in solution was detected by the very sensitive spectrophotometric determination of the iron phenanthroline complex (13). H_2O_2 was determined iodometrically (13) using a coulometer for the back titration of the excess thiosulfate. All chemicals were reagent grade. An optical microscope and a Scanning

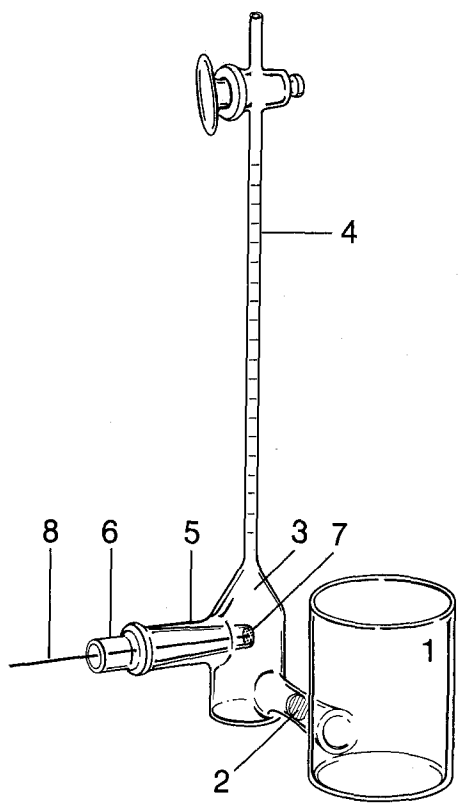

Fig. 1. A closed cell for oxygen collection. 1. Counter and reference electrode compartment. 2. Fritted glass separator. 3. Working electrode compartment. 4. 2 ml calibrated burette. 5. Female ground glass joint sealed to working compartment. 6. Demountable male ground gloss joint. 7. Working electrode sealed to front surface of the male joint. 8. Copper wire lead.

* Electrochemical Society Active Member.
Key words: photoelectrolysis, α-Fe_2O_3, photoanodes, faradaic efficiency, oxygen faradaic efficiency.

Electron Microscope (SEM) Autoscan (Etec Corporation) were used to examine the electrode surface.

Results and Discussion

Current-potential characteristics.—Current potential curves for an α-Fe_2O_3 anode in 1M NaOH and 1M H_2SO_4 are shown in Fig. 2. The curves are very similar in shape and magnitude suggesting that the rate-limiting step is identical in both solutions. The photocurrent as well as the dark current in 1M H_2SO_4 are shifted 0.98 ± 0.05V in the anodic direction compared to 1M NaOH. This represents a shift of ~70 mV/pH, somewhat larger than the expected shift of the flatband potential (V_{FB}), which is 59 mV/pH. This discrepancy may be understood in the following way. The onset of steady-state photocurrent which occurred a few tenths of a volt anodic to V_{FB} represents the situation when sufficient band bending has been established in the semiconductor space charge layer that hole transfer to the reduced species in the solution competes efficiently with other processes. These competing processes include electron-hole recombination and electron capture from the conduction band by the oxidized species in solution. Hence, the discrepancy between the 59 mV/pH expected for V_{FB} and the 70 mV/pH found experimentally for the onset of the steady-state photocurrent may suggest that more band bending is required in acidic solution to overcome electron-hole recombination and/or significant back-reaction. Although the discrepancy between 59-70 mV/pH is not large the proposed hypothesis is also supported by transient photocurrents. Significant transient photocurrents were observed cathodic to the onset of the observed steady-state photocurrent.

Figure 3 shows photocurrent-potential curves in four different acidic solutions. It is evident from the figure that the photocurrent onset in a solution that contains Cl^- is more cathodic than in solutions containing SO_4^{2-}. It was also observed that photocurrent-potential curves in $HClO_4$ media were very similar to those in H_2SO_4. While the electrode reaction in H_2SO_4 or $HClO_4$ was shown to be the oxidation of water to oxygen, as will be discussed later, oxidation of chloride (to chlorine) was responsible for part of the photocurrent in HCl. The competition between halogens and water on photo-oxidation at α-Fe_2O_3 will be reported in a future paper.

The ability of Cl^- to shift the photocurrent curve to more cathodic potentials at a given pH was observed throughout the pH range 0-12.4, but no effect was found in 1M NaOH. A similar effect has been observed at a WO_3 electrode (14).

This shift can be explained in two ways. First, a direct shift of the V_{FB} due to specific adsorption may occur, and second, Cl^- may improve the charge transfer to the solution, possibly by deactivating surface recombination centers. The fact that the steady-state photocurrent curve in 1M HCl is shifted exactly 59 mV/pH from the one in 1M NaOH may suggest that Cl^- is as efficient as OH^- in capturing the hole from

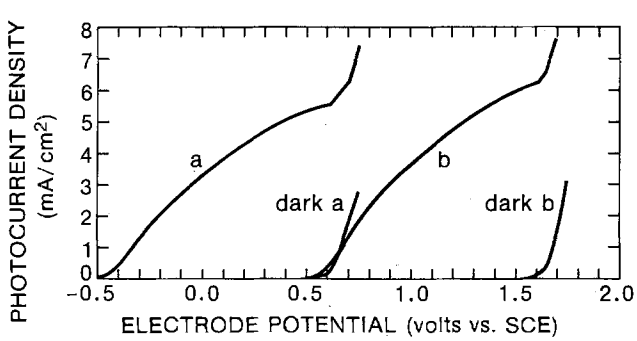

Fig. 2. Current-potential curves for a polycrystalline α-Fe_2O_3 electrode. (a) 1M NaOH; (b) 1M H_2SO_4.

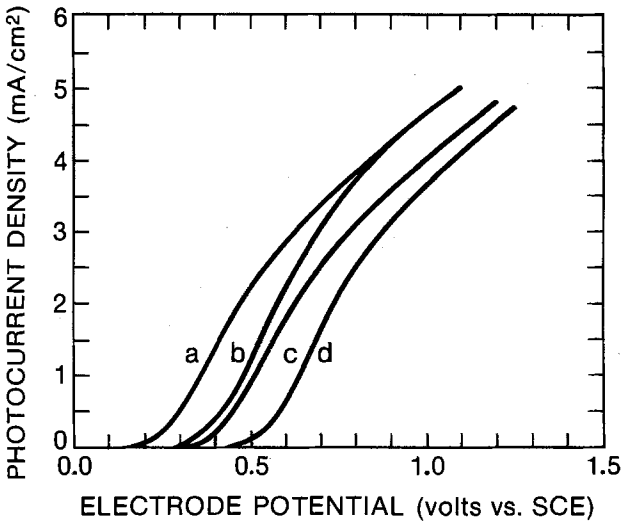

Fig. 3. Photocurrent density vs. electrode potential in various acidic solutions. (a) 0.5M NaCl + HCl, *pH* 3.0; (b) 1M HCl, *pH* 0.3; (c) 0.25M Na_2SO_4 + H_2SO_4, *pH* 3.0; (d) 1M H_2SO_4, *pH* 0.2. Dark current was negligible for the potential range given.

the valence band while SO_4^{2-}, HSO_4^-, ClO_4^-, and water are not. The photocurrent-potential curves in more neutral solutions (pH 3-12) were frequently more complex and will be reported in a later paper.

Anodic dark current, demonstrated to be formation of oxygen, began ~0.9V more positive than the onset of photocurrent in both 1M NaOH and 1M H_2SO_4. A cathodic dark current started at < -0.55V *vs.* SCE in 1M NaOH and $< +0.5$V *vs.* SCE in 1M H_2SO_4. The cathodic dark current was high when oxygen was still present on the electrode surface. However, if the electrode potential was scanned further in the cathodic direction, additional cathodic dark current was observed which dropped with time but did not completely disappear. This dark current was probably a direct reduction of the electrode itself

$$Fe^{3+} + e^- \rightarrow Fe^{2+} \qquad [1]$$

Subsequent to this cathodic dark current, an anodic dark current was observed if the electrode potential was scanned back to more positive values. By holding the electrode at a potential anodic to the onset of photocurrent for a few minutes, it was usually possible to recover the performance of the electrode, and the anodic dark current disappeared. Performance did not recover, indicating a more severe damage, when the electrode was held at < 0V *vs.* SCE in acidic media or < -1V *vs.* SCE in basic media for more than a few minutes.

Oxygen collection.—Previous studies showed that oxygen bubble collection from an open cell using a burette with a broad opening did not give 100% faradaic efficiency even when there was no evidence for another product. Collection efficiency of 30-70% was usually obtained. It was also observed that collection efficiency usually increased with current density and that for each new solution there was an induction time in which a lower collection efficiency was obtained before reaching the plateau value. Other investigations have also reported low collection efficiency (10-93%) for oxygen at α-Fe_2O_3 and TiO_2 anodes (7, 14, 15), except for 100 ±10% reported for very high light intensity conditions (16).

These observations led us to assume that some of the oxygen bubbles are being formed in the bulk solution and, thus, are not collected by the burette. To confirm this assumption we constructed a closed cell (Fig. 1) that collected all oxygen formed anywhere in the cell after saturation with O_2. Indeed, after a few hours' induction time, a faradaic efficiency of 100

± 5% was obtained in several solutions which were tested including 1M NaOH, borax buffer (pH ~ 9.2), 0.5M H_2SO_4, 1M $HClO_4$, and 5M H_2SO_4. A faradaic efficiency of 100 ± 5% for oxygen production was also obtained in the dark at a potential of ~ 1V *vs.* SCE for 1M NaOH and at 1.9V *vs.* SCE for 0.5M H_2SO_4. The induction time could be greatly reduced if the solution was saturated with oxygen before electrolysis in a fresh solution.

Two possible mechanisms (a) and (b) could account for the low efficiencies reported in the past

(a) $2\,OH^- + 2h^+ \rightarrow H_2O_2$ (electrode surface) [2]

$H_2O_2 \rightarrow H_2O + \frac{1}{2}\,O_2$ (bulk solution) [3]

(b) $2\,OH^- + 2h^+ \rightarrow H_2O + \frac{1}{2}\,O_2(aq)$ (electrode surface) [4]

$\frac{1}{2}\,O_2(aq) \rightarrow \frac{1}{2}\,O_2(g)\uparrow$ (bulk solution) [5]

To distinguish between these two pathways, we have carried out the three following experiments. First, the working solution was tested for the presence of H_2O_2. In all cases, the amount found in acidic solution represented < 0.3% of the coulombs passed. Second, when a known amount of H_2O_2, comparable to the amount that would be generated in reaction [2], was added to the acidic solution, 60% of it decomposed in 20 hr during which the electrode was photoelectrolyzing water at 1.3V *vs.* SCE. Third, when this same amount of H_2O_2 was added to the solution for the same period of time while the electrode was at open circuit, no decomposition of the H_2O_2 was observed.

Experiment three indicated that reaction [3] can be ignored, and, hence, mechanism (b) is likely to be responsible for the low collection efficiency observed with an open cell at least in acidic solutions.

However, the above tests do not mean that H_2O_2 is not an intermediate product of the photoelectrolysis. In fact, small amounts of H_2O_2 were consistently found in the working solution and could not come from the Pt auxiliary electrode compartment which was isolated by a double fritted glass separator in these experiments. This observation suggests that H_2O_2 is an intermediate product of the photoelectrolysis, but due to the favorable energetics of the H_2O_2/O_2 couple compared to that of the H_2O/O_2 couple (shown in experiment two), most of the H_2O_2 undergoes further oxidation before having time to diffuse away from the electrode.

Stability.—Figure 4 shows photocurrent *vs.* time curves for three α-Fe_2O_3 electrodes in various acidic solutions. Stable photocurrents are evident although a small drop (~10%) was usually observed in the first few hours when an electrode was transferred from a basic to an acidic medium. This drop was probably due to a slow adsorption/desorption process and/or slow diffusion of some species along grain boundaries and is not surprising for polycrystalline materials. After the small initial decay, photocurrents were stable for several days of continuous operation during which > 600C were transferred. Electrodes have been used intermittently for over 3 months without any damage provided they were always held anodic to the onset of cathodic dark current.

Current-potential curves were generally reproducible after the initial decay. Current-potential curves in basic solution could also be reproduced after the electrodes had been used in acidic media. There was no observable change in the surface appearance, which was examined using optical and scanning electron microscopy.

As a final test of stability the electrolyte solution was analyzed for the presence of Fe^{3+} ions. The analysis technique is quite sensitive allowing the detection of 3 μg Fe^{3+} in the 30 ml electrolyte solution.

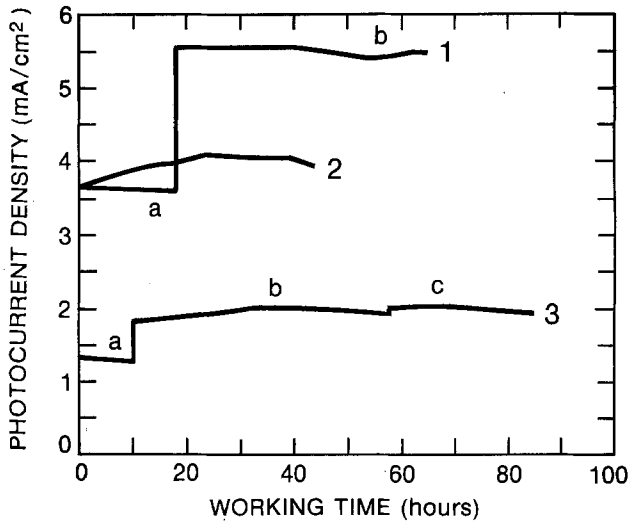

Fig. 4. Photocurrent density *vs.* working time for polycrystalline α-Fe_2O_3 in acidic solutions. Curve 1: (a) 0.5M H_2SO_4; 1.2V *vs.* SCE, and (b) 1M HCl; 1.4V *vs.* SCE. Curve 2: 0.5M H_2SO_4; 1.3V *vs.* SCE. Curve 3: (a) 10M H_2SO_4; 1.5V *vs.* SCE, (b) 1.5M Na_2SO_4 + 0.5M H_2SO_4 pH 2.0; 1.4V *vs.* SCE, and (c) 0.5M H_2SO_4; 1.4V *vs.* SCE. Light intensity for electrode 3 was about one-half the light intensity for electrodes 1 and 2.

Some of the results are shown in Table I. In agreement with Hardee and Bard (1), we found slow dissolution of the electrodes in all acidic media tested under open-circuit conditions in the dark (row VII in Table I). The amount of dissolution was the least in 1M $HClO_4$ (~2 μg/cm² in 24 hr), larger in 0.5M H_2SO_4 (4-30 μg/cm² in 24 hr), and the largest in 1M HCl and 5M H_2SO_4 (~300-600 μg/cm² for 24 hr). These values varied from electrode to electrode with the more porous electrodes (< 80% theoretical density) being more susceptible to dissolution. Higher dissolution rates were generally observed under working conditions (row VI in Table I). Light intensity at the electrode surface was ~500 mW/cm², and the potential was 1-1.5V *vs.* SCE for these experiments. Subtraction of the amount (as μeq) of Fe^{3+} found in solution at open circuit from that found in solution under working conditions and dividing by μeq of electrical charge (row VIII of Table I) represents a measure of photocorrosion.

It is important to note that at least part of the increase in the dissolution rate under working conditions could be due to the intense mixing effect of the electrolyte at the electrode surface by the oxygen bubbles, and not involving a direct photocorrosion. Possible evidence for this mechanism is the lack of any significant difference in the corrosion rate between columns c and d when the amount of current was reduced by a factor of three. Therefore, row VIII should be taken as an upper limit of photocorrosion. These results demonstrate that photocorrosion in 1M $HClO_4$ and 0.5M H_2SO_4 is certainly <0.1%, and probably < 0.01% of the total charge passed through the cell.

The open-circuit dissolution of iron oxide in acidic solutions can be described by the following reaction

$$Fe_2O_3 + 6H^+ \rightleftharpoons 2Fe^{3+}(aq) + 3H_2O$$

$$\Delta G^\circ = -1.97\ \text{kcal/mol} \quad [6]$$

On the other hand according to Scaife (17), the photodissolution of iron oxide to give a monoferric species is given in reaction [7]

$$6h^+ + Fe_2O_3 + 2yH_2O \rightleftharpoons 2Fe(OH)_y^{3-y} + 3/2\,O_2 + 2yH^+ \quad [7]$$

where the value of y depends upon the pH of the

Table I. Amount of Fe^{3+} found in solution for several α-Fe_2O_3 electrodes in various acidic solutions[a]

		a	b	c	d	e	f	g
I	Electrode No.	1	2	3	3	3	3	4
II	Electrolyte	0.5M H_2SO_4	0.5M H_2SO_4	0.5M H_2SO_4	0.5M H_2SO_4	1M $HClO_4$	0.5M H_2SO_4	1M HCl
III	Average current (mA)	3.95	3.8	4.25	1.4	4.6	2.7	1.88
IV	Working time (hr)	44	25	23.25	23	20.8	15	47
V	Electrical charge (μeq)	6480	3550	3690	1200	3570	1510	3300
VI	Fe^{3+} found in solution (μg)	70	39	55	42	12.2	227	818
VII	Fe^{3+} found in solution at open circuit for the same time period (μg)	60	25	3.8	3.8	1.5	77	465
VIII	Percentage photocorrosion (μeq Fe^{3+} in working solution—μeq Fe^{3+} at open circuit)/ μeq charge	0.008%	0.021%	0.075%	0.17%	0.016%	0.53%	0.57%

[a] Electrode area: 1 cm^2; electrode weight: 0.3g; solution volume: 30-1000 ml.

electrolyte. At pH = 0, Fe^{3+}(aq) is expected to be the dominant Fe(III) species, and reaction [7] can be written for $y = 0$

$$6h^+ + Fe_2O_3 \rightleftharpoons 2Fe^{3+}(aq) + 3/2\ O_2 \qquad [7a]$$

Reaction [7a] is different in essence from reaction [6] because the driving force for corrosion is a strong oxidizing agent, *i.e.*, a hole in the valence band (approximately 2V *vs.* SCE). This hole is thermodynamically capable of oxidizing the semiconductor, causing dissolution.

The question of the stability of n-type semiconductors toward photocorrosion has been discussed by Gerischer (18) and by Bard and Wrighton (19). A decomposition potential, E_D, has been assigned for reactions like reaction [7]. Perfect thermodynamic stability of the semiconductor toward anodic photocorrosion requires that E_D be more positive than the valence bandedge avoiding the possibility that the hole will oxidize the semiconductor. Practically all semiconductors that have been studied to date as photoanodes in photoelectrochemical cells do not have this characteristic. Bard and Wrighton (12) have suggested that long-term stability can be achieved if the Fermi level of the redox couple in solution will be more negative than E_D. According to this, model n-type semiconductors will be stable toward photocorrosion provided the oxidized species of the redox couple is thermodynamically incapable of oxidizing the semiconductor.

Figure 5 shows the E_D values for reactions like reaction [7] as a function of the pH of the electrolyte for y values of 0-4. Only monoferric species are considered here, the data are taken from Latimer (20), and a similar scheme was given by Scaife (17).

The figure demonstrates that with respect to the Bard and Wrighton criterion, α-Fe_2O_3 should be stable toward photoelectrolysis at pH > 0 but will exhibit photocorrosion at pH < 0 when the O_2/H_2O level crosses the E_D level of reaction [7a]. However, thermodynamic energy levels are not explicit levels but represent a distribution of levels, and some photocorrosion will be expected even when $E_D > E_{redox}$ (19). Further examination of Fig. 5 shows that $E_D^* - E_{redox} \leq 0.12$V throughout the pH range −1-14 (E_D^* is defined as the most negative E_D value from all type [7] reaction at a given pH). Hence, the effect of pH on the thermodynamic stability of Fe_2O_3 (Bard and Wrighton criterion) is only moderate.

Clearly kinetics also have to be taken into account. Our experimental results which demonstrate that the fractional photocorrosion around pH > 0 is only $< 0.1\%$ and may be much less than this, and that the fractional photocorrosion at pH < 0 when the photocorrosion reaction is thermodynamically favored was still $< 0.5\%$, suggest that complex kinetics inhibit the photocorrosion of α-Fe_2O_3 electrodes.

The mechanistic pathway for either photocorrosion or photoelectrolysis is not known. Both processes require four holes per molecule of O_2 produced, and the experimental results suggest that the photodecomposition reaction must go through a higher activation barrier. One such barrier could possibly involve the Fe^{3+} ion before it has been stabilized by hydration, this kind of barrier should be less pronounced for ions with smaller charge, and lower valent metal oxide semiconductors may exhibit less stability.

The results as presented in Fig. 4 and Table I indicate that in contrast to what was believed before (12), iron oxide is probably more stable toward photocorrosion than wider bandgap materials like WO_3 (21), $SrTiO_3$ (22, 23), and is comparable to TiO_2 (24, 25). Scaife's analysis is in excellent agreement with these findings (17).

We would further like to compare our results to those of Hardee and Bard (1, 2). These authors reported a rapid dissolution of the CVD film at −0.5V *vs.* SCE in pH 4.5, and slow dissolution of the film under open-circuit conditions at pH < 4.

It should be noted regarding the dissolution reaction that interface energetics at pH 4.5 will be shifted by $\sim$ +0.55V compared to the situation at pH 14. Hence, a bias of −0.5V *vs.* SCE at pH 4.5 is comparable to −1.05V *vs.* SCE at pH 14. Our electrodes showed high cathodic dark currents and deteriora-

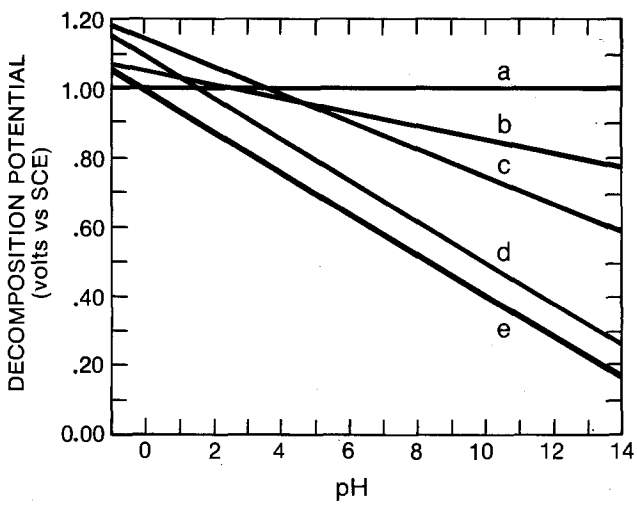

Fig. 5. Decomposition potentials for reaction [7] as a function of pH. (a) $y = 0$; $6h^+ + Fe_2O_3 \rightleftharpoons 2Fe^{3+}aq + 3/2\ O_2$; $E_D = 1.0 + 0\ pH$, (b) $y = 1$; $6h^+ + Fe_2O_3 + 2H_2O \rightleftharpoons 2Fe(OH)^{2+} + 3/2\ O_2 + 2H^+$; $E_D = 1.048\text{-}0.0197\ pH$, (c) $y = 2$; $6h^+ + Fe_2O_3 + 4H_2O \rightleftharpoons 2Fe(OH)_2^+ + 3/2\ O_2 + 4H^+$; $E_D = 1.141\text{-}0.0394\ pH$, (d) $y = 3$; $6h^+ + Fe_2O_3 + 6H_2O \rightleftharpoons 2Fe(OH)_3 + 3/2\ O_2 + 6H^+$; $E_D = 1.096\text{-}0.0592\ pH$, and (e) The oxidation of water to O_2: $6h^+ + 3H_2O \rightleftharpoons 6H^+ + 3/2\ O_2$; $E = 0.99\text{-}0.0592\ pH$.

tion of performance under both conditions, which are possibly already cathodic to V_{FB}. Hence, the corrosion at −0.5V *vs.* SCE is not really meaningful or unique to acidic solution conditions.

With regard to the open-circuit dissolution, we have found a typical rate of dissolution under open circuit of 3-7 μm in 24 hr. Hardee and Bard's films varying in thickness from 1-6 μm should, therefore, exhibit short life. The stable photocurrent observed in this work clearly shows the advantages of using thick electrodes. However, the observed stable performance also means that the new surface exposed to the electrolyte as the electrode dissolved was not significantly different from the initial outer surface. If the stability that was observed in this work for over 80 hr continues, inexpensive sintered polycrystalline electrodes could last for several years while photoelectrolyzing water in acidic media.

Acknowledgments

This work is supported by the Division of Chemical Sciences, Office of Basic Energy Sciences, U.S. Department of Energy. The authors also thank Mr. Don Zak from the Electrical Engineering Department of the University of California, Santa Barbara, for generous technical assistance.

Manuscript submitted Aug. 9, 1982; revised manuscript received Nov. 22, 1982.

Any discussion of this paper will appear in a Discussion Section to be published in the December 1983 JOURNAL. All discussions for the December 1983 Discussion Section should be submitted by Aug. 1, 1983.

Publication costs of this article were assisted by the University of California.

REFERENCES

1. K. L. Hardee and A. J. Bard, *This Journal*, **123**, 1024 (1976).
2. K. L. Hardee and A. J. Bard, *ibid.*, **124**, 215 (1977).
3. R. K. Quinn, R. D. Nasby, and R. J. Baughman, *Mater. Res. Bull.*, **11**, 1011 (1976).
4. L. S. R. Yeh and N. Hackerman, *This Journal*, **124**, 833 (1977).
5. J. H. Kennedy and K. W. Frese, *ibid.*, **125**, 709 (1978).
6. J. H. Kennedy and K. W. Frese, *ibid.*, **125**, 723 (1978).
7. H. H. Kung, H. S. Jarrett, A. W. Sleight, and A. Ferretti, *J. Appl. Phys.*, **48**, 2463 (1977).
8. K. G. McGregor, M. Calvin, and J. W. Otvos, *ibid.*, **50**, 369 (1979).
9. J. S. Curran and W. Gissler, *This Journal*, **126**, 56 (1979).
10. J. H. Kennedy, R. Shinar, and J. D. Ziegler, *ibid.*, **127**, 2307 (1980).
11. J. H. Kennedy, M. Anderman, and R. Shinar, *ibid.*, **128**, 2371 (1981).
12. L. A. Harris and R. H. Wilson, *Ann. Rev. Mater. Sci.*, **8**, 99 (1978).
13. D. A. Skoog and D. M. West, "Analytical Chemistry," 2nd ed., Holt, Rinehart and Winston, Inc., New York (1974).
14. W. A. Gerrard, *J. Electroanal. Chem.*, **86**, 421 (1978).
15. M. S. Wrighton, D. S. Ginley, P. T. Wolczanski, A. B. Ellis, D. L. Morse, and A. Linz, *Proc. Natl. Acad. Sci. U.S.A.*, **72**, 1518 (1975).
16. M. S. Wrighton, A. B. Bocarsley, and J. M. Bolts, *Prog. Astronaut. Aeronaut.*, **61**, 613 (1978).
17. D. E. Scaife, *Solar Energy*, **25**, 41 (1980).
18. H. Gerischer, *J. Electroanal. Chem.*, **82**, 133 (1977).
19. A. J. Bard and M. S. Wrighton, *This Journal*, **124**, 1706 (1977).
20. W. M. Latimer, "Oxidation Potentials," 2nd ed., Prentice Hall, New York (1952).
21. K. D. Quarto, A. D. Daula, and C. Samser, *Electrochim. Acta*, **26**, 1177 (1981).
22. C. W. de Kreak, J. L. B. De Groot, and A. Mackor, *Sol. Energy Mater.*, **5**, 437 (1981).
23. R. E. Schwerzel, E. W. Brooman, H. J. Byker, E. J. Drauglis, D. D. Levy, L. E. Vaaler, and V. E. Wood, in "Photoeffects at Semiconductor/Electrolyte Interfaces," A. J. Nozik, Editor, ACS Symposium Series **146**, 191 (1981).
24. L. A. Harris and R. H. Wilson, *This Journal*, **123**, 1010 (1976).
25. L. A. Harris, D. R. Cross, and M. E. Gerstner, *ibid.*, **124**, 839 (1977).

The Relation Between Performance and Stability of Cd-Chalcogenide/Polysulfide Photoelectrochemical Cells

I. Model and the Effect of Photoetching

R. Tenne and N. Müller[1]

Department of Plastics Research, The Weizmann Institute of Science, Rehovot 76100, Israel

Y. Mirovsky and D. Lando

Department of Structural Chemistry, The Weizmann Institute of Science, Rehovot 76100, Israel

ABSTRACT

Photoetching of CdS, CdSe, and CdTe electrodes, which is known to improve their quantum efficiency in electrochemical solar cells, is found to improve the electrode stability in polysulfide electrolyte, even though the photocurrent is increased after the photoetching (under constant illumination intensity). A simple model for the performance and the stability of Cd-chalcogenide/polysulfide photoelectrochemical cells is suggested, according to which any parameter that increases the quantum efficiency of the photoelectrode will also increase the electrode stability. Any impediment on the flow of holes into the electrolyte will lead to increased photocorrosion and surface recombination. The validity of this model is tested by measuring the quantum efficiency, electrode stability, and photocurrent transients at various light intensities and electrolyte concentrations.

Photocorrosion of semiconductor electrodes is one of the main obstacles in the development of photoelectrochemical solar cells (PEC's) (1-3). As thermodynamic arguments show (1, 2), all n-type semiconductors tend to photocorrode in aqueous electrolytes, but they can still be stabilized by kinetic means, *e.g.* by a fast redox reaction which takes over the photogenerated holes

[1] Presently on leave of absence as Mineral Fellow, Fritz-Haber Institute of the Max Planck Gesellschaft, Berlin, Germany.

Key words: photocorrosion, quantum efficiency, photoelectrochemical etching.

before they can perform the decomposition reactions (3). A well-known example is the stabilization of Cd-chalcogenide electrodes by polysulfide solutions (4-7). It has been shown that the stabilization of PEC's of this type is not an absolute one, with the consequence that exchange reactions take place at the semiconductor-electrolyte interface, leading, *e.g.*, to the formation of a CdS layer on the top of a CdSe electrode in contact with a polysulfide electrolyte (8-11).

Experimental investigations of electrode stability showed that photocorrosion increases with increasing light intensity and decreasing concentration of the reduced species in the electrolyte (12-14). Furthermore, it has been observed that, after a photoetching treatment of CdSe electrodes the long range stability is considerably enhanced, compared with the chemically-etched electrodes when the same initial photocurrent is drawn from the cell (15, 16). Taking into account the increase in the quantum yield of the cell after photoetching (17, 18), it was tempting to try to see whether this correlation between the quantum yield of the cell and its output stability is of much broader bearings. Thus, in this work we substantiate this notion by studying the effect of photoetching, light intensity, and electrolyte concentration on the performance and the stability of these cells. A simple kinetic model of the cell stability and performance is proposed. The experimental results are compared qualitatively with the model. Quantitative tests of this model by computer simulation are in progress. In subsequent papers we will report the effect of photoelectrode potential and electrolyte temperature on cell stability, and discuss these effects using the model proposed in this paper.

Experimental

The experiments were carried out in a conventional photoelectrochemical setup. Materials, electrode preparation, etc. were as described previously (3). The photoetching treatment was carried out with a (0.3:9.7:90% by volume) HNO_3:HCl:H_2O mixture with carbon rod as a counterelectrode (17). Subsequently the electrode was immersed in polysulfide (to dissolve any free Se) and rinsed with water. The laser experiments were carried out with a 7 mW CW Radiation He-Ne laser and calibrated Si photodiode was used for the determination of the absolute quantum efficiency. A lock-in detection technique was used to avoid the dark current contribution. The transient (peak/steady) measurements were carried out with a homemade detector with 1 μsec resolution.

Results

Saturation of the short-circuit current *vs.* light intensity proved to be a good indication for slow kinetics of the hole-electrolyte reaction leading to photocorrosion (3, 19). Figure 1 shows how photoetching modifies the photocurrent *vs.* light intensity behavior. It can be seen that under conditions where the short-circuit current (J_{sc}) of the chemically etched electrodes showed saturation with the light intensity (ϕ), a linear dependence of J_{sc} *vs.* ϕ was still observed with the photoetched electrode. Operation of the chemically etched electrode at current densities above the saturation level brought about a fast deactivation (photocorrosion), while the photoetched electrode was found to be stable at these light intensities.

Figure 2 shows the dependence of the quantum efficiency on light intensity as measured with an He-Ne laser. The quantum efficiency decreases for both the etched and the photoetched electrode with increasing light intensity. Under same conditions the photoetched electrode exhibits bigger quantum efficiencies, especially at high illumination intensities and small electrolyte concentrations. Note that even under the most favorable conditions, *i.e.*, photoetched electrode, high electrolyte concentration, and small illumination intensity, the quantum efficiency does not exceed 85%, due probably to surface recombination.

In prevous publications of this laboratory (12, 15) it was shown that both the surface area and the light intensity play an important role in determining the output stability of these cells. As reported earlier (15), the stability of a CdSe photoelectrode was found to decrease with increasing illumination intensities (Fig. 3). Transient measurements were carried out to compare the short-circuit photocurrent at the onset of illumination (where we expect complete coverage of the electrode surface with sulfide ions) with the photocurrent after reaching a steady value (partial coverage by sulfide ions). The result of such a measurement is shown in Fig. 4. Whereas the steady-state photocurrent saturates with light intensity, the peak current is linear with light intensity. We found that electrode deactivation is very rapid at light intensities where the steady-

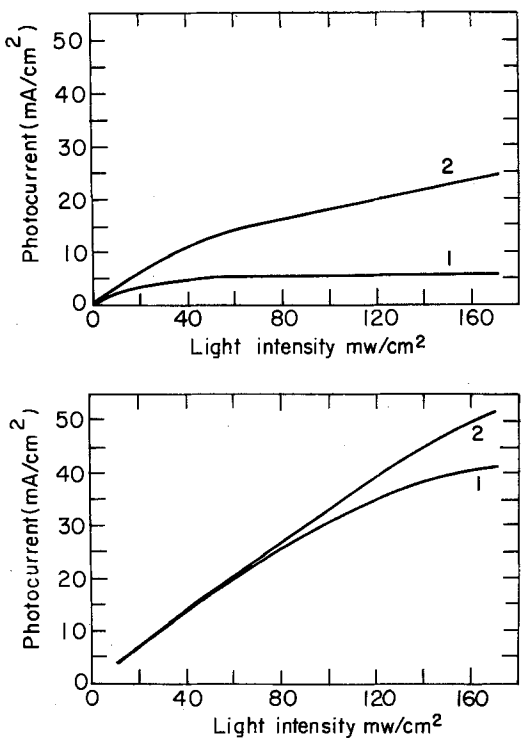

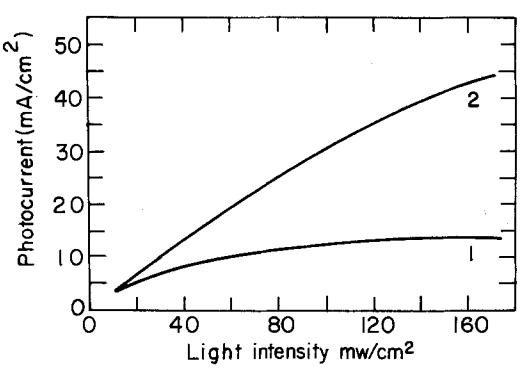

Fig. 1. Photocurrent *vs.* light intensity of etched, 1, and photoetched, 2, CdSe in different polysulfide solutions. (a, upper left) (0.1:0.1:0.1)M with respect to OH^-; $S^=$ and S^-, respectively. (b, lower left) (1:1:1) solution, and (c, upper right) (2:2:2) solution.

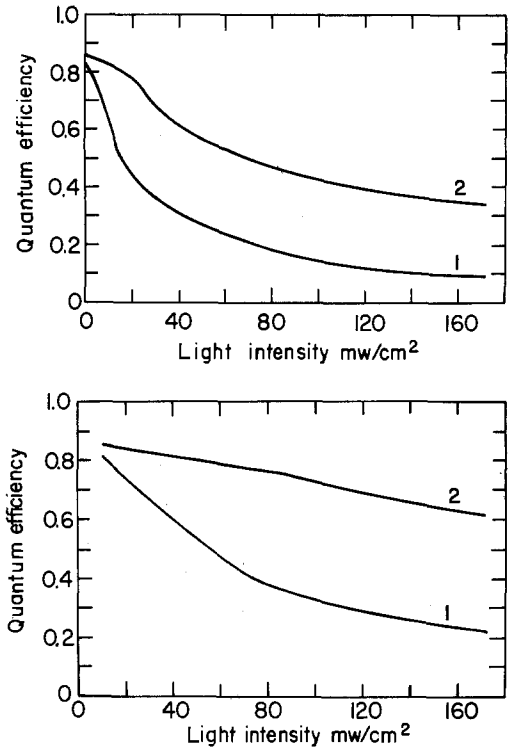

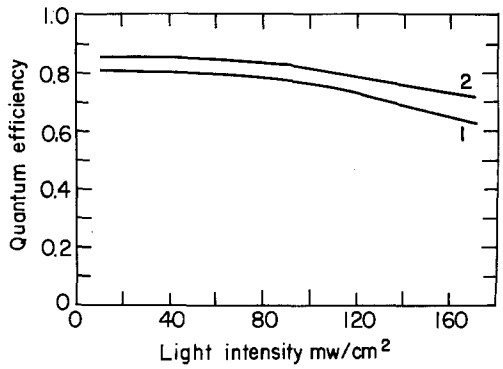

Fig. 2. Quantum yield vs. light intensity of etched, 1, and photoetched, 2, CdSe in different polysulfide solution. a, upper left, b, lower left, and c, upper right and the light source as in Fig. 1.

state photocurrent saturates The effect of the electrolyte concentration on electrode stability was elaborated in numerous publications (6, 8, 13, 19, 20). Figure 5 shows an example of the increase in electrode stability at higher electrolyte concentrations.

In all experiments reported earlier (15), the comparison of the stability of chemically etched and photoetched CdSe electrodes has been performed under the condition of identical initial photocurrent, which means that the chemically etched electrode has been illuminated at a higher light intensity. To check, if the improved stability of the photoetched electrode is not only due to the lower illumination intensity, we repeated these experiments under the condition of identical illumination intensity. In Fig. 7 it is shown that also in this case the photoetched electrode is more stable than the chemically etched one, though the initial photocurrent of the former is higher. The gain in electrode stability with photoetching is not restricted to CdSe electrodes, as can be seen from Fig. 8 and 9, which show stability tests of CdS and CdTe electrodes in polysulfide electrolyte. In these tests the illumination intensity was kept constant again: the photoetched electrodes show a higher photocurrent and a lower electrode deactivation than after a chemical etch.

Discussion

Working hypothesis.—Our working hypothesis is that photocorrosion arises from the discrepancy between the flux of holes arriving at the surface of the electrode and the reaction rate between these surface holes and adsorbed sulfide ions at the electrode surface.

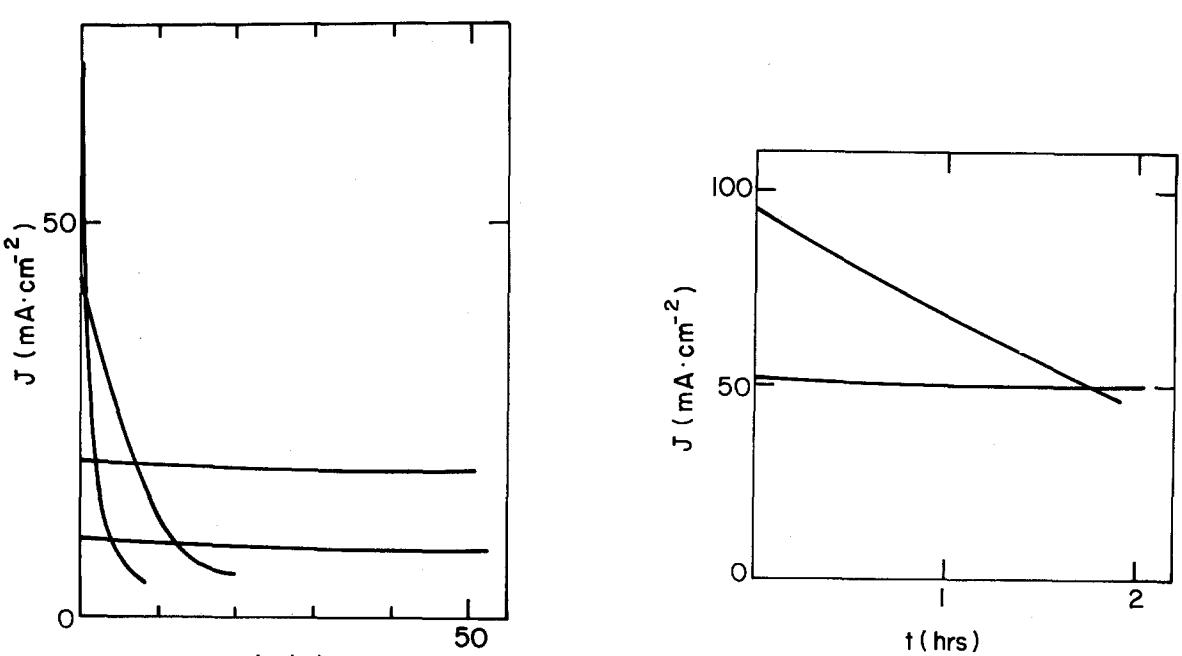

Fig. 3. Photocurrent of etched CdSe vs. time (output stability) at different light intensities. (a, left) (1:1:1) polysulfide; (b, right) (2:2:2) polysulfide.

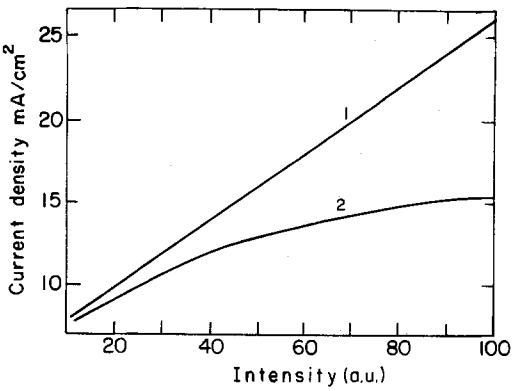

Fig. 4. Peak, 1, and steady-state, 2, photocurrents as a function of light intensity for polycrystalline CdSe electrode in solution of 1M $S^=$ and 1M OH^- and 0.3M S.

A depletion of adsorbed sulfide ions may occur due to a slow adsorption rate resulting from low bulk concentration, or due to a slow desorption rate (dissolution of oxidized sulfide), which diminishes the number of available adsorption sites.

Increasing the roughness of the electrode (by photoetching) has the effect of reducing the effective surface concentration of the holes per unit area of the junction. This ensures an adequate supply of adsorbed sulfide ions, which results in an improved stability. By increasing the light intensity we deplete the sulfide ions from the interface. Therefore the following holes have no redox electrolyte to oxidize and they are impeded on the electrode surface, so that their probability to recombine or to oxidize the crystal increases. If we increase the concentration of the electrolyte, the surface density (coverage) of the oxidizable species of the electrolyte increases and, in addition, the kinetics of the sulfur dissolution from the electrode surface is improved so that the output stability is improved.

Correlation between quantum yield and output stability—a model and its experimental verification.—The model described here takes into account the self-oxidation of the electrode (photocorrosion) in addition to the electrolyte oxidation and surface recombination. The hole flux arriving at the semiconductor surface, J_ϕ which is proportional to the illumination intensity, ϕ, is consumed by three different routes: the holes can oxidize the electrolyte which leads to a regenerative photocurrent, J_{reg}; they can participate in corrosion reaction which leads to the corrosion current, J_{cor}, and they can recombine at the electrode surface leading to the recombination current, J_{rec}.[2] Hence, we have

$$J_\phi = J_{reg} + J_{cor} + J_{rec} \quad [1]$$

The first two currents are connected with a flow of charges through the external circuit so that the total photocurrent which we read is

$$J_{ph} = J_{reg} + J_{cor} \quad [2]$$

We define the normalized current yield as

$$q_n = J_{ph}/J_\phi \quad [3]$$

which shows the compatibility between the hole flux arriving to the semiconductor surface and the ionic flux into the electrolyte. Note that q_n can be determined directly under reverse bias only where $W > \alpha^{-1}$ (W = the width of the space charge layer, α = absorption coefficient) and all the incident light is absorbed in the space charge region, since in this case bulk and space charge recombination are negligible. In this case the photogenerated holes are effectively swept toward the semiconductor surface. Nevertheless q_n is not nec-

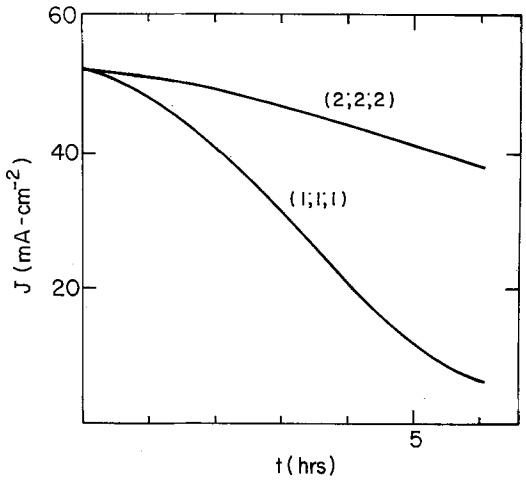

Fig. 5. Output stability of etched CdSe in two concentrations of the polysulfide electrolyte.

[2] The recombination current consists of a radiationless part and a radiative part, the latter being exceedingly small, however (21).

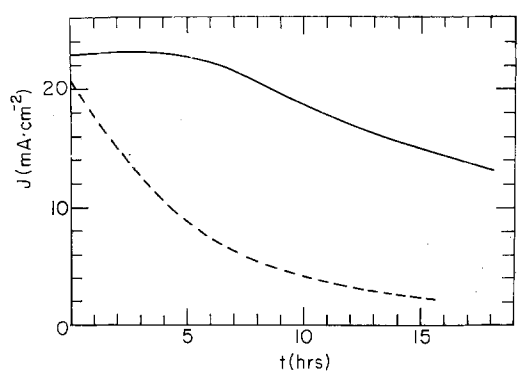

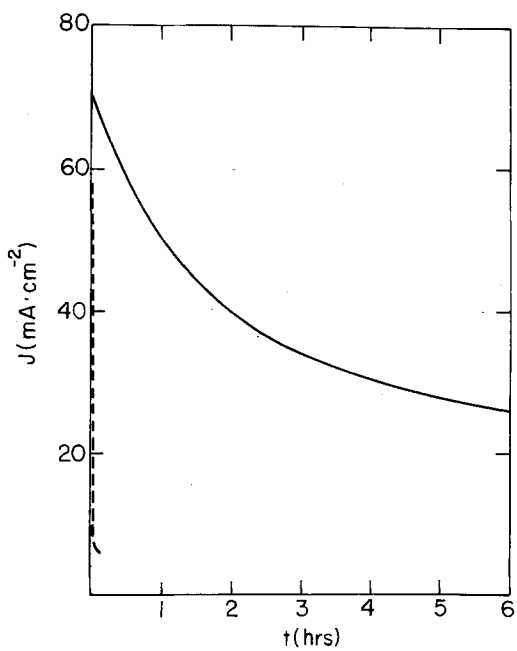

Fig. 6. Schematic representation of semiconductor-electrolyte junction with uneven surface of the electrode

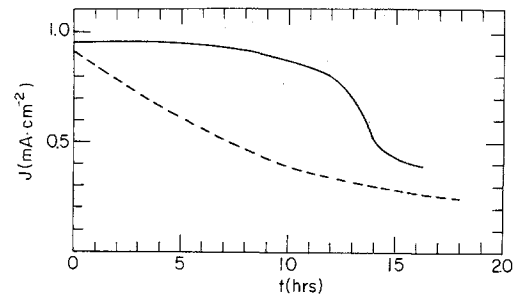

Fig. 7. Comparison of the output stabilities of etched (- - -) and photoetched (——) CdSe in (1:1:1) polysulfide in two light intensities: a. 2 AM1; b. ~7 AM1.

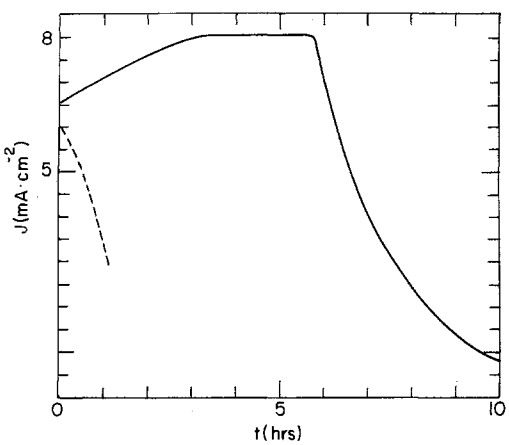

Fig. 8. Comparison of the output stabilities of etched (- - -) and photoetched (——) CdS electrode in sulfide solution containing 1M $S^=$ and OH^-.

essarily equal to 1 in this case, as surface recombination still might occur, as suggested by the quantum efficiencies in Fig. 2.

Consider the following sequence of reactions occurring at the semiconductor-electrolyte interface under illumination at short-circuit conditions.

$$AB \xrightarrow{J_\phi} AB + h^+ + e^- \quad \text{(generation)} \quad [4]$$

$$AB + e^- + h^+ \xrightarrow{Sr} AB \quad \text{(surface recombination)} \quad [5]$$

$$AB + h^+ \xrightarrow{k_1} A^+ + B \quad \text{(photocorrosion)} \quad [6]$$

$$C_{ads}^{2-} + h^+ \xrightarrow{k_2} C^- \quad \text{(electrolyte oxidation)} \quad [7]$$

$$C^{2-} \xrightarrow{k_3} C_{ads}^{2-} \quad \text{(adsorption)} \quad [8]$$

In this scheme AB is the semiconductor; e^- and h^+ are the photogenerated electrons and holes; Sr is the surface recombination velocity;[3] k_1 and k_2 are the rate

[3] Here we include surface and near surface (space charge) recombinations between which we cannot discriminate in the present experiments.

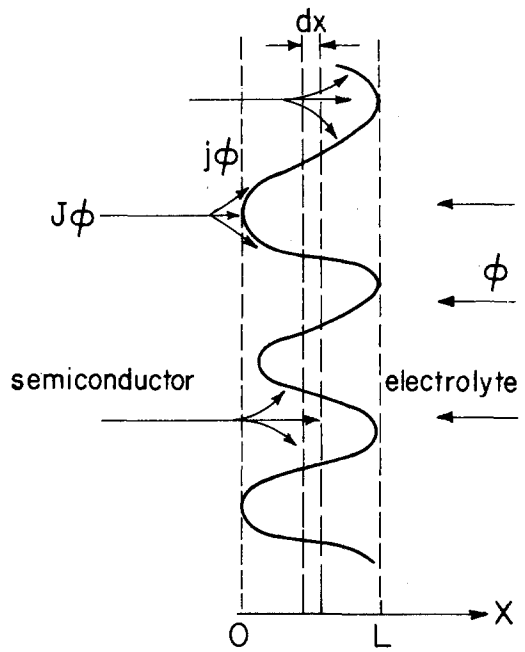

Fig. 9. Comparison of the output stabilities of etched (- - -) and photoetched (——) CdTe electrode under ~0.33 AM1 light intensity. Solution is 5M with respect to OH^- and S and 1.5M with respect to $S^=$.

constants for the photocorrosion reaction and for the regenerative oxidation of the adsorbed electrolyte, C_{ads}^{2-}, respectively. It has been shown that the rate-determining factor at an illuminated Cd-chalcogenide/polysulfide interface is the exchange rate of the oxidized species by its reduced counterpart (20). In the model presented here we assume that the rate-determining step is the adsorption of the reduced species at the electrode surface (Eq. [8]). A probably more realistic model, in which the rate of desorption of the oxidized species is limiting the regenerative photocurrent under moderate and high illumination intensities, is presented in the Appendix. Both models predict the same behavior for the parameters studied in this work. As the simple model (Eq. [4] to [8]) includes fewer rate constants and is more comfortable to deal with we preferred to utilize it for the interpretation of our experimental results.

In this model we assume that all the new species which are formed under illumination (A^+, B, and C^-) are removed fast from the electrode surface. Also since we consider the stability of our cell under short-circuit conditions ($V = 0$) we do not take into account the cathodic dark current. Note that the present model deals with one hole transfer because detailed mechanism for the Cd-chalcogenide/polysulfide cells is not available at present.

A top insulating layer of CdS, which usually forms under illumination, is not taken into account in this model, which therefore strictly speaking describes a highly idealized case, and is valid for times shortly after the onset of illumination only. However, it is shown below, that this simple model can be used to predict trends in the stability behavior of our cells in general. The reason for this is that the top CdS layer can be considered as a mediator for the charge injection into the electrolyte, but it does not alter the basic kinetic conditions of the interface as presented here.

In the operation of a PEC considered in this work we can differentiate between two distinct time scales. Whereas a quasistationary steady state is established in a matter of seconds or less, an observable electrode deactivation occurs after hours of illumination and is very slow (unless we work at high intensities and low concentration of the electrolyte). This argument justi-

fies the use of a quasi-steady-state solution for the model. Thus, we may write for the excess concentration of holes on the surface p_s^* [$p_s^* = p_s - p_s(\phi = 0)p_s^*$ is given in units of cm^{-2}] the following expression

$$O = \frac{dp_s^*}{dt} = J_\phi - Srp_s^* - k_1 p_s^* - k_2 p_s^* \theta_{red} \quad [9]$$

Here θ_{red} is the relative surface concentration (coverage) of the reduced species of the electrolyte ($\theta_{red} = C_{ads}^{2-}/M$, where M is the total density of adsorption sites on the surface). In Eq. [9] and [13b] we have assumed that the rate of recombination is independent of the surface concentration of electrons (22). This assumption is supported by the fact that the quantum efficiency of the etched CdSe electrode close to short circuit does not exceed 85% and is potential independent (in reverse bias), even under low light intensities. One possible explanation is that the chemically etched electrode contains large density of surface states with a broad distribution. If these states have good communication with the bulk of the semiconductor, the rate of recombination at the surface does not depend on the position of the Fermi level, but on the density of the surface states. This notion is further supported by the large increase in the quantum efficiency observed after the photoetching as a result of the "cleaning" of the surface. From Eq. [9] we obtain

$$p_s^* = J_\phi/(Sr + k_1 + k_2\theta_{red}) \quad [10]$$

Similarly we can write for the time derivative of θ_{red}

$$O = \frac{d\theta_{red}}{dt} = k_3(C_{red})(1 - \theta_{red}) - k_2\theta_{red}p_s^* \quad [11]$$

Here (C_{red}) is the concentration of C^{2-} in the solution. Note that the rate of C^{2-} adsorption on the electrode surface is proportional to the available fraction of unoccupied sites $1 - \theta_{red}$. We find

$$\theta_{red} = \frac{k_3(C_{red})}{k_3(C_{red}) + k_2 p_s^*} \quad [12]$$

The different routes for the consumption of the holes on the surface of the electrode are given by

$$J_{reg} = k_2 p_s^* \theta_{red} \quad [13a]$$

$$J_{rec} = S_r p_s^* \quad [13b]$$

and

$$J_{cor} = k_1 p_s^* \quad [13c]$$

The normalized current yield is then

$$q_n = (J_{reg} + J_{cor})/J_\phi = \frac{k_2\theta_{red} + k_1}{S_r + k_1 + k_2\theta_{red}} \quad [3a]$$

Using the results of this kinetic model we will discuss now the experimental results which demonstrate the correlation between the performance and the stability of Cd-chalcogenide/polysulfide solar cells. We discuss the effect of the light intensity, surface roughness, removal of surface defects, and the effect of the electrolyte concentration upon the performance and the stability of these cells.

Effect of light intensity.—In the simplest case J_ϕ is proportional to ϕ (23). We examine two extreme cases when ϕ is very small and very large ϕ's. When $\phi \to 0$ the coverage of the surface by the reduced species is complete ($\theta_{red} \to 1$). In this domain p_s^* increases linearly with the light intensity. Therefore, the light induced currents in Eq. [13] are also proportional to the light intensity and the quantum efficiency is a constant. These conclusions are substantiated by the results of the experiments shown in Fig. 1 and 2. In these experiments we used an He-Ne light source of 632.8 nm. Under somewhat larger light intensities θ_{red} decreases linearly with the light intensity

$$\theta_{red} = 1 - \frac{k_2}{k_3(C_{red})} \cdot \frac{J_\phi}{S_r + k_1 + k_2} + O(\phi^2) + \ldots \quad [14a]$$

The regenerative photocurrent shows sublinear dependence on the light intensity (or p_s^*)

$$J_{reg} = k_2 p_s^* \left(1 - \frac{k_2 p_s^*}{k_3(C_{red})} + \ldots\right) \quad [14b]$$

and the quantum yield decreases with increasing light intensity

$$q_n = q_n^o \left(1 - \frac{k_2 p_s^*}{k_3(C_{red})} + \ldots\right) \quad [14c]$$

For a very strong light intensity $k_2 p_s^* >> k_3(C_{red})$ so that

$$\theta_{red} = \frac{k_3(C_{red})}{k_2 p_s^*} \quad [15a]$$

and

$$J_{reg} = k_3(C_{red}) \quad [15b]$$

On the other hand J_{rec} and J_{cor} increase indefinitely with the light intensity. Since $S_r >> k_1$ (*i.e.*, corrosion is negligible compared to recombination), most of the holes that do not contribute to J_{reg} will recombine so that under strong light intensities the observed photocurrent tends to saturate with the light intensity, as is shown in Fig. 1. In addition, the rate of deactivation of the photoelectrode increases with the light intensity as was shown before (12) and as can be seen also from Fig. 3 for an etched CdSe electrode.

The assumption $S_r >> k_1$ is justified by the observation that under conditions where the rate of electrode deactivation is very slow the quantum efficiency does not exceed 85% so that surface (or space charge) recombination is very large. Equation [15b] suggests a linear relation between the photocurrent and the electrolyte concentration at high illumination intensities. In the experiment, however, we see a hyperlinear behavior (cf. Fig. 1). The reason for this probably lies in the fact that not only sulfide ions but also oligomers of polysulfide serve as acceptors of holes at the electrode surface. The average rate constant for the exchange of oxidized species by reduced species from the solution is improved by increasing the concentration of the electrolyte (20). An increased series resistance of the cell under high illumination intensities, which is neglected in our model, should not be expected below photocurrent densities of about 30 mA/cm^2.

As to the series resistance of the electrolyte itself it is difficult to assess it accurately. Under strong light intensities when the photocurrent of the etched CdSe electrode is saturated, the photocurrent of the photoetched CdSe electrode still rises with light intensity, which shows that series resistance due to insufficient rate of mass transport of the electrolyte may occur in the vicinity of the interface, but it cannot be distinguished at present from the limiting rate of sulfur dissolution.

A more refined model of the cell must take into account also the flattening of the bands in the space charge region as a result of the fast depletion of the adsorbed $S^=$ ions from the surface of the electrode. This band flattening is not negligible under strong light intensities, as numerical analysis of similar cells suggests (24).

The peak photocurrent under weak and moderate light intensities depends mostly on the supply of holes to the surface of the electrodes so that

$$J^p = k_2 J_\phi/(S_r + k_1 + k_2) \quad [16]$$

This peak photocurrent is linear in the light intensity and is always larger than the steady-state photocurrent $J^s = J_{ph}$ as is confirmed in Fig. 4. Under very strong light intensities the peak photocurrent also

saturates as a result of the flattening of the energy bands. A correlation between the normalized ratio $NR = (J^p - J^s)/J_p$; the rate of sulfur dissolution in a polysulfide electrolyte and the stability of CdSe photoelectrodes in this electrolyte have been reported earlier (20). Under small light intensities NR is small and it increases with the light intensity. This increase in NR, which goes along with the decrease in the quantum yield and the stability, is connected to the inadequate supply of hole acceptors to the surface of the electrode, which is the result of slow rate of sulfur dissolution.

A word of caution is necessary here concerning the time resolution of our photocurrent transient measurements. In view of the recent fast transient measurements carried out on Cd-chalcogenide/polysulfide PEC's (25), in which response times on nanoseconds time scales were monitored, it is clear that the measurements carried out in this laboratory on a milliseconds time scale are rather crude. But as the rate-determining step in the regenerative photocurrent can be monitored with our time resolution (20), these transient measurements are very useful in detecting trends and effects of different parameters on the response of our system, and these results can be correlated quite well to the performance and the output stability of the PEC cells under investigation.

The conclusion that emerges from this discussion is that under small light intensities, the quantum efficiency of the cell and its output stability are the highest and they decrease with the light intensity, but in a nonlinear manner, as was formerly observed (13, 19).

Effect of electrolyte concentration.—The effect of the electrolyte concentration is evident in the present model. When $(C_{red}) \rightarrow 0$ then θ_{red} vanishes and therefore J_{reg} vanishes too. The corrosion and recombination currents are given by

$$J_{cor} = \frac{k_1 J_\phi}{S_r + k_1} \qquad [17a]$$

and

$$J_{rec} = \frac{S_r J_\phi}{S_r + k_1} \qquad [17b]$$

But since $S_r >> k_1$ then most of the surface holes recombine and the photocurrent is small. However, the rate of electrode deactivation is relatively fast even under small light intensities. Comparison of the quantum efficiencies of etched CdSe electrodes at three electrolyte solutions (Fig. 1 and 2) demonstrates the effect of the electrolyte concentration upon the performance of the cell. Figure 5 shows the effect of the electrolyte concentration upon the output stability of a cell containing etched CdSe electrode, as was shown before (20). In the measurement reported here we used solutions with the same ratio $OH^-:S^=$ and S (1/1/1). This ensures a monotonic increase of the active species of the electrolyte with increasing concentration of the different components.

When C_{red} is very large $\theta_{red} \rightarrow 1$, and $p_s^* = J_\phi(S_r + k_1 + k_2)$ attains its lowest value, J_{rec} and J_{cor} attain their lowest values and J_{reg} is a maximum. Therefore, in this limit both cell performance and its output stability are the highest. Most probably the increase of C_{red} increases k_2 as well so that the stability and the performance of the cell are further improved.

Effect of photoetching.—Deliberate photocorrosion of the semiconductor surface for short periods (photoetching) improves the performance of many photoelectrochemical cells (17, 18). We can discriminate between two cases. In CdSe and CdTe crystals the main effect of the photoetching is due to the formation of pits which increase the surface area of the junction by about 50%. This increase in the surface area of the junction reduces the reflectivity of the surface by about 10% and improves the rate of the hole-electrolyte reaction considerably. The surface of CdS does not show any observable changes, and the large effect of the short photoetching is mainly due to the removal of surface imperfections. Let us examine in detail how photoetching improves the performance and the stability of photoelectrochemical cells.

In Fig. 6 we give a schematic representation of a junction between electrolyte and a semiconductor electrode with uneven surface area. We use an approach equivalent to the macrohomogeneous model which was found useful for the description of the kinetics of reactions in porous electrodes (26). We consider an idealized case in which all the pores have even shapes so that the flow of holes from the bulk of the semiconductor into the surface is essentially uniform. We restrict ourselves to a quasi-unidimensional approach in which the complicated y-z plan kinetics is taken into account by the macroscopic terms S_p(cm^2/cm^3), which gives the specific surface area of a unit volume of the electrode close to the electrode surface ($0 \leq x \leq L$). The surface roughness parameter of the junction is given by the integral

$$s = \int_0^L dx S_p \qquad [18]$$

We can formulate the model through s or S_p but we prefer the former, since we consider here surface phenomena rather than a phenomenon of the bulk as in porous electrodes. The parameter s expresses the roughness of the electrode surface. It is the ratio between the real surface area of the junction and its geometrical surface area. By increasing the roughness of the surface area we increase the density of sites by a factor, $s > 1$, so that the coverage (per geometrical area) increases from θ_{red} to $s\theta_{red}$. Inserting this new value of coverage into Eq. [9] we obtain

$$O = \frac{dp_s^*}{dt} - J_\phi - S_r p_s^* - k_1 p_s^* - k_2 p_s^* \theta_{red} s \qquad [9a]$$

so that

$$p_s^* = J_\phi/(S_r + k_1 + k_2 \theta_{red} s) \qquad [19]$$

Hence we can write for the regenerative mode

$$J_{reg} = k_2 p_s^* \theta_{red} \cdot s = s \frac{k_2 J_\phi \theta_{red}}{(S_r + k_1 + k_2 \theta_{red} \cdot s)} \qquad [20a]$$

so that the regenerative photocurrent increases with an increase of the surface roughness, s. On the contrary

$$J_{rec} = \frac{J_\phi S_r}{k_1 + S_r + k_2 \theta_{red} \cdot s} \qquad [20b]$$

and

$$J_{cor} = \frac{J_\phi k_1}{k_1 + S_r + k_2 \theta_{red} \cdot s} \qquad [20c]$$

decrease with s as was confirmed experimentally.

Note that if recombination and corrosion would not exist so that the only possible mode would be the regenerative one, because photoetching (or s) would have no effect on the quantum efficiency.

An indirect effect of s on the light induced currents of Eq. [20] comes through the intrinsic surface coverage θ_{red} which increases as a result of the decrease in p_s^*. Therefore, J_{reg} increases with s more significantly as exhibited by Eq. [20a], whereas J_{cor} and J_{rec} decrease even further with s. The effect of the photoetching on the photocurrent of CdSe/polysulfide cell is exhibited in Fig. 1 and 2, especially under strong light intensities and in the dilute solutions. Whereas the photocurrent of the etched electrode is almost independent of the light intensity, the photocurrent of the photoetched electrode continues to rise with the intensity of illumination almost linearly. Furthermore, the photoetching decreases considerably the normalized ratio, NR, so that the difference between the steady-

state photocurrent and the peak photocurrent is smaller.

The increase of the surface area of the electrode was reported to decrease substantially the polarization of the oxidation reaction of polysulfide on inert electrodes (27). It was shown that platinized platinum had substantially smaller polarization values than all other inert electrodes.

In Fig. 7 we compare the output stability of an etched and a photoetched CdSe electrode under the same intensity of illumination. It is observed that the photoetched electrode has larger initial photocurrent and greater stability than the etched one as expected from Eq. [20a] and [20c].

In CdS the effect of the photoetching on the I-V curve of the cell was explained as resulting from the removal of surface imperfections (17b). These surface imperfections impede the holes on the surface of the semiconductor and increase their probability to recombine with the abundant electrons. The main effect of the photoetching here is therefore to reduce the recombination velocity S_r. In addition, surface imperfections are generally connected with loosely attached lattice atoms which are prone to photocorrosion reaction (28). Thus, the removal of these imperfections also decreases, k_1, so that the stability of photoetched CdS is better than the etched electrode as is confirmed in Fig. 8 for two distinct light intensities.

The stability of etched and photoetched CdTe in polysulfide is shown in Fig. 9. Here (17c) short photoetching leads to pitting of the electrode surface as in CdSe, and the photocurrent and the fill factor are improved. The improved stability of the photoetched electrode is in accordance with the present model.

In polycrystalline CdSe (17) and $CdSe_xTe_{1-x}$ (18) electrodes, the density of surface imperfections on the surface of the electrode is considerable, and therefore the effect of the photoetching is dominant on the performance and stability of the cell under moderate light intensities.

Conclusions

In this work we tried to show that there exist correlations between the different routes by which the photogenerated holes, which are collected on the semiconductor (CdX)-electrolyte (polysulfide interface are consumed. In particular any factor which will impede the crossing of the holes into the electrolyte will have an adverse effect on the (real) quantum yield by increased recombination and on the stability (enhanced corrosion currents) of the cell.

The stability of Cd-chalcogenide/polysulfide based PEC solar cells can be improved by photoetching. Considering the high stability of polycrystalline thin film CdSe electrode (29) which can be further improved by adding elemental Se (30) or indifferent salts (31) to the electrolyte, it might be possible to apply concentrated sunlight on CdSe/polysulfide based PEC's.

Recently we have shown that by lowering the temperature of the CdSe/polysulfide cell both the quantum efficiency and the stability of the cell deteriorate, in accordance with the present model (32).

In subsequent publications we will discuss the effect of the bias in the light of this interpretation. Furthermore we will show that it is possible to further improve the stability of these cells by chopping the light incident on the cell as can be anticipated from the present discussion.

Acknowledgments

This research was partly supported by a BMFT grant through KFA Jülich. J. Manassen, D. Cahen, and B. Vainas are acknowledged for the discussions and the suggestions they gave while preparing this work.

Manuscript submitted May 21, 1981; revised manuscript received Dec. 17, 1981.

Any discussion of this paper will appear in a Discussion Section to be published in the December 1983 JOURNAL. All discussions for the December 1983 Discussion Section should be submitted by Aug. 1, 1983.

APPENDIX

We present here a model which describes the Cd-chalcogenide/polysulfide cells more realistically but is more complicated than the one presented in the text. The rate-determining step in this model is not the rate of adsorption of the reduced species, but rather the rate of desorption of the oxidized species, following the hole capture from the semiconductor. This model is being employed now for the numerical verification of the ideas of the present work. The following scheme of reactions is assumed to take place on the interface

$$AB \xrightarrow{J_\phi} AB + h^+ + e^- \qquad [A\text{-}1]$$

$$AB + e^- + h^+ \xrightarrow{S_r} AB \qquad [A\text{-}2]$$

$$AB + h^+ \xrightarrow{k_1} A^+ + B \qquad [A\text{-}3]$$

$$C_{ads}^- + h^+ \xrightarrow{k_2} C_{ads} \qquad [A\text{-}4]$$

$$C^- \underset{k_{-3}}{\overset{k_3}{\rightleftharpoons}} C_{ads}^- \qquad [A\text{-}5]$$

$$C^- + C_{ads} \xrightarrow{k_4} C_2^- \qquad [A\text{-}6]$$

In relatively stable cells B is formed in minute quantities so that its removal from the surface is of no kinetic implication. However the removal of sulfur is the rate-limiting process (20) and is represented in Eq. [A-6]. Assuming steady state for p_s^*, θ_{red}, and θ_{ox} we obtain for them the following expressions

$$p_s^* = J_\phi/(S_r + k_1 + k_2\theta_{red}) \qquad [A\text{-}7]$$

$$\theta_{red} = \frac{k_3(C_{red})(1 - \theta_{ox})}{k_3(C_{red}) + k_{-3} + k_2 p_s^*} \qquad [A\text{-}8]$$

and

$$\theta_{ox} = \frac{k_2 p_s^* \theta_{red}}{k_4(C_{red})} \qquad [A\text{-}9]$$

Substituting [A-9] into [A-8] we obtain for θ_{red}

$$\theta_{red} = \frac{k_3(C_{red})}{k_3(C_{red})\left(1 + \frac{k_2 p_s^*}{k_4(C_{red})}\right) + k_{-3} + k_2 p_s^*} \qquad [A\text{-}10]$$

Therefore the three photocurrents

$$J_{rec} = S_r p_s^* \qquad [A\text{-}11a]$$

$$J_{cor} = k_1 p_s^* \qquad [A\text{-}11b]$$

and

$$J_{reg} = k_2 p_s^* \theta_{red} \qquad [A\text{-}11c]$$

can be expressed by Eq. [A-7] and [A-10].

To see the usefulness of that model we examine some limit cases

$$\phi \to \infty \quad \text{(strong light intensity)}$$

In this limit

$$p_s^* \to \infty \quad \text{and} \quad \theta_{red} \to 0$$

and from Eq. [A-8] $\theta_{ox} \to 1$. Whereas J_{cor} and J_{rec} increase indefinitely, $J_{reg} = k_4(C_{red})$ since $k_{-3} >> k_4$, so that the regenerative mode depends on the rate of removal of the oxidized species from the electrode surface.

We see that whereas the rate of C_{red} adsorption determined J_{reg} under strong light intensity in the model presented in the text, here C_{ox} desorption is determining J_{reg}, which shows the equivalence between these two processes in the two models.

Other limit cases can be handled similarly. For example, when $C^- \to \infty$ then $\theta_{red} \to 1$ and $\theta_{ox} \to 0$. Under these conditions the density of holes on the semiconductor surface is minimal, $p_s^* = J_\phi/(S_r + k_1 + k_2)$,

the rate of hole transfer across the interface J_{reg} is maximum and J_{rec} and J_{cor} are minimal.

REFERENCES

1. H. Gerischer, *J. Electroanal. Chem.*, **82,** 133 (1977); *Faraday Discuss.*, **70,** 6 (1980).
2. A. J. Bard and M. S. Wrighton, *This Journal,* **124,** 1706 (1977).
3. D. Cahen, J. Manassen, and G. Hodes, *Sol. Energy Mater.*, **1,** 343 (1979).
4. G. Hodes, J. Manassen, and D. Cahen, *Nature* (London), **261,** 403 (1976); *Bull. Isr. Phys. Soc.*, **22,** 100 (1976).
5. A. B. Ellis, S. W. Kaiser, and M. S. Wrighton, *J. Am. Chem. Soc.*, **98,** 1635, 6418, 6855 (1976).
6. B. Miller and A. Heller, *Nature* (London), **262,** 680 (1976); *This Journal,* **124,** 697 (1977).
7. H. C. Chang, A. Heller, B. Schwarz, S. Menezes, and B. Miller, *Science,* **196,** 1097 (1977).
8. D. Cahen, G. Hodes, and J. Manassen, *This Journal,* **125,** 1623 (1978).
9. H. Gerischer and J. Gobrecht, *Ber. Bunsenges. Phys. Chem.*, **82,** 520 (1978).
10. R. Noufi, P. A. Kohl, J. W. Rogers, J. M. White, and A. J. Bard, *This Journal,* **126,** 949 (1979).
11. K. T. L. Desilva and D. Haneman, *ibid.*, **127,** 1554 (1980).
12. G. Hodes, J. Manassen, and D. Cahen, *J. Am. Chem. Soc.*, In press.
13. T. Inoue, T. Watanabe, A. Fujishima, and K. Honda, *Bull. Chem. Soc. Jpn.*, **52,** 1243 (1979).
14. F. Cardon, W. P. Gomes, F. Vanden Kerchove, D. Vanmaekelbergh, and F. Van Overmeire, *Faraday Discuss.*, **70,** 7 (1980).
15. G. Hodes, J. Manassen, and D. Cahen, *This Journal,* Submitted.
16. D. Cahen, G. Hodes, J. Manassen, and R. Tenne, in ACS Series, A. J. Nozik, Editor, **146,** 369 (1980).
17. (a) R. Tenne and G. Hodes, *Appl. Phys. Lett.*, **37,** 428 (1980); (b) R. Tenne, *Appl. Phys.*, **25,** 13 (1981); (c) N. Müller and R. Tenne, *Appl. Phys. Lett.*, **39,** 283 (1981).
18. G. Hodes, *Nature* (London), **285,** 29 (1980).
19. M. Russak, J. Reichman, H. Witzke, S. K. Deb, and S. N. Chen, *This Journal,* **127,** 725 (1980).
20. D. Lando, J. Manassen, G. Hodes, and D. Cahen, *J. Am. Chem. Soc.*, **101,** 3969 (1979).
21. A. B. Ellis and B. R. Karas, *Adv. Chem. Ser.*, **184,** 185 (1980), and other references of that group.
22. Y. Nashimoto, S. Fuyuki, T. Akutagawa, and S. Hayakawa, *Jpn. J. Appl. Phys.*, **20,** 565 (1981).
23. W. W. Gartner, *Phys. Rev.*, **116,** 84 (1959).
24. R. H. Wilson, *This Journal,* **126,** 1187 (1979).
25. Z. Harzion, N. Groitoru, and S. Gootesfeld, *ibid.*, **128,** 551 (1981).
26. J. S. Newmann and C. W. Tobias, *ibid.*, **109,** 1183 (1962).
27. P. L. Allen and N. Hickling, *Trans. Faraday Soc.*, **53,** 1626 (1957).
28. K. W. Freese, Jr., M. J. Madou, and S. R. Morrison, *J. Phys. Chem.*, **84,** 3172 (1980).
29. G. Hodes, J. Manassen, and D. Cahen, *Sol. Energy Mater.*, **4,** 373 (1981).
30. A. Heller, G. P. Schwartz, R. G. Vadimsky, S. Menezes, and B. Miller, *This Journal,* **125,** 1156 (1978).
31. R. Tenne, *ibid.*, **129,** 142 (1982).
32. N. Müller, R. Tenne, and D. Cahen, *J. Electroanal. Chem.*, In press.

Competition Reactions at α-Fe_2O_3 Photoanodes

Ruth Shinar and John H. Kennedy*

Department of Chemistry, University of California, Santa Barbara, California 93106

ABSTRACT

Photoanodic oxidation of iodide and bromide ions at polycrystalline doped α-Fe_2O_3 electrodes in competition with oxygen production was investigated in the *p*H range 0-13 in aqueous media. It appears that at high *p*H values only iodide oxidation could compete effectively with water oxidation. However, in addition to the photoelectrochemical oxidation of iodide, evidence for secondary reactions involving electrogenerated species was observed mainly in highly basic solutions. Adsorption of I^- plays a significant role in the reaction as well as in the photoelectrochemical properties of α-Fe_2O_3. α-Fe_2O_3 photoanodes were found to be stable under illumination in solution at *p*H 0 with or without the presence of bromide ions.

Competition reactions involving halide and hydroxide ions have been studied by Fujishima *et al.* (1) and by Hirano and Bard (2). These investigations were carried out at TiO_2 electrodes at relatively low *p*H values.

The I_2/I^- couple was also studied at n-$MoSe_2$ layer-type crystals (3-5). Measurements indicated a specific surface reaction between the I_2/I^- couple and n-$MoSe_2$, and as a result of this interaction, induced a negative shift in the flatband potential.

Halide ions were also used to stabilize ZnO photoanodes in aqueous solutions (6). Halide ion oxidation competed with the decomposition of ZnO, and the competitive processes depended on light intensity. Effects of illumination intensity on competitive oxidation of halide ions were also studied at stable photoanodes (7). However, experiments were performed mainly on TiO_2 electrodes at low *p*H values. Preliminary results on the competitive oxidation of halides at α-Fe_2O_3 photoanodes in the *p*H range 9-13 were presented previously (8).

In the present work we have studied the competitive oxidation of halide and hydroxide ions over a wide *p*H range at 1 atom percent (a/o) TiO_2- and 1 a/o SiO_2-doped α-Fe_2O_3 photoanodes. Current-potential curves and spectral response for these electrodes have been reported previously (9).

Experimental

Electrodes were prepared from high purity α-Fe_2O_3 (Apache Chemical Company and Alfa Products). The high purity α-Fe_2O_3 was doped with 1 a/o TiO_2 and 1 a/o SiO_2 by mixing appropriate amounts in acetone for about 24 hr. The acetone evaporated while mixing. The dry powder (0.2-0.5g) was pressed at 10,000 psi. The TiO_2-doped pellets were sintered at 1300°C for 4 hr and the 1 a/o SiO_2-doped pellets were sintered at 1360°C for about 20 hr. After sintering, the pellets were quenched to room temperature. A copper wire was attached to the electrodes by applying silver epoxy. The electrode and the wire were then sealed in a glass tube with epoxy resin. The resistances of the electrodes, as measured with a conductivity bridge at 1 kHz, were about 1-2 kΩ.

Experiments were carried out in a two-compartment cell separated by a fritted glass disk. One compartment contained the semiconductor electrode facing a quartz window, and the other compartment contained a

* Electrochemical Society Active Member.

Key words: halides, iron oxide, oxygen photoelectrochemical cells.

platinum counterelectrode. In order to collect the oxygen evolved at the electrode efficiently we have also used a cell in which the compartment containing the semiconductor electrode was closed. The upper part of this compartment was a burette in which the oxygen was collected.

The light source was a 150W Xe lamp. Light was focused on the semiconductor electrode by means of a quartz lens. A light intensity of 380 mW/cm^2 was usually used.

Photocurrents *vs.* potential plots were taken using a PAR Model 174 and an X-Y recorder. Chemical reactions were investigated under constant potential, and the photocurrent was recorded as a function of time.

The amount of iodine (and other possible oxidation products such as IO^- and IO_3^- that will yield I_2 in acid in the presence of an excess of I^-), was measured by adding an excess of thiosulfate to the acidified solution and back-titrating using a constant current coulometer until the blue starch-iodine end point was reached. I_2 disproportionates rapidly in base to give I^- and IO^-, and IO^- further disproportionates to produce IO_3^-. However, in the acidified solution iodate will react with excess of iodide to yield iodine which is then detected by the above procedure. Hydrogen peroxide, bromine, and/or bromate concentrations were determined by adding an excess of iodide to the solution and then following the above procedure.

Results

α-Fe_2O_3 photoanodes are known to be stable over a wide *p*H range (10). Recently (11), stability in highly acidic solutions, containing no added redox couples, has been reported.

The amount of O_2 collected accounted for 100% (within experimental error) of the photocurrent in H_2SO_4, KOH, and buffered K_2SO_4 solutions in the *p*H range 0-14. Quantum yields have been reported previously (12) and were about 25-50% at 400 nm. However, the main objective in this study was the competition between different chemical reactions and was carried out using polychromatic light. No significant amount of H_2O_2 was detected even in the highly acidic solutions. The percentage of oxygen collected was independent of the applied voltage (for conditions of zero dark current) or of the light intensity in the range 70-800 mW/cm^2.

All the photoelectrochemical experiments were carried out under conditions where the dark current was practically zero. No oxygen was produced in the dark.

The competition between O_2 production and iodide oxidation was investigated in the *p*H range 9-13. Experiments were normally carried out in air-saturated solutions, but saturating the solutions with N_2 did not alter the results in this *p*H range. At *p*H values lower than 9, iodide was easily oxidized by dissolved oxygen or by oxygen produced at the electrode under an N_2 atmosphere.

The iodide concentration was varied from 0-1.8M, and the contribution of its oxidation to the photocurrent was measured in both stirred and unstirred solutions as shown in Fig. 1 for a 1 a/o TiO_2-doped electrode at *p*H 13. The amount of iodate (which was probably the main product in highly basic solutions) in the stirred solutions was measured after 1.5 hr of illumination, except for the lowest concentration of I^- where a longer irradiation period was used. Surprisingly, a stirring effect was observed even when high concentrations of iodide were used, and the percentage of iodate produced was higher the longer the irradiation period. It should be noted that the current density *vs.* potential was the same for stirred and unstirred solutions. Essentially the same results were obtained at 1 a/o SiO_2-doped electrodes.

A decrease in the oxygen percentage with time was observed in stirred solutions. This decrease was followed by an increase in the iodate amount. Such a behavior was not observed in unstirred solutions. Table I shows the percentage of oxygen production as a function of the illumination period for a 1 a/o SiO_2-doped electrode in a stirred solution.

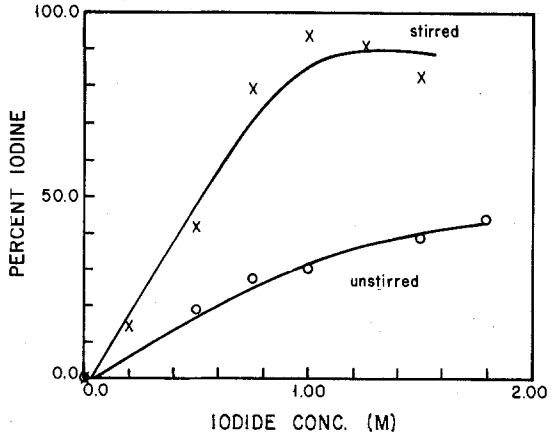

Fig. 1. Percentage of iodide oxidation as a function of iodide concentration in 0.1M NaOH for stirred and unstirred solutions. 1 a/o TiO_2-doped α-Fe_2O_3 electrode.

Blank experiments utilizing a disconnected electrode at *p*H 13 containing up to 1.7M KI and lasting up to 20 hr indicated that no oxidation occurred while stirring the solution under illumination. Also, no oxidation occurred in the dark for electrodes biased at a potential at which no dark current was observed. The amount of oxidation was also checked in iodide solutions through which oxygen was bubbled for about 5 hr. No oxidation was detected. However, small amounts of iodate ($\sim$ 2 μequiv. in 20 ml of 0.25M KI/0.1M NaOH) were detected in the dark and under illumination when, in addition to oxygen bubbling, a disconnected electrode was inserted into the solution. After completing this series of experiments photocurrents *vs.* potential plots were recorded again in 0.1M NaOH, and the photocurrents were found to be unchanged.

The influence of light intensity was checked by using neutral density filters. Photocurrent was directly proportional to light intensity down to $\sim$ 9% of the full light, the lowest intensity studied.

Measurements were also carried out in solutions containing bromide ion. At high *p*H (0.1M NaOH) neither bromine nor bromate was produced in solutions containing up to 1.5M KBr in unstirred or stirred solutions. Oxygen formation accounted for 100% of the photocurrent.

Following these experiments, iodine and bromine production were investigated at *p*H 9. Their contribution to the photocurrent as a function of the halide concentration is shown in Fig. 2 and 3, respectively, for a 1 a/o TiO_2-doped electrode. The bromine production increased slowly with bromide concentration and little or no stirring effect was apparent. The rest of the current was accounted for by O_2 production.

Plateau photocurrents at a 1 a/o TiO_2-doped electrode, at *p*H 9, were higher than at *p*H 13 and reached

Table I. Percentage of oxygen measured for different time intervals during illumination. 1 a/o SiO_2-doped α-Fe_2O_3 electrode. Solution: 0.5M KI/0.1M NaOH.

Total illumination time (hr)	Time interval (hr)	% Oxygen produced for the given time interval
0.7	0.7	74
1.1	0.4	62
2.0	0.9	34
4.0	2.0	19
5.0	1.0	14
21.0	16.0	6

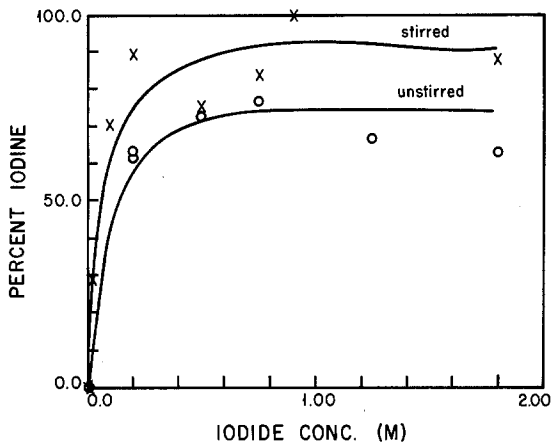

Fig. 2. Iodine production as a function of iodide concentration at pH 9 for stirred and unstirred solutions. 1 a/o TiO_2-doped α-Fe_2O_3 electrode.

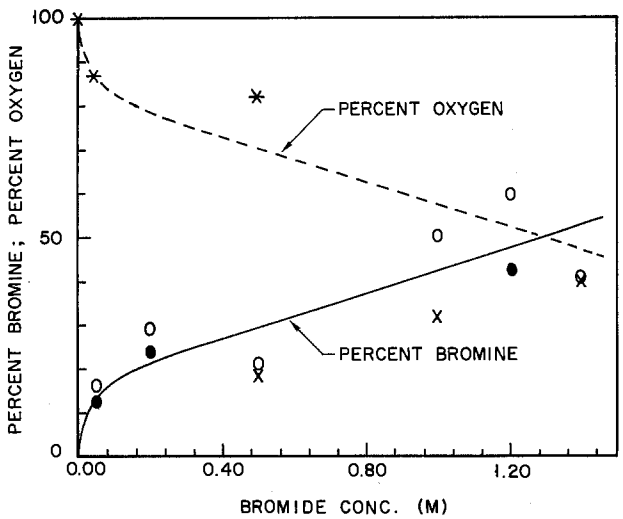

Fig. 3. Bromine (○, ×, ●) and oxygen (*) percentage as a function of bromide concentrations at pH 9 for stirred and unstirred solutions. ○, Stirred solutions at 1 a/o TiO_2-doped electrode; ×, unstirred solutions at 1 a/o TiO_2-doped electrode; ●, unstirred solutions at 1 a/o SiO_2-doped electrode; *, unstirred solutions at 1 a/o SiO_2-doped electrode. Broken line: calculated O_2% assuming O_2% = 100-Br_2%.

a value of 4.2 mA/cm² at 0.9V *vs.* SCE in 0.75M KI solutions, compared to a value of 1.3 mA/cm² in the basic solution.

The competitive oxidation of iodide was also measured as a function of pH while keeping the iodide concentration at 0.75M KI. The pH was maintained with mixtures of borax and NaOH, and results for a 1 a/o TiO_2-doped electrode are shown in Fig. 4.

Following these experiments photocurrents *vs.* potential were remeasured in 0.1M NaOH. An increase by a factor of three was observed at 0.9V *vs.* SCE for the 1 a/o TiO_2-doped electrode. Iodate percentage in a stirred basic solution was as before (77% compared to 79%), after ~ 1.5 hr of illumination, but in the unstirred solution an increase from 28 to 64% was observed. This, too, is shown in Fig. 4.

Washing the electrode with water and immersing it in water for 48 hr had no effect, and the photocurrents remained relatively high. On the other hand, heating the electrode to ~130°C for about 1 hr reduced the photocurrents back to their original values. The dark currents remained the same after all treatments. It was also noted that the increase in the photocurrents was not a result of a decrease in the electrode's resistance. This enhanced photocurrent was stable for over 3 months and even after working in different electrolytes

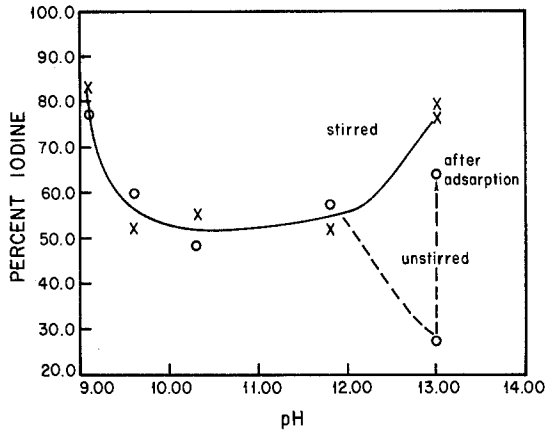

Fig. 4. Iodine and iodate production as a function of pH in stirred (×) and unstirred (○) solutions at 1 a/o TiO_2-doped electrode. The vertical line shows the change in iodate percentage in an unstirred solution after treatment with iodide at pH 9.

iodine was still present on the electrode's surface according to surface analysis results.

Blank experiments at pH 9 were carried out in 0.1M KI for up to 16 hr as described before for pH 13. No iodine was detected. At higher iodide concentrations some iodine was produced probably by air oxidation during long periods of irradiation. Amounts of iodine were therefore determined after a maximum of 2 hr of illumination. In these short periods no iodine was detected in blank experiments nor in the dark.

Bromide oxidation was also studied at pH 0. Results for a 1 a/o SiO_2-doped electrode are shown in Fig. 5. No deterioration of the electrode was observed in this solution. A calculated curve of O_2 percentage, assuming only O_2 and Br_2 production by the photogenerated holes, is also shown in Fig. 5, while the points are experimental values. No dependence on light intensity or applied potential was observed.

Discussion

Iodide solutions at pH 13 remained colorless during the course of oxidation under illumination. This may be due to a rapid disproportionation of iodine at pH 13 or to a direct formation of higher oxidized forms such as IO^- and IO_3^-. A yellow color was formed at the electrode's surface at pH $\leq$ 12 clearly indicating the formation of iodine at the surface under these conditions.

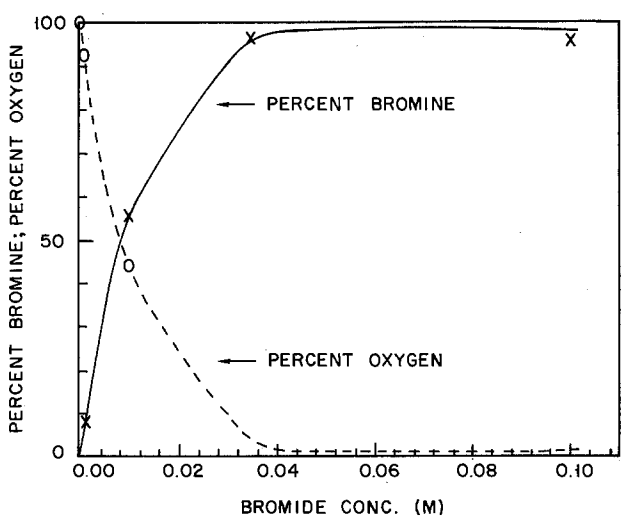

Fig. 5. Bromine and oxygen percentage as a function of bromide concentration in 1M H_2SO_4 solutions. 1 a/o SiO_2-doped α-Fe_2O_3 electrode. Broken line: calculated O_2% assuming O_2% = 100-Br_2%.

Figures 1-3 and 5 show that the competitive oxidation of halide ion is dependent on the halide concentration in solution. However, in the case of iodide ion the production of iodate and/or iodine increases rapidly with increasing iodide concentration especially in stirred solutions while in the case of bromide ion the production of bromine and/or bromate increases only slowly at pH 9 with increasing bromide concentration.

Little difference was seen between stirred and unstirred solutions for iodide oxidation at pH 9 and for bromide oxidation at all pH values investigated. Thus, it is apparent that oxidation of iodide at pH 13 is a more complicated process. It should be noted that the chemical product at pH 13 is IO_3^-, and the oxidation of I^- to IO_3^- would require 6 photogenerated holes. One likely intermediate in this oxidation is IO^-, which can be produced as shown in Eq. [1]

$$I^- + 2\,OH^- + 2h \rightarrow IO^- + H_2O \qquad [1]$$

IO^- is known to disproportionate to give IO_3^-

$$3IO^- \rightarrow IO_3^- + 2I^- \qquad [2]$$

However, IO^- is also an oxidizing agent ($E^\circ = +0.49$V *vs.* NHE) and could react with oxygen species such as ·OH at the electrode to give O_2. Therefore, stirring of the solution could remove IO^- from the electrode surface eliminating surface reactions and allow reaction [2] taking place in the bulk to predominate.

The effect of time on the oxygen percentage shown in Table I is not clearly understood. However, reaction [2] is certainly not simple and, if self-catalyzed, would increase in speed as the IO_3^- concentration in solution increased. Other plausible explanations could be envisaged for the observed effect.

The increase in iodate percentage at pH 13 in an unstirred solution after exposure of the electrode to iodide solutions at pH 9 (Fig. 4) can be explained by viewing the α-Fe_2O_3 as a chemically modified electrode. The strongly adsorbed I^- allows the electrode to behave as if it were in a solution at the lower pH and containing iodide ion leading to higher currents and greater I^- oxidation percentage. Thus, surface effects appear to play an important role in this system. It should be realized that in a 0.1M base adsorption of OH^- may be preferred over adsorption of I^-. At pH 9, on the other hand, the hydroxide concentration is only 10^{-5}M and I^- adsorption may compete effectively. The photocurrent enhancement observed after soaking an electrode in KI solutions at pH 9 required about 3 weeks to reach a plateau value (9). Such a slow process may reflect not only adsorption on the surface but also penetration of I^- into the bulk of the electrode along grain boundaries. One other observation should be noted. The enhancement varied with the electrode. Electrodes which exhibited low photocurrents initially showed greater enhancement than those exhibiting high photocurrents initially. Thus it appears that the iodide treatment removes sites leading to inefficiency. For example, adsorption may occur at surface imperfections which act as recombination sites. Similar observations have been made by Ginley and Butler in their study of $SrTiO_3$ aged in KF (13).

In unstirred iodide solutions at pH 13 the relative contributions of iodide and hydroxide oxidation to the photocurrent were the same for different illumination periods. Thus, it appears that in the unstirred solutions iodide ions were mainly oxidized by photogenerated holes, however, some contribution from the secondary reaction cannot be ruled out.

Somewhat surprisingly the α-Fe_2O_3 electrodes appear to be stable under illumination (>100 hr) at pH 0 with or without added bromide ion. No Fe(III) was found in solution after irradiation. All photocurrent could be accounted for by H_2O or Br^- oxidation as shown in Fig. 5. In solutions containing >0.04M Br^-, essentially all photocurrent resulted in Br^- oxidation.

Oxidation of Cl^- does not compete with OH^- oxidation in neutral or basic solution while in acid solution it appears more complicated than I^- or Br^- oxidation. Little O_2 was observed while at the same time only ~15% of the current could be attributed to production of Cl_2. Intermediates formed and final products are presently under study using RRDE techniques.

Acknowledgments

The authors thank the Division of Chemical Science, Office of Basic Energy Science, U.S. Department of Energy for financial support of this project. The authors also thank Professor Somorjai and Dr. Langell at the Lawrence Berkeley Laboratories for carrying out the surface analysis experiments.

Manuscript submitted Aug. 2, 1982; revised manuscript received *ca.* Nov. 15, 1982.

Any discussion of this paper will appear in a Discussion Section to be published in the December 1983 JOURNAL. All discussions for the December 1983 Discussion Section should be submitted by Aug. 1, 1983.

Publication costs of this article were assisted by the University of California.

REFERENCES

1. A. Fujishima, T. Inoue, and K. Honda, *J. Am. Chem. Soc.*, **101**, 5582 (1979).
2. K. Hirano and A. J. Bard, *This Journal*, **127**, 1056 (1980).
3. H. Tributsch, *Ber. Bunsenges. Phys. Chem.*, **82**, 169 (1978).
4. H. Tributsch, H. Gerischer, C. Clemen, and F. Bucher, *ibid.*, **83**, 655 (1979).
5. H. Tributsch, *Solar Energy Mater.*, **1**, 257 (1979).
6. T. Kobayashi, H. Yoneyama, and H. Tamura, *Chem. Lett.*, 457 (1979).
7. T. Kobayashi, H. Yoneyama, and H. Tamura, *J. Electroanal. Chem. Interfacial Electrochem.*, **122**, 133 (1981).
8. J. H. Kennedy, R. Shinar, and J. P. Ziegler, Third International Conference on Photochemical Conversion and Storage of Solar Energy, Paper X-3, University of Colorado, Boulder, Colorado, August 1980.
9. J. H. Kennedy, R. Shinar, and J. P. Ziegler, *This Journal*, **127**, 2307 (1980).
10. K. G. McGregor, M. Calvin, and J. W. Otvos, *J. Appl. Phys.*, **50**, 369 (1979).
11. J. H. Kennedy and M. Anderman, *This Journal*, **130**, 848 (1983).
12. R. Shinar and J. H. Kennedy, *Solar Energy Mater.*, **6**, 323 (1982).
13. D. S. Ginley and M. A. Butler, Third International Conference on Photochemical Conversion and Storage of Solar Energy, Paper IX-2, University of Colorado, Boulder, Colorado, August 1980.

Technical Notes

Spectroscopic Evidence for the Formation of Polysulfide Species during Charging of an Li-Al/S Couple

Victor A. Maroni and Zygmunt Tomczuk*

Argonne National Laboratory, Chemical Technology Division, Argonne, Illinois 60439

The purpose of this communication is to report recently obtained absorption spectrophotometric evidence for the formation of polysulfide species during the charging of Li-Al/S cells with molten LiCl-KCl electrolyte. The results are part of an ongoing series of studies to characterize the electroactive species present in Li-Al/metal sulfide battery systems during various stages of charge/discharge, with particular emphasis on those species that may be contributing to self-discharge.

There have been numerous prior studies of the formation of polysulfide species in molten salts (1-5) and in other aprotic media such as dimethyl sulfoxide (6). Gruen *et al.* (1) reported maxima at 31,400, 25,600, and 16,800 cm^{-1} in the absorption spectra of solutions of Li_2S-sulfur mixtures in LiCl-KCl. Their studies, carried out between 600° and 800°C, indicated an equilibrium involving sulfur (S_2), sulfide (S^{2-}), S_2^-, and S_3^-. They assigned the bands at 25,600 and 16,800 cm^{-1} to S_2^- and S_3^-, respectively, but did not make a specific assignment of the band at 31,400 cm^{-1}. Giggenbach (2) observed maxima at 25,000 and 17,000 cm^{-1} in both molten KSCN and borated glasses that were doped with sulfur prior to quenching. The two bands were attributed to S_x^{2-} and S_2^-, respectively. Martin *et al.* (6) studied solutions of Na_2S_x ($x = 4, 6, 8$) in dimethyl sulfoxide. They reported a maxima at 16,200 cm^{-1} for all values of x, and a second maxima which shifted from 20,000 to 24,000 cm^{-1} as the value of x decreased.

Bodewig and Plambeck conducted both electrochemical (3) and spectroelectrochemical (4) studies of the S(l)/LiCl-KCl/Li cell. In their experiments, they generated polysulfide ions by electrochemically discharging a pool of liquid sulfur in contact with LiCl-KCl. They monitored the absorption spectrum of the electrolyte phase as a function of the extent of discharge (presumably corresponding to production of increasing amounts of S^{2-}), and observed the steady growth in absorbance of a band at 17,100 cm^{-1}. They attributed this absorption to one or more unspecified polysulfide anions since there was evidence in their data for an equilibrium involving more than one such species.

More recently, Chivers (7) has evaluated a wide body of data on polysulfides (including those discussed above) and has rather soundly argued that the band at 16,700 ± 500 cm^{-1} is due to S_3^-, a species which generally characterizes the deep blue color of a variety of alkali polysulfide-containing media. In a recently published paper, Fehrmann *et al.* (5) present unequivocal evidence from ESR, Raman, and absorption spectrophotometric studies (on sulfide-containing CsCl-$AlCl_3$ melts) to affirm this argument.

Experimental

The experiments conducted in our laboratory have been of two basic types. In one type of experiment, we prepared solutions of Li_2S and Li_2S-FeS mixtures in LiCl-KCl and generated polysulfide species *in situ* by stepwise oxidation of the S^{2-} to S° using controlled additions of oxygen. In the second type of experiment, a solution of Li_2S in LiCl-KCl was subjected to electrolysis to again oxidize S^{2-} to S°. The samples were prepared using high purity Li_2S and FeS and polarigraphic-grade LiCl-KCl eutectic (8). Solutions were pre-equilibrated in a helium atmosphere glove box (H_2O < 1 ppm), filtered through fine quartz frits under helium pressure, and then loaded into 1 cm path-length quartz spectrophotometer cells. In the case of the chemical oxidation experiments, dry air was admitted to the gas plenum above the melt in the spectrophotometer cell.

For the electrochemical experiments, a 1.6 mm molybdenum rod was used as the positive electrode and aluminum mesh packed in a boron nitride sleeve and attached to a molybdenum rod was used as the negative electrode. The electrodes were placed in a 10 mm path-length quartz spectrophotometer cell fused to a 200 mm long, 20 mm diam quartz tube. The quartz tube terminated with a 29/42 male ground joint. A mating female cap containing gasketed feed throughs to accommodate the electrode leads and a valved evacuation port were used to seal the cell. Current was supplied and coulombs counted with a Model 173 Princeton Applied Research Potentiostat. Absorption spectra were recorded with a Cary 17-H Spectrophotometer. A furnace assembly designed specifically for high temperature measurements with the Cary 17-H was used in this study.

Results and Discussion

The results of a typical chemical oxidation experiment are shown in Fig. 1. In this experiment, a solution of Li_2S-FeS in LiCl-KCl eutectic at approximately 10% of the saturation limit was examined by absorption spectroscopy at 400° ± 5°C. The initial solution (curve a in Fig. 1) was green in color and was characterized by a sharp absorption band at ~25,600 cm^{-1}, which we presume is due to S_2^- following the work of Gruen *et al.* (1). Upon introduction of successive aliquots of dry air, this band gradually gave way to a second band at 17,200 cm^{-1}, which is indicative of S_3^- according to Chivers (7). In fact, the solution corresponding to curve d in Fig. 1 was the deep blue color described by Gruen (1), Chivers (7), and others (4-6). With continued addition of dry air, the LiCl-KCl solution eventually became colorless, and there was evidence of some sulfur condensation in the cold end of the plenum region above the salt melt.

The spectroelectrochemical measurement was made in an optical configuration similar to that used by Bodewig and Plambeck (4). The molybdenum positive electrode was inserted in the cell along one of the rectangular corners and extended all the way to the bottom of the cell. This was done so that any absorbing species formed along the surface of the posi-

* Electrochemical Society Active Member.
Key words: cell, inorganic, spectroscopy, polysulfide.

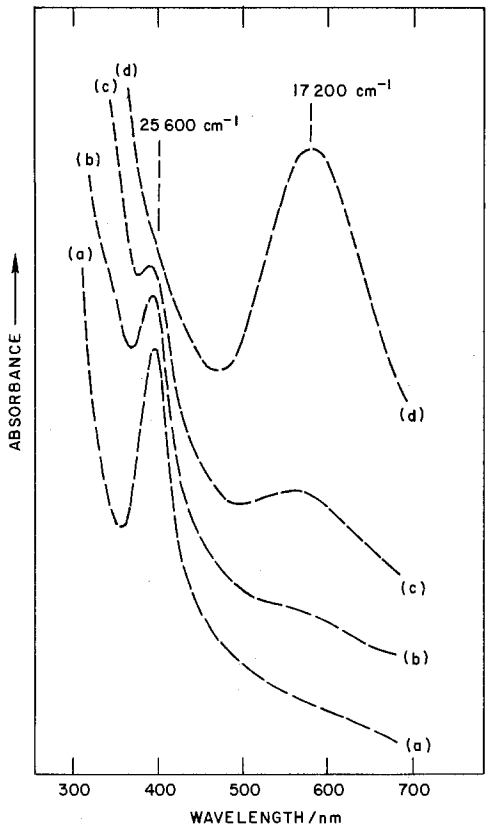

Fig. 1. Electronic absorption spectra of an Li_2S-FeS solution in LiCl-KCl eutectic as-prepared (curve a) and after successive oxygen additions (curves b through d). All spectra recorded at 400° ± 5°C.

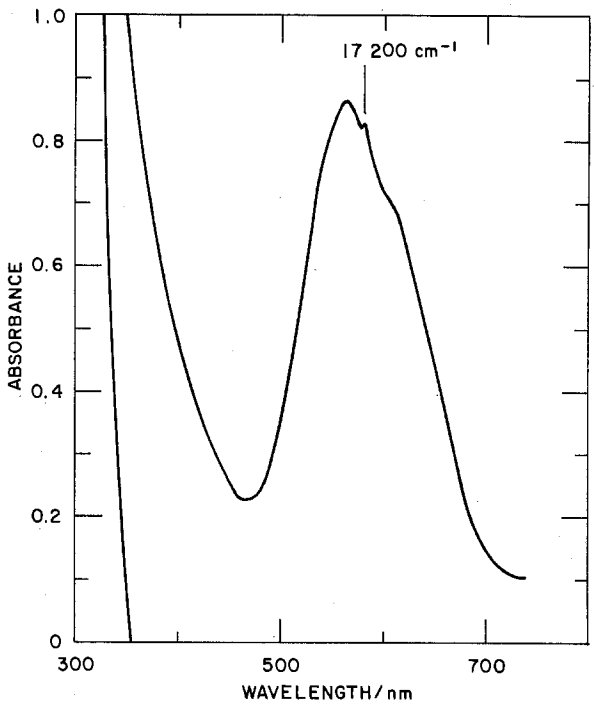

Fig. 2. *In situ* electronic absorption spectrum of the species produced during charging of an Li-Al/LiCl-KCl/S electrochemical cell employing molybdenum current collectors. Total number of coulombs charged was 5.8.

tive electrode would be in the optical path of the spectrophotometer source beam. The tip of the negative electrode (aluminum electrode) was immersed in the salt melt to a level just a few millimeters below the surface. At this point it was several centimeters above the optical path of the source beam. The melt studied was a near-saturated solution of Li_2S in LiCl-KCl. The absorption spectrum of this melt obtained after charging the Li-Al/LiCl-KCl/S couple to ~2.2V (IR included) is shown in Fig. 2. This spectrum is very much the same as that reported by Bodewig and Plambeck (4) and that shown in Fig. 1, curve d. The difference between this experiment and the one performed by Bodewig and Plambeck is that the negative electrode was Li-Al (instead of pure Li), and there was very little excess sulfur at the positive electrode. The state of charge at which the deep blue color began to appear (as evidenced by the absorption band at ~17,200 cm^{-1}) indicates that the polysulfide species does not form until the sulfur activity at the positive electrode is high enough to generate a potential >2.0V *vs.* Li-Al.

The results of these experiments are in agreement with those of Gruen (*et al.*) (1) and Bodewig and Plambeck (4). The data in Fig. 1 support the contention of the previous studies that there exists an equilibrium involving more than one sulfide/polysulfide species. During the spectroelectrochemical experiment (*e.g.*, Fig. 2), there was no evidence for the formation of the species giving rise to the 25,600 cm^{-1} absorption in Fig. 1. We deduce from the results in Fig. 1 that this latter species corresponds to a lesser state of charge of the Li-Al/S couples than S_3^- (17,200 cm^{-1}), but the range of S/S^{2-} activity over which it dominates the absorption spectrum may be quite narrow. Also, although the S^{2-}/Fe ratio used in the air oxidation experiment was quite high and the amount of iron in solution was very small (~8 ppm), we have not yet entirely eliminated the possibility that the 25,600 cm^{-1} band is due to an iron sulfide complex.

We conclude from these experiments that at higher sulfur activities one can expect increasingly greater amounts of soluble polysulfide species in both Li-Al/S and Li-Al/MS_x cells (M = *e.g.*, Fe, Co, Ni). These species will tend to diffuse toward the Li-Al electrode where they can react with lithium (in the electrolyte or at the Li-Al electrode surface) to form the less soluble species Li_2S. Work on this research activity is continuing in an effort to more thoroughly characterize the sulfide-species equilibria in Li-Al/metal sulfide electrochemical cells.

Acknowledgments

The authors would like to express their gratitude to D. R. Vissers, F. A. Cafasso, R. K. Steunenberg, and D. L. Barney for their support of this work. This work was conducted under the auspices of the U.S. Department of Energy, Office of Energy Systems Research and Office of Basic Energy Sciences.

Manuscript submitted Oct. 27, 1982; revised manuscript received *ca.* Dec. 15, 1982.

Any discussion of this paper will appear in a Discussion Section to be published in the December 1983 JOURNAL. All discussions for the December 1983 Discussion Section should be submitted by Aug. 1, 1983.

Publication costs of this article were assisted by Argonne National Laboratory.

REFERENCES

1. D. M. Gruen, R. L. McBeth, and A. J. Zielen, *J. Am. Chem. Soc.*, **93**, 6691 (1971).
2. W. Giggenbach, *Inorg. Chem.*, **10**, 1308 (1971).
3. F. G. Bodewig and J. A. Plambeck, *This Journal*, **116**, 607 (1969).
4. F. C. Bodewig and J. A. Plambeck, *ibid.*, **117**, 904 (1970).
5. R. Fehrman, S. Von Winbush, G. N. Papatheodorou, R. W. Berg, and N. J. Bjerrum, *Inorg. Chem.*, **21**, 3396 (1982).
6. R. P. Martin, W. H. Doub, Jr., J. L. Roberts, Jr., and D. T. Sawyer, *ibid.*, **12**, 1921 (1973).
7. T. Chivers, *Nature*, **252**, 32 (1974).
8. Z. Tomczuk, S. K. Preto, and M. F. Roche, *This Journal*, **128**, 760 (1981).

Thermodynamics of Aqueous Sulfur Species to 300°C and Potential-*p*H Diagrams

Richard C. Murray, Jr.*

Gould Laboratories, Rolling Meadows, Illinois 60008

and Daniel Cubicciotti*

Electric Power Research Institute, Palo Alto, California 94303

Equilibria involving sulfur-containing species in high temperature water are important for understanding corrosion processes in water-cooled systems such as nuclear power reactors (1). For these applications, it is helpful to utilize the most current data even if some estimations are involved. Biernat and Robins (2) presented potential-*p*H diagrams for the stable sulfur species systems up to 300°C based on the room temperature thermodynamic data available at the time and the Criss-Cobble method for estimating high temperature heat capacities. Since that time, Cobble, Murray, and co-workers (3) have critically assessed available experimental heat of solution and equilibrium constant data to present improved estimates for heat capacities to 300°C. Also, the room temperature data have been re-evaluated by Wagman *et al.* in two reports (4, 5).

In the present paper, whenever possible, we have used the experimentally based heat capacities evaluated in Ref. (3) with the room temperature data of Ref. (4) and (5) to calculate the free energies of formation of aqueous sulfur species. In other cases, the free energy changes for relevant reactions were evaluated from free energies measured over moderate temperature ranges and extrapolated to 300°C using the "Principle of balance of identical like charges" (6). This type of extrapolation is felt to be an improvement over the Criss-Cobble method, which is adequate to 200°C, but is less reliable at higher temperatures (7). The electrode potentials presented below reflect the revised free energy of formation of $S_2O_3^{-2}$ given in Ref. (5) and, thus, differs somewhat from the potentials in Ref. (3). The heat capacity of $S_2O_3^{-2}$ was assumed to be the same as that for SO_4^{-2}, and that of $S_2O_8^{-2}$ the same as for $S_4O_6^{-2}$, to estimate the high temperature values.

Gibbs energies of formation for the aqueous species from Ref. (3-5) are given in Table I. The quantity tabulated ($\Delta\bar{G}^*$) is the standard Gibbs energy of formation of the substance referred to the elements in their standard states at 298 K. The reference states for the elements are not elevated temperature ones. This distinction is important when these values are combined with data from other sources. When values are combined with others in the table for a given temperature to obtain a balanced half or whole reaction, the room temperature reference states cancel so that the resultant Gibbs energy change represents the elevated temperature value. Also, since these are "standard" values, they represent dissolved substances at unit activity.

The Gibbs energies evaluated as above can be used to calculate standard electrode potentials for the half-cell reactions listed in Table II. These potentials, being standard values, refer to unit activity for each species in the half reaction. For dissolved substances, the activity coefficients are taken to be unity at infinite dilution.

Acid dissociation constants can also be evaluated from the Gibbs energy values. These are presented in Table III. It is interesting to note the increase of the *p*K values with temperature increase. This increase reflects the general decrease of stability of ionic species relative to un-ionized species or to less highly charged ionic species as temperature increases, which is primarily a result of the decrease of the dielectric constant of water (3).

The data in Tables II and III can be used to construct diagrams that present the conditions of electrochemical potential and acidity for which various species are stable. Such diagrams are generally called potential-*p*H diagrams or Pourbaix diagrams (9). Figure 1 is the diagram for the thermodynamically stable species at unit activities in the S-H_2O system at 300°C calculated from the present data. Figures 2-4 give the diagrams for individual sulfur-containing species relative to sulfide. Although these species are generally unstable with

Table I. Standard Gibbs energies of formation for aqueous sulfur species and related substances

	$\Delta\bar{G}^*$ (cal/mol)				
t (°C)	H_2S (aq)	HS^- (aq)	S(rh, mono, l)[a]	$HS_2O_3^-$ (aq)	$S_2O_3^{-2}$ (aq)
25	−6,660	2,880	0	−127,250	−124,900
50	−7,430	2,550	−200	−128,170	−125,250
			rhomb - - - - mono		
100	−9,190	2,100	−620	−130,030	−125,610
			mono - - - - liq		
150	−11,240	1,930	−1,120	−131,740	−125,420
200	−13,530	1,990	−1,700	−133,220	−124,610
250	−16,030	2,260	−2,310	−134,330	−123,070
300	−18,730	2,730	−2,970	−135,000	−120,760

t (°C)	$S_4O_6^{-2}$(aq)	H_2SO_3(aq)	HSO_3^-(aq)	SO_3^{-2}(aq)
25	−248,700	−128,560	−126,160	−116,300
50	−250,240	−130,010	−126,980	−116,062
100	−253,280	−133,260	−128,600	−115,226
150	−256,130	−136,940	−130,180	−113,919
200	−258,650	−141,000	−131,730	−111,854
250	−260,720	−145,400	−133,250	−108,664
300	−262,250	−150,100	−134,750	−104,184

t (°C)	HSO_4^-(aq)	SO_4^{-2}(aq)	$S_2O_8^{-2}$(aq)
25	−180,680	−177,970	−266,500
50	−181,330	−178,010	−267,960
100	−182,660	−177,790	−270,850
150	−183,980	−177,140	−273,540
200	−184,960	−175,770	−275,910
250	−185,460	−173,560	−277,820
300	−185,770	−170,830	−279,190

t (°C)	$H_2(g)$[a]	H_2O(l)	OH^-(aq)	$O_2(g)$[a]	e^-[b]
25	0	−56,687	−37,596	0	0
50	−790	−57,122	−37,498	−1,232	−395
100	−2,400	−58,096	−37,157	−3,737	−1,200
150	−4,060	−59,191	−36,650	−6,291	−2,030
200	−5,760	−60,392	−35,924	−8,888	−2,880
250	−7,500	−61,688	−34,890	−11,524	−3,750
300	−9,270	−63,069	−33,430	−14,197	−4,635

[a] Data from Ref (8).

[b] Values for H^+(aq) were taken to be zero at each temperature. On the basis of that convention, the standard Gibbs energy of formation of the conventional electron takes on the values shown, which are ½ of the values for H_2(g). (Note: The free energy of the conventional electron as used in electrode reactions is not to be confused with the free energy of a real electron in any state.)

* Electrochemical Society Active Member.

Key words: Pourbaix diagrams, sulfide, sulfate, sulfite, thiosulfate.

Table II. Half reactions and standard electrode potentials at elevated temperatures

A. Half reactions for reduction

(a) $S(c,l) + 2H^+(aq) + 2e^- = H_2S(aq)$
(b) $S_2O_3^{-2}(aq) + 6H^+(aq) + 4e^- = 2S(c,l) + 3H_2O(l)$
(c) $HS_2O_3^-(aq) + 5H^+(aq) + 4e^- = 2S(c,l) + 3H_2O(l)$
(d) $2H_2SO_3(aq) + 2H^+(aq) + 4e^- = S_2O_3^{-2}(aq) + 3H_2O(l)$
(e) $2H_2SO_3(aq) + 3H^+(aq) + 4e^- = HS_2O_3^-(aq) + 3H_2O(l)$
(f) $HSO_4^-(aq) + 3H^+(aq) + 2e^- = H_2SO_3(aq) + H_2O(l)$
(g) $HSO_4^-(aq) + 9H^+(aq) + 8e^- = H_2S(aq) + 4H_2O(l)$

B. Standard electrode potentials in acid solution[a] (reduction potentials)

t (°C)	Half reaction a	b	c	d	e	f	g
25	0.14	0.490	0.464	0.410	0.436	0.10	0.286
50	0.14	0.487	0.456	0.380	0.411	0.11	0.279
100	0.13	0.489	0.441	0.310	0.358	0.14	0.267
150	0.13	0.502	0.433	0.228	0.296	0.18	0.259
200	0.13	0.525	0.432	0.133	0.226	0.23	0.255
250	0.14	0.560	0.438	0.025	0.147	0.31	0.251
300	0.14	0.605	0.451	0.095	0.059	0.39	0.261

[a] These potentials are consistent in sign with those used by Pourbaix (9) but are opposite in sign to the standard oxidation potentials used in Section 3 of Ref. (3) or by Latimer (10). The standard electrode potential for the hydrogen couple is assumed to be zero at any temperature.

Table III. Acid dissociation constants

A. Reactions

a $H_2S(aq) = HS^-(aq) + H^+(aq)$
b $HS_2O_3^-(aq) = S_2O_3^=(aq) + H^+(aq)$
c $H_2SO_3(aq) = HSO_3^-(aq) + H^+(aq)$
d $HSO_3^-(aq) = SO_3^=(aq) + H^+(aq)$
e $HSO_4^-(aq) = SO_4^=(aq) + H^+(aq)$
f $H_2O = H^+(aq) + OH^-(aq)$

B. pK values[a]

t (°C)	a	b	c	d	e	f
25	6.99	1.72	1.76	7.23	1.99	13.99
50	6.75	1.97	2.05	7.38	2.25	13.27
100	6.61	2.59	2.73	7.83	2.85	12.26
150	6.80	3.26	3.49	8.40	3.53	11.64
200	7.17	3.98	4.28	9.18	4.25	11.30
250	7.64	4.70	5.08	10.27	4.97	11.20
300	8.18	5.43	5.85	11.66	5.70	11.30

[a] $pK = -\log_{10}$ (equilibrium constant of reaction as written in A).

respect to sulfate (especially at low concentrations of sulfate), they may, nevertheless, be present in finite concentrations at equilibrium, or as metastable species (*i.e.*, present in significant quantities because their reactions are slow), and are, therefore, worth consideration.

The boundaries between the stability regions were calculated by the methods indicated in Ref. (9). Boundaries between regions that involve a change in oxidation state of sulfur are defined by equations of the type

$$\mathbf{E} = \mathbf{E}^\circ - fk\,p\mathrm{H} + gk \log C_{ox} - hk \log C_{red}$$

in which E is the electrochemical potential; $\mathbf{E}^\circ$ the standard potential given in Table II; f, g, and h are the stoichiometric coefficients of the hydrogen ion, the oxidized dissolved species, and the reduced dissolved species, respectively, in the pertinent half reaction; C_{ox} and C_{red} are the activities (assumed equal to molar concentrations) of the oxidized dissolved species and the reduced dissolved species; and k is the usual Nernst electrochemical coefficient, namely, 2.303 $RT/n\mathbf{F}$ with n equal to the number of electrons in the half reaction ($k = 0.1136/n$ at 300°C). Boundaries between regions that involve only acid dissociation are vertical in the diagrams. The pH of each vertical boundary is equal to the pK for the corresponding acid dissociation as given in Table III.

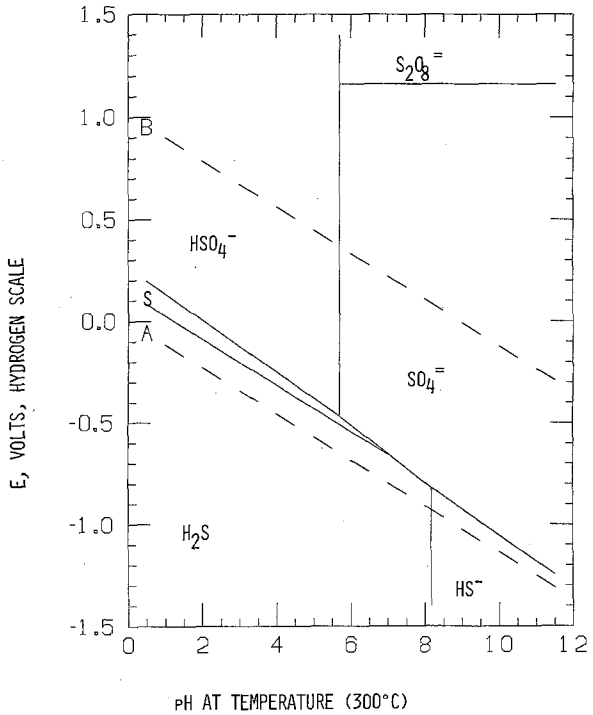

Fig. 1. Stability diagram for S-H_2O system at 300°C for thermodynamically stable species. Boundary lines indicate conditions for unit activity of each species. Dashed lines A and B are the electrode potentials for H_2 and O_2 in water.

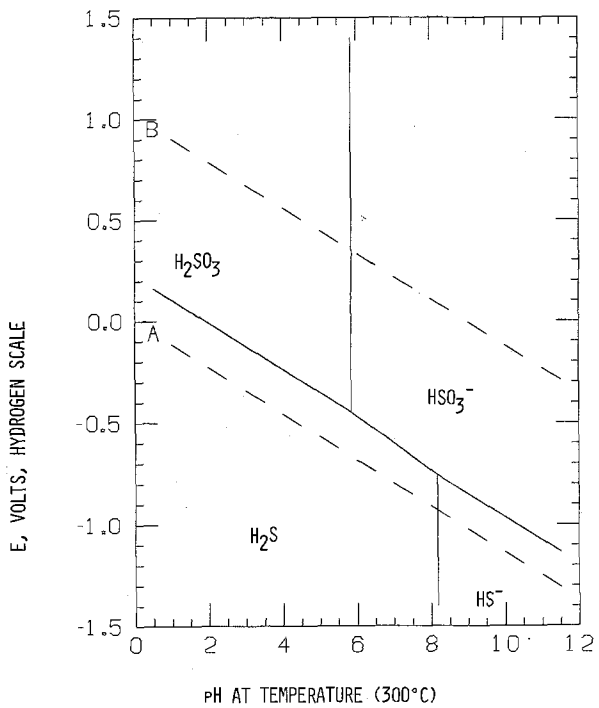

Fig. 2. Potential-pH diagram considering sulfite species as the only oxidized form. Boundary lines indicate conditions for equal concentrations (activities) of corresponding dissolved species.

No stability region for the S^{-2} ion is presented. Ellis and Giggenbach (11) have pointed out that at elevated temperatures S^{-2} is a sufficiently strong base that it hydrolyses to HS^- at all pH's below about 14. Therefore, we have not included a field for S^{-2}.

Heat capacity data for aqueous polysulfide species (*i.e.*, S_n^{-2}) above room temperature are not available, so those species were not considered for the present diagrams (Fig. 1-4). Nevertheless, estimates of the free energies and equilibrium constants for the formation of the various polysulfide species can be made using

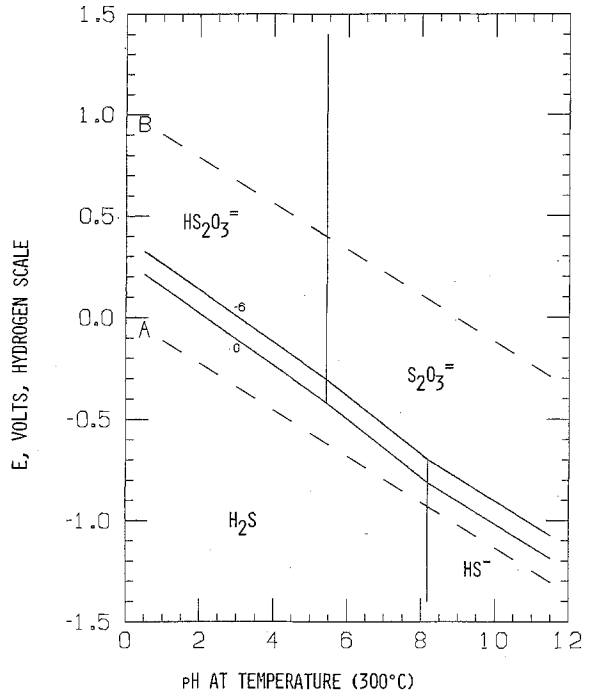

Fig. 3. Potential-pH diagram considering thiosulfate species at the only oxidized form. Lines identified by 0 and −6 refer to solutions with total concentration (activity) of dissolved sulfur species of one and 10^{-6} molar, respectively.

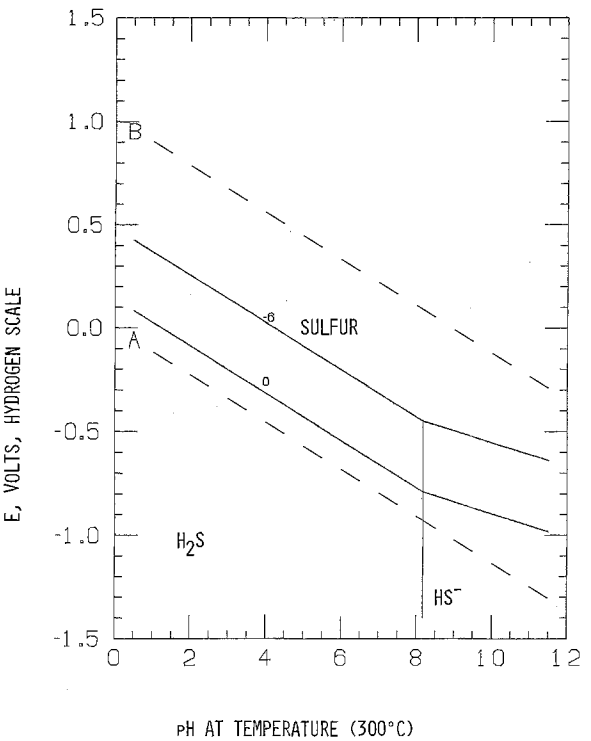

Fig. 4. Potential-pH diagram considering elemental sulfur as the only oxidized form. Lines corresponding to 0 and −6 refer to solutions of one and 10^{-6} molar (activity) sulfide.

data from Ref. (4) and assuming ΔCp is zero in each case. The thermodynamic data used and the estimated pK values are presented in Table IV. The equilibrium constants are seen to decrease with increasing temperature. The concentrations of polysulfide ions are small at room temperature when the activity of total dissolved sulfide is small (because the S^{-2}/HS^- ratio is small), see Ref. (9), and Table IV shows that the concentrations are even smaller at elevated temperatures. Furthermore, Giggenbach (12) has found experimentally that polysulfides are not important above about 240°C. A stability field for $HS_2O_8^{-1}$ was not included in the diagrams because of insufficient information about its acid dissociation constant.

Table IV. Estimated thermodynamics for polysulfide species

Reactions	$\Delta G°(298)$ (cal mol^{-1})	$\Delta S°(298)$ (cal mol^{-1} deg^{-1})
1) $S(s,l) + S^{-2}(aq) = S_2^{-2}(aq)$	−1500	2.7
2) $S(s,l) + S_2^{-2}(aq) = S_3^{-2}(aq)$	−1400	1.4
3) $S(s,l) + S_3^{-2}(aq) = S_4^{-2}(aq)$	−1100	1.3
4) $S(s,l) + S_4^{-2}(aq) = S_5^{-2}(aq)$	−800	1.3

Equilibrium constants

t (°C)	pK_1[a]	pK_2[a]	pK_3[a]	pK_4[a]
25	−1.10	−1.03	−0.81	−0.59
100	−1.00	−0.88	−0.70	−0.53
200	−0.91	−0.76	−0.61	−0.48
250	−0.88	−0.72	−0.58	−0.46
300	−0.86	−0.68	−0.56	−0.44

[a] pK_1 = −log of equilibrium constant for reaction; assuming $\Delta Cp = 0$ and $\Delta H = 0$ for melting for sulfur.

Detailed comparison of Fig. 1-4 indicates that the lower stability boundary of the species relative to oxidation state −2 increases slightly in the order S, H_2SO_3, HSO_4^-, $HS_2O_3^-$ in acid solutions (although for low H_2S activities the order is H_2SO_3, S, HSO_4^-, $HS_2O_3^-$) and $SO_4^=$, $SO_3^=$, $S_2O_3^=$, S in basic solutions. That is, their relative thermodynamic stabilities at 300°C decreased in that order.

The diagram given by Biernat and Robins for 300°C [Fig. 7 of Ref. (2)], which was based entirely on Criss-Cobble extrapolation of room temperature thermodynamic data, differs somewhat from the present diagram (Fig. 1), based on improved data. The most significant difference is that in the Biernat and Robins treatment, the stability field for HS^- has disappeared from the diagram so that H_2S goes directly to $S^=$ for pH greater than 7.3, while in the present treatment, H_2S is converted to HS^- at pH 8.1. Also, the transition from HSO_4^- to $SO_4^=$ occurs at pH 6.5 in the Biernat and Robins diagram and at 5.7 in the present treatment. (Note also that the E_T scale used by Biernat and Robins is shifted by +0.103V compared to the scales used in the present paper. Thus, the $E°$ for hydrogen reduction in unit activity of H^+ is 0.103V on the Biernat and Robins scale at 300°C and 0.0V in the present paper. The difference occurs because of differences in convention. We assume the hydrogen half-cell has a standard electrode potential of zero at any temperature. Biernat and Robins assume the standard Gibbs energy for electrons is zero at all temperatures; thus, the hydrogen electrode potential is not zero except at 298 K.) Diagrams for other temperatures can be constructed from the data given in Tables II and III. The diagrams tend to show a gradual transition of features from the room temperature diagram given in Ref. (9) to the present Fig. 1.

Acknowledgment

The authors would like to thank Prof. James W. Cobble, of San Diego State University, for his support and for providing many helpful comments in connection with the data used in this report.

Manuscript submitted Sept. 22, 1982; revised manuscript received Dec. 6, 1982.

Any discussion of this paper will appear in a Discussion Section to be published in the December 1983 JOURNAL. All discussions for the December 1983 Discussion Section should be submitted by Aug. 1, 1983.

Publication costs of this article were assisted by the Electric Power Research Institute.

REFERENCES

1. "Water Chemistry of Nuclear Reactor Systems 2," British Nuclear Energy Society, London (1981).
2. R. J. Biernat and R. G. Robins, *Electrochim. Acta*, **14**, 809 (1969).
3. J. W. Cobble, R. C. Murray, Jr., P. J. Turner, and K. Chen, "High Temperature Thermodynamic Data for Species in Aqueous Solution," EPRI Report NP 2400, Electric Power Research Institute, Palo Alto, CA (May 1982).
4. D. D. Wagman, W. H. Evans, V. B. Parker, I. Halow, S. M. Bailey, and R. H. Schumm, "Selected Values of Chemical Thermodynamic Properties," NBS Technical Note 270-3, U.S. Dept. of Commerce, Washington, DC (1968).
5. Revision to Ref. 4 in Appendix of NBS Technical Note 270-8, 1981.
6. R. C. Murray and J. W. Cobble, in "Proceedings of the 41st International Water Conference," p. 295, Pittsburgh, Pennsylvania (1980).
7. D. J. Turner, in "Thermodynamics of Aqueous Systems with Industrial Applications," S. A. Newman, Editor, pp. 653-679, ACS Symposium Series 133, American Chemical Society, Washington, DC (1980).
8. JANAF Thermochemical Tables, National Bureau of Standards, NSRDS-NBS 37, U.S. Govt. Printing Office, Washington, DC (1971).
9. M. Pourbaix, "Atlas of Electrochemical Equilibria in Aqueous Solutions," "Sulfur," Section 19.2, National Association of Corrosion Engineers, Houston, TX (1974).
10. W. M. Latimer, "The Oxidation States of the Elements and their Potentials in Aqueous Solution," 2nd ed., Prentice-Hall, Inc., Englewood Cliffs, NJ (1952).
11. A. J. Ellis and W. Giggenbach, *Geochim. et Cosmochim. Acta*, **35**, 247 (1971).
12. W. Giggenbach, *Inorg. Chem.*, **13**, 1724 (1974).

Electrodeposition of Conducting Transition Metal Oxide/Hydroxide Films from Aqueous Solution

Dennis Tench and Leslie F. Warren

Rockwell International, Microelectronics Research and Development Center, Thousand Oaks, California 91360

Metal oxide/hydroxide films formed by electrochemical or chemical growth on the corresponding metal electrode have been investigated extensively. Many of these oxy-hydroxides are of considerable practical interest because of their charge storage capabilities (Ni, Mn), electrochromic activity (Ni, Rh, Ir), electrocatalytic properties (Ru), and photoelectrochemical activity (Cu, Ni, Fe), A simple method for the controlled application of such films onto substrates other than the metals themselves (*e.g.*, onto semiconductors) does not appear to have been developed. We report here our preliminary results describing a general technique for the electrochemical deposition of oxide/hydroxide films of copper, nickel, cobalt, iron, and manganese from aqueous solution. The general properties of these materials, some of which are new, are also discussed.

Films were typically deposited on a 0.5 cm^2 rotating platinum disk electrode (400 rpm), either by voltage cycling (50 mV/sec) or at constant electrode potential from buffered solutions (*p*H 6.5-7.5). A sodium acetate buffer was used since, at the metal ion concentrations employed (0.10-0.25*M*), other common buffering agents either precipitate the metal hydroxide or strongly complex the metal ion (increase the overpotential for deposition). All potentials are given relative to the saturated calomel electrode (SCE).

Figure 1 shows voltammograms associated with nickel oxy-hydroxide deposition. On the first anodic sweep (dashed line), only a slowly increasing anodic current is evident. On each subsequent cycle, beginning at the positive limit, corresponding reduction and oxidation peaks, for which the associated (equivalent) charge increases with each cycle, were observed. The cathodic/anodic peaks correspond to reduction/oxidation of the nickel oxy-hydroxide film, which is deposited by oxidation of Ni^{2+} to Ni^{3+} and precipitates on the electrode surface, presumably as NiO(OH). Although the equations are not balanced, the overall reaction can be schematically represented as

$$Ni^{2+} \xrightarrow{-e^-} Ni^{3+} \xrightarrow{OH^-} NiO(OH) \underset{-e^-}{\overset{+e^-}{\rightleftharpoons}} Ni(OH)_2 \qquad [1]$$

Key words: metal oxides/hydroxides, electrodeposition procedures, electrochemical properties.

The current then increases on each cycle as new Ni^{2+} is oxidized and deposited, and the oxide deposit is cycled between NiO(OH) and $Ni(OH)_2$

Nickel oxy-hydroxide films prepared by this potential cycling technique appear to be uniform and smooth, are electrically conducting, and exhibit electrochromic properties, rapidly turning from transparent to dark brown at well-defined potentials. Figure 2 shows a linear plot of film thickness, measured by ellipsometry, *vs.* the integrated peak charge. Approximate calculations of the film thickness based on the voltammetry peak charge (Fig. 1), assuming a cubic lattice and Ni-O bond distance of 4.2Å, gave comparable numbers to those derived from the ellipsometry measurements. Electrochemically, the electrodeposited films resemble

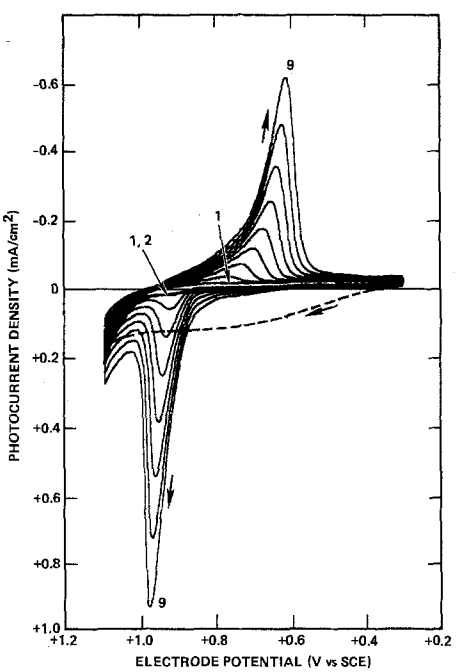

Fig. 1. Cyclic voltammograms (50 mV/sec) for a rotating Pt disk electrode (400 rpm) in an aqueous solution containing 0.13M $NiSO_4$, 0.1M Na_2SO_4, and 0.13M sodium acetate (pH 7.1).

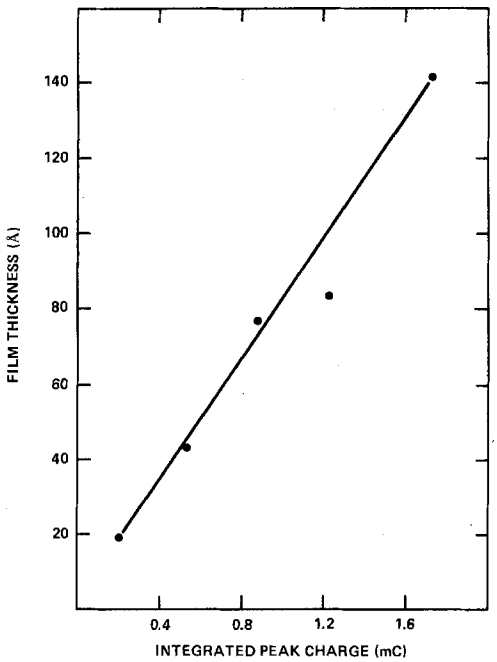

Fig. 2. Plot of the thickness of electrodeposited nickel oxy-hydroxide films measured by ellipsometry vs. the integrated peak area (form Fig. 1).

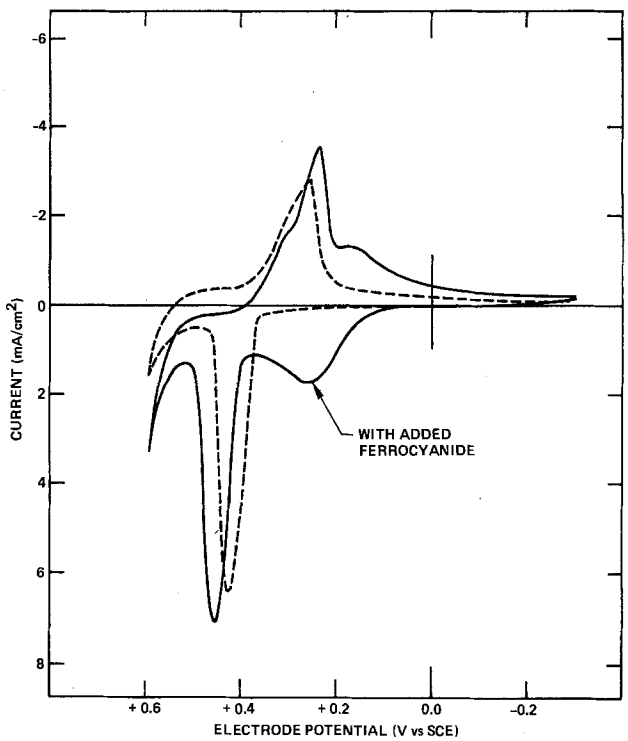

Fig. 3. Cyclic voltammograms at 50 mV/sec for a stationary electrodeposited nickel oxy-hydroxide film (100Å) on Pt in 0.1M NaOH with (solid curve) and without (dashed curve) added ferrocyanide (0.01M).

the thick anodic hydrous oxide films grown on nickel electrodes in neutral or basic electrolytes (1), rather than the passive film (2). Films having similar electrochemical properties have been prepared by cathodic deposition from aqueous nickel nitrate solutions (3-5), where nitrate reduction to form hydroxide seems to be involved. The structures of nickel oxy-hydroxides have been previously investigated (3, 4, 6).

The good electrical conductivity of the nickel oxy-hydroxide films prepared by anodic electrodeposition is evident from the voltammograms in Fig. 3. Note that, in this basic electrolyte, the redox properties of the film, as reflected in the general shape of the voltammograms, changes somewhat with potential cycling (4). The current waves corresponding to ferri-ferrocyanide reduction/oxidation on the oxide-covered electrode in this system (onset at 0.1V) are virtually identical to those observed for the bare platinum electrode.

Other oxide/hydroxide films prepared by electrodeposition from acetate-buffered solutions and the deposition conditions are listed in Table 1. At a potential of 1.1V, manganese oxy-hydroxide can also be deposited from acidic electrolytes (0.2*M* H_2SO_4). It should be noted that manganese oxide for use in dry batteries has been prepared by anodic deposition for some time (7, 8), but the deposition potential at higher pH with the acetate buffer is considerably lower. Passivating iron oxy-hydroxide films prepared anodically from Fe^{2+} solutions have also been described previously (9). Film thicknesses reported below were derived from calculations similar to those used for nickel oxy-hydroxide films.

Copper oxide films deposited cathodically at constant potential under the conditions given in Table I are orange and can be grown to a nominal thickness of about 5000Å; above this limit, the deposition current rapidly decays. The film structure was investigated by x-ray diffraction which yielded a sharp peak corresponding to a lattice spacing of 2.468 nm and two smaller peaks (2.137 and 1.510 nm), suggesting a structure of Cu_2O with a preferred orientation. The deposition process probably involves reduction of Cu^{2+} in solution and dehydration of the deposited oxide, which can be represented schematically as

$$Cu^{2+} \xrightarrow[OH^-]{+e^-} CuOH \xrightarrow{-H_2O} Cu_2O \qquad [2]$$

Consistent with other work (10), these films were found to undergo oxidation/reduction and to gradually

Table I. Deposition conditions for metal oxide/hydroxide films

Metal	Solution composition	pH	Electrodeposition conditions	Probable film composition
Ni	0.13*M* $NiSO_4 \cdot 6H_2O$ 0.13*M* NaOAc 0.10*M* Na_2SO_4	7.14	Potential cycled between +0.3 and +1.1V at 50 mV/sec; anodic deposition	$Ni(OH)_2/NiO(OH)$
Cu	0.1*M* $Cu(OAc)_2 \cdot 2H_2O$ 0.8*M* NaOAc (Nitrogen saturated)	6.45	Constant potential at 0.0V; cathodic deposition	Cu_2O
Co	0.1*M* $CoSO_4 \cdot 6H_2O$ 0.1*M* NaOAc 0.1*M* Na_2SO_4	7.52	Constant potential at 1.0V; anodic deposition	Hydrous CoO_x ($x < 2$)
Fe	0.1*M* $Fe(NH_4)_2(SO_4)_2 \cdot 6H_2O$ 0.2*M* NaOAc 0.1*M* Na_2SO_4 (Nitrogen saturated)	6.80	Constant potential at −0.1V; anodic deposition	Hydrous FeO_x ($x < 1.5$)
Mn	0.1*M* $Mn(OAc)_2 \cdot 4H_2O$ 0.1*M* Na_2SO_4	7.50	Constant potential at +0.4V; anodic deposition	Hydrous MnO_x ($x < 2$)

Where Ac = acetate.

dissolve during potential cycling in aqueous solutions. However, electrodeposited copper oxide films appear to be stable in acetonitrile electrolytes, where oxidation/reduction of the film itself is not observed, but the ferrocene/ferricenium redox reaction (E° = +0.4V) occurs reversibly on the film-covered electrode.

Under illumination, electrodeposited copper oxide films exhibit p-type semiconducting behavior. The electrolyte used to demonstrate this effect was the acetonitrile-phthalonitrile (o-$C_6H_4(CN)_2$) system utilized with p-type Cu_2O by Nagasubramanian, *et al.* (10). Figure 4 shows the current-potential characteristics of the film-covered electrode under illumination with chopped light (tungsten-halogen lamp, 80 mW/cm^2). Note that photocurrents in the 100 μA/cm^2 range were observed, a remarkable result considering the unoptimized nature of these as-formed films. The p-type behavior observed for the electrodeposited material substantiates the assignment of Cu_2O as its structure.

Cobalt oxy-hydroxide films anodically deposited at constant potential under the conditions given in Table I are deep yellow (thinner films exhibit interference colors) and appear to have high electrical conductivity. Black films approaching a nominal thickness of 1 μm can be deposited with no observable decay in the deposition current. Deposits formed at +0.8V appear to be much less conducting, which suggests that a Co(IV) species may be responsible for the high conductivity of films deposited at more positive potentials (11). X-ray diffraction studies indicated that such films are amorphous. As shown by the voltammograms in Fig. 5, in the presence of ferrocyanide, reversible $Fe(CN)_6^{3-/4-}$ redox waves are superimposed on the voltammetric features corresponding to oxidation/reduction of the cobalt oxy-hydroxide film in alkaline solution. The voltammograms shown are stable, but slow changes are observed for sweeps to more negative potentials.

Iron oxy-hydroxide films anodically deposited at constant potential under the conditions given in Table I are pale yellow and can be grown to a nominal thickness of ~ 300Å, above which the deposition current decays. On films below this apparent limiting thickness, the ferro-ferricyanide reaction proceeds reversibly, whereas thicker films appear to be insulating. Stable voltammograms with potential cycling between +0.6 and −0.8V were obtained for thinner films in 0.1M NaOH. No photoresponse was observed for electrodeposited iron oxy-hydroxide in any of various electrolytes tested. The film thickness was apparently too small to permit determination of the structure by x-ray diffraction.

Like cobalt oxy-hydroxide, manganese oxy-hydroxide films (orange) anodically deposited under the conditions given in Table I are highly conducting, as evidenced by the stable deposition currents at film

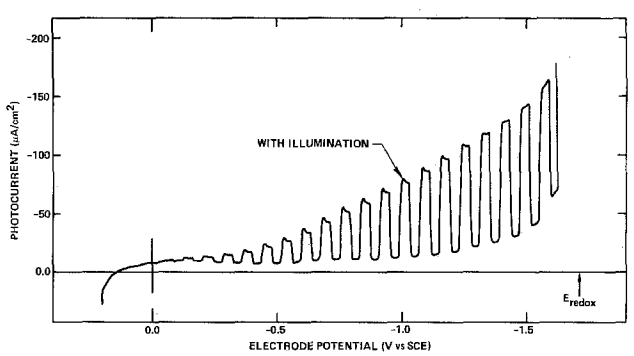

Fig. 4. Voltammetric behavior at 50 mV/sec of a stationary electrodeposited copper oxide film (5000Å) on platinum under illumination with chopped light (80 mW/cm^2) in acetonitrile solution containing 0.1M phthalonitrile and 0.1M $NaClO_4$.

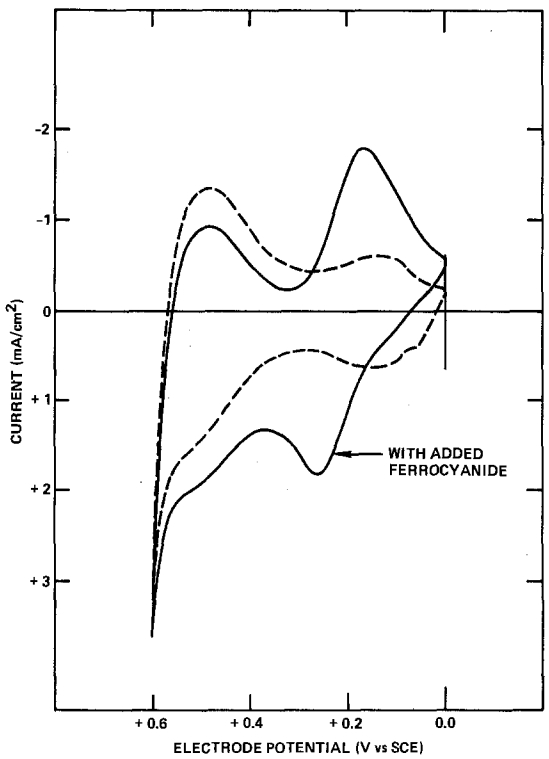

Fig. 5. Cyclic voltammograms at 50 mV/sec for a stationary electrodeposited cobalt oxy-hydroxide film (600Å) on Pt in 0.1M NaOH, with (solid curve) and without (dashed curve) added ferrocyanide (0.01M).

thicknesses approaching the 1 μm range. X-ray diffraction studies indicated an amorphous film structure. Under potential cycling, these films slowly dissolve in acidic or basic electrolytes, but are apparently stable in neutral 0.1M Na_2SO_4 (pH 7.5) at potentials between +1.0 and 0.0V. Figure 6 shows voltammograms ob-

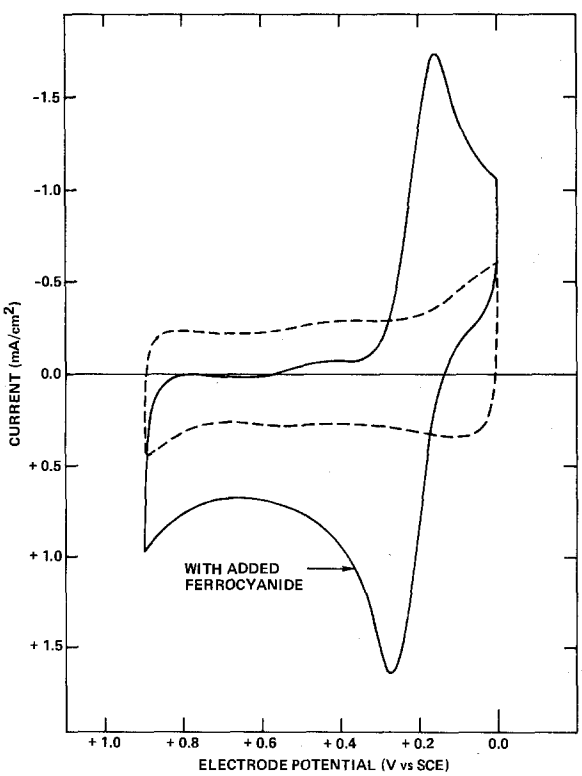

Fig. 6. Cyclic voltammograms at 50 mV/sec for a stationary electrodeposited manganese oxy-hydroxide film (600Å) on Pt in 0.1M Na_2SO_4, with (solid curve) and without (dashed curve) added ferrocyanide (0.01M).

tained for manganese oxy-hydroxide films in the latter electrolyte, with and without added ferrocyanide ion. The good conductivity of the film is also evident from the reversible $Fe(CN)_6^{3-/4-}$ redox wave.

In conclusion, thin uniform metal oxide/hydroxide films of copper, nickel, cobalt, iron, and manganese can be electrodeposited onto conducting substrates from acetate-buffered aqueous solutions. The as-formed copper oxide films exhibit p-type photoactivity. In most cases, the other electrodeposited oxide/hydroxide films are electrically conducting, especially those of manganese and cobalt. The nickel oxy-hydroxide exhibits electrochromic behavior.

Acknowledgment

The authors gratefully acknowledge support of this work by the Solar Energy Research Institute under Subcontract No. XG-O-9276.

Manuscript submitted Aug. 23, 1982; revised manuscript received ca. Dec. 7, 1982.

Any discussion of this paper will appear in a Discussion Section to be published in the December 1983 JOURNAL. All discussions for the December 1983 Discussion Section should be submitted by Aug. 1, 1983.

Publication costs of this article were assisted by Rockwell International.

REFERENCES

1. B. MacDougall and M. J. Graham, *This Journal*, **128**, 2321 (1981).
2. S. M. Wilhelm and N. Hackerman, *ibid.*, **128**, 1668 (1981).
3. J. L. Ord, *Surf. Sci.*, **56**, 413 (1976).
4. L. D. Burke and T. A. M. Twomey, *J. Electroanal. Chem.*, **134**, 353 (1982).
5. S. H. Glarum and J. H. Marshall, *This Journal*, **129**, 535 (1982).
6. R. E. Carbonio, V. A. Macagno, M. C. Giordano, J. R. Vilche, and A. J. Arvia, *J. Appl. Electrochem.*, **12**, 121 (1982).
7. C. C. Liang, in "Encyclopedia of Electrochemistry of the Elements," Vol. I, A. Bard, Editor, p. 349, Marcel Dekker, New York (1973).
8. E. Barchese, H. C. Chagas, and S. Wolynec, *An. Acad. Brasil. Ciênc.*, **53**, 309 (1981).
9. M. Cohen, D. Mitchell, and K. Hashimoto, *This Journal*, **126**, 442 (1979).
10. G. Nagasubramanian, A. S. Gioda, and A. J. Bard, *ibid.*, **128**, 2158 (1981).
11. L. D. Burke, M. E. Lyons, and O. J. Murphy, *J. Electroanal. Chem.*, **132**, 247 (1982).

Tin(IV)-Based Photoselective Metal Deposition of Cobalt and Nickel from Alkaline Baths

I. Kiflawi*

Precision Electronic Components Limited, Toronto, Ontario Canada M6M 2V6

and M. Schlesinger*

Department of Physics, University of Windsor, Windsor, Ontario Canada N9B 3P4

The electroless method for thin metal film deposition continues to maintain and even to expand its important role in many industrial applications. The physics and chemistry of the processes involved, however, still elude exact explanations. Of the aspects that on the one hand are easily exploitable but on the other are difficult to fully understand is photoselective deposition. In a series of publications (1, 2, 3) from our research group in Windsor we showed that aged Sn(IV) chloride solution can serve as a sensitizer for electroless copper plating and for nickel plating from an acidic bath. For nickel (or cobalt) plating from an alkaline bath it was observed that an additional reducing bath is necessary between the activation step and the last rinse.

Ultraviolet irradiation of the substrate after Sn(IV) sensitization and Pd(II) activation was shown to have a marked effect on subsequent metal plating. In a copper bath plating was found to occur only on the irradiated surface producing a sharp negative image of the photomask. In an acidic nickel bath plating was observed to occur only on the nonirradiated surface producing a sharp positive image. It was found possible to achieve a positive image of the photomask using an alkaline nickel (cobalt) bath if ultraviolet was applied before the reducing bath.

The purpose of the present paper is twofold. First we report that the production of a negative photoimage using alkaline nickel or cobalt metallizing baths is also possible. Second, we attempt to further clarify possible mechanisms for the influence of ultraviolet irradiation on subsequent metal deposition.

* Electrochemical Society Active Member.

Experimental

All chemicals were ACS reagent grade supplied by Fisher or Canlab and were used without further purification.

Sensitizer.—The stock solution we used was made by dissolving 10g $SnCl_4 \cdot 5H_2O$ in 12.5 ml concentrated HCl. To prepare a sensitizer bath 2.5 ml of this stock solution was diluted to 200 ml using distilled water.

Aging of the sensitizer solution was monitored using optical absorption. When the optical density reached $D = 0.1\ cm^{-1}$ at $\lambda = 5200$Å the aging process was complete and the performance quality of the solution was at its best (usually after about 24 hr). It was possible to maintain good performance for periods of a few months by periodically adding HCl or water as needed to maintain the optical density at its stated value.

Activator.—To 1g $PdCl_2$ we added 1 ml concentrated HCl and 10 ml H_2O. After complete dissolution we diluted 1 ml of the above in 50 ml of H_2O. This was the stock solution. Any of the following 3 activators work equally well. They differ only in the ensuing deposition rate.

deposition rate of No. 1 < deposition rate of No. 2 < deposition rate of No. 3

Activator bath No. 1: 5 ml stock + 95 ml H_2O

Activator bath No. 2: 10 ml stock + 90 ml H_2O

Activator bath No. 3: 15 ml stock + 85 ml H_2O.

Alkaline nickel and cobalt baths.—The composition of these are given in Table I. The metallizing baths

Table I. Composition of metallizing baths (quantities given for 1 liter of solution)

	Ni	Co
$CoSO_4 \cdot 7H_2O$		35g
$NiSO_4 \cdot 6H_2O$	30g	
$NaH_2PO_2 \cdot H_2O$	17g	40g
Na_3- citrate	100g	35g
NH_4Cl	53.6	
$(NH_4)_2SO_4$		70g
pH (adjusted with NH_4OH)	8.5	9.1 → 9.5

were used at 62°C. Other baths were used at room temperature.

Substrate.—Two different substrates were used with similar results. The one were Esco precleaned Borosilicate microscope slide glasses. The other were 3M(Al Si) ceramic plates.

Irradiation.—Ultraviolet irradiation was carried out using a 5W mercury vapor lamp held at a distance of about 5 cm from the substrate.

Results

Samples in the present study were dipped in aged Sn(IV) sensitizer for 3 min, rinsed, dipped in Pd(II) activator for 2 min, and left until dried at room temperature. The designation [Sn(IV) · Pd(II)] refers to the catalytic substance present on the substrate after these steps have been completed.

If the above steps are followed and an alkaline Ni or Co bath is used no plating is obtained. No plating is obtained even if the temperature of the metallizing bath is raised as high as 85°C. Although, once the *p*H of the bath has fallen to around 6.5, due to ammonia evolution, it was possible to obtain Ni or Co plating. Further, irradiation with u.v. light resulted in a positive image (*i.e.*, the irradiated areas did not plate).

Ultraviolet irradiation for about 10 min followed by a short rinse in distilled water and subsequent immersion in alkaline (*p*H ≧ 7) Ni bath produces metal deposition on the irradiated area only. That is, one obtains a clear negative image of the photomask. In the case of an alkaline Co bath the same results are obtained, except that for best results, *i.e.*, clear negative, a higher *p*H value (about 9.1 and up) is advisable.

As mentioned in the previous section, the metallizing baths were used in the temperature range 60° ≦ temp ≦ 65°; usually 62°C.

In order to demonstrate that by merely changing the *p*H of the metallizing bath one can obtain either a negative or a positive photoimage, we performed the following. First we produced a negative image with the Ni bath at about *p*H 8. Second, by keeping the bath at 60°C the *p*H fell eventually to about 6.6. At this *p*H value we produced a positive image. Finally, by adding NH_4OH or NaOH, the *p*H of the bath rose again to around 8 and another negative image was produced (see Fig. 1).

In Fig. 2 we present the resistance values of a semicircularly shaped, negative nickel, strip. They are given as a function of rotation angle from one edge. The linear character of the function is an indication of the uniformity of the deposit. Similar results were obtained for a strip of positive nickel deposited with the help of an appropriate mask.

Discussion

In Ref. (1) and (2) we have suggested that the reason tin(IV) sensitizer is effective for Ni plating from an acidic bath but not for Cu plating bath is that the hypophosphite (in the acidic Ni bath) can reduce the attached Pd(II) to Pd(0), but formaldehyde (in the basic Cu bath) cannot. Our present results together with those of Ref. (3) indicate that a reduction of the catalyst [Sn(IV) · Pd(II)] does occur prior to

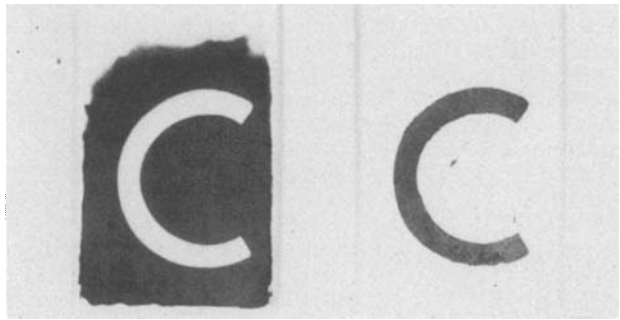

Fig. 1. Positive and negative photoimages of a mask made from the same electroless nickel bath by varying the *p*H.

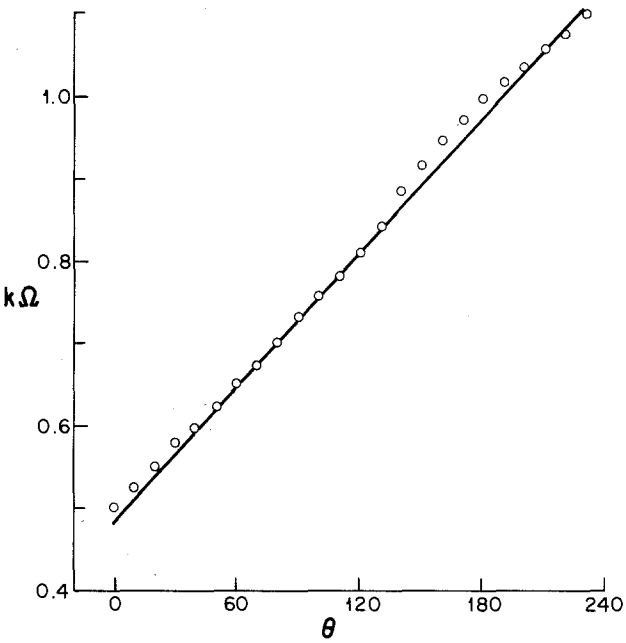

Fig. 2. Resistance vs. angle of rotation from one edge of a semicircularly shaped strip of electroless nickel, deposited as negative.

Ni and Co plating, and that this reduction can proceed in acidic hypophosphite, but not in neutral or basic hypophosphite.

Our results of producing negative-positive-negative from the same Ni bath by changing the *p*H value makes it clear that it is the change in *p*H that determines whether reduction of Pd(II) and hence plating occurs onto the catalyst. Now, the effect of raising the *p*H on hypophosphite is to increase its reduction potential [see Ref. (4)]. However, Pd(II) is much harder to reduce in basic solution than in acid because it forms $Pd(OH)_2$ which has a lower reduction potential than $PdCl_2$. Thus we infer that the reason no plating occurs on nonirradiated [Sn(IV) · Pd(II)] in basic plating baths is that $Pd(OH)_2$ forms which cannot be reduced and cannot initiate metal plating. It has been observed (5) that some time in the alkaline metallizing bath is necessary before the material present on the substrate offer Sn(II) sensitization and Pd(II) activation is capable of catalyzing Cu plating. This probably indicates that even for the [Sn(II) · Pd(II)] system reduction in the metallizing bath is a necessary step in producing an active catalyst.

In his excellent review "Photochemical Selective Activation for Electroless Metal Deposition on Nonconductors," Paunovic (6) has suggested chemical paths associated with different photoelectrochemical processes. These were offered in conjunction with Sn(II) related electroless systems. Our present work

refers to Sn(IV) photochemistry and we have to content ourselves with a generalized picture.

The specific effect of u.v. light on [Sn(IV) · Pd(II)] is still not known but it is plausible to assume that it renders [Sn(IV) · Pd(II)] capable of catalyzing Ni or Co plating from a warm alkaline bath, by reducing it to [Sn(IV) · Pd(0)] as suggested in Ref. (3).

The ultraviolet light's effect is such that in an acidic medium (*i.e.*, pH $\leq$ 7) no metal plating occurs on the irradiated areas. This is in harmony with the assumption that the ultraviolet light reduces [Sn(IV) · Pd(II)] into [Sn(IV) · Pd(0)]. In the alkaline bath where no further reduction occurs, deposition will be initiated. In the acidic bath further reduction into a (crystalline?) form of palladium not capable of initiating deposition will occur (3, 5, 7).

In conclusion, we have demonstrated that an efficient Sn(IV) based system for electroless metal deposition exists, which is capable of producing both positive and negative images of a photomask of high uniformity. We are led to the assumption that the sensitization/activation stage is extended into the metallizing bath step, and the latent image is not completely determined (6) even after the palladium bath.

Acknowledgments

This research was supported by the Natural Sciences and Engineering Research Council and the National Research Council of Canada. The skillful technical contributions of Miss S. Varevorakul, Mr. R. Cancian, and Mr. A. Busuttil are gratefully acknowledged.

Manuscript submitted Sept. 21, 1982; revised manuscript received Nov. 19, 1982. This was Paper 318 presented at the Denver, Colorado, Meeting of the Society, Oct. 11-16, 1981.

Any discussion of this paper will appear in a Discussion Section to be published in the December 1983 JOURNAL. All discussions for the December 1983 Discussion Section should be submitted by Aug. 1, 1983.

Publication costs of this article were assisted by the University of Windsor.

REFERENCES

1. B. K. W. Baylis, A. Busuttil, N. E. Hedgecock, and M. Schlesinger, *This Journal*, **123**, 348 (1976).
2. B. K. W. Baylis, A. Busuttil, N. E. Hedgecock, and M. Schlesinger, *ibid.*, **123**, 1376 (1976).
3. B. K. W. Baylis, N. E. Hedgecock, and M. Schlesinger, *ibid.*, **124**, 346 (1977).
4. "Handbook of Chemistry and Physics," 51st ed., p. D112, Chemical Rubber Co., Cleveland, Ohio (1970); W. M. Latimer, "The Oxidation States of the Elements and their Potentials in Aqueous Solutions," Prentice-Hall, New York (1952).
5. R. L. Meek, *This Journal*, **122**, 1478 (1975).
6. M. Pavnovic, *ibid.*, **127**, 441C (1980).
7. J. J. Kelly and J. K. Vondeling, *ibid.*, **122**, 1103 (1975).

The Determination of Nitrite Ion in Copper Pyrophosphate Plating Solution

Thomas M. Tam* and Greg A. Fung

Lockheed Missiles and Space Company, Process Control Engineering, Sunnyvale, California 94086

Copper pyrophosphate plating solutions are widely used by the electronic industry to manufacture printed wiring boards. This solution has been extensively used in the past 20 years; however, an easy method to maintain the optimum operation of the solution is still desirable. Although the fundamental chemistry of this solution is fairly well understood (1, 2, 3, 4), the effects of impurities are less well defined.

Recently, Ogden and Tench (5) developed a cyclic voltammetric technique for determining effective brightener (PY61-H, M&T Chemicals Incorporated) concentration. Such a method has been adopted to control our plating solution routinely. A cyclic voltammogram similar to the one published can be obtained from a freshly prepared solution. However, a different voltammogram is obtained from a used solution (1½ years), where a large current density (5 mA/cm^2, 0.8V) begins at 0.65V[1] (tail) as shown in Fig. 1. This voltammogram has been previously published (6), but the chemical species that cause the tail have not been defined. The intent of this paper is to report the work that identify this chemical species.

Experimental Section

Material and solution.—Copper pyrophosphate solutions were prepared from Unichrom C10XB and C11XB (M&T Chemicals Incorporated). The pH was adjusted to 8.65 by concentrated NH_4OH or pyrophosphoric acid. A typical solution contains: $[Cu(P_2O_7)_2^{6-}] \cong$ 0.4M and $[NH_3] \cong$ 0.05M. Used plating solutions were obtained from the plating shop. Solutions with added PY61-H (M&T Chemical Incorporated) were aged at 55°C for at least 16 hr. ACS grade potassium nitrite was washed with ethanol-water (10:1) and dried at 100°C for 3 hr, then stored in a desiccator.

Cyclic voltammetric measurements.—A 250 ml Brinkmann titration vessel was used to hold the working, auxiliary, and reference electrodes. The working electrode was prepared by pressing a ⅛ in. D platinum rod into a ⅜ in. D stainless steel rod. The electrode body was sealed by using Microstop (Michigan Chrome & Chemical Corporation), and the exposed platinum surface was polished with GRIT 600 silicon

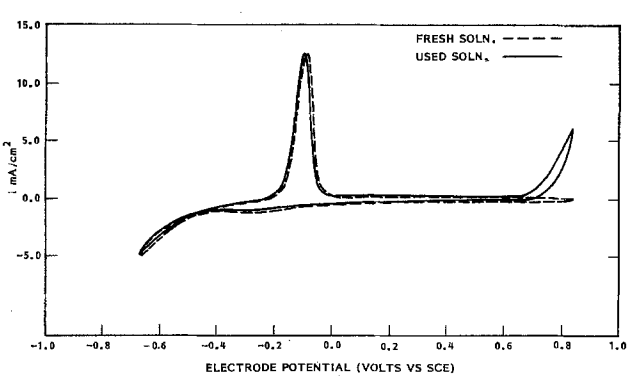

Fig. 1. Cyclic voltammogram of copper pyrophosphate solution. a. $[Cu(P_2O_7)_2^{6-}] \cong$ 0.4M; pH = 8.65 ± 0.05. b. Temperature = 25° ± 1°C. c. Sweep rate = 40 mV/sec; rotational speed = 3000 rpm.

* Electrochemical Society Active Member.
Key words: voltammetry, visible, impurity.
[1] All voltages reported herein are with respect to saturated calomel electrode (SCE).

carbide grinding paper. A Dietzan motor equipped with a rotating mercury contact (Mercotac Incorporated) was used to rotate the electrode at 3000 rpm (with this setup, we are limited to one reproducible speed). The potential was driven by a cyclic voltammetric unit (7). A Soltec X-Y recorder (UP 6432S) was used to record the voltage and current change. The potential was scanned between −0.65 and 0.85V at a rate of 40 mV/sec.

Spectroscopic measurement.—Spectroscopic measurements were made with an HP8450A u.v. vis spectrophotometer.

Results and Discussion

The voltammogram of a used copper pyrophosphate solution exhibits a pronounced raised tail at about 0.65V which increases with bath usage. This phenomenon has been observed, but never clearly defined. Ogden and Tench (5, 6, 8) suggested that this tail can be related to the concentration of the brightener's breakdown products and other organic impurities. We have a different explanation based upon the following results: (*i*) An old tank solution (1½ years) was carbon treated twice to remove the organic impurities (9), but the intensity of the tail did not change at all. (*ii*) Excess PY61-H (~10 ml/liter) was added to a fresh copper pyrophosphate solution and heated at 50°C for over 2 weeks. Free sulfur (one of the breakdown products) precipitated, but no tail was observed at 0.65V. (*iii*) One liter of freshly prepared copper pyrophosphate solution with and without added PY61-H was dummy plated using a copper anode and a stainless steel cathode at 25 A/ft² overnight. The cyclic voltammogram of the resulting solution clearly shows a tail at the region of interest.

Based upon the results of these three experiments described, we concluded the electroactive species responsible for the high current density in the region of interest are not due to thermal decomposition of the additive or any other organic impurities. In this case, it is due to the electrochemical decomposition of the inorganic chemicals that come with the solutions. The possibility of deplating different transition metals at this anodic potential is unlikely. The major transition element in solution is copper, which is easily deplated at −0.2V. Other transition elements exists only in ppm levels (*i.e.*, iron ~40 ppm, analyzed by atomic absorption spectroscopy). This low level of impurities does not account for the high current density observed.

The exact concentration of any other chemical species in solution is not known, since it is a proprietary solution. Dini (1), however, indicated that addition of ammonium nitrate (NH_4NO_3) in copper pyrophosphate increases the permissible current density and improves the quality of copper deposits, and indeed a large quantity of NO_3^- (10) was found in the solution. Latimer (11) has suggested that nitrate, NO_3^-, in basic solution is easily reduced electrolytically at the copper cathode to give nitrite, NO_2^-. Potassium nitrite, KNO_2, was added to the copper solution, and the same voltammogram as that of the used solution was observed. The intensity of this tail is directly proportional to the amount of KNO_2 added. Figure 2 displays the linear relationship between the anodic current density, *i* mA/sec² at 0.8V *vs.* $[NO_2^-]$M.

Spectroscopic study.—Figure 3 displays the spectra of a fresh copper pyrophosphate solution and a solution which has been heavily used for 1½ years. The spectrum of the old solution exhibits an absorption peak at 356 nm. By adding KNO_2 to the fresh solution, the same peak is obtained. The absorbance of this peak is directly proportional to the concentration of NO_2^-. Table I lists the optical properties of KNO_2 in potassium pyrophosphate and copper pyrophosphate solutions. This data agrees well with literature value; we, therefore, conclude that NO_2^- in

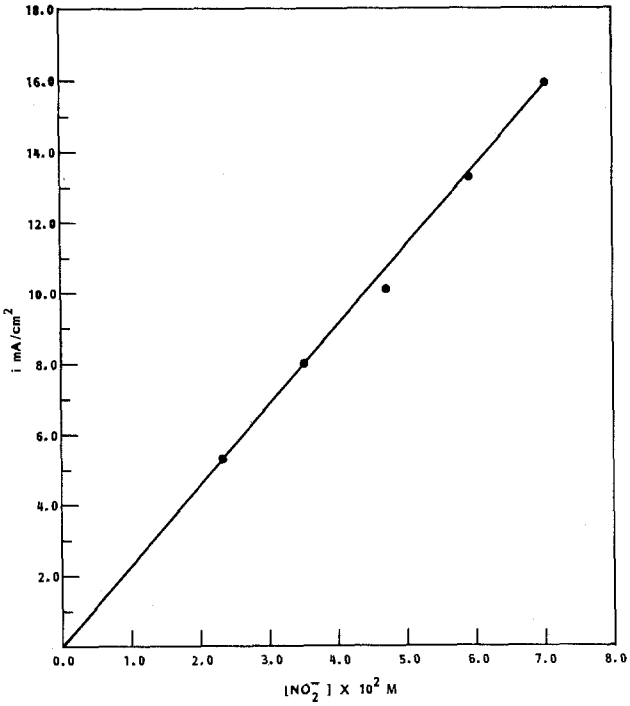

Fig. 2. Dependence of current density (0.8V vs. SCE) on $[NO_2^-]$M. Experimental conditions are given in Fig. 1.

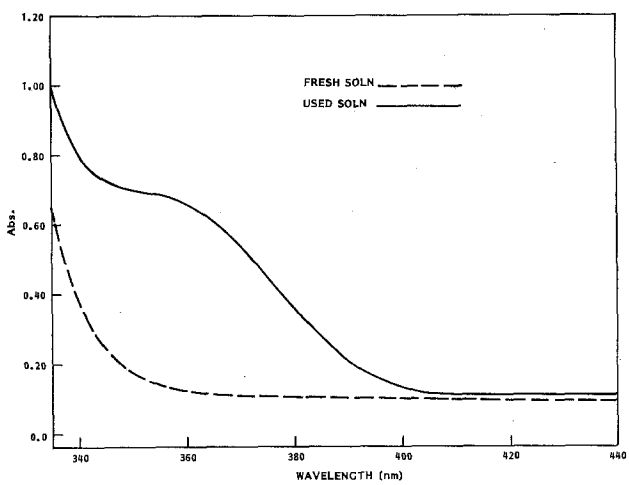

Fig. 3. Visible spectrum of copper pyrophosphate solution. a. $[Cu(P_2O_7)_2^{6-}]$ = 0.4M; pH = 8.65 ± 0.5. b. Temperature = 23° ± 1°C. c. Cell-length = 1 cm.

copper pyrophosphate solution exists as a noncomplexed anionic species.

From the above evidence, it is clear that as the bath is used extensively, NO_2^- builds up due to the reduction of NO_3^-. The concentration of NO_2^- can be accurately measured either by cyclic voltammetric or spectroscopic techniques. A used sample solution was analyzed for NO_2^- by cyclic voltammetry and a different analytical technique (13). The results are 2.5 and 2.2 g/liter, respectively, which are in good agreement.

The effect of NO_2^- on the chemistry of the solution was studied by adding 7.0 mmol of KNO_2 to 100 ml copper pyrophosphate solutions containing different amounts of PY61-H. The ratio of rotational (3000 rpm) to static stripping peak areas was plotted against the volume of PY61-H added. This plot was compared to a plot generated in the same manner by adding PY61-H only. No apparent shift of maximum is observed (5). Thus, we conclude that the effect of NO_2^- on the function of the brightener is either

Table I. Optical properties of NO_2^- in copper pyrophosphate and pyrophosphate solution

Solution	λ_{max} nm	$\epsilon_{cm^{-1}\,M^{-1}}$
Potassium pyrophosphate + KNO_2[a]	356 ± 1	21.1 ± 0.8
Copper pyrophosphate + KNO_2[a]	356 ± 1	24.1 ± 0.8
Sodium nitrite (8)	355	23.3 ± 0.8

[a] $[NO_2^-]$ = 0.02-0.07M; pH = 8.65; temperature = 23° ± 1°C.

insignificant or undetectable by cyclic voltammetric technique.

Conclusion

The cyclic voltammogram of a used copper pyrophosphate solution shows a distinct tail beginning at approximately 0.65V. We have concluded that this tail is due to the oxidation of NO_2^- ions. The source of NO_2^- is the reduction of NO_3^- during electroplating. The concentration of NO_2^- can be accurately measured by cyclic voltammetric and spectroscopic techniques. Ogden and Tench (4) have found that the effective concentration of the brightener is changed in a used solution. Based upon our study, this change cannot be due to the buildup of NO_2^-. The effect could be due to organic impurities or to the buildup of orthopyrophosphate (14).

Acknowledgment

The authors would like to thank Lockheed Missiles & Space Company's summer hire program in supporting G. A. Fung.

Manuscript submitted Sept. 9, 1982; revised manuscript received Dec. 21, 1982.

Any discussion of this paper will appear in a Discussion Section to be published in the December 1983 JOURNAL. All discussions for the December 1983 Discussion Section should be submitted by Aug. 1, 1983.

Publication costs of this article were assisted by Lockheed Missiles and Space Company.

REFERENCES

1. T. W. Dini, in "Modern Electroplating," 3rd ed., F. A. Lowenheim, Editor, p. 205, Wiley-Interscience, New York (1974).
2. J. I. Watters and A. Aaron, *JACS*, **75**, 611 (1953).
3. O. Radovici, C. Vass, and I. Solacolu, *Rev. Roum. Chim.*, **18**, 8, 1325 (1973).
4. C. Ogden and D. Tench, *This Journal*, **128**, 539 (1981).
5. C. Ogden and D. Tench, *ibid.*, **125**, 194 (1978).
6. C. Ogden and D. Tench, *Plating Surf. Fin.*, **66**, 45 (1979).
7. A. M. Bond, "Modern Polarographic Methods in Analytical Chemistry," p. 47, Marcel Dekker, Inc., New York (1980).
8. C. Ogden and D. Tench, *Plating Surf. Fin.*, **66**(9), 30 (1979).
9. J. B. Mohler, "Metal Finishing," p. 252, Metals and Plastics Publications Inc., New York (1982).
10. W. J. Blaedel and V. W. Moloche, "Elementary Quantitative Analysis," p. 379, Harper and Row Inc., New York (1963).
11. W. M. Latimer, "The Oxidation States of the Elements and Their Potentials in Aqueous Solutions," 2nd ed., p. 94, Prentice-Hall Inc., Englewood Cliffs, New Jersey (1959).
12. J. H. Watters and K. L. Ughim, *Anal. Chem.*, **42**, 335 (1970).
13. "Methods for Chemical Analysis of Water," March 1979 Environmental Monitoring and Support Laboratory Office of Research and Development, U.S. E.P.A., Cincinnati, Ohio.
14. B. F. Rothschild, *Met. Fin.*, **49** (1978).

The Effect of *p*H on Electroless Copper Deposition

John Duffy, Lester Pearson,[1] and Milan Paunovic*

Kollmorgen Corporation, PCK Technology Division, Melville, New York 11747

Electroless copper deposition is affected by pH in two distinct ways. First, the OH^- ions are reactants in the overall and the partial anodic reaction and thus affect these reactions in a direct way (primary pH effects). Second, pH effects various phenomena associated with the structure and composition of the metal-solution interphase. The major phenomena include: (*i*) adsorption, (*ii*) potential of zero charge (pzc), (*iii*) structure of the double layer, (*iv*) structure of the copper species in the solution, and (*v*) the ionic strength of the solution. All these phenomena effect the rate of electroless copper deposition in an indirect way (secondary pH effects).

The primary pH effect is expressed in terms of the reaction order with respect to OH^- ions, p_{OH^-}, and graphically as a rate *vs.* pH function. Reported values for p_{OH^-} by different authors (1-6) varied from −0.70 to 0.37. There are probably three major reasons for these differences among the authors. (*i*) The disagreement originates from the use of the chemical instead of the electrochemical definition for the order of reaction. The constant potential at the electrode, $\Delta\phi$, is an essential part of the definition of the electrochemical reaction order (7, 8). This restriction was removed when p_{OH^-} was determined on the basis of the chemical definition. However, it is well known that the mixed potential varies with pH (between −610 and −780 mV *vs.* SCE) and with the type and concentration of the ligand used in complexing the copper ions (9, 10). Thus, the removal of the restriction $\Delta\phi$ = const. could result in a rough approximation. (*ii*) The second reason for disagreement could stem from the neglect of the dependence of reaction order on adsorption (8). (*iii*) The third reason for the disagreement originates from the characteristic shape of the plating rate *vs.* pH curve. A plot of the logarithm of the plating rate against the logarithm of the OH^- concentration is not a straight line. Analysis of different segments of the curve produces different results.

Plots of the experimentally observed plating rates *vs.* pH show an initial increase, a maximum, and then decrease of the rate with increasing pH. The initial increase of the rate is due to the primary pH effect. The maximum and the decrease of the rate at high pH values were interpreted in terms of secondary pH effects. Two secondary effects were suggested so far: (*i*) change of the relative concentration of the methylene glycol and the hydroxide ions with pH due to the dissociation of methylene glycol (11), and (*ii*) variation of the transfer coefficient for the oxidation of formaldehyde with pH (12). It was shown that dissociation of methylene glycol is an important factor in electroless deposition of copper, but it is not sufficient to explain the pH effect (12).

Additional experimental data are needed in order to formulate a well-documented theory of the rate *vs.* pH function. We have selected two approaches in the

* Electrochemical Society Active Member.
[1] Present address: Pall Corporation, Glen Cove, New York 11542.
Key words: interfaces, spectra, additive, catalysis.

present study: electrochemical and spectroscopic. In the electrochemical approach, we have investigated the effect of pH on the rest potentials and the transfer coefficients for partial processes composing electroless copper deposition. In the spectroscopic approach, we have investigated the effects of pH on the composition of the adsorption film on the substrate. The importance of these studies is twofold: to elucidate the dependence of the rate of electroless copper deposition on pH and to interpret the dependence of the effect of additives on pH (13-16). The accelerating effect of an additive is usually observed in the range of the peak in the rate *vs.* pH function. The inhibiting effect of the same additive is observed at the lower and the higher pH values (16). For these reasons, Auger spectra have been taken for three characteristic values around the maximum.

Experimental

The solutions were prepared with analytical grade reagents and deionized water. An EDTP [ethylenedinitrilo-tetra-2-propanol, or N,N,N^1,N^1,-tetrakis-2 (2-hydroxypropyl) ethylenediamine][2] type electroless copper bath was used for these studies (10). The electroless copper solution contained 0.05M $CuSO_4$, 0.15M EDTP, 0.07M (para) formaldehyde, and NaOH to give a desired pH. Oxygen was removed by bubbling argon through the solution.

Gravimetric experiments were carried out in a glass beaker placed in a constant temperature bath regulated at 25°C (± 0.5°). Approximately 500 ml of the electroless copper solution was used. The stainless steel plate sample had a surface area of 30 cm^2. The steel plate samples were activated in $PdCl_2$ prior to immersion into the plating solution in order to avoid effects of the variable induction time (10). During plating, argon was passed above the solution. After 30 min of deposition, the steel plate was taken out of the solution, dried, and the amount of the deposited copper was determined by weighing.

In electrochemical experiments an all-glass, single compartment cell with three electrodes was used. The test electrode was a platinum sheet of 2.32 cm^2 in area, and the auxiliary electrode a platinum sheet (2.5 cm^2), both electroplated with copper. Plating was done in an acid copper solution (17) at 10 mA/cm^2. A saturated calomel electrode (SCE) was used as a reference electrode.

Galvanostatic experiments were performed using Hewlett Packard 6177C Precision Constant Current Source. The potential-time curves were recorded on a Hewlett Packard 70004A recorder. The recorded potential-time (E-t) curves, in duration between 1 and 2 sec, were extrapolated to $t = 0$ and so measured values of overpotential were used to construct the current-potential (i-E) curves.

Auger spectra were obtained with the V.G. Scientific Scanning Auger Microscope attached to a V.G. ESCA unit.

Results

The pH effect on the over-all reaction.—The rate of electroless copper deposition as a function of pH is shown in Fig. 1. It can be seen from Fig. 1 that the maximum rate of deposition is obtained at pH 12.5.

The pH effect on the partial anodic reaction.—The two pH functions characteristic for the rest potential due to the partial anodic reaction were recorded. First, the rest potentials of the copper electrode as a function of pH were recorded in the solution containing formaldehyde and a supporting electrolyte (in order to minimize ionic strength variation with variation in pH). Then, the rest potentials as a function of pH were recorded in the solution containing formaldehyde, supporting electrolyte, and EDTP in order to see the influence of ligand. Results are shown in Fig. 2. The

[2] Commercially available as, *e.g.*, "Quadrol," BASF Wyandotte Corporation.

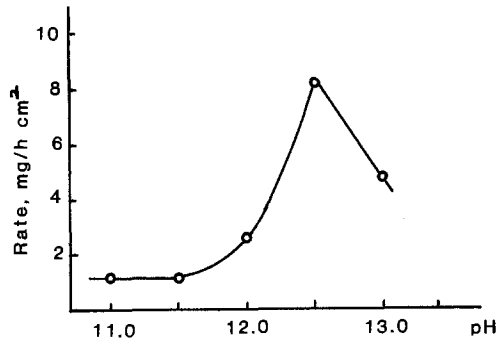

Fig. 1. Rate of electroless copper deposition as a function of pH

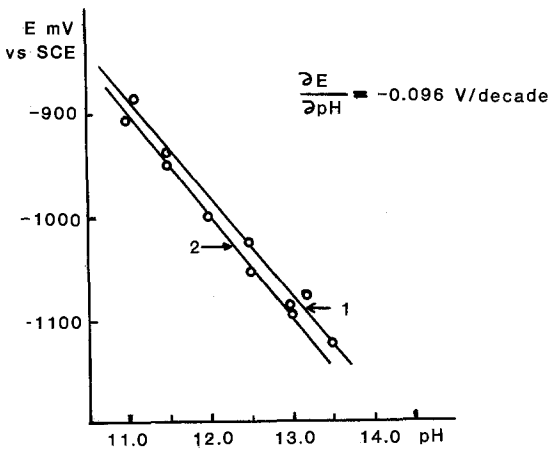

Fig. 2. The rest potential of a copper electrode in 0.13M formaldehyde and 1.0M KCl as a function of pH. Curve 1, the absence of ligand; curve 2, the presence of 0.05M EDTP.

average slope $\partial E/\partial(pH)$ of experimental functions in Fig. 2 is −0.096 V/decade.

The rate of oxidation of formaldehyde at the single electrode (absence of copper ions) as a function of pH, expressed in terms of the transfer coefficient α_F, is shown in Fig. 3. Transfer coefficients were calculated from Tafel slopes of current-potential curves obtained by the galvanostatic technique. Overpotentials up to 400 mV were recorded. It can be seen from Fig. 3 that the transfer coefficient for the anodic oxidation of formaldehyde α_F first increases, passes through a maximum, and then decreases when the pH is varied. This is the same type of dependence as for the overall process of copper deposition.

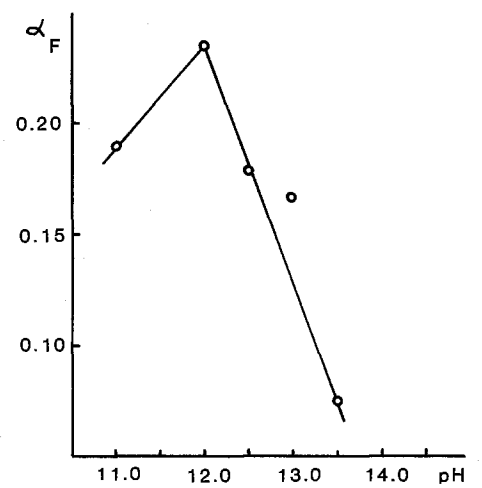

Fig. 3. The transfer coefficient of the anodic oxidation for formaldehyde in 0.25M KCl, 0.13M CH_2O as a function of pH. Copper electrode.

The pH effect on the partial cathodic reaction.—A plot of the rest potential of the copper electrode in a solution of cupric ions, as a function of pH, in the presence of complexing agent is shown in Fig. 4. The average slope $\partial E/\partial(pH)$ of this function is −0.066 V/decade.

The pH dependence of the transfer coefficient for the cathodic reduction of complexed copper ions, α_{CuL}, is shown in Fig. 5. Transfer coefficients were calculated from Tafel slopes of the current-potential relationship. The relationship is of the same type as for the $\alpha_F = f(pH)$ function.

Surface analysis of copper deposit by Auger electron spectroscopy.—Copper deposits obtained from solutions at pH values of 11.5, 12.5, and 13.0, in the air atmosphere, and in the presence of sodium 2-mercaptobensothiazole (MBT) were analyzed. Analysis was carried out *ex situ* in the as-deposited condition (sample exposed to air atmosphere after deposition) and after a very light etch (20 sec, 6 keV) to remove the adsorbed contaminant layer.

Wide scans (1100-100 eV) were used to identify the species present. Narrow scans were carried out for transitions in the core states for O and N (600-300 eV) and Cu (1050-750 eV). Results are shown in Table I. The valence band transition for Cu was observed in order to determine the oxidation state of the copper. Results are shown in Table II. It can be seen from Table II that the copper deposit from the solution at pH 12.5 shows smallest signal for sulfur, carbon, nitrogen, and sodium. The largest signals for the same elements, sulfur, carbon, nitrogen, and sodium were observed for the sample deposited at pH 11.5. It is interesting to note that the sample deposited at pH 13.0 shows a new carbon peak at 256 eV in addition to the peak at 275 eV. Carbon (275 and 256 eV) and sulfur (150 eV) peaks for three samples are shown in Fig. 6. Copper Auger spectra from valence band regions (67.5 eV) are shown in Fig. 7. The shift of −2 eV observed (pH 11.5 and 13.0) here (Table II and Fig. 7) is in agreement with that observed earlier (18, 19). Auger electron spectra of copper for transitions in the core states did not develop the Auger peak at 916.7 eV corresponding to the Cu-MBT complex (20).

Table I. Species observed and the peak-to-peak heights in the etched samples of electroless copper (0.05M $CuSO_4$, 0.15M EDTP, 0.07M CH_2O, 2 mg/liter MBT)

pH of electroless solution	Element						
	Na	Cu	O	N	C	C′	S
11.5	7	45	28	25	134		72
12.5		118	36	3	48		15
13.0	4	104	60	4	40	56	48

Table II. Auger spectra from valence band region

	Standards	eV*	
	Cu	67.5	
	Cu_2O	65.0	
	CuO	63.0	
Samples	eV*	Shift, eV	Inference
pH 11.5	65.5	−2.0	Cu_2O
pH 12.5	68.0		Cu
pH 13.0	65.5	−2.0	Cu_2O

* Relative to C Auger peak 277 eV.

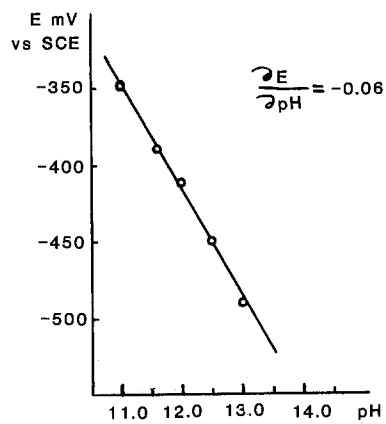

Fig. 4. The rest potential of a copper electrode in 0.1M $CuSO_4$, 0.175M EDTP, and 0.25M KCl as a function of pH.

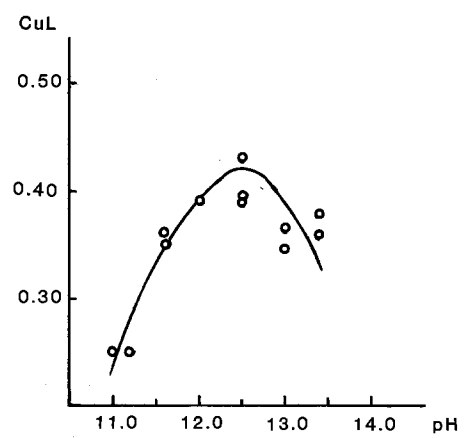

Fig. 5. The transfer coefficient for cathodic reduction of Cu(II) ions in 0.1M $CuSO_4$, 0.175M EDTP, and 0.25M KCl.

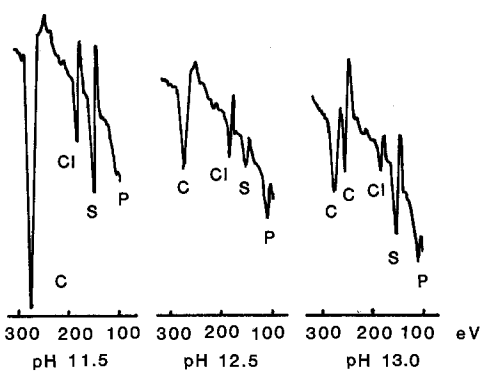

Fig. 6. Auger electron spectra of electrolessly deposited copper. Electroless solution: 0.05M $CuSO_4$, 0.15M EDTP, 0.07M CH_2O, 2 mg/liter MBT.

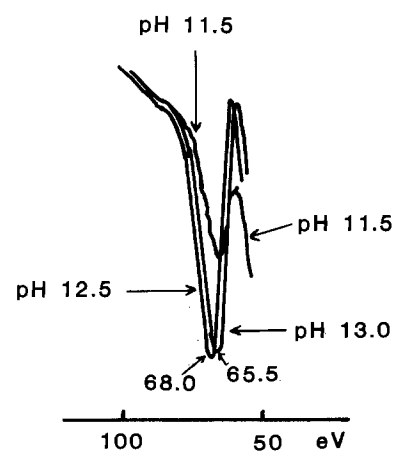

Fig. 7. Auger electron spectra of copper, valence band region

Discussion

The pH effect on the partial anodic reaction.—It was shown that the straight line representing the rest potential for the copper electrode in the alkaline solution containing formaldehyde as a function of pH has the slope ($\partial E/\partial$pH) of −0.096 V/decade. There are two possible reactions that can control this rest potential and the slope. According to Buck and Griffith (21) the anodic oxidation of formaldehyde at the Pt electrode in an alkaline solution proceeds according to the reaction

$$CH_2O + 3\,OH^- \rightarrow HCOO^- + 2H_2O + 2e^- \quad [1]$$

In this kinetic scheme the adsorbed hydrogen formed in the dissociative adsorption of the electroactive species $CH_2(OH)O^-$ is desorbed in the electrochemical reaction. In a modified Buck and Griffith mechanism (22), applicable to the Cu electrode, the adsorbed hydrogen is desorbed in a chemical reaction and the anodic oxidation of formaldehyde then proceeds according to the reaction

$$CH_2O + 2\,OH^- \rightarrow HCOO^- + H_2O + 1/2\,H_2 + e^- \quad [2]$$

The rest potential as a function of pH, at 25°C, is given by the Nernst equation (23)

$$E = E_o' - 0.059\ (m/n)\ pH \quad [3]$$

and the slope by

$$\partial E/\partial(pH) = -0.059\ m/n \quad [4]$$

where E_o' combines the standard electrode potential E_o and the concentration term in the Nernst equation, m is the number of H^+ (or OH^-) ions, and n is the number of electrons participating in the reaction. Application of Eq. [4] to reactions [1] and [2] yields the slopes of −0.089 and −0.118 V/decade, respectively. Since the average slope of curves in Fig. 2 is −0.096 V/decade it appears that both mechanisms, [1] and [2], are controlling the rest potential and its pH dependence.

The expected Tafel slopes ($b = 0.059/\alpha n$), at 25°C and assuming $\alpha = 0.5$, for reactions [1] and [2] are 0.059 and 0.118 V/decade, respectively. The experimentally observed Tafel slopes for oxidation of formaldehyde at the Cu electrode, at 25°C and pH 12.50, are in the range between 0.290 and 0.330 V/decade (17). Tafel slopes between 0.205 and 0.840 V/decade were observed in this work when pH was varied. It was shown in Fig. 3 that the transfer coefficient α_F increases, passes through a maximum, and then decreases when the concentration of sodium hydroxide varied. The same type of pH dependence was observed for the pH effect in the overall copper deposition process (Fig. 1).

Tafel slopes higher than 0.118 V/decade are not unusual in oxidations of organic compounds (24-26). One cause for high slopes is the formation of films of adsorbed intermediates and the anodic products on the electrode surface (27-29). Systems with surface films can be treated on the basis of the dual barrier model of the interphase where an overall transfer coefficient is used to describe the current-potential relationship (28).

Electrochemical systems where a film of adsorbed intermediates is formed at the surface of the substrate have two important characteristics, besides a high Tafel slope. These characteristics are a transition region in the current-potential relationship (27, 28) and an arrest in the galvanostatic potential time curves (27). A transition region is characteristic of barrier layer films and corresponds to an onset of a passive behavior (29). Transition regions in systems that we have studied are between overpotentials of 0.15 and 0.25V, depending on conditions. In the lower region ($\eta < 0.2$V) Tafel slopes are smaller, with transfer coefficients between 0.3 and 0.5. In the higher η region ($\eta > 0.2$V) Tafel slopes are larger and transfer coefficients smaller, as reported above. Arrests in the galvanostatic charging curves (E-t) correspond to less than a monolayer coverage by an adsorbed species (*e.g.*, about 100 μC/cm^2 for 0.8 mA/cm^2).

All the above data indicate that the anodic oxidation of formaldehyde does not proceed according to the simple kinetic scheme represented by reactions [1] or [2] but by a more complicated scheme based on a double barrier model. According to this model, transfer coefficients presented in this paper are overall transfer coefficients given by

$$\alpha = (\alpha_F\alpha_s/\alpha_F + \alpha_s) \quad [5]$$

where α_F is the transfer coefficient for the field-dependent migration of the charge carriers and α_s that for the electrochemical charge transfer (28).

The pH effect on the partial cathodic reaction.—The slope $\partial E/\partial(pH)$ of the straight line representing the rest potential of the copper electrode in the alkaline solution of Cu^{2+} and EDTP as a function of pH is found to be −0.066 V/decade. This slope is in conformity with at least four possible reactions in this system

$$Cu + H_2L' = CuL' + 2H^+ + 2e^- \quad [6]$$

where L = EDTP, L′ = EDTP − 2H$^+$ (30, 31)

$$2Cu + H_2O = Cu_2O + 2H^+ + 2e^- \quad [7]$$

$$Cu + H_2O = CuO + 2H^+ + 2e^- \quad [8]$$

$$Cu + 2H_2O = Cu(OH)_2 + 2H^+ + 2e^- \quad [9]$$

All these reactions show the following potential-pH dependence

$$E = E^\circ - 0.059pH \quad [10]$$

and the slope $\partial E/\partial(pH) = -0.059$/decade (32). The experimentally observed slope of −0.066 V/decade is in good agreement with this value. In addition, systems that are relevant to this study, Cu_2O-CuO, Cu_2O-$Cu(OH)_2$, and Cu_2O-Cu^{2+} show the same −0.059 pH dependence (30). Thus, the rest potential of the copper electrode in the aqueous alkaline solution of cupric ions is probably a mixed potential.

The transfer coefficient for the cathodic reduction of complexed copper ions (α_{CuL}) shows the same type of pH dependence (Fig. 5) as α_F (Fig. 3) and the over-all deposition rate-pH function (Fig. 1). A comparison of Fig. 3 and 5 shows that the cathodic sites at the surface are less inhibited than the anodic sites.

Surface analysis.—The surface analysis of a copper deposit by Auger electron spectroscopy showed that the deposit obtained at pH 12.5 had the least amount of chemisorbed species at the surface. The thinnest chemisorbed film at the pH 12.5 can be correlated to the maximum values for α_F, α_{CuL}, and the rate of deposition. It appears that the dual barrier model (28) is plausible for systems described in this study.

The above electrochemical and spectroscopic results point to the importance of adsorption, inhibition, and passivation phenomena in electroless copper deposition and need for more studies in this direction.

Acknowledgments

The authors are grateful to Professor Clive R. Clayton, Department of Materials Science and Engineering, State University of New York, Stony Brook, New York, for the scanning Auger microprobe analysis and discussion of Auger spectra. Messers R. Arndt, G. Combes, and D. Vitkavage are thanked for confirmatory electrochemical measurements.

Manuscript submitted June 29, 1981; revised manuscript received Sept. 22, 1982. This was Paper 493 presented at The Electrochemical Society Meeting, Minneapolis, Minnesota, May 10-15, 1981.

Any discussion of this paper will appear in a Discussion Section to be published in the December 1983 JOURNAL. All discussions for the December 1983 Discussion Section should be submitted by Aug. 1, 1983.

Publication costs of this article were assisted by the Kollmorgen Corporation.

REFERENCES

1. F. Donahue, *Oberflaeche-Surf.*, **13,** (12), 301 (1972).
2. F. L. Shippey and F. M. Donahue, *Plating*, **60,** 43 (1973).
3. J. Dumesic, J. A. Koutsky, and T. W. Chapman, *This Journal*, **121,** 1405 (1974).
4. A. Molenaar, M. F. E. Holdrinet, and L. K. H. van Beek, *Plating*, **61,** 238 (1974).
5. S. M. El-Raghy and A. A. Abo-Salama, *This Journal*, **126,** 171 (1979).
6. F. M. Donahue, K. L. M. Wong, and R. Bhalla, *ibid.*, **127,** 2340 (1980).
7. J. O'M. Bockris and A. K. N. Reddy, "Modern Electrochemistry," p. 1009, Plenum Press, New York (1970).
8. E. J. Rudd and B. E. Conway, *Trans. Faraday Soc.*, **67,** 440 (1971).
9. F. Donahue and F. L. Shippey, *Plating*, **60,** 135 (1973).
10. M. Paunovic, *This Journal*, **124,** 349 (1977).
11. L. N. Schoenberg, *ibid.*, **119,** 1491 (1972).
12. M. Paunovic, *ibid.*, **125,** 173 (1978).
13. H. Fischer, *J. Electroanal. Chem. Interfacial Electrochem.*, **62,** 163 (1975).
14. S. Sathyanarayan, *ibid.*, **50,** 195 (1974).
15. E. Dutkiewitz and A. Puacz, *ibid.*, **100,** 974 (1979).
16. F. Nuzzi, *Plating Surf. Finishing*, In press.
17. M. Paunovic, *Plating*, **55,** 1161 (1968).
18. G. Schön, *Surf. Sci.*, **35,** 96 (1973).
19. B. G. Baker, in "Modern Aspects of Electrochemistry," Vol. 10, J. O'M. Bockris and B. E. Conway, Editors, Plenum Press, New York (1975).
20. D. Chadwick and T. Hashemi, *Surf. Sci.*, **89,** 649 (1979).
21. R. P. Buck and L. R. Griffith, *This Journal*, **109,** 1005 (1962).
22. M. Saito, *Met. Surf. Technol. Jpn.*, **16,** 300 (1965).
23. J. O'M. Bockris and A. K. N. Reddy, "Modern Electrochemistry," p. 1121, Plenum Press, New York (1970).
24. A. A. Humffray, in "Modern Aspects of Electrochemistry," Vol. 8, J. O'M. Bockris and B. E. Conway, Editors, Plenum Press, New York (1972).
25. B. J. Piersma and E. Gileadi, in "Modern Aspects of Electrochemistry," Vol. 4, J. O'M. Bockris, Editor, Plenum Press, New York (1966).
26. B. E. Conway, "Theory and Principles of Electrode Processes," Ronald Press, New York (1964).
27. B. E. Conway and M. Dzieciuch, *Can. J. Chem.*, **41,** 21, 38, 55 (1963).
28. J. J. MacDonald and B. E. Conway, *Proc. R. Soc. London*, **269,** 414, 419 (1962).
29. D. Gilroy and B. E. Conway, *J. Phys. Chem.*, **69,** 1259 (1965).
30. J. L. Hall, R. F. Jones, C. E. Delchamp, and C. W. McWilliams, *J. Am. Chem. Soc.*, **79,** 3361 (1957).
31. D. A. Keyworth, *Talanta*, **2,** 383 (1959).
32. M. J. N. Pourbaix, "Thermodynamics of Dilute Aqueous Solutions," p. 55, Edward Arnold & Co., London (1949).

Standard Free Energy of Formation of Iron Iodide

Ashok Khandkar,* V. B. Tare, and J. Bruce Wagner, Jr.**

Center for Solid State Science, Arizona State University, Tempe, Arizona 85281

Although solid electrolytes are being increasingly used for the determination of thermodynamic properties of compounds, there are surprisingly few reports on the use of silver iodide for this purpose. Silver iodide is known to exist in two stable crystallographic forms: α-AgI (stable above 147°C) is known to be a superionic conductor with an electronic transport number approximately 10^{-8} times the ionic transport number. β-AgI (stable below 147°C) exhibits a very small total conductivity and is also reported to be predominantly an ionic conductor (1).

Thus by using silver iodide as a solid electrolyte it is possible to formulate a galvanic cell

$$\text{Ag} \mid \text{AgI} \mid \text{Fe-FeI}_2 \qquad [\text{I}]$$

to determine the free energy of formation of iron iodide. The thermodynamic stability of FeI_2 is not known precisely, but it appears to be less stable than AgI. Thus if the cell satisfies the criteria for reversibility, the open-circuit emf is related to the free energy change of the cell reaction by

$$\Delta G_{\text{cell}} = -nE\mathbf{F} = 2\Delta G^\circ_{\text{AgI}} - \Delta G^\circ_{\text{FeI}_2} \qquad [1]$$

where n is number of electrons transferred during the cell reaction, E the emf in volts, and F the Faraday constant. The overall cell reaction is

$$2\text{Ag} + \text{FeI}_2 = 2\text{AgI} + \text{Fe} \qquad [2]$$

The standard free energy of formation of AgI is known and hence it is possible to estimate the standard free energy of formation of iron iodide by measuring the open-circuit emf of the above cell as a function of temperature.

A mixture of iron and iron iodide was prepared by mixing iron powder, −200 mesh and 99.999% pure, with 99.9% pure iodine in the weight ratio of 5:1. The mixture was sealed in an evacuated silica tube and heated initially to 200°C for 8 hr. The completion of the reaction of iodine with excess iron was evident from the disappearance of the violet iodine vapors. The mixture was subsequently heated to 600°C for 2 hr, examined by x-ray powder diffraction for phase identification, ground to a fine powder, and pressed into a pellet of 12 mm diam and 6 mm thick in a steel die under hydrostatic pressure of 5 tons/in.^{2}. The pellet was annealed in purified argon for 12 hr at 400°C. Iron iodide is hygroscopic. It is therefore essential to avoid contact with water vapor.

An electrolyte pellet of similar dimensions was prepared by pressing AgI (99.999% pure purchased from Aldrich Chemicals) powder under hydrostatic pressure of 5 tons/in.^{2}. The pellet was lightly polished on a fine emery paper and sandwiched between two electrode pellets, one of which was a pure silver disk, 12 mm diam and 3 mm thick, and the other was a pellet of Fe-FeI_2 prepared as described above. The whole assembly was placed between two platinum disks each with a spot-welded platinum lead wire and held together by means of a spring pressure assembly. The spring-loaded cell was introduced into a quartz tube in which a steady continuous flow of dried and purified argon was maintained. The quartz tube was kept in a Nichrome wire-wound furnace with a constant temperature zone of about 2 in. The temperature of the furnace was controlled to ± 0.5°C by a proportional controller. The temperature of the cell was measured

* Electrochemical Society Student Member.
** Electrochemical Society Active Member.

independently by a Pt-Pt + 10% Rh thermocouple placed very near the cell. The open-circuit emf of the cell was measured by a Hewlett Packard digital multimeter with an input impedance of ≈ 10 MΩ.

Before starting the measurements, the cell was annealed at 150°C for about 10 hr after which steady, nondrifting emf values were obtained. The cell satisfied all the usual criteria of reversibility. Emf was measured at temperatures which were varied in a random fashion. Preliminary investigations showed that emf drifted rapidly at temperatures above 230°C. Similarly below 110°C the cell took an unusually long time for obtaining steady values, and emf values between different runs were not consistent. On keeping the cell for a very long time (> 12 hr) at temperatures above 230°C, visible signs of reaction at the AgI/Fe + FeI_2 interface were seen as black spots on the AgI pellet surface in contact with Fe + FeI_2. The measurement of emf on the cell was therefore restricted to the temperature range 115°-230°C. After the measurements in this temperature range, the surfaces of the electrolyte pellet as well as the Fe-FeI_2 electrode were examined by x-ray powder diffraction technique for any possible reactions. Emf readings were regarded as reliable only when there was no change in the electrolyte and the electrodes after the measurement.

The cell responded quickly to changes in temperatures above 150°C. Steady emf values were obtained within 10-15 min after obtaining a constant temperature. The response below 150°C was found to be very slow. Usually 60 min or more were required to obtain steady emf values.

Table I gives the emf's at various temperatures measured on three different cells. The same data are plotted in Fig. 1. The data can be represented by two linear relationships between emf and temperature.

The linear regression analysis of the data gave the following two expressions

$$E_{volts} + 0.09072(\pm 0.00774) + 1.2(\pm 1.9) \times 10^{-5}T \quad \text{for } T < 422.5\text{ K} \quad [3]$$

$$E_{volts} + 0.02017(\pm 0.00225) + 1.79(\pm 0.05) \times 10^{-4}T \quad \text{for } T > 422.5\text{ K} \quad [4]$$

The temperature at which the change in slope occurs is estimated from these two equations to be 422.5 K. This temperature T_{trans} corresponds to the change in crystal structure of silver iodide from β at lower temperatures to α at higher temperatures. The enthalpy change for this transformation ΔH_{trans} can be estimated from the difference in slopes of these lines by using the relationship

$$\Delta H_{trans} = n\mathbf{F}\Delta\text{slope} \times T_{trans} \quad [5]$$

where $n = 1$ per mol of AgI. This is calculated to be 1630 ± 250 cal/mol.

Table I. Cell emf in mV at various temperatures*

Cell 1		Cell 2		Cell 3	
Temp (°C)	Emf (mV)	Temp (°C)	Emf (mV)	Temp (°C)	Emf (mV)
156	97.40	155	95.42	152	97.28
172	99.50	189	102.14	203	105.05
144	96.07	176	100.27	172	99.50
217	107.64	217	107.64	139	94.82
198	103.80	207	106.69	181	101.18
209	106.22	170	99.50	186	102.48
227	109.53	191	103.00	219	108.07
203	140.77	202	105.83	152	97.28
189	101.97	224	109.45	161	98.38
131	95.68	155	95.62	178	100.69
166	98.95	132	95.23	213	107.60
119	95.75	125	95.45	128	95.25
		148	96.80	135	95.50

* Values are reported in the order in which they were measured.

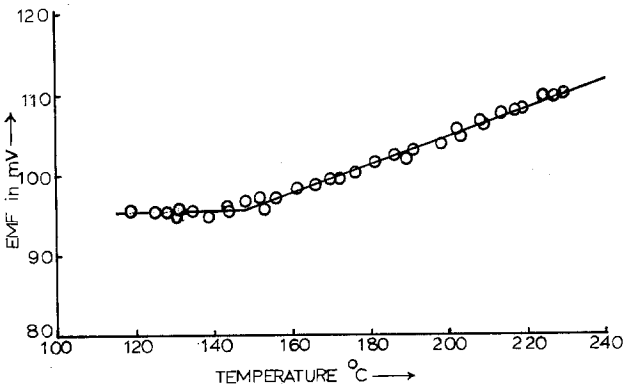

Fig. 1. Open-circuit emf of a galvanic cell Ag|AgI|Fe-FeI_2 as a function of temperature.

As mentioned earlier the values of emf obtained at temperatures below 150°C took a long time to stabilize. The range of temperature of measurement below 150°C is also very small (≈ 40°). The errors in slope are therefore expected to be large. In spite of this, the agreement between the temperature and enthalpy of transformation reported in the literature (2, 3) as 421 K and 1.47 ± (0.1) K cal/mol, respectively, and the one estimated from the present data is good. However, to estimate the standard free energy of formation of FeI_2, only the data above the transition temperature have been used. This is because at these temperatures AgI is a superionic conductor (σ sp $\approx 10\ \Omega^{-1}\ cm^{-1}$ at 200°C) and is ideal for use as a solid electrolyte. At temperatures below transition the total conductivity is very small (σ sp $\approx 10^{-6}\ \Omega^{-1}\ cm^{-1}$ at 25°C) (3). The transport numbers of electrons, holes, and ions in this temperature range have not so far been uniquely determined. Available data indicate that the electronic transference number is only an order of magnitude lower than the ionic transference number (1, 4). Our inability to obtain reliable data at lower temperatures is probably due to these considerations.

Using Eq. [1] and [4], one obtains

$$\Delta G_{cell} = -930(\pm 104) - 8.25(\pm 0.23)T \text{ cal/mol} \quad [6]$$

To obtain standard free energy of formation of FeI_2 from this expression, the standard free energy of formation of silver iodide has to be known precisely.

For this purpose recent compilation of thermodynamic data of Barin and Knacke (5) has been used. From these data an expression for the standard free energy of formation of α-AgI above 422 K has been obtained as

$$\Delta G°_{AgI} = -19857 + 7.955T \text{ cal/mol} \quad [7]$$

The error limits for the values of $\Delta G°_{AgI}$ have not been reported. However, since the data is based on the values reported by Kelley (6) who has claimed the accuracy to be only 5%, the maximum error in the values of $\Delta G°_{AgI}$ can be estimated to be ± 1000 cal/mol.

Using Eq. [1], [6], and [7] the standard free energy of formation of FeI_2, from solid iron and iodine at 1 atm pressure has been estimated to be

$$\Delta G°_{FeI_2} = -38784 + 24.165T \text{ cal/mol} \quad [8]$$

To estimate the errors in the values of $\Delta G°_{FeI_2}$ one has to take into account the errors in the values of $\Delta G°_{AgI}$ as well as the errors estimated in Eq. [6]. The maximum error in the latter in the temperature range investigated is calculated to be ± 200 cal. Combining this error with the one reported for $\Delta G°_{AgI}$ one can estimate the maximum error limits in the values of $\Delta G°_{FeI_2}$ obtained from the present investigation to be ± 2500 cal/mol. One may, however, note that these

large error limits are primarily because of the uncertainties in the values reported for $\Delta G°_{AgI}$.

The standard free energy of formation of FeI_2 can also be estimated from the data given by Barin, Knacke, and Kubaschewski (7) as well as those given in the JANAF Tables (8). These values are based on the measurement of decomposition pressures of iodine over FeI_2 in this temperature range (9) and also on the data obtained by solution calorimetry (10). On the basis of error limits reported for $\Delta H°_f$ and $S°_f$ the error limits in the calculated values of $\Delta G°_{FeI_2}$ are estimated to be ± 5000 cal/mol.

An expression for the standard free energy of formation of FeI_2 has been given by Kubaschewski and Alcock (2) with estimated error limits in the values of $\Delta G°_{FeI_2}$ as ± 5000 cal/mol. Figure 2 shows these data along with the data obtained in the present investigation. Our data are much closer to those reported by Barin, Knacke, and Kubaschewski (7). The data obtained in the present investigation can, however, be considered to be more accurate because of the smaller uncertainties and the consistency and the reliability of the technique used. It may be emphasized, however, that the uncertainties in the values of $\Delta G°_{FeI_2}$ obtained from the present investigations would be greatly reduced if more accurate data for $\Delta G°_{AgI}$ become available.

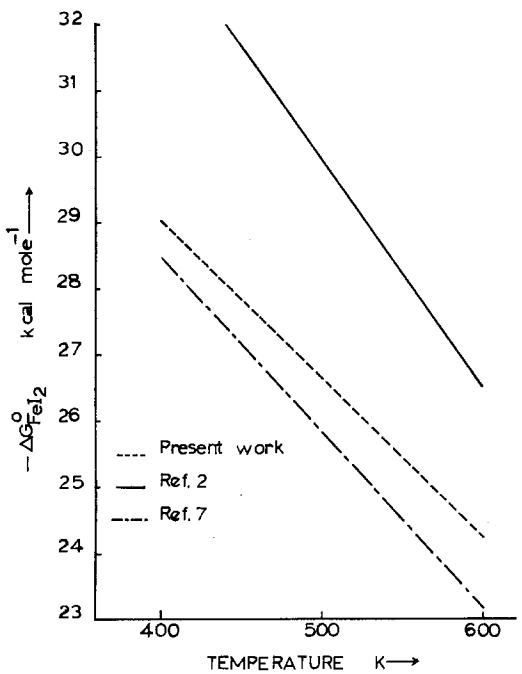

Fig. 2. Standard free energy of formation of FeI_2 as a function of temperature.

Acknowledgments

This work was initiated under NASA Contract No. NAS8-32937 and subsequently funded by a grant from the Center for Solid State Science, Arizona State University.

Manuscript submitted Aug. 2, 1982; revised manuscript received Oct. 5, 1982.

Any discussion of this paper will appear in a Discussion Section to be published in the December 1983 JOURNAL. All discussions for the December 1983 Discussion Section should be submitted by Aug. 1, 1983.

Publication costs of this article were assisted by Arizona State University.

REFERENCES

1. B. Ilschner, *J. Chem. Phys.*, **28**, 1109 (1958); J. Mizusaki, K. Fueki, and T. Mukaibo, *Bull. Chem. Soc. Jpn.*, **51**, 694 (1978).
2. O. Kubaschewski and C. B. Alcock, "Metallurgical Thermochemistry," p. 268, Pergamon Press, New York (1979).
3. J. C. Bazan and E. A. Dayen, *Z. Phys. Chem.* (NF), **105**, 64 (1977).
4. K. Shahi and J. B. Wagner, Jr., *Phys. Rev. B*, **23**, 6417 (1981).
5. I. Barin and O. Knacke, "Thermochemical Properties of Inorganic Substances," Springer-Verlag (1973).
6. K. K. Kelley, *U.S. Bur. Mines Bull. No. 476* (1949) and *584* (1960).
7. I. Barin, O. Knacke, and O. Kubaschewski, "Thermochemical Properties of Inorganic Substances," Supplement, Springer-Verlag (1977).
8. JANAF Thermochemical Tables, U.S. Department of Commerce, National Bureau of Standards/ Institute of Applied Technology, Michigan (1965-1968).
9. W. E. Zaugg and N. W. Gregory, *J. Phys. Chem.*, **70**, 486 (1966).
10. W. Hieber and A. Woerner, *Z. Electrochem.*, **40**, 287 (1934).

Evaluation of Tetrafluoroethane-1,2-Disulfonic Acid as a Fuel Cell Electrolyte

Philip N. Ross, Jr.*

Lawrence Berkeley Laboratory, Materials and Molecular Research Division, Berkeley, California 94720

It has been demonstrated in a number of investigations that the kinetics of oxygen reduction on Pt are significantly higher in trifluoromethane sulfonic acid (TFMSA) solutions than in phosphoric acid (1-3). These differences appear to be due to the higher oxygen solubility and the lower specific adsorption of anions in TFMSA (4). However, the further investigation of TFMSA as a fuel cell electrolyte has revealed the undesirable physical properties of this material that may limit its usefulness. TFMSA solutions more concentrated than *ca.* 7M have wetting contact angles on polytetrafluoroethylene (PTFE) surfaces, ionic conductivities lower than desirable, and high acid vapor pressure (5). The wetting of PTFE causes loss of the hydrophobic gas-diffusion electrode structure essential for low transport losses at high current density, and the high vapor pressure represents a life limitation and/or maintenance problem. Pure hydrogen-air fuel cells using 6M TFMSA at 60°C have shown improved performance relative to state-of-the-art phosphoric acid fuel cells, but use with hydrogen containing carbon monoxide at levels above *ca.* 0.01% severely poisons the Pt electrode at such a low temperature (6). Use of less volatile higher homologs of TFMSA was suggested by Baker and co-workers (7), particularly the dimeric form of TFMSA, tetrafluoroethane-1,2-disulfonic acid

* Electrochemical Society Active Member.
Key words: oxygen reduction, Pt electrocatalyst, carbon monoxide poisoning.

(TFEDSA). The purpose of this communication is to report some physical properties of TFEDSA relevant to fuel cell use and preliminary examinations of this electrolyte in fuel cells with hydrogen containing carbon monoxide.

Experimental

Tetrafluoroethane-1,2-disulfonic acid was supplied by KOR (Cambridge, Massachusetts) as a 50 weight percent (w/o) solution. The acid was purified by repeated vacuum refluxing (200°C) with intermittent peroxide treatment and recrystallization of what was presumed to be the dihydrate, $(CF_2SO_3H \cdot H_2O)_2$; elemental analysis was consistent with this assumption. The purification did not, however, appear to have a significant effect on the physical properties measured here, as equivalent results were obtained with the as-received solutions concentrated by evaporation. Solutions were prepared by weight additions of water to the purified acid hydrate, or by concentration of the as-received solution to a known weight loss. Specific gravity at 25°C was used as an internal standard for concentration measurement. The conductivity of the acid solutions was measured in a thermostated microconductivity cell (cell constant 0.5 cm^{-1}) using an a-c impedance bridge (Wayne-Kerr). The vapor pressure of the acid solutions was measured using the isoteniscope technique (8). The properties of the acid as a fuel cell electrolyte were observed using a small (1 cm^2 active area) free electrolyte cell (1.5 ml), fabricated out of PTFE with phosphoric acid fuel cell standard supported Pt catalyst fabricated into PTFE-bonded fuel cell type electrodes (9). PTFE capillary tubing connected the cell to an external hydrogen electrode in the same electrolyte (all potentials are referenced to this RHE). The Pt loading on both electrodes was 0.25 mg/cm^2. The PTFE content of the hydrogen electrode was fixed at 25 w/o, with a curing temperature 20°-30°C below the melting point of TFE-30B (327°C). Optimum results were obtained for the oxygen electrode using slightly higher PTFE content with a curing temperature of 320°C. A hydrogen-carbon dioxide-carbon monoxide mixture of calibrated composition 80 H_2:19 CO_2:1 CO was purchased from Matheson, and diluted with an 80 H_2:20 CO_2 calibrated mixture (Matheson Ultra-Pure Grade) to produce mixtures containing 0.1% CO and 0.01% CO. The composition of the dilution gases was checked on a mass spectrometer using the calibrated mixture as standard. The accuracy of the CO content was estimated to be ±0.05 and ±0.005%, respectively. Fuel cell polarization data were obtained using a PAR 173D Potentiostat, usually in the controlled-current mode, with *IR*-corrections by current interception using a mercury-wetted relay.

Results

The vapor pressure data are shown in Fig. 1. For intermediate temperatures of 80°-160°C, the vapor over the acids was water with no detectable acid content. Vapor pressure data for pure H_2O (10), and 85 and 98 w/o H_3PO_4 solutions (11) are added for reference purposes. Practical fuel cell experience indicates that H_2O vapor pressures greater than *ca.* 200 Torr create a problem in water balance in the cell. Most of the water in an acid fuel cell is carried out by the air stream, and the cathode polarization is reduced by use of more than stoichiometric air flow (12). Simple material balances indicate vapor pressures more than *ca.* 200 Torr require air flows close to stoichiometric, resulting in a polarization penalty. TFEDSA solutions of 60-70 w/o have water vapor pressures comparable to 85 w/o H_3PO_4, which is *ca.* 200 Torr at 100°-110°C. For use at higher temperature, both TFEDSA and H_3PO_4 must become considerably more concentrated to be in equilibrium with H_2O vapor at 200 Torr. At 170°C, for example, the H_3PO_4 concentration would be about 98 w/o, while

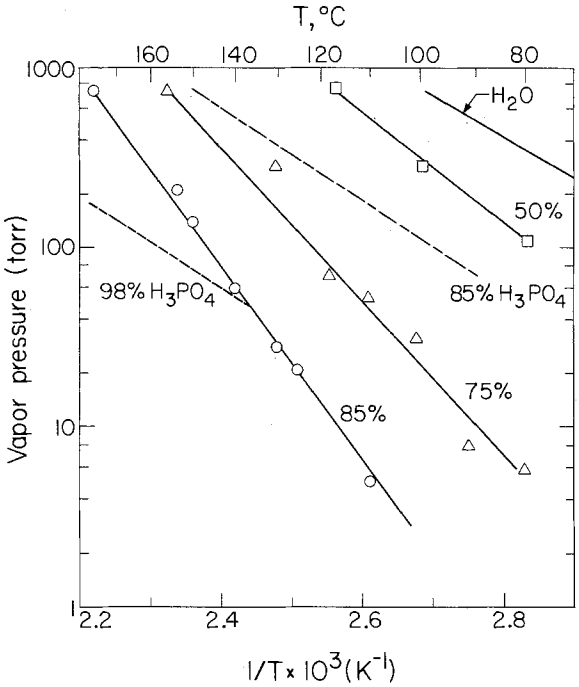

Fig. 1. Vapor pressure of water over TFEDSA solutions

for TFEDSA the concentration would be about 88-90 w/o, which is nominally the composition of the hydrate of the acid.

Quantitative measurements of contact angle have not yet been made. However, less precise observations of the wetting of cleaved PTFE surfaces were made for 70-85 w/o TFEDSA electrolyte at 100°C. The contact angles appeared to be greater than 90°, indicative that a hydrophobic structure would be obtained with these electrolytes in a PTFE-bonded electrode.

The conductivity data is shown in Fig. 2. As expected, solutions more concentrated than 40 w/o are on the descending side of the conductivity-concentration curve. At an equivalent normality of 6*N* and at 80°C, TFEDSA appears to have about the same conductivity (*ca.* 0.4 Ω^{-1} cm^{-1}) as TFMSA (5). The

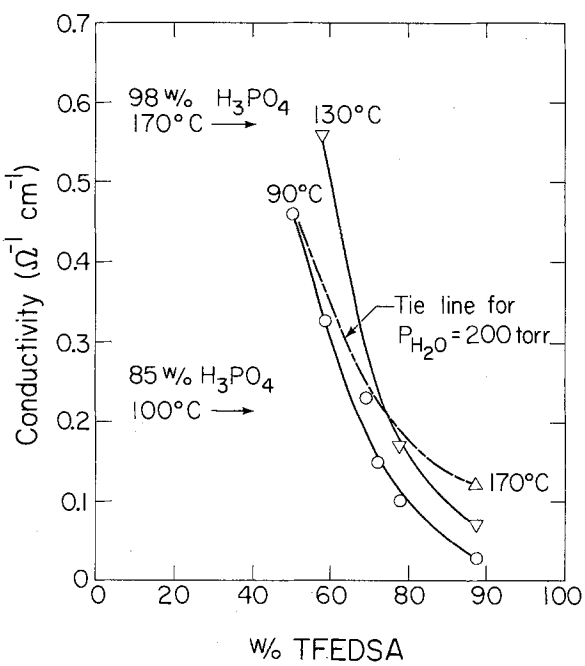

Fig. 2. Conductivity of TFEDSA solutions as a function of concentration and temperature. Tie represents the acid in equilibrium with 200 Torr H_2O vapor over the range 90°-170°C.

conductivity of these acids at 6*N* is significantly higher than that for 6M H_3PO_4 (11), which might be expected from the stronger acidity. However, H_3PO_4 exhibits the unusual and desirable property that the conductivity remains high even in extremely concentrated form, *e.g.*, the conductivity of 98 w/o H_3PO_4 at 170°C is 0.6 Ω^{-1} cm^{-1}. That is not the case with either TFMSA or TFEDSA solutions, as the data in Fig. 2 show clearly. The tie-line drawn in Fig. 2 represents (approximately) the concentration and conductivity of acid in equilibrium with H_2O vapor at 200 Torr in the temperature range of 90°-170°C. In comparison to H_3PO_4 solutions, comparable or superior conductivity is observed only for 60-70 w/o at 100°-110°C. At 170°C, the conductivity of TFEDSA in equilibrium with 200 Torr H_2O vapor is only 0.12 Ω^{-1} cm^{-1}, a factor of five lower than in 98 w/o H_3PO_4 at this temperature. The technological consequences of this lower conductivity are severe. In a full-scale H_3PO_4 fuel cell, the internal resistance losses due to resistance in the electrolyte matrix are *ca.* 40 mV at rated load (13); increasing this by a factor of five by substitution of TFEDSA would mean the nonohmic polarization would have to be reduced by about 200 mV just to break even (!). Laboratory fuel cell tests have confirmed that optimum cell voltages were obtained when this electrolyte was used at the lower temperatures of 100°-110°C.

Fuel cell cathode polarization in 70 w/o TFEDSA was compared with that observed in TFMSA and H_3PO_4 electrolytes. The type of electrode used in this study was similar to that described by Kunz and Gruver (14), using a wet-proofed Stackpole carbon paper substrate with the catalyst layer applied by direct filtration. The catalyst was 10 w/o Pt on Vulcan XC-72R carbon black supplied by Prototech and used as-received. The PTFE content and the curing conditions for the cathodes were optimized for each electrolyte by trial and error. In general, in these acids, optimum polarization was achieved by the use of lower PTFE content and lower curing temperatures than is usual practice for phosphoric acid fuel cells, *e.g.*, 25 w/o TFE-30 cured 10 min at 320°C *vs.* 40 w/o TFE-30 cured 15 min at 350°C. The resulting polarization curves are shown in Fig. 3 on an *IR*-free basis, but all three electrolytes have about the same conductivity at the conditions shown (ca. 0.3 Ω^{-1} cm^{-1}). The polarization behavior in TFEDSA was intermediate between that for 85 w/o H_3PO_4 and that for 60 w/o TFMSA. The polarization curves shown in Fig. 3 are not necessarily representative of the relative kinetics of oxygen reduction on Pt in these electrolytes, so that other workers using different gas-diffusion electrodes might observe different relative polarization. More quantitative kinetic measurements in concentrated TFEDSA (and TFMSA as well) were attempted using the rotating disk method, but electrolyte impurity problems prevented definitive determinations. It is also possible that impurities are reducing the performance of the cathode in TFEDSA, but this seems unlikely since the Pt surface to electrolyte volume ratio in a fuel cell is about 5 orders of magnitude higher than in a rotating disk cell. Since a reasonably exhaustive optimization of the polarization characteristics of gas-diffusion electrodes in these electrolytes was made, it was concluded that the curves in Fig. 3 are representative of electrode structures with a high degree of Pt wetting and an effective transport of oxygen into the catalyst layer, and that the relative polarizations are, in fact, indicative of the relative kinetics. The polarization curve for TFEDSA in Fig. 3 is probably close to (within 30 mV or less) the best technologically achievable polarization in this electrolyte with this particular catalyst.

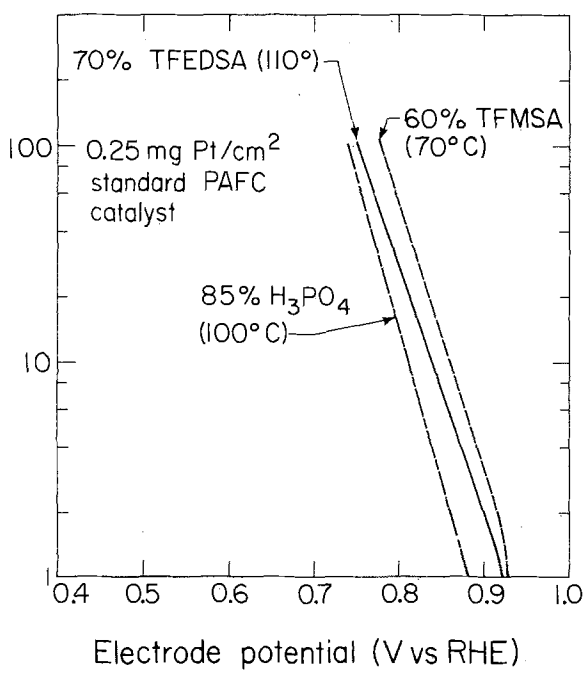

Fig. 3. Oxygen electrode polarization curves (*IR* corrected) in H_3PO_4, TFMSA, and TFEDSA.

Anode polarizations in the simulated reformed hydrocarbon fuels are summarized in Table I. CO poisoning of 0.25 mg Pt/cm^2 anodes is severe at 70°C in TFMSA even with CO levels as low as 0.01%. Raising the temperature 40°C had a dramatic effect on polarization, as would be expected from the CO absorption isotherms reported by Stonehart and Ross (15). The anode polarization of 20 mV in TFEDSA at 110°C on 0.1% CO is about the same as in 98 w/o H_3PO_4 at 170°C on 2% CO with the same electrode. In the case of methanol as fuel, CO levels as low as 0.1% can be achieved using a combination of thermal cracking and low temperature shift conversion (16). The polarization results of Fig. 3 and Table I, together with conductivity data in Fig. 2, indicate that it should be possible to operate a reformed methanol (0.1% CO) fuel cell using 70% TFEDSA at 110°C, and achieve 0.63-0.64V per cell on air at 200 mA/cm^2 with 0.75 mg Pt/cm^2 of catalyst. This performance level is about 30 mV better than what would be observed with H_3PO_4 at 110°C, but is about the same as what is observed in phosphoric acid fuel cells at 170°-180°C (13).

There has been some controversy in the literature (17) over the stability of TFMSA and its possible reduction at Pt electrodes at the reversible hydrogen potential. We have examined this problem ourselves both for TFMSA and TFEDSA, and our findings are in agreement with the comments of Adams and Foley (17). An impurity in TFMSA appears to be the source of sulfur produced at a hydrogen electrode in unpurified acid; the impurity is probably SO_3. Early samples of TFEDSA from KOR were badly contaminated with sulfur oxides (and possibly CS_2); but improvements in the synthesis eliminated these impurities for the most part. Purified forms of either TFMSA or TFEDSA showed no chemical instability in the fuel cell tests in this laboratory.

The conclusion of our study of TFEDSA as a fuel cell electrolyte is that because of poor conductivity at high concentration it offers no advantage over H_3PO_4

Table I. Polarization* relative to pure hydrogen for 80 H_2:20 CO_2 mixtures containing various levels of CO

	CO level (vol %)			
	1%	0.1%	0.01%	No CO
TFMSA (70°C)	>300	>300	245	5
TFEDSA (110°C)	60	20	10	5

* In mV at 200 mA/cm^2 and low utilization of hydrogen.

in fuel cell applications where systems considerations favor cell temperatures above *ca.* 120°C.

Acknowledgment

This work was supported by the Electric Power Research Institute under contract RP-1676-2 through an agreement with the Assistant Secretary for Fossil Energy under contract No. DE-AC03-76SF00098.

Manuscript submitted Aug. 16, 1982; revised manuscript received *ca.* Nov. 15, 1982.

Any discussion of this paper will appear in a Discussion Section to be published in the December 1983 JOURNAL. All discussions for the December 1983 Discussion Section should be submitted by Aug. 1, 1983.

Publication costs of this article were assisted by the Lawrence Berkeley Laboratory.

REFERENCES

1. A. Adams, R. Foley, and H. Barger, *This Journal*, **124**, 1228 (1977).
2. A. Appleby and B. Baker, *ibid.*, **125**, 404 (1978).
3. R. Foley, in Extended Abstracts of the National Fuel Cell Seminar, Bethesda, MD, June 1979.
4. O. Petrie, S. Vasina, and L. Lukyanycheva, *Sov. Electrochem.*, **17**, 1144 (1982).
5. M. George, Technical Report, U.S. Army Mobility Equipment Research and Development Command Contract No. DAAK70-78-C-0103, December 1979.
6. W. Vogel, J. Lundquist, P. Ross, and P. Stonehart, *Electrochim. Acta*, **20**, 79 (1975).
7. B. Baker, Final Technical Report, U.S. Army Mobility Equipment Research and Development Command, Contract No. DAAK02-73-C-0084, February 1975.
8. W. Moore, "Physical Chemistry," 3rd ed., p. 106, Prentice-Hall, Englewood Cliffs, NJ (1962).
9. P. Ross, EPRI Final Report EM-1553, September 1980.
10. "Lange's Handbook of Chemistry," 11th ed., J. A. Dean, Editor, McGraw-Hill, New York (1973).
11. D. MacDonald and J. Boyack, *J. Chem. Eng. Data*, **14**, 380 (1969).
12. R. Iczkowski and M. Cutlip, *This Journal*, **127**, 1433 (1980).
13. L. Christner, Final Technical Report, NASA Lewis Research Center, Contract DEN3-67.
14. H. Kunz and G. Gruver, *This Journal*, **122**, 1279 (1975).
15. P. Stonehart and P. Ross, *Electrochim. Acta*, **21**, 441 (1976).
16. J. McElroy, Final Report, Los Alamos Scientific Laboratory Contract No. 9-L61-3863V-1.
17. Discussion Section, *This Journal*, **129**, 2646 (1982).

The Determination of Ionic Transport Numbers by Use of Radiotracers

Peter J. Smith and Trevor L. Jones

Imperial Chemical Industries PLC, Mond Division, Technical Department, Winnington Laboratory, Winnington, Northwich, Cheshire CW8 4DJ, England

Transport phenomenon in ion exchange membranes can be investigated by a variety of techniques. In this paper we report details of a recirculating transport cell for the determination of sodium ion transport numbers by radioactive tracer methods. The construction and operation of the transport cell are discussed and, in order to illustrate the scope of the transport cell, data concerning sodium ion transport in a 1200 equivalent weight Nafion membrane are presented. The ion transport data are interpreted in terms of membrane electrolyte sorption and membrane water content.

Cation exchange membranes are used widely as cell separators in the electrolysis of sodium chloride solutions (1). Suitable membranes are resistant to chlorine and strong alkali and are capable of selectively transporting sodium ions. In addition to chemical stability and high sodium ion specificity it is desirable that a membrane has low electrical resistance, so that minimum power dissipation is caused by the separator. An indication of the overall commercial suitability of a chlor-alkali membrane can be obtained from a knowledge of the sodium ion transport number (selectivity) and the membrane voltage drop (power dissipation). For this reason it is important that reliable methods of determining the sodium ion transport number and membrane voltage drop are developed.

In the present communication we report details of a small cell for use in the determination of sodium ion transport numbers. The cell system can also be used, in specific situations, to measure membrane voltage drop. The apparatus is such that it is possible to obtain accurate transport number information, from a small piece of membrane, in a relatively short period of time. The cell has been used to investigate sodium ion transport in the absence of and presence of concentration differences across membranes, and to illustrate the scope of the apparatus we present results of an investigation concerning a 1200 equivalent weight Nafion[1] membrane. The cell has also been used to investigate properties of membranes that have been used in commercial chlor-alkali cells.

Methods used to investigate transport numbers in membranes fall broadly in two categories (2, 3): membrane potential measurement and electrolysis measurement. The magnitude of the membrane potential can be used to infer a value of an apparent transport number whereas electrolysis studies provide a true transport number. The value of the apparent transport number is not identical to that found in the electrolysis situation and it is difficult to relate quantitatively the apparent and real transport numbers (4). The membrane potential technique is not capable of being applied to situations where a membrane separates two similar electrolytes of equal concentration and it is also not readily applicable to bi-ionic systems. In addition, the inference of apparent transport number from membrane potential measurement relies on an accurate knowledge of electrolyte activities, water activities, and membrane-water transfer coefficient. For these reasons we choose not to use membrane potential measurement for the investigation of transport numbers in membranes.

The true sodium ion transport number found in a conventional chlor-alkali cell can be measured using a steady-state electrolysis cell

$$\oplus \text{ titanium-coated anode/NaCl } (m_1)\text{/membrane/}$$
$$\text{NaOH } (m_2)\text{/nickel cathode } \ominus$$

Key words: transport, chlor-alkali, electrolysis, radio activity.

[1] Registered trademark of E. I. du Pont de Nemours.

In this type of cell, electrolyte and water are generally fed continuously to the anode and cathode chambers and the sodium ion transport number (t_+) is obtained by determining the number of mols of sodium hydroxide produced per Faraday of charge passed, *i.e.*, t_+ = mols of sodium hydroxide produced/number of Faradays of charge passed.

Calculation of the number of mols of sodium hydroxide produced, in a given time interval, requires a knowledge of the sodium hydroxide concentration (which can be obtained easily by volumetric analysis) and an accurate measure of the exit catholyte flow rate. If the exit catholyte flow rate is not known accurately, then catholyte liquor must be collected over a long period of time (at least 16 hr for flow rates less than 25 cm^3/hr) to minimize errors in flow measurement. For most small cells, exit catholyte flow is not well defined and hence a long sodium hydroxide collection time is required. This means that a rapid measurement of transport number is not possible with the steady-state electrolysis procedure.

The steady-state electrolysis cell procedure has been refined by the application of radiotracers. Early work carried out in the 1960's by Meares (5) resulted in a transport cell where ionic fluxes were inferred from radiotracer movements and not from conventional volumetric analysis. This transport cell was complex, as it incorporated several membranes to eliminate diffusional effects, but it did provide accurate data in a short period of time and it could be used in situations where the membrane separated identical solutions. The technique of radioactive flux measurements provides an inherently elegant way of determining sodium ion transport numbers and because of this our present apparatus is based on this technique.

Recent workers have also used radiotracers to determine sodium ion transport numbers in perfluorinated membranes. However, both the work of Burkhardt (6) and of Yeager (7) involves a procedure where samples of catholyte liquor are withdrawn from the cell and analyzed separately. Such a procedure is tedious and not amenable to automation. The method described here involves continuous monitoring of radioactivity in recirculated catholyte liquor. With this method, a sample of the recirculating liquor passes through a flow cell and the level of activity is recorded by a nucleonic scaler/ratemeter which is controlled by an Apple[2] II microprocessor.

The Apple is programmed to record the catholyte activity level at a preselected time interval, display a graph of activity *vs.* elapsed time, and calculate the rate of increase of activity with time by means of a least squares fit technique. In addition to this, the microprocessor collects data on membrane current density, cell voltage, voltage drop across the membrane, and cell temperature. By interpreting additional information on the level of radioactivity in the anolyte liquor the microprocessor calculates sodium ion flux through the membrane and determines a value for the sodium ion transport number.

The radiotracer technique is very sensitive and results can be obtained rapidly. This means that the activity in the catholyte liquor is always very much less than the activity in the anolyte liquor and that a linear relationship between transport of sodium ions and transport of radioactivity can therefore be assumed. In addition, because the calculation of transport numbers is based on the rate of increase of radioactivity and not on the absolute level of radioactivity, consecutive measurements can be made on the system without changing cell liquors.

Apparatus and Procedure

A schematic representation of the transport cell is shown in Fig. 1. The cell, which is made of Fluon,[3] is placed in a water bath and preheated anolyte and catholyte liquors are circulated by means of a bellows PTFE pump. The recirculating hot liquors ensure rapid temperature equilibration and facilitate good mixing of the bulk electrolyte (there are about 25 volume changes a minute). The entry ports to the cell are designed to promote fluid mixing as this diminishes concentration polarization effects and the cell exit ports are large to enable gas, formed during electrolysis, to be swept from the cell by the flowing liquor. The cation exchange membrane (area $\simeq$ 4 cm^2) is sandwiched between the two half-cells using neoprene rubber gaskets and clamped between brass end plates with threaded bolts.

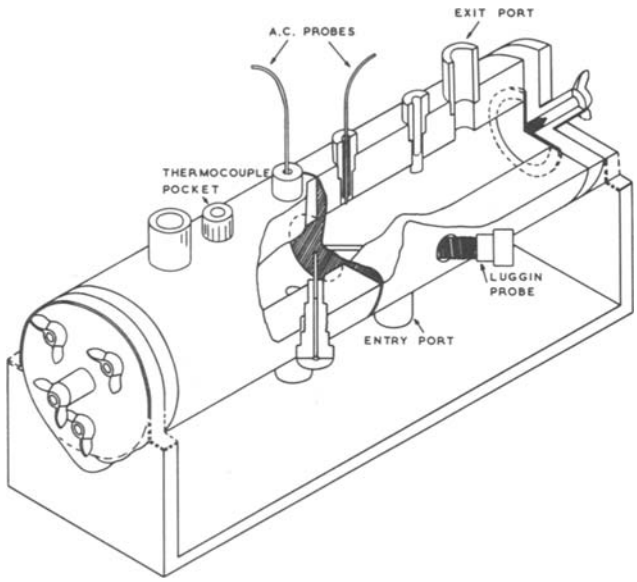

Fig. 1. Diagram of the cell used to measure sodium ion transport numbers.

The interior of each half-cell is cylindrical as it was observed that conical compartments, although helping gas release, caused an uneven distribution of the electric field lines. Irregular current distributions may influence transport number data and an irregular current distribution precludes the use of the cell for determining meaningful membrane voltage drop. In addition to a thermocouple pocket, each half-cell is equipped with a Luggin probe directed toward the membrane. These Luggin probes, which are attached by double junctions to standard calomel electrodes, can be used to infer membrane voltage drop. The working electrodes are made of platinum sheet as early experiments with coated electrodes resulted in problems from corrosion. The cell is also equipped with two platinum probes to facilitate measurement of membrane a-c resistance.

The apparatus for continuous monitoring of the transfer of radioactive sodium ions through the membrane is shown schematically in Fig. 2. The procedure for carrying out the measurements is as follows.

Reservoirs A and B are filled with equal, known volumes of the liquors under investigation. Reservoir A contains sodium 22 at a concentration of 10 kilobecquerel/cm^3. The membrane, which has been equilibrated in catholyte liquor for a minimum period of 24 hr, is positioned in the cell. The cell and the reservoirs are then placed in the water bath and allowed to attain the required temperature. A sample is removed from reservoir A, the activity per gram ion of sodium per cm^3 is measured (x_1), and an equivalent volume of nonactive liquor is added to reservoir A. The pump, which circulates the catholyte liquor through the flow cell, and the recirculation pumps from the anolyte and catholyte reservoirs are switched on and the required current is set on the constant current device. The microprocessor program is initiated by selecting the re-

[2] Registered trademark of Apple Computer Incorporated.
[3] Registered trademark of Imperial Chemical Industries PLC.

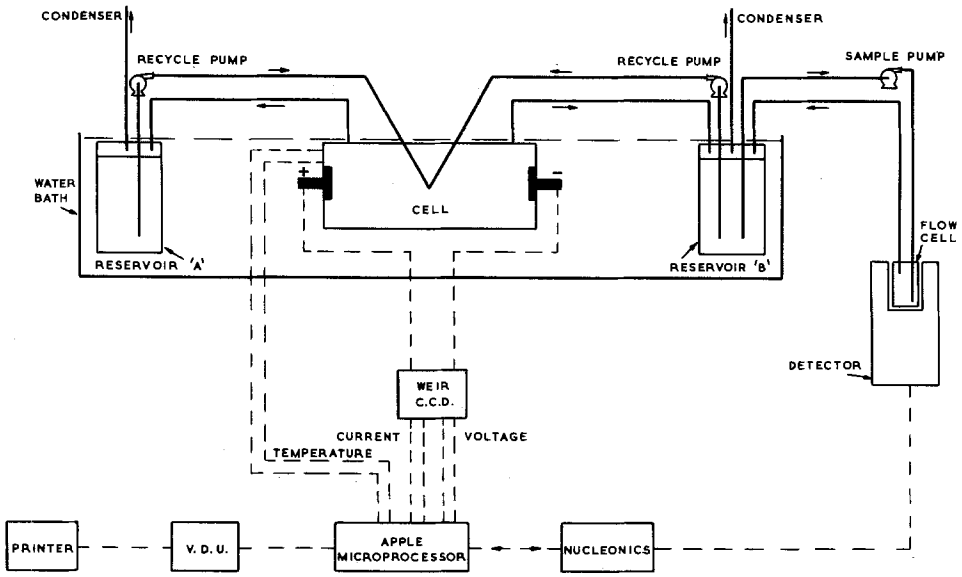

Fig. 2. Schematic representation of transport cell system.

quired time interval and data points are collected. At the end of each time interval (typically 60 or 100 sec) the activity in reservoir B, the membrane current density, the voltage across the membrane, and the cell temperature are recorded and the nucleonic counting system restarted.

When sufficient data points have been collected to define the slope of the graph of activity *vs.* time, within preselected statistical limits, the run is terminated by switching off the applied current and the recirculating pumps. All of the accumulated data are transferred to storage on a disk and hard copy is displayed on a printer. A further sample is removed from reservoir A, the activity per gram ion of sodium per cm^3 is measured, and an equivalent volume of nonactive liquor is added to reservoir A. As it is the rate of increase of activity in B which is of interest and not the absolute level of activity (provided that activity A is very much greater than activity B), further measurements can now be made on this system either at the same or at different current densities.

At the end of a series of measurements, the flux (J_i) of sodium ions through the membrane at each current density and temperature are calculated by entering the individual "standard" activities

$$J_i = \frac{Y_i}{X_i} \text{ g-ions sodium/sec}$$

where X_i = standard activity in becquerels/g-ion sodium of the ith run and Y_i = slope in becquerels/sec of the ith run.

The sodium ion transport number t_i is related to the sodium ion flux J_i by an expression of the form

$$t_i = \frac{J_i F}{I_i \times 23}$$

where **F** is the Faraday constant, I_i is the ith current measured in amperes, and t_i has units of mol/**F**.

This simple expression was used to calculate the transport number and it ignores the influence of back-diffusion. Omission of a correction for back-diffusion is justified as at the high current densities employed (> 2 kAm^{-2}) this correction was shown to be negligible.

The standard deviation of the individual points on the graph of sodium ion flux *vs.* time, which is used to calculate the transport number, varies with the amount of activity in the catholyte compartment and, at worst is $\pm 2\%$ of the count rate. In most instances, and for all measurements of over 2 hr duration, it is better than $\pm 1\%$.

Water sorption measurements were carried out by a conventional gravimetric procedure. Samples of polymer (*ca.* 2g) were cut from a large sheet and allowed to equilibrate with one molal sodium hydroxide at ambient temperature. The membranes were then washed with copious quantities of water and dried in a vacuum oven (< 2 Torr 100°C) for 16 hr. Samples of dry polymer of known mass were then equilibrated in electrolyte at elevated temperature. After attainment of equilibrium the samples were removed from the equilibrating electrolyte, surface washed, dried, and weighed rapidly. The weighed sample of membrane was then transferred to the vacuum oven and dried for a further 16 hr. Finally, the mass of dry polymer plus sorbed solid electrolyte was measured. From a knowledge of the initial mass of dry polymer, the mass of polymer/water/electrolyte, and the mass of polymer/solid electrolyte, values for membrane water uptake and sorbed electrolyte concentration were calculated.

The validity of the above procedure was checked by carrying out standard titration experiments to determine the quantity of sorbed electrolyte. It was found that the simpler gravimetric procedure gave results that were similar to the volumetric method.

Application of the Transport Cell

It is of little value to determine a transport number rapidly if the measured value is not characteristic of the equilibrium transport number. We have investigated this point for a 1200 equivalent weight Nafion membrane. The anolyte and catholyte chambers of the cell were charged with sodium hydroxide solution and the transport cell was then used to determine the sodium ion transport number of 1200 equivalent weight Nafion immersed in 8 molal sodium hydroxide at 90° ± 1°C. Values of the transport number were deduced at 30 min intervals and Fig. 3 is a plot of the sodium ion transport number against time. From the data displayed in Fig. 3 it is evident that the transport number measured after the 30 min electrolysis is similar (± 2%) to that obtained after the 24 hr electrolysis. In view of this we are confident that transport numbers measured rapidly are characteristic of steady-state values.

The relationship between the sodium ion transport number and temperature for two different sodium hydroxide concentrations is displayed in Fig. 4. Temperature does not have a major influence on transport number; in the 8 molal case a change in temperature from 25° to 90°C results in a 6% reduction in the sodium ion transport number. The weak temperature dependence is in agreement with the observations of Yeager (7). Although the greater part of our investigations were carried out at 90°C it is interesting to consider reasons for the small temperature dependence of the sodium ion transport number.

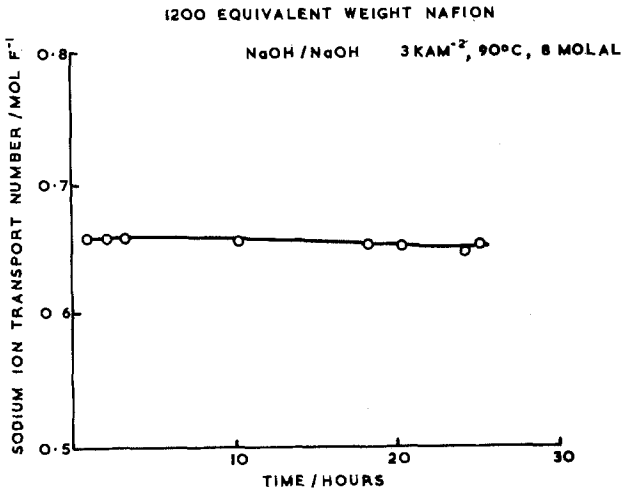

Fig. 3. Variation of sodium ion transport number with time

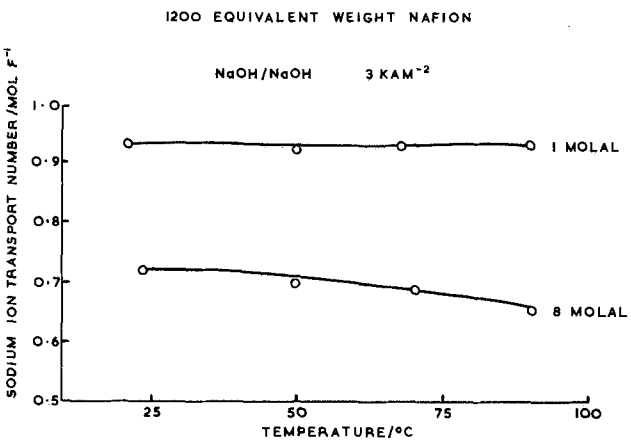

Fig. 4. The relationship between sodium ion transport number and temperature.

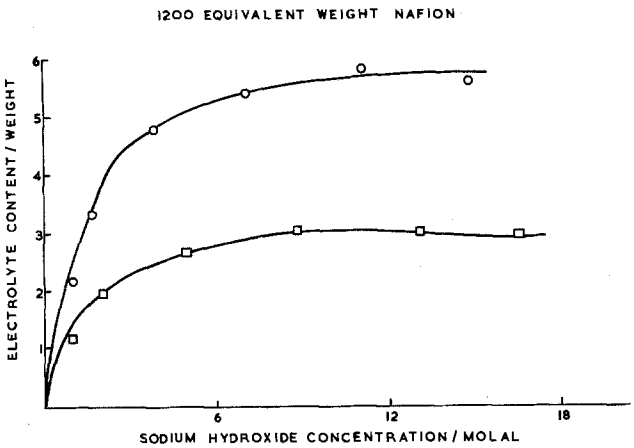

Fig. 5. The dependence of sorbed electrolyte content on external sodium hydroxide concentration. ○ 90°C, □ 25°C.

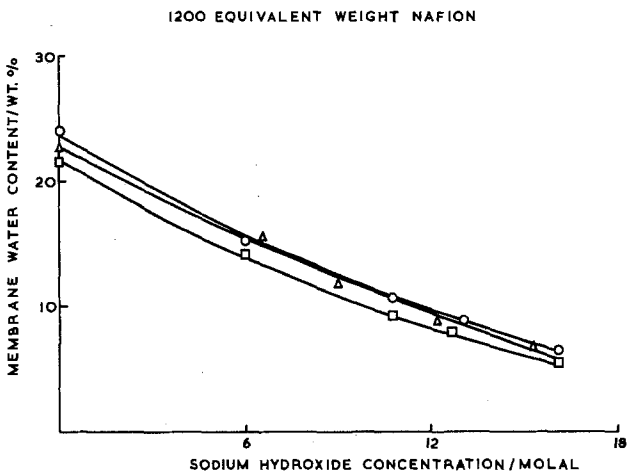

Fig. 6. The variation of membrane water content with external sodium hydroxide concentration. □ 50°C, △ 70°C, ○ 90°C.

The magnitude of the sodium ion transport number depends, in part, on the quantity of sorbed sodium hydroxide and on the water content of the membrane. High water contents and large quantities of sorbed sodium hydroxide favor hydroxyl ion transport and hence produce low sodium ion transport numbers. The quantity of sodium hydroxide sorbed by the 1200 equivalent weight ionomer, in several sodium hydroxide solutions at two temperatures, is shown in Fig. 5. The quantity of sorbed sodium hydroxide, expressed as a weight percent of the dry membrane, increases only slightly with increasing external sodium hydroxide concentration and with temperature. The membrane water uptake in sodium hydroxide solution is presented in Fig. 6. The water uptake, which increases with temperature in the range 25°-90°C, declines steadily with increasing sodium hydroxide concentration. The weak temperature dependence of sorbed sodium hydroxide and of polymer water content is responsible for the slight decline of transport number with increasing temperature.

The dependence of the sodium ion transport number on external sodium hydroxide concentration for a membrane immersed in only sodium hydroxide is presented in Fig. 7. The transport number does not decline monotonically with increasing sodium hydroxide concentration. Between 1 and 8 molal sodium hydroxide, the transport number falls, but after this there is a small increase in transport number followed by a further decline.

The diminution of the transport number in the concentration range 1-8 molal is associated with increasing sorbed electrolyte concentration (4). In the middle concentration range (8-14 molal) the quantity of water sorbed by the membrane declines. The mechanism of hydroxyl ion transport, in this concentration range, may be a conventional diffusion mechanism and this will enhance the sodium ion transport number. When the external sodium hydroxide solution is very concentrated (> 17 molal) there is only minimal water in the membrane. In order that each ionic species present in the membrane has as many water molecules associated with it as is possible "ion pair" formation occurs. This results in the counterions associating closely with the fixed sulfonic acid sites and hence a rapid decline in sodium ion selectivity occurs. Evidence for ion pair formation in perfluorosulfonic acid membranes has been presented previously by Mauritz (8).

The concentration dependence of the transport number is not in agreement with the results reported by Yeager (7) for 1150 equivalent weight Nafion. In this other study no evidence was found for a minimum in the sodium ion transport number. No explanation can be given for the differences between the two sets of results.

The sodium ion transport number of 1200 equivalent weight Nafion immersed in sodium hydroxide solution is compared with the transport number found when the membrane is used to separate 4 molal sodium chloride and varying sodium hydroxide concentrations in Fig. 8. Although the general shape of the two curves is broadly similar, the mixed electrolyte graph has more pronounced curvature than the single electrolyte data. The mixed electrolyte sodium ion transport number is smaller than that obtained while using only sodium hydroxide. The deviation between the two transport numbers is largest in the concentration range

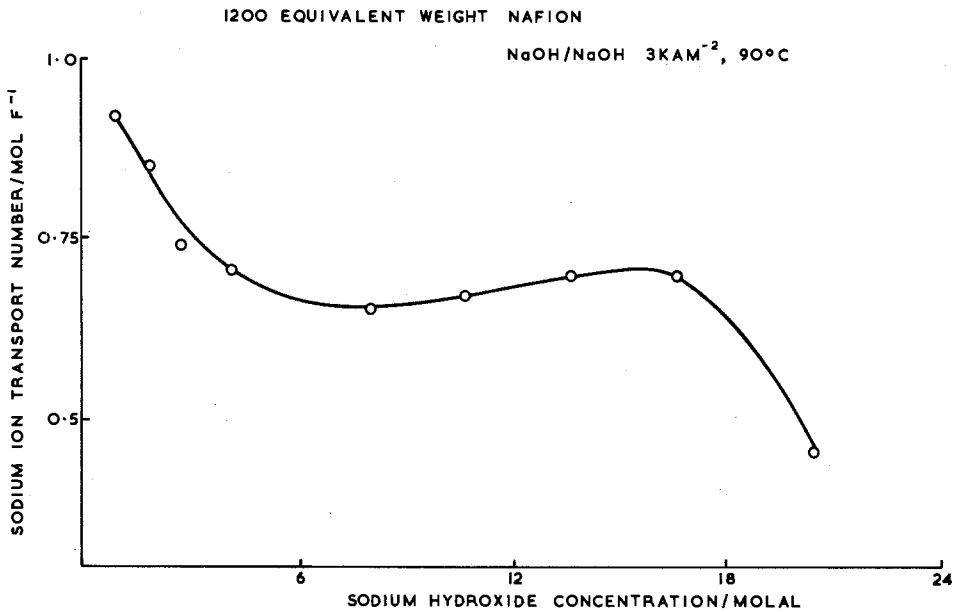

Fig. 7. The variation of sodium ion transport number with external sodium hydroxide concentration.

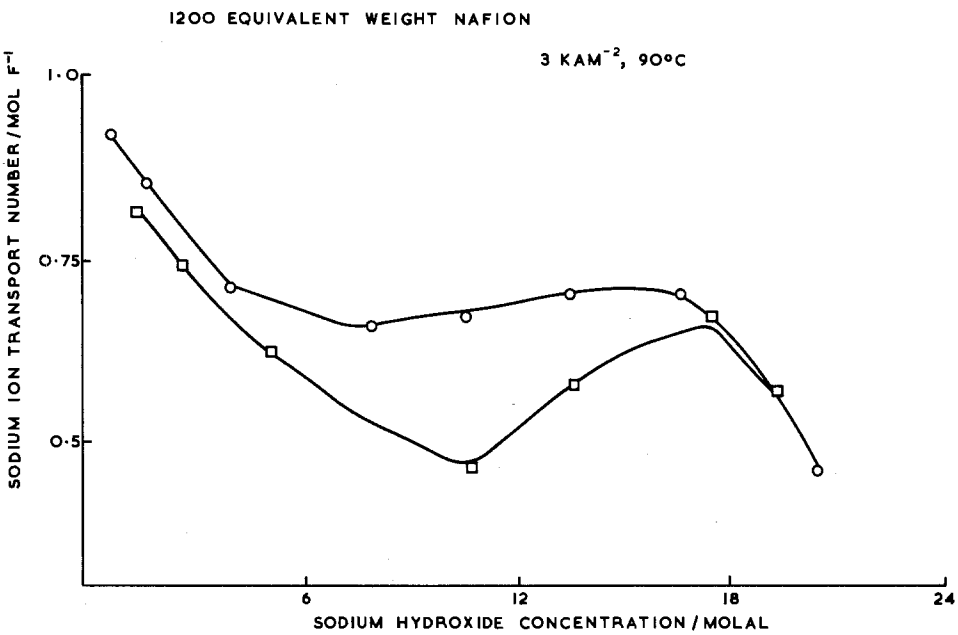

Fig. 8. Comparison of sodium transport number for NaOH/NaOH and NaCl/NaOH systems. ○ NaOH/NaOH, □ 4M NaCl/NaOH.

8-12 molal. In the range 0-8 molal the mixed electrolyte sodium ion transport number is about 5% smaller than that found with the sodium hydroxide system. It is suggested that the difference between the two transport numbers can be explained in terms of polymer water content.

The water content of the anolyte face of the membrane contains more water when it is in equilibrium with brine solution than when in equilibrium with sodium hydroxide solutions. It may be that this increased water content is responsible for the difference in transport number found with dilute sodium hydroxide. As the external sodium hydroxide concentration increases the concentration of sorbed hydroxide ion increases and this further reduces the sodium ion transport number. The sodium ion transport number does not decline continually with increasing external sodium hydroxide concentration because as the osmotic water flux increases this causes the frictional interaction between migrating hydroxyl ion and water molecules to increase. At concentrations above 12 molal a large frictional interaction between hydroxyl ion and water may reduce the transport of hydroxyl ion and the sodium transport number increases (9). At very high sodium hydroxide concentration contact ion pairs form in the membrane and selectivity toward sodium ion declines.

Conclusion

We have developed a transport cell suitable for the determination of sodium ion transport numbers. The apparatus makes use of a small sample of membrane and is capable of providing accurate transport number data rapidly. The transport cell has applications in examining samples of commercially used chlor-alkali membranes.

Acknowledgments

We wish to express our thanks to B. D. Young and J. A. Kelly for experimental assistance and to thank ICI (Mond Division) PLC for permission to publish this paper.

Manuscript submitted June 17, 1982; revised manuscript received *ca.* Nov. 23, 1982.

Any discussion of this paper will appear in a Discussion Section to be published in the December 1983 JOURNAL. All discussions for the December 1983 Discussion Section should be submitted by Aug. 1, 1983.

Publication costs of this article were assisted by Imperial Chemical Industries.

REFERENCES
1. K. H. Simmrock, E. Griesenbeck, J. Jonssen, and R. Rodermund, *Chem. Ing. Tech.*, **53**, S10 (1981).
2. N. Lakshminarayanaiah, "Transport Phenomena in Membranes," Academic Press, New York (1969).
3. F. Helfferich, "Ion Exchange," McGraw-Hill Co. Inc., New York (1962).
4. M. Suhara and Y. Oda, Paper 631 presented at The Electrochemical Society Meeting, Hollywood, Florida, Oct. 5-10, 1980.
5. P. Meares and A. H. Sutton, *J. Colloid Interface Sci.*, **28**, 118 (1968).
6. S. F. Burkhardt, Paper 440 presented at The Electrochemical Society Meeting, Atlanta, Georgia, Oct. 9-14, 1977.
7. H. L. Yeager, B. O'Dell, and Z. Twardowski, Papers 413 and 414 presented at The Electrochemical Society Meeting, Minneapolis, Minnesota, May 11-15, 1981.
8. R. A. Komoroski and K. A. Mauritz, *J. Am. Chem. Soc.*, **100**, 7487 (1978).
9. S. G. Cutler, "Advances in Chemistry Series 187," American Chemical Society, Washington (1980).

In Situ Raman Spectroscopic Studies of the Rechargeable Low Temperature Molten Salt Cell

Na/Beta″-Alumina/S(IV) in $AlCl_3$-NaCl

K. Tanemoto, A. Katagiri,* and G. Mamantov*

Department of Chemistry, University of Tennessee, Knoxville, Tennessee 37996

The rechargeable cell

$$Na/\beta''\text{-alumina/S(IV) in } AlCl_3\text{-NaCl}$$

is operated at 180°-250°C and has an open-circuit voltage of 4.2V (1-3). High energy densities and long cycle life have been achieved. The two discharge plateaus (3) correspond to the formation of elemental sulfur and sulfide as shown by the simplified equations below

$$SCl_4 + 4Na = S + 4NaCl$$

$$S + 2Na = Na_2S$$

Although these equations do not include solvent species such as $AlCl_4^-$ and $Al_2Cl_7^-$, it is apparent that the melt chloro acidity decreases during the discharge process until the melt becomes saturated with NaCl.

Electrochemical, u.v.-visible, and electron spin resonance spectroelectrochemical studies of relatively dilute solutions of sulfur in chloroaluminate melts (4-7) have provided evidence for several intermediates formed in the oxidation of sulfur to tetravalent sulfur in acidic ($AlCl_3$-rich) and to monovalent sulfur in basic (NaCl saturated) melts. The Raman spectroscopic studies described in this paper were undertaken to provide a better understanding of the chemistry that takes place during discharge and charge processes in the positive electrode compartment. Raman spectral studies of chloroaluminate melts containing tetravalent sulfur (8, 9), elemental sulfur (10), and sulfide (11) have been reported previously.

Experimental

Melt preparation and a number of experimental procedures have been reported previously (12, 13). Tetravalent sulfur was added to $AlCl_3$-NaCl (68.3-31.7 mol percent (m/o)) melt as SCl_3AlCl_4 (9); its concentration was 0.74*F*. The electrochemical cell was similar to that described previously (2, 3); the positive mix of the above composition was separated from the sodium electrode by means of a β-alumina tube (from General Electric Company). The cell was discharged or charged at a low current density (1.4 mA/cm^2) at 200°C. Raman spectra were obtained using either the 514.5 nm excitation from an argon ion laser (Spectra-Physics Model 171) or the 587.2 nm line from a Rhodamine-6G dye laser (Spectra-Physics Model 375). A Jobin-Yvon Ramanor 2000M spectrometer was used to record the spectra. The cell was positioned so that the incident laser beam illuminated the sample just above the reference compartment [see Fig. 1 of Ref. (2)]. Scattered light

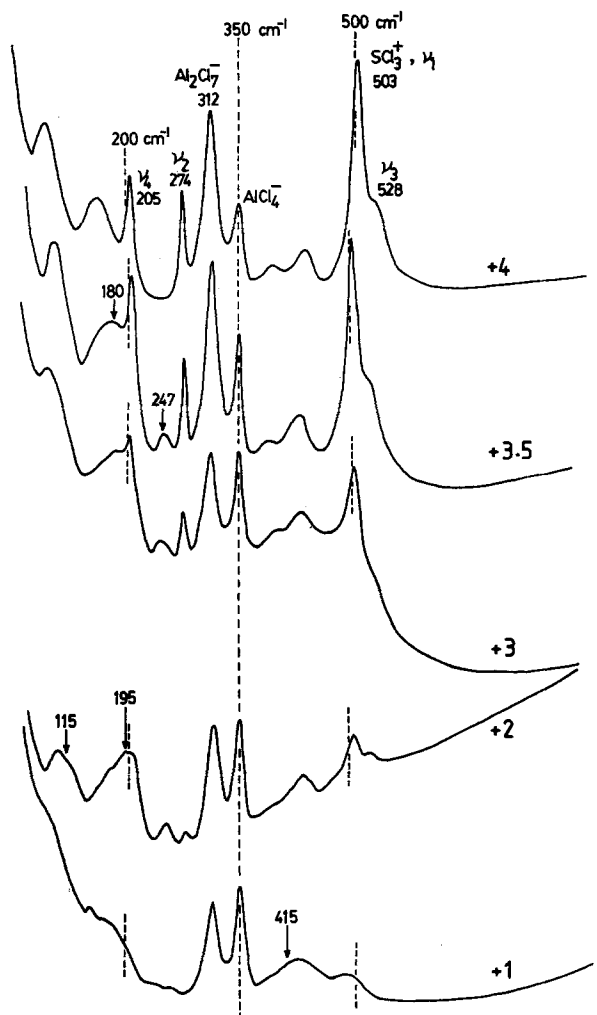

Fig. 1. Raman spectra of the positive mix in the cell Na/β-alumina/S(IV) in molten $AlCl_3$-NaCl, at different stages of discharge. The FOXS is shown on each spectrum. Excitation for top three spectra 514.5 nm; for bottom two spectra 587.2 nm. Temperature 140°C.

* Electrochemical Society Active Member.
Key words: fused salts, spectra, energy storage, battery.

was observed at right angles to the exciting beam. Polarization measurements were made by rotating 90° the plane of polarization of the laser beam.

Results and Discussion

Raman spectra of the positive mix taken at selected points of the first discharge plateau (2, 3) are shown in Fig. 1. The formal oxidation state of sulfur (FOXS) calculated from the amount of SCl_3AlCl_4 used and the amount of electricity passed through the cell, is indicated for each spectrum. Spectrum corresponding to a fully charged cell (Fig. 1, +4) is a summation of the spectral features of $Al_2Cl_7^-$ (strongest band at 312 cm^{-1}), $AlCl_4^-$ (strongest band at 350 cm^{-1}), and SCl_3^+ (strongest band at 503 cm^{-1}) (9, 12). Spectra taken at different stages of the first discharge plateau (Fig. 1, +3.5 to +1) clearly show the disappearance of SCl_3^+, the increase of $AlCl_4^-$, and the decrease of $Al_2Cl_7^-$ bands. All of the bands along with assignments are tabulated in Table I. Several weak Raman bands shown in Fig. 1 could not be assigned; for example, bands at ~180 and 247 cm^{-1} at FOXS = +3.5 and +3, shoulders at 115 and 195 cm^{-1} at FOXS = +2 and +1, and shoulder at 415 cm^{-1} at FOXS = +1. It is worth noting that a Raman spectrum of S_2Cl_2 dissolved in the $AlCl_3$-NaCl (63-37 m/o) melt has a weak band at 415 cm^{-1} which may be due to the species S_2Cl^+ (5).

It is interesting that at FOXS = +2, SCl_3^+ is still present in the melt. We have previously (14) obtained a Raman spectrum of SCl_2 dissolved in the $AlCl_3$-NaCl (63-37 m/o) melt; the only sulfur species that could be detected in the melt was SCl_3^+. Freezing of the cell at the point corresponding to FOXS = +2 resulted in the formation of a yellow liquid in a cooled side arm. The Raman spectrum of the yellow liquid showed the liquid to be S_2Cl_2. Thus, SCl_2 is unstable in acidic $AlCl_3$-NaCl melts disproportionating to SCl_3^+ and S_2Cl_2.

The Raman spectra obtained after the first discharge plateau are shown in Fig. 2; the observed bands are given in Table II. At FOXS = 0 and −1, weak bands at 149, 217, and 476 cm^{-1} may be attributed to S_8 (10). In addition, a shoulder at ~ 304 cm^{-1} is present at FOXS = −1 besides the 312 cm^{-1} band of $Al_2Cl_7^-$. The band at 305 cm^{-1} is clearly evident at FOXS = −2 (Fig. 2c) since the 312 cm^{-1} band of $Al_2Cl_7^-$ is no longer present. The intensity of the 305 cm^{-1} band decreases markedly upon overdischarge (formation of aluminum) (Fig. 2d); it may be calculated that at this point the melt has become basic and saturated with NaCl. A shoulder at ~ 333 cm^{-1} is also observed in Fig. 2d in addition to the spectral features of $AlCl_4^-$.

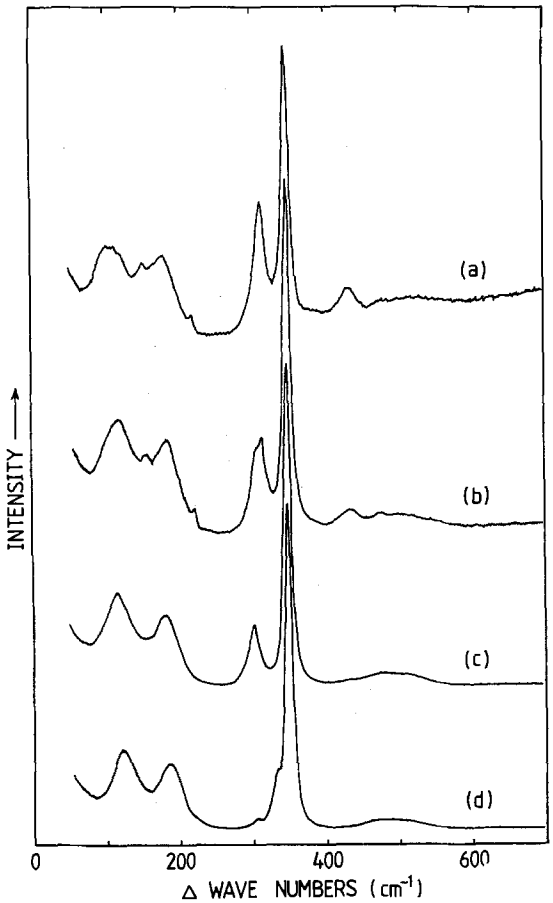

Fig. 2. Raman spectra of the positive mix in the cell Na/β-alumina/S(IV) in molten $AlCl_3$-NaCl, at different stages of discharge. The formal oxidation state of sulfur corresponding to each spectrum is: (a) 0, (b) −1, (c) and (d) −2. Excitation 514.5 nm. Temperature 175°C.

The Raman spectra of sulfide containing basic chloroaluminates have been reported by Berg *et al.* (11) who attribute the band at ~300 cm^{-1} to the solvated polymeric $(AlSCl)_n$ and the band at ~330 cm^{-1} to the solvated polymeric $(AlSCl_2^-)_n$; the values of n are believed to be ~3-4 in dilute melts. Similar species have been postulated by Robinson *et al.* (15).

Our results are in accord with those of Berg *et al.* (11). Based on their assignments, there is good evidence that the sulfide ions produced by discharge interact chemically with the solvent resulting in oligomeric entities. Formation of such species as well as the

Table I. Raman spectral data (cm^{-1}) obtained at selected points of the first discharge plateau

FOXS	+4	+3.5	+3	+2	+1
	98 m dp $AlCl_4^-$ + $Al_2Cl_7^-$	99 m dp $AlCl_4^-$ + $Al_2Cl_7^-$	99 m dp $AlCl_4^-$ + $Al_2Cl_7^-$ (115)	99 m dp $AlCl_4^-$ + $Al_2Cl_7^-$ 115 w dp ?	(99) mw $AlCl_4^-$ + $Al_2Cl_7^-$ (115) ? (152)
	163 m dp $AlCl_4^-$ + $Al_2Cl_7^-$	163 m dp $AlCl_4^-$ + $Al_2Cl_7^-$ (180) w	(163) m $AlCl_4^-$ + $Al_2Cl_7^-$ (180) w (195)	(165) m $AlCl_4^-$ + $Al_2Cl_7^-$ (180) w 195 w	165 $AlCl_4^-$ + $Al_2Cl_7^-$ (180) ? (195) w
	205 m dp SCl_3^+, ν_4	203 m dp SCl_3^+, ν_4 247 w	202 mw dp SCl_3^+, ν_4 247 w	205 w SCl_3^+, ν_4 251 w dp ?	(247) ? (261) ?
	274 m p SCl_3^+, ν_2 311 s p $Al_2Cl_7^-$ 349 mw p $AlCl_4^-$ 391 w $Al_3Cl_{10}^-$?	274 m p SCl_3^+, ν_2 312 s p $Al_2Cl_7^-$ 348 m p $AlCl_4^-$ 385 w $Al_3Cl_{10}^-$?	274 mw p SCl_3^+, ν_2 311 s p $Al_2Cl_7^-$ 348 s p $AlCl_4^-$ 390 vw $Al_3Cl_{10}^-$?	276 vw SCl_3^+, ν_2 315 s p $Al_2Cl_7^-$ 350 s p $AlCl_4^-$ (415)	313 s p $Al_2Cl_7^-$ 350 s p $AlCl_4^-$ (415) mw
	434 mw p $Al_2Cl_7^-$	432 mw p $Al_2Cl_7^-$	432 mw p $Al_2Cl_7^-$	434 mw p $Al_2Cl_7^-$	434 mw $Al_2Cl_7^-$ 490 mw (broad) $AlCl_4^-$
	503 vs p SCl_3^+, ν_1 528 w dp SCl_3^+, ν_3	503 s p SCl_3^+, ν_1 528 w dp SCl_3^+, ν_3	502 s p SCl_3^+, ν_1 528 vw SCl_3^+, ν_3	506 m p SCl_3^+, ν_1 528 vw SCl_3^+, ν_3	

s, strong; m, medium; w, weak; v, very; p, polarized; dp, depolarized. Bands shown in parentheses are very weak or poorly defined.

Table II. Raman spectral data (cm^{-1}) obtained after the first discharge plateau

FOXS	0	−1	−2	−2 (basic melt)
	105 m $AlCl_4^-$ + $Al_2Cl_7^-$	113 m dp $AlCl_4^-$ + $Al_2Cl_7^-$	116 m dp $AlCl_4^-$, ν_2	117 m dp $AlCl_4^-$, ν_2
	149 w S_8, ν_8	151 w dp S_8, ν_8		
	180 m $AlCl_4^-$ + $Al_2Cl_7^-$	181 m dp $AlCl_4^-$ + $Al_2Cl_7^-$	183 m dp $AlCl_4^-$, ν_4	183 m dp $AlCl_4^-$, ν_4
	217 w S_8, ν_2	218 w p S_8, ν_2		
		304 mw p $(AlSCl)_n$	305 m p $(AlSCl)_n$	304 w p $(AlSCl)_n$
	311 ms $Al_2Cl_7^-$	313 m p $Al_2Cl_7^-$		
				333 m (sh.) p $(AlSCl_2^-)_n$
	347 s $AlCl_4^-$	350 s p $AlCl_4^-$	349 s p $AlCl_4^-$, ν_1	349 s p $AlCl_4^-$, ν_1
	431 mw $Al_2Cl_7^-$	435 mw p $Al_2Cl_7^-$		
	476 w S_8, ν_1 and ν_7	477 w p S_8, ν_1 and ν_7		
	490 w (broad) $AlCl_4^-$	490 w (broad) $AlCl_4^-$	490 w (broad) dp $AlCl_4^-$, ν_3	490 w (broad) dp $AlCl_4^-$, ν_3

s, strong; m, medium; w, weak; v, very; p, polarized; dp, depolarized. Bands shown in parentheses are very weak or poorly defined.

Table III. Observed Raman bands due to sulfur-containing species in the positive compartment of the cell Na/β-alumina/S(IV) in $AlCl_3$-NaCl

Formal oxidation state of sulfur								
4	3.5	3	2	1	0	−1	−2	−2
Al(III)/(Al(III) + Na(I)), %								
70.0	68.0	66.4	63.2	60.3	57.7	55.2	52.3	49.0
Estimated melt composition ($AlCl_3$ m/o) (Raman data)								
~70	~68	~66	~63	~60	~57.7	~54.5	~50.3	~49.8*
Observed Raman bands due to sulfur-containing species (cm^{-1})								
		(115)	115	(115)?				
				(152)	149	151		
	180	180	180	(180)?				
		(195)	195	195				
205	203	202	205					
					217	218		
	247	247	251	(247)?				
				(261)?				
274	274	274	276					
						304	305	304
								333
			(415)	415				
					476	477		
503	503	502	506					
528	528	528	528					

* NaCl-saturated melt.

presence of elemental sulfur as S_8 may be responsible for the pronounced electrochemical irreversibility of the sulfur/sulfide couple in chloroaluminate melts (4, 5, 16).

Finally, it is worth noting that the melt compositions estimated from the intensities of the Raman bands of $Al_2Cl_7^-$ at 312 cm^{-1} and $AlCl_4^-$ at 350 cm^{-1} are in reasonable agreement with melt compositions calculated from the stoichiometry of the electrochemical process (Table III). This Table also includes all bands that may be attributed to the sulfur-containing species.

Acknowledgments

This research has been supported by the Department of Energy, University of California Subcontract 4502810. The Raman spectrometer used for these studies was obtained through partial support by the National Science Foundation Grant No. CHE-8006315. We are grateful to Dr. R. W. Powers, General Electric Company, for providing β-alumina tubes for this research.

Manuscript submitted Aug. 23, 1982; revised manuscript received *ca.* Dec. 7, 1982.

Any discussion of this paper will appear in a Discussion Section to be published in the December 1983 JOURNAL. All discussions for the December 1983 Discussion Section should be submitted by Aug. 1, 1983.

Publication costs of this article were assisted by The University of Tennessee.

REFERENCES

1. G. Mamantov and R. Marassi, U.S. Pat. 4,063,005 (1977).
2. G. Mamantov, R. Marassi, M. Matsunaga, Y. Ogata, J. P. Wiaux, and E. J. Frazer, *This Journal*, **127**, 2319 (1980).
3. G. Mamantov, R. Marassi, Y. Ogata, M. Matsunaga, and J. P. Wiaux, in "Proceedings of the 15th Intersociety Energy Conversion Engineering Conference," Vol. I, 809107, American Institute of Aeronautics and Astronautics, Seattle, Washington, August 18-22, 1980.
4. R. Marassi, G. Mamantov, and J. Q. Chambers, *This Journal*, **123**, 1128 (1976).
5. R. Marassi, G. Mamantov, M. Matsunaga, S. E. Springer, and J. P. Wiaux, *ibid.*, **126**, 231 (1979).
6. V. E. Norvell, K. Tanemoto, G. Mamantov, and L. N. Klatt, *ibid.*, **128**, 1254 (1981).
7. K. Tanemoto, R. Marassi, C. B. Mamantov, Y. Ogata, M. Matsunaga, J. P. Wiaux, and G. Mamantov, *ibid.*, **129**, 2237 (1982).
8. H. E. Doorenbos, J. C. Evans, and R. O. Kagel, *J. Phys. Chem.*, **74**, 3385 (1970).
9. G. Mamantov, R. Marassi, F. W. Poulsen, S. E. Springer, J. P. Wiaux, R. Huglen, and N. R. Smyrl, *J. Inorg. Nucl. Chem.*, **41**, 260 (1979).
10. R. Huglen, F. W. Poulsen, G. Mamantov, R. Marassi, and G. M. Begun, *Inorg. Nucl. Chem. Lett.*, **14**, 167 (1978).
11. R. W. Berg, S. von Winbush, and N. J. Bjerrum, *Inorg. Chem.*, **19**, 2688 (1980).
12. G. Torsi, K. W. Fung, G. M. Begun, and G. Mamantov, *ibid.*, **10**, 2285 (1971).
13. R. Marassi, J. Q. Chambers, and G. Mamantov, *J. Electroanal. Chem. Interfacial Electrochem.*, **69**, 345 (1976).
14. K. Tanemoto and G. Mamantov, Unpublished work.
15. J. Robinson, B. Gilbert, and R. A. Osteryoung, *Inorg. Chem.*, **16**, 3040 (1977).
16. K. A. Paulsen and R. A. Osteryoung, *J. Am. Chem. Soc.*, **98**, 6866 (1976).

Stability of Semiconducting TiO_2 Photoanodes

Fu-Tai Liou and Chiang Y. Yang

Department of Energy and Environment, Brookhaven National Laboratory, Upton, New York 11973

and Sumner N. Levine*

Department of Materials Science and Engineering, State University of New York at Stony Brook, Stony Brook, New York 11794

As shown in the extensive study by Harris and Wilson (1), TiO_2 photoanodes tend to undergo aging effects characterized by changes in the action spectra, quantum efficiency, and surface capacitance. Specifics of the aging effect, as well as photoelectrochemical behavior in general, depend on the method of anode preparation (2-4). Migration of interstitial Ti^{+3} (5) and hydrogen ions (2, 4) has been proposed as contributing to the effect although the detailed mechanisms remain obscure. The situation with hydrogen-loaded specimens is complicated by the observations that hydrogen in both TiO_2 single crystals (6) and sputtered films (7) appears to occupy different sites not all of which are electrochemically active.

Reported here are some striking aging effects observed with relatively highly doped TiO_2 anodes which have been exposed in the dark to alkaline solutions for somewhat over 100 hr. No detailed explanation for the effects noted is available at this time.

Single crystals of TiO_2 (National Lead Corporation) oriented in the (110) plane were employed. These were polished with 0.3μ Al_2O_3 abrasive and then converted to n-type material by heating to 700°C in hydrogen for 20 min. While a number of specimens were so prepared, we report on a sample with a carrier concentration of $4.8 \times 10^{19}/cm^3$ as determined by the Mott-Schottky method. The reliability of the carrier concentration was checked with resistivity measurements using the Van derPauw technique (8). These gave a calculated mobility of 1.87 cm^2/V-sec at room temperature, in agreement with the value reported in the literature (9). Indium solder and silver-plated copper wires provided ohmic contacts to the samples. The contacts were protected by a coating of silicone rubber and a glass tube. The cell was fabricated of Pyrex and provided with a quartz window to admit illumination. A platinum counterelectrode and a saturated calomel reference electrode (SCE) were employed. The electrolyte used was 0.1*N* NaOH.

* Electrochemical Society Active Member.
Key words: photoelectrochemistry, ellipsometry.

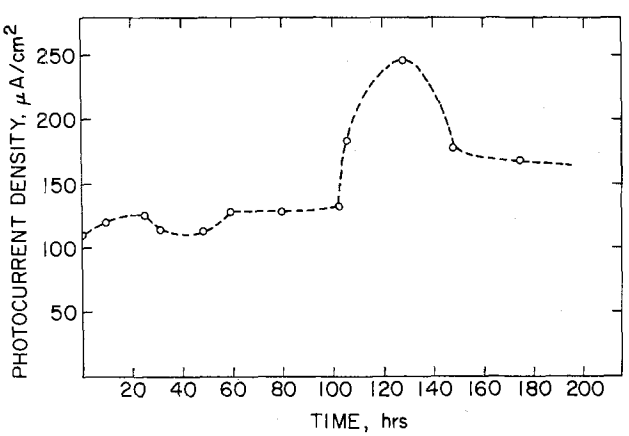

Fig. 1. The photocurrent vs. time of a single crystal TiO_2 for the long-term stability study. The electrode was biased at 0.5V (SCE). Electrolyte, 0.1*N* NaOH. Xenon illumination, 25 mW/cm^2.

Illumination was provided by a Schoeffel LH151N/Z 1000W xenon lamp employing a Schoeffel GM 252

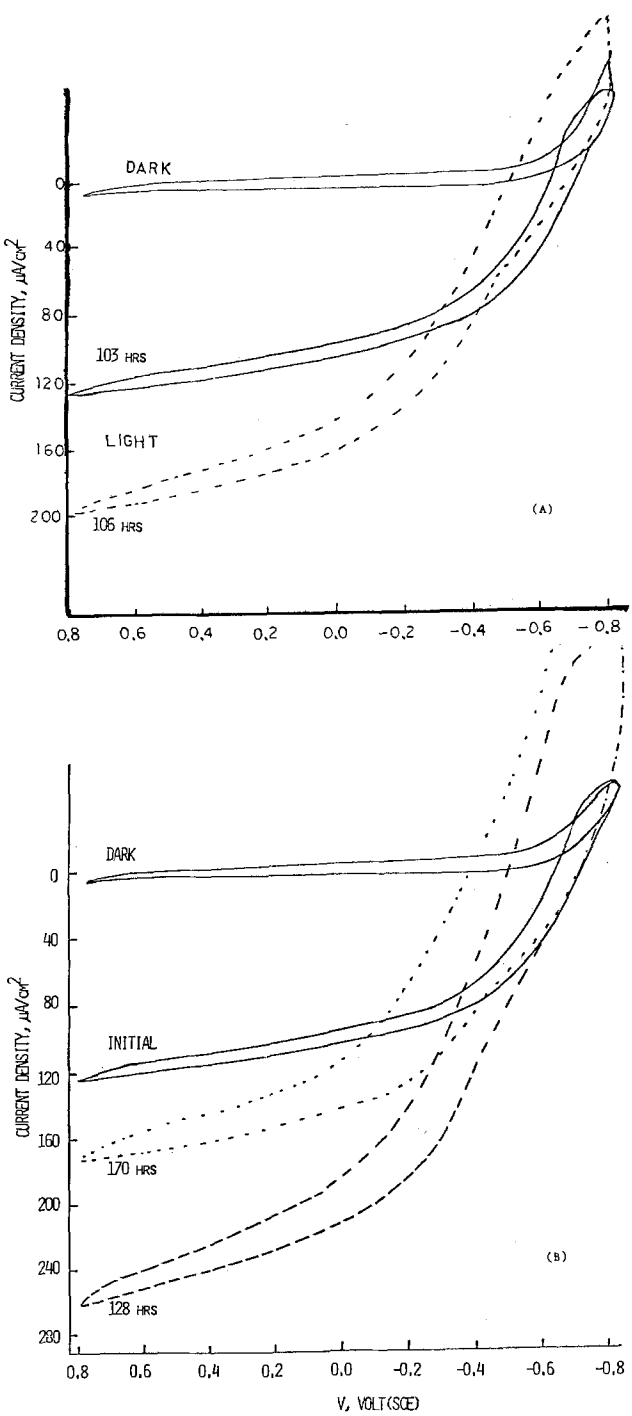

Fig. 2. *I-V* curves at the TiO_2 electrode at different stages in the long-term stability study. (A) shows the most dramatic variation between 103 and 106 hr. (B) shows the eventual decrease of the current density. Electrolyte, 0.1*N* NaOH; sweep rate, 50 mV/sec. Xenon illumination, 25 mW/cm^2.

monochrometer. Light intensity was measured with an EPLAB Model 901 thermopile. Current voltage plots were made with the aid of a PAR 175 Universal programmer, a PAR 173 potentiostat, and an HP 7044A X-Y recorder. Mott-Schottky measurements were made at 1 kHz with a surface impedance bridge.

A fast automatic ellipsometer was used to analyze the variation of the surface properties of the sample *in situ* during a long-term operation. The ellipsometer arrangement was similar to that reported in the literature (10). The wavelength used, employing a tungsten-halogen lamp, was 5461Å and the analyzer was a Rudolph Model RR 2000. The ellipsometric angles Δ and Ψ were recorded from the digital readout of the analyzer. The angles describe the differences in phase and amplitude between the reflection coefficients for light polarized in the plane of incidence to that for light polarized in the plane of the surface, *i.e.*, $R/R_1 =$ tan Ψ exp ($i\Delta$). The initial Ψ and Δ of the sample measured in air were 234.0 and 8.2, respectively. The corresponding real and imaginary indexes of refraction of the sample were n = 2.404 and k = 0.495, respectively.

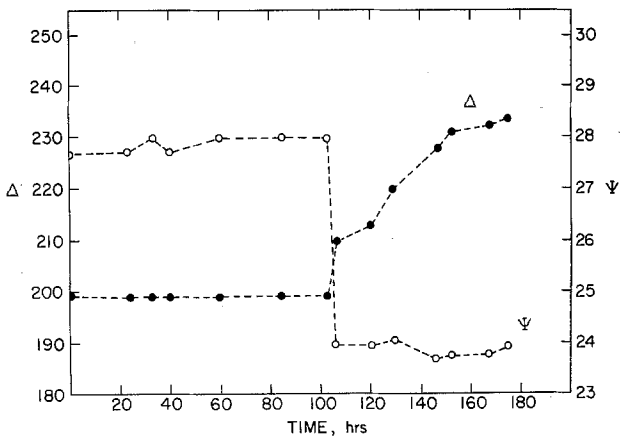

Fig. 4. The corresponding ellipsometry data of Fig. 1

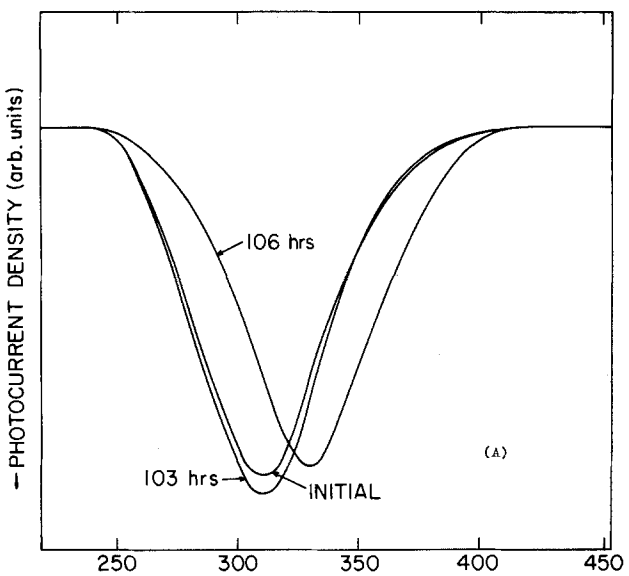

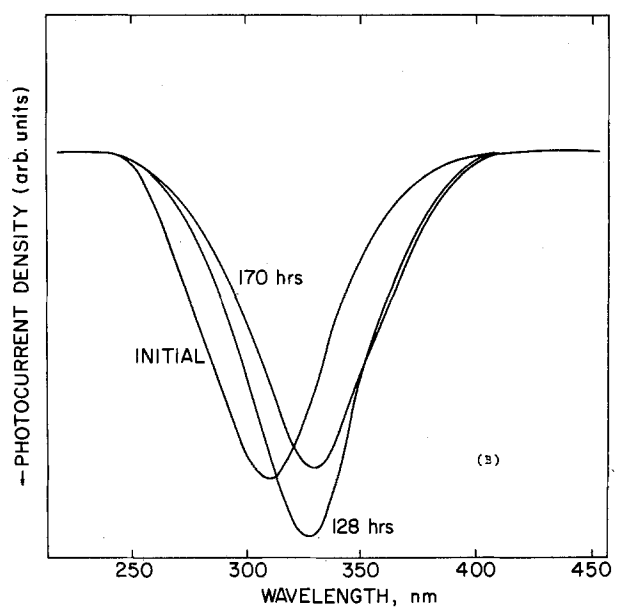

Fig. 3. The corresponding photocurrent spectra of Fig. 2 at different stages.

Figure 1 shows the effect of long-term operation for the sample that was heavily doped with a carrier concentration of 4.8 × 10^{19}/cm^3. The sample was kept in the dark and biased at 0.5V (SCE) at all times except when the measurements of *I-V* curves, photocurrent spectra under xenon illumination, or of ellipsometric data under tungsten-halogen illumination were made. In the first 103 hr, there were only minor fluctuations of the photocurrent (measured at 0.5V SCE). However, after 103 hr, the photocurrent increased substantially to more than twice the original value. After 108 hr, the photocurrent started to decrease. Figure 2 shows the *I-V* curves under illumination at different stages of the experiment. The large change between 103 and 106 hr is quite dramatic. The corresponding spectral dependence of the photocurrent is shown in Fig. 3. There is an apparent shift to longer wavelengths between 103 and 106 hr. Mott-Schottky measurements were also made at different stages during the stability experiments. The measured junction capacitance as a function of biased potential is listed in Table I. Again, there is a drastic change between 103 and 106 hr indicative of an increase in positively charged species at the surface. The ellipsometric data shown in Fig. 4 exhibit the similar abrupt variation between 103 and 106 hr for both Δ and Ψ. After 106 hr, Δ continued changing while Ψ showed only slight variation. Inspection of the surface of the TiO_2 anode under the scanning electron microscope before and after the experiment indicated that there were no observable changes.

It appears that at 103 hr structural changes may have been initiated at the TiO_2 surface characterized by a narrowing of the bandgap and shifts in the refractive index. These structural changes may have resulted from a buildup in the concentration of positively charged species (such as Ti^{+3} or H^+) that would be

Table I. C(μF/cm^2)

V (V) (SCE)	Time (t) (hr) 0	25	60	85	103	106	122	147	170
−0.9	25.0	27.0	29.0	29.0	28.0	11.0	14.0	12.5	12.0
−0.8	15.0	17.5	15.0	17.0	17.0	8.3	9.5	8.4	8.2
−0.7	12.0	13.5	10.5	10.6	10.0	4.7	5.0	4.9	4.7
−0.6	11.0	11.9	9.5	9.6	9.1	3.3	3.4	3.0	3.0
−0.5	10.0	11.4	9.0	8.9	8.6	3.0	3.1	2.6	2.5
−0.4	9.5	10.8	8.5	8.5	8.0	2.8	2.9	2.4	2.3
−0.3	9.1	10.5	8.3	8.2	7.8	2.7	2.8	2.3	2.2
−0.2	8.9	10.2	8.0	7.8	7.5	2.6	2.6	2.2	2.1
0	8.6	9.5	7.6	7.3	7.1	2.4	2.4	2.0	2.0

expected to migrate toward the surface when the electrode is under positive bias.

Work is underway to clarify the mechanism of the above-described effect.

Acknowledgment

This research was performed under the auspices of the U.S. Department of Energy under Contract No. DE-AC02-76CH00016.

Manuscript submitted July 2, 1982; revised manuscript received Oct. 6, 1982.

Any discussion of this paper will appear in a Discussion Section to be published in the December 1983 JOURNAL. All discussions for the December 1983 Discussion Section should be submitted by Aug. 1, 1983.

Publication costs of this article were assisted by the State University of New York at Stony Brook.

REFERENCES

1. L. A. Harris and R. H. Wilson, *This Journal*, **123**, 1010 (1976).
2. L. A. Harris, M. E. Gerstner, and R. H. Wilson, *ibid.*, **126**, 850 (1979).
3. R. H. Wilson, L. A. Harris, and M. E. Gerstner, *ibid.*, **126**, 844 (1979).
4. L. A. Harris and R. Schumacher, *ibid.*, **126**, 844 (1979).
5. M. A. Butler, *ibid.*, **126**, 338 (1979).
6. D. S. Ginley and M. L. Knotek, *ibid.*, **126**, 2163 (1979).
7. M. F. Weber, L. C. Schumacher, and M. J. Dignam, *ibid.*, **129**, 2022 (1982).
8. L. J. Van derPauw, *Philips Res. Rep.*, **13**, 1 (1958).
9. Z. M. Jarzebsk, "Oxide Semiconductors," Pergamon Press (1972).
10. F. McCrackin, E. Passaglia, R. Stromberg, and H. Steinberg, *J. Res. Natl. Bur. Standards, A, Physics and Chemistry*, **67**, No. 4 (1963).

Effects of the Helmholtz Layer Capacitance on the Potential Distribution at Semiconductor/Electrolyte Interface and the Linearity of the Mott-Schottky Plot

Kohei Uosaki* and Hideaki Kita

Department of Chemistry, Faculty of Science, Hokkaido University, Sapporo 060, Japan

The knowledge of the potential distribution of the semiconductor/electrolyte interface is essential for understanding the photoelectrochemical behavior of the semiconductor electrode. It is usually assumed that the Helmholtz layer capacitance is so large compared with the space charge layer capacitance that the total capacitance measured can be treated as the space charge layer capacitance and all potential change occurs within the space charge layer, *i.e.*, bandedge is pinned (1). Recently, however, Bard *et al.* and Wrighton *et al.* have shown that if a significant amount of surface states is present all the potential change occurs in the Helmholtz layer, *i.e.*, Fermi level is pinned, contrary to the above assumption (2-4). The bandedge pinning and the Fermi level pinning are the two extreme situations of the potential distribution at the semiconductor/electrolyte interface, and usually the applied potential with respect to the flatband potential distributes partly in the space charge layer and partly in the Helmholtz layer (5).

The linearity of the Mott-Schottky plot is often considered to be evidence of the bandedge pinning (6), although De Gryse *et al.* have shown, by solving the Poisson equation for a depletion layer with Mott-Schottky approximation (7), that the linearity holds even when the bandedge movement occurs.

In this note we examine the effects of the Helmholtz layer capacitance on the bandedge movement and the linearity of the relation between $1/C^2$ and the applied voltage when no surface states are present by the calculation of the potential dependence of the Helmholtz layer capacitance and the potential change in the Helmholtz layer without many approximations.

To obtain the potential distribution of semiconductor/electrolyte interface, the following Poisson equation must be solved (8)

$$\frac{d^2\phi}{dx^2} = -\frac{e}{\epsilon_0\epsilon}\left[p_0 \exp\left\{-\frac{e(\phi-\phi_b)}{kT}\right\} - n_0 \exp\left\{\frac{e(\phi-\phi_b)}{kT}\right\} + N_D - N_A\right] \quad [1]$$

where e is the elementary charge, ϵ_0 is the dielectric constant of the vacuum, ϵ is the relative dielectric constant of the semiconductor, ϕ and ϕ_b are the potential of the semiconductor at x from the semiconductor/electrolyte interface and in the bulk, p_0 and n_0 are the concentration of holes and electrons in the bulk, and N_D and N_A are the concentration of donor and acceptor levels, respectively. When the charge at the semiconductor/electrolyte interface is distributed continuously and does not consist of separate point charges, the evaluation gives the following equation for the space charge in the semiconductor, Q_{sc}, from the Eq. [1] (8)

$$Q_{sc} = \epsilon\epsilon_0\left(\frac{d\phi}{dx}\right)_{x=0} = \pm\sqrt{2\epsilon\epsilon_0 kT\{-(N_D-N_A)y_s + p_0(e^{-y_s}-1) + n_0(e^{y_s}-1)\}} \quad [2]$$

Here

$$y_s = \frac{e(\phi_s-\phi_b)}{kT} \quad [3]$$

where ϕ_s is the potential of the semiconductor at the surface. The plus sign appears in front of the root when $y_s < 0$ and the minus when $y_s > 0$. The differential capacitance of the space charge layer, C_{sc}, is obtained by differentiation of Eq. [2] as

* Electrochemical Society Active Member.

Key words: semiconductor, Mott-Schottky plot, Helmholtz layer capacitance.

$$C_{sc} = e\sqrt{\frac{\epsilon\epsilon_0}{2kT}} \frac{|-(N_D - N_A) - p_o e^{-y_s} + n_o|}{\sqrt{-(N_D - N_A)y_s + p_o(e^{-y_s} - 1) + n_o(e^{y_s} - 1)}} \quad [4]$$

The measured capacitance, C, can be written as

$$C^{-1} = C_{sc}^{-1} + C_H^{-1} \quad [5]$$

where C_H is the differential capacitance of the Helmholtz layer, and the electrode potential of the semiconductor electrode, V, with respect to the flatband potential, V_{FBP}, can be written as

$$V - V_{FBP} = \Delta\phi_{sc} + \Delta\phi_H \quad [6]$$

where $\Delta\phi_{sc}$ is the potential change in the space charge layer, *i.e.*, $\Delta\phi_{sc} = \phi_b - \phi_s$, and $\Delta\phi_H$ is the potential change in the Helmholtz layer, *i.e.*, $\Delta\phi_H = \phi_{H,V} - \phi_{H,FBP}$, where $\phi_{H,V}$ and $\phi_{H,FBP}$ are the potential drop in the Helmholtz layer at potential V and at the flatband potential, respectively. By assuming the variation of C_H as a function of the electrode potential is negligible, $\Delta\phi_H$ can be expressed as

$$\Delta\phi_H = Q_{sc}/C_H \quad [7]$$

The usual assumption is $|\Delta\phi_{sc}| >> |\Delta\phi_H|$, *i.e.*, the bandedge is pinned. By using Eq. [2], [3], and [7], the ratio of $\Delta\phi_H$ to $\Delta\phi_H + \Delta\phi_{sc}$, *i.e.*, the total potential change, is calculated as a function of $(\Delta\phi_H + \phi\Delta_{sc})$ by assuming $C_H = 10\ \mu\mathbf{F} \cdot \mathrm{cm}^{-2}$ and the results are shown in Fig. 1. The contribution of $\Delta\phi_H$ is surprisingly high, particularly at the potentials near the flatband potential. De Gryse *et al.* have derived the following equations for n-type semiconductors by using the Mott-Schottky approximation and demonstrated that the linearity of the Mott-Schottky plot holds even when C_H and $\Delta\phi_H$ are taken into account (7)

$$Q_{sc} = \frac{2e\epsilon\epsilon_0}{N_D}\left(\Delta\phi_{sc} - \frac{kT}{e}\right) \quad [8]$$

$$C_{sc} = \frac{e\epsilon\epsilon_0 N_D}{2} \cdot \frac{1}{\sqrt{\Delta\phi_{sc} - \frac{kT}{e}}} \quad [9]$$

$$C^{-2} = C_H^{-2}\left\{1 + \frac{2C_H^2}{e\epsilon\epsilon_0 N_D}\left(V - V_{FBP} - \frac{kT}{e}\right)\right\} \quad [10]$$

The comparison is made between $\Delta\phi_H/(\Delta\phi_{sc} + \Delta\phi_H)$ obtained by using Eq. [2], [3], and [7] and one obtained by using Eq. [7] and [8] in Fig. 2. When the potential change is relatively large, two calculations give similar results, but the difference is significant when $(\Delta\phi_{sc} + \Delta\phi_H) < 0.15$V.

It is interesting to see how C_H and $\Delta\phi_H$ affect the plot of C^{-2} *vs.* $(V - V_{FBP})$, *i.e.*, Mott-Schottky plot. The values of C^{-2} obtained by using Eq. [4] and [5] with $C_H = 10\ \mu\mathbf{F} \cdot \mathrm{cm}^{-2}$ and ∞ are plotted against $(\Delta\phi_{sc} + \Delta\phi_H)$ in Fig. 2. $\Delta\phi_H$ is calculated by using Eq. [2], [3], and [7]. The values of C^{-2} obtained by Eq. [10] with $C_H = 10\ \mu\mathbf{F} \cdot \mathrm{cm}^{-2}$ are also plotted against $(\Delta\phi_{sc} + \Delta\phi_H)$ in Fig. 2. In this case $\Delta\phi_H$ is calculated by using Eq. [7] and [8]. Again the difference between the plot with (curve 4) and without (curve 3) the approximation becomes significant at small bias potentials. The relation between C^{-2} and $(\Delta\phi_{sc} + \Delta\phi_H)$ obtained by Eq. [2], [3], and [7] is linear when potential change is large but curved when $(\Delta\phi_{sc} + \Delta\phi_H) <$ *ca.* 0.3V. The slope of the linear portion of the relation (curve 3) is almost the same as that of C^{-2} *vs.* $(\Delta\phi_{sc} + \Delta\phi_H)$ relation when C_H and $\Delta\phi_H$ are neglected (curve 5) as demonstrated by De Gryse *et al.* (7).

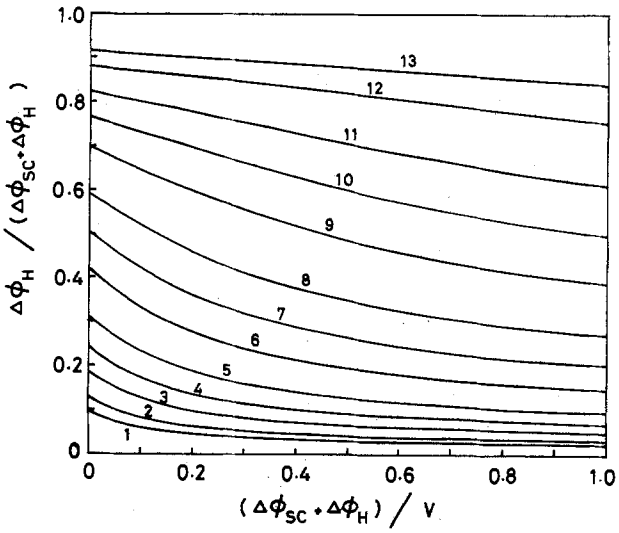

Fig. 1. The ratio of the potential in the Helmholtz layer to the total potential change as a function of the total potential change. $\epsilon = 173$. $C_H = 10\ \mu\mathrm{F} \cdot \mathrm{cm}^{-2}$. Carrier densities are: 1. 10^{16} cm^{-3}, 2. 2×10^{16} cm^{-3}, 3. 5×10^{16} cm^{-3}, 4. 10^{17} cm^{-3}, 5. 2×10^{17} cm^{-3}, 6. 5×10^{17} cm^{-3}, 7. 10^{18} cm^{-3}, 8. 2×10^{18} cm^{-3}, 9. 5×10^{18} cm^{-3}, 10. 10^{19} cm^{-3}, 11. 2×10^{19} cm^{-3}, 12. 5×10^{19} cm^{-3}, 13. 10^{20} cm^{-3}.

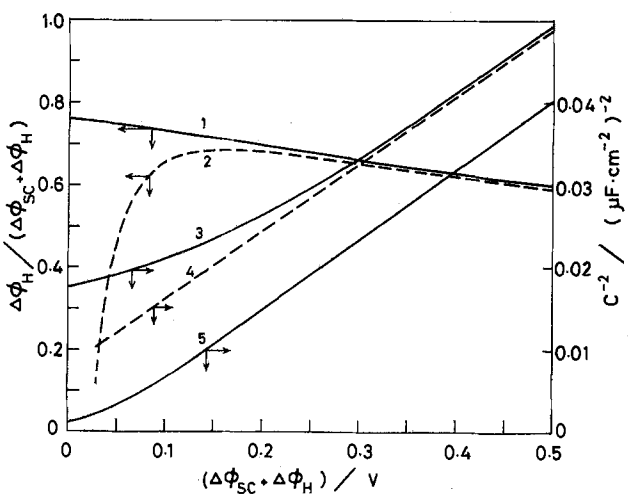

Fig. 2. Dependence of the ratio of the potential change in the Helmholtz layer to the total potential change and of C^{-2} as a function of total potential change. $\epsilon = 173$. Carrier density is 10^{19} cm^{-3}. 1. $\Delta\phi_H/(\Delta\phi_H + \Delta\phi_{sc})$ vs. $\Delta\phi_H + \Delta\phi_{sc}$ calculated by using Eq. [2], [3], and [7]. 2. As curve 1 but calculated by using Eq. [7] and [8]. 3. C^{-2} vs. $\Delta\phi_H + \Delta\phi_{sc}$ calculated by using Eq. [2], [3], [4], [5], and [7], $C_H = 10\ \mu\mathrm{F} \cdot \mathrm{cm}^{-2}$. 4. As curve 3 but calculated by using Eq. [7], [8], and [10]. 5. As curve 3 but $C_H = \infty$.

Thus, although the linearity between C^{-2} *vs.* $(\Delta\phi_{sc} + \Delta\phi_H)$ does not hold at relatively small bias and the extrapolation of the linear portion of the relation to $C^{-2} = 0$ does not give $V_{FBP} + \frac{kT}{e} - \frac{e\epsilon\epsilon_0 N_D}{2C_H^2}$, the general conclusion of De Gryse *et al.* is supported, because usually the Mott-Schottky plot is presented for relatively large bias potentials.

The following conclusion can be drawn from the above. (*i*) C_H and $\Delta\phi_H$, *i.e.*, the movement of bandedge, cannot be neglected even when no surface state is present, particularly at highly doped semiconductors. (*ii*) C^{-2} *vs.* $V - V_{FBP}$ plot is linear at relatively large bias potentials but curved at small bias potentials and the slope of the linear portion is almost the same as that of C^{-2} *vs.* $V - V_{FBP}$ without taking into account C_H and $\Delta\phi_H$. Thus, the linearity of the Mott-Schottky

plot at relatively large bias potentials cannot be used as evidence of bandedge pinning. (*iii*) To obtain an accurate picture of the potential distribution of the semiconductor/electrolyte interface, one must measure the differential capacitance-potential relation for a wide potential range, particularly at small bias potentials, calculate the carrier density from the slope of the linear portion of C^{-2} *vs.* potential plot, and compare the C^{-2} *vs.* potential relation calculated by using the carrier density thus obtained and Eq. [2]-[7] for certain values of V_{FBP} and C_H, with the experimentally observed C^{-2} *vs.* potential plot.

Acknowledgment

This work was partly supported by a grant-in-aid for scientific research, Ministry of Education, Science and Culture, No. 57470001.

Manuscript submitted Sept. 21, 1982; revised manuscript received Dec. 1, 1982.

Any discussion of this paper will appear in a Discussion Section to be published in the December 1983 JOURNAL. All discussions for the December 1983 Discussion Section should be submitted by Aug. 1, 1983.

Publication costs of this article were assisted by Hokkaido University.

REFERENCES

1. R. H. Wilson, in "Semiconductor Liquid-Junction Solar Cells," A. Heller, Editor, p. 67, The Electrochemical Society Softbound Proceedings Series, Princeton, NJ (1977).
2. A. J. Bard, A. B. Bocarsly, F.-R. F. Fan, E. G. Walton, and M. S. Wrighton, *J. Am. Chem. Soc.*, **102**, 3671 (1980).
3. F.-R. F. Fan and A. J. Bard, *ibid.*, **102**, 3677 (1980).
4. A. B. Bocarsly, D. B. Bookbinder, R. N. Dominey, N. S. Lewis, and M. S. Wrighton, *ibid.*, **102**, 3683 (1980).
5. J. O'M. Bockris, K. Uosaki, and H. Kita, *J. Appl. Phys.*, **52**, 808 (1981).
6. J. A. Turner and A. J. Nozik, *Appl. Phys. Lett.*, **41**, 101 (1982).
7. R. De Gryse, W. P. Gomes, F. Cardon, and J. Vennik, *This Journal*, **122**, 711 (1975).
8. V. A. Myamlin and Yu. V. Pleskov, "Electrochemistry of Semiconductors," Plenum Press, New York (1967).

JOURNAL OF THE ELECTROCHEMICAL SOCIETY

SOLID-STATE SCIENCE AND TECHNOLOGY

APRIL 1983

Evolution of Scale Microstructure and the Pressure Dependence of the Sulfidation Rate of Iron

R. A. McKee and R. E. Druschel

Oak Ridge National Laboratory, Oak Ridge, Tennessee 37830

ABSTRACT

The sulfidation rate of iron to $Fe_{1-x}S$ has been measured, and the microstructural features of this sulfide have been carefully studied. The measurements were made at 700°C in pure sulfur vapor covering the pressure range from 1-10^3 Pa; 700°C is a temperature in the midrange of previous measurements, and was selected to facilitate a study of the general aspects of the microstructure and growth rate of this highly nonstoichiometric sulfide of iron. We find that the growth direction and microstructure of the scale are pressure dependent, and contrary to previously reported results, we find no evidence to suggest that the growth rate of iron sulfide is any different in pure sulfur vapor than in H_2/H_2S mixtures.

In a series of experiments, we have measured the sulfidation rate of iron in pure sulfur vapor. From the literature that is available, there is a clear indication that microstructural as well as physical property characteristics are influenced by gas purity and composition. Our effort has not been simply to survey the reaction kinetics (*i.e.*, to determine the complete temperature and pressure dependence), but to look very carefully at a temperature in the midrange of data that exist and to investigate the pressure dependence thoroughly. Therefore, we have been extremely careful in measuring the specimen reaction temperature and fixing the sulfur pressure in a reliable and reproducible manner. Two aspects of the iron-sulfur reaction were of particular importance when we initiated our study. First, both Fryt, Bhide, Smeltzer, and Kirkaldy (1) and Narita and Nishida (2) had suggested that a transformation in growth direction of the scale forming on the metal occurred as the pressure was varied; this is not a common occurrence in metal oxidation and we felt that it was important to verify this observation. Second, it also had been suggested that hydrogen, ionizing in hydrogen-hydrogen sulfide mixtures [see Worrell and Turkdogan (3) and Zelouf and Simkovich (4)] might somehow play a part in the sulfide defect structure; this idea is important to the overall evaluation of sulfidation processes, and can be tested by carefully comparing measurements in H_2/H_2S and pure sulfur vapor; we have provided accurate measurements in sulfur vapor for such a comparison.

Toward these aims then we report our results of a study using pure iron[1] in which we measured the rate of sulfidation using a multispecimen technique, to insure reproducibility and to provide specimens for microstructural observations. The sulfur pressure was varied from 0.1 to 1000 Pa, and a systematic comparison of the pressure dependence of the microstructure is now available.

Experimental

We describe several features of our experimental technique that we believe are important in considering the merit of our overall results. The three principle areas are (*i*) the measurement of the specimen temperature, (*ii*) the general care that went into assuring that the sulfur pressure was specified and reproducible, and (*iii*) the use of a multispecimen technique that allows for a clear demonstration of the reproducibility of the sulfidation rate data and the time evolution of the scale microstructure. An additional feature, which is not at all minor, is specimen purity.

Specimen temperature measurement.—In Fig. 1, a schematic of our apparatus shows that a Pt/Pt-10% RH thermocouple was used directly as a hang-down or suspension wire for the iron specimen. We were able to weld the thermocouple directly to the specimen and monitor its temperature throughout the run. This had several advantages for our experimental method, and it made it possible to keep a continuous specimen temperature-time record. Some of our experiments were short time (~1 min) experiments; our measuring technique allowed the normal sort of temperature overshoot from self-heating that occurs at the initiation of the reaction to be recorded, so that time-at-temperature corrections could be applied. Moreover, since this same thermocouple was the measuring couple as well as the input signal and the furnace controller, any tendency for overshooting from self-heating could be minimized if not eliminated altogether.

Figure 2 shows the results that were regularly and frequently obtained as an *in situ* calibration check of our thermometry methods. In Fig. 2, we plot the temperature of the iron specimen heated in vacuum through the α-γ phase transformation. The accepted temperature range for this transformation is 910°-912°C (5). As is demonstrated in this figure, a thermal arrest occurs at 911.2° ± 0.5°C. As a result of this and numerous other tests, we believe that we know the actual reaction temperature of the specimen to ±2°C. The methods that were used in this experimental temperature measurement are largely the result of our experiences in recent work done at this laboratory on the high temperature oxidation of zirconium and its alloys (6-8).

Sulfur pressure specification.—Numerous studies of iron sulfidation are available in the literature (1, 2, 9-11), but it seems safe to say that very few show

[1] Marz grade iron, supplied by MRC, total metal impurities less than 10 ppm, oxygen + carbon less than 60 ppm.

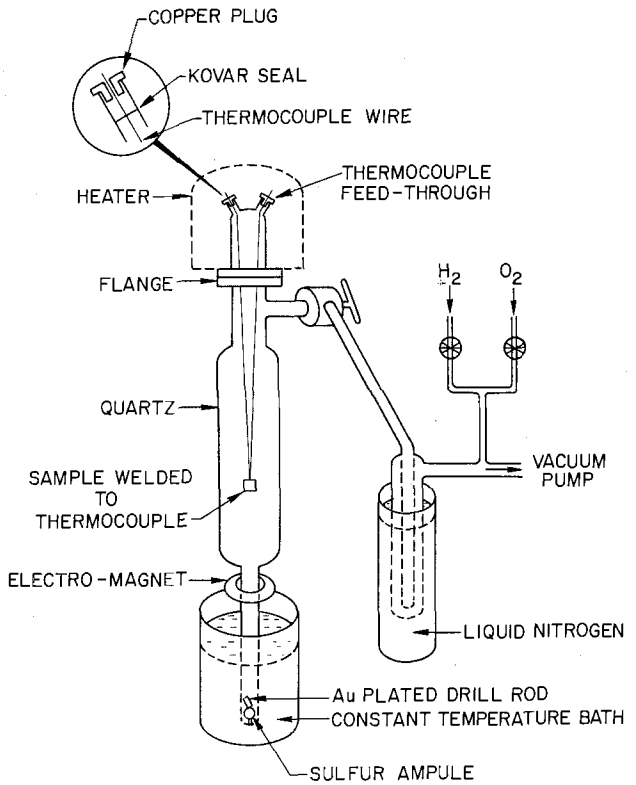

Fig. 1. Schematic of reaction chamber and supporting apparatus for sulfidation measurements.

anything more than qualitative agreement. In all these studies, there are both absolute rate variations and real microstructural differences that are very likely due to poor specification of the sulfur pressure. The two questions that we have sought to answer in our study both require that the sulfur pressure be reliably fixed. Perhaps the most important is the "a" to "c" growth direction change that occurs as the pressure changes (1, 2), and since this has had no mechanistic explanation, an accurate specification of the sulfur pressure is essential to describe the range of pressure over which the transition occurs.

Our experimental apparatus is shown schematically in Fig. 1. Every segment of the quartz furnace liner and reaction chamber were heated either by the furnace itself or by external heat sources. Thermocouples placed at intervals along the apparatus were monitored throughout an experiment to assure that no point on the reaction chamber surface was cooler than the saturated vapor temperature that was maintained in the oil or salt bath. Moreover, while developing our apparatus, we used several methods of isolating the sulfur until the reaction was started. The first method was the breaking of an ampul break-off tip with subsequent sulfur egress into the reaction chamber. We found this method unsatisfactory because unpredictable tip size openings gave problems associated with the sulfur egress and limitation of the reaction rate. An example of the complications that arise from this effect is shown in Fig. 3a. The specimen illustrated in this electron micrograph was exposed to sulfur vapor at a pressure, nominally 1 Pa, that subsequent tests proved to be much lower than expected. The scale morphology, the manner in which the grains of the scale arrange themselves in "colonies," and the overall scale thickness are typical of scale formation at sulfur pressures much lower than 1 Pa. Figure 3b is the

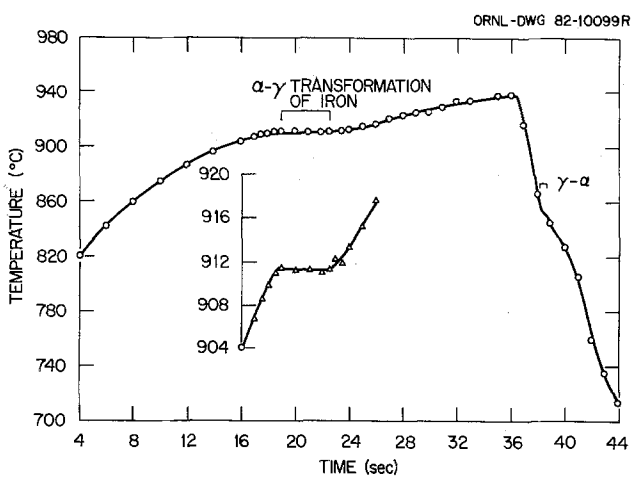

Fig. 2. Time-temperature profile for *in situ* thermometry checks showing the α-γ phase transformation and thermal arrest at 911.1° ± 0.5°C.

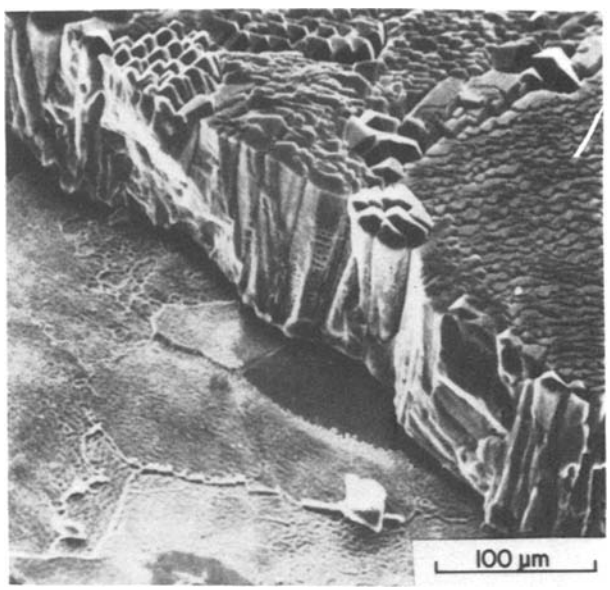

Fig. 3a. Scale morphology and colony structure that formed when cold spots in the apparatus left the sulfur pressure lower than the assumed equilibrium 1 Pa vapor pressure. This micrograph shows the specimen surface with a portion of the scale popped off to illustrate the scale surface, scale cross section, and the underlying metal surface; reaction time, 1 hr.

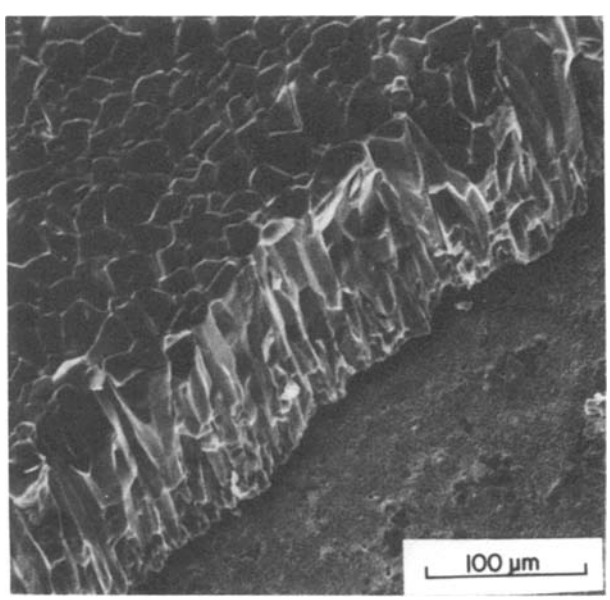

Fig. 3b. Scale morphology that truly represents steady-state growth for an equilibrium sulfur vapor pressure of 1 Pa; reaction time, 10 min.

microstructure morphology and scale structure that results when FeS is grown to the same thickness as that obtained for the specimen in Fig. 3a, except that the pressure is truly 1 Pa. Note the differences not only in the time of sulfidation but in the morphology of the scale-gas interface. The problem just described was eliminated, and the method used to release sulfur into the reaction chamber was to first contain the sulfur in an ampul or bulb and then to shatter the ampul by a breaker dropped from an electromagnet. If the ampul is broken in this manner, the sulfur can establish thermal contact with the entire surface area of the reaction chamber that is immersed in the bath. The sulfur actually achieves the bath temperature, and this was confirmed by suspending a thermocouple into this reaction chamber area, and monitoring the glass surface temperature before the ampul is shattered and after it is shattered. Under no conditions did we ever find the inside surface of the reaction chamber or the sulfur that was exposed to it when the ampul was ruptured to vary by more than ±0.5°C from the bath temperature.

The actual bath temperature was controlled to ±0.1°C and monitored throughout the experiment. The bath temperature was measured with a permanently installed Pt/Pt-10% RH thermocouple connected to a continuous digital readout. The absolute bath temperature was determined and set against periodic measurements using a platinum resistance thermometer. On an absolute basis, the bath temperatures were known to be within ±0.5°C and controlled to ±0.1°C. We record the bath temperatures directly in Table I along with the sulfur pressure values taken from Ref. (12) that correspond to these saturated vapor temperatures. Other vapor pressure-temperature sources are available, and although Ref. (12) seems entirely adequate, we make no statement of support for these values against any others. Finally, we subjected these general precautions in experimental technique for sulfur pressure specification to a critical test. The Fe/S ratio is known as a function of sulfur pressure for this material, see Fryt *et al.* (1). When iron specimens were sulfidized to completion in our apparatus at the pressures used in our study, the Fe/S ratios compiled and reported by Fryt *et al.* (1) that had been determined using H_2/H_2S mixtures were reproduced to 1 part in 10^3.

Multi-specimen technique.—To determine the rate of sulfur attack, we ran individual specimens for a fixed time in separate experiments and ran enough specimens in this manner to obtain a rate curve. Figure 4 shows our data for several pressures plotting the scale thickness squared against time. Every point on this figure represents a separate experiment on a separate specimen. Doing our measurements in this manner requires reproducibility in specimen preparation, specimen purity, reaction temperature, and sulfur pressure. This method insures self-consistency of the data and permits the time evolution of the microstructure to be studied.

Specimen purity.—We have used Marz grade iron supplied by the Materials Research Cooperation: we used analysis data supplied by them and did analyses of our own. Metallic impurities were limited to a total of less than 10 atomic ppm. By using a fast neutron analysis, we find that oxygen is below 30 ppm in this material, confirming the analysis supplied by MRC. We

Table I.

Bath temperature (°C)	Saturated vapor pressure of sulfur (Ref. 13) (Pa)
95	1
130	10
175	100
235	1000

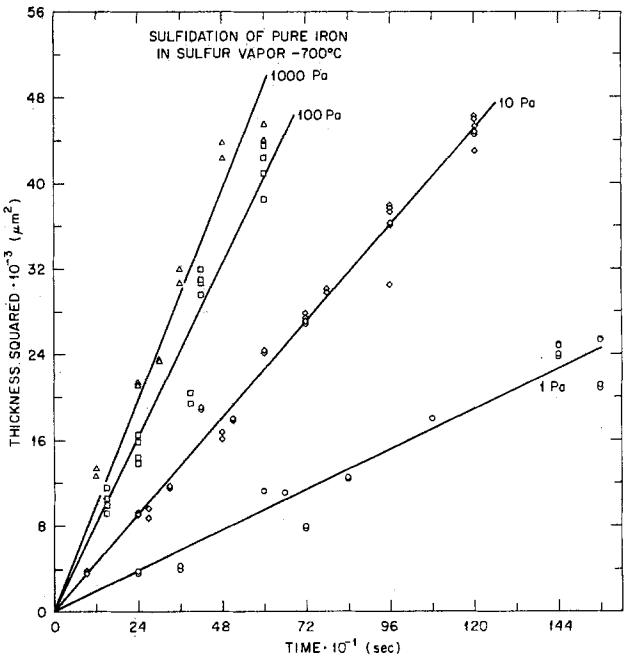

Fig. 4. Sulfidation rate data as a function of pressure at 700°C. Each point represents a separate experiment on a different specimen. These data illustrate the reproducibility of specimen preparation, specimen purity, reaction temperature, and sulfur pressure.

have looked at this material's microstructure, and bright field optical light microscopy shows features in the iron that are said to be (13) precipitates; silicates, sulfides, and oxides of Fe and Mn. Optical light microscopy shows that these particles are roughly spherical and ½-1 μm in diameter. By examining these particles with an electron microprobe, we can detect Si and Fe. The microprobe is not capable of analyzing for oxygen, but sulfur detection is clearly within its capabilities: no sulfide is detected, and Mn is apparently not in the particles, or if it is, it is at a level of 500 ppm or less in the particle itself. It seems very likely that the particles observed in our material are silicates and iron oxides. These particles do not dissolve or undergo any detectable coarsening in the heat-treatments that occur in our experiments, *i.e.*, 30 min-1 hr at temperatures of 700°-800°C. Probably more so than the overall level of impurities that might be dissolved in the growing sulfide, the density of these precipitate particles could be a major factor in influencing the growth kinetics of a material like iron sulfide, *i.e.*, the particles accumulate at the Fe-FeS interface during scale growth.

Experimental procedure.—Finally, we conclude this section by giving a detailed description of the experimental procedure. Basically, the system (see Fig. 1) is a reaction chamber which contains two heat zones: (*i*) the bath controls the sulfur temperature, and (*ii*) the furnace controls the specimen temperature. The reaction chamber is separated from a high vacuum system by bakable, metal, high-vacuum valves. To begin with, the specimen is welded to the thermocouple hang-down wire and a flange with thermocouple feed-throughs is bolted onto the reaction chamber. All connections are helium leak tested. Then the system is pumped down until the ionization gauge reads below 5×10^{-7} Pa. The high vacuum valve is blanked off, and the system is backfilled and purged with hydrogen several times. Then all parts of the sulfidation chamber are baked under vacuum at temperatures from 50°-100°C above the temperature that corresponds to the sulfur vapor temperature for the particular run condition. Then the system is once again evacuated, backfilled with hydrogen to a pressure of approximately 100 Pa, and the

specimen is raised to a temperature of 700°C and annealed for 20-30 min. Finally, the hydrogen is pumped from the system while everything is up to temperature, *i.e.*, the bath at the required vapor-pressure temperature and the specimen at 700°C. Under these conditions, the system is pumped until the ionization gauge once again reads lower than 5×10^{-7} Pa. This usually takes between 10 and 20 min. Once this ultimate pressure is reached, the high-vacuum system is blanked off, the sulfur ampul is broken, and the experiment is started. The experiment is terminated by abruptly opening the reaction chamber to the vacuum system and shutting off the furnace power. The bath is lowered to allow the sulfur to cool. We used a radiant-heating furnace, and the specimen temperature drops from 700° to 400°C in approximately 1 min, finally cooling to room temperature in approximately 10 min. The specimen is then removed from the apparatus, sectioned, and polished by standard methods in preparation for a thickness measurement of the FeS scale.

Results and Discussion

To determine the rate of sulfidation, we ran our experiments with many specimens, every one of which was sulfidized at a constant temperature and sulfur pressure continuously until some time, t, had elapsed. These specimens were exposed to sulfur individually and then removed from the furnace. The scale thickness was measured after the specimen had been mounted and polished using standard metallographic techniques[2] and a series of specimens was run to obtain different thicknesses. Figure 4 shows the results obtained by this method for four pressures, 1, 10, 100, and 1000 Pa. The scale growth rate is clearly parabolic. (Experiments were also run at 0.1 Pa; however, at this pressure the mean-free path of sulfur is so long that geometrical restrictions in our furnace chamber caused a sulfur limitation growth. The data obtained at this pressure are not relevant to our present discussion.)

Microstructure.—In Fig. 5-10, we present a microstructure study that illustrates several features of the sulfidation of pure iron. We discuss the pressure dependence at constant thickness, the time dependence at constant pressure, and the interface features at both the scale-metal and the scale-gas interfaces. Bright field, polarized light, and SEM micrographs are used. By first popping off a scale segment, we were able to take the SEM pictures, and then the same specimen was mounted and polished for the bright field and polarized light microscopy.

The pressure dependence at constant thickness can be illustrated by comparing Fig. 5 and 6. The scale thickness in both cases is approximately 100 μm, but the sulfur pressure was 1 Pa for the specimen shown in Fig. 5 and 10 Pa for that in Fig. 6.

The scale grown at 1 Pa is highly columnar, having a broom straw type of morphology. This is illustrated more clearly in the higher magnification of this same specimen shown in Fig. 7. Notice that this micrograph shows a compact, nonporous, crack-free scale. The scale did separate from the metal on cooling, but from a close examination of the scale-metal interface in this figure, and in others that we shall discuss subsequently, it is apparent that the scale grew adherent to the metal with an integral match between scale and metal microstructural features. A pole figure analysis indicates that the scale is highly oriented with the major growth axis being the "a" direction of the hexagonal crystal, *i.e.*, {102}. This result is entirely consistent with the data from Fryt *et al.* (2), although their data only extend to 0.1 Pa at 700°C.

[2] Metallography technique: (*i*) mount in epoxy, (*ii*) grind through 600 grit paper, (*iii*) polish on Pellon cloth with Linde A and ethylene glycol, and (*iv*) polish on nylon cloth with ½ micron diamond and ethylene glycol.

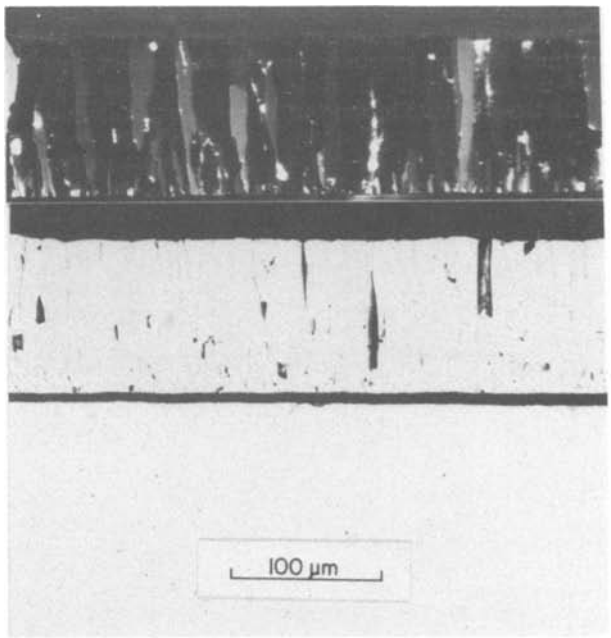

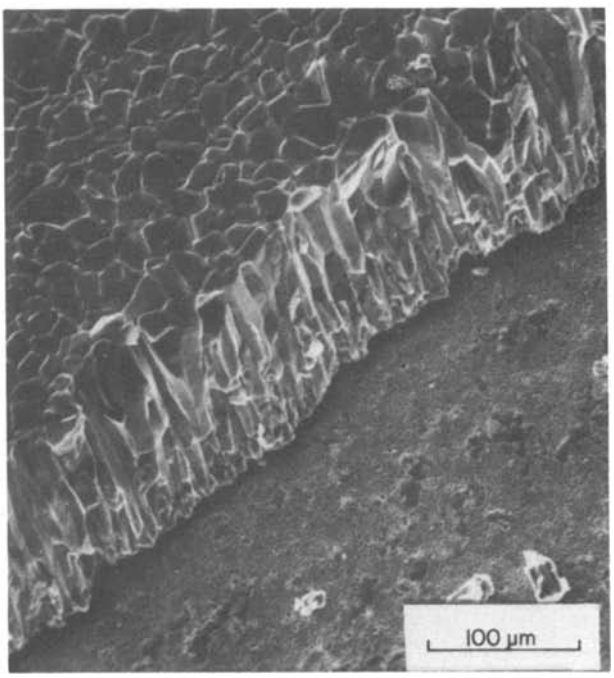

Fig. 5. FeS scale on iron, growth at 700°C and 1 Pa sulfur pressure. The upper portion of the figure shows the scale in cross section, and the lower portion shows the scale C at a 45° angle to the surface with a portion of the scale popped off, revealing the metal underlayer.

In comparison to the 1 Pa result, the scale grown at 10 Pa and shown in Fig. 6 is still columnar in nature but has a much larger grain size. This micrograph, like that in Fig. 5, also shows a compact, nonporous, crack-free scale. There is the inadvertent polishing artifact that occurs when grain segments pull out on polishing; however, it is apparent from an examination of these features that they are not intrinsic to the scale growth. A pole figure analysis of this scale shows a change from that obtained for the 1 Pa result. The scale is still highly oriented, but its major growth direction has changed to some 20 deg off the "c" direction. Therefore, by increasing the pressure only one order of magnitude, the growth direction has

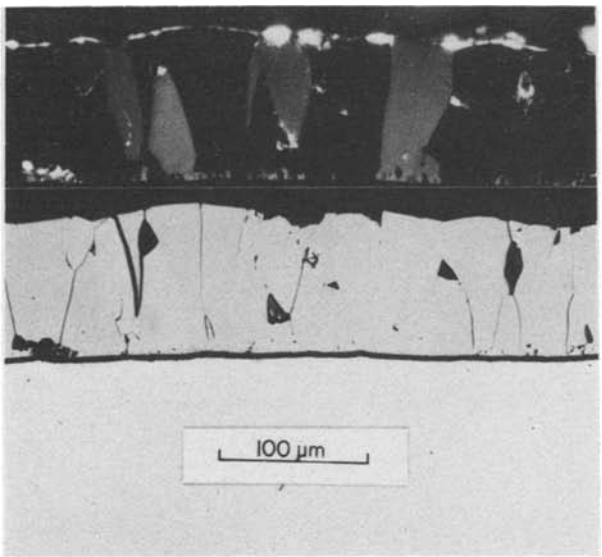

Fig. 6. FeS scale iron, grown at 700°C and 10 Pa sulfur pressure

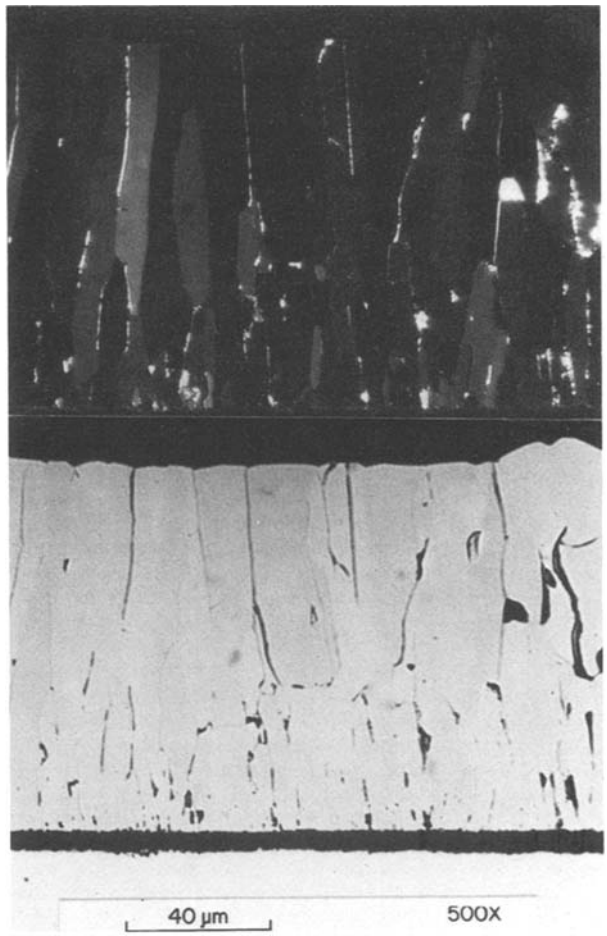

Fig. 7. FeS scale on iron, grown at 700°C and 1 Pa. This is the same specimen as shown in Fig. 5, but at a higher magnification to show the scale details. The polarized light picture is the same segment as the bright field image of the scale shown immediately below it.

made a rather substantial change. Moreover, by increasing the pressure again from 10 to 100 Pa, we find a complete change to "c" direction growth. After that, the microstructure is essentially that shown in Fig. 6, a large grained, compact, nonporous, crack-free scale.

Changing now to a discussion of the time dependence of scale microstructure at constant pressure, we consider Fig. 6 and 8. The scale thickness in Fig. 8 is twice that for the scale in Fig. 6. The important thing to note is that all features shown in Fig. 8 seem to be like a magnification of those in Fig. 6. The grains have coarsened in time, the scale-gas interface has evolved, and as a result Fig. 8 appears to be a magnification of Fig. 6. The observation that suggests itself from this result is that the transport mechanism is not related to grain boundary diffusion. From Fig. 4, we see that at all pressures, the scale growth rate was constant with time and that scale growth was parabolic. With this rather marked reduction in grain boundary area, associated with the grain growth process, would come a change in growth rate if the grain boundaries were important in the growth process. This same time dependence of the microstructure is found at all pressures investigated.

The final aspects of the microstructure that we discuss are the morphological features at the scale-gas and scale-metal interfaces. At the scale-gas interface, the surface exposed to the sulfur vapor is always heavily faceted. Significant surface rearrangement occurs as a result of what apparently is a rather high rate of surface diffusion as opposed to volume diffusion. The grain diameter varies from near 10 to 50 μm depending on pressure and time of exposure, but the faceted features such as grain boundary grooves on the scale-gas interface are often as large in dimensional aspect as the grain diameter itself. Similarly, the scale-metal interface is far from flat, but while the faceting on the scale-gas interface is directly related to grain boundaries, the irregularities at the scale-metal interface are apparently unrelated to the grain boundaries, as can be seen by an examination of Fig. 9. The scale segment shown in Fig. 9 is shown at a lower magnification in Fig. 6 and has broken off the main scale segment and lies on the metal surface. Figure 9 illustrates the adherent, "cup-and-cone" feature of the scale-metal interface.

Kinetics.—At 700°C, there are no measurements of the sulfidation rate of iron in pure sulfur vapor over the pressure range we have covered. Fryt *et al.* (1) used H_2/H_2S at 700°C, but stopped at 0.1 Pa for the sulfur partial pressure. Meussner and Birchenall (9) attempted, but were unable, to measure a sulfidation

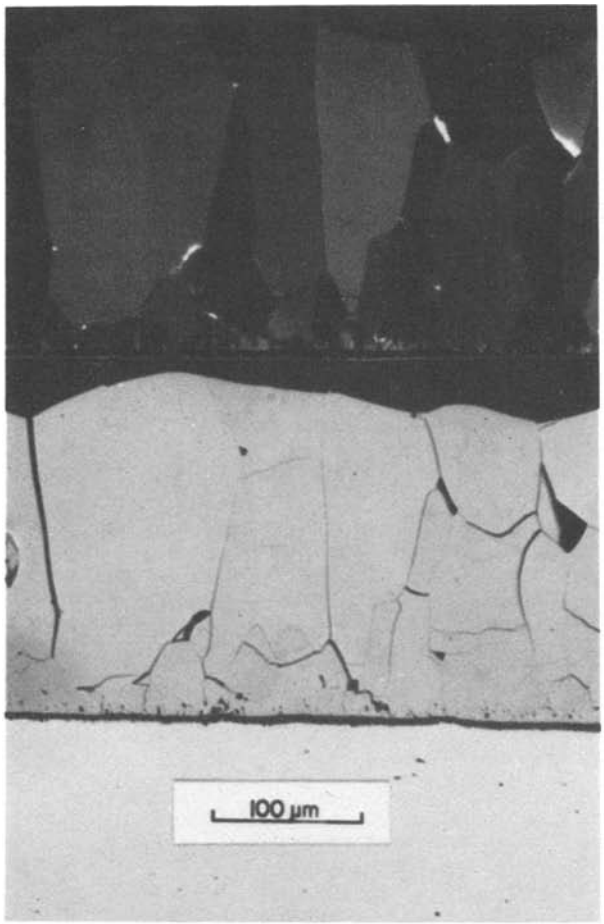

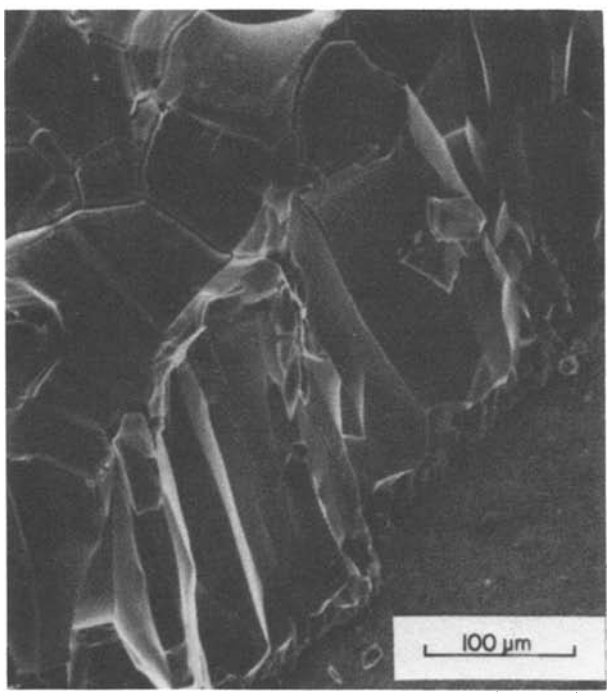

Fig. 8. FeS scale on iron, grown at 700°C and 1 Pa, but for a longer time to illustrate the time evolution of the scale microstructure.

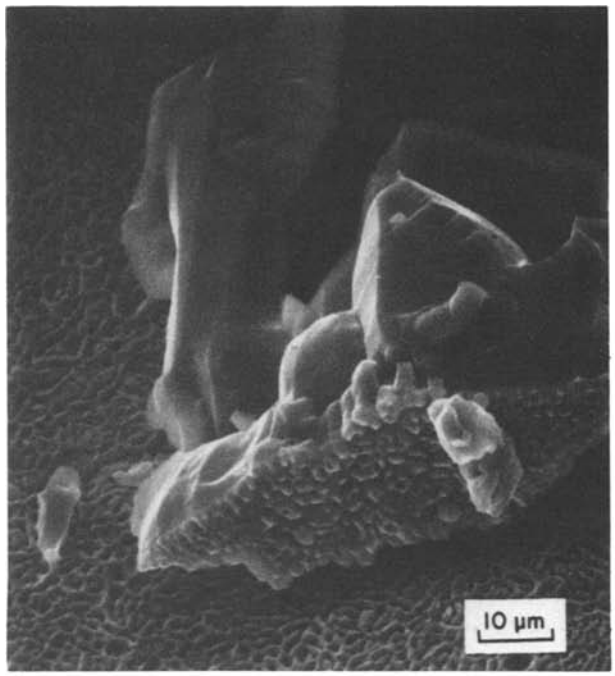

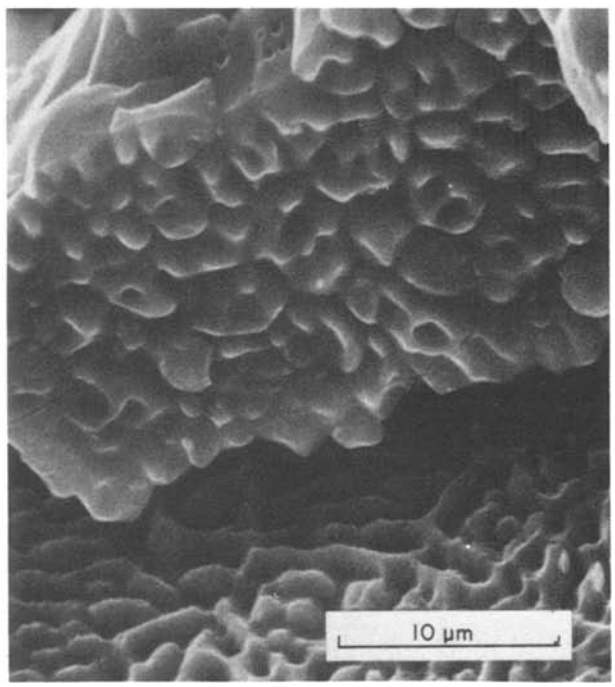

Fig. 9. Scale segment illustrating scale metal interface

rate below 10 Pa, and the pressure dependence they report is not reliable until the pressure exceeds 100 if not 1000 Pa. Narita and Nishida (2) did measure the sulfidation rate from 10^3 to 10^5 Pa, and Mrowec (10) has reported limited measurements at 10^4 Pa. We have measured the thickness of FeS formed on iron as a function of time, and from an examination of Fig. 4, the data are parabolic, implying a diffusion-controlled sulfidation rate.

When data in Fig. 4 are converted from the rate constant k defined with

$$(\text{thickness of FeS})^2 = kt \qquad [1]$$

where t is the time, to the rate constant k_p for sulfur uptake defined from

$$(\text{weight of sulfur gain})^2 = k_p t \qquad [2]$$

our data can be compared with similar data from Fryt *et al.* (1), Narita and Nishida (2), and Mrowec (10). Such a comparison is shown in Fig. 10, and we can

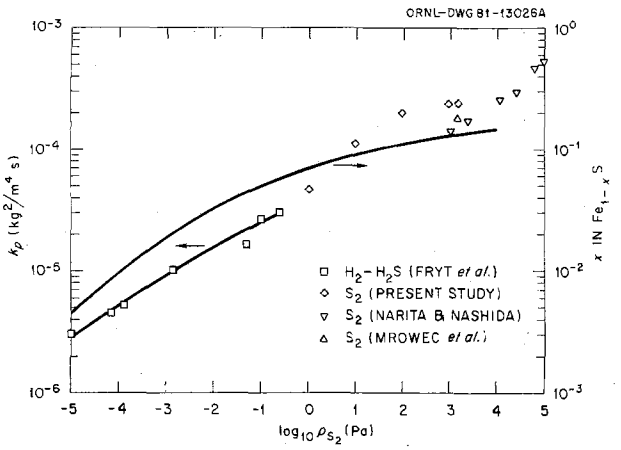

Fig. 10. Rate constant data for sulfidation of iron in H_2/H_2S and pure sulfur vapor, along with the pressure dependence of stoichiometry data for iron sulfide.

use this to discuss the reported (3, 4) "hydrogen effect" and the anisotropy in growth direction (2).

The suggestion that ionized hydrogen influences the defect structure of FeS, discussed by Worrel and Turkdogan (3) and Zelouf and Simkovich (4), is not apparent in these data. Except for the increased rate of sulfidation when the growth direction changes from "a" to "c" in this hexagonal material, it is reasonable to conclude that our measurements in pure sulfur vapor are simply a continuation to higher pressure of the data for sulfidation in H_2/H_2S mixtures, *i.e.*, no hydrogen effect.

The other aspect of the iron-sulfur reaction that we can discuss by reference to data in Fig. 10, is the transformation in growth direction of the scale forming on the metal as the sulfur pressure is varied. Narita and Nishida (2) reported such an effect, and although their data span the range of 10^3 to 10^5 Pa and our measurements are from 1 to 10^3 Pa, the data are qualitatively similar. The transformation they report is some three to four orders of magnitude higher in pressure than when we observe it, but we believe that there are at least two explanations for this discrepancy. First, the pressure specification in the Narita-Nishida study could be in error: they reported no effort to document or prove that the sulfur pressure was what they reported. This is not unimportant since it is so difficult to insure that cold spots do not change the expected pressure specification; for an example, see the work by Meussner and Birchenall (9) where nothing more than a tarnishing film was observed at a reported pressure of 10 Pa. Cold spots in an apparatus will reduce the pressure to some lower value than it is otherwise thought to be; hence, Narita and Nashida's (2) data could be translated to lower pressures on a plot like Fig. 10. The second and equally likely cause is specimen purity. The microstructure reported by Narita and Nishida and other studies as well, [see Ref. (1, 9)] is duplex in that a small equiaxed layer exists underneath overgrowing columnar grains. We have demonstrated that this microstructural feature is directly a result of specimen purity and that it effects the pressure range where the "a" to "c" growth transformation occurs. This matter will be discussed in detail in a subsequent publication.

A final remark on the growth kinetics can be made in light of this discussion of the pressure dependence of the scale growth direction. In Fig. 10, we plot the pressure dependence of rate constants for sulfidation and the pressure dependence of δ in $Fe_{1-\delta}S$. In the study by Fryt *et al.* (1) it was found that the growth rate was simply proportional to δ in $Fe_{1-\delta}S$. We similarly find this result, and thus confirm the tracking of k_p and δ. This has important manifestations in considerations of diffusion in this nonstoichiometric compound.

Conclusion

We have demonstrated that the growth direction for FeS forming on Fe does change as a function of pressure, and that when experiments are done carefully, there is no apparent difference between the sulfidation rate of iron in pure sulfur vapor and sulfur reacting from H_2/H_2S mixtures. Moreover, it seems that the result that was reported by Fryt *et al.* is confirmed: namely, the rate constant tracks the variation in Fe/S ratio.

Acknowledgments

Research was sponsored by the Materials Sciences Division, U.S. Department of Energy, under Contract W-7405-eng-26 with the Union Carbide Corporation.

Manuscript submitted June 25, 1982; revised manuscript received Nov. 25, 1982.

Any discussion of this paper will appear in a Discussion Section to be published in the December 1983 JOURNAL. All discussions for the December 1983 Discussion Section should be submitted by Aug. 1, 1983.

Publication costs of this article were assisted by the Oak Ridge National Laboratory.

REFERENCES

1. E. M. Fryt, V. S. Bhide, W. W. Smeltzer, and J. S. Kirkaldy, *This Journal*, **126**, 683 (1979).
2. T. Narita and K. Nishida, *Trans. Jpn. Inst. Met.*, **15**, 314 (1974).
3. W. L. Worrel and E. T. Turkdojan, *Met. Trans.*, **1**, 299 (1970).
4. S. Zelouf and G. Simkovich, *ibid.*, **245**, 875 (1969).
5. R. Hultgren, P. D. Desir, T. H. Hawking, M. Gleiser, K. K. Kelly, and D. D. Wagman, "Am. Soc. Met.," Metals Park, OH (1973).
6. R. E. Pawel, J. V. Cathcart, and R. A. McKee, *This Journal*, **126**, 1105 (1979).
7. R. E. Pawel, J. V. Cathcart, and R. A. McKee, *Oxid. Met.*, **14**, 1 (1980).
8. R. E. Pawel, R. A. Perkins, R. A. McKee, J. V. Cathcart, G. J. Yurek, and R. E. Druschel, ASTM STP 633, A. L. Lowe, Jr. and G. W. Parry, Editors, p. 119, ASTM, Philadelphia (1977).
9. R. A. Meussner and C. E. Birchenall, *Corrosion*, **13**, 677 (1957).
10. S. Mrowec, A. Stoklosa, and M. Danielewski, *Oxid. Met.*, **11**, 355 (1977).
11. K. Hauffe and A. Rahmel, *Z. Phys. Chem.*, **199**, 152 (1952).
12. "International Critical Tables of Numerical Data in Physics, Chemistry and Technology," Vol. III, p. 201, McGraw-Hill, New York (1928).
13. "Metals Handbook," Vol. 7, p. 516, American Society for Metals, Metals Park, OH (1972).

Downstream Atomic Monitoring for Absolute Etch Rate Determinations

David A. Danner,*,[1] Daniel L. Flamm, and John A. Mucha*

Bell Laboratories, Murray Hill, New Jersey 07974

ABSTRACT

Monitoring optical emission has become a valuable tool for the plasma processing of semiconductor materials. We have extended this technique by monitoring atomic emission from etch products excited in an auxiliary discharge located downstream of the plasma processing region. In this configuration, process monitoring can be achieved even in the absence of a reactive plasma, and emission intensities are independent of the plasma characteristics in the process discharge. The method is applied to the determination of the absolute etch rate of silicon by atomic fluorine.

Changes in the intensity of optical emission from reactants (1) and etch products (2-5) in plasma reactors are valuable for process end-point detection. Although these absolute intensities reflect the process chemistry and aid in its optimization, they are difficult to relate to quantitative etch rates because emission from excited states is a complex function of the plasma composition and the electrical gas discharge parameters. Thus, it would be extremely useful to employ a monitoring system in which the relationship between intensity and etch rate is simple in form. Clearly, the monitoring of products rather than etching species would be most useful, since one requires no detailed chemical information to relate emission from product to the etch rate. Ideally, the monitoring system should also be applicable to simple gas-solid reactors (no-plasma) as well, since recent III-V etching studies (6) have demonstrated that feature morphology and anisotropy can be controlled by a combination of plasma etching and etching with undissociated molecular halogens.

Mass spectrometry offers some of these characteristics; however, the instrumentation is often complex, expensive, and insensitive when the partial pressure of product species is low. We describe a product monitoring technique based on optical emission excited downstream of the reactor, which shows promise of satisfying all the criteria. Using the etching reaction of atomic fluorine with silicon (7) as a model system, we have demonstrated the measurement of absolute etch rate with this technique using a simple calibration procedure.

Experimental

Etching was done with the discharge flow system used in our silicon etching study (7). As a result, the degree of dissociation of molecular fluorine (total flow = 50 sccm, p = 0.5 Torr) in the 14 MHz rf discharge could be controlled, producing well-defined etch rates for the ~1 cm^2 silicon (100) substrate. As before, the substrate was mounted on a temperature-controlled sample holder located far downstream of the discharge zone. For these experiments, rf power was 40W, yielding an atomic fluorine density (n_F) of 4.0 $\times$ 10^{15} atoms/cm^3 in the reaction cell as determined by the chemiluminescent titration of F atoms with Cl_2.

The system was modified to incorporate a sampling system and second discharge as shown in Fig. 1. A leak valve ~30 cm downstream of the reaction cell was used to extract a small sample (~0.1 sccm) of the etch product effluent, which was then diluted in a 100 sccm flow of argon. An auxiliary liquid nitrogen trapped vacuum pump and throttle valve were used to maintain the pressure in the downstream sampling system at 0.25 Torr. Atomic emission from silicon in the argon/product mixture was excited in a 2450 MHz discharge produced using an Evenson-type microwave cavity (8) at 50W net power. The emission was monitored through a sapphire window, dispersed with a 0.3M monochromator (optical band pass ~0.15 nm), located 28 cm from the discharge cavity, and detected using a simple photomultiplier-picoammeter strip-chart recording system.

Spectral scans between 250-253 nm were recorded, and the Si I emission lines at 251.61 and 252.85 nm (9) were used as an indicator of silicon concentration (predominantly SiF_4) sampled from the main flow tube. Under the present discharge conditions, the 251.61 nm line had approximately twice the intensity of the 252.85 nm line and was preferred for concentration monitoring. Interference from Ar emission at 251.68 and 251.56 nm (9) was negligible as shown by observing emission from the discharge with the sampling valve closed.

It is desirable to monitor emission at a single wavelength. Unfortunately, we were unable to do this because of the presence of background emission from silicon contamination and a slow continuous drift in the optical zero. The optical zero drift was due to the detection electronics and can be eliminated; however, background contamination is a more serious problem. Although we measured the intensity and variability of background silicon emission, we have been unable to unambiguously isolate the source. It originated in the main flow tube and varied from run to run, but the intensity was reasonably constant throughout a given experiment. To minimize the effect of background interference in our measurements, spectral traces of the silicon emission region were taken before introducing calibrant gas in calibration experiments and with the main flow tube discharge alternately on and off in etching experiments. The difference in Si I emission intensity was used as an indicator of concentration.

Calibration of the emission intensity per unit flow of Si into the sampling system was achieved by diluting a standard 1% SiH_4 in Ar mixture (0.6-8.5 sccm) with the etchant gas (50 sccm) in the reactor. Since the standard SiH_4/Ar mixture was added to the main flow in the reactor, it is not necessary to accurately know the sampling rate, provided it is constant during a series of measurements. As a result, simple standard addition methods (10) can be employed during etching, which greatly simplifies the determination of absolute etch rates. In this case, SiH_4 is a suitable calibrant since it is converted to SiF_4 before the sampling valve. Ideally, the calibration mixture should contain the final etch product.

Results and Discussion

Calibration curves for the two Si emission lines, with standard additions and no substrate in the reaction cell, are shown in Fig. 2. The emission intensity scales linearly with the silicon flow rate in the main flow tube, but exhibits a small intercept. We believe the offset is attributable to a combination of low sig-

* Electrochemical Society Active Member.
[1] Present address: Department of Chemical Engineering, University of California at Berkeley, Berkeley, California 94720.
Key words: silicon, luminescence, discharge, spectra.

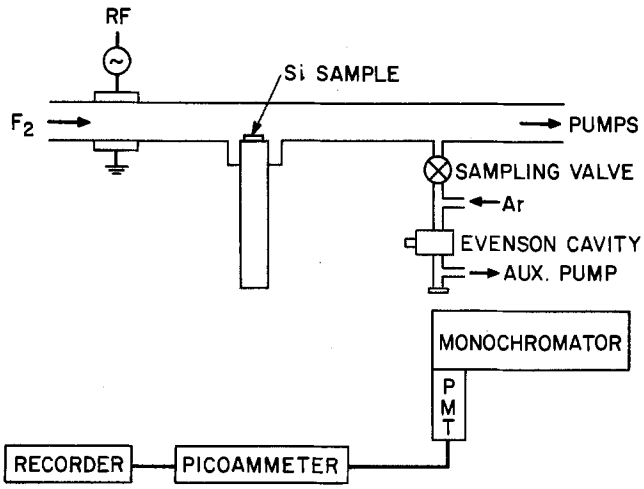

Fig. 1. Diagram of discharge flow reactor including downstream atomic monitoring network.

nal-to-noise in the recorded intensities (error bars in Fig. 2), and contaminant emission levels contributing nearly half of the total intensity of the highest calibration points.

The 251.61 and 252.85 nm emission intensities during etching of a 1 cm^2 silicon (100) substrate at room temperature (298 K) were measured under identical pressure and flow conditions used during calibration. These data are indicated as crosses in Fig. 2, and correspond to silicon flow rates during etching of 0.048 and 0.057 sccm, respectively. Based on the substrate area, these flows give etch rates of 2740 Å/min (251.61 nm) and 3400 Å/min (252.85 nm), in excellent agreement with a rate of 3040 Å/min, calculated using the etch rate [Eq. [8] of Ref. (7)] from previous studies (7).

To demonstrate the feasibility of monitoring relative etch rate changes under variations in process parameters, we monitored Si I intensity as a function of substrate temperature. Arrhenius plots based on several such experiments exhibited activation energies of 0.07-0.13 eV which were in reasonable agreement with 0.108 eV (7) obtained previously. Higher precision was initially anticipated, but small changes in pressure drop during sample heating led to variability in the sampling rate. This sensitivity was also observed without heating by intentionally introducing small pressure changes, and doubtlessly could be reduced by using closed loop pressure control with a sensor located at the sampling point.

Based on this experience with the downstream monitoring system, several improvements can be suggested. Increasing the diameter of tubular laboratory reactors in addition to locating the pressure control sensor at the sampling point would help. In larger scale industrial etching, the pressure effects would be minimal, and sensor location may not be critical. In addition, the monitor discharge should be operated at as low a pressure as possible in order to minimize sensitivity to process stream pressure. Finally, to guard against perturbation of the electron energy distribution function in the monitor discharge from diluted process gas, etchant could be deliberately added to the Ar or He carrier (perhaps 1% by volume) so the sample stream etchant contribution (0.1% by volume here) is negligible. These precautions should ensure that the monitoring discharge properties are totally independent of the etching reactor.

The signal-to-noise ratio observed in this study (error bars in Fig. 2) indicates a minimum etch rate of a few hundred Å/min per cm^2 substrate area can be measured by downstream atomic monitoring. From simple solid angle considerations, we anticipate sensitivity could be improved a hundred-fold by optimizing the optical collection efficiency. Furthermore, in the absence of overlapping emission from the etchant

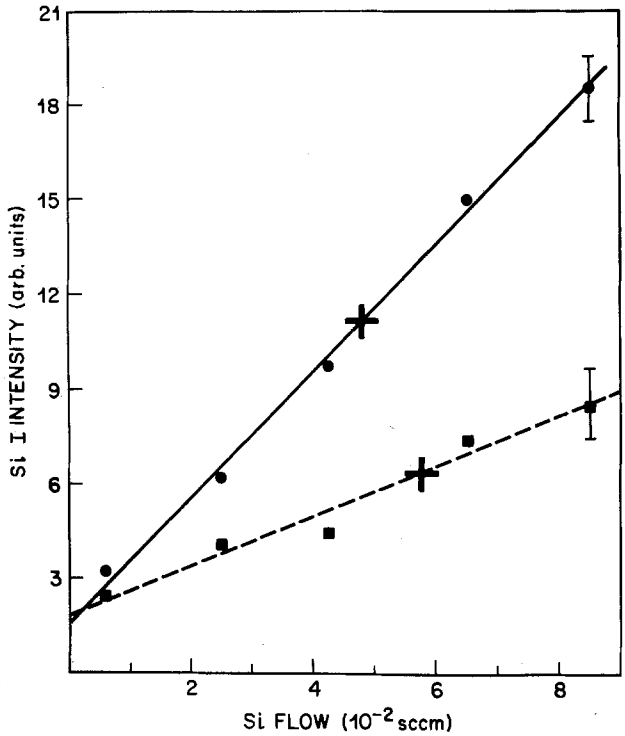

Fig. 2. Calibration curves for Si I emission at 251.6 nm (●) and 252.8 nm (■). Ordinate values represent intensities corrected for background contamination, and crosses indicate emission levels observed for etching of 1 cm^2 Si sample under conditions noted in the text. Error estimates are indicated for the highest intensity data points.

and sample diluent gas species, optical bandpass filters can be used instead of a monochromator to increase sensitivity and simplify the detection system. This type of apparatus could easily be added to production reactors for etch rate monitoring and end-point detection.

Conclusions

A new method for monitoring etch processes has been described using atomic emission from products excited downstream of the reaction zone. Quantitative *in situ* etch rate measurements have been demonstrated, and the technique should be valuable for the rapid measurement of etch rates. Background interference was present which required correction; however, it arose from contamination and may be absent in other systems. Downstream atomic monitoring can be easily applied to end-point detection and is a useful diagnostic for gas phase etching with molecular species (no discharge).

Manuscript submitted July 6, 1982; revised manuscript received Nov. 3, 1982.

Any discussion of this paper will appear in a Discussion Section to be published in the December 1983 JOURNAL. All discussions for the December 1983 Discussion Section should be submitted by Aug. 1, 1983.

Publication costs of this article were assisted by Bell Laboratories.

REFERENCES

1. W. R. Harshbarger, R. A. Porter, T. A. Miller, and P. Norton, *Appl. Spectrosc.*, **31**, 201 (1977).
2. E. O. Degenkolb, C. J. Mogab, M. R. Goldrick, and J. E. Griffiths, *ibid.*, **30**, 520 (1976).
3. B. J. Curtis and H. J. Brunner, *This Journal*, **125**, 829 (1978).
4. M. N. Bosyakov, N. N. Nikiforenko, and A. A. Labuda, *Soviet J. Appl. Spectrosc.*, **30**, 434 (1979) [Translated from *Zhur. Prikl. Spektrosk.*, **30**, 622 (1979)].
5. K. Hirobe and T. Tsuchimoto, *This Journal*, **127**, 234 (1980).
6. D. A. Danner, D. L. Flamm, J. A. Mucha, and D. E.

Ibbotson, To be published; D. E. Ibbotson, V. M. Donnelly, D. L. Flamm, and B. S. Duncan, To be published.
7. D. L. Flamm, V. M. Donnelly, and J. A. Mucha, *J. Appl. Phys.*, **52**, 3633 (1981).
8. F. C. Fehsenfeld, K. M. Evenson, and H. P. Broida, *Rev. Sci. Instrum.*, **36**, 294 (1965).
9. A. N. Zaidel', V. K. Prokof'ev, S. M. Raiskii, V. A. Slavnyi, and E. Ya. Shreider, "Tables of Spectral Lines," Plenum Publishing Corporation, New York (1970).
10. J. A. Mucha, *Appl. Spectrosc.*, **36**, 393 (1982).

Observation of Nickel Inclusions in Thermally Grown NiO Scales

D. Quinn, G. L. Leatherman,* R. K. MacCrone, and S. R. Shatynski*

Department of Materials Engineering, Rensselaer Polytechnic Institute, Troy, New York 12181

ABSTRACT

Films of NiO thermally grown at 900°C in various oxygen pressures were examined using magnetic resonance techniques. The NiO films were grown in Ar-O_2 gas mixtures which varied from 0.1 to 1 atm oxygen pressure. Samples were then removed from the nickel substrate and examined using magnetic resonance. These experiments detected discrete cigar or pancake particles of metallic nickel embedded in the NiO scale. Careful examination of these films using optical microscopy also revealed the presence of nickel particles in the NiO external scale. From these results, a model for the oxidation of nickel based upon grain boundary oxidation was developed which incorporates the formation of metallic nickel inclusions in NiO scale. Such results add further insight into the mechanism of oxidation of nickel and reveal further deviation from simple bulk diffusion growth models.

The high temperature oxidation of nickel has been extensively studied over the years for obvious reasons. Since only one oxide, NiO, is formed, this system is an excellent candidate for mechanistic studies of oxidation. Its position is further enhanced by the realization that a dilute solution of point defects exists in pure NiO. Direct correlations between defect populations and oxide growth are then possible since there will be little defect-defect interactions. Furthermore, since nickel is a common base metal for many high temperature superalloys, measurement of its high temperature corrosion resistance is of extreme practical importance.

Thermogravimetric studies of nickel oxidation generally display simple parabolic growth, thus making the growth of NiO on Ni a typical case for Wagner's model of bulk diffusion controlled growth (1-2). The supposed predominant point defect is generally agreed to be vacancies in the nickel sublattice. More investigations agree that doubly charged vacancies of nickel V''_{Ni} are the predominant defect (3, 4). These studies are based on a $P_{O_2}^{1/6}$ dependence on conductivity. However, other studies have shown a $P_{O_2}^{1/4}$ dependence, indicative of singly charged nickel vacancies V'_{Ni} (5, 6). Morphological studies however, indicate serious complications (7-27). Very pure nickel samples when oxidized develop an equiaxed grain with increased porosity adjacent to the metal/oxide interface. If impure samples are used then the morphology changes dramatically. The oxide develops a two layered microstructure of single phase of NiO. The outer layer is now columnar grained whereas the inner layer remains equiaxed and porous. Marker studies are even more confusing. If only an equiaxed grain structure is prevalent, then the markers remain at the metal/oxide interface indicating growth is due to transport of nickel through the oxide, and consequent flux of nickel vacancies. Marker studies on two layered NiO scales, show the markers move to the columnar grain/equiaxed grain interface. This indicates that mixed transport perhaps also involving oxygen is occurring. Tracer diffusion studies have shown that besides outward diffusion of nickel ions, there can also be inward diffusion of oxygen (17). This inward diffusion can be either long term or occur upon initial oxidation with short-circuit transport down grain boundaries or line dislocations. Consequently, the parabolic rate law is often violated when measured at short times by thermogravimetric techniques or at low temperatures. Below 900°C oxidation rates are faster than the parabolic rate (1). An added complication also arises as oxide scale formation may vary from compact to duplex causing void formation and a variation in oxidation rate (14).

As a result of the complications involved with measuring oxide growth rates by thermogravimetric techniques, we have undertaken a magnetic study to further characterize NiO films carefully grown under controlled conditions, to provide additional insight into the growth and provide comparison with the implications of TGA analysis.

Experimental Procedure

Nickel wafers, > 99.998% nickel, 12 mm in diameter, 1.0 mm thick, and ASTM grain size 3 were cut from a rod using a wafering saw with a diamond blade. The surfaces were polished on 240 grit abrasive paper. After cleaning and degreasing in trichloroethylene, samples were washed in ethanol. Oxidation was carried out by suspending the samples from platinum wire in a furnace or by oxidation in alumina boats in a tube furnace. Oxidation was carried out in a flowing Ar-O_2 gas atmosphere thus setting the oxygen partial pressure (P_{O_2}). Both gases were cleaned using Ascarite and Drierite. After oxidation the circumference of the sample was removed by grinding to expose the unoxidized nickel. The sample was placed in hot 50% HNO_3 to dissolve the metallic nickel, leaving intact NiO films. The films were mechanically robust and showed very little tendency to curl.

Magnetic resonance experiments were performed using a homodyne spectrometer operating at X-band (~ 9.5 GHz). Provision was made to orient the films with respect to the applied magnetic field as required.

Static magnetization measurements were performed using a vibrating specimen magnetometer, aligning the films parallel or perpendicular to the applied field as required. The temperature of measurement in both systems could be set (±1 K) over the 30-300 K range.

Results

A typical magnetic resonance of an NiO film is shown in Fig. 1. This oxide was grown 24 hr at 0.1 atm P_{O_2} at 900°C.

In determining to what the resonance is due, it is of interest to consider: (*i*) the correlation if any, of the

* Electrochemical Society Active Member.
Key words: NiO, magnetic resonance, inclusions.

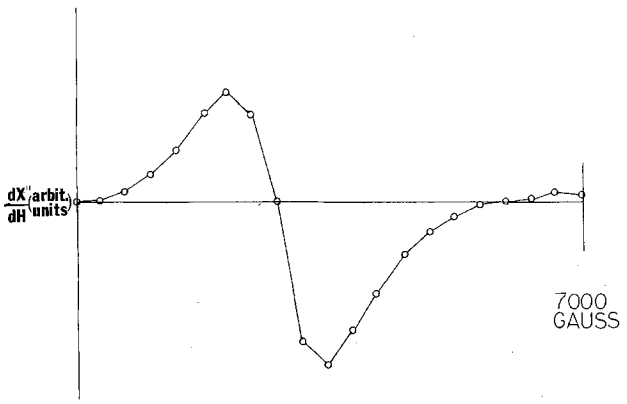

Fig. 1. NiO film resonance

resonance to thermogravimetric measurements; (*ii*) the dependence of the magnitude of the resonance on P_{O_2} and the time of oxidation; (*iii*) the temperature dependence of the resonance; (*iv*) the shape of the resonance and its dependence on the orientation of the film with respect to the magnetic field; (*v*) the correlation between resonance and the static magnetization.

Aspects (*i*) and (*ii*) are concerned with establishing whether or not the resonating entities are related to conventionally accepted growth theory, such as the parabolic rate constant as monitored by thermogravimetric measurements and the P_{O_2} dependence, to decide whether this observation is a perturbation of the accepted theory or a more serious deviation.

Items (*iii*), (*iv*), and (*v*) are concerned with investigating, by magnetic means, the structure of the resonating entities with the purpose of developing ideas concerning their formation.

Aspects (i) and (ii): Magnitude of resonance vs. P_{O_2}. —Figure 2 shows the magnitude of the resonance *vs.* P_{O_2} on a log-log plot. As can be seen, there is considerable scatter in the data. However, at high pressures ($0.1 \leq P_{O_2} \leq 1.0$) the magnitude of the resonance increases with decreasing pressure. At low pressures (< 0.01 atm) the resonance is absent. The concentration of vacancies as deduced from thermogravimetric measurements are plotted in Fig. 3. As can be seen, the dependence on oxygen pressure is completely different. We conclude from the rather different behavior that the two experiments are not simply connected.

On heating a given film in oxygen the resonance disappears (Fig. 4). This is evidence that Fig. 1 shows the ferromagnetic resonance of metallic nickel inclusions in the as-grown film. These inclusions are completely surrounded by oxide since they remain after the oxide is removed from the metal by acid. Direct evidence for the nickel inclusions is shown in Fig. 5, a

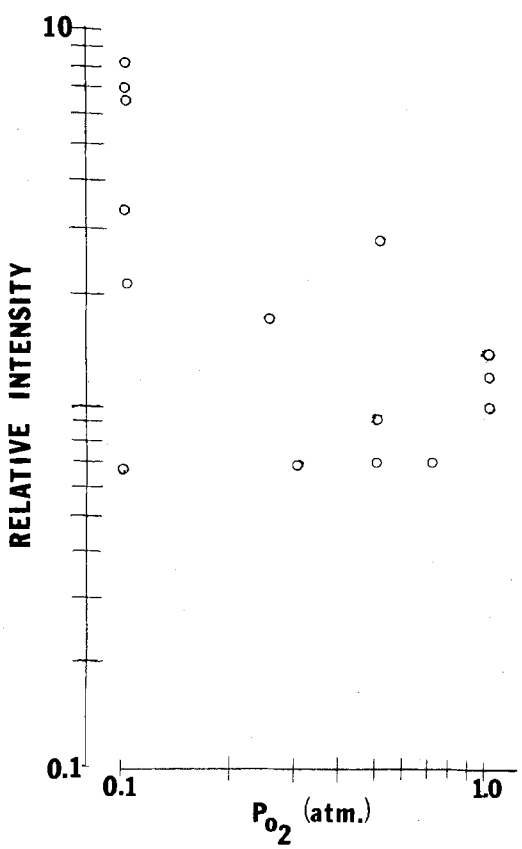

Fig. 2. Magnitude of NiO resonance *vs.* partial pressure of oxygen

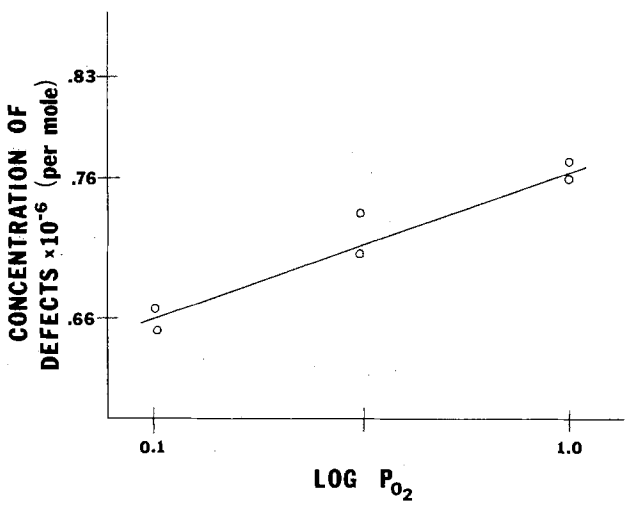

Fig. 3. Vacancy concentration in NiO films *vs.* partial pressure of oxygen.

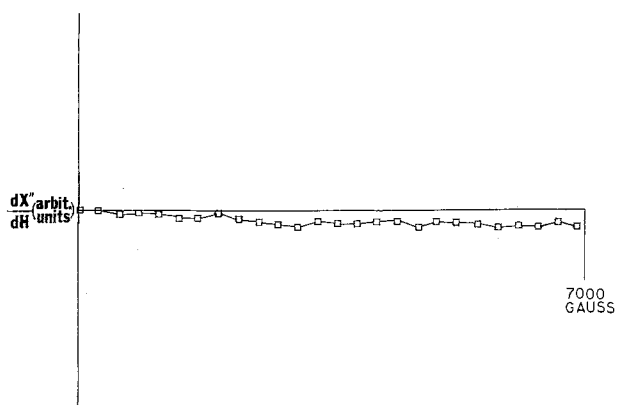

Fig. 4. NiO film resonance after annealing in oxygen

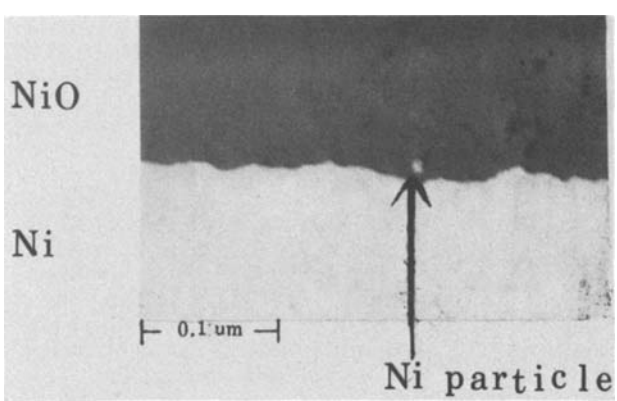

Fig. 5. Optical micrograph of cross section of NiO grown on pure Ni at 900°C, 1 atm oxygen pressure for 1 week. Note the existence of a small particle (designated by an arrow) near the metal oxide interface (magnification 1250×).

photomicrograph of an NiO film grown at 0.1 atm for 160 hr at 900°C.

Aspects (iii), (iv), and (v): Nature of the resonance. —For ferromagnetic systems, the value of the magnetic field of resonance is dependent upon the magnetocrystalline anisotropy constants and also on the shape of the particles through the demagnetizing factors. The anisotropy of the resonance field here has been studied by varying the angle of the magnetic field with respect to the normal to the plane of the films. The results are shown in Fig. 6.

The shift in resonance field to lower fields as the magnetic field approaches the orientation of lying in the plane of the film indicate that the nickel particles have longer dimensions in the plane of the film compared to normal to the plane of the film. Using the ferromagnetic equation of resonance (28), the deduced demagnetizing factors give a particle shape that is either pancake-like, with an axial ratio of 0.82, or cigar-like, with an axial ratio of 0.75. We note that the shift in the resonance field with orientation observed here is too large to be accounted for by crystalline anisotropy effects.

The width of the resonance is also very large, again too large to be ascribable to the effects of magnetocrystalline anisotropy of nickel. Figure 7 shows the single crystal resonance width of nickel obtained by computer simulation (29) using the accepted values for the anisotropy energies. Polycrystalline samples would lead to a broadening of this width but not be over an order of magnitude as is the case here.

Experimentally, the nickel containing films were simulated by mixing special nickel powder, referred to as "sponge nickel," with alumina to act as an inert matrix. The resulting resonance of a 1% nickel powder in Al_2O_3 is shown in Fig. 8. The possibility exists that the large line width here is due to dipole-dipole interactions between Ni particles and the powder. To show that this is not the case, the prepared Ni-Al_2O_3 mixture was further diluted and the resonance observed. The diluted sample produced a curve of decreased intensity but the general shape remained unchanged.

As mentioned above, the width of the resonance cannot be due to the anisotropy energy, but must arise from the distorted particles of high porosity which can produce line widths several thousands of gauss wide (30). Their morphology is shown in Fig. 9. Thus we conclude that the nickel particles in our films have a very irregular and porous surface structure.

A characteristic feature of ferromagnetic resonance in metals is the decrease in the size of the resonance with decreasing temperature. The decrease is a result of the microwave penetration depth, the "skin-depth," decreasing with decreasing temperature as the conductivity increases. The effect is indeed present and is shown in Fig. 10. This is additional and strong evidence that the resonance is ferromagnetic in nature and "simple" to temperatures above 50 K. At low temperatures, < 50 K, the resonance changes qualitatively to give a line of unusual shape. This indicates that a different spin interaction in the inclusion, or between the metal and the oxide, becomes important at low temperatures.

The existence of this new low temperature effect is also manifest in the static magnetization measure-

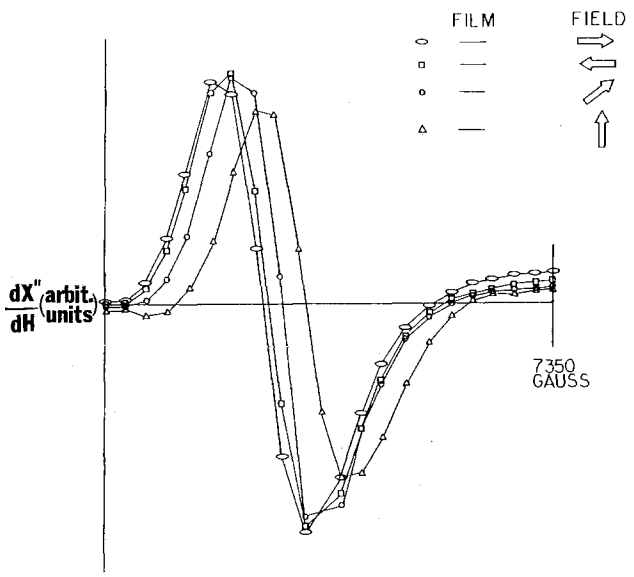

Fig. 6. Orientation dependence of sample on resonant field

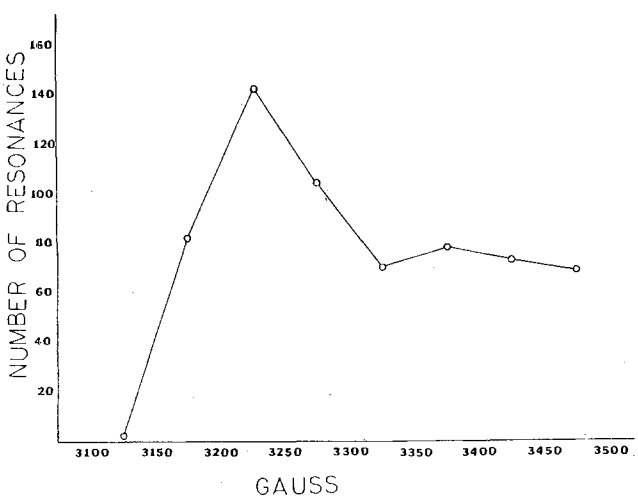

Fig. 7. Computer simulated nickel resonance based on nickel magnetocrystalline anisotropies.

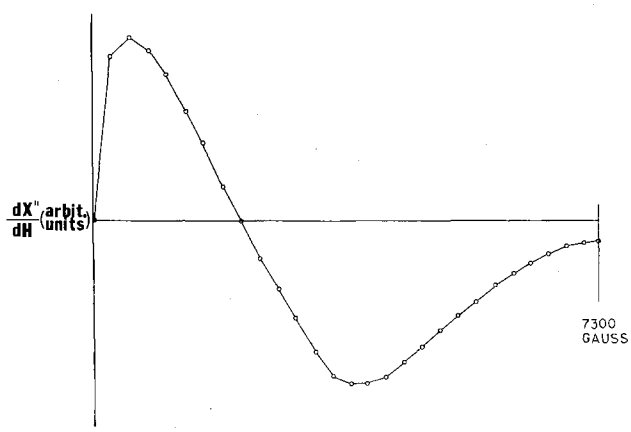

Fig. 8. 1% nickel in Al_2O_3 resonance

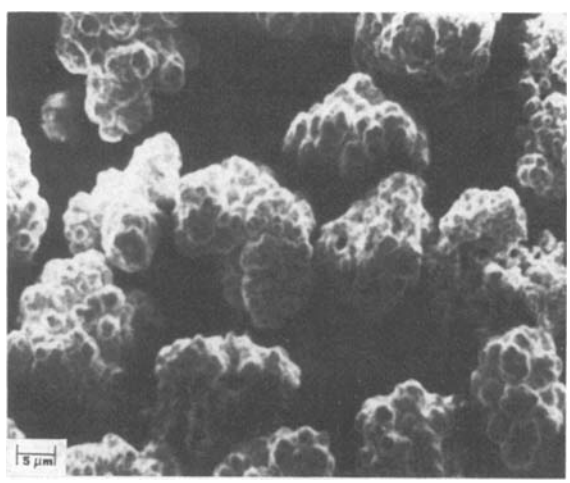

Fig. 9. Photomicrograph of nickel powder mixed with Al_2O_3

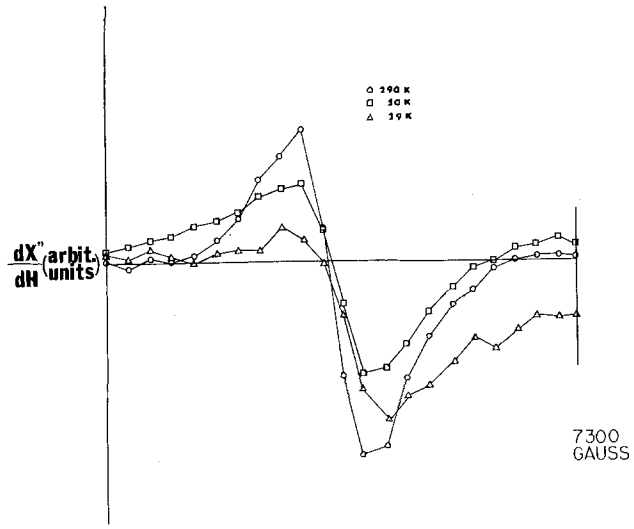

Fig. 10. Temperature dependence of NiO resonance

ments. Figure 11 shows the magnetic moment/unit area as a function of applied magnetic field at various temperatures. As can be seen there is a qualitative difference in the magnetization curve at temperatures below 50 K. At low temperatures the change in slope is much more gradual, and the linear transition decreases as the temperature decreases.

At both high and low temperatures, the static magnetization is quite anomalous. First, the temperature independence of the magnetization at low field suggests domain wall motion and the expectation that the magnetization should saturate at high fields. However, the magnetization at high fields is a monotonically increasing function of applied field and surprisingly independent of temperature. It is interesting to notice that the magnetization of the films with the applied field parallel and perpendicular to the surface shows a shape anisotropy as in the resonance experiments. Films whose surfaces are perpendicular to the field exhibit the change in slope at higher field. Films parallel show the change at lower fields; the shape anisotropy in this orientation is the direction of easy magnetization. The elasticity of the magnetization, together with the lack of temperature dependence, indicates that there is strong exchange coupling between the Ni inclusions and the oxide matrix. This interesting observation is worthy of further study using torque measurements such as those of Berkowitz *et al.* (31). The magnetization of a thin disk of pressed Ni-Al_2O_3 powder is perfectly conventional. The results are shown in Fig. 12.

Discussion

The existence of metallic nickel in the NiO scale implies a mechanism more complex than simple bulk diffusion of nickel vacancies in NiO. Indeed, there is abundant evidence in the literature that under particular conditions, (low temperatures ~ 800°C and high oxygen pressures ~0.1 atm) oxygen diffusion down the oxide grain boundaries or cracks is responsible for a duplex grain structure (1, 14, 32). This consists of fine equiaxed grains closest to the Ni, changing abruptly to long columnar grains closest to the gas interface. Platinum markers remain stationary at the interface between the grain types (3, 13, 14). The transport of oxygen into the film has been directly verified by tracer studies (17). Sartell and Li (2) found that there was an abrupt stoichiometry difference between the oxide adjacent to the metal (green oxide) and the oxide adjacent to the oxygen gas (black oxide) and that the markers were situated at the interface between the two types of oxide. Our observations add another dimension to the process, namely, the existence of small platelets of Ni metal, in the oxide. This morphology also only occurs under specific conditions.

Some speculations on the mechanism of formation are given: The generation of metallic nickel in the scale may be related to significant contributions of grain boundaries in the metal to the scale growth. Given that oxygen penetrates the scale by gaseous diffusion down cracks or void networks in the oxide film, substantial amounts of oxygen could result at the NiO-Ni interface. Rapid transport down the metallic Ni grain boundaries would occur, resulting in precipitation of NiO in the boundary upon exceeding the solubility product of NiO in Ni. Stress generation due to NiO nucleation at the grain boundaries would therefore enhance this effect. The grain boundaries would then continue to accelerate the nucleation of NiO precipitation. Figure 13 schematically illustrates the enhanced and continually accelerating grain boundary nucleation of NiO. Because of such preferential paths the grain then becomes completely surrounded by oxide, and is incorporated as a particle in the oxide film. Further, if oxidation of the Ni particles requires bulk diffusion through the surrounding NiO (33, 34) the inherently slow process allows transitory existence of such particles. On the other hand, close to the Ni metal where such inclusions are being formed, the cation vacancy concentration is also presumably small, also allowing the transitory existence of the entities in question. Eventually the nickel particles will be oxidized to NiO. Furthermore, the *in situ* oxidation of such particles would be another source of stress in the oxide and may contribute to the generation of the

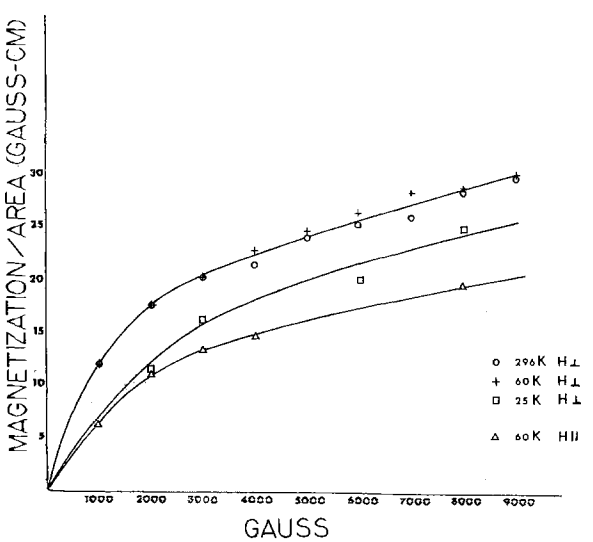

Fig. 11. Temperature and orientation dependence of d-c magnetization of NiO films.

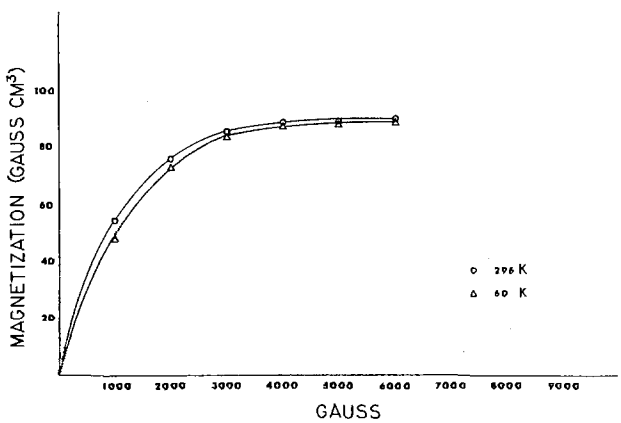

Fig. 12. D-C magnetization curve of 1% nickel in Al_2O_3

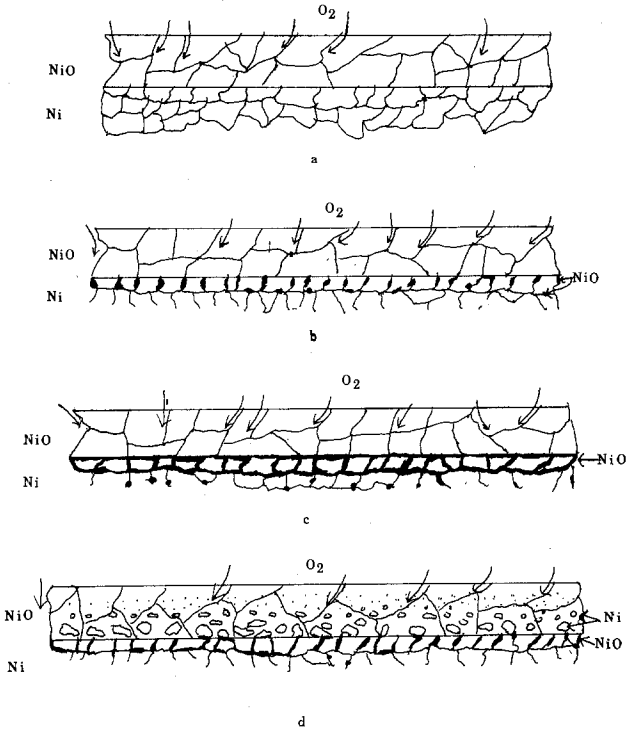

Fig. 13. Schematic illustration of grain boundary enhanced oxidation and the generation of metallic nickel inclusions. (a) Preferred transport of oxygen occurs down grain boundaries in NiO. (b) This will then lead to nucleation of small NiO particles in the grain boundaries. (c) Enhanced oxidation along grain boundaries occurs resulting in NiO surrounding the grain. (d) Further oxidation of each grain interior results in nickel inclusions within the NiO scale.

observed morphology of NiO growing on Ni. Fairly strong evidence in favor of this model is provided by our observation that cold rolling the metal substrate before oxidation greatly increases the number of metal inclusions found in oxide.

A second possible mechanism can also be visualized. Generation of a localized nonequilibrium condition in the NiO may result in the decomposition of the NiO resulting in the generation of voids and metallic nickel particles. Although no experimental evidence for such conditions exists, nevertheless, such conditions may be generated from models of vacancy wind effects or diffusional fluxes around inert second phase particles. In such cases it may be possible to generate locally very low oxygen pressures thus decomposing *in situ* the existing NiO.

The observed metal inclusions in the oxide film cannot be the result of a steady-state planar growth model; some large change in the mechanism or boundary conditions must have occurred to produce the nonequilibrium inclusions we observe.

The metallographic observations of a columnar oxide layer above an equiaxed layer is suggestive of a significant change in growth mechanism and defect concentration at the interface between the two regions. At some state, a difference in flux across the boundary could produce a precipitation of nickel metal. The result that cold-worked surfaces produce films with a significantly larger number of inclusions suggests that dislocations or sub-boundaries are important; perhaps these determine the size of the oxide grains.

Another possibility is that increased vertical cracking occurs with thicker films. The rapid diffusion of oxygen down these cracks to regions closer to the metal-oxide interface may drastically increase the cation vacancy concentration on the crack surface. Lalauze and Meunier (35, 36) have shown that the sudden exposure of NiO to oxygen increases the cation vacancy to such an extent that cation diffusion is significantly suppressed by electric fields. This may induce the formation of the metal inclusions here.

Conclusions

We have shown that under the oxidation conditions $T = 900°C$ and $0.1 < P_{O_2} < 1$, nickel oxide scales formed on nickel metal contain metallic nickel inclusions. These inclusions are within the oxide and are cigar or pancake shaped, with the long axis lying parallel to the plane of the film.

The understanding of the mechanism by which the metal inclusions are formed and their relation to the complexities of the oxide growth at these pressures and temperatures must await a careful study of the microstructure of the metal substrate, the microstructure of the oxide film, and the relationship of these two factors to the number of metal inclusions.

Acknowledgment

The authors are pleased to acknowledge support of this research by the U.S. Department of Energy, Division of Basic Sciences, under Contract No. DE-ACO2-79ER10428.

Manuscript submitted Jan. 28, 1982; revised manuscript received Nov. 5, 1982.

Any discussion of this paper will appear in a Discussion Section to be published in the December 1983 JOURNAL. All discussions for the December 1983 Discussion Section should be submitted by Aug. 1, 1983.

Publication costs of this article were assisted by Rensselaer Polytechnic Institute.

REFERENCES

1. G. C. Wood, I. G. Wright, and J. M. Ferguson, *Corros. Sci.*, **5**, 645 (1965).
2. J. A. Sartell and C. H. Li, *J. Inst. Metals*, **90**, 92 (1961-1962).
3. F. S. Pettit and E. J. Felton, *This Journal*, **111**, 135 (1964).
4. A. Preece and G. Lucas, *J. Inst. Metals*, **81**, 219 (1952).
5. S. Mrowec and T. Werber, *This Journal*, **105**, 363 (1958).
6. L. Czerski, S. Mrowec, and T. Werber, *ibid.*, **109**, 273 (1962).
7. H. H. Uhlig, J. Pickett, and J. MacNairn, *Acta. Metall.*, **7**, 111 (1959).
8. E. A. Gulbransen and K. F. Andrew, *This Journal*, **104**, 334 (1957).
9. W. J. Moore and J. K. Lee, *J. Chem. Phys.*, **19**, 225 (1951).
10. J. Paidassi, J. Berry, and R. Darras, *C. R. Acad. Sci. Paris*, **264**, 361 (1967).
11. C. Wagner and K. Zimens, *Acta Chim. Scand.*, **1**, 574 (1947).
12. J. Deren and J. Novotny, *Oxid. Met.*, **1**, 73 (1969).
13. K. Godlewski, A. Stoklosa, and T. Walec, *Bull. Acad. Pol. Sci.*, **26**, 951 (1978).
14. F. N. Rhines and J. S. Wolf, *Metall. Trans.*, **1**, 1701 (1970).
15. F. Morin, *Oxid. Met.*, **6**, 79 (1973).
16. W. W. Smeltzer and D. J. Young, *Prog. Solid State Chem.*, **10**, 17 (1975).
17. A. Atkinson, R. I. Taylor, and P. D. Goode, *Oxid. Met.*, **13**, 519 (1979).
18. M. J. Graham, *Can. Metall. Q.*, **18**, 283 (1979).
19. C. M. Osburn and R. W. Vest, *J. Phys. Chem. Solids*, **32**, 1331 (1971).
20. I. Bransky and N. M. Tallan, *J. Chem. Phys.*, **49**, 1243 (1968).
21. A. J. Bosman and C. Crevecoeur, *Phys. Rev.*, **144**, 763 (1966).
22. J. Novotny and J. B. Wagner, *Bull. Acad. Pol. Sci. Ser. Sci. Chim.*, **21**, 12 (1973).
23. G. H. Meier and R. A. Rapp, *Z. Phys. Chem.*, **74**, 168 (1971).
24. Z. M. Jarzebski and S. Mrowec, *Oxid. Met.*, **1**, 267 (1969).
25. S. Pizzini and R. Morloffi, *This Journal*, **115**, 1179 (1967).

26. S. P. Mitoff, *J. Chem. Phys.*, **35**, 882 (1961).
27. M. I. Volpe and J. Reddy, *J. Chem. Phys.*, **53**, 1117 (1970).
28. C. Kittel, *Phys. Rev.*, **73**, 155 (1948).
29. D. L. Griscom, E. J. Friebele, and D. B. Shimm, *J. Appl. Phys.*, **50**, 2402 (1979).
30. E. A. Turov, *Ferromagn. Reson.*, **184**, (1966).
31. A. E. Berkowitz and J. H. Grenier, *J. Appl. Phys.*, **36**, 3330 (1965).
32. F. N. Rhines and R. G. Connel, in "Properties of High Temperature Alloys," Z. A. Foroulis and F. S. Pettit, Editors, Vol. 77-1, p. 154, The Electrochemical Society Softbound Proceedings Series, Princeton, NJ (1977).
33. K. Fuecki and B. Wagner, *This Journal*, **113**, 386 (1965).
34. G. J. Kael and P. J. Gellinger, *Oxid Met.*, **5**, 185 (1972).
35. R. L. Lalauze and J. H. Meunier, *ibid.*, **12**, 183 (1978).
36. R. L. Lalauze and J. H. Meunier, *ibid.*, **13**, 301 (1979).

Highly Sensitive Positive Electron Resists Consisting of Halogenated Alkyl α-Chloroacrylate Series Polymer Materials

Tsukasa Tada[1]

VLSI Technology Research Association, Cooperative Laboratories, Takatsu, Kawasaki, 213, Japan

ABSTRACT

Halogenated alkyl α-chloroacrylate series polymer materials, designed based on the molecular orbital theory, have been investigated as positive electron resists. Both high sensitivity and good thermal stability are accomplished at the same time for these positive resists. Detailed studies of an EBR-9 positive electron resist are also presented.

With the increase in integrated circuit density and the miniaturization of devices, advanced technology, such as electron beam or x-ray lithography, has been introduced. In particular, electron beam lithography is now in the production level for photomask fabrication. One important problem in electron beam lithography is its throughput as well as its practical reliability. Since resist sensitivity is one of the important factors which determine the throughput of electron beam exposure systems, highly sensitive and reliable electron resists are required, and many highly sensitive electron resists have been reported so far.

In the previous communication (1), we reported a highly sensitive positive electron resist EBR-9 consisting of poly(trifluoroethyl α-chloroacrylate). This paper describes the same series of halogen-containing positive electron resists and more detailed studies of EBR-9.

Molecular Design Consideration

In developing practical electron resists, the following important items should be taken into consideration: (*i*) performance, (*ii*) processability, and (*iii*) supply. The first concerns sensitivity, resolution, etch resistance, and so forth, which are known to be major factors of electron resists. The second concerns process tolerance or easiness for processing, such as insensitiveness to humidity or little postpolymerization effect. The third concerns easiness for quality control, easiness for material synthesis, cost, etc. Although the first item always laid emphasis in evaluating electron resists in comparison with the other two items, practical electron resists are based on a good balance of these three items. PMMA is a typical example of such good balanced electron resists. It should be stressed that these three items are equivalently important for practical electron resists.

Considering the above three items, one of the most appropriate polymer groups is acrylate series polymer materials. This is because acrylate series polymers are easy to be synthesized, easy for the molecular weight control, and have been widely employed for practical use. They also have a high tolerance in selecting their coating solvents or developers. Due to the COO moiety, they generally have a good or moderate adhesion to various substrates. These properties of acrylate series polymers may be closely connected with the fact that most of the reported electron resists consist of acrylate series polymers.

Therefore, selecting acrylate series polymers, we have intended their molecular structural optimization for electron resists by modifying the α-substituent A and the ester side chain B, as shown in Fig. 1. Sensitive and practical positive electron resists are desired to satisfy the following conditions: (*i*) high scission efficiency for ionizing radiation, (*ii*) good solubility characteristics, and (*iii*) good thermal stability. Therefore, substituents A and B should be selected to meet the above conditions. One may anticipate that high scission efficiency is inconsistent with good thermal stability. However, molecular orbital theory indicates that scission efficiency by ionizing radiation is not always correlated with that by heating. Extended Hückel calculations (2) suggest that α-Cl substituent enhances scission efficiency of the C-C main chain bond for ionizing radiation while maintaining relatively good thermal stability. They suggest that poly(α-chloroacrylate) has almost the same thermal stability as poly(methacrylate) does. At the same time, it is also suggested that halogen substitution into the ester side chain mainly improves solubility characteristics. α-Cl substituent is also expected to enhance glass transition temperature by suppressing Micro-Brownian motion of polymers. Therefore, the combination of α-Cl substituent and halogenated alkyl ester side chain satisfies the above three conditions.

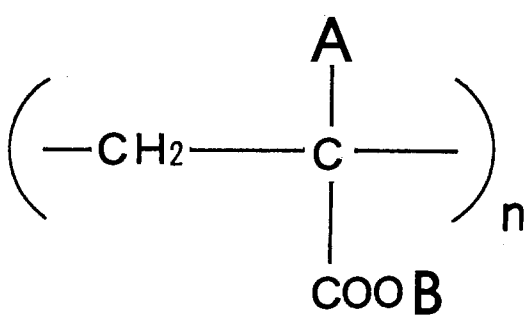

Fig. 1. Molecular structure of acrylate series polymers

[1] Present address: Toshiba Research and Development Center, Saiwai, Kawasaki, 210, Japan.

Key words: films, integrated circuits, current density, etching.

Based on the calculated results (2) and the above speculations, we have designed halogenated alkyl α-chloroacrylate series polymer materials as highly sensitive positive electron resists with good thermal stability, as shown in Fig. 2.

Experimental

Differential thermal analysis (DTA) and thermogravimetric analysis (TGA) were carried out for the synthesized polymers to measure their grass transition temperature (*Tg*) and initial thermal degradation temperature (*Tdi*), respectively. ^{13}C NMR spectra were recorded at 25.05 MHz with the condition of suppressed Nuclear Overhauser Effect (NOE) using JEOL FX-100 FT-NMR spectrometer. Pulse width and pulse repetition time were 7 μsec and 11 sec, respectively. X-ray photoelectron spectra were recorded on Kokusai Denki ES-200 spectrometer using aluminum Kα radiation. Electron beam exposure was carried out at 20 kV accelerating voltage by using JEOL JBX-5AR or VL-R1 (3) electron beam exposure systems. Dry etching experiments were performed by using NEVA DEM-451 reactive ion etching or IPC 2010 T plasma etching systems.

Resist Properties of Halogenated Alkyl α-Chloroacrylate Series Polymer Material

Various halogenated alkyl α-chloroacrylate series polymers were synthesized by conventional radical polymerization. The synthesized polymers are listed in Table I together with their electron beam sensitivity, developers, thermal properties and intrinsic viscosities [η]. PMMA's resist properties are also added to Table I as reference data. The synthesized polymers were dissolved in methyl cellosolve acetate except for EBR-3 [poly(trichloroethyl α-chloroacrylate)] which was dissolved in dioxan. The dissolved polymers were spin coated on a silicon substrate with a thickness of 0.5 μm. After being prebaked for 1.0 hr at 190°-250°C, the resist films were exposed to an electron beam at 20 kV accelerating voltage by using JEOL JBX-5AR electron beam exposure system. Subsequently, the exposed films were developed and rinsed to selectively remove the exposed area. In Table I, electron sensitivity is defined as the minimum electron charge density to completely remove the exposed area without decrease in resist thickness.

As shown in Table I, the synthesized resist materials consist of halogenated alkyl α-chloroacrylate series polymers. The resist materials of EBR-3 to EBR-11 consist of fluorinated or chlorinated alkyl α-chloroacrylate series homopolymers. EBR-12 to EBR-95 consist of fluorinated alkyl α-chloroacrylate series copolymers. In particular, EBR-90 series are trifluoroethyl α-chloroacrylate series copolymers.

Among them, EBR-3 is the only properties consisting of chlorinated alkyl α-chloroacrylate series homopolymer, and corresponds to a modified type of EBR-1 (4) [poly(trichloroethyl methacrylate)]. In spite of similarity in chemical structure, EBR-3 has some different properties from EBR-1. Firstly, EBR-3 does not

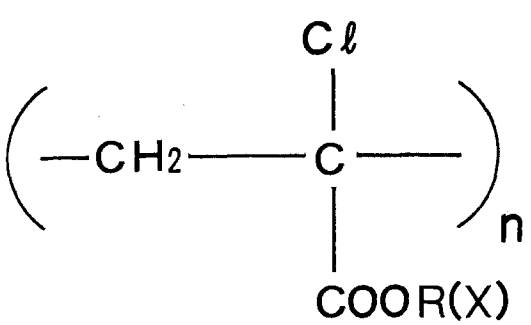

Fig. 2. Molecular structure of halogenated alkyl α-chloroacrylate series polymers.

Table I. Resist properties of halogenated alkyl α-chloroacrylate series polymers

Polymers	[η] (25°C, MEK)	Tdi (°C)	Tg (°C)	Developers	Sensitivity (μC/cm²)
PMMA	0.90	220	105	MIBK	50.00
EBR-3	0.60	230	142	ECS-PA 70-30	1.50
9	0.92	230	133	MIBK-IPA 70-30	0.75
10	1.20	220	120	MIBK-IPA 50-50	0.20
11	0.49	240	120	MIBK-IPA 35-65	3.50
12	0.44	230	138	MIBK-IPA 55-45	4.00
13	0.59	220	—	MIBK-IPA 60-40	1.75
91	0.78	225	139	MIBK-IPA 65-35	1.00
92-1	1.20	220	143	MIBK-IPA 90-10	1.50
92-2	0.80	225	144	MIBK-IPA 70-30	2.00
93	0.98	230	145	MIBK-IPA 60-40	1.75
94	1.45	300	108	ECS-BCS 80-20	1.75
95	1.56	270	136	MCS	4.00

EBR-3: poly(trichloroethyl α-chloroacrylate)
EBR-9: poly(trifluoroethyl α-chloroacrylate)
EBR-10: poly(trifluoroisopropyl α-chloroacrylate)
EBR-11: poly(trifluoro-t-butyl α-chloroacrylate)
EBR-12: poly(heptafluorobutyl α-chloroacrylate-Co-phenyl α-chloroacrylate) (62:38)
EBR-13: poly(1,1-dimethylheptafluorobutyl α-chloroacrylate-Co-n-butyl α-chloroacrylate) (50:50)
EBR-91: poly(trifluoroethyl α-chloroacrylate-Co-methyl methacrylate) (95:5)
EBR-92-1: poly(trifluoroethyl α-chloroacrylate-Co-phenyl α-chloroacrylate) (75:25)
EBR-92-2: poly(trifluoroethyl α-chloroacrylate-Co-phenyl α-chloroacrylate) (50:50)
EBR-93: poly(trifluoroethyl α-chloroacrylate-Co-methacrylic acid) (94:6)
EBR-94: poly(trifluoroethyl α-chloroacrylate-Co-t-butyl methacrylate) (60:40)
EBR-95: poly(trifluoroethyl α-chloroacrylate-Co-t-butyl α-chloroacrylate) (70:30)
MIBK: methyl isobutyl ketone
ECS: ethyl cellosolve
BCS: butyl cellosolve
MCS: methyl cellosolve
PA: propyl acetate
IPA: isopropyl alcohol

thermally cross-link, while EBR-1 is easily cross-linked by heating. In this respect, EBR-3 shows a marked contrast to EBR-1. This difference is suggestive that α-methyl group in EBR-1 plays an important role in intermolecular cross-linking of EBR-1. Secondly, EBR-3 has a higher cross-linking point than EBR-1 does, when exposed to an electron beam. In the case of EBR-1, cross-linking is observed in the dose region of more than 25 μC/cm². On the other hand, EBR-3's cross-linking point is enhanced up to 50 μC/cm². Therefore, EBR-3 can be employed as a positive electron resist in the dose region of less than 50 μC/cm². This result suggests that α-Cl atom rather suppresses the intermolecular cross-linking of polymers in comparison with α-CH_3 group, at least in the case of trichloroethyl acrylate series polymers.

Other resist materials consist of fluorinated alkyl α-chloroacrylate series polymers. In this series of resist materials, the following trends are observed. Firstly, as the number of fluorine atom in alkyl group is increased, solubility to organic solvent is deteriorated and it becomes difficult to select the coating solvents or developers. In this respect, it is undesirable to employ the polymers containing exceedingly many fluorine atoms. Secondly, as the size of fluorinated alkyl group is increased, it becomes difficult to synthesize sufficiently high molecular weight polymers. Yet it can be observed that there is no trend in which the polymers with large fluorinated alkyl ester side chains are particularly highly sensitive. So the polymers with exceedingly large fluorinated alkyl group are not desirable as highly sensitive and practical positive electron resists. In general, these fluorinated alkyl α-chloroacrylate series polymers do not cross-link in the dose region of less than 400 μC/cm². In this respect, these fluorine containing polymers are in a sharp contrast to EBR-3. This difference can be easily attributed to the chemical reactivity difference between C-F and C-Cl bonds in alkyl group. As is evident from Table I, these resist materials gen-

erally have high sensitivity which is one or two orders magnitude higher than that of PMMA, indicating that these halogen containing resists satisfy the high-throughput EB exposure system. Their *Tg* and *Tdi* data in Table I show that their thermal stability is nearly equal to or better than that of PMMA. In particular, their *Tg* is higher than that obtained with PMMA. This is an indication that they have a high process tolerance to thermal processes such as post-baking or plasma etching processes.

Because of easiness for polymer synthesis, various trifluoroethyl α-chloroacrylate series copolymers were synthesized as EBR-90 series. Their resist properties are almost the same as those obtained with EBR-9, except for EBR-94 and 95, which are thermally cross-linked type positive resists like poly(methacrylic anhydride) (PMAH) (5). Due to t-butyl ester side chains, EBR-94 and 95 are thermally cross-linked and become insoluble to organic solvent by conventional prebaking process (250°C, 1 hr). The most likely explanation for this phenomenon is that heating process generates inter or intramolecular C(=O)—O—C(=O) bonds by the elimination of t-butyl group. Their fairly high *Tdi* values are easily explained by their inter or intramolecular cross-linking. Concerning EBR-91 to 93, although some deterioration in sensitivity is observed, they are generally highly sensitive and have higher *Tg* and better adhesion than those obtained with EBR-9. Their relatively high *Tg* values can be attributed to their phenyl group (EBR-92) or carboxyl group (EBR-93) which suppress their micro-Brownian motion. EBR-92 is also expected to have a higher dry etch resistance than EBR-9 does.

As mentioned above, halogenated alkyl α-chloroacrylate series positive resists have high sensitivity which is one or two orders magnitude higher than that of PMMA. Yet they have almost the same or better thermal stability than PMMA does. Namely, although highly sensitive positive electron resists have tended to be thermally unstable, both high sensitivity and good thermal stability are accomplished at the same time for these halogen containing positive resists, as suggested by the molecular orbital calculations (2). Therefore, these halogenated alkyl α-chloroacrylate series polymers can serve as practical positive electron resists for VLSI.

Some Properties of EBR-9 Positive Resist

Since EBR-9 is most easily synthesized and a typical example of halogenated alkyl α-chloroacrylate series resists discussed in the previous section, EBR-9, in particular, has been studied in detail as a positive electron resist. This section presents more detailed studies of EBR-9 as a representative sample of halogenated alkyl α-chloroacrylate series positive resists.

NMR and XPS analyses.—In order to identify the synthesized poly(trifluoroethyl α-chloroacrylate) (EBR-9), ^{13}C-FT NMR measurements were carried out with the condition of suppressed NOE. Figure 3 shows ^{13}C NMR spectrum of the synthesized poly(trifluoroethyl α-chloroacrylate) dissolved in acetone-d_6. From the quartet splitting due to three equivalent fluorine nuclei in trifluoroethyl group and analogy to NMR spectra of other acrylate series polymers, each carbon atom constituting a polymer unit is easily assigned, as shown in Fig. 3. The measured signal positions and ^{13}C-^{19}F, ^{13}C-C-^{19}F coupling constants are listed in Table II. Since FT-NMR spectra were measured with the suppressed NOE condition, we can obtain quantitative information about each carbon atom ratio by integrating their signals (6). The estimated carbon atom ratios are A: B: C: D: E: = 1.00: 0.99: 1.00: 1.04: 0.86. The relatively small value of carbonyl carbon atom can be attributed to the remaining small NOE due to the relatively large T_1 value of carbonyl carbon atom. Therefore, these carbon atom ratios confirm that poly(trifluoroethyl α-chloroacrylate) homopolymer has been almost perfectly synthesized. The NMR spectrum in Fig. 3 also suggests that the synthesized polymer is an usual atactic polymer.

Table II. ^{13}C NMR spectroscopic data of poly(trifluoroethyl α-chloroacrylate)

Carbon positions[a]	Signal positions (ppm)	C-F coupling constants (Hz)
A	50.3, 51.68, 53.53, 54.04, 55.48	
B	63.40	$J(^{13}C\text{-}C\text{-}^{19}F) = 36.8$
C	67.5, 67.80, 68.29, 68.46, 68.56	
D	124.08	$J(^{13}C\text{-}^{19}F) = 276.5$
E	168.0, 168.33, 168.44, 168.65, 169.0	

[a] Carbon positions are indicated in Fig. 3.

Figure 4 shows a wide scan XPS (x-ray photoelectron spectroscopy) spectrum of poly(trifluoroethyl α-chloroacrylate). From the XPS spectrum in Fig. 4, we can get a general view of the electronic structure of EBR-9. As shown in Fig. 4, valence band and Cl 2p, Cl 2s, C 1s, O 1s, F 1s core electron levels are observed in the energy region of 800-1400 eV (KE). In the energy region of less than 800 eV, signals of F, O, C, and Cl Auger electrons are observed overlapped with the signals of secondary electrons. The analyzed binding energies of each level are summarized in Table III.

Since XPS spectra also provide direct information about the photoionization cross section of each energy level, one can estimate effective high energy electron sources for Al Kα x-ray radiation. As evident from Fig. 4, photoionization cross section of valence electrons, which contribute to the formation of chemical bonding in EBR-9, is considerably lower compared with those of other core electrons, indicating that most of the high energy electrons are generated from the inner core electrons of each atom. Particularly, F 1s photo-

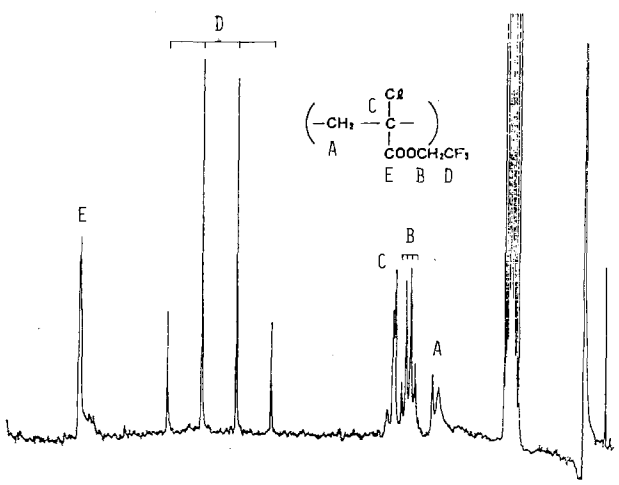

Fig. 3. ^{13}C-NMR spectrum of synthesized poly(trifluoroethyl α-chloroacrylate).

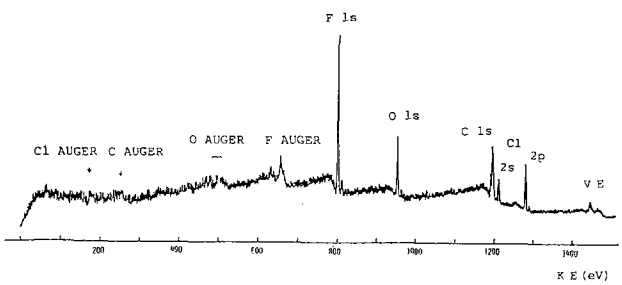

Fig. 4. Wide scan XPS spectrum of poly(trifluoroethyl α-chloroacrylate).

Table III. Binding energies of each molecular orbital level in poly(trifluoroethyl α-chloroacrylate)

Energy levels	Binding energies (eV)
Valence band	11.0 ~ 38.6
Cl 2p(3/2)	206.2
2s	277.1
C 1s A[a]	291.3
B, C[a]	293.1
D[a]	298.6
E[a]	295.2
O 1s C—O—C	538.7
C=O	540.4
F 1s	694.6

[a] Carbon positions are indicated in Fig. 3.

ionization cross section is observed to be fairly high. This suggests that incorporation of fluorine atoms is effective for enhancement of resist sensitivity in the case of Al Kα x-ray lithography.

EB exposure characteristics.—We have studied three different EBR-9 samples, named as EBR-9(1), 9(2), and 9(3), whose intrinsic viscosity [η] (25°C, MEK) are 0.60, 0.92, and 1.91, respectively. Of these samples, EB exposure characteristics of EBR-9(1) were already reported in the previous communication (1). Figure 5 shows EB exposure characteristics of the three EBR-9 samples (when developed with relatively strong condition without resist thickness loss). As has been often pointed out (7, 8), the factor of high molecular weight is favorable in obtaining highly sensitive positive electron resists. As shown in Fig. 5, EBR-9 sensitivity is enhanced with the increase in molecular weight. Particularly in the case of EBR-9(3), its sensitivity goes as high as 0.25 μC/cm² after being developed with methyl isobutyl ketone (MIBK) for 30 min. However, as the molecular weight is increased, it becomes difficult to uniformly coat the resist film or to filter the resist solution, and the resist film becomes liable to swell in the developing process. These troubles bring on serious problems for practical use.

Figure 6 shows EB exposure characteristics of EBR-9 (2) with moderate molecular weight, where developing time and developer composition are changed. Two kinds of developers, 6:4 MIBK-IPA [Fig. 6(a)] and 7:3 MIBK-IPA [Fig. 6(b)] mixtures, are employed, in which MIBK and isopropyl alcohol (IPA) correspond to a good solvent, and a nonsolvent for EBR-9, respectively. As shown in Fig. 6, EB exposure characteristics considerably differ according to the developing condition. EBR-9's sensitivity is increased in proportion to the developing time in both developers. Although the same trend is also observed in PMMA, EBR-9's γ-value (slope of the sensitivity curve) is fairly independent of developing time, while PMMA's γ-value tends to be

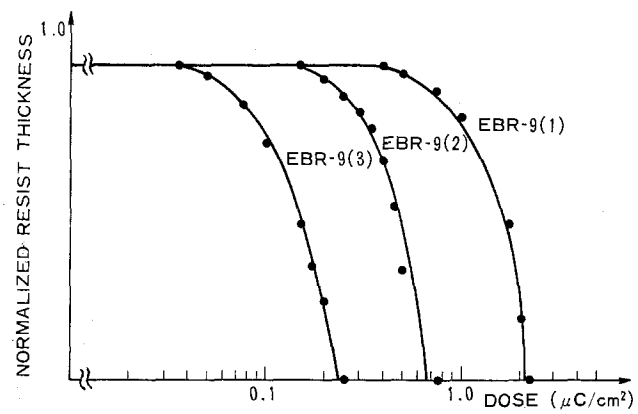

Fig. 5. EB exposure characteristics of three different EBR-9 samples, developing conditions: EBR-9(1): 6:4 MIBK-IPA(22°C) 20 min, EBR-9(2): 7:3 MIBK-IPA(22°C) 20 min, EBR-9(3): MIBK(22°C) 30 min; initial resist thickness: 0.5 μm.

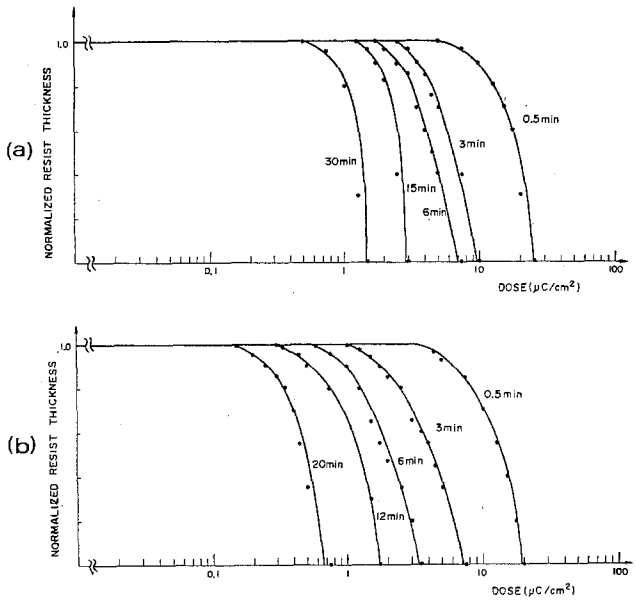

Fig. 6. EB exposure characteristics of EBR-9(2), (a) 6:4 MIBK-IPA developer (22°C), (b) 7:3 MIBK-IPA developer (22°C); initial resist thickness: 0.5 μm.

decreased with developing time. In this point, EBR-9 shows a sharp contrast to PMMA. Concerning the developer composition, developing rate and sensitivity are increased with MIBK composition. In the case of 6 min developing time, for example, 7.0 and 3.5 μC/cm² sensitivity are obtained with 6:4 MIBK-IPA and 7:3 MIBK-IPA developers, respectively. On the other hand, the γ-value tends to be decreased with MIBK composition.

Since degradation predominates at least in the dose region of less than 400 μC/cm², EBR-9 can be employed as a positive working resist in this dose region. Therefore, by controlling developing conditions such as composition or time, the EBR-9 resist system can be adjusted to various optimum charge densities differing from system to system. In other words, EBR-9, like PMMA, has a high process tolerance to electron beam dosages in contrast to negative electron resists. Due to the relatively high *Tg*, EBR-9 is good in thermal stability and is easily processed. Like PMMA, EBR-9's resolution depends on the electron beam diameter or electron beam sharpness. However, submicron resolution can be easily obtained by using a fine electron beam with the diameter of less than 0.5 μm. By using a sufficiently fine electron beam, 0.1-0.2 μm resolution can be obtained. Figures 7 and 8 show the 0.3 μm line-0.7 μm space EBR-9 resist profile, and the 0.2 μm-0.5 μm cross-line pattern, respectively. As is evident from Fig. 7 and 8, EBR-9 is fully capable of fabricating submicron feature size. Figures 9 and 10 show the 1 μm-rule EBR-9 resist patterns delineated by the VL-R1 electron beam exposure system. As shown in Fig. 9 and 10, EBR-9 can be employed for the fabrication of 1 μm-rule VLSI. EBR-9 is successfully employed for the photomask fabrication. Figures 11 and 12 show the chromium mask patterns etched through EBR-9 positive resist. Both wet and dry etching processes are applicable for EBR-9. Because of its high resolution, EBR-9 is suitable for the fabrication of high quality photomasks.

Dry etch resistance.—As described in the previous section, EBR-9 has almost the same thermal stability as PMMA does. Therefore, one may expect that EBR-9 has almost the same dry etch resistance as PMMA does. However, EBR-9's dry etch resistance fairly differs from that of PMMA. Its relative etch resistance (*vs.* PMMA) strongly depends on etching conditions such as etching gases or etching methods. Table IV

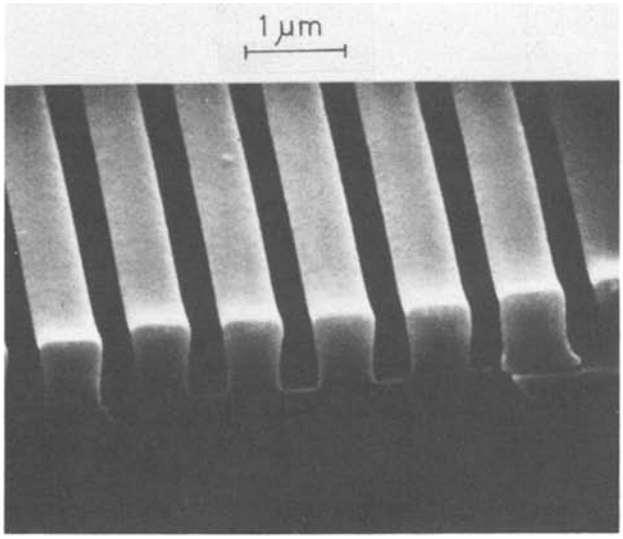

Fig. 7. SEM photograph of a 0.3 μm line-0.7 μm space EBR-9 resist profile.

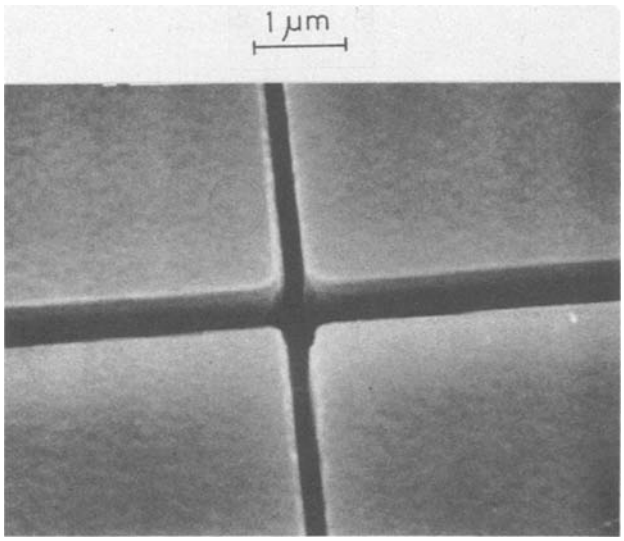

Fig. 8. SEM photograph of a 0.2 μm-0.5 μm cross line EBR-9 resist pattern.

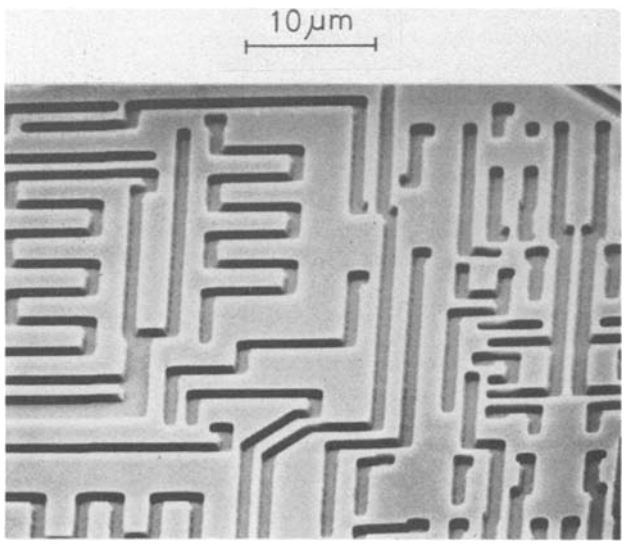

Fig. 9. SEM photograph of a 1 μm-rule EBR-9 resist pattern delineated by VL-R1 at a dose of 10 μC/cm².

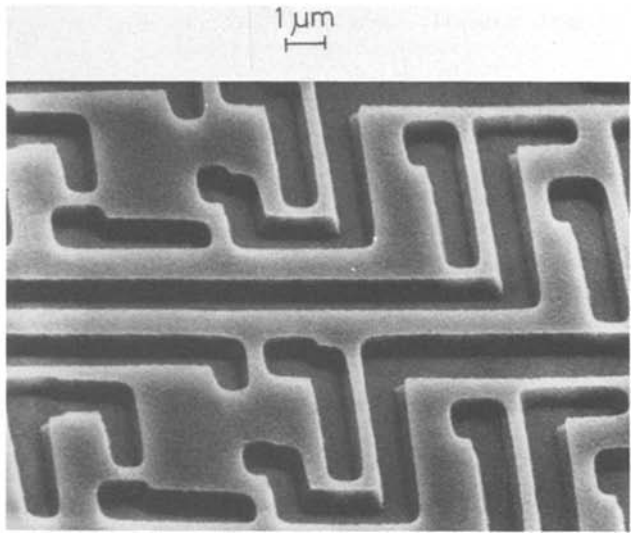

Fig. 10. SEM photograph of a 1 μm-rule EBR-9 resist pattern delineated by VL-R1 at a dose of 8 μC/cm².

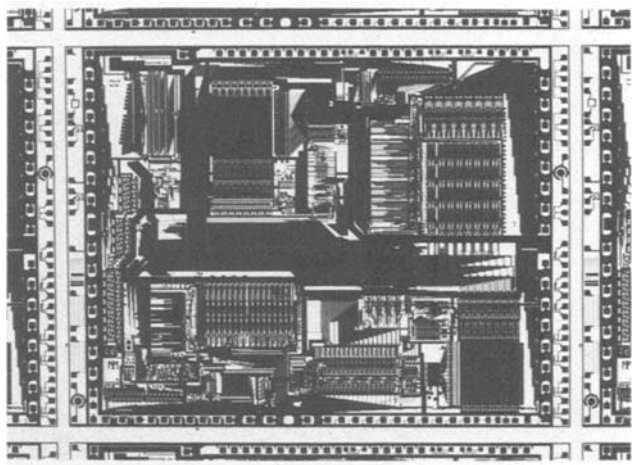

Fig. 11. Photomicrograph of an LSI chromium mask pattern (8.85 × 6.66 mm microprocessor chip) wet-etched through EBR-9 positive resist.

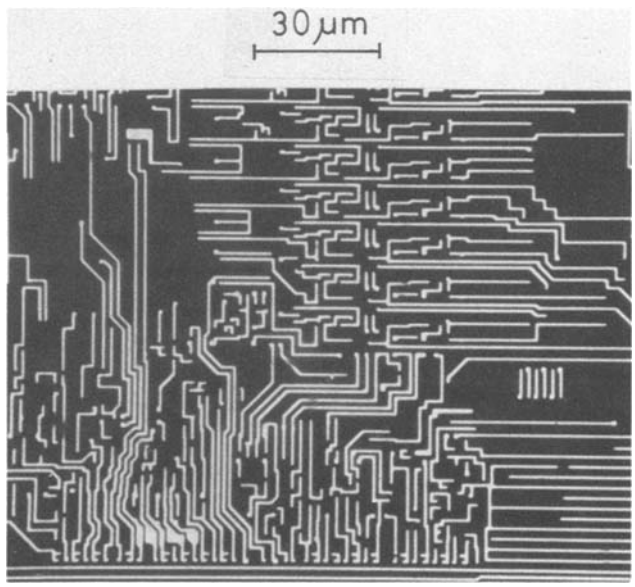

Fig. 12. Photomicrograph of a chromium mask pattern dry-etched through EBR-9 positive resist.

summarizes the measured etching rate ratios of EBR-9 and PMMA, where dry etching is performed in the three different etching conditions. The employed dry etching systems are NEVA DEM-451 reactive ion etching system and IPC 2010 T plasma etching system. The former is a parallel plate type system capable of per-

Table IV. Measured etching rate ratios of EBR-9 and PMMA in various etching conditions

Etching system / etching gas / Resists	NEVA DEM-451 CCl_4-air (7:10)	IPC 2010T O_2	IPC 2010T CF_4-O_2 (96:4)
EBR-9	1.9	0.9	0.7
PMMA	1.0	1.0	1.0

forming anisotropic etching, and the latter is a conventional plasma etching system which isotropically etches the substrate. The employed etching gases are O_2 gas and CF_4-O_2 (96:4) mixture gas for plasma etching, and CCl_4-air (7:10) mixture gas for reactive ion etching. The experimental results in Table IV show that EBR-9 has higher etch resistance to isotropic plasma etching than PMMA does. In the case of CF_4-O_2 mixture gas, for example, EBR-9's etch rate is 7/10 of that of PMMA. However, an opposite result is observed in the case of reactive ion etching. EBR-9's etch rate is nearly two times higher than that of PMMA when DEM-451 system is employed.

In so-called dry etching process, it is considered that the following two types of chemical reactions proceed on the surface of substrates or resists: (*i*) Chemical reactions caused by the interaction between plasma-induced reactive species and substrate atoms or resist molecules, and (*ii*) Radiation induced chemical reactions. In isotropic plasma etching, the first type is considered to predominate. However, in the case of reactive ion etching, the above two types of chemical reactions are considered to proceed competitively. In this case, the relative magnitude of the two types of chemical reactions strongly depends on the etching conditions.

Since EBR-9's molecular structure is designed to be easily degraded by ionizing radiation, it is expected that EBR-9 shows a relatively low dry etch resistance in the etching condition when the second type of chemical reactions predominate. On the other hand, in the etching condition when the first type of chemical reactions predominate, EBR-9 is expected to show a relatively high dry etch resistance. From this point of view, the experimental results in Table IV are easily understood. In other words, the experimental results suggest that there exists little radiation induced chemical reaction in the plasma etching process, and that the relative magnitude of radiation induced chemical reactions is large in the reactive ion etching condition listed in Table IV. Therefore, it is expected that EBR-9 tends to have a relatively low etch resistance to reactive ion etching. However, if anisotropic dry etching is performed in the etching condition when the first type of chemical reactions predominate, EBR-9 is expected to have a moderate dry etch resistance. We suggest that EBR-9 is applicable to the reactive ion etching process by carefully controlling the etching conditions. From this point of view, the development of more advanced anisotropic dry etching systems which minimize the resist or substrate damage is desired.

Acknowledgments

The author would like to acknowledge M. Ninomiya for electron beam exposure by VL-R1, and Toray Basic Research Laboratories for the polymer synthesis.

Manuscript received Sept. 23, 1982.

Any discussion of this paper will appear in a Discussion Section to be published in the December 1983 JOURNAL. All discussions for the December 1983 Discussion Section should be submitted by Aug. 1, 1983.

Publication costs of this article were assisted by VLSI Technology Research Association.

REFERENCES

1. T. Tada, *This Journal*, **126**, 1829 (1979).
2. T. Tada, *ibid.*, **128**, 1791 (1981).
3. M. Sumi, M. Ninomiya, F. Chiba, M. Nakasuji, S. Sano, and Y. Takeishi, in Proceedings of the 10th Conference on Solid-State Devices, p. 303 (1978).
4. T. Tada, *This Journal*, **126**, 1635 (1979).
5. A. Miura and S. Hideyama, *J. Vac. Sci. Technol.*, **16**, 1996 (1979).
6. G. A. Gray, *Anal. Chem.*, **47**, 547A (1975).
7. M. Hatzakis, C. H. Ting, and N. Viswanathan, in Proceedings of the 6th International Conference on Electron and Ion Beam Science Technology, p. 542 (1974).
8. M. J. Bowden, L. F. Thompson, and J. P. Ballantyne, *J. Vac. Sci. Technol.*, **12**, 1294 (1975).

Microstructure and Electro-Optical Properties of Evaporated Indium-Oxide Films

Z. Ovadyahu,[1] B. Ovryn,[2] and H. W. Kraner

Brookhaven National Laboratory, Upton, New York 11973

ABSTRACT

The microstructures and electro-optical properties of thermally evaporated indium-oxide films are given and discussed. It is shown that highly transparent and conducting films can be prepared at relatively low (~150°C) substrate temperatures, with and without doping by tin. Results of stoichiometry measurements in conjunction with the Hall effect and crystal structure data suggest the existence of indium atoms with different valences in these films. This implies that the conduction mechanism in this material may be more complicated than hitherto assumed.

Films of indium-oxide and indium-oxide doped with tin (ITO) have a wide range of application in the field of optoelectronic devices. These materials are fair conductors of electricity (with room temperature conductivity, $\sigma \approx 10^3$-10^4 $(\Omega\,\mathrm{cm})^{-1}$) and are highly transparent in the visible (~90% integrated transmission). Most of the preparation methods currently known (1-5) involve a relatively high substrate temperature ($\gtrsim$ 300°C) for a reasonably good conductivity to be obtained. This requirement may be somewhat restrictive; for example, photovoltaic devices based on amorphous silicon may seriously deteriorate at elevated temperatures (6).

In this paper, we describe the properties of e-gun evaporated indium oxide and ITO films. The choice of an e-gun for the process was largely motivated by the

[1] Present address: Department of Physics, Ben-Gurion University of the Negev, Beer-Sheva, Israel.
[2] Permanent address: Department of Physics and Astronomy, University of Rochester, Rochester, New York 11972.

work of Pan and Ma. (5). These authors have shown that the high quality films can be obtained by thermally evaporating In_2O_3 + 10% In from Al_2O_3 crucibles onto substrates held at 320°-350°C. The high quality of the films was attributed to the inclusion of metallic indium in the process. It can be argued that if the coevaporated indium plays a nontrivial role in the evaporation kinetics, it is probably related to the quantitative ratio of the chemical species involved. We note that the vacuum species observed when In_2O_3 is evaporated from Al_2O_3 crucibles are In_2O, In, and O_2 in descending order of abundance (7). If there is indeed an inherent advantage to be gained by increasing the relative In content, then an e-gun evaporation might prove beneficial. The vacuum species observed when In_2O_3 is evaporated from nonreactive supports (and an e-gun should act like one) contain more (8) In than In_2O. Furthermore, since the latter procedure involves fewer independent degrees of freedom, it should result in an easier to control method of preparation that hopefully would make feasible the use of lower substrate temperatures. This goal has presumably been achieved; high quality films are shown to be easily obtainable at substrate temperatures as low as ~ 150°C. The feasibility of this preparation method for amorphous-silicon-based devices has already been demonstrated (9).

The detailed conduction mechanism in this material is not well understood at present. It is generally recognized (3, 5, 10) that oxygen vacancies play a dominant role in this respect even when the material is doped. Some attempts have been made to determine the actual amount of these vacancies but the results were not accurate enough (1) to warrant a meaningful interpretation. In the course of characterizing our films, we have carried out Rutherford back scattering experiments with the purpose of elucidating these questions. The results for the actual films' stoichiometry, thus, obtained, in conjunction with data from electrical measurements and crystal structure data, lead us to some interesting ideas concerning the conduction mechanism as well as the source of scattering in this material.

Experimental

Samples have been thermally evaporated from an e-gun in an oil-diffusion vacuum system operating at a base pressure of 5×10^{-7} Torr. Dry O_2 (purity 99.9%) was admitted through a needle valve maintaining a partial pressure of $2\text{-}6 \times 10^{-4}$ Torr during material deposition. The evaporated material was a hot-pressed target of optical-electronic grade In_2O_3 or In_2O_3 + 9 (or less) mol percent (m/o) SnO_2 (both of purity 99.997% or better by Cerac, Incorporated). Deposition rate and film thickness were measured *in situ* with a quartz crystal monitor that was calibrated against an optical interferometer. Unless otherwise mentioned, microscope glass-slides were used as substrates. The substrates were mechanically clamped to an aluminum resistively heated stage, equipped with a thermocouple to monitor substrate temperature. The sample stage was set about 50 cm from the e-gun and slightly displaced from its center so as to block the radiative heat originating from the filament. Therefore, the only source of radiative heat was the electron-bombarded In_2O_3 whose temperature, as determined by an optical pyrometer, was 1250° ± 50°C, for a deposition rate of 0.5 ± 0.25 A/sec which was typical.

In most evaporation runs, an electron-microscope copper grid (precoated with ~ 100Å of amorphous carbon) was attached to the substrate stage in close proximity with the sample so that structural analysis was performed on virtually the same material used for electrical or optical measurements (*i.e.*, problems associated with removal of the film off the substrate were eliminated). The electron microscopy was done in a JEM-100C microscope operated at 100 kV.

The relative In/Sn content in the evaporant was probed by x-ray fluorescence, while the stoichiometry of the resulting films was analyzed by Rutherford backscattering. For the latter, samples were deposited on thin carbon layers supported by a metal frame. A source of energetic α-particles was used for this experiment in the BNL research Van de Graaf (11). A 241 Am α-source measured concurrently with accurate pulser measurements allowed the energy scale to be calibrated to ~ 1 keV. Optical measurements in the range 0.3-0.65 μm were made using an Applied Physics Corporation (Cary 14) Recording Spectrophotometer.

Electrical measurements were made on samples that were shaped (by use of masks) into strips of 5 × 1 cm with two current leads on either side and two pairs of "clover leaf" Hall contacts along the strip. The latter doubled as voltage contacts for d-c four-probe resistivity measurements. Both the resistivity and the Hall constant were measured as a function of temperature from 290 K down to 1.1 K. Hall effect data were taken in a standard way employing fields of ± 5000 Oe. (The readings of the Hall voltage were averaged on the two perpendicular field orientations, to cancel effects due to nonideal geometry or a nonuniform current distribution.)

Results and Discussion

Microstructure.—The films' microstructure was probed by transmission electron microscopy. Characteristic micrographs and diffraction patterns are shown in Plates 1A-1E and Plates 2A and 2B. One feature, immediately seen from these micrographs, is the large diversity in crystallites size and shape obtained under different deposition conditions. We have found that the partial O_2 pressure during deposition plays a crucial role in the growth process. For example, a clear tendency towards a dendritic growth is observed once the O_2 partial pressure is lowered below the nominal pressure. (See Plate 1B.) Apparently, the lack of building material forces the growing crystal to maximize its surface to volume ratio. Not surprisingly, such a film is also characterized by low light transmission (Fig. 1) and poor electrical conductivity ($\sigma \sim 10^2$ $(\Omega\text{-cm})^{-1}$) although the carrier concentration can be rather high

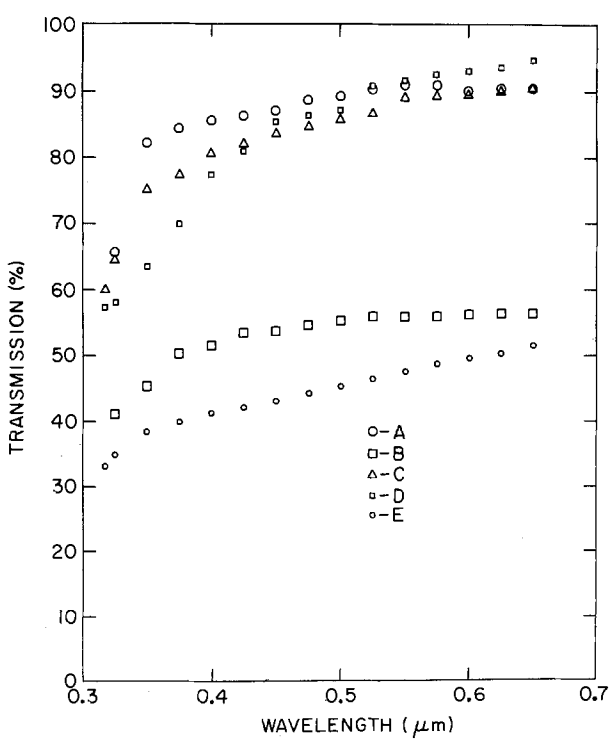

Fig. 1. Optical transmission of five characteristic samples [refer to Plates 1-A-1-E for sample identification].

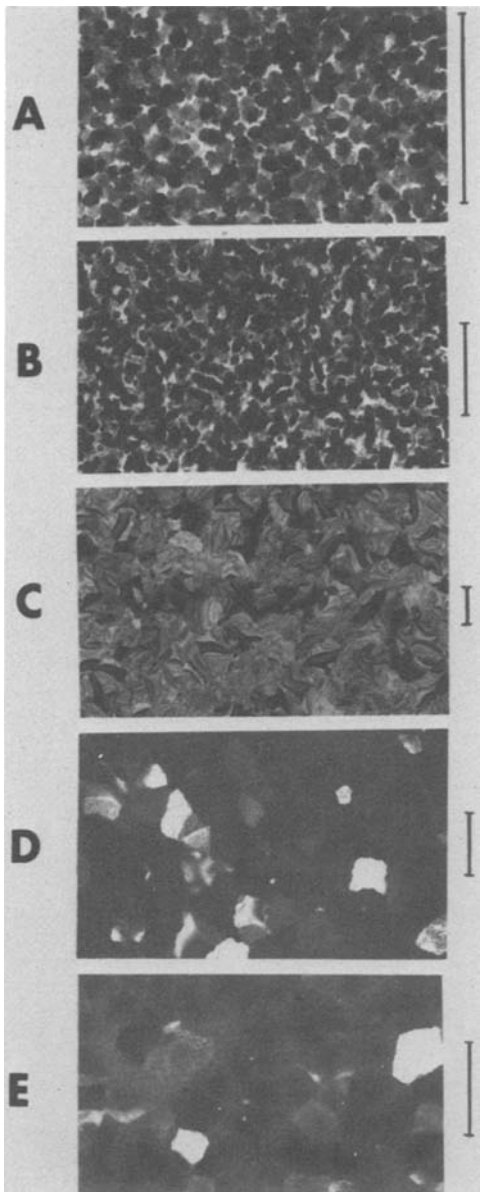

Plate 1. Transmission electron micrographs of five typical samples (thickness 250-300Å) 1-A: prepared at ~300°C substrate temperature using In_2O_3 + 9 m/o SnO_2 as the evaporant. 1-B: same as 1-A but with O_2 reduced to $2\text{-}10^{-5}$ Torr. 1-C: prepared at 150°C using pure In_2O_3 as the evaporant. 1-D: prepared at 150°C using In_2O_3 + 3 m/o SnO_2 as the evaporant (dark field). 1-E: same as 1-D except that In_2O_3 + 7 m/o SnO_2 was used as the evaporant (dark field). The black bar on the right of each plate is equivalent to 0.5 μm.

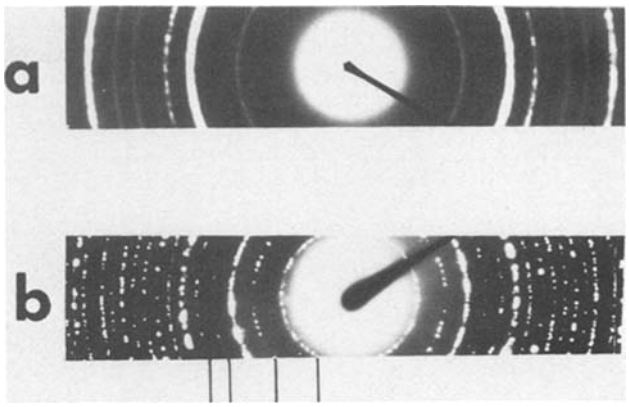

Plate 2. Electron diffraction patterns of evaporated pure indium oxide films: A—close to stoichiometry, B—prepared under nominal conditions. The four "extra" reflections (see text) are marked by black lines.

(4×10^{20} cm^3). On the other hand, a too high O_2 pressure, though resulting in a film of excellent optical transmission (~ 90% in the visible), has presumably too few oxygen vacancies (*i.e.*, "donors") to act as charge carriers. The critical role of the partial O_2 pressure can, thus, be naturally explained as resulting from the conflicting requirements of introducing enough oxygen vacancies without creating too many grain boundaries in the process.

The substrate temperature seems to be less critical in this respect. Reasonably good conductivity [$\sigma \sim 10^3$ $(\Omega\text{-cm})^{-1}$] is easily and reproducibly obtained for substrate temperature as low as 130°C using pure In_2O_3 as the evaporant. In fact, for undoped films, increasing this temperature to 250°C has no apparent advantage for either the electrical conductivity or the transparency of the films. Interestingly, the largest grain-size and the best coverage properties (judged by the thickness at which physical continuity is reached) are obtained at the lower substrate temperature. The near-perfect planar growth affected at ~ 150°C can be seen from the thickness-interference fringes (Plate 1C).

Essentially, the same behavior is observed for films doped with tin except that the grain size is somewhat reduced (see Plate 1D). We have found that the SnO_2 content in the starting material should be considerably smaller than the 9 m/o usually used in sputtering targets. In fact, such high concentration of the dopant material resulted in films of very poor quality unless the substrate temperature was increased to ~ 300°C. The source of the problem seems to be connected with the appearance of an additional, quasi-amorphous phase that was identified from the diffraction pattern as Sn_3O_4. By dark field imaging techniques, this phase is seen to reside mainly along grain boundaries (Plate 1E). Note that even though this quasi-amorphous (and highly resistive) phase has very small relative volume, it has a marked detrimental effect, not only on electrical conductivity, but on optical transmission as well (Fig. 1). Similar problems were encountered in Ref. (4) where sputtering techniques were employed. We have found an obvious correlation between the SnO_2 content in the starting material (as determined by x-ray fluorescence) and the severity of the effect. Either an increased substrate temperature (300°C for 10 m/o) or a reduced SnO_2 content (3 m/o for 150°C) were found effective in eliminating this problem. We have also noticed a monotonous decrease of the Sn/In contents ratio (measured by x-ray fluorescence) in the evaporant that is attributed to a preferential sublimation of SnO_2. This effect was more apparent for targets containing $\geq$ 9 m/o SnO_2 for which a reduction of ~ 3 m/o in the latter per hour of evaporation was observed. Unless a continuous feed method is employed, problems of inhomogeneities are, therefore, likely to be encountered during prolonged evaporations.

The crystal structure of the evaporated In_2O_3 films is basically identical with the bulk structure. There are, nevertheless, some subtle differences reflected in the electron diffraction patterns (Plates 2A and 2B). The diffraction lines observed in a typical conducting sample (Plate 2A) are listed in Table I. Note that all the observed reflections can be indexed on the basis of a bcc symmetry with a lattice parameter a = 10.09A (found from high angle x-ray diffraction experiments on these films) which is only 0.3% smaller than the respective bulk value (12). The four reflections (110), (200), (220), and (310) which are extinct in the bulk (13) are very clearly observed. We believe that these reflections are real since dark field micrographs, taken from any of them, were identical to one taken from the "legitimate" (222) ring. Further, a diffraction pattern similarly taken from a highly resistive (presumably

Table I. Diffraction lines observed in a typical conducting film of evaporated In_2O_{3-x} (cf Plate 1-B) indexed on a bcc basis with lattice parameter of 10.09Å

d (Å)	(hkl)
7.13	(110)
5.04	(200)
4.125	(211)
3.57	(220)
3.20	(310)
2.921	(222)
2.70	(321)
2.52	(400)
2.38	(411)
2.25	(420)
2.15	(332)
2.06	(422)
1.98	(431)

close to stoichiometry) film (Plate 2B) is in very good agreement with the bulk reflections in terms of intensities. These extra lines appear for doped films as well but their relative intensity is somewhat weaker.

Optical measurements.—Optical transmission curves for the five representative thin films mentioned above are shown in Fig. 1. Note that except where structural complications interfere, the integrated transmission in the visible is very high and is presumably limited only by scattering (for energies above the optical gap). This conjecture was supported by measurements on thicker films that gave similar results to those obtained by Fan and Bachner (4) in the 0.3-0.65μ range, in particular, interference fringes were clearly observed. The refractive index was calculated from the position of the minimum reflectance as a function of thickness for films deposited on silicon wafers. The value of the refractive index thus obtained ($n = 2 \pm 0.1$) is in agreement with values found by other researchers (4, 5).

Stoichiometry.—A typical spectrum obtained from a Rutherford backscattering experiment on an undoped film is shown in Fig. 2. The oxygen and indium peaks as well as those due to (12) C (undoubtedly coming from the backing film) are clearly observed. By measuring the kinematic factor, the narrow peak in midscale is identified as sulfur, and the broad peak above indium is presumably tungsten. The tungsten peak is broadened to the same extent as the oxygen and indium peaks indicating that this contaminant (3×10^{-4} that of the indium content on an atom basis) resides within the film. Most probably, this contaminant comes from the e-gun filament. Apparently, the precaution taken to block the radiative heat generated by the e-gun filament is not very effective in this respect. We have indeed noticed the accumulation of a yellow deposit at the filament supports after prolonged evaporations. This fact presumably means that filament contamination (though hopefully minimized) is still possible with the present evaporation geometry. The sulfur peak (4×10^{-3} that of indium on an atom basis) is relatively narrow compared to the energy-loss-broadened O, In, and W peaks which is distinctly indicative of surface contamination.

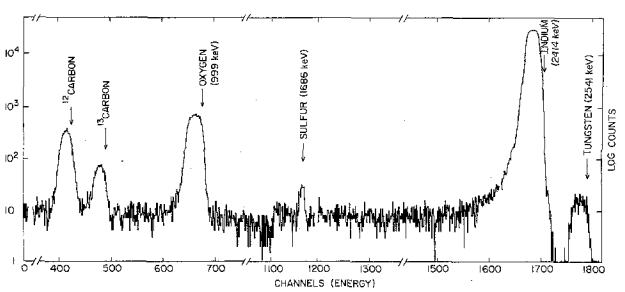

Fig. 2. Typical Rutherford backcscattering spectrum for a ~1000Å undoped In_2O_{3-x} film. .

Results of three machine runs at energies 2.25, 2.08, and 1.28 meV gave for the In/O atomic ratio values of 0.755, 0.755, and 0.76, respectively, with an accuracy of ~ 1%. It is interesting to note that similar values (derived by a less accurate method) were reported for tin-doped indium-oxide films sputtered at low powers (4).

Electrical measurements.—The room temperature resistivity, ρ, free carriers density, N, and Hall mobility, μ_H, for doped and undoped In_2O_{3-x} films are listed in Table II. The quoted ranges of these parameters are typical of what is obtainable for a given class (*i.e.*, pure and tin doped indium oxide) using the present technique. These values are based on at least 20 samples in each group and are characteristic of samples whose thickness is $\geq$ 140Å. Films thinner than ~ 100Å may not be yet physically continuous, and naturally, their resistivity was found to be thickness dependent.

The resistance of a typical film decreased by 10-15% upon cooling down from room temperature to ~ 100 K. We have found that this weak temperature dependence can be fitted by $R(T) = R_o + AT^5$ in the 100-200 K temperature range. Such a dependence is consistent with phonon scattering at temperatures which are much lower than the Debye temperature, θ_D. This is presumably the case here; from the heat capacity data (14) we estimate, using the Debye approximation, that θ_D in this material is ~ 1000 K.

At low temperatures ($T < 100$ K), various anomalous transport properties associated with disorder scattering such as negative TCR and magnetoresistance were observed (15). The Hall constant, however, was found to be temperature independent down to ~ 1 K. This is a clear indication of a metallic (*i.e.*, nonactivated) conduction mechanism and should have been anticipated considering the high ($\sim 10^{20}$ cm^{-3}) density of carriers. The elastic mean free path in these conducting films was estimated from the low temperature measurements (15) to be 40-80Å. These values are considerably smaller than even the smallest grain size actually observed (Plates 1A-1E). Grain boundaries and surface irregularities are, therefore, not likely to be the major source of scattering in this material.

The room temperature resistivity of films prepared under the conditions outlined above was found to change little with time, typically less than ± 20% over a period of a year, independent of storage conditions. In contrast, samples prepared at substrate temperature < 110 C, had considerably lower free-carrier densities; $N \approx 8 \cdot 10^{18}$-$5 \cdot 10^{19}$ (and respectively lower conductivities) and their resistivity was strongly influenced by the storage environment even at room temperature. When kept in the laboratory atmosphere, the resistivity drifted towards higher values in a matter of days, a trend that could be easily reversed by storing the sample in an evacuated system. Hall effect measurements indicated that this resistivity change is essentially a reflection of N changing in the above range (presumably due to oxygen atoms diffusing in and out of the material). This feature of the latter class of films, while clearly undesirable for most applications, is very useful for studies of the metal-insulator transition which is of much current interest.

Discussion.—In this section, we want to address the question of the basic conduction mechanism in indium-oxide films when the density of free carriers is large enough for the assumption of degeneracy to be justified

Table II. The range of room temperature electrical parameters of thermally evaporated indium-oxide films

	ρ (cm)	N (10^{20} cm^{-3})	μ_H (cm^2/Vsec)
Undoped In_2O_{3-x}	$8\text{-}16 \times 10^{-4}$	0.5-1.1	60-95
In_2O_{3-x} doped with Sn	$1.5\text{-}10 \times 10^{-4}$	2-6	45-70

(*i.e.*, $\geq 10^{19}$ cm^{-3}). The electro-optical properties of the In_2O_{3-x} films described above appear, in most respects, to be similar to those prepared by other methods. We, therefore, believe that the following considerations should apply to such films in general regardless of their preparation method. Nevertheless, one should bear in mind that the Rutherford backscattering measurements, on which the following discussion hinges in an essential way, were performed only on pure indium-oxide films prepared under the prescribed conditions.

The oxygen deficiency we observe is quite significant, amounting to an average of 5-6 oxygen atoms leaving each unit cell. If one adopts the simple picture that each missing oxygen atom "leaves behind" two electrons in the conduction band, one expects to have a density of $\sim 10^{22}$ cm^{-3} electrons, rather than the 10^{20} actually observed, given this deviation from stoichiometry (which is much larger than the impurity content) and the fact that the basic crystal structure and lattice spacing value are close to the "bulk" values.

One is forced to the conclusion that in each unit cell some of the In atoms must have a valency different than 3 (to preserve chemical neutrality). It is quite possible that this may also account for the somewhat reduced crystal symmetry we observe in the electron diffraction patterns (Plate 2-B). In fact, it is difficult to understand the coherent change in crystal symmetry for such large grains unless the oxygen deficiency is substantial (*i.e.*, a number of atoms per each unit cell). If such is the case, it becomes natural to assume that the basic conduction mechanism involves charge transfer between indium atoms of different valencies. In other words, In_2O_{3-x} appears to be a defect structure, similar to the more familiar case of Fe_3O_4[16] except that in the latter, band structure effects make it a semiconductor, whereas the former exhibits metallic behavior (a semi-metal?). Band structure effects may be important in In_2O_{3-x} too; this may explain the high degree of compensation observed as the latter is unaccountable by any foreign acceptor agent (the impurity contents detected being only $\sim 10^{18}$ cm^{-3}). A somewhat related question and one that is of practical importance is the scattering mechanism of these films. Our best samples show peak Hall mobilities of the order of 90 cm^2/Vsec for $N \sim 10^{20}$ cm^{-3}. This value of the mobility seems to be disorder-limited and suggests an elastic mean, free of the order of path ~ 80Å. As noted before, the grain size observed in these films is at least an order of magnitude larger than that, and, therefore, grain boundaries cannot account for this restricted mobility. Neutral impurity scattering is not likely to be important either; for that case the mobility is given by (17)

$$\mu = \frac{m^* e^3}{20\, h^3 N_i \epsilon} \qquad [1]$$

where N_i is the impurities concentration and ϵ the dielectric constant. Using $m^* \sim 0.3\ m_0$ and $\epsilon = 4$, we get $N_i \sim 10^{21}$ cm^{-3} for $\mu = 90$ cm^2/Vsec, which is about two orders of magnitude higher than the concentration of foreign impurities actually measured. Apparently, the main source of scattering is of intrinsic nature, most likely involving the disorder associated with the oxygen vacancies themselves; some disorder must originate from the fact that the vacancies spatial distribution is partially random. This simply follows from a stoichiometry that cannot be reconciled with the basic crystal symmetry.

An obvious corollary of this point of view is that a drastic improvement in mobility (and therefore conductivity) can be expected only if an oxygen-deficient structure of a definite favorable stoichiometry could be coaxed from nature. To date, most of the efforts made to improve the conductivity of the material focused on increasing the effective number of free carriers via doping. Although this method has been somewhat successful, it is clearly self-limited: Insofar as the dopant atoms occupy random sites in the host lattice, the process of doping while increasing N certainly impairs the mobility. This results in an optimum conductivity of the order of 5000 $(\Omega\ \text{cm})^{-1}$. The work of Pan and Ma (5), as well as the present study, have demonstrated that comparable conductivities can be easily achieved by thermally evaporating pure In_2O_3. In both works, the improved conductivity was obtained due to enhanced mobilities (by as much as a factor of 2) over other preparation methods. In our view, a closer control over deposition parameters (especially the rate to oxygen-pressure ratio) may conceivably result in even higher mobilities than those presently obtained.

Acknowledgments

We are grateful to O. F. Kammerer for x-ray diffraction measurements and to L. Wielopolski for the x-ray fluorescence analysis of our samples and for many instructive discussions. This research was performed under the auspices of the U.S. Department of Energy under Contract No. ACO2-76CH00016.

Manuscript submitted April 19, 1982; revised manuscript received Dec. 8, 1982.

Any discussion of this paper will appear in a Discussion Section to be published in the December 1983 JOURNAL. All discussions for the December 1983 Discussion Section should be submitted by Aug. 1, 1983.

Publication costs of this article were assisted by Brookhaven National Laboratory.

REFERENCES

1. R. Groth, *Phys. Status Solidi*, **14**, 69 (1966).
2. H. K. Muller, *ibid.*, **27**, 723 (1968).
3. D. B. Fraser and H. D. Cook, *This Journal*, **119**, 1368 (1972).
4. J. C. C. Fan and F. J. Bachner, *ibid.*, **122**, 1719 (1975).
5. C. A. Pan and T. P. Ma, *Appl. Phys. Lett.*, **37**, 163 (1980).
6. J. McMillan and E. Peterson, *J. Appl. Phys.*, **8**, 5238 (1979).
7. "Condensation and Evaporation of Solids," E. Rutner, P. Goldfinger, and J. P. Hirth, Editors, p. 255, Gordon and Breach, Science Publishers, Inc., New York (1966).
8. L. Holland, "Vacuum Deposition of Thin Films," p. 466, John Wiley and Sons, Inc., New York (1961).
9. Z. Ovadyahu and H. Wiesman, *J. Appl. Phys.*, **52**, 5865 (1981).
10. W. W. Molzen, *J. Vac. Sci. Technol.*, **12**, 99 (1975).
11. A. Rohatgi, S. R. Butler, F. J. Feigl, H. W. Kraner, and K. W. Jones, *This Journal*, **126**, 143 (1979).
12. R. W. G. Wyckoff, "Crystal Structures," Vol. II, 2nd ed., p. 2, John Wiley and Sons, Inc., New York (1964).
13. L. Pauling and M. D. Shappell, *Z. Kristallogr.*, **75**, 128 (1930).
14. "Handbook of Chemistry and Physics," R. C. Weast, Editor, CRC Press, (1929).
15. Z. Ovadyahu and I. Imry, *Phys. Rev. B*, In press.
16. L. V. Azaroff, "Introduction to Solids," McGraw-Hill, Inc., New York (1960).
17. C. Erginsoy, *Phys. Rev.*, **79**, 1013 (1950).

Precipitation as the Phenomenon Responsible for the Electrically Inactive Arsenic in Silicon

D. Nobili, A. Carabelas,[1] G. Celotti, and S. Solmi

CNR, Istituto LAMEL, 40126 Bologna, Italy

ABSTRACT

The physical nature of the electrically inactive arsenic in silicon was investigated by annealing experiments performed on specimens doped in a wide range of concentration, up to 4×10^{21} cm^{-3}, obtained by ion implantation and laser annealing. Thermal treatments of these alloys at temperatures of 800°, 900°, and 1000°C provided solid solubility values which correspond to the carrier density in equilibrium with excess dopant. Additional confirmation that the electrically inactive arsenic is a precipitated phase was obtained by the kinetics of the annealing process. The occurrence of precipitation in an amount which is consistent with that of the electrically inactive dopant was confirmed by small angle x-ray scattering which provided also details on the size and shape of the particles. The latter are in form of thin platelets and match the structure of the silicon lattice. These results clearly contradict the models developed to account for the difference between carrier and arsenic concentration which hypothesize the formation of a high equilibrium concentration of complex point defects making the excess dopant electrically inactive.

The carrier concentration of silicon crystals doped with arsenic by thermal diffusion shows an upper limit which increases with temperature attaining values of the order of 3×10^{20} cm^{-3} (1, 2). The excess dopant is electrically inactive.

The formation of complex point defects in thermal equilibrium is the commonly accepted cause of the discrepancy between the density of carriers and that of arsenic atoms at high dopant concentration (3-7). A small dependence of the carrier density on the chemical concentration, occurring in heavily doped layers, was in fact reported, although the values determined by different authors differ markedly (4, 7).

The variety of models which have been proposed reflects the discrepancy of the experimental results. Tsai *et al.* (4) proposed the formation of a complex which becomes neutral at room temperature following the equilibrium reaction.

$$3As^+ + e^- \rightleftharpoons As_3^{++} \xrightarrow{25°C} As_3$$

On the other side, the formation of an arsenic-vacancy complex

$$2As^+ + V + 2e^- \rightleftharpoons As_2V$$

was proposed by Fair (3, 7).

The hypothesis of complex point defects in thermodynamic equilibrium is in agreement with Rutherford backscattering (RBS) and channeling results which showed that a large fraction of the excess arsenic still keeps the substitutional lattice site (2, 8). Accurate determinations put into evidence a limited displacement (0.15Å) from the substitutional position, an effect which was attributed to the formation of the neutral complex defect As_2V (8). Moreover, no observation was until now reported in literature of rings or spots in the x-ray or electron diffraction patterns of heavily doped specimens, which can be attributed to the formation of an additional crystal structure.

On the other side, thermal equilibrium experiments performed by Leitoila *et al.* (2, 9) on ion implanted and laser annealed layers, put into evidence that the electrically active concentration depends only on temperature. The above result supports the hypothesis of a two-phase equilibrium, *i.e.*, a precipitation process. Transmission electron microscopy (TEM) examinations performed on these speciments by using the bright field technique evidenced dislocation lines and loops, but could not provide clear confirmation of precipitation, although "rod shaped structures" were observed after annealing at 900°C. These authors conclude that "the values to which the active concentration relaxes at different temperatures are the true solubilities of arsenic as an electrically active, non complexed dopant." Therefore, the hypothesis of complex defects is still present in their interpretation.

Yamamoto *et al.* (10) observed precipitate-like defects, by TEM examinations of ion implanted electron beam annealed specimens subsequently heated at 700°C. At higher temperature, the occurrence of dislocation loops was noticed, which coalesce and disappear concomitant with the electrical activation of the dopant.

Recent research work on the electrically inactive phosphors in silicon provided conclusive evidence that the solid solubility corresponds to the carrier density equilibrium with excess dopant. This statement was confirmed by TEM examinations which allowed the observation of precipitated coherent particles in an amount consistent with that of the inactive phosphors (11). These findings and the strict chemical likeness of these two elements suggests that a similar behavior could be presented by arsenic.

The present work, performed on the same line of the above mentioned one (11), aims at clarifying the nature of the electrically inactive arsenic in silicon. It was performed on specimens doped by ion implantation followed by laser annealing. The hypothesis of an equilibrium between point defects leading to the formation of a complex was tested by using silicon single crystals doped in a very broad range of concentrations. Thermal treatments followed by electrical measurements and x-ray examinations provided conclusive evidence that a precipitation phenomenon takes place, and that arsenic solubility corresponds to the electrically active concentration in equilibrium with excess dopant.

Experimental

For our experiments, we used <100> oriented, CZ pulled, dislocation-free silicon slices, about 300 μm thick and mirror finished on one side. Wafers were p-type of nominally 1 Ω cm resistivity.

Implantation of crystals with As^+ ions was carried out in random direction operating at an energy of 100 keV, with doses ranging from 5×10^{15} up to 1×10^{17} cm^{-2}. The process was performed by a Lintott III acceleration that provides a doping uniformity better than 2%.

Laser annealing was performed by a 20 nsec light single pulse delivered by a Q-switched ruby oscillator with amplifier operating in multimode regime. An optical guide was used to yield a uniform light spot, 14 mm diam, with an energy density of 1.8 J/cm^2.

[1] Permanent address: Democritus University of Thrace, Faculty of Engineering of XANTHI, Greece.

Key words: electrically inactive arsenic in silicon, arsenic precipitation, small angle x-ray scattering, laser annealing.

For the determination of the electrical profile the Van der Pauw geometry was etched on the specimen's surface by a photolithographic process. Sheet resistance and Hall effect measurements were performed after anodic oxidation, in steps of 200A, and oxide stripping. To minimize measurement errors, these values were calculated averaging eight determinations obtained by inverting current, magnetic field, and interchanging current and voltage contacts. More details on the experimental apparatus used are reported elsewhere (12).

Carrier concentration profiles after laser annealing were determined for all the implanted doses. The fractional standard deviation, calculated in the plateau region of the profiles after thermal annealing (see Fig. 1-3) was less than 10%.

The equilibrium conditions of these alloys and the related kinetics were studied by heat-treating the laser-annealed wafers in the temperature range 300°-1000°C. Treatments were performed in an open-tube furnace with nitrogen atmosphere and were followed by Hall effect and resistivity measurements, using the above detailed techniques. Extraction from the furnace was rapid. Specimens were allowed to cool in an air stream, and a quartz boat of low thermal capacity was used. The laser-induced recovery of radiation damage was controlled by TEM examinations.

The structural features of the precipitates were studied by small-angle x-ray scattering (SAXS) experiments performed in a Kratky camera (13-14), equipped with a proportional counter and point-by-point intensity strip-chart recorder. The width of the main slit, defining the incident beam, was 60 μm; a sample-to-counter distance of 230 mm was employed and the scattered intensity was recorded every 50 μm of counter displacement (corresponding to 0.0125° of 2θ) from 200 to 10,000 μm (0.05°-2.50° of 2θ), with a fixed counting time of 400 sec.

X-ray beam was generated by a broad-focus (2 × 12 mm) Cu anode tube, with extra-large (ϕ 20 mm) window, especially designed for Kratky scattering camera and operated at 40 kV and 40 mA.

Specimens for small-angle scattering transmission examinations were cut from Si single crystals in rectangular pieces 10 mm wide and 30 mm long, then they were mechanically thinned and chemically polished up to thicknesses varying in the range 70-90 μm, which should result in a reduction to $1/e$ of the intensity of incident beam; in fact, the calculated value for Si and CuKα radiation is 70-75 μm, according to the different values reported in literature for the mass absorption coefficient (15, 16). The samples were mounted in the slot of the sample holder by silicone grease, to avoid any kind of mechanical stress.

To gather more information about the eventual presence of well-defined crystallographic phases, we examined the same specimens also with a Wallace-Ward cylindrical texture camera (17), using Cr Kα radiation and a glancing angle as low as 10°. In this way, the x-ray penetration is limited to about 1.5 μm, enhancing the diffraction contributed from the surface implanted layer and avoiding at the same time an excessive spread of the incident beam.

Results and Discussion

Annealing experiments.—Comparison between the implanted dose and that deduced from the corresponding electrical profiles after laser annealing, showed that all arsenic was made electrically active up to a dose of 5×10^{16} cm^{-2}, corresponding to a maximum concentration of 4×10^{21} cm^{-3}. TEM examinations showed that, up to this limit, the crystal lattice was free of observable defects.

With higher doses only a fraction of the dopant resulted electrically active, and structural defects were clearly noticed. Similar results were reported by Natsuaki *et al.* (18).

Dopant concentration profiles of our specimens, including that for the highest dose (5×10^{16} cm^{-2}) are shown in Fig. 1-3. Thermal annealing of these samples was performed to test the hypothesis of an equilibrium between point defects leading to the formation of complexes.

We report in the same figures the results after thermal treatments: in Fig. 1, the carrier profiles after 10 min at 1000°C, in Fig. 2, those after 30 min at 900°C, and in Fig. 3, those after 6 hr at 800°C.

Our determinations confirm that the electrically active concentration which is in equilibrium with the inactive dopant depends only on temperature; in fact, within the precision of the measurements, it is independent of the total dopant concentration.

The measured equilibrium values are 2.2×10^{20} cm^{-3} at 1000°C, 1.8×10^{20} cm^{-3} at 900°C, and 1.2×10^{20} cm^{-3} at 800°C. These values coincide with those previously determined on polycrystalline silicon films heavily doped by different techniques (19), and are slightly lower than those reported by Leitoila (2).

These experiments clearly contradict the hypothesis of an equilibrium leading to the formation of a complex. In fact, considering the wide range of dopant concentration which was explored, a constant equilibrium concentration of As$^+$ cannot result from a point defect reaction. Only a two-phase equilibrium, that is the formation of precipitates, is compatible with these results.

Further support to this conclusion was provided by the study of the kinetics of the process performed by isochronal and isothermal annealing of our alloys. Isochronal treatments were performed in the temperature range 300°-800°C, in steps of 50°C. After each

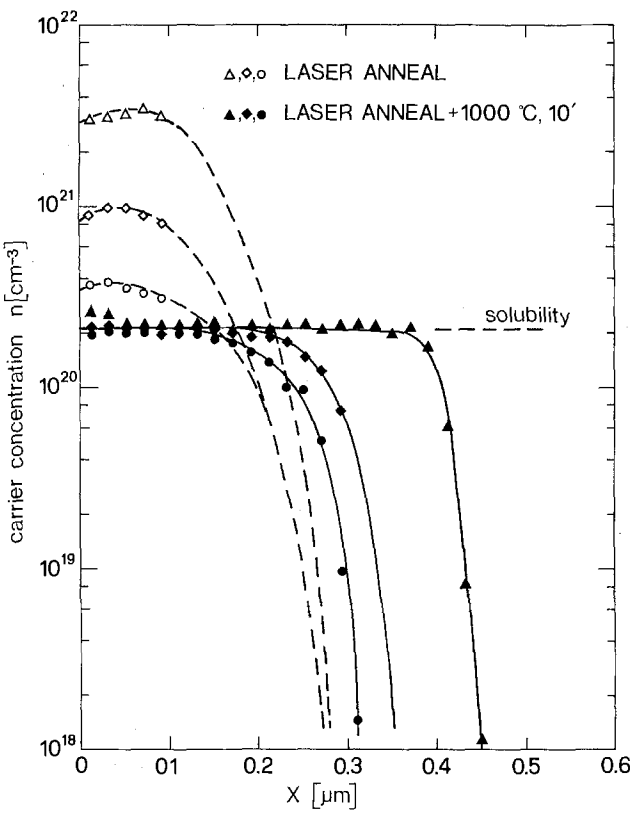

Fig. 1. Carrier density profiles of iron implanted and laser annealed specimens for three widely different As concentrations. Open symbols (△, ◇, ○) refer to the initial conditions when all dopant is electrically active, and black symbols (▲, ◆ ●) to those after equilibration (10 min at 1000°C). Maximum electrically active concentrations, in equilibrium with the inactive dopant results the same within the precision of the measurement. For sake of clarity, only the first experimental points of the laser-annealed profiles are reported.

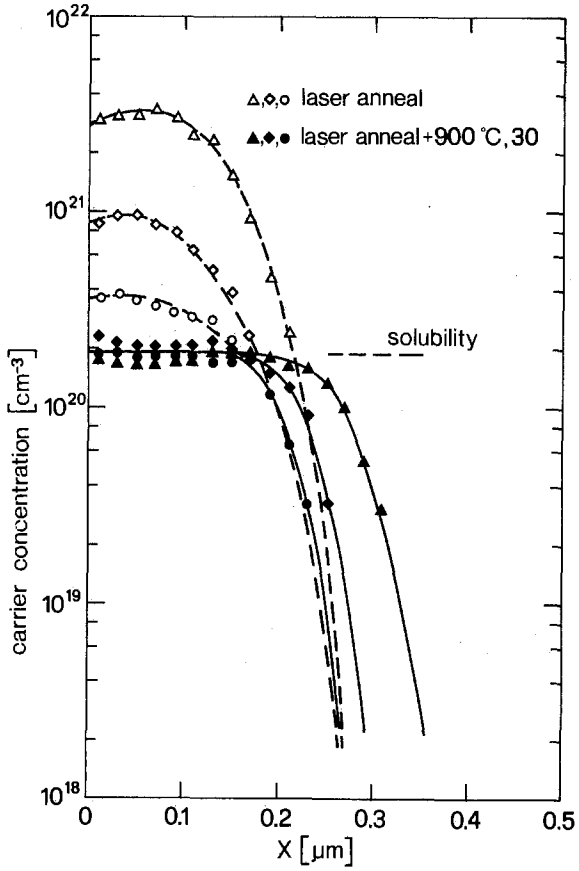

Fig. 2. Carrier density profiles in the initial conditions and after equilibration (30 min at 900°C). The notations are the same as those in Fig. 1.

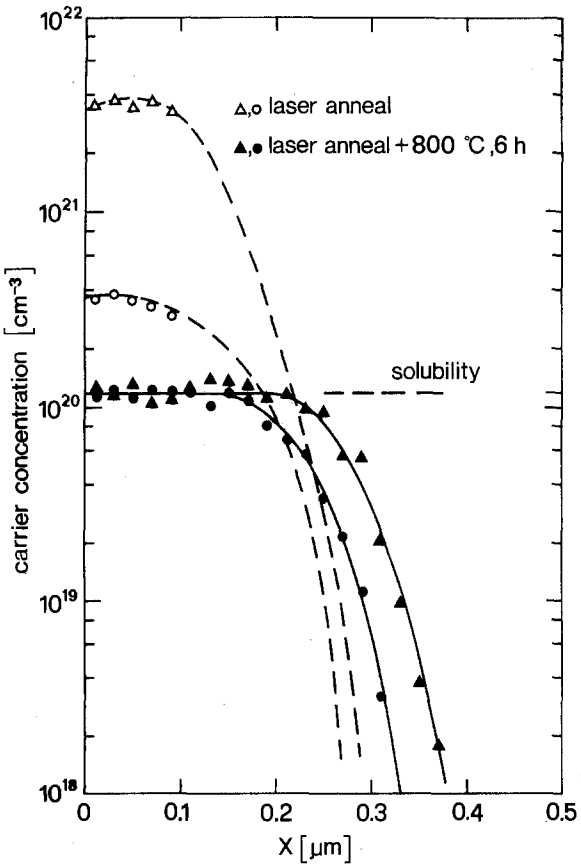

Fig. 3. Carrier density profiles in the initial conditions and after equilibration (6 hr at 800°C). The notations are the same as those in Fig. 1.

step, the carrier concentration per unit surface and the sheet resistance were determined.

We report in Fig. 4 the carrier concentration per unit surface *vs.* isochronal annealing temperature for the upper and lower dose. The trend shown in this figure, where intermediate compositions were omitted for sake of clarity, puts into evidence that the thermal stability of these alloys decreases with increasing dopant concentration.

The dilute alloy is fairly stable up to 400°C, while, at the same temperature, the heavily doped one undergoes a carrier concentration decrease of about 75%. In addition, both compositions present the reverse annealing effect, that is an increase of carrier concentration occurring at high temperatures. As is shown in Fig. 4, the occurrence of this phenomenon starts at temperatures which decrease with increasing dopant concentration.

The minima observed in the two curves depend on dopant concentration and, therefore, are not equilibrium values. As an additional confirmation of this statement, it has to be noticed that further annealing at 650°C for 30 hr of the most heavily doped specimens after completion of their cycle, gave rise to a further remarkable concentration decrease attaining the value arrowed in Fig. 4.

The isochronal annealing behavior of arsenic is, therefore, quite similar to that previously observed and discussed for phosphorus (11, 20), and is typical of a precipitation process.

Also, in this case, the precipitation and the associated phenomenon of reversion were put in clearer evidence by a step increase in temperature. Specimens that had been partially annealed at a temperature T_1 were subsequently annealed at higher temperature T_2.

As is shown in Fig. 5, where T_1 and T_2 are 650° and 750°C, respectively, increasing the temperature gives rise to a transient increase of the concentration of carriers, which subsequently decreases towards the equilibrium value. Also experiments performed between 800° and 900°C showed the occurrence of reversion. A similar behavior was presented by phosphorus (11).

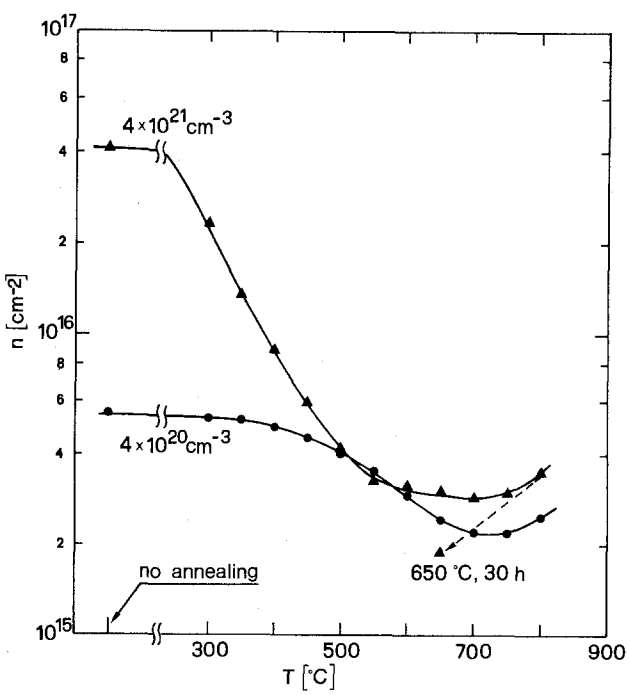

Fig. 4. Carrier density per unit surface *vs.* isochronal annealing temperature for two specimens having maximum arsenic concentrations in the profile of 4 × 10^{21} (▲) and 4 × 10^{20} (●) cm^{-3}, respectively.

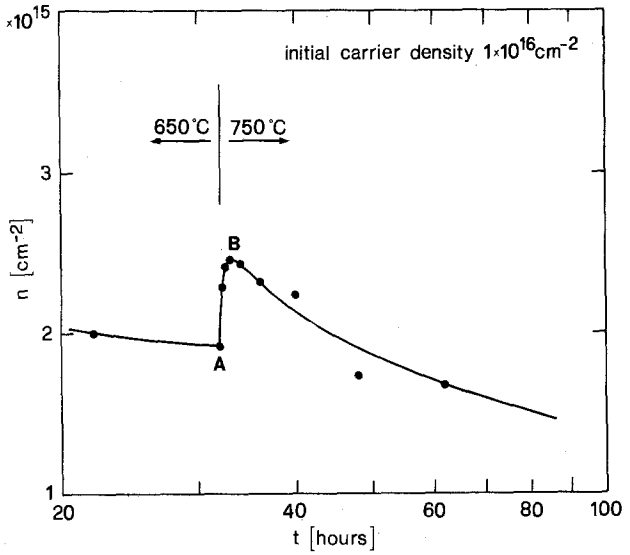

Fig. 5. Carrier density per unit surface vs. heating time in an As implanted and laser-annealed specimen (Maximum concentration 1×10^{21} cm^{-3}). Isochronal treatments were performed at 650°C up to 32h (point A) and subsequently at 750°C. Point B shows reverse annealing after 1 hr heating at the higher temperature.

As was discussed in our previous paper, only the occurrence of precipitates can account for the reversion process (11, 20). If the population consists of precipitates of different free energy, increasing the temperature makes the higher energy particles redissolve, while the remaining more stable population, still in conditions of supersaturation, gives rise to further precipitation (21, 22).

In the absence of this phenomenon, the temperature increase should, on the contrary, give rise to an increase in the annealing rate, that is to a steeper slope.

The occurrence of precipitation is compatible with the channeling results (2, 8) if the silicon arsenide precipitates are coherent, *i.e.*, they keep the lattice structure of silicon, or match it closely. In this case as a large fraction of the arsenic atoms belonging to the precipitates still occupy substitutional sites in the silicon lattice, the channeling analysis detects an amount of precipitated dopant which is unavoidably markedly less than the true one.

The observation of precipitates of this type by TEM techniques should also be hindered; a difficulty which is further increased by the similarity of the tetrahedral radius of silicon (1.17Å) with that of arsenic (1.13-1.15Å). The latter values were obtained by double crystal x-ray determinations, performed on the same ion implanted laser annealed specimens (dose 5×10^{16} cm^{-2}) (23).

On the other side, given the largely different atomic numbers, 33 and 14, respectively, of these elements, the occurrence of precipitation can be analyzed by SAXS techniques.

SAXS examinations.—By comparing the experimental SAXS curves obtained from samples implanted with As (dose 5×10^{16} cm^{-2}) and laser annealed, and from the same ones further thermally annealed 30 min at 900°C, it was found that the thermal treatment gives rise to a remarkable intensity scattered at small angles.

This effect provides clear evidence of the formation of precipitates. As is well known (24), the scattered intensity is proportional to $(\Delta\rho)^2$, with $\Delta\rho$ indicating the difference in electron density between the matrix and the precipitates.

To make one sure that other phenomena giving rise to scattering at small angles, like clustering of intrinsic defects (25), were absent or negligible, blank experiments were performed on specimens implanted with phosphorus (same dose and energy), laser annealed in the same conditions, and subsequently heat-treated in the same way at 900°C.

The choice of phosphorus was made in order to obtain a situation quite similar to that with arsenic (same annealing behavior, Fermi level, etc.) but with precipitates which cannot contribute appreciable scattered intensity because the atomic number is very near to that of silicon.

Examination of these specimens before and after the heat-treatment at 900°C did not reveal any difference in the SAXS curves. This result leaves the formation of As-rich precipitates as the only source of the observed scattered intensity.

Thus, it is justified to deduce the formation of "particles" and to work out the net observed intensity data accordingly (26, 27). In Fig. 6, the classical Guinier-plot (log I *vs.* h^2, with $h = (4\pi \sin\theta)/\lambda$) is reported. We neglected interparticle interference effects, for which no clear evidence was found; in fact, the total scattered intensity, as shown by its continuous decrease with increasing scattering angle, is proportional to that relative to a single particle. The marked deviation of the graph from linearity in the small h region, immediately indicates that we have a pronounced degree of polydispersity (*i.e.*, the particle size is far from uniform and the radius of gyration of the particles (26) is not unique).

This concave upwards scattering curve can be treated with the simple graphical breakdown of the subtraction of the successive less sloped tangents (28, 29), in such a way the particle size distribution, in terms of volume, is obtained as a set of discrete fractions. Although this admittedly is a decided compromise in the interpretation of the data, it yields results which have a physical meaning and appear useful in practice. The analysis performed on this basis is also shown in Fig. 6; the experimental curve is fully explained by three different groups of particles, whose radii of gyration $R1$, $R2$, and $R3$ can be calculated from the observed slopes p through the relation: $R = 0.4183\ \lambda \sqrt{-p}$, where λ is the x-ray wavelength.

A more rigorous determination of this particle size statistical distribution can be obtained in form of a continuous function (see Appendix A). The resulting distribution curve is reported in Fig. 7.

In the same figure, we have drawn also, in correspondence of the three different values for radius of gyration obtained from the slopes of tangents, a schematic bar-diagram representing the discrete fractions of particles of radius R in terms of numbers of particles, $u(R)$, under the hypothesis that density is in-

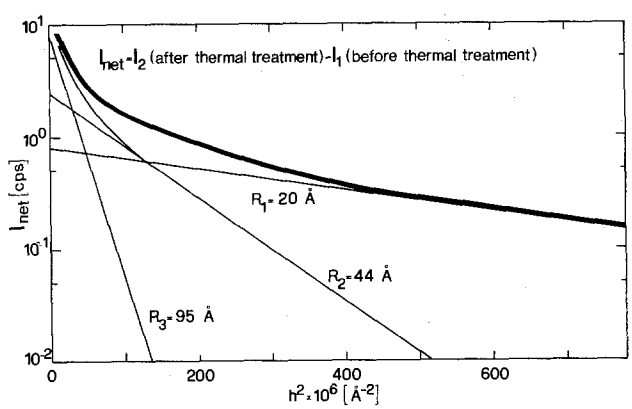

Fig. 6. Guinier-plot of the small-angle intensity produced by thermal treatment at 900°C or ion implanted and laser annealed specimen, having maximum arsenic concentration in the profile 4×10^{21} cm^{-3}. The analysis by the method of subtraction of successive less sloped tangents is also outlined with proper values for radii of gyration indicated.

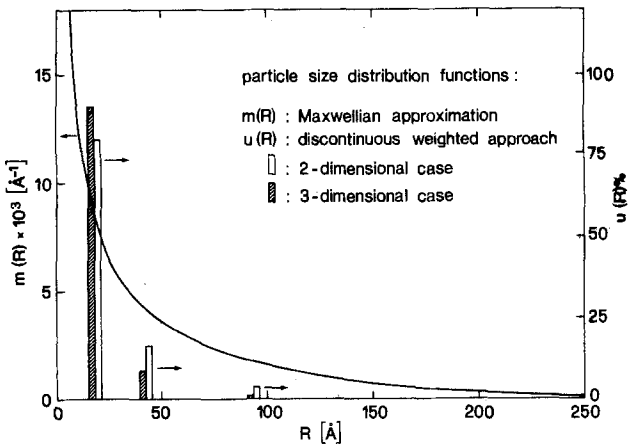

Fig. 7. Particle size statistical distributions: the curve $m(R)$ represents the Maxwellian continuous distribution, while the bars refer to the discrete numerical fractions $u(R)$ obtained from the tangents method for three- and two-dimensional approaches.

dependent of size, for the three-dimensional and two-dimensional interpretation of the Guinier-plot data. One can see that, in spite of the approximation introduced considering the particle proportions as a discrete set of discontinuous maxima, the agreement between trends of the two different distributions has to be considered rather satisfactory.

Another important conclusion that may be drawn from SAXS intensity data is the shape of particles (30); in Fig. 8, the log I *vs.* log h plot, necessary for this determination, is shown. The theoretical slopes in the h range, intermediate between those of validity of Guinier's and Porod's approximations (24), calculated for some elementary shapes, are also reported (needles represent the limiting case of one-dimensional rod-like particles, platelets for two-dimensional disk-like ones, and spheres for three-dimensional globular ones, *i.e.*, with not too different extension along three orthogonal axes in space). By comparing the experimental value with those calculated, one can see that we have nearly flat-shaped particles. The value, slightly lower than −2, means that the thickness of our platelets is not quite negligible in respect to their diameter. It must be pointed out that a single atomic layer represents a sufficient thickness to deviate significantly from the geometrical two-dimensional

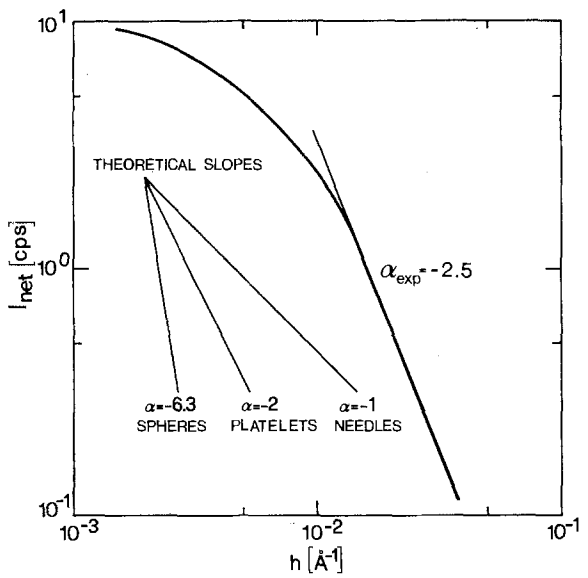

Fig. 8. Bilogarithmic plot to obtain information about particle shape; theoretical slope values for main simple limiting cases are reported for comparison.

limiting case; especially when the mean particle diameter is not too large.

The mean value of the radius of gyration, obtained for the continuous distribution is $R = 30$Å, whereas for the discontinuous ones, the most significant weighted value is $R = 27$Å (from $u(R)$) for the two-dimensional case, which better approximates the present situation. It is hardly worth of mention the fact the real radius r of the platelets (supposed of negligible thickness) is related to the radius of gyration by $r = \sqrt{2}R$. Therefore, the mean radius of the particles turns out to be ~40Å.

Moreover, under the hypothesis of a nearly equiatomic stoichiometry (SiAs) of precipitates, and of platelets with thickness corresponding to that of a single atomic layer, a quantitative estimate of the particles' volume fraction can be made employing the absolute value of the limiting ($h = 0$) intensity. By this method (see Appendix B for details), we found that $\sim 5 \times 10^{16}$ cm^{-2} of arsenic atoms are present in the precipitates, a number fairly well corresponding to the total electrically inactive arsenic concentration in the implanted layer (4.5×10^{16} cm^{-2}), as evaluated by the corresponding profiles shown in Fig. 2.

Additional experiments and remarks.—By our glacing angle x-ray experiments, no diffraction effect other than Si substrate spots was revealed, even after 24 hr exposure of the samples rotating around an axis normal to their surface. If an Si-As phase were present with its own crystallographic structure, due to the sensibility of the employed technique (usually in the range of 0.5-1 volume percent) and the high concentration of precipitated arsenic in the surface layer, we would have recorded some of its characteristic diffraction lines or spots.

These findings, even allowing for the uncertainties due to the large broadening expected on the reflections owing to the small average dimensions and to the platelet-like shape of the crystallites of the precipitated phase, suggest that the precipitates have to be essentially of coherent type, with arsenic atoms mostly occupying lattice sites of the silicon matrix. Therefore, they lead only to local variations in the silicon lattice parameter, necessarily small on account of the negligible difference in atomic size between arsenic and silicon. As was noticed previously, the coherent nature of the precipitates makes the occurrence of precipitation fully compatible with the results of channeling observations reported in literature (2, 8).

The small size of these particles, which was deduced from SAXS analysis, can account for the reversion effects evidenced in Fig. 5, as well as for those shown in Fig. 4, where the minimum in the carrier density *vs.* temperature plot is higher for the most heavily doped specimens. Increasing the supersaturation raises the nucleation frequency leading to smaller precipitates (22), an effect which was clearly noticed also in phosphorus-doped samples (11, 20). A smaller size of the precipitates corresponds to higher solubility; this is the well-known Gibbs-Thomson effect which is significant only for very small particles (22).

Accordingly, further heat-treatments, giving rise to coalescence of the precipitates, can reduce the equilibrium dopant concentration, as is shown by the value arrowed in Fig. 4. The Gibbs-Thomson effect, and an insufficient heat-treatment, can account for the slight increase of the carrier density with increasing excess dopant concentration which was reported by some author (4, 7). These findings, which are contradicted by our equilibrium values reported in Fig. 1-3, contributed markedly to originate the hypothesis of a point defect reaction.

Considering now the diffusivity of arsenic, we notice that the displacement of the profiles after heat-treatments, shown in Fig. 1-3, was much larger for the most heavily doped specimens. The larger concentra-

tion gradient should not account for this behavior because as is shown in Fig. 4, the precipitation rate increases strongly with the initial supersaturation; hence, the initial difference in the concentration gradient should vanish in time which is short, as compared to that of the thermal treatment. The larger diffusivity should, therefore, be attributed to the precipitation process. The occurrence of this phenomenon, which was in fact observed in the case of phosphorus, should be confirmed by further investigation.

Finally, we point out that the Boltzmann-Matano analysis of the diffusivity from a concentration profile must satisfy the basic requirement that the diffusion process obeys the second Fick's law, hence, it is invalid if precipitation takes place. As a consequence, the values of the diffusivity of arsenic in supersaturated solutions, based on this analysis, are incorrect.

Conclusions

This work, performed on ion implanted laser annealed silicon slices, doped with arsenic in a wide range of concentration, shows that the carrier density in equilibrium with excess dopant depends only on temperature. This finding, which is in agreement with the results reported by other authors (2, 9), leads to the conclusion that a two-phase equilibrium takes place and that the electrically active arsenic concentration corresponds to the solubility.

The formation of a precipitated phase was evidenced not only from these thermal equilibrium experiments but also from the isochronal heating behavior which is quite similar to that presented by phosphorus-doped specimens and is typical of a precipitation process. Moreover, also arsenic-doped alloys showed reversion, that is the redissolution process occurring by a step increase in temperature during the anneal of samples with a carrier density which exceeds the equilibrium value (see Fig. 4 and 5). The occurrence of this phenomenon provides clear evidence of precipitation.

These precipitates were in fact detected by SAXS' a technique which is suitable due to the markedly different atomic numbers of silicon and arsenic. These determinations provided information on the size distribution and the shape of these particles, which are in form of thin disks.

Moreover, the quantitative elaboration of SAXS data (see Appendix B), under the hypothesis that the composition of the precipitates corresponds to that of the conjugate phase SiAs, shows that the extent of precipitation is consistent with the concentration of electrically inactive dopant.

X-ray glancing angle patterns did not show lines or spots due to additional phases, and this suggests that the precipitates, or most of them, maintain the structure of the silicon lattice. Due to this feature and to the similarity of the tetrahedral radii of silicon and arsenic, only a fraction of the precipitated dopant is observable by channeling determinations. The same features hinder their observation by TEM techniques.

The hypothesis of the formation of a high concentration of complex point defects which make the excess arsenic electrically inactive, and account for the difference between dopant concentration and the carrier density, is clearly contradicted by our results. As a consequence, the diffusivity models based on data obtained by the Boltzmann-Matano analysis of the concentration profiles are also contradicted; in fact this method is invalid for any diffusion process involving precipitation.

Acknowledgments

The authors wish to thank A. Armigliato and M. Servidori for useful discussion and criticisms, and P. De Luca, E. Gabilli, A. Garulli, R. Lotti and P. Negrini for their technical assistance and cooperation. Thanks are also due to A. Ripamonti and M. Roveri of the Institute "G. Ciamician" of the University of Bologna for having made the SAXS Kratky camera available and for their skillful assistance.

Manuscript received July 12, 1982.

Any discussion of this paper will appear in a Discussion Section to be published in the December 1983 JOURNAL. All discussions for the December 1983 Discussion Section should be submitted by Aug. 1, 1983.

Publication costs of this article were assisted by CNR, Istituto LAMEL.

APPENDIX A

Determination of the Statistical Distribution of the Particles

Under the following hypotheses: (*i*) geometrical similarity of all particles, (*ii*) scattering curves of different types of particles representable by an exponential relation, and (*iii*) distribution of the radii of gyration given by a Maxwellian function; the distribution of the radii of gyration R of the particles can be represented by the following expression

$$m(R) = \frac{2}{q^{n+1}\,\Gamma\left(\frac{n+1}{2}\right)} R^n e^{-R^2/q^2}$$

where $m(R)dR$ represents the proportion of the particles whose radius of gyration is between R and $R + dR$. By means of only two parameters, q (dimensionally a length) and n (pure number), we can satisfactorily describe a wide range of distributions. The arithmetic mean of the radii of gyration is given by

$$\bar{R} = q\Gamma\left(\frac{n+2}{2}\right) \Big/ \Gamma\left(\frac{n+1}{2}\right)$$

The experimental SAXS intensity curve may be likewise expressed in terms of these parameters as follows

$$I(h) = \frac{\text{constant}}{[1 + (hq)^{2/3}]^{(n+4)/2}}$$

It can be immediately seen that the above constant corresponds to the value $I(0)$ of the limiting intensity scattered at $h = 0$ and not accessible to direct experimental evaluation. The determination of q and n is usually performed with the method proposed by Hosemann (28), which is based on the use of a curve h^2I *vs.* h: in our case we found $n = -0.75$, $q = 156.5$Å. When $n < 0$, the distribution $m(R)$ no more presents a maximum, but assumes a hyperbolic-type shape, with proportion of particles monotonically decreasing as their radius increases.

As our experimental SAXS curves present an intensity monotonically decreasing with scattering angle, the value of polydispersity has to be higher than the packing density of the particles (27).

The polydispersity, which gives the fractional standard deviation from the mean of the radii of gyration, in this Maxwellian statistical approach is approximately given by: $\sqrt{\overline{\Delta R^2}}/R \simeq 1/\sqrt{2(n+1)}$, and in our case it is found to be as high as $\sqrt{2}$. Such a value results in any case much higher than the particle packing density, (*i.e.*, the ratio between the volume occupied by particles and the total irradiated volume contributing to SAXS information), which is limited by the obvious impossibility to be > 1.

APPENDIX B

Evaluation of the Volume Fraction Occupied by the Particles

The determination of the number (or concentration) of particles in a sample, involves a simple formula only under rather restrictive hypotheses (26); in the cases of identical and sufficiently separated particles, the equation for the limiting intensity is

$$I(0) = I_e(0) N n^2$$

where I_e, the intensity scattered by one electron, can be calculated as a function of the incident intensity I_o by means of Thomson's equation ($I_e(0) = 7.9 \times 10^{-26}\, I_o D^{-2}$, D being the distance in cm between sample and

receiver); N is the total number of particles in the irradiated volume and n the number of electrons per particle. The absolute primary energy I_o can be determined with the help of a calibrated Lupolen sample (31), supplied as accessory of the Kratky camera.

If we want to apply such an equation, under the same hypotheses, to nonidentical particles, an approximate value (neglecting again any interference effect) can be obtained introducing necessary modifications in the above relation

$$I(0) = I_e(0)\bar{N}\sum_k f_k\overline{n_k^2}$$

with f_k indicating the proper fractions of different groups of particles. $I(0)$ cannot be determined directly by experiment, but if the curve log $I(h^2)$ has a linear portion at low angles it can be easily obtained by extrapolation. Furthermore, if the shape of the particles is known, the mean volume of the particles, and, thus, n_k (supposing a particular stoichiometry), can be determined from the radii of gyration: in such a case the x-ray measurement gives the value of $\bar{N}$. In this way, the number of particles (or their concentration) in the irradiated volume of a sample can be estimated.

In our practical case, we obtain $I_o = 2.6 \times 10^7$ counts/sec, and consequently, for $D = 23$ cm, $I_e(0) = 3.9 \times 10^{-21}$ counts/sec. It is easy to evaluate (by approximating the particles as thin disks of radius $r = \sqrt{2}R$ and thickness $t = 2.35$Å, corresponding to one atomic layer) $\sum_k f_k\overline{n_k^2} = 2.0 \times 10^9$, and V the average volume of the particle, which turns out to be 2.0×10^{-20} cm^3. From the Guinier plot, we can extrapolate $I(0) = 10$ counts/sec. Therefore, we have: $N = 1.3 \times 10^{12}$, and the total average volume occupied by particles results: $V_{tot} = NV = 2.6 \times 10^{-8}$ cm^3. The sample irradiated area contributing to recorded scattering in our experiments is $S_{irr} = 1.2 \times 10^{-2}$ cm^2, corresponding to the beam dimensions projected on the sample, so it follows immediately $V_{tot}/S_{irr} = 2.2 \times 10^{-6}$ cm^3 of particles for each cm^2 of sample irradiated surface. Such a specific volume occupied by particles, without any assumption about their distribution in depth, but maintaining the same atomic density of the Si matrix in the coherent precipitates, corresponds to 1.1×10^{17} atoms/cm^2. Since we have supposed a nearly equiatomic stoichiometry and Si and As atoms are very similar in size, half of this value ($\sim 5 \times 10^{16}$ atoms/cm^2) has to be considered as pertaining to arsenic atoms.

Allowing for the fact that the precipitates can really be found only within a surface layer about 2500Å thick, we obtain: $V_{irr} = 3.0 \times 10^{-7}$ cm^3 for the irradiated volume, which corresponds to a particle volume fraction (in the layer interested by As implantation) of about 9%.

REFERENCES

1. R. B. Fair and J. C. C. Tsai, *This Journal*, **122**, 1689 (1975).
2. A. Lietoila, J. F. Gibbons, and T. W. Sigmon, *Appl. Phys. Lett.*, **36**, 765 (1980).
3. R. B. Fair and G. R. Weber, *J. Appl. Phys.*, **44**, 273 (1973).
4. M. Y. Tsai, F. F. Morehead, J. E. E. Baglin, and A. E. Michel, *ibid.*, **51**, 3230 (1980).
5. J. Murota, K. Arai, K. Kobayashi, and K. Kudo, *ibid.*, **50**, 804 (1979).
6. S. M. Hu, in "Atomic Diffusion in Semiconductor," D. Shaw, Editor, Plenum Press, London (1972).
7. R. B. Fair, in "Semiconductor Silicon 1981," H. R. Huff, R. J. Kriegler, and Y. Takeishi, Editors, p. 963, The Electrochemical Society Softbound Proceedings Series, Pennington, NJ (1981).
8. W. K. Chu and B. J. Masters, A.I.P. Conference Proc. 50, p. 305, American Institute of Physics, New York (1978).
9. A. Leitoila, J. F. Gibbons, T. G. Magee, I. Peng, and J. D. Hong, *Appl. Phys. Lett.*, **35**, 532 (1979).
10. Y. Yamamoto, T. Inada, T. Sugiyama, and S. Tamura, *J. Appl. Phys.*, **53**, 276 (1982).
11. D. Nobili, A. Armigliato, M. Finetti, and S. Solmi, *ibid.*, **53**, 1484 (1982).
12. F. Moust, P. Ostoja, and L. Passari, *ibid.*, **45**, 4576 (1974).
13. O. Kratky, *Makromol Chem.*, **35A**, 12 (1959).
14. O. Kratky, in "Small Angle X-ray Scattering," H. Brumberger, Editor, p. 63, Gordon & Breach, New York (1967).
15. J. L. Lawrence, *Acta Crystallogr. Section A*, **33**, 343 (1977).
16. G. Hildebrandt, *ibid.*, **35**, 696 (1979).
17. C. A. Wallace and R. C. C. Ward, *J. Appl. Crystallogr.*, **8**, 255 (1975); *ibid.*, **8**, 545 (1975).
18. N. Natsuaki, M. Tamura, and T. Takuyama, *J. Appl. Phys.*, **51**, 3373 (1980).
19. S. Solmi, M. Severi, R. Angelucci, L. Baldi, and R. Bilenchi, *This Journal*, In press.
20. M. Finetti, P. Negrini, S. Solmi, and D. Nobili, *ibid.*, **128**, 1313 (1981).
21. A. Kelly and R. B. Nicholson, *Prog. Mater. Sci.*, **10**, 149 (1963).
22. J. W. Christian, "The Theory of Transformations in Metals and Alloys," Pergamon Press, New York (1975).
23. M. Servidori, Private communication.
24. V. Gerold, in "Small-angle X-ray Scattering," H. Brumberger, Editor, p. 277, Gordon & Breach, New York (1967).
25. V. Gerold and G. Kostorz, *J. Appl. Crystallogr.*, **11**, 376 (1978).
26. A. Guinier and G. Fournet, "Small-angle Scattering of X-ray," John Wiley and Sons, New York (1955).
27. A. Guinier, "Théorie et Technique de la Radiocristallographie," p. 637, Dunod, Paris (1964).
28. R. Hosemann and S. N. Bagchi, "Direct Analysis of Diffraction by Matter," North-Holland, Amsterdam (1962).
29. M. H. Jellinek, E. Solomon, and I. Fankuchen, *Ind. Eng. Chem. (Anal. Ed.)*, **18**, 172 (1946).
30. J. C. Grosskreutz, in "Handbook of X-rays," E. F. Kaelble, Editor, p. 16-1, McGraw Hill, New York (1967).
31. O. Kratky, I. Pilz, and P. J. Schmitz, *J. Colloid Interface Sci.*, **21**, 24 (1966).

Electrical Properties of Post-annealed Thin SiO_2 Films

Simon S. Cohen

General Electric Company, Corporate Research and Development, Schenectady, New York 12301

ABSTRACT

Very thin films of silicon dioxide grown in a conventional dry oxidation process often suffer from poor electrical quality due to the presence of various defects. A low dielectric breakdown is, in particular, detrimental to the operation of many electronic devices. We have attempted to improve this situation by modifying the dry oxidation process. We show that oxides grown in oxygen ambient and under atmospheric pressure, which are postannealed for a long period of time in an inert atmosphere and then reoxidized for a short time, have considerably improved values of both the magnitude and distribution of the electric field at the dielectric breakdown. Very few low-field dielectric breakdown events are encountered and the breakdown field histogram assumes a very narrow shape.

Films of silicon dioxide grown from single crystal silicon have been extensively used in metal oxide semiconductor (MOS) device technology, primarily due to their excellent electrical insulating properties. However, in such films, localized conducting channels which are due to either the presence of various defects (1) or local crystalline regions in the amorphous oxide (2), can cause failure in such devices. The density of oxide defects for films grown under identical conditions may be higher in thinner films than in thicker ones. Hence, one may expect poorer electrical performance in thinner layers of silicon dioxide (3). In particular, a high defect density may, under certain operating conditions, give rise to a time dependent breakdown phenomenon resulting in the lowering of the median breakdown field. It has been known for some time (4) that for oxides $\gtrsim$ 50 nm in thickness, the median of the dielectric breakdown field increases with the thickness. However, recently, higher breakdown fields were reported for thinner oxides that were prepared under special conditions (5). Thus, it seems that the method of preparation as well as the thickness is important in determining the electrical properties of an oxide film.

The study of failure-causing mechanisms in silicon dioxide films has proceeded through the examination of breakdown phenomena (4, 6) and conduction measurements (7). Hot electron injection into the oxide layer (8) and sodium contamination (3) were cited as main reasons for the oxide failure. Sodium contamination, in particular, is believed to cause lowering of the barrier height at the silicon-silicon dioxide interface (8, 9) which increases electron injection into the film and results in a time-dependent breakdown under continued electric field stress conditions. Conduction measurements (7, 10) have shown that this is limited by Fowler-Nordheim tunneling into the oxide from either the silicon or metal electrode in an MOS capacitor structure. The applied electric field influences the tunneling process as does the presence of a positive charge within the oxide. This field effect may be enhanced by the presence of hillocks, edge and screw dislocations, surface fractures, and other structural and geometrical defects (11, 12) at the interface.

In the present study we have attempted to eliminate the failure-causing defects that develop in thin oxide films during the oxidation step by performing a long-time postoxidation annealing in an inert atmosphere. Short postannealing treatments have become an accepted practice for decreasing the value of the fixed charge in the oxide layer (13). The new feature of our study is that long-time postannealing causes the breakdown field to increase considerably, and the number of low-field breakdowns to decrease. This long-time postannealing step was performed in N_2 and Ar ambients. At the anneal temperature of 900°C we were unable to detect any effect due to the annealing atmosphere. This situation is different than that reported by Vromen (14), who observed serious degradation in the electrical (dielectric breakdown) properties when oxides were annealed in N_2 at elevated temperatures. No such effect took place when the annealing treatment was performed in Ar. In Ref. (14) the annealing was done at 1050°C. At this temperature N_2 is known to react with silicon at the silicon-silicon dioxide interface (15). To avoid this nitridation reaction we performed all oxidations and anneals at 900°C. This is also compatible with the lower temperature treatments required in very large scale integration technology.

Experimental

The oxidation experiments were all carried out at 900°C, using Monsanto p-type, (100) orientation, 4-6 Ωcm, 2 in. silicon wafers. All wafers were chemically cleaned prior to the oxidation step. Oxygen was passed through a cold trap (a mixture of alcohol and dry ice) at a rate of 2 liters/min. The purpose for this cold trap is to ensure the removal of any water molecules that may otherwise be carried into the furnace with one of the gases used. A small amount of water molecules is, nevertheless, known to be present during the oxidation step. As discussed by Irene (16), the oxygen that is supplied from boil-off of a liquid contains trace amounts of methane. In our O_2 supply system this has been measured to be ~10 parts per million (ppm). At the oxidation temperature used, the methane combusts to form H_2O and CO_2. The H_2O molecules may assist in forming traps that could effect the dielectric properties of the thin oxide (16, 17). We shall return to this point when we come to discuss our results. When the oxidation step was completed, 1 μm of pure Al was evaporated on the sample and patterned with 0.051 cm diam dots so as to form the metal electrode. Next, back-side oxide was etched and 0.5 μm of Al was evaporated on the back of the wafers to ensure a good contact. The wafers were then annealed in a hydrogen atmosphere at 450°C for 60 min.

Some wafers were postannealed in nitrogen at the growing temperature, while other wafers were postannealed in an argon ambient. When the oxidation step was completed, the wafers were left in the furnace at the oxidation temperature for the postannealing step, which lasted in some cases up to 3 hr, and then removed in a conventional manner. Thermal stress effects that are due to a sudden change in temperature such as that experienced by the silicon wafer when pulled out of the furnace, may result in a lower oxide quality. To study this effect, we have slowly cooled down the oxidation furnace to room temperature in one particular experiment. In this experiment the postanneal cool-down step lasted about 10 hr.

Prior to metal deposition on the samples, the oxide thickness throughout the wafer's area was measured on a Rudolph Research AutoEl Ellipsometer. The repeatability of the measurements was better than ±2Å and was frequently checked against a standard sample. Only those wafers whose oxide films were essen-

tially uniform were selected for further processing. Recorded variations in thickness in those chosen were less than ±3%. Breakdown voltage measurements were performed using a microcomputer-controlled semiconductor wafer test station. A limiting current of 1 μA was taken as a definition for a total dielectric breakdown. High frequency (10^6 Hz) C-V measurements were also made.

Results and Discussion

We surmised that the postannealing treatment, if performed at not too high a temperature, would reduce some thermal stress effects and other defects by allowing thermal relaxation to take place. Such defects may be responsible for the formation of conduction channels in the oxide film. The uniform and homogeneous oxide film that may thus be obtained would have fewer pinholes and other degrading structures.

Since a too-fast pull out step (from the furnace) may increase the defect density, it was decided to first perform a slow cool-down experiment. The silicon wafers that were chemically cleaned were first oxidized for 32 min at 900°C. Following the oxidation, nitrogen was introduced to the system, and the furnace heaters were shut down. The wafers were left in this condition until the furnace reached room temperature, which took roughly 10 hr. The thickness of the thermally grown oxide films were found to be ~14.5 nm.

In Fig. 1, a histogram depicting the number of breakdown events *vs.* the applied field is presented. A total of 360 breakdown events were recorded from five identically treated 2 in. wafers. We note the remarkably high breakdown fields achieved by this postannealing process. The value of the median field is 17 mV/cm, as compared with the 7.8 mV/cm value obtained in a control experiment (Table I) involving only the conventional 30 min postanneal in N_2. In a similar experiment to our control, Irene (16) obtained a value of 9 mV/cm with broad tails in both directions. An interesting feature of the results shown in Fig. 1 is the narrow distribution of the breakdown fields, and the absence of any low field breakdowns. It thus seems that the combination of postannealing and a slow cooling may result in high quality oxides that are more homogeneous and presumably of low porosity.

High frequency (1 MHz) capacitance-voltage measurements have been made on some of these samples. Figure 2 depicts a typical C-V curve obtained from these MOS capacitors. A hysteresis is evident. This hysteresis must be due to the postannealing process. It could be due to a thin oxynitride (SiO_xN_y) layer in the vicinity of the interface that may have been created during the prolonged treatment in nitrogen. However, a temperature of 900°C is too low for a reaction of N_2 with either Si or SiO_2. The hysteresis in the C-V curve could also be explained by the formation of a thin layer of SiO at the interface. This may result from the reduction of SiO_2 by Si during the prolonged annealing at the elevated temperature and in the absence of oxygen in the ambient atmosphere. A very thin layer of oxygen-deficient oxide (SiO_x; $x < 2$) is known to always exist at the Si-SiO_2 interface. Under the present experimental conditions, such a layer would probably increase in thickness and thus cause its effect on the electrical properties of the insulator to become more visible. The thickness of this layer, however, is not sufficiently high to enable its characterization by ellipsometry.

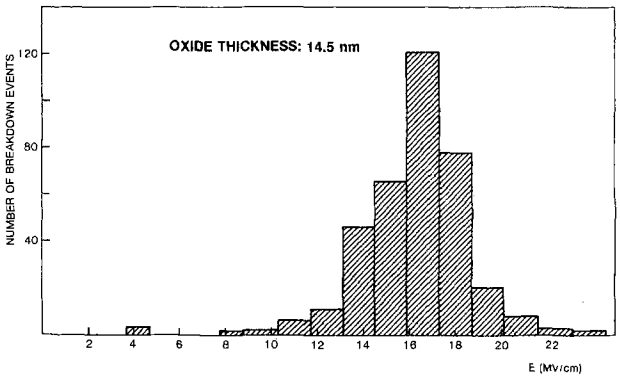

Fig. 1. A plot of the number of dielectric breakdown events *vs.* the applied field for thin oxides that were postannealed in nitrogen ambient and slowly cooled down to room temperature.

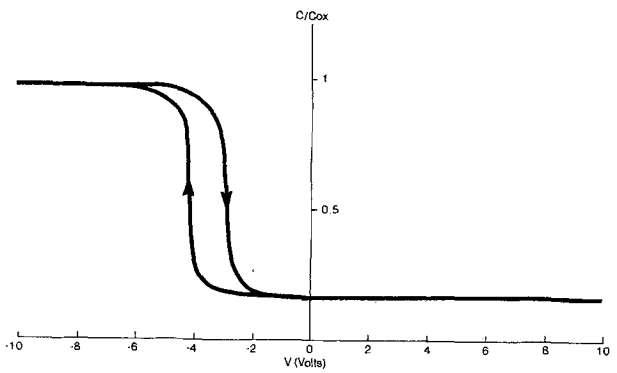

Fig. 2. High frequency C-V plot of MOS capacitors that were fabricated utilizing the thin oxides mentioned in Fig. 1. Note the appearance of a broad hysteresis and the large shift in the flatband voltage, both indicative of the presence of charges at the interface.

The effect of postannealing on the electrical properties of thin oxides without slow cooling was studied in several experiments. Both nitrogen and argon gases were used for the postannealing step. First, a control experiment was performed. In this study the oxidation was done as in all other experiments but the postannealing was limited to 30 min. The results of the dielectric breakdown measurements are shown in Fig. 3. A C-V measurement on the control samples showed that no hysteresis exists. From these measurements we have also determined the level of the fixed positive charge to be ~5 × 10^{10} charges/cm^2. In a typical long-time annealing experiment, nitrogen annealing was applied for 3 hr at the oxide growing temperature of 900°C. The histogram in Fig. 4(a) shows the number of breakdowns encountered as a function of the applied field. The results of this experiment are improved electric field distribution for the dielectric breakdown events, a higher median field compared with that obtained in a conventional process, and very

Table I. Results of dielectric breakdown and C-V measurements on 2060 MOS capacitors fabricated in seven different experiments

Experiment No.	Oxidation time (min)	N_2 anneal time (min)	Reoxidation time (min)	Average oxide thickness (nm)	Average breakdown field (10^6 V/cm)	Standard deviation (10^6 V/cm)	% Breakdown below 4 × 10^6 V/cm	Hysteresis in C-V?	No. of capacitors tested
1	32	~600 (cool down)	—	14.5	17.0	2.00	0.9	Yes	360
2	40	—	—	17.5	8.0	2.30	10.0	No	300
3	40	30	—	17.5	7.8	2.10	11.0	No	300
4	40	180	—	16.5	11.4	1.20	0.5	Yes	200
5	40	180	10	19.5	11.5	0.92	0.0	No	300
6	40	90	10	19.0	9.4	0.90	0.0	No	200
7	70	180	10	24.0	10.1	1.50	0.0	No	400

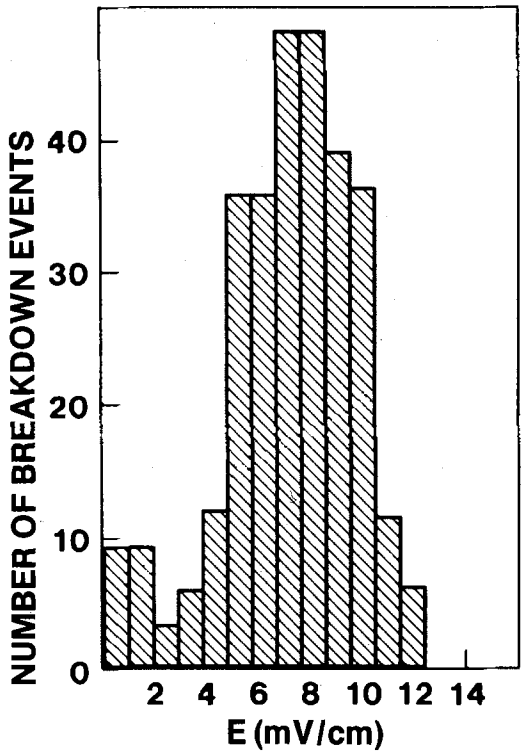

Fig. 3. The number of dielectric breakdown events *vs.* the applied field for control samples that were postannealed in N_2 for 30 min. The oxide thickness is 17.5 nm.

few low-field breakdowns. In particular, the distribution becomes extremely narrow, indicating an even more homogeneous oxide layer than in the previous case. The median field value is roughly 12 mV/cm which is lower than that recorded in the previous case. Very few low-field breakdowns (at 1-3 mV/cm) that are believed to be due to small crystalline regions in the amorphous oxide (2) were recorded. Similar dielectric breakdown results to these were recently reported for thin oxides that were grown under very low pressure (0.25-1.0 Torr) conditions, with possibly some unintentional postannealing in nitrogen (5). In the measurements reported in Ref. (5) the limiting current was set to be ≥ 10 μA. The oxidation time was much longer than used in the present study in achieving the same oxide thickness. As was the case in the slow cool-down experiment, we have again found hysteresis in the *C-V* plot. Figure 4(b) shows the form of the hysteresis. It is of type b in the terminology of Ref. (18) which indicates the existence of charge trapping sites in the oxide or at the interface.

Comparable breakdown characteristics were previously obtained by Irene (16) for H_2O grown thin oxides that were either not annealed or annealed for a long time in an argon ambient. Attempts to do even a short-time N_2 anneal (30 min) to this H_2O grown thin oxide resulted in a considerable deterioration of the breakdown properties. This situation is very similar to that reported by Vromen (14) for the dry oxidation process which, in some cases, included 2% HCl in the ambient. In both studies, the possibility of an N_2 reaction with the substrate is more likely owing to the higher oxidation-anneal temperatures, and in the study of Ref. (16) also possibly owing to the presence of reactive chemical species (such as OH radicals) at the interface. As noted earlier, traces of water molecules are also present in our oxidizing ambient. We do not believe, however, that the small amounts of H_2O molecules involved in our experiment have affected the electrical properties of the thin oxides to any great extent. This is based on the fact that, unlike in other reported cases, we have not been able to record any difference between N_2 and Ar as ambients in our long-time postannealing treatments. Further,

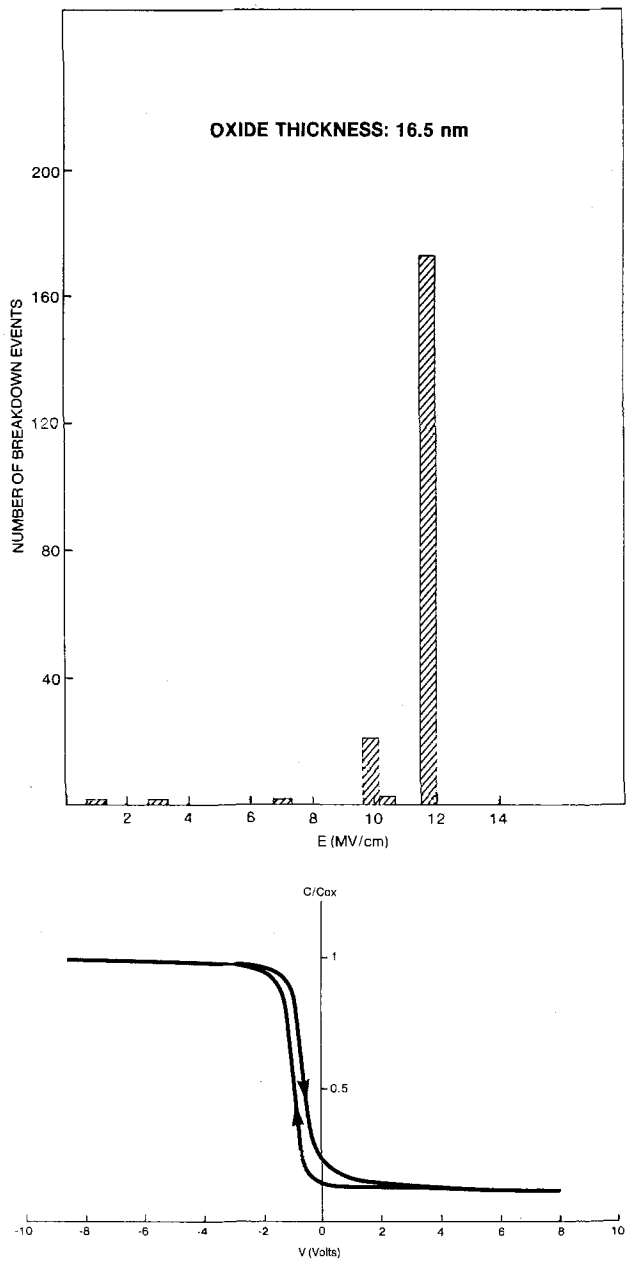

Fig. 4. Results of dielectric breakdown (a, top) and *C-V* (b, bottom) measurements related to thin oxides that were postannealed in nitrogen for 3 hr at the oxide growing temperature. In case b a hysteresis is seen again. This, however, is not as broad as was the case in Fig. 2, and the flatband voltage is shifted only slightly.

no detrimental effects could be associated with the use of N_2. In fact, the long-time annealing in these ambients resulted in improved breakdown characteristics as compared with those of the control case (*cf.* Table I). Thus it seems that the effect owing to the long-time postannealing treatment is additional to any other effect observed previously, such as may be due to H_2O generated trapping sites.

As already mentioned, argon was used in similar experiments to provide the ambient atmosphere during the postannealing steps. The electrical properties of the resulting oxide were very much the same as those reported above using nitrogen. We have also attempted to use oxygen itself for the postannealing step. This was done by lowering the furnace temperature from 900° to 600°C, and holding the wafers there for several hours. The dielectric breakdown characteristics obtained in this experiment were very unsatisfactory, being no better than those usually recorded in conventionally grown oxides. No hysteresis in the C-V plot appeared in this case. This last result seems to sup-

port the hypothesis of the SiO formation during the long-time postanneal in an inert atmosphere, since the availability of oxygen in this last experiment would prevent any reduction of the silicon dioxide at the interface.

Similar results to those presented in Fig. 4(a) and 4(b) were also obtained in several other experiments in which the postannealing time lasted only 90 min. In this case the median breakdown field tends to fall at a slightly lower value (see Table I). Other postanneal times employed were those of 60 and 40 min. In very few cases we did get good breakdown characteristics even for the 40 min postanneal case, but these seem to be the exception while for annealing times of $\geq$90 min the improved characteristics are the rule.

The postanneal process has proved to result in better quality oxides in the sense that their breakdown characteristics were superior to those usually obtained. This, however, was accompanied by an unusual and unwanted C-V behavior. Since the usual C-V characteristics were thought to be due to enhanced surface states which are possibly due to an SiO intermediate layer, we have attempted to cure this situation by applying a short-time reoxidation step immediately following the long-time postanneal. In a typical experiment the reoxidation step lasted 10 min, otherwise the experiment was identical to that described in Fig. 4(a) and 4(b). We found that, while there was no change in the breakdown characteristics, the C-V behavior returned to normal. This result seems to further establish the hypothesis on the SiO formation during the anneal step. These experiments show that a long-time

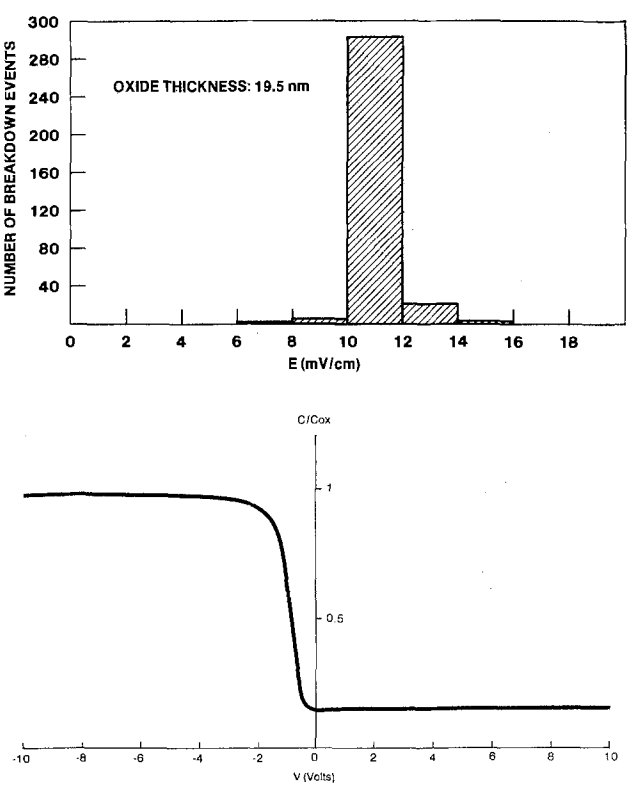

Fig. 5. Results of an experiment similar to that described by Fig. 4(a) and 4(b) except for the additional reoxidation step for 10 min following the long-time postanneal step. (a) Top, (b) bottom.

postannealing treatment of a dry oxide followed by a short-time reoxidation results in highly desired electrical properties, as summarized in Fig. 5(a) and 5(b). Finally, Table I summarizes the results of several other experiments which clearly show the advantage of the proposed oxidation sequence over the regular process in a dry oxidation process. In all, over 2000 capacitors were tested in the present set of experiments.

In summary, a simple process amenable for the fabrication of high quality thin oxides utilizing dry oxidation conditions has been described. The temperature of 900°C has been used throughout the present study. The process essentials are: (*i*) oxidation in dry O_2 atmosphere at 900°C, (*ii*) long-time postannealing in an inert atmosphere to reduce the effects of pinhole and conduction-causing defects, and (*iii*) reoxidation for a short length of time to remove charges built up in the vicinity of the interface during the postannealing treatment. These charges are believed to be due to the presence of a thin SiO layer, which may be formed as a result of the reduction of SiO_2 by Si in the absence of oxygen.

Acknowledgments

Discussions with Dr. D. M. Brown and Dr. M. Garfinkel are gratefully acknowledged. The author is indebted to Dr. H. G. Parks and Dr. K. G. Vosburgh for reading the manuscript and to Mr. G. Gildenblat for his assistance with the C-V measurements.

Manuscript submitted Feb. 22, 1982; revised manuscript received Sept. 27, 1982.

Any discussion of this paper will appear in a Discussion Section to be published in the December 1983 JOURNAL. All discussions for the December 1983 Discussion Section should be submitted by Aug. 1, 1983.

Publication costs of this article were assisted by the General Electric Company.

REFERENCES

1. F. J. Alinger, *J. Mater. Sci.*, **1**, 1 (1966).
2. C. Fritzsche, *Z. Agnew. Phys.*, **24**, 48 (1967).
3. N. J. Chou and J. M. Eldridge, *This Journal*, **117**, 1287 (1970).
4. N. Klein, *IEEE Trans. Electron. Dev.*, **ed-13**, 281 (1966).
5. A. C. Adams, T. E. Smith, and C. C. Chang, *This Journal*, **127**, 1787 (1980).
6. N. Klein, *IEEE Trans. Electron. Dev.*, **ed-13**, 788 (1966).
7. M. Lanzlinger and E. H. Snow, *J. Appl. Phys.*, **40**, 278 (1969).
8. T. H. Di Stephano, *Appl. Phys. Lett.*, **19**, 280 (1971).
9. S. I. Raider, *ibid.*, **23**, 34 (1973).
10. C. M. Osburn and E. J. Weitzmann, *This Journal*, **119**, 603 (1972).
11. A. K. Zakzouk, R. Stuart, and W. Eccleston, *ibid.*, **123**, 1551 (1976).
12. R. M. Anderson and D. R. Kerr, *J. Appl. Phys.*, **48**, 4834 (1977).
13. B. E. Deal, M. Sklar, A. S. Grove, and E. H. Snow, *This Journal*, **114**, 266 (1967).
14. B. H. Vromen, *Appl. Phys. Lett.*, **27**, 152 (1975).
15. S. I. Raider, R. A. Gdula, and J. R. Petrak, *Appl. Phys. Lett.*, **27**, 150 (1975).
16. E. A. Irene, *This Journal*, **125**, 1708 (1978).
17. D. R. Young, E. A. Irene, D. J. DiMaria, and R. F. Keersmaecker, *J. Appl. Phys.*, **50**, 6366 (1979).
18. P. V. Gray, *Proceedings, IEEE*, **57**, 1543 (1969).

The Effect of Implantation of Phosphorus into Sputtered $MoSi_2$ Thin Films

T. P. Chow,* C. S. Grant,* W. Katz, G. Gildenblat, and R. F. Reihl

General Electric Corporation Research and Development, Schenectady, New York 12301

ABSTRACT

The effect of phosphorus implantation into d-c magnetron sputtered $MoSi_2$ thin films is studied. The structural, compositional, and electrical properties are examined with x-ray diffraction, secondary ion mass spectrometry (SIMS), sheet resistance, and MOS measurements. A higher hexagonal to tetragonal $MoSi_2$ phase transition temperature is observed for implanted films than for unimplanted ones. At high fluence (5×10^{16} ions/cm^2), MoP is detected, with a significant increase in sheet resistance. Isothermal and isochronal annealing indicates a minimum temperature of 950°C, and a maximum fluence of 2×10^{16} ions/cm^2 can be used. Comparative *C-V* measurements show similar MOS characteristics between unimplanted and implanted films.

In the course of development of a refractory and highly conductive interconnection system for very-large-scale-integrated (VLSI) circuits, several refractory metal silicides, such as $MoSi_2$(1-5), WSi_2 (6-9), and $TaSi_2$ (10, 11), are under study as an alternative to the widely used doped polycrystalline silicon (poly-Si). These metal silicides, unlike the metals, have resistance to high temperature oxidation and to most chemicals routinely encountered during device fabrication.

Since the gate metal is often used as ion implantation mask during the source/drain doping in a self-aligned process, the effect of implantation of various group III and V ions, phosphorus, arsenic, and boron, on the properties of silicide thin films needs to be studied. Also, recently, it has been reported (12, 13) that doping $MoSi_2$ films with phosphorus can help stabilize silicide-gate threshold voltage and form low resistant and reliable contacts between silicide and silicon substrates. In that study, doped silicide films were deposited by using an Mo/Si target in a phosphine/argon atmosphere. In this paper, the effect of phosphorus implantation on the structural, compositional, and electrical characteristics of sputtered molybdenum disilicide thin films is investigated. Also, its effect on the flatband voltage and threshold stability of silicide-gate MOS capacitors is studied.

Experimental Procedure

Molybdenum disilicide films, nominally 3000Å thick, were deposited onto oxidized silicon substrates. The sputtering was done in an MRC 603 system using d-c magnetron from an alloy target of stoichiometric proportion. The parameters used were 2 kW of power and 3μ of argon pressure. Then, phosphorus was implanted into the silicide films with a dose ranging from 10^{15} and 5×10^{16} ions/cm^2. The implantation energy was calculated using an interpolation program based on Brice (14). Silicon and molybdenum were used as interpolating points. The density of $MoSi_2$ was assumed to be 5.7 g/cm^3, which was measured on sputtered thin films (15) and was less than the values of 5.9-6.3 g/cm^3 reported for bulk silicide (16). The projected range and straggle, R_p and ΔR_p, were calculated for boron (B^{11}), phosphorus (P^{31}), arsenic (As^{75}), and antimony (Sb^{121}), using their range data in Si and Mo given by Smith (17). These are shown in Fig. 1 and 2, respectively, up to 500 keV. The corresponding values in silicon are also shown. Except when noted, the energy used was 140 keV throughout this experiment. Unimplanted samples were also included for comparison. Subsequently, a silicon dioxide (silox) layer was deposited at 350°C on top of $MoSi_2$ in order to prevent outdiffusion of phosphorus ions during the high temperature annealing steps. Also, it protects the silicide from oxidation by any trace of oxygen in the annealing ambient. The wafers were annealed in nitrogen between 900°-1000°C for times up to 1 hr. The oxide layer was later removed with buffered HF. Sheet resistance was measured using a four-point probe before and after implantation as well as after annealing and removal of the oxide cap.

MOS capacitors were made on (100), n-type, phosphorus-doped wafers. Various thicknesses (<2000Å) of oxide were grown at 1000°C in dry oxygen. The 3000Å thick silicide films were then sputtered. Half of the samples were implanted with phosphorus at 5×10^{15} ions/cm^2 and 50 keV while the rest were not implanted. The silicide films were then patterned into 20 mil diam dots with photoresist and etched in a planar plasma etcher with NF_3 (18, 19). A 5000Å thick oxide layer was then deposited in a low pressure system and subsequently the samples were annealed at 900°C for 1 hr. Another patterning step defined the contact holes and buffered HF was used to etch

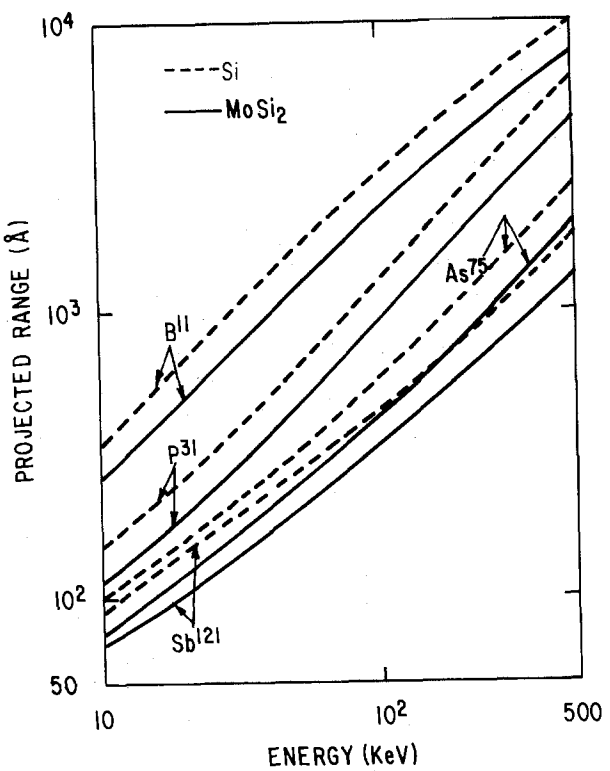

Fig. 1. Calculated projected range of B^{11}, P^{31}, As^{75}, and Sb^{121} in silicon and $MoSi_2$.

* Electrochemical Society Active Member.
[1] Summer student from Yale University, New Haven, Connecticut.
Key words: refractories, ion implantation, resistivity, phase transformation.

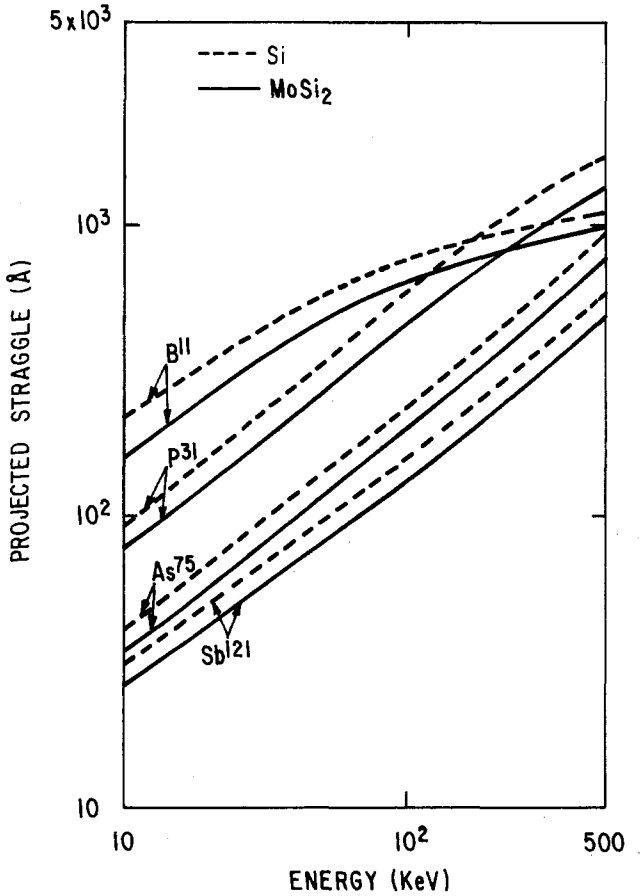

Fig. 2. Calculated projected straggle of B^{11}, P^{31}, As^{75}, and Sb^{121} in silicon and $MoSi_2$.

the oxide. Aluminum was then put on both sides of the wafers. The front side was patterned and etched in H_3PO_4/HNO_3 solution. A final annealing step in H_2 at 400°C finished the process.

Structure and Composition

X-ray diffraction measurements were made with a Siemens D500 automated powder diffractometer. After deposition or ion implantation, the silicide films were essentially amorphous. The x-ray diffraction pattern only showed a small and broad peak around 2θ of 41.6°, corresponding to the (111) peak of the hexagonal and low temperature phase of $MoSi_2$. This confirms that during ion implantation, little recrystallization took place. However, annealing these films at high temperatures resulted in significant structural changes, as shown in Fig. 3 and 4. Figure 3 shows the major diffraction peaks for the silicide films which are (a) unimplanted, and implanted with (b) 10^{15}, (c) 2×10^{16} phosphorus ions/cm^2. These films were then annealed at 900°C for 1 hr. The unimplanted film had tetragonal $MoSi_2$ (t-$MoSi_2$) as the major phase, with small traces of hexagonal $MoSi_2$ (h-$MoSi_2$), and Mo_2C or carbon-stabilized, hexagonal Mo_5Si_3 [Mo_5Si_3(C)] phases. For the film implanted with 10^{15} ions/cm^2, h-$MoSi_2$ appeared as a significant minor phase [Fig. 3(b)]. When the implantation dosage exceeded 2×10^{16} ions/cm^2, major structural difference can be observed. h-$MoSi_2$ became the major phase, with t-$MoSi_2$ as a minor, though significant, phase. Also, for the most heavily implanted (5×10^{16} ions/cm^2) case, MoP was detected in significant amounts. Furthermore, the level of Mo_2C or Mo_5Si_3(C) remained about the same inferring that it was a contaminant from the sputtering target and not a product of the implantation process.

In Fig. 4, the diffraction peaks for films implanted with the same fluences but were then annealed at 1000°C for 1 hr are shown. The unimplanted film had

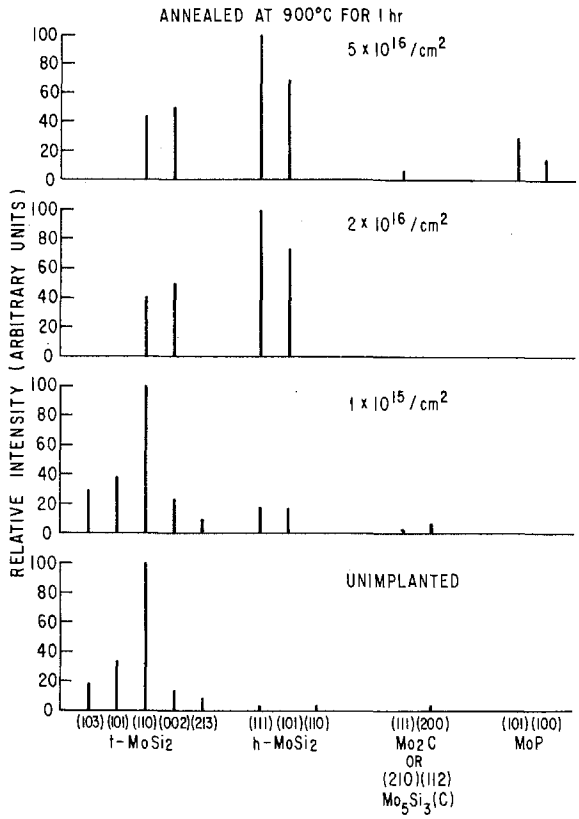

Fig. 3. Major x-ray diffraction peaks (peak intensities, not corrected for background and normalized to the highest silicide peak) for various $MoSi_2$ films after implantation and annealing at 900°C for 1 hr.

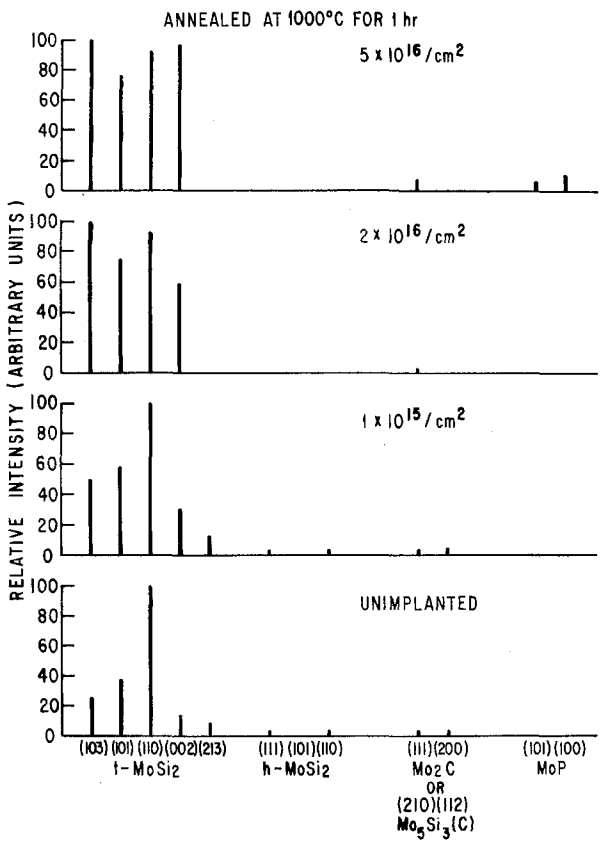

Fig. 4. Major x-ray diffraction peaks for various $MoSi_2$ films after implantation and annealing at 1000°C for 1 hr.

the same features as the 900°C case, with the (110)-oriented, t-$MoSi_2$ as the major phase [Fig. 4(a)]. Little change was seen for the 10^{15} ions/cm^2 implanted

film, except the amount of h-MoSi decreasing to trace level [Fig. 4(a) *vs.* Fig. 4(b)]. On the other hand, for the two heavily implanted samples, the predominant phase was changed from h-$MoSi_2$ into t-$MoSi_2$. Also, the t-$MoSi_2$ appears to be more randomly oriented than the undoped or lightly doped films. Moreover, MoP was again observed for the film implanted with 5×10^{16} ion/cm^2 case but not the one with 2×10^{16} ions/cm^2.

There are several interesting observations that can be made from the diffraction data just described. Firstly, the presence of phosphorus in the silicide apparently increases the hexagonal to tetragonal $MoSi_2$ phase transition temperature. For the undoped film, it has been shown to be ~800°C (20). This is also confirmed by our present data for the undoped film which, after annealed at 900°C for 1 hr, had mostly t-$MoSi_2$ phase. For the silicide film implanted with 10^{15}/cm^2, the transition was almost completed at 900°C. But increasing the dosage to over 2×10^{16} ions/cm^2 has made the transformation take place between 900° and 1000°C. Secondly, the main contaminant observed here is Mo_2C or $Mo_5Si_3(C)$. Mo_2C has a face-center cubic structure and a bulk resistivity of 65 $\mu\Omega$-cm at 300 K (21). Hexagonal Mo_5Si_3, similar to its niobium counterpart (22), has only been found in the presence of carbon (23) but its resistivity has not been reported. Thirdly, while no molybdenum/phosphorous compound was detected at low dosage, MoP was detected at a dosage of 5×10^{16} ions/cm^2. The occurrence of this compound has been mentioned previously in a phosphorus-ion-induced silicide formation study (24). Molybdenum phosphide has a bulk resistivity of 0.9 mΩ-cm at 300 K (25), several orders of magnitude higher than that of the silicide.

Secondary ion mass spectrometry (SIMS) was performed with a Cameca IMS 3-f ion microscope with an O_2^+ beam of an impact energy of 10.5 kV. Figure 5 shows the depth profiles of various positive ions obtained from SIMS for the unimplanted sample and two as-implanted samples. Specifically, the ions are molybdenum ($^{96}Mo^+$), silicon ($^{28}Si^{++}$), phosphorus ($^{31}P^+$), carbon ($^{12}C^+$), and argon ($^{40}Ar^+$). Since oxygen ions were used for depth profiling, its level in the various layers of thin films (oxide and silicide) cannot be determined. Molybdenum and silicon are the main constituents and their intensity ratio is fairly constant throughout the film. The presence of carbon further confirms the x-ray data earlier. It was probably incorporated during the high temperature metallurgical step in the alloy target fabrication. On the other hand, argon was entrapped in the film during sputtering since it was used as the sputtering gas. The presence of argon and carbon in alloy-sputtered silicide films has also been observed in the case of $NbSi_2$ (22). Figure 5(a) is for the unimplanted film, whereas the profiles for silicide films implanted with phosphorus fluence of 1×10^{15}/cm^2 and 5×10^{16}/cm^2 are shown in Fig. 5(b) and (c), respectively. For all three films, high intensity of mass 31 in the surface oxide film is not attributed to phosphorus ions. Instead, it is probably due to molecules such as SiH. At a dose of 1×10^{15}/cm^2, the phosphorus ions were just detectable [compare Fig. 5(a) with 5(b)]. Also, the peak of the phosphorus ions can be seen very close to the middle of the silicide films, as simulated.

The peak intensity of phosphorus ions (mass 31) in the silicide is correlated with the peak phosphorus concentration as calculated from the dosage and projected straggle, as shown in Fig. 6. A linear relationship is observed for dosage at or above 5×10^{15} ions/cm^2.

The high temperature annealing did not significantly change the relative percentage of molybdenum, silicon, and argon but redistributed phosphorus and carbon. Only the profiles for the unimplanted sample and the sample implanted with 5×10^{16} ions/cm^2, after annealing at 900°C, are shown in Fig. 7(a) and (b), respectively. Though the level of phosphorus became fairly uniform within the film, it accumulated at the outer interface. Also, the saturation level apparently depended on the implantation dosage. Fast outdiffusion of phosphorus through WSi_2 has also been observed (26). The distribution of carbon is even more interesting. Initially, it was uniform but, after annealing it became localized or clustered, particularly for the implanted samples. Since Mo_2C or $Mo_5Si_3(C)$ was detected after annealing, the variation of the carbon ions is probably related to the nucleation of these carbide phases. Finally, there is no distinguishing difference between films annealed at 900° and 1000°C.

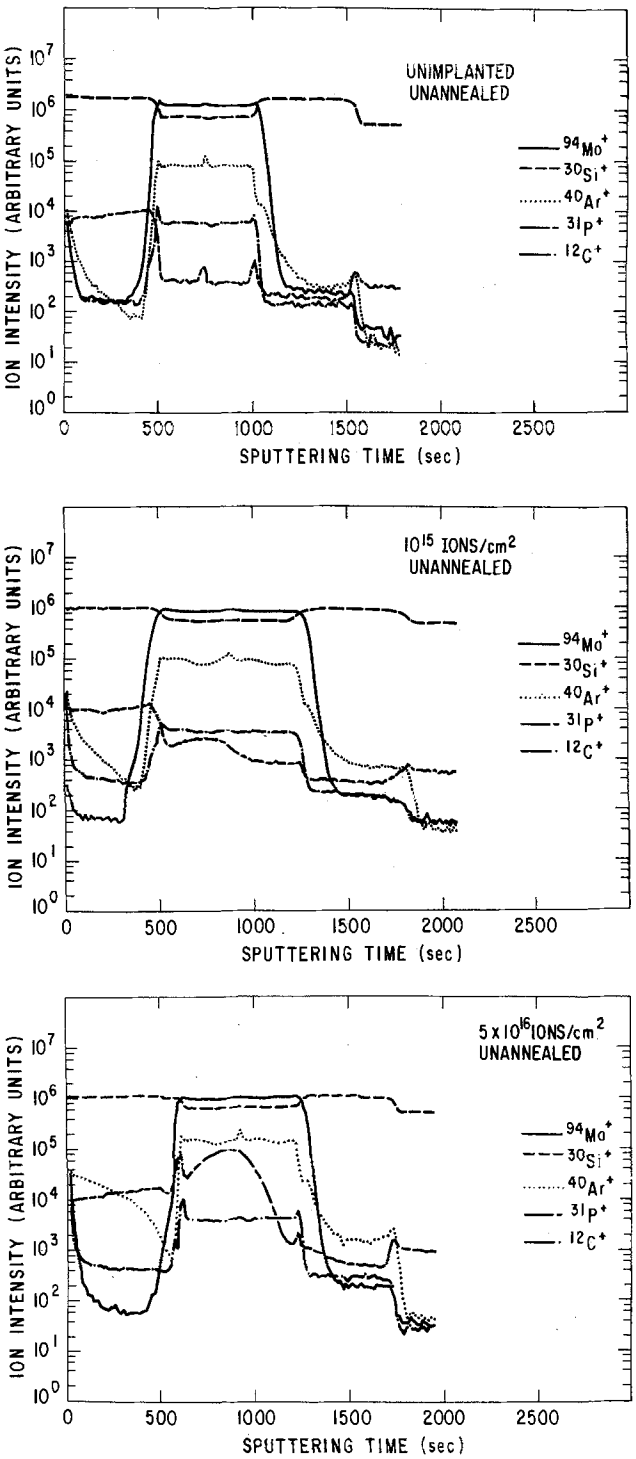

Fig. 5. As-implanted SIMS depth profiles for $MoSi_2$ films which were (a) unimplanted, and phosphorus implanted with (b) 10^{15}, and (c) 5×10^{16} ions/cm^2.

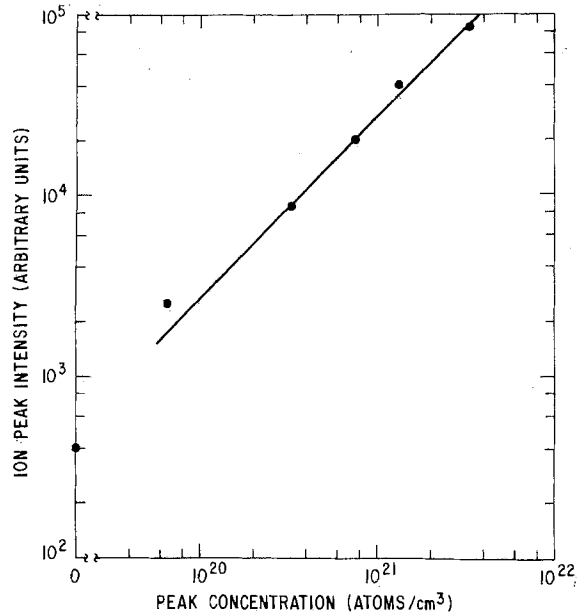

Fig. 6. Mass 31 ion peak intensity as a function of calculated peak concentration of implanted phosphorus.

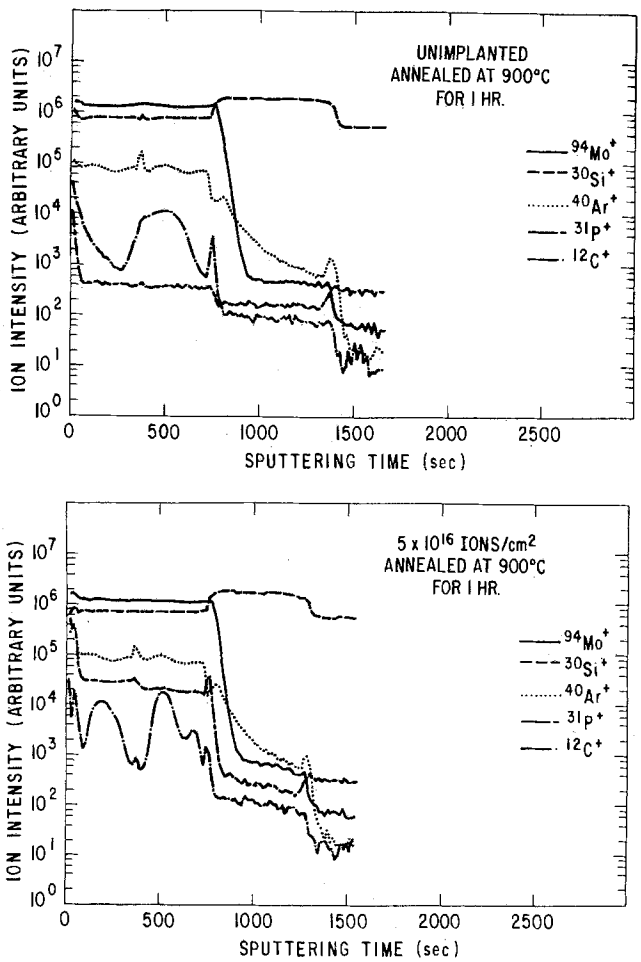

Fig. 7. SIMS depth profiles for silicide films which were (a) unimplanted and (b) implanted with 5 × 10^{16} phosphorus ions/cm², and then annealed at 900°C for 1 hr.

Resistivity

Electrical properties of these silicide films were characterized with sheet resistance measurements. As illustrated in Fig. 8, sheet resistance was studied as a function of annealing temperature for various films annealed for 1 hr in nitrogen. The as-planted films all had sheet resistance of approximately 30 Ω/sq. In general, the sheet resistance decreased with increasing temperature up to 950°C. Beyond that, the variation of sheet resistance with temperature was small. However, the sheet resistance of the sample implanted with 5 × 10^{16} ions/cm² was approximately twice that of the rest. Specifically, the sheet resistance of the most heavily implanted sample dropped from 33-7 Ω/sq after 1 hr at 950°C, while the rest from 28-31 to 3.8-4.5 Ω/sq. After 1 hr at 1000°C, the sheet resistance was essentially the same in either case as those annealed at 950°C.

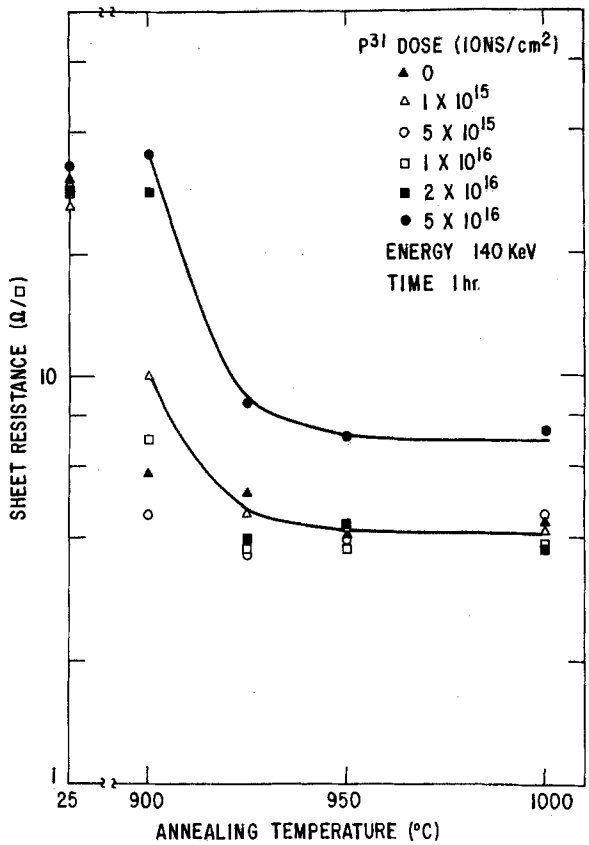

Fig. 8. Sheet resistance as a function of annealing temperature for various silicide films annealed for 1 hr.

In the case of isothermal annealing, the sheet resistance was measured as a function of annealing time up to 1 hr at 1000°C for various dosages, as shown in Fig. 9. Generally, the sheet resistance dropped off abruptly during the first 15 min of annealing. Thereafter, the change of sheet resistance with time was small. In particular, the unimplanted film and the films implanted up to 2 × 10^{16} ions/cm² all decreased their sheet resistance from 26-33 to 3.3-5.5 Ω/sq after 15 min at 1000°C. After 1 hr of annealing, the sheet resistance was between 4 and 4.8 Ω/sq. On the other hand, in the case of implantation with 5 × 10^{16} ions/cm², a sheet resistance of 7.5 Ω/sq was obtained after 15 min, leveling off only to 7 Ω/sq after 1 hr. Furthermore, the reason for the apparent slight increase in sheet resistance when the annealing time exceeded 15 min has not been found.

To understand the annealing characteristics of these silicide films, the structural data obtained from x-ray diffraction are correlated with the sheet resistance measurements. After implantation, even at the heaviest fluence used here, the films were essentially amorphous, as reflected in the fairly high sheet resistance (26-33 Ω/sq). This indicates little heating occurred in this step. After annealing at 900°C for 1 hr, the unimplanted sample was recrystallized into mostly (110)-oriented t-$MoSi_2$, and hence the decrease in sheet resistance to 5.8 Ω/sq. The silicide film which was implanted with 10^{15} ions/cm² also had (110)-oriented

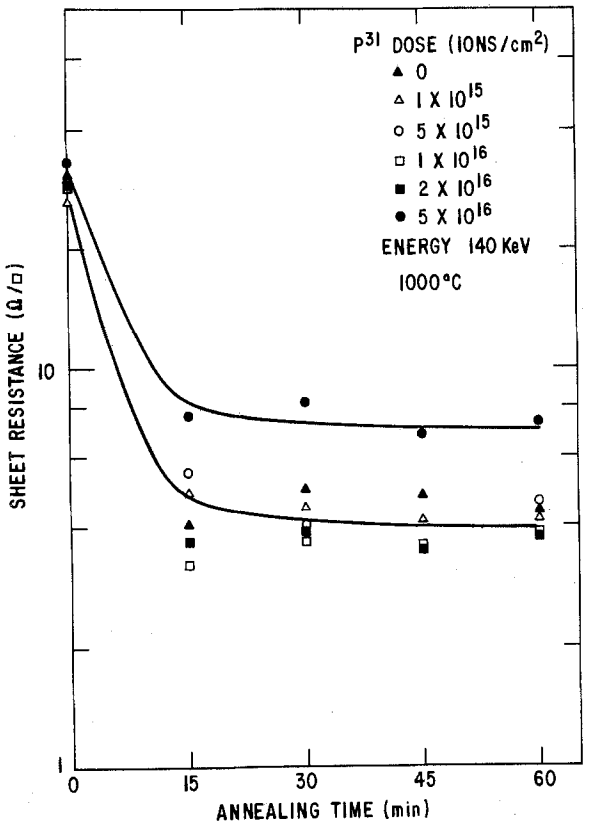

Fig. 9. Sheet resistance as a function of annealing time at 1000°C for silicide films implanted with various dosage of phosphorus.

t-$MoSi_2$ as the predominant phase. In this case, the higher resistance measured (10 Ω/sq) may be attributed to the presence of h-$MoSi_2$. When the silicide films were implanted with over 2×10^{16} ions/cm^2 and annealed at 900°C for 1 hr, they contained mostly h-$MoSi_2$ and also t-$MoSi_2$. Hence, still higher sheet resistance (31-35 Ω/sq) was measured. In the case of 5×10^{16} ions/cm^2, MoP, which has resistivity several orders of magnitude higher than that of the silicide, also contributed to the higher resistance here.

When the annealing temperature was increased to 1000°C, the undoped showed little change in diffraction pattern or sheet resistance. The disappearance of h-$MoSi_2$ in the film implanted with 10^{15} ions/cm^2 resulted in decreased sheet resistance (from 10 to 4 Ω/sq). The annealing behavior for the films implanted with 2×10^{16} and 5×10^{16} ions/cm^2 differed in that, despite h-$MoSi_2$ was transformed into t-$MoSi_2$ in both cases, the presence of MoP in the latter but not the former resulted in a nearly two-fold increase in sheet resistance (7 *vs.* 4 Ω/sq). In this way, one can see the effect of implantation of phosphorus on the structure and resistivity of these films. Furthermore, it is noted that the effect of phosphorus implantation on grain growth, which can also affect resistivity (15), has not been studied here.

MOS Properties

To investigate the effect of these properties on device characteristics, MOS capacitors were fabricated and tested. The work function, threshold voltage stability, and breakdown voltage were studied with comparative C-V measurements. The flatband voltages determined from C-V measurements are shown in Fig. 10(a) and (b), for the unimplanted and implanted

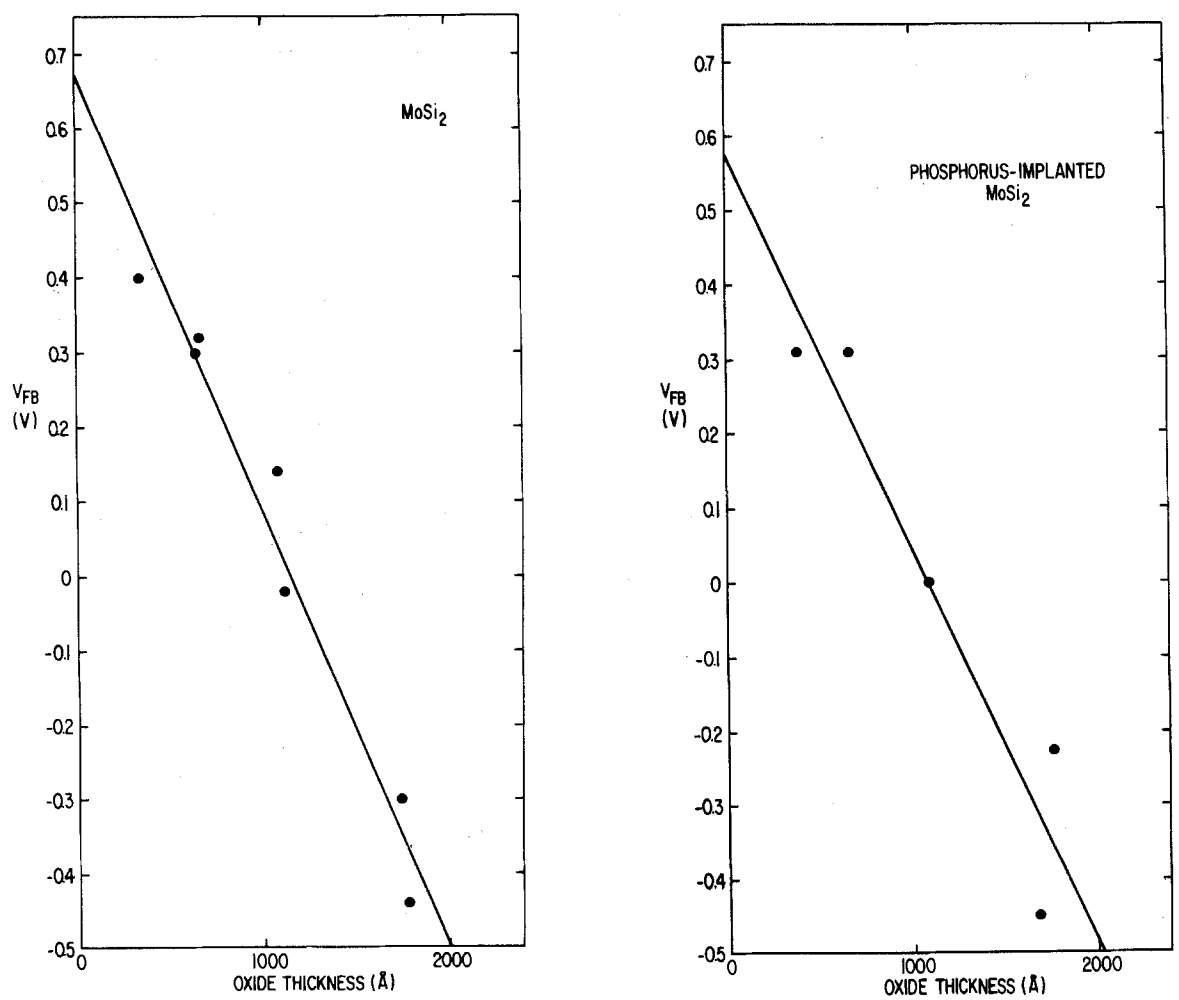

Fig. 10. Flatband voltage *vs.* oxide thickness for (a) unimplanted and (b) phosphorus-implanted silicide-gate MOS capacitors.

samples, respectively. Since extrapolation of the flatband voltage to zero oxide thickness from least squares fitting yields ϕ_{MS} values of 0.67 and 0.57 eV, the work functions are hence 4.93 and 4.83 eV, respectively. The corresponding total charge densities calculated from the slope of the V_{FB} *vs.* t_{ox} dependence were 1.26×10^{11} and $1.24 \times 10^{11}/cm^2$. Also, temperature-bias stress measurements, performed with +10V at 200°C for 15 min on these devices resulted in negligible flatband voltage shift, indicating threshold voltage stability. Furthermore, breakdown voltage measurements also yielded similar results for these two types of devices. For the case of 400Å thick oxide, the breakdown field distributions are shown in Fig. 11(a) and (b), for unimplanted and implanted gates, respectively. On the average, the breakdown field of ~7 mV/cm was observed. Based on these results, the implanted silicide film, in the case of implantation fluence of 5×10^{15} ions/cm^2, showed little difference in MOS properties when compared with the unimplanted ones.

Summary

The effect of phosphorus implantation into molybdenum disilicide thin films has been studied. The structural, compositional, and electrical properties of these films were investigated with x-ray diffraction, secondary ion mass spectrometry, and sheet resistance measurements. Implanted films showed a higher hexagonal to tetragonal $MoSi_2$ phase transition temperature than the unimplanted one. Also, at high fluence (5×10^{16} ions/cm^2), MoP was detected, within a sheet resistance value twice that of the unimplanted or lightly implanted films. Isothermal and isochronal annealing indicated a minimum temperature of 950°C and a maximum fluence of 2×10^{16} ions/cm^2 can be used. Comparative C-V measurements showed similar MOS characteristics between the unimplanted and implanted silicide films.

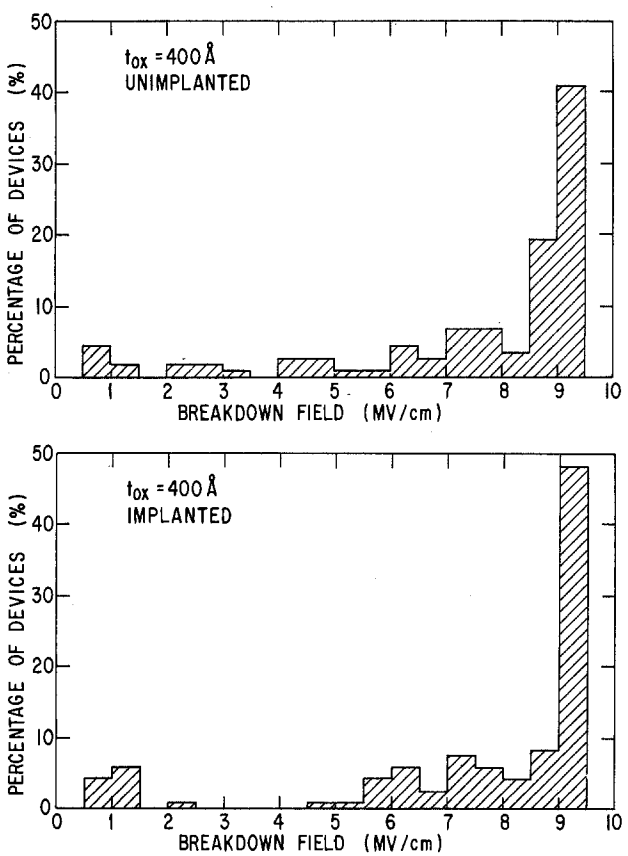

Fig. 11. Gate oxide breakdown field distribution for (a) unimplanted and (b) phosphorus-implanted silicide-gate MOS capacitors.

Manuscript submitted Aug. 13, 1982; revised manuscript received Nov. 22, 1982. This was Paper 301 presented at the Montreal, Que., Canada, Meeting of the Society, May 9-14, 1982.

Any discussion of this paper will appear in a Discussion Section to be published in the December 1983 JOURNAL. All discussions for the December 1983 Discussion Section should be submitted by Aug. 1, 1983.

Publication costs of this article were assisted by the General Electric Company.

REFERENCES

1. T. Mochizuki, K. Shibata, T. Inoue, and K. Ohuchi, *Jpn. J. Appl. Phys.*, **17**, Supp. 17-1, 37 (1978).
2. T. P. Chow and A. J. Steckl, *Appl. Phys. Lett.*, **36**, 297 (1980).
3. P. Shah, D. Laks, and A. Wilson, *IEEE IEDM, Tech. Dig.*, 465 (1979)
4. T. Mochizuki, T. Tsujimaru, M. Kashiwagi, and Y. Nishi, *IEEE Trans. Electron Devices*, **ed-27**, 1431 (1980).
5. T. P. Chow, A. J. Steckl, and R. T. Jerdonek, *IEEE Electron Device Letters*, **edl-3**, 37 (1982).
6. B. L. Crowder and S. Zirinsky, *IEEE Trans. Electron Devices*, **ed-26**, 369 (1979).
7. F. Mohammadi and K. C. Saraswat, *This Journal*, **127**, 450 (1980).
8. H. J. Geipel, Jr., N. Hsieh, M. H. Ishaq, C. W. Koburger, and F. R. White, *IEEE Trans. Electron Devices*, **ed-27**, 1417 (1980).
9. M. Y. Tsai, H. H. Chao, L. M. Ephrath, B. L. Crowder, A. Cramer, R. S. Bennett, C. J. Lucchese, and M. R. Wordeman, *This Journal*, **128**, 2207 (1981).
10. S. P. Murarka, *J. Vac. Sci. Technol.*, 17, 775 (1980).
11. A. K. Sinha, W. S. Lindenberger, D. B. Fraser, S. P. Murarka, and E. N. Fuls, *IEEE Trans. Electron Devices*, **ed-27**, 1425 (1980).
12. S. Inoue, N. Toyokura, T. Nakamura, and H. Ishikawa, *IEEE IEDM Tech. Dig.*, 152 (1980).
13. S. Inoue, N. Toyokura, T. Nakamura, and H. Ishikawa, *This Journal*, **128**, 2402 (1981).
14. D. K. Brice, "Ion Implantation Range and Energy Deposition Distributions," Vol. 1, p. 12 (1975).
15. P. Cappelletti, T. Mori, G. Pignatel, G. Ferla, F. Nava, and G. Ottaviani, in "Semiconductor Silicon 1981," H. R. Huff, R. J. Kriegler, and Y. Takeishi, Editors, p. 608, The Electrochemical Society Softbound Proceedings Series, Princeton, NJ (1981).
16. G. V. Samsonov, "Silicides and their Uses in Engineering," (translated), Aca. Sci. UkrSSR, Kiev (1959)
17. B. Smith, "Ion Implantation Range Data for Silicon and Germanium Device Technologies," Research Studies Press, Inc. (1977).
18. T. P. Chow and A. J. Steckl, *IEEE IEDM Tech. Dig.*, 149 (1980).
19. T. P. Chow and A. J. Steckl, *J. Appl. Phys.*, **53**, 5531 (1982).
20. S. Yanagisawa and T. Fukuyama, *This Journal*, **127**, 1150 (1980).
21. Y. S. Touloukian, Editor, "Thermophysical Properties of High Temperature Solid Materials," Vol. 5, p. 79 (1967). Standard Powder Diffraction Pattern 15-457.
22. C. D. Rude, T. P. Chow, and A. J. Steckl, *J. Appl. Phys.*, **53**, 5570 (1982).
23. H. Schachner, E. Cerwenka, and H. Nowotny, *Mh. Chem.*, **85**, 245 (1954). Standard Diffraction Pattern 8-429.
24. S. W. Chiang, T. P. Chow, R. F. Reihl, and K. L. Wang, *J. Appl. Phys.*, **52**, 4027 (1981).
25. R. L. Ripley, *J. Less-Common Met.*, **4**, 496 (1962).
26. P. Pan, N. Hsieh, H. J. Geipel, Jr., and G. J. Slusser, *J. Appl. Phys.*, **53**, 3059 (1982).

Alignment Signals from Symmetrical Silicon Marks for Electron Beam Lithography

Yi-Ching Lin,[1] Andrew R. Neureuther,* and William G. Oldham*

Department of Electrical Engineering and Computer Sciences and the Electronics Research Laboratory, University of California, Berkeley, California 94720

ABSTRACT

This paper discusses the experimental observations of alignment signals from symmetrical U-, V-, and W-shaped silicon marks. Solid-state detectors are used to measure alignment signals by collecting electrons backscattered in different takeoff angle regions. The results indicate several methods for improving the signal quality. The effects on the alignment signals due to the resist coatings are measured particularly for PMMA coated on V-marks at different positions on the wafer. The experimentally observed resist profile is characterized by the degree of planarization, which in turn is used to evaluate the reduction of the signal level due to the coated resist thickness. The detection uncertainty error due to the asymmetry of the resist profile at a peripheral position of the wafer is evaluated. The accuracy in locating the alignment marks is also calculated as a function of the expanded signal-to-noise ratio, the number of scans of the electron beam, and the depth of the mark. Simple design rules are given for characterizing the effects of resist thickness, the incident beam voltage, and the mark depth in terms of the Bethe range.

The direct exposure of wafers in electron beam lithography (EBL) requires the capability of accurately overlaying the pattern to be exposed to the processed pattern already on the wafer. For this purpose, alignment marks are typically fabricated at the four corners of each chip. The alignment process is carried out by scanning the electron beam across the alignment marks, and collecting backscattered electrons which penetrate the resist layer. To avoid additional process steps it is desirable to align without removal of the resist coated over the alignment marks.

Many authors (1-9) have contributed to characterizing alignment signals. Wolf *et al.* (1) reported measurements of alignment signals for silicon pedestals, silicon dioxide channels, and gold marks. Friedrich *et al.* (2) considered the alignment signals from V-shaped silicon marks. Iida and Everhart (3) examined anisotropically etched silicon holes as alignment marks. Davis *et al.* (4) discussed the optimization of the alignment mark detection process from U-shaped silicon marks. Stickel (5) developed a qualitative model to describe the effects of the separation between the two sidewalls of a U-shaped mark on the signals observed experimentally using solid-state detectors in four quadrants. A more quantitative technique based on Monte Carlo (MC) simulations has been used by Aizaki (6) to explore the total backscattered signals from step, V-, and W-shaped grooves in silicon. In a similar study, Stephani (7) investigated the backscattered signals in different takeoff and azimuthal angles from rectangular steps, pedestals, and grooves.

The authors have also employed the MC method to characterize the alignment signals (8-9) formed by electrons backscattered from tapered silicon steps both with and without resist coatings. In our investigations, we have found that the preferred detector configurations collect the low takeoff angle electrons within $0 < \theta_L < 30°$. For a fixed beam voltage, the preferred resist thickness is less than 40% of the Bethe range of the incident beam in the PMMA resist (denoted as R_{PMMA}) so that the backscattered electrons will reflect the effect of the silicon marks themselves. For a resist layer thicker than 0.4 R_{PMMA}, the backscattered electrons will sense primarily the resist topography.

The uncertainty in locating the exact position of a single step mark is not only caused by the resist coverage but also affected by the accurate definition of the mark during the fabrication process. The processing uncertainty in defining the mark patterns in the oxide mask for anisotropic etching (10) will eventually be transferred to the Si step masks themselves. These uncertainties may be minimized by using symmetrical marks, because the uncertainty from individual edges of the marks may be reduced through averaging and only asymmetrical processing errors remain.

This paper presents experimental observations of alignment signals for the U-, V-, and W-shaped symmetrical silicon marks, and discusses the relationship between the signal-to-noise ratio and alignment error. The experiment was conducted in a ETEC autoscan scanning electron microscope (SEM). It is shown that many aspects of the resultant alignment signals are controlled by the manner in which the resist covers the alignment marks. In particular, the actual resist profile on V-marks and its effect on the alignment signals are characterized experimentally. A guideline to determine the selection of beam voltage, resist thickness, and mark depth is also developed.

Alignment Signals from Bare Silicon Marks

Secondary electron signals.—Examples of symmetrical silicon alignment marks are the U-, V-, and W-shaped marks shown in Fig. 1(a)-(d), respectively. These experimental structures were fabricated by etching (100)-Si anisotropically. The sidewalls of these samples were smooth and uniform, and the rough appearance here at a tilt angle of 82° is due to the finite focal depth of the SEM. The signals in Fig. 1(a)-(d) are secondary electron signals for a 20 kV electron beam. The slight asymmetry in these secondary electron signals stems from the asymmetrical position of the scintillator detector.

The effects on the electron signal of the various geometrical components of a mark can be seen from this sequence of alignment signals. The signal from a U-shaped mark given in Fig. 1(a) consists of two parts corresponding to two steps of the mark, which interfere with each other at the trench of the mark. The interference is stronger for a narrower trench. As the width of the trench eventually vanishes to become a V-shaped mark, it leads to a sharp minimum in signal of the V-mark, as is evident with Fig. 1(b). Therefore, the detection of the exact position of the bottom of a V-groove can be much more accurate than the detection of a single step mark. If two V-marks are brought to within the Grün range of the primary electron beam, an interference between the two corresponding V-shaped signals occurs (5, 8), as can be seen in Fig. 1(c). When the separation is so small that two V-marks indeed become a W-shaped mark, as shown in Fig. 1(d), then signal enhancement takes place at the center of the W-mark. Because it has two sharp minima

* Electrochemical Society Active Member.
[1] Present address: Central Research Laboratory, Texas Instruments, Incorporated, Dallas, Texas 75265.

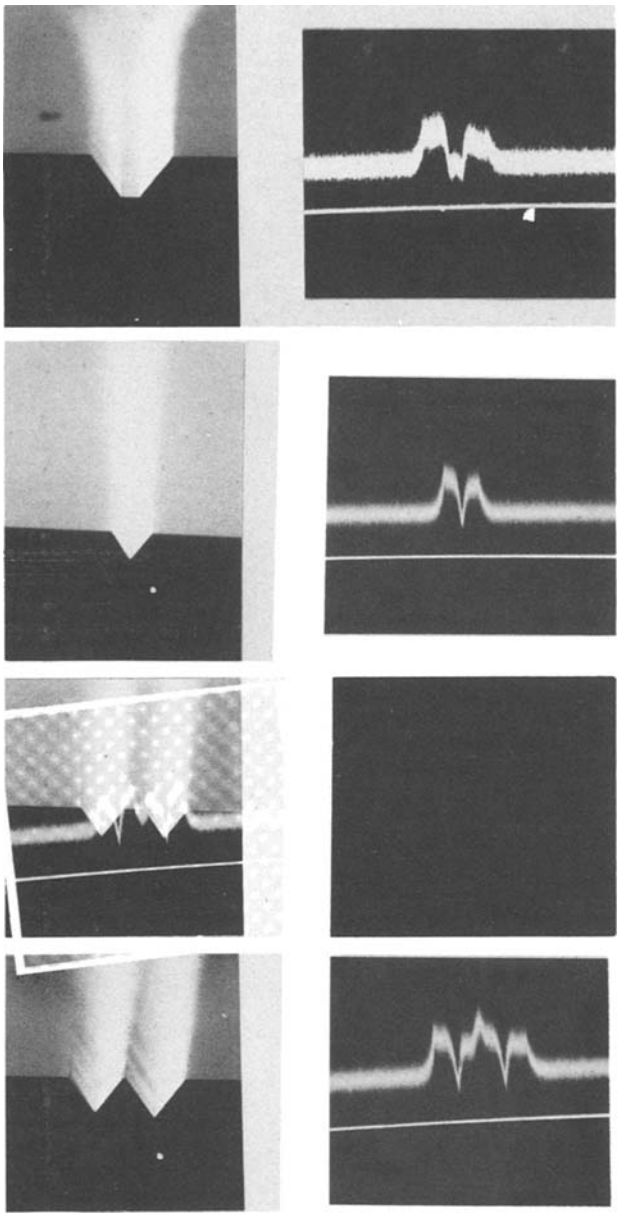

Fig. 1. (a) Symmetrical U-shaped alignment mark of 7 μm depth at 82° tilt. The secondary electron signals were recorded using 20 kV beam with a line scan mode available in SEM. (b) Symmetrical V-shaped alignment mark of 4.86 μm depth. (c) Symmetrical W-shaped alignment can be regarded as two V-shaped grooves close to one another, and (d) symmetrical W-shaped alignment mark gives a sharp maximum in the recorded secondary electron signals.

and one sharp maximum available in the signal, the W-shaped mark is potentially very effective for precise mark detection.

Backscattered electron signals.—The alignment signals obtained by collecting the backscattered electrons from bare silicon symmetrical marks are shown in Fig. 2, 3, and 4 for U-, V-, and W-shaped marks, respectively. In each figure, case (a) is the "total" backscattered electron signal detected by using a copper detector, and cases (b) and (c) are the signals from collecting electrons backscattered into low, medium, and high takeoff angle regions with solid-state detectors. The latter are proportional to the signal energy, whereas the copper detector is sensitive only to the number of backscattered electrons.

The solid-state detector consisted of a 0.82 mm^2-area p-n junction diode with a guard ring to reduce the dark current. The diode was centered at 13°, 41°, and 79° for the low θ_L, medium θ_M, and high θ_H takeoff

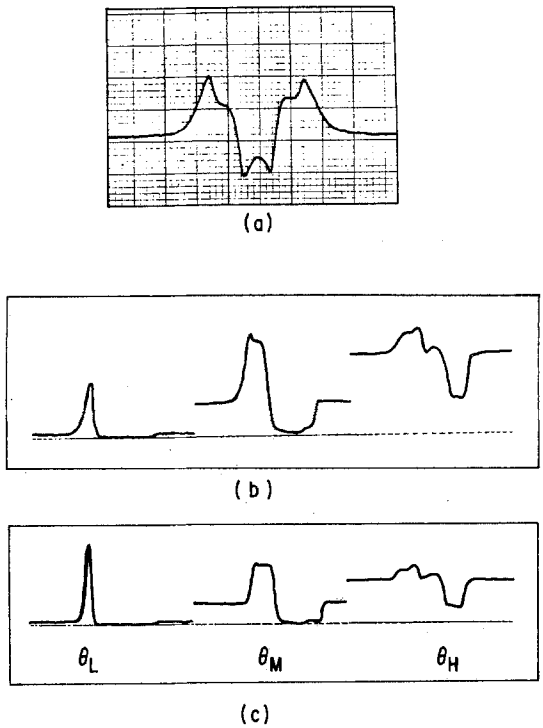

Fig. 2. Alignment signals for a symmetrical U-shaped mark of depth 7 μm. The signals in this and the following two figures are (a) "TOTAL" backscattered electron signal collected by the copper detector for a 30 kV beam, and (b) Signals from the solid-state detectors in θ_L, θ_M, and θ_H positions, respectively. The beam voltage is 30 kV, (c) Same as (b), except the beam voltage is 20 kV.

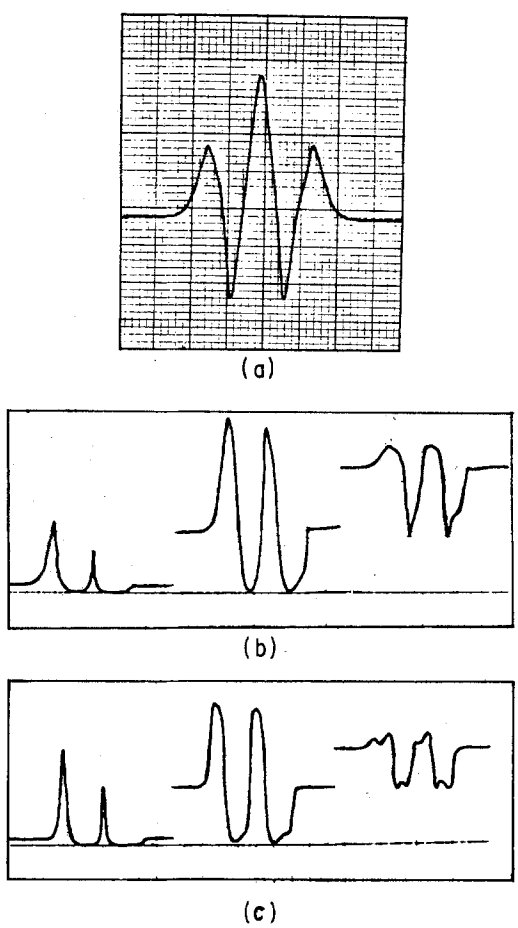

Fig. 3. Alignment signals for a symmetrical V-shaped mark of depth 4.0 μm.

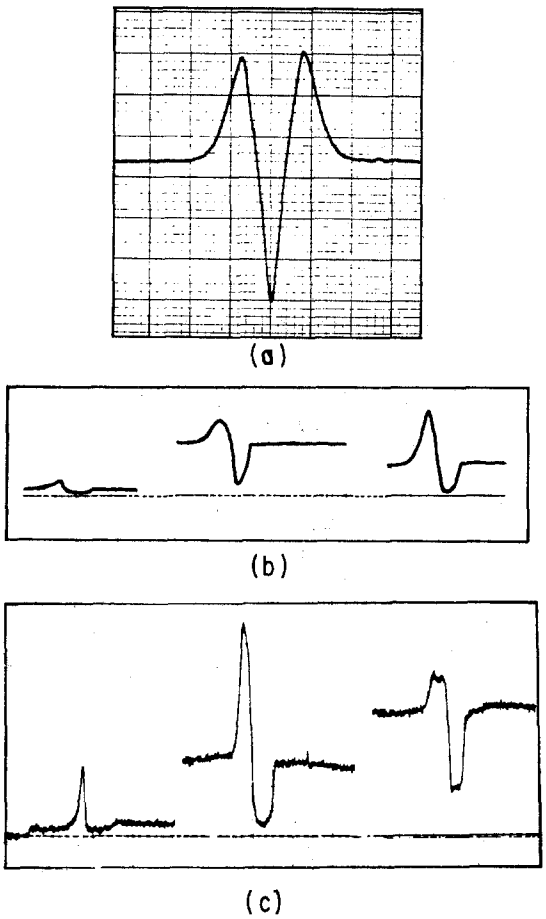

Fig. 4. Alignment signals for a symmetrical W-shaped mark of depth 4.86 μm.

angle ranges, respectively. With respect to each case, the solid angle subtended by the detector was 0.011, 0.0048, and 0.0071 s.r. The copper detector was an annular plate which collected the current of backscattered electrons for takeoff angles in the range $13° < \theta < 67°$. The plate was painted with aquadag (a carbon suspension) to suppress secondary electron emission, and a negative 45V bias between the copper plate and the specimen was used to eliminate the collection of low energy secondary electrons. In recording alignment signals from these detectors, the collected output current was measured by using a Keithley 610C electrometer, and was then plotted on a chart recorder. A computer-controlled electron beam was scanned across the alignment mark with 10 msec dwell time on each picture element. The bandwidth of this system was limited by the chart recorder to about 100 Hz.

The signals shown here in (b) and (c) of Fig. 2, 3, and 4 are from detection of the scanning beam. Because of the symmetry of marks, the signal in ϕ_3 quadrant which ranges from 135° to 225° is a mirror image of that in ϕ_1, as has been confirmed experimentally. The beam voltage used for both cases (a) and (b) is 30 kV, while for case (c) it is 20 kV. The "total" backscattered signals resemble the actual mark shapes, while the signals at θ_L, θ_M, and θ_H are more complicated, and differ significantly from the original mark shapes. In general, the signal at θ_L has a simple signal shape and θ_H has the most complex signal shape. The signal level at θ_L is usually lower because of the geometrical shadowing effect.

The shape of the collected signal is also affected by the beam voltage and the mark depth. These effects can be combined into a normalized mark depth z which is the ratio of the physical mark depth s to the Bethe range R_{Si} of the primary beam in Si. When z increases, the modulation S in the signal at θ_L increases, while ΔS in the signals at θ_M and θ_H may decrease.[2] This effect can be explained as follows. The maximum of the signal is generated when the beam is incident at the top corner of these symmetrical marks. The increase of z (smaller beam voltage and/or greater mark depth) makes the electron scattering at the top corner closer to that of a single isolated step; therefore the signal increase is enhanced in the low takeoff angle regions, as is evident from the angular distribution of backscattered electrons shown in Ref. (8). The minimum of the signal is mainly caused by attenuation and shadowing effects (8), which are most pronounced for the low takeoff angle electrons. Therefore, ΔS, which is the difference between the maximum and minimum in signal, is enhanced toward θ_L for larger z. If z is greater than unity, undesirable plateaus appear in the regions of the sloped edges of the mark and make the collected signals (particularly for θ_M and θ_H) more complex. Hence, it is desirable that the mark depth should be no greater than R_{Si}.

Note that the spread of the signals at θ_L is usually smaller than that at θ_M and θ_H. Despite the fact that the signal level may be lower, the signal at θ_L is generally preferred because of the simple signal shape and the small spread.

Both the total signal (TOTAL) and the sum signal of ϕ_1 and ϕ_3 (SUM) have a signal shape similar to the original mark. For V-marks, the TOTAL and SUM signals are particularly useful because of the sharp minimum which corresponds to the bottom of the V-groove. The determination of the mark position can be made very accurately by using this sharp minimum. Similarly, two sharp minima and one sharp maximum available in W-marks make them potentially very effective for precise mark detection. But this advantage for W-marks disappears in the difference signal between signals ϕ_1 and ϕ_3 (DIFFERENCE). The DIFFERENCE signal from U-, V-, and W-marks gives a symmetrical zero-crossing signal, which may be more useful if the zero-crossing detection technique is used for further signal processing.

Detection uncertainty error.—The detectability of the marks and the accuracy of locating them are limited by the noise level in the alignment signal associated with the electron beam and the detection system. A high signal-to-noise ratio (SNR) is imperative for achieving precise overlay of patterns. Techniques to improve the SNR have been reviewed elsewhere (4, 8). A higher SNR can be obtained by decreasing the scan rate of the electron beam or by increasing the incident beam current. The SNR can also be improved by using larger detectors and placing them closer to the specimen. To minimize the noise, the bandwidth of the system during alignment should not be larger than necessary to pass the alignment signal without distortion. In addition, the ensemble average of M individual scans can be used to reduce the noise by a factor of $\sqrt{M}$ (11).

The accuracy in locating the alignment marks increases with the SNR. As an example, consider that a "peak" detection (including the maximum and minimum in the signal) is used to process the collected alignment signals and to locate the position of a V-shaped mark. From MC simulations (6, 12), the maximum and the minimum correspond to the top corner and the sharp bottom of the V-mark. Due to the background noise N_b, the detection uncertainty δ for one mark edge is equal to the noise divided by the average signal slope $\Delta S/W$ where W is the horizontal distance between the maximum and minimum in the signal. That is, δ is proportional to W divided by the expanded signal-to-noise ratio ΔSNR, which is defined as

[2] Note that signal amplitudes in Fig. 3(c) must be reduced by a factor of 2/5 in order to be compared with signals in Fig. (b), due to a change in recording scale on the chart recorder during the experiment.

$$\Delta\text{SNR} = \frac{\Delta S}{N_b} \quad [1]$$

Generalizing for an ensemble of M individual scans, K V-marks per single scan, and two sidewalls per V-mark, one obtains the following expression for the detection uncertainty δ as has been derived by following the approach of Davis (4)

$$\delta = \frac{W}{\sqrt{2MK}\,(\Delta\text{SNR})} = \frac{s}{2\sqrt{MK}\,(\Delta\text{SNR})} \quad [2]$$

Here the horizontal distance W is related to the physical mark depth s by a factor of $\tan 54.7° = \sqrt{2}$.

Figure 5(a) depicts the detection uncertainty δ *vs.* the expanded SNR for $s/2\sqrt{MK} = 0.4$ μm, which is the case for using 25 individual scans on one single V-mark of 4 μm depth. It shows that for δ to be less than 0.02 μm, a relatively high ΔSNR (greater than 20) is required. In practice, more scans over the same mark for averaging can be used to improve the accuracy with a tradeoff in slower throughput. Figure 5(b) shows δ as a function of the number of scans for $s/2\sqrt{K}\,(\Delta\text{SNR}) = 0.5$ μm, which is the case for using one single V-mark of 2 μm depth and a beam current corresponding to $\Delta\text{SNR} = 2$.

This result may be cast into a different form which displays the dependence of alignment precision on alignment time. Let T be the total scan time (equal to MKt_s where t_s is the time to scan one mark), m be the fractional modulation in the alignment signal ($\Delta S/s$), and I_s be the average signal current. Then assuming that the system bandwidth is $0.37/f\tau_s$ (where f is the ratio of the mask width to the scan length) and the noise is α times the theoretical shot noise limit, it is straightforward to derive

$$\delta = \frac{\alpha s}{2m}\sqrt{\frac{0.74q}{fTI_s}} \quad [3]$$

in which q is the electronic charge (1.6×10^{-19}C). For example if we assume 50% modulation, an α of 5, an alignment mask duty cycle f of 0.01, and an alignment time of 0.25 msec per mark, then a signal current of 6 pA is required to achieve an alignment precision of $s/50$. The signal losses due to the backscattered electron coefficient n and detector collection efficiency f require the incident beam current to be about two orders of magnitude larger ($1/nf$).

Generally the average slope of the signal from the maximum to the minimum is steeper than that of the decrease of the signal with distance along the top of the silicon away from the mark. This top silicon signal has a spread proportional to the Grün range (8). Since it does not decay as rapidly as the maximum-to-minimum signal, its use will result in a greater uncertainty in the edge location. Such will be the case for a threshold detection scheme which examines only the peak of the signal. Alternative detector methods based on differentiation would be limited by a relative error related to the slope. Typically for 30 kV and $s = 4$ μm, the average slope of the maximum-to-minimum signal could be about a factor of 4.6 higher than the slope on the silicon side near the peak, and would also be about a factor of 1.6 higher than the average of the two slopes near the peak. Therefore, from a consideration of signal slopes, the peak-to-valley detection scheme is preferred over threshold detection scheme.

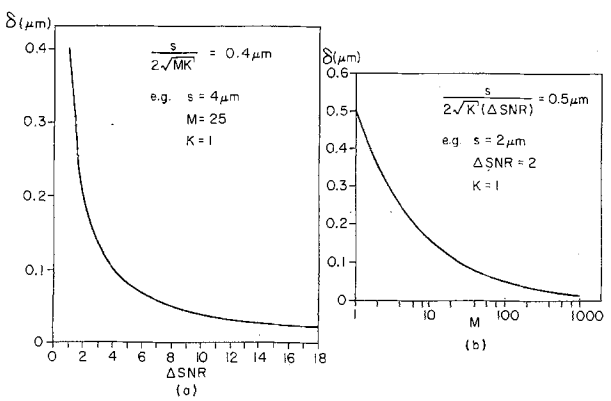

Fig. 5. (a) Detection uncertainty δ as a function of ΔSNR for $s/2\sqrt{MK} = 0.4$ μm, and (b) δ as a function of the number of scans M for $s/2\sqrt{K}(\Delta\text{SNR}) = 0.5$ μm.

V-Shaped Marks with Resist Coverage

Resist profile.—A micrograph showing a side view of a ~1.6 μm PMMA resist layer coated on a 7 μm deep V-shaped silicon mark is given in Fig. 6. The resist coverage profile is smooth and curved to a minimum at the bottom of the V-mark, where the resist is thickest. The resist becomes thinner near the two top corners of the V-mark. The region of thickness nonuniformity depends on the coating conditions, the resist thickness, and the groove depth, and can extend at least 10 μm away from the mark. In general, the resist profile becomes more planar for shallower groove depths and thicker resist film. Following the definition given by Rothman (13), the degree of planarization D is expressed as

$$D = 1 - \frac{d}{s} \quad [3]$$

where s denotes the groove depth and d is the distance between the maximum and minimum of the resist profile. Figure 7 illustrates D *vs.* resist thickness t for two V-shaped grooves with depths 4.86 and 7.04 μm, respectively. Data from Yamamoto *et al.* (14) for U-shaped marks of depth 0.24 μm are also shown in Fig. 7 for comparison. D increases as the resist becomes thicker, and eventually approaches unity which implies a flat surface. By studying the PMMA resist coverage on U-shaped marks of depth of 0.14 and 0.24 μm, Yamamoto *et al.* (14) concluded that the coated resist surface becomes flat when the coating thickness of PMMA resist exceeds ~2.3 times the groove depth. Our experimental results in Fig. 7 indicate that for

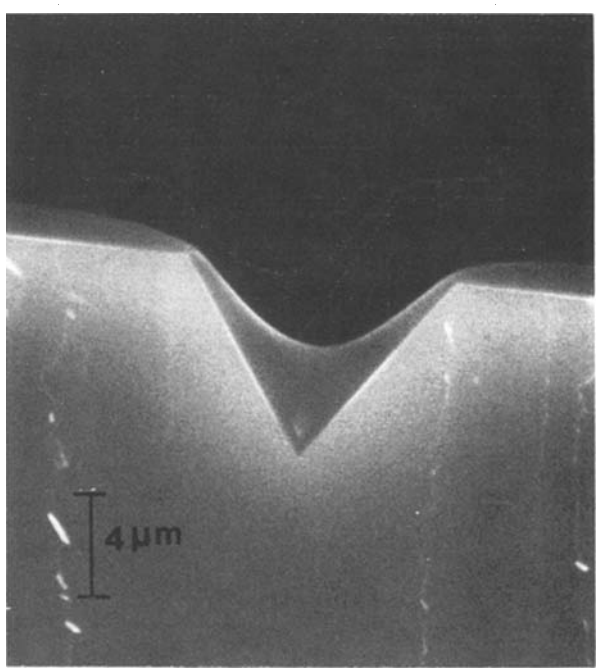

Fig. 6. Cross section of 1.6 μm PMMA resist coated on a V-mark of 7 μm depth.

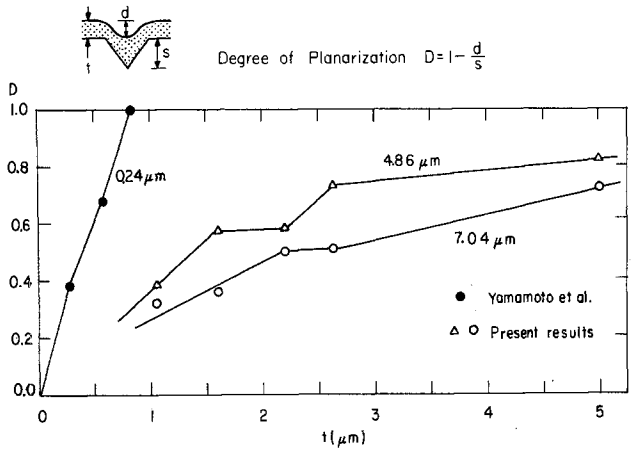

Fig. 7. Degree of planarization *D* vs. coated resist thickness *t*, with mask depth as a parameter.

V-shaped marks with depths of 4-7 μm, a conclusion similar to that of Yamamoto *et al.* can be drawn; namely, for $t \lesssim 2.3s$, $D \cong 1$.

The thickness uniformity of spun-on resist in different locations on the wafer has been reported in the literature (15). It is a function of resist viscosity, dispense volume, spin speed, and wafer diameter. Figure 8 shows resist profiles of 0.6 μm PMMA coated on V-marks of the same depth 4.4 μm at two different locations on a 50 mm wafer. At position A, the resist flows in a direction parallel to the line (radial mark), while at point B, the resist flows perpendicular to the line (peripheral mark), from right to left, as sketched in the figure legend. Both A and B are ~ 1.9 cm away from the center of the wafer. As expected, the resist profile is more symmetrical for case A than for case B. The asymmetry in profile B may arise from the fact that the resist in attempting to flow out of the groove builds up on the outbound side. The slight asymmetry in profile B may cause a detectable difference in the alignment signals between case B and case A, and may become significant for a thicker resist coverage ($t \gtrsim 1$ μm). Radial alignment marks are clearly preferred, but in general are not possible if chip by chip alignment is to be used.

Resist effects.—The effects of a resist layer coating the alignment marks are to reduce the amplitude and to broaden the peaks of the alignment signals. This

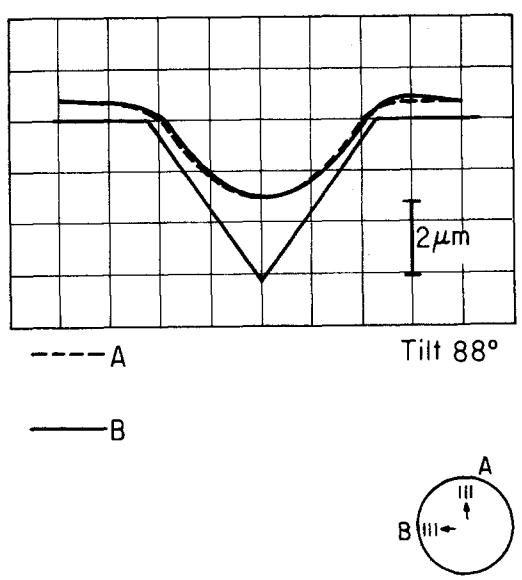

Fig. 8. Resist profiles at different locations on the wafer (see text).

degradation of the alignment signals makes the mark detection more difficult and less accurate. The undesirable "bubbling" and charging (4, 16) worsen the problem even further. It has been shown in a previous study (9) that both thickness and profile shape of the resist layer can affect the alignment signals. In addition, for a resist layer thicker than 0.4 R_{PMMA}, the alignment signal is dominated by the resist topography.

Figure 9 shows typical alignment signals derived from the copper detector. These signals were recorded for a 20 kV beam incident on a V-shaped silicon mark of about 4 μm depth. The resist thickness increases from zero (bare Si mark) on the left to ~ 1.6 μm on the right. As expected, the effect of the resist coating is a reduction in the alignment signal amplitude. Notice the asymmetry in the alignment signals in cases (d) and (e) in Fig. 9. This is primarily due to the asymmetry in the resist profiles for the marks in the peripheral position B on the wafer, as depicted in Fig. 8. In addition, the sharp minimum in the signal rounds off with the coated resist thickness. These observations suggest that the alignment signal follows closely the resist profile, particularly for thick resist coverage. The rate of reduction in the signal modulation ΔS depends on the resist thickness (particularly at the bottom and top corner of the V-mark) as well as the profile shape of the resist. From Fig. 7 and 9, we observe that for $t \cong s/8$ and $D \cong 0.2$, ΔS decreases to $\sim 60\%$ of the value on a bare Si V-mark signal, while $t \cong s/2$ and $D \cong 0.6$, ΔS decreases to only $\sim 25\%$ of the value in a bare Si mark signal. (s is the mark depth, t is the coated resist thickness, and D is the degree of planarization.)

The minimum in the alignment signal corresponds to the sharp bottom for a V-mark without resist coating, as predicted from the MC simulations (6, 12). However, the asymmetry of the resist profile coated on a peripheral V-mark at position B of the wafer (see Fig. 8) can cause deviations. This introduces some error in assuming the signal minimum to be the bottom of the V-mark. Figure 10 plots observed average error of this type *vs.* the coated resist thickness. The average error in locating the bottom mark position increases with increasing resist thickness, and is 0.48 μm for 1.6 μm thick PMMA.

The experimental observations of Fig. 7 suggest that the resist profile becomes planar when the coating thickness of PMMA exceeds ~ 2.3 times the groove depth. Furthermore, the alignment signal is contributed mainly from the resist profile if the resist is thicker than 0.4 R_{PMMA}, where R_{PMMA} is the Bethe range of the incident beam in PMMA. These features determine the minimum beam voltage for a given resist coating thickness or the maximum resist coating thickness for a given beam voltage if the depth of V-mark is fixed. Specifically, with a 20 kV beam which has a Bethe range of 7.55 μm in PMMA, the thickness of resist should be less than 3 μm. If a resist layer thicker than 3 μm is required for the device fabrication process, then either a beam voltage greater than 20 kV is needed or the groove should be deeper than 1/2.3 times the resist thickness.

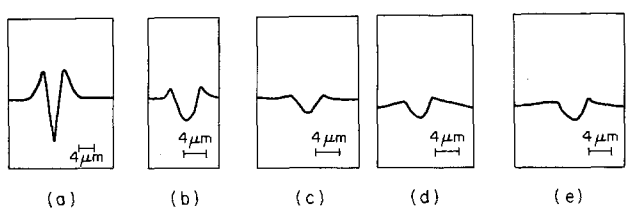

Fig. 9. Detected alignment signals using the copper detector with a 20 kV beam. The depth of the V-mark is 4.03 μm. The coated resist is (a) zero, (b) 0.83 μm, (c) 1.03 μm, (d) 1.20 μm, and (e) 1.61 μm.

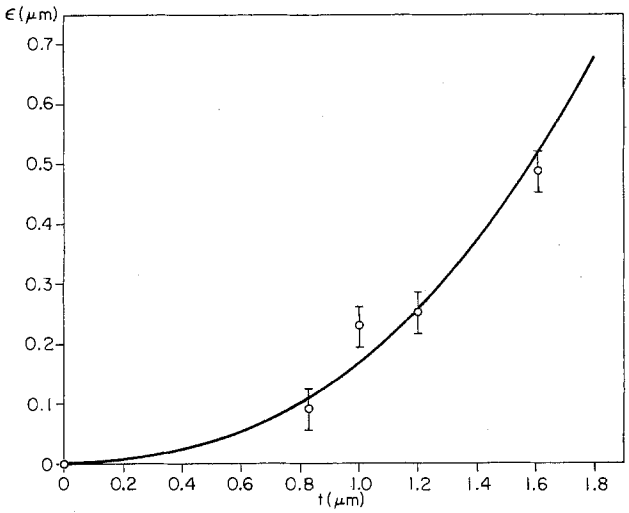

Fig. 10. Average shift in signal minimum relative to the bottom of the V-mark due to asymmetrical resist coating profile.

Conclusion

Alignment signals for both bare and resist coated symmetrical U-, V-, and W-shaped marks have been investigated. Several detector configurations have been considered. On bare silicon, although the signal level may be smaller, the low takeoff angle signals are most useful in the determination of the mark position because of the simple signal shape and the small signal spread. The TOTAL and the SUM of signals taken at various azimuthal angles resemble the original mark shape. They offer sharp maximum and sharp minimum in the signals which are potentially very effective for a precise mark detection. The DIFFERENCE signals may be more advantageous if the zero-crossing detection techniques is used for signal processing. The situation for resist coated marks is quite similar except that the signal level for the low takeoff angle signal decreases much faster with increasing resist thickness than the medium and high takeoff angle signals (9).

The resist effects were evaluated particularly for PMMA coated on V-marks. If the resist is thicker than 2.3 times the mark depth, the resist surface becomes essentially flat. The position of the V-marks on the wafer is also critical for the coated resist profile. Radial V-marks are preferred, because peripheral V-marks have asymmetry in their coated resist profiles. For a given beam voltage, the resist thickness should be less than 0.4 R_{PMMA} so that the backscattered electrons will reflect the geometry of the silicon marks themselves. A resist layer thicker than 0.4 R_{PMMA} can be used if required by the device fabrication processes, but the alignment signal will be derived primarily from the resist topography. In that case, the depth of a groove mark must be significantly greater than 1/2.3 of the resist thickness so that there will be sufficient resist topography for detection. For bare silicon marks, an inclination angle of tapered steps of value between $60° \sim 70°$ maximizes the electron backscatter coefficient (8). For resist coated marks, a steeper sidewall angle will likely be preferred as it will generally give a steeper resist profile slope. This is particularly true for thick resist coating where the backscattered signal primarily reflects the resist topography. The true optimum angle is apt to depend on the nature of the resist profiles in the coating process and requires a specific characterization.

Acknowledgments

We would like to thank Dr. I. Adesida, Dr. C. H. Ting, Professor D. W. Hess, and Professor T. Van Duzer for many helpful discussions. This research was sponsored by the Joint Services Electronics Program under Contract No. F49620-79-C-0178.

Manuscript received Nov. 5, 1981.

Any discussion of this paper will appear in a Discussion Section to be published in the December 1983 JOURNAL. All discussions for the December 1983 Discussion Section should be submitted by Aug. 1, 1983.

REFERENCES

1. E. D. Wolf, P. J. Coane, and F. S. Ozdmir, *J. Vac. Sci. Technol.*, **12**, 1266 (1975).
2. H. Friedrich, H. U. Zeitler, and H. Birnenke, *This Journal*, **124**, 627 (1977).
3. Y. Iida and T. E. Everhart, *J. Vac. Sci. Technol.*, **15**, 917 (1978).
4. D. E. Davis, R. D. Moore, M. C. Williams, and O. C. Woodard, *IBM J. Res. Develop.*, **21**, 498 (1977); also, D. E. Davis, *IBM J. Res. Dev.*, **24**, 545 (1980).
5. W. Stickel, *J. Vac. Sci. Technol.*, **15**, 901 (1978).
6. N. Aizaki, *Jpn. J. Appl. Phys.*, **18**, Suppl. 18-1, 319 (1979).
7. D. Stephani, *J. Vac. Sci. Technol.*, **16**, 1739 (1979).
8. Y. C. Lin, I. Adesida, and A. R. Neureuther, *Appl. Phys. Lett.*, **36**, 672 (1980); also Y. C. Lin, A. R. Neureuther, and I. Adesida, *J. Appl. Phys.*, To be published.
9. Y. C. Lin and A. R. Neureuther, *IEEE Trans. Electron Dev.*, To be published.
10. R. M. Finne and D. L. Klein, *This Journal*, **114**, 965 (1967).
11. A. D. Wilson, T. H. P. Chang, and A. Kern, *J. Vac. Sci. Technol.*, **12**, 1240 (1975).
12. Y. C. Lin, Ph.D. Thesis, University of California, Berkeley, CA (1981).
13. L. B. Rothman, *This Journal*, **127**, 2216 (1980).
14. S. Yamamoto, K. Kobayashi, and Y. Toyama, *Fujitsu Sci. Tech. J.*, **14**, No. 2, 143 (1978).
15. F. L. Givens and W. J. Daughton, *This Journal*, **126**, 269 (1979).
16. R. K. Watts, W. Fichtner, E. N. Fulf, L. R. Thiebault, and R. L. Johnson, in 1980 IEDM Technical Digest, p. 772, December 1980.

Electron Beam Induced Damage in Poly-Si Gate MOS Structures and Its Effect on Long-Term Stability

Masakazu Shimaya, Noboru Shiono, Osaake Nakajima, Chisato Hashimoto, and Yutaka Sakakibara

Nippon Telegraph and Telephone Public Corporation, Musashino Electrical Communication Laboratory, Musashino-shi, Tokyo, Japan, 180

ABSTRACT

Repeated electron beam irradiation and annealing processes are shown to enhance radiation damage in the gate SiO_2, compared to only one irradiation and annealing cycle. Repeated irradiation with 20 keV electrons causes an introduction of more positive charge, neutral traps, and interface traps. Neutral trap density gradually increases with increasing repeated cycles, even after 700°C annealing in dry N_2, though these traps are removed completely by only one cycle. Positively charged and neutral traps are determined by avalanche hot-electron injection, and interface traps at the SiO_2-Si interface are determined by quasistatic C-V measurements. Long-term stability for electron beam irradiated MOS capacitors has been examined through positive and negative bias-temperature (BT) stress aging. Devices annealed at 450° and 700°C result in faster and larger V_{FB} shifts and interface trap generation under BT stress than those for devices annealed at 1000°C. Around 1000°C annealing is found necessary to completely remove structural defects in the oxides induced by ionizing radiation and to assure good long-term stability for MOS devices fabricated by electron beam lithography.

The demand for achieving submicron pattern delineation has been recently increased for fabricating high performance LSI's. For this purpose, electron beam lithography and reactive ion etching (RIE), for example, have been used extensively. However, these high energy particles, or concurrently generated x-rays, create damage in the gate oxides, as they pass through the surface layers in the devices. Radiation damage studies are important, because radiation induced positive charge and neutral traps in the gate oxides of MOSFET's degrade device characteristics (1, 2) and enhance hot-electron induced instabilities (3). Therefore, there have been several studies made concerning characterization and annealing effect of radiation induced charge and traps (4-8). They are, however, concerned mainly with the annealability of radiation damage by only one time postmetallization annealing after irradiation. In an actual fabrication process, there are many irradiation and annealing processes. Therefore, it is practically important to understand the nature of the damage in the gate oxides and annealability of the damage by repeated irradiation and annealing processes.

This paper shows that repeated irradiation and annealing processes cause unremovable neutral traps to be generated, even at 700°C annealing, though they are annealed out completely by one irradiation and annealing cycle. In addition to the initial characterization of radiation damage in the repeated process, long-term stability of radiation damaged devices under bias-temperature stress was also examined, focusing on the annealing temperature effect.

Experimental

Sample preparation.—The devices were polysilicon gate MOS capacitors fabricated on p-type (100) silicon substrates with a resistivity of 0.1-0.2 Ωcm. Such a high doped substrate is necessary for the uniform injection of minority carriers, when the capacitors are avalanched (9). All MOS capacitors were fabricated by conventional photolithography and chemical etching. After forming thick field oxides and removing oxides in the gate area of 2.5×10^{-3} cm², a 30 nm thick gate SiO_2 was grown in a dry O_2 ambient at 950°C. Arsenic doped polysilicon electrodes were 450 nm thick, chemical vapor deposited at 730°C in an SiH_4-H_2-AsH_3 ambient, followed by annealing in a dry N_2 ambient at 900°C. After etching off polysilicon outside the gate area, CVD SiO_2 was deposited for surface passivation. Finally, CVD SiO_2 was removed in a contact region on the field oxides.

Key words: radiation damage, neutral trap, interface trap, MOS devices, long-term stability.

Some of the capacitors in a wafer were irradiated directly through CVD SiO_2 and polysilicon electrodes in an electron beam lithography system, while others were kept as unirradiated controls. The gate area of individual capacitors was scanned by a 20 keV electron beam. Dosages were varied in steps between 2×10^{-6} and 2×10^{-3} C/cm², where a standard irradiation dosage is about 2×10^{-5} C/cm² in our laboratory (10).

Annealing after electron beam irradiation was carried out in a dry N_2 ambient for 30 min. Annealing temperatures were varied between 400° and 1000°C. N_2 annealing, instead of forming gas annealing, was used because it is a widely used method in MOS fabrication processes, except for postmetallization annealing. In addition to the only one time irradiation and annealing experiment, repeated irradiation and annealing cycles were carried out considering actual MOS fabrication processes, *i.e.*, there are many irradiation and annealing processes after gate oxide formation.

Wafer samples were used for evaluating the annealing effect of radiation damage, whereas packaged devices were used for examining long-term stability of radiation damaged MOS capacitors. After electron beam irradiation and annealing at various dosages and temperatures, aluminum contacts to the polysilicon electrodes were made via a contact hole located on the thick field oxides. Aluminum was deposited by resistant heated evaporation. After contact pad formation, wafers were given a postmetallization annealing for 30 min in a forming gas at 450°C. Diced chips were, then, encapsulated in TO-5 packages. These samples were, therefore, given an additional forming gas annealing after post electron beam irradiation annealing in a dry N_2 ambient.

Evaluation method.—The densities of positively charged and neutral traps in the gate oxides and interface trap density at the SiO_2-Si interface were determined at various points during the experiments, *i.e.*, before irradiation and after a series of irradiations and annealings.

High frequency C-V curves were measured to determine the radiation-induced flatband voltage shift. Densities of neutral traps as well as positively charged traps were determined by uniformly injecting hot-electrons from the substrate into the gate oxides, and measuring the flatband voltage shift. The electron current through the gate oxides was generated by avalanche injection technique (11, 12). Avalanche injection was obtained by using repetitive double pulses (13) with a 20 μsec period. A positive injection pulse (5 μsec) was applied to the gate electrode, following

immediately after opposite polarity pulse (5 μsec), which sweeps minority carriers that accumulate at the inversion layer during a previous injection pulse. A constant average d-c current was maintained during avalanche injection by automatic adjustment of injection pulse voltage. Small current (4×10^{-8} A/cm^2) was used to fill the traps with large cross sections. As these traps saturated, the current was gradually raised to populate the remaining traps at an acceptable rate, but the current was restricted below 4×10^{-5} A/cm^2 to eliminate the generation of interface traps and oxide traps caused by hot-electron injection into the gate oxides. The injection was stopped periodically and flatband voltage and total injection charge was recorded directly into a computer. A large amount of data, about 500 data points, were recorded to obtain reliable values of cross sections and effective trap densities. By analyzing the relation of flatband voltage shift *vs.* injection charge, effective densities, and cross sections of various oxide traps may be obtained (14).

The distribution of interface trap density in the forbidden bandgap was determined by quasistatic C-V method (15, 16), which was also automated. Long-term stability was examined through BT stress aging, that is the aging of positive or negative bias applied to the gate electrodes at an elevated temperature. Stress biases were 3.5 MV/cm (+BT) and −3 MV/cm (−BT) and temperatures were 200°-300°C. Aging time was extended to 1000 hr. V_{FB} and interface trap density distribution were determined at a scheduled aging period at room temperature, after the samples were cooled to room temperature with the bias applied.

Results and Discussion

One time irradiation and annealing.—Figure 1 shows V_{FB} shifts before and after annealing for electron beam irradiated MOS capacitors, given as a function of irradiation dosages and annealing temperatures. Positive oxide charge induced by irradiation was reduced by annealing; 700°C annealing was found necessary to remove the positive oxide charge, when irradiation dosages are large.

The results of electron injection measurement are shown in Fig. 2. In this figure, the change in V_{FB}, which occurs as injected electrons are captured, is plotted against the number of injected electrons, as a function of annealing temperatures. The initial V_{FB} shift observed at less than 10^{14}/cm^2 injected electrons occurs due to electron trapping at positively charged traps. The subsequent V_{FB} shift, according to an increase in injected electrons, corresponds to the charging of neutral traps.

From the detailed analysis of the curve, six distinct trap cross sections were resolved for irradiated samples. Their cross sections and effective trap densities are shown in Table I for irradiated, annealed, and control samples. Traps A and B are identified as positively charged centers, because of their large cross sections. In fact, an estimated V_{FB} shift from the

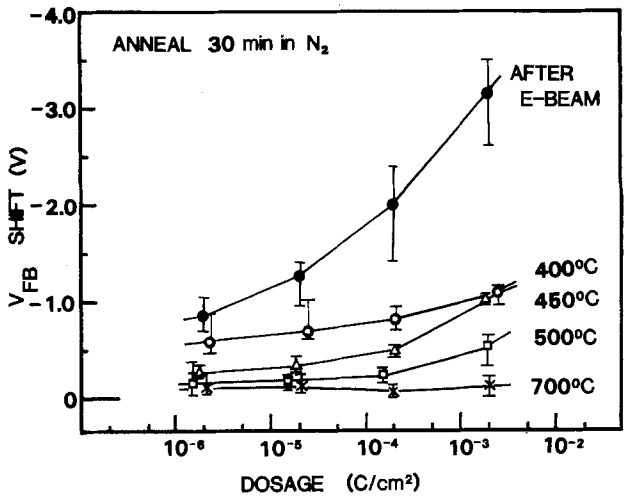

Fig. 1. Flatband voltage shift from preirradiation state for irradiated and annealed MOS capacitors, as a function of irradiation dosages.

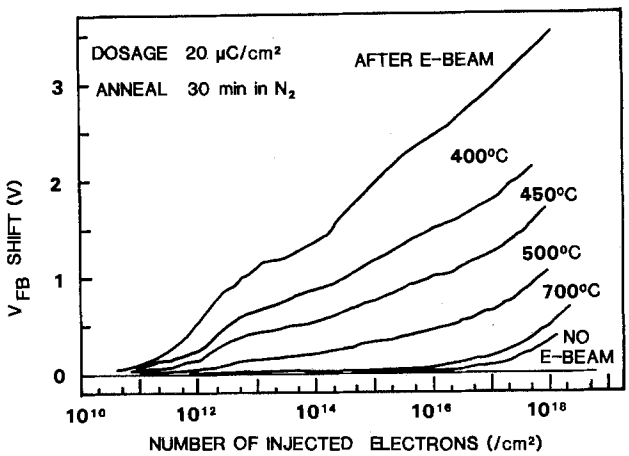

Fig. 2. Flatband voltage shift due to avalanche hot-electron injection into the gate oxides for irradiated, annealed after irradiation, and unirradiated MOS capacitors.

effective trap densities of traps A and B for irradiated samples, is in good agreement with the actual V_{FB} shift after irradiation. Trap A is also found to be removed easily by low temperature annealing, compared to trap B. From their cross sections, traps C and D are believed to be radiation induced neutral traps (5). Traps E and F exist even in the unirradiated samples. These traps have been discussed extensively and are thought to be water-related defects in the oxides (12, 17).

Interface traps over the entire bandgap were also generated due to electron beam irradiation. The density increased as irradiation dosage was increased. At 20 μC/cm^2 dosage, interface trap density at midgap

Table I. Trapping parameters for irradiated, annealed, and control devices

Trap	Charge	Cross section σ_1 (cm^2)	Effective density (cm^{-2})			
			Irradiated*	Annealed** 450°C	Annealed** 700°C	Control
A	+	$1\text{-}3 \times 10^{-13}$	5×10^{11}	—***	—	—
B	+	$3\text{-}7 \times 10^{-14}$	5×10^{11}	3×10^{11}	—	—
C	0	$6\text{-}9 \times 10^{-16}$	5×10^{11}	3×10^{11}	—	—
D	0	$5\text{-}9 \times 10^{-17}$	5×10^{11}	2×10^{11}	—	—
E	0	$3\text{-}5 \times 10^{-18}$	5×10^{11}	2×10^{11}	1×10^{11}	9×10^{10}
F	0	$2\text{-}5 \times 10^{-19}$	6×10^{11}	4×10^{11}	3×10^{11}	3×10^{11}

* 20 μC/cm^2 at 20 keV.
** 30 min in dry N_2.
*** Less than 1×10^{10}.

was about 3×10^{11} eV^{-1} cm^{-2}. These interface traps were removed completely by annealing at above 450°C.

From these measurements, it is concluded that, for polysilicon gate MOS structures, annealing at above 700°C is necessary to remove radiation induced positive charge and neutral traps, although 450°C annealing is enough to remove interface traps. This result is almost the same as Aitken's result (5), although a little higher temperature than 550°C is required for completely removing positive charge and neutral traps in the experiment.

Repeated irradiation and annealing.—Flatband voltage shifts due to avalanche hot-electron injection in the repeated irradiation and annealing processes for 700°C annealing is shown in Fig. 3. It is obvious that repeated irradiation causes considerable increase in radiation induced positive charge and neutral traps and that unremoved neutral traps after annealing gradually increase with repeated cycles.

Figure 4 shows the annealing temperature dependence of V_{FB} shifts and neutral trap density induced by repeated irradiation and annealing processes. Unremoved positive charge after annealing gradually increased as cycle proceeded for 450°C annealing. On the other hand, for 700° and 1000°C annealing, there was no increase in positive charge, as shown in Fig. 4(a). Neutral trap density after annealing also gradually increased for samples annealed at 450° and 700°C, whereas samples annealed at 1000°C did not show that increase, as shown in Fig. 4(b). It is noticeable that 700°C annealing is not enough to remove neutral traps induced by the repeated processes, though neutral traps are completely removed by the first irradiation and annealing cycle.

Figure 5(a) shows a typical change in interface trap density distribution after repeated irradiation and annealing processes, for 450°C annealing. Larger interface traps, mainly in the upper half of the bandgap, were generated by irradiation in the second and third cycles. Interface trap density peak, appeared at around 0.7 eV from the valence bandedge, is the same feature as reported by Ma (7). This peak seems to be caused by Si-O bond breaking near the SiO_2-Si interface under irradiation, because the recent theoretical work by Sakurai (18) has pointed out that stretched Si-O bonds cause interface trap generation in the upper half of the bandgap. An increase in interface traps generated by repeated irradiation may be attributed to the easiness of Si-O bond breaking, due to insufficient annealing in the repeated irradiation and annealing processes.

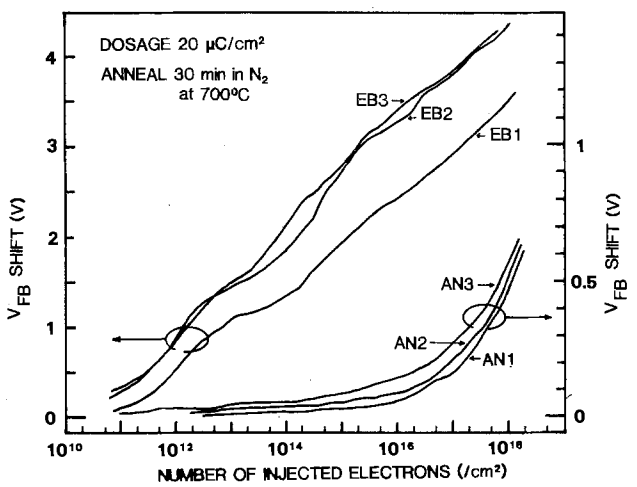

Fig. 3. Flatband voltage shift due to avalanche hot-electron injection into the gate oxides in repeated irradiation and annealing processes. EBn and ANn represent the nth cycle for electron beam irradiation and annealing, respectively.

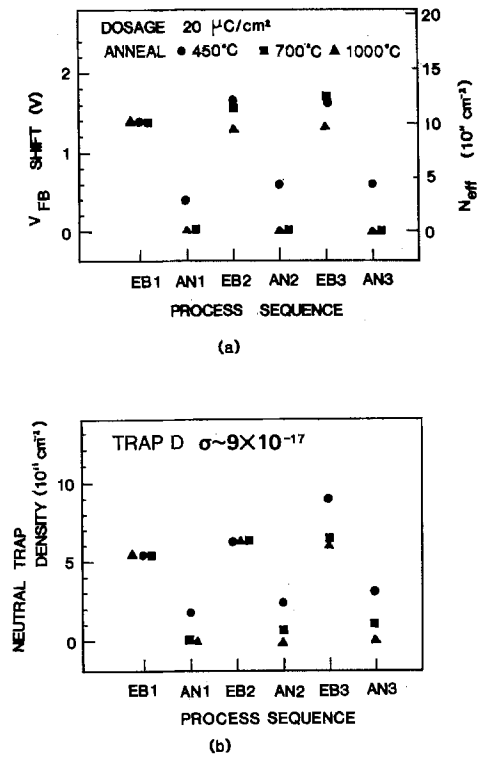

Fig. 4. Repeated irradiation and annealing processes: (a) flatband voltage shift and (b) neutral trap density. V_{FB} shifts are measured from preirradiation state.

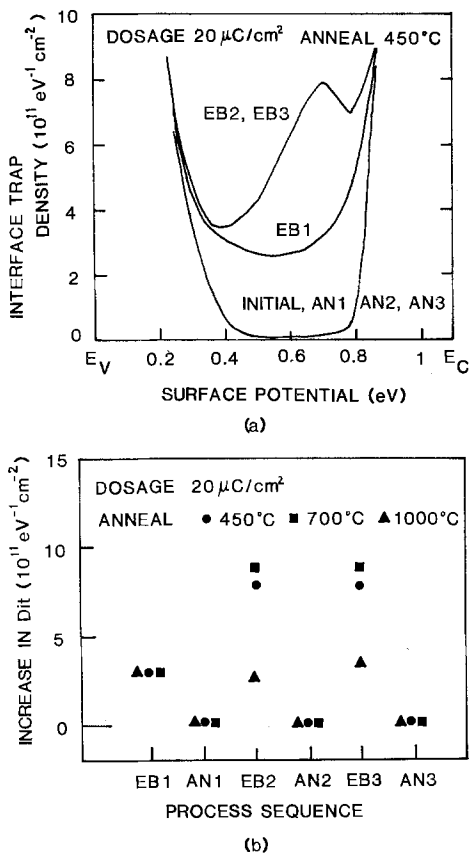

Fig. 5. Increase in interface trap density in repeated irradiation and annealing processes: (a) change in interface trap density distribution for 450°C annealing and (b) increase in interface trap density peak appeared at around 0.7 eV from the valence bandedge, as a function of annealing temperatures.

Annealing temperature dependence of interface trap generation in the repeated processes is shown in Fig. 5(b), where interface trap density peak is plotted

after various process steps. Larger interface traps were generated after irradiation in the second and third cycles, for samples annealed at 450° and 700°C, whereas samples annealed at 1000°C did not show any increase. On the other hand, in the annealing steps, interface traps were annihilated completely at above 450°C annealing temperatures, even after the third irradiation.

A remarkable fact in the experiment is that residual damage exists even at such a high temperature annealing as 700°C in the repeated irradiation and annealing processes, although radiation induced positive charge and neutral traps are removed completely at the first irradiation and annealing cycle. Measurements of residual stresses on SiO_2 films on silicon substrate have shown that structural defects induced by electron beam irradiation are removed by thermal annealing at such a high temperature as 800°C (19). Neutral traps are thought to be associated with these structural defects in the SiO_2 (5). The experiment reveals that structural defects induced by ionizing radiation require annealing temperature around 1000°C, and that 700°C is not sufficient to remove these defects, when taking into account repeated irradiation and annealing processes. This is consistent with the result reported by EerNisse (19).

Long-term stability.—In addition to the initial characterization of electron beam irradiation damage, long-term stability for damaged devices was examined, focusing on the annealing temperature effect.

The devices used in the experiment were passed through an additional forming gas annealing at 450°C after aluminum metallization. Table II displays the initial V_{FB} and average neutral trap density of traps C and D. Interface trap density at midgap were less than 1×10^{10} eV^{-1} cm^{-2} for all annealed samples. Comparing Fig. 1 and Table II, the additional forming gas annealing is found to reduce residual positive charge to about a half of that density, for samples annealed at 450° and 700°C, when compared to only N_2 annealing. On the other hand, neutral trap density was not changed, even after forming gas annealing.

Flatband voltage shift under bias-temperature stress aging.—Figure 6 shows V_{FB} shifts *vs.* aging time under positive and negative BT stress aging. A positive V_{FB} shift was observed under positive BT stress for only devices annealed at 450°C. Negative BT stress results in a negative V_{FB} shift for all devices. It is clearly seen that devices annealed at lower than 700°C revealed larger V_{FB} shifts, compared to devices annealed at 1000°C. V_{FB} shifts for unirradiated samples were almost the same as those for samples annealed at 1000°C.

A positive V_{FB} shift under positive BT stress is believed to be caused by electron trapping in the oxides, because electrons would inject from the substrate into the gate oxides under a positive bias applied to the gate at an elevated temperature. Since positive charge acts as electron trapping centers with large cross section, devices having large positive charge density would show appreciable positive V_{FB} shifts under positive BT stress. In fact, measurable V_{FB} shifts were observed for devices annealed at 450°C, which had large residual positive charge density, as shown in Table II.

Table II. Initial state for long-term stability experiment

Electron beam irradiation	Annealing* (°C)	Flatband voltage V_{FB} (V)	Effective density** of neutral traps (cm^{-2})
	450	−1.28	2×10^{11}
20 keV	700	−1.21	—***
2×10^{-5} C/cm²	1000	−1.18	—
20 keV	450	−1.33	5×10^{11}
	700	−1.22	5×10^{10}
2×10^{-3} C/cm²	1000	−1.17	—

* 30 min in dry N_2 at each temperature + 30 min at 450°C in forming gas.
** Average density of traps C and D.
*** Less than 1×10^{10}.

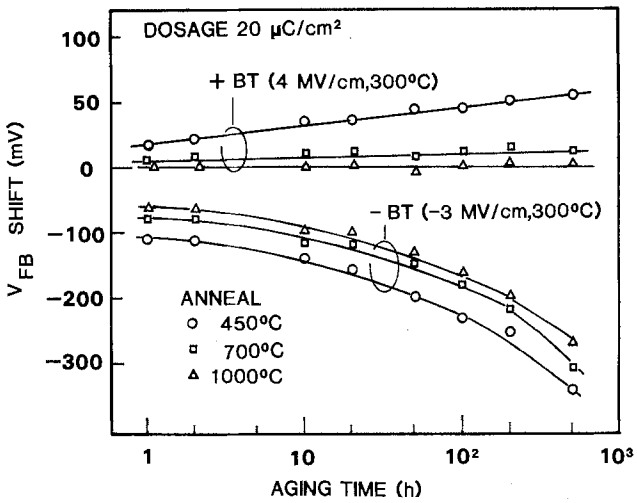

Fig. 6. Flatband voltage shifts *vs.* aging time under positive and negative BT stress aging for MOS capacitors annealed at various temperatures.

The presumption of the electron trapping in the positively charged centers is verified by the comparison of the V_{FB} shift due to avalanche hot-electron injection between nonstressed and stressed devices. The density of positively charged trapping center (trap B) was reduced from 8×10^{10} to 2×10^{10} cm^{-2} for devices annealed at 450°C after 2×10^{-3} C/m^2 irradiation, due to positive BT stress (4 mV/cm, 300°C and 1000 hr). This reduction is attributed to electron trapping at the positively charged centers under positive BT stress. The difference in trap density between nonstressed and stressed devices corresponds to about 70 mV V_{FB} difference. This estimated value is in good agreement with the actual V_{FB} shift of 100 mV.

It is well known that the negative V_{FB} shift accompanied with interface trap generation is revealed by negative BT stress, and is sometimes called slow trapping instability (20, 21). The negative V_{FB} shift is also known to be greater when the initial positive oxide charge density is large (20). Devices annealed at lower temperatures show larger negative V_{FB} shifts under negative BT stress in the experiment. This is accounted for by the fact that devices annealed at lower temperatures revealed larger positive oxide charge density in the prestressed state, as shown in Table II.

Interface trap generation under bias-temperature stress aging.—The BT stress also causes interface trap generation. Figure 7 shows typical changes in interface trap density distribution under positive and negative BT stress. Positive BT stress induces interface trap generation mainly in the upper half of the bandgap, its peak appears at around 0.7 eV from the valence bandedge. This is a common phenomenon, irrespective of device fabrication processes, although an increase in interface trap density depends on the gate oxide quality (22, 23). On the other hand, interface traps are generated mainly in the lower half of the bandgap under negative BT stress. This is also a common feature (21-23).

Figure 8 shows an increase in interface trap density (D_{it}) peak against aging time under positive BT stress, for devices annealed at various temperatures. In addition to the aging temperature dependence of the increase in D_{it} peak, as shown in Fig. 8, the aging bias field dependence for that increase was also examined.

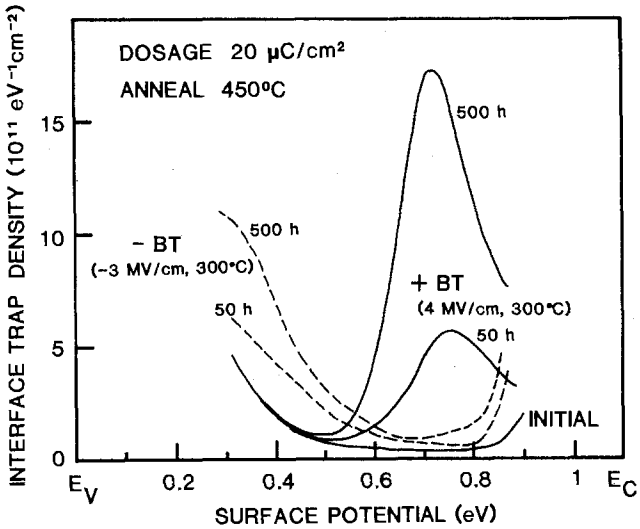

Fig. 7. Typical change in interface trap density distribution under positive and negative BT stress aging.

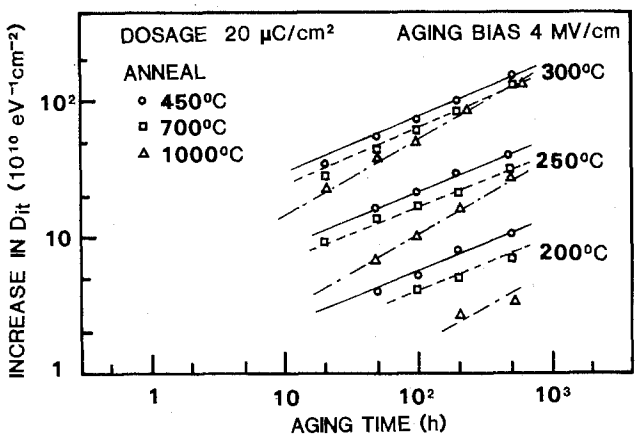

Fig. 8. Increase in interface trap density peak, which appeared at around 0.7 eV from the valence bandedge, vs. aging time under positive BT stress aging, as a function of annealing temperatures.

From these experimental curves of D_{it} increase *vs.* aging time, the increase in D_{it} peak (ΔD_{it}) is found to be expressed approximately as the following equations

450°C annealed

$$\Delta D_{it} \sim 1.5 \times 10^4\, t^{0.40} \exp\,(-0.65/kT + 3.0\sqrt{E_{ox}}) \quad [1]$$

700°C annealed

$$\Delta D_{it} \sim 1.2 \times 10^4\, t^{0.40} \exp\,(-0.65/kT + 3.0\sqrt{E_{ox}}) \quad [2]$$

1000°C annealed

$$\Delta D_{it} \sim 3.2 \times 10^5\, t^{0.55} \exp\,(-0.85/kT + 3.0\sqrt{E_{ox}}) \quad [3]$$

where the units for each quantity are ΔD_{it} (10^{10} eV^{-1} cm^{-2}), aging time t (hr), thermal voltage kT (eV), and aging bias field E_{ox} (MV/cm). These equations are in good approximation under below 5 MV/cm aging bias and at temperatures below 300°C.

These equations and Fig. 8 lead to the conclusion that devices annealed at 450° and 700°C show fast and large D_{it} increase at relatively low temperature stress, due to rather weak time dependence and low activation energy for the D_{it} generation, when compared to the dependence for devices annealed at 1000°C.

The interface trap generation in the upper half of the bandgap results in a positive threshold voltage shift for n-channel MOSFET's (22) and is called positive BT instability. Therefore, devices annealed at lower than 700°C are found to have enhanced positive BT instability. This enhancement may be attributed to the incomplete annealing out of structural defects near the SiO_2-Si interface, after electron beam irradiation. Since this BT instability is probably caused by breakng or stretching of strained Si-O bonds near the interface, incomplete annealing leads to more easily broken or stretched bonds.

Larger interface trap generation under negative BT stress was also observed with lowering annealing temperatures. Devices annealed at 450°C showed about two times larger D_{it} increase than devices annealed at 1000°C.

Conclusion

It has been shown that residual radiation damage in the form of neutral electron traps exists in the oxides for MOS capacitors, even after 700°C annealing in the repeated irradiation and annealing processes. The densities of neutral traps and interface traps at the SiO_2-Si interface after irradiation increase with repeated irradiation and annealing cycles. Devices annealed at lower than 700°C have been shown to reveal larger V_{FB} shifts and faster and larger interface trap generation under positive and negative BT stress aging. This BT instability is believed to be enhanced by residual structural defects near the SiO_2-Si interface, caused by incomplete annealing after irradiation. Annealing temperature around 1000°C is required to remove all the damage in the oxides and assure good long-term stability for the MOS devices fabricated by electron beam lithography. Removal of radiation induced structural defects, therefore, is difficult in MOS structures after aluminum metallization. It is urgently required to develop a more efficient low temperature annealing method or a new process for preventing electron penetration into the gate oxides during electron beam lithography.

Acknowledgments

The authors would like to thank Drs. T. Matsumoto, E. Arai, and T. Kitayama for their advice and encouragement. They are also indebted to members of the High Density Integration Section and the Patterning Technology Section for sample preparations.

Manuscript submitted Sept. 3, 1982; revised manuscript received Nov. 20, 1982. This was Paper 219 presented at the Montreal, Que., Canada, Meeting of the Society, May 9-14, 1982.

Any discussion of this paper will appear in a Discussion Section to be published in the December 1983 JOURNAL. All discussions for the December 1983 Discussion Section should be submitted by Aug. 1, 1983.

Publication costs of this article were assisted by Nippon Telegraph and Telephone Public Corporation.

REFERENCES

1. J. M. Aitken, *IEEE Trans. Electron Devices*, **ed-26,** 372 (1979).
2. J. M. Aitken, *J. Non-Cryst. Solids*, **40,** 31 (1980).
3. T. H. Ning, P. W. Cook, R. H. Dennard, C. M. Osburn, S. E. Schuster, and H. N. Yu, *IEEE Trans. Electron Devices*, **ed-26,** 346 (1979).
4. R. A. Gdula, *ibid.*, **ed-26,** 644 (1979).
5. J. M. Aitken, D. R. Young, and K. Pan, *J. Appl. Phys.*, **49,** 3386 (1978).
6. T. H. Ning *ibid.*, **49,** 4077 (1978).
7. T. P. Ma, G. S. Scoggan, and R. Leone, *Appl. Phys. Lett.*, **27,** 61 (1975).
8. Y. Sakakibara, E. Arai, H. Yoshino, T. Kobayashi, H. Akiya, and K. Hirata, *Jpn. J. Appl. Phys. Suppl.* **18-1,** 311 (1979).
9. E. H. Nicollian, A. Goetzberger, and C. N. Berglund, *Appl. Phys. Lett.*, **15,** 174 (1969).
10. Y. Sakakibara, T. Ogawa, K. Komatsu, S. Moriya, M. Kobavashi, and T. Kobavashi, *IEEE Trans. Electron Devices*, **ed-28,** 1279 (1981).
11. E. H. Nicollian and C. N. Berglund, *J. Appl. Phys.*, **41,** 3052 (1970).
12. E. H. Nicollian, C. N. Berglund, P. F. Schmidt, and

J. M. Andrews, *ibid.*, **42**, 5654 (1971).
13. M. Bakowski, R. H. Cockrum, N. Zamani, J. Maserjian, and C. R. Viswanathan, *IEEE Trans. Nucl. Sci.*, **ns-25**, 1233 (1978).
14. T. H. Ning and H. N. Yu, *J. Appl. Phys.*, **45**, 5373 (1974).
15. M. Kuhn, *Solid-State Electron.*, **13**, 873 (1970).
16. N. Shiono and T. Yashiro, *Jpn. J. Appl. Phys.*, **18**, 1087 (1979).
17. F. J. Feigl, D. R. Young, D. J. Dimaria, S. Lai, and J. Calise, *J. Appl. Phys.*, **52**, 5665 (1981).
18. T. Sakurai and T. Sugano, *ibid.*, **52**, 2889 (1981).
19. E. P. EerNisse and C. B. Norris, *ibid.*, **45**, 6196 (1974).
20. B. E. Deal, M. Sklar, A. S. Grove, and E. H. Snow, *This Journal*, **114**, 266 (1967).
21. A. Goetzberger, A. D. Lopez, and R. J. Strain, *ibid.*, **120**, 90 (1973).
22. N. Shiono and C. Hashimoto, *IEEE Trans. Electron Devices*, **ed-29**, 361 (1982).
23. N. Shiono, O. Nakajima, and C. Hashimoto, *This Journal*, **130**, 138 (1983).

XPS Study of Annealed SiO_2/GaAs Interfaces

U. König and E. Sasse

AEG-TELEFUNKEN Forschungsinstitut Ulm, D-7900 Ulm, Germany

ABSTRACT

SiO_2 has been deposited pyrolytically on GaAs of different orientations. The effects of annealing on these samples has been investigated with XPS. Between SiO_2 and GaAs, additional layers of Ga_2O_3 and As have been formed. Ga diffusion into SiO_2 is found. Orientation effects are discovered: the Ga amount in SiO_2 rises in the sequence from (111)B over (111)A to (100) and the As accumulation at the interface is more pronounced for (100). A simple model for oxidation and diffusion is proposed.

During many processes of device technology, surfaces of III-V semiconductors passivated with SiO_2 are submitted to the various annealing steps, such as contacts formation (1, 2), diffusion process (3), post implantation annealing (4), and sealing of semiconductor to glass (5). These processes are usually performed under vacuum, hydrogen, or nitrogen atmosphere. Extremely purified gases are seldomly used, so that a certain amount of oxygen and water may be present. They can easily reach the semiconductor surface due to the higher diffusion rate in unordered pyrolytical or sputtered SiO_2 in comparison with thermal SiO_2 (6-8). Additionally, oxygen is supplied by the unbridged oxygen in pyrolytically deposited SiO_2 (9). Our study, established by x-ray photoelectron spectroscopy (XPS), shows how the semiconductor interface and the composition of the passivation film are changed during annealing. In addition, we investigated a polarity effect, *i.e.*, the influence of the crystal orientation on the composition of the passivation film.

Experimental

(100), (111)A, and (111)B surfaces of GaAs, heavily Zn doped ($\approx 2 \cdot 10^{18}$ cm^{-3}), polished, and wet chemically cleaned, were covered with a 130 nm thick layer of SiO_2 during a conventional pyrolytic process using silane, nitrogen, and oxygen (10 min at 700 K). This was followed by annealing at 940 K during 1, 2, or 4 hr in an open reactor under nitrogen ambient (less than 1% impurities).

The XPS measurements were conducted with a Leybold LHS surface analysis system equipped with hemispherical analyzer and employing Mg-Kα x-rays. For evaluation, we predominantly used the Ga-3d, Ga-2p, As-3d, O-1s, and Si-2p lines. The small Ga content of the SiO_2 layer could only be detected with the intense Ga-Auger line. Peak overlapping of Si-2p and Ga-3p at the SiO_2/Ga_2O_3 interface required using the Si-2s line. The peaks were plotted on an X-Y recorder and integrated. Relative sensitivity factors for the quantitative determination of the profiles were obtained from samples of SiO_2, Ga_2O_3, and GaAs. No attempt was made to deconvolve the Ga-3d peak at the interface. Depth profiling was accomplished by Ar-ion sputtering. Sputter rates for SiO_2 and GaAs were found to be 1.6 and 2.5 nm min^{-1}, respectively. The depth resolution at the SiO_2/GaAs interface was about 11 nm.

Key words: GaAs passivation, gallium-oxide, orientation effects.

Results

Figure 1 shows the XPS result of an unannealed SiO_2 film which is typical for all substrate orientations. An abrupt interface (within the experimental depth resolution) is found for all components (Ga, As, Si, O). Figure 2 represents the change taken place near the interface and within the SiO_2 film after annealing. Situated in front of the stoichiometric semiconductor GaAs, a more or less pronounced accumulation of As is observed, depending on the orientation.

The As maximum approximately coincides with a Ga intensity minimum. Here, a transition occurs of the oxidation states of Ga, marked by the presence of two Ga-2p peaks, one with a higher kinetic energy be-

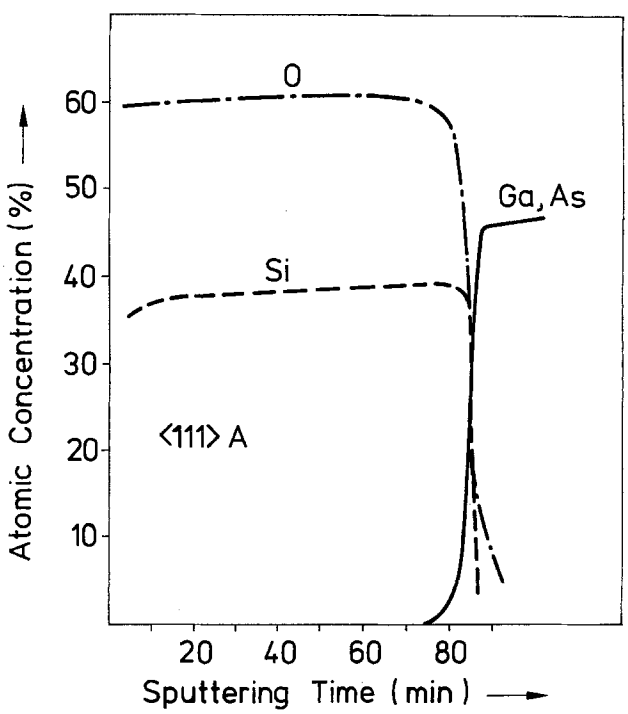

Fig. 1. XPS profile of the structure SiO_2/GaAs before annealing. Surface carbon is not indicated.

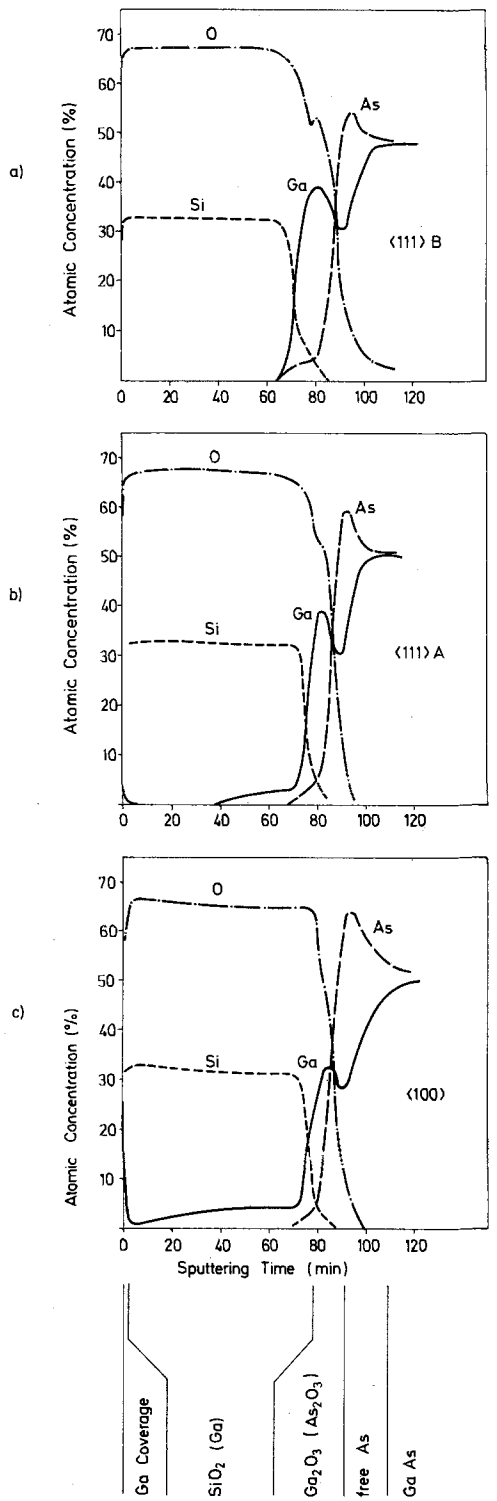

Fig. 2. Annealing influence on the SiO_2/GaAs structure evaluated by XPS. Annealing time 4 hr, annealing temperature 940 K. Substrate orientations are: (a) (III)B, (b) (III)A, and (c) (100). Surface carbon is not indicated. The resulting layer sequence is depicted at the bottom.

longing to GaAs, the other belonging to oxidized Ga in the following layer. The chemical shift cannot be deduced accurately due to charging effects.

This transition region is followed by a thin gallium-oxide layer (manifested by the Ga accumulation and the step in the flank of the oxygen profile), containing minor amounts of As and Si (owing to the less steep lower ends of the respective flanks). The atomic concentrations of Ga and O identify the gallium-oxide as Ga_2O_3. The gallium-oxide layer is apparently thicker for (111)B than for the other orientations. Furthermore, the bulk of the SiO_2 film is changed in its composition. It contains an increasing amount of Ga, rising in the sequence from (111)B over (111)A to (100). A Ga pile-up on the outer SiO_2 surface indicates that the surface collects the gallium species coming through the SiO_2 film. No phenomenological difference is established for different annealing times, apart from an increasing Ga quantity in SiO_2 with the annealing time.

Discussion

Let us first consider reactions at the oxide/semiconductor interface. When oxygen reaches the interface, it thermally oxidizes GaAs. For all orientations studied here, the final oxidation products ought to be Ga_2O_3 and As_2O_3. However, Ga_2O_3 dominates, mixed only with a minor quantity of As, most likely As_2O_3 (see Fig. 2). This is due to the fact that in the presence of GaAs the arsenic oxide is regarded as relatively unstable and is converted to Ga_2O_3 and elemental As (10, 11). The thicker Ga_2O_3 layer on (111)B probably reflects differential sputtering effects due to the more pronounced roughness of oxidized (111)B surfaces (12), and/or sputtering differences due to the varying composition of gallium-oxide on the differently orientated gallium-arsenide samples. The accumulation of free As between Ga_2O_3 and GaAs is found to be more intense on (100) than on other orientations, as similarly found with Auger analysis on free GaAs surfaces (13). Arsenic can be detached more easily from a (100) crystal, because there is equal preference for Ga and As each being doubly bonded. The diffuse transition between the free As layer and the stoichiometric (100) GaAs points to an intermediate layer of As-rich GaAs. Finding similar As quantities on (111)A and (111)B is in agreement with conclusions pertaining to oxidation rates at room temperature (10, 12). In this respect, our results verify that SiO_2-protected GaAs surfaces during annealing react like free GaAs surfaces.

We now turn to the characterization of the annealing influence on the SiO_2 protective layer. The Ga_2O_3 layer prevents diffusion of elemental As (14). Elemental Ga and/or Ga_2O, suspected of being the diffusing species (15), can easily be transported through Ga_2O_3 and enter the SiO_2 film. Both are also able to diffuse through SiO_2 [D (940 K) $\approx 1.8 \cdot 10^{-13}$ cm^2/sec (15)] and can reach the outer SiO_2 surface, similarly as found in backscattering experiments (16). The different amounts of Ga in SiO_2, depending on the orientation, reflect the individual reaction kinetics. When a (111)B orientation is used, the oxygen finds As triply bonded to the crystal. Due to the two "free" electrons of As, see Ref. (17), the oxidation leads predominantly to As_2O_3, which is subsequently converted to Ga_2O_3 and As (see above). No gallium species are formed, which would be capable of diffusion through SiO_2, as confirmed by Fig. 2a. It cannot be excluded, however, that a small amount of oxygen reacts with the underlying Ga leading at most to diffusion of a gallium species below the detection limit of XPS. Contrary to this, gallium-oxides (Ga_2O, Ga_2O_3) are formed directly, when the (111)A or (100) surfaces (these being constituted wholly or partly of Ga) are exposed to oxygen.

Furthermore, at our annealing temperature, free Ga exists in equilibrium with both gallium oxides (18). Therefore, Ga_2O and/or free Ga are responsible for the observed diffusion in SiO_2. The doubly bonded Ga in (100) can be more easily detached than the triply bonded Ga in (111)A. This raises the probability of generating diffusing Ga species for (100) and explains the larger quantity of Ga established in SiO_2 films on (100) (compare Fig. 2b and c).

Conclusion

We have observed oxidation of SiO_2 protected GaAs interfaces. On the source of the oxygen, either from

water or oxygen impurities in the nitrogen ambient during annealing of the SiO_2/GaAs system or from unbridged oxygen in the pyrolytically deposited SiO_2, no decision could be made. The observed variation in the SiO_2 composition and the ultrathin Ga_2O_3 and As layers at the interface may be responsible for changes in the optical parameters of the SiO_2/GaAs structure. Indeed a color change, depending on the respective substrate orientation, points to this: the starting pyrolytical SiO_2 film appears royal blue, the annealed layer on (100) alters its color to light blue, the one on (111)B lies between metallic and yellow-green, and that one on (111)A turns to yellow-green (19). In addition, it has been qualitatively found that the optical transmission of a layer annealed on (100) is better than on (111)A (20). A detailed study of optical and electrical criteria like refractive index and breakdown voltage of such layers is planned.

Acknowledgments

The authors wish to thank Dr. E. Kasper for useful discussions and critical reading, and W. Keck for sample preparation.

Manuscript submitted Sept. 23, 1982; revised manuscript received Nov. 30, 1982.

Any discussion of this paper will appear in a Discussion Section to be published in the December 1983 JOURNAL. All discussions for the December 1983 Discussion Section should be submitted by Aug. 1, 1983.

Publication costs of this article were assisted by AEG-TELEFUNKEN.

REFERENCES

1. T. Ito and Y. Saki, *Solid-State Electron.*, **17**, 751 (1974).
2. A. K. Sinha, *Appl. Phys. Lett.*, **26**, 171 (1975).
3. J. A. Turner, in "Proc. of the First Intern. Symp.," p. 213, Inst. of Phys. Soc., London (1966).
4. J. S. Harris, F. H. Eisen, B. Welch, J. D. Haskell, R. D. Pashley, and J. W. Mayer, *Appl. Phys. Lett.*, **21**, 601 (1972).
5. G. A. Antypas and J. Edgecumbe, *Appl. Phys. Lett.*, **26**, 371 (1975).
6. F. J. Norton, *Nature*, **191**, 701 (1961)
7. E. J. Williams, *J. Am. Ceram. Soc.*, **48**, 190 (1965).
8. R. Pfeffer and M. Ohring, *J. Appl. Phys.*, **52**, 777 (1981).
9. M. Kuisl, *Z. Angew. Phys.*, **28**, 342 (1970).
10. C. W. Wilmsen, *J. Vac. Sci. Technol.*, **19**, 279 (1981).
11. X. Wang, A. Reyes-Mena, and D. Lichtman, *This Journal*, **129**, 851 (1982).
12. K. Löschke and K. Kühn, *Krist. Tech.*, **10**, K 45 (1975).
13. J. Shiota, N. Miyamoto, and J. Nishizawa, *This Journal*, **124**, 1405 (1977).
14. C. W. Wilmsen, R. W. Kee, and K. M. Geib, *J. Vac. Sci. Technol.*, **16**, 1434 (1979).
15. S. Wagner and E. J. Povilonis, *This Journal*, **121**, 1487 (1974).
16. J. Gyulai, J. W. Mayer, J. V. Mitchell, and V. Rodriguez, *Appl. Phys. Lett.*, **17**, 332 (1970).
17. B. Truck, *J. Mater. Sci.*, **10**, 321 (1975).
18. J. A. Sheka, J. S. Chaus, and T. T. Mityurewa, "The Chemistry of Gallium," Elsevier Publishing Company, Amsterdam, Holland (1966).
19. W. Keck, Personal communication.
20. S. Weber, Personal communication.

Properties of Sputtered Molybdenum Silicide Thin Films

T. P. Chow,* D. H. Bower,*,[2] R. L. Van Art,[1] and W. Katz

General Electric Corporate Research and Development, Schnectady, New York 12301

ABSTRACT

The structural, compositional, and electrical properties of molybdenum silicide (with an Si/Mo ratio between 2 and 2.3) thin films either sputtered from a hot-pressed, composite target or cosputtered from elemental targets are compared. Structural and compositional examination was performed with x-ray diffraction, Rutherford backscattering spectrometry (RBS), and secondary ion mass spectrometry (SIMS). X-ray diffraction revealed that the as-deposited silicide films were essentially amorphous but, after high temperature annealing, contained mostly tetragonal $MoSi_2$. SIMS depth profiling showed that the concentration of carbon and argon is lower in the cosputtered films but that of oxygen is higher than the alloy-sputtered films. This difference is attributed to the target purity and sputtering system configuration. Isothermal and isochronal annealing resulted in a minimum resistivity of ~100 $\mu\Omega$-cm in both cases. C-V measurements of silicide-gate capacitors with both types of films yielded similar values of work function and surface-state density.

Molybdenum silicide is one of several refractory metal silicides which are being actively investigated as highly conductive gate and interconnection material for very large scale integrated (VLSI) circuits (1-12). It has a high melting point (2030°C), low resistivity [21.6 $\mu\Omega$-cm for bulk samples (13)], small grain size, oxidation resistance, and inertness with most chemicals used in semiconductor processing. Various deposition methods have been reported: sputtering from composite or mixed metal/silicon targets (1-8), cosputtering or coevaporation from doped or undoped elemental sources (4, 9, 10), and reactive sputtering with phosphine or silane and argon (11, 12). Since thin film properties of these silicides are highly dependent on the deposition conditions, optimization of various parameters is needed for each method. In this paper, the properties of molybdenum silicide films sputtered from a hot-pressed target and cosputtered from molybdenum and phosphorus-doped silicon targets are discussed and compared.

* Electrochemical Society Active Member.
[1] Present address: General Electric Microelectronic Center, Research Triangle Park, North Carolina 27709.
[2] Present address: NCR Corporation, Colorado Springs, Colorado 80907.
Key words: refractories, phases, resistivity, capacitor.

Experimental Procedure

Molybdenum silicide films were deposited onto, unless otherwise stated, oxidized or unoxidized silicon substrates by either sputtering from a hot-pressed, composite target (MRC, MOS Grade, 99.7%) in a planar system (MRC603) or cosputtering from separate molybdenum (Varian, 99.99%) and phosphorus-doped silicon (Varian, 99.9999%, 0.005-0.009 Ω-cm) targets in an S-Gun system (Varian 3140). In the load-locked, planar magnetron system (MRC603), the wafers are vertically mounted on a susceptor which is closely (~2 cm) coupled to the target. The loading procedure here involves placing the susceptor onto a load lock port which is then pumped down to 100 mTorr. Then, the susceptor is exchanged into the main chamber which is pumped to less than 5×10^{-7} Torr with a cyropump prior to sputtering. Typically, with a d-c power level of 3 kW and an argon pressure of 3 mTorr, a deposi-

tion rate of ~1000 Å/min was measured. In the batch, S-Gun system, the wafers are mounted onto a rotating planetary which is about 20 cm away from the targets. Before each deposition, the system is pumped down to 2×10^{-6} Torr, baked out at 200°C for 20 min, and further pumped to less than 5×10^{-7} Torr, also with a cyropump. An argon pressure of 4 mTorr was selected here to maximize the deposition rate while reducing arcing and cracking in the doped silicon target. A typical rate of 85 Å/min was obtained.

RBS was performed with a 2 MeV $^4He^+$ beam from a linear accelerator. X-ray diffraction was done on a Siemens D500 automated diffractometer and SIMS on a Cameca IMS 3-f ion microscope with a cesium beam of 17 kV.

MOS capacitors were made on (100), n-type, 8-12 Ω-cm wafers for silicide films sputtered from a composite target and on (100), p-type, 4-6 Ω-cm ones for cosputtered films. Various thicknesses (< 3000Å) of oxide were grown at 1000°C in dry oxygen.

Structure and Composition

RBS.—For cosputtered films, the silicon-to-molybdenum atomic ratio needs to be carefully monitored to insure run-to-run reproducibility and uniformity. Here, the ratio has been estimated from RBS, and rate and density considerations. Figure 1 shows the relationship between this ratio as determined from RBS and rate ratio estimated from the target power levels used in prior, separate molybdenum and silicon calibration runs. A fairly linear dependence can be observed. In comparison, the silicide film from the composite target had an Si/Mo ratio of 2.1, as determined from RBS.

X-ray diffraction.—Molybdenum disilicide is known to exist in either a body-centered-tetragonal (t-$MoSi_2$) or a hexagonal (h-$MoSi_2$) structure. The hexagonal-to-tetragonal transition has been shown to take place at ~800°C (14). The unit cell of the tetragonal phase is depicted in Fig. 2. Each molybdenum atom is surrounded by ten silicon atoms and each silicon atom similarly by five molybdenum and five silicon atoms. The Mo-Si and Si-Si bond distance is 2.617Å, leading to a valence of 5.50 for molybdenum and 4.45 for silicon. Since molybdenum and silicon usually have a valence of 6 and 4, respectively, a transfer of valence

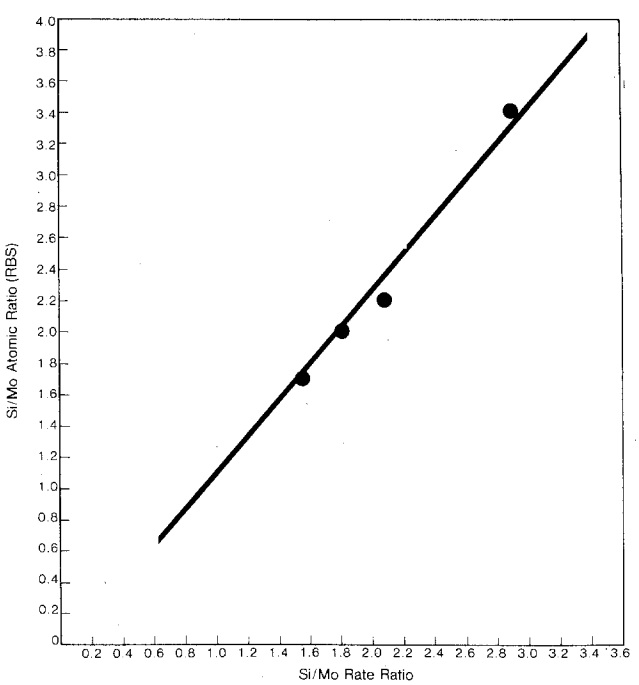

Fig. 1. Silicon-to-molybdenum atomic ratio as determined from RBS as a function of Si/Mo deposition rate ratio.

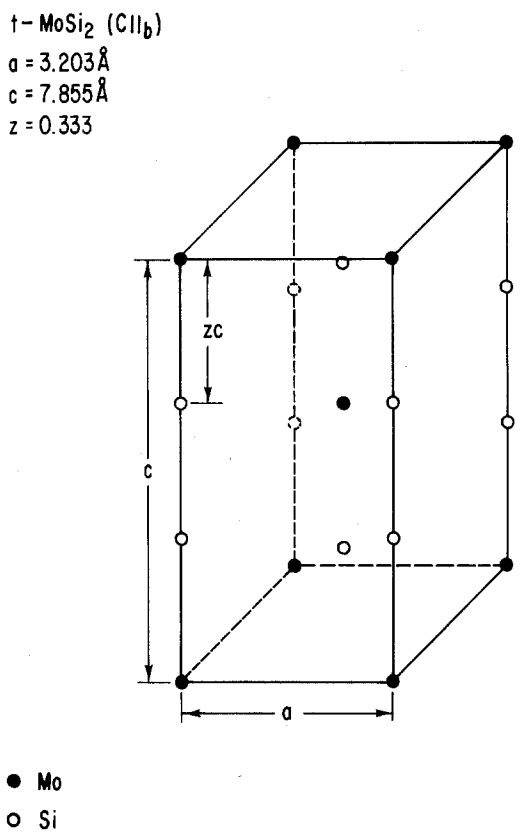

Fig. 2. The unit cell of tetragonal $MoSi_2$

electrons from molybdenum to silicon atoms is suggested (15). As deposited, both alloy-sputtered and cosputtered films had very small crystallites. In Fig. 3(a), the x-ray diffraction pattern of a 3000Å thick $MoSi_2$ film deposited from a composite target is shown. Other than the reflection from the Si (111) substrate, there is only a broad peak around 2θ of 41.6°, corresponding to the (111) peak of h-$MoSi_2$. A grain size of 12Å is estimated from the diffraction line broadening. Upon annealing at 1000°C for 1 hr, significant recrystallization took place, resulting in a pattern shown in Fig. 3(b). The film had tetragonal $MoSi_2$ as the major phase, with small traces of hexagonal $MoSi_2$ and Mo_2C or carbon-stabilized, hexagonal Mo_5Si_3 (8). The diffraction peaks of the minor phases were at 38.1, 38.9, 42.3, and 44.1°, corresponding to d spacings of 2.36, 2.31, 2.13, and 2.05Å, respectively. These weak peaks can be correspondingly attributed to either Mo_2C (111), h-$MoSi_2$ (110) and (111), and Mo_2C (200), or the (210), (102), (211), and (112) peaks of hexagonal Mo_5Si_3. In comparison, the diffraction pattern of a cosputtered sample with an Si/Mo ratio of 2.2, after annealing at 1000°C for 1 hr, is shown in Fig. 3(c). This spectrum is very close to that of the alloy-sputtered film and can also be matched to t-$MoSi_2$. Comparing both diffraction patterns with the standard powder pattern, it can be seen that these silicide thin films have a (110)-orientation. However, in contrast, no trace of either carbide phase was detected. Also, the presence of any silicon grain cannot be unambiguously determined because of interference from the silicon substrate. Furthermore, there are significant differences in SIMS depth profiles, as is shown below.

SIMS.—SIMS depth profiles were obtained to detect compositional uniformity and contaminants present. Here, the cosputtered sample had an Si/Mo ratio of 2.0, as determined from RBS. The relative intensities of various ions, carbon ($^{12}C^-$), oxygen ($^{16}O^-$), silicon ($^{30}Si^{--}$), argon ($^{40}Ar^-$), and molybdenum ($^{92}Mo^-$), were measured as a function of cesium ion milling

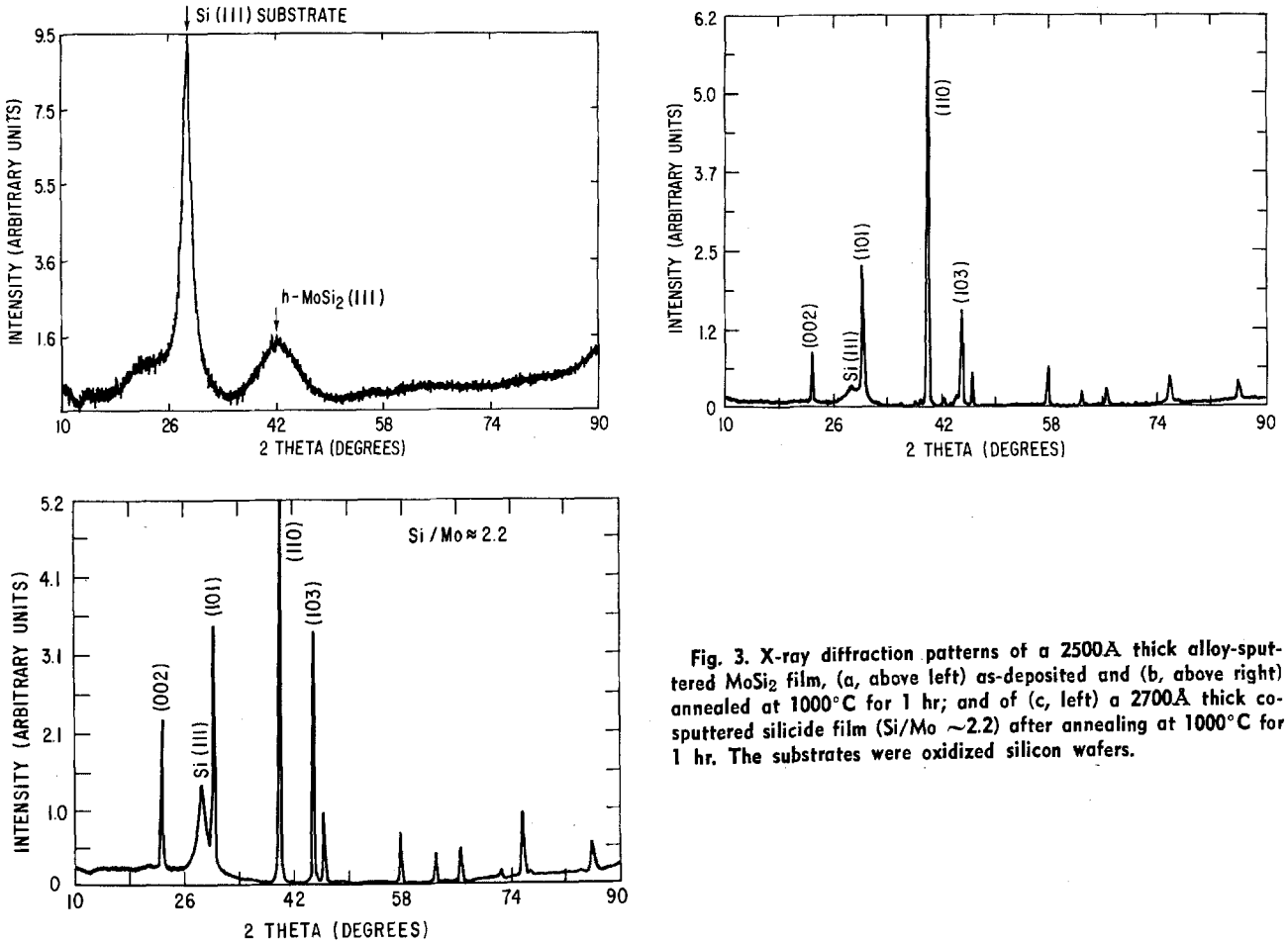

Fig. 3. X-ray diffraction patterns of a 2500Å thick alloy-sputtered $MoSi_2$ film, (a, above left) as-deposited and (b, above right) annealed at 1000°C for 1 hr; and of (c, left) a 2700Å thick co-sputtered silicide film (Si/Mo ~2.2) after annealing at 1000°C for 1 hr. The substrates were oxidized silicon wafers.

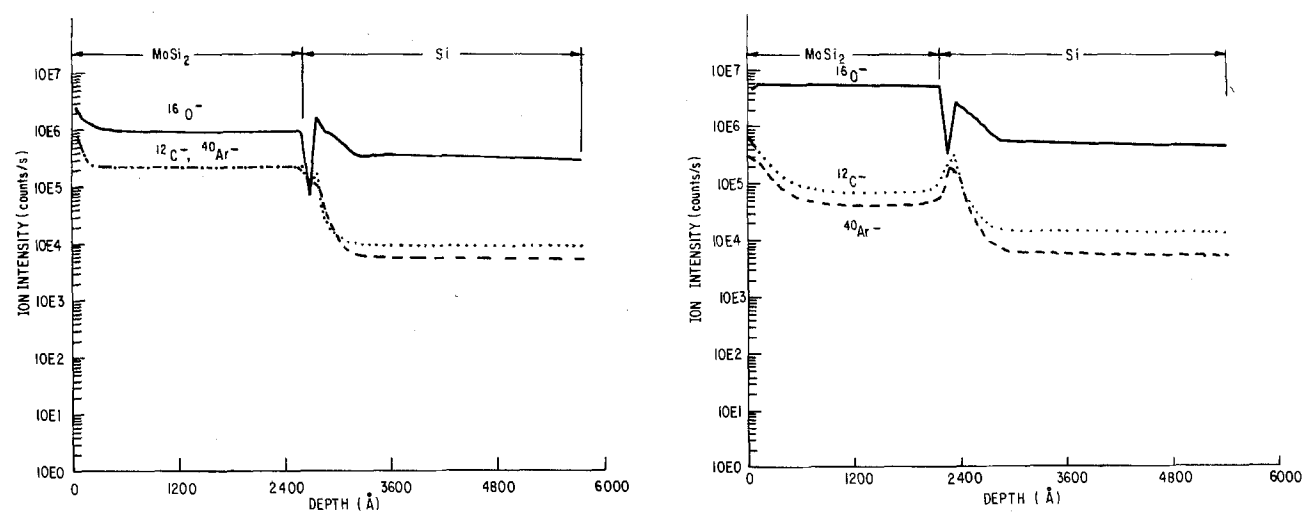

Fig. 4. SIMS depth profiles of various contaminants (oxygen, carbon, and argon) of (a, left) alloy-sputtered and (b, right) cosputtered (Si/Mo ~2.0) silicide film on silicon substrate.

time or depth. In both types of films, the Si/Mo ratio is fairly constant throughout. However, the level of containment differs greatly, as shown in Fig. 4(a) and (b), where the ion intensity of carbon, oxygen, and argon is shown as a function of depth. The ratios of these levels are listed in Table I. The amounts of carbon and argon are 3-6 times lower in the co-sputtered sample but that of oxygen is 6 times higher than the alloy-sputtered sample. The decrease of argon content can be attributed to the difference in the sputtering system configuration. In the planar system used for sputtering from a hot-pressed target, the substrates and the target (cathode) are more closely spaced (~2 cm) than in the S-Gun. In the latter, the substrates are situated in the planetaries far (~20 cm) from the target assembly. Since similar vacuum conditions were maintained for both systems, the higher level of oxygen in the cosputtered films can

Table I. Ratios of contaminant levels in alloy-sputtered and cosputtered molybdenum silicide thin films

Element	Ratio (alloy-sputtered/cosputtered)
Oxygen	1/6
Carbon	3
Argon	6

be explained by the lower deposition rate (85 *vs.* 1000 Å/min). The lower concentration of carbon, on the other hand, is due to the higher purity obtainable from elemental targets. Finally, phosphorus is also incorporated into the cosputtered films from the doped silicon target. Its concentration has been estimated to be ~8 × 10^{19}/cm^3 (16). Similar levels of contaminants have been observed for niobium silicide films sputtered from a composite target (17).

Electrical Properties

To monitor the electrical properties of these silicide films, the sheet resistance and MOS characteristics were measured with four-point probe and high-fre-

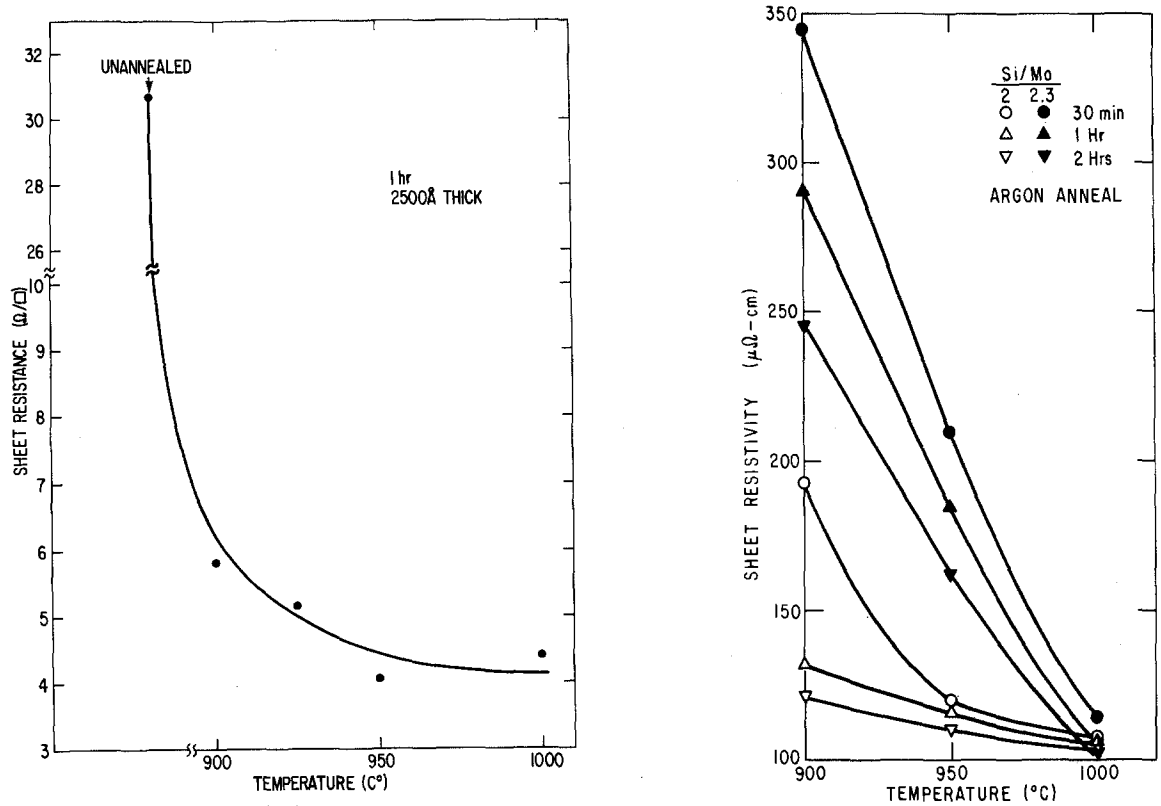

Fig. 5. Sheet resistance or resistivity of (a, left) alloy-sputtered and (b, right) cosputtered (Si/Mo ~2.0 and 2.3) silicide films as a function of annealing temperature.

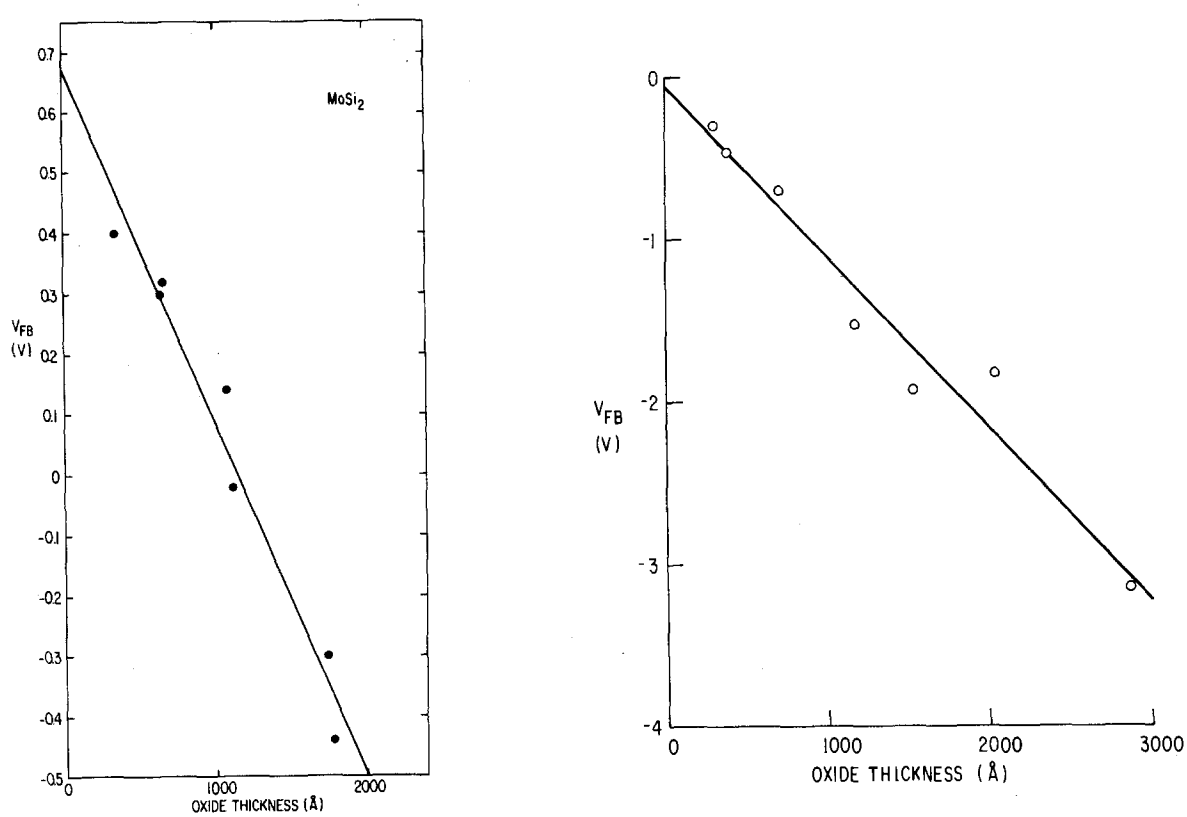

Fig. 6. Flatband voltage of (a, left) alloy-sputtered and (b, right) cosputtered (Si/Mo ~2.2) silicide-gate MOS capacitors vs. oxide thickness.

quency capacitance-voltage (C-V) techniques, respectively.

Resistivity.—$MoSi_2$ is a p-type metallic conductor (18), a result of its band characteristics (19). A fairly small effective carrier concentration of 0.2 per molecule and a Hall mobility of 58.9 cm^2/V-sec has been measured for bulk t-$MoSi_2$. Thin films deposited from a composite target had a resistivity of ~900 $\mu\Omega$-cm, but high temperature annealing lowered it significantly, consistent with the recrystallization described earlier. The isochronal annealing of a 2500Å thick film is shown in Fig. 5(a). The sheet resistance was decreased from 31 to 4.1-5.6 Ω/square between 900°-1000°C after 1 hr. The isochronal annealing of cosputtered silicide films was studied for two Si-to-Mo ratios, 2 and 2.3. In Fig. 5(b), the sheet resistivity of a 2700Å thick film with an Si/Mo ratio of 2 and a 4150Å thick film with Si/Mo ~2.3 are plotted *vs.* annealing temperature for times up to 2 hr. The cosputtered silicide films had as-deposited resistivity of 1200 and 2400 $\mu\Omega$-cm for $MoSi_2$ and $MoSi_{2.3}$, respectively. After 2 hr at 900°C, the corresponding values were 245 and 120 $\mu\Omega$-cm. However, at 1000°C, the resistivity decreased to approximately the same value of 100 $\mu\Omega$-cm. Clearly, the 1000°C heat-treatment is necessary to minimize the resistivity within a reasonable time period.

C-V measurements.—To compare the characteristics of MOS devices with both types of films, capacitors were fabricated with varying oxide thicknesses (300-3000Å). High-frequency C-V measurements yielded flatband voltage. Then, the silicide work function and surface-state density can be deduced from the V_{FB} *vs.* t_{ox} relationship, which is shown in Fig. 6(a) and (b), where Fig. 6(a) is taken from Ref. (8). Similar work function values of 4.9 and 4.8 eV and surface-state densities of 1.3×10^{11} and $2.3 \times 10^{11}/cm^2$ were obtained for alloy-sputtered and cosputtered silicide-gate devices, respectively.

Summary

The structural, compositional, and electrical properties of molybdenum silicide thin films sputtered from a composite target and cosputtered from separate metal and doped silicon targets are compared. The level of carbon and argon is higher in the alloy-sputtered films while that of oxygen is lower due to the difference in target purity and sputtering system configuration. Similar values of resistivity (~100 $\mu\Omega$-cm) was obtained after high-temperature annealing. Also, comparative C-V measurements yielded similar work function and surface-state density values. Finally, it will be interesting to comparatively study the effect of differences in impurity and contaminant levels on other properties, such as oxidation and etching.

Manuscript submitted Aug. 25, 1982; revised manuscript received Dec. 2, 1982.

Any discussion of this paper will appear in a Discussion Section to be published in the December 1983 JOURNAL. All discussions for the December 1983 Discussion Section should be submitted by Aug. 1, 1983.

Publication costs of this article were assisted by the General Electric Company.

REFERENCES

1. T. Mochizuki, K. Shibata, T. Inoue, and K. Ohuchi, *Jpn. J. Appl. Phys.*, **17**, Supp. 17-1, 37 (1978).
2. T. P. Chow and A. J. Steckl, *Appl. Phys. Lett.*, **36**, 297 (1980).
3. T. Mochizuki, T. Tsujimaru, M. Kashiwagi, and Y. Nishi, *IEEE Trans. Electron Devices*, **ed-27**, 1431 (1980).
4. R. S. Nowicki and J. F. Moulder, *This Journal*, **128**, 562 (1981).
5. P. Cappelletti, T. Mori, G. Pignatel, G. Ferla, F. Nava, and G. Ottaviani, in "Semiconductor Silicon 1981," H. R. Huff, R. J. Kriegler, and Y. Takeishi, Editors, PV 81-5, p. 608, The Electrochemical Society Softbound Proceedings Series, Pennington, NJ (1981).
6. T. Tanaka, H. Ishiuchi, Y. Takeuchi, M. Ishikawa, T. Mochizuki, and O. Ozawa, *IEEE IEDM, Technical Digest*, 659 (1981).
7. T. P. Chow, A. J. Steckl, and R. T. Jerdonek, *IEEE Electron Device Letters*, **edl-3**, 37 (1982).
8. T. P. Chow, C. S. Grant, W. Katz, G. Gildenblat, and R. F. Reihl, Abs. 301, p. 494, The Electrochemical Society Extended Abstracts, Vol. 82-1, Montreal, Que., Canada, May 9-14, 1982.
9. H. J. Geipel, Jr., N. Hsieh, M. H. Ishaq, C. W. Koburger, and F. R. White, *IEEE Trans. Electron Devices*, **ed-27**, 1417 (1980).
10. S. P. Murarka, D. B. Fraser, T. F. Retajczyk, Jr., and T. T. Sheng, *J. Appl. Phys.*, **51**, 5380 (1980).
11. S. Yanagisawa and T. Fukuyama, *This Journal*, **127**, 1120 (1980).
12. S. Inoue, N. Toyokura, T. Nakamura, and H. Ishikawa, *ibid.*, **128**, 2402 (1981).
13. N. S. Neshpor and G. V. Samsonov, *Fiz. Tverd. Tela*, **2**, 2202 (1960).
14. S. Yanagisawa and T. Fukuyama, *This Journal*, **127**, 1150 (1980).
15. L. Pauling, in "Molybdenum Compounds," D. Killifer and A. Linz, Editors, p. 95, Interscience Publishers, NY (1952).
16. T. P. Chow, Ph.D. Thesis, Rensselaer Polytechnic Institute, Troy, New York, p. 35 (1982).
17. C. D. Rude, T. P. Chow, and A. J. Steckl, *J. Appl. Phys.*, **53**, 5703 (1982).
18. V. S. Neshpor and G. V. Samsonov, in "Refractory Transition Metal Compounds; High Temperature Cements," G. V. Samsonov, Editor, p. 162, Translated, Academic Press Inc., New York (1964).
19. H. Schenk and U. Dehlinger, *Acta Metall.*, **4**, 7 (1956).

A Raman Study of Etching Silicon in Aqueous KOH

E. D. Palik, H. F. Gray, and P. B. Klein

Naval Research Laboratory, Washington, D.C. 20375

ABSTRACT

Orientation-dependent etching of silicon by aqueous KOH is a standard procedure in the microelectronics industry. We have measured the etching products by recording the Raman spectra in real time as the etching of {100} silicon progressed in a 5M KOH solution. The primary etching species has been determined to be OH^-, and the etching products have been determined to be the silicate $SiO_2(OH)_2^=$. Isopropyl alcohol does not appear to participate chemically in the etching process.

Aqueous KOH is used as an orientation-dependent etching solution (1) throughout the microelectronics industry to make a variety of silicon devices such as V-grooves for VMOS transistors (2, 3), pyramids for field-emitter arrays (4), small holes for ink jets (5), and thin-wall Josephson junctions (6). Previously re-

ported etching studies (7-10) suggested that the final etch products might be $SiO_3^=$, $SiO_4^=$, or K_2SiO_3, and plausible chemical reaction equations were put forth. We have suggested (11) that monolayers of silicon dioxide or silicates can coat each atomic plane differently, thereby, causing the orientation dependence.

In this study, we monitored the etching process *in situ* in real time by Raman spectroscopy as the etching progressed. Unfortunately, we were unable to monitor the surface reaction directly by reflection Raman scattering because the number of adsorbed molecules was probably below the detection sensitivity of our instrumentation.

Experimental

The Raman excitation source was a CW Argon-ion laser emitting the 4880Å line. Power incident on the cell was about 300 mW after elimination of the plasma lines by a diffraction grating. A Jarrell Ash Model 25-100 double monochromator with a cooled RCA C31034A GaAs photomultiplier and photon counting electronics were used to obtain the Raman spectra. The spectra were stored in a Nicolet Model 1070 multichannel analyzer and plotted out on an X-Y recorder.

The etching container was a fused quartz cell, 1 × 1 × 4.5 cm^3, with polished sides and bottom. This cell was heated by a tungsten wire which was encapsulated in a thin quartz tube and inserted into the cell in such a way that the laser light path was not affected. The etching solution was an aqueous 5M KOH (3.0×10^{21} KOH molecules/cm^3) solution. Etching was performed at 62°C to provide a sufficient etch rate. Etching of the quartz container was estimated to be about 2.5×10^{-4} that of the silicon sample (11-13) and, thus, was considered to be negligible.

Each silicon sample consisted of a piece of a standard {100} silicon wafer, 1 × 5 × 0.03 cm^3, n-type (phosphorus doped), 10 Ω cm (1×10^{15}/cm^3). The silicon sample was placed into the cell in such a way that the incident beam, propagating vertically into the cell (and parallel to the monochromator slit), was focused 1-2 mm in front of the sample surface. The 90° scattered light was focused into the monochromator. The spectral resolution was set at 4 cm^{-1} because the spectra were recorded rather rapidly and because the spectral linewidths were usually greater than 20 cm^{-1}. The laser light was polarized in the horizontal plane and perpendicular to the propagation directions of both the incident and scattered beams. No analyzing polarizer was used in the collecting system, so the resulting data were unpolarized.

Results

Aqueous 5M KOH solution.—The Raman spectrum of a fresh 5M KOH etching solution is shown in Fig. 1a. This spectrum is characteristic of liquid H_2O with the addition of OH^- ions (14, 17) which give rise to the molarity-dependent sharp line at 3610 cm^{-1}. The four major water features are as follows. The broad line at 3420 cm^{-1} is due to the bond-stretching vibration mode (15), the weak broad line near 2120 cm^{-1} is due to a short-range intermolecular mode (16), the line at 1640 cm^{-1} is an angle-bending mode, and the broad line at about 550 cm^{-1} is due to a librational mode. The large increase in intensity below 300 cm^{-1} is probably due to a combination of Rayleigh scattering and Raman scattering of low-frequency modes (18). Although Fig. 1a was taken at 21°C, the spectrum taken at 62°C was essentially identical.

After a silicon sample was immersed into the etching solution, several minutes of etching were required to remove the native oxide. Silicon etching commenced when hydrogen bubbles (7) were visibly observed. Etch rates at 62°C were measured to be about 3000 Å/min (by measuring the sample thickness with a micrometer), which is comparable to a reported

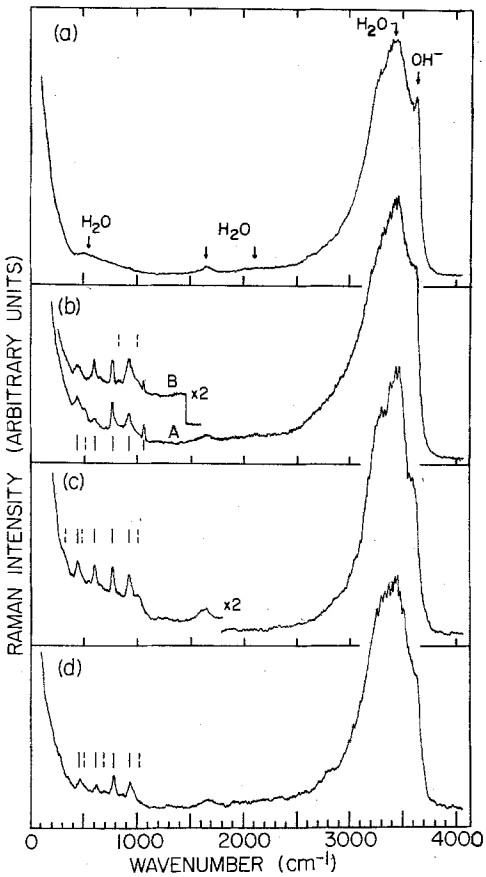

Fig. 1a. Raman spectrum of an aqueous 5M KOH etching solution at 21°C. Arrows indicate H_2O and OH^- vibrational bands. The background is due primarily to elastically scattered light and photomultiplier noise; 1b. A Raman spectrum of an aqueous 5M KOH etching solution at 62°C which contains about 0.11g of dissolved silicon (6×10^{20} Si/cm^3) at the beginning of the run. Silicon lines appear and grow in the low-frequency region. Curve B is a 62°C spectrum started after about 0.35g of Si dissolved (2×10^{21} Si/cm^3). The solid vertical bars indicate the definite line positions listed in Table I. The dashed vertical bars refer to unresolved structures, and these are marked with a (?) in Table I; 1c. A Raman spectrum of an aqueous 2.8M $Na_2SiO_3 \cdot 9H_2O$ solution at 62°C which shows silicate lines at low frequency. Note the similarity to curve B of Fig. 1b except for the sharp line at 1058 cm^{-1} in curve B; 1d. A Raman spectrum of an aqueous 2.8M $Na_2SiO_3 \cdot 9H_2O$ solution at 62°C containing about 0.4g of dissolved KOH (1×10^{21} KOH molecules/cm^3). Note the similarity with curve A of Fig. 1b except for the sharp line at 1058 cm^{-1} in curve A.

value of about 4000 Å/min (1). Recording of spectra commenced 30 min after immersion to insure temperature stabilization. Typically, 66 min were required to cover the complete 50-4050 cm^{-1} spectral range. Curve A of Fig. 1b is the Raman spectrum started after about 0.11g of silicon had been dissolved (6×10^{20} Si/cm^3). It is to be noted that the OH^- line decreased appreciably, and six new lines at 442, 515, 600, 766, 920, and 1058 cm^{-1} were observed. These lines and their assignments to various silicate structures are listed in Table I. Table I also contains a number of published Raman assignments to various silicates (19, 21-26). Curve B of Fig. 1b is the Raman spectrum started after about 0.35g of silicon had been dissolved (2×10^{21} Si/cm^3). The main difference between curves A and B is the large increase in intensity of the 600 cm^{-1} line.

Interestingly, in one experiment, we dissolved approximately 0.7g of silicon (4×10^{21} Si/cm^3) with the result that the solution became viscous and the Raman lines altered considerably by broadening and shifting. Hence, it was quite evident that a silicate had formed.

Table I

Present KOH etch with Si	Present $Na_2SiO_3 \cdot 9H_2O$	Present $Na_2SiO_3 \cdot 9H_2O$ with KOH	Ref. (19) Various silicates $SiO_2(OH)_2^=$	Ref. (19) Various silicates Polymers	Ref. (26) Na_2SiO_3 $SiO_2(OH)_2^=$	Ref. (19) Various silicates $SiO_3(OH)^\equiv$
				~180		
			260			
	~340(?)		350	350		350
			430			430
442*	445*	450*	450		456	450
			460			460
~515	~485(?)	~500(?)		550		
600*	602*	603*		600	614	
		675(?)		~650		
						~740
766*	770*	770*	780		779	
~830(?)			825			
						865
920*	923*	925*	930		937	
			985			~980
~1005(?)	~1007(?)	~1025(?)		1020	1030	
1058				1045		

This table compiles the Raman vibrational lines for aqueous KOH etching solutions and for various aqueous silicate solutions. Our lines are accurate to ±5 cm^{-1}. Consequently, lines marked with an (*) are considered to be coincident. (?) represents a shoulder or a weak feature which is not very conclusive. Assuming the published data has an accuracy similar to ours, we conclude that the primary etch product is $SiO_2(OH)_2^=$.

In fact, when the temperature decreased from 62° to 21°C, the solution jelled.

Figure 1c is a Raman spectrum of a 2.8M aqueous solution of $Na_2SiO_3 \cdot 9H_2O$ which compares favorably with published spectra (19). The silicate spectral lines are listed in Table I for comparison and reference. When 0.4g of KOH crystals were added to the solution (1×10^{21} KOH/cm^3), the spectrum shown in Fig. 1d was obtained, with the silicate lines listed in Table I. Note that the sharp line at 1058 cm^{-1} is always missing in the sodium metasilicate spectrum, although a 600 cm^{-1} line, assigned as a polymer (19), is present. Because $SiO_3(OH)^\equiv$ has a line at 740 cm^{-1}, which was never observed in any solution that we studied, this species is not considered to be an etching product. While K_2SiO_3 has been postulated as a product of etching (1), we saw no absorption features creditable to it (28, 29). Also, there was no evidence for undissociated KOH (30). In fact, we found no spectral structure related to any feasible potassium compound, even though a structure consisting of a K^+ cation surrounded by 6 waters of hydration has been postulated (17, 32). We also searched for the H_2 vibrational band near 4160 cm^{-1} without success, probably because our sensitivity was adversely affected due to the bubbles.

Using the results listed in Table I, especially the analysis of Freund (19) who discussed the concentration of various species of $SiO_x(OH)_{4-x}$ as a function of molarity in sodium silicate solutions, we conclude that $SiO_2(OH)_2^=$ is the primary etching product of {100} silicon in aqueous 5M KOH. Based on the appearance of a sharp additional line at 1058 cm^{-1} and a line at 600 cm^{-1} (19), we further conclude that this silicate polymerizes.

Aqueous 5M KOH solution with isopropyl alcohol.— When aqueous KOH solutions are used to etch silicon for integrated circuits, these solutions are often "buffered" with isopropyl alcohol (IPA). This procedure alters the etch-rate ratio between the {100} and {111} surfaces, and it slows down the etch rate in general (1). It has been suggested (21) that the OH group of the IPA molecule attaches itself to silicon dioxide. Since the IPA molecule has the form

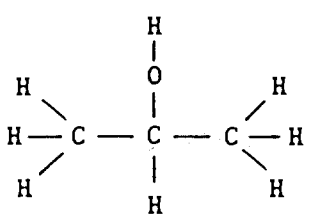

the OH bond might be altered by other groups attaching themselves to it, or the molecule could undergo a chemical reaction during etching. Both of these effects might be observed by Raman spectroscopy. Consequently, IPA was added to 2M KOH until a layer of IPA was formed over the KOH solution. The pure IPA unpolarized Raman line positions and relative intensities that we observed were in good agreement with published values (33-35). Furthermore, no temperature effects were observed from 21°-62°C. In fact, the Raman spectra for pure IPA and for IPA in aqueous KOH were very similar. In addition, the OH peak was scarcely perturbed by the IPA. After about 0.25g of silicon (1×10^{20} Si/cm^3) was etched, the Raman spectrum was measured. No change in the main IPA lines was observed. Using the results of normal-mode analysis (33, 35) to identify the lines, we found no change in the C-C-C stretch bond (819 cm^{-1}), the CH_3 deformation (1452 cm^{-1}), or the CH_3 stretch bonds (2882, 2920, and 2975 cm^{-1}). We could not see the weaker IPA lines. We conclude, therefore, that the IPA molecules in solution remain intact and unperturbed. Because IPA does not seem to participate in a chemically destructive manner in the etching process, its role might be to coat the surface in such a way as to prevent OH^- from etching Si directly, or it might change the diffusion of OH^- to, or etching products from, the silicate layer.

The degree to which IPA is miscible in aqueous KOH is determined by the molarity. In order to determine the amount of IPA in our etching solutions, we compared the intensity of the IPA lines from our 5M KOH etching solution to those from pure IPA. From these measurements, we estimate that we had about 6% IPA uniformly distributed vertically in the KOH solution, in reasonable agreement with published values (1). This corresponds to about 4×10^{20} IPA molecules/cm^3. Presumably, if IPA were taking part chemically in the etching reaction, one should observe changes in the Raman spectra after a similar amount of silicon is dissolved. We might ask whether IPA molecules are "destroyed" and replaced by new molecules entering the solution from the top where excess IPA floats. To answer this, we dissolved about 0.11g of Si (6×10^{20} Si/cm^3) and observed no differences from the original 5M KOH Raman spectra as far as relative intensities go. However, when more than 0.3g of Si (2×10^{21} Si/cm^3) was dissolved, we noticed an overall decrease in intensity of the IPA peaks showing that the IPA concentration had dropped to about 1%. Furthermore, the solution was now viscous and far beyond any typical etching condition.

Discussion and Conclusions

Raman spectroscopy is sensitive enough for studying etching dynamics in aqueous KOH solutions with a molarity greater than about 0.1M. Nevertheless, our measurements have told us little about the actual chemical reactions going on at the etching interface since we observed only the final etch products in solution.

The vibrational bands seen in all our etching solutions bear a close resemblance to the bands observed in our spectra of aqueous solutions of $Na_2SiO_3 \cdot 9H_2O$ and the literature spectra of aqueous solutions of Na_2SiO_3 (19, 26). Furthermore, all the clear Raman lines that we observed at 442, 600, 766, 920, and 1058 cm^{-1} are assignable to the species $SiO_2(OH)_2^=$ and polymers of it (19). The line at 515 cm^{-1}, seen in the early etch spectrum (Fig. 1b, curve A), is not assigned although shoulders in the general region are seen in the silicate spectra. The erratic behavior of the polymer lines in the 1000-1060 cm^{-1} region is puzzling, especially the sharp line in the etch solution, which was not clearly seen by us in any other silicate solution.

Since the OH^- line substantially decreases in intensity during etching, we infer that the active etching species is the OH^- ion, which is continually depleted. Based on our etching solution results, our sodium silicate spectra, and on published Raman spectra (19, 26), we conclude that the main etch product is ultimately $SiO_2(OH)_2^=$ with subsequent polymerization.

Because we see no significant differences in the Raman spectra from pure IPA and IPA in aqueous KOH, and because we do not see any significant changes in the IPA spectrum during etching as the silicon concentration in solution increases, we conclude that IPA added to the etchant does not participate chemically in the etching process. Rather, we feel that IPA probably coats the surface, thereby preventing OH^- ions in the solution from reaching the Si or silicate-covered surface, thereby modifying the etch rate for each crystallographic orientation.

Acknowledgments

We thank R. F. Greene of the Naval Research Laboratory and J. W. Faust, Jr.. of the University of South Carolina for many useful discussions.

Manuscript submitted March 3, 1982; revised manuscript received Dec. 22, 1982.

Any discussion of this paper will appear in a Discussion Section to be published in the December 1983 JOURNAL. All discussions for the December 1983 Discussion Section should be submitted by Aug. 1, 1983.

Publication costs of this article were assisted by the Naval Research Laboratory.

REFERENCES

1. J. B. Price, in "Semiconductor Silicon." H. R. Huff and R. R. Burgess, Editors, p. 339, Electrochemical Society Softbound Proceedings Series, Princeton, NJ (1973).
2. K. E. Bean, *IEEE Trans. Electron Devices*, **ed-25,** 1185 (1978).
3. D. B. Lee, *J. Appl. Phys.*, **49,** 4569 (1969).
4. H. F. Gray, To be published.
5. E. Bassous and E. F. Baran, *This Journal*, **125,** 1321 (1978).
6. C. L. Huang and T. Van Duzer, *Appl. Phys. Lett.*, **25,** 753 (1974).
7. S. O. Izidonov, T. I. Borisova, and V. I. Veselovskii, *Russ. J. Phys. Chem.*, **36,** 659 (1962); *Zh. Fiz. Khim.*, **36,** 1246 (1962).
8. M. Hurd and P. T. Wrotenbery, *Ann. NY Acad. Sci.*, **101,** 876 (1963).
9. D. R. Turner, *This Journal*, **107,** 810 (1960).
10. S. O. Izidinov, *J. Appl. Chem. USSR*, **44,** 1660 (1971); *Zh. Prikl. Khim.*, **44,** 1642 (1971).
11. E. D. Palik, J. W. Faust, Jr., H. F. Gray, and R. F. Greene, *This Journal*, **129,** 2051 (1982).
12. I. Bergman and M. S. Paterson, *J. Appl. Chem.*, **11,** 369 (1961).
13. D. L. Kendall, *Ann. Rev. Mater. Sci.*, **9,** 373 (1979); *Appl. Phys. Lett.*, **26,** 195 (1975).
14. W. R. Busing and D. F. Hornig, *J. Phys. Chem.*, **65,** 284 (1961).
15. J. R. Scherer, in "Advances in Infrared and Raman Spectroscopy," Vol. V, R. J. H. Clark and R. E. Hestger, Editors, p. 149, Heyden, London (1978).
16. D. A. Draegert, N. W. B. Stone, B. Curnutte, and D. Williams, *J. Opt. Soc. Am.*, **56,** 64 (1966).
17. P. Rhine, D. Williams, G. M. Hale, and M. R. Querry *J. Phys. Chem.*, **78,** 1405 (1974).
18. O. Faurskow Nielsen, *Chem. Phys. Lett.*, **60,** 515 (1979).
19. E. Freund, *Bull. Soc. Chim. France*, **7-8,** 2238, 2244 (1973).
20. J. Etchepare, *Spectrochim. Acta, Part A*, **26,** 2147 (1970).
21. R. K. Iler, "The Chemistry of Silica," p. 657, Wiley-Interscience, New York (1979).
22. H. C. Marsmann, *Z. Naturforsch., Teil A*, **29,** 495 (1974).
23. G. Engelhardt, D. Zeigan, H. Jancke, D. Hoebbel, and W. Wieker, *Z. Anorg. Allg. Chem.*, **418,** 17 (1975).
24. R. K. Harris and R. H. Newman, *J. Chem. Soc. Faraday Trans.*, **73,** 1204 (1977).
25. D. Fortnum and J. O. Edwards, *J. Inorg. Nucl. Chem.*, **2,** 264 (1956).
26. J. E. Earley, D. Fortnum, A. Wojcicki, and J. O. Edwards, *J. Am. Chem. Soc.*, **81,** 1295 (1959).
27. V. V. Strelko, *Theor. Exp. Chem.*, **10,** 277 (1974); *Teor. Eksper. Khim.*, **10,** 359 (1974).
28. F. A. Miller, G. L. Carlson, F. F. Bentley, and W. H. Jones, *Spectrochim. Acta*, **16,** 135 (1960).
29. F. A. Miller and C. H. Wilkins, *Anal. Chem.*, **24,** 1266 (1952).
30. R. G. Snyder, J. Kumamoto, and J. A. Ibers, *J. Chem. Phys.*, **33,** 1171 (1960).
31. G. W. Brady and J. T. Krause, *ibid.*, **27,** 304 (1957).
32. G. W. Brady, *ibid.*, **28,** 464 (1958).
33. H. A. Szymanski, "Interpreted Infrared Spectra," Vol. II, p. 111, Plenum Press, New York (1966).
34. B. Schrader and W. Meier, "Raman/Infrared Atlas or Organic Compounds," Vol. I, Verlag Chemie, Weinheim (1974).
35. C. Tanaka, *Nippon Kagaku Zasshi*, **83,** 521 (1962).

Optimum Conditions for Baking of Indium

Mats Janson

Institute of Microwave Technology, S-100 44, Stockholm, Sweden

ABSTRACT

Calculations of SiO partial pressure over an indium melt with dissolved silicon in a moist hydrogen atmosphere are reported. The results are given as a function of temperature, water vapor pressure, and concentration of silicon in the melt, both with and without SiO_2 present. The influence of the total pressure in the baking system is considered, and the calculations indicate that by using a pressure lower than atmospheric, the efficiency of the baking should be significantly increased. The time constant of the baking process is, furthermore, shown to be critically dependent on water vapor partial pressure. These results should be valuable when one wants to find the optimum baking procedure to remove residual silicon from indium.

In the growth of InP and GaInAsP by LPE, silicon is normally the dominant residual donor. The reason for this is its high distribution coefficient ($\approx$ 30 for InP) (3). The source of the silicon can be both the starting materials (especially the indium) and the growth apparatus which normally has a quartz reaction tube. It is possible, however, to reduce the silicon content in the melt by adjusting the water vapor pressure in the growth system and thereby oxidize the silicon to SiO or SiO_2 (3-5).

To our knowledge, the work done so far on this problem (both for GaAs, InP, and GaInAsP) (1-5) has only considered the case where SiO_2 is present at the baking temperature. In this case, one finds that at equilibrium, the silicon content in the indium melt is determined by the temperature and the water content of the atmosphere. By modifying the system so that the only silicon that takes part in the reaction comes from the melt, it should be possible to increase the efficiency of the process significantly. One way to achieve this condition is to use a quartz tube with cold walls and to heat the melt by rf induction (6).

To be able to optimize the baking process, it is necessary to understand the thermodynamics of the chemical reactions between the Si, In, and the moist hydrogen atmosphere. Since the silicon is transported from the melt in the form of SiO (which has a much higher vapor pressure than SiO_2), an important part of the optimization is to find the relationship between SiO partial pressure and the variables of the system.

In this paper, calculations of the equilibrium SiO pressure as a function of H_2O partial pressure, melt silicon concentration, and temperature are reported and some conclusions for optimizing the purification process are given.

Calculation of SiO Partial Pressure

Consider the situation shown in Fig. 1. At the inlet of the reactor tube, which is assumed to be inert, a mixture of hydrogen and water vapor is introduced. This gas mixture passes over a melt of indium which contains some dissolved silicon and possibly some solid silicon dioxide on the surface. The melt is contained in an inert crucible. The gas phase above the indium melt contains silicon monoxide, water vapor, and hydrogen. The amount of all other possible reaction products are assumed to be small enough to be neglected.

The net reactions to be considered are

$$\{Si\} + (H_2O) = (SiO) + (H_2) \quad K_1, \Delta G^\circ_1 \quad [1]$$

and

$$(SiO) + (H_2O) = \langle SiO_2\rangle + (H_2) \quad K_2, \Delta G^\circ_2 \quad [2]$$

K is the equilibrium constant, and ΔG° the standard free energy of reaction. The same notation as in Ref. (6) is used, where $\langle\ \rangle$ indicates solid, $\{\}$ liquid, and $(\ )$ gaseous.

The chemical system considered contains the elements Si, O, H, and In. According to the phase rule, the number of degrees of freedom are in the first case four since there are two different phases (the liquid In with dissolved Si and the gas phase). In the second case, there are only three degrees of freedom since one more phase (the solid SiO_2) is present. The state of the system is thus in the first case fully determined by the temperature, total pressure, H_2O partial pressure, and melt Si-concentration, and in the second case by the temperature, total pressure, and the H_2O partial pressure.

From basic chemical thermodynamics (8)

$$\Delta G^\circ = -RT \ln K$$

where R is the gas constant and T the absolute temperature. For reaction [1], one has

$$K_1 = ([SiO] \cdot [H_2])/([Si] \cdot [H_2O])$$

[ ] indicates the activity. This can be rewritten (the H_2 pressure is assumed to be 1 atm)

$$K_1 = P_{SiO}/([Si] \cdot P_{H_2O}) = \exp(-\Delta G^\circ_1/RT)$$

P_{SiO} and P_{H_2O} are the partial pressures of SiO and H_2O, respectively.

The activity of the dissolved silicon can be written

$$[Si] = \gamma \cdot X_{Si} \quad [2a]$$

X_{Si} is the atom fraction of silicon in the indium and γ the activity coefficient.

Similarly one obtains for reaction [2]

$$K_2 = 1/(P_{SiO} \cdot P_{H_2O}) = \exp(-\Delta G^\circ_2/RT) \quad [3]$$

To calculate ΔG°_1 and ΔG°_2 reactions [1] and [2] are divided into subreactions. For reaction [1]

$$(H_2) + \tfrac{1}{2}(O_2) = (H_2O) \quad \Delta G^\circ_1 \quad [1a]$$

$$\langle SiO_2\rangle = \langle Si\rangle + (O_2) \quad \Delta G^\circ_2 \quad [1b]$$

$$\langle SiO_2\rangle + \langle Si\rangle = 2(SiO) \quad \Delta G^\circ_3 \quad [1c]$$

$$\langle Si\rangle = \{Si\} \quad \Delta G^\circ_4 \quad [1d]$$

The standard free energies of reaction for [1a]-[1d] are obtained from Ref. (7) and are (T is the temperature in degrees Kelvin)

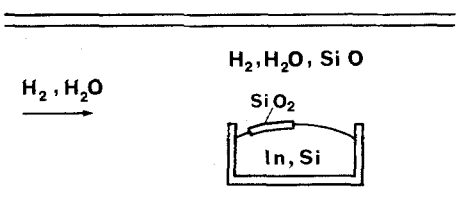

Fig. 1. The system under consideration. The reaction tube walls and the melt crucible are assumed to be inert.

[1] Present address: LM Ericsson, S-126 25, Stockholm, Sweden.
Key words: semiconductor, doping, epitaxy.

$$\Delta G^{\circ}{}_1 = -58{,}900 + 13.1T \quad \text{cal/mol}$$

$$\Delta G^{\circ}{}_2 = 215{,}600 - 41.5T \quad \text{cal/mol}$$

$$\Delta G^{\circ}{}_3 = 169{,}600 + 12.9T \log T - 124.3T \quad \text{cal/mol}$$

$$\Delta G^{\circ}{}_4 = 12{,}100 - 7.2T \quad \text{cal/mol}$$

The standard free energy of reaction for reaction [1] is then

$$\Delta G^{\circ}{}_1 = -\Delta G^{\circ}{}_1 - \tfrac{1}{2}\Delta G^{\circ}{}_2 + \tfrac{1}{2}\Delta G^{\circ}{}_3 - \Delta G^{\circ}{}_4$$

$$= 23{,}800 + 6.45T \log T - 47.3T \text{ cal/mol}$$

From Eq. [1] and [2]

$$\log (P_{SiO}/P_{H_2O}) - \log X_{Si} = (\log e/RT)(RT \ln \gamma - \Delta G^{\circ}{}_1)$$

From Ref. (8)

$$RT \ln \gamma = 11{,}450 - 3.37T \quad \text{cal/mol}$$

This gives

$$\log (P_{SiO}/P_{H_2O}) - \log X_{Si} = (\log e/RT) \cdot (-12{,}350 - 6.45T \log T + 43.9T) \quad [4]$$

Reaction [2] can be divided correspondingly into reactions [1a]-[1c], and the free energy of reaction of reaction [2] obtained as

$$\Delta G^{\circ}{}_2 = -\Delta G^{\circ}{}_1 - \tfrac{1}{2}\Delta G^{\circ}{}_2 - \tfrac{1}{2}\Delta G^{\circ}{}_3 =$$

$$- 133{,}700 - 6.45T \log T + 69.8T \text{ cal/mol}$$

From Eq. [3]

$$\log (P_{SiO} \cdot P_{H_2O}) = (\log e/RT) \cdot \Delta G^{\circ}{}_2 \quad [5]$$

Equations [4] and [5] are summarized in Fig. 2 where the lines with negative slope describe the system according to Eq. [5] which is valid when SiO_2 is present. The perpendicular lines describe the system when the water vapor pressure is lower than the limit for SiO_2 formation at the actual temperature and melt silicon concentration (Eq. [4]). From Fig. 2, it is clear that the SiO pressure can be maximized by choosing the optimum H_2O pressure, and that the latter is a function of the silicon concentration in the melt.

Note that the H_2O pressure here is the equilibrium pressure over the indium melt. This is, however, approximately equal to the H_2O pressure at the inlet as long as the pressures of other oxides (SiO and In_2O) formed in the system are small compared with the H_2O pressure. As Fig. 2 shows $P_{SiO} << P_{H_2O}$ for the P_{H_2O} temperature combinations of interest here. From values of the free energy of formation of In_2O from Ref. (9) and $\Delta G^{\circ}{}_1(T)$ given above P_{In_2O}/P_{H_2O} is found to be smaller than $5 \cdot 10^{-2}$ for $T < 1000°C$.

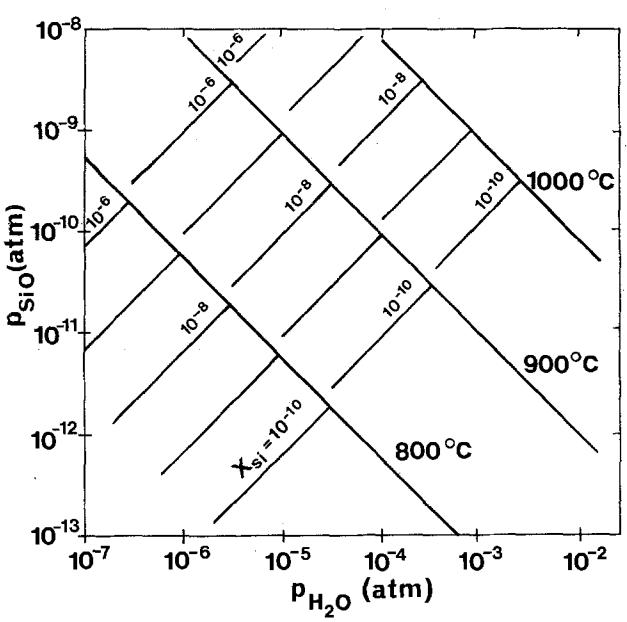

Fig. 2. SiO partial pressure as a function of temperature and silicon concentration in the indium (X_{Si}). The curves with negative slope describe the system when SiO_2 is present. The perpendicular curves are valid when the P_{H_2O} and X_{Si} combinations are such that no SiO_2 forms.

Aspects on the Reaction Rate

In the following discussion, we assume that the rate limiting factor is the removal of the silicon monoxide, and consider the influence of gas flow rate and total pressure.

The cooling of the quartz tube has two important aspects. First, it allows H_2O and SiO pressures which are not on the curves (Fig. 2) describing equilibrium with SiO_2 (Eq. [5]). There is also no risk that the reaction goes backwards and that silicon is transported from the quartz tube to the melt. Second, all the SiO in the exhaust gas stream comes from the indium melt which of course is important for the efficiency of the process.

The relative rate of silicon removal can be written

$$(dX_{Si}/dt)/X_{Si} = (F_e \cdot K)/(22.4 \cdot M_{In}) = 1/\tau$$

Where F_e is the effective flow rate measured at 300 K in liter/min, $K = P_{SiO}/X_{Si}$, and M_{In} is the amount of indium in mols. Figure 3 shows some values of τ *vs.* X_{Si} and T for $F_e = 1$ liter/min and $M_{In} = 0.1$ mol. As can be seen, the baking times can be quite long if the initial silicon-concentration is above approximately 1 ppm.

To see what happens if one changes the total pressure in the system, we rewrite Eq. [1] and [3]

$$K_1 = (P_{SiO} \cdot P_{H_2})/([Si] \cdot P_{H_2O}) \quad [1']$$

$$K_2 = P_{H_2}/(P_{SiO}\, P_{H_2O}) \quad [3']$$

P_{SiO} is maximum when Eq. [1'] and [3'] give the same value. This gives

$$(P_{SiO})_{max} = (K_1 \cdot [Si]/K_2)^{1/2}$$

for

$$P_{H_2O}/P_{H_2} = (1/(K_1 \cdot K_2 \cdot [Si]))^{1/2}$$

This means that $(P_{SiO})_{max}$ is independent of the total pressure in the system as long as P_{H_2O}/P_{H_2} is kept constant. By decreasing the pressure, the relative concentration of SiO in the gas stream (P_{SiO}/P_{H_2}) will be increased, and the removal rate of SiO will be higher at a given H_2 flow rate (measured at atmospheric pressure). Decreasing the pressure will also reduce kinetic barriers (i.e., diffusion through boundary layers),

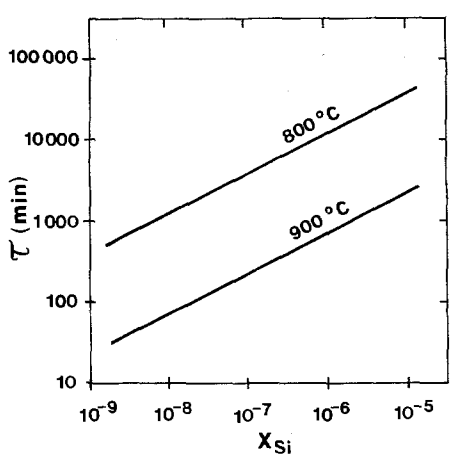

Fig. 3. Time constant for the silicon removal as a function of silicon concentration when the H_2O partial pressure is adjusted for maximum SiO partial pressure. The effective flow rate is 1 liter/min and the size of the melt is 0.1 mol.

and this will probably also contribute to reducing the necessary baking time.

Discussion and Conclusions

From Fig. 2, the optimum H_2O pressure for a given baking temperature and melt silicon concentration can be found. It is clear from the figure that the removal rate of silicon is critically dependent on the H_2O pressure, and also that the optimum H_2O pressure is a function of melt silicon concentration. Thus, to minimize the baking time, the H_2O pressure should be adjusted (increased) during the baking as the silicon concentration in the melt decreases. It is also seen that a high baking temperature is advantageous. The temperature will, however, be limited by indium evaporation.

It is assumed in the above calculations that the removal rate of silicon from the indium melt is limited by gas flow transport of gaseous SiO. If the water vapor partial pressure is above the critical value for SiO_2 formation, the silicon will not be removed from the system but bound in the form of SiO_2 in contact with the melt, and the reaction will go backwards rapidly when the water pressure is decreased with the silicon going back into solution.

To further reduce the baking time, one can reduce the total pressure in the system. This does not change the value of the optimum P_{H_2O}/P_{H_2} ratio. Thus, controlled mixing of the hydrogen and water vapor can be done at atmospheric pressure, and the mixture fed to the low pressure baking chamber. No accurate control of the pressure in the chamber is necessary to maintain the conditions for maximum SiO pressure.

When small amounts of arsenic, gallium, and phosphorus are added to the indium as is done when a melt for LPE growth of GaInAsP is prepared, the above results are expected to still be a good approximation since the activity coefficient of silicon is not expected to change very much, and the possible new oxides are less stable than SiO_2.

Acknowledgments

This work was financed by L. M. Ericsson and the Swedish Board of Technical Development.

Manuscript submitted Sept. 20, 1982; revised manuscript received Nov. 29, 1982.

Any discussion of this paper will appear in a Discussion Section to be published in the December 1983 JOURNAL. All discussions for the December 1983 Discussion Section should be submitted by Aug. 1, 1983.

Publication costs of this article were assisted by the Institute of Microwave Technology.

REFERENCES

1. H. G. B. Hicks and P. D. Greene, in Proc. of 3rd International Symposium on GaAs and Related Compounds, p. 92, Institute of Physics (1970).
2. M. E. Weiner, *This Journal*, **119**, 496 (1972).
3. V. L. Wrick, K. T. Ip, and L. F. Eastman, *J. Electron. Mater.*, **7**, 253 (1978).
4. S. H. Groves and M. C. Plonko, in Proc. of 7th International Symposium on GaAs and Related Compounds, pp. 71-77, Institute of Physics (1979).
5. J. D. Oliver and L. F. Eastman, *J. Electron. Mater.*, **9**, 693 (1980).
6. O. Kubaschewski, E. L. L. Evans, and C. B. Alcock, "Metallurgical Thermochemistry," Pergamon Press, Inc., Elmsford, NY (1967).
7. R. A. Swalin, "Thermodynamics of Solids," John Wiley & Sons, Inc., New York (1962).
8. C. D. Thurmond and M. Kowalchik, *Bell Syst. Tech. J.*, 169 (1960).
9. K. A. Kleindinst and D. A. Stevenson, *J. Chem. Thermodyn.*, **5**, 21 (1973).

Optical and Electrical Properties of Yttria Stabilized Zirconia (YSZ) Crystals

R. C. Buchanan and S. Pope

Department of Ceramic Engineering, University of Illinois at Urbana-Champaign, Urbana, Illinois 61801

ABSTRACT

Optical transmission spectra (λ = 0.3-50 μm) and d-c conductivity (25° -1000°C) data were obtained on yttria stabilized zirconia (YSZ) single crystals commercially grown by the skull-melting process. The crystals were doped with up to 2.0 w/o rare earth (Ce, Nd, Er, Pr) and transition (Mn, Fe, Cr, Ni) metal ions, and a few were annealed. Dopant effects were most pronounced in the visible region, but were evident throughout much of the spectral range. Annealing and dopant ions Ce and Er showed significant absorption effects attributed to the Ce^{3+} ion. Electrical conductivity was only marginally affected by doping.

The system ZrO_2-Y_2O_3 (YSZ) has been much studied (1, 2). This reflects the importance of ZrO_2 (stabilized) as a refractory material for solid electrolyte and fuel cell applications, and more recently as precise oxygen sensors for use in automotive and steel manufacture.

The effect of the Y_2O_3 additions is to stabilize the high temperature cubic ZrO_2 phase. Without adequate stabilization, the cubic fluorite phase transforms on cooling below ~2300°C to the tetragonal form, which in turn transforms to the stable low temperature monoclinic phase below ~1150°C. This latter phase change is accompanied by a 4-5 volume percent increase, which is disruptive of the structure.

It is now generally agreed that ~9 mol percent (m/o) Y_2O_3 addition is sufficient to fully stabilize the cubic ZrO_2 phase. In practice, the ZrO_2-9 m/o Y_2O_3 composition has also been found to have the highest electrical conductivity in the system. As a result, it is widely used for oxygen (gas) sensor applications, where high electrical conduction is a necessary design parameter.

Electrical conduction in the system ZrO_2-Y_2O_3 above 700°C is due almost entirely to high anion mobility ($t_{O^{2-}} > 0.99$) via vacancies (3-7). With 9 m/o Y_2O_3, ~4.1% anion vacancies are created. The high electrical conduction observed for this relatively low anion vacancy concentration, therefore, reflects minimal defect interactions. Significant electronic conduction below 500°C has, however, been reported for YSZ doped with Fe^{3+} and other multivalent cations (8).

Single crystals of YSZ have recently been prepared by the skull-melting process (9, 10). This technique

Key words: ceramics, conduction, defects.

allows the growth of relatively large crystals of refractory dielectric materials (YSZ crystals > 15 cm diam have been grown). A water-cooled crucible or "skull" is used to contain the molten dielectric within a crust or jacket (~1 mm thick) of its own composition. The skull is shaped such that radio frequency energy can pass through into the batch to heat and melt the powder charge. In the case of YSZ, initial heating of the dielectric powder is provided by Zr metal susceptors placed in the middle of the batch. At temperatures above ~900°C, where the YSZ powder becomes sufficiently conducting, the metal is no longer needed and oxidizes to augment the batch composition. Columnar crystals, often twinned, are obtained from the melt by directional solidification during cooling. Different colored crystals may be produced in this process, by incorporating low concentrations [< 2.0 weight percent (w/o)] of multivalent or rare earth oxides into the batch.

Detailed studies by Aleksandrov (11, 12) on optical homogeneity of the skull-grown YSZ crystals showed the most characteristic defect to be cords running perpendicular to the crystal growth axis [011]. Small concentrations of such oxides as CeO_2, Er_2O_3, and Nd_2O_3 were found to generate particulate defects in the range 0.03-8.0 μm, which acted as scattering sites. Annealing of the crystals above 1200°C in an oxidizing atmosphere reduced the stresses as well as the defect level and dislocation density, making the crystals essentially isotropic. The refractive index (n) measured for the 9 m/o Y_2O_3 crystals was in the range 2.11-2.17, with coefficient of dispersion, $\nu \sim 31.50$. These values decreased for higher Y_2O_3 content, and varied to a lesser extent with heat-treatment and the amount of added rare earth or transition element. Optical absorption spectra for a number of these elements at oxide concentrations of ~0.5 w/o were also recorded between 0.22-1.0 μm. Characteristic absorption peaks were obtained which could be modified by irradiation or annealing treatment.

As indicated, the YSZ crystals possess a high refractive index and dispersion, close to that of diamond ($n = 2.42$, $\nu = 27$). The crystals are also transparent throughout the visible and near infrared spectral ranges ($\lambda = 0.35$-7.0 μm). With a hardness factor in the range 7.5-8.5 mhos, depending on Y_2O_3 content, this combination of properties makes good quality YSZ crystals an attractive synthetic substitute for gem quality diamonds, for which purpose they are mainly used. Other uses include lenses, prisms, laser applications, and infrared sensors or windows, this latter because of the high spectral transmission in the range $\lambda = 3$-7 μm. YSZ crystals have also been considered for oxygen sensor and for fuel cell applications.

Little data exist, however, on the electrical properties of the YSZ crystals, particularly when doped with rare earth and multivalent cations. Likewise, the effect of this doping on the infrared transmission spectra has not been determined. The object of this study, therefore, was to characterize the effects of the various dopants on the optical and electrical properties of YSZ crystals.

Samples used in this study were 9.5 m/o Y_2O_3 (YSZ) crystals prepared by Ceres Corporation, Waltham, Massachusetts, using the aforementioned skull-melting process. Rare earth and transition element dopants up to 2 w/o oxide were incorporated into the crystals. A few samples were also annealed. A 12 m/o Y_2O_3 crystals was used for comparison. Optical transmission spectra were developed for the range $\lambda = 0.3$-50 μm for each of the samples. Electrical resistivity (d-c) measurements were made up to 1000°C.

Experimental Procedures

Composition.—As indicated, single crystal YSZ samples used in this study were prepared by the skull-melting process and were supplied by the Ceres Corporation, Waltham, Massachusetts. Composition of the various samples are given in Table I. The base compositions of the crystals was ZrO_2-9.5 m/o Y_2O_3, to which small concentrations of dopant or coloring oxides were added, as detailed in Table I. The dopant cations have all been shown to cause the development of color in the cubic ZrO_2-Y_2O_3 single crystal lattice (9), and the different combinations were designed to develop particular colors. Several samples contained CeO_2 (typically 0.1 w/o but also at 1.0 and 2.0 w/o) alone or in combination with other dopants. The CeO_2 aided in the control of the various colors. Most samples were supplied in the unannealed state, whereby some cerium ions would be in the reduced (Ce^{3+}) state (11). Two samples (No. 1 and 8, Table I) were received in the annealed state. This had been carried out in air at 1200°C/ 24 hr, and was intended to reoxidize any reduced ions as well as reduce the overall defect levels in the crystal. This allowed direct comparison with samples 1, 2 and 7, 8, which were of identical composition.

Optical spectra.—Samples for optical evaluation were prepared from each crystal. The samples were cut plane parallel about 2 mm thick in a direction normal to the growth axis. Nominal diameters were about 2.0 cm. The samples were polished on both sides to transparency using 600 SiC (Carborundum) grit and 15 and 6 μm diamond paste. Care was taken to avoid too reflective a surface on the specimen faces.

Table I. Composition of YSZ (9.5 m/o Y_2O_3)

		Single crystal samples								
		Dopant/concentration (w/o)								
Sample	Color	CeO_2	MoO_2	FeO	CoO	NiO	Pr_2O_3	Nd_2O_3	Er_2O_3	Cr_2O_3
1*	Clear	0.1	—	—	—	—	—	—	—	—
2	Orange	0.1	—	—	—	—	—	—	—	—
3	Red-org.	2.0	—	—	—	—	—	—	—	—
4	Straw	—	0.1	—	—	—	—	—	—	—
5	Lt. yell.	—	0.05	—	—	—	—	—	—	0.5
6	Yellow	—	—	0.1	—	—	—	—	—	—
7	Dark violet	—	—	—	0.2	—	—	—	—	—
8*	Violet	—	—	—	0.2	—	—	—	—	—
9	Dk. red	1.0	—	—	0.3	—	—	—	—	—
10	Amber	0.1	—	—	—	0.1	—	—	—	—
11	Salmon	—	—	—	—	0.1	—	—	1.0	—
12	Pink	0.1	—	—	—	—	—	—	1.0	—
13	Gold. yel.	—	—	—	—	—	0.2	—	—	—
14	Clear	0.1	—	—	—	—	—	0.22	—	—
15	Lt. gray	0.1	—	—	—	—	—	0.44	—	—
16**	Clear	—	—	—	—	—	—	—	—	—

* Air annealed 1200°C/24 hr.
** YSZ (12 m/o Y_2O_3).

Each sample was optically scanned over the spectral range 0.3-50 μm, incorporating both the visible and infrared ranges. For the infrared ranges (50-2.5 μm), a Beckman Infrared-12 Spectrophotometer was used in the double-beam mode. A Nicolet FT-Infrared Spectrophotometer was also used over the same infrared range and permitted more accurate interpretation of the data. Wavelengths spanning the near infrared and visible regions (2.5-0.65 μm) and (0.65-0.3 μm) were scanned using a Cary-14 Spectrophotometer.

Electrical conductivity.—Samples for electrical conductivity measurements were cut plane parallel as described previously and shaped geometrically to approximately 1 × 1 × 0.2 cm. Electrodes were applied to both faces of the sample using platinum paste which was fired at 800°C for 10 min. Measurements were carried out as a function of temperature to ~1000°C using a Keithley 610-B electrometer. The specimens were heated in a vertical, shielded platinum-wound tube furnace up to 1000°C at a heating rate of ~10°C/min. A flat platinum stage (supported on Al_2O_3) served as contact base and a spring-loaded platinum tipped probe as the upper electrode. The temperature sensing thermocouple was positioned next to this probe.

Results and Discussion

Visible spectra.—Table I shows the wide spectrum of coloration imparted to the basic YSZ crystals by the various dopants. Grouping of these dopants could be made according to the colors produced in the crystals which, in general, were similar to the colors produced in glasses. Yellow hues, for examples, were predominantly produced by Mo, Cr, Fe, and Pr dopants, generally in the absence of Ce. These ions would likely be present in the 3^+ state. Transmission spectra in the visible range are given for these dopants in Fig. 1. Numbering of the curves in the figures correspond to the data inTable I.

Relative transmission values may not be strictly comparable, however, due to differences in sample thickness and surface finish. The spectra show generally good transmission in the range 4500-6500Å, with the absorption edge around 3400Å (~1.4 eV), except for Fe doping (curve 6) which showed a significant shift of the absorption edge to ~4100Å. This is in line with the well-known absorption of the blue (ultraviolet) end of the spectrum by Fe^{3+} ions in glasses. Other than the shift of absorption edge, no significant absorption peaks were observed in this spectral region.

The basic YSZ crystals were clear or colorless (sample 16 in Table I) and moderately transmitting in the visible region, as shown in Fig. 2. Addition of Nd also gave clear crystals which became progressively more gray with increase in Nd content (samples 14 and 15).

Doping with Ce imparted an orange coloration to the crystal (sample 2) tending to red (sample 3) as the Ce concentration was increased. Annealing of the Ce-doped crystals removed the coloration and gave a normal spectra (sample 1, Fig. 2). The spectra for the unannealed sample show high transmission in the red region and significant absorption at ~4700Å, attributed to a significant concentration of Ce^{3+} ions. The similarity of the spectra for samples 1, 16, and 4 (Mo/Cr) would suggest that the ions substitute on regular cation sites in YSZ lattice.

Apart from Ce^{3+}, the only strong absorption peaks observed were for Er doping (samples 11 and 12). Figure 3 shows these spectra where strong absorption peaks were obtained in the ranges 5200-4900Å and 3800-3500Å. Again, this was attributed to absorption by the Er^{3+} ions.

A strong deep blue color was obtained with Co doping which became lighter after annealing (samples 7 and 8), reflecting the decrease impurity level. Combination of Ce with Co produced a dark ruby red crystal (sample 9).

Infrared spectra.—Figures 4, 5, and 6 show infrared spectra for the different crystals in near (0.65-2.5 μm), medium (2.5-10 μm), and far (7.0-50 μm) infrared regions, respectively. Figure 4 shows transmission in the near infrared range to be relatively high, with little absorption activity except for crystals 1, 11, 16, and 12.

Considering the sample compositions, the absorption peaks in the region of 1.5 μm seem clearly associated with the presence of Ce and Er since both are missing in the undoped sample 16. Peaks at ~1.2 and 2.2 μm would seem to be associated with the presence of Y^{3+} in the ZrO_2 lattice (11). This area of the spectrum has not been well studied.

Figure 5 shows the infrared transmission up to 10 μm for the crystals studied. All showed an infrared

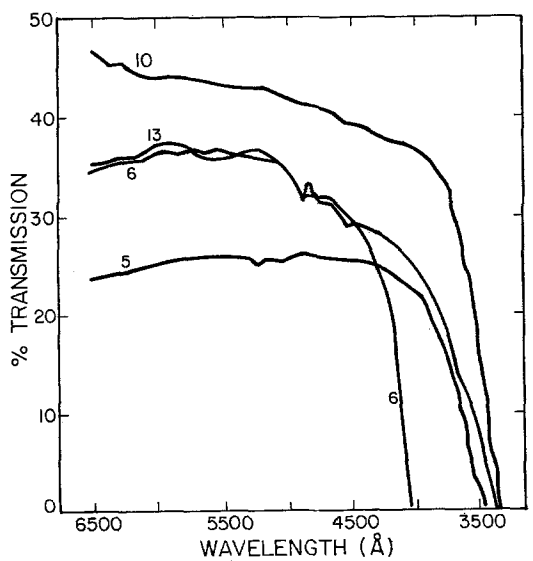

Fig. 1. Optical transmission spectra for YSZ crystals with dopants 5(Mo/Cr), 6(Fe), 10(Ce/Ni), and 13(Pr) as given in Table I.

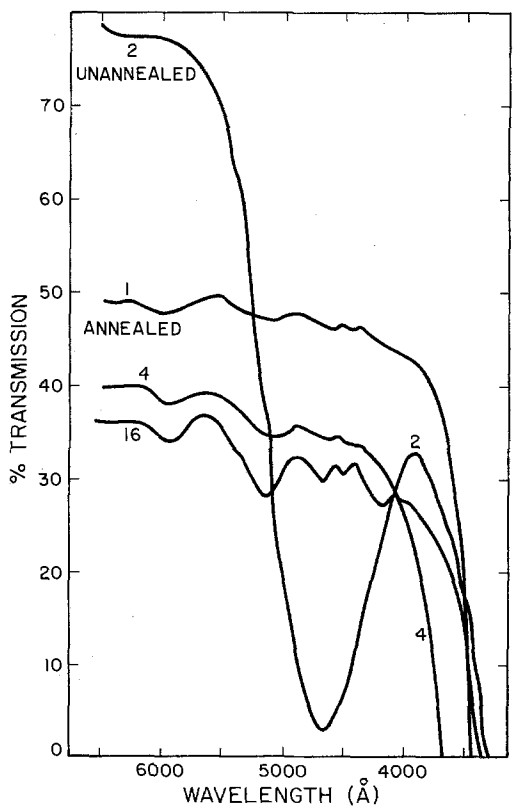

Fig. 2. Optical transmission spectra for YSZ crystals with dopants 1(Ce), 2(Ce), 4(Mo), and 16(none) as given in Table I.

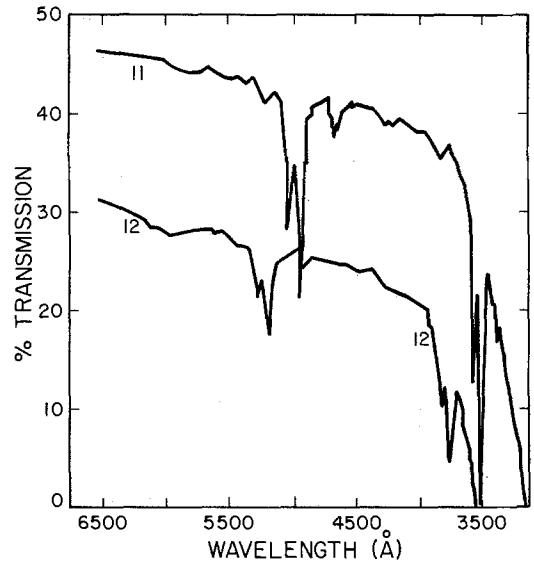

Fig. 3. Optical transmission spectra for YSZ crystals with dopants 11(Ni/Er) and 12(Ce/Er) as given in Table I.

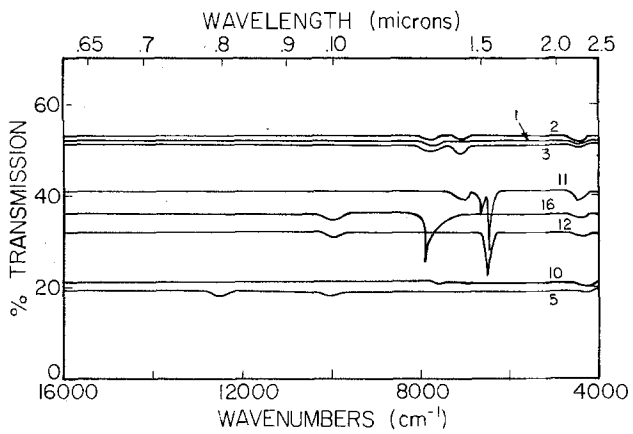

Fig. 4. Near infrared transmission spectra for YSZ crystals No. 1, 2, 10, 11, 12, and 16 in Table I.

cutoff at ~7 μm. Highest transmitting crystals were numbers 2 and 1 (low Ce) and lowest numbers 10 (Ce/Ni) and 5 (Mo/Cr), attributed to the presence of the transition metal ions. In general, any dopant addition to the YSZ crystals tended to decrease the infrared transmission in this range. Significant absorption peaks were observed only for samples 3 and 9, reflecting the relatively high Ce content in these crystals (2, 11).

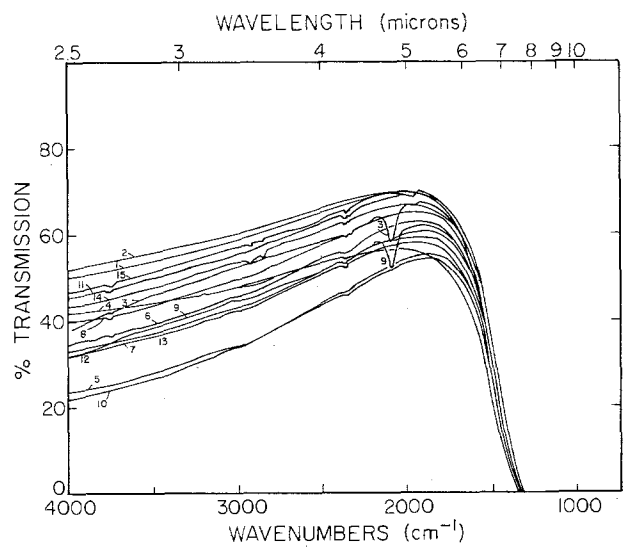

Fig. 5. Medium infrared transmission spectra for the YSZ crystals in Table I.

Figure 6 shows a generalized curve for the crystals in the infrared range 7-50 μm, since the transmission characteristics were essentially identical for all samples. The crystals were essentially opaque up to ~17 μm and showed significant transmission at the longer wavelengths (2). The fine structure of the spectra represents bonding characteristics within the fluorite structure.

Electrical conductivity.—Table II gives electrical conductivity data at 200°, 500°, 800°, and 1000°C for the different YSZ samples with dopants including activation energy values. For the 9.5 m/o YSZ samples, dopant level or type dopant was found to have little direct effect on conductivity of the crystals. The annealed Ce (sample 1) and those with transition metal (Fe, Mo, Cr, Ni) dopants gave slightly lower conductivities, but activation energy values were comparable.

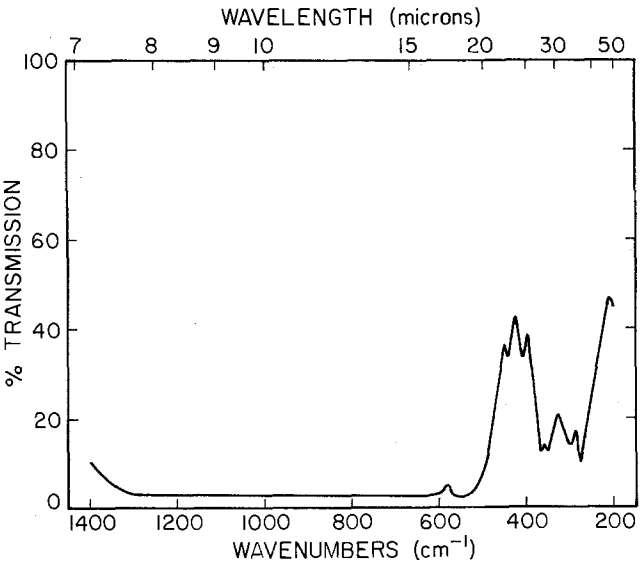

Fig. 6. Typical far infrared transmission spectra for the YSZ-(9.5 m/o Y_2O_3) single crystals.

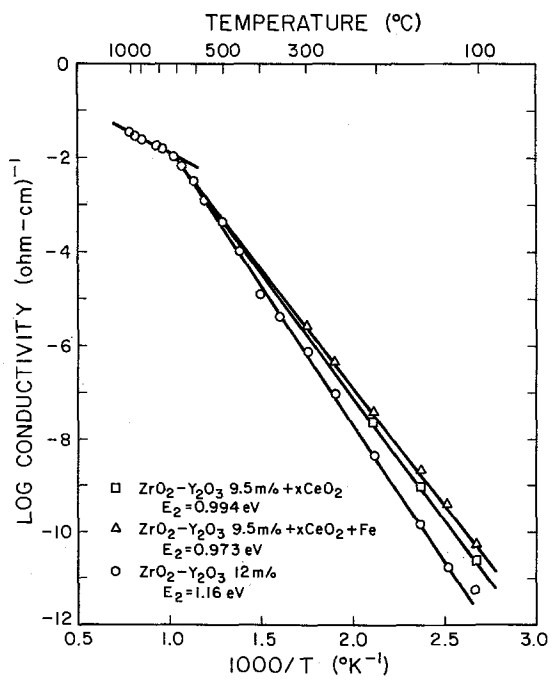

Fig. 7. Log conductivity *vs.* reciprocal temperature for YSZ (12.0 m/o Y_2O_3) and YSZ (9.5 m/o) crystals with different dopants. Activation energies, E_2, were calculated from data below 800°C.

Table II. Electrical conductivity for YSZ crystals with temperature

Sample	Dopants	Conductivity-(Ω-cm)$^{-1}$ 200°C	500°C	800°C	1000°C	E_a (eV)
1*	CeO_2	4.71×10^{-8}	7.37×10^{-4}	7.06×10^{-2}	1.28×10^{-1}	1.02
2	CeO_2	2.89×10^{-8}	3.77×10^{-4}	2.42×10^{-2}	3.99×10^{-2}	0.99
3	CeO_2	2.82×10^{-8}	5.25×10^{-4}	2.47×10^{-2}	3.56×10^{-2}	1.01
4	MoO_2	6.17×10^{-9}	3.36×10^{-4}	2.89×10^{-2}	4.95×10^{-2}	1.05
5	MoO_2/Cr_2O_3	1.59×10^{-8}	2.31×10^{-4}	1.42×10^{-2}	2.06×10^{-2}	1.00
6	FeO	4.89×10^{-8}	7.13×10^{-4}	1.94×10^{-2}	3.89×10^{-2}	0.97
7	CoO	2.74×10^{-8}	5.37×10^{-4}	2.84×10^{-2}	4.35×10^{-2}	1.02
8*	CoO	3.64×10^{-8}	2.26×10^{-4}	2.48×10^{-2}	3.64×10^{-2}	1.00
9	CeO_2/CoO	2.30×10^{-8}	1.67×10^{-4}	2.38×10^{-2}	4.63×10^{-2}	1.02
10	CeO_2/NiO	1.13×10^{-8}	2.23×10^{-4}	1.67×10^{-2}	2.5×10^{-2}	1.03
11	NiO/Er_2O_3	2.65×10^{-8}	3.63×10^{-4}	1.63×10^{-2}	2.49×10^{-2}	1.01
12	CeO_2/Er_2O_3	1.60×10^{-8}	4.21×10^{-4}	2.63×10^{-2}	3.86×10^{-2}	1.05
13	Pr_2O_3	1.19×10^{-8}	2.00×10^{-4}	2.35×10^{-2}	3.7×10^{-2}	1.05
14	CeO_2/Nd_2O_3	1.77×10^{-8}	2.76×10^{-4}	1.92×10^{-2}	3.22×10^{-2}	0.99
15	CeO_2/Nd_2O_3	2.02×10^{-8}	2.03×10^{-4}	1.60×10^{-2}	2.18×10^{-2}	0.99
16**	None	4.32×10^{-9}	4.32×10^{-4}	1.75×10^{-2}	2.32×10^{-2}	1.16

* Air annealed 1200°C/24 hr.
** YSZ (12 m/o Y_2O_3).

The 12 m/o YSZ samples gave a lower value for the conductivity and correspondingly higher activation energy, as expected.

Figure 7 shows a plot of log conductivity *vs.* reciprocal temperature for the 9.5 YSZ sample with dopants and the undoped 12 m/o YSZ sample. Only the latter showed any significant difference in activation energy, indicated by the steeper slope below ~800°C. The change of slope in the conductivity curve above 800°C had not previously been reported for YSZ. Below 800°C, both conductivity and activation energy values were comparable (1, 2, 6).

Conclusions

For YSZ samples containing 9.5 m/o Y_2O_3, dopant and annealing effects were particularly noticeable in the visible spectra. Ce, Er, Fe, and Co doping showed the most significant changes. Effect of annealing was apparently to reduce Ce^{3+} and defect concentration.

The infrared spectra appeared less affected by dopants, except in the near infrared. Relatively high transmission was obtained for all crystals up to ~7 μm cutoff. Dopant influence on electrical conductivity was not significant.

Changes in the Y_2O_3 content had a greater effect. Measured activation energy for conduction of ~1.0 eV and conductivity of $\sim 2 \times 20^{-2}$ (Ω-cm)$^{-1}$ at 800°C, were typical of the YSZ samples.

Acknowledgments

This work was supported by the Office of Naval Research under Contract No. N-00014-80-K-0969 and in part by the National Science Foundation under NRL grant DMR-80-20250.

Manuscript received Sept. 21, 1982.

Any discussion of this paper will appear in a Discussion Section to be published in the December 1983 JOURNAL. All discussions for the December 1983 Discussion Section should be submitted by Aug. 1, 1983.

Publication costs of this article were assisted by the University of Illinois at Urbana-Champaign.

REFERENCES

1. C. B. Choudhary, H. S. Maiti, and E. C. Subbarao, in "Solid Electrolytes and Their Applications," E. C. Subbarao, Editor, pp. 37-43, Plenum Press, New York and London (1980).
2. K. S. Mazdiyasni, C. T. Lynch, and J. S. Smith II, *J. Am. Ceram. Soc.*, **50**, 432 (1967).
3. T. K. Gupta, R. B. Grekila, and E. C. Subbarao, *This Journal*, **128**, 929 (1981).
4. L. W. Niedrach, *ibid.*, **127**, 2122 (1980).
5. A. Kumar, D. Rajdev, and D. L. Douglas, *J. Am. Ceram. Soc.*, **55**, 439 (1972).
6. D. W. Strickler and W. G. Carlson, *ibid.*, **47**, 122 (1964).
7. L. S. Alekseenko, G. Yu. Koifman, E. D. Posokhova, and D. M. Shakhtin, *Izv. Akad. Nauk SSSR, Neorg. Mater.*, **10**, 2006 (1974).
8. R. V. Wilhelm, Jr. and D. S. Howarth, *Am. Ceram. Soc. Bull.*, **58**, 228 (1979).
9. V. I. Aleksandrov, V. V. Osiko, V. M. Tatarintsev, and V. T. Udovenchik, *Izv. Akad. Nauk SSSR, Neorg. Mater.*, **9**, 236 (1973).
10. K. Nassau, *J. Lapidary*, **31**, 900, 922 (1977); **32**, 2136 (1979).
11. V. I. Aleksandrov, S. Kh. Batygov, Yu. K. Voron'ko, B. I. Denker, E. E. Lomonova, V. V. Osiko, and V. M. Tatarintsev, *Izv. Akad. Nauk SSSR, Neorg. Mater.*, **11**, 664 (1975).
12. V. I. Aleksandrov, V. F. Kalabukhova, E. E. Lomonova, V. V. Osiko, and V. I. Tatarintsev, *ibid.*, **13**, 2192 (1977).

Technical Notes

Influence of Impurities on Lateral Polysilicon pn Diodes

M. Dutoit[1]

Centre Electronique Horloger S.A., CH 2000 Neuchâtel, Switzerland

Lateral pn diodes in thin films of polycrystalline Si (1, 2) have found widespread uses in CMOS integrated circuits (3, 4) and other applications (5). The reverse current of 10 μm-wide diodes fabricated with a typical low power CMOS process reaches a few nA at 1.5V. This property allows one to employ these devices as high-value area-saving resistors not easily integrated otherwise. Moreover, even though they are fairly leaky, compared to pn junctions in single crystal Si, they can be used in noncritical applications to maintain a logic level. Lateral polysilicon diodes are completely isolated from the substrate.

Their electrical characteristics have been ascribed to field-enhanced emission via grain boundary traps, in addition to the classical mechanisms of generation and recombination of minority carriers (2, 6). They are, therefore, very sensitive to factors that influence the density and occupation of these traps, among them grain size (7-9) and resistivity (2) of the polysilicon layer. Since the advent of LPCVD for growing polysilicon films and ion implantation for doping them, these two parameters are well under control. Nevertheless, unexpected increases in the average reverse current of the devices on some batches of wafers may occur on occasion, mainly after periodic cleaning and maintenance work on the LPCVD reactor, even though no changes in deposition conditions, structure, etch rate, optical and electrical parameters are recorded.

The purpose of this work is to show that gaseous pollutants, which may inadvertently be present in the reactor during deposition, can significantly alter the properties of polysilicon diodes. The impurities most likely to be found are H_2, O_2, and HCl. H_2 is a by-product of the pyrolysis of SiH_4; O_2 may be introduced by leaks or be adsorbed on the walls of the tube while the reactor is opened to room ambient, and HCl is used before each deposition to clean the wafers.

It is easy to introduce O_2 (in the form of N_2O, to avoid the premature reaction with SiH_4 to form SiO_2) and HCl directly into the reactor. Significant amounts of H_2 can be incorporated into polysilicon films by annealing them in an H^+ plasma at about 500°C. Yet, our preliminary results with this last method remain inconclusive.

Experimental

Polysilicon films were deposited in a Tempress LPCVD reactor at 190 mTorr and 620°C from 100% SiH_4 (Air Liquide, N50) on 1 μm-thick SiO_2 layers thermally grown on 2 in. (100) Si wafers. SiH_4 flow rate was 50 sccm. Small amounts of N_2O (Air Liquide, N45) or HCl (Pittsburgh Materials and Chemicals, N45) were admitted to the reaction chamber during deposition through a calibrated mass flow controller. In both cases, the growth rate was reduced from its value under normal conditions (Fig. 1). The deposition time was adjusted to yield 0.5 μm thick films.

[1] Present address: Institute for Microelectronics, Swiss Federal Institute of Technology, CH 1015 Lausanne, Switzerland.

The structure of these films was examined by transmission electron microscopy (TEM). A novel batch process was developed for rapidly preparing rugged TEM samples that are easy to handle (10). It consists in chemically etching circular holes in the substrate underneath the polysilicon layer (Si and SiO_2) by using a Cr/Au film as a mask. Thickness and optical properties were evaluated with an ellipsometer.

Our conventional CMOS process (2, 4) served to fabricate lateral p^+n^+ diodes. The sheet resistivity of both p^+- and n^+-doped layers with no HCl or N_2O added, was about 100 $\Omega/\square$.

Results

Average grain size is decreased by addition of small amounts of either N_2O or HCl, even though the growth rate diminishes (Table I). Normally, the opposite would be expected. Yet, this result confirms previous work which showed that N_2 and O_2 retard grain growth (11, 12). The thickness of films prepared with N_2O or HCl is less uniform than without. The angle ψ determined by ellipsometry is reduced by several degrees. In our experience with standard production runs, this indicates a roughened surface rather than a change in optical constants of the film. Yet, we have not checked this point in the present case.

Figures 2 and 3 show the variation of sheet resistivity ρ_S and average reverse current I_R with flow rate of N_2O and HCl, respectively. In the first case, these parameters vary rapidly even for small flow rates. By extrapolating our results, we infer that I_R can decrease by an order of magnitude without a significant change in ρ_S. With HCl, ρ_S varies little and I_R goes through a maximum at 1 sccm. This increase could be due, as well, to the incorporation of chlorine in the films, as to precipitations on the wafers of metal impurities dissolved upstream by HCl in the presence of traces of H_2O.

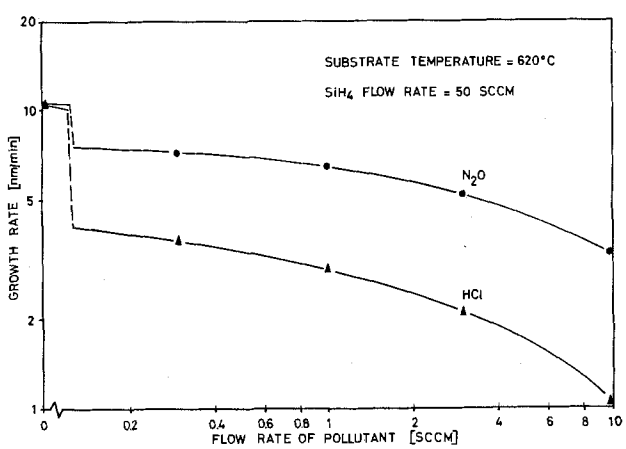

Fig. 1. Variation of LPCVD polysilicon film growth rate due to N_2O and HCl.

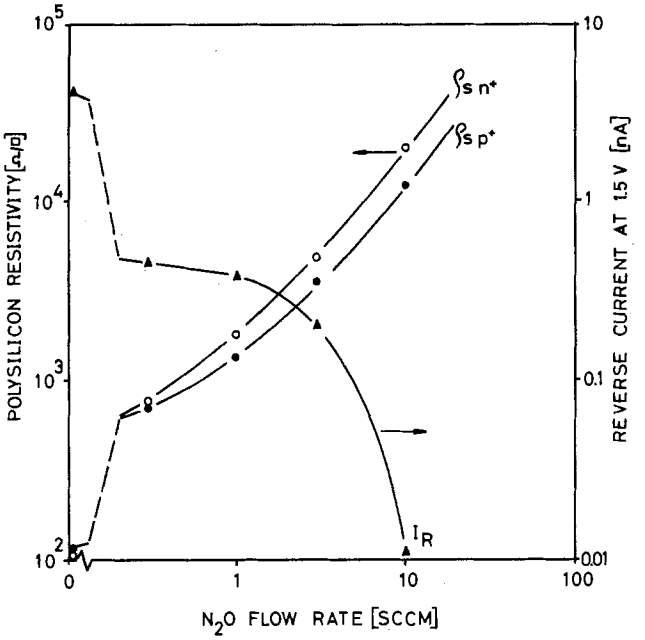

Fig. 2. Sheet resistivity of p^+- and n^+-doped polysilicon and of reverse current at 1.5V (10 μm-wide diodes) *vs.* flow rate of N_2O.

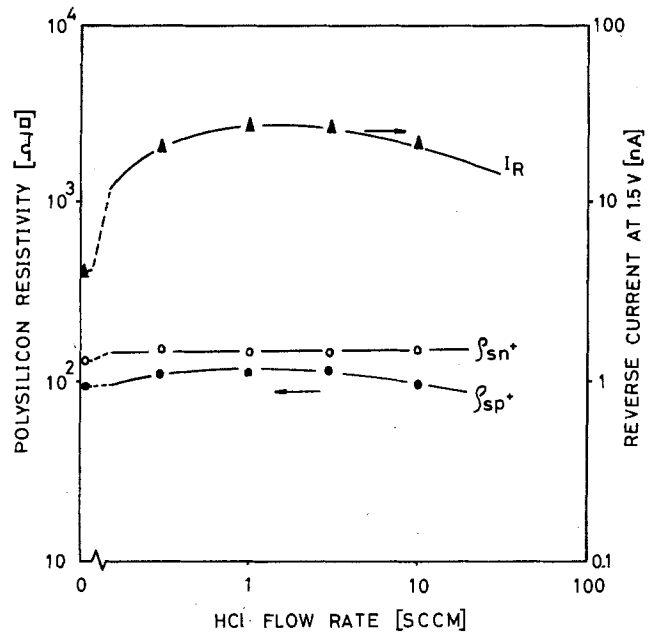

Fig. 3. Sheet resistivity of p^+- and n^+-doped polysilicon and of reverse current at 1.5V (10 μm-wide diodes) *vs.* flow rate of HCl.

These results show that lateral polysilicon diodes are very sensitive to minute amounts of pollutants in the LPCVD reactor. Changes in reverse current after maintenance work can be explained by the gradual shift of the O_2 adsorption-desorption equilibrium of the silicon layer deposited on the walls of the reactor tube or by small leaks. These effects can be sufficiently weak so as not to affect the other properties of the polysilicon film. In order to obtain reproducible results, contamination and leakage need to be carefully controlled. On the other hand, the characteristics of polysilicon diodes could be intentionally modified by closely monitored additions of these impurities during deposition.

Table I. Average grain size (nm) after diffusion (N_2, 1000°C, 45 min)

Flow rate (sccm)	N_2O	HCl
	Grain size (nm)	
0	110	110
0.3	80	80
1.0	—	55
3.0	30	55

Acknowledgments

Helpful discussions with F. Leuenberger, F. Sollberger, M. E. Roulet, and J. M. Moret are gratefully acknowledged.

Manuscript received Sept. 17, 1982.

Any discussion of this paper will appear in a Discussion Section to be published in the December 1983 JOURNAL. All discussions for the December 1983 Discussion Section should be submitted by Aug. 1, 1983.

Publication costs of this article were assisted by Centre Electronique Horloger S.A.

REFERENCES

1. J. Manoliu and T. I. Kamins, *Solid-State Electron.*, **15**, 1103 (1972).
2. M. Dutoit and F. Sollberger, *This Journal*, **125**, 1648 (1978).
3. H. Oguey and B. Gerber, U.S. Pat. 4,041,522 (1977).
4. E. A. Vittoz, Proceedings of ESSCIRC 80, p. 174, Grenoble, Sept. 22-25, 1980.
5. H. C. de Graaff and J. G. de Groot, IEDM, Washington, DC, Dec. 8-10, 1980, Technical Digest, Paper 3.1.
6. H. C. de Graaff, M. Hybers, and J. G. de Groot, *Solid-State Electron.*, **25**, 67 (1982).
7. M. E. Roulet, M. Dutoit, W. Lüthy, and K. Affolter, *Appl. Phys. Lett.*, **37**, 737 (1980).
8. R. R. Shah, D. R. Hollingsworth, G. A. de Jong, and D. L. Crostwait, *IEEE Electron Device Lett.*, **edl-2**, 159 (1981).
9. G. E. J. Eggermont and J. G. de Groot, *ibid.*, **edl-3**, 156 (1982).
10. F. Mauron, Unpublished results.
11. R. M. Anderson, *This Journal*, **120**, 1540 (1973).
12. M. Hamasaki, T. Adachi, S. Wakayama, and M. Kikuchi, *J. Appl. Phys.*, **49**, 3987 (1978).

Transmission Electron Microscopic Observation of Precipitates in Si^+ Ion-Implanted GaAs

G. Das[1]

Systems Research Laboratories Incorporated, Dayton, Ohio 45440

and Y. S. Park

Avionics Laboratory, Air Force Wright Aeronautical Laboratories, Wright-Patterson Air Force Base, Ohio 45433

Radiation damage in the form of dislocation loops and an amorphous layer was observed in Si^+ ion-implanted GaAs by transmission electron microscopy (TEM) and reflection electron diffraction (1). Precipitates in heavily Si^+ ion-implanted GaAs were observed at room temperature. These precipitates are matched with those of $SiAs_2$.

Bridgman-grown semi-insulating Cr-doped GaAs single crystals (resistivity $\sim 10^8\ \Omega \cdot cm$) having the <100> orientation were obtained in the form of polished wafers from Crystal Specialties, Incorporated. These wafers were implanted with Si^+ ions at 120 keV at room temperature using a dose rate of 6.25×10^{11} ions/cm^2 sec to two different doses, namely, 3×10^{13} and 3×10^{15}/cm^2. For TEM studies, specimens having $\sim 4 \times 4 \times \frac{1}{2}$ mm dimensions were cut from the implanted wafers by a diamond scriber along the {110} cleavage plane. These specimens were mechanically ground from the unimplanted side using 400-grit SiC paper to a thickness of $\sim 150\ \mu m$. The corners of the specimen were ground to provide a diameter of 3 mm (for fitting into the TEM holder). The implanted surface was protected by an Apiezon wax coating, and the specimen was chemically polished in a bromine-methanol solution (1:99 by volume) at room temperature in a commercially available twin jet polisher, using only one jet to strike the unimplanted side. Just prior to perforation, the specimen was removed from the solution, and the Apiezon wax was removed by trichloroethylene. The specimen was again polished using one jet as before until perforation was achieved. The specimen was then rinsed in methanol, dried, and examined in a Philips EM 300 electron microscope operated at 100 kV at room temperature.

A typical electron micrograph from a Cr-doped GaAs specimen implanted with Si^+ ions to a dose of 3×10^{13}/cm^2 is shown in Fig. 1. The electron micrograph had rather a mottled appearance and contained small defect clusters. The diffraction pattern showed neither extra reflections resulting from precipitation nor evidence of diffuse rings, characteristic of an amorphous layer.

Figure 2 is a typical electron micrograph and the corresponding selected-area diffraction pattern obtained from Cr-doped GaAs specimen implanted with Si^+ ions to a dose of 3×10^{15}/cm^2. The specimen contained a high density of black spots. The majority of them exhibited black-white contrast, and a few exhibited double-arc contrast with a line of no contrast. The selected-area diffraction pattern revealed the presence of extra reflections [marked by x in the schematic diagram, Fig. 2(c)] resulting from precipitates. The d-spacings corresponding to the extra reflections A, B, and C can be matched with the (210), $(\bar{1}21)$, and $(\bar{3}12)$ planes, respectively, of $SiAs_2$ which has the cubic structure (Table I). Good agreement between the measured and calculated angles of the different planes due to precipitates can be observed (Table II).

Key words: transmission electron microscope, precipitation, ion implantation, semiconductor.

[1]Present address: Super Semi Conductor (P) Ltd., Sch. IVM, Beliaghata, Calcutta-700010, India.

The dark-field technique using the extra reflections to delineate the precipitates in the implanted region was attempted; however, because of the very weak intensity of these reflections, these attempts were unsuccessful. Consequently, the precipitates present in the implanted area could not be separated from other black spot damage such as dislocation loops.

As in the case of low-dose (3×10^{13}/cm^2) Si^+ ion implants, no evidence of the amorphous ring pattern was found in the diffraction pattern obtained from the specimen implanted with Si^+ ions to a dose of 3×10^{15}/cm^2 [see Fig. 2(b)]. A few as-grown dislocation lines were also observed, as shown in Fig. 2(a).

Selected-area diffraction patterns taken from thin foils of Cr-doped GaAs implanted with Si^+ ions to a

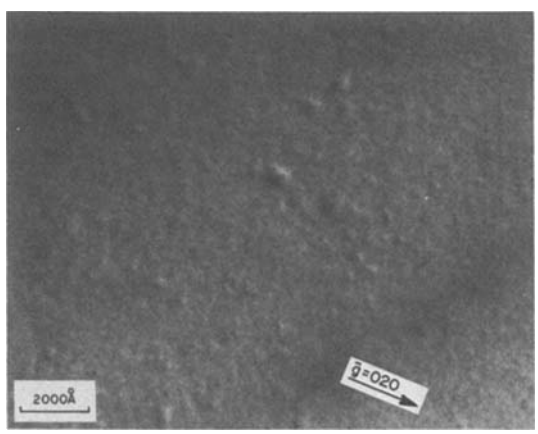

Fig. 1. Electron micrograph showing a few defect clusters (shown by an arrow) in the background of a "mottled" structure in GaAs:Cr implanted with Si^+ ions (120 keV) at room temperature. Total dose: 3×10^{13}/cm^2. Foil orientation is very close to (100).

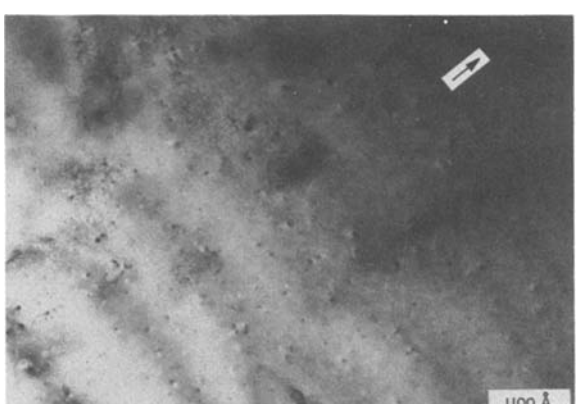

Fig. 2. (a) Electron micrograph showing point-defect clusters, precipitates, and as-grown dislocations (shown by an arrow) in GaAs:Cr implanted with Si^+ ions (120 keV) at room temperature. Total dose: 3×10^{15}/cm^2.

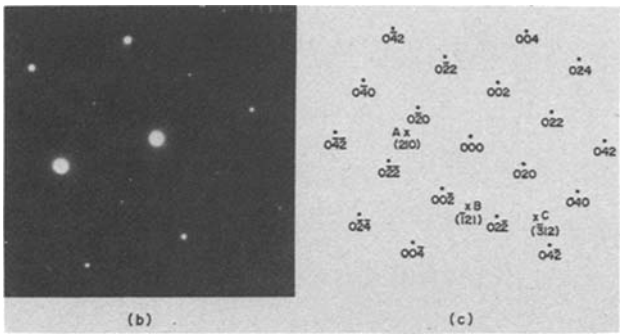

Fig. 2. (b), (c) Selected-area diffraction pattern and its schematic diagram showing the presence of extra spots (x) due to precipitates. Foil orientation is very close to (100).

dose of $3 \times 10^{15}/cm^2$ showed extra spots which were found to match those of $SiAs_2$ precipitates. According to Shimanoe *et al.* (2, 3), doping of silicon to a concentration of $2.5 \times 10^{18}/cm^3$ is possible in GaAs. A silicon concentration value of $2.4 \times 10^{20}/cm^3$ is obtained in the implanted layer of GaAs through implantation of Si^+ ions at 120 keV to a dose of $3 \times 10^{15}/cm^2$ (projected range = 1030Å, standard deviation = 510Å). This value is considerably higher than the solubility limit, and the excess silicon should precipitate. However, precipitation in the form of $SiAs_2$, and not in the form of elemental silicon, was observed, suggesting that the precipitation process is rather complex during ion implantation. In contrast, Tamura *et al.* (1) found no evidence of precipitation in GaAs implanted with 50 keV Si^+ ions to a dose of $10^{15}/cm^2$, corresponding to a silicon concentration of $1.6 \times 10^{20}/cm^3$ in the implanted layer. This difference is not well understood. Although defect clusters in the form of black spots were observed in specimens of Si^+ implanted to a dose of $3 \times 10^{13}/cm^2$ (*i.e.*, a silicon concentration of $2.4 \times 10^{18}/cm^3$) in the present study, no extra spots due to precipitates were observed, suggesting that the Si concentration is still within the solid solubility limit of GaAs. Alternatively, the absence of extra spots may be due to an insufficient volume fraction of precipitates in the low-dose samples capable of producing extra spots in the diffraction pattern.

Another interesting difference between the present study and that of Tamura *et al.* (1) is the absence of diffuse rings arising from amorphization of the implanted layer in the selected-area diffraction patterns taken from 120 keV Si^+ ions implanted into GaAs, to doses of 3×10^{13} and $3 \times 10^{15}/cm^2$ at room temperature. Tamura *et al.* (1) observed the presence of an amorphous layer by the reflection electron diffraction method in GaAs implanted with 50/170 keV Si^+ ions at room temperature to doses ranging from 10^{12} to $10^{15}/cm^2$. The origin of this discrepancy may lie in the methods used to detect the amorphous layer in these two investigations. When reflection electron diffraction is used to study the nature of the surface layer, diffraction will be produced mainly from the surface and the thin amorphous implanted surface layer can be recognized easily, as observed by Tamura *et al.* (1). On the other hand, in the TEM mode, the electron beams pass through the crystalline as well as the amorphous implanted layer. The strong intensities of the diffraction beams, coupled with the absence of diffuse rings in the present study, suggest that the electron beam is passing mainly through the crystalline material; and the amorphous layer, even if it is present, is too thin to produce observable diffuse ring in the selected-area diffraction pattern. It should be mentioned, however, that Tamura *et al.* (1) did not report observation of the amorphous layer in their TEM characterization of similar implanted materials.

Table I. Measured d-spacings from extra reflections and their assignment based upon the $SiAs_2$ structure

Measured d-value of precipitate from origin (Å)	Calculated d-value of $SiAs_2$ (Å) plane)
d_A 2.679	2.693 $(\bar{2}10)$
d_B 2.418	2.458 $(\bar{1}\bar{2}1)$
d_C 1.617	1.606 $(\bar{3}\bar{1}2)$

Table I. Comparison of measured and calculated angle (based upon the $SiAs_2$ structure) of different planes due to precipitates

Plane	Measured angle (deg)	Calculated angle (deg)
$(210) \wedge (\bar{1}21)$	90	90.0
$(210) \wedge (\bar{3}12)$	~130	126.7
$(\bar{1}21) \wedge (\bar{3}12)$	~42	40.2

Manuscript submitted March 2, 1982; revised manuscript received Dec. 3, 1982.

Any discussion of this paper will appear in a Discussion Section to be published in the December 1983 JOURNAL. All discussions for the December 1983 Discussion Section should be submitted by Aug. 1, 1983.

Publication costs of this article were assisted by Systems Research Laboratories, Incorporated.

REFERENCES

1. M. Tamura, T. Miyazaki, and N. Natsuaki, *Suppl. J. Jpn. Soc. Appl. Phys.*, **43**, 504 (1974).
2. T. Shimanoe, T. Murotani, M. Nakatani, M. Otsubo, and S. Mitsui, *Surf. Sci.*, **86**, 126 (1979).
3. T. Murotani, T. Shimanoe, and S. Mitsui, *J. Cryst. Growth*, **45**, 302 (1978).

A Simple Technique for the Estimation of the Bulk Resistivity of Powdered Materials

J. R. Whyte, Jr.

Freeport Minerals Company, Research and Development Center, Belle Chasse, Louisiana 70037

and K. Seshan

Department of Metallurgical Engineering, University of Arizona, Tucson, Arizona 85721

Recently, a study was undertaken to establish the relationship between the efficiency of a particulate collection device, the Electrostatic Precipitator (ESP), and the nature of the particles which were to be collected. The electrical resistivity of the particles is a parameter which was deemed worthy of investigation in this regard. It was thus desired to develop a technique and device for resistivity measurements on bulk particulate or powdered samples.

The resistivity measurements were only to be a small part of the complete study, a requirement for utmost simplicity was imposed on the technique and device. Measurements were to be made at room temperature to prevent phase changes in the material being tested. It was desired to measure the bulk powder resistivity as the sample was subjected to various compacting pressures, to take advantage of the diagnostic capabilities of such a procedure. A bulk resistivity close to the resistivity of individual particles would be obtained by a final application of an extremely high compacting pressure. Finally, the technique and device would have to be suited to measurement of a wide range of resistivities, from perhaps as low as 10^{-8} Ωcm and up to 10^{15} Ωcm.

Review of the Literature

The bulk of the literature pertaining to measurement of particle (powder) resistivity dealt with three major particle groups. These were battery materials, powder metallurgy materials, and coal fly ash. Resistivity measurement techniques used for battery materials were deemed most adaptable to measurements on particles of wide-ranging resistivity, and these techniques are discussed exclusively hereafter.

The devices used for electrical resistivity measurements on battery materials were generally capable of making such measurements with the test material under high compacting pressure (1, 2, 3). Electrical contact with the sample was usually accomplished by probes which were pressed against the sample by the compacting pressure; thus minimizing contact resistance between the metal probe and a semiconducting or insulating sample. A few of the more common cell designs were excerpted from the excellent review article by Euler and appear in Fig. 1.

All of the techniques in Fig. 1 involved measurement of the voltage induced by a current passed longitudinally through the sample or vice versa. Nanba (4) used a van der Pauw (5) technique with a four-point probe, but performed measurements on heated compacts at only modest pressures. Nanba's device is shown in Fig. 2. The van der Pauw technique had the advantage of being less sensitive than other techniques to uneven pressure distributions within the sample, which may be hard to avoid at high compacting pressures.

It was decided to combine some of the features of the above techniques into a simple technique utilizing a four-point probe arrangement and a sample cell designed for measurements at very high pressures at room temperature.

Key words: estimation of bulk resistivity of powdered materials, four-point probe, PbO, ZnO, CuS.

Design and Use of the Resistivity Cell

The van der Pauw resistivity cell used in this study is pictured schematically in Fig. 3. The device is based on four probes arranged on a circle concentric with the edges of a circular compact. This probe arrangement was first used by Nanba (4), and the method of compaction is similar to many of the techniques reviewed by Euler (1).

To perform a measurement, sample powder was loaded into the sample chamber and compacted with an aluminum rod plunger on a 15-ton capacity Carver laboratory press. The plunger was removed during electrical measurements. Samples were compacted successively at pressures of from 5,000 to 75,000 psi (35-530 MPa) in 5,000 psi (35 MPa) intervals. Since it is known that the rate of compaction can affect the resistivity of a powder compact, and that values closer to bulk values are obtained with small rates of compaction (1), each incremental pressure increase was performed over a time span of about 30 sec. Resistivities were measured after each pressure increment, and their measurement was based on the theory given in the following paragraphs (5).

If a current I_{ab} is passed through the two adjacent probes a and b in Fig. 2, a voltage drop V_{cd} will be induced between probes c and d. A resistance $R_{ab,cd}$ is defined as the voltage drop between probes c and d, per unit of current through probes a and b. Thus

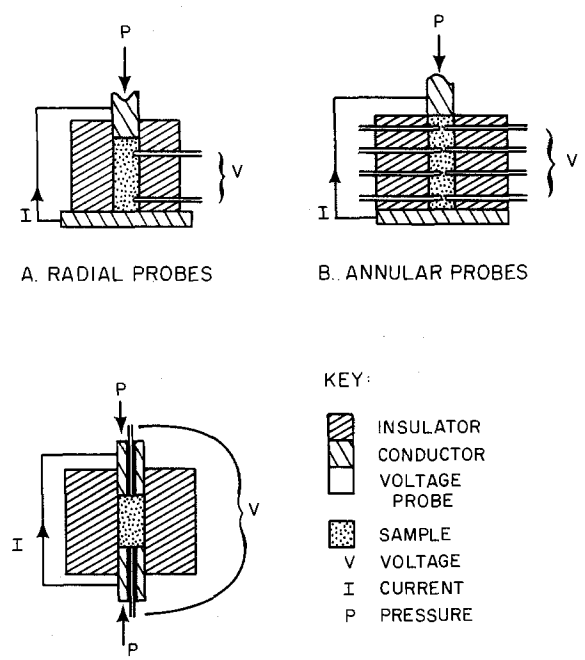

Fig. 1. Schematic illustrations of some devices conventionally used for powder resistivity measurements. In these devices, current is parallel to applied pressure. Illustrations excerpted from Euler (1).

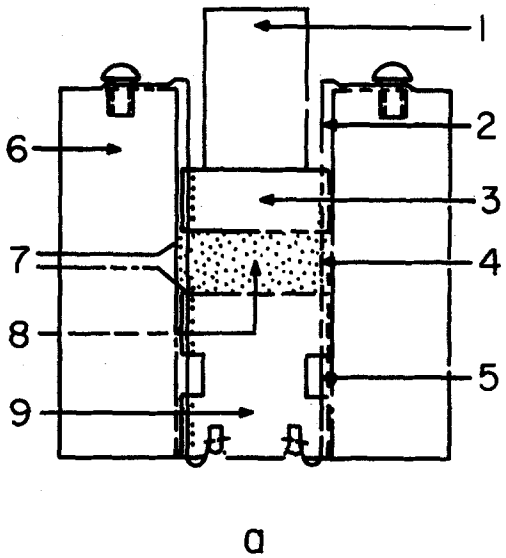

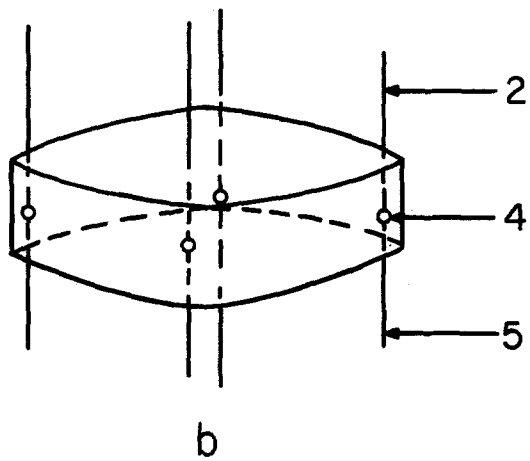

Fig. 2. The device used by Nanba (4) to prepare compacts for resistivity measurements on powders. (a) mold; (b) a fabricated compact with embedded probes. (1) stripper die; (2) Pt wire; (3) upper punch; (4) junction point; (5) Pt-13% Rh wire; (6) die body; (7) eyelet; (8) powder; (9) lower punch. Dimensions (larger numbers) are in mm.

$$R_{ab,cd} = V_{cd}/I_{ab} \quad [1]$$

A resistance $R_{bc,da}$ is defined in a similar manner. The resistivity of the compact is then given by

$$\rho = \frac{2\pi d}{c}(R_{ab,cd} + R_{bc,da}) \cdot F \quad [2]$$

where

D = height of compact, varied from 3/32 to 1/4 in. (0.24-0.64 cm)

$$C = 4(r_1^2 + r_2^2)^4/(r_1^4 + r_1^4 + r_2^4)^2 \quad [3]$$

and r_1 = radius of compact, 1/4 in. (0.64 cm)

r_2 = distance from any probe to the center of the compact, 3/16 in. (0.48 cm)

For the device used in this study

$$\rho = 361d(R_{ab,cd} + R_{bc,da}) \cdot \mathbf{F} \quad [4]$$

The factor **F** depends on the ratio of the two resistances, and is given by the plot in Fig. 4 excerpted from van der Pauw (5).

The applied d-c voltage (provided by a Heathkit power supply) was selected so as to give a measurable current, and thus ranged between 0.1 and 50V. The resultant voltage gradient of less than 50 V/cm was below the level at which the gradient would have a substantial (*i.e.*, order of magnitude) effect on the measured resistivity (1). The induced voltage was measured by applying the voltage across an external resistance and measuring the resultant current. Current

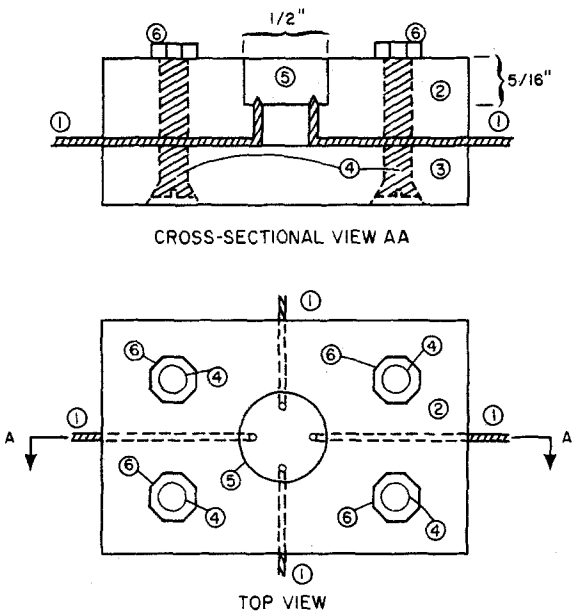

Fig. 3. Schematic drawings of the new van der Pauw type powder resistivity measurement cell. (1) 0.052 in. copper wire probes, sharpened into 45° cones on contact end; (2) cloth-based phenolic insulating sample chamber support block; (3) polyvinyl chloride (PVC) insulating and support block; (4) countersunk flathead clamping screws; (5) sample chamber; (6) hexagonal nuts.

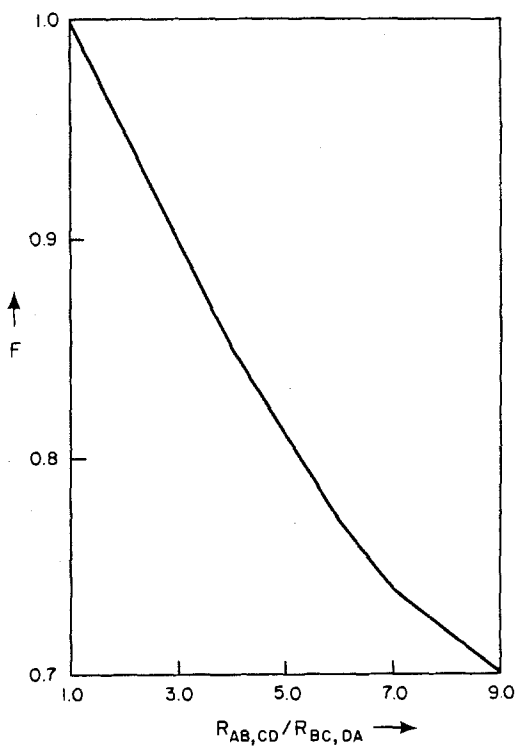

Fig. 4. The geometric factor, *F*, used in powder resistivity determinations, plotted against the resistivity ratio. Taken from van der Pauw (5).

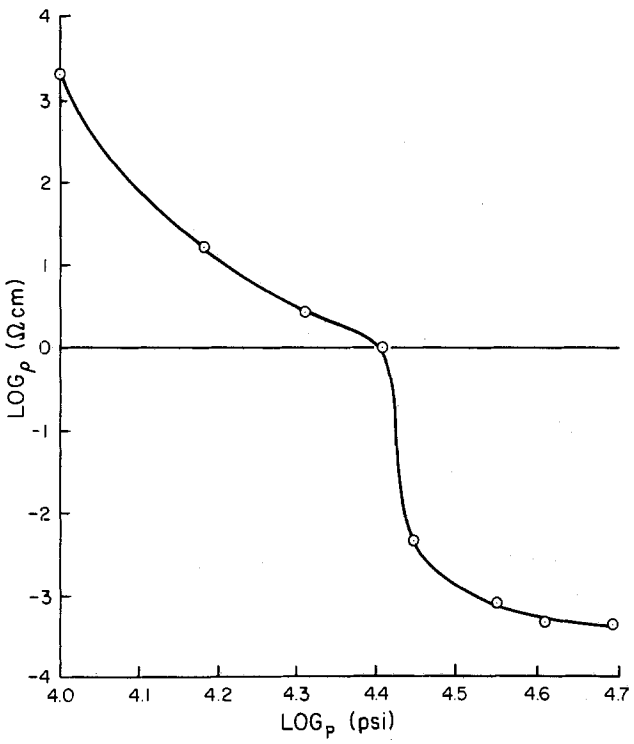

Fig. 5. Reagent grade Cu_2S powder resistivity (ρ) vs. compacting pressure (P) measured with the new van der Pauw type resistivity cell.

measurements were made with a Keithley micromicroammeter.

Resistivity Measurements on the Standard Substances

Reagent grade powders of ZnO, Cu_2S, and PbO (yellow) were used as calibrating substances for the resistivity cell. The powders were tested in the as-received condition without regard to particle size. The bulk resistivities of these materials was found from the literature, for comparison with the planned powder resistivity measurements. Log-log plots of resistivity against compacting pressure for the reagent grade powders of Cu_2S, PbO (yellow), and ZnO are shown in Fig. 5, 6, and 7, respectively. The plots all show an initial linear region, then becoming asymptotic to a resistivity value which was taken as the absolute resistivity of the sample.

Discussion

The measured resistivities are compared with published values for minerals and single crystals in Table I. The measured values are in good agreement with published values, with the exception of ZnO, the resistivity of which is notoriously difficult to measure in the powdered form without the aid of lubricants (1). The fact that an uneven pressure distribution was probably responsible for the poor results for ZnO is evidenced by the fact that the resistivity ratio, $R_{ab,cd}/R_{bc,da}$, which was close to one for PbO and Cu_2S, was very large for ZnO, as shown in Table II. It should

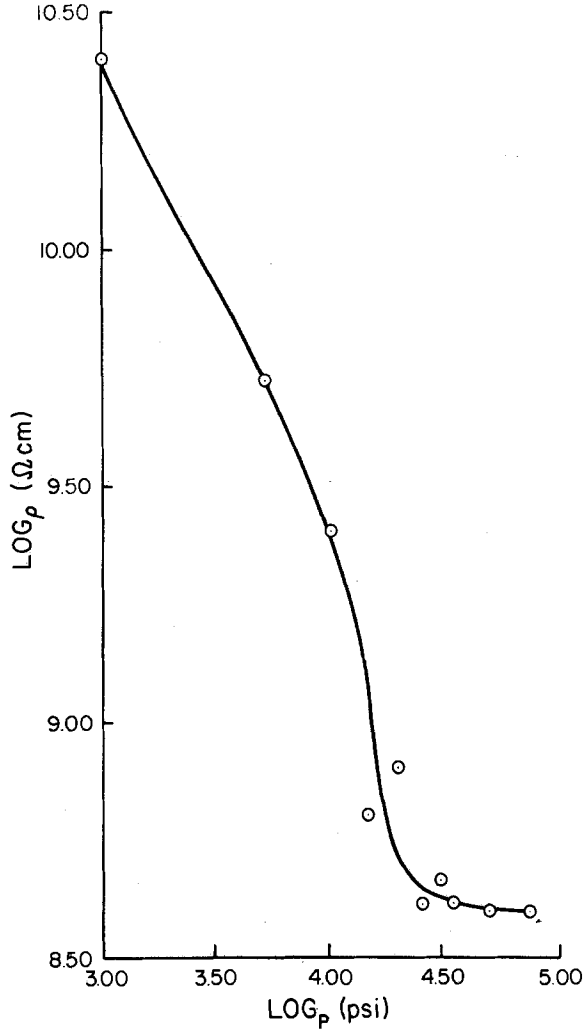

Fig. 6. Reagent grade PbO powder resistivity (ρ) vs. compacting pressure (P) measured with the new van der Pauw type resistivity cell.

be noted that resistivity measurements on uncompacted samples gave very erratic results and are not reported. Only resistivities measured on powders under pressures equal to or greater than 5000 psi (35 MPa) are reported.

The values of the pressure exponent, γ, for the three calibrating substances are given in Table III. The exponents for ZnO and PbO are within the range which would be expected for multicomponent particles. Since these reagent grade powders are not multicomponent, it was concluded that their pressure exponents differed from 0.66 due to nonspherical particle shape (6). The value for γ for Cu_2S was far greater than would be expected for typical single or multicomponent spherical particles (6). This extraordinarily large pressure exponent may be explained if the Cu_2S was coated with a thin layer of highly insulating CuO_2 (1).

Table I. Comparison of room temperature resistivities of the standard materials, measured on reagent grade powders with the new van der Pauw type resistivity cell, to those reported in the literature for bulk natural minerals and single crystals

Calibrating substance	Measured resistivity (Ω-cm)	Reported resistivity range (Ω-cm)	Reference
Cu_2S	9×10^{-4}	4×10^{-4}-10^{2}	(7)
ZnO	5×10^{8}	7×10^{8}-10^{11}	(8)
PbO (yellow)	5×10^{8}	7×10^{8}-10^{11}	(9, 10)

Table II. Resistivity ratio, $R_{ab,cd}/R_{bc,da}$, for the three calibrating substances at the two highest compacting pressures applied to each substance

Compound	Compacting pressure psi (MPa)	$R_{ab,cd}/R_{bc,da}$
ZnO	7.5×10^{4} (530)	2.32
	5.0×10^{4} (350)	4.83
Cu_2S	7.5×10^{4} (530)	1.50
	5.0×10^{4} (350)	1.20
PbO	7.5×10^{4} (530)	1.10
	5.0×10^{4} (350)	1.20

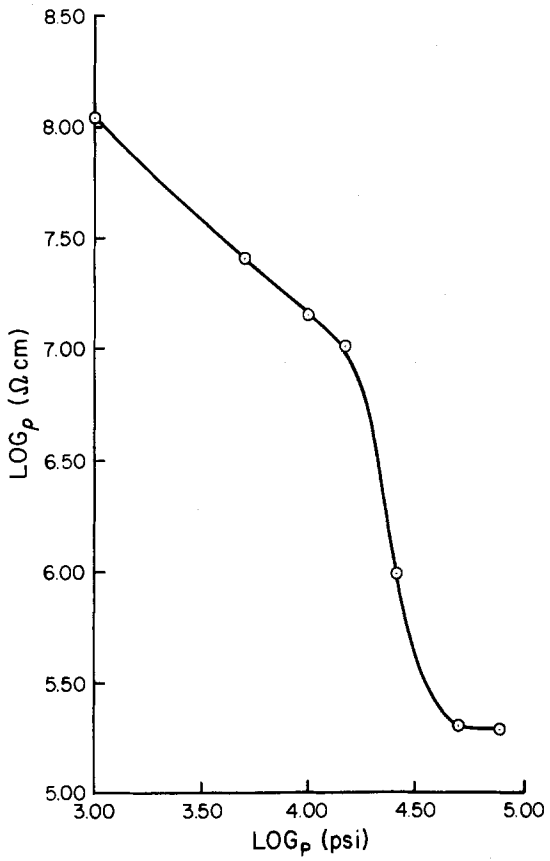

Fig. 7. Reagent grade ZnO powder resistivity (ρ) vs. compacting pressure (P) measured with the new van der Pauw type resistivity cell.

Conclusions

A simple technique to accurately measure the bulk resistivity of powdered substances has been developed. The technique provides some structural information as well as electrical properties information about the powder under test.

Acknowledgments

The authors would like to thank the U.S. Department of HEW, AMAX Base Metals R&D Corporation, and the Phelps-Dodge Division of Environmental Engineering and Research for their support of Mr. Whyte's M.S. Thesis work from which this study arose. Dr. G. H. Geiger also receives our thanks for reviewing the manuscript and providing useful comments and discussion.

Work done in partial fulfillment of the degree of Master of Science at the Department of Metallurgical Engineering, University of Arizona, and supported by the Phelps Dodge Corporation.

Manuscript submitted June 8, 1981; revised manuscript received Jan. 20, 1982. This was Paper 479 presented at the Minneapolis, Minnesota, Meeting of the Society, May 10-15, 1981.

Any discussion of this article will appear in a Discussion Section to be published in the December 1983 JOURNAL. All discussions for the December 1983 Discussion Section should be submitted by Aug. 1, 1983.

Publication costs of this article were assisted by Freeport Minerals Company.

Table III. Comparison of pressure exponents (γ) obtained from room temperature resistivity measurements made on the various reagent grade calibrating substances with the new von der Pauw type resistivity cell

Calibrating substance	Measured resistivity (Ω-cm)	$\gamma = d \log \rho / d \log P$
Cu_2S	9×10^{-4}	10.0
ZnO	2×10^{4}	1.8
PbO (yellow)	5×10^{8}	1.1

REFERENCES

1. K. J. Euler, *J. Power Sources*, **3**, 117 (1978).
2. N. S. Lidorenko, O. M. Narva, L. D. Dudka, and R. S. Ecofeev, *Izv. Akad. Nauk SSSR, Neorg. Mater.*, **6**, 2112 (1970).
3. D. P. Snowden and H. Saltisburg, *Rev. Sci. Instrum.*, **34**, 1263 (1963).
4. N. Nanba, *Jpn. J. Appl. Phys.*, **17**, 445 (1978).
5. L. J. van der Pauw, *Philips Res. Rep.*, **13**, 1 (1958).
6. K. J. Euler, *Bull. Schweit ETV*, **63**, 1498 (1972).
7. R. T. Shuey, "Semiconducting Ore Minerals," Elsevier Scientific Pub. Co., New York (1975).
8. N. Sakagama and M. Wada, *Electron. Commun. Jpn.*, **60**, 100 (1977).
9. G. P. Mohanty and L. V. Azoroff, *J. Chem. Phys.*, **35**, 1268 (1961).
10. S. B. Brody, F. A. Chambers, and M. Seitelman, *ibid.* **52**, 100 (1970).

JOURNAL OF THE ELECTROCHEMICAL SOCIETY

ACCELERATED

—BRIEF COMMUNICATIONS—

APRIL

1983

An Infrared Absorption Study of LTCVD Silicon Dioxide

C. Pavelescu and C. Cobianu

R&D Center for Semiconductors (CCSITS), R-72996, Bucharest, Romania

A. Vancu

IFTM, POB MG, 76900, Magurele-Bucharest, Romania

Introduction: The absorption band at 880 cm^{-1} has been assigned to a Si-H bond in the LTCVD silicon dioxide from silane and oxygen and it has been observed that the absorbance decreased with increasing deposition temperature (1). The aim of the present work is to investigate the behavior of the maximum absorption coefficient corresponding to this band with respect to CVD conditions in order to get an insight in the complex mechanism of silane oxidation.

Experimental: The silicon substrates we used were 2 inches in diameter, 20 mils thick, with a (111) orientation, p-type with a resistivity of 10-12 ohm cm. Their front surfaces was polished, the back surface was etched in order to reduce roughness, i. e. light losses by scattering, and avoid interference effects (2). The silicon dioxide over one half of each wafer used in infrared measurements was removed by etching in standard $HF-NH_4F$ buffer solution. This half-wafer was placed in the reference beam of the spectrophotometer during the measurements, in order to compensate for silicon lattice absorption and light scattering at the back surface.

The silicon dioxide was deposited on a nozzle-type reactor from silane and oxygen diluted in nitrogen at atmospheric pressure, at different temperatures in the 125-400°C range, by keeping constant at 45 cm^3/min the silane flow rate, (with different oxygen/silane ratios obtained by variing the oxygen flow rate), and with a total flow rate of 8.2 l/min. The thicknesses of the films measured with an Alpha-Step profilometer were in 0.1-0.7 μm range.

Infrared transmission spectra were recorded with a double-beam spectrophotometer Grubb-Parsons Spectromaster MK2E, in the 5-13 μm wavelength range. The attenuator in the sample beam was used at each run to adjust the initial transmission value for each sample at approximately 100 % at the wavelength of 5 μm (3).

Results: Infrared spectra obtained with our LTCVD silicon dioxide films (Fig. 1) are similar to the spectra reported in (1). The apparent absorption coefficient α_{app} corresponding to the minimum transmission at 880 cm^{-1}(11.36 μm) was calculated after the Lambert-Bouguer law (4):

$$\alpha_{app}=(2.3/d)\log(I_o/I) \qquad [1]$$

were d is the oxide thickness, I is the minimum value of the transmission and I_o is a transmission value taken by using the base line technique (5).

Fig. 2 represents α_{app} as a function of the oxygen/silane ratio with the deposition temperature (between 125 and 400°C) taken as a parameter. An increase-maximum-decrease variation is observed up to 350°C. At this tem-

perature this dependence disappears and at 400°C the 880 cm^{-1} Si-H band is observed only for low oxygen/silane ratios. In our transmission spectra the other Si-H absorption band at 2230 cm^{-1} was masked by the broad band of atmospheric carbon dioxide at 2350 cm^{-1} (6).

We found that $1/(\alpha_{app\ max})$ for each temperature presents an exponential variation with reciprocal absolute temperature and the activation energy associated with this dependence shows a break at 250°C (Fig. 3). For 350°C we have taken $1/o_{app}$ corresponding to the oxygen /silane ratio which gives the maximum deposition rate (7).

Discussion: The increase-maximum -decrease dependence of the absorption coefficient α_{app} at 880 cm^{-1} upon the oxygen/silane ratio, with the deposition temperature as a parameter (Fig. 2) is similar to the dependence we previously found for the rate of deposition upon the same variables. The oxygen/ silane ratios giving maximum absorption coefficient $\alpha_{app\ max}$ for different temperatures below 350 °C are closed to those which give maximum deposition rates at the same temperatures. However, with increasing temperature, the variation flattens out and even disappears above 350°C. The break at 250°C in the activation energy associated with $1/\alpha_{app\ max}$ observed by us (Fig. 3) as well as in (1) correlates with the break we previously observed at the same temperature in the activation energy of the oxygen/silane ratio corresponding to the maximum deposition rate (7).

The present absorption data give further evidence to our previous conclusion that there is a change at 250°C in the adsorption mechanism of the reactant gases, which can be understood in terms of the bimolecular surface reactions theory applied to the kinetics of LT CVD silicon dioxide deposition (7).

This change is responsible for the similar behaviour with deposition temperature of the oxygen /silane ratio corresponding to maximum deposition rate and of the absorption coefficient α_{app} at 880 cm^{-1}.

The absorption band at 880 cm^{-1} in our LTVCD silicon dioxide films obtained from silane oxidation can be attributed to a bending mode of SiH_2 group, in agreement with the assignment made for the same band in amorphous Si deposited by plasma decomposition of silane (8,9). (In the infrared spectrum of gaseous silane (10) an absorption band at about 900 cm^{-1} was attributed to a bending vibration mode SiH bond (9)).

This assignment is supported by the following considerations. We have shown that our silicon dioxide deposition takes place by a bimolecular surface reaction. This reaction can be preceded by a gas phase dissociation of silane near the surface (11). The resulting SiH_2 radicals are adsorbed on surface sites and some of them remain incorporated, without being oxidized, into the silicon dioxide structure thus giving rise to the absorption band observed at 880 cm^{-1}.

Conclusions: Our study has shown that a strong correlation exists between the hydrogen incorporation in the LTCVD silicon dioxide films deposited in the temperature range 125 to 350°C and the kinetics of film deposition.

The absorption band at 880 cm^{-1} is attributed to bond-bending vibration mode of the SiH_2 group. The SiH_2 radicals incorporated into the silicon dioxide structure are silane dissociation products adsorbed on surface sites and remained unoxidized.

This paper was presented at 162 nd Meeting of The Electrochemical Society, Detroit, Michigan, October 17-21,1982,Abstract No. 192.

Manuscript received Nov. 19, 1982.

References:
1. E.A. Taft, J. Electrochem. Soc. ,126, 1782 (1979).
2. A.C. Adams, T.E. Smith, and C.C. Chang, ibid, 127, 1787 (1980).
3. J.E. Dial, R.E. Gong, and J.N. Fordemwalt, ibid, 115, 326 (1968).
4. J. Wong, J. Electronic Mater., 5, 113 (1976).
5. W.J. Potts Jr., Chemical Infrared Spctroscopy, vol. I, John Wiley, New York, 1963, p. 165.
6. Grubb Parsons Instruction Manual, p. 3.
7. C. Cobianu and C. Pavelescu, Abstr. No. 208, Electrochem. Soc. Ext. Abstr. (Montreal, May 1982).
8. M.H. Brodsky, M. Cardona, and J.J. Cuomo, Phys. Rev. (B) 16, 3556 (1977).
9. J.C. Knights, G. Lucovsky, and R.J. Nemanich, Phil. Mag. (B), 37, 469 (1978).
10. K. Strater, RCA Rev., 29, 618 (1968).
11. P. Pascal, Nouveau Traité de Chimie Minerale, Tome VIII, p. 328, Mason et Cie, Editeurs Paris 1965.

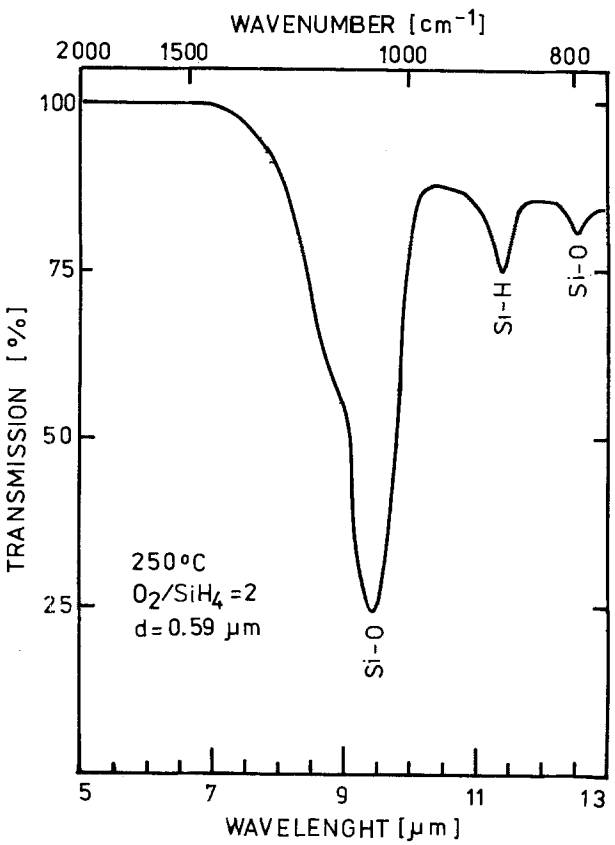

Fig.1. Infrared absorption curve for CVD SiO_2 deposited at 250 °C

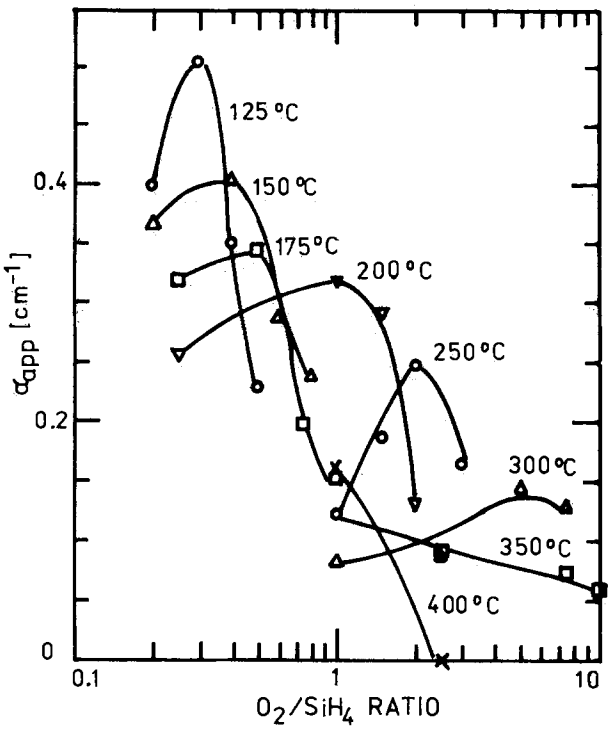

Fig.2. Absorption coefficient α_{app}, vs. O_2/SiH_4 ratio with deposition temperature as a parameter

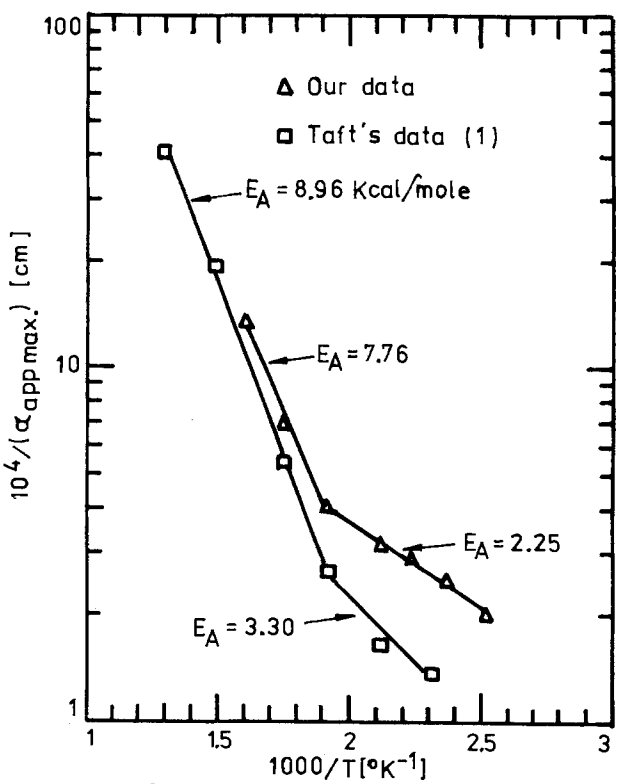

Fig.3. Reciprocal maximum absorption coefficient vs. reciprocal absolute temperature

Size Effect on Contact Resistance and Device Scaling

S. S. Cohen, G. Gildenblat, and D. M. Brown*

ıeral Electric Company, Corporate Research and Development, Signal Electronics Laboratory, Schenectady, New Yo 12301

ABSTRACT

We have measured the size effect on the contact resistance (R_C) to shallow junctions in silicon utilizing two different metallization systems. $R_C(W)$, where W stands for the contact widths, is found to display a non-quadratic dependence. Thus, our experimental observations show that the commonly used device scaling theory which assumes that contact impedance increases inversely with the square of the scaling factor is incorrect.

In recent years use of the four-terminal Kelvin resistor test structure has been suggested in order to characterize the contact resistance of metal-to-semiconductor contacts.[1-4] Such a structure, however, cannot yield unambiguous values of the contact resistance because, as depicted in Figure 1, only a portion of the contact carries the largest fraction of the total current. This situation is common to other methods of contact resistance measurement and was discussed previously.[5] Nevertheless, the four-terminal Kelvin resistor contact structure[2] is very interesting because of its similarity to actual device contacts. Also, this method of contact resistance measurement is particularly reliable for a comparative study of different metallizations since it involves only one particular contact area during the measurement. In this communication we shall describe results obtained using this structure to measure the contact impedance for a range of contact sizes. The results will show that the commonly used LSI device scaling theory[6-8] which assumes that contact impedance increases inversely with the square of the scaling factor is incorrect.

*Electrochemical Society Active Member. Key Words: size effect, contact resistance.

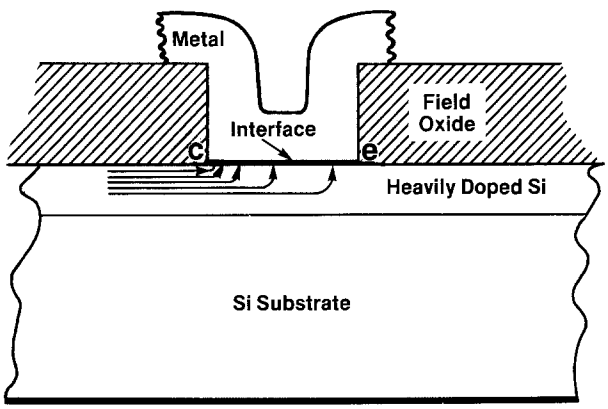

Figure 1. Cross section of a typical contact opening. A suitable metallization system is usually in contact with a heavily doped region of the semiconductor material. The lines and arrows depict the current crowding and bending effects.

The mask utilized in the present study to measure the contact impedance as a function of contact size contains 8 individual Kelvin structures with contact sizes of $2X2\mu m^2$, $3X3\mu m^2$, $4X4\mu m^2$, $5X5\mu m^2$, $6X6\mu m^2$, $7X7\mu m^2$, $8X8\mu m^2$ and $10X10\mu m^2$ within an active area 30 μm wide, made by ion implantation. The samples were fabricated using the processing sequence previously described.[2] The ion implantation doses for forming the n^+p and p^+n junctions were $8X10^{15}$ cm^{-2} As and $6X10^{15}$ cm^{-2} B resulting in final surface concentration of $3X10^{20}$ cm^{-3} As and $7X10^{19}$ cm^{-3} B respectively. The contacting metals used were an Al(0.9%Si) alloy and PtSi.

The contact impedance measurements are plotted in Figures 2 and 3. Notice that the impedance increases more

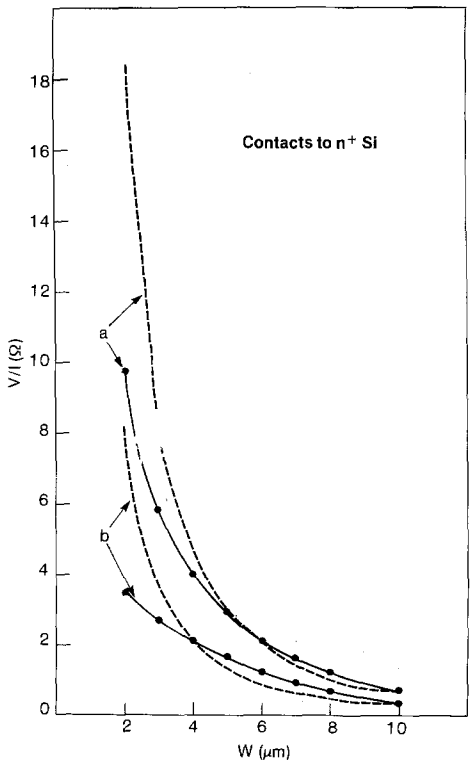

Figure 2. The solid lines describe the experimental results for contacts made to n^+Si plotted as V/I vs. the contact width, W. The broken lines represent the calculated results based on the scaling theory and assuming the value for the 10 μm contact as a reference. Case (a) depicts the results obtained utilizing an Al-0.9% Si alloy and case (b) shows the results for a system composed of a thin PtSi layer and a thick Al-0.9% Si overlayer.

slowly than predicted by the scaling theory.[7,8] In fact, the contact impedance of p^+ regions increases only a factor of two compared to the scaling theory prediction of twenty-five in going from 10 to 2 μm contact size. Similarly, the n^+ contact impedance increases 9 and 12 fold for the PtSi and Al contacts respectively. An example of the behavior of the normalized contact resistance (with respect to the contact area) is shown in Figure 2b. This experimentally-derived quantity is seen to be a non-constant function of the contact area.

Figure 1 is a representation of the

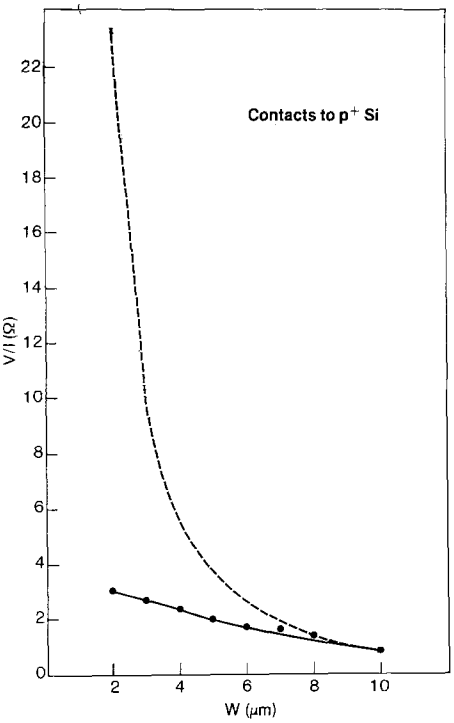

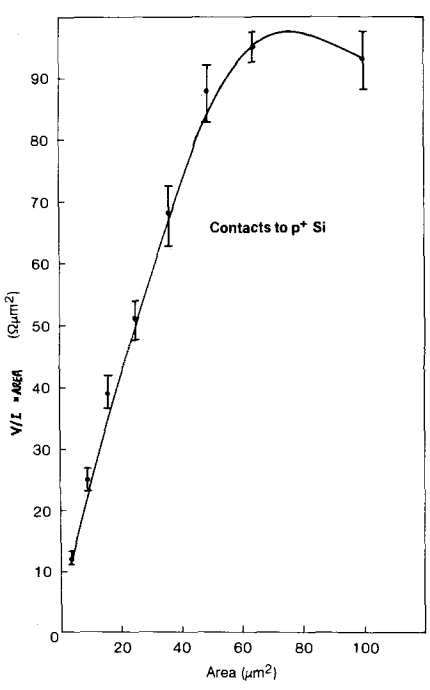

Figure 3. Case (a) is similar to that of Figure 2 for contacts to p^+Si utilizing the Al-0.9% metallization system. Figure 3(b) shows the results for the contact resistance normalized to the contact area (V/I x area), as a function of contact area.

vertical current density distribution at the contact. Since the contact area is smaller than the heavily doped region there also is a lateral non-uniform current distribution. The existance of a junction underneath the contact interface that has a finite depth and sheet resistance values, and the presence of current crowding effects are the reasons behind the contact resistance size effects shown in Figures 2 and 3. However, the type of square contacts described here are similar to those used for small aspect ratio MOSFETs. Hence, the values of R_C obtained here should be of direct relevance. Obviously there can also be a dependency of the contact resistance on the contact shape. We have not investigated this possibility in the present study as our interest is in contacts to VLSI devices where square contact apertures are the rule.

In present Kelvin-type contact resistance structures it is difficult to isolate the impedance of the metal-semiconductor interface, from "parasitic" contributions such as the current crowding in the material directly beneath the contact. Even though the four-terminal Kelvin resistor suffers from these current crowding effects, it has certain advantages over other methods of contact resistance measurements. One advantage stems from the fact that in the measurement process only one particular contact is involved. Hence, independent values for R_C can be obtained for each contact without having to assume that several of the contacts are identical in order to be able to deduct such a value by some difference method. This then leads to another advantage, i.e., the ability to determine very low values for R_C. Obviously in discussions of contact resistance extreme care must be utilized in the presentation of the data. Without this care confusion results. A method for the unambiguous interpretation of the data is essential before any determinations of specific interface resistance can be made. Only in the special case where the contact size is equal to that of the implanted bar, an attempt has been made to determine the specific contact resistance as defined in Ref. [9]. This assumes, of course, that the contact metallurgy is uniform across the contact area.

A final word about scaling theory as it relates to contact resistance is in order. When scaling device dimensions by a factor K, scaling theory[6-8] states that the contact impedance would scale as K^{-2}. However, as we have shown, for contact areas of the scale currently employed in semiconductor technology, this is not the case. The measured contact resistance scales with a factor less than K^{-2}. The practical implication of this non-quadratic scaling of R_C may include less pressure for developing ultra-low contact resistance metallization systems for VLSI circuits and may also require a revision of estimates of achievable VLSI design rules.

REFERENCES

1. R.M. Anderson and T.M. Reith, This Journal, 122, 1337 (1975).
2. S.S. Cohen, G. Gildenblat, M. Ghezzo and D.M. Brown, This Journal, 129, 1335 (1982).
3. S.S. Cohen, G. Gildenblat and D.M. Brown, Proceedings of the ECS Annual Meeting, Montreal, Canada, May 1982.
4. S.J. Proctor and L.W. Linholm, IEEE Electron Device Lett. EDL-3, 294, (1982).
5. H. Murrmann and D. Widmann, IEEE Trans. Electron Devices, ED-16, 1022 (1969).
6. R.H. Dennart, F.H. Gaensslen, Hwa-Nien Yu, V. Leo Rideout, E. Bassous and A.R. LeBlanc, IEEE J. Solid State Circuits, 256 (1974).
7. D.C. Mayer, VLSI, Design, 50, May/June (1982).
8. T.L. Paince in "Very Large Scale Integration," D.G. Barbe Ed., p. 76, Springer-Verlag, NY (1980).
9. C.Y. Chang, Y.K. Fang and S.M. Sze, Solid State Electron. 14, 541 (1971).

Manuscript received Feb. 2, 1983.

Publication costs of this article were assisted by the General Electric Company.

JOURNAL OF THE ELECTROCHEMICAL SOCIETY

ELECTROCHEMICAL SCIENCE
— AND TECHNOLOGY

MAY
1983

A Comparison of Procedures Used in Assessing the Anodic Corrosion of Metal Matrix Composites and Lead Alloys for Use in Lead-Acid Batteries

C. M. Dacres,* R. A. Sutula,* and B. F. Larrick

Naval Surface Weapons Center, Materials Division White Oak, Silver Spring, Maryland 20910

ABSTRACT

The anodic corrosion of lead at 70°C in sulfuric acid was studied at a potential of 1.226V *vs.* Hg/Hg_2SO_4 where both the oxidation of lead to PbO_2 and the oxidation of water are thermodynamically possible. These parallel anodic reactions can be the cause of a decrease in the faradaic efficiency. The faradaic corrosion current efficiency can be defined as a fraction of the total charge passed which is used to transport metal ions into solution. The faradaic efficiency can affect the corrosion process in several ways. The most obvious of these is the corrosion time which increases with decreasing efficiency. The extent of corrosion was measured in terms of weight loss of lead and the current density of the corrosion layer. It is believed that some of the current is going towards oxygen evolution, which makes it inexact to use electrochemical capacities alone to predict accurately the corrosion rates for this system. Weight loss values are compared with those from Faraday's laws and data are presented on mass changes and corrosion currents.

Pure lead is a very desirable positive electrode grid material for rechargeable lead-acid batteries because it resists corrosion. However, its use is limited by lack of mechanical strength and ability to resist deformation. As a consequence, metal matrix materials have been developed with the idea of combining the noncorrosive properties of pure lead with the increased mechanical strength provided by nonmetallic fiber reinforcement. The corrosion resistance of lightweight high strength lead metal matrix composites under conditions that simulate their use as grid materials in lead-acid batteries has been studied using a comparison of data on mass changes and data on measured corrosion currents. The aim of this study is to develop a relationship between the corrosion current measured and the actual current going towards the oxidation of lead.

Lander (1-3), Willihnganz (4), and Weininger's (5) early results clearly demonstrate the importance of weight loss determinations in alloy evaluation, especially in the oxygen evolution region where it is somewhat inaccurate to compute the corrosion rate from Faraday's laws alone. It is also essential to examine the specimens for intergranular penetration which may be more catastrophic than the weight loss or current density would indicate. Corrosion rate *vs.* time relationships also provide information on the corrosion mechanism provided the test is of adequate duration. It is also important to realize that the electrode reactions are heterogeneous processes with potential-dependent rate constants. The potential characterizes the interfacial conditions and the net reaction is proportional to the current density

The Burbank diagram (6, 7) of reactions in the lead-sulfuric acid system indicates that at the potential used in these studies (1.226V *vs.* Hg/Hg_2SO_4) both the oxidation of lead to PbO_2 by

$$Pb + 2H_2O \rightarrow PbO_2 + 4H^+ + 4e^- \qquad [1]$$

and the oxidation of water by the reaction

$$2H_2O \rightarrow 4H^+ + O_2 + 4e^- \qquad [2]$$

are possible. Some of the current is being used up possibly by reaction [1] or [2], and maybe other reactions. It is possible, if not inaccurate, to have data with comparable values between measured mass loss and that calculated from Faraday's law using total charge passed will be equal when the faradaic efficiency is 100%. Even through the mass loss may not correspond to the current passed, a high current will indicate a high rate of corrosion and also indicate a very poor faradaic efficiency (*i.e.*, a low oxygen overpotential). Reproducibility of the data may be poor because more than one corrosion reaction is occurring simultaneously.

The composition and potential dependence of the corrosion product layer has been extensively studied by a number of workers using various analytical techniques, and the data have been presented in terms of thermodyanmic equilibrium diagrams and corrosion models (8, 9, 10). However, the major limitation of this approach is that the figures do not contain kinetic information and, therefore, cannot be used to predict corrosion rates. Nevertheless, a knowledge of equilibrium conditions required for the formation of the compounds found in the corrosion product layer is a necessary background for the understanding of the corrosion kinetics.

The technique of constant potential measurements offers many advantages in both theoretical investigations and practical alloy development. These advantages are well illustrated in the much quoted data of Lander (1, 2, 3) obtained during his studies of lead alloys and reported in the 1950's for different acid concentrations.

For this system, the corrosion rate may be controlled by concentration polarization (*e.g.*, oxygen diffusion). The equation (11)

* Electrochemical Society Active Member.
Key words: anodic corrosion, power sources, lead-acid batteries, metal matrix composites, lead alloys, faradaic efficiency.

$$\left[\frac{d(\Delta E)}{di}\right]_{\Delta E=0} = R_p = \frac{b_a}{2.3 i_{corr}} \quad [3]$$

should apply, where $\Delta E = E - E_{corr}$ = overvoltage, E = specimen potential, E_{corr} = corrosion potential, b_a = anodic Tafel constant, and i_{corr} = corrosion current density.

A plot of log R_p *vs.* log i_{corr} should give a straight line of the predicted slope. A reasonable estimate of corrosion rate can, therefore, be rapidly made without knowing more about the corroding system other than that it is part of the electrochemical phenomenon.

It is assumed that the current going towards the production of Pb^{+4} is constant. The faradaic relationship used to calculate the corrosion rate is as follows (12)

$$\text{corrosion rate (mpy)} = 0.1288 I\ \mu\text{A/cm}^2 \frac{\text{equiv. wt (g)}}{\rho(\text{g/cm}^3)} \quad [4]$$

where I = the corrosion current density, ρ = specimen density, and equiv. wt = specimen equivalent weight, and the relationship used to equate weight loss to corrosion rate is as follows (12)

$$\text{mpy} = \frac{534W\ (\text{mg})}{\rho(\text{g/cm}^3) A\ (\text{in.}^2)\ t\ (\text{hr})} \quad [5]$$

where W = weight loss, ρ = specimen density, A = specimen area, and, t = exposure time.

The mechanism of corrosion is extremely complex in a homogeneous chemical system. Not only are several different compounds of each element present or formed during the corrosion process, but there are also surface effects to consider. For this reason, corrosion rate measurements must be made rather nonspecific with regard to the element in the metal or alloy. For example, rate measurements by weight loss determination require no presumption of the actual identity of the corroding species.

Experimental Procedures

Accelerated corrosion studies were performed in a 1.285 specific gravity sulfuric acid electrolyte at 70°C. The experimental methods, apparatus, and techniques employed have been described previously (13). The potential was measured against an Hg/Hg_2SO_4 reference electrode in the electrolyte of the corroding cell. The current flowing between the working electrode and the counterelectrode was recorded as a direct measure of the instantaneous corrosion rate. Data were collected on mass change, and the corrosion which is attributable to the current flow according to the Faraday laws. Mass changes were obtained by weighing the specimens before corrosion and weighing after corrosion when the corrosion products had been removed by stripping in a warm alkali-hydrazine-mannitol bath.

Results and Discussion

The composition of the lead samples tested are listed in Table I. The corrosion resistance of the alloy is dependent on its metallurgy, the physical and mechanical properties, as shown in its structure and chemistry, as well as the electrochemical factors which need to be considered when it reacts with the corrosive environment. There is a predominance of information in the electrochemical literature on the initial film formation processes without consideration being given to substantial corrosion film growth (6, 7, 9, 10). Reported testing of alloys is often limited to hours or a few days; whereas, in practice, the life of lead components is measured in years. Our tests were performed for a prolonged time, usually until the electrode fell apart. Figure 1 is a plot of the average corrosion current densities *vs.* the time the specimens were on test.

Table I. Composition of materials

Material	v/o				w/o		
	Al_2O_3	C	Glass	Si/C	Ca	Sn	Ag
Fiber composites							
Lead alumina (FP)	15						
Lead alumina (FP)	10						
Lead alumina (FP)	5						
Lead carbon		4					
Lead glass-quartz			9.5				
Lead silicon carbide				6.8			
alloys							
Lead calcium					0.07		
Lead calcium tin					0.065	0.66	
Lead tin						0.20	
Lead silver							0.02
Pure lead							

The corrosion rates obtained from mass change measurements and the corrosion rates obtained from the total corrosion current measured along with the percentage of this current that is attributable to the dissolution of lead are reported in Table II.

The corrosion rates obtained from the corrosion currents through Faraday's laws are much higher than those obtained from average weight loss measurements. Figure 1 has plots of all the samples listed in Table II. The corrosion current densities are a measure of the relative corrosion because the faradaic efficiencies are roughly equal (~33% from Table II).

Figure 2 is a plot of the log $(\Delta E/\Delta I)$ *vs.* log i_{corr} for the specimens listed in Table I. From this, the anodic Tafel constants are calculated and are listed in Table III.

The observation of gassing at the surface of the test samples strongly supports the possibility of the occurrence of Eq. [2]. Hence, at high potentials, oxygen evolution may, then, be contributing to the current. The relationship

$$I_{corr} = i_{Pb} + i_{O_2} \quad [6]$$

where

I_{corr} = total measured corrosion current density
i_{Pb} = current density due to dissolution of lead obtained from weight loss determinations
i_{O_2} = current density due to the decomposition of water

appears to be possible. The fraction of current referred to in Table II as $\%i_{Pb} \rightarrow Pb^{+4}$ can be used to develop the relationship

$$(0.1288)\ (0.33 \pm 0.005)\ I\ \mu\text{A/cm}^2 \frac{\text{equiv. wt. (g)}}{\rho(\text{g/cm}^3)} = \frac{534W\ (\text{mg})}{\rho(\text{g/cm}^3) A\ (\text{in.}^2) t\ (\text{hr})} \quad [7]$$

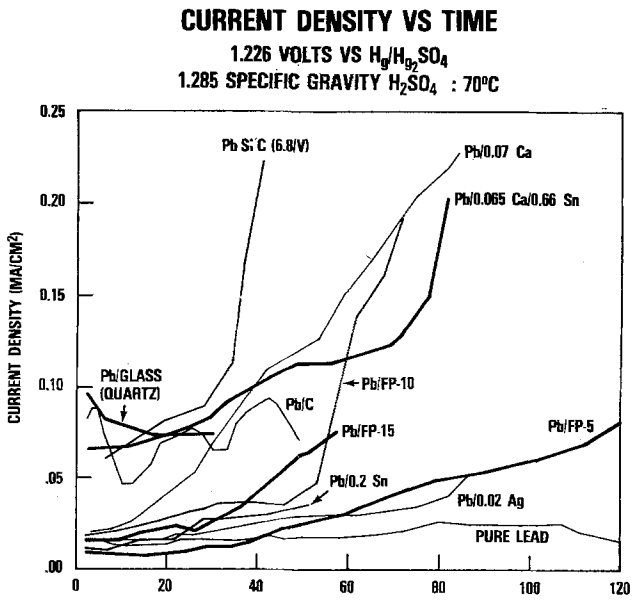

Fig. 1. Plots of the average corrosion current densities *vs.* time

Table II. Corrosion rates

Sample	Gravimetric (mpy)	Faradaic (mpy)	% I $Pb \rightarrow Pb^{+4}$
Pb	2.05	6.09	33.66
Pb/Ca	14.74	39.17	27.63
Pb/Ca/Sn	19.33	52.96	36.72
Pb/Sn			
Pb/Ag			
Pb/alumina (FP)—15			
Pb/alumina (FP)—10	2.92	9.67	30.20
Pb/alumina (FP)— 5	1.30	4.01	32.42
Pb/C	17.00	43.32	29.24
Pb/glass-quartz	9.40	24.50	38.37
Pb/SiC	9.80	30.20	32.45

Table III. Tafel constants

Sample	Tafel constant
Pb	5.74
Pb/Ca	3.48
Pb/Ca/Sn	4.87
Pb/Sn	4.48
Pb/Ag	5.03
Pb/alumina (FP)—15	3.80
Pb/alumina (FP)—10	3.47
Pb/alumina (FP)— 5	3.58
Pb/C	7.63
Pb/SiC	4.48

The value (0.33 ± 0.005) can be termed the faradaic efficiency. Hence, to use current density measurements or weight loss measurements in the initial stages of the experiment to determine accurate corrosion rates could be misleading and inaccurate.

Also, the initial stage of the experiment is the portion where the PbO_2 film is established. This film is not completely established for the first 12 hr or so depending to a considerable extent on the type of alloy being tested. From Fig. 3, it can be concluded that at high potential testing, a protective film of PbO_2 is built up gradually at the lead surface. During this time, there are numerous changes of complex form proceeding on the Pb surface, on the metallic heavily doped PbO_2, as well as in systems of grain boundaries which are present.

A measure of the corrosion rate is the corrosion current density, i_{corr}, which is defined in Eq. [3]. Under applied constant potential conditions in the absence of cracks or pores through the PbO_2 layer, the corrosion rate is apparently controlled by a solid-state diffusion process. The composition of the alloy determines the

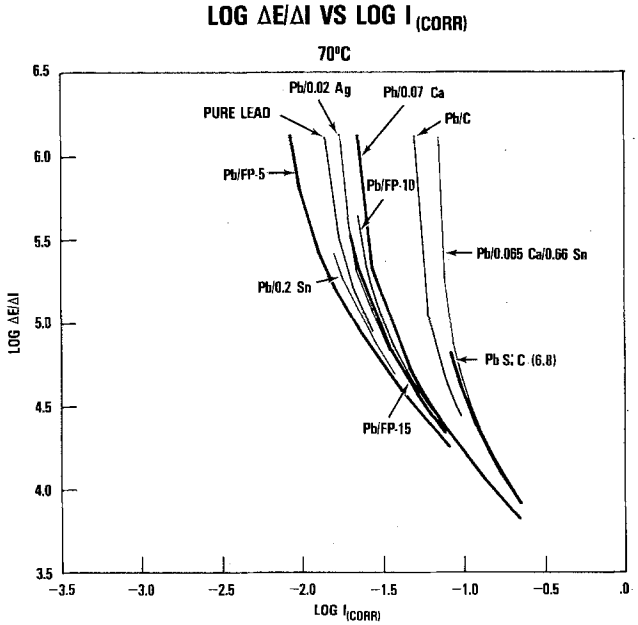

Fig. 2. Plots of log ($\Delta E/\Delta I$) vs. log i_{corr}

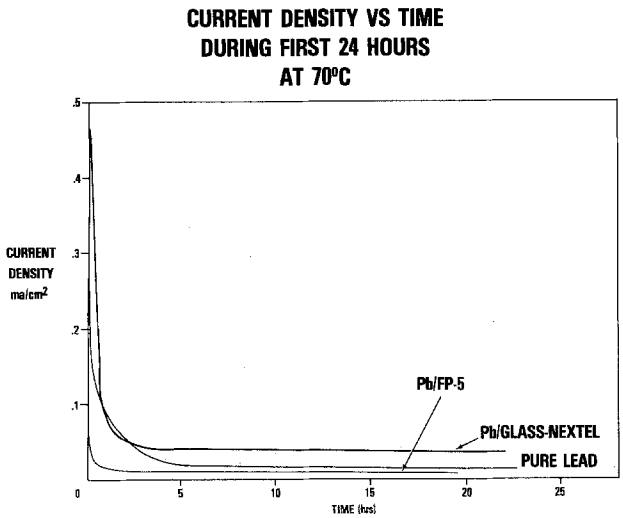

Fig. 3. Current density vs. time during first 24 hr for 3 samples at 70°C.

structure of the lead dioxide substrate, and it is significant to note that the alloys tend to give a linear/rate of corrosion under constant voltage conditions; whereas, the fiber composites exhibit a logarithmic or parabolic rate (13). In the latter case, it has not been established if the reaction rate-determining step is diffusion through the film or diffusion in the metal, but obviously metallurgical factors such as grain size, grain boundary composition, and related problems of corrosion resistance of eutectic compositions where intermetallic compounds become increasingly important in controlling the life of the component.

Fig. 4. SEM of corroded Pb/Ca/Sn

Leaching of selected phases from the alloy will give rise to a roughening surface with porosity into the metal grain boundary, or even dissolution within the grain, which is clearly observed by sectioning the samples followed by microscopic examination. Figures 4, 5, 6, 7, and 8 are sections of samples observed. The metallurgical properties of alloys tested are similar and are considered together although the calcium alloys have received greater attention than the other systems. These examples illustrate the interaction between alloy composition and operating voltage, and again emphasize the increasing use of potentiostatic control in corrosion testing.

In the fiber composites, corrosion at constant potential increased with increased fiber content. Wetting between the lead and the fiber is very important to prevent premature failure of the specimen due to crevice corrosion at the interface of the fiber and lead (11). Although the weight loss does not truly indicate the extent of the damage due to corrosion, a microscopic examination of the specimen cross section clearly points up the problem (Fig. 9). These specimens also undergo considerable increases in volume when they are penetrated by the electrolyte, and there is corrosion product build up. Any change in volume of these materials could severely affect their utility.

Equation 3 is valuable from both a theoretical and an experimental point of view, since it relates the corrosion rate and the Tafel slopes to polarization measurements close to the corrosion potential. Thus, low current polarization measurements combined with corrosion rate data permit a calculation of the Tafel slope. This is of great value when concentration polarization of *IR* drop effect interfaces with measurements at the higher currents. In addition, measurements are made close to the corrosion potential, thus eliminating any surface changes which may result from high current polarization.

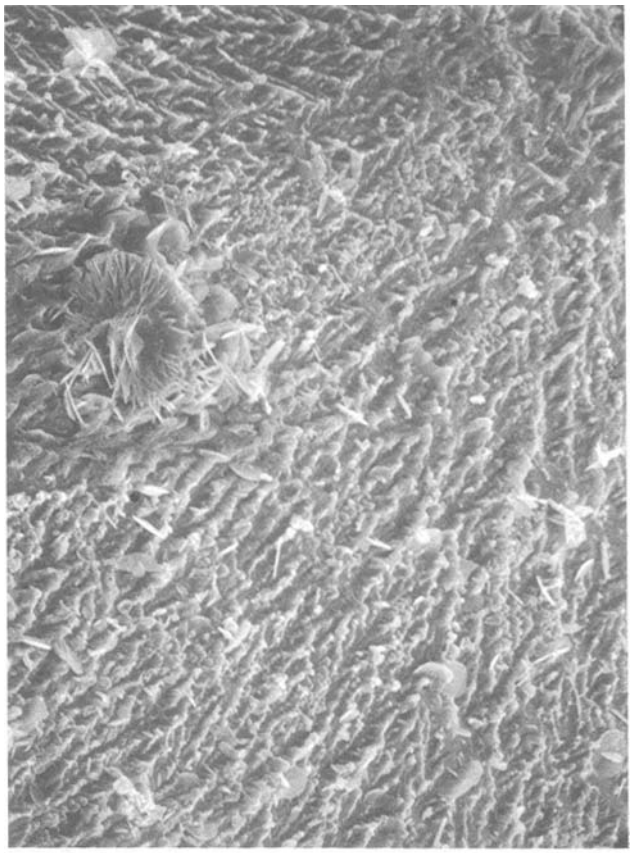

Fig. 6. SEM of corroded Pb/quartz

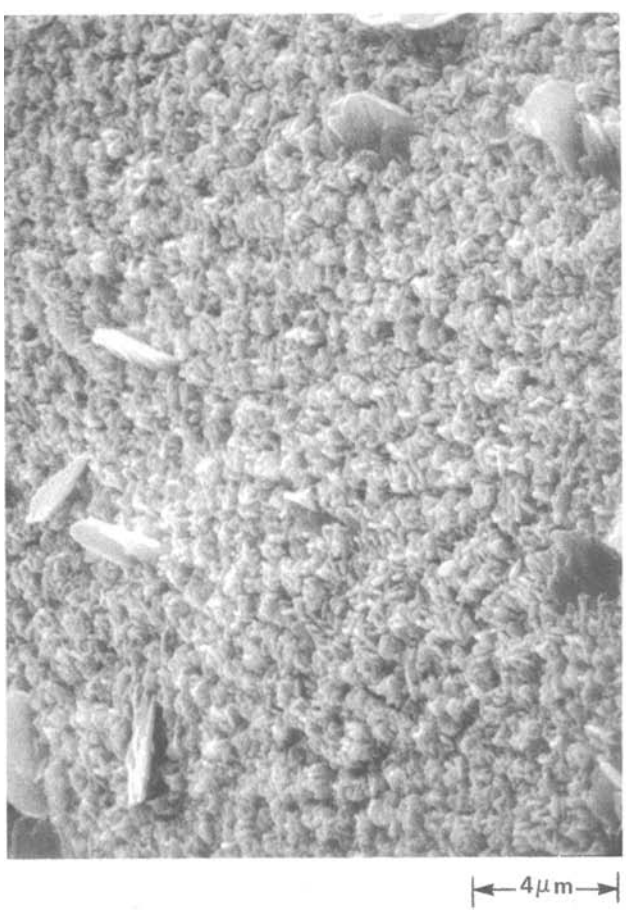

Fig. 5. SEM of corroded Pb/Ag

Fig. 7. SEM of corroded Pb/Ca. The final form of the surface corresponds to tetragonal rutile structure deposits.

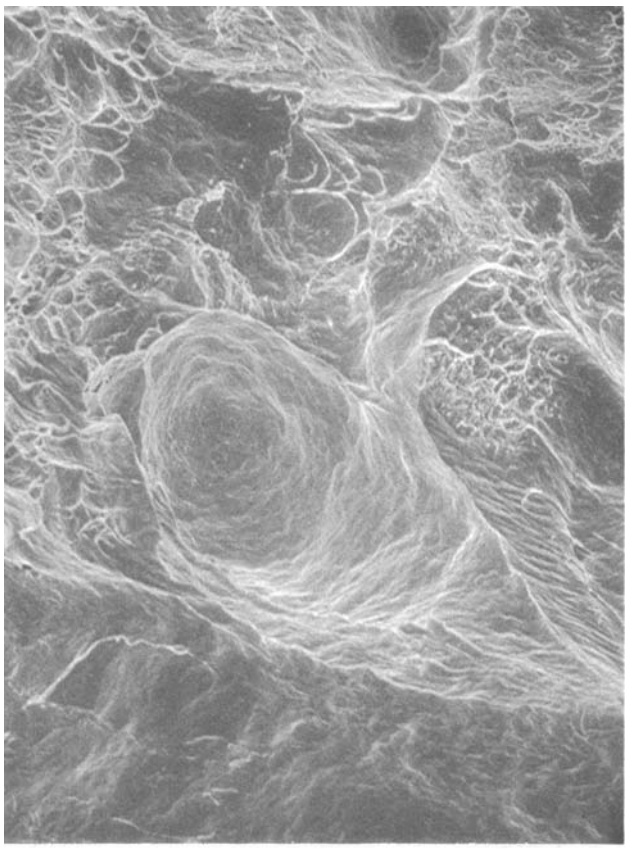

Fig. 8. SEM showing corrosion along grain boundaries of Pb/Ca/Sn specimen.

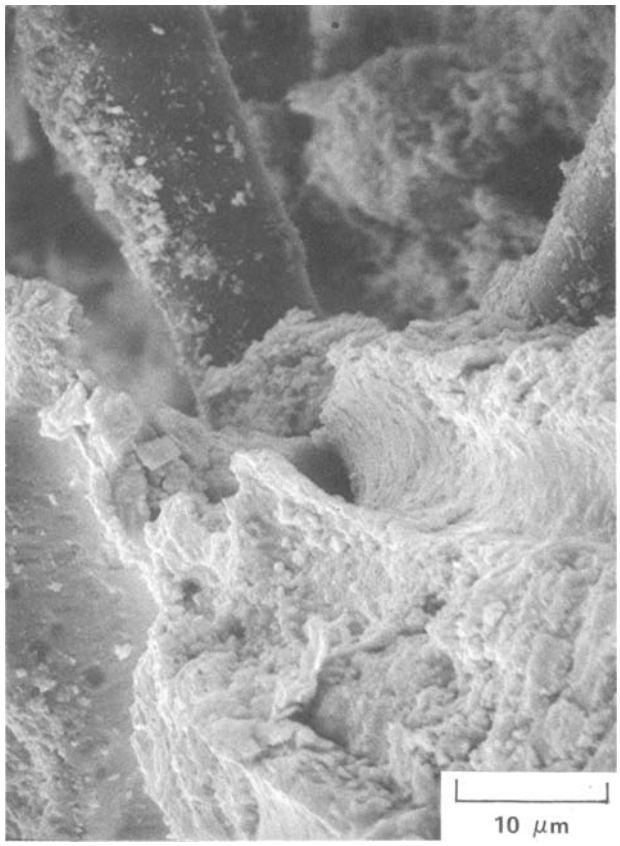

Fig. 9. SEM showing corrosion of lead reinforced with glass fibers

Conclusion

Anodic corrosion of lead in sulfuric acid was studied at a high potential (1.226V *vs.* Hg/Hg_2SO_4). In general, the phenomena that were expected were observed. The assumption was made that at this high potential only two reactions were occurring simultaneously. These reactions are expressed in Eq. [1] and [2]. Data were interpreted to show: (*i*) The corrosion behavior of Pb/alumina (FP)—5 displayed the best properties and could be acceptable for use in lead-acid batteries. (*ii*) Oxygen evolution contributes to the total corrosion current observed. Only about 0.33 of the total current is contributing to the reaction where lead is going into solution. (*iii*) Weight loss results when compared with values calculated from Faraday's laws, and the current density time traces indicated that some of the current was being used by other reactions. Presumably, the other reaction is oxygen generation; this is what makes the faradaic efficiency for lead dissolution low. (*iv*) To use current density values as absolute values to indicate corrosion rates, the value of the faradaic efficiency should be determined for that set of corrosion reactions. (*v*) The Eq. [7] derived relates the average current densities to the weight loss measurements. This type of relationship could prove valuable when considering the effect of parasitic reactions in a corroding system.

Manuscript submitted Aug. 11, 1982; revised manuscript received *ca.* Dec. 27, 1982.

Any discussion of this paper will appear in a Discussion Section to be published in the December 1983 JOURNAL. All discussions for the December 1983 Discussion Section should be submitted by Aug. 1, 1983.

Publication costs of this article were assisted by Naval Surface Weapons Center.

REFERENCES

1. J. J. Lander, *This Journal*, **98**, 213 (1951).
2. J. J. Lander, *ibid.*, **98**, 220 (1951).
3. J. J. Lander, *ibid.*, **103**, 1 (1956).
4. E. Willihnganz, *Electrochem. Technol.*, **6**, 338 (1968).
5. J. L. Weininger and R. C. Morelock, *This Journal*, **122**, 1161 (1975).
6. J. Burbank, *ibid.*, **106**, 369 (1959).
7. J. Burbank, A. C. Simon, and E. Willihnganz, "Advances in Electrochemistry and Electrochemical Engineering," Vol. VIII, P. Delahay, Editor, p. 157, Wiley Interscience, London and New York (1971).
8. M. Pourbaix, "Atlas of Electrochemical Equilibria in Aqueous Solutions," Cabeleor, Brussels (1966).
9. P. Ruetschi, *This Journal*, **120**, 331 (1973).
10. P. Ruetschi and R. T. Angstadt, *ibid.*, **111**, 1323 (1964).
11. M. Stern and A. L. Geary, *ibid.*, **104**, 56 (1957).
12. W. H. Ailor, "Handbook of Corrosion Testing and Evaluation," pp. 173-174, John Wiley & Sons, Inc., New York (1971).
13. C. M. Dacres, S. M. Reamer, R. A. Sutula, and I. A. Angres, *This Journal*, **128**, 2060 (1981).

Expected Cycle Life *vs.* Depth of Discharge Relationships of Well-Behaved Single Cells and Cell Strings

Lawrence H. Thaller*

National Aeronautics and Space Administration, Lewis Research Center, Cleveland, Ohio 44135

ABSTRACT

The factors that might influence the cycle life *vs.* depth of discharge relationship are examined. This is done first at the single cell level using a progressively more complex cell life model. This is then extended to multicell battery strings where the stochastic aspects associated with groupings of cells are introduced. These relationships are important when considering the weight, cost, and life of battery packs. The results of this theoretical study are compared with a recent review of actual cell-cycling data. The factors examined are the rate of capacity loss, the amount of excess capacity built into the cells, and the penalty in capacity loss resulting from the use of deep depths of discharge. This study suggests that the relationship between cycle life and depth of discharge is not one that can be varied or significantly improved by cell research. The relationship appears to be determined by certain more or less fixed cell parameters. Among multicell strings, the standard deviation, as expected, plays an important role in determining overall battery life.

Large battery packs for high energy (kW-hr) storage, operating at deep depths of discharge, are required for aerospace and terrestrial applications. The desirability of high voltage levels will require a significant number of individual cells to be connected electrically in series. The cycling of such battery packs will be influenced not only by the stochastic variations associated with the grouping of items, but also by the cycle life *vs.* depth of discharge characteristics of the single cells from which the battery packs are assembled. A recent review (1) of this latter subject pointed out the semilogarithmic relationship of cycle life as a function of depth of discharge. Although the actual performance of these single cells and three- or six-cell modules ranged from good to poor, a relationship of the form $L = L_0 e^{\alpha(1-D)}$ could always be fitted to the data. The term, L_0, is the cycle life at 100% depth of discharge, and D is the fractional depth of discharge. The term, L, is then the cycle life at any fractional depth of discharge. The exponent α is determined by plotting corresponding values of ln L and D. Reference (1) showed how important the value of α is in determining what the most cost effective depth of discharge would be.

This article examines what factors might influence the cycle life *vs.* depth of discharge relationship, first at the single cell level and then at the battery level. The factors examined are the rate of loss of cell capacity, the amount of excess capacity built into the cells, and the penalty in capacity loss resulting from the use of deep depths of discharge. What might be called "first principles" have been used to develop a cell life model for somewhat arbitrary conditions. This model is then used to estimate the cycle life *vs.* depth of discharge relationships (and thereby α) for "well behaved" single cells. The stochastic variations associated with groupings of single cells are then introduced to the battery pack cycle life model.

For the purposes of this paper, a "well behaved" single cell is one that does not suffer any abrupt failure mode during the course of its operation. It gradually loses capacity for any number of the usual reasons at a rate that is the product of the fractional depth of discharge and a factor which is characteristic of the cell under consideration. This approach to be reported here would suggest that the slope of the semilogarithmic life *vs.* depth of discharge relationship is fixed by the value of certain cell parameters such as the amount of excess reactive material, or the penalty related to deep depths of discharge, and is not a factor that can be varied or improved over a wide range. What might be improved is the rate of capacity loss once it is fully understood for the particular cell chemistry under consideration. All of this can be done without the necessity of evaluating lengthy life cycle test programs of actual cell hardware, using techniques that are outlined in the following sections.

* Electrochemical Society Active Member.

Background

The electric vehicle application has proven to be a very severe and challenging one for near-term electrochemical systems. Although cycle life requirements are rather modest (1000-2000 cycles), the depths of discharge (DOD) to which these batteries will be cycled (up to 80% DOD) are not usually associated with long life. A complicating factor associated with this application results from the desirability of using high voltage strings of cells and modules to attain battery pack voltages around 100V. The inherent stochastic variations accompanying the grouping of items from a population of certain average properties and the standard deviation thereof, can very easily lead to cell reversal, overcharging, or other undesirable occurrences that would tend to shorten the overall life of the battery pack. A recent review article, Ref. (1), covering the cycle life *vs.* depth of discharge relationships of near-term single cells and three- or six-cell batteries has been published. Besides being a fine compilation of cycling data and a thorough discussion of failure modes, this article showed how most of this cycling information could be fitted to a semilogarithmic relationship of the form $L = L_0 e^{\alpha(1-D)}$. That is, the cycle life L, at any fractional depth of discharge D, is a function of its cycle life at 100% depth of discharge L_0, and an exponent α determined from the slope of semilog plot of the actual cycle life data at various DOD's. An important deduction of this prior review was related to a derivation of an expression for the vehicle miles traveled as a function of the depth of discharge to which the battery is cycled. Since this value is related to the cycle life L and the fractional depth of discharge D, then it appears reasonable that there would be a maximum in that product. This maximum was shown to occur at $D = 1/\alpha$. The value of α is thus very important in determining the most cost-effective depth of discharge. Although there were some anomalies, the exponents for various lead-acid and nickel-zinc devices from various manufacturers generally fell within the range of 3.0-6.0. This would suggest that DOD's of 17-33% would be the most cost effective. Since the value of α was determined from a curve-fitting process and was not assigned any physical significance, it is not immediately obvious whether it is subject to alteration or by how much. The desired end, of course, would be to develop cells which have an α value of 2.0 or less. This would result in the most cost effective DOD being 50% or greater.

The objective of this effort is to examine the possibility that indeed α does have some degree of physical significance and can be derived, although ever so crudely, from some pseudo first principles. The Lewis Research Center has been conducting an effort under the title "Synthetic Battery Cycling" (2), which has as its objective the prediction of the cycle lives of large battery packs as a function of the stochastic distribution of certain cell characteristics and the rate of capacity loss. In essence, a cycle life *vs.* DOD relationship is built into a single cell performance model and then the cycle life of a group of such cells subject to random variations of certain characteristics is projected. An equality is established between α, the slope of the semilog plot of the Seiger relationship, and the midrange slope of the similar plot of this paper's single cell performance model. By determining the effect of specific cell characteristics on the latter slope, some inferences are made as to the likelihood of achieving α's smaller than the 3.0-6.0 range defined by Seiger for actual cells. Conclusions are then reached concerning how best to approach the development of long-lived battery systems.

The Cell Model and the Cycling Mode

The cells to be described here are hypothetical and are not meant to represent any particular technology. They will be assumed to have a nominal capacity of 100 A-hr. Their total capacity will depend on what additional fraction, F, of this nominal capacity is available as reserve capacity at the beginning of life. Figure 1 depicts the significance of the terminology used here. The total capacity at the beginning of life is then $(1 + F) \times 100$ A-hr. In later sections, the parameter F will be assigned a range of values and will also take on a certain degree of variability around each value. Parameters that vary will be taken from populations of normal distributions of mean, m, and standard deviation, σ.

The cells will not be assigned a failure mode as such but it will be assumed that there is a certain capacity loss rate. The parameter, A, multiplied by the fractional DOD to which the cell is cycled, D, will represent the amount of capacity that is lost in each cycle. The parameter A can be assigned any constant small number or be a parameter with a certain mean and standard deviation when considering a string of cells. It will be shown later that variations in A for this capacity-loss model do not lead to changes in the corresponding α's. A third parameter P will be introduced later which will simulate a higher rate of capacity loss at deeper DOD's and will have an effect on the corresponding α's.

The method of cycling these cells requires a certain degree of explanation. It will be assumed that a fixed number of ampere hours are removed from the cell on discharge and replaced on charge. Overcharging may or may not be used depending on the cell chemistry under consideration. Even in the case of overcharging, there is a finite amount of permanent capacity loss, and it is this gradual accumulation of permanent capacity loss that is being considered here.

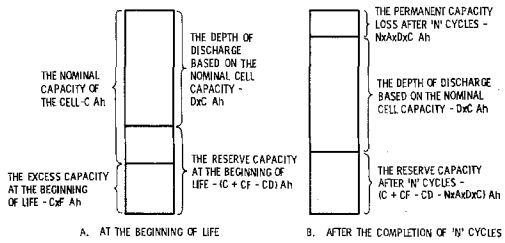

Fig. 1. Schematic diagram of the cycling terms

Reference (2) contains a fuller explanation of these matters. The capacity loss per cycle in the simplest case will be $A \times D \times 100$. The cell has a certain degree of reserve capacity, depending on the fractional DOD and the amount of active material put in the cell at the beginning of life. When the number of cycles times the value of $A \times D \times 100$ equals the reserve capacity, then the cell will no longer be able to deliver $100 \times D$ A-hr and the cell will be considered "failed." This cycling mode is not the usual one when considering single cells, but is representative of a cell in a cell string where individual cell switching is not used. More often, constant voltage or constant current with a subsequent taper are used in single cell testing.

The following sections, in a sequential way, examine the cycle lives of single cells and then cell strings, given an increasingly complex format of assumptions and variations of parameters that can be assigned to cells and populations of cells. The effect of these variations on the resultant slope of the semilogarithmic relationship between cycle life and depth of discharge are examined in an attempt to explore the possibility of reducing the α value of these relationships.

The Simplest Case

In this case the actual cell capacity and the nominal capacity will be the same. The F parameter is thus 0.0 and the reserve capacity is $(1 - D) \times 100$ A-hr. The loss factor A will be assigned a value of 0.001. The capacity lost per cycle will be $0.001 \times D \times 100$ A-hr. Therefore, cell life is defined as reserve capacity divided by the capacity loss per cycle, or, $L = 1 - D$ divided by AD (see Table I). Figure 2 is a plot of this relationship. Since there are no wet-stand limitations or failure modes hypothesized other than loss of capacity as a function of DOD, very high cycle lives are predicted at low DOD's and very low cycle lives are predicted at deep DOD's. In fact, using this simple model and assumptions, this simplest case would predict a cycle life of 1 at a DOD of 100%, since failure is defined as the absence of any remaining reserve capacity. Added to the figure is a straight line drawn tangent to the midportion of the curve. This straight line can be expressed by $L = L_0 e^{\alpha(1-D)}$, per Ref. (1). The value of α is equal to the whole integer 4.0. This is to be compared to the α values of 3.0-6.0 as experimentally observed in commercially available hardware. Thus, the simple model does give a realistic result.

Table I. Equations and slopes for various cases

Case	Equation	Slope $\frac{d(\ln L)}{dD}$	Slope at $D = 0.5$	Slope at $D = 0.5$ $F = 0.5$	Slope at $D = 0.5$ $F = 0.5$ $P = 1.0$
Seiger (Ref. 1)	$L = L_0 e^{\alpha(1-D)}$	$-\alpha$	α	α	α
Simplist	$L = \frac{1-D}{AD}$	$-\frac{1}{D(1-D)}$	-4	NA	NA
Excess reactants	$L = \frac{1+F-D}{AD}$	$-\frac{1+F}{D(1+F-D)}$	NA	-3	NA
DOD penalty	$L = \frac{1+F-D}{A(1+PD)D}$	$-\frac{1}{D} - \frac{1}{1+F-D} - \frac{P}{1+PD}$	NA	NA	-3.66

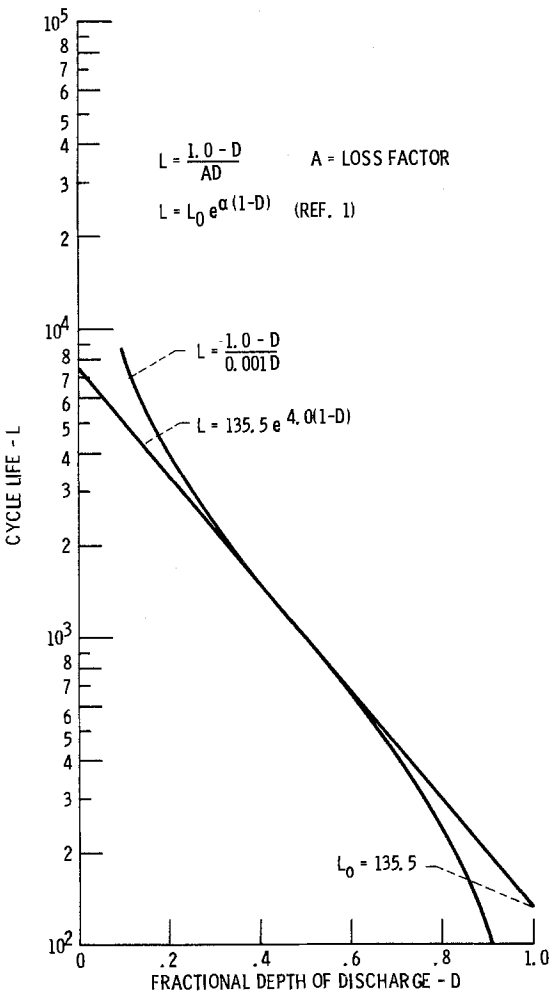

Fig. 2. Cycle life *vs.* depth of discharge relationships predicted by two different models described in the text.

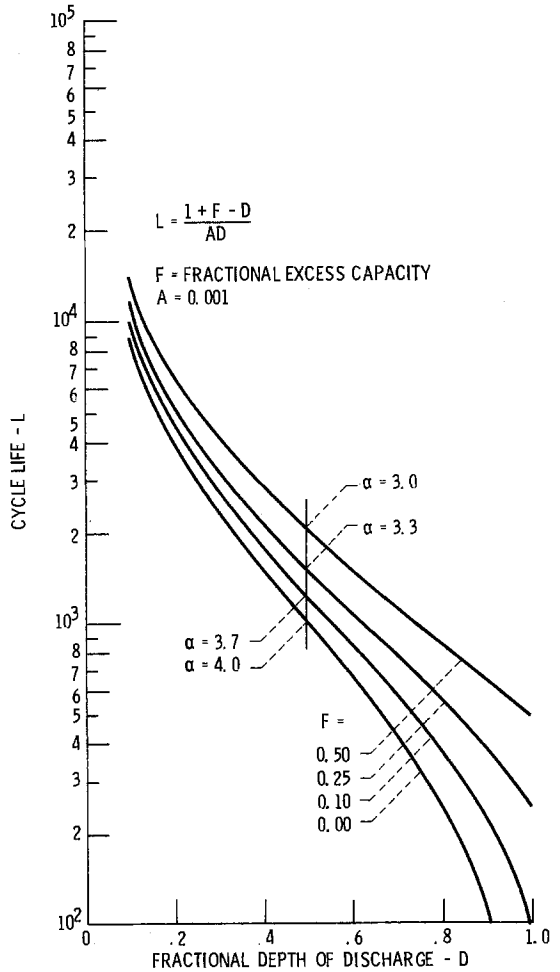

Fig. 3. Cycle life *vs.* depth of discharge as function of the fractional excess capacity, *F*, defined in the text.

Cells with Added Capacity

Quite often cells are built with extra active material so that at the beginning of life they would be able to deliver more than their rated or nominal capacity. Figure 3 assumes that 10, 25, and 50% excess capacity is available at the begining of life. The reserve capacity of these cells takes the form of $(1 + F - D) \times 100$, while the capacity loss per cycle remains as in the preceding case. The cycle lives are again the quotient of the reserve capacity and the loss per cycle. These curves not only show (as one would expect) that the cycle lives are increased by having excess capacity, but the equivalent α value (at 50% DOD) is reduced from 4.0-3.0 as the F factor is increased from 0-0.5 (50% excess capacity). The droop at deep DOD's is removed at the higher values of F. For the remainder of the cases to be examined in this paper, it will be assumed that cells have $F = 0.5$. Figure 4 shows the relationship between the equivalent α value at 50% DOD as a function of F. The effect diminishes as F increases, and it is problematic what benefits could be derived by having cells with very high excess capacities, even though α's less than 3.0 can be thus attained.

Cells of Different Loss Rates

The preceding figures were constructed assuming cells for which the loss rate was assigned a value of 0.001. Figure 5 is constructed for the cases where the parameter A is varied over several orders of magnitude. The reserve capacities at the beginning of life are all $(1 + 0.5 - D) \times 100$ A-hr, and the loss rates take on the A values as noted on the curves of Fig. 5. These curves are seen to be simple vertical translations of the base case shown in Fig. 3. Thus there is no change in the equivalent α value, but the effect on the cycle life of the cell is very significant.

Additional Penalty for Deeper Depths of Discharge

Deeper depths of discharge are known to introduce an additional rate of loss of cycle life that is above and beyond the loss rate associated with simple charging inefficiencies. This additional penalty at deep DOD's is caused by higher shedding rates and rates of grain growth, more severe mass transport environments, higher mechanical stresses due to differential expansion, *etc.* This effect is introduced to the model by assigning a value to the penalty factor P. The loss rate becomes $A \times (1 + PD) \times D \times 100$ A-hr where P can be assigned various values. In Fig. 6, a series of cycle life *vs.* DOD relationships are plotted where the value of P is varied from 0.0-2.0. The equivalent values are seen to increase from 3.0-4.0 (see Table I). The introduction of P into the model shows that real cells are more likely to have α values closer to 6.0 than to the desired value of 2.0.

The above sections cover the most obvious factors that can assume or be assigned various values. The single cell cycle lives are seen to vary over several orders of magnitude, and the values for α range from 3.0-4.0. It would appear that the most significant factor in producing long cycle lives is the loss factor, A. Since this does not affect α, it however does not result in a deep DOD value for the most cost-effective one. This modeling exercise suggests that the most cost-effective DOD will remain where it has been found to be using experimental procedures; that is, between 25-33% DOD.

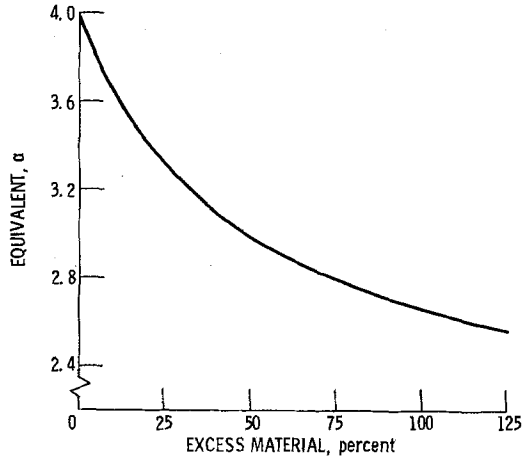

Fig. 4. Equivalent value of α at 50% DOD vs. percentage of excess reactive material.

Battery Strings

Cells are usually connected in series to yield the proper combination of capacity and voltage level. Going from a single cell for which single values of A, F, and P can be assumed to a multicell string where A, F, and P may be assigned distributive functions, introduces a different level of problems. By assuming that these factors are normally distributed about means of A, F, or P with various values of standard deviation, a wide variety of plots could be generated. The factors F and P will be covered first since they only introduce second-order effects.

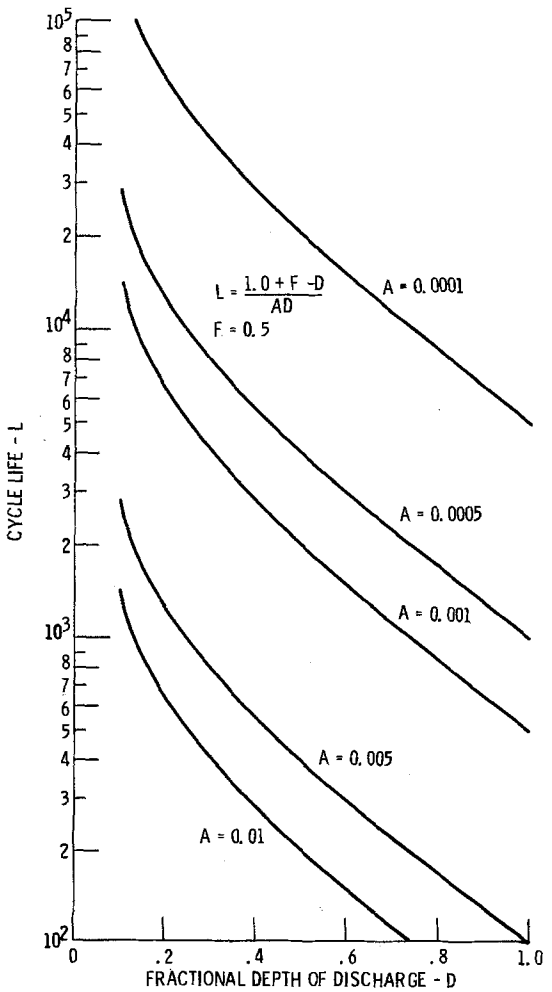

Fig. 5. Cycle life vs. depth of discharge as a function of the loss factor, A, defined in the text.

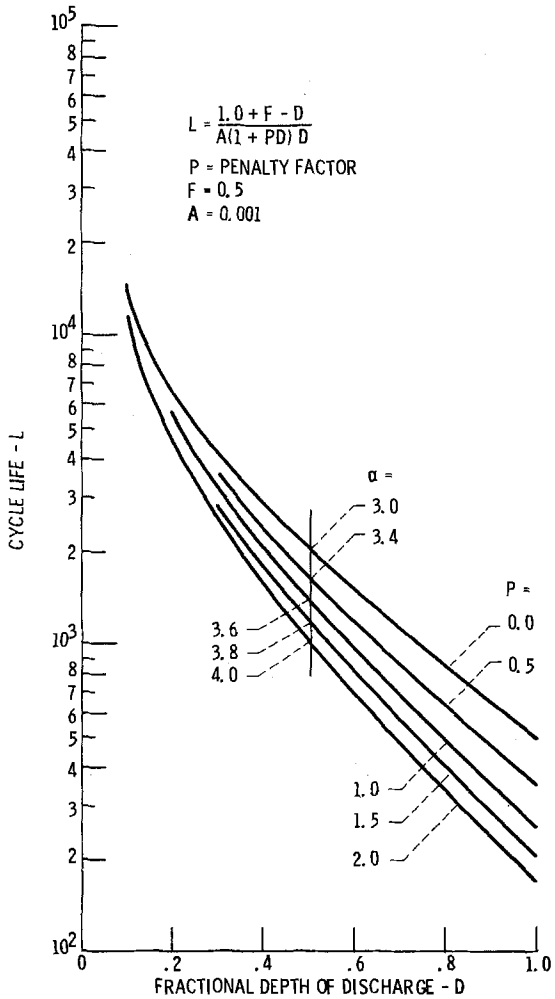

Fig. 6. Cycle life vs. depth of discharge as a function of a penalty factor, P, for depth of discharge described in the text.

If a string of cells were to be made of ones where there was a variation in the amount of active material, there would be a distribution of the value $(1 + F)$ around its mean. If, for example, this distribution were to have a standard deviation, σ, of 0.05 $(1 + F)$, the cell that would fail first would of course be the one with the smallest amount of capacity. This would be equivalent to a cell where F now takes the new value of $F - 0.05 \times (1 + F) \times 2$, if it is assumed that the selected population is bounded by 2σ on either side of the mean value. For the case of F nominally being 0.5, the equivalent F for the worst cell is 0.35. This of course would result in a slightly lower cycle life of the string. This definition of string failure may be arguable, but all the following comments will use it and will therefore be on a consistent basis.

For the case where the factor P is varied about an average value, the factor $[1 + (P + 2\sigma)D]$ is not too far from $(1 + PD)$, given reasonable values for the standard deviation around the mean. The resultant values of the cycle life and α would not change very much. The A factor is somewhat different since the variation is usually assigned or viewed in terms of the efficiency, $(1 - A)$. For an A value of 0.001, it can be stated that a cell is 99.9% efficient in the recovery of the capacity during any one cycle. For the case of an efficiency 99.9% $\pm$ 0.1%, there would result a distribution of A from 0.002-0.000. An A value of 0.000 would result in a cycle life of infinity. For the following examples the cell efficiency will be assumed to be normally distributed about a mean of $1 - A$ with a standard deviation that will take on a variety of values. For the string life, only the cycle life of the cell with the largest value A need be considered.

Furthermore, it will be assumed that cells beyond 2σ can be culled out of any battery pack. Figure 7 is for strings of cells made up from populations of various values of σ. The number of cells in the string is immaterial since its cycle life is fixed by the worst cell in the string (the 2σ cell). The main feature of this figure is that the resultant string lives are simple vertical translations of the single cell relationship. Although there is no change in the equivalent value of α, it is obvious that battery life is strongly affected by the stochastic character of the cell population.

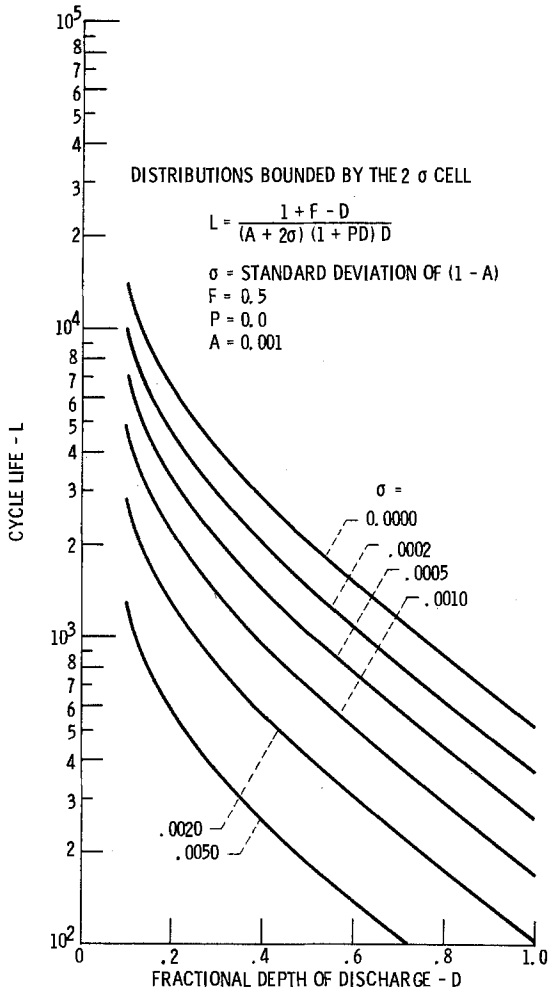

Fig. 7. Cycle life vs. depth of discharge in battery strings as a function of the deviation, σ, in the cycling efficiency.

Concluding Remarks

The subject of cycle life *vs.* depth of discharge has been explored from a theoretical standpoint first at the single cell level and then the multicell battery level. A technique was illustrated that permits the study of the effect of a number of parameters on the shape of the cycle life *vs.* depth of discharge relationship of cells. The equivalent values for α were found to vary over only a very narrow range similar to those found in actual life cycle testing. No potential variable or parameter was found to have a significant influence on the value of α.

The factors that had the greatest influence on the cycle life were the value of the parameter that represented the rate of capacity loss and the standard deviation of value for the cycle efficiency. Even though desirable, finding conditions for an α value of 2.0 does not appear too probable. It would thus appear that battery string cycle lives approaching 1000 can only be achieved by assembling those strings from a very close population of single cells that would have cycle lives of several thousand if tested as single cells. The ratio of cycle life obtainable at 20% DOD to that at 80% DOD will remain about five and possibly higher.

Manuscript submitted Sept. 22, 1982; revised manuscript received *ca.* Dec. 13, 1982. This was Paper 40 presented at the Detroit, Michigan, Meeting of the Society, Oct. 17-22, 1982.

Any discussion of this paper will appear in a Discussion Section to be published in the December 1983 JOURNAL. All discussions for the December 1983 Discussion Section should be submitted by Aug. 1, 1983.

Publication costs of this article were assisted by NASA-Lewis Research Center.

REFERENCES

1. H. N. Seiger, in "Proceedings of the 16th Intersociety Energy Conversion Engineering Conference," American Society of Mechanical Engineers, p. 102, New York (1981).
2. L. H. Thaller, in "Proceedings of the 16th Intersociety Energy Conversion Engineering Conference," American Society of Mechanical Engineers, p. 667, New York (1981).

A Systematic Application of the Potentiostatic Scratch Method in Order to Determine the Pitting Corrosion Resistance of Traditional and Advanced Stainless Alloys

Dany Sinigaglia

Dipartimento di Chimica Fisica Applicata, Politecnico di Milano, Piazza Leonardo da Vinci, 32, 20133 Milano, Italy

Bruno Vicentini and Giorgio Taccani

Istituto per la Tecnologia dei Materiali Metallici non Tradizionali del C. N. R., Via Induno, 10, 20092 Cinisello B, Milano, Italy

Gabriele Salvago

Dipartimento di Chimica Fisica Applicata, Politecnico di Milano, Piazza Leonardo da Vinci, 32, 20133 Milano, Italy

and Giampaolo Dallaspezia

Istituto per la Tecnologia dei Materiali Metallici non Tradizionali del C. N. R., Via Induno, 10, 20092 Cinisello B, Milano, Italy

ABSTRACT

The potentiostatic scratch method has been systematically applied to rank the pitting corrosion (PC) resistance of commercial and laboratory austenitic, superaustenitic, and extra low interstitial ferritic stainless steels in chloride solutions simulating the aggressivity of the human body and seawater. This technique was generally shown to be reliable and reproducible when the pits were associated with the scratched regions. In this case, it was possible to confirm that deformation-induced martensitic transformation does not have any effect upon the PC behavior of metastable austenitic stainless steels. On the contrary, when the pits are formed on the unscratched regions, the scratch technique does not provide an accurate way of determining the pitting potential. In this latter case, the nonmetallic inclusions seem to be more critical sites for pitting development than the bare scratched regions.

For some time now, many advanced laboratory methods have been proposed for evaluating the PC resistance of stainless alloys (1-3). Of these, potentiokinetic and cyclic potentiokinetic methods have undergone the most extensive development. In fact, Schwenk (4) has shown that the most reliable way of evaluating susceptibility to pitting corrosion is to use a potentiostatic technique in which a constant potential is applied for given time, and a constant surface condition is used for each sample (this conclusion was based on the observation of the pitting induction time-potential ratio). Unfortunately, this potentiostatic method is very time consuming and is, thus, of limited practical use.

With kinetic polarization methods, the following data can generally be obtained: the potential at which the passive film breaks down locally and pitting corrosion begins (E_p); the potential below which pits, regardless of how they were formed and propagated, are deactivated or repassivated (E_{pr}).

E_p and E_{pr} have been widely discussed (1-3) and utilized for ranking stainless alloys (5), etc. with regard to pitting corrosion resistance. It has generally been recognized that these potentials do not represent an intrinsic property of the composition and structure of metal or of the test environment, but rather, they greatly depend upon the experimental conditions adopted (for example, the polarization rate) (6). In particular, from the point of view of practical applications, it must be emphasized that E_p may be more noble with respect to the static pitting potential, because pitting initiation can be a very slow process (7); on the other hand, E_{pr} depends upon the extent of localized attack propagation and, therefore, to the local chemical modification inside pits.

Key words: potentiostatic scratch method, pitting corrosion, protection potential, extra low interstitial ferritic stainless steels, martensite α'.

Pessall and Liù (8) have proposed an improved approach to the measurement of pitting potential that does not depend on the time of pit initiation, but instead focuses on the repassivation process (9). In this method, the passive surface, whose pitting potential (labeled E_p^s) is to be determined, is scratched at various potentials set by a potentiostat. If the scratched surface repassivates (*i.e.*, the anodic current rapidly decreases with time), the imposed potential is less noble than the E_p^s; if repassivation does not occur (*i.e.*, the anodic current remains high or does not decrease with time), then the imposed potential is more noble than the E_p^s (Fig. 1).

Therefore, the potentiostatic scratch method identifies the intrinsic capacity of a given alloy to repassivate in a given aggressive environment when the passive film is broken down locally. Its unquestionable advantages over kinetic methods are the following: (*i*)

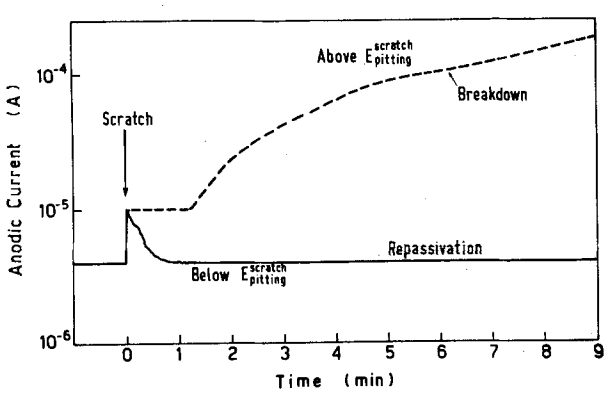

Fig. 1. Scratch technique current-time curves for specimens held at potentials above E_p^s (breakdown) and below E_p^s (repassivation) (8).

This technique eliminates film breakdown time as a variable in the determination of pitting potential; therefore, E_p^s is more negative than E_p. (*ii*) This technique is better applicable to practical pitting corrosion problems because it more closely resembles a real structure which is very likely to be scratched or otherwise have its surface oxide film damaged during use. (*iii*) According to Pessall and Liù, the E_p^s is interchangeable with the protection potential E_{pr}^s if changes in solution concentrations within the pit are prevented by rapidly stirring the solution. For static solutions, E_p^s does not coincide with E_{pr}^s, but tends to be more noble (8).

According to Syrett (10), the cyclic potentiokinetic method does not provide any information on the kinetics of pitting initiation and a propagation between E_p^s and E_{pr}^s, while the potentiostatic scratch method presents the disadvantage that the bare surface exposed by the scratch is not "*a priori*" and "always" the most favorable site for pitting initiation. In fact, it has been experimentally shown that some precipitates and above all nonmetallic inclusions as such (11), or via the effects of their microcrevices (12, 13), can constitute extremely favorable sites for the insurgence of PC. It may, therefore, be that PC begins in such favorable sites at relatively less noble values of the imposed potential, and that PC is not affected by the scratch. According to Barbosa and Scully (14), the scratch technique can be successfully used only in metals with a high degree of purity, *e.g.*, when PC does actually result from the breakdown of the passive film. When PC preferentially nucleates at nonmetallic inclusions, the scratch technique is not applicable.

In order to overcome the above-mentioned limitations, Syrett has developed a method for measuring the pitting propagation rate (≡ PPR) as a function of the imposed potential (Fig. 2) (11). This electrochemical technique is analogous to what is used in stress corrosion phenomena where the crack propagation rate, da/dt, can be established as a function of the stress intensity factor K_I (15). With Syrett's technique, the meaning of the measured protection potential at zero current density is analogous to that of the threshold stress intensity K_{ISCC} and, like the da/dt-K_I curves obtained on precracked specimens, the pitting rate-potential curves of the PPR method are obtained on prepitted specimens.

The PPR method has, thus far, been applied for characterizing TRIP steels. It is a rather long and laborious method and, based on preliminary tests that we conducted on some stainless steels, it presents considerable difficulties in the microscopic evaluation of the total projected area when the pits are numerous and very small. Therefore, it is not easily adaptable to a rapid ranking of passive alloys.

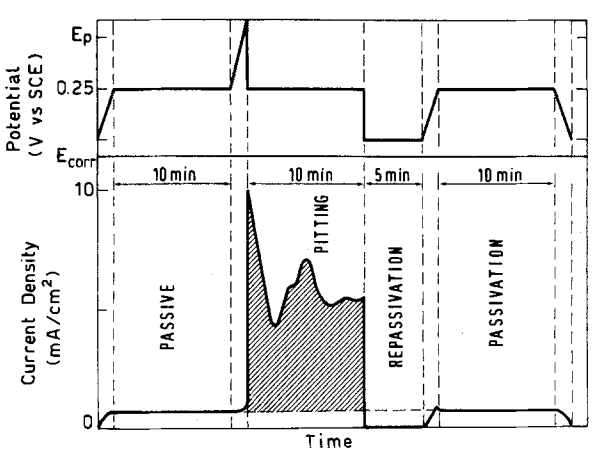

Fig. 2. Schematic diagram of potential-time and current-time cycles used to determine the anodic behavior of growing pits (10).

The above-mentioned reasons and the data in the available literature indicate that the scratch method is very popular and profitable due to the fact that it requires relatively little time and is generally believed to provide accurate values for pitting potentials. We, thus, decided to conduct a more in-depth study of the scratch method, first of all, by improving the experimental apparatus, particularly with regard to controls upon the manner in which the scratch would be executed. After this improvement, the method was, then, systematically applied to a series of traditional and advanced stainless alloys that are already available on the market or which can be produced in the laboratory. These alloys are of great technological interest for use in chloride environment such as seawater and physiological solutions simulating the aggressivity of human body fluids.

Experimental Method

Materials.—Table I indicates the chemical composition of the alloys that were investigated. They were basically three categories of stainless steels: (*i*) Commercial and laboratory produced austenitic stainless steels (type AISI 316L; 16Cr-14Ni-2Mo); (*ii*) superaustenitic stainless steels (type 20Cr-25Ni-4.5Mo-Cu; type 20Cr-18Ni-6Mo-Cu); and (*iii*) extra low interstitial ferritic and superferritic commercial stainless steels (type 18Cr-2Mo-Ti; 21Cr-3Mo-Ti; 26Cr-1Mo-Ti; 25Cr-4Ni-4Mo-Ti; 26Cr-2.5Ni-3Mo-Ti; 28Cr-4Ni-2Mo-Nb) and those laboratory produced (Cr = 21-28%; Ni = 2.5-4%; Mo = 2.5-4%; Ti, Ti + Nb, Nb; Heats ITM 37 to 42, CSM 1039 and 10848).

A series of tests, limited to an artificial "physiological" solution, was conducted on AISI 316L and on type 16Cr-14Ni-2Mo subjected to cold plastic deformation by rolling (10, 30, and 50% reduction in the cross-sectional area) at room temperature and at −196°C, according to the procedure previously described (13, 19).

The laboratory produced alloys were cast and hot rolled according to the procedures already described in previous papers (16), and, then, underwent a final heat-treatment which allowed a metallurgical state to be obtained which was free of second phases; this was afterwards referred to as the "annealed" condition. The commercial alloys were tested in the mill-received condition.

Specimen preparation.—The specimens (disks of 20 mm diam) were ground with wet paper up to 1000 mesh and, then, polished with diamond paste up to 3 μm. They were, then, degreased with ethyl alcohol or acetone (ultrasonically). Finally, they were passivated by immersion in 20% nitric acid for 5 min at room temperature to overcome the crevice susceptibility at the specimen electrode assembly interface.

Aggressive environment.— For tests conducted on annealed and mill-received alloys, a deaerated 3.5% (0.6M) sodium chloride (analytical grade chemical) solution was used. This solution was maintained at a constant temperature (25°, 40°, 60°, 80°, 100°C) (16). For test conducted on work-hardened steels, a deaerated artificial "physiological" solution was used of the following chemical composition: 0.15M (8.74 g/liter) NaCl; $4.16 \cdot 10^{-3}$M (0.35 g/liter) $NaHCO_3$; $3.37 \cdot 10^{-4}$M (0.06 g/liter) $Na_2HPO_4 \cdot 2H_2O$; $5 \cdot 10^{-4}$M (0.068 g/liter) $NaH_2PO_4 \cdot H_2O$. This solution was buffered to a *p*H of 7, and its temperature was maintained at 40°C (13). The solutions were always deaerated with oxygen-free nitrogen.

Equipment.—The potentiostatic scratch test was conducted in a cell with separate compartments, as already described in a previous paper (16). The scratching device was perfected through a series of preliminary tests (17). As illustrated in Fig. 3, the device consisted of a cone-shaped sapphire stylus, (tip radius: 15-18 μm), fixed to the end of a Teflon arm with epoxy

Table I. Chemical composition (w/o) of stainless steels investigated

Grade	Alloy type / Element	C	N	Cr	Ni	Mo	Ti	Nb	Cu	Mn	Si	O	P	S	C + N (ppm)
Austenitic (commercial)	AISI 316 L	0.0260	0.0340	16.1	10.9	2.20	—	—	—	1.24	0.41	0.046	0.008	0.011	600
Austenitic (laboratory)	16Cr-14Ni-2Mo	0.0020	0.0034	16.5	13.8	2.02	—	—	—	1.99	0.83	0.005	0.003	0.009	54
Superaustenitic (commercial) A	20 Cr-25Ni-4.5Mo-Cu (Uranus B 6)	0.0160	0.0250	20.1	24.6	4.47	—	—	1.35	1.33	0.68	0.0040	0.025	0.010	310
Superaustenitic (commercial) B	20 Cr-25Ni-4.5Mo-Cu (Avesta 254 SLX)	0.0155	0.0207	20.0	25.0	4.37	—	—	1.50	1.70	0.74	0.0020	0.020	0.0014	362
Superaustenitic (commercial) C	20 Cr-18Ni-6Mo-Cu-N (Avesta 254 SMO)	0.0171	0.1200	20.0	17.8	6.10	—	—	0.70	0.48	0.33	0.0015	0.017	<0.0005	1371
ELI ferritic (commercial)	18Cr-2Mo-Ti	0.0190	0.0120	19.5	0.3	2.30	0.47	—	—	0.17	0.20	0.0030	0.020	0.013	310
ELI ferritic (commercial)	21Cr-3Mo-Ti	0.0380	0.0073	21.3	—	2.90	0.73	—	—	0.50	0.52	0.0030	0.020	0.008	453
ELI ferritic (commercial)	26Cr-1Mo-Nb (Orion)	0.0010	0.0095	26.1	0.13	1.02	—	0.06	—	0.01	0.21	0.0030	0.010	0.010	105
ELI ferritic (commercial)	26Cr-2.5Ni-3Mo-Ti (Sea cure)	0.0140	0.0058	24.4	2.0	2.95	0.42	Abs.	—	—	0.16	0.0015	0.027	0.0017	198
ELI ferritic (commercial)	25Cr-4Ni-4Mo-Ti (Monit)	0.0160	0.0044	26.1	4.0	3.50	0.34	—	—	—	0.33	<0.0010	0.030	0.0017	204
ELI ferritic (commercial)	28Cr-4Ni-2Mo-Nb (Remanit)	0.0090	0.0140	28.3	3.9	2.37	—	0.42	—	0.22	0.39	N.D.	0.023	0.0070	230
ELI ferritic (laboratory)	ITM 37	0.0115	0.0090	21.7	2.6	2.82	—	—	—	—	0.08	0.0065	0.014	0.0070	205
ELI ferritic (laboratory)	ITM 38	0.0030	0.0090	22.3	2.6	2.80	0.30	—	—	—	0.07	0.0030	0.010	0.0070	120
ELI ferritic (laboratory)	ITM 39	0.0095	0.0130	24.5	3.6	3.45	0.29	—	—	—	0.06	0.0030	0.014	0.0070	225
ELI ferritic (laboratory)	ITM 40	0.0080	0.0130	24.4	3.5	3.30	0.28	0.22	—	—	0.06	0.0030	0.011	0.0073	210
ELI ferritic (laboratory)	ITM 41	0.0085	0.0080	24.9	3.6	3.72	—	0.26	—	—	0.08	0.0096	0.015	0.0070	165
ELI ferritic (laboratory)	ITM 42	0.0065	0.0120	26.0	3.9	3.99	—	0.42	—	—	0.07	0.0100	0.012	0.0022	185
ELI ferritic (laboratory)	CSM 1039*	0.010	0.0162	25.1	0.48	3.00	—	0.21	—	0.08	0.15	0.0165	0.013	0.014	362
ELI ferritic (laboratory)	CSM 1084 B*	0.024	0.0200	28.5	3.15	3.90	0.21	0.22	—	0.27	0.29	0.0050	N.D.	0.010	440

* Laboratory steels supplied in the annealed condition by the Centro Sperimentale Metallurgico.

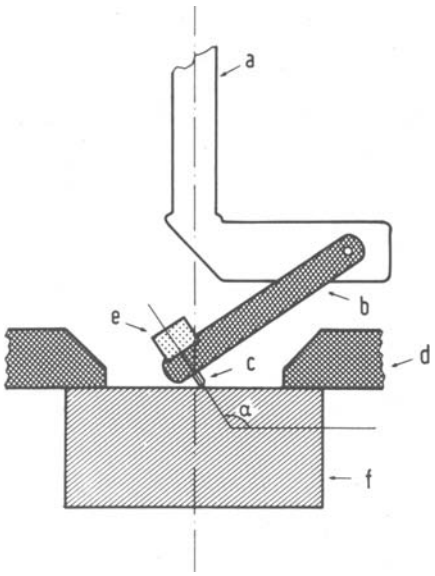

Fig. 3. Schematic drawing of the scratching device: a) Teflon arm; b) Teflon lever; c) cone-shaped sapphire stylus; d) Teflon specimen holder; e) tantalum weight; f) specimen.

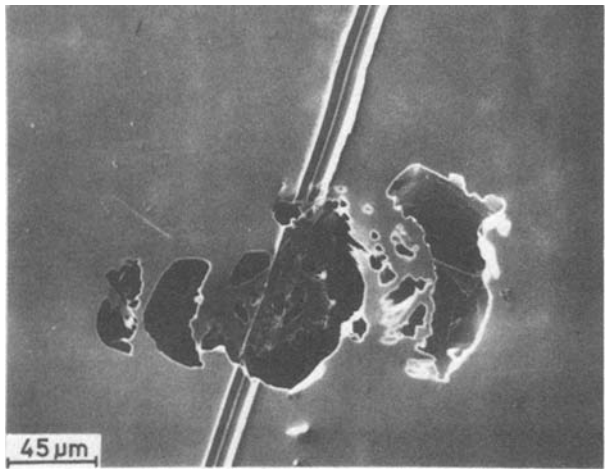

Fig. 4. Example of the specimen surface at the end of the test

resin (Araldite). The stylus can scratch the specimen surface through a vertical manual movement of the glass rod supporting the arm.

The scratches were continuous, of a controlled and reproducible length and depth, and did not have any marks at the ends. These conditions were obtained by tilting the stylus at an obtuse angle in relation to the specimen surface and by attaching a tantalum weight (approximately 10g) to the extreme end of the arm (17). Figure 4 is an example of the specimen surface at the end of the test, showing the regularity of the scratch obtained and the typical pit morphology. Each pitting potential determination was repeated following the procedure already described in a previous paper (16); in many cases, the tests were repeated from three to five times.

The measured potentials were referred to the normal hydrogen electrode (NHE); the interliquid junction was minimized by using an agar-agar bridge saturated with KCl. The thermogalvanic effect was not taken into consideration.

Results and Discussion

Table II shows a comparison of the PC behavior of cold rolled AISI 316L and the analogous high purity austenitic stainless steel 16Cr-14Ni-2Mo in the artificial physiological solution. Their behavior was tested in relation to temperature and degree of rolling as well as the orientation (with respect to the rolling direction) of the exposed surface to the aggressive environment. On the basis of these data, the following observations can be made. (*i*) For laboratory austenitic stainless steel 16Cr-14Ni-2Mo PC resistance does not depend on the degree of cold working, nor on the rolling temperature, nor on the orientation of the surface. This demonstrates, on the one hand, that the very small amount of inclusions [sulfide inclusions and especially, mixed sulfide-oxide inclusions (11)] eliminates the anisotropic behavior with regard to the PC of the surface exposed to the aggressive environment, as already noted by Scotto *et al.* (18) for two stainless steels (18Cr-9Ni and 17Cr-11Ni-2Mo), and by one of the present authors for type AISI 316L and AISI 304L stainless steels (16); on the other hand, it clearly establishes that martensite α', induced by deformation in metastable austenitic stainless steels (19), does not affect pitting initiation. (*ii*) For commercial stainless steel type AISI 316L it was reconfirmed that resistance to PC depends on the degree of work hardening and the rolling temperature only when the long transversal (LT) or short transversal (ST) surface is exposed to the aggressive environment. In fact, these are the only two surfaces which show a decreasing resistance to PC (the E_p^s becomes less noble) as the degree of deformation at room temperature increases. The LT surface, for room temperature deformation, demonstrates worse behavior than the ST surface.

At low deformation temperature, the resistance of the LT and ST surfaces to PC is reversed (the second surface demonstrates worse behavior than the first). With regard to the ST surface, it should be emphasized that, on the one hand, the measurements are extremely difficult to reproduce and, on the other hand, pitting initiation corresponds to the heterogeneity of the surfaces (*i.e.*, inclusions), and it is also characterized by the formation of solid corrosion products which usually cover the mouth of the pit, as illustrated in Fig. 5.

Table II. Pitting potential (mV vs. NHE) of work-hardened (room temperature and −196°C) AISI 316 L and 16Cr-14Ni-2Mo in deaerated physiological solution at 40°C

Surface	Deformation degree (%) / Alloy	0%	10%		30%		50%	
			RT	−196°C	RT	−196°C	RT	−196°C
Longitudinal	AISI 316 L	630	630	590	605	650	595	610
	16Cr-14Ni-2Mo		630	630	630	570	630	670
Long transverse	AISI 316 L	605	480	610	430	630	405	650
	16Cr-14Ni-2Mo		570	590	570	630	610	670
Short transverse	AISI 136 L	630	590	480*	515	480*	505	430*
				430*		430*		350*
				490*		410*		370*
				510*		510*		
				610				
				500 avg		460 avg		380 avg
	16Cr-14Ni-2Mo	—	550	590	570	630	590	650

* Pits on the electrode surface; no pits at the scratched site.

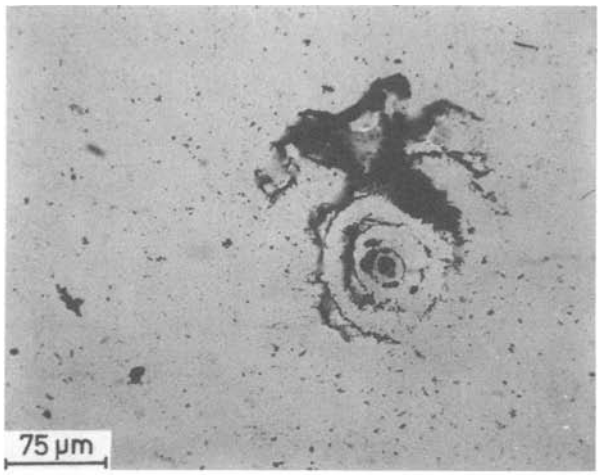

Fig. 5. Pit morphology on the ST surface of cold rolled AISI 316L after removing corrosion products.

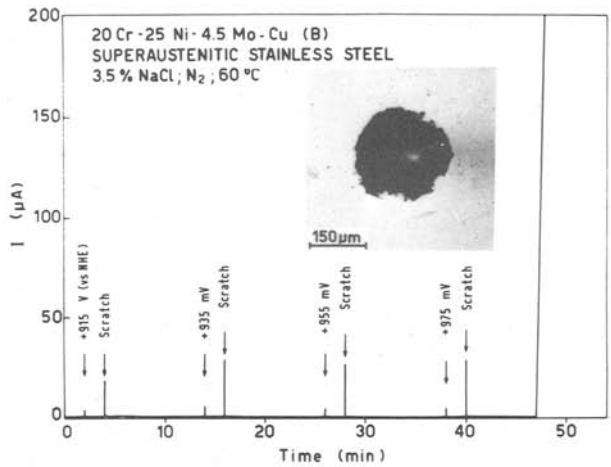

Fig. 6. Scratch technique current-time plot for the superaustenitic stainless steel B in chloride solution.

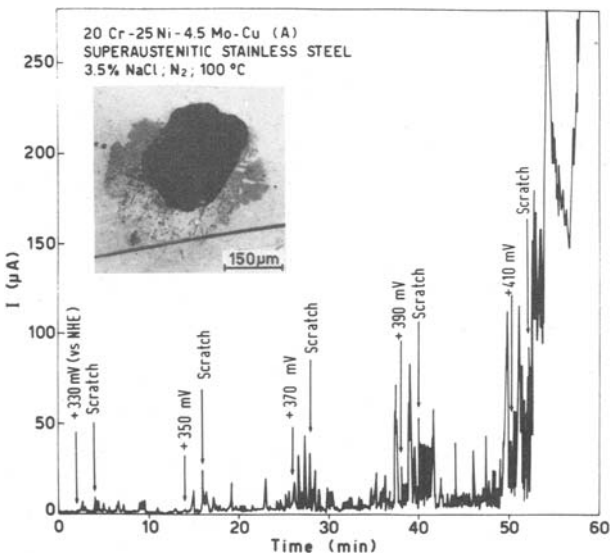

Fig. 7. Scratch technique current-time plot for the superaustenitic stainless steel A in chloride solution.

The anisotropic behavior with regard to the PC resistance of AISI 316L steel, rolled at room temperature [the quantity of martensite-α' is less than 1% (19)], can be explained by the different morphology quantity and distribution of the inclusion appearing on the surface (microcrevice effect). On the other hand, the anisotropic behavior to the PC resistance of AISI 316 steel, rolled at −196°C [the quantity of martensite-α' is greater than 25% (19)], is influenced not only by the morphology, quantity, and distribution of the inclusions (as was the case for alloys deformed at room temperature), but also by the morphology, quantity, and distribution of the deformation bands (and, thus, of the martensite-α') which can be susceptible to selective dissolution phenomena (6).

Table III offers a comparison of the pitting corrosion behavior of some commercial superaustenitic steels as a function of the temperature of the chloride solution. Figures 6 and 7 illustrate two particularly significant current-time curves. The results thus far obtained can be summarized as follows: (*i*) None of the three steels (labeled A, B, and C) manifested pitting initiation at room temperature (25°C), despite the damage to the passive film by scratching; instead, transpassivity and/or oxygen evolution were attained. Such behavior was also found at 40°C for one of the

Table III. Pitting potentials (mV *vs.* NHE) of some commercial superaustenitic stainless steels in 3.5% sodium chloride deaerated solution

T (°C) \ Alloy	20Cr-25Ni-4.5Mo-Cu (A)	20Cr-25Ni-4.5Mo-Cu (B)	20Cr-18Ni-6Mo-Cu-N (C)
25	1095°	1185°	—
	1095°	1175°	—
	1095 avg	1180 avg	—
40	605*	1165	—
	595*	1145	—
	600 avg	1155 avg	—
60	525*	975*	1155°
	545**	935	1155°
	535 avg	955 avg	1155 avg
80	495**	735*	1165°
	485*	775	1135°
			1165°
			1165°
	490 avg	755 avg	1160 avg
100	410*	540*	1160**
	400*	530	1150*
			1000
			920*
	405 avg	535 avg	1060 avg

° No pits formed on the electrode surface (transpassive and/or oxygen evolution region).
* Pits formed on the electrode surface, but no pits at the scratched site.
** Pits formed at the scratched site after repassivation of this latter.

20Cr-25Ni-4.5Mo-Cu type steels (steel B) and at up to 80°C for the 20Cr-18Ni-6Mo-Cu type steel (steel C). Under these conditions, the potentials of Table III were read at an anodic current of about 10 μA which has been conventionally considered to be the current limiting the passivity field at more noble potentials. (*ii*) At higher temperatures, PC normally originates either on the unscratched region or on the scratched region after repassivation of scratched region itself. In these two cases, the current-time relationships show the same shape (Fig. 6 and 10). (*iii*) In particular, for steel A, the passivity field is characterized by a series of sharp anodic current "blips" which increase together with the average values of the anodic current as the potential increases (Fig. 7). These "intrinsic" blips indicate that the oxide film breaks down locally followed by immediate repassivation of the incipient pits. The scratch determines an anodic current blip which cannot be easily distinguished from the "intrinsic" blips. Under these conditions, Table III shows the values of potential above which pitting was observed on the specimen surface. (*iv*) The pitting corrosion resistance of the alloys decreases as the temperature increases; in any case it follows the order: steel A < steel B < steel C.

Finally, Table IV shows the results regarding pitting corrosion resistance of ELI commercial and laboratory ferritic stainless steels. Figures 8, 9, and 10 illustrate some of the most significant current-time curves. The

Table IV. Pitting potnetials (mV vs. NHE) of commercial and laboratory ELI ferritic stainless steels in 3.5% sodium chloride deaerated solution

Alloy \ T (°C)	25	40	60	80	100
18Cr-2Mo-Ti		635	505	405	300
	815	635	495	395	280
	795	625			
		615			
	805 avg	625 avg	500 avg	400 avg	290 avg
21Cr-3Mo-Ti	1075°	795	530	495	330
	1095°	815	530	485	320
			505	490	
	1085 avg	805 avg	520 avg	490 avg	325 avg
26Cr-1Mo	1285°	785	565	395	280
	1255°	795	535	375	300
		825			
		865			
	1270 avg	820 avg	550 avg	385 avg	290 avg
26Cr-2.5Ni-3Mo-Ti	—	1235°	975*	655	370
		1215°	955	625	390
		1225 avg	965 avg	640 avg	380 avg
25Cr-4Ni-4Mo-Ti	—	—	1125°	815	490
			1005°	835	510
			915*	815	440
			1015 avg	820 avg	480 avg
28Cr-4Ni-2Mo	—	—	1215°	645	400
			1205°	605	400
ITM 37	1225*	885	615	445	380
	1155*	835	625	455	370
					370
	1190 avg	860 avg	620 avg	450 avg	375 avg
ITM 38	1345°	995	635	465	340
	1295°	985	645	455	320
	1320 avg	990 avg	640 avg	460 avg	330 avg
ITM 39	—	1375°	1275*	795	410
			1195**	815	460
					435 avg
ITM 40	—	1235°	1065*	665	380
		1225°	1085	675	400
		1230 avg	1075 avg	670 avg	390 avg
ITM 41	—	—	1185°	835	490
			1165	845	520
			1175 avg	840 avg	505 avg
ITM 42	—	—	1165°	1195°	590
			1175°	965	620
			1170 avg		605 avg
CSM 1039	—	1195°	845	545	350
		1185°	835	525	370
CSM 104	—	—	1175°	1175°	520
			1205°	1155°	520

° No pits formed over electrode surface (transpassive and/or oxygen evolution region).
* Pits formed over the electrode surface, but no pits at the scratched site.
** Pits formed at the scratched site, after repassivation of this latter.

following conclusions can be drawn from these data: (*i*) As was the case for superaustenitic alloys, each ELI ferritic stainless steels, despite the damage to the passive film, revealed a different temperature value below which potential of transpassivity and/or oxygen evolution is reached without pitting initiation (see Fig. 8). This critical temperature rises as the intrinsic PC resistance of the steels tested increases. So for type 18Cr-2Mo-Ti steel, it is below 25°C, while for the other alloys, it is higher than room temperature. (*ii*)

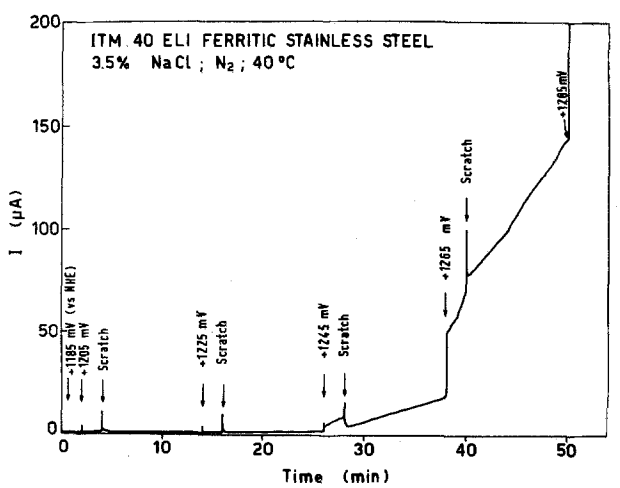

Fig. 8. Scratch technique current-time plot for the laboratory produced ELI ferritic stainless steel in chloride solution. No pits on the scratched and unscratched regions.

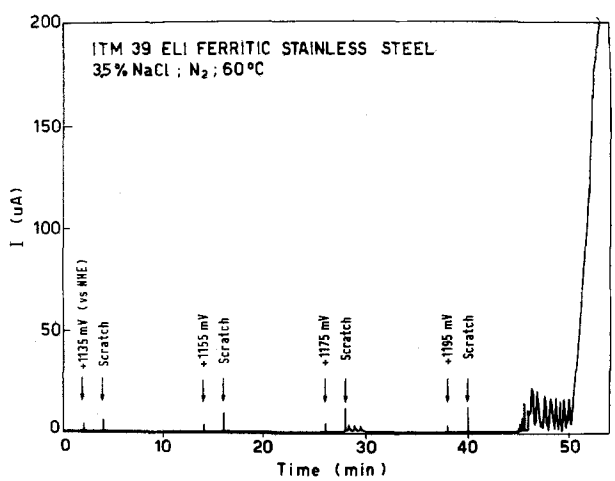

Fig. 9. Scratch technique current-time plot for the laboratory produced ELI ferritic stainless steel in chloride solution.

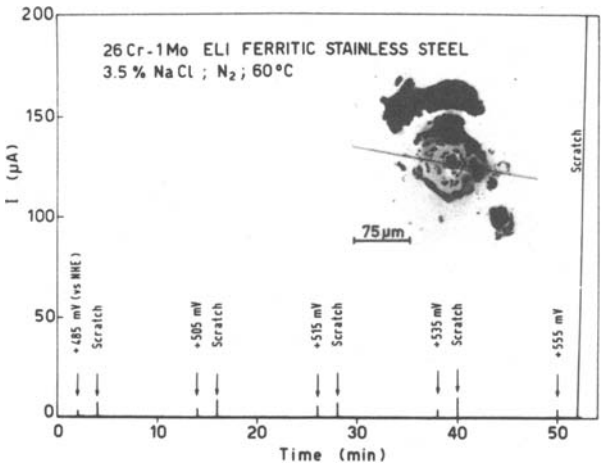

Fig. 10. Scratch technique current-time plot for the 26Cr-1Mo ELI ferritic stainless steel in chloride solution.

Generally, above the critical temperature, pits nucleate and develop at the scratched site and E_c^s shows a good reproducibility (Table IV). In these conditions, the scratch technique provides a very reliable way of identifying the maximum service temperature of the alloys themselves in a chloride solution, beyond which there is a sharp drop in the PC resistance (see for example type 28Cr-4Ni-2Mo-Nb; ITM 39 to 42; CSM 1039 and 1084). (*iii*) For some ELI ferritic stainless alloys (26Cr-2.5Ni-3Mo-Ti; ITM 39 and ITM 40), pitting in some tests does not initiate along the scratch, or it only occurs after repassivation of the scratch itself (Fig. 9). This behavior is to be found when the potentials are very noble (Table IV).

Conclusions

The improved potentiostatic scratch method was systematically applied in order to rank the PC resistance of a series of traditional and advanced stainless steels in solutions simulating the aggressivity of seawater and of the human body. The principal results obtained were the following: (*i*) The scratch method was generally shown to be reliable and reproducible when pitting nucleation is associated with the scratched regions (±25 mV). In this case, the E_p^s, defined by Pessal and Liù as the potential at which the repassivation time is equal to infinity, becomes useful for ranking the alloys with regard to the PC resistance. (*ii*) The scratch method seems to confirm that the deformation-induced martensitic transformation does not have any effect upon the PC behavior of metastable austenitic stainless steels in solution simulating aggressivity of the human body. (*iii*) For each alloy investigated, despite the breakdown of the passivity film caused by scratching, below certain temperature values of the aggressive environment a potential region of transpassivity and/or oxygen evolution is reached without nucleation and development of its pitting phenomena. This temperature value rises as the intrinsic PC resistance of the steel tested increases. (*iv*) For some alloys, which are particularly resistant to PC, the pits could nucleate either on the unscratched region (case I) or on the scratched region after repassivation of the bare scratched region itself (case II). This behavior is shown especially by the superaustenitic stainless steels (Table III) and is also found in particularly "defective" alloys, such as the ST surface of AISI 316L steel, rolled at −196°C (Table II). (*v*) Our results seem to indicate that the scratch method usually offers an accurate means of determining the pitting potential; this was especially the case of ELI ferritic stainless steels (Table IV). However, this method does not give precise results if on the alloy surface there are particularly favorite sites for pitting nucleation [*i.e.*, nonmetallic inclusions of sulfides (microcrevices) (11)], where pits could nucleate and develop without regard to the performed scratch. If this is the case, the obtained values are not a measure of E_p^s; these results should be disregarded as Bond and Lizlov did (5). However, also these results were reported by us to give more evidence of the fact that, if pits do not start at the scratched sites, a great irreproducibility should be expected. Our conclusions agree with those of Syrett (10) and Barbosa (14, 20).

Acknowledgments

The authors wish to express their sincere thanks to Dr. J. Kruger of the National Bureau of Standards of Washington, DC for his critical reading of the manuscript and helpful suggestions.

Manuscript submitted Oct. 18, 1982; revised manuscript received Jan. 7, 1983.

Any discussion of this paper will appear in a Discussion Section to be published in the December 1983 JOURNAL. All discussions for the December 1983 Discussion Section should be submitted by Aug. 1, 1983.

Publication costs of this article were assisted by the Instituto per la Technologia dei Materiali Metallici non Tradizionali, CNR.

REFERENCES

1. VV.AA., "Localized Corrosion," Nace 3, R. W. Staehle *et al.*, Editors, NACE, Houston (1974).
2. P. E. Morris, "Galvanic and Pitting Corrosion," ASTM-STP 576, R. Babonian *et al.*, Editors, pp. 261-275, ASTM, Philadelphia (1976).
3. R. Babonian and G. S. Haynes, "Electrochemical Corrosion Testing," ASTM-STP 727, F. Mansfeld and U. Bertocci, Editors, pp. 274-282, ASTM, Philadelphia (1981).
4. W. Schwenk, *Corros. Sci.*, **5**, 254 (1965).
5. L. A. Lizlovs and A. P. Bond, *Corrosion*, **31**, 219 (1975).
6. G. Salvago, G. Fumagalli, and D. Sinigaglia, *Corros. Sci.*, In press.
7. J. Kruger, "Passivity and Its Breakdown on Iron Base Alloys," R. W. Staehle and H. Okada, Editors, p. 91, NACE, Houston (1976).
8. N. Pessal and C. Liu, *Electrochim. Acta*, **16**, 1987 (1971); *Corrosion*, **30**, 381 (1974).
9. J. Kruger, "Corrosion and Degradation of Implant Materials," ASTM-STP 684, pp. 118-119, ASTM, Philadelphia (1979); G. M. Ugiansky and J. Kruger, *Corrosion*, **30**, 63 (1974); J. Kruger, "Electrochemical Techniques for Corrosion," R. Babonian, Editor, p. 37, NACE, Houston (1978).
10. B. G. Syrett, *Corrosion*, **33**, 221 (1977); "Electrochemical Techniques for Corrosion," R. Babonian, Editor, pp. 93-100, NACE, Katy (1978).
11. Z. Szklarska-Smialowska and E. Lunarska, *Werkst. Korros.*, **32**, 478 (1981); A. Szummer and M. Janik-Czachor, *ibid.*, **33**, 150 (1982).
12. D. Brookobank and K. W. Andrew, *J. Iron Steel Inst.*, **206**, 595 (1968).
13. A. Cicada *et al.*, "Corrosion and Degradation of Implant Materials," ASTM-STP 684, B. C. Syrett and A. Acharya, Editors, pp. 144-160, ASTM, Baltimore (1979).
14. M. Barbosa and J. C. Scully, "Environment Sensitive Fracture of Engineering Materials," Z. A. Foroulis, Editor, pp. 91-113, AIME, Warrendale (1979).
15. D. Sinigaglia, G. Re, and P. Pedeferri, "Cedimento per Fatica e Ambientale dei Materiali Metallici," Clup, Milano (1979).
16. D. Sinigaglia *et al.*, *Werkst. Korros.*, **31**, 851 (1980); B. Vicentini *et al.*, *ibid.*, **33**, 92 (1982); D. Sinigaglia *et al.*, *ibid.*, **33**, 592 (1982).
17. G. Dallaspezia, Internal Report Istituto Tecnologia Materiali Metallici non Tradizionali, C.N.R. No. 80/7, Cinisello B Milano.
18. V. Scotto, G. Ventura, and E. Traverso, *Corros. Sci.*, **19**, 237 (1979).
19. G. Re, D. Sinigaglia, D. Wenger, and A. Benvenuti, *La Met. Italiana*, **71**, 382 (1979).
20. M. Barbosa and J. C. Scully, *Corros. Sci.*, **22**, 1025 (1982).

Effect of Laser Surface Melting on Some Corrosion Characteristics of an Iron-Chromium Alloy

P. T. Cottrell,[1] R. P. Frankenthal,* G. W. Kammlott, and D. J. Siconolfi*

Bell Laboratories, Murray Hill, New Jersey 07974

and C. W. Draper

Western Electric Company, Engineering Research Center, Princeton, New Jersey 08540

ABSTRACT

The effect of laser surface melting (LSM) on the breakdown of the passivating film and subsequent pitting of a ferritic stainless steel has been studied. An Fe-19%Cr alloy was subjected to LSM by pulses from a Q-switched Nd-YAG (1.06 μm) laser. The composition of the native oxide film was analyzed by Auger electron spectroscopy. Although LSM enriches the surface oxide film in chromium, it degrades its electrochemical behavior, for there is premature breakdown of the passivating film and subsequent pitting when the electrochemical potential is swept from the passive region into the active region in 1*N* H_2SO_4. The premature breakdown occurs at sites associated with inclusions. Stresses introduced in the surface by LSM affect pit growth rates and morphology in the same manner as when they are introduced by mechanical means.

Recently there have been several studies of the effect of laser surface melting (LSM) on the electrochemical properties of metals and alloys. McCafferty *et al.* (1) showed that LSM improved the resistance of an Al-1%Mn alloy to general corrosion but did not improve its resistance to pitting corrosion. Ayers *et al.* (2) reported that LSM improved the corrosion resistance of sprayed titanium coatings to seawater. Draper and co-workers (3) showed that LSM improved the corrosion resistance of aluminum bronze to acidified chloride solutions. Anthony and Cline (4) using LSM changed the susceptibility of Type 304 stainless steel to intergranular attack by redistributing chromium in the surface region. Since no studies of the effect of LSM on the breakdown of the passivating film and pitting of ferritic stainless steels have been reported, we have undertaken such an investigation.

Many studies of the breakdown of the passivating film on ferritic stainless steels and their subsequent pitting exist in the literature and have been reviewed by Galvele (5). Most common is pitting induced by aggressive anions, such as halides, at potentials in the passive region. However, local film breakdown and crystallographic pitting have been reported for iron-chromium alloys (Cr $>$ 12%) that are subjected to a slow potential sweep from the passive potential region into the active region in sulfuric acid solutions that do not contain any aggressive anions (6, 7). The rate of pitting and the crystallography of the pits are affected by the manner in which the surface has been prepared (7).

We report here on the effect of LSM on the breakdown of the passivating film and pitting of an iron-chromium alloy during potential sweeps from the passive potential region into the active region in 1*N* H_2SO_4.

Experimental

An Fe-19%Cr alloy, whose composition, analysis, and heat-treatment have been reported previously (7), was investigated. Electrodes were machined and mechanically polished as previously described (7).

Laser surface melting was accomplished with an acousto-optically Q-switched Nd-YAG (1.06 μm) laser. The laser output consists of a train of pulses with a pulse length of 150 nsec, repetition rate of 10 kHz, and incident power density of ~100 MW/cm^2. Optical spot sizes are between 10 and 20 μm in diameter. Under these conditions, the molten layer did not reach the boiling point, except at some sites that are associated with second phase particles. The depth of the melt layer is estimated, from a thermal model by Hsu *et al.* (8), to be 0.8 to 1 μm. A computer-controlled, high precision linear induction table was used to raster scan the sample, thereby producing uniform large area coverage. Melt spots are typically 5-10 μm in diameter. The spot-to-spot and line-to-line overlap are typically about 5 μm each. It should be emphasized that for these pulse lengths and repetition rates each melt spot resolidifies several orders of magnitude faster than the arrival of the next laser event.

The electrolyte solution was 1*N* H_2SO_4 made from electronic grade acid and distilled water. A conventional three-compartment electrochemical cell was used, the compartments being separated by fine porosity, fritted disks.

A PAR Model 173 potentiostat with a PAR Model 176 current-to-voltage converter or a PAR Model 376 logarithmic current converter was used. IR-compensation was applied when the current density exceeded 1 mA /cm^2. For potentiodynamic experiments, a PAR Model 175 waveform generator programmed the potential output of the potentiostat. All experiments were conducted at room temperature. Potentials were measured relative to the saturated calomel electrode and are reported relative to the standard hydrogen electrode (SHE).

Alloy surfaces were examined for film breakdown and pitting by optical microscopy and by scanning electron microscopy with a Cambridge Stereoscan. The composition of surface oxide films was determined by Auger electron spectroscopy (AES). All spectra in the $dN(E)/dE$ mode were obtained with a Physical Electronics Industries Thin Film Analyzer system. Normal operating conditions were 5 kV electron gun voltage, 10 μA beam current, and 2 eV modulation amplitude. For sputtering, argon was used at a pressure of 7 mPa (5 $\times$ 10^{-5} Torr); the ion beam voltage and emission current were 2 kV and 30 mA, respectively.

Results and Discussion

Native oxide composition.—The composition of the native oxide was determined by AES for both the LSM-treated and the untreated conditions. Typical spectra are shown in Fig. 1. These spectra were obtained after ion sputtering for a few seconds to remove surface carbon contamination. It is evident that LSM has increased the chromium content of the oxide. Since the oxygen (O 510 eV) and chromium (Cr 529 eV) peaks overlap (9), a quantitative determination of the

* Electrochemical Society Active Member.
[1] Present address: Department of Chemistry, Florida A&M University, Tallahassee, Florida 32307.
Key words: iron-chromium alloys, lasers, melting, corrosion, passivity.

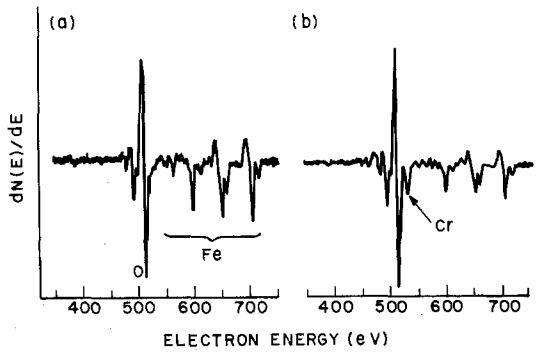

Fig. 1. AES spectra of the native oxide on (a) the untreated control and on (b) the LSM specimen, showing that LSM enhances the Cr content of the film.

oxide composition cannot be obtained from these spectra. The intensity of the Cr 529 eV peak, relative to the intensity of the Fe 703 eV peak, is plotted in Fig. 2 as a function of ion sputtering time. The sputter rate and, hence, the depth are not known. It is seen that LSM not only increases the chromium content of the oxide but also shifts the maximum in chromium content toward the air/oxide interface, thereby making the surface richer in chromium oxide. Papagno and Scarmozzino (10) also found enrichment of chromium in the surface region when they irradiated Type 304 stainless steel with multiple short (30 nsec) laser pulses. It is not clear, however, whether the excess chromium they found was in the alloy or in the surface oxide. In the present study, the oxide/alloy interface lies between 2 and 3 min sputter time for both the treated and untreated specimens, based on their oxygen depth profiles. The Fe/Cr intensity ratio of the LSM alloy changes only slightly after this time and reaches a steady state in about 8 min. The Fe/Cr intensity ratio of the control, however, is at a minimum after 8 min and then increases slowly until it becomes equal to this intensity ratio for the treated alloy.

Electrochemical properties.—Each specimen was initially subjected for 5 min to a potential of −0.50V in 1*N* H_2SO_4. The LSM specimens exhibit a cathodic current two orders of magnitude lower than the untreated ones. To achieve approximately equivalent cathodic currents, the applied potential for the LSM specimens has to be changed to −0.70V. In the passive potential region at +0.50V, the anodic current for the LSM specimens is about one order of magnitude less than that for the untreated specimens. The native oxide on the LSM specimens is not reduced by the cathodic treatment, as evidenced by the low anodic and cathodic currents that are unaffected by the time of the cathodic treatment. It has previously been shown that the oxide film on untreated iron-chromium alloys cannot be completely reduced cathodically (11). Since the oxide films on both the treated and untreated specimens are approximately of equal thickness, the lower cathodic and anodic currents on the LSM specimens most likely result from a lower ionic and electronic conductivity of the oxide, due to its enrichment in chromium. The lower conductivity is also the reason that the oxide on the treated specimen cannot be reduced.

Film breakdown and pitting.—To study breakdown of the passivating film during a potential sweep from the passive into the active potential region, the alloy surface was passivated at +0.50V for 90 min; the potential was then changed at a rate of 0.10 V/hr into the active potential region. The *E-i* curves for the LSM specimen and for the untreated control are shown in Fig. 3. The curve for the control was reported previously (7). The cathodic loop for the untreated specimen is due to hydrogen evolution prior to film breakdown (6). It is not observed for the LSM specimen because of the low cathodic reaction rate (see above). The major difference between the two curves is the hump on the positive potential side of the anodic loop of the LSM specimen, which indicates that film breakdown occurs more easily on the treated specimen. The breakdown potential for the control is −0.128 ± 0.002V. For the LSM specimen, there are two breakdown potentials. The first is at −0.078 ± 0.005V, while the second at the inflection point is the same as that observed for the control.

An SEM examination was made of the breakdown sites for an LSM specimen held at a potential between −0.078 and −0.128V, *i.e.*, in the region of the hump, (Fig. 4) and for one held at a potential negative of −0.128V (Fig. 5). For the former, corrosion is observed only at sites that result from a coupling of the laser radiation with inhomogeneities in the alloy surface, causing excessive heating, evaporation, and crater formation. A correlation was found between the number density of chromium oxide inclusions and the number density of these craters. It is concluded that these craters are formed at inclusion sites, as has also been observed at carbide inclusions in Type 304 stainless steel (12). Corrosion at these sites produces noncrystallographic pits, whose shape is governed by

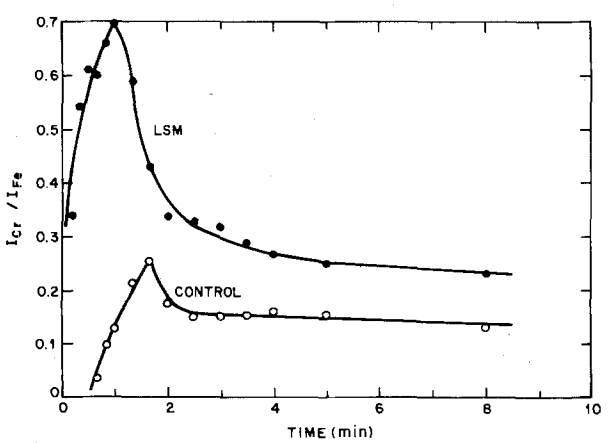

Fig. 2. Depth profiles through the native oxide films on the untreated and LSM treated specimens, showing that LSM enhances Cr content of the film and shifts the maximum Cr content toward the air/oxide interface.

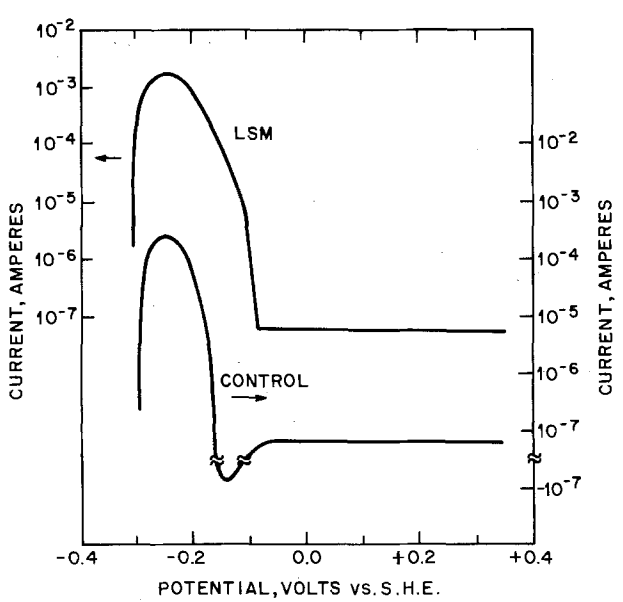

Fig. 3. *E-i* curves for the untreated and LSM treated specimens, showing the hump on the positive potential side of the anodic loop for the treated specimen.

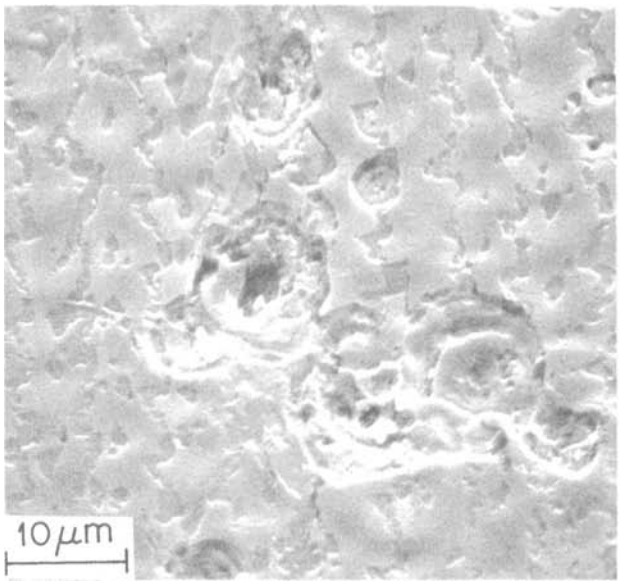

Fig. 4. Breakdown sites for an LSM specimen polarized at a potential between −0.078 and −0.128V, the region of the hump. Film breakdown and pitting occurred at sites resulting from a coupling of laser radiation with inclusions in the surface.

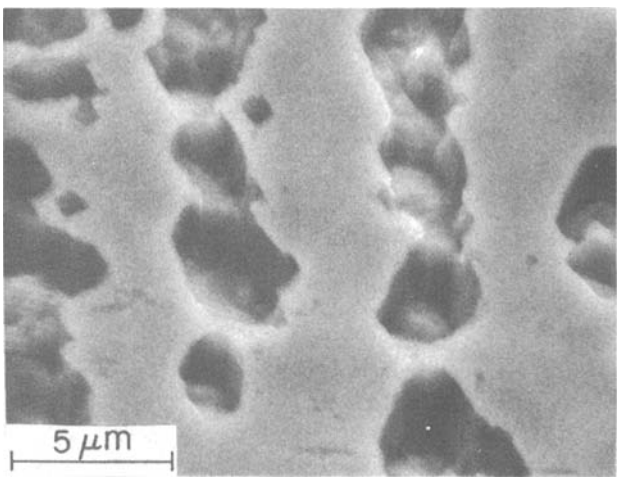

Fig. 5. Film breakdown sites and pitting for an LSM specimen polarized at a potential negative of −0.128V, showing crystallographic pitting.

unknown factors. For the specimen held at a potential negative of −0.128V, the pits are mostly crystallographic (Fig. 5). The pitting in this regime appears to be identical to that previously described (6, 7).

The crystallographic pits in the LSM specimens nucleate on ridges, where melt spots overlap (Fig. 6) and develop in parallel rows that correspond to the rows of the melt spots (Fig. 7). Nucleation most likely occurs at points of stress that arise at the sites exposed to multiple melt events. As these pits grow, their bottoms become flat (Fig. 8). After each pit has grown to a certain depth, it continues to grow laterally, but growth in the direction normal to the surface is greatly diminished. In Fig. 8, the smaller of the two pits has a flat bottom, while the larger one is flat at its periphery but has deepened slightly in the center and appears to be changing its morphology as it deepens. This phenomenon of a reduced growth rate normal to the surface and a change in morphology was also observed when this alloy with a mechanically polished surface was pitted under the same conditions (7). It was shown that the surface layer was deformed by the polishing and that the rate of dissolution was faster and the pit morphology was different in the deformed layer than in the annealed substrate. In the present study, the irradiated surface was deformed or damaged by transient thermomechanical stresses that introduced defects (13, 14), like those caused by mechanical polishing. As a result, pitting occurs at a faster rate and with a different morphology in the melt layer than in the annealed bulk. The depth of the smaller pit, *i.e.*, the flat bottomed one, in Fig. 8 is 1 μm, which is approximately the same as the melt depth, in agreement with this hypothesis.

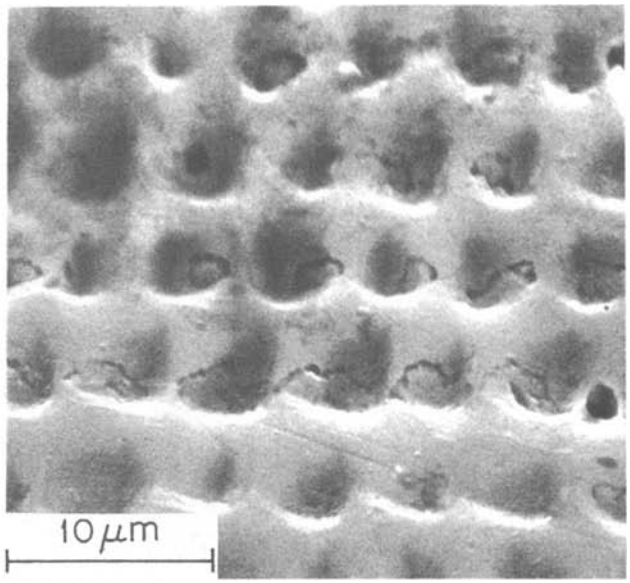

Fig. 6. Pit nucleation sites on an LSM specimen

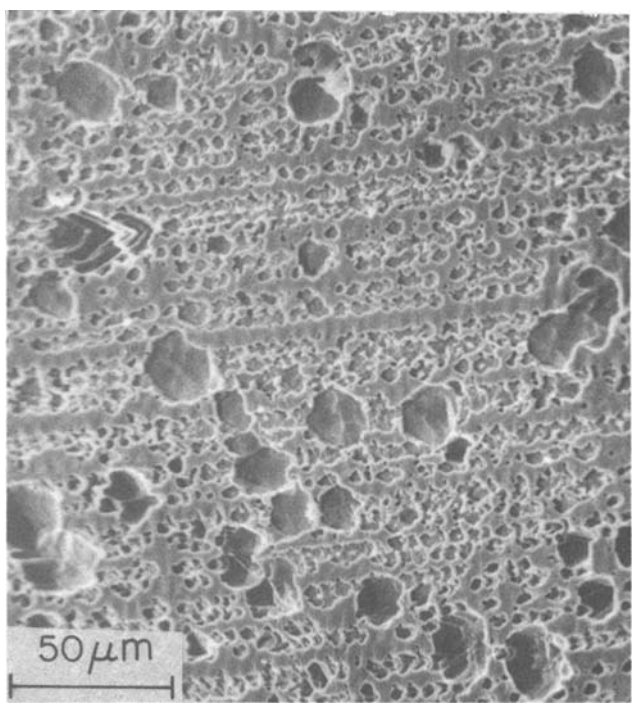

Fig. 7. Pits on an LSM specimen developing in rows that correspond to rows of melt spots.

Conclusions

Laser surface melting enriches the native oxide film in chromium oxide. Despite this, LSM has a detrimental effect on the resistance of an Fe-19%Cr alloy to film breakdown in H_2SO_4, when the potential is swept from the passive into the active potential region. Premature film breakdown occurs at sites that are as-

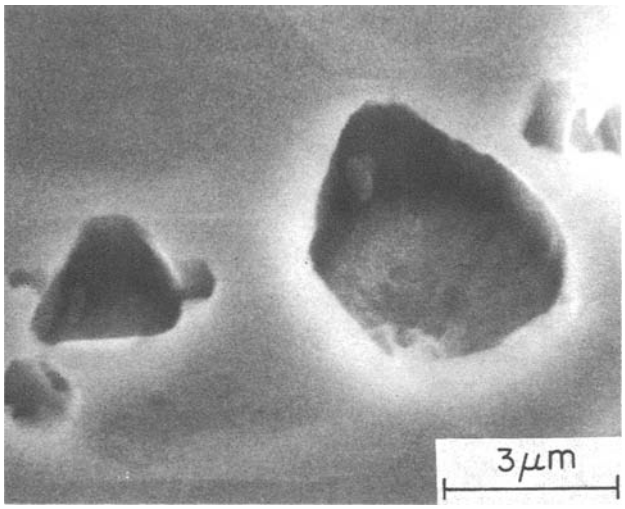

Fig. 8. Crystallographic pits that after a period of growth become flat bottomed (a, left) and then change morphology as they grow further (b, right).

sociated with inclusions in the surface region. In the absence of the inclusions, it appears that LSM would cause little or no improvement in the alloy's resistance to breakdown, even though the surface oxide film has been enriched in chromium, because the breakdown potential is only a weak function of the chromium content of the alloy for Cr > 20% (15).

LSM introduces strains and defects into the melt layer, resulting in faster pit growth and a change in pit morphology compared to that observed for the annealed bulk material. This effect is similar to that caused by mechanical deformation of the surface layer.

Acknowledgments

The technical assistance of Messrs. P. P. Solan and R. F. Shinkle is greatly appreciated.

Manuscript submitted Aug. 18, 1982; revised manuscript received Nov. 29, 1982.

Any discussion of this paper will appear in a Discussion Section to be published in the December 1983 JOURNAL. All discussions for the December 1983 Discussion Section should be submitted by Aug. 1, 1983.

Publication costs of this article were assisted by Bell Laboratories.

REFERENCES

1. E. McCafferty, P. G. Moore, and G. T. Peace, *This Journal*, **129**, 9 (1982).
2. J. D. Ayers, R. J. Schaefer, F. D. Bogar, and E. McCafferty, *Corrosion*, **37**, 55 (1981).
3. C. W. Draper, R. E. Woods, and L. S. Meyer, *ibid.*, **36**, 405 (1980).
4. T. R. Anthony and H. E. Cline, *J. Appl. Phys.*, **49**, 1248 (1978).
5. J. R. Galvele, in "Passivity of Metals," R. P. Frankenthal and J. Kruger, Editors, p. 285, The Electrochemical Society, Princeton, NJ (1978).
6. H. W. Pickering and R. P. Frankenthal, *This Journal*, **112**, 761 (1965).
7. R. P. Frankenthal, *Corros. Sci.*, **8**, 491 (1968).
8. S. C. Hsu, S. Chakravorty, and R. Mehrabian, *Metall. Trans. B*, **9**, 221 (1978).
9. R. P. Frankenthal and D. E. Thompson, in "Passivity of Metals," R. P. Frankenthal and J. Kruger, Editors, p. 262, The Electrochemical Society, Princeton, NJ (1978).
10. L. Papagno and R. Scarmozzino, *Thin Solid Films*, **75**, 221 (1981).
11. R. P. Frankenthal, *This Journal*, **114**, 542 (1967).
12. C. W. Draper, In preparation.
13. K. Meyer and W. Meier, *Kristall. Techn.*, **3**, 399 (1968).
14. H. M. Musal, in "Laser Induced Damage in Optical Materials," H. E. Bennett, A. J. Glass, A. H. Guenther, and B. E. Newnam, Editors, NBS Special Publication 568, p. 159 (1980).
15. H. J. Rocha and G. Lennartz, *Arch. Eisenhüttenw.*, **26**, 117 (1955).

Dissolved Metal Species Mechanism for Initiation of Crevice Corrosion of Aluminum

I. Experimental Investigations in Chloride Solutions

Kurt Hebert* and Richard Alkire**

Department of Chemical Engineering, University of Illinois, Urbana, Illinois 61801

ABSTRACT

Experiments on initiation of crevice corrosion were carried out on Al specimens in dilute aqueous NaCl solutions at ambient temperature. Transient current distributions within crevices were measured by a sectioned electrode technique, and microsampling was used to monitor dissolved aluminum, *p*H, and [Cl^-] composition changes within the crevice prior to breakdown. Auxiliary (noncrevice) experiments were carried out in solutions having various *p*H, [Cl^-], and dissolved aluminum concentration. Initiation was found to occur upon exceeding a minimum concentration of dissolved aluminum inside the crevice. Mechanisms for initiation based on acidification within the crevice were excluded.

Crevice corrosion occurs at restricted locations which are part of a metal structure, for example, at flange couplings and under gaskets. When such crevices are immersed in electrolyte solution, rapid corrosion may occur. This accelerated dissolution arises because the crevice restricts mass transport of dissolved corrosion products away from the metal surface. Consequently, the chemical composition of the crevice electrolyte changes with time; species which are aggressive to the metal surface accumulate there. The present work seeks to determine the specific change in crevice solution composition which causes breakdown of the initially protective oxide layer on the metal.

The system under study is aluminum in dilute aerated aqueous sodium chloride solution at room temperature. Although the crevice corrosion of aluminum in salt water has been noted in practical applications (1, 2), it is not as common or as destructive

* Electrochemical Society Student Member.
** Electrochemical Society Active Member.
Key words: corrosion, aluminum, chloride, crevice.

as, for example, crevice corrosion of steels or titanium alloys (3). However, previous work on the aluminum/chloride system by Siitari and Alkire (4) has identified it as an excellent model system for study of crevice corrosion initiation: the chemistry of the system is simple and it yields experimental results which are reproducible. The experimental and theoretical techniques developed in this work can, thus, be tested on aluminum/chloride before being applied to other, more complex, systems.

Several mechanisms have been proposed for breakdown in crevice corrosion, all of which involve three basic components alone or in combination: differential aeration, localized acidification, and migration of chloride ions into the crevice. It should be noted that the word "mechanism" as used here refers to events taking place in the crevice solution which lead to the "critical" aggressive solution for breakdown. In this work, "mechanism" is not associated with the surface reactions by which the aggressive solution destroys the protectiveness of the oxide film. For more complete reviews of the crevice corrosion literature, the reader is referred to works of France (3) and Rosenfeld (2). It should be noted that most of the crevice corrosion literature to date concerns stainless steels. While various metal/electrolyte systems have many features in common, one should exercise caution in extending these mechanisms to aluminum systems (4-6).

Historically, differential aeration was the first mechanism advanced for corrosion in occluded cells (7). However, the time of oxygen depletion is small compared to the initiation time (8-12), so that while deaeration of the crevice is not a cause of breakdown, it may be a prerequisite for activation. More recent models cite localized acidification within the crevice and chloride ion migration into the crevice as factors causing breakdown. Some investigators (9) interpret the effect of pH based on the kinetics of stainless steel in the active potential region. The work of Rosenfeld, Danilov, and Oranskaya (13) is especially promising for the acidification mechanism. *In situ* crevice potential measurements were coupled with measurements of the corrosion potential of stainless steel in solutions of various pH and chloride concentration, and the conclusion was drawn that acidification, and not chloride accumulation, is the dominant cause of breakdown. Many authors, including Fontana and Greene (11), hypothesize that a buildup of aggressive anions within the crevice is in part a cause of breakdown. Chloride ions migrate into the crevice to balance the otherwise increasingly positive charge owing to metal ion concentration. The procedure by which aggressive ions participate in the activation of the surface is unknown.

The above discussion indicates that the pH and chloride concentration in the crevice may play roles in the breakdown mechanism. However, the results of work like Rosenfeld's, which shows promise for stainless steels, may not apply to the aluminum system. It is, therefore, worthwhile to examine the aluminum corrosion literature to determine the possible effects of pH and chloride concentration on aluminum dissolution kinetics.

For comprehensive reviews of aluminum corrosion, the reader is referred to those of Kaesche (14, 15). Typical polarization curves for aluminum are found therein as well as in Ref. (16-20). In general, the anodic current density/potential curve for aluminum in nearly neutral chloride solutions consists of two branches, a horizontal branch near zero current density, and a near-vertical branch at the critical pitting potential, E_p. The fundamental meaning of E_p is a subject of much controversy. It is generally thought that E_p depends on chloride ion concentration in a logarithmic fashion, and that it is independent of pH (14). For aluminum crevice corrosion, pH is not a likely candidate for the activating agent because, in the range of pH values expected within crevices before breakdown, the aluminum dissolution kinetics are independent of pH. According to Kaesche, the passive current density in basic chloride solutions increases with pH, but it becomes negligible in neutral solutions (14). This conclusion has been confirmed with polarization curves on aluminum in 0.05M NaCl solutions of pH 3-6 (19).

The reported dependence of aluminum dissolution kinetics on chloride concentration also contradicts the chloride migration mechanism of breakdown. The empirical dependence of E_p on chloride concentration

$$E_p = A - B \log [Cl^-] \quad [1]$$

where a typical value of B is 0.12V (21), ($[Cl^-]$ taken in M). If there were significant chloride accumulation prior to breakdown, Eq. [1] would predict that the electrode potential within the crevice would decrease steadily after immersion of the crevice, and that the measured current density would therefore rise steadily. However, the observed behavior is that both potential and current density are constant before breakdown, and then change sharply. Furthermore, the accumulation of chloride ion within the crevice may actually be quite small, since before breakdown the potential difference between the crevice and the open metal is on the order of 5 mV. Siitari (5) measured the average chloride concentration within the crevice after breakdown, and found that it had risen to 0.07M from the initial concentration of 0.05M. Equation [2] predicts that the change in E_p would have been only 18 mV, while the observed change in the crevice potential after breakdown was 60 mV. Thus, chloride migration alone cannot explain observed current density and potential behavior.

Since both chloride migration and local acidification have been discounted as sole causes of breakdown, other possibilities must be considered. In 1959, Hagyard and Santhiapillai (22) discovered that upon immersion of an aluminum specimen in 0.1*N* stoichiometric aluminum chloride solution (pH 3.5), the corrosion potential remained constant for about 1 hr, and then fell 200 mV within 15 min. Aluminum in a sodium chloride solution adjusted to the same pH did not become active but remained at the initial potential for at least 2.5 hr. This behavior could certainly account for breakdown in aluminum crevice corrosion. That is, during the prebreakdown period, the concentration of dissolved aluminum in the crevice may become large enough to activate the metal surface in this fashion. If it does, it would explain the observed rapid changes in potential and current density. The corrosion of aluminum in aluminum salts has also been studied by Sotoudeh *et al.* (23).

The present work, the activating effect of aluminum chloride solutions is explored further (19). On the basis of measurement of [Al], $[Cl^-]$, and pH within a crevice, and of measurements of the effects of these factors on aluminum dissolution kinetics, a mechanism is proposed for the initiation of crevice corrosion of aluminum. This mechanism is, then, incorporated into a mathematical model of crevice corrosion initiation described in the paper which follows. The model includes all effects considered in that of Siitari (5). as well as the hydrolysis equilibrium of Al^{+3} ions and migration of Al^{+3}, H^+, Na^+, Cl^-, and hydrolyzed aluminum ions. To test the accuracy of the initiation mechanism, the model is compared to experimental transient current density distribution measurements.

Experimental Details

The metal/electrolyte system studied in this work was Al in 0.05M NaCl. To keep the chemistry of the system simple, there were no buffers or inhibitors in the electrolyte, and no alloying elements in the metal. The electrolyte concentration was low so that dilute

solution theory could be used in the model. Aluminum was selected for study in preference to iron because it gave superior reproducibility in crevice corrosion experiments (4-6). The electrode material was 99.9% purity aluminum (Research Organic/Inorganic Chemical Corporation). Specimens were polished down to 0.3μ alumina following procedures given elsewhere (4, 5, 19).

All electrolytes were prepared from analytical grade reagents and deionized-distilled water stored in a tin-lined receiver. The solutions used in crevice corrosion experiments were not preaerated. In the kinetic studies, solutions were deaerated by bubbling nitrogen (Linde Dry Grade) through them for at least 1 hr before the experiment.

For the purpose of determining the effect of solution composition on the kinetics of the aluminum electrode, experiments were carried out in solutions of controlled composition. These experiments were similar to those of Hagyard and Santhiapillai (22), in which the corrosion potential of the aluminum electrode was monitored as a function of time. The corrosion potential, though, was determined by the kinetics of both anodic and cathodic reactions, and it was desired to isolate the anodic reaction. Therefore, a constant current density of 32 μA/cm^2 was applied to the electrode. This current density was chosen to greatly exceed the expected cathodic reaction current densities, so that cathodic kinetics would play no role in determining the measured electrode potential. The galvanostatic polarization also mimics conditions within the crevice, where the aluminum metal is poised at constant current by oxygen reduction outside the crevice. To increase the knowledge gained about the anodic kinetics, potentiodynamic polarization curves at 1.0 mV/sec were measured both before and after activation of the metal. Many workers prefer to use a potentiostatic technique to measure polarization curves in pitting systems. However, the potential scan rate used in this work should have no effect on the qualitative shape of the i/E curve, and is, then, sufficient for this study (17).

The controlled solution experiments were carried out with an aluminum working electrode, platinum flag counterelectrode, saturated calomel reference electrode (Corning Glass Works, Ct. No. 476109), pH electrode (Orion 91-05 combination pH electrode), and gas dispersion tube for deaeration with nitrogen. The aluminum electrode was constructed from an aluminum disk of 0.64 cm diam embedded with epoxy in a Plexiglas tube. The disk was cut from the same 99.9% Al specimen used for the sectioned electrodes.

The crevice corrosion cell used in this work was developed originally by Siitari (5) and only its salient features are discussed here. Figure 1 shows the cell, which was fashioned from a microscope stand. The crevice is the clearance between the metal electrode surface and the bottom surface of a Plexiglas cylinder (⅞ in. diam) fixed to the lens mount of the microscope. A photograph of the sectioned aluminum electrode is shown in Fig. 2, where the dimensions of the electrode sections are given in the caption. The sections of the metal electrode were connected to a set of operational amplifier current followers (Analog Devices 233K, chopper stabilized with 10^5 Ω feedback resistors). The voltage signals from the current followers were measured with a multipoint recorder (Leeds and Northrup, Speedomax W).

Samples of the crevice solution were taken through a polyethylene tube (PE 50, inner diameter 0.023 in.) embedded in the center of the upper surface. The first 10 μl of solution was rejected since the volume of the sampling tube was 11 μl. A sample of 25 μl was then withdrawn. Samples were analyzed for aluminum and chlorine by neutron activation. Ion-sensitive electrode measurements were also made with commercial miniature reference and pH electrodes (Microelectrodes, MI-401 and MI-405). Because a typical crevice volume was about 60 μl, and since the measurement techniques required a minimum sample size of 25 μl, an experiment was stopped after withdrawing one sample. To obtain information on the crevice solution composition as a function of time, experiments of varying durations were carried out, and samples taken at the end of each. This method required that the experiments be quite reproducible, a condition that was met in this work.

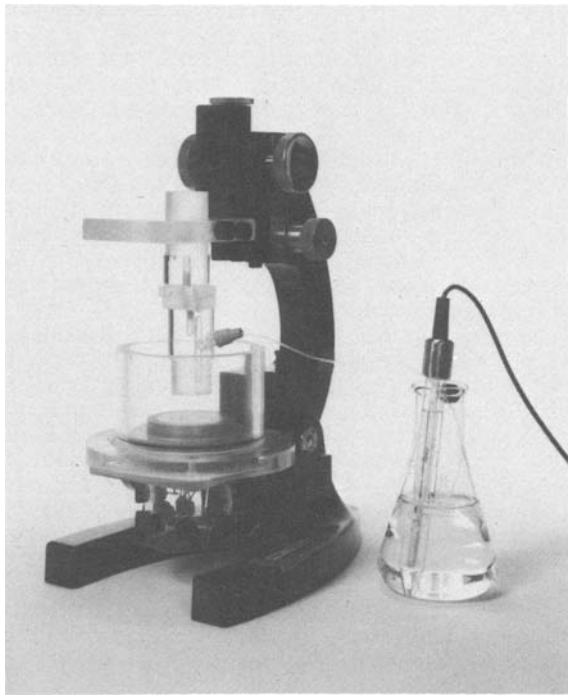

Fig. 1. Crevice corrosion cell described in detail in Ref. (5)

Experimental Results and Discussion

Experiments on aluminum in controlled solutions.— In most of the following experiments, the aluminum electrode was immersed in test solutions and anodically polarized at 32 μA/cm^2. The electrode potential was monitored as a function of time. The principal aim of these experiments was determination of the range of solution compositions which can activate the

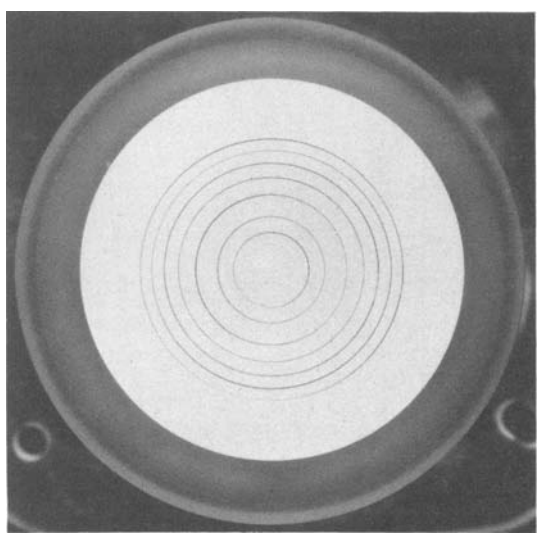

Fig. 2. Sectioned electrode, showing concentric sections separated by thin insulating rings. Outer diameters of the sections are 0.719, 1.02, 1.44, 1.77, 2.04, 2.29, 2.51, and 4.19 cm

aluminum electrode. Results of polarization measurements on aluminum are also reported in this section.

Figure 3 shows the results of the base case controlled solution experiment. The solution (0.05*N* $AlCl_3$, pH 3.9) was deaerated and stirred during the experiment. After the electrode was placed in solution, there was a rapid increase in potential from −0.82 to −0.66V (all potentials are referenced to SCE). The potential remained near this value for about 30 min (the induction time), and, then, gradually fell to −0.76V. The results of an experiment carried out under identical conditions, also given in Fig. 3, show this behavior is reproducible.

To confirm the results of Hagyard and Santhiapillai (22), a potential transient was measured in 0.05*N* HCl adjusted to pH 3.9 by addition of NaOH. All conditions were the same as those of the base case experiment, except that the test solution contained no aluminum. Figure 3 displays the results of this experiment. The potential did not become active, but remained at −0.66V. It is concluded that the presence of dissolved aluminum is a prerequisite for activation.

To determine the specific effect of activation on aluminum dissolution kinetics, polarization curves, at 1.0 mV/sec, were measured on the aluminum electrode both before and after activation. These curves appear in Fig. 4. Note that the conditions at which these curves were taken differ from those of the previous sections: the solution is aerated and quiescent, rather than deaerated and stirred. However, it is shown elsewhere (19) that these conditions should not alter the potential/time curves. The polarization measurements show that activation changes the form of the current/potential curve: it is not simply a change in the pitting potential.

The postactivation polarization curve is corroborated by results reported by De Micheli (20). A stationary-potential polarization curve was measured in deaerated 0.10*N* $AlCl_3$ solution. As shown in Fig. 5, its form was quite similar to that of the results reported here.

As mentioned above, the potential/time transients have a unique shape: a sharp rise in potential, followed by an induction time in which the potential falls to the active potential. The rise in potential upon immersion may be explained by the two polarization curves shown in Fig. 6. Both curves were measured in a 0.05*N* Cl^- medium at *p*H 4.1 and were taken at 1.0 mV/sec. One curve was taken immediately after the electrode was placed in solution; the other was measured 1 hr after immersion. It is seen that the passive current density is quite large (about 100 $\mu A/cm^2$) when the electrode is immersed, but decreases to about zero current after 1 hr. The passive current density is determined by the rate of anodic reaction through the oxide

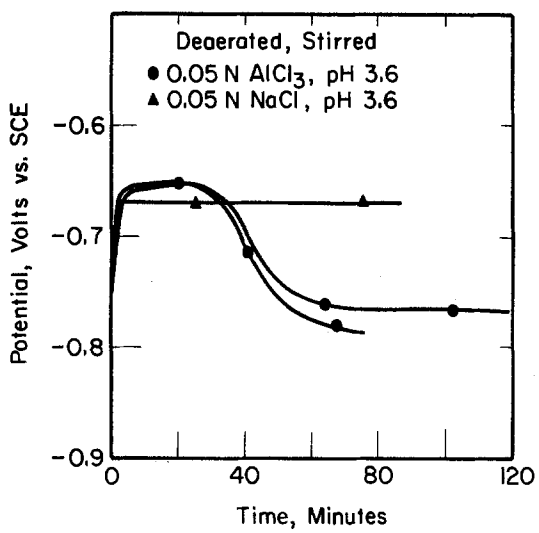

Fig 3. Galvanostatic dissolution of Al in deaerated stirred solutions

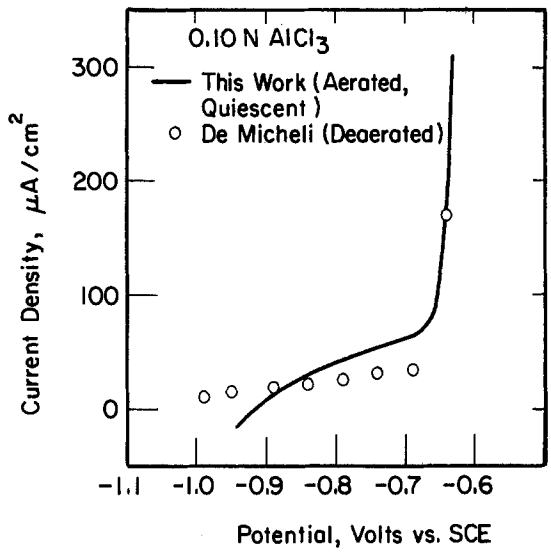

Fig. 5. Comparison of aluminum polarization curve (potential scanned at 1.0 mV/sec) with results of De Micheli (18).

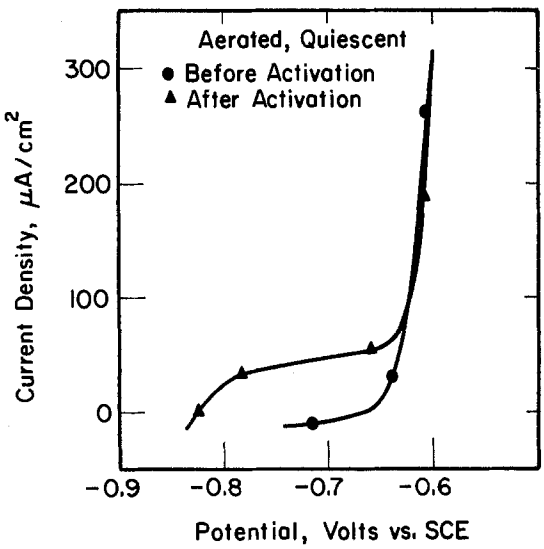

Fig 4. Polarization curves of Al electrode before and after activation in $AlCl_3$ solution (potential scanned at 1.0 mV/sec).

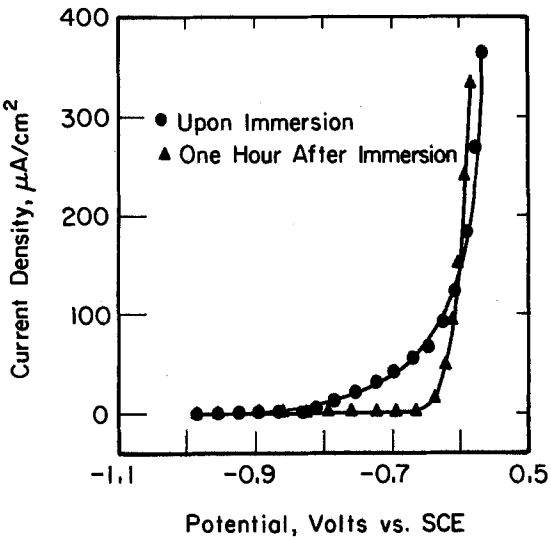

Fig. 6. Effect of immersion time on aluminum polarization curve (potential scanned at 1.0 mV/sec).

layer, and, according to Kaesche (15), the air-formed oxide is "sealed" after immersion in aqueous solution by formation of hydroxide on top of the oxide. Thus, while this process takes place, the passive current drops, causing the potential at $i = 32$ $\mu A/cm^2$ to rise rapidly to the pitting potential.

In order to establish that dissolved aluminum is responsible for breakdown in crevice corrosion, it was necessary to determine the lowest aluminum concentration which activated the electrode. Figure 7 gives the results of three controlled solution experiments: aluminum in solutions of 0.005*N* Al, 0.025*N* Al, and the base case experiment, 0.05*N* Al. In all three experiments, the solution was deaerated and stirred, and the chloride ion concentration was kept at 0.05*N* by addition of NaCl. The pH of the three solutions was not controlled but was determined by hydrolysis alone. The results show that the induction time, but not the active potential, was strongly affected by aluminum concentration. In the 0.025*N* Al solution, the steady active potential of −0.76V was reached after about 2 hr, compared to half that time in the 0.05*N* Al solution. The 0.005*N* Al solution experiment showed no potential change at all after 2 hr. Each of these experiments was repeated, and the reproducibility of results was found to be good. Thus, it was concluded that the minimum aluminum concentration for activation is between 0.005 (2×10^{-3}M) and 0.025*N* (8×10^{-3}M).

If accumulation, by migration, of chloride ions within the crevice is significant, it is possible that the activation behavior would depend upon [Cl^-]. To test for this possibility, the experiments were carried out with the chloride concentration doubled to 0.10*N* by addition of NaCl. The results are displayed in Fig. 8. It is seen that the behavior in the 0.025*N* and 0.05*N* Al solutions was largely unaffected, except that in the latter solution, the active potential was decreased to 0.84V. However, the 0.005*N* Al, 0.10*N* Cl solution activated the electrode, while the 0.005*N* $AlCl_3$ solution did not. Evidently, increased chloride concentrations in the crevice may affect the critical aluminum concentration for breakdown. Based on the chloride measurement of Siitari (5) though, it is doubtful that migration alone can increase the chloride concentration by a factor of two.

Evidently, activation is a reaction on the metal surface which involves aluminum species in solution. If the reaction is fast, the concentration of dissolved aluminum close to the metal surface may differ significantly from the bulk aluminum concentration. Concentration gradients may also arise from the electrochemical dissolution of aluminum at constant current.

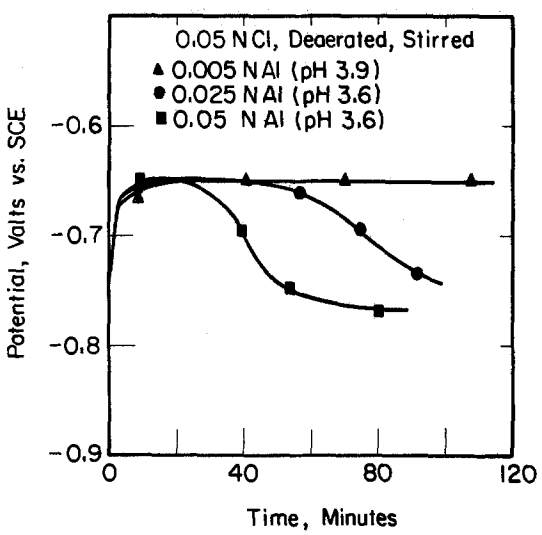

Fig. 7. Effect of dissolved aluminum concentration on activation of aluminum specimen.

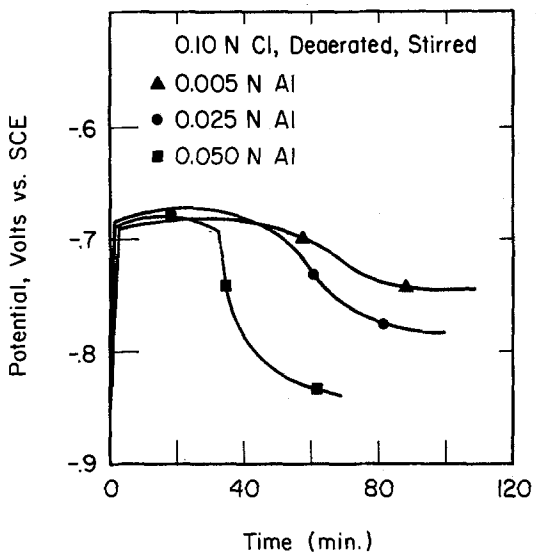

Fig. 8. Effect of chloride ion concentration on activation of aluminum specimen.

Thus, it will be difficult to relate the activation behavior of the electrode to the known bulk concentration. A concentration boundary layer can be detected by noting the effect of stirring on the time needed for activation to occur: if a concentration gradient exists, the rate of the activation reaction should be enhanced by an increased mass transport rate at the surface. Therefore, an experiment was carried out in deaerated, unstirred 0.05*N* $AlCl_3$. The induction time was about 10 min longer than for the experiments with stirring. Given the accuracy of these experiments, however, the difference is not large enough to conclude that mass transfer control exists. It will be assumed that the surface and bulk concentration of dissolved aluminum are the same.

In his crevice corrosion experiments, Siitari (4, 5) noticed that once the breakdown process had begun, its subsequent progress was unaffected when the crevice was temporarily raised and the solution stirred. This behavior indicates that the activation process is in a sense irreversible, that the electrode does not immediately deactivate when the solution concentrated in aluminum is washed away, and the nonaggressive bulk solution is introduced.

Crevice corrosion experiments.—The foregoing experiments have established that the aluminum electrode becomes active when the solution contains dissolved aluminum in excess of a critical concentration of between 2×10^{-3}M and 8×10^{-3}M Al. They also demonstrated that a chloride concentration buildup inside the crevice, if significant, would lower this critical concentration. In this section, results of aluminum and chloride concentration measurements within a crevice are presented. If the dissolved aluminum mechanism of breakdown is correct, the aluminum concentration should be within the range specified above just before breakdown. The chloride measurements assess the importance of chloride migration in the breakdown mechanism.

Figures 9 and 10 show the aluminum and chloride concentration measurements. The data in both figures are scattered. The sampling technique relied on the reproducibility of the crevice corrosion experiments; this is one possible source of error.

In spite of the scatter, some conclusions may be drawn from the data. In the crevice corrosion experiments done by Siitari under identical conditions [Fig. 24 in Ref. (5)], breakdown occurs at 6 hr under the conditions of our experiments. The projected aluminum concentration at breakdown is about 3×10^{-3}M Al which falls within the range of possible values for

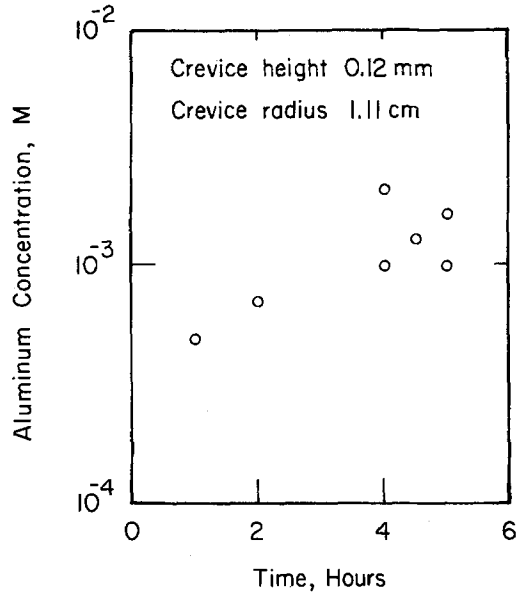

Fig. 9. Dissolved aluminum concentration found in crevices prior to breakdown.

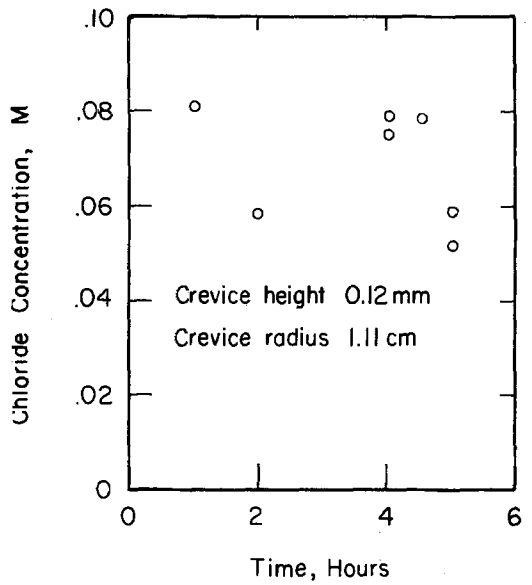

Fig. 10. Average chloride ion concentration found in crevices prior to breakdown.

the critical concentration. Thus, the sampling results are promising for the dissolved aluminum breakdown mechanism.

The chloride measurements are even less precise than the aluminum measurements, but two conclusions can be drawn. First, these data place an upper limit on the accumulation of chloride before breakdown, an increase of about 40%. This value seems rather high, however, since Siitari measured an increase of only 20% after breakdown, when the rate of migration would become much larger. Second, the data show no clear rise in chloride concentration, as did the aluminum data. The data are scattered around a constant average concentration of 0.066M. Thus, it is possible that the concentration increase observed reflects an offset error more than an accumulation by migration.

It is not clear whether the limiting 40% increase in chloride concentration is sufficient to affect the activation behavior of the aluminum electrode. For the purposes of the following mathematical model, it will be assumed that the chloride concentration is not a variable in determining breakdown behavior.

Table I. Crevice pH measurements

Time, hr	pH
2	4.2
2	4.3
3	4.6

The pH of solution within the crevice was meaured as reported in Table I. The measurements fall within the general range of Siitari's pH measurements (5). The pH of the bulk 0.05*N* NaCl solution was about 5.5; thus, there is appreciable acidification of the crevice electrolyte before breakdown.

Conclusions

In order to determine the conditions responsible for activation of aluminum metal within a crevice, an aluminum electrode was exposed to a number of simulated crevice solutions. The change in electrode kinetics upon exposure to these environments of various pH, [Cl^-], and [Al] was monitored with galvanostatic and potentiostatic experiments. Acidification alone had no effect on the electrode. The metal became activated in solutions containing greater than a critical concentration of aluminum. This critical concentration has some dependence on the chloride concentration of the solution. Mechanisms for crevice corrosion initiation based on hydrogen or chloride ion buildup are, therefore, excluded. In addition, further experiments (19) showed that the presence of oxygen in solution does not hinder the activation process, so deaeration of the crevice is not a precondition for breakdown.

Aluminum and chloride concentrations were measured in a crevice during the initiation period prior to breakdown. The aluminum concentration at breakdown agreed with the critical value previously established. The chloride concentration in the crevice increased by no more than 40% over that in the bulk solution.

In the accompanying paper, a mathematical model for the initiation of crevice corrosion is presented for the aluminum/chloride system. The model incorporates a critical aluminum concentration as its mechanism for breakdown. Through comparison with crevice corrosion experiments (4, 5), the dissolved aluminum mechanism is further tested in the following paper, and the significance of chloride accumulation is assessed.

Acknowledgments

This work was supported by the National Science Foundation (Grant NSF-DMR 77-28285) and by the fellowships from National Steel Corporation and from Gulf Oil Chemicals. Computer costs were assisted by the Research Board of the University of Illinois.

Manuscript submitted March 30, 1982; revised manuscript received *ca.* Jan. 12, 1983. This was Paper 144 presented at the Denver, Colorado, Meeting of the Society, Oct. 11-16, 1981.

Publication costs of this article were assisted by University of Illinois at Urbana-Champaign.

REFERENCES

1. H. P. Godard, W. B. Jepson, M. R. Bothwell, and R. L. Kane, "The Corrosion of Light Metals," John Wiley and Sons, New York (1967).
2. I. L. Rosenfeld, in "Localized Corrosion," R. W. Staehle *et al.*, Editors, p. 373, NACE, Houston (1974).
3. W. D. France, in "Localized Corrosion—Cause of Metal Failure," ASTM STP 516, p. 164, American Society for Testing and Materials, Philadelphia (1972).
4. D. W. Siitari and R. C. Alkire, *This Journal*, **129**, 481 (1982).
5. D. W. Siitari, Ph.D. Dissertation, University of Illinois at Urbana-Champaign, Urbana, IL (1979).

6. R. Alkire and D. Siitari, *This Journal*, **129**, 488 (1982).
7. U. R. Evans, *J. Inst. Met.*, **30**, 239 (1923).
8. I. L. Rosenfeld and I. K. Marshakov, *Corrosion*, **20**, 115 (1964).
9. G. Karlberg and G. Wranglen, *Corros. Sci.*, **11**, 499 (1971).
10. J. W. Oldfield and W. H. Sutton, *Br. Corros. J.*, **13**, 104 (1978).
11. M. G. Fontana and N. D. Greene, "Corrosion Engineering," McGraw-Hill, New York (1978).
12. R. R. Salem, E. M. Zaretskii, and I. Ya. Klinov, *Trudy Moskov. Inst. Khim. Mashinostroenie*, **22**, 60 (1960).
13. I. L. Rosenfeld, I. S. Danilov, and R. N. Oranskaya, *This Journal*, **125**, 1729 (1978).
14. H. Kaesche, in "Passivity of Metals," R. P. Frankenthal and J. Kruger, Editors, p. 935, The Electrochemical Society, Princeton, NJ (1978).
15. H. Kaesche, in "Localized Corrosion," R. W. Staehle *et al.*, Editors, p. 516, NACE, Houston (1974).
16. R. Ergang, G. Masing, and M. Möhling, *Z. Elektrochem.*, **56**, 8 (1952).
17. A. Broli and H. Holtan, *Corros Sci.*, **13**, 237 (1973).
18. B. N. Stirrup, N. A. Hampson, and I. S. Midgely, *J. Appl. Electrochem.*, **5**, 229 (1975).
19. K. R. Hebert, M.S. Thesis, University of Illinois at Urbana-Champaign, Urbana, IL (1981).
20. S. M. De Micheli, *Corros. Sci.*, **18**, 605 (1978).
21. J. R. Galvele, in "Passivity of Metals," R. P. Frankenthal and J. Kruger, Editors, p. 285, The Electrochemical Society, Princeton, NJ (1978).
22. T. Hagyard and J. R. Santhiapillai, *J. Appl. Chem.*, **9**, 323 (1959).
23. K. Sotoudeh, T. H. Nguyen, R. T. Foley, and B. F. Brown, *Corrosion*, **37**, 358 (1981).

Dissolved Metal Species Mechanism for Initiation of Crevice Corrosion of Aluminum

II. Mathematical Model

Kurt Hebert* and Richard Alkire**

Department of Chemical Engineering, University of Illinois, Urbana, Illinois 61801

ABSTRACT

A mathematical model for the initiation of crevice corrosion was developed based on the hypothesis that, for Al in 0.05*N* NaCl, initiation occurs when the concentration of dissolved metal exceeds a certain minimum critical value. This hypothesis was tested experimentally in the preceding qualitative paper. The model accounts for crevice geometry; for electrode reactions of aluminum, oxygen, and hydronium ion; for homogeneous hydrolysis equilibria; and for transport by unsteady-state diffusion and migration. The predictions of the model, made with use of literature data for all parameters, were found to compare favorably with experimental observations reported in the previous paper. The model predicts rapid depletion of O_2 and rapid acidification of the crevice solution, followed by the gradual buildup of dissolved metal species which eventually trigger breakdown. The model also predicts that there is negligible accumulation of Cl^- within the crevice prior to breakdown.The model accurately predicts the influence of crevice geometry upon breakdown time.

Crevice corrosion is one of the most commonly encountered forms of localized corrosion. It occurs on shielded regions of metal surface which are in contact with small volumes of electrolytic solution. After immersion in solution, dissolved corrosion products accumulate in the crevice, since the crevice impedes transport away from the metal surface. The resulting change in solution composition somehow leads to the acceleration of corrosion in the crevice.

Several investigators have observed events following the formation of a crevice (1-8). The onset of rapid corrosion, called breakdown, occurs after an induction time of several hours. The geometry of the crevice is found to exert a significant effect on the length of the initiation time (1, 3). This result may be explained by the idea that breakdown occurs when a critical concentration of some aggressive species is exceeded inside the crevice (4, 9, 10). The time required to generate this critical concentration is, then, determined by the relative rates of dissolution within the crevice and transport out of the crevice, both of which depend on crevice geometry. With knowledge of the reaction and transport processes and the critical species responsible for breakdown, the initiation period of crevice corrosion may be mathematically modeled.

Alkire and Siitari (9) designed a mathematical model for comparison with their experiments on the aluminum/sodium chloride system. Their experimental corrosion cell had been built so that one-dimensional transport equations and simple initial and boundary conditions could be used in the model. Also, the authors employed accurate mathematical expressions for transport in the crevice and cathodic reaction kinetics. The breakdown mechanism used in the model was based on a critical pH of the crevice solution, and the predicted initiation times were about one-half of those observed in experiments. The results of the model, thus, pointed to the need for improved understanding of the mechanism of breakdown.

The experiments of Hebert and Alkire (11) aimed at elucidation of the activation mechanism. It was found that, in $AlCl_3$/NaCl solutions with an aluminum molarity greater than about 2×10^{-3}, the potential of aluminum dissolution became more active. This concentration compared favorably with the aluminum concentration measured in a crevice just prior to breakdown. In addition, it was observed that acidification of a sodium chloride solution did not activate the aluminum electrode, so that pH alone cannot be the agent of breakdown. Rather, they concluded that crevice corrosion was initiated by concentration in the crevice electrolyte of dissolved aluminum.

The model presented in this paper differs from that of Alkire and Siitari principally in its incorporation of the dissolved aluminum mechanism of breakdown. The initiation times predicted by the present model for various crevice geometries are compared to the results of the corresponding experiments of Siitari and Alkire (1). The model, thus, serves as an independent check of the proposed initiation mechanism, which was tested experimentally with measurements of the crevice alu-

* Electrochemical Society Student Member.
** Electrochemical Society Active Member.
Key words: corrosion, model, aluminum, crevice, chloride.

minum concentration. This confirmation is important, since the crevice sampling measurements were relatively imprecise. In addition, the model is used to evaluate the significance of accumulation of chloride ion in the crevice by migration, a question which was not resolved experimentally in previous work.

The mathematical model was employed in this study as a quantitative instrument for testing scientific hypotheses of mechanism. However, a successful mathematical model is also an end in itself: once firmly established, it can be applied to predict behavior in conditions different from those for which experimental data are available. A model like the one presented here can determine *a priori* whether or not a given crevice geometry and environment is susceptible to localized corrosion.

Theoretical Model

The sequence of events leading to the inception of crevice corrosion begins with the formation of the crevice, which is shown schematically in Fig. 1. Before the crevice is formed, the aluminum surface is corroding uniformly at a low rate. Anodic aluminum dissolution

$$Al \rightarrow Al^{+3} + 3e^- \qquad [1]$$

proceeds everywhere at the same local current density as the cathodic reactions, hydrogen ion reduction, and oxygen reduction

$$H^+ + e^- \rightarrow \tfrac{1}{2} H_2 \qquad [2]$$

$$O_2 + 4H^+ + 4e^- \rightarrow 2H_2O \qquad [3]$$

As corrosion within the crevice progresses, aluminum species are concentrated in the crevice, and oxygen is depleted from it. When cathodic reactant has, thus, been removed from the crevice, there results a net anodic reaction within the crevice, which is balanced by oxygen reduction on outside metal. Chloride ions migrate into the crevice in response to the potential gradient which now exists. The hydrolysis of aluminum ions

$$Al^{+3} + nH_2O \leftrightarrows Al(OH)_n^{+3-n} + nH^+ \qquad [4]$$

causes acidification of the crevice. Eventually, the aluminum concentration at some point may exceed the critical concentration for activation, as described in more detail in the preceding paper. If this occurs, breakdown is initiated.

Some features present in the experimental system are omitted or simplified in the following mathematical model. The major assumptions implied in the model equations are: (*i*) The potential and species concentrations at the edge of the crevice are at the uniform corrosion potential and bulk concentrations, respectively. This assumption should introduce little error, since before breakdown the current densities arising in crevices are quite low. Also, the form of the potential boundary condition used here allows direct comparison with cathodic protection experiments, in which the potential at the crevice edge is controlled. (*ii*) The hydrolysis behavior of the model is idealized in that only one hydrolysis reaction is included ($n = 1$), and that reaction is assumed to be instantaneous, so that equilibrium is always in effect

$$K_h = \frac{[Al(OH)_n^{+3-n}]\,[H^+]^n}{[Al^{+3}]} \qquad [5]$$

(*iii*) The experimental crevice exhibits radial symmetry and has a large diameter-to-height ratio (0.56 cm/0.0015 cm = 400 in the experiments of Ref. (1)). Hence, the model includes spatial variations only in the radial direction. Also, the geometry of the crevice is unaffected by dissolution during the time span of the model. (*iv*) Only the period prior to breakdown is considered; after breakdown, the above assumptions are no longer valid. This restriction is permissible, because this work focuses on the cause of breakdown.

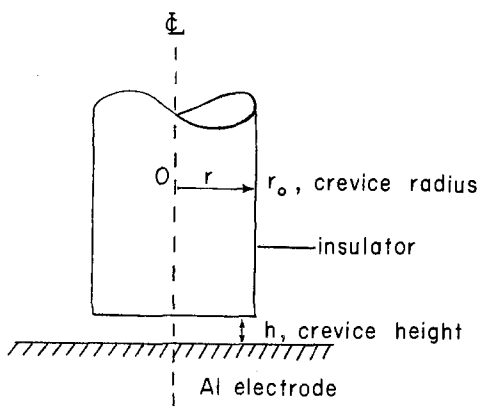

Fig. 1. Geometry and coordinate system of theoretical model

The model geometry and coordinate system is given in Fig. 1. In the equations listed below, the dependent variables are $[Al^{+3}]$, $[H^+]$, $[O_2]$, $[Al(OH)_n^{+3-n}]$, $[Na^+]$, $[Cl^-]$, and the electrode potential, ϕ.

The kinetic rate expressions for aluminum dissolution, hydrogen reduction, and oxygen reduction are

$$j_1 \begin{cases} = A\,(\phi - \phi_{R1}) & ;\ \phi \geqq \phi_{R1} \\ = 0 & ;\ \phi < \phi_{R1} \end{cases} \qquad [6]$$

$$j_2 \begin{cases} = -\,i_{0,2}\dfrac{c_2}{c_{2,0}} \exp\left\{\dfrac{-\alpha_2 \mathbf{F}}{RT}(\phi - \phi_{R2})\right\} & ;\ \phi \leqq \phi_{R2} \\ = 0 & ;\ \phi > \phi_{R2} \end{cases} \qquad [7]$$

$$j_3 \begin{cases} = -\,i_{3,0}\dfrac{c_3}{c_{3,0}} \exp\left\{\dfrac{-\alpha_3 \mathbf{F}}{RT}(\phi - \phi_{R3})\right\} & ;\ \phi \leqq \phi_{R3} \\ = 0 & ;\ \phi > \phi_{R3} \end{cases} \qquad [8]$$

The kinetics of the hydrogen and oxygen reduction reactions are assumed to follow the Tafel form; the expression for the aluminum corrosion kinetics is taken from typical polarization curves in neutral and mildly acidic solutions (12-14). In this pH range, dissolution of aluminum below ϕ_{R1}, the pitting potential, is negligible (15). Also, only prebreakdown behavior is of interest, so the enhanced dissolution below ϕ_{R1} in concentrated aluminum solutions is neglected. Above ϕ_{R1}, linear kinetics are assumed, since, as will be seen below, the potential range before initiation is within a few mV of ϕ_{R1}. The parameter A is determined from experimental polarization curves (12). The hydrogen reaction kinetic parameters are uncertain, because, in the range of potentials inside the crevice, the hydrogen reaction is obscured by aluminum dissolution. The oxygen reaction parameters were chosen so that the calculated potential of uniform corrosion is in agreement with the corresponding experimental value.

The partial differential equations resulting from the species balances for Al^{+3}, H^+, O_2, $Al(OH)_n^{+3-n}$, Na^+, and Cl^- are listed below

Al^{+3}, $Al(OH)_n^{+3-n}$

$$\frac{\partial c_1}{\partial t} + \frac{\partial c_4}{\partial t} = D_1 \nabla^2 c_1 + D_4 \nabla^2 c_4 + \frac{\nu_{11} a}{n_1 \mathbf{F}} j_1 \qquad [9]$$

H^+, $Al(OH)_n^{+3-n}$

$$\frac{\partial c_2}{\partial t} - n\frac{\partial c_4}{\partial t} = D_2\nabla^2 c_2 - nD_4\nabla^2 c_4 - \frac{\nu_{22}a}{n_2\mathbf{F}}j_2 - \frac{\nu_{23}a}{n_3\mathbf{F}}j_3 \quad [10]$$

O_2

$$\frac{\partial c_3}{\partial t} = D_3\nabla^2 c_3 - \frac{\nu_{33}a}{n_3\mathbf{F}}j_3 \quad [11]$$

Cl^-

$$\frac{\partial c_5}{\partial t} = -\mathbf{F}u_5c_5\nabla^2\phi - \mathbf{F}u_5\frac{\partial c_5}{\partial r}\frac{\partial \phi}{\partial r} + D_5\nabla^2 c_5 \quad [12]$$

Na^+

$$\frac{\partial c_6}{\partial t} = \mathbf{F}u_6c_6\nabla^2\phi + \mathbf{F}u_6\frac{\partial c_6}{\partial r}\frac{\partial \phi}{\partial r} + D_6\nabla^2 c_6 \quad [13]$$

These conservation equations account for unsteady-state behavior involving diffusion, migration, and reaction by both homogeneous and heterogeneous processes. The diffusion and migration fluxes are written in accordance with the theory of infinitely dilute solutions. Conductivities predicted by dilute solution theory were found to agree with literature values for NaCl concentrations near 0.05M (12, 16, 17). An additional variable, the instantaneous rate of the hydrolysis reaction, has been eliminated by adding the $Al(OH)_n^{+3-n}$ species balance to that for Al^{+3}, and by subtracting the $Al(OH)_n^{+3-n}$ species balance from the H^+ balance. The set of equations is closed with the hydrolysis equilibrium relation, (5), and the electroneutrality relation

$$0 = \sum_i z_ic_i \quad [14]$$

The initial conditions are

$$c_i = c_{i,0}; \quad i = 1, 6$$
$$\phi = \phi_0 \quad [15]$$

$c_{1,0}$, $c_{2,0}$, $c_{3,0}$, $c_{5,0}$, and $c_{6,0}$ are fixed by experimental conditions. $c_{4,0}$ is calculated from $c_{1,0}$, $c_{2,0}$, and the hydrolysis equilibrium relation. The potential of uniform corrosion, ϕ_0, is calculated from the condition of no net electrode current density

$$j_1(\phi_0) + j_2(\phi_0, c_{2,0}) + j_3(\phi_0, c_{3,0}) = 0; \quad t = 0 \quad [16]$$

The boundary conditions at $r = 0$ are radial symmetry

$$\frac{\partial c_i}{\partial r} = 0; \quad i = 1, 6$$
$$\frac{\partial \phi}{\partial r} = 0 \quad [17]$$

At $r = r_0$, the edge of the crevice, the boundary conditions are

$$c_i = c_{i,0}; \quad i = 1, 6$$
$$\phi = \phi_0 \quad [18]$$

Breakdown is triggered in the model by exceeding a critical aluminum concentration within the range identified by experiment (11). The activation of the aluminum metal in the crevice at breakdown is represented by a decrease in ϕ_{R1}, the aluminum rest potential. This representation is artificial, since the alteration of the Al polarization curve is more complex than a simple shift in ϕ_{R1} (11). In order to predict the crevice behavior during breakdown, it would be necessary to obtain more knowledge on the effect of dissolved aluminum on aluminum dissolution kinetics below the pitting potential. However, this information was not sought in this work: only the time of breakdown was considered to be of interest.

Dimensionless equations.—In reducing the mathematical model equations to dimensionless form, the following variables are defined

$$R = \frac{r}{r_0} \quad \tau = \frac{tD_1}{r_0^2} \quad \Phi = \frac{\phi - \phi_{R1}^0}{\phi_0 - \phi_{R1}^0}$$
$$C_i = \frac{c_i}{c_{i,0}} \quad [19]$$

Upon insertion of these expressions into the dimensional equations, the following set of dimensionless model equations is formed

$$\frac{\partial C_1}{\partial \tau} + H_1\frac{\partial C_4}{\partial \tau} = \nabla^2 C_1 + \pi_4 H_1\nabla^2 C_4 + \nu_{11}\chi_{11}(\Phi - \Phi_{R1}) \quad [20]$$

$$\frac{\partial C_2}{\partial \tau} - nH_2\frac{\partial C_4}{\partial \tau} = \nabla^2 C_2 - n\pi_4 H_2\nabla^2 C_4 + \nu_{23}\chi_{23}\delta_3 C_3\, e^{-\zeta_3\Phi} + \nu_{22}\chi_{22}\delta_2 C_2^{\alpha_2+1}\, e^{-\zeta_2\Phi} \quad [21]$$

$$\frac{\partial C_3}{\partial \tau} = \pi_3\nabla^2 C_3 - \nu_{33}\chi_{33}\delta_3 C_3\, e^{-\zeta_3\Phi} \quad [22]$$

$$\frac{\partial C_5}{\partial \tau} = -\epsilon_5 C_5\nabla^2\Phi - \epsilon_5\frac{\partial C_5}{\partial R}\frac{\partial \Phi}{\partial R} + \pi_5\nabla^2 C_5 \quad [23]$$

$$\frac{\partial C_6}{\partial \tau} = \epsilon_6 C_6\nabla^2\Phi + \epsilon_6\frac{\partial C_6}{\partial R}\frac{\partial \Phi}{\partial R} + \pi_6\nabla^2 C_6 \quad [24]$$

$$\sum_i z_ic_{i,0}C_i = 0 \quad [25]$$

$$C_1 = C_2^n C_4 \quad [26]$$

The boundary conditions in dimensionless form are

$$\frac{\partial C_i}{\partial R} = 0; \quad i = 1, 6$$
$$\frac{\partial \Phi}{\partial R} = 0 \quad [27]$$

at $R = 0$, and

$$C_i = 1; \quad i = 1, 6$$
$$\Phi = 1 \quad [28]$$

at $R = 1$. At $\tau = 0$, we have

$$C_i = 1; \quad i = 1, 6$$
$$\Phi = 1 \quad [29]$$

The dimensionless parameters contained in Eq. [20]-[26] are the following

$$\Phi_{R1} = \frac{\phi_{R1} - \phi_{R1}^0}{\phi_0 - \phi_{R1}^0} \qquad \zeta_j = \frac{\alpha_j\mathbf{F}(\phi_0 - \phi_{R1})}{RT}$$
$$\delta_2 = \frac{\alpha_2}{c_{2,0}}\exp\left[\alpha_2\mathbf{F}(\phi_{R2} - \phi_{R1}^0)/RT\right]$$
$$\delta_3 = \exp\left[\alpha_3\mathbf{F}(\phi_{R3} - \phi_{R1}^0)/RT\right]$$
$$H_i = \frac{c_{4,0}}{c_{i,0}} \qquad \epsilon_i = \frac{\mathbf{F}u_i(\phi_0 - \phi_{R1}^0)}{D_1}$$
$$\pi_i = \frac{D_i}{D_1} \qquad \chi_{11} = \frac{A(\phi_0 - \phi_{R1}^0)r_0^2 a}{n_1 c_{1,0} D_1\mathbf{F}}$$
$$\chi_{ij} = \frac{r_0^2 i_{0,j}a}{n_j D_1\mathbf{F}c_{i,0}} \quad [30]$$

The parameters χ_{ij} and π_i were introduced by Alkire and Siitari (9) in a previous attempt to model this system. Values of the dimensionless groups calculated

from typical system parameters may be used to assess the relative importance of the diffusion, migration, and generation terms. The ratio $\nu_{ij}x_{ij}\delta_j/\pi_i$ indicates the significance of reaction as compared to diffusion. Also, since ϵ_i/π_i is about 0.1 for all species, migration terms were omitted in all equations except the Na^+ and Cl^- species balances. When all migration terms were included, there was no perceptible change in the results.

Method of solution.—The equations of the mathematical model form a set of seven coupled, nonlinear equations. The nonlinear terms were linearized about a trial solution, according to the scheme given by Newman (17). The linearized equations were then written in Crank-Nicolson finite difference form, and solved numerically. The following computational procedure was used: (*i*) Equation [16] was solved for the potential of initial uniform corrosion, which was subsequently used as the potential scale. For the solution of this nonlinear equation, the IMSL (International Mathematical Subroutine Library) subroutine ZSYSTM, which uses Brown's method, was employed (18). (*ii*) At each time step, the trial solution was initially set to the solution at the former time step. (*iii*) The resulting system of linear algebraic equations was stored in band matrix form, and solved using the IMSL subroutine LEQT2B. (*iv*) Iteration was performed on the trial solution until a convergence criterion was met. The criterion was

$$\text{Max}_{(j)}\left[\frac{\sum_j (X_{ij}^{k+1} - X_{ij}^{k})}{\sum_j X_{ij}^{k}}\right] < \Delta \qquad [31]$$

where X_i denotes a dependent variable, j a mesh point, and k an iteration number. Δ was usually chosen to be 10^{-6}. Three iterations were usually required for convergence.

Near time zero and after breakdown, the variables changed very rapidly with time, while for most of the prebreakdown time the transients were much slower. Thus, it was desirable to employ a nonlinear time grid. From $t = 0$ to about 15 min, and also after breakdown, a geometric series was used to calculate time steps. Elsewhere, the time step was taken to be constant. Ten spatial finite difference nodes were employed. Doubling the number of nodes did not significantly affect the results. All computations were made on a CDC Cyber 175 computer. Typical values of the execution time and core usage were 60 CP seconds and 19 K words, respectively.

Results and Discussion

The results of the mathematical model for the base case system parameters are given in Fig. 2-7. Table I lists values of these parameters. The numbers appearing on the plots refer to sections of the experimental sectioned electrode (11); values of variables are taken at the inner radii of electrode sections (see Table I). In Table II, theoretically predicted breakdown times for a varity of crevice geometries are compared to the experimental results in Ref. (1). The concentration, current and potential distributions predicted for these crevice geometries are qualitatively similar to those for the base case crevice.

The current density and potential are both highest in the outer section, and decrease monotonically toward the center of the crevice, as illustrated in Fig. 2 and 3. Ohmic effects are responsible for this trend. The net electrode current is anodic, and current flows radially outward through the solution. Thus, the solution potential is highest at $r = 0$ and decreases in the radial direction. The trend in the electrode potential is the opposite, *i.e.*, increases with increasing radius. Since the net reaction current density is dominated by the anodic aluminum dissolution reaction, whose kinetics depend only on electrode potential, the current density

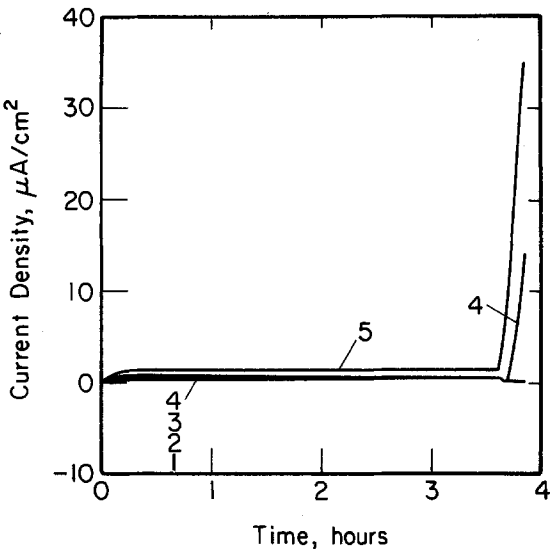

Fig. 2. Base case current distribution

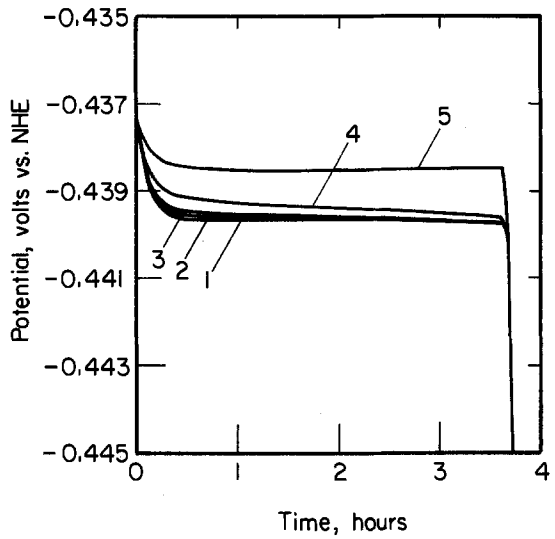

Fig. 3. Base case potential distribution

is greatest at the edge of the crevice. The current distributions measured by Siitari and Alkire (1) displayed the same trend (Fig. 8).

Before breakdown, the variation in potential within the crevice is at most 2 mV, and the current densities are, correspondingly, only a few $\mu A/cm^2$. This behavior is caused by the high slope of the aluminum polarization curve [see Fig. 4 of Ref. (11)]. Since the electrode potential increases with increasing radius, the potential must be less than the uniform corrosion potential of −0.437V, which is the boundary condition at the edge of the crevice. But the electrode potential must also be greater than the aluminum reaction rest potential. Because the rate of aluminum dissolution rises so sharply with potential, this allowed variation is only 3 mV. The potential gradient in the crevice, and, thus, the current flowing from the crevice, are limited to small values until breakdown, when the aluminum rest potential becomes more negative.

The computed concentrations of reactive species change quite rapidly in the first few minutes after the crevice is formed, and, then, change at a much slower rate until breakdown. This behavior is related to the numerical stiffness of the model equations; that is, the eigenvalues of the Jacobian matrix for the system differ by orders of magnitude. Initially, the rates of diffusion and migration are negligible. No concentration gradients exist to drive diffusion, and

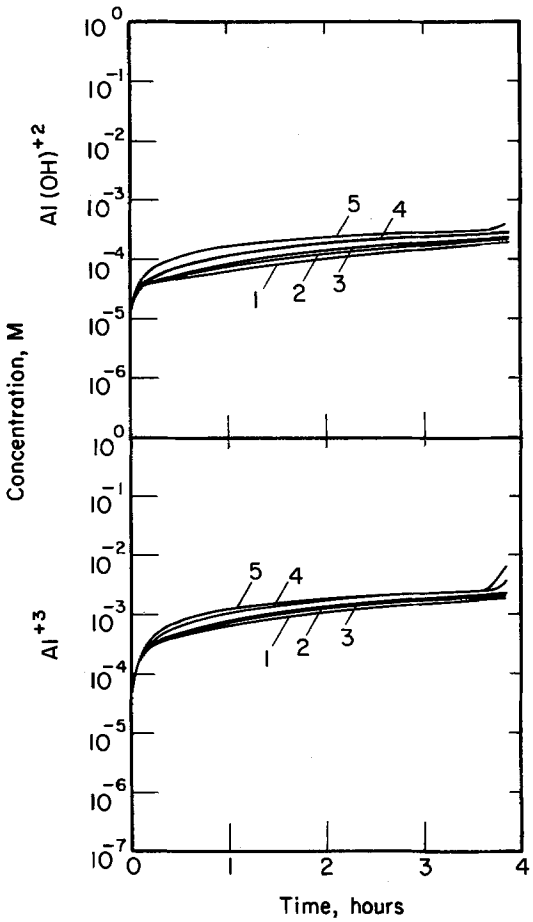

Fig. 4. Base case aluminum concentration distributions

the migration rates are small because the concentrations of ionic reaction products are low. As species are depleted or concentrated within the crevice, transport increases in importance, so that the crevice composition changes much less rapidly. Thus, the hydrogen ion and oxygen concentrations become practically constant, while the aluminum concentration slowly increases, approaching a steady value.

The results of the mathematical model are now compared to previous experimental results given in Ref. (1 and 11). The discussion is divided into the following topics: (*i*) breakdown time, (*ii*) aluminum concentration, (*iii*) pH behavior, (*iv*) current transients, and (*v*) chloride migration.

Table I. Parameter values used in the base case model calculations

Geometry	$h = 0.12$ mm	$r_o = 1.11$ cm
Kinetics	$A = 1.0 \times 10^{-3}$ A/V-cm^2	$\phi_{R1} = -0.44$V NHE
	$i_{o,2} = 1.0 \times 10^{-11}$ A/cm^2	$i_{o,3} = 2.0 \times 10^{-12}$ A/cm^2
	$\alpha_2 = 0.25$	$\alpha_3 = 0.50$
	$\phi_{R2} = 0.00$V NHE	$\phi_{R3} = 0.29$V NHE
Stoichiometry	$n_1 = 3$	$n_2 = 1$
	$n_3 = 4$	$\nu_{11} = 1$
	$\nu_{22} = -1$	$\nu_{23} = 0$
	$\nu_{33} = -1$	
Transport	$D_1 = 6.6 \times 10^{-6}$ cm^2/sec	$D_2 = 9.3 \times 10^{-5}$ cm^2/sec
	$D_3 = 2.0 \times 10^{-5}$ cm^2/sec	$D_4 = 1.0 \times 10^{-5}$ cm^2/sec
	$D_5 = 2.03 \times 10^{-5}$ cm^2/sec	$D_6 = 1.66 \times 10^{-5}$ cm^2/sec
	$u_5 = 8.2 \times 10^{-9}$ cm^2-mol/J-sec	$u_6 = 5.38 \times 10^{-9}$ cm^2-mol/J-sec
Initial concentrations	$c_{1,0} = 1.0 \times 10^{-7}$M	$c_{2,0} = 5.0 \times 10^{-6}$M
	$c_{3,0} = 2.5 \times 10^{-4}$M	$c_{5,0} = 0.05$M
	$c_{6,0} = 0.05$M	
Breakdown	$c_b = 2.0 \times 10^{-3}$M	
Hydrolysis	$K_h = 6.3 \times 10^{-6}$M	$n = 1$
Electrode section radii	$r_1 = 0.362$ cm	$r_2 = 0.513$ cm
	$r_3 = 0.723$ cm	$r_4 = 0.888$ cm
	$r_5 = 1.020$ cm	

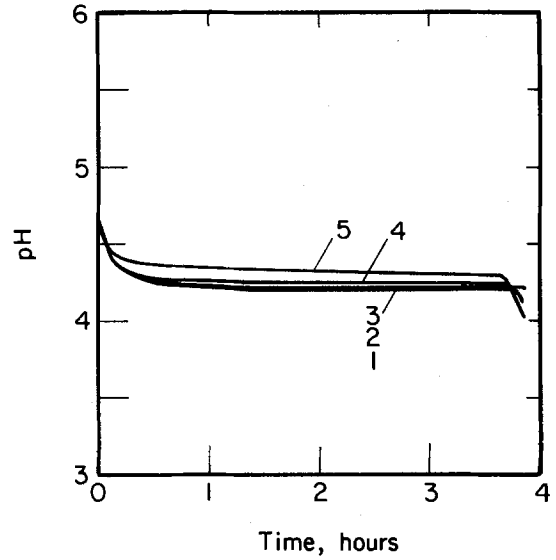

Fig. 5. Base case pH distribution

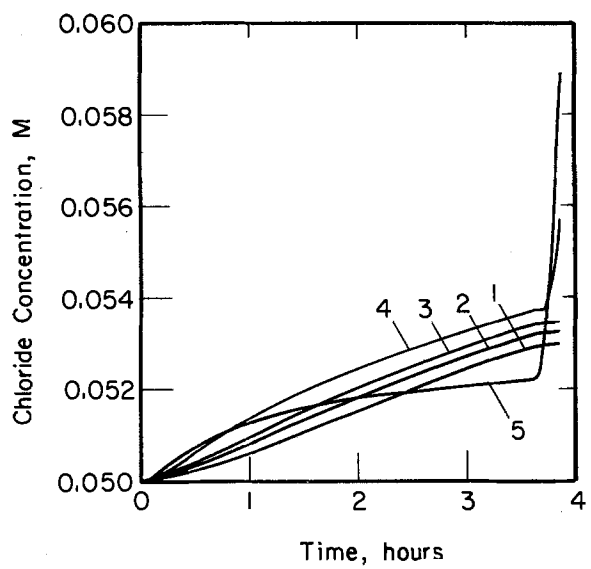

Fig. 6. Base case chloride ion concentration distribution

Times of breakdown.—The time to initiate crevice corrosion is the most important prediction of the model. If the concentrations of species inside the crevice have been modeled accurately, agreement with experimentally measured breakdown times reflects the choice of the proper activating species. A critical dissolved aluminum concentration of 2×10^{-3}M was taken as the criterion for breakdown in the model. The range of possible critical aluminum concentrations identified by experiment (11) was 2-8 $\times 10^{-3}$M. However, the crevice sampling experiments in the preceding paper show that the aluminum concentration at breakdown is about 1-2 $\times 10^{-3}$M. The value of c_{Al}* selected for the model is, then, reasonable.

Table II. Effect of crevice geometry of initiation time

Height (mm)	Radius (cm)	Theoretical time to reach critical concentration (hr)	Experimental initiation time (hr)	Difference (hr)
0.03	1.11	0.6	2.1	1.5
0.12	1.11	1.9	3.0	1.1
0.215	1.11	3.0	4.0	1.0
0.12	0.955	1.9	2.5	0.6
0.12	0.11	1.9	3.0	1.1
0.12	1.59	2.0	3.3	1.3
			Average difference =	1.1 hr

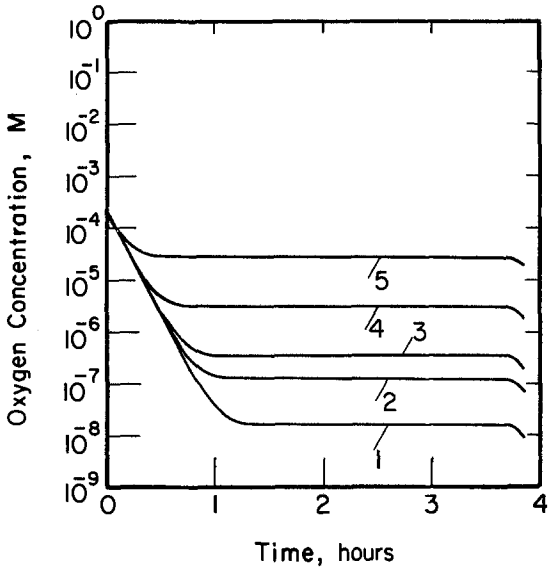

Fig. 7. Base case oxygen concentration distribution

Table II shows, for a variety of crevice sizes, the predicted time to reach c_{Al}^*, and, for comparison, breakdown times measured in the corresponding experiments of Siitari and Alkire (1). These times cannot be compared directly, because experiments show that, when an aluminum electrode is placed in an activating solution, there is an induction time of some minutes before activation is observed (see Fig. 7 of the preceding paper). It would then be expected that some time would elapse after the critical concentration is attained in the crevice before breakdown initiates. From Table II, the average difference between the experimental breakdown time and the theoretical critical time is 1.1 hr, which, according to Fig. 7 of Ref. (11), is a reasonable induction time. This agreement between experimental and calculated results is consistent with the proposed mechanism of breakdown. As the crevice height or radius increases, both experimental and theoretical times increase, although the dependence on radius is weaker than in experiments. Decreasing the crevice height enhances the electrochemical reaction term for generation of aluminum ions, thus, diminishing the time needed to reach the critical concentration. The dependence of breakdown time on crevice radius is less straightforward.

Aluminum concentration.—The predicted dissolved aluminum concentration, shown in Fig. 4, can be compared only indirectly to the sampling measurements of Ref. (11) (Fig. 9 therein). The presence of a sampling port in the crevice necessitated the use of plexiglass as the material for the upper surface of the crevice. Siitari (2) observed that when plexiglass was substituted for quartz as the material for the upper surface, breakdown times were increased by a factor of 2. This might be attributed to adsorption onto or leaching from the plexiglass. In all respects other than breakdown time, the quartz and plexiglass experiments were similar. Because of the difference in initiation times, though, the sampling results cannot be compared quantitatively with the model, whose predicted breakdown times agreed with the quartz experiments. At any rate, the model predicts the observed slow increase of aluminum concentration with time before breakdown, as well as the correct magnitude of the concentration. This is evidence that the reaction and transport of aluminum has been modeled correctly.

pH behavior.—Experimental measurements (1, 11) indicate that the pH rises sharply to about 7 from the initial value of 5.5, and then declines gradually to 4.0-4.5 prior to breakdown. The initial pH spike is not

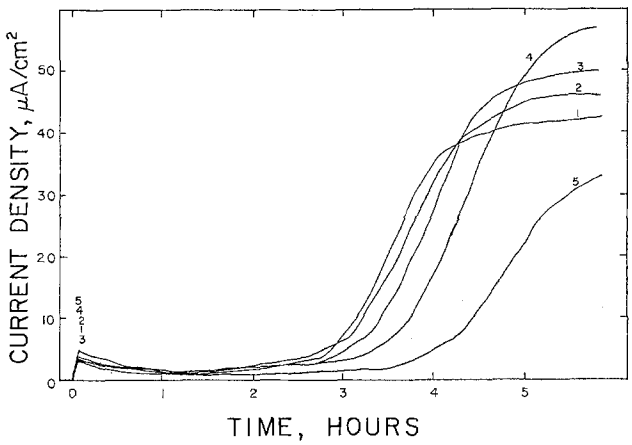

Fig. 8. Experimental base case current distribution [from Ref. (1)] $h = 0.12$ mm, $r_0 = 1.11$ cm.

present in the theoretical results shown in Fig. 5. When the consumption of hydrogen ions by the oxygen reaction was included in the model, the spike was found. However, this rapid transient caused computational difficulties for the finite difference code, so the stoichiometric parameter ν_{23} was set to zero. To account for the consumption of charge by the oxygen reaction, the electroneutrality equation was differentiated with respect to time and a term proportional to the rate of oxygen reduction added to it. These changes had no effect on the pH behavior except in the initial moments, because the rate of oxygen reduction very quickly became negligible.

Prediction of hydrogen ion concentration in the crevice requires knowledge of both the hydrolysis of aluminum ions and the kinetics of hydrogen ion reduction. The modeling of each of these effects is subject to uncertainty. If $Al(OH)^{+2}$ was assumed to be the only hydrolyzed species, the pH calculated at various aluminum concentrations agreed well with published pH/[$AlCl_3$] data (19). Substitution of a hydrolysis number of 2 did not appreciably influence the crevice pH, because the hydrolysis constant is about five orders of magnitude smaller than that for $n = 1$ (20). The hydrogen ion reduction kinetics were found to exert a significant influence on the pH behavior. Exchange current densities of 10^{-11}, 10^{-9}, and 10^{-7} A/cm² were tested, and the resulting pH transients are shown in Fig. 9. It is seen from these results that the pH agrees with experiment only if $i_{0,2}$ is less than 10^{-11} A/cm². This low exchange current density is

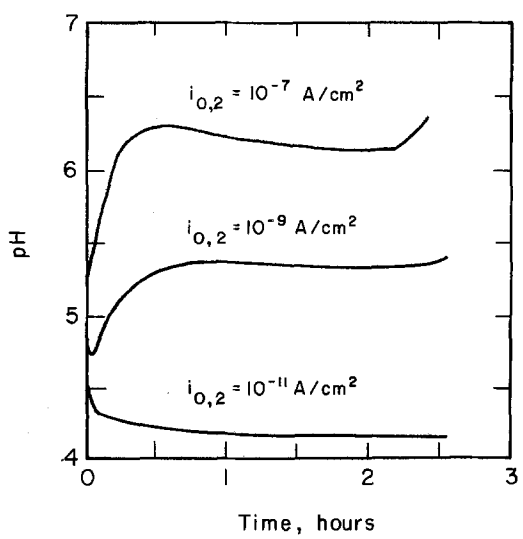

Fig. 9. pH transients at center of crevice for various hydrogen reduction exchange current densities.

reasonable for an oxide-filmed aluminum electrode. The value of 10^{-7} A/cm^2 is close to that obtained from polarization curves for potentials negative of −0.56V NHE. It does not, however, necessarily reflect the hydrogen kinetics in the region of interest, which is from −0.445 to −0.435V.

Current transients.—All the crevice corrosion experiments done by Siitari and in the present work exhibit unique initial current density and potential transients (Fig. 8). The current densities rise to a peak of usually 5-10 μA/cm^2, and then fall to the steady prebreakdown current densities. Concurrently with the current density peak, the electrode potential within the crevice reversibly dips about 10 mV. The model current densities do not show this initial peak. Evidently, the factors responsible for the initial transients are not included in the mathematical model.

In view of the established potential dependence of the aluminum reaction kinetics, it is difficult to see how these kinetics could predict a rise in current if the electrode potential falls by 10 mV. The electrode potential within the crevice is bounded by the aluminum rest potential and the uniform corrosion potential, a range of no more than 5 mV. Thus, if the potential were to fall 10 mV, the anodic reaction rate would be zero.

An explanation for this ambiguity (15, 21) may be that the passive aluminum kinetics increase with pH as the pH becomes more basic. The initial rapid rise in pH may cause the passive current density of the aluminum reaction to rise, accounting for the rise in current density and drop in potential. The increase in aluminum ion production would then increase the rate of hydrolysis, causing the pH to fall and the kinetics to return to their original state.

Discrepancies between the experimental and theoretical current transients are also present after breakdown. The currents predicted by the model rise much more sharply than those observed experimentally. Also, in the model, when activation occurs at some electrode section, the current from the other sections drops to zero. This behavior was not observed experimentally. However, as has already been mentioned, the mathematical formulation for activation used in the model is artificial. After the critical aluminum concentration is reached, an induction time passes after which the aluminum rest potential is made more negative. No attempt was made to accurately predict the experimental current transients after breakdown.

Chloride migration.—The theoretical results shown in Fig. 6 indicate that accumulation of chloride ion by migration is not large enough to influence breakdown. The largest chloride concentration increase before breakdown was from 0.05 to 0.055M (10%), while the average increase was about 8%. Experiments have shown that the critical aluminum concentration for activation is somewhat reduced if the chloride concentration were to increase by 100% (11). Although the effect of an 8% increase in [Cl^-] was not investigated, it seems unlikely that the critical concentration would be significantly altered.

Conclusions

A mathematical model was developed to evaluate a hypothesis for initiation of crevice corrosion of aluminum in dilute aqueous chloride electrolyte. The model contained mathematical expressions for reaction and transport processes occurring in crevices during the initiation period. The central feature of the hypothesis of mechanism was that the metal in the crevice becomes activated when the concentration of dissolved aluminum species in the solution exceeds a certain minimum critical value. This breakdown mechanism had been established qualitatively by experiments described previously.

The mathematical model was used in pursuit of scientific understanding by predicting localized behavior during initiation of crevice corrosion, including such salient features as oxygen depletion, acidification, accumulation of dissolved aluminum, hydrolysis, unsteady-state diffusion, and migration of all species including chloride. That these model predictions compared favorably with the experimental data of the previous paper lends credence to the validity of the hypothesis of dissolved metal species mechanism upon which the model was based. In addition, the model illustrated that alternative initiation mechanisms based on chloride migration must be excluded for the behavior of Al in 0.05*N* NaCl.

The model was also used in pursuit of engineering goals such as scale-over and corrosion prevention. For example, the model accurately predicted the initiation time observed in crevices of different geometry. One could also utilize the model to predict system configurations under which crevice corrosion could not occur, as well as to explore methods for corrosion prevention with use of impressed current. That is, once a mathematical model is established by experimental tests, it then becomes a predictive tool and may be used for engineering design of corrosion-resistant configurations.

Because localized corrosion is complex and involves many processes which occur simultaneously, the analysis of experimental observations is rarely straightforward. A mathematical model is particularly helpful in organizing complex hypotheses of mechanism, and in upgrading ability to address increasingly sophisticated experimental tests of that hypothesis. Models are particularly useful in studying corrosion processes which involve reaction and transport along surfaces. Corrosion phenomena which have salient features that lend themselves to such a modeling approach include pitting, stress corrosion cracking, erosion, cavitation, impingement, and inhibition, in addition to crevice corroson investigated here.

Acknowledgments

This work was supported by the National Science Foundation (Grant NSF DMR 77-28285) and by fellowships from National Steel Corporation and Gulf Oil Chemicals. Computer costs were assisted by the Research Board of the University of Illinois.

Manuscript submitted March 30, 1982; revised manuscript received *ca.* Jan. 12, 1983. This was Paper 144 presented at the Denver, Colorado, Meeting of the Society, Oct. 11-16, 1981.

Any discussion of this paper will appear in a Discussion Section to be published in the December 1983 JOURNAL. All discussions for the December 1983 Discussion Section should be submitted by Aug. 1, 1983.

Publication costs of this article were assisted by University of Illinois at Urbana-Champaign.

LIST OF SYMBOLS

A	kinetic parameter of aluminum dissolution reaction, A/V-cm^2
a	specific surface area of crevice, $1/h$, cm^{-1}
C_i	concentration of species i, dimensionless
c_i	concentration of species i, M
$c_{i,0}$	initial or bulk concentration of species i, M
c_b	critical concentration of dissolved aluminum for activation, M
D_i	diffusion coefficient of species i, cm^2/sec
$\mathbf{F}$	Faraday's constant, coulombs/equivalent
H_i	initial concentration parameter for species i, dimensionless
h	clearance of crevice, cm
$i_{0,j}$	exchange current density of reaction j, A/cm^2
j_i	electrode current density of reaction j, A/cm^2
K_h	equilibrium constant of aluminum ion hydrolysis, M
n	hydrolysis number

n_j number of electrons involved in reaction j
R radial position, dimensionless (also gas constant, J/mol K)
r radial position, cm
r_0 crevice radius, cm
T temperature, K
t time, sec
u_i electrochemical mobility of species i, cm^2-mol/J-sec
z_i ionic charge of species i

Greek characters

α_j charge transfer coefficient of reaction j
δ_j kinetic parameter of reaction j, dimensionless
ϵ_i dimensionless parameter for migration of species i
ζ_j kinetic parameter of reaction j, dimensionless
ν_{ij} stoichiometric coefficient for species i and reaction j
π_i diffusion coefficient of species i, dimensionless
τ time, dimensionless
Φ electrode potential, dimensionless
ϕ electrode potential, V NHE
ϕ_0 potential of initial uniform corrosion, V NHE
ϕ_{Rj} rest potential of reaction j
ϕ_{R1}^0 rest potential of Al dissolution before activation, V NHE
x_{ij} dimensionless parameter representing production of species i by reaction j

Subscripts

i species: 1-Al^{+3}, 2-H^+, 3-O_2, 4-$Al(OH)_n^{+3-n}$, 5-Cl^-, 6-Na^+
j electrochemical reaction: 1-aluminum dissolution, 2-hydrogen ion reduction, 3-oxygen reduction

REFERENCES

1 D. W. Siitari and R. C. Alkire, *This Journal*, **129**, 481 (1982).
2. D. W. Siitari, Ph.D. Dissertation, University of Illinois at Urbana-Champaign, Urbana, IL (1979).
3. I. L. Rosenfeld, in "Localized Corrosion," R. W. Staehle *et al.*, Editors, p. 373, NACE, Houston (1974).
4. I. L. Rosenfeld, I. S. Danilov, and R. N. Oranskaya, *This Journal*, **125**, 1729 (1978).
5. G. Karlberg and G. Wranglen, *Corros. Sci.*, **11**, 499 (1971).
6. J. W. Oldfield and W. H. Sutton, *Br. Corros. J.*, **13**, 104 (1978).
7. J. F. Bates, *Corrosion*, **29**, 28 (1973).
8. B. Vicentini, D. Sinigaglia, and G. Taccani, *Corros. Sci.*, **15**, 479 (1975).
9. R. C. Alkire and D. W. Siitari, *This Journal*, **129**, 488 (1982).
10. J. W. Oldfield and W. H. Sutton, *Br. Corros. J.*, **13**, 13 (1978).
11. K. R. Hebert and R. C. Alkire, *This Journal*, **130**, 1001 (1983).
12. K. R. Hebert, M.S. Thesis, University of Illinois at Urbana-Champaign, Urbana, IL (1981).
13. R. Ergang, G. Masing, and M. Möhling, *Z. Elektrochem.*, **56**, 8 (1952).
14. A. Broli and H. Holtan, *Corros. Sci.*, **13**, 237 (1973).
15. H. Kaesche, in "Passivity of Metals," R. P. Frankenthal and J. Kruger, Editors, p. 935, The Electrochemical Society, Princeton, NJ (1978).
16. T. W. Chapman and J. Newman, "A Compilation of Selected Thermodynamic and Transport Properties of Binary Electrolytes in Aqueous Solution," University of California, Lawrence Radiation Laboratory, Berkeley, CA (1968).
17. J. Newman, "Electrochemical Systems," Prentice-Hall, Englewood Cliffs, NJ (1973).
18. "IMSL Library Reference Manual," IMSL, Inc., Houston (1980).
19. T. Hagyard and J. R. Santhiapillai, *J. Appl. Chem.*, **9**, 323 (1959).
20. C. F. Baes and R. E. Mesmer, "The Hydrolysis of Cations," John Wiley and Sons, New York (1978).
21. K. E. Heusler and W. Allgaier, *Werkst. Korros.*, **22**, 297 (1971).

Space Charge Effects on the Growth of Anodic Oxide Films on Zirconium Metal

Francesco Di Quarto, Salvatore Piazza, and Carmelo Sunseri

Istituto di Ingegneria Chimica, Università di Palermo, Viale delle Scienze, 90128 Palermo, Italy

ABSTRACT

The kinetics of growth of anodic oxide films in different electrolytic solutions, and in a range 1-32 mA cm^{-2} of current density has been investigated. By interferometric measurements an increase in the electrical field strength has been measured with increasing film thickness at all current densities and in all solutions. This finding has been attributed to the existence of a mobile ionic space charge. A test of this hypothesis has been made by fitting the $1/C_{OX}$ *vs.* V_E curves on the basis of Fromhold's theory. Nonlinear Tafel plots have been obtained in sulfuric acid and in carbonate solutions while a straight line behavior was observed in sulfamic acid solutions. Lower dielectric constant values also have been measured for films formed in the former two solutions which are known to give incorporation of anions in ZrO_2 films. No incorporation of anions seems to occur when anodization process is performed in sulfamic acid solutions. Some discrepancies between experimental results and the existing theory have been pointed out.

The anodic behavior of zirconium in different solutions has been investigated by numerous workers (1). As a result of these studies some unique features of the anodization process of zirconium electrodes have been reported. Two aspects seem to distinguish this metal with respect to other valve metals: (*i*) a very low transport number for the metal ions in a relatively large range of current density ($t_M \leq 0.05$ at $i \leq 10$ mA cm^{-2}) (2, 3); and (*ii*) the large incorporation of electrolytic species particularly in sulfate and carbonate solutions and its strong dependence on the current density and pH used during the anodization process (4-6). The strong influence of the anions in solutions in determining the kinetics of growth as well as the breakdown of the zirconium oxides is also well known (1, 5, 7-10). By comparison of the literature data some discrepancies can be noted between the experimental results reported by different authors which could be attributed both to the different experimental techniques and purity of zirconium metal. Bearing in mind these possible sources of discrepancies, some experimental results still remain conflicting between them. In fact a nonlinearity in the log i *vs.* electric field (E) plots has been reported by Willis *et al.* and Ortega *et al.* (11, 12) for anodization in sulfate or citrate solutions respectively. Both these solutions have been reported to give incorporation of anions in the ZrO_2

Key words: films, electrode, passivity, reflectance.

films. Moreover Ortega and Siejka claimed that the onset of the nonlinearity in the $E = f(\log i)$ plots was independent of the incorporation but strictly dependent on a critical electric field value ($E = 4.2\ 10^6$ V cm^{-1}). On the other hand, other authors (13, 14) reported linear log i *vs.* E plots in a wide range of current density ($10^{-5} \leq i \leq 10^{-2}$ A cm^{-2}) and in different solutions containing sulfate, carbonate, and phosphate ions. According to different authors all these anions are to various extents incorporated into the films during the growth (4-6).

Another controversial aspect is the possible dependence of the electric field on the thickness of the films. Young (15) attributed the variation of electric field with thickness to the presence of a mobile ionic space charge, while Rogers *et al.* (5) attributed this variation to the incorporation of species contained in the solutions. More recently this last hypothesis has been confirmed by Hopper *et al.* (14) in a study performed in 0.1M Na_2CO_3 solution and in the range of current density (C.D.) ($10^{-5} \leq i \leq 5 \times 10^{-4}$ A cm^{-2}) where a very low incorporation of anions as well as a very low current efficiency have been reported (5). In order to check some of the previous hypotheses a detailed study of the influence of the different solutions on the kinetics of growth and on the breakdown of anodic ZrO_2 films was performed.

In this paper we report a study of the kinetics of growth of ZrO_2 films in some selected solutions where the highest efficiency of formation was observed. The experimental results will be interpreted on the basis of Fromhold's theory of growth of anodic films in the presence of high mobile space charge and by taking into account the experimental findings on the incorporation of anions into the films.

Experimental

The samples were prepared by using zirconium rods (0.5 cm diam purchased from Goodfellow Metal, Cambridge, England) 99.8+ purity sealed to Teflon cylinders with epoxy resins (Torr Seal, Varian Associates, Palo Alto, California) or forced into heated (100°C) Teflon cylinders (0.45 cm inner diameter). The surface exposed to the solution was mechanically polished before each experiment with very fine abrasive paper, ultrasonically cleaned in distilled water, and then chemically etched.

The chemical etching was performed in HF:H_2O:HNO_3 mixture (1:4:2 in volume) (16). During the etching procedure the electrode was rotated at constant rotation speed. In this way a better finish of the electrode surface was obtained as evidenced by a mirror-like final surface and uniform interference colors after anodization. The ohmic contact was ensured by silver paste sealed to the back-side of the electrode.

The galvanostatic measurements were performed using a Keithley Model 227 constant current generator. The cell voltage, V_E, was monitored with a Keithley Model 610C electrometer and recorded on a PAR Model RE 0074 X-Y Recorder. A Simpson Model 360 digital multimeter was used in the experiments where voltage values higher than 118V were reached.

The reflectance measurements were carried out by using a 632.8 nm wavelength of an He-Ne Laser Mod. 138/01 Spectra Physics. The intensity of the reflected light was measured by an RCA Model 5819 photomultiplier tube.

Both the cell voltage and the output current from the photomultiplier were recorded, respectively, on the x and y axes of the recorder.

The capacitance of the metal/oxide/electrolyte system was measured by monitoring the 90° out-of-phase component of the a.c. with a PAR Model 124A/116/ lock-in amplifier.

The internal oscillator of the lock-in drove the PAR system formed by Model 175 universal programmer and Model 173/178 potentiostat. The a.c. was obtained by superimposing a 20 mV peak-to-peak a-c voltage on the triangular waveform which modulated the working electrode potential U_E. The frequency of the a-c voltage was usually 1 kHz and the sweep rate was 10 mV sec^{-1}.

All the capacitance measurements were performed in 1N H_2SO_4 solutions, the counterelectrode was a 10 cm^2 Pt foil and the reference electrode was Hg/Hg_2SO_4 (1N H_2SO_4). The capacitance values were obtained by comparison with a decade capacitor HP Model 4440B. The current density was calculated on the basis of the apparent area ($S = 0.196$ cm^2). Solutions were prepared from distilled water and analytical grade reagents. All experiments were carried out at room temperature (20° ± 2°C).

Experimental Results

A preliminary study on the influence of the electrolytic solutions on the anodic behavior of zirconium electrodes was performed by investigating the voltage *vs.* time (V_E *vs.* t) curves at constant C.D. (charging curves). In this way the influence of the C.D. as well as of the electrolytic solutions on the efficiency of film formation was obtained. The most significant parameters in determining the efficiency were the nature of the anions in solutions and the C.D. used during the anodization. A similar behavior was observed both in acidic and neutral solutions containing the same anions.

A good efficiency of film formation current was observed in solutions containing sulfate, carbonate, sulfamate, and borate anions in a relatively large range of C.D.'s and cell voltages. For this reason and for a better comparison of our results with the literature a detailed analysis of the kinetic data was restricted to the experiments performed in 0.1N H_2SO_4, 0.1N NH_2SO_3H, and 1N Na_2CO_3 solutions.

A small bubbling on the electrode surface was visible at high voltages during the anodization in these last solutions. As a general trend a decrease in the efficiency was observed by decreasing the C.D. value or by increasing the cell voltage above ~80V. The decrease in the efficiency was, however, faster in solutions containing carbonate in comparison with the sulfuric or sulfamic acid ones. In Fig. 1 the average efficiency η is reported as a function of the C.D. The η values were calculated on the basis of the average slopes measured from the charging curves and the average electric fields obtained by the interferometric measurements (see below). The range of cell voltages in which these measurements were performed was that corresponding to the appearance of the first maximum in the interference curves (see Fig. 2).

The film formation efficiency was calculated by the following relation

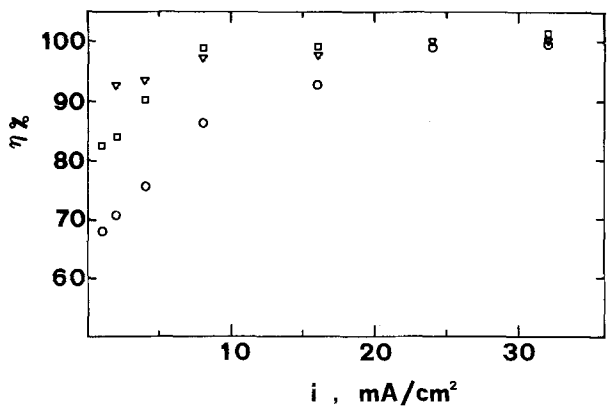

Fig. 1. Efficiency of film formation, calculated between the origin and the first maximum of the interference patterns, *vs.* current density for various solutions: ▽ NH_2SO_3H 0.1N; □ H_2SO_4 0.1N; ○ Na_2CO_3 1N.

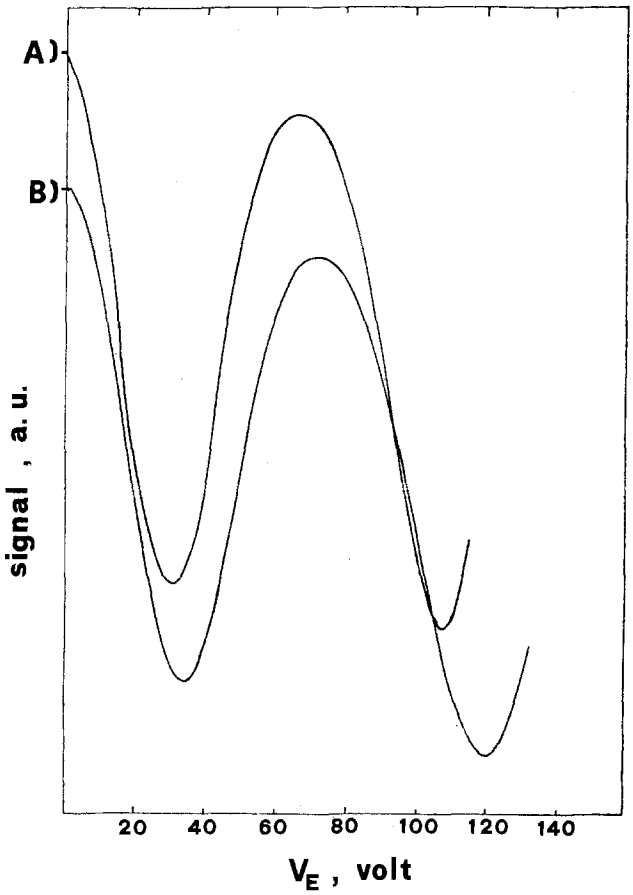

Fig. 2. Interference patterns of the light reflected during the growth of films in 0.1*N* NH_2SO_3H solutions. Curve a: $i = 4$ mA cm^{-2}; curve b: $i = 24$ mA cm^{-2} ($\lambda = 6328$Å, $\phi_0 = 27°$).

$$\eta = \frac{i_{ion}}{i_{tot}} \times 100 = \frac{ZF\rho\, \Delta v/\Delta t}{M\overline{E}_{opt}\, i_{tot}} \times 100 \qquad [1]$$

where ρ and M are respectively the density and the molecular weight of the films, assumed independent of the C.D., $\Delta v/\Delta t$ is the average slope measured on the charging curves at each C.D., $\overline{E}_{opt}$ is the average electric field measured between the origin and the first maximum of the interference curves, and i_{tot} is the apparent C.D. used in the anodization process. The values reported in Fig. 1 were normalized by assuming a unitary efficiency for the highest C.D. used in our experiments ($i = 32$ mA cm^{-2}). In this way a ρ/M value equal to 0.046 ± 0.002 in fairly good accordance with those reported in the literature (5, 9, 11, 15) was found. As reported in Fig. 1, higher film formation efficiency was found in sulfuric or sulfamic acid solutions with respect to the carbonate ones.

These results agreed very well with visual inspection of the bubbling on the electrode surface showing a poor gas evolution in sulfamic and sulfuric solution until very high voltages at all C.D. used. On the other hand, the bubbling phenomenon occurred earlier and at more sustained rate in carbonate solutions.

Interferometric Measurements

Due to the variable efficiency of film formation current, an interferometric method was chosen for determining the film thickness and then the anodizing electric field during the galvanostatic experiments.

Typical interference patterns of the light reflected during the growth of ZrO_2 films at two different C.D.'s in 0.1*N* NH_2SO_3H solutions are reported in Fig. 2.

Often the second minimum of the interference curves was hard to obtain or scarcely reproducible because of breakdown phenomena or copious bubbling on the electrode surface. For this reason kinetic data is discussed in detail for all the solutions in the range of film thicknesses limited to the appearance of the first maximum in the interference curves. The thickness of the film was obtained by using the relationship (17)

$$\Delta D = \frac{\lambda}{2(n_1^2 - \sin^2 \phi_0)^{1/2}} \qquad [2]$$

where ΔD is the change in film thickness D corresponding to two adjacent maxima or minima in the interference patterns, n_1 is the refractive index of the film, λ is the vacuum wavelength, and ϕ_0 the angle of incidence of the light.

The film thickness can be determined by this method if the value of the refractive index n_1 is known at the light wavelength employed. In our case the value $n_1 = 2.17$ was used according to Hopper *et al.* (14) for $\lambda = 6328$Å. Two approximations were made in the analysis of the interference patterns: (*i*) the n_1 value was assumed equal in all anodizing solutions; and (*ii*) the optical absorption of the films at $\lambda = 6328$Å was considered negligible in the investigated range of films thicknesses.[1]

A possible source of error in the above assumptions could come from the incorporation into the films of the anions contained in the solutions. This phenomenon has been reported for sulfate and carbonate solutions and it is very much dependent on the C.D. (5). As for the incorporation of the sulfamic anion, no experimental data are reported, to our knowledge, in the literature. However the experimental results discussed below and the poor adsorption of this anion (18) seem to point in the direction of absence of incorporation of this anion in the ZrO_2 films. If this is true, at least in sulfamic acid solutions, the n_1 value can be assumed constant in the whole range of investigated thickness according to the results reported by Banter (19) and Wilkins (20).

Bearing in mind this assumption the results in Fig. 2 can be interpreted by assuming an increase of the electric field of anodization with the thickness. This increase is visible by using twice Eq. [2] for the maxima and minima of the interference curves of Fig. 2. In this way it was possible to calculate, at least, two incremental electric fields E_1 and E_2. With the aid of Eq. [2] an average electric field $\overline{E}_{12}$ was also estimated from the maxima of the interference curves. The large bubbling observed at the higher cell voltages in carbonate solutions did not allow recording with sufficient accuracy the second minimum in the interference curves. In sulfuric or sulfamic acid solutions it was still possible to record a second minimum in the interference patterns, although the corresponding cell voltages showed a low reproducibility at different current densities, probably related to the parasitic reaction of oxygen evolution. For these reasons the log i *vs.* electric field plots reported in Fig. 3 were restricted to the E_1, E_2, and E_{12} values measured in a range of film thicknesses below 1500Å.

In all solutions an increase in the electric field strength was recorded with increasing thickness. This aspect is evidenced in Fig. 3 where the log i_{ion} *vs.* E plots were reported in the different range of film thicknesses. The experimental uncertainty on the measured electric field values was estimated to be less than $\pm 2\%$ after correction for the ohmic drop in the measured cell voltages.

As shown in the figures, a straight line behavior is observed in the log i *vs.* E plots only for the sulfamic acid solutions. In the sulfate and carbonate anion containing solutions a nonlinear behavior is observed. It is meaningful to observe that the curvature in the log

[1] A numerical computation, made by taking into account the complex refractive index reported in Ref. (14), gives very small changes in the measured film thickness, which are largely below the experimental uncertainty.

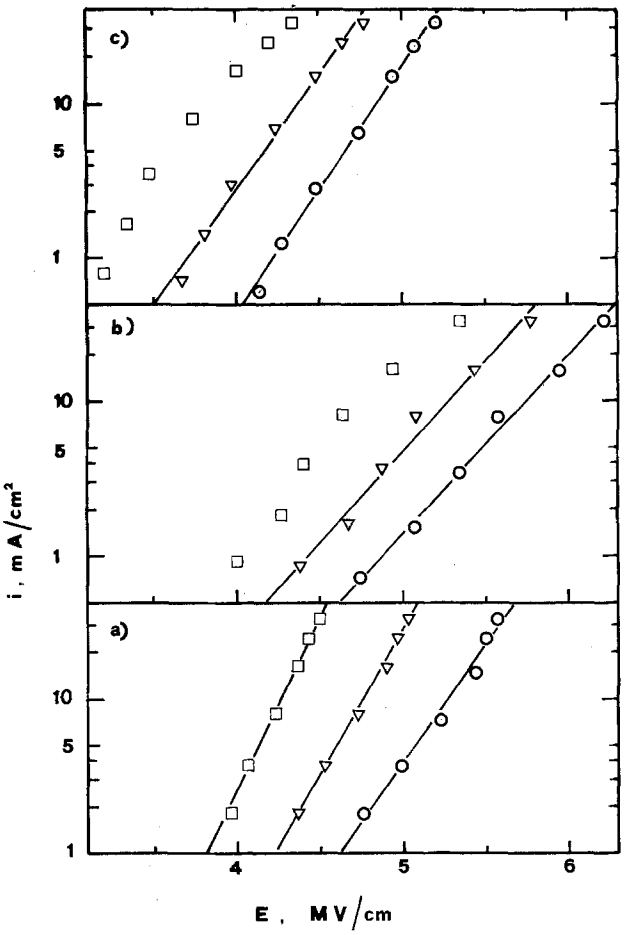

Fig. 3. Influence of film thickness on the log i_{ion} *vs.* average electric field plots for films formed in: a) 0.1*N* NH_2SO_3H, b) 0.1*N* H_2SO_4, c) 1*N* Na_2CO_3. □ 0-745Å average electric field; ▽ 0-1490Å average electric field; ○ 745-1490Å average electric field. A thickness-dependent efficiency was used to determine the i_{ion} values. The straight lines are the least squares fitting.

i vs. E plots is much more visible at lower thicknesses than at the higher ones. Moreover, the experimental data show that there is not a threshold value of electric field where the nonlinearity starts. In the same figures we report the curves, obtained by the least squares method, which fitted the experimental points. It is worth noting that at the higher thicknesses the experimental points obtained in sulfuric acid or carbonate solutions can be fitted in the investigated range of C.D. by using either a parabolic or a linear interpolation.

The linear Tafel plots reported in Fig. 3a for the anodizations performed in sulfamic acid solution as well as the above mentioned poor absorbability of this anion suggest that the growth of ZrO_2 anodic films in these solutions could happen without incorporation of this anion.

Capacitance Measurements

Capacitance measurements of the anodic films grown at different C.D.'s were carried out in order to get more information on the effects of anion incorporation on the dielectric constant of the film, as well as of space charge on the $1/C_{ox}$ *vs.* V_E curves. The capacitance measurements were performed soon after the anodization process. The thickness of the films was changed by interrupting the galvanostatic experiments at different preselected cell voltages.

A preliminary study of the influence of the a-c frequency as well as of the electrode potential U_E on the capacitance values showed that: (*i*) the differential capacitance of ZrO_2 electrodes was frequency dependent in the range 10 Hz-30 kHz (21); and (*ii*) a nearly constant *C* value, slightly increasing in the negative electrode potentials range, was measured by decreasing U_E from +3.0 to −1.4V *vs.* MSE when a large drop in the measured capacitance was observed.

Such a behavior can be attributed to the electrical behavior as insulators of the ZrO_2 anodic films (22) analogously to the reported findings on HfO_2 anodic films (23). A very small hysteresis in the C *vs.* U_E plots was recorded in the reversal scans of the potential sweeps in accordance with the observed time-dependence of the ZrO_2 films/electrolyte interface capacitance. The measured capacitance was corrected by assuming a value of 20 $\mu F \cdot cm^{-2}$ (24) for the Helmholtz double layer capacitance. The *C* values reported in the $1/C_{ox}$ *vs.* V_E plots were all measured at U_E = 3.0V (MSE) and at f = 1 kHz. In Fig. 4-5 are reported the $1/C_{ox}$ *vs.* V_E plots for films grown in the investigated solutions at different C.D.'s. The large drop in the efficiency measured in carbonate and sulfuric acid solutions dissuaded us from making capacitance measurements of the films grown above 160V or at lower C.D.

On the other hand, the higher breakdown voltage and the good efficiency measured in sulfamic solutions permitted us to extend the capacitance measurements in 0.1*N* NH_2SO_3H solutions until 190V. In this range of voltage no bubbling was observed and still linear charging curves were recorded for C.D. values ranging between 8 mA cm^{-2} and 32 mA cm^{-2}. A good linearity was found in the $1/C_{ox}$ *vs.* V_E plots for films grown until about 130V regardless of the anodizing solutions.

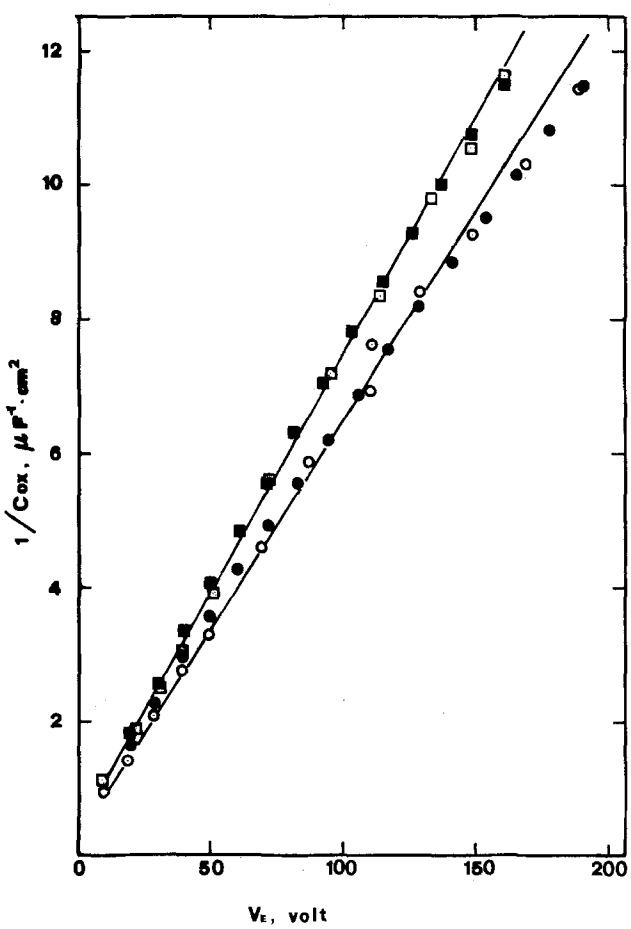

Fig. 4. Reciprocal capacitance value *vs.* final film formation voltage V_E, for films grown in NH_2SO_3H 0.1*N* at i = 8 mA cm^{-2} (circles) and in Na_2CO_3 1*N* at i = 32 mA cm^{-2} (squares). Open symbols: experimental points; closed symbols: theoretical points calculated on the basis of the theory of mobile ionic space charge (see text).

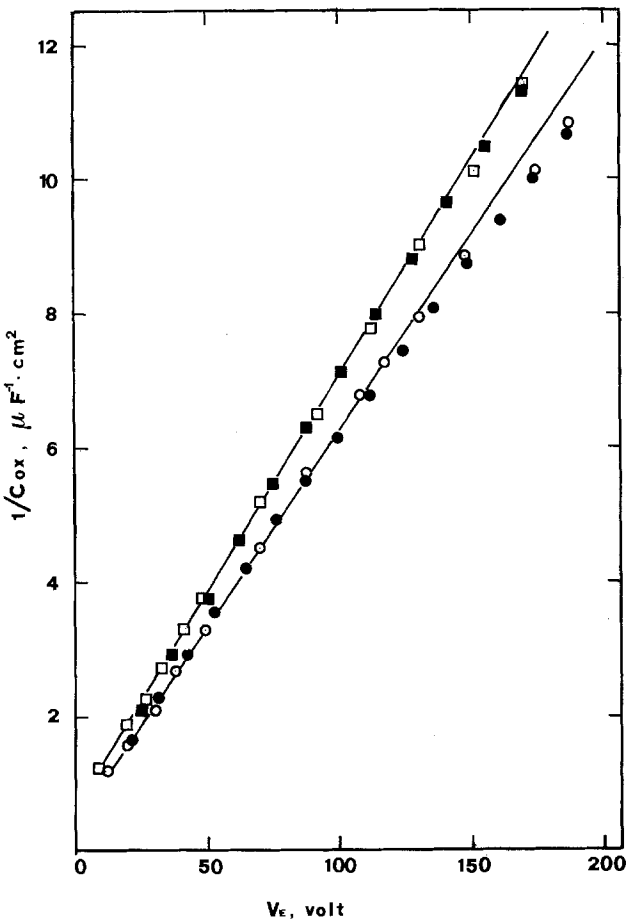

Fig. 5. Reciprocal capacitance value *vs.* final film formation voltage, V_E, for films grown in NH_2SO_3H 0.1*N* (circles) and H_2SO_4 0.1*N* (squares) at $i = 32$ mA cm^{-2}. Open symbols: experimental points; closed symbols: theoretical points calculated on the basis of the theory of mobile ionic space charge (see text).

At higher anodization voltages the $1/C_{ox}$ values fall below the extrapolated straight-line behavior for sulfamic acid solution, while they show a tendency to fall on the straight line in carbonate as well as in sulfuric acid solutions.

In Fig. 4-5, we report also the theoretical points of the $1/C_{ox}$ *vs.* V_E curves obtained on the basis of the V_E *vs.* thickness relationship given by Fromhold (see discussion section) for the growth of anodic films in presence of high space charge. The dielectric constant value used for the fitting procedure, ϵ_{fit}, is reported in Table I together with the other fitting parameters. A more detailed discussion of these findings will be made in the following section.

Discussion

The experimental results previously outlined agree, in our opinion, with the hypothesis of growth of the ZrO_2 anodic films in the presence of a high space charge due to the mobile ionic species (15). The importance of the effects of mobile space charge in the growth of anodic films, originally stressed by Dewald (25), has been more extensively discussed by Fromhold in the last years (26, 27). However a clear experimental evidence in favor of the existence of such ionic space charge has not been drawn until now.

In the case of the anodization of zirconium electrodes the most important experimental finding reported until now in favor of the existence of space-charge effects is, according to Young (15), the increase with film thickness of the electric field strength. In our experiments an increase in the average electric field was observed in all solutions and investigated C.D.'s (1-32 mA cm^{-2}). These experimental findings are partially conflicting with the results of Draper *et al.* (5) who reported a constancy in the electric field strength during the anodization of zirconium in carbonate and sulfuric acid solutions at 1 mA cm^{-2}.

More recently the constancy in the electric field strength has been reported by De Smet *et al.* (14) for anodization in carbonate solutions at still lower current densities ($i \leq 0.5$ mA cm^{-2}).

These findings could suggest that the increase of the electric field strength with thickness is to some extent related to the phenomenon of the incorporation of anions from the electrolytic solutions (5), which is very sensitive to the value of C.D. used in the galvanostatic experiment. Although this hypothesis cannot be excluded, *a priori*, it seems incompatible with the experimental results obtained in sulfamic acid solution. In this last solution linear Tafel plots and higher values of dielectric constant (see below) were measured in the same range of C.D. Both these facts suggest that the incorporation of sulfamic ions into the zirconium oxide films should be absent or very small. A very small incorporation of sulfur containing species cannot be excluded due to the tendency of the sulfamic acid to hydrolyze according to the reaction

$$NH_2SO_3H + H_2O \rightarrow NH_4HSO_4 \qquad [3]$$

This tendency has been reported (28) to be very small at room temperature so that it seems reasonable to exclude the incorporation of anions as a cause of the increase of the electric field strength in the experiments performed in sulfamic acid solution. A further experimental proof in favor of the hypothesis of high mobile space charge in ZrO_2 films comes from our experimental data reported in Fig. 4 and 5. In fact in the figures an evident nonlinearity in the $1/C_{ox}$ *vs.* V_E plots appears at the higher thicknesses. This nonlinearity agrees very well with the theoretical expectations of Fromhold's theory.

In order to check further the validity of this hypothesis a series of numerical calculations were performed on the basis of Fromhold's model (26, 27) of growth of anodic films in galvanostatic experiments.

The starting point was the use of the equations (see Ref. (26), Eq. [21]-[22])

$$V(L) = -E_0 L + E^* \ln Q \qquad [4]$$

Table I. Numerical values of the parameters used for fitting the experimental $1/C_{ox}$ *vs.* V_E plots and the $V(L)$ *vs.* L curves

Electrolyte	C.D., mA cm^{-2}	x^*, A	E_0, V cm^{-1} × 10^6	E^*, V cm^{-1} × 10^6	V^{calc}, V	V^{exp}, V	ϵ_{fit}
Na_2CO_3, 1*N*	32	10.0	2.229	0.620	112.0	127.5	30.5
H_2SO_4, 0.1*N*	32	10.0	2.603	0.796	138.0	147.0	27.0
	8	10.0	1.806	0.800	120.5	134.0	30.0
NH_2SO_3H, 0.1*N*	32	10.0	1.794	0.800	119.5	122.0	34.5
	16	10.0	1.579	0.820	116.7	121.0	34.5
	8	10.0	1.404	0.830	113.8	118.0	34.5
	4	2.7	1.002	0.660	107.2	107.5	34.5

Abbreviations: x^* = space-charge screening parameter; E_0 = surface charge electric field; $E^* = kT/zea$; V^{calc} = electrode potential values estimated by using Eq. [4] and [5] at the second minimum of the interference curves; and V^{exp} = experimentally measured cell voltage in the interference curves corrected for the ohmic drop.

with

$$\ln Q = 1 - (x^*/L)(1 + L/x^*) \ln (1 + L/x^*) \quad [5]$$

where E_0 is the surface charge electric field at the defect injecting interface, x^* is the "space charge screening parameter" representing the distance within the growing film in which the concentration of mobile species falls to one-half of its largest value, $E^* = kT/zea$ with ze the electric charge carried by the mobile species, a the half-hopping distance for the diffusing species, and L the actual film thickness at the electrode potential $V(L)$. Equations [4] and [5] were used twice in connection with the cell voltage values measured at the first minimum and successive maximum of the interference curves.

In this way it should be possible to determine independently the values of two parameters by assuming a value for the third one. This last parameter was chosen as an adjustable one in order to have the best fitting both the cell voltage values at the second minimum of the interference curves (see Table I) and of the experimental $1/C_{ox}$ *vs.* V_E plots. From the numerical computations we become aware that the best choice was to use as adjustable parameter x^* because a good fitting of the experimental curves was possible by varying x^* within an order of magnitude ($3 \leq x^* \leq 30$Å). Moreover by using as a guideline the theoretical expectations we tried to use the same value of x^* for the fitting of the different curves $1/C_{ox}$ *vs.* V_E obtained at different C.D.'s. According to Fromhold's analysis (27), in fact, a nearly constant x^* value can be expected for a ratio of C.D.'s equal to 20, which is about the ratio of C.D. exploited in our measurements.

The whole fitting procedure was, then, the following: (*i*) determination on the basis of the experimental measurements and by a trial and error method of the essential parameters of Fromhold's theory E_0, E^*, x^*, and construction of a voltage *vs.* thickness curve to be used in the $1/C_{ox}$ *vs.* V_E curve; and (*ii*) fitting of the $1/C_{ox}$ *vs.* V_E experimental curves by using both the values of film thicknesses calculated by Eq. [4]-[5] for any assigned electrode potential value, and a value of dielectric constant which assured the best fitting in the whole range of the measured capacitance values.

The results of the fitting procedure for different experimental conditions (*e.g.*, anions, C.D.'s) are summarized in Table I, where both the fitting parameters and the experimental cell voltages, V^{exp}, measured at the second minimum of the interference curves are reported. In the same table are reported the electrode potential values V^{calc}, at the corresponding thickness, extrapolated by using Eq. [4]-[5] and related fitting parameters. The agreement between V^{calc} and V^{exp} is always better than 90% for any solution and it becomes still better if we restrict our attention to the experiments performed in sulfamic acid where it varies between 96 and 99%. It is not surprising that the agreement is better for the data relative to the sulfamic acid solutions in which the anodization process occurs with the lowest bubbling until very high voltages. This finding suggests that the scanty agreement observed in the other solutions could be ascribed to the higher electronic currents (higher bubbling) as well as to the incorporation of anions previously discussed. It must be considered, moreover, that the reading of the cell voltages at the second minimum of the interference curves was strongly influenced by gas evolution on the electrode surface.

By looking to Fig. 4 and 5 it is possible to see the good agreement between the experimental curves and the fitting curves in the plots $1/C_{ox}$ *vs.* V_E. An aspect which we like to stress on the basis of these curves is that a linear $1/C_{ox}$ *vs.* V_E plot cannot be assumed as a proof of absence of space-charge effects particularly if the range of investigated thickness is relatively narrow.

Our results show unequivocally that a pseudolinear $1/C_{ox}$ *vs.* V_E plot can be obtained in a relatively large range of thickness by using the relationship V_E-thickness (*e.g.*, Eq. [4]-[5]) valid in presence of space charge together with an acceptable value of dielectric constant. Moreover by taking into account the possibility of a decreasing efficiency in the film formation current at the highest thicknesses, it is not surprising that in several cases the curvature predicted by the space-charge effects in the higher thicknesses region can be missed in the $1/C_{ox}$ *vs.* V_E plots.

As previously mentioned the final step in the fitting procedure was to get a dielectric constant value which allowed the best fitting of the $1/C_{ox}$ *vs.* V_E curves provided that it was in reasonable agreement with the literature data. The data of dielectric constant in Table I as well as the ϵ_{ox} *vs.* thickness plots reported in Fig. 6 show that: (*i*) the values ϵ_{fit} used are in fairly good agreement with the literature data obtained in similar experimental conditions (15); (*ii*) the experimental ϵ_{ox} values are practically independent of the film thickness provided that space-charge effects are taken into account by using the correct V_E *vs.* thickness relationship; and (*iii*) lower ϵ_{ox} values are obtained in sulfuric acid and carbonate solutions than in sulfamic acid.

Moreover, in the last solution the dielectric constant values are independent of the C.D., while they depend on the C.D. in sulfuric acid solution (see Table I). All these findings agree with the results of Rogers *et al.* (5) regarding the incorporation of sulfate and carbonate anions in the ZrO_2 anodic films. The lower values of the dielectric constant measured in these two solutions can be attributed to the incorporation phenomenon as reported by different authors (29, 30). As for Young's statement on an existing influence of the thickness on the "effective" dielectric constant of the ZrO_2 films, it is not confirmed in our work. In fact by looking to Fig. 6 it seems to us that a correct interpretation of these plots can be made on the basis of a constancy in the ϵ_{ox} values at different thicknesses. It is not surprising, moreover, that a larger scattering in the experimental points around the ϵ_{fit} value is observed in the region of smaller thicknesses where larger variations in the measured capacitance are found for a small thickness increment.

Some further comments must be devoted to the Tafel plots reported in Fig. 3. Although the limited range of investigated C.D.'s does not allow us to reach final conclusions, the results of Fig. 3 seem to confirm the hypothesis suggested by Dell'Oca and Young (31)

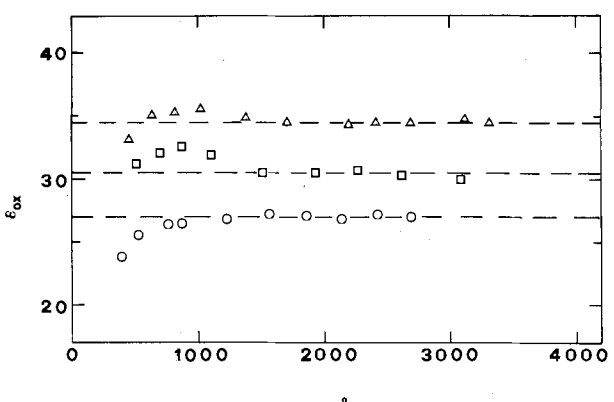

Fig. 6. Dielectric constant values *vs.* film thickness for films formed in various solutions at $i = 32$ mA cm^{-2}. △ NH_2SO_3H 0.1*N*; □ Na_2CO_3 1*N*; ○ H_2SO_4 0.1*N*. The ϵ_{ox} values were obtained by using the formula of the plane capacitor in connection with the Eq. [4]-[5] for the calculation of the thicknesses at different voltages. The experimental capacitance values have been corrected for the Helmholtz double layer capacitance $C_H = 20$ μF cm^{-2}.

that the incorporation of anions into the anodic films could be the source of nonlinearity in the Tafel plots. The progressive linearization at higher thicknesses of the Tafel plots reported in Fig. 3b and 3c could be ascribed to the mechanism of incorporation and growth of the ZrO_2 anodic films. It is tempting to correlate, in fact, the linearization of the Tafel plots with the results of Rogers *et al.* (5) showing a duplex structure in the ZrO_2 films formed in carbonate or sulfate solutions, with the inner layer near the metal/oxide interface incorporation free. This could suggest that a change in the rate-determining step from the oxide/electrolyte interface toward the bulk of the oxide films is occurring during the growth of the films. In the presence of a mobile space charge and then of an increasing electric field at the opposite injecting interface (26, 27), the previous suggestion should mean that the oxygen transport occurs via a vacancy-type mechanism. Such a mechanism has been suggested for calcia stabilized zirconia (CSZ) (32) as well as for ZrO_2 anodic films. By using the relationship $i = A \exp BE$ and Tafel plots of Fig. 3a, the A and B parameters were calculated and reported in Table II. The values of the half-hopping distances a were estimated according to the expression $B = zea/kT$ and to the hypothesis that only the oxygen ions are mobile in the films. This last assumption could be questioned at the highest current density ($i > 10$ mA cm^{-2}). However the agreement between the data of Table II and the A and B values reported in the literature (9, 11-15) is fairly good. The agreement with the literature data is still good if we compare the data of Table III(a) relative to the linear interpolation of the Tafel plots reported in Fig. 3b and 3c, for sulfuric acid and carbonate solutions, respectively. A direct comparison with other experimental data is not possible for the parabolic interpolation of the Tafel plots [see also Table III(b)].

An estimation of the activation energy at zero field, W (26, 27), has been carried out for films grown in HNH_2SO_3 solution on the basis of the parameter values reported in Tables I and II, and by assuming a value of 10^{13} sec^{-1} for the jump frequency of the migrating species in the film. The W values vary in the range (1.02-1.1) ± 0.04 eV.

These values of activation energy are not too far from the value reported by Croset *et al.* (33) for CSZ ($W = 1.18 \pm 0.02$ eV) and obtained by measurements of a-c electrical conductivity at high temperatures ($T \geq 200°C$). This fact seems a further proof that the same mechanism of ionic conduction is operating in CSZ as well in the films of ZrO_2 anodically grown.

A discrepancy between experimental data and theoretical ones comes out by comparing the hopping distances obtained on the basis of the Tafel plots and those obtained from the data of E^* values reported in Table I. From the results of Table I a half-hopping distance varying between 1.50 and 2.0Å in good agreement with the theoretically estimated value of 1.66Å given by Young (15) is found. These values should be compared with the a values obtained by using the experimental Tafel plots [see Tables II and III(a)]. The significance of these discrepancies between theory and experimental data are, at the moment, not clear to us. However we recall that analogous discrepancies in the half-hopping distances are common to other valve metals too.

Table II. Values of the parameters A and B obtained by the least squares method for the relationship $i = A \exp BE$ plotted in Fig. 3a at different thicknesses. The corresponding a values were calculated according to the relation $B = zea/kT$, with $z = 2$ and $kT/e = 0.025$V

Film thickness range, A	A, A cm^{-2}	B, cm V^{-1}	a, A
0-745	3.8×10^{-12}	5.09×10^{-6}	6.4
745-1490	9.2×10^{-11}	3.51×10^{-6}	4.4
0-1490	2.0×10^{-11}	4.2×10^{-6}	5.3

Table III(a). Values of the parameters A and B calculated by the least squares method for the relationship $i = A \exp BE$ plotted in Fig. 3b and 3c. The corresponding a values were calculated according to the relation $B = zea/kT$, with $z = 2$ and $kT/e = 0.025$V

Film thickness range A	A, A cm^{-2}	B, cm V^{-1}	a, A	
745-1490	2.8×10^{-9}	2.62×10^{-6}	3.3	
0-1490	7.0×10^{-9}	2.68×10^{-6}	3.4	H_2SO_4 0.1N
745-1490	1.71×10^{-10}	3.68×10^{-6}	4.6	
0-1490	3.04×10^{-9}	3.42×10^{-6}	4.3	Na_2CO_3 1N

Table III(b). Numerical values of the parameters calculated by the least squares method for the relationships $i = i_0 \exp ze(\alpha E - \beta E^2)/kT$ interpolating data of Fig. 3b and 3c at different thicknesses. The α and β values were calculated by assuming $z = 2$ and $kT/e = 0.025$V

Film thickness range, A	i_0, A cm^{-2}	α, A	β, A/10^7 V cm^{-1}	
0-745	1.1×10^{-17}	14.89	11.60	
745-1490	1.48×10^{-11}	5.70	2.20	H_2SO_4 0.1N
0-1490	3.89×10^{-15}	10.50	7.03	
0-745	2.14×10^{-19}	21.45	23.22	
745-1490	2.04×10^{-17}	13.15	9.15	Na_2CO_3 1N
0-1490	5.3×10^{-19}	17.70	15.90	

Summary

The kinetics of growth of ZrO_2 anodic films in the investigated solutions occurs in presence of mobile ionic space charge. This fact can explain both the reported increase with film thickness of the electric field strength and the shape of the $1/C_{ox}$ *vs.* V_E plots. The curvature of these plots observed at the higher thicknesses for films grown in sulfamic acid solution at different C.D.'s, together with the constancy in the measured ϵ_{ox} values, agree with the hypothesis of Fromhold's model of oxide growth in the presence of a high mobile space charge. The same model has been used in the fitting of the $1/C_{ox}$ *vs.* V_E plots for films grown in presence of incorporation of anions like sulfate and carbonate.

In these last solutions the curvature in the log i *vs.* E plots seems related with the effect of anions incorporation. This effect can also explain the lower ϵ_{ox} values measured for the films grown in these solutions as well as their dependence on the anodization current density.

Acknowledgments

This work has been financially supported by the Technological Committee of the C.N.R. (Roma). Part of this work has been performed by Salvatore Piazza in partial fulfillment of the requirements for the Chemical Engineering degree at the University of Palermo, March 1981.

Manuscript submitted June 7, 1982; revised manuscript received Dec. 10, 1982.

Any discussion of this paper will appear in a Discussion Section to be published in the December 1983 JOURNAL. All discussions for the December 1983 Discussion Section should be submitted by Aug. 1, 1983.

Publication costs of this article were assisted by the Universita di Palermo.

REFERENCES

1. L. Young, "Anodic Oxide Films," pp. 257-265, Academic Press, New York (1961), and references therein.

2. J. A. Davies, B. Domeij, J. P. S. Pringle, and F. Brown, *This Journal*, **112**, 675 (1965).
3. J. L. Whitton, *ibid.*, **115**, 59 (1968).
4. J. C. Banter, *ibid.*, **114**, 508 (1967).
5. G. T. Rogers, P. H. G. Draper, and S. S. Wood, *Electrochim. Acta*, **13**, 251 (1968).
6. J. S. L. Leach, C. Panagpoulos, and B. R. Pearson, Abstract 28, p. 91, The Electrochemical Society Extended Abstracts, Minneapolis, MN, May 10-15, 1981; J. S. L. Leach and C. Panagpoulos, 32nd I.S.E. Meeting, Extended Abstracts, Vol. II, p. 1002, Cavtat, September (1981).
7. V. A. Gilman and Ya. M. Kolotyrkin, *Zashch. Met.*, **2**, 360 and 1103 (1966).
8. B. Cox, *This Journal*, **117**, 654 (1970).
9. V. R. Howes, *Corros. Sci.*, **14**, 491 (1974).
10. G. C. Palit and K. Elayaperumal, *ibid.*, **18**, 169 (1978).
11. G. C. Willis, G. B. Adams, P. Van Rysselberghe, *Electrochim. Acta*, **9**, 79 (1964).
12. C. Ortega and J. Siejka, Abstract 55, p. 157, The Electrochemical Society Extended Abstracts Minneapolis, MN, May 10-15, 1981.
13. F. F. Faizullin, G. I. Yakhvarov, and V. V. Mosolov, *Elektrokhimiya*, **9**, 1508 (1973).
14. H. A. Hopper, J. A. Wright, and D. J. De Smet, *This Journal*, **124**, 44 (1977).
15. L. Young, *Trans. Faraday Soc.*, **55**, 632 (1959).
16. L. C. Archibald and J. S. L. Leach, *Electrochim. Acta*, **22**, 15 (1977).
17. O. S. Heavens, "Optical Properties of Thin Films," p. 114, Dover Publications, Inc., New York (1965).
18. R. Piontelli, in Symposium Proceedings on Sulphamic Acid and its Electrometallurgical Applications," pp. 175 and 437, A.I.M. Milano, Milan, May (1966).
19. J. C. Banter, *This Journal*, **112**, 388 (1965).
20. N. J. M. Wilkins, *Corros. Sci.*, **4**, 17 (1964); *ibid.*, **5**, 3 (1965).
21. L. Young, *Trans. Faraday Soc.*, **55**, 842 (1959).
22. N. Ramasubramanian and T. Trottier, *This Journal*, **119**, 1375 (1972).
23. C. Bartels, J. W. Schultze, U. Stimming, and M. A. Habib, in 32nd I.S.E. Meeting, Vol. II, p. 607, Cavtat, September (1981); *Electrochim. Acta*, **27**, 129 (1982).
24. J. W. Schultze and K. J. Vetter, *Ber. Bunsenges. Phys. Chem.*, **75**, 470 (1971).
25. J. F. Dewald, *This Journal*, **102**, 1 (1955).
26. A. J. Fromhold, *ibid.*, **124**, 538 (1977).
27. A. J. Fromhold, in "Oxides and Oxide Films," Vol. 3, J. W. Diggle and A. K. Vijh, Editors, pp. 1-271, Marcel Dekker, New York (1976).
28. L. Peraldo Bicelli, in "Symposium Proceedings on Sulphamic Acid and its Electrometallurgical Applications," Milan, May 1966, A.I.M. Milano (1966).
29. J. J. Randall, W. J. Bernard, and R. R. Wilkinson, *Electrochim. Acta*, **10**, 183 (1965).
30. F. Di Quarto, A. Di Paola, and C. Sunseri, *This Journal*, **127**, 1016 (1980).
31. C. J. Dell'Oca and L. Young, *ibid.*, **117**, 1548 (1970).
32. J. Perrière, J. Siejka, and M. Croset, *ibid.*, **128**, 530 (1981).
33. M. Croset, J. P. Schnell, and G. Velasco, *J. Appl. Phys.*, **48**, 775 (1977).

The Morphology of Silicon Electrodeposits on Graphite Substrates

Dennis Elwell,* Robert S. Feigelson, and Gopalakrishna M. Rao*,[1]

Center for Materials Research, Stanford University, Stanford, California 94305

ABSTRACT

Silicon electrodeposited on a dense, pyrolytic carbon, and on a graphite with 22% porosity are compared. Deposits with strongly developed <111> texture and apparently free from voids and inclusions can be made on both substrate materials. Deposits on vertical surfaces are normally free from inclusions and voids, in contrast to those on horizontal surfaces, even when the cathode is rotated.

In a previous paper (1) the conditions were described for the electrodeposition of dense, well-adherent silicon layers on graphite cathodes. The graphite in that case was mainly in rod form (Ultracarbon) and the deposits generally studied were those on the cylindrical surfaces of the rods as they were dipped to a depth of about 1 cm into K_2SiF_6/LiF/KF melts. Deposits were up to 1 mm thick on the side wall and 2 mm thick at the edge of the rod. The grain size was normally up to 250 μm and the best purity was 99.99%.

Silicon for solar cell applications is required in the form of uniform layers 100-200 μm in thickness. A 200 μm thick layer is required to absorb 95% of the solar spectrum at sea level (2). A major aim of this investigation was therefore to study the feasibility of achieving large grain size silicon electrodeposits when the thickness was restricted to only 100-200 μm. Electrodeposition offers the prospect of preparing silicon layers for solar cells in a single stage process starting with an inexpensive raw material (K_2SiF_6). The formation of the cell would be achieved by dopant diffusion or epitaxial layer deposition to form a p-n junction, or forming a Schottky barrier cell, for example by spraying a coating of indium oxide onto the silicon surface. In either case, the graphite would provide a back contact to the cell and would give the cell enough mechanical strength for easy handling.

The cost of the graphite could be a significant part of the solar cell cost, and so this investigation was undertaken to determine whether coherent, inclusion- and void-free deposits could be obtained on an inexpensive grade of graphite. The study reported here is a comparative study of electrodeposition on a low-grade graphite and on high-grade pyrolytic carbon. In addition, results are reported of electrodeposition studies using graphite rod cathodes rotated about a vertical axis.

Experimental

The apparatus, chemicals, and conditions used in this investigation were described previously (1) except where specified. The graphite chosen for this investigation was Great Lakes Carbon grade HLM, which has a density of 1.74 g cm^{-3} and a resistivity of 6-10 $\mu\Omega$ cm. Since the x-ray density of graphite is 2.24 g cm^{-3}, this material has an average porosity of 22.3%, which is expected to be an adverse factor for the electrodeposition of uniform layers. The purity of the HLM graphite was 99.7%, the main impurities being Ca, Fe, S, and Si. This material is sold at about \$1 per lb (\$0.45 per kg).

* Electrochemical Society Active Member.
[1] Present address: Inorganic & Metals Research Division, Dow Chemicals. Freeport, Texas 77541.
Key words: polycrystalline silicon, electrocrystallization, semiconductor, solar cell, graphite.

In order to investigate the influence of the surface finish, sheets of HLM graphite were polished by the manufacturer to No. 32, No. 125, and No. 250 grit finish, respectively. Figure 1 shows the microstructure of the materials with No. 32 and No. 240 finish ,and illustrates the high degree of porosity and roughness characteristic of the surfaces. The cathodes were normally 1-2 cm in width, 3 mm thick, and 5 cm long, and were immersed to a depth of about 1.5 cm. Vitreous carbon or graphite crucible materials were used as anode; the gap between the anode and the cathode was normally about 3 cm. However, for cylindrical cathodes larger than the 1 cm diam rods employed in our rotating cathode experiments, the gap was smaller; for example the cathode cylinder of 3 cm diam was placed at a distance 1.5 cm from the side wall and 2 cm from the bottom of the crucible. Each new cathode was cleaned by an acid dip, distilled water rinse, ultrasonic agitation in ethanol, and was then dried prior to each deposition experiment. Silicon was electrodeposited at a current density of about 10 mA cm^{-2} in a three-electrode configuration. In a typical experiment the potential dropped from an initial value of -0.80 ± 0.05V to a steady-state value of -0.65 ± 0.05V (*vs.* Pt) during the course of an experiment.

Rotating cathode experiments were performed using a modified furnace in which the cathode was mounted axially with a shaft which could be rotated through a Chevron seal. The rotation range normally employed was from 10-80 rpm, and the cathodes used in this case were rods of graphite of much higher density than that used in the stationary cathode experiments. The diameter of these cathodes was varied from 0.6-2.6 cm.

Results

Stationary electrodes.—A selection of typical deposits on both pyrolytic graphite and on the HLM material is shown in Fig. 2. Fairly uniform coverage was obtained on the pyrolytic graphite and on one other sample, but the two other examples illustrate typical problems encountered. It has been reported earlier (3) that electrodeposited silicon on both silver and graphite tends to nucleate nonuniformly, leaving rather large voids (up to 1 mm or so in size) which are filled in only as growth continues over a period of about 4 hr. This problem appears to be exaggerated by the rough nature of the graphite surface, and the deposit next to the pyrolytic sample in Fig. 2 is an extreme case of this problem. In addition to roughness, the impurity level within the melt appears to influence the uniformity of deposition; successive deposits from the same melt tend to be smoother, with better grain development than the previous deposits.

Figure 3 shows the cross section of two samples of HLM graphite on which thin films of silicon were deposited. The deposits vary in thickness from about 100 μm near the top to about 200 μm near the bottom, and are generally coherent (crack free) in spite of large voids in the graphite substrate material. The deposits follow major irregularities in the graphite surface rather than filling them in to give a smooth surface, as can be particularly seen on the right-hand sample where there is a large indentation on the side facing the second sample. The bottom surface is nor-

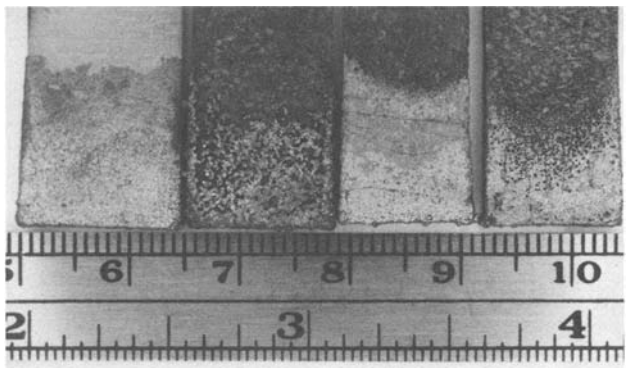

Fig. 2. Typical silicon electrodeposits on pyrolytic carbon (left-hand sample) and HLM graphite cathodes.

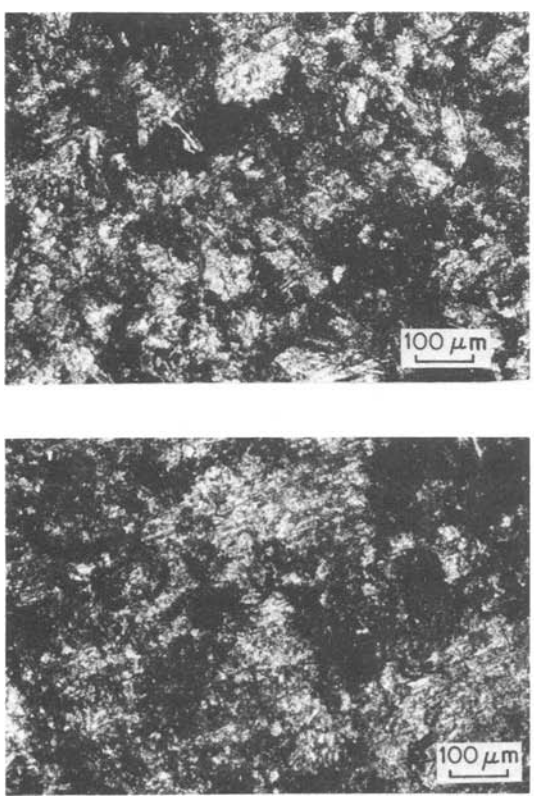

Fig. 1 Optical micrograph of (a) No. 32, (b) No. 240 finish HLM graphite substrate materials.

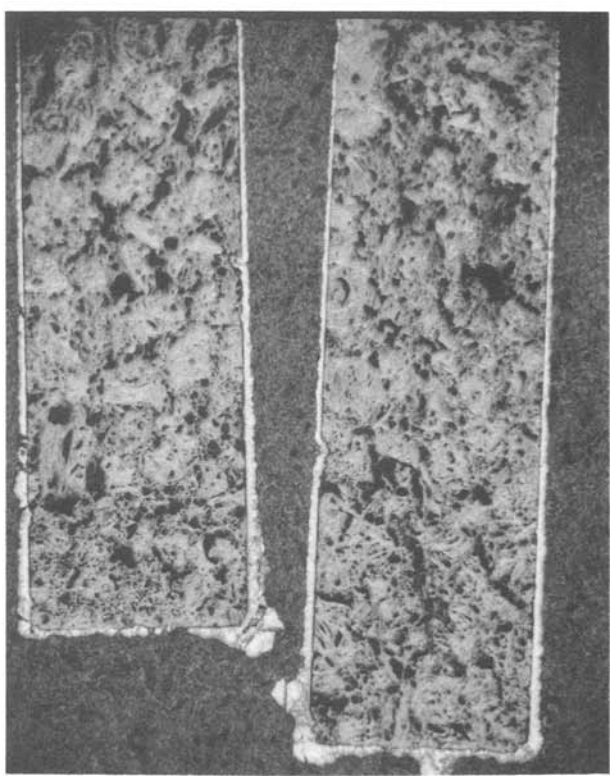

Fig. 3. Cross section through HLM graphite electrodes showing silicon deposits. The electrodes are 3.2 mm in thickness.

mally less uniform in thickness and there are large protuberances at the corners of the sample. This latter effect is common in any process of crystallization from solution, and arises from the greater access of solute to the corners in comparison with points on a flat surface.

Substrate surface finish clearly has an influence on the morphology of the deposit, since major perturbations in film thickness arose from the larger irregularities on the graphite surface, and occasional voids in the film could be associated with corresponding voids in the surface (see Fig. 3). On the whole, however, the quality of the silicon layers on the rather porous graphite was remarkably good. The average quality of films on the pyrolytic graphite, as judged by thickness uniformity, grain size, and incidence of voids, was better on the pyrolytic carbon than on the HLM graphite as expected. However, many of the best films were deposited on the HLM material.

The growth of silicon layers of large grain size depends not on the nucleation process but on the preferential growth of relatively few grains at an early stage of deposition. Cross-sectional studies have shown that the initial grain size is extremely small; observations using a scanning electron microscope (SEM) normally reveal a grain size of about 1 μm or less at the interface between the silicon and graphite or silver substrate. However, grain selection can be extremely rapid when the current density is maintained at a low level and especially during the third or subsequent deposits from the same melt.

Figure 4 is an example which shows the tendency towards columnar growth. Observations normal to the surface (Fig. 5) show clearly that the films tend to grow with {111} orientation. This same tendency is shown by deposits on both pyrolytic carbon and HLM graphite surfaces. The average grain size is about 150 μm and the layers in this case are continuous.

The average deposition efficiency, determined as the ratio of the mass of silicon deposited to that expected from the number of coulombs passed, was 49%. The highest value recorded was 67%.

No strong systematic differences were seen in deposition efficiency or the characteristics of the silicon deposits on the grit size used to polish the HLM graphite. In fact, the rougher 32 grit finish gave larger grain size deposits with better developed {111} facets than those on 240 or 120 finish surfaces, but the 32-finish material appeared to have a lower porosity than the material polished with the finer grit size, and this may be a more significant parameter. Purity of the melts may also be significant since it was notable that subsequent deposits from the same melt were normally more uniform and of better-developed {111} texture.

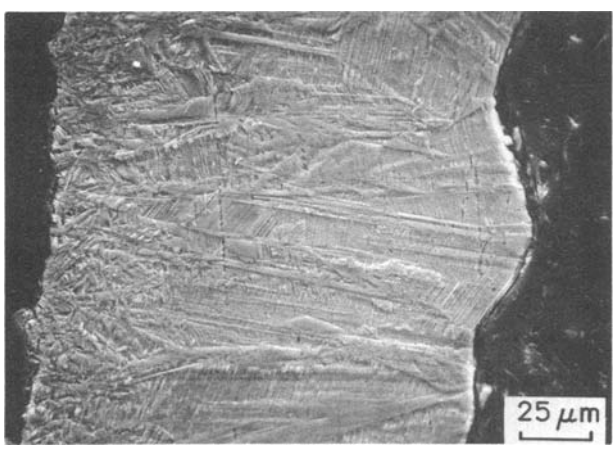

Fig. 4. Scanning electron micrograph of etched cross section of silicon electrodeposit. The graphite substrate is on the left-hand side, and the relatively fine grain size at this stage can be observed.

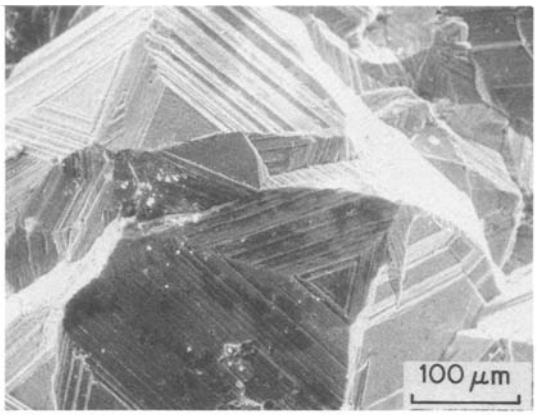

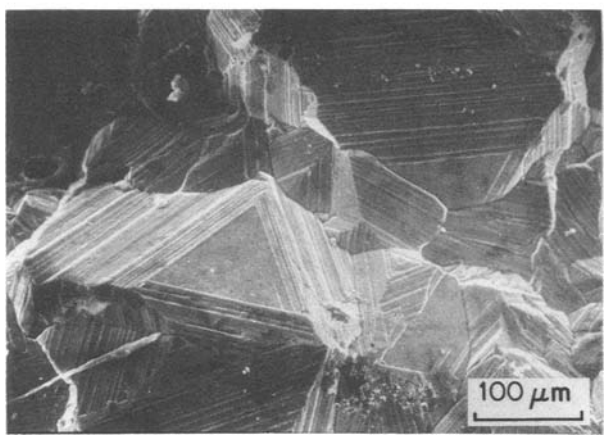

Fig. 5. Scanning electron micrographs of the surface of silicon deposits on HLM graphite, showing the <111> texture.

Rotating electrodes.—When the larger diameter cathodes were used (> 1 cm) it was not convenient to use a reference electrode during the rotating cathode experiments because of space limitations in a 6 cm diam crucible. During two-electrode deposition with a graphite anode, the deposition potential required to give a current density of around 10 mA cm^{-2} was normally found to increase sharply from about −1.6 to −2.8V *vs.* a vitreous carbon anode (the crucible), after a time which depends on the current density, rotation speed, and previous history of the bath. This effect has been attributed to traces of moisture in the melt, leading to a reduction in cell voltage, as oxygen rather than fluorine is liberated at the anode (4). It does not appear to have a serious influence on the efficiency of deposition for durations longer than 8 hr, although some hydrogen will be liberated at the cathode until the moisture traces are removed.

Figure 6 shows a series of deposits on the bottom surface of some rotated cathodes of various diameters. Deposits on rotating cathodes were normally of nonuniform cross section in spite of the theoretical expectation of a uniform boundary layer in contact with a horizontal rotating disk or cylinder (5). Figure 7 shows a typical cross section which shows that the thickness at the edges is roughly twice that at the center. In addition, this photograph shows that the silicon deposit contains a high concentration of voids, especially in the region near the center of the cathode face. A magnified view of a typical cluster of voids is shown in Fig. 8. The formation of the voids is probably associated with small gas bubbles (probably CF_4) which are trapped between grains. The

Fig. 6. Bottom surface of graphite rods used as rotating electrodes, showing silicon electrodeposits.

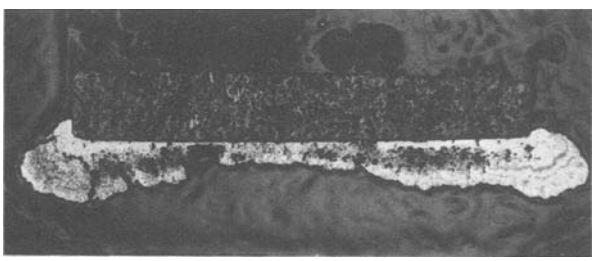

Fig. 7. Cross section through end of graphite electrode and silicon deposit, showing voids in the silicon. The cathode is 9.3 mm in diameter.

external surfaces of thicker deposits were often continuous with large grain size, as in the case of the stationary cathodes. However, a typical deposit was porous and dull in appearance at the center, with shiny appearance at the raised edges due to larger grain size and lower or zero porosity there. In a few cases the porosity was so high that no adhesion was obtained. This problem was particularly severe with the larger diameter cathodes, 1.9-2.6 cm across, and in no case was a coherent and well-adherent deposit achieved on these large diameter rods.

In contrast to the porous deposits at the face centers, the deposits at the corners and especially on the vertical edges of the rotating cathodes were coherent, with well-formed grains. An example is shown in Fig. 9. The {111} texture was less apparent in such deposits, but the average grain size was around 100 μm.

Discussion

From the practical viewpoint, the most encouraging result of this investigation was the deposition of coherent, inclusion-free silicon layers of acceptable grain size for solar cells on very porous graphite substrates. Mechanically polishing the graphite with different grit sizes appeared to have little influence on the morphology of the deposit, although the presence of major irregularities in the graphite surface leads to corresponding variations in the film and so should be avoided.

Nucleation of silicon by electrodeposition at controlled current density, even at the low value of 10 mA cm^{-2}, gives very fine particles even on relatively smooth surfaces like silver or pyrolytic graphite. Independent of the roughness of the substrate surface, columnar growth occurs with the development of {111} grains. The development of a <111> texture is presumably a kinetic effect, the {111} faces being the slowest growing, so that this texture develops whatever the surface finish on the material.

Although the deposits of largest grain size were made on the porous HLM graphite, this material also showed greater variations in the quality of the deposit than those on pyrolytic carbon. A lower porosity material than the HLM graphite appears desirable for practical fabrication of solar cells, in order to improve reproducibility and to reduce variations in the flatness of the surface. Coating the graphite with a thin layer of pyrolytic carbon prior to deposition would be beneficial and should not contribute substantially to the cost of the device.

With both stationary and rotating electrodes, deposits on vertical surfaces were of significantly better quality (as judged by absence of porosity) than those on horizontal surfaces. This difference is attributed to gas bubbles which are easily trapped in irregularities between grains on a horizontal downward-facing surface. Although the quality of deposits on the vertical surfaces of rotating cathodes was not better than that on the stationary materials, agitation of the electrolyte appears very desirable as a means of improving the uniformity in the thickness of the deposit as a function of the position below the surface. The thickness tapering seen in deposits on stationary elec-

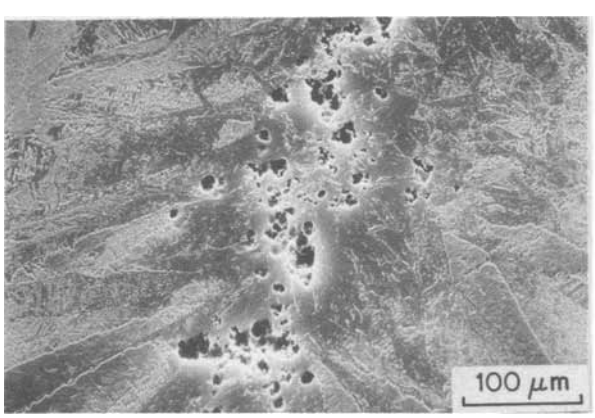

Fig. 8. SEM photograph showing voids in silicon electrodeposited on bottom surface of rotating electrode.

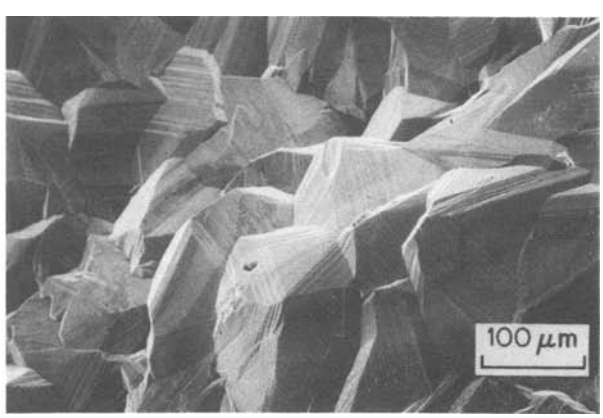

Fig. 9. SEM photograph of surface of silicon deposited on vertical sides of a rotating electrode.

trodes (Fig. 3) is attributed to variations in concentration of solute and vibration of the cathode, or gentle rocking of a rectangular trough containing the electrolyte is envisaged for future experiments.

The relative ease of production of films having an average grain size above 100 μm is encouraging for applications of electrodeposited silicon in solar cells. Although the scale of experiments performed to date is too small for fabrication of test cells, the electrical properties of the deposits appear promising (6). The purity of the best deposits as determined by emission spectroscopy is greater than 99.999%. Undoped samples are n-type with a carrier concentration of $\approx 10^{17}$ cm^{-3}, carrier mobility of 100 cm^2 V^{-1} sec^{-1}, and resistivity up to 3 Ω cm. The reduction of impurity level from 1-2% in the K_2SiF_6 starting material to 8-10 ppm in the deposited silicon was achieved by purely electrolytic means, using a sacrificial predeposition for at least 24 hr to purify every new melt. It was noted that successive deposits normally showed improved uniformity and grain size, and this improvement is attributed to the higher purity of the melt as deposition continues. Prepurification of the starting chemicals appears worthy of investigation in future studies.

Conclusions

1. An inexpensive and rather porous grade of graphite can give silicon deposits of over 100 μm average grain size and which are apparently free from voids and inclusions.

2. The surface finish of the graphite has little effect on the morphology of the deposit but a high degree of porosity leads to more variability in the deposits.

3. The deposits show a well-developed <111> texture.

4. Deposits on vertical surfaces are of much better quality than on horizontal, even when the cathode is rotated.

5. A stirred bath, with vertical plate electrodes, appears to be the most favorable condition for deposition of void-free layers of uniform thickness.

Acknowledgments

This work was supported by the Division of Advanced Energy Projects (Dr. R. Gajewski) of the Department of Energy under contract number DE-A503-76SF-0326 PA67. Some use was made of facilities made available to the Stanford Center for Materials Research by the National Science Foundation through its MRL program. We are grateful to Great Lakes Carbon Corporation for the HLM graphite used in this investigation, and to Mss. R. Koch and M. M. Simkins for the figures.

Manuscript submitted March 15, 1982; revised manuscript received Oct. 6, 1982. This was Paper 537 presented at the Denver, Colorado, Meeting of the Society, Oct. 11-16, 1981.

Any discussion of this paper will appear in a Discussion Section to be published in the December 1983 JOURNAL. All discussions for the December 1983 Discussion Section should be submitted by Aug. 1, 1983.

REFERENCES

1. G. M. Rao, D. Elwell, and R. S. Feigelson, *This Journal*, **128**, 1708 (1981).
2. R. N. Hall, *Solid-State Electron.*, **24**, 595 (1981).
3. G. M. Rao, D. Elwell, and R. S. Feigelson, *Surf. Technol.*, **13**, 331 (1981).
4. D. Elwell and G. M. Rao, To be published.
5. V. C. Levich, *Russ. J. Phys. Chem.*, **18**, 335 (1944).
6. G. M. Rao, D. Elwell, and R. S. Feigelson, *Sol. Energy Mater.*, **7**, 15 (1982).

Voltammetric Study of the Anodic Oxidation of Sulfide Ions in Molten Fluorides

Nguyen Quang Minh* and Neng-Ping Yao*

Argonne National Laboratory, Chemical Engineering Division, Argonne, Illinois 60439

ABSTRACT

The electrochemical oxidation of sulfide ions has been studied in LiF-NaF eutectic by linear sweep voltammetry using graphite electrodes at 1023 K. The oxidation is found to be reversible and diffusion controlled. A detailed analysis of the experimental results suggests the following mechanism for the oxidation of sulfide ions $2S^{2-} \rightleftarrows S_2^{2-} + 2e^-$. The average apparent diffusion coefficient for sulfide ions is calculated to be 1.47×10^{-5} cm^2/sec at 1023 K.

The electrochemical behavior of sulfide ions in molten salts is of considerable interest from both fundamental and applied viewpoints. The oxidation of of sulfide ions in molten salts offers challenging fundamental research. To date, the mechanism of the reaction is still controversial and cannot be interpreted in an unambiguous manner (1). From the applied viewpoint, knowledge of the electrochemical reaction of sulfide ions is important for (*i*) battery technology such as high temperature secondary batteries (2) and (*ii*) metallurgical molten-salt processes such as metal electrowinning from sulfides (3).

The electrochemical oxidation of sulfide ions has been studied in chloride melts (4-25), mainly LiCl-KCl, $PbCl_2$-NaCl, and $AlCl_3$-NaCl. In LiCl-KCl eutectic, different oxidation mechanisms have been proposed by various investigators. This can be illustrated by the following two examples of mechanisms proposed for the sulfide oxidation. Weaver and Inman (7) found that the oxidation of sulfide ions was overall diffusion controlled and reversible. However, it appeared to be controlled by the extensive formation of a polymeric sulfur film, and a mixture of various soluble polysulfides was ultimately formed. These authors proposed either one of the following three types of reaction mechanism to account for the observed behavior (*i*)

$$S^{2-} \xrightarrow{-2e^-} S(\rightarrow S_x);\ S \xrightarrow{S^{2-}} S_2^{2-},\ (ii)\ S^{2-} \xrightarrow{-2e^-} S \rightarrow S_x \rightarrow S_y;\ S_x \xrightarrow{} S_{x+1}^{2-},$$

or (*iii*) the reaction is similar to mechanism (*ii*) with a soluble product passivation model. On the other hand, the reactions postulated by Kam and Johnson (11) for sulfide ions are

$$2S^{2-} \xrightarrow{-2e^-} S_2^{2-} \xrightarrow{-e^-} S_2^{-} \xrightarrow{-e^-} S_2$$

* Electrochemical Society Active Member.

Key words: voltammetry, oxidation, fused salts, sulfide ions, fluorides, mechanism.

The oxidation of sulfide in PbS-$PbCl_2$-alkali chloride melts has been studied by several workers to obtain a better understanding of the anode reaction in the electrowinning of lead (14-22). It was generally found that the reaction involves a chemical reaction subsequent to the oxidation. For example, Skyllas and Welch (16) showed that the oxidation of PbS occurred via an irreversible two-electron process in $PbCl_2$-NaCl at 713 K. The oxidation product reacted with the melt to form a new product that was not electrochemically reduced. The followup reaction was first order, with a rate constant of 8 sec^{-1}.

Other workers have investigated the behavior of sulfide in $AlCl_3$-NaCl melts. They found the absence of polysulfides in these melts and the oxidation of S into cationic species S^{n+}. In $AlCl_3$-NaCl melt saturated with NaCl, Marassi *et al.* (24) observed two steps for the oxidation of sulfide ions. The oxidation product was either S_2^{2+} or S^{2+} depending on temperature.

Recently, in connection with research on the production of aluminum via the electrolysis of Al_2S_3, the present authors (26) studied the mechanism of the anodic oxidation of sulfide ions in molten $MgCl_2$-NaCl-KCl eutectic at 1023 K. The results show that the oxidation proceeds via a mechanism based on two steps: $S^{2-} \xrightarrow{-2e^-} S$ followed by $S + S \rightarrow S_2(g)$. The electrochemical reaction is reversible and diffusion controlled. The dimerization of sulfur atoms to elemental sulfur is very fast and very much displaced toward S_2. The electrochemical behavior of sulfide in molten LiF-NaF was also studied by the present authors and is the subject of the present paper. The objective of this study is to evaluate the feasibility of the LiF-NaF melt as solvent for the electrolysis of Al_2S_3.

Literature search shows that no work has been reported on the oxidation of sulfide ions in molten fluorides. The only related information is limited to the electrolysis of Al_2S_3 (3, 27-29) and ZnS (30) in fluoride and mixed fluoride-chloride melts. In these cases, sulfur was reported to be the principal anode product. However, the details of the reaction are not known, and the mechanism has not been elucidated. In the present paper, the results obtained from a voltammetric study of the electrochemical oxidation of sulfide in LiF-NaF eutectic (61-39 mol percent (m/o), mp 922 K) at 1023 K are presented. A reaction mechanism consistent with the experimental data has been suggested for the oxidation.

Experimental

Procedure.—General procedures for experimental work have been reported elsewhere (26). In the present work, the electrolytic cell consisted of a pyrolytic boron nitride crucible (5.2 cm diam, 7.2 cm high, Union Carbide) containing molten LiF-NaF eutectic and three electrodes. The cell was operated inside a VAC helium atmosphere glove box and heated in a single-zone Lindberg furnace as previously described (26). Standard voltammetric instrumentation was employed. Voltammograms were recorded with a Hewlett-Packard X-Y recorder. All measurements were made at 1023 K.

Electrodes.—All potentials were measured with respect to a Pt wire immersed in the melt as a quasi-reference electrode. The working electrode was a graphite rod (0.63 cm diam, Union Carbide, Grade ECV) insulated with hot-pressed boron nitride (carborundum) so that only a defined surface area was exposed to the molten salt. Another graphite rod immersed in the melt served as the counterelectrode.

Chemicals.—The molten salt electrolyte (LiF-NaF eutectic) was prepared from pure LiF and NaF crystals (Harshaw Chemical); Al_2S_3 and Na_2S (Cerac Pure) were used without further purification.

Results and Discussion

A typical background curve for LiF-NaF (61-39 m/o) melt (with no added solute) at 1023 K is shown in Fig. 1. The cathodic limit as indicated by the steeply rising current at about −0.8V (all potentials given *vs.* Pt reference electrode) can be assigned to the reduction of sodium ions. The anodic peak located at about +2.3V was the so-called critical current, *i.e.*, the maximum current which is attained before the normal anode reaction is superseded by the anode effect which is attributable to dewetting of the electrode by fluorocarbon compounds. Another small anodic peak was observed at about +1.1V. This might be due to the presence of residual impurities. The "impurity" peak even remained unchanged after a few hours of purification by pre-electrolysis.

On the addition of Al_2S_3 to the melt, two additional peaks were observed on the voltammogram. A typical voltammogram is shown in Fig. 2. (In this figure, the observed increase in the anodic current near the cathodic limit is not associated with S^{2-} but instead is due to the oxidation of any products formed from the deposition of aluminum or sodium.) These additional peaks were attributable to the oxidation of sulfide ions and, on the reverse scan, to the reduction of its product. The identification of sulfide peaks was confirmed by the addition of Na_2S to the melt containing Al_2S_3. The Na_2S addition enhanced the sulfide peaks. No peaks were attributable to the presence of aluminum ions in the LiF-NaF eutectic melt. The absence of any aluminum waves was probably due to the small potential separation between the aluminum deposition and the cathodic limit, the aluminum waves being undistinguishable from the cathodic limit. As can be seen from Fig. 1 and 2, the "impurity" peak appears to have no effect on the sulfide oxidation. This finding was easily confirmed by reversing the poten-

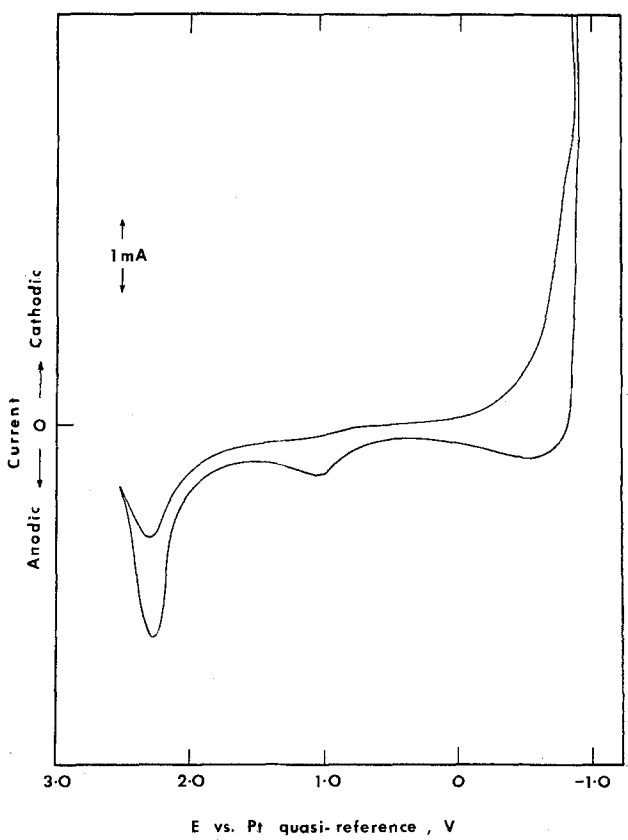

Fig. 1. Voltammogram of LiF-NaF melt background. T = 1023 K, electrode area = 0.32 cm^2, v = 100 mV/sec.

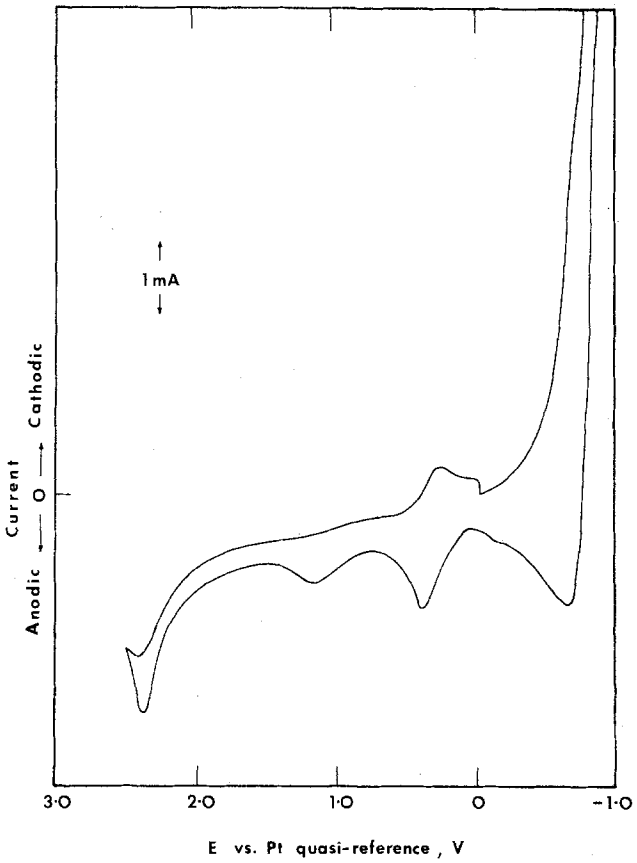

Fig. 2. Voltammogram of Al_2S_3 in LiF-NaF eutectic melt. T = 1023 K, electrode area = 0.32 cm^2, v = 100 mV/sec, Al_2S_3 concentration = 4.47 × 10^{-6} mol/cm^3.

tial at a value more cathodic than the oxidation potential of the "impurity"; the sulfide peaks remained unchanged. However, it is desirable to prevent impurities from being deposited on the electrode since the deposition can change the nature of the working electrode. In these voltammetric experiments, the cathodic potential was limited to about +1V, well before the "impurity" deposition.

The oxidation of sulfide ions was studied at three different Al_2S_3 concentrations: 4.47 × 10^{-6}, 6.61 × 10^{-6}, and 8.49 × 10^{-6} mol/cm^3. Voltammograms were obtained for the oxidation at sweep rates of 0.02-1 V/sec. Typical linear sweep voltammograms for different sweep rates at the graphite working electrode are shown in Fig. 3. The peak currents of the recorded voltammograms, i_p, were measured and are plotted as a function of the square root of the sweep rate, $v^{1/2}$, in Fig. 4. These plots resulted in straight lines. Although these lines appear to have a small intercept at the peak current axis, it is not unreasonable to assume that the plots pass through the origin considering experimental error and uncertainty (±10%) from peak current measurements. Also, the slope of the plots is proportional to the concentration of sulfide ions. These results indicate that the electrochemical reaction is diffusion controlled. The reversibility of the reaction is confirmed by the constancy of the peak potential as the sweep rate is varied, as seen in Fig. 3. It was found that the peak potential for the sulfide oxidation shifts anodically with increasing sulfide concentration in the melt. It was also found that the rest potential of the working electrode becomes more anodic as the sulfide concentration is increased. This could explain the shift of the peak potential.

For diffusion-controlled, reversible electrochemical processes, potential separations such as peak-to-half-peak potential, ΔE_p, and peak-to-half-wave potential, ΔE (the half-wave potential is measured at the potential corresponding to 0.85 i_n), are useful for kinetic

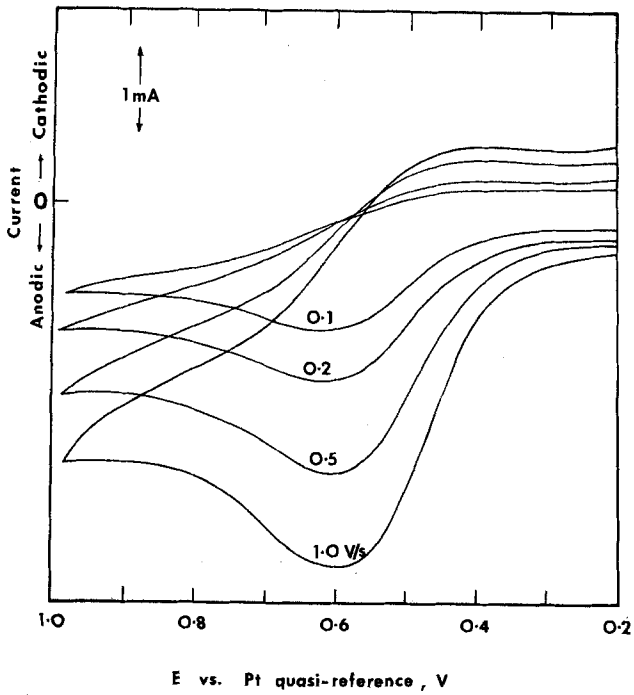

Fig. 3. Voltammograms of the oxidation of sulfide ions in LiF-NaF melt at different sweep rates. T = 1023 K, electrode area = 0.32 cm^2, Al_2S_3 concentration = 4.47 × 10^{-6} mol/cm^3.

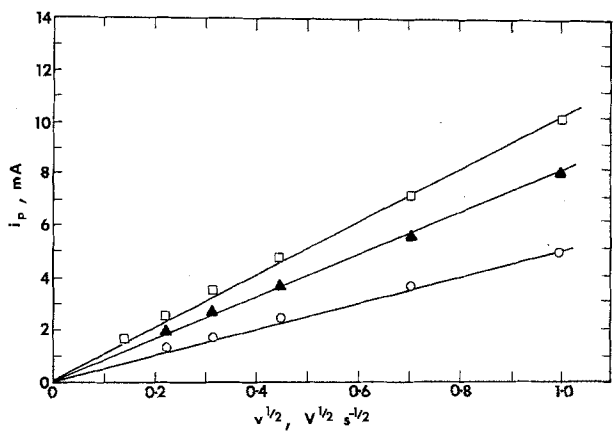

Fig. 4. Plots of i_p vs. $v^{1/2}$ for the oxidation of sulfide ions in LiF-NaF melt. T = 1023 K, electrode area = 0.32 cm^2, □ = 8.49 × 10^{-6} mol/cm^3 Al_2S_3, ▲ = 6.61 × 10^{-6} mol/cm^3 Al_2S_3, ○ = 4.47 × 10^{-6} mol/cm^3 Al_2S_3.

diagnostic purposes. Table I summarizes the experimental data obtained for ΔE_p and ΔE at the different sulfide concentrations studied.

It can be seen from Table I that ΔE_p and ΔE are independent of potential sweep rate. For a simple electrochemical reaction that is reversible and first order ($R \rightleftarrows O + ne$), ΔE_p and ΔE at 1023 K are 193.9/n and

Table I. Data for peak-to-half-peak and peak-to-half-wave potential for the oxidation of sulfide ions in LiF-NaF eutectic at 1023 K

	Al_2S_3 concentration					
	4.47 × 10^{-6} (mol/cm^3)		6.61 × 10^{-6} (mol/cm^3)		8.49 × 10^{-6} (mol/cm^3)	
v (mV/sec)	ΔE_p (mV)	ΔE (mV)	ΔE_p (mV)	ΔE (mV)	ΔE_p (mV)	ΔE (mV)
20					135	60
50	135	60	140	65	140	65
100	140	60	140	65	140	65
200	135	65	140	70	145	65
500	140	65	145	70	145	75
1000	145	70	145	65	145	60

97.7/n mV (31), respectively, where n is the number of electrons involved in the process. If the above mechanism were applicable to the oxidation of sulfide ions in the present study, n would lie between 1 and 2. Since the experimental results show that the oxidation proceeds via a single, reversible, diffusion-controlled step, that mechanism cannot be applied. The experimental voltammetric curves obtained were broader than the theoretically expected first-order curve. Schuman (32) has considered the theory of diffusion-controlled electrode processes, $qR \rightleftarrows mO + ne$, where one or both of the stoichiometric numbers q and m are integers greater than unity. His results have shown that as the reaction order increases, the voltammogram becomes less peak-shaped in nature and lower in peak current. In the case of a second-order process, $2R \rightleftarrows O + ne$, $\Delta E_p = 279.4/n$ mV and $\Delta E = 123.6/n$ mV (32). The data shown in Table I fit this mechanism, assuming $n = 2$. It is, therefore, hypothesized that the oxidation of sulfide ions in LiF-NaF eutectic at 1023 K involves

$$2S^{2-} \rightleftarrows S_2^{2-} + 2e^- \quad [1]$$

No prior spectroscopic or related physicochemical studies have been reported for S_2^{2-} species in molten fluorides. However, the species S_2^{2-} has been found to form in the oxidation of sulfide ions in LiCl-KCl (6, 7) and $PbCl_2$-NaCl melts (16). There is also spectroscopic evidence that S_2^{2-} species exist in molten chlorides (33). The existence of S_2^{2-} in LiF-NaF suggested by the present electrochemical study is, thus, tentative and should be proved by spectroscopic measurements of characteristic absorption frequencies.

If the mechanism for the sulfide oxidation in LiF-NaF eutectic is represented by Eq. [1], then the peak current is given as (32)

$$i_p = 0.3533 \frac{n^{3/2}\mathbf{F}^{3/2}}{R^{1/2}T^{1/2}} A_s D^{1/2} C^\circ v^{1/2} \quad [2]$$

where $\mathbf{F}$ is the Faraday (C), R is the universal gas constant (J/mol · K), T is the temperature (K), A_s is the electrode area (cm^2), D is the diffusion coefficient (cm^2/sec), and C° is the concentration of the electroactive species (mol/cm^3). The diffusion coefficients of sulfide ions in LiF-NaF eutectic at 1023 K were calculated to be 1.41×10^{-5} cm^2/sec at 4.47×10^{-6} mol/cm^3 Al_2S_3, 1.48×10^{-5} cm^2/sec at 6.61×10^{-6} mol/cm^3, and 1.52×10^{-5} cm^2/sec at 8.49×10^{-6} mol/cm^3, with an estimated experimental error of ±10%. Within this uncertainty, the concentration dependence of the diffusion coefficient cannot be defined.

Since previous works reported in the literature indicate that the electrolysis of metal sulfides in fluoride melts produces sulfur at the anode, it is interesting to know whether this is the case for the electrolysis of Al_2S_3 in this melt. The electrolysis was conducted with 2 weight percent Al_2S_3 in LiF-NaF as the electrolyte, using the cell assembly previously described (34). Sulfur was detected (by x-ray analysis) during the electrolysis. For such electrolysis, the sulfide reaction at the anode is represented by Eq. [1] or

$$S^{2-} \rightleftarrows S + 2e^- \quad [3]$$

$$S + S^{2-} \rightleftarrows S_2^{2-} \quad [4]$$

Sulfur atoms formed by reaction [3] dissolve in the melt by chemical reaction [4]. When the saturation of S_2^{2-} is reached, S combines to give elemental sulfur, as detected during the electrolysis experiment.

One interesting observation is that the LiF-NaF melt was colorless, but turned reddish brown on the addition of enough Al_2S_3. The intensity of the color increased with increasing Al_2S_3 concentration. Addition of Na_2S to the melt gave similar results.

In summary, the voltammetric study has shown that the anodic oxidation of sulfide ions in LiF-NaF eutectic is reversible and diffusion controlled. The experimental results were in best agreement with the mechanism $2S^{2-} \rightleftarrows S_2^{2-} + 2e^-$.

Acknowledgment

This work was performed under the auspices of the U.S. Department of Energy, Division of Electrochemical Energy Storage Systems.

Manuscript submitted Sept. 7, 1982; revised manuscript received *ca.* Dec. 7, 1982.

Any discussion of this paper will appear in a Discussion Section to be published in the December 1983 JOURNAL. All discussions for the December 1983 Discussion Section should be submitted by Aug. 1, 1983.

Publication costs of this article were assisted by Argonne National Laboratory.

REFERENCES

1. R. P. Tischer and F. A. Ludwig, in "Advances in Electrochemistry and Electrochemical Engineering," Vol. X, H. Gerischer and C. W. Tobias, Editors, p. 391, John Wiley and Sons, New York (1977).
2. J. L. Sudworth, in "Electrochemical Power Sources, Primary and Secondary Batteries," M. Barak, Editor, p. 403, The Institution of Electrical Engineers, London (1980).
3. N. Q. Minh and N. P. Yao, in "Advances in Molten Salt Chemistry," Vol. V, G. Mamantov, Editor, Elsevier, New York, To be published.
4. G. Delarue, *Bull. Soc. Chim. Fr.*, 906 (1960).
5. G. Delarue, *ibid.*, 1654 (1960).
6. F. G. Bodewig and J. A. Plambeck, *This Journal*, **116**, 607 (1969).
7. M. J. Weaver and D. Inman, *Electrochim. Acta*, **20**, 929 (1975).
8. B. Cleaver, A. J. Davis, and D. J. Schiffrin, *ibid.*, **18**, 747 (1973).
9. J. P. Bernard, A. de Haan, and H. van der Poorten, *C. R. Acad. Sci., Ser. C*, **276**, 587 (1973).
10. J. R. Birk and R. K. Steunenberg, in "Advances in Chemistry Series," No. 140, p. 186, American Chemical Society, Washington, DC (1975).
11. K. W. Kam and K. E. Johnson, *J. Electroanal. Chem. Interfacial Electrochem.*, **115**, 53 (1980).
12. D. Warin, Z. Tomczuk, and D. R. Vissers, *This Journal*, **130**, 64 (1983).
13. V. I. Lysin, V. F. Zinchenko, Z. N. Belous, and A. A. Velikanov, *Chem. Abstr.*, **93**, 122570b (1980).
14. P. L. King, Ph.D. Thesis, The University of New South Wales, Sydney, Australia (1971).
15. B. J. Welch, A. J. Cox, and P. L. King, in "Physical Chemistry of Process Metallurgy: The Richardson Conference," J. H. E. Jeffes and R. J. Tait, Editors, p. 33, The Institution of Mining and Metallurgy, London (1974).
16. M. Skyllas and B. J. Welch, *Electrochim. Acta*, **23**, 1157 (1978).
17. P. H. Davies, E. J. Frazer, M. Skyllas, and B. J. Welch, in "Trends in Electrochemistry," J. O'M. Bockris, D. A. J. Rand, and B. J. Welch, Editors, p. 253, Plenum Press, New York (1977).
18. V. Plichon, A. de Guibert, and M. N. Moscard-Levelut, in "Ionic Liquids," D. Inman and D. G. Lovering, Editors, p. 387, Plenum Press, New York (1981).
19. A. de Guibert and V. Plichon, *J. Electroanal. Chem. Interfacial Electrochem.*, **90**, 399 (1978).
20. A. de Guibert, V. Plichon, and J. Badoz-Lambling, *ibid.*, **105**, 143 (1979).
21. A. de Guibert, V. Plichon, and J. Badoz-Lambling, *This Journal*, **126**, 1902 (1979).
22. D. Lelievre, A. de Guibert, and V. Plichon, *Electrochim. Acta*, **24**, 1243 (1979).
23. K. A. Paulsen and R. A. Osteryoung, *J. Am. Chem. Soc.*, **98**, 6866 (1976).
24. R. Marassi, G. Mamantov, and J. Q. Chambers, *This Journal*, **123**, 1128 (1976).
25. G. Mamantov and R. A. Osteryoung, in "Characterization of Solutes in Non-Aqueous Solvents," G. Mamantov, Editor, p. 223, Plenum Press, New York (1978).

26. N. Q. Minh, R. O. Loutfy, and N. P. Yao, *J. Electroanal. Chem. Interfacial Electrochem.*, **131**, 229 (1982).
27. E. I. Khazanov and A. I. Belyaev, *Legk. Met.*, **4**, 1 (1935).
28. E. I. Khazanov and N. I. Komarov, *Tsvetn. Metall.*, **2**, 68 (1940).
29. P. Rontgen and K. Giesen, in "Abhandlungen Institut fur Metallhuttenwesen und Elektrometallurgie der Technischen Hochschule, Aachen,' Vol. V, P. Rontgen, Editor, Aachen, Germany (1940).
30. H. T. Fullam and J. N. Hartley, "Zinc Production by the Direct Electrolysis of Sphalerite Dissolved in a Molten Salt, Phase I," Battelle Pacific Northwest Laboratories, Richland, WA (1978).
31. P. Delahay, "New Instrumental Methods in Electrochemistry," Interscience, New York (1954).
32. M. S. Schuman, *Anal. Chem.*, **41**, 142 (1969).
33. D. M. Gruen, R. L. McBeth, and A. J. Zielen, *J. Am. Chem. Soc.*, **93**, 6691 (1971).
34. N. Q. Minh, R. O. Loutfy, and N. P. Yao, in "Light Metals 1982," J. E. Andersen, Editor, p. 267, The Metallurgical Society of AIME, Warrendale, PA (1982).

Electrochemistry of Coal Slurries

II. Studies on Various Experimental Parameters Affecting Oxidation of Coal Slurries

Patrick M. Dhooge and Su-Moon Park*

Department of Chemistry, The University of New Mexico, Albuquerque, New Mexico 87131

ABSTRACT

The anodic oxidation of coal slurries has been studied under various experimental conditions. Results obtained from various experiments support the mechanism of the catalytic oxidation of coal slurries by iron (III) in solution, followed by the oxidation of reduced iron (II) to iron (III) at the electrode. The oxidation of coal slurries by iron (III) in solution is found to be a first-order process with respect to both reactants, *i.e.*, coal and iron (III), from concentration dependency studies, indicating that the overall reaction may consist of a sequence of one-election transfers. It may also be concluded from various experimental results that the electrolysis reaction proceeds through the sequential formation, first of carbon oxides on the coal surface, and then of carbon dioxide as a final product. Of various catalyst oxidants studied, bromine and cerium (IV) appear to have the largest pseudo first-order catalytic rate constants with 1.1×10^{-3}sec^{-1} and 4.1×10^{-4}sec^{-1}, respectively. Redox potentials of the catalyst pairs appear to be the most important parameter in determining catalytic reaction rates.

In our previous report (1), we described findings which indicated that coal slurries were catalytically oxidized by metal ions, iron(III) or cerium (IV). The reactions were represented as an oxidation of coal in solution by catalyst oxidants

$$4Fe^{3+} + C + 2H_2O \rightarrow CO_2 + 4Fe^{2+} + 4H^+$$

or

$$4Ce^{4+} + C + 2H_2O \rightarrow CO_2 + 4Ce^{3+} + 4H^+$$

followed by the reoxidation of reduced catalyst ions at the electrode

$$Fe^{2+} \rightarrow Fe^{3+} + e$$

or

$$Ce^{3+} \rightarrow Ce^{4+} + e$$

We had concluded that the continuous electrolysis current of coal slurries observed in original experiments by Coughlin and Farooque (2-4) and others (5, 6) was explained by the cyclic nature of the above reactions, as the catalyst ions were continuously reduced by coal to form surface oxides on it. Studies of coals and acid-washed coals in the presence of iron(III) and cerium(IV) confirmed the idea of an electrocatalytic mechanism for coal oxidation (1). Reaction rates and activation energies were determined for some systems and found to be reasonable for the proposed mechanism of oxidation by metal ion. However, the electrolytic coal oxidation reaction should almost surely proceed by a multistep mechanism, since it is highly improbable for reactions involving one-step multielectron transfer to occur.

Our previously reported experiments left many unanswered questions. The orders of the reaction with respect to the metal ion, the coal, and water were not determined. Also, we had used only one type of coal, the subbituminous San Juan coal, as a reactant, leaving questions about whether the oxidation reaction would proceed as we had described on a harder coal which would not contain so many impurities. This paper attempts to address these and other questions in electrocatalytic coal oxidation by further experimentation on this electrochemical coal gasification reaction.

* Electrochemical Society Active Member.
Key words: coal slurry, electrochemical coal gasification, catalytic oxidation, solution catalysts, hydrogen production.

Experimental

The coals used in this study were from the San Juan Basin, northwestern New Mexico, and from the Pittsburgh Seam No. 8, a sample PSOC-1099 obtained from Pennsylvania State Coal Sample Bank and Data Base, Coal Research Section of Pennsylvania State University. Elemental analysis of the coals showed 44.81% C, 3.91% H, 0.47% N, 3.1% Fe_2O_3, less than 0.01% S, and 33.0% ash in the San Juan coal, and 73.02% C, 4.94% H, 1.34% N, and 11.15% ash in the Pennsylvania coal (both as received). Alfa Chemical's graphite powder (<325 mesh) and VWR's activated Norit A were used as other carbonaceous compounds.

Baker's ceric sulfate and Lindsay's cerous chloride were used as received as sources of cerium(IV) and cerium(III). Baker's AR ferric sulfate and ferrous sulfate were sources of iron(III) and iron(II). The potassium sulfate, boric acid, sodium hydroxide, and the sulfuric, phosphoric, hydrochloric, and perchloric acids used as supporting electrolytes were all reagent grade chemicals as received. Bromine, potassium ferricyanide, and potassium ferrocyanide were also used "as is" from bottles of Baker and Mallinckrodt AR grade. Eastman Organic's p-benzoquinone, 2-naphthol and anthroquinone, Mallinckrodt's AR phenol, Fischer's certified benzoic acid, Matheson Coleman and Bell's practical grade 1,4-naphthoquinone, K&K Laboratories' anthracene-2-carboxylic acid, and Aldrich's mellitic acid and 2-naphthoic acid were used as "model" compounds for coal, all used as received. The gas standard used to calibrate for analysis of carbon dioxide and carbon monoxide was obtained from Scientific Gas Products and was certified to contain

270 ppm by volume CO_2 and 31 ppm by volume CO in nitrogen.

The electrochemical cell used for many of the studies has been described to some extent in our previous paper (1). A diagram of the cell for product (CO_2) analysis is presented in Fig. 1. The reference electrode used in all studies was mercury/mercurous sulfate/saturated potassium sulfate, separated from the cell by an agar/K_2SO_4 bridge. The results, however, were all presented against a normal hydrogen electrode (NHE) unless otherwise stated. The counterelectrode compartment was isolated by a salt bridge and used a gold-plated bronze screen electrode. The working electrode was a 10 cm^2 platinum foil with electrical contact made by a press-fitted clip of heavy platinum wire. Due to the back pressure of the effluent gas scrubbing system (concentrated sulfuric acid was used to remove water from the effluent gas), the counterelectrode compartment and the reference electrode had to be maintained at the same pressure as the working cell. Temperatures in the working electrode compartment were maintained by a thermostated water bath with circulator.

A Princeton Applied Research (PAR) Model 173 galvanostat-potentiostat with a PAR 176 I/E converter, or a Pine Instrument bipotentiostat, were used for electrochemical measurements. Gas samples were taken in a 10 cm path length gas cell with KBr windows and analyzed by the Fourier transform infrared (FTIR) method. All infrared analyses were conducted on the Nicolet Model 6000 computerized FTIR system. The PAR 179 digital coulometer was used to count the charge passed for electrolysis.

Results and Discussion

Coal and metal ion concentration effects.—By way of comparison of the reactions of Pennsylvania *vs.* San Juan coal, see Fig. 2(a) and (b). The current levels obtained by addition of iron(III) and cerium(IV) were very similar for both coals. Currents for Norit A and graphite powder are also included. High background currents were obtained with Norit A, perhaps due to sulfide oxidation. The current increases for both of these more pure carbons were appreciable for reaction with cerium(IV), but quite low for reaction to reduce iron(III). The coal contains reactive sites which can be oxidized by iron(III), that may not exist in any appreciable amounts in carbon sources such as Norit A and graphite powder. However, cerium(IV) does oxidize these purer carbons, undoubtedly due to the higher standard electrode potential of the cerium(IV)/cerium(III) redox couple [~ 1.45V *vs.* 0.69V for iron(III)/iron(II)]; this same conclusion was presented in our previous paper (1). The type

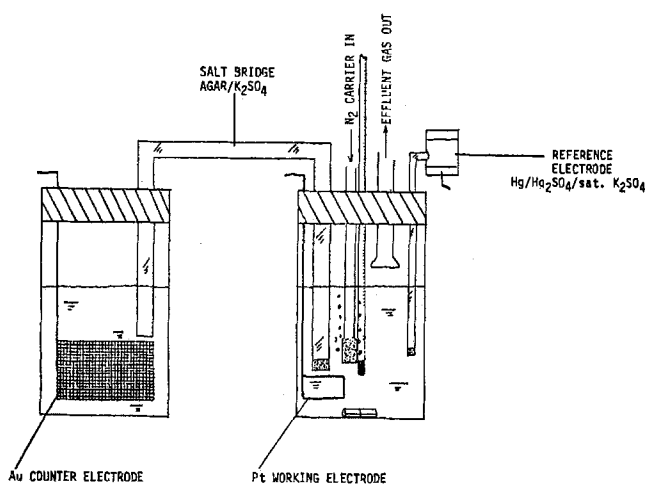

Fig. 1. Electrochemical cell used for the oxidation product analysis

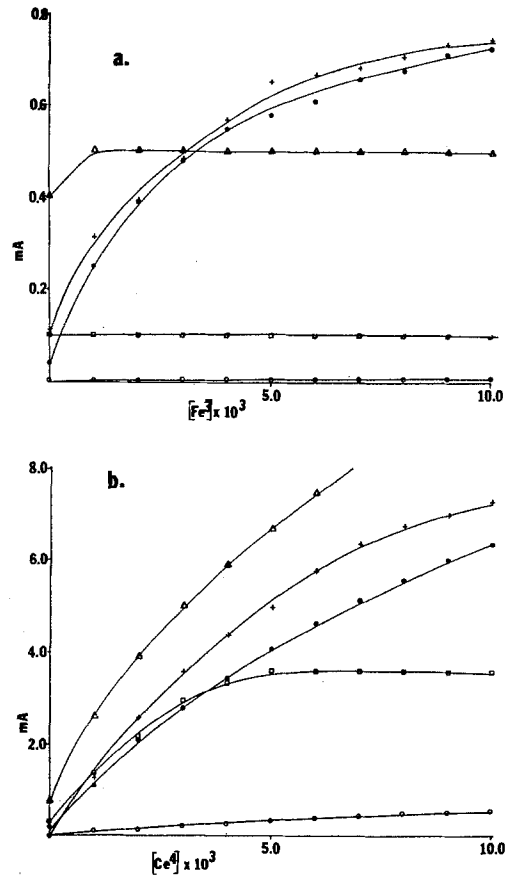

Fig. 2 (a) Current at +1.0V *vs.* iron(III) concentration at 20°C for: ●-acid washed San Juan coal, +-acid-washed Pennsylvania coal, △-Norit A, □-Alfa Chemicals powdered graphite, and ○-blank. 2.0g of carbonaceous compound in 75.0 ml 1.0M H_2SO_4. The electrode area was about 10 cm^2. (b) Current at +1.5V *vs.* cerium(IV) concentration. Symbols and experimental conditions are the same as in (a).

of coal used apparently mattered little in its reactive qualities over the relatively short period of this test.

Note further that the current increased roughly linearly with metal ion concentration, indicating an order of one with respect to the metal ion in the redox reaction. This is true only when the carbonaceous compounds react with metal ions and at lower concentrations of metal ions. This suggests that the redox reaction to produce CO_2 from coal is a stepwise process of one-electron transfers, one of which is rate controlling.

Kinetics of the reactions of the Pennsylvania coal with iron(III) and cerium(IV) were determined in the same manner as described previously (1). Rate constants for reactions with iron(III) and cerium(IV) were 1.9×10^{-5} sec^{-1} and 9.6×10^{-5} sec^{-1}. Thermodynamic measurements gave the activation energies as 12.0 kcal/mol and 6.6 kcal/mol, respectively. These compare quite favorably with the values for these reaction parameters reported for San Juan coal in our previous report (1). The two coals react in a very similar manner with these two metal ion oxidants, despite the fact that they are of different ranks.

The effect of coal loading on the slurry is shown graphically in Fig. 3. Increase in oxidation current was approximately linear with the weight of coal added to the slurry. The higher order Pennsylvania coal did not increase reaction rate with loading as quickly as the San Juan coal, indicating reaction saturation at lower total reaction amount. These studies were run both to determine the order of the reaction with respect to the coal and to clarify the effect of coal loading. In experiments by Farooque and Coughlin (2), a practical limit of current increase with coal

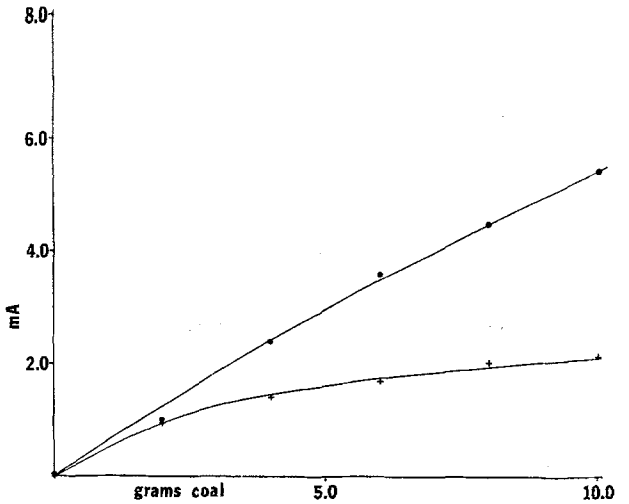

Fig. 3. Current at +1.0V vs. coal loading at 20°C, iron(III) concentration 0.1M in 75 ml 1.0M H_2SO_4 for: +-Pennsylvania coal and ●-San Juan coal.

loading was achieved at about 100g coal/liter. Our experiments show about the same results reported by Farooque and Coughlin, a practical limit of about 100g coal/liter with a concentration of 0.1*M* metal ion. San Juan coal allows higher loading capability due to its higher reactivities. Loading can undoubtedly be increased with higher metal ion concentrations, although a limit will be reached at which slurry agitation becomes difficult.

The reaction order for coal is about one, as was found for the metal ion. This is reassuring in that one metal ion should not be able to react with more than one coal functionality simultaneously.

Effect of pH.—To date no experiments have been reported determining the *p*H dependence of the coal oxidation reaction. This is important for several reasons. The coal, if it undergoes the electrochemical reaction according to the stoichiometry proposed by Coughlin and Farooque, *i.e.*

$$C + 2H_2O \rightarrow CO_2 + 4H^+ + 4e^-$$

should have a reaction equilibrium potential shift of −59 mV/*p*H unit. If, however, iron(III) oxidizes coal catalytically, the equilibrium potential should be independent of change in *p*H, since the electrochemical step does not involve the hydronium ion. Furthermore, the anodic current should decrease drastically when the *p*H is sufficiently high to precipitate iron ions. Experiments were run using a 0.5*M* K_2SO_4 solution. Two grams of coal were added to 150 ml of the solution, and *p*H was adjusted to the desired value using 1.0*M* H_2SO_4 and 1.0*M* NaOH for *p*H = 0-4. For higher values of *p*H 0.10*M* boric acid was added to provide a buffer. For comparison purposes, experiments were also performed on a solution containing $1 \times 10^{-3}M$ iron(III)/$1 \times 10^{-3}M$ iron(II) in 0.5*M* K_2SO_4 at various *p*H values.

The *i*-*E* curves were recorded for coal from *p*H = 0-10 (Fig. 4). The equilibrium potential (0.6 ~ 0.7V *vs.* NHE) did not change significantly over this *p*H range, indicating that the reaction at the electrode does not involve water or ions derived from water, *i.e.*, H^+ or OH^-. The oxidation current at +1.0V *vs.* NHE generally increased when going to lower *p*H values. Both anodic and cathodic currents on electrode polarization appeared to improve with lower solution *p*H. This may simply be due to increased solubilities of iron ions leached from the coal under more acidic conditions, and not necessarily to a faster coal/iron(III) reaction. The oxidation current became quite small, and was almost nonexistent at or higher than *p*H = 7.0. Some oxidation current

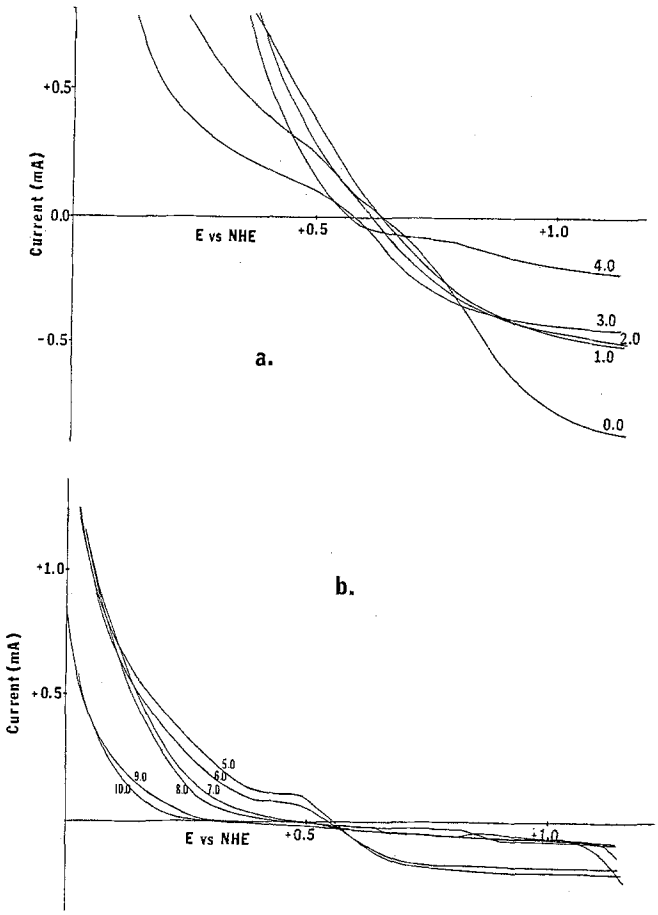

Fig. 4. *p*H dependencies of coal oxidation. (a) *p*H = 0 ~ 4, and (b) *p*H = 5 ~ 10.

was seen at *p*H = 9.0 and 10.0 at potentials more positive than 1.1V *vs.* NHE; this is most likely water oxidation at these *p*H values. Reduction current of considerable magnitude was seen at higher *p*H's. This is presumably due to reducible species from the coal that are solubilized in basic media (7, 8).

Similar results were obtained for the iron(III)/iron(II) solutions at various *p*H values. The equilibrium potential for the iron solution is almost identical to the coal solution, showing that the metal ion is the species reacting at the electrode. The only difference was that the iron(III)/iron(II) solution did not show as high currents as shown by coal slurries at higher *p*H's. Small amounts of oxidizable organic compounds from coal may be responsible for this difference.

Other oxidation catalysts.—Both iron(III) and cerium(IV) have been found to possess the necessary characteristics for electrocatalytic agents in the coal oxidation reaction. The potentials of the iron(III)/iron(II) and cerium(IV)/cerium(III) couples are positive enough to react with oxidizable sites on the coal, both species are soluble to a large extent (at least in acid solution), and the oxidation reaction at the electrode proceeds reasonably fast. Other more efficient oxidants may be found, however, which have faster reaction rates with coal.

One would like to find some redox catalyst with as low a standard electrode potential as possible which would still oxidize coal at a fast rate. This redox pair must also be soluble in water or acid solution to a large extent, be stable over a long period of time, have a relatively large heterogeneous electron transfer rate constant at the electrode, and be relatively inexpensive.

We tested catalytic activities of a few species under various experimental conditions. In Fig. 5 are plotted the oxidation currents monitored at various times for

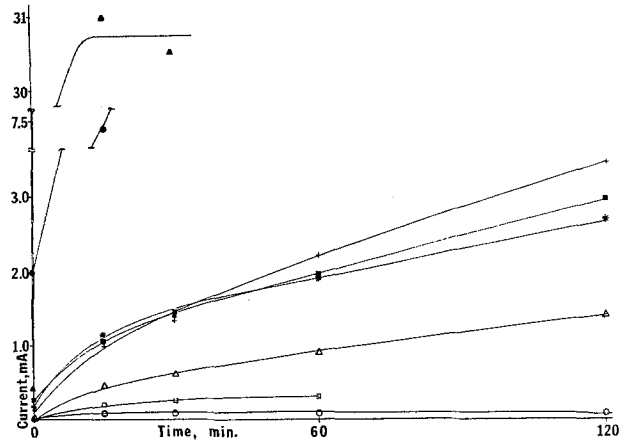

Fig. 5. Intermittently measured limiting oxidation current vs. time for 2.0g washed San Juan coal in 75 ml of ○-1.0 × 10^{-2}M iron(III) in 1.0M H_3PO_4, □-1.0 × 10^{-2}M ferricyanide in sat. K_2SO_4, △-1.0 × 10^{-2}M iron(III) in 1.0M H_2SO_4, *-1.0 × 10^{-2}M ferricyanide in 1.0M H_2SO_4, ■-1.0 × 10^{-2}M iron(III) in 1.0M HCl, +-1.0 × 10^{-2}M iron(III) in 1.0M $HClO_4$, ●-1.0 × 10^{-2}M cerium(IV) in 1.0M H_2SO_4, and ▲-1.0 × 10^{-2}M bromine in 1.0M H_2SO_4. The final current for Ce (IV) is in the range not shown in this figure.

the amount of a reductant produced when an oxidation catalyst is added to the coal slurry. In this experiment no current was passed except for a short period when measurements were made. Thus the currents reflect the amount of reductant produced due to the reaction

$$\text{coal} + \text{oxidant} \rightarrow \text{products} + \text{reductant}$$

Two points which are immediately apparent are that bromine and cerium(IV) had by far the fastest reaction rates with coal, and that iron(III) in 1.0*M* H_3PO_4 reacted very slowly, if at all, with coal under these conditions. Since the current response of each reductant is expected to be different, a known concentration (1.0 × 10^{-3}*M*) of the reduced species was measured in the same cell. These values were used to calculate the amount of oxidant reacted with the coal, and thus the reaction rates.

Table I lists the calculated reaction rates and standard potentials for the oxidative systems studied. The rate constants listed in Table I compare favorably with the one reported earlier (1), which was determined using different methods. Between 0.44 and 0.68V, the reaction rate increases more than ten times. Yet between 0.68 and 0.77V, the reaction rate increases by only 1.5-2.0 times. The range between 0.77 and 1.06V shows a ~ 50-fold increase in the reaction rate, which seems relatively level to +1.45V (cerium(IV) shows ~ 20-fold increase over iron(III) in 1.0*M* HCl). These values seem to indicate that some specific functional groups on the coal are reacting with the oxidants. This view is supported by the current data for coals

Table I. Standard electrode potentials and catalytic reaction rate constants of several solution catalysts

System	E° or $E^{\circ\prime}$	k_c at 20°C, sec^{-1}
$Fe(CN)_6^{-3}$ in sat. K_2SO_4	0.36	3.6×10^{-6}
Fe(III) in 1.0*M* H_3PO_4	0.44	7.3×10^{-7}
Fe(III) in 1.0*M* H_2SO_4	0.68	9.6×10^{-6}
$Fe(CN)_6^{-3}$ in 1.0*M* H_2SO_4	0.72	2.1×10^{-5}
Fe(III) in 1.0*M* $HClO_4$	0.75	1.9×10^{-5}
Fe(III) in 1.0*M* HCl	0.77	1.6×10^{-5}
Br_2 in 1.0*M* H_2SO_4	1.06	1.1×10^{-3}
Ce^{4+} in 1.0*M* H_2SO_4	1.45	4.1×10^{-4}

* The rate constants were determined from Fig. 5 by following reductant concentrations through first hour. Not all data points used for the calculation are shown in the earlier time zone of Fig. 5.

vs. carbon powders [Fig. 2(a) and (b)], where the carbon powders seemed to lack some type of functionality which reacts with iron(III). These reactive functional groups may be oxidized at around +0.6V and around +0.9V, according to our results here.

Various investigators have found electroactive groups on graphites and carbons used as electrodes (9-13). The most common groups appear as oxidation waves at ~0.5-0.6V and at ~0.9V. These waves have been assigned by various investigators to quinone and hydroquinone-like functionalities. Other studies (11) have shown that cerium(IV) forms an oxide film on carbons, which is also electroactive at a potential which has been determined to be quinoid groups. We now have good reason to believe that coal oxidation proceeds through the oxidation, and preceding oxidative formation, of quinoid groups.

In rate studies with iron(III) in the presence of o-phenanthroline, the reaction rate was found to be no faster than with iron(III) in 1.0*M* H_2SO_4. A faster reaction rate was found for ferricyanide in 1.0*M* H_2SO_4, as well as iron(III) in 1.0*M* HCl, and 1.0*M* $HClO_4$. Part of this effect is undoubtedly due to the increased formal electrode potential of iron(III) in HCl and $HClO_4$. However, complexation may play some role, since ferricyanide in 1*M* H_2SO_4 had a reaction rate twice as fast as iron(III) in 1*M* H_2SO_4, even though the formal potentials for these two systems are virtually identical. Ferricyanide was also reacted with washed coal in saturated K_2SO_4; the reaction rate is also listed in Table I. It is much lower than for ferricyanide in 1.0*M* sulfuric acid, more on the order of the rate found for iron(III) in 1.0*M* phosphoric acid. The standard electrode potential of the ferricyanide/ferrocyanide pair is +0.36V *vs.* NHE with both ions fully dissociated, whereas the formal potential of the same pair is 0.71V in 1*F* HCl or 0.72 in 1*F* $HClO_4$ or H_2SO_4 (14, 15). This is due to the acid-base equilibrium reaction of the redox pair, *e.g.*

$$Fe(CN)_6^{4-} + H^+ = HFe(CN)_6^{3-} \qquad pK = 4.30$$

and

$$HFe(CN)_6^{3-} + H^+ = H_2Fe(CN)_6^{2-} \qquad pK = 3.00$$

Thus, the overwhelming parameter determining reaction rates in coal oxidation appear to be the standard electrode potential for the oxidant/reductant pair. Also, the fact that ferricyanide is sufficiently stable to keep the iron in solution while the aquocation is sorbed on the coal surface may explain this difference, as reviewer II suggested.

Current efficiency of carbon dioxide production.— Previously reported values for the current efficiency of CO_2 production from coal oxidation have varied widely (2, 5, 6). In order to determine the identity and quantity of gases being produced in the reaction cell, we have resorted to the use of Fourier transform infrared (FTIR) spectrometry. This technique

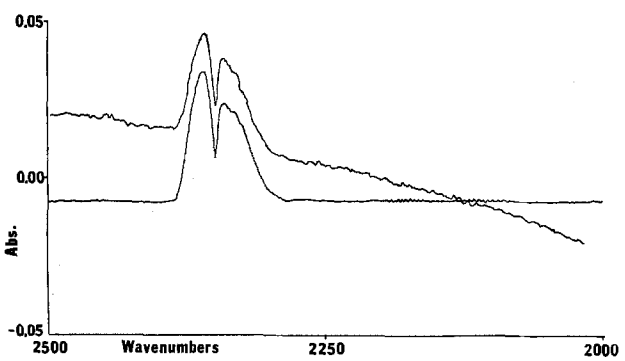

Fig. 6. Absorbance vs. wavenumber for: lower curve, 270 ppm CO_2 and 31.0 ppm CO in nitrogen, 1000 scans, and, higher curve, sample of coal oxidation effluent gas, 32 scans.

can identify and quantitate the two gaseous products produced in any significant amount in the reaction vessel.

Long-term current efficiency in production of CO_2 was measured using San Juan coal. Typical spectra of the standard gas mixture and a gas sample of the electrolysis product are shown in Fig. 6. Samples of effluent gas were collected from the vessel containing 0.10*M* iron(III) and 20g coal in 150 ml of 1.0*M* H_2SO_4 (70°C), and electrolyzed at +1.0V *vs.* NHE at the 10 cm^2 Pt working electrode. Initial currents were of the order of 60 mA but decreased gradually to about 10 mA during the extent of the experiment. During this time over 5000C were passed. The gaseous nitrogen purge flow rate was about 50 cm^3/min. The only product seen over the course of the test was CO_2. No CO was detected. Figure 7 plots the current efficiency of CO_2 production as a function of the total charge passed, assuming four electrons per CO_2 molecule produced. The current efficiency gradually increased over the course of the experiment. This may be due to saturation of oxide surface sites to the point where more of the oxidations lead to the production of CO_2.

In Fig. 8 the CO_2 production, reflected by its concentration in the effluent gas stream, is plotted for 20g coal with 0.10*M* iron(III) in 150 ml 1.0*M* H_2SO_4

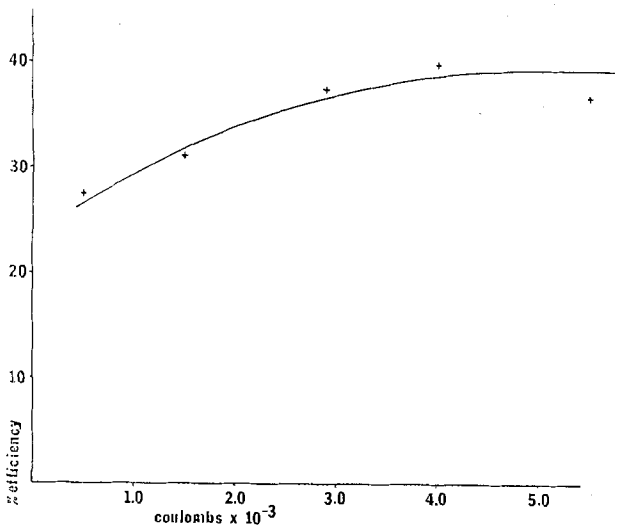

Fig. 7. Percent CO_2 production current efficiency vs. total charge passed at +1.0V in coal oxidation cell, 20g San Juan coal, and 0.10M iron(III) in 150 ml 1.0M H_2SO_4 at 70°C.

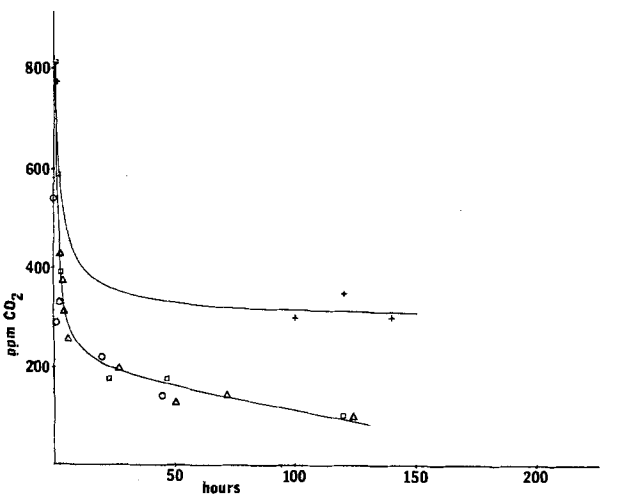

Fig. 8. Ppm CO_2 in 50 cm^3/min N_2 carrier for 150 ml 1.0M H_2SO_4 at 70°C and 20g San Juan coal + 0.10M iron(III) with anodic current at +1.0V, □-20g San Juan coal + 0.10M iron(III) without anodic current, △-20g San Juan coal with no anodic current, and, ○-20g acid-washed San Juan coal with no anodic current.

at +1.0V *vs.* NHE, and for 20g of coal in 150 ml 1.0*M* H_2SO_4 under no current, with no added iron(III) and no current, and with washed coal under no current. The results clearly show the increased CO_2 production from coal when the iron(III) concentration was maintained by oxidative electrolysis. The amount of CO_2 being produced in the cell with anodic current after 100 hr was approximately three times that in the cell without current. Initial CO_2 production rates with and without current were approximately equivalent. Apparently, even an acid-washed coal can produce some CO_2 over quite a long period of time in acid solution. This baseline rate of CO_2 production may be due to some spontaneous oxidation of coal functionalities; it is seriously doubted that inorganic carbonates are the source of this CO_2, since the coal used was washed in 1:1 sulfuric acid for more than 50 hr, which should be sufficient to remove all inorganic carbonates. The same two experiments described above were run again using Pennsylvania coal, with approximately the same results, although at lower CO_2 production levels and lower current levels. Current efficiency values were higher, however, approaching 50%. We speculate that compounds on the coal surface somehow undergo an acid-catalyzed decomposition to CO_2. This was confirmed by detecting CO_2 in the product gas from p-benzoquinone in 1*M* H_2SO_4 at an elevated temperature, 70°C (see later section on model compound studies).

If the reaction of coal with iron(III) and other oxidants is a continuing process and not due to some initial reaction which then exhausts a source of CO_2 on the coal, then addition of further iron(III) should give an increase in CO_2 production. Unwashed San Juan and Pennsylvania coals were placed in 1.0*M* H_2SO_4 (20g/150 ml) and the initial burst of CO_2 production was allowed to level off. Addition of 0.20*M* iron(III) gave a new burst of CO_2 production, as is shown in Fig. 9. This experiment should leave no doubt about the source of the CO_2 produced in such coal oxidation experiments. It is a direct product of the oxidation of coal by a suitable oxidant, in this case iron(III). This system was not connected to an electrical source; the CO_2 was produced purely by chemical oxidation.

The current efficiency and current *vs.* time were measured with San Juan coal both in the presence of iron(III) and in the presence of cerium(IV). Results are shown graphically in Fig. 10. In the presence of cerium(IV), the amount of CO_2 produced was 5-10 times larger than with iron(III). The increased CO_2 production reflects the increased reaction rate with cerium(IV) seen in the rate studies. Note also the higher current efficiency for CO_2 production achieved with cerium(IV); the cerium(IV) is apparently able to completely oxidize (*i.e.*, to CO_2) functional groups more readily than iron(III), resulting in higher current efficiencies. This conclusion is further supported by the current *vs.* time curve for cerium(IV) compared to iron(III). The iron(III) curve shows an initially high current, which dropped off rather rapidly as the more easily oxidizable species on the coal surfaces were depleted. Cerium(IV) maintained at high current for a much longer period, showing an ability to react with functional groups unavailable to iron(III).

Particle size vs. current and current efficiency with time.—Farooque and Coughlin have run experiments measuring the current *vs.* time with coal particle size (2). However, there was no control of the amount of oxidant in those experiments. The amount of iron in various particle size fractions of a coal may vary considerably due to differences in mineral content in softer *vs.* harder coal particles.

In order to remove this variable, we ran a series of tests using a large excess of iron(III) to eliminate any effects of variation in natural iron content of the

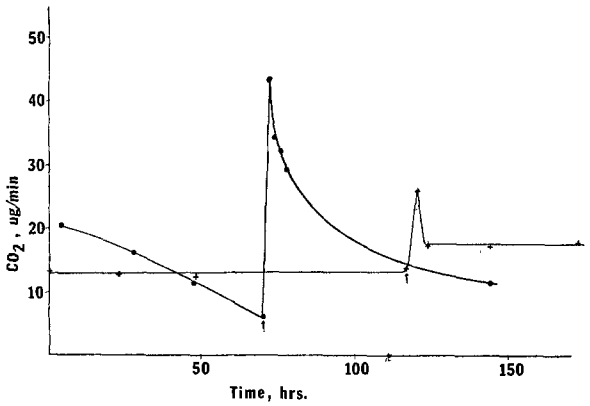

Fig. 9. CO_2 production vs. time for 150 ml 1.0M H_2SO_4 at 70°C and: ●-20.0g San Juan coal and +-20.0g Pennsylvania coal. 0.20M iron(III) added at arrow mark. No current flowed.

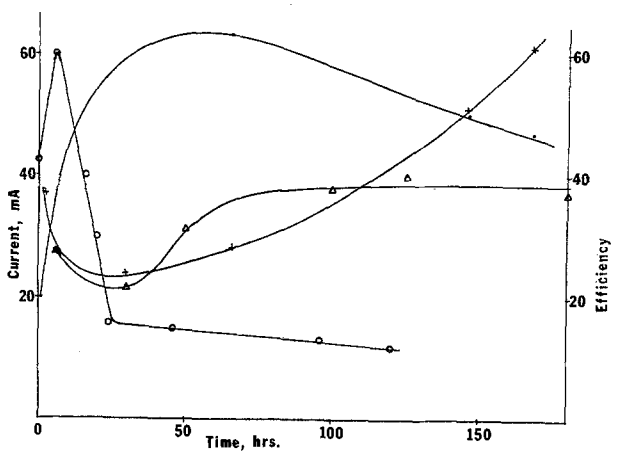

Fig. 10. 20g San Juan coal in 150 ml 1.0M H_2SO_4 at 70°C: ○-anodic current at +1.0V with 0.10M iron(III), △-CO_2 production efficiency with 0.1M iron(III), ●-anodic current at 1.5V with 0.10M cerium(IV), +-CO_2 production efficiency with 0.10M cerium(IV).

coal. Our tests were done with 5.0g of the appropriate size fraction of coal in 150 ml of 1.0*M* H_2SO_4 containing 0.20*M* iron(III) at 70°C. The particle sizes used were 45-50 mesh, 140-170 mesh, and 230-270 mesh. In Table II we list the calculated parameters for different mesh sizes of coal, based on spherical particles.

These experiments were run for about 100 hr each, giving not only the initial reaction rates (*e.g.*, oxidation currents), but the currents after a certain period of time. The current efficiency of CO_2 production was also measured. As in other experiments, no CO was detected.

Figures 11 and 12 show the data from these tests for different particle sizes of San Juan (Fig. 11) and Pennsylvania (Fig. 12) coal using iron(III) as an electrocatalyst. Data from the San Juan coal is easier to interpret. The initial current increased with decreasing particle size, which is consistent with a reaction rate dependent on coal surfaces exposed to the solution. The initial fast rise in iron(II) oxidation current indicates a process with which the electrode reaction cannot keep up. This phenomenon was also seen in other of our studies. This fast rise was followed by a decrease in current as the readily reactive sites on the coal were depleted and the reaction rate dropped. Admittedly, some of the current seen initially may be due to iron(II) leached from the coal, but calculations based on iron content of the coal show that not all the current drop should be due to depletion of leached ions.

Note that initially (30 min after coal is added to the hot acid) there was relatively high CO_2 production current efficiency. This may be due to several reasons. First is the reaction of free carbonates with the hot acid to form CO_2. This reaction should proceed quickly, and there is some doubt on our part that this reaction would still be producing CO_2 at that time. Another possibility would be that the readily oxidizable groups on the coal, which we postulate are responsible for the sudden rise in iron(II) concentration initially, are oxidized completely to CO_2. Also, the acid catalyzed decomposition of benzoquinone-like functional groups may contribute to the production of CO_2, as already pointed out.

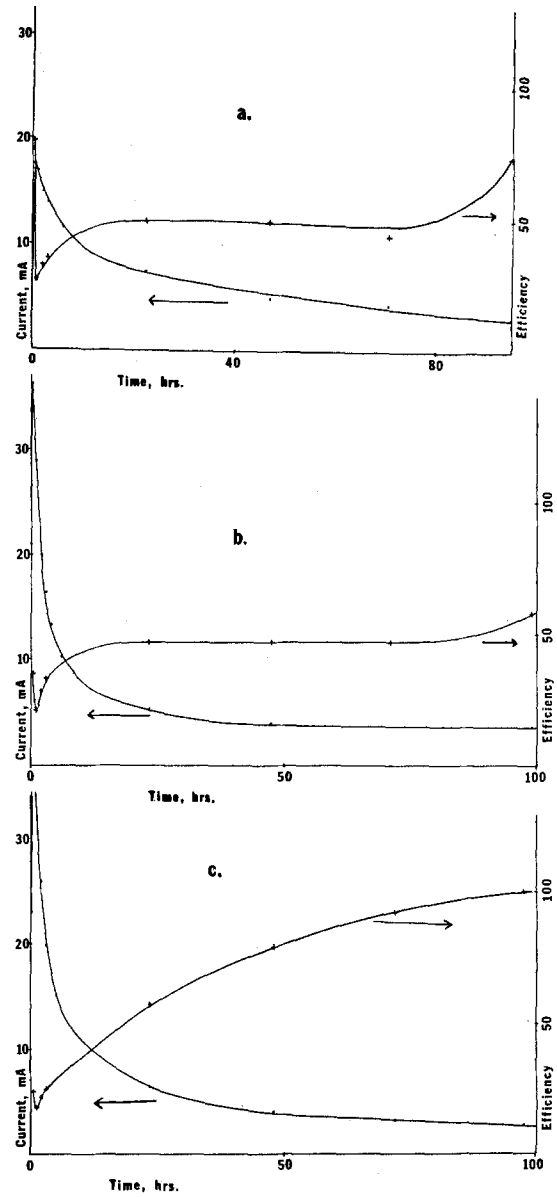

Fig. 11. 5.0g San Juan coal in 150 ml 1.0M H_2SO_4 + 0.20M iron(III) at 70°C: ●-anodic current at +1.0V and +-CO_2 production efficiency; a) 45-50 mesh coal, b) 140-170 mesh coal, and c) 230-270 mesh coal.

CO_2 production current efficiency then dropped to a minimum and increased to a somewhat constant value which we feel reflects the nature of the coal/

Table II. Various parameters for different particle sizes

Mesh size	Diameter of particles (cm)	Average particle area (cm^2)	Average particle volume (cm^3)	Area per wt *vs.* 45-50 mesh
~45-50	0.035-0.0300	3.3×10^{-3}	1.8×10^{-5}	1.00
140-170	0.0105-0.0088	2.9×10^{-7}	4.7×10^{-7}	3.37
230-270	0.0062-0.0053	1.0×10^{-4}	1.0×10^{-6}	5.49

metal ion reaction. Since the order of the reaction has been shown to be about one with respect to the coal and the metal ion, we believe that not all metal ion reactions with the coal produce CO_2; that is, some of the reactions are partial oxidations which do not immediately lead to CO_2. Eventually the surface will become saturated with these partially oxidized sites, and CO_2 production current efficiency will increase. We believe we were seeing this at longer times in these experiments, when current efficiency began to increase somewhat. Also, note the larger CO_2 production efficiencies for the smallest mesh size of San Juan coal.

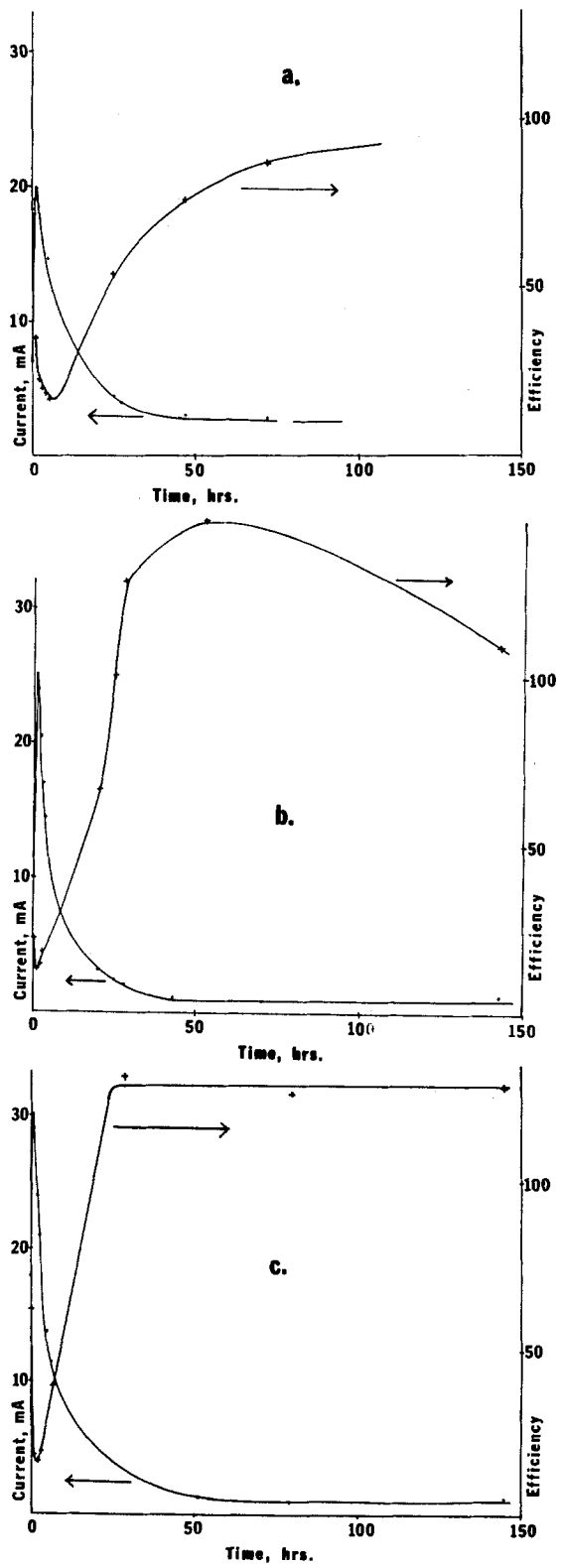

Fig. 12. Same as Fig. 11 for Pennsylvania coal

The data for the Pennsylvania coal is somewhat more difficult to interpret, although some features are very similar to San Juan coal. Again, the iron(II) oxidation current increased quickly and peaked at a relatively high current value, followed by a decrease to a much lower and fairly stable current. Steady-state currents for the Pennsylvania coal are 2-4 times lower than for San Juan coal; we believe this to be due to a lesser amount of reactive sites on the higher order coal. Current efficiency values for CO_2 production again had an initial high value and went through a minimum. This minimum seems to indicate a phase of the reaction where oxidation of the coal is occurring without CO_2 generation, although part of this effect may be due to iron(II) leached from the coal. As with the San Juan coal, the smaller mesh sizes of Pennsylvania coal gave higher CO_2 production current efficiencies. Undoubtedly the smaller particles represent the softer fractions of the coal, and as such should produce more CO_2 per oxidation. This indeed seems to be the case. Efficiencies of over 100% are not unexpected, as they can result from CO_2 production from partially oxidized functionalities; our efficiency calculations assume four electrons per CO_2 molecule.

These experiments lend further support to our postulate that some specific functional groups are responsible for the reduction of iron(III) or other suitable oxidizing agent. Our results also demonstrate that no great increase in reaction rate can be obtained by using smaller particle sizes of coals; for the Pennsylvania coal, smaller particle sizes give less steady-state current.

Oxidation of model compounds.—In order to better understand what type of functional groups might be involved in the coal oxidation, we performed some experiments using compounds which we believe might simulate, or model, the behavior of coal in the presence of oxidants. This type of study has been carried out by other investigators employing chemical oxidants such as hypochlorite (16). All tests were run with ~0.1*M* of the model compound (dissolved or slurried) in 150 ml 1.0*M* H_2SO_4 at 70°C. CO_2 production was measured with and without ~0.1*M* of oxidant.

In Fig. 13 see the CO_2 production rate of p-benzoquinone with and without iron(III). This was the only one of the model compounds tested which produced CO_2 in the presence of iron(III); it also produced CO_2 in the acid solution without any oxidant added at 70°C. This is significant in that we have seen in the coals CO_2 production without oxidant which also increases in the presence of the oxidant. The other model compounds, phenol, benzoic acid, mellitic acid, 1,4-naphthoquinone, 2-naphthol, 2-naphthoic acid, anthroquinone, and 2-anthranoic acid, showed no significant CO_2 production with or without iron(III).

With cerium(IV) an entirely different situation occurred. Many of the model compounds produced some CO_2 in the presence of cerium(IV), in particular p-benzoquinone, 2-naphthoic acid, and 1,4-naphthoquinone. As has been stated previously, cerium(IV) has the ability to oxidize many more types of compounds than iron(III), and that fact is demonstrated here. Also shown is the preference of quinones and acids to react with these oxidizing agents to produce CO_2. In general, the compounds with larger aromatic structures are more stable to oxidation to CO_2 due to the stabilization of intermediate species of oxidation by aromatic rings. The less aromatically stabilized quinones reacted more quickly here, as would be expected.

The model compounds studied show that some organic compounds, in particular quinones, are similar to coal in reactive properties in the presence of oxidizing agents such as iron(III) and cerium(IV).

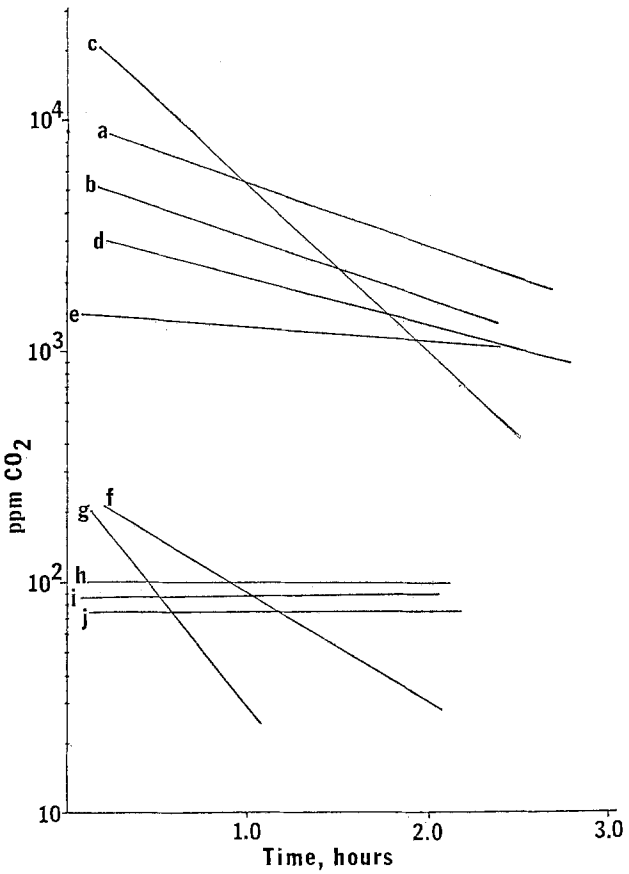

Fig. 13. CO_2 generation in 50 cm^3/min N_2 purge gas for 150 ml 1.0M H_2SO_4 at 70°C with: a-0.10M p-benzoquinone + 0.20M iron(III), b-0.10M p-benzoquinone, c-0.10M p-benzoquinone + 0.20M creium(IV), d-0.10M 2-naphthoic acid + 0.20M cerium(IV), e-0.10M 1,4-naphthoquinone + 0.20M cerium(IV), f-0.10M 2-anthranoic acid + 0.20M cerium(IV), g-0.10M 2-naphthol + 0.20M cerium(IV), i-0.10M benzoic acid + 0.20M cerium(IV), and j-0.10M mellitic acid + 0.20M cerium(IV).

Coal apparently contains functionalities which are considerably more reactive than many of these compounds, the exception being p-benzoquinone. The evidence of water's role in the reaction indicates that there may be reactive sites on coal which easily form quinones by an oxidative mechanism, at least in aqueous solution (17).

Conclusions

We have demonstrated the oxidation of coal by electrocatalysts utilizing redox couples such as iron(III)/iron(II) and cerium(IV)/cerium(III). The reaction would seem to proceed through the sequential formation, first of oxygen compounds on the coal surface, and finally carbon dioxide. This mechanism resembles that of chemical oxidation (18). Our evidence suggests that quinoids may be intimately involved in the oxidation process as an intermediate oxidation product. Apparently any coal is suitable for electrocatalytic oxidation although less pure coals react more readily due to their greater number of reactive sites.

Our studies show that the determining factor in catalytic reaction rate is the thermodynamics of the system. That is, the redox potential of the electrocatalyst pair employed appears to be the most important in determining catalytic reaction rates. The cerium(IV)/cerium(III) couple shows much promise as a practical agent for this reaction. Perhaps complexation of the cerium ions to increase their reaction kinetics could further increase the reaction rate, as we found was the case for ferricyanide/ferrocyanide. The bromine/bromide couple also produces a fast reaction. When a proper solution catalyst is discovered, the production of hydrogen gas in this manner may be feasible. It may also be possible to use this concept for production of hydrogen from waste organic material. Our experiments with model compounds indicate that many carbonaceous wastes could be oxidized electrochemically with the production of hydrogen as a useful product.

Acknowledgments

Grateful acknowledgment is made to the U.S. Department of Energy, Fossil Fuel Program for support of this research under contract, DE—AC21-81MC16377. The FTIR Spectrometer, Nicolet 6000 FTIR, was purchased through an instrumentation grant from the National Science Foundation to our department (CHE 8007979).

Manuscript submitted July 26, 1982; revised manuscript received Dec. 16, 1982.

Any discussion of this paper will appear in a Discussion Section to be published in the December 1983 JOURNAL. All discussions for the December 1983 Discussion Section should be submitted by Aug. 1, 1983.

Publication costs of this article were assisted by The University of New Mexico.

REFERENCES

1. P. M. Dhooge, D. E. Stilwell, and S.-M. Park, *This Journal*, **129**, 1719 (1982). This paper is the paper I of this series.
2. M. Farooque and R. W. Coughlin, *Fuel*, **58**, 705 (1979).
3. M. Farooque and R. W. Coughlin, *Nature*, **279**, 301 (1979).
4. R. W. Coughlin and M. Farooque, *ibid.*, **280**, 666 (1979).
5. G. Okada, V. Gruswamy, and J. O'M. Bockris, *This Journal*, **128**, 2097 (1981).
6. K. E. Johnson, L. Verdet, F. W. Yerhoff, S. Baiton, and C. Dhem, Abstract 456, p. 746, The Electrochemical Society Extended Abstracts, Montreal, Que., Canada, May 9-14, 1982.
7. F. R. Mayo and N. A. Kirshen, *Fuel*, **58**, 698 (1979).
8. A. A. Lappin and G. A. Pereversev, *Solid Fuel Chem.*, **11**, 46 (1977).
9. K. F. Blurton, *Electrochim. Acta*, 18, 869 (1973).
10. K. Kinoshita and J. A. S. Bett, *Carbon*, **11**, 403 (1973).
11. G. Mamantov, D. B. Freeman, F. J. Miller, and H. E. Zittel, *J. Electroanal. Chem.*, **9**, 305 (1965).
12. H. Binder, A. Kohling, K. Richter, and G. Sandstede, *Electrochim. Acta*, **9**, 255 (1964).
13. K. Kinoshita and J. Bett, *Carbon*, **11**, 237 (1973).
14. W. M. Lattimer, "The Oxidation States of the Elements and Their Potentials in Aqueous Solutions," 2nd ed., Prentice-Hall, Englewood Cliffs, NJ (1952).
15. E. H. Swift and E. A. Buttler, "Quantitative Measurements and Chemical Equilibria," Freeman, San Francisco, CA (1972).
16. F. R. Mayo, *Fuel*, **54**, 273 (1975).
17. P. M. Dhooge and S.-M. Park, *This Journal*, In press.
18. H. C. Howard, in "Chemistry of Coal Utilization," H. H. Lowry, Editor, John Wiley and Sons, New York (1945).

Parallel Plate Electrochemical Reactor Model

R. E. White*

Chemical Engineering Department, Texas A&M University, College Station, Texas 77843

Mike Bain

Ashland Oil, Ashland, Kentucky 41101

and Mike Raible

Texas Eastman Company, Longview, Texas 75601

ABSTRACT

A model is presented for a parallel plate electrochemical reactor which has electrodes that are the same size and are close together. That is, the distance between the electrodes (S) is much smaller than the length (L) or width (W) of the electrodes. Consideration of the material balance equations in light of this small aspect ratio (S/L) condition leads to predictions of derived quantities of interest (*e.g.*, current efficiency) that depend on the product of the aspect ratio and the Peclet number, where $Pe = 2v_{avg}S/D_R$. Predictions of such derived quantities are made for electrolysis of an aqueous, hydrochloric acid solution containing copper in a cell with no separator.

The design of a parallel plate electrochemical reactor (see Fig. 1) often requires predicting such quantities as the current and energy efficiency for multiple electrode reactions, the conversion per pass of a reactant or product, and the selectivity of a desired product. For example, in a cell with no separator, the electrode reactions for electrowinning of copper from a chloride solution might be

$$CuCl_3^{2-} \rightarrow CuCl^+ + 2Cl^- + e^- \quad \text{(anode, reaction 1)}$$

$$CuCl^+ + 2Cl^- + e^- \rightarrow CuCl_3^{2-} \quad \text{(cathode, reaction 2)}$$

$$CuCl_3^{2-} + e^- \rightarrow Cu + 3Cl^- \quad \text{(cathode, reaction 3)}$$

Note that $CuCl_3^{2-}$, or Cu(I) reacts at both electrodes and $CuCl^+$, or Cu(II), is a product at the anode and a reactant at the cathode. This scheme is presented here as a hypothetical illustration of a complex system. The possibility of Cu(II) reacting with copper deposited on the cathode was ignored for convenience. Many, if not most, electrochemical processes of interest are similarly complicated and often it is some aspect of the complexity that dictates the performance of the system.

The design of an electrochemical cell based on the above reactions should include predictions of the current and energy efficiency for copper deposition, the conversion per pass of both Cu(I) and Cu(II), and the selectivity of copper deposition. These predictions would be expected to depend on, among other things, the cell potential, the flow rate of the electrolyte through the cell, and the length of the electrodes at a fixed separation. Classical design techniques [see Ref. (1), *e.g.*] cannot be used to make these predictions because they do not include the capabilities to handle the complexities due to the above reactions.

Pickett (1), for example, presents models for parallel plate cells which are based on the assumption that only one electrode reaction is important and that it is mass transfer controlled. He does present a method for including an undesired side reaction, but it is cumbersome to use. In a different work, he and Stanmore (2) do present a model for the case where different electrode reactions occur at the anode and cathode but do not include multiple electrode reactions.

Other more complicated (3-10) models have been presented for parallel plate cells, but they are also not suitable here for one reason or another. Sakellaropoulos and Francis (3-5) present a model for a parallel plate cell which does include both series and parallel electrode reactions at one electrode, but does not include the reaction at the other electrode nor the effect of the separation of the electrodes. Parrish and Newman (6) present a model for a parallel plate cell which includes the electrode separation and the kinetics of the electrode reactions (same reaction at both electrodes), but does not include multiple electrode reactions. Caban and Chapman (7) present essentially the same model as Parrish and Newman, but set the cell potential instead of the cell current. Caban (8) extends their model to include multiple electrode reactions (and, consequently, the ability to predict current efficiencies), but not the conversion per pass of a reactant or product. Lee and Selman (9) extend Caban and Chapman's work to include a separator in the cell and nonisopotential electrodes, but do not include the conversion per pass. Lee (10) extends their work to include multiple electrode reactions and a heterogeneous reaction at one of the electrodes and a method for predicting ap-

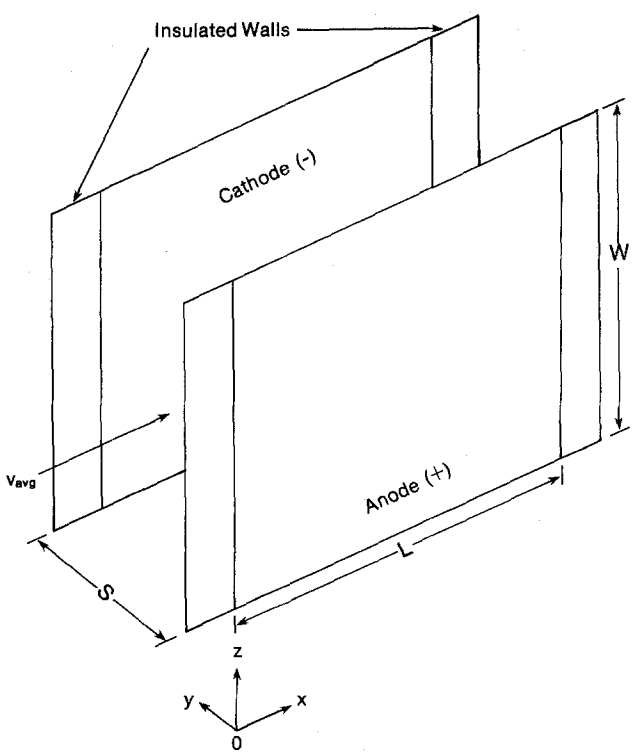

Fig. 1. Schematic of a parallel plate electrochemical reactor

* Electrochemical Society Active Member.
Key words: metals, cell, current efficiency, mass transport.

proximately the conversion per pass based on a quasi-steady-state approach. Their method is, however, limited to cases where the conversion per pass is small.

Models based on the Parrish and Newman approach are sometimes referred to as thin diffusion layer models. They are referred to as such because it is assumed in the development of the models that the concentration of a reactant is constant in the bulk solution over the entire length of the reactor and that the reactant concentration differs from its bulk value only within thin diffusion layers on the electrodes. This assumption is reasonable if the conversion per pass of a reactant is small, but this is often not the case. Another assumption used in the thin diffusion layer models is that Laplace's equation governs the potential distribution within the bulk solution and within the thin diffusion layers on the electrodes. This assumption is also questionable because, as shown by White *et al.* (11), the potential at an electrode predicted by Laplace's equation can be different from that predicted by utilizing dilute solution theory, which includes the effect of ionic migration. This difference may be small but important because the predicted current density depends exponentially on the potential difference between the electrode and the adjacent solution. It is worth reiterating, perhaps, that the major limitation of thin diffusion layer models is that they cannot be used to predict the conversion per pass of a reactant because of the requirement that the bulk concentration of a reactant remain the same over the length of the reactor.

To eliminate these assumptions, a model was developed for a parallel plate cell which includes the effect of ionic migration in the flux expression for species i and uses the electroneutrality condition as a constraint to determine the potential in the solution. This method was used by Alkire and Ng (12, 13) for a model of a porous, flow-by electrode. The approach removes the limitations of the thin diffusion layer model and provides a method that includes the capability of predicting the quantities mentioned above. Also, the approach could be extended to handle even more complicated cases. The model consists of assumptions, material balance equations, the electroneutrality condition, boundary conditions, and parameters.

Model

The assumptions made in the development of the model are presented first followed by the equations.

Assumptions

The following assumptions apply to the model presented here:

1. Isothermal conditions exist.
2. Gas generation effects are ignored.
3. Newtonian electrolyte.
4. Constant physical and transport parameters.
5. Nernst-Einstein equation ($u_i = D_i/RT$) applies.
6. The length (direction of flow) and width of both electrodes are large relative to the gap between the electrodes.
7. Dilute solution theory (14) applies.
8. Well-developed laminar flow.
9. The Butler-Volmer equation can be used to describe each electrode reaction.
10. No heterogeneous or homogeneous chemical reactions occur.
11. Steady-state conditions exist.

Assumptions 8, 9, 10, and 11 could be modified easily to account for turbulent flow, other types of electrode reactions, heterogeneous or homogeneous (or both) chemical reactions, and dynamic behavior.

Equations

In the absence of homogeneous reactions, the steady-state material balance equation for species i is (14)

$$\nabla \cdot \mathbf{N}_i = 0 \qquad [1]$$

where

$$\mathbf{N}_i = -D_i \nabla c_i - z_i u_i F c_i \nabla \Phi + \mathbf{v} c_i \qquad [2]$$

The velocity distribution within the reactor is assumed to be well-developed laminar flow and is given by (1)

$$v_x = 6 v_{avg} \left(\frac{y}{S} - \frac{y^2}{S^2} \right) \qquad [3]$$

and

$$v_y = 0 \qquad [4]$$

Since the Nernst-Einstein equation

$$u_i = \frac{D_i}{RT} \qquad [5]$$

is assumed to be valid, substitution of Eq. [2], [3], [4], and [5] into Eq. [1] yields

$$6 v_{avg} \left[\frac{y}{S} - \frac{y^2}{S^2} \right] \frac{\partial c_i}{\partial x} = D_i \left[\frac{\partial^2 c_i}{\partial x^2} + \frac{\partial^2 c_i}{\partial y^2} \right] + \frac{z_i D_i F}{RT} \left[c_i \frac{\partial^2 \Phi}{\partial x^2} + \frac{\partial c_i}{\partial x} \frac{\partial \Phi}{\partial x} + c_i \frac{\partial^2 \Phi}{\partial y^2} + \frac{\partial c_i}{\partial y} \frac{\partial \Phi}{\partial y} \right] \qquad [6]$$

The electroneutrality condition

$$\sum_i z_i c_i = 0 \qquad [7]$$

completes the set of $i + 1$ equations needed to determine values for the $i + 1$ unknowns (c_i and Φ) for $x > 0$ and $0 \leq y \leq S$.

Equation [6] can be simplified since the aspect ratio (α)

$$\alpha = S/L \qquad [8]$$

is assumed to be small. This can be seen by substituting the dimensionless variables

$$\zeta = x/L \qquad [9]$$

$$\eta = y/S \qquad [10]$$

$$\theta_i = c_i/c_{i,ref} \qquad [11]$$

into Eq. [6] to obtain

$$6 S v_{avg} (\eta - \eta^2) \frac{\partial \theta_i}{\partial \zeta} = D_i \left(\alpha^2 \frac{\partial^2 \theta_i}{\partial \zeta^2} + \frac{\partial^2 \theta_i}{\partial \eta^2} \right) + \frac{z_i D_i F}{RT} \left[\alpha^2 \left(\theta_i \frac{\partial^2 \Phi}{\partial \zeta^2} + \frac{\partial \theta_i}{\partial \zeta} \frac{\partial \Phi}{\partial \zeta} \right) + \frac{\partial^2 \Phi}{\partial \eta^2} + \frac{\partial \theta_i}{\partial \eta} \frac{\partial \Phi}{\partial \eta} \right] \qquad [12]$$

which shows by inspection that α^2 is a coefficient of the terms that contain derivatives in the axial direction. These terms are negligibly small if α is small and the derivatives in the axial direction are of the same order of magnitude as those in the normal direction.[1] Assuming that these conditions exist reduces Eq. [12] to

$$3 \frac{D_R}{D_i} Pe \alpha (\eta - \eta^2) \frac{\partial \theta_i}{\partial \zeta} = \frac{\partial^2 \theta_i}{\partial \eta^2} + \frac{z_i F}{RT} \left[\theta_i \frac{\partial^2 \Phi}{\partial \eta^2} + \frac{\partial \theta_i}{\partial \eta} \frac{\partial \Phi}{\partial \eta} \right] \qquad [13]$$

where the Peclet number (Pe) is

$$Pe = \frac{2 S v_{avg}}{D_R} \qquad [14]$$

(Equation [14] is reasonable because the Peclet number is defined to be

$$Pe = \frac{D_e v_{avg}}{D_R} \qquad [15]$$

[1] For the case where α is not small, Eq. [12] should be used for the material balance equation for species i, the initial conditions replaced by the appropriate boundary conditions, and the IAD-Newman (15) or similar technique used to solve the equations.

and for flow in a rectangular channel

$$D_e = \frac{4SW}{2(S+W)} \quad [16]$$

which, since $W >> S$, becomes $D_e = 2S$.)

Specification of the initial and boundary conditions completes the system of equations. The initial conditions are simply that

$$\text{at } \zeta = 0 \qquad \theta_i = 1 \qquad \sum_i z_i c_{i,ref}\, \theta_i = 0 \quad [17]$$

and the boundary conditions are

at $\eta = 0$ (anode)

$$\sum_j \frac{s_{ij}\, i_{nj}}{n_j F} = -N_{ni} \quad [18]$$

at $\eta = 1$ (cathode)

$$\sum_j \frac{s_{ij}\, i_{nj}}{n_j F} = N_{ni} \quad [19]$$

and at both $\eta = 0$ and $\eta = 1$

$$\sum_i z_i c_i = 0 \quad [20]$$

It should be pointed out that the derivatives in the flux expression for species i (N_{ni}) are defined to be in the positive y direction (from the anode to the cathode), and the signs used for N_{ni} in Eq. [21] and [22] are consistent with the sign convention that positive current leaves the anode and enters the solution and negative current leaves the solution and enters the cathode.

The normal component of the current density for reaction j (i_{nj}) is assumed to be given by the Butler-Volmer equation and is shown here for reaction j at the anode

$$i_{nj} = i_{oj,ref} \left\{ \prod_i \left(\frac{c_{i,o}}{c_{i,ref}} \right)^{p_{ij}} \exp\left[\frac{\alpha_{aj} F}{RT} (V_a - \Phi_{oa} - U_{j,ref}) \right] - \prod_i \left(\frac{c_{i,o}}{c_{i,ref}} \right)^{q_{ij}} \exp\left[\frac{-\alpha_{cj} F}{RT} (V_a - \Phi_{oa} - U_{j,ref}) \right] \right\} \quad [21]$$

where

$$U_{j,ref} = U^\theta_j - U^\theta_{re} - \frac{RT}{n_j F} \sum_i s_{ij} \ln\left(\frac{c_{i,ref}}{\rho_o} \right) + \frac{RT}{n_{re} F} \sum_i s_{i,re} \ln\left(\frac{c_{i,re}}{\rho_o} \right) \quad [22]$$

Equation [21] can be used for the cathode reactions by changing V_a and Φ_{oa} to V_c and Φ_{oc}, respectively. Substitution of Eq. [21] and its counterpart for the reactions at the cathode into Eq. [18] and [19] yields a system of equations for the dependent variables θ_i and $F\Phi/RT$ in terms of the independent variables ζ and η and parameters (kinetic, geometric, physical, thermodynamic, transport, reference concentrations, and the cell potential).

Parameter Values

The utility of the model can be demonstrated by calculating the potential and concentration distributions within the reactor for the hypothetical case given above with HCl included as a supporting electrolyte.

The fixed parameter values used here are given in Table I for this system of species and reactions. The variable parameter values are the average velocity of the electrolyte (v_{avg}), the length of the reactor (L), and the potential of the anode (V_a) relative to the half-cell potential of reaction 1 evaluated at the appropriate reference concentrations. Note, however, that according to Eq. [13], Peα is the important independent variable and not S, v_{avg}, or L separately. Thus, for the case where S and D_R are constants, v_{avg} and L can be replaced by Peα. Also, note that the cell potential ($E_{cell} = V_a - V_c$) is actually the independent variable, not V_a. That is, even though V_a and V_c can be varied independently within the model, the results depend only on their difference, not their individual values.

Consideration of the above boundary conditions written in dimensionless form gives rise to the following fixed dimensionless parameters

$$\xi_{ij} = \left| \frac{s_{ij}\, i_{oj,ref}\, S}{n_j\, c_{i,ref}\, D_i F} \right| \quad [23]$$

The magnitudes of these dimensionless parameters provide a qualitative guide to the relative rates of charge transfer to mass transfer as shown in Table II. (Note that both ξ_{ij} and Peα depend on S.)

Table I. Fixed parameter values

Kinetic and thermodynamic

Reaction (j)	$10^8 i_{oj,ref}$ (A/cm²)[a]	α_{aj}	α_{cj}	n_j	U_j^θ (V)[b]	$U_{j,ref}$ (V)[c]
1	1.0	0.5	0.5	1	0.438	0
2	1.0	0.5	0.5	1	0.438	0
3	100.0	0.5	0.5	1	0.233	0.1143

T = 298.15 K

Component (i)	Reactions 1 and 2 (j = 1, 2) s_{ij}	p_{ij}	q_{ij}
H^+	0	0	0
Cl^-	−2	0	2
Cu(I)	1	1	0
Cu(II)	−1	0	1

Component (i)	Reaction 3 (j = 3) s_{ij}	p_{ij}	q_{ij}
H^+	0	0	0
Cl^-	3	3	0
Cu(I)	−1	0	1
Cu(II)	0	0	0

$V_{cathode}$[d] = 0.0V

Geometric

S = 0.1 cm

Transport and reference concentrations

Component (i)	z_i	$10^5 D_i$[e] (cm²/sec)	$10^3 c_{i,ref}$ (mol/cm³)
H^+	1	9.312	1.000
Cl^-	−1	2.032	1.000
Cu(I)[f]	−2	0.720	0.500
Cu(II)	1	0.720	0.100

[a] Chosen arbitrarily.
[b] See Ref. (11, 16).
[c] The open-current potential of reaction j at the reference concentrations ($U_{j,ref}$) was chosen for convenience to be relative to reaction 1 (i.e., re = 1 in Eq. [22]).
[d] Relative to the half-cell potential of reaction 1 evaluated at the reference concentrations of Cl^-, $CuCl_3^{2-}$, and $CuCl^+$ (i.e. an imaginary reference electrode at which reaction 1 occurs and the reactants that participate in reaction 1 are at their reference concentrations).
[e] Taken from Ref. (14, 11).
[f] Designated as the limiting reactant.

Table II. Fixed dimensionless parameters

$$\xi_{ij} = \left| \frac{s_{ij}\, i_{oj,ref}\, S}{n_j\, c_{i,ref}\, D_i F} \right|$$

Component (i)	Reactions 1 and 2	Reaction 3
H^+	0.00000	0.000
Cl^-	0.01020	1.530
$CuCl_3^{2-}$	0.00288	0.288
$CuCl^+$	0.01440	0.000

Results and Discussion

Once the fixed and variable parameters have been set, the above set of equations can be solved for $\theta_i(\zeta, \eta)$ and $\Phi(\zeta, \eta)$ using an implicit stepping technique (17) in the axial (ζ) direction and Newman's technique (14, 18) in the normal (η) direction. The accuracy of the values obtained for θ_i and Φ depends on the number of mesh points used in both the ζ and η directions. The results reported here are accurate to three significant digits. This accuracy was obtained by adding additional mesh points in both the η and ζ directions until the results no longer changed to within three significant digits. It is worth noting that the potential distribution does not depend on specification of a reference state. That is, it is not necessary to specify the value of Φ at any point. As mentioned above, it is only necessary to fix the potential difference between the anode and the cathode and use the electroneutrality condition at both electrodes (Eq. [20]) to obtain the potential distribution between the electrodes. For the results reported here the values obtained for Φ varied only slightly (approximately 5-10 mV) both across the cell and over the length of the electrodes, as would be expected for well-supported solutions. The concentration and potential distributions obtained can then be used to calculate derived information of interest, such as the current density distribution for each electrode reaction along each electrode.

These current density distributions can be used to obtain another quantity of interest λ which is defined as the ratio of the average current density to the average limiting current density

$$\lambda = \frac{i_{avg}}{i_{llm,avg}} \qquad [24]$$

where for each electrode

$$i_{avg} = \sum_j i_{nj,avg} \qquad [25]$$

with j ranging over the electrode reactions which occur at that particular electrode. The average normal current density of reaction j ($i_{nj,avg}$) can be obtained by utilizing the calculated surface concentration and potential distributions and the appropriate Butler-Volmer equation as follows

$$i_{nj,avg} = \frac{1}{L}\int_0^L i_{nj}(x)\, dx \qquad [26]$$

The average limiting current density for the limiting reactant (as designated by the subscript R, Cu(I) here) at the cathode for a one-electron reaction can be obtained from integration of Eq. [26] with $i_{nj}(x)$ replaced by $i_{lim}(x)$ (19)

$$i_{lim}(x) = \frac{-FD_R c_{R,ref}}{(1-t)\Gamma(4/3)}\left(\frac{6v_{avg}}{9SD_R x}\right)^{1/3} \qquad [27]$$

where the transference number (t) for the limiting reactant is assumed to be zero here due to the well-supported solution considered. The result of the integration and this assumption is that

$$i_{lim,avg} = \frac{-3^{2/3}FD_R c_{R,ref}}{2L\Gamma(4/3)}\left(\frac{Pe}{\alpha^2}\right)^{1/3} \qquad [28]$$

Note that the value of $i_{lim,avg}$ and, consequently, values of λ depend on the choice of the limiting reactant and its reference concentration. Here Cu(I) is chosen to be the limiting reactant and its feed concentration is chosen to be its reference concentration. These choices make $i_{lim,avg}$ the maximum average current density obtainable for this cell so that λ is always less than or equal to one.

Equation [28] can be used to normalize the predicted current density distributions

$$i_{nj}^*(x) = \frac{i_{nj}(x)}{i_{lim,avg}} \qquad [29]$$

as shown in Fig. 2 for a given set of parameter values.[2] Figure 2 shows that the current density distributions are highly nonuniform for reactions 1 and 3 as expected since the average current density is only slightly less than the average limiting current density (λ = 0.946).

The predicted current density distributions can also be used to derive local and average current efficiencies which are defined here as follows

$$CE_j(x) = i_{nj}(x)/i_{avg} \qquad [30]$$

and

$$CE_{j,avg} = i_{nj,avg}/i_{avg} \qquad [31]$$

Figure 3 presents predicted local current efficiencies for copper deposition at a fixed value of Peα for various cell potentials. The case where the cell potential varies from 0.4 to 0.6V is for a linear change in the anode potential from 0.4V at ζ = 0 to 0.6V at ζ = 1. Note that the 0.4-0.6V case gives a more uniform current efficiency than the 0.6V case. Figure 4 presents the average current efficiency for copper deposition as a function of Peα for various values of the cell potential. Here the average current efficiency for the 0.4-0.6V case is higher than either the 0.5 or 0.6V case. This means that the current efficiency (or the energy consumption per unit mass of product which is simply related to the current efficiency and cell potential) of a process may be improved by designing the electrodes to have a desired potential drop.

Another derived quantity of interest is the bulk average concentration of species i

$$c_{i,avg}(x) = \frac{1}{S}\int_0^S c_i(x, y)\, dy \qquad [32]$$

[2] Again the fixed parameter values are given in Table I and the variable parameter values are given in the figures. Note that S is held fixed. If Peα is varied by varying S then the figures do not apply unless the ξ_{ij} values are held fixed by changing $i_{oj,ref}$.

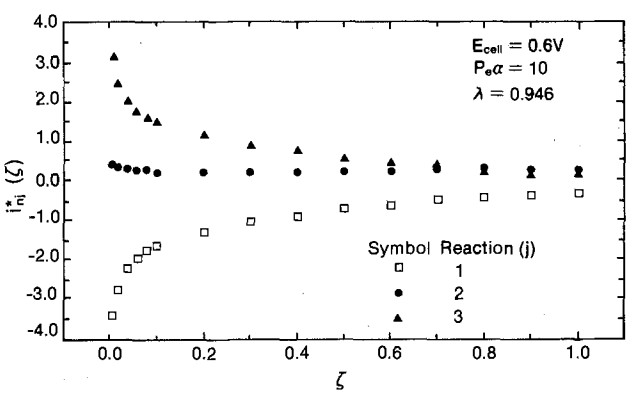

Fig. 2. Normalized current density distributions

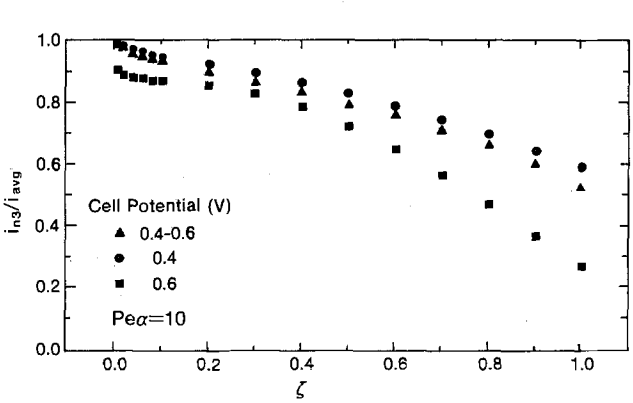

Fig. 3. Local current efficiency for reaction 3

which can be written in dimensionless form as

$$\theta_{i,avg}(\zeta) = \frac{c_{i,avg}(x)}{c_{i,ref}} \qquad [33]$$

Figures 5 and 6 present the dimensionless bulk average concentrations of Cu(I) and Cu(II), respectively, as well as their dimensionless concentrations at the electrodes.

These bulk average concentrations can be used to predict the conversion per pass for a particular species which is defined here as

$$CPP_i = | 1 - \theta_{i,avg}(\zeta = 1) | \qquad [34]$$

Figure 7 shows how the conversion per pass for Cu(I) depends on the values of Peα and the cell potential. Note that a mild maximum is predicted for the case where the cell potential is 0.6V.

Finally, the selectivity of copper is defined here as

$$\text{Cu selectivity} = \frac{\text{mols of Cu produced}}{\text{mols of Cu(II) produced}}$$

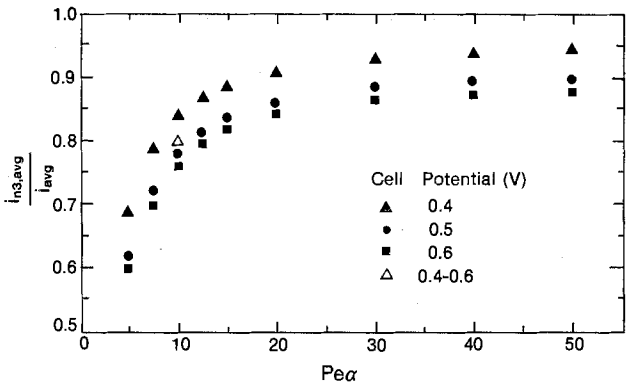

Fig. 4. Average current efficiency for reaction 3

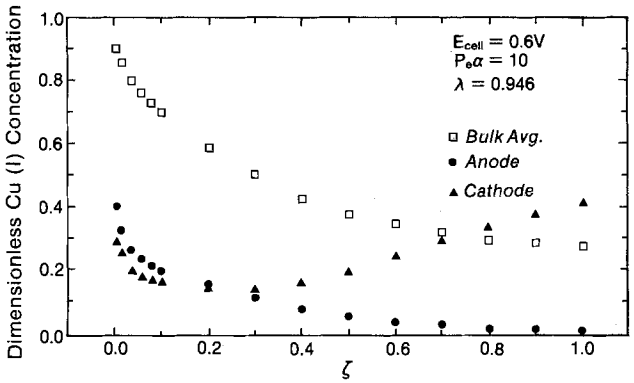

Fig. 5. Dimensionless Cu(I) concentration distribution

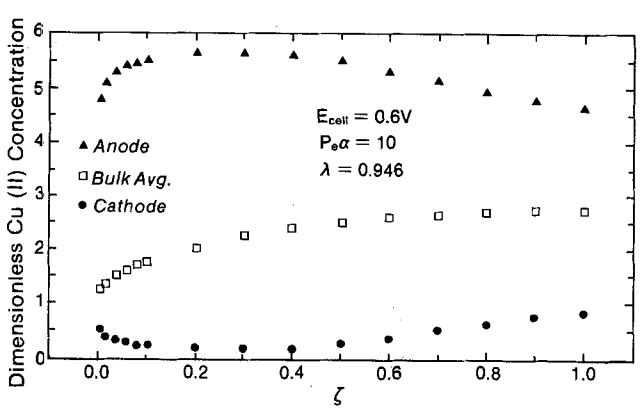

Fig. 6. Dimensionless Cu(II) concentration distribution

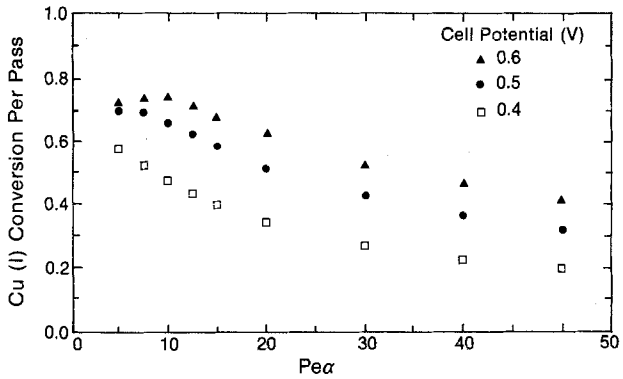

Fig. 7. Cu(I) conversion per pass

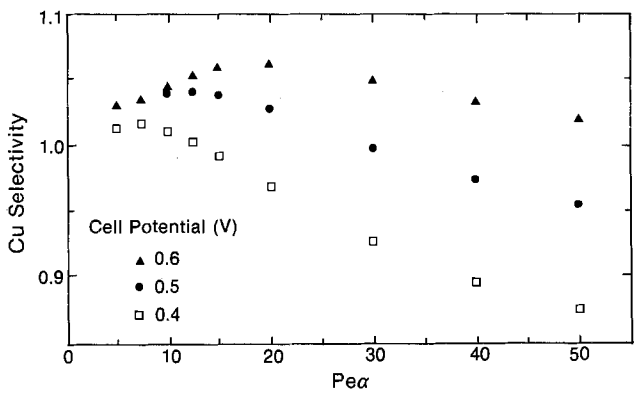

Fig. 8. Copper selectivity

$$\text{Cu selectivity} = \frac{\text{mols of Cu(I) produced} - \text{mols of Cu(II) produced}}{\text{mols of Cu(II) produced}}$$

$$\text{Cu selectivity} = \left| \frac{1 - \theta_{CuCl_3^{2-},avg}(\zeta = 1)}{\theta_{CuCl^+,avg}(\zeta = 1) - 1} \right| \left(\frac{c_{CuCl_3^{2-},ref}}{c_{CuCl^+,ref}} \right) - 1 \qquad [35]$$

and is shown in Fig. 8 as a function of Peα for various cell potentials. Note that a mild maximum is predicted for the 0.6V cell potential case at Pe$\alpha \approx 20$.

Conclusion

The parallel plate electrochemical reactor model presented here may be useful for design purposes if the necessary parameter values are known. Alternatively, the model may be useful for determining some of the unknown kinetic or transport parameter values for a system of interest by using the model, experimental data, and a nonlinear least squares fitting technique; however, it should be pointed out that such a procedure is not well developed.

Manuscript submitted Aug. 16, 1982; revised manuscript received ca. Dec. 10, 1982.

Any discussion of this paper will appear in a Discussion Section to be published in the December 1983 JOURNAL. All discussions for the December 1983 Discussion Section should be submitted by Aug. 1, 1983.

LIST OF SYMBOLS

$c_{i,o}$	concentration of species i at the electrode surface, mol/cm^3
$c_{i,ref}$	concentration of species i at the reactor inlet (reference), mol/cm^3
D_i	diffusion coefficient of species i, cm^2/sec
D_e	equivalent diameter of the reactor (= 2S here), cm

D_R diffusion coefficient of the limiting reactant, cm^2/sec
F Faraday's constant, 96,487 C/mol
i_{avg} average current density, A/cm^2
i_{lim} limiting current density, A/cm^2
$i_{lim,avg}$ average limiting current density, A/cm^2
i_{nj} normal component of current density due to reaction j, A/cm^2
$i_{nj,avg}$ average normal current density due to reaction j, A/cm^2
$i_{oj,ref}$ exchange current density of reaction j at reference concentrations, A/cm^2
L electrode length, cm
$\mathbf{N}_i$ flux vector of species i, $mol/cm^2/sec$
N_{ni} normal component of the flux of species i, $mol/cm^2/sec$
p_{ij} anodic reaction order of species i in reaction j
Pe Peclet number ($= 2Sv_{avg}/D_R$)
q_{ij} cathodic reaction order of species i in reaction j
R gas law constant, 8.3143 J/mol K
s_{ij} stoichiometric coefficient of species i in reaction j
S electrode gap, cm
T temperature, K
u_i mobility of species i, $cm^2mol/J\text{-}sec$
$U_{j,ref}$ open-circuit potential of reaction j at reference conditions, V
$\mathbf{v}$ electrolyte velocity vector, cm/sec
v_{avg} average velocity of the electrolyte, cm/sec
v_x velocity of the electrolyte in the x direction, cm/sec
v_y velocity of the electrolyte in the y direction, cm/sec
V_a anode potential, V
V_c cathode potential, V
W electrode width, cm
x axial coordinate, cm
y normal coordinate, cm
z_i charge number of species i

Greek

α S/L
α_{aj} anodic transfer coefficient for reaction j
α_{cj} cathodic transfer coefficient for reaction j
$\Gamma(4/3)$ the gamma function of $4/3 = 0.89298$
ζ dimensionless axial coordinate (x/L)
η dimensionless normal coordinate (y/S)
θ_i dimensionless concentration
λ average current density relative to the average limiting current density ($i_{avg}/i_{lim,avg}$)
ξ_{ij} dimensionless parameter (see Eq. [23])
ρ_o solvent density, kg/cm^3
Φ solution potential, V
Φ_{oa} solution potential at the anode, V
Φ_{oc} solution potential at the cathode, V

REFERENCES

1. D. J. Pickett, "Electrochemical Reactor Design," 2nd ed., Elsevier Scientific Publishing Co., New York (1979).
2. D. J. Pickett and B. R. Stanmore, Institute of Chemical Engineers Symposium on Electrochemical Engineering, Newcastle upon Tyne, England (1971).
3. G. P. Sakellaropoulos, *AIChE J.*, **25**, 781 (1979).
4. G. P. Sakellaropoulos and G. A. Francis, *This Journal*, **126**, 1928 (1979).
5. G. P. Sakellaropoulos and G. A. Francis, *J. Chem. Tech. Biotechnol.*, **30**, 102 (1980).
6. W. R. Parrish and J. S. Newman, *This Journal*, **117**, 43 (1970).
7. R. Caban and T. W. Chapman, *ibid.*, **123**, 1036 (1976).
8. R. Caban, Ph.D. Dissertation, University of Wisconsin, Madison, WI (1976).
9. J. Lee and J. R. Selman, *This Journal*, **130**, 1670 (1982).
10. J. Lee, Ph.D. Dissertation, Illinois Institute of Technology (1981).
11. R. White, J. A. Trainham, J. Newman, and T. W. Chapman, *This Journal*, **124**, 669 (1977).
12. R. Alkire and P. K. Ng, *ibid.*, **121**, 95 (1974).
13. R. Alkire and P. K. Ng, *ibid.*, **124**, 1220 (1977).
14. J. S. Newman, "Electrochemical Systems," Prentice-Hall, Inc., Englewood Cliffs, NJ (1973).
15. J. Van Zee, M. A. Edmund, and R. E. White, *Ind. Eng. Chem. Fundam.*, **19**, 438 (1980).
16. R. E. White, Ph.D. Dissertation, University of California, Berkeley, CA (1977).
17. B. Carnhan, H. A. Luther, and J. O. Wilkes, "Applied Numerical Methods," John Wiley & Sons, Inc., New York (1969).
18. R. E. White, *Ind. Eng. Chem. Fundam.*, **17**, 367 (1978).
19. W. R. Parrish and J. Newman, *This Journal*, **116**, 169 (1969).

Degradation of Sodium β''-Alumina: Effect of Microstructure

Andrew C. Buechele, Lutgard C. De Jonghe, and David Hitchcock

Materials and Molecular Research Division, Lawrence Berkeley Laboratory, and Department of Materials Science and Mineral Engineering, University of California, Berkeley, California 94720

ABSTRACT

The effect of microstructure on failure initiation of sodium beta"-alumina solid electrolytes have been investigated by acoustic emission detection. Mode I failure initiation follows Weibull statistics with a modulus of about 2.5. The observed average critical current densities were 145 and 640 mA/cm^{-2} for large and for small grained electrolytes, respectively. Nonuniform secondary current distributions near the electrode edges were considered and were found to lead to minor corrections to these values. The conditions under which nonuniformity of current would affect failure statistics have been considered in the Appendix. Considerations of failure statistics indicate conditions where proof testing may be necessary to achieve sufficient reliability. These considerations assume complete equivalence between mechanical and electrolytic failure; the indication is, however, that such equivalence is not valid.

When sodium-beta or beta" alumina solid electrolytes are subjected to ionic charge transfer in sodium/sodium or in sodium/sulfur cells, degradation of the electrolytes may occur. This electrochemical degradation may take different forms, as was recently discussed by De Jonghe *et al.* (1). Mode I degradation involves the cathodic plating of Na into a pre-existing surface flaw on the sodium side of the electrolyte, causing crack extension above some critical value of the current density. This was first discussed by Armstrong *et al.* (2) (ADT). Several workers have considered refinements of the ADT treatment, attempting to derive theoretically the critical current density thresholds at which the Mode I crack propagation initiates or propagates (3-6). All calculations, however, lead to predicted current density thresholds that are orders of magnitude higher than the observed ones (6). To fully understand the factors that determine the onset of Mode I degradation, it is first necessary to measure the critical current density thresholds

with some accuracy and to determine which factors affect this threshold. Several experiments were done by Armstrong *et al.* (2) indicating that imperfections in the surface of the electrolyte indeed played a role. Further experiments on initiation of Mode I degradation were performed by Richmann and Tennenhouse (4) and by Virkar *et al.* (3, 5). These experiments involved strength measurements after electrolysis. A more sensitive method for the detection of initiation of crack propagation is acoustic emission detection. Acoustic emission detection during current flow through solid electrolytes was first reported by Worrell and Redfern (7). The technique was adopted in the present work. Na/Na cells, using Na-beta" solid electrolytes, were tested at 350°C, and the acoustic activity was monitored. Two types of electrolytes, with the same composition but different microstructures, were examined. Additionally, some electrolytes used in extended Na/S cell testing were also examined for evidence of correlation between microstructure and Mode I degradation. The results indicate that large grained electrolyte has a significantly lower current density threshold for Mode I initiation.

Materials

The Na/Na cell tests were performed on Na-beta" alumina tubes prepared by Ceramatec, Incorporated, Salt Lake City, Utah. The electrolyte composition was: 8.85 weight percent (w/o) Na_2O; 0.75 w/o Li_2O; balance Al_2O_3. The tubes had a wall thickness of 1.3 mm and a diameter of 19 mm. The microstructural data are summarized in Table I, and the microstructures are shown in Fig. 1. The microstructure of the coarse grained material, "300," is strongly bimodal. The fine grained material, "10," was also bimodal, but the volume fraction of grains with a size larger than 10 μm was less than 0.01, as indicated in Table I. The grain sizes reported here were determined by a random intercept method, in which the number of grain boundaries are counted intercepting a random straight line on a micrograph. The largest grain dimensions were measured directly on individual grains.

Some used electrolytes were also obtained from British Rail, Research and Development Division, Derby, England. The electrolyte reported on here had a nominal composition of 8.12 w/o Na_2O; 0.7 w/o Li_2O; balance Al_2O_3. The electrolyte had been subjected to 195 cycles in an Na/S cell, over a period of 97 days, for a total (charge + discharge) charge transfer of 121 A-hr/cm^{-2} at 350°C, between 50 and 100 mA/cm^{-2}.

Experimental

When electrolytes fail by initiation and propagation of cracks, stress waves are generated as a result of the sudden stored energy release. These stress waves, or acoustic emissions, can be monitored by a sensitive ultrasonic transducer, and either the cumulative events or the number of acoustic events per second can be recorded. In the present work the increase in count rate appeared to be the clearest indication of the onset of acoustic activity. A similar method was used by Worrell and Redfern (7).

An acoustic emission detection system, manufactured by Acoustic Emission Technology Corporation, Sacramento, California, was used. An acoustic transducer was coupled to the specimen via an alumina wave-

Table I. Microstructural comparison

	Material	
	"10"	"300"
Average grain size	1.1 μm	5.2 μm
Volume fraction grains larger than 10 μm	<0.01	0.83
Average small grain size	0.94 μm	1.1 μm
Average length of large grains >10 μm	14 μm	54 μm

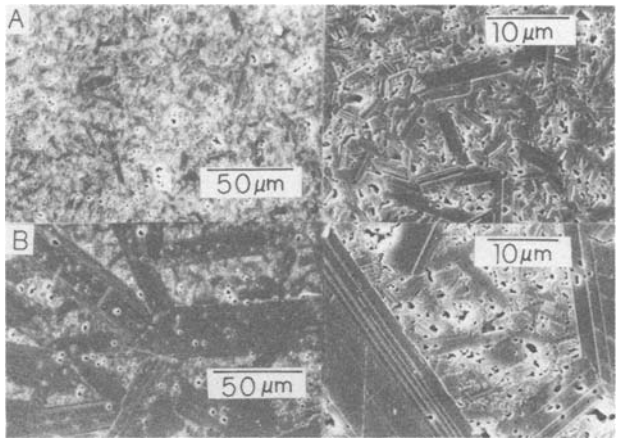

Fig. 1. Comparison of the electrolyte microstructures. Scanning electron micrograph of electrolyte etched in H_3PO_4.

guide rod. The signals were amplified to 106 dB by the instrument amplifier, Model 204A, operating in a bandwidth between 100 and 250 kHz. It was important to ensure excellent contact at the various mechanical interfaces in the system, and to eliminate electrical and mechanical interference.

The sodium/sodium cells were constructed from rings cut under the Na beta" alumina tubes. The rings were cut under kerosene to a height of approximately 15 mm and sealed to a small disk and to a tube of α-alumina with a sealing glass (Owens-Illinois Electronic Materials Center, Toledo, Ohio). The setup is shown in Fig. 2. Prior to joining the electrolyte rings to the α-alumina tubes, they were carefully washed in dry ethanol and acetone and heated in air for 30 min to about 700°C to remove all organic matter and water. In the joining operation, the external surfaces of the rings were covered with sealing glass, except for a small, roughly circular area of about 0.2 cm^2 left exposed for current flow. This area acted as the sodium

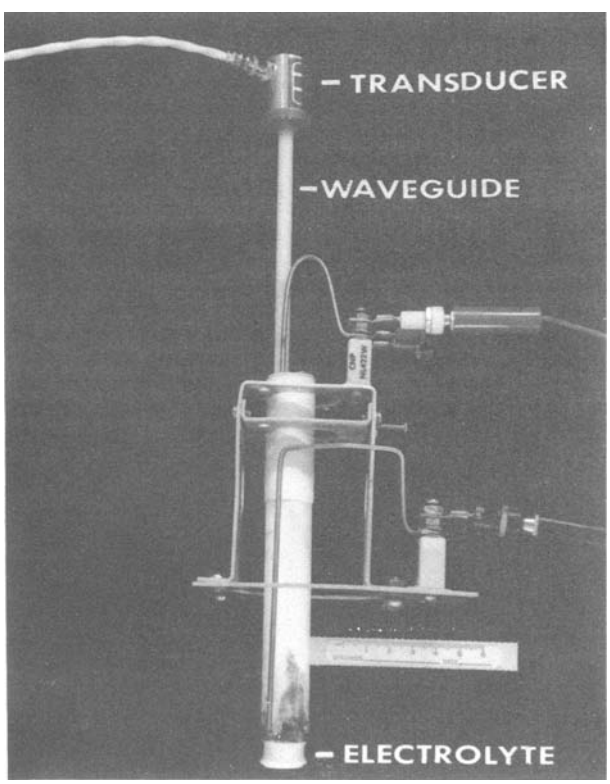

Fig. 2. Setup for the acoustic emission detection experiments in Na/Na cells.

exit surface during the test. The Na/Na cells were set up in an argon glove box. The sodium was obtained from Fisher Scientific Company, Fairlawn, New Jersey. Although the oxygen contamination of the glove box was below 5 ppm, it was sufficient to saturate the sodium with oxygen since Na_2O was observed to form on the surface of molten sodium. Oxygen saturation of the sodium is unavoidable in glove box experiments, as the Na/Na_2O equilibrium oxygen pressure is about 10^{-55} atm at 300°C.

To verify the sensitivity of the acoustic emission detection system, some electrolytes were cooled through the freezing point of sodium under a current of about 40 mA cm^{-2}, and the acoustic emission rates were compared to those of samples cooled without current passage.

The possibility of large grains acting as initiation sites for Mode I degradation was examined on electrolytes with the "300" microstructure with a polished surface section. These cells were then subjected to increasing currents until failure, with the polished section acting either as a sodium exit or a sodium entrance surface only. After this cycle, the cells were removed from the Na, washed in methanol, stained with $AgNO_3$ (8), and examined in the optical microscope.

Results and Discussions

Verification of the acoustic emission detection method.—At low current densities, below 50 mA/cm^2, Mode I degradation is unlikely above the melting point of sodium. However, as the sodium becomes solid, Mode I degradation should be expected to occur. The onset of Mode I degradation should, therefore, be manifested as an increased acoustic emission rate at the freezing point of sodium when the current is maintained. Figure 3 shows the increase of the acoustic activity in the immediate vicinity of the freezing point of sodium. Specimens cooled through the freezing point of sodium in the same setup without current did not exhibit any increased acoustic activity. Some additional tests at room temperature were done on bar-shaped samples of the electrolyte with a negative electrode of evaporated gold and a positive electrode of Hg-Na amalgam. The electrolyte next to the negative electrode could, then, be observed during the test. Increasing currents were passed through the sample until a sudden increase in acoustic activity occurred. Moments later, after a current increase of about 5 to 10%, the usual rapid darkening, indicative of the appearance of a sodium filled crack, could be seen emanating from the negative electrode. These experiments demonstrated that acoustic emission monitoring

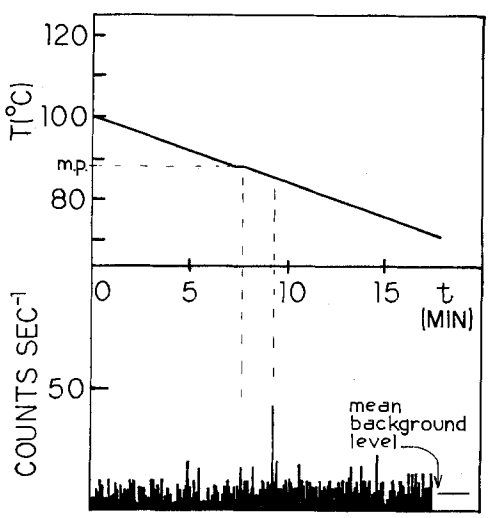

Fig. 3. Increase in acoustic activity at the freezing point of sodium under constant current of 40 mA/cm^{-2}.

was suitable for the study of the initiation of Mode I breakdown.

Microstructure dependence of Mode I initiation.—The observed critical current density for initial crack propagation will be related to the distribution of pre-existing active flaws in the surface of the electrolyte in contact with the negative sodium electrode, and to the current distribution on the electrode. The statistical nature of the active flaw distribution should lead to a corresponding distribution of the current densities necessary to initiate Mode I degradation. The largest flaw will grow first so that the critical current distribution should be treated with extreme value statistics. Weibull statistics are appropriate for describing such statistics and are widely used in the analogous problem of distribution of failure strengths for brittle solids subjected to a mechanical stress, σ. If the failure-initiating flaws are strictly confined to the sample surface (of area A), then the standard treatment (9) gives the probability of survival, P_s, of a sample subjected to a nonuniform applied stress σ, as

$$P_s \equiv 1 - P_f = \exp\left[-\oint_A ((\sigma - \sigma_u)/\sigma_o)^m dA \right] \quad [1]$$

where $P_f \equiv 1 - P_s$ is the failure probability, σ_u and m are materials parameters, and σ_o is a normalizing parameter. By analogy, the distribution of critical current densities might be represented as

$$P_s = \exp\left[-\oint_A ((i - i_u)/i_o)^n dA \right] \quad [2]$$

where A is the active electrode area containing the flaw distribution, i is the current density, which may be a function of position on the electrode, and i_u and n are again materials parameters. It will be assumed here that the current density below which $P_s \equiv 1$, *i.e.*, j_u, is zero. This assumption has the effect that extrapolation of data to electrode areas many times larger than the test area leads to a vanishing survival probability at finite current densities. Since large electrolyte tubes are known to survive finite current densities, the assumption that $j_u = 0$ is not justified as it would lead to significant errors upon extrapolation. From the tests reported here, j_u could not be determined, and the data should, therefore, not be used to extrapolate to large electrolyte tubes; they can, however, be used for mutual comparison and for putting an upper bound on j_u. Since the electrodes in the present experiments were of a finite size, the current density was not uniform. Very close to the edges of the electrode, the current density will rise sharply. The primary current distribution has a singularity at the electrode edge; the secondary current distribution is somewhat more difficult to calculate but remains finite at the electrode edge. The effect of the current concentration at the electrode edges is that failure occurs at an average current density, j, that is lower than if the electrode current density were uniform. The secondary current distribution and its effect on P_s are described in the Appendix. If at failure $j = I/A$, where I is the total current through the cell and A is the electrode area, then it is shown in the Appendix that a current density of $C^{1/n} \cdot j$ would actually have to be applied to cause the same failure if the electrode current density had been completely uniform. The correction factor $C^{1/n}$ depends significantly on the magnitude of the Weibull modulii, n, on the electrode size, and on the exchange current density. The values for P_s corresponding to a uniform electrode current density have been drawn as dashed lines in Fig. 6; the corrections appear to be rather small in this case. It is interesting to note that $C^{1/n}$ increases with increasing n, as is shown in Fig. 11, implying that the electrode edge becomes the more likely source of failure initiation. Increase in cell size enhances this tendency, as

evident from Fig. 12 and 13. For an actual Na/S cell, this would mean that failures tend to originate from the seal/electrolyte interface for those seal configurations that lead to current enhancement. This is shown qualitatively in Fig. 14 [after Newman (17)]. Control of the local seal geometry at the seal/electrolyte junction could, thus, reduce significantly the edge current concentrations and hence the edge related seal failure. Such local seal junction geometries could be achieved with glasses that do not wet the electrolyte well.

Each electrolyte tested to failure provides one value for the failure current density, j. The survival probability, P_s^i, associated with the ith test is determined by arranging the values found for the N individual tests in increasing order. The median rank position of the ith datum is then (9)

$$P_s^i = 1 - [(i - 0.3)/(N + 0.4)] \quad [3]$$

Two different criteria were used to mark the onset of Mode I degradation: the first definition uses the first significant acoustic emission above background; the second definition uses the start of sustained acoustic activity. The reason for considering two different criteria follows from the general acoustic activity pattern when tests are performed with increasing current densities. The first significant acoustic activity occurs at a current density well below the onset of sustained emission, as is shown in Fig. 4. This may be interpreted as follows. An initial flaw population exists in the surface of the electrolyte. Current passage will activate some of these flaws leading to a first flaw extension The beta aluminas are, however, microstructurally very anisotropic, and it should be expected that local variations in K_{IC}, the critical stress intensity factor, should be encountered by the crack tip. These variations in K_{IC} are especially significant when the flaws are on the order of the grain size, in early flaw growth. Even modest local variations in K_{IC} would strongly affect j_{crit} for that flaw of size l, as follows from the recently derived relation (6)

$$j_{crit} \propto K_{IC}^4/l \quad [4]$$

One could, therefore, interpret the acoustic activity patterns such as the one shown in Fig. 4 as due to the establishing of a new flaw population as a result of current passage. When the acoustic emission resumes after the first flaw extension, it is sustained by increasing current densities and many more events are detected than the number of active flaws detected by staining methods after the test. This clearly indicates that the sustained acoustic emission involves flaw extension. The number of active flaws can, however, not be determined from the acoustic emission data.

The results of the critical current testing are shown in Fig. 5 and 6. Figure 5 shows a Weibull plot of the current densities at the first acoustic emission, while

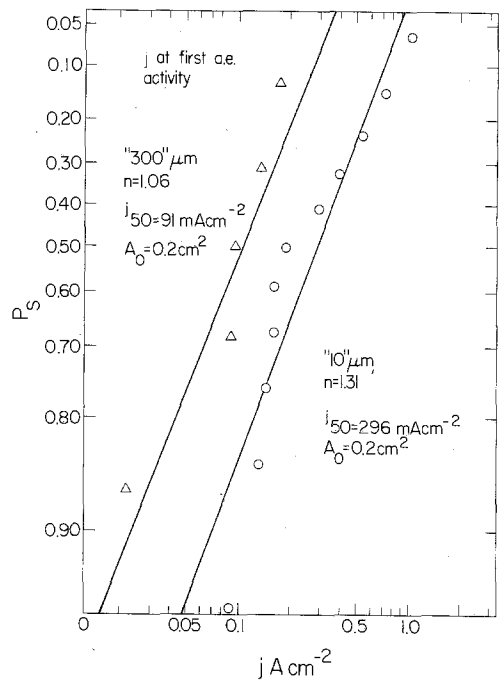

Fig. 5. Weibull plot of the current densities at which the first, significant acoustic events are observed.

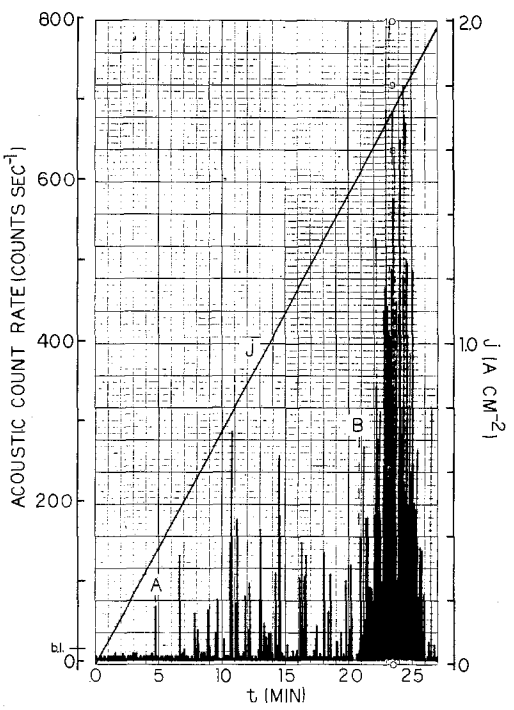

Fig. 4. Typical acoustic activity as a function of time at 350°C, with current density increasing at a constant rate. The first significant acoustic events occur at a constant density, A, that is significantly lower than that for sustained emission, B.

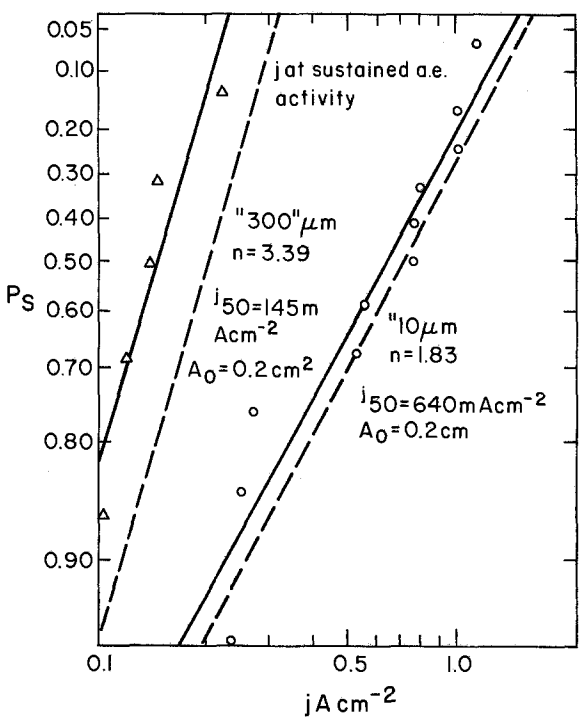

Fig. 6. Weibull plots of the current densities at the onset of sustained acoustic emission. The solid lines are for $j = I/A$; the dashed lines are calculated for uniform electrode current densities.

Fig. 6 shows a similar plot for the onset of sustained acoustic activity. Each data point represents a test on a different cell. The differences between the large and the small grain size electrolytes are evident for both data groups. The average critical current densities for the 0.2 cm^2 test specimens were 145 and 640 $mAcm^{-2}$ for the large and the small grain size electrolytes, respectively, at the first sustained acoustic activity. The correction for the nonuniformity of the current distribution due to the finite electrode size puts these values at 240 and 700 $mAcm^{-2}$ (see Appendix). The differences for the onset of first acoustic activity are not as large. The data clearly show that Mode I breakdown is initiated at lower average current densities for larger grain size electrolyte. It is interesting to note that the ratio of the average critical current densities is comparable to that of the average grain size or average largest grain dimension. This would actually be expected on the basis of Eq. [4]. The lowest initial current density observed in the set of experiments on the fine grain size material, taking the onset of sustained acoustic activity as the significant initiation of Mode I failure, is 250 $mAcm^{-2}$. This would put an upper bound on j_u (Eq. [2]) of about 20 $mAcm^{-2}$.

Microstructural examination.—The sodium entrance and exit surfaces of polished, large grained electrolytes were examined after electrolysis. Figure 7A shows a silver stained sodium exit surface after a unidirectional charge transfer of 22 A-hrcm^{-2}, at 350°C, with a current density increasing uniformly in time from 0 to 7.5 A/cm^{-2}. The micrograph reveals preferential degradation along the grain boundaries of large grains. Figure 7B is a stained cross section of this sample showing how such Mode I degradation extends into the interior of the electrolyte. The silver decoration of similarly used sodium entrance surfaces did not show this type of grain boundary degradation. These observations are in agreement with the acoustic emission data showing lower critical current densities for large grained electrolytes.

The effect of large grains on failure initiation is in general agreement with the trend of mechanical strength reported by Virkar and Gordon (10) on β''-aluminas of similar composition but with differing microstructures. In their observation, the fracture strength of the solid electrolytes decreases significantly when a substantial fraction of large grains (>120 μm) is present. Recently, the involvement of large grains was also demonstrated directly by De Jonghe *et al.* (13).

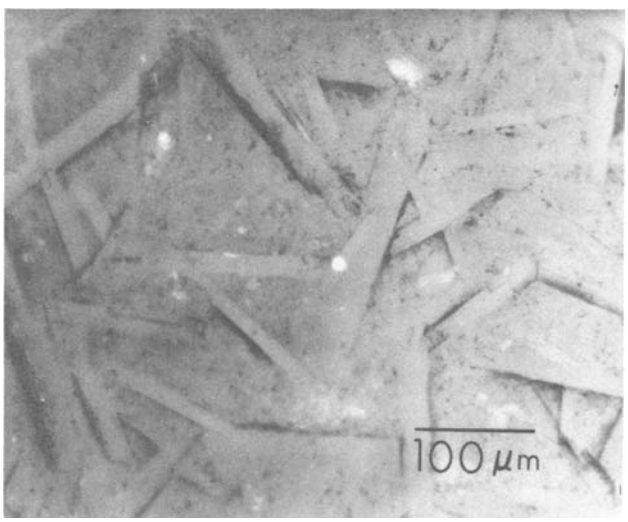

Fig. 7A. Silver stained sodium exit surface after a unidirectional charge transfer of 22 A-hr/cm^{-2}, at 350°C. The current density increased at a constant rate from 0 to 7.5 A/cm^{-2}.

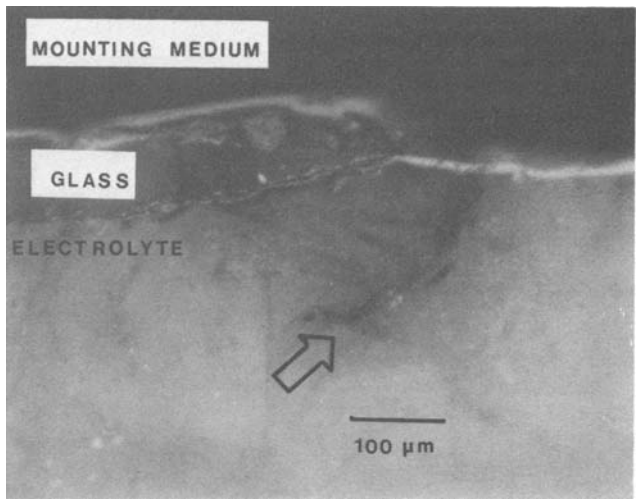

Fig. 7B. Stained cross section of sample shown in Fig. 7A, showing Mode I degradation extending into the interior of the electrolyte.

Further support for the conclusion that large grains have a significant role as preferred sites or paths for Mode I breakdown was found in electrolytes used in the long-term Na/S cell test of British Rail. Figure 8 shows an optical micrograph of a polished and stained cross section under reflected light, Fig. 8A, to reveal the microstructure, and with crossed polarizers to reveal the decoration of a Mode I type degradation, Fig. 8B. This degradation appears to have followed a string of large grains emerging at the Na electrode interface. It is not possible to specify when this Mode I degradation occurred.

Frequently, Mode I cracks that have not reached the sulfur electrode interface are found in used electrolytes. This strongly suggests that slow subcritical sodium dendrite growth occurs during Na/S cell cycling. It is interesting to note here that in purely mechanical testing Shetty *et al.* (3) did not find evidence for a stress-corrosion effect, strongly suggesting that mechanical and electromechanical degradation cannot be considered equivalent.

Discussion

Although the observations indicate that mechanical and electromechanical failure are not equivalent, it is, nevertheless, useful to discuss briefly the significance of Eq. [2] and [4] in the context of the present find-

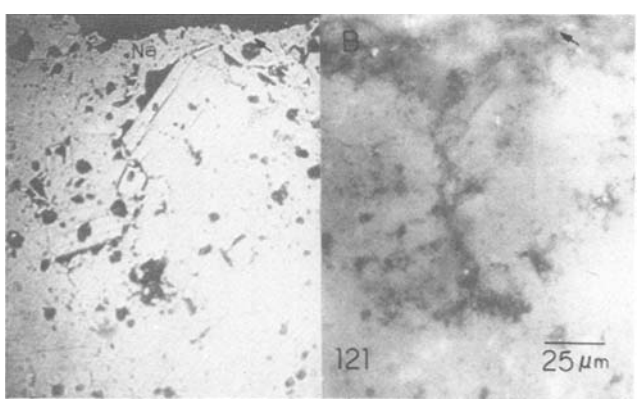

Fig. 8. (A, left) Optical micrograph of electrolyte cross section (Na electrode side) from Na/S cell after 121 A-hr/cm^{-2} of charge transfer. Reflected light to reveal microstructure. (B, right) Same area as in Fig. 8A, crossed polarizers to reveal Mode I degradation. The degradation has followed a string of large grains in the middle of the micrograph. The arrow points at a common area in Fig. 8A and B.

ings. The particular dependence of j_{crit} on K_{IC}, Eq. [4], permits a comparison of the mechanical reliability, expressed by m in Eq. [1], and electrical reliability expressed by n in Eq. [2]. It follows from Eq. [1], [2], and [4] that $m = 4n$. If, for example, one would operate a tube at a current density j_{op}, which is a factor B below the 50% failure probability current, j_{50}, then one could specify n, and, hence, m, for a particular level of required survival P_R. Assuming that the survival probabilities, P_s, pertain to tests for which the electrode current distribution is uniform and $j_u = 0$, the manipulation of Eq. [2] leads to

$$n = \left(\ln\ln\frac{1}{P_R} - \ln\ln\frac{1}{0.5}\right) \Big/ \ln B \qquad [5]$$

Table II lists some examples for m and n, calculated with Eq. [5], when B is 10, 5, or 2, and P_R is 0.95 or 0.99. It is evident from this table that the requirements on reproducibility of mechanical properties of large electrolyte tubes would become very stringent if $B = j_{50}/j_{op}$ becomes less than 5, and an initial crack initiation level of less than 5% cannot be tolerated. Alternatively, one might eliminate the weaker electrolyte tubes by subjecting them to a uniform mechanical proof stress, σ_p, related to the average fracture strength, $\bar{\sigma}$, by

$$\left(\frac{\bar{\sigma}}{\sigma_p}\right)^{4n} = -\ln P_R/\ln 2 \qquad [6]$$

The considerations are analogous to those of mechanical proof testing (11) and follows from combining Eq. [1], [4], and [5] with the assumption that $\sigma_u = 0$. Proof stress testing of electrolytes has also been proposed by Virkar (12). The present discussion clearly points out what is required of the electrolyte tubes if mechanical and electrical failure were identical. In the case where n, B, and P_R are fixed by materials and economic operating conditions, then a mechanical or electrical proof testing would be a necessity when, as follows from Eq. [5]

$$|\ln B| < \left|\ln\ln\frac{1}{P_R} - \ln\ln\frac{1}{0.5}\right| \Big/ n \qquad [7]$$

Equation [6] is represented graphically in Fig. 9 for survival probabilities between 0.800-0.999. Each line of constant P_R separates domains of n and B values in which proof testing is or is not necessary. Since actual ceramics have m (Eq. [1]) range between 5-20, with $m = 10$ a common value for reasonably well prepared ceramics, one should expect n to be in the neighborhood of 2 or 3, as appears to be the case in the present tests. For a 99% absence of crack initiation events, Fig. 9 then indicates that B should be between 5 and 10. Since the Na/S batteries are usually operated around 80-100 mA/cm^{-2}, this would have to put the average Mode I failure initiation around 1 A/cm^{-2}. The present experiments, performed on small electrode areas, show an average Mode I initiation threshold approaching this value. Requirements of a low incidence of crack initiation event probability would, therefore, appear to require either electrical or mechanical proof testing. The most reliable method for proof testing would in fact be one in which the Weibull parameters n and m, and the average failure current density, j_{50}, and average fracture stress, σ, are determined on electrolyte specimens that

Table II.

B	$P_R = 0.95$		$P_R = 0.99$	
	n	m	n	m
10	1.1	4.4	1.8	7.2
5	1.6	6.4	2.6	10.4
2	3.75	15.0	6.1	24.0

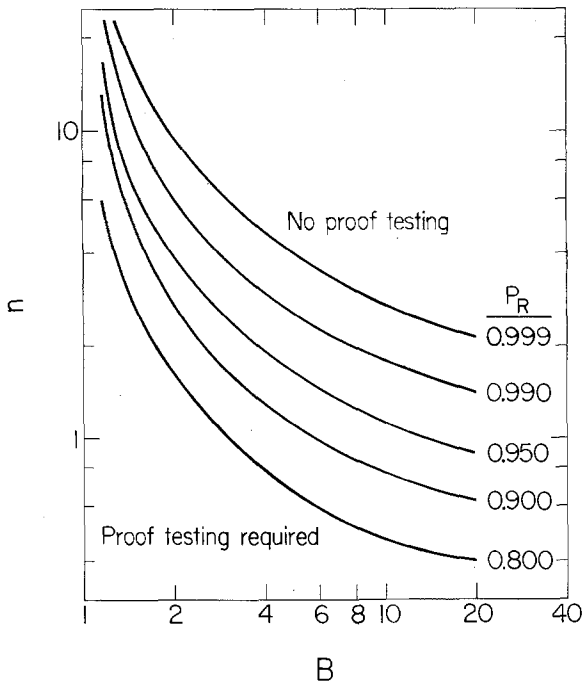

Fig. 9. Graphic representation of Eq. [7] for the different required survival probabilities, P_R, as a function of Weibull exponent, n, and B (defined in text).

are identical to those used in the batteries. The mechanical testing would be one in which the entire tube is stressed uniformally, so that extrapolation of data is minimal.

A first point that must be emphasized is that the above considerations are only valid under the conditions of strict equivalence of mechanical and electrolytic failure. While all our observations seem to indicate that such equivalence does not fully prevail, it should be stressed that the mechanical properties strongly affect the electrical ones. Since the exact correspondence has not yet been established, we should take the above considerations only as a possible worst case, underscoring the necessity for collecting statistical data on full or nearly full scale cells.

A second point that needs some discussion is the definition of electrolyte failure. While the electrolytes used in Na/S cells and so far examined in this laboratory nearly all showed some Mode I cracks, even after relatively short use (~20 A-hr/cm^{-2}), they are known to function with virtually no detectable deterioration in cell performance for extended periods. Thus, the critical current density thresholds reported here use a different failure initiation definition than a battery developer would. Typically, a technological definition uses the appearance of a specified level of nonfaradaic behavior as a failure criterion. Nonfaradaic currents in Mode I failure are the result of electronic shorting through the sodium filled crack. In laboratory Na/Na cell tests, this is manifested by an abrupt voltage drop at constant cell current. These abrupt voltage drops were also observed in the present experiments but they occurred at average current densities of around 1-1.5 A/cm^{-2}. The electronic shorting was in most cases only partial, and the apparent cell resistance change in many cases would be no more than 10%. The correlation between Mode I initiation in laboratory test such as reported here and technologically meaningful electrolyte failure in an Na/S cell is, therefore, not yet established. However, the present experiments can be considered suitable for comparison of the effects of microstructure, and for the evaluation of the ade-

quacy of models proposed for the initiation current density thresholds of Mode I degradation.

Acknowledgments

This work was supported by the Assistant Secretary for Conservation and Renewables, Office of Advanced Conservation Technology, Electrochemical Systems Research Division of the U.S. Department of Energy under Contract No. DE-AC03-76SF000098. Major funding for this work was provided by the Electric Power Research Institute. Dr. L. Feldman of the Aerospace Corporation is thanked for the verification of the acoustic emission detection method. Dr. Sudworth of British Rails is thanked for providing the electrolytes used in experimental sodium/sulfur cells.

Manuscript submitted Feb. 22, 1982; revised manuscript received Jan. 7, 1983.

Any discussion of this paper will appear in a Discussion Section to be published in the December 1983 JOURNAL. All discussions for the December 1983 Discussion Section should be submitted by Aug. 1, 1983.

Publication costs of this article were assisted by Lawrence Berkeley Laboratory.

APPENDIX

To calculate the correction to the average failure initiation current density $j = I/A$, where I is the total cell current and A is the negative electrode area, the cell was assumed to consist of a thin electrolyte plate with an infinitely extending positive electrode and a circular negative electrode. The plate thickness, h, and the negative electrode diameter, L, were chosen such that they corresponded to those of the actual electrolyte ($h = 0.13$ cm and $L = 0.5$ cm). This approximated the experimental configuration fairly well. The secondary current distribution on the negative electrode was then computed by numerical methods, similar to those of Parrish and Newman (14), from the solution to Laplace's equation using the appropriate boundary conditions. The secondary current distribution takes into account the surface overpotential. In general, eight parameters are required to define the problem, as discussed by Parrish and Newman (14). In our case, concentration gradients in the electrolyte can be ignored, and the Butler-Vollmer equation relating current to overpotential, η_s

$$i = i_o\left[\exp\left(\frac{Z\alpha_a\mathbf{F}}{RT}\eta_s\right) - \exp\left(\frac{-Z\alpha_c\mathbf{F}}{RT}\eta_s\right)\right] \qquad [A\text{-}1]$$

can be linearized to give

$$i = (\alpha_a + \alpha_c)(Z\mathbf{F}/RT)i_o\eta_s \qquad [A\text{-}2]$$

Since the reduction of Na^+ to Na is a simple reaction, it should be expected that $(\alpha_a + \alpha_c)\eta = 1$ (16). The exchange current density i_o needed to be found experimentally. It was determined using a method suggested by Sundheim (15). For this purpose, a separate Na/Na cell was constructed, with a reference electrode placed as shown in Fig. 10. The only overpotentials expected in this cell are the ohmic resistance overvoltage of the electrolyte and the surface overpotentials. The ohmic resistance overvoltage was determined by passing a small a-c current between the reference and the negative electrode. At frequencies in excess of 50 Hz, the ohmic contribution was independent of frequency so that the ohmic overpotential could be determined. For the surface overpotential determination, the potential difference between the working and the reference electrodes was measured as a function of current density. From these measurements, and Eq. [A-2], it was determined that i_o was about 5 A/cm^{-2}. A large exchange current density was expected because nonlinear polarization was not observed even at current densities of several hundred mA/cm^{-2}. The parameter used in the numerical computations were, then: $Z = 1$, $L = 0.5$ cm, $T = 600$ K, $K_\infty = 0.25^{-1}$ Ωcm^{-1}, $J = 200$ (at 5 A/cm^{-2}). K_∞ is the electrolyte resistivity, and J is the dimensionless exchange current density defined by

$$J = \frac{Z\mathbf{F}L\,i_o}{RT\,K_\infty} \qquad [A\text{-}3]$$

The secondary current distribution was also calculated for various values of i_o, h/L, and L. Once the current density was found the integral in Eq. [1] could be evaluated numerically, leading to an integrated expression of the form

$$P_s = \exp\left[-A/A_o\left(\frac{j}{j_o}\right)^n C\right] \qquad [A\text{-}4]$$

C does not depend on the average current density $j = I/A$; it is a function of the current distribution and of the Weibull modulus, n. For a uniform current distribution (or for $n = 1$), $c = 1$. Then, if a cell were considered for which the electrode current density is uniform and equal to j, with all other factors identical, one would have

$$P_s\,(\text{uniform}) = \exp\left[-\frac{A}{A_o}\left(\frac{j}{j_o}\right)^n\right] \qquad [A\text{-}5]$$

or, from Eq. [A-2] and [A-3]

$$P_s\,(\text{uniform}) = P_s^{1/C} \qquad [A\text{-}6]$$

or, at constant failure probability

$$j\,(\text{uniform}) = j \cdot C^{1/n} \qquad [A\text{-}7]$$

In a Weibull plot, the values of P_s will then all be

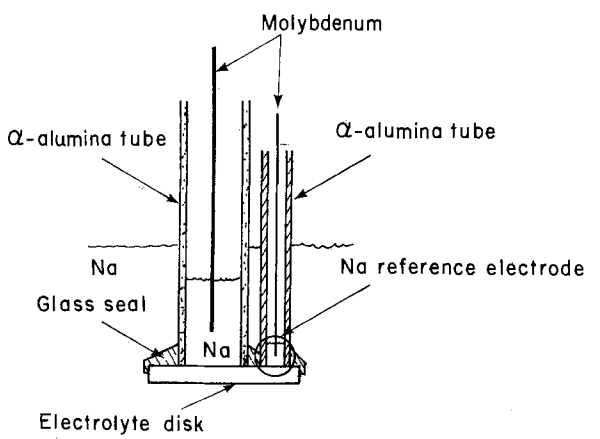

Fig. 10. Setup for determination of the exchange current density

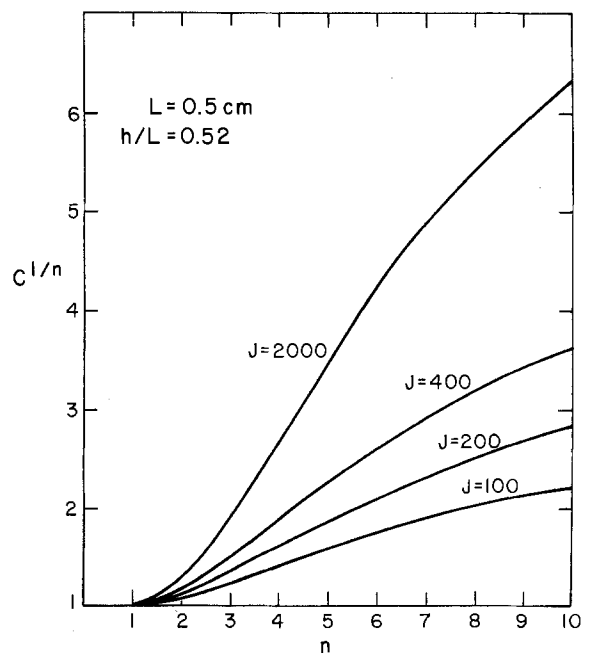

Fig. 11. $C^{1/n}$ vs. n for the cell geometry corresponding to the experimental one, at various values of the dimensionless exchange current density J.

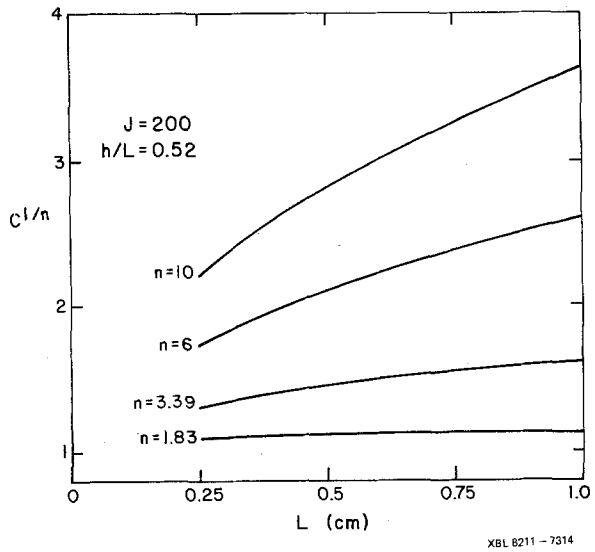

Fig. 12. Dependence of $C^{1/n}$ on electrode dimension, L, at constant h/L for various values of the Weibull modulus, n, with $J = 200$.

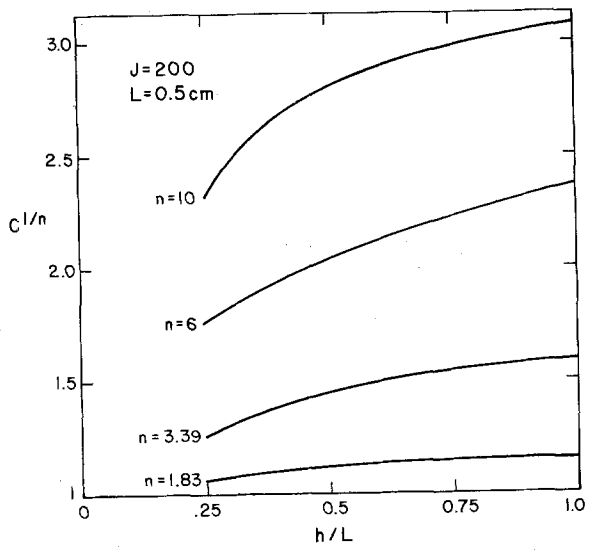

Fig. 13. Dependence of $C^{1/n}$ on electrode dimension, h/L, at constant electrode diameter L, for various values of n, at $J = 200$.

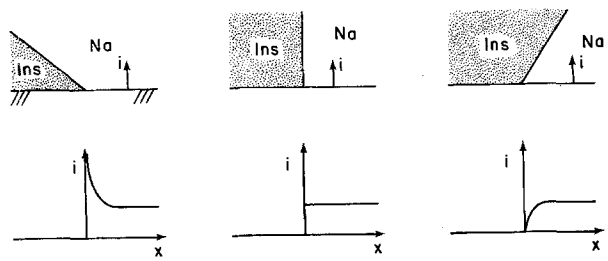

Fig. 14. Qualitative dependence of the electrode edge current concentration for different local geometries; see e.g., Ref. (17).

displaced by the same factor, log C, towards lower values if one corrects for the nonuniformity of the current distribution. C was calculated for several values of n, L, h/L, and J. The results are shown in Fig. 11, 12, and 13. Figure 11 shows that $C^{1/n}$ increases as n increases and that the rate of increase is greater for large values of the exchange current density. Figures 12 and 13 show the dependence of C on cell dimensions for some values of n.

LIST OF SYMBOLS

A	electrode area
B	j_{op}/j_{50}
$\mathbf{F}$	Faraday constant
h	electrode thickness
i	local electrode current density
i_o	exchange current density
I	total cell current
j	current density at failure, averaged over electrode
j_u, σ_u	values of j and σ below which $P_s \equiv 1$
j_{op}, j_{50}	operating current density and average failure current density
J	dimensionless exchange current density
K_{IC}	critical stress intensity factor
K_∞	electrolyte conductivity
l	flaw length
L	electrode diameter
m, n	Weibull moduli
P_s	$1 - P_f$ = survival probability
P_f	failure probability
P_R	required survival probability
R	gas constant
T	absolute temperature
Z	valence of transported species (+ 1 for sodium ions)
α_a, α_c	transfer coefficients
η_s	surface overpotential
σ	mechanical stress
$\bar{\sigma}$, σ_p	average failure stress, and proof stress

REFERENCES

1. L. C. De Jonghe, L. Feldman, and A. Buechele, *J. Mater. Sci.*, **16**, 780 (1981).
2. R. D. Armstrong, T. Dickinson, and I. Turner, *Electrochim. Acta*, **19**, 187 (1974).
3. D. H. Shetty, A. V. Virkar, and R. S. Gordon, in "Fracture Mechanics of Ceramics," Vol. 4, Proceedings of an International Symposium on Fracture Mechanics of Ceramics, R. C. Bradt, *et al.*, Editors, pp. 651-665 (1978).
4. R. H. Richmann and G. J. Tennenhouse, *J. Am. Ceram. Soc.*, **58**, 63 (1975).
5. A. Virkar and L. Viswanathan, *ibid.*, **62**, 528 (1979).
6. L. Feldman and L. C. De Jonghe, *J. Mater. Sci.*, **17**, 885 (1982).
7. C. A. Worrell and B. A. W. Redfern, *ibid.*, **13**, 1515 (1978).
8. L. C. De Jonghe and L. Feldman, *Mater. Res. Bull.*, **15**, 777 (1980).
9. R. N. Davidge, in "Mechanical Behaviour of Ceramics," Cambridge Univ. Press, Cambridge (1979).
10. A. Virkar and R. S. Gordon, *J. Am. Ceram. Soc.*, **58**, 63 (1975).
11. A. G. Evans and J. M. Wiederhorn, *Int. J. Fracture*, **10**, 379 (1974).
12. A. Virkar and G. Miller, in "Fast Ion Transport in Solids," P. Vashishta, J. N. Mundy, and G. K. Shenoy, Editors, pp. 87-90, Elsevier North-Holland, New York (1979).
13. L. C. De Jonghe, A. Buechele, and K. H. Yoon, Lawrence Berkeley Laboratory Report LBL-14150, March 1982.
14. W. R. Parrish and J. S. Newman, *This Journal*, **117**, 43 (1970).
15. B. R. Sundheim, *ibid.*, **115**, 158 (1969).
16. J. S. Newman, "Electrochemical Systems," pp. 171-178, Prentice-Hall, Englewood Cliffs, NJ (1973).
17. J. S. Newman, "Electrochemical Systems," pp. 342-343, Prentice-Hall, Englewood Cliffs, NJ (1973).

Photoactivated Electrolysis on Nonporous Chlorogallium Phthalocyanine Thin Film Electrodes

C. Linkous, T. Klofta, and N. R. Armstrong*

Department of Chemistry, University of Arizona, Tucson, Arizona 85721

ABSTRACT

Various metal and semiconductor substrates demonstrated greatly enhanced activity toward the electrolysis of the benzoquinone (Q) hydroquinone (H_2Q) redox couple when coated with multimolecular layers of chlorogallium phthalocyanine (GaPc-Cl) and irradiated with visible wavelength light. These electrodes were nearly reversible toward H_2Q in the light, but were quite inert in the dark, even suppressing corrosion of the metal when silver substrates were used. Exchange current densities on GaPc-Cl/Au electrodes irradiated with approximately 100 mW/cm^2 polychromatic light were *ca.* 10^3 times greater than on plain Au. The improved voltammetric response of these electrodes over other Pc film electrodes are attributable in part to the sublimation conditions employed, distinguished primarily by a deposition rate of tens of angstroms per minute or less. Varying degrees of film porosity were obtained as evidenced by cyclic voltammetry and x-ray photoelectron spectroscopy. The role of GaPc-Cl in activating the substrate surface is briefly discussed, contrasting the behavior of GaPc-Cl/Au electrodes to plain Au, which shows two distinct rates of Q/H_2Q electrolysis, depending on electrochemical pretreatment.

Research in our laboratory has been directed toward elucidating the photoelectrochemical reactions of organic dye-sensitizing films on wide bandgap semiconductors such as n-TiO_2 and n-SnO_2. Phthalocyanine (Pc) modified electrodes were fabricated which showed quantum efficiencies (electrons injected per photon absorbed) on the order of a few percent for the photoassisted oxidation of hydroquinone in aqueous electrolytes (1). The power conversion or overall energy efficiency of a closed cycle photovoltaic cell using quinone/hydroquinone (Q/H_2Q) however, was considerably less, since a few monolayers of even the most highly absorbent dyes will only absorb a small fraction of the light incident upon it. We have sought to increase the portion of incident radiation absorbed by these electrodes by increasing the Pc film thickness, while at the same time maintaining long-range molecular order within the film. The idea is to use an optically dense material whose conductivity is high enough to pass current without significant ohmic loss. Phthalocyanines have been widely used as dye sensitizers (1-15) and are well known for their chemical and thermal stability, high molar absorptivity in the optimal region of solar irradiance, and ability to catalyze electrode reactions. While phthalocyanines exhibit rather low electrical conductivity by themselves, this conductivity can be improved by incorporating acceptor species such as Br, I, chloranil, and TCNE into the lattice (17-21).

The phthalocyanine derivative of interest in this report is chlorogallium phthalocyanine (GaPc-Cl) consisting of a trivalent Ga center with a single chloride counterion. GaPc-Cl may have been overlooked in the past as a sensitizing molecule because it is a precursor for the other halide derivatives, which have interesting properties of their own. GaPc-Br and GaPc-I have been shown to have high dark conductivity (17-20), while GaPc-F possesses a linear polymeric crystal structure (22). We have found, however, that GaPc-Cl itself is unusual in its photoelectrochemical properties.

When GaPc-Cl/SnO_2 electrodes were used to study the photoassisted oxidation of H_2Q, it was noted that the onset potential for oxidative current flow was *ca.* 150 mV negative of the $E^{\circ\prime}$ for the H_2Q/Q redox couple (1). It was of interest to determine whether this photoactivity was due to true dye sensitization of the SnO_2 substrate, or to a photoassisted increase in the rate of the normally slow $H_2Q \rightarrow Q$ oxidation on SnO_2 (1). Since SnO_2 electrodes can behave as nearly degenerate semiconductors, we decided to expand our explorations to the photoresponse on metal substrates. In this report, we show that gold, silver, and even brass substrates that have been modified with thin films of GaPc-Cl, show a remarkably enhanced rate of Q/H_2Q and ferro-/ferricyanide electrolysis when illuminated with polychromatic visible light. The rate of this electrochemical process is controlled over several orders of magnitude by the incident photon flux. The phthalocyanine-modified electrode acts essentially as a light-activated electrochemical switch.

The rate of quinone electrolysis on unmodified bulk and thin film gold electrodes is quite slow in $pH = 4$ electrolytes. Electrochemical oxidation and reduction of the gold surface immediately followed by voltammetric examination of the quinone electrolysis showed a substantial increase in the reaction rate. Similar rates of reaction are observable on illuminated GaPc-Cl modified gold surfaces.

Experimental

Instrumentation

Cyclic voltammetric measurements were made with a conventional three-electrode potentiostat, X-Y recorder (Houston Instruments), and digital voltmeter (Keithley). The potential scale was referenced to the Ag/AgCl electrode. A spectroelectrochemical cell designed to accommodate optically transparent electrodes on both front and back faces was employed.

The radiation source consisted of the output of a 450W Xe arc lamp (Oriel) through a 470 nm longpass filter (Oriel), creating a polychromatic (470-900 nm) light intensity of approximately 100-150 mW/cm^2. A PHM 84 Research *p*H meter (Radiometer/Copenhagen) was used to measure the open-circuit photopotential. Optical spectra were taken with a Bausch and Lomb Shimadzu Spectronic 210 u.v. spectrophotometer. X-ray photoelectron spectroscopic data were taken with a GCA McPherson ESCA 36, using Mg Kα radiation at 270W.

Electrode Preparation

Substrates.—Bulk gold substrates were in the form of a rotating disk electrode, mechanically polished with 5 micron alumina and, then, chemically cleaned in several portions of triply distilled water. Au and Ag substrates were cut from Intrex films obtained from the Sierracin Corporation. They consisted of vapor deposited thin (30 nm) metal film on a transparent polyester or polycarbonate sheet, forming a metallized plastic which we utilize as optically transparent electrodes (MPOTE) (23). The substrate electrodes were ultrasonicated 15 min each in ethanol and water,

* Electrochemical Society Active Member.

Key words: quinone electrolysis, photoconductivity, molecular metals.

and let dry before use. The brass substrates were cut from a sheet (0.010 in.) and polished with increasingly fine abrasives, finishing with 50,000 mesh diamond dust. They were then ultrasonicated successively in CH_2Cl_2 and in ethanol before use. n-SnO_2 was obtained as a 500-700 nm thick film on glass plate from Pittsburgh Plate Glass. Roughly ¾ in. square electrodes were cut and ultrasonicated in ethanol and water before use. Mott-Schottky capacitance measurements indicated a carrier density on the order of 10^{20} cm^{-3}, indicative of a heavily doped semiconductor.

Deposition of nonporous GaPc-Cl films.—Since the difference between voltammetric results in this report and others may be due to the film deposition procedure, it will be described in detail. Several milligrams of GaPc-Cl were spread evenly across the base of a 2 in. diam sublimation cylinder. The electrode substrates were held on an aluminum masking plate which was supported by three indents in the walls of the vessel, 2 in. above the GaPc-Cl source on the bottom of the cylinder. The vessel was placed in a 500 ml heating mantle (Glas-Col), with glass wool packed around the vessel, filling the volume of the mantle. Temperature was measured by a thermometer inserted through the glass wool packing as near to the base of the vessel as possible. The vessel was evacuated down to 10^{-6} Torr, and a variable transformer was used to apply 55V to the heating mantle. The temperature increased typically at 10°C/min until a steady state was approached around 300°. While some sublimation occurred as low as 200°, the rate only became appreciable near the steady state. Some heat is unavoidably transferred to the electrode substrates through the walls of the vessel and the masking plate during the course of deposition. Electrodes made by slower sublimation rates routinely produce porous highly crystalline GaPc-Cl films, which will be described in more detail elsewhere.

While the deposition rate was nonuniform through the course of each sublimation trial, we can estimate a mean rate for the final 10 min of sublimation on the order of 1-10 nm/min, which is less than other rates reported in and calculated from the literature (3, 6, 12). When the deposition was completed, the sublimation vessel was immediately removed from the heating mantle and the vacuum line and allowed to cool, still evacuated. The vessel was then opened, and the electrodes made ready for use.

The solution and solid film optical absorption spectra of GaPc-Cl in the visible/near infrared region are shown in Fig. 1. While solution spectra always gave an absorbance maximum at 683 nm in pyridine, the predominant maximum for the solid phase spectra varied between 760-810 nm. Thus, we were unable to directly measure relative film thicknesses to any degree of accuracy. We could, however, accurately obtain the number of mols of GaPc-Cl contained in the film by dissolving the film off a substrate with a measured volume of pyridine and comparing the peak absorbance values to prepared standards. Since we undoubtedly did not have single crystal films, we did not use available crystallographic data to calculate film thicknesses. Instead, we define an "equivalent monolayer" as an array of phthalocyanine molecules lying side by side, flat on the substrate surface. We calculated that each Pc macrocycle would occupy about 150Å^2 surface area. By calculating the number of equivalent monolayers deposited on a substrate, we could develop a reasonable molecular picture of the film against which voltammetric and electron spectroscopic results could be compared.

Reagents

GaPc-Cl was synthesized in our laboratory by solvating stoichiometric amounts of the metal trichloride and phthalonitrile (practical grade from Eastman, recrystallized from benzene) in dry benzene and adding the solution dropwise to a few milliliters of nitrobenzene heated to 180°C. The product was then purified by thorough washing with benzene and subliming at 300°C and 10^{-5} Torr. H_2Q was obtained from Eastman and recrystallized from ethanol. The pH 4 buffered electrolyte was made with deionized water, doubly distilled from permanganate, and with potassium hydrogen phthalate, KHP, obtained from MCB Chemicals and used without further purification. Potassium ferrocyanide was obtained from Mallinckrodt and used without further purification. All solutions were purged of O_2 before use.

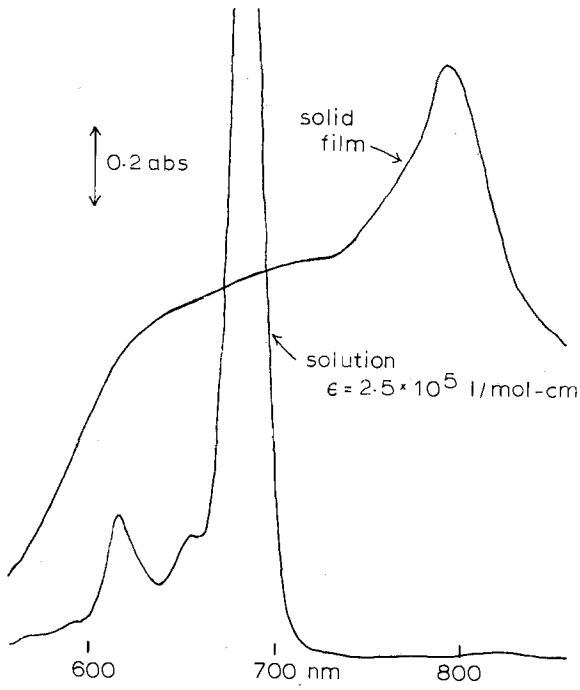

Fig. 1. Solution and solid film absorption spectra of GaPc-Cl solution is 1.52 × 10^{-5}, GaPc-Cl in pyridine. Solid phase is a 493 equivalent monolayer deposition on glass.

Results and Discussion

Visible spectral response.—Films of GaPc-Cl, sublimed onto SnO_2, Au, or Ag semitransparent substrates or glass, always give the type of visible spectrum shown in Fig. 1. The series of phthalocyanines which include AlPc-Cl, AlPc-F, GaPc-Cl, GaPc-I, and GaPc-F; CuPc, CoPc, FePc, VOPc, and H_2Pc have been explored as thin films on SnO_2 and gold in this laboratory. Those Pc-films which show a strong red-shifted and broadened visible spectral response (GaPc-Cl, GaPc-I, GaPc-F, AlPc-Cl, VOPc) are also those films which are most efficient in the photoelectrochemical reactions of hydroquinone (1). By inference to other ordered Pc-systems (24), we hypothesize that this spectral response is due to several coexisting polymorphs of the GaPc-Cl in the solid film. In the range of porosity or thickness of the GaPc-Cl films explored here, the visible spectrum of each film was similar to that shown in Fig. 1.

GaPc-Cl film porosity.—The porosity of our prepared GaPc-Cl films was variable, as indicated by scanning electron microscopy (SEM) and by voltammetry, as shown in Fig. 2. Two GaPc-Cl/Au electrodes, prepared with small differences in sublimation rate in separate trials, demonstrate the extremes in film porosity obtainable. Using the $Fe(CN)_6^{3-,4-}$ redox couple as a probe, we voltammetrically characterized the GaPc-Cl films as to their degree of porosity. $Fe(CN)_6^{4-}$ reaching the Au substrate would react reversibly in the light or in the dark. In Fig. 2a we see the dark

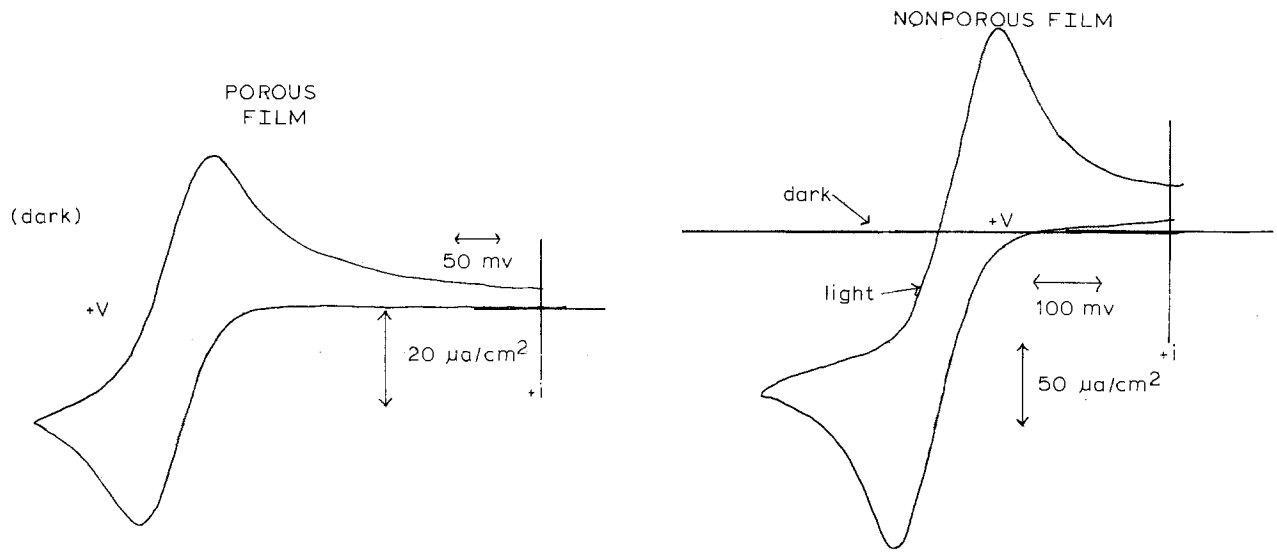

Fig. 2. Cyclic voltammogram for: (a, left) porous (506 equivalent monolayers) and (b, right) nonporous (493 equivalent monolayers) GaPc-Cl/Au electrodes. Scan rate: 50 mV/sec. Electrolyte: 1 mM $Fe(CN)_6^{4-}$ 0.1M KHP (aq).

cyclic voltammogram for a 506 equivalent monolayer porous GaPc-Cl/Au electrode. The voltammogram is similar in shape but the currents are a factor of 2.5 smaller compared to that which would be obtained for an unmodified Au-MPOTE. The Pc restricts but does not eliminate the activity of the underlying Au substrate. In contrast, the cyclic voltammograms for a 493 equivalent monolayer nonporous GaPc-Cl/Au electrode is shown in Fig. 2b. Note that the current scale is larger than for the porous electrode. Here the dark current is negligibly small, while under irradiation the voltammogram becomes appreciably reversible and as reversible as that for ferrocyanide oxidation on the plain Au electrode. The peak current is 1.5 times larger than on the plain Au electrode.

Reports which will follow will detail the differences between the porous and nonporous Pc films on the Au MPOTE. Preliminary scanning electron micrographs show that both film types are composed of large crystallites, with dimensions on the order of 0.5-1.0 microns, length and width. These crystallites are widely separated on the porous GaPc-Cl films and are tightly packed on the nonporous films. At 11,000× magnification, the nonporous GaPc-Cl film still shows considerable surface roughness, while the Au MPOTE substrate at the same magnification shows no discernable surface features. A surface roughness factor of 1.5 for the illuminated GaPc-Cl/Au electrode is not unreasonable; however, the increased voltammetric currents cannot be explained based on this enhanced surface area, since the diffusion layer thickness in the voltammetric experiment exceeds the dimensions of the surface roughness. Preliminary photothermal spectroscopic investigations of these films in this laboratory indicate considerable heat loss from the film following visible wavelength illumination. It is quite possible that the enhanced currents seen under illumination of the nonporous GaPc-Cl/Au electrode are due to a small thermally induced convection from the radiationless decay pathways within the film.

To corroborate the voltammetric data, x-ray photoelectron spectra were taken of electrodes prepared in the same sublimation vessel at the same time as those used in Fig. 2. In Fig. 3, the XPS data for a high resolution scan of the Au(4f) transition for the porous and the nonporous GaPc-Cl/Au electrodes are shown, along with that of a plain Au-MPOTE. Since the thickness of the Pc films (greater than 300Å) must be greater than the escape depth of an Au-4f electron through the Pc film, any Au signal must be due to pinholes or other imperfections in the phthalocyanine film. No Au signal is observed for the nonporous electrode, while for the porous electrode a signal is observed. The Au signal on the porous GaPc-Cl film is still much less than on the plain Au-MPOTE and is diminished more than the electrochemical response of the Au substrate was diminished. A porous Pc-film will be more "transparent" to a diffusion-controlled, electrochemical process, than will electron spectroscopy of the Au substrate. In the XPS experiment, electrons escaping from the Au substrate must follow a collision-free trajectory to the detector in the spectrometer, thus, their intensity is expected to be low with a thick, porous overlayer.

Quinone electrolysis.—In Fig. 4, the cyclic voltammograms for the electrolysis of H_2Q on nonporous GaPc-Cl film electrodes in the dark and under illumination are presented. Also shown is the response for each of the bare substrates: Au, Ag, brass, and n-SnO_2.

The electrodes made from nonporous GaPc-Cl films on Au and Ag (Fig. 4a and 4b, respectively) show almost no activity in the dark; the reaction of H_2Q

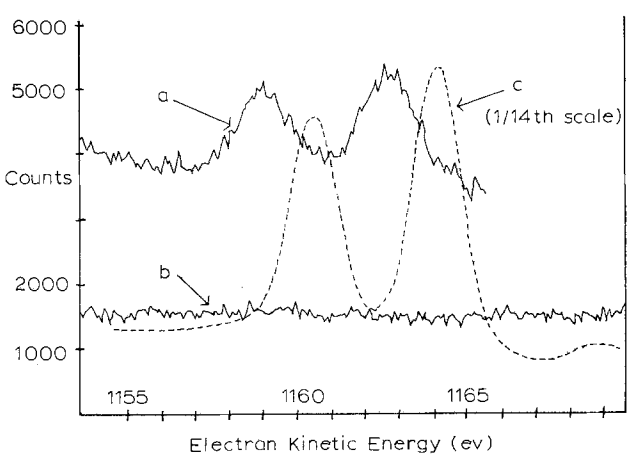

Fig. 3. XPS spectra of the Au-4f transition for: a) porous and b) nonporous GaPc-Cl electrodes; c) plain Au-MPOTE, drawn to 1/14th scale. Scans a) and b) correspond to electrodes identical to those in a) and b) of Fig. 3, respectively. None of these scans have been charge-shift corrected, hence, the difference in Au(4f) peak position.

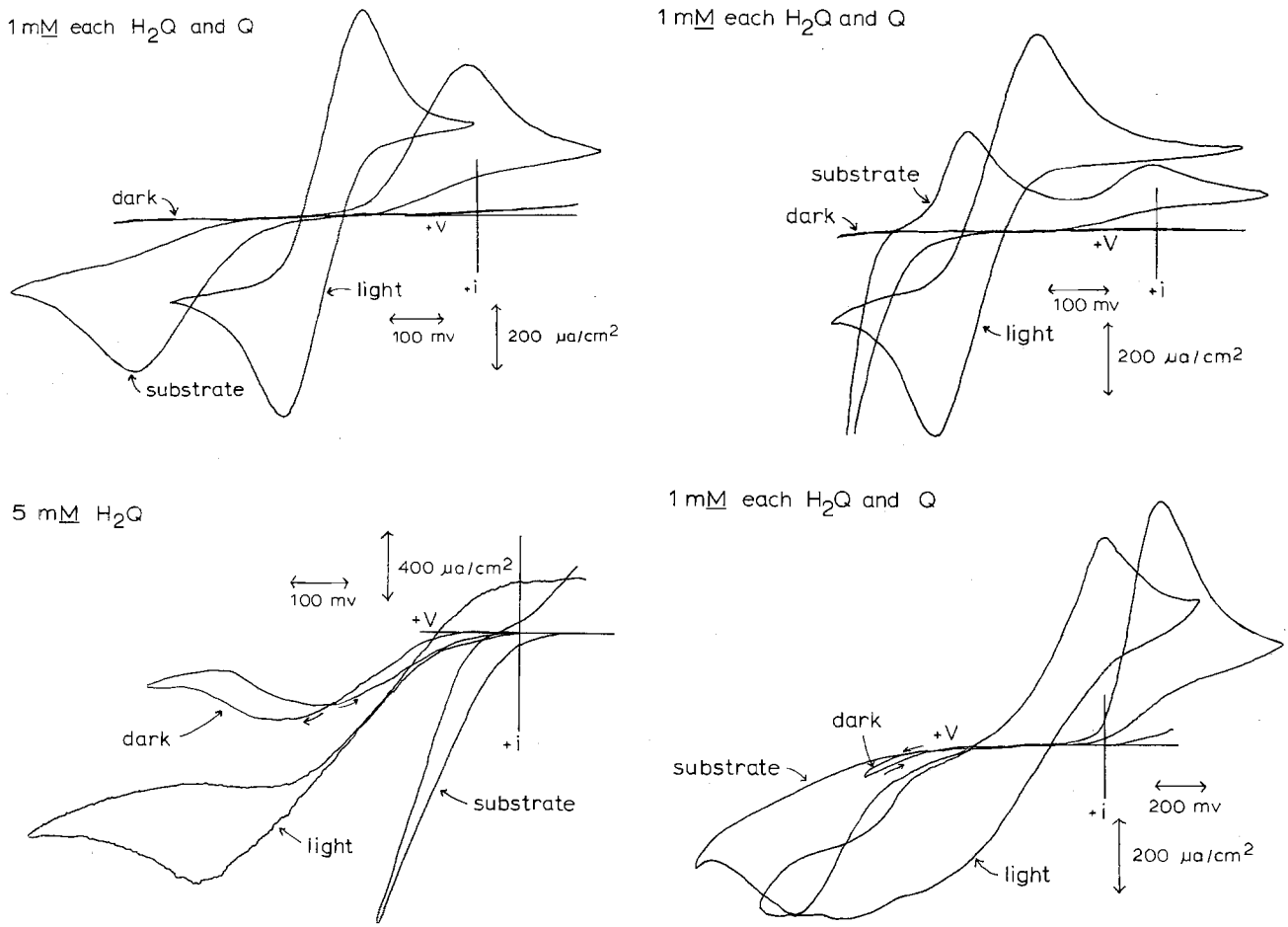

Fig. 4. Cyclic voltammograms for GaPc-Cl films deposited on various substrates. a, top left) Au; b, top right) Ag; c, bottom left) brass; d, bottom right) n-SnO_2. Scan rate: 50 mV/sec; electrolyte: H_2Q and/or Q, as marked in 0.1M KHP (aq).

on Au is suppressed. This suppression of anodic activity is even more significant for Ag, because the current-voltage curve remains flat even past the oxidative decomposition potential of the Ag film. This implies that the films were truly nonporous; neither H_2Q nor water was in contact with the metallic surfaces.

With unattenuated visible wavelength irradiation (450-900 nm) from the xenon arc lamp, the H_2Q electrolysis shows appreciable reversibility. In the case of the GaPc-Cl/Au electrode, the rate of reaction exceeded that of the Au substrate itself. This type of electrochemical reversibility is seen on the Au substrates in the pH range from 1 to 7. Figure 5 shows the dependence of light intensity on the shape of the voltammetric curve for H_2Q oxidation on the GaPc-Cl modified Au electrode. The apparent electrochemical reaction rate was controlled by the photon flux to the surface. This photon dependence was further quantitated by observing that the photocurrent at any potential was linear with the incident photon flux from an He-Ne laser (632.8 nm, 5.6-0.056 mW/cm²). Using light from the He-Ne laser source, the photoelectrochemical quantum efficiency (n_e/n_p) was calculated. Here n_e represents the photoinitiated electron flow, and n_p represents the photon flux. At 632.7 nm, $n_e/n_p = 0.08$-0.1%. It should be noted that this wavelength is not within the maximum absorbance envelope for the film, where it is believed the most photoconductive phases absorb. Further studies are underway using monochromatic sources near 800 nm; however our preliminary studies using broad band sources in this region show that n_e/n_p is in the range of 1-5% (1). Through Tafel plot data, we calculated the exchange current density of 10^{-3}M H_2Q on Au in pH = 4 buffered electrolyte to be 0.27 μA/cm². This value is in reasonable agreement with the data of Vetter for quinone electrolysis on Pt (24). The resistivity of the illuminated organic film made it difficult to obtain accurate Tafel data for the GaPc-Cl electrodes using monochromatic irradiation sources. We did, however, estimate a lower limit for the exchange current density through the method of cyclic voltammetric peak separation (Fig. 4a) as described by Nicholson (26). We obtained a value of 1-2 × 10^{-4} A/cm², about three orders of magnitude greater on the illuminated GaPc-Cl/Au surface that for plain Au. For GaPc-Cl/Ag (Fig. 4b), it can be remarked that the H_2Q electrolysis proceeded as reversibly as on GaPc-Cl/Au electrodes

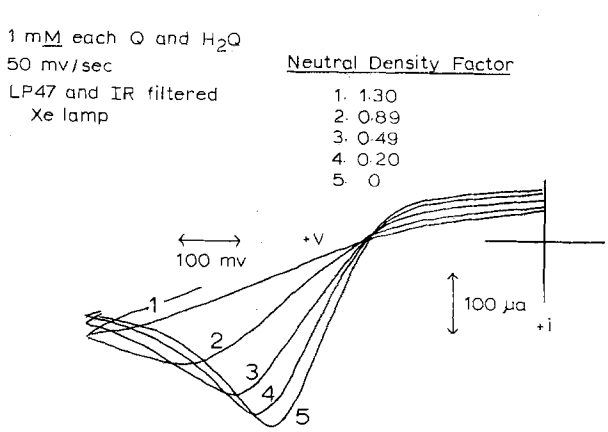

Fig. 5. Effect of light intensity of H_2Q oxidation on a nonporous GaPc-Cl/Au electrode. The polychromatic output of the xenon arc lamp was neutral density filtered to give the fractions of full light intensity shown in the drawing.

in a potential range where the Ag electrode itself would have decomposed.

Pursuing the idea of extending the anodic limit of the substrate material, we tested GaPc-Cl films on brass. As shown in Fig. 4c, we were not completely successful in preparing a stable nonporous GaPc-Cl film on brass substrates. The presence of the film apparently mass transport-limits the dissolution of brass, but the current crossover on the return sweep must also mean steady erosion of the GaPc-Cl layer. At this point, we are not sure whether film porosity on brass compared to Au and Ag Intrex is due to unavoidable differences in surface preparation (see Experimental section) or to fundamental differences in adsorption characteristics of the phthalocyanine that cause variability in film growth. XPS data from our laboratory on the Intrex films indicate a small concentration of organic functionalities incorporated in the metal surface, which may facilitate good adhesion and crystal growth of the GaPc-Cl (23). It is clear, nevertheless, that the GaPc-Cl/brass electrodes under irradiation can successfully electrolyze H_2Q at potentials several hundred millivolts past the oxidative limit of plain brass. Attempts to corrosion-protect other semiconductor photoelectrodes with nonporous films of these phthalocyanines are currently underway in our laboratory.

In Fig. 4d, the cyclic voltammetry for a GaPc-Cl film on n-SnO_2 is shown. While H_2Q was not quite as reversible on the irradiated GaPc-Cl/SnO_2 electrode as on GaPc-Cl/Au, the difference in activity compared to the substrate is more pronounced; a very large overpotential is required to drive H_2Q oxidation on bare n-SnO_2. Sweeping too far in the anodic direction can desorb the Pc film, as shown by the current wave obtained in the dark.

The concentration dependence of the H_2Q photocurrent response of the nonporous GaPc-Cl/Au was tested in the range from 10^{-5}M to 5×10^{-2}M. At the lowest concentrations, the photocurrent was linear with H_2Q solution concentration, as the solution concentration was increased up to 10^{-3} to 10^{-2}M, the photocurrent response reached a near-plateau. This response is consistent with a weak surface interaction between H_2Q and the GaPc-Cl surface.

The nature of the enhancement of quinone electrolysis on the illuminated, Pc-modified metallic substrates was further explored by testing the reason for the apparently slow kinetics on the unmodified Au substrate. There are several literature sources which support the idea that H_2Q/Q redox chemistry is reversible at low *p*H and that the rate of reaction (k_s or exchange current density, i_o) decreases markedly as *p*H is increased (25). Recent thin layer electrochemical experiments by Hubbard and co-workers on platinum in various aqueous environments show that quinones tend to adsorb tenaciously to the noble metal substrate (27). Their results suggest that the solution redox chemistry on Pt occurs through this adsorbed quinone layer.

The manner in which the Au metal substrate of these experiments is activated prior to the voltammetric experiment is of importance as shown in the experiment of Fig. 6. "Cleaned" and polished bulk Au substrates showed a markedly irreversible H_2Q/Q redox voltammogram (curve 1) until the electrode was poised at a potential sufficient to oxidize the Au surface. Subsequent reduction of the gold oxide layer (curve 2) resulted in a decidedly enhanced rate of quinone reduction and subsequent hydroquinone oxidation. This reversible voltammetric activity could be sustained for many minutes as the electrode remained immersed in the electrolyte. Exposure of the electrode to the atmosphere and return to the electrolyte always resulted in the voltammetric activity of curve 1. Nearly identical results were obtained on the Au-MPOTE substrates used for the photoelectrochemical experiments which were never polished, only cleaned as described in the Experimental section. Further characterization of this electrode surface reactions is underway in a surface analysis system with vacuum transfer capabilities.

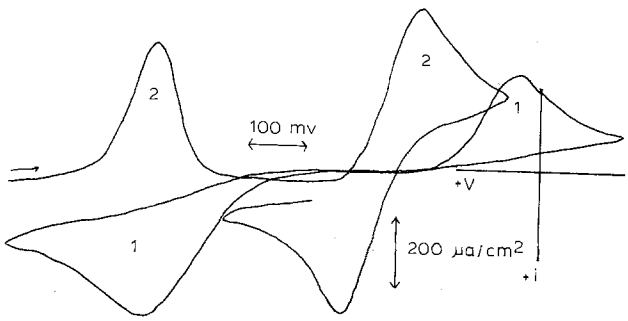

Fig. 6. Voltammetric response toward H_2Q of a mechanically cleaned and rinsed Au substrate (curve 1) and the same electrode following gold oxide formation and reduction (curve 2). 50 mV/sec, 0.1M KHP, 1.4 mM H_2Q.

Conclusions

The observation of reversible ferro/ferricyanide and hydroquinone/quinone electrolysis on the illuminated nonporous GaPc-Cl film electrode raises several interesting questions regarding the mechanism of charge transfer within the Pc layer, and the applicability of these dye films to semiconductor sensitization. At low surface coverages of the phthalocyanine on an n-type semiconductor, it is expected that the phthalocyanine will act strictly as a sensitizer with high photoconductivity. Within the confines of the Gerischer model (28) design of a GaPc-Cl sensitized semiconductor system would appear to be optimized by the use of a nonporous film, with a thickness of *ca.* 400 equivalent monolayers. The optical density of such a film is *ca.* 1.0, at 800 nm, which is still not as high as we would like to optimize the power conversion efficiency of a single electrode.

Since the thin GaPc-Cl films are acting primarily to conduct the electron and hole to the electrode and electrolyte interfaces respectively, any energy conversion (*i.e.*, generation of a photopotential) that occurs must be controlled by the relative electron affinity of the semiconductor substrate and the formal potential of the solution redox couple. When GaPc-Cl films of the surface coverages reported here are placed on a metallic substrate (Au, Ag) small (less than 50 mV) or no detectable photopotential was produced, confirming this mainly photoconductive nature of the Pc film. To our knowledge, this is the best example of photoinitiated, reversible, electrolysis on Pc films reported to date. The reason for this enhanced photoelectrochemical behavior seems to lie in (*i*) the choice of a phthalocyanine which tends to aggregate to form polymorphs with high photoconductivity and red-shifted spectral response and (*ii*) sublimation rates that are controlled and slow enough to permit the growth of large Pc crystallites, thereby, lowering the number of recombination events occurring at edge-sites and defects that would otherwise lower the photoelectrochemical efficiency.

In our most recent studies, carefully grown GaPc-Cl films of much greater thickness than reported here (on the Au-MPOTE) have shown sizable photopotentials for several different redox couples, indicating that semiconductor-like properties of the Pc film can be obtained when the molecular ordering and the crystallite dimensions become even greater (29). This photopotential response appears similar to that observed for other photoconductors which have been built up to sufficient surface coverages to facilitate energy conversion through the formation of a barrier layer (30).

This apparently dual nature of phthalocyanine film electrodes has been observed previously. Some rectification of the current voltage response has been seen for monolayers to multilayer quantities of Pc's on SnO_2 and TiO_2 surfaces (1, 7-9). In most of these cases, however, some photocurrent response was observed in a potential region where the basic sensitization model would predict no current flow. Bard and coworkers explained this observation with the existence of a different mechanism for each direction of current flow: photoreduction was due to the p-type character of the phthalocyanine, and photo-oxidation was due to dye sensitization of the n-type substrate (8). Faulkner and co-workers (10, 11) observed quite reversible voltammograms for ferro/ferricyanide electrolysis, in the dark, on FePc and ZnPc films of several thousand angstroms thickness. The existence of as yet uncharacterized surface states has been invoked to explain facile charge transfer in both directions (8, 10, 11).

In addition to the highly desirable photoconductivity and corrosion-inhibiting capabilities of the nonporous GaPc-Cl films, a slow electrolysis rate for the H_2Q/Q couple is photoenhanced by up to three orders of magnitude. From the experiments described in Fig. 6, it is clear that the reasons for this enhancement are complex. The hydroquinone oxidation has a high overpotential on the Au substrate, apparently because of the incompatibility of solution H_2Q with this surface. It is not clear at this time whether adsorbed reactant is responsible for this retarded electrolysis rate. Our control experiments in a number of aqueous electrolytes and pH ranges show the generality of this inhibition, and tend to demonstrate that less than detectable concentrations of solution impurities may be one of the causes for this slow electrolysis (29). Activation of the Au substrate can be achieved by either the formation and reduction of the gold surface oxide or by application of a GaPc-Cl layer and its illumination. The action of the phthalocyanine may be to (*i*) block all of the Au surface sites to provide only a GaPc-Cl surface for electrolysis and/or (*ii*) provide a unique chemical environment for the multielectron multiproton transfer steps to occur. Further studies of this redox chemistry on the GaPc-Cl/Au electrodes are underway to clarify this issue.

Acknowledgments

This research was supported by a grant from the National Science Foundation, CHE 80-17571 and in part by a grant from the Sierracin Corporation. The authors wish to thank Professor Art Hubbard and Dr. Manuel Soriaga for sharing preprints of their work and for several stimulating discussions.

Manuscript submitted June 30, 1982; revised manuscript received *ca.* Dec. 17, 1982.

Any discussion of this paper will appear in a Discussion Section to be published in the December 1983 JOURNAL. All discussions for the December 1983 Discussion Section should be submitted by Aug. 1, 1983.

Publication costs of this article were assisted by the University of Arizona.

REFERENCES

1. T. M. Mezza, C. L. Linkous, V. R. Shepard, N. R. Armstrong, R. Nohr, and M. Kenney, *J. Electroanal. Chem.*, **124**, 311 (1981); N. R. Armstrong, ACS Symposium on Chemically Modified Surfaces, ACS Publications, In press.
2. K. Tamaru and S. Meshitsuka, *J. Chem. Soc., Fl*, **73**, 236, 760 (1977).
3. W. M. Ayers, *Faraday Discuss. Chem. Soc.*, **70**, 247 (1980).
4. N. Minami, T. Watanabe, A. Fujishima, and K. Honda, *Ber. Bunsenges. Phys. Chem.*, **83**, 476 (1979).
5. N. Minami, *J. Chem. Phys.*, **72**, 6317 (1980).
6. Y. Nakato, M. Shioji, and H. Tsubomura, *ibid.*, **85**, 1670 (1981).
7. F. F. Fan and A. J. Bard, *J. Am. Chem. Soc.*, **101**, 6139 (1979).
8. C. D. Jaeger, F. F. Fan, and A. J. Bard, *ibid.*, **102**, 2592 (1980).
9. A. Giraudeau, F. F. Fan, and A. J. Bard, *ibid.*, **102**, 5137 (1980).
10. F. Fan and L. R. Faulkner, *ibid.*, **101**, 4779 (1979).
11. H. Tachikawa and L. R. Faulkner, *ibid.*, **100**, 4379 (1978).
12. Yu. S. Shumov, V. I. Sevast'yanov, and G. G. Kommissarov, *Biofizika*, **18**, 47 (1973).
13. G. S. Alferov and V. I. Sevast'yanov, *Zh. Fiz. Khim.*, **49**, 214 (1976).
14. Yu. S. Shumov, S. S. Chakhmakhchyan, V. I. Mityaev, and G. G. Kommissarov, *Zh. Fiz. Khim.*, **53**, 1834 (1979).
15. V. R. Shepard, Jr. and N. R. Armstrong, *J. Phys. Chem.*, **83**, 1268 (1979).
16. H. Meier, W. Albrecht, U. Tschirwitz, E. Zimmerhackl, and N. Geheeb, *Ber. Bunsenges. Phys. Chem.*, **81**, 592 (1977).
17. J. L. Peterson, C. S. Schramm, D. R. Stojakovic, B. M. Hoffman, and T. J. Marks, *J. Am. Chem. Soc.*, **99**, 286 (1977).
18. C. J. Schramm, R. P. Scaringe, D. R. Stojakovic, B. M. Hoffman, J. A. Ibers, and T. J. Marks, *ibid.*, **102**, 6702 (1980).
19. W. A. Orr and S. C. Dahlberg, *ibid.*, **101**, 2875 (1979).
20. Y. Yamamoto, K. Yoshino, and Y. Inuishi, *J. Phys. Soc. Jpn.*, **47**, 1887 (1979).
21. H. Meier, W. Albrecht, and U. Tschirwitz, *Ber. Bunsenges. Phys. Chem.*, **73**, 795 (1969).
22. J. P. Linsky, T. R. Paul, R. S. Nohr, and M. E. Kenney, *Inorg. Chem.*, **19**, 3131 (1980).
23. R. Cieslinski and N. R. Armstrong, *Anal. Chem.*, **51**, 565 (1979).
24. J. H. Sharp and M. Oardon, *J. Phys. Chem.*, **72**, 3230 (1968); J. H. Sharp and M. Mokowitz, *ibid.*, **77**, 477 (1973).
25. K. J. Vetter, *Zeit. Elektrochem.*, **56**, 797 (1952).
26. R. S. Nicholson, *Anal. Chem.*, **37**, 1351 (1965).
27. M. P. Soriaga and A. T. Hubbard, *J. Am. Chem. Soc.*, **104**, 2735, 2742 (1982).
28. H. Gerischer and F. Willig, *Top. Curr. Chem.*, **61**, 31 (1976).
29. C. Linkous and N. R. Armstrong, Manuscript in preparation.
30. G. S. Calabrese, M.-S. Lin, J. Dresner, and M. S. Wrighton, *J. Am. Chem. Soc.*, **104**, 2412 (1982).

Impedance Measurements and Photoeffects on Ni Electrodes

Marc J. Madou and Michael C. H. McKubre*

SRI International, Menlo Park, California 94025

ABSTRACT

Depending on the electrode potential an n-type or a p-type semiconducting oxide can be present at a Ni electrode surface giving rise, respectively, to anodic or cathodic photocurrents under illumination. Impedance measurements show that a solid-state diffusion process, presumably of protons through the oxide film, dominates the impedance behavior for the charged electrode; for the discharged electrode, the impedance behavior is dominated by the space charge inside the p-type oxide. A flatband potential and donor density estimate could be made for the p-type semiconducting oxide.

For several decades the work on the Ni electrode has been oriented to its battery applications (1). Recent publications have focused attention on more fundamental problems associated with this electrode. The electrochemical processes at the Ni electrode are greatly influenced by the presence of surface oxides. Both the charged and discharged state of the Ni electrode are oxides of nickel, and a number of studies have been performed to determine the influence of lithium ions on the solid-state properties of these passivating oxide films. The a-c response of nickel oxides have been studied in detail by, for example, Glarum *et al.* (2) and Zimmerman *et al.* (3). Ellipsometric measurements of oxide films on Ni were performed by Hopper *et al.* (4). MacArthur determined a proton diffusion coefficient for the nickel hydroxide electrode (5). Cyclic voltammetry on the Ni electrodes has been carried out extensively by, for example, Arvia *et al.* (6-8). The different theories put forward to explain the positive influence of lithium hydroxide on capacity, potential, and life of the nickel oxide electrode rely on solid-state properties of the passivating films. In this context Tichenor (9) pointed out that the lithium influence could be explained as a doping effect of Li in NiO, under the assumption that the oxide involved is a p-type semiconductor. Tuomi (10), on the other hand, pointed out that the effect cannot be explained on the basis of the p-type character of one of the oxides since the important oxide in the charged region (β-NiOOH) is an n-type semiconductor. Chernykh and Yakovleva (11) found both anodic and cathodic photocurrents at oxidized Ni electrodes. These photocurrents were attributed to n- and p-type nickel oxides, respectively, but no details about wavelength and chopper speed dependence of the photocurrents were given. Angelini *et al.* (12) show anodic and cathodic photopotentials for Ni and discuss a fast and a slow component of the observed photopotential. They assume that the faster photopotential component is due to the separation of electron-hole pairs within the electric field in the oxide and that the slow process is due to decomposition of surface oxides.

In view of the importance of the solid-state properties of the oxide films in understanding the Ni electrode behavior we thought it to be interesting to approach the study of the Ni electrode using methods which reveal more about the bulk and surface properties of the nickel oxides. The experimental methods used in the present study were principally as follows: photocurrent measurements as a function of voltage, wavelength, and chopper speed, and a-c impedance measurements as a function of frequency and voltage. Measurements were performed on surface-formed passivating oxides and on electrodeposited films. It was anticipated that semiconductor effects would be more readily observed when dealing with thicker films.

Experimental

An all-Teflon cell was used for performing impedance measurements, coulometry, and cyclic voltammetry. The reference electrode [in most cases a Zn/Zn(II) couple] was placed in an external reservoir to prevent contamination of the working electrolyte. As a counterelectrode we used a Pt wire also placed in a separate compartment. Provision was made in the working electrode chamber to sparge with high purity N_2 to eliminate dissolved O_2 and exclude CO_2. For the light experiments an all quartz cell was used with all three electrodes in the same compartment. The light source was a mercury vapor pressure lamp (PEK Model 912-0, power supply M702). Potentials were recalculated to be expressed with respect to the standard hydrogen electrode (SHE).

Electrodeposited nickel oxide films of different thickness on Ni were prepared according to a procedure described by Briggs *et al.* (13). The room temperature electrodeposition of the oxide by this method is effected by anodic/cathodic cycling the metal substrate in an aqueous solution containing 0.1*N* $NiSO_4$, 0.1*N* NaAC, and 0.001*N* KOH ("Briggs' solution"). Depending on the cycling procedure a different thickness of deposit can be obtained. The films mostly used in our experiments were those described by Briggs as procedure C and procedure F films. To determine qualitatively the relative thickness of the oxide films on Ni, we used coulometry; the amount of charge under the large anodic peak in cyclic voltammograms such as shown in Fig. 1 was measured. It is accepted in the literature (14) that this peak corresponds to the oxidation of $Ni(OH)_2$ to β-NiOOH (charging peak). Typically for the bare Ni surface cycled in a 35 weight percent (w/o) KOH solution, at a sweep rate of 100 mV sec^{-1}, 11 mC cm^{-2} would be associated with this peak (see Fig. 1b), 62 mC cm^{-2} for a C-type film (see Fig. 1a), and 176 mC cm^{-2} for an F-type film (not

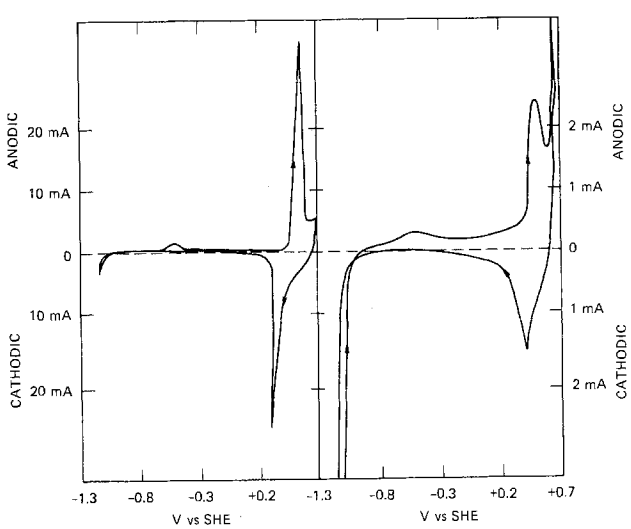

Fig. 1. Cyclic voltammograms, 100 mV sec^{-1}, 35 w/o KOH, surface area = 0.452 cm^2. (a, left) Treated sample (C-type film, observe y-axis) and (b, right) untreated sample.

* Electrochemical Society Active Member.
Key words: semiconductor, battery, discharge, passivity.

shown). The smaller anodic peak in Fig. 1 has been associated with oxidation of Ni to $Ni(OH)_2$ and the single cathodic (discharge) peak has been attributed to the reduction of β-NiOOH back to $Ni(OH)_2$.

Measurements of the electrochemical transfer function (15, 16) (the "a-c impedance") of the Ni oxide/electrolyte system were performed using a Solartron Model 1172/1183/1185 Frequency Response Analyzer (FRA). Figure 2(a) shows schematically the experimental configuration employed for impedance measurements. The FRA is controlled by an Apple II microcomputer via an IEEE-488 bus (17). In this way it is possible to perform measurements over a range of frequencies (10^{-4}-10^4 Hz) and d-c voltages in a single experiment, thus facilitating the determination of Mott-Schottky plots (18). The software written to control the FRA and for subsequent data reduction and deconvolution is presented in Ref. (19).

A Princeton Applied Research Model 175/173 potentiostat was used for both potentiodynamic cycling and a-c impedance studies. In order to offset inherent limitations of the potentiostat and FRA, a novel interface between these units was designed and built. The circuit diagram is shown as Fig. 2(b), and the function is described in detail in Ref. (19). The important features of this unit briefly are as follows: (*i*) Provides automatic "back-off" of the d-c component of the voltage applied between the working and reference electrodes, thus allowing greater precision in the measurement of the a-c signal. (*ii*) Measures the current as the voltage drop across an *R-C* parallel standard, in series with the counterelectrode. This minimizes the double limitations of poor high frequency response of the PAR current-to-voltage converter (17), and the difficulty of handling large voltages which occur at high frequencies under potentiostatic conditions when the current is transduced by a resistor or simple current clamp. (*iii*) Attenuates the FRA a-c output, allowing measurement to be made with <10 mV excitation. (*iv*) Provides the high input impedance and low input capacitance necessary for the determination of semiconductor impedances.

Results and Discussion

Photoeffects on Ni electrodes.—Crystalline NiO is known to be a p-type semiconductor (20), β-NiOOH is reported to be an n-type semiconductor (10). The sign of the photocurrents found on the Ni electrode under study should indicate of which type the passivating oxides on Ni are. With the bandgap of NiO around 3.7 eV (21), light of wavelengths shorter than 3314Å will be absorbed by a material containing NiO. We could not find a value for the bandgap of β-NiOOH.

Depending on the applied potential, we observed both large anodic and large cathodic photocurrents when illuminating a filmed Ni electrode with u.v. light. With the filmed Ni electrode polarized negative with respect to the solution (close to and into the hydrogen evolution range) we found cathodic photocurrents. In this discharge range the electrode behaves as if it were covered with a p-type semiconducting oxide. With the electrode polarized positive (in the $Ni(OH)_2$ → β-NiOOH charge region), large anodic photocurrents were observed, pointing to an n-type passivating oxide layer. We discuss the cathodic photoeffect first.

The measurements represented in Fig. 3 were performed on a filmed Ni electrode (F-type film; see experimental) in the Briggs' solution (0.1*N* $NiSO_4$, 0.1*N* NaAc, and 0.001*N* KOH). The light was chopped at a relatively high constant frequency while the potential was progressively made more negative. Clearly, the current amplitude increases as the potential becomes more negative. Since the oxide involved here is a p-type oxide this behavior was not unexpected, indeed the more negative the applied voltage, the more efficiently electron-hole pairs are separated and the more photocurrent can be expected. The feature that was less easily understood, in terms

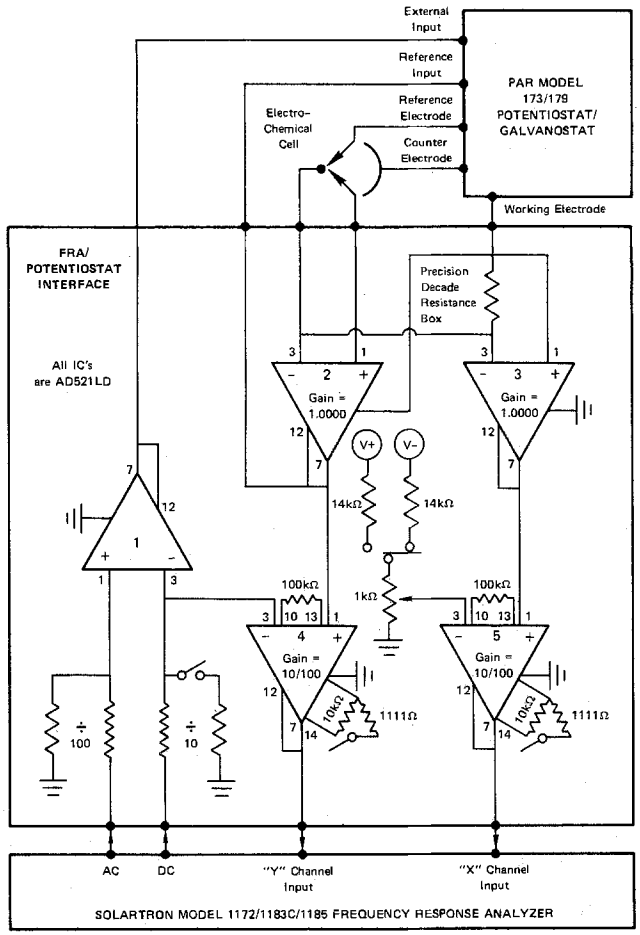

Fig. 2. (b) Impedance measurement system

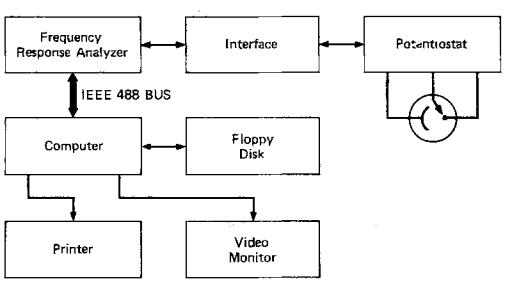

Fig. 2. (a) Impedance measurement circuit

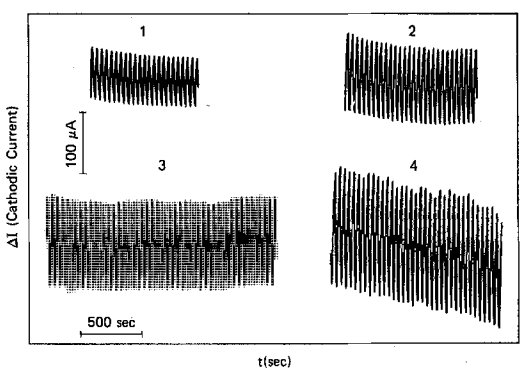

Fig. 3. Photocurrent (ΔI) vs. time at constant chopper speed: 1, −1.112V *vs.* SHE; 2, −1.200V *vs.* SHE; 3, −1.250V *vs.* SHE; 4, −1.350V *vs.* SHE. Solution: 0.1*N* $NiSO_4$, 0.1*N* NaAc, 0.001*N* KOH (Briggs' solution). F-type film (explanation see Experimental).

of simple p-type semiconductor behavior, is shown in Fig. 4. In this figure we present the measured photocurrent as a function of chopper speed for a filmed Ni electrode (C-type film) at a negative potential (−1.35V *vs.* SHE). A very strong dependence of the photocurrent magnitude on chopper speed is observed. The lower the chopper speed the higher the photocurrent. At the highest and also at the lowest chopper speeds the photocurrents finally became constant, the amplitude being almost an order of magnitude smaller at the highest chopper speeds. The above seems to indicate that there are two processes involved in the photoresponse of the Ni electrode; a fast responding photocurrent associated with a semiconducting oxide layer and a much slower not yet explained process. This is in accordance with the observations by Angelini *et al.* (12) (see also the beginning of this paper) that there are two components to the photopotential at a Ni electrode. The photocurrent disappears with a filter absorbing u.v. (transmission lower than 0.5% at wavelengths shorter than 3650Å) and transmitting visible light inserted in the light path. This indicates that we are dealing with a u.v. induced photocurrent. With a combination of other light filters we attempted to measure approximately the absorption edge. With u.v. transmitting clear filters (transmission at $\lambda =$ 3314Å higher than 85%) in place there was little or no decrease of the photocurrent. For a filter with a transmission lower than 0.5% for $\lambda <$ 3340Å there was a substantial decrease in photocurrent. The data above can accommodate the 3314Å for the absorption edge of NiO. In the future a monochromator in combination with a differential technique for measuring the photocurrent will be used to obtain more quantitative data on the absorption edge.

The same photoeffects as shown in Fig. 3 and 4 were found in 5*N* KOH and in 35 w/o KOH. More surprisingly, the photoeffect was still present after etching of a filmed electrode using a 50 w/o HCl solution. In all cases the photocurrents showed the same potential dependence and chopper speed dependence as discussed above for the filmed electrodes. The alkaline solutions used here were chosen because of their practical importance for use in batteries, but obviously the effects described here are rather independent of the solutions used.

Our tentative explanation for the two kinds of photoresponses differs from that presented by Angelini *et al.* (12) and is as follows. Electrons excited by light into the conduction band of a thin layer of oxide reduce mainly protons to hydrogen but also reduce some Ni(II) oxide to metal at the NiO/electrolyte interface; this corresponds to the fast photoresponse. The overpotential for hydrogen evolution on Ni in the Ni(II) oxide matrix is expected to be lower than on the passivated Ni surface. The longer the period of time the light is on the more Ni forms and the rate of hydrogen evolution increases; this leads to the slow "photoresponse." When the light is turned off the Ni slowly passivates again, resulting in an accompanying slow decay of the hydrogen evolution. So we suggest that illumination of the Ni electrode gives rise to two distinctively different processes: (a) A fast responding primary photoeffect.—Generation of electron/hole pairs in the semiconducting Ni(II) oxide by u.v. light, leads, under negative polarization, to increased hydrogen evolution and to some oxide reduction at the oxide/electrolyte interface. (b) A slow responding pseudophotoeffect.—Increased current due to hydrogen formation through the reduction of protons on the Ni formed in process (a).

Obviously it is unnecessary to deliberately grow a thick Ni(II) oxide film to see the effects described above. A native oxide seems sufficient to produce the same effects. In the last section of this paper the thermodynamic feasibility of the photoreduction of Ni(II) oxide is discussed.

It should be noted that it is generally assumed (14) that Ni(II) oxide cannot be reduced by Ni. We have indirect proof here that such a reduction can occur with optically excited conduction band electrons. In the second paper in this series (22) we describe evidence based on cyclic voltammetry data that Ni(II) oxide can, under certain conditions, be rereduced to Ni even in the dark.

As stated above, at sufficiently large anodic potentials (in the charging region), a large anodic photocurrent can be observed. This photocurrent for an Ni electrode with an F-type film is shown in Fig. 5. Clearly the oxide behaves as an n-type semiconductor in this potential range. As in the case of the cathodic photocurrents, here also a slow and a fast photoresponse are observed. The measurements shown in Fig. 5 were performed in the Briggs' solution, the same kind of photoresponse was observed in 5*N* KOH or with unfilmed surfaces. Using the light effect as a probe to determine the nature of the mixed oxide in the charging region as a function of voltage might be very useful in understanding the more fundamentally important electrode reactions involved in the charge/discharge of the Ni electrode. The photocurrents seen here might be attributed to n-type β-NiOOH described by Tuomi (10).

Impedance measurements on Ni electrodes.—Impedance measurements on native nickel oxide electrode films in strong alkali are reported here as a function of frequency and applied potential. We show that the reduced film (discharged region) exhibits a much smaller capacitance than the oxidized film (charged region), moreover the capacitance of the reduced film is potential dependent and this is not so for the oxidized film. Recently Glarum and Marshall (2) published similar findings. In our work, though, we analyzed the data in terms of the semiconductor properties of the Ni(II) oxide film.

Figure 6 shows a typical Nyquist plot for a discharged electrode (−0.32V *vs.* SHE). By expanding the high frequency region of this plot (see Fig. 7),

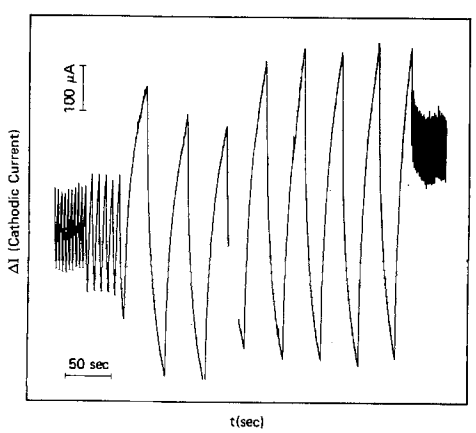

Fig. 4. Photocurrent (Δ*I*) *vs.* time at different chopper speeds but constant potential (−1.350V *vs.* SHE). Solution: 0.1*N* $NiSO_4$, 0.1*N* NaAc, 0.001*N* KOH (Briggs' solution). C-type film (explanation see Experimental).

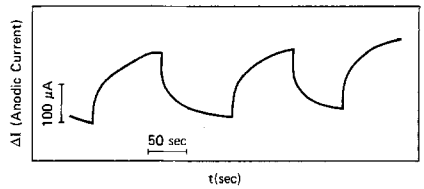

Fig. 5. Photocurrent (Δ*I*) *vs.* time at constant potential (+1.25V *vs.* SHE). Solution: 0.1*N* $NiSO_4$, 0.1*N* NaAc, 0.001*N* KOH (Briggs' solution). F-type film (explanation see Experimental).

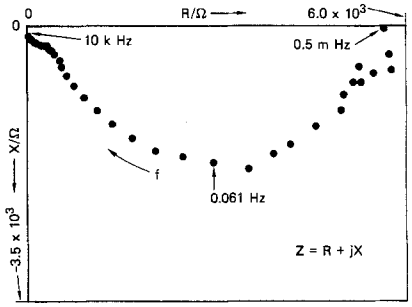

Fig. 6. Nyquist plot for applied potential of −0.32V *vs.* SHE. Solution: 5*N* KOH. Surface area: 0.452 cm².

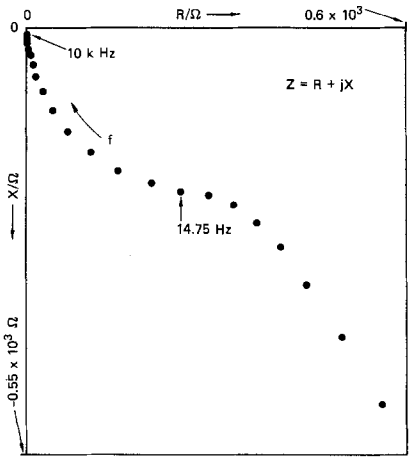

Fig. 7. Expanded Nyquist plot for applied potential of −0.32V *vs.* SHE. Solution: 5*N* KOH. Surface area: 0.452 cm².

we see that it exhibits two semicircles. At more negative applied d-c bias, the two semicircles become increasingly well resolved. At a more positive d-c bias the first semicircle gradually merges with the second. The latter is clearly illustrated for the charged electrode in Fig. 8 (+0.61V *vs.* SHE), in which case only the onset of one semicircle is to be seen. This same figure illustrates also that the Nyquist plot in this case describes a diffusional process (45° angle), whereas the first semicircle in, for example, Fig. 7, describes a single *R-C* parallel combination (90° angle).

The above is even more evident when observing a Bode plot at, say, −0.785V *vs.* SHE, as shown in Fig. 9. In the frequency range of the first semicircle in a Nyquist plot, the corresponding Bode plot exhibits a slope approaching −1 (capacitive behavior, phase → −90°). In the region of the second semicircle, the slope is close to −½ (diffusional process, phase −45°). The more positive the voltage at which the impedance measurements were made the more the region with slope −½ prevails. The Bode plot corresponding to the Nyquist plot shown in Fig. 8 shows only one line with slope

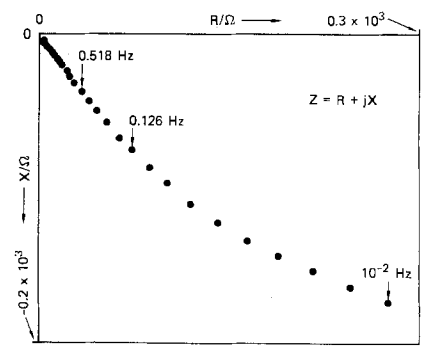

Fig. 8. Nyquist plot for applied potential of +0.61V *vs.* SHE. Solution: 5*N* KOH. Surface area: 0.452 cm².

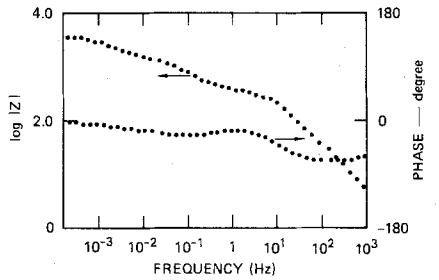

Fig. 9. Bode plot for applied potential of −0.785V *vs.* SHE. Solution: 5*N* KOH. Surface area: 0.452 cm².

−½, and the phase is −45° over the whole frequency range (see Fig. 10). The origins of these different processes are considered separately.

1. The first semicircle which is best resolved in the discharged region can be attributed to a simple *R-C* circuit, with *C* the capacitance of the space charge layer of the Ni(II) oxide film and *R* the interfacial reaction, charge transfer resistance. In the discharged region, the nickel oxide electrode shows a much smaller capacitance than in the charged region. Moreover, this small capacitance is very voltage dependent, whereas the capacitance measured for the charged electrode is voltage independent. This is illustrated in Fig. 11, which shows a plot of X^2 *vs.* *V*, at 1000 Hz (X = imaginary component of the impedance). At 1000 Hz we can say to a good approximation that $X = -1/\omega C$.

From semiconductor theory, it is expected that in the presence of a space charge, the voltage dependence of the capacitance of that space charge will

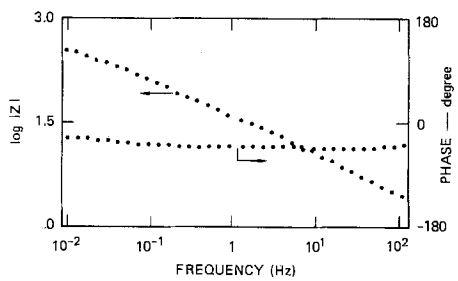

Fig. 10. Bode plot for applied potential of +0.614V *vs.* SHE. Solution: 5*N* KOH. Surface area: 0.452 cm².

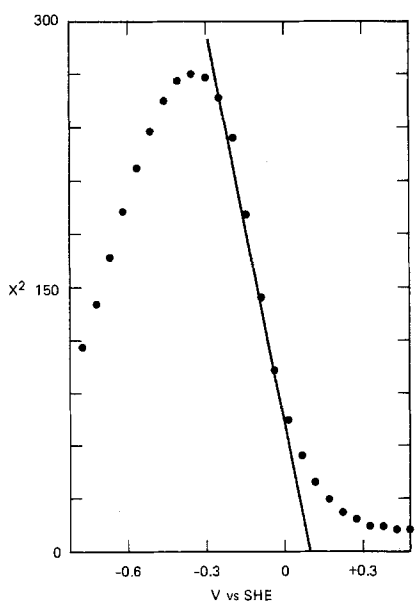

Fig. 11. Plot of X^2 *vs.* *V* *vs.* SHE for an Ni electrode in 35 w/o KOH. $X = \frac{1}{2}\pi fC$, f = 1000 Hz.

follow a Mott-Schottky relationship. This relation is given by

$$\frac{1}{C^2} = \frac{2}{eN_A\epsilon_0\epsilon_A}\left(-V + V_{FB} - \frac{kT}{e}\right) \quad \text{(for a p-type)}$$

or

$$\frac{1}{C^2} \propto V \text{ (and thus } X^2 \propto V)$$

In this formula, N_A is the acceptor density in the semiconductor, V_{FB} is the flatband potential, ϵ_A is the dielectric constant of the semiconductor, and ϵ_0 is the dielectirc constant in vacuum. The linear portion in the X^2 *vs.* V plot might indicate that space charge effects indeed play some role in the discharged nickel oxide electrode impedance behavior.

The flatband potential determined in 35 w/o KOH for our kind of electrodes was +0.100V *vs.* SHE. From work on crystalline NiO by Tench and Yeager (20) the following expression could be deduced for the flatband potential of their highest doped material as a function of pH

$$V_{FB} = 1.490 - 0.100\,pH$$

Assuming a pH of 14.5 for the solution used in the experiment described in Fig. 11, we predict on the basis of this formula that

$$V_{FB} = +0.040\text{V } vs.\text{ SHE}$$

The correspondence with our value of +0.100V for V_{FB} is remarkably good in view of the approximations and extrapolations involved in obtaining V_{FB}. Both values, on the other hand, are only in fair agreement with the 0.215V *vs.* SHE for V_{FB} calculated with the expression given by Rouse and Weiniger (23)

$$V_{FB} = 0.94 - 0.050\,pH$$

The shortness of the voltage range, over which the depletion region governs the impedance behavior, presumably has to do with the high doping level of the oxide. This is already obvious from the relative high capacitance for the nickel oxide even in depletion. At high doping levels, tunneling through the space charge layer is likely to occur at relatively low reverse bias, at which point the Mott-Schottky relation breaks down. An extensive discussion of the potential distribution across a highly doped NiO/electrolyte interface was given by Tench and Yeager (20). It turns out that their theoretical predictions for a highly doped material such as studied here indicate that only at extremely large cathodic potentials (< -2V *vs.* V_{FB}) all the potential change occurs across the space charge region and can linearity be expected in the $1/C^2$ *vs.* V plot. The fact that, despite this, a linear $1/C^2$ *vs.* V was observed at much less negative potentials (as observed in their work and the present study) they explain by the effect of specifically adsorbed cations, for example, H^+, which cause an exhaustive depletion layer to exist by strongly repelling the p-carriers (Ni^{3+}).

Ideally, the photocurrent onset at an intensely illuminated Ni electrode should correspond to the flatband potential. Thus we have another independent means of checking if we are measuring a true flatband potential with our Mott-Schottky plots. Angelini *et al.* (12) report that the electrode potential corresponding to the reversal in sign of the photoeffect is in agreement with that reported by Rouse and Weiniger (23) for the NiO flatband potential. In a borate buffer of pH = 8.7 they determined for the photoeffect sign invasion +0.55V *vs.* SHE and based on Rouse and Weiniger's expression for the flatband −0.505V *vs.* SHE was expected. In 5*N* KOH and 35 w/o KOH solution we found for the onset of the cathode photocurrent under high intensity illumination ~ +0.06V *vs.* SHE corresponding well with the +0.10V *vs.* SHE we found for the flatband potential in 35 w/o KOH. As the pH decreases it is expected that the flatband potential and thus also the photocurrent onset shift toward more anodic values. Extrapolating our value for the photocurrent onset to the value expected in a solution of pH = 8.1, we get either +0.590V *vs.* SHE [using the 0.100 V/pH slope given by Tench and Yeager (20)] or +0.325V *vs.* SHE [using the 0.05 V/pH slope given by Rouse and Weiniger (23)]. The former of the two value is close to +0.550V *vs.* SHE given by Angelini (12).

The concentration of the dopant can be calculated from the slope of the Mott-Schottky relation. In view of the above, the concentration is expected to be high. Taking into account a roughness factor of 1.5 we calculate an acceptor concentration of 4×10^{20} cm^{-3}. This is a very high doping level and constitutes almost the limit of applicability of the Mott-Schottky relation. We propose that the nonstoichiometric and/or the highly imperfect nature of the oxide film is responsible for its high conductivity. This doping level is almost the same as that reported by Tench and Yeager for their highest doped material (2.4×10^{20} cm^{-3}). Both slope and intercept of our Mott-Schottky plots are acceptable and justify our assumption of the existence of a space charge in a cathodically polarized Ni electrode, a point which is also in accordance with the cathodic photocurrent in that potential region.

2. Because the impedance spectrum is observed to be independent of electrode rotation speed, the diffusional process responsible for the second semicircle in the Nyquist plot is most likely to be associated with the diffusion of ions within the oxide. Recently Zimmerman *et al.* (3) published impedance data on nickel-cadmium cells. Their results pointed also to solid-state diffusion in a surface film. Because the measurements were done on an NiCd cell, it was difficult for them to assign processes definitively, but an H^+ diffusion inside the NiO film was considered as possibly explaining one of the two solid-state diffusion processes they describe. Assuming that the cell impedance is predominantly controlled by diffusion, σ, the Warburg coefficient can be determined from a plot of the impedance *vs.* the square root of ω ($=2\pi f$). The Warburg coefficient σ can be represented by (24)

$$\sigma = \frac{RT}{n^2\mathbf{F}^2c_0\sqrt{2D}}$$

where c_0 is the concentration of diffusing species and D is the diffusion coefficient. Zimmerman *et al.* (3) estimate the following values of $c_0\sqrt{D}$ for the two diffusion processes they assume: 1×10^{-7} mol cm^{-2} sec$^{1/2}$ for process 1 and 1×10^{-6} mol cm^{-2} sec$^{1/2}$ for process 2. From our data we calculate $c_0\sqrt{D}$ 5.7×10^{-9} mol cm^{-2} sec$^{-1/2}$ which points toward process 1 being the solid-state diffusion inside the nickel oxide. The large discrepancy between our value and their value for $c_0\sqrt{D}$ is presumably due to the difference in d-c current density in the respective experiments. The currents in our experiments were much smaller than in their experiments and in that case a larger σ or smaller $c_0\sqrt{D}$ can be anticipated as explained in Ref. (3).

Energy diagram for the interface Ni(II) oxide electrolyte.—Following Gerischer's approach (25), we now discuss the thermodynamic feasibility of the proposed photoreduction of Ni(II) oxide. For a reductive decomposition of a semiconductor to be possible, it is necessary that the associated decomposition energy fall within the bandgap of the material. The same holds for the anodic decomposition of the material. First, we construct an energy diagram for the Ni(II) oxide electrode. Unfortunately, data on flatband potentials, necessary to construct such a diagram, are scarce and somewhat contradictory. Since our value

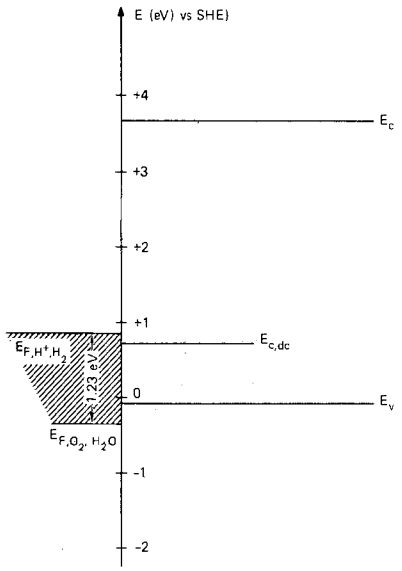

Fig. 12. Energy diagram for Ni(II) oxide at pH = 14 together with Fermi levels for cathodic decomposition ($E_{c,dc}$), H^+/H_2 and O_2/H_2O.

for the flatband potential was close to the value predicted by using the formula $V_{FB} = 1.490 - 0.100\ pH$ derived from Tench and Yeager's work (20), we use this value to construct the energy diagram. Since the Ni(II) oxide electrode is very highly doped, we can let the Fermi level coincide with the top of the valence band, and since the band width is supposed to be about 3.7 eV for NiO, the following energy diagram at pH = 14 (Fig. 12) results. In this figure, $E_{c,dc}$ is the cathodic decomposition energy for Ni(II) oxide. The standard potential found in the literature (25) for the reduction of Ni(II) oxide in the reaction

$$Ni + H_2O = NiO + 2H^+ + 2e^-$$

is 0.110V *vs.* SHE. The energy level corresponding to the above potential for oxidation of pH = 14 is indicated in the diagram as $E_{c,dc}$. This level is well within the bandgap. Therefore, from a thermodynamic point of view, the cathodic reduction is possible because electrons excited to the conduction band are above the $E_{c,dc}$ level and can fall into that level, leading to the reductive decomposition of Ni(II) oxide. This reduction mechanism is impossible in the dark since, under that condition, there are no electrons in the conduction band. In that case reduction of H^+ or Ni(II) oxide is only possible by polarizing the electrode far enough negative so that valence band electrons can tunnel to the empty H^+ or Ni(II) oxide levels. For a highly doped material, as the oxide under investigation here, this will readily occur.

Acknowledgment

Funding was provided by the Department of Energy under Contract EM-78-C-01-5159. The authors wish to thank Dr. F. R. McLarnon of DOE for his continued interest in this study.

Manuscript submitted Oct. 11, 1982; revised manuscript received *ca.* Dec. 21, 1982.

Any discussion of this paper will appear in a Discussion Section to be published in the December 1983 JOURNAL. All discussions for the December 1983 Discussion Section should be submitted by Aug. 1, 1983.

Publication costs of this article were assisted by SRI International.

REFERENCES

1. S. U. Falk and A. J. Salkind, "Alkaline Storage Batteries," John Wiley & Sons, Inc., New York (1969).
2. S. H. Glarum and J. H. Marshall, *This Journal*, **129**, 535 (1978).
3. A. H. Zimmerman, M. R. Martinelli, M. C. Jarnecki, and C. C. Badcock, *ibid.*, **129**, 289 (1981).
4. M. A. Hopper and J. L. Ord, *ibid.*, **120**, 183 (1973).
5. D. M. MacArthur, *ibid.*, **117**, 729 (1970).
6. R. S. Schrebler Guzman, J. R. Vilche, and A. J. Arvia, *ibid.*, **125**, 1578 (1978).
7. V. A. Macagno, J. R. Vilche, and A. J. Arvia, *ibid.*, **127**, 301 (1980).
8. R. S. Schrebler Guzman, J. R. Vilche, and A. J. Arvia, *J. Appl. Electrochem.*, **9**, 183 (1979).
9. R. L. Tichenor, *Ind. Eng. Chem.*, **44**, 973 (1952).
10. D. Tuomi, *This Journal*, **112**, 1 (1965).
11. Yu. N. Chernykh and A. A. Yakovleva, *Sov. Electrochem.*, **6**, 1595 (1970).
12. E. Angelini, M. Maja, and P. Spinelli, *J. Phys.*, **C-5**, 261 (1977).
13. G. W. D. Briggs, E. Jones, and W. F. K. Wynne-Jones, *Trans. Faraday Soc.*, **51**, 1433 (1955).
14. A. J. Arvia and D. Posadas, in "Encyclopedia of Electrochemistry of the Elements," Vol. III, A. J. Bard, Editor, Marcel Dekker, New York (1973).
15. M. Sluyters-Rehbach and J. H. Sluyters, in "Electroanalytical Chemistry," Vol. 4, A. J. Bard, Editor, pp. 1-128, Marcel Dekker, New York (1970).
16. D. D. Macdonald and M. C. H. McKubre, in "Modern Aspects of Electrochemistry," Vol. 14, J. O'M. Bockris, B. E. Conway, and R. E. White, Editors, pp. 61-150, Plenum, New York (1982).
17. M. C. H. McKubre and D. D. Macdonald, in "A Treatise of Electrochemistry," Vol. 5, E. Yeager, J. O'M. Bockris, and R. E. White, Editors, To be published.
18. M. J. Madou, K. Kenoshita, and M. C. H. McKubre, Submitted to *Electrochim. Acta.*
19. M. C. H. McKubre, "Temperature Limitation of Primary and Secondary Alkaline Battery Electrodes. Part III, The Mechanisms of Dissolution and Passivation of Iron and Zinc in Concentrated Potassium Hydroxide Solutions," SRI Report prepared for the Department of Energy under Contract 450561, August 1981.
20. D. M. Tench and E. Yeager, *This Journal*, **120**, 164 (1973).
21. J. L. McNatt, *Phys. Rev. Lett.*, **23**, 915 (1969).
22. M. J. Madou and M. C. H. McKubre, Submitted to *This Journal.*
23. T. O. Rouse and J. L. Weiniger, *This Journal*, **113**, 184 (1966).
24. P. Drossbach and J. Schultz, *Electrochim. Acta*, **9**, 1391 (1964).
25. H. Gerischer, in "Semiconductor Liquid-Junction Solar Cells," A. Heller, Editor, p. 1, PV 77-3, The Electrochemical Society Softbound Proceedings Series, Princeton, NJ (1977).
26. M. Pourbaix, "Atlas of Electrochemical Equilibria in Aqueous Solutions," Pergamon-Cebelcor, Brussels (1966).

Surface Recombination at n-TiO_2 Electrodes in Photoelectrolytic Solar Cells

Withana Siripala and Micha Tomkiewicz*

Department of Physics, Brooklyn College of The City University of New York, Brooklyn, New York 11210

ABSTRACT

The photocurrent-potential behavior of n-TiO_2 photoelectrodes in liquid junction configuration is investigated. The Gartner model is modified to include the surface recombination. Impedance and photocurrent-potential measurements reveal the presence of a high density of surface states at the interface, covering more than half a monolayer. A total of four parameters are used to characterize the surface states. Two of these parameters appear in the expression for both the quantum efficiency-potential dependence and the expression for the capacitance due to these states. The other two parameters appear separately in conjunction with each experiment. The model is tested by perturbating the steady state of the system by strong background illumination which induces higher injection rate of carriers. The effect of the background illumination is interpreted as the change in the equilibrium distribution of the surface states which will result in the increase in surface recombination of photocarriers.

Since Fujishima and Honda reported (1) photoelectrolysis of water using TiO_2, many researchers (2-5) have extensively studied TiO_2 and other semiconductors in liquid junction configurations. Among the factors that determine the efficiency of the process are thickness of the space charge layer at a specified potential, the flatband potential, the efficiency of the back reactions, the optical properties of the semiconductor, and recombination mechanisms of the photogenerated carriers. Since all these effects will strongly influence the shape of the light-induced current-potential curve, and since this is the most sought after system response, there were numerous attempts in the literature to formulate a unified theory of charge transfer across the interface that can be tested against the experimentally observed response. The difficulty in this approach is the relative scarcity of information on the current-potential curve which makes it an insensitive tool for identification of the predominant mechanism in the charge transfer process.

The minority carrier flux originates from carriers generated in the bulk of the semiconductor and those generated within the space charge layer. Direct recombination of these carriers can take place in the bulk, in the space charge layer, and on the surface of the electrode.

In the Gartner model (6) as applied by Butler (7), it is assumed that bulk recombination processes are the only important recombination mechanism. At a sufficiently positive potential with n-type semiconductors, this approximation is valid for many systems. This simple model was later modified to include surface recombination (8, 9), recombination at the space charge layer (10, 11), and both (12). In this paper we present an attempt at delineating some of these processes without adjusting any system parameters. We will concentrate on effects of surface recombination on the current-potential behavior. We will use highly doped TiO_2 to minimize the effects of processes within the space charge layer. Since in such systems, the penetration depth of light exceeds the thickness of the space charge layer throughout the potential range, it can serve as a useful probe for monitoring the interdependence of the charge separation processes in the bulk of the material and at the interface with the electrolyte. We hope that the methodology and the results that are presented here will help in the understanding of the performance of more efficient, lower doped systems, at a potential range near the flatband potential, which is the most useful regime from a device standpoint and least understood because of failure of extrapolation from more positive potentials. Our interpretation of the current-potential behavior of highly doped TiO_2 was tested by perturbation of the steady-state conditions with higher injection rate background illumination. The use of two beams to study interface properties was previously reported (13-15). The results were interpreted in terms of light-induced modification of the potential distribution in the space charge layer. Since we have chosen a system in which the charge separation in the space charge layer plays a minor role, we can identify the effects of the background illumination as due to changes in the equilibrium distribution of the surface states. We hope that these experiments will contribute in understanding the effects of light intensity on performance characteristics of more efficient, lighter doped photoelectrodes.

* Electrochemical Society Active Member.

Key words: photocurrent-potential response, dark current.

Experimental

For the two-beam experiments 1000W xenon lamp (Oriel) with an infrared filter made of $CuSO_4$ solution was used for the background illumination. The beam was filtered through a 320 nm bandpass filter. The intensity of the beam was changed using neutral density filters and the intensity was monitored using an Epply thermopile. The scanning beam was obtained from 150W xenon lamp (Oriel) that passed through a high intensity Jarrel-Ash monochromator. This beam was chopped at 26 Hz with an Ithaco Model 382 B chopper. The electrochemical cell was previously described (9). PAR Models 173 and 175 potentiostat and programmer were used to operate the cell in a potentiostatic mode. The output of the current to voltage converter was fed to the input of PAR Model HR-8 lock-in amplifier with a reference signal taken from the chopper.

Measurements were taken under nitrogen atmosphere under conditions identical to the ones previously described (9). TiO_2 single crystals were purchased from Atomergic, sawed, and measured perpendicular to the c-axis. They were doped with H_2/Ar at 850°C for 30 min, polished to 0.3 μm, boiled in 1*N* H_2SO_4 for 30 min, and then washed with distilled water. All the chemicals were analytical grade and were used without further purification. Sample opening area was kept constant at 0.07 cm^2.

Impedance measurements were carried out by the previously described technique (16) of relaxation spectrum analysis to evaluate the doping density of the samples and the surface-state capacitance.

Results

Figure 1 shows a typical photocurrent-potential behavior as a function of background illumination. The scanning beam was held at 350 nm while the electrode potential was scanned. Pronounced effects

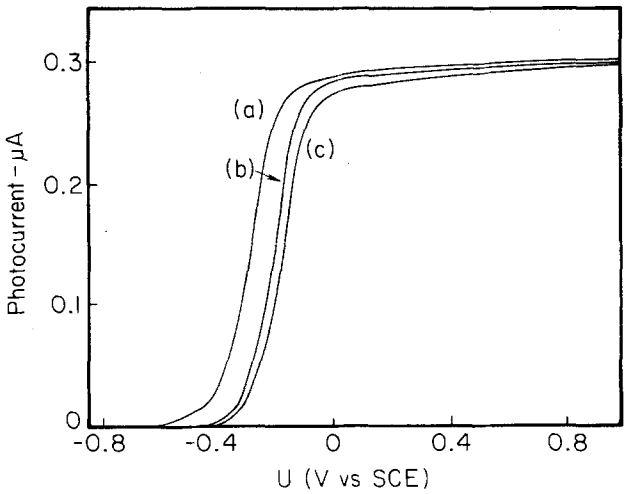

Fig. 1. Typical photocurrent-potential behavior of n-TiO_2 in phosphate buffer as a function of background illumination. pH = 6.5. (a) Without background illumination. (b), (c) With background illumination of intensity 2.1 and 5.0 mW/cm², respectively.

of background illumination were observed in the descending region of the photocurrent-potential curve, namely, at forward bias. This was true up to the highest intensity of background illumination that was measured here (16 mW/cm²). More detailed measurements of this region are shown in Fig. 2. Special care was taken to eliminate the possibility that the effects which were observed in Fig. 1 and 2 are due to a potential shift caused by infrared drop due to the d-c photocurrent which is being induced by the background illumination. It was observed that infrared electronic compensation was practically not required for the electrochemical cell that we used here. Data were taken by placing the reference electrode close to the working electrode by using a Luggin capillary. There was no change observed. The decrease in photocurrent at the electrode potential of −0.30 (V *vs.* SCE), due to the background illumination, was measured as function of the distance between the working electrode and the reference electrode. The decrease in photocurrent was independent of the position of the reference electrode. All these experiments have shown conclusively that the effect of background illumination cannot be traced to a potential shift caused by infrared drop.

Figure 3 shows the spectral response as function of background illumination. These curves are corrected

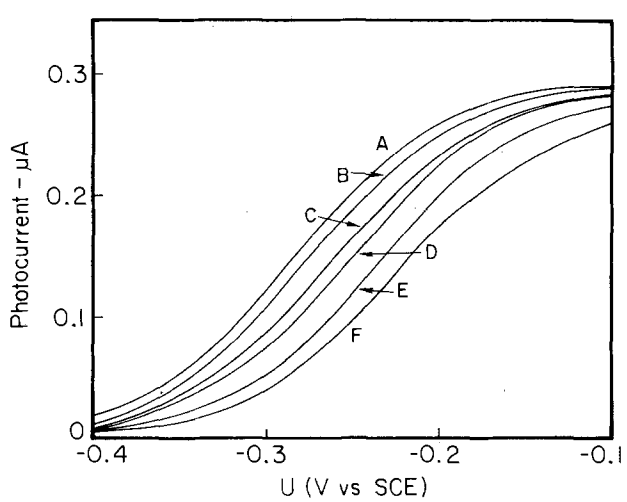

Fig. 2. Detailed measurements of background illumination effect in the potential region where it is pronounced. A, Without background illumination. B-F, With background illumination of intensity 0.1, 1.3, 2.1, 8.1, and 16.2 mW/cm², respectively.

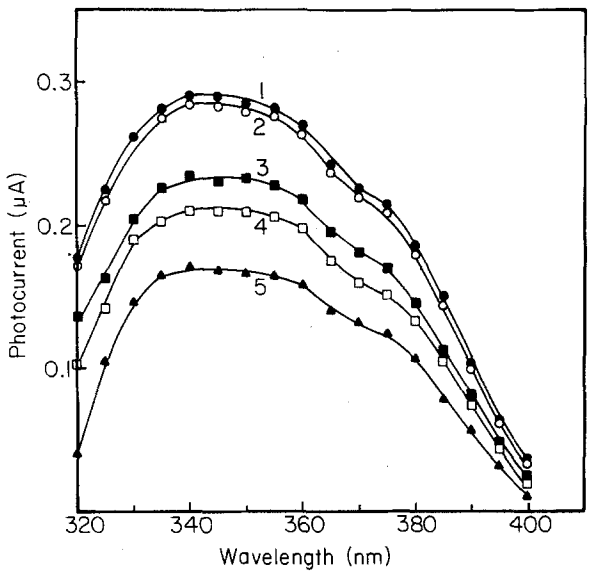

Fig. 3. Spectral response of n-TiO_2 in phosphate buffer, pH = 6.5, as a function of background illumination. U = −0.25V vs. SCE. Curve 1 without background illumination. Curves 2-5 with background illumination of intensity 0.1, 2.1, 3.9, and 16.2 mW/cm², respectively.

for the spectral intensity distribution at the monochromator output. The shape of the spectral response curves does not change with background illumination but the efficiency decreases sharply with increased intensity of the background illumination. Harris and Wilson (17) have reported previously that under intense background illumination the spectral response is changed due to an aging effect. We repeated the spectral response measurements after exposing them to the background illumination. We could not observe any significant difference before and after the illumination. This eliminates the possibility that the observed decline of photoresponse was due to an aging effect. Figure 4 shows the Mott-Schottky plot of the space charge layer capacitance and the potential de-

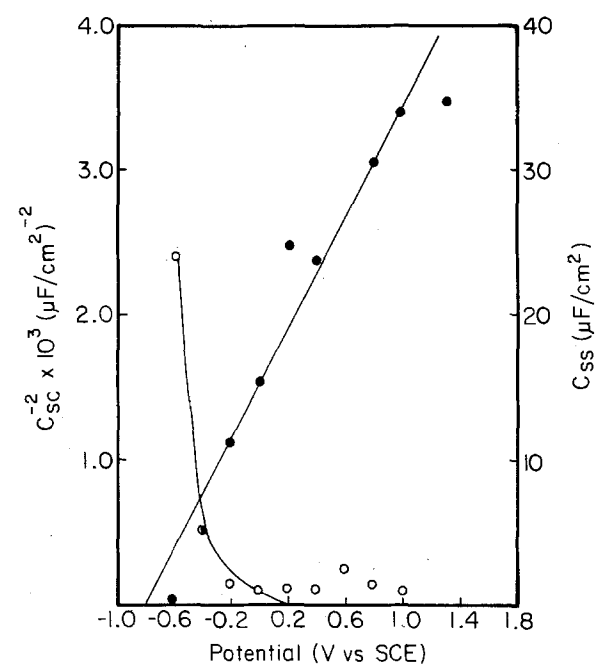

Fig. 4. Mott-Schottky plot of space charge capacitance (●-C_{sc}, left scale), and the variation of the surface-state capacitance (○-C_{ss}, right scale). The solid line is the best fit to the gaussian line shape for C_{ss}, given by Eq. [3], with the following parameters: U_t = −1.0V vs. SCE, σ = 0.21V, and N_t = 6.6 × 10¹⁴/cm².

pendence of the surface-state capacitance. The equivalent circuit of this crystal is similar to the one described earlier (16).

Discussion

Photocurrent-potential response with no background illumination.—In the Gartner model (6) modified for surface recombination (8, 9), the quantum efficiency for anodic photocurrent is expressed as (4)

$$\phi = \frac{S_t}{S_t + S}\left[1 - \frac{e^{-\alpha d}}{1 + \alpha L}\right] \quad [1]$$

where S_t is the potential independent, pseudo first-order rate constant for charge transfer across the interface, S is the rate constant for surface recombination, α is the absorption coefficient, L is the minority carrier diffusion length, and d is the thickness of the space charge layer that can be approximated by (18)

$$d = (2\epsilon\epsilon_0/eN_D)^{1/2}(U - U_{FB})^{1/2} \quad [2]$$

where N_D is the doping level, e is the electronic charge, ϵ_0 is the permittivity of free space, ϵ is the relative dielectric constant, U_{FB} is the flatband potential, and U is the electrode potential. The assumptions which are involved in the derivation of Eq. [1] were previously discussed (4).

The capacitance of the surface states, shown in Fig. 4, closely resembles the capacitance of the states which were artificially introduced by chemical modification (9). Following the assumptions which were made there, the surface-state capacitance is given by

$$C_{ss} = \frac{eN_t}{\sigma\sqrt{2\pi}} \exp\left[-(U - U_t)^2/2\sigma^2\right] \quad [3]$$

where U_t is the potential of the surface states, N_t is their concentration, and σ is the standard deviation in the Gaussian energy distribution. The solid line in Fig. 4 is the best fit to this equation with the following parameters: $U_t = -1.0$V *vs.* SCE, $\sigma = 0.21$V, and $N_t = 6.6 \times 10^{14}$/cm^2. This situation, where U_t is more negative than the flatband potential and N_t corresponds to more than half a monolayer of coverage, closely resembles the situation where states were artificially introduced on the surface of TiO_2 (9). It differs from our previous observations (19, 20) for different samples where much lower concentration of states, located within the gap and created dynamically by the back reaction, were observed. The situation here, which prevails only for highly doped samples and even in this category varies from sample to sample, is more characteristic of tailing of the conduction band at the surface than the classical description of broadening the energy distribution of discrete states. Following again Ref. (9), the surface recombination rate is given by

$$S = \frac{1}{2} k_r^h N_t \left(1 - \mathrm{erf}\left(\frac{U - U_t}{\sigma\sqrt{2}}\right)\right) \quad [4]$$

where k_r^h is the second-order rate constant for the recombination process. Figure 4 also shows the Mott-Schottky plot of space charge layer capacitance from which $N_D = 2.2 \times 10^{20}$/cm^3 and $U_{FB} = -0.8$V *vs.* SCE. Taking $\epsilon = 173$ for the (001) face of TiO_2 we obtain from Eq. [2]

$$d \approx (U + 0.8)^{1/2}\ 10^{-6}\ \mathrm{cm}$$

From Eq. [1], knowing α and d, L can be evaluated at positive potentials in which $S = 0$. For $\lambda = 350$ nm and $\alpha = 10^4$ cm^{-1} (21), $L = 5.5 \times 10^{-6}$ cm. The ratio between the thickness of the space charge layer and the minority carrier diffusion length will be $d/L = (U + 0.8)^{1/2}/5.5$.

At the maximum positive potential employed here, *e.g.*, $U = 1$V *vs.* SCE and $d/L = 0.24$, the charge separation in the space charge layer will contribute only 24% of the total charge separation. At the potential of 0V *vs.* SCE where the various competing mechanism start to operate, this contribution is reduced to 16%. We now include the contribution of surface recombination: the best fit between experiment and theory is shown in Fig. 5 for the following parameters: $U_t = -1.0$V *vs.* SCE, $\sigma = 0.21$V, and

$$k_r^h N_t/2S_t = K/2 = 3.5 \times 10^3 \quad [5]$$

Two of the parameters are identical to the parameters which were obtained from Fig. 4, so the only new adjustable parameter is $k_r^h N_t/2S_t$, which describes the relative rate of the surface recombination and the charge transfer process.

Photocurrent-potential response with background illumination.—Since both the probe beam and the background illumination have energies above the bandgap of TiO_2, they will be absorbed and will induce formation of carriers in a similar way. From Fig. 2 and 3 it is evident that the background illumination reduces the quantum efficiency in a similar way, as shifting the electrode potential toward flatband, and since we have shown already that surface recombination is the dominant recombination mechanism at potentials in which the sharp drop in quantum efficiency is observed, we are being forced to conclude that the dominant effect of the background illumination is through its contribution to surface recombination. In what follows, we will attempt to quantify this statement and test it for agreement with the experimental results.

The conventional interpretation of photoeffects on semiconducting electrodes assumes contribution from light-induced minority carriers only. The argument is that because of the high concentration of majority carriers, their incremental contribution is undetected. Recently, it was recognized that at negative potentials, close to flatband, light-induced majority carriers can penetrate through the barrier and make a contribution to the photoeffects (22, 23).

A schematic diagram of the electron and hole fluxes at the interface is shown in Fig. 6. We do not know *a priori* what is the mechanism of penetration of majority carriers, through or around the barriers, to interact with the electrolyte. Regardless of the mechanism, we can expect it to follow a generalized Tafel-type equation

$$J_e = J_{oo} \exp(-\beta\Delta U) \quad [6]$$

where the value of β will change according to the

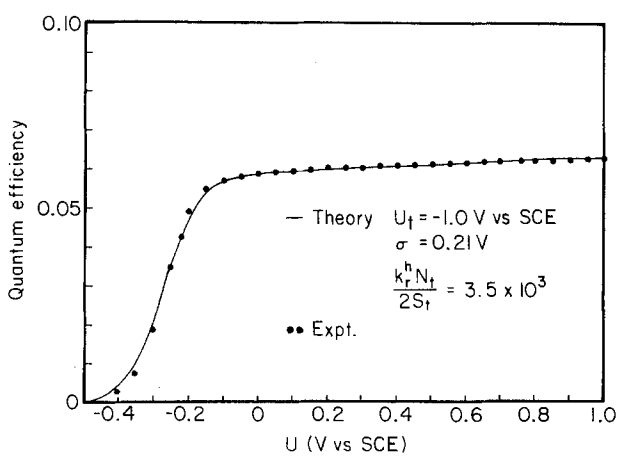

Fig. 5. Quantum efficiency *vs.* electrode potential of n-TiO_2 in phosphate buffer, pH = 6.5. Dashed curve is experimental measurement obtained from Fig. 2 when there is no background illumination. Solid curve is calculated using $\alpha = 10^4$ cm^{-1}, $L = 5.5 \times 10^{-6}$ cm, and a gaussian distribution of surface states with the parameters: $U_t = -1.0$V *vs.* SCE, $\sigma = 0.21$V, and $k_r^h N_t/2S_t = 3.5 \times 10^3$.

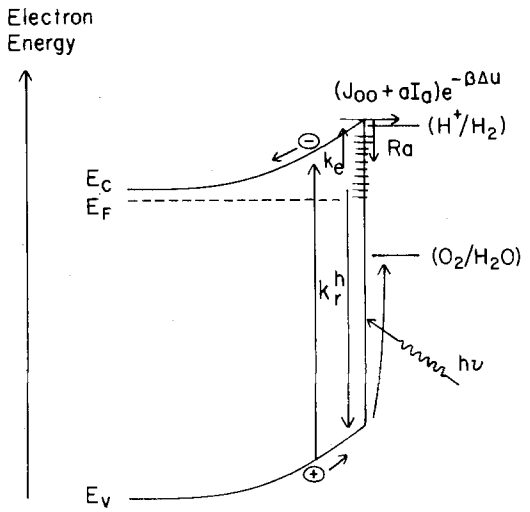

Fig. 6. Schematic diagram of the electron and hole fluxes at the semiconductor-electrolyte interface.

mechanism of charge transfer across the barrier, J_{oo} is the exchange current at $\Delta U = 0$, $\Delta U = U - U_{FB}$ is the barrier height, and J_e is the dark current. We will assume only that when the semiconductor is illuminated, a certain fraction of the light-induced majority carriers will also penetrate the same barrier and flow to the surface. This methodology has been used before (23) to explain the decrease in collection efficiency for strongly absorbed light in Schottky diodes. Thus with this contribution, Eq. [6] will be modified to yield

$$J = (J_{oo} + aI_a) \exp(-\beta\Delta U) \quad [7]$$

where a is the quantum efficiency for light-induced electrons to reach the surface when $\Delta U = 0$.

The electrons that will reach the surface will either interact with the electrolyte or will be captured by empty surface states. Let $\phi_{s.s}$ be the probability that these electrons be captured by the surface states when all the available states are empty, then the rate of filling of the surface states, R_a, will be given by

$$R_a = \phi_{s.s}\frac{(N_t - n_t)}{N_t}(J_{oo} + aI_a)\exp(-\beta\Delta U) \quad [8]$$

where n_t is the density of occupied states. The emission rate of the electrons from the occupied surface states can be either emission to the conduction band at the rate of $k_e n_t$ or recombination with minority carriers at the rate of $k_r^h P_s n_t$, where P_s is the hole density at the surface. Since the anodic photocurrent can be represented as (24)

$$J_a = eS_t P_s \quad [9]$$

and the quantum efficiency as

$$\phi = J_a/eI_a = S_t P_s/I_a \quad [10]$$

and

$$k_r^h P_s = (k_r^h \phi/S_t) I_a = \gamma I_a \quad [11]$$

the total emission rate is

$$k_e n_t + \gamma I_a n_t \quad [12]$$

At steady state the emission rate will be equal to the rate of filling of the states and from Eq. [8] and [12] we arrive at

$$\phi_{s.s}\frac{(N_t - n_t)}{N_t}(J_{oo} + aI_a)\exp(-\beta\Delta U) = k_e n_t + \gamma I_a n_t \quad [13]$$

$$\frac{n_t}{N_t} = \frac{(J_{oo} + aI_a)\,\phi_{s.s}\exp(-\beta\Delta U)}{N_t k_e + N_t\gamma I_a + (J_{oo} + aI_a)\phi_{s.s}\exp(-\beta\Delta U)} \quad [14]$$

For $I_a \to 0$

$$\frac{n_t^\circ}{N_t} = \frac{J_{oo}\,\phi_{s.s}\exp(-\beta\Delta U)}{k_e N_t + J_{oo}\exp(-\beta\Delta U)} \quad [15]$$

and combining [14], [15], and [11]

$$n_t = \frac{J_{oo} + aI_a}{J_{oo}/n_t^\circ + aI_a/N_t + \dfrac{k_r^h\,\phi I_a}{S_t\phi_{s.s}}\exp(-\beta\Delta U)} \quad [16]$$

From Eq. [1]

$$\phi = \frac{S_t}{S + S_t}\phi_{s=0} \quad [17]$$

and following the assumptions made in Ref. (9)

$$S = k_r^h n_t \quad [18]$$

$$k_r^h n_t = S_t\left(\frac{\phi_{s=0}}{\phi} - 1\right) \quad [19]$$

From Eq. [5]

$$k_r^h N_t/S_t = K = 7 \times 10^3$$

$$Kn_t = N_t\left(\frac{\phi_{s=0}}{\phi} - 1\right) = N_t\Gamma \quad [20]$$

and

$$Kn_t^\circ = N_t\left(\frac{\phi_{s=0}}{\phi_o} - 1\right) = N_t\Gamma_o \quad [21]$$

where ϕ_o is the quantum efficiency extrapolated to zero light intensity with no background illumination. Substituting Eq. [20] into [16] and rearranging the terms will yield

$$\frac{\Gamma^2 + (1 - \Gamma_o)\Gamma - \Gamma_o}{(1 - \Gamma^2/K)\,I_a} = \frac{a\Gamma_o}{J_{oo}}\left[1 - 1/K - \frac{\phi_{s=0}\exp(\beta\Delta U)}{a\phi_{s.s}}\right]\frac{\Gamma}{(1 - \Gamma^2/K)} + a\Gamma_o/J_{oo} \quad [22]$$

The linear relations between the left-hand side of Eq. [22] and $\Gamma/(1 - \Gamma^2/K)$, at various electrode potentials, are shown in Fig. 7. Γ and Γ_o were evaluated from Fig. 1 and 2. From Eq. [22], the ratio between the slopes and intercept of the straight lines should give

$$\frac{\text{slope}}{\text{intercept}} = 1 - 1/K - \frac{\phi_{s=0}\exp(\beta\Delta U)}{a\phi_{s.s}} \quad [23]$$

For $\delta = 1 - 1/K - \dfrac{\text{slope}}{\text{intercept}}$

$$\ln(\delta/\phi_{s=0}) = -\ln(a\phi_{s.s}) + \beta\Delta U \quad [24]$$

This relation is shown in Fig. 8. From the slope in Fig. 8, β was found

$$\beta = 13.1\text{V}^{-1}$$

The extent of the validity of the assumptions that were made in Eq. [6] and [7] can be tested by direct measurements of the dark current.

Dark Current

The potential dependence of the dark current is shown in Fig. 9. The logarithmic presentation of this current is shown as insert in the same figure. From both presentations one can clearly distinguish between two distinct mechanisms for the dark current, one which operates at potentials negative to -0.3V *vs.* SCE and one at potentials positive to that potential. Calculations that we have made on tunneling probability in this system (25) have revealed that independent of the shape of the potential barrier assumed, tunneling starts to play a dominant role at potentials negative to -0.3V *vs.* SCE.

Where tunneling does not play an important role, $\beta = 15.4\text{V}^{-1}$ corresponds to a diode quality factor (18)

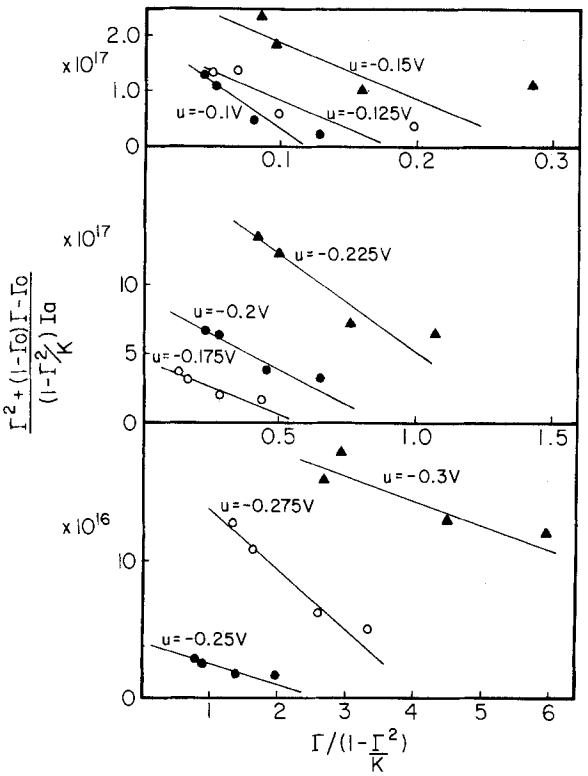

Fig. 7. $\frac{\Gamma^2 + (1 - \Gamma_0)\Gamma - \Gamma_0}{(1 - \Gamma^2/K)\, I_a}$ vs. $\frac{\Gamma}{(1 - \Gamma^2/K)}$ at different electrode potentials, measured with respect to SCE. For more details see the text, Eq. [22].

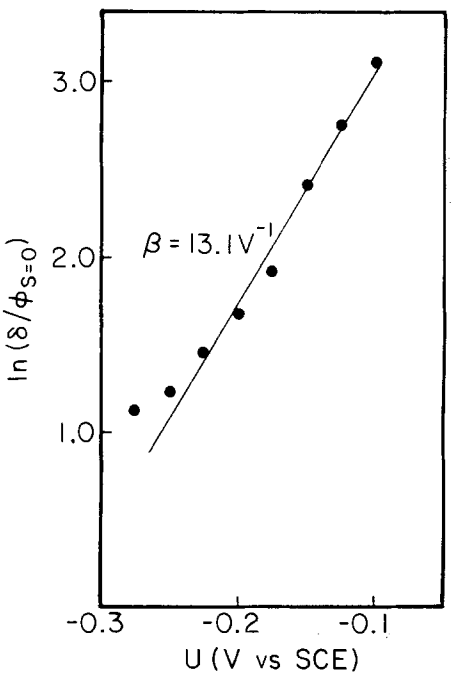

Fig. 8. ln $(\delta/\phi_{S=0})$ vs. U. For more details see the text, Eq. [24]

of 2.5 which suggests a dominant role for diffusion as a mechanism for the back reaction at this potential region.

It is evident also from Fig. 8 that the linear relation which is predicted by Eq. [24] breaks down near $U = -0.3$V *vs.* SCE. This is not surprising since Eq. [6] invokes only single mechanism for the back reaction.

Despite these complications, the agreement in β between Fig. 8 and 9 is gratifying.

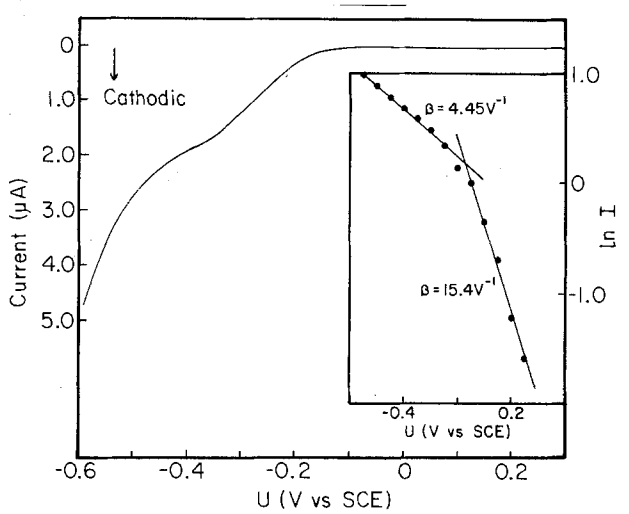

Fig. 9. Potential dependence of dark current, I, of n-TiO_2 electrodes in phosphate buffer, pH = 6.5. In the insert, logarithm of the dark current, ln I, is plotted against the electrode potential.

It is, of course, possible to extract from Fig. 7, 8, and 9 the other parameters that appear in the model. However, in spite of the close agreement in β between Fig. 8 and 9, the 15% discrepancy found between Fig. 8 and 9 and the exponential dependence on β makes such an evaluation unwarranted.

Conclusions

A total of four parameters were used to characterize the surface states with no background illumination. Two of these parameters appear in the expression for both the quantum efficiency-potential dependence and the expression for the capacitance due to these states. The other two parameters appear separately in conjunction with each experiment. The nonlinear nature of the response in both experiments and the good agreement between theory and experiment are strong arguments in favor of the uniqueness of the mechanism presented here. Furthermore, upon further perturbation, we have avoided making new assumptions and *a priori* parameters were not introduced. We were able to linearize the equations at every stage and check them against experiment. The final step in this procedure enabled us to predict the rate of change of the dark current with electrode potential which agrees well with direct measurements of the dark current.

The system offers the opportunity of direct evaluation of charge transfer parameters of minority and majority carriers at the interface, but efforts in this direction should involve explicit introduction of the full expression for the dark current in the system and more detailed background illumination experiments. Regardless of the success or failure of such an approach, it is still gratifying to be able to subject the system to four different experiments, all involving different steady states of carriers and quantitatively accounting for the results with one comprehensive and simple model which is a trivial extension of the abrupt junction model.

Acknowledgments

This work was partially supported by NASA Grant No. NAGI-44 and we gratefully acknowledge the support of the Exxon Education fellowship for new research initiatives for partial support of this work.

Manuscript submitted Aug. 21, 1982; revised manuscript received Oct. 11, 1982.

Any discussion of this paper will appear in a Discussion Section to be published in the December 1983 JOURNAL. All discussions for the December 1983 Discussion Section should be submitted by Aug. 1, 1983.

Publication costs of this article were assisted by Brooklyn College of The City University of New York.

REFERENCES

1. A. Fujishima and K. Honda, *Nature (London)*, **238**, 37 (1972).
2. A. J. Nozik, *Ann. Rev. Phys. Chem.*, **22**, 189 (1978).
3. L. A. Harris and R. H. Wilson, *Ann. Rev. Mater. Sci.*, **8**, 99 (1978).
4. M. Tomkiewicz and H. Fay, *Appl. Phys.*, **18**, 1 (1979).
5. M. A. Butler and D. S. Ginely, *J. Mater.*, **15**, 1 (1980).
6. W. W. Gartner, *Phys. Rev.*, **116**, 84 (1959).
7. M. A. Butler, *J. Appl. Phys.*, **48**, 1914 (1977).
8. R. H. Wilson, *ibid.*, **48**, 4292 (1977).
9. M. Tomkiewicz, *This Journal*, **127**, 1518 (1980).
10. J. Reichman, *Appl. Phys. Lett.*, **36**, 574 (1980).
11. H. S. Jarrett, *J. Appl. Phys.*, **52**, 4681 (1981).
12. F. El. Guibaly, K. Colbow, and D. L. Funt, *ibid.*, **52**, 3480 (1981).
13. A. Heller, K. C. Chang, and B. Miller, *This Journal*, **124**, 697 (1977).
14. D. Laser and S. Gottesfeld, *ibid.*, **126**, 475 (1979).
15. W. D. Gill and R. H. Bube, *J. Appl. Phys.*, **41**, 3731 (1970).
16. M. Tomkiewicz, *This Journal*, **126**, 2220 (1979).
17. L. A. Harris and R. H. Wilson, *ibid.*, **123**, 7 (1976).
18. S. M. Sze, "Physics of Semiconductor Devices," Wiley-Interscience, New York (1969).
19. W. Siripala and M. Tomkiewicz, *This Journal*, **128**, 2491 (1981).
20. W. Siripala and M. Tomkiewicz, *ibid.*, **129**, 1240 (1982).
21. F. Moller, H. J. Tolle, and R. Memming, *ibid.*, **121**, 1160 (1974).
22. M. P. Dare-Edwards, A. Hamnett, and J. B. Goodenough, *J. Electroanal. Chem. Interfacial Electrochem.*, **119**, 109 (1981).
23. M. Lavagna, J. P. Pique, and Y. Marfaing, *Solid State Electron.*, **20**, 235 (1977).
24. A. L. Vanden Berghe, F. Cardon, and W. P. Gomes, *Surf. Sci.*, **39**, 368 (1973).
25. W. Siripala and M. Tomkiewicz, Unpublished results.

Improvements of CdS Film Photoanodic Behavior by Sulfur Organic Reducing Agents

P. Josseaux and A. Kirsch-De Mesmaeker*

Université Libre de Bruxelles, Faculté des Sciences, Service de Chimie Organique, 1050 Bruxelles, Belgium

and J. Riga, and J. Verbist

Université Notre-Dame-de-la-Paix, Laboratoire de Spectroscopie Electronique, 5000 Namur, Belgium

ABSTRACT

The influence of aromatic sulfur reductants on the photoanodic behavior of CdS films is examined. Thiocresol does not substantially improve the characteristics of the *i/V* curve, contrary to p-mercaptobenzoic acid which increases the fill factor during illumination. XPS shows that the disulfide and the cadmium salt of thiocresol are formed on the CdS, blocking the charge transfer across the electrode-solution interface. On the other hand, the binding of p-mercaptobenzoic acid to the CdS after irradiation, evidenced by XPS, would be responsible for the enhancement of the photoconversion yield.

The photoanodic behavior of thin CdS films, prepared by chemical precipitation, has been studied previously (1) in the presence of alkaline cysteine (I) solutions. It turned out that cysteine is oxidized into cystine at the illuminated CdS and inhibits the CdS photocorrosion, but not completely. On the other hand, very interestingly, besides the role of reductant, cysteine (I) also acts as a photoetching agent. Indeed, under illumination and in the presence of cysteine 1 mol · dm^{-3}, the characteristics of the CdS *i/V* curves are improved: the photocurrent at 0 mV (SCE) increases by factors of 4 and the fill factor is enhanced. For smaller cysteine concentrations, improvements of the *i/V* curves are also observed but to a lesser extent (2).

These observations led us to study the origins of these favorable effects (2) which depend, among other factors, on the characteristics and preparation method of the CdS films. The chemically precipitated CdS presents inhomogeneity of grain size and a low degree of crystallinity. Therefore, the cysteine effects on this amorphous CdS may be attributed to the elimination or passivation of recombination centers, which are numerous in this type of material. The XPS analysis of the electrode, after the cysteine treatment, indicates that cysteine is not incorporated into the CdS lattice, but that degradation products of the CdS itself, such as hydroxylated cadmium, accumulate from the surface to some thickness into the CdS layer.

The sulfide ions S^{2-}, on the other hand, do not affect as favorably the CdS photoanodic behavior (1, 3). This difference originates most probably from their ability to solubilize the CdS photocorrosion products. Indeed, although both S^{2-} and cysteine easily dissolve the S° from the CdS decomposition, the S^{2-} ions reprecipitate the Cd^{2+} ions freed from the lattice, whereas cysteine solubilizes the Cd^{2+} ions into cadmium cysteinate which is very soluble in aqueous basic solution. This explains why cysteine photoetches the surface. However, up to now, the origin of the favorable cysteine effect is not yet quite clear.

An approach to obtain a deeper insight into the influences of sulfur reductants is to carry out comparative CdS photoelectrochemical studies with sulfur containing organic reducing agents, presenting different physicochemical properties. We selected the aromatic reductants thiocresol (II) and p-mercaptobenzoic acid (III), whose adsorption and solubility properties are very different.

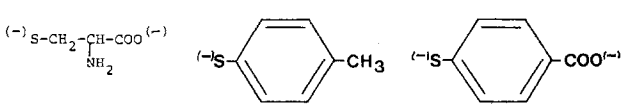

(I) (II) (III)

(E_{p} +0.7V vs. SCE) (E_{p} +0.2V vs. SCE) (E_{p} +0.6V vs. SCE)

* Electrochemical Society Active Member.

Key words: CdS, photoanode, x-ray photoelectron spectroscopy, sulfur reductants.

Concerning their oxidation potentials, we have to mention that these three reductants present quite irreversible oxidation waves at a Pt electrode in basic medium, which make them unsuitable for photovoltaic electrochemical cells (the peak potentials at 200 mV/sec in NaOH at pH 14 are indicated for each compound). Nevertheless, taking into account the important improvement of the CdS when treated with (I) under illumination, it was interesting to test the CdS behavior in the presence of (II) and (III), in order to clarify the origins of this improvement.

In this paper, we present the photoelectrochemical results obtained with (II) and (III) and draw conclusions concerning the origin of their effects on the CdS behavior.

Experimental

Photoelectrochemical measurements.—The CdS is obtained as described previously (1) by four successive precipitations from a $CdCl_2$ plus thiourea solution, thermostated at 26°C, according to the method of Pavaskar, Menezes, and Sinha (4). These CdS films have an average thickness of 1.5μ with a resistivity of the order of $10^5\ \Omega \cdot$ cm; the grain size is inhomogeneous. The degree of crystallinity of the CdS film is low and close to an amorphous structure. We have to note here that, because of this low crystallinity, it is not possible to determine the CdS flatband potential as a function of concentrations of (II) or (III), by Mott-Schottky plots ($1/C^2$ *vs.* V) because these are not linear. For this reason, and also as mentioned above, because the redox potentials of (II) and (III) cannot be determined, a band diagram of the semiconductor with respect to the redox levels in solution cannot be represented.

The electric contact is made with gold painted on the SnO_2 support before the CdS precipitation; the contact wire is glued afterward with silver paint (Elecolit 340). The film degradation is followed by optical density measurements of the electrode (2.5 cm diam) with a Cary 319 spectrophotometer. Electrodes of 20 mm^2 are used for the potentiostatic measurements at a constant applied potential or in cyclic voltammetry.

The electrode is glued on a glass support (glue Dow Corning 730 RTV). The CdS is illuminated through the solution with a 2000W halogen lamp (OSRAM 64788) and only a part of the beam is focused by lenses on the optical glass of the cell. For the quantum yield measurements at 468 nm, the intensity of the monochromatic light, selected by a High Intensity Bausch & Lomb monochromator, is determined by actinometry with potassium ferrioxalate (5). The photocurrents, at a constant applied potential, are measured with a Philips PM 8202 recorder; in cyclic voltammetry the photocurrents are recorded on a Philips PM 3210 oscilloscope, at 200 mV/sec.

Preparation of chemical reagents.—All the reagents are of analytical grade. Water is tridistilled and acetone is distilled twice, with the first distillation on $KMnO_4$. The Fe^{3+} ions are eliminated from NaOH by coprecipitation with $Mg(OH)_2$ by adding $MgSO_4$ to the basic aqueous solution. The commercial thiocresol (99%) is purified by sublimation.

The p-mercaptobenzoic acid is synthesized according to two different methods, one described by Smiles and Harrison (6) and the other by Campaigne and Wendell (7) which leads to a better yield. The p-mercaptobenzoic acid disulfide is obtained as an intermediate product during the synthesis of p-mercaptobenzoic acid by Campaigne and Wendell (7).

Mass spectrometry.—The mass spectra are recorded with a V.G. micromass 7070F spectrometer. The main peaks originating from the fragmentation of p-cresyldisulfide correspond to the following m/z values: 246 ($M^{\cdot+}$, 100%), 155 (2%), 123 (85%), 108 (4%), 91 (10%). Moreover at masses greater than 246, polymers of thiocresol are detected: a trimer and a tetramer at 368 and 490 mass units, respectively.

XPS.—X-ray photoelectron spectra are recorded on a Hewlett-Packard 5950A spectrometer, using the monochromatic Al $K\alpha_{1,2}$ radiation ($h\nu = 1486.6$ eV). The samples are studied at the normal operating temperature (≈ 320 K) and during the analysis the vacuum in the spectrometer is in the $1 \cdot 10^{-9}$ Torr range. The XPS spectra have been calibrated by the gold decoration technique (E_B Au $4f_{7/2} = 84.0$ eV) (8). This procedure yields a value of 405.4 eV for the Cd $3d_{5/2}$ component coming from the CdS substrate. The samples have an area of 1.2 × 1 cm and a thickness of 0.1 cm, the analyzed area is about 0.2 cm^2.

Results and Discussion

Complexity of the CdS Photoanodic Behavior with Thiocresol (II)

Thiocresol has been chosen because it oxidizes (at a Pt electrode) at less positive potential than (I) (see beginning of paper); besides it oxidizes very quickly into the disulfide when the solution is exposed to the air. We thus expected (II) to behave as a better reductant than (I) and thus as a more efficient photocorrosion inhibitor of the CdS.

We tested (II) as corrosion kinetic inhibitor and also as a possible modification agent of the CdS surface.

Behavior with thiocresol in H_2O/NaOH pH 14.—Thiocresol is less soluble than cysteine in aqueous base, the highest reliable thiocresol concentration corresponds to $3 \cdot 10^{-2}$ mol $\cdot$ dm^{-3} at pH 14. For higher concentrations, even under nitrogen, a very fast formation of disulfide occurring during the solution preparation turns the solution turbid and decreases the light intensity reaching the electrode; we thus never exceeded this limiting concentration.

With thiocresol $3 \cdot 10^{-2}$ mol $\cdot$ dm^{-3}, the first i/V curve obtained by cyclic voltammetry at 200 mV/sec, before illumination at a constant applied potential, is shifted to negative potentials, relative to the one in NaOH alone (compare curve A with B in Fig. 1); both curves A and B present a dependence of the photocurrent on the applied potential. The negative shift can find different explanations. The most obvious one is of course that (II), being a reductant, traps the holes at the interface before their recombination with the electrons, at potentials slightly anodic to the flatband potential. Another possibility is that (II) adsorbs on the CdS surface, charging the interface negatively, which leads to a negative shift of the flatband potential. It is shown indeed that (II) remains adsorbed on the CdS surface once the electrode has been dipped in a basic aqueous solution of (II) and

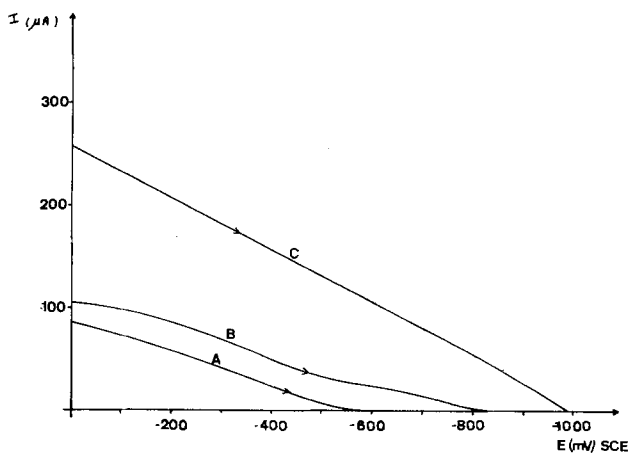

Fig. 1. Photocurrent-applied potential curves recorded at the first scan at 200 mV/sec in NaOH pH 14 (A), with thiocresol $3 \cdot 10^{-2}$ mol $\cdot$ dm^{-3} pH 14 (B), and with p-mercaptobenzoic acid $3 \cdot 10^{-2}$ mol $\cdot$ dm^{-3} pH 14 (C). Illuminated area $\approx$ 20 mm^2.

washed afterward in NaOH. The presence of thiocresol on the surface is evidenced by dissolving the adsorbed reductant in cyclohexane and by analyzing the dissolved product by mass spectrometry.

At the first scan of the *i/V* curve (Fig. 1, curve B), the photocurrents with (II) are rather low, scarcely greater than in NaOH alone; the photocurrent quantum yields measured at 468 nm and at −0.2V *vs.* SCE with a light intensity of $1.4 \cdot 10^{-10}$ E · sec^{-1} cm^{-2} reach only 10%. Moreover, the photocurrent evolution with time at constant applied potential (0 mV *vs.* SCE) (Fig. 2, curve A) starts decreasing continuously from 750 sec toward a value approaching zero after 1 hr. On the other hand, when the *i/V* curves at 200 mV/sec are recorded after different illumination times at the applied potential of 0 mV (SCE), there are no improvements of the curve characteristics and the photocurrents do not decrease importantly (Fig. 3A). The discrepancy between the photocurrent evolution with time at 0 mV (SCE) in Fig. 2 and 3A is due to the fact that while recording the *i/V* curves of Fig. 3A, the application of negative potentials close to the photocurrent onset potential cleans the electrode and removes the anodic decomposition products, which is not the case in Fig. 2. This effect of cyclic voltammetry had already been discussed previously for the cysteine study (2). A surprising result is the increase of the optical density (O.D.) of the CdS film during illumination (see Table I) whereas in NaOH alone (Table I) the O.D. decreases continuously indicating some CdS photocorrosion.

The reasons for these abnormal and nonencouraging results described above become obvious when the electrode is examined by optical microscopy after a long illumination time with (II); one observes crystals which are formed inhomogeneously on the surface (Fig. 4). These crystals are responsible for the O.D. shift of the CdS film, not because they absorb light in the CdS bandgap absorption region (they start absorbing only from 300 nm), but because of the enhanced reflectivity of the surface covered by the crystals. When these crystals are dissolved in cyclohexane, the film O.D. is found to be smaller than before the illumination, indicating some CdS photocorrosion, in spite of the presence of the reductant (II) in the solution. Moreover once these crystals are dissolved in cyclohexane, the photocurrent increases again to its initial value, thus suggesting that these crystals

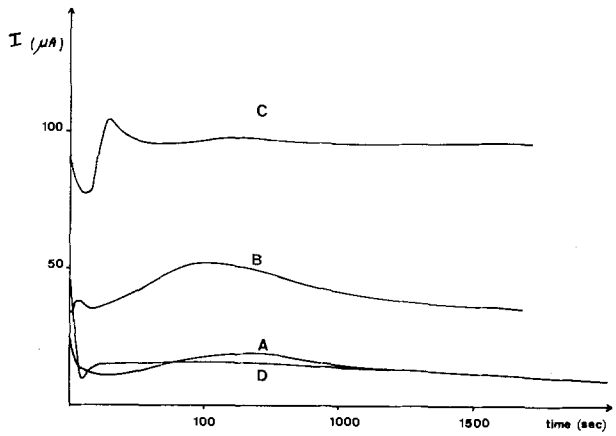

Fig. 2. Photo-oxidation current as a function of time at a constant applied potential of 0 mV (vs. SCE), in NaOH pH 14 + thiocresol $3 \cdot 10^{-2}$ mol · dm^{-3} (A), in NaOH pH 14/40% acetone + thiocresol $3 \cdot 10^{-2}$ mol · dm^{-3} (B), in NaOH pH 14/40% acetone + thiocresol $5 \cdot 10^{-2}$ mol · dm^{-3} (C), and in NaOH pH 14 (D), the photocurrent for NaOH/40% acetone has the same magnitude as curve D. Illuminated area ≈ 20 mm^2.

are responsible for the continuous current drop with time by blocking the charge transfer across the interface.

The crystals formed on the electrode were dissolved in acetone and their mass spectrum compared with that of an authentic sample, leading to the conclusion that these crystals correspond to p-cresyldisulfide (M = 246) (see experimental section) and to polymers of mass 368 and 490 which would be, respectively, trimers and tetramers of thiocresol radicals. The p-cresyldisulfide originates obviously from the oxidation of the ionized thiocresol (II) at the illuminated CdS. The disulfide is indeed insoluble in an aqueous basic solution and precipitates on the electrode during the irradiation. We did not succeed in measuring the faradaic yield for the formation of p-cresyldisulfide, *i.e.*, the ratio of the number of mols of disulfide formed over the number of coulombs passed during a certain illumination time; the amount of disulfide is determined by u.v. spectrometry of the crystals dissolved in cyclohexane (λ_{max} = 244 nm, ϵ_{max} = 20.620 mol^{-1} dm^3 cm^{-1}), and the obtained values are irreproducible and

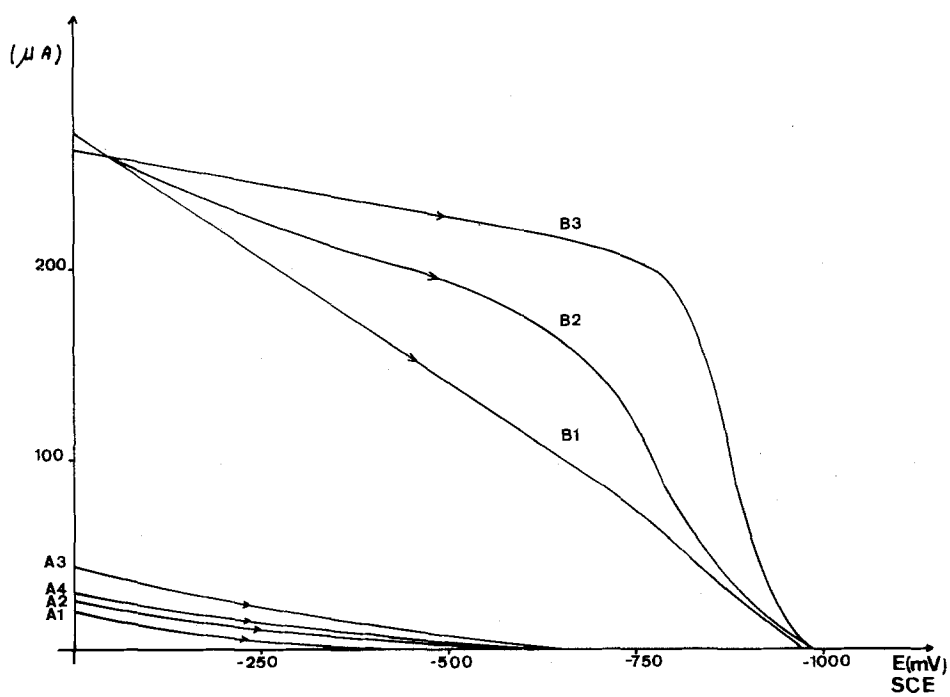

Fig. 3. Photocurrent-applied potential curves recorded at 200 mV/sec; illuminated area ≈ 20 mm^2. A: with thiocresol $3 \cdot 10^{-2}$ mol · dm^{-3} in NaOH pH 14 at the first scan (A1), after 45 sec (A2), 3 min (A3), and 9 min (A4) of illumination at 0 mV (SCE). B: with p-mercaptobenzoic acid $3 \cdot 10^{-2}$ mol · dm^{-3} in NaOH pH 14 at the first scan (B1), at the second scan (B2), and after 80 sec (B3) of illumination at 0 mV (SCE).

Table I. Photoelectrochemistry (A) in H_2O/NaOH pH 14 and (B) in H_2O/NaOH pH 14/acetone 40%. O.D. at 468 nm of the CdS film before and after illumination, with different thiocresol concentrations; illuminated area = 3.5 cm^2

Concentration of thiocresol (mol · dm^{-3})		O.D. Initial	O.D. End	O.D. Δ(%)	Consumed (C)	Illumination time (hr)
0	(A)	0.84	0.46	−45	—	5
0.01	(A)	1.05	1.05	0	—	5
0.02	(A)	1.00	1.08	+8	—	5
0.04	(A)	1.04	1.20	+15	—	4
0.04	(A)	1.05	1.26	+20	—	6
0	(B)	1.13	0.92	−12	$33 \cdot 10^{-3}$	5
0.05	(B)	1.12	0.90	−20	$119 \cdot 10^{-3}$	5¾

too high, probably because of the presence of the polymers which introduce errors in the determination.

From all the observations concerning the CdS behavior in the presence of thiocresol (II) in H_2O/NaOH, we may conclude that (II) is not favorable to the CdS photoelectrochemistry since the oxidation products block the electrode. However in this case, the accumulation of disulfide on the electrode allows us to prove without ambiguity that the thiocresol is actually oxidized to the disulfide at the illuminated CdS and acts as a reductant toward the photogenerated holes.

Behavior with thiocresol in H_2O/NaOH/40% acetone.—In order to avoid the blocking problem of the electrode by the oxidation products of (II), we added 40% acetone to the aqueous basic solution. This percentage of acetone is high enough to solubilize the disulfide but still sufficiently low to remain miscible with the aqueous basic solution. In these conditions, no products are detected in the mass spectrometric analysis of the acetone used to wash the irradiated surface. It should be noticed that this absence of products does not mean that there is no adsorption at all of (II) or of its disulfide on the electrode in the presence of 40% acetone since an adsorbed monolayer can probably not be detected by mass spectrometry.

In these experimental conditions, where crystals can no more block the electrode, one could expect *a priori* an improvement of the photoelectrochemical characteristics as observed with cysteine. However, by adding $3 \cdot 10^{-2}$ mol · dm^{-3} of (II) to H_2O/acetone, the photocurrents of the *i/V* curve, recorded at the first scan at 200 mV/sec, increase only by a factor of 2 and the potential of photocurrent onset is only slightly negatively shifted (from −800 to −850 mV). Moreover at 0 mV (SCE) (curve B, Fig. 2), after a slight increase at the beginning, the photocurrent still decreases with the illumination time, indicating probably another blocking effect on the electrode. In this case, the blocking could be attributed to some accumulation of sulfur S° from the CdS photocorrosion, which is not dissolved rapidly enough by the reductant or the solvent.

When the thiocresol concentration is increased to $5 \cdot 10^{-2}$ mol · dm^{-3}, which can now be reached thanks to the presence of acetone, at the first scan of the *i/V* curve, the photocurrent quantum yield reaches 50% (at 468 nm and −200 mV *vs.* SCE, with a light intensity of $1.4 \cdot 10^{-10}$ E · sec^{-1} cm^{-2}) and the potential of the photocurrent onset is negatively shifted to −1V *vs.* SCE. Moreover, with $5 \cdot 10^{-2}$ mol · dm^{-3} in (II), as is seen from Table I, the CdS photocorrosion is slightly inhibited. Indeed, for a same decrease of the CdS O.D. (Table I), the number of coulombs passed in the presence of (II) is four times greater than in NaOH plus acetone alone, indicating some stabilization by the reductant, however, not sufficient to completely inhibit the photocorrosion.

With $5 \cdot 10^{-2}$ mol · dm^{-3} in (II), when the photocurrent is recorded at constant applied potential (0 mV *vs.* SCE) as a function of time (curve C, Fig. 2), after a slight decrease, followed by a slight enhancement, the photocurrent rather quickly reaches a constant value. This suggests that the electrode surface is no longer blocked either by the disulfide (cf. curve A, Fig. 2) or by the sulfur S° from the CdS photocorrosion (cf. curve B, Fig. 2), which is more rapidly dissolved by thiocresol $5 \cdot 10^{-2}$ mol · dm^{-3}. Moreover, in spite of the fact that there is no more blocking product which covers the electrode, the characteristics of the *i/V* curve do not improve significantly during illumination. We thus conclude that even in the presence of acetone, thiocresol (II) cannot importantly improve the CdS behavior.

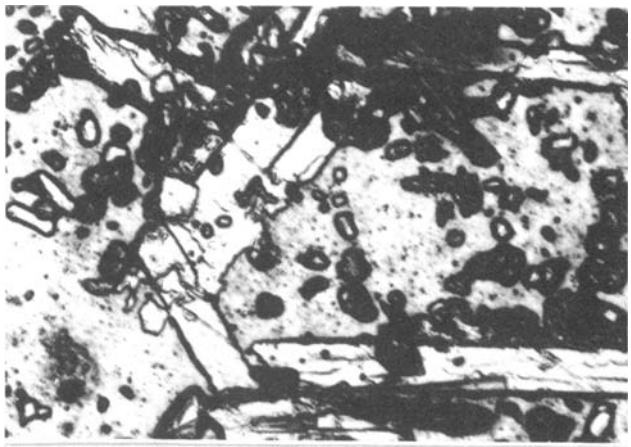

Fig. 4. Optical microscopy of the electrode surface after illumination with thiocresol $3 \cdot 10^{-2}$ mol · dm^{-3} in NaOH pH 14, magnification 12.5 × 12.5.

Analysis of the CdS by XPS, after illumination with thiocresol in H_2O/NaOH/40% acetone.—The difference between thiocresol and cysteine could be attributed to a different solubility of the cadmium salt of the two reductants. Indeed, with thiocresol (II) in H_2O/NaOH/acetone, even if there is no accumulation of the disulfide on the electrode surface, the cadmium salt of thiocresol can be formed and precipitate onto the surface; such a coverage by the salt is indeed possible since we know that the photocorrosion is not completely inhibited (see Table I) and that the Cd^{2+} ions freed from the lattice could give rise to cadmium thiocresolate, which is completely insoluble in H_2O/NaOH/acetone. This possibility cannot be verified by a mass spectrometry analysis of the acetone used to wash the electrode since this salt is not soluble in acetone. Therefore, we analyzed the electrode surface after illumination, by x-ray photoelectron spectroscopy (XPS). It has to be noted that because of the charge effects we cannot use the absolute values of the signal energies, but we have to compare energy differences.

First, we compared the XPS spectrum of a nonilluminated CdS electrode with the one obtained after illumination with thiocresol in H_2O/NaOH without acetone, in order to be sure that when the electrode is covered by p-cresyldisulfide, it can easily be detected by XPS. After illumination, we observe broad Cd 3d and C 1s signals and the occurrence of a very broad sulfur massive extending from 161 to 170 eV, without structure. A direct comparison of this XPS spectrum with the one obtained with the reference p-cresyldisulfide (Table II), where only one S peak at 163.8 eV is detected, shows that these broadenings cannot be attributed only to the presence of disulfide but also to other products which are responsible for additional peaks which make the spectrum unanalyzable.

We then analyzed the surface after illumination with thiocresol in H_2O/NaOH plus 40% acetone, after irradiation times corresponding to constant values of the photocurrent (curve C, Fig. 2). Before each XPS

Table II. Cd $3d_{5/2}$ and S $2p_{3/2}$ signals of reference compounds and CdS electrodes before and after illumination with thiocresol $5 \cdot 10^{-2}$ mol · dm^{-3} in H_2O/NaOH/40% acetone. (1), (2), (3) correspond to three different S or Cd signals. (*) means that the Cd $3d_{5/2}$ signal has been positioned at 405.4 eV

Samples	$Cd^{(1)}$ $3d_{5/2}$ (eV)	$Cd^{(2)}$ $3d_{5/2}$ (eV)	$S^{(1)}$ $2p_{3/2}$ (eV)	$S^{(2)}$ $2p_{3/2}$ (eV)	$S^{(3)}$ $2p_{3/2}$ (eV)	ΔE(Cd $3d_{5/2}$-S $2p_{3/2}$) $Cd^{(1)}$-$S^{(1)}$	$Cd^{(2)}$-$S^{(2)}$	$Cd^{(1)}$-$S^{(3)}$
Nonilluminated CdS	405.4	—	161.7	—	169.4	243.7	—	—
Illuminated CdS + (II)	405.4	406.8	161.7	163.9	169.4	243.7	242.9	237.4
Disulfide of II	—	—	163.8	—	—	—	—	—
Cadmium salt of (II)	405.4*	—	162.5	—	—	242.9	—	—

spectrum, the electrode is washed with H_2O/NaOH/acetone to ensure the complete dissolution of the remaining adsorbed disulfide. As shown in Fig. 5 and Table II, we detect a splitting of the Cd $3d_{5/2}$ line and the relative intensities of the two Cd $3d_{5/2}$ signals depend on the irradiation time. Moreover, we observe three doublets on the S 2p spectrum (Fig. 6). Their components are located, respectively, at E_B = 161.7, 163.9, and 169.4 eV for the S $2p_{3/2}$ levels (Fig. 6, Table II) and at E_B = 162.9, 165.0, and 170.6 eV for the S $2p_{1/2}$ ones. The S $2p_{3/2}$ line at E_B = 161.7 eV is associated with the Cd $3d_{5/2}$ signal at 405.4 eV and arises from the CdS electrode (Table II). The intensity of the two new S peaks increases also with the illumination time. It has to be noticed that the S signal detected at high binding energy (E_B S $2p_{3/2}$ = 169.4 eV) was also present after illumination with cysteine. It would correspond to a sulfur atom in a high oxidation state, originating from CdS oxidation (9).

The S $2p_{3/2}$ signal at E_B = 163.9 eV increases with illumination and with the Cd $3d_{5/2}$ shoulder (406.8 eV) indicating that the new S $2p_{3/2}$ signal is associated with the new cadmium species. To determine the origin of these new S $2p_{3/2}$ and Cd $3d_{5/2}$ signals, XPS spectra of the cadmium thiocresolate have been recorded (Table II). It appears that in this salt, the binding

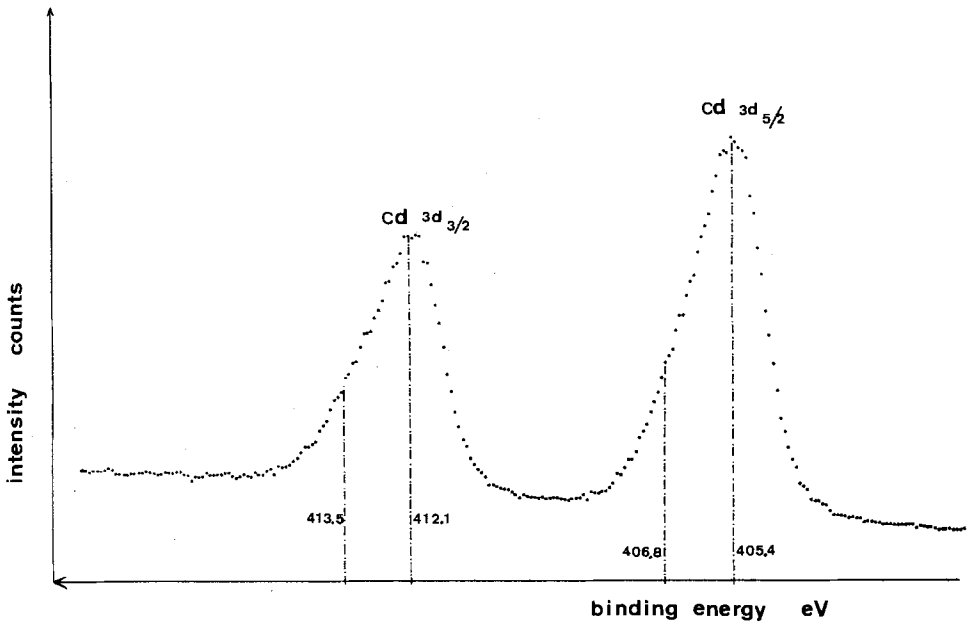

Fig. 5. Cd 3d XPS spectrum of the CdS electrode after illumination with thiocresol $5 \cdot 10^{-2}$ mol · dm^{-3} in NaOH pH 14/40% acetone.

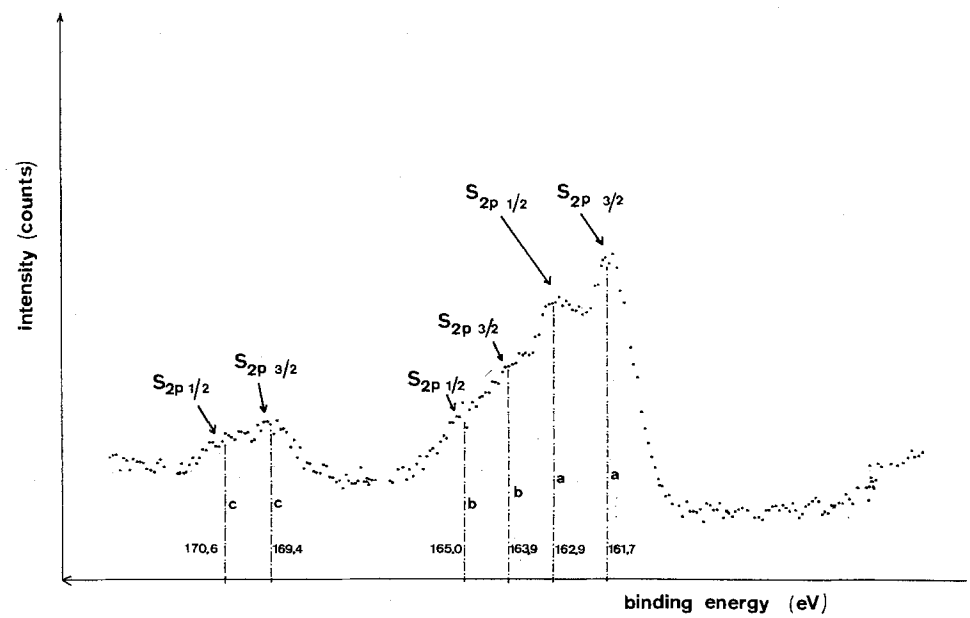

Fig. 6. S 2p XPS spectrum of the CdS electrode after illumination with thiocresol $5 \cdot 10^{-2}$ mol · dm^{-3} in NaOH pH 14/40% acetone. (a) S 2p levels from CdS, (b) S 2p levels from salt (cadmium thiocresolate), (c) S 2p levels from oxidized CdS (probably $CdSO_4$).

energy difference E_B Cd $3d_{5/2}$ — E_B S $2p_{3/2}$ (405.4-162.5) (Table II) is equal to 242.9 eV. This value corresponds quite well to the binding energy difference of the new S $2p_{3/2}$ (163.9 eV) and Cd $3d_{5/2}$ (406.8 eV) signals, equal to 242.9 eV, which leads to the conclusion that during the illumination the thiocresol cadmium salt precipitates onto the CdS electrode. Moreover when a flood gun is used during the scanning of the CdS XPS spectrum, the new Cd and S peaks appearing under illumination, are shifted toward lower energies indicating that these peaks do not correspond to a compound incorporated into the CdS lattice. This behavior suggests that the new peaks correspond probably to an adsorbed or precipitated derivative, in agreement with the formation of the thiocresol cadmium salt on the electrode surface.

Conclusion.—The results obtained with thiocresol show that the CdS behavior is rather complex and that thiocresol, contrary to cysteine, does not appreciably improve the photoanodic behavior of the CdS films. In H_2O/NaOH, the origin of the poor efficiency of the reductant can simply be attributed, as mentioned previously, to the blocking by p-cresyldisulfide and its polymers. However, by adding acetone, which dissolves the blocking products, the photocurrent does not increase appreciably with time and the fill factor of the *i/V* curve is not improved. One could wonder why, even in these conditions, thiocresol does not favorably influence the CdS behavior as observed with cysteine. A possible reason could be that thiocresol does not act as a photoetching agent. Indeed, as evidenced by the XPS results, the cadmium salt of the thiocresol remains on the electrode whereas the cadmium cysteinate is very soluble and leads to a continuous cleaning of the electrode during the photocorrosion. Does the cadmium thiocresolate formed on the electrode influence the CdS behavior? Up to now, the effect of this salt is not yet clear. However, this salt does not seem to block the electrode as the disulfide since once a constant value of the current is reached, it remains constant with time in spite of the continued production of the salt on the electrode.

Improvements of the CdS Photoanodic Behavior with p-Mercaptobenzoic Acid (III)

In order to avoid the problems encountered with thiocresol (II), we tested p-mercaptobenzoic acid (III) *vs.* the CdS photoanodic behavior.

This derivative is not only more soluble than thiocresol in an aqueous basic solution but its oxidation product (the disulfide) and its cadmium salt are also soluble. Consequently, the addition of acetone is not more necessary for dissolving the oxidation products. Moreover, (III) also dissolves the sulfur from the CdS decomposition. With (III) we should thus obtain the same photoetching effects as with cysteine (I).

Photoelectrochemical characteristics with (III).—When p-mercaptobenzoic acid (III) $3 \cdot 10^{-2}$ mol · dm^{-3} is added to an NaOH solution at *p*H 14, *i/V* curve recorded at the first scan (curve C, Fig. 1) is shifted negatively, compared to the one with NaOH alone. This effect is explained similarly to the thiocresol one (curve B, Fig. 1). However, in this case, the photocurrent magnitudes are greater, indicating that, as expected, the electrode blocking by the oxidation products is absent or less important. Besides, even after a long illumination period, no precipitate can be detected on the electrode by optical microscopy or by mass spectrometry.

When the *i/V* curves are recorded in cyclic voltammetry as a function of the illumination time with (III) $3 \cdot 10^{-2}$ mol · dm^{-3}, the characteristics show major improvements (Fig. 3B), contrary to the *i/V* curve evolution in the presence of (II) (Fig. 3A). The maximum modification of the *i/V* curve with (III) is reached after 80 sec illumination. We have to note, however, that this improvement of the *i/V* curve does not persist after three scans in NaOH alone. Figure 3B shows also that at 0 mV, the photocurrent does not change very much from curve B_1 to B_3, whereas at −800 mV, it increases importantly. This is better pointed out when the photocurrents are measured as a function of the illumination time at the constant applied potentials of 0 mV (curve A, Fig. 7) and −800 mV (curve B, Fig. 7). This different behavior at 0 and −800 mV was not observed with (II): at 0 mV, as described previously, the photocurrent decreases continuously (from ± 750 sec) (curve A, Fig. 2) and at −800 mV, it drops very quickly to 0 (curve C, Fig. 7). In NaOH alone at −800 mV, there is no photocurrent (cf. Fig. 1, curve A).

It has to be noted that the different rate of photocurrent increase with (III) at −800 mV in Fig. 7 and in Fig. 3B, should be attributed to the type of measurement: in cyclic voltammetry (Fig. 3B), the modification is always faster than at a fixed applied potential (Fig. 7). This difference was observed previously with cysteine (2).

CdS analysis by XPS after illumination with (III).—Under illumination with (III), the produced disulfide and cadmium salt of (III) should not be detected by

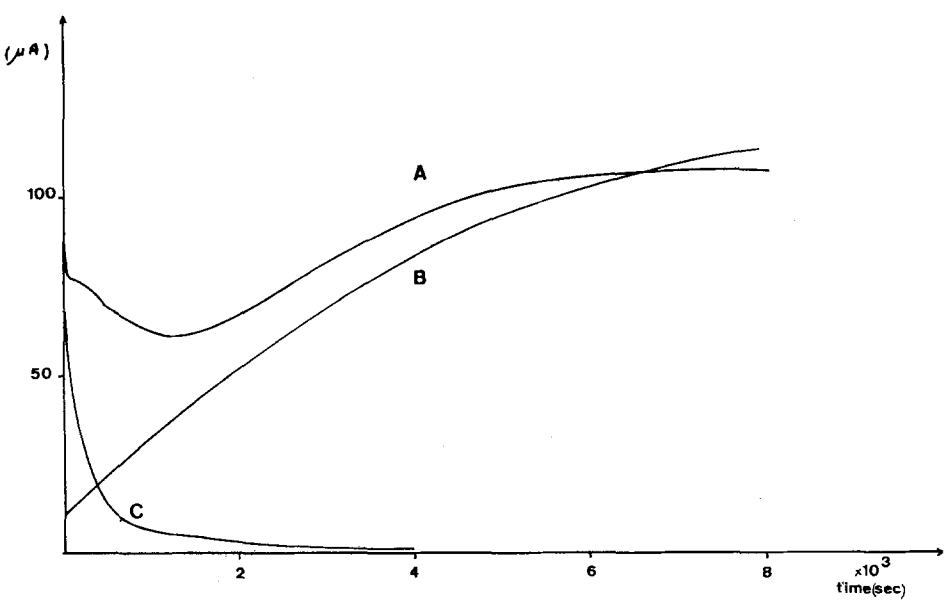

Fig. 7. Photocurrent vs. time at a constant applied potential. A: with p-mercaptobenzoic acid $3 \cdot 10^{-2}$ mol · dm^{-3} in NaOH *p*H 14 at 0 mV (SCE); B: with p-mercaptobenzoic acid $3 \cdot 10^{-2}$ mol · dm^{-3} in NaOH *p*H 14 at −800 mV (SCE); C: with thiocresol $3 \cdot 10^{-2}$ mol · dm^{-3} in NaOH *p*H 14 at −800 mV (SCE). Illuminated area ≈ 20 mm^2.

Table III. Cd $3d_{5/2}$ and S $2p_{3/2}$ signals of reference compounds and CdS electrodes. (1), (2), (3), (4) correspond to four different S $2p_{3/2}$ signals. (*) means that the Cd $3d_{5/2}$ signal has been positioned at 405.4 eV

Samples	$Cd^{(1)}$ $3d_{5/2}$ (eV)	$S^{(1)}$ $2p_{3/2}$ (eV)	$S^{(2)}$ $2p_{3/2}$ (eV)	$S^{(3)}$ $2p_{3/2}$ (eV)	$S^{(4)}$ $2p_{3/2}$ (eV)	ΔE(Cd $3d_{5/2}$-S $2p_{3/2}$) $Cd^{(1)}$-$S^{(1)}$	$Cd^{(1)}$-$S^{(2)}$
Illuminated CdS at 0 mV + (III)	405.4	161.7	164.0	169.3	—	243.7	241.4
Illuminated CdS at −800 mV + (III)	405.4	161.6	163.9	169.2	167	243.8	241.5
Cd salt of (III)	405.4*	162.7	—	—	—	242.7	242.7
CdS dipped in (III), no illumination	405.4	161.9	—	169.1	167.3	243.5	—
Illuminated CdS in NaOH at 0 mV	405.4	161.6	—	168.9	—	243.9	—
Disulfide of (III)	—	163.5	—	—	—	—	—

XPS since both products are soluble in aqueous basic solution. However, we also performed an analysis after illumination with (III) to detect possible chemical modifications of the electrode which could be responsible for the improvements of the i/V characteristics (Fig. 3B) and for the important photocurrent increase at −800 mV (Fig. 7). Before each XPS measurement, the electrode is thoroughly washed in NaOH (pH 14) for half an hour.

After CdS illumination with (III), contrary to what was observed with (II), the splitting of the two Cd peaks (as in Fig. 5) is no longer observed. The only noticeable effect is a broadening of the Cd peaks. However, this broadening occurs only when the electrode is polarized at 0 mV and not under a polarization at −800 mV. From a width of 1.2 eV before illumination, it becomes 1.7 eV after irradiation at 0 mV and a Cd signal shoulder appears in the lower energy range under flood gun. On the contrary, after illumination at −800 mV, the Cd signal remains unchanged even under flood gun. Concerning the S peaks, one observes the same type of evolution of the S 2p peaks as with (II) (Table III); *i.e.*, the occurrence of new S $2p_{3/2}$ components at 164.0 and 169.3 eV, the latter being attributed to a sulfate-type sulfur. There is however a quantitative difference between the S signals observed after illumination at 0 and −800 mV. At 0 mV, the S $2p_{3/2}$ signal at 164.0 eV represents 1-4% of the Cd $3d_{5/2}$ signal whereas at −800 mV, it represents 13-16%. Moreover, for some samples, after longer irradiation times at −800 mV, the component at 164.0 eV of the S $2p_{3/2}$ signal is even more important than the component at 161.7 eV, corresponding to the S $2p_{3/2}$ signal of the CdS. At −800 mV (Table III), a fourth component of the S $2p_{3/2}$ signal also appears at 167 eV, but with a very low intensity. All these S $2p_{3/2}$ components, except the one at 161.7 eV associated with the CdS, move in energy under flood gun.

The first question which arises is: what is responsible for the S $2p_{3/2}$ component at 164.0 eV? The first possibility is to attribute this peak to the cadmium salt of (III), as we did for (II). This is, however, little probable for two reasons. The first one is that the energy difference between the Cd $3d_{5/2}$ (405.4 eV) and S $2p_{3/2}$ (164.0 eV) signals of the illuminated sample is equal to 241.4 eV (Table III) which, contrary to the thiocresol case, does not correspond to the difference Cd $3d_{5/2}$ (405.4 eV) − S $2p_{3/2}$ (162.7 eV) = 242.7 eV of the cadmium salt of (III). The second reason for not attributing the 164.0 eV signal to the Cd salt of (III) is that this salt is much more soluble in H_2O/NaOH than the Cd salt of (II). Indeed, it has not been possible to prepare the Cd salt of (III) in H_2O/NaOH even with a very concentrated solution; the salt had to be prepared in an ammoniacal solution by evaporation of ammonia. Another possible origin of the 164.0 eV signal would be the sulfur S° accumulated on the electrode from the CdS anodic decomposition. However, this second possibility should also be excluded because of the absence of this peak on the CdS electrode illuminated in NaOH alone (Table III). The only remaining possibility would be to attribute the 164.0 eV signal to (III) or a derivative which has been attached photoelectrochemically to the surface. In this case, the Cd $3d_{5/2}$ broadening at 0 mV would be attributed to $Cd(OH)_2$ or CdO from the CdS photocorrosion which is more important at 0 mV than at −800 mV where the Cd signal remains unchanged. Moreover, since the 164.0 eV signal is more important at −800 mV than at 0 mV, it would mean that there is a greater amount of (III) attached to the electrode at −800 mV. It has still to be noted that the presence of an S $2p_{3/2}$ signal at 167.3 eV on a CdS electrode dipped in (III) without illumination or polarization (Table III) and originating probably from (III) remaining adsorbed on the CdS surface, would indicate that the S $2p_{3/2}$ signal at 164.0 eV on the illuminated electrode would not originate from (III) physically adsorbed on the surface but rather bound to the CdS.

Conclusions.—From the XPS analysis with (III), we may conclude that (III) or a derivative is photoelectrochemically attached to the surface under a polarization of 0 or −800 mV (SCE). The higher amount of (III) on the electrode when it is polarized at −800 mV could be correlated to the more important photocurrent increase at −800 mV than 0 mV. The attachment of (III) on the CdS could thus be responsible for the i/V curve characteristic improvements (Fig. 3B), especially the photocurrent enhancement around −750 mV. The way (III) is attached to the electrode is not clear. However among different possibilities, the attachment of (III) by its sulfide, to a CdS sulfur, would not be in disagreement with the XPS results. Indeed, in this case, the Cd signal would not be influenced by (III) and would remain insensitive to the flood gun; on the other hand, the perturbation of the CdS S signals by the reaction of (III) on the surface cannot be pointed out because of the complexity of the S signals.

The effect of (III) on the CdS could be explained in the same way as Ru^{3+} on GaAs (10). Heller *et al.* (10) explain these favorable Ru^{3+} effects by a splitting of surface-state energy levels into higher and lower levels, due to the interaction with the Ru^{3+} ions. The shifted surface states lead to a cell efficiency increase because they can no longer intervene as shunt or electron-hole pair recombination centers.

The behavior of (III) at illuminated CdS is different from (II). Probably because the insoluble Cd salt of (II) masks any possible effects of other surface modification and does not improve the i/V curve characteristics. The behavior of (III) is also different from the behavior of (I) since, as mentioned earlier, (I) cannot be detected on the electrode by XPS after illumination. The sulfur containing organic compound behavior at an illuminated CdS electrode is thus quite different from one derivative to the other.

Acknowledgments

P. Josseaux thanks the "Institut pour l'Encouragement de la Recherche Scientifique dans l'Industrie et l'Agriculture" (IRSIA) for a fellowship.

Manuscript submitted July 26, 1982; revised manuscript received *ca.* Jan. 5, 1983. This was Paper 570 presented at the Electrochemical Society Meeting, Denver, Colorado, Oct. 11-16, 1981.

Any discussion of this paper will appear in a Discussion Section to be published in the December 1983 JOURNAL. All discussions for the December 1983 Discussion Section should be submitted by Aug. 1, 1983.

REFERENCES

1. A. Kirsch-De Mesmaeker, A. M. Decoster, and J. Nasielski, *Solar Energy Mater.*, **4**, 203 (1981), and references therein.
2. A. Kirsch-De Mesmaeker, P. Josseaux, J. Nasielski, and C. Defosse, *ibid.*, **6**, 429 (1982).
3. A. B. Ellis, S. W. Kaiser, and M. S. Wrighton, *J. Am. Chem. Soc.*, **98**, 1635, 6855 (1976); A. B. Ellis, S. W. Kaiser, J. M. Bolts, and M. S. Wrighton, *ibid.*, **99**, 2839 (1977); G. Hodes, J. Manassen, and D. Cahen, *Bull. Isr. Phys. Soc.*, **22**, 100 (1976); *Nature*, **261**, 403 (1976).
4. N. B. Pavaskar, C. A. Menezes, and A. P. B. Sinha, *This Journal*, **124**, 743 (1977).
5. C. G. Hatchard and C. A. Parker, *Proc. R. Soc. London, Ser. A*, **235**, 518 (1956).
6. S. Smiles and D. C. Harrison, *J. Chem. Soc.*, **121**, 2025 (1922).
7. E. Campaigne and W. Wendell, *J. Org. Chem.*, **27**, 2835 (1962).
8. (a) G. Johansson, J. Hedman, A. Berndtsson, M. Klasson, and R. Nilsson, "Calibration of Electron Spectra," UUIP Rep. No. 769 (March 1972). (b) J. Delhalle, J. M. Andre, S. Delhalle, J. J. Pireaux, R. Caudano, and J. J. Verbist, *J. Chem. Phys.*, **60**, 595 (1974).
9. M. Lichtensteiger, C. Webb, and J. Lagowski, *Surf. Sci.*, **97**, L375 (1980).
10. A. Heller and B. Miller, *Electrochim. Acta*, **25**, 29 (1980); B. A. Parkinson, A. Heller, and B. Miller, *This Journal*, **126**, 954 (1979); *Appl. Phys. Lett.*, **33**, 521 (1978).

EMF Measurements on the Li-Al/Ni_3S_2 Couple in Molten Salt Electrolytes

Z. Tomczuk,* L. Redey,* and D. R. Vissers*

Argonne National Laboratory, Chemical Technology Division, Argonne, Illinois 60439

ABSTRACT

The (emf) *vs.* temperature curve for the Li-Al/Ni_3S_2 couple was determined in 58.2 mol percent (m/o) LiCl-41.8 m/o KCl (eutectic electrolyte), 49.1 m/o LiCl-50.9 m/o KCl (KCl-rich electrolyte), 69.6 m/o LiCl-30.4 m/o KCl (LiCl-rich electrolyte), and in 22 m/o LiF-31 m/o LiCl-47 m/o LiBr electrolyte. The results indicate that with these electrolytes the emf value of the couple at a given temperature is independent of the electrolyte composition. Equilibrium emf values were obtained instantaneously upon heating or cooling at rates of ~0.2°C/min, while at higher rates (~0.5°C/min) equilibrium values were obtained after ~1½ hr at a given temperature. X-ray diffraction analyses of the positive electrodes from the cells tested indicate that the only nickel-sulfur phase formed in the electrode reaction is Ni_3S_2. Thermochemical analyses also suggest Ni_3S_2 as the active nickel sulfide phase.

The Ni/Ni_3S_2 micro-reference electrode developed at this laboratory (1) continues to be used in both basic laboratory research studies and in compact Li-Al/FeS cells to investigate the polarization characteristics of the respective electrodes (2-3). The micro-reference electrode has been found to have excellent long-term stability, within ±1 mV over a time period of several months (4).

In characterizing the electrode, the electromotive force (emf) *vs.* temperature response for the Ni/Ni_3S_2 electrode *vs.* (α + β)-Li-Al was determined in the LiCl-KCl eutectic electrolyte (1). However, since the present Li-Al/FeS engineering cells (>100 A-hr capacity) are operated in LiCl-rich electrolyte (67 mol percent (m/o) LiCl-33 m/o KCl) and since the composition of the electrolyte has been shown theoretically and experimentally to vary during cell operation (5-7), it is important that the emf *vs.* temperature curve for the Li-Al/Ni_3S_2 couple be established in electrolytes of differing compositions. Otherwise, it is possible that significant errors might develop in making working electrode potential measurements with the reference electrode if the LiCl-KCl electrolyte interacts with the Ni/Ni_3S_2 electrode to form sulfide phase or phases which would have emf values differing from that of Ni_3S_2 *vs.* LiAl. Such electrolyte interaction has already been demonstrated with the FeS electrode where a phase of composition $LiK_6Fe_{24}S_{26}Cl$ forms (8).

In this paper, we report the results of our measurements of the emf *vs.* temperature curves of the Li-Al/Ni_3S_2 couple in a variety of electrolyte systems each saturated with Li_2S. These systems included the LiCl-KCl eutectic (58.2 m/o LiCl), the LiCl-rich electrolyte[1] (69.6 m/o LiCl), the KCl-rich electrolyte (49.1 m/o LiCl), and the LiF-LiCl-LiBr electrolyte (22 m/o LiF-31 m/o LiCl-47 m/o LiBr). The electrolyte systems were chosen to cover the compositional ranges of the LiCl-KCl electrolyte which might be encountered in a cell, and to examine the response characteristics of the Li-Al/Ni_3S_2 couple in the LiF-LiCl-LiBr electrolyte now being used in the starved electrolyte cells with MgO powder separators by Gould Incorporated (9).

Experimental

The LiCl-KCl eutectic, LiF-LiCl-LiBr electrolyte, and LiCl were of polarographic grade and were obtained from Anderson Physics Laboratory. The KCl was Baker reagent grade and was vacuum dried at 400°C for several hours before use. The Li-Al alloy was obtained from Kawecki Berylco Industries Incorporated, and the Li_2S was obtained from Eagle-Picher Industries. The LiCl-rich and KCl-rich LiCl-KCl electrolytes were prepared by adding weighed amounts of either LiCl or KCl to the eutectic electrolyte.

The cell design was identical to that described elsewhere (8), except that the graphite cup for the positive electrode was eliminated and replaced by a nickel-200 rod (0.6 cm diam, active area 2.5 cm^2) which was anodized in the respective Li_2S saturated electrolytes to form the Ni/Ni_3S_2 electrode. To avoid the need for thermal emf corrections, the negative electrode also utilized a nickel-200 lead. An experimental check of the thermal emf generated for the cell hardware over the temperature range of interest was made and the measured values were less than 0.01 mV over the temperature region of interest. The negative electrode contained 5 A-hr Li-Al alloy (40 atomic percent (a/o) Li). At this composition both the α-Al and β-LiAl phases are present which fixes the emf of the electrode (10). The preparation of the Li-Al

* Electrochemical Society Active Member.

Key words: electrode, emf, fused salts, cell.

[1] The LiCl and KCl-rich designations refer to electrolytes which contain higher concentrations of LiCl or KCl than contained in the eutectic electrolyte. Values in parentheses are the actual compositions tested.

electrodes has been described earlier (8). The positive electrodes were formed *in situ* as described above. The amount of Ni_3S_2 formed electrochemically on the rod was varied; however, no differences in the results were observed between 2-400 C/cm^2. The quantity of Li_2S added to each electrolyte investigated was in excess of 10,000 ppm, a value which is considerably greater than that needed for saturation of the electrolytes (12, 13). The amount of electrolyte used for each test was ~200g.

The procedure consisted of measuring the emf of the Ni/Li-Al/electrolyte, $Li_2S(c)/Ni_3S_2/Ni$ cell at a given temperature using a Keithley Model 191 digital multimeter (input impedance $>10^9\Omega$) for periods which, in some cases, were in excess of 100 hr. Checks on the reversibility were made by measuring the emf's under increasing and decreasing temperature scans. Measurements were also made on the response of the cell emf to changes in rates of temperature increase or decrease. The cell temperature was monitored using calibrated Chromel-Alumel thermocouples. At the end of each cell test, the positive electrode was cooled to room temperature, and a portion of the reaction product was analyzed by x-ray diffraction.

Results and Discussion

A linear regression analysis of the data was made for the different electrolyte systems tested, and the results are summarized in Table I. The equation relating the emf (in mV) to temperature in this table is based on a composite of all the long-term points (>90 min at a given temperature). Note that the emf at a given temperature is independent of the electrolyte composition. The experimental points for the LiCl-KCl eutectic electrolyte are shown in Fig. 1. The scatter of the data is typical of that for the other electrolyte compositions as well.

Although the emf expression given in Table I for the LiCl-KCl eutectic electrolyte summarizes the test results, slightly different equations can be derived from the experimental data if the data are broken down according to (*i*) those data points which were obtained on the initial charge of the cell, (*ii*) those points which are obtained after a slight discharge of the cell, and (*iii*) those points which were obtained after the cell had been operated for ~5 cycles. The equation developed from the data of (*i*) is

$$E(\text{mV}) = 1366.6 + 0.0865(T\text{-}700\ \text{K}) \quad [1]$$

while the equation developed from the data in (*ii*) is

$$E(\text{mV}) = 1367.0 + 0.079(T\text{-}700\ \text{K}) \quad [2]$$

and the equation representing the data for (*iii*) is

$$E(\text{mV}) = 1367.4 + 0.094(T\text{-}700\ \text{K}) \quad [3]$$

The slight differences in Eq. [1]-[3], however, do not cause significant differences in the absolute value of the emf for a given temperature. For example, at temperatures of 400° and 500°C, respectively, Eq. [1] yields values of 1.3643 and 1.3729V, respectively; Eq. [2] yields values of 1.3649 and 1.3728V, respectively; and Eq. [3] yields 1.3649 and 1.3743V, respectively. Thus no significance should be attached to the differences in the respective equations.

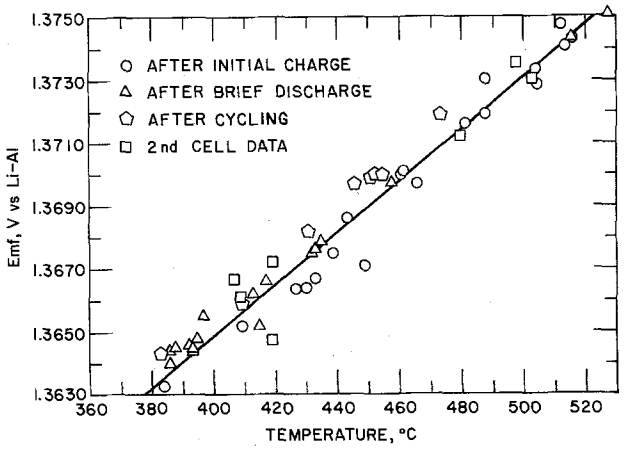

Fig. 1. Emf *vs.* temperature data for the Li-Al/Ni_3S_2 couple in LiCl-KCl eutectic electrolyte. Individual data points shown were obtained in a separate temperature scan sequence.

The response of the cell emf to temperature changes was rapid. Figures 2 and 3 show that the cell emf changed rapidly with temperature changes. However, higher than equilibrium emf values were obtained when heating rates greater than 0.5°C/min were used and lower than equilibrium emf values were obtained when cooling rates greater than 0.5°C/min were used. When lower cooling or heating rates (~0.2°C/min) were used, the instantaneous cell emf was the equilibrium value. These results might be explained by assuming that, at the high heating rates, the dissolution rate of Li_2S in the electrolyte was slower than the heating rate and thus the solution was unsaturated with respect to Li_2S, and that the respective electrolyte became supersaturated with Li_2S during rapid cooling. At any temperature-rate change tested, however, the equilibrium emf value was obtained within 1½ hr. For that reason, all of the data points used to generate Table I were obtained after at least 1½ hr at temperature.

The stability of the cell emf *vs.* time at a given temperature was excellent. Typical results are shown in Fig. 4. The data in Fig. 4 indicate that over a 50 hr time period, the cell emf fluctuated no more than 0.4 mV. Similar results were obtained over longer time periods (>100 hr).

The x-ray diffraction examinations of the respective positive electrodes from the cells tested showed that Ni_3S_2 was the only nickel sulfide phase present. The optical microscopy examinations showed that the Ni_3S_2 had formed as an adherent reaction layer. There was no evidence for the formation of $K_2Ni_3S_4$ which is known to exist (14). These x-ray results confirm that the overall cell reaction is the same in all of the electrolytes tested, namely

$$4\text{Li-Al} + Ni_3S_2 \leftrightarrow 2Li_2S + 3\text{Ni} + 4\text{Al} \quad [4]$$

These x-ray results also explain the independence of the cell emf with electrolyte composition.

Our emf results for the LiCl-KCl eutectic electrolyte compare well with those reported earlier using the

Table I. Summary of emf data

Electrolyte	Composition	Number of cells tested	Total number of points	Emf (mV) as function of temperature	Temperature range tested, K
LiCl-KCl eutectic	58.2 m/o LiCl-41.8 m/o KCl	2	60	1366.9 + 0.082 (*T*-700 K) correlation coefficient = 0.993	653-793
KCl-rich LiCl-KCl	49.1 m/o LiCl-50.9 m/o KCl	2	42	1366.6 + 0.073 (*T*-700 K) correlation coefficient = 0.929	656-796
LiCl-rich LiCl-KCl	69.6 m/o LiCl-30.4 m/o KCl	1	23	1367.1 + 0.073 (*T*-700 K) correlation coefficient = 0.983	671-793
LiF-LiCl-LiBr	22 m/o LiF-31 m/o LiCl-47 m/o LiBr	2	21	1365.5 + 0.092 (*T*-700 K) correlation coefficient = 0.963	735-793

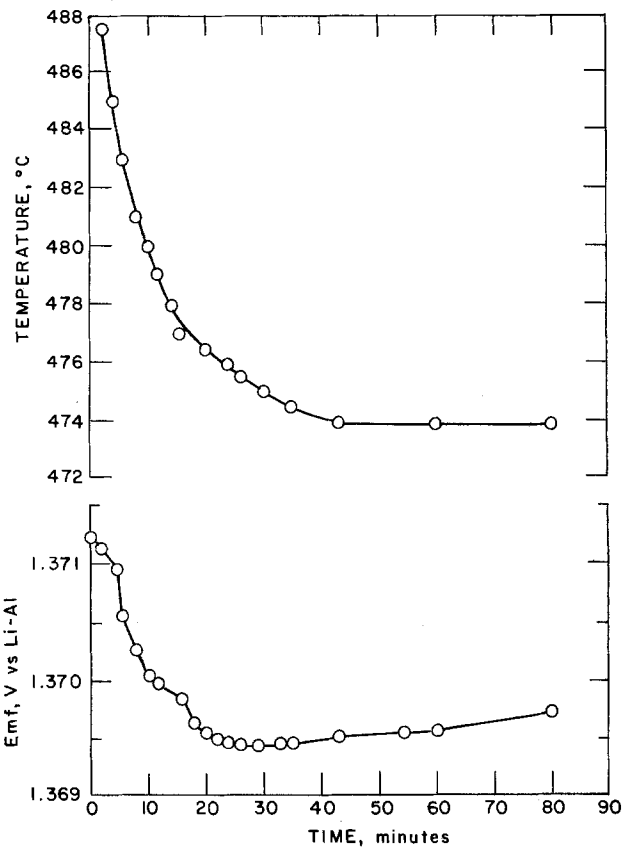

Fig. 2. Response of the Li-Al/Ni_3S_2 couple upon cooling at an average rate of 0.5°C/min.

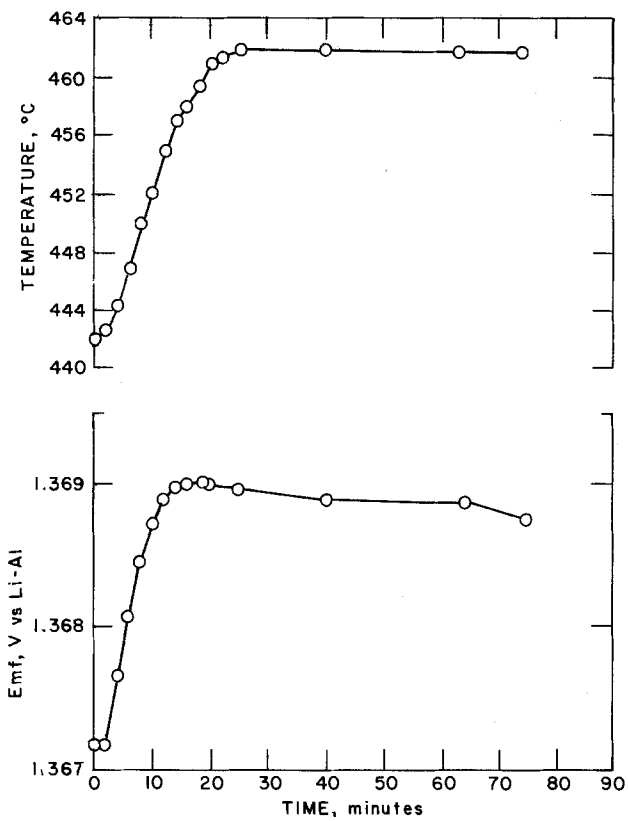

Fig. 3. Response of the Li-Al/Ni_3S_2 couple upon heating at an average rate of 0.5°C/min.

micro Ni/Ni_3S_2 electrode (1). For example, at 400° and 500°C our results are 1.3647 and 1.3729V, respectively, while the previous results were 1.3649 and

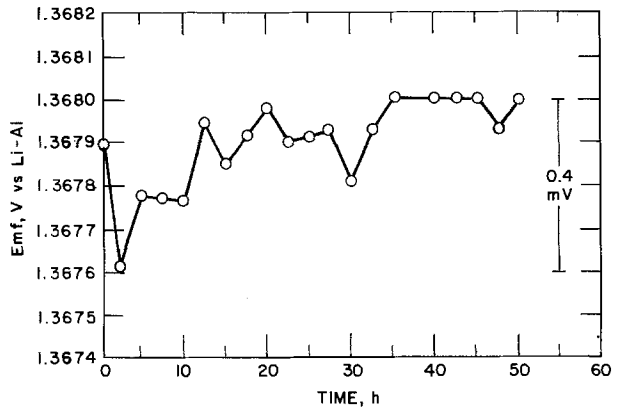

Fig. 4. Emf stability of the Li-Al/Ni_3S_2 couple vs. time

1.3746V, respectively. The slight difference at 500°C is within the scatter of the experimental data shown in Fig. 1.

The experimental emf results compare well with that calculated for reaction [4] using available thermochemical data, where the calculated value is 1.3703V at 700 K while the measured value was 1.3669V. For this comparison, the available free energy data for Li-Al (10), Li_2S (11), and Ni_3S_2 (15) were used. Alternatively, we can calculate the free energy of formation of Ni_3S_2 at 700 K from the emf data and the thermochemical data for Li-Al and Li_2S. This calculation yields a value of −47.02 kcal/mol, a value which is in excellent agreement with the thermochemically reported value of −46.66 kcal/mol (15). The measured emf value at 700 K for reaction [4] and the published free energy values for Li-Al (10) and Ni_3S_2 (15) can be combined to yield the free energy of formation of Li_2S. This calculation yields a value of −100.06 kcal/mol, a value which is also in agreement with the reported value of −100.22 kcal/mol (11).

Conclusions

The emf of the Li-Al/Ni_3S_2 couple was found to be essentially independent of the electrolyte composition in the systems evaluated. The response of the emf of the couple to temperature changes was rapid with equilibrium values being obtained almost instantaneously when temperature change rates of ~0.2°C/min were used. When high temperature change rates were used, nonequilibrium values were observed; however, equilibrium values were observed after the system had been at a given temperature for ~1½ hr. When one considers that the emf and the temperature response characteristics of the Li-Al/Ni_3S_2 couple are the same in the different electrolyte systems investigated, it is not surprising that the x-ray diffraction analyses of the positive electrodes of the respective cells show only one nickel sulfide phase, Ni_3S_2. It should also be noted that a thermochemical analysis of the cell reaction which assumes Ni_3S_2 to be the active nickel sulfide phase is in excellent agreement with the observed cell emf.

Acknowledgments

The authors would like to express their gratitude to B. Tani for the x-ray diffraction analyses, and to Drs. D. L. Barney and R. K. Steunenberg for their support during this work. This work was conducted under the auspices of the Department of Energy.

Manuscript submitted July 6, 1982; revised manuscript received *ca.* Sept. 23, 1982.

Any discussion of this paper will appear in a Discussion Section to be published in the December 1983 JOURNAL. All discussions for the December 1983 Discussion Section should be submitted by Aug. 1, 1983.

Publication costs of this article were assisted by Argonne National Laboratory.

REFERENCES
1. L. Redey and D. R. Vissers, *This Journal*, **128**, 2703 (1981).
2. L. Redey and D. R. Vissers, Paper 20 presented at The Electrochemical Society Meeting, Detroit, Michigan, Oct. 17-22, 1982.
3. L. Redey, S. Higuchi, T. Kaun, F. Martino, and D. R. Vissers, in "Lithium Batteries," H. V. Venkatasetty, Editor, p. 392, The Electrochemical Society Softbound Proceedings Series, Pennington, NJ (1981).
4. L. Redey and D. R. Vissers, *This Journal*, **130**, 231 (1983).
5. R. Pollard and J. Newman, *This Journal*, **128**, 491 (1981).
6. C. E. Vallet and J. Braunstein, *ibid.*, **125**, 1193 (1978).
7. C. E. Vallet, D. E. Heatherly, and J. Braunstein, Abstract 437, p. 718, The Electrochemical Society Extended Abstracts, Montreal, Que., Canada, May 9-14, 1982.
8. Z. Tomczuk, S. K. Preto, and M. F. Roche, *This Journal*, **128**, 760 (1981).
9. B. A. Askew, in Progress Report for October 1979-September 1980, Argonne National Laboratory Report ANL-80-128, p. 48 (1981).
10. C. J. Wen, B. A. Boukamp, R. A. Huggins, and W. Weppner, *This Journal*, **126**, 2258 (1979).
11. Z. Tomczuk, M. F. Roche, and D. R. Vissers, *ibid.*, **128**, 2255 (1981).
12. D. Warin, Z. Tomczuk, and D. R. Vissers, *This Journal*, **130**, 64 (1983).
13. Z. Tomczuk, D. R. Vissers, and M. L. Saboungi, Argonne National Laboratory, To be published.
14. W. Bronger, J. Eycle, W. Ruedonff, and A. Stoessel, *Z. Anorg. Allg. Chem.*, **375**, 1 (1970).
15. "Sulfide Mineralogy," P. H. Ribbe, Editor, Southern Printing Co., VA (1974).

Synergism in Hydrogen Evolution at Metal Sulfide/Tungsten Trioxide (WO_3) in Neutral Solution

A. I. Onuchukwu*

Department of Chemistry, Bayero University, Kano, Nigeria

ABSTRACT

Tungsten trioxide (WO_3) is a poor electrocatalyst for hydrogen evolution, but its use as a support for iron sulfide has been found to enhance the activity of the latter for hydrogen evolution in neutral solution. This synergism, *i.e.*, the reaction between the hydrogen atoms and tungsten trioxide giving rise to conducting hydrogen tungsten bronze, H_xWO_3 ($0 < x < 1$), has been observed to decrease due to shedding of the catalyst/tungsten trioxide at high sulfide loading and at increased temperature of the electrolytic system.

A support, as a dispersion medium for catalyst, can act either as a diluent or conjointly with the catalyst for improved performance. Enhancement of catalytic activity of a material, by inclusion of an active substrate, is a phenomenon that has been under extensive study recently (1-3). Previous studies based on polarization curves of electrodes fabricated from various platinized substrates indicated a synergistic mechanism on tungsten trioxide (3, 4). In an earlier work, Tseung and Hobbs (5) have shown that the anodic oxidation of hydrogen at platinized WO_3 electrodes occurred by a synergistic mechanism involving predissociation of molecular hydrogen on the platinum, followed by migration of H atoms into the WO_3 lattice to form hydrogen tungsten bronzes (H_xWO_3). A mechanism was proposed to elucidate the participation of these bronzes in the anodic oxidation of hydrogen, thereby enhancing the output of the electrodes using Pt/WO_3 catalysts (6, 7).

Thus, for hydrogen oxidation two routes were postulated by Tseung *et al.* (8) and Hibberts *et al.* (9):

a normal route

$$H_2 + 2Pt \rightarrow 2Pt - H \cdot \quad [1]$$

$$Pt - H \rightarrow Pt + H^+ + e \quad [2]$$

and a bronze route

$$xPt - H + WO_3 \rightarrow Pt + H_xWO_3 \quad [3]$$

$$H_xWO_3 \rightarrow xH^+ + xe + WO_3 \quad [4]$$

The rate of reaction, compared to that on pure platinum is, thus, enhanced if synergism (Eq. [3]) and the subsequent reaction of tungsten bronze are fast.

This paper contains a report of the results of experiments which show synergism for hydrogen evolution in 3.5% sodium chloride solution, seawater NaCl content (10), on earlier reported (11) iron sulfide hydrogen cathode with WO_3 active support and comment on the possible mechanism of this "spillover" effect.

Experimental

Catalyst preparation.—The preparation and characterization of the hydrogen cathode, FeS_y ($0 < x < 1$) have been described in detail elsewhere (11). Tungsten trioxide (WO_3) was prepared by the action of dilute hydrochloric acid on a weak solution of Analar sodium tungstate; the pale yellow precipitate obtained was washed several times with distilled water until the residue was sodium chloride-free. In order to produce a uniform dispersion of the FeS_y on the tungsten trioxide, impregnation was carried out by varying loading sulfide weight (*i.e.*, 5-60 mg/80 mg of oxide) in an agate mortar, and the mix was kept in a sample bottle mechanically agitated for 24 hr. This mixed powder was pressed into tablet form at 100 kg/cm^2 in a Metaserv mounting Press Model Minor Type C 190, then sintered at 200°C for 3 hr. The tablet was ground into fine powder in the mortar. The x-ray d-spacings and relative intensities of reflection on FeS_y/WO_3 powder after the impregnation were compared with those given for the same material in the ASTM powder reference. The major phases present were, therefore, determined. Although the preponderant amount of WO_3 in each sample partially eclipsed the sulfide coconstituent, the d-plane spacings for the various sulfides were fairly distinguishable. Thus, Debye-Scherrer powder diffraction photographs showed the presence of the troilite (FeS_{1-y}) and the pyrrholite ($Fe_{1-x}S$) as well as the FeS_2. These were the major constituents of FeS_y, as reported earlier (11). This confirms no appreciable loss of

* Electrochemical Society Active Member.
Key words: catalysis, gas, electrode.

sulfide constituent during the impregnation process. This procedure was adequate as the freeze drying technique proved difficult due to loss of sulfur during the vacuum drying stage of the process.

Electrode preparation.—Electrodes of the polytetrafluorethylene (PTFE) bonded type, having very similar physical structure but significantly different sulfide loading, were prepared according to an optimized procedure described by Tseung *et al.* (8, 12): weighed quantities of impregnated WO_3/FeS_y powder were slurried with aqueous PTFE dispersion and pasted onto 100 mesh nickel screen. The electrodes were dried at 100°C for 1 hr, followed by final curing in an oven at 300°C for 1 hr. These electrodes were 1.0 cm^2/geometric area in all cases, and 0.1 cm thick nickel wire was spot welded onto each to facilitate current collection.

It must be mentioned that a complete transfer of the mix to the screen was impossible, and the FeS_y loadings were, therefore, estimated from the screen weight changes before and after fabrication, assuming that the component of the catalyst/PTFE paste was transferred in the same ratio as the original pot mix.

Sulfide loadings were kept low to avoid masking any substrate activity by the intrinsic FeS_y activity. An oxide loading of about 80 mg/geometric cm^2 of screen was used, with FeS_y contents ranging between 5-60 mg/cm^2 electrode.

Electrode testing.—Electrochemical measurements were made using a three compartment electrolyte cell, described in detail in the previous work (11). A graphite rod was the counterelectrode. A cyclic voltammogram on the sulfide/tungsten trioxide-PTFE bonded electrode showed that H_2-evolution commenced at −750 mV *vs.* SCE in 3.5% sodium chloride solution at 50 rev/min scan rate at 30°C. Steady-state polarization measurements were made from the high applied overvoltage, and the cell current density (A/cm^2), corresponding to each value of applied overvoltage, was monitored through an externally connected digital multimeter. The electrode had initially been cathodized at −300 mV, H_2 overvoltage with continuous nitrogen gas purging for 5 hr. At the end of 5 hr H_2 charging, a fresh deaerated solution (3-5% NaCl) was introduced. Further, H_2 was charged for 10 min prior to the electrochemical measurement. The potentiostatic polarization measurement was accomplished within 300 sec for each electrode sample. The temperature of the electrolyte was varied between 30°-70°C by partial submersion of the electrolytic cell into a water bath. A Sycopel Scientific Model 703C-3A potentiostat was employed for this study.

The IR (arising possibly from catalyst loading, electrolyte, gas evolution within the micropores, and location of the Luggin capillary, etc.) was observed to be pronounced at high H_2 overvoltage. An interruptor circuit arrangement was used to correct for IR drop. The limits of experimental error were determined from the maximum spread of measurements obtained from several samples made from each batch of catalyst loading.

Results

The extent of support participation in the electrode reaction can be determined in the presence of these complicating structural effects by examining the relationship between electrode activity and sulfide loading, the support loading being held constant. Thus, assuming all the electrode current at a given overvoltage originates from the FeS_y, the specific activity of an electrode (J) can be defined as the current density at a given overvoltage divided by the FeS_y loading, expressed in milliampere per square centimeter per milligram of FeS_y as postulated for Pt/WO_3 electrode by Tseung *et al.* (8)

$$J = \frac{i(\eta)}{W_s} \qquad [5]$$

where $i(\eta)$ is the electrode current density at a fixed overvoltage(η), in $mAcm^{-2}$ and W_s is the sulfide loading (mg).

Therefore, for a system in which the support (WO_3) plays no part, J($mAcm^{-2}$ mg^{-1}) is constant with sulfide loading as defined by Eq. [5]. If, however, the support also contributes to the electrode current, J will apparently increase as the sulfide loading decreases. Figure 1 shows the comparative steady-state hydrogen polarization curves, and the contributive effect of the WO_3 support over pure FeS_y performance under the same experimental conditions. Figure 2 shows a series of curves of (J) against sulfide loading for electrodes at different overvoltages. Identical results were obtained for several electrodes, the reproducibility being 12.5% between different electrodes. The electrode prepared from pure WO_3 gave negligible current at the overvoltage investigated, but the characteristic blue color of hydrogen tungsten bronze (13) was conspicuous on all electrodes.

The temperature dependence of the current at $\eta = -20$ mV for an electrode of sulfide loading of 0.4 weight percent (w/o) is shown in Fig. 3. The performance was observed to decrease at above 50°C. As there is no appreciable pH change at the cathode compartment, this could not be responsible for the decrease in FeS_y/WO_3 electrode performance. This decrease was attributed to loss of FeS_y and WO_3 support to the base of the electrolytic cell due to shedding which was also evident at high overvoltage.

Discussion

The enhanced performance of the FeS_y/WO_3 electrode over the performance of pure FeS_y hydrogen cathode in the steady-state polarization curves, Fig. 1, suggests a spillover effect. Similarly, the existence of a maximum in the profile of (J) against sulfide loading at 0.4 w/o FeS_y also indicates a synergistic effect. The fall in activity at low sulfide loading may be correlated with the number of particles of FeS_y and WO_3. At 0.1-0.3 w/o FeS_y, a simple estimate shows that the number of FeS_y particles just equals the number of tungsten trioxide particles. Therefore, below this loading, WO_3

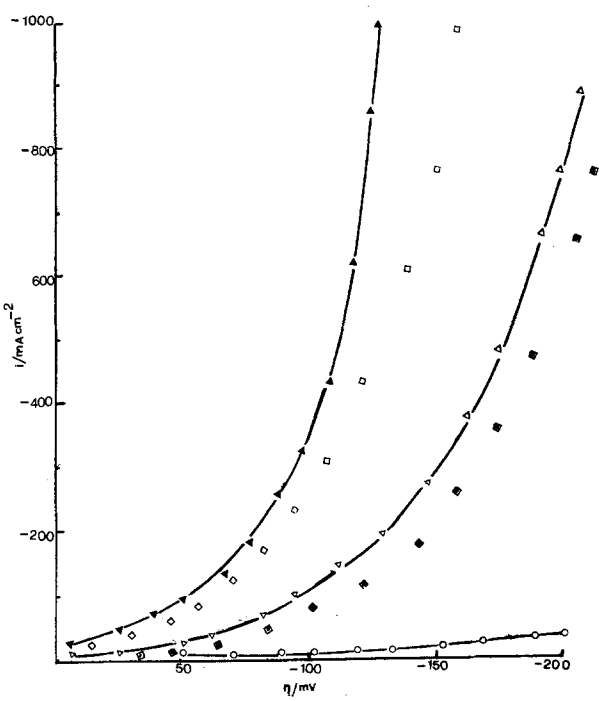

Fig. 1. I-V polarization performances for (i) ○—○ pure tungsten trioxide, (ii) △—△ pure iron sulfide (FeS_y), and (iii) ▲—▲ iron sulfide/tungsten trioxide electrodes at 50 mg loading each. In 3.5% NaCl solution, at 30°C, IR corrected ▲ △ ○, and IR not corrected □ ⊡.

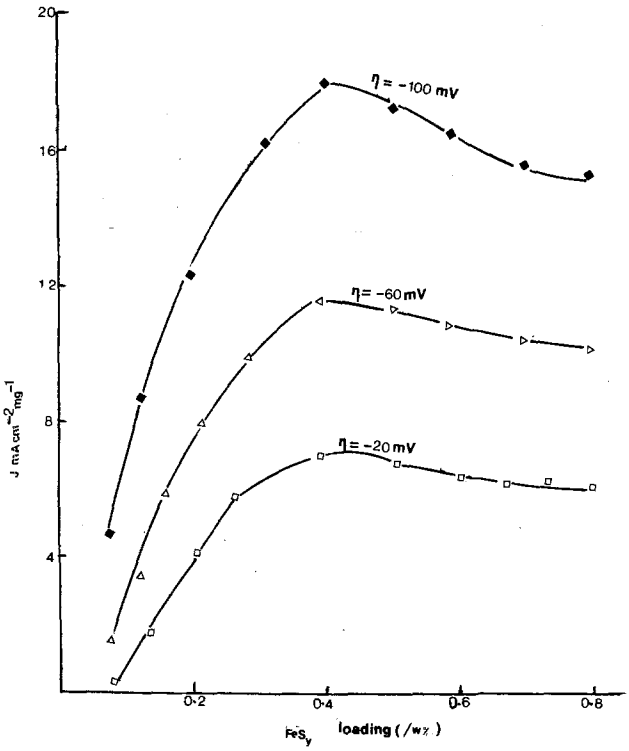

Fig. 2. Variation of specific activity (J) of iron sulfide/tungsten trioxide electrode with iron sulfide loading at variable overvoltage. IR corrected.

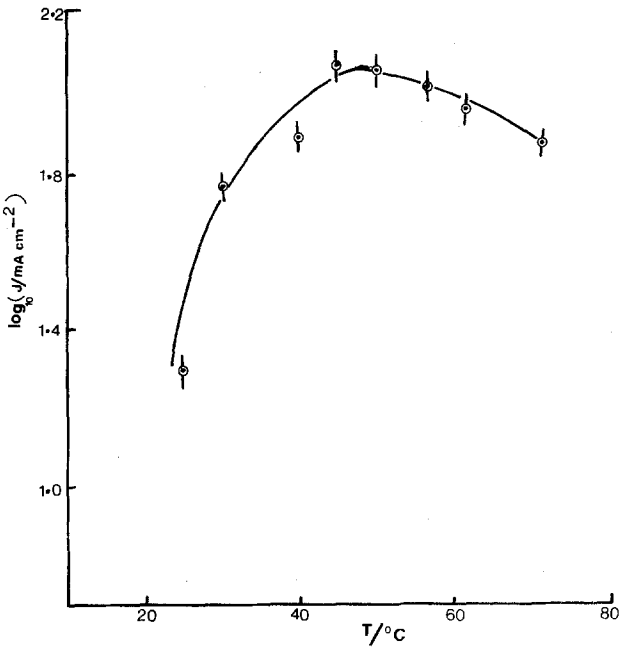

Fig. 3. Variation in current density from FeS_y/tungsten trioxide electrode (FeS_y loading 0.4 w/o) with increasing temperature. $\eta = -20$ mV in 3.5% NaCl solution. IR corrected.

particles exist which are not in contact with FeS_y, and may not contribute to the activity if the migration of hydrogen atoms between tungsten trioxide particles is slow.

The simple scheme to elucidate synergism (spillover) in this system may be postulated in which adsorbed H atoms on iron sulfide (FeS_y = MS) may react immediately to give hydrogen (Eq. [7]) or migrate onto tungsten trioxide to give a tungsten bronze (Eq. [8])

$$MS + H^+ + e \rightarrow MS - H \quad [6]$$

$$2MS - H \rightarrow 2MS + H_2 \quad [7]$$

or

$$MS - H + WO_3 \rightarrow MS + H_xWO_3 \quad [8]$$

$$H_xWO_3 \rightarrow x/2H_2 + WO_3 \quad [9]$$

Thus, it is possible the tungsten bronze (Eq. [9]) may decompose or act as an H_2 evolution catalyst *per se*. The inactivity of pure tungsten trioxide at low overvoltage, even though the blue color of the hydrogen bronze was observed, suggests the latter step does not contribute greatly. Bockris *et al.* have shown that the rate-determining step of H_2 evolution reaction on platinum is hydrogen recombination (14). Use has been made of this mechanism in the previous work (11). Therefore, a fractional coverage of H-atoms on FeS_y electrode surface would ultimately allow spillover to occur easily and, thus, facilitates synergism.

The initial increase in activity (Fig. 3) suggests an endothermic decomposition of the hydrogen bronze in which the determination of the energy of activation could be of interest.

Conclusion

Hydrogen bronze (H_xWO_3), formed in FeS_y/WO_3 hydrogen electrodes, contributes to the net cathode current density, being formed chemically by H-atom migration from the FeS_y to the WO_3 and recombined chemically. Thus, the reaction site is extended onto the support, and the overall electrode activity is increased. Therefore, the commercialization of this principle could be optimized to an advantage for cheaper H_2 evolution, provided a less cumbersome impregnation technique of the sulfide/tungsten trioxide is introduced.

Acknowledgments

The author is grateful to Research and Higher Degree committee of Bayero University, Kano, Nigeria for approving the research grant that made this work possible, and he is also indebted to Dr. A. M. Qureshi for useful discussion.

Manuscript submitted June 2, 1982; revised manuscript received Nov. 22, 1982.

Any discussion of this paper will appear in a Discussion Section to be published in the December 1983 JOURNAL. All discussions for the December 1983 Discussion Section should be submitted by Aug. 1, 1983.

REFERENCES

1. N. F. Taylor, M. Boudart, and A. W. Aldag, *J. Catal.*, **18**, 46 (1970).
2. G. E. Gardens, G. M. Pajonk, and S. J. Teichna, *ibid.*, **33**, 145 (1974).
3. J. C. Shlater and M. Boudart, *ibid.*, **5**, 307 (1966).
4. W. L. Neikan and M. A. Venice, *ibid.*, **27**, 207 (1972).
5. A. C. C. Tseung and B. S. Hobbs, *Platinum Met. Rev.*, **13**, (4), 146 (1969).
6. B. S. Hobbs and A. C. C. Tseung, *This Journal*, **119**, 580 (1972).
7. B. S. Hobbs, Ph.D. Thesis, The City University, London (1970).
8. B. S. Hobbs and A. C. C. Tseung, *This Journal*, **120**, 766 (1973).
9. D. B. Hibberts, N. Thomas, and A. C. C. Tseung, *J. Chem. Soc., Chemical Comm.*, **1**, 193 (1977).
10. T. H. Rogers, "An Introduction to Marine Corrosion," 2nd ed., Pergamon Press, London (1976).
11. A. I. Onuchukwu, *Electrochim. Acta*, **27**, 529 (1982).
12. P. R. Vassie and A. C. C. Tseung, *ibid.*, **20**, 759, 763 (1975).
13. A. C. C. Tseung and B. S. Hobbs, *This Journal*, **122**, 1174 (1975).
14. J. O'M. Bockris and A. K. N. Reddy, "Modern Electrochemistry," Vol. II, p. 1231, Plenum Publishing Corp., New York (1976).

Electrochromic Polymers Covalently Anchored to Electrode Surfaces. Optical and Electrochemical Properties of a Viologen-Based Polymer

Dana C. Bookbinder and Mark S. Wrighton*

Department of Chemistry, Massachusetts Institute of Technology, Cambridge, Massachusetts 02139

ABSTRACT

Smooth Pt and optically transparent SnO_2 electrodes can be functionalized with redox active polymeric material derived from the hydrolytically unstable {N,N'-bis[-3-(trimethoxysilyl)propyl]-4,4'-bipyridinium}dibromide, **I**. The redox polymer on the surface $[(PQ^{2+})_n]_{surf.}$ is reversibly reducible to $[(PQ^{+})_n]_{surf.}$ in either CH_3CN/ or H_2O/electrolyte solutions, and in CH_3CN the reduction of $[(PQ^{+})_n]_{surf.}$ to $[(PQ^{\circ})_n]$ is reversible. The $E^{\circ\prime}[(PQ^{2+/+})_n]_{surf.} = -0.55 \pm 0.05$V *vs.* SCE, and -0.45 ± 0.05V *vs.* SCE in H_2O and CH_3CN, respectively. The $E^{\circ\prime}[(PQ^{+/\circ})_n]_{surf.} = -0.85 \pm 0.05$V *vs.* SCE in CH_3CN. The optical properties of $[(PQ^{2+})_n]_{surf.}$ (colorless), $[(PQ^{+})_n]_{surf.}$ (purple, $\lambda_{max} \approx 545$ nm, $\epsilon_{545\ nm} \approx 10^7$ cm^{2}mol^{-1}), and $[(PQ^{\circ})_n]_{surf.}$ (yellow, $\lambda_{max} \approx 375$ nm, $\epsilon_{375\ nm} \approx 4 \times 10^7$ cm^{2}mol^{-1}) depend somewhat on solvent/electrolyte. The optical spectral features associated with the three redox states of the surface polymer are easily distinguishable with the naked eye for coverages corresponding to $>10^{-8}$ mol/cm^2 of redox active centers. Electrodes bearing $[(PQ^{2+/+})_n]_{surf.}$ are very rugged and do not deteriorate upon repeated cycling between $[(PQ^{2+})_n]_{surf.}$ and $[(PQ^{+})_n]_{surf.}$. Potential step/chronoamperometry experiments establish that the current for oxidation/reduction of the polymer is nearly proportional to $t^{-1/2}$, indicating that the rate of oxidation or reduction is controlled by a diffusion process with a diffusion constant, D, of 10^{-9} to 10^{-10} cm^2/sec depending on electrolyte and its concentration. In practical terms a potential step from 0.0 to -0.80V *vs.* SCE results in ~50% reduction of $[(PQ^{2+})_n]_{surf.}$ to $[(PQ^{+})_n]_{surf.}$ in a time as short as 5×10^{-3} sec at a coverage of 1×10^{-8} mol/cm^2.

The electrode surface derivatizing reagent **I** (1-6) is related to N,N'-dialkyl-4,4'-bipyridinium reagents that are known to become intensely

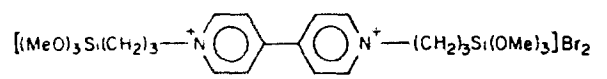

I

colored upon one-electron reduction (7). Electrochromic display systems based on the reversible reduction of N,N'-dialkyl-4,4'-bipyridinium reagents have been proposed (8-10). Typically the chemistry can be represented by Eq. [1]

$$n\,HV^{2+}_{(soln)} \underset{-ne^-}{\overset{ne^-}{\rightleftharpoons}} (HV^{+})_{n(ppt)} \qquad [1]$$

colorless — purple

where $HV^{2+}_{(soln)}$ represents solution N,N'-di-*n*-heptyl-4,4'-bipyridinium (heptylviologen) that can be reduced to HV^+ that aggregates and precipitates onto the cathode to form purple $(HV^{+})_{n(ppt)}$ from the colorless starting material. We report herein the results of a study of the electrochromic behavior of electrodes derivatized with reagent **I**. While the optical and certain electrochemical properties should be similar to those for other N,N'-dialkyl-4,4'-bipyridinium systems, the electrochromic material from **I** is confined to the surface. Representing the surface redox polymer from **I** by $[(PQ^{2+})_n]_{surf.}$, the reduction of $[(PQ^{2+})_n]_{surf.}$ to $[(PQ^{+})_n]_{surf.}$ depends on ions moving in or out of the polymer to balance charge in the polymer.

A great deal of work has now been published on surface-confined, redox active polymers (11-25), some of which undergo large optical spectral changes upon oxidation or reduction, including systems (12-15) closely related to $[(PQ^{2+})_n]_{surf.}$. Our work and the collective work of others suggest that electrochromic display systems based on surface-confined redox active species could prove to be practical. Speed, durability, color, potential required, and coloration per unit of charge are all important factors that are considered here.

Experimental

General procedures.—Cyclic voltammetry and potential step/chronoamperometry data were obtained using a PAR Model 173 potentiostat equipped with a Model 179 Digital Coulometer and a Model 175 Voltage Programmer. For cyclic voltammetry, the data were recorded on a Houston Instruments X-Y recorder. Chronoamperometric data were recorded by a Tektronix Model 564B storage oscilloscope and a Biomation Model 2805 Waveform Digitizer. Experiments were performed in a single compartment Pyrex cell with a saturated calomel reference electrode (SCE), Pt gauze counterelectrode (area ~30 cm^2), and the appropriate working electrode. Spectral measurements, using an electrochemical cell fitted with quartz windows, were performed on a Cary 17 u.v.-vis-nir spectrophotometer. Reflection data were obtained using a ~6 mW Aerotech Model LS5P He-Ne laser detected by a Xenon Corporation Model F-107 photomultiplier tube-based detector. Light intensity striking the photomultiplier was attenuated by passing the beam of the laser through neutral density filters. Solutions were made using doubly distilled deionized H_2O. Electrolytes used were analytical grade. All experiments were carried out in deoxygenated solutions and kept under Ar.

Electrodes.—SnO_2, Sb-degenerately doped, coated glass (~3500Å thick film, resistivity of 21-24 Ω-cm) was generously donated by Corning Glass Works. Electrodes were made by cutting the glass into 7 × 15 mm pieces. Ohmic contact was achieved by rubbing Ga-In eutectic on the surface of the SnO_2. A copper wire was attached using conducting Ag epoxy. The copper wire lead was threaded through 5 mm diam tubing, then the assembly was insulated with ordinary epoxy leaving only the SnO_2 exposed. Pt electrodes were made from smooth foil (0.004 in. thick) cut into small sheets (~5 × 6 mm).

Synthesis of **I**.—Synthesis and characterization of **I** is as follows: Dry 4,4'-bipyridine (1.0g, 0.67 mmol) (Aldrich) in dry CH_3CN (600 ml) was added to 1-bromo-3-trimethoxysilylpropane, **II**, (12.5g, 0.05 mol) [prepared by reacting 4 equivalents of $HC(OMe)_3$ with 1-bromo-3-trichlorosilylpropane (Petrach Company) then fractionally distilling **II** (bp 85°C/10 mm Hg)]. The mixture was refluxed for 14 days, cooled to 298 K and filtered to collect **I**. The product **I** was then recrystallized twice from CH_3CN/Et_2O and isolated as a solid pale yellow bromide salt, yield 90%. Compound **I** readily dissolves in D_2O (accompanied by hydrolysis) to give the following ^1H NMR: (δ, D_2O, 90 MHz): 0.84 (4H, m), 2.24 (4H, m), 3.37 (18H, s), 4.78 (4H, t, $J = 7$ Hz), 8.61 (4H, D, $J = 7$ Hz), 9.17 (4H, d, $J = 7$ Hz).

* Electrochemical Society Active Member.

Key words: electrochromism, modified electrodes, redox polymers, surface-confined polymers.

Prominent infrared absorptions for **I** in a KBr pellet are at 1637 (m), 1385 (vs), 1196 (m), and 1080 (s) cm^{-1}. The electronic absorption spectrum of **I** shows a strong band at 262 nm ($\epsilon \approx 30{,}000$ $lmol^{-1}$ cm^{-1}) in CH_3CN. Elemental analysis (Schwartzkopf): [calc. (found)]: C, 41.14 (40.63); H, 5.96 (5.81), N, 4.36 (4.23); Si, 8.74 (8.76); Br, 24.87 (24.68).

Surface attachment of **I**.— Surface pretreatment of Pt for chemical modification with **I** is as previously outlined (26). Pretreatment of SnO_2 consisted of immersing the electrode in 10*M* NaOH for 10 min followed by rinsing with distilled H_2O and air drying. After the appropriate pretreatment, functionalization with **I** is accomplished by either (*i*) potentiostating the electrode at −0.74V *vs.* SCE in aqueous 0.20*M* KCl/0.10*M* K_2HPO_4 (*p*H = 8.9), containing ~3 m*M* **I** or (*ii*) linearly cycling the electrode potential in the above solution between 0.0 and −0.78V *vs.* SCE. The solutions are kept under Ar and not stirred. Both of these methods work on the principle of surface adsorption followed by covalent attachment discussed in the text. Derivatization to the desired coverage of the polymer, $[(PQ^{2+})_n]_{surf.}$, from **I**, is accomplished in less than 2 hr. The electrodes are removed from the derivatizing solution with the polymer in the oxidized, $[(PQ^{2+})_n]_{surf.}$ form, rinsed with distilled H_2O and allowed to air dry. The surface coverage for the polymer, $[(PQ^{2+})_n]_{surf.}$, from **I**, is determined by integration of cyclic voltammetric waves for reduction of $[(PQ^{2+})_n]_{surf.}$ to $[(PQ^{+})_n]_{surf.}$ or for the reverse oxidation process. The scan rate, typically 50 or 100 mV/sec, was sufficiently low that all electroactive material was detected. This has been established by measuring charge passed as a function of scan rate from 5-100 mV/sec. Generally, in this range the charge passed is independent of scan rate.

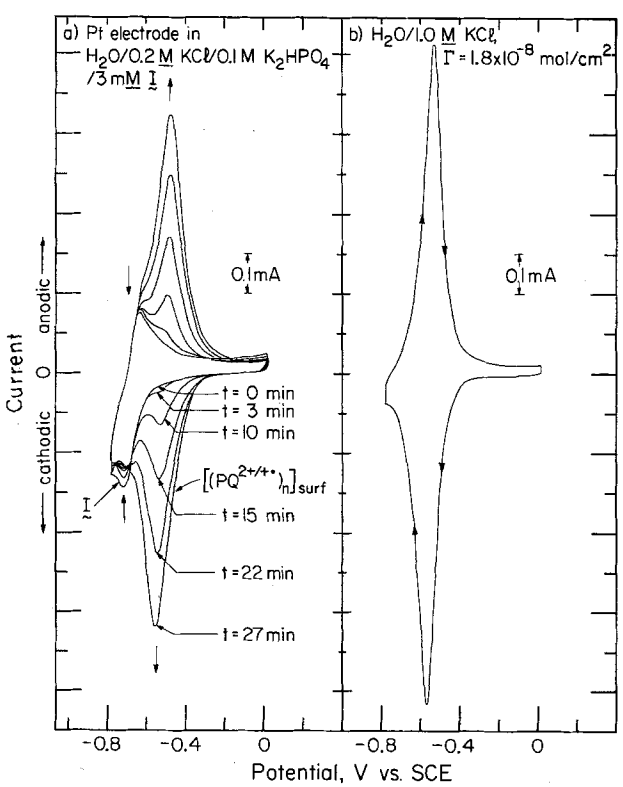

Fig. 1. (a) Cyclic voltammetry, 100 mV/sec, as a function of time illustrating the attachment of redox active material from I to a pretreated Pt surface. During the time $t = 0$ to $t = 27$ min, the potential is being swept between 0.00 and −0.75V *vs.* SCE. Most of the scans are omitted for clarity. The wave present at $t = 0$ at ~ −0.7V *vs.* SCE is associated with ~3 mM I and at increasing times a feature grows at −0.55 attributable to attached material $[(PQ^{2+})_n]_{surf.}$. (b) Cyclic voltammetry, 100 mV/sec of electrode in (a) after $t = 27$ min in a solution containing no electroactive material. After removing from the derivatizing solution at 0.00V *vs.* SCE the electrode was rinsed with H_2O and dried in air.

Polymer thickness measurements were obtained using a Sloan Dektak 9000 Surface Profile Measuring System. Films of $[(PQ^{2+} \cdot 2Cl^{-})_n]_{surf.}$ prepared on SnO_2 electrodes and the polymer step are formed by either a simple masking of the electrode with tape or by mechanical removal of the film with a razor blade. All thickness measurements were made for dry films of $[(PQ^{2+} \cdot 2Cl^{-})_n]_{surf.}$.

Results and Discussion

Electrode derivatization with **I**.—Surface pretreatment of SnO_2 and Pt presumably yields surface-O^- or surface-OH functionality that can lead to the covalent attachment of reagents bearing reactive $-Si(OR)_3$ groups (11), (Eq. [2]). Forming surface-confined polymers from reagents having $-Si(OR)_3$ groups

$$\text{surface—OH} + R'Si(OR)_3 \rightarrow \text{surface—O—}\underset{\displaystyle R'}{\overset{\displaystyle |}{Si}}(OR)_2 + ROH \quad [2]$$

depends on the hydrolysis to form silanols that lead to the formation of $\diagup\!\!\diagdown Si—O—Si\diagup\!\!\diagdown$ linkages, Eq. [3] and [4]. Another, perhaps more likely

$$\text{surface—O—Si(OR)}_2 + H_2O \rightarrow \text{surface—O—}\overset{\displaystyle R}{\overset{\displaystyle O}{\overset{\displaystyle |}{Si}}}(OH) \quad [3]$$

$$\text{surface—O—}\overset{\displaystyle R}{\overset{\displaystyle O}{\overset{\displaystyle |}{Si}}}(OH) + R'Si(OR)_3 \rightarrow \text{surface—O—}\overset{\displaystyle R}{\overset{\displaystyle O}{\overset{\displaystyle |}{Si}}}\text{—O—Si(OR)}_2 \quad [4]$$

route to the $\diagup\!\!\diagdown Si—O—Si\diagup\!\!\diagdown$ linkages is the prior partial hydrolysis of $R'Si(OR)_3$, Eq. [5], followed by reaction of two silanols, Eq. [6]

$$R'Si(OR)_3 + H_2O \rightarrow R'Si(OR)_2(OH) \quad [5]$$

$$\text{surface—O—}\overset{\displaystyle R}{\overset{\displaystyle O}{\overset{\displaystyle |}{Si}}}(OH) + R'Si(OR)_2(OH) \rightarrow \text{surface—O—}\overset{\displaystyle R}{\overset{\displaystyle O}{\overset{\displaystyle |}{Si}}}\text{—O—Si(OR)}_2 \quad [6]$$

Whatever the mechanism for the formation of the Si—O—Si links it is plausible that a high concentration of the Si-containing molecules can speed the rate of polymerization. With this in mind, coupled with the knowledge that N,N'-dialkyl-4,4'-bipyridinium can ag-

gregate onto a cathode upon reduction, we have employed the technique of electroadsorption to promote the formation of covalently attached redox active polymer from **I**. Deposition of a redox active polymer onto electrode surfaces has been previously described (16), but our procedure involves adsorbing the monomer to concentrate it in order to accelerate polymerization and covalent attachment.

As described in the Experimental, potentiostating an electrode at −0.74V *vs.* SCE in aqueous ~3 m*M* **I** leads to the persistent attachment of redox active material, $[(PQ^{2+})_n]_{surf.}$. Alternatively, linearly cycling the electrode potential between 0.00 and −0.74V *vs.* SCE effects derivatization in a similar fashion, and at the same time buildup of covalently anchored material can be monitored, Fig. 1. That production of the reduced material is important in bringing about covalent attachment, is established by the fact that immersing pretreated, but unpotentiostated electrodes in aqueous ~3 m*M* **I** does not lead to any electrode functionalization on the same time scale. Promotion of the attachment and polymerization by the reduction may be attributable to faster hydrolysis rates for the reduced form of **I**. Despite a role for adsorption in derivatizing electrodes, the cyclic voltammetry of **I** does not reveal significant wave distortion. In any event, as Fig. 1b shows, persistently attached, electroactive material is present on the Pt electrode surface after the cycling of the electrode for 27 min in ~3 m*M* **I**. Stirring the electrolyte solution does not affect the cyclic voltammetry shown in Fig. 1b, consistent with the presence of a surface-confined, electroactive polymer. To the naked eye the coverage of material is quite uniform with an obvious purple coloration occurring when cycling from 0.00 to −0.74V *vs.* SCE. The same procedures have been employed to uniformly coat either Pt or SnO_2 electrodes from ~0.1 to ~30 cm^2 in exposed area.

Cyclic voltammetry, durability, and redox potentials for $[(PQ^{2+/+})_n]_{surf.}$ *and* $[(PQ^{+/0})_n]_{surf.}$.—Taking $E^{o\prime}[(PQ^{2+/+})_n]_{surf.}$ and $E^{o\prime}[(PQ^{+/0})_n]_{surf.}$ to be given by the average positions of the appropriate anodic and cathodic peaks in a cyclic voltammogram, we have determined that in H_2O/electrolyte the $E^{o\prime}[(PQ^{2+/+})_n]_{surf.} = -0.55 \pm 0.05$V *vs.* SCE and is independent of *p*H. Generally, the reduction of $[(PQ^{+})_n]_{surf.}$ to $[(PQ^{o})_n]_{surf.}$ is not reversible in H_2O electrolyte; potential excursions out to −1.0V *vs.* SCE in 1.0*M* KCl always show a cathodic peak at ~ −0.9V *vs.* SCE, but this reduction to presumably form $[(PQ^{o})_n]_{surf.}$ is only sometimes reversible. Large coverages and neutral, unbuffered aqueous media tend to give a reversible $[(PQ^{+/o})_n]_{surf.}$ redox system, but such durability is not always encountered. In CH_3CN solvent both $[(PQ^{2+/+})_n]_{surf.}$ and $[(PQ^{+/o})_n]_{surf.}$ are reversible. Figure 2 shows representative cyclic voltammetry in H_2O and CH_3CN solvent. The $E^{o\prime}[(PQ^{2+/+})_n]_{surf.} = -0.45$V *vs.* SCE and $E^{o\prime}[(PQ^{+/o})_n]_{surf.} = -0.85$V *vs.* SCE in CH_3CN/0.1*M* $[n\text{-}Bu_4N]ClO_4$. Table I summarizes the $E^{o\prime}$s for

Table I. Formal potentials for $[(PQ^{2+/+})_n]_{surf.}$ and relevant solution species[a]

System	Solvent	$E^{o\prime}$, V *vs.* SCE
$[(PQ^{2+/+})_n]_{surf.}$	H_2O/pH = 1-8.6	−0.55 ± 0.05
$[(PQ^{2+/+})_n]_{surf.}$	CH_3CN	−0.45 ± 0.05
$[(PQ^{+/0})_n]_{surf.}$	CH_3CN	−0.85 ± 0.05
$I_{soln.}$ (2+/+)	H_2O	−0.68 ± 0.03
$I_{soln.}$ (2+/+)	CH_3CN	−0.45 ± 0.03
$I_{soln.}$ (+/0)	CH_3CN	−0.85 ± 0.03
$MV^{2+/+}$	H_2O/pH = 1-8.6	−0.69 ± 0.03
$MV^{2+/+}$	CH_3CN	−0.45 ± 0.03
$MV^{+/0}$	CH_3CN	−0.85 ± 0.03

[a] All data are from 25°C solvent/electrolyte. $E^{o\prime}$s are the average positions of the oxidation and reduction peaks in cyclic voltammograms at 50 mV/sec. Data apply to a variety of electrolytes. $E^{o\prime}$s are essentially independent of electrolyte. The solution species MV^{2+} and **I** were measured at ~1 m*M* concentration.

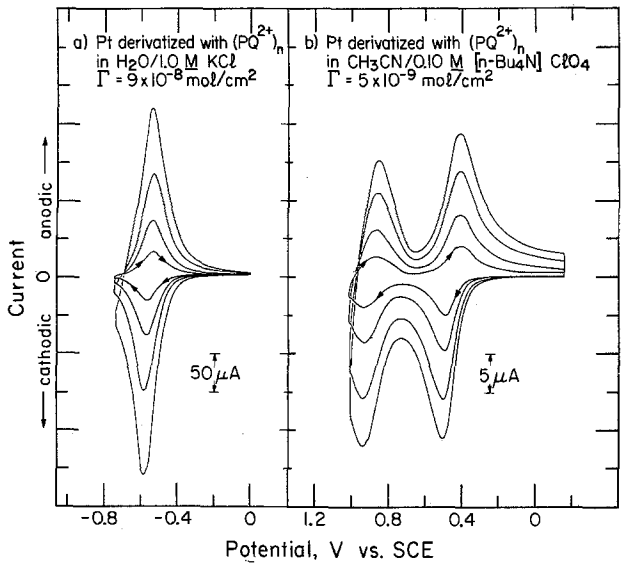

Fig. 2. (a) Cyclic voltammetry in aqueous electrolyte at different scan rates (least current 20 mV/sec), 20, 50, 100, and 200 mV/sec, for a Pt electrode bearing 9 × 10^{-8} mol/cm² of electroactive centers. (b) As in (a) except CH_3CN electrolyte and coverage is 5 × 10^{-9} mol/cm².

relevant solution and surface-bound bipyridinium reagents.

As can be seen in Fig. 1 and 2, the cyclic voltammetry for $[(PQ^{2+})_n]_{surf.}$ reveals symmetrical waves having a generally small potential separation between the anodic and cathodic peaks. The charge passed associated with the anodic wave is the same as that for the cathodic wave and remains roughly constant for scan rates below 200 mV/sec. Also, the peak-to-peak separation is unaffected by scan rate for scan rates less than 200 mV/sec. At scan rates faster than 200 mV/sec the cyclic voltammetry begins to reveal departure from the ideal behavior expected from a surface-confined, fast, one-electron redox reagent (11a). Such nonideality is common for surface-confined redox polymers and reflects slow ion movement and/or slow self-exchange among the redox units of the polymer (11-25). The rate of reduction of the $[(PQ^{2+})_n]_{surf.}$ system has been examined by potential step chronoamperometry and is discussed below.

One interesting fact concerning the $E^{o\prime}$ of the $[(PQ^{2+/+})_n]_{surf.}$ system is that it is ~150-200 mV more positive than for the solution species **I**. This discrepancy is revealed in the comparison of the cyclic voltammetry of **I** and $[(PQ^{2+})_n]_{surf.}$, Fig. 1a. The wave for the solution species is obviously more negative than for the surface-confined system. We attribute the difference in $E^{o\prime}$s to interactions between the PQ^+ centers. For example, N,N′-dimethyl-4,4′-bipyridinium, MV^{2+}, is known to yield dimers, $(MV^+)_2$, upon reduction, Eq. [7] (27). The magnitude of the equilibrium constant for the

$$2MV^{2+} \underset{-2e^-}{\overset{+2e^-}{\rightleftarrows}} 2MV^{+} \rightleftarrows (MV^{+})_2 \qquad [7]$$

reversible dimerization of MV^+ is of the order expected for a 150-200 mV positive shift in potential for $MV^{2+/+}$ to $MV^{2+}/(MV^+)_2$. Generally, however, cyclic voltammetry is done for solution species at sufficiently low concentration that $(MV^+)_2$ is not important. When the redox center is confined to the electrode surface the effects of interactions would be expected to be significant, owing to the high effective concentration of redox centers.

The $[(PQ^{2+/+})_n]_{surf.}$ system is durable under all conditions except that O_2 must be excluded (28). Figure 3 shows a plot of coverage of electroactive $[(PQ^{2+})_n]_{surf.}$

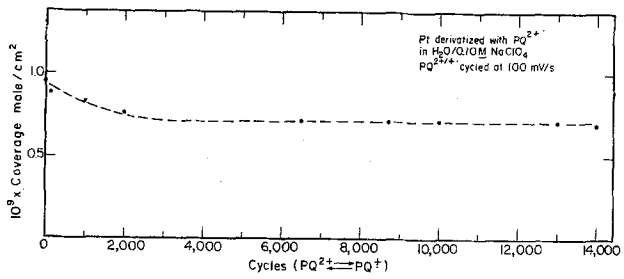

Fig. 3. Coverage of $[(PQ^{2+})_n]_{surf.}$ as a function of the number of cycles of reduction and oxidation. The Pt electrode was scanned between 0.00 and −0.70V vs. SCE at 100 mV/cm under Ar at 25°C.

on a Pt electrode as a function of the number of complete reduction/oxidation cycles $[(PQ^{2+})_n]_{surf.} \rightleftarrows [(PQ^{+})_n]_{surf.}$. The first few hundred cycles generally give a declining coverage, but the coverage is then observed to remain constant essentially indefinitely. Even holding the electrode at a potential where $[(PQ^{+})_n]_{surf.}$ is present leads to no significant deterioration, provided O_2 is excluded. Indeed, we have held the polymer in the one-electron reduced state for periods of the order of four weeks without deterioration.

Optical properties of electrodes modified with **I**.—As indicated above, the functionalization of Pt or SnO_2 electrodes obviously leads to electrochromic material, since negative potential excursions from 0.0 to −0.74V *vs.* SCE produce a purple colored surface that is obvious to the naked eye when the coverage of $[(PQ^{2+})_n]_{surf.}$ is sufficiently large. Figures 4 and 5 show optical transmission spectra of SnO_2 electrodes derivatized with **I** at electrode potentials where $[(PQ^{2+})_n]_{surf.}$, $[(PQ^{+})_n]_{surf.}$, or $[(PQ^{\circ})_n]_{surf.}$ is present. Comparing the spectrum of $[(PQ^{+})_n]_{surf.}$ in H_2O, Fig. 4, and in CH_3CN, Fig. 5, it is clear that there is a

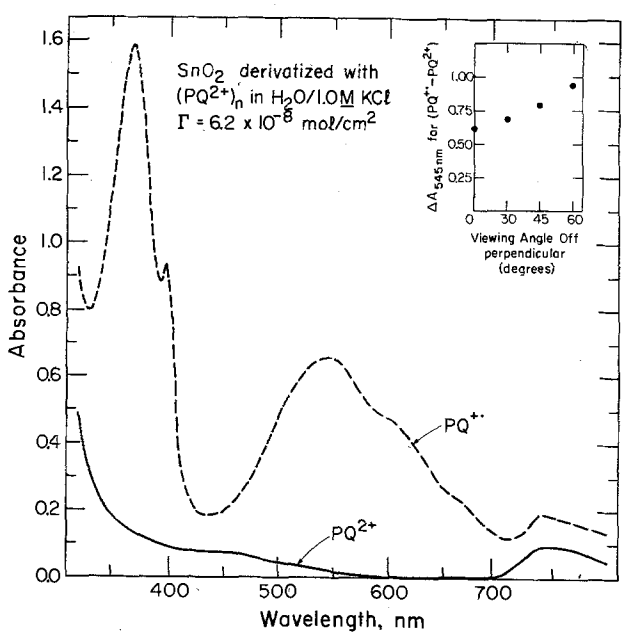

Fig. 4. Near u.v.-vis absorption spectrum of an optically transparent SnO_2 electrode derivatized with I. The smooth curve (———) shows the absorption of the electrode held at 0.00V vs. SCE while immersed in aqueous 1.0M KCl under Ar corresponding to $[(PQ^{2+})_n]_{surf.}$, and the dashed curve (- - - -) is for the same system but at an electrode potential of −0.70V vs. SCE where $[(PQ^{+})_n]_{surf.}$ is present. The inset at the upper right shows the difference in absorbance at 545 nm between the $[(PQ^{2+})_n]_{surf.}$ and $[(PQ^{+})_n]_{surf.}$ as a function of the angle of the incident beam measured degrees off the perpendicular (90° incidence).

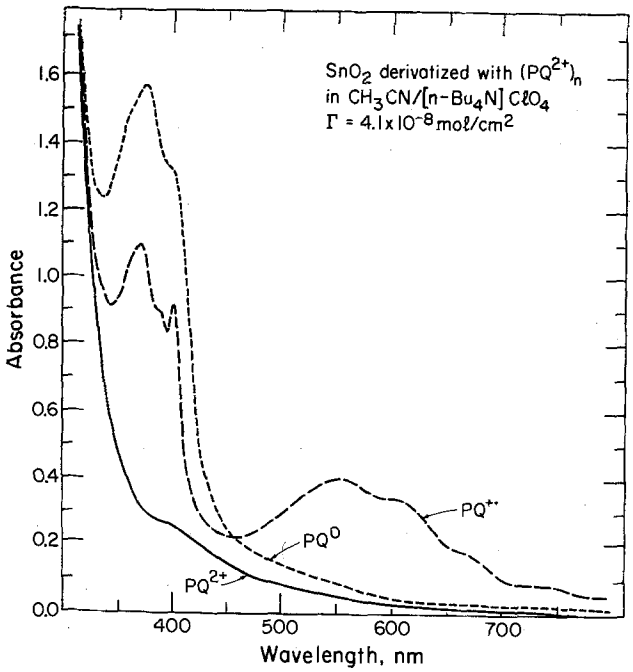

Fig. 5. Comparison of the spectra of $[(PQ^{2+})_n]_{surf.}$, $[(PQ^{+})_n]_{surf.}$, $[(PQ^{0})_n]_{surf.}$ on a derivatized SnO_2 electrode at 0.00, −0.70, and −1.00V vs. SCE in CH_3CN/electrolyte under Ar.

large visible absorption in either solvent that maximizes at ~545 nm, accounting for the purple color of electrodes bearing $[(PQ^{+})_n]_{surf.}$. The $[(PQ^{+})_n]_{surf.}$ shows an even more intense absorption in the near u.v. at ~375 nm. The relative intensities of the 545 and 375 nm features are somewhat different in H_2O compared to CH_3CN. Further, close examination of the spectra in Fig. 4 and 5 shows that the visible absorption centered at 545 nm differs in CH_3CN and H_2O such that there is more low energy absorption in CH_3CN than in H_2O. This difference in spectral properties has the consequence of making the surface appear to be more of a blue-purple in CH_3CN compared to purple in H_2O.

The distribution of absorption attributable to the one-electron reduced form of the polymer is independent of the extent to which the polymer is reduced, within experimental error. That is, except for the actual absorbance, the absorption spectrum associated with PQ^{+} centers is independent of the $PQ^{2+/+}$ ratio. This is an interesting finding inasmuch as the sort of interaction responsible for the difference in E°"s of solution **I** and $[(PQ^{2+/+})_n]_{surf.}$ could give large spectral changes. For example, dilute solutions of MV^{+} are blue, $\lambda_{max} = 603$ nm, whereas concentrated solutions of MV^{+}, where dimer $(MV^{+})_2$ is present, are purple, $\lambda_{max} = 550$ nm.

As shown in Fig. 6, the absorbance of $[(PQ^{+})_n]_{surf.}$ is directly proportional to the measured electrochemical coverage. Roughly, the optical density for optically transparent SnO_2 electrodes depends on the angle of incidence of the beam in a manner consistent with longer path lengths when the beam is not 90° to the plane of the electrode, as illustrated by the inset in Fig. 3. From 90° beam incidence measurements the absorptivity of $[(PQ^{+})_n]_{surf.}$ is determined to be $\approx 10^7$ cm^2/mol at 545 nm in H_2O. This value is in rough accord with reported molar extinction coefficients for MV^{+}. Table II summarizes the optical properties for appropriate solution and surface-bound reagents including the two-electron reduced species that are durable in nonaqueous media.

As an additional part of the characterization of $[(PQ^{2+})_n]_{surf.}$ we have measured the thickness of the polymer layer at known electrochemical coverages

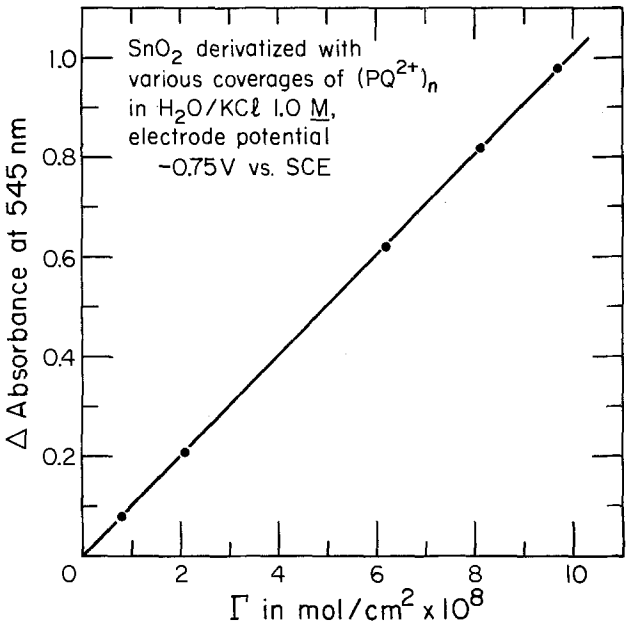

Fig. 6. Absorbance at 545 nm for $[(PQ^{+})_n]_{surf.}$ as a function of coverage on an optically transparent SnO_2 electrode.

using a Dektak surface profile measuring system, Table III. An electrochemical coverage of 6.0×10^{-8} mol/cm² is found to yield a dry thickness of 2000Å ± 10%. This thickness was measured for SnO_2 coated electrochemically; the surface system was the air-dried $[(PQ^{2+} \cdot 2Cl^{-})_n]_{surf.}$. With the known coverage 6.0×10^{-8} mol/cm² having a thickness of 2000Å we determine that there are 1.81×10^{21} PQ^{2+} centers per cm³ of polymer. Effectively the polymer is thus 3.0*M* in PQ^{2+} centers. Taking the molar absorptivity of PQ^{+} from solution measurements to be 1.0×10^{4} $lmol^{-1}$ cm^{-1}, concentration to be 3.0 mol/liter as determined above, and l to be 2×10^{-5} cm for the film, we calculate an adsorbance of 0.60 for the film, that is very close to the observed value for an electrode bearing 6.0×10^{-8} mol/cm² of $[(PQ^{2+})_n]_{surf.}$, Fig. 6. The close agreement between the measured absorbance and that calculated from the solution absorptivity and concentration of PQ^{2+} centers in the polymer establishes consistency between all measurements, and further substantiates the finding that the PQ^{2+} centers in the polymer are not significantly perturbed by the attachment and polymerization on the surface.

Table II. Optical properties for $[(PQ^{2+})_n]_{surf.}$, $[(PQ^{+})_n]_{surf.}$, and relevant solution species

Species	Solvent/electrolyte, conc. *M*	Band maxima (absorptivity, cm²/mol)
$[(PQ^{2+})_n]_{surf.}$	H_2O/1.0*M* KCl	Tail absorption only for λ >350 nm
	CH_3CN/0.1*M* $[n\text{-}Bu_4N]ClO_4$	
$[(PQ^{+})_n]_{surf.}$	H_2O/1.0*M* KCl	545 (1.0×10^7); 370 (2.5×10^7)
	CH_3CN/0.1*M* $[n\text{-}Bu_4N]ClO_4$	550 (0.8×10^7); 375 (2×10^7)
$[(PQ^{0})_n]_{surf.}$	CH_3CN/0.1*M* $[n\text{-}Bu_4N]ClO_4$	375 (3×10^7)
$I_{soln.}$ (2+)	H_2O/1.0*M* KCl	261 (3×10^7)
	CH_3CN/0.1*M* $[n\text{-}Bu_4N]ClO_4$	262 (3×10^7)
$I_{soln.}$ (+)[a]	H_2O/1.0*M* KCl	540 (1.0×10^7); 370 (2.5×10^7)
	CH_3CN/0.1*M* $[n\text{-}Bu_4N]ClO_4$	603 (1.2×10^7); 395 (2×10^7)
$I_{soln.}$ (0)	CH_3CN/0.1*M* $[n\text{-}Bu_4N]ClO_4$	384 (2.5×10^7)
MV^{2+}	H_2O/1.0*M* KCl	258 (2.1×10^7); 228 (3×10^7)
	CH_3CN/0.1*M* $[n\text{-}Bu_4N]ClO_4$	248 (3×10^7)
MV^{+}[a]	H_2O/1.0*M* KCl	553 (9.4×10^3); 395 (2.4×10^7)
	CH_3CN/0.1*M* $[n\text{-}Bu_4N]ClO_4$	603 (1.2×10^7); 390 (2×10^7)
MV^{0}	CH_3CN/0.1*M* $[n\text{-}Bu_4N]ClO_4$	380 (2.5×10^7)

[a] Measured at 1.0×10^{-3}*M*. Spectra are dependent on concentration due to dimer formation, see text.

Table III. Molar concentration of $[(PQ^{2+} \cdot 2Cl^{-})_n]_{surf.}$ films on SnO_2 as a function of coverage

Γ, mol/cm²[a]	Film thickness, cm[b]	$(PQ^{2+} \cdot 2Cl^{-})_{conc.}$,[c] *M*
6.00×10^{-8}	2.0×10^{-5}	3.0
7.4×10^{-8}	2.5×10^{-5}	3.0
1.8×10^{-7}	6.0×10^{-5}	3.0

[a] All coverages of $[(PQ^{2+})_n]_{surf.}$ on SnO_2 were determined electrochemically by integration of cyclic voltammogram, 5 mV/sec, in 1.0*M* KCl for $[(PQ^{2+})_n]_{surf.} \rightarrow [(PQ^{+})_n]_{surf.}$.
[b] Film thickness taken using a Sloan Dektak surface profile measuring system. All measurements ±10%.
[c] Concentration, mol/liter, of $(PQ^{2+} \cdot 2Cl^{-})$ redox centers in a dry surface-bound film.

Rate of $[(PQ^{2+})_n]_{surf.} \rightleftarrows [(PQ^{+})_n]_{surf.}$.—The data so far establish the $[(PQ^{2+/+})_n]_{surf.}$ redox system to be electrochromic and sensibly durable in H_2O. The optical properties are quite similar to those for solution viologen species, Table II, and hence the degree of coloration per unit of charge is about the same as with solution viologen systems. Further, the redox potential associated with surface system is nearly the same as that for the solution system, Table I. We now consider the rate of the $[(PQ^{2+})_n]_{surf.} \rightleftarrows [(PQ^{+})_n]_{surf.}$ interconversion. We have examined this both by monitoring the current and the optical spectral changes associated with the redox process. The rate data have been collected for smooth, shiny Pt surfaces bearing $[(PQ^{2+})_n]$ immersed in an aqueous electrolyte. The optical properties were monitored in the arrangement represented by Scheme I. In such an arrangement the light beam reflected off the Pt surface, passes through the polymer twice, giving at least twice the absorbance per unit of charge as for the optically transparent SnO_2 electrodes characterized by data in Fig. 4-6 for a 90° beam incidence angle.

Figure 7 shows the cyclic voltammogram and associated change in 632.8 nm reflected light intensity for a shiny Pt electrode bearing $[(PQ^{2+/+})_n]_{surf.}$. As can be seen, the current associated with the reduction results in the coloration expected. In the relatively slow scan depicted by Fig. 7, the kinetics for the $[(PQ^{2+/+})_n]_{surf.}$ are sufficiently good that the reduction/oxidation is only controlled by the imposed sweep rate. Potential step experiments, described below, have been used to establish the maximum rates of reduction and oxidation of $[(PQ^{2+})_n]_{surf.}$.

Following a potential step, the current, charge, and absorbance can be determined. Figure 8 shows some representative data following a potential step from 0.00 to −0.80V *vs.* SCE for a shiny Pt electrode bearing $[(PQ^{2+})_n]_{surf.}$. As shown in the inset for the current *vs.* time, *i vs. t* data, the current is nearly proportional to $(time)^{-1/2}$. Thus, the current-time profile reveals "Cottrell behavior" where the diffusion constant, *D*, for the Cottrell equation, [7], is in the range of 0.4-3 × 10^{-10} cm²/sec, Table IV, for a

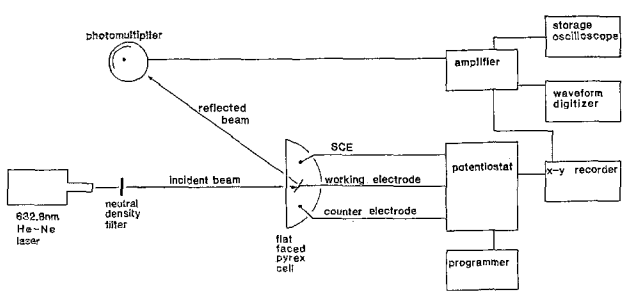

Scheme I. Diagram of apparatus for monitoring electrochromic electrodes.

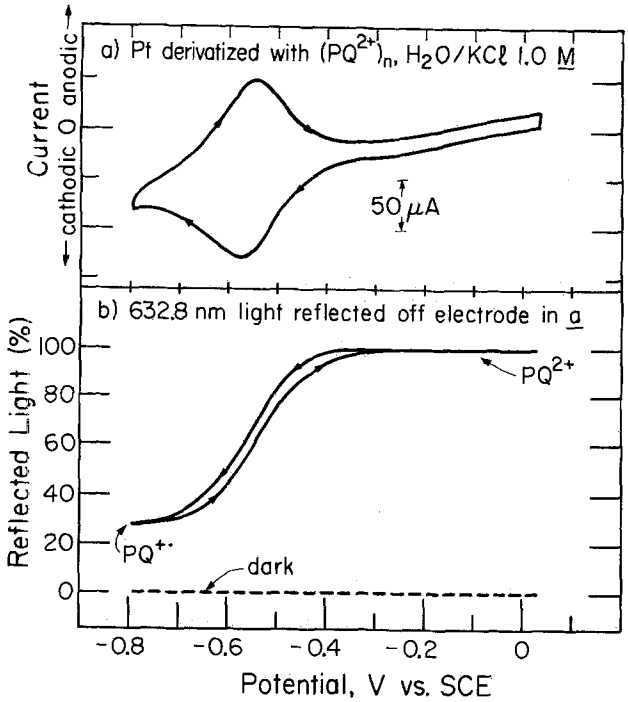

Fig. 7. Cyclic voltammetry (a), 100 mV/sec, with an initial potential of 0.00V *vs.* SCE and relative intensity of reflected 632.8 nm laser beam during the same scan (b) for a derivatized Pt electrode. The dashed line is the signal from the PMT detector (cf. Scheme I) when the laser beam is blocked; 100% is the intensity when the $[(PQ^{2+})_n]_{surf.}$ is present.

$$i(t) = \frac{nFAD^{1/2}C}{\pi^{1/2}t^{1/2}} \qquad [7]$$

variety of electrolytes and electrolyte concentrations. For a given electrode coverage, the value of D should be regarded as having an error of ±20%. These values of D are ~ two orders of magnitude higher than for a surface-confined polybenzylviologen system (12). In Eq. [7] n is the number of electrons involved in the procass, $\mathbf{F}$ is the Faraday constant, A is the electrode area, and $i(t)$ is the observed current at time = t (29). The concentration, C, is taken to be the molarity of

Table IV. Optical response time, T, for the $[(PQ^{2+/+})_n]_{surf.}$ system under various conditions in aqueous solutions

Γ, mol/cm²[a]	Electrolyte, conc., M[b]	T_{red}, msec[c]	T_{ox}, msec[c]	D, 10^{10} cm²/sec[d]
1.0×10^{-8}	LiCl, 0.1	32.0	28.0	0.37
	LiCl, 0.5	13.0	11.0	0.97
	LiCl, 1.0	9.0	9.0	1.40
	LiCl, 4.0	4.7	3.9	2.10
	$LiClO_4$, 1.0	12.0	10.0	1.10
	LiBr, 1.0	11.0	10.0	0.85
	Li_2SO_4, 1.0	10.0	10.0	0.97
	NaCl, 1.0	11.0	10.0	1.10
	KCl, 1.0	9.0	10.0	1.60
	$[(CH_3)_4N]Cl$, 1.0	10.0	10.0	1.10
	$MgSO_4$, 1.0	15.0	15.0	0.75
7.6×10^{-9}	KCl, 1.0	4.0	4.0	3.30
3.0×10^{-8}	KCl, 1.0	36.0	34.0	3.40
6.0×10^{-8}	KCl, 1.0	54.0	48.0	3.30

[a] Electrochemically determined coverage of $[(PQ^{2+})_n]_{surf.}$ on shiny Pt from integration of slow sweep, 50 mV/sec, cyclic voltammogram in 1.0*M* KCl for $[(PQ^{2+})_n]_{surf.} \rightarrow [(PQ^{+})_n]_{surf.}$.

[b] All data are for unbuffered aqueous solutions at 25°C.

[c] T_{red} and T_{ox} refer to the response time for $[(PQ^{2+})_n]_{surf.} \rightarrow [(PQ^{+})_n]_{surf.}$ and $[(PQ^{+})_n]_{surf.} \rightarrow [(PQ^{2+})_n]_{surf.}$, respectively. T is taken to be the time necessary to reach 50% of the eventual absorbance change after a potential step. For all data shown here the step is from 0.00 to −0.80V *vs.* SCE to give complete reduction or from −0.80 to 0.00V *vs.* SCE to give complete oxidation. Thus, for these cases T is the time required to achieve 50% reduction of all $[(PQ^{2+})_n]_{surf.}$ present or 50% oxidation of $[(PQ^{+})_n]_{surf.}$. The ΔO.D. is measured at 632.8 nm using the apparatus sketched in Scheme I.

[d] Diffusion coefficient, D, in cm²/sec, as calculated from Eq. [7] in text from slope of Cottrell plots.

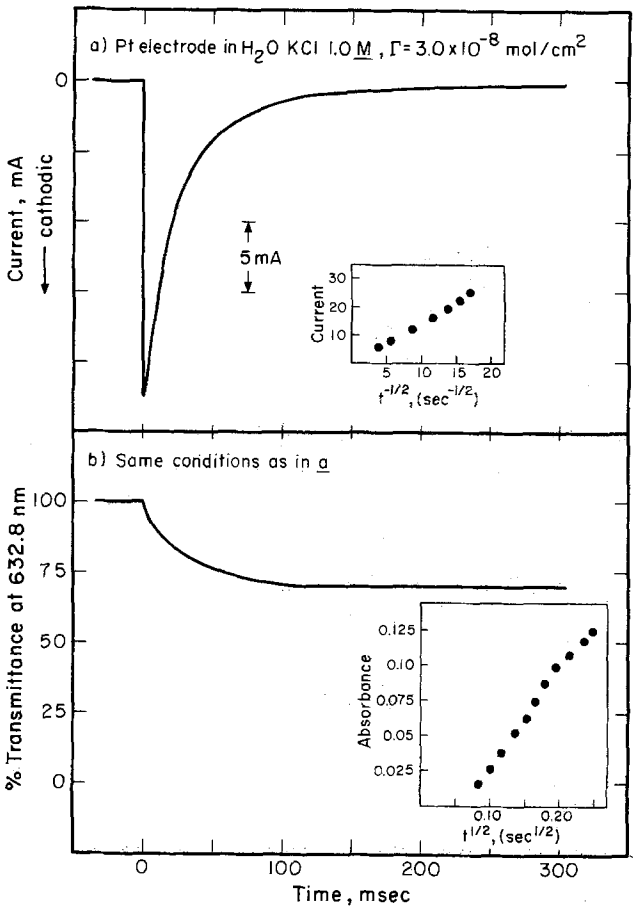

Fig. 8. (a) Plot of current *vs.* time upon a potential step of an electrode bearing 3×10^{-8} mol/cm² of $[(PQ^{2+})_n]_{surf.}$ from 0.00 to −0.80V *vs.* SCE. The inset shows a plot of current *vs.* (time)$^{-1/2}$ for experiment in (a). (b) Plot of % T for a single pass of the 632.8 nm light through the $[(PQ^{2+/+})_n]_{surf.}$ (cf. Scheme I) *vs.* time for experiment in (a); the inset shows absorbance *vs.* (time)$^{1/2}$ for the same experiment.

PQ^{2+} centers, *i.e.*, 3.0*M* as described above. As others have pointed out, the diffusion process can be regarded as the migration of electrons from redox center to redox center (self-exchange) by a hopping mechanism (11-25). This "diffusion" process can be treated mathematically as a usual diffusion process. Also, it is possible that the diffusion of ions through the polymer could be the diffusioin process. However, it seems logical that the self-exchange among the $PQ^{2+/+}$ centers of the polymer could in fact be the limiting rate, inasmuch as the redox centers are relatively fixed (compared to solution species) geometrically relative to one another. Using the procedure applied to an electroactive polyvinylferrocene film (24), our values of D give a self-exchange rate constant for the $PQ^{2+/+}$ centers of $\geq 10^5\ M^{-1}\ sec^{-1}$, a value well below the estimated self-exchange of $MV^{2+/+}$ of $\sim 10^8\ M^{-1}\ sec^{-1}$ solution (30).

Since we are concerned here with electrochromic films, it is easy to determine that the current observed is due to the $[(PQ^{2+})_n]_{surf.} \rightarrow [(PQ^{+})_n]_{surf.}$ reduction upon a potential step from 0.00 to −0.80V *vs.* SCE. As illustrated in Fig. 8, the potential step results in optical changes concommitant with current flow. Since absorbance has been established to be directly proportional to the surface coverage of $[(PQ^{+})_n]_{surf.}$, Fig. 6, the absorbance change, ΔO.D., is directly proportional to the charge, Q, passed. The integrated Cottrell equation, [8] (29). can thus be related to observed optical spectral

$$\Delta O.D. \propto Q = \frac{2nFAD^{1/2}Ct^{1/2}}{\pi^{1/2}} \qquad [8]$$

changes (12). The constant of proportionality will be dependent on the wavelength, but the point is that a plot of ΔO.D. *vs.* $t^{1/2}$ should be linear. As the inset in Fig. 8 shows, there is nearly a linear ΔO.D. *vs.* $t^{1/2}$ plot. The fact that the ΔO.D. seems to somewhat lag the current at the shortest times possibly indicates that some of the initial current is in fact due to charging (non-faradaic current). But this non-faradaic current does not appear to dominate the observed current, since integration of current *vs.* time plot is equal, within experimental error, to the charge needed to reduce $[(PQ^{2+})_n]_{surf.}$ to the extent found in the optical measurement. Another explanation is that there is loss of potential control at the early times in the experiments.

In comparing the electrochromic behavior of $[(PQ^{2+})_n]_{surf.}$ we have found it illustrative to compare the response time by measuring the time, τ, required to deplete $[(PQ^{2+})_n]_{surf.}$ to 50% of the value possible after a potential step from 0.00V to some negative potential where $[(PQ^{+})_n]_{surf.}$ can be formed. For example, stepping to −0.80V vs. SCE should (ultimately) lead to complete reduction of the $[(PQ^{2+})_n]_{surf.}$; in such a case τ is the time required to obtain 50% reduction of the $[(PQ^{2+})_n]_{surf.}$. As Fig. 8 shows, 50% reduction appears to be a regime where Eq. [8] approximates the dependence of charge passed on time after the potential step. Significantly beyond 50% reduction, however, cannot be accurately described using Eq. [7] and [8] because the polymer system cannot be regarded as semi-infinite; *i.e.*, the $[(PQ^{2+})_n]_{surf.}$ concentration obviously (ultimately) goes completely to zero in all regions of the polymer. Thus, the τ we define is arbitrary but does give qualitative insight into parameters affecting coloration rate of the redox polymer.

Data in Table IV show values of τ measured by ΔO.D. measurements following a potential step from 0.00 to −0.80V vs. SCE to effect $[(PQ^{2+})_n]_{surf.} \rightarrow [(PQ^{+})_n]_{surf.}$ or from −0.80-0.00V *vs.* SCE to effect $[(PQ^{+})_n]_{surf.} \rightarrow [(PQ^{2+})_n]_{surf.}$. In all cases, the chronoamperometric or the chronocoulometric measures of the sort given in Fig. 8 show behavior consistent with application of Eq. [7] and [8], and the data are in qualitative accord with the values of D given in Table IV from the chronoamperometric data. Note that the data in Tables IV and V are for Pt electrodes, not optically transparent SnO_2 electrodes. For the optically transparent electrodes optical density measurements would be more accurate, but slow electrochromic behavior is found owing to the high resistance of the SnO_2. On Pt we believe that the electrochromic response is controlled by the charge and ion transport properties of the surface-confined polymer.

First, it is noteworthy that τ's from the reduction and oxidation under a given set of conditions are, within experimental error, the same. We can interpret this to mean that the polymer does not undergo significant structural change upon interconverting between oxidized and reduced state. Second, for the range of electrolytes examined, there does not appear to be a major variation in τ for variation in the electrolyte at a fixed coverage of $[(PQ^{2+})_n]_{surf.}$ and at similar ionic strength. Other studies have shown that the anions, SO_4^{2-}, ClO_4^-, Br^-, and Cl^- are all extremely labile with respect to exchange processes such as that represented by Eq. [9] (3), and there is

$$[(PQ^{2+} \cdot 2Cl^-)_n]_{surf.} + 2n\text{KBr} \rightleftarrows [(PQ^{2+} \cdot 2Br^-)_n]_{surf.} + 2n\text{KCl} \quad [9]$$

little difference among these anions with respect to the energy associated with electrostatic binding. Large complex anions such as transition metal complexes $Fe(CN)_6^{4-}$, $Mo(CN)_8^{4-}$, etc. do bind relatively strongly and once bound do not rapidly exchange with solution anions. The $[(PQ^{2+})_n]_{surf.} \rightleftarrows [(PQ^{+})_n]_{surf.}$ is thus slow in a solution of 0.1*M* $K_4Fe(CN)_6$. Inasmuch as the large, highly charged anions may electrostatically bind at concentrations in the micromolar range, some care must be exercised to avoid such species in electrolytes in order to maintain fast redox properties of $[(PQ^{2+})_n]_{surf.}$. The data show further that for 1.0*M* M^+Cl^- there is no significant effect on τ upon varying M^+ among Li^+, Na^+, K^+, $(CH_3)_4N^+$. The positively charged polymer logically repels the cation of the bulk electrolyte and geometrically large or small cations or large and small charges on the cation are not significant in determining rate of $[(PQ^{2+})_n] \rightleftarrows [(PQ^{+})_n]_{surf.}$ interconversion.

The two parameters that clearly do affect τ are electrolyte concentration and coverage of $[(PQ^{2+})_n]_{surf.}$. Variation of LiCl concentration from 0.1-4.0*M* changes τ_{red} from 32 to 4.7 msec for the same electrode. The effects of electrolyte and concentration charges are completely reversible; note that all experiments for coverage of 1.0×10^{-8} mol/cm² in Table IV are for the same electrode. The data are very reproducible and the electrodes showed no deterioration in properties with use. The faster time for coloration at the high LiCl concentration could be attributed to the fact that the self-exchange can be faster at high ionic strength, however, when the concentration of PQ^{2+} centers is 3.0*M* the Cl^- concentration in the polymer is 6.0*M*. Thus, it is not obvious that 4.0*M* LiCl in the bulk solution gives any advantage in the polymer film. We therefore attribute the better response, at least partly, to better ionic conductivity. It might appear that the value of τ would be even shorter at higher concentrations of LiCl. However, increasing the concentration leads to greater solution viscosity and response time actually becomes slower at very high concentrations. In 1.0*M* KCl it is clear that larger coverage of $[(PQ^{2+})_n]_{surf.}$ leads to larger values of τ, as would be expected for a redox process controlled by diffusion.

Data in Table V illustrate the effect on τ_{red} from changing the final potential in the potential step beginning from 0.00V *vs.* SCE to some negative potential where reduction of $[(PQ^{2+})_n]_{surf.}$ can occur. For example, upon stepping from 0.00 to −0.55V *vs.* SCE eventually 50% of the PQ^{2+} centers will be reduced to PQ^+, since −0.55V *vs.* SCE is very close to the formal potential, we have defined τ, remember, as the time required to achieve one-half of the possible reduction. Not unexpectedly, there is a driving force dependence on τ_{red}. The driving force originates from the fact that at say −0.55V *vs.* SCE the $PQ^{2+/+}$ adjacent to the electrode only come to a 1/1 ratio, whereas at −0.75V *vs.* SCE this ratio should be ~1/1000 or ~180 mV of driving force. However, for final poten-

Table V. Dependence of τ on the final potential in potential step experiments[a]

Final potential	Ultimate % reduction[b]	τ_{red}, msec[c]
−0.56	50	108
−0.58	69	77
−0.60	83	65
−0.62	91	57
−0.64	96	52
−0.66	>98	49
−0.68	>99	48
−0.70	>99	46
−0.72	>99	43
−0.74	>99	41
−0.76	>99	34
−0.78	>99	32
−0.80	>99	31

[a] All data are for shiny Pt bearing 2.5×10^{-8} mol/cm² of $[(PQ^{2+})_n]_{surf.}$ in aqueous 1.0*M* KCl at 25°C. The initial potential is 0.00V *vs.* SCE and τ_{red} is measured by determining ΔO.D. for 632.8 nm light using the apparatus sketched in Scheme I.
[b] Experimentally observed % reduction of PQ^{2+} centers to PQ^+ at times long after the potential step.
[c] Time required to achieve one-half of the eventual ΔO.D., see text.

tials sufficient to achieve >99% reduction, there is less than a factor of two change in τ_{red}, consistent with a reduction process limited by some diffusion process where the electrode potential can no longer be useful in achieving larger rates.

Conclusions

The $[(PQ^{2+})_n]_{surf.}$ redox system is a durable, surface electrochromic material that exhibits fast response and coloration per unit of charge expected for a viologen-based chromophore in a variety of aqueous electrolyte systems. The rate of interconversion between $[(PQ^{2+})_n]_{surf.}$ and $[(PQ^{+})_n]_{surf.}$ is controlled by diffusion when the coverage is $\geq 1 \times 10^{-8}$ mol/cm^2 with D in the range 0.4-3 $\times 10^{-10}$ cm^2/sec leading to a minimum calculated self-exchange rate of 10^5 M^{-1} sec^{-1} for the $PQ^{2+/+}$ centers in the polymer. The system exhibits optical properties that are similar to those associated with the electrodeposition of HV^{+} from solutions of HV^{2+}. Roughly the same amount of charge must be passed to $[(PQ^{2+})_n]_{surf.}$ to color it (to the same color) to the same absorbance as for the $HV^{2+/+}$ system. The possible advantages of the $[(PQ^{2+})_n]_{surf.}$ electrochromic include the facts that (*i*) the electrochromic is covalently anchored to the surface, (*ii*) the $PQ^{2+/+}$ centers are more or less rigidly held relative to one another tending to prevent irreversible polymerization of the bipyridinium centers, and (*iii*) the system will work in a variety of solvent/electrolyte combinations and presumably over a fairly wide range of temperatures.

Acknowledgments

We thank the M.I.T. Laboratory for Computer Science, IBM Fund, for support of this research. Generous assistance from James C. Mitchener in carrying out ΔO.D. *vs.* time concommitant with current *vs.* time is gratefully acknowledged. D.C.B. acknowledges support as an M.I.T. NPW Fellow, 1981-1982.

Manuscript submitted May 3, 1982; revised manuscript received Nov. 17, 1982.

Any discussion of this paper will appear in a Discussion Section to be published in the December 1983 JOURNAL. All discussions for the December 1983 Discussion Section should be submitted by Aug. 1, 1983.

Publication costs of this article were assisted by the Massachusetts Institute of Technology.

REFERENCES

1. D. C. Bookbinder and M. S. Wrighton, *J. Am. Chem. Soc.*, **102**, 5123 (1980).
2. D. C. Bookbinder, J. A. Bruce, R. N. Dominey, N. S. Lewis, and M. S. Wrighton, *Proc. Nat. Acad. Sci., U.S.A.*, **77**, 6280 (1980).
3. J. A. Bruce and M. S. Wrighton, *J. Am. Chem. Soc.*, **104**, 74 (1982).
4. R. N. Dominey, N. S. Lewis, J. A. Bruce, D. C. Bookbinder, and M. S. Wrighton, *ibid.*, **104**, 467 (1982).
5. N. S. Lewis and M. S. Wrighton, *Science*, **211**, 944 (1981).
6. J. A. Bruce, T. Murahashi, and M. S. Wrighton, *J. Phys. Chem.*, **86**, 1552 (1982).
7. A. Ledwith, *Acc. Chem. Res.*, **5**, 133 (1972).
8. (a) M. S. Simon and P. T. Moore, *J. Polym. Sci. Polym. Chem. Ed.*, **13**, 1 (1975); (b) C. J. Schoot, J. J. Ponjee, H. T. van Dam, R. A. van Doorn, and P. T. Bolwijn, *Appl. Phys. Lett.*, **23**, 64 (1973); (c) H. T. van Dam and J. J. Ponjee, *This Journal*, **121**, 1555 (1974).
9. (a) B. Reichman, F.-R. F. Fan, and A. J. Bard, *This Journal*, **127**, 333 (1980); (b) R. J. Jasinski, *ibid.*, **124**, 637 (1977); *ibid.*, **125**, 1619 (1978); and *ibid.*, **126**, 167 (1979); (c) J. Bruinink, C. G. A. Kregting and J. J. Ponjee, *ibid.*, **125**, 1297 (1978); (d) J. Bruinink, C. G. A. Kregting, and J. J. Ponjee, *ibid.*, **124**, 1854 (1977); (e) I. F. Chang, B. L. Gilbert, and T. I. Sun, *ibid.*, **122**, 955 (1975); (f) T. Kawata, M. Uakamoto, M. Tajima, and T. Nakano, *Jpn. J. Appl. Phys.*, **14**, 725 (1975); (g) S. Fletcher, L. Duff, and R. G. Barradas, *J. Electroanal. Chem. Interfacial Electrochem.*, **100**, 759 (1979); (h) R. C. Cieslinski and N. R. Armstrong, *This Journal*, **127**, 2605 (1980).
10. (a) D. J. Barclay, C. L. Bird, and D. H. Martin, *J. Electron. Mater.*, **8**, 311 (1979); D. J. Barclay, C. L. Bird, D. H. Kirkman, D. H. Martin, and F. T. Moth, *SID 80 Digest*, 124 (1980).
11. (a) R. W. Murray, *Acc. Chem. Res.*, **13**, 135 (1980); (b) K. D. Snell and A. G. Keenan, *Chem. Soc. Rev.*, **8**, 259 (1979).
12. K. W. Willman and R. W. Murray, *J. Electroanal. Chem. Interfacial Electrochem.*, **133**, 211 (1982).
13. H. Akahoshim, S. Toshima, and K. J. Itaya, *J. Phys. Chem.*, **85**, 818 (1981).
14. A. Facter and T. O. Rouse, *This Journal*, **127**, 1313 (1980).
15. H. D. Abruna and A. J. Bard, *J. Am. Chem. Soc.*, **103**, 6898 (1981).
16. A. Merz and A. J. Bard, *ibid.*, **100**, 3222 (1978).
17. L. L. Miller and M. R. Van De Mark, *ibid.*, **100**, 3223 (1978).
18. R. Nowak, F. A. Schultz, M. Umana, H. Abruna, and R. W. Murray, *J. Electroanal. Chem. Interfacial Electrochem.*, **94**, 219 (1978).
19. (a) N. Oyama and F. C. Anson, *This Journal*, **127**, 247 (1980); *Anal. Chem.*, **52**, 1192 (1980); (b) K. Shigehara, N. Oyama, and F. C. Anson, *Inorg. Chem.*, **20**, 518 (1981).
20. N. Oyama, K. Sato, and H. Matsuda, *J. Electroanal. Chem. Interfacial Electrochem.*, **115**, 149 (1980).
21. (a) A. H. Schroeder and F. G. Kaufman, *J. Electroanal. Chem. Interfacial Electrochem.*, **113**, 209 (1980); (b) A. H. Schroeder, F. G. Kaufman, V. Patel, and E. M. Engler, *ibid.*, **113**, 193 (1980); (c) F. B. Kaufman, A. H. Schroeder, E. M. Engler, S. R. Kramer, and J. Q. Chambers, *J. Am. Chem. Soc.*, **102**, 483 (1980).
22. F. C. Anson, *J. Phys. Chem.*, **84**, 3336 (1980).
23. C. P. Andrieux, J. M. Dumas-Bouchiat, and J. M. Saveant, *J. Electroanal. Chem. Interfacial Electrochem.*, **114**, 159 (1980).
24. (a) P. Daum and R. W. Murray, *ibid.*, **103**, 289 (1979); (b) *J. Phys. Chem.*, **85**, 389 (1981).
25. R. W. Murray, *Philos. Trans. Roy. Soc.*, In press and private communication.
26. J. R. Lenhard and R. W. Murray, *J. Electroanal. Chem. Interfacial Electrochem.*, **78**, 195 (1977).
27. E. M. Kosower and J. L. Cotler, *J. Am. Chem. Soc.*, **86**, 5524 (1964).
28. (a) J. A. Farrington, A. Ledwith, and M. F. Stam, *J. Chem. Soc. Chem. Commun.*, 259 (1969); (b) E. J. Nanni, Jr., C. T. Angelis, J. Dickson, and D. T. Sawyer, *J. Am. Chem. Soc.*, **103**, 4268 (1981).
29. A. J. Bard and L. R. Faulkner, "Electrochemical Methods," Wiley, New York (1980).
30. C. R. Bock, J. A. Conner, A. R. Gutierrez, T. J. Meyer, D. G. Whitten, B. P. Sullivan, and J. K. Nagle, *Chem. Phys. Lett.*, **61**, 522 (1979).

An Admittance Study of the Tin Electrode

S. H. Glarum* and J. H. Marshall

Bell Laboratories, Murray Hill, New Jersey 07974

ABSTRACT

Voltammetric and admittance measurements for tin deposition at a rotating disk electrode from sulfuric and fluoboric acid Sn^{++} solutions have been analyzed. Apparent exchange current densities *ca.* 10 A/cm² are reduced 100-fold upon addition of polyethylene glycol. With or without the additive, the conductance representing the exchange process varies with potential directly as the surface Sn^{++} concentration. Localized three-dimensional concentration polarization zones in the electrolyte phase arising from discrete growth sites form the preferred interpretation, although an alternative kinetic process occurring prior to charge transfer cannot be excluded as the rate-limiting step.

The reversibility and supposed simplicity of tin electrodeposition in acid media has made it an attractive subject for fundamental electrochemical investigations (1). Previous studies have attempted interpretations in terms of the two-electron reduction of Sn^{++} to Sn, expressed through an exchange current density and symmetry coefficient for a charge transfer process. Reported values for the former parameter range over 4-5 decades depending on the means of measurement, electrode nature (tin or tin amalgam), and complexes of the stannous ion present (2-11). Generally a-c or pulse measurements have given the highest exchange currents (2-4). Plating additives have been found to reduce these currents substantially at both tin and amalgam electrodes, bringing them into a more accessible experimental range (9-11).

The collective disagreement among these studies suggests additional factors may be important. We have attempted a systematic examination of the tin deposition and dissolution processes combining voltammetric and a-c admittance meaurements over a range of frequencies and potentials. Through rapid measurements on a common electrode surface it is possible to reduce some of the uncertainties involved in comparisons of disparate measurements. Although the effective exchange current densities we observe fall among the highest reported, we find evidence for an aging process which markedly retards surface kinetics, particularly in fluoboric acid solutions. Whether additives are present or not, the potential dependence for the limiting kinetic step is compatible not with a charge transfer process but rather a preceding stage.

Experimental

Inorganic reagents were used as supplied. Polyethylene glycol (Polysciences) had an average molecular weight of 1540 or about 35 monomer units per molecule. $SnSO_4$ was added directly to the acid in the cell after argon degassing and its concentration was determined gravimetrically. For most fluoboric acid solutions $SnSO_4$ also served as the Sn(II) source, although no difference was observed when the fluoborate was substituted.

Platinum disk electrodes, 1/16 in. diam, provided the substrate for tin deposition and these were polished prior to each series of runs (12). A tin wire mounted in rigid glass capillary tubing served as the reference electrode. The cell was thermostated at 25°

The experimental apparatus and procedures have been previously described (12). Two types of admittance measurements, $Y^*_\eta(\omega)$ and $Y^*_\omega(\eta)$, were used in this work. For the former the admittance was measured at a fixed d-c potential and the frequency swept between 100 Hz and 200 kHz. The complex potential differences between the working and reference electrodes and across a reference resistor were measured, their ratios then giving complex admittances. The $Y^*_\omega(\eta)$ measurements were taken at a fixed frequency and increasing potential during cycling. These measurements furnish a better picture of the potential dependence of electrode parameters. All measurements reported herein involved potential scan rates of 13 mV/sec and disk rotation speeds of 100 rad/sec.

Basic Theory

To establish an initial framework for our results and analysis, we suppose that the current-voltage behavior of the deposition process is described by the Butler-Volmer equation (anodic current defined as a positive parameter)

$$I = I_o\,[e^{(1-\alpha)ze\eta/kT} - (c(0)/c_o)e^{-\alpha ze\eta/kT}]$$

$$c(0)/c_o = 1 + I/I_{lim} \quad [1]$$

The limiting cathodic current density, I_{lim}, is defined as a positive quantity, and the steady-state solution is

$$I = I_o\frac{\exp(ze\eta/kT) - 1}{(I_o/I_{lim} + \exp(\alpha ze\eta/kT)} \quad [2]$$

Overpotential modulation perturbs both the current and the surface concentration and conventional analysis leads to Randles' circuit shown in Fig. 2, to which an electrolyte resistance, R_e, and double layer capacitance, C_{dl}, have been added (13). The two circuit elements contributed by deposition are

$$W = zFD^{1/2}\,(\partial c(0)/\partial\eta)_I \quad [3]$$

$$G = (\partial I/\partial\eta)_{c(0)}$$

The admittance of the Warburg element varies with frequency as $(i\omega)^{1/2}W$. At low frequencies (*ca.* 1 Hz) with periods near the diffusional transit time through the Nernst layer, the frequency dependence of this element is more complex, and at sufficiently low frequencies it becomes resistive with the circuit admittance approaching the slope of the current-voltage curve. Several papers have discussed this transition region for impedance studies at the rotating-disk electrode (14-16). The frequencies used in this work lie well above the transition region, and the high frequency Warburg expression given by Eq. [3] suffices for our studies. High frequency impedance values will be independent of disk rotational speed at the equilibrium potential. However, the impedance generally depends on surface concentrations and, at other potentials, impedances will vary with disk rotation. The rotating disk is therefore recommended for the establishment of steady-state concentration profiles.

The complementary information in I-η and G-η plots is illustrated by several limiting cases. For $\eta = 0$

$$(\partial I/\partial\eta)_{\eta=0} = (ze/kT)\,I_oI_{lim}/(I_o + I_{lim})$$

$$G_{\eta=0} = (ze/kT)\,I_o \quad [4]$$

$$(\partial \ln G/\partial\eta)_{\eta=0} = (ze/kT)\,[(1-\alpha) - \alpha I_oI_{lim}/(I_o + I_{lim})]$$

* Electrochemical Society Active Member.

In the cathodic limit, $\eta \to -\infty$

$$I = -I_{lim}$$
$$G = \alpha(ze/kT)I_{lim} \quad [5]$$

Both Butler-Volmer parameters may be found from $G(\eta)$ measurements near the equilibrium potential, whereas $I(\eta)$ measurements yield only I_o provided this parameter is not too much greater than I_{lim}.

When $I_o >> I_{lim}$ the equations for I and G reduce to

$$I = I_{lim}[\exp(ze\eta/kT) - 1]$$
$$G = (ze/kT)I_o \exp[(1-\alpha)ze\eta/kT] \quad [6]$$

In this limit the current-voltage curve furnishes no information about the Butler-Volmer parameters, whereas both may be deduced from ln G *vs.* overpotential data. That these plots are useful for finding I_o and α in intermediate situations is best demonstrated by plots using the general solution to Eq. [1] and [3] (Fig. 1A and B). Slopes yield reliable values for α in the vicinity of $\eta = 0$. At increasing cathodic potentials G deviates from a simple exponential variation, approaching the limiting value given by Eq. [5].

The complex impedance diagram for the circuit of Fig. 2 has a high frequency real axis intercept at R_e, a high frequency dispersion determined by G and C_{dl}, and a low frequency dispersion due to W (16). The former dispersion appears as a semicircle and the latter as a 45° line. When these dispersions overlap their graphical separation may not be clearcut. Figure 2 shows several plots for typical experimental conditions and indicates the detectable range of G values. The low frequency expansion for the impedance is

$$Z' + iZ'' = R_e + G^{-1} - C_{dl}/W^2 + (i\omega)^{-1/2}W^{-1} + \ldots \quad [7]$$

and W can be found from Z'' values in the region where data lie on the 45° asymptote

$$-Z'' = 1/(2\omega)^{1/2}W \quad [8]$$

Whether the real-axis intercept for this line is greater or less than R_e depends on the relative magnitudes of G, W, and C_{dl}, and a value for C_{dl} is needed before G can be evaluated.

Usually R_e can be accurately found (0.5%) from high frequency extrapolations of complex impedance plots.

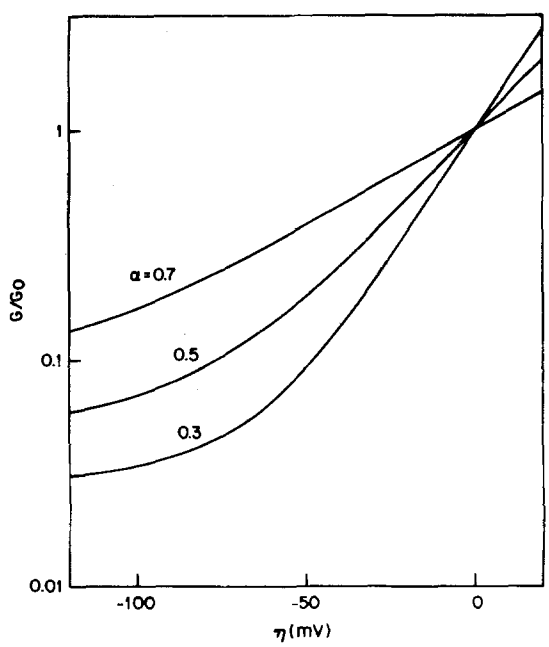

Fig. 1A. Theoretical plots for the potential variation of G (Eq. [3]) for $I_o/I_{lim} = 10$ and various transfer coefficients. The plots have been normalized with respect to the value at the equilibrium potential, G_o.

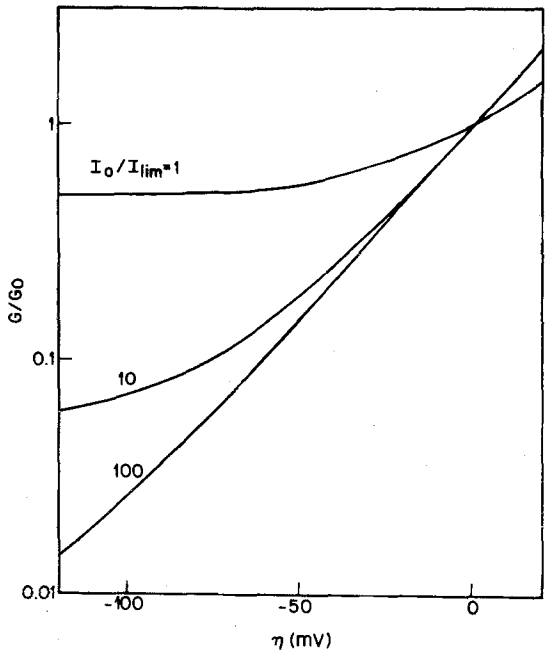

Fig. 1B. Plots of G for $\alpha = 0.5$ and various I_o/I_{lim} ratios

Results at other electrode potentials may be used in questionable cases, for R_e is independent of surface processes. To evaluate C_{dl} we make use of complex capacitance plots after subtraction of R_e

$$C^* = C' + iC'' = [i\omega(Z^* - R_e)]^{-1} \quad [9]$$

The low frequency graph of this function is also a 45° line given by the asymptotic equation

$$C' + iC'' = C_{dl} - W^2/G + (i\omega)^{-1/2}W + \ldots \quad [10]$$

C_{dl} is found from the extrapolated high frequency intercept of these plots, W from the linear low frequency portion in which

$$-C'' = (2\omega)^{-1/2}W \quad [11]$$

and G from the difference between C_{dl} and the extrapolated intercept of the low frequency linear section. For the circuit of Fig. 2 this asymptotic line always lies to the left of a 45° line through C_{dl} by an amount W^2/G.

The foregoing procedures have proved most useful for analyzing real data obtained from a-c measure-

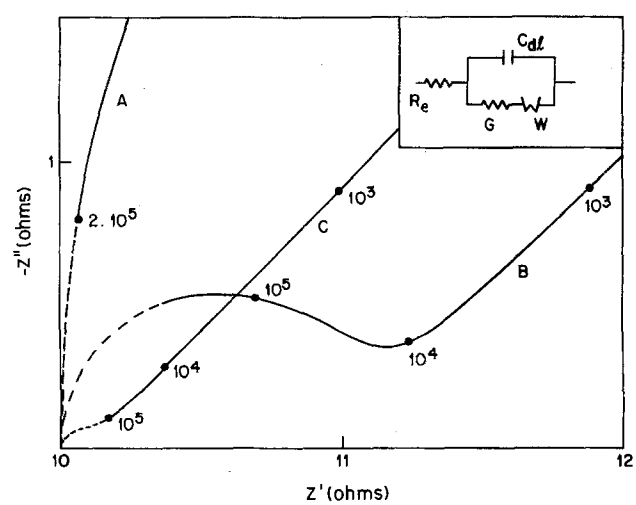

Fig. 2. The inset defines the elements of Randles' equivalent circuit. Complex impedance plots are shown for typical experimental conditions, $R_e = 10\Omega$, $C_{dl} = 1\ \mu F$, $W = 0.01$ mho-sec$^{1/2}$, and $G = 0.1$ (A), 1.0 (B), and 10.0 (C) mhos. Frequencies in Hz are given for several points.

ments in this study. The shapes of complex-plane plots are especially helpful in establishing the domain of validity of an equivalent circuit model and illustrating the frequency ranges most sensitive to contributions from individual equivalent circuit elements.

Results

Sulfuric acid.—A plating/stripping cyclic voltammogram typical of this work, Fig. 3, shows a flat cathodic limiting current region and an abrupt anodic current drop upon the completion of stripping. Deposits characterized by such curves were adherent, uniform, and granular in appearance (20×). For Sn^{++} concentrations greater than 20 mM, currents exceeding the limiting current developed due to dendritic growths which penetrated the Nernst diffusion layer and upset the disk convective flow pattern (18). The deposit thickness obtained from coulometry in a mean geometric area approximation was *ca.* 10^{-5} cm. Greater potential excursions led to irregular stripping and deposits were not usually adherent once the electrode had been so treated. Consequently this study has been restricted to concentrations below 20 mM and potentials within 100 mV of the reversible Sn/Sn^{++} potential.

The limiting current was found to be proportional to $[Sn^{++}]$ and the square root of disk rotational speed. Diffusion coefficients calculated from numerous voltammetric measurements ranged 6.7 ± 0.5 cm²/sec and agree with published values for Sn^{++} (19, 20). The slope of the current-voltage curve at $\eta = 0$ after correction for electrolyte resistance equaled $2eI_{lim}/kT$ within 5%. Thus from Eq. [4], the exchange current density must exceed the limiting current density by at least an order of magnitude. Plots of log $(I + I_{lim})$ *vs.* potential were linear with slopes of 30-34 mV/decade.

Admittance data were taken at selected potentials in the cathodic region. Figure 4 is a representative complex capacitance plot for 14 mM $SnSO_4$/1M H_2SO_4 at −30 mV. Below 10 kHz this plot shows the 45° line predicted by a diffusion model, and the average of 24 points between 0.1 and 10 kHz gives 0.0616 ± 0.0005 mho/sec½ cm² for the Warburg coefficient W (Eq. [11]). The extrapolated intercept of the linear portion falls at 30 μF/cm². Above 20 kHz the data deviate from the 45° line and appear to approach the real axis perpendicularly with an apparent intercept between 80 and 100 μF/cm². The "curl" in the plot above 100 kHz can be explained by a lead inductance of 0.1 μH. An empirical correction would improve the appearance of the plot in this region, but the gains would be illusory

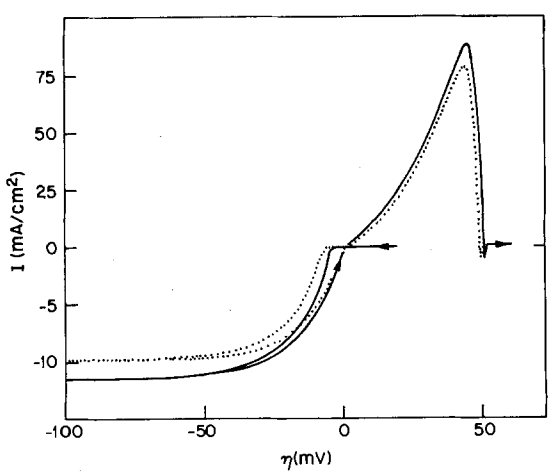

Fig. 3. Plating and stripping cyclic voltammogram for 12.7 mM $SnSO_4$/1M H_2SO_4, scan 13 mV/sec, and rotational speed 100 rad/sec. The solid curve was recorded before PEG addition and the dotted curve immediately after. Note the compressed anodic current scale.

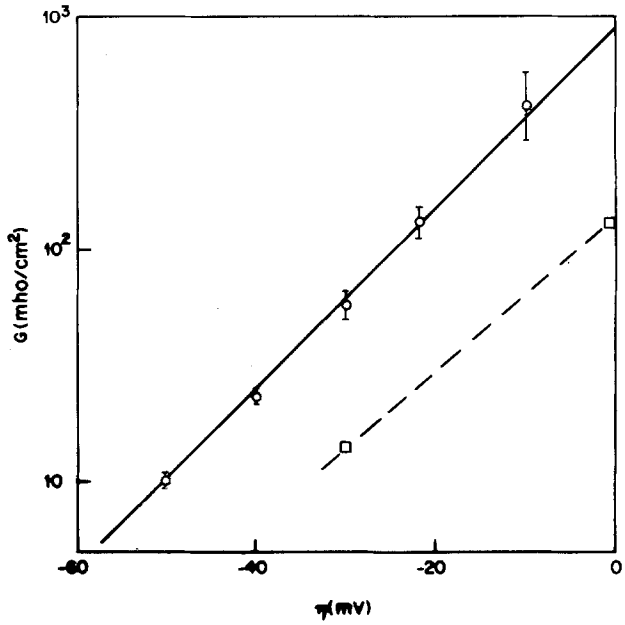

Fig. 4. Experimental complex-plane plots for 14 mM $SnSO_4$/1M H_2SO_4 at −30 mV. Curve A is the complex impedance (lower scale), B the complex capacitance (upper scale), and C a 5× expansion of the high frequency portion of B. Frequencies are indicated in kHz.

for other systematic errors such as current distribution corrections, synthesizer waveform, and phase detector response appear in this frequency regime where the measurement is dominated by electrolyte resistance.

The difference between C_{dl} and the extrapolated intercept of the linear asymptote gives $G = 43 \pm 5$ mho/cm² (Eq. [10]). Figure 5 plots the variation of G with potential based on analogous measurements, revealing a 26 mV/decade slope. Unfortunately the value at $\eta = 0$ is too large to be measured diirectly, but extrapolation suggests ~10^3 mho/cm² or $I_o \sim 13$ A/cm² for $Z = 2$ (Eq. [4]). The principal difficulty in obtaining credible values for large exchange currents lies not so much in the electrolyte resistance as in the double layer capacitance, and the uncertainty in this parameter deter-

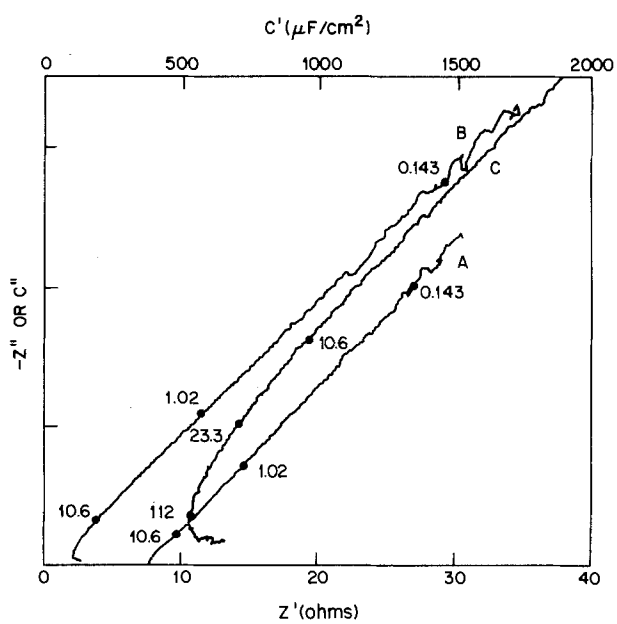

Fig. 5. Semilog plot for G obtained from Fig. 4 and its homologues. The dashed line shows results with a 5 mM $SnSO_4$ for two consecutive measurements taken without an intervening time delay for data analysis.

mines the error in evaluating large conductances at high frequencies.

Frequency-swept admittance measurements required about 10 sec and during this interval plating inevitably created changes in the surface, complicating a comparison of measurements taken at different potentials. Admittance measurements made at a fixed frequency during potential cycling offer a more consistent picture of how the elements of Randles' circuit vary with potential, provided this frequency is chosen to isolate the contribution of a particular element. Log plots for the variation of Y' are shown in Fig. 6 at several frequencies. All show an extensive linear region with Y' proportional to $\omega^{1/2}$ and a 34 mV/decade slope. Within this frequency-potential range Y' is principally determined by W. The slope of the current-voltage curve is also shown and corresponds to an extrapolated 1 Hz plot, the frequency where the high frequency Warburg approximation breaks down.

Figure 7 indicates the variation of C' at several frequencies with potential. In the cathodic limit the curves approach a common value of 40 μF/cm^2, typical of values expected for the double layer capacitance for the metal-electrolyte with a moderately rough surface. With increasing potential the curves diverge because of contributions from an increasing Warburg admittance. Some variation of C_{dl} with potentials is evident but its form is not well-defined, requiring data at higher frequencies than were available.

Sulfuric acid/PEG.—Addition of the brightening agent polyethylene glycol (PEG) to the sulfuric acid bath produces distinctive changes in both voltammetric and admittance measurements. The former remain similar to those for the additive-free bath, but a reduction in the limiting current appears immediately after addition (Fig. 3). Admittance changes are more marked. The 45° line is no longer evident, being replaced by a well-defined semicircle in complex impedance plots (Fig. 8). Only at the lowest frequencies does one begin to see indications of the Warburg contribution. In terms of Randles' circuit these plots

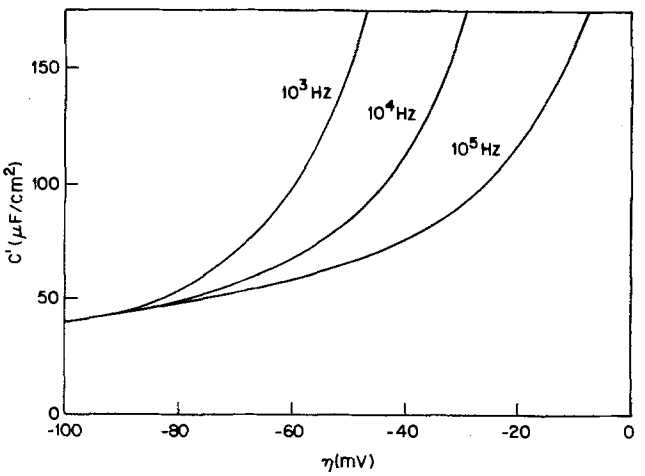

Fig. 7. Dependence of $C'_\omega(\eta)$ for the runs of Fig. 6

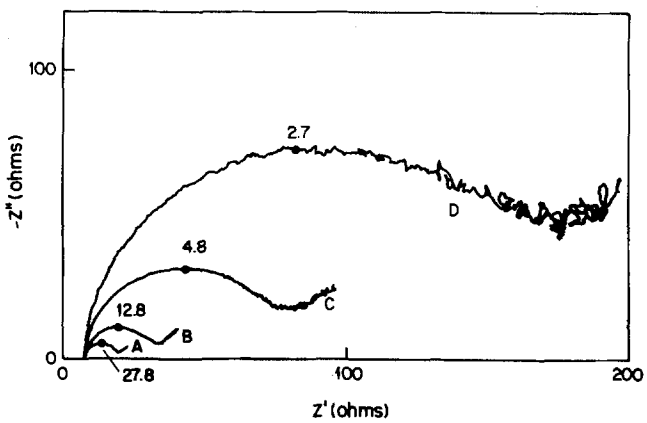

Fig. 8. Complex impedance plots for 9.6 mM $SnSO_4$/1M H_2SO_4 after addition of PEG (1.2 mM monomer) for overpotentials 0 mV (A), −10 mV (B), −20 mV (C), and −30 mV (D). Frequencies (kHz) for the dispersion maxima are shown.

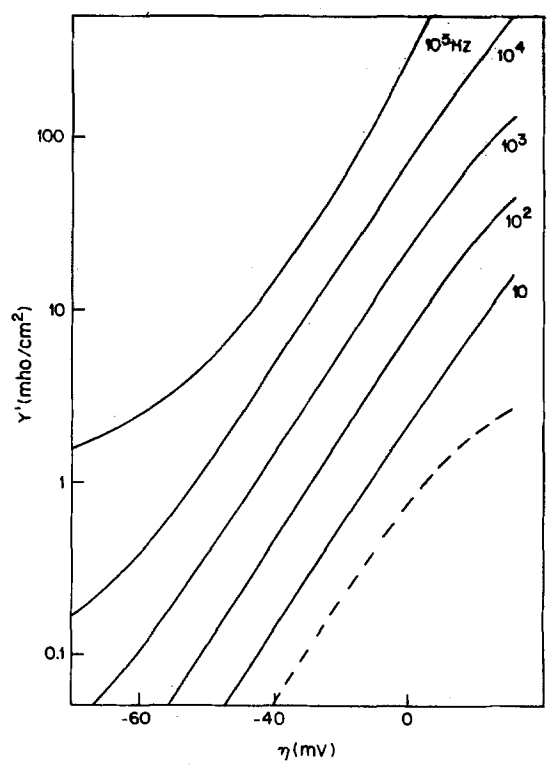

Fig. 6. Semilog plot of $Y'_\omega(\eta)$ for 11.7 mM $SnSO_4$/1M H_2SO_4 at several frequencies. The dashed line gives the slope of the current-voltage curve.

show quite clearly that $G << W$ and that G increases rapidly with potential. At higher frequencies after subtraction of the electrolyte resistance, the effective circuit reduces to a parallel G-C circuit and the variations of these parameters with potential can be ascertained from admittance *vs.* potential measurements at appropriate frequencies. Log plots of Y' *vs.* potential are given in Fig. 9 at 10 and 100 kHz for several additive concentrations. The close agreement between these curves, in contrast to Fig. 6, bears out the presence of a true resistive contribution. (The slight difference appears because the semicircle in Fig. 8 is slightly depressed and not centered on the real axis.)

The 31 mV/decade slopes of these plots are similar to those found for the additive-free solutions (Fig. 5), although values at $\eta = 0$ yield exchange current densities of only 0.18, 0.10, and 0.05 A/cm^2. It should be remembered that Fig. 9 corresponds to a variation of G, whereas Fig. 6 reflects that of W in the additive-free solution. Values for C' in this region were also independent of frequency and are plotted in Fig. 10.

A brief series of measurements was made in sulfuric acid using camphor as an additive (10, 11). Voltammetric and admittance changes were similar to those found with PEG, *e.g.*, G varied at a 26 mV/decade rate with potential and is not discussed further. These experiments do suggest that the behavior of PEG as a plating additive is typical rather than unique.

Fluoboric acid.—Measurements in this acid were complicated by irreproducibility due to the gradual growth of a film which remained visible on the surface after stripping. This film could be seen even when the maximum anodic potential excursion lay within 10 mV

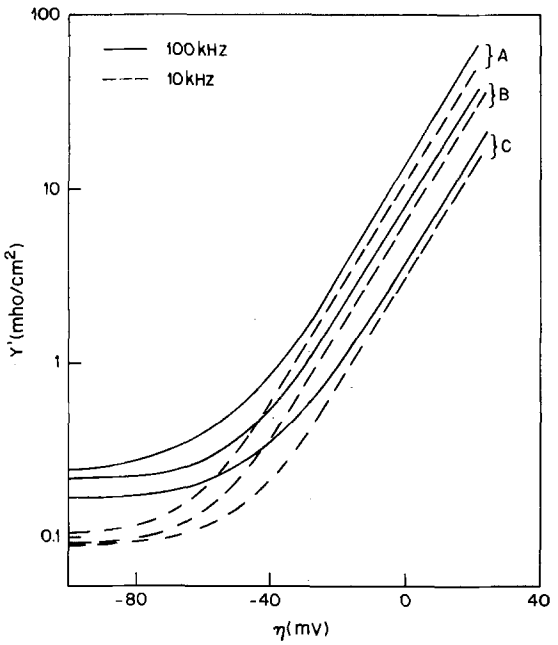

Fig. 9. Dependence of $Y'_\omega(\eta)$ at 100 and 10 kHz for 16.1 mM $SnSO_4$/1M H_2SO_4 and PEG monomer concentrations of 0.62 mM (A), 1.2 mM (B), and 6.2 mM (C).

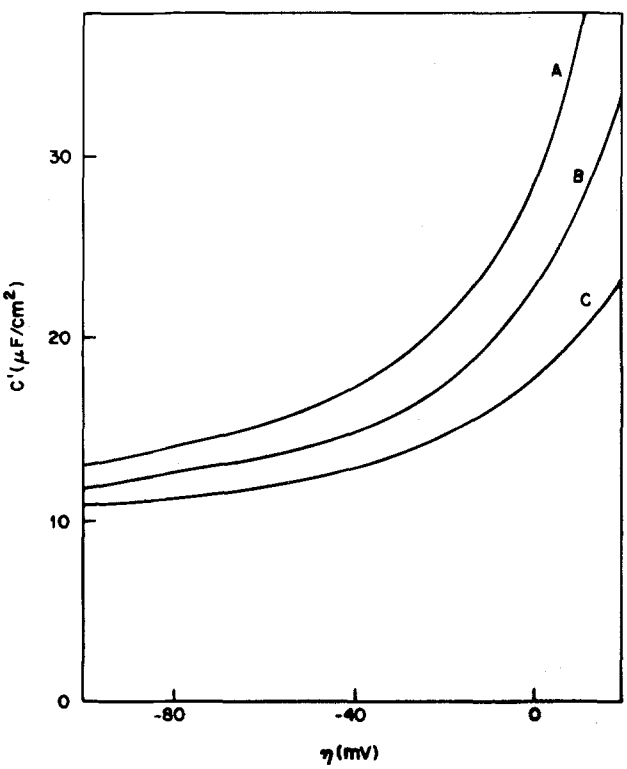

Fig. 10. Dependence of $C'_\omega(\eta)$ for the solutions of Fig. 9 at 100 kHz. 10 kHz data were coincident over most of this range.

of the reversible Sn potential. Addition of 1M boric acid to complex free fluoride did not suppress film formation. Reproducible measurements were only obtained with immediate experiments on a freshly polished platinum substrate. Results were similar to those for sulfuric acid and are briefly summarized.

Current-voltage plots indicated a somewhat larger diffusion coefficient, $9 \pm 1 \times 10^{-6}$ cm²/sec, and had slopes at $\eta = 0$ of $2eI_{lim}/kT$ after correction for solution resistance. Semilog plots of $Y'(\eta)$ exhibited 34-36 mV/decade slopes, $(\omega)^{1/2}$ dependence, and values at $\eta = 0$ corresponding to diffusion coefficients of 8-9 $\times$ 10^{-6} cm²/sec. Complex-plane plots showed the 45° linear behavior characteristic of diffusion-controlled kinetics and high frequency capacitance values near 50 μF/cm² at −100 mV. Exchange current densities appeared to be at least as large as found in the sulfuric acid solutions.

When film growth became perceptible, typically after 0.5 hr of experimentation, a-c results were irreproducible, impedances increasing with time without apparent limiting behavior. $Y'(\eta)$ plots then had slopes of 45-50 mV/decade. Values at $\eta = 0$ were reduced more than an order of magnitude and were no longer consistent with a diffusion process. High frequency capacitances dropped to about 25 μF/cm². The continuous change in a-c parameters during film formation frustrated attempts to study these electrodes more systematically.

Fluoboric acid/PEG.—Polyethylene glycol additions produced changes similar to those reported in sulfuric acid solutions, but film formation was encountered and marked aging changes were seen in cyclic voltammetric experiments. Prior to PEG addition the cathodic branch of the cyclic voltammogram shows a flat cathodic limiting current region (Fig. 11). Immediately following addition the current level in this region is reduced and the plot acquires a positive slope which increases gradually with time. Eventually the portion of the curve following the nucleation region appears to consist of two components and cathodic currents are markedly less. This reduction is accompanied by a slow relaxation process. If, after such a voltammogram has developed, the potential sweep is halted at −100 mV, the steady-state current decays to 10-20% of its initial value. The shape of the anodic stripping curve also suggests a complex behavior with dissolution of the metal deposit becoming more difficult. By tinkering with the sweep conditions a stripping curve showing two maxima was sometimes observed. Repolishing the platinum surface restored the original voltammetric behavior with aging then occurring as before.

PEG altered complex-plane plots in the manner observed with H_2SO_4 solutions. Semilog plots of $Y'(\eta)$ exhibited 47-49 mV/decade slopes and limiting cathodic values (Fig. 12), although aging complicated a direct comparison between separate measurements. High frequency capacitance measurements gave limiting cathodic values of 15-20 μF/cm² for these solutions.

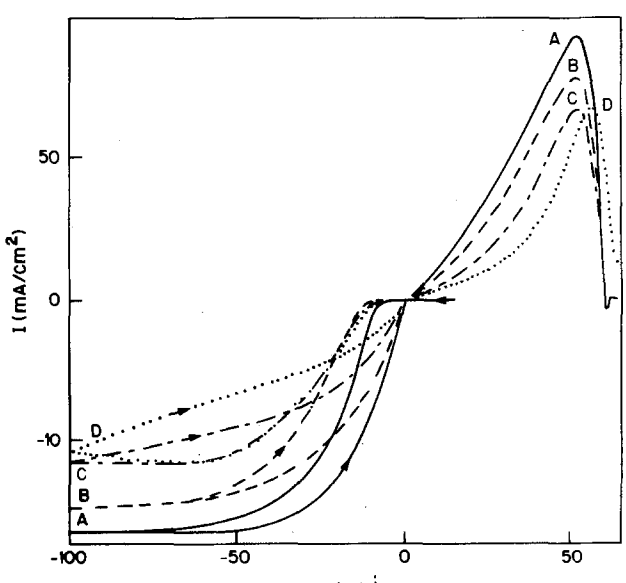

Fig. 11. Plating and stripping cyclic voltammograms for 9.6 mM $SnSO_4$/1M HBF_4 before (A) and immediately after (B) PEG addition (1.2 mM monomer). Curves C and D show aging changes over 1 hr.

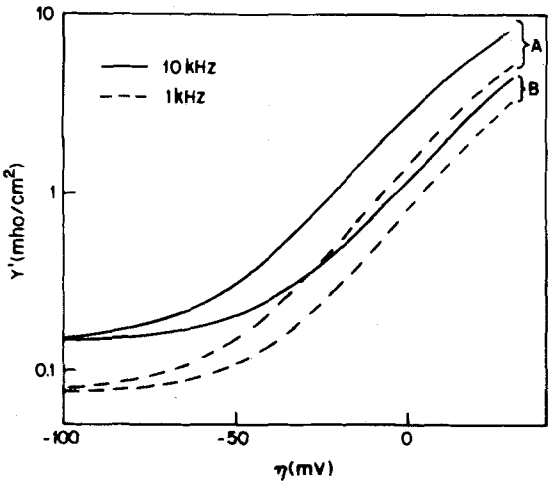

Fig. 12. Aging effects on $Y'_\omega(\eta)$ for 11.5 mM $SnSO_4$/1M HBF_4 and 1.2 mM PEG (monomer). Measurements were taken in the sequence 10 kHz (A), 1 kHz (A), 10 kHz (B), and 1 kHz (B) at 15 min intervals. The electrode was stripped at +10 mV between runs and at no time did the anodic potential exceed this value.

Discussion

The cyclic voltammograms for additive-free acid solutions bear no surprises, confirming tin deposition to be a rapid process limited primarily by Sn^{++} diffusion (1). The somewhat greater diffusion coefficient in fluoboric acid solutions may reflect formation of complexes such as SnF_3^-. The hydrolysis reaction (21)

$$BF_4^- + H_2O \rightleftharpoons HF + BF_3OH^- \qquad [12]$$

leads to free F^- which forms a series of strong Sn^{++} complexes (22).

A-C measurements verify kinetic control by a diffusion process at low frequencies and independently yield diffusion coefficients agreeing with those derived from RDE limiting currents. The variation of a-c parameters with potential and frequency provides additional information regarding the diffusion process. When $I_o >> I_{lim}$, the Warburg coefficient reduces to

$$W = (z^2e\mathbf{F}/kT)D^{1/2}c(0) \qquad [13]$$

and directly measures the surface concentration. The 34 mV/decade slopes seen in Fig. 7 lie close to the 30 mV/decade value expected for an "ideal" divalent species, although the source of the reproducible discrepancy is conjectural.

A survey of reported exchange current densities for tin deposition indicates a highly variable parameter, with not even order-of-magnitude consistency (1). Our values fall among the highest and those were obtained at Hg rather than Sn electrodes. The diversity of results suggests the rate may depend on "active" site densities determined either by morphological variations or impurity poisoning. Our measurements, which have been made immediately on freshly deposited surfaces, may contain a greater density of growth sites or be less sensitive to contamination. With respect to the circuit elements of Fig. 2, we have observed reproducible values for all parameters except G when experimental runs were separated by more than 20 min. Inevitably G values decreased with time whether the electrode was cycled, potentiostated at $\eta = 0$, or held at open circuit during the interval between measurements. No visible evidence of film formation was seen during this period, and cyclic voltammograms were unaltered.

The data shown in Fig. 5 were taken in order of increasing cathodic potential and aging would tend to increase the slope of this plot. It was experimentally possible to acquire two frequency-sweep runs at different potentials before a 15-20 min delay for data analysis. Pairs of such measurements, one of which is also shown in Fig. 5, had slopes of 30-35 mV/decade. Despite aging uncertainties, the variation of G with potential appears far more rapid than expected for a two-electron process with $\alpha = 0.5$ (60 mV/decade). The apparent α value from Eq. [4] is only ~0.1, indicating that the height of the barrier limiting the cathodic partial current is but slightly potential dependent, with most of the applied potential bias occurring between the metal surface and the barrier (cf. Eq. [1]). Rate limitation by processes preceding cathodic charge transfer (or following anodic charge transfer) will lead to low α-values provided the associated barrier lies on the electrolyte side of the Helmholtz layer.

Measurements with PEG solutions offer a more convincing demonstration for the potential dependence of G. They do not depend on the analysis of small experimental differences and can be directly plotted from admittance *vs.* potential data taken at fixed frequencies (Fig. 9). The exchange current density is reduced by a factor of 100, but the 33 mV/decade slope remains consistent with results for additive-free solutions. Bearing in mind that the Warburg coefficient also varies at this rate, it appears that the cathodic partial current is independent of potential and only an explicit function of $Sn^{++}(0)$ or from Eq. [1], $\alpha \simeq 0$.

The cathodic limiting values in Fig. 9 are not indicative of the limit expressed by Eq. [5], for they are frequency dependent. At 100 Hz only a linear plot is found down to $Y' \simeq 10^{-2}$ mho/cm², and from Eq. [5], $\alpha < 0.01$. A null value is also consistent with the apparent limiting current decrease seen in Fig. 3 upon PEG addition. According to Eq. [2] a cathodic limiting current unequal to the diffusion-limited value exists when $\alpha = 0$. From the magnitude of the reduction observed, Eq. [2] gives $I_o \simeq 10^2$ mA/cm², a figure in accord with a-c results. The limit in Fig. 9 probably arises from currents flowing in a path parallel to the deposition process (Fig. 2). In this potential region the surface admittance is dominated by the double layer, and resistive contributions arise if this is not an ideal capacitor.

The exchange currents measured with PEG present are comparable to or greater than most results obtained for additive-free tin deposition, and 2-3 orders of magnitude greater than results found in other additive studies. In particular, Meibuhr *et al.* have studied the polarization effects of a variety of polyglycols and found no influence with PEG, although polypropylene glycol (PPG) led to a dramatic polarization increase with exchange current densities *ca.* 10^{-3}-10^{-4} A/cm² and low α-values (9). Their polarization curves also exhibit a constant current region before entering a Tafel region beyond −200 mV.

We have confirmed the greater effect of PPG and also found Tafel regions with similar slopes and intercepts. Unfortunately, the cathodic currents in this region exceeded the Sn^{++} limiting current densities established at the RDE prior to additive addition by more than a factor of 2. Hydrogen evolution, possibly modified by the deposition process, seems the most plausible interpretation. Stannane formation is not expected on thermodynamic grounds until more negative potentials are reached (23). Experiments using bulk tin electrodes ruled out the possibility that the platinum substrate was involved via a porosity path.

Meibuhr *et al.* suggest that additives influence deposition through the formation of a blocking film, with the rate then controlled by migration through this layer. Comparison of capacitance results in Fig. 7 and 10 reveals a threefold reduction which can be attributed to this layer, although roughness changes might account for a portion of the difference. The principal difficulty we see for this interpretation is the similar potential dependence of G for solutions with and without PEG, despite a change in absolute rate by 2-3 orders of magnitude. If a common mechanism under-

lies both systems, an alternative interpretation is that the surface film drastically reduces the number of available sites for deposition and dissolution rather than kinetics at these sites.

The observation of film formation in fluoboric acid solutions introduces further possible complications in tin deposition. Thermodynamically Sn(II) and Sn(IV) hydrous oxides are only stable in pH $\simeq$ 0 solutions at potentials 100 mV anodic to the reversible deposition potential in 10 mM Sn^{++} solutions (23). No bulk films were found with sulfuric acid solutions below this limit. We postulate the formation of a somewhat more stable oxyfluoride film. This film is not removed by anodic stripping and develops continuously. Additives do not suppress its formation, although their presence renders it less adherent, for these films could be removed readily by lightly wiping the surface. Additive-free deposits required metallurgical polishing to expose the platinum substrate. While bulk films were not encountered with sulfuric acid solutions, the irreversible formation of monolayer or submonolayer films could explain aging drifts and account for the diversity of reported exchange current densities.

Complex-plane plots (Fig. 4) show deviations from linear low frequency behavior beginning near 20 kHz, with a complete breakdown at 100 kHz. During the corresponding periods Sn^{++} ions will have diffused 500-1000Å, raising questions about the influence of surface roughness upon diffusion measurements at short times. De Levie has modeled the influence of roughness upon the double layer capacitance and commented upon the diffusional aspects of roughness (24). The capacitance values we find at −100 mV, 40-50 μF/cm^2, are frequency independent and suggest roughness factors, s, of 2-3 (true area/geometric area). For the prevailing RDE conditions the effective Nernst layer thickness is 15μ, substantially greater than the deposit thickness of 0.1-0.2μ. Let us heuristically suppose that d characterizes a distance at which surfaces of equal concentration shift between micro- and macrosurface parallels. To model the a-c response we make use of the analogy between diffusion and the GC transmission line with series conductance G and shunt capacitance C per unit length. The characteristic impedance and propagation constant of this line are related to diffusional parameters by

$$Z = (i\omega CG)^{-1/2} = 1/(i\omega)^{1/2}W \qquad [14]$$

$$\gamma = (i\omega C/G)^{1/2} = (i\omega D)^{1/2}$$

Consider the input impedance of a transmission line composed of an input segment, length d, with parameters γ_s and Z_s terminated by an infinite line with impedance Z_o

$$Z^* = Z_s(Z_o + Z_s \tanh \gamma_s d)/(Z_s + Z_o \tanh \gamma_s d) \qquad [15]$$

The input or surface line elements are enhanced by the roughness factor so that $C_s = sC_o$ and $G_s = sG_o$ or $Z_s = Z_o/s$ and $\gamma_s = \gamma_o$.

The solution for the complex capacitance becomes

$$C^* = (i\omega Z^*)^{-1} = s(i\omega)^{-1/2}W$$

$$[s - (s^2 - 1)/(s + \tanh (i\omega\tau)^{1/2})] \qquad [16]$$

where $D\tau = d^2$. At high frequencies $C^* = sW/(i\omega)^{1/2}$, while at low frequencies

$$C^* = (i\omega)^{-1/2}W + (s - 1/s)W\tau^{1/2} + \ldots \qquad [17]$$

Although this inhomogeneous transmission line model is necessarily simplified, it does exhibit the asymptotic behaviors expected as $\omega \to 0, \infty$, $d \to 0$, and $s \to 1$. Normalized C^* plots in Fig. 13 illustrate the changes to be seen in the complex plane as the Warburg coefficient shifts between its micro- and macrolimits.

The abrupt transition postulated overstates the case and tapered transitions will broaden the transition region. We feel, however, this elementary model suffices

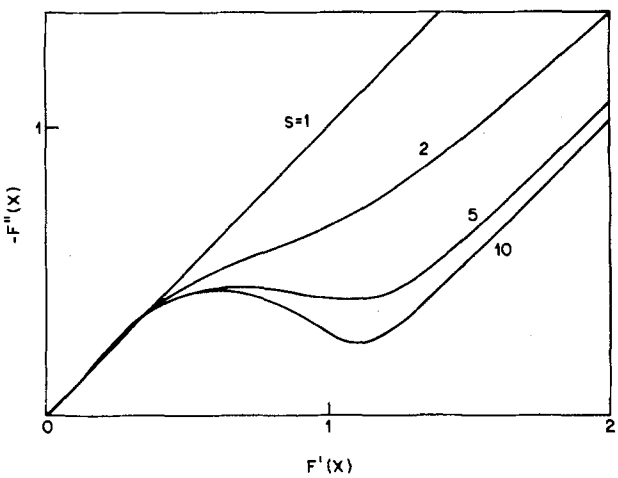

Fig. 13. The influence of surface roughness, s, and concentration polarization on the shape of C^* plots according to the inhomogeneous transmission line model. Plotted is the normalized function $F^* = (W/s\sqrt{\gamma})C^*$.

to illustrate some general expectations. In particular, roughness increases the intercept obtained by extrapolation of the low frequency asymptote. This increase is a direct measure of the number of diffusing ions within the roughness layer. For a 14 mM Sn^{++} solution at −30 mV, c(0) is reduced to 1.4 mM and, for $s = 2$ and $d = 500$Å, the added capacitance is 160 μF/cm^2.

Examination of results for numerous experiments at different concentrations and potentials revealed only one instance in which the extrapolated capacitance intercept lay outside the range 50-100 μF/cm^2 and this result was not reproduced within the same experimental sequence. The 550 μF/cm^2 value corresponded to a roughness length of 180Å for $s = 2$ (Eq. [17]). This length represents a weighted average over a distribution of parallel diffusion paths and not necessarily a peak-to-valley separation. The weighting function depends on a more explicit model for surface contours, but should be dominated by contributions from microsurface regions of greatest concentration gradients, *i.e.*, near asperities.

The foregoing picture presumes uniform charge transfer across the microsurface. If, instead, current sources and sinks are localized, resistive effects arise from concentration polarization at these sites (25). The concentration perturbation in the vicinity of a point source is given by (26)

$$i\omega c^* = \frac{D}{r^2}\frac{\partial}{\partial r}\left(r^2\frac{\partial c^*}{\partial r}\right) \qquad [18]$$

with the solution

$$c^*(r) = c^*(a)(a/r)\exp[-(i\omega/D)^{1/2}(r - a)] \qquad [19]$$

where $c^*(a)$ is the boundary value at an idealized inner spherical surface of radius a. The current modulation for a hemispherical source equals

$$I^* = -z\mathbf{F}D(2\pi a^2)\left(\frac{\partial c^*}{\partial r}\right)_{r=a} \qquad [20]$$

and the corresponding admittance becomes

$$Y^* = (z^2e\mathbf{F}D/kT)(2\pi a)c(0)[1 + (i\omega/D)^{1/2}a]N \qquad [21]$$

where N is the surface density of sources. At very high frequencies Y^* varies as $(i\omega)^{1/2}$ but, for lower frequencies permitting diffusion over distances greater than a, Y^* turns into a resistive element. Provided the separation of sources is sufficient, the admittance remains resistive until diffusion in the macroscopic Nernst layer becomes the limiting factor. If d is the effective separation, $N = 1/d^2$, then minimally $d > 4a$.

For our result $G \simeq 10^3$ mho/cm^2 at $c = 10$ mM, Eq. [21] gives $d^2/a = 6.6 \times 10^{-6}$ cm, or for $a = 5$-10Å, $d = 60$-80Å. There thus appears to be a marginal numerical window to support the hypothesis that the apparent exchange current is a limiting current due to a high density of spherical diffusion zones on the microsurface. This model has been invoked on a macroscale for cadmium deposition (27).

The advantages of this interpretation are an explanation of the parallel potential dependences of G and the surface concentration, the involvement of surface morphology, and the avoidance of an independent kinetic surface process such as charge transfer. The difficulties are the absence of roughness effects is still unexplained, *i.e.*, the macroscopic Warburg coefficient remains constant to high frequencies, and the model is specific to point-like sources. The former objection may be qualitatively surmounted by noting that roughness deviations in C^* plots lie in the opposite direction to those for localized concentration polarizations.

A hemicylindrical or line source does not analytically lead to resistive limiting behavior but may appear to do so for practical purposes. For this case the expression equivalent to Eq. [21] is

$$Y^* = (z^2e\mathbf{F}/kT)\,(i\omega D)^{1/2}c(0)\pi L K_1(x)/K_0(x) \quad [22]$$

where $x = (i\omega a^2/D)^{1/2}$, L is the total length of sources per unit area, and K_η's, are modified Bessel functions. At low frequencies ($x << 1$)

$$Y^* = (z^2e\mathbf{F}/kT)\,Dc(0)\pi L[-2/\ln\,(i\omega a^2/D)] \quad [23]$$

For $a = 5$Å, the modulus of the last factor varies only 0.13-0.23 for frequencies 10^2-10^5, while the phase angle ranges 5°-10°, so the admittance is approximately resistive. Our value for G then gives $L = 1.6 \times 10^6$ cm/cm^2, suggesting linear source spacings of 100-200Å.

If the point polarization interpretation is extended to the PEG solutions, the additive effect must be to reduce the density of active sites to $d \simeq 10^3$Å, a distance commensurate with film thickness. This conclusion need not imply deposition only at such remote sites. Should the kinetics for the creation and annihilation of growth sites be independent of potential, the a-c measurement will be uncorrelated with these fluctuations and respond only to their mean value. Further, lattice growth during the diffusion period will move the growth site, and the effective value for a which best describes the polarization configuration should be larger than atomic dimensions.

A definitive model for tin deposition cannot be deduced from present experimental data and an alternative interpretation to the localized concentration polarization model cannot be ruled out. The potential dependence of G could be attributed to an unusual charge-transfer step, $\alpha \simeq 0$, but a rate-limiting step prior to charge transfer seems preferable. As one possibility a surface disproportionation reaction

$$Sn^{++} + Sn \rightleftharpoons 2[Sn(I)]_s \quad [24]$$

involving a monovalent tin species followed by a rapid charge-transfer step is technically consistent if the surface species concentration varies as exp $(e\eta/kT)$. This model, however, also predicts a pseudocapacitance, $C = (e\mathbf{F}/kT)\,[Sn(I)]_s$, not evident in our measurements. If $C < 50$ μF/cm^2, then $[Sn(I)]_s < 10^{-11}$ M/cm^2. Rate limitation due to reactions following the charge-transfer step, on the other hand, does not lead to the experimental potential dependence, ruling out adatom processes.

The alteration of the potential dependence of the rate-limiting step by a bulk surface film suggests a modification of the surface potential gradient, bringing the limiting barrier within the electrically polarized region. One may conjecture that the film reduces the surface potential gradient so that the energy of an intermediate within the film becomes an explicit function of potential. The test of this hypothesis requires more reproducible methods for controlling film development and thickness before meaningful quantitative results can be obtained.

Reconciliation of our results, particularly the null transfer coefficient, with previous studies generally reporting values of 0.4-0.6 raises awkward questions. Our results are based on perturbations of the electrode under steady-state polarization conditions at specified overpotentials. Surface conditions may differ from those following a large potential jump to this potential from equilibrium, apart from macroscopic concentration polarization differences. Impurity effects in our work seem an unlikely explanation in as much as we find exchange current densities for 10 mM solutions considerably greater than those reported at even higher concentrations, and double-layer capacitance values rule out anomalous microsurface areas.

A direct comparison with amalgam studies may be inappropriate because of differences in Sn° activity and morphology. In acid chloride solutions the basic chloride has been predicted to be thermodynamically stable in the potential range for tin deposition (28), and aging effects ascribed to the formation of such a film have been reported (8). We note that plots for measurements with surface films present lead to finite α-values, *i.e.*, for Fig. 12 $\alpha = 0.38$. Continued aging would decrease this slope and the value at $\eta = 0$, leading to an exchange current density and transfer coefficient in better agreement with published data.

Summary

At long times tin deposition is limited by diffusion of stannous ions in the electrolyte phase. At shorter times the process is limited by a resistive step which appears to be similar whether or not additives are present, although the additive PEG reduces the rate by factors of 100-1000. The potential dependence of this rate, equivalent to a null transfer coefficient, is not that expected for conventional charge-transfer processes and implies a barrier on the electrolyte side of the Helmholtz layer, with the cathodic partial current being directly proportional to the surface concentration of Sn^{++}. Localized concentration polarization zones at discrete growth sites are consistent with this potential dependence. No direct evidence, such as a large pseudocapacitance, indicates the existence of surface intermediates. Additive effects are most easily explained by large reductions in the density of available growth sites, and the irreversible formation of surface oxides may be responsible for the variability of literature results.

Manuscript submitted June 17, 1982; revised manuscript received *ca.* Sept. 13, 1982.

Any discussion of this paper will appear in a Discussion Section to be published in the December 1983 JOURNAL. All discussions for the December 1983 Discussion Section should be submitted by Aug. 1, 1983.

Publication costs of this article were assisted by Bell Laboratories.

REFERENCES

1. Z. Galus, in "Encyclopedia of Electrochemistry of the Elements," Vol. IV, A. J. Bard, Editor, Marcel Dekker, New York (1975).
2. G. G. Kostryukova, O. I. Ratkov, V. A. Kazakov, A. M. Ginberg, and A. T. Vagramyan, *Elektrokhimiya*, **5**, 571 (1969).
3. J. Amose, P. Carle, and M-J. Barbier, *C.R. Acad. Sci., Paris*, **268C**, 784 (1969).
4. A. Kozlowska, P. K. Wrona, and Z. Galus, *Bull. Acad. Pol. Sci., Ser. Sci. Chim.*, **22**, 917 (1974).
5. R. Tunold and A. Broli, *Corros. Sci.*, **13**, 361 (1973).
6. V. V. Gorodetskii, I. P. Slutskii, K. A. Mishenina, and V. V. Losev, *Elektrokhimiya*, **12**, 1798 (1976).
7. B. N. Stirrup and N. A. Hampson, *J. Electroanal. Chem. Interfacial Electrochem.*, **67**, 57 (1976).
8. B. N. Stirrup and N. A. Hampson, *J. Appl. Electro-*

chem., 6, 353 (1976).
9. S. Meibuhr, E. Yeager, A. Kozawa, and F. Hovorka, *This Journal*, **110**, 190 (1963).
10. V. V. Gorodetskii, I. P. Slutskii, and V. V. Losev, *Elektrokhimiya*, **8**, 1401 (1972).
11. I. P. Slutskii, V. V. Gorodetskii, and V. V. Losev, *ibid.*, **13**, 205 (1977).
12. S. H. Glarum and J. H. Marshall, *This Journal*, **128**, 968 (1981).
13. J. E. B. Randles, *Discuss. Faraday Soc.*, **1**, 11 (1947).
14. C. Deslouis, I. Epelboin, M. Keddam, and J. C. Lestrade, *J. Electroanal. Chem. Interfacial Electrochem.*, **28**, 57 (1970).
15. D. A. Scherson and J. Newman, *This Journal*, **127**, 110 (1980).
16. K. Tokuda and H. Matsuda, *J. Electroanal. Chem. Interfacial Electrochem.*, **82**, 157 (1977); **90**, 149 (1978); **95**, 147 (1979).
17. R. D. Armstrong, M. F. Bell, and A. A. Metcalfe, "Electrochemistry—Spec. Period, Rpts.," Vol. 6, The Chemical Society, London (1978).
18. P. A. Kohl, *This Journal*, **129**, 1196 (1982).
19. A. Vincente and S. Bruckenstein, *Anal. Chem.*, **44**, 297 (1972).
20. H. P. Agarwal and S. Qureshi, *Electrochim. Acta*, **21**, 465 (1976).
21. C. A. Wamser, *J. Am. Chem. Soc.*, **70**, 1209 (1948).
22. A. M. Bond and R. J. Taylor, *J. Electroanal. Chem. Interfacial Electrochem.*, **28**, 207 (1970).
23. M. Pourbaix, "Atlas of Electrochemical Equilibria," Pergamon, London (1966).
24. R. de Levie, *Electrochim. Acta*, **10**, 113 (1965).
25. M. Fleischmann and J. A. Harrison, *ibid.*, **11**, 749 (1966).
26. H. Gerischer, *Z. Phys. Chem.*, **198**, 286 (1951).
27. J. A. Harrison and D. R. Sandbach, *J. Electroanal. Chem. Interfacial Electrochem.*, **85**, 125 (1977).
28. T. D. Hoar, *Trans. Faraday Soc.*, **33**, 1152 (1937).

A Model of the Bromine/Bromide Electrode Reaction at a Rotating Disk Electrode

R. E. White* and S. E. Lorimer*

Department of Chemical Engineering, Texas A&M University, College Station, Texas 77843

ABSTRACT

A mathematical model is presented for the Br_2/Br^- electrode reaction at a rotating disk electrode. The model includes current density-overpotential expressions for the electrode reaction according to either the Volmer-Heyrovsky (V-H) or the Volmer-Tafel (V-T) mechanism and the transport equations including the effect of ionic migration. The model is used to predict current-overpotential curves for various cases of interest. Qualitative comparison of the model predictions to literature data shows that either the V-H or the V-T mechanism, with V controlling, may be acceptable for the Br_2/Br^- reaction.

Table I presents a summary of the investigations of the kinetics of the Br_2/Br^- electrode reaction. The three mechanisms that have been proposed frequently are the Volmer-Heyrovsky (V-H), Volmer-Tafel (V-T), and the Heyrovsky-Tafel (H-T), which can be written as follows

V-H mechanism

$$(V) \quad Br^- \rightleftarrows Br_{ads} + e^- \qquad [1]$$

$$(H) \quad Br_{ads} + Br^- \rightleftarrows Br_2 + e^- \qquad [2]$$

V-T mechanism

$$(V) \quad 2(Br^- \rightleftarrows Br_{ads} + e^-) \qquad [3]$$

$$(T) \quad 2Br_{ads} \rightleftarrows Br_2 \qquad [4]$$

H-T mechanism

$$(H) \quad 2(Br_2 + e^- \rightleftarrows Br^- + Br_{ads}) \qquad [5]$$

$$(T) \quad 2Br_{ads} \rightleftarrows Br_2 \qquad [6]$$

Table I includes the kinetic mechanism(s) proposed by each group, the type of electrode material, and the technique used to determine the kinetics. Also included in the table are comments concerning each group's approach to handling the tribromide ion formation reaction

$$Br_2 + Br^- \underset{k_b}{\overset{k_f}{\leftrightarrows}} Br_3^- \qquad K_{eq} = \frac{k_f}{k_b} \qquad [7]$$

and assumptions made concerning the degree of coverage of the electrode surface with adsorbed bromine (θ) or the rate of adsorption-desorption processes.

Essentially, four different methods have been used to study the kinetics of the Br_2/Br^- electrode reaction. The four methods are: galvanostatic or potentiostatic, impedance, preexponential factor, and coulostatic. Three groups (1, 2, and 3, see Table I) used current density-potential curves produced either galvanostatically or potentiostatically to study the Br_2/Br^- reaction. The kinetic mechanism was selected by comparing the experimentally determined slopes of Tafel curves and reaction orders to those values predicted for each possible electrode kinetic mechanism. Three other groups (4, 5, and 6) measured the impedance of the electrode as a function of the frequency of an applied alternating current and used this to determine the exchange current density. They then determined the dependence of the exchange current density on concentration and overpotential to select the electrode kinetic mechanism. Allard and Parsons (7) used experimentally determined values of the preexponential factor to study Br_2/Br^- electrode kinetics. The order of magnitude of the experimental value of the preexponential factor, which can be determined from measurements of the exchange current density at

Table IA. Summary of Br_2/Br^- kinetic studies

Investigator(s)	Technique	Electrode
1. Osipov *et al.* (1)	Potentiostatic	Platinum RDE
2. Janssen and Hoogland (2)	Galvanostatic	Graphite Stationary
3. Faita, Fiori, and Mussini (3)	Potentiostatic	Platinized Ti RDE
4. Llopis and Vazquez (4)	Impedance	Platinum Stationary
5. Cooper and Parsons (5)	Impedance	Platinum RDE
6. Albery *et al.* (6)	Impedance	Platinum RRDE
7. Allard and Parsons (7)	Preexponential	Platinum RDE
8. Rubinstein (8)	Coulostatic	Platinum Stationary

* Electrochemical Society Active Member.
Key words: battery, migration.

Table 1B. Summary of Br_2/Br^- kinetic studies

Investigator(s)	Proposed mechanism	Rate-controlling step	Comments
1	V-H	Both equally	Ignored tribromide ion formation and adsorption effects
2	V-H	V	Ignored tribromide ion formation; included surface coverage
3	V-H	Both equally	Low surface coverage assumed; ignored tribromide ion formation
4	Slightly modified H-T	H	Ignored tribromide ion formation; experimental data indicated adsorption did not effect electrode reaction rate
5	V-H or V-T (Low surface coverage)	V	Ignored tribromide ion formation
	V-T or H-T (High surface coverage)	T	
6	V-H or V-T	V	Reaction thought to occur in sparsely filled second layer on top of an electrode surface completely covered with a layer of unreactive bromine atoms.
7	V-T	V	Corrections made for tribromide ion formation; estimate made of the degree of surface coverage
8	V-T or V-H (Oxidized electrodes)	V	Used a combined isotherm approach to account for adsorption
	Slightly modified V-T or V-H (Reduced electrodes)	V	

different temperatures, was then used to identify the rate-determining step of various mechanisms. Rubinstein (8) used the coulostatic method which consists of charge injection followed by an open-circuit transient analysis to obtain the kinetic parameters. As before, these parameters are then compared to those predicted by the proposed mechanisms to determine acceptable mechanisms.

As can be seen from Table I, no single electrode kinetic mechanism is supported by all of the investigators. The V-H and V-T mechanisms are, however, suggested more often than the H-T mechanism. Table I also shows that most workers neglected the formation of tribromide ion. This is unfortunate because at the very least this causes confusion concerning the bulk concentrations of the reacting species (Br_2 and Br^-). Finally, Table I entries and other studies reveal that considerable confusion exists over the role of adsorbed bromine in the electrode reaction. Equilibrium values for the degree of coverage of platinum surfaces with adsorbed bromine indicate that as many as 55-60% of the available adsorption sites are covered (9, 10). Also, bromine is known to be strongly chemisorbed on platinum (11-13). On the other hand, the values of the preexponential factor for the bromine electrochemical reaction measured by Allard and Parsons (7) indicate that the degree of surface coverage is low and that the adsorbed species has a high degree of mobility across the electrode surface. Also, the impedance measurements made by Llopis and Vazquez (4) indicated that the rate of the bromine/bromide reaction is not affected by adsorption. To explain these apparently conflicting results, Allard and Parsons (7) proposed that the electrode reaction involves a loosely adsorbed reactive bromine species existing in a sparsely filled layer on top of a layer of unreactive bromine adsorbed directly on the electrode surface. Albery *et al.* (6) and Rubinstein (8) support this proposal.

It is clear that there is still uncertainty concerning the Br_2/Br^- electrode reaction. The kinetic mechanism and associated issues such as the effect of the homogeneous tribromide formation reaction and the role of adsorption-desorption processes in the electrode reaction are still unresolved.

A model is presented here which may be useful for analysis of potentiostatic RDE data. The model includes rate expressions for either the V-H or the V-T mechanisms and is used here to predict current-potential curves for both mechanisms for various cases of interest.

Model

Figure 1 presents a schematic of the RDE system in which the position of the reference electrode is shown. The model presented here consist of current-overpotential expressions for either the V-H or the V-T mechanisms, the transport equations, and the boundary conditions for the RDE system. The model is presented by first listing the assumptions and then the equations.

Assumptions

1. The rates of the individual steps in each of the reaction mechanisms are equal (*i.e.*, $i_V = i_H$ and $i_V = i_T$). Also, for the V-H mechanism, $i = i_V + i_H$ and for V-T mechanism, $i = i_V = i_T$ (14).
2. The double layer is ignored by assuming that it is infinitely thin.
3. Equilibrium adsorption of the adsorbed bromine (Br_{ads}) follows the Langmuir isotherm and is very small ($\theta_o << 1$).
4. The rates of the adsorption-desorption process are rapid enough to not interfere with the rates of the charge transfer steps.
5. The electrolyte is an ideal solution (*i.e.*, concentrations instead of activities are used).
6. Infinitely dilute solution theory (15) applies.
7. The RDE is an equipotential electrode and is uniformly accessible.
8. Steady-state conditions exist.
9. Isothermal conditions exist.

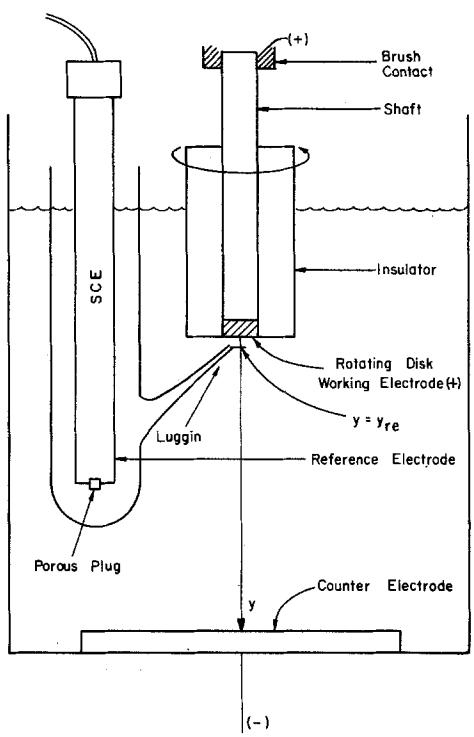

Fig. 1. Schematic of a rotating disk electrode system

10. The electrolyte is Newtonian and the physical and transport properties are constants.
11. The Nernst-Einstein equation ($u_i = D_i/RT$) is a valid approximation.
12. The reaction orders are given by the stoichiometry of the individual steps of the overall reaction.

Kinetic Equations

The above assumptions and the rate expressions given by Jansson and Hoogland (14) for the Cl_2/Cl^- electrode reaction can be used to derive current density-potential expressions for the V-H and V-T mechanisms, as discussed by Lorimer (16). Essentially the method consists of using assumption 1 to obtain an expression for the current density i for each mechanism which depends on, among other things, the surface coverage and the equilibrium surface coverage of adsorbed bromine atoms. These equations can then be simplified by using assumption 3. The resulting expressions for the V-H and V-T mechanisms are as follows

V-H mechanism

$$i = 2i_{\text{Oref,H}} \exp\left(\frac{(1+\alpha_H)\mathbf{F}}{RT}(\Phi_{\text{met}} - \Phi_o - U_{\text{ref}})\right) \times \frac{\left[\left(\frac{c_{\text{Br}^-,o}}{c_{\text{Br}^-,\text{ref}}}\right)^2 - \left(\frac{c_{\text{Br}_2,o}}{c_{\text{Br}_2,\text{ref}}}\right)\exp\left(\frac{-2\mathbf{F}}{RT}(\Phi_{\text{met}} - \Phi_o - U_{\text{ref}})\right)\right]}{\left[1 + \frac{i_{\text{Oref,H}}}{i_{\text{Oref,V}}}\left(\frac{c_{\text{Br}^-,o}}{c_{\text{Br}^-,\text{ref}}}\right)\exp\left(\frac{(1-\alpha_V+\alpha_H)\mathbf{F}}{RT}(\Phi_{\text{met}} - \Phi_o - U_{\text{ref}})\right)\right]} \quad [8]$$

V-T mechanism

$$i = A + \left[A^2 - \left(i_{\text{Oref,V}}\left(\frac{c_{\text{Br}^-,o}}{c_{\text{Br}^-,\text{ref}}}\right)\exp\left(\frac{\alpha_V\mathbf{F}}{RT}(\Phi_{\text{met}} - \Phi_o - U_{\text{ref}})\right)\right)^2 + \left(i_{\text{Oref,V}}\left(\frac{c_{\text{Br}_2,o}}{c_{\text{Br}_2,\text{ref}}}\right)^{1/2}\exp\left(\frac{-(1-\alpha_V)\mathbf{F}}{RT}\right)(\Phi_{\text{met}} - \Phi_o - U_{\text{ref}})\right)^2\Bigg]^{1/2} \quad [9]$$

where

$$A = i_{\text{Oref,V}}\left(\frac{c_{\text{Br}^-,o}}{c_{\text{Br}^-,\text{ref}}}\right)\exp\left(\frac{\alpha_V\mathbf{F}}{RT}(\Phi_{\text{met}} - \Phi_o - U_{\text{ref}})\right) + \left(\frac{i_{\text{Oref,V}}}{2i_{\text{Oref,T}}}\right)^2\exp\left(\frac{-2(1-\alpha_V)\mathbf{F}}{RT}(\Phi_{\text{met}} - \Phi_o - U_{\text{ref}})\right) \quad [10]$$

The exchange current densities ($i_{\text{Oref,H}}$, $i_{\text{Oref,V}}$, and $i_{\text{Oref,T}}$) are based on the reference concentrations used in the analysis. These reference exchange current densities are the values that would be obtained from comparison of the predicted and experimental current density-potential curves. Once values for $i_{\text{Oref,j}}$ have been determined they can be adjusted to a standard electrolyte composition by using the following expression

$$i_{\text{Ostd,j}} = i_{\text{Oref,j}} \prod_i \left(\frac{c_{i,\text{std}}}{c_{i,\text{ref}}}\right)^{\gamma_{ij}} \quad [11]$$

where the values of γ_{ij} used here are based on the stoichiometry of the reactions (15, 16) and are presented in Table II. (Even though Br_2 does not participate in the Volmer reaction, Eq. [1], a value for $\gamma_{\text{Br}_2,\text{V}}$, as given in Table II, arises because of the use of assumption 3 in the derivation of Eq. [8] and [9]). The open-circuit potential U_{ref} is based on the reference concentrations and is given by

Table II. Concentration dependence of the exchange current densities

Reaction j	Species i	γ_{ij}
V	Br^-	$1 - \alpha_V$
V	Br_2	$\alpha_V/2$
H	Br^-	$1 - \alpha_H$
H	Br_2	$(1 + \alpha_H)/2$
T	Br^-	0
T	Br_2	1

$$U_{\text{ref}} = U^\theta - U^\theta_{\text{re}} - \frac{RT}{n\mathbf{F}}\sum_i s_i \ln\left(\frac{c_{i,\text{ref}}}{\rho_o}\right) + \frac{RT}{n_{\text{re}}\mathbf{F}}\sum_i s_{i,\text{re}} \ln\left(\frac{c_{i,\text{re}}}{\rho_o}\right) \quad [12]$$

where $c_{i,\text{re}}$ represents the concentration of species i in the reference electrode compartment and both $c_{i,\text{ref}}$ and $c_{i,\text{re}}$ must be in mols/liter in Eq. [12]. This dependence of the open-circuit potential on the reference concentration instead of the surface concentration arises naturally in the derivation of Eq. [8] and [9] due to the concentration dependence of the exchange current density. Also, it should be pointed out that U_{ref} is for the overall reaction ($2Br^- \rightleftarrows Br_2 + 2e^-$).

The above current density-potential expressions can be simplified by assuming that one of the steps is rate controlling or that both steps proceed at approximately the same rate. Table III presents the simplified forms of the rate equations where

$$\eta_{\text{ref}} = \Phi_{\text{met}} - \Phi_o - U_{\text{ref}} \quad [13]$$

Entries IA and IB can be obtained by considering the denominator of Eq. [8]. For $i_{\text{Oref,H}} >> i_{\text{Oref,V}}$ and $|\eta_{\text{ref}}| \leq \sim 0.1$V the term containing the exponential is large relative to one; however, when $|\eta_{\text{ref}}| \geq \sim 0.1$V, the term containing the exponential is small relative to one. The reason for this depends on whether η_{ref} is negative or positive. When η_{ref} is negative and is made to be more and more negative, eventually the exponential becomes so small that the entire term is small relative to one. On the other hand, if η_{ref} is positive and is made more positive, eventually the surface concentration of the bromide ion ($c_{\text{Br}^-,o}$) becomes so small that the entire term is small relative to one, assuming, of course, that the bromide ion is not present in the electrolyte in abundance. The kinetic parameters from these simplified forms are presented for convenience in Table IV and V for cathodic and anodic values of η_{ref}, respectively.

These simplified equations and parameters are presented for completeness and to aid in understanding the system. However, the simplified equations are not necessary for determination of the kinetic rate constants. Again, the kinetic rate constants should be determined by comparison of the experimental data (current density at a set potential difference between the RDE and a reference electrode) to predicted values from the complete expressions.

Transport Equations

The steady state, no homogeneous reaction material balance equation for species i is (15)

Table III. Simplified forms of the V-H and V-T current density expressions for limiting cases

I. Volmer-Heyrovsky mechanism (Eq. [8])

A. Volmer reaction rate controlling, low η_{ref} ($i_{oref,H} >> i_{oref,V}$, $|\eta_{ref}| \leq \sim 0.1V$)

$$i = 2i_{oref,V}\left[\left(\frac{c_{Br^-,O}}{c_{Br^-,ref}}\right)\exp\left(\frac{\alpha_V F}{RT}\eta_{ref}\right) - \left(\frac{c_{Br_2,O}}{c_{Br_2,ref}}\right)\left(\frac{c_{Br^-,O}}{c_{Br^-,ref}}\right)^{-1}\exp\left(\frac{-(2-\alpha_V)F}{RT}\eta_{ref}\right)\right]$$

B. Volmer reaction rate controlling, high η_{ref} ($i_{oref,H} >> i_{oref,V}$, $|\eta_{ref}| \geq \sim 0.1V$)

$$i = 2i_{oref,H}\left[\left(\frac{c_{Br^-,O}}{c_{Br^-,ref}}\right)^2\exp\left(\frac{(1+\alpha_H)F}{RT}\eta_{ref}\right) - \left(\frac{c_{Br_2,O}}{c_{Br_2,ref}}\right)\exp\left(\frac{-(1-\alpha_H)F}{RT}\eta_{ref}\right)\right]$$

C. Heyrovsky reaction rate controlling ($i_{oref,V} >> i_{oref,H}$)

$$i = 2i_{oref,H}\left[\left(\frac{c_{Br^-,O}}{c_{Br^-,ref}}\right)^3\exp\left(\frac{(1+\alpha_H)F}{RT}\eta_{ref}\right) - \left(\frac{c_{Br_2,O}}{c_{Br_2,ref}}\right)\exp\left(\frac{-(1-\alpha_H)F}{RT}\eta_{ref}\right)\right]$$

D. Both reactions approximately equally rate controlling ($i_{oref,V} \approx i_{oref,H}$)

1. Cathodic overpotential (anodic back reaction neglected)

$$i = -2i_{oref,H}\left(\frac{c_{Br^-,O}}{c_{Br^-,ref}}\right)\exp\left(\frac{(1+\alpha_H)F}{RT}\eta_{ref}\right)$$

2. Anodic overpotential (cathodic back reaction neglected)

$$i = 2i_{oref,V}\left(\frac{c_{Br^-,O}}{c_{Br,ref}}\right)\exp\left(\frac{\alpha_V F}{RT}\eta_{ref}\right)$$

II. Volmer-Tafel mechanism (Eq. [9] and [10])

A. Volmer reaction rate controlling ($i_{oref,T} >> i_{oref,V}$)

$$i = i_{oref,V}\left[\left(\frac{c_{Br^-,O}}{c_{Br^-,ref}}\right)\exp\left(\frac{\alpha_V F}{RT}\eta_{ref}\right) - \left(\frac{c_{Br_2,O}}{c_{Br_2,ref}}\right)^{1/2}\exp\left(\frac{-(1-\alpha_V)F}{RT}\eta_{ref}\right)\right]$$

B. Tafel reaction rate controlling ($i_{oref,V} >> i_{oref,T}$)

$$i = i_{oref,T}\left[\left(\frac{c_{Br^-,O}}{c_{Br^-,ref}}\right)^2\exp\left(\frac{2F}{RT}\eta_{ref}\right) - \left(\frac{c_{Br_2,O}}{c_{Br_2,ref}}\right)\right]$$

C. Both reactions approximately equally rate controlling ($i_{oref,V} \approx i_{oref,T}$)

1. Cathodic overpotentials (anodic back reaction neglected)
No simplified form of the V-T current density expression is available for this case except near limiting current where

$$i = -i_{oref,T}\left(\frac{c_{Br_2,O}}{c_{Br_2,ref}}\right)$$

2. Anodic overpotentials (cathodic back reaction neglected)

$$i = i_{oref,V}\left(\frac{c_{Br^-,O}}{c_{Br^-,ref}}\right)\exp\left(\frac{\alpha_V F}{RT}\eta_{ref}\right)$$

$$-\frac{dN_i}{dy} = 0 \qquad [14]$$

where N_i is the flux of species i. The flux of species i occurs by three mass transfer processes: ionic migration, diffusion, and convection and is given by

$$N_i = -z_i\frac{D_i F c_i}{RT}\frac{d\Phi}{dy} - D_i\frac{dc_i}{dy} + v_y c_i \qquad [15]$$

Newman (15), for example, shows that at high Schmidt numbers, the component of fluid velocity in

Table IV. Electrode kinetic parameters from simplified forms of current density expressions for cathodic η_{ref}

Kinetic mechanism	Rate-determining step	2.303 / Tafel slope (in volts)	Tafel line intercept	Reaction orders q_{Br_2}	Reaction orders q_{Br^-}
V-H	Volmer, $-\eta_{ref} \leq \sim 0.1V$	$\frac{(2-\alpha_V)F}{RT}$	$2i_{oref,V}$	1	−1
	Volmer, $-\eta_{ref} \geq \sim 0.1V$	$\frac{(1-\alpha_H)F}{RT}$	$2i_{oref,H}$	1	0
	Heyrovsky	$\frac{(1-\alpha_H)F}{RT}$	$2i_{oref,H}$	1	0
	Approximately equal	$\frac{(1-\alpha_H)F}{RT}$	$2i_{oref,H}$	1	0
V-T	Volmer	$\frac{(1-\alpha_V)F}{RT}$	$i_{oref,V}$	½	0
	Tafel	0	$i_{oref,T}$	1	0
	Approximately equal	0	$i_{oref,T}$	1	0

Table V. Electrode kinetic parameters from simplified forms of current density expressions for anodic η_{ref}

Kinetic mechanism	Rate determining step	2.303 / Tafel slope (in volts)	Tafel line intercept	Reaction orders p_{Br_2}	Reaction orders p_{Br^-}
V-H	Volmer, $\eta_{ref} \leq \sim 0.1V$	$\frac{\alpha_V F}{RT}$	$2i_{oref,V}$	0	1
	Volmer, $\eta_{ref} \geq \sim 0.1V$	$\frac{(1+\alpha_H)F}{RT}$	$2i_{oref,H}$	0	2
	Heyrovsky	$\frac{(1+\alpha_H)F}{RT}$	$2i_{oref,H}$	0	2
	Approximately equal	$\frac{\alpha_V F}{RT}$	$2i_{oref,V}$	0	1
V-T	Volmer	$\frac{\alpha_V F}{RT}$	$i_{oref,V}$	0	1
	Tafel	$\frac{2F}{RT}$	$i_{oref,T}$	0	2
	Approximately equal	$\frac{\alpha_V F}{RT}$	$i_{oref,V}$	0	1

the directional normal to the electrode surface is given by

$$v_y = -a\Omega(\Omega/\nu)^{1/2}y^2 \quad [16]$$

where y is the distance from the electrode into the electrolyte in a direction normal to the electrode surface. This coordinate can be rewritten in dimensionless form as

$$\xi = y\left(\frac{\nu_a}{3D_R}\right)^{1/3}\left(\frac{\Omega}{\nu}\right)^{1/2} \quad [17]$$

or

$$\xi = y/\delta_D \quad [18]$$

where δ_D is the diffusion layer thickness and is given by

$$\delta_D = \left(\frac{3D_R}{\nu_a}\right)^{1/3}\left(\frac{\nu}{\Omega}\right)^{1/2} \quad [19]$$

Substitution of Eq. [15], [16], and [18] into Eq. [14] yields

$$D_i\frac{d^2c_i}{d\xi^2} + 3D_R\xi^2\frac{dc_i}{d\xi} + \frac{z_iD_iF}{RT}\left[c_i\frac{d^2\Phi}{d\xi^2} + \frac{dc_i}{d\xi}\frac{d\Phi}{d\xi}\right] = 0 \quad [20]$$

which is the material balance equation used here for species i. The electroneutrality condition

$$\sum_i z_ic_i = 0 \quad [21]$$

completes the set of i + 1 equations to be solved subject to the boundary conditions to obtain c_i and Φ.

Boundary Conditions in the Bulk Solution

Bulk solution conditions are assumed to exist at $y = y_{re}$ where y_{re} is the normal distance from the RDE to the reference electrode (see Fig. 1). The concentration of species i in the bulk solution is designated as $c_{i,ref}$ and the potential in the bulk solution at $y = y_{re}$ is designated as Φ_{re}.

Thus, the boundary conditions in the bulk solution are:

at $y = y_{re}$

$$c_i = c_{i,ref} \quad [22]$$

$$\Phi = \Phi_{re} = \text{a set value (0.01V, } e.g.\text{)} \quad [23]$$

where $c_{i,ref}$ must satisfy the electroneutrality condition (Eq. [21]).

Boundary Conditions at the Electrode Surface

The boundary conditions at the electrode surface are as follows:

at $y = 0$

$$\frac{s_ii}{nF} = -N_i \quad [24]$$

$$\sum_i z_ic_i = 0 \quad [25]$$

$$\Phi_{met} = \text{a set value (0.1V, } e.g.\text{)} \quad [26]$$

where N_i is given by Eq. [15] with $v_y = 0$ and i is given by either Eq. [8] or [9].

The potentials in the boundary conditions given by Eq. [23] and [26] are shown schematically in Fig. 2 for a rotating disk electrode being operated anodically. Note that the potential difference between the working electrode and the reference electrode ($\Phi_{met} - \Phi_{re}$) is the quantity set by a potentiostat. In the model, however, both Φ_{met} and Φ_{re} are set independently such that their difference is equal to that set by the potentiostat.

Solution Technique

The i + 1 set of governing equations for c_i and Φ (Eq. [20] and [21]) can be solved numerically subject to the boundary conditions (Eq. [22]-[26]) once values have been specified for the following parameters: $c_{i,ref}$, D_i, ρ_o, ν, T, U^θ, s_i, n, type of reference electrode, $s_{i,re}$, $c_{i,re}$, y_{re}, $i_{Oref,j}$, α_V, α_H, (if necessary) Ω, and Φ_{met}, and Φ_{re} (again, only $\Phi_{met} - \Phi_{re}$ is important). Newman's (15) numerical technique [see also White (17)] can be used to solve this set of equations which yields values for the variable quantities Φ_o, $c_{Br^-,o}$, and $c_{Br_2,o}$. These values together with either Eq. [8] or [9] and the values for Φ_{met}, Φ_{re}, and the calculated value U_{ref} yield values for the current density i at a specified value of $\Phi_{met} - \Phi_{re}$ or η_{ref} calculated according to Eq. [13].

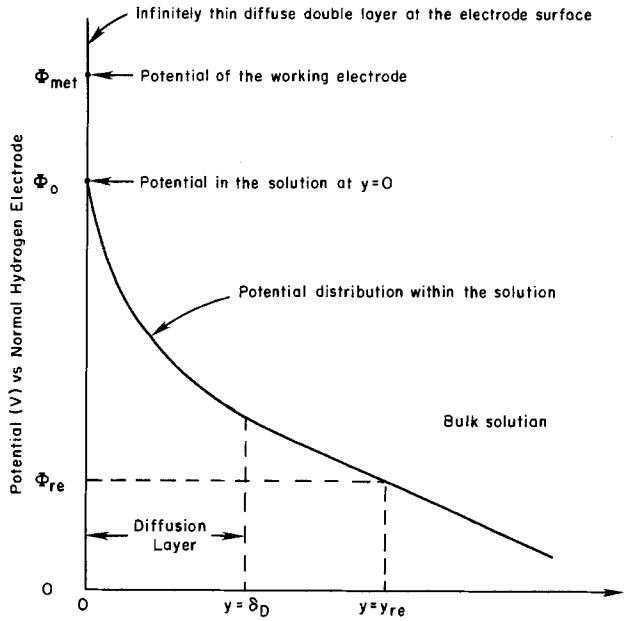

Fig. 2. Schematic of the solution potential profile near an electrode

Results and Discussion

The model presented above can be used to predict the current density for a set potential difference between the working electrode and a reference electrode ($\Phi_{met} - \Phi_{re}$) once the parameter values have been set. Alternatively, the model could be used to determine the kinetic parameters by comparing the predicted current density values to observed values and finding the parameter values that minimize the sum of the squares of the difference between the predicted and measured current densities. However, the model is used here to present predicted current density-potential curves which illustrate some of the capabilities of the model. Also, to simplify the presentation, the tribromide ion formation reaction is neglected completely (additional work which includes the formation of Br_3^- may be presented in the future).

Table VI presents the fixed parameter values used in the model to produce the predicted current-potential curves shown in Fig. 3-7. Figure 3 presents the effect of varying the magnitude of the exchange current densities in the V-H mechanism with $i_{Oref,H}/i_{Oref,V} = 1.0$. As shown in Fig. 3, an order of magnitude change in the exchange current densities yields noticeably different cathodic current-potential curves. Figure 4 shows the effect of the magnitude of the exchange current densities for the V-T mechanism with the Volmer step controlling ($i_{Oref,V}/i_{Oref,T} = 0.01$). Notice that the predicted limiting current densities depend on the magnitude of the exchange current densities even though the Volmer step is rate controlling. Note also that the limiting current density predicted by Levich equation (15)

$$i_{LD} = -0.62Fc_{Br_2,ref}(\Omega\nu)^{1/2}\left(\frac{D_{Br_2}}{\nu}\right)^{2/3}$$

Table VI. Fixed parameter values

Parameter	Value
Reference concentrations	$c_{K^+,ref} = 2.01 \times 10^{-3}$ mol/cm³ $c_{Br^-,ref} = 1.0 \times 10^{-5}$ mol/cm³ $c_{SO_4^{2-},ref} = 1.0 \times 10^{-3}$ mol/cm³
Diffusion and stoichiometric coefficients	$D_{K^+} = 1.957 \times 10^{-5}$ cm²/sec[a] $s_{K^+} = 0$ $D_{SO_4^{2-}} = 1.065 \times 10^{-5}$ cm²/sec[a] $s_{SO_4^{2-}} = 0$ $D_{Br^-} = 2.084 \times 10^{-5}$ cm²/sec[a] $s_{Br^-} = 2$ $D_{Br_2} = 1.2 \times 10^{-5}$ cm²/sec[b] $s_{Br_2} = -1$
Miscellaneous:	
Pure solvent density (ρ_0)	1.0 g/cm³
Kinematic viscosity (ν)	1.0×10^{-2} cm²/sec
Temperature (T)	298.15 K
Equilibrium electrode potential (U_{ref})	0.904V, for reference concentrations and a saturated calomel reference electrode
Reference electrode position[c] (y_{re})	0.01 cm

[a] Newman (15).
[b] Osipov *et al.* (1).
[c] Picked for convenience.

is not obtained until the values of the exchange current densities are larger than expected. This means that the exchange current density for the Tafel reaction is probably larger than the exchange current density for Volmer reaction by more than two orders of magnitude.

Figure 5 shows the effect of the Heyrovsky transfer coefficient (α_H) in the V-H mechanism for the case where the Heyrovsky step is rate controlling and Fig. 6 shows the effect of α_V when the Volmer step is controlling. Both figures show that transfer coefficients change the shape of the entire curve.

Figure 7 presents the effect of α_V on the predicted current density-potential curves for the V-T mechanism. Notice that the small exchange current density for the Tafel step indicating that it is the rate-controlling step prevents a noticeable change in the curve when α_V is changed from 0.1 to 0.9.

Qualitative comparison of predicted current density-potential curves based on the model presented here to those given by Osipov *et al.* (1) reveals that either the V-H or the V-T mechanism with the Volmer step rate controlling may be an acceptable mechanism for the Br_2/Br^- electrode reaction. Additional raw data are necessary for a complete comparison which may permit a more definitive statement about the Br_2/Br^- mechanism.

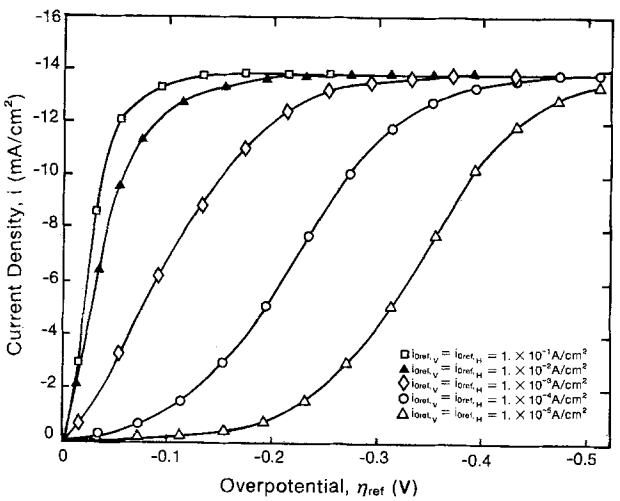

Fig. 3. Effect of the magnitude of the exchange current densities for the V-H mechanism with $i_{Oref,H}/i_{Oref,V} = 1.0$, $\alpha_V = \alpha_H = 0.5$, rotation speed = 1000 rpm.

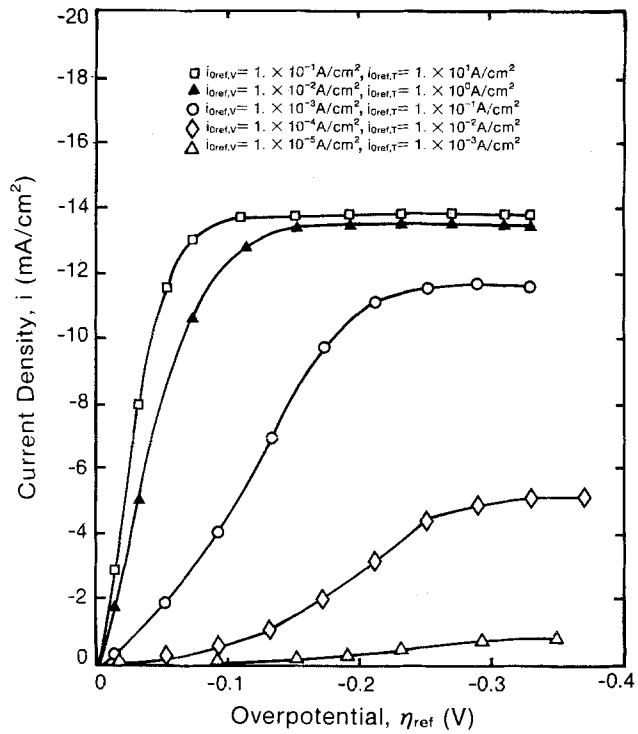

Fig. 4. Effect of a change in the exchange current density magnitude on cathodic current density curves predicted with the model for V-T kinetics. Volmer reaction rate controlling. $\alpha_V = 0.5$, rotation speed = 1000 rpm.

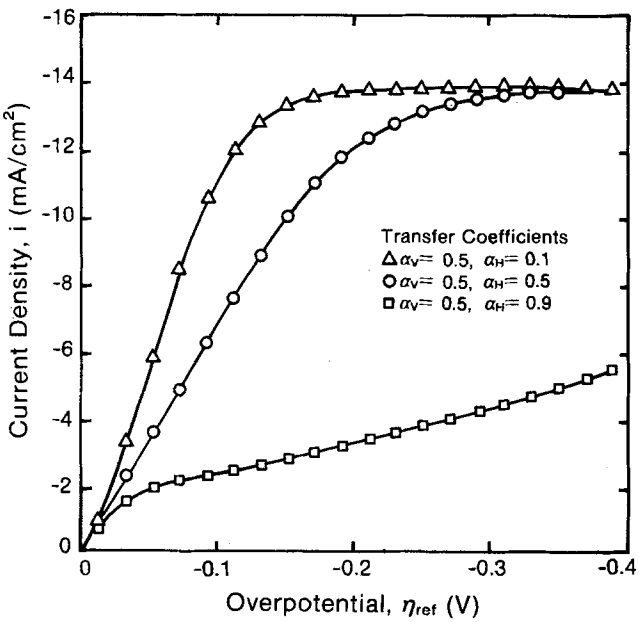

Fig. 5. Effect of a change in Heyrovsky transfer coefficient value on cathodic current density curves predicted with the model for V-H kinetics. Heyrovsky reaction rate controlling. $i_{Oref,V} = 1 \times 10^{-1}$ A/cm², $i_{Oref,H} = 1 \times 10^{-2}$, rotation speed = 1000 rpm.

Conclusion

The current density expressions presented here for the V-H and V-T mechanisms can be used to predict current density-overpotential curves which are similar to data. Qualitative comparison of the predictions of the model presented here to data shows that either the V-H mechanism or the V-T mechanism with the Volmer reaction controlling is an acceptable mechanism for the Br_2/Br^- reaction.

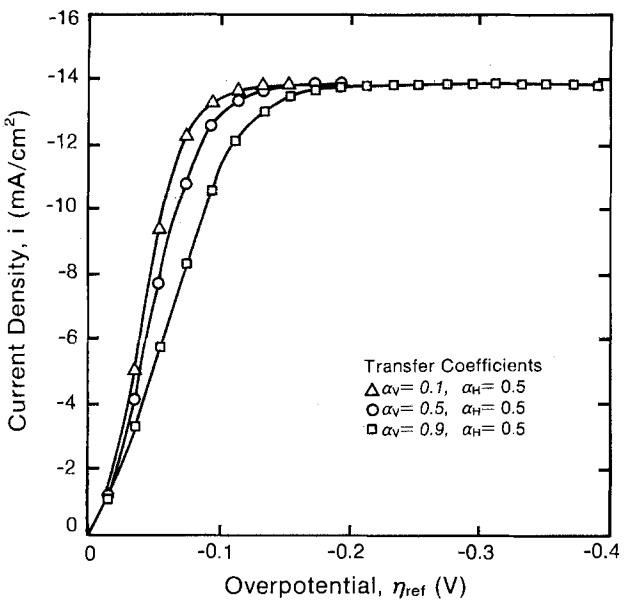

Fig. 6. Effect of a change in Volmer transfer coefficient value on cathodic current density curves predicted with the model for V-H kinetics. Volmer reaction rate controlling. $i_{Oref,V} = 1 \times 10^{-3}$ A/cm², $i_{Oref,H} = 1 \times 10^{-1}$ A/cm², rotation speed = 1000 rpm.

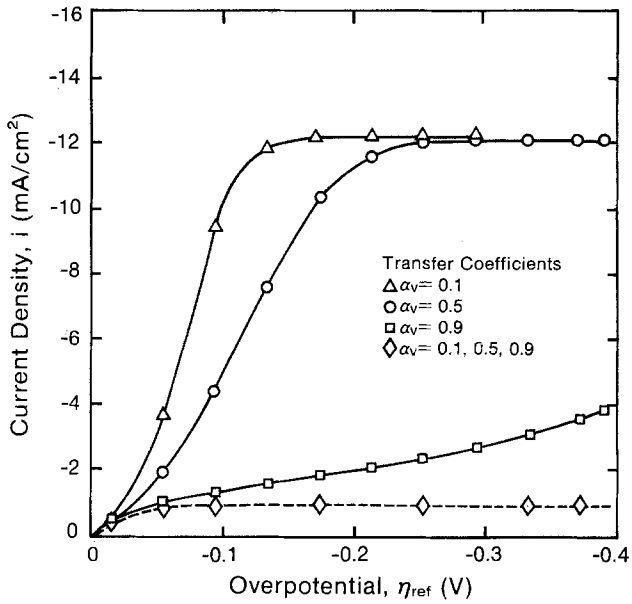

Fig. 7. Effect of a change in Volmer transfer coefficient value on cathodic current density curves predicted with the model for V-T kinetics using two sets of exchange current density values. $i_{Oref,V} = 1 \times 10^{-1}$ A/cm², $i_{Oref,T} = 1 \times 10^{-3}$ A/cm² (- - -); $i_{Oref,V} = 1 \times 10^{-3}$ A/cm², $i_{Oref,T} = 1 \times 10^{-1}$ A/cm² (———).

Acknowledgments

This work was supported by NSF Grant Number ENG-7908071 and by the Center for Energy and Mineral Resources of Texas A&M University.

Manuscript submitted Oct. 14, 1982; revised manuscript received Jan. 3, 1983.

Any discussion of this paper will appear in a Discussion Section to be published in the December 1983 JOURNAL. All discussions for the December 1983 Discussion Section should be submitted by Aug. 1, 1983.

LIST OF SYMBOLS

a	0.51023
$c_{i,std}$	standard concentration of species i (mol/cm³)
$c_i(y)$	concentration of species i at distance y from electrode (mol/cm³)
D_i	diffusion coefficient of species i (cm²/sec)
D_R	diffusion coefficient of limiting reactant (cm²/sec), chosen to be Br_2 here
$\mathbf{F}$	Faraday's constant, 96,487 C/mol
i	current density (A/cm²)
i_{LD}	limiting current density determined by convection and diffusion, value given by Levich equation (A/cm²)
$i_{Ostd,j}$	exchange current density for reaction j at standard concentrations (A/cm²)
$i_{Oref,j}$	exchange current density for reaction j at reference concentrations (A/cm²)
K_{eq}	equilibrium constant for homogeneous tribromide formation reaction (cm³/mol)
k_b	backward reaction rate constant for tribromide homogeneous reaction (sec⁻¹)
k_f	forward reaction rate constant for tribromide homogeneous reaction (cm³/mol-sec)
N_i	flux of species i (mol/cm²-sec)
n	number of electrons transferred in the overall electrode reaction ($n = 2$ here)
p_i	anodic reaction order of species i
q_i	cathodic reaction order of species i
R	universal gas constant, 8.3143 J/mol K
s_i	stoichiometric coefficient for species i in overall electrochemical reaction
T	temperature (K)
U	standard potential of an electrode reaction on hydrogen electrode scale (V)
U^θ_{re}	standard potential of reference electrode reaction on hydrogen electrode scale (V)
U^θ_{ref}	equilibrium potential difference between working electrode and reference electrode evaluated with chosen reference concentrations (V)
u_i	mobility of species i (cm²-mol/J-sec)
v_y	component of velocity of electrolyte flow in a direction normal to the electrode surface (cm/sec)
y	distance from electrode in a direction normal to the electrode surface (cm)
z_i	charge on species i
α_j, $(1 - \alpha_j)$	anodic and cathodic transfer coefficients of reaction j
γ_{ij}	power on concentration term for species i in reaction j in expressions for exchange current densities
δ_D	diffusion layer thickness (cm)
η_{ref}	overpotential expressing departure of electrode reaction driving force ($\Phi_{met} - \Phi_o$) from equilibrium value corresponding to chosen reference concentrations (V)
θ_o	equilibrium surface coverage of adsorbed bromine
ν	kinematic viscosity of the electrolyte (cm²/sec)
ξ	dimensionless distance from electrode surface (y/δ_D)
ρ_o	pure solvent density (g/cm³)
Φ	potential in the solution as sensed by a reference electrode (V)
Φ_{re}	potential in the bulk solution at the reference electrode as sensed by a reference electrode at $y = y_{re}$ (V)
Φ_o	potential in the electrolyte immediately adjacent to working electrode surface as sensed by a reference electrode (V)
Φ_{met}	potential of the working electrode (RDE) with respect to the same thermodynamic potential scale as the reference electrode in the solution (V)
Ω	disk rotational speed (rad/sec)

Subscripts

H	identifies the value of a quantity associated with the Heyrovsky reaction
R	denotes quantity associated with the limiting reactant
re	refers to the reference electrode
ref	identifies a value associated with a chosen set of reference concentrations (*e.g.*, $c_{i,ref}$, $i_{Oref,j}$)
std	identifies a value associated with a chosen set of standard concentrations
T	identifies the value of a quantity associated with the Tafel reaction
V	identifies the value of a quantity associated with the Volmer reaction
o	subscript, denoting a quantity which is evaluated with the concentration adjacent to the electrode surface (except for θ_o and ρ_o)

REFERENCES

1. O. R. Osipov, M. A. Novitskii, Yu. M. Povarov, and P. D. Lukovtsev, *Elektrokhimiya*, **8**, 327 (1972).
2. L. J. J. Janssen and J. G. Hoogland, *Electrochim. Acta*, **15**, 1677 (1972).
3. G. Faita, G. Fiori, and T. Mussini, *ibid.*, **13**, 1765 (1968).
4. J. Llopis and M. Vasquez, *ibid.*, **6**, 167, 177 (1962).
5. W. D. Cooper and R. Parsons, *Trans. Faraday Soc.*, **66**, 1968 (1970).
6. W. J. Albery, A. H. Davis, and A. J. Mason, *Faraday Discuss. Chem. Soc.*, **56**, 317 (1973).
7. D. Allard and R. Parsons, *Chem.-Ing.-Tech.*, **44**, 201 (1972).
8. I. Rubinstein, *J. Phys. Chem.*, **85**, 13 (1981).
9. V. S. Vilinskaya and M. R. Tarasevich, *Elektrokhimiya*, **7**, 1515 (1971).
10. V. S. Bagotzky, Yu. B. Yassilyev, J. Weber, and J. N. Pirtskhalava, *J. Electroanal. Chem. Interfacial Electrochem.*, **27**, 31 (1970).
11. M. W. Breiter, *Electrochim. Acta*, **8**, 925 (1963).
12. N. A. Balashova and K. E. Kazarinov, *Electroanal. Chem.*, **3**, 135 (1969).
13. R. F. Lane and A. T. Hubbard, *J. Phys. Chem.*, **79**, 808 (1975).
14. L. J. J. Janssen and J. G. Hoogland, *Electrochim. Acta*, **15**, 941 (1972).
15. J. S. Newman, "Electrochemical Systems," Prentice-Hall, Englewood Cliffs, NJ (1973).
16. S. E. Lorimer, M.S. Thesis, Texas A&M University, College Station, TX (1982).
17. R. E. White, *Ind. Eng. Chem. Fundam.*, **17**, 367 (1978).

Technical Notes

A Technique for Calculating Shunt Leakage and Cell Currents in Bipolar Stacks Having Divided or Undivided Cells

E. A. Kaminski and R. F. Savinell*

Department of Chemical Engineering, The University of Akron, Akron, Ohio 44325

The design of high-output voltage electrochemical batteries calls for series electrical connection of separate cells. Likewise, in scaling up electrosynthesis processes, simplicity of construction may warrant the building of reactors containing several cells arranged in series. A convenient design for supplying reactants to a cell assembly is to parallel feed the cells with electrolyte distributed by an inlet manifold and collected by an outlet manifold. The electrolyte-filled piping furnishes secondary series electrical connections among the cells. Consequently, the ionic currents generated by electrode processes are driven by the intercell potential gradients of the assembly through conductive paths in the piping. These ionic shunt or bypass currents short-circuit each cell in the assembly causing power loss, corrosion, current inefficiency, and nonuniform cell-to-cell current distribution. The magnitude of the bypass current in an assembly is a function of the number of cells in the assembly, cell voltage (which includes current dependent polarizations), conductivity of the electrolyte, and the geometry of the electrolyte feed system. Thus, bypass current is a parameter in the design of assemblies.

Analysis of bypass current proceeds by applying Kirchhoff's laws to electrical circuit analogs of assemblies. The analog circuits are devised to represent current flow paths by standard electrical components. Most investigators (1) model assemblies by linear, passive, d-c networks, the work of Katz (2) and Onishchuk (3) being exceptions. Katz incorporates into the analog imaginary Zener diodes with different polarization characteristics in the forward and backward current direction. The diodes account for the polarizations of the anodic and cathodic reactions which occur at the ends of the shunt paths. Onishchuk (3) models a cell by a voltage source in series with a nonlinear current dependent resistive element.

Analysis of the analog results in a large set of simultaneous linear or nonlinear equations. Two methods have usually been employed in obtaining solutions. One is simultaneous solution of the governing equations (1, 2, 4, 5). The other is approximating the system of equations by a single differential equation (3, 6). The continuous approximations apply to assemblies with a sufficiently large number of cells.

This study presents a treatment of bypass current based on the solution of finite difference equations. The formalism is applied to assemblies of divided and undivided cells. The analysis yields a set of compact equations for determining branch currents in the circuit analog. Implementation of this computational procedure requires a minimum of programming effort and computer storage as simultaneous solution of equations is avoided. The same equations can be used to simulate an assembly of cells operating as energy or substance producers.

Theory

Circuit analogs are constructed making the usual assumptions (2, 4, 5, 6). Surfaces of the electrolyte distribution system are nonconducting. The electrolyte flow paths are conducting and are represented by resistor elements. All resistance paths between the cells and a manifold are identical, and each manifold segment between a pair of branches is represented by an identical resistor. Cells of assemblies are assumed to have a linear polarization characteristic, while each cell is represented as an ideal voltage source in series with this resistor. Electrodes offer no resistance to current flow. The electrolyte in a cell compartment is assumed to be at a uniform potential throughout.

An analog circuit of an N cell assembly of two-compartment cells which incorporates these assumptions

* Electrochemical Society Active Member.
Key words: shunt currents, bipolar cell, separated cells, current distribution.

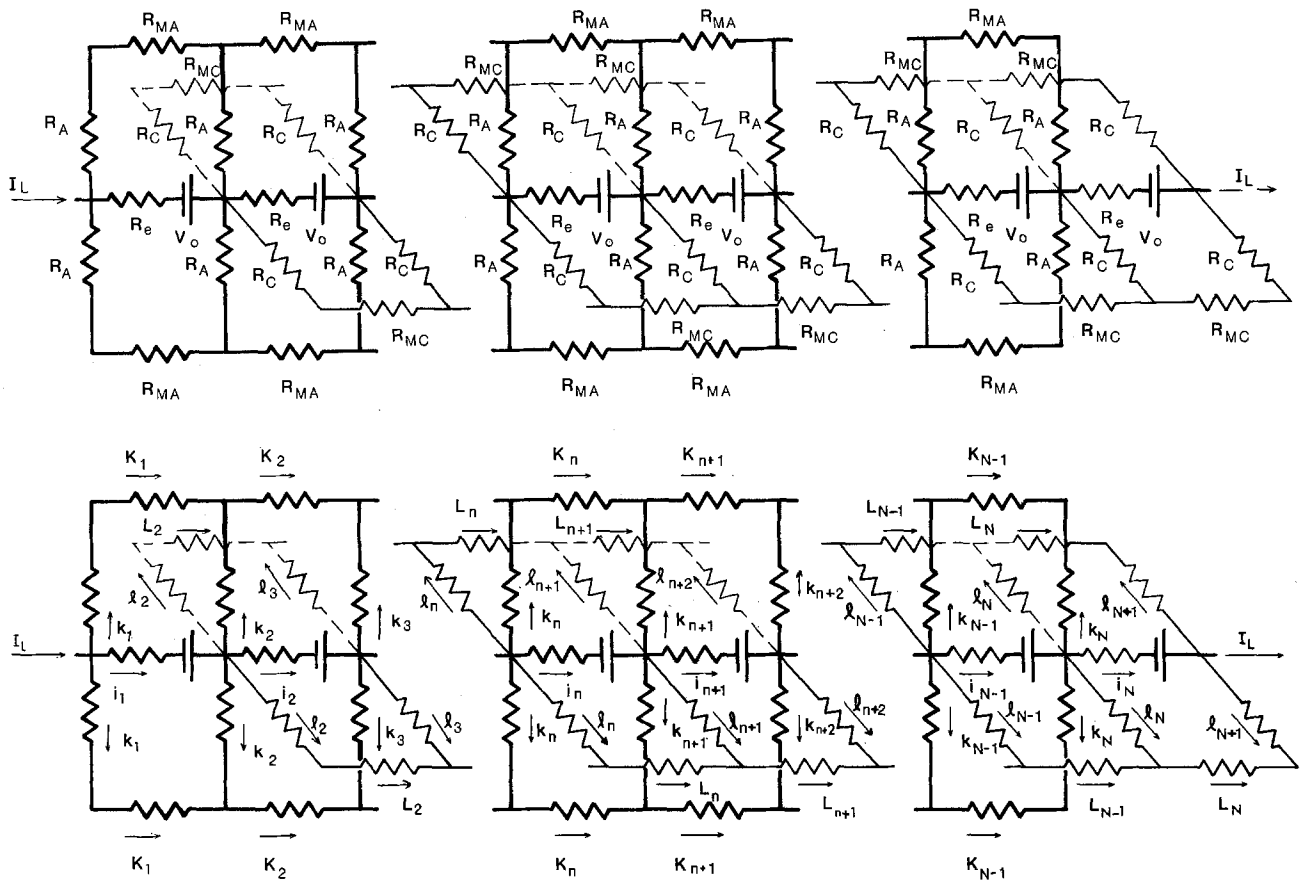

Fig. 1. Analog circuit of an N assembly of two-compartment cells

is shown in Fig. 1. Note that the circuit is symmetric with respect to the analogs of the inlet and outlet piping for both the anolyte and catholyte. The symmetry is taken advantage of in the model. However, the figure is presented without simplification so that the currents computed may retain physical significance. The assembly as described is assumed to be under a current load I_L, and branch currents are positive as defined in the figure.

Application of Kirchhoff's laws to this symmetric network at the nth cell analog results in a set of five linear constant coefficient difference equations. The first two are summations of currents at the junctions of the anolyte and catholyte manifold segments which are given as

$$K_{n+1} - K_n - k_{n+1} = 0 \quad [1]$$

$$L_{n+1} - L_n - l_{n+1} = 0 \quad [2]$$

The third equation is the summation of currents at the junctions of the nth and $n+1$ cell analogs

$$i_{n+1} - i_n + 2k_{n+1} + 2l_{n+1} = 0 \quad [3]$$

Finally, the summation of potential drops around the loops formed by the nth cell analog element and elements of the anolyte and catholyte feed systems results in

$$-R_{MA}K_n + R_A(k_{n+1} - k_n) + R_e i_n - V_o = 0 \quad [4]$$

$$-R_{MC}L_n + R_C(l_{n+1} - l_n) + R_e i_n - V_o = 0 \quad [5]$$

The system of Eq. [1]-[5] is solved in the standard way (7) and has the complete solution, for details regarding the solution, see Ref. (8).

$$k_n = \sum_{j=1}^{4} C_j r_j^n \quad [6]$$

$$l_n = \sum_{j=1}^{4} C_j D_j r_j^n \quad [7]$$

$$K_n = \sum_{j=1}^{4} C_j \frac{r_j^{n+1}}{r_j - 1} + \frac{R_e}{R_{MA}} C_5 - \frac{V_o}{R_{MA}} \quad [8]$$

$$L_n = \sum_{j=1}^{4} C_j D_j \frac{r_j^{n+1}}{r_j - 1} + \frac{R_e}{R_{MC}} C_5 - \frac{V_o}{R_{MC}} \quad [9]$$

$$i_n = -2 \sum_{j=1}^{4} C_j (1 + D_j) \frac{r_j^{n+1}}{r_j - 1} + C_5 \quad [10]$$

In the above equations the C's are arbitrary independent constants to be determined from boundary conditions. The r's and D's are solution parameters which are related to the coefficients of Eq. [1]-[5]. To obtain the four r's, define

$$A = 4R_A R_C + R_A(R_{MC} + 2R_e) + R_C(R_{MA} + 2R_e) \quad [11]$$

$$B = 6R_A R_C + 2[R_A(R_{MC} + 2R_e) + R_C(R_{MA} + 2R_e)] + R_{MA}R_{MC} + 2R_e(R_{MA} + R_{MC}) \quad [12]$$

$$C = R_A R_C \quad [13]$$

with a and b defined as

$$a = (A/C + \sqrt{(A/C)^2 - 4(B/C - 2)})/2 \quad [14]$$

$$b = (A/C - \sqrt{(A/C)^2 - 4(B/C - 2)})/2 \quad [15]$$

the r's are

$$r_1 = \frac{a}{2} + \sqrt{\left(\frac{a}{2}\right)^2 - 1} \quad [16]$$

$$r_2 = \frac{a}{2} - \sqrt{\left(\frac{a}{2}\right)^2 - 1} \quad [17]$$

$$r_3 = \frac{b}{2} + \sqrt{\left(\frac{b}{2}\right)^2 - 1} \quad [18]$$

$$r_4 = \frac{b}{2} - \sqrt{\left(\frac{b}{2}\right)^2 - 1} \quad [19]$$

For each r, a corresponding D is defined to be

$$D_j = \frac{R_A(r_j - 1)^2 - (R_{MA} + 2R_e)r_j}{2R_e r_j} \quad j = 1, 2, 3, 4 \quad [20]$$

To determine the arbitrary constants, (the C's), the boundary conditions are written in terms of solution forms as

$$K_o = \sum_{j=1}^{4} C_j \frac{r_j}{r_j - 1} + \frac{R_e}{R_{MA}} C_5 - \frac{V_o}{R_{MA}} = 0 \quad [21]$$

$$K_{N+1} = \sum_{j=1}^{4} C_j \frac{r_j^{N+1}}{r_j - 1} + \frac{R_e}{R_{MA}} C_5 - \frac{V_o}{R_{MA}} = 0 \quad [22]$$

$$L_1 = \sum_{j=1}^{4} C_j D_j \frac{r_j^2}{r_j - 1} + \frac{R_e}{R_{MC}} C_5 - \frac{V_o}{R_{MC}} = 0 \quad [23]$$

$$L_{N+1} = \sum_{j=1}^{4} C_j D_j \frac{r_j^{N+2}}{r_j - 1} + \frac{R_e}{R_{MC}} C_5 - \frac{V_o}{R_{MC}} = 0 \quad [24]$$

$$i_1 + 2k_1 = \sum_{j=1}^{4} 2C_j \left(r_j - \frac{(1 + D_j)r_j^2}{r_j - 1} \right) + C_5 = I_L \quad [25]$$

Equations [21]-[25] are a linear algebraic system in the arbitrary constants. Branch currents defined in the analog circuit are calculated by Eq. [6]-[10] using values of solution parameters and arbitrary constants calculated as indicated.

The case of the one compartment cell assembly is treated similarly. Figure 2 is the analog circuit for this assembly. The governing difference equations are

$$K_{n+1} - K_n - k_{n+1} = 0 \quad [26]$$

$$L_{n+1} - L_n - l_{n+1} = 0 \quad [27]$$

$$i_{n+1} - i_n + k_{n+1} + l_{n+1} = 0 \quad [28]$$

$$-R_{MI}K_n + R_{EI}(k_{n+1} - k_n) + R_e i_n - V_o = 0 \quad [29]$$

$$-R_{ME}L_n + R_{EE}(l_{n+1} - l_n) + R_e i_n - V_o = 0 \quad [30]$$

with complete solution being given as (see Ref. (8) for details)

$$k_n = \sum_{j=1}^{4} C_j r_j^n \quad [31]$$

$$l_n = \sum_{j=1}^{4} C_j D_j r_j^n \quad [32]$$

$$K_n = \sum_{j=1}^{4} C_j \frac{r_j^{n+1}}{r_j - 1} + \frac{R_e}{R_{MI}} C_5 - \frac{V_o}{R_{MI}} \quad [33]$$

$$L_n = \sum_{j=1}^{4} C_j D_j \frac{r_j^{n+1}}{r_j - 1} + \frac{R_e}{R_{ME}} C_5 - \frac{V_o}{R_{ME}} \quad [34]$$

$$i_n = -\sum_{j=1}^{4} C_j(1 + D_j) \frac{r_j^{n+1}}{r_j - 1} + C_5 \quad [35]$$

The C's again are arbitrary constants, and the r's and D's are solution parameters. The r's are calculated as before with A, B, and C now defined as

$$A = 4R_{EI}R_{EE} + R_{EI}(R_{MI} + R_e) + R_{EE}(R_{ME} + R_e) \quad [36]$$

$$B = 6R_{EI}R_{EE} + 2[R_{EI}(R_{MI} + R_e) + R_{EE}(R_{ME} + R_e)] + R_{MI}R_{ME} + R_e(R_{ME} + R_{MI}) \quad [37]$$

$$C = R_{EI}R_{EE} \quad [38]$$

and the D's in this case are defined to be

$$D_j = \frac{R_{EI}(r_j - 1)^2 - (R_{MI} + R_e)r_j}{R_e r_j} \quad j = 1, 2, 3, 4 \quad [39]$$

The arbitrary constants are determined from the boundary conditions which gives the following set of expressions

$$K_o = \sum_{j=1}^{4} C_j \frac{r_j}{r_j - 1} + \frac{R_e}{R_{MI}} C_5 - \frac{V_o}{R_{MI}} = 0 \quad [40]$$

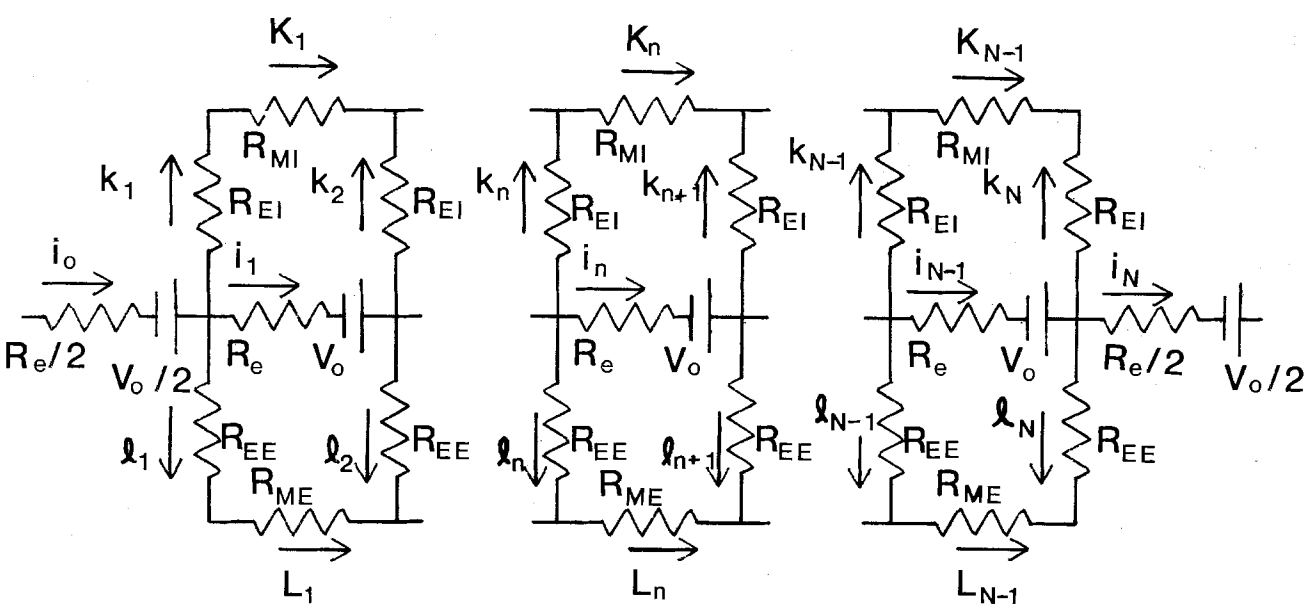

Fig. 2. Analog circuit of an N assembly of one-compartment cells

$$K_N = \sum_{j=1}^{4} C_j \frac{r_j^{N+1}}{r_j - 1} + \frac{R_e}{R_{MI}} C_5 - \frac{V_o}{R_{MI}} = 0 \quad [41]$$

$$L_0 = \sum_{j=1}^{4} C_j D_j \frac{r_j}{r_j - 1} + \frac{R_e}{R_{ME}} C_5 - \frac{V_o}{R_{ME}} = 0 \quad [42]$$

$$L_N = \sum_{j=1}^{4} C_j D_j \frac{r_j^{N+1}}{r_j - 1} + \frac{R_e}{R_{ME}} C_5 - \frac{V_o}{R_{ME}} = 0 \quad [43]$$

$$i_0 = -\sum_{j=1}^{4} C_j (1 + D_j) \frac{r_j}{r_j - 1} + C_5 = I_L \quad [44]$$

Branch current for the one-compartment cell assembly analog are calculated using Eq. [31]-[35] with values of solution parameters and arbitrary constants.

Discussion

The simplicity of this algorithm can be demonstrated with the following example. Consider a battery of 20 two-compartment cells working under a current load. Values of the resistances, the open-circuit cell voltage, and the load current are listed in Table I. Solution parameters obtained with the assumed resistances are shown in the table together with values for the intermediate constants. The arbitrary constants of the solution are obtained by solving the following linear system (Eq. [21]-[25] written in matrix form)

$$\begin{bmatrix} 20.013881 & -19.013881 & 26.136081 & -25.136081 & 0.10000000 \\ 55.788173 & -6.8211873 & 57.029356 & -11.519657 & 0.10000000 \\ 11.999132 & -10.288886 & -59.639768 & 53.052666 & 0.20000000 \\ 33.447269 & -3.6911150 & -130.13494 & 24.313597 & 0.20000000 \\ -64.026029 & 58.605537 & 67.007372 & -55.833169 & 1.00000000 \end{bmatrix} \begin{bmatrix} C_1 \\ C_2 \\ C_3 \\ C_4 \\ C_5 \end{bmatrix} = \begin{bmatrix} 0.15000000 \\ 0.15000000 \\ 0.30000000 \\ 0.30000000 \\ 0.50000000 \end{bmatrix}$$

The above system is inverted using Crout's algorithm which is particularly suited for implementing on a hand held calculator because storage requirements are minimized. The result of the calculation gives

$$C_1 = 1.2281475 \times 10^{-3}$$

$$C_2 = -3.7421141 \times 10^{-3}$$

$$C_3 = -3.6207009 \times 10^{-4}$$

$$C_4 = 9.4561370 \times 10^{-4}$$

$$C_5 = 8.7500000 \times 10^{-1}$$

The values for the currents defined in the analog circuit are calculated using Eq. [6]-[10] and the given solution parameters and constants. Plots of three subdistributions are given in Fig. 3 and 4. The magnitude of the manifold currents, K_n, as a function of cell position is shown in Fig. 3. The shunt current in the manifold flows in the direction opposing the current in the battery and is maximum in the center portion of the assembly. Also, in this figure is shown the distribution of battery currents, i_n. All the battery currents are greater than the load current and reach a maximum at the center of the assembly. Individual cell voltages

Table I. Parameters and intermediate constants for example of bypass current distribution for an assembly of 20 two-compartment cells

$R_A = 5 \times 10^3\Omega$	$R_C = 4 \times 10^3\Omega$	$R_e = 1\Omega$	$I_L = 0.5A$
$R_{MA} = 10\Omega$	$R_{MC} = 5\Omega$	$V_o = 1.5V$	$N = 20$

$A = 8.0083000 \times 10^7$	$a = 2.0026272$
$B = 1.2016608 \times 10^8$	$b = 2.0015227$
$C = 2.0000000 \times 10^7$	
$r_1 = 1.0525931$	$D_1 = 0.56958426$
$r_2 = 0.95003468$	$D_2 = 0.56958447$
$r_3 = 1.0397834$	$D_3 = -2.1945858$
$r_4 = 0.96173871$	$D_4 = -2.1945856$

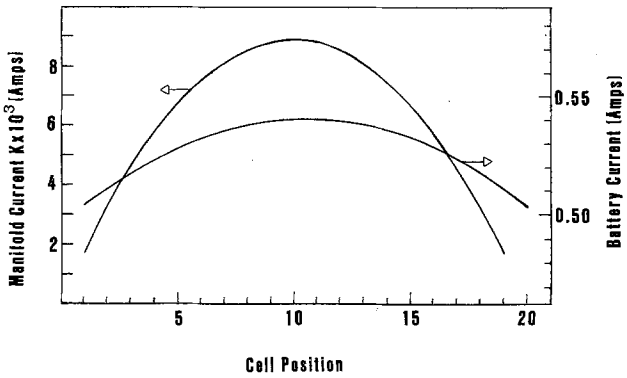

Fig. 3. Distribution of manifold currents and battery currents of the example calculation for a two-compartment cell stack.

are, thereby, reduced as is the voltage of the battery as a whole.

Figure 4 shows the distribution of current, k_n, flowing in the manifold connecting paths. These currents are largest at the two ends of the assembly and decrease toward the center. Currents flowing in the connecting paths are always opposite in direction for the two halves of the assembly. The characteristics of current distributions predicted by this procedure are in agreement with those predicted by other investigators using a linear model (3, 4, 6).

When implementing the algorithm described here, some caution must be exercised. For example, it is possible to encounter a set of model parameter values such that rounding errors resulting from finite representation of numbers by calculating machines causes a model to predict inconsistent results. This is especially a problem when the resistances are such that the values of the parameters a and b approach each other. The significance of this problem becomes apparent when the imposed boundary conditions are not sufficiently met. Caution is particularly needed when the ratios $R_{MA}R_{MC}/R_AR_C$, $R_{MA}R_e/R_AR_C$, and $R_{MC}R_e/R_AR_C$ are all uniformly small (as on the order of 10^{-8}). This leads to the computing of a singular coefficient matrix. Further, illconditioning of the coefficient matrix can occur for N sufficiently large. In this case, Gauss elimination with pivoting is recommended. However, this

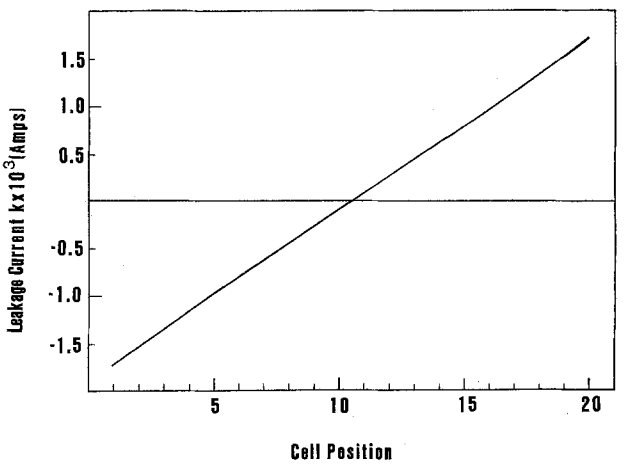

Fig. 4. Distribution of currents in the manifold connecting paths of the example calculation for a two-compartment cell stack.

condition is met in circumstances rare to industrially important processes.

The technique presented here can be used to calculate other cell stack parameters of interest. For example, the terminal voltage of a cell stack under load can be easily calculated. In the case of a stack undergoing constant load discharge, this technique can be conveniently included in an iterative procedure to calculate the terminal voltage and load current (consequently delivered power). One of the added advantages of using this technique (as compared to solving a large set of simultaneous equations) is that once the coefficients are known, it is a trivial matter to compute any or all the currents. Finally, it should be recognized that in certain cases the solution forms of this technique can be cast into an analytical form. For example, this can be done for the single compartment system as described in Fig. 2. However, the forms of the solution are complex, and any physical interpretations of the resulting equations are difficult to make.

Conclusions

A compact procedure for calculating current distributions in assemblies with parallel electrolyte feed has been developed. Assemblies of both divided and undivided cells were considered. The technique presented requires little programming effort or storage.

Acknowledgment

The authors wish to acknowledge the helpful discussions with L. Thaller during the early stages of this work.

Manuscript submitted Sept. 20, 1982; revised manuscript received *ca.* Nov. 29, 1982.

Any discussion of this paper will appear in a Discussion Section to be published in the December 1983 JOURNAL. All discussions for the December 1983 Discussion Section should be submitted by Aug. 1, 1983.

REFERENCES

1. A. F. Kuhn and J. S. Booth, *J. Appl. Electrochem.*, **10**, 233 (1980).
2. M. Katz, *This Journal*, **125**, 515 (1978).
3. V. A. Onishchuk, *Elektrokhimiya*, **8**, 698 (1972).
4. P. R. Prokopius, "Model for Calculating Electrolytic Shunt Path Losses in Large Electrochemical Conversion Systems," NASA TMX-3359 (1976).
5. I. Rouser and V. Cezner, *This Journal*, **121**, 648 (1974).
6. O. S. Ksenzhek and N. D. Koshel, *Elektrokhimiya*, **7**, 353 (1970).
7. C. Jordan, "Calculus of Finite Differences," Chelsea Publishing Company, London (1956).
8. E. A. Kaminski, M.S. Thesis, University of Akron, Akron, OH (1983).

Elastomeric Binders for Electrodes

S. P. S. Yen,* D. H. Shen, and R. B. Somoano*

Jet Propulsion Laboratory, California Institute of Technology, Pasadena, California 91109

An important problem affecting the performance of ambient temperature secondary lithium cells is the poor mechanical integrity of the cathode. Upon repeated charge and discharge of an intercalatable cathode, *e.g.*, TiS_2, the small expansion and contraction of the TiS_2 lattice gives rise to stresses which disturb the electrode structure and can contribute to capacity loss. Our studies, using cathode fabrication procedures as described in the literature (1), indicate that the use of an inelastic binder material, such as Teflon, exacerbates this problem, *e.g.*, leads to electrode disruption and poor TiS_2 particle-particle contact. The fabrication process utilizing Teflon is unduly complicated, requiring high temperature and pressure. The resulting electrodes are brittle, nonflexible plates. We have investigated the use of elastomers as TiS_2 binder materials. These rubbery materials are used in place of Teflon (a hard, leathery material) and result in room temperature-atmospheric pressure preparation of cathodes which exhibit improved performance.

Experimental

There are several beneficial properties which an elastomer should possess for use in a secondary lithium cell. The material should have a low glass transition temperature, T_g, to ensure flexibility at the cell operation temperature. For example, if one wishes to operate a cell at −40°C, the binder material should have a $T_g < -60$°C. It should be chemically and electrochemically stable in the presence of lithium and the electrolyte environment. It should be soluble in common solvents which are inert to TiS_2, yet be insoluble (but wettable) in the electrolyte. It is also desirable to be able to cross-link the material (*e.g.*, by γ-radiation), if necessary, to tailor the mechanical or thermal characteristics to a given application. Finally, a high molecular weight encourages the formation of a viscous dilute polymer solution, and thus, facilitates electrode fabrication.

Figure 1 shows the chemical structure of a typical elastomeric binder which we have used in TiS_2 cathodes for ambient temperature secondary lithium cells. The polymer, ethylene-propylene-diene-terpolymer (EPDM) is a common copolymer which is available from several commercial sources. The norborene group can be used for cross-linking. Our material had a $T_g \sim -60$°C and a molecular weight of 100,000-200,000.

The first step of the cathode fabrication involves dissolving the EPDM polymer in a common inert solvent, such as cyclohexane, to form a 1 weight percent (w/o) solution of suitable viscosity. This solution is then added to TiS_2 to yield a mixture containing ~1-5 w/o binder. Because of the high molecular weight of the binder, this mixture has a paste-like consistency which enables it to be easily brushed onto nickel exmet screen at room temperature. The cathode is, then, dried *in vacuo* to remove any remaining solvent. Slight pressure can be applied to the finished electrode to optimize the smoothness of the electrode surface, but this is normally not necessary.

It is not necessary to use trial and error, or guessing, to identify a suitable elastomer for a given electrolyte

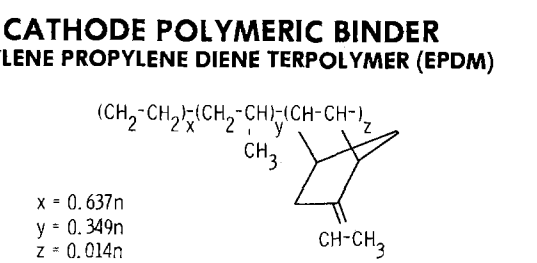

Fig. 1. Chemical structure of ethylene-propylene-diene terpolymer

* Electrochemical Society Active Member.

solution. One can use the solubility parameter, δ, to provide guidance to achieve good wettability between the binder and solvent. Two materials are wettable when their free energies of mixing, $\Delta F_{mix} \sim (\delta_a - \delta_b)^2$ are minimized, *i.e.*, $\delta_a - \delta_b \rightarrow 0$ (2). The solubility parameter of each component is given by

$$\delta_a = (\Delta E_a/V_a)^{1/2} \sim \gamma_a^{0.43}$$

where ΔE_a is the molar energy of vaporization, V_a is the molar volume, and γ_a is the surface tension of component a. The solubility parameter of the solvent and the elastomer may be readily calculated or obtained from tables (3, 4). Table I shows some calculated and measured values of δ for typical materials (5). It is desirable that the solubility parameters of the solvent and binder material be as close as possible. This ensures good solubility and wettability. However, it should be reiterated that the binder should not be soluble in the electrolyte. Dissolution of the binder in the electrolyte solvent is not cause for great concern since cross-linking the elastomer binder in the finished cathode, or the addition of an electrolyte salt leading to salting out effects, minimizes solubility while not compromising the wettability. As can be seen in Table I, 2-MeTHF wets EPDM much better than Teflon as indicated by the similar solubility parameters. We have measured a contact angle of 30°-32° at 21°C of 1.5M $LiAsF_6$/2-MeTHF electrolyte with respect to a EPDM film. There was no observable dissolution of the EPDM. This is much lower than the contact measured with Teflon, 50°-52°, indicating the superior wettability of the EPDM binder material. If it is desired to use propylene carbonate, a more suitable elastomer with a $\delta \sim 11$ should be utilized.

Results

The resulting elastomeric TiS_2 cathodes exhibit excellent flexibility and allow one to use spiral or cylindrical wound electrodes. Figure 2 shows the cathodes before and after cycling. The cathodes exhibit an excellent surface morphology after 120 cycles. Very similar results have been obtained with Li/1.3M $LiAsF_6$-3MeS/TiS_2 after 350 cycles (6). 3-MeS is three-methyl sulfolane. Thus, these cathodes look and perform much better than Teflon-bonded cathodes fabricated in our laboratory (*e.g.*, ~50 cycles with planar Teflon-bonded cathodes). It is believed that the improved mechanical integrity plays an important role in achieving high cycle life with the $LiAsF_6$/3-methyl sulfolane system.

Table I. Solubility parameters of typical materials

Example	Propylene carbonate	Cyclohexane	2-MeTHF	EPDM	Teflon
δ_{calc} (cal-cm^3)$^{1/2}$	11.1	8.07	8.06	8.42	6.66
$\delta_{measured}$ (cal-cm^3)$^{1/2}$	13.5[5] (b)	8.2[5] (b)		8.165[a]	6.2[5] (a)

Table II. Effect of thickness of TiS_2 cathode utilization

Cell No.	Current density for cell cycling (mA/cm^2)	Cathode thickness (mil)	% Cathode utilization (based on TiS_2 conc)	Cell capacity per unit area (mA-hr/cm^2)
1*	1	12.5	99.6	9.6
2*	1	20	97.6	19.3
3*	1	24	80.9	24.9
1'*	2	17	97.4	15.6
2'*	2	23	80.0	23.5
3'**	2	27	80.0	29.4
1''*	3	13.5	83.3	12.2
2''*	3	23	70.0	21.1
3''*	3	24	72.6	23.4

* EPDM binder conc = 2 w/o, pressure for cathode fabrication: 5000 psi.
** EPDM binder conc = 4 w/o, no pressure used for cathode fabrication.

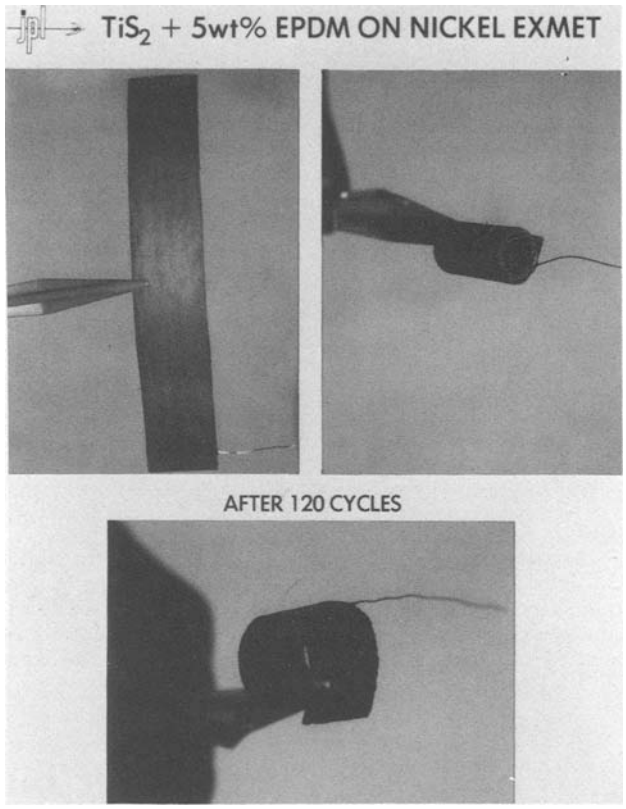

Fig. 2. TiS_2 elastomeric cathodes before and after cycling

Table II demonstrates the effect of thickness on the elastomeric cathode utilization. The experimental data shown in Table II indicates that an increase in the cathode thickness or current density results in a decrease in the percent cathode utilization (based on TiS_2 concentration). Note that the thick (27 mil) TiS_2 cathode (particle size ~1 μm), containing 4% elastomeric binder with 29.4 mA-hr/cm^2 cell capacity per unit area, exhibits the same cathode utilization as the 23 mil cathode containing 2% binder. This may reflect increased porosity due to the lower TiS_2 cathode bulk density of the thicker electrode. A pressure of ~5000 psi was used to prepare these cathodes in order to ensure thickness homogeneity. Pressure is not required for cathode fabrication, and because of the rubbery nature of the binder, the cathode performance is not affected, as shown in the table (*e.g.*, see 2'* and 3'**).

Conclusions

Elastomeric binders provide an effective way to simplify rechargeable cathode fabrication. The marked improvement in the mechanical integrity of the cathode structure contributes to prolonged cycle life. The solubility parameter can serve as a useful guide to selecting an elastomeric binder which will be compatible with a given electrolyte solvent. In addition, this technique can be used to prepare other types of electrode structures, such as microelectrodes and composite electrodes, from powdery electroactive materials for use in electrochemical studies.

Acknowledgments

It is a pleasure to thank Boyd Carter, Roger Williams, Harvey Frank, Dave Lawson, and Barrie Brummer for

useful discussions. This work represents one phase of research performed by the Jet Propulsion Laboratory, California Institute of Technology, sponsored by the National Aeronautics and Space Administration, Contract NAS7-918.

Manuscript submitted Sept. 7, 1982; revised manuscript received *ca.* Dec. 22, 1982. This was Paper 71 presented at the Denver, Colorado, Meeting of the Society, Oct. 11-16, 1981.

Any discussion of this paper will appear in a Discussion Section to be published in the December 1983 JOURNAL. All discussions for the December 1983 Discussion Section should be submitted by Aug. 1, 1983.

Publication costs of this article were assisted by Jet Propulsion Laboratory.

REFERENCES

1. G. L. Holleck and J. R. Driscoll, *Electrochim. Acta*, **22**, 647 (1977); L. P. Klemann and G. H. Newman, *This Journal*, **128**, 13 (1981); K. M. Abraham, J. L. Goldman, and D. L. Natwig, *This Journal*, **129**, 2404 (1982).
2. J. H. Hildebrand and R. L. Scott, "The Solubility of Nonelectrolytes," ACS Monograph Series, No. 17 (1950).
3. R. F. Fedors, *Polymer Engineering and Science*, **14**, 147 (1974).
4. R. F. Fedors, *ibid.*, **14**, 472 (1974).
5. J. M. G. Cowie, "Polymers: Chemistry and Physics of Modern Materials," p. 145, Intext Educational Publishers, New York (1974); "Polymer Handbook," 2nd Section IV, p. 337, John Wiley and Sons, New York (1975).
6. R. Somoano, *NASA Conference Publication*, **2217**, 123 (1981).

Dissolution of Copper Chloride in Concentrated LiCl Solution

R. L. Brossard*

Institut de Recherche d'Hydro-Québec (IREQ), Materials Department, Varennes, Quebec, Canada J0L 2P0

In a previous paper (1), the dissolution of copper chloride formed by the electrochemical oxidation of copper in aqueous lithium chloride was studied. The bulk of the experiments were carried out at a low LiCl concentration, *e.g.*, 0.02M LiCl. The complete dissolution of the anodically formed CuCl coincides with a rapid drop in potential which allows the transition time τ to be defined from which the dissolution rate of CuCl can be calculated.

It is difficult to predict whether the dissolution process of the film formed during the electrochemical oxidation is the same at 0.02M and at higher LiCl concentrations, *e.g.*, 0.02M, since Moreau (2) and Braun and Nobe (3) pointed out that the mechanism of the electrodissolution of copper is different, depending on Cl^- concentration values close to 0.1M. It is tentatively ascribed by them to the different nature of the complexed ions possibly formed during the dissolution of copper. The aim of the present work is to extend the previous study (1) to solutions having up to 1M LiCl.

Experimental

The electrochemical cells, their accessories, and the test procedures have been described in detail in a previous paper (1). In the present investigation, two cells were used: cell 1 for electrode oxidation and cell 2 for dissolution of CuCl. Cell 2 was similar to cell 1 except it only contained the working electrode (on open circuit) and the reference electrode.

The solution in cell 1 contained 0.05M of dissolved LiCl at pH = 4. A potassium phthalate-buffer was used to stabilize the pH. The LiCl concentration in cell 2 was adjusted from 0.02 to 1M while no buffer was used to stabilize the pH. Solutions in cells 1 and 2 were carefully deaerated by nitrogen bubbling, which was discontinued prior to the experiments.

The experimental technique recently developed (1) to measure the dissolution rate of copper chloride was the same, except that the copper electrode was removed from cell 1 after oxidation to be quickly immersed in cell 2. Unless otherwise noted, all electrode potential values are given in relation to the saturated-calomel electrode. Dissolution rates were measured on both stationary and rotating electrodes.

Results and Discussion

It was established (1) that the copper electrode becomes covered by a CuCl precipitate during the oxidation stage when a constant potential of 50 mV is imposed for 8 min. Its characteristics and its dissolution rate (v) are unaffected by contact with the atmosphere for several days. Therefore, the transfer of the oxidized copper electrode from cell 1 to cell 2 should not influence its behavior as a working electrode. In addition, the constant value of v during the dissolution of copper chloride was confirmed from the reduction of the precipitate at −300 mV after different periods of contact with the solution (Fig. 1). The difference between the charge required for complete film reduction at $t = 0$ and at $t = t$ is ascribed to the dissolution of CuCl during time t. It was assumed that a cathodic charge of 96,500C is required to decompose 1 g/molecule of this compound, because copper ions have a valency of +1 in this compound. The slope of the curve in Fig. 1 corresponds to v; its value is 1.4×10^{-8} mol cm^{-2} sec^{-1} in 0.6M LiCl. The amount of CuCl on the electrode surface is zero as soon as $t = \tau$ where v becomes zero.

The main characteristics of the behavior of the copper electrode covered by CuCl on its surface are the following: (*i*) The value of the open-circuit potential (E_{oc}) obtained immediately after electrode immersion is shown in Fig. 2 as a function of Cl^- concentration. It may be noted that the E_{oc} ($t = 0$) decreases as the

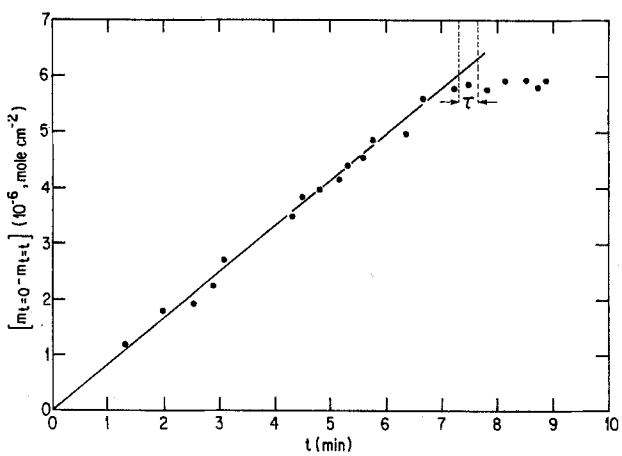

Fig. 1. The amount of precipitate dissolved from the electrode surface (m) after contact with 0.6M LiCl solution. $m_{t=0}$: m at $t = 0$. $m_{t=t}$: m at $t = t$. τ: duration of transient. No stirring in the solution.

* Electrochemical Society Active Member.
Key words: film dissolution, dissolution rate.

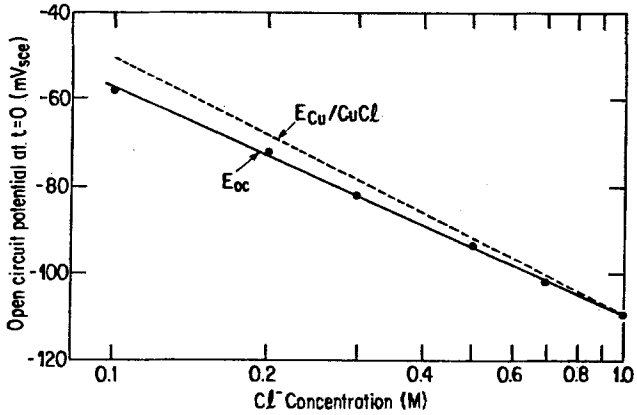

Fig. 2. The open-circuit potential upon immersion of the working electrode as a function of Cl^- concentration. Oxidation: +50 mV in 0.05M LiCl with $Q_{OXIDATION}$ = 600 mC/cm². No stirring in the solution. Dashed line: theoretical values.

Cl^- concentration increases and is just several mV below the equilibrium potential (4) $|E_{Cu/CuCl}|$ for the reaction

$$Cu + Cl = CuCl + 1\,e \qquad [1]$$

which is shown by a dashed line. (*ii*) Figure 3 illustrates the dissolution rate as a function of electrode rotation rate when the electrode was rotated. Linearity between v and $\omega^{1/2}$ is observed over a wide range of angular velocity, while v is relatively small when $\omega = 0$. In this illustration, the solution is 0.2M LiCl. (*iii*) v is directly proportional to Cl^- concentration as illustrated in Fig. 4. (*iv*) Between +22° and +80°C, values of the apparent heat of activation $\Delta H^{\neq}$, equal to 7.5 ± 0.4 kcal/mol, where determined from Arrhenius plots log v – T^{-1} (Fig 5) from various data sets. Values of $\Delta H^{\neq}$ were independent of Cl^- concentration for the range 0.02-0.2M in Cl^- and were unaffected by the method employed to calculate v, *i.e.*, from transient measurements (τ) or from the rate of enrichment of the solution in copper during the copper chloride dissolution. The other curve for which $\Delta H^{\neq}$ is equal to 6.7 kcal/mol will be commented upon further.

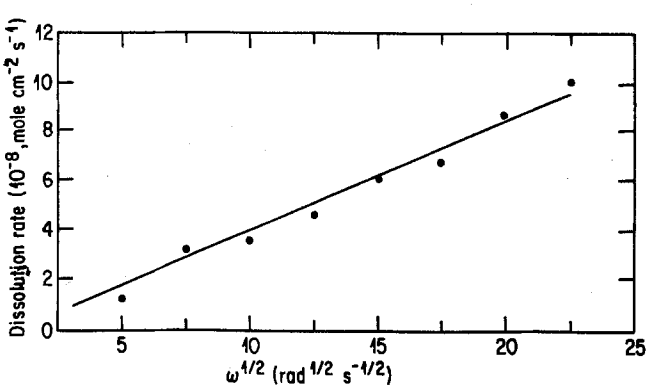

Fig. 3. Dependence of the dissolution rate from rotating electrode on the angular velocity of the electrode. Solution: 0.2M LiCl.

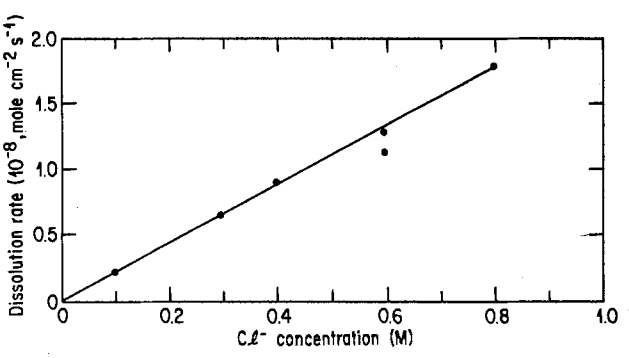

Fig. 4. Dissolution rate on a copper wire electrode *vs.* Cl^- concentration. No stirring in the solution.

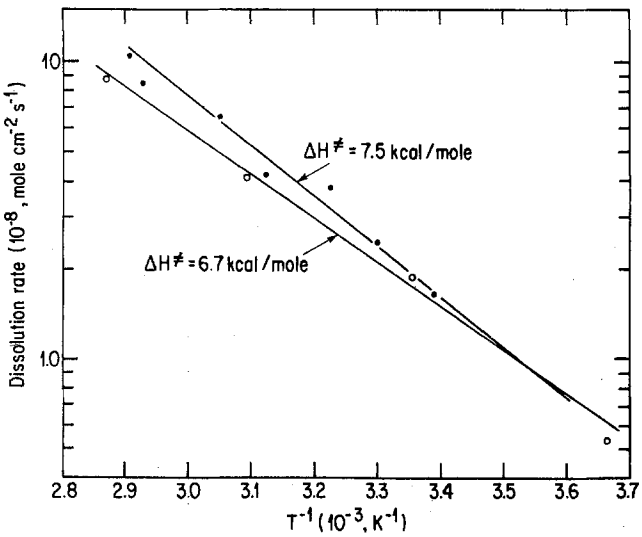

Fig. 5. Dependence of the rate of dissolution on the temperature of the solution of 0.2M LiCl. • Experimental values. o Relative values calculated from Eq. [5].

The characteristics (*i*), (*ii*), and (*iii*) are similar to those previously found concerning the dissolution of copper chloride in solutions with a low Cl^- concentration (1). Accordingly, the dissolution process is

$$CuCl + Cl^- = (CuCl_2^-)_i \qquad [2]$$

$$(CuCl_2^-)_i \rightarrow (CuCl_2^-)_s \text{ rds} \qquad [3]$$

where the subscripts i and s refer to concentrations at the electrode solution interface and the bulk solution, respectively. The rate-determining step [2] is the diffusion transport of $CuCl_2^-$ from the interface to the bulk solution. The first step [2], the oxidation of CuCl to $CuCl_2^-$, is assumed to be in equilibrium. The dissolution rate of a rotating electrode should be given by the following application of the Levich equation

$$v = 0.035\ D_{CuCl_2}{}^{-2/3}\nu^{-1/6}\omega^{1/2}[Cl^-] \qquad [4]$$

In this equation, v is in mol cm^{-2} sec^{-1}; $D_{CuCl_2^-}$ is the diffusion coefficient of $CuCl^{2-}$, ν the kinematic viscosity of the solution, and ω the angular velocity of the electrode.

Values of the diffusion coefficient deduced from the slopes of v *vs.* $\omega^{1/2}$ were calculated assuming that the diffusing species is $CuCl_2^-$ or Cl^- (Table I). These experimental values are in good agreement with those given in the literature for $D_{CuCl_2^-}$ and were far away from D_{Cl^-} values commonly accepted in the literature.

Table I. $D_{CuCl_2^-}$ and D_{Cl^-} values calculated from the slope of v – $\omega^{1/2}$ curves

[Cl⁻] (M)	$D_{CuCl_2^-}$ (cm²/sec)	D_{Cl^-}[a] (cm²/sec)	D_{Cl^-}[b] (cm²/sec)
0.11	1.68 × 10⁻⁵*		
0.2	0.81 × 10⁻⁵**	0.011 × 10⁻⁵	1.9 × 10⁻⁵
0.31	1.45 × 10⁻⁵*		
0.5	1.1 × 10⁻⁵**	0.015 × 10⁻⁵	1.9 × 10⁻⁵
0.83	1.2 × 10⁻⁵*		
0	0.77 × 10⁻⁵**	0.011 × 10⁻⁵	1.8 × 10⁻⁵

* $D_{CuCl_2^-}$ given in the literature for NaCl aqueous solutions (5).
** Calculated from the slope of v-$\omega^{1/2}$ curves. ν was assumed to be 0.96 × 10⁻² cm/sec (6, 7) and the activity of Cl⁻ was used rather than concentration (8).
[a] D_{Cl^-} was calculated from the slope of v-$\omega^{1/2}$ curves assuming that the dissolution process is controlled by diffusion of Cl⁻ ions.
[b] D_{Cl^-} given in the literature for NaCl aqueous solutions (8).

The relative values of the dissolution rate corresponding to the curve for which $\Delta H\neq$ is equal to 6.7 kcal/mol in Fig. 5 were calculated on the assumption that the change of v with the temperature is due to the variation of both the diffusion coefficient of $CuCl_2^-$ and the solubility of copper chloride in the solution. From Eq. [4], the relative values of v are given by (1)

$$v\alpha D_{CuCl_2}{}^{-2/3}\,[CuCl_2^-] \qquad [5]$$

The values of $D_{CuCl_2}-$ at different solution temperatures were calculated from the equation (9)

$$\frac{D\mu}{T} = \text{constant} \qquad [6]$$

where μ is the viscosity of the solution, given in Ref. (7). The data on the solubility of copper chloride in solutions were borrowed from Ref. (10). The relative values of v are plotted against T^{-1} in Fig. 5. The slope of this curve gives a $\Delta H\neq$ value equal to 6.7 kcal/mol which is close to the experimental value of 7.5 kcal/mol. Therefore, the change of v with temperature is entirely ascribed to the variation of both $D_{CuCl_2}-$ and the solubility of copper chloride in the solution.

In summary, the rate-determining step for the dissolution of CuCl formed during the anodic dissolution of copper in solutions ranging from 0.05 to 1M in dissolved LiCl can be entirely attributed to the diffusion of $CuCl_2^-$ from the electrode surface to the bulk electrolyte.

Acknowledgment

The author extends his grateful thanks to Dr. G. Bélanger of IREQ for useful discussions.

Manuscript submitted June 7, 1982; revised manuscript received Jan. 4, 1983.

Any discussion of this paper will appear in a Discussion Section to be published in the December 1983 JOURNAL. All discussions for the December 1983 Discussion Section should be submitted by Aug. 1, 1983.

Publication costs of this article were assisted by Institut de Recherche d'Hydro-Quebec (IREQ).

REFERENCES

1. L. Brossard, *Can. J. Chem.*, **60**, 616 (1982).
2. A. Moreau, *Electrochim. Acta*, **26**, 497 (1981).
3. M. Braun and K. Nobe, *This Journal*, **126**, 1666 (1979).
4. N. Van Muylder, N. De Zoubov, and M. Pourbaix, *Cebelcor Tech. Rep.*, **101**, 000 (1962).
5. I. A. Semenov, V F. Lazarev, and A. I. Levin, *Sov. Electrochem. II*, 1013 (1975).
6. R. Parsons, "Handbook of Electrochemical Constants," p. 77, Butterworths Sci. Publ., London (1959).
7. R. P. Bird, W. E. Stewart, and E. M. Lightfoot, "Transport Phenomena," p. 8, John Wiley & Sons, New York (1960).
8. R. Parsons, "Handbook of Electrochemical Constants," p. 80, Butterworths Sci. Publ., London (1959).
9. J. G. Perry, "Chemical Engineering Handbook," 4th ed., McGraw-Hill, New York (1963).
10. I. N. Utkina, T. Ikunin, and A. A. Shutov, *Izv. Vyssh. Ucheb. Zaved, Khim. Technol.*, **12**, 7068 (1969).

Copper Deposition on Metal Filled Polymers Through Augmentative Replacement: New Method

A. Auerbach, C. W. Eichelberger, and R. J. Wojnarowski

General Electric Company, Research and Development Center, Schenectady, New York 12345

A new process has been developed (1) for bonding low resistivity copper onto a screen-printable polymer. This is accomplished by loading a polymer resin (novalac epoxy, curing agent, and a wetting agent) with a fine metal powder (−325 mesh) to upwards of eight times the resin weight. The metal powder consists of a nickel (75% by weight: Apache Chemicals, Incorporated): zinc (25% by weight: Apache Chemicals, Incorporated) mix. Although various ratios and mesh sizes were investigated, the adhesion of the copper to the polymer is best with the above mixture. To facilitate the high loading ratio and good printability a solvent is required (2). We used ethylene glycol ethyl ether acetate. The loaded polymer resin is then screen printed onto a substrate (glass, metal, phenolic, porcelainized steel, etc.) and oven cured. The solvent evaporates during the cure cycle. A cure schedule which we have used, when bonding to a glass substrate, is 30 min at 95°C followed by 1 hr at 180°C. Afterwards, the sample is cooled, and immersed from 2-7 min into an acidified copper plating bath. The bath consists of ⅝M $CuSO_4 \cdot 5H_2O$ (Fisher Chemicals), ½M H_2SO_4 (reagent grade), and ¼M HNO_3 (reagent grade). The bath temperature is maintained at 55°C. Here too, various bath mixtures and temperatures were investigated; the above bath composition and temperature was chosen since it provided both good copper plating and a reasonably long bath life.

Key words: polymer, electrode, SEM, reduction.

The sample is removed from the bath, rinsed with tap water, and dried. A low resistivity, bright copper coating is deposited on the screen printed substrate via the augmentative replacement reaction. The copper is contiguous as is readily obvious from the scanning electron microscope (SEM) print (Fig. 1). The surface resistivity is comparable to that of fired noble metal conductors (3-10 milliohms per square). The adhesion of the conductor to the polymer is excellent; in most cases more than 20 Newtons per square millimeter are required to sever the conductor from the polymer. Since the conductor is readily solderable without leaching, the adhesion test is easily performed.

We refer to the above process as augmentative replacement, since the contiguous copper conductor augments the metal available on the surface prior to the plating, to generate a surface conductor having a very low resistivity. The SEM print in Fig. 1 is representative of what occurs before, during, and after the plating. The left frame depicts the metal-filled polymer surface. Here the spherical particles are zinc; the granules are nickel. Both particle types are bonded to the polymer. The next frame shows the surface after the sample was immersed in the plating bath. The dark spots represent the zinc which is rapidly dissolved; the light spots are the nickel flakes covered in numerous places with copper. The final frame depicts the surface, now covered by the copper conductor, after a 4 min "electrodeless" plating. When compared with

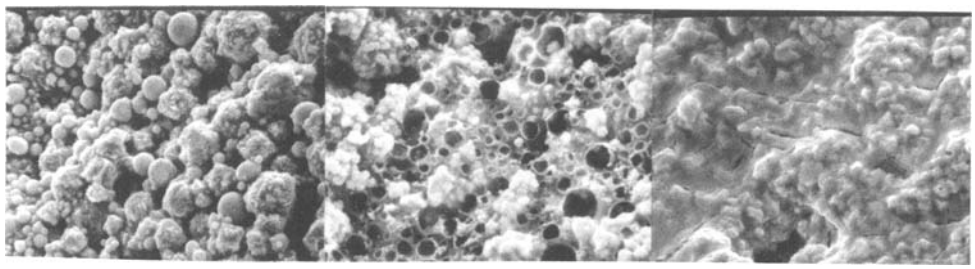

Fig. 1. An SEM print (2500×) of the augmentative replacement process. Left to right: zinc-nickel metallized epoxy, surface just after immersion into the plating solution, contiguous copper conductor after 5 min.

conventional autocatalytic electroless plating techniques, our method is extremely rapid. Figure 2 is a cross-sectional view of one screen printed sample. The thickness of the epoxy base is estimated at 50 μm. The copper conductor is from 5-10 μm thick. The conductor was deposited in only 4 min! It would take upwards of 1 hr to do this via conventional electroless plating.

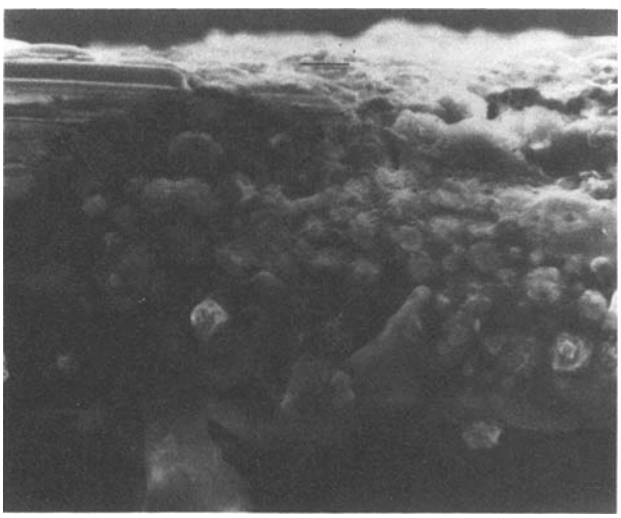

Fig. 2. Cross-sectional view (1000×) of the copper coated epoxy. The thickness of the epoxy base is *ca.* 50 μm; the copper conductor (region A) is *ca.* 8 μm thick.

Although our process is "electrodeless," it more closely resembles electrodeposition of copper in quantity per unit time. This can be explained by the microbattery action obtained from dissimilar metals. The process involves a replacement of the electronegative metals nickel and zinc by the electropositive copper. As the zinc dissolves, the liberated electrons reduce the copper ions contained in the bath.[1] The reduction occurs readily on all conductive surfaces. In the plate shown in Fig. 2 this would include both the nickel flakes and the deposited copper. This has been verified by monitoring both the surface potential of the metallized polymer and the resultant current as the augmentative replacement process occurs (3).

In summary, we report a new method for producing contiguous copper conductors on a variety of substrates having: surface resistivities rivaling those of conventional thick film noble metal conductors, excellent surface adhesion, and solderability without leaching. Although the process is "electrodeless", plating occurs rapidly, within 2-7 min. Furthermore, the process costs substantially less than alternative thick film methods. Possible future applications are manifold.

[1] Although the nickel also dissolves, it does so at a much slower rate under the conditions used. A more detailed discussion will be in a future publication.

REFERENCES

1. C. W. Eichelberger and R. J. Wojnarowski, Patents submitted.
2. H. Lee and K. Neville, in "Handbook of Epoxy Resins," McGraw-Hill, New York (1967).
3. In preparation.

Mechanisms of Electroless Metal Plating

I. Application of the Mixed Potential Theory

Perminder Bindra* and Judith Tweedie

IBM, T. J. Watson Research Center, Yorktown Heights, New York 10598

The Wagner and Traud (1) theory of mixed potentials postulates that the rate of a faradaic process is independent of other faradaic processes occurring simultaneously at the electrode and, thus, depends only on the electrode potential. Hence, the polarization curves for independent anodic and cathodic processes may be added to predict the overall rates and potentials which exist when more than one reaction occurs simultaneously at an electrode. More recently, it has been suggested (2) that the same concept applies to electroless plating processes and that plating mechanisms can be predicted from the polarization curves for the partial processes. This has given rise to some controversy (3, 4) as the two partial reactions in electroless plating processes are not entirely independent of each other.

* Electrochemical Society Active Member.
Key words: electroless plating, mixed potential, rotating disk electrode.

During the course of measurements to establish the validity or otherwise of the mixed potential theory for electroless plating processes, we have used a technique which allows determination of the polarization curve for one of the partial reactions during electroless plating, *i.e.*, while the other partial reaction is occurring simultaneously. This technique is similar to a technique used earlier by Makrides (5) to study the dissolution of iron in sulfuric acid. It is a very simple technique and involves observation of the mixed potential of the plating system as a function of agitation and as a function of the concentration of the reductant or oxidant. It is based on the classification of electroless plating processes according to their overall mechanisms. Electroless plating of metals invariably involves a reaction proceeding at a rate limited by diffusion. For example, the plating rate of copper in a copper-formaldehyde bath is determined, to a large extent, by the rate of diffusion of copper to the plating surface

(6). The technique described here allows a clear distinction between those reactions whose rate is controlled by the rate of diffusion of reactants to the plating surface, and those reactions whose rate is limited by some slow electrochemical step.

Since each partial reaction is under diffusion control or under electrochemical (activation) control, the overall reaction scheme consists of four possible combinations. This is a simplified view of the situation as it is perfectly possible for a partial reaction to be under mixed control, *i.e.*, under diffusion plus activation control. In this paper however, the case in which the cathodic partial reaction is entirely diffusion controlled, and the anodic partial reaction totally activation controlled is described. This case applies to the copper-formaldehyde plating bath.

Theoretical Aspects

We assume that the electroless plating reaction is composed of the following partial reactions

$$R^{o} \rightarrow R^{z+} + Ze^{-} \quad \text{(anodic)} \qquad [1]$$

and

$$M^{z+} + Ze^{-} \rightarrow M^{o} \quad \text{(cathodic)} \qquad [2]$$

When these two reactions are at steady state, the Wagner-Traud postulate applies and the plating rate, i_p, is given by

$$i_p = i_R = |i_M| \qquad [3]$$

where i_R and i_M are the anodic and cathodic partial currents (with opposite signs). The potential associated with this equilibrium condition is the mixed potential E_{MP}. The current due to the diffusion of metal ions to a rotating disk is given by (7)

$$i_M = B_{M'} (C_M^{\infty} - C_M^{a}) \sqrt{\omega} \qquad [4]$$

where C_M^{∞} is the bulk concentration of metal ions, C_M^{a} the surface concentration, and $B_{M'}$ is a diffusion parameter given by (8)

$$B_{M'} = 0.62\, n_M F D_M^{2/3} \nu^{-1/6} A \qquad [5]$$

In Eq. [5], D_M = diffusion coefficient of the metal ions; ν = kinematic viscosity; n_M = number of electrons involved in the metal deposition reaction; F = Faraday, and A = area of the disk. For diffusion-controlled cathodic partial reaction, $C_M^{a} = 0$, and the limiting current i_M^{D} is independent of potential and takes the form

$$i_M^{D} = B_{M'} C_M \sqrt{\omega} \qquad [6]$$

When the anodic partial reaction is under electrochemical control, the current-voltage curve is described by the equation

$$E = E_R^{o} - b_R \ln n_R F k_R - b_R \ln C_R^{\infty} + b_R \ln i_R \qquad [7]$$

where k_R is the apparent rate constant; n_R is the number of electrons involved in the anodic reaction, and the Tafel slope $b_R = RT/(1 - \alpha_R) n_R F$. Then combining Eq. [6] with Eq. [7] by means of Eq. [3] gives

$$E_{MP} = E_R^{o} - b_R \ln n_R F k_R - b_R \ln C_R^{\infty} + \frac{b_R}{2} \ln B_{M'}^{2} \omega + b_R \ln C_M^{\infty} \qquad [8]$$

Equation [8] describes the dependence of E_{MP} on experimental parameters such as ω and C_M^{∞} for the case in which the cathodic partial reaction is diffusion controlled and anodic partial reaction is activation controlled. It is clear that E_{MP} is a linear function of ln ω and ln C_M^{∞}. This case is represented graphically in the symbolic diagram of Fig. 1.

Results

The measurements were performed in a copper EDTA-formaldehyde plating solution which consisted of $4 \times 10^{-2} M$ $CuSO_4$, $1.2 \times 10^{-1} M$ EDTA, and $0.0784 M$ formaldehyde. The operating temperature was 70°C, and the solution pH was maintained at a value of 11.7 with NaOH. In order to achieve conditions of controlled mass transfer, the measurments were performed with a rotating disk electrode. The data obtained is shown in Fig. 2 and 3. It is clear that the experimental points in each one of these plots group around straight lines. The slopes of the straight lines were determined by least squares analysis. We note that the mixed potential increases with both the rotation rate ω and the metal ion concentration C_M^{∞} while it decreases with the concentration C_R^{∞} of formaldehyde in the plating solution. This behavior meets the criteria of a diffusion-controlled cathodic partial reaction coupled with an activation-controlled partial anodic reaction as indicated in Eq. [8]. Further verification for this overall mechanism was obtained by comparing the measured slope of the rotation rate dependence dE_{MP}/d ln ω with the concentration dependences dE_{MP}/d ln C_M^{∞} and dE_{MP}/d ln C_R^{∞}. The experimental slopes have

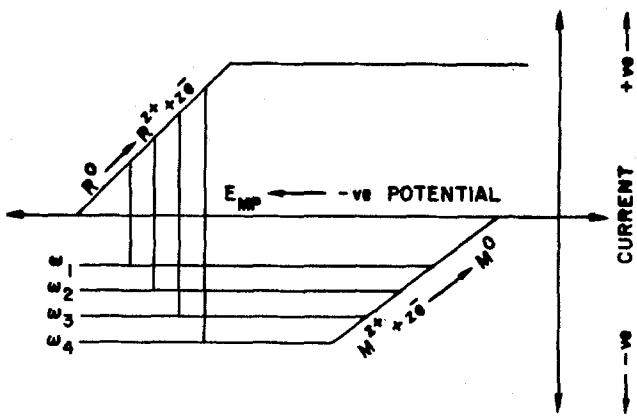

Fig. 1. Symbolic representation of the overall reaction scheme for electroless metal deposition in which the cathodic partial reaction is diffusion controlled and the anodic partial reaction activation controlled.

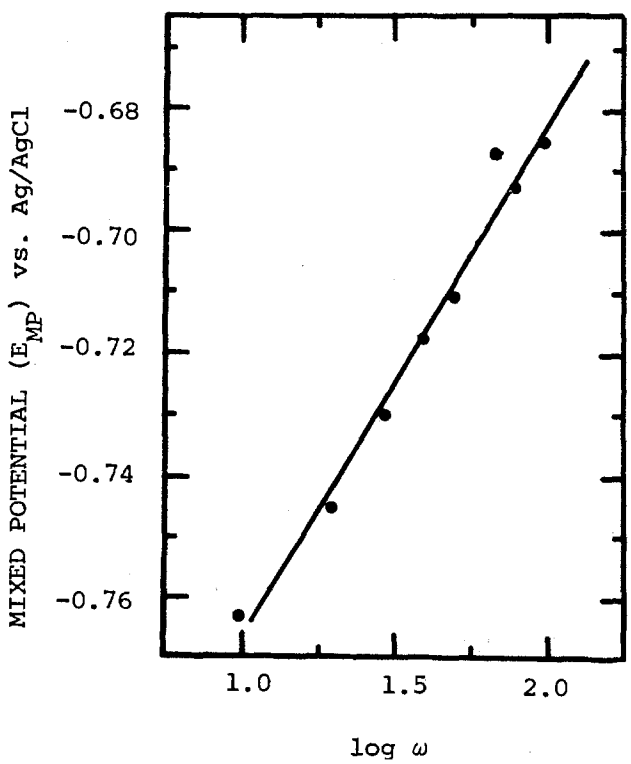

Fig. 2. Plot of the mixed potential of the plating solution as a function of rotation rate. Temperature = 70°C; pH = 11.7.

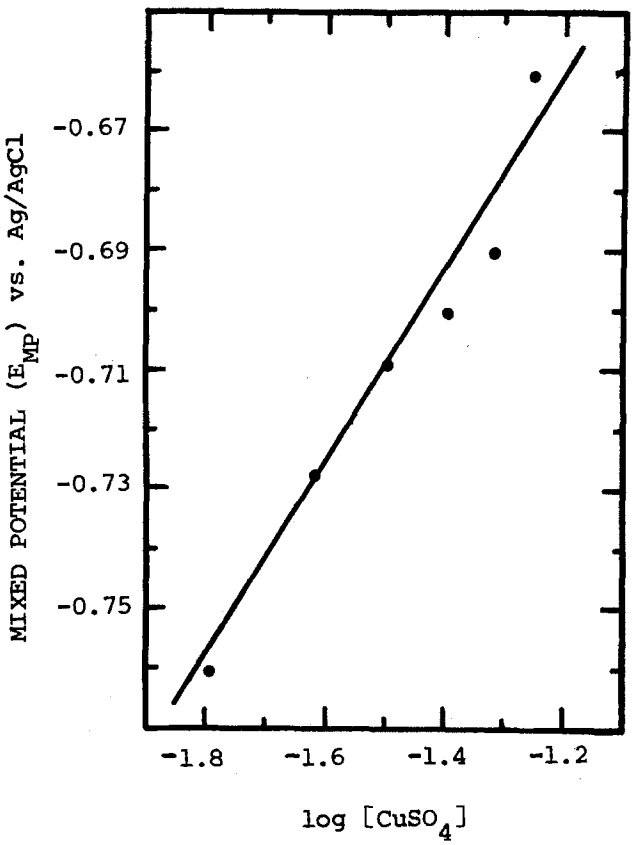

Fig. 3. A plot of the mixed potential of the plating solution against the logarithm of the $CuSO_4$ concentration. Temperature = 70°C; pH = 11.7.

the relationship

$$\frac{dE_{MP}}{d \ln C_R^{\infty}} = \frac{dE_{MP}}{d \ln C_M^{\infty}} = 2 \times \frac{dE_{MP}}{d \ln \omega} \quad [9]$$

which is also predicted by Eq. [8]. A Tafel slope of 170 mV/decade for formaldehyde oxidation obtained in the plating solution is slightly lower than the value obtained in the anolyte alone. This is due to the interdependence of the two partial reactions in the plating solution. Nonetheless, a Tafel slope of 170 mV/decade corresponds to a value of 0.41 for the anodic transfer coefficient. Deviation of the transfer coefficient from 0.5 is known to occur when the reacting species are specifically adsorbed. Such behavior is characteristic of catalytic reactions.

Manuscript submitted Sept. 7, 1982; revised manuscript received Nov. 15, 1982.

Any discussion of this paper will appear in a Discussion Section to be published in the December 1983 JOURNAL. All discussions for the December 1983 Discussion Section should be submitted by Aug. 1, 1983.

Publication costs of this article were assisted by IBM T. J. Watson Research Center.

REFERENCES

1. C. Wagner and W. Traud, *Z. Electrochem.*, **44**, 391 (1938).
2. M. Paunovic, *Plating*, **51**, 1161 (1968).
3. S. M. El-Raghy and A. A. Abo-Salama, *This Journal*, **126**, 171 (1979).
4. F. Donahue, *ibid.*, **119**, 72 (1972).
5. A. C. Makrides, *ibid.*, **107**, 869 (1960).
6. F. M. Donahue, *ibid.*, **127**, 51 (1980).
7. V. G. Levich, "Physicochemical Hydrodynamics," Prentice-Hall, Englewood Cliffs, NJ (1962).
8. A. C. Riddiford, "Advances in Electrochemistry and Electrochemical Engineering," Vol. IV, Interscience, New York (1966).

Time-Resolved Laser Interferometric Investigation of the Growth of Diffusion Layer during an Electrodeposition of Pyrrole Polymer

R. N. O'Brien

Department of Chemistry, University of Victoria, Victoria, British Columbia, Canada V8W 2Y2

and K. S. V. Santhanam

Tata Institute of Fundamental Research, Bombay, India

Laser interferometry has been shown to be a useful technique for the investigations of the growth of diffusion layers at the electrode-solution interface during electrochemical processes such as metal ion deposition (1, 2), but its applicability to the study of organic electrode processes such as polymer deposition has not yet been explored. Polymer deposition on an electrode involves several steps including, for example, formation of free radicals, propagation and termination of the polymeric chains. A few polymers such as polypyrrole exhibit the property of electronic conduction and are being considered as replacements of conventional electrode materials (3, 4). We wish to report in this communication on the growth of the diffusion layer during the electrodeposition of polypyrrole on a gold electrode and the use of such a polymer as an electrode material in the investigation of electrochemical oxidation and reduction.

The electrodeposition of polypyrrole was carried out galvanostatically from an acetonitrile (anhydrous) bath containing 0.1M $(C_4H_9)_4NClO_4$ and 60 mM freshly distilled pyrrole. The electrochemical cell consisted of two gold-plated copper blocks (length 11 mm, thickness 1.78 mm) separated by either 7.5 or 5.0 mm fitted into a Teflon cell holder. A few experiments were also carried out using gold-plated glass electrode pieces (deposited by vacuum deposition) (length 30.0 mm, thickness 5.0 mm) separated by a fixed distance of 6.60 mm. The cell itself acted as a Fabry-Perot interferometer (5). The gold plating of the copper blocks and glass pieces was done by the sputtering technique or by vacuum deposition for a maximum period of 5 min. In all cases the electrodes were in the deep vertical configuration (V) so that the greater dimension (length) is the depth of solution and the lesser dimension (thickness) is the solution thickness the laser light traverses. The interferometric multiple beam fringes were formed using dielectric-coated flats separated by the thickness of the electrodes (1.78 mm) having a finesse of about 7. The light source was a nominal 1 mW He-Ne laser. The fringes were arranged by suitably tightening the cell clamps and the concentration-perturbed fringe patterns were recorded at intervals with a 35 mm Nikon camera. The experi-

Key words: interferometry, diffusion, polypyrrole, polymer coated, nonaqueous.

mental runs were also videotaped through the Nikon's view finder with verbal comments audio recorded.

The deposition of pyrrole polymer was carried out at different current densities (C.D.'s) in the range of 0.10 mA cm^{-2} for a duration ranging from 3 to 15 min. The thickness of the deposits ranged from about 80 nm to 20 μm depending on the duration and current passed in the electrolysis.

The progress of the electrodeposition was followed by time-resolved laser interferometry using vertical electrodes in the electrochemical interferometric cell. Figure 1 shows the interference fringes before starting the electrolysis. Equally spaced dark and bright fringes show that the refractive index of the medium remains constant throughout the solution except for the central, expanded dark fringe to be discussed later. When the electrolysis was started, the fringes at the cathode and anode regions bend as shown in Fig. 1b, indicating the development of diffusion layers at the cathode and anode. The central optical disturbance now shows up as the area at which some convection is beginning and below which there is limited deposition. The deposition of the polymer occurred on the anode ($E_{pyrrole}^{o'} \approx 1.22V$ *vs.* SCE) (6) and the corresponding cathodic process was the reduction of tetra-n-butyl ammonium ($(C_4H_9)_4N^+$) ion. The electrochemistry of the quaternary ammonium ion in nonaqueous solvents has previously been reported (7, 8) and the one-electron reduction produces a neutral radical. The neutral radical undergoes a cleavage reaction ultimately producing $(C_4H_9)_3N$ ($n_o = 1.4252$) and C_4H_{10} (g). The development of the diffusion layer at the anode can be seen in Fig. 1b and c (c is a gold on glass electrode discussed below). From the very beginning of the electrolysis, fringes begin to bend upward (the result of oxidation as previously explained) and this growth continues up to about 60 sec. The fringes at the cathode show a bending downward (increase in refractive index and increase in concentration of the reduction product). The two, odd diverging fringes in the figure, which are seen from the start of the electrolysis, are caused by the darker part of the gold plating during sputtering. Portions below the diverging fringes had an uneven mixture of gold and presumably some oxides or intermetallics. The appearance of the sputtered surface and the divergence of the fringe suggests a very slight potential difference between the two electrodes at this point and between top and bottom of the electrodes resulting in a small amount of local electrochemical activity (corrosion of the bottom part). The electrodeposition of the polymer in this region was not adherent. This problem was overcome by using a glass substrate for gold which yielded uniform fringes (Fig. 1c). As the electrolysis proceeds, at about 30 sec, a fringe shift at the cathode of 6 was observed while at the anode a fringe shift of 5 was observed using a C.D. of 0.66 mA cm^{-2}. The change in refraction index and hence the concentration change is found from the modified Bragg equation, $2n + \cos\theta = N\lambda$ (1), where n is the refractive index, t is the thickness of the cell, N is the order of interference, and λ is the laser light wavelength. At the cathode $N_o = N_0 + 6$ and the appropriate Δn can be found and thence ΔC. At higher C.D.'s (5 mA cm^{-2}), a rapid production of the intermediates at the anode in the polymerization process results in the accumulation of products near the electrode surface which cuts off part of the fringes. This cutoff region increases with time and, interestingly during the course of the electrolysis, a development of hydrodynamic flow pro-

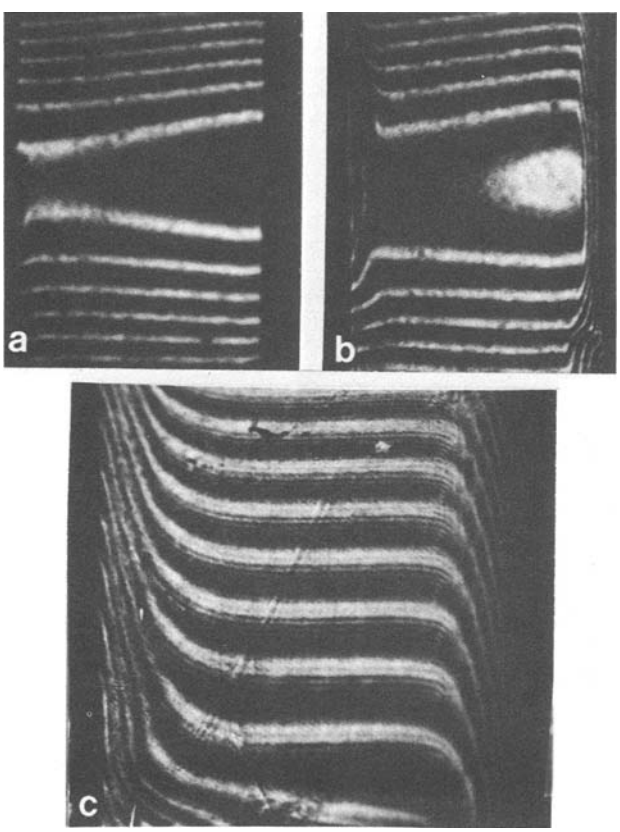

Fig. 1. Interferograms showing concentration gradients during deposition of the pyrrole polymer from an acetonitrile bath containing 0.1M $(C_4H_9)_4NClO_4$ and 60 mM pyrrole. (a) 0, (b) 30 sec $i_0 = 5.0$ mA cm^{-2}. Left side, Au anode; right side, Au cathode. (c) 60 sec at $i_0 = 0.66$ mA cm^{-2}. (Glass substrate.)

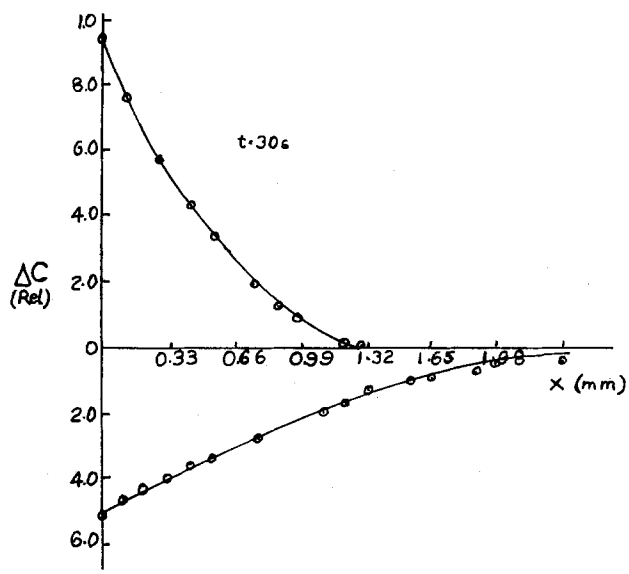

Fig. 2. Changes in interfacial concentrations during electrodeposition at anode or cathode. i_0, 5.0 mA cm^{-2}. Elapsed time in electrolysis, 30 sec. Top, at cathode; bottom curve, at anode.

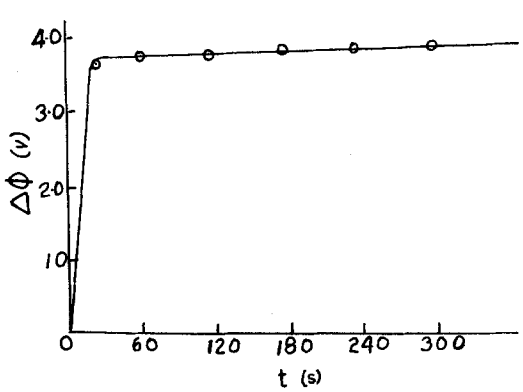

Fig. 3. The changes in the cell voltage during the progress of electrolysis of pyrrole. i_0, 5.0 mA cm^{-2}.

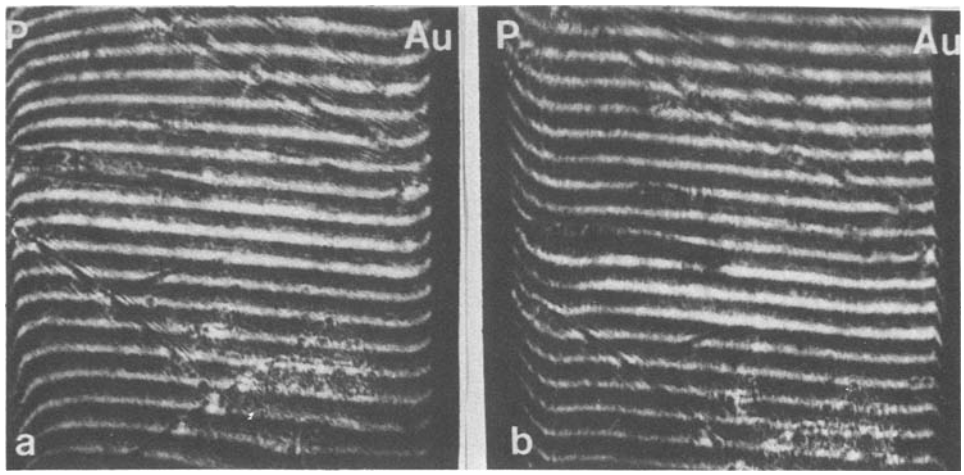

Fig. 4. Interferograms obtained during electrolysis of 0.1M $(C_4H_9)_4NClO_4$ in acetonitrile at a pyrrole polymer (p) at 2.5 m cm^2 and 30 sec. Panel (a) shows the polymer (p) coated electrode as the cathode and panel (b) the polymer electrode as the anode.

duced near the cathode due to the movement of tiny bubbles near the electrode surface can be observed. There is evidence for this flow in the contorted fringe pattern. This flow completely disrupts the fringes below the pure gold part of the electrode. This type of disturbance is negligible at lower C.D.'s and, at the end of this electrolysis, a smooth adherent deposit was obtained on the gold surface similar to anodic film formation (9).

The growth of the diffusion layer in the first 30 sec of deposition at 5 mA cm^{-2} and for longer periods of 300 sec at a lower C.D. of 0.66 mA cm^{-2} can be observed in the recordings. Figure 2 shows the pyrrole depletion with distance from the electrode during an electrolysis. The optical anomalies, reported by Ibl (10) and later treated by Beach (11), resulting from unequal refraction of the light in a concentration gradient would cause less than 1% error (the electrode thickness is small). The depletion region at the anode extends to 2.35 mm while at the cathode, the refractive index gradient is sharper and extends to about 1.32 mm. We did not investigate in detail the cause of the sharp gradient of the cathode, although it appears to be caused by the hydrodynamics (convection) at this electrode and the production of $(C_4H_9)_3N$ (7). Whether the direction of the fringe bending was caused by an increase or decrease in refractive index in the actual experiment was decided by injecting pyrrole in the anode or cathode region. This introduction of pyrrole produced a fringe bending downward at the anode (increase in concentration), which is in the same direction as in the real experiment at the cathode. The current-voltage (galvanostatic condition) curve for the polymer deposition is shown in Fig. 3.

The performance of the polymer-coated electrode was examined by using acetonitrile containing 0.1M $(C_4H_9)_4NClO_4$. The polymer-coated electrode (20 μm) was washed well with acetone followed by acetonitrile before using it in the experiment. The counterelectrode was a gold-plated glass electrode. The development of the interference fringe pattern during electrolysis at a C.D. of 2.50 mA cm^{-2} is shown in Fig. 4. The fringes at the cathode show a smooth downturn (increase in refractive index, increase in concentration) during the progress of the electrolysis and the concentration changes occurring at this electrode are shown in Fig. 5. The polymer electrode was used in an experiment following the one whose results are shown in Fig. 5. The concentration changes at this electrode were about five times smaller than was observed at the Au electrode. Nevertheless, the conducting nature of the polymeric electrode is clearly demonstrated in these experiments. The oxidation of perchlorate ion at the anode was not examined in detail because it undergoes a catalytic and cyclic reaction (12).

The studies conducted here show that polymer depositions in nonaqueous media can be followed by laser

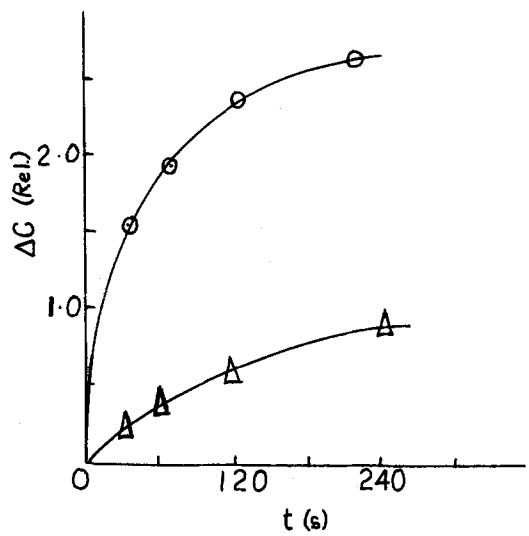

Fig. 5. The interfacial concentration changes during the progress of the electrolysis of 0.1M $(C_4H_9)_4NClO_4$ in acetonitrile at a polymer electrode. ○ at cathode (Au), △ polymer cathode i_0, 2.50 mA cm^{-2}.

interferometry and the depletion in the regions at the electrode surfaces (diffusion/hydrodynamic layer) can be determined. When pyrrole oxidation produces a conducting polymer on the electrode surface, some of the intermediate radicals appear to diffuse away from the electrode as expected (7). The polymeric pyrrole coatings show good conducting properties and show promise as an electrode material (3).

Acknowledgments

The authors wish to acknowledge the support for this work by Natural Sciences and Engineering Research Council of Canada and the help of Teddy Robert Gathwright and N. S. Sundaresan.

Manuscript submitted Aug. 25, 1982; revised manuscript received Nov. 15, 1982.

Any discussion of this paper will appear in a Discussion Section to be published in the December 1983 JOURNAL. All discussions for the December 1983 Discussion Section should be submitted by Aug. 1, 1983.

Publication costs of this article were assisted by the University of Victoria.

REFERENCES

1. R. N. O'Brien, in "Techniques of Chemistry, Physical Methods," Vol. 1, A. Weissberger and B. Rossiter, Editors, Part IIIA, Chap. 1, Wiley-Interscience, New York (1972).
2. R. N. O'Brien, B. B. Kulkarni, W. Michalik, and K. S. V. Santhanam, *Can. J. Chem.*, **59**, 1933 (1981).
3. *Chem. Eng. News*, 29 (April 19, 1982).

4. G. Towsillon and F. Garnier, *J. Electroanal. Chem. Interfacial Electrochem.*, **135**, 173 (1982) and references therein.
5. R. N. O'Brien, *This Journal*, **124**, 96 (1977).
6. N. S. Sundaresan and K. S. V. Santhanam, *Trans. SAEST*, **16**, (3), 117 (1981); C.A., 211882, **95**, (1981).
7. S. D. Ross, M. Finklestein, and R. C. Patterson, *J. Am. Chem. Soc.*, **82**, 1582 (1960).
8. L. Horner and H. Lund, "Organic Electrochemistry," M. M. Baizer, Editor, p. 743, Marcel Dekker, New York (1973).
9. S. Fletcher and R. G. Barradas, *This Journal*, **125**, 1960 (1978); J. D. Porter, *Can. J. Chem.*, **55**, 4037 (1977).
10. N. Ibl, in "Proceedings of the 7th Meeting C.I.T.C.E., Lindan," Butterworths, London (1955).
11. K. Beach, Ph.D. Thesis, University of California, Lawrence Radiation Laboratory, Berkeley, Calif., UCRL-20324, AEC Contract-W 7405, Eng. 48.
12. A. H. Maki and D. H. Geske, *J. Chem. Phys.*, **30**, 1356 (1959).

The Electrolytic Synthesis of Hydrogen Peroxide in a Dual Membrane Cell

Christa Kuehn,[1] Frederic Leder, Raymond Jasinski,* and Kathy Gaunt[2]

Occidental Research Corporation, Irvine, California 92713

Hydrogen peroxide is a chemical of continuing and growing commercial interest. Hydrogen peroxide is presently manufactured by an organic auto-oxidation process with anthraquinone derivatives and by electrochemical oxidation of sulfuric acid via peroxydisulfuric acid (1). Investigation of new methods to obtain hydrogen peroxide directly from oxygen has received recent attention (2-7). Alkaline solutions of hydrogen peroxide can be prepared by the electroreduction of oxygen at carbon electrodes in caustic media (2-7), and alkaline peroxide solutions can be used as sodium hydroperoxide solutions for on-site bleaching (4). However, these solutions are not sufficiently stable for storage or shipping and are unsuitable for making concentrated solutions of neutral hydrogen peroxide by steam distillation. Acidic hydrogen peroxide has been produced electrochemically only on an electroanalytical scale (*e.g.*, 8, 9). We describe here a dual-membrane plate-and-frame electrochemical cell for the direct production of relatively concentrated acidic hydrogen peroxide solutions (Fig. 1). A thin center compartment is defined by a cation and an anion exchange membrane. Caustic peroxide is generated at the carbon cathode by the reduction of oxygen and is concentrated in the center compartment by electrodialysis across the ion-exchange membrane. Water is oxidized simultaneously at the anode, forming oxygen and protons. These protons migrate across the cation-exchange membrane at the same rate anions migrate across the anion-exchange membrane, neutralizing OH^- and HO_2^-. The electrolyte (acid) concentration in the center is not altered and only oxygen and water are consumed to make hydrogen peroxide.

Experimental

The circular dual-membrane plate-and-frame cell was fabricated from Plexiglas. The cathode (63 mm diam, 380 millimicrons thick) was a porous carbon black-Teflon gas-diffusion electrode on nickel screen backing (Giner Incorporated, Waltham, Massachusetts). The circular anode was a DSA electrode with an IrO_2/Ta_2O_5 coating on titanium (TIR-2000, Diamond Shamrock, Ohio). The anode was imbedded in the Plexiglas and only one surface was exposed to solution. The cation exchange membrane was Nafion 415 (du Pont), 0.30 mm thick. A variety of anion exchange membranes was used: Ionac MA 3148 (0.33 mm thick) (Ionac, Birmingham, New Jersey), Permion 4025 and 4035 (RAI Research Corporation, Hauppauge, New York). The 4035 membrane has pyridinium functions, radiation grafted to Teflon. Ionac MA 3148 is a polymerized polyvinylpyridinium material.

The cell was assembled with the cation membrane spaced 1.5 mm from the anode, the cation and anion membranes spaced 3 mm apart, and the anion membrane spaced 8 mm from the cathode. Each of the three compartments had a separate reservoir of electrolyte solution which was recirculated through the compartment at 120 ml/min. The catholyte volume was 200 ml, the anolyte volume was 100 ml, and the center compartment solution volume was usually 60-100 ml. The specific concentrations are given in Table I. The current was controlled at 5A with an HP 6286 A Power Supply, resulting in cathode and anode current densities of 394 A/m^2. The cell voltage varied between 2 and 4V using Nafion 415 and Permion 4035 membranes and between 4 and 10V using Ionac 3148 membranes. The oxygen was introduced at the porous cathode at 1.1 kPa gauge. Water was added to the anolyte and catholyte solutions to maintain constant volume, and the product solution was withdrawn from the center compartment in order to maintain a constant volume. The temperature of all the solutions was maintained at approximately 15°C by keeping the reservoir solutions in an ice bath.

The peroxide concentration in the center and catholyte solutions was determined by titrating 0.500 ml aliquots (acidified with 100 ml 0.3M H_2SO_4) with 0.100M standard ceric ammonium sulfate solution (GF Smith). The electrolyte solutions were made up using reagent grade sodium hydroxide (MCB) and sulfuric acid (VWR) and deionized water. Compressed oxygen gas was 99.8% O_2 (Matheson).

Results

The experimental data are summarized in Table I; the term "final H_2O_2 concentration" is taken to represent total peroxide, *i.e.*, HO_2^- as well as neutral peroxide. The time-peroxide concentration profile of Run 2 is shown in Fig. 2. Oxygen was reduced at the gas-diffusion cathode to hydroperoxide ion. Over the duration of the experiment the concentration of peroxide in the center compartment increased from 0 to 11.1%, while the concentration of peroxide in the catholyte remained approximately constant. In all runs the final catholyte peroxide concentration approximated the original concentration of the KOH electrolyte (Table I). No hydrogen peroxide was detected in the anolyte. (If any neutral peroxide had passed through the cation-exchange membrane, it would have been oxidized at the anode and thus would not have been detected.)

The concentration-time curves with electrolytes other than sulfuric acid in the center compartment (Runs 9

* Electrochemical Society Active Member.
[1] Present address: P.O. Box 7728, Newport Beach, California 92660.
[2] Present address: Burroughs Corporation, Westlake Village, California 91361.
Key words: hydrogen peroxide, electrochemical synthesis, ion exchange membranes.

Table I. Summary of peroxide generation experiments (3 compartment cell; M H_2SO_4 anolyte)

Experiment No.	Initial electrolyte composition		Final H_2O_2 concentration		
	Center	Catholyte (M KOH)	Center (M)	w/o	Catholyte (M)
1	0.1M H_2SO_4	0.1	1.6	5.4	0.09
2	0.1M H_2SO_4	0.5	3.2	10.8	0.51
3	0.1M H_2SO_4	1.0	1.9	6.4	0.90
4	1.0M H_2SO_4	1.0	1.7	5.7	0.80
5	0.6M H_2O_2 + 0.1M H_2SO_4	1.0	2.1	7.1	0.50
6	1.5M H_2O_2 + 0.1M H_2SO_4	1.0	2.6	8.8	0.75
7	2.9M H_2O_2 + 0.1M H_2SO_4	1.0	2.9	9.9	—
8	1.0M H_2SO_4	0.3	1.6	5.4	0.30
9	0.1M NaOH	0.5	1.4	4.8	0.60
10	0.1M Na_2SO_4	1.0	1.7	5.7	0.75

and 10) were similar to Fig. 2. However, these experiments were deliberately terminated before the plots had approximated plateaus and thus these "final" concentration values do not necessarily represent limiting values. Nevertheless the data (Table I) show that hydroperoxide ion can be transferred into electrolytes other than sulfuric acid.

The concentration of peroxide attainable in the center sulfuric acid compartment depended on the size (volume) of the center compartment solution as well as the rate of decomposition of peroxide, the rate of attack of all elements by peroxide, and the diffusion of neutral peroxide out of the center compartment. The role of the center compartment volume was shown as follows: For Run 2, the starting solutions were anolyte 1M H_2SO_4 (100 ml), center solution 0.1M H_2SO_4 (65 ml), and catholyte 0.5M KOH (200 ml). This volume of the center solution, 65 ml, was the minimum volume practical in our particular experiments. When the volume of the center solution was 100 ml, or 1.5× greater, the concentration of the peroxide obtained in the center compartment was correspondingly less, *i.e.*, ≃7 weight percent (w/o) (Run 3).

The anion membrane was visibly deteriorated after all experiments; new anion membranes were used for each experiment. The rate of membrane attack was not studied in detail since the best of the membranes survived only a few hours, far too short to be of interest for an industrial process. The RAI Permion 4035 was more stable than the others tried (Run 2). Using RAI Permion 4035, the cell voltage for a single experiment remained essentially constant at 3-3.3V; the current efficiency varied between 100 and 73%. When the Ionac 3148 membrane was used, the cell voltage changed from 4 to 9V, and the current efficiency was substantially lower. The Nafion 415 cation membrane was reused in all our experiments. It appeared stable and virtually unchanged from experiment to experiment.

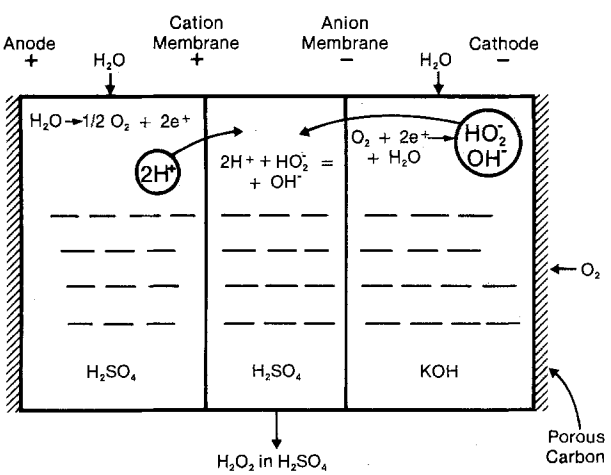

Fig. 1. This is a schematic representation of the operating cell emphasizing the transfer by electrodialysis of OH^-, HO_2^-, and $2H^+$ produced by electrolysis in the anolyte and catholyte.

Discussion

Oxygen is reduced at a carbon gas-diffusion cathode to hydroperoxide anion and hydroxide anion

$$O_2 + H_2O + 2e \rightarrow OH^- + HO_2^-$$

By virtue of the anion membrane, K^+ is restricted to the catholyte. To maintain electrical neutrality, anions must therefore exit the catholyte in numbers equal to those produced by electrolysis. OH^- is the more mobile anion [192 Ω^{-1} eq^{-1} cm^2, *vs. ca.* 50 for HO_2^- (11)] and is expected to leave the catholyte preferentially. However, electrolysis continues to inject HO_2^- into the catholyte, eventually yielding an HO_2^- concentration equal to the original potassium ion concentration. At this point, both OH^- and HO_2^- produced by electrolysis must exit the catholyte and enter the center

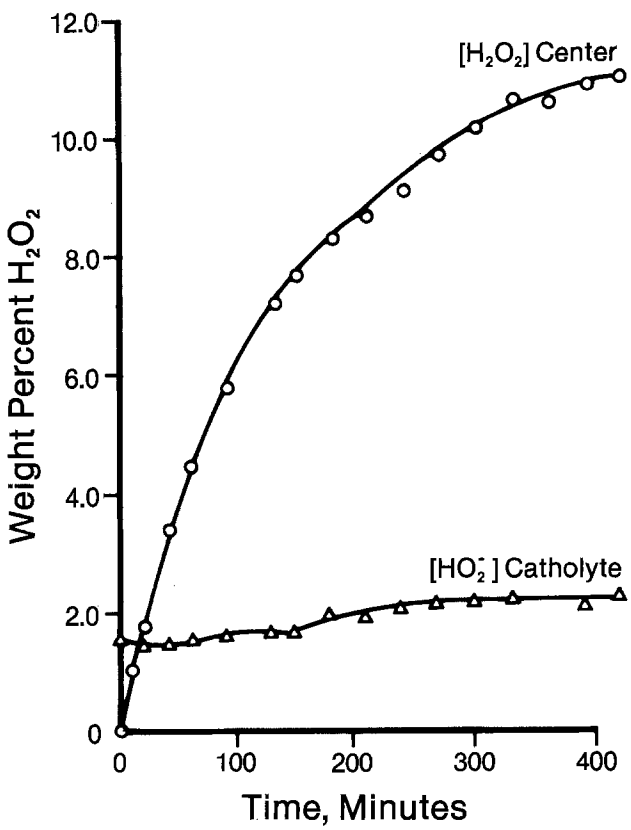

Fig. 2. Shown here are the concentrations of H_2O_2 measured in the catholyte and in the center compartment solution *vs.* time. The initial solutions were a catholyte of 200 ml, 0.5M KOH, and a center compartment solution of 65 ml, 0.1M H_2SO_4. This was Run 2 of Table I.

compartment where both are neutralized by protons entering from the anolyte. Thus at steady state, one molecule of H_2O and one molecule of H_2O_2 accumulate in the center compartment solution per molecule of O_2 electrolyzed at the cathode. By this electrolysis/dialysis technique we were able to generate *ca.* 11% peroxide from oxygen and 0.1M H_2SO_4.

The chemistry of the receiving solution had little effect on cell performance within the concentration ranges studied. Peroxide was concentrated into sulfuric acid, sodium hydroxide, and sodium sulfate. Hydroperoxide salt precipitation would be expected at higher sodium salt concentrations than referenced in Table I. It is to be expected that some neutral H_2O_2 will diffuse out of the center compartment into the anolyte and catholyte by virtue of the concentration gradient. Measurements of this effect were not made.

This electrolysis/dialysis model suggests that the maximum hydroperoxide concentration in the catholyte should approximate the original potassium ion concentration. As shown in Table I this is indeed the case.

Peroxide concentrations (center compartment)/time curves were calculated based on this simple model of electrolysis, dialysis, and charge balance, ignoring diffusion of neutral peroxide. Shown in Fig. 3 are two such curves calculated for 70 and 100% net efficiency, compared with the curve for Run 3. Clearly this simple model of electrolysis and dialysis explains at least the gross features of the experiment. The theoretical maximum hydrogen peroxide concentration in the center calculates as 22M, assuming a center compartment solution formed only from the water and peroxide generated by electrolysis/dialysis/neutralization. This concentration is determined solely by dilution of H_2O_2 by water formed from neutralized OH^-, *i.e.*, $(H_2O_2)/[(H_2O_2) + (H_2O)] = 34/(34 + 18)$. Such a situation is achievable in principle by starting with a center compartment solution of any volume, but at 22M H_2O_2. Product peroxide would result in a net increase in center compartment solution volume. It should also be possible, in principle, to build up the concentration of electrolytic peroxide from zero to commercially attractive values (variously estimated as greater than 15 or 20%) by using low center solution volumes, thin center campartment, and by cascading several cells in series.

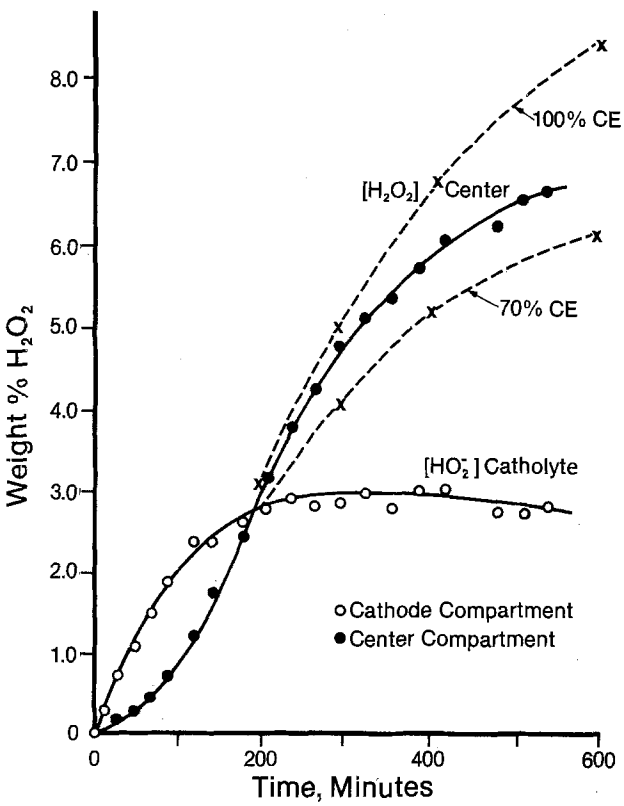

Fig. 3. An experimental center compartment peroxide concentration/time curve is compared with two calculated curves (- - -), based on a model of electrolysis and dialysis. The variable in the calculation was current efficiency. Also shown is the catholyte accumulation curve. This was Run 3 of Table I.

However, the chemical stability of present anion-exchange membranes limits the commercially accessible peroxide concentrations to less than the 10-12% (nominally 3.3M) achieved in these experiments. At these concentrations state-of-the-art anion exchange membranes break down within a few hours. The Nafion cation membranes, on the other hand, were stable for the duration of these experiments. They are fluorocarbon polymers, functionalized with sulfonic acid groups. An anion-exchange fluorocarbon membrane is not commercially available. The use of radiation-grafted Teflon (with pyridinium function) did show an improvement over conventional hydrocarbon backbone membranes. However, our results imply that oxidative attack also takes place on the pyridinium linkage. Quaternary-ammonium-salt membranes with hydrocarbon backbones were rapidly deteriorated.

Manuscript submitted Aug. 31, 1982; revised manuscript received Dec. 1, 1982.

Any discussion of this paper will appear in a Discussion Section to be published in the December 1983 JOURNAL. All discussions for the December 1983 Discussion Section should be submitted by Aug. 1, 1983.

Publication costs of this article were assisted by Occidental Research Corporation.

REFERENCES

1. W. C. Schumb, C. N. Sattefield, and R. L. Wentworth, "Hydrogen Peroxide," Reinhold Publ. Corp., New York (1955).
2. C. Oloman and A. P. Watkinson, *J. Appl. Electrochem.*, **9**, 117 (1979).
3. C. Oloman and A. P. Watkinson, U.S. Pat. 3,969,201 (1976); U.S. Pat. 4,-18,305 (1978).
4. C. Oloman, *Can. Pulp Pap. Ind.*, **63-64** (July 1980).
5. J. A. McIntyre and R. F. Phillips, Paper 399 presented at The Electrochemical Society Meeting, Montreal, Que., Canada, May 9-14, 1982.
6. O. Spalek and J. Balej, *Collect. Czech. Chem. Commun.*, **46**, 2052 (1981) and references therein.
7. J. Balej, K. Balogh, and O. Spalek, *Chem. Zvesti*, **30**, 384 (1976).
8. H. Behret, W. Clauberg, and G. Sandstede, *Ber. Bunsenges. Phys. Chem.*, **81**, 54.
9. T. Geiger and F. C. Anson, *J. Am. Chem. Soc.*, **103**, 7489 (1981).
10. D. A. Skoog and D. M. West, "Fundamentals of Analytic Chemistry," Holt, Rinehart, Winston, New York (1969).
11. W. Schumt, C. Satterfield, and R. Wentworth, "Hydrogen Peroxide," p. 259, ACS Monograph Series, Reinhold Publ. Corp., New York (1955).

Removal of Chloride from 4-Chlorobiphenyl and 4,4′-Dichlorobiphenyl by Electrocatalytic Reduction

Thomas F. Connors and James F. Rusling*

Department of Chemistry, University of Connecticut, Storrs, Connecticut 06268

Polychlorinated biphenyls (PCB's) are widespread environmental pollutants (1, 2). They can be dechlorinated by chemical (2-6), photochemical (2, 3, 7), or electrochemical (8-10) means. Such methods are potentially useful to detoxify materials contaminated with PCB's, but extreme conditions and/or excess amounts of reagents are often necessary. Recent interest in the electrocatalytic reduction of aryl halides (11-15) has led us to investigate similar reactions for chlorobiphenyls. We describe here the electrocatalytic C-Cl cleavage of 4-chlorobiphenyl (4-CB) and 4,4′-dichlorobiphenyl (4,4′-DCB), which yields biphenyl.

Scheme I has been proved for electrocatalytic reduction of aryl halides (13-15)

$$A + e \rightleftharpoons A^{\cdot-} \qquad E^\circ \qquad [1]$$

$$A^{\cdot-} + BX \underset{k_{-1}}{\overset{k_1}{\rightleftharpoons}} A + BX^{\cdot-} \qquad [2]$$

$$BX^{\cdot-} \xrightarrow{k} B^{\cdot} + X^- \qquad [3]$$

$$A^{\cdot-} + B^{\cdot} \rightarrow A + B^- \qquad [4]$$

Scheme I

Here, A is the catalyst reduced at the electrode to its radical anion $A^{\cdot-}$. The aryl halide BX reacts with $A^{\cdot-}$ in [2] to yield radical anion $BX^{\cdot-}$, which decomposes in reaction [3]. Reaction [4] gives B^-, which is protonated in later steps to yield hydrocarbon. Under pseudo first-order conditions with [2] as rds, the sigmoid-shaped, linear-sweep voltammograms obtained are described by (14, 16-18)

$$i = i_{l,c}/(1 + \theta) \qquad [5]$$

where i is the current at potential E, and $\theta = \exp[(\mathbf{F}/RT)(E - E^\circ)]$. The limiting current, $i_{l,c}$, is proportional to $k_1^{1/2}$. These results were used to analyze our voltammetric data on chlorobiphenyls.

Cyclic voltammetry (CV) was carried out with a PAR 174A Polarographic Analyzer. The cell contained a hanging-drop mercury working electrode (HDME) of area 0.018 cm², an Ag/AgI reference, and a Pt counterelectrode. N,N′-dimethylformamide (DMF) was treated with alumina (19) and purged with nitrogen before use. The electrolyte was 0.1M Bu_4NI. Catalysts anthracene, 9, 10-diphenylanthracene (9, 10-DPA), and α-naphthonitrile were reversibly reduced to anion radicals in DMF (13, 19, 20). When excess 4,4′-DCB was added to 0.10 mM solutions of catalyst, cathodic voltammograms were sigmoid shaped and showed an increase in current over those of the catalyst alone. Anodic peaks disappeared, suggesting a reaction of the electrogenerated anion radical with 4,4′-DCB. For the reduction of 4-CB, anthracene gave similar CV's, but only a small catalytic effect was observed with 9, 10-DPA.

Table I summarizes the voltammetric results. $E_{1/2}$ was independent of scan rate (ν) and $i_{l,c}/i_d$ varied inversely with ν, as expected (14, 16-18) for pseudo first-order electrocatalytic reduction with [2] as rds. Potentials for reduction of chlorobiphenyls shifted positive by 0.27-0.48V (ΔE) compared to direct electrochemical reduction. The rate constant k_1 increased as ΔE decreased.

Table I. Voltammetric results

Catalyst[a]	ν (V/sec)	$-E_{1/2}$ (V[b])	$i_{l,c}/i_d$[c]	Avg[d] log k_1 (M^{-1} Ls^{-1})
	4,4′-dichlorobiphenyl			
Anthracene	0.05	1.91	5.14	
(ΔE = 0.27V, γ = 40)	0.10	1.91	3.53	3.1
	0.20	1.90	2.83	
	0.50	1.90	1.49	
9,10-DPA	0.10	1.84	1.35	
(ΔE = 0.33V, γ = 100)	0.20	1.83	1.25	2.0
	0.50	1.83	1.17	
α-naphthonitrile	0.05	1.83	1.93	
(ΔE = 0.34V, γ = 100)	0.10	1.83	1.63	2.0
	0.20	1.82	1.35	
	0.50	1.82	1.23	
	4-chlorobiphenyl			
Anthracene	0.05	1.92	1.70	
(ΔE = 0.41V, γ = 100)	0.10	1.91	1.62	2.1
	0.20	1.91	1.27	
9,10-DPA	0.10	1.82	1.15	0.6[e]
(ΔE = 0.48V, γ = 200)	0.20	1.81	1.13	

[a] Concentration 0.10 mM. $\Delta E = E^\circ - E_p^{CB}$, where E_p^{CB} is the peak potential of the chlorobiphenyl at 0.20 V/sec. $\gamma = C_{BX}{}^\circ/C_A{}^\circ$.
[b] V *vs.* SCE.
[c] Avg; i_d is peak current for catalyst alone.
[d] Calc. from $i_{l,c}$ as in (17).
[e] Estimated from ratio of anodic current in the presence and absence of BX using working curves in Fig. 12 of Ref. (16).

Data from sigmoid-shaped voltammograms were analyzed by nonlinear regression (21) onto Eq. [5]. Good agreement between theory and experiment was obtained (Fig. 1). Average values of $RT/\mathbf{F}$ for curves

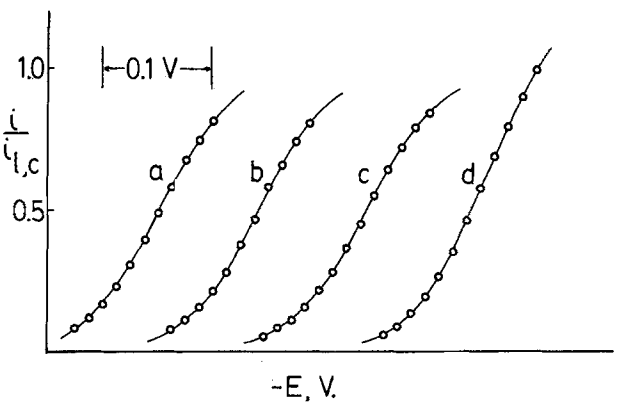

Fig. 1. Voltammograms for electrocatalytic systems at a scan rate of 0.20 V/sec. Circles are experimental data; solid line calculated by nonlinear regression onto Eq. [5] for a, b, and c. Data in d contain a contribution from the uncatalyzed reduction wave and were fitted to

$$i = i_{l,c}/(1 + \theta) + i' \exp[(\alpha n\mathbf{F}/RT)(E' - E)] \qquad [6]$$

where i' is the background current at an arbitrary potential E'. Deviation-pattern recognition was used to demonstrate the validity of Eq. [6] for 16 sets of data (22). (a) 0.10 mM 9,10-DPA with 100-fold excess 4,4′-DCB, (b) 0.10 mM α-naphthonitrile with 100-fold excess 4,4′-DCB, (c) 0.10 mM anthracene with 100-fold excess 4-CB, and (d) 0.10 mM anthracene with 40-fold excess 4,4′-DCB.

* Electrochemical Society Active Memeber.
Key words: catalysis, organic, free radicals, voltammetry.

at 0.10 and 0.20 V/sec were: 0.0246 ± 0.0008V for 4,4'-DCB/anthracene, 0.0258 ± 0.0001V for 4,4'-DCB/9,10-DPA, 0.0232 ± 0.0018V for 4,4'-DCB/α-naphthonitrile, and 0.0276 ± 0.0017V for 4-CB/anthracene, in acceptable agreement with the theoretical value at 25°C of 0.0257V. All results are consistent with reduction of the chlorobiphenyl by Scheme I.

To determine products, chlorobiphenyls were electrocatalytically reduced at a stirred-mercury-pool (17 cm^2 area) electrode in a divided cell using a three-electrode potentiostat. Solutions 0.10 mM in catalyst and 2 mM in 4,4'-DCB were electrolyzed at a potential on the rising portion of the catalytic wave. Average current densities were 0.25-0.10 mA cm^{-2}. Concentrations were monitored by high-pressure liquid chromatography (HPLC). With anthracene as the catalyst, 17 mg 4,4'-DCB reacted in 30 min (Fig. 2). The concentration of 4-CB increased early in the electrolysis, reached a maximum, and then decreased. This shows that 4-CB is an intermediate in the formation of biphenyl. The amount of biphenyl corresponded to 86% yield after 50 min, when 4-CB accounted for 8% yield. Similar results were obtained with 9,10-DPA as catalyst, but 7.5 hr were required to convert 4,4'-DCB to about 50% each of 4-CB and biphenyl, in accord with differences in rate constants (Table I). Some catalyst was destroyed during electrolysis, possibly by radical coupling (23). Nevertheless, the predominant reaction of 4,4'-DCB under our conditions is stepwise replacement of chloride with hydrogen. Each step follows Scheme I.

Thus, dechlorination of 4-CB and 4,4'-DCB can be carried out electrocatalytically at low overpotentials and current densities when compared to direct (8-10) electrochemical reduction. These reactions require less than 5% of the stoichiometric amount of catalyst. We are presently extending this work to other halogenated biphenyls.

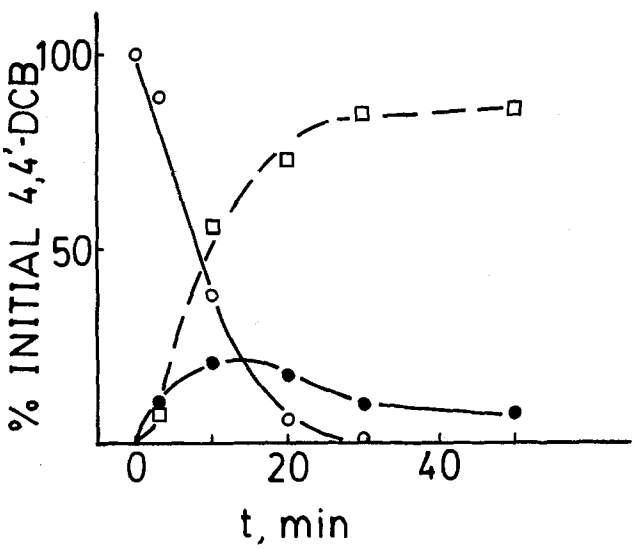

Fig. 2. Concentrations of reactants and products during controlled-potential electrolysis. Potential was −1.34V vs. Ag/AgI (−1.88V vs. SCE). Concentrations determined by HPLC using a reversed-phase (C-18) column and ultraviolet detector. Eluant was acetonitrite:water (7:3) at a flow rate of 2.0 ml/min. □ Biphenyl (4.8 min), ● 4-CB (6.8 min), and ○ 4,4'-DCB (9.6 min). Retention times in parentheses.

Acknowledgments

We thank James Arena for experimental assistance and J. D. Stuart for suggesting the HPLC method.

Manuscript received Sept. 10, 1982.

Any discussion of this paper will appear in a Discussion Section to be published in the December 1983 JOURNAL. All discussions for the December 1983 Discussion Section should be submitted by Aug. 1, 1983.

Publication costs of this article were assisted by the University of Connecticut.

REFERENCES

1. T. C. Cairns and E. C. Siegmund, *Anal. Chem.*, **53**, 1183A (1981).
2. O. Hutzinger, S. Safe, and V. Zitko, "The Chemistry of PCB's," CRC Press, Cleveland, Ohio (1974).
3. K. Tsujimoto, S. Tasaka, and M. Ohashi, *JCS Chem. Commun.*, 758 (1975).
4. A. Oku, K. Yasufku, and H. Kataoka, *Chem. Ind.*, **21**, 841 (1978).
5. W. H. Dennis, Y. H. Chang, and W. J. Cooper, *Bull. Env. Contam. Toxicol.*, **22**, 750 (1979).
6. R. B. LaPierre, L. Guczi, W. L. Kranich, and A. H. Weiss, *J. Catal.*, **52**, 230 (1978).
7. L. O. Ruzo and M. J. Zabik, *Bull. Env. Contam. Toxicol.*, **13**, 181 (1975).
8. S. O. Farwell, F. A. Beland, and R. D. Geer, *Anal. Chem.*, **47**, 895 (1975).
9. S. O. Farwell, F. A. Beland, and R. D. Geer, *J. Electroanal. Chem.*, **61**, 315 (1975).
10. M. Maruyama and K. Murakami, *Nippon Kagaku Kaishi*, **536**, (1976).
11. H. Lund, M.-A. Michel, and J. Simonet, *Acta Chem. Scand.*, **B29**, 217 (1975); *ibid.*, **B29**, 489 (1975).
12. H. Lund, M.-A. Michel, and J. Simonet, *Acta Chem. Scand.*, **B28**, 900 (1974); H. Lund and J. Simonet, *J. Electroanal. Chem.*, **65**, 205 (1975).
13. C. P. Andrieux, C. Blocman, J. M. Dumas-Bouchiat, and J. M. Saveant, *J. Am. Chem. Soc.*, **101**, 3431 (1979).
14. C. P. Andrieux, C. Blocman, J. M. Dumas-Bouchiat, J. M'Halla, and J. M. Saveant, *J. Electroanal. Chem.*, **113**, 19 (1980).
15. C. P. Andrieux, C. Blocman, J. M. Dumas-Bouchiat, F. M'Halla, and J. M. Saveant, *J. Am. Chem. Soc.*, **102**, 3806 (1980).
16. R. S. Nicholson and I. Shain, *Anal. Chem.*, **36**, 706 (1964).
17. J. M. Saveant and E. Vianello, *Electrochim. Acta*, **10**, 905 (1965).
18. J. M. Saveant and E. Vianello, in "Advances in Polarography," Vol. I, I. Longmuir, Editor, pp. 367-374, Pergamon Press, London, England (1960).
19. B. S. Jensen and V. D. Parker, *JCS Chem. Commun.*, 367 (1974).
20. J. Perichon, in "Encyclopedia of Electrochemistry of the Elements," Vol. XI, A. J. Bard and H. Lund, Editors, pp. 71-161, Marcel Dekker, New York (1978).
21. L. Meites, "The General Multiparametric Curve-Fitting Program CFT4A," Computing Laboratory, Clarkson College, Potsdam, New York (1976); L. Meites, *Crit. Rev. Anal. Chem.*, **8**, 1 (1979).
22. J. F. Rusling and T. F. Connors, *Anal. Chem.*, In press.
23. N. L. Holly, *Chem. Rev.*, **74**, 243 (1974).

Ionization and Dissociation Equilibria in Liquid SO_2

XIV. Dissociation Constant and Limiting Conductance of $(n\text{-}C_5H_{11})_4NI$ in Liquid SO_2 at 0.0°C

Norman N. Lichtin*

Department of Chemistry, Boston University, Boston, Massachusetts 02215

and John F. Reardon*

Department of Chemistry, University of Massachusetts, Boston, Massachusetts 02125

Tetraalkylammonium ions have served as model cations of low and varying charge density to probe the nature of ion-solvent interactions in a variety of solvents and solvent mixtures. In general, the conductance of R_3N^+ cations, where R represents alkyl or aryl groups, decreases as the size of R increases in contrast to the behavior of the alkali metal cations (1) which display solvation effects in many nonaqueous solvents while the quaternary ammonium ions generally do not seem to be solvated except possibly for the Me_4N^+ ion in solvents such as dimethyl sulfoxide (2).

As part of a series of studies (3, 4, 5) of the physical chemistry of SO_2 solutions, we have previously reported on the conductance behavior of quaternary ammonium halides, $R_4N^+X^-$, in which R spanned the series with R = n-alkyl from methyl to n-hexyl with the exception of the n-amyl salt, $(n\text{-}C_5H_{11})_4N^+$. The study reported here was carried out to close the gap and to furnish a series of limiting ionic conductances in liquid SO_2 at 0.0°C for all the $(n\text{-}R)_4N^+$ ions from methyl to n-hexyl in the belief that this information will contribute to elucidation of ion-solvent interactions.

Experimental

The experimental procedures and the bridge have been described (6) previously as has the cell and thermostat (7). Eastman White Label tetrapentylammonium iodide was recrystallized four times by precipitation from acetone by addition of ethyl ether and dried *in vacuo* at 60°C over P_2O_5 for 2 days, found 29.91% I and calculated 29.83% I. Analysis was carried out by Galbraith Laboratories.

Results and Discussion

Data of a typical experiment are presented in Table I. Application of Shedlovsky's method (8) to the data provided $K_d = 61.4 \pm 11.4 \times 10^{-4}$ mol/liter and $\Lambda_o = 182.5 \pm 0.6$ mho cm²/mol, where the indicated uncertainties were calculated from the slope and intercept of the linear Shedlovsky plot. Only data at dilutions up to 70,000 liters/mol were employed, so that solvent conductivity was less than 1% of total solution conductivity. The values of the dielectric constant and viscosity of sulfur dioxide employed in the calculations were taken from Ref. (9)

$$\epsilon = 95.12 \exp [-6.676 \times 10^{-3} T\,(K)]$$

and

$$1000\eta = 4.03 - 0.0363t\ (°C)$$

and were 15.35 at 273.15 K and 4.03 mP, respectively.

The Bjerrum distance of closest approach, a_{BJ}, calculated (10) from K_d is 13.02 ± 0.96Å as compared to the sum of ionic radii, $r_+ + r_- = 5.29 + 2.17 = 7.46$Å (11). The limiting equivalent conductance calculated from Stokes' law for perfect sticking (12), and the aforementioned ionic radii is 132, 28% lower than the experimental value. Since SO_2 is known to solvate anions (5), the observed conductance can be attributed to the unsolvated state of the $(n\text{-}Am)_4N^+$ ion.

By a Fuoss-Coplan division of the limiting equivalent conductance of $(i\text{-}Am)_4NB(i\text{-}Am)_4$, we have evolved a series of single ion conductances in SO_2 at 0.0°C (4) including a value of $\lambda_o^- = 124.2 \pm 0.2$ mho cm²/equiv. for iodide. Subtracting this value from the value of $\Lambda_o = 182.5 \pm 0.6$ for $(n\text{-}Am)_4NI$ yields a value of 58.3 ± 0.8 for the value of λ_o^+ of the $(n\text{-}Am)_4N^+$ ion. Substitution of this value of λ_o^+ in the Stokes slip equation, $\lambda_o\eta_o = (1.20/z_i/)R_s$, yields a value of $R_s = 5.11$Å to be compared with the value of 5.29Å proposed by Robinson and Stokes (13) for the radius of the $(n\text{-}Am)_4N^+$ ion. As expected, there is no solvation of the $(n/Am)_4N^+$ ion in liquid SO_2 at 0.0°C.

For the salt $(i\text{-}Am)_4NI$, we have previously reported (4) a K_d value of 46.0 ± 5.0 × 10^{-4}M and a Λ_o value of 186.5 ± 0.6 mho cm²/mol, both at 0.0°C. The somewhat smaller $(i\text{-}Am)_4N^+$ ion, $r_+ = 5.12$Å (11), produces a tighter ion pair and a slightly more mobile solute species than the $(n\text{-}Am)_4N^+$ ion, $r_+ = 5.29$Å. This behavior may be compared with K_d and Λ_o reported for solutions in methanol at 25°C ($\epsilon = 32.70$) (14)

$(i\text{-}Am)_4NI$ $\quad K_d = 7.81 \times 10^{-2}$M

$\Lambda_o = 98.04$ mho cm²/mol

$(n\text{-}Am)_4NI$ $\quad K_d = 6.25 \times 10^{-2}$M

$\Lambda_o = 97.42$ mho cm²/mol

For the individual R_4N^+ cations, we have determined λ_o^+ to be 62 mho cm²/mol for R = n-Bu, 62 for R = *i*-Am, and 58 for R = n-Am in SO_2 at 0.00°C (4). In methanol (15) at 25°C, the corresponding values are 39.0 mho cm²/mol for R = n-Bu, 35.4 for R = *i*-Am, and 34.8 for R = n-Am. The smaller values of λ_o^+ in methanol are probably due primarily to the higher viscosity of methanol (CH_3OH, 5.44 mP, 298.15 K; SO_2, 4.03 mP, 273.15 K) (16).

For two other sulfur-containing solvents of some current interest, dimethyl sulfoxide $(CH_3)_2SO$ (ϵ = 46.7, 298.15 K) and sulfolane $(CH_2)_4SO_2$ (ϵ = 43.3, 303.15 K) (16), less data are available. The limiting ionic conductances in DMSO at 298.15 K (15) are, respectively, 11.8 mho cm²/mol for R = n-Bu, 11.0 for R = *i*-Am, and 10.8 for R = n-Am; while in sulfolane

Table I. Data of a typical conductance run

Volume (liter/mol)	Λ_o (mho cm²/mol)
2172	160.1
3195	164.1
4700	167.6
6913	170.6
10170	172.9
14960	174.7
22005	176.5
33370	177.2
47617	177.4

* Electrochemical Society Active Member.

at 303.15 K (15), the corresponding values are 2.76 for R = n-Bu and 2.51 for R = n-Am. Both $(i\text{-Am})_4NI$ and $(n\text{-Am})_4NI$ are regarded as dissociated in DMSO at 298.15 K (2). For sulfolane, no data are available, but because of the high dielectric constant, high temperature of measurement, and behavior of similar R_4N^+ salts (17), we assume that they are both completely dissociated.

Manuscript submitted April 12, 1982; revised manuscript received ca. Aug. 6, 1982.

Any discussion of this paper will appear in a Discussion Section to be published in the December 1983 JOURNAL. All discussions for the December 1983 Discussion Section should be submitted by Aug. 1, 1983.

REFERENCES

1. M. Spiro, "Physical Chemistry of Organic Solvent Systems," A. K. Covington and T. Dickinson, Editors, p. 636, Plenum Press, New York (1973).
2. J. N. Butler, *J. Electroanal. Chem.*, **14**, 89 (1967).
3. N. N. Lichtin and J. F. Reardon, *J. Phys. Chem.*, **84**, 2398 (1980).
4. N. N. Lichtin and J. F. Reardon, *ibid.*, **84**, 2946 (1980).
5. N. N. Lichtin and J. F. Reardon, *ibid.*, **85**, 1590 (1981).
6. N. N. Lichtin and M. J. Vignale, *J. Am. Chem. Soc.*, **79**, 579 (1957).
7. N. N. Lichtin and H. Glazer, *ibid.*, **73**, 5537 (1951).
8. T. Shedlovsky, *J. Franklin Inst.*, **225**, 739 (1938).
9. D. F. Burow, in "Chemistry of Nonaqueous Solvents," Vol. III, J. Lagowski, Editor, p. 305, Academic Press, New York (1970).
10. R. A. Robinson and R. H. Stokes, "Electrolyte Solutions," p. 396, Butterworths, London, England (1959).
11. M. Spiro, "Physical Chemistry of Organic Solvent Systems," A. K. Covington and T. Dickinson, Editors, pp. 261 and 637, Plenum Press, New York (1973).
12. R. L. Kay, in "Water, A Comprehensive Treatise," Vol. III, F. Frank, Editor, Chap. 4, Plenum Press, New York (1973).
13. R. A. Robinson and R. H. Stokes, "Electrolyte Solutions," p. 125, Butterworths, London, England (1959).
14. R. Fernandez-Prini, "Physical Chemistry of Organic Solvent Systems," A. K. Covington and T. Dickinson, Editors, p. 588, Plenum Press, New York (1973).
15. M. Spiro, in "Physical Chemistry of Organic Solvent Systems," A. K. Covington and T. Dickinson, Editors, p. 679, Plenum Press, New York (1973).
16. "Physical Chemistry of Organic Solvent Systems," A. K. Covington and T. Dickinson, Editors, p. 5, Plenum Press, New York (1973).

Prediction of the Current Density at an Electrode at Which Multiple Electrode Reactions Occur under Potentiostatic Control

R. E. White,* S. E. Lorimer,* and R. Darby

Chemical Engineering Department, Texas A&M University, College Station, Texas 77843

It is often desirable to be able to predict the total current density at an electrode when multiple electrochemical reactions occur there under potentiostatic control. It is also sometimes desirable to include the effect of ionic migration within the diffusion layer upon the predicted total (1) and partial current densities (2). A procedure for doing this can be illustrated by considering the rotating disk electrode (RDE) system and the associated potential distribution near the RDE as shown in Fig. 1 and 2. For simplicity, it is assumed that the concentration of species i in the solution (c_i) and the potential of the solution (Φ) depend only on the normal coordinate y as shown in Fig. 1. This assumption is reasonable for well-supported solutions and small radius disks. Also, it is assumed that no potential drop exists between the reference electrode within its own compartment and the tip of the Luggin capillary tube.

The procedure consists of writing the Butler-Volmer equation for any general electrochemical reaction j in a particular way, including the effect of ionic migration in the flux expression for species i, and writing the boundary conditions for the concentration of species i and the potential in the solution in a specific manner.

Butler-Volmer Equation

The Butler-Volmer equation for electrochemical reaction j can be written as follows

$$i_j = i_{oj,o}\left[\exp\left(\frac{\alpha_{aj}\mathbf{F}}{RT}\eta_{sj}\right) - \exp\left(\frac{-\alpha_{cj}\mathbf{F}}{RT}\eta_{sj}\right)\right] \quad [1]$$

where

$$\eta_{sj} = V - \Phi_o - U_{j,o} \quad [2]$$

$$U_{j,o} = U_j^\theta - \frac{RT}{n_j\mathbf{F}}\sum_i s_{ij}\ln\left(\frac{c_{i,o}}{\rho_o}\right) - U^\theta_{RE} + \frac{RT}{n_{RE}\mathbf{F}}\sum_i s_{i,RE}\ln\left(\frac{c_{i,RE}}{\rho_o}\right) \quad [3]$$

$$i_{oj,o} = i_{oj,ref}\prod_i\left(\frac{c_{i,o}}{c_{i,ref}}\right)^{\gamma_{ij}} \quad [4]$$

and

$$i_{oj,ref} = i_{oj,data}\prod_i\left(\frac{c_{i,ref}}{c_{i,data}}\right)^{\gamma_{ij}} \quad [5]$$

As shown in Eq. [1], anodic and cathodic current densities are defined here to be positive and negative, respectively. Also, s_{ij} is positive for an anodic reactant and negative for a cathodic reactant. As shown by Eq. [2], the current density i_j depends upon the difference between the potential of the electrode (V) and the potential in the solution adjacent to the electrode surface (Φ_o) relative to the open-circuit potential for reaction j ($U_{j,o}$) evaluated at the surface concentrations of species i ($c_{i,o}$). The values of the potentials V, Φ, U_j^θ, and U^θ_{RE} are all relative to the standard hydrogen reference electrode potential which is defined to be zero for convenience. Thus, if the reference electrode used in the experiment is a standard hydrogen reference electrode, $U_{j,o}$ is simply the Nernst equation (1) evaluated at $c_{i,o}$. Note that i_j depends on $c_{i,o}$ through both $U_{j,o}$ and the concentration dependence of the exchange current density as given by Eq. [4], which shows that the exchange current density of reaction j evaluated at the surface concentrations ($i_{oj,o}$) can be written in terms of reference concentrations ($c_{i,ref}$). Also note that Eq. [5] can be used to determine a value for $i_{oj,ref}$ assuming values are known for $i_{oj,data}$, $c_{i,data}$, and γ_{ij}. The open-circuit potential $U_{j,o}$

* Electrochemical Society Active Member.

Key words: interfaces, mass transport, kinetics.

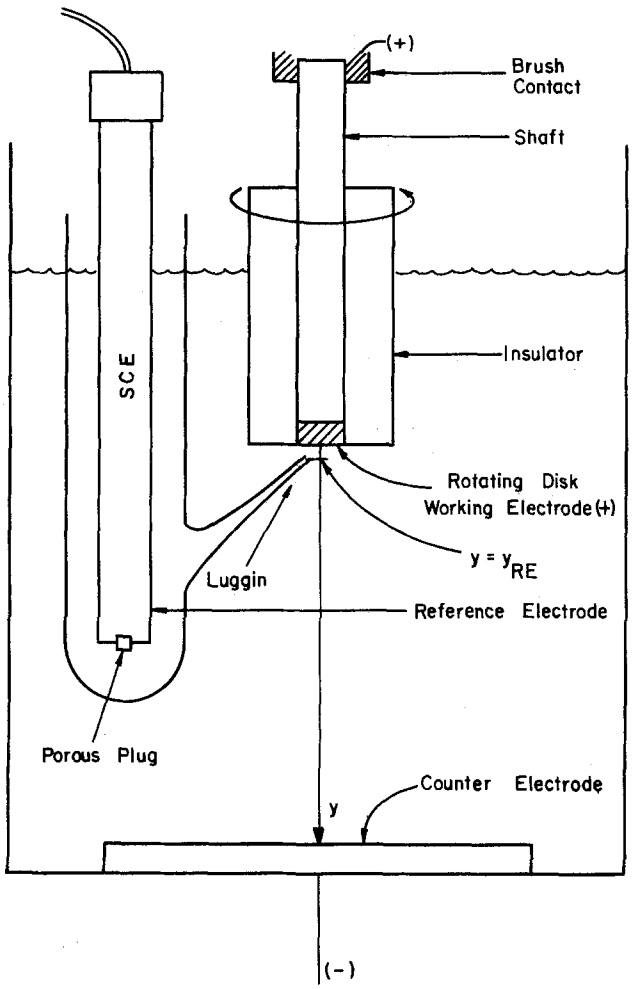

Fig. 1. Schematic of a rotating disk electrode system

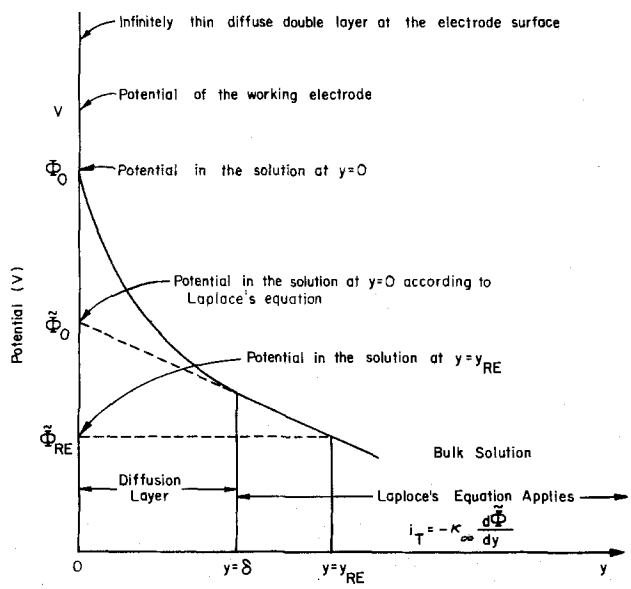

Fig. 2. Schematic of the solution potential profile near an electrode being operated anodically.

can be written in terms of the reference concentrations by adding and subtracting the following term to Eq. [3]

$$\frac{RT}{n_j F}\sum_i s_{ij}\ln\left(\frac{c_{i,ref}}{\rho_o}\right) \qquad [6]$$

The result is

$$U_{j,o} = U_{j,ref} - \frac{RT}{n_j F}\sum_i s_{ij}\ln\left(\frac{c_{i,o}}{c_{i,ref}}\right) \qquad [7]$$

where

$$U_{j,ref} = U_j^\theta - \frac{RT}{n_j F}\sum_i s_{ij}\ln\left(\frac{c_{i,ref}}{\rho_o}\right) - U^\theta_{RE} + \frac{RT}{n_{RE}F}\sum_i s_{i,RE}\ln\left(\frac{c_{i,RE}}{\rho_o}\right) \qquad [8]$$

Also, the potential difference $V - \Phi_o$ in Eq. [2] can be written in terms of the applied or set potential difference $V - \tilde{\Phi}_{RE}$ as follows

$$V - \Phi_o = V - \tilde{\Phi}_{RE} - (\Phi_o - \tilde{\Phi}_{RE}) \qquad [9]$$

where $\tilde{\Phi}_{RE}$ is the potential in the solution at $y = y_{RE}$ (see Fig. 1 and 2).

Now, Eq. [2], [4], [7], and [9] can be used to rewrite Eq. [1] in the desired form

$$i_j = i_{o,jref}\left\{\frac{\pi}{i}\left(\frac{c_{i,o}}{c_{i,ref}}\right)^{p_{ij}}\exp\left(\frac{\alpha_{aj}F}{RT}[V - \tilde{\Phi}_{RE} - (\Phi_o - \tilde{\Phi}_{RE}) - U_{j,ref}]\right) - \frac{\pi}{i}\left(\frac{c_{i,o}}{c_{i,ref}}\right)^{q_{ij}}\exp\left(\frac{-\alpha_{cj}F}{RT}[V - \tilde{\Phi}_{RE} - (\Phi_o - \tilde{\Phi}_{RE}) - U_{j,ref}]\right)\right\} \qquad [10]$$

where

$$p_{ij} = \gamma_{ij} + \frac{\alpha_{aj}s_{ij}}{n_j} \qquad [11]$$

and

$$q_{ij} = \gamma_{ij} - \frac{\alpha_{cj}s_{ij}}{n_j} \qquad [12]$$

It is useful at this point to compare the potential differences in the arguments of the exponentials in Eq. [10]

$$V - \tilde{\Phi}_{RE} - (\Phi_o - \tilde{\Phi}_{RE}) - U_{j,ref} \qquad [13]$$

to those used commonly by others (3) in similar expressions. Typically, the potential differences used by others (3) are

$$E_{appl} - E_{eq} - i_T A R_s \qquad [14]$$

where E_{appl} is defined to be the potential difference between the working electrode and a reference electrode placed in the bulk solution with current being passed in the cell, E_{eq} is that same potential difference when no current is being passed, and $i_T A R_s$ is the ohmic potential drop in the solution between the working and reference electrodes. It should be pointed out that the potential in the solution at y_{RE} depends upon the current being passed; it is not a constant as is often assumed (3). The potential differences given by Eq. [13] and [14] are not the same because, even though

$$E_{appl} = V - \tilde{\Phi}_{RE} \qquad [15]$$

and for a single electrode reaction

$$E_{eq} = U_{j,ref} \qquad [16]$$

the ohmic drop through the diffusion layer is different. That is

$$i_T A R_s \neq \Phi_o - \tilde{\Phi}_{RE} \qquad [17]$$

The ohmic potential drops are not the same because the specific conductivity (κ_∞) of the electrolyte is not constant through the diffusion layer as is often assumed by others (3). That is, if it is assumed that both i_T and κ_∞ are constants through the diffusion layer, then Laplace's equation

$$i_T = -\kappa_m \frac{d\tilde{\Phi}}{dy} \quad [18]$$

can be integrated to give

$$\frac{i_T y_{RE}}{\kappa_m} = \tilde{\Phi}_o - \Phi_{RE} \quad [19]$$

which can be rewritten in terms of the solution resistance (R_s) by using the following equation (3)

$$R_s = \frac{y_{RE}}{\kappa_m A} \quad [20]$$

Thus, by using Eq. [20], Eq. [19] becomes

$$i_T A R_s = \tilde{\Phi}_o - \tilde{\Phi}_{RE} \quad [21]$$

Comparison of Eq. [17] and [21] shows that $\Phi_o \neq \tilde{\Phi}_o$ as illustrated schematically in Fig. 2. Typically, it is assumed, however, that $\Phi_o = \tilde{\Phi}_o$, which is often not true (2, 4).

It should be noted that both E_{appl} and $V - \tilde{\Phi}_{RE}$ depend upon the type of reference electrode used, since they both represent the same physical quantity. (It can be seen that $V - \tilde{\Phi}_{RE}$ must depend upon the type of reference electrode used in the experiment since at equilibrium

$$V - \tilde{\Phi}_{RE} = U_{j,ref} \quad [22]$$

and $U_{j,ref}$ depends upon the type of reference electrode used. (Note that the potential difference $\Phi_o - \tilde{\Phi}_{RE}$ is equal to zero at equilibrium.) In addition, E_{eq} and $U_{j,ref}$ depend in the same manner upon the type of reference electrode used (3). Consequently, the difference between $V - \tilde{\Phi}_{RE}$ and $U_{j,ref}$ is independent of the type of reference electrode used in the experiment, as is $E_{appl} - E_{eq}$.

Governing Equations and Boundary Conditions for c_i and Φ

The governing equation for the concentration of species i at steady-state conditions and no homogeneous reactions is (1)

$$\frac{dN_i}{dy} = 0 \quad [23]$$

where

$$N_i = -D_i \frac{dc_i}{dy} - z_i \frac{D_i c_i F}{RT} \frac{d\Phi}{dy} + v c_i \quad [24]$$

and the governing equation for the potential in the solution is the electroneutrality condition (1)

$$\Sigma z_i c_i = 0 \quad [25]$$

The boundary conditions for a single electrode reaction are as follows

at $y = 0$

$$\Sigma z_i c_i = 0 \quad [26]$$

$$V = \text{a set constant } (e.g., 0.2\text{V}) \quad [27]$$

$$\frac{s_{ij} i_j}{n_j F} = -N_i \quad [28]$$

where N_i is given by Eq. [24] with $v = 0$ and i_j is given by Eq. [10]

at $y = y_{RE}$

$$c_i = c_{i,ref} \quad \text{where} \quad \Sigma_i z_i c_{i,ref} = 0 \quad [29]$$

$$\Phi = \tilde{\Phi}_{RE} = \text{a set constant } (e.g., 0.1\text{V}) \quad [30]$$

It is important to note that both V and $\tilde{\Phi}_{RE}$ must be set such that their difference $(V - \tilde{\Phi}_{RE})$ is equal to the value set by the potentiostat.

Once values have been set for the parameters of the system, the solution of Eq. [23] and [25] subject to Eq. [26]-[30] yields values for $c_i(y)$ and $\Phi(y)$. The values of c_i and Φ at $y = 0$ ($c_{i,o}$ and Φ_o) can then be used together with the kinetic parameters to predict the current density of reaction j according to Eq. [10].

If more than one electrode reaction occurs, Eq. [28] must be changed to

$$\sum_j \frac{s_{ij} i_j}{n_j F} = -N_i \quad [31]$$

where i_j is given by Eq. [10] with the appropriate kinetic parameters. The total predicted current density (i_T) can, then, be obtained by solving the equations and summing the current densities due to the individual reactions as follows

$$i_T = \sum_j i_j \quad [32]$$

It is worth noting that even if the effect of ionic migration is negligible, the procedure presented here is useful because it permits the direct use in the model of the set potential difference between the working electrode and a reference electrode in the bulk solution, and it provides a method of predicting the current densities of the individual reactions when multiple electrode reactions occur.

Finally, it should be mentioned that a less direct method could be used for a single electrode reaction but would be difficult to apply for multiple electrode reactions. The procedure would consist of setting i_j in Eq. [28] and, then, determining Φ_o by solving the transport problem. This value of Φ_o could, then, be used in Eq. [10] to obtain $V - \tilde{\Phi}_{RE}$ which could be compared to the observed value and a new i_j selected, if necessary. Since this would be an iterative procedure, it would be difficult to implement particularly for multiple electrode reactions, especially if the current densities due to the individual reactions were not equal, as is often the case.

Manuscript submitted Aug. 9, 1982; revised manuscript received Jan. 3, 1983.

Any discussion of this paper will appear in a Discussion Section to be published in the December 1983 JOURNAL. All discussions for the December 1983 Discussion Section should be submitted by Aug. 1, 1983.

LIST OF SYMBOLS

A	area of the electrode, cm^2
c_i	concentration of species i, mol/cm^3
$c_{i,o}$	local surface concentration of species i, mol/cm^3
$c_{i,data}$	data concentration of species i, mol/cm^3
$c_{i,ref}$	reference concentration of species i, mol/cm^3
D_i	diffusion coefficient of species i, cm^2/sec
E_{appl}	potential of working electrode relative to potential of a reference electrode of a given kind, V
E_{eq}	potential of working electrode relative to potential of a reference electrode of a given kind when no current is passed, V
F	Faraday's constant, 96,487 C/mol
i_j	current density due to reaction j, A/cm^2
$i_{oj,data}$	exchange current density at concentrations reported in the literature ($c_{i,data}$), A/cm^2
$i_{oj,ref}$	exchange current density at reference concentrations, A/cm^2
i_T	total current density, A/cm^2
n_j	number of electrons transferred in reaction j
p_{ij}	anodic reaction order of species i in reaction j
q_{ij}	cathodic reaction order of species i in reaction j
R	universal gas constant, 8.3143 J/mol K
R_s	solution resistance, Ω
s_{ij}	stoichiometric coefficient of species i in reaction j
T	absolute temperature, K
$U_{j,o}$	theoretical open-circuit potential for reaction j

at the surface concentrations of the species i which participate in reaction j, V

$U_{j,ref}$ theoretical open-circuit potential evaluated at reference concentrations, V

U_j^θ standard electrode potential for reaction j, V

V potential of the working electrode, V

y normal coordinate, cm

y_{RE} position of the reference electrode, cm

z_i charge number of species i

Greek Symbols

α_{aj} anodic transfer coefficient for reaction j

α_{cj} cathodic transfer coefficient for reaction j

γ_{ij} exponent in the composition dependence of the exchange current density

δ diffusion layer thickness, cm

ρ_o pure solvent density, kg/cm^3

Φ potential in the solution within the diffusion layer, V

$\tilde{\Phi}$ potential in the bulk solution, V

Φ_o solution potential adjacent to electrode surface, V

$\tilde{\Phi}_o$ potential in the solution at $y = 0$ obtained by integrating Laplace's equation with constant i_T and κ_∞, V

$\tilde{\Phi}_{RE}$ potential in the bulk solution at y_{RE}, V

κ_∞ bulk solution specific conductivity, Ω^{-1} cm^{-1}

Subscripts

o at the electrode surface

RE reference electrode

ref reference conditions

REFERENCES

1. J. S. Newman, "Electrochemical Systems," Prentice-Hall, Inc., Englewood Cliffs, NJ (1973).
2. R. E. White, J. A. Trainham, J. Newman, and T. W. Chapman, *This Journal*, **124**, 669 (1977).
3. A. J. Bard and L. R. Faulkner, "Electrochemical Methods: Fundamentals and Applications," John Wiley & Sons, New York (1980).
4. R. E. White, Ph.D. Thesis, University of California, Berkeley (1977).

JOURNAL OF THE ELECTROCHEMICAL SOCIETY

SOLID-STATE SCIENCE AND TECHNOLOGY

MAY 1983

Hydrogen and Phosphorus Ion Beam Exposure Characteristics of PMMA

Yasuo Wada,* Masatoshi Migitaka, Kozo Mochiji, and Hidehito Obayashi

Hitachi, Limited, Central Research Laboratory, Kokubunji, Tokyo 185 Japan

ABSTRACT

Hydrogen and phosphorus ion beam exposure characteristics of PMMA are investigated as functions of dose and acceleration energy. PMMA shows both positive and negative exposure characteristics depending on the ion dose. A hydrogen ion dose of 1.6×10^{-6} C/cm^2 is required to reveal positive exposure characteristics with a contrast of 3, which indicates that PMMA is about two orders of magnitude more sensitive to ions than to electron beam. More than a 4×10^{-5} C/cm^2 ion dose affords negative exposure characteristics with a contrast of about 1. The positive exposure characteristics of PMMA are mainly determined by the amount of energy deposited per unit volume. On the other hand, the negative exposure characteristics are mainly determined by the total energy that the surface region receives. The projected ranges and projected deviations of hydrogen and phosphorus ions in PMMA are experimentally determined from the exposure characteristics and are about one order of magnitude smaller than the calculated results. Patterns as narrow as 1 μm on a stencil mask are neatly replicated in a PMMA layer by a 180 keV hydrogen ion beam, and demonstrate the applicability of ion beam lithography to the submicrometer VLSI fabrication.

The technological innovations of lithography in the semiconductor industry have lead to a reduction of the minimum dimensions utilized in LSI's by about 30% every three years (1). The extrapolation of this trend should bring the semiconductor industry to the stage where novel submicrometer lithographic technology is indispensable by about 1985. Recently, ion beam lithography has gathered attention for its capability to fabricate fine patterns. The experimental results of fine line formation in poly(methylmethacrylate) (PMMA) by gallium ion beams (2) and hydrogen ion beams (3, 4) as well as the results of calculated energy deposition of a hydrogen ion beam (5) together with the ion beam sensitivity investigations of PMMA (8, 19) suggest that ion beam lithography should provide very high resolution in replicating mask patterns.

This paper reports the exposure characteristics of PMMA by hydrogen and phosphorus ion beams, placing emphasis on the experimental verification of the energy deposition of these ions in PMMA. It also reports the capability of fine-line formation by replication of a stencil mask, with as narrow as 1 μm wide patterns.

Experimental Procedures

A p-type, (100) oriented silicon wafer was used as a substrate. PMMA was spun on the substrate to a thickness of around 0.85 μm, then prebaked in a nitrogen atmosphere at 200°C for 30 min. The average molecular weight (Mw) of the PMMA was 600,000. Hydrogen or phosphorus ions were implanted into the PMMA layer at an energy of between 30-180 keV by an ion implanter. The dose range utilized in this experiment was between 10^{-8} and 10^{-3} C/cm^2. Charge up effect on the resist during ion implantation was negligible, which has been experimentally demonstrated previously (17). The substrate temperature during ion exposure was kept below 50°C, by a suitable choice of dose rate and acceleration energy (6), so that the substrate heating does not affect the exposure characteristics of PMMA. Then, the sample was immersed in a PMMA developer, composed of methyl ethyl ketone and isopropanol, at 25°C for 3 min. The residual resist thickness was measured by an ellipsometer, a film thickness analyzer, and/or a Dektak (Sloan). The error of these measurements was less than 5%. Contrast of the resist, γ, was defined by the slope of the residual resist thickness and exposure relationship, as explained in the literature (18).

A stencil mask, made of around 1 μm thick electroplated nickel foil was used to demonstrate the capability of hydrogen ion beam lithography. Patterns of as narrow as 1 μm wide on the stencil mask were replicated on PMMA layer by a 180 keV hydrogen ion beam. Then the sample was coated with gold to a thickness of several tens of nanometers, and these patterns were observed by an SEM.

Results and Discussion

Hydrogen ion dose dependence of PMMA exposure characteristics.—A 180 keV hydrogen ion beam exposure characteristic of PMMA is shown in Fig. 1. An ion dose of around 1.6×10^{-6} C/cm^2 is required to fully expose the resist layer, which indicates that PMMA is about two orders of magnitude more sensitive to a hydrogen ion beam than to an electron beam (8, 19). Therefore, PMMA can be used as a high sensitivity resist for hydrogen ion beam lithography. The contrast, γ, of the positive exposure characteristics is around 3, which suggests that PMMA should provide high contrast patterns.

A hydrogen ion dose of more than 4×10^{-5} C/cm^2 affords negative exposure characteristics. Similar positive to negative inversion phenomenon is also observed in high dose electron beam exposure (7). The total energy (acceleration voltage $\times$ dose) that the PMMA layer receives is about 7 J/cm^2. The increase of refractive index from 1.48 to more than 1.80 with the increase of ion dose, shown by the broken line in Fig. 1, suggests that PMMA is changed into an amorphous carbon-like substance by the heavy ion

* Electrochemical Society Active Member.
Key words: semiconductor, integrated circuits, ion implantation.

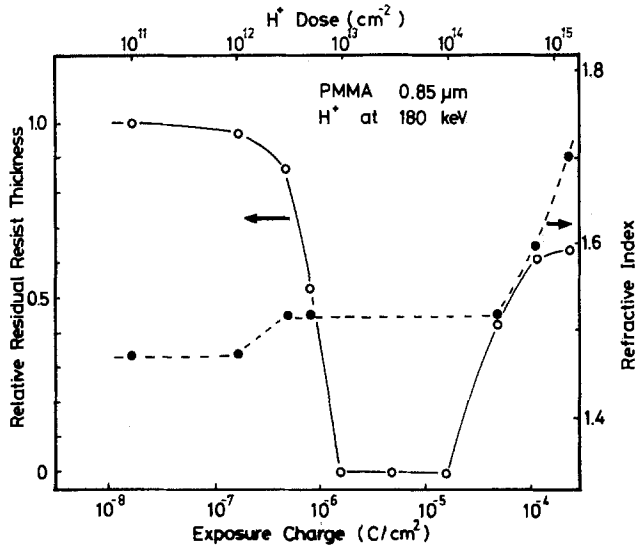

Fig. 1. A 180 keV hydrogen ion dose dependence of PMMA exposure characteristics; ○ resist thickness, ● refractive index.

dose. This phenomenon would provide other applications, such as ion modification of PMMA into more plasma stable material (14, 16). Additional flood hydrogen ion exposure of 3×10^{-6} C/cm² makes the rest of the PMMA region soluble to developer, and negative patterns are obtainable by conventional development processing. The contrast of the negative exposure characteristics is around 1.0, which is about 1/3 of that of positive side. Therefore, together with the low sensitivity, PMMA would not be a useful negative ion beam resist for practical applications.

Hydrogen ion energy dependence of PMMA exposure characteristics.—The hydrogen ion energy dependence of PMMA exposure characteristics was investigated to clarify the appropriate ion acceleration energy range for practical applications. Typical results are shown in Fig. 2, where it is depicted that an acceleration energy of 60 keV is not high enough to fully expose the 0.85 μm thick PMMA layer. It also suggests that the projected range of hydrogen ions in PMMA at 60 keV should be around 0.7 μm, which is about an order of magnitude smaller than the calculated results based on LSS theory in AZ 111 (9). Recently, Karapiperis, *et al.*, (5) calculated the projected ranges of hydrogen ions in PMMA by Monte Carlo method, and the typical values are around 0.35, 0.68, and 0.96 μm at 30, 60, and 90 keV, respectively.

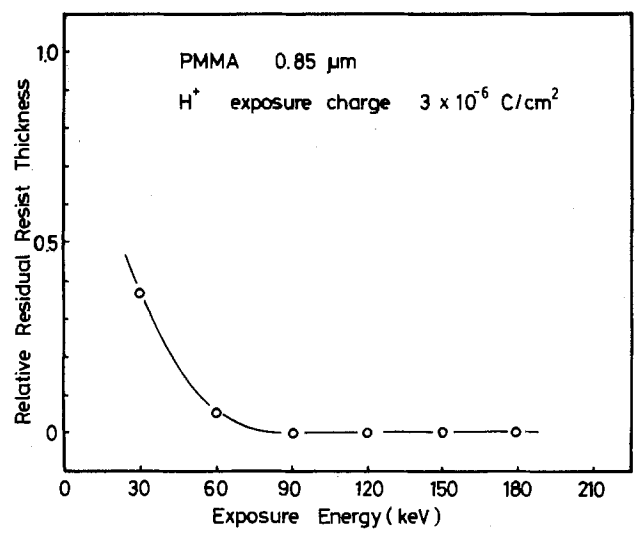

Fig. 2. Hydrogen ion energy dependence of residual PMMA film thickness (3×10^{-6} C/cm² hydrogen ion dose).

Assuming the similar energy deposition curves reported in their article, the exposed depth in the PMMA layer should be around 0.38, 0.74, and 1.05 μm at 30, 60, and 90 keV, respectively. These results coincide well with the present experimental results shown in Fig. 2.

Assuming that the surface topography of the semiconductor devices does not change very much from that of the present one, but follows the scale-down principle (1), a corrugation of around 0.8 μm high should exist in the coming submicrometer devices. Then, the minimum resist thickness for practical lithography processing should be around 1.0 μm from the resist coverage requirement at the edge of the corrugations. In this case, the resist thickness should reach 1.8 μm at the edge of the step. Therefore, the results shown in Fig. 2, as well as the simulation (5), suggest that an acceleration energy of around 180 keV is required for the practical hydrogen ion beam exposure machine for integrated circuit fabrications.

Phosphorus ion beam exposure characteristics of PMMA.—Provided that the ion species are electrically active in silicon semiconductors, the projected range and projected deviation of ions in PMMA can be experimentally derived by measuring the flatband voltage shifts of MOS capacitors covered with PMMA of various thicknesses (11, 12). Figure 3 shows the ion acceleration energy dependence of phosphorus ion projected ranges and projected deviations in PMMA thus determined. These results indicate that the projected ranges of phosphorus ions in PMMA are also about one order of magnitude smaller than that of the calculated results in AZ 111 (9).

The phosphorus ion exposure characteristics of PMMA was derived assuming the following and compared with experiment. (*i*) PMMA layer is exposed and become soluble to a developer when it receives a certain amount of energy per unit volume. (*ii*) The energy deposition of the implanted ions decrease slightly from the surface of PMMA layer to the ion profile peak, and, beyond the peak, it is almost proportional to the ion profile as shown in Fig. 4 of Ref. (5). The latter assumption is schematically shown in Fig. 4, where the solid line represents the ion profile, while the broken line represents the energy deposition profile (5).

The calculated exposure characteristics of PMMA by a 120 keV phosphorus ion beam, in which the projected range and projected deviation are 0.12 μm and 0.04 μm, respectively, are shown in Fig. 5 by the dot-dash line. The experimentally obtained exposure characteristics of PMMA by a 120 keV phosphorus ion beam are also shown in Fig. 5 by a solid line. The PMMA film was exposed to about half of its thickness by a dose of 3×10^{-6} C/cm², which coincides very well with the calculated results. Therefore, the posi-

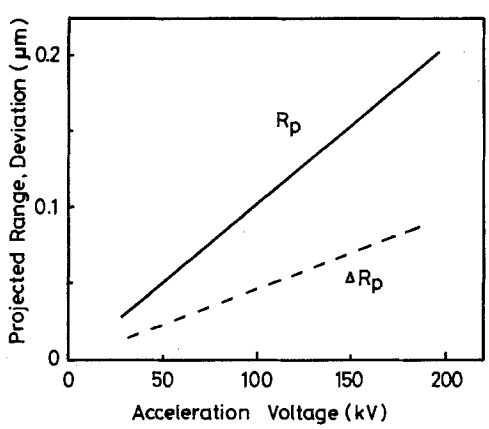

Fig. 3. Acceleration energy dependence of projected range (Rp) and projected deviation (ΔRp) of phosphorus ions in PMMA (experimentally obtained).

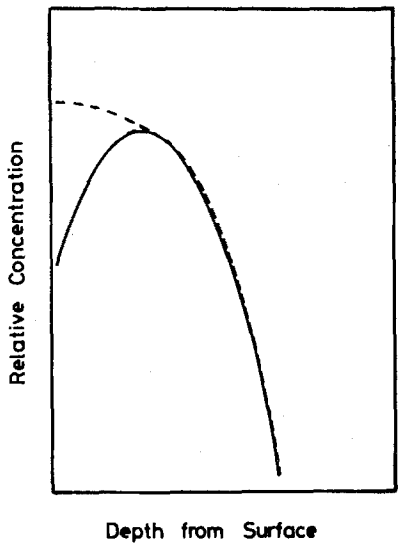

Fig. 4. Schematic representation of energy deposition profile (— — — —) and ion profile (————) in PMMA (assumed).

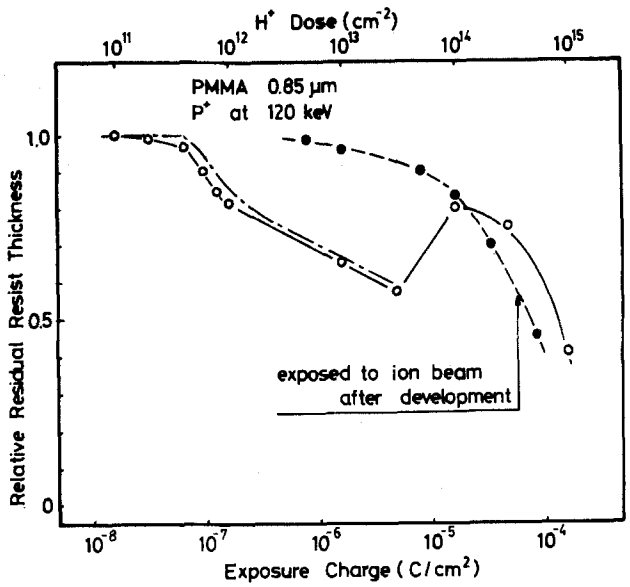

Fig. 5. A 120 keV phosphorus ion dose dependence of PMMA exposure characteristics.

tive exposure characteristics of PMMA are mainly determined by the energy deposition of the exposing ions as described above in the assumptions (*i* and *ii*). In other words, the projected range and projected deviation of ions in PMMA can be determined by fitting the positive exposure characteristics with the calculated energy deposition curve.

The negative exposure characteristics of PMMA by more than a 2×10^{-4} C/cm² phosphorus ion dose (total energy 5 J/cm²) are almost identical to that of by hydrogen ion exposure.

The film thickness reduction phenomenon of PMMA by more than a 4×10^{-5} C/cm² phosphorus ion dose was analyzed on the basis of PMMA decomposition by the exposing ions. Phosphorus ion dose dependence of PMMA film thickness reduction is also shown in Fig. 5 by a broken line. The results coincide well with the film thickness reduction phenomenon by more than the threshold dose of the negative exposure characteristics, shown by the solid line. In other words, the differences of with or without development processing following phosphorus ion exposure has negligible effect on the film thickness reduction phenomenon. Therefore, the PMMA film, which is heavily exposed by an ion beam and shows the negative exposure characteristics, is quite stable against organic solvents. These results suggest the possibility of ion modification of PMMA and other organic films into a very tough stable layer against severe atmospheres, such as reactive ion etching (14, 16).

Exposure characteristics of PMMA by relatively low energy hydrogen ion beam.—The exposure characteristics of PMMA by relatively low energy hydrogen ion beam was investigated to ascertain the PMMA exposure mechanism as well as the projected range and projected deviation determination method discussed in the preceding section. The dose dependence of residual resist thickness by a 30 keV hydrogen ion beam is shown in Fig. 6. An ion dose of around 1.6×10^{-6} C/cm² is required to expose the surface region of PMMA layer to a depth of around 0.4 μm (0.85 μm × 0.5).

The projected range of hydrogen ions in PMMA was derived from the dose dependence of relative residual resist thickness shown in Fig. 6, following the assumptions ascertained in the preceding section. The dotted line depicted in Fig. 6 indicates the exposure characteristics of PMMA calculated for a 30 keV hydrogen ion beam, assuming the projected range and projected deviation to be 0.32 and 0.1 μm, respectively. The calculated curve agrees very well with the experimentally obtained results, which indicates that the exposure of PMMA by a hydrogen ion beam is also mainly determined by the energy deposition of the exposing ions on the PMMA layer.

An ion dose of greater than 1×10^{-4} C/cm² (3 J/cm²) is required to reveal the negative exposure characteristics, which is about 2.5 times higher than that for a 180 keV hydrogen ion beam exposure. These results suggest that the total energy (acceleration energy × dose) deposited on the unit area of the surface layer could be used as an indicator to forecast the required dose to reveal the negative exposure characteristics.

Fine pattern formation on PMMA.—Patterns of as narrow as 1 μm wide on a stencil mask were replicated on PMMA by hydrogen ion beam. The acceleration energy for the exposure was 180 keV, which was chosen for the following reasons. (*i*) The scattering of ions in resist layer becomes manifest when the ions lose their energy (5). (*ii*) Backscattering from the substrate silicon should show a small effect on the total ion scattering at high energies (13). (*iii*) Complete penetration of ions through the resist layer should be assured in the corrugated structure of the coming submicrometer VLSI's.

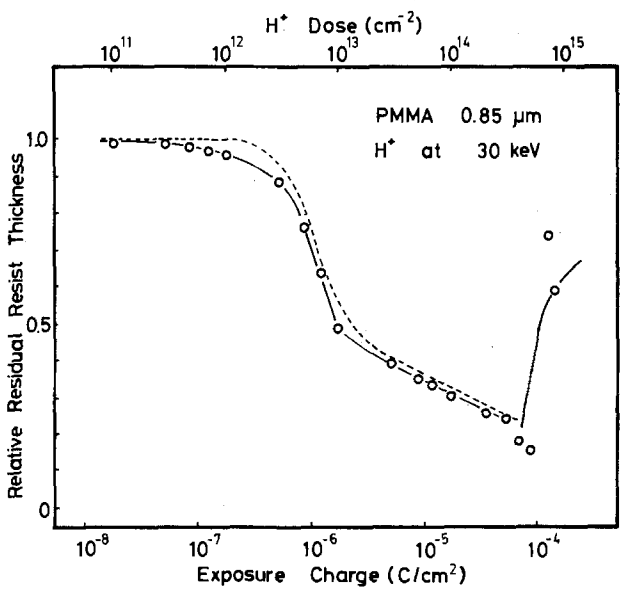

Fig. 6. Dose dependence of residual PMMA film thickness exposed by a 30 keV hydrogen ion beam.

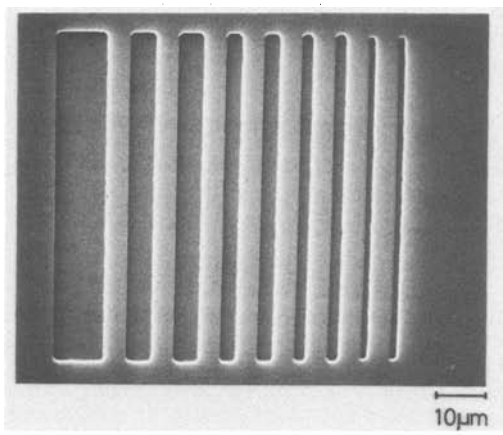

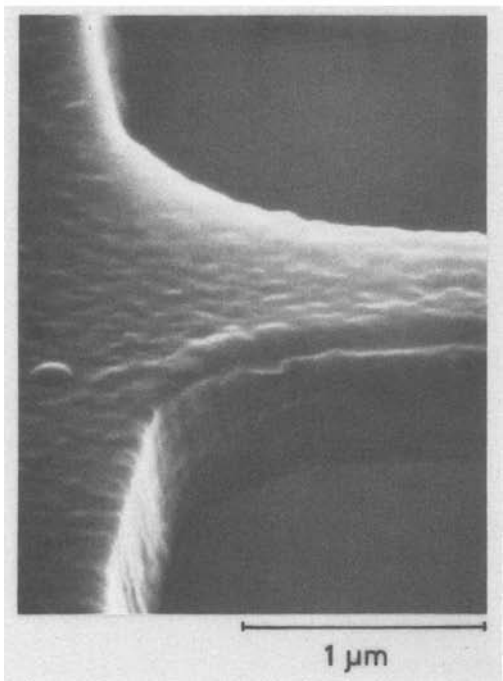

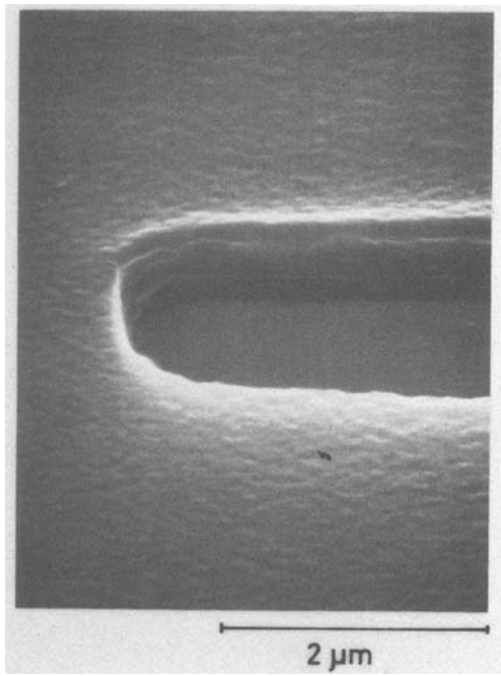

Fig. 7. SEM micrographs of 0.85 μm thick PMMA patterns replicated by a 180 keV hydrogen ion beam (3×10^{-6} C/cm^2 hydrogen ion dose): (a, upper left) low magnification micrograph showing the patterns of between 1 μm and 10 μm width, (b, right) a 2 μm wide pattern (hole) edge depicting the almost vertical edge profile, and (c, lower left) a 1 μm wide pattern (line) edge also showing the almost vertical edge profile.

Typical results are depicted in Fig. 7a through 7c, where patterns of as narrow as 1 μm wide are neatly replicated on PMMA layer. In the figures, the hydrogen ion dose was 3×10^{-6} C/cm^2, and the PMMA thickness was 0.85 μm. A sharp edge profile with almost vertical gradient was obtained in PMMA patterns, which indicates the negligible scattering effect of the exposing ions, and the small proximity effect in the ion beam lithography. These results suggest the submicrometer resolution capability of hydrogen ion beam lithography. Together with the reactive ion etching resistant resists (15), the hydrogen ion beam lithography should provide a method for realizing the coming submicrometer VLSI's.

Conclusions

Hydrogen and phosphorus ion beam exposure characteristics of PMMA were investigated as functions of acceleration energy, ion dose, and ion species. PMMA shows both positive and negative exposure characteristics depending on the dose and energy. Projected ranges and projected deviations of hydrogen and phosphorus ions were reported, and were almost one-third to one-tenth of the calculated values based on simple LSS theory, but coincide very well with the calculated results based on Monte Carlo method. A 1 μm wide pattern was neatly replicated on PMMA layer by a 180 keV hydrogen ion beam, and demonstrates the applicability of ion beam lithography to submicrometer VLSI fabrication.

Acknowledgments

The authors wish to express their thanks to Dr. T. Tokuyama and Dr. N. Hashimoto for their continuous encouragement and fruitful discussions. SEM micrographs made by Y. Yoneda are gratefully acknowledged.

Manuscript submitted Dec. 30, 1981; revised manuscript received *ca.* Dec. 8, 1982.

Any discussion of this paper will appear in a Discussion Section to be published in the December 1983 JOURNAL. All discussions for the December 1983 Discussion Section should be submitted by Aug. 1, 1983.

Publication costs of this article were assisted by Hitachi, Limited.

REFERENCES

1. G. E. Moore, Paper 1-3, International Electron Device Meeting, Washington, DC (1975).
2. R. L. Seliger, R. L. Kubena, R. D. Olney, J. W. Ward, and V. Wang, *J. Vac. Sci. Technol.*, **16**, 1610 (1979).
3. D. B. Rensch, R. L. Seliger, G. Csanky, R. D. Olney, and H. L. Stover, *ibid.*, **16**, 1897 (1979).
4. N. P. Economou, D. C. Flanders, and J. P. Donnelly, in "Proceedings of the 16th Symposium Electron, Ion and Photon Beam Technology," Dallas, Texas (1981).
5. L. Karapiperis, I. Adesida, C. A. Lee, and E. D. Wolf, in "Proceedings of the 16th Symposium Electron, Ion, and Photon Beam Technology," Dallas, Texas (1981).
6. Y. Wada, H. Usui, and M. Ashikawa, *Jpn. J. Appl. Phys.*, **14**, 1351 (1975).
7. "Fine Line Lithography," R. Newman, Editor, p. 21, North Holland, New York (1980).
8. R. G. Brault and L. J. Miller, in "Proceedings of the 15th Symposium Electron, Ion, and Photon Beam Technology," Boston, Massachusetts (1979).
9. "Projected Range Statistics," J. F. Gibbons, W. S. Johnson and S. W. Mylroie, Editors, Dowder, Hutchington and Roth, Inc., Stroudsburg, PA (1975).
10. Y. Wada and M. Ashikawa, *Jpn. J. Appl. Phys.*, **15**, 1725 (1976).
11. S. Furukawa and H. Ishiwara, *J. Appl. Phys.*, **43**, 1268 (1972).
12. O. Kudoh, K. Nakamura, and M. Kamoshida, *ibid.*, **45**, 4514 (1974).
13. J. A. Davis, J. Denhartog, L. Eriksson, and J. W. Mayer, *Can. J. Phys.*, **45**, 4053 (1967).
14. K. Mochiji, Y. Wada, and H. Obayashi, *This Journal*, **129**, 2556 (1982).
15. Y. Wada, K. Mochiji, and H. Obayashi, *This Journal*, **130**, 187 (1983).
16. Y. Iida, H. Okabayashi, and K. Shimizu, *Jpn. J. Appl. Phys.*, **16**, 1313 (1977).
17. Y. Wada and K. Sato, *ibid.*, **15**, 2289 (1976).
18. "Fine Line Lithography," R. Norman, Editor, p. 17, North Holland, New York (1980).
19. M. Komuro, N. Atoda, and H. Kawakatsu, *This Journal*, **126**, 483 (1979).

Process for Forming Passivated Metal Interconnection System with a Planar Surface[1]

L. B. Rothman*

IBM General Technology Division, East Fishkill, Hopewell Junction, New York 12533

ABSTRACT

The planarization characteristics of polyimide films were investigated for use in a multilevel, metal-insulator structure. Results showed that planarization is dependent on the geometry of the metal pattern. Therefore, a simple coating and etchback technique does not produce planarization over a typical metallization pattern. This paper describes a new, experimental process for fabricating a multilevel, metal-insulator structure with a planar surface. As a result of the planar structures, uniform narrow linewidths can be maintained on all levels of metallization. Good edge coverage of metal and insulators is also obtained on all levels.

The increase of circuit density on chips necessitates increased wirability. The dimensional limitation of the active area in a semiconductor chip dictates that vertical interconnections be made through multilevel metallization. In conventional multilevel structures, a great deal of topography results from the metal lines and etched via holes. The yield and reliability of these structures become a concern because of thinning metal and poor insulator coverage at steps. Linewidth variation is another problem resulting from topography. A planar surface is necessary in order to obtain high resolution lines of uniform widths and to ensure good edge coverage of metal and insulators on all levels. Polyimide was chosen as the insulator for several reasons. Polyimide has good thermal stability, chemical resistance, and dielectric properties. Polyimide is inexpensive to process, compared to sputtered SiO_2. Polyimide reportedly (1) provides planarization over a metal pattern: the simplest multilevel interconnection process described by Sato *et al.* (1) involves using polyimide to competely planarize the underlying metal pattern, followed by an etchback of the polyimide to expose the "bumps" or "studs" used to make contact to the next level of metal (Fig. 1). As discussed in a previous paper (2), the degree of planarization depends on the type of polyimide (solids content and molecular weight) and also on the dimensions of the lines and spaces to be planarized. The planarization characteristics of polyimide must be understood in order to develop a process for fabricating a planar multilevel, metal-insulator structure.

Planarization

A previous paper (2) discusses polyimide planarization characteristics, illustrated in Fig. 2 and 3. Thin lines with narrow spaces result in better planarization than wide lines. However, as shown in Fig. 3, a group of closely spaced lines, widely separated from other lines, act as one wide line. Since total planarization was unobtainable with any of the commercially available polyimides investigated, the use of multiple coat-

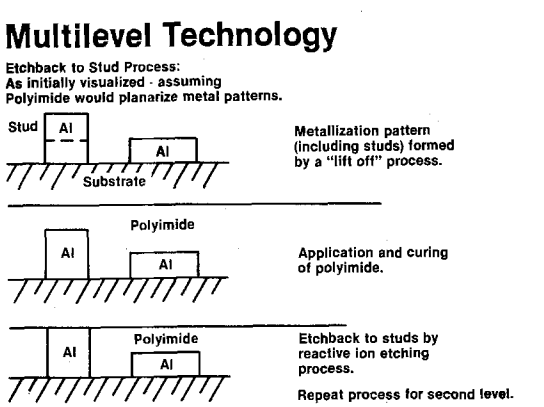

Fig. 1. Etchback to stud process, as initially visualized assuming polyimide would planarize metal patterns.

* Electrochemical Society Active Member.
[1] L. Zielinski, U.S. Pat. 3,985,597 (1975).
Key words: insulator, polyimide, metal, edge, planarization.

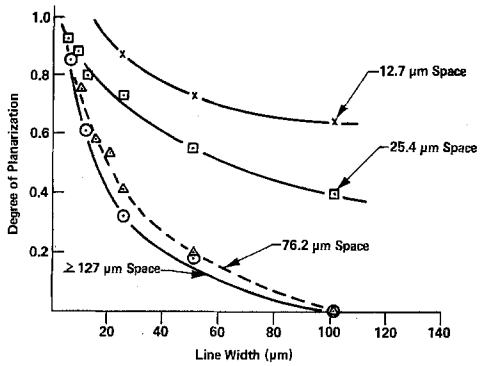

Fig. 2. Polyimide planarization as a function of linewidth and space

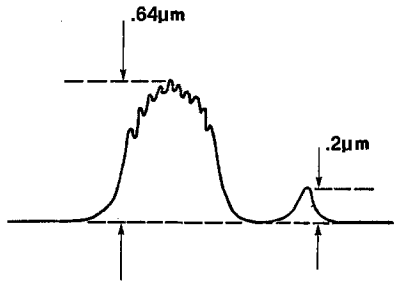

Fig. 3. Polyimide planarization for group lines vs. single isolated line. 5 μm width lines with 5 μm spaces, isolated 5 μm line with 125 μm space (Polyimide C).

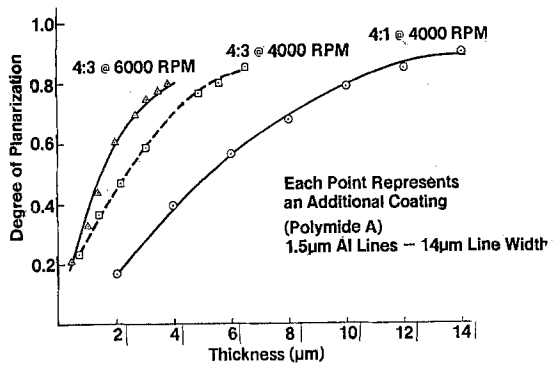

Fig. 4. Planarization as function of multiple coatings of polyimide

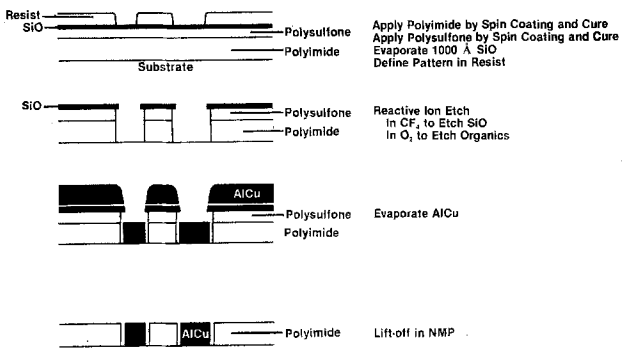

Fig. 5. Process description for forming first level metal

ings was studied. Figure 4 shows the results of multiple coating of a polyimide film. The degree of planarization seems to be more dependent on the number of coatings than the total thickness. Since the polyimide films are cured between coats, this becomes relatively time-consuming. Also, total planarization of all the geometries of a typical metallization pattern seems almost impossible, especially over large probe pads. Unfortunately, this geometry dependence violates the most basic requirement for a multilevel structure: that the insulator should have uniform thickness over the metal lines where via holes are located. Even if all the lines under the vias are of the same width, the spacing and grouping will still affect the planarization and result in varying thickness over metal lines. If a structure could be found that had small, uniform spaces and very narrow lines, total planarization would be achieved. This concept led to the discovery of this multilevel metal insulator process. The process is based on the principle that a small gap is created during evaporation through a lift-off mask: that this gap is uniform in size no matter what the geometry of the metallization pattern; and that the gap is so small that total planarization is achieved when a layer of polyimide is applied.

Process Description

The process is summarized in Fig. 5-7. A polyimide film is applied to the substrate by spin coating and then fully cured. The polyimide and metal thicknesses are the same (~1 μm). The polysulfone is spin coated and baked on hot plates. The polysulfone acts as a lift-off layer. Next, a thin film of SiO is evaporated. Other inorganic materials such as plasma-deposited oxides or nitrides can be used in place of the SiO, which serves as a masking layer. The resist is then coated and the first level metal pattern is defined, either by E-beam or optical lithography. The pattern is transferred into the underlying structure by reactive ion etching in CF_4 to etch the SiO and then in O_2 to etch the polysulfone and polyimide. A diode-type reactive ion etching system is used as described previously (3). The undercut of the organic layer is obtained by operating at relatively high O_2 pressure. The amount of undercut can be controlled by the O_2 pressure (3). After the reactive ion etching, a solution of buffered HF removes any residue (3), as shown in Fig. 8.

First-level metal is evaporated and then the lift-off is performed in warm n-methyl pyrrolidone (NMP).

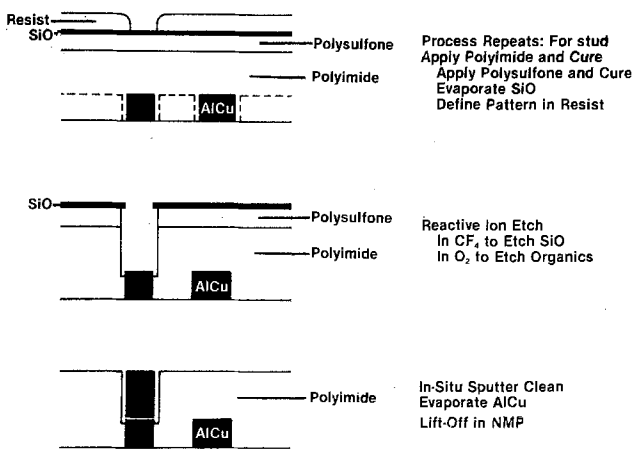

Fig. 6. Process repeats for forming first stud level

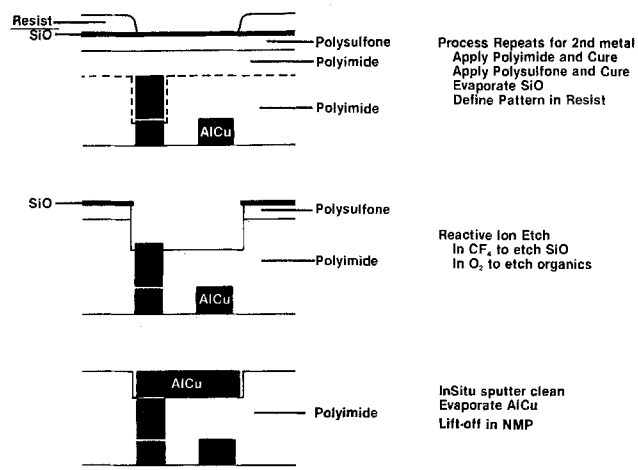

Fig. 7. Process repeats for forming second level metal

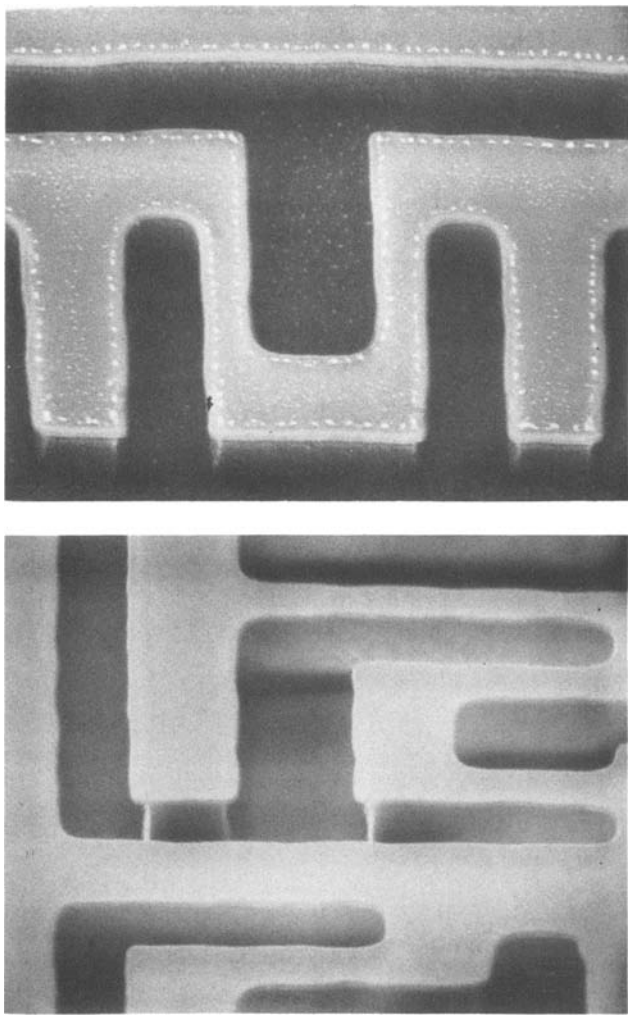

Fig. 8. Scanning electron micrographs illustrating structure (a, top) after RIE and (b, bottom) after 10 sec dip in buffered HF clean-up to remove residue. 8200×.

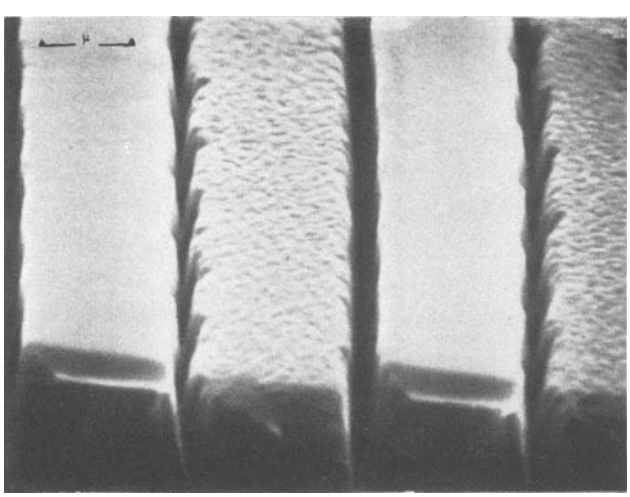

Fig. 9. SEM showing first metal completed

At this point, a basically planar structure remains with small "gaps" between the metal and the polyimide (Fig. 9). As illustrated in Fig. 2, planarization is dependent on the dimensions of the line or space to be planarized. Because the gaps are very small, total planarization of these gaps occurs as the next layer of polyimide is coated. The process for forming the stud is identical to the first metal formation except that the thickness of the polyimide and metal increases and an rf sputter clean is done prior to metal evaporation.

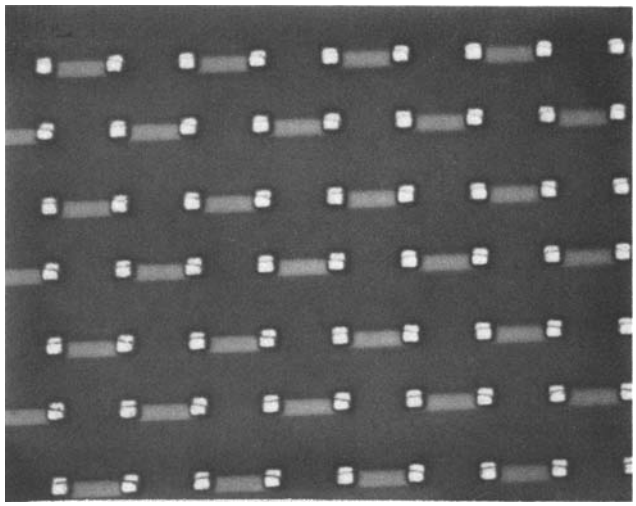

Fig. 10. Optical micrograph of structure with first level metal and studs.

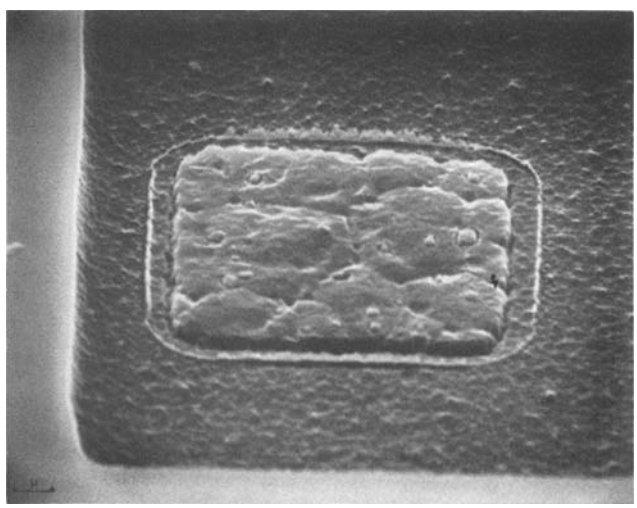

Fig. 11. SEM after RIE for second level metal

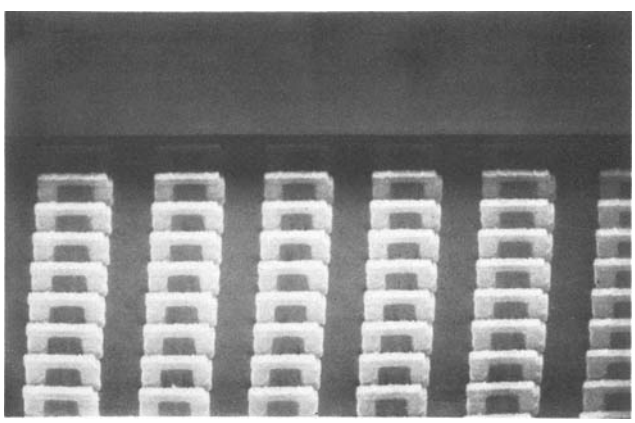

Fig. 12. SEM of via (stud) chain. The polyimide has been removed by RIE to illustrate planarity.

Figure 10 shows the structure with studs on top of the first metal. The processing continues for the second metal. The reactive ion etching is monitored using an optical end-point detect to insure that overetching of the polyimide is minimized, as shown in Fig. 11. The reactive ion etching of the polyimide also provides a slightly roughened surface which improves the metal-to-polyimide adhesion.

The contact resistance between the first and second levels of the metal of a single stud structure, using a

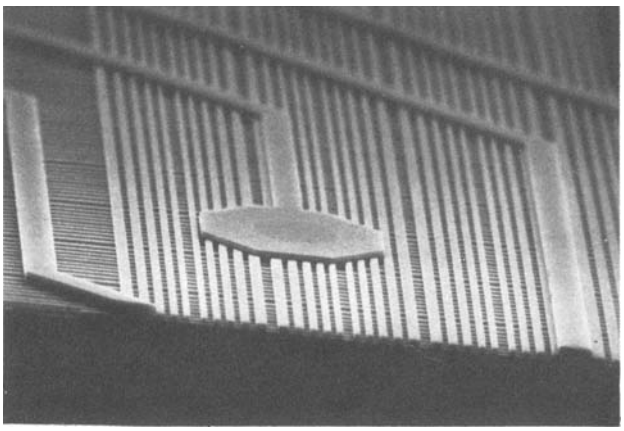

Fig. 13. SEM after four levels of metal completed. The polyimide removed to illustrate planarity.

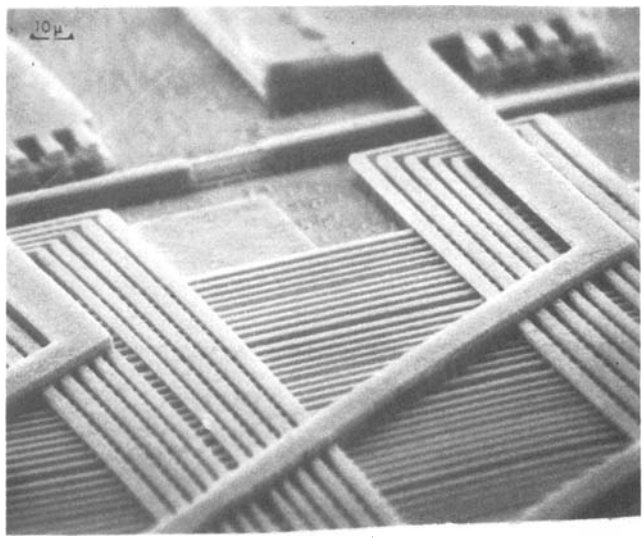

Fig. 14. SEM after four levels of metal completed. The polyimide removed to illustrate planarity.

four-point probe measurement, is approximately 20 mΩ. The rf sputter cleaning prior to metal evaporation is necessary for good contact. This is especially true since there are two interfaces per via (or stud) inter-

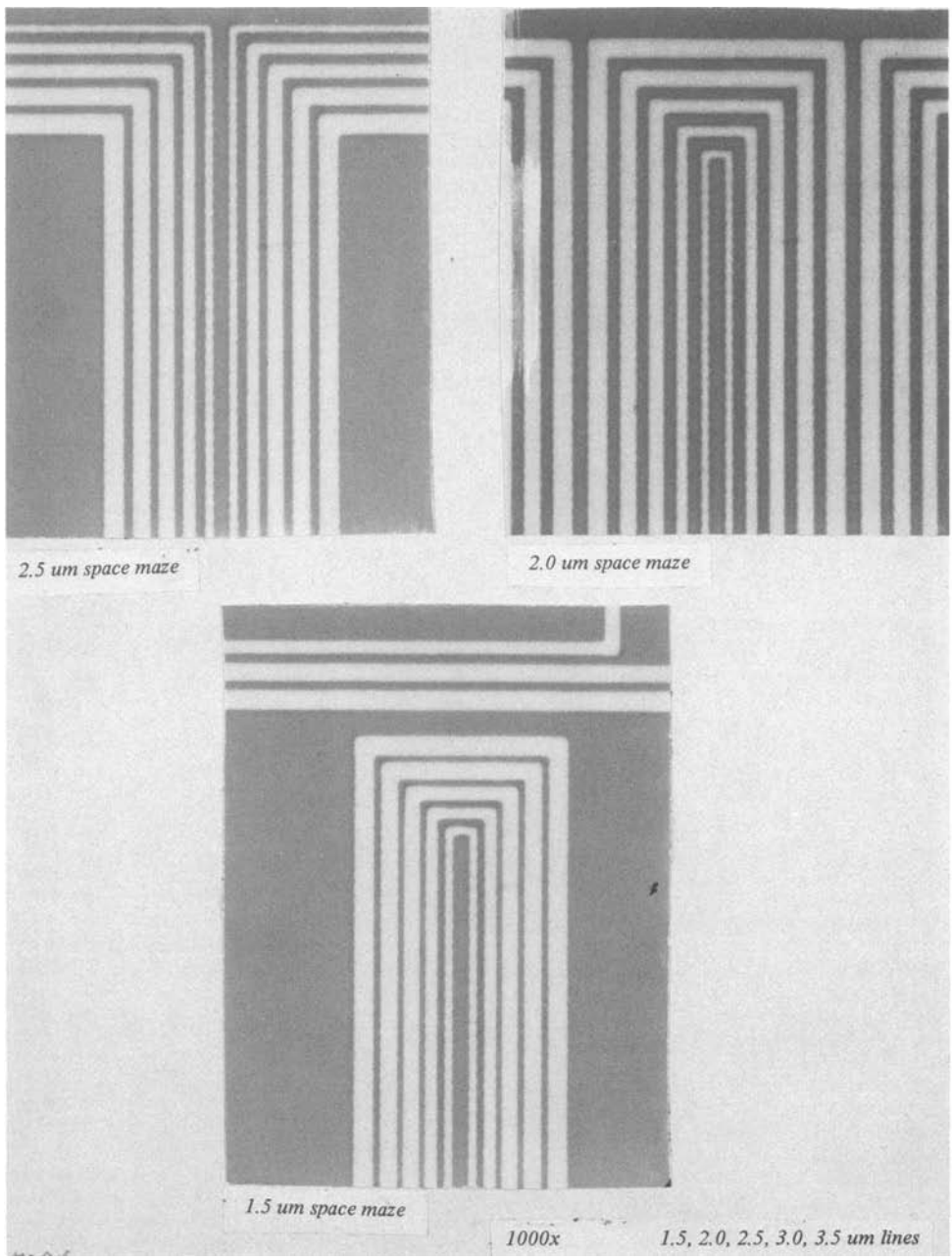

Fig. 15. Optical micrograph of metal maze pattern.

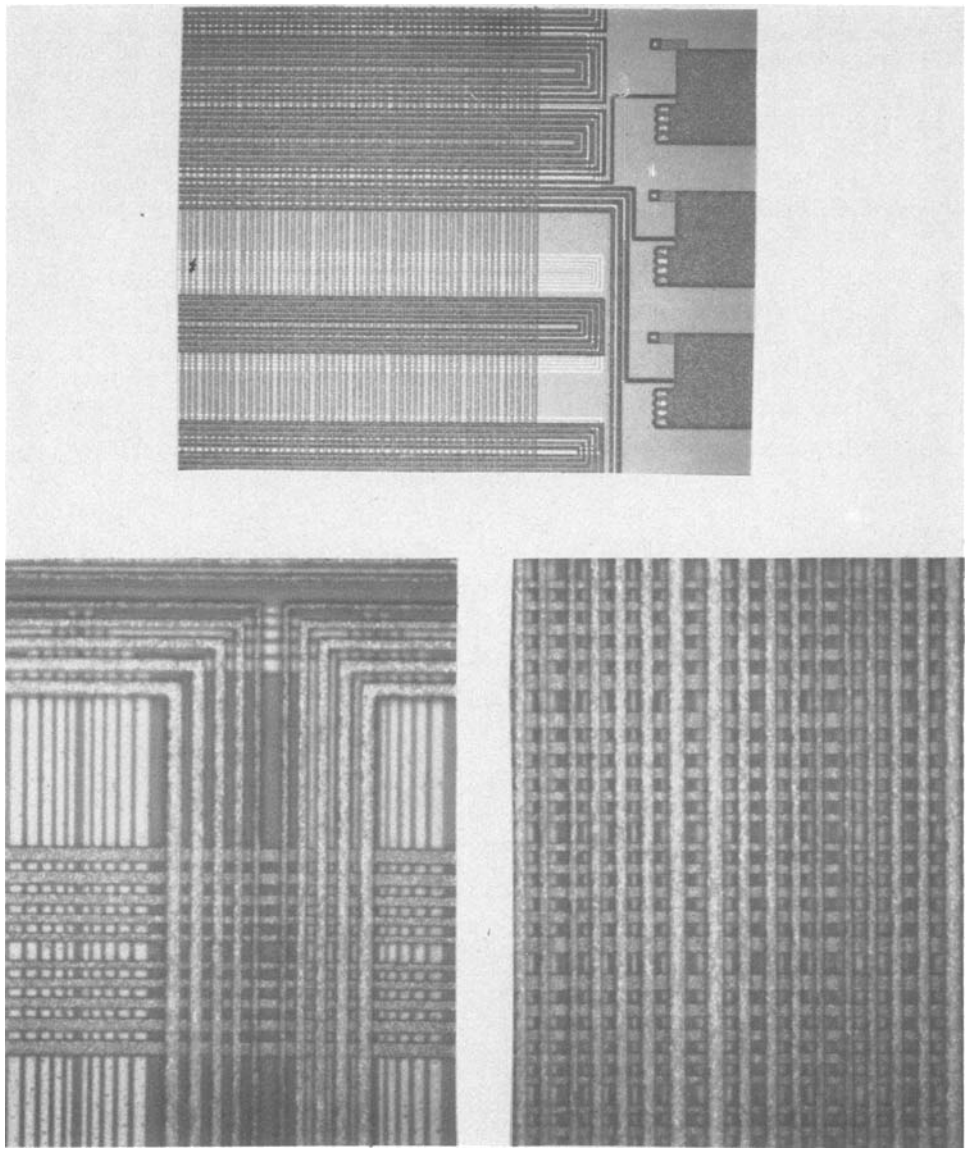

Fig. 16. Optical micrographs of metal maze structure after three levels of metal.

connection, in contrast to one interface for a normal via process.

The process is repeated for the second stud, third metal, third stud, and fourth metal. Illustrations show the planarization achieved with this process.

The structure can be seen more accurately if the polyimide is removed. The following SEM's were taken after removing the polyimide around the metal pattern by reactive ion etching in an O_2 plasma. Figure 12 shows a via (or stud) chain. Figures 13 and 14 show the planarization with four levels of metal.

Since the structure remains planar at all levels, it is possible to maintain uniform narrow linewidths. Figure 15 shows a test site first-level metal pattern. There are three mazes with varying linewidths and spaces. Figure 16 shows that these dimensions can be maintained on all three levels of metallization. Another advantage that a planar structure provides is good edge coverage of metal and insulators on all levels, as illustrated in Fig. 17.

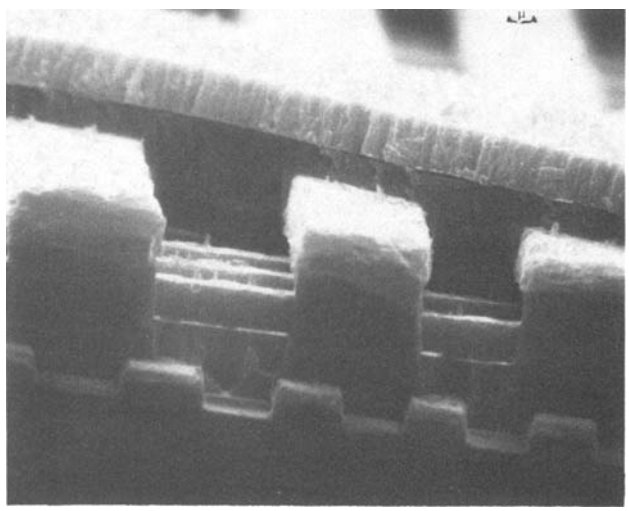

Fig. 17. SEM with four levels of metal to illustrate good edge coverage.

Conclusion

With the polyimides investigated, it did not seem feasible to completely planarize a typical metal pattern of a semiconductor device by simply applying a layer of polyimide. The degree of planarization is geometry dependent. However, making use of certain geometry effects, such as narrow spaces or "gaps," a process was developed for fabricating a planar multilevel, metal-insulator structure. The advantages of this planar structure are that narrow linewidths can be maintained on all levels and good edge coverage of metal and insulators is obtained.

Manuscript submitted Jan. 21, 1982; revised manuscript received *ca.* Dec. 15, 1982. This was Paper 243 presented at the Denver, Colorado, Meeting of the Society, Oct. 11-16, 1981.

Any discussion of this paper will appear in a Discussion Section to be published in the December 1983 JOURNAL. All discussions for the December 1983 Discussion Section should be submitted by Aug. 1, 1983.

Publication costs of this article were assisted by IBM Corporation.

REFERENCES

1. K. Sato, S. Harada, A. Saiki, T. Kimura, T. Okubo, and K. Mukai, *IEEE Trans. Parts, Hybrids, Packg.*, **php-9**, 176 (1973).
2. L. B. Rothman, *This Journal*, **127**, 2216 (1980).
3. L. B. Rothman, J. L. Mauer, G. C. Schwartz, and J. S. Logan, in "Plasma Processing," R. G. Frieser and C. J. Mogab, Editors, p. 193, PV 81-1, The Electrochemical Society Softbound Proceedings Series, Pennington, NJ (1981).

An XPS Study of Cu_xS Formed on $Zn_{0.15}Cd_{0.85}S$

P. N. Uppal, D. W. Dwight, and L. C. Burton

Departments of Electrical and Materials Engineering, Virginia Polytechnic Institute and State University, Blacksburg, Virginia 24061

ABSTRACT

X-ray photoelectron spectroscopy (XPS) was applied to the surface chemical characterization of $Cu_xS/Zn_{0.15}Cd_{0.85}S$ and C_xS/CdS heterojunctions with emphasis upon the effects of the ambient (oxygen and water vapor in particular) on chemical species present at or near the Cu_xS surface. Elevated temperature during or subsequent to formation of a junction promoted migration of Zn and Cd toward the Cu_xS surface. When formed on CdS, the Cu_xS surface was found to contain CdO (or $Cd[OH]_2$), CuO, $CuSO_4 \cdot nH_2O$ and $CdSO_4 \cdot nH_2O$. Preferential segregation of ZnO to the Cu_xS surface was observed in specimens formed on $Zn_yCd_{1-y}S$. For $Zn_{0.15}Cd_{0.85}S$ substrates, ZnO was the predominant species, with the Cu and Cd compounds present in lesser amounts. Also, development of djurleite and diginite Cu_xS phases during heat-treatments was verified by x-ray diffraction.

During fabrication, cells of the $Cu_xS/Zn_yCd_{1-y}S$ type (including Cu_xS/CdS) receive extensive heat-treatment. A number of chemical phenomena related to the Cu_xS/CdS junction have been documented which effect cell response and which should also occur for the $Cu_xS/Zn_yCd_{1-y}S$ junction. Some of these are diffusion of copper into the CdS (1), oxidation of Cu_xS (2, 3), cross diffusion of cadmium and zinc into the Cu_xS (4), phase changes of Cu_xS (1, 5), and copper ion migration in the Cu_xS (1, 6). It has been found that heat-treatments increase cadmium and zinc concentrations both in and on the Cu_xS layer (4). However, most compositional measurements of Cu_xS/CdS and $Cu_xS/Zn_yCd_{1-y}S$ junctions have dealt only with elemental analyses. In this work, we have used XPS combined with ion-milling to determine the chemical species that exist in and on Cu_xS layers formed on CdS and ZnCdS substrates, when aged under different conditions. This is the first report of this type that we are aware of, and could be of importance with respect to a better understanding of potential degradation mechanisms.

Experimental Techniques

$Cu_xS/Zn_yCd_{1-y}S$ heterojunctions ($y = 0$, 0.15) were formed using aqueous (wet) and solid-state (dry) ion-exchange reactions. These were standard formation procedures that have been reviewed elsewhere (7). Effective Cu_xS thicknesses comparable to those for solar cells ($\approx$ 0.2-0.3 μm) were used. All junctions received heat-treatment in a hydrogen ambient (150°C, 16 hr) subsequent to formation. Some samples were then measured after air storage at room temperature. For accelerated studies, junctions were heat-treated in air saturated with water vapor (150°C). XPS measurements were performed with a Perkin-Elmer 550 instrument, using an Mg anode source (1253.6 eV) operating at 400W (10 kV, 40 mA). Surface milling was performed *in situ* with a rastered 5 kV Ar^+ ion beam. Phase changes that occurred as a result of aging were determined by means of x-ray diffraction (8). X-ray measurements were done in a Siemens Model M386-A7 diffractometer, using Cu Kα radiation ($\lambda = 1.542$Å).

Results and Discussion

The x-ray diffraction pattern in Fig. 1A shows that the Cu_xS film is originally chalcocite ($X \geq 1.996$). When exposed to air, chalcocite oxidizes and transforms into more stable copper-deficient phases, indicated by the diffraction pattern in Fig. 1B. The transformation from chalcocite to djurleite is detrimental to

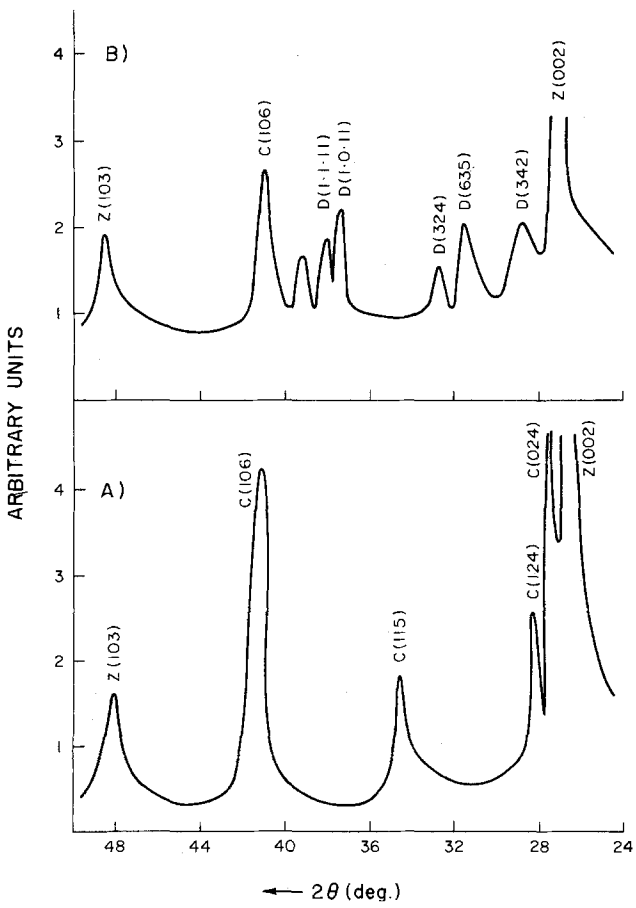

Fig. 1. X-ray diffraction patterns before A) and after B) heat-treatment (air, 150°C, 3 hr). C = chalcocite; D = djurleite; Z = ZnCdS substrate.

photovoltaic response, and it occurs much more rapidly in the presence of moisture (8).

To ascertain composition *vs.* depth through the heterojunctions, angular dependent x-ray photoemission results were correlated with Auger electron spectroscopy combined with ion milling.

We used powder standards, of the following compounds: Cu_2S, CuS, ZnS, CdS, Cu_2O, CuO, ZnO, CdO, $CuSO_4 \cdot 5H_2O$, and $CdSO_4$. These powders were pressed to aluminum foil and mounted, and spectra were taken under the same conditions employed for the thin films.

Figure 2 shows three typical high resolution spectra from in-depth study of a dry formed and 150°C steam heat-treated heterojunction. In Fig. 2A, the spectrum was collected at normal exit angle, and three sulfur oxidation states can be assigned as follows: the peak at ~172 eV is $Cd(SO_4) \cdot nH_2O$, the peak at ~168 eV is $CuSO_4$, and the largest peak at ~161 eV is Cu_xS. The same three assignments pertain to Fig. 2B, but there is greater relative intensity in the sulfate peak components. This spectrum was collected at grazing photoelectron exit angle, and the indication is that sulfates are located in the very top layer or two of the Cu_xS.

The peak assignment at 172 eV was made after analyzing the S 2p spectra collected on oxidized CdS powder and on $CdSO_4$ powder. In addition, the Cd photoelectron and Auger spectra were used for compound identification. These results are consistent with other reports in the literature (9, 10). Amalnerkar *et al.* (9) report S 2p spectra at 162.6 and 172.8 eV, which are attributed to the sulfide and the sulfate, respectively, for oxidized CdS films. In addition, they attribute a peak located at 179.7 eV to SO_2^{-}-like species. (The energy of the latter peak was slightly out of our observational window.)

The undulating appearance of the S 2p spectrum taken at grazing angle (Fig. 2B) could be due to the low count rate and the fact that the collection time for this spectrum was the same as for the others. This appearance is not attributed to charging effects, since it was not seen for any other spectrum (*i.e.* Cu, O, Cd, Zn).

Figure 2C demonstrates that only sulfide remains after brief Ar^+ ion sputtering (5 kV Ar^+ ions at intensity of 2×10^{11} cm^{-2} sec^{-1}). All other peak shapes remained constant, and the carbon intensity diminished by about 3 times.

A separate experiment was carried out to determine if the sulfate was being reduced by the Ar^+ ion beam. Sputtering of $CdSO_4$ using Ar^+ of the same energy and intensity noted above did not result in significant peak modification. Thus, we believe that sulfates are present only at the very top atom layers.

Many of the copper spectra showed signs of shake-up satellite structure, indicative of the cupric oxide, but the majority contaminants made this result uncertain. Therefore, a Cu_xS film was vacuum evaporated onto a glass substrate, and Fig. 3 shows the Cu $2p_{3/2}$ XPS spectra before (B) and after (A) steam treatment. (It should be noted that the reason oxygen 1s peaks were not used as a basis for chemical identification is because of the difficulty in unambiguous interpretation. Oxygen is bound to every other element, and some of the 1s peaks collected were unusually broad and difficult to interpret.) Here the appearance of the shake-up structures, as well as small shift and broadening of the main peak, typical of Cu^{+2}, are unambiguous (11, 12).

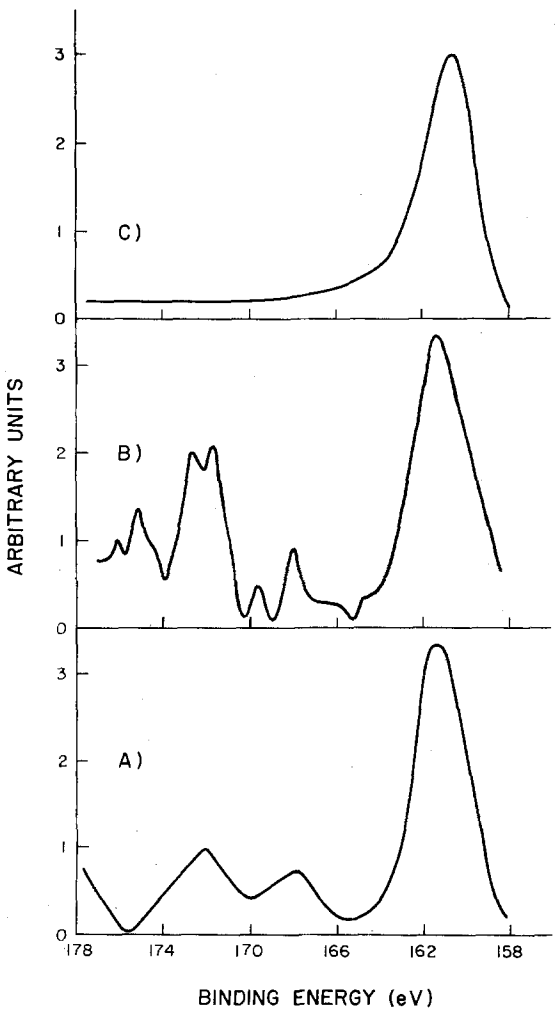

Fig. 2. Sulfur 2p spectra taken from dry-formed Cu_xS/$Zn_{0.15}Cd_{0.85}S$ surfaces A) initial normal angle; B) before Ar^+ ion milling, grazing angle; C) after milling, normal angle.

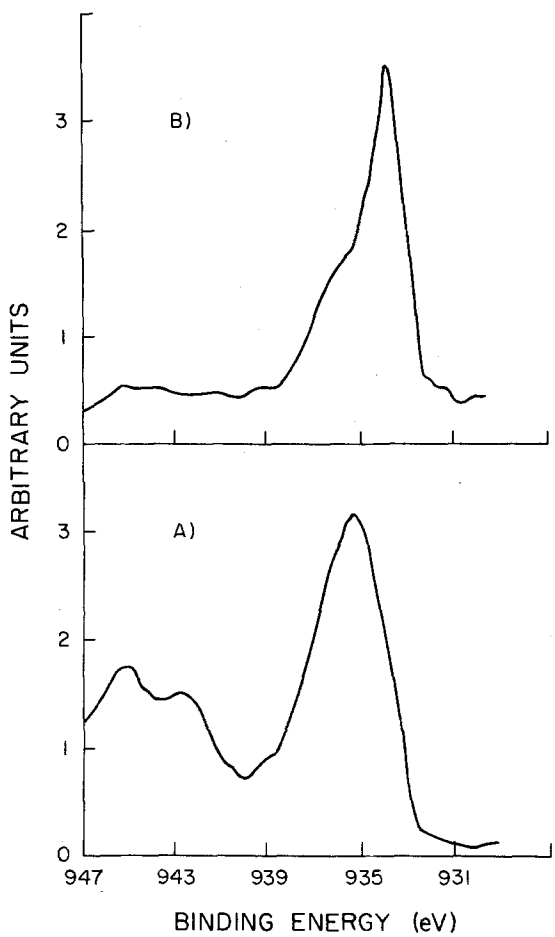

Fig. 3. Copper $2p_{3/2}$ spectra taken from evaporated Cu_xS on glass A) after, and B) before heat-treatment (wet air, 150°C, 4 hr).

Table I. XPS peak positions and relative compositions for various $Cu_xS/Zn_{0.15}Cd_{0.85}S$ surfaces

Sample formation/ post-treatment	X-ray photoelectron spectral analysis									
	Cu $2p_{3/2}$ (λ = 0.8 nm)		Zn $2p_{3/2}$ (λ = 0.6 nm)		Cd $3d_{5/2}$ (λ = 1.7 nm)		O 1s (λ = 1.5 nm)		S 2p (λ = 1.9 nm)	
	BE (eV)	%	BE (eV)	%	BE (eV)	%	BE (eV)	%	BE (eV)	%
Dry evaporated/heated in H_2	931.6	0.3	1021.6	73	405.2	0.6	530.6	25	160.8	0.6
									168.6	0.1
Dry evaporated/steam	932.6	4	1022.6	48	406.0	9	532.2	33	162.0	4
									168.0	0.4
									172.4	0.6
Wet ion exchange/heated in H_2	932.9	20	1022.6	46	405.6	5	532.2	19	161.8	9
									172.2	0.3
Wet ion exchange/steam	931.8	8	1022.0	15	405.0	15	531.4	50	161.2	10
									168.2	1
									171.4	1

Peak assignments were made by comparison to standard references (11), and by studying the standard compounds noted above in powder form. We found that the surfaces of several of the controls had contaminants of the same type as appeared on our heterojunctions. For example, the S 2p spectrum of CdS showed two strong peaks at about 162 and 171 eV, respectively, but the S 2p spectrum of $CdSO_4$ had only the peak at 171 eV. Similarly, $CuSO_4$ was found on the Cu_2S powder.

In order to make meaningful comparisons between the XPS peak intensities, the integrated peak areas were divided by published empirical sensitivity factors that take into account spectrometer constants, photoelectron cross sections, and mean-free path values (13). Then, the effect of variable contamination layers, indicated by a large carbon 1s peak, was removed by assuming a uniform overlayer model and a 4λ total sampling depth (individual values of λ are shown in Table I). The results of these calculations were self-consistent in terms of overlayer thickness, and also correlated well with XPS peak intensities observed after a slight argon ion sputtering that removed most of the carbon.

The trends in surface composition and bonding can be discerned from the results on four typical specimens (wet- and dry-formed Cu_xS; H_2 or H_2O post-treated) shown in Table I. The relative atom fraction values were calculated by the method described above and should be used for comparison purposes only. The binding energy values do show small chemical shift effects that corroborate the conclusions based upon the peak intensity analysis. Most striking is the fact that no specimen is composed of a majority of the desired Cu_xS absorber species; contaminants involving oxides and sulfates, as well as Zn^{+2} and Cd^{+2}, always dominate the top surface. Dry-formed heterojunctions have ZnO as the principal top-surface component, probably because of the higher formation temperature which promotes both a Zn excess (14) and enhanced Zn diffusion. Auger electron spectroscopy with ion milling gave composition profile results similar to those obtained by XPS for wet and dry-formed specimens.

Steam treatment promotes the migration of cadmium to the surface, mostly as the sulfate, and also copper sulfate and oxide are mixed with the still-dominant zinc oxide. Wet-forming yields the largest amount of Cu_xS at the surface, but ZnO, $CdSO_4$, and CdO contaminants still dominate. Cadmium and oxygen show the greatest increase after steam treatment; the sulfates and oxides of cadmium and copper exceed the ZnO surface concentration in this case only.

Oxidation of Cu_2S is believed to proceed according to the reaction (15)

$$2Cu_2S + 5\,O_2 \rightarrow 2CuSO_4 + 2CuO$$

Cadmium and zinc can be viewed as diffusing through Cu_xS as Cd^{+2} and Zn^{+2}. Some of these ions may combine with S^{-2}, and then, as oxidation proceeds some of these sulfides in the top atom layers transform into sulfates. It has been reported that during the initial stages of CdS oxidation, oxygen bonds to sulfur preferentially, forming $CdSO_4$ (9), and as oxidation proceeds, an increasing amount of oxygen is bonded to cadmium (10).

These results are consistent with other reports in the literature. It is known that cadmium segregates on Cu_xS formed on CdS (16), and that both cadmium and zinc segregate on Cu_xS formed on ZnCdS (4).

Increased sulfate formation for Cu_xS heated in humid air has also been reported (17). Our results indicate that cadmium and zinc will exist on the Cu_xS surface mainly as oxides after exposure to dry air at room temperature. Subsequent exposure to humid air at elevated temperatures results in increased sulfates of copper and cadmium, with Cu_xS near the surface (within $\approx$ 10Å) reduced to almost zero. It is apparent from these results that H_2O is the prime cause of sulfate formation at the Cu_xS surface.

In conclusion (*i*) For all Cu_xS surfaces measured, the following species were identified: CuO, Cu_xS, $CuSO_4$, CdO, and $CdSO_4$. (*ii*) For ZnCdS substrates, ZnO is an additional species. $ZnSO_4$ was not unambiguously identified. (*iii*) Following humid air heat-treatment, copper signals decreased for wet formed samples, with $CdSO_4$ becoming predominant. (*iv*) The main effect of water in the ambient is increased formation of sulfates ($CdSO_4$ and $CuSO_4$). (*v*) Sputter etch verified that the cadmium and zinc compounds are surface species. Postsputtering XPS into the bulk revealed large copper increases, with sulfur then identified as mainly Cu_xS. (*vi*) Development of the djurleite and diginite phases was seen via x-ray diffraction upon exposure to air, being much enhanced by the presence of water. (*vii*) For samples aged in humid air, only Cu^{+2} is detected at the surface (contrasted to Cu^{+}).

Acknowledgments

We would like to acknowledge the Solar Energy Research Institute for supporting this work, and the reviewers for their helpful comments.

Manuscript submitted June 22, 1982; revised manuscript received Jan. 4, 1983. This was Paper 81 presented at the Montreal, Que., Canada, Meeting of the Society, May 9-14, 1982.

Any discussion of this paper will appear in a Discussion Section to be published in the December 1983 JOURNAL. All discussions for the December 1983 Discussion Section should be submitted by Aug. 1, 1983.

REFERENCES

1. L. R. Shiozawa *et al.*, Rep. ARL 69-0155 (Clevite Final Report), Clevite Corp., Cleveland, OH (1969).
2. L. C. Burton and H. M. Windawi, *J. Appl. Phys.*, **47**, 4621 (1976).
3. J. Besson *et al.*, 11th IEEE Photovoltaic Specialists Conference, p. 38, IEEE, New York (1975).
4. L. C. Burton, P. N. Uppal, and D. W. Dwight, *J. Appl. Phys.*, **53**, 1538 (1982).
5. R. Hill, in "Active and Passive Thin Film Devices," T. J. Coutts, Editor, Chap. 10, Academic Press, New York (1978).

6. H. L. Zwicker *et al.*, 15th IEEE Photovoltaic Specialists Conference, p. 787, IEEE, New York (1981).
7. L. C. Burton, *Solar Cells*, **1**, 159 (1980).
8. P. K. Roy and S. J. Lusczs, 15th IEEE Photovoltaic Specialists Conference, p. 1025, IEEE, New York (1981).
9. D. P. Amalnerkar *et al.*, *Appl. Phys. Lett.*, **41**, 270 (1982).
10. M. Lichtensteiger *et al.*, *Surf. Sci.*, **97**, L375 (1980).
11. "Handbook of X-ray and Ultraviolet Photoelectron Spectroscopy," D. Briggs, Editor, Heyden, London (1977).
12. D. C. Frost, A. Ishtiani, and C. A. McDowell, *Molecular Phys.*, **24**, 861 (1972).
13. "Handbook of X-Ray Photoelectron Spectroscopy," Physical Electronics Division, Perkin-Elmer Corp., Eden Prairie, MN (1979).
14. L. C. Burton, *Appl. Phys. Lett.*, **35**, 780 (1979).
15. "Encyclopedia of Chemical Reactions," Vol. III, C. Jacobson, Editor, p. 432, Reinhold, New York (1949).
16. J. V. Florio *et al.*, 15th IEEE Photovoltaic Specialists Conference, p. 793, IEEE, New York (1981).
17. G. S. Frents and E. I. Novikova, Issled. Metal. v Zhidkom i Tverd. Sostoyaniyakh, Akad, Nauk SSSR, Inst. Met., pp. 55-64 (1964).

Low Pressure Nitrided-Oxide as a Thin Gate Dielectric for MOSFET's

S. S. Wong,[1] and C. G. Sodini,[1] T. W. Ekstedt, H. R. Grinolds,* K. H. Jackson, and S. H. Kwan

Hewlett-Packard Laboratories, Palo Alto, California 94304

and W. G. Oldham

University of California, Berkeley, California 94720

ABSTRACT

SiO_2 films were nitrided in an NH_3 ambient or an NH_3 plasma between 925° and 1050°C for less than 2 hr. From the etching and the oxidation properties, along with the Auger analysis, the resulting film composition was determined and the reaction kinetics were postulated. Capacitors and n-channel MOSFET's were fabricated on the nitrided-oxide films. Effects of the nitridation step on the interfacial characteristics were examined.

Thin gate dielectrics of about 10 nm have been of increasing interest during the past few years. When channel lengths of MOSFET's are scaled down to one micron or below, gate dielectrics of 10-20 nm thick are required for constant field scaling (1). In single transistor dynamic random access memory cells, a thin dielectric can increase the charge stored. Circuit margins are increased, refresh time is improved, and soft error problems are reduced (2). In the case of electrically erasable, read only memories the programming voltage can be reduced when thin tunneling dielectrics are adopted (3).

The requirements on MOSFETs' gate dielectrics suitable for present or future MOS technology are very stringent. The dielectric must be homogeneous and uniform with low defect density throughout the entire fabrication sequence. It should ideally be an effective diffusion barrier against dopants, metals, and impurities. It must have low trap density for physical durability and reliability. Finally, a dielectric-substrate interface with low interface fixed and trapped charge densities is needed for high performance MOSFET's. In order to enhance the properties of SiO_2 dielectrics, nitridation in NH_3 ambients has been explored (4-8). However, most of the work reported involves extended cycles at high temperature. This paper emphasizes nitridation performed at 925°-1050°C for less than 2 hr in an NH_3 ambient or an NH_3 plasma. First, a method of forming the nitrided-oxide films in low pressure ambients is presented. The nitrided-oxide films are characterized with chemical etch rates and oxidation resistance, and are analyzed with Auger electron spectroscopy. The ability of the nitrided-oxide films to prevent boron diffusion is confirmed. Finally, the interfacial characteristics of the nitrided-oxide films are compared to those of SiO_2 films.

* Electrochemical Society Active Member.
[1] Also at the University of California at Berkeley, Berkeley, California.
Key words: nitrided-oxide, gate dielectric, MOSFET, interface, mobility.

Growth of Low Pressure Oxide and Nitrided-Oxide Films

A furnace depicted in Fig. 1 was specifically developed for growing low pressure SiO_2 films and for nitriding these films. The quartz tube is resistively heated and can be evacuated by a mechanical pump. At the source end of the tube, two electrodes are used to capacitively couple 13.56 MHz rf power and excite a plasma discharge, if desired.

All wafers used were p-type, <100>-oriented and with resistivity of 5-9 Ω-cm. The wafers were cleaned in $H_2SO_4 + H_2O_2$ solution followed by a dip in diluted HF. Oxidation in a reduced pressure ambient of 10 Torr O_2 at 950°C was chosen to grow the initial 10 nm oxide (9). Due to the slow oxidation rate as shown in Fig. 2, uniformity of ±0.2 nm on a wafer and reproducibility of ±0.3 nm across run has been achieved. The SiO_2 films were then annealed in 1 Torr N_2 ambient for 30 min during which the furnace temperature was ramped from 950°C to the nitridation temperature. The typical nitridation step was carried out at 925°C in 1 Torr NH_3 ambient or NH_3 plasma ambient for 2 hr. Nitridation temperature, time, and rf power were varied to allow further understanding of the kinetics. After the nitridation step, there was no

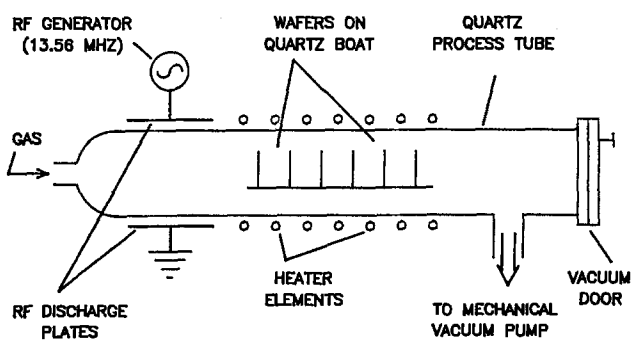

Fig. 1. Schematic drawing of furnace

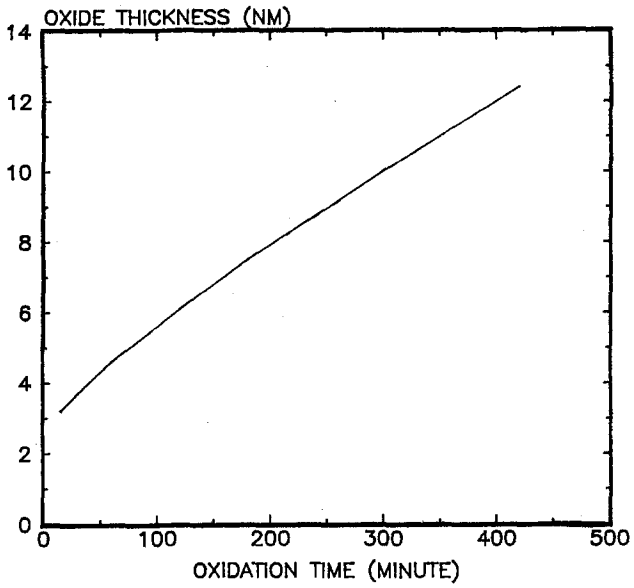

Fig. 2. SiO_2 thickness vs. growth time in 10 Torr O_2 at 950°C

change in the apparent film thickness which was measured with a Rudolph Auto EL 3 ellipsometer. The index of refraction was forced to be 1.45 owing to the difficulty in resolving both thickness and index of refraction in the 10 nm range.

Film Composition

The composition of the low pressure SiO_2 film, NH_3 nitrided-oxide film, and plasma-enhanced nitrided-oxide film were analyzed by etching the films in 100-1 buffered HF (100:1 = NH_4F:HF). The etch profiles are shown in Fig. 3a. The SiO_2 film has a constant etch rate of 0.14 nm/sec down to about 2 nm from the film-substrate interface. The apparently slower etch rate observed below 2 nm owes largely to the effects of fluorine bonds and native oxide on the ellipsometric measurement (HF cleaned "bare" silicon has a time-dependent ellipsometric delta which corresponds to an effective oxide thickness of 0.5-2 nm). It is also possible that the silicon-rich SiO_2 near the interface actually has a slower etch rate than pure SiO_2. For both types of nitrided-oxide films, a top layer of about 1 nm in thickness etches slower than the SiO_2 film Throughout the bulk of the nitrided-oxide films, the etch rates are similar to that of pure SiO_2. About 3 nm from the film-substrate interfaces, the etch rates start to decrease. These results indicate that the nitridation step only alters the surface and the interface regions. When comparing the two types of nitrided-oxide films, the one that was nitrided in an NH_3 plasma exhibits more development of the surface layer. No quantita-

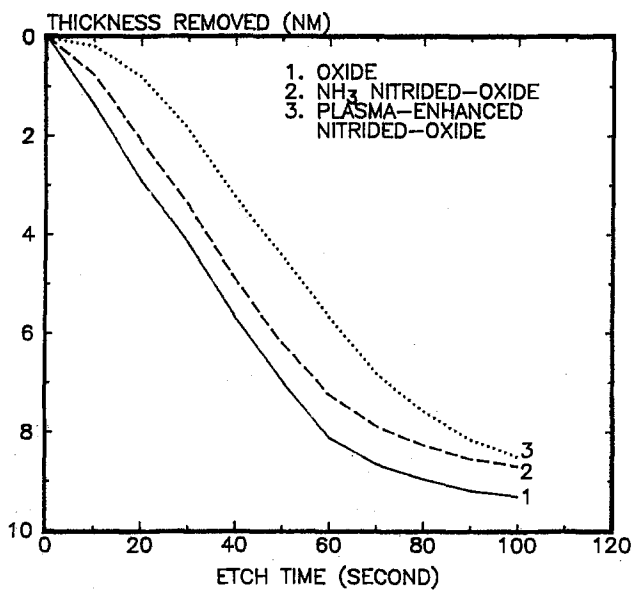

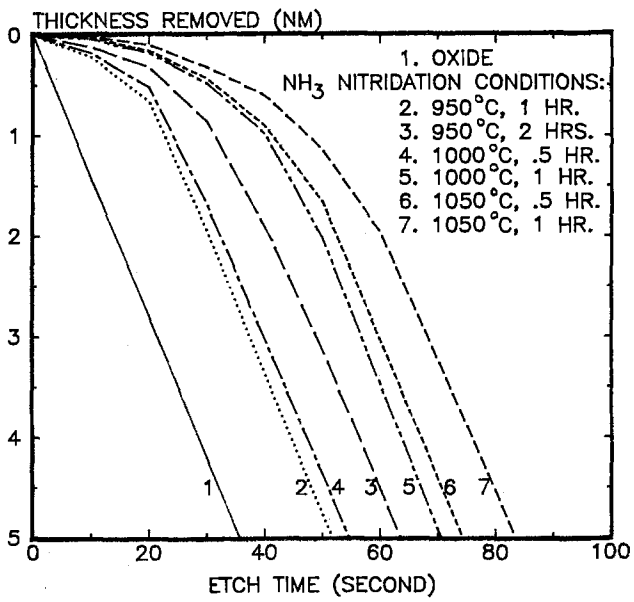

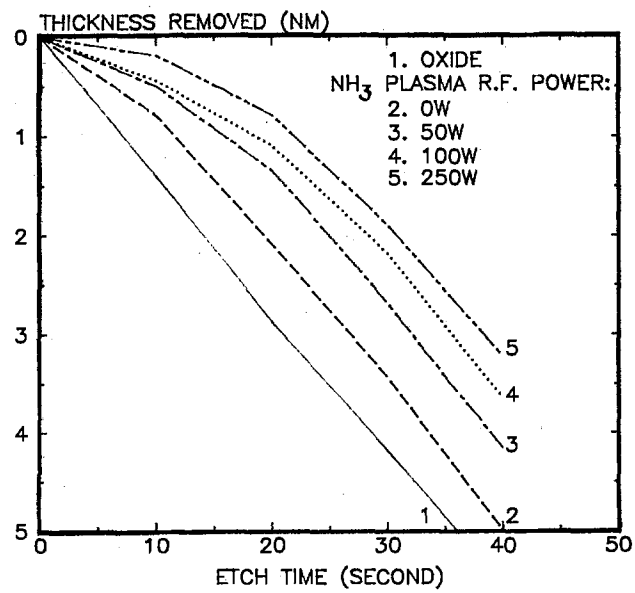

Fig. 3. Etch behavior of oxide and nitrided-oxide films in 100:1 = NH_4F:HF. (a, top left) Comparison of three film types: low-pressure SiO_2, NH_3 nitrided-oxide and plasma-enhanced nitrided-oxide. Nitridation was performed at 925°C for 2 hr. (b, top right) Comparison of NH_3 nitrided-oxide films for various time-temperature conditions. (c, bottom left) Comparison of plasma-enhanced nitrided-oxide films (nitridation was performed at 925°C for 2 hr) at various rf power levels.

tive conclusion can be made about the interface regions because the apparent etch rates are influenced by the factors discussed earlier. As expected, the surface layer becomes more etch resistant for higher nitridation temperature and longer nitridation time, as shown in Fig. 3b. The etch rates of the bulk regions, however, are the same as that of the SiO_2 even for the most severe nitridation condition. In Fig. 3c, the surface etch profiles of plasma-enhanced nitrided-oxide films with different rf power are shown. There is more development of the etch-resistant surface layer when higher rf power is used. At present, the species responsible for the surface reaction have not yet been identified. From the gradual change of the surface characteristic with increasing rf power, it would appear that the plasma does not introduce new nitridation species, but rather just increases the population of the species over that which is obtained thermally.

The films were also analyzed with Auger electron spectroscopy. The incident electron beam was 0.5 μA at 8 keV. Sputtering was accomplished with a 0.5 keV argon beam. A sputtered Auger-depth profile of the plasma-enhanced nitrided-oxide film is shown in Fig. 4a. Strong nitrogen signals are detected at the surface and at the interface regions. Nevertheless, nitrogen is also detected throughout the bulk of the film. The combination of the noise level of the system and the forward sputtering process through which argon knocks the surface nitrogen further into the film can account for this bulk signal. To confirm the above reasoning, a composite film of 10 nm CVD Si_3N_4 deposited onto 10 nm thermally grown SiO_2 was analyzed. The Auger-depth profile is shown in Fig. 4b. Nitrogen is detected even in the SiO_2 region. Surface Auger scans were also performed on some chemically etched-back plasma-enhanced nitrided-oxide samples. The data are plotted *vs.* film thickness measured by ellipsometry as shown in Fig. 4c. Nitrogen atoms are detected only at the surface and at the interface regions, but not in the bulk region. These results agree with the etch profiles. The surface and interface etch resistance observed is due to the presence of nitrogen in both regions. The inevitable surface contamination on all etched-back samples causes the atomic ratio shown in Fig. 4c to be only qualitative.

In order to compare the amount of nitrogen at the surface and the interface regions, the oxidation resistance of the films was studied. A series of 12 nm low pressure oxide films were grown and were nitrided using various temperature, time, and rf power conditions. These thicker films were, then, chemically etched back to about 10 nm to remove the top nitrided layer. All samples were then oxidized in atmospheric O_2 ambient at 950°C for 15 min. The increase in film thickness is shown in Fig. 5. The film, as expected, becomes more oxidation resistant when nitridation is performed at higher temperature and for longer time. The films with only the nitrided interface have almost

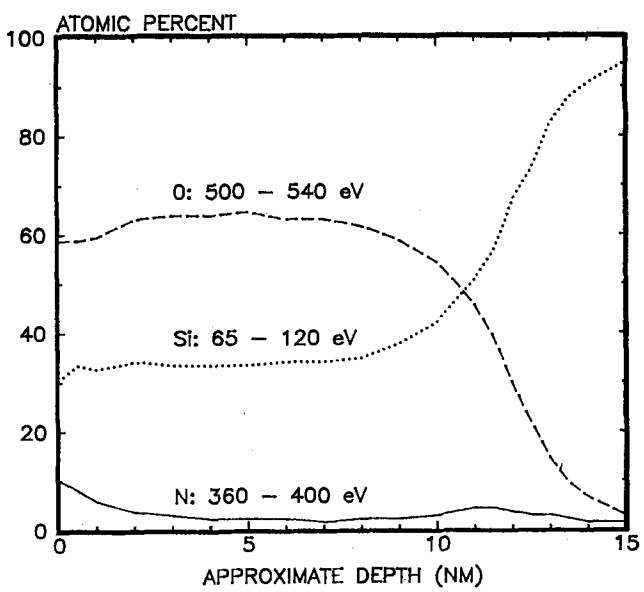

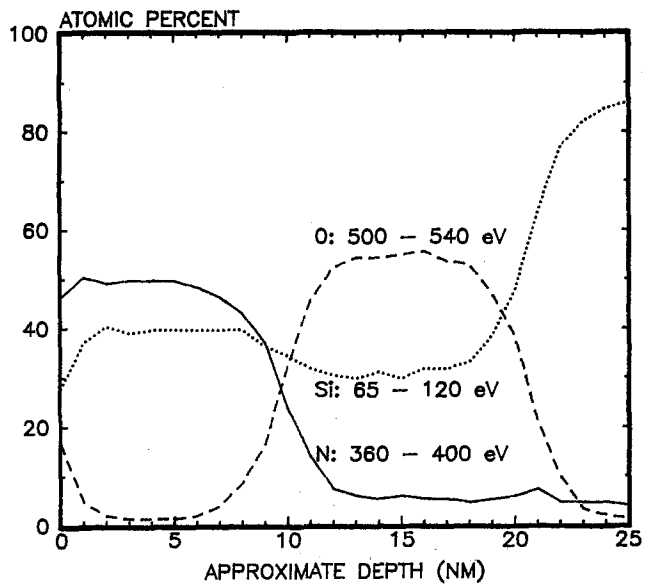

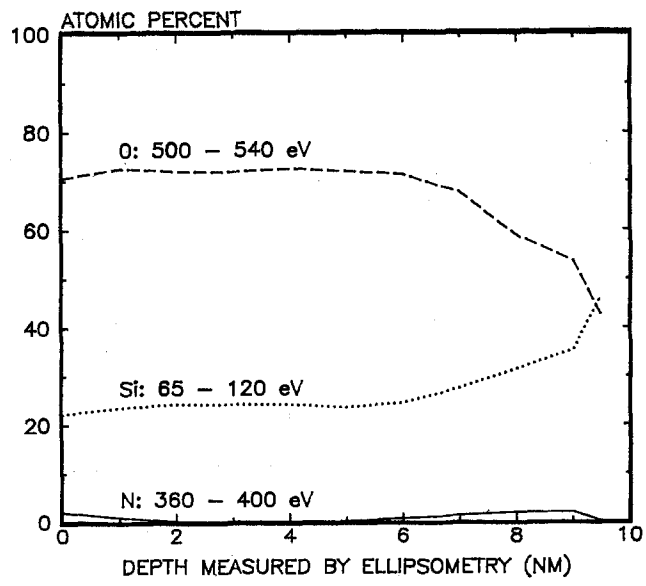

Fig. 4. (a, top left) Auger-depth profile of plasma-enhanced nitrided-oxide film (nitridation was performed at 925°C for 2 hr with 250W rf power). (b, top right) Auger-depth profile of composite film consisted of 10 nm CVD Si_3N_4 on 10 nm thermal SiO_2. (c, bottom left) Depth profile of plasma-enhanced nitrided-oxide film obtained by surface Auger scans of chemically etched-back samples.

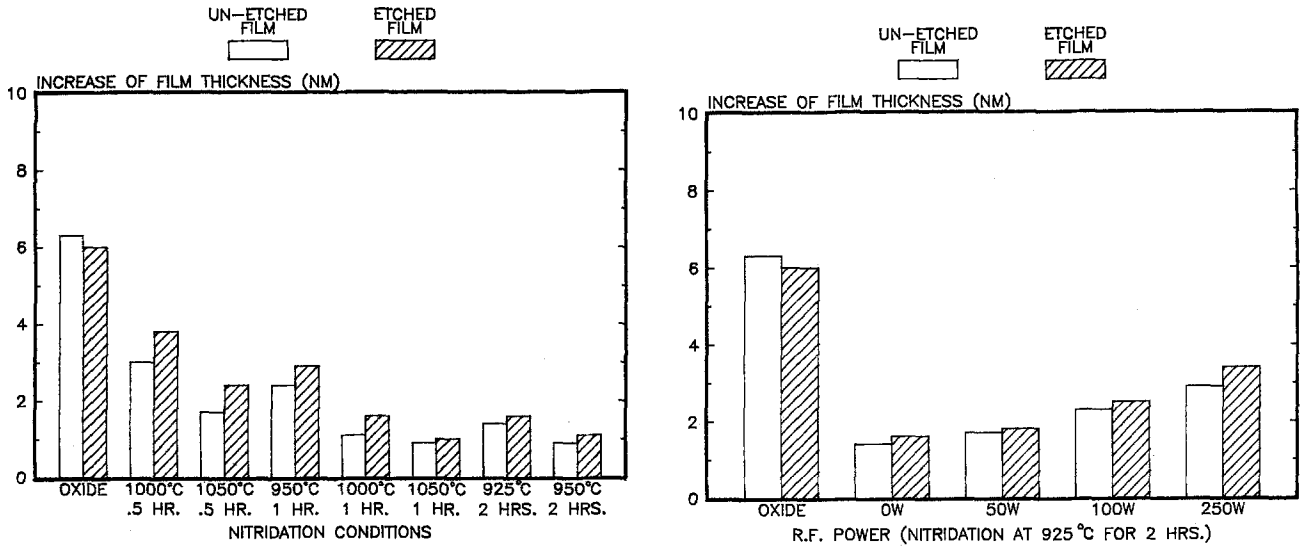

Fig. 5. Increase of film thickness after 15 min O_2 oxidation. (a, left) Comparison of NH_3 nitrided-oxide films for various time-temperature conditions. (b, right) Comparison of plasma-enhanced nitrided-oxide films (nitridation was performed at 925°C for 2 hr) at various rf power levels.

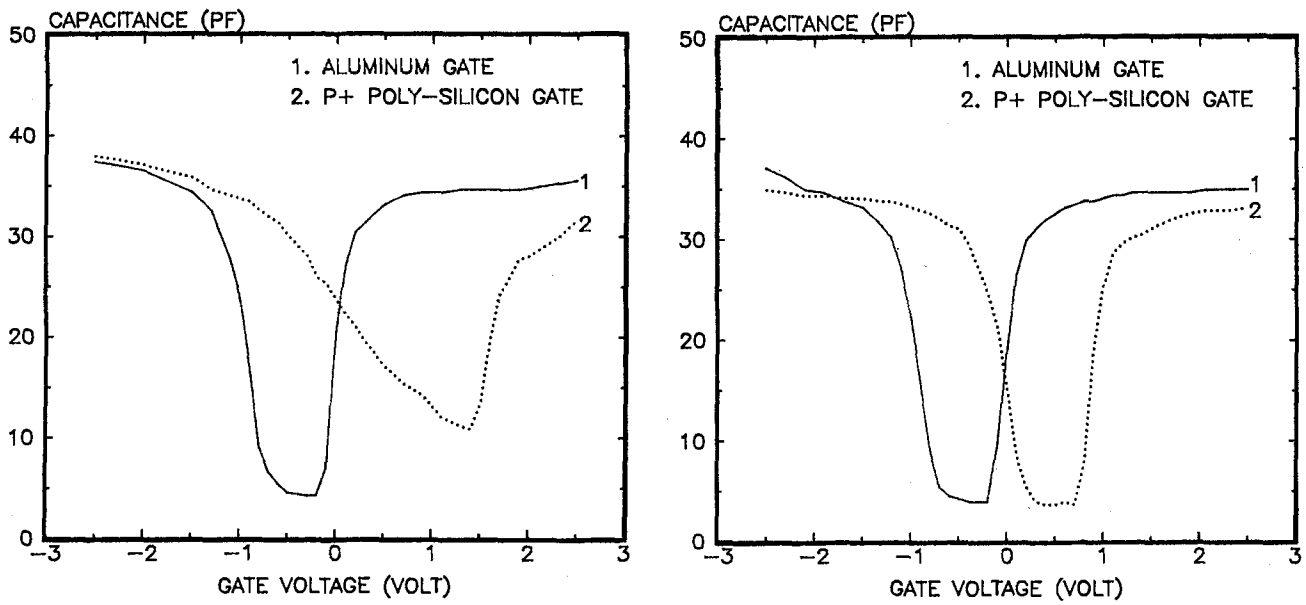

Fig. 6. Quasi-static C-V plots of capacitors fabricated on (a, left) SiO_2 and (b, right) plasma-enhanced nitrided-oxide (nitridation was performed at 925°C for 2 hr with 250W rf power).

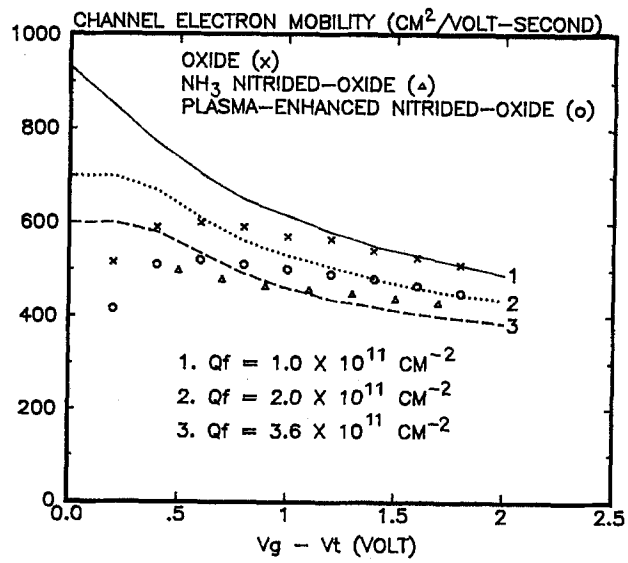

Fig. 7. Channel electron mobility as a function of gate drive. The three reference lines are calculated with data of Ref. (14).

the same oxidation resistance as the corresponding unetched films. This indicates more nitrogen is present at the interface than at the surface, and/or that the interface region resembles stoichiometric Si_3N_4 which is known to be more resistant to oxidation than the surface oxy-nitride layer (10). The formation of a thin Si_3N_4 layer at the interface has been postulated under even less thermodynamically favorable conditions (11). Comparing the various plasma-enhanced nitrided-oxide films, the oxidation resistance decreases with increasing rf power. This phenomenon is probably due to the more rapid formation of the surface nitrided layer, which constitutes a barrier against the diffusion of nitridation species towards the interface region, when higher rf power is employed.

Capacitors and n-Channel MOSFET's

To investigate the ability of the nitrided-oxide films to prevent boron diffusion, capacitors were fabricated with both aluminum and polysilicon electrodes. The polysilicon was implanted with B_{11}^+ at 25 keV for a dose of 3×10^{15} cm^{-2}. The implant was annealed for 1 hr in N_2 at 950°C. The aluminum sintering cycle was 30 min in H_2 at 450°C. Quasi-static C-V measurements

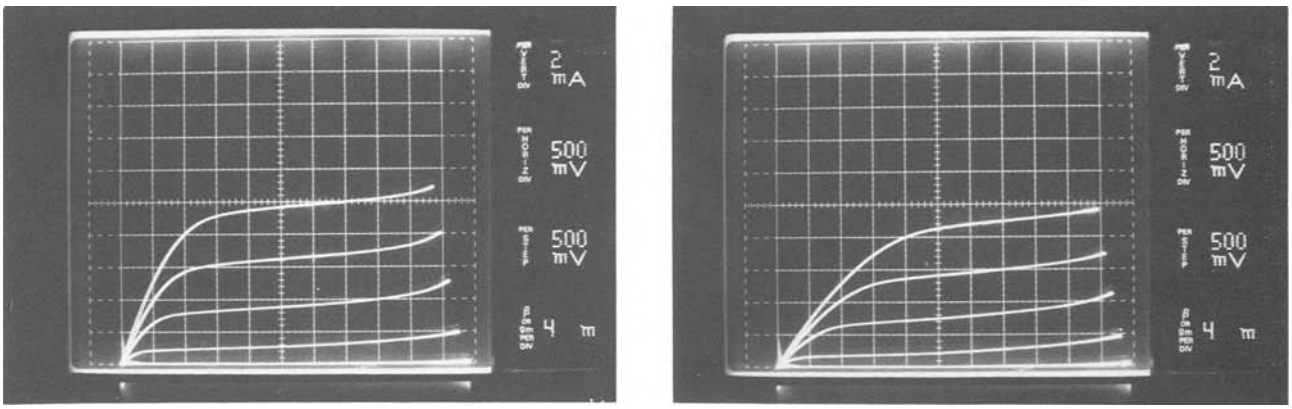

Fig. 8. I-V characteristics of n-channel MOSFET's. $W = 50$ μm, Leff ≈ 1.5 μm and gate voltage is 0.5V/step above the threshold voltage. (a, left) Low pressure SiO_2 gate dielectric with arsenic-doped gate ($Vt = 0.09$V). (b, right) Plasma-enhanced nitrided-oxide gate dielectric (nitridation was performed at 925°C for 2 hr with 250 W rf power) with boron-doped gate ($Vt = 1.02$V).

were performed on the capacitors, and the results are shown in Fig. 6. Comparing the two types of SiO_2 capacitors, the polysilicon capacitor exhibits a smaller change of capacitance with respect to gate voltage. Also, the threshold voltage of the polysilicon capacitor is more than 1.1V higher than that of the aluminum one (the work function of P^+ polysilicon is about 1.1 eV larger than that of aluminum). The additional threshold difference indicates that about 1×10^{12} cm^{-2} boron atoms have diffused through the SiO_2 film into the channel region of the capacitor. In the case of the nitrided-oxide films, no boron diffusion can be detected, either by the threshold voltage shift or by the distortion in the depletion region of the C-V characteristic. The exact nature and location of the diffusion barrier has not been identified. Even if boron atoms have diffused into the dielectric but are stopped by the interfacial nitrided layer, the presence of a small amount of boron in the dielectric has not been reported to degrade the dielectric quality. The nitridation steps also did not significantly degrade the film-substrate interface. Accurate determinations of the interface fixed or trapped charge densities are difficult because a charge of 1×10^{11} cm^{-2} only contributes to a voltage shift of 50 mV for 10 nm oxide. The fluctuation of just the flatband voltage due to processing conditions has been reported to be more than 50 mV (12). Relative comparisons, however, can be made. The plasma-enhanced nitrided-oxide film has about 1×10^{11} cm^{-2} more interface fixed charge when compared to the SiO_2 film. This point is elaborated further below in the discussion of electron mobility in n-channel MOSFET's.

Large geometry n-channel MOSFET's (100×100 μm) were built on all three types of dielectrics. The SiO_2 MOSFET's had arsenic-doped polysilicon gates whereas the nitrided-oxide MOSFET's had boron-doped polysilicon gates. Channel doping was about 1×10^{15} cm^{-3} for all the devices. Electron mobilities *vs.* gate voltage were measured with the charge accumulation method (13). It has been shown that channel electron mobility depends not only on the vertical electric field, but also on the interface fixed charge (14). These published data are replotted in Fig. 7. The mobility of the SiO_2 MOSFET corresponds to an interface fixed charge of about 1×10^{11} cm^{-2}. Although this number seems high, it agrees with what has been observed for thin SiO_2 (15). The plasma-enhanced nitrided-oxide film has an interface fixed charge of about 2×10^{11} cm^{-2}. The NH_3 nitrided-oxide film has even higher interface fixed charge and, hence, the lowest electron mobility. The interface fixed charge density correlates with the amount of nitrogen at the interface determined by the oxidation resistance experiment discussed earlier. Interestingly, a similar degradation of oxide interface properties has been observed after a prolonged nitrogen anneal cycle (16).

Short channel MOSFET's with channel length down to about one micron were also built and typical I-V characteristics are shown in Fig. 8. These high performance MOSFET's have been discussed elsewhere (17).

Conclusions

Nitridation of SiO_2 film in 1 Torr NH_3 ambient or NH_3 plasma between 925°-1050°C for less than 2 hr results in the incorporation of nitrogen only at the surface and at the film-substrate interface regions. The surface region is of an oxynitride structure; whereas, the interface region resembles a thin Si_3N_4 layer. The NH_3 plasma enhances the surface reaction and, as a consequence, retards the interface reaction. The nitrided-oxide films are slightly resistant to HF-based etchant, slightly oxidation resistant and very effective against boron diffusion. The nitrogen at the film-substrate interface introduces additional interface fixed charge resulting in lower channel electron mobility. Application of the nitrided-oxide film as a thin gate dielectric has been demonstrated by the successful fabrication of short channel MOSFET's.

Acknowledgments

The authors wish to thank L. Martinez for assistance in fabricating the devices, Y. Strausser and C. Franklin for performing the Auger analysis. The support of D. Bartelink and F. Schwettmann is appreciated. S. Wong and C. Sodini are partially supported by DARPA grant N00039-81-K-0251.

Manuscript submitted Nov. 5, 1982; revised manuscript received Jan. 8, 1983.

Any discussion of this paper will appear in a Discussion Section to be published in the December 1983 JOURNAL. All discussions for the December 1983 Discussion Section should be submitted by Aug. 1, 1983.

Publication costs of this article were assisted by Hewlett-Packard Corporation.

REFERENCES

1. R. H. Denard, *IEEE J. Solid-State Circ.*, **sc-9, 256** (1974).
2. C. A. Benevit, J. M. Cassard, K. J. Dimmler, A. C. Dumbri. M. G. Mound, and F. J. Procky, *IEEE ISSCC Tech. Digest*, **25,** 76 (1982).
3. W. S. Johnson, G. Perlegos, A. Renninger, G. Kuhn, and T. R. Ranganath, *ibid.*, **23,** 152 (1980).
4. T. Ito, T. Nozaki, and H. Ishikawa, *This Journal*, **127,** 2053 (1980).
5. T. Ito, H. Arakawa, T. Nozaki, and H. Ishikawa, *ibid.*, **127,** 2248 (1980).
6. M. Naimen, F. Terry, J. Burns, J. Raffel, and R. Aucoin, *IEEE IEDM Tech. Digest,* 562 (1980).

7. T. Ito, T. Nakamura, and H. Ishikawa, *This Journal*, **129**, 184 (1982).
8. Y. Hayafuji and K. Kajiwara, *ibid.*, **129**, 2102 (1982).
9. A. C. Adams, T. E. Smith, and C. C. Chang, *ibid.*, **127**, 1787 (1980).
10. J. Hui, T. Y. Chiu, S. Wong, and W. G. Oldham, *IEEE Electron Device Letts.*, **edl-2**, 244 (1981).
11. E. Kooi, J. G. van Lierop, and J. A. Appels, *This Journal*, **123**, 1117 (1976).
12. R. R. Razonk and B. E. Deal, *ibid.*, **129**, 806 (1982).
13. C. G. Sodini, T. W. Ekstedt, and J. L. Moll, *Solid State Electron.*, **25**, 833 (1982).
14. S. C. Sun and J. D. Plummer, *IEEE Trans. Electron Devices*, **ed-27**, 1497 (1980).
15. H. P. Vyas, G. D. Kirchner, and S. J. Lee, *This Journal*, **129**, 1757 (1982).
16. B. E. Deal, *ibid.*, **121**, 198C (1974).
17. C. G. Sodini, S. S. Wong, and T. W. Ekstedt, 40th Device Research Conference, Fort Collins, CO (1982).

Plasma Etch Anisotropy—Theory and Some Verifying Experiments Relating Ion Transport, Ion Energy, and Etch Profiles

C. B. Zarowin*

The Perkin-Elmer Corporation, Norwalk, Connecticut 06856

ABSTRACT

A model of plasma etch anisotropy is presented which shows that the ionic component of the chemical etch process produces etch profiles that vary with E/p, where E is the electric field controlling the ion transport to the etch surface and p is the etch gas pressure. From a relation derived here between E and the observable rf current density, J_{rf}, this model predicts that the profiles will vary continuously from isotropically to anisotropically produced as the parameter J_{rf}/p is increased. This behavior reflects the directionality of the ion kinetic energy transported to the etch surface and the effect of the ion energy in reducing the surface reaction activation energy. The one-to-one correspondence between ion energy and ion transport or etch directionality shown by this model clarifies the compromise required between etch anisotropy and the adverse effects of such high ion energy, such as reduced resist survival and selectivity against other materials in addition to the possibility of increased substrate damage. Another important practical consequence of this work is the establishment of a theoretical basis for extending the conventional wisdom that low pressures (<10 Pa) are required for anisotropic plasma etching to the more general requirement of a sufficiently high E/p ratio. Thus, this theory shows, and a wide range of experiments verify, that equally anisotropic etch profiles are obtainable at high (*e.g.*, 1000 Pa) or low pressures from the same J_{rf}/p ratios. Alternatively, it will be shown that reactive ion etching is a low pressure limiting case of plasma etching, both of which are able to produce identically anisotropic etch profiles, although the latter is capable of considerably higher etch rates. Finally, this model predicts a dependence of the anisotropy on the ion-neutral scatterer collision cross section and/or mass ratio, which is experimentally confirmed here by previously unpublished data.

Plasma etching has become an important technique for the fabrication of VLSI semiconductor devices because of its high etch selectivity and ability to replicate submicron mask pattern features, stemming partly from its relatively low resist erosion rate and partly from its ability to etch anisotropically, *i.e.*, without mask undercut. To date, however, the theoretical understanding of the parameters controlling such anisotropic etching has been proven inadequate, frequently leading to inconsistencies between model and experiment.

The following four experimental results are somewhat inconsistent with or, at least, show some incompleteness in our understanding of the mechanisms of anisotropic plasma etching: (*i*) the wide variety of conditions yielding anisotropic plasma etching at pressures too high to preclude collision dominated charged particle transport across the plasma sheath (1-6); (*ii*) the increase in etch anisotropy as rf power density increases (2, 6), excitation frequency decreases (3, 4) and/or etch gas pressure decreases (1, 5, 6); (*iii*) the observed ability to modify etch profiles at constant rf power, pressure, and frequency by application of d-c voltages to one of the reactor electrodes (2); and, finally, (*iv*) that the ratio of the isotropic and anisotropic vertical etch rates, under conditions of (*iii*) above, are significantly less than that of the etch depth to mask undercut (2).

Such inconsistencies and experimental results are the motivation for the model of anisotropic plasma etching presented in this paper. We begin by identifying the generic neutral and ionic species reactions with the etch solid. These two reaction rates are related by assuming (7) that the ionic reaction activation energy is smaller than the neutral reaction activation energy by an amount proportional to the kinetic energy obtained by the ion while crossing the sheath electric field. This assumption further stems (7) from the smaller slopes obtained on Arrhenius plots for reactive ion etching (RIE) and plasma etching (PE) than for similar reactions in the absence of plasma ion bombardment.

* Electrochemical Society Active Member.

Key words: anisotropic etching, ion transport, plasma electric fields, ion-assisted chemistry.

The Generic Neutral and Ionic Chemistry in Plasma Etching

The generic neutral and ionic chemical reactions involved in plasma etching are taken as

$$S + A \underset{k_B}{\overset{k_F}{\rightleftharpoons}} B$$

and

$$S + A^+ + e^- \underset{k_B^+}{\overset{k_F^+}{\rightleftharpoons}} B$$

respectively, where S is the etch solid, A is the neutral reactant species "prepared" in the plasma by excitation or disassociation, A^+ is the ionic reactant species ionized in the plasma, e^- is the electron produced during this ionization, and B is the volatile product compound of this reaction. The limiting rates, respectively, for the neutral and ionic reactions are $R_o = k_F[A]$ and $R_+ = k_F^+[A^+]$ at sufficiently high product removal rates, so that the total rate is $R = R_o + R_+$. The rate constant for the neutral reaction is $k_F = \kappa e^{-E_F/kT}$ and for the ionic reaction is $k_F^+ = \kappa e^{-(E_F - U)/kT}$, where the neutral reaction activation energy is E_F and the ion reaction activation energy is reduced from that of the neutral reaction by an

amount U, taken as proportional to the ion kinetic energy (7). The total etch rate R, can then be written

$$R = \kappa[A]e^{-E_F/kT}\,(1 + \alpha_+ e^{U/kT}) \qquad [1a]$$

where $\alpha_+ = [A^+]/[A]$ is the degree of ionization of the reactant A. It can be seen that the rate is negligibly ion assisted when $\alpha_+ e^{U/kT} << 1$ and strongly ion assisted when $\alpha_+ e^{U/kT} >> 1$.

Taking the logarithm of R, we obtain

$$\ln R = \ln \kappa[A] - E_F/kT + \ln (1 + \alpha_+ e^{U/kT}) \qquad [1b]$$

from which we see that the slope of $\ln R$ *vs.* $1/T$ is given by $-E_F/k$ when negligibly ion assisted and $-(E_F - U)/k$ when strongly ion assisted. Observed values of $(E_F - U)$ are between 0.2 and 0.6 eV while E_F is about 1 eV; so that U is between 0.4 and 0.8 eV. Thus, with $\alpha_+ \sim 10^{-7}$ (see Appendix), the ratio of the ionic to neutral reaction rates $R_+/R_o = \alpha_+ e^{U/kT}$ can be estimated as between unity and 10^7, *i.e.*, the surface conditions that cause U to change from 0.4 to 0.8 eV can cause the reaction to change from weakly to strongly ion assisted. Impurities in the gases can also affect (1, 2) this ratio by modifying α_+ as when the impurity is more electronegative and U, by impurity adsorption on the etch surface.

By taking U as an increasing function of the ion kinetic energy, any differences in the ion kinetic energy with direction will result in etch rate changes with direction, *i.e.*, an etch directionality defined as $\delta = R_x/R_y$ will be less than unity ($\delta = 1$ for isotropy), where R_x and R_y are, respectively, the etch rates horizontally and vertically. The etch directionality δ can be expressed in terms of Eq. [1a] as follows

$$\delta = \frac{1 + \alpha_+ \exp (U_x/kT)}{1 + \alpha_+ \exp (U_y/kT)} = \exp\{(U_x - U_y)/kT\}\,\frac{1 + \{\alpha_+ \exp (U_x/kT)\}^{-1}}{1 + \{\alpha_+ \exp (U_y/kT)\}^{-1}} \qquad [2a]$$

for $U_x/U_y \leq 1$. When $\alpha_+ e^{U_x/kT}$ and $\alpha_+ e^{U_y/kT} << 1$, as for a negligibly ion assisted reaction, $\delta \cong 1$ or only isotropic etching is possible, while when $\alpha_+ e^{U_x/kT}$ and $\alpha_+ e^{U_y/kT} >> 1$ as for strongly ion assisted etching, Eq. [2a] reduces to

$$\delta \cong e^{(U_x - U_y)/kT} = \exp \beta\,\frac{\rho^2 - 1}{\rho^2} \qquad [2b]$$

where $\beta = U_x/kT$, $0 < \beta < 1$, and having defined the ion transport directionality, $\rho^2 \equiv U_x/U_y$.

When $\rho^2 \to 1$, as for isotropic ion transport ($U_x = U_y$), $\delta \to 1$ and the strongly ion assisted etching approaches isotropy, while when $\rho^2 \to 0$ as for anisotropic ion transport ($U_x << U_y$), $\delta \to 0$ and the etching is anisotropic. As will be shown in the next section, ρ^2 is a function of the parameter α, proportional, among other things, to the sheath electric field to pressure ratio, so that Eq. [2b] implicitly depends on E_s/p.

Relating the Sheath Electric Field and Gas Pressure to the Ion Transport Directionality

In a sheath field, E_s, ions of mass m_+ and charge e, experience collisions with neutral species of mass, m_o, so that, at steady state, the force on the charged ion eE_s, is equal to the mean momentum loss per unit time, $\mu \bar{u} \nu$, where μ is the reduced mass of the ion-neutral collision pair given by $1/\mu = 1/m_+ + 1/m_o$, $\bar{u}$ is the mean directed velocity, and ν is the collision frequency. The collisions occur primarily with neutral scatterers of number density n_o because the plasma is weakly ionized ($\alpha_+ \sim 10^{-7}$, see Appendix). When $m_+/m_o << 1$, *e.g.*, for electrons colliding with atoms $\mu \cong m_o$ while when $m_+/m_o >> 1$, as for "heavy" ions in a "light" diluent gas, *e.g.*, Cl^+ in He, $\mu \cong m_+$, exhibiting the "persistance of velocity" effects for the "heavier" species. Thus the mean directed velocity $\bar{u}$ is

$$\bar{u} = e\bar{E}_s/\mu\nu \qquad [3a]$$

The product of the ion collision frequency ν and the ion mean free path between collisions, λ, is the root mean square total ion velocity, $\sqrt{\langle v^2\rangle}$. Since $\bar{v} = \bar{u} + \bar{w}$ and $\langle v\rangle = \bar{u} + \langle w\rangle = \bar{u}$, where $\langle w\rangle = 0$ is the mean random velocity of the ion and $\bar{u}$ is the mean directed velocity, $\langle v^2\rangle = u^2 + \langle w^2\rangle + 2\bar{u}\cdot\langle w\rangle = u^2 + \langle w^2\rangle$. Thus, $\lambda\nu = \sqrt{\langle w^2\rangle}\sqrt{1 + u^2/\langle w^2\rangle}$, permitting Eq. [3a] to be written as

$$\bar{u} = \frac{e\bar{E}_s\lambda}{\mu\sqrt{\langle w^2\rangle}} \cdot \frac{1}{\sqrt{1 + u^2/\langle w^2\rangle}} \qquad [3b]$$

This can be rewritten as

$$(u/\sqrt{\langle w^2\rangle})\,\sqrt{1 + u^2/\langle w^2\rangle} = eE_s\lambda/\mu\langle w^2\rangle \equiv \alpha$$

Squaring this expression and defining $\rho^2 = (1 + u^2/\langle w^2\rangle)^{-1}$ as the ion kinetic energy transport directionality, for which we obtain an expression in terms of the parameter α

$$\rho^2 = 2/(1 + \sqrt{1 + (2\alpha)^2}) \qquad [4]$$

Replacing $\lambda = 1/n_oQ$, where n_o is the neutral scatterer number density, Q is the ion-neutral collision cross section, and recognizing that $m_+\langle w^2\rangle/2 = 3kT_+/2$ is the ion thermal energy, the parameter α is

$$\alpha = \left(\frac{e}{3kT_+}\right)\left(\frac{E_s}{n_o}\right)\left(\frac{1 + m_+/m_o}{Q}\right) \qquad [5]$$

In addition to the dependence of α on the sheath electric field to pressure ratio E_s/n_o, the effect of the ion-neutral mass ratio and cross section on α should be noted. When $(1 + m_+/m_o)/Q$ is larger, the magnitude of E_s/n_o required to achieve the same α, and, therefore, the same ρ^2, is reduced. We shall return to this point later when an experimental verification of this effect is discussed.

For $\alpha << 1$, Eq. [4] reduces to $\rho^2 \cong 1 - \alpha^2$ and for $\alpha >> 1$, to $\rho^2 \cong 1/\alpha$, so that as $\alpha \to 0$, $\rho^2 \to 1$, or isotropic ion transport directionality, and as $\alpha \to \infty$, $\rho^2 \to 0$, or anisotropic (strongly directional) ion transport. This is summarized schematically in Fig. 1.

Defining $E_* = (3kT_+/e)n_oQ/(1 + m_+/m_o)$ as the sheath electric field for which $\alpha = E/E_* = 1$, or for which $\rho^2 \cong 0.62$, (mostly isotropic), we may estimate the magnitude of $E_* \cong 300$ V/cm from $Q \sim 2 \times 10^{14}$ cm^2 (8), $\eta_o \sim 10^{17}$ cm^{-3} ($\sim$1 Torr), $m_+/m_o \cong 1$, and $kT_+/e \cong 10^{-1}$V. Typical experimental measurements of current density at which etch anisotropy (2) just begins, $J_{rf} \cong 75$ A/m^2, or an rf power density of about 10^{-1} W/cm^3, yields a sheath electric field of about 10^3 V/cm at 13.56 MHz, using an equation (Eq. [7]) to be derived in the next section. This specifies $\rho^2 \cong 1/3$ and is in good agreement with this model. Alternately, for strongly anisotropic etching some 750 A/m^2 or 10 W/cm^3 is required (2) yielding a sheath field of about 10^4 V/cm, or $E/E_* \cong 30$, and $\rho^2 \cong 1/30$, also in agreement.

Identifying the amount by which the activation energy of the ionic reaction is reduced as proportional to the ion kinetic energy, $U \propto \langle v^2\rangle$, $U_x/U_y = \langle w^2\rangle/(u^2 + \langle w^2\rangle)$ which is recognized as ρ^2, the ion transport directionality defined above in connection with Eq. [2b]. The etch directionality $\delta = R_x/R_y$, following Eq. [2] can, then, be written as

$$\delta = \exp\left[-\frac{3\beta}{4}\,(\sqrt{1 + (2\alpha)^2} - 1)\right] \qquad [6]$$

when the process is strongly ion assisted and with $\beta = U_x/kT_+$ as the fraction of the ion energy by which

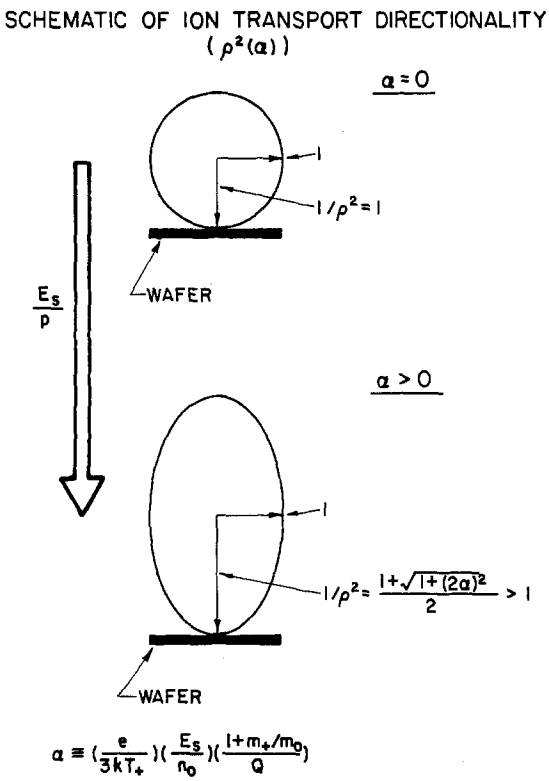

Fig. 1. Schematic representation of ion transport directionality variation with α or E/p.

the activation energy is reduced. When $\alpha \to \infty$, $\delta \to 0$, or the etching is anisotropic. A plot of Eq. [6] is given in Fig. 2a with β as a parameter (the fraction of ion energy reducing the etch reaction activation energy) and in Fig. 2b with the electric field scaling factor defined above, $E_* = (3kT_+/e)n_0Q/(1 + m_+/m_0)$, as a parameter. Such a plot against α will be shown in the next section as equivalent to one against E_S, J_{rf} or $\sqrt{P_{rf}/Sl_p}$ where P_{rf}/Sl_p is the rf power density. Since E_* is proportional to the pressure (n_0), and the cross section and mass ratio $[Q/(1 + m_+/m_0)]$, this parameter displays the behavior of the etch directionality as these change at fixed rf current or power density, J_{rf} or $\sqrt{P_{rf}/Sl_p}$. Alternatively, plotting this equation against $\phi = 1/\alpha$, is equivalent to plotting the etch directionality δ, against the pressure or the cross section and mass ratio, as shown in Fig. 3a, with β as the parameter and Fig. 3b with increasing E_* as a parameter.

An alternative, and in some ways more informative plot, is shown in Fig. 4. By plotting E_S, J_{rf} or $\sqrt{P_{rf}}$ *vs.* $(1 + m_+/m_0)/n_0Q$, where the latter is, among other things, inversely proportional to the pressure, equilateral hyperbolas result which are loci of constant ion energy ($eE_S\lambda$) and etch directionality because α is constant on these curves. The ion energy increases and the etch profiles become more anisotropic as the hyperbolas move away from the coordinate axes. At the coordinate axes, the ion energy is thermal and their transport and etching is isotropic. This shows, for example, that the rf power density for which anisotropic etching is required increases for increasing pressure but that on these hyperbolas the ion energy remains fixed. It also shows that the reduction of the pressure at constant power density increases the anisotropy. Also, perhaps more importantly, this plot makes the compromise required between etch directionality and the adverse effects of increasing ion energy very clear. These adverse effects include resist erosion, loss of chemical selectivity of the etch process and possibly, substrate radiation damage. For example, three values of ion energy (1, 3, and 7.2 arbitrary energy units) and etch directionality (δ = 0.9, 0.5, and 0.1) are shown on this plot, respectively, almost isotro-

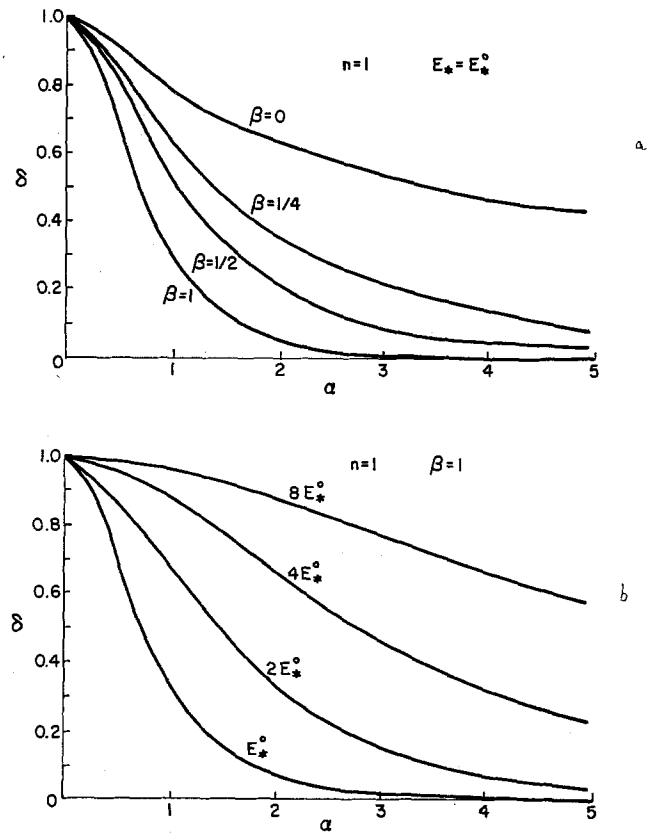

Fig. 2. (a, top) Plot of etch directionality *vs.* $\alpha = E_S/E_*$, $E_* = 3kT/e\ [Qn_0/(1 + m/m_0)]$ (α proportional to $\sqrt{P_{rf}}$, J_{rf}, E_S) with β as parameter. (b, bottom) Plot of etch directionality *vs.* $\alpha = E_S/E_*$, $E_* = 3kT/e\ [Qn_0/(1 + m/m_0]$ (α proportional to $\sqrt{P_{rf}}$, J_{rf}, E_S) with E_* as parameter.

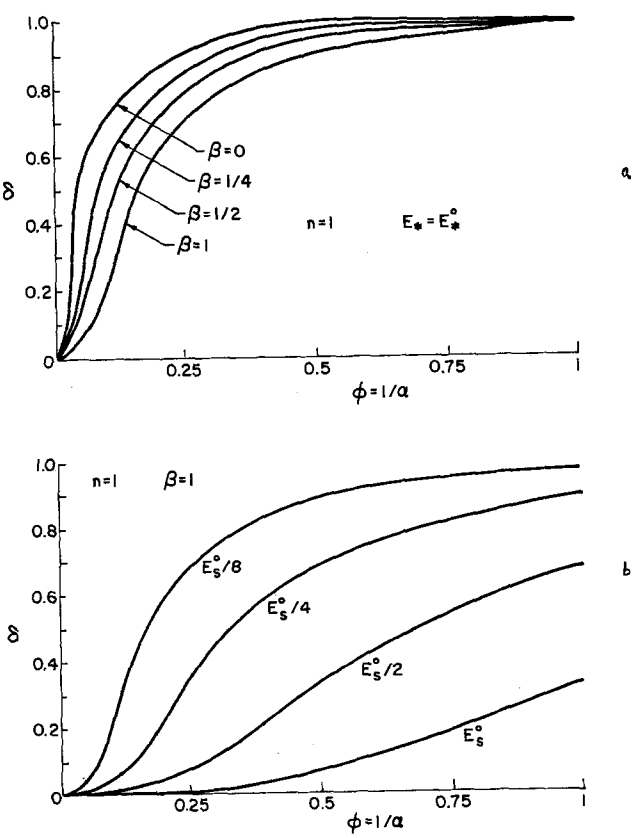

Fig. 3. (a, top) Plot of etch directionality *vs.* ϕ $(= 1/\alpha) = E_*/E_S$ with β as parameter (ϕ proportional to pressure). (b, bottom) Plot of etch directionality *vs.* ϕ $(= 1/\alpha) = E_*/E_S$ with E_S (or $\sqrt{P_{rf}}$, J_{rf}) as parameter.

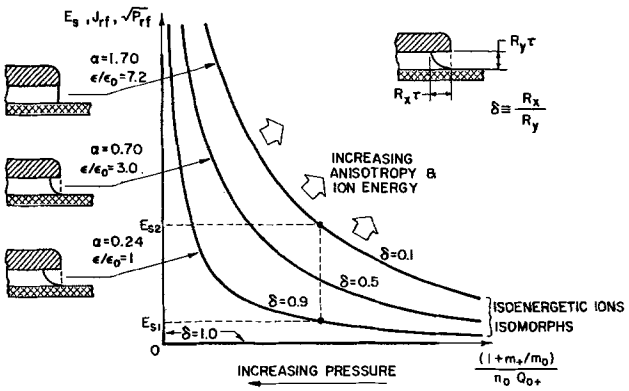

Fig. 4. Plot of sheath electric field, rf current density, or square root of rf power vs. reciprocal pressure showing ion isoenergies and profile isomorphs.

pic, partly anisotropic, and moderately anisotropic, so that more than seven times the ion energy is required to achieve 10:1 anisotropy than is required to achieve 1.1:1 (almost isotropic). It is interesting to note that for polysilicon the etch rates are only about two or three times greater for about seven times the ion energies (2).

As can be seen from Eq. [5], the effect of a larger cross section for collisions between the ions and neutrals and of smaller ion-neutral mass ratio is equivalent to the requirement of larger E_s, J_{rf}, or $\sqrt{P_{rf}}$ to p ratios for the same etch directionality. A lower value of this parameter (*e.g.*, E_s/p) is then expected for the plasma etching of polysilicon with chlorine as a mixture with 90% He and 10% Cl_2, than for HCl and still less than for pure Cl_2 gas. This holds true to the extent that the chemistry remains the same, and only the transport of the ions in the background gas dominates the behavior.

Relating the RF Current Density and the Excitation Frequency to the Electric Field Controlling Ion Transport

In this section, we derive a relation between the electric field which determines the anisotropy of the ion transport and the observable rf current density at some excitation frequency. This relation is required because of the relative inaccessibility of the electric fields to experiment. Such a result will provide a connection to an observable parameter, which together with the pressure, prescribes the ion transport properties discussed above. To obtain this relation and identify the excitation frequency regime in which it applies, we begin by constructing a discharge equivalent circuit.

The Discharge equivalent circuit.—Application of an rf voltage of sufficient amplitude causes the gas between electrodes to become conducting. This can be represented as a change of the passive components of its equivalent circuit from capacitors to capacitors shunted by resistors. This discharge consists of two characteristic regions: the plasma body which has approximately equal electron and ion densities, and a sheath region having an electron density much smaller than the ion density. These sheaths separate the body of the plasma from each electrode or other walls. The sheath region is formed to compensate for the greater loss of electrons than ions to the electrodes due to the greater mobility of the electrons. The mean voltage generated across the sheath because of this excess electron to ion loss achieves its steady-state value as these losses become equal. For the sake of simplicity, this is not explicitly accounted for in the equivalent circuit, but it could by introduction of a voltage source in series with the sheath resistors to be introduced in this equivalent circuit. This is discussed further in the Appendix.

The passive electrical characteristics of each of these regions can be summarized in terms of an equivalent circuit consisting of a capacitor shunted by a resistor, having suppressed inductive effects, as shown in Fig. 5. The discharge equivalent circuit, then, consists of a plasma resistor, R_p, shunted by a capacitor, C_p, in series with two sheath capacitors, C_{s1} and C_{s2}, each shunted by sheath resistors, R_{s1} and R_{s2}. The current density, J, in each of these regions, then, consists of a conductive and a displacement component, *i.e.*, $J = (\sigma + j\omega\epsilon_0)\bar{E}$, where σ is the conductivity, ω is the angular frequency of the exciting voltage, ϵ_0 is the vacuum dielectric constant, and $\bar{E}$ is the electric field in that region.

The frequency characteristics of the discharge.—For each region of the discharge, remembering that we have ignored inductive effects, there are two frequency regimes: when $\omega >> \sigma/\epsilon_0$ and $\omega << \omega_0 = \sigma/\epsilon_0$, respectively, when they are displacement and conduction dominated; the conductivity is given (8) by $\sigma = ne^2/m\nu$, where n is the pertinent charge carrier number density, m is its mass, e is the charge it carries, and ν is its collision frequency with the dominant neutral. The collision frequency is approximately given by $\nu_\pm = n_0 Q_\pm \sqrt{kT_\pm/m_\pm}$, where n_0 is the number density of the neutrals, $Q_\pm$ is the collision cross section, and $kT_\pm$ is the charge carrier mean thermal energy (ion +, or electron −). The charge carrier plasma frequency is defined (8) as $\omega_{p\pm} = (n_\pm e^2/m_\pm \epsilon_0)^{1/2}$, so that the ratio (frequency) $\omega_{0\pm} = \sigma_\pm/\epsilon_0 = \omega^2_{p\pm}/\nu_\pm$. Thus, each plasma region has two frequency regimes defined by whether ω is less than or greater than ω_0. From a knowledge of the appropriate plasma and collision frequencies, the equivalent circuit for each region can, for simplicity, be reduced to a single passive component for each regime.

Evaluation of the equivalent circuit parameters.—In the Appendix to this paper, it is shown that the degree of ionization $n_\pm/n_0$, is about 10^{-7} for typical etching discharges, so that for $n_0 = 10^{17}$ cm^{-3} (~ 150 Pa), the electron-ion density in the plasma is about 10^{10} cm^{-3}. In the plasma sheath, the ion density is roughly comparable to that in the plasma body, but as long as the electron density in the sheath is less than 1% of the ion density (see Appendix), the conduction current is carried dominantly by the ions. In the plasma body, the rough equality between ion and electron densities means that the electrons dominate as current carriers because of their greater mobility. In other words, while the dielectric properties are taken as those of the vacuum in the sheath the conductivity is ion dominated, or $\sigma_s = \sigma_+ = n_+e^2/m_+\nu_+$, and in the body of the plasma it is electron dominated so that $\sigma_p = \sigma_- = n_-e^2/m_-\nu_-$.

Thus, for the sheath region when $\omega >> \omega_{0+}$, the equivalent circuit reduces to a capacitor, and the dominant current through the sheath is displacement current. When $\omega << \omega_{0+}$, the equivalent circuit reduces to a resistor, and the dominant current is conductive. Taking the ion-neutral collision cross section

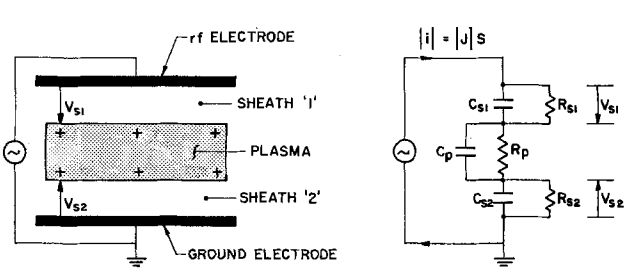

Fig. 5. Schematic of plasma diode and circuit equivalent

as (8) $Q_+ = 5 \times 10^{-15}$ cm^2, $n_o = 10^{17}$ cm^{-3}, and $\sqrt{kT_+/m_+} = (4 \times 10^4)$ cm sec^{-1}, $_+ = 2 \times 10^7$ sec^{-1}, with $n_+ = 10^{10}$ cm^{-3} and $m_+ = 10^{-22}$ g, $\omega_{o+} = 1.7 \times 10^7$ sec^{-1} [$\cong 2\pi(2.7)$ MHz]. Above about 2.7 MHz, the sheath is dominantly capacitive and below it, the sheath is resistive. Since the electrons dominate the charge transport in the plasma, a similar calculation yields $\nu_- = 7 \times 10^{10}$ sec^{-1}, for (8) $Q_- = 5 \times 10^{-15}$ cm^2, $kT_- = 12$ eV (see Appendix), and $m_+/m_- = 10^5$; also $\omega_{o-} = 4.8 \times 10^8$ sec^{-1} [$\cong 2\pi(77)$ MHz], so that as long as the excitation frequency is less than some 77 MHz, the plasma appears resistive.

If we restrict ourselves to frequencies of plasma excitation between 2.7 and 77 MHz, the discharge equivalent circuit consists of two sheath capacitors coupling the plasma resistance to the electrodes as shown in Fig. 6a. Below about 2.7 MHz, the sheaths and the plasma are dominantly resistive as shown in Fig. 6b.

Relations between electric fields and current densities.—Having established the appropriate equivalent circuit at "high" (2.7-77 MHz) and "low" (less than 2.7 MHz) frequencies, we may now deduce the relations between the electric fields and the current density. For simplicity, the two sheaths are lumped together in the following discussion. In the "high" frequency regime, $\omega^2_{p+}/\nu_+ << \omega << \omega^2_{p-}/\nu_-$, the sheath current density, $\bar{J}_s = \epsilon_o\omega\,|\,\bar{E}_s\,|$, and the plasma current density, $\bar{J}_p = \sigma_p \bar{E}_p$ are equal to each other. When the source and load impedances are matched, they are also equal to the observable rf current density, $\bar{J}_{rf} = \bar{I}_{rf}/S$, where S is the cross-sectional area of the plasma. Thus, $|\bar{E}_s|/|\bar{E}_p| = (\sigma/\epsilon_o\omega) = (\omega^2_{p-}/\omega\nu_-) >> 1$ using values obtained in the section above; *i.e.*, the sheath field is very much greater than the plasma electric field. Also, the sheath field is given by

$$|\bar{E}_s| = \bar{J}_{rf}/\epsilon_o\omega \qquad [7a]$$

In terms of the rf power density, since $P_{rf}/Sl_p = J^2_{rf}/\sigma_p$

$$|\bar{E}_s| = (\sqrt{\sigma_p}/\omega\epsilon_o)\sqrt{P_{rf}/Sl_p} \qquad [7b]$$

This shows the one-to-one correspondence between rf current or power density and the sheath electric field.

In the "low" frequency regime, $\omega << \omega^2_{p+}/\nu_+$, the sheath current density is given by $\bar{J}_s = \sigma_+ E_s$, the conduction, rather than the displacement current, dominates. Because the currents in the different plasma regions are equal, the ratio of the sheath to the plasma field in the "low" frequency regime is $E_s/E_p \cong 25$. This was obtained by using the above section values of the collision frequencies and mass ratios and by taking the ratio of electron to ion densities as close to unity. Furthermore, the sheath field is

$$\bar{E}_s = \bar{J}_{rf}/\sigma_- \qquad [7c]$$

where a corresponding rf power dependence is applicable as for Eq. [7b]. The ratio of the sheath fields of the "high" and "low" frequency regimes, $|E_{sh}|/|E_{sl}|$, can be estimated by taking the ratio of Eq. [7a] and [7c] at equal current densities, demonstrating that $|\bar{E}_{sh}|/|\bar{E}_{sl}| << 1$. This shows that the "high" frequency sheath field is very much smaller than that of the "low" frequency sheath field at equal current densities. In addition, since the ions are also mobile in this regime, the sheath thickness is smaller than in the "high" frequency regime where they are essentially immobile. In sum, these two effects combine such that in the low "frequency" regime, the ions can be expected to be much more energetic and anisotropically transported to the etch surface.

In an asymmetric plasma reactor diode, where the electrode areas are different, the two sheath fields can be shown from the above arguments to be different. Since the two sheath currents I_{S1} and I_{S2} are in series, they must be equal, so that $I_{S1} = J_{S1}S_1 = J_{S2}S_2 = I_{S2}$ where $J_{S1,2}$ are the sheath current densities and $S_{1,2}$ are the electrode areas. Thus, using Eq. [7a], the ratio of the sheath fields are

$$E_{S1}/E_{S2} = S_2/S_1 \qquad [7d]$$

This shows that for a fixed pressure, the sheath field to pressure ratio at the larger electrode will be smaller than that at the smaller electrode. Remembering that the E/p dependence derived above for the ion transport directionality and its relation to etch directionality, this explains why isotropic etching can be observed at the larger area electrode while anisotropic etching occurs at the smaller area electrode at some rf powers and etch gas pressures. This can be generalized in terms of Fig. 4, showing that at a given pressure and rf current or power density, the sheath electric fields at electrode "1" may be significantly lower than at electrode "2," yielding, for example, an etch directionality $\delta_2 = 0.1$ on a wafer supported by electrode "2" and $\delta_1 = 0.9$ at the other.

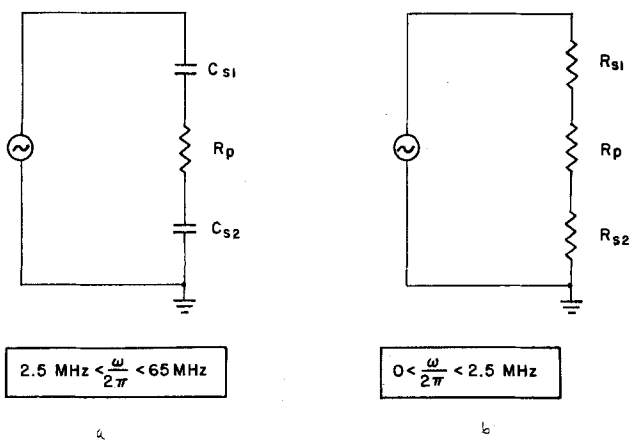

Fig. 6. (a, left) Schematic of plasma diode and circuit equivalent at "high" frequencies (~ 2.7-77 MHz). (b, right) Schematic of plasma diode and circuit equivalent at "low" frequencies (< 2.7 MHz).

Discussion

The most important of the inconsistencies between experiment and existing models is the idea that high pressures precludes anisotropic plasma etching. Such anisotropic etching had been thought to require the low pressures (< 10 Pa) or relatively collisionless (and, hence, highly directional), ion transport employed in earlier ion assisted chemical etch processes. On the other hand, as the model presented above shows, both low and high pressures (at least up to 1000 Pa) are capable of anisotropic etching if sufficiently high plasma sheath electric fields are generated. Under these circumstances, we have seen that the directionality of the ion transport, or the ratio of (electric field induced) directed motion to random (thermal) motion controls the directionality of the ionic component of chemical etching. The connection between ion transport and etch directionalities has been shown to derive from the effect of the energy of ion bombardment in reducing the activation energy of the ion assisted chemical reaction (7) and thus increasing the reaction rate.

In addition to the greater pressure at which the anisotropic profiles are obtained in PE, the etch wafer is supported on the grounded electrode rather than the rf electrode as in RIE (see Fig. 7). These two positions differ only in the voltage across the plasma sheath in which the wafer is immersed. As has been shown (2) (also, see Eq. [7d]), the two sheath voltages V_{S1} and V_{S2} increase as the square root of the rf power density, and the ratio V_{S1}/V_{S2} is some increas-

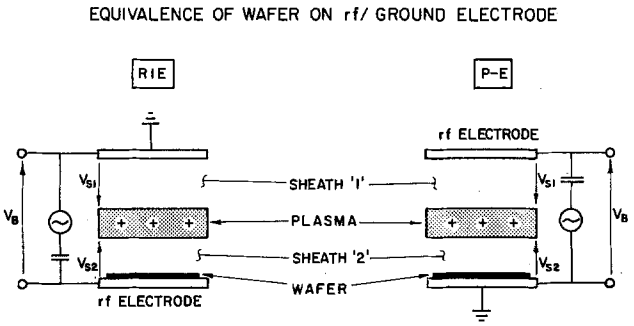

Fig. 7. Equivalence of wafer on rf driven (RIE) and ground (PE) electrode.

ing function (9) of the electrode area ratio $(S_2/S_1)^{-1}$. Consequently, for equal areas, these voltages are equal, but, as is frequently the case, when $S_1/S_2 > 1$, $V_{S1}/V_{S2} < 1$. For such a case, if the wafer is immersed in the sheath with voltage drop V_{S2}, the ions striking its surface will be more energetic and directed in their motion than those striking the one immersed in the other (V_{S1}). This is also shown in Fig. 4.

An experimental demonstration of the relation between the sheath voltage and anisotropic etching has been described in Ref. (2). For plasma etching of polysilicon in a chlorine gas mixture at a total pressure of about 66 Pa, it was found (2) that the mask undercut decreased as the 13.56 MHz rf power density increased as shown in Fig. 8. In Fig. 9, we see that application (2) of a d-c voltage of positive polarity at constant rf power to the rf driven electrode increases the anisotropy (decreases the undercut), with the wafer on the grounded electrode, while negative polarity decreases the anisotropy. Furthermore, addition of only 1% of the rf power by applying such d-c voltage reproduces the etch profile effects which otherwise require more than 30% changes in rf power. Since changes in the sheath voltage caused by the rf power and the application of d-c voltage were comparable, it was concluded that the sheath voltage, not the plasma composition or the degree of ionization was responsible for such profile changes. From this, we can further conclude that similar sheath voltages and pressures of a given gas should give similar etch

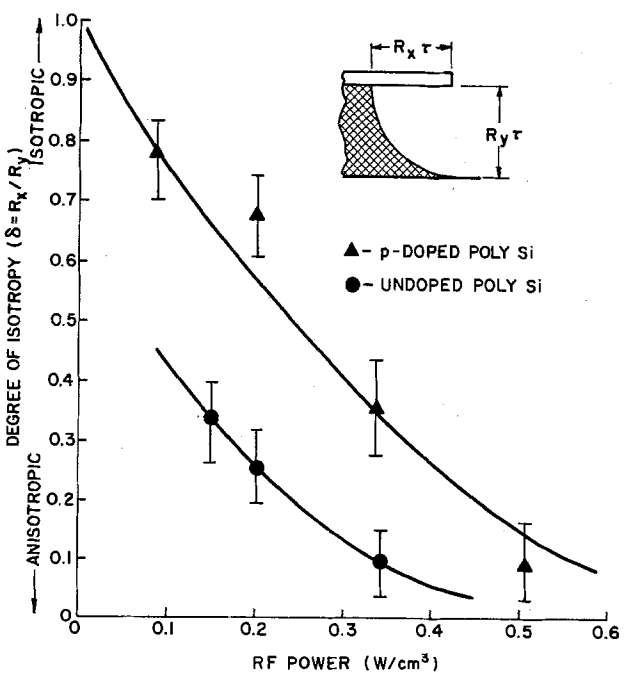

Fig. 8. Degree of isotropy vs. rf power density for HCl-CCl_4-N_2 plasma etching of polysilicon (2).

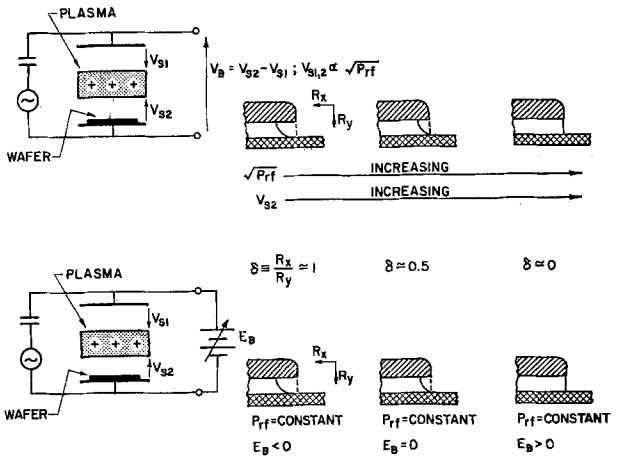

Fig. 9. Comparison (2) of rf and applied d-c produced sheath electric field effect on etch anisotropy.

anisotropy, whether achieved by changing the rf power density, application of d-c voltage, or by changing the electrode area ratios. This conclusion is consistent with the model given here, and its generalization as shown in Fig. 4, which plots the sheath electric field against the reciprocal of the pressure (among other things) and shows that a fixed relation exists between the etch anisotropy and the electric field to pressure ratio. This plot further demonstrates that the asymmetric diode reactor can give anisotropic etching on one electrode while producing isotropic etching at the other, because the sheath fields are proportional to the reciprocal of the electrode area, as shown in above section of this paper.

The model presented in the paper removes the inconsistency between experiment and the idea of plasma etching as the superposition of an isotropic thermochemical and a completely anisotropic ionic chemical process. This latter idea leads to the inconsistency by requiring that the etch rate ratio between isotropic and anisotropic etching be the same as the ratio of undercut to etch depth, in considerable disagreement with experiment (2). We can make this inconsistency explicit by defining the etch directionality $\delta = R_x/R_y$, where R_x is the horizontal and R_y the vertical etch rate with y along the sheath electric field. By proposition, the horizontal rate R_x can only be due to the isotropic thermochemical rate R_o, while the vertical rate R_y is the sum of the thermochemical and ionic rates, $R_o + R_+$, since the ionic component is taken to be completely anisotropic (directed only along y). R_o is a function of temperature and reactant pressure and is, thus, constant, but R_+ may depend on degree of ionization and ion energy, which vary with rf power. Thus, the etch directionality $\delta \equiv R_x/R_y = R_o/(R_o + R_+)$. The vertical etch rate when the etching is isotropic is $R_y^I = R_o$ ($R_+ = 0$) and when anisotropic, $R_y^A = R_o + R_+$. Thus, for an etch directionality $\delta = 1/10$ (moderate anisotropy), $R_y^A = R_o + R_+^A = 10R_o$, and for $\delta = 1$ (isotropy) $R_y^I = R_o$, requiring that $R_y^A/R_y^I = 10$. This rate ratio has been found (2) experimentally to be less than 3 for the plasma etching of polysilicon in 66 Pa of a chlorine gas mixture excited at 13.56 MHz. In spite of this inconsistency, the reasonable assumption of the superposition of the neutral and ionic chemistry was kept in this paper's model by recognizing that the ionic component need not be completely anisotropic, *i.e.*, that the ion transport can vary from isotropic to anisotropic as the sheath electric field overcomes the random motion due to ion collisions with the neutral scatterers.

In this paper, we accounted for the effect of the sheath field on the ion kinetic energy transport across the sheath. This yields the result that the ion energy transport was isotropic at low field-pressure ratios

(E/p) and anisotropic at high values of this ratio, *i.e.*, equal to the ion thermal energy in all directions at low E/p and much greater than thermal energy along the field direction at high E/p. This ion energy transport anisotropy was, then, related to the etch anisotropy through the etch rates perpendicular and parallel to the sheath electric field. A natural outcome of this model leads to an ion-neutral mass ratio and collision cross-sectional dependence of the E/p ratio that is experimentally verifiable.

Finally, since the sheath electric fields are not conveniently observable, we related them to the observable rf current or power density from a relatively simple discharge equivalent circuit. The relations obtained between sheath fields, plasma fields, and rf current or power densities in the plasma naturally manifests the frequency behavior of the PE/RIE discharges, showing that the discharge exhibits a low frequency regime, below 2.7 MHz, and a high frequency regime, between 2.7-77 MHz, with somewhat different properties. In the former regime, the sheath electric fields are much greater than in the latter. In both regimes, the fields in the body of the plasma are much less than in the sheaths.

Comparison with Experiment

Behavior with pressure and power density.—While many plasma etch experiments describe results (3, 4, 5) in qualitative agreement with the predictions of this model, there are only three reports of experimental results with respect to pressure and rf power density (1, 2, 6) on etch profiles that are sufficiently detailed to permit reasonably quantitative comparison. At 13.56 MHz, the rf power density of 0.4 W/cm^3 produces an increased undercut with increased pressure of CF_4 for the plasma etching of doped polysilicon (1). Twice this power density permits still higher pressure for the same undercut, as shown in Fig. 10 at pressures between 30-130 Pa. Comparison of this result with the predicted behavior shown in Fig. 3a and b is reasonably good. Equivalent behavior is observed (2) for the plasma etching of both doped and undoped polysilicon in an entirely different gas, a mixture of N_2, HCl, and CCl_4 at a total pressure of 66 Pa, when the rf power density at 13.56 MHz was increased from 0.1 to 0.5 W/cm^3. At the lower power density, the mask was undercut and at the higher power the undercut was negligible as summarized in Fig. 8, which compares quite favorably with the predicted behavior shown in Fig. 2a and b. As mentioned at the beginning of the paper and explored in more detail in the Discussion section, the ratio of the etch rates measured in these experiments at $\delta \simeq 1$ (isotropic) and $\delta \simeq 0.1$ (anisotropic) were found (2) to be less than 3:1, precluding an explanation based simply on a change from a thermochemical (isotropic) to an ionic (anisotropic) etch

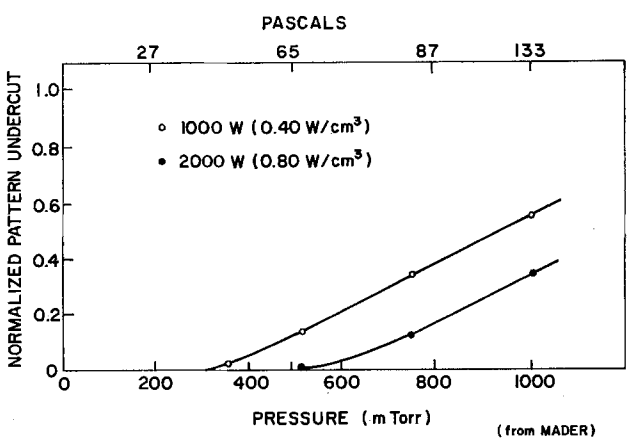

Fig. 10. Normalized pattern undercut vs. pressure for CF_4 plasma etching of polysilicon (2).

reaction. A discussion of the experimental difficulties in evaluating this etch rate increase is given in Ref. (2). The lower power density required to produce anisotropic etching of undoped polysilicon reported in this reference (2), coupled with the observed lower etch rates at comparable conditions may be explained as due to the different surface conditions of the undoped polysilicon. This may be caused by a different effective reaction activation energy, E_F, either because the unbombarded activation energy or its reduction by the ion energy U is different (a different β).

Experimental verification of the ion-neutral scatterer. —Cross section and mass ratio effect on etch anisotropy.—The ion-neutral collision cross section and mass ratio effects on the E_s/p, J_{rf}/p or $\sqrt{P_{rf}}/p$ required to achieve a given etch anisotropy, δ, summarized by Eq. [2b] and [5] have been verified (6) for chlorine based plasma etching of polysilicon. Decreasing the factor $(1 + m_+/m_o)/Q$ in Eq. [5] can be seen from the data (6) summarized in Table I and Fig. 11 to increase the parameter $\sqrt{P_{rf}}/p$ required for similar profiles when the ion (Cl^+ or Cl_2^+) is dominantly scattered by He, HCl, and Cl_2, in reasonable agreement with expected cross sections and mass ratios. In all three etch gases, at a variety of rf powers and pressures, the etch anisotropy increases from 1.1 to 2 from 2 to 10, always accompanied by the same ratio of changes in $\sqrt{P_{rf}}/p$, of about 1.4. This behavior has been shown (6) to be valid over a range of pressure between some 66 and 1000 Pa.

The effects of "low" and "high" frequencies on the experimentally observed etch anisotropy.—As shown in the section discussing the electric fields in the plasma, the sheath field in the "low" frequency regime (less than about 2.7 MHz) is very much larger than that at plasma excitation frequencies well above 2.7 MHz ("high"), in addition to which, the sheath thickness at the lower frequencies is smaller because of the greater ion motion permissible at these frequencies. The ion transport would be expected to be much more anisotropic, both because of the larger fields at similar rf powers and because the smaller sheath thickness decreases the number of collisions the ions can make while in such a higher field. The observed increase in etch anisotropy with lower excitation frequencies at the same power is well documented (3, 4). The effect of these lower frequencies in increasing the resist erosion (3, 4, 6), and reducing the process selectivity (or increasing the sputtering) is also well known.

Summary

The model presented here for (ion assisted) anisotropic plasma etching is in agreement with experiments and explains the following behavior:

(*i*) As rf power density is increased at fixed gas pressure, the mask undercut decreases continuously, approaching zero undercut (anisotropic etching) asymptotically.

Table I. Effect of ion-neutral scatterer cross section and mass ratio on required E_s/p, J_{rf}/p or $\sqrt{P_{rf}}/p$ for etch directionality, δ SEM photographs shown in Fig. 11.

0.1 Cl_2-0.9 He	HCl	Cl_2	
	$\sqrt{P_{rf}}/p$ (W$^{1/2}$ – Torr^{-1})		$1/\delta$
$\sqrt{50}/10 \simeq 0.7$	$\sqrt{50}/2 \simeq 3.5$	$\sqrt{25}/0.5 \simeq 10$	1.1
$\sqrt{25}/5 \simeq 1.0$	$\sqrt{100}/2 \simeq 5.0$	$\sqrt{50}/0.5 \simeq 14$	2
$\sqrt{50}/5 \simeq 1.4$	$\sqrt{200}/2 \simeq 7.0$	$\sqrt{100}/0.5 \simeq 20$	10

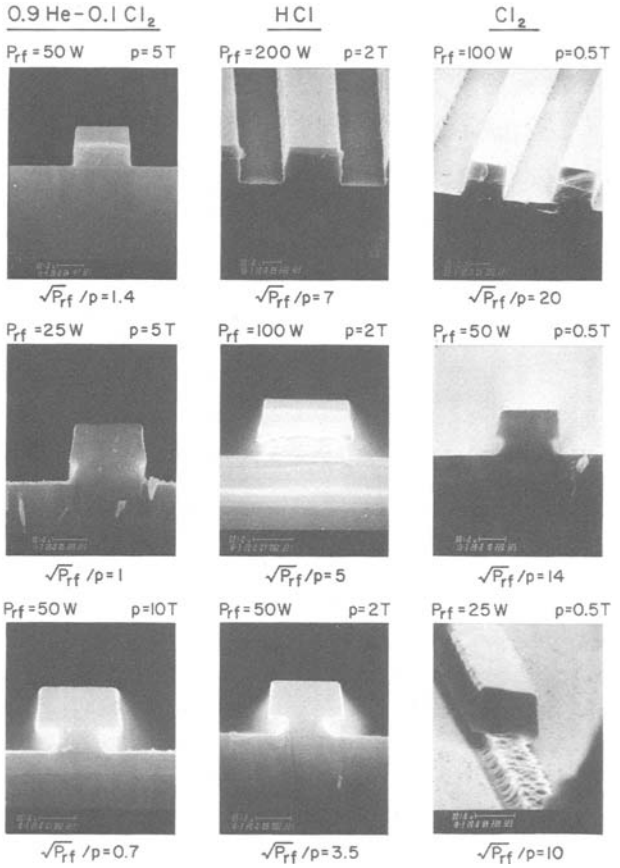

Fig. 11. Polysilicon etch profiles in 10% Cl_2-90% He, HCl, and Cl_2 showing ion-neutral scatterer cross section and mass ratio effect in modifying $\sqrt{P_{rf}}/p$ required for anisotropy.

(*ii*) As gas pressure is increased at fixed rf power or current density, the mask undercut increases continuously, approaching an undercut equal to the etch depth (isotropic etching) at sufficiently high pressures.

(*iii*) The preceding behavior can be summarized in terms of the ratio of the rf current density J_{rf} or the square root of the rf power density, $\sqrt{P_{rf}}$, and pressure p as a single parameter (J_{rf}/p or $\sqrt{P_{rf}}/p$), where the etching becomes more anisotropic as these ratios increase and more isotropic as they decrease. Identical profile changes are produced by changing either the rf current density or the gas pressure to achieve the same ratio. A plot of J_{rf}, $\sqrt{P_{rf}}$ or E_s *vs.* $1/p$ (Fig. 4), gives the hyperbolic loci which are ion isoenergies and profile isomorphs. This one-to-one correspondence between ion energy and etch anisotropy requires that a compromise be made between sufficient high etch anisotropy and low ion energy, in the interest of low resist erosion and high etch selectivity.

(*iv*) An estimate of the sheath field required to observe the onset of anisotropic etching is some 300 V/cm, in agreement with the observed plasma current density of 75 A/m^2 or power density of 0.1 W/cm^3 at 66 Pa.

(*v*) The transport properties of ions crossing the plasma sheath, which control this behavior depend on the ratio of directed velocity to the random velocity of these ions, and not only on the change from an isotropic thermochemical etch reaction to an anisotropic ionic etch reaction. This is concluded from the inconsistency between the 10:1 etch anisotropy observed for the less than 3-1 etch rate ratios when anisotropic and isotropic, respectively.

(*vi*) Whether the ions enhance the etch rate directly (as if decreasing the surface reaction activation energy) or by removal of a passivating layer deposited on the etch surface from the plasma, is shown to be moot; anisotropic etching in both cases requires that the ion transport be suitably anisotropic. On the other hand, as is sometimes the case, when a thermochemical nonionic and an intrinsically isotropic reaction dominates the etch rate, such a surface passivation may be required to permit an ionic reaction to dominate the etch rate. Without the anisotropy of the ion transport to the etch surface, the etching cannot achieve the required anisotropy, since the passivation is essentially isotropic.

(*vii*) Larger ion-neutral scatterer mass ratios and smaller cross sections are predicted by this model to reduce the sheath electric field to pressure ratios E/p required for a given degree of anisotropy. This is demonstrated experimentally by varying the neutral scatterer from He to HCl to Cl_2 for either the Cl^+ or Cl_2^+, with result that the He exhibits the lowest required E/p, for a given etch anisotropy, while the HCl and Cl_2 gases exhibit progressively increasing E/p, as expected from this model, with their cross sections and mass ratios.

(*viii*) In agreement with observation, the ion energy and etch anisotropy are much greater in the "low" frequency regime of plasma excitation (less than 2.7 MHz) than in the "high" frequency regime (between 2.7 and 77 MHz). The above frequency dependence of the ion energy and etch anisotropy is deduced from the electrical properties of the discharge which is summarizable in terms of different equivalent circuits in the "low" and "high" frequency regimes.

Acknowledgments

The author is grateful to J. Dalle Ave for very capable technical assistance and to D. A. Huchital, J. F. Nester, D. H. Tracy, A. R. Reinberg, and other colleagues at this laboratory for constructive criticism that improved the clarity of this paper.

Manuscript submitted Sept. 27, 1982; revised manuscript received Jan. 5, 1983.

Any discussion of this paper will appear in a Discussion Section to be published in the December 1983 JOURNAL. All discussions for the December 1983 Discussion Section should be submitted by Aug. 1, 1983.

Publication costs of this article were assisted by Perkin-Elmer Corporation.

APPENDIX

The ion density in the plasma sheath, to a good approximation, is equal to the electron density in the body of the plasma. To estimate this density, the electron mean energy, kT_-, is required. This can be obtained from a knowledge of the sheath voltage, V_s. At the boundary between the plasma and the sheath, the ion and electron flux can be taken as roughly equal (8), so that

$$\Gamma_+ \simeq n_+\sqrt{kT_+/m_+}\ \exp\ (+\ eV_s/kT_-)$$

$$\simeq \Gamma_- \simeq n_-\sqrt{kT_-/m_-}\ \exp\ (-\ eV_s/kT_-)$$

where $\exp\ (\pm\ eV_s/kT_-)$ accounts for the effect of the sheath voltage in reducing the electron loss and enhancing the ion loss from the plasma, with the approximation that the ion and electron velocities are $\sqrt{kT_\pm/m_\pm}$. Since $n_+ = n_-$ in the plasma up to the boundary with the plasma sheath, this yields

$$\frac{\gamma}{x} - \ln x = \ln\frac{m_+}{m_-}$$

where $\gamma = 4\ eV_s/kT_+$ and $x = kT_-/kT_+$. Since $m_+/m_- = 10^5$ and $V_s \cong 50$V from the measured (2, 6) peak rf voltage (see discussion in connection with Eq. [7a] and [7b]), we obtain $kT_-/kT_+ \simeq 120$, or for $kT_+ \simeq 0.1$ eV, $kT_- \simeq 12$ eV.

The electron density in the body of the plasma and the ion density in the sheath can be estimated from the measured rf current and power density, since the plasma conductivity, $\sigma_p = J_{rf}^2/(P_{rf}/l_pS) = n_-e^2/m_-\nu_-$,

where n_- is the electron density, e the electron charge, m_- is its mass, and ν_- is the electron elastic collision frequency. The collision frequency can be estimated from $\nu_- = n_0 Q_- \sqrt{kT_-/m_-}$, where n_0 is the dominant neutral species number density (4×10^{16} cm^{-3} at 1 Torr), $Q_- = 10^{-15}$ cm^2 (8), and the mean electron velocity is taken as approximately $\sqrt{kT_-/m_-}$. With the electron mean energy obtained earlier in this Appendix, the collision frequency is about 5.8×10^9 sec^{-1}. Measured (2, 6) rf current density, $J_{rf} = 750$ A/m^2 and power density $P_{rf}/Sl_p = 10^7$ W/m^3, then gives a plasma conductivity $\sigma_p \simeq 5.6 \times 10^{-2}\ \Omega^{-1}$m^{-1}, so that the electron density in the plasma and the ion density in the sheath is: $n_- = \sigma_p m_- \nu_- / e^2 \simeq 1.2 \times 10^{16}$ m^{-3}. Thus, at 1 Torr (133 Pa), where the neutral density is 4×10^{22} m^{-3}, the fractional ionization is about 10^{-7}.

The sheath thickness, l_s, can be estimated from the electric field and ion density in the sheath. $\nabla \cdot \bar{E}_s = e(n_+ - n_-)/\epsilon_0$ becomes $dE_s/dy \simeq n_+ e/\epsilon_0$ since $n_-/n_+ << 1$ in the sheath. Integration of this expression gives

$$\int_{E_s(o)}^{E_s(l_s)} dE_s \simeq \frac{n_+}{\epsilon_0} \int_0^{l_s} dy$$

$$E_s(l_s) - E_s(o) \simeq (n_+ e/\epsilon_0) l_s$$

where $E_s(o)$ is the field at the plasma-sheath boundary. Since the field in the plasma was shown in the neutral and ionic chemistry section to be small compared to the sheath field, we take $E_s(l_s) - E_s(o) \simeq E_s(l_s)$, and the sheath thickness, l_s, is given by

$$l_s \cong \epsilon_0 E_s(l_s)/n_+ e$$

where $E_s(l_s)$ is the field in the vicinity of the electrode surface. From the estimate of the sheath field given at the end of the neutral and ionic chemistry section, $10^3 < E_s < 10^4$ V/cm, when etching varies from isotropic to anisotropic, and with $n_- \simeq 10^{10}$ cm^{-3} from this Appendix, the range of sheath thicknesses is $0.05 < l_s < 0.5$ cm, in good accord with observed values (2).

Since ions and electrons can both contribute to the conduction current, *i.e.*, $J = (\sigma_- + \sigma_+)E$, the dominating current carrier is determined by whether the conductivity ratio, σ_+/σ_-, is greater or less than unity. These conductivities are given by $\sigma_\pm = n_\pm e^2/m_\pm \nu_\pm$, where it will be remembered that the charge carrier-neutral scatter collision frequency is approximately given by $\nu_\pm \cong n_0 Q_\pm \sqrt{kT_\pm/m_\pm}$. Thus, the ratio

$$\sigma_+/\sigma_- = (n_+/n_-)(m_-/m_+)(Q_-/Q_+)\sqrt{kT_-/m_-}\sqrt{m_+/kT_+}$$

$$= (n_+/n_-)(Q_-/Q_+)\sqrt{kT_-/kT_+}\sqrt{m_-/m_+}$$

so that, for (8) $Q_-/Q_+ \sim 1$, $kT_-/kT_+ \sim 10^2$ (from this Appendix), and $m_-/m_+ \sim 10^{-5}$, we obtain $\sigma_+/\sigma_- \cong 0.03\ n_+/n_-$. When $n_+/n_- \simeq 1$, as in the body of the plasma, $(\sigma_+/\sigma_-)_p \simeq 0.03$ and the electrons conduct most of the current. On the other hand, when $n_+/n_- \simeq 10^3$ as occurs in the sheath, $(\sigma_+/\sigma_-)_s \simeq 30$, or the conduction current in the sheath is dominantly carried by the ions.

REFERENCES

1. H. Mader, Paper 104 presented at The Electrochemical Society Meeting, St. Louis, MO, May 11-16, 1980.
2. C. B. Zarowin *et al.*, Paper 264 presented at The Electrochemical Society Meeting, Denver, CO, Oct. 11-16, 1981.
3. A. R. Reinberg *et al.*, Paper 275 presented at The Electrochemical Society Meeting, Denver, CO, Oct. 11-16, 1981.
4. R. H. Bruce *et al.*, "High Rate Anisotropic Etching," Tech. Digest, IEDM, Dec. 1981.
5. T. Mizutani *et al.*, "A New Aluminum Plasma Etching Technology," Tech. Digest, IEDM, Dec. 1981.
6. C. B. Zarowin and J. Dalle Ave, Paper 154 presented at The Electrochemical Society Meeting, San Francisco, CA, May 8-13, 1983.
7. C. B. Zarowin, *Thin Solid Films*, **85**, 33 (1981).
8. V. E. Golant *et al.*, in "Fundamentals of Plasma Physics," S. C. Brown, Editor, pp. 48-51, 66, 150-152, John Wiley and Sons, New York (1979).
9. H. R. Koenig and L. I. Maissel, *IBM J. Res. Dev.*, **14**, 168 (1970).

Characterization of Oxide-Nitride Interface Charges in MNOS Devices

K. Rajkanan* and J. S. Multani*

General Instrument Corporation, Microelectronics Division, Hicksville, New York 11802

ABSTRACT

Effects of Si_3N_4 deposition processes on SiO_2-Si_3N_4 interface charges in MNOS devices have been studied. The deposition of Si_3N_4 on SiO_2 (400-500Å) introduces 1-3 $\times 10^{12}$ cm^{-2} fixed positive charges located at SiO_2-Si_3N_4 interface. The fixed positive charges are introduced during the initial stages of nitride deposition and appear to be localized to a nonstoichiometric region of the order of a couple of hundred angstrom thickness. An H_2 anneal at 900°-950°C reduces the density of these positive charges to almost half of the unannealed value.

Dual-dielectric MNOS logic devices are quite common in nonvolatile integrated memory circuits based upon memory properties of silicon nitride-silicon oxide composites (1, 2). The dual-electric gates usually consist of thermally grown silicon oxide and CVD silicon nitride, both of several hundred angstrom thickness. Several theoretical models, based upon the conduction mechanisms in nitride and oxide layers, have been proposed to explain the electrical behavior of MNOS memory devices which have thin (50Å) oxide (3-8). However, it is a common practice to use an equivalent oxide thickness based upon the dielectric constant ratio of Si_3N_4 and SiO_2, in simulating the electrical behavior of the MNOS logic devices having thick (500Å) oxide, in circuit simulation programs like SPICE. Thus, the effects of oxide-nitride interface are ignored. One of the reasons for this simplification is that little is known about the exact nature of the oxide-nitride interface. In MNOS devices with 300Å oxide, it has been shown that the flatband voltages of these devices shift with gate bias and stress period (9-11). This shift is primarily attributed to the charge injection from the gate electrode and charge movement through the nitride (10, 11). In this paper, the effects of the oxide-nitride interface on MNOS devices with about 500Å of oxide, are examined.

Experimental Results

MNOS capacitors and n-channel enhancement-mode devices were fabricated on (100) orientation, 10-12

* Electrochemical Society Active Member.
Key words: MNOS, interface charges, dielectrics, silicon nitride.

Ω-cm p-type Si. All the enhancement-mode devices had 50 × 50 μm drawn channel regions and the capacitor area was 475 × 475 μm. The gate electrode in both enhancement devices and capacitors was E-beam evaporated aluminum.

The dual dielectric structure was obtained by first oxidizing the silicon in wet oxygen at 950°C. HCl gettering was used to reduce the mobile oxide charge density at Si-SiO_2 interface. Final oxide thickness was typically 450-500Å. Silicon nitride was then deposited in an LPCVD system using an SiH_2Cl_2 and NH_3 mixture at 675°C. The oxide and nitride thicknesses were monitored optically, nitride thickness being monitored on an area of the test circuit where nitride was deposited on bare Si. Refractive index of 1.45 for oxide and 2.00 for nitride was used at 550 nm wavelength for these measurements.

In enhancement devices, boron was implanted in channel regions through oxide prior to gate oxidation, to obtain the device threshold around 1V. The implant oxide was then etched away from the channel area, and dual-dielectric gates were obtained as described above.

The electrical parameters of oxide and nitride layers were monitored at various points of processing, by 1 MHz capacitance-voltage characteristics, measured by using a mercury-wetted gold probe (12, 13). By monitoring the flatband voltages, it was determined how the deposition of nitride affects the fixed charge density associated with the MNOS structure.

Results and Discussion

Flatband voltages for 470Å thermally grown oxide on 10-12 Ω-cm, uniformly doped, (100) p-type Si was measured to be about −0.05V for gold-mercury (Au-Hg) probe (curve A in Fig. 1). This corresponds to

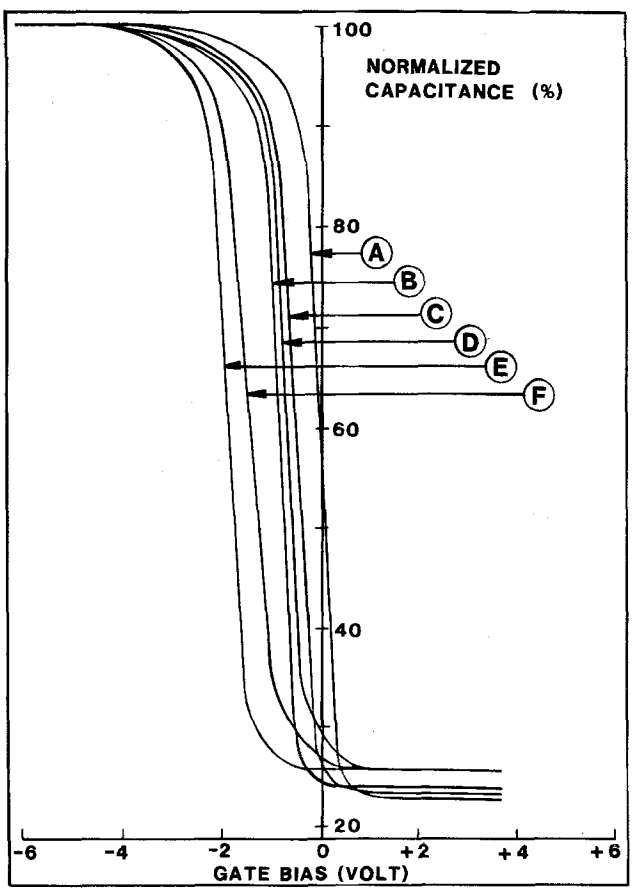

Fig. 1. Room temperature C-V characteristics for various MNOS structures with Au-Hg gate probe. Substrate is 10-12 Ω-cm <100> p-type silicon. A: 470Å gate oxide, B: 463Å nitride, C: 475Å oxide + 300Å nitride, D: 473Å oxide + 500Å nitride, E: 476Å oxide + 550Å nitride, F: 1000Å oxide + 525Å nitride.

fixed positive oxide charge density at the Si-SiO_2 interface, Q_{ss}, of 1.4×10^{10} cm^{-2}. The measured oxide dielectric constant was 3.55 E_o. Here, E_o is the dielectric constant of the vacuum. The dielectric constant of nitride layers was also calculated from the accumulation capacitance of oxide-nitride dual dielectric structure by accounting for the oxide capacitance. The dielectric constant of nitride cannot be easily extracted from the C-V characteristics of a metal-nitride-silicon capacitor directly, due to charge injection from the gate electrode. The measured dielectric constant for the nitride layers of different thicknesses are listed in Table I. It is interesting to note that the dielectric constant of the nitride increases with thickness and tends to saturate to a value of around 11 E_o after 300Å nitride is deposited. This indicates a potential stoichiometric variation in the nitride layer with thickness.

In Fig. 1, the C-V characteristics of various MNOS structures obtained using the Au-Hg probe are shown. It can be seen that the flatband voltages have changed significantly, compared to MOS structure C-V, even if only about 100Å of nitride is deposited. This immediately suggests the existence of positive charges at the SiO_2-Si_3N_4 interface. Using these flatband voltages and the previously measured dielectric constants of nitride and oxide, the charge density located at the SiO_2-Si_3N_4 interface, Q_i, can be calculated using

$$Q_i = (V_{FB} - \phi_{ms})(E_n/t_n) + Q_{ss}(1 + E_n t_{ox}/E_{ox} t_n)$$

where V_{FB} is the flatband voltage, ϕ_{ms} is the work function difference between the gate electrode and silicon, t_n and t_{ox} are nitride and oxide thicknesses, respectively, and E_n and E_{ox} are dielectric constants for nitride and oxide, respectively.

The values of Q_i are listed in Table I for different thicknesses of the deposited nitride. It is important to note that although the dielectric constant of Si_3N_4 varies significantly with the thickness, the fixed positive charge density at the SiO_2-Si_3N_4 interface is always 1-3 × 10^{12} cm^{-2} and almost independent of nitride and oxide thicknesses.

The additional flatband shift caused by positive charges at the SiO_2-Si_3N_4 interface has important consequences for the dual-dielectric logic MNOS devices. If two n-channel enhancement mode devices, one MOS type and the other MNOS type, have equivalent dielectric thickness and silicon resistivity, the MNOS device should have lower threshold voltage due to additional positive charges at SiO_2-Si_3N_4 interface. In other words, to obtain the same threshold in MOS and MNOS n-channel enhancement mode devices, with equivalent dielectric thicknesses, the silicon resistivity in the MNOS device has to be lower. Because of lower resistivity silicon requirement and additional surface scattering caused by higher density of surface charges in MNOS devices, the channel mobility, and, hence, the gain factor, K', in MNOS devices will be lower compared to MOS devices with similar threshold voltages. This effect can be seen in Table II in which three types of n-channel enhancement mode devices are compared. Devices in group 3 are MNOS devices with 450Å oxide and 450Å nitride as gate dielectric, and have threshold voltage of about 1V. To obtain the

Table I. Dielectric constant of Si_3N_4, E_{nit}, and positive charge density at the SiO_2-Si_3N_4 interface, Q_i, as a function of nitride thickness

Oxide thickness (Å)	Deposited nitride thickness (Å)	E_{nit}/E_o	Q_i (cm^{-2})
476	550	11 ± 1	2.4×10^{12}
473	500	10.5 ± 1	1×10^{12}
468	400	11 ± 1	1.3×10^{12}
475	300	11 ± 1	1.5×10^{12}
476	200	8 ± 2	3.5×10^{12}
463	120	5 ± 1	2×10^{12}
1000	525	10.5 ± 1	2×10^{12}

Table II. Comparison of threshold voltage, V_T, and gain factor, K', of different 50 × 50m n-channel enhancement devices

Group	Gate dielectric	Boron implant through 5000Å oxide	V_T (V)	K' (μA/V)
1	650Å oxide	1.6×10^{12} cm^{-2} at 178 keV	1 ± 0.1	28 ± 1
2	680Å oxide	2.3×10^{12} cm^{-2} at 164 keV	1.2 ± 0.1	27 ± 1
3	450Å oxide + 450Å nitride	2.3×10^{12} cm^{-2} at 164 keV	1 ± 0.1	24 ± 1

same threshold, devices in group 1 with similar equivalent dielectric thickness needed a significantly lower dose of boron implant, and K' for group 1 is significantly higher than for group 3. In group 2, the boron implant is the same as for group 3, and equivalent oxide thickness is also comparable. However, because of the absence of a nitride layer, group 2 shows higher threshold and higher K'. A close look at K' of these three groups also suggests that a major degradation in K' value, and, hence, the channel mobility, is due to the nitride layer rather than due to a difference in the implant.

It is, therefore, clear that nitride deposition on oxide causes about $1\text{-}3 \times 10^{12}$ cm^{-2} positive charges, resident near the SiO_2-Si_3N_4 interface, regardless of oxide and nitride thickness, and they cause lowering in threshold voltage and channel mobility in MNOS devices. The question still remains: how do these charges originate, and can they be annealed in some fashion? Results on MNOS devices with 300Å oxide suggest charge injection from the gate electrode (9-11). If such effect is present, enhancement device thresholds would shift under temperature-bias stress. Our devices with about 450Å of oxide did not exhibit any drift under temperature-bias stress, and it has been confirmed over many lots of MNOS devices. Thus, some other mechanism is responsible for charges at the oxide-nitride interface. It is conceiveable that the positive charges are caused by some kind of mixed interface of SiO_2 and Si_3N_4, probably SiO_xN_y in nature (15-16). There is some evidence available which suggests such possibility. First of all, as seen in Table I, the structure is plotted against time. For the first 15 min, the etch rate of the top nitride layer is about 0.55 Å/sec in 10:1 water-diluted HF, after which the etch rate keeps on increasing for about the next 1 min and then saturates to about 6 Å/sec, which is the oxide etch rate. A separate sample of similar nitride thickness on silicon took 16 min to etch completely at a constant rate of about 0.55 Å/sec. Therefore, between the 15-16 min period, the increasing etch rate must be due to the nonstoichiometric region in the nitride/oxide structure. Integration of each rate curve in this time period indicates a thickness of about 250Å. It should be noted that this thickness was measured as oxide thickness using a refractive index of 1.45 at 550 nm wavelength, which may not be true for the nonstoichiometric region. In fact, it can be expected that the refractive index of this region would also change with thickness as much as the dielectric constant. This would mean that the actual thickness of the nonstoichiometric region may be somewhat different than the above calculated thickness. However, it is interesting to note that this thickness is about the same as the thickness of nitride layer after which the value of dielectric constant saturates. It is also worth mentioning here that the C-V characteristics of the oxide, after completely etching the top nitride and nonstoichiometric region, indicates a Q_{ss} of about 2×10^{10} cm^{-2}, close to the value for the virgin oxide layer. This further confirms that the additional charges observed after nitride deposition are indeed located near the SiO_2-Si_3N_4 interface. At this stage, we have not attempted to find the energy distribution of the positive charges at the SiO_2-Si_3N_4 interface, as they tend to behave like fixed charges over a wide range of gate potential, much like the fixed charges at the Si-SiO_2 interface. It should be mentioned here that the density of these dielectric constants is much lower for the first few hundred angstroms of nitride. It should be borne in mind that the optical thickness of thin nitride layers, used to calculate these dielectric constants, may be in some error due to variation in refractive index. However, this error is not expected to be more than 10%; thus, lower dielectric constant for this nitride layer is real. This lower dielectric constant is consistent with the possibility that the two dielectrics are intermixed to form a nonstoichiometric region (14). A separate experiment was performed to determine whether this nonstoichiometric region is formed during actual deposition of Si_3N_4 layer or during the NH_3 purge step which precedes the introduction of SiH_2Cl_2 into the system to prevent any silicon particle deposition. An oxidized Si wafer on which C-V measurements were already done, was introduced in the LPCVD system and pulled out after the NH_3 purge step without allowing any Si_3N_4 deposition. No measureable difference in the C-V plot could be observed after this treatment. However, deposition of very thin Si_3N_4 layers causes flatband shift, indicating the presence of positive charges at the SiO_2-Si_3N_4 interface, as seen in Table I. It is then obvious that the presence of positive charges at the SiO_2-Si_3N_4 interface is related to the nonstoichiometric region formed during the initial stages of nitride deposition. Since the dielectric constant of the nitride layer saturates after about 300Å of nitride is deposited, it can be expected that the nonstoichiometric region would be of the same order of magnitude in thickness.

A further estimate of the nonstoichiometric region thickness can be obtained by studying the etch rates. In Fig. 2, the etch rate of 525Å nitride + 1000Å SiO_2 charges can be reduced from $1\text{-}3 \times 10^{12}$ cm^{-2} to about 5×10^{11} cm^{-2} by H_2 anneal. In Fig. 3, the C-V characteristics of Al-gate MOS capacitors, which were fabricated on 10-12 Ω-cm p-Si implanted with 2.25×10^{12} cm^{-2} dose of boron at 160 keV, are shown, before H_2 anneal and after a 30 min H_2 anneal at 900°C and 950°C. The H_2 anneal was performed before Al deposition and subsequent alloy at 440°C in forming gas. It can be noticed that the flatband voltage is almost reduced to half the value as a result of the H_2 anneal. This is further evidenced by the increases in the threshold voltage of enhancement mode devices fabricated and annealed together with the above capacitors. The threshold voltages V_T, and device gain factors, K', are listed in Table III, and a definite increase in V_T and K' is noticed after H_2 anneal. We anticipate that the mechanism of reduction in the SiO_2-Si_3N_4 interface charges is similar to the mechanism of reduction in Si-SiO_2 interface charges, *i.e.*, by saturation of dangling bonds at the interface. It is interesting to note here that high temperature hydrogen annealing also improves the retentivity of MNOS memory devices (17).

Conclusions

In summary, the LPCVD deposition process of Si_3N_4 on thick SiO_2, to form MNOS devices, introduces fixed positive charges of the order of $1\text{-}3 \times 10^{12}$ cm^2 in density. These charges are localized in about a 250Å

Table III. Effect of H_2 anneal on MNOS n-channel enhancement device threshold, V_T, and gain factor, K'

Parameter	No H_2 anneal	30 min H_2 anneal 900°C	30 min H_2 anneal 950°C
V_T (V)	0.8 ± 0.1	1.1 ± 0.1	1.1 ± 0.1
K' (μA/V)	24 ± 1	29 ± 1	30 ± 1

Device size: 50 × 50 μm.
Gate: 450Å oxide + 450Å nitride gate, Al gate.

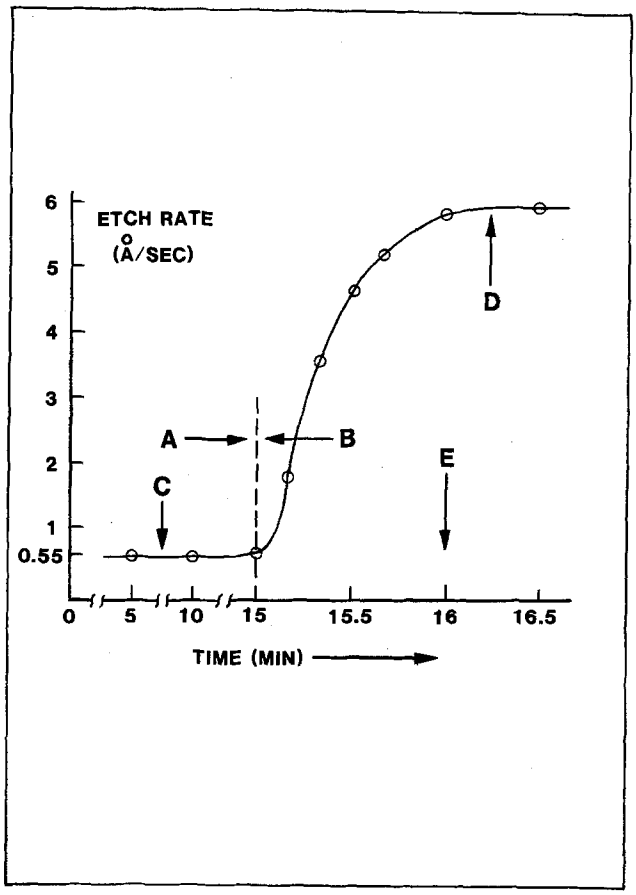

Fig. 2. Room temperature etch rate of 525Å nitride on 1000Å oxide as a function of time. Etchant was 10:1 solution of H_2O and HF (49%). As long as the etch rate of nitride + oxide system matched with the etch rate of nitride layer alone, on a monitor wafer, the etch rate was calculated by the change in the nitride thickness (region A). Once the etch rate of the nitride + oxide system started deviating from the etch rate of the nitride layer alone, the etch rate was calculated by the change in the effective oxide thickness (region B). C: nitride etch rate, about 0.5 Å/sec, D: oxide etch rate, about 6 Å/sec, E: time to completely etch 525Å nitride alone, on a monitor wafer.

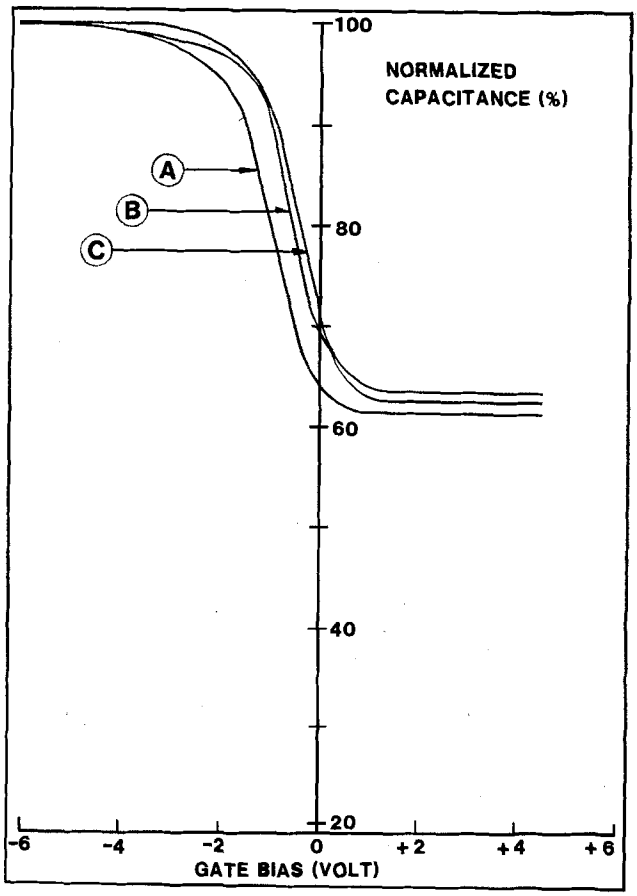

Fig. 3. Room temperature C-V characteristics before and after H_2 anneal. Substrate was 10-12 Ω-cm <100> p-type silicon with 2.25 × 10^{12} cm^{-2} dose of boron implanted at 160 keV. Gate dielectric was a combination of 450Å of oxide and 450Å of nitride. A: No H_2 anneal, B: 30 min H_2 anneal at 900°C, C: 30 min H_2 anneal at 950°C.

thick nonstoichiometric region which forms during the initial stages of nitride deposition. The dielectric constant and the etch rate of this region varies with the thickness. The positive charge density is independent of oxide and nitride thickness and can be reduced to almost half by annealing the device in H_2 ambient at 900°-950°C before metallization. Because of these positive charges at the SiO_2-Si_3N_4 interface, the threshold voltage and gain factors of MNOS devices are significantly different compared to MOS devices fabricated on Si with equivalent oxide as gate dielectric.

It would be interesting to study the exact composition of the nonstoichiometric region near the SiO_2-Si_3N_4 interface, to obtain the energy distribution of interface states present at this interface, and to relate this information to the reliability of MNOS logic devices. Experiments are underway in this direction.

Manuscript submitted July 12, 1982; revised manuscript received Dec. 21, 1982.

Any discussion of this paper will appear in a Discussion Section to be published in the December 1983 JOURNAL. All discussions for the December 1983 Discussion Section should be submitted by Aug. 1, 1983.

Publication costs of this article were assisted by General Instrument Corporation.

REFERENCES

1. M. Kalet, J. Multani, K. Rajkanan, and A. Sass, *Electronics*, **54,** 152 (1981).
2. J. J. Chang, *Proc. IEEE*, **64,** 1039 (1976).
3. M. H. White and J. R. Cricchi, *IEEE Trans. Electron Devices*, **ed-19,** 1280 (1972).
4. K. I. Lundstrom and C. M. Svensson, *ibid.*, **ed-19,** 826 (1972).
5. H. C. Card and M. I. Elmasry, *Solid-State Electron.*, **19,** 863 (1976).
6. J. J. Chang, *IEEE Trans. Electron Devices*, **ed-24,** 511 (1977).
7. A. V. Ferris-Prabhu, *ibid.*, **ed-24,** 524 (1977).
8. M. E. Beguwala and T. L. Gunckel, *ibid.*, **ed-25,** 1023 (1978).
9. A. P. Turley, R. M. McLouski, P. R. Reid, and D. H. McCann, *This Journal*, **123,** 117 (1976).
10. L. A. Kasprzak, A. K. Gaind, and A. Hornung, *ibid.*, **124,** 1631 (1977).
11. P. K. Chaudhari, *ibid.*, **125,** 1657 (1978).
12. J. S. Multani, B. B. Kosicki, and J. S. Sandhu, *IEEE Trans. Electron Devices*, **ed-25,** 1072 (1978).
13. J. S. Multani and J. S. Sandhu, *This Journal*, **126,** 1084 (1979).
14. K. Rajkanan, *Mater. Res. Bull.*, **14,** 207 (1979).
15. J. S. Johannessen, C. R. Helms, W. E. Spicer, and Y. E. Strausser, *IEEE Trans. Electron Devices*, **ed-24,** 547 (1977).
16. S. Thomas and R. J. Mattox, *This Journal*, **124,** 1942 (1977).
17. Y. Yatsuda, S. Minami, R. Kondo, T. Hagiwara, and Y. Itoh, *Jpn. J. Appl. Phys.*, **19-1,** 219 (1980).

Computer Simulation and Controlled Growth of Large Diameter Czochralski Silicon Crystals

K. M. Kim,* A. Kran, P. Smetana, and G. H. Schwuttke[1]

IBM East Fishkill Laboratories, Hopewell Junction, New York 12533

ABSTRACT

Computer simulation leading to controlled large diameter Czochralski crystal growth is discussed. A simple mathematical model, which describes the different crystal growth phases including neck-in, fast flat top, roll-over to constant diameter bulk growth, and tail-off is presented. This model, in conjunction with a computer-implemented simulator, is used to simulate silicon crystal growth. Good agreement between simulation results and experimental crystal growth is obtained.

Large diameter silicon single crystals free of dislocations are routinely grown from the melt by using the Czochralski (CZ) technique. This paper presents a simple mathematical model which describes the behavior of the crystal radius during all phases of 125 mm CZ silicon crystal growth. This model is the basis for a computer simulation of the crystal growth process. The simulation includes the initial neck-in growth after seeding, which represents a standard procedure for elimination of dislocations; then fast flat growth, also called shoulder growth, roll-over to constant diameter bulk growth, and finally, the tail-off procedure to terminate crystal growth. The simulation results are compared to actual growth of 125 mm diam silicon crystals. This modeling effort is an integral part of a larger program directed toward complete interactive digital computer control of the CZ crystal growth process.

Modeling of 125 mm Diameter Silicon Crystal Growth

Fluctuations of crystal diameter during growth are caused by variations both in crystal pull rate and thermal conditions. In principle, it should be possible to obtain insight into a cause and effect relationship of crystal diameter variations during growth through thermal analysis. To the best of our knowledge, such an analysis has not yet been performed. Thermal analyses of the CZ crystal growth process have been made by several investigators. However, the efforts reported are concerned with other aspects of crystal growth, such as temperature distributions in the crystal and/or at the solid-liquid interface (1-7), and crystal pull rate limits (8, 9). This paper provides insight into crystal diameter variations during crystal growth, through development of a mathematical model in conjunction with a computer simulation comprising all phases of the growth process. This insight is gained through a comparison between simulated and actual crystal growth data. The simulation is based on the model described in the following sections.

Mathematical model.—The sequence of large diameter CZ silicon crystal growth is schematically illustrated in Fig. 1. The radius (R) of the growing crystal is a function of the crystal pull rate (V) and of the temperature (T) of the system. T is defined here as the difference between the crucible wall temperature and the melting point (1412°C) of silicon. Experimentally, it is found that R is inversely proportional to V and T. The behavior of R prevails during neck-in, constant diameter bulk growth, and tail-off. During fast flat top growth, R is assumed to increase exponentially in time (9). During this phase, T and V are kept close to constant. The exponential increase of R during the flat growth is physically due to the radiational heat loss mechanism prevailing during this phase of crystal growth. Both the latent heat of solidification and the heat conducted to the solid-liquid growth interface from the melt is radiated primarily from the surface area of the growing flat top. As the surface area increases, the radiational loss increases. This in turn results in an exponential increase of R with time (t) (9).

On the basis of these assumptions, we state a relationship of R as a function of V, T, and t as follows

$$R(V,T,t)_L = F(V,T)G(t) \quad [1]$$

The functions $F(V,T)$ and $G(t)$ are expressed as follows

$$F(V,T) = 1/(V + A) + B/T \quad [2]$$

$$G(t) = \exp(\alpha t) \quad [3]$$

The total length of the crystal pulled is expressed as

$$L = L_0 + \Sigma V_i t_i \quad [4]$$

where we have R = radius (mm) of the crystal, L = length (mm) of the growing crystal, L_0 = length (mm) of the seed, V = crystal pull rate (mm/min),

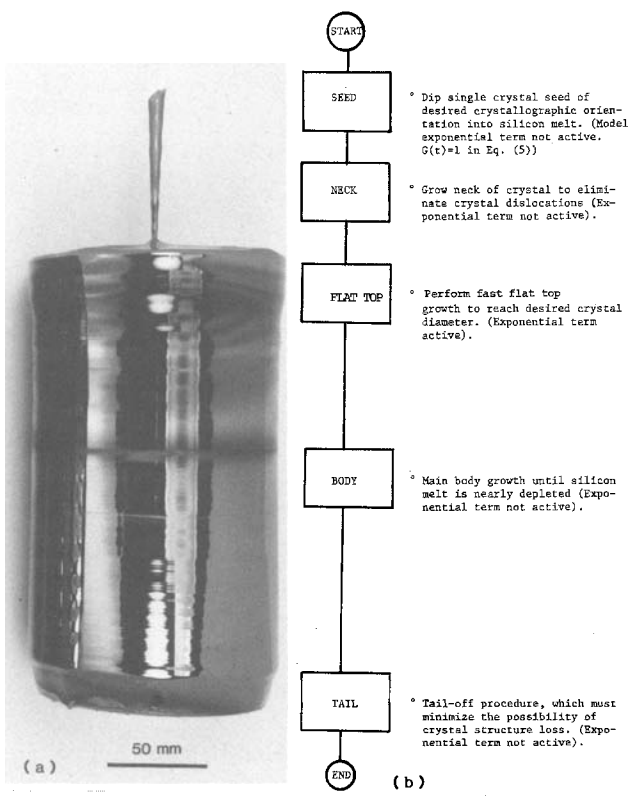

Fig. 1. (a) Photograph of a typical large diameter 125 mm CZ silicon crystal. (b) Crystal growth sequence described by the mathematical model.

* Electrochemical Society Active Member.
[1] Formerly with IBM. Now retired.
Key words: mathematical modeling of CZ silicon growth, CZ silicon crystal growth, computer simulation.

t_i = time of growth (min) for a crystal section, T = difference of temperature between crucible wall and melting point (1412°C) of silicon, t = time (min) for the flat growth, and $G(t)$ = exponential function operative during the flat growth; A, B, and α: constants. Thus, the radius R of the CZ silicon crystal, during the four sequential growth steps, namely, (*i*) neck-in, (*ii*) flat top roll-over, (*iii*) constant diameter bulk, and (*iv*) tail-off can be reproduced by using Eq. [1]-[3] as a function of time, establishing crystal length L. The constants A, B, and α are evaluated from boundary conditions, which are being used during typical 125 mm CZ silicon crystal growth.

Evaluation of the constants A and B in Eq. [2].—The constants A and B are evaluated from boundary conditions prevailing during neck-in growth, where both the diameter of the crystal and the melt temperature are continually decreased while the crystal pull rate is ramped up. This procedure is aimed at eliminating dislocations. Programmed variations of crystal pull rate and temperature during neck-in and subsequent growth of the other crystal segments are reproduced in Fig. 2a. The programming of the pull rate and the temperature used for the evaluation of the constants and for the development of the mathematical model were chosen to be as close as possible to the values used during 125 mm CZ crystal growth (see Fig. 2b).

At the start of neck-in growth, thermal equilibrium is achieved by first establishing contact between the 3.2 mm seed and the melt. Then the seed is left in that position for 10-15 min before seed lift is initiated. The boundary conditions at seeding are R = 3.2 mm, T = 50°C above melting point of Si, and V = 0. Since the exponential radial growth function [$G(t)$] is not operative during neck-in growth, $G(t)$ consequently is 1. Thus, at seeding, from Eq. [1] and [2] we have

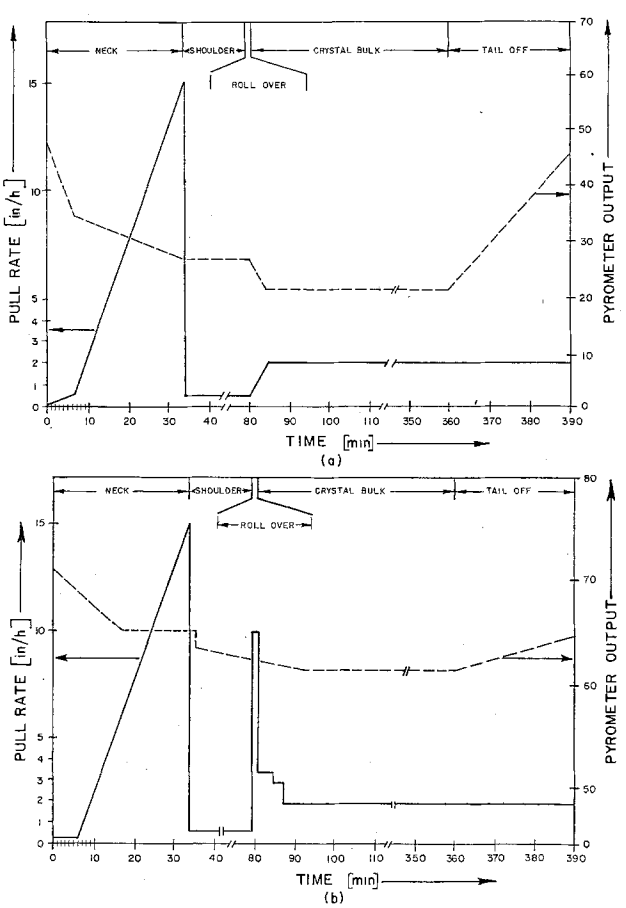

Fig. 2 (a) Histogram of the crystal pull rate, and of the temperature programming used for the development of the mathematical model and for the computer simulation. (b) Histogram similar to (a) but representing the actual growth of 125 mm CZ crystal.

$$R_1 = 3.2 = \frac{1}{A} + \frac{B}{50} \qquad [5]$$

At the end of neck-in growth, the crystal pull rate is at its maximum, V = 6.35 mm/min, while the temperature difference has decreased to T = 27.6°C. This has caused crystal radius to be reduced to 1.6 mm (see Fig. 1a). Thus, at the end of neck-in, from Eq. [2] we get

$$R_2 = 1.6 = \frac{1}{6.35 + A} + \frac{B}{27.6} \qquad [6]$$

Solving Eq. [5] and [6] simultaneously, we obtain for the constants A = 0.417 mm/min and for B = 40.1 mm deg C; thus Eq. [2] becomes

$$F(V, T) = 1/(V + 0.417) + 40.1/T \qquad [7]$$

Equation [7] also applies to both constant diameter bulk growth as well as to the tail-off procedure. Here, T gradually increases in order to decrease the diameter of the crystal from a cylinder to a point. This is necessary for achieving separation of the crystal from the melt without generating dislocations in the crystal, which may propagate upward into the bulk. For reasons of dimensional consistency, the numerator of the first term in Eq. [7] is set to a constant of unit value with the dimension of mm²/min.

Evaluation of the constant α of the exponential flat top growth term G(t) (*Eq.* [3]).—At the end of neck growth, the pull rate is decreased stepwise from 6.35 to 0.21 mm/min. The temperature difference is kept constant, at T = 27.6°C. As a result, crystal radius increases within 1 min from 1.6 to 3.05 mm and from then on increases exponentially with time. While R increases to 63.0 mm in 45 min, V and T stay constant during flat growth at V = 0.21 mm/min and T = 27.6°C, respectively (see Fig. 2a). From Eq. [1] and the boundary conditions, R = 63.0 = (3.05) exp (45α) and results in α = 0.0673 min^{-1}.

All three constants A, B, and α have been evaluated. The mathematical model Eq. [1] can be restated as follows

$$R = [1/(V + 0.417) + 40.1/T] \exp (0.0673)(t) \qquad [8]$$

In summary, Eq. [8] is the mathematical expression that describes the behavior of crystal radius during large diameter (125 mm) CZ silicon crystal growth.

Computer Simulation of 125 mm Diameter Crystal Growth

The simulator.—The crystal growth simulator consists of a computer and an application software system (10). It was developed to support and advance silicon crystal growth technology. The simulator produces graphical representations of a "growing" crystal on a vector graphics display screen in a highly interactive manner. For instance, a simulation session is initiated by executing one main function. All functions are subsequently called from that function in a tree-like fashion.

The simulator is deterministic, and consists of approximately 20 subroutines (functions) written for this application. It is coded in APL, which is a high level, interpretive programming language, and utilizes GRAPHPAK, an IBM developed software system, for producing the graphical representation. Conceptually, the simulator can be compared to a CZ crystal growth furnace, except that it produces a simulated, rather than real, crystal from input data representing temperature and growth rate. The simulator input data can be derived from a number of sources such as: (*i*) mathematical model as described in the previous section, (*ii*) data gathered by the crystal growers during an actual run, and (*iii*) data collected automatically and stored on flexible disk during crystal growth.

In this paper we first simulate crystal growth based upon input data obtained by utilizing the mathematical model Eq. [8], and then compare the simulation results with the actual (125 mm) CZ silicon crystal growth.

Details of computer simulation of various crystal segments based upon mathematical model.—The computer simulation model translates the mathematical model parameters, which define the crystal's physical shape, into a graphical representation of the crystal. Like actual crystal growth, the model is divided into distinct phases as shown in Fig. 1. From analysis of actual 125 mm crystal growth runs, the temperature and growth rate *vs.* time profiles depicted in Fig. 2a were developed. Applying Eq. [7] and [8] to the growth conditions defined in that profile results in data used by the simulator. Equations [7] and [8] are evaluated once a minute during simulated growth time, and a "wafer" is "grown" (plotted) accordingly. For instance, as can be observed from horizontal line spacings (Fig. 1a), neck growth proceeds much faster than main body growth, which in turn is faster than the flat growth.

Simulation for the growth of various crystal segments based upon our mathematical model in conjunction with the histogram of V and T given in Fig. 2a are described in this section.

Simulation of neck-in growth.—Radius of the crystal during neck-in growth is simulated using Eq. [7]. Crystal pull rate and temperature are linearly varied in 1 min time intervals, as follows

$$R = \frac{1}{V + 0.417} + \frac{40.1}{T}$$

For t = 0-6 (min), $V = (0.0353)(t)$ (mm/min), $T = 50 - [(2.5)(6)]$ (°C), and $L_i = [L_o + \Sigma(0.0177)(t_i^2)]$ (mm). Subsequently, for t = 1-28 (min), $V = [(0.2192)(t) + 0.21]$ (mm/min), $T = [35 - (0.264)(t)]$ (°C), $L_1 = [L_i + \Sigma(0.21)(t_i) + \Sigma(0.11)(t_i^2)]$ (mm), and L_i = length of the crystal segment growing during slow ramping of V.

Transition to fast flat top growth.—At the end of neck-in growth, *i.e.*, at a time of (34 + 1) = 35 min from the start of crystal growth, V is decreased to 0.21 from 6.14 mm/min. The details of the simulation are as follows

$$R = \frac{1}{V + 0.417} + \frac{40.1}{T}$$

where we have V = 0.21 (mm/min), T = 27.6 (°C), or r = 3.05 mm, and $L_2 = [L_1 + (0.21)(1)]$ (mm).

The radius increases to 3.05 from 1.6 mm in 1 min as the result of the stepwise decrease in V. Starting from R = 3.05 mm, the radius increases exponentially in time.

Fast flat top growth.—At a time of 35 min from the start of crystal growth, after the radius increased to 3.05 mm, R increases exponentially. The exponential radial growth function $[G(t)]$ becomes operative. Equation [8] is used to simulate the flat growth as follows

$$R = \left(\frac{1}{V + 0.417} + \frac{40.1}{T}\right) \exp(\alpha t)$$

where we have V = 0.21 (mm/min), T = 27.6 (°C), α = 0.0673 (min^{-1}), t = 0-45 min, and $L_3 = L_2 + (0.21)(t)$ (mm).

Transition to constant diameter bulk crystal growth.—At a time of 45 min from the start of the flat growth, when the desired or target radius of 63.0 mm is reached, pull rate is ramped up for a period of 4 min to arrest the exponential radial increase. The slow-down of the exponential growth with the sudden increase in V occurs, physically, because of increased generation of the latent heat of solidification. In order to control the radial decrease and prevent it from becoming too abrupt, the temperature is programmed. The details of the simulation are as follows

$$R = \left(\frac{1}{V + 0.417} + \frac{40.1}{T}\right) (\exp \alpha t)$$

where we have $t = [45 + x]$ (min), x = 1,2,3,4, $V = (0.21)(x)$ (mm/min), $T = [27.6 - (2)(x - 1.5)]$ (°C), α = 0.0673 (min^{-1}), and $L_4 = \left[L_3 + \frac{2.1}{20}x^2\right]$ (mm).

At x = 3, the radial flat growth starts to stabilize instead of increasing exponentially. From this time on, *i.e.*, $t = 45 + 3 = 48$ min from the start of flat growth, $G(t)$ is assumed to be a constant term, *i.e.*, $G(t) = \exp[(\alpha)(48)] = 25.29$. This value remains constant during growth of the subsequent crystal segments.

Constant diameter bulk crystal growth.—From the time of (80 + 4) = 84 min after seeding started, constant diameter bulk crystal growth proceeds with a radius R = 64.9 mm. Pull rate and temperature stay constant throughout the bulk crystal growth. The details of the simulation are as follows

$$R = \left(\frac{1}{V + 0.417} + \frac{40.1}{T}\right) \Big/ (25.29)$$

where we have $V = (0.21)(4) = 0.84$ (mm/min), $T = 27.6 - (2)(4\text{-}1.5) = 22.6$ (°C), r = 64.9 mm, and $L_5 = [L_4 + (0.84)(t)]$ (mm) (t = 1, 2, 3, . . .).

Tail-off.—After a sufficiently long constant diameter bulk crystal is grown, a gradual decrease of crystal diameter, called tail-off, is accomplished by ramping up the temperature. Simultaneously, the pull rate can be also ramped up. The details of the simulation are as follows

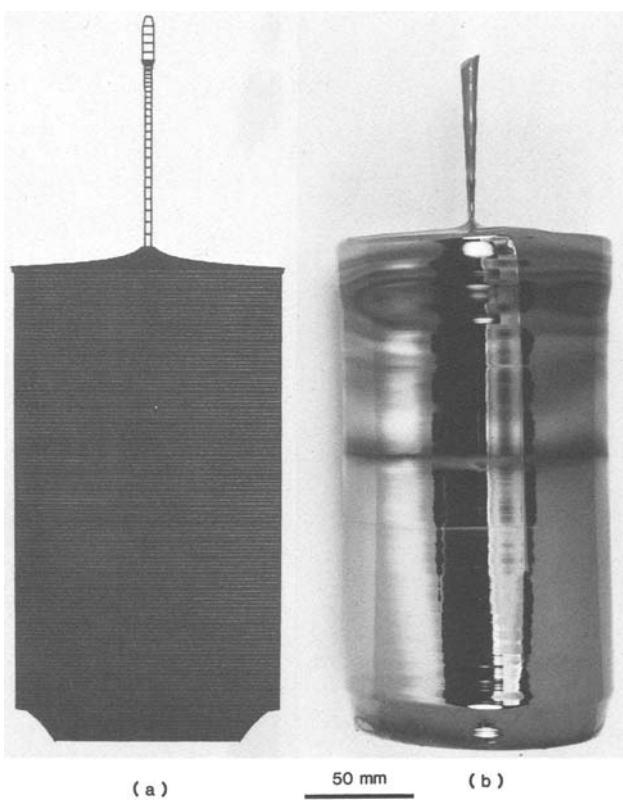

Fig. 3. (a) Computer print-out of a 125 mm diam silicon crystal obtained by simulation. (b) Photomicrograph of a grown 125 mm crystal.

Table I. Calculated and experimentally measured values of the radius R of a 125 mm silicon crystal during neck-in, fast flat top, constant diameter bulk crystal growth, and tail-off as a function of the crystal length L

Crystal section	L (mm)	R (mm) Calculated	R (mm) Measured
Neck-in	14.0 (seed)	3.1	(4.4)*
	14.1	2.94	(4.4)
	14.5	2.75	(4.4)
	16.1	2.10	(4.4)
	18.0	1.85	(4.4)
	19.3	1.78	(4.4)
	24.6	1.65	(4.4)
	28.0	1.61	4.4
	34.0	1.58	3.8
	40.0	1.57	3.4
	49.0	1.55	3.4
	57.0	1.55	2.8
	65.0	1.55	2.5
	71.0	1.56	2.4
	77.0	1.57	2.0
	83.0	1.58	2.1
	92.0	1.59	1.8
	96.0	1.59	1.5
	99.0	1.60	1.5
Transition	100.0	3.2	2.4
Fast top	101	4.0	4.0**
	102.0	6.2	6.8
	103.0	8.5	13.5
	104.0	11.7	22.2
	105.0	16.4	30.2
	106.0	23.0	39.7
	107.0	30.0	49.2
	108.0	42.1	57.9
	109.0	58.9	63.5
	109.3	64.1	66.7
	109.5	66.9	—
Transition (Roll-over)	109.8	64.7	—
	110.5	66.4	—
	111.3	66.2	—
	112.1	65.0	67.8
Constant diameter bulk crystal	119	65.0	68.0
	127	65.0	67.8
	134	65.0	67.0
	139	65.0	66.6
	143	65.0	66.0
	149	65.0	65.8
	156	65.0	65.7
	164	65.0	65.5
	176	65.0	65.6
	186	65.0	65.8
	194	65.0	65.8
	200	65.0	65.8
	210	65.0	65.5
	215	65.0	65.2
	224	65.0	65.2
	234	65.0	65.3
	244	65.0	65.3
	253	65.0	65.4
	268	65.0	65.6
	276	65.0	65.6
	284	65.0	65.7
	291	65.0	66.0
	300	65.0	66.0
	312	65.0	66.0
	222	65.0	66.4
	234	65.0	66.4
	240	65.0	66.5
	247	65.0	66.6
Tail-off	251	57.6	64.4
	253	53.6	63.0
	256	51.2	61.8
	361	46.3	60.8
	364	45.2	59.8
	369	40.2	59.4

* Initial seed section was broken, and the values in the parentheses are estimated.
** Radii of the "Fast Flat Top" crystal segments were measured during growth at 1 min intervals, for a constant crystal pull rate of 0.2 mm/min.

$$R = \left(\frac{1}{V + 0.417} + \frac{40.1}{T} \right) \quad (25.29)$$

where we have $T = T_0\,[1 + (0.03)(t)]$ (°C), $V_0 = 0.84$ (mm/min), $T_0 = 22.6$ (°C), $t = 1, 2, 3, \ldots, \sim 35$ min), and $L_6 = L_5 + (0.84)(t)$.

Computer simulation and comparison with actual 125 mm CZ crystal growth.—125 mm diameter silicon crystals simulated by our mathematical model and actually grown with growth conditions described in Fig. 2 are reproduced in Fig. 3a and 3b, respectively. For the computer simulation, crystal growth was updated at 1 min intervals. Actual 125 mm crystals were grown from a Siltec Model 860-D puller, using a 254 mm OD crucible and 10 kg silicon charge. A partial vacuum of 20 Torr argon was applied during crystal growth. The computer and control system are based upon Intel single-board computer hardware, and programmed to run under the RMX-80 real-time multi-tasking executive (11). Using this system, a higher degree of crystal growth reproducibility and better control of crystal diameter, with relatively small fluctuation of the pull rate, was achieved as compared to utilizing a conventional analog CZ control system. Details of this computerization effort of CZ silicon crystal growth will be reported separately in the future.

As seen from Fig. 3, the mathematical model simulates actual 125 mm crystal growth well. In order to make a quantitative comparison, the diameter of the actual 125 mm crystal was measured as the function of length starting from seed to tail end. The measured and calculated values of crystal radius based on the mathematical model are summarized in Table I. They are plotted in Fig. 4 as a function of crystal length. A good quantitative, first-order of magnitude agreement is found between the calculated and measured radius values of these crystal sections; neck-in, fast flat, and constant diameter bulk crystal growth. For the tail-off, the agreement is less good, but the model still describes the main features.

Discussion

The crystal growth model, defined in Eq. [1] or [8], expresses crystal radius R as a composite function of $F(V,T)$ and $G(t)$. It reproduces actual large-diameter silicon CZ crystal growth quite well. This proves the validity of the assumptions: (*i*) $F(V,T)$ and $G(t)$ are operative primarily during the neck-in and fast flat growth, respectively; (*ii*) $G(t)$ stays constant at a value when the flat growth is finished and the roll-over growth starts; (*iii*) subsequent growth sequences including constant diameter bulk crystal growth and tail-off is controlled by $F(V,T)$, with $G(t)$ remaining constant.

The mathematical model is general, and can be applied to digital computer controlled systems aimed at automation of the entire CZ silicon crystal growth

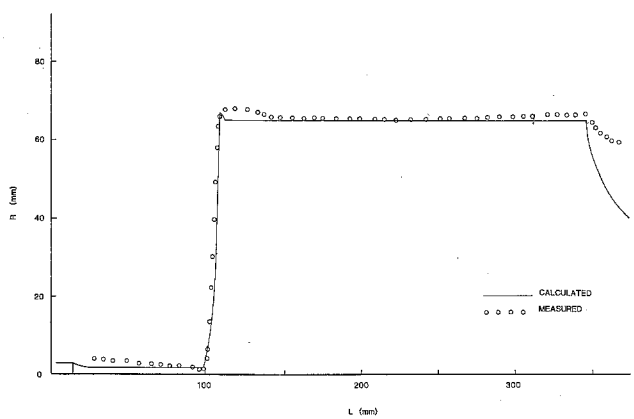

Fig. 4. Comparison of calculated and measured values of the crystal radius R vs. the length (L) of a 125 mm diam CZ silicon crystal as shown in Fig. 3.

process including neck-in, flat, constant diameter bulk growth, and tail-off. Furthermore, effects of pull rate and/or temperature variation on crystal radius can be simulated by using the model. These variations are generally periodic with respect to time. The effect of the time delay on radius in case of temperature variation relative to pull rate can be also simulated.

Summary

A simple mathematical model has been developed to simulate 125 mm diameter CZ silicon crystal growth. In the model, crystal radius is expressed as a function of growth rate, temperature, and an exponential function *vs.* time. The latter growth function is operational only during shoulder growth. By using growth rate and temperature programming, which is similar to real 125 mm crystal growth, the simple mathematical model simulates actual 125 mm diameter CZ silicon crystal growth. The result is a quantitative, first order of magnitude, agreement.

Manuscript submitted Aug. 9, 1982; revised manuscript received Jan. 27, 1983.

Any discussion of this paper will appear in a Discussion Section to be published in the December 1983 JOURNAL. All discussions for the December 1983 Discussion Section should be submitted by Aug. 1, 1983.

Publication costs of this article were assisted by IBM Corporation.

REFERENCES

1. T. Arizumi and N. Kobayashi, *J. Cryst. Growth*, **13/14**, 615 (1972).
2. N. Kobayashi and T. Arizumi, *Jpn. J. Appl. Phys.*, **9**, 361 (1970).
3. W. R. Wilcox and R. L. Duty, *J. Heat Transfer*, Trans. ASME, **88C**, 45 (1966).
4. V. H. S. Kuo and W. R. Wilcox, *J. Cryst. Growth*, **12**, 191 (1972).
5. J. C. Brice, *ibid.*, **2**, 395 (1968).
6. E. Billig, *Proc. R. Soc. London, Ser. A*, **235**, 37 (1956).
7. V. A. Borodin, L. B. Dadidova, V. N. Erofeev, A. V. Shdanov, S. A. Startsev, and V. A. Tatarchenko, *J. Cryst. Growth*, **46**, 757 (1979).
8. S. N. Rea, *ibid.*, **54**, 267 (1981).
9. W. R. Runyan, "Silicon Semiconductor Technology," pp. 40-44, McGraw-Hill Book Co., New York (1965).
10. A. Kran, K. M. Kim, K. Riedling, P. Smetana, and G. H. Schwuttke, *This Journal*, To be submitted.
11. K. Riedling, *J. Cryst. Growth*, To be submitted.

Gate Oxide Defects Connected to Submicron Isolation Regions Subjected to Selective Oxidation

Manabu Itsumi, Osaake Nakajima, and Kazushige Minegishi

Nippon Telegraph and Telephone Public Corporation, Musashino Electrical Communication Laboratory, Musashino, Tokyo, 180 Japan

ABSTRACT

Defect detection of gate oxide films thermally grown on Si substrates subjected to selective oxidation for isolation oxides has shown that gate oxide defects are induced in the active device regions adjacent to small size isolation oxide regions. The size of the small regions proves to be less than 1 μm. The isolation oxide thickness and also the bird's beak length are suppressed to a great extent. A simple semiquantitative model, derived from the bird's beak configuration, is presented to account for the bird's beak length suppression and the gate oxide defects. The gate oxide defects are attributed to gate oxide thinning which results from some Si nitride formed on the Si substrate during selective oxidation.

The selective oxidation method (1-4) for device isolation is becoming a standard in Si LSI. According to this method, isolation oxides are formed through selective thermal oxidation using an Si_3N_4 mask over the silicon surface regions that will later become gate oxide areas. As pointed out by several researchers, this method has a few problems (4-10) to be solved. The most important problem associated with selective oxidation is that selective oxidation followed by gate oxidation often results in a thinning of the gate oxides. Kooi, Lierop, and Appels (5) found gate oxide thinning that is locally situated in the regions next to isolation oxides. On the other hand, Nakajima, Shiono, Muramoto, and Hashimoto (7) found gate oxide thinning that is randomly distributed throughout gate oxide areas. The gate oxide thinning reported so far is believed to be caused by thin oxidation-masking material such as some silicon nitride generated on the Si substrate during selective oxidation (5-10).

The present paper is intended to describe another gate oxide thinning resulting from selective oxidation. This gate oxide thinning is associated with the gate oxide regions next to submicron isolation regions. A semiquantitative model derived by combining masking Si_3N_4 stiffness and bird's beak suppression is described. The gate oxide defects are discussed with bird's beak suppression observed using scanning electron micrographs.

Key words: gate oxide defects, selective oxidation, submicron region, small size effect, bird's beak suppression.

Experimental Procedure

The silicon wafers used in the present study were CZ-p type, (100), 3 in. diam. The wafers were cleaned in aqueous solutions (11) of NH_4OH-H_2O_2, HCl-H_2O_2, and HF, and then rinsed in deionized water. Pad oxide (200Å) between masking Si_3N_4 (1500Å) and Si substrate is for relief of the stress within the Si_3N_4. Silicon nitride was deposited on the pad oxide at 920°C. Photolithography or electron beam direct writing followed by Si_3N_4 dry etching was performed. Subsequently, selective oxidation was conducted at 1000°C for 0.75 μm thick selective oxides. Wet oxidation was carried out by direct reaction of H_2 and O_2 in a pyrogenic system. After removal of oxynitride on the Si_3N_4, the Si_3N_4, and the underlying oxides, sacrificial oxidation (6, 7, 9, 10) followed by etchback of the resultant oxides was performed. Dry oxidation at 1000°C was used for sacrificial oxidation (350Å) (9). Thereafter, 300Å dry oxide films were grown thermally at 950°C in a double-walled quartz oxidation tube through which pure O_2 was passed. Oxygen gas for the dry oxidations was supplied from a liquid source. The H_2O content in the oxygen gas was less than 1 ppm. Defects in the gate oxide films were detected by using the copper decoration method (7, 9, 12, 13). Mobile

charge concentration in thermally grown SiO_2 films was $< 1 \times 10^{10}$ cm^{-2}.

Electron beam (EB) direct writing technology (14) was used for the patterning of small isolation regions responsible for the gate oxide defects. The accelerating voltage used for the EB direct writing was 20 kV. The resist material was negative resist CMS (13), which has high durability for dry etching processes.

Results and Discussion

Submicron-size isolation regions.—During oxide defect detection of samples subject to selective and gate oxidations, it was noticed that gate oxide defects were correlated with the pattern size of the isolation oxide regions. Representative optical micrographs of copper decorations at the gate oxide defects are shown in Fig. 1. Conventional ultraviolet photolithography was used for patterning in the present experiment. Figures 1a, b, and c portray several stripe patterns of 3.8 μm wide isolation regions and many dot patterns of isolation regions of different sizes. The sizes of the dot patterns are 2.5 $\times$ 3.1 μm, 1.3 $\times$ 1.5 μm, and less than 0.8 $\times$ less than 0.8 μm for Fig. 1a, b, and c, respectively. These three photographs depict regions on a single wafer after oxide defect detection with copper decoration. From Fig. 1c, it can be readily seen that gate oxide defects are situated next to the isolation oxide regions with areas below 1 μm^2. Here, it should be emphasized that isolation oxide regions with areas above 1 μm^2 are not responsible for gate oxide defects, as shown in Fig. 1a and b.

These gate oxide defects are also observed in several other wafers prepared in the same run. The gate oxide defect generation is not directly connected to the photolithographic step itself, because the gate oxide defects are generated also through EB direct writing technology, as will be mentioned in a later section. From the results, the authors are forced to conclude that a direct correlation is present between gate oxide defect generation and isolation region size.

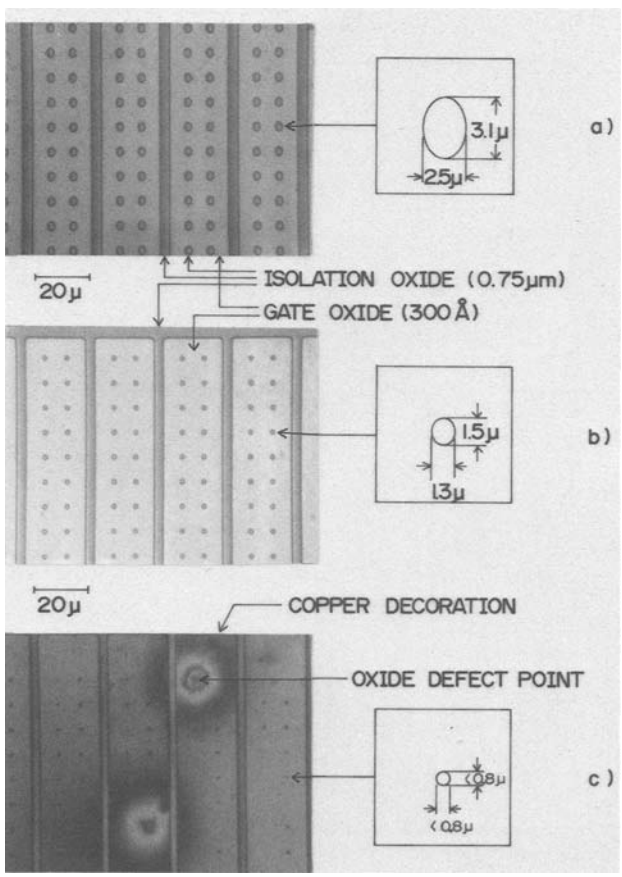

Fig. 1. The influence of pattern size of isolation oxide regions on gate oxide defect generation. In (a), (b), and (c), the isolated regions have an area of about 6 μm^2, about 1.5 μm^2, and smaller than 0.5 μm^2, respectively.

SEM Observation of Oxide Thinning Region

In order to obtain an accurate description of the gate oxide defects, an EB direct writing method (14) was introduced for the patterning of selective oxide regions. Extremely small regions (~0.1 μm diam) were formed on the extension of one side of rectangular regions (2 $\times$ 3 μm). Figure 2 shows typical copper-decorated gate oxide defects on the samples. We observed that all of the gate oxide defects seen in Fig. 2 are associated with the submicron patterns. The actual gate oxide defects themselves were hardly detectable by optical microscopy. Scanning electron micrographs of the gate oxide defect regions in the same wafer shown in Fig. 2 are presented in Fig. 3 at low and high magnifications. These pictures were taken after the removal of the decorated copper. Some thinning of the gate oxides is seen just outside the very small-sized isolation oxide region. In addition, the bird's peak associated with the isolation oxide region is scarcely

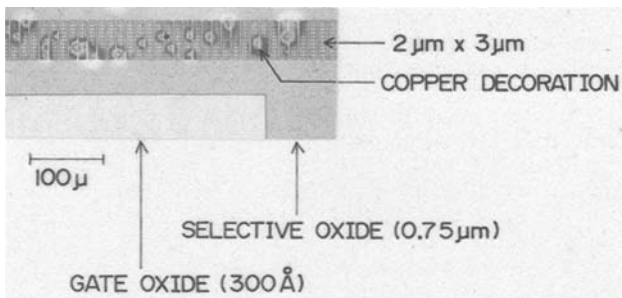

Fig. 2. Top view of copper-decorated gate oxide defects. The defects correspond with the submicron selective oxide regions intentionally formed by using electron beam direct writing technology.

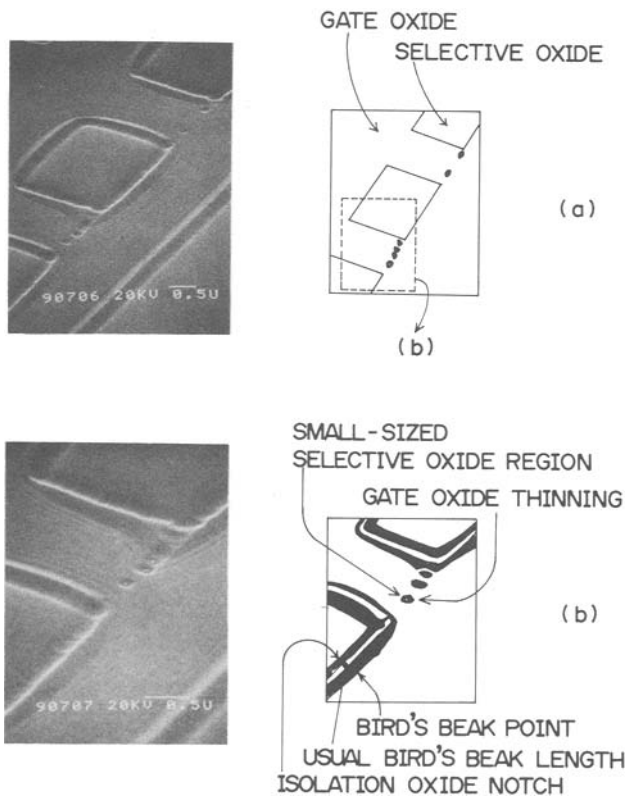

Fig. 3. Scanning electron micrographs of gate oxide defect regions (sample from the same wafer as that shown in Fig. 2). (a): A bird's eye view. (b). Higher magnification micrograph of the region surrounded by the dotted line shown in (a). Note small selective oxide points in the center of oxide thinning regions in (b).

found, differing from the usual bird's beak of large isolation regions (2 × 3 μm).

The bird's beak length is about 0.6 μm for the 0.75 μm thick isolation oxides with larger isolation regions. The length of bird's beak next to the rectangular selective oxide regions (2 × 3 μm) is similar to that for the selective oxides with large areas, as is seen in Fig. 3a. It is noteworthy that the length of the bird's beak situated at the corner of the selective oxide region seems smaller than that at the other portions. This is also assumed to be related to the stress of the masking Si_3N_4.

Figure 4 illustrates the dependence of bird's beak length on the diameter of the selective oxide region for a given selective oxidation. The bird's beak length is markedly reduced when the diameter is less than 1 μm. From these experimental findings, we assume that the complete suppression of both the bird's beak formation and the selective oxide growth observed for extremely small isolation regions is associated with the generation of the gate oxide defects.

Thinning Mechanism in Oxides

The question arises as to how submicron-size isolation regions only are responsible for the gate oxide defects. Assuming that a mechanism similar to that proposed by Kooi *et al.* (5) takes place in those local regions, it is feasible that NH_3 species could reach the silicon surface in much higher concentration due to the small size of the local regions and that subsequent reaction of NH_3 with Si is enhanced. The resultant thicker Si nitride will act as an oxidation-masking material during selective oxidation, which may result in the suppression of the selective oxidation. This is presumably the reason why only small size isolation oxide regions are responsible for the suppression of the selective oxide growth and the bird's beak formation. The short bird's beak length leads to higher concentration of NH_3 species at the silicon surface and to resulting thicker Si nitride. It is assumed that a kind of a positive feedback like this occurs during selective oxidation.

Another plausible mechanism we propose for the observed phenomena involves the geometrical effect of the surrounding Si_3N_4 film edge and volume increase along with oxide growth. The suppression of the oxide growth observed for the small regions reminds us of the results of Shen *et al.*, who showed that oxides were sometimes thinned by 20-30% in regions very close to thick-oxide wall. They also suggested that the oxide thinning was due to the geometrical effect of the thick-oxide wall acting as a partial barrier which limits the oxidation rate in that local region. It is assumed that these phenomena are associated with the continuity of oxide growth adjacent to each other. Considering this effect, it seems reasonable that oxide growth in the region close to the Si_3N_4 mask edge is suppressed. In addition, the small size isolation regions are surrounded by Si_3N_4 mask edge (that is to say, two-dimensional) and, therefore, the geometrical effect can be stronger. A simple configuration involving the bird's beak structure is shown in Fig. 5, which illustrates a case for a circle pattern. Here, it should be emphasized that inner SiO_2 growth under the Si_3N_4 mask edge enlarges the effective perimeter of the Si_3N_4 mask edge. When the radius of the selective oxide region in sufficiently large, as compared with the increase in the peripheral length, the increase will not necessarily be harmful. When the radius of the selective oxide region is sufficiently small, on the other hand, the increase will result in a relatively large expansion of the Si_3N_4 mask edge perimeter. Conversely, if the Si_3N_4 mask edge perimeter is difficult to expand and the expansion is small, both bird's beak length and the thickness of selective oxides close to the edge will be small along with the small expansion. This may be the mechanism for the suppression of both the selective oxides and the bird's beak seen in Fig. 3.

In any case, the bird's beak length and the selective oxide thickness are closely connected to the perimeter expansion of the Si_3N_4 mask edge.

Next, we will derive a relationship among selective oxide thickness, bird's beak length, and radius of selective oxide region, using a simple model, which is illustrated in Fig. 6. Let us assume that (*i*) there is no change in the Si_3N_4 film length in the radius direction of the circle, before and after bird's beak oxide growth under the Si_3N_4 edge, *i.e.*, BC = BC′ (= *d*), and (*ii*) the bird's beak is defined as a triangular shaped structure with an angle θ independent of bird's beak length. These assumptions result in the following formula

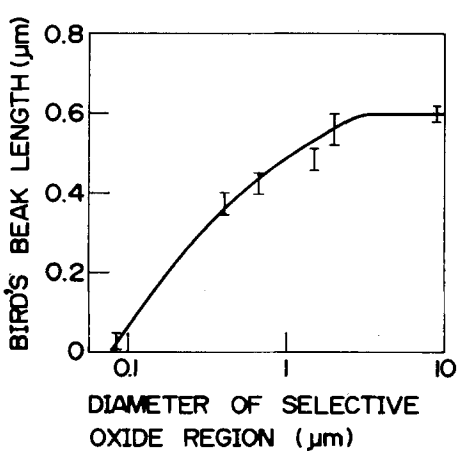

Fig. 4. Variation in bird's beak length as a function of diameter of selective oxide region. Selective oxidation was carried out at 1000°C in a mixture of H_2 and O_2 for 235 min.

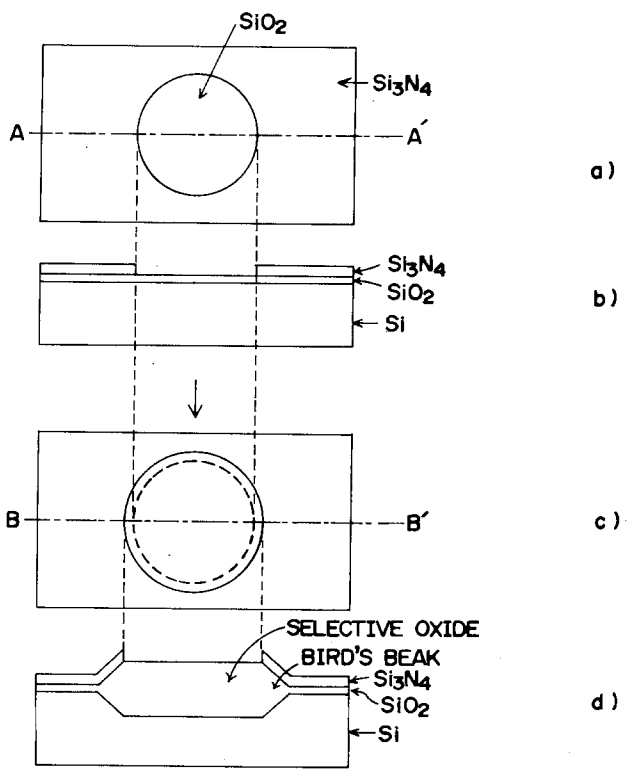

Fig. 5. Inner perimeter expansion of masking Si_3N_4 edge next to growing selective oxides. (a) Top view of a circular area surrounded by a masking Si_3N_4 before selective oxidation; (b) Vertical cross-sectional view along the line A-A′ shown in (a). (c) Top view of a circular selective thick oxide surrounded by an extended oxide beak under the edge of the Si_3N_4 film; (d) Vertical cross-sectional view along the line B-B′ shown in (c).

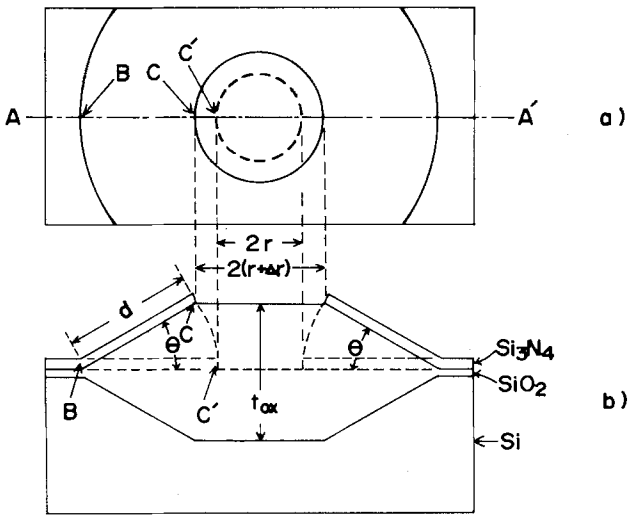

Fig. 6. Selective oxide structure surrounded by an extended oxide beak under the edge of the Si_3N_4 film. (a) Top view of the selective oxide; (b) Vertical cross-sectional view along the line A-A' shown in (a).

$$\Delta r = (r + \Delta r) - r$$
$$= d\,(1 - \cos\theta) \qquad [1]$$

where r or $r + \Delta r$ is the radius of the circle for the Si_3N_4 mask edge before or after selective oxidation, respectively, d is the distance between the bird's beak point and the Si_3N_4 mask edge after selective oxidation. Since the SiO_2 film thickness is divided approximately equally above and below the original silicon surface, the selective oxide thickness t_{ox} can be written as

$$t_{ox} = 2d \sin\theta \qquad [2]$$

The expansion coefficient of the perimeter of the Si_3N_4 mask edge, ξ, is defined by

$$\xi = [2\pi(r + \Delta r) - 2\pi r]/(2\pi r) \qquad [3]$$

By combining Eq. [1] and [2], we obtain

$$\xi = (1 - \cos\theta)\, t_{ox}/(2r \sin\theta) \qquad [4]$$

The selective oxide thickness t_{ox} is given by radius r through the relation

$$t_{ox} = 2\xi r \sin\theta/(1 - \cos\theta) \qquad [5]$$

As will be discussed in the following section, ξ is of the order of 0.05 and $\theta \sim 20°$. The result is

$$t_{ox} \sim 0.6\, r \qquad [6]$$

The bird's beak length, L_{BB}, can be given by

$$L_{BB} = d \cos\theta$$
$$= t_{ox} \cos\theta/(2 \sin\theta) \qquad [7]$$

Substituting Eq. [6] into [7] leads to the relation

$$L_{BB} \sim 0.8\, r \qquad [8]$$

The bird's beak length predicted from Eq. [8] is plotted in Fig. 7 as the solid line along with data. Relatively good agreement between the model and the experimental findings has been shown.

From these results, it is found that the bird's beak length is considerably suppressed along with the exceptional suppression of selective oxide thickness. Assuming that a mechanism similar to that proposed by Kooi *et al.* (5) takes place for this gate oxide thinning, it is feasible that NH_3 species could reach the silicon surface in much higher concentration due to the short bird's beak length, and that subsequent reaction of NH_3 with Si is enhanced. The resultant thick Si nitride will act as an oxidation-masking material during gate oxidation, which results in gate oxide thinning. This

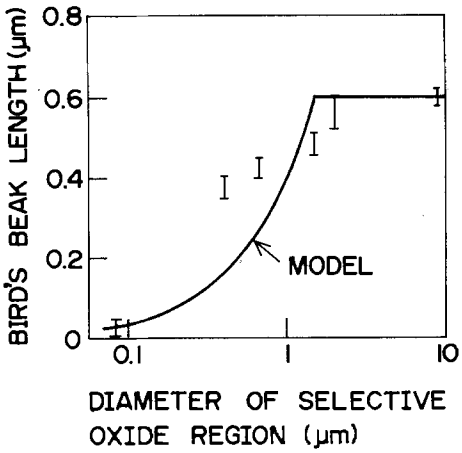

Fig. 7. Model results for bird's beak length vs. diameter of selective oxide region. The solid line represents the model calculation. The experimental data points are from Fig. 4.

is presumably the reason why only isolation oxide regions with areas below 1 μm^2 are responsible for the gate oxide defects.

An Estimation of Si_3N_4 Edge Expansion Coefficient

In this section, we will evaluate the Si_3N_4 edge expansion coefficient, using the Si_3N_4 film deformation associated with usual bird's beak formation. As mentioned in the previous section, along with the lateral oxidation under the edge of the Si_3N_4 mask during selective oxidation, the Si_3N_4 film is strained and tends to bend. Figure 8a shows an SEM micrograph of a cross section of a bird's beak structure with 1500Å Si_3N_4 film over regions that will later become active device areas. The curvature of the strained Si_3N_4 film is of

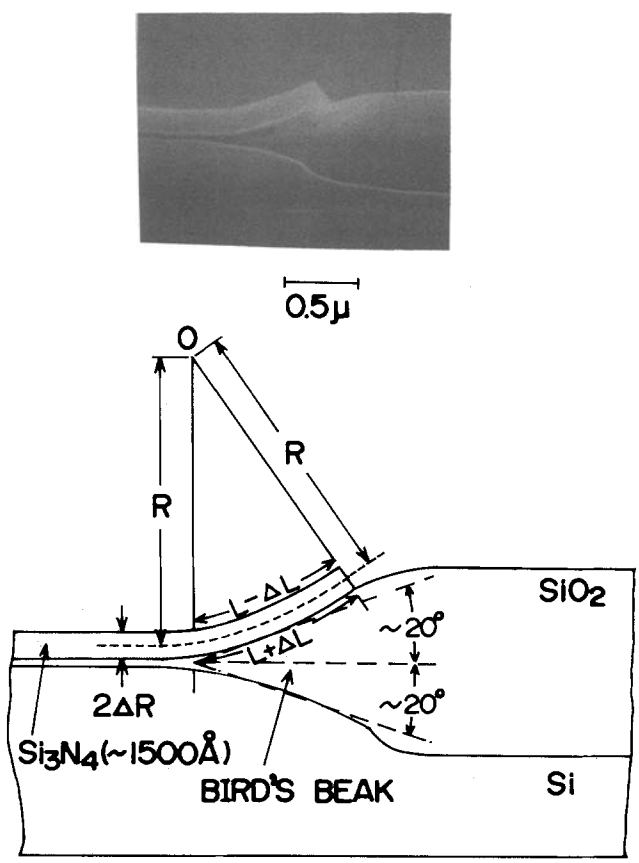

Fig. 8. Cross-sectional view of bird's beak and Si_3N_4 strain attributed to bird's beak. (a) Scanning electron micrograph. (b) A diagram used for roughly estimating Si_3N_4 edge expansion coefficient. The shape of the strained Si_3N_4 is approximated by a circular arc. The center of the circle is represented by O.

the order of 1 μm, as is seen from the figure. It is assumed that the top layer or the bottom layer of the strained Si_3N_4 film is under compressive or tensile stress, respectively. For the simple geometry in Fig. 8b, the strain on the top or bottom layer is given by

$$\Delta L/L = \Delta R/R \sim 0.05 \quad [9]$$

where $2\Delta R = 1500$Å and R is assumed to be ~ 1.6 μm. This value was used for the analysis given in the previous section. This value is only approximate, since the estimation is on the basis of the simple model illustrated in Fig. 8b.

The angle θ related to the triangular shaped bird's beak structure can be estimated from Fig. 8, and the value is $\sim 20°$. It must be noted that the influence of selective oxide thickness on the angle θ is relatively small. The value of 20° is used for the analysis described above.

Conclusions

Gate oxide defect detection after isolation and gate oxidations shows that small dimensions of the isolation oxide regions seem responsible for the gate oxide defects. The area of the regions is found to be smaller than 0.5 μm^2. SEM observation of submicron-size isolation oxide regions reveals that both the bird's beak extension and isolation oxide thickness are suppressed to a great degree. Masking Si_3N_4 films surrounding the submicron regions are inferred to have an important role in causing these phenomena. A simple model that combines isolation region dimensions, bird's beak suppression, and subsequent gate oxide defects was presented. Relatively good agreement between this model and experimental results was shown.

Acknowledgments

The authors are indebted to M. Kondo, E. Arai, K. Kiuchi, and Y. Yoriume for their encouragement, and to Y. Sakakibara for his contributions in electron beam direct writing. The helpful contributions of a number of colleagues in the High Density Integration Section of Musashino Electrical Communication Laboratory in the sample preparation are also gratefully acknowledged.

Manuscript submitted Sept. 17, 1982; revised manuscript received Jan. 24, 1983.

Any discussion of this paper will appear in a Discussion Section to be published in the December 1983 JOURNAL. All discussions for the December 1983 Discussion Section should be submitted by Aug. 1, 1983.

Publication costs of this article were assisted by Nippon Telegraph and Telephone Public Corporation.

REFERENCES

1. J. A. Appels, E. Kooi, M. M. Paffen, J. J. H. Schatorjé, and W. H. C. G. Verkuylen, *Philips Res. Rept.*, **25**, 118 (1970).
2. J. A. Appels and M. M. Paffen, *ibid.*, **26**, 157 (1971).
3. E. Bassous, H. N. Yu, and V. Maniscalco, *This Journal*, **123**, 1729 (1976).
4. I. Magdo and A. Bohg, *ibid.*, **125**, 932 (1978).
5. E. Kooi, J. G. van Lierop, and J. A. Appels, *ibid.*, **123**, 1117 (1976).
6. T. A. Shankoff, T. T. Sheng, S. E. Haszko, R. B. Marcus, and T. E. Smith, *ibid.*, **127**, 216 (1980).
7. O. Nakajima, N. Shiono, S. Muramoto, and C. Hashimoto, *Jpn. J. Appl. Phys.*, **18**, 943 (1979).
8. D. W. Ormond and J. R. Gardiner, *IBM J. Res. Dev.*, **24**, 353 (1980).
9. M. Itsumi and F. Kiyosumi, *This Journal*, **129**, 800 (1982).
10. C. A. Goodwin and J. W. Brossman, *ibid.*, **129**, 1067 (1982).
11. W. Kern and D. A. Puotinen, *RCA Rev.*, 187 (1970).
12. W. J. Shannon, *ibid.*, 431 (1970).
13. W. Kern, *ibid.*, 655 (1973).
14. Y. Sakakibara, T. Ogawa, K. Komatsu, S. Moriya, M. Kobayashi, and T. Kobayashi, *IEEE Trans. Electron Devices*, **ed-28**, 1279 (1981).
15. T. T. Sheng and R. B. Marcus, *This Journal*, **125**, 432 (1978).

Reactive Ion Beam Etching of $MoSi_2$ in CCl_4

R. A. Powell

Varian Associates, Incorporated, Corporate Solid State Laboratory, Palo Alto, California 94303

ABSTRACT

Dry etching of sputter-deposited $MoSi_2$ films using (RIBE) derived from a CCl_4 plasma is reported. The RIBE rates increase linearly with both ion current density (0.1-1 mA/cm²) and ion energy (0.4-1 keV) and are lower than those obtained using inert Ar^+ bombardment. Postdeposition annealing in Ar (900°C, 20 min) reduced the RIBE etching rate by ~15%. Profiles of etched $MoSi_2$/Si(100) samples are anisotropic (~5:1 aspect ratio), exhibit no undercutting of the Si under the silicide, and show only minimal trenching. Typical etching rate ratios of $MoSi_2$ to Si or SiO_2 are ~1:2.

The emergence of VLSI technology has led to the development of new materials and new processing techniques in IC fabrication. For example, it is widely appreciated that doped polysilicon, because of its limiting high resistivity, is not the optimal material for gate electrodes and interconnects in VLSI devices (1). As a replacement for polysilicon in these device applications, refractory metal silicides have attracted much attention (2). One of the most promising is $MoSi_2$ which has a sheet resistance about ten times lower than heavily doped polysilicon and can withstand high temperature oxidizing ambients. Already, gates of $MoSi_2$ and $MoSi_2/n^+$-polysilicon, *i.e.*, molycide gates, have been used in the fabrication of high performance NMOS and CMOS devices (3-6). In order to process devices such as these, a compatible dry etching technique capable of patterning $MoSi_2$ with submicron definition is required.

Key words: semiconductor, integrated circuits, etching.

Relatively little has been reported on dry etching of $MoSi_2$ or molycide structures; however, several dry etching techniques have been tried. These include plasma etching (barrel-type reactor) in CF_4/O_2 mixtures (4, 7, 8), plasma etching (planar-type reactor) in CF_4/O_2 (9) or in NF_3/Ar (8), and reactive ion etching (RIE) in CF_4/O_2 (4, 5) or SF_6/He (10) mixtures. Recently, a two-step dry process for patterning molycide gates was described (5), consisting of RIE of $MoSi_2$ in $CF_4/C_2F_6/O_2$, followed by RIE of the n^+-Si using CCl_2F_2/C_2F_6.

Reactive ion beam etching (RIBE) is a relatively new dry etch technique which offers a high degree of process flexibility (11, 12). In RIBE, unlike RIE, the ion energy and flux density can be independently

varied. In addition, the etching profile can be changed by varying the incident angle of the impinging ions. One also has some control over the contribution of ion-assisted gas-surface chemistry to the etch process. In this paper, we report the first use of RIBE to dry etch $MoSi_2$ films.

Experimental

$MoSi_2$ films were deposited by simultaneously S-gun™ sputtering Si and Mo onto 3 in. silicon (100) substrates using a Varian 3125 batch coater. Argon ($\sim 3 \times 10^{-3}$ Torr) was used to cosputter the disilicide from elemental Si and Mo targets. Prior to codeposition, the Si substrate was sputter etched in Ar to remove any native oxide. As-deposited films were ~2500Å thick and had a sheet resistivity of ~55 Ω/□. To reduce this resistivity in device applications, co-sputtered $MoSi_2$ films are normally postannealed (2). Therefore, selected samples were given a 900°C, 20 min furnace anneal in Ar, which reduced the sheet resistivity to ~5 Ω/□ and increased the average grain size to $\gtrsim$ 1000Å. Samples were spin-coated with 1.5 μm of AZ 1350J resist and photolithographically masked with a resolution test pattern. After dry etching, samples were cleaved and observed by scanning electron microscopy (SEM). With the resist stripped, step heights were measured with an interferometer or a profilometer, and etching rates determined.

Etching was carried out using a Varian Associates reactive ion beam etching system (Model RE-580) previously described in Ref. (11). The stainless steel vacuum chamber was diffusion pumped to a base pressure of $\sim 5 \times 10^{-7}$ Torr. Reagent-grade CCl_4 was introduced by a precision metering valve/mass-flow controller into a Kaufman-type ion source to achieve a stable d-c plasma discharge. A hollow cathode (Ion Tech Model HC-500) was used in place of the hot-wire filament typically used in Kaufman-type sources. Research-grade argon was flowed (~2 sccm) through the hollow cathode and a d-c Ar discharge established. Electrons were extracted from this inert gas discharge to establish a reactive CCl_4 discharge in the source.

CCl_4 flow rates were ~5 sccm, and chamber pressure during etching was $\sim 1\text{-}2 \times 10^{-4}$ Torr, as measured with a hot cathode ionization gauge. Ion beam diameter was ~15 cm at the source, with ~10° total beam divergence. The distance from extraction grids to sample was $\simeq$ 22 cm. Sample charging and beam divergence were minimized by injection of low energy electrons into the beam from a pair of tantalum neutralizing filaments. Incident ion current density (typically ~0.1-1 mA/cm²) was measured with a Faraday cup. Samples were clamped against a freon-cooled wafer platen, and argon flowed between the sample back surface and cooled platen to insure good thermal contact in the vacuum ($\sim 2 \times 10^{-4}$ Torr) ambient. This gas-assisted cooling allowed incident ion beam power densities of $\lesssim$ 1 W/cm² to be used without damage to the photoresist.

Results and Discussion

Before presenting data obtained using reactive ion beams, we first consider inert ion beam etching of $MoSi_2$. In Fig. 1, the etching rate of $MoSi_2$ under inert Ar^+ bombardment is presented as a function of ion beam energy from 400-1000 eV. To obtain this data, Ar gas was introduced directly into the Kaufman source instead of CCl_4. The sputtering rate (Å/min) was, as expected, proportional to incident Ar^+ ion current density (mA/cm²) and is, therefore, given in Fig. 1 in units of Å/min/mA/cm². The $MoSi_2$ etching rate is seen to increase with increasing ion energy above 400 eV and to level off above ~700 eV. From Fig. 1, the sputtering rate of $MoSi_2$ at 500 eV is 1000 Å/min-mA/cm², giving a sputtering yield of 1.9 atoms (either Mo or Si) per incident Ar^+ ion. By comparison, the sputtering yields of Si and Mo are much lower. From data supplied by manufacturers of ion beam milling equipment (13, 14), sputtering rates of Si and Mo under 500 eV Ar^+ bombardment (normal incidence) are in the range of 300-500 Å/min-mA/cm². Taking 400 Å/min-mA/cm² as a representative value, sputtering yields of Si and Mo at 500 eV are $\simeq$ 0.5 and 0.7 atoms/ion, respectively.

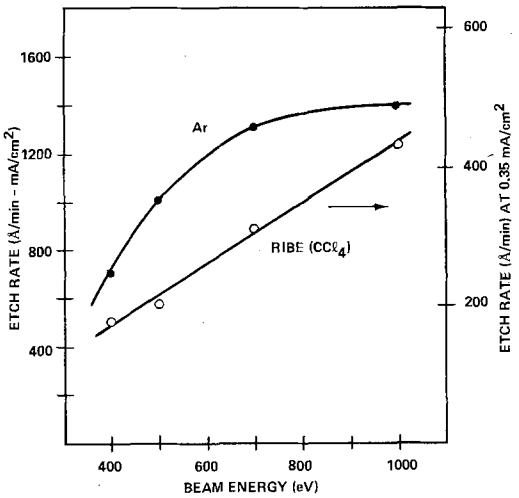

Fig. 1. Inert Ar^+ ion beam etch rate of $MoSi_2$ as a function of beam energy. The etching rate is normalized to incident ion current density. These data are also shown in comparison with RIBE data (CCl_4 plasma) taken at a constant ion current density of 0.35 mA/cm².

We now present data obtained from $MoSi_2$ under bombardment with ions extracted from a CCl_4 plasma. The predominant reactive ionic species extracted from a CCl_4 discharge in a Kaufman-type source are believed to be Cl^+ and Cl_2^+ (15); however, in the present case, some Ar^+ is probably present in the extracted beam as well. This inert ion component arises from (*i*) argon introduced directly into the ion source from the hollow cathode, and (*ii*) argon used for gas-assisted wafer cooling which leaks into the etching chamber, diffuses to the source extraction grids, and is ionized. In order to assess the influence of this inert ion component, RIBE was also carried out without gas-assisted cooling and with a hot-cathode electron source instead of a hollow cathode. With all argon, thus, removed from the system, RIBE rates at 500 eV were found to be nearly the same as before when argon was present.

In addition to reactive (Cl_2^+, Cl^+) and inert (Ar^+) ion bombardment, the sample also experiences a flux of neutral particles. This neutral flux is comprised of ambient gas molecules, CCl_4 and Ar, as well as free radicals which diffuse from the ion source through the graphite extraction grids, and, if suitably long-lived, reach the sample surface. The collective interaction of these energetic ions and neutral species with the sample surface, in the presence of visible and u.v. radiation from the ion source, determine the nature of the RIBE process.

Figure 2 presents etching rates of $MoSi_2$ under RIBE with CCl_4. Unlike the case of inert ion beam milling, RIBE rates do not, in general, scale with incident ion beam current density. Such nonlinear behavior has been observed in RIBE of both Si and SiO_2 using fluorocarbon gases CF_4, C_3F_8, and C_2F_6 (16). For this reason, the etching rates in Fig. 2 are plotted *vs.* ion current density at selected beam energies from 400-1000 eV. Data below $\simeq$ 0.1 mA/cm² could not be obtained due to unstable operation of the Kaufman source at low discharge currents.

The data in Fig. 2 suggest that the RIBE rate of $MoSi_2$ increases linearly with ion current density for energies in the range 500-1000 eV, although this is not as conclusive at 500 eV due to scatter in the data at low beam currents. The data shown in Fig. 2 were obtained from as-deposited $MoSi_2$ samples; however,

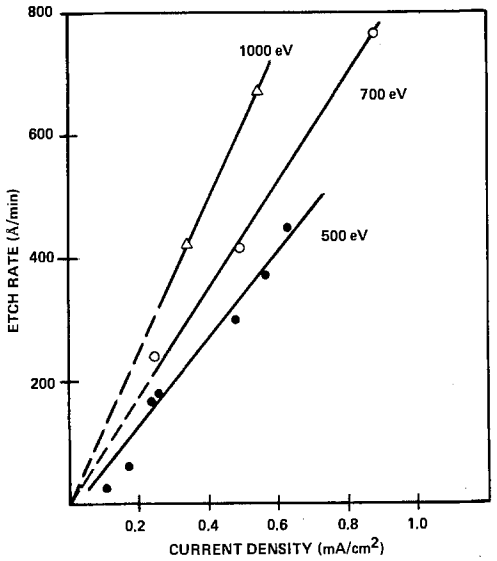

Fig. 2. RIBE rate of $MoSi_2$ as a function of incident ion current density for selected ion energies. The reactive ions are extracted from a CCl_4 d-c plasma discharge.

RIBE was performed as well on samples which were given a conventional furnace anneal (950°C, 20 min) following sputter deposition. For the beam energies employed (500-700 eV), the RIBE rate was found to decrease slightly (~15%) following a postanneal. Other workers have observed similar behavior using CF_4/O_2 plasma etching (barrel reactor) (7). They found that postdeposition annealing of sputtered $MoSi_2$ films decreased the dry etching rate slightly (~10-20%), a result which they connected with the amorphous-to-crystalline phase transition occurring during the annealing process.

RIBE data obtained at constant current densities (0.35 mA/cm²) from 400-1000 eV are compared in Fig. 1 with Ar^+ sputtering data at the same current density. The energy dependence of the inert and reactive ion beam etching rates are seen to be quite different with the RIBE rate increasing linearly with beam energy. This linear dependence of etching rate on beam energy is not a characteristic of RIBE *per se*, as studies of Si and SiO_2 RIBE etched in C_2F_6 demonstrate (6). Nevertheless, such behavior has been observed under RIBE conditions for a variety of etching gas/substrate combinations such as GaAs (17) and AlCu (4%) Si (1.5%) (11) etched in CCl_4, and Si or SiO_2 etched in C_3F_6 (16).

Figure 1 also shows that the removal rate of $MoSi_2$ under RIBE is suppressed relative to the Ar^+ sputtering rate. For example, at 500 eV the RIBE rate is lower by 40%. We note that this behavior was not observed in RIBE of either Mo or Si. In the case of Mo, both RIBE and Ar^+ sputtering gave comparable etching rates at 500 eV, while in the case of Si, the etch rate under RIBE was greater than that of Ar^+ by a factor of $\simeq$ 2. The suppressed RIBE rate of $MoSi_2$ may be the result of a protective coating (carbon?) which accumulates on the sample surface and impedes the formation of volatile reaction products. A possible source of such contamination is the interaction of the incident ion beam with CCl_4 at the sample surface or with hydrocarbons present in the diffusion-pumped vacuum chamber. This possibility is suggested by studies of Si etched in ion beams derived from fluorocarbon plasmas (16) (CF_4, C_2F_6, C_3F_8) in which the RIBE rate was suppressed from the Ar^+ ion milling rate, a fact attributed to carbon buildup on the Si surface by ion beam-enhanced decomposition of species such as CF_3^+.

At energies $\gtrsim$ 700 eV, the sputtering rate of $MoSi_2$ in Ar^+ is seen to level off while the RIBE rate continues to increase, possibly because at these energies, the removal rate of surface contamination by physical sputtering is increasing faster than its deposition rate.

Figure 3 presents SEM images of a patterned $MoSi_2$/Si(100) sample which has been RIBE etched in CCl_4 at 500 eV and 0.6 mA/cm². Etching has proceeded through the 2500Å $MoSi_2$ film and about 1 μm into the underlying Si substrate. The photoresist has been stripped before electron microscopy. Note that the etched profile displays good anisotropy (aspect ratio of ~5:1) with minimal trenching and no undercutting of the Si under the silicide. Lateral photoresist mask erosion during etching may have contributed to the slope of the etched profile (~11° from the vertical). At 500 eV and 1 mA/cm² incident ion beam current density, the RIBE rate of 1350J photoresist is $\simeq$ 600 Å/min, comparable to that of $MoSi_2$ and about half that of Si. Angular divergence of the incident ion beam may also have contributed to the etched sidewall profile.

Although refractory metal silicides by themselves have been used as gate metallizations, VLSI devices will probably use a multilevel polycide structure in which the silicide is deposited over a heavily doped polysilicon layer (1). With regard to $MoSi_2$, therefore, one must consider patterning an $MoSi_2/n^+$-polysilicon/SiO_2 structure. Ideally, the etching process should etch anisotropically both silicide and polysilicon layers with high selectivity relative to a thin (~200-400Å) gate

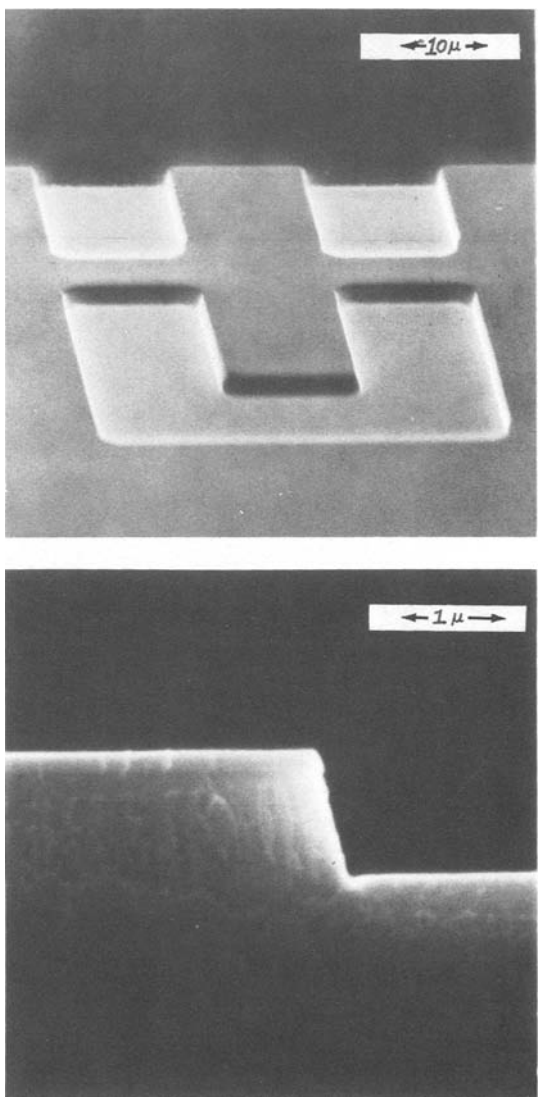

Fig. 3. SEM photographs of a sample consisting of a 2500Å $MoSi_2$ film over Si(100) which has been patterned, RIBE-etched (CCl_4, 500 eV, 0.6 mA/cm²), and cleaved. The 1350J photoresist was removed prior to electron microscopy.

oxide. In the past, RIBE has been shown capable of producing highly anisotropic features. For example, 0.5 μm diam contact windows have been patterned in 1 μm thick SiO_2 films using RIBE with C_2F_6 (16). The present results show that RIBE in CCl_4 can etch anisotropically an $MoSi_2$/Si structure with etched sidewalls having an aspect ratio of ~5:1. Although RIBE of heavily doped polysilicon was not carried out in the present experiments, anisotropic RIBE profiles of n^+-polysilicon have been observed by other workers (11, 16). In addition, the RIBE rate of heavily doped polysilicon is comparable to that of single crystal Si (16, 18).

Unfortunately, however, the selectivity of RIBE Si or doped poly-Si relative to SiO_2 with CCl_4 is not high. Using CCl_4 at 500 eV, *e.g.*, the etching rate of $MoSi_2$, is about half that of Si, while the etching rates of Si and SiO_2 are nearly equal. A calculation of the etching rate ratio of polysilicon-to-oxide required to pattern polycide gate structures in an MOS integrated circuit has been presented by Wang *et al.* (19). In like manner, we estimate this ratio for an $MoSi_2$ (1500Å)/polysilicon (1500Å)/SiO_2 (300Å) structure. We assume that the polysilicon and $MoSi_2$ films conformally coat the sloped, transition region of the adjacent thick field oxide, and that this sloped region makes a 30° angle to the horizontal. Film thickness and RIBE rate nonuniformities are taken as ±5% and ±2%, respectively. We also assume that one can tolerate 80% of the gate oxide's thickness being etched above the source and drain regions. A simple calculation (19) then gives the desired RIBE rate ratio of polysilicon-to-oxide as ~5:1, which is several times larger than observed in the present study.

As with other dry etching techniques, the selectivity of RIBE is influenced by a variety of parameters including: beam energy and current density, etching gas and gas mixture, ion source design, etc. For example, by using C_2F_6 instead of CCl_4 in RIBE, Si:SiO_2 etching rate ratios as low as 1:6 have been reported (16), while the use of $SiCl_4$ increases the ratio to ~3:1 (20). This latter value is still not sufficiently large for reliable etching of molycide structures in VLSI applications, and more work needs to be done to increase the selective etching of polysilicon over SiO_2. If such a reactive gas chemistry can be developed, however, RIBE then offers the attractive possibility of a one-step polycide etching process.

Summary

In summary, we have reported the first use of RIBE to etch $MoSi_2$ films. Using reactive ion beams extracted from a CCl_4 plasma, etching rates appear to increase linearly with both beam energy (400-1000 eV) and ion current density (0.1-1 mA/cm^2). These etching rates are lower than those obtained using inert Ar^+ bombardment and are lowered slightly more (~15%) by post deposition annealing of the cosputtered $MoSi_2$ films. RIBE etching was anisotropic with little evidence of trenching or other sputtering artifacts. Etching was not highly selective, however, and typical etching rate ratios of $MoSi_2$ to Si were about 1:2.

Acknowledgments

Useful conversations with R. L. Bell, R. T. Fulks, and D. Downey during the course of this work are gratefully acknowledged. D. Nichols deposited the $MoSi_2$ films described in this paper.

Manuscript submitted Sept. 27, 1982; revised manuscript received Dec. 27, 1982.

Any discussion of this paper will appear in a Discussion Section to be published in the December 1983 JOURNAL. All discussions for the December 1983 Discussion Section should be submitted by Aug. 1, 1983.

Publication costs of this article were assisted by Varian Associates, Incorporated.

REFERENCES

1. J. L. Vossen, *J. Vac. Sci. Technol.*, **19**, 761 (1981).
2. S. P. Murarka, *J. Vac. Sci. Technol.*, **17**, 775 (1980).
3. T. Mochizuki, K. Shibata, T. Inoue, and K. Ohuchi, *Jpn. J. Appl. Phys.*, **17-1**, 37 (1978).
4. T. Mochizuki, T. Tsujimaru, M. Kashiwagi, and Y. Nishi, *IEEE Trans. Electron Devices*, **ed-27**, 1431 (1980).
5. E. C. Whitcomb and A. B. Jones, *Solid-State Technol.*, **3**, 121 (1982).
6. T. P. Chow, A. J. Steckl, and R. T. Jerdonek, *IEEE Electron. Device Lett.*, **edl-3**, 37 (1982).
7. T. P. Chow and A. J. Steckl, *Appl. Phys. Lett.*, **37**, 466 (1980).
8. T. P. Chow and A. J. Steckl, in "Proceedings of the International Electron Device Meeting," p. 149, Washington, DC, Dec. 8-10, 1980.
9. S. Inoue, N. Toyokura, T. Nakamura, and H. Ishikawa, in "Proceedings of the International Electron Device Meeting," p. 152, Washington, DC, Dec. 8-10, 1980.
10. W. Beinvogel and B. Hasler, Abstract 233, p. 586, The Electrochemical Society Extended Abstracts, Vol. 81-1, Minneapolis, Minnesota, May 10-15, 1981.
11. D. Downey, W. R. Bottoms, and P. R. Hanley, *Solid-State Technol.*, **2**, 121 (1981).
12. B. A. Heath, *ibid.*, **2**, 75 (1981).
13. Ion Tech. Incorporated, Ft. Collins, CO.
14. Commonwealth Scientific Corporation, Alexandria, VA.
15. D. Downey, Private communication.
16. B. A. Heath, *This Journal*, **129**, 396 (1982).
17. R. A. Powell, *Jpn. J. Appl. Phys.*, **21**, L170 (1982).
18. D. F. Downey, "Reactive Ion Beam Etching for VLSI Device Fabrication," Varian Associates, Semiconductor Equipment Operations Report No. 18, January 1982.
19. K. L. Wang, T. C. Holloway, Z. P. Sobczak, W. R. Hunter, and A. F. Tasch, Jr., *IEEE Trans. Electron Devices*, **ed-29**, 547 (1982).
20. S. Matsuo and Y. Adachi, *Jpn. J. Appl. Phys.*, **21**, L4 (1982).

Phosphorus Depth Profiles in Thermally Oxidized P-Doped Polysilicon

C. C. Chang, T. T. Sheng, and T. A. Shankoff

Bell Laboratories, Murray Hill, New Jersey 07974

ABSTRACT

Phosphorus concentrations in the oxide and in the poly-Si after thermal oxidation of heavily phosphorus-doped poly-Si were investigated using Auger analysis. Dry oxides were found to contain less phosphorus than steam oxides grown to the same thickness using commonly utilized oxidation temperatures. If the first dry oxide was etched off and a second dry oxide was grown, the second oxide contained less phosphorus than the first. The phosphorus concentrations in the oxide and poly-Si were qualitatively consistent with the present theory of the phosphorus segregation coefficient for single crystal silicon. Based on these results, the merits of several schemes for minimizing the P content in the oxide are discussed.

The phosphorus content of thermal oxides grown from heavily phosphorus-doped polycrystalline silicon (poly-Si) was investigated for applications in integrated circuit processing. These thermal oxides have many uses; for example, as mask oxide for patterning the poly-Si, or as an intermediate dielectric. Control of the phosphorus content in the oxide is important for photoresist adhesion and line definition, as well as for providing inter-level oxides with optimum dielectric properties. For example, the oxide and poly-Si etch rates depend on the phosphorus concentration. It is in general desirable to grow oxides on poly-Si with the lowest possible phosphorus content so as to take advantage of the excellent dielectric, chemical, and other properties of pure SiO_2.

We begin by briefly examining transmission electron microscope (TEM) pictures of two level poly-Si structures that demonstrate the importance of the dielectric properties of the oxide. Then, measurements of the phosphorus concentrations in the oxide and poly-Si are described. These measurements were carried out using Auger spectroscopy combined with ion milling.

It is not possible to provide a straight forward quantitative analysis of the phosphorus concentration in SiO_2 using Auger spectroscopy for the low concentrations encountered in this work. This difficulty is examined in some detail below because there is little discussion of this subject in the literature. For this work, a special technique was devised to circumvent this problem.

Experimental

The samples studied are listed in Table I. Sample 1 is an integrated circuit code (a charge coupled device, or CCD) requiring two levels of poly-Si, which was processed up to "P-glass flow" (see bottom of table). This sample was examined by transmission electron microscopy.

Samples 2 and 3 of the table were also wafers with device chips that were processed up to the deposition of the first level poly-Si, phosphorus doping, and 15:1 H_2O:HF etch (to remove the phosphorus-rich oxide grown during doping). All the phosphorus dopings of this work were accomplished by heating the wafers in a furnace at 950°C for 30 min with flowing PBr_3 mixed with a carrier gas (N_2, O_2, mixture). The PBr_3 was introduced by flowing N_2 gas through a PBr_3 bubbler at 30°C. After removing the surface P-glass, the samples were then given a single or a double dry oxidation to grow about 700Å of oxide for each oxidation. These were used for evaluating the effects of the first and second dry oxidations on the phosphorus distribution in the oxide and in the poly-Si.

Samples 4 and 5 are oxidized Si wafers on which poly-Si was deposited, then doped with phosphorus, and then oxidized, as detailed in Table I. These were studied to compare the phosphorus concentrations in steam and dry oxides.

TEM pictures were obtained from thin cross-sections of device samples cut perpendicular to the plane of the wafer. Details of the sectioning technique are reported elsewhere (1, 2).

The methods and instrumentation for Auger spectroscopy have been previously reviewed (3). The apparatus used in this work was a (Varian) cylindrical mirror analyzer with energy resolution of 0.25% and equipped with a 10 keV integral electron gun. Data were acquired in the "derivative" mode using incident electron currents near 10 μA and a-c modulation of 2-5 eV (peak-to-peak). Chemical depth profiles were generated by measuring the surface composition with Auger spectroscopy while simultaneously ion milling the surface with a (Varian) Ar ion gun operated at 2 keV. The ion and electron beams were mutually perpendicular, and both were at 45° with the sample surface normal. Ion milling rates of about 200Å/min were used.

Measurement of the phosphorus content of oxides on silicon using Auger analysis is at best difficult above about 1 atomic percent (a/o) and effectively impossible below 1 a/o, because both the electron beam used for Auger excitation and the ion beam used for milling (to obtain the depth profiles) cause movement of phosphorus within the oxide, and they decompose the P-oxide (4, 5). These problems are aggravated when different oxides must be examined, because these artifacts are dependent on the dielectric and chemical properties of the oxide.

An example of the electron bombardment induced artifact is presented in Fig. 1. The incident electron current was 20 μA over an area 100 microns diam. Note the rapid initial increase in the surface phosphorus concentration caused by electron irradiation. The phosphorus peak monitored is the peak for elemental phosphorus so that not only is the phosphorus

Table I. List of samples

Sample No.	Sample preparation			
1	CCD code (two level poly-Si), processed to P-glass flow.*			
2	n-MOS code processed to poly-Si doping with phosphorus and first oxidation (1000°C, 40 min, dry oxygen, ≅700Å).			
3	Different wafer from lot of sample 2, after first oxide strip and second oxidation (1000°C, 40 min, dry oxygen, ≅700Å).			
	Phosphorus doping (°C, min)	Sheet resistance (Ω/sq)	Thermal oxidation (°C, min)	Oxide thickness (Å)
4	1000, 35	15	1000, 90, dry	1045
5	950, 45	44	950, 12, steam	1025

* P-glass is highly P-doped SiO_2; it is "flowed" at high temperature (about 1100°C) to smooth out the top contour of the IC chip in order to reduce the step coverage problems with subsequently deposited layers.

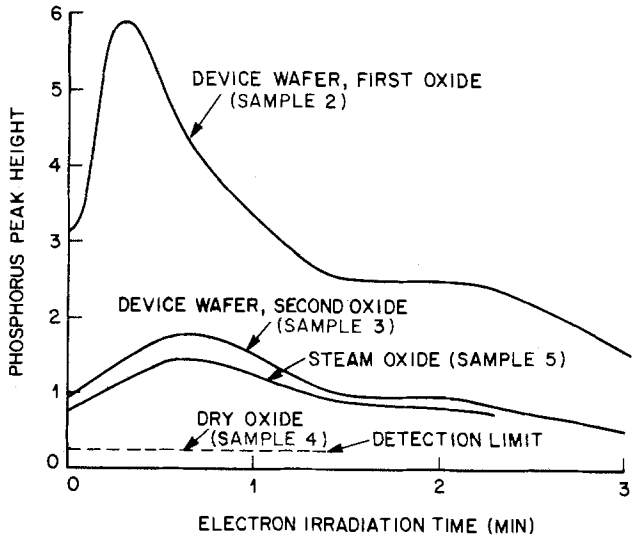

Fig. 1. Variation of the phosphorus Auger signal from the oxide surface during irradiation by the electron beam used for Auger analysis.

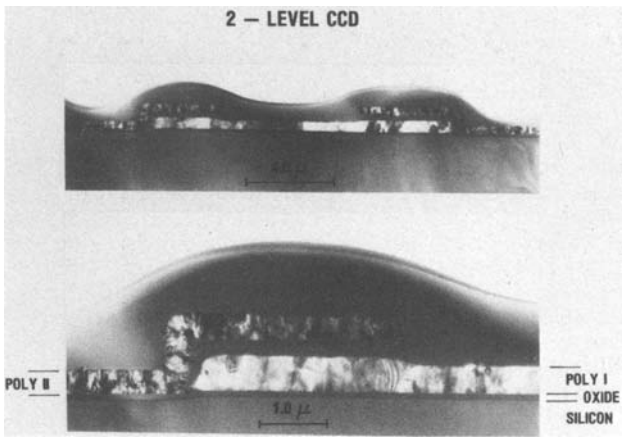

Fig. 2. Transmission electron micrograph of two-level poly-Si structure, sample 1. The lower micrograph is a magnified photograph of another part of the same chip, showing an area corresponding to the left side hump in the upper picture. Note the regions of thin oxide and sharp poly-Si protrusions.

brought out to the surface, but it is also reduced to elemental form. The mechanisms behind these surface processes are complex and not well understood. Chemical reduction can occur because electron and ion irradiations readily break chemical bonds, enabling oxygen molecules to form and diffuse out of the oxide (6, 7). These irradiations also create high densities of energetic phonons, as well as vacancies and interstitials, so that rapid diffusion processes become possible with no intentional heating (8). Moreover, the electron and ion beams create sheets of charge near the surface that can attract or repel variously charged species in the oxide. The Auger spectra from P in SiO_2 have already appeared in the literature (5).

In Fig. 1, the apparent surface phosphorus concentration eventually begins to decline with continued electron irradiation. We propose that this decline is due to electron stimulated desorption of some phosphorus containing species; *i.e.*, as the phosphorus is depleted from the oxide, the accumulation rate decreases and eventually becomes smaller than the desorption rate.

For this work, a simple method of monitoring the phosphorus concentration in the oxide was devised by turning the accumulation problem discussed above to advantage. This phenomenon in fact offers the possibility of extracting a large fraction of the phosphorus from the oxide and concentrating it on the surface, thus greatly increasing the sensitivity and at the same time eliminating the need for ion-mill depth profiling. Therefore, the amounts of phosphorus in the various oxides studied here were compared by measuring the phosphorus outdiffusion to the surface upon electron irradiation, and assuming that the amount diffusing to the surface is approximately proportional to the overall phosphorus content of the oxide. This assumption should be valid provided the qualities of the oxides are not very different, and their thicknesses are comparable (as they are here).

Results

TEM analysis.—An example of a two-level poly-Si CCD structure demonstrating the critical nature (9) of the poly-Si and dielectric geometries is displayed in Fig. 2. This is a TEM micrograph of a thin cross-section cut perpendicular to the plane of the chip. The first level poly-Si is the structure with the larger crystallite grain size (it received a more extensive heat-treatment). Note, incidentally, the well-rounded contour of the flowed P-glass above the poly-Si. The lower photograph is a magnified picture which reveals the sharp poly-Si projections and apparent thin spots in the isolation oxide separating the two levels. Obviously, any weakness in the oxide at these locations will be a potential reliability problem in the finished device.

Analysis of the phosphorus content.—The major results of this work were obtained by measuring the amounts of phosphorus that diffused to the surface of the thermally grown oxides during electron irradiation. Results from two experiments are displayed in Fig. 1. The first experiment compares the phosphorus outdiffusion from steam and dry oxides (samples 4 and 5). The second compares the phosphorus outdiffusion rates for the first and second dry oxides (samples 2 and 3).

Comparison of data from samples 4 and 5 in Fig. 1 shows that more phosphorus outdiffuses to the surface for the steam oxide than for the dry oxide. If we assume that the phosphorus outdiffusion kinetics are similar for steam and dry oxides, we can conclude from these data that the steam oxide contains more phosphorus. Although we have not determined the relative outdiffusion rates for steam and dry oxides, we demonstrate below that rapid phosphorus outdiffusion, comparable to that observed for the steam oxide, does also occur for dry oxides, if the phosphorus concentration in the dry oxide is sufficiently high.

The phosphorus content in the poly-Si has also been measured in this work and is shown in Fig. 3 and 4. There are no known electron or ion induced artifacts

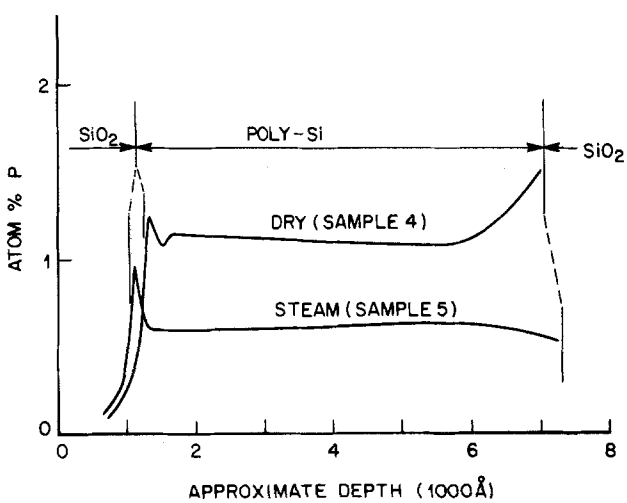

Fig. 3. Phosphorus depth profile through samples 4 and 5

with the determination of phosphorus in poly-Si, as there are for SiO_2. In Fig. 3, we demonstrate that the phosphorus content in the poly-Si of sample 4 is about twice that in sample 5. This difference is due to the higher phosphorus doping temperature used for sample 4 (see Table I). Note how the phosphorus concentrations in the poly-Si (Fig. 3) correlate quite nicely with the sheet resistivities given in Table I. In spite of the higher phosphorus content in the poly-Si film of sample 4, the subsequently grown dry oxide exhibited no detectable phosphorus outdiffusion (Fig. 1); whereas the phosphorus outdiffusion was easily detectable on the steam oxide of sample 5. This observation reinforces our conclusion that steam oxides contain more phosphorus than dry oxides.

The phosphorus outdiffusion comparison for the first and second dry oxidations can be made by reference to the top two curves of Fig. 1 (samples 2 and 3). It is clear that there is more phosphorus in the first dry oxide than in the second. Measurements of the oxide thicknesses from Fig. 4 show that the first oxide (750Å) is thicker than the second (650Å). Thus the oxidation rate of poly-Si with higher phosphorus content is faster (10).

The phosphorus depth profiles in the poly-Si, presented in Fig. 3 and 4, reveal some additional useful information. First, the phosphorus concentrations in the oxide are much lower than in the poly-Si and the data are consistent with published values of the phosphorus segregation coefficient (11) of about 10. This appears to hold in spite of the different degrees to which the phosphorus "pile-up" effect causes the phosphorus to accumulate near the oxide/silicon interface.

Second, this pile-up effect is clearly evident; it is caused only partly by the large value of the segregation coefficient (12). How this excess phosphorus is distributed along the plane of the oxide-Si interface is not known. If this distribution is uneven, *i.e.*, the phosphorus concentrations are locally higher over the poly-Si grain boundaries, then the local oxidation rate and phosphorus concentration will depend strongly on the grain structure of the poly-Si.

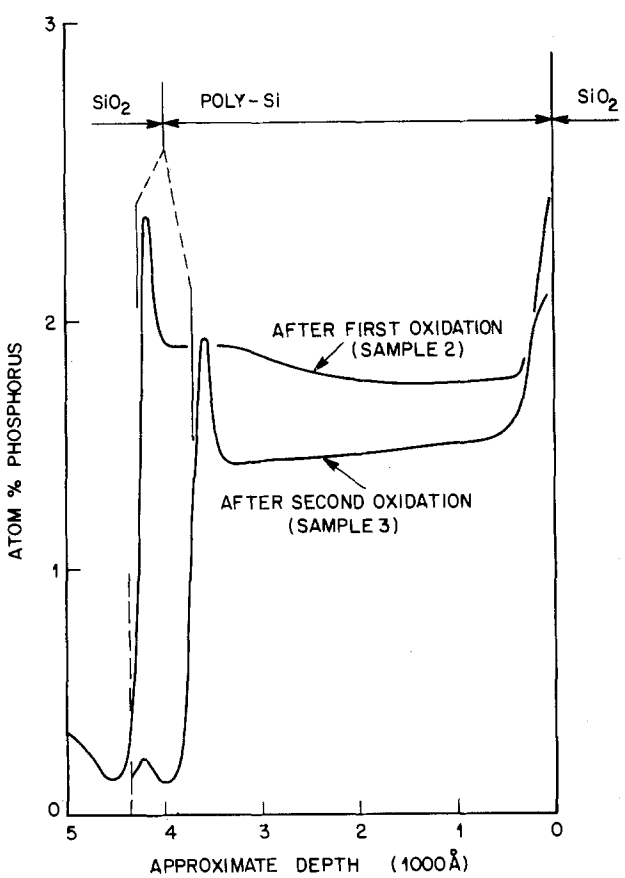

Fig. 4. Phosphorus depth profile through samples 2 and 3

Note that in Fig. 3 and 4, the phosphorus profiles are essentially flat within the poly-Si. That is, the phosphorus indiffusion is not limited by the diffusion rate in the poly-Si (as it partially is, in the case of single crystal silicon), but by some limiting process at the poly-Si surface. The flatness of the profiles is also due at least in part to the relatively fast diffusion of phosphorus along the poly-Si grain boundaries, compared to the diffusion within each grain.

Discussion

We have found that the second oxide grown on phosphorus doped poly-Si contains less phosphorus than the first. Therefore, photoresist adhesion should be better, and the etch rate slower, for the second oxide.

Our explanation for the high phosphorus concentration in the first oxide is as follows. During phosphorus doping, the poly-Si surface is in direct contact with a P-glass that has high phosphorus content. Therefore, a phosphorus-rich skin forms on the poly-Si. Initial oxidation of this layer produces an oxide with high phosphorus concentration. As oxidation proceeds, some of the accumulated phosphorus is driven into the poly-Si so that the extent of accumulation decreases, leading to a lower phosphorus concentration in the second oxide. This explanation for the difference in phosphorus concentration between the first and second dry oxide leads to the conclusion that a third oxidation after second oxide strip will not result in a further reduction of the phosphorus concentration in the oxide. In fact, successive oxidations will cause the phosphorus concentration in the poly-Si to rise because of the large segregation coefficient of phosphorus. This increase occurs also because phosphorus diffusion in SiO_2 is much slower than in silicon near 1000°C (13), so that the rate of phosphorus loss from the oxide during oxidation should be negligible. We conclude that the double dry oxidation process produces one of the best oxides on poly-Si.

The results of this work allow us to consider alternative methods (for which we present no experimental data in this report) to the double dry oxidation process for reducing the phosphorus content in the oxide. One approach is to remove some poly-Si by a chemical etch. This method has the advantage that it is not required to "fight" the large phosphorus segregation coefficient encountered in oxidation, and in fact should preferentially remove phosphorus-rich poly-Si regions. In addition, there is no "piled-up" phosphorus in the poly-Si surface region after a chemical etch. Therefore, during subsequent oxidation, phosphorus must be resupplied to the interface to create a new pile-up layer; this process should further reduce the phosphorus concentration in the growing oxide. The chemical etch method is also simpler than thermal oxidation and can be used to remove any amount of poly-Si, but does not have the extra cleaning effect and uniform removal property of double oxidation. It might appear that a first steam oxidation and strip should be more effective for reducing the phosphorus in the second oxide than a first dry oxidation and strip, because of the larger amount of phosphorus incorporated into the first oxide. However, the effectiveness of this approach may depend on the extent of phosphorus pile-up for the two methods of oxidation, and Fig. 3 suggests that the pile-up may be greater after steam oxidation. Thus, whether first steam or dry oxidation is more beneficial may well depend on the exact time and temperature of that first oxidation.

In Fig. 1, there is an apparent contradiction against our conclusion that steam oxides contain more phosphorus than dry oxides, because the curves for sam-

ples 2 and 3 (dry oxides) show more phosphorus outdiffusion than for the steam oxide of sample 5. The most important factor responsible for this apparent contradiction is the higher phosphorus concentration in the poly-Si of samples 2 and 3, compared to that of sample 5 (see Fig. 3 and 4). Therefore, the exact phosphorus concentration in the poly-Si can exert a disproportionately large influence on the phosphorus concentration in the oxide. We speculate, on the basis of the data of Fig. 3 and 4 and other data not discussed in this work, that there is a critical phosphorus concentration in the neighborhood of 1 a/o above which this disproportionate influence is observed. The critical concentration may be related to the onset of extensive grain boundary segregation of phosphorus that takes place when the solid solubility limit of P in Si is exceeded. These possibilities are obviously important points to consider when attempts are made to control the phosphorus concentration in the oxide.

Our observation of the higher phosphorus concentration in steam oxides compared to dry oxides grown on similarly prepared poly-Si can be explained on the basis of the faster oxidation rate in steam (see the oxidation times in Table I). Thus, our results are consistent with established segregation theory (11).

Conclusions

The steam oxides of this work contained more phosphorus than dry oxides grown to the same thickness on similarly prepared phosphorus-doped poly-Si.

The first dry oxide grown on phosphorus-doped poly-Si contained more phosphorus than the second dry oxide grown after etch removal of the first oxide. Thus, the double dry oxidation method results in minimal P concentration in the oxide. We suggest two alternative methods for reducing the P content in the oxide: (*i*) chemical etching of the first few hundred angstroms of the poly-Si followed by dry oxidation, and (*ii*) steam oxidation followed by dry oxidation. The advantages and disadvantages of all three methods were discussed.

The phosphorus depth profiles in the oxide and poly-Si are qualitatively consistent with the segregation theory developed for single crystal silicon.

Acknowledgments

The authors are grateful to A. K. Sinha and R. B. Marcus for their assistance in carrying out this work.

Manuscript submitted May 1, 1980; revised manuscript received April 28, 1981.

Any discussion of this paper will appear in a Discussion Section to be published in the December 1983 JOURNAL. All discussions for the December 1983 Discussion Section should be submitted by Aug. 1, 1983.

Publication costs of this article were assisted by Bell Laboratories.

REFERENCES

1. T. T. Sheng and C. C. Chang, *IEEE Trans. Electron Devices*, **ed-23,** 531 (1976).
2. T. T. Sheng and R. B. Marcus, *This Journal*, **127,** 737 (1980).
3. C. C. Chang, in "Characterization of Solid Surfaces," P. F. Kane and G. B. Larrabee, Editors, Chap. 20, Plenum Press, New York (1974).
4. C. C. Chang, A. C. Adams, G. Quintana, and T. T. Sheng, *J. Appl. Phys.*, **45,** 252 (1974).
5. G. Queirolo and G. Pignatel, Paper 343 presented at The Electrochemical Society Meeting, Los Angeles, CA, Oct. 14-19, 1979.
6. B. A. Joyce and J. H. Neave, *Surf. Sci.*, **34,** 401 (1973).
7. M. Kaminsky, in "Atomic and Ionic Impact Phenomena on Metal Surfaces," p. 151, 218, Academic Press, New York (1965).
8. J. R. Lloyd and S. Nakahara, *Thin Solid Films*, **45,** 441 (1977).
9. A. K. Sinha, T. T. Sheng, T. A. Shankoff, W. S. Lindenberger, E. N. Fuls, and C. C. Chang, in "Proceedings of the 17th IEEE Reliability Physics Symposium," p. 35, San Francisco, CA (1979).
10. C. P. Ho and J. D. Plummer, *This Journal*, **126,** 1516 (1979).
11. A. S. Grove, "Physics and Technology of Semiconductor Devices," p. 72, 74, John Wiley and Sons, New York (1967).
12. S. A. Schwarz, C. R. Helms, W. E. Spicer, and N. J. Taylor, *J. Vac. Sci. Technol.*, **15,** 227 (1978).
13. A. S. Grove, "Physics and Technology of Semiconductor Devices," p. 39, John Wiley and Sons, New York (1967).

Ion Beam Processing Using Metal on Polymer Masks

E. L. Hu, R. E. Howard, P. Grabbe, and D. M. Tennant

Bell Laboratories, Holmdel, New Jersey 07733

ABSTRACT

We describe the use of multilayer metal-on-polymer stencils as masks for reactive ion etching (RIE) and ion implantation. The thin metal film allows deep features to be transferred into the substrate during etching, or acts as a high contrast mask during ion implantation. The underlying polymer allows the clean removal of the stencil in organic solvents which do not attack the substrate. When combined with E-beam lithography, the method is capable of extremely high resolution. We show examples of submicron features transferred into Si and GaAs using these masks.

Ion beam processes such as reactive ion etching (RIE) ion beam lithography, and ion implantation are integral parts of current semiconductor device fabrication. More emphasis has been placed on these techniques as more stringent requirements are set on reduced device dimensions, linewidth accuracy, and alignment tolerance. Pattern stencils to be used in ion processing should be capable of replicating high resolution features, be durable, and be easily removed without damaging the substrate.

We have designed multilevel metal-on-polymer (MOP) masks that satisfy the above requirements. E-beam patterned MOP's have been used as masks for transferring ~200 nm features into GaAs and Si substrates by RIE. MOP stencils incorporating Au metal have been successfully used as masks for selective area proton bombardment of InGaAs, as well as for As implants into silicon. In all cases, the stencils were cleanly and easily removed after use without damage to the underlying substrate.

Though typical polymer resists are easily applied, patterned, and removed without damage to the substrate they mask, they are often unsatisfactory for use as high resolution masks. For ion etching applications, the relatively high etching or sputtering rate of the polymers makes it difficult to obtain etched structures having high aspect ratios. For ion implantation, the low ion stopping power of polymers neces-

sitates very high aspect ratio masks for submicron features. Both of these problems can be eliminated by replacing the polymer masks with thin metal layers. Fine-grained films of NiCr alloys have etch rates between 10-100 times slower than semiconductors such as Si or GaAs (1). High density metals such as Au have stopping powers for high energy ions at least 10 times larger than polymers and are in this respect much better than SiO_2 as masks for ion implantation. Difficulty may arise in removing metal masks that have been deposited directly on the substrate, without damaging the substrate itself. The MOP technique we describe combines the resolution and durability of the metal film masks with the easy removal of the polymer stencils.

The MOP technique is especially attractive for III-V semiconductor applications where projected ion ranges (2) are short, requiring higher implant energies. The correspondingly thicker masking material, usually resist, SiO_2, or Si_3N_4, must have high aspect-ratio edge profiles to insure sharp edged implant profiles. These geometries can be difficult to control and will ultimately limit the minimum implant feature that may be patterned. Thin high stopping power materials (*e.g.*, high density metals) can be patterned with much higher resolution, rendering edge effects unimportant. As a specific example, consider a $^{14}Si^+$ implant in GaAs. An implant energy of 300 kV is needed to provide a peak impurity concentration at 0.25 μm below the substrate surface. Typically, the mask for such an implant must be sufficiently thick that it extends 3σ beyond the concentration peak (where σ is the standard deviation of the gaussian implant distribution). This masking can be accomplished by using 1.9 μm of resist, 0.6 μm of SiO_2, 0.44 μm of Si_3N_4, or 0.3 μm of Au. Among these, the patterned metal is the most promising for submicron device fabrication, yet only the resist is easily removed without attacking the substrate. However, by depositing this metal on a thin polymer layer, this high resolution option is retained even when the mask metal is not appropriate for the final device configuration.

We describe here the process sequence for the fabrication of an optical and E-beam MOP mask. In both cases, the initial layer spun on is polyimide, a high glass temperature (320°C) polymer (3). This is useful in maintaining pattern integrity, and ensuring clean resist removal under processing conditions of high local heating (4) (for example, due to high local incident ion flux). In the case of the optical MOP, the polyimide was spun on to a thickness of 0.3 μm and baked at 160°C for 1 hr. 1.3 μm of positive photoresist, AZ1350J (5) was spun on top of the polyimide and baked at 70°C for 30 min. Since the solvents of the polyimide and AZ1350J are dissimilar, there is no need of an intermediate layer to prevent interdiffusion of the two resists. The resist is exposed in the desired pattern, and an undercut profile developed in the upper layer optical resist using a chlorobenzene hardening process (6). A blanket exposure is given to the resist and a metal film thermally evaporated through the openings in the upper resist layer. The undercut profile of the optical resist facilitates clean liftoff of the evaporated metal film. Liftoff is achieved by soaking the sample in AZ developer to dissolve the fully exposed upper layer of resist, leaving the underlying polyimide intact. The MOP stencil is completed by RIE in an oxygen plasma to transfer the resist pattern into the polyimide layer. The use of RIE here allows control of the profile of the lower layer polymer and maintains the resolution of the original pattern.

The top of Fig. 1 is an SEM micrograph of a MOP stencil atop a GaAs substrate. The stencil is comprised of ~60 nm Ni(Cr) on 0.3 μm polyimide. The substrate was subsequently etched in a mixture of

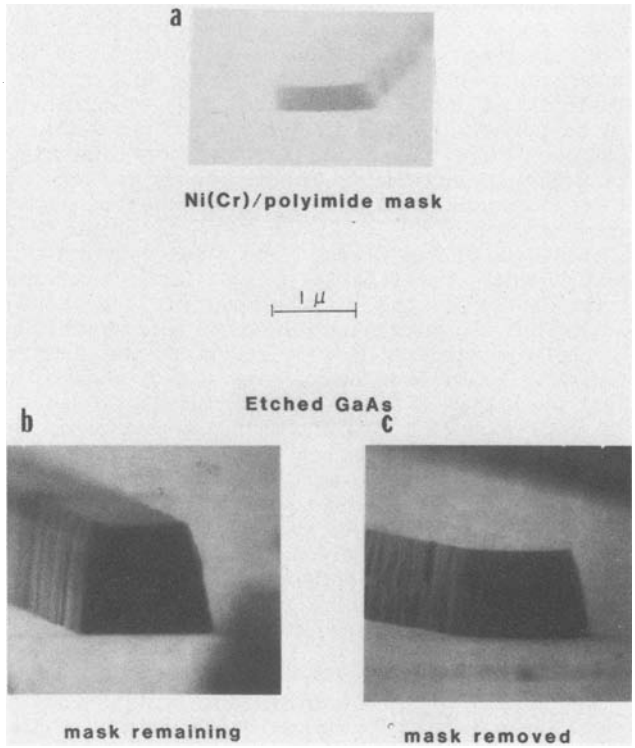

Fig. 1. (a) MOP stencil on GaAs substrate. (b) Etched GaAs pedestal with MOP mask in place. (c) Etched pedestal after removal of MOP mask.

CCl_2F_2, argon, and oxygen (7), and the resulting etched feature with the MOP mask remaining is shown in the lower left portion of Fig. 1. Note that the MOP stencil remains in excellent condition after etching the GaAs to a total depth of approximately 1 μm. The final micrograph of Fig. 1 shows the clean GaAs structure after removal of the MOP stencil.

We are interested in using the E-beam patterned MOP's to produce lateral features much finer than those obtained with the optical MOP's. Accordingly, the total thickness of the resist stencil must be thinner to avoid unreasonably high aspect ratios that would prevent the achievement of good liftoff metal patterns. For these stencils, the initial layer of polyimide was spun on to a thickness of ~0.2 μm, and then baked at 200°C for 1 hr. The "upper layer" resist in this case is actually a high resolution E-beam bilevel resist that has been previously described (8). The bilevel comprised approximately 100 nm of polymethylmethacrylate (PMMA) atop 200 nm of a copolymer of methylmethacrylate and methacrylic acid [P(MMA-coMAA)]. The E-beam patterns were written at 30 keV using an SEM; an undercut pattern was developed into the bilevel using a 3:7 solution of cellosolve:methanol. A 5 nm layer of Cr and a 30 nm layer of Ni(Cr) were evaporated through the stencil, the unwanted portions of the mask were, then, lifted off by immersion in acetone, and the stencil completed, as for the optical MOP, by RIE in O_2. Figures 2 and 3 show fine structures etched into Si and GaAs substrates, respectively, using the E-beam MOP's as masks. The Si patterns were formed by RIE in CF_3Br at 30 mTorr pressure and 400V bias, and the GaAs patterns were etched in a CCl_2F_2/Cl_2 gas mixture at 5 mTorr pressure and 150V bias voltage.

Figure 4 shows an optically patterned MOP used as a mask for ion implantation. The three scanning electron micrographs illustrate the major processing steps used to form the MOP implant mask. The top micrograph shows the undercut resist profile with the evaporated metal films (Cr/Au/Cr) cleanly broken across the edge. The thin top layer of Cr is used to prevent sputtering of the Au mask. The middle micro-

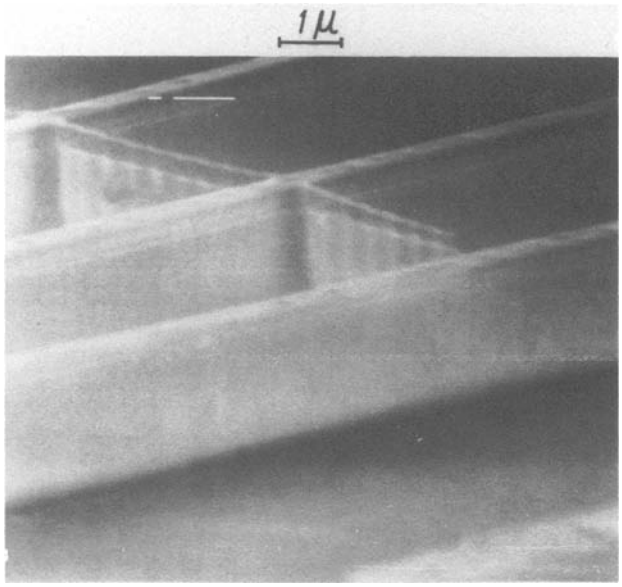

Fig. 2. Patterns etched in silicon using RIE in CF_3Br plasma through an E-beam defined MOP mask.

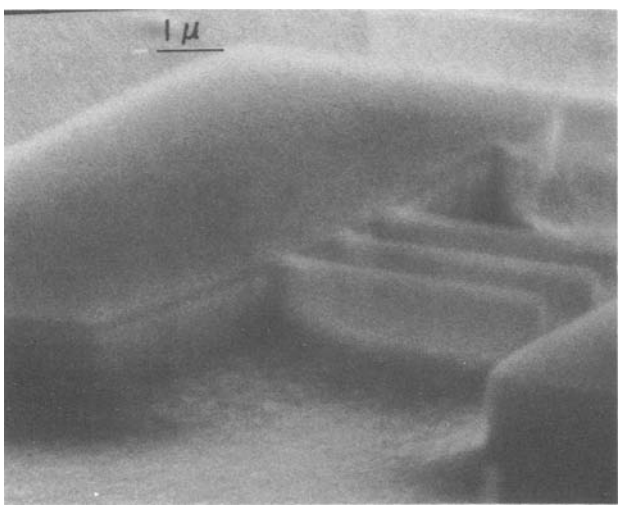

Fig. 3. Patterns etched in GaAs using RIE in a $CCl_2F_2/Ar/O_2$ plasma through an E-beam defined MOP mask.

graph shows the metal pattern on the thin polyimide layer. The bottom micrograph shows the completed MOP profile after reactive ion etching the polyimide in the exposed areas.

The MOP structures form easily applied and easily removed implantation masks that are useful for a wide variety of material substrates. The control of the stencil profile, achieved using RIE, allows potentially greater control of the implantation profile. By using a thin highly absorbing gold film atop of a fairly thin resist layer, the total thickness of the implantation mask can be kept thin enough to allow fine lateral features without having the aspect ratio of the mask so large that it promotes excess ion scattering.

Metal films offer greatly improved contrast over polymer films for application to processes like ion implantation and RIE. MOP masks combine these features with the ease of removal of polymer layers. High-aspect-ratio etching and high contrast masking

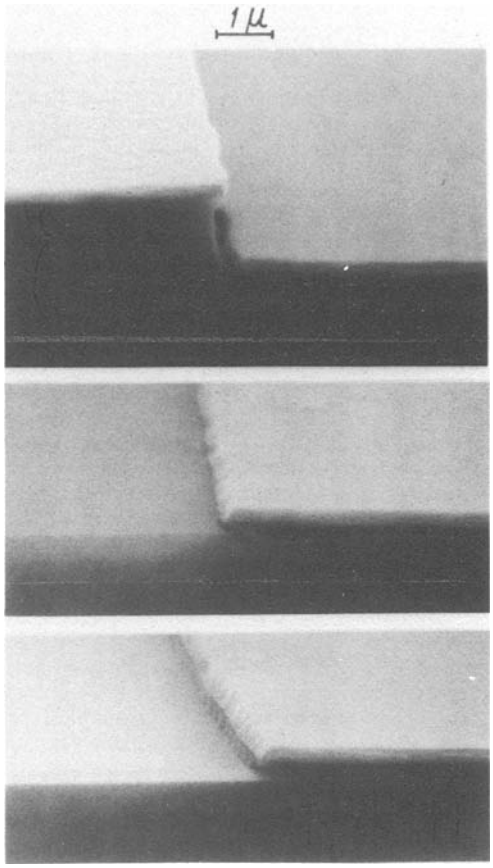

Fig. 4. Steps in formation of (Cr/Au/Cr)-on-polyimide MOP mask for ion implantation. (a) Undercut resist profile with evaporated metal broken cleanly across resist edge. (b) Metal pattern on polyimide layer. (c) Completed MOP stencil, after RIE of polyimide.

for ion implantation have been demonstrated using this process.

Acknowledgment

We wish to thank J. M. Moran for supplying the polyimide used in this study.

Manuscript received Nov. 9, 1982.

Any discussion of this paper will appear in a Discussion Section to be published in the December 1983 JOURNAL. All discussions for the December 1983 Discussion Section should be submitted by Aug. 1, 1983.

Publication costs of this article were assisted by Bell Laboratories.

REFERENCES

1. D. Prober, Personal communication.
2. J. F. Gibbons, W. S. Johnson, and S. W. Mylroie, "Projected Range Statistics of Semiconductors and Related Materials," 2nd ed., Dowder, Hutchinson, and Ross, Inc., Stroudsburg, PA (1975).
3. Polyimide XU218, CIBA-GEIGY Corp., Resins Dept., Ardsley, NY.
4. P. Grabbe, E. L. Hu, and R. E. Howard, *J. Vac. Sci. Technol.*, **21**, 33 (1982).
5. Shipley Company, Newton, MA.
6. M. Hatzakis, B. J. Canavello, and J. M. Shaw, *IBM J. Res. Dev.*, **24**, 452 (1980).
7. E. L. Hu and R. E. Howard, *Appl. Phys. Lett.*, **37**, 1022 (1980).
8. R. E. Howard, E. L. Hu, L. D. Jackel, P. Grabbe, and D. M. Tennant, *ibid.*, **36**, 592 (1980).

Properties of Mo-Silicides in Si-Gate Technology

F. Neppl, G. Menzel, and U. Schwabe

Siemens Research Laboratories, Munich, Germany

ABSTRACT

For low interconnect resistance at the gate level, refractory metal disilicides have been suggested. There are, however, silicide phases with higher metal concentration promising lower electrical resistivity. In this paper, properties of the metal-rich Mo-silicide Mo_3Si and the disilicide $MoSi_2$ are compared. In particular, stress, resistivity, sensitivity to residual gas conditions during deposition, chemical reactions, and MOS characteristics of $MoSi_2$- and Mo_3Si-polycide gate devices are considered. The applicability of Mo_3Si is restricted by its high sensitivity to processing, *e.g.*, to residual gas composition, sintering atmosphere, standard chemicals, and thermal reoxidation. Differences between sputtered and evaporated films are discussed.

Silicides are widely used to reduce the sheet resistance at the poly-level of MOS devices (1). So far, the work on silicides for this application in Si-gate technology largely concentrated on the disilicides of metals such as Ti (2), Ta (2), W (3), and Mo (4). For these metals, however, there are silicide phases with higher metal concentration which promise lower electrical resistivity. In this paper, we present the results of experiments with the metal-rich Mo-silicide Mo_3Si and, for comparison with the corresponding disilicide $MoSi_2$. The second metal-rich Mo-silicide, Mo_5Si_3, was very often mechanically unstable and will not be considered in detail here. In the course of our silicide work, we have also looked for differences between silicide films deposited by coevaporation and sputtering. After some experimental notes in the first section, individual film properties of $MoSi_2$ and Mo_3Si will be compared. In the third section, the behavior of $MoSi_2$ and Mo_3Si polycide gate MOS devices will be discussed.

Experimental Notes

The typically 200 nm thick silicide layers were deposited on oxidized 3 in. (100) Si wafers with (polycide) or without 300 nm highly phosphorus-doped poly-Si. Coevaporation was carried out using two E-gun sources of high purity. The Si:Mo atomic ratio in the films was adjusted by the ratio of the respective evaporation rates. A defined increase of the N_2-, O_2-, or H_2O-partial pressure was possible through an adjustable gas leak. The composition of the residual gas was determined by a quadrupole mass analyzer.

For rf sputtering (p_{Ar} = 20 mTorr; power = 850W, substrate bias 70V), we used mosaic targets, *i.e.*, high purity Si-targets with inserted Mo-pieces of appropriate area.

For sputtering, as well as for evaporation, the deposition time was chosen to be about 5 min for 200 nm of silicide. The composition of the deposited Mo/Si films was checked by electron microprobe. Usually a 900°C sinter step in N_2 or forming gas was carried out to crystallize the amorphous Mo/Si mixtures. The crystalline structure was studied by x-ray diffraction and TEM. Quoted macroscopic stress values result from laser interferometer measurements on 3 in. wafers.

Film Properties

First of all, the properties of evaporated $MoSi_2$ and Mo_3Si are compared. Subsequently, differences between evaporated and sputtered films are pointed out. After deposition, high temperature sintering was necessary to obtain crystalline films with low resistivity. In particular, films with high Mo content were extremely sensitive to traces of oxygen in the sintering atmosphere which caused them to tarnish. When we evaporated Mo and Si in the ratio corresponding to the stoichiometry of $MoSi_2$ or Mo_3Si, respectively, the main phases detected by x-ray diffraction were indeed the tetragonal $MoSi_2$ or the cubic Mo_3Si. In addition, in each case, traces of Mo_5Si_3 and, at high Mo-concentrations, also of Mo were found. Obviously, no complete reaction to the desired silicides took place. In the following, we shall name the silicide films corresponding to the respective main phase. The typical grain size of polycrystalline Mo-silicide films was up to 1 μm for $MoSi_2$ and $\approx$0.2 μm for Mo_3Si. These results apply to films on oxide as well as on poly-Si. Consequently, also a reaction between metal-rich films and poly-Si yielding disilicide seems to be impeded, probably because of oxygen pile-up at the silicide/poly-Si interface, as it was observed by Campelletti *et al.* (5).

Polycrystalline disilicide films on Si-wafers are usually in a state of strong tensile stress, which is attributed to volume shrinkage during the silicide formation and to the mismatch of thermal expansion coefficients. During sintering, we measured a decrease in film thickness of about 15% for $MoSi_2$, but of only 3-5% for Mo_3Si. From this, we conclude a smaller volume contraction in the metal-rich films. Furthermore, the thermal expansion coefficient of Mo_3Si, which is about 4×10^{-6} K^{-1}, matches much better that of Si(3×10^{-6} K^{-1}). In these films, therefore, much less stress is expected to build up during sintering. We found out, however, that this advantage is compensated by a higher intrinsic stress already existent in the as-deposited layers. Thus, Mo_3Si and $MoSi_2$ end up with about the same total tensile stress of order 2×10^9 N/m^2.

One might anticipate that the strain caused by these high stresses influences the alignment accuracy of subsequent structure levels in device fabrication. We have checked this for the misregistration of the poly or polycide edge with respect to the "locos" (*i.e.*, field oxide) edge of MOS devices using test structures, which allow electrical misalignment measurements. The result is shown in Fig. 1. Plotted is the average maximum misalignment of poly-edge to "locos" edge of MOS devices for batches made by contact printing with and without silicide. It is obvious that the silicide inherent strain has no significant effect on the total misalignment, at least for the 3 in. wafers used. The high stress, however, probably caused the occasionally poor adhesion of the Mo-silicide films.

A major criterion in choosing a silicide for Si-gate technology is an electrical resistivity ρ which is as low as possible. Figure 2 shows ρ of as-deposited amorphous Mo/Si-films *vs.* Mo-concentration (ρ is calculated from sheet resistance $R_\square$ and film thickness). ρ is in the range of several hundred $\mu\Omega$cm, and decreases with increasing Mo-concentration. The steepness of the curve over a wide range of Mo-concentration provides an easy control of the metal concentration directly after deposition.

Figure 3 shows the decrease of sheet resistance of $MoSi_2$ during sintering at various temperatures, caused

Key words: films, integrated circuits, gates, resistivity.

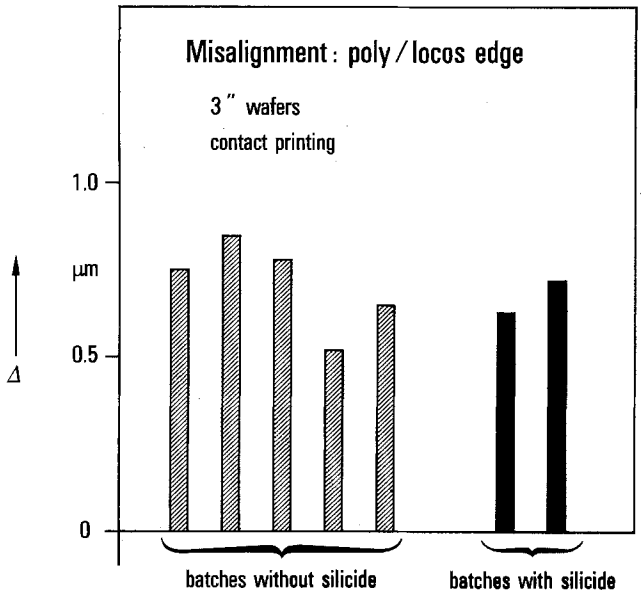

Fig. 1. The misalignment △ between gate and "locos" edge measured on wafers with and without silicide on top of poly-Si.

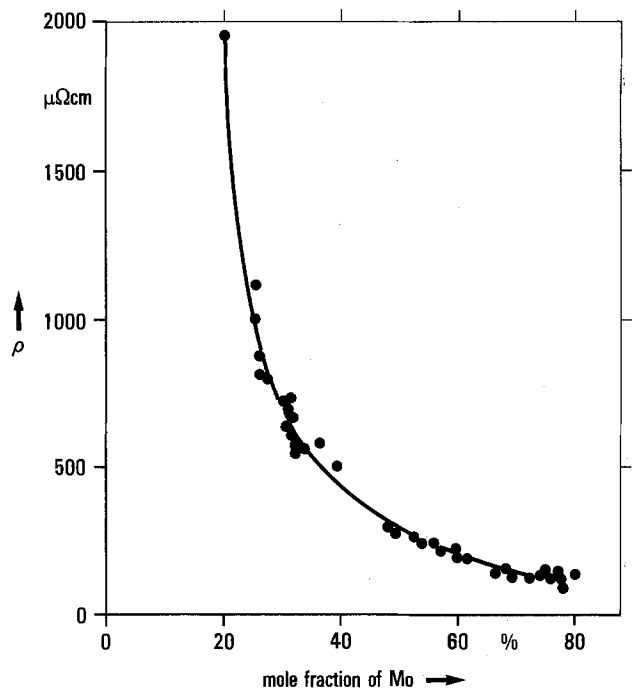

Fig. 2. Resistivity of as-deposited Mo/Si layers (d = 200 nm) vs. Mo-concentration.

by the transition from the amorphous to the polycrystalline state. Temperatures considerably lower than 900°C are obviously not suitable. Sintering at 1000° instead of 900° still leads to lower resistance indicating an advanced crystallization. Similar behavior is observed for Mo_3Si. Figure 4 shows ρ of Mo/Si-layers after 1 hr sintering at 900°C as a function of the Mo-concentration. At the stoichiometry of $MoSi_2$ (33.3% Mo), we found the relatively low value of about 70 $\mu\Omega$cm. The strong dependence of ρ on the Mo-concentration. At the stoichiometry of $MoSi_2$ etry of $MoSi_2$ makes it favorable to use a Mo-concentration somewhat above 33.3 a/o, if a silicide with low metal content is desired. Then, slight scatter of the metal concentration does not affect the sheet resistance. Around the stoichiometry of Mo_3Si (75% Mo), ρ is about a factor of 2 lower than for the disilicide. Values as low as 25 $\mu m\Omega$cm have been observed, making this metal-rich silicide highly attrac-

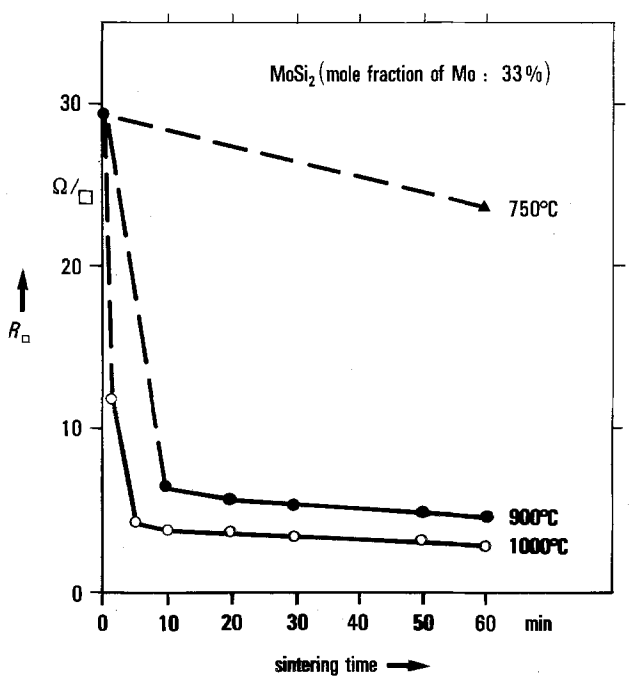

Fig. 3. Sheet resistance of Mo/Si layers with 33% Mo (mol fraction corresponding to the stoichiometry of $MoSi_2$) vs. sintering time for various sintering temperatures.

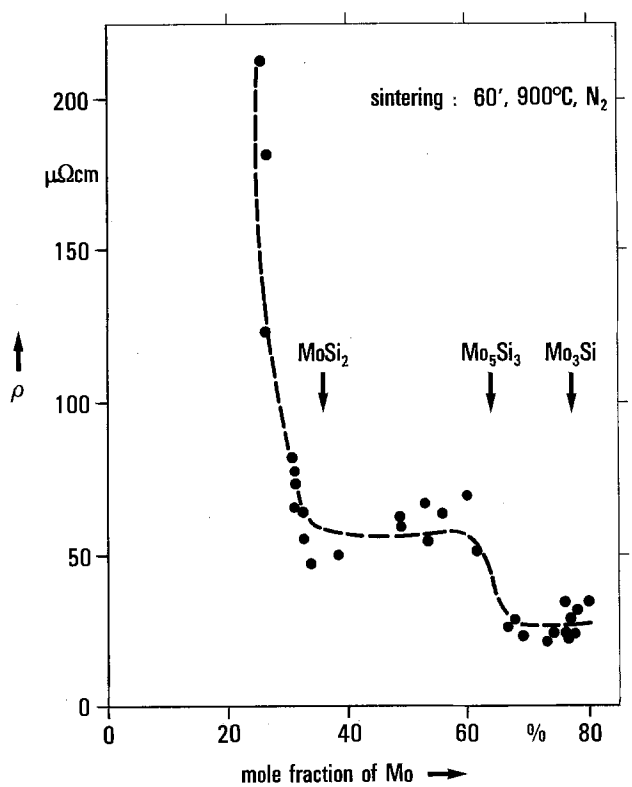

Fig. 4. Resistivity of sintered Mo/Si layers (d = 200 nm) vs. Mo-concentration.

tive. The choice of the substrate (oxide or poly-Si) had no influence on the silicide resistance.

The relatively large scatter of ρ-values at high Mo-concentration may suggest an enhanced sensitivity to sintering ambients or the residual gas conditions during film deposition. Therefore, we investigated in more detail the influence of the residual gas and its composition on the properties of Mo_3Si and $MoSi_2$. We evaporated silicide films after adding partial pressures of about 1.6×10^{-6} Torr of O_2, N_2, or H_2O to the normal base pressure of about 3×10^{-7} Torr.

These three gases are main constituents of the residual gas in a vacuum system. Figure 5 shows the resistivity of Mo_3Si-layers as a function of sintering time at 900°C for the different conditions. In all cases, ρ drops rather quickly to a certain saturation value; obviously, there is no retardation in crystallization but a fast formation of different stable states characterized by different values of ρ. The sensitivity of ρ is highest to H_2O, but there is also an increase of ρ for N_2- and O_2-rich atmospheres during evaporation.

Figure 6 shows analogous results for the disilicide $MoSi_2$. In contrast to Mo_3Si, there is practically no change in resistivity for deposition in O_2- or N_2-rich atmosphere. On the other hand, the influence of elevated H_2O partial pressure is much stronger for the disilicide. Here, an H_2O-partial pressure of 1.6×10^{-6} Torr caused ρ to rise by more than a factor of two. This was correlated with a 30% increase in tensile stress.

The x-ray diffractometer spectra revealed but a texture in the $MoSi_2$-films, which varied with the impurity atoms incorporated. No significant change in lattice constants or in the widths of the Bragg reflections was found. In particular, the drastic effect of H_2O on stress and resistivity did not correspond to major changes in the crystalline structure and, therefore, is likely to be a grain boundary effect or possibly is caused by amorphous phases present in the crystalline silicide. No deterioration of the film adhesion was found with varying impurity gas conditions during deposition.

Another requirement of silicides for use in Si-gate technology is that they should withstand standard process chemicals. We found that both Mo_3Si and $MoSi_2$ are not measurably attacked by HF. However, cleaning solutions containing HCl or NH_4OH destroyed the metal-rich silicide layers. $MoSi_2$ was resistant to these chemicals. Both $MoSi_2$ and Mo_3Si polycide structures have been etched by reactive ion etching in SF_6. The details have been reported by Beinvogl and Hasler (6).

Growing a thermal oxide from the polycide structures was possible only with $MoSi_2$ (7). Mo_3Si readily

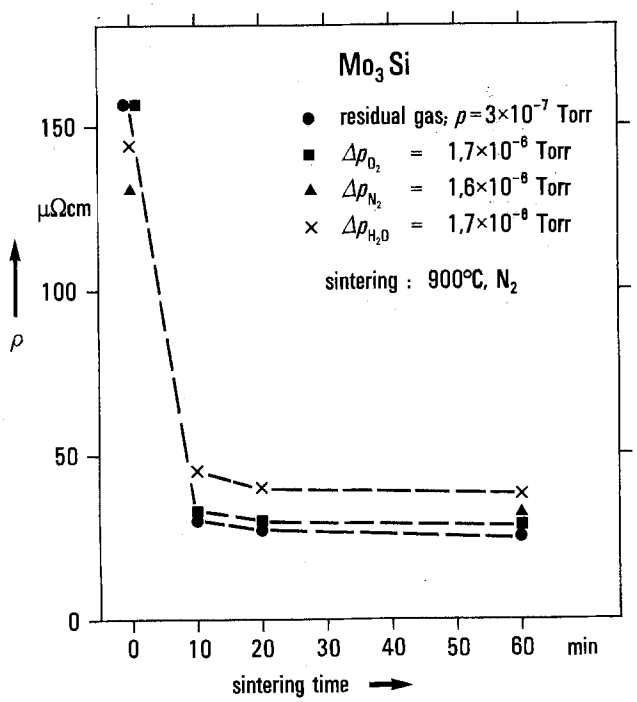

Fig. 5. Sintering time dependence of the resistivity of Mo/Si layers with 75% Mo (mol fraction corresponding to the stoichiometry of Mo_3Si), evaporated in a O_2-, N_2- and H_2O-rich residual gas atmosphere, respectively.

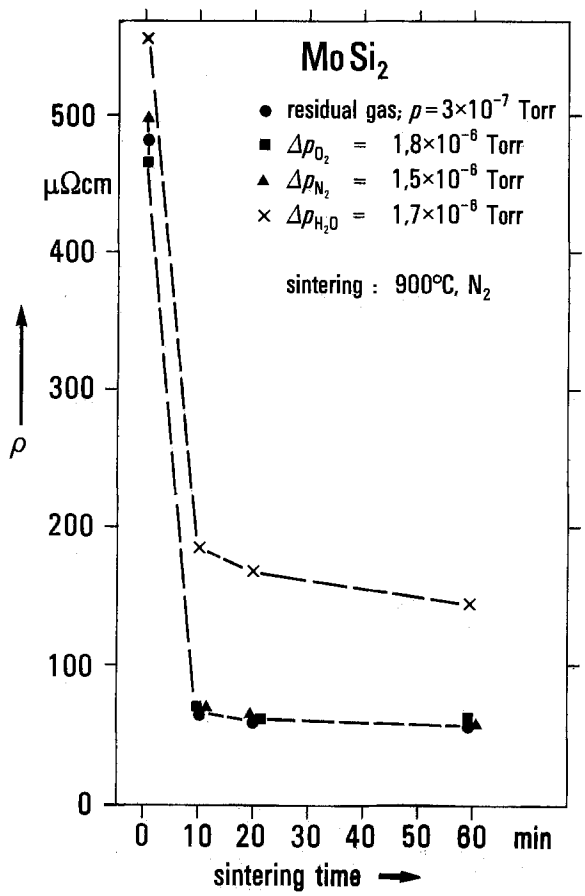

Fig. 6. Sintering time dependence of the resistivity of Mo/Si layers with 33% Mo (mol fraction corresponding to the stoichiometry of $MoSi_2$), evaporated in O_2-, N_2-, and H_2O-rich residual gas atmosphere, respectively.

decomposed in oxidizing ambients, probably under formation of volatile Mo-oxide. Most of the results reported so far also apply to films sputtered under comparable residual gas conditions (except for the necessary amount of Ar) and equal deposition rates, which should imply similar incorporation of impurities other than Ar. The only significant difference occurred with ρ. Once again, an enhanced sensitivity of the metal-rich films became apparent.

In Fig. 7, $R_\square$ of evaporated and sputtered Mo_3Si films of equal thickness is plotted *vs.* sintering time. Whereas, $R_\square$ of evaporated films readily decreased to a low saturation value, $R_\square$ of sputtered films, after a less pronounced fast decrease in the first few minutes, still continues to decrease slowly. Nevertheless, after 60 min at 900°, $R_\square$ of sputtered films is still about twice as high as for evaporated ones. As is seen from the values after 4 hr, even extended sintering did not eliminate this difference, caused possibly by Ar incorporation or impurity gases made more reactive by the glow discharge in the sputtering system. For $MoSi_2$, no such effect was observed confirming the lower sensitivity of silicon-rich layers (see Fig. 8).

Device Parameters

$MoSi_2$ and Mo_3Si polycide gate devices were fabricated by a standard silicon gate process with the exception that a CVD oxide was used instead of thermal reoxidation. Table I summarizes the results of test chip measurements.

What we did not expect was the result on the resistivity of Mo_3Si which is given here for evaporated films only. On the fully processed wafers, we measured $R_\square$ as high as 2.6 l/□ whereas at least 1.5 Ω/□

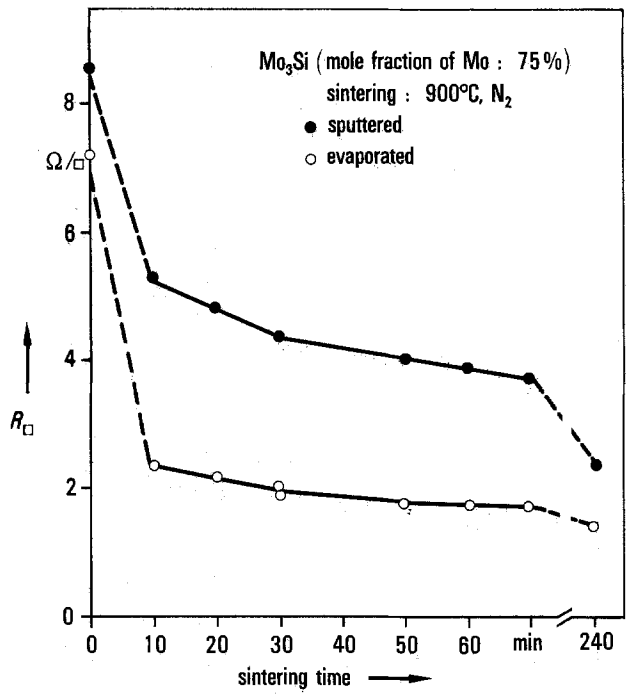

Fig. 7. Sheet resistance of evaporated and sputtered Mo/Si films with 75% Mo (mol fraction corresponding to the stoichiometry of Mo_3Si).

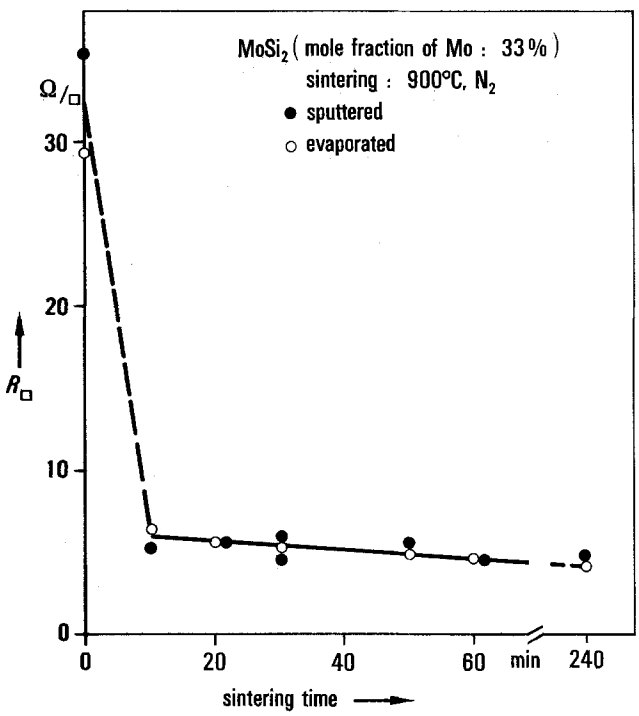

Fig. 8. Sheet resistance of evaporated and sputtered Mo/Si films with 33% Mo (mol fraction corresponding to the stoichiometry of $MoSi_2$).

was expected. Further experiments showed that the reason for this discrepancy was the insufficient annealing of the As-implantation damage in Mo_3Si or possibly incorporation of As as such. Thus, the big advantage of Mo_3Si, the low resistivity, in particular of evaporated films, is partly lost again during processing. A remarkable feature is the low contact resistance from polycide to the Al/Si metallization, which is about one order of magnitude lower than for poly-Si devices. As far as the other properties listed in the table are concerned, no essential differences were found either between the two kinds of polycide

Table I.

property	$MoSi_2$-polycide	Mo_3Si-polycide	poly-Si
$R_□$	3.5 Ω/□ (as expected)	2.6 Ω/□ (expected: 1.5 Ω/□)	25 Ω/□
gate oxide breakdown (d_{ox} = 50 nm)	43 V	42 V	45 V
N_{ss}	$< 10^{10}$ cm^{-2}	$< 10^{10}$ cm^{-2}	$< 10^{10}$ cm^{-2}
τ_g	~ 100 µsec	~ 100 µsec	~ 100 µsec
stability to T/U-stress	good	good	good
U_T (L_{eff})	← equal →		
leakage current of MOSFETs	$\leqslant 10^{-14}$ A/µm	$\leqslant 10^{-14}$ A/µm	$\leqslant 10^{-14}$ A/µm
contact resistance to Al/Si (4×4 µm^2)	$\leqslant$ 0.1 Ω very stable	$\leqslant$ 0.1 Ω very stable	~ 1 Ω

Table II.

property	$MoSi_2$-polycide	Mo_3Si-polycide
resistivity	−	+
sintering	+	−
N_2-sensitivity	+	−
O_2-sensitivity	+	−
H_2O-sensitivity	− −	−
compatibility with standard chemicals	+	−
thermal reoxidation	+	−
sputtering/evaporation	+	−
MOS-device parameters	+	+

or between the polycide and the poly-Si devices. The resistance of Mo_3Si excepted, these results apply to both evaporated and sputtered silicide layers.

Conclusions

We have compared the highly conductive Mo_3Si with $MoSi_2$ as possible candidates for Si-gate technology. An assessment for this application is made in Table II using "+" and "−" signs. With Mo_3Si, one indeed obtains a lower $R_□$ than with $MoSi_2$, though not as low as expected, without significant influence on the MOS parameters. For this, however, one has to regard the enhanced sensitivity to processing (N_2, O_2 in residual gas, sintering, cleaning, sputtering), and one has to dispense with thermal reoxidation. In contrast, for $MoSi_2$, once again the high compatibility with the Si-gate process has been confirmed, as is obvious from a large number of "+" signs in Table II. In particular, the $MoSi_2$ layers have been shown to be insensitive to the deposition technique (evaporation or sputtering) and even to high amounts of N_2 and O_2 in the residual gas during evaporation. Only water vapor pressure has to be kept as low as possible, if the lowest ρ is required.

Acknowledgments

The authors wish to thank Mr. J. Gorniak for technical assistance, Dr. A. Politycki and Dr. U. Bürker for valuable discussions and our colleagues for preparation of the wafers.

Manuscript submitted Dec. 14, 1981; revised manuscript received March 3, 1982.

Any discussion of this paper will appear in a Discussion Section to be published in the December 1983 JOURNAL. All discussions for the December 1983 Discussion Section should be submitted by Aug. 1, 1983.

Publication costs of this article were assisted by Siemens Research Laboratory.

REFERENCES

1. S. P. Murarka, *J. Vac. Sci. Technol.*, **17**, 775 (1980).
2. S. P. Murarka, D. B. Fraser, A. K. Sinha, and H. J. Levinstein, *IEEE Trans. Electron Devices*, **ed-27**, 1409 (1980).
3. B. L. Crowder and S. Zirinsky, *IEEE J. Solid-State Circuits*, **sc-14**, 291 (1979).
4. T. Mochizuki, K. Shibata, T. Inoue, and K. Ohuchi, *Jpn. J. Appl. Phys.*, **17-1**, 37 (1978).
5. P. Campelletti *et al.*, "Proceedings of the 4th Int. Symposium on Silicon Materials, Science, and Technology," p. 608, Minneapolis, Minnesota, May 1981.
6. W. Beinvogl and B. Hasler, "Proceedings of the 4th Int. Symposium on Silicon Materials, Science, and Technology, p. 648, Minneapolis, Minnesota, May 1981.
7. D. Pawlik, Unpublished results.

Solidification-Front Modulation to Entrain Subboundaries in Zone-Melting Recrystallization of Si on SiO_2

M. W. Geis, Henry I. Smith,[1] D. J. Silversmith,* and R. W. Mountain

Lincoln Laboratory, Massachusetts Institute of Technology, Lexington, Massachusetts 02173

and C. V. Thompson

Research Laboratory of Electronics, Massachusetts Institute of Technology, Cambridge, Massachusetts 02139

ABSTRACT

In zone-melting recrystallization of Si films on SiO_2, encapsulated with SiO_2/Si_3N_4, subboundaries form which correspond to small angular deviations $< 1°$. These have been entrained to form along parallel lines underneath a photolithographically-defined optical absorber pattern. Models for the generation and entrainment of subboundaries and grain boundaries are presented and supported by experimental results. Subboundary entrainment requires control of the temperature gradient, the modulation of the isothermal contours and the azimuthal crystallographic orientation.

Zone-melting recrystallization is a process in which a narrow molten zone produced in a thin film on a substrate is scanned across the sample (1-6), resulting in a film consisting of one or more large grains. Recent work has focused almost exclusively on Si over SiO_2 (4-6); whereas, earlier work dealt with Ge and InSb (2-3). The zone-melting recrystallization process is a simple solidification from the melt, and for this reason, the molten zone can be produced by any of several methods: laser, electron beam, arc lamp, hot wire, or (as in most of our work) graphite strip-heater (4-6). To confine the molten zone and prevent agglomeration or "balling up," an encapsulation layer is generally necessary, unless the zone is so narrow that agglomeration does not occur. Zone-melting recrystallization of Si on an SiO_2 substrate produces films composed of a few large grains, ~1 mm wide, extending the full length of the region scanned and having (100) texture (6). The <100> directions are generally within ~15° of the scan direction. Films of a single orientation have been produced by seeding from a single crystal (7-9), by zone-melting through planar constrictions (10, 11), and by so-called cross-seeding (5). In all cases, the films contain subboundaries which are arrays of dislocations or, equivalently, low-angle grain boundaries. (We use the term subboundary to refer to those low-angle boundaries which form during solidification from a single seed. We use the term grain boundary to refer to the region where crystals grown from two different seeds meet.) Subboundaries can be revealed by chemical etching. The crystallographic angular deviation across a subboundary is generally less than 1° (6, 12). The density of subboundaries can be substantially reduced by repeated melting and resolidification (13). This technique has been used to laser-recrystallize Si stripes, ~50 μm wide, essentially free of subboundaries (14). Subboundaries have also been eliminated by zone melting Si patterned into stripes (11).

Subboundaries have only a small effect on electron transport and do not inhibit the fabrication or operation of metal-oxide-silicon field-effect transistors that have minimum linewidths of several micrometers (15, 16). At present, it is not clear what effect subboundaries will have on other classes of devices. In this paper, we describe the entrainment of subboundaries and grain boundaries in strip-heater zone-melting recrystallization of Si using photolithographically-defined patterns that modulate the solidification front, and present models to explain the experimental results. Coligne *et al.* (17, 18) have used a patterned antireflection coating in conjunction with laser recrystallization to achieve grain boundary localization, although in this case, crystallographic texture was not controlled. The localization of subboundaries at well-defined positions gives one the option of building electronic devices between subboundaries in dislocation-free material. Moreover, the entrained subboundaries could perhaps play a beneficial role as gettering sites for certain mobile impurities and defects.

Method of Entrainment

Subboundaries arise when large facets form at the solid-liquid interface, as in the case of zone-melting recrystallization of Si with a graphite strip-heater. The subboundaries originate at the interior corners of the faceted front where two (111) planes meet (6), as shown in Fig. 1 and discussed more fully in the next section. Ordinary grain boundaries also locate at the interior corners. To entrain subboundaries and grain boundaries, one needs to control the positions of the

* Electrochemical Society Active Member.
[1] Also the Department of Electrical Engineering and Computer Science, Massachusetts Institute of Technology, Cambridge, Massachusetts 02139.
Key words: semiconductor, crystallography, solidification, crystallization.

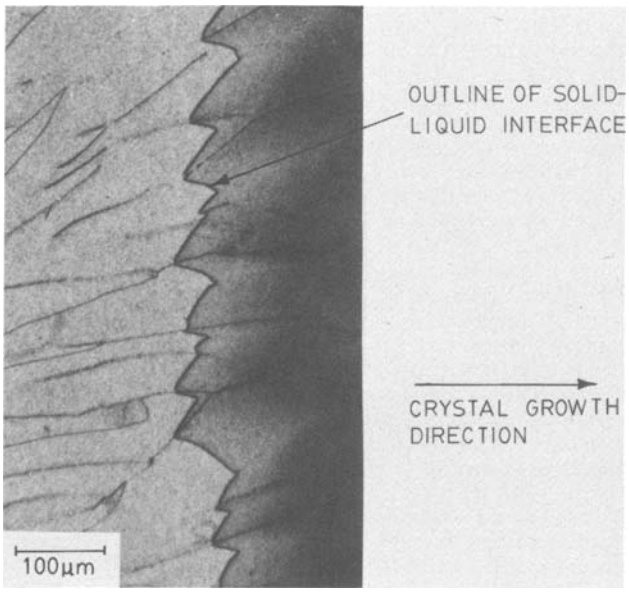

Fig. 1. Micrograph showing faceting of the solidification front in zone-melting recrystallization, and the formation of subboundaries at the interior corners. The means used to obtain the micrograph (6) is such that only the general morphology is revealed, not the instantaneous interface.

facet intersections during zone-melting recrystallization. One technique we have used for doing this is to spatially modulate the temperature at the solid-liquid interface. This can be done by forming a grating on top of the sample that locally enhances either the absorption or reflection of the radiation incident from above (19). Figure 2a illustrates schematically the use of a patterned optical absorber for subboundary entrainment. Figure 2b indicates entrainment of subboundaries underneath the absorber stripes. Because of the enhanced optical absorption, the Si is hotter under the middle of the absorber stripe than at any other lateral position, and hence, this is the last place to solidify. For this reason, the interior corners of the faceted solidification front, and hence, the subboundaries, align with the middle of the absorber, as depicted in Fig. 2b. As an optical absorber, we have used carbonized photoresist. Some results are shown in Fig. 3a. The Si film was 1 μm thick, the substrate was 1 μm of SiO_2 over a (100) Si wafer, the encapsulant was 2 μm SiO_2 and 30 nm Si_3N_4, and the entrainment pattern was a grating of carbonized photoresist (AZ1350 J, Shipley Company, Newton, Massachusetts, initially ~7 μm thick) of 100 μm period and 50 μm linewidth. The zone melting was carried out at a scanning speed of 0.5-1 mm/sec, as described in detail in Ref. (5, 6). The Si between entrained subboundaries is free of dislocations, as determined by chemical etching, and no carbon contamination was detected by Auger analysis, implying that any contamination must be $<10^{19}$ atom/cm^3. Figure 3b shows the typical pattern of subboundaries from an area of an identical sample that did not have an entrainment pattern.

Figure 4 illustrates the use of a grating of thin Si stripes imbedded in an encapsulation layer to achieve entrainment. The thin Si stripes reflect incident radiation at the high temperature used in zone melting, and, as a result, subboundaries entrain between the Si stripes.

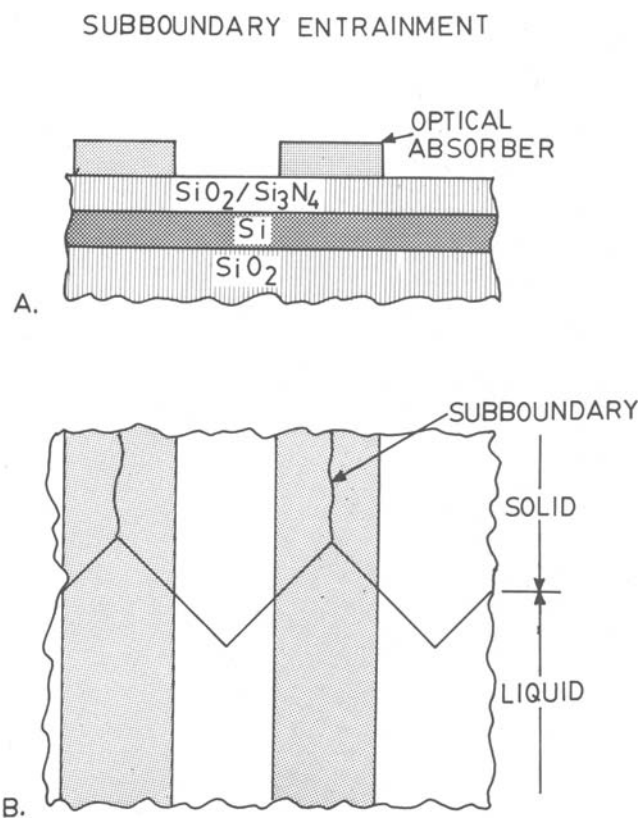

Fig. 2. (a) Schematic illustration of the use of a grating of optical absorber stripes on top of an encapsulation layer to modulate the temperature profile and entrain subboundaries. (b) Illustration of the entrainment of subboundaries under the middle of the optical absorber stripes.

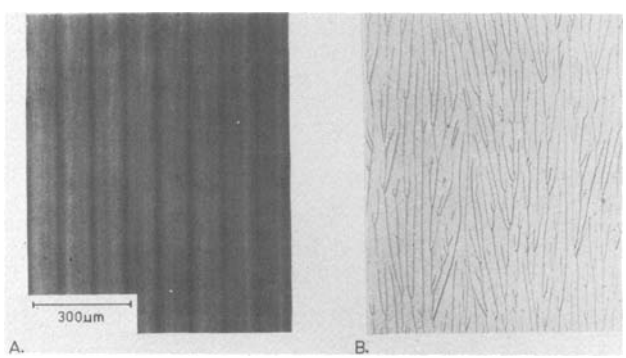

Fig. 3. (a) Entrainment of subboundaries in a 1 μm thick Si film using a 100 μm period, 50 μm linewidth, grating of carbonized photoresist. (b) Typical pattern of subboundaries in an identical sample recrystallized without an entrainment pattern.

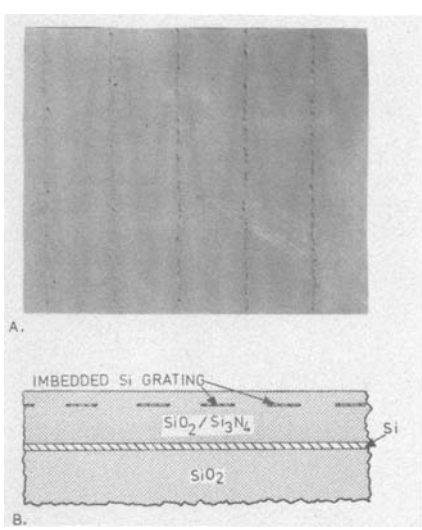

Fig. 4. (a) Entrainment obtained with a grating of Si stripes imbedded in an encapsulation layer. The stripes are reflecting and, as a result, entrainment occurs in between stripes. (b) Schematic illustration of the imbedded Si reflector stripes.

Mechanism of Subboundary Entrainment

The results presented in the previous section demonstrate the feasibility of entraining subboundaries. In this section, we present a model to explain the characteristic morphology of subboundaries, and support this with experimental evidence. Following that, we develop a model for subboundary entrainment and present experimental results which indicate that the modulation depth, temperature gradient, and azimuthal crystallographic orientation must be controlled within narrow ranges in order to entrain subboundaries. Such control has been difficult to achieve with current strip-heater techniques, and, as a result, we have not been able to entrain subboundaries over an entire sample, or to get consistency from run to run. Despite this lack of consistency, we believe our results point the way to further improvements in subboundary entrainment.

Figure 1 shows that the solid-liquid interface of Si is faceted in zone-melting recrystallization. (To obtain this micrograph the molten zone was rapidly quenched with a jet of He gas during scanning (6). This method reveals the general morphology of the solid-liquid interface but does not provide an instantaneous demarcation as given, for example, in Fig. 6 below.) A faceted interface is consistent with Jackson's criterion (20, 21) and also indicates that growth occurs by the addition of atoms at ledges or steps which sweep rapidly across the facets. Subboundaries originate at the interior corners of the faceted solid-liquid interface. Figures 1 and 3b show the typical morphology of subboundaries. The initiation of new subboundaries between two approximately parallel subboundaries and the coalescence of two subboundaries to form a "Y" or "wishbone" pattern are characteristic morphological features. Figure 5 depicts a simplified model of the solid-liquid interface at three consecutive times, and indicates how new subboundaries originate and form the characteristic "wishbone" patterns. The Si film is assumed to have a (100) texture with <100> direction parallel to the direction of zone motion. The facets at the liquid-solid interface are (111) planes,

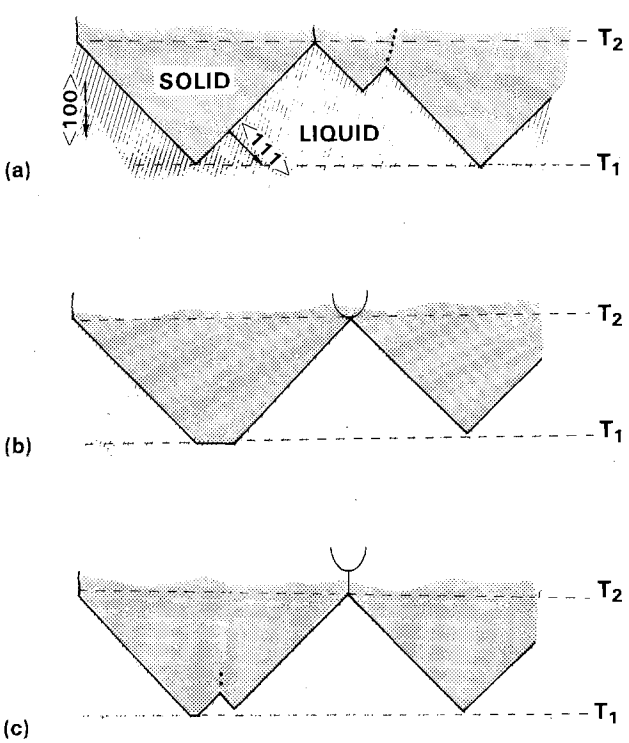

Fig. 5. Simplified model of the solid-liquid interface, shown as a top view, at three consecutive times. The isothermal contours, T_1 and T_2, are defined in the text. Subboundaries are shown originating at interior corners. The characteristic Y or "wishbone" pattern is due to the coalescence of two interior corners.

and, thus, their intersections with a plane parallel to the substrate form 90° angles. The distance a chevron-shaped pair of facets extends into the liquid silicon, which determines the distance between the subboundaries originating at the interior corners, is limited by two temperatures, T_1 and T_2, shown as dotted isothermal contours in Fig. 5. T_2 is the temperature at which the generation of new ledges occurs at such a rate that the forward advance of the (111) facets just matches the imposed zone-scanning velocity. At temperatures close to T_2, the speed with which ledges sweep across a (111) facet is much greater than the rate of forward advance of the solidification front; hence, the rate of forward advance is determined by the rate of generation of new ledges at T_2. The velocity of ledge motion decreases as a ledge encounters higher and higher temperatures. Eventually, when T_1 is reached, the forward velocity of the ledge just matches the zone-scanning velocity. T_1 is probably very close to the melting temperature of Si, T_m. Liquid silicon can, of course, be undercooled more than $T_m - T_2$. At higher undercoolings, however, ledge nucleation at reentrant corners, and at the intersection of the crystalline silicon with the cap and substrate, will be even more copious than at T_2, and for this reason, the solidification front should not fall behind T_2. One might propose other mechanisms (22, 23) but regardless of which mechanism operates, we believe Fig. 5 depicts a reasonable working model of the behavior of the solid-liquid interface. If impurities are present in the molten Si, they would tend to segregate at interior corners, thus, lowering the local solidification temperature, causing cul-de-sacs to form that trail behind the T_2 contour.

Subboundaries tend to be parallel to the direction of zone motion but small perturbations can cause them to move laterally. When the distance between adjacent subboundaries becomes so large that the chevron formed by a pair of facets would extend beyond T_1, the front of the chevron becomes flattened, as indicated in Fig. 5b. This flattened face is not stable and soon dimples and develops into an interior corner which becomes a source of dislocations, as depicted in Fig. 5c. This interior corner will not advance at the imposed scanning velocity but instead will fall back until it contacts the contour T_1. Figures 5a-c also illustrate the coalescence of two subboundaries to create the characteristic wishbone pattern. Note that the apex of a wishbone is parabolic rather than angular. This indicates that some mechanism causes interior corners to pull together when they come within a few micrometers of one another.

Figure 6 provides experimental evidence for the model presented in Fig. 5, showing both formation of new subboundaries by the flattening-dimpling mechanism and the coalescence of subboundaries to form a wishbone. The micrograph was obtained from an Si film which was etched after zone-melting recrystallization to delineate subboundaries, which appear as dark vertical lines, and dopant variations in the film, which appear as zig-zag horizontal lines. The dopant variations were obtained by pulsing the upper heater strip at 120 Hz to demark the instantaneous solid-liquid interface. (This technique was previously used by Holmes *et al.* (24) for the case of conventional crystal growth from the melt.) Approximately every twelfth demarcation line in Fig. 6 is traced in ink to clarify the time evolution of the solidification front. The formation of cul-de-sacs at the interior corners can also be inferred from the slight curvature of certain demarcation lines as they near the interior corners. The protrusions frequently observed along subboundaries (6, 12, 25) are also consistent with cul-de-sac formation and delayed solidification. Leamy *et al.* have presented evidence for cellular growth in strip-heater zone-melting recrystallization at high impurity content (26, 27). Our observations of the zone-melting recrystallization of Si films heavily doped with As are

Fig. 6. Micrograph of an Si film recrystallized by zone-melting showing experimental evidence in support of the model presented in Fig. 5. The instantaneous solid-liquid interface was demarked by pulsing the upper strip-heater at 120 Hz. Approximately every twelfth demarcation line is traced in ink to clarify the time evolution of the solidification front. Seam direction is from top to bottom.

consistent with this (6). However, Fig. 10 of Ref. (6) showed that increased speed of zone motion led to an increase in subboundary spacing in undoped Si, which argues against a cellular-growth mechanism of subboundary formation. Faceting similar to that shown in Fig. 6 has been observed in bulk crystal growth (28).

When an absorbing or reflecting grating pattern is located above a film being recrystallized by the zone-melting technique, the temperature profile is modulated. Figures 7a and b depict two different depths of sinusoidal modulation that have the same temperature gradient (*i.e.*, the same distance between T_2 and T_1 contours). In Fig. 7a, the depth of modulation is small, subboundaries form between entrained subboundaries, and move laterally. We have frequently observed patterns of subboundaries that can be explained by the model of Fig. 7a. In Fig. 7b, the depth of modulation is large enough to prevent the formation of subboundaries between those that are entrained. The portion of the solid-liquid interface located along the isothermal contour T_2 does not give rise to dislocations or subboundaries, and, hence, we assume it is microscopically faceted and able to follow the curvature of the contour, as depicted in Fig. 7b. According to this model, entrainment without the generation of additional, non-entrained subboundaries requires a modulation of the T_2 contour given by

$$Y \geqq (0.22D) \sin (2\pi X/D)$$

where the distance, Y, is in the direction of zone motion, D is the period of the entrainment pattern, and X is a distance measured perpendicular to the direction of zone motion. Unfortunately, we have not been able to directly monitor the temperature contours or the entrained solidification fronts and, hence, could not confirm our models experimentally. However, we did

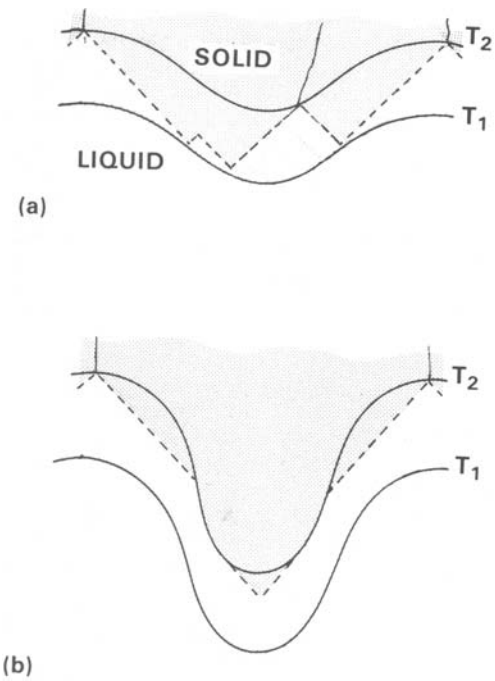

Fig. 7. Schematic illustration of a model for the solid-liquid interface when the isothermal contours are sinusoidally modulated. (a) Depth of modulation is insufficient to achieve full entrainment. (b) Depth of modulation is sufficient to induce entrainment.

observe that entrainment was favored by increased temperature modulation.

Control of the temperature gradient is important in subboundary entrainment. Before discussing this, it is helpful first to clarify the relationship between temperature gradient and subboundary spacing. As discussed above and in Ref. (6), the average separation between subboundaries in zone-melting recrystallization depends upon the distance a chevron-shaped pair of facets extends into the molten Si, which in turn depends upon the temperature gradient, specifically the distance between the T_1 and T_2 contours. This was confirmed experimentally, as shown in Fig. 8. In Fig. 8a, the upper heater was a single strip of graphite, whereas, in Fig. 8b, two strips were used to reduce the temperature gradient. As shown in the micrographs, the average subboundary spacing increases as the gradient is decreased. (A similar result was reported in Ref. (6), Fig. 10, where decreased tempera-

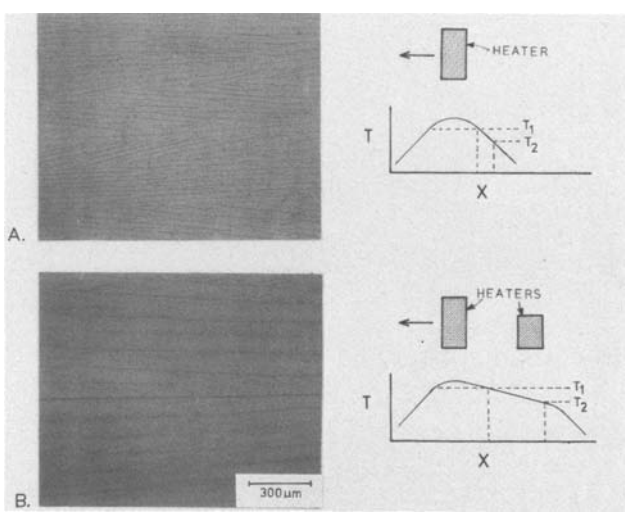

Fig. 8. Dependence of subboundary spacing on temperature gradient. (a) A single strip-heater yields a normal subboundary spacing (6). (b) A shallower temperature gradient, produced by a pair of strip-heaters, yields an increased subboundary spacing.

ture gradient was achieved by increasing the speed of zone motion.) We were able to get entrainment only when the period of the entrainment pattern, D, was at least a factor of 2 larger than the average separation between subboundaries, reflecting the need for a steep thermal gradient to achieve entrainment.

Figure 9 illustrates the importance of azimuthal crystallographic orientation in entrainment. The grid of etch pits (29) shows that two crystal grains are present and that the grain boundary is entrained. On the lower side of the grain boundary, the <100> direction is parallel to the lines of the entrainment pattern. On the upper side, the <100> direction is at an angle of ~40° to the entrainment lines. As a result of this azimuthal misorientation, the pattern of subboundaries has an asymmetric "feathered" appearance due to subboundaries that originate in between the entrained boundaries and run roughly parallel to the $<0\bar{1}0>$ direction until they coalesce with the entrained boundaries. Figure 10 presents a simplified model, for the case where the <100> direction is rotated approximately 25° from the growth direction, illustrating how this asymmetric pattern of subboundaries probably occurs. At time, t_1, a single interior corner is shown, located on the T_2 contour. This interior corner and the region where the chevron facet is tangent to the T_2 contour are sources of ledges which sweep across the facets of the chevron, causing it to grow. When the tip of the chevron encounters the T_1 contour a new interior corner is formed, as depicted at t_2. (This dimpling mechanism was discussed in connection with Fig. 5.) The newly formed interior corner falls back until it encounters the T_2 contour, as depicted at t_3. Since an interior corner cannot trail behind the T_2 contour, the forward motion of the contour causes the interior corner to move to the left, as shown at t_4. As an interior corner approaches the peak of the contour the leftward movement ceases and coalescence with

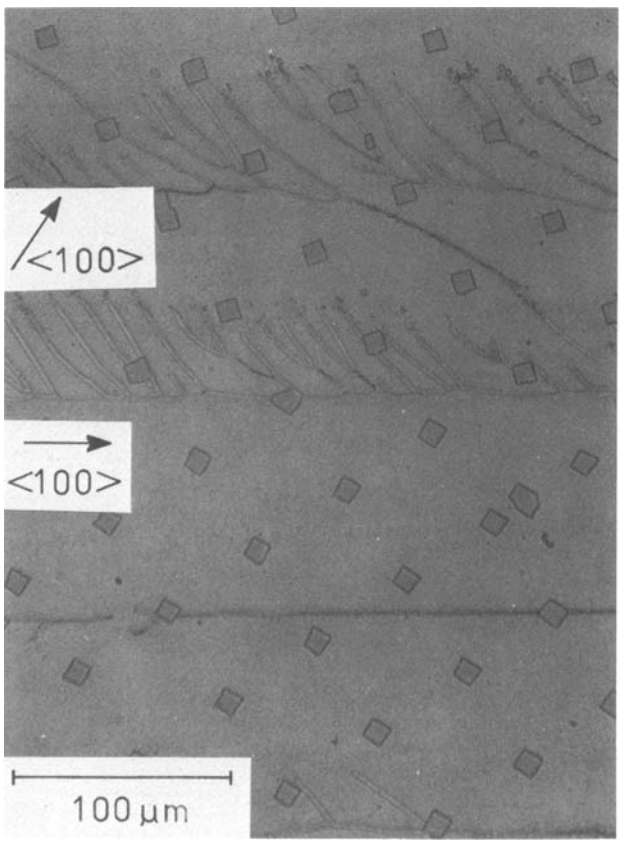

Fig. 9. Optical micrograph showing the dependence of entrainment on azimuthal crystallographic orientation. The diagonals of the etch pits are <100> directions.

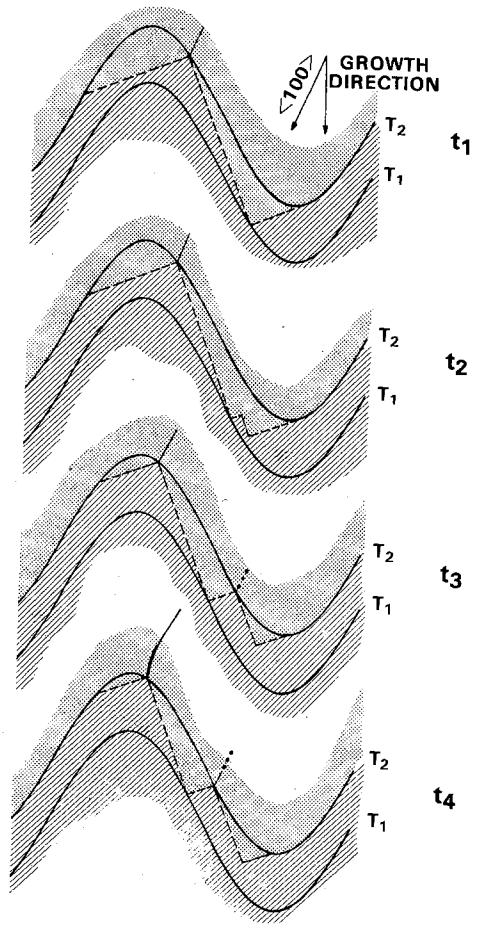

Fig. 10. Schematic illustration of a model for the solid-liquid interface at four consecutive times, t_1, t_2, t_3, and t_4, when the <100> crystallographic direction is at an angle relative to the direction of zone motion. The direction of zone motion is parallel to the entrainment pattern axis.

an interior corner entrained at the peak should occur (not shown in Fig. 10). A subboundary traces the path of the interior corner from which it originates. Thus, subboundaries are initially parallel to the <100> direction but as they approach the peak of the T_2 contour they follow the growth direction and coalesce. This model is certainly a simplification but predicts a subboundary pattern reasonably close to that observed in Fig. 9.

Conclusions

We have described the entrainment, by means of photolithographically defined patterns, of subboundaries and grain boundaries in zone-melting recrystallization of Si over SiO_2. A model for the generation and characteristic morphology of subboundaries was presented, and we showed that entrainment requires a high degree of control over the temperature gradient, the modulation of the isothermal contours, and the azimuthal crystallographic orientation. Recrystallized samples of Si-on-SiO_2 in which the subboundaries are entrained may be ideal for integrated electronic circuits because critical regions of devices could be arranged to avoid the subboundaries, and subboundaries could serve as getter sites.

Acknowledgments

The authors are grateful to C. L. Doherty, K. E. Krohn, J. M. Lawless, and G. H. Foley for technical assistance, and M. Finn for Auger analysis. This work was sponsored by the Defense Advanced Research Projects Agency, the Department of the Air Force, and the Department of Energy.

Manuscript submitted Sept. 15, 1982; revised manuscript received Jan. 3, 1983.

Any discussion of this paper will appear in a Discussion Section to be published in the December 1983 JOURNAL. All discussions for the December 1983 Discussion Section should be submitted by Aug. 1, 1983.

Publication costs of this article were assisted by Massachusetts Institute of Technology.

REFERENCES

1. E. Leitz, British Pat. 691,335 (1953).
2. J. Maserjian, *Solid-State Electron.*, **6**, 477 (1963).
3. A. R. Billings, *J. Vac. Sci. Technol.*, **6**, 757 (1969).
4. E. W. Maby, M. W. Geis, Y. L. LeCoz, D. J. Silversmith, R. W. Mountain, and D. A. Antoniadis, *Electron. Device Lett.*, **edl-2**, 241 (1981).
5. M. W. Geis, H. I. Smith, B-Y. Tsaur, J. C. C. Fan, E. W. Maby, and D. A. Antoniadis, *Appl. Phys. Lett.*, **40**, 158 (1982).
6. M. W. Geis, H. I. Smith, B-Y. Tsaur, J. C. C. Fan, D. J. Silversmith, and R. W. Mountain, *This Journal*, **129**, 2813 (1982); M. W. Geis, H. I. Smith, B-Y. Tsaur, J. C. C. Fan, D. J. Silversmith, R. W. Mountain, and R. L. Chapman, in "Proceedings of the 1982 Materials Research Society Conference," Boston, MA, November 1982.
7. J. C. C. Fan, M. W. Geis, and B-Y. Tsaur, *Appl. Phys. Lett.*, **38**, 365 (1981).
8. B-Y. Tsaur, M. W. Geis, J. C. C. Fan, D. J. Silversmith, and R. W. Mountain, *ibid.*, **39**, 909 (1981).
9. R. F. Pinizzotto, H. W. Lam, and B. L. Vaandrager, *ibid.*, **40**, 388 (1982).
10. H. I. Smith, H. A. Atwater, and M. W. Geis, Paper 159 presented at The Electrochemical Society Meeting, Montreal, Que., Canada., May 9-14, 1982.
11. H. A. Atwater, H. I. Smith, and M. W. Geis, *Appl. Phys. Lett.*, **41**, 747 (1982).
12. H. W. Lam, R. F. Pinizzotto, D. S. D. Malhi, and B. L. Vaandrager, *ibid.*, **41**, 1083 (1982).
13. K. A. Jackson and C. E. Miller, *J. Cryst. Growth*, **42**, 364 (1977).
14. G. K. Celler, L. E. Trimble, K. K. Ny, H. Baumgart, and H. J. Leamy, Paper 151 presented at the Electrochemical Society Meeting, Montreal, Que., Canada, May 9-14, 1982.
15. E. W. Maby and D. A. Antoniadis, *Appl. Phys. Lett.*, **40**, 158 (1982).
16. B-Y. Tsaur, J. C. C. Fan, M. W. Geis, D. J. Silversmith, and R. W. Mountain, *IEEE Electron Device Lett.*, **edl-3**, 79 (1982).
17. J. P. Colinge, G. Auvert, and J. M. Temerson, Paper 147 presented at The Electrochemical Society Meeting, Montreal, Que., Canada, May 9-14. 1982.
18. J. P. Colinge, E. Demoulin, D. Bensahel, and G. Auvert, *Appl. Phys. Lett.*, **41**, 346 (1982).
19. M. W. Geis, H. I. Smith, B-Y. Tsaur, J. C. C. Fan, D. J. Silversmith, and R. W. Mountain, Electronic Materials Conference, Fort Collins, CO, June 1982.
20. D. P. Woodruff, "The Solid-Liquid Interface," Chap. 3, Cambridge University Press, New York (1973).
21. K. A. Jackson, in "Nucleation and Atomic Kinetics," North Holland, New York (1979).
22. D. E. Ovsienko and G. A. Alfinstev, in "Crystals Growth, Properties, and Applications," pp. 119-170, Springer-Verlag, Berlin, Heidelberg, New York (1980).
23. J. W. Cahn, *Acta Metall.*, **8**, 554 (1960).
24. D. E. Holmes and H. C. Gatos, *J. Appl. Phys.*, **52**, 2971 (1981).
25. J. C. C. Fan, B-Y. Tsaur, R. L. Chapman, and M. W. Geis, *ibid.*, **41**, 186 (1982).
26. H. J. Leamy, C. C. Chang, H. Baumgart, R. A. Lemons, and J. Chang, *Mater. Lett.*, **1**, 33 (1982).
27. R. A. Lemons, M. A. Bosch, J. Cheng, and H. J. Leamy, Electronic Materials Conference, Fort Collins, CO, June 1982.
28. W. Bardsley, J. S. Boulton, and D. T. J. Hurle, *Solid-State Electron.*, **3**, 395 (1962).
29. K. A. Bezjian, H. I. Smith, J. M. Carter, and M. W. Geis, *This Journal*, **129**, 1848 (1982).

Mass Spectrographic Analysis and SEM Investigation of α-HgI_2 Crystals Grown by Static Sublimation

T. Kobayashi,[1] J. T. Muheim, P. Waegli, and E. Kaldis

Laboratorium für Festkörperphysik, ETHZ, 8093 Zürich, Switzerland

ABSTRACT

In this paper, the applicability of spark-source mass spectrographic analysis and SEM investigations for α-HgI_2 is demonstrated. The influence of the chemical history of the material on the spectrum of the impurities has been investigated by comparing materials synthesized in three different ways. Static sublimation was used to grow single crystals, which had an appreciable average linear growth rate (10^{-6} cm/sec) and relatively low etch pit density (10^3/cm^2 or less). Synthesis from "suprapur" elements after additional purification of iodine gave the most pure crystals, which still contained 1700 ppm at. of impurities. The spark source mass spectrographic analysis on α-HgI_2 reveals abundant distributions which are conspicuously characteristic of the crystal properties (valence, structure, composition, etc.) for elemental impurities, and crystal structure characteristic for the hydrocarbon fragments. Overall abundances for sublimated α-HgI_2 vary according to the material source. Morphological investigation of uncoated crystal surfaces (as grown, etched, or cleaved) was possible by low temperature SEM investigation. They showed that most etch pits are flat bottomed at up to 10,000× magnification. Emergence points of dislocations are not visible; dislocations appear only in the form of a few pyramidal etch pits.

Red tetragonal mercuric iodide (α-HgI_2) has been receiving much attention as a material for room temperature operable semiconductor detectors for low energy x- and γ-rays (1-3). This is due to its unique physical properties. Its wide bandgap of 2.1 eV, and the large atomic numbers of the components (80 for Hg and 53 for I) result in low dark current at room temperature and high photoionization efficiency (1, 2). A medical application was exemplified by a small HgI_2 detector mounted inside an injection needle (4). Application to computer tomography is highly desirable if small size HgI_2 detectors could replace the currently used large scintillation detectors. In this way, the local resolution of the tomograms would be improved.

In the last six years, considerable progress has been made in crystal growth of α-HgI_2 and detector fabrication. However, the detector performance of HgI_2 tends to suffer from insufficient collection of the electrons and holes, produced by the interaction of an incident photon with the crystal. This is due to rather

[1] Permanent address: The Graduate School at Nagatsuta, Tokyo Institute of Technology, Midori-Ku Jokohama 227, Japan.

Key words: α-HgI_2, single crystals by static sublimation, impurities in, mass spectrographic analysis of, SEM investigation on cold stage, spark source mass spectrographic analysis of HgI_2, sublimation, static, of αHgI_2, vapor growth rate of α-HgI_2 single crystals.

small values of the $\mu\tau$ (mobility $\times$ lifetime) product of the charge carriers, particularly for holes. An open question for the moment is which material parameter can be changed in order to improve the charge carrier collection efficiency. Recent studies of iodine treatment of the starting material (5), seeded solution growth (6), and poisoned vapor growth (7) have suggested that both nonstoichiometry and structural defects introduced during growth and detector fabrication may be responsible for incomplete charge carrier collection. Evaluation of the relative importance of these two factors is difficult at present because reliable information on the phase diagram, and methods for exact determination of the composition are not available.

From the point of view of structural perfection, a clear correlation was reported between etch pit density and detector performance (8). However, a more detailed morphological investigation is desired in order to decide if all etch pits result from dislocations. This and a general morphological investigation of the growth steps at the interface could be optimally performed with the scanning electron microscope (SEM). However, such investigations have been very difficult up to now (9) due to the high volatility of HgI_2 ($p \sim 10^{-5}$ Torr at 25°C).

Another drawback of the HgI_2-research is that no impurity effects on the detector performance have been systematically investigated. This is surprising in view of the great efforts for the analysis and elimination of impurities in silicon and compound semiconductors. One reason for this stagnating situation is that the impurities of HgI_2 crystals are close to the detection limit of emission spectroscopy (9), the only method for chemical analysis which has been used up to now. Mass spectrography has not been utilized effectively, in spite of its potential advantages of simultaneous determination of a large number of elements with much higher sensitivity than the spectrochemical analysis.

Recently, we have started an investigation of the applicability of the spark source mass spectrographic analysis and the SEM technique to HgI_2 (10). In this paper, we report some of these results in connection with SEM morphological investigations of as-grown crystal faces and the crystal growth and purification conditions. As most of the vapor growth investigations have used the temperature oscillation methods, we preferred crystal growth by static sublimation, hoping to accumulate some data for this rather neglected method. As we were particularly interested in small HgI_2 crystals as detectors for tomography, no special attempt was made to grow large crystals.

Purification of the Raw Material and Crystal Growth

The batches of α-HgI_2 used in this investigation as a starting material were obtained from three different sources (*i*) Merck analytical grade HgI_2 powder, (*ii*) analytical grade (Merck) Hg and I_2, from which the compound was synthesized, and (*iii*) "suprapur" grade (Merck) elements used also to synthesize the compound. The synthesis was carried out by reacting Hg and I_2 (slight excess of I_2). The elements were brought to reaction in an evacuated Pyrex ampul at temperatures up to 220°C for 12 hr (10b). The material from each of these sources was purified by repeated sublimation (11) in Pyrex ampuls with 40 mm ID and 220 mm length which were sealed under a vacuum of 10^{-5} Torr. Up to five consecutive purification steps, each in a separate ampul, were performed, the temperature differences ΔT and absolute temperature T varying in steps from ΔT = 130°-90°C = 40°C (for the first purification) to ΔT = 90°-30°C = 60°C (for the last purification). The rate of mass transport ranged from 8 to 4 g/day.

Segregation of impurities became visible in the form of residue, which remained in the evaporation zone after the more volatile fraction was transported. The appearance of the residue changed with the material source; yellow powder for the Merck HgI_2 powder and dark-brown, tarlike substance for the two batches of material synthesized from the elements. After the third (for Merck HgI_2) or fourth (for the synthesized materials) purification, no residue was visible.

Single crystals of α-HgI_2 were grown by static sublimation in which the ampul position in a vertical furnace and the temperature profile remained unchanged during growth. In order to minimize the temperature fluctuations due to convection of the air, the two-zone furnace was placed in an evacuated glass chamber with brass lids carrying the connections for vacuum (10^{-2} Torr), power, and thermocouples (Fig. 1).

The experiments were conducted under a supersaturation of about 60% ($P_1 - P_2/P_2$) = 0.6 corresponding to an undercooling of $\Delta T = T_1 - T_2 = 5$°C at a growth temperature ranging from 90° to 110°C. The temperature of the upper zone was kept higher than that of the lower zone until the latter reached the desired temperature. After the above-mentioned supersaturation was established, nucleation started simultaneously on many sites. Some crystallites intergrew, while others resulted in well separated single crystals. Crystals grown in ampuls of 75 mm ID and 200 mm length are shown in Fig. 2a. Figure 2b shows a crystal grown in a purification ampul on a seed.

The average linear growth rate (ALGR) of the single crystals shown in Fig. 2a was of the order of 10^{-6} cm/sec. This is a typical value for diffusion controlled growth from the vapor phase (12) and larger than the value previously reported (11). Schieber *et al.* observed for crystals grown by static sublimation a growth rate of the order of 500 μm/week (ALGR $\sim 8 \times 10^{-8}$ cm/sec).

Some preliminary growth experiments were performed using HgI_2 of technical grade without any purification. Sizable crystals without macroscopic faults could be grown but the growth rate was time dependent. Observation of the crystal size (by a stereomicroscope) as a function of time gave the results shown in Fig. 3. From the measured length of the largest edge of the C-plane, we can conclude the following growth rates. Assuming a linear slope for the first 18 hr of growth, we can estimate an ALGR

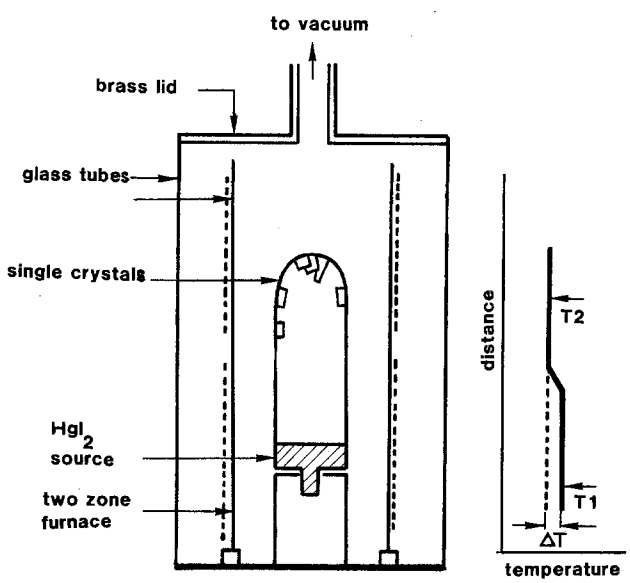

Fig. 1. Schematic drawing of the apparatus used for crystal growth of α-HgI_2 by static sublimation.

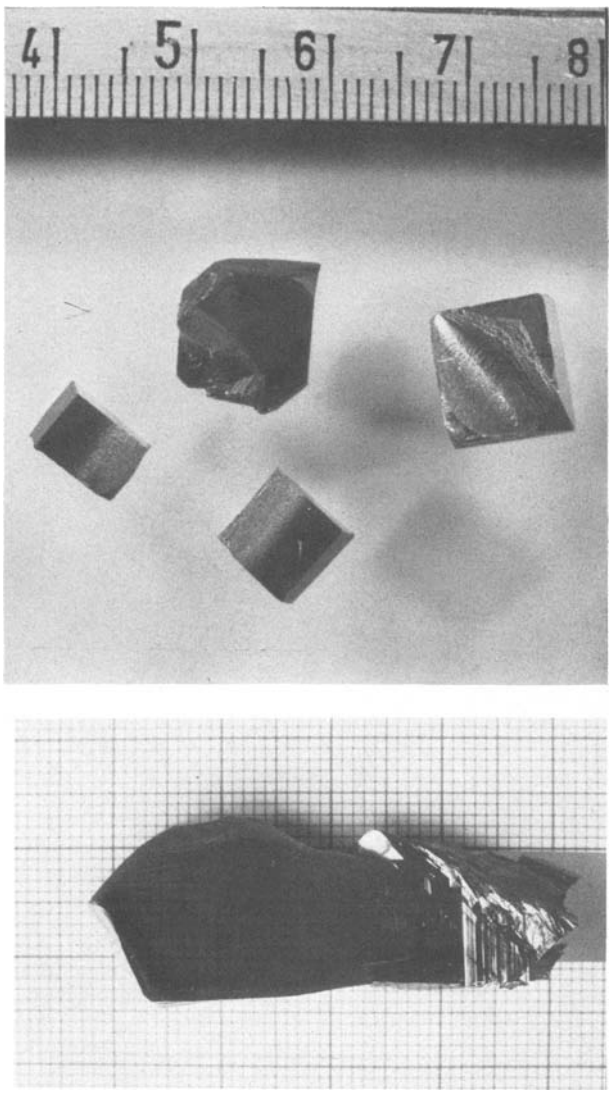

Fig. 2. Single crystals of α-HgI_2 grown by static sublimation. (Smallest subdivisions in 2a and 2b are millimeters.)

of 7×10^{-6} cm sec^{-1}. Between 5-10 days, several measurements exist, so that the approximate linear slope allows the calculation of the effective linear growth rates (LGR) of 0.7×10^{-6} cm sec^{-1} and 0.5×10^{-6} cm sec^{-1} for two different individuals. The growth rate along the C-axis is approximately half of this value. We can, therefore, conclude that the growth rate decreases by approximately one order of magnitude during the growth experiment. These measurements were made at approximately constant temperature conditions ($T_1 = T_{evap.} = 110° \pm 2°C$) and undercooling ($\Delta T = 6° \pm 1°C$), corresponding to a supersaturation of $(P_{110°C} - P_{104°C})/P_{104°C} = 0.67$. We, therefore, tend to attribute this transient growth rate to poisoning of the growth steps due to the high concentration of impurities (see the following section). We will continue these measurements for pure crystals in order to study the growth rate in the absence of impurities.

It is interesting that in solution growth the reported rates (6) are $0.3\text{-}0.6 \times 10^{-6}$ cm sec^{-1} for the <100> and one order of magnitude less for the <001> at a supersaturation of approximately 5×10^{-3}. In conclusion, it can be said that static sublimation results in substantial growth rates. The suggested influence of the impurities on the growth rate was an additional stimulus for the investigation of the impurities in HgI_2 of various sources.

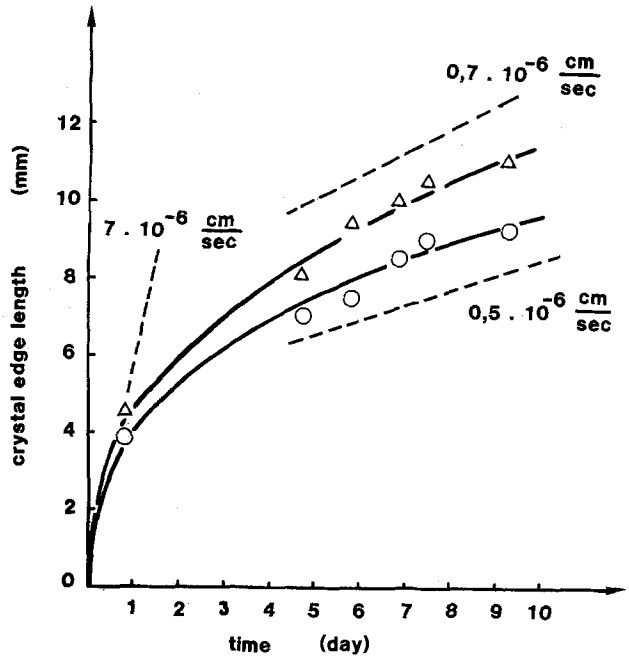

Fig. 3. Linear dimensions of α-HgI_2 crystals as a function of growth time. The two solid curves correspond to the largest edge of the c-plane of two different individuals. The dashed lines correspond to the given values of linear growth rates.

Spark-Source Mass Spectrographic Analysis

The mass spectrographic analyses have been performed with a spark-source mass spectrograph MS-702 of Associated Electrical Industries Limited. In an initial attempt, small single crystals of α-HgI_2 used as electrodes could not be rf sparked. In order to solve this problem, coaxial electrodes were developed in which an α-HgI_2 rod, cut from a single crystal, was embedded into high purity silver powder and compacted under pressure. This electrode design has an advantage over a compact homogeneous mixture of HgI_2 and silver powder, because it minimizes the effect of silver; sparking occurs mainly from the HgI_2 core. In all cases, the source pressure before sparking was relatively high, 2×10^{-6} Torr before the first and 2×10^{-7} Torr before the second, as compared with a more usual value of 5×10^{-8} Torr when dealing with other materials. This effect is due to partial evaporation of the electrode substance (HgI_2 plus impurities). The amount of α-HgI_2 sample consumed in an experiment was of the order of 5 mg corresponding to an integrated current of 5 nC. The photographically detected mass spectra were evaluated by means of a Joyce-Loebel microdensitometer. All concentrations stated in this paper refer to Hg as an internal standard and are given in ppm atomic unless otherwise stated. The Ag used for the compound electrode contains only C(28 ppm), N(10), O(55), and CH_3(11) as impurities in concentration more than 10 ppm. However, they do not conflict with the sample data.

Assuming constant sparking conditions, carbon inhomogeneities were very often observed in terms of anomalous relationships between plate exposure and line darkening. These inhomogeneities occurred on sample amounts ranging from 0.1 to 1.0 mg, the local concentration deviating from the average by a factor of as much as 10 in either direction. It is important to note that this behavior was true even for single crystals grown from four-times sublimated material. Further, it was found that small parts of the crystals were enriched mainly in Na and/or K. However, no abrupt changes of the line darkening as a function of the exposure were observed for these impurities.

Table I. Comparison of the total concentration of seventeen typical impurities for two measurements in each of eight specimens

Material source	Specimen	No.	Concentration relative to Hg, ppm at. Measurement 1	Measurement 2	Average
HgI_2 powder	As supplied	1	15000	3000	9000
	Single crystal 4 × sublimated	29	6900	5000	6000
"Suprapur" elements	Polycrystalline 1 × sublimated	40	35000	3700	20000
	Polycrystalline 4 × sublimated	39	3600	5300	4500
	Polycrystalline purified I_2 1 × sublimated	38	1700	3200	2500
Analytical grade elements	Single crystal 4 × sublimated	31-1	4200	1400	2800
		31-2	10000	1300	5700
		31-3	2700	4800	3800

These results, together with the fact that a compound electrode system (Ag + HgI_2 was used, make the discussion of analytical "reproducibility" difficult. A general impression can be given from the total concentrations of impurities shown for material from different sources in Table I. Experiments No. 31-1, 2, 3 were made with three sets of electrodes cleaved from the same crystal. Specimens No. 31-1 and 31-3 showed a reproducibility better than a factor of two. Specimen No. 31-2 showed a very high concentration of Na(2000 ppm at.) and K(2800 ppm at.) which indicated the above mentioned enrichment. All other samples showed total impurities compatible with their purification efficiency: Sample No. 1 was taken from the as-supplied powder of HgI_2 (Merck analytical grade) without further purification. Sample No. 29 had the same source but it was single crystal sublimated four times. Samples No. 38, 39, 40, all polycrystalline, were synthesized from "suprapur" grade elements (Merck). No. 40 was sublimated once and No. 39 four times; No. 38 was sublimated once but synthesized from twice-sublimated "suprapure" iodine. Samples No. 31 were all single crystals cut from the same piece, but the starting material was synthesized from analytical grade (Merck) elements, and it was sublimated four times.

The results of a second measurement performed with the same set of electrodes after an interval of about one hour are also shown in Table I. It is interesting that these second measurements showed neither inhomogeneities nor enriched parts. Also, they do not reflect clearly the above mentioned purification history of the samples. It is possible that under the complex conditions of sparking, a desorption of impurities intercalated in the layer structure of HgI_2 takes place. On the other hand, sample inhomogeneities or a possible change of the sparking mode of the compound electrode (as HgI_2 was preferentially consumed, the second sparking occurred from electrodes with a crater geometry) can be the reason for the difference between the values of the first and the second measurements.

Unfortunately, little information about systematic investigations of the reproducibility of spark source mass spectrography exists in the literature, partly due to a lack of sufficiently-homogeneous materials. However, whatever the reason for the difference between the first and the second measurements may be, an overall "effective reproducibility" of the order of a factor 2-3 can be derived from Table I.

A comparison of the spectrum of typical impurities among the as-supplied material, the residue, and the purification products was possible only for the commercial HgI_2 powder (Merck, analytical grade). For the material synthesized from the elements, no mass spectrographic analysis for the as-supplied Hg(liquid) and I_2(volatile) could be made. Table II allows a comparison for the three fractions of the above mentioned material. The raw material and residue show clearly the enrichment of impurities in the latter. The contamination of the raw material with NO_3^- ions was revealed only by the analysis of the residue (detection of NO_2^+ and NO^+ ions). The high concentration of N and O is probably due to the fragmentation of these molecular ions.

As a first approximation, the fingerprint or spectral shape of the impurities is the same between the source material, the residue, and the single crystal. Na and K were the most abundant metallic impurities, and the hydrocarbon spectra ranging from CH_3 to C_4H_8 as typical fragments had maxima at C_3H_3 and C_4H_7 with a minimum at C_4H_4. This strongly suggests that not only hydrocarbon spark fragment spectra are characteristic of the crystal structure (15) but that also elemental impurities have in principle abundance distributions characteristic of the matrix crystal. The minimum of abundance at the mass of the relatively unstable plane-cyclobutadiene is not unexpected, and it is probably indicative of the microscopically-uneven layer structure formed by the large Hg and I ions (16).

The residues resulting from the sublimation of material synthesized from the elements, both of "suprapur" and analytical grade, had different impurity spectra. No ions resulting from NO_3^- were observed, and both B and Si had ten times lower intensities. Also single crystals grown after four purifications from each of these three starting materials had different impurity spectra. These spectrographic fingerprints are shown in Fig. 4. The peaks for metallic impurities, especially Na and K, are very strong in both single crystals and residue for Merck HgI_2 (Fig. 4a). Metallic and organic impurities have rela-

Table II. Mass spectrographic analyses for Merck analytical grade HgI_2; concentration relative to Hg in ppm at., and ppm wt in brackets

Impurity as positive ions	ppm at. (ppm (wt)) Raw material	Residue	Single crystal after 4 × sublimated
B		11000 (260)	
C	1900 (50)	30000 (790)	290 (7.7)
N	72 (2.2)	510000 (16000)	65 (2.0)
O	160 (5.6)	870000 (31000)	87 (3.1)
O_2		31000 (2200)	
NO		76000 (5000)	
NO_2		23000 (2300)	
F		170 (7.1)	
Na	1400 (71)	63000 (3200)	820 (42)
Al	94 (5.6)	3300 (200)	120 (7.1)
Si		110000 (6800)	
K	7700 (660)	1400000 (120000)	2500 (220)
Ca	490 (43)	3000 (270)	200 (18)
Cr	270 (31)	4800 (550)	93 (11)
Mn	5.7 (0.7)	610 (74)	3.5 (0.4)
Fe	400 (49)	11000 (1400)	130 (16)
CH_3	240 (7.9)	970 (32)	230 (7.6)
C_2H_3	520 (31)	2300 (140)	530 (32)
C_3H_3	740 (63)	2600 (220)	780 (67)
C_3H_4	320 (28)	1200 (110)	310 (27)
C_4H_4	100 (11)	540 (62)	93 (11)
C_4H_7	200 (24)	760 (92)	490 (59)
C_4H_8	100 (12)	920 (110)	120 (15)
Total	15000 (2000)		6900 (550)

The values listed refer to the first measurements (Table I).

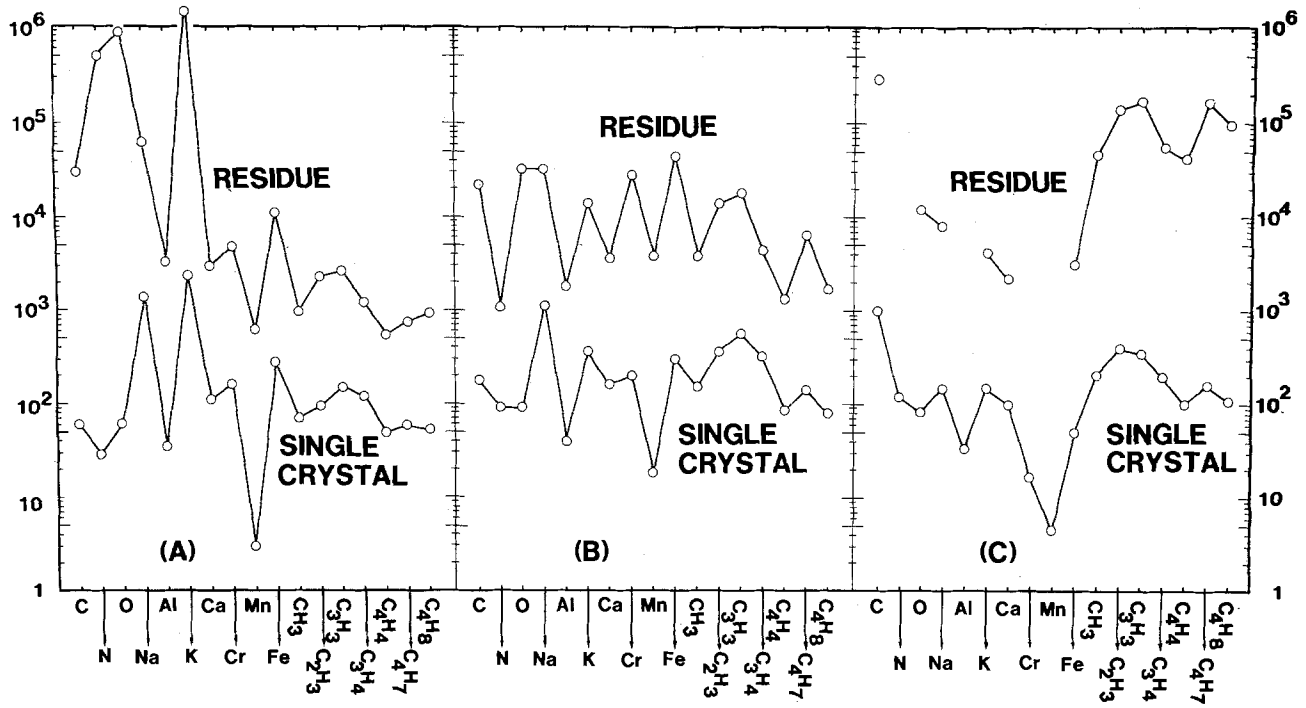

Fig. 4. Mass spectra of 17 typical impurities for single crystals grown from four times sublimated materials and the corresponding residues. A: Analytical grade HgI_2 (Merck). B: Synthesized from analytical grade elements (Merck). C: Synthesized from as-supplied "suprapur"-grade elements (Merck). Spectral overlap due to strong intensities of hydrocarbon ions precluded the determination of N^+, Al^+, Cl^+, and Mn^+ in the residue.

tively comparable concentrations for the material synthesized from analytical grade elements (Fig. 4b). A striking feature of the HgI_2 synthesized from "suprapur" grade elements (Fig. 4c) is that both C and hydrocarbon concentrations are extremely high as compared with the other two groups of materials.

As I_2 was suspected to be the source of the organic impurities, the as-purchased "suprapur" I_2 was purified by sublimation (ΔT = 40°-25°C = 15°C). A large amount of hydrocarbon droplets was found to remain on the glass wall of the ampul near the evaporation zone. Twice sublimated I_2 was used for the synthesis of another batch of HgI_2.

Table III shows the sums of the four important groups of impurities and the total amount for four different samples. Table IV shows the detailed analyses. In agreement with the above, the material from "suprapur" source shows the highest concentration of carbon and hydrocarbons. A decrease by a factor of twenty takes place when once-sublimated I_2 is used. It is interesting that single crystals, grown from four times sublimated commercial HgI_2 (Tables III and IV, sample No. 29) and material synthesized from analytical grade elements (Tables III and IV, sample No. 31-1) show more impurities. Therefore, we conclude that synthesis from purified elements should be considered for future work. In view of the influence of impurities on the charge carrier mobility, no top performance can be expected from α-HgI_2 detectors with the impurities concentration shown in Tables III and IV.

In this paper, we do not discuss the problem of the nonstoichiometry of HgI_2 crystals. However, in view of the results of Fig. 4 and Tables III and IV, it has to be kept in mind that treatment of the crystals with iodine may greatly increase the carbon and hydrocarbon content unless mass spectrographically pure iodine is used.

Etch Pits and Surface Morphology by SEM and OM

As-grown and cleaved HgI_2 crystals, before and after etching, were investigated with SEM and for supplementary observations with an optical microscope (OM).

In view of the lack of morphological investigations with SEM, a very effective tool for the study of crystal growth and dissolution phenomena, we have tried to overcome the experimental difficulties associated with a volatile compound like HgI_2. It was reported in the past (9) that a layer by layer evaporation induced by the electron beam does not allow reliable studies of the as-grown surface morphology. For this reason, we have used a cooling stage (81114-0001) in conjunction with the Cambridge Stereoscan Mark IIA. This allowed (with some minor drawbacks) the observation of the surface morphology at a temperature near that of liquid nitrogen. Our investigations showed that some important morphological features can be observed and

Table III. Total amount and concentrations of four groups of impurities in samples from material of four different sources

Material source	Specimen	No.	Concentration relative to Hg, ppm at.				
			Total	C	N + O	Total hydrocarbon	Total metallic
HgI_2 powder	Single crystal 4 × sublimated	29	6900	290	150	2600	3900
Analytical pure elements	Single crystal 4 × sublimated	31-1	4200	180	180	1700	2200
As supplied "Suprapur" element	Polycrystalline 1 × sublimated	40	35000	11000	690	20000	3800
As above, but with I_2 after 2 × sublimated	Polycrystalline 1 × sublimated	38	1700	17	38	660	980

Table IV. Spark source mass spectrum of the purest polycrystalline α-HgI_2 (No 38) as compared with the spectra of two single crystals grown from different source material

Impurity (as positive ions)	Concentration relative to Hg, ppm at. HgI_2 powder single crystal 4 × sublimated (no 29)	Analytical elements single crystal 4 × sublimated (no 30-1)	"Suprapur" elements, I_2 purified polycrystalline 1 × sublimated (no 38)
C	290	180	17
N	65	91	25
O	87	88	13
Na	820	1100	610
Al	120	41	27
K	2500	360	110
Ca	200	160	98
Cr	93	200	47
Mn	3.5	18	1.6
Fe	130	300	82
CH_3	230	150	61
C_2H_3	530	360	130
C_3H_3	780	560	260
C_3H_4	310	320	98
C_4H_4	93	86	26
C_4H_7	490	140	52
C_4H_8	120	80	35
Total	6900	4200	1700

that only a few monolayers evaporation takes place during an experiment of several hours.

The minor drawbacks referred to above are (*i*) the tilting of the specimen is appreciably hindered when using the cooling stage, so that only magnifications up to about 10,000 can be effectively used, and (*ii*) some condensation of impurities takes place on the specimen. As we will see, however, the latter effect leads, under certain conditions, to decorations which appreciably increase the resolving power of the instrument.

Despite the low conductivity of HgI_2, it was not necessary to coat the surface with a metal film prior to the SEM observation. Charging effects were avoided if all the surfaces of the specimen, except the one to be investigated, were covered with conducting carbon paint.

Evacuation and cooling procedures required a compromise between evaporation of the HgI_2 specimen and deposition of the residual gases. When cooled with liquid nitrogen after normal vacuum ($1\text{-}2 \times 10^{-5}$ Torr) was attained, the sample suffered some evaporation during evacuation. On the other hand, the simultaneous start of evacuation and cooling resulted in deposition of a fair amount of white particles, presumably ice crystals, on the specimen. The best result was obtained by a few minutes evacuation by the forepump followed by cooling with liquid nitrogen. Evacuation by the diffusion pump started after the sample reached the low temperature desired

In order to establish a bridge to the existing observations using optical microscope (5, 6, 9, 13), we have investigated the same as grown surface, both with OM and SEM. This surface was then etched and again investigated, first with OM and then with SEM. In addition, cleaved surfaces were investigated before and after etching. The etching solution used was 0.2% Br_2 solution in methanol (14), applied to the surface after polishing with 20% KI aqueous solution.

The main results of our investigation are the following: (*i*) Several forms of etch pits were observed. The results of the SEM investigation indicate that not all of them may be attributed to dislocation pits (6, 8, 13). (*ii*) Crystals grown by static sublimation even without particularly good temperature stabilization seem to be dislocation poor, showing many parts with dislocation densities of 10^3 cm^{-2}. (*iii*) Crystal growth on the (001) plane takes place, at least sometimes, via spiral dislocations.

Figure 5 is an optical micrograph in reflection mode of an as-grown crystal face (001), at a magnification of about 70 times. The crystal was taken from a charge which contained intentionally added polyethylene (7). It is probably due to bunching of the spiral steps that we can see them at this low magnification. Figures 6a and b show at two different magnifications of the SEM of the same crystal face. Some evaporation has taken place during the evacuation of the SEM and a residue (white) decorated the surface. It probably originates from the impurities contained in the crystal and some contamination from the microscope. That many monolayers have been evaporated, is seen also from the optical micrograph (Fig. 7, taken after the SEM investigation). The step height has decreased down to the border of the optical resolution of the microscope, so that the position of the steps becomes visible only

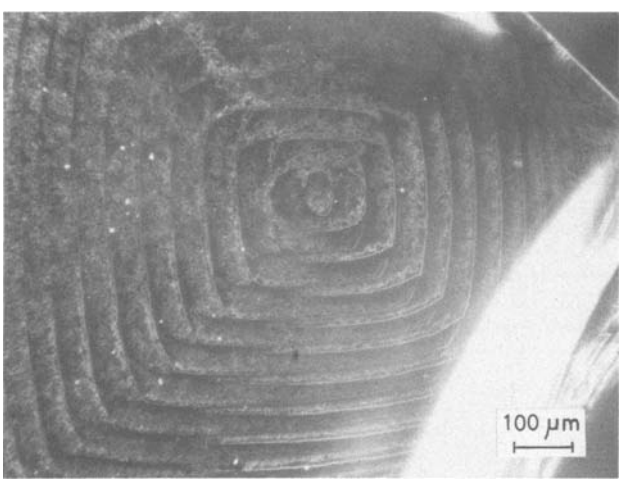

Fig. 5. An optical micrograph of an as-grown (001) facet, showing the spiral pattern, of an α-HgI_2 crystal grown in the presence of polyethylene dopant.

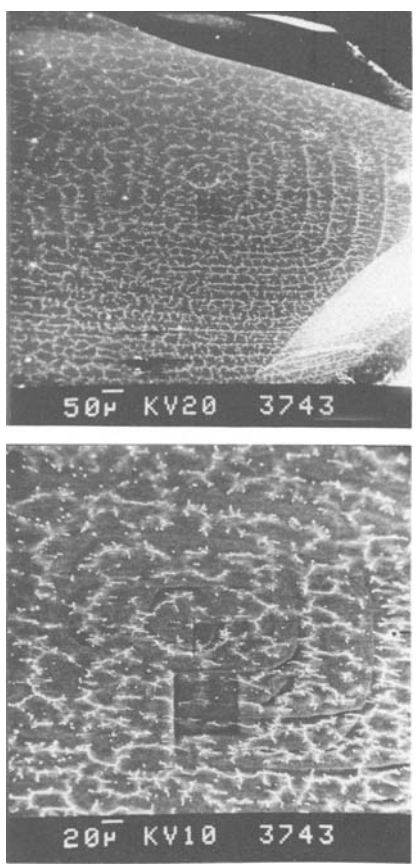

Fig. 6. SEM photographs of the same crystal face as in Fig. 5, taken by using a cold stage. Partial evaporation and decoration took place due to evacuation and cooling with liquid nitrogen.

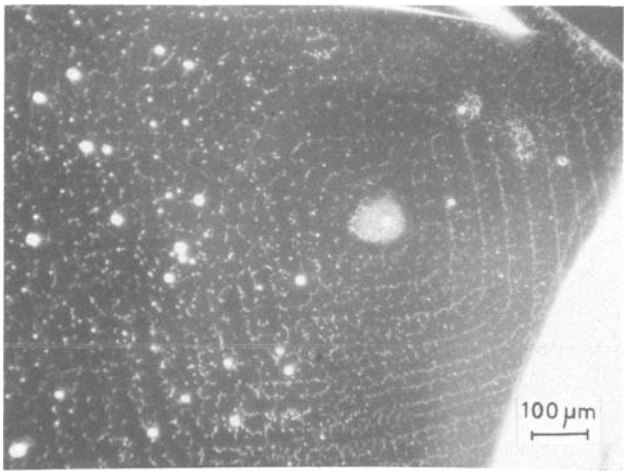

Fig. 7. An optical micrograph of the same crystal face as in Fig. 5, taken after the SEM observation. It shows the weak spiral pattern decorated with impurities. The central part suffered damage by the electron beam bombardment.

from the traces of the residue. After polishing and etching for 30 sec, many etch pits appeared (Fig. 8) on the surface originally covered by the spiral steps. Figures 9a and b are SEM micrographs of these pits. They are flat bottomed and do not show the point of emergence of a dislocation. Clearly these etch pits appear not only on electron bombarded surfaces but also on etched as-grown surfaces (Fig. 10).

Among these flat bottomed pits, there are some others which show an emergence point of a dislocation. Figures 11a and b are SEM, and Fig. 12a and b optical micrographs of such etch pits. A cluster of pronounced pyramidal pits was also sometimes observed in cleaved and etched imperfect surfaces (Fig. 13).

A typical concentration of etch pits for crystals grown by static sublimation is shown in Fig. 14. The figure shows an as-grown crystal surface after polishing and etching for 30 sec. The central part of the crystal contains a low number of pyramidal etch pits, corresponding to a dislocation density of 10^3 cm^{-2}. It is quite common that larger areas of the crystal do not contain any etch pits so that much lower etch pit densities can be calculated.

The outer zone of this crystal shows a high concentration (bands) of flat bottomed pits. This can be the result of increasing impurities towards the end of the growth experiment. This explanation is in agreement with the decrease of growth rate in long duration experiments (Fig. 3), which was explained also with high concentrations of impurities at the last stage of growth.

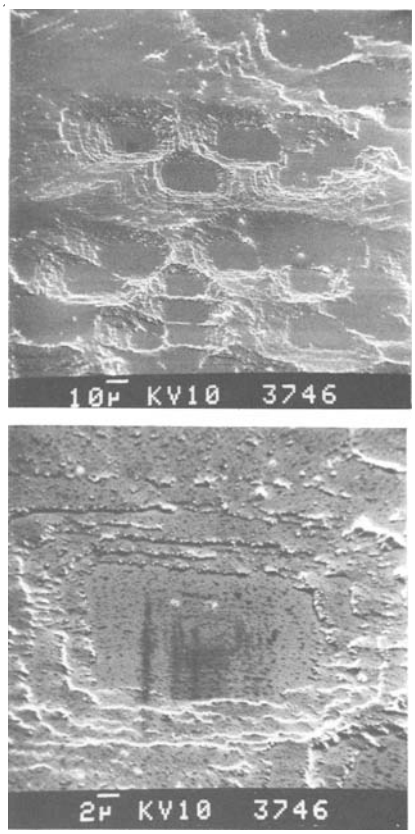

Fig. 9. SEM micrographs of the etch pits shown in Fig. 8. Flat bottomed pits can be clearly seen in a, and b.

Conclusions

The applicability of spark-source mass spectrographic analysis and SEM investigations in α-HgI_2 was demonstrated, using single crystals grown by static sublimation as well as polycrystalline material. Spectrum and concentration of impurities are greatly influenced by those of the starting material, even after repeated sublimations. These reduce of course the concentration of impurities of the commercial starting material, but purer samples can be obtained from material synthesized from pure elements.

Even "suprapur" iodine introduces large amounts of hydrocarbons in the HgI_2 crystals. These impurities are greatly reduced if the iodine is repeatedly subli-

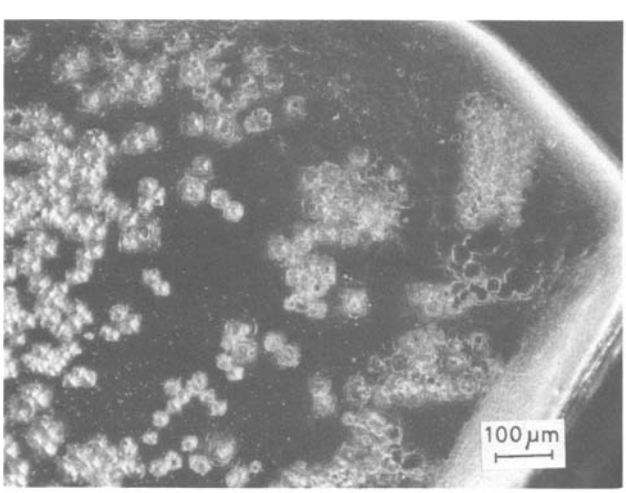

Fig. 8. An optical micrograph of the same crystal face as in Fig. 7, taken after etching with 0.2% Br_2 in methanol.

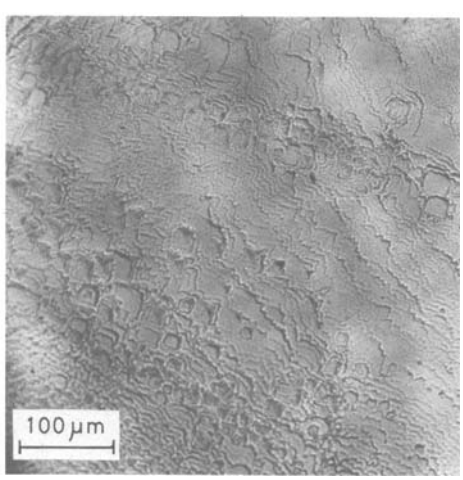

Fig. 10. Flat bottomed etch pit clusters on an etched as-grown surface (optical micrograph).

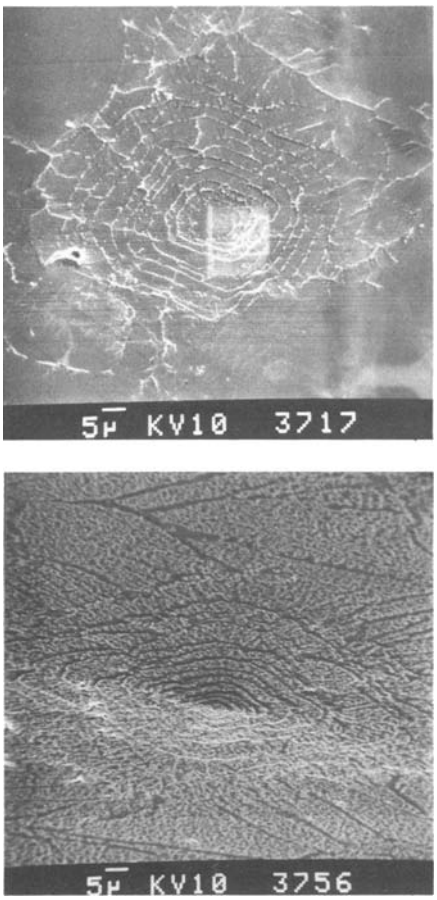

Fig. 11. SEM micrographs which show emergence points possibly due to dislocations. The white square in Fig. 11a is due to the scan of the electron beam.

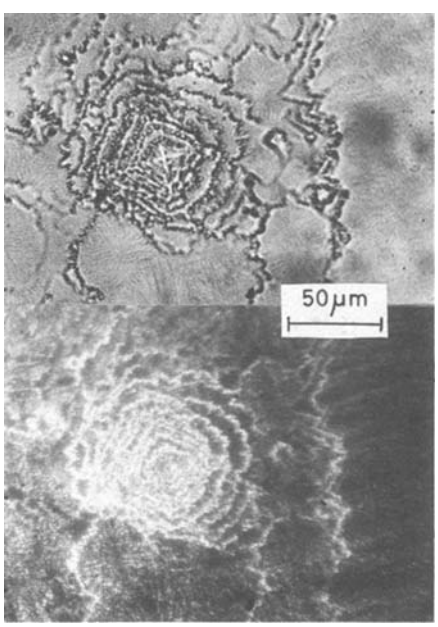

Fig. 12. Pyramidal etch pits which may be due to dislocations. (a, top) Optical micrograph in transmission mode, (b, bottom) in reflection mode.

mated. We may conclude, therefore, once more, that not the claimed purity, but only the one proved by mass spectrography is decisive for the preparation of pure material. High concentrations of impurities and carbon containing inclusions have been found even in single crystals, indicating possible intercalation of the layer structure of α-HgI_2. Growth experiments of

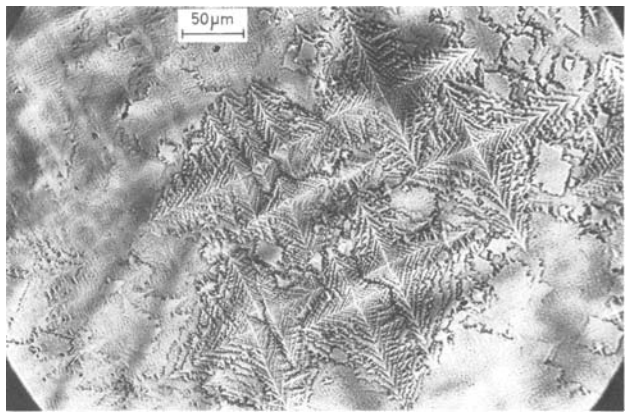

Fig. 13. A cluster of pronounced pyramidal etch pits on an etched cleaved surface.

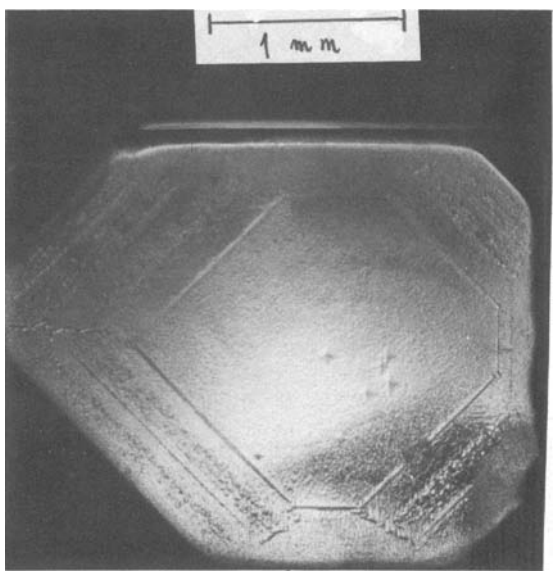

Fig. 14. As-grown crystal surface after polishing and etching. Notice the low concentration of pyramidal etch pits in the central part corresponding to a dislocation density of 10^3 cm^{-2}. Bands with high concentration of flat bottomed etch pits appear at the outer parts.

long duration with technical grade material show a decrease of the growth rate as a function of time by one order of magnitude. It is probable that this is the result of step-poisoning by impurities. Crystals grown by static sublimation show an appreciable linear growth rate (10^{-6} cm/sec) and low dislocation density (10^3 or less/cm^2). SEM investigations at liquid nitrogen temperature revealed that most etch pits are flat bottomed and do not show the point of emergence of a dislocation. Such flat bottomed etch pits appear in crystal surfaces after SEM investigations (probably as the result of electron bombardment) but also in as-grown surfaces.

Acknowledgments

One of us (E.K.) wishes to express his thanks to the Schweizerische Volkswirtschafts-Stiftung for a grant which enabled the above investigation. All authors are indebted to Prof. H. R. Hohl and Mr. U. Jauch (Institute of Plantbiology, University of Zürich) for allowing the use of the SEM-cooling stage.

Manuscript submitted Aug. 31, 1982; revised manuscript received Jan. 7, 1983.

Any discussion of this paper will appear in a Discussion Section to be published in the December 1983 JOURNAL. All discussions for the December 1983 Discussion Section should be submitted by Aug. 1, 1983.

REFERENCES

1. R. C. Whited and M. Schieber, *Nucl. Instrum. Methods*, **162**, 113 (1979).
2. P. Siffert, *J. de Phys. Coll., C3*, **39**, C 3-40 (1978).
3. C. Scharager, P. Siffert, A. Holzer, and M. Schieber, *IEEE Trans. Nucl. Sci.*, **ns-27**, 276 (1980).
4. S. Caine, A. Holzer, I. Beinglass, M. Schieber, and E. Lowenthal, *ibid.*, **ns-25**, 649 (1978).
5. M. Schieber, I. Beinglass, G. Dishon, A. Holzer, and G. Yaron, *Nucl. Instrum. Methods*, **150**, 71 (1978).
6. Y. F. Nicolau and J. P. Joly, *J. Cryst. Growth*, **48**, 61 (1980).
7. S. P. Faile, A. J. Dabrowski, G. C. Huth, and J. S. Iwanczyk, *ibid.*, **50**, 752 (1980).
8. P. T. Randtke and C. Ortale, *IEEE Trans. Nucl. Sci.*, **ns-24**, 129 (1977).
9. M. Schieber, *Nucl. Instrum. Methods*, **144**, 469 (1977).
10. (a) J. T. Muheim, T. Kobayashi, and E. Kaldis, in "Proceedings of the 5th International Workshop on α-HgI_2, Jerusalem (1972), to appear in *Nucl. Instrum. Methods*; (b) G. G. Gospodinov, T. I. Godzhevurgova, and D. S. Barkov, *J. Appl. Chem. USSR*, **51**, 520 (1978).
11. M. Schieber, R. C. Carlston, H. A. Lamonds, P. T. Randtke, and F. W. Schnepple, *J. Cryst. Growth*, **24/25**, 205 (1974).
12. E. Kaldis, in "Crystal Growth, Theory and Techniques," Vol. I, H. L. Goodman, Editor, pp. 49-191, Plenum Press, London (1974).
13. J. P. Ponpon, R. Stuck, and P. Siffert, *IEEE Trans. Nucl. Sci.*, **ns-22**, 182 (1975).
14. M. Schieber, I. Beinglass, G. Dishon, and A. Holzer, in "Current Topics in Materials Science," Vol. II, E. Kaldis and H. J. Scheel, Editors, pp. 280-300, North Holland, Amsterdam (1977).
15. G. Busch, E. Kaldis, J. T. Muheim, and R. Bischof, *J. Less-Common Metals*, **24**, 453 (1971); J. T. Muheim, *Helv. Phys. Acta*, **48**, 444 (1975).
16. J. T. Muheim, *Spectra 2000*, **8**, 55 (1980).

Growth and Characterization of $Ga_{0.47}In_{0.53}As$ Films on InP Substrates Using Triethylgallium, Triethylindium, and Arsine

J. S. Whiteley[1] and S. K. Ghandhi*

Electrical, Systems, and Computer Engineering Department, Rensselaer Polytechnic Institute, Troy, New York 12181

ABSTRACT

Lattice matched epitaxial layers of $Ga_{0.47}In_{0.53}As$ on InP substrates are of current interest in a number of device applications. In this paper, we report on the growth of such epitaxial layers using organometallic chemical vapor deposition with triethylgallium (TEG), triethylindium (TEI), and arsine (AsH_3) for the reactant species. A conventional, atmospheric pressure reactor system was used for these experiments. The depletion reaction between TEI and arsine has been modeled and a theory predicting the epitaxial layer composition as a function of the reactant pressures at the inlet has been developed, based on this model. The inclusion of an *in situ* substrate etching step has been found to significantly improve the surface morphology of the grown layer and resulted in mirror-like surfaces. The effect of lattice mismatch is shown to be much worse for layers in tension than for layers in compression.

Lattice matched $Ga_{0.47}In_{0.53}As$ epitaxial layers on indium phosphide substrates are currently of interest for the fabrication of detectors for optical fibers operating at the transmission loss minimum, near 1.6 microns wavelength (1). This material also has been demonstrated to have improved electron transport properties over GaAs (2), making it attractive for use in high frequency field effect transistors (3, 4).

In a previous paper (5), we have demonstrated the feasibility of using organometallic chemical vapor deposition (OMCVD), with trimethylgallium (TMG), triethylindium (TEI), and arsine (AsH_3) to grow $Ga_{0.47}In_{0.53}As$ on InP in a reactor operating at atmospheric pressure. An *in situ* etching process for the indium phosphide substrates was also presented, and the improvement in epitaxial layer morphology which resulted from its use was demonstrated.

A number of advantages can be realized if triethylgallium (TEG) is used as the gallium source instead of TMG. The vapor pressure of TEG is significantly lower than that of TMG (6) allowing better control of the gas phase concentration of the gallium species. The incorporation rate of gallium into the epitaxial layer is also lower when TEG is used, as has been observed previously (7). Together, these effects make it possible to obtain greater control of the epitaxial layer composition and growth of lattice matched layers over a wider range of conditions than is the case for TMG.

In this paper we report the growth of $Ga_{0.47}In_{0.53}As$ on InP substrates in an atmospheric pressure reactor, by the reaction of TEG, TEI, and AsH_3. The effect of *in situ* substrate etching prior to epitaxy on the electrical properties of the layers is also described.

A major complication in the use of organoindium compounds as reactant sources is their depletion due to a low temperature reaction with arsine (8, 9). This paper also presents a model for this depletion which allows prediction of the effect of the reactant particle pressures on the composition of the epitaxial layer.

Experimental Apparatus and Procedure

The reactor system used in these experiments has been described previously (10). The only modification to this system was the substitution of TEG[2] for TMG. The other reactant sources, TEI and arsine,[3] and the procedure for preparing the indium phosphide[4] substrates were identical to that in our previous paper (5). Throughout this work the TEG and TEI bubblers were maintained at 10° and 24°C, respectively.

All the epitaxial $Ga_{1-x}In_xAs$ layers reported in this paper were grown with a total gas flow of 6.0 standard liters/min and a total organometallic flow rate (TEI and TEG) of 0.54 standard cm^3/min (sccm).[5] These flow rates were calculated assuming that equilibrium saturation was achieved in the bubblers and all partial pressures were calculated assuming ideal gas behavior. Epitaxial layer composition (x) was varied by adjusting the ratio of TEI to TEG (P_{TEI}/P_{TEG}) in the inlet stream.

* Electrochemical Society Active Member.
[1] Present address: MA-COM, Gallium Arsenide Products Company, Burlington, Massachusetts 01803.

[2] Alfa-Ventron, Danvers, Massachusetts 01923.
[3] Matheson Gas Products, E. Rutherford, New Jersey 07074.
[4] Varian Associates, Palo Alto, California 94303.
[5] Throughout this paper, all flows are quoted in terms of the flow of pure gas.

Epitaxial layers were grown both on substrates which were etched *in situ* prior to epitaxy and on substrates which were not etched. Experiments without the *in situ* substrate etching step consisted of heating the substrate to the desired growth temperature, typically 700°C, with a phosphine flow of 36 sccm ($p_{PH_3} = 6.0 \times 10^{-3}$ atm) added to the required flows of hydrogen and arsine. Control experiments have shown these conditions to be sufficient to prevent substrate decomposition at temperatures less than 750°C. After stabilization at the desired growth temperature, the phosphine flow was terminated. The organometallic flows were begun, initiating layer growth, after a 1 min interval to allow the phosphine to be purged from the reactor.

Anhydrous hydrogen chloride gas was the etching agent in experiments where *in situ* substrate etching was used. Details of this process have been given in an earlier paper (5). In summary, however, a 1% mixture of electronic grade HCl in hydrogen[6] was used as the etchant source for InP substrates at 750°C. The etching was carried out with a phosphine overpressure of 1.3×10^{-2} atm to prevent substrate decomposition. An HCl flow of 1.77 sccm was used to remove about 25 microns of substrate in 2 min, providing a featureless surface on which the epitaxial $Ga_{1-x}In_xAs$ was subsequently grown.

Epitaxial Layer Growth

Precise control of the composition of the $Ga_{1-x}In_xAs$ epitaxial layer is required for obtaining lattice matching on InP substrates From an experimental point of view, use of TEG as the gallium reactant source was advantageous, since it allowed the growth of closely lattice matched layers over a much wider range of conditions than was possible using TMG.

It was necessary to develop (11) a mathematical model describing the depletion of TEI from the gas stream in order to understand the effect of the partial pressures of the three reactant sources, TEG, TEI, and AsH_3. The depletion of TEI was assumed to occur by a first-order, bimolecular reaction with AsH_3

$$TEI_{(g)} + AsH_{3(g)} \rightarrow Complex_{(s)} \qquad [1]$$

The product of this reaction condensed on the walls of the reaction chamber upstream of the reaction zone, resulting in less TEI arriving to the substrate. The rate of this depletion reaction can be written as

$$\frac{dp_{TEI}}{dt} = -K p_{TEI}(t)\, p_{AsH_3}(t) \qquad [2]$$

Expressing the partial pressures as functions of time

$$p_{TEI}(t) = p^\circ_{TEI} - \delta(t) \qquad [3]$$

$$p_{AsH_3}(t) = p^\circ_{AsH_3} - \delta(t) \qquad [4]$$

where p°_{TEI} and $p^\circ_{AsH_3}$ are the reactant partial pressures before any depletion occurs, and $\delta(t)$ represents the amount of product formed, in units of its pressure, if it were an ideal gas. These equations can be combined and solved using direct integration after algebraic manipulation, giving

$$p_{TEI}(t) = p^\circ_{TEI} \frac{1 - p^\circ_{TEI}/p^\circ_{AsH_3}}{\exp\left[K\,(p^\circ_{AsH_3} - p^\circ_{TEI})\,t\right] - \dfrac{p^\circ_{TEI}}{p^\circ_{AsH_3}}} \qquad [5]$$

The composition of $Ga_{1-x}In_xAs$ layers will depend on the partial pressures of the gallium and indium reactant species near the substrate. Earlier experiments in this study, as well as literature data (5, 8, 9), indicate that the mol fractions of gallium and indium in the solid are proportional to the partial pressures of TMG and TEI in the inlet stream. This behavior is also expected to hold for the growth of $Ga_{1-x}In_xAs$ using TEG, so that

$$\frac{x}{1-x} = K_2 \left.\frac{p_{TEI}}{p_{TEG}}\right|_{Substr.} = K_2 \frac{p^\circ_{TEI}}{p^\circ_{TEG}} \frac{p^\circ_{TEI}/p^\circ_{AsH_3}}{\exp\left[K_1(p^\circ_{AsH_3} - p^\circ_{TEI})\right] - p^\circ_{TEI}/p^\circ_{AsH_3}} \qquad [6]$$

In this equation, K_1 is a phenomenological constant that groups together the depletion reaction rate and the transit time from the inlet to the vicinity of the substrate. Its calculation would require knowledge of the flow pattern and thermal gradients encountered within the reaction chamber.

The effect of the TEI/TEG ratio on the epitaxial layer composition is shown in Fig. 1 for layers grown at 600° and at 700°C. The arsine partial pressure was 8.3×10^{-4} atm for the 600°C experiments, and 4.2×10^{-4} atm for the 700°C experiments. The solid curves shown on this figure were calculated from the theoretical equation. The agreement between the predictions and the experimental data indicates that the assumption of proportionality between the gas phase and the solid phase compositions is valid. The linearity of the curves in Fig. 1 is due to the narrow range of TEI partial pressures used in these experiments and the large TEI to AsH_3 ratios (9.5-26.3).

Comparison with the previous results obtained using TMG indicates the gallium incorporation is reduced when TEG is the reactant source. The relative transport ratio may be defined as the quotient of the solid-phase indium to gallium ratio to that of the gas phase at the inlet, *i.e.*, $(x/1-x)/(p^\circ_{TEI}/p^\circ_{TEG})$. In the present experiments this ratio was approximately 2.36 for layers grown at 600°C, and 1.66 for those grown at 700°C. In our earlier work with TMG at 700°C this ratio was 0.22.

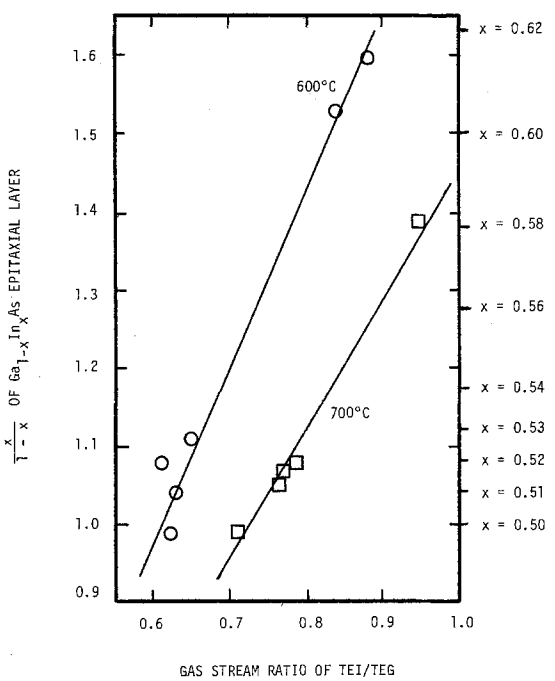

Fig. 1. Effect of the TEI/TEG pressure ratio at the inlet on the composition of $Ga_{1-x}In_xAs$ layers. These experiments had a total flow rate of 6000 sccm, and a total organometallic flow rate (TEG + TEI) of 0.54 sccm. The 700°C experiments had an arsine partial pressure of 4.2×10^{-4} atm while those at 600°C are for 8.3×10^{-4} atm.

[6] Synthatron Corporation, Parsippany, New Jersey 07054.

We have indicated that the presence of TMG inhibits the depletion reaction of AsH_3 and TEI (5). It is possible that the use of TEG further inhibits this reaction, since it is present as a larger fraction of the input mixture. No definitive judgment can be made on this issue, however.

Figure 2 shows the inlet gas phase TEI-TEG ratio required to grow $Ga_{0.47}In_{0.53}As$, as a function of the arsenic partial pressure. Note that this depletion begins to occur at the point of mixing, but continues throughout the travel of reactants in the hot zone. Thus, the combined effects of temperature, temperature gradient, and transit time cooperate in this process. In our work, this change is relatively small (about 46% for a temperature range from 600°-750°C). We do not believe that the incorporation ratios of the individual elements change significantly with temperature, since growth of either pure GaAs or pure InAs (9) is essentially mass transport limited in this range. The solid curves indicate the theoretically predicted behavior and were calculated using the constants K_1 and K_2, which yielded the best fit to the experimental data. At 700° these were $K_1 = 1.23 \times 10^2$ $atom^{-1}$, $K_2 = 1.45$; while at 600°C, $K_1 = 2.98 \times 10^2$ $atom^{-1}$, $K_2 = 2.35$. The correlation between the theory and the data in this case indicates that the bimolecular depletion model predicts with reasonable accuracy the effect of arsine partial pressure on the extent of depletion of TEI.

The substrate temperature had little effect on the growth rate of the epitaxial layers. Over the range of 550°-750°C, the apparent activation energy associated with the epitaxy of $Ga_{0.47}In_{0.53}As$ was approximately 2.3 kcal/mol. This value is typical of processes in which the rate is limited by the gaseous diffusion of reactants or products through a boundary layer (12), and is an order of magnitude below what would be expected if the rates were kinetically controlled (13). In these experiments therefore, it appears that the growth rate is mass transport limited by diffusion.

In Fig. 3, the relative transport ratio, $(x/1-x)/(p_{TEI}/p_{TEG})$, is shown as a function of susceptor temperature, for layers grown with an arsine partial pressure of 4.2×10^{-4} atm. The decrease in the relative transport ratio at temperatures above 600°C can be explained by the increasing depletion of TEI from the inlet gas stream at higher temperatures. Here, the depletion of indium is clearly seen to be greater at 700° than at 600°C. Note, however, that a fourfold change in AsH_3 pressure changes the requirements on the TEI/TEG ratio by only 1.6. This serves to emphasize that temperature is only one term in controlling the indium depletion reaction, and that kinetic factors are also important.

The fall in this ratio at temperatures below 600°C could be due to small differences in the desorption rates of the indium and gallium species at the surface, or to differences in the temperature dependences of the gaseous diffusion rates. This data serves to emphasize the importance of accurate temperature control for the growth of closely lattice matched epitaxial layers, even though the growth process is mass transport limited.

The primary effect of *in situ* substrate etching prior to epitaxy on the growth process was to improve the morphology of the epitaxial layers. The degree of surface roughness was much smaller for layers grown on etched substrates than in layers grown without a substrate etching step. However, *in situ* substrate etching had no effect on either the composition (5) (as determined by gravimetric methods) or the growth rate of epitaxial layers. Smooth surfaces, with few visual defects, were obtained for layers grown at temperatures between 600° and 750°C. At lower temperatures the films became increasingly faceted and exhibited a large density of visual defects. The partial pressure of arsine used during growth did not appear to affect the morphology of these layers, therefore, it

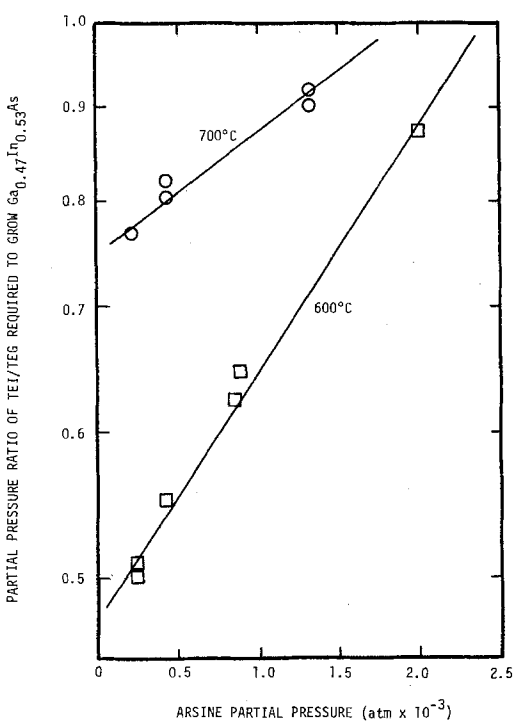

Fig. 2. Effect of the arsine partial pressure on the TEI/TEG ratio required to grow $Ga_{0.47}In_{0.53}As$. The experiments had a total flow rate of 6000 sccm and a combined (TEG + TEI) flow of 0.54 sccm.

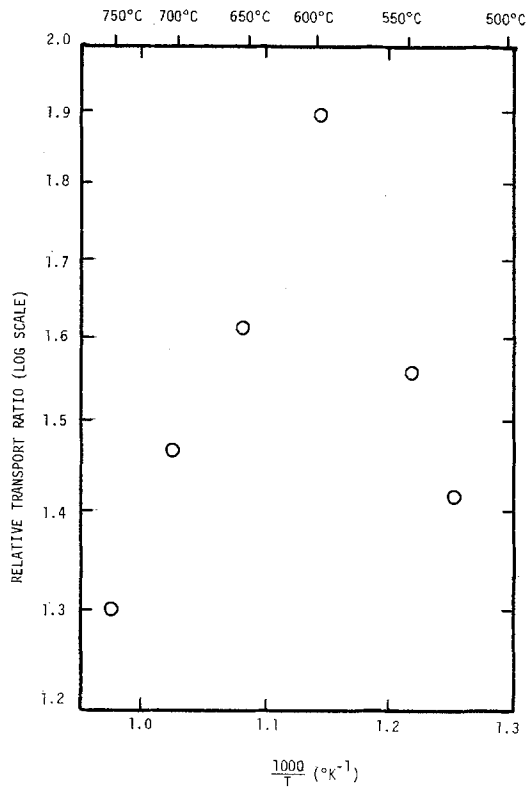

Fig. 3. Effect of growth temperature on the relative transport ratio

$$\left[\left(\frac{x}{1-x}\right)\Big/\left(\frac{p_{TEI}}{p_{TEG}}\right)\right]$$

Experiments were conducted with a total flow of 6000 sccm, a total organometallic flow (TEG + TEI) of 0.54 sccm, and an arsine pressure of 4.2×10^{-4} atm.

appears that the growth rate is mass transport limited by diffusion.

Electrical Characteristics

All epitaxial layers grown in this study were n-type with carrier concentrations of between 10^{16} cm^{-3} and 1.5×10^{17} cm^{-3} due to residual impurities in the reactant sources. The electron mobility and concentration in these layers were measured from the Hall effect using the van der Pauw technique, with layers grown on semi-insulating Fe^+ doped InP. The Hall mobility measured by this technique typically ranged from 6000 cm^2/V-sec ($n = 5 \times 10^{16}$ cm^{-3}) at room temperature to 10,000 cm^2/V-sec at 77 K. Note that these values are averaged over the entire layer. Sequential etch and van der Pauw measurements showed that the layer mobility was nonuniform, and fell off in the vicinity of the episubstrate interface (14). Lattice matched epitaxial $Ga_{1-x}In_xAs$ layers were grown at temperatures between 550° and 750°C, and at growth rates from 0.07-0.1 μm/min.

Figure 4 shows the electron mobility, measured at 300 K, for layers grown over this temperature range. As shown in this figure, the electron mobility improved with increasing growth temperature up to about 700°C, but decreases at temperatures greater than this value. We believe that this is due to two competing factors. First, growth at increasing temperatures leads to increased crystalline perfection in the epitaxial layer, due to the enhanced diffusion effects of reactant species on the surface. On the other hand, residual impurity incorporation would also be expected to increase with temperature, as has been shown for the organometallic growth of GaAs (15). Thus, the observed decline in mobility above 700°C can most probably be attributed to the effects of increased impurity scattering, resulting from this latter effect.

Lattice matched epitaxy is desirable in order to minimize the effects of interfacial defects on the electrical properties of the epitaxial layer. The effect of the composition, and hence the lattice mismatch, on the electron mobility of as-grown epitaxial layers is shown in Fig. 5. Here, the composition of the epilayers was determined by optical transmission measurements in the range $1.1 < \lambda < 2$ μm, which were used to determine the absorption coefficient, and extrapolated to find the direct bandgap (5). The composition was calculated from

$$E_g(x) = 0.36 + 0.629\,(1 - x) + 0.436\,(1 - x)^2 \quad [7]$$

which is a best quadratic fit to photoluminescence and optical absorption data in the literature. The lattice parameter was next calculated by the use of Vegard's law. The carrier concentration of these films showed no correlation with layer composition and was in the mid-10^{16} cm^{-3} range for each of the data points shown. All layers were approximately 4 microns thick. As can be seen, the electron mobility of epitaxial layers with $|\Delta a/a_0| < 10^{-3}$ did not vary significantly with composition. Films within this range have been considered to be lattice matched (16). Additionally, films under compressive stress ($x > 0.53$) exhibited high electron mobilities even though their lattices were only poorly matched to the substrate. Indium-deficient layers which were under tensile stress, to the extent that their unstrained lattice constants exceeded the above criterion, exhibited decreased electron mobilities. Similar results have been reported for layers grown by both liquid phase epitaxy (16) and molecular beam epitaxy (17), and have been attributed to the greater probability of dislocation formation and "microcracking" in layers under tensile stress than in those under compressive stress (18).

Conclusions

We have shown that device quality $Ga_{0.47}In_{0.53}As$ can be grown on InP by OMCVD at atmospheric pressure. The use of TEG as the gallium reactant source provided several advantages over TMG; among these are its lower vapor pressure and lower incorporation rate, which together act to provide greater control of the growth process. As a result of the wider range of conditions possible, epitaxial layers with electrical characteristics comparable to those reported for thin films grown by low pressure OMCVD (19) and MBE (20) have been obtained.

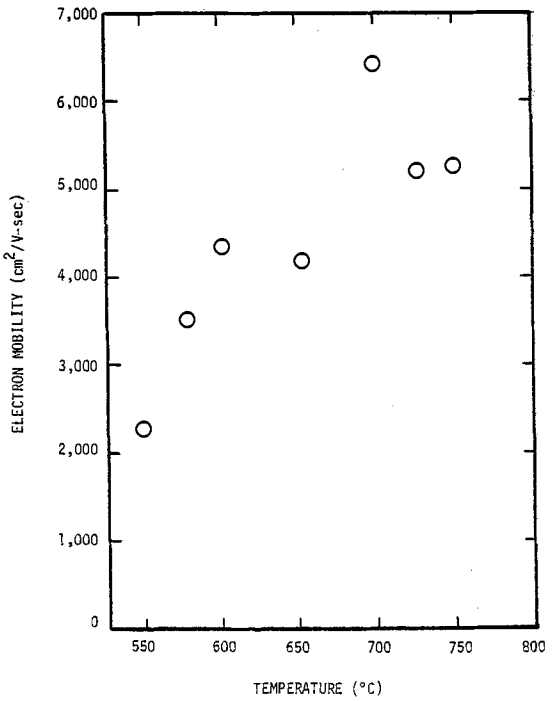

Fig. 4. Effect of growth temperature on the electron mobility of lattice matched $Ga_{1-x}In_xAs$ epitaxial layers grown on InP.

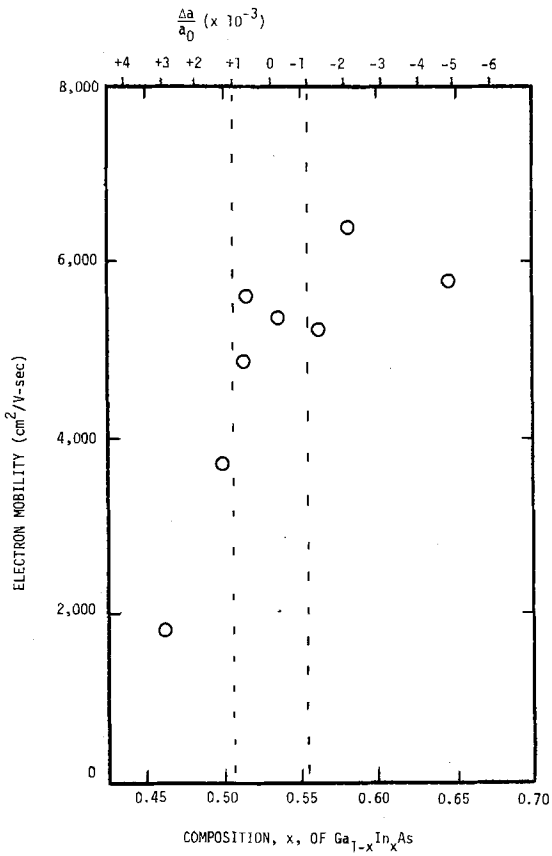

Fig. 5. Effect of the composition (x) of $Ga_{1-x}In_xAs$ layers grown on InP on the electron mobility. These layers were grown at 700°C and were all approximately 4 microns thick.

A model of the depletion reaction between TEI and AsH_3, which is a major complication in the OMCVD of $Ga_{1-x}In_xAs$, has been developed and shown to predict the composition of the epitaxial layer as a function of the reactant partial pressures. This model, along with our experimental results, demonstrates the requirement of precise flow and temperature controls for the attainment of closely lattice matched epitaxial layers, even though the growth process appears to be diffusive mass transport limited.

The results of our electrical measurements have shown that, whereas lattice matching is important in obtaining the best electrical performance, slightly mismatched films under compressive stress are preferable to those under tensile stress. Additionally, the incorporation of an *in situ* substrate etching step immediately prior to epitaxy was found to substantially improve the surface morphology of the grown layers.

Acknowledgments

The authors would like to thank R. C. Reep for assistance in manuscript preparation. This work was partially supported by Grant No. DAAG29-76-G-0127 from the U.S. Army Research Office, Durham, North Carolina.

Manuscript submitted Aug. 6, 1982; revised manuscript received Jan. 25, 1983.

Any discussion of this paper will appear in a Discussion Section to be published in the December 1983 JOURNAL. All discussions for the December 1983 Discussion Section should be submitted by Aug. 1, 1983.

Publication costs of this article were assisted by Rensselaer Polytechnic Institute.

REFERENCES

1. T. P. Pearsall, *IEEE J. Quantum Electron.*, **qe-16,** 709 (1980).
2. S. Bandy, C. Nishimoto, Shyder, and C. Hooper, *Appl. Phys. Lett.*, **38,** 817 (1981).
3. A. Cappy, B. Garnez, R. Fauquemberques, G. Salmer, and E. Constant, *IEEE Trans. Electron. Dev.*, **ed-27,** 2158 (1980).
4. J. Barnard, H. Ohno, C. E. Wood, and L. F. Eastman, *IEEE Electron. Dev. Lett.*, **edl-1,** 179 (1980).
5. J. S. Whiteley and S. K. Ghandhi, *This Journal*, **129,** 383 (1982).
6. V. K. Vanchagova, A. D. Zorin, and V. A. Umilin, *J. Gen. Chem. U.S.S.R., Engl. Transl.*, **46,** 985 (1976).
7. G. B. Stringfellow and H. T. Hall, Jr., *J. Cryst. Growth*, **43,** 47 (1978).
8. H. M. Manasevit and W. I. Simpson, *This Journal*, **120,** 135 (1973).
9. B. J. Baliga and S. K. Ghandhi, *ibid.*, **121,** 1642 (1974).
10. R. Bhat and S. K. Ghandhi, *ibid.*, **124,** 1447 (1977).
11. J. S. Whiteley, Ph.D. Thesis, Rensselaer Polytechnic Institute, Troy, NY, 1982.
12. D. W. Shaw, in "Crystal Growth," Vol. 1, C. H. L. Goodman, Editor, Plenum Press, New York (1974).
13. K. J. Laidler, "Chemical Kinetics," McGraw-Hill, New York (1965).
14. J. S. Whiteley and S. K. Ghandhi, *J. Thin Solid Films*, Submitted.
15. S. J. Bass and P. E. Oliver, "Gallium Arsenide and Related Compounds, 1976,," Inst. Phys. Conf. Ser. No. 33b, p. 1 (1977).
16. J. D. Oliver, Jr. and L. F. Eastman, *J. Electron. Mater.*, **9,** 693 (1980).
17. B. I. Miller and J. H. McFee, *This Journal*, **125,** 1310 (1978).
18. G. H. Olsen and M. Ettenberg, in "Crystal Growth," Vol. 2, C. H. L. Goodman, Editor, Plenum Press, New York (1978).
19. J. P. Hirtz, J. P. Duchemin, P. Hirtz, B. deCremoux, and T. Pearsall, *Electron. Lett.*, **16,** 275 (1980).
20. H. Asahi, H. Okamoto, M. Ikeda, and Y. Kawamura, *Jpn. J. Appl. Phys.*, **18,** 565 (1979).

Molybdenum Nitride Film Formation

M. J. Kim, D. M. Brown,* and W. Katz

General Electric Company, Corporate Research and Development, Schenectady, New York 12301

ABSTRACT

A molybdenum nitride film was developed by direct reaction of the molybdenum film with ammonia or forming gas. The nitride film made above 800°C in pure ammonia showed dominance of the δ-phase MoN, having hexagonal structure which makes it very brittle with a large volumetric expansion. The Mo film can be partially converted to molybdenum nitride by reacting molybdenum with diluted ammonia in the temperature range 500°-700°C. The low temperature film was found to be dominantly γ-phase Mo_2N, with a mixed structure of face-centered cubic and hexagonal. The film retained metallic luster and strength. The ammonia reaction is enhanced by the presence of monatomic nitrogen. Partial conversion of the molybdenum film was found to be easily controlled. The low temperature Mo_2N phase appears suitable for use in VLSI and microelectronic interconnection.

Refractory metal gates to produce self-aligned source/drain MOSFET's were introduced in 1966 (1). Molybdenum or tungsten metal gates have the advantage of high intrinsic conductivity compared to doped polysilicon (2). In addition, the metal gates can be patterned directly using photoresist and simple metal etchants, whereas the polysilicon gate required that an oxide transfer mask be applied for the case of wet etching the gate pattern (3), although direct patterning using plasma etching is generally used for recent processing. Furthermore, polysilicon could be self-passivated using thermal oxidation. High purity silane used for chemical vapor deposition of polysilicon was also readily available and the source/drain diffusions could be formed using conventional high temperature gaseous dopant sources because of the self-passivation properties of polysilicon. These properties made polysilicon gate integrated circuits easily manufacturable. Furthermore, early integrated circuits did not require the high speed capabilities of molybdenum or tungsten gates and interconnections. With a widespread adoption of ion implantation doping, high yield, high frequency molybdenum gate structures became easily fabricable (4). However, passivation against oxidation and protection from mobile ion contamination was still accomplished using doped glasses (4), which can actually getter impurities from the columnar grain structure of molybdenum films (5). Because of higher speed and density requirements, refractory metal materials are assuming a higher degree of importance in VLSI applications.

Various metal silicides have been recently investigated. Platinum, tantalum, molybdenum, and tungsten silicides are being extensively studied. These silicides are about one order of magnitude more conductive than polysilicon, whereas the conductivity of refractory metals is about two orders of magnitude higher.

The purpose of this work is to improve the properties of molybdenum films in order to overcome some of the previous difficulties described above. For instance, it has been reported that molybdenum nitride is a better barrier to mobile ions, has better masking capability against ion implantation, and reduces the possibility of oxidation of the molybdenum underlying the molybdenum nitride layer (6). The nitride layers in Ref. (6) were formed by reactive sputtering.

In this work the molybdenum film was reacted with ammonia and/or forming gas to form molybdenum nitride, with temperatures and gas compositions being varied to find an optimum process. The films were thoroughly characterized by means of SIMS, x-ray diffraction, SEM, and resistivity measurement.

Experimental Procedure

Sample preparation.—The starting material used was 10 Ω-cm p- and n-type Si wafers with (100) orientation. The wafers were oxidized at 1000°C in dry oxygen to grow 500-1000Å of SiO_2. A molybdenum film of 3000Å was sputtered in an S-gun system using argon. The substrate was heated to 250°C to promote adhesion. The center of the wafer was patterned with 20 mil dots for C-V measurements, leaving molybdenum sheets at the edge for the evaluation of changes in physical property. Using photoresist as an etch mask, molybdenum etching was performed in standard Al etch (4). The resist was stripped off in acetone, followed by cleaning in hot phosphoric acid. The initial sheet resistivity was in the range of 0.4-0.5 Ω/sq before nitride formation.

Nitriding in forming gas.—Molybdenum nitride was made by a direct reaction with nitrogen in a mixture of hydrogen gas using an open furnace tube. Since molybdenum is readily oxidized in trace amounts of oxygen or moisture, commercial forming gas had to be cleaned. This was done by passing the forming gas through a Deoxo unit and a subsequent liquid nitrogen trap. A nitride film could be formed in 20 min in the temperature range between 700° and 800°C. This nitride was very thin, (<600Å), as determined by SIMS depth profiling, but could not be made reproducibly.

Nitriding in ammonia.—With the use of ammonia the nitride could be made reproducibly in the temperature range between 500° and 900°C. Initial experiments were performed in a vertical rf reactor with high purity electronic-grade ammonia. A slow heating was required to prevent nonuniform heating, which occasionally causes part of the film to lift. An open tube furnace was found to be more convenient. The nitride films were extensively evaluated using SIMS, x-ray, SEM, and four-point probing techniques.

Results and Discussion

The different thicknesses of molybdenum nitride could be made by varying the temperature, time, and ammonia concentration. Above 700°C, the total thickness (3000Å) of molybdenum could be converted to nitride in 10 min with pure ammonia. In these instances the surface became rough because of the large crystal grain volumetric expansion which occurs during the formation of the nitride. When ammonia was diluted with nitrogen, the reaction rate was reduced, and complete conversion did not take place until 10 min reaction time in the furnace at 750°C had been completed. In the lower temperature range, from 500° to 700°C, a surface layer of the film was converted to nitride, without losing any surface smoothness or luster.

When 10 min nitriding is performed using 10% anhydrous ammonia mixed with 90% dry nitrogen by volume, the temperature is found to be a very useful parameter to control the nitride thickness and structure. Under these conditions the 3000Å Mo can be partially converted to nitride in the temperature range 500°-750°C. The dominant nitride phases are γ-phase

* Electrochemical Society Active Member.

Key words: metals, integrated circuits, conductivity, phase transformation.

Mo_2N (face-centered cubic) in the temperature range of 500°-800°C, and δ-phase MoN (hexagonal) above 800°C. The increase in ammonia concentration or nitriding time showed a similar effect of temperature increase.

MoN (δ-phase) film.—Figure 1 shows SIMS depth profiles of the molybdenum nitride film made by the reaction with 100% ammonia at 800°C for 10 min. Data were taken using a Cameca IMS 3-f ion microscope using Cg^+ primary ions. In order to maximize detection sensitivity, the species profiled were $^{60}Si_2^-$, $^{92}Mo^-$, and $^{112}MoN^+$. In Fig. 1 one notes the conversion of the molybdenum film to MoN. Also, the SiO_2 layer is seen between the MoN film and silicon substrate. This type of SIMS profile was typical for all of the wafers reacted in pure ammonia above 700°C. When the reaction time was extended to 1 hr, similar results were obtained at 650°C. The exact time required to complete the conversion at any given lower temperature was not determined. X-ray traces were obtained with a Siemens D500 diffractometer equipped with Cu target and a graphite-receiving crystal beam monochromator. The traces were run with a Θ angle of the diffractometer offset by 2° to minimize the strong single crystal Si reflections. When this is done, the Si peaks give the appearance of a broad, diffuse profile. Figure 2 shows the x-ray diffraction spectrum of a molybdenum nitride film grown under the same conditions. The strong peak at $2\Theta = 36.554°$ is the (200) diffraction of hexagonal δ-phase MoN with $a = 5.725Å$ and $C = 5.608Å$; $C/A = 0.980$. These data show that almost all of the Mo has been converted to the nitride. The small peak at higher angle suggests the face-centered cubic Mo_2N. There is also a trace of Mo appearing at $2\Theta = 40.802°$, caused by (110) Mo reflection. In any case, δ-phase MoN is the dominant phase in the high temperature process. When the relative intensities of the dominant δ-phase are compared to those given by the JCPDS, (200) preferential orientation is obvious. The δ-phase also contains small amounts of the superlattice structure (7) with 8 atoms per cell.

When δ-phase MoN is formed across the total thickness, the surface becomes hazy, losing the original metallic luster. Figure 3 shows an SEM photomicrograph of the rough surface which develops at 800°C as ammonia concentration is increased (*e.g.*, 20% from 5% in volume). Figure 4 is an SEM photomicrograph of the nitride film made in pure ammonia at 800°C, which shows a localized development of the superlattice embedded in a simple hexagonal sublattice and the generation of cracks along the edge of the islands caused by tension. The severe crack sometimes lifts a part of the film, as presented in Fig. 4. The microscopic observation indicates that the superlattice is not formed uniformly from the beginning of the nitride process when the nitrogen content is low. Since low angle reflection of the thin film is more intense than higher angle, we could not observe the superlattice reflection obtained at the higher angle (7). The new structure, shown in Fig. 4 and 5, starts after the completion of δ-phase transformation without adding any

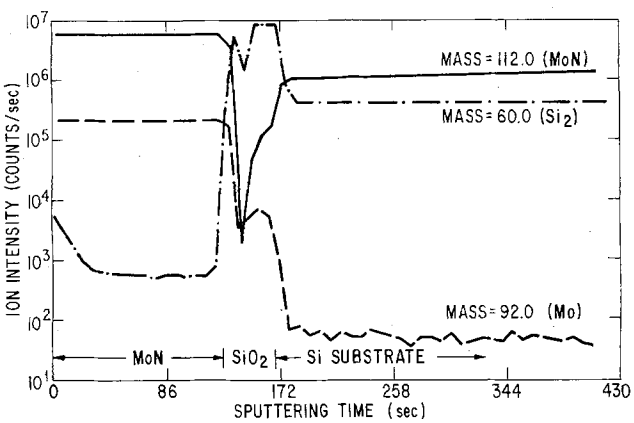

Fig. 1. SIMS composition depth profile of molybdenum nitride film made at 800°C for 10 min in 100% ammonia, showing a complete conversion of 3000Å molybdenum to molybdenum nitride.

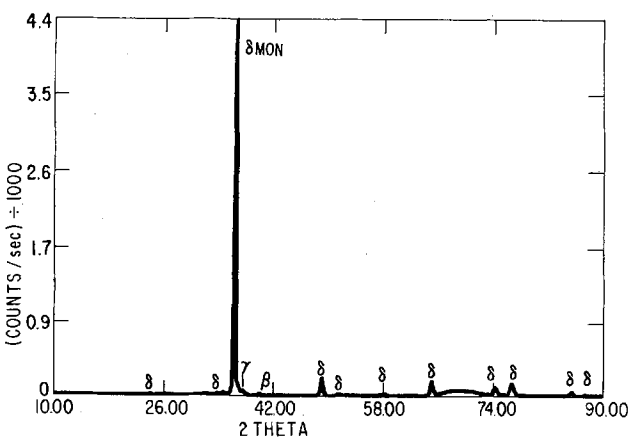

Fig. 2. X-ray diffraction spectrum of the molybdenum nitride made at 800°C for 10 min in 100% ammonia. δ-phase MoN (peak 5) is dominant with a possible trace of Mo_2N.

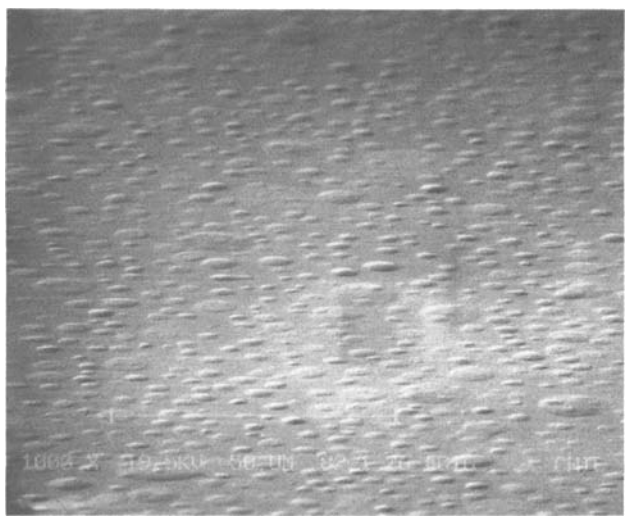

Fig. 3. SEM photomicrograph which shows physical change of the nitride surface. The surface roughness increases with ammonia concentration.

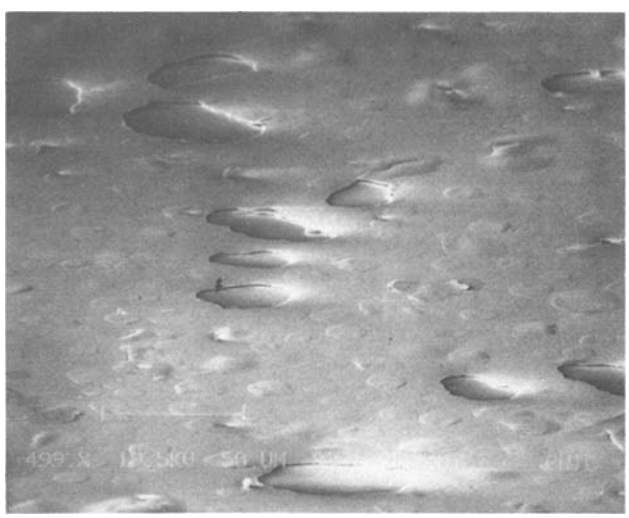

Fig. 4. SEM photomicrograph of the nitride film made in pure ammonia at 800°C, which shows the development of the hexagonal superlattice and cracks along its edge caused by severe tension.

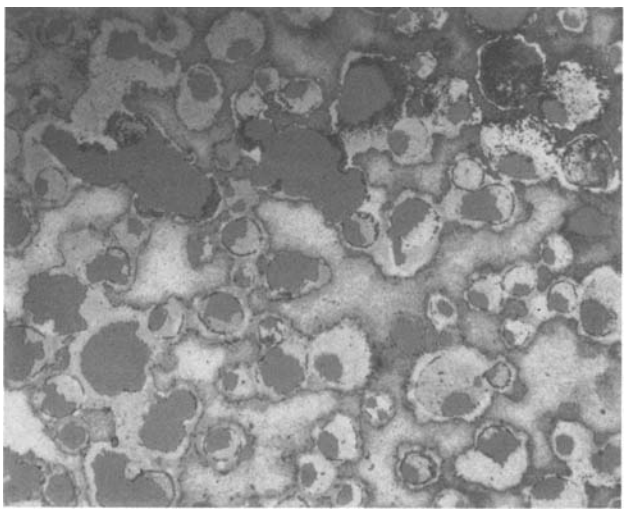

Fig. 5. Nitride film remainder after etching in concentrated nitric acid. The superlattice has less chemical resistance than the surrounding nitride.

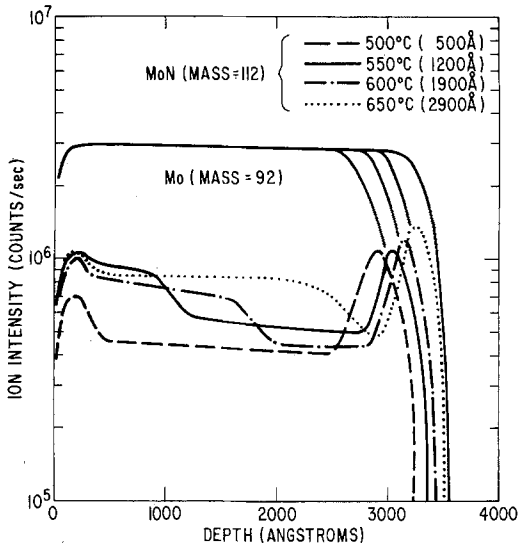

Fig. 6. SIMS profile of molybdenum nitride for different nitriding temperatures in rf reactor with 10% ammonia; the film thickness increases with the reaction temperature.

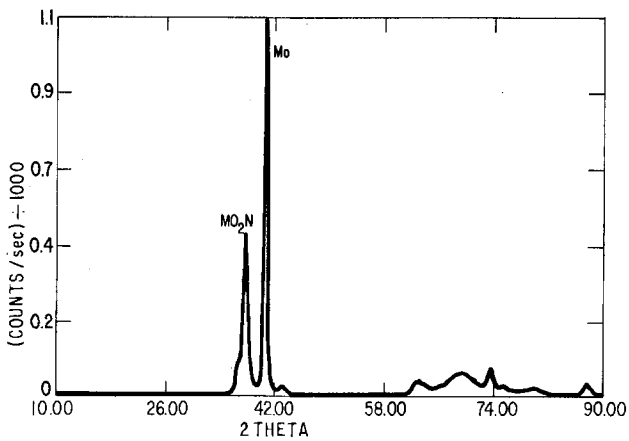

Fig. 7. X-ray diffraction spectrum of the partially converted Mo_2N/Mo double layer made at 600°C for 10 min in 10% ammonia.

significant diffraction peak at the low angle. Therefore, this structure can be linked to the hexagonal superlattice. As the nitrogen concentration increases, the transformation occurs locally. This is clearer in Fig. 5, where the superlattice structure disappears much faster than the surrounding sublattice during the etching, because the sublattice nitrides react at a slower rate in the etchant. In the δ-phase, the smaller nitrogen atoms occupy the interstitial position, but they seem not to be distributed in the ordered interstices of the lattice because there is no extra visible reflection in the x-ray spectrum. The nitrogen atoms may be situated at the centers of trigonal prisms of molybdenum atoms (8), which displace the molybdenum atoms from the normal position of the sublattice. From the lattice constants, the volume of the unit superlattice hexagonal cell can be calculated to be 1.60×10^{-22} cm^3. The volume expansion is 27.7% when compared with the unit cell volume of pure molybdenum. The large volume expansion makes the surface rough. This, together with the inherent property of hexagonal structure, makes the film brittle.

Mo_2N (multiphase) film.—The physically strong and smooth films required for device applications were achieved by partial conversion with 10% ammonia in nitrogen. The ideal temperature range was determined to be 500°-700°C with ammonia gas concentrations of less than 10%.

Figure 6 shows a SIMS depth profile of the nitride grown for 10 min at 500°, 550°, 600°, and 650°C in an rf reactor. Under these conditions part of the 3000Å of molybdenum converts to molybdenum nitride. These profiles show the increasing Mo_2N thickness as a function of nitriding temperature. From these results the molybdenum nitride film thicknesses were determined to be 500, 1200, 1900, and 2900Å for the 500°, 550°, 600°, and 650°C nitriding conditions, respectively. The nitride films are smooth with high luster.

Figure 7 shows a typical x-ray diffraction spectrum of an Mo film after being nitrided in this temperature range. The sample shown in Fig. 7 was made at 600°C under the same conditions. The spectrum indicates major peaks at 2θ diffraction angles of 37.847° and 40.802°, which, respectively, represent Mo_2N and molybdenum. These results show that the film is a composite of molybdenum and molybdenum nitride, a finding which is in qualitative agreement with the SIMS result. The strong 37.847° peak is very close to (111) diffraction of γ-phase Mo_2N with 2.404Å interplanar spacing and (112) diffraction of body-centered tetragonal (bct) β-phase Mo_2N with 2.370Å interplanar spacing. All the x-ray data with samples prepared at higher nitriding temperature showed γ-phase near the diffraction angle, *i.e.*, 37.477°. Since the discrepancy in diffraction angle of 0.37° is within the experimental error and since a 2° offset is applied to suppress Si peaks, we concluded that the major nitride phase at 600°C is γ-phase Mo_2N with face-centered cubic (fcc) structure. The superimposed peak at 36.727° represents (200) diffraction of the hexagonal δ-phase MoN. The small peak at $2\theta = 43.303°$ may be a (200) diffraction of the fcc phase for a lattice parameter of 4.163Å. The broad peaks in the range from 62° to 72° are caused by the silicon substrate underneath the film.

At the low temperature the dominant phase is γ-Mo_2N with a small trace of δ-MoN. When the nitriding temperature is raised to near 800°C, δ-phase MoN increases significantly, as presented in Fig. 9. When the temperature reaches 850°C, δ-phase MoN becomes the major nitride phase, as shown with the x-ray diffraction analysis in Fig. 10. Therefore, a multiphase mixed with γ-phase and δ-phase coexists in the temperature range 500°-850°C under the nitriding condition. This mixed phase makes the nitride structure appear to be a partially disordered form (9).

It should be noted that, since these data are from textured thin films, the relative intensities cannot be directly compared to JCPDS values. For example, for thin films the low angle lines will appear more intense than higher angle lines. Further, peak positions will be slightly moved due to the 2° offset used to minimize the Si peaks, as previously discussed.

The above analysis suggests that instead of the dominance of a single phase at a given temperature, there are several phases coexisting. Depending upon the local content of nitrogen, fcc or face-centered tetragonal (fct) phases are formed whose lattice parameters also change with nitrogen content. As previously mentioned the nitrogen atoms will not make a completely ordered structure but randomly occupy the largest interstices. In the fcc unit cell, there are eight equivalent interstitial positions: (1/4 1/4 1/4), (1/4 1/4 3/4), (1/4 3/4 1/4), (3/4 1/4 1/4), (3/4 3/4 1/4), (3/4 1/4 3/4), (1/4 3/4 3/4), and (3/4 3/4 3/4), while four molybdenum atoms can be situated at (000), (1/2 1/2 0), (1/2 0 1/2), and (0 1/2 1/2). For the unit cell, about 1.36 nitrogen atoms equivalent to 34 atomic percent can go to the eight identical positions. Thus, a random occupancy of nitrogen is expected, which makes it easy to form different phases. Therefore, some properties are expected to be related to the amount of nitrogen content, as illustrated later by resistivity measurements.

Kinetics and related properties.—The formation of metal nitrides requires several thermal energies: the heat of dissociation of the nitrogen molecule or ammonia, ΔH_D, and the heat of solution of the nitrogen in the metal, ΔH_S. Assuming that monatomic nitrogen reacts with the metal to form the nitride, the value of ΔH_D is a critical factor determining the nitriding temperature. When molybdenum is heated in the nitrogen gas, the nitrogen molecule dissociates as described by

$$1/2\ N_2 = N,\ K_p = P_N/P_{N_2}^{1/2} \qquad [1]$$

where K_p is the equilibrium constant, P_{N_2} the pressure of nitrogen gas, and P_N the partial pressure of the monatomic nitrogen. ΔH_D associated with reaction [1] is very high: 113 kcal/mol (10), and log K_p at 800°C is −27.744, which means that there is a negligible amount of the monatomic nitrogen existing at this temperature range. Thus, no nitride was observed to form by heating molybdenum in pure nitrogen. When forming gas was used, a nitride formed, implying that the dissociation kinetics favored monatomic nitrogen formation. This conclusion assumes a significant reduction of ΔH_D in forming gas as has been reported for the nitriding of chromium in an N_2-H_2 mixture (11). The equilibrium nitrogen pressure, P_{N_2}, was found to be related by the relationship: $\log P_{N_2} = -11{,}080/T + 5.32$ in the temperature range 1100°-1310°C. From this one can easily estimate ΔH_D as 50.7 kcal/mol. Thus, it is thermodynamically possible to form metal nitride in forming gas at relatively low temperatures (700°-800°C), as described previously.

In the case of the new ammonia nitriding process, higher concentrations of nitrogen monatomics dissociate from NH_3. The pure ammonia is easily dissociated due to the low free energy of formation, *i.e.*, 3.9 kcal/mol at room temperature (12). The reaction with pure ammonia was too fast to control the thickness. Thus, we used ammonia mixed with dry nitrogen. The degree of dissociation of the mixed ammonia, α, can be expressed (13) as

$$\alpha = \frac{\alpha_1 - n(1 - \alpha_1)}{2 - \alpha_1} \qquad [2]$$

where $n = V_{N_2}/V_{NH_3}$ is the volumetric ratio of nitrogen to ammonia at the inlet, and α_1 is the normal degree of dissociation of the pure ammonia in parts by volume. For 10% ammonia, α is about 20%, making the active nitrogen volume ratio to the total gas only 2%. This degree of dilution produces thin uniform nitride films.

In the previous section, it was formulated that the nitrogen atoms randomly occupy interstitial positions of the molybdenum nitride lattice and that the lattice parameter of the molybdenum nitride continuously expands as the nitrogen concentration increases over the temperature range of 500°-700°C. It was found that the sheet resistance of the composite film continuously increases with nitrogen content, from 0.47 Ω/sq for pure molybdenum to 3.8 Ω/sq for pure nitride.

Figure 8 shows the average sheet resistance change as a function of temperature during the isochronal nitriding in diluted ammonia.

The sheet resistance, ρ_s, increases gradually in the temperature range of 500°-700°C. As the nitriding temperature approaches 750°C, ρ_s increases rapidly. ρ_s reaches a maximum at 800°C, after which it decreases slightly followed by another increase. SIMS analysis shows complete film conversion to nitride around 750°C. The ρ_s minimum is caused by the phase transformation to hexagonal MoN from fct Mo_2N. This is verified by the x-ray analysis in Fig. 9 and 10. In Fig. 9 the dominant phase is Mo_2N. The sample made at 850°C near the resistivity minimum has the reversed dominance of the phase, as shown in Fig. 10, where MoN is the major phase. Therefore, the resistivity maximum occurs due to the resistivity reduction as γ-phase Mo_2N is converted to δ-phase MoN. When the temperature is further increased, more nitrogen is expected to be dissolved to increase the resistivity.

Since molybdenum expands its volume upon nitriding, it is convenient to express the molybdenum and

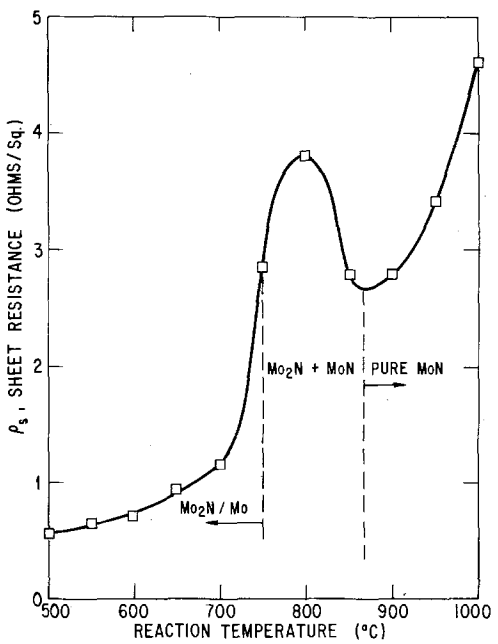

Fig. 8. Sheet resistance change as a function of nitriding temperature: increases slowly for Mo_2N/Mo double layer, peaks near the complete conversion to Mo_2N, and shows a minimum as MoN phase transformation occurs.

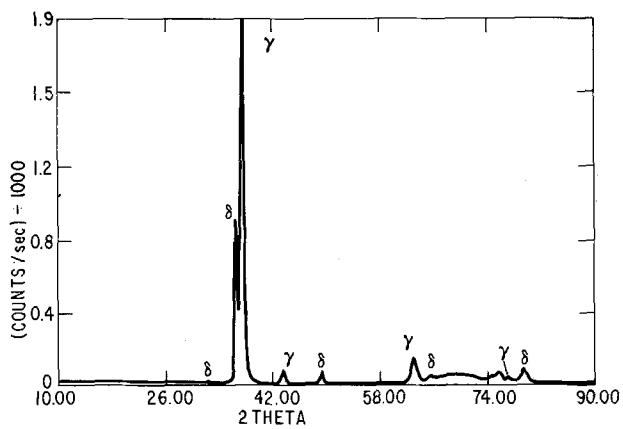

Fig. 9. X-ray diffraction spectrum of a nitride film made at 800°C by nitriding with 10% ammonia for 10 min in an open tube furnace. The major component is Mo_2N with MoN as the minor.

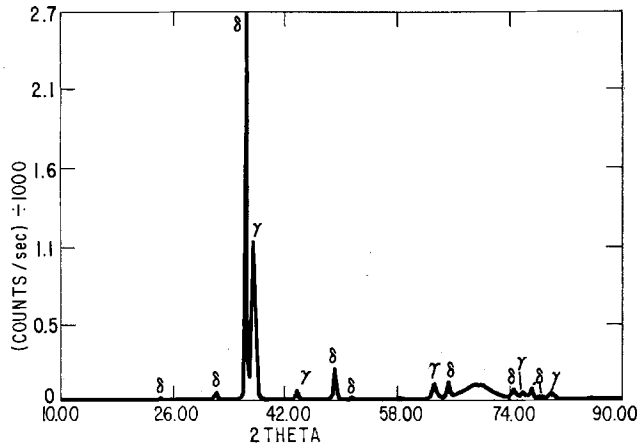

Fig. 10. X-ray diffraction spectrum of a nitride film made at 850°C by nitriding with 10% ammonia for 10 min in an open tube furnace, which shows the reversal of the major phase in Fig. 9 from Mo_2N to MoN.

nitride thickness in terms of measurable values. Let d_o, d_N, d_{Mo}, and d_T, respectively, be the initial film, nitride, remaining molybdenum, and total thickness. Then

$$(d_o - d_{Mo})\ (1 + V) = d_N \qquad [3]$$

where V is the fraction of the linear expansion that occurs when the molybdenum is converted to nitride. From the relationship of $d_T = d_{Mo} + d_N$

$$d_{Mo} = \frac{(1 + V)d_o - d_T}{V}, \quad d_N = \frac{(d_T - d_o)(1 + V)}{V} \qquad [4]$$

since d_o and d_T can easily be measured, d_{Mo} and d_N can be calculated by using either the theoretical or experimental value of V.

Figure 11 shows the film thickness changes as a function of temperature. The total measured thickness, d_T, increases continuously with temperature until 800°C. Thereafter the increase is retarded due to the phase transformation of the δ-phase. This thickness discontinuity agrees very well with the resistivity maximum in Fig. 8. The curve with circular dots represents the remaining molybdenum thicknesses measured by SIMS, which showed the complete conversion at 750°C. In this case, Eq. [3] becomes $V = d_T/d_o - 1$, where d_T is 3620Å from Fig. 11 and d_o is 3078Å, which gives 0.176 for V. The calculated d_{Mo} ($d_{Mo} = d_T - d_N$) value was plotted in Fig. 11, which agrees with the SIMS observation except for the small nitride thickness region where measurement error was high. The triangular curve represents the observed d_{Mo} for samples nitrided in the rf reactor.

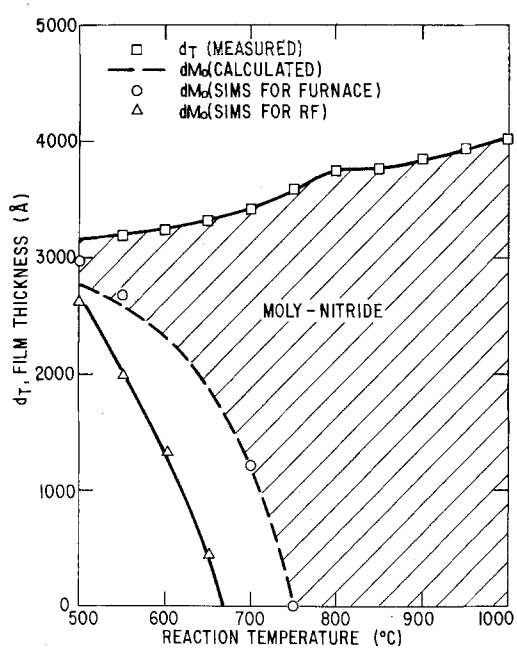

Fig. 11. Relative film thickness change as a function of nitriding temperature for 10 min isochronal reaction with 10% ammonia. The nitriding rate in the rf reactor is faster than that in the open tube furnace. The film thickness expansion rate is reduced above 800°C, where MoN phase transformation occurs.

Conclusion

A molybdenum nitride process has been developed to passivate molybdenum gates and interconnections. The film can be made by a direct reaction of the molybdenum with either ammonia or forming gas. The Mo_2N multiphase made with the diluted ammonia is more reproducible and produces high quality films. The formation of MoN δ-phase is more enhanced as the reaction temperature, time, and concentration of ammonia are increased. However, MoN causes the film surface to become very rough and makes the film brittle when complete conversion occurs at high temperatures. The important conclusion is that molybdenum nitride formation must be restricted to the Mo_2N phase for thin film electronic applications.

Acknowledgments

The authors wish to thank E. A. Taft, T. J. Soltys, and T. P. Chow for their constructive advice and permission to use their equipment. The authors appreciate the help of P. Piacente, C. Logan, and D. Bower with processing. The authors are also grateful to J. Norton for the SEM photos, G. A. Smith for the SIMS analysis, and R. P. Goehner and C. H. Reilly for the x-ray diffraction analysis.

Manuscript submitted May 3, 1982; revised manuscript received Dec. 3, 1982.

Any discussion of this paper will appear in a Discussion Section to be published in the December 1983 JOURNAL. All discussions for the December 1983 Discussion Section should be submitted by Aug. 1, 1983.

Publication costs of this article were assisted by the General Electric Company.

REFERENCES

1. D. M. Brown, W. E. Engeler, M. Garfinkel, and P. V. Gray, *This Journal*, **115**, 874 (1966); *Solid State Electron.*, **11**, 1105 (1968).
2. W. E. Engeler and D. M. Brown, *IEEE Trans. Electron Devices*, **ed-19**, 54 (1972).
3. J. C. Sarace, R. E. Kerwin, D. L. Klein, and R. Edwards, *Solid-State Electron.*, **11**, 653 (1968).
4. D. M. Brown and R. J. Connery, *IEEE Trans. Electron Devices*, **ed-25**, 1302 (1978).
5. T. Nozaki and H. Okabayashi, *This Journal*, **128**, 175 (1981).
6. H. Okabayashi, K. Higuchi, and T. Nozaki, Abstract 302, p. 753, The Electrochemical Society Extended Abstracts, Minneapolis, MN, May 10-15, 1981.
7. H. Schönberg, *Acta Chem. Scand.*, **8**, 204 (1954).
8. G. Hägg, *Z. Phys. Chem. B*, **7**, 339 (1930).
9. R. W. G. Wyckoff, "Crystal Structures," 2nd ed., Vol. 1, p. 381, John Wiley & Sons, Inc., New York (1963).
10. A. G. Gaydon, "Dissociation Energies," Chapman and Hall, London (1955).
11. K. Schwerdtfeger, *Trans. Met. Soc. AIME*, **239**, 1432 (1967).
12. M. C. Sneed and R. C. Brasted, "Comprehensive Inorganic Chemistry," Van Nostrand, New York (1953).
13. L. V. Beloruchev, V. V. Dembovski, and I. M. Morshteniei, *Themicheskaya Obrabotka Metallov.*, No. 3, 67 (1968).

Ellipsometric Characterization of Si Surface Damage Induced by Sputter Etching

F. Ohira

Nippon Telegraph and Telephone Public Corporation, Musashino Electrical Communication Laboratory, Musashino-shi, Tokyo 180 Japan

ABSTRACT

Surface characterization using spectroscopic ellipsometry is applied to sputter etched Si surfaces. It is elucidated by spectrum measurement that broadening of the refractive index spectrum occurs due to crystal damage induced by sputter etching. As more damage is introduced by increasing the rf power, the spectrum peaks in n and k are broadened, and especially for the extinction coefficient k. Thus, the extinction value can be a measure of the degree of damage. For crystal damage evaluation, ellipsometric measurement at a wavelength of 4200-4500Å is effective and reasonable. Comparing the results of ellipsometry with those of RHEED patterns and electrical properties, it is verified that the degree of broadening is compatible with that of blurring in RHEED patterns and increase in leakage current in Schottky type diodes constructed on the etched surfaces. It is concluded that surface quality can be assessed numerically by measuring the change in refractive index.

Developments in MOS process technology have made surface characterization of Si wafer more important because of the great influence of the surface layer on device properties (1). Several methods have been presented for characterizing the Si wafer, *e.g.*, lifetime measurement (2), reflection electron diffraction (RHEED) (3), light reflection measurement (4), electron beam induced conductivity measurement (5), and oxidation Sirtl etching to reveal stacking faults (OS check (6).

These methods possess individual advantages, but they also have disadvantages in that they are destructive, they can be disturbed by the natural oxide layer, they have low sensitivity, and they are difficult to evaluate quantitatively.

It is well known that the surface crystal damage causes variations in the optical parameters of the processed surface regions (7, 8). As ellipsometry can determine the refractive indexes of the substrate in spite of the natural oxide film, it is considered useful for characterizing the Si surface.

Recently, ellipsometry has been applied for estimating damage by Ohira (9), Watanabe (10), and other researchers (11-14) because of its ability to determine refractive indexes precisely. They measured the changes in the ellipsometric parameters Δ and ψ, or calculated the refractive indexes n and k for the Si wafer surfaces processed in various ways.

In the previous paper (15), the author measured the changes in the refractive index spectrum, and reported that the refractive indexes at 5461Å, especially the extinction coefficient k, increased with the crystal damage. This was deduced from the broadening of the k spectrum. The author showed that ellipsometry was useful because of its nondestructive and highly sensitive characterization of Si wafer surfaces. However, the physical meaning of the changes in the refractive indexes was not clarified, and comparison of the results obtained by this method with those of other characterization methods were not reported.

In this paper, the author measures and discusses spectrum changes in the refractive indexes for rf sputter etched, annealed, and plasma deposited Si surfaces concerning the surface damage. The results are compared with those obtained from RHEED and electrical properties of the processed Si surfaces. Experimental results show that the results are compatible with each other, and, therefore, that ellipsometry is a useful technique for assessing Si surface damage.

Experimental

Three inch diameter 380 μm thick (100) oriented p-type Si wafers are used in this experiment. Si wafer surfaces are mechanochemically polished (MCP), and are undamaged. Thereafter, they are rf sputter etched (RFS) using Ar gas to introduce surface damage. rf power of 100, 150, and 250W, a gas pressure of 10 Pa, and an etching time of 3 min are employed. As it is generally supposed that rf sputter etched surface has a damaged layer in the amorphous state, an amorphous Si (a-Si) surface formed by plasma deposition is also examined for comparison.

In order to estimate the effect of heat-treatment annealing on crystal damage, RFS surfaces and a-Si surfaces are heated in an Ar ambient at 300°-800°C for 60 min. The MCP and RFS specimens are characterized by RHEED, electrical properties, and spectroscopic ellipsometry. Comparison of these results are made and discussed. Also, the heated specimens are characterized by RHEED and ellipsometry, and the comparisons between them are carried out.

Furthermore, in order to investigate the effect of the formation and the removal of the native oxide layer on the damaged surface after a long time exposure in an atmosphere, the RFS surfaces are exposed in an atmospheric condition for three months. Thereafter, the surfaces are assessed by spectroscopic ellipsometry. The RHEED equipment is JEOL Model JEM-100S, and a 100 kV electron beam is chosen to obtain the RHEED patterns.

For the electrical properties concerning device characteristics, current-voltage characteristics for the processed surfaces are examined. For the measurement of I-V characteristics, an ohmic contact must be formed on the back surface of Si wafer. For this purpose, Al metallization by vacuum evaporation and heat-treatment is usually used. However, the heat-treatment may cause a change in the crystallographic structure, and the damage introduced by RFS cannot be characterized correctly. Therefore, the back surface of the processed wafer is metallized with Al by ion plating, and an ohmic contact is formed to the Si wafer without heat-treatment (16). Circular electrodes, 2 mm diam, are vacuum evaporated on the Si surface, and Schottky type diodes are constructed for the test.

The ellipsometer used is the Shimazu polarimetric spectrometer Model EP-10. All ellipsometric measurements are carried out with an incident angle of 70°. For spectroscopic measurement, a Bausch and Lomb monochromator, tungsten light source, and Babinet-Soleil compensator are used. The measurement wavelength ranges from 3600 to 6328Å.

Figure 1 shows a model of the Si wafer surface used in the experiment. There is a native oxide film with nonabsorbing refractive index n_1 and thickness d on the Si substrate with complex refractive index $\tilde{n}_2 = n_2$

Key words: ellipsometry, damage, surface, sputter etching.

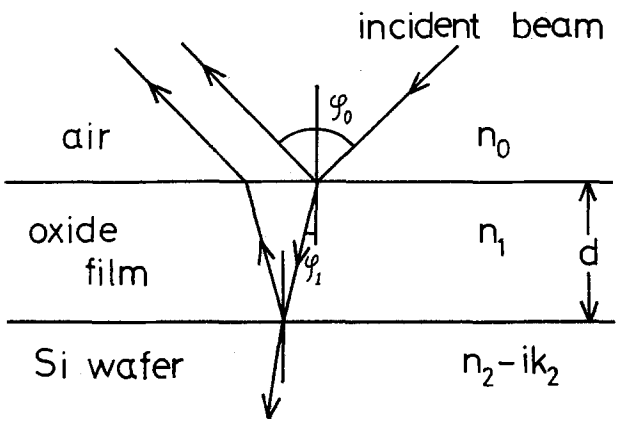

Fig. 1. Model of Si wafer surface. There is a natural oxide film with nonabsorbing refractive index n_1 and thickness d on the Si substrate with complex refractive index $\tilde{n}_2 = n_2 - ik_2$.

$- ik_2$. When monochromatic light of wavelength λ is incident on the surface from the ϕ_0 direction, ellipsometric parameters Δ and ψ and refractive indexes n_1, n_2, k_2, etc. are related by Eq. [1] (17)

$$\tan\psi \exp(i\Delta) = \frac{(r_{1p} + r_{2p}\exp(-2i\delta))(1 + r_{1s}r_{2s}\exp(-2i\delta))}{(1 + r_{1p}r_{2p}\exp(-2i\delta))(r_{1s} + r_{2s}\exp(-2i\delta))} \quad [1]$$

$$\delta = 2\pi n_1 \cos\phi_1 d/\lambda$$

where δ is the phase change in the reflection of light, n_0 is the refractive index of the ambient (air), and r_{1p}, r_{1s}, r_{2p}, and r_{2s} are the Fresnel reflection coefficients.

The other symbols are the ones normally used in the ellipsometry. Parameters Δ and ψ are directly measured by ellipsometry. They correspond to the phase shift and relative attenuation of the electric field parallel or perpendicular to the plane of incident light, respectively. When the values of Δ, ψ, ϕ_0, n_0, n_1, and d are given, n_2 and k_2 can be calculated from Eq. [1] assuming isotropic, homogeneous plane boundaries. For experimental convenience, native oxide layers on the Si surfaces are removed by chemical etching just before the ellipsometric measurement, using 3% aqueous solution of hydrofluoric acid (HF) for 1 min. The refractive indexes of the Si substrate are determined from Eq. [1] with $d = 0$. It is well known that the native oxide regrows quickly in an atmosphere. However, measuring the refractive indexes in UHV in order to assess the surface quality is not practical. Therefore, in the present study, the refractive indexes are measured in an atmosphere as a practical method. The errors of the refractive indexes caused by ignoring the thickness d will be discussed in the next paragraph. The surfaces, except for the surfaces exposed for three months, are measured immediately after the sputter etching or heat-treatment.

Results and Discussion

Figure 2 shows RHEED patterns for MCP and RFS surfaces. A Kikuchi pattern clearly appears on the MCP surface. It is evident that the surface has good crystallographic quality. The patterns become unclear as rf power increases. It is estimated from the pattern that a surface processed at 250W is in an almost amorphous state.

The current *vs.* voltage characteristics for the Schottky type diodes constructed on processed surfaces are shown in Fig. 3. It is apparent that the backward (leakage) current increases as rf power increases. For MCP surface, the level of leakage current density stays at an almost constant value of 1.9-2.0 $\times$ 10^{-8} A/mm^2 in the applied voltage range between 0.1-10.0V. However, with the RFS surface, the current is larger than that for MCP surface, and the current also increases as the voltage increases. For example, for 250W RFS surface, the current level at 0.1V is 1.5 times as large as for MCP. The current level markedly increases at 10V, and reaches as more than 20 times large as for MCP. By the experimental result, it is evident that the damage induced by sputter etching results effectively on the current *vs.* voltage characteristics of the specimens.

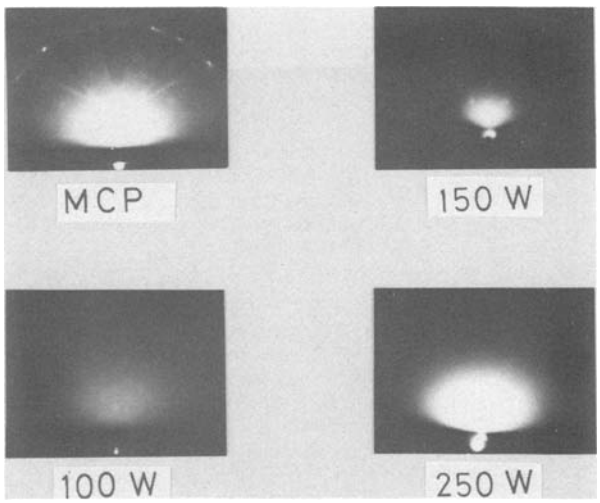

Fig. 2. Changes in RHEED patterns by rf sputter etching

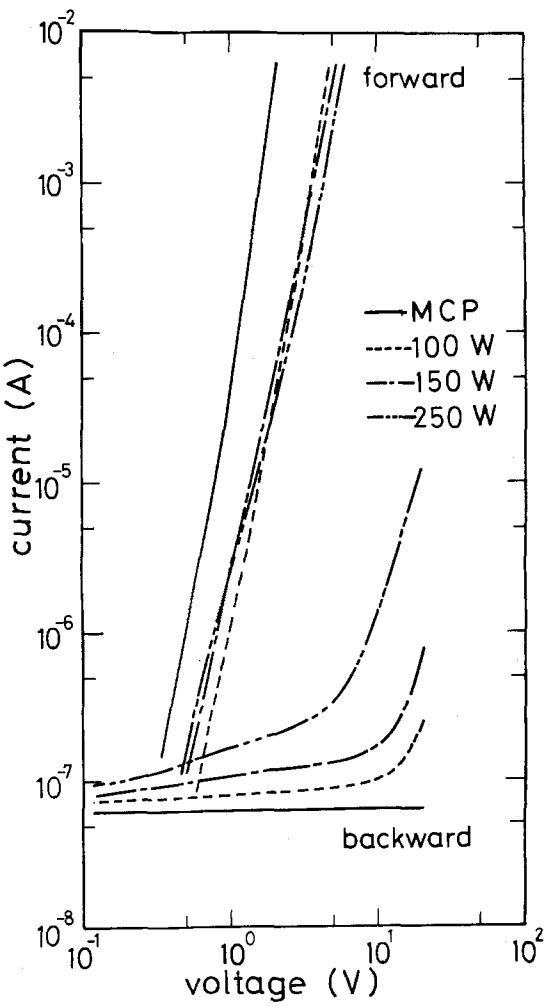

Fig. 3. Changes in I-V characteristics by rf sputter etching

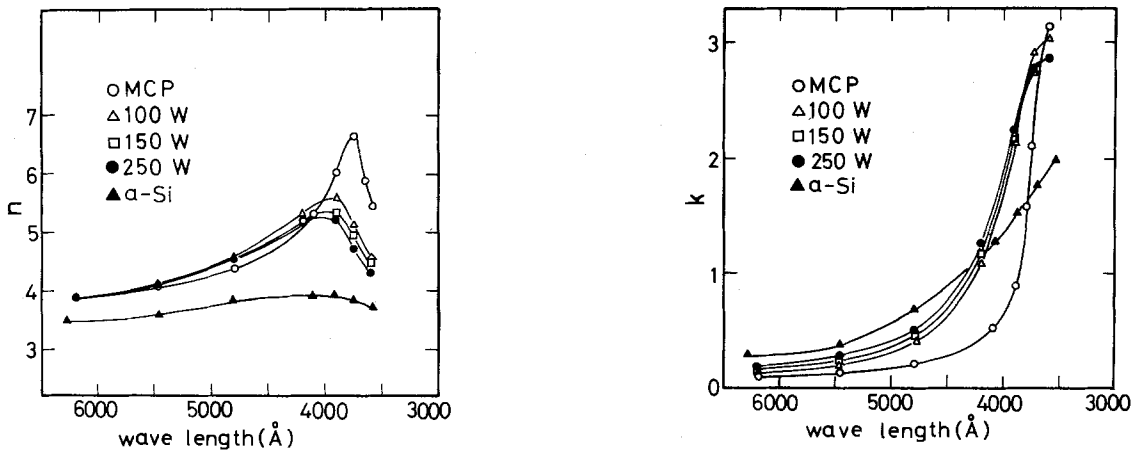

Fig. 4 Changes in refractive indexes by rf sputter etching

Figure 4 shows the spectra of the refractive indexes for Si wafer surfaces processed by MCP, RFS, and plasma deposition. It is known that n and k spectra have an intrinsic peak at about 3750 and 3550Å, respectively, in a single crystal Si surface (18). The MCP surface shows these sharp peaks. However, RFS surfaces tend to broaden the spectra. The tendency is pronounced as the rf power increases for the sake of introducing damage.

Judging from the fact that RFS surface spectra approach those of the a-Si surface, the RFS surface is estimated to be in an amorphous-like state. Looking at the k value at 5461Å, the value increases monotonically with increase in damage. The extinction coefficient k has a peak at 3550Å (3.5 eV), which corresponds to the direct transition in Si. When the band structure is disordered by rf sputter etching, the peak may shift according to the lattice disorder. If the lattice disorder includes both tensile and compressive strain, or is in an amorphous state, the peak shift is estimated to occur at energies slightly higher and lower than 3.5 eV (19). Thus, the spectrum broadens its peak. As a result, the spectrum peak drops, and the absorption edge is broadened. Therefore, the coefficient value can be larger at a wavelength away from the spectrum peak, say at 5461Å. This indicates that it is reasonable to assess the degree of surface damage by the k value at 5461Å. It is clear from Fig. 4 that the evaluation via k value at a wavelength of about 4500Å is more sensitive for Si surface damage.

Furthermore, it is possible to estimate from Fig. 4 that evaluation at wavelength in the ultraviolet region give a more sensitive indication of damage than in the visible wavelength region. The results of ellipsometric measurement are closely compatible with those of RHEED patterns and I-V characteristics.

As the refractive indexes are affected by various factors, their accuracy or error arising from the factors is discussed for these specimens. The main factors in the errors are (*i*) measuring errors of the ψ and Δ values, and (*ii*) the effect of the native oxide layer.

Firstly, the effect of ψ and Δ values is examined. It is experimentally verified that reading errors of ψ and Δ values are within $\pm 0.05°$. The errors caused by using the monochromator and compensator in order to measure the spectra are estimated by comparing the values of ψ and Δ found by using the monochromator and compensator with those determined by the UHV mercury lamp and $\lambda/4$ plate. In this experiment, differences in ψ and Δ values between the results found using the two methods are experimentally confirmed to be $\pm$ 0.1°. Therefore, the errors in n and k values caused by the ψ and Δ errors of $\pm$ 0.1° are calculated and discussed at 5461Å, which is the wavelength usually used to characterize the refractive indexes of Si surfaces. The error of $\pm$ 0.1° in the ψ value causes errors of 0.015 for MCP and 250W RFS in n, and 1.8×10^{-3} for MCP and 3.9×10^{-3} for 250W RFS in k. The error of $\pm$ 0.1° in the Δ value causes errors of 3.5×10^{-4} for MCP and 8×10^{-4} for 250W RFS in n, and 3×10^{-3} for MCP and 250W RFS in k.

These errors are very small, and it is apparent that that the ψ and Δ errors do not introduce effective errors in the refractive indexes and that the ranking of the refractive indexes for these specimens remains the same. Errors in n and k at different wavelengths are also calculated, and the results show that errors are very small, and the ranking of the refractive indexes for these specimens remains the same. As discussed above, the errors in n and k caused by errors in ψ and Δ are very small, and, therefore, the difference in the n and k spectra is significant.

Secondly, the effect of the native oxide layer is examined. It is generally supposed that Si surface is covered with a very thin oxide layer. In this experiment, the maximum Δ value is 176.2° after the removal of the layer by HF etching. Comparing the Δ value with that of Archer, the Si surface is estimated to be covered with the natural oxide layer of 10Å thickness (20, 21). Accordingly, the effect of the oxide layer thickness on the n and k is discussed. It is verified that by taking into account the thickness, the n value becomes higher, and the k value becomes smaller in comparison with cases in which the effect of the thickness is ignored. It is also revealed that the shift is pronounced for the shorter wavelength region. The shift in the n value when the oxide layer thickness is taken into account is small especially at the region of 4200-6328Å. For example, the shift is about 0.004 for MCP, 0.013 for 250W RFS surfaces at 5461Å, and, therefore, the ranking of the calculated n value for each specimen remains the same. The k value calculated by taking into account the thickness decreases to about the same values at the same wavelength especially at the region of 4200-6328Å. That is, the k value only shifts about the same amount for each specimen at the same wavelength especially in the region of 4200-6328Å. For example, the k value at 5461Å shifts to 0.091 for MCP, and 0.094 for 250W RFS surface when the oxide layer thickness is taken into account. The ranking of the k values remains the same for the MCP and 100, 150, 250W RFS specimens. Therefore, relative damage evaluation through the k value is meaningful.

When samples are rf sputter etched, the native oxide may also be damaged. It is reported that Si surface may be covered with SiO_{2-x} ($0 < x < 1$) (12). In the present study, the refractive index of the native oxide is assumed to be 1.45 in the analysis. The errors arising from assuming the value to be 1.45 are calculated and discussed. The refractive index

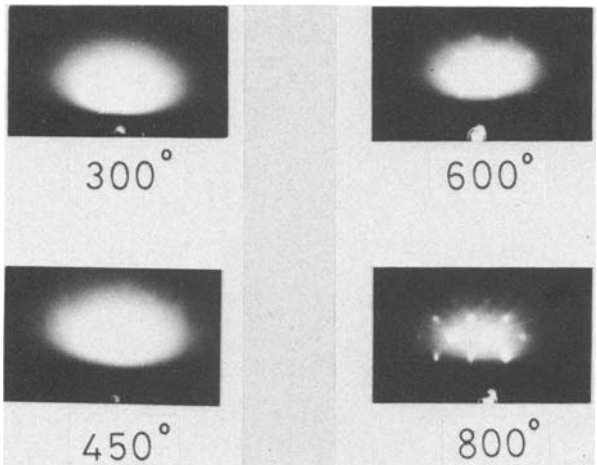

Fig. 5. Changes in RHEED patterns for rf sputter etched surfaces by heat-treatment.

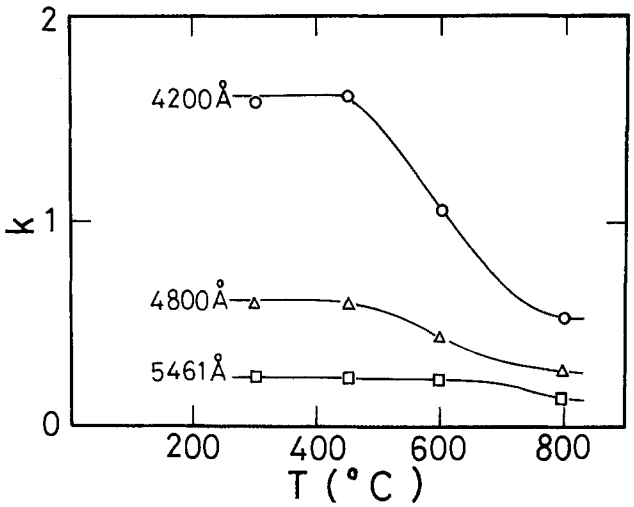

Fig. 7. Effect of heat-treatment on k tor rt sputter etched surfaces

value of the damaged native oxide on the damaged surface is not clear. The differences in the refractive indexes of damaged Si between assuming the value 1.45 and assuming it 1.8 are 8.6×10^{-4}-3.5×10^{-3} in n, and 0.02 in k for MCP, 100, 150, and 250W rf sputter etched surfaces at 5461Å. It is apparent that these differences are very small.

As discussed above, although there are certain errors caused by ignoring the oxide layer, the k value shifts to about the same value at the same wavelength. Therefore, it is considered that the relative damage assessment through the change in the refractive indexes is reasonable, and that ellipsometry can be conventionally used for such damage assessment. Then, in the present experiment, surface quality is assessed by using refractive index values on the assumption that $d = 0$Å as in the conventional method for all specimens.

Figure 5 shows the effect of annealing due to heat treatment on crystal damage as examined by RHEED. Surfaces rf sputter etched at 250W are heated at 300°, 450°, 600°, and 800°C in an Ar ambient for 60 min. With heat-treatment at 300° and 450°C, the patterns show no change, however, at 600°C, it shows spots, and at 800°C, the pattern approaches that of a single crystal surface, which means recovery for the single crystal.

Figure 6 shows the corresponding refractive index spectrum changes examined by ellipsometry. Though heated surfaces at 300° and 450°C show no change in the spectra, the surface heated at 600°C shows a little change, and the surface heated at 800°C shows a sharp peak. This indicates the recovery of the crystal damage. The single crystal spectra are recovered only when the slices are heated above the temperature of about 800°C, which agrees with the result reported by Sachse (23). This means that recovery of the damage induced by RFS, in spite of the low bias voltage, requires the same heat-treatment as the case by the ordinary ion implantation.

Figure 7 is rewritten from Fig. 6, and shows the change in the k value due to the heat-treatment. The change in the k value at about 600°C can be clearly recognized. In the figure, it is also evident that the characterization at a wavelength of 4200Å is very effective.

As shown in Fig. 5 and 6, changes in RHEED patterns and the spectra show the recovery of the surface crystallographic structure and are closely compatible with each other. As shown in Fig. 4 an amorphous Si surface has broadened spectra. The annealing effect is also studied for amorphous Si surfaces.

Figure 8 shows the annealing effect for heat-treated amorphous Si surfaces. By heat-treatment at 450°C, no change is shown, but at 600°C a little change is shown, and at 800°C, recovery to some extent is shown. However, even at 800°C, the same pattern as for a single crystal surface is not shown.

Figure 9 shows the corresponding refractive index spectrum for heat-treated amorphous Si surfaces. Both n and k spectra change greatly owing to the heat-treatment, and show recovery of the surface crystal structure. However, even with the heat-treatment at 800°C, complete recovery is not shown for the single crystal.

All these results are closely compatible with each other. The RFS surface is estimated to have a very thin damaged layer. Therefore, it is thought that the formation and the removal of the native oxide layer

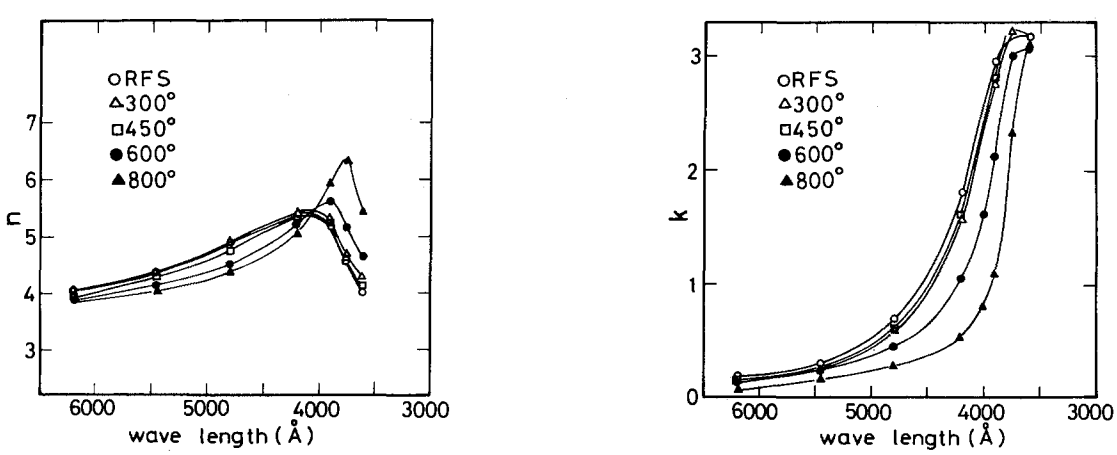

Fig. 6. Changes in refractive indexes for rf sputter etched surfaces by heat-treatment

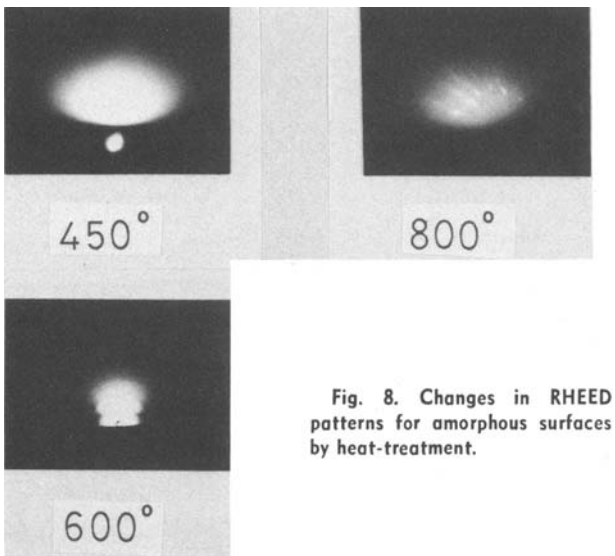

Fig. 8. Changes in RHEED patterns for amorphous surfaces by heat-treatment.

influences the degree of surface damage. As ellipsometry is expected to be able to assess a very thin damaged layer, this method is examined to evaluate the change in degree of surface damage resulting from the formation and the removal of the native oxide layer.

Figure 10 shows the changes in the spectra for sputter etched surfaces after exposure in an atmosphere for three months. The ψ value decreases and Δ value increases at 5461Å after the removal of a very thin surface layer, which means the recovery of damage. Though the difference in the spectra between the 100-250W specimens still remains, both the spectra show sharper peaks. The thickness of the native oxide layer is estimated to be about 20 or 30Å after three months exposure in an atmosphere (24). This means that the removal of a very thin layer is effective for the recovery of sputter etched surface damage. The recovery of damage resulting from the removal of a very thin surface layer is clearly detected by this method.

Conclusion

Surface characterization using spectroscopic ellipsometry is applied to an Si wafer processed by sputter etching. To confirm the relation between spectra changes of the refractive indexes and crystallographic quality, ellipsometry is applied to Si surfaces characterized by RHEED or I-V characteristics. Results are summarized in the next paragraph.

It is elucidated by the spectrum measurement that the increase in k value, the extinction coefficient, at 5461Å, is the result of the broadening of the k spectrum due to crystal damage. For crystal damage characterization, ellipsometric measurement at a wavelength of 4200-4500Å is effective and reasonable.

Comparing the results of ellipsometry with those for RHEED patterns and electrical properties, it is verified that the spectrum changes are closely compatible with results from other characterization methods. Therefore, it is concluded that surface quality can be assessed numerically by measuring the change in refractive indexes. Change in the damage degree of a very thin surface layer can be clearly detected by this method.

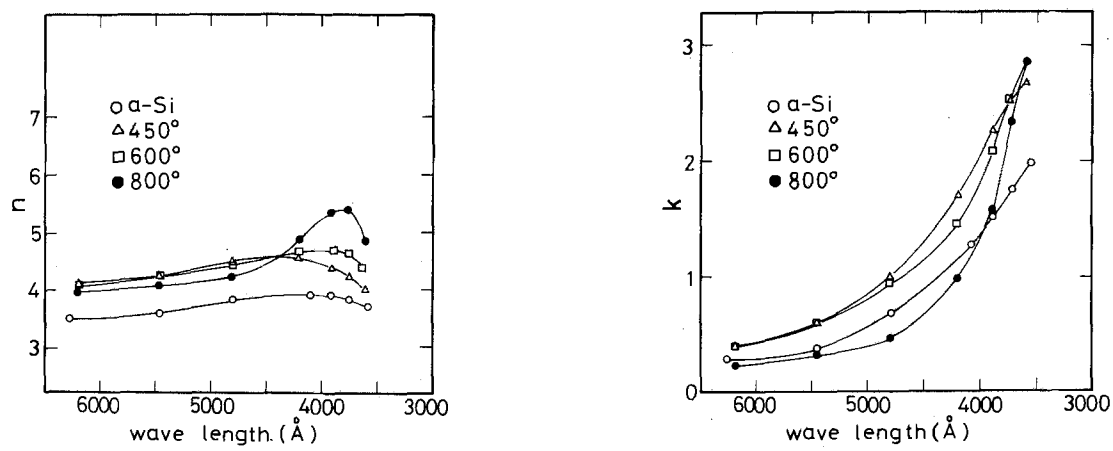

Fig. 9. Changes in refractive indexes for amorphous surfaces by heat-treatment

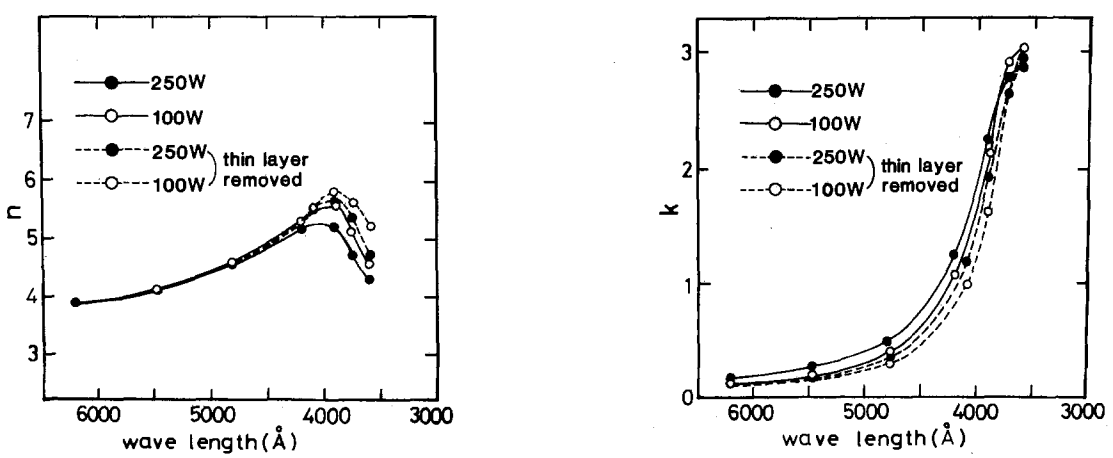

Fig. 10 Changes in refractive indexes for sputter etched surfaces by the removal of thin surface layer

Acknowledgments

The author wishes to thank Mr. M. Itakura for useful discussions.

Manuscript submitted Oct. 26, 1981; revised manuscript received Feb. 3, 1983.

Any discussion of this paper will appear in a Discussion Section to be published in the December 1983 JOURNAL. All discussions for the December 1983 Discussion Section should be submitted by Aug. 1, 1983.

Publication costs of this article were assisted by Nippon Telegraph and Telephone Public Corporation.

REFERENCES

1. H. Kressel, *RCA Rev.*, **28**, 175 (1967).
2. M. Zerbst, *Z. Angew. Phys.*, **22**, 30 (1960).
3. S. Ino, *J. Appl. Phys.*, **16**, 891 (1977).
4. T. C. McGill, S. L. Kurtin, and G. A. Shifrin, *ibid.*, **41**, 246 (1970).
5. K. V. Ravi, C. J. Varker, and C. E. Volk, *This Journal*, **120**, 533 (1973).
6. H. J. Queisser and P. G. G. van Loon, *J. Appl. Phys.*, **41**, 246 (1970).
7. M. Miyao, T. Miyazaki, and T. Tokuyama, *Jpn. J. Appl. Phys.*, **17**, 955 (1978).
8. R. R. Hart and O. J. Marsh, *Appl. Phys. Lett.*, **14**, 225 (1969).
9. F. Ohira and M. Itakura, *Jpn. J. Appl. Phys.*, **18**, 1243 (1979).
10. K. Watanabe, M. Miyao, I. Takemoto, and N. Hashimoto, *Appl. Phys. Lett.*, **34**, 518 (1979).
11. K. Vedam, *Surf. Sci.*, **56**, 221 (1976).
12. M. M. Ibrahim and N. M. Bashara, *ibid.*, **30**, 632 (1972).
13. A. Kučírková, *Radiat. Eff.*, **28**, 129 (1976).
14. J. R. Adams, *Surf. Sci.*, **56**, 307 (1976).
15. F. Ohira and M. Itakura, *Appl. Phys. Lett.*, **37**, 398 (1980).
16. M. Itakura and F. Ohira, in "Proceedings of the Third Symposium on Ion Sources and Application Technology," p. 127, Tokyo (1979).
17. P. Drude, "Lehrbuch der Optik," S. Hirzel, Leipzig (1912).
18. H. R. Philipp and E. A. Taft, *Phys. Rev.*, **120**, 37 (1960).
19. H. Y. Fan, M. L. Shepherd, and W. Spitzer, in "Photoconductivity Conference," p. 190, John Wiley & Sons, Inc., New York (1954).
20. R. J. Archer, *J. Opt. Soc. Am.*, **52**, 970 (1962).
21. R. J. Archer, *This Journal*, **104**, 619 (1957).
22. S. I. Raider and R. Flitsch, *J. Vac. Sci. Technol.*, **13**, 58 (1976).
23. G. W. Sachse, W. E. Miller, and C. Gross, *Solid-State Electron.* **18**, 431 (1975).
24. F. Lukes, *Surf. Sci.*, **30**, 91 (1972).

The Vaporization of Realgar, As_4S_4

R. D. Brittain, K. H. Lau, and D. L. Hildenbrand

SRI International, Menlo Park, California 94025

ABSTRACT

The vaporization behavior of As_4S_4 has been investigated by mass spectrometry and mass-loss torsion-effusion. The results of these studies indicate that the primary constituent of the vapor above crystalline As_4S_4 is molecular As_4S_4, but that minor amounts of As_4S_5, As_4S_3, As_2S_3, As_2S_2, AsS, and S_2 are also present. The enthalpy and entropy of vaporization at 450 K are 30.7 (± 0.9) kcal/mol and 41.9 (± 2.0) cal/K mol, respectively. The value of the enthalpy of sublimation at 298.15 K is calculated as $\Delta H°_{298}$ = 31.6 (± 2.0) kcal/mol. The results of this study are compared with those of previous investigations, and ambiguities resulting from the slow phase transition between α- and β-As_4S_4 are addressed.

The vaporization behavior of As_4S_4 has been investigated previously by Munir, Street, and Winters (1), who employed the techniques of mass spectrometry and torsion-effusion to determine the vapor species and absolute vapor pressures above both synthetic and mineral samples of realgar, As_4S_4. They reported that $As_4S_4(g)$ was the primary vapor phase component, but that $As_4S_5(g)$, $As_4S_3(g)$, $As_4(g)$, and $As_2(g)$ were also present in minor amounts, although the vapor phase composition was not determined quantitatively. Since melting point and x-ray diffraction analyses indicated that the sample remaining after the vaporization experiments was pure $As_4S_4(s)$, they concluded that the compound sublimed stoichiometrically, and the proportion of $As_4S_4(s)$ which sublimed to give $As_4S_4(g)$ was estimated to be at least 75% or as much as 90%. From measurements of the temperature dependence of the absolute vapor pressures by the torsion-effusion method, the second law enthalpy and entropy changes for the vaporization process were derived by assuming that the predominant vapor component was $As_4S_4(g)$. The $As_4S_4(s)$ samples used in the torsion-effusion studies did not transform from the original β form to the thermodynamically more stable α form, even though the measurements were made well below the phase transition temperature of 540 K. Johnson, Papatheodorou, and Johnson (2) have recently reported the enthalpy of formation and high temperature thermodynamic functions of β-As_4S_4; they assumed that the samples studied by drop calorimetry did not revert to the α form during temperature equilibration. At about the same time, however, it was reported by Blachnik, Hoppe, and Wickel (3) that β-As_4S_4 transformed to the α form under slow cooling rates in differential scanning calorimetry. The disagreement over the reversibility of the phase transitions in realgar and uncertainty about the vapor composition cast doubt on the interpretation of thermodynamic data determined for both solid and vapor states. Consequently, we have undertaken a study to reevaluate the vaporization behavior of As_4S_4.

Key words: thermodynamics, vaporization, sublimation.

Experimental

The apparatus and experimental procedures employed in Knudsen cell mass spectrometry and mass-loss torsion-effusion experiments have been described in previous articles (4-8). Torsion-effusion experiments were carried out in two alumina cells with orifice diameters of 1.05 and 1.50 mm. The initial runs in the cells employed β-phase As_4S_4 as received from Alfa Products. At the completion of the torsion measurements, however, x-ray diffraction analysis indicated the residual sample to be α-phase As_4S_4. Another torsion run was then made on the residual α-phase material with the 1.5 mm orifice cell. Mass-loss data were collected at several points in one run so that the average molecular weight of the effusate could be determined. The performance of the apparatus was checked by measurement of the vapor pressure of crystalline KCl; the resulting pressures were within

3%, and the experimental enthalpy of vaporization within 0.5 kcal/mol, of the accepted values (9).

Mass spectrometry was performed with both the magnetic sector instrument described in Ref. (4) and (5) and with an Extranuclear quadrupole mass filter system equipped with a furnace and beam source similar in design to that of the magnetic instrument. The quadrupole mass filter has a mass range of 800 amu and is equipped with an ion energy programmer to minimize mass discrimination. Species effusing from the Knudsen cell in either mass spectrometer were distinguished from background species by the displacement of an Inconel beam-defining slit. Neutral vapor species above As_4S_4(s) were identified primarily from the threshold appearance potentials of ions in the mass spectrum of the effusion beam. The relative abundances of parent species were measured at 3 eV above the ionization potential in the magnetic sector instrument; relative abundances of all detectable species were measured in both instruments in order to compare our results with those of Munir, Street, and Winters (1). The same sample of α-As_4S_4 was used successively in the quadrupole filter and magnetic sector instruments; the α-phase sample was the residue from a torsion-effusion run performed earlier.

Results

Mass spectrometry.—The appearance potentials of species found in the vapor above the As_4S_4 sample in the magnetic sector instrument are compared with those of Munir, Street, and Winters (MSW) in Table I; the relative intensities of vapor species at 18 eV for our two instruments are compared with the MSW quadrupole results in the same table. We do not report the appearance potentials of the atomic and molecular arsenic ions because the background signal was much higher than the signal from the Knudsen cell, making an accurate determination of the appearance potential of the sample component difficult. It was not possible, however, to find sample components of As^+, As_2^+, and As_4^+ signals when they were measured at 3 eV above the known ionization threshold of those ions (10), so we believe that signals observed for these species at 18 eV result from fragmentation processes. The comparatively high levels of As_4^+ and As_2^+ observed by MSW probably include large background components which were not separated from the sample beam signals in the MSW experiments. We were also unable to obtain accurate appearance potentials for AsS_2^+ and As_2S^+ because of the low signal levels observed.

Based on the appearance potentials of the remaining ions, we have identified 7 parent ions in the vapor above As_4S_4(s): S_2^+, AsS^+, $As_2S_2^+$, $As_2S_3^+$, $As_4S_3^+$, $As_4S_4^+$, and $As_4S_5^+$. This identification is justified in part by comparison with the spectrum of As_2S_3 (11), where we found S_2^+, $As_2S_3^+$, $As_4S_4^+$, and $As_4S_5^+$ parent ions with comparable AP's. In the vaporization of As_4S_4, we found significantly lower AP's for AsS^+, $As_2S_2^+$, and $As_4S_3^+$, consistent with the values expected for such open shell molecules. The measured AP or AsS is in fact within 0.1 eV of the value reported for AsS generated by two different methods in Ref. (11). An interesting phenomenon observed in the magnetic sector instrument which lends additional support to this assignment is the observed instantaneous slit effect reported in Table II as I_o/I_f for each of the parent ions. The instantaneous slit effect is illustrated in Fig. 1 for $As_4S_5^+$, $As_4S_4^+$, and $As_4S_3^+$ signals at 475 K. The fact that the $As_4S_4^+$ and $As_4S_3^+$ signals continued to decrease slowly after the slit was moved to block the direct path of molecules from the Knudsen cell into the ion source is ascribable to low condensation coefficients for these molecules on the surfaces of the ion source region. The behavior of the As_4S_5 molecules, by contrast, indicates a very high condensation coefficient. The ratio I_o/I_f varies significantly from one ion to the next in Table I indicating clearly that these ions result from different neutral precursors; several of the ions, S_2^+, $As_2S_2^+$, $As_4S_3^+$, and $As_4S_4^+$, behave almost as permanent gases. It should be noted that the effects of low condensation coefficients on slit effects are barely discernable in the quadrupole measurements, most likely because a more open ion source with a higher pumping speed is employed in that instrument. Also reported in Table II are the relative intensities of the parent ions at 418 and 475 K, where measurements are made 3 eV above the ionization threshold of the respective ions and the absolute intensities, I_o^+, are based on the instantaneous slit effects. We believe that the mass spectrum obtained at low ionizing energy gives a reliable measure of actual vapor composition.

The temperature dependence of ion signals for $As_4S_4^+$ and $As_4S_5^+$ at 18 eV, measured in the temperature range 427-475 K, is shown in Fig. 2, based on the data in Table III. The second law enthalpy derived for the vaporization of $As_4S_4^+$ is 32.8 ($\pm$0.2) kcal/mol, while that for $As_4S_5^+$ is 31.0 ($\pm$0.2) kcal/mol. Although there is not a significant difference be-

Table I. Appearance potentials and relative intensities in the mass spectrum of vapor above As_4S_4

Ion	AP, eV: This work	AP, eV: Ref. (1)	Relative intensity, 18 eV: Magnetic sector, 450 K	Relative intensity, 18 eV: Quadrupole 450 K	Relative intensity, 18 eV: Ref. (1) 400 K
S_2^+	9.5	12.0	0.3	0.08	3.0
As^+		<10		0.03	1.0
AsS^+	8.4	9.0	32.0	15.0	6.0
AsS_2^+			0.3	0.06	0.1
As_2^+		9.7		0.2	15.0
As_2S^+			0.1	1.1	2.0
$As_2S_2^+$	9.0	9.0	16.0	5.4	5.0
As_3^+		12.0	1.5	0.5	3.0
$As_2S_3^+$	10.5		0.6	0.2	0.18
As_3S^+	11.5	10.0	21.0	10.0	15.0
$As_3S_2^+$	10.8	11.0	6.3	2.5	8.0
As_4^+		8.5	0.3	0.2	25.0
$As_3S_3^+$	10.2	9.0	71.0	49.0	30.0
$As_3S_4^+$	9.7		3.0	2.3	4.0
$As_4S_3^+$	8.6	8.7	2.3	0.3	30.0
$As_4S_4^+$	8.9	9.0	100.0	100.0	100.0
$As_4S_5^+$	9.0		1.4	1.0	4.0

Table II. Relative intensities and instantaneous slit effects for parent vapor species above As_4S_4 at 418 and 475 K*

Ion	T = 418 K: I_o^+(mV)	T = 418 K: I_o/I_f	T = 418 K: Relative intensity	T = 475 K: I_o^+(mV)	T = 475 K: I_o/I_f	T = 475 K: Relative intensity
S_2^+				0.9	0.3	3.3
AsS^+				0.02	1.0	0.01
As_2S_2				0.14	0.6	0.05
$As_2S_3^+$				0.50	0.9	0.18
$As_4S_3^+$	0.054	0.6	1.2	9.0	0.4	3.3
$As_4S_4^+$	4.65	0.7	100.0	275.0	0.7	100.0
$As_4S_5^+$	0.045	1.0	1.0	3.1	1.0	1.1

* All measurements made in the magnetic sector instrument at approximately 3 eV above the ionization potential of each ion.

Table III. Temperature dependence of ion signals for $As_4S_4^+$ and $As_4S_5^+$ *

T (K)	I^+ (As_4S_4)	I^+ (As_4S_5)
427.08	7.7	0.22
439.35	23.5	0.63
449.41	51.6	1.30
464.06	158	3.72
475.44	360	8.31

* Ion intensities were measured at 3 eV above threshold, and are reported in arbitrary units.

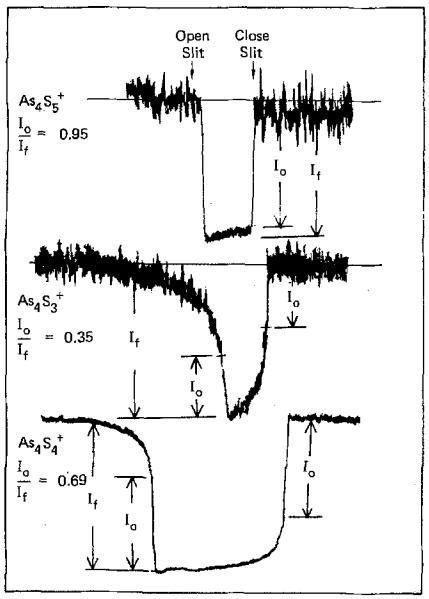

Fig. 1. Instantaneous and total slit effects observed in the magnetic sector instrument.

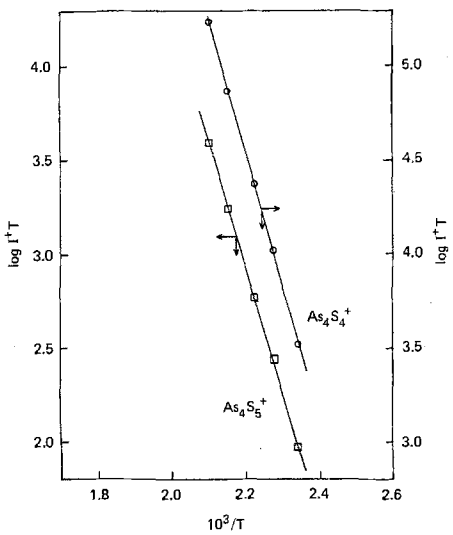

Fig. 2. Temperature dependence of ion signals for As_4S_4 and $As_4S_5^+$ observed in the magnetic sector instrument.

tween the enthalpy values for the two ions, the signals were measured at only 3 eV above the ionization thresholds in each case so that only parent ions could contribute to the signals.

Torsion-effusion measurement.—The vapor pressure above As_4S_4 was measured in the range 410-465 K; the results are reported in Tables IV and V for alumina cells with orifice diameters of 1.05 and 1.5 mm, respectively. Total pressures are derived from the observed deflection angles by the relation

$$P = K \cdot \theta \qquad [1]$$

where K is a constant based on the geometry of the effusion cell and the torsion constant of the fiber. Vapor molecular weight is calculated from the experimental data from the expression

$$M = C \cdot T \cdot (\dot{w}/\theta)^2 \qquad [2]$$

where T is the absolute temperature, $\dot{w}$ is the rate of mass loss, and C is another constant derived from cell geometry.

The original torsion-effusion runs in each cell employed β-As_4S_4 as received from Alfa Products. X-ray analysis of the residues from the two runs showed that the samples had converted to the α-phase by the end of the run, in contrast with the results of MSW, who did not observe the transition in their torsion-effusion runs. A second run was performed in cell AlO2 (1.5 mm orifices) using residual α-As_4S_4 from the first run; the absolute pressures were in excellent agreement with those of the AlO2 run with β-As_4S_4 as the starting material. The second law enthalpy derived from the slope of the pressure measurements in cell AlO3 (1.05 mm orifices) was 29.5 (±0.15) kcal/mol; the results for the runs starting with β- and α-As_4S_4 in cell AlO2 were 29.6 (±0.47) and 30.9 (±0.20) kcal/mol, respectively. Figure 3 is a plot of the vapor pressure *vs.* inverse temperature for the two cells. The least squares line obtained by MSW is included for comparison; the least squares equations for our data are in Tables IV and V.

Table IV. Total vapor pressure above As_4S_4 measured in cell AlO-3 (1.05 mm)

T (K)	θ Radians	− Log P (atm)
458.68	0.16252	5.5763
437.09	0.03268	6.2730
414.49	0.00518	7.0727
427.32	0.01493	6.6130
449.76	0.08385	5.8637
454.65	0.11990	5.7084
442.44	0.04732	6.1122
420.95	0.00854	6.8560
431.46	0.02062	6.4730
427.32	0.01554	6.5957
450.35	0.08790	5.8432
464.74	0.24876	5.3914
434.59	0.02761	6.3461

Log P (atm) = 8.470 − 6445/T(K)
ΔH(T Avg) = 29.5 (± 0.15) kcal/mol
ΔS(T Avg) = 38.8 (± 0.35) cal/mol K

Table V. Total vapor pressure of As_4S_4 measured in cell AlO-2 (1.5 mm)

	Set I — Start with β −As_4S_4			
K	θ Radians	− Log P (atm)	Mass loss (mg/hr)	Mol wt
425.49	0.03493	6.6402	0.768	407.2
435.78	0.07719	6.2958	1.724	430.3
435.18	0.07201	6.3260	1.576	412.6
446.23	0.16572	5.9640	3.632	424.3
410.80	0.00960	7.2010		
432.18	0.05714	6.4264		
449.53	0.19782	5.8871	4.424	445.1
435.18	0.06779	6.3522		
441.61	0.10905	6.1457	2.448	440.5
419.00	0.01732	6.9448		
424.38	0.02746	6.7447		
412.53	0.01004	7.1815		

Log P (atm) = 8.527 − 6470/T(K)
ΔH(T Avg) = 29.6 (± 0.47) kcal/mol
ΔS(T Avg) = 39.0 (± 1.1) cal/mol K

	Set II — Start with α −As_4S_4	
436.26	0.07698	6.2970
415.22	0.01236	7.0914
425.12	0.03097	6.6924
446.59	0.17416	5.9424
440.90	0.11063	6.1395
428.55	0.04031	6.5780

Log P (atm) = 9.192 − 6758/T(K)
ΔH(T Avg) = 30.9 (± 0.2) kcal/mol
ΔS(T Avg) = 42.0 (± 0.5) cal/mol K

Discussion

The mass spectra of As_4S_4 vapor found in our two instruments and in the quadrupole instrument of MSW are summarized in Table I; the most striking differences in the results are the lower intensities we observed for S_2^+, As^+, As_2^+, and As_4^+. Reactions of arsenic sulfides in the hot ion source region of the mass filter probably account for the greater ion intensities found for these species in the MSW study, emphasizing the importance of using a beam-defining

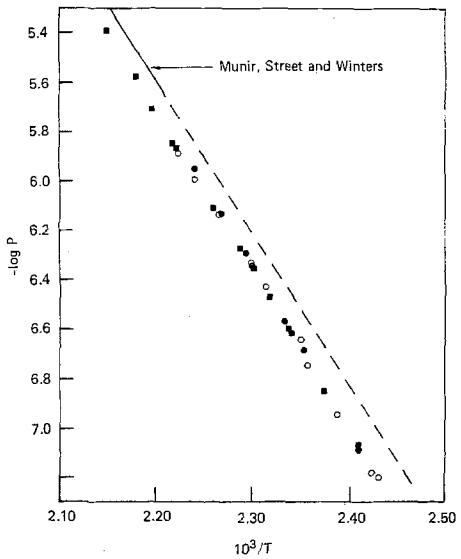

Fig. 3. Vapor pressures above As_4S_4 observed by torsion-effusion (= β-As_4S_4 in cell AlO3, O = α-As_4S_4 in cell AlO2, O = β-As_4S_4 in cell AlO2).

slit for positive identification of ion signals originating in the Knudsen cell. The results of the three sets of measurements are in fair agreement for other ion signals with the exception of $As_4S_3^+$, for which a much higher signal was also reported by MSW.

We feel that the relative abundance of neutral species effusing from the Knudsen cell is reflected most accurately by observing all parent ions at the same small energy increment above the IP of the neutral, as we have done for the As_4S_4 sample in Table II. If the energy is chosen at only 2-3 eV above the ionization threshold, contributions from fragmentation processes are minimized. A more complete discussion of these points was given recently in our work on As_2S_3 (11). The results in Table II clearly show that $As_4S_4(g)$ is the dominant vapor species above solid As_4S_4. Assuming that differences in the ionization cross sections for the neutral species are not large, As_4S_4 comprises at least 90% of the effusate; the molecular weights derived from the mass-loss torsion-effusion results corroborate the mass spectral data, since the average, 427 ± 20, is in close agreement with the molecular weight of As_4S_4 (427.94).

Since the primary process is the sublimation of As_4S_4, the second law enthalpy of vaporization measured by torsion effusion can be used to evaluate the thermochemical properties of $As_4S_4(g)$. Averaging the three slope enthalpies derived from the torsion-effusion measurements (29.5, 29.6, 30.9 kcal/mol) with the value obtained by mass spectrometry (32.8 kcal/mol), we obtain a value of 30.7 (±0.9) kcal/mol for the sublimation enthalpy of As_4S_4 at 450 K. The average entropy change for the sublimation process is 41.9 (±2.5) cal/K mol at that temperature.

The results of our torsion-effusion measurements are in good agreement with those of MSW, although we obtain a somewhat higher enthalpy of sublimation for As_4S_4. Our measured pressure is 20% lower than the MSW torsion-effusion pressure at 465 K, the upper temperature limit of our measurements.

MSW observed a transformation from β-As_4S_4 starting material to α-As_4S_4 residual after free evaporation experiments but the residue from their torsion-effusion runs was β-phase. They did observe the same vapor pressures in the free evaporation studies whether the original sample was α- or β-phase, in agreement with our observations. MSW observed that vapor pressures derived from free evaporation measurements were about a factor of two lower than torsion-effusion results; they attributed this effect to a kinetic barrier in the evaporation process.

It is also possible that the lower pressures reported in the free evaporation studies result from an artifact in the experiment. In an ideal free evaporation experiment, molecules leaving the sample surface are removed to infinity; whereas, in real systems, it is possible for a portion of the molecular flux from the surface to rebound from nearby surfaces in the system to recondense on the sample pellet. The recondensation reduces the net torque on the torsion fiber so that calculated pressures in the experiment are too low. By extrapolating results from experiments on samples of different surface area to zero surface area, the true free evaporation pressure may be derived. This correction cannot be performed on the data of MSW since free evaporation experiments were performed for only one sample area. The presence of a significant kinetic barrier to vaporization of As_4S_4 is not indicated by our torsion-effusion results, since the vapor pressures were virtually identical for vaporization from cells with orifice areas differing by a factor of two. With this difference in orifice sizes, such an effect would be observed only when the condensation coefficient is less than or equal to 0.10.

In an extension of our analysis, we have calculated the thermodynamic functions of As_4S_4 from the geometry and bond lengths deduced from electron diffraction by Lu and Donohue (12) and the vibrational frequencies reported by Scheuermann and Ritter (13) from laser-Raman spectra of single crystal As_4S_4. The calculated thermal functions are given in Table VI. It should be empasized that the vibrational modes reported for the solid may include lattice modes which would differ in energy from fundamental frequencies of the gas phase As_4S_4 molecule, but the spectrum of $As_4S_4(g)$ has not been reported. In any event, the assigned frequencies (13) appear quite reasonable. The data of Johnson *et al.* (12) for the enthalpy of formation and high temperature thermodynamic functions of β-As_4S_4 were assumed actually to apply to α-As_4S_4 since during temperature equilibration for drop calorimetry experiments the phase transition probably occurred.

From the calorimetric and sublimation data, we derive an experimental entropy of 121.8 ± 2.0 cal/K mol for $As_4S_4(g)$ at 450 K, compared to the value 124.6 cal/K mol calculated from spectroscopic and molecular constants. Overall, the agreement between calculated and experimental entropies is reasonably good, considering the error limits on the latter and possible misassignment of some of the vibration frequencies. Until the vibrational spectrum of $As_4S_4(g)$

Table VI. Ideal gas thermodynamic functions of $As_4S_4(g)$

T, K	$-(G-H°_{298})/T$, cal/K mol	S, cal/K mol	$H°_T - H°_{298}$, kcal/mol	C_p, cal/K mol
300	107.94	108.18	0.72	39.29
400	109.51	119.77	4.10	41.11
500	112.52	129.05	8.27	42.01
600	115.94	136.76	12.49	42.52
700	119.39	143.34	16.76	42.83
800	122.75	149.07	21.06	43.04
900	125.96	154.15	25.37	43.18
1000	129.01	158.71	29.69	43.28
1100	131.90	162.83	34.02	43.35
1200	134.64	166.61	38.36	43.41
1300	137.24	170.09	42.70	43.46
1400	139.70	173.31	47.05	43.49
1500	142.04	176.31	51.40	43.52

$H°_{298} - H°_0 = 7.89$ kcal/mol

Input data: ground state statistical weight = 1.
Product of the moments of inertia: $I_aI_bI_c = 7.683 \times 10^{-111}$ g³cm⁶.
Vibrational frequencies — (cm^{-1})

194	221	234	246	263
276	290	304	322	341
353	368	403		

is clarified, the calculated thermal functions in Table VI should be useful in thermodynamic calculations on the As-S system.

The sublimation enthalpy of As_4S_4 is converted to 298.15 K by using the derived values of $H°_T - H°_{298}$ for $As_4S_4(g)$ and the data of Johnson *et al.* for $As_4S_4(s)$, with a resultant value of $H°_{298}$ of 31.6 (±2.0) kcal/mol. The estimated error reflects uncertainty in both experimental slope determinations and spectroscopic constants of $As_4S_4(g)$. Adding this value to that for the formation of $As_4S_4(s)$, we obtain for the enthalpy of formation of $As_4S_4(g)$, $\Delta Hf°_{298} = -1.4$ (±2.6) kcal/mol. The enthalpy of atomization of $As_4S_4(g)$ may then be calculated employing $\Delta Hf°_{298}$ of As(g) reported by Rau (15) and that of S(g) in the JANAF Thermochemical Tables (16) as revised in 1977. The value for the enthalpy of atomization so derived is 590.4 kcal/mol.

Molecular As_4S_4 consists of a tetrahedron of arsenic atoms, each of which is bonded to two sulfur atoms and one arsenic atom, so that there are two As-As bonds and eight As-S bonds. The As-As bond length is 2.49Å in $As_4S_4(g)$ (12) as compared to 2.43Å in $As_4(g)$ (17); we may assume that the As-As bond energy in $As_4S_4(g)$ is similar to that in $As_4(g)$, about 39.5 kcal/mol. With this assumption, we derive a value of 57.7 kcal/mol for the As-S bond energy in $As_4S_4(g)$. This is considerably weaker than the dissociation energy of AsS at 89.8 kcal/mol (11), the difference accounted for in part by high strain energy in the As_4S_4 molecule. The average As-O bond is similarly lowered from 113.4 kcal/mol for AsO(g) to 78 kcal/mol in $As_4O_6(g)$ (18).

While As_4S_4 is the dominant vapor species above solid As_4S_4, the observation of five other arsenic-sulfur species indicates that this system may exhibit a complexity similar to that recently observed for the arsenic-oxygen system (14). We plan further studies of arsenic sulfide vapor species over a wider temperature range by mass spectrometry in order to elucidate the bonding patterns and bond dissociation energies.

Acknowledgments

This research was supported by the National Science Foundation under Grant DAR 79-12296.

Manuscript submitted Aug. 27, 1982; revised manuscript received Dec. 20, 1982.

Any discussion of this paper will appear in a Discussion Section to be published in the December 1983 JOURNAL. All discussions for the December 1983 Discussion Section should be submitted by Aug. 1, 1983.

Publication costs of this article were assisted by SRI International.

REFERENCES

1. Z. A. Munir, G. B. Street, and H. F. Winters, *J. Chem. Phys.*, **55**, 4520 (1971).
2. G. K. Johnson, G. N. Papatheodorou, and C. E. Johnson, *J. Chem. Thermodyn.*, **12**, 545 (1980).
3. R. Blachnik, A. Hoppe, and U. Wickel, *Z. Anorg. Allg. Chem.*, **463**, 78 (1980).
4. D. L. Hildenbrand, *J. Chem. Phys.*, **48**, 3657 (1968); **52**, 5751 (1970).
5. D. L. Hildenbrand, *Int. J. Mass Spectrom. Ion Phys.*, **4**, 75 (1970); **7**, 255 (1971).
6. D. L. Hildenbrand and D. T. Knight, *J. Chem. Phys.*, **51**, 1260 (1969).
7. K. H. Lau, D. Cubicciotti, and D. L. Hildenbrand, *ibid.*, **66**, 4532 (1977).
8. D. L. Hildenbrand and W. F. Hall, *J. Phys. Chem.*, **67**, 888 (1963); **69**, 989 (1964).
9. D. L. Hildenbrand, W. F. Hall, F. Ju, and N. D. Potter, *J. Chem. Phys.*, **40**, 2882 (1964).
10. H. M. Rosenstock, K. Draxl, B. W. Steiner, and J. T. Herron, "Energetics of Gaseous Ions," National Bureau of Standards, Washington, DC (1977).
11. K. H. Lau, R. D. Brittain, and D. L. Hildenbrand, Submitted to *J. Phys. Chem.*
12. C. S. Lu and J. Donohue, *J. Am. Chem. Soc.*, **66**, 818 (1944).
13. W. Scheuermann and G. J. Ritter, *Z. Naturforsch*, **21**, 408 (1969).
14. R. D. Brittain, K. H. Lau, and D. L. Hildenbrand, Submitted to *J. Phys. Chem.*
15. H. Rau, *J. Chem. Thermodyn.*, **7**, 27 (1975).
16. D. R. Stull, H. Prophet, *et al.*, "JANAF Thermochemical Tables," NSRDS-NBS 37, U.S. GPO, Washington, D.C., (1971); Supplement No. 49 (1977).
17. Tables of Interatomic Distances and Configurations in Molecules and Ions, Special Publication No. 11, The Chemical Society, London, England (1958).
18. K. H. Lau, R. D. Brittain, and D. L. Hildenbrand, *Chem. Phys. Lett.*, **81**, 227 (1981).

Thermal Oxidation of Reactively Sputtered Titanium Nitride and Hafnium Nitride Films

I. Suni,[1] D. Sigurd,[2] K. T. Ho, and M-A. Nicolet*

California Institute of Technology, Pasadena, California 91125

ABSTRACT

The oxidation behavior of reactively sputtered TiN and HfN thin films was investigated for oxide formation in dry and wet oxidizing ambient in the temperature range of 425°-800°C. For both cases, formation of a single-oxide phase, rutile TiO_2 for oxidized TiN and monoclinic HfO_2 for oxidized HfN, was observed. The oxidation process is thermally activated, and it has a parabolic time dependence, except in the case of wet oxidized HfN where nonuniform oxidation behavior was observed. The parabolic time dependence of the oxide growth is attributed to a transport-controlled process which is limited by the diffusivity of the oxidant in the oxide. The dry oxidation of TiN is much faster than the dry oxidation of HfN at a given temperature. The oxidation rate is always higher in a wet than in a dry ambient.

Many interstitial compounds such as nitrides and carbides of the relatively large transition metals have refractory properties, yet they are metallic. This combination has suggested their use as stabilizing barriers in metallization structures for semiconductor devices.

An attractive compound among the transition metal nitrides is titanium nitride (TiN) which has been successfully used in devices such as insulated gate field effect transistors (1) and beam lead devices (2). Good

* Electrochemical Society Active Member.
[1] Permanent address: Technical Research Centre of Finland, Otakaari 5A, SF-02150 Espoo 15, Finland.
[2] Permanent address: Institute of Microwave Technology, S-100 44 Stockholm 70, Sweden.
Key words: titanium nitride, hafnium nitride, oxidation, reactive sputtering, refractory compounds.

barrier performance has been reported also for tantalum nitride (TaN) (3) and hafnium nitride (HfN) (4). It has further been shown that TiN, TaN, and HfN provide good electrical contacts to heavily doped silicon (5).

In spite of their refractory properties, the transition metal nitrides transform to oxides at elevated temperatures in oxidizing ambients. This can be understood by comparing the heats of formation for nitrides and oxides of group IV and V transition metals (see Table I). The average gain of energy in the oxidizing reaction is in the order of 150 kcal/g · mol/metal atom.

Apart from being interesting from the point of view of materials properties and characterization, the behavior of these nitride layers in an oxidizing ambient is relevant in assessing their possible applications. The oxidation kinetics of TiN thin films has recently been reported by Sigurd *et al.* (7) and Wittmer (8) for oxidation in dry O_2 ambient. In both studies, the oxide growth followed a square root of time dependence in the temperature range of 500°-650°C. This result has been interpreted in terms of oxidant diffusion through the growing oxide as the rate-limiting step. The parabolic rate of oxidation was found to be thermally activated with an activation energy $E_a \approx 2.1$ eV. More complicated kinetics are generally observed during the oxidation of pure transition metals where the oxidation proceeds through dissolution of oxygen into the metal and formation of intermediate oxide phases (9). Nonparabolic kinetics have been found for low temperature oxidation of tantalum nitrides. Brady *et al.* (10) have reported that the kinetics for oxidation of hcp Ta_2N, fcc TaN_x, and bcc Ta changes with temperature. At 250°-350°C, they observe a quartic ($\sim t^{1/4}$) time dependence, but they found a parabolic time dependence for similar films which were annealed at 400°-525°C.

In this study, we report the oxidation behavior of sputter-deposited TiN and HfN films for dry and wet oxidation at 425°-800°C. The results are based on direct observation of changes in the oxide thickness by backscattering spectrometry (BS).

Experimental Procedures

Titanium nitride and hafnium nitride films were deposited on chemically cleaned single crystal <100> oriented silicon substrates. All films were reactively sputtered from metallic titanium (99.9% Ti) and hafnium (94 atomic percent (a/o) Hf + 6 a/o Zr) targets. The deposition rates and the substrate bias voltage were adjusted to obtain oxygen-free nitride layers with low resistivity and minimum stress. The film resistivity, which depends on the stoichiometry and the oxygen concentration, was below 100 μΩcm for TiN and below 250 μΩcm for HfN. The sputtering rate and the substrate bias, which both affect the film resistivity, did not seem to alter the oxidation behavior of the films. The film thicknesses were in the order of 2500Å for the deposited nitride films yielding an approximately 4000Å thick oxide layer after a complete oxidation.

The deposited nitride films were subsequently oxidized in an open-ended quartz tube furnace with an O_2 gas flow. The wet oxidation was carried out in the same furnace by bubbling the O_2 gas through a bottle of hot deionized water prior to entering the furnace. The oxidation temperatures ranged from 425° to 600°C for TiN and from 450° to 800°C for HfN.

Table I. Heats of formation for mononitrides and oxides of group IV and V transition metals according to Goldschmidt [Ref. (6)]

Group	Metal	ΔH_f (kcal/g · mol per metal atom) Nitride	Oxide
IV	Ti	TiN −80.4	TiO_2 −219
	Zr	ZrN −87.3	ZrO_2 −259
	Hf	HfN −88.2	HfO_2 −272
V	V	VN −52.0	V_2O_5 −192
	Nb	NbN −59.0	Nb_2O_5 −232
	Ta	TaN −59.0	Ta_2O_5 −250

The oxidized layers were analyzed by 2 MeV $^4He^+$ ion BS. A series of BS spectra from an unoxidized TiN layer and layers oxidized for different times at 595°C are shown in Fig. 1. The reduced BS yield in the leading edge of the Ti signal is due to the energy loss by oxygen atoms in the oxide layer. The oxide thickness was calculated from the energy width of the oxidized TiN layer.

The approximate composition of the layers was determined from the height ratios of signals corresponding to the oxidized and unoxidized layers, respectively. The crystal structures were identified by x-ray diffraction analysis. Optical properties of fully oxidized layers on silicon substrates were determined by ellipsometry.

Results

Titanium nitride.—An oxidized surface layer is formed on the TiN films after a short time of annealing at about 500°C in an oxidizing ambient. The well-defined signals in the BS spectrum (see Fig. 1) indicate that the composition of the oxide is relatively uniform in depth. The atomic ratio between the metal and oxygen is found to be Ti:O = 0.5 ± 0.03 as determined from the signal heights of the BS analysis. This corresponds to the stoichiometric formula TiO_2 of titanium dioxide. The crystal structure of the oxide layer was determined by x-ray diffraction analysis. Only the tetragonal rutile structure of TiO_2 could be identified by this analysis. No diffraction lines due to the other polymorphic forms of TiO_2 (*i.e.*, anatase or brookite) or the intermediate oxide phases (*i.e.*, Ti_3O_2, TiO, Ti_2O_3, or Ti_3O_5) could be detected. The structures of both dry and wet oxidized TiN layers were identical. Details of the x-ray data have been reported in Ref. (7).

The kinetics of the oxide growth were investigated by measuring the oxide thickness after various times of isothermal oxidation for several temperatures. An example of a gradual increase in the oxide thickness is shown in Fig. 1 for dry oxidation of TiN at 595°C. A parabolic time dependence of oxide thickness was observed for both dry and wet oxidized TiN layers, as can be seen in Fig. 2 where the thickness of the oxide grown in a wet ambient at 500°C is plotted as a function of the square root of time. The data can be fitted to a straight line

$$W = (K \cdot t)^{1/2} \quad [1]$$

where W is the oxide thickness, t is the oxidation time, and K is the parabolic rate constant of oxidation. The corresponding linear relationship for dry oxidation at 500°C is shown as a dashed line based on data given in Ref. (7). The oxidation rate is much faster for the wet than for the dry oxygen ambient over the temperature range of this study. The rate constants corresponding to the slopes of the linear plots in Fig. 2 are K_{dry} (500°C) = $2.21 \cdot 10^3$ Å²/min and K_{wet} (500°C) = $2.25 \cdot 10^4$ Å²/min.

The values of the rate constant K are presented on a logarithmic scale as a function of reciprocal temperature in Fig. 3. The linear fit of the data corresponds to the exponential Arrhenius relationship of the form

$$K = K_o \exp(-E_a/kT) \quad [2]$$

where K_o is a temperature independent factor, E_a is the thermal activation energy associated with the parabolic oxidation process, and k is the Boltzmann coefficient. The values for K_o and E_a, derived from an exponential regression analysis of the data given in Fig. 3, are presented in Table II. K_o and E_a for wet oxidation of TiN are lower than the corresponding values for dry oxidation. Consequently, the relative difference between the oxidation rates increases toward low temperatures.

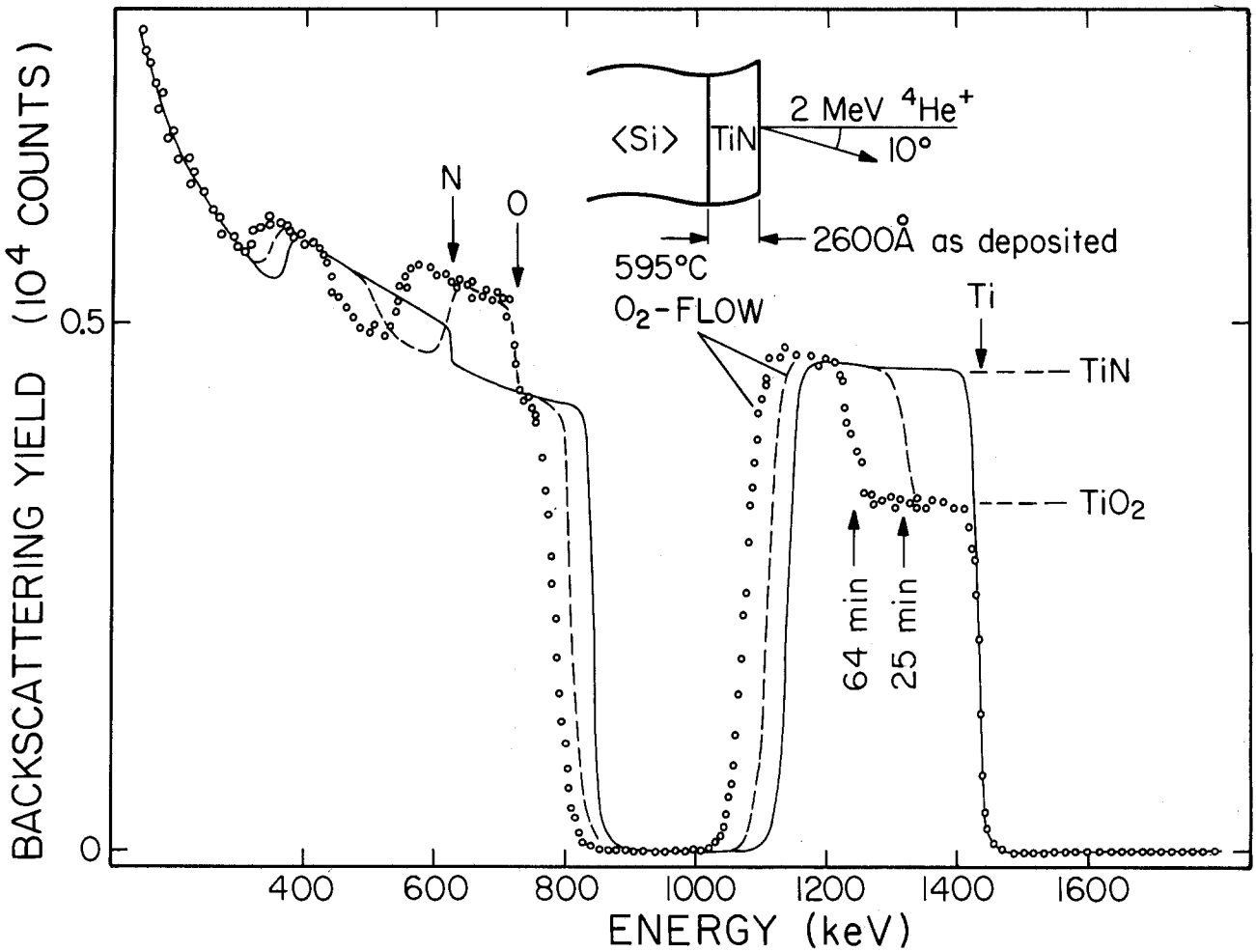

Fig. 1. Backscattering spectra of a titanium nitride layer as-deposited (———) and subsequently dry oxidized at 595°C for 25 (- - -) and 64 min (○ ○ ○).

The refractive index of the fully oxidized TiN layers was determined with an ellipsometer operating at the wavelength of an He-Ne laser (632.8 nm). The measured value $n = 2.3 \pm 0.05$ is lower than those given for bulk TiO_2 ($n_o = 2.6$, $n_e = 2.9$) (11), but comparable to the value reported for vacuum evaporated TiO_x films ($n = 2.4$) (12).

Hafnium nitride.—Hafnium nitride films annealed in oxygen ambient show oxidized surface layers similar to those found in oxidized TiN samples. Backscattering spectrometry indicates that the composition is given by the ratio Hf:O = 0.5 ± 0.02 which corresponds to the stoichiometric formula of HfO_2.

Hafnium dioxide is known to have several polymorphs, but only the monoclinic form which is a derivative of the fluorspar structure remains stable at room temperature (13). This is also the only phase identified by x-ray diffraction analysis of oxidized HfN films. Possible monoclinic ZrO_2 phases due to the known Zr impurity contained in the sputtering target and the resulting nitride layers cannot be separated in the x-ray diffraction spectra taken with a Read camera because of the almost identical d-spacings to those of HfO_2. The detailed data are given in Table III.

Table II. Constants K_o and E_a related to the parabolic oxidation rate $K = K_o \exp(-E_a/kT)$ for TiN and HfN

	K_o (A^2/min)	E_a (eV)
TiN (dry)	$2.2 \cdot 10^{17}$	2.1
TiN (wet)	$2.2 \cdot 10^{14}$	1.5
HfN (dry)	$4.0 \cdot 10^{17}$	2.5

The oxidation kinetics were investigated in a similar fashion as in the case of TiN. The dry oxidation was studied at a slightly higher temperature range because the oxidation rates were found to be lower compared to those of TiN at a given temperature. A parabolic time dependence of oxidation was again observed for dry oxidized HfN. This is demonstrated by the linear thickness *vs.* square root of time plots in Fig. 4 for two different temperatures. A completely different behavior was observed for the wet oxidation of HfN. The initially slow oxidation rapidly increases after a certain

Table III. X-ray analysis of fully oxidized HfN films. The measured d-spacings are compared to those given for monoclinic systems of HfO_2 and ZrO_2 [Ref. (14)]

d-spacings (A)			
Measured	HfO_2	ZrO_2	hkl
4.96	5.07	5.04	100
3.63	3.61	3.63	110
3.13	3.15	3.16	$11\bar{1}$
2.82	2.82	2.83	111
2.53	2.59	2.62	002, 020
2.52	2.52	2.54	200
2.30	2.32	2.33	012, $02\bar{1}$, 120
2.19	2.20	2.21	$21\bar{1}$
1.99	2.00	2.01	112
1.84	1.84	1.84	$21\bar{2}$, 022
1.79	1.79	1.80	$12\bar{2}$
1.68	1.68	1.69	300, 202
1.64	1.63	1.66	013, $03\bar{1}$, $11\bar{3}$
1.58	1.58	1.59	$13\bar{1}$
1.53	1.53	1.54	131, 302

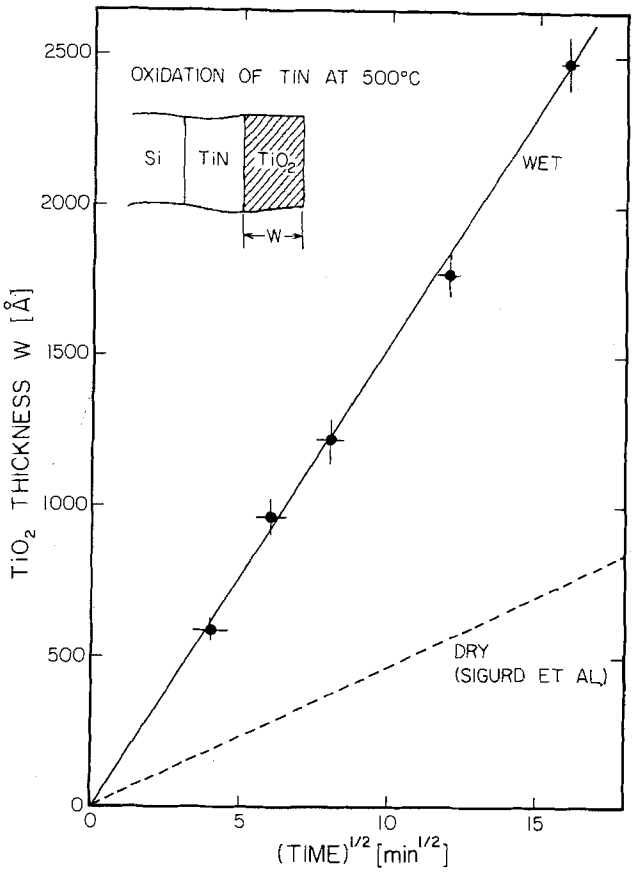

Fig. 2. The thickness, W, of the oxidized layer on titanium nitride plotted as a function of the square root of time for dry (- - -) and wet (——) oxidation at 500°C.

time delay as shown by the dashed line in Fig. 4. At the same time, severe pitting is observed in the oxidized layer. Because of the limited thickness of the sputtered nitride layers, this oxidation process could not be followed in detail. The Arrhenius plot of the parabolic rate constant K for dry oxidation of HfN is shown in Fig. 3. K_0 and E_a are given in Table II. The pre-exponential factor K_0 for HfN is in the same order of magnitude as for dry oxidized TiN. The activation energy E_a is higher, however, resulting in a much slower oxidation rate for HfN compared to that of TiN.

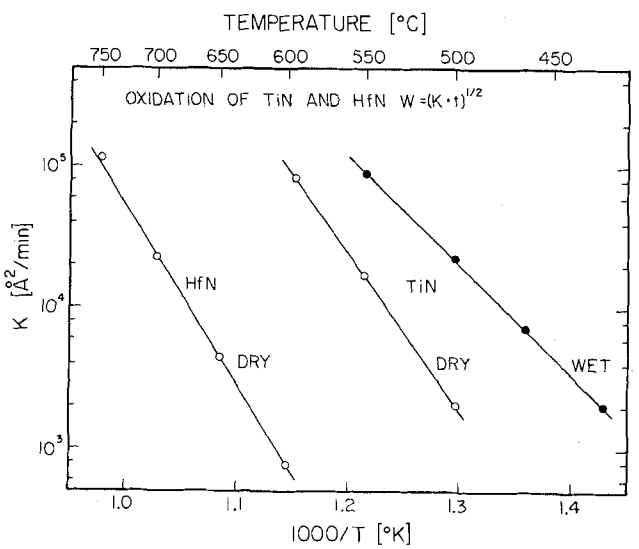

Fig. 3. The parabolic rate constant K [$W = (K \cdot t)^{1/2}$] for the oxidation of sputtered TiN and HfN layers as a function of reciprocal temperature. The values of K_0 and E_a for $K = K_0 \exp(-E_a/kT)$ are given in Table II.

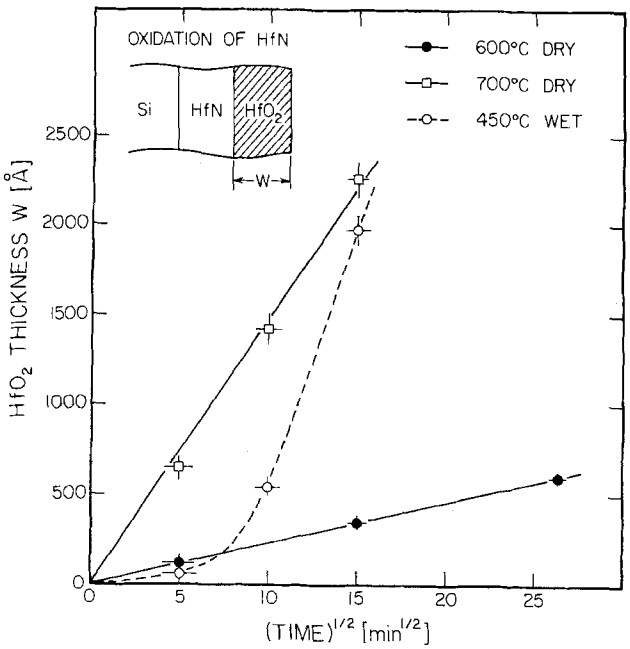

Fig. 4. The thickness, W, of the oxidized layer on hafnium nitride plotted as a function of the square root of time for dry oxidation at 600° and 700°C and wet oxidation at 450°C.

The refractive index of the fully oxidized HfN layers measured ellipsometrically was $n = 1.9 \pm 0.05$ at $\lambda = 632.8$ nm. This again is lower than the values reported for bulk HfO_2 ($n \approx 2.2$). The refractive index of reactively sputtered HfO_2 thin films is known to vary with the oxygen concentration of the sputtering gas and the deposition rate ($n = 1.8 \ldots 2.1$), the lower values corresponding to lower deposition rates and presumably lower film densities (15).

Discussion

Transition metal nitrides show basically similar oxidation behavior as the metals themselves. The observed parabolic time dependence for the dry oxidation of TiN and HfN suggests that the process is limited by the atomic transport through the oxidized surface layer. In the case of pure metals, this oxidation mechanism involves oxygen dissolution and formation of intermediate oxide phases as shown for Ti (9) and Ta (16). For nitrides where the octahedral interstitial sites are filled with nitrogen atoms, the solubility of oxygen is probably very low. In such a case, the oxidation is likely to lead directly to the more stable higher oxides. This assumption is also supported by the experimental fact that only one oxide phase has been observed for oxidized TiN films. A sharp oxide-nitride interface is visible in the backscattering spectra of partially oxidized TiN and HfN layers. For the Hf-O system, stable lower oxides do not exist and the oxidation should eventually result in the formation of HfO_2.

A growth of a compound layer that is proportional to $t^{1/2}$ is usually taken to indicate a transport-limited process. Which atomic species dominates in the transport, if any, cannot be derived from such information. Refractory metal oxides tend toward nonstoichiometric structure due to oxygen deficiency. Consequently, the atomic transport during the oxidation has been attributed to the oxygen diffusion (9). If it is assumed that this same diffusion mechanism controls oxidation of our TiN and HfN films, the dominant diffusing species must be oxygen. This same hypothesis has been advanced for the oxidation of bcc Ta, β-Ta, and Ta_2N thin films (18).

The activation energies derived from the oxidation rates (see Table II) are those of the parabolic rate constants. The value $E_a = 2.05$ eV, recently reported by Wittmer (8) for the dry oxidation of TiN is in good

agreement with our data although it was related to the diffusivity rather than the rate constant. However, even if a single dominant diffusion process is assumed, one cannot arrive at the diffusivity from the rate constant without the knowledge of the concentration difference of the diffusing species at the boundaries of the oxide layer. In general, this gradient depends on the equilibrium solubility of oxygen in the oxide (19). The role of solubility is, thus, important for understanding the difference in kinetics for dry and wet oxidation. Whether the fast rate of wet oxidation of TiN should be attributed to the high diffusivity (E_a = 1.5 eV) or the high solubility of the oxidant is not clear. A complex solubility and transport behavior of water in silica has been reported for thermal oxidation of silicon (20). A similar mechanism accounting for the catalytic role of water in the oxide may also explain the wet oxidation behavior of titanium nitride.

The activation energy observed for dry oxidation of HfN (E_a = 2.5 eV) is higher than the corresponding value for TiN. The oxide structures of HfO_2 and TiO_2 have basically similar atomic arrangements. Hence, the solubilities of oxygen are likely to be similar in these oxides. The lower oxidation rate in the case of HfN then implies a lower diffusivity of oxygen in HfO_2 compared to that in TiO_2.

The complicated behavior of the wet oxidation of HfN can possibly be explained by changes in the surface morphology of the oxide layers. When the oxide layer breaks up, the oxidant has available sufficiently broad grain boundaries and pores for rapid transport to the reaction front so that phase-boundary reactions instead of diffusion became rate limiting (21). Kofstad (16) has observed a similar effect of "breakaway" oxidation which was associated with Ta_2O_5 formation during thermal oxidation of bulk Ta at 400°C. For the oxidation of nitride layers such as TiN and HfN, the outdiffusion of nitrogen has to be emphasized as a possible reason for the changes in surface morphology. Particularly at low temperatures, the outdiffusion may be considerably impeded resulting in severe blistering of the brittle oxide and nitride films similar to that observed in HfN films wet-oxidized at 450°-500°C.

The optical properties of the TiO_2 and HfO_2 films indicate that the oxidation of nitride layers leads to a structure slightly different from that of bulk oxides. The lower values of refractive index for the oxidized nitride layers suggest that the film density is lower than the bulk density. Both the optical (ellipsometer) and mechanical (Sloan-Dektak) measurements yield larger film thicknesses than the BS analysis using bulk density values for the oxides and stopping cross sections for the elements given in Ref. (22). The deviation between the mechanical and BS thicknesses amounts to approximately 10% for both TiO_2 and HfO_2. Similar thickness deviations were also observed for the initial nitride films. Because x-ray analysis has confirmed the correct lattice structure, it is believed that the films are relatively porous.

Conclusion

Reactively sputtered titanium nitride films transform to titanium dioxide when annealed in an oxidizing ambient at 425°-600°C. The oxide thickness follows parabolic time dependence both for the dry and wet oxidation. The activation energies associated with the parabolic rate constant are 2.1 eV for the dry oxidation and 1.5 eV for the wet oxidation, respectively. A single oxide phase, the rutile structure of TiO_2 has been observed.

The dry oxidation of hafnium nitride at 600°-800°C leads to the formation of monoclinic hafnium dioxide. Also in this case, a parabolic oxidation kinetics is observed. The activation energy is 2.5 eV, and the oxidation rate is much slower than the rate for TiN at a given temperature. In both cases, the rate-limiting process is believed to be the diffusion of oxidant through the oxide layer. The wet oxidation of HfN at 450°-500°C results in a nonuniform oxide layer with a rough surface morphology. The observed fast oxidation mode is attributed to a reaction controlled process.

Acknowledgments

We thank B. X. Liu (Caltech) for the x-ray analysis of our samples, M. B. Chamberlain (Sandia National Laboratories, Albuquerque, New Mexico) for critical comments, and R. Gorris (Caltech) for technical assistance. This work was financially supported by the Department of Energy and monitored by Sandia Laboratories, Albuquerque, New Mexico (L. Beavis and M. B. Chamberlain).

Manuscript submitted Nov. 15, 1982; revised manuscript received *ca.* Jan. 5, 1983. This was Paper 356 presented at the Denver, Colorado, Meeting of the Society, Oct. 11-16, 1981.

Any discussion of this paper will appear in a Discussion Section to be published in the December 1983 JOURNAL. All discussions for the December 1983 Discussion Section should be submitted by Aug. 1, 1983.

Publication costs of this article were assisted by the Department of Energy.

REFERENCES

1. P. R. Fournier, U.S. Pat. 3,879,746 (1976).
2. W. J. Garceau and G. K. Herb, *Thin Solid Films*, **60**, 237 (1979).
3. M. Wittmer, *Appl. Phys. Lett.*, **36**, 456 (1980).
4. I. Suni, M. Mäenpää, M-A. Nicolet, and M. Luomajärvi, *This Journal*, **130**, 1215 (1983).
5. M. Mäenpää, I. Suni, M-A. Nicolet, F. Ho, and P. Iles, in "Proceedings of the 15th IEEE Photovoltaic Specialists Conference," p. 518 (1981).
6. H. J. Goldschmidt, "Interstitial Alloys," pp. 218, 356, Plenum Press, New York (1967).
7. D. Sigurd, I. Suni, L. Wieluński, M-A. Nicolet, and H. von Seefeld, *Solar Cells*, **5**, 81 (1981-1982).
8. M. Wittmer, J. Noser, and H. Melchior, *J. Appl. Phys.*, **52**, 6659 (1981).
9. K. Hauffe, "Oxidation of Metals," p. 209, Plenum Press, New York (1965).
10. D. P. Brady, F. N. Fuss, and D. Gerstenberg, *Thin Solid Films*, **66**, 287 (1980).
11. N. G. Driscoll and W. Vaughan, "Handbook of Optics," pp. 7-100, McGraw-Hill, New York (1978).
12. M. Koltun, "Selective Optical Surfaces for Solar Energy Converters," p. 80, Allerton Press, New York (1981).
13. H. J. Goldschmidt, "Interstitial Alloys," p. 369, Plenum Press, New York (1967).
14. ASTM Powder Diffraction File. 6-0318 and 13-307.
15. I. Suni, Unpublished results.
16. P. Kofstad, *J. Inst. Metals*, **91**, 209 (1962-1963).
17. N. Cabrera and N. F. Mott, *Rept. Progr. Phys.*, **12**, 163 (1948).
18. C. A. Steidel and D. Gerstenberg, *J. Appl. Phys.*, **40**, 3828 (1969).
19. D. E. Deal and A. S. Grove, *ibid.*, **36**, 3770 (1965).
20. D. R. Wolters, *This Journal*, **127**, 2072 (1980).
21. K. Hauffe, "Oxidation of Metals," p. 217, Plenum Press, New York (1965).
22. W. K. Chu, J. W. Mayer, and M-A. Nicolet, "Backscattering Spectrometry," p. 362, Academic Press, New York (1978).

Thermal Stability of Hafnium and Titanium Nitride Diffusion Barriers in Multilayer Contacts to Silicon

I. Suni,[1] M. Mäenpää,[1] and M-A. Nicolet*

California Institute of Technology, Pasadena, California 91125

and M. Luomajärvi

Department of Physics, University of Helsinki, SF-0070 Helsinki 17, Finland

ABSTRACT

The thermal stability of reactively sputtered hafnium nitride (HfN) and titanium nitride (TiN) thin films is investigated for the application as diffusion barriers in metallic contacts to silicon. The temperature range of interest is from 400°-800°C. The dominating failure mechanism is associated with loss of adhesion and blistering of the barrier layers. The extent of the failure is related to the compressive stresses in the sputtered nitride layers. With proper constraints imposed on the deposition process, HfN and TiN can perform as effective diffusion barriers up to 800°C.

Metallization schemes used in semiconductor contact technology show various degrees of failure when subjected to elevated temperatures during device processing. The degradation of an unstable metal-semiconductor or a metal-metal system can be retarded by introducing a diffusion or reaction barrier to the critical interface (1, 2). An ideal diffusion barrier for a contact metallization is a chemically stable and electrically conductive layer that inhibits interdiffusion between two contact metals or a metal and the semiconductor substrate. Most of the metallic elements fail as diffusion barriers by forming intermetallic compounds or solid solutions with one or both of the separated materials. Even in immiscible systems, rapid short circuit diffusion along the grain boundaries may deteriorate the contact structure. Some refractory compounds such as nitrides, carbides, and borides have high electrical conductivity and chemical stability, which are properties that make them attractive as materials for diffusion barriers. Some of these compounds have been successfully applied to practical devices such as insulated gate field effect transistors (3) and beam lead devices (4). A potential application of titanium nitride (TiN) as diffusion barrier in solar cells has also been demonstrated (5). It has been shown further that titanium nitride, tantalum nitride, and hafnium nitride (HfN) provide good electrical contacts on heavily doped silicon substrates (6). In the specific application for solar cells, these materials have sufficiently low contact resistivities to satisfactorily handle current densities typical for solar cells operating at 100-fold concentration of solar irradiation.

The diffusion barrier properties of TiN in a metal-silicon system have been studied in detail by Cheung *et al.* (7). The failure temperatures of a TiN barrier interposed between a silicon substrate and a metallic overlayer of Au, Al, Ag, Pd, or Cu were related to the specific metal-silicon eutectic temperatures ranging from 370°C for Au to 830°C for Ag. The cause of failure was attributed to the grain boundary diffusion or the transport through defects such as pinholes. The nature and the source of these defects were not specified, however.

For reactively sputtered TiN, large variations in the electrical resistivity and the atomic composition have been reported as a result of varying the deposition parameters (8, 9). How these variations affect the barrier performance of sputtered TiN has not yet been established.

* Electrochemical Society Active Member.
[1] Permanent address: Semiconductor Laboratory, Technical Research Centre of Finland, Otakaari 5A, SF-02150 Esoo 15, Finland.
Key words: hafnium nitride, titanium nitride, diffusion barriers, thermal stability, reactive sputtering, sputtering, metallization, refractory compounds.

To gain insight into the actual failure mechanism and the constraints for the deposition of reliable diffusion barriers, we have investigated the thermal stability of diffusion barrier systems containing a layer of either HfN or TiN interposed between a silicon substrate and a metallic overlayer of Pd, Cu, or Au.

Experimental Procedures

The samples consist of a multilayer structure with a reactively sputtered HfN or TiN barrier layer interposed between the top metal layer (Pd, Cu, or Au) and the polished Si<100> substrate. Before the deposition of nitride layers, the substrates passed through organic cleaning and etching in a dilute HF solution. In electrical measurements, it was found that this cleaning procedure improves the contact between the nitride layer and the silicon substrate, presumably eliminating partly the adverse effect of the native SiO_2 layer at the interface (6).

The HfN and TiN layers were deposited by reactive rf sputtering in a vacuum chamber equipped with 7.5 cm in diameter, planar magnetron cathodes. Target plates of nominally 99.9% pure Ti and Hf [in fact 94 atomic percent (a/o) Hf + 6 a/o Zr], placed in contact with the water cooled cathode surface, served as sources for nitride deposition. The chamber was evacuated with a liquid nitrogen trapped oil diffusion pump to a background pressure less than 2×10^{-6} Torr prior to the deposition. The layers were sputtered in a premixed Ar-N_2 gas ambient on samples placed at a distance of 7 cm from the target. The substrate holder was isolated from the ground potential and connected to a d-c bias voltage supply. Deposition rates and substrate bias conditions were adjusted to obtain nitride layers with controlled film properties. Typical sputtering conditions are given in Table I for the deposition of HfN and TiN, respectively.

The sample preparation was completed by evaporating the top metal layer on the sputtered nitride layers in an electron beam evaporation system. In some cases, the metallized areas were confined with a

Table I. Deposition parameters used for reactive sputtering of HfN and TiN layers

	HfN	TiN
Total pressure (10^{-3} Torr)	10	8
Gas composition	70% Ar 30% N_2	80% Ar 20% N_2
RF power (W)	500	200 500
Deposition rate (Å min^{-1})	400	30 150
Substrate bias (VDC)	−50	0 −50

shadow mask to an area less than that of the sputtered sample, to avoid reactions at the edge of the samples during the annealing.

To test the metallizations for interdiffusion and possible reaction at elevated temperatures, the samples were annealed for 15 min in the temperature range of 400°-800°C in vacuum of better than 1×10^{-6} Torr. Scanning electron micrographs of the sample surfaces were taken after annealing to find any visible failure patterns. The atomic depth profiles were also obtained by 2 MeV $^4He^+$ backscattering spectrometry.

Hafnium Nitride Barriers

The electrical resistivity of reactively sputtered HfN is a sensitive function of the partial pressure of nitrogen introduced to the deposition process. Rapid increase in the resistivity is associated with an increasing amount of nitrogen incorporated to the growth film in excess to the stoichiometric composition of HfN (10). The lowest resistivity of reactively sputtered HfN thin films has been reported as 90 $\mu\Omega$ cm by Smith (10) for slightly nitrogen deficient layers. To obtain layers with low electrical resistivity and low concentration of impurities at a fixed gas pressure, high deposition rates are preferred. In the present study, the deposition rate was adjusted to a value of 400 Å/min, which yields a film resistivity of 240 $\mu\Omega$ cm on biased substrates (see Table I). The film thickness of HfN was 1500Å.

Palladium on HfN.—Scanning electron micrographs (SEM) shown in Fig. 1 demonstrate the failure mechanism of Pd-HfN metallizations annealed at various temperatures. Protrusions appear on the surface in the form of blisters that are evidently the result of a local loss of adhesion (delamination) during the heat-treatment. The blisters become visible on samples annealed at 500°C for 15 min and a large fraction of the surface area shows delamination after annealing at 550°C. The delamination of the blisters takes place at the Si/HfN interface. The evidence supporting this conclusion is that: (*i*) blisters appear also without a metal overlayer, and (*ii*) the Si substrate can be observed microscopically where the delaminated layer is removed. This conclusion applies to all films described here. The blistering that appears on the SEM micrograph is not visible in the depth profiles obtained by $^4He^+$ ion backscattering, which indicates that the films retain their layered configuration over the blisters.

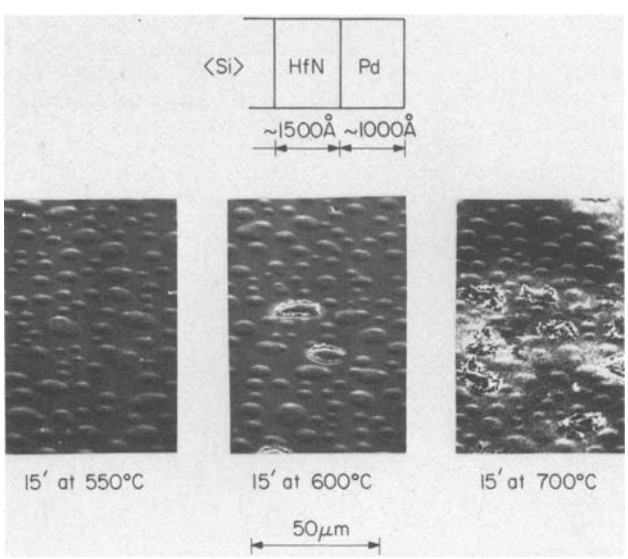

Fig. 1. Scanning electron micrographs indicating the laterally nonuniform failure mechanism of Si-HfN-Pd contacts annealed isochronically at temperatures 550°, 600°, and 700°C.

At higher temperatures, the integrity of the bilayer film is lost locally, presumably as a result of fracturing along the blister circumference, as shown in Fig. 1 for the sample annealed at 600°C.

The reaction between the metal layer and the silicon substrate initiates at these fractures and proceeds by extended lateral diffusion. At 700°C, the lateral integrity of the film structure has severely degraded over large areas of the sample (see Fig. 1). Backscattering now shows that large amounts of material have been transported across the film interfaces.

Copper on HfN.—Blistering of the film structure occurs in this case at 500°C in a similar fashion as for Si-HfN-Pd during annealing. When fracturing sets in, the fractures seem to provide less effective diffusion paths for Cu compared to the case of Pd, where backscattering analysis shows extended interdiffusion already at 700°C. For Si-HfN-Cu system, the laterally nonuniform interdiffusion is detectable after annealing at 750°C.

Gold on HfN.—In contrast to Pd and Cu, Au forms only a eutectic with silicon (at a low 370°C). The failure of HfN barriers in contact with Au follows a pattern similar to that for Pd and Cu, except that blistering and lateral spread of the failure occur fairly abruptly after delamination at 500°C.

Titanium Nitride Barriers

Three different types of barrier layers indicated by sample numbers 1-3 were tested for thermal stability (see Table II). Increasing the deposition rate from 30 Å/min to 150 Å/min improves the conductivity of TiN layers by 60% when a constant substrate bias of −50 VDC is used. At a fixed deposition rate of 150 Å/min, a negative bias voltage of −50 VDC applied to the substrate holder improves the conductivity by 55% (from 170 to 75 $\mu\Omega$ cm) compared to the films deposited on substrates held at the ground potential. It is therefore evident that changing the deposition parameters can result in large variations of film properties. These presumably include changes in the chemical composition and the microstructure of the films (8).

Palladium on TiN.—The degradation of TiN barriers proceeds in a similar fashion as it was found to occur for HfN layers. Blisters appear on sample 1 annealed at 550°C. Some of the blisters are fractured at 600°C (see Fig. 2). At 650°C, backscattering analysis shows extensive interdiffusion between Pd and Si. Again, the failure is laterally nonuniform as indicated by a long tail of the Pd signal in the backscattering spectrum. Spectra of sample 2 show only minor interdiffusion at the TiN-Pd interface at 650°C. For this sample, the interdiffusion is detectable at 700°C and it proceeds gradually when the annealing temperature is increased. In sample 2, the delaminated areas are relatively small and less numerous than in sample 1 after annealing at 600°C, as shown by the SEM micrograph in Fig. 2. The SEM micrograph taken from sample 3 annealed at 650°C is featureless, indicating that the lateral integrity of the film structure is preserved. For this sample, backscattering analysis shows interdiffusion between Pd and Si during annealing when the temperature is raised to 750°C.

Table II. Data for deposition and film properties of TiN barriers

Sample No.	No. 1	No. 2	No. 3
Thickness (Å)	1000	1000	500
Resistivity ($\mu\Omega$ cm)	75	425	<100
Deposition rate (Å/min)	150	30	150
Substrate bias (VDC)	−50	0	−50

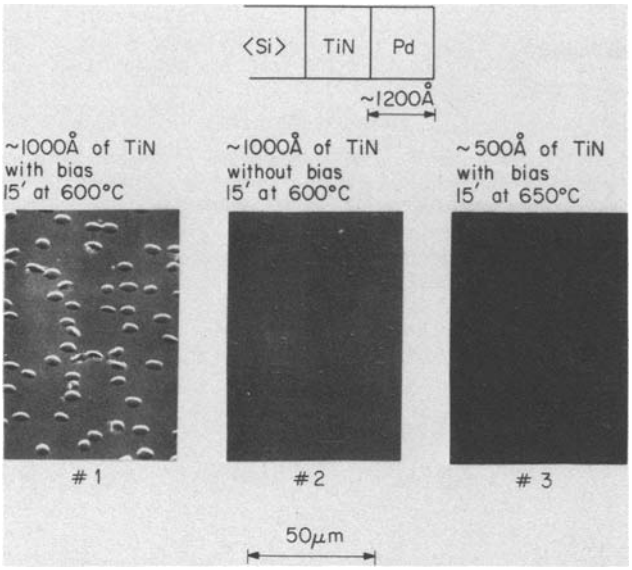

Fig. 2. Scanning electron micrographs indicating the effect of deposition parameters on the failure pattern of Si-TiN-Pd contacts for samples No. 1, No. 2, and No. 3 annealed at 600° (No. 1 and No. 2) and 650°C (No. 3).

Copper on TiN.—Scanning electron micrographs of samples 1 and 2 after annealing at 750°C are shown in Fig. 3. Loss of adhesion and blistering are visible on sample 1. Backscattering analysis shows hardly any transport of Cu or Si across the barrier at this temperature. The interdiffusion becomes noticeable at 800°C, however. In sample 2, diffusion of Cu into Si starts at 650°C The interdiffusion proceeds much faster than in sample 1. After 15 min at 800°C, the Cu layer has completely reacted with the Si substrate. The SEM (Fig. 3) indicates that the penetration of Cu through the TiN layer is more uniform than in sample 1. Protrusions are visible along the crystal planes of the underlying Si<100>

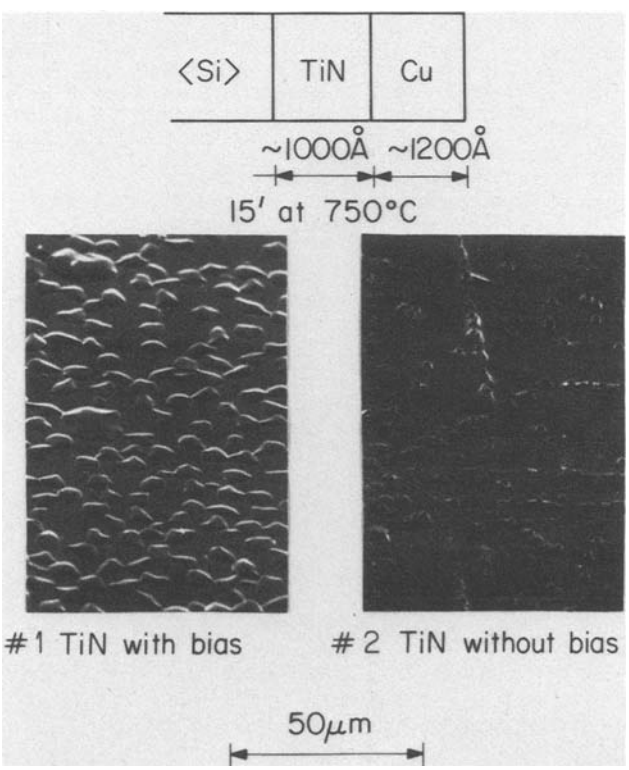

Fig. 3. Scanning electron micrographs of failure patterns on Si-TiN-Cu contacts with TiN barriers deposited with (No. 1) and without (No. 2) substrate bias.

substrate. In sample 3, no delamination was observed up to 750°C. Backscattering analysis shows interdiffusion at 800°C. Similar substrate-related decoration patterns as in sample 2 are visible on this sample after annealing.

Gold on TiN.—Blistering of Au-TiN contacts is found in sample 1 after annealing at 400°C. Isolated failure patches appear at the edges of the sample. The patches expand slightly at higher temperatures. The central part retains its layer structure up to 550°C as indicated by the backscattering analysis. On sample 2, scattered failure patches of 50-70 microns in diameter, not observable by backscattering, are found after the heat-treatment at 550°C. The patches consist of a small central protrusion and a wide circular zone depleted of gold. The protrusions presumably indicate the Au-Si reaction through a small defect in the TiN barrier. The reaction is limited by the depletion of the gold film around the defect. Cheung *et al.* (7) have found evidence of a similar failure mode at lower temperature. There the Si-TiN-Au system failed completely at 500°C after 10 min with resolidified Au droplets balling up on the sample's surface.

In sample 3, no blisters or fractures are observed after 15 min annealing at 800°C. Backscattering analysis does not show any evidence of interdiffusion of contact layers in this sample.

Discussion

Two distinctly different failure mechanisms are found in multilayer contacts with a thin layer of HfN or TiN interposed between the contact metal and the silicon substrate: (*i*) Blistering and fracture of the barrier layer at the edges of the delaminated areas is the primary failure mechanism when 1000-1500Å thick barrier layers are deposited by high rate reactive sputtering using a negative substrate bias. The failure occurs during annealing at temperatures as low as 400°C for 15 min (Au on TiN). (*ii*) Interdiffusion of the contact metal and the silicon initiates through defects in the diffusion barrier. The rate of contact degradation depends on the density and the size of these defects identified as pinholes, cracks on blister edges or other discontinuities in the film structure. The local diffusion zones expand laterally with increasing time or temperature, eventually overlapping each other if the defect density is large enough. At sufficiently high temperatures, failures occur abruptly via eutectic reactions between the contact metal and silicon. The failure temperature is specific to each metal-silicon pair and related to the lowest eutectic temperature of the system. Much higher failure temperatures can be observed if the lateral integrity of the diffusion barrier is preserved and the direct contact between metal and silicon can be prevented. Our results indicate that a 500Å thick TiN layer can inhibit the eutectic reactions between Au and Si (T_e = 370°C) during annealing at 800°C for 15 min.

For most of our results which show interdiffusion below 600°C, the failure starts by delamination of the barrier layer and proceeds by reactions through open fractures in the film. At higher temperatures one has to anticipate the possibility of volume and grain boundary diffusion across the barrier. Diffusion studies in Cu-TiN thin film couples indicate that the effective diffusivity of Cu in TiN is $D_{eff} = 9 \times 10^7 \exp(-4.43\ eV/kT)\ cm^2/sec$ as determined from diffusion profiles at 608°, 635°, and 700°C (11). According to this the diffusion length $L_d = 2\sqrt{Dt}$ is ~10Å for annealing at 600°C for 15 min. Diffusion of Cu through a 1000Å thick TiN barrier would then be negligible at this temperature. The mechanisms of Cu diffusion were not reported to be bulk processes, however.

For metals with very high melting temperatures comparable to that of TiN (~ 2900°C), diffusivity along the grain boundaries is predicted to be 10-15 orders of magnitude higher than the volume diffusivity in the temperature range of 600°-800°C. These fast diffusion paths constitute the mechanism responsible for most of the atomic transport in the temperature range below one-half of the melting temperature. Effective bulk diffusivity and a simple erfc profile would therefore strongly underestimate the number of diffusing species at large distances from the interface.

Macroscopic defects seem to remain the most important reason for contact failures. We have observed large compressive stresses, in the order of 10^{10} dyne · cm^{-2}, in both HfN and TiN layers which fail by delamination. Blisters are the characteristic relief mechanism of these high stresses. The following general statements can be made: (*i*) The compressive stress is more severe in the nitride films deposited with negative substrate bias than without (although negative bias improves the electrical conductivity). (*ii*) Delamination caused by the compressive stress decreases with decreasing film thickness as the result of reduced shear at the film interface.

Curvature measurements on samples with reactively sputtered nitride layers on thin Ni or Si cantilever substrates indicate that the stress distribution is nonuniform in depth, and the total stress is 2-3 times higher in the films sputtered with −40V substrate bias compared to the films deposited on grounded substrates. The initial compressive stress increases during annealing as a result of the mismatch between the thermal expansion coefficients of HfN ($\alpha \simeq 5 \times 10^{-6}$ K^{-1}) or TiN ($\alpha \simeq 6 \times 10^{-6}$ K^{-1}) and Si ($\alpha \simeq 3 \times 10^{-6}$ K^{-1}). We have not studied in detail the functional dependence of the stress on various deposition parameters, such as deposition rate and argon pressure. However, stress behavior similar to that observed in reactively sputtered nitride films has been reported for sputter-deposited refractory metals (12-14) and compounds (15). The compressive state of stress has been related to argon entrapment during the film growth (16) or peening by energetic neutral atoms (17). We have indeed observed that both the film stress and the amount of entrapped argon in rf-diode sputtered HfN films increase rapidly with increasing substrate bias voltage.

Conclusion

Our results suggest that the thermal stability of HfN and TiN diffusion barriers ultimately depends on the mechanical film properties and consequently, on the method of deposition. The dominating failure mechanism is associated with loss of adhesion and blistering of the barrier layers. The extent of the failure is related to compressive stresses present in reactively sputtered nitride films. Stresses are more pronounced in films deposited with a negative substrate bias, and blistering occurs when the film thickness exceeds a critical value. Because the barrier performance depends on the physical integrity of the film, narrow constraints need to be imposed on the deposition process. The best results in this study have been obtained for 500Å thick TiN films which effectively prevent the eutectic reaction between Au and Si at 800°C.

Acknowledgments

We thank R. W. Hoffman (Case Western Reserve University) for his collaboration in evaluating the stress in our samples, M. B. Chamberlain (Sandia National Laboratories, Albuquerque, New Mexico) for providing diffusion data and for critical comments, and R. Fernandez and R. Gorris (Caltech) for their technical assistance. This work was financially supported by the Department of Energy and monitored by Sandia National Laboratories, Albuquerque, New Mexico (H. T. Weaver and M. B. Chamberlain).

Manuscript submitted Feb. 8, 1982; revised manuscript received *ca.* Jan. 19, 1983. This was Paper 357 presented at the Denver, Colorado, Meeting of the Society, Oct. 11-16, 1981.

Any discussion of this paper will appear in a Discussion Section to be published in the December 1983 JOURNAL. All discussions for the December 1983 Discussion Section should be submitted by Aug. 1, 1983.

Publication costs of this article were assisted by the Department of Energy.

REFERENCES

1. M-A. Nicolet, *Thin Solid Films*, **52**, 415 (1978).
2. M-A. Nicolet and M. Bartur, *J. Vac. Sci. Technol.*, **19**, 786 (1981).
3. P. R. Fournier, U.S. Pat. 3,879,746 (1976).
4. W. J. Garceau and G. K. Herb, *Thin Solid Films*, **60**, 237 (1979).
5. N. W. Cheung, H. von Seefeld, M-A. Nicolet, F. Ho, and P. Iles, *J. Appl. Phys.*, **52**, 4297 (1981).
6. M. Mäenpää, I. Suni, M-A. Nicolet, F. Ho, and P. Iles, in "Proceedings of the 15th IEEE Photovoltaic Specialists Conference," 518 (1981).
7. N. W. Cheung, H. von Seefeld, and M-A. Nicolet, in "Thin Film Interfaces and Interactions," J. E. E. Baglin and J. M. Poate, Editors, p. 323, The Electrochemical Society Softbound Proceedings Series, Princeton, N.J. (1980).
8. M. Mäenpää, H. von Seefeld, N. Cheung, M-A. Nicolet, and A. G. Cullis, in "Thin Film Interfaces and Interactions," J. E. E. Baglin and J. M. Poate, Editors, p. 316, The Electrochemical Society Softbound Proceedings Series, Princeton, N.J. (1980).
9. M. Wittmer, B. Studer, and H. Melchior, *J. Appl. Phys.*, **52**, 5722 (1981).
10. F. T. J. Smith, *ibid.*, **41**, 4227 (1970).
11. M. Chamberlain, *Thin Solid Films*, **91**, 155 (1982).
12. R. S. Nowicki, J. M. Harris, M-A. Nicolet, and I. V. Mitchell, *ibid.*, **53**, 195 (1978).
13. R. S. Nowicki, W. D. Buckley, W. D. Mackintosh, and I. V. Mitchell, *J. Vac. Sci. Technol.*, **11**, 675 (1974).
14. F. M. d'Heurle, *Trans. Am. Inst. Min., Metall. Pet. Eng.*, **236**, 321 (1966).
15. K. Kuwahara, T. Sumomogi, and M. Kondo, *Thin Solid Films*, **78**, 41 (1981).
16. H. F. Winters and E. Kay, *J. Appl. Phys.*, **38**, 3928 (1967).
17. D. W. Hoffman and J. A. Thornton, *Thin Solid Films*, **45**, 387 (1977).

Effect of Crosslinking and Doping on Thermoluminescence of U.V.-Irradiated Polymers

M. Ladang, J. Vanderschueren,[1] J. Niezette, and R. Vanderschueren

Department of Physical Chemistry, Université de Liège, Sart-Tilman, B4000 Liege, Belgium

ABSTRACT

The thermoluminescence (TL) of elastomeric materials modified by doping and chemical or γ-induced crosslinking was measured following irradiation with u.v. light at 77 K and compared with the thermally stimulated depolarization currents (TSDC) obtained during warmup of samples previously polarized from 298 to 77 K, stressing the comparison of luminescence and current peaks observed in the glass transition range. Significant shiftings of the TL peaks were found as a function of degree of crosslinking and nature of the dopant, even though the glass transition temperature and the position of the TSDC peaks were not affected, showing that the kinetics of the light-emitting process is not only governed by the thermal motions of the polymer units but also critically depends on the nature of traps and luminescent species. Generally speaking, the TL method appears to be much more sensitive than the classical relaxation methods to any structural, morphological, or environmental change of the macromolecular chains and seems, thus, particularly attractive to obtain valuable information on new aspects of polymer relaxation.

The thermoluminescence (TL), which involves measuring and analyzing light emitted during warmup of materials previously irradiated at low temperature, is generally considered as a useful means for studying molecular motion and structural transitions occurring in polymeric solids (1-5). On the basis of significant correlations observed between the TL glow curves and the relaxation peaks obtained by mechanical or dielectric loss measurements, it is usually assumed that the luminescence emission depends on the molecular mobility either because the macromolecular chains can act as effective carrier traps (*e.g.*, via formation of dielectric cavity traps defined by the chains themselves) or because the release of charge carriers from other traps (such as free radicals or neutral molecules with positive electron affinity) can only occur as a result of the onset of local motion involving molecules located in the immediate vicinity of the trap (1-5). As an alternative to the detrapping phenomenon, it has been sometimes postulated that charge recombination can occur by physical approach and reaction of a radical ion with the parent ion or any other neighboring positive ion (3). In principle, such a process should be also closely related to structural changes in the polymeric matrix because it is likely to arise only in a temperature range where large scale motion sets in, *i.e.*, in the vicinity of the glass transition temperature T_g. Whatever the exact trapping and detrapping mechanisms involved and the nature of luminescence centers, the macromolecular motions are, thus, expected to contribute significantly to the light-emitting processes in such a way that the TL glow curve could be considered as reflecting the relaxation itself and could be used to determine the transition temperatures.

We have recently shown, however, that, at least in certain polymers, the type of impurity present in the matrix can also play a prevailing role in thermoluminescence, and that an observed glow curve is often typical of a given dopant-polymer system rather than of the polymer itself (6-9). In doped poly(bisphenol-A carbonate) for example, the TL peaks observed at low temperature ($T < 273$ K) after u.v.-irradiation do not generally correspond with the characteristic relaxation spectra obtained by other methods. In fact, a reasonable agreement between TL and loss peaks was only found with one of 22 dopants tested; moreover, some specific dopants give rise to additional large TL peaks which did not correspond to any known intrinsic relaxation (7, 8).

In our opinion, an advisable way for testing more precisely the relations between TL and molecular motions is now to compare the respective evolutions of TL and loss characteristics observed in a well-defined relaxation region whose properties are systematically varied as a result of morphological, environmental, or chemical modifications of the macromolecular structure. To this end, it is necessary to select polymers characterized by a well-resolved relaxation spectrum and a pronounced TL peak appearing in a temperature range corresponding to a well-known structural transition. These conditions are satisfactorily fulfilled for elastomers based on butadiene or isoprene, particularly in the glass transition region. It is the object of this paper to report results obtained on such materials before and after modifying them by doping and chemical or γ-induced crosslinking. Thermally stimulated depolarization currents (TSDC) has been chosen as a reference for relaxation properties because it can work at heating rates similar to that used in TL measurements, which allows a direct comparison of the peak positions (10-13).

Experimental

All the polymers investigated are characterized by glass transition temperatures located in the 170-270 K range. These are: (*i*) a methyl methacrylate-butadiene random copolymer (MMA-B) with a butadiene content of 70 weight percent (w/o) ($T_g = 268$ K); (*ii*) a styrene butadiene random copolymer (SB) with a butadiene content of 55 w/o ($T_g = 243$ K); (*iii*) a styrene butadiene radial block copolymer (SBb) with a butadiene content of 70 w/o (T_g of the polybutadiene phase = 186 K); (*iv-v*) two styrene-isoprene-styrene triblock copolymers with respective isoprene contents of 28 (SIS 28) and 67 w/o (SIS 67) (T_g of the isoprene phase = 255 K) and (*vi*) a polybutadiene (PB) with 98% 1-4 cis content ($T_g = 183$ K). The butadiene-based polymers were commercial materials: PB and MMA-B were supplied by Polymer Corporation Polysar (Taktene 1202 and Butakon ML 577, respectively), SB by Texus (Sympol 8000) and SBb by Phillips Petroleum (Solprene 416). The SIS copolymers were prepared at the Ecole d'Application des Hauts Polymères (Strasbourg, France) from n-butyllithium catalysts in benzene as described elsewhere (14).

To remove impurities such as catalyst residues and antioxidants, all these polymers were purified by repeated reprecipitations of benzene or hexane solutions in methanol. They were subsequently vacuum dried at 373 K for 1 day. The powdered materials

[1] Research Associate of the National Fund for Scientific Research, Belgium.

Key words: elastomers, glass transition, thermally stimulated currents, molecular relaxation.

were, then, compression molded at 370-420 K into disks of about 100 μm thick which were stored at room temperature under vacuum for at least 1 week.

The doped samples were obtained by, first, swelling the polymer films in solvent-nonsolvent mixtures containing the dopant and then deswelling at 373 K under vacuum for 48 hr. The dopant content in the dried material was always lower than 0.1 w/o in order to not significantly alter the polymer structure. Lightly crosslinked samples were obtained either by curing with 1 w/o dicumyl peroxide or by γ-irradiation from ^{60}Co source in degassed and sealed glass ampuls with total doses ranging from 10^5 to 10^8 rad.

The TL experiments were carried out in a classical cryostat provided with a cold finger and a temperature programmer allowing the sample temperature to be linearly varied between 85 and 373 K. Irradiations were always performed under vacuum at 77 K using a 450W xenon lamp (XBO 450 Osram). The light output was measured with a Hamamatsu R376 photomultiplier (bias 1000V; the light intensity unit given in the figures corresponds to a 5×10^{-10}A current).

The TSDC measurements were carried out with a three-terminal electrode system under controlled nitrogen flow (25 cm^3/min) in the dielectric test cell of a relaxation spectrometer (Unirelax, Tetrahedron). The heating and cooling rates were controlled by the Tetrahedron Wizard 1501 programming system. The thermal cycles of polarization and depolarization consisted essentially of the following steps: (*i*) application of a d-c electric field E_p = 10-30 kV/cm for a time t_p = 30 min at a temperature T_p = 298 K; (*ii*) cooling in the field to a temperature T_o = 77 K at a rate of 10 K/min; (*iii*) disconnecting the d-c supply and linear heating of the short-circuited samples at a rate of 5 K/min.

Results

Doping of butadiene-based copolymers.—Figure 1 shows the TSDC and TL results obtained for SBb samples before and after doping them with some classical dyes. All the curves have the same general shape and are characterized by two distinct peaks which are conventionally labeled β and α in order of increasing temperatures.

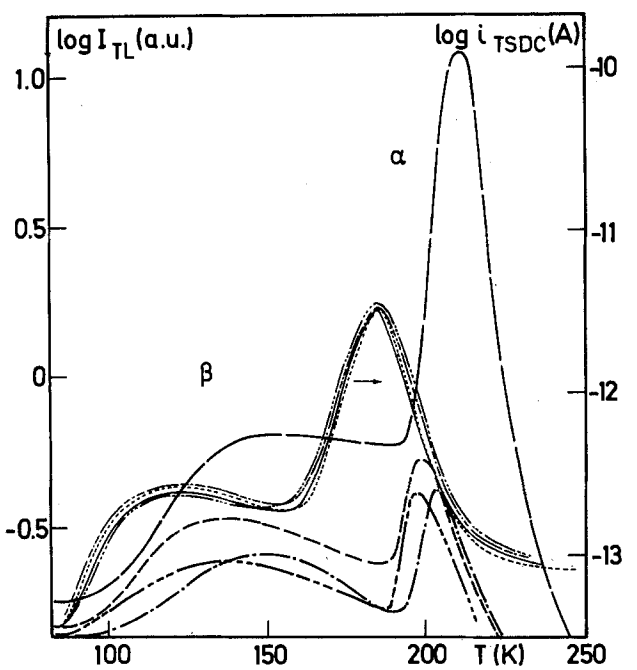

Fig. 1. TSDC and TL of SBb copolymer undoped (TSDC: ——; TL: — - - - —) and doped with rhodamine 6G (TSDC: — — — —; TL: — · —) 9,10-phenanthrenequinone (TSDC: — · · · —; TL: —— ——), and crystal violet (TSDC':— - · · —; TL: — — —).

In the TSDC case, these two peaks reflect essentially the two main relaxation ranges typical of diene elastomers (15). The α peak appears close to the glass transition temperature as determined by differential scanning calorimetry (T_g = 186 K) and can, thus, be related to microBrownian motions of chain segments (α relaxation) involving in particular rotation of cis and vinylbutadiene isomers (effective dipole moment = 8.2×10^{-31} Cm) (16) while the β peak corresponds well to the low temperature complex peak observed in pure polybutadiene by dynamic mechanical measurements and can, thus, be ascribed to local chain motions (β relaxation) (17). The precise mechanism responsible for the β relaxation is not yet well understood. According to Morgan *et al.* (17), it involves principally motions of the trans units of the butadiene chains, but this explanation can hardly hold for the TSDC peak because the trans isomer is dielectrically inactive, and the current intensity observed in various types of SB random copolymers is not related to the concentration of the trans units (15). Since the present study is mainly focused on the glass transition, this problem of origin and variations of the β relaxation will not be further discussed in this paper.

From the curves shown in Fig. 1, it is clear that these TSDC relaxations are insensitive both in position, shape, and amplitude to dye-doping the samples. Moreover, they are no more affected by other types of impurities provided that the concentration remains lower than 0.1 w/o (18).

The TL glow curve of the undoped SBb sample shows a close similarity with the TSDC spectrum, and it is, thus, certain that some correlation exists between the onset of molecular motion and the light-emitting process. It is significant however, that the TL peak appears at a higher temperature (maximum temperature T_M = 197 K) than the TSDC peak (T_M = 183 K). This phenomenon, which seems quite general in polymers (18, 19), will be discussed in connection with results obtained in doped and crosslinked materials.

In doped SBb samples, the properties of the TL α peak are markedly influenced by the nature of the added dye. Disregarding the luminescence intensity, which is obviously expected to depend strongly on the dopant, important variations in shape and position are observed. The shifts of T_M, in particular, are quite significant (10-15 K), more especially as they appear similarly when other excitation modes are used (9), and they can, thus, be considered as characteristic of the dopant-polymer system. Entirely similar results have been obtained with the other materials tested. In doped MMA-B and SB random copolymers for example, T_M variations of 10-25 K with respect to the undoped samples were commonly observed.

This behavior implies as an important consequence that the TL method can hardly be used for determining precise values of T_g in polymers since in most of them, it is well known that the observed emission does not result from the macromolecular matrix itself but rather from impurities or additive molecules lying between the chains (1).

Selective doping of SIS block copolymers.—Figure 2 shows the effect of a selective doping of the polyisoprene blocks on the TSDC and TL properties of the SIS 67 copolymer (in these experiments, the materials were doped by swelling and then deswelling the samples by using n-decane or isooctane as a specific solvent containing the dopants). Again the TSDC α peak, which corresponds to the glass transition of the polyisoprene phase (T_g = 222 K), remains unaffected while the TL α peak, which appears some 10-15 K higher, is markedly reduced and shifted.

More interesting is the result of a selective doping of the polystyrene phase (using tetrahydrofurfuryl alcohol as specific solvent) on the TL characteristics of the SIS 28 copolymer (Fig. 3). As a matter of fact,

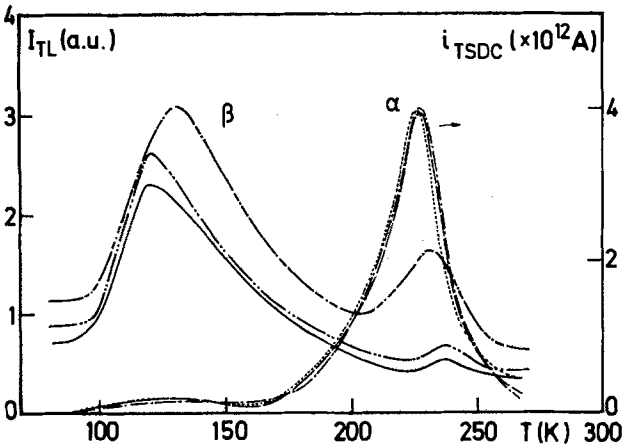

Fig. 2. TSDC and TL of SIS 67 copolymer undoped (TSDC: —— ——; TL: — · · —) and doped in the polyisoprene blocks with phenanthrene (TSDC: · · · ·; TL — · · —) and benzophenone (TSDC: — · —; TL: ——).

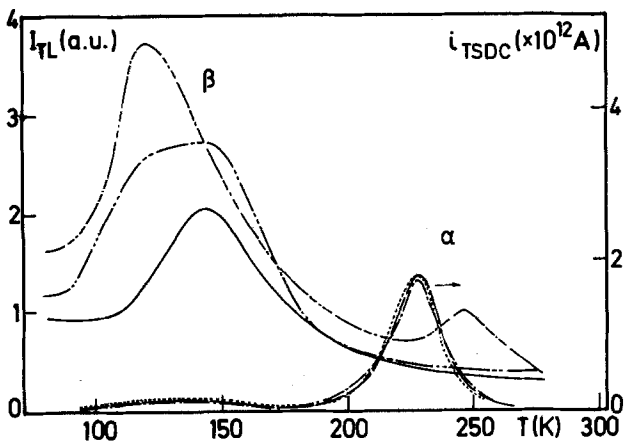

Fig. 3. TSDC and TL of SIS 28 copolymer undoped (TSDC: —— ——; TL: — · · —) and doped in the polystyrene blocks with phenanthrene (TSDC: · · · · ·; TL: — · · —) and benzophenone (TSDC: — · —; TL: ——).

while no significant change is observed in the TSDC properties, the TL α peak is now completely canceled though it is related to the glass transition process taking place in the polyisoprene blocks, *i.e.*, the undoped phase. Two essential consequences directly follow from this observation: (*i*) the most important part of the TL obtained in this temperature range is of interfacial origin and (*ii*) a TL peak is not systematically associated with a structural transition of the polymer.

Effect of crosslinking.—In order to study the effect of introducing crosslinkages without affecting markedly the molecular packing, slight conditions of curing or irradiation were applied to polybutadiene samples; the curing time at 420 K ranged from 5 to 30 min, and the γ radiation doses varied from 10^5 to 10^8 rad. Under these conditions, no increase in T_g is detectable by DSC, and no shift of the dielectric α dispersion towards higher temperatures is obtained in TSDC measurements, which obviously means that the chain length between crosslinks remains important with regard to the chain length necessary to observe a glass transition.

Some results obtained for γ-crosslinked samples are represented in Fig. 4 (only the TSDC curve related to the unirradiated sample is shown as a reference since no significant variation is obtained with the radiation doses used). The TL intensity of the α peak, which again appears at a higher temperature than the corresponding TSDC peak, is a clearly decreasing function of the radiation dose. In addition, important shifts of about 20 K are observed first towards higher

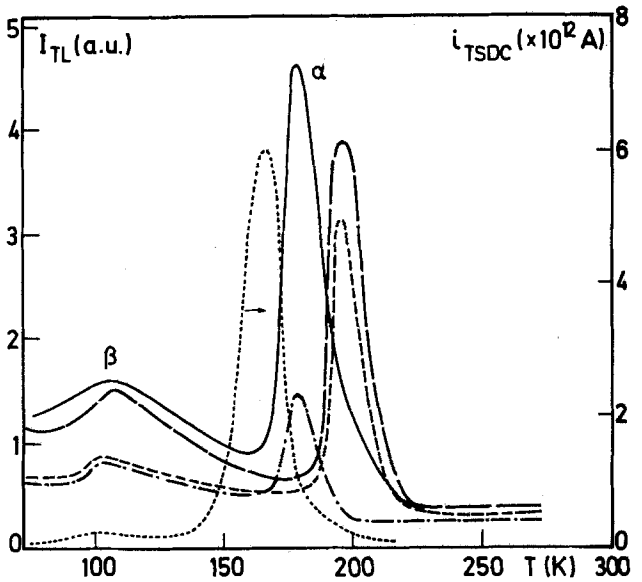

Fig. 4. TL of polybutadiene before (——) and after γ-irradiation with 10^5 Rad (— —), 10^6 rad (· · ·) and 10^8 Rad (— · —). The dotted curve shows the TSDC reference spectrum.

temperatures and then towards lower temperatures. If an unequivocal interpretation of this phenomenon is not possible at this time, the mere existence of such marked shifts confirms unambiguously that a TL peak can be greatly affected by specific factors to which the classical methods of T_g determination are completely insensitive.

Finally, some examples of glow curves obtained from chemically crosslinked PB are reported in Fig. 5, together with the TSDC reference spectrum. In these samples, the position of the TL α peak is not much influenced by the degree of crosslinking. On the other hand, the luminescence intensity drastically decreases, so that the peak entirely disappears well before the glass transition temperature is affected. This behavior is somewhat similar to that observed in selectively doped SIS 28 copolymers.

Discussion

The comparative TSDC and TL study of undoped diene elastomers based on butadiene or isoprene shows

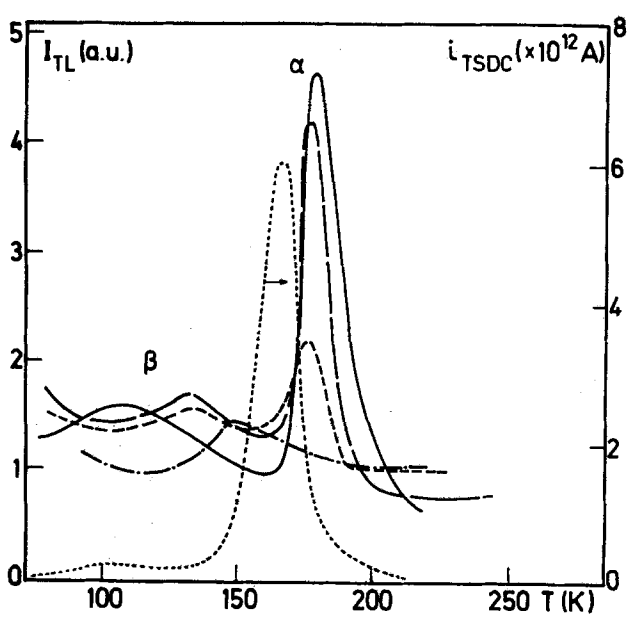

Fig. 5. TL of polybutadiene before (——) and after crosslinking obtained by curing the samples with 1 w/o dicumyl peroxide during 5 min (—— ——), 15 min (· · ·) and 30 min (— · —). The dotted curve shows the TSDC reference spectrum.

that in general, a well-defined TL peak appears in the glass transition range which, in principle, affords evidence for a significant contribution of the molecular motions to the carrier-detrapping or any other light-emitting processes. However, the fact that the TL peak is systematically shifted towards higher temperatures, even though it is recorded at a heating rate similar to that used in TSDC experiments, shows that the luminescence emission follows after the structural transition and, thus, does not reflect the transition itself, probably because the thermal energy necessary to lift the carriers over the barrier potential of the traps or to erode the traps themselves is reached only beyond the glass transition temperature.

Moreover, the important variations of the TL properties, observed in samples slightly doped or crosslinked in such a way that the glass transition is not affected, seem to show that the kinetics of the light-emitting process is not only governed by the thermal motions of the molecular units but also depends critically on the nature of traps and luminescent species. In this view, the effect of crosslinking on the TL properties could be due to the appearance of new specific defects in the immediate vicinity of the new C—C bonds formed, which could affect the position of the glow curve without interfering with the glass transition process, while the influence exercised by doping could be related to differences in excitation energy transfer. It also appears from these results that a TL peak is not automatically associated with the increase of molecular mobility taking place during a structural transition. Such is the case for example in chemically crosslinked PB and in SIS copolymers doped in the polystyrene blocks where no TL peak is detectable in the glass transition range even though this transition remains perfectly distinguishable by other techniques.

Generally speaking, the systematic shifts of the TL peaks observed in doped samples also imply, on one hand, that the TL method cannot be used to determine precise values of T_g in polymers since it seems now well established that in most of them the thermoluminescence does not result directly from excitation of polymeric species but rather from impurities to which the excitation energy is guided by energy transfer (1) and, on the other hand, that it can hardly be expected that the characteristic parameters deduced from TL curves (activation energy, frequency factor . . .) can be directly related to molecular motions.

Obviously, this is not to say that the TL method cannot be considered as a useful tool for studying the molecular motions in polymers. On the contrary, the fact that it is much more sensitive than the classical methods to any structural, morphological, or environmental change of the macromolecular chains renders it particularly attractive as a means of obtaining valuable information on new aspects of relaxation processes.

Acknowledgments

Three of us thank the Fonds National de la Recherche Scientifique and The Institut pour l'Encouragement de la Recherche Scientifique dans l'Industrie et l'Agriculture for financial assistance.

Manuscript submitted Nov. 1, 1982; revised manuscript received ca. Jan. 4, 1983. This was Paper 479 presented at the Montreal, Que., Canada, Meeting of the Society, May 9-14, 1982.

Any discussion of this paper will appear in a Discussion Section to be published in the December 1983 JOURNAL. All discussions for the December 1983 Discussion Section should be submitted by Aug. 1, 1983.

REFERENCES

1. R. H. Partridge, in "The Radiation Chemistry of Macromolecules," Vol. I, M. Dole, Editor, Chap. 10, Academic Press, New York (1972).
2. G. G. A. Bohm, K. R. Lucas, and W. G. Mayes, *Rubber Chem. Technol.*, **50**, 714 (1977).
3. G. G. A. Bohm, *J. Polym. Sci.*, **14**, 437 (1976).
4. L. Y. Zlatkevich, *Rubber Chem. Technol.*, **49**, 179 (1976).
5. Y. Takai, K. Mori, T. Mizutani, and M. Ieda, *J. Polym. Sci.*, **B16**, 1861 (1978).
6. A. Linkens, J. Vanderschueren, S.-H.-Chor, and J. Gasiot, *Eur. Polym. J.*, **12**, 141 (1976).
7. A. Linkens and J. Vanderschueren, *J. Electrostatics*, **3**, 149 (1977).
8. A. Linkens and J. Vanderschueren, *J. Polym. Sci.*, **B15**, 41 (1977).
9. A. Linkens and J. Vanderschueren, *J. Appl. Polym. Sci.*, **22**, 3081 (1978).
10. "Thermally Stimulated Relaxation in Solids, Topics in Applied Physics," Vol. 37, P. Braunlich, Editor, Springer Verlag, Berlin (1979).
11. J. Vanderschueren and J. Gasiot, "Thermally Stimulated Relaxation in Solids, Topics in Applied Physics," Chap. 4, Vol. 37, Springer Verlag, Berlin (1979).
12. J. Van Turnhout, "Topics in Applied Physics," Vol. 33, G. M. Sessler, Editor, Chap. 3, Springer Verlag, Berlin (1980).
13. R. Chen and Y. Kirsh, "Analysis of Thermally Stimulated Processes," Pergamon Press, Oxford, England (1981).
14. L. Beaudoin, *Rev. Gen. Caoutch. Plast.*, **51**, 225 (1974).
15. J. Vanderschueren, M. Ladang, and J. M. Heuschen, *Macromolecules*, **13**, 973 (1980).
16. A. M. North, R. A. Pethrick, and A. D. Wilson, *Polymer*, **19**, 913 (1978).
17. R. J. Morgan, L. E. Nielsen, and R. Buchdahl, *J. Appl. Phys.*, **42**, 4653 (1971).
18. A. Linkens, Ph.D. Thesis, University of Liège, Liège, Belgium (1979).
19. M. Ladang, Ph.D. Thesis, University of Liège, Liège, Belgium (1982).

Technical Note

A Slow Selective Etch for GaInAsP Grown on InP

G. A. Ferrante, J. P. Donnelly, and C. A. Armiento

Lincoln Laboratory, Massachusetts Institute of Technology, Lexington, Massachusetts 02173

The technology for fabricating laser diodes, detectors, and optical waveguides in GaInAsP/InP epitaxial wafers requires the use of suitable etching techniques for providing smooth damage-free surfaces, precise pattern geometries, and preferential and

Key words: chemical etching, selective etch, InGaAsP, InP.

reproducible removal of specific layers. Several previous publications have reported slow controllable etches for InP (1-4) and etches for selectively removing InP layers grown over GaInAsP (5). Several etches have been used to selectively (6-9) etch GaInAsP on InP, but only a limited amount of information on etch rate and the degree of selectivity has been reported. This paper presents etch rate and surface morphology results obtained using a dilute sulfuric acid, hydrogen peroxide, and water etch, which has proven to be a slow selective etch for GaInAsP.

Slow controllable etches suitable for removing thin layers of InP are generally not usable with GaInAsP. For example, we found that iodic acid etches (2) GaInAsP in a nonuniform manner, leaving very badly pitted surfaces. Potassium-ferrocyanide potassium-hydroxide solutions, which are often used to delineate p-n junctions in the III-V compounds, etch GaInAsP faster than InP and have been used as selective etches (6, 7). The etch rates for most GaInAsP compositions tend to be fairly fast (greater than several μm/min) (7). In addition, the etch rates and resultant selectivity appear to depend on the doping of the InP and GaInAsP, as well as the composition of the etch solution, and little information on these variations has been published.

Sulfuric acid-peroxide-based etches, which are commonly used as fast polishing etches for GaAs, etch InP only slowly (10). For example, we have found that a 3 H_2SO_4:1 H_2O_2:1 H_2O solution at room temperature etches InP at about 200 Å/min. This etch (8) has been used to etch GaInAsP on InP, since the etch rate increases with increasing amounts of Ga and As in the material. A 1 H_2SO_4:6 H_2O_2:10 H_2O solution at 50°C has been used to etch mesas in GaInAs on InP (9). In both cases, details of the etch rate and selectivity were not reported. We have found that by decreasing the relative volume of H_2SO_4 compared to the standard GaAs etches and increasing that of water, while leaving that of H_2O_2 fixed, the etch rate in InP can be reduced to a negligible value while maintaining a reasonable etch rate for most GaInAsP lattice-matched compositions, except those very close to InP. As shown below, a 1 H_2SO_4:1 H_2O_2:10 H_2O solution at room temperature appears to be particularly suitable as a slow selective etch for the most commonly used GaInAsP compositions.

The samples used in these experiments were (100) liquid phase epitaxial (LPE) grown GaInAsP/InP heterojunction wafers in which the quaternary composition was either $Ga_{0.27}In_{0.73}As_{0.63}P_{0.37}$ (having a bandgap, E_g, of 0.95 eV, $\lambda = 1.3$ μm), $Ga_{0.17}In_{0.83}As_{0.59}P_{0.61}$ ($E_g = 1.08$ eV, $\lambda = 1.15$ μm), or $Ga_{0.10}In_{0.90}As_{0.04}P_{0.96}$ (E_g 1.24 eV, $\lambda = 1.04$ μm). Each etch solution used was placed in a clean 200 ml Pyrex beaker which was modified for mounting a microscope slide inside. Since a great deal of heat is generated when sulfuric acid etches are mixed, some care must be taken to insure that the solution returns to room temperature, 21° ± 1°C, before etching samples. If this is not done, higher etch rates than reported in this paper will be obtained. The solution was stirred continuously by means of a Teflon-coated magnetic stirrer. Part of each sample to be etched was masked with SiO_2 to provide a step in order to measure etch depth. For etching, the sample was mounted on a microscope slide using Apiezon wax. After etching, the mask was removed, the sample rinsed, dried, and inspected. The etch depth was measured with a Dek-tak surface profiler.

The etch depth *vs.* etch time obtained on a (100) $Ga_{0.27}In_{0.73}As_{0.63}P_{0.37}$ ($\lambda = 1.3$ μm) sample in a 1 H_2SO_4:1 H_2O_2:10 H_2O room temperature solution is shown in Fig. 1. As determined from this data, the etch rate is a very constant 1000 Å/min. The etched GaInAsP surface appeared to be free of any etch

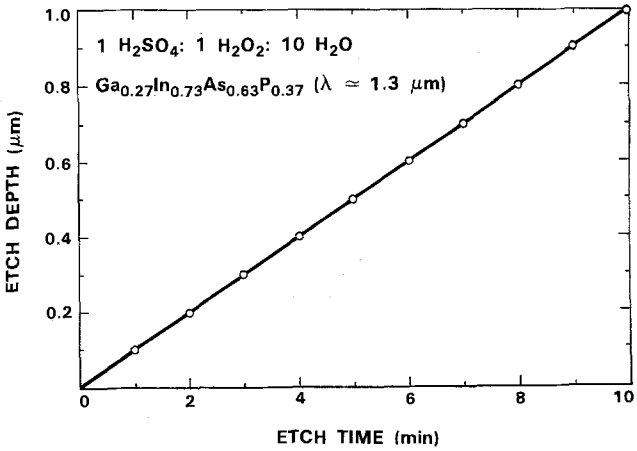

Fig. 1. The etch depth *vs.* etch time obtained on a $Ga_{0.27}In_{0.73}As_{0.63}P_{0.37}$ ($\lambda = 1.3$ μm) layer etched in a room temperature 1 H_2SO_4:1 H_2O_2:10 H_2O solution.

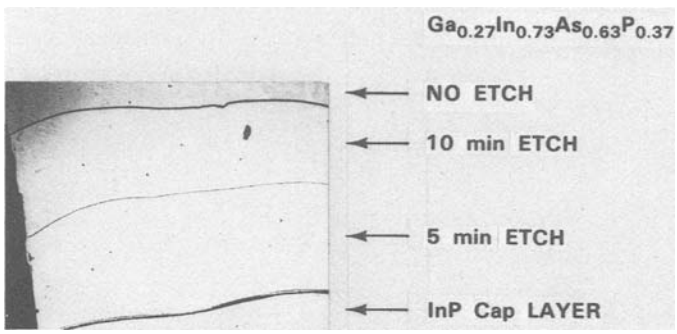

Fig. 2. Photomicrograph of a $Ga_{0.27}In_{0.73}As_{0.63}P_{0.37}$/InP double heterojunction wafer in which most of the top InP was removed in concentrated HCl and different areas of the quaternary layer etched for the times indicated (no etch, 5 min etch and 10 min etch) in a 1 H_2SO_4:1 H_2O_2:10 H_2O solution.

related defects. Figure 2 shows a photomicrograph of a double heterojunction wafer in which the top InP layer was removed from most of the wafer using concentrated HCl, a selective etch which etches (100) InP at 5.4 μm/min while having a negligible etch rate on 1.3 μm bandgap GaInAsP. Different areas of the GaInAsP layer were then etched for different times using 1 H_2SO_4:1 H_2O_2:10 H_2O. The etched surfaces have the same surface texture as the originally exposed quaternary surface.

Table I lists the etch rate measuered for several different GaInAsP compositions and InP. The errors in the etch rates are estimated to be less than ±10 Å/min. For (100) $Ga_{0.17}In_{0.83}As_{0.59}P_{0.61}$ ($\lambda \pm 1.15$ μm), the etch rate is 420 Å/min, while for (100) $Ga_{0.10}In_{0.90}As_{0.04}P_{0.96}$ ($\lambda = 1.04$ μm), the etch rate decreases further to 75 Å/min. The etch depth on (100) InP could not be measured after an hour's etch time although a fine demarcation line between the etched and unetched areas of the samples was observed. The surface quality of the InP exposed to the dilute sulfuric acid etch was good (see InP surface in Fig. 2, which was exposed to the dilute sulfuric acid etch). The same result was obtained on (100)-oriented liq-

Table I. Etch rate of InP and various compositions of GaInAsP in a 1 H_2SO_4:1 H_2O_2:10 H_2O solution at room temperature

Material		Etch rate
(100)	$Ga_{0.27}In_{0.73}As_{0.63}P_{0.37}$ ($\lambda = 1.3$ μm)	1000 Å/min
(100)	$Ga_{0.17}In_{0.83}As_{0.59}P_{0.61}$ ($\lambda = 1.15$ μm)	420 Å/min
(100)	$Ga_{0.10}In_{0.90}As_{0.04}P_{0.96}$ ($\lambda = 1.04$ μm)	75 Å/min
(100)	InP	Negligible
(111)B	InP	30 Å/min

uid encapsulated Czochralski (LEC) InP samples doped with either Zn and Sn to concentrations greater than 10^{18} cm^{-3}. On (111)B InP, however, an etch rate of $\approx$30 Å/min was measured. The higher etch rate on the (111)B plane is consistent with the results reported in Ref. (9).

In conclusion, a room temperature solution of 1 H_2SO_4:1 H_2O_2:10 H_2O etches (100) InP at a negligible rate while it etches most lattice-matched compositions of GaInAsP at a reasonable rate leaving a good surface morphology. This etch should prove useful as a slow selective etch in a variety of applications.

Acknowledgments

The authors would like to thank S. H. Groves, Z. L. Liau, M. C. Plonko, and D. E. Mull for supplying the GaInAsP layers used in these experiments. This work was sponsored by the Department of the Air Force.

Manuscript submitted Oct. 5, 1982; revised manuscript received Dec. 14, 1982.

Any discussion of this paper will appear in a Discussion Section to be published in the December 1983 JOURNAL. All discussions for the December 1983 Discussion Section should be submitted by Aug. 1, 1983.

Publication costs of this article were assisted by Massachusetts Institute of Technology.

REFERENCES

1. R. Becker, *Solid-State Electron.*, **16,** 1241 (1973).
2. A. R. Clawson, D. A. Collins, D. I. Elder, and T. J. Monroe, NOSC Technical Note 592, Naval Ocean Systems Center, San Diego, California, Dec. 13, 1978.
3. S. Adachi and H. Kawaguchi, *This Journal,* **128,** 1342 (1981).
4. S. Adachi, H. Kawaguchi, and G. Iwane, *J. Mater. Sci.*, 16, 2449 (1981).
5. S. B. Phatak and G. Kelner, *This Journal,* **126,** 287 (1979).
6. Z. L. Liau and J. N. Walpole, *Appl. Phys. Lett.*, **40,** 56 (1982).
7. K. L. Conway, A. G. Dentai, and J. C. Campbell, *J. Appl. Phys.*, **53,** 1836 (1982).
8. J. J. Hsieh and C. C. Shen, *Appl. Phys. Lett.*, **30,** 429 (1977).
9. T. P. Pearsall and M. Papuchon, *ibid.*, **33,** 640 (1978).
10. Y. Nishitani and T. Kotani, *This Journal,* **126,** 2269 (1979).

JOURNAL OF THE ELECTROCHEMICAL SOCIETY

ACCELERATED

—BRIEF COMMUNICATIONS—

MAY

1983

Rechargeable Li/$Li_{1+x}V_3O_8$ Cells

S. Panero, M. Pasquali, and G. Pistoia

Centro di Studio per la Elettrochimica e la Chimica, Fisica delle Interfasi del C.N.R., 00161 Rome, Italy

The research for substitutes of TiS_2 as cathodes for rechargeable Li cells has been recently aimed at transition metal oxides with particular attention for the V compounds of formula V_6O_{13+y} ($y < 0.2$) (1,2). These materials have greater enerby densities than TiS_2 and need not keep to a strict stoichiometry for optimum performance. Their cycling behavior at current densities around 1 mA/cm^2 is characterized by high and stable (after the first few cycles) specific capacities (2), i.e., 0.16-0.20 Ah/g of pure material. However, an important drawback is reported for both V_6O_{13} (so-called stoichiometric) and, especially, $V_6O_{13.16}$ (nonstoichiometric). At 1.6 V a reduction process occurs which inhibits further rechargeability (2). This probably stems from irreversible structure reorganizations connected with the high Li^+ content (2.37 Li^+/V).

Such a drawback could discourage the use of these materials in practical Li cells. We have attempted to overcome it by using a material which, while retaining the basic electrochemical features of V_6O_{13+y}, would be able to undergo overdischarges without structural damage. The $Li_{1+x}V_3O_8$ phase investigated by Wadsley (3) is closely related in structure to V_6O_{13}. Initial cycling tests have shown that cathodes based on this phase could be overdischarged to voltages as low as 1.0 V without a decrease in the cycling efficiency. Indeed, contrarily to what happens for V_6O_{13+y}, no voltage plateaus were observed below 1.8 V and a minor amount of capacity was recovered between this value and 1.0 V. At the same time, other pleasant features were noticed with these materials, ease of preparation (at 680°C in the air from Li_2CO_3 and V_2O_5) and high rate capability.

$Li_{1+x}V_3O_8$ has a structure characterized by two kinds of coordination for V, i.e., octahedral and trigonal bipyramidal (3). Strings of bipyramids and ribbons of octahedra are linked together (by common corners) forming puckered sheets. The sheets are linked by Li^+ ions residing in both octahedral and tetrahedral sites. The presence of Li^+ ions in the network increases the number of M-O bonds. This reduces the electron density on O^{2-}, thus reducing the possibilities for the latter to form strong (partly covalent) Li-O bonds with the ions entering the lattice during discharge (4). Such a situation contributes, besides geometrical factors, to a fast Li^+ diffusion between sites.

Murphy has compared the behavior of glassy and crystalline LiV_3O_8 (5) in Li cells with $LiAsF_6$-PC as electrolyte. At 0.25 mA/cm^2 and 1.9 V cut-off, the capacity obtained in the 1st discharge was not particularly impressive for either form (0.13 Ah/g for the glassy form and 0.11 Ah/g for the crystalline one). Futhermore, marked capacity losses were soon noticed upon cycling.

However, especially for low x values in $Li_{1+x}V_3O_8$, we have obtained high capacities and good cycling efficiencies in prismatic Li cells containing 1 M $LiClO_4$-PC/DME (1:1). The cathode (100-150 mg) was obtained by mixing the compound with 30% of a 2:1 carbon black-Teflon mixture. The resistivity of the material was initially relatively low (~10 ohm·cm), but increased upon lithiation, so that addition of conductive diluents was essential for good performance.

In the first low rate discharge (0.2 mA/cm^2) it was observed that, at 1.0 V cut-off, 3 Li^+ could be incorporated per formula weight, corresponding to 0.28 Ah/g. A specific energy of 620 Wh/kg was calculated in this experiment on the basis of anode and cathode weight. Further experiments were performed at 1 and 2 mA/cm^2 for both charge and discharge. In Fig. 1, the typical shape of the first and second discharge are shown when the upper

Key words: Li batteries, V oxides.

discharge limit was fixed at 3.8 V. It is remarkable that the stepped discharge curve is followed by a linear charge curve which remains below 3.0 V for 65% of the charging time. However, in order to recover the rest of the capacity, one has to go on charging up to 3.8 V. We believe that some of the Li^+ inserted in the lattice are strongly bound to O^{2-} non-coordinating Li^+ pre-exisiting in the lattice. Therefore an energy surplus is required to remove them. By overcharging some cells, it was observed that the electrolyte could be oxidized only at ca. 4.5 V after a steep potential increase at ca. 4.0 V.

Typical cyclings are reported in Tables I and II for a material of nominal composition $Li_{1.05}V_3O_8$. Even at 2 mA/cm^2 the cells cycled satisfactorily. Furthermore, capacity losses were limited, especially when recharging up to 3.8 V. Calculations of the energy densities for the 2nd cycle are given 0.37 Wh/g and 0.49 Wh/g for the experiments in Tables I and II, respectively. For stoichiometric V_6O_{13}, which in long cycling tests has been shown to outperform the non-stoichiometric variety (2), the energy density in Li cells containing $LiAsF_6$ in 2Me-THF was reported to be 0.39 Wh/g. We have prepared stoichiometric V_6O_{13} and tested it in both $LiClO_4$-PC/DME and in $LiAsF_6$-2Me-THF. Its capacity in the 1st cycle was equal to that of $Li_{1.05}V_3O_8$ but tended to decrease faster than $Li_{1.05}V_3O_8$ when cycled at 1 mA/cm^2.

In some experiments, the lower limit for $Li/Li_{1.05}V_3O_8$ cells was set at 1.0 V. The cells could still be cycled extensively even when the upper limit was set at 4.0 V. More than 50 cycles have been obtained in prismatic cells without excess electrolyte. Cell failure in all cases was due to anode degradation (dendrites and mechanical instability). We believe that this exceptional electrochemical performance is due to the structural stability of this compound as shown by x-ray analyses.

On the basis of these preliminary observations, inclusion of these new materials with those challenging TiS_2 seems justified and are now being given the highest priority.

ACNOWLEDGEMENT

This work has been entirely supported by the Consiglio Nazionale delle Ricerche (C.N.R.) of Italy.

REFERENCES

1. D.W. Murphy, P.A. Christian, F.J. DiSalvo, J.N. Carides, and J.V. Waszczak, This Journal, 128, 2053 (1981).
2. K.M. Abraham, J.L. Goldman, and M.D. Dempsey, This Journal, 128, 2493 (1981).
3. A.D. Wadsley, Acta Cryst., 10, 261 (1957).
4. H.Y.-P. Hong, J. Power Sources, 5, 137 (1980).
5. K. Nassau and D.W. Murphy, J. Non-Cryst. Solids, 44, 297 (1981).

Manuscript received June 2, 1982.

Publication costs of this article were assisted by Centro di Studio per la Elettrochimica e la Chimica Fisica delle Interfasi del C.N.R.

TABLE I

Cycling of a $Li/Li_{1.05}V_3O_8$ cell between 3.3-3.4 and 1.8-1.9 V.

Cycle No.	c.d. (mA/cm^2)	Capacity (Ah/g)
1	1	0.18
2	1	0.14
4	1	0.14
5	2	0.12
16	2	0.10
18	1	0.14
20	0.5	0.16

TABLE II

Cycling of a $Li/Li_{1.05}V_3O_8$ cell between 3.8-3.9 and 1.8 V.

Cycle No.	c.d. (mA/cm^2)	Capacity (Ah/g)
1	1	0.18
2	1	0.18
4	1	0.18
5	2	0.14
9	2	0.13
17	1	0.16
26	1	0.15
35	1	0.15

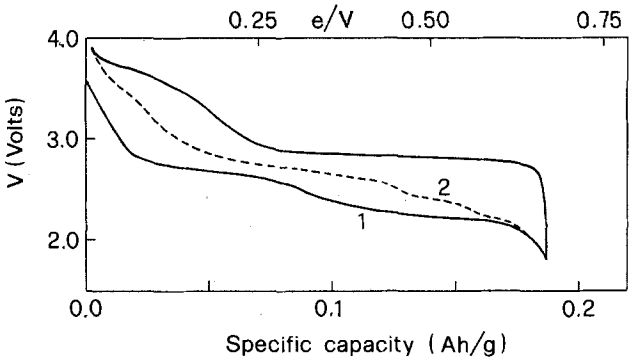

Fig. 1. Initial cycling of a $Li/LiClO_4$-PC/DME/$Li_{1.05}V_3O_8$ cell at 1 mA/cm^2.

Photoeffect on SiAs Electrodes

H. J. Lewerenz* and H. Wetzel

Hahn-Meitner-Institut für Kernforschung Berlin, Bereich Strahlenchemie, D-1000 Berlin 39, Germany

We report here first electrochemical measurements on SiAs (1), a layered semiconductor with different structure and bonding compared to the hitherto investigated group VI chalcogenides (2,3). A schematic illustration of the bonding geometry is given in Fig.1 (4). Two silicon atoms bound to each other are confined to an octahedron built by arsenic atoms. The somewhat distorted octahedra are bound to each other along one side and this consecutive attachment forms the layers. The interlayer forces are largely due to van der Waals attraction and the material can be cleaved along the layers.

Experiments were performed using standard potentiostatic configuration with a carbon rod as counterelectrode. All potentials are referred to the saturated calomel electrode(SCE) used as reference. Photocurrents were obtained with lock-in technique. All experiments were done in N_2-saturated sulfate solution. The electrodes were freshly cleaved, ohmic contacts were made using a Pt laquer (Demetron 308) and subsequent Ag epoxy (Scotchcast 3M M100) for attachment of the samples to a brass holder. The samples were then encapsulated with insulating epoxy (Scotchcast 3M XR5241). After cleavage, before immersion, the crystals were etched in N_2 saturated 1M HCl in order to remove residual As_2O_3, which has been claimed to form on SiAs in contact with air (5), from the surface. All solutions were made using triple distilled water and analytical grade chemicals. Illumination was provided from a tungsten-iodine lamp.

The dark I-V curves show reasonably good diode behavior with an anodic peak setting in at 0 V (SCE) and a cathodic maximum starting at about -1.2 V (SCE) (see insert in Fig.2). Differential capacitance measurements in the potential region of low dark current are shown in Fig.2. The resulting Mott-Schottky plots yield good linear behavior over a potential range of 0.6 V and allow a quite accurate extrapolation of the flat band potential (V_{fb}) at + 0.2 V. The material is p-type with an approximate acceptor concentration of 4×10^{17} cm^{-3}. Fig.3 shows the dependence of cathodic photocurrent on applied potential. The photocurrent onset potential coincides with the measured value of V_{fb}. The increase of current with cathodic bias is rather sluggish up to -0.5 V, rises steeply around -0.7 V and saturates at larger cathodic potential.

A photocurrent spectrum is shown in Fig. 4. In the long wavelength region a relatively small increase of current with photon energy is observed, indicating indirect electron transitions at photon energies near the semiconductor band gap at 1.42 eV (6). Around 500 nm a shoulder is observed and at 400 nm a steep increase in photocurrent is noted. This maximum is attributed to direct transitions in SiAs associated with a high oscillator strength.

The almost ideal energetic location of the SiAs band gap and the low material costs could make this semiconductor a promising candidate for solar energy conversion. The indirect character of the energy gap, however, associated with a low absorption coefficient, might present material preparation problems due to high minority carrier diffusion length needed for efficient energy conversion. In photoelectrochemical solar cells, stability problems might occur since the highest valence band in SiAs is not derived from intrametallic d-bands as in group VI layered photoelectrodes.

---

* Electrochemical Society Active Member

Keywords: SiAs, Photoelectrochemistry

REFERENCES

1. The authors thank Dr.Hönle for donating the crystals
2. H.Tributsch, this Journal, 125,1086(1978)
3. H.J.Lewerenz,A.Heller, and F.J.Disalvo, J.Am.Chem.Soc. 102, 1877 (1980)
4. T.Wadsten, Acta Chem.Scand. 19, 1232 (1965)
5. T.Wadsten, J.Mat.Sci. 12, 841 (1977)
6. J.I.Pankove, "Optical Processes in Semiconductors", Dover Publ.Inc., New York (1971)

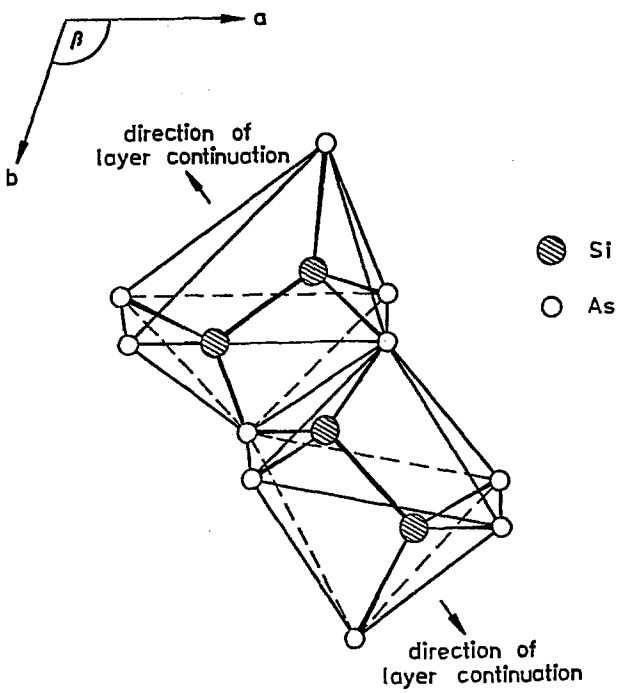

Figure 1.
Crystal structure of SiAs after Ref.4

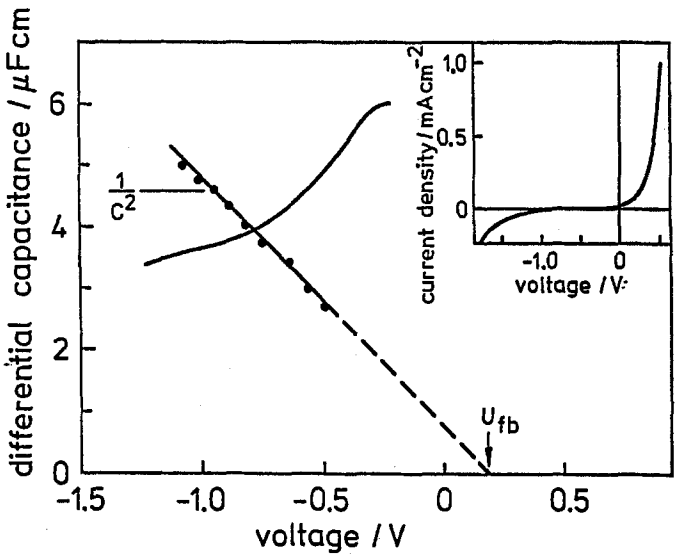

Figure 2.
Differential capacitance of p-SiAs vs. potential (full curve), 630 Hz; Mott-Schottky plot with extrapolation of flat band potential U_{fb} ($1/c^2$); insert: dark I-V characteristic of p-SiAs; electrolyte: 0.5 M K_2SO_4

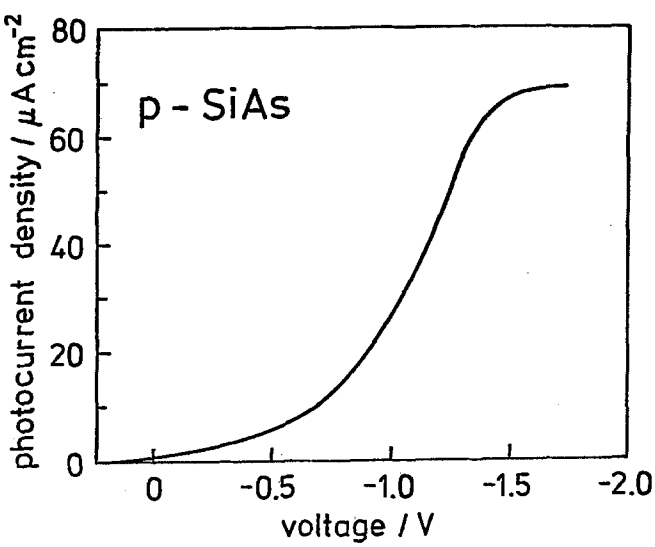

Figure 3.
Photocurrent vs. electrode potential; electrolyte: 0.5 M K_2SO_4; illumination intensity 10 mW/cm^2

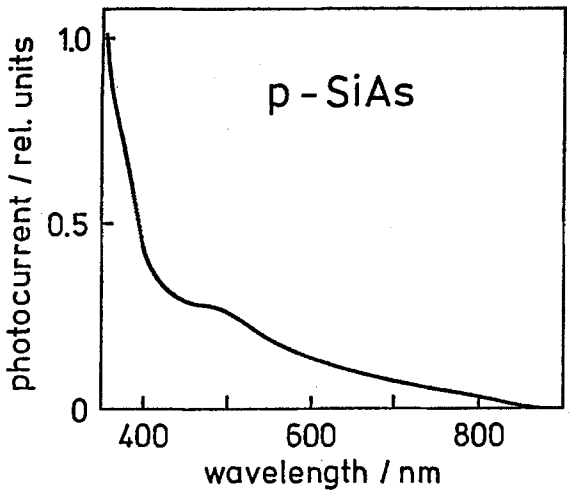

Figure 4.
Photocurrent spectrum of p-SiAs electrode; 0.5 M K_2SO_4

Manuscript received Jan. 25, 1983.

Publication costs of this article were assisted by Hahn-Meitner-Institut fur Kernforschung Berlin.

JOURNAL OF THE ELECTROCHEMICAL SOCIETY

REVIEWS AND NEWS

MAY 1983

Electrochemical Utilization of Metal Hydrides

H. F. Bittner* and C. C. Badcock*

The Aerospace Corporation, Chemistry and Physics Laboratory, Los Angeles, California 90009

ABSTRACT

Fundamental and applied works involving the electrochemical utilization of metal hydrides are reviewed. In the first part of the paper, studies that investigated metal hydrides for hydrogen storage in nickel hydrogen batteries are reviewed. These studies showed that use of hydrides lowered the operating pressures in nickel hydrogen cells, which could lead to improved energy density. However, results regarding degradation of the hydriding material in an aqueous medium were conflicting. In the second part of the paper, the use of metal hydrides as reversible hydrogen electrodes is discussed. Studies reviewed included thermodynamic and kinetic investigations of a variety of hydriding materials. Conflicting results among studies are reconciled where possible, and conclusions are drawn regarding the feasibility of electrochemical utilization of metal hydrides, with suggestions for further work.

The interaction between hydrogen and metals has been extensively investigated from both fundamental and practical viewpoints. Oesterreicher (1) recently reviewed fundamental properties of intermetallic hydrides and Cohen and Wernick (2) reviewed their technological applications. Not included in either review, however, was a discussion of work performed in the last decade involving electrochemical utilization of hydrides.

The application of hydrides in electrochemical systems involves the use of hydrogen in hydrogen/oxidizer cells, such as hydrogen/metal oxide cells (3). The half-cell reaction at the hydrogen electrode can be represented as

$$\tfrac{1}{2}\,H_2 + OH^- \rightleftharpoons H_2O + e^- \qquad [1]$$

Conventional hydrogen/metal oxide cells use hydrogen gas stored in pressure cylinders. One application of hydrides replaces gaseous hydrogen storage with metal hydride hydrogen storage, with hydrogen produced by the following reaction

$$MH_x \rightleftharpoons \frac{x}{2}H_2 + M \qquad [2]$$

where M is an intermetallic compound or alloy capable of reversibly absorbing hydrogen. The thermodynamic characteristics of a hydriding material are usually described by their sorption isotherms, shown in Fig. 1 for $LaNi_5$ (4). A second application makes use of the metal hydride directly as a reversible hydrogen electrode according to the following reaction

$$MH_x + OH^- \rightleftharpoons H_2O + MH_{x-1} + e^- \qquad [3]$$

The use of hydrides in each application shows technological promise; however, results in the literature have often been contradictory. Further experimental work is required to resolve the contradictions.

Hydride Hydrogen Storage in Hydrogen Metal Oxide Cell

Hydrogen/metal oxide batteries, developed primarily for aerospace application, provide high reliability and long cycle life (3). Present batteries use a nickel oxide cathode and pressurized hydrogen gas with Pt catalyst as the anode; the required pressure cylinder limits volumetric energy density. Storage of the hydrogen as metal hydride allows lower pressure, lower volume cells, and a prismatic design with superior packing and heat management capabilities. However, degradation of cycling capability of the hydride material in a cell environment that contains water vapor and oxygen is a primary concern and has been a focus of research in this area.

Earl and Dunlop (5, 6, 7) were the first to investigate hydride hydrogen storage for Ni/H_2 cells. $LaNi_5$, one of the most extensively studied hydrogen storage materials (4), was used in their system. These workers initially constructed a 1.6 A-hr cell that included a sintered nickel hydroxide positive electrode, a polypropylene separator, a platinum catalyzed hydrogen negative electrode, and 5.29g of $LaNi_5$. The stoichiom-

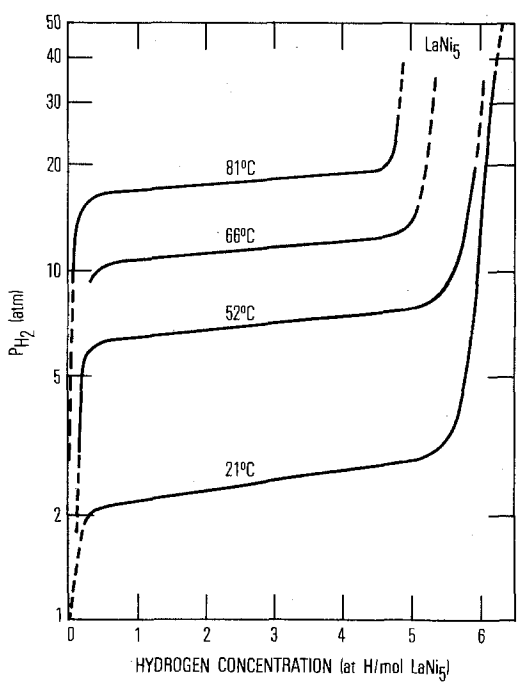

Fig. 1. Desorption isotherms for $LaNi_5$ at various temperatures, from Ref. (4); (1 atm = 1.02 × 10^5 kPa).

* Electrochemical Society Active Member.
Key words: interfaces, electrode, thermodynamics, oxidation.

etry of the hydride was $LaNi_5H_{4.8}$, which corresponded to a capacity of 1.57 A-hr for this amount of $LaNi_5$. The cell was cycled through over 1000 charge-discharge cycles; the pressure range during cycling was consistently 2.5-6 atm per cycle. A comparison of the cell operating pressure with and without the hydride, after 1000 cycles, is shown in Fig. 2. The consistency of the pressure indicated that no decomposition of the hydride material occurred. Subsequently, a 15 A-hr cell was constructed that utilized a nonwoven nylon separator and 66.47g of $LaNi_5$, produced by a different supplier. The $LaNi_5$ absorbed hydrogen to a stoichiometry $LaNi_5H_{6.5}$, which corresponded to 26.7 A-hr capacity (the authors reported 29.0 A-hr capacity). The cell was successfully subjected to one charge-discharge cycle, the pressure ranging from 2.0-6.5 atm. Further cycling, if performed, was not reported. They concluded that $LaNi_5$ hydrogen storage in Ni/H_2 batteries was feasible without reduction in high cycle-life expectancy.

Holleck *et al.* (8) constructed 5 A-hr D size Ni/H_2 cells that utilized $LaNi_5$ hydrogen storage. The hydride was completely separated from the electrolyte by means of a microporous Teflon membrane, and a large catalytic surface recombined O_2 with H_2 to prevent oxygen from reaching the hydride. The cell was cycled at a low rate (22 hr per half-cycle) to about 85% depth of discharge, accompanied by a hydrogen pressure range of approximately 1.5-4.5 atm. After 20-40 cycles, the maximum hydrogen pressure began to rise, which suggested gradual degradation of the hydride. These investigators performed separate hydride cycling experiments in order to characterize the hydride degradation. For these experiments, 25g samples of $LaNi_5$ from three different suppliers were activated by repeated exposure to 60 atm dry H_2. Cycling experiments were performed by using controlled-flow hydrogen absorption and desorption between pressure limits of 12 and 0.5 atm. Humidity was simulated by a pool of 30% KOH placed in the pressure vessel, producing approximately 10 Torr water vapor. A relatively rapid decrease in hydrogen storage capacity was found with increasing cycle number. The rate of degradation was significantly dependent on the lot (supplier) of the $LaNi_5$. In Fig. 3, results are shown for $LaNi_5$ from three different suppliers. These workers concluded that advantages of hydride hydrogen storage in Ni/H_2 cells were compromised by the continual decrease of hydrogen storage capacity in $LaNi_5$ in the presence of water vapor.

Other investigations have been performed to determine the effects of oxygen and water vapor on the hydrogen absorption properties of various materials. Although these works were not performed specifically in regard to battery studies, the results are applicable to this review. Goodell and Sandrock (9) measured the effects of 300 ppm H_2O and O_2 on $LaNi_5$, FeTi, and on $Fe_{0.85}Mn_{0.15}Ti$. After 30 absorption-desorption cycles, they found approximately a 50% reduction in hydrogen storage capacity for FeTi and $Fe_{0.85}Mn_{0.15}Ti$. However, $LaNi_5$ exhibited initially a small capacity loss, which was recovered after approximately 10 cycles, and then exhibited immunity to degradation from both H_2O and O_2. Substantial reactivation of FeTi and $Fe_{0.85}Mn_{0.15}Ti$ was accomplished by further cycling with ultrapure hydrogen. These workers concluded that O_2 and H_2O poisoned the alloy surface by formation of complex oxides, inhibiting the catalytic H_2 dissociation and/or hydrogen penetration. In the case of $LaNi_5$, these films disproportionated into stable oxides and metallic Ni, which acted to restore the catalytic activity of the surface. This behavior is in line with results found by Schlapbach *et al.* (10, 11) who found similar surface disproportionation and concomitant surface catalytic activity for hydrogen absorption in $LaNi_5$.

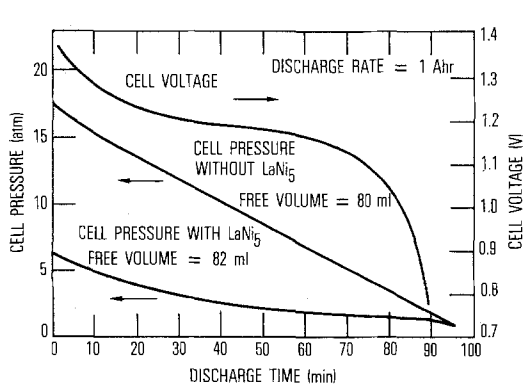

Fig. 2. Cell pressure and voltage for complete discharge with and without $LaNi_5$, from Ref. (6).

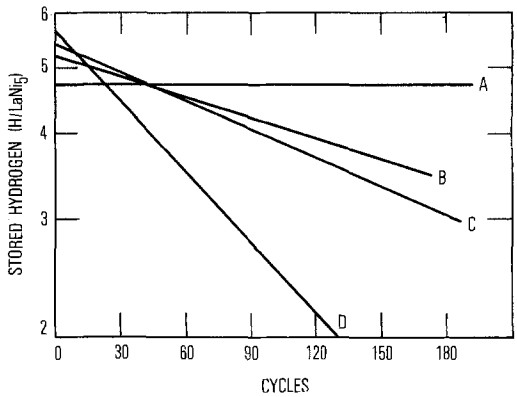

Fig. 3. Hydrogen storage capacity of $LaNi_5$ during absorption-desorption cycling. A, research chemicals alloy, dry H_2; B, C, and D, ergenics, research chemicals, and molycorp alloys, respectively, H_2 + about 10 Torr H_2O vapor, from Ref. (8).

The explanation for the contradictory results found by Earl and Dunlop (5) and Holleck *et al.* (8) may lie in differences in the $LaNi_5$ or in different procedures employed in the use of the $LaNi_5$. In each case, the $LaNi_5$ was obtained from different suppliers. Holleck *et al.* (8) found a marked difference in hydride degradation among samples from different suppliers; it may be that the material used by Earl and Dunlop (5) was more degradation resistant than the materials used by Holleck *et al.* (8). The result of Goodell and Sandrock (9) that $LaNi_5$ showed long-term immunity to small concentrations of H_2O and O_2 indicates that at least under certain conditions $LaNi_5$ does not significantly degrade in the presence of water. The procedures used by Earl and Dunlop (5) and Holleck *et al.* (8) were different. Factors that might affect hydride performance include pressure, temperature, cycle time, physical separation of the hydride from the aqueous medium, and heat conduction from the hydride. The cell design of Earl and Dunlop (5) allowed for a more significant separation of the hydride from the electrochemical cell and probably had better heat conduction from the hydride, which may account for the superior performance of the cell. Further work is required to understand the nature of the hydride degradation, and must include careful characterization of the starting materials, the cycling procedures, and a study of the surface and bulk characteristics of the degraded materials.

Metal Hydrides as Reversible Hydrogen Electrodes

Certain intermetallic hydrides function as hydrogen electrodes, absorbing and desorbing hydrogen electrochemically without formation of gaseous hydrogen. Utilization of such electrodes in metal oxide/H_2 cells may provide higher energy density, higher efficiency, and faster reaction kinetics over cells that utilize gaseous hydrogen. Use of these electrodes in fuel cells may also be of interest (12). In Table I, theoretical

Table I. Theoretical energy densities of various electrochemical couples (12, 27, 28)

Couple	Reaction	Theoretical energy density (W-hr/kg)
Pb/H_2SO_4	$Pb + PbO_2 + 2H_2SO_4 \rightarrow 2PbSO_4 + 2H_2O$	161
Ni/Cd	$2NiOOH + Cd + 2H_2O \rightarrow 2Ni(OH)_2 + Cd(OH)_2$	209
$Ni/LaNi_5H_6$	$6Ni(OH)_2 + LaNi_5 \rightarrow 6NiOOH + LaNi_5H_6$	275
Ni/H_2	$Ni(OH)_2 \rightarrow NiOOH + \frac{1}{2}H_2$	378
$LaNi_5H_6$-air	$LaNi_5H_6 + 3/2\ O_2 \rightarrow 3H_2O + LaNi_5$	458
Na/S_2	$Na + S_2 \rightarrow NaS_2$	980
MgH_2-air	$MgH_2 + \frac{1}{2}\ O_2 \rightarrow H_2O + Mg$	1900

energy densities are given for various electrochemical couples; some hydride-air fuel cell couples are included. Research has been performed on electrochemical properties of three hydriding materials and their derivatives, such as the Ti-Ni system, $LaNi_5$-based compounds, and Fe-Ti-based materials.

Ti-Ni system.—Among the first researchers to investigate the use of hydriding materials as reversible electrodes were Justi *et al.* (13). They chose $Ti_{1-x}Ni_x$ alloys because of their relatively low specific weight, high hydrogen absorption capacity, and good oxidation resistance. Electrodes with various values x in $Ti_{1-x}Ni_x$ were cathodically charged in 6M KOH at 0.4 mA/cm² to a capacity of from 300 to 500 mA-hr/g. Subsequent anodic discharge showed that all capacity was recovered for electrodes where $x = 0.5$, and only about 60% was recovered for electrodes where $x = 0.33$. The difference in the x values in $Ti_{1-x}Ni_x$ corresponded to different ratios of the two phases present, Ti_2Ni and TiNi. TiNi can be charged completely reversibly, whereas Ti_2Ni apparently forms two hydride phases, one which cannot be anodically discharged. These researchers also reported that pure TiNi exhibits much greater oxidation resistance than Ti_2Ni in alkaline medium. However, pure TiNi is very hard and could not be ground to make sintered electrodes. By alloying TiNi with small amounts of a third element, the material became brittle and could be ground. Electrodes were fashioned from this material, and extrapolation of the slope of the capacity *vs.* cycle number indicated more than 1000 charge-discharge cycles could be attained before 50% degradation of the initial capacity occurred. However, the discharge kinetics were slow.

Gutjahr *et al.* (14) studied electrochemical charging of sintered mixtures of Ti_2Ni-TiNi. Reversible capacities in excess of 300 mA-hr/g were found. The highest capacity measured was 320 mA-hr/g, which corresponded to discharging 84% of the hydrogen from 940 mV OCV to 740 mV *vs.* Hg/HgO (for 1 atm H_2, $E° = -926$ mV *vs.* Hg/HgO). Under optimal conditions, 450 charge-discharge cycles were obtained at 80% depth of discharge. Shallow cycling (<10% capacity) under high loads (3-5C rate, *i.e.*, a rate where total capacity C would be discharged in 1/3 to 1/5 hr) resulted in more than 20,000 cycles. In contrast to the findings of Justi *et al.* (13), Gutjahr *et al.* (14) found an interaction between the two phases Ti_2Ni and TiNi that resulted in almost complete discharge of the hydrogen. From x-ray diffraction measurements of the electrodes during charge-discharge cycles, a model of the hydrogen transfer mechanism was proposed. During electrochemical discharge, hydrogen diffuses from the mixture $Ti_2NiH_{2.5}$ + TiNiH to the hydride/electrolyte phase boundary. As TiNi is formed, hydrogen is also transferred from Ti_2NiH_x to TiNi; the irreversibly absorbed hydrogen in Ti_2NiH_x described by Justi *et al.* (13) is apparently mostly discharged by transfer to TiNi and then to the solid and liquid phase boundary. Gutjahr *et al.* (14) reported no kinetic difficulties for hydrogen transfer in the TiNi phase. It is likely that the presence of Ti_2Ni in the alloy had a catalytic effect on the discharge of TiNi. In contrast, Justi *et al.* (13) reported slow discharge kinetics for a pure TiNi phase. However, their "pure" TiNi was actually alloyed with a third element to allow grinding, which may have contributed to its slow discharge kinetics.

Miles (15) studied the hydrogen and oxygen evolution reactions in 30% KOH at 80°C for a number of electrode materials, including TiNi and Ti_2Ni. Results showed that reduction of water occurred somewhat more readily for TiNi than for pure Ti or Ni, however, no hydrogen evolution was observed; it was assumed that hydride formation took place. As in the case of pure Ni, a large increase in the hydrogen overvoltage following anodic treatment for TiNi indicated formation of an oxide film. Results for Ti_2Ni were similar to those for TiNi, except that the overvoltage for water reduction was smaller.

$LaNi_5$.—Ewe, Justi, and Stephan (16) investigated the use of $LaNi_5$ as a reversible hydrogen storage electrode. Electrodes were fashioned from 3g $LaNi_5$ of particle size <80μ and 6g of electrolytic copper, hot pressed together. The electrode was charged and discharged at 22°C and 4 mA/cm² (between 50 and 300 mV *vs.* standard hydrogen electrode), and reached a specific capacity of 100 mA-hr/g after about 10 cycles, which remained constant up to 100 cycles, the highest number performed. Higher temperatures lowered the capacity, and higher pressures seemingly had no effect on the capacity. Interestingly, higher current densities, about 500 mA for the entire electrode, raised the capacity to about 200 mA-hr/g. These capacities are low in comparison with the 370 mA-hr/g expected from the stoichiometry $LaNi_5H_6$ produced by gas charging techniques. The differences in capacity were attributed to differences in preparation of the $LaNi_5$ material.

Will (17) obtained a patent for a battery with an $LaNi_5$ hydride anode. He reported an open-circuit voltage of 1.3V and current densities up to 50 mA/cm². A polarization of 300 mV was observed at 25 mA/cm². No cycling was performed, and no other data were reported.

Bronoel *et al.* (18) studied the electrochemical capacity of $LaNi_5$ and $LaNi_5$-based electrodes in unpressurized cells. The electrodes consisted of 50 mg powdered alloy, of approximately 10μ particle size, compressed between a vitreous carbon collector and porous separator wetted with 5*N* KOH electrolyte. The potential was measured *vs.* a standard calomel electrode (SCE), and a gold sheet was used as the counterelectrode. The working electrode was charged for 16 hr at 1.5 mA (current density estimated at 0.04 mA/cm²) and 20°C; after charge, the potential was found to be −1160 mV/SCE. The electrode was anodically polarized at −1000 mV/SCE, and the change in current *vs.* time was measured. The method of alloy preparation was found to affect its electrochemical capacity. Preparation of $LaNi_5$ in an alumina crucible (which produced Al contamination in the alloy) yielded a capacity of only 250 mA-hr/g, whereas cold-crucible melts (no contamination) yielded a capacity of 320 mA-hr/g. $LaNi_{5+x}$ electrodes of various compositions x were prepared, from $x = -0.3$ to $+0.5$. A plateau in capacity of approximately 320 mA-hr/g was found for $-0.3 \leq x \leq 0.0$, with a decrease for $x > 0.0$ to about 250 mA-hr/g for $x = 0.5$. Higher temperatures were accompanied by a decrease in capacity. These results can be explained in terms of equilibrium pressure; by modifying the alloy composition or by raising the temperature, the hydrogen equilibrium pressure can be increased. In an unsealed cell, the hydrogen will escape when the equilibrium pressure is greater than 1 atm, and the capacity will be reduced.

Percheron-Guegan *et al.* (19, 20) of the same laboratory later investigated the effects of substitution of Yb, Ca, Mg, Y, Ti, Mn, Cr, and Cu for La or Ni in $LaNi_5$. Generally, a maximum in electrochemical capacity was observed at small amounts of each substituent. $LaMn_{0.5}Ni_{4.5}$ showed a capacity of 390 mA-hr/g at 20°C, and $LaMn_{0.75}Ni_{4.25}$ showed a capacity of 335 mA-hr/g at 70°C, both significantly higher than pure $LaNi_5$. It was stated that electrodes shaped from materials could undergo a great many charge-discharge cycles between −10° and 50°C with a capacity higher than 300 mA-hr/g. Sarradin *et al.* (21) of the same laboratory constructed hydride-air secondary batteries by using $LaNi_5$ and reversible air electrodes with equilibrium potentials of −100 mV *vs.* SCE. They found energy densities of 100 W-hr/kg. During discharge at 40 mA/cm², a cell voltage of 0.7V was observed.

Markin *et al.* (22) studied the use of $LaNi_5$ in both small and full-sized cells. For the small cells, electrodes were fashioned from 70 mg $LaNi_5$ plus binder on 0.5 cm² Ni grids, and were immersed in a cell with 35% KOH, Pt counterelectrode, and SCE reference electrode. Cycling was performed at 0°C by charging the electrodes at 15 or 30 mA to a capacity of 250 mA-hr/g, then discharging to 0.7V. After 10 cycles, the reversible capacity rose to 230 to 240 mA-hr/g, and remained constant to 50 cycles, at which time the experiment was terminated. Full-sized cells were fabricated by using electrodes consisting of 8g $LaNi_5$ (corresponding to a hydrogen absorption capacity of 1.42 A-hr) separated from an $Ni(OH)_2$ positive electrode (1.1 A-hr) by a nylon separator. This cell reached 1.1 A-hr after 14 cycles at C/2, and retained this capacity for 517 cycles. Some loss of capacity occurred between 517 and 947 cycles, corresponding to 0.06 A-hr or 4.2% per 100 cycles. This loss was attributed entirely to degradation of the $LaNi_5$ electrode through reaction with oxygen generated at the end of charge and during overcharge. The degradation was assumed to have occurred also during the first 517 cycles, when the cell was cathode-limited, and would not have shown the loss in anode capacity. Cycling of a six cell 8 A-hr stack fully immersed in electrolyte and equipped with a Pt catalyst in the gas phase to effect the $H_2 + O_2$ recombination led to increased hydrogen pressure with cycle number, because of inefficiencies of hydrogen absorption. After removing the excess electrolyte so that the back of each $LaNi_5$ electrode was exposed to gaseous H_2, a more severe pressure rise resulted. This was attributed to degradation of the $LaNi_5$ by oxygen transferred via the gas phase. The primary means of $LaNi_5$ degradation is, therefore, reaction with oxygen transferred across the separator or via the gas phase. A thin layer of Pt black painted on the surface of the $LaNi_5$ catalyzed the $H_2 + \frac{1}{2} O_2$ recombination reaction, and reduced the capacity loss to 0.01 A-hr/100 cycles.

Van Rijswick (23) studied $LaNi_5$, $LaNi_4Cu$, and $LaNi_4Cr$. Electrodes were prepared by mixing the crushed active materials with fine copper or carbonyl-nickel powder and cold pressing the mixture into a pellet. Cells were constructed with Ni counterelectrodes, Ag/AgCl or SCE as reference electrodes, and 6*N* KOH electrolyte. Both unsealed and pressurized cells were used for determining the electrochemical capacities. In a sealed cell, $LaNi_5$ showed a capacity of 350 mA-hr/g, which did not vary appreciably from room temperature to 55°C. (In contrast, Percheron-Guegan *et al.* (19) found a reduction in capacity for $LaNi_5$ in an open cell to less than 50 mA-hr/g at 40°C; apparently the hydrogen escaped owing to the high equilibrium pressure for $LaNi_5$ at 40°C). The capacity of $LaNi_4Cu$ was determined in an open cell to be 270 at 20°, 210 at 40°, and 160 mA-hr/g at 60°C, respectively. $LaNi_4Cr$ showed a capacity of 280 mA-hr/g at 20° and 40°C ,which decreased slightly to 265 mA-hr/g at 60°C. These results can be explained in terms of the lower equilibrium pressures for the Cu- and Cr-substituted $LaNi_5$ derivatives and are discussed further at the end of this section.

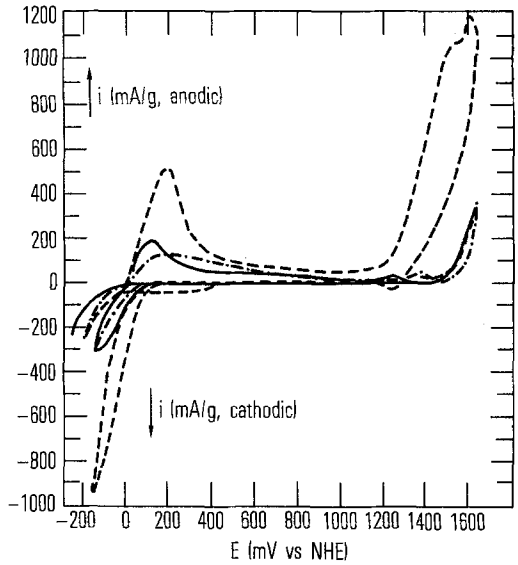

Fig. 4. Cyclic voltammograms of $LaNi_5$, $LaNi_4Cu$, and $LaNi_4Cr$. (Solid curve, $LaNi_5$; dot-dashed curve, $LaNi_4Cu$, and dashed curve, $LaNi_4Cr$.) Scan rate, 1 mV/sec, from Ref. (23).

Van Rijswick (23) also performed cyclic voltammetry for the same electrodes; results are shown in Fig. 4. For $LaNi_5$, hydrogen was absorbed in the cathodic direction to −150 mV NHE, then oxidized at +100 mV in the anodic direction; above +200 mV, oxidation of the Ni occurred (with small currents) to $Ni(OH)_2$; and at +1350 mV, oxidation to NiOOH occurred. Above +1450 mV, oxygen evolution began. In the cathodic direction, NiOOH was reduced at +1230 mV. Apparently a layer of NiOOH, which was not cathodically reducible, retarded hydrogen production to −50 mV, which was absorbed by the metal, and hydrogen evolution began at −250 mV. $LaNi_4Cu$ behaved in a very similar manner, with an extra peak at +450 mV, attributed to oxidation of the Cu. $LaNi_4Cr$ showed an intense oxidation peak at +1200 mV, which did not passivate the material. Extended exposure to this potential severely reduced the hydrogen storage capacity after returning to the hydrogen potential, and this material was, therefore, deemed unacceptable as an electrode.

Van Rijswick (23) further studied the kinetics of electrochemical charging and discharging. It was concluded that two processes may be rate limiting, charge transfer at the metal/electrolyte interface and hydrogen transport in the metal. For small particles, hydrogen transport is not rate limiting owing to the short diffusion path, and, therefore, charge transfer is rate limiting; for large particles, the diffusion path increases and transport in the metal becomes rate limiting. However, because equilibration by diffusion is slow, any real discharge for large particles will be rate limited initially by charge transfer and in the end by diffusion. This phenomenon was shown experimentally for $LaNi_4Cu$. By calculating the exchange current and by using the Tafel relationship, a value for the exchange current density of 0.5 mA/cm² was found, comparable to the highly catalytic electrodes Pd and Pt.

Folonari *et al.* (24) studied $LaNi_5$, $MmNi_5$ (Mm ≡ Mischmetal), and $CaNi_5$ electrodes. The powdered materials (diameter less than 100 μm) were placed on graphite collectors and dipped in 30% KOH, and electrochemical capacities were measured. $LaNi_5$ showed a capacity of 250 mA-hr/g, and $MmNi_5$ had a capacity of 170 mA-hr/g with slower kinetics. $CaNi_5$

showed an instability in potential and was, therefore, considered unacceptable as an electrode material. A $LaNi_5$ hydride-air fuel cell was constructed by using an anionic membrane as the electrolyte ($LaNi_5$ was found to undergo anodic dissolution in the presence of acidic membranes, whereas it was found to be stable in an alkaline environment), sandwiched between an air cathode and a pressed $LaNi_5$ powder electrode or a composite electrode of $LaNi_5$ bonded by a polymeric resin. Polarization characteristics of the cell were obtained, and the characteristics of the cell were extrapolated to define future prototypes, yielding an energy density of 64 W-hr/kg.

Kitamura *et al.* (25) studied the hydrogen evolution reaction at $LaNi_5$ and $MmNi_5$ electrodes in 1M KOH at 30°C. These electrodes showed lower overvoltages than pure La, Mm, or Ni electrodes. The logarithmic current densities, obtained by extrapolating the Tafel lines to the hydrogen equilibrium potential (−0.926V *vs.* Hg/HgO), were −3.5 for $LaNi_5$, −3.7 for $MmNi_5$, and −5.1 for Ni. The activities for hydrogen evolution for the $LaNi_5$ and $MmNi_5$ electrodes were, therefore, comparable to those for Pt and Pd electrodes, with logarithmic current densities of −3.0 and −3.9, respectively.

TiFe.—Fukushima and Tanabe (26) studied TiFe and TiFe-$Nb_{6.8}$ a/o (presumably this corresponded to $Ti_{0.466}Fe_{0.466}Nb_{0.068}$) by several methods including potentiometric, galvanostatic, dynamic impedance, alternating current impedance, and rotating disk electrode techniques. Their results indicated that TiFe-Nb was somewhat more reactive to the hydrogen reaction than TiFe, because hydrogen absorption occurred on cathodic sweep at more positive potentials. In the potential range where hydrogen evolution occurs, addition of Nb to TiFe increased the rate of hydrogen evolution by 10 times. They concluded that the reaction rate was controlled by two factors: formation of an active site between the electrode surface and the adsorbed hydrogen, and recombination of adsorbed hydrogen atoms. The former corresponds to the charge transfer reaction described by Van Rijswick (23) as a rate-controlling step. Fukushima and Tanabe (26) did not consider hydrogen transport in the metal, an important rate-controlling step reported by Van Rijswick (23). Combining results from these two works, three rate-controlling steps emerge: (*i*) recombination (or dissociation) of hydrogen at the metal surface; (*ii*) charge transfer at the metal-electrolyte interface; and (*iii*) diffusion in the metal.

Many of the results regarding hydride electrodes can be understood in terms of equilibrium sorption isotherms, such as shown for $LaNi_5$ in Fig. 1. The electrochemical capacity of a hydride electrode of course depends on the amount of reversibly absorbed hydrogen in the hydriding material. The amount of hydrogen contained in the material can be changed by altering the environmental conditions (*i.e.*, temperature and pressure) or by altering the material itself and, therefore, the characteristics of the isotherm. The works by Percheron-Geugan *et al.* (19) and Van Rijswick (23) demonstrated the effects of changing environmental conditions. In those works, higher temperatures in unpressurized cells led to desorption of some of the hydrogen with a resulting loss in capacity. However, higher temperatures in pressurized cells merely increased the equilibrium hydrogen pressure, and had little or no effect on capacity. Along these lines the low capacity found for $LaNi_5$ by Ewe *et al.* (16) might be attributed to their unsealed cells. However, their statement that higher pressures did not increase capacity is not consistent with other works. The low capacity might be attributable to differences in preparation of the $LaNi_5$, as the authors suggested. The works by Bronoel *et al.* (18), Percheron-Guegan *et al.* (19), and Van Rijswick (23) demonstrated the effects on capacity of changing the hydriding material. It was shown that either by changing the stoichiometry in $LaNi_5$ or by substituting various elements into $LaNi_5$, the electrochemical capacity could be changed. This was due partly to a change in the equilibrium hydrogen pressure and partly to a change in the maximum hydrogen takeup for these new materials.

Similar arguments apply to the Ti_2Ni-TiNi system. The equilibrium hydrogen pressure for this material is sufficiently low at room temperature that no hydrogen desorbs from unsealed cells. In fact, the irreversibly absorbed hydrogen in Ti_2Ni described by Justi *et al.* (13) is probably a consequence of the extreme stability, or low hydrogen equilibrium pressure, of this hydride.

As a consequence of these phenomena, it is noted here that either hydrides with low equilibrium pressures or hydrides in sealed cells are necessary to retain the maximum electrochemical capacity available. However, lower equilibrium pressures result in lower cell voltages according to the Nernst equation. As a guideline, the potential gained from forming the hydride must be significantly less than the potential required to evolve hydrogen [$E_o = -0.828$V *vs.* standard hydrogen electrode (SHE)]. For example, hydrides with free energies of formation less exothermic than −19.1 kcal/mol H_2 (-7.99×10^4 kJ/mol H_2) will result in voltages more positive than −0.424 *vs.* SHE.

In addition to the equilibrium properties of the hydride material, degradation of the hydride was found to influence performance of the hydride electrode. Losses in capacity that were attributed to degradation were reported by Justi *et al.* (13), Markin *et al.* (22), and Van Rijswick (23). Markin attributed degradation of his $LaNi_5$ electrode to reaction with oxygen during overcharge. In other works, no capacity losses were reported, although extensive cycling was not performed in these works. From a thermodynamic viewpoint, oxidation of the hydride material is likely to occur. However, by correctly choosing the hydride material and by carefully managing charge and discharge cycling, it would appear possible to minimize the degradation.

In choosing a hydriding material for electrochemical utilization, thermodynamic, kinetic, and degradation-resistant properties must all be considered. Pure elements that form hydrides are generally not suitable because their hydrides are too stable. The number of intermetallic alloys and compounds that absorb hydrogen is virtually limitless; however, some guidelines can be applied in choosing appropriate materials. Materials with heats of hydriding between −7 and −19 kcal/mol H_2 (-3×10^4 and -8×10^4 kJ/mol H_2) are desirable. More positive heats of formation could be tolerated; however, hydrogen pressures become greater than atmospheric. Materials containing significant amounts of Fe, Mn, or Cr appear to degrade in alkaline environments. $LaNi_5$ and other materials with this structure ($CaCu_5$-type) show promising results, and further work is needed to optimize stoichiometry or substituents. However, many other materials fit these guidelines and have yet to be investigated.

Conclusions

The application of hydride hydrogen storage and hydride electrodes for electrochemical cells shows technological promise. For either application, the hydride material must show stability in an alkaline environment that contains water and oxygen. The materials expand on absorption and may disintegrate, and the cells need to be designed accordingly. The hydrogen equilibrium pressure must fall in an appropriate range, and the cells must be sealed to prevent loss of the hydrogen. $LaNi_5$ appears to be the

most promising material studied to date; however, other known hydriding materials have yet to be investigated. Definitive studies that include carefully controlled conditions and long-term cycling are required.

Acknowledgment

This work was supported by the Space Division, United States Air Force, under Contract No. F04701-81-C-0082.

Manuscript submitted May 11, 1982; revised manuscript received Aug. 5, 1982.

Any discussion of this paper will appear in a Discussion Section to be published in the December 1983 JOURNAL. All discussions for the December 1983 Discussion Section should be submitted by Aug. 1, 1983.

Publication costs of this article were assisted by The Aerospace Corporation.

Note added in proof: Schultze and Antoine recently published results on hydride hydrogen storage in silver hydrogen cells (J. P. Schultze and P. Antoine, "Application of Hydrides to Silver Hydrogen System," SAFT Report #SAS-224/82-JPS/MD, SAFT Aerospace Department, Romainville, France, April 1982). These researchers constructed a 7.5 A-hr Ag/H_2 cell with $LaNi_{4.7}$ hydride hydrogen storage. The cell was cycled at a C/10 charge rate and a C/2.6 discharge rate at 50% depth of discharge. The cell underwent 2000 cycles with no apparent hydride degradation. These researchers also constructed a prototype 90 A-hr common pressure vessel Ag/H_2 cell with $La_{0.8}Ce_{0.2}Ni_5$ hydride hydrogen storage. The use of hydrides in this cell resulted in a 40% increase in the volumetric energy density.

REFERENCES

1. H. Oesterreicher, *Appl. Phys.*, **24**, 169 (1981).
2. R. L. Cohen and H. Wernick, *Science*, **214**, 1081 (1981).
3. J. D. Dunlop, J. Stockel, and G. Van Ommering, in "Power Sources," Vol. V, D. H. Collins, Editor, p. 315, Academic Press, New York (1975).
4. H. H. Van Mal, H. K. J. Buschow, and A. R. Miedema, *J. Less-Common Met.*, **35**, 65 (1974).
5. M. W. Earl and J. D. Dunlop, *COMSAT Technical Review*, **3**, 437 (1973).
6. M. W. Earl and J. D. Dunlop, in "Proceedings of the 26th Power Sources Symposium," Atlantic City, N.J., The Electrochemical Society, Inc., p. 24 (1974).
7. J. D. Dunlop, M. W. Earl, and G. V. Ommering, U.S. Pat. 3,959,018 (1976).
8. G. L. Holleck, J. R. Driscoll, and B. E. Paul, *J. Less-Common Met.*, **74**, 379 (1980).
9. P. D. Goodell and G. P. Sandrock, *ibid.*, **73**, 161 (1980).
10. L. Schlapbach, A. Seiler, H. C. Siegmann, T. V. Waldkirch, P. Zurcher, and C. R. Brundle, 2nd World Hydrogen Energy Conference, Zurich, Switzerland (1978).
11. H. C. Siegmann, L. Schlapbach, and C. R. Brundle, *Phys. Rev. Lett.*, **40**, 972 (1978).
12. K. Videm, "Hydrides for Energy Storage," A. F. Andresen and A. J. Maeland, Editors, p. 463, Pergamon Press, Oxford (1978).
13. E. W. Justi, H. H. Ewe, A. W. Kalberlah, N. M. Saridakis, and M. H. Schaefer, *Energy Conver.*, **10**, 183 (1970).
14. M. A. Gutjahr, H. Buchner, K. D. Beccu, and H. Saufferer, "Power Sources," Vol. IV, D. H. Collins, Editor, p. 79, Oriel Press, Newcastle Upon Tyne, England (1973).
15. M. H. Miles, *Electroanal. Chem. Interfacial Electrochem.*, **60**, 89 (1975).
16. H. Ewe, E. W. Justi, and K. Stephan, *Energy Conver.*, **13**, 109 (1973).
17. F. G. Will, U.S. Pat. 3,874,928 (1975).
18. G. Bronoel, J. Sarradin, M. Bonnemay, A. Percheron, J. C. Achard, and L. Schlapbach, *Int. J. Hydrogen Energy*, **1**, 251 (1976).
19. A. Percheron-Guegan, F. Briaucourt, H. Diaz, J. C. Achard, J. Sarradin, and G. Bronoel, in "Proceedings of the 12th Rare Earth Research Conference," C. E. Lundin, Editor, p. 300, Vail, CO (July 1976).
20. A. Percheron-Guegan, J. C. Achard, J. Sarradin, and G. Bronoel, "Hydrides for Energy Storage," A. F. Andresen and A. J. Maeland, Editor, p. 485, Pergamon Press, Oxford, England (1978).
21. J. Sarradin, G. Bronoel, A. Percheron-Guegan, and J. C. Achard, "Power Sources," Vol. VII, J. Thompson, Editor, p. 345, Academic Press, London (1979).
22. T. L. Markin, N. J. Bridger, R. Bennett, and R. M. Dell, in "Proceedings of the 28th Power Sources Symposium," Atlantic City, NJ, June 12-15, 1978, The Electrochemical Society, Inc., p. 136 (1978).
23. M. H. J. Van Rijswick, "Hydrides for Energy Storage," A. F. Andresen and A. J. Maeland, Editors, p. 261, Pergamon Press, Oxford, England (1978).
24. C. Folonari, G. Iemmi, F. Manfredi, and A. Rolle, *J. Less-Common Met.*, **74**, 371 (1980).
25. T. Kitamura, C. Iwakura, and H. Tamura, *Chem. Lett.*, 965 (1981).
26. S. Fukushima and H. Tanabe, in "Proceedings of the 3rd World Hydrogen Energy Conference," June 1980, T. N. Veziroglu, K. Fueki, and T. Ohta, Editors, p. 897, Pergamon Press, New York (1981).
27. M. Klein and M. George, in "Proceedings of the 26th Power Sources Symposium," Atlantic City, NJ, The Electrochemical Society Inc., p. 18 (1974).
28. S. U. Falk and A. J. Salkind, "Alkaline Storage Batteries," p. 435, John Wiley and Sons, Inc., New York (1969).

Sputter Depth Profiling of Microelectronic Structures

Ernst Zinner[1]

Institut für Allgemeine Elektrotechnik und Elektronik und Institut für Analytische Chemie, Technische Universität Wien, 1040 Wien, Austria

ABSTRACT

Reviewed are the principles and applications of sputter depth profiling for the analysis of semiconductor and microelectronic materials. Various techniques are based on sputter removal whereby either the sputtered species (in SIMS, SCANIIR) or the remaining surface (AES, XPS, ISS) are investigated. In spite of its increasing importance, there are many problems associated with sputter etching. After a general survey of the principles, a detailed discussion is devoted to the many effects which can distort sputter depth profiles and limit depth resolution. These effects can be caused by instrumental factors (nonuniformity of erosion, beam impurities, vacuum contaminants) and the sample composition or can be due to the analysis method used (information depth, matrix effects, detection limit, sample consumption). Most important are the effects caused by the sputtering ion beam itself. Among these are notably preferential sputtering, atomic mixing, surface roughness as a result of the sputter process, sample charging, surface transport, and chemical reduction. The review of applications concentrates on the measurement of the distribution of dopants and impurities in semiconductors, on the study of insulating films (in particular the Si/SiO_2 interface and the oxidation of GaAs), and on the metallization problem in Si and GaAs technology.

The ever-increasing miniaturization of electronic devices in VLSIC technology (1) places new demands on analytical techniques for their characterization (2, 3). Of special interest is the measurement of elemental distributions, in particular the measurement of dopant distributions in the semiconductor substrate (4, 5) and the analysis of diffusive and reactive processes between metal, semiconductor, and dielectric films (6, 7) which are the basic elements of microelectronic structures. The analytical requirements for measurement techniques include good spatial resolution as well as elemental sensitivity and specificity. Although there are interesting questions to be asked with respect to lateral dimensions, because of the planar structure of most microelectronic devices, methods for the measurement of elemental concentrations as a function of depth are of special importance. An example for the requirements for the depth resolution of such methods is given in Fig. 1 which shows calculated depth distributions of dopants in base and camel collector of a monolithic hot electron transistor (MHET) with an extremely shallow barrier raising implant.

An overview of methods for the measurement of depth profiles is given in Table I. The so-called nondestructive techniques are so named not because they necessarily leave the sample undamaged, but because the sample surface does not have to be removed in order to obtain information about the inside. The sample interior is rather probed with penetrating ion or electron beams whereby the depth information is obtained via the energy loss experienced by the particles while traversing the sample. Rutherford backscattering spectroscopy (RBS) is based on the kinematical energy loss of light ions (p,He) elastically scattered from atoms in the analyzed sample (9). The method is best suited for the determination of the depth distribution of heavy elements in a light matrix.

In nuclear reaction analysis (10-12), a method sensitive mainly for light elements, the energy of the bombarding ions can be varied in such a way that the energy for a nuclear reaction with a sharp resonance in the cross section like, *e.g.*, $^{27}Al(p,\gamma)^{28}Si$ is reached at a given depth. The intensity of the γ-signal is monitored as function of proton energy. Alternatively, the energy of reaction products can be measured if the nuclear reaction results in monoenergetic nuclei. The measurement of B via the reaction $^{10}B(n,\alpha)^{7}Li$ is an example.

Through variation of the take-off angle of the Auger or photoelectrons with respect to the sample surface in AES or XPS analysis (13-16), depth information is obtained because of the variation of the effective escape depth of the electrons.

The destructive methods rely on the removal of the surface. This is usually done in subsequent flat layers, but sometimes a nonflat crater is excavated from the sample. In the latter case ("crater edge profiling") the crater bottom is analyzed in different spots representing different depths by a surface sensitive technique with good lateral resolution (*e.g.*, scanning Auger microscopy) (17, 18). Surface removal can be accomplished by small angle lapping (19-21) or ball cratering (22, 23). Chemical microsectioning techniques include straight chemical dissolution (24, 25) or anodic sectioning (26). Especially the latter method is prominently used for electronic materials like Si (27-29), GaAs (30, 31), or Ta (32). In the last decade surface removal by sputtering with heavy ions with energies of 1-20 keV has become increasingly important.

In all destructive methods either the remaining sample surface or the removed material can be analyzed. Neutron activation analysis (33) is still in use for depth profiling because of its precision and sensitivity for certain elements (4, 34). Particle induced x-ray emission (PIXE) leads to elemental analysis by measurement of characteristic x-rays (35, 36). This technique has good sensitivity compared to electron microprobe analysis, but suffers from poor depth resolution.

The requirement of good depth resolution makes surface sensitive techniques most important that use electrons or low energy ions to probe only a few atomic layers of the sample surface. Both Auger electron spectroscopy (AES) (37-40) and x-ray photoelectron spectroscopy (XPS) (41-44)

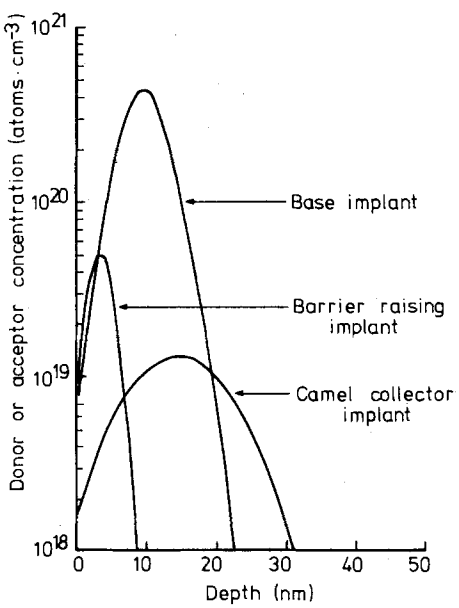

Fig. 1. Depth distribution of ion implantation profiles for the fabrication of a monolithic hot electron transistor. From Ref. (8).

[1] Permanent address: McDonnell Center for the Space Sciences, Washington University, St. Louis, Missouri 63130.

Key words: AES profiling, SIMS profiling, profile distortions, semiconductor materials, insulating films.

Table I. Methods for elemental depth profiling

I. Nondestructive
  A. Energy loss of ions: RBS, nuclear reactions
  B. Attenuation of electron signal: varying take-off angle in AES and XPS
II. Destructive
  Removal of surface:
  A. Mechanical: small angle lapping, ball cratering
  B. Chemical: chemical etching, anodic sectioning
  C. Sputter etching
  For all destructive methods:
  1. Analysis of the remaining material or surface: PIXE, NAA, AES, SAM, XPS, ISS
  2. Analysis of the removed material: SIMS, SNMS, GDMS, SCANIIR, GDOS

are based on the measurement of the energy distribution of electrons that in the first case are resulting from Auger transitions induced by electron or photon bombardment, in the second case are photoelectrons ejected by x-ray or u.v. (UPS) illumination. In AES and XPS fairly large areas (up to 1 mm in diameter) are analyzed. In scanning Auger microscopy (SAM) a finely focused electron beam is used and a lateral resolution of less than 100 nm can be achieved. Finally, there is ISS or ion scattering spectroscopy (45-48). In this analysis technique the energy distribution of low energy ions scattered from the first atomic layer of the sample is measured.

Whereas with above methods sputter etching is only one of several possible ways to uncover new layers below the sample surface, the following analytical techniques rely on the sputter process as an integral part since the sputtered species itself is subject to analysis. Sputtered ions are measured by mass spectrometry in SIMS (secondary ion mass spectrometry) (49-52), while sputtered neutrals are postionized and analyzed in SNMS (secondary neutral mass spectrometry) (53-55) or in GDMS (glow discharge mass spectrometry) (56-58). A second approach is to measure the light emitted by the sputtered atoms or ions. Analysis of impact radiation is called SCANIIR (surface composition by analysis of neutral and ion impact radiation) (59, 60), but also SIPS (sputter induced photon spectroscopy) (61) or ORSP (optical radiation of sputtered particles) (62). GDOS stands for glow discharge optical spectroscopy (63-65). For completeness also to be mentioned is IXE (ion induced x-ray emission) (66, 67).

This review is concerned with depth profiling by ion sputtering. Since its first introduction less than two decades ago (68, 69), sputter sectioning has become the most widely used method for depth profiling. The main reasons for this development are simplicity and speed. A further major advantage, which has been recognized since the first combination of sputter etching with AES analysis (70, 71), is the fact that microsectioning and analysis can be performed in the same high vacuum environment, thus minimizing atmospheric effects.

In spite of its great successes there are some serious complications inherent to the method of sputter depth profiling. One has to be aware of the fact that sputtering, being just one manifestation of a complex physical process which affects not only the very surface of the sample, introduces a variety of important changes in the sample being analyzed. Although the problems associated with sputter etching have been repeatedly dealt with (72-75), a generally uncritical attitude has prevailed in many applications. On the other side, only a few years ago, Smith (76) arrived at the following judgment: "Ion-sputter AES profiles are entirely misleading if interpreted as quantitative concentration profiles, but are very informative as to qualitative analysis and when properly understood reveal physical and chemical non-isotropy within the films." Fortunately, it can be said that matters are much better today, but it also has to be emphasized that problems of quantification and the presence of artifacts are intrinsic features of sputter profiling and have to be understood if quantitative measurements are desired. Only then the optimum information will be obtained from this powerful method.

A sizable number of reviews have been concerned with various aspects of surface analysis methods (72, 77-79), with sputter depth profiling in general (73, 74, 80-85) or with AES (14, 86, 87) and SIMS (75, 88, 131) depth profiling specifically. Other articles have dealt with applications to thin film and interface analysis (89, 90) or with the study of electronic materials by surface analysis techniques (2, 3). This paper tries to give a comprehensive review of the problems of sputter profiling of microelectronic structures from the present level of our understanding. The first part is devoted to a thorough discussion of the principles of sputter depth profiling. Special attention is paid to the various problems encountered during experimental measurements. The second part gives a survey of applications to the analysis of semiconductor materials and microelectronic devices. It focuses on the more recent literature in an attempt to give a representative overview of this rapidly expanding field.

Principles of Sputter Depth Profiling

Fundamental Concepts

What is measured in any sputter depth profile is a signal as a function of time. It is the task of any quantitative analysis method to convert this signal *vs.* time relationship into a concentration *vs.* depth relationship (81, 86, 91). The questions to be answered are if and how this conversion can be accomplished and what the limitations are on the precision of the measurement of concentration and depth.

Time into depth—The relationship between time t and depth z is given by

$$z = \int_0^t \dot{z}(\tau)d\tau$$

where $\dot{z}$ is the erosion rate. It is related to the sputter yield S by

$$\dot{z} = \frac{j_p \cdot S}{N \cdot e}$$

with j_p the primary current density and N the atomic number density. In the simplest case, for a sample with constant erosion rate, the determination of depth from $z = \dot{z} \cdot t$ is reduced to a measurement of $\dot{z}$. This can be accomplished by measuring the crater depth after prolonged sputtering of polished surfaces by optical interference or mechanical stylus techniques (92-94). Another approach is to sputter through a film of known thickness (95-97) or through a film containing a marker at known depth (98). A large number of experiments have been performed in order to measure the sputter yield of many different materials. The erosion rate is not only a function of projectile species, energy, and incident angle, but also depends strongly on the chemical composition of the target. Specifically for multielement compounds it is not possible to relate the total erosion rate of the sample in a simple manner to the erosion rates of the elemental constituents (72, 99-101).

In many samples, however, the erosion rate is not constant but varies with depth (81, 86, 97, 102-104). This is especially the case in heterogeneous structures. Figure 2 shows a depth profile through Ni/Cr multilayers of equal thickness. In this intensity *vs.* time plot the Cr layers appear thicker than the Ni layers, which is due to the erosion rate of Cr being smaller than that of Ni. This is also reflected in the distribution of nitrogen used for sputtering that is implanted into the sample. Its concentration is higher in the slower eroding Cr. What makes the depth measurement in such structures difficult is the fact that, because of beam induced mixing between different films, the erosion rate does not change abruptly at the interface between layers. Considerable effort has been devoted to the study of the depth profile shape obtained from a sharp interface (97, 102, 105) and to the question of what function would best be fitted to the changing erosion rate (86). The most accurate depth determination can be obtained if the varying $\dot{z}$ is measured during sputtering *in situ*. Kempf (106) has measured the depth of the crater bottom during analysis by laser interferometry, while another group of experimenters (97, 102, 104, 107) has used the emission of x-rays from a thin film to determine its varying thickness under the sputtering ion beam and, thus, measure $\dot{z}$.

Intensity into concentration—The conversion of intensity into elemental concentration is the subject of the quantification of the various surface analysis techniques (108). It is not within the scope of this paper to deal with this question and the reader is referred to the literature re-

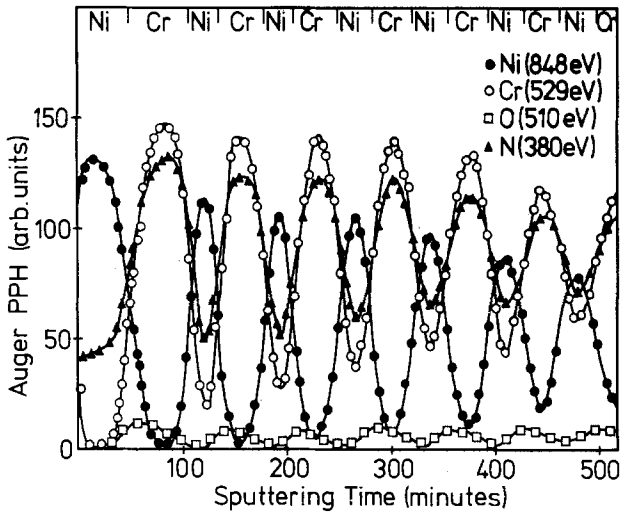

Fig. 2. AES sputter depth profile of an Ni/Cr multilayer sample. Each layer is 11.5 nm thick. Plotted are the peak to peak height amplitudes of Ni, Cr, O, and N Auger lines. Ion beam 1 keV N_2^+. From Ref. (103).

viewing the quantification of AES and XPS (86, 109, 110), SIMS (49, 111, 112), and ISS (113). The considerations, discussions, and examples in the rest of this paper are almost exclusively based on these four methods. Common to all of them is that the factor relating the signal intensity to the concentration of the measured element depends on this concentration itself as well as on the concentration of other elements present. This so-called matrix effect is most serious in SIMS analysis where the ionization probability strongly depends on sample composition (75, 114-117). This makes SIMS depth profiling best suited for homogeneous samples with low concentrations of the elements to be measured (50), but of much lesser value for the study of heterogeneous structures (95, 96). Matrix effects are less of a problem in AES and XPS that are, thus, better suited for the study of the interface between films of different composition, but even here one has to be aware that artifacts due to matrix effects can occur.

Distorting Effects

In the previous section the idealized assumption has been made that there are simple relationships between time and depth and between signal intensity and elemental concentration. In reality, there is a large number of factors that may contribute to the distortion of the "true" depth profile, affecting either the measurement of depth or the measurement of concentration. Table II shows a list of factors that can distort depth profiles in one way or another. It is the task of the skillful experimenter to minimize these effects and, if they cannot be eliminated completely, to correct for them in the analysis. The distortion of the depth scale generally results in profile broadening. If the resolution function of this broadening is known, the original profile can be obtained by deconvolution of the measured profile (81, 118-120).

1. Instrumental effects.—Edge effects.—To obtain good depth resolution one has to make sure that the signal comes from the flat portion of the crater bottom (121). A number of papers have been devoted to correction procedures for nonideal crater shapes (119, 122, 123). However, any measurement from a nonflat crater is accompanied by a loss of information since the signal contains contributions from different layers. Means to assure a uniform erosion include defocusing of the ion beam (124) or rastering of it over the sample surface (125). To exclude edge effects only the central portion of the crater is probed in AES or XPS analysis (83) [an exception is the already mentioned crater-edge profiling (17, 18)]. In SIMS or ISS analysis this can be achieved by electronic gating of the signal (46, 126-128) or by using an electrostatic lens system in SIMS instruments to image only the central part of the crater onto the entrance of the mass spectrometer (129, 130). How much depth resolution and background of a B-profile in Si are improved by a combination of measures is seen in Fig. 3. Since by

Table II. Factors affecting depth profiling by ion sputtering

I. Instrumental
- Time constancy of the ion beam
- Uniformity of ion beam
- Edge effects
- Ion beam composition: impurities
- Neutral component of beam
- Residual gas contamination: adsorption
- Redeposition of sputtered material: memory effect

II. Sample effects
- Multiple phases: preferential erosion
- Compounds, alloys: preferential sputtering, decomposition
- Polycrystalline samples: faceting
- Crystal defects, contamination: cone formation
- Layered structures: cone formation
- Surface roughness

III. Ion beam effects
- Preferential sputtering
- Atomic mixing
- Sputter-induced surface roughness
- Radiation-induced diffusion
- Implantation effects: effects on erosion rate, signal, dilation
- Ion beam heating effects
- Structural changes
- Chemical effects induced by sputtering: reduction, compound formation
- Charging effects
- Surface transport

IV. Effects depending on analysis method
- Information depth
- Backscattering in AES
- Matrix effects
- Chemical effects in SIMS
- Noise, detection limits, sample consumption
- Electron stimulated desorption
- Electron beam induced diffusion
- Interferences

minimizing all other factors depth resolutions of less than 1% can be achieved, flatness of the crater can be the limiting factor in practical analysis (131).

Beam impurities.—Neutrals and the unfocused component, which may be a considerable fraction of the total ion beam, give rise to the undesired halo effect in SIMS (121, 129, 132). Neutrals can be eliminated by use of a magnetic sector primary beam filter (133, 134) or by bending of the beam line (129, 135). The effect of both components is further reduced by ion imaging and/or electronic gating of the secondary signal. In some cases, however, neutrals are used for sputtering in order to reduce charging of insulating samples (136, 137). Mass analysis of the primary beam is also used to exclude other impurities that otherwise would be implanted into the sample. Only by such measures is it possible to obtain the large dynamic range enjoyed in modern SIMS instruments (135, 138).

Adsorption and redeposition.—An important consideration for sputter profiling is the cleanliness of the vacuum

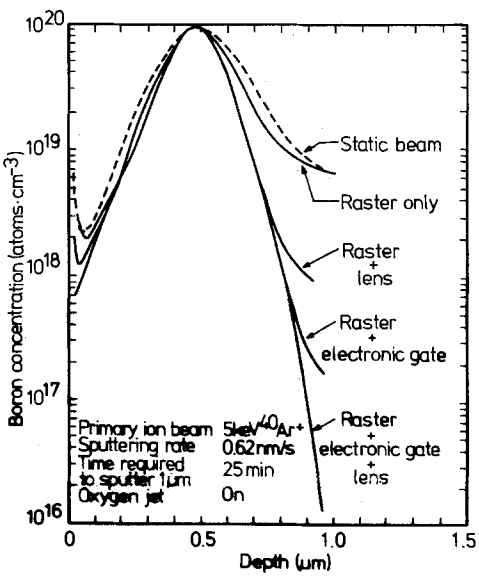

Fig. 3. SIMS depth profiles of 150 keV B implanted into Si demonstrating the improvements of depth resolution and background suppression obtained by a series of primary beam techniques and secondary ion optics. From Ref. (129).

environment during analysis. Adsorption of residual gas results in a background. If sputtering and analysis (by AES and XPS) are performed simultaneously, a steady state between adsorption and sputter removal is obtained (139). Mathieu and co-workers (140, 141) found that depth resolution in AES depth profiling is reduced if the background-gas adsorption exceeds the sputter removal rate. As a rule of thumb the gas pressure p (in Torr) should be

$$p << 10^{-5} j_p$$

if j_p is measured in mA/cm². High erosion rates (up to 1 nm/sec) or low pressure UHV systems are employed to satisfy this condition. Contaminants (mainly carbon compounds) in the vacuum system can also be deposited onto the sample surface by the analyzing electron beam. This has led in one case to the formation of carbides under the combined influence of ion and electron bombardment (142).

Adsorption of reactive background gas contaminants is a special problem in SIMS because of the strong chemical effect (116, 143). Adsorbed species are incorporated into subsurface layers of the sample either by diffusion (144) or by recoil implantation (145, 146) and can thus have an effect on the secondary ion yield. On the other hand, adsorption can result in an undesired background of atomic species like H, N, and O (147, 148) or, most importantly, of molecular species like hydrides and oxides (149, 150). The use of UHV SIMS systems with pressures as low as 10^{-10} Torr (150, 151) is one approach to minimize molecular interferences like SiH, Si_2O, and O_2 and thereby to reduce detection limits for P, As, and S. Alternatively, it is often desirable to control the chemistry of the sample surface during SIMS analysis by increasing the partial pressure of oxygen in the sample chamber in order to saturate the secondary ion signal (152).

Another source of background results from material sputtered from the crater edge or halo zone, as well as from other faces of the sample chamber, that is redeposited on the crater bottom (132, 153). This can be sputtered material deposited on the extraction lens system now resputtered by secondary ions or electrons ("memory effect"). Sputtering of areas outside the analyzed spot can yield a background also in other ways. Powell (154) reports that a background during AES depth profiling resulted from the $Al_{L_{2,3}MM}$ Auger transition excited by Ar bombardment of the Al sample tray.

2. Summary of remedies.—To minimize instrumental effects the erosion of the probed area should be kept as uniform as possible employing either an electronic aperture or ion imaging or both (129). Beam impurities and neutrals can be eliminated by beam filtering. UHV technology and cooling of components close to the sample reduce contaminants from the vacuum.

Sample effects.—The sputtering beam causes a variety of structural, compositional, chemical, and topographical changes of the sample surface, all of which can affect depth profiling measurements. The detailed nature of these changes depends on the sample composition and structure. In this section only topographical effects are considered which are called macroroughness in order to distinguish them from a roughness on an atomic scale resulting from the statistical nature of the sputter process.

An uneven erosion of the sample surface has several consequences for sputter depth profiling: (*i*) degradation of depth resolution; (*ii*) the sensitivity of analysis depends on surface topography (155-158); and (*iii*) the total erosion rate changes with changing surface topography (99, 159). There is a bizarre variety of surface forms produced by ion sputtering: steps, ridges, facets, pyramids, cones, and needles. A large number of experimental studies [see Ref. (72, 159-161)] as well as theoretical treatments have been devoted to this phenomenon. Depending on which sample is bombarded, different causes can produce these forms.

Multiple phases.—Different phases making up the sample will in general have different erosion rates. This means that a stationary state will be reached only at a sputtered depth which is a few times the grain size (99).

Polycrystalline samples.—Since the sputter yield depends on the crystal orientation (162, 163), sputtering of a polycrystalline surface leads to facets and similar features (99, 160). Channeling, the main reason for this orientational dependence of the erosion rate, can lead also to other effects: beam implantation depths are different for different crystal directions, saturation concentrations may vary from one crystal grain to the next. This can result in large differences in the secondary ion yield in SIMS analysis if a reactive species like oxygen is used for sputtering.

Single crystals.—Pronounced topographical features produced by ion sputtering can be also observed in single crystals. Small impurities with low sputter yield situated on the surface or imbedded in the sample cause cone formation (160, 161, 164-166). Cone formation is also frequently observed for the same reason at the interface between films of different composition (96, 167) if the breakthrough from one layer to the next is not uniform and the sputter rate of the two films is very different.

However, surface roughness develops even in pure single crystals without any contamination (99, 161, 168) as can be seen in Fig. 4 that shows an extensive pattern of pyramids produced by Ar sputtering of a single Cu crystal. The cause for the development of surface topography can be crystal defects that influence the sputter rate (162, 169). Hermanne (162) has observed an increase of the sputter yield from single crystals above "extensive defects" that result from the agglomeration of point defects created by the ion bombardment. The structural response of single crystals to irradiation with heavy ions varies considerably. The semiconductors Si, Ge, GaAs, and InP become amorphous (161, 170). The surfaces of these materials remain smooth or, at worst, show a slightly wavy structure (161, 171). Cones or needles are observed only due to contamination. The semiconductors GaP, InSb, CdS, and CdTe, on the other hand, retain their crystalline structure. The same is true for many metals (170). In these cases (*e.g.*, Cu in Fig. 4) crystallinity is the dominant factor for the development of surface topography; facets and cones are formed irrespective of the presence of contaminants (168).

The mechanism which produces the observed topographical features on surfaces with contaminants, grain boundaries, or crystal defects is the variation of the sputter rate with the angle of incidence (172-174). A whole series of theoretical models to predict surface topography under sputtering are based on this effect (175-177). Littmark and Hofer (159) consider angular variation and recapture of sputtered material, whereas Carter (178) includes thermal/and radiation-enhanced diffusion into his model.

Initial sample roughness.—Any original surface roughness of the sample is usually accentuated by ion bombardment and thus degrades depth resolution. A number of experimental studies on thin sandwich and multilayer films have shown how the depth resolution depends on the roughness of the substrate (118, 179, 180). This effect is strongly enhanced during depth profiling of porous structures like Al oxides (155, 181).

Multilayered films, interfaces.—Cones, needles, and ridges have been observed in a large number of cases during depth profiling analysis of heterogeneous layers (96, 103, 166, 167,

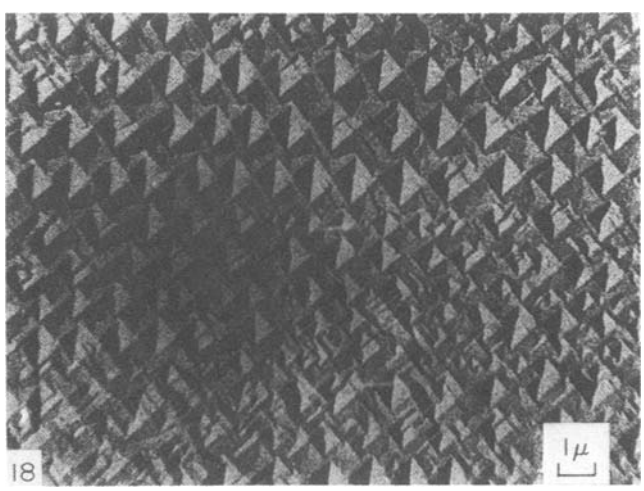

Fig. 4. Surface of a Cu <100> grain bombarded with 10^{18} Ar ions/cm² at energy of 5 keV. From Ref. (160).

182-184), because of nonuniform erosion and change of sputter rate. Since the analysis of such structures is one of the main applications of sputter profiling, the loss in depth resolution accompanying these topographical features poses a serious problem.

Remedies.—A number of precautions and measures can be taken to reduce surface roughness and thereby increase depth resolution. Rotating the sample bombarded by a beam not normally incident onto the sample surface leads to a more uniform erosion by averaging over different bombardment directions. For the same reason the use of two ion guns has led to improvements (181). In some cases reduction of surface roughness has been reported if the ion energy is decreased (185). The original sample surface should be as flat and smooth (180), but also as clean, as possible. Williams *et al.* (166), for example, could obtain a much better depth reolution for measuring the interface of $In_xGa_{1-x}As_yP_{1-y}$-InP heterojunctions after removing trace metals from the surface by chemical etching.

The use of oxygen or nitrogen for sputtering ("chemical sputtering") or the increase of the partial pressure of one of these gases in the sample chamber ("backfilling") have been shown to successfully decrease surface roughness on poly- and single crystals (169, 186-188). The reason is thought to be the formation of an amorphous oxide or nitride layer which eliminates sputter effects due to crystallinity. This technique has been especially beneficial in improving the depth resolution for profiling of the interface between metal layers with AES (103, 183, 184) or SIMS (96, 167, 189). In the most systematic study of chemical sputtering, Blattner *et al.* (183) showed that O is to be preferred over N which in turn produces much better results than Ar. That measurement conditions also play a role is shown by the fact that Hofer and Martin (96) observed an improved depth resolution when profiling V/Ti layers with N instead of Ar, while Hofmann *et al.* (103) report that results are very similar for these two gases.

3. Ion beam effects.—Distortions of depth profiles caused by the ion beam are the most important ones since they are intimately tied to the sputtering process itself. A large body of experimental and theoretical work has been devoted to the study of sputtering phenomena (174, 190-193). Experiments indicate that the sputter process in most materials is best described by the collision cascade formalism as first formulated by Sigmund (194). Since then most theoretical work has been based on this concept (195-197). However, in certain cases (*e.g.*, for the sputtering of many oxides and halides) the collision cascade model fails to account for observed effects (198-202) and has been replaced by a thermal spike model (203). Still, in essentially all practical applications of depth profiling to the analysis of microelectronic materials the collision model describes the effects most realistically (204).

For pure elements there is good agreement between theory and experiment (174, 205, 206). In Sigmund's theory the sputter yield S is given as function of projectile energy by

$$S(E) = f\left(\frac{M_2}{M_1}\right) s_n(E)/U_o$$

where f is a function of the projectile mass M_1 and target mass M_2, of $s_n(E)$, the nuclear stopping power of the incident ion, and of U_o, the surface binding energy of the target (heat of sublimation). An important quantity for the theory is the product $S(E)U_o$ which is proportional to the deposited energy distribution function at the target surface. Sigmund's theory strictly applies only to amorphous targets and does not take any lattice effects (channeling) into considerations.

The sputtering from multielement alloys and compounds is more complicated. The reason is "preferential sputtering," an effect which leads to a compositional change in a layer whose thickness roughly equals the penetration range of the bombarding ions. The "altered layer" is established by extensive "atomic mixing" in the collision cascade but also by radiation enhanced diffusion. Both preferential sputtering and atomic mixing have strong effects on depth profiling, the first by way of a change in surface composition, the second by the smearing of sharp concentration gradients. Both are closely connected by their common basic physical mechanism.

Preferential sputtering.—Preferential sputtering occurs when the constituents of a multielement target are sputtered in proportions that are different from their relative concentrations in the layer from which the sputtered particles originate. Alternatively to this definition that defines "preferential" with respect to the surface composition (207), some authors use the term with respect to the bulk composition (73). Preferential sputtering results in a change of surface composition until a stationary state is reached (208), in which the sputter rates of the components are proportional to their bulk concentrations ("stoichiometric sputtering"). For a binary compound or alloy A + B, the surface concentrations C_A^s and C_B^s in the stationary state are related to the bulk concentrations by

$$\frac{C_A^s}{C_B^s} = \frac{S_A\, C_A^b}{S_B\, C_B^b}$$

where S_A and S_B are the sputter yields of the elements. The effect of this compositional change on the analysis by a surface sensitive technique is different, depending on whether the sputtered particles or the surface composition are measured (Fig. 5). In the first case (*e.g.*, with SIMS), the signal from the fresh surface is modified by the sputter yield of the element in question, while the true bulk concentration is measured in the stationary state. The situation is exactly the opposite for methods like AES and XPS that measure the changed surface composition in the stationary state.

The study of preferential sputtering has been the subject of a large number of papers [see Ref. (72, 99-101)]. Information on which the component is enriched or depleted at the surface has been obtained for many binary and ternary targets [for a compilation of data see Ref. (72, 99)]. Methods for the study of the changed surface composition include AES (209, 210) and RBS analysis (205, 211-213). Whereas with AES only a limited amount of depth information can be obtained by using Auger lines with different energies and thus escape depths, RBS allows the study of the composition of the altered layer with depth, albeit with limited depth resolution. Several causes have been considered for explaining the observed changes of surface composition (72, 99, 207, 214): (*i*) mass difference of the constituents; (*ii*) sputter yield of the pure elements; (*iii*) binding energy; and (*iv*) vapor pressure. The relative importance of these factors depends on the sputter mechanism in question (101, 214). Within the linear cascade regime (196) of the collision theory of sputtering for compound targets (215), several reasons lead one to expect enrichment of the heavier component: (*i*) more energy is imparted to the lighter atoms enabling them to leave the surface preferentially (216, 217); (*ii*) lighter atoms have a larger range and can be ejected from deeper layers in the sample as compared to heavy atoms (218); and (*iii*) lighter atoms are subject to a higher degree of direct knock-on ("recoil implantation") than heavy ones (89, 214, 219, 220). This last effect does not result in an enrichment in the stationary state, but leads to a transient when sputtering is started from a fresh surface.

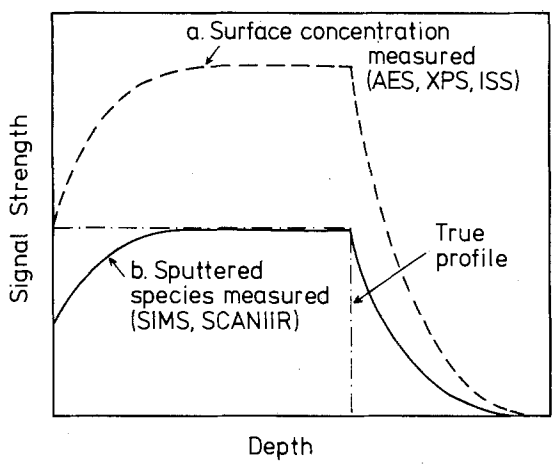

Fig. 5. Sputter depth profiles of a square shape true profile for a component which is surface enriched by preferential sputtering obtained (a) by a technique which measures sample surface concentration, (b) by a technique which measures the sputtered species.

Most observations agree with these considerations and show heavy element enrichments. However, there are a number of exceptions to this rule. For example, in the binary alloys Cu-Ni and Pd-Ni the lighter Ni is enriched, as is Pd in Au-Pd (221). In all these cases, the enriched component has the lower sputter yield as an element. Betz (100) concluded that changes in surface composition of alloys are governed by the binding energy as long as the recoil energy densities U_0S of the two components are very similar: the component with the higher sputter yield as an element is sputtered preferentially. For compounds with very different recoil densities of the components the mass effect dominates and the surface becomes enriched in the heavy component, as required by the linear cascade collision model.

In thermal sputtering bonding effects are dominant (101). A special case is the sputtering of oxides and halides (72, 99, 201) which results generally in a deficiency of the volatile component. In the case of oxides that would fit the mass effect concept although also here there are some notable exceptions like Cr_2O_3 and Ti_2O_3 (222). It must be concluded that there is still no detailed understanding of preferential sputtering in the sense that one would be able to predict the direction and magnitude of surface enrichments for a multielement system. The experimenter thus has to rely on calibration measurements performed on standards as the basis for any quantitative correction procedure of the preferential sputter effect.

Preferential sputtering not only changes the surface composition but establishing this composition takes time leading to a transient during depth profiling. An example is seen in Fig. 6 that shows the changes in the Pd and Ag AES signals obtained from an Ag-Pd alloy when the Xe bombardment energy is changed from 0.5 to 5 keV and back again. These changes are explained by assuming an altered layer whose thickness is different for different energies. During sputtering at lower energy, Pd is enriched in a thin layer. After switching to 5 keV energy, atomic mixing takes place throughout a deeper zone that initially dilutes Pd at the surface (decrease of Pd signal). In the steady state the whole thicker layer is enriched in Pd, the enrichment factor being larger at 5 keV than at 0.5 keV. After changing back from 5 to 0.5 keV Xe, the surface is enriched from an already enriched layer leading to an initial rise until the altered layer formed under 5 keV bombardment is sputtered away and the original state is reestablished.

The depth of the transient in binary compounds is generally comparable to the thickness of the altered layer (72), but depends also on the ratio of the sputter yields S_A/S_B and concentrations C_A/C_B (223, 224). Exceptions are samples in which phase changes occur or compounds with a low concentration of a species with low effective sputter yield. Then sputtering has to proceed to a depth corresponding to many altered layers before a steady state is reached (99). The same is true if thermal and/or radiation-enhanced diffusion plays a role (225-227).

There have been various attempts to model the evolution of the surface composition of a multielement target under ion sputtering and to develop correction methods for depth profiling analysis. The first step of this undertaking was to include a "sputter correction factor" in AES analysis (86, 228). Early kinetic models (229, 230) have considered the change of only the topmost atomic layer, neglecting any depth effects. Also Werner (231) took only changes in the composition of the very surface into account in a sequential layer removal model for the transient.

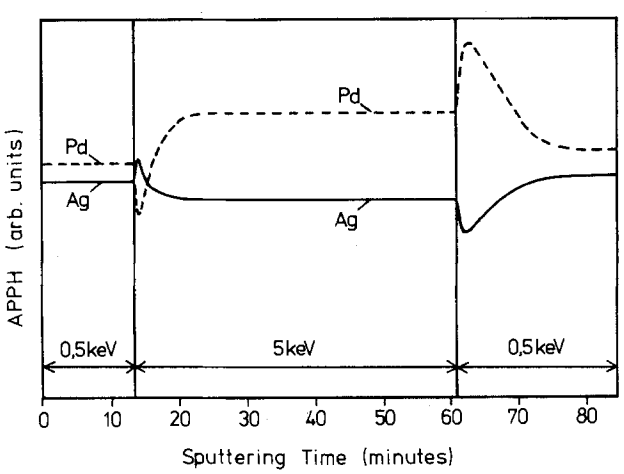

Fig. 6. Changes in the Auger peak to peak heights of Pd (326/330 eV) and Ag(351/356 eV) with time in an 80 a/o Ag-Pd alloy when the energy of the bombarding Xe beam is changed. From Ref. (209).

All kinetic surface evolution models are based on the mass balance in the altered layer (211, 224, 227, 232). Included are the mass fluxes of material removed by sputtering and replenished from the bulk as surface and altered layer recede into the sample. For a binary alloy A + B the change of the surface concentration of one component (A) is described by the equation

$$\frac{d}{dt}(NdC_A^s) = j_p[S_AC_A^sC_A^b + S_B(1 - C_A)C_A - S_AC_A]$$

Here C_A^s and C_A^b are as before the atomic concentrations of component A in the altered layer and the bulk, N is the average atomic number density of the compound, N_A the density for pure element A, d is the thickness of the altered layer, and S_A and S_B are the sputter yields of elements A and B in the alloy. The three terms on the right represent the replacement of a sputtered atom A by another atom A, the replacement of a sputtered atom B by atom A, and the loss of A by sputtering. A critical evaluation of this approach can be found in Ref. (224).

A series of phenomenological models have assumed a finite thickness of the altered layer and have included it as a parameter into the theory (217, 223, 232, 233). Later models have added information about the thickness of the altered layer by considering specific mechanisms for its generation. Liau *et al.* (211) and Haff (218) based their models on collisional mixing. Other workers included diffusion, either radiation-enhanced or not, into models for surface changes (227, 234-236). There is experimental evidence that at least radiation-enhanced diffusion contributes to changes of the surface composition (237, 238).

Sigmund (219) considered only recoil implantation by direct knock-on for modeling the concentration transient under ion sputtering. How important the altered layer is for the preferential sputtering transient depends on the efficiency of the mechanism (cascade mixing, diffusion) establishing the layer. If this efficiency is low, then surface preferential sputtering and recoil implantation are the dominant factors for depth profiling transients. Sigmund's model predicts an initial surface enrichment of the heavy component while later a layer enriched in the light component is encountered. In contrast to preferential sputtering the sputtered species is never enriched in the light component.

Besides the effect of preferential sputtering on the concentration measurement there is also an effect on the instantaneous erosion rate of the sample surface which, strictly speaking, has to be taken into account during conversion of time into depth but is usually ignored. Existing transient models apply only to the simplest cases (224), and it is not always possible to use them for practical cases like, *e.g.*, profiling through an interface between different layers. One then would have to interpolate between simple sputter correction factor regimes (steady-state regimes). However, the understanding of the preferential sputtering effect helps in averting wrong interpretations of measured depth profiles. The use of low ion energy and a large angle of incidence minimizes the depth of the transient in the profile.

Collisional mixing.—Besides the important role ion beam induced mixing plays for preferential sputtering, it leads to another distorting effect during depth profiling by changing the depth distribution of the element of interest below the sample surface before it is measured. First the effect of this relocation caused by collisional mixing is considered. Various authors (89, 239, 240) distinguish between "cascade mixing" and "recoil mixing" by direct knock-on. Both lead to a broadening as well as a shift of measured distributions during depth profiling. Figure 7 shows SIMS depth profiles of a 5 nm thick P-rich layer imbedded below the surface of a Ta_2O_5 film, obtained with different ion energies. These profiles display various features characteristic of

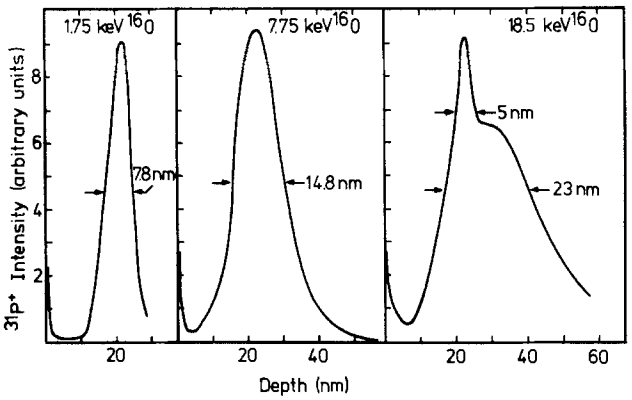

Fig. 7. SIMS phosphorus depth profiles in a Ta_2O_5 film containing a 5 nm thick ^{31}P-rich layer imbedded 23 nm below the surface. The profiles were obtained with ^{16}O sputtering beams of varying energy at normal incidence. From Ref. (121).

collisional mixing: asymmetric broadening, energy dependence of broadening, distinction between cascade and knock-on mixing (at 18.5 keV beam energy), and gradual fall-off of the P-concentration.

Experimental studies of the altered layer have in many cases been restricted to indirect effects. To be mentioned are measurements of buried layers (121, 241) and implantation profiles (242, 243). The most widely used approach has been to measure the broadening of a sharp interface between layers of different composition (102, 244-248). A more direct method is to study the formation of the altered layer and to measure its thickness by RBS (207, 211-213, 217, 249). These experiments have established that the formation of the altered layer is in most cases very efficient, which means that the surface material is thoroughly mixed before much of it has been sputtered. This is not surprising since at energies typical for depth profiling many atoms are moved in the collision cascade for each sputtered atom. The mixing efficiency ratio F (number of displaced atoms per sputtered atom) depends besides the beam energy E on the ratio of surface binding energy U_0 to effective displacement energy for bulk atoms E_d (239)

$$F \propto EU_0/E_d$$

If the mixing efficiency is high, the thickness of the altered layer d is approximately equal to the projected ion range R_p (211, 249) and the broadening Δz of a sharp interface proportional to E (217). This, however, is not always observed in studies which measure Δz as function of beam energy (102, 244-247). If the formation of the altered layer is slow, sputter erosion of the surface limits its thickness to less than the ion range. A simple model predicts $\Delta z \propto \sqrt{E}$ in this case (239). The thickness d depends on the relative importance of mixing and sputtering and is approximately $D/\dot{z}$ (211), where D is the diffusion constant that can be used to describe the mixing process and $\dot{z}$ the surface erosion rate. Experiments at low total ion fluences (212) show that it is valid to describe the collision cascade mixing mechanism by such a "diffusive picture."

Differences in the efficiency of ion mixing for elements of such similar mass as Hf and Pt (237) are evidence that collisional mixing is not always solely responsible for the formation of the altered layer. Radiation-induced diffusion can be more important in some cases (212). The thickness of the altered layer can be measured by RBS only if it is of the order of several tens of nanometers. The measurement of the thickness of thinner layers (down to 1 nm) can be accomplished by depth profiling of a film of known thickness on a substrate and recording the moment when the front of the altered layer reaches the interface (131, 250).

Various theoretical approaches have been taken to predict the broadening effects of collisional mixing during depth profiling. Hofmann (81) uses a simple phenomenological model combining broadening with forward displacement to calculate the expected profile shape of a thin single sandwich layer ("tracer") in a foreign matrix. It has been pointed out that peak shifts of impurity distributions due to collisional mixing can occur in either direction (251, 252). Of a more fundamental nature are the models of a number of authors who treat the movement of atoms in the collision cascade as a diffusion-type random walk problem (218, 239, 246, 253, 254). The energy of the bombarding ion is assumed to be shared among the atoms of the cascade, each of which receives the displacement energy E_d. It follows then that the broadening Δz of a sharp feature is

$$\Delta z \approx \sqrt{4Dt} \approx R\sqrt{\frac{E}{S \cdot E_d}}$$

where R, the range of the cascade recoils, is of the order of the distance between nearest neighbors.

The analytical cascade theory (transport theory) is used by other authors to model collisional mixing (240, 251, 255, 256). An asymmetric broadening of a sharp step is obtained even if only the isotropic part of the collision cascade is taken into account (240, 255). This fact is due to the inward motion of the cascade because of the sputter erosion of the surface. A thin tracer buried below the surface experiences a shift and broadening. A tracer at the surface yields an exponentially decaying depth profile (251) which is observed experimentally (248) (see Fig. 14). More sophisticated models include anisotropic cascade mixing (251, 256) and the effect of the implanted primaries (251), but these additions lead to only small modifications of the results.

Cascade mixing dominates over primary recoil implantation for heavy impurities in light matrices whereas the latter mechanism plays a role for light impurities in heavy targets bombarded with light projectiles (239, 256). Phosphorus in Ta_2O_5 under O bombardment is such a case (Fig. 7). Recoil implantation is included besides cascade mixing in a series of models (240, 251, 256) or is assumed to be alone responsible for the redistribution of atoms (219, 220, 257-259).

Recoil implantation has found special attention because it plays an important role for the redistribution of implanted ions by subsequent irradiation (243, 260-262) or for the redistribution of atoms from thin surface films into the substrate during implantation through these films (257, 263). Studied was the recoil implantation of O into Si during implantation of P, As, or Kr through SiO_2 layers (264-268) and of N onto Si during implantation through Si_3N_4 (262, 269).

Monte Carlo calculations by computer have also been used to predict the broadening of depth profiles by collisional mixing (270-272). Specifically treated was the case of a B-layer in Si and its broadening as a function of beam energy and angle of incidence.

Collisional cascade mixing seems to dominate in most practical applications, especially in cases where low concentrations of impurities or thin layers are concerned (212, 254). Given this situation, the effect of atomic mixing is reduced by all measures that minimize the thickness of the altered layer. As far as this thickness is determined by the primary ion range, this entails: use of low ion energy, large angle of incidence, high ion mass (*e.g.*, Cs), or molecular ions. Since the sputter rate decreases with decreasing bombarding energy, there is a practical lower limit to the ion energy. Still, an altered layer thickness of less than 1 nm can be achieved in practical depth profiling (131).

Collisional mixing has not been considered a drawback in all cases, but has been used to an advantage in the "cascade dilution technique" (273). In this method mixing serves to eliminate matrix effects by reducing relevant concentrations during SIMS measurement of impurities like H, C, and F in deeply buried interfaces.

Radiation-enhanced diffusion.—In many cases it is impossible to distinguish experimentally between the relative contributions of diffusion and collisional mixing. A variety of beam-induced mechanisms can contribute to bulk diffusion (252, 274-276). The most important one is the production of mobile defects, mainly vacancies and interstitials, and their thermally activated migration. Temperature effects (212, 238, 252) or chemical effects (237) have been observed in atomic mixing, indicating the presence of diffusive processes. Besides defects, ion-induced compressive stress gradients can lead to diffusion (277) that can also occur along extended defects (252). The creation of defects also affects the migration of the implanted beam ions or can give rise to diffusion of adsorbed gas from the surface into the sample (144).

In addition to bulk diffusion that worsens depth resolution during profiling, ion bombardment also increases surface diffusion. The latter tends to smooth out surface roughness (178, 278), thus improving depth resolution. Since all diffusive processes are time-dependent, their effect depends on the rate at which the surface is eroded. This leads to beam current density effects (278).

Sputter-induced surface roughness.—This surface roughness originates from the statistical nature of the sputter removal process. Benninghoven (279) calculated the depth broadening caused by this "microroughness" by assuming uncorrelated sputtering of surface atoms in his "sequential layer sputtering" (SLS) model (90). The predicted broadening Δz has a square root dependence on the sputtered depth z

$$\Delta z = 2(az)^{1/2}$$

where a is the thickness of a monolayer. A number of early measurements of sputter broadening seemed to agree with this model (83, 280). Hofmann (281) presented a series of experimental examples in support of the claim that the SLS term dominated Δz.

In time, however, various arguments arose against the SLS model. The assumption of uncorrelated sputtering was criticized as being unrealistic (282), and it was pointed out that because of beam implantation effects the sputtered surface cannot be considered to be undisturbed (283). Wittmaack and Schulz (282) compiled evidence against the model by showing that depth resolutions achieved by sputter depth profiling were much better than the limit set by the SLS theory. A collection of a large number of depth resolution measurements (284) supports this argument. It was suggested to consider differential sputter probabilities and to include surface and bulk diffusion to make the model more realistic (282).

These findings prompted a series of modifications. The inclusion of conditional probabilities (285) yields

$$\Delta z \propto z^{1/2}(1 + S)^{1/2}$$

which, because of the energy dependence of the sputter yield S for small energies, leads to a depth resolution that depends on the primary beam energy. Another treatment is based on the observation that the sputter yield of an individual atom is not site independent. The sputter probability is assumed to be inversely proportional to the surface bonding which results in a constant depth resolution Δz of the order of 1-2 nm (286). A third attempt to improve the SLS model involves the inclusion of surface transport processes (178, 278). This addition results in a decrease of Δz whose value now depends on the ratio of the sputter erosion rate $\dot{z}$ to the surface transport velocity. For the case in which the second quantity dominates, a constant Δz is obtained also in this model.

Another mechanism leading to surface roughness has been considered by Sigmund (287), namely, the local difference in the sputter yield due to the nonuniform energy deposition by an ion in the presence of surface features of dimensions of the deposition zone.

Beam implantation effects.—If sputter profiling starts from a fresh surface, implantation of the bombarding species results in a buildup of its concentration until an equilibrium is reached between implantation and sputtering (88, 144, 283, 288). The change of the implanted concentration during the preequilibrium phase has a series of consequences on depth profiling measurements, leading to transients at the surface or at interfaces between films of different composition. A change of the sputter rate with total ion dose has been observed in various studies (97, 205, 289-291). Figure 8 shows the variation of the sputter yield of Si under Ar bombardment. Displayed also is the total implanted Ar concentration and the Ar surface concentration. Lowering of the average binding energy (292, 293) is considered to be the most likely cause for the observed dose effect.

Dilution of substrate atoms and lattice dilation due to beam implantation also influence depth profiles (89). Chou and Shaffer (224) have included ion impregnation effects in their phenomenological model of preferential sputtering for SIMS and AES depth profiling. Because of the strong matrix effect (116, 117) the variation of the implanted beam concentration can have especially drastic consequences in SIMS analysis. If a reactive species like O or Cs is used for sputtering, the gradual increase of the O or Cs concentration leads to a change in the secondary ion yield and thus to a transient even in homogeneous samples (88, 121, 294, 295). This can also be the case with backfilling (144). Transients in SIMS profiles due to implantation concentration effects are common for interfaces (296) since the implanted beam concentration depends on the sputter yield which generally changes from one layer to the next.

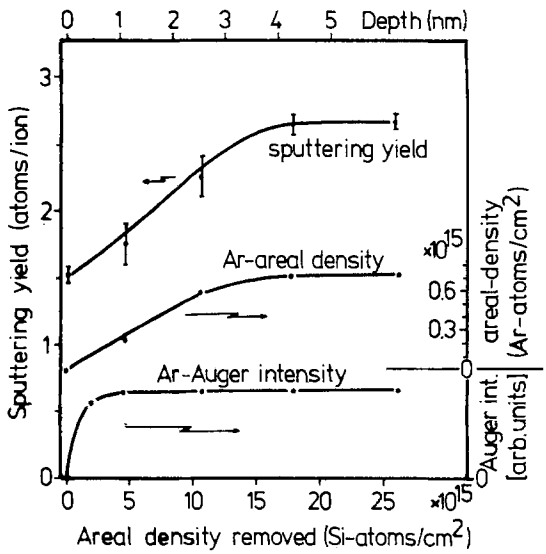

Fig. 8. Variation of the Si sputter yield, the Ar areal density, and Ar Auger intensity during bombardment of amorphous Si by 3 keV Ar^+ as function of amount of removed material. From Ref. (97).

Ion beam heating.—Heating can contribute to changes in the sputter rate (102, 202, 203) in materials where sputtering is governed by a thermal spike mechanism or thermal evaporation of decomposed target material. Heating can also increase diffusion (252) but causes usually only small effects for ion bombardment and poses a much more serious problem in AES analysis.

Structural changes.—Ion bombardment can cause different structural changes in different samples. Many materials, especially metals, but also semiconductors, retain their crystalline structure (99, 160, 161). Common is the amorphization of originally crystalline samples for semiconductors as well as oxides and nonmetallic compounds (99, 161, 170). However, also the opposite transformation is observed in several materials (170). For practical depth profiling structural changes are mostly important as far as they affect the development of surface roughness.

Chemical effects.—XPS and AES are methods that allow the experimenter to obtain information on the chemical state of the analyzed sample via the energy shifts of the emitted electrons (297-299). Chemical information can also be obtained by ISS (300), although to a much lesser extent. Chemical reactions are one of the results of ion bombardment (170, 301, 303). As a consequence, the chemical information obtained from the sputtered surface by AES or XPS analysis during depth profiling does not necessarily always reflect the chemical state of the sample interior before it is exposed by sputtering.

Ion bombardment can induce the formation of compounds from unmixed layers (303), ranging from intermetallic compounds like $AlPd_2$ to metal-semiconductor eutectic systems like Au-Ge (304). Silicide formation by ion beams has been studied most thoroughly (211, 237, 305-307) because of the importance of silicides for the metallization schemes of integrated circuits (308). Ion beam sputtering by Ar or Kr leads to reduction at the sample surface as has been documented extensively (72, 170). The resulting effect has been observed during "chemical depth profiling" in many instances. Metal oxides are reduced to lower oxides or metal, *e.g.*, in Ti-oxide films (142, 309-311) TiO_2 is reduced to Ti_2O_3. Reduction is also observed in oxides of GaAs: As_2O_5 changes to As_2O_3 and As_2O_3 to As (312, 313) under the influence of the Ar beam.

Besides energy shifts, changes in the chemical state lead also to changes of the line shape of XPS and AES spectra (314, 315). Because of this effect the customarily used peak to peak amplitude of the first derivative of AES spectra is not a reliable measure of the elemental concentration. The use of peak heights is preferable, but the best approach is to measure the total Auger current (area under the peak). This can be achieved by digital integration but also by a tailored modulation technique (TMT) (316, 317).

Charging effects.—Charging of the sample surface of insulators due to the ion beam can have several detrimental consequences for the analysis during depth profiling. During AES or XPS analysis in combination with sputtering, charging leads to energy shifts of the emitted electrons, in SIMS to a shift and a broadening of the energy distribution of secondary ions that results in a change of overall transmission (318). If charging is uniform over the irradiated area, energy shifts can be compensated for by biasing the sample potential (319, 320). Charging also causes electromigration of mobile ion species (321). A common problem is the migration of alkalis in SiO_2 films (319, 322, 323).

A variety of remedial measures have been tried to reduce surface charging. Since the effect depends crucially on the emission of secondary electrons, negative ion bombardment has been used successfully in SIMS (324), often in combination with a conducting grid (321), diaphragm (325-328), or metal coating (114). The use of a neutral beam has already been discussed (136, 137). In many cases an electron flood gun is used to control surface charging during depth profiling by positive ion sputtering (318, 329-332). By carefully matching the ion and electron current density it is often possible to eliminate charging effects. Figure 9 shows an example where the electromigration of Na implanted into an SiO_2 film on Si could be avoided with the help of charge neutralization by electron flooding.

Surface transport.—Besides transport processes induced by ion bombardment like collisional mixing and radiation-enhanced diffusion there are other processes which are not always caused by the ion beam directly but which, in combination with sputtering, can give rise to distortions and artifacts. Equilibrium segregation can lead to effects very similar to preferential sputtering. Because of segregation, in many alloys the surface composition in thermal equilibrium differs from the bulk composition (333, 334). Sputtering changes this composition and a new dynamic equilibrium between preferential sputtering and surface segregation is established (335-338) that depends on the ratio of sputter rate and segregation rate, the second one being a function of the sample temperature. Any change in this equilibrium leads to a change of surface concentrations and the corresponding signals during analysis. A drastic case is seen in Fig. 10 which shows the changes in the AES signals from an Ag-Cu alloy when the sputtering Ar beam is turned off and on again (337). The relative increase of the Ag signal during absence of sputtering is inversely proportional to the Ag bulk concentration, which implies a coverage of the surface by about 1-2 atomic layers of Ag independent of the bulk composition. In many cases surface enrichments due to equilibrium segregation are opposite those caused by preferential sputtering (339, 340). However, it has been pointed out that with steady-state surface concentration measurements (*e.g.*, AES) it is impossible to distinguish between surface segregation and preferential sputtering (99).

Defects produced by ion bombardment can lead to radiation-enhanced segregation (341, 342). The redistribution of solutes is driven by the flow of point defects toward sinks, away from the irradiation regions with high defect production rates. Lam *et al.* (343-345) included both preferential sputtering and radiation-induced segregation (RIS) into a model for the change of surface composition during sputtering of dilute binary alloys.

The role of surface diffusion on the improvement of depth resolution has been discussed previously. An example of how surface diffusion of a component adsorbed from the vacuum can affect surface analysis is shown in Fig. 11. The surface of pure Si was analyzed in a CAMECA IMS 3F SIMS instrument with ion beams rastered over different areas at constant beam current. An area much larger than $100 \times 100\ \mu m$ had been presputtered in order to exclude surface contamination effects. The measured species SiH, K, and C all derive from adsorption from the vacuum. In case of K, surface migration is seen in addition. Whereas the C^+ and SiH^+ signals experience a sudden decrease after a reduction of the ion beam area and remain low, the K^+ signal originally decreases but rises again to the original level.

Summary of remedies.—Low energy, large angle of incidence, and high mass of the bombarding ions minimize atomic mixing effects, *i.e.*, reduce broadening of concentration gradients and the depth of the preferential sputtering transient. Negative ions, neutral beams, and electron flooding are used to control sample charging. A high sputter rate limits rate-dependent effects like segregation and

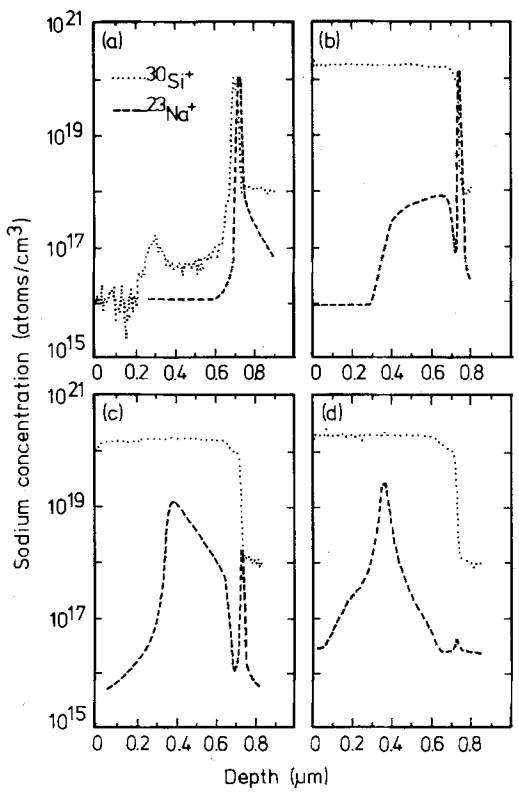

Fig. 9. The effect of charge neutralization by electron flooding on the SIMS depth profile of Na implanted at 150 keV into SiO_2/Si (total dose 1.5×10^{14} atoms/cm^2). (a) No charge neutralization: 98% of Na pushed to SiO_2/Si interface, (b) 500 eV electrons: 89% of Na at SiO_2/Si, (c) 1000 eV electrons: 1% Na at SiO_2/Si, (d) 2000 eV electrons: 0.06% Na at SiO_2/Si interface. Notice that the $^{30}Si^+$-signal is already normal in cases (b) and (c). From Ref. (329).

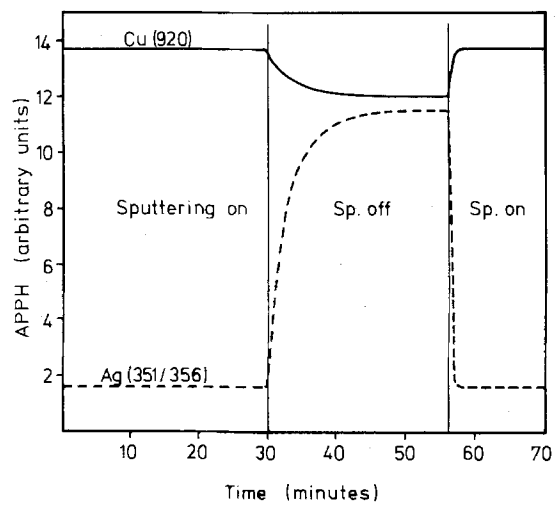

Fig. 10. Changes of the Ag and Cu Auger peak heights for a 5 a/o Ag-95 a/o Cu sample due to the effects of sputtering and surface segregation. From Ref. (337).

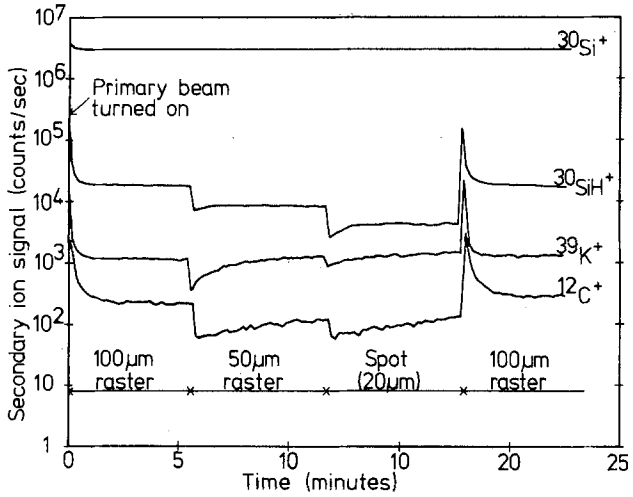

Fig. 11. Changes of the secondary ion signals of vacuum derived components (C, SiH, K) from a pure Si sample when the size of the primary beam raster area is changed. Primary beam 15 nA O_2^+ at 8 keV energy.

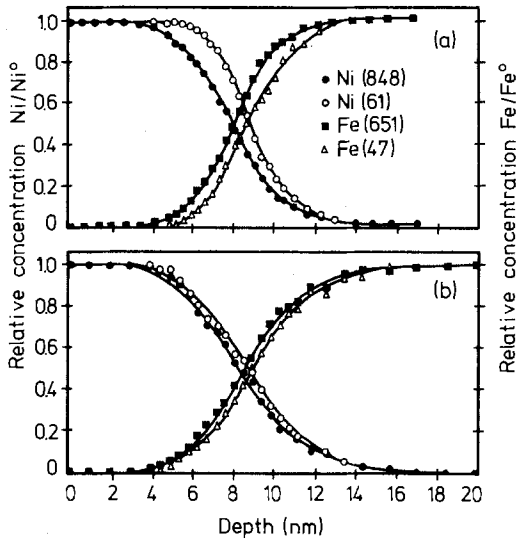

Fig. 12. AES sputter depth profiles of an 8 nm thick Ni film on Fe substrate obtained by using different Auger peaks. The bombarding Ar^+ energies were 0.5 keV in case (a) and 1.5 keV in case (b). From Ref. (244).

surface transport whereby the latter effect might be welcome to reduce sputter-induced surface roughness.

Effects Depending on Analysis Method.—Information depth.—One fundamental limit to the depth resolution is given by the depth from which the signal originates. This depth varies from technique to technique. In ISS analysis ions are scattered only from the top monolayer of the sample (45); in this respect the method achieves the maximally possible intrinsic depth resolution. In SIMS secondary ions are emitted mostly from the first 3-4 atomic layers of the surface (51, 194, 251, 270). This depth depends only weakly on the ion energy. Since other broadening effects are usually dominant, this limit imposed onto the depth resolution is not of practical importance.

In AES and XPS λ, the escape depth of the electrons, depends on their energy and varies from less than 1 nm at ~30-50 eV to 3-5 nm at higher energies and more than 30 nm at very low (~1 eV) energies (346-348). The signal at the surface is composed of contributions from layers at different depth (38, 349)

$$I_{Ai} = f \int_0^\infty C_A(z) \exp(-z/\lambda_{Ai}) dz$$

Here I_{Ai} is the Auger or photoelectron current, respectively, for a given line i of element A and C_A is the elemental concentration as a function of depth z. The factor f contains all other parameters like instrumental transmission, excitation cross section, and electron current (photon flux). It is most conveniently determined from measurements on pure elemental standards. The concentration depth profile $C_A(z)$ is obtained by deconvolution of the intensity depth profile $I_A(z)$. In first order this deconvolution is given by the expression (107, 349, 350)

$$C_A(z) = \frac{1}{f}\left[\frac{I_{Ai}(z)}{\lambda_{Ai}} - \left(\frac{dI_{Ai}}{dz}\right)_z\right]$$

The finite escape depth λ causes a broadening and a shift to lesser depths of the true profile (14, 97, 102). Figure 12 shows AES depth profiles of an Ni/Fe interface obtained from Auger lines of different electron energies. Besides showing the λ-effect, the figure also demonstrates the broadening effect of collisional mixing at higher beam energies. At ion energies of more than 2 keV the λ-effect is already dominated by atomic mixing. For a sharp interface the shift amounts to 0.7λ and the broadening to 1.6λ (14), the form of the profile is an exponential function (82). Some authors (97) point out that the use of high energy lines with larger corresponding escape depths λ is an advantage in locating the position of the interface. This is because the interface can be "observed" over a larger depth range and the exponential intensity function be fitted more reliably. A practical example of the λ-effect is the AES depth profiling of MOS structures where, without correction, the O signal was found to depend on the oxide thickness (350).

Backscattering in AES.—In the above expression for I_{Ai} the excitation flux density was assumed to be independent of depth. This assumption is usually satisfied. However, because of backscattering, the exciting electron flux density may depend on the composition of the sample well below the electron escape depth (351, 352), especially if substrate and overlayer are very different in atomic number Z (353). The backscattering effect is taken into account by introduction of a backscattering correction factor $1 + r_B$ which is included into the expression for I_{Ai} (352, 354).

During depth profiling through layers of very different atomic mass, backscattering can lead to transients as well as to a loss of lateral resolution in SAM. An example of a transient due to backscattering is given in Fig. 13 that shows an AES depth profile through a Ta_2O_5/Ta interface. The profile shape can be well approximated by model calculations. This latter fact demonstrates the increasingly sophisticated quantification procedures for AES depth profiling. These procedures progressed in steps: (*i*) sensitivity factors (86, 228); (*ii*) preferential sputter correction factor (86, 228, 229); (*iii*) models for λ-effect (14, 85, 280, 349); and (*iv*) depth broadening models for preferential sputter transients and atomic mixing [see Ref. (227, 232, 251) and references cited in the relevant sections].

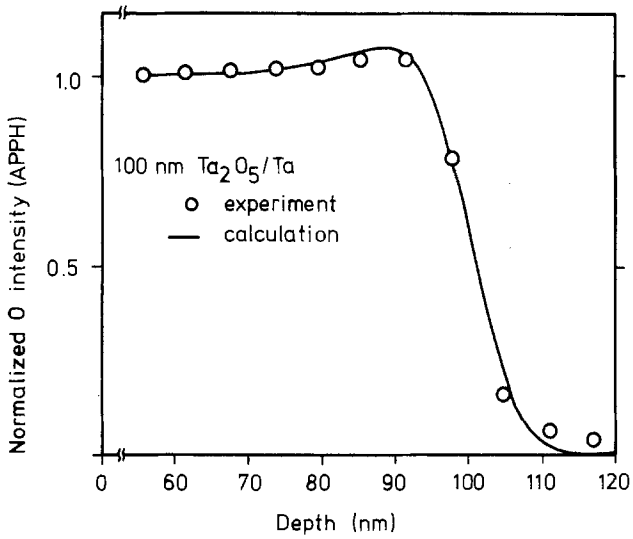

Fig. 13. AES sputter depth profile (5 kev Ar^+ ions) of a Ta_2O_5/Ta interface. Plotted is the O(510 eV) intensity vs. depth assumed to be proportional to sputter time. Calculated profile obtained with $\lambda = 1.29$ nm, $(1 + r_{Ta})/(1 + r_{Ta_2O_5}) = 1.3$, a sputter broadening $\Delta z = 7$ nm, and a step approximation by layers of 2.5 nm thickness. From Ref. (81).

Matrix effect.—All analysis methods are afflicted with matrix effects of different origins and magnitude. These can contribute to distortions of depth profiles in various ways when the composition of the sample changes, especially during profiling of interfaces. In AES analysis, backscattering is a particular example of the matrix effect. Also mention has already been made of peak shifts and line shape changes in AES and XPS at the transition between different layers (*e.g.*, SiO_2/Si) which can lead to artifacts if the proper corrections are not made (316, 317).

Matrix effects are particularly complicated in SIMS analysis where the ion yield of a given element depends, often strongly, on the chemical composition of the sample. Correction procedures for matrix effects are the central aim of quantification in SIMS analysis (112, 355). One traditionally distinguishes between matrix effects proper (355-357) and the "chemical effect" which is the enhancement of the secondary yield of positive or negative ions due to the presence of reactive species like N, O, or Cs, respectively (114, 358). Deline *et al.* (116, 117) have shown that a certain part of the first effect can be reduced to the second one because of the dependence of the concentration of the implanted primary beam species on the sputter erosion rate of the sample.

The affinity of different elements for oxygen can lead to strong chemical effects during depth profiling of heterogeneous layers. A series of SIMS depth profiles of metal films deposited on semiconductor substrates measured with oxygen bombardment shows very different features (Fig. 14). The profile of Mo on Si behaves more or less as expected, the initial rise reflects the effect of the increasing concentration of implanted O. The depth profile of Au on Si looks entirely different. First there is no effect due to the O implantation, the Au^+ signal is constant throughout the Au film. As soon as the Si substrate is reached, however, the Au^+ signal increases by more than an order of magnitude before it starts to decay. The Au profile displays the same features when O backfilling is used, the Au^+ increase being even more pronounced. This dramatic increase is due to the fact that O adheres strongly to Si but not to Au, so that the chemical effect of the increased O concentration is experienced only in the Si layer. A film of Au on GaAs, on the other hand, does not show any increase of the Au^+ signal at the interface reflecting the much smaller sticking coefficient of O to GaAs. The often-advocated control of surface chemistry by chemical sputtering or backfilling is in the case of Au not sufficient to avoid artifacts because of the chemical effect. A common feature of all profiles in Fig. 14 is the exponential falloff with depth of the metal signal inside the semiconductor substrate due to atomic mixing. The characteristic length of this decay depends on the relative sputter yields of the elements involved (see the section on preferential sputtering).

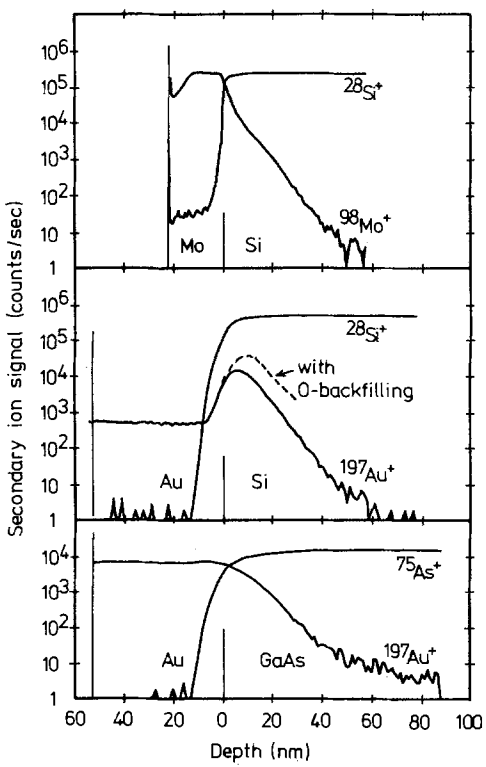

Fig. 14. SIMS depth profiles of Mo and Au layers on Si and GaAs substrates. Primary O_2^+ beam of 5.5 keV energy. (a) 40 nm Mo on Si, (b) 54 nm Au on Si, profiles with and without O backfilling, (c) 54 nm Au on GaAs.

These examples show that the many different possible artifacts plaguing SIMS depth profiling make this method often less than ideal for probing heterogeneous structures.

Sample consumption, detection limits.—If the sputtered atoms are analyzed, a certain sample volume must be consumed so that a statistically meaningful signal (*e.g.*, a certain number of counted ions) can be obtained. This requirement places a limitation on the depth resolution which is expressed by the relation (88, 133)

$$\Delta z = 1.6 \times 10^{-23} n/A\gamma TC$$

which gives the depth interval Δz from which a total number of n ions is detected if A is the analyzed area, γ the ionization yield, T the overall instrumental transmission, and C the concentration of the element in question. From this equation the detection limit $C_{min.}$ can be obtained. There exists an exclusive relationship between depth resolution, lateral resolution, and detection limit. To quote a detection limit is thus, strictly speaking, only meaningful in the context of a given set of instrumental and measurement conditions (3). For a given noise level of the detection system an increase of the erosion rate improves the S/N ratio, however, such a demand could run counter to the requirement for the reduction of the erosion rate in order to minimize beam heating effects. In some circumstances the best one can do is to find a good compromise.

Electron beam effects in AES.—One of the complications experienced in AES analysis is electron-stimulated desorption (ESD) (337). The electron beam leads to dissociation or decomposition and subsequent desorption of the sample, particularly of halides (359, 360) and of oxides (76, 142, 310, 361). Of interest is the electron-induced reduction effect in SiO_2 during the AES depth profiling of MOS structures (362-365). As can be seen in Fig. 15, the desorption of O and the production of reduced Si depends on the stoichiometry of the Si oxide. Electron beam irradiation can, on the other hand, enhance the oxidation of surfaces from the background gas (366, 367), or lead to the adsorption of other species like carbon (142). An increase of the ion sputter rate has been observed in the electron beam bombarded area (310, 363).

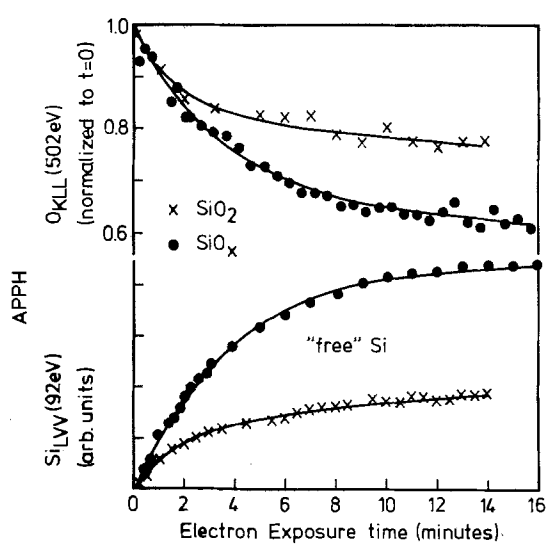

Fig. 15. The effect of electron stimulated desorption on the O_{KLL} and Si_{LVV} lines from SiO_2 and SiO_x (x = 1.4). The normalized peak to peak height amplitudes are plotted as a function of irradiation time for a beam flux larger than 2×10^{17} electrons/cm²/sec. The desorption effect increases with decreasing stoichiometry factor x. From Ref. (364).

Electron beam induced diffusion.—Electron beam induced diffusion is mainly related to beam heating (226, 368). Charging of insulators can be a serious problem especially if the secondary electron emission coefficient is smaller than one. This results in a buildup of negative charge which cannot be compensated (38).

Depth Resolution

It has been seen that there are many factors that result in a broadening of the original concentration profile during the measurement. All these different contributions can be combined into a single depth broadening (14, 83, 281, 369, 370)

$$\Delta z = \sqrt{\sum_i (\Delta z_i)^2}$$

Of interest is the magnitude and depth dependence of the different contributions Δz_i.

The broadening Δz is best determined by measuring the width of the depth profile of a sharp interface. There are different definitions of this width to be found in the literature (81, 244):

1. Δz(0.1-0.9), the depth for the signal to decrease from 90 to 10%.

2. Δz(0.16-0.84). This definition assumes the interface profile shape to be an error function (83, 85, 280, 371), for which $\Delta z(0.16\text{-}0.84) = 2\sigma$.

3. $\Delta z = 1/S$, the inverse maximum slope of the profile (244).

4. Δz(FWHM), the full width at half maximum of the resolution function $g(z - \zeta)$ which relates the measured profile $I(z)$ to the true one (118)

$$I(z) = \int_{-\infty}^{+\infty} C(\zeta) g(z - \zeta) d\zeta$$

For a step function of the concentration C the resolution function is the derivative of the interface profile, for an error function this derivative is Gaussian.

The assumption that the interface profile is best represented by an error function is not always a good one. Many measurements show the profile to be asymmetric (97, 102, 107). This asymmetry can be caused by different factors: (*i*) different sputter rates of the two layers, (*ii*) the λ-effect for AES depth profiling, and (*iii*) atomic mixing (102, 240, 255) (see Fig. 7 and 14). For asymmetric profiles the use of the 50% point tends to underestimate film thicknesses measured by sputtering through the interface.

Seah and Lea (179) have derived the broadening from depth profiles of multilayer sandwich samples by using the envelope shape of the signals measured in individual layers.

A variety of layered samples have been used for Δz measurements: evaporated films of metals and semiconductors, epitaxial heterojunctions and superlattices of semiconductors and garnets, and oxide layers, mostly produced by anodization, on metals and semiconductors. Table III gives a survey of depth resolution measurements performed by different techniques and under different experimental conditions.

The contributions to Δz caused by different mechanisms show different depth dependences:

$\Delta z/z$ = constant: edge effects, inhomogeneous beam current density, macroroughness

$\Delta z/z \propto z^{-1/2}$: statistical sputter removal (SLS)

$\Delta z/z \propto z^{-1}$: preferential sputtering, atomic mixing, information depth, enhanced diffusion, surface transport

Honig and Magee (284) have compiled a large number of $\Delta z/z$ *vs.* z measurements that show that in several cases $\Delta z/z$ falls off as $1/z$. The magnitude of the constant in this $1/z$ term is mainly given by the atomic mixing depth and is thus a function of the beam energy and angle of incidence. This constant determines at what depth the term $\Delta z/z$ = constant will begin to dominate. Under appropriately chosen conditions, the atomic mixing depth can be made smaller than 1 nm (131); the practical limit to the depth resolution presently seems to come from instrumental factors (nonuniform beam erosion).

Table III. Measurements of depth resolution

Material	Method	Ion	Energy (keV)	Reference
Ni/Cr sandwiches	AES	Ar^+	1.0	(103, 180, 280)
Mo/W	AES	Ar^+	0.2-0.5	(372)
Ni/Cu, Nb/Ge, Cu/Nb, Mo/Ge	AES	Ar^+	2.0	(183)
Co/Mo, Ni/Mo	AES	Ar^+	?	(373)
Ni/Cu, Au/Cu, Cu/SiO_2, Co/SiO_2	GDMS	Ar^+	0.1	(58)
Cu/Ni, Au/Ag/Au	AES	Ar^+	1.0	(118)
Au/Ni	AES	Ar^+	0.5-2.0	(185)
Cu/Ni	SIMS	Ar^+, N_2^+	11.0	(167)
V/Ti sandwiches	SIMS	Ar^+, N_2^+	11.0	(96)
Au/Si	AES	Ar^+	2.0, 2.7	(374)
Si/C	AES, x-ray	Ar^+	0.5-5.0	(97)
Ge/Si	AES, x-ray	He^+, Ne^+ Ar^+, Kr^+ Xe^+	0.5-5.0	(102, 107)
$Ga_{1-x}Al_xAs$-GaAs superlattice	AES	Ar^+	1.5	(375)
Ta_2O_5/Ta, NbO/Nb	SNMS	Ar^+	0.4	(54)
Ta_2O_5/Ta	SNMS	Ar^+	0.1-0.6	(55, 376)
Ta_2O_5/Ta	SIMS	Cs^+	3.0	(296)
Ta_2O_5/Ta	SIMS	Ar^+	3-12	(247)
Ta_2O_5/Ta	SIMS	Ar^+	5.0	(129)
Ta_2O_5/Ta, Al_2O_3/Al TiO_2/Ti	AES	Ar^+	0.5	(309)
Ta_2O_5/Ta, SiO_2/Si	SIMS	Ar^+	2.0	(377)
SiO_2/Si	AES	Ne^+, Ar^+ Xe^+	0.5-5.0	(246)
SiO_2/Si	AES	Ar^+	1.0	(364, 369, 378)
Y-garnet	SIMS	Ar^+	12.0	(128)
Gd-garnet	SIMS	O^-	15.0	(325)
N implanted into Co	AES	Ar^+	1.0	(379)
D, H implanted into α-Si	SIMS	Ar^+	5.0	(380)

Applications

This second part provides a survey of sputter depth profiling measurements in microelectronic structures. A detailed discussion of all measurements is impossible within the framework of this paper, but attention is given to a number of characteristic problems. The essential question addressed is the measurement of elemental distributions in substrates, films, and interfaces. The first section deals with dopants and impurities in semiconductors. The second section is devoted to measurements of insulating films including the study of the insulator/semiconductor and insulator/metal interface. The third section is concerned with measurements of metal films, the metal/semiconductor, and metal/metal interface.

Dopant and Impurity Distributions in Semiconductors

In order to be able to control doping profiles in semiconductor devices, it is essential to understand the factors that affect the depth distribution of dopant elements. This includes dopants contained in the substrate or introduced by ion implantation and diffusion from the surface or added during epitaxial growth. The information sought, which forms the imput for process modeling programs (381, 382), is the original depth distribution of implants and the diffusive redistribution and electrical activation during annealing. It is sometimes equally important to know the concentration and distribution of unwanted impurities introduced during crystal growth or in subsequent processing steps, whose presence or absence might be decisive for the functioning of a given electronic device.

The measurement of dopant and impurity distributions by sputter depth profiling is almost exclusively the domain of SIMS (50, 75, 383). There are only very few exceptions where implantation profiles have been measured by AES (384-386), IXE (67), GDOS (65), or SCANIIR (61, 62, 387). The reason is the by far superior sensitivity of SIMS. Whereas for the other examples given elemental detection limits lie in the concentration range of 10^{18}-10^{19} atoms/cm^3, the detection limits of SIMS can be as low as 5×10^{13} atoms/cm^3 in certain cases. It has already been pointed out that detection limits during depth profiling depend on the lateral and depth resolution. The capability of a modern SIMS instrument in this respect is demonstrated in Fig. 16 which shows a B-depth profile from an area of only 1 μm in diameter. The reason for the extremely high sensitivity achieved in this measurement is the value for the transmission T which is much larger than that of most other instruments (388).

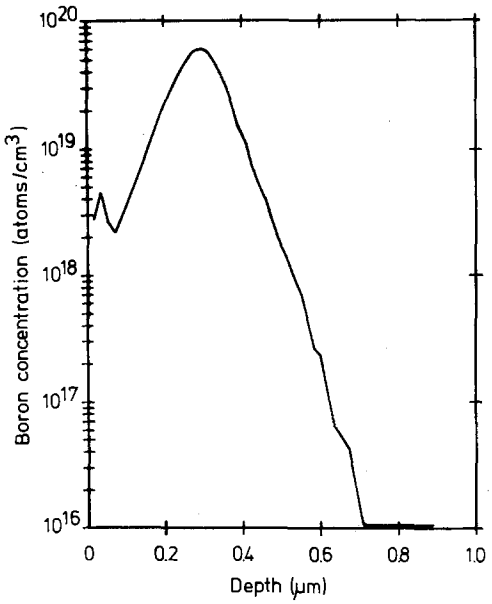

Fig. 16. SIMS depth profile of 10^{15} atoms/cm² $^{10}B^+$ implanted into Si at 100 keV energy measured in a CAMECA IMS 3F. The secondary ion signal is collected from an area of 1 μm diam (7.85×10^{-9} cm²) on the sample surface, selected by a diaphragm in the secondary beam. Each value in the depth profile is obtained from a layer of 18 nm depth. The concentration limit of 10^{-16} atoms/cm³ represents 1.4 counts from the corresponding volume of 1.4×10^{-14} cm³. Under the experimental conditions of this measurement γT, the product of the ionization probability of B and the instrument transmission is 8.3×10^{-3}.

In most applications depth distributions are measured in much larger areas. Under such conditions, detection limits are usually not determined by the depth and lateral resolution but by other factors like the background from the vacuum, interferences, beam impurities, memory effects, etc. Only in this case detection limits for depth profiling with high depth resolution are the same as those for bulk analysis, although experimenters quoting detection limits are not always careful to make this distinction. Table IV is a compilation of SIMS detection limits of various elements in Si and GaAs. Different instrumental designs are used to deal with the problem of interferences. Two typical examples are the measurement of P in Si (interference of ^{30}SiH) and As in Si (interference of $^{29}Si^{30}SiO$). The background from these interferences can be either reduced by working in a UHV of 10^{-10} Torr (129, 138, 398) and using Cs^+ bombardment detecting P^- or $AsSi^-$ ions or by employing high mass resolution or energy filtering, respectively, (34, 50) in an instrument which offers these capabilities (130).

SIMS measurements in silicon.—In the past Si has been the most widely investigated semiconductor. While there are almost no SIMS depth profiling measurements in Ge (399), SIMS measurements in Si include studies of the distribution of the most common impurities C and O (400, 401), studies of the diffusion of H, C, N, and O in α-Si (150, 390, 402), diffusion measurements of Ga (403), P (404), or Si (405) introduced from the surface, segregation studies of C, P, and Fe in laser-annealed Si (406), the study of the solid phase epitaxial growth (SPEG) of α-Si (407), and measurements of the gettering of O upon annealing into damage regions produced by mechanical abrasion (408). Most important are, however, the measurements of implantation profiles from which many different kinds of information can be obtained [for a more detailed discussion see Ref. (75)].

Table IV. Sims detection limits of impurities in semiconductors

Matrix	Element	Detected species	Ion beam	Detection limit (atoms/cm³)	Reference
Si	H	H^-	Cs^+	5×10^{17}	(389)
	C	C^-	Cs^+	8×10^{17}	(390)
	N	SiN^-	Cs^+	10^{17}	(390)
	O	O^-	Cs^+	6×10^{18}	(390)
	B	B^+	O_2^+	10^{14}	(391)
	P	P^-	Cs^+	5×10^{15}	(151, 50)
	P	P^+	O_2^+	5×10^{15}	(34)
	As	$AsSi^-$	Cs^+	3×10^{15}	(392)
	As	As^+	O_2^+	2×10^{16}	(34)
GaAs	O	O^-	Cs^+	5×10^{17}	(393)
	Si	Si^+	O_2^+	3×10^{15}	(394)
	S	S^-	Cs^+	10^{15}	(395)
	Cr	Cr^+	O_2^+	5×10^{13}	(396)
	Mn	Mn^+	O_2^+	4×10^{13}	(383)
	Fe	Fe^+	O_2^+	5×10^{14}	(397)
	Zn	Zn^+	O_2^+	10^{16}	(138)
	Se	Se^-	Cs^+	3×10^{13}	(395)
	Te	Te^-	Cs^+	2×10^{13}	(394)

The measurement of implanted range distributions serves for the determination of the electronic (389, 409-412) or nuclear (413, 414) stopping power. These as well as the more phenomenological range moments provide the data for improvements of existing range theories [see, *e.g.*, Ref (415) and references there]. Range data are complemented by channeling measurements (409, 412, 416, 417). Important also is the study of recoil implantation (264, 265, 267-269). In many cases dopants like P or As are implanted into Si through films of SiO_2 or Si_3N_4. The resulting recoil implantation of O or N can have far-reaching consequences for the redistribution of dopants during subsequent annealing.

Many factors govern the redistribution of implants and/or of other dopants present during the annealing step: crystal damage caused by the implantation and its annealing (418, 419), amorphization and recrystallization (420-422), dopant precipitation (417), and/or clustering (34), as well as the presence of other impurities (421, 423, 424). On the basis of careful SIMS measurements, often in combination with electrical measurements, it is possible to disentangle some of the complex processes taking place during annealing (417) and to improve on diffusion models for process simulation (382, 425).

Another example is the study of the segregation of dopants and impurities during oxidation (426), annealing under encapsulation (427), or during recrystallization of the melt zone produced by laser annealing (406). Laser annealing of ion-implanted semiconductors (428) has become increasingly popular. Q-switched lasers cause surface melting with subsequent perfect recrystallization (429) leading to electrical activation but also to some diffusive redistribution of the dopant. Annealing by CW laser occurs without melting and achieves essentially complete electrical activation without any diffusion (430). SIMS depth profiles have been measured of B (420, 431-434), C, and O (401), P (433, 434), and As (434, 435) implants in Si after pulsed laser annealing as well as B and As in Si after CW laser annealing (430, 436-438).

SIMS measurements in GaAs.—In recent years increased attention has been focused on ion implantation in III-V compounds (439) and specifically in GaAs (440). This is reflected by the large number of SIMS depth profiling measurements performed in this semiconductor. Table V gives a survey of measurements of implants in GaAs.

For dopants like Be or Se original implant distributions and annealing distributions have been studied. The example of Se demonstrates the complexity of diffusion processes in GaAs. Se is implanted into GaAs in order to create shallow n-type layers for active regions in microwave Schottky-gate FET's. During Se implantation radiation-enhanced diffusion is observed leading to implantation distributions which are different for different implantation temperatures (395, 461). In contrast to Si, GaAs does not become amorphous during implantation at room temperature. Radiation damage anneals during implantation at elevated temperatures facilitating diffusion of Se. Redistribution during annealing involves also the annealing of defects produced by the implantation (460). The results of a series of experiments which combine electrical with SIMS measurements (395, 460-463) are the basis of a model (462) according to which there are at least four chemically different species of Se in GaAs: (*i*) interstitial Se, (*ii*) substitutional Se, (*iii*) Se complexed with a Ga vacancy, and (*iv*) precipitated Se. Only substitutional Se is a donor whereas only complexes of Se and Ga vacancies can diffuse through the GaAs lattice.

In many cases the diffusive redistribution of implanted dopants cannot, by itself, explain the observed electrical behavior of implanted and annealed GaAs. The reason is to be found in the migratory behavior of compensating impurities. The implantation of inactive ions like H, B, and As into Cr-doped GaAs causes the formation of depletion

Table V. SIMS measurements of implantation profiles in GaAs

Implanted element	Information sought by measurement	Reference
Be	Implanted ranges	(441)
	Redistribution during annealing	(411, 442, 443)
B	Implanted ranges	(444)
	Redistribution during annealing	(444-446)
	Redistribution of Cr during annealing (capped and capless), gettering	(447-449)
C, Ge, Sn	Amphoteric dopant behavior	(450)
O	Redistribution of Cr during annealing	(393)
Si	Implanted ranges	(151, 451-453)
	Channeled range distribution	(394)
	Redistribution during annealing	(453, 454)
	Amphoteric dopant behavior	(450)
	Redistribution of Cr during annealing	(452, 453)
S	Implanted ranges	(151, 441, 453)
	Ranges as function of implantation temperature	(395)
	Channeled range distribution	(394, 395)
	Redistribution during annealing	(395, 441, 453)
	Distribution of Cr	(455)
	Redistribution of Cr during annealing	(453, 455, 456)
Cr	Implanted ranges	(427, 457, 458)
	Redistribution during annealing	(427, 456-459)
Se	Implanted ranges	(460)
	Ranges as function of implantation temperature	(395, 461)
	Channeled range distribution	(394, 395)
	Redistribution during annealing	(395, 460, 462)
	Solid solubility limits	(463)
	Redistribution of Cr during annealing	(302, 464, 465)
Zn	Redistribution of Cr during annealing	(302)
Te	Channeled range distribution	(394)

zones in the electrical density profiles after annealing (445, 449). Similarly, p-type conduction layers ("surface conversion") are formed in Cr-doped substrates without implantation after annealing under Si_3N_4 encapsulation (466, 467).

A large number of SIMS depth profiling measurements has been performed to study the diffusive behavior of Cr, but also Mn and Fe, in doped substrates (396, 464, 468-473), in doped epitaxial layers (45, 397, 474, 475) and in samples implanted with Cr but also many other ions (see Table V). These measurements were performed after annealing under different conditions (capped and capless).

The picture which emerges from these studies is the following: Cr in GaAs is a very mobile impurity whose redistribution during annealing is governed by several factors.

1. In the presence of an implant the Cr distribution during low temperature (<800°C) annealing depends on the damage produced by the implant (455, 456, 464, 465). Parameters which play a role are the fluence of the implant (448, 449, 456) and the Cr background concentration (455). Gettering of Cr occurs in several regions of residual damage which are successively emptied during annealing at increasing temperatures.

2. At higher temperatures (>800°C) Cr accumulates at the GaAs/encapsulant interface if annealing takes place under an encapsulating film of Si_3N_4 (427, 447, 466, 469), SiO_2 (455, 456, 471), or SiO_2/Si_3N_4 (464, 465, 476). Cr depletion in a near-surface zone produces a conducting layer. Gettering of Cr occurs due to the encapsulation stress during annealing. Outdiffusion of Cr can be minimized by capless CAT (controlled atmosphere technique) annealing in an H_2/AsH_3 or H_2/As_4 atmosphere where the As partial pressure can be adjusted (470, 471).

3. Cr gettering can occur because of back-surface damage caused by mechanical abrasion (468, 472). Pregettering of substrates reduces Cr diffusion into VPE layers during epitaxial growth (474).

4. Cr can be trapped by other impurities like O as was shown by implanting O into Cr-doped substrates (393).

Because of this complicated behavior of Cr it is not always simple to use Cr-doped semi-insulating substrates for FET or other IC structures.

Besides SIMS measurements in GaAs there are only a few studies in other III-V or II-VI semiconductors: implantation profile measurements of H (477), Be (478, 479), or Si (478) in InP, of Be in $GaAs_xP_{1-x}$ (480), or of diffusion studies of Sn in SnTe (481) and PbSe (482) and of Te in SnTe (483).

Heterojunctions and superlattices.—Heterojunctions play an important role for opto-electronic devices. Sputter depth profiling has been applied to the measurement of the transition width and to the study of the distribution of contaminants. For interface width measurements a high sensitivity is not required. As a consequence, most measurements of this type have used AES depth profiling. The AES depth profiles of a GaAs-$Ga_{1-x}Al_xAs$ superlattice by Ludeke *et al.* (375) are a beautiful demonstration of the depth resolution which can be achieved by this method. The interface widths of GaAs-$Ga_{1-x}Al_xAs$ heterojunctions grown by different epitaxial techniques, VPE (vapor phase epitaxy), LPE (liquid phase epitaxy), and MBE (molecular beam epitaxy), have been measured and compared (245, 484-486). The narrowest interface (1.3 nm) is obtained by the MBE method (245).

SIMS depth profiling of heterojunctions has been used in cases where the distribution of dopants and impurities between the layers was sought (484, 487). Figure 17 shows an example of a SIMS depth profile through GaAs-$Ga_{1-x}Al_xAs$ sandwich layers in an experimental study of the redistribution of Te and Cr during epitaxial growth by MBE.

Measurements of the interface width by AES depth profiling have also been performed in InAs-$InAs_xSb_yP_{1-x-y}$ superlattices (488) and InP-$In_xGa_{1-x}As_yP_{1-y}$ heterojunctions (166). The interface of the PbS-Si heterojunction has been investigated with respect to the presence of contaminants (489, 490). In the structure GaP-$In_xGa_{1-x}P$-GaAs the LPE-grown $In_xGa_{1-x}P$ buffer layer was studied for its chemical composition by SIMS and AES profiling (491).

AES depth profiles were also measured in $Cu_{2-x}S$-Cds (492, 493) and in $CuInSe_2$-CdS and $CuInS_2$-CdS (494) junctions. Studied was the interdiffusion of Cu and Cd between the layers and its influence on device stability.

Insulating Films

Insulating films fulfill a large variety of functions in semiconductor devices: as protective films, doping masks, dielectric layers in MIS, MOS, or MNOS structures, encapsulants during annealing, or as diffusion and reaction barriers. There are many properties of insulating films which determine electrical and mechanical device performance. The chemical composition of the films is important as is the detailed chemical and morphological structure and the width of the interface between insulator and semiconductor or metal, respectively. Significant also is the distribution of dopants or impurities in the film. The

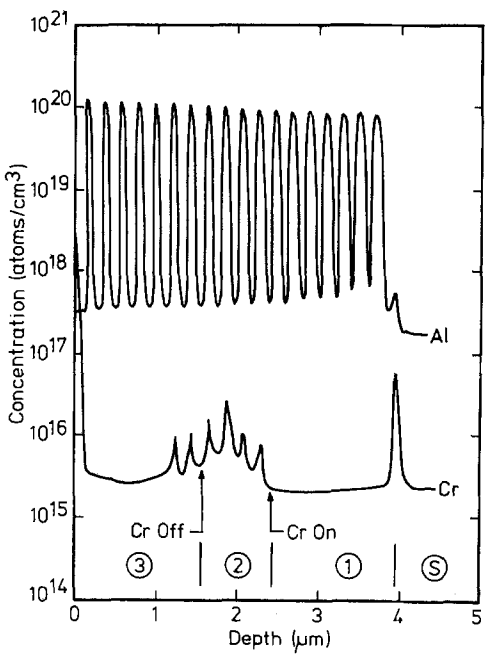

Fig. 17. SIMS depth profiles of Cr and Al in a three-layer structure of GaAs grown by MBE. The layers consist of 1.5 μm undoped GaAs, 1, on the Te-doped substrate (S); 0.8 μm Cr-doped GaAs, 2; and a 1.5μm undoped film, 3, on top. In order to study the Cr segregation and redistribution during the growth, $Ga_{0.7}Al_{0.3}As$ layers of 3 nm thickness were introduced every 0.2 μm of growth. The arrows indicate when the Cr cell shutter was turned on and off, respectively. From Ref. (487).

interdiffusion between different layers sometimes leads to device failure (*e.g.*, diffusion barrier breakdown).

Sputter depth profiling is one of the major tools for studying these properties, especially in conjunction with AES and XPS analysis which can provide information about the chemical binding of different elements (297, 299). Figure 18 shows an example of "chemical depth profiling" by XPS. It displays the XPS spectra of Ga and P during sputtering through an oxide/GaP interface. Although the warnings in the section principles of sputter depth profiling about the possibility of chemical changes by Ar bombardment should be heeded, chemical depth profiling has been successfully applied to many different cases (Table VI). Most of these examples are concerned with the oxide/semiconductor interface, but there are also other interesting cases. It has, *e.g.*, been possible to distinguish between the oxide of GaP and O-implanted GaP (298).

The SiO_2/Si interface.—The SiO_2/Si interface has been most extensively studied (525). Depth profiling has helped in gaining an understanding of the oxidation mechanism and has provided information on the interface structure and composition for different oxidation methods and conditions.

The width of the interface has been measured mainly by AES depth profiling (182, 317, 364, 365, 369, 370, 378, 496, 526, 527). Since the SiO_2/Si interface is very sharp, these measurements have taxed the depth resolution of the analysis method (364, 369). High resolution (2Å) TEM and RBS channeling indicate that this interface is atomically sharp.

Other studies have been concerned with the segregation of dopants during oxidation. It has been shown that B migrates into the oxide layer (495, 532, 533), where as P (531) and As (534) are pushed out of the oxide and pile up at the interface. Other impurities like alkalis are similarly found to be preferentially concentrated at the interface (319, 526). Because of the required sensitivity most measurements of impurity distributions were made by SIMS (329, 526, 535-537) which was also used to study the distribution of D after wet oxidation (538) or after annealing in a D-atmosphere (539): the presence of H at the interface crucially affects its electronic properties in Si field-effect devices.

Besides SiO_2/Si, the Si_3N_4/SiO_2 interface has also been the subject of a number of studies on MNOS memory devices. Among them are AES (350, 362, 365, 540) and XPS (125) profiling measurements of its stoichiometry and chemical structure. The O impurity distribution was measured in

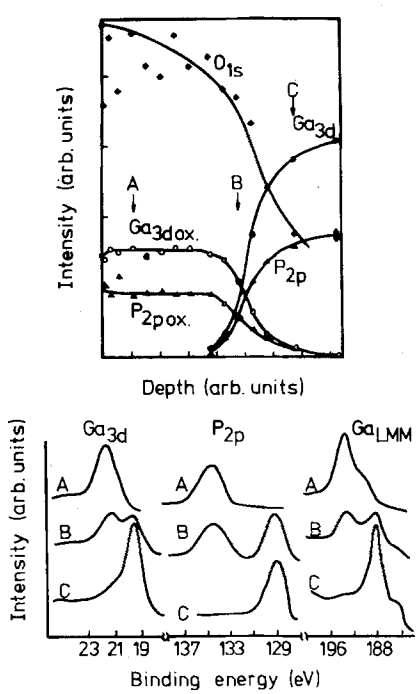

Fig. 18. XPS chemical sputter depth profile (5 keV Ar^+ bombardment) through thermally grown oxide on GaP. Shown are also XPS spectra at different depths A, B, and C indicated by arrows in the depth profile. From Ref. (298).

Table VI. Chemical depth profiling by XPS and AES

Interface studied	Method	Reference
Si/SiO_2	AES	(317, 364, 365, 495-498)
	XPS	(30)
Si/Si_3N_4	AES	(317, 365)
$Si/SiO_2/Si_3N_4$	XPS	(125)
Al/SiO_2	AES	(499)
Si/silane	AES	(500)
SiC/oxide	AES	(501)
GaAs/oxide	AES	(502-505)
	XPS	(30, 31, 312, 313, 504) (506-514)
GaP/oxide	AES	(515)
	XPS	(298, 506)
InP/oxide	XPS	(508, 516)
InSb/oxide	XPS	(506)
GaSb/oxide	XPS	(506)
InAs/oxide	XPS	(517)
Metal/silicide/Si	AES	(518)
Sr, Ba/oxide	AES	(519)
Te in $Hg_{0.8}Cd_{0.2}Te$/oxide	XPS	(520)
Al/Al_2O_3	AES	(105, 316, 497)
Ta/Ta_2O_5	XPS	(521)
Fe, Ni, Cr/oxide	XPS	(522)
Pd/Ge/GaAs	AES	(523)
Au/GaAs	XPS	(504)
Ti/SiO_2, Ti/Al_2O_3	AES + XPS	(524)

Si_3N_4 produced by CVD (541). To be added are measurements on the Si_3N_4/Si interface (317, 542).

The oxidation of GaAs and other III-V compounds.—In contrast to Si, there exists no stable oxide passivation system for GaAs. Considerable effort has been spent on the examination of different oxidation methods (thermal, anodic, and plasma techniques) for GaAs with the hope of finding a process by which a stable oxide film could be formed. Correspondingly, there is a large number of depth profiling studies to characterize the oxide layers and to investigate the detailed mechanism of oxide formation (Table VII).

During oxidation of GaAs a layer is formed which consists of Ga_2O_3 with varying amounts of As_2O_3, elemental As, and some As_2O_5. The relative abundances of these components and their variation with depth depend on method and conditions of oxidation. Dry thermal oxidation produces a rather uniform layer of Ga_2O_3 with a pileup of As at the interface (312, 502-504, 507). Wet oxidation, but also oxidation in an As-rich atmosphere, results in the addition of As_2O_3 and As_2O_5 (312, 507). Plasma oxidation also yields a mixture of Ga_2O_3 and As_2O_3, but with less pileup of elemental As (502, 503). Yamasaki *et al.* (543) have measured SIMS depth profiles by using ^{18}O marking in order to study the O transport in the oxide. The chemical structure of anodically grown oxides depends on a number of parameters like the composition of the electrolyte used, its *p*H value, and the applied current density during anodization (508). Variations of these parameters result in a variation of the Ga_2O_3/As_2O_3 ratio, of the amounts of elemental As, and of the depth distributions of these components. Some investigators (508) have concentrated on the study of the early stages of oxidation (nucleation and island growth). Others (30, 31) have studied thin native oxides on GaAs since anodically grown oxide films may have compositions far from interfacial equilibrium.

Of other III-V compounds, depth profiles (all XPS) were measured of anodically (506, 515) and thermally (298) grown GaP-oxide, anodically (508) and thermally (516) grown InP-oxide, and the thermally grown oxides of InAs (517), GaSb, and InSb (506). Additional SIMS and AES profiles were obtained of the InP/oxide interface (516) to study the distribution of impurities. Also the oxides of these compounds show a complex structure which depends on formation conditions. Whereas, *e.g.*, the anodically grown oxide of InP shows a uniform distribution of In_2O_3 and P_2O_5 (508), buildup of elemental P is observed at the interface of the thermally grown oxide (516).

Other interfaces in MOS, MIS, and MNO structures and encapsulations.—Several depth profiling studies have been concerned with the insulator/metal interface. Examples are AES measurements of SiO_2 on Mo, Ta, and W (545) in order to study the barrier breakdown of the oxide layer which serves to prevent silicide formation in an MOS structure. Other examples are AES studies of the SiO_2/Al (365), Si_3N_4/Al (546), and Cr_2O_3/Cu (547) interface as well as SIMS

Table VII. Depth profiling measurements of oxidized GaAs

Oxidation technique	Electrolyte (if anodic oxidation)	Analysis method	Reference
Native		XPS	(30, 31)
Thermal		AES, XPS, SIMS	(503, 504, 507)
		XPS	(312, 509)
		AES, SIMS	(502)
Plasma		AES, SIMS	(502)
		AES, XPS, SIMS	(503)
		SIMS	(543)
Anodic	$K_2Cr_2O_7$ in $HOCH_2 \cdot CH_2OH$	XPS	(313)
	Tartaric acid in propylene glycol	XPS	(312, 313, 508, 509, 511-513)
	Tartaric acid in propylene glycol	AES, SIMS	(502)
	Tartaric acid in propylene glycol	AES, XPS, SIMS	(503)
	Arsenic acid in propylene glycol	XPS	(313)
	H_3PO_4 in water	AES	(505)
	Na_3PO_4 in diethylene glycol	ISS	(514, 544)
Anodic	$(NH_4)_2HPO_4$ in water (saturated with As_2O_3)	XPS	(510)
	$(NH_4)_2HPO_4$ in glycol	XPS	(512)
	H_3PO_4 in water	XPS	(513)
	0.1N $KMnO_4$; 0.1N KOH; 30% H_2O_2	XPS	(506)

studies of barrier layers in the structures $Ni/Ta_2N/Al_2O_3$ (383) and Ti/TiN/Pt (548).

Because of the lack of stable oxides of III-V compounds, films of Si_3N_4 and SiO_2 are used as encapsulants during annealing. Of interest is whether diffusion occurs between semiconductor and encapsulant. AES depth profiling measurements showed diffusion of Si into GaAs (549) as well as loss of P from InP (550) under Si_3N_4 encapsulation. To circumvent diffusion of Si into GaAs, AlO_xN_y was used instead of Si_3N_4 although it could not completely prevent outdiffusion of As (551). Another study deals with SiO_2 on InP (386).

Metal oxide layers.—Like Si oxide and nitride, metal oxides are frequently used as barrier films and as dielectric material in electronic devices. Table VIII gives a survey of depth profiling measurements which have been performed on such films. The problems studied are similar to those investigated in oxides of semiconductors: oxidation mechanisms, width of interface, chemical structure and composition of oxide film and interface, and distribution of impurities. The analysis method used has to correspond to the problem at hand; AES is preferred but ISS is also used more frequently than for other film structures.

Metal Films

Metal contacts are essential components of all semiconductor devices either as ohmic contacts or as Schottky barriers (562). The formation of a contact with desired electrical and mechanical properties requires a certain amount of interdiffusion between the metal and the semiconductor. The miniaturization of LSIC device technology demands that reactions between contact and semiconductor be kept limited in order to prevent, *e.g.*, penetration of shallow junctions by diffusion of contacting metal. Different metallization schemes may place different requirements on the planar film technology. Basic demands are good electrical contact and mechanical bonding as well as stability against device degradation due to interdiffusion and compound formation at elevated operating temperatures and during exposure to atmosphere. Production control makes the understanding of reactive and diffusive processes between films (6) in a given device essential. Sputter depth profiling plays an important role for studying these processes (563). Unlike for oxide films which are frequently analyzed by XPS, AES is the preferred technique for the depth profiling of metal/semiconductor and metal/metal interfaces.

Contacts in silicon technology.—For Si IC's, Al and Au are preferentially used as contact metals and several corresponding AES studies are devoted to them (374, 499, 564, 565). In practice multiple films are used to prevent excessive diffusion between contact metal and Si and to improve mechanical bonding. The first objective is accomplished by using a diffusion barrier between active layers. The barrier properties of a variety of metal films have been investigated by depth profiling: Al/TiW/Si (566, 567), Au/Ta/Si (568), Au/Ni/Cu (569, 570), Au/Mo/Si (571), and Cu/Mo/Si (46). All measurements used AES profiling except for the last (ISS). The diffusion of Au and Si through Mo could be prevented if N was added to Mo by reactive sputter deposition (571).

Mechanical adhesion is improved by interspersed layers of metals like Pd or Cr. Depth profiles have served to study bonding mechanisms and causes of failure. Examples are measurements of $Au/PdAg/Al_2O_3$ (572), Hf/Al_2O_3 (573), $Au/Cr/Al_2O_3$ (574), or Pd between Ti and Cu in the sandwich structure Ti/Cu/Ni/Au (575).

In order to achieve a controlled contact, silicide layers, mainly PtSi and Pd_2Si, are widely used in metallization schemes for Si (308). Sputter depth profiling studies of silicide formation and depth compositional measurements of silicide films were performed for Pd (306, 307, 518, 576-578), Ni (518, 563, 576, 579-581), Ti (305, 307, 518), V (518, 579), Mo (306, 307, 582), Ta (306, 307), and W (583) as well as Nb, Zr, Pt, and Rh (518). Usually thermal annealing is used for silicide formation, but it can also be achieved by ion bombardment (305-307). The influence of oxide layers and other contaminants on contacts has also been studied by AES depth profiling (564, 584).

Besides investigations of the "classical" metallization schemes, depth profiling measurements have been reported also on the film structures Al/Au/Si (104), Cu/Au (585), Ag/Pt (584), $Au/Ag/SiO_2$ (586), Hf/Al_2O_3 (573), Ti/SiO_2 and Ti/Al_2O_3 (524), and Ta/SiO_2 and Ta/Al_2O_3 (587).

Contacts in gallium arsenide technology.—Ohmic contacts to N-type GaAs require a region of high carrier density under the metal. This is achieved by alloying a eutectic of AgInGe or AuGe to the GaAs surface.

The mechanism of Ge doping has been studied by AES and XPS depth profiling for the AgInGe contact (588). Heating of the contact results in diffusion of Ge to the alloy/GaAs interface accompanied by the preferential outdiffusion of Ga to the alloy surface. Ge by replacing Ga acts as a donor, creating the required doped layer. Contacts of Pt/AuGe (589) and Ni/AuGe (590) have been similarly studied by AES depth profiling: melting above the eutectic temperature is necessary to prevent formation of a rectifying contact due to diffusion of Ni to the GaAs. In the case of Pt/AuGe a good ohmic contact could be achieved by electron beam irradiation (589).

Table VIII. Depth profiling measurements of metal/oxide films

Metal	Analysis method	Reference
Ta	SNMS	(54, 55, 376)
	ISS, SIMS	(552)
	SIMS	(129, 247, 296, 377)
	AES	(309)
Al	AES	(105, 155, 309, 316, 553)
	ISS, SIMS	(552)
Ti	AES	(309, 310)
	AES, SIMS	(554)
Cu	ISS	(555)
Nb	SNMS	(54)
Ba, Sr	AES	(519)
PdAuSi-alloy	AES	(556)
AlCu-alloy	ISS	(557)
FeCr-alloy	ISS	(558)
CuBe-alloy	XPS, AES	(559)
TiMo-alloy	AES	(560)
BeCu-alloy	SIMS	(561)

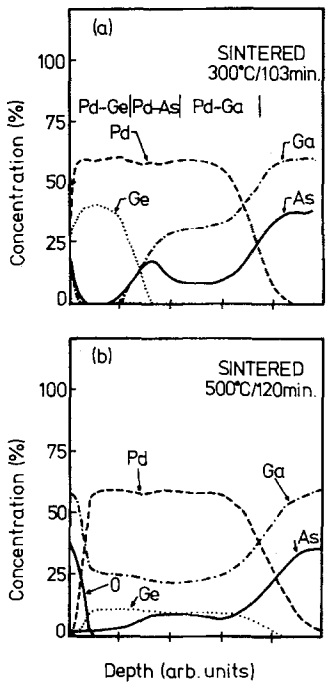

Fig. 19. AES depth profiles of films of 110 nm Pd and 37 nm Ge on GaAs after sintering at (a) 300°C for 103 min and (b) 555°C for 120 min. From Ref. (523).

Another ohmic metallization scheme that avoids melting of the contact is based on Pd (591) or Pd/Ge (592). The ohmic contact is produced by sintering. The diffusive processes and chemical reactions in the Pd/Ge/GaAs metallization were studied by SIMS, AES, and XPS (523). Figure 19 shows AES depth profiles through the contact film after sintering at different temperatures. At lower temperatures interdiffusion of Pd and Ge occurs leading to the formation of Pd_2Ge and PdGe. At higher temperatures further solid-phase reactions between Pd and the substrate result in the formation of the compounds $PdAs_2$ and PdGa. The contact remains rectifying up to sintering temperatures of >400°C. The onset of ohmic behavior is characterized by penetration of Ge to the GaAs interface (Fig. 19b).

Measurements of depth profiles have also been performed to test different metals for Schottky barriers. Gold contacts were measured by SIMS (593) and XPS (594), the second study included also GaSb and InP. Another SIMS study investigated the metals, Pt, Ni, Al, Cr, Ti, Ta, Mo, and W (595), whereas SIMS, AES, and XPS were combined to study the interdiffusions and reactions of Au and Ag contacts with GaAs (504).

Other measurements of metal films.—Sputter depth profiling has been employed to study metal films and their interfaces in various other applications listed in Table IX. The first group deals with contacts on II-VI compounds which play a role for solar cells and photoconductive devices, the second group with films of magnetic alloys. NiCr alloys are used for resistive films.

There exist many other sputter depth profiling measurements of metal film layers which are concerned with the study of the measurement technique (see Table III). These do not apply directly to practical problems in electronic device technology and are therefore not listed here.

Table IX. Examples of sputter depth profiling of metal films and their interfaces

Film structure	Problem studied	Analysis method	Reference
Al/Cu_xS/CdS	Contacts for solar cells	AES	(184)
Cr/CdSe	Metallization	AES, XPS	(596)
Cr/CdSe, Al/CdSe	Metallization	AES	(597)
Co/GdFe	Contacts on magnetic alloys	AES	(598)
Cr/CoNi	Contacts	AES	(599)
GdCo	Composition of film	AES	(600)
Ni/Cr	Composition of films, contaminants	AES	(17, 103, 180) (601-603)

Conclusion

From the large number of diverse applications of sputter depth profiling it must have become clear what an important role this powerful technique plays for semiconductor device technology. What has not been duly emphasized so far and should be done here is the fact that in many cases the solution of the problem at hand is obtained only by a combination of different methods and approaches. This includes combinations of different sputter depth profiling techniques, combinations with other techniques like RBS, but also combinations with SEM, TEM, x-ray diffraction and, very importantly, with a variety of electrical measurements.

Acknowledgments

The author is grateful to the Techniker-Cercle, the Verband der Freunde der Technischen Universität Wien, the Österreichische Forschungsgemeinschaft, and to the Electrochemical Society for financial help which made the attendance at the Symposium on "Surface and Thin Film Analysis of Semiconductor Materials" possible. The Fond zur Förderung der wissenschaftlichen Forschung provided financial support for this research. Thanks are due to F. Paschke and W. Fallmann for active interest and support during this work. Also gratefully acknowledged is the splendid collaboration with M. Grasserbauer during the author's stay at his institute. G. Stingeder provided the sample for Fig. 16 and G. Stangl prepared the film sandwiches measured in Fig. 14. U. Sammt is responsible for the preparation of the figures and B. Wilcox helped with the preparation of the manuscript. This paper would not have been possible without the resources of the Zentralbibliothek der Physikalischen Institute der Universität Wien.

Manuscript submitted May 18, 1982; revised manuscript received Dec. 13, 1982. This was Paper 346 presented at the Denver, Colorado, Meeting of the Society, Oct. 11-16, 1981.

Any discussion of this paper will appear in a Discussion Section to be published in the December 1983 JOURNAL. All discussions for the December 1983 Discussion Section should be submitted by Aug. 1, 1983.

REFERENCES

1. B. E. Deal and J. M. Early, *This Journal*, **126**, 20C (1979).
2. P. H. Holloway and G. E. McGuire, *Appl. Surf. Sci.*, **4**, 410 (1980).
3. H. W. Werner, *Mikrochim. Acta, Suppl.*, **8**, 25 (1979).
4. H. Ryssel and I. Ruge, "Ionenimplantation," B. G. Teubner, Stuttgart (1978).
5. G. Dearnaley, J. H. Freeman, R. S. Nelson, and J. Stephen, "Ion Implantation," North Holland Publishing Co., Amsterdam and London (1973).
6. J. M. Poate, K. N. Tu, and J. W. Mayer, Editors, "Thin Films—Interdiffusions and Reactions," John Wiley & Sons, New York (1978).
7. J. E. Baglin and J. M. Poate, Editors, "Thin Film Interfaces and Interactions," The Electrochemical Society Softbound Proceedings Series, Princeton, NJ (1980).
8. J. M. Shannon, *Nucl. Instrum. Methods*, **182/183**, 545 (1981).
9. W. K. Chu, J. W. Mayer, and M. A. Nicolet, "Backscattering Spectrometry," Academic Press, New York (1978).
10. E. A. Wolicki, J. W. Butler, and P. A. Treado, Editors, "Ion Beam Analysis," North-Holland Publishing Co., Amsterdam (1978).
11. A. Cachard, J. P. Thomas, and E. Ligeon, in "Materials Characterization Using Ion Beams," J. P. Thomas and A. Cachard, Editors, p. 367, Plenum Press, New York (1978).
12. K. L. Dunning, in "ARPA/NBS Workshop IV, Surface Analysis for Silicon Devices," NBS SP 400-23, p. 95, U. S. Dept. Commerce, Washington D. C. (1976).
13. M. Pijolat and G. Hollinger, *Surf. Sci.*, **105**, 114 (1981).
14. S. Hofmann, *Analysis*, **9**, 181 (1981).
15. M. P. Seah, *Surf. Sci.*, **32**, 703 (1972).
16. M. F. Ebel, *J. Electron Spectrosc. Relat. Phenom.*, **14**, 287 (1978).

17. A. Zalar and S. Hofmann, *Surf. Interface Anal.*, **2,** 183 (1980).
18. A. van Oostrom, *Surf. Sci.*, **89,** 615 (1979).
19. C. Lea and M. P. Seah, *Thin Solid Films*, **75,** 67 (1981).
20. M. L. Tarng and D. G. Fisher, *J. Vac. Sci. Technol.*, **15,** 50 (1978).
21. R. A. Chappell and C. T. H. Stoddart, *J. Mater. Sci.*, **12,** 2001 (1977).
22. V. Thompson, H. E. Hintermann, and L. Chollet, *Surf. Technol.*, **8,** 421 (1979).
23. J. M. Walls, D. D. Hall, and D. E. Sykes, *Surf. Interface Anal.*, **1,** 204 (1979).
24. R. Kelly, *J. Appl. Phys.*, **39,** 5298 (1968).
25. J. P. S. Pringle, *This Journal*, **119,** 482 (1972).
26. M. T. Shehata and R. Kelly, *ibid.*, **127,** 579 (1980).
27. J. A. Davies, G. C. Ball, F. Brown, and B. Domej, *Can. J. Phys.*, **42,** 1070 (1964).
28. W. Przyborski, J. Roed, J. Lippert, and L. Sarholt-Kristensen, *Radiat. Eff.*, **1,** 33 (1969).
29. J. A. Adams, *Surf. Sci.*, **56,** 307 (1976).
30. F. J. Grunthaner, P. J. Grunthaner, R. P. Vasquez, B. F. Lewis, J. Maserjian, and A. Mad Hukar, *J. Vac. Sci. Technol.*, **16,** 1443 (1979).
31. P. J. Grunthaner, R. P. Vasquez, and F. J. Grunthaner, *ibid.*, **17,** 1045 (1980).
32. R. E. Pawel, *Rev. Sci. Instrum.*, **35,** 1066 (1964).
33. D. DeSoete, R. Gijbels, and J. Hoste, "Neutron Activation Analysis," Wiley-Interscience, New York (1972).
34. M. Grasserbauer, G. Stingeder, E. Guerrero, H. Poetzl, R. Tielert, and H. Ryssel, in "SIMS III, Proceedings of 3rd International Conference, Budapest," p. 321, Springer, Berlin (1982).
35. S. A. E. Johansson and T. B. Johansson, *Nucl. Instrum. Methods*, **137,** 437 (1976).
36. F. Folkmann, *J. Phys. E.*, **8,** 429 (1975).
37. J. M. Morabito, *Surf. Sci.*, **49,** 318 (1976).
38. A. Joshi, L. E. Davis, and P. W. Palmberg, in "Methods of Surface Analysis," A. W. Czanderna, Editors, p. 159, Elsevier, Amsterdam (1975).
39. C. C. Chang, in "Characterization of Solid Surfaces," P. F. Kane and G. R. Larrabee, Editors, p. 509, Plenum Press, New York (1974).
40. J. M. Morabito and P. M. Hall, in "Scanning Electron Microscopy/1976," O. Johari, Editor, p. 221, Illinois Institute of Technology Research Institute, Chicago (1976).
41. K. Siegbahn, *J. Electron Spectrosc. Relat. Phenom.*, **5,** 3 (1974).
42. W. M. Riggs and M. J. Parker, in "Methods of Surface Analysis," A. W. Czanderna, Editor, p. 103, Elsevier, Amsterdam (1975).
43. L. Fiermans, J. Vennik, and W. Dekeyser, Editors, "Electron and Ion Spectroscopy of Solids," Plenum Press, New York (1978).
44. M. P. Seah, *Surf. Interface Anal.*, **2,** 222 (1980).
45. E. N. Haeussler, *ibid.*, **2,** 134 (1980).
46. G. C. Nelson, *J. Colloid Interface Sci.*, **55,** 289 (1976).
47. T. M. Buck and J. M. Poate, *J. Vac. Sci. Technol.*, **11,** 289 (1974).
48. E. Taglauer and W. Heiland, *Appl. Phys.*, **9,** 261 (1976).
49. H. W. Werner, *Surf. Interface Anal.*, **2,** 56 (1980).
50. R. J. Blattner and C. A. Evans, Jr., "Scanning Electron Microscopy/1980," Vol. IV, p. 55, SEM Inc., Chicago (1980).
51. A. Benninghoven, *Surf. Sci.*, **35,** 427 (1973).
52. S. J. B. Reed, *Scanning*, **3,** (2) (1980).
53. H. Oechsner and W. Gerhard, *Surf. Sci.*, **44,** 480 (1974).
54. H. Oechsner and E. Stumpe, *Appl. Phys.*, **14,** 43 (1977).
55. E. Stumpe, H. Oechsner, and H. Schoof, *ibid.*, **20,** 55 (1979).
56. J. W. Coburn and E. Kay, *Appl. Phys. Lett.*, **19,** 350 (1971).
57. J. W. Coburn, E. Taglauer, and E. Kay, *J. Appl. Phys.*, **45,** 1779 (1974).
58. J. W. Coburn, E. W. Eckstein, and E. Kay, *ibid.*, **46,** 2828 (1975).
59. I. S. T. Tsong, C. A. Houser, N. A. Yusuf, R. F. Messier, W. B. White, and J. W. Michels, *Science*, **201,** 339 (1978).
60. N. H. Tolk, I. S. T. Tsong, and C. W. White, *Anal. Chem.*, **49,** 16A (1977).
61. C. W. White, *Nucl. Instrum. Methods*, **149,** 497 (1978).
62. M. Brown, B. Emmoth, and R. Buchta, *Radiat. Eff.*, **28,** 77 (1976).
63. J. E. Green, F. Sequeda-Osorio, and B. R. Natarajan, *J. Appl. Phys.*, **46,** 2701 (1975).
64. G. T. Marcyk and B. G. Streetman, *J. Vac. Sci. Technol.*, **14.** 1165 (1979).
65. Y. S. Park, W. M. Theis, and J. T. Grant, *Appl. Surf. Sci.*, **4,** 445 (1980).
66. J. A. Cairns, D. F. Holloway, and R. S. Nelson, *Radiat. Eff.*, **7,** 167 (1971).
67. F. Bernhard, H. Kerkow, and F. Kudella, *ibid.*, **49,** 107 (1980).
68. H. Lutz and R. Sizmann, *Phys. Lett.*, **5,** 113 (1963).
69. H. Heinen and R. Sizmann, *Z. Angew. Phys.*, **17,** 356 (1964).
70. P. W. Palmberg and T. N. Rhodin, *J. Appl. Phys.*, **39,** 2455 (1968).
71. P. W. Palmberg and H. L. Marcus, *Trans. ASM*, **62,** 1016 (1969).
72. J. W. Coburn, *Thin Solid Films*, **64,** 371 (1979).
73. J. W. Coburn, *J. Vac. Sci. Technol.*, **13,** 1037 (1976).
74. J. W. Coburn and E. Kay, *CRC Crit. Rev. Solid State Sci.*, **4,** 561 (1974).
75. E. Zinner, *Scanning*, **3,** 57 (1980).
76. T. Smith, *Surf. Sci.*, **55,** 601 (1976).
77. C. J. Powell, *Appl. Surf. Sci.*, **1,** 143 (1978).
78. C. A. Evans, Jr., *Anal. Chem.*, **47,** 818A (1975).
79. A. W. Czanderna, Editor, "Methods of Surface Analysis," Elsevier, Amsterdam (1975).
80. J. W. Mayer and J. M. Poate, in "Thin Films-Interdiffusions and Reactions," P. M. Poate, K. N. Tu, and J. W. Mayer, Editors, p. 119, John Wiley & Sons, New York (1978).
81. S. Hofmann, *Surf. Interface Anal.*, **2,** 148 (1980).
82. S. Hofmann, *Mikrochim. Acta, Suppl.*, **8,** 71 (1979).
83. S. Hofmann, *Appl. Phys.*, **9,** 59 (1976).
84. G. K. Wehner, in "Methods of Surface Analysis," A. W. Czanderna, Editor, p. 5, Elsevier, Amsterdam (1975).
85. S. Hofmann, Le Vide-Les Couches Minces, Numero Spec., p. 259 (1979).
86. P. M. Hall and J. M. Morabito, *CRC Crit. Rev. Solid State Mater. Sci.*, **8,** 53 (1978).
87. D. M. Holloway, *J. Vac. Sci. Technol.*, **12,** 392 (1975).
88. H. Liebl, *ibid.*, **12,** 385 (1975).
89. P. H. Holloway and R. S. Bhattacharya, *Surf. Interface Anal.*, **3,** 118 (1981).
90. A. Benninghoven, *Thin Solid Films*, **39,** 3 (1976).
91. B. Gruzza, J. M. Guglielmacci, and E. Gillet, *ibid.*, **52,** 103 (1978).
92. P. Laty, D. Seethanen, and F. Degreve, *Surf. Sci.*, **85,** 353 (1979).
93. R. S. Blewer and J. W. Guthrie, *ibid.*, **32,** 743 (1972).
94. K. Wittmaack, *Appl. Phys.*, **12,** 149 (1977).
95. W. O. Hofer and H. Liebl, in "Ion Beam Surface Layer Analysis," O. Meyer, G. Linker, and F. Kaeppeler, Editors, p. 659, Plenum Press, New York (1976).
96. W. O. Hofer and P. J. Martin, *Appl. Phys.*, **16,** 271 (1978).
97. J. Kirschner and H. W. Etzkorn, *Appl. Surf. Sci.*, **3,** 251 (1979).
98. C. A. Evans, Jr. and J. P. Pemsler, *Anal. Chem.*, **42,** 1060 (1970).
99. G. Betz and G. K. Wehner, in "Sputtering by Particle Bombardment," Vol. 2, R. Behrisch, Editor, Springer, Berlin, In press.
100. G. Betz, *Surf. Sci.*, **92,** 283 (1980).
101. R. Kelly, *ibid.*, **100,** 85 (1980).
102. H. W. Etzkorn and J. Kirschner, *Nucl. Instrum. Methods*, **168,** 395 (1980).
103. S. Hofmann and A. Zalar, *Thin Solid Films*, **60,** 201 (1979).
104. J. Kirschner and H. W. Etzkorn in "Proceedings of 7th International Vacuum Congress," p. 2213, Vienna (1977).
105. A. van Oostrom, *J. Vac. Sci. Technol.*, **13,** 224 (1976).
106. J. Kempf, in "SIMS II, Proceedings of 2nd International Conference, Stanford," p. 97, Springer, New York (1979).
107. H. W. Etzkorn, U. Littmark, and J. Kirschner, in "Proceedings of Symposium on Sputtering, Perchtoldsdorf/Vienna," P. Varga, G. Betz, and F. P. Viehboeck, Editors, p. 542 (1980).
108. C. J. Powell, *Appl. Surf. Sci.*, **4,** 492 (1980).
109. P. M. Hau and J. M. Morabito, *Surf. Sci.*, **83,** 391 (1979).
110. M. P. Seah, *Analusis*, **9,** 171 (1981).
111. D. H. Smith and W. H. Christie, *Int. J. Mass Spectrom. Ion Phys.*, **26,** 61 (1978).
112. D. E. Newbury, *Scanning*, **3,** 110 (1980).
113. T. M. Buck, in "Methods of Surface Analysis," A. W. Czanderna, Editor, p. 75, Elsevier, Amsterdam (1975).
114. G. Slodzian, *Ann. Phys.*, **9,** 591 (1964).
115. T. Narusawa, I. Satake, and S. Komiya, *J. Vac. Sci. Technol.*, **13,** 514 (1976).

116. V. R. Deline, W. Katz, C. A. Evans, Jr., and P. Williams, *Appl. Phys. Lett.*, **33,** 832 (1978).
117. V. R. Deline, C. A. Evans, Jr., and P. Williams, *ibid.*, **33,** 578 (1978).
118. P. S. Ho and J. E. Lewis, *Surf. Sci.*, **55,** 335 (1976).
119. D. W. Hoffman, I. S. T. Tsong, and G. L. Power, *J. Vac. Sci. Technol.*, **17,** 613 (1980).
120. S. Hofman and J. M. Sanz in "Proceedings of 8th International Vacuum Congress," p. 90, Cannes (1980).
121. J. A. McHugh, in "Secondary Ion Mass Spectrometry," p. 179, NBS SP-427, U. S. Dept. of Commerce, Washington D. C. (1975), and "Methods of Surface Analysis," A. W. Czanderna, Editor, p. 223, Elsevier, Amsterdam (1975).
122. I. S. T. Tsong, G. L. Power, D. W. Hoffman, and C. W. Magee, *Nucl. Instrum. Methods*, **168,** 399 (1980).
123. F. Storbeck, *Krist. Tech.*, **13,** 331 (1978).
124. R. J. Blattner, J. E. Baker, and C. A. Evans, Jr., *Anal. Chem.*, **46,** 2171 (1974).
125. L. Bradley, Y. M. Bosworth, D. Briggs, V. A. Gibson, R. J. Oldman, A. C. Evans, and J. Franks, *Appl. Spectrosc.*, **32,** 175 (1978).
126. P. Williams and C. A. Evans, Jr., *Int. J. Mass Spectrom. Ion Phys.*, **22,** 327 (1976).
127. W. O. Hofer, H. Liebl, G. Roos, and G. Staudenmaier, *ibid.*, **19,** 327 (1976).
128. K. Wittmaack, *Appl. Phys.*, **12,** 149 (1977).
129. C. W. Magee, W. L. Harrington, and R. E. Honig, *Rev. Sci. Instrum.*, **49,** 477 (1978).
130. M. Lepareur, *Rev. Tech. Thomson-CSF*, **12,** 225 (1980).
131. C. W. Magee, *Surf. Interface Anal.*, **4,** 35 (1982).
132. J. H. Schilling and P. A. Buerger, *Int. J. Mass Spectrom. Ion Phys.*, **26,** 163 (1978).
133. H. Liebl, *Scanning*, **3,** 79 (1980).
134. F. G. Ruedenauer and W. Steiger, *Mikrochim. Acta*, **1981II,** 375 (1981).
135. K. Wittmaack and J. B. Clegg, *Appl. Phys. Lett.*, **37,** 285 (1980).
136. F. M. Devienne and J. C. Roustan, *C. R. Acad. Sci., Ser. B*, **283,** 397 (1976).
137. G. Borchardt, S. Scherrer, and S. Weber, *Mikrochim. Acta*, **1981II,** 421 (1981).
138. J. B. Clegg, *Surf. Interface Anal.*, **2,** 91 (1980).
139. P. H. Holloway and H. J. Stein, *This Journal*, **123,** 723 (1979).
140. H. J. Mathieu and D. Landolt, *J. Microsc. Spectrosc. Electron.*, **3,** 113 (1978).
141. H. J. Mathieu, Le Vide-Les Couches Minces, Numero Spec., p. 273 (1979).
142. H. J. Mathieu, J. B. Mathieu, D. E. McClure, and D. Landolt, *J. Vac. Sci. Technol.*, **14,** 1023 (1977).
143. C. A. Andersen, *Int. J. Mass Spectrom. Ion Phys.*, **3,** 413 (1970).
144. W. Wach and K. Wittmaack, *Nucl. Instrum. Methods*, **149,** 259 (1978).
145. T. Ishitani, H. Tamura, and T. Shinmiyo, *Surf. Sci.*, **55,** 179 (1976).
146. K. Wittmaack, in "Inelastic Ion-Surface Collisions," p. 153, Academic Press, San Francisco and London (1977).
147. W. Wach and K. Wittmaack, in "SIMS II, Proceedings of 2nd International Conference, Stanford," p. 85, Springer, New York (1980).
148. P. Williams, R. K. Lewis, C. A. Evans, Jr., and P. R. Hanley, *Anal. Chem.*, **49,** 1399 (1977).
149. K. Wittmaack, *Appl. Phys. Lett.*, **29,** 552 (1976).
150. G. J. Clark, C. W. White, D. D. Allred, B. R. Appleton, C. W. Magee, and D. E. Carlson, *ibid.*, **31,** 582 (1977).
151. C. W. Magee, *This Journal*, **126,** 660 (1979).
152. G. Slodzian and J. F. Hennequin, *C. R. Acad. Sci., Ser. B*, **263,** 1246 (1966).
153. H. W. Werner, *Acta Electron.*, **19,** 53 (1976).
154. R. A. Powell, *J. Vac. Sci., Technol.*, **15,** 125 (1978).
155. T. S. Sun, D. K. McNamara, J. S. Ahearn, J. M. Chen, B. Ditchek, and J. D. Venables, *Appl. Surf. Sci.*, **5,** 406 (1980).
156. P. H. Holloway, *J. Electron Spectrosc. Relat. Phenom.*, **7,** 215 (1975).
157. H. H. Brongersma and J. B. Theeten, *Surf. Sci.*, **54,** 519 (1976).
158. G. C. Nelson, *J. Appl. Phys.*, **47,** 1253 (1976).
159. U. Littmark and W. O. Hofer, *J. Mater. Sci.*, **13,** 2577 (1978).
160. B. Navinsek, *Progr. Surf. Sci.*, **7,** 49 (1977).
161. I. H. Wilson, *Radiat. Eff.*, **18,** 95 (1973).
162. N. Hermanne, *ibid.*, **19,** 161 (1973).
163. R. S. Bhattacharya, D. Basu, and S. B. Karmohapatro, *ibid.*, **21,** 275 (1974).
164. G. K. Wehner and D. J. Hajicek, *J. Appl. Phys.*, **42,** 1145 (1971).
165. J. L. Whitton, G. Carter, M. J. Nobes, and J. S. Williams, *Radiat. Eff.*, **32,** 129 (1977).
166. R. S. Williams, R. J. Nelson, and A. R. Schlier, *Appl. Phys. Lett.*, **36,** 827 (1980).
167. W. O. Hofer and H. Liebl, *Appl. Phys.*, **8,** 359 (1975).
168. J. L. Whitton and G. Carter, in "Proceedings of Symposium on Sputtering, Perchtoldsdorf/Vienna," P. Varga, G. Betz, and F. P. Viehboeck, Editors, p. 552 (1980).
169. R. D. Webber and J. M. Walls, *Thin Solid Films*, **57,** 201 (1979).
170. H. M. Naguib and R. Kelly, *Radiat. Eff.*, **25,** 1 (1975).
171. I. H. Wilson, in "Ion Surface Interaction, Sputtering and Related Phenomena," R. Behrisch, W. Heiland, W. Poschenrieder, P. Staib, and H. Verbeek, Editors, p. 217, Gordon and Breach, London, New York, Paris (1973).
172. A. D. G. Stewart and M. W. Thompson, *J. Mater. Sci.*, **4,** 56 (1969).
173. C. Catana, J. S. Colligon, and G. Carter, *ibid.*, **7,** 467 (1972).
174. G. M. McCracken, *Rep. Progr. Phys.*, **38,** 241 (1975).
175. G. Carter, J. S. Colligon, and M. J. Nobes, *J. Mater. Sci.*, **6,** 115 (1971).
176. D. J. Barber, F. C. Frank, M. Moss, J. W. Steeds, and I. S. T. Tsong, *ibid.*, **8,** 1030 (1973).
177. S. S. Makh, R. Smith, and J. M. Walls, *Surf. Interface Anal.*, **2,** 115 (1980).
178. G. Carter, *J. Mater. Sci.*, **11,** 1091 (1976).
179. M. P. Seah and C. Lea, *Thin Solid Films*, **81,** 257 (1981).
180. S. Hofmann, J. Erlewein, and A. Zalar, *ibid.*, **43,** 275 (1977).
181. D. E. Sykes, D. D. Hall, R. E. Thurstans, and J. M. Walls, *Appl. Surf. Sci.*, **5,** 103 (1980).
182. C. F. Cook, Jr., C. R. Helms, and D. C. Fox, *J. Vac. Sci., Technol.*, **17,** 44 (1980).
183. R. J. Blattner, S. Nadel, C. A. Evans, Jr., A. J. Braundmeier, and C. W. Magee, *Surf. Interface Anal.*, **1,** 32 (1979).
184. H. M. Windawi, J. R. Katzer, and C. B. Cooper, *Phys. Lett. A*, **59,** 62 (1976).
185. H. J. Mathieu, D. E. McClure, and D. Landolt, *Thin Solid Films*, **38,** 281 (1976).
186. V. Naundorf and M. P. Macht, *Nucl. Instrum. Methods*, **168,** 405 (1980).
187. M. Bernheim, *Radiat. Eff.*, **18,** 231 (1973).
188. M. Bernheim and G. Slodzian, *Int. J. Mass Spectrom. Ion Phys.*, **12,** 93 (1973).
189. P. A. Buerger, F. Blum, and J. H. Schilling, *Z. Naturforsch., Teil A*, **32,** 144 (1977).
190. G. Carter and J. S. Colligon, "Ion Bombardment of Solids," American Elsevier, New York (1968).
191. P. D. Townsend, J. C. Kelly, and N. E. W. Hartley, "Ion Implantation, Sputtering and their Application," Academic Press, London (1976).
192. H. Oechsner, *Appl. Phys.*, **8,** 185 (1975).
193. R. Behrisch, Editor, "Sputtering by Particle Bombardment," Vol. 1, "Sputtering of Single Elements," Springer, Berlin, Heidelberg, New York (1981).
194. P. Sigmund, *Phys. Rev.*, **184,** 383 (1969).
195. D. P. Jackson, in "Proceedings of Symposium on Sputtering, Perchtoldsdorf/Vienna," P. Varga, G. Betz, and F. P. Viehboeck, Editors, p. 2 (1980).
196. P. Sigmund, in "Sputtering by Particle Bombardment," Vol. 1, "Sputtering of Single Elements," R. Behrisch, Editor, p. 9, Springer, Berlin, Heidelberg, New York (1981).
197. M. T. Robinson, in "Sputtering by Particle Bombardment," Vol. 1, "Sputtering of Single Elements," A. Behrisch, Editor, p. 73, Springer, Berlin, Heidelberg, New York (1981).
198. H. L. Bay, H. H. Andersen, W. O. Hofer, and O. Nielsen, *Nucl. Instrum. Methods*, **132,** 301 (1976).
199. H. M. Naguib and R. Kelly, *Radiat. Eff.*, **25,** 79 (1975).
200. R. W. Ollerhead, J. Bottiger, J. A. Davies, J. L'Ecuyer, H. K. Haugen, and N. Matsunami, *ibid.*, **49,** 203 (1980).
201. R. Kelly and N. Q. Lam, *ibid.*, **19,** 39 (1973).
202. M. Szymonski, H. Overeijnder, and A. E. de Vries, *ibid.*, **36,** 189 (1978).
203. R. Kelly, *ibid.*, **32,** 91 (1977).
204. G. Carter, D. G. Armour, and K. J. Snowdon, *ibid.*, **35,** 175 (1978).
205. H. H. Andersen and H. L. Bay, *ibid.*, **19,** 139 (1973).
206. H. H. Andersen and H. L. Bay, *J. Appl. Phys.*, **46,** 1919 (1975).
207. H. H. Andersen, *J. Vac. Sci. Technol.*, **16,** 770 (1979).
208. E. Gillam, *J. Phys. Chem. Solids*, **11,** 55 (1959).
209. G. Betz, M. Opitz, and P. Braun, *Nucl. Instrum. Meth-*

ods, **182/183,** 63 (1981).
210. W. Faerber and P. Braun, *Vakuum-Technik,* **23,** 239 (1974).
211. Z. L. Liau, B. Y. Tsaur, and J. W. Mayer, *J. Vac. Sci. Technol.*, **16,** 121 (1979).
212. S. Matteson, B. M. Paine, M. G. Grimaldi, G. Mezey, and M.-A. Nicolet, *Nucl. Instrum. Methods,* **182/183,** 43 (1981).
213. Z. L. Liau, W. L. Brown, R. Homer, and J. M. Poate, *Appl. Phys. Lett.*, **30,** 626 (1977).
214. R. Kelly, *Nucl. Instrum. Methods,* **149,** 553 (1978).
215. N. Andersen and P. Sigmund, *Mat. Fys. Medd. Dan. Vid. Selskab,* **39,** 1 (1974).
216. H. F. Winters and P. Sigmund, *J. Appl. Phys.*, **45,** 4760 (1974).
217. Z. L. Liau, J. W. Mayer, W. L. Brown, and J. M. Poate, *ibid.*, **49,** 5295 (1978).
218. P. K. Haff, *Appl. Phys. Lett.*, **31,** 259 (1977).
219. P. Sigmund, *J. Appl. Phys.*, **50,** 7261 (1979).
220. S. Dzioba and R. Kelly, *J. Nucl. Mater.*, **76/77,** 175 (1978).
221. P. Braun, F. Ruedenauer, and F. P. Viehboeck, *Adv. Electronics Electron Phys.*, **57,** 231 (1981).
222. K. S. Kim, W. E. Baitinger, J. W. Amy, and N. Winograd, *J. Electron Spectrosc. Relat. Phenom.*, **5,** 351 (1974).
223. H. F. Winters and J. W. Coburn, *Appl. Phys. Lett.*, **28,** 176 (1976).
224. N. J. Chou and M. W. Shafer, *Surf. Sci.*, **92,** 601 (1980).
225. H. M. Nitz, O. Ganschow, U. Kaiser, L. Wiedmann, and A. Benninghoven, *ibid.*, **104,** 365 (1981).
226. K. Roell, W. Losch, and C. Achete, *J. Appl. Phys.*, **50,** 4422 (1979).
227. P. S. Ho, *Surf. Sci.*, **72,** 253 (1978).
228. P. M. Hall and J. M. Morabito, *ibid.*, **67,** 373 (1977).
229. H. Shimizu, M. Ono, and K. Nakayama, *ibid.*, **36,** 817 (1973).
230. L. Holland and C. R. D. Priestland, *Vacuum,* **22,** 133 (1972).
231. H. W. Werner and N. Warmholtz, *Surf. Sci.*, **57,** 706 (1976).
232. P. S. Ho, J. E. Lewis, H. S. Wildman, and J. K. Howard, *ibid.*, **57,** 393 (1976).
233. P. S. Ho, J. E. Lewis, and J. K. Howard, *J. Vac. Sci. Technol.*, **14,** 322 (1977).
234. H. W. Pickering, *ibid.*, **13,** 618 (1976).
235. R. Collins, *Radiat. Eff.*, **37,** 13 (1978).
236. M. Arita and M. Someno, in "Proceedings of 7th International Vacuum Congress," p. 2511, Vienna (1977).
237. B. Y. Tsaur, Z. L. Liau, and J. W. Mayer, *Appl. Phys. Lett.*, **34,** 168 (1979).
238. W. K. Chu, J. K. Howard, and R. F. Lever, *J. Appl. Phys.*, **47,** 4500 (1976).
239. H. H. Andersen, *Appl. Phys.*, **18,** 131 (1979).
240. P. Sigmund and A. Gras-Marti, *Nucl. Instrum. Methods,* **168,** 389 (1980).
241. J. A. McHugh, *Radiat. Eff.*, **21,** 209 (1974).
242. F. Schulz, K. Wittmaack, and J. Maul, *ibid.*, **18,** 211 (1973).
243. E. Zinner, R. M. Walker, J. Chaumont, and J. C. Dran, in "Proceedings of 7th Lunar Science Conference," p. 953 (1976).
244. T. J. Chuang and K. Wandelt, *IBM J. Res. Dev.*, **22,** 277 (1978).
245. C. M. Garner, C. Y. Su, Y. D. Shen, C. S. Lee, G. L. Pearson, W. E. Spicer, D. D. Edwall, D. Miller, and J. S. Harris, Jr., *J. Appl. Phys.*, **50,** 3383 (1979).
246. S. A. Schwarz and C. R. Helms, *J. Vac. Sci. Technol.*, **16,** 781 (1979).
247. T. Ishitani, R. Shimizu, and H. Tamura, *Appl. Phys.*, **6,** 277 (1975).
248. P. Williams, *Appl. Phys. Lett.*, **36,** 758 (1980).
249. R. R. Hart, H. L. Dunlop, and O. J. Marsh, *J. Appl. Phys.*, **46,** 1947 (1975).
250. I. S. T. Tsong, J. R. Monkowski, and D. W. Hoffman, *Nucl. Instrum. Methods,* **182/183,** 237 (1981).
251. U. Littmark and W. O. Hofer, *ibid.*, **168,** 329 (1980).
252. S. M. Myers, *ibid.*, **168,** 265 (1980).
253. P. K. Haff and Z. E. Switkowski, *J. Appl. Phys.*, **48,** 3383 (1977).
254. S. Matteson, B. M. Paine, and M.-A. Nicolet, *Nucl. Instrum. Methods,* **182/183,** 53 (1981).
255. W. O. Hofer and U. Littmark, *Phys. Lett. A,* **71,** 457 (1979).
256. P. Sigmund and A. Gras-Marti, *Nucl. Instrum. Methods,* **182/183,** 25 (1981).
257. R. Kelly and J. B. Sanders, *Surf. Sci.*, **57,** 143 (1976).
258. A. Gras-Marti and P. Sigmund, in "Proceedings of Symposium on Sputtering, Perchtoldsdorf/Vienna," P. Varga, G. Betz, and F. P. Viehboeck, Editors, p. 512 (1980).
259. L. A. Christel, J. F. Gibbons, and S. Mylroie, *J. Appl. Phys.*, **51,** 6176 (1980).
260. A. Grob, J. J. Grob, N. Mesli, D. Salles, and P. Siffert, *Nucl. Instrum. Methods,* **182/183,** 85 (1981).
261. U. Littmark and W. O. Hofer, *ibid.*, **170,** 177 (1980).
262. T. Hirao, K. Inoue, and S. Takayanagi, *Appl. Phys. Lett.*, **31,** 505 (1977).
263. A. D. Marwick and R. C. Piller, *Nucl. Instrum. Methods,* **182/183,** 121 (1981).
264. T. Hirao, G. Fuse, K. Inoue, S. Takayanagi, Y. Yaegashi, S. Ichikawa, and T. Izumi, *J. Appl. Phys.*, **51,** 262 (1980).
265. T. Hirao, K. Inoue, Y. Yaegashi, and S. Takayanagi, *Jpn. J. Appl. Phys.*, **18,** 647 (1979).
266. R. A. Moline, G. W. Reutlinger, and J. C. North, in "Atomic Collisions in Solids," S. Datz, B. R. Appleton, and C. D. Moak, Editors, p. 159, Plenum Press, New York and London (1975).
267. T. J. Magee, C. Leung, H. Kawayoshi, L. J. Palkuti, B. K. Furman, C. A. Evans, Jr., L. A. Christel, J. F. Gibbons, and D. S. Day, *Appl. Phys. Lett.*, **39,** 564 (1981).
268. A. C. Yen, *J. Vac. Sci. Technol.*, **18,** 895 (1981).
269. T. Hirao, K. Inoue, S. Takayanagi, and Y. Yaegashi, *J. Appl. Phys.*, **50,** 193 (1979).
270. T. Ishitani and R. Shimizu, *Appl. Phys.*, **6,** 241 (1975).
271. S. T. Kang, R. Shimizu, and T. Okutani, *Jpn. J. Appl. Phys.*, **18,** 1987 (1979).
272. R. Shimizu, in "Proceedings of 7th International Vacuum Congress," p. 1417, Vienna (1977).
273. P. Williams and J. E. Baker, *Appl. Phys. Lett.*, **36,** 842 (1980).
274. J. C. Bourgoin and J. W. Corbett, *Radiat. Eff.*, **36,** 157 (1978).
275. R. Sizmann, *J. Nucl. Mater.*, **69/70,** 386 (1978).
276. Y. Adda, M. Beyeler, and G. Brebec, *Thin Solid Films,* **25,** 107 (1975).
277. G. Dearnaley, *Appl. Phys. Lett.*, **28,** 244 (1976).
278. J. Erlewein and S. Hofmann, *Thin Solid Films,* **69,** L39 (1980).
279. A. Benninghoven, *Z. Phys.*, **230,** 403 (1970).
280. S. Hofmann, in "Proceedings of 7th International Vacuum Congress," p. 2613, Vienna (1977).
281. S. Hofmann, *Appl. Phys.*, **13,** 205 (1977).
282. K. Wittmaack and F. Schulz, *Thin Solid Films,* **52,** 259 (1978).
283. J. M. Walls, A. D. Martin, and H. N. Southworth, *Surf. Sci.*, **50,** 360 (1975).
284. R. E. Honig and C. W. Magee, in "Proceedings of 26th Annual Conference on Mass Spectrometry," p. 207, St. Louis (1979).
285. R. Shimizu, *Appl. Phys.*, **18,** 425 (1979).
286. M. P. Seah, J. M. Sanz, and S. Hofmann, *Thin Solid Films,* **81,** 239 (1981).
287. P. Sigmund, *J. Mater. Sci.*, **8,** 1545 (1973).
288. P. Blank and K. Wittmaack, *Radiat. Eff.*, **27,** 29 (1975).
289. H. H. Andersen, in "Physics of Ionized Gases," V. Vujnivic, Editor, p. 361, Institute of Physics, Zagreb (1974).
290. H. H. Andersen, *Radiat. Eff.*, **19,** 257 (1973).
291. H. H. Andersen and H. L. Bay, *J. Appl. Phys.*, **46,** 2416 (1975).
292. R. S. Nelson, *Radiat. Eff.*, **32,** 19 (1977).
293. G. Carter, R. Webb, and R. Collins, *ibid.*, **37,** 21 (1978).
294. R. K. Lewis, J. M. Morabito, and J. C. C. Tsai, *Appl. Phys. Lett.*, **23,** 260 (1973).
295. K. Wittmaack, *Int. J. Mass Spectrom. Ion Phys.*, **17,** 39 (1975).
296. C. W. Magee, S. A. Cohen, D. E. Voss, and D. K. Brice, *Nucl. Instrum. Methods,* **168,** 383 (1980).
297. H. H. Madden, *J. Vac. Sci. Technol.*, **18,** 677 (1981).
298. R. Nishitani, H. Iwasaki, Y. Mizokawa, and S. Nakamura, *Jpn. J. Appl. Phys.*, **17,** 321 (1978).
299. G. E. McGuire, in "ARPA/NBS Workshop IV, Surface Analysis for Silicon Devices," NBS SP 400-23, p. 175, U. S. Dept. Commerce, Washington D. C. (1976).
300. R. C. McCune, *J. Vac. Sci. Technol.*, **18,** 700 (1981).
301. S. Storp and R. Holm, *J. Electron Spectrosc. Relat. Phenom.*, **16,** 183 (1979).
302. P. N. Favennec and H. L'Haridon, *Appl. Phys. Lett.*, **35,** 699 (1979).
303. J. W. Mayer, B. Y. Tsaur, S. S. Lau, and L. S. Hung, *Nucl. Instrum. Methods,* **182/183,** 1 (1981).
304. S. S. Lau, B. Y. Tsaur, M. von Allmen, J. W. Mayer, B. Stritzker, C. W. White, and B. Appleton, *ibid.*, **182/183,** 97 (1981).
305. K. L. Wang, F. Bacon, and R. F. Reihl, *J. Vac. Sci. Technol.*, **16,** 130 (1979).
306. K. L. Wang and H. A. Storms, in "SIMS II, Proceedings of 2nd International Conference, Stanford," p. 110, Springer, New York (1979).

307. K. L. Wang, F. Bacon, and R. F. Reihl, *J. Vac. Sci. Technol.*, **16,** 1909 (1979).
308. K. N. Tu and J. W. Mayer, in "Thin Films-Interdiffusions and Reactions," J. M. Poate, K. N. Tu, and J. W. Mayer, Editors, p. 359, John Wiley & Sons, New York (1978).
309. H. J. Mathieu and D. Landolt, in "Proceedings of 7th International Vacuum Congress," p. 2023, Vienna (1977).
310. S. Thomas, *Surf. Sci.*, **55,** 754 (1976).
311. T. E. Parker and R. Kelly, *J. Phys. Chem. Solids,* **36,** 379 (1975).
312. Y. Mizokawa, H. Iwasaki, R. Nishitani, and S. Nakamura, *Jpn. J. Appl. Phys., Suppl.,* **17-1,** 327 (1977).
313. Y. Mikozawa, H. Iwasaki, R. Nishitani, and S. Nakamura, *This Journal,* **126,** 1370 (1979).
314. S. Evans, *Proc. R. Soc. London, Ser. A,* **360,** 427 (1978).
315. T. E. Gallon, in "Electron and Ion Spectroscopy of Solids," L. Fiermans, J. Vennik, and W. Dekeyser, Editors, p. 230, Plenum Press, New York (1978).
316. J. T. Grant and M. P. Hooker, *Surf. Sci.*, **60,** 1 (1976).
317. J. T. Grant, R. G. Wolfe, M. P. Hooker, R. W. Springer, and T. W. Haas, *J. Vac. Sci. Technol.*, **14,** 232 (1977).
318. W. Reuter, M. L. Yu, M. A. Frisch, and M. B. Small, *J. Appl. Phys.*, **51,** 850 (1980).
319. A. Hurrle and G. Sixt, *Appl. Phys.*, **8,** 293 (1975).
320. T. A. Whatley, R. L. Conrad, and R. D. Fralick, in "Proceedings of 8th Conference on X-ray Optics Microanalysis and 12th Annual Conference of Microbeam Analysis Society," p. 135A (1977).
321. D. V. McCaughan and R. A. Kushner, in "Characterization of Solid Surfaces," P. F. Kane and G. R. Larrabee, Editors, p. 627, Plenum Press, New York and London (1974).
322. H. L. Hughes, R. D. Baxter, and B. Phillips, *IEEE Trans. Nucl. Sci.*, **ns-19** (6), 256 (1972).
323. G. Larrabee and R. Dobrott, NBS-GCS-79-158, Report (1979).
324 C. A. Andersen, H. J. Roden, and C. F. Robinson, *J. Appl. Phys.*, **40,** 3419 (1969).
325. A. E. Morgan, H. W. Werner, and J. M. Gourgout, *Appl. Phys.*, **12,** 283 (1977).
326. H. W. Werner and A. E. Morgan, *J. Appl. Phys.*, **47,** 1232 (1976).
327. R. Stefani, *Adv. Mass Spectrometry,* **7A,** 729 (1976).
328. E. Zinner, in "Proceedings of 13th Annual Conference of Microbeam Analysis Society," p. 32A (1978).
329. C. W. Magee and W. L. Harrington, *Appl. Phys. Lett.*, **33,** 193 (1978).
330. C. P. Hunt, C. T. H. Stoddart, and M. P. Seah, *Surf. Interface Anal.*, **3,** 157 (1981).
331. G. Mueller, *Appl. Phys.*, **10,** 317 (1976).
332. K. Wittmaack, *J. Appl. Phys.*, **50,** 493 (1979).
333. H. H. Brongersma, M. J. Sparnaay, and T. M. Buck, *Surf Sci.*, **71,** 657 (1978).
334. A. Crucq, L. Degols, G. Lienard, and A. Frennet, *ibid.*, **80,** 78 (1979).
335. S. Hofmann and J. Erlewein, *ibid.*, **77,** 591 (1978).
336. M. Yabumoto, K. Watanabe, and T. Yamashina, *ibid.*, **77,** 615 (1978).
337. P. Braun, W. Farber, G. Betz, and F. P. Viehboeck, *Vacuum,* **27,** 103 (1977).
338. S. Hofmann, *Mater. Sci. Eng.*, **42,** 55 (1980).
339. S. Hofmann, G. Blank, and H. Schultz, *Z. Metallk.*, **67,** 189 (1976).
340. R. Kelly, in "Proceedings of Symposium on Sputtering, Perchtoldsdorf/Vienna," P. Varga, G. Betz, and F. P. Viehboeck, Editors, p. 390 (1980).
341. R. S. Averback, L. E. Rehn, P. R. Okamoto, and R. E. Cook, *Nucl. Instrum. Methods,* **182/183,** 79 (1981).
342. A. D. Marwick and R. C. Piller, *Radiat. Eff.*, **47,** 195 (1980).
343. N. Q. Lam, P. R. Okamoto, and R. A. Johnson, *J. Nucl. Mater.*, **78,** 408 (1978).
344. N. Q. Lam, G. K. Leaf, and H. Wiedersich, *ibid.*, **85/86,** 1085 (1979).
345. N. Q. Lam, G. K. Leaf, and H. Wiedersich, *ibid.*, **88,** 289 (1980).
346. M. P. Seah and W. A. Dench, *Surf. Interface Anal.*, **1,** 2 (1979).
347. C. J. Powell, *Surf. Sci.*, **44,** 29 (1974).
348. J. Szajman, J. G. Jenkin, J. Liesegang, and R. C. G. Leckey, *J. Electron Spectrosc. Relat. Phenom.*, **14,** 41 (1978).
349. H. Iwasaki and S. Nakamura, *Surf. Sci.*, **57,** 779 (1976).
350. P. Pan, P. C. Velasquez, and R. W. Douse, *Surf. Interface Anal.*, **3,** 106 (1981).
351. D. M. Smith and T. E. Gallon, *J. Phys. D,* **7,** 151 (1974).
352. J. Kirschner, in "Scanning Electron Microscopy/1976," O. Johari, Editor, p. 215, Illinois Institute of Technology Research Institute, Chicago (1976).
353. G. Queirolo, *Thin Solid Films,* **56,** L21 (1979).
354. P. W. Palmberg, *Anal. Chem.*, **45,** 549A (1973).
355. A. Havette and G. Slodzian, *J. Phys.*, **41,** L247 (1980).
356. N. Shimizu, M. P. Semet, and C. J. Allegre, *Geochim. Cosmochim. Acta,* **42,** 1321 (1978).
357. J. S. Colligon and G. Kiriakidis, *Vacuum,* **29,** 357 (1979).
358. V. Krohn, *J. Appl. Phys.*, **33,** 3523 (1963).
359. P. W. Palmberg and T. N. Rhodin, *J. Phys. Chem. Solids,* **29,** 1917 (1968).
360. N. Itoh, *Nucl. Instrum. Methods,* **132,** 201 (1976).
361. B. Carriere and B. Lang, *Surf. Sci.*, **64,** 209 (1977).
362. J. S. Johannessen, C. R. Helms, W. E. Spicer, and Y. E. Strausser, *IEEE Trans. Electron Dev.*, **ed-24,** 547 (1977).
363. J. Ahn, C. R. Perleberg, D. L. Wilcox, J. W. Coburn, and H. F. Winters, *J. Appl. Phys.*, **46,** 4581 (1975).
364. J. S. Johannessen, W. E. Spicer, and Y. E. Strausser, *ibid.*, **47,** 3028 (1976).
365. J. S. Johannessen, W. E. Spicer, and Y. E. Strausser, *J. Vac. Sci. Technol.*, **13,** 849 (1976).
366. J. P. Coad, H. E. Bishop, and J. C. Riviere, *Surf. Sci.*, **21,** 253 (1970).
367. Y. Margoninski, *J. Appl. Phys.*, **47,** 3868 (1976).
368. S. Hofmann and A. Zalar, *Thin Solid Films,* **56,** 337 (1979).
369. C. R. Helms, W. E. Spicer, and N. M. Johnson, *Solid State Commun.*, **25,** 673 (1978).
370. C. R. Helms, C. M. Garner, J. Miller, I. Lindau, S. Schwarz, and W. E. Spicer, in "Proceedings of 7th International Vacuum Congress," p. 2241, Vienna (1977).
371. R. E. Honig and W. L. Harrington, *Thin Solid Films,* **19,** 43 (1973).
372. M. L. Tarng and G. K. Wehner, *J. Appl. Phys.*, **43,** 2268 (1972).
373. K. Roell and C. Hammer, *Thin Solid Films,* **57,** 209 (1979).
374. J. Gandon, J. C. Joud, and P. Desre, *J. Microsc. Spectrosc. Electron.*, **3,** 131 (1978).
375. R. Ludeke, L. Esaki, and L. L. Chang, *Appl. Phys. Lett.*, **24,** 417 (1974).
376. H. Oechsner, H. Schoof, and E. Stumpe, *Surf. Sci.*, **76,** 343 (1978).
377. K. Wittmaack, *ibid.*, **68,** 118 (1977).
378. C. R. Helms, N. M. Johnson, S. A. Schwarz, and W. E. Spicer, *J. Appl. Phys.*, **50,** 7007 (1979).
379. J. B. Malherbe and S. Hofmann, *Surf. Interface Anal.*, **2,** 187 (1980).
380. D. E. Carlson and C. W. Magee, *Appl. Phys. Lett.*, **33,** 81 (1978).
381. S. Selberherr, A. Schuetz, and H. W. Poetzl, *IEEE Trans. Electron Dev.*, **ed-27,** 1540 (1980).
382. D. A. Antoniadis, S. E. Hansen, and R. W. Dutton, Computer program SUPREM II-05, Integrated Circuits Laboratory, Stanford Electronics Laboratories.
383. A. Huber, G. Morillot, and P. Merenda, *J. Microsc. Spectrosc. Electron.*, **4,** 493 (1979).
384. J. R. Adams, *Surf. Sci.*, **56,** 307 (1976).
385. Y. S. Park, J. T. Grant, and T. W. Haas, *J. Appl. Phys.*, **50,** 809 (1979).
386. T. Nishioka and Y. Ohmachi, *ibid.*, **51,** 5789 (1980).
387. C. W. White and N. H. Tolk, *J. Nucl. Mater.*, **63,** 506 (1976).
388. A. E. Morgan, H. A. M. de Grefte, and H. J. Tolle, *J. Vac. Sci. Technol.*, **18,** 164 (1981).
389. C. W. Magee and C. P. Wu, *Nucl. Instrum. Methods,* **149,** 529 (1978).
390. C. W. Magee, J. C. Bean, G. Foti, and J. M. Poate, *Thin Solid Films,* **81,** 1 (1981).
391. T. W. Sigmon, in "SIMS II, Proceedings of 2nd International Conference, Stanford," p. 80, Springer, New York (1979).
392. P. Williams and C. A. Evans, Jr., *Appl. Phys. Lett.*, **30,** 559 (1977).
393. P. N. Favennec, M. Gauneau, H. L'Haridon, B. Deveaud, C. A. Evans, Jr., and R. J. Blattner, *ibid.*, **38,** 271 (1981).
394. R. G. Wilson and V. R. Deline, *ibid.*, **37,** 793 (1980).
395. R. G. Wilson and D. M. Jamba, *ibid.*, **39,** 715 (1981).
396. A. M. Huber, G. Morillot, P. Merenda, J. Perrocheau, J. L. Debrun, M. Valladon, and D. Koemmerer, *Inst. Phys. Conf. Ser. No. 56,* 579 (1981).
397. A. M. Huber, G. Morillot, P. Merenda, and N. T. Linh, in "SIMS II, 2nd International Conference, Stanford," p. 91, Springer, New York (1979).
398. C. W. Magee, in "SIMS II, 2nd International Conference, Stanford," p. 88, Springer, New York (1979).

399. N. G. Nakhodkin, A. F. Bardamid, A. I. Shaldervan, and S. P. Chenakin, *Thin Solid Films*, **65**, 209 (1980).
400. G. Mezey, E. Kotai, T. Nagy, L. Lohner, A. Manuba, J. Gyulai, V. R. Deline, C. A. Evans, Jr., and R. J. Blattner, *Nucl. Instrum. Methods*, **167**, 279 (1979).
401. H. Koyama, *J. Appl. Phys.*, **51**, 3202 (1980).
402. D. L. Staebler and J. I. Pankove, *Appl. Phys. Lett.*, **37**, 609 (1980).
403. S. Haridoss, F. Beniere, M. Gauneau, and A. Rupert, *J. Appl. Phys.*, **51**, 5833 (1980).
404. E. Fogarassy, R. Stuck, J. C. Muller, A. Grob, J. J. Grob, and P. Siffert, *J. Electron. Mater.*, **9**, 197 (1980).
405. R. Seguin and G. Brebec, *J. Microsc. Spectrosc. Electron.*, **5**, 243 (1980).
406. J. Chikawa and F. Sato, *Jpn. J. Appl. Phys.*, **19**, L159 (1980).
407. Z. L. Liau, S. S. Lau, M.-A. Nicolet, J. W. Mayer, R. J. Blattner, P. Williams, and C. A. Evans, Jr., *Nucl. Instrum. Methods*, **149**, 623 (1978).
408. T. J. Magee, C. Leung, H. Kawayoshi, B. K. Furman, and C. A. Evans, Jr., *Appl. Phys. Lett.*, **38**, 891 (1981).
409. J. Comas and R. G. Wilson, *J. Appl. Phys.*, **51**, 3697 (1980).
410. K. Inoue, T. Hirao, Y. Yaegashi, and S. Takayanagi, *Jpn. J. Appl. Phys.*, **18**, 367 (1979).
411. W. V. McLevige, K. V. Vaidyanathan, B. G. Streetman, J. Comas, and L. Plew, *Solid State Commun.*, **25**, 1003 (1978).
412. W. K. Hofker, H. W. Werner, D. P. Oosthoek, and H. A. M. de Grefte, *Radiat. Eff.*, **17**, 83 (1973).
413. W. K. Chu, R. H. Kastl, and P. C. Murley, *ibid.*, **47**, 1 (1980).
414. D. Fuller, J. S. Colligon, and J. S. Williams, *Surf. Sci.*, **54**, 647 (1976).
415. S. Kalbitzer and H. Oetzmann, *Radiat. Eff.*, **47**, 57 (1980).
416. A. Desalvo, R. Galloni, R. Rosa, and F. Zignani, *J. Appl. Phys.*, **51**, 1994 (1980).
417. W. K. Hofker, H. W. Werner, D. P. Oosthoek, and N. J. Koeman, *Appl. Phys.*, **4**, 125 (1974).
418. D. K. Sadana, M. Strathman, J. Washburn, C. W. Magee, M. Maenpaa, and G. R. Booker, *Appl. Phys. Lett.*, **37**, 615 (1980).
419. R. G. Wilson and J. Comas, *Radiat. Eff.*, **47**, 137 (1980).
420. J. C. Muller, J. J. Grob, A. Grob, R. Stuck, and P. Siffert, *ibid.*, **48**, 115 (1980).
421. M. Y. Tsai and B. G. Streetman, *J. Appl. Phys.*, **50**, 183 (1979).
422. M. Y. Tsai, D. S. Day, B. G. Streetman, P. Williams, and C. A. Evans, Jr., *ibid.*, **50**, 188 (1979).
423. D. Lecrosnier, G. Pelous, and F. Richou, *Radiat. Eff.*, **48**, 101 (1980).
424. G. J. Van Gurp, J. W. Slotbloom, F. J. B. Smolders, W. T. Stacy, and Y. Tamminga, *This Journal*, **127**, 1813 (1980).
425. R. Tielert, *IEEE Trans. Electron Dev.*, **ed-26**, 490 (1979).
426. D. Fuoss and J. A. Topich, *Appl. Phys. Lett.*, **36**, 275 (1980).
427. F. Simondet, C. Venger, G. M. Martin, and J. Chaumont, *Appl. Phys.*, **23**, 21 (1980).
428. C. W. White, J. Narayan, and R. T. Young, *Science*, **204**, 461 (1979).
429. G. K. Celler, J. M. Poate, and L. C. Kimerling, *Appl. Phys. Lett.*, **32**, 464 (1978).
430. A. Gat, T. J. Magee, J. Peng, V. R. Deline, and C. A. Evans, Jr., *Solid State Technol.*, **22** (11), 59 (1979).
431. W. H. Christie, R. J. Warmack, C. W. White, and J. Narayan, in "SIMS II, Proceedings of 2nd International Conference, Stanford," p. 100, Springer, New York (1979).
432. W. H. Christie and C. W. White, *Surf. Sci.*, **100**, 43 (1980).
433. C. W. White, W. H. Christie, P. P. Pronko, B. R. Appleton, S. R. Wilson, R. T. Young, J. C. Wang, R. F. Wood, and J. Narayan, *Radiat. Eff.*, **47**, 37 (1980).
434. C. W. White, W. H. Christie, B. R. Appleton, S. R. Wilson, P. P. Pronko, and C. W. Magee, *Appl. Phys. Lett.*, **33**, 662 (1978).
435. J. F. Gibbons, J. L. Regolini, A. Lietoila, T. W. Sigmon, T. J. Magee, J. Peng, J. D. Hong, W. Katz, and C. A. Evans, Jr., *J. Appl. Phys.*, **50**, 4388 (1979).
436. A. Gat, L. Gerzberg, J. F. Gibbons, A. Lietoila, N. M. Johnson, T. J. Magee, J. Peng, V. Deline, P. Williams, and C. A. Evans, Jr., *Radiat. Eff.*, **48**, 195 (1980).
437. A. Gat, J. F. Gibbons, T. J. Magee, J. Peng, V. R. Deline, P. Williams, and C. A. Evans, Jr., *Appl. Phys. Lett.*, **32**, 276 (1978).
438. A. Gat, J. F. Gibbons, T. J. Magee, J. Peng, P. Williams, V. R. Deline, and C. A. Evans, Jr., *ibid.*, **33**, 389 (1978).
439. F. H. Eisen, *Radiat. Eff.*, **47**, 99 (1980).
440. J. P. Donnelly, *Inst. Phys. Conf. Ser. No. 33b*, 166 (1977).
441. J. Comas and L. Plew, *J. Electron. Mater.*, **5**, 209 (1976).
442. K. S. Lee, J. M. Ess, M. A. Littlejohn, R. B. Benson, Jr., and J. Comas, *ibid.*, **9**, 185 (1980).
443. G. K. Hubler, J. Comas, and L. Plew, *Nucl. Instrum. Methods*, **149**, 635 (1978).
444. B. Toulouse, P. N. Favennec, A. Guivarc'h, and G. Pelous, *Inst. Phys. Conf. Ser. No. 45*, 501 (1979).
445. E. V. K. Rao, N. Duhamel, P. N. Favennec, and H. L'Haridon, *J. Appl. Phys.*, **49**, 3898 (1978).
446. C. G. Hopkins, V. R. Deline, R. J. Blattner, C. A. Evans, Jr., and T. J. Magee, *Appl. Phys. Lett.*, **36**, 989 (1980).
447. T. J. Magee, K. S. Lee, R. Ormond, R. J. Blattner, and C. A. Evans, Jr., *ibid.*, **37**, 447 (1980).
448. T. J. Magee, K. S. Lee, R. Ormond, C. A. Evans, Jr., R. J. Blattner, and C. Hopkins, *ibid.*, **37**, 635 (1980).
449. T. J. Magee, R. D. Ormond, C. A. Evans, Jr., R. J. Blattner, R. M. Malbon, D. S. Day, and R. Sankaran, *ibid.*, **38**, 559 (1981).
450. H. Krautle, *Nucl. Instrum. Methods*, **182/183**, 625 (1981).
451. D. H. Lee and R. M. Malbon, *Appl. Phys. Lett.*, **30**, 327 (1977).
452. A. Masuyama, M.-A. Nicolet, I. Golecki, J. L. Tandon, D. K. Sadana, and J. Washburn, *ibid.*, **36**, 749 (1980).
453. S. G. Liu, E. C. Douglas, C. P. Wu, C. W. Magee, S. Y. Narayan, S. T. Jolly, F. Kolondra, and S. Jain, *RCA Rev.*, **41**, 217 (1980).
454. S. G. Liu, E. C. Douglas, C. W. Magee, F. Kolondra, and S. Jain, *Appl. Phys. Lett.*, **37**, 79 (1980).
455. P. K. Vasudev, R. G. Wilson, and C. A. Evans, Jr., *ibid.*, **36**, 837 (1980).
456. P. K. Vasudev, R. G. Wilson, and C. A. Evans, Jr., *ibid.*, **37**, 308 (1980).
457. R. G. Wilson, P. K. Vasudev, D. M. Jamba, C. A. Evans, Jr., and V. R. Deline, *ibid.*, **36**, 215 (1980).
458. R. G. Wilson, *J. Appl. Phys.*, **52**, 3954 (1981).
459. B. Deveaud and P. N. Favennec, *Solid State Commun.*, **24**, 473 (1977).
460. A. Lidow, J. F. Gibbons, V. R. Deline, and C. A. Evans, Jr., *Appl. Phys. Lett.*, **32**, 15 (1978).
461. A. Lidow, J. F. Gibbons, V. R. Deline, and C. A. Evans, Jr., *ibid.*, **32**, 149 (1978).
462. A. Lidow, J. F. Gibbons, V. R. Deline, and C. A. Evans, Jr., *J. Appl. Phys.*, **51**, 4130 (1980).
463. A. Lidow, J. F. Gibbons, V. R. Deline, and C. A. Evans, Jr., *Appl. Phys. Lett.*, **32**, 572 (1978).
464. P. M. Asbeck, J. Tandon, B. M. Welch, C. A. Evans, Jr., and V. R. Deline, *IEEE Electron Dev. Lett.*, **edl-1**, 35 (1980).
465. Y. Makita, H. Nojiri, T. Tsurushima, H. Tanoue, and J. Shimada, *Appl. Phys. Lett.*, **35**, 293 (1979).
466. R. C. Eden, B. M. Welch, R. Zucca, and S. I. Long, *IEEE J. Solid State Circuits*, **cs-14**, 221 (1979).
467. J. P. Donnelly, C. O. Bozler, and W. T. Lindley, *Solid State Electron.*, **20**, 273 (1977).
468. T. J. Magee, J. Hung, V. R. Deline, and C. A. Evans, Jr., *Appl. Phys. Lett.*, **37**, 53 (1980).
469. A. M. Huber, G. Morillot, N. T. Linh, P. N. Favennec, B. Deveaud, and B. Toulouse, *ibid.*, **34**, 858 (1979).
470. J. Kasahara and N. Watanabe, *Jpn. J. Appl. Phys.*, **19**, L151 (1980).
471. V. Eu, M. Feng, W. B. Henderson, H. B. Kim, and J. M. Whelan, *Appl. Phys. Lett.*, **37**, 473 (1980).
472. T. J. Magee, J. Peng, J. D. Hong, C. A. Evans, Jr., and V. R. Deline, *Phys. Status Solidi A*, **55**, 169 (1979).
473. P. E. R. Nordquist, P. B. Klein, S. G. Bishop, and P. G. Siebermann, *Inst. Phys. Conf. Ser. No. 56*, 569 (1981).
474. T. J. Magee, J. Peng, J. D. Hong, C. A. Evans, Jr., V. R. Deline, and R. M. Malbon, *Appl. Phys. Lett.*, **35**, 277 (1979).
475. M. Feng, V. Eu, T. Zielinski, H. B. Kim, and J. M. Whelan, *ibid.*, **38**, 688 (1981).
476. A. Lidow, J. F. Gibbons, T. J. Magee, and J. Peng, *J. Appl. Phys.*, **49**, 5213 (1978).
477. D. Mathiot, A. M. Huber, J. Perrocheau, and G. Morillot, *Inst. Phys. Conf. Ser. No. 56*, 689 (1981).
478. K. V. Vaidyanathan, C. L. Anderson, H. L. Dunlap, and D. E. Holmes, *Nucl. Instrum. Methods*, **182/183**, 631 (1981).
479. W. J. Devlin, K. T. Ip, D. P. Leta, L. F. Eastman, G. H. Morrison, and J. Comas, *Inst. Phys. Conf. Ser. No. 45*, 510 (1979).
480. W. V. McLevige, K. V. Vaidyanathan, B. G. Streetman, J. Comas, and L. Plew, *J. Electron. Mater.*, **7**, 547 (1978).
481. H. Scherrer, G. Pineau, and S. Scherrer, *Phys. Lett. A*, **75**, 118 (1979).
482. G. Pineau, H. Scherrer, and S. Scherrer, *ibid.*, **75**, 234 (1980).

483. H. Scherrer, S. Weber, and S. Scherrer, *ibid.*, **77,** 189 (1980).
484. F. Hottier, J. Hallais, and F. Simondet, *J. Appl. Phys.*, **51,** 1599 (1980).
485. A. van Oostrom, L. Augustus, W. Nijman, and W. Leswin, *J. Vac. Sci. Technol.*, **17,** 40 (1980).
486. C. M. Garner, Y. D. Shen, J. S. Kim, G. L. Pearson, W. E. Spicer, J. S. Harris, Jr., and D. D. Edwall, *J. Appl. Phys.*, **48,** 3147 (1977).
487. H. Morkoc, C. Hopkins, C. A. Evans, Jr., and A. Y. Cho, *ibid.*, **51,** 5986 (1980).
488. T. Fukui and Y. Horikoshi, *Jpn. J. Appl. Phys.*, **19,** L551 (1980).
489. H. Elabd and A. J. Steckl, *J. Appl. Phys.*, **51,** 726 (1980).
490. H. Elabd and A. J. Steckl, *J. Electron. Mater.*, **9,** 525 (1980).
491. D. G. Fisher and G. H. Olsen, *J. Appl. Phys.*, **50,** 2930 (1979).
492. M. Iwami, S. Kim, I. Matsuo, and A. Hiraki, *J. Cryst. Growth*, **45,** 467 (1978).
493. K. J. Matysik and F. G. Ramos, *J. Vac. Sci. Technol.*, **18,** 372 (1981).
494. L. L. Kazmerski, *Thin Solid Films*, **57,** 99 (1979).
495. G. Moore, H. Guckel, and M. G. Lagally, *J. Vac. Sci. Technol.*, **14,** 70 (1977).
496. J. F. Wager and C. W. Wilmsen, *J. Appl. Phys.*, **50,** 874 (1979).
497. C. C. Chang and D. M. Boulin, *Surf. Sci.*, **69,** 385 (1977).
498. H. Frenzel and P. Balk, *J. Vac. Sci. Technol.*, **16,** 1454 (1979).
499. Y. E. Strausser and K. S. Majumder, *ibid.*, **15,** 238 (1978).
500. J. Cain and E. Sachet, *J. Colloid Interface Sci.*, **67,** 538 (1978).
501. A. Suzuki, H. Matsunami, and T. Tanaka, *This Journal*, **125,** 1896 (1978).
502. K. Watanabe, M. Hashiba, and T. Yamashina, *Jpn. J. Appl. Phys., Suppl.*, **17-1,** 335 (1977).
503. K. Watanabe, M. Hashiba, Y. Hirohata, M. Nishino, and T. Yamashina, *Thin Solid Films*, **56,** 63 (1979).
504. L. L. Kazmerski and P. J. Ireland, *Surf. Interface Anal.*, **1,** 144 (1979).
505. C. C. Chang, B. Schwartz, and S. P. Murarka, *This Journal*, **124,** 922 (1977).
506. H. J. Bilz, G. Leonhardt, G. Kuhn, K. Loschke, and A. Meisel, *Krist. Tech.*, **13,** 363 (1978).
507. L. L. Kazmerski, P. J. Ireland, S. S. Chu, and Y. T. Lee, *J. Vac. Sci. Technol.*, **17,** 521 (1980).
508. K. M. Geib and C. W. Wilmsen, *ibid.*, **17,** 952 (1980).
509. Y. Mizokawa, H. Iwasaki, R. Nishitani, and S. Nakamura, in "Proceedings of 7th International Vacuum Congress," p. 631, Vienna (1977).
510. G. P. Schwartz, G. J. Gaulteri, G. W. Kammlott, and B. Schwartz, *This Journal*, **126,** 1737 (1979).
511. C. W. Wilmsen, R. W. Kee, and K. M. Geib, *J. Vac. Sci. Technol.*, **16,** 1434 (1979).
512. P. Breeze, H. L. Hartnagel, and P. M. A. Sherwood, *This Journal*, **127,** 454 (1980).
513. C. W. Wilmsen and R. W. Kee, *J. Vac. Sci. Technol.*, **15,** 1513 (1978).
514. M. Croset, J. Diaz, D. Dieumegard, and L. M. Merandalli, *This Journal*, **126,** 1543 (1979).
515. A. Okada, *Appl. Phys. Lett.*, **33,** 447 (1978).
516. L. L. Kazmerski, P. J. Ireland, P. Sheldon, T. L. Chu, S. S. Chu, and C. L. Lin, *J. Vac. Sci. Technol.*, **17,** 1061 (1980).
517. D. A. Baglee, D. K. Ferry, C. W. Wilmsen, and H. H. Wieder, *ibid.*, **17,** 1032 (1980).
518. J. A. Roth and C. R. Crowell, *ibid.*, **15,** 1317 (1978).
519. J. Verhoeven and H. van Doveren, *Thin Solid Films*, **77,** 367 (1981).
520. T. S. Sun, S. P. Buchner, and N. E. Byer, *J. Vac. Sci. Technol.*, **17,** 1067 (1980).
521. H. Bispinck, O. Ganschow, L. Wiedmann, and A. Benninghoven, *Appl. Phys.*, **18,** 113 (1979).
522. N. S. McIntyre and D. G. Zetaruk, *J. Vac. Sci. Technol.*, **14,** 181 (1977).
523. H. R. Grinolds and G. Y. Robinson, *Solid State Electron.*, **23,** 973 (1980).
524. C. P. Lofton and W. E. Swartz, Jr., *Thin Solid Films*, **52,** 271 (1978).
525. S. T. Pantalides, Editor, "The Physics of SiO_2 and Its Interfaces," Pergamon, New York (1978).
526. I. Barsony, D. Marton, and J. Giber, *Thin Solid Films*, **51,** 275 (1978).
527. C. R. Helms, Y. E. Strausser, and W. E. Spicer, *Appl. Phys. Lett.*, **33,** 767 (1978).
528. J. M. Hill, D. G. Royce, M. Mehta, C. S. Fadley, L. F. Wager, and F. J. Grunthaner, *J. Vac. Sci. Technol.*, **14,** 376 (1977).
529. F. J. Grunthaner and J. Maserjian, *IEEE Trans. Nucl. Sci.*, **ns-24,** 2108 (1977).
530. S. I. Raider and R. Flitsch, in "Proceedings of International Topical Conference on the Physics of SiO_2 and Its Interfaces," p. 384, Pergamon, New York (1978).
531. S. A. Schwarz, C. R. Helms, W. E. Spicer, and N. J. Taylor, *J. Vac. Sci. Technol.*, **15,** 227 (1978).
532. J. W. Colby and L. E. Katz, *This Journal*, **123,** 409 (1976).
533. B. Blanchard, N. Hilleret, and J. B. Quoirin, *J. Radioanal. Chem.*, **12,** 85 (1972).
534. V. R. Deline, P. Williams, and C. A. Evans, Jr., in "Proceedings of 13th Annual Conference of Microbeam Analysis Society, p. 5A (1978).
535. K. L. Wang and P. Gray, *This Journal*, **123,** 1392 (1976).
536. A. Benninghoven, W. Sichtermann, and S. Storp, *Thin Solid Films*, **28,** 59 (1975).
537. K. Wittmaack, *Surf. Sci.*, **68,** 118 (1977).
538. J. C. Mikkelsen, Jr., *Appl. Phys. Lett.*, **39,** 601 (1981).
539. N. M. Johnson, D. K. Biegelsen, M. D. Moyer, V. R. Deline, and C. A. Evans, Jr., *ibid.*, **38,** 995 (1981).
540. J. Liday, R. Harman, and M. Vesely, *Vacuum*, **27,** 129 (1977).
541. V. J. Kapoor, R. S. Bailey, and S. R. Smith, *J. Vac. Sci. Technol.*, **18,** 305 (1981).
542. G. J. Slusser and J. S. Slattery, *ibid.*, **18,** 301 (1981).
543. K. Yamasaki and T. Sugano, *ibid.*, **17,** 959 (1980).
544. M. Croset, J. Diaz, D. Dieumegard, and L. M. Mercandalli, in "Proceedings of 7th International Vacuum Congress," p. 2551, Vienna (1977).
545. A. J. Bevolo, G. J. Campisi, H. R. Shanks, and F. A. Schmidt, *J. Appl. Phys.*, **51,** 5390 (1980).
546. H. Ogata, K. Kanayama, M. Ohtani, K. Fujiwara, H. Abe, and H. Nakayama, *Thin Solid Films*, **48,** 333 (1978).
547. S. V. Krishnaswamy, L. L. Tongson, N. Said, and R. Messier, *J. Vac. Sci. Technol.*, **18,** 401 (1981).
548. W. J. Garceau, P. R. Fournier, and G. K. Herb, *Thin Solid Films*, **60,** 237 (1979).
549. L. E. Bradley and J. R. Sites, *J. Vac. Sci. Technol.*, **16,** 189 (1979).
550. T. Inada, S. Taka, and T. Hara, *Nucl. Instrum. Methods*, **182/183,** 641 (1981).
551. H. Birey, S.-J. Pak, J. R. Sites, and J. F. Wager, *J. Vac. Sci. Technol.*, **16,** 2086 (1979).
552. R. C. McCune, *ibid.*, **15,** 31 (1978).
553. H. M. Hindam and W. W. Smeltzer, *Oxid. Met.*, **14,** 337 (1980).
554. M. B. Chamberlain and R. J. Lederich, *Thin Solid Films*, **41,** 167 (1977).
555. A. W. Czanderna, A. C. Miller, H. H. G. Jellinek, and H. Kachi, *J. Vac. Sci. Technol.*, **14,** 227 (1977).
556. C. C. Lo and H. G. Tompkins, *J. Appl. Phys.*, **47,** 3496 (1976).
557. H. H. Strehblow and D. L. Malm, *Corros. Sci.*, **19,** 469 (1979).
558. R. P. Frankenthal and D. M. Malm, *This Journal*, **123,** 186 (1976).
559. Y. Fujii, F. Kanematsu, T. Koshikawa, and E. Sugata, *J. Vac. Sci. Technol.*, **17,** 1221 (1980).
560. D. Laser and H. L. Marcus, *This Journal*, **127,** 763 (1980).
561. F. Nakao, M. Birakawa, and T. Yamamoto, *J. Vac. Sci. Technol.*, **16,** 1017 (1979).
562. B. Schwartz, Editor, "Ohmic Contacts to Semiconductors," The Electrochemical Society, New York (1969).
563. K. E. Singer, *Thin Solid Films*, **57,** 115 (1979).
564. S. M. Goodnick, M. Fathipour, D. L. Ellsworth, and C. W. Wilmsen, *J. Vac. Sci. Technol.*, **18,** 949 (1981).
565. C. C. Chang, T. T. Sheng, D. V. Speeney, and D. B. Fraser, *J. Appl. Phys.*, **47,** 1790 (1976).
566. P. B. Ghate, J. C. Blair, C. R. Fuller, and G. E. McGuire, *Thin Solid Films*, **53,** 117 (1978).
567. L. D. Hartsough, A. Koch, J. Moulder, and T. Sigmon, *J. Vac. Sci. Technol.*, **17,** 392 (1980).
568. J. K. Howard and P. L. Garbarino, *ibid.*, **15,** 243 (1978).
569. T. E. Brady and C. T. Hovland, *ibid.*, **18,** 339 (1981).
570. H. G. Tompkins and M. R. Pinnel, *J. Appl. Phys.*, **48,** 3144 (1977).
571. R. S. Nowicki and I. Wang, *J. Vac. Sci. Technol.*, **15,** 235 (1978).
572. N. T. Panoussis, *Thin Solid Films*, **64,** 41 (1979).
573. J. L. Vossen, J. J. O'Neill, Jr., O. R. Mesker, and E. A. James, *J. Vac. Sci. Technol.*, **14,** 85 (1977).
574. L. S. Weinman, T. W. Orent, and T. S. Liu, *Thin Solid Films*, **72,** 143 (1980).
575. C. T. Kemmerer and R. H. Mills, *J. Vac. Sci. Technol.*, **16,** 352 (1979).
576. V. Atzrodt, T. Wirth, and H. Lange, *Phys. Status Solidi A*, **62,** 531 (1980).

577. H. Grinolds and G. Y. Robinson, *J. Vac. Sci. Technol.*, **14,** 75 (1977).
578. J. N. Miller, S. A. Schwarz, I. Lindau, W. E. Spicer, B. DeMichelis, I. Abbati, and L. Braicovich, *ibid.*, **17,** 920 (1980).
579. H. Kotake, Y. Oana, and I. W. Watanabe, *Thin Solid Films*, **75,** 247 (1981).
580. G. L. P. Berning, K. H. Yoon, G. Lewis, S. Sinsharoy, and L. Levenson, *ibid.*, **45,** 141 (1977).
581. E. Hokelek and G. Y. Robinson, *ibid.*, **53,** 135 (1978).
582. R. S. Nowicki and J. F. Moulder, *This Journal*, **128,** 562 (1981).
583. A. J. Bevolo, F. A. Schmidt, H. R. Shanks, and G. J. Campisi, *J. Vac. Sci. Technol.*, **16,** 13 (1979).
584. R. K. Quinn, M. L. Knotek, N. R. Armstrong, and N. E. Vanderborgh, *This Journal*, **123,** 1794 (1976).
585. A. C. Miller and A. W. Czanderna, *Appl. Surf. Sci.*, **4,** 481 (1980).
586. A. W. Czanderna and R. Summermatter, *J. Vac. Sci. Technol.*, **13,** 384 (1976).
587. K. Hieber and E. Lautenbacher, *Thin Solid Films*, **66,** 191 (1980).
588. G. E. McGuire, W. R. Wisseman, R. D. Ragle, and J. H. Tregilgas, *J. Vac. Sci. Technol.*, **16,** 141 (1979).
589. C. P. Lee, J. L. Tandon, and P. J. Stocker, *Electron. Lett.*, **16,** 849 (1980).
590. G. Y. Robinson, *Solid State Electron.*, **18,** 331 (1975).
591. A. Oustry, M. Caumont, A. Escaut, A. Martinez, and B. Toprasertpong, *Thin Solid Films*, **79,** 251 (1981).
592. A. K. Sinha, T. E. Smith, and H. J. Levinstein, *IEEE Trans. Electron Dev.*, **ed-22,** 218 (1975).
593. T. J. Magee, J. Peng, J. D. Hong, V. R. Deline, and C. A. Evans, Jr., *Appl. Phys. Lett.*, **35,** 615 (1979).
594. P. W. Chye, I. Lindau, P. Pianetta, C. M. Garner, C. Y. Su, and W. E. Spicer, *Phys. Rev. B*, **18,** 5545 (1978).
595. S. D. Mukherjee, D. V. Morgan, M. J. Howes, J. G. Smith, and P. Brook, *J. Vac. Sci. Technol.*, **16,** 138 (1979).
596. S. J. Ingrey, F. R. Shepherd, and W. D. Westwood, *ibid.*, **17,** 481 (1980).
597. F. R. Shepherd, H. Nentwich, W. D. Westwood, and S. J. Ingrey, *ibid.*, **17,** 485 (1980).
598. H. S. Gill and J. H. Judy, *J. Appl. Phys.*, **50,** 1648 (1979).
599. L. F. Herte and A. Lang, Jr., *J. Vac. Sci. Technol.*, **18,** 153 (1981).
600. S. Yasugi, S. Honda, M. Ohkoshi, and T. Kusuda, *J. Appl. Phys.*, **52,** 2298 (1981).
601. S. Hofmann and A. Zalar, *Thin Solid Films*, **39,** 219 (1976).
602. A. Zalar, A. Banovec, and S. Hofmann, in "Proceedings of 7th International Vacuum Congress," p. 2303, Vienna (1977).
603. M. L. Yu and W. Reuter, *J. Vac. Sci. Technol.*, **17,** 36 (1980).

JOURNAL OF THE ELECTROCHEMICAL SOCIETY

ELECTROCHEMICAL SCIENCE AND TECHNOLOGY

JUNE 1983

The Li/Cl_2 in SO_2Cl_2 Inorganic Battery System

III. High Rate Performance, Storability, and Safety Characteristics

R. M. Murphy*,[1] and C. C. Liang*,[1]

Electrochem Industries (E · I) Incorporated, Clarence, New York 14031

ABSTRACT

A study to determine the high rate performance, storability, and safety characteristics for the Li/Cl_2 in SO_2Cl_2 (Li/CSC) inorganic battery system was conducted. The results for practical, spirally wound D cells discharged under constant current conditions at different temperatures show no significant differences in realized capacities (*e.g.*, 10.0 and 10.2 A-hr for cells discharged at the 12.0A rate at −2° and +25°C, respectively). Comparison of the performance characteristics for D cells discharged under constant current (1.0-15.0A) and constant load (3.00-0.14Ω) conditions at 25°C shows an increase in realized capacities as well as load voltage levels for those cells discharged under constant load conditions. Investigation of the storability and voltage delay characteristics for 1.5 year old prototype DD cells shows little or no loss in realized capacity for cells discharged under loads of 3.00-0.59Ω, but do exhibit decreased realized capacities when discharged under heavier loads (*e.g.*, 21.0 A-hr realized capacity to a 2.0V cutoff level under a 0.24Ω load at 25°C). Safety and hazards characterization relative to high rate testing show that D cells will vent when discharged under constant current conditions above 6.0A. When cells were discharged under constant load conditions, however, only those cells under loads of 0.24Ω and lower (*i.e.*, greater than the 12A rate) vented through a cracked glass to metal seal. Additional safety/hazards characteristics relative to the Li/CSC system are discussed.

The low-to-medium rate performance, safety, and storability characteristics for practical cells of the Li/Cl_2 in SO_2Cl_2 (Li/CSC) system have been reported previously (1-3). These results indicate that Li/CSC cells have high current delivering capabilities, high energy densities, exceptional safety characteristics, and low self-discharge rates. It has become increasingly apparent that the Li/CSC system is being considered as an attractive power source candidate in many applications requiring high power and energy densities. A study was initiated, therefore, to investigate the performance and, just as importantly, the safety characteristics relative to discharge at high rates (*i.e.*, 0.1-1.5C) at temperatures of −2° and +25°C under both constant current and constant load conditions. Further, a study to determine the effect of increased geometric surface area of the carbon electrode on the discharge/safety characteristics at −2°C under constant current conditions of 15.0A showed that those cells having the increased surface area not only yielded higher capacities and load voltage levels, but also vented at a voltage level one volt below that observed for the state-of-the-art cell.

In addition to the safety/hazard characteristics associated with high rate discharge conditions, safety testing has been extended beyond the scope of forced overdischarge, short circuit, the sequence of forced overdischarge/charge, incineration, and shock sensitivity testing to include crushing, penetration (high and low velocity), and localized heating. It has been found that specific combinations of two or more usually nonhazardous abusive conditions may result in cell venting, rupture, and/or explosion.

The storability characteristics for the Li/CSC system have been discussed previously (1, 2). It was found that the self-discharge predictions based upon microcalorimetry data did not correlate with the results obtained from performance testing of stored cells (1). Further, no correspondence in the self-discharge rate could be made between storage at elevated temperatures (*i.e.*, 72°C or higher) with subsequent discharge at 25°C and ambient temperature storage for extended periods of time (2). The performance results obtained from long-term ambient temperature storage showed that little or no decrease in realized capacity was observed when cells were discharged at low to medium rates, but cells did show some capacity loss when discharged at moderately high rates. Additionally, a lowered rate capability was observed for all cells tested with the exception of those cells under very low discharge rates. This work has been extended to include high rate performance testing of prototype Li/CSC DD cells stored for 1.5 years. Comparison of the results obtained following storage to those obtained from fresh prototype Li/CSC DD cells, as well as the present state-of-the-art Li/CSC DD cells, show little loss in capacity for loads as heavy as 0.59Ω (approximately 5.5A) but do indeed show a significant decrease in realized capacity when discharged under heavier loads of 0.50Ω or less.

Experimental

Details relative to the preparation of the Cl_2 in SO_2Cl_2 codepolarizer solution and cell fabrication were given previously (2). The optimum concentrations of Cl_2 and $LiAlCl_4$ in SO_2Cl_2 were found to be 0.45 and 1.45 M, respectively. The electrolyte solution fill weights for Li/CSC D and DD cells used in this investigation were 43 ± 1g and 89 ± 1g, respectively.

Two types of spirally wound Li/CSC D cells were fabricated for use in these studies. The first represents the state-of-the-art standard production cell having a carbon electrode (Shawinigan black, 50% compressed) geometric surface area of 239 cm^2 (25.4 cm length × 4.7 cm height × 2 sides). Two current collector tabs were welded to the extremities of the electrode. The second type of D cell was used in the study to determine the effect of increased carbon electrode geometric

* Electrochemical Society Active Member.
[1] Present address: OMNION, Incorporated, Clarence, New York 14031.
Key words: battery, inorganic, electrolyte, discharge.

surface area on the performance and safety characteristics under high discharge rates. The carbon electrode in these cells had an 80% increase in surface area (430 cm^2, 45.7 cm^2 length × 4.7 cm height × 2 sides). These electrodes also possessed two current collector tabs at the electrode extremities.

The prototype Li/CSC DD cells used in the voltage delay/storability studies represented initial efforts to fabricate a high rate cell. The carbon electrode geometric surface area for these cells was 448 cm^2 (22.9 cm length × 9.8 cm height × 2 sides). In contrast to the carbon electrodes for the D cells, only one current collector tab was welded to that electrode extremity comprising the innermost windings of the cell body. For comparative purposes relative to high rate performance characteristics, present state-of-the-art Li/CSC DD cells were fabricated. The carbon electrode geometric surface area in these cells is 33% greater than that in the prototype cells (*i.e.*, 597 cm^2, 30.5 cm length × 9.8 cm height × 2 sides). Two current collector tabs are located at the extremes of the electrode body.

The constant current battery discharge system consisted of a 5.0V power supply and eleven constant current circuits: two each of 0.5, 1.0, 2.0, 4.0, and 5.0A, and one adjustable 0.0-0.5A circuit. The circuits may be connected in parallel to provide a total current of 25A. Current measurement was effected through use of a 25A/50 mV meter shunt with an output of 0.5 A/mV. The current was monitored by either chart recorder or oscilloscope.

The resistors chosen for the constant load discharge tests were at least 100% above the calculated power dissipation values required for cell discharge. This assured that the resistance values did not vary significantly from the values measured prior to cell testing. Further, the resistors were attached directly across the cell terminals. The load voltages for both the constant current and constant load tests were measured across the terminals of the cell and displayed on a strip-chart recorder. Unless otherwise noted, all realized capacities cited herein were obtained to a 2.0V voltage cutoff level. All performance and safety/hazards testing was performed using cells with no electrical or thermal protective devices (*i.e.*, electrical fuses, diodes, or thermal fuses).

Results and Discussion

Spirally wound state-of-the-art Li/CSC D cells (carbon electrode geometric surface area: 239 cm^2) were equilibrated at −2° ± 2°C and discharged under constant currents of 1.0-15.0A. The performance results for fresh cells (less than 3 months old) are presented in Fig. 1. At the comparatively lower rates of 1.0, 3.0, and 6.0A, the realized capacities differ very little (13.6, 13.0, and 12.5 A-hr, respectively). However, as the discharge rate increases, the realized capacities decrease. For cells discharged at 9.0, 12.0, and 15.0A, the realized capacities were 10.7, 10.0, and 8.7 A-hr, respectively. It is apparent from the initial stages of the discharge curves that the load voltage levels decrease rapidly until the cells can be warmed through I^2R heating. As the cell temperature increases throughout the discharge period, the load voltage levels attain equilibrium values and discharge at that level until the end of life is neared. A plot of realized capacity *vs.* log *I* (4) for approximately 250 cells discharged under constant current conditions of 1.0-15.0A at −2° ± 2°C is given in Fig. 2. Included in these data are the results obtained for cells discharged under rates as low as 25 mA. Throughout the current range of 25 mA to approximately 3A, very little variability in realized capacity exists. However, as the discharge rate increases to 6.0A, the capacity gradually decreases until, at the 15.0A level, a capacity of 8.7 ± 0.5 A-hr is realized. This latter value, nonetheless, corresponds to approximately 62% of the realized capacities of 14.0-14.5 A-hr obtained under the lower discharge rates.

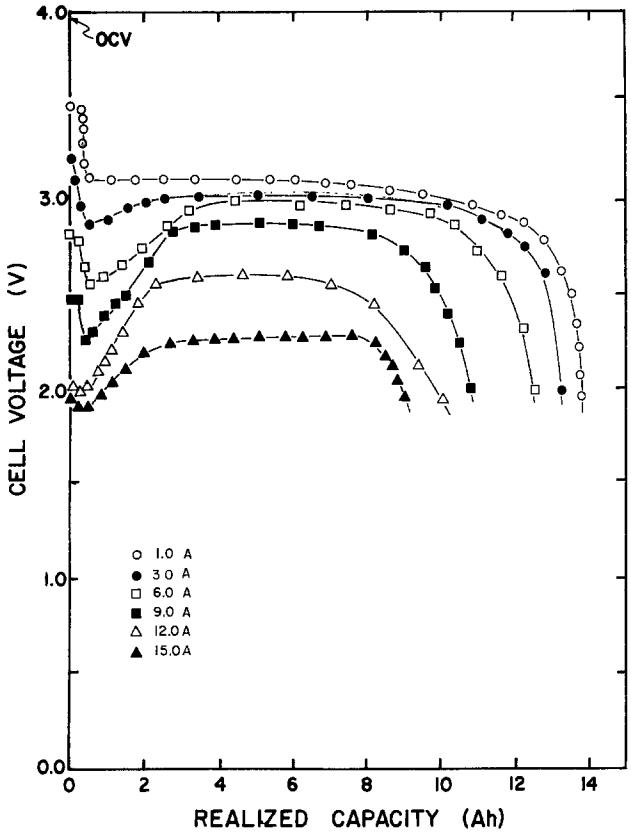

Fig. 1. Constant current discharge characteristics for fresh, state-of-the-art Li/CSC D cells at −2° ± 2°C.

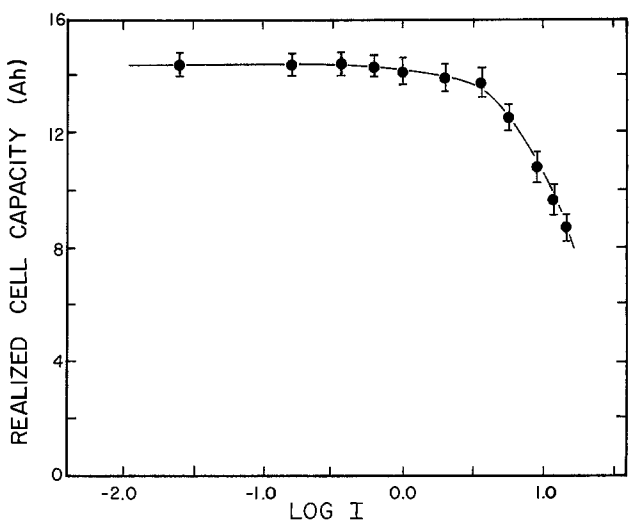

Fig. 2. Realized capacity *vs.* log *I* (Selim-Bro plot) for fresh, state-of-the-art Li/CSC D cells discharged under constant current conditions at −2° ± 2°C.

It was found that, as the discharge rate increased to the 15.0A level, the performance behavior at such high rates became increasingly varied. The cell-to-cell high rate performance variability for fresh state-of-the-art Li/CSC D cells at −2° ± 2°C is shown in Fig. 3. The results shown for cell 1 typify the performance for the majority of the cells tested at the 15.0A rate. At the initial stages of the discharge, the load voltage level decreased to 2.0V and remained at that level for the first minute. An abrupt decrease in load voltage to approximately 1.9V was then noted. The load voltage then recovered gradually during the following four minute period to approximately 2.1V. Dur-

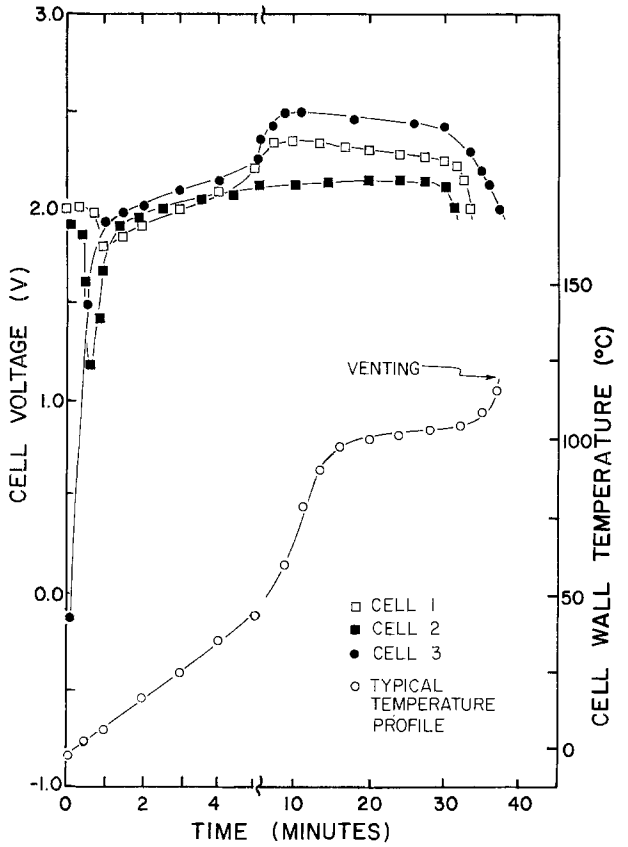

Fig. 3. Variation of performance for fresh, state-of-the-art Li/CSC D cells discharged at a constant current of 15.0A at −2° ± 2°C.

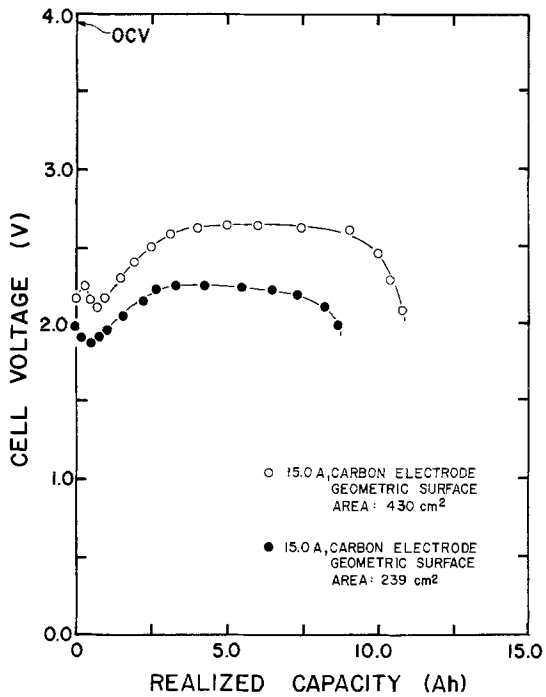

Fig. 4. Comparison of the high rate performance characteristics at −2° ± 2°C for state-of-the-art Li/CSC D cells (carbon electrode geometric surface area: 239 cm^2) to experimental Li/CSC D cells (carbon electrode geometric surface area: 430 cm^2).

ing the second five minutes of discharge, the cell voltage level attained a plateau at 2.35-2.40V until the end of life was reached. The total realized capacity for such cells was 8.7-9.0 A-hr. The discharge results for cells 2 and 3 not only exhibited more severe initial polarization at the initial stages of discharge, but also recovered to equilibrium plateau voltages more rapidly than cell 1. The results for cells 2 and 3 also emphasized the variability in plateau voltage levels (2.1 and 2.5V, respectively). The realized capacities, however, did not differ significantly from those obtained for cell 1 (8.2 and 9.6 A-hr for cells 2 and 3, respectively). The cell wall temperature was monitored on each cell discharged under these constant current conditions. A typical temperature profile is shown in Fig. 3. During the first five minutes of cell discharge, the cell wall temperature increased from −2° to approximately 45°C and continued to increase during the following 10 min. For the remainder of the discharge, the cell wall temperature was nearly constant at 95°-105°C. As the cell voltage level approached 2.0V, there was noted a rapid increase in the temperature to 120°C whereupon the cell vented through a cracked glass to metal seal. Venting typically occurred in all cells tested when cell wall temperatures reached 120° ± 10°C.

Experimental Li/CSC D cells were fabricated to determine the effect of increased carbon electrode surface area on the high rate performance and safety characteristics. These D cells contained carbon electrodes having an 80% increase in geometric surface area of 430 cm^2 compared to 239 cm^2 for the state-of-the-art Li/CSC D cells. The typical performance results for the 15.0A constant current discharge at −2° ± 2°C for these cells are presented in Fig. 4. It can be seen that the initial load voltages for the experimental D cell were only 0.15 to 0.20V higher than those for the state-of-the-art D cell. However, as the discharge proceeded, the load voltages for the cell having the higher surface area increased to approximately 2.65V, a difference of 0.30-0.35V higher than the state-of-the-art D cell. Also, the realized capacities obtained to a 2.0V cutoff level differed markedly for the two cell types: 10.8 and 8.7 A-hr for the experimental and state-of-the-art Li/CSC D cells, respectively. The current densities at the carbon electrodes for the two cell types were 35 and 63 mA cm^{-2} throughout the 15.0A constant current discharge for the experimental and the state-of-the-art D cells, respectively. These performance results for the experimental D cells may also be compared to the results obtained for the 9.0A constant current discharge of state-of-the-art D cells (Fig. 1) based upon the respective current densities of 35.0 and 37.7 mA cm^{-2}. The initial load voltage levels differed by approximately 0.30V, but as cell discharge proceeded, the difference between the load voltages decreased to 0.20V throughout the plateau region of discharge. It is believed that these disparities are due not only to less efficient current collection with increased carbon electrode length but also to the decreased carbon electrode thickness attendant with increased surface area. The realized capacities for the state-of-the-art cells discharged at 9.0A and experimental cells discharged at 15.0A were found to be 10.8 and 10.7 A-hr, respectively. Both cells also vented at approximately 120°C after attaining voltage levels of +0.8V. This result is in marked contrast to the venting results previously noted for the state-of-the-art D cells discharged at the 15.0A rate at −2° ± 2°C.

Li/CSC state-of-the-art D cells were also discharged under constant current conditions at +25°C. Figure 5 shows the performance characteristics for cells discharged at rates from 1.0 to 20.0A. It is apparent that the results are markedly similar to those obtained at −2°C (Fig. 1). For the cells discharged at lesser rates of 1.0-6.0A, the load voltage levels are slightly higher than those observed for cells discharged at −2°C. The results obtained from cells discharged at the 9.0 and 12.0A rates show virtually no significant differences in load voltage levels or realized capacities when compared to the performance characteristics for cells discharged at −2°C. For cells discharged at the rate of

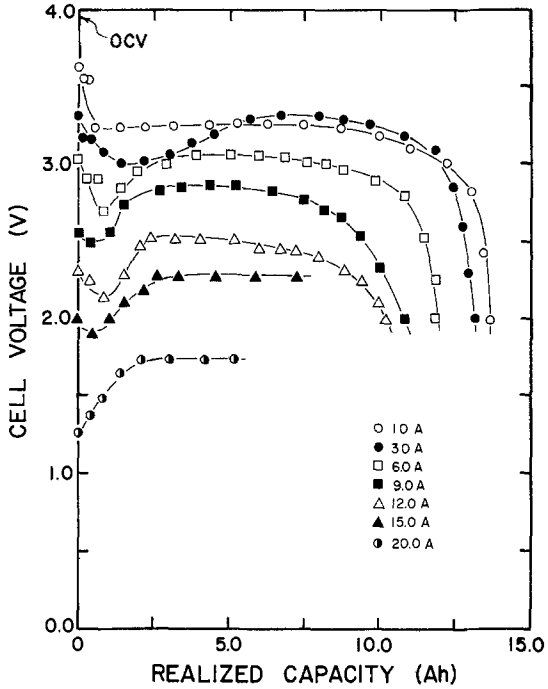

Fig. 5. Constant current discharge characteristics for fresh, state-of-the-art Li/CSC D cells at +25° ± 2°C.

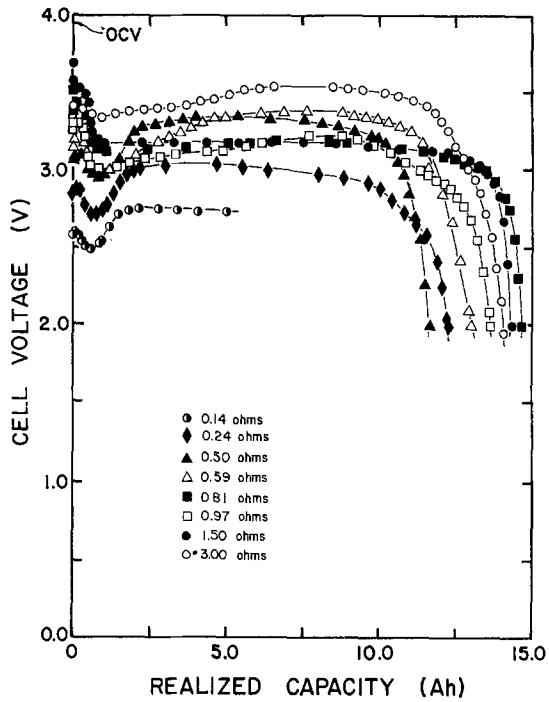

Fig. 6. Constant load discharge characteristics for fresh, state-of-the-art Li/CSC D cells at +25° ± 2°C.

15.0A, however, there was venting observed (*i.e.*, the glass-to-metal seals cracked as the cell wall temperature rose to 125°C) prior to the cell load voltage reaching the 2.0V cutoff level. The realized capacities for cells discharged at the 15.0A rate at 25°C were less (7.3 ± 0.5 A-hr) than those obtained for cells discharged at −2°C (8.7 ± 0.5 A-hr). Five Li/CSC state-of-the-art D cells were also discharged at the 20.0A rate at 25°C. The typical results are given in Fig. 5. The load voltages for all of the cells tested did not reach the 2.0V level. Nonetheless, the average plateau voltages did reach approximately 1.75V and continued to discharge at that voltage level for 15-18 min. The realized capacities observed for the discharge at the above load voltage levels varied from 5.0 to 6.0 A-hr. After the 15-18 min period, the cell wall temperatures reached approximately 125°C with resultant cell ventings.

It is important to note that cell venting will take place for those cells discharged under constant current conditions at rates above 6.0A. The venting is effected through a cracked glass-to-metal seal. The occurrence of venting is dependent upon discharge rate. For example, cells discharged at the 6.0, 9.0, 12.0, and 15.0A rates at 25°C will reach the venting temperature at approximately 0.0, 0.8, 1.3, and 2.3V levels, respectively. No ventings occurred for cells discharged at the 1.0 and 3.0A rates. The resultant toxic gases (*i.e.*, Cl_2, SO_2Cl_2, and SO_2) form corresponding acids in a normal environment. Approximately 500 Li/CSC D cells have been discharged under such high rates and in no instance was the mode of failure a cell rupture, explosion, or violent venting resulting in hazards to personnel.

For comparison purposes, fresh state-of-the-art Li/CSC D cells were discharged under constant loads of 0.14-3.00Ω at 25° ± 2°C. The results are presented in Fig. 6 and represent the typical discharge curves for approximately 200 cells tested in this phase of the study. The realized capacities differ very little whether the discharge load is 3.00Ω (14.4 A-hr to a 2.0V cutoff level) or 0.59Ω (13.0 A-hr). However, the realized capacities decrease as the loads become heavier. For example, for cells discharged under 0.50Ω loads the average realized capacities obtained were 11.7 A-hr. The results are presented for one cell discharged under the 0.24Ω load and show the effect of a mild venting on the discharge characteristics. During the discharge period, the cell load voltage reached a plateau value of approximately 3.0V. As the realized capacity and load voltage approached 9.3 A-hr and 2.9V near the end of life, respectively, the cell experienced a mild venting. The cell continued to discharge until the 2.0V cutoff level. As a result, the realized capacity for this one cell is higher (12.3 A-hr) than the average values for cells discharged under the lighter load of 0.50Ω (11.7 A-hr). This phenomenon has also been observed when cells were short circuited across a 0.040Ω load (5). Cells discharged under 0.14Ω loads also experienced venting after a discharge period of approximately 15 min. It is interesting to note that only those cells discharged under the heavier loads of 0.14 and 0.24Ω (approximate currents: 19.0 and 12.0A, respectively) experienced venting. Venting was not observed for cells discharged under the lighter loads.

In addition to the safety/hazards characteristics associated with Li/CSC cell discharge at high rates as discussed herein, safety studies have been extended beyond the scope of short circuit, forced overdischarge, the sequence of forced overdischarge/charge, incineration, and shock sensitivity testing (2, 3), to include penetration, crushing, and localized heating. Extensive testing relative to the high and low velocity penetration of Li/CSC D cells has been performed. The effect of bullet or nail penetration results in a massive internal short circuit causing the melting of the lithium metal with subsequent cell rupture or exposion. Cells have also been crushed using a hydraulic press. In every instance of longitudinal crushing, the D cells ruptured or exploded after sufficient pressure was applied to decrease the cell height to approximately two-thirds the initial height. Further, crushing cells at the radial axis results initially in a cracked glass to metal seal followed by a rapid venting and cell rupture. State-of-the-art Li/CSC cells vent mildly when incinerated above a naphtha flame (2, 3) or when heated to temperatures above approximately 115°C either by self-heating under high discharge rates or by exposure to external heat sources such as ovens or operating environments. The heating in the above instances is uniform throughout the cell. A study was conducted to determine the effect of localized heating on the safety/hazards characteristics of

the cell. In an effort to simulate an attempt to solder leads or connections to the cell wall, D cells were positioned above a small pinpoint heat source or heated locally using resistance wire. In some cases, the cells vented in a similar manner as described above, but in approximately 50% of the tests the cells vented violently or exploded.

Extensive studies in this laboratory have shown that Li/CSC cells exhibit exceptionally safe features when subjected to specific, individual abusive conditions. It is believed, however, that many incidents involving lithium batteries (*i.e.*, venting, cell/battery ruptures, or explosions) which pose hazards to personnel are not necessarily the result of cells or batteries exposed to one singular abusive condition, but are the result of a combination of two or more abusive conditions. Preliminary results in this laboratory relative to cells of the Li/CSC system have shown that ventings or cell ruptures will occur when cells are subjected to at least two normally nonhazardous abusive conditions. For example, Li/CSC cells may vent when force-overdischarged at moderate rates while being simultaneously heated at a high rate by an external source.

It is also believed that the experimentally determined safety characteristics for one specific cell size should not be extended to other cell sizes (*e.g.*, D cell *vs.* DD cell or C cell) or to cells of the same size fabricated with electrodes having greater geometric surface areas (*e.g.*, D cells having carbon electrodes of 239 cm^2 *vs.* 430 cm^2, as described herein).

The storability characteristics for the Li/CSC system have been investigated using microcalorimetry (1) and high temperature storage (74°C) for various time periods followed by cell discharge at 25°C (2). Neither method proved satisfactory relative to the characterization of the self-discharge properties for cells of the Li/CSC system. The room temperature performance results obtained from Li/CSC cells stored for extended periods of time at ambient temperature or for specific periods of time at elevated temperatures (*i.e.*, 1 week, 1 month, etc.) show that little or no realized capacity was lost for cells discharged under low to moderate rates. However, the results also showed that both the realized capacity, and the rate capability decreased when cells were discharged under high rates.

An investigation was initiated to determine the realized capacity loss and voltage delay characteristics for prototype Li/CSC DD cells stored at 25° ± 5°C for 1.5 years. These cells represent initial efforts to produce a high rate/high capacity cell. The carbon electrode geometric surface area was 448 cm^2 (22.9 length × 9.8 cm height × 2 sides). In contrast to state-of-the-art Li/CSC D and DD cells, these prototype cells only had one current collector tab welded to the electrode extremity comprising the innermost windings of the cell body. The ambient temperature performance characteristics were determined for these cells one week after fabrication. The results are shown in Fig. 7. It can be seen that for constant loads of 0.50-10.0Ω (approximate rates of 6.5-0.36A, respectively), the realized capacities to a 2.0V cutoff comprise a narrow band with values of 28.5-31.5 A-hr. Other Li/CSC prototype DD cells were stored under uncontrolled ambient temperature conditions (25° ± 5°C) and discharged at 25° ± 2°C under similar constant load conditions. The results given in Fig. 8 show cell polarization immediately upon load application. For example, the minimum load voltage observed immediately after application of a 0.50Ω load was 0.17V. The cell voltage for this cell rose to 2.0V within 20 sec. The voltage continued to increase to approximately 3.25V for the remainder of the discharge. The realized capacities for cells discharged under the lighter loads of 0.59-3.00Ω exhibit the same narrow band and are only slightly less than those observed for newly fabricated cells (Fig. 7). The realized capacity for the 1.5 year old cell discharged under 0.50Ω was 23.9 A-hr, a decrease of 4.6 A-hr from that obtained for newly fabricated cells. Comparison of Fig. 7 and 8 also shows a decrease in the rate capability for cells discharged under identical loads. Thus, the effect of storage for prototype Li/CSC DD cells at 25° ± 5°C for as long as 1.5 years results in a loss of rate capability, no significant loss in realized capacity for cells discharged under lighter loads of 0.59Ω (approximately 5.6A rate), and does result in a realized capacity loss for cells

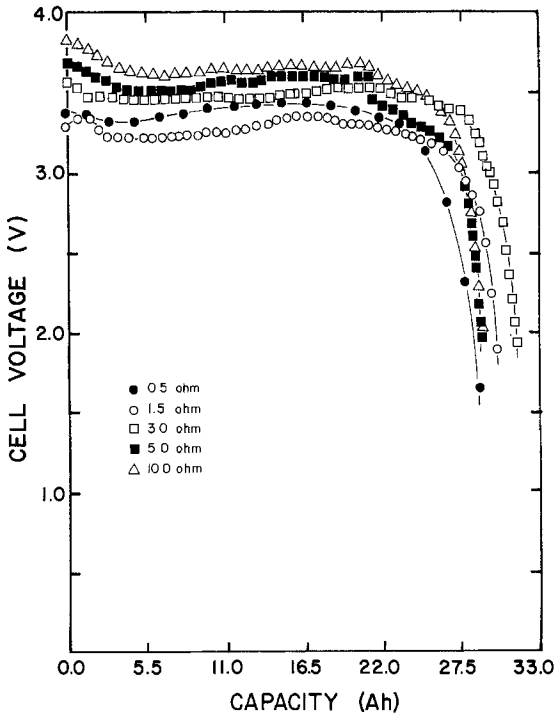

Fig. 7. Constant load discharge characteristics for fresh, prototype Li/CSC DD cells at 25° ± 2°C (carbon electrode geometric surface area: 448 cm^2).

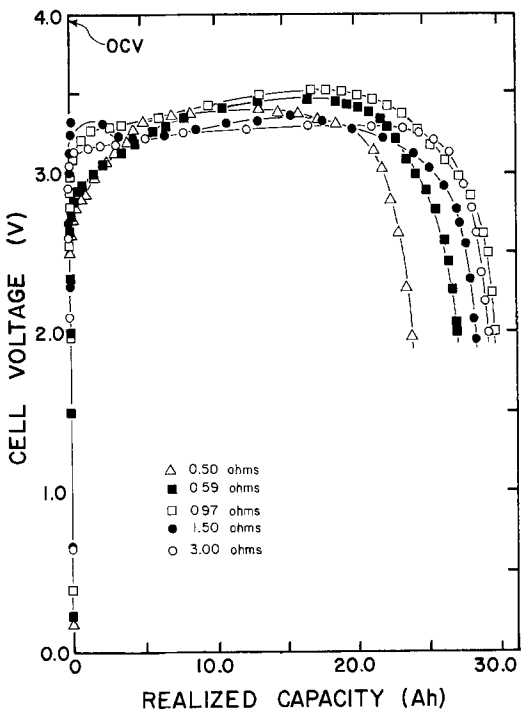

Fig. 8. Ambient temperature constant load discharge characteristics for prototype Li/CSC DD cells stored 1.5 years at 25° ± 5°C (3.00-0.50Ω loads).

discharged under heavier loads of 0.50Ω or less (*i.e.*, greater than 6.5A rate).

Stored Li/CSC DD cells were also discharged under the especially heavy loads of 0.14-0.31Ω. Examination of the results presented in Fig. 9 show that the cells experienced severe initial polarization, but recovered rapidly to load voltages greater than 2.5V. The average realized capacities for cells discharged under the 0.24 and 0.31Ω loads were 21.0 and 21.9 A-hr, respectively. These values represent approximately 75 and 78%, respectively, of those capacities obtained for stored cells discharged under the lighter loads (Fig. 8). The performance results for cells discharged under 0.14Ω loads indicate that venting occurred after approximately 15-18 min of operation (4.5-5.5 A-hr).

All stored Li/CSC DD cells experienced severe cell polarizations and voltage delays immediately upon load application. These results are summarized in Table I. The initial, minimum load voltages range from 0.07 to 0.65V for cells under loads of 0.14-3.00Ω, respectively. The total elapsed time for the load voltages to reach the 2.0, 2.5, and 3.0V levels are also given. It can be seen that for the lighter loads (*e.g.*, 3.00-0.97Ω) the voltage delays to the 2.0V level were 10 sec or less. For cells discharged under loads as heavy as 0.24Ω, the voltage delays to the 2.0V level were all found to be less than 60 sec. One notable exception was found for the cells discharged under 0.14Ω loads: the average voltage delays to the 2.0 and 2.5V levels were 101 and 433 sec. The load voltages for these cells did not reach the 3.0V level for any of the test cells. Further, the cells discharged under 0.24Ω loads (approximately 12A) did not reach the 3.0V load voltage level for approximately 900 sec. It can also be seen that for moderately heavy loads of 0.59-0.31Ω, the voltage delay to the 3.0V level varies from 260 to 840 sec. However, these results for the voltage delay and realized capacities obtained for these stored cells are exceptionally good when the storage time and cell construction characteristics are considered.

The present state-of-the-art Li/CSC DD cells differ significantly from those used in the storability/voltage delay studies as described above. Improvements relative to the carbon electrode geometric area and current collection means have optimized the performance characteristics of the Li/CSC DD cell. The carbon electrode geometric surface area for state-of-the-art Li/CSC DD cells was increased 33%, from 448 to 597 cm^2 (30.5 length × 9.8 cm height × 2 sides). In addition, two carbon electrode tabs located at the electrode extremities presently comprise the current collection means in the state-of-the-art cell. The ambient temperature performance results for fresh cells are given in Fig. 10. The realized capacities for cells discharged under 1.50-0.50Ω loads comprise a very narrow band with values between 29.6-28.7 A-hr, respectively. As the load increased to 0.24 and 0.14Ω, the realized capacities decreased to 26.5 and 24.0 A-hr, respectively. Cells discharged under 0.14Ω loads vented mildly before reaching the 2.0V voltage cutoff level. It is believed that because of the improvements relative to the carbon electrode geometric surface area and current collection means, the storability and voltage delay characteristics would correspondingly be improved.

Table I. Average values of the voltage delay and performance characteristics for Li/CSC93 DD cells discharged under constant loads at 25° ± 2°C following storage for 1.5 years at 25° ± 5°C

Load (Ω)	Initial, minimum load voltage (V)	Total elapsed time to reach the 2.0V level (sec)	Total elapsed time to reach the 2.5V level (sec)	Total elapsed time to reach the 3.0V level (sec)	Realized capacity to a 2.0V cutoff level (A-hr)
0.14	0.07	101	433	—†	4.7*
0.24	0.10	44	280	900	21.0
0.31	0.14	31	64	840	21.9
0.50	0.17	20	42	780	23.9
0.59	0.23	20	38	260	27.1
0.97	0.39	10	19	76	29.8
1.50	0.65	6	14	38	28.4
3.00	0.65	9	16	33	29.3

† Load voltages did not reach the 3.0V level under the 0.14Ω load for any of the test cells.
* Cells vented mildly at load voltages of 2.55-2.70V.

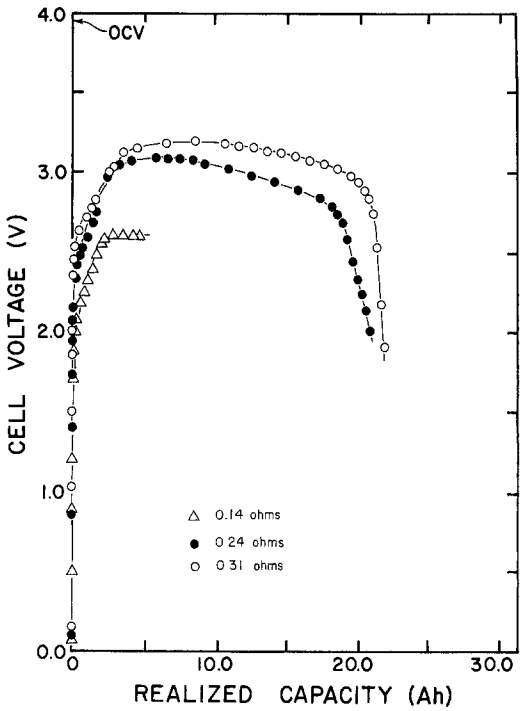

Fig. 9. Ambient temperature constant load discharge characteristics for prototype Li/CSC DD cells stored 1.5 years at 25° ± 5°C (0.31-0.14Ω loads).

Conclusions

The Li/CSC system possesses especially high rate capability and exceptional storability characteristics. It

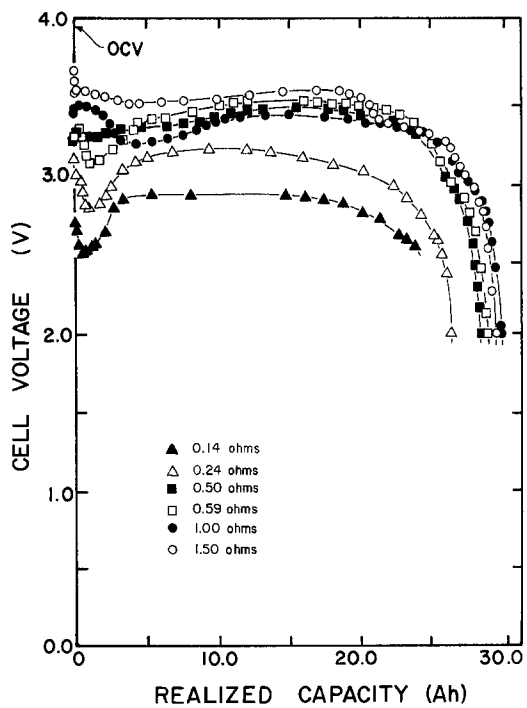

Fig. 10. Ambient temperature constant load discharge characteristics for fresh, present state-of-the-art Li/CSC DD cells (carbon electrode geometric surface area: 597 cm^2).

has been shown that Li/CSC D cells may be discharged at rates as high as 15A under constant current conditions at −2° and +25°C and under loads as heavy as 0.14Ω at 25°C. However, cells will vent mildly when discharged at rates above 6A and under loads of 0.24Ω and heavier. In a normal environment, the corresponding acids of the resultant gases are expected to be formed. Results of safety testing have shown that cell penetration, crushing, and localized heating will result in venting, cell rupture, or explosion. Further, cells of the Li/CSC system are abuse resistant when subjected to individual hazardous conditions. However, the combination of two or more safety test conditions may result in cell venting or case rupture. The storability/voltage delay characteristics as determined from cells stored under actual storage time conditions show that little or no realized capacity is lost when cells are discharged under even moderately high rates, but do indeed show a realized capacity loss when discharged under especially high rates. Further, there is a noted rate capability loss for all cells discharged with the exception of cells discharged under comparatively low rates.

Acknowledgment

The authors wish to thank Ms. M. E. Bolster and Ms. L. S. Wolcott for their technical assistance during these investigations. The authors also gratefully acknowledge the contributions of Messrs. M. J. Bakos, J. J. Christen, and J. G. Grotke relative to the fabrication of the electronic devices used in these studies.

Manuscript submitted July 13, 1982; revised manuscript received Jan. 18, 1983.

Any discussion of this paper will appear in a Discussion Section to be published in the December 1983 JOURNAL. All discussions for the December 1983 Discussion Section should be submitted by Aug. 1, 1983.

Electrochem Industries, Incorporated assisted in meeting the publication costs of this article.

REFERENCES

1. C. C. Liang, M. E. Bolster, and R. M. Murphy, in Proceedings of the 29th Power Sources Conference," Atlantic City, NJ, June 9-12, 1980, The Electrochemical Society, Inc., p. 144 (1981).
2. C. C. Liang, M. E. Bolster, and R. M. Murphy, *This Journal*, **128**, 1631 (1981).
3. R. M. Murphy, P. W. Krehl, and C. C. Liang, in "Proceedings of the 16th Intersoc. Energy Conv. Eng. Conf.," **1**, 97 (1981).
4. R. Selim and P. Bro, *This Journal*, **118**, 829 (1971).
5. R. F. Bis and J. D. Jensen, Private communication.

Electrode Corrosion in a Compartmented Flow Cell by Diffusion from the Counterelectrode

Johnsee Lee*[1] and J. R. Selman*

Department of Chemical Engineering, Illinois Institute of Technology, Chicago, Illinois 60616

ABSTRACT

Electrode corrosion by a soluble species diffusing from the counterelectrode in a circulating flow cell has been analyzed. The net rate of corrosion and its distribution along the electrode are found to be governed by two dimensionless parameters, representing ratios of mass transfer and kinetic resistances. Application of this analysis to a zinc-bromine flow cell indicates that corrosion of the zinc electrode by dissolved bromine is mass-transfer controlled. Using the experimentally measured bromine diffusion coefficient and an estimated kinetic rate constant, the average zinc corrosion rate in a typical zinc-bromine cell is calculated to be in the range of 1 mA/cm², if a typical bromine concentration in the positive channel (10 g/liter) is assumed.

In some electrochemical reactors, the negative electrode may be corroded by the reaction product of the positive electrode. For example, in a zinc-halogen battery cell, the zinc electrode may be corroded by dissolved halogen produced at the positive electrode during charging (1, 2). This corrosion reaction causes the battery to lose charge continually at a slow rate and thereby reduces the capacity of the battery. Similarly, corrosion by zinc-halogen recombination occurs when the cell is in the charge (or electrolysis) mode. As a parasitic reaction, the corrosion consumes a fraction of the product of electrolysis reaction, thereby lowering the net energy efficiency of the cell or battery. In this paper, the rate of the parasitic corrosion and its distribution during electrolysis (charging) in a parallel-plate electrochemical cell with circulating electrolyte is analyzed.

As shown in Fig. 1, the cell under consideration consists of a positive electrode, a microporous separator, and a negative electrode. The positive and negative electrolytes flow separately through the rectangular channel formed by the separator and the electrodes. During electrolysis, the halogen or other corrosive species is produced at the positive electrode and dissolved in the positive electrolyte. Its concentration in this electrolyte, often limited by solubility (in the case of chlorine) or by the presence of complexing agents (in the case of bromine), remains unchanged throughout most of the operational period. The rate processes associated with the parasitic corrosion are: the diffusion of the corrosive species through the separa-

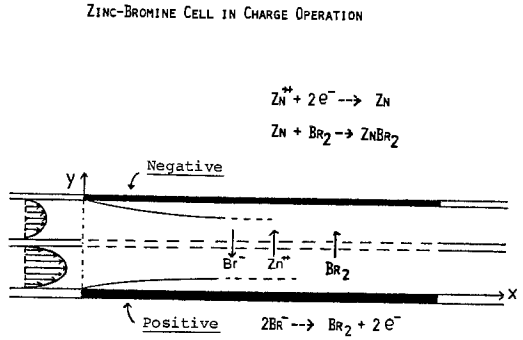

Fig. 1. Two-dimensional representation of a parallel-plate zinc-bromine flow cell. The negative electrode is cathode during charge, while the positive electrode is anode.

* Electrochemical Society Active Member.
[1] Present address: Argonne National Laboratory, Chemical Technology Division, Argonne, Illinois 60439.
Key words: electrode corrosion, self-discharge, flow cell, bromine diffusion, zinc-bromine cell, flow battery.

tor, its transport across the negative electrolyte channel, and the kinetics of the corrosion reaction. The net corrosion rate at the negative electrode depends on the overall rate of these three consecutive processes.

Mathematical Formulation

To analyze the rate processes and the distribution of parasitic corrosion in the flow cell of Fig. 1, the following assumptions are made: (*i*) Both the electrolysis (charging) operation and the corrosion process have reached steady (or quasi-steady) state. (*ii*) The concentration of corrosive species in the positive electrolyte remains constant and uniform during electrolysis; its concentration in the inlet stream of negative electrolyte also reaches a steady value due to the recirculation of electrolyte. (*iii*) No concentration gradients of corrosive species exist near the interfaces between the separator and either electrolyte. This assumption is reasonable since the transport through the separator, purely by molecular diffusion, is usually much slower than the convective transport from the bulk solution to the surface of the separator, and reverse. (*iv*) The Peclet number with respect to the corrosive species is large for the negative electrolyte so that concentration variation is confined to a thin diffusion layer very near the surface of the negative electrode (3). A typical concentration profile of the corrosive species across the flow cell is shown in Fig. 2. (*v*) The velocity profile in the negative electrolyte channel corresponds to fully developed laminar flow. (*vi*) The physical and transport properties are constant. For a further discussion of these assumptions, see Ref. (4).

Following molecular diffusion theory, the transport rate of the corrosive species through the separator may be written as

$$N_{sep} = D_{sep}\frac{C_{\infty,A} - C_{\infty,K}}{H_{sep}} \quad [1]$$

where D_{sep} is the effective diffusivity of the corrosive species in the separator, and is taken to be related to its bulk-solution diffusivity by (5)

$$D_{sep} = D_{\infty}\epsilon^{1.5} \quad [2]$$

Note that $C_{\infty,K}$ in Eq. [1], the steady-state bulk concentration of corrosive species in the negative electrolyte channel, is not known *a priori*.

The transport of corrosive species across the negative electrolyte is governed by the two-dimensional convective diffusion equation (3) applied to the thin diffusion layer near the negative electrode (schematically indicated in Fig. 1)

$$v_x\frac{\partial C}{\partial x} = D\frac{\partial^2 C}{\partial y^2} \quad [3]$$

subject to the following boundary conditions

$$C = C_{\infty,K}, \text{ at } x = 0; \text{ for all } y \quad [4]$$

$$C = C_{\infty,K}, \text{ at } y = \infty; \text{ for } 0 \leq x \leq L \quad [5]$$

$$D\frac{\partial C}{\partial y} = r, \text{ at } y = 0; \text{ for } 0 \leq x \leq L \quad [6]$$

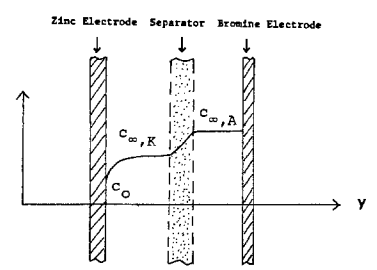

Fig. 2. Typical concentration profile of the corrosive species across a flow cell.

Here r is the reaction (corrosion) rate at the surface of the negative electrode.

The velocity v_x in Eq. [3] follows from the assumption of laminar flow in the negative channel. The corrosion reaction, for example

$$Zn(s) + R_n(aq) \rightarrow Zn^{2+}(aq) + nR^-(aq) \quad [7]$$

may be regarded as a combination of two faradaic reactions: $Zn \rightarrow Zn^{2+} + ne^-$, and $R_n + ne^- \rightarrow nR^-$, in a mixed potential process. Its reaction rate is then related to the equilibrium potential and the exchange current density of each reaction. Because of the high exchange current density of zinc dissolution and the mass-transfer resistance of $R_n(aq)$ toward the zinc surface, the corrosion potential in this example will be much closer to the zinc equilibrium potential than to that of R_n/R^-, and the corrosion rate will be relatively insensitve to potential. Therefore, this corrosion reaction may be considered as a direct chemical reaction with the kinetic expression

$$r = kC_o(x) \quad [8]$$

where k is a chemical reaction rate constant; $C_o(x)$ is the concentration of the corrosive species R_n at various locations along the surface of the negative electrode.

At steady state, the diffusion flux through the separator may be related to the corrosion rate at the negative electrode by the mass balance in the negative flow channel

$$N_{sep} = \frac{H<v>}{L}[C_{\infty}(L) - C_{\infty}(o)] + \frac{1}{L}\int_0^L kC_o(x)dx \quad [9]$$

In most electrochemical flow cells with recirculation, the first term on the right-hand side is very small compared to the second. For example, in the zinc-bromine battery, the coefficient $H<v>/L$ is 10^{-6} m/sec under typical conditions (Table I), while the bromine concentration in the negative electrolyte is approximately 5 kmol/m^3 (0.005 mol/liter). On the other hand, the corrosion current density is of the order of 1 mA/cm^2 (6). Therefore, we may simplify equation [9] to

$$N_{sep} = \frac{1}{L}\int_0^L kC_o(x)dx \quad [9a]$$

The corrosion rate along the negative electrode can be calculated by solving Eq. [1], [3]-[6], [8], and [9] simultaneously. In order to allow a generalized analysis, the following dimensionless variables and groups are defined

$$\zeta = \frac{x}{L} \quad [10]$$

$$C_o^*(\zeta) = \frac{C_o(\zeta)}{C_{\infty,K}} \quad [11]$$

$$C_{\infty}^* = \frac{C_{\infty,K}}{C_{\infty,A}} \quad [12]$$

$$K_1 = \frac{kC_{\infty,K}}{<N_{lim}>} = \frac{2k\Gamma(4/3)}{3D}\left(\frac{2<v>}{3DH_KL}\right)^{-1/3} \quad [13]$$

Table I. Typical conditions of a zinc-bromine cell

	Positive	Negative
Electrode length (m)	30×10^{-2}	30×10^{-2}
Channel height (m)	0.3×10^{-2}	0.3×10^{-2}
Flow rate (m/sec)	0.5×10^{-2}	0.25×10^{-2}
Zinc bromide concentration (M)	1.0	1.0
Dissolved bromine concentration (M)	0.05	
Microporous separator:		
Thickness (m)	0.05×10^{-3}	
Porosity	0.5	
Bromine diffusivity (m^2/sec)	0.988×10^{-9}	
Corrosion rate constant (m/sec)	1.40×10^{2}	

$$K_2 = \frac{k}{D\epsilon^{1.5}/H_{sep}} \quad [14]$$

Note that in Eq. [13], $<N_{lim}>$, the average limiting flux due to convective mass transfer in the negative electrolyte, can be written as (7)

$$<N_{lim}> = \frac{3DC_{\infty,K}}{2\Gamma(4/3)}\left(\frac{2<v>}{3DH_K L}\right)^{1/3} \quad [15]$$

As defined by [13] and [14], the dimensionless group K_1 measures the relative magnitude of mass transfer resistance in the negative electrolyte to the kinetic resistance of the corrosion reaction at the negative electrode, while K_2 represents the relative importance of mass transfer resistance through the separator to the kinetic resistance of cororsion. A nondimensional corrosion rate is also defined

$$r^*(\zeta) = kC_o(\zeta)/<N_{lim}> = K_1 C_o^*(\zeta) \quad [16]$$

i.e., the corrosion rate normalized by the average limiting mass transfer rate.

Solutions of Governing Equations

Using the superposition principle (8), Eq. [3] and boundary conditions [4]-[6] can be written in integral form as

$$C_o^*(\zeta) = 1 - \frac{3\sqrt{3}}{4\pi} K_1 \int_0^{\zeta} \frac{C_o^*(\bar{\zeta})}{(\zeta - \bar{\zeta})^{2/3}} d\bar{\zeta} \quad [17]$$

Note that the distribution of dimensionless surface concentration $C_o^*(\zeta)$ is solely a function of parameter K_1. The solution of Eq. [17] for various values of K_1 is shown in Fig. 3. At large values of K_1, the surface concentration approaches zero along the electrode, and the rate of corrosion is controlled by convective mass transfer; at small values of K_1, the surface concentration approaches unity, and the corrosion is under kinetic control. These results may also be represented in terms of average surface concentration

$$<C_o^*> = \int_0^1 C_o^*(\zeta) d\zeta \quad [18]$$

as in Fig. 4. The transition from kinetic control to mass transfer control occurs as K_1 increases from 0.1 to 100.

From the solution to Eq. [17], the distribution of the corrosion rate at various values of K_1 may be calculated as shown in Fig. 5. Here the dimensionless rate, $r^*(\zeta)$, defined by Eq. [16], is used. At large K_1, the corrosion rate is very high near the flow entrance $\zeta = 0$, and the distribution is similar to that for mass-transfer limiting current; at small K_1, the corrosion rate becomes much smaller than the limiting mass-transfer rate, and its distribution becomes more uniform.

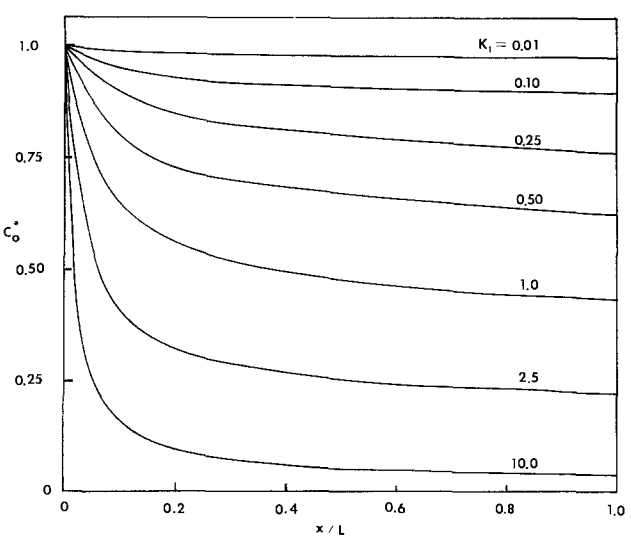

Fig. 3. Dimensionless concentration distribution of the corrosive species along the negative electrode at various values of K_1. The ordinate is the concentration at the electrode divided by the bulk concentration in the negative channel.

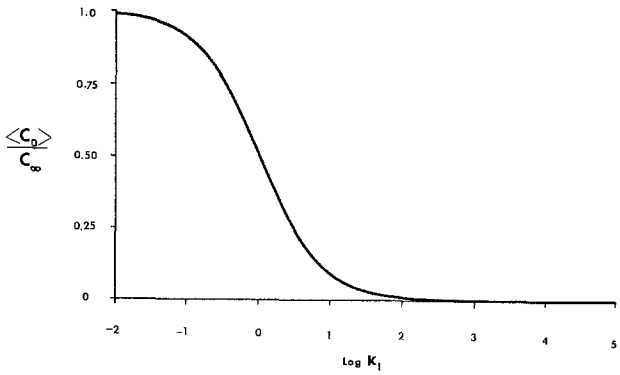

Fig. 4. The ratio of average surface concentration to bulk concentration in the negative channel as a function of log K_1.

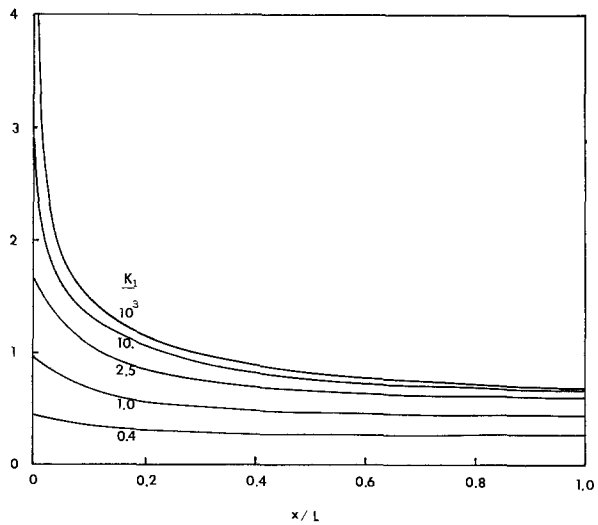

Fig. 5. Dimensionless corrosion rate distribution along the negative electrode at various values of K_1. The ordinate is the local corrosion rate normalized by the average limiting flux.

Although the distribution of the dimensionless rate r^* is determined solely by the value of K_1, the actual rate of corrosion depends on the bulk concentration $C_{\infty,K}$, which is governed by the diffusion rate through the separator as well as the mass balance Eq. [9]. By combining Eq. [1] and [9] and substituting dimensionless variables, one obtains

$$C_\infty^* = \frac{1}{1 + K_2 \int_0^1 C_o^*(\zeta) d\zeta} \quad [19]$$

where $C_o^*(\zeta)$ is the solution of Eq. [17]. Thus, the ratio C_∞^* is function of both K_1 and K_2.

The solutions of Eq. [17] and [19] at various K_1 and K_2 are represented by a three-dimensional graph (Fig. 6). In this graph, two plateaus are observed. The upper plateau represents the region where the separator is not effective in preventing crossover of the corrosive species from positive to negative channel. At the lower plateau, the majority of the corrosive species are stopped by the separator, and the ratio of its concentration in the negative electrolyte to that in the positive one approaches zero. For any given cell design and operating conditions, the ratio C_∞^* can be estimated from Fig. 6 when the parameters K_1 and K_2 are known. The bulk concentration in the negative electrolyte $C_{\infty,K}$

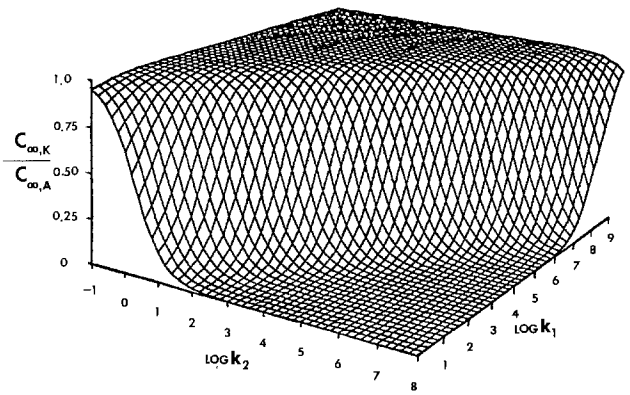

Fig. 6. The ratio of the bulk concentration in the negative electrolyte to the bulk concentration in the positive electrolyte as a function of log K_1 and log K_2.

can be calculated from C_∞* and the given concentration in the positive electrolyte $C_{\infty,A}$.

Application to Zinc-Bromine Flow Cell

The zinc-bromine battery is a promising device for energy storage because of its attractive theoretical energy density, relatively low electrode polarization, and the low cost and wide availability of the active materials (1). The unit cell of the zinc-bromine battery consists of a zinc negative electrode, a microporous separator, and a bromine positive electrode. The negative and positive electrolytes are circulated through the flow channels formed by the separator and the respective electrodes.

During charging of the battery, the reaction product at the positive electrode is liquid bromine, which is highly water-soluble and would diffuse across the flow channel to the zinc electrode where it would react according to

$$Zn(s) + Br_2(aq) \rightarrow Zn^{2+}(aq) + 2Br^-(aq) \quad [20]$$

or

$$Zn(s) + Br_3^-(aq) \rightarrow Zn^{2+}(aq) + 3Br^-(aq) \quad [20a]$$

Therefore, the main function of the separator is to prevent crossover of bromine. To suppress corrosion further, an organic complexing agent, such as a quaternary ammonium halide, is added to the electrolyte of the positive electrode. In this way, the concentration of bromine in the anolyte is reduced to 5-10 kg/m^3 (5-10 g/liter). However, a small amount of bromine still diffuses through the separator and corrodes the zinc electrode. During the charge operation, the current efficiency is thus reduced by this parasitic reaction.

To use the method presented above, one first calculates the parameters K_1 and K_2 as defined by Eq. [13]-[15], for the typical cell dimensions and flow conditions as shown in Table I. The only unknown quantities are the bromine diffusion coefficient D, and the corrosion kinetic constant k. For preliminary calculation, D is assumed to be the common value 10^{-9} m^2/sec used in aqueous solutions; k is estimated, by Evans' method (9), to be approximately 1.4×10^2 m/sec based on the exchange current densities and the oxidation-reduction potentials of zinc and bromine electrodes (10, 11).

Substitution of these values into Eq. [13]-[15], yields $K_1 \approx 10^7$, while K_2 ranges from 10^7 to 10^8 depending on the thickness of separator H_{sep}. Referring to Fig. 4, the average surface concentration of the corrosive species approaches zero, and the overall corrosion rate is controlled by the convective diffusion process. Under these conditions, the distribution of the corrosion rate along the electrode is similar to the limiting current distribution.

Although not affecting the distribution of dimensionless corrosion rate along the zinc electrode, the value of K_2 determines the bulk concentration of the corrosive species in the negative electrolyte. Only when this concentration is known can the actual zinc corrosion rate be calculated. Furthermore, one may estimate C_∞*, the ratio of the bulk concentration of bromine in the negative electrolyte to that in the positive, by using Fig. 6 and the magnitudes of K_1 and K_2. For example, with the parameters of Table I, this ratio turns out to be very small (about 0.1). Apparently, the presence of the separator effectively reduces the zinc corrosion rate by drastically reducing the concentration of bromine in the negative electrolyte.

Since the above analysis indicates a more important role of mass transfer than kinetics, an accurate measurement of the bromine diffusion coefficient in the zinc bromide electrolyte becomes essential for estimating the corrosion rate of the zinc electrode in a zinc-bromine flow cell. This can be accomplished by measuring the mass-transfer limiting current of bromine reduction at an electrode under well-defined laminar flow condition. For example, at a rotating disk electrode, the diffusion limiting current is related to the bromine flux by the Levich equation (3). This method was used by White *et al.* (12).

Alternatively, one may determine the bromine diffusion coefficient by measuring zinc weight loss due to bromine corrosion under mass-transfer limiting condition. For example, Kim and Jorne (13) have calculated the chlorine diffusion coefficient by measuring the weight loss of a rotating zinc hemisphere submerged in a chlorine-containing zinc chloride solution. In either the limiting-current or the weight-loss method, what is determined is an effective bromine diffusion coefficient, which implicitly includes the effects of migration and the presence of complex species such as Br_3^- and possibly $ZnBr_3^-$ or $ZnBr_4^{2-}$.

To facilitate the calculation of zinc corrosion rate in a practical zinc-bromine flow cell, the bromine diffusion coefficients in various concentrations of zinc-bromide solution were measured using the weight-loss method. The rotating zinc hemisphere consists of a Teflon support rod and a replaceable zinc hemispherical head (Fig. 7). The diameter of the Teflon rod is 1.82 cm. A zinc hemisphere (99.999% zinc from Metron Incorporated, New Jersey) is embedded in the Teflon rod. The diameter of the zinc hemisphere varies from 0.97 to 1.0 cm. Zinc-bromide solution is prepared by dissolving zinc-bromide powder (Fisher, certified grade) into double distilled water. The solution is, then, deaerated by sparging nitrogen gas over a 30 min period. Bromine liquid (Fisher, reagent grade) is

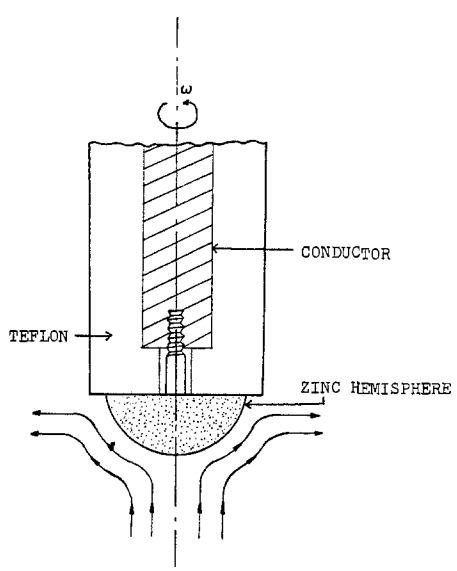

Fig. 7. The rotating zinc hemisphere for bromine diffusivity measurement.

added to the zinc bromide solution, and the pH of the solution adjusted to 4.5. A 1000 ml Pyrex flask is used to contain the prepared solution.

At the beginning of each experiment, the zinc hemisphere is pretreated, and then attached to a rotator (Pine Instrument, Grove City, Pennsylvania). As the rotating zinc hemisphere is submerged into the bromine-containing zinc bromide solution, the corrosion reaction [20] occurs. Since the corrosion kinetics is so fast (as discussed above), the process becomes mass transfer limited at moderate rotation rate. Under this condition, the mass transfer rate and hence the diffusion coefficient of dissolved bromine can be obtained from the experimental corrosion rate, using the equation of Chin (14), corrected by Newman (15)

$$N_{\text{lim}} = 0.4508\, C_\infty \nu^{-1/6} D^{2/3} \omega^{1/2} \qquad [21]$$

Here C_∞ is the bulk concentration of the dissolved bromine, ν is the kinematic viscosity of solution, D is the effective diffusion coefficient; ω is the angular velocity of rotating zinc hemisphere. The mass transfer flux is determined from the weight loss $\Delta\overline{W}$ of the zinc hemisphere over a time period $\Delta\tau$ by

$$N = \frac{\Delta\overline{W}}{\overline{M}\Delta\tau S} \qquad [22]$$

where $\overline{M}$ is the molecular weight of zinc; S is the surface area of the hemisphere. Equating Eq. [21] with [22], one obtains

$$\frac{\Delta\overline{W}\nu^{1/6}}{0.4508\, SC_\infty \overline{M}\Delta\tau} = D^{2/3}\omega^{1/2} \qquad [23]$$

All the quantities on the left-hand side of the equation are directly measurable in each experiment. Therefore, by plotting the left-hand side of Eq. [23] *vs.* $\omega^{1/2}$, the diffusion coefficient of bromine can be calculated from the slope of the plot.

These experiments have so far been conducted in 0.5 and 1.0M concentrations of zinc bromide solutions. Additional measurements are in progress and will be reported on separately. The details of experimental procedure have also been described elsewhere (4, 10). From the obtained weight-loss data, the left-hand side of Eq. [23] at various rotation speeds was calculated, and plotted in Fig. 8. Data points for either 0.5 or 1.0M zinc-bromide solutions form a fairly straight line. From the slope of line b and c, bromine diffusion coefficients are calculated, and are listed in Table II. For comparison, line a in Fig. 8 is drawn based on the reported bromine diffusivity in water (16). At rotation speeds higher than 5000 rpm, the Reynolds number of the hemisphere becomes so large that Eq. [21] is no longer valid.

Using these diffusion coefficients, one can now calculate the average corrosion rate of zinc based on the mass-transfer limiting flux [15], with $C_{\infty,K}$ obtained from Eq. [19]. The results are shown in Fig. 9, for various values of the separator thickness and porosity. They agree well with the range of self-discharge rates (0.5-1.5 mA/cm²) reportedly observed in advanced zinc-bromine flow cells (6).

Conclusion

Electrode corrosion by a species diffusing from the counterelectrode in a circulating flow cell has been analyzed. Two dimensionless groups, K_1 and K_2, are found to govern the net corrosion rate and its distribution along the electrode. K_1 represents the ratio of mass transfer resistance in the negative flow channel to the kinetic resistance of the corrosion process at the negative electrode. K_2 is the ratio of diffusion resistance in the separator to the kinetic corrosion resistance. For a given electrochemical cell, the concentration of the corrosive species and its corrosion rate can be readily estimated from Fig. 3-6, provided that K_1 and K_2 are known.

Application of this analysis to a zinc-bromine flow cell indicates that the corrosion of the zinc electrode by dissolved bromine during electrolysis is mass-transfer controlled. The effective diffusion coefficient of bromine in the zinc-bromide solution has been determined experimentally to be close to 1.0×10^{-9} m²/sec.

Table II. Effective diffusivities of dissolved bromine in various zinc bromide solutions

$ZnBr_2$ (M)	pH	T (°C)	$D \times 10^9$ (m/sec)
0		25	1.30
0.5	4.5	25	1.118
1.0	4.3	25	0.988

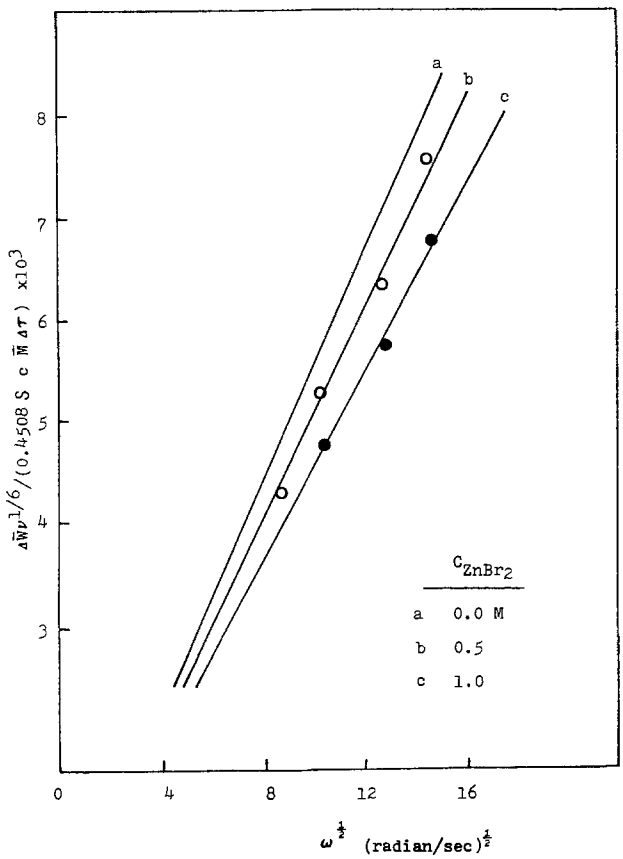

Fig. 8. Plot of the left-hand side of Eq. [23] *vs.* $\omega^{1/2}$

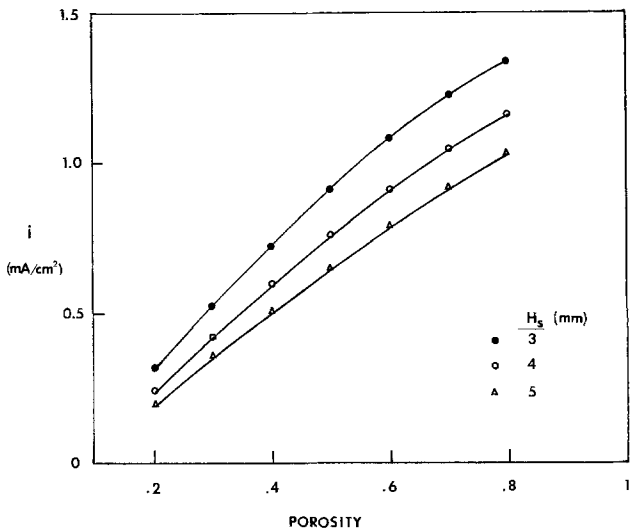

Fig. 9. Effects of the porosity and thickness of separator on the corrosion current density. See Table I for cell design and operating conditions.

Using this coefficient and the estimated kinetic rate constant, the average zinc corrosion rate in a typical zinc-bromine flow cell is in the range of 1 mA/cm^2 (1.6 μm/hr), if a typical concentration of bromine in the positive channel (10 g/liter) is assumed.

Acknowledgments

The authors would like to thank Mr. E. Moore and Mr. S. L. Lee for their assistance in experimental work. This work was supported by the Electric Power Research Institute, Palo Alto, California, under contract RP-1198-3 and by the U.S. Department of Energy (Berkeley Electrochemical Research Center, Lawrence Berkeley Laboratory, Berkeley, California) under subcontract 4512010. Equipment support by the National Science Foundation Grant CPE-7923967 is gratefully acknowledged.

Manuscript submitted May 21, 1982; revised manuscript received Jan 31, 1983.

Any discussion of this paper will appear in a Discussion Section to be published in the December 1983 JOURNAL. All discussions for the December 1983 Discussion Section should be submitted by Aug. 1, 1983.

The Illinois Institute of Technology assisted in meeting the publication costs of this article.

LIST OF SYMBOLS

C	concentration, kmol/m^3
$<C>$	average concentration, kmol/m^3
D	diffusion coefficient, m^2/sec
$\mathbf{F}$	Faraday's constant, 96,500 C/equivalent
H	channel height or thickness of separator, m
I	total current, A
k	reaction rate constant, m/sec
L	length of electrode, m
$\overline{M}$	molecular weight, kg/mol
N	mass flux, kmol/m^2-sec
$<N>$	average mass flux, kmol/m^2-sec
n	number of electrons per reaction
R	represents chlorine (Cl_2) or bromine (Br_2)
r	reaction rate, kmol/m^2-sec
S	total surface area, m^2
v	flow velocity, m/sec
$<v>$	average velocity, m/sec
$\Delta\overline{W}$	weight loss, kg
x	distance along electrode, m
y	distance perpendicular to electrode, m
ϵ	porosity
$\Gamma(x)$	complete gamma function of x
$\Delta\tau$	total reaction time, sec
ν	kinematic viscosity, m^2/sec
ω	angular velocity, rad/sec

Subscripts

A	refers to positive electrode or electrolyte
K	refers to negative electrode or electrolyte
lim	refers to mass transfer limiting flux
sep	refers to separator
o	refers to electrode surface
∞	refers to bulk solution

Superscripts

*	dimensionless variable

REFERENCES

1. "Zinc/Bromine Battery Feasibility Assessment," Gould Inc., Rolling Meadows, IL, EPRI EM-1059 (1979).
2. "Development of the Zinc-Chloride Battery for Utility Applications," Energy Development Associates, Madison Heights, WI, EPRI EM-1051 (1979) & EPRI EM-1417 (1980).
3. V. G. Levich, "Physicochemical Hydrodynamics," Prentice-Hall, Englewood Cliffs, NJ (1962).
4. J. Lee, Ph.D. Thesis, Illinois Institute of Technology (1981).
5. T. K. Sherwood, R. L. Pigford, and C. R. Wilke, "Mass Transfer," McGraw-Hill, New York (1975).
6. P. Grimes, Private communication.
7. J. Newman, "Electrochemical Systems," Prentice-Hall, Englewood Cliffs, NJ (1973).
8. F. G. Hildebrand, "Advanced Calculus for Applications," Prentice-Hall, Englewood Cliffs, NJ (1962).
9. J. O'M. Bockris and A. K. N. Reddy, "Modern Electrochemistry," Plenum Press, New York (1970).
10. J. R. Selman and J. Lee, in "Zinc Electrodeposition and Dendritic Growth from Zinc Halide Electrolytes," EPRI Contract No. RP-1198-3, Final Report EM-2393 (1982).
11. K. J. Vetter, "Electrochemical Kinetics," Academic Press, New York (1967).
12. S. E. Lorimer and R. E. White, Abstract 492, p. 1213, The Electrochemical Society Extended Abstracts, Vol. 81-1, Minneapolis, MN, May 10-15, 1981.
13. J. T. Kim and J. Jorne, *This Journal*, **125**, 89 (1978).
14. D. T. Chin, *ibid.*, **118**, 1434 (1971).
15. J. Newman, *ibid.*, **119**, 69 (1972).
16. "Chemical Engineer's Handbook," 5th ed., J. H. Perry, Editor, McGraw-Hill, New York (1973).

Reaction of Palladium with Chlorine and Hydrogen Chloride

S. P. Sharma* and E. S. Sproles, Jr.

Bell Laboratories, Columbus, Ohio 43213

ABSTRACT

A laboratory study has been conducted of the reactions of palladium with chlorine and HCl vapors at various relative humidities (RH). Reaction kinetics have been studied employing quartz crystal oscillators coated with palladium by electron beam evaporation. Corrosion films were analyzed by electron spectroscopy for chemical analysis (ESCA). It has been found that no reaction is detectable between palladium and air containing 1.8 ppm chlorine at room temperature (RT) and relative humidities less than 60%, but a film formation reaction occurs at higher relative humidities. The film is believed to be $PdCl_2 \cdot 2H_2O$. An ambient containing 10 ppm HCl at high relative humidity forms a film on Pd which largely desorbs in dry air. ESCA analysis after exposure to HCl revealed no significant chloride film. The similarity of the corrosion film formed in chlorine at high relative humidity with films formed on palladium samples placed in field environments suggests that an accelerated laboratory environmental test for palladium can be developed utilizing chlorine at high relative humidity.

Palladium and its alloys are being considered as replacements for gold platings in separable connectors. Palladium offers significant cost savings and has been used on relay contacts in the Bell System with favorable results.

Palladium is a precious metal and has been mentioned in the literature to withstand the effects of corrosive gases in the atmosphere. Extensive studies have been conducted in Bell Laboratories on the interactions of Pd with flowers of sulfur and other sulfur containing gases (H_2S and SO_2). No significant contact resistance changes were observed in the tests on Pd exposed to S_8 vapors (1). In recent studies at Bell

* Electrochemical Society Active Member.
Key words: corrosion, palladium chloride, electrical contacts, tarnishing of metals.

Laboratories, Pd coupons were exposed to various indoor and outdoor environments in different parts of the country. The indoor ambients included telephone central offices with well controlled temperature and humidity as well as other more poorly controlled environments. Some of these coupons developed high contact resistances (2). A careful investigation of these surfaces revealed the composition of the films to be $PdCl_2 \cdot 2H_2O$ (3). This observation is consistent with the fact that all base materials exposed in similar locations also showed chloride film formation (4). The film thickness developed on Pd coupons is greatest in an uncontrolled environment (5). This raises a significant concern about the use of Pd on the connector contacts. In order to understand the reaction of Pd with Cl_2 and HCl (two prominent chlorine containing pollutants), a study was conducted in an environmental chamber at very high concentrations of Cl_2 and HCl and at different relative humidities.

Experimental

The samples were prepared by electron beam evaporation of a film of 1 μm thick Pd onto 5 MHz AT-cut quartz crystals. In addition, coupons of wrought Pd were cut from a thin sheet of Pd strip (99.9% purity) and exposed to the same pollutant gases. The exposure was done in a permeation tube apparatus described earlier (6). A fluorinated ethylene propylene (FEP) Teflon tube is filled with Cl_2 in the liquid state and sealed. After an initial induction period, permeation of the chemical through the tube proceeds at a very constant rate (7). The system flow rate was adjusted so that the calculated Cl_2 concentration in the reaction chamber remained at 1.8 ppm, and the relative humidity could be varied from 0% to 80%. The actual Cl_2 concentration in the reaction chamber may be less than 1.8 ppm. All measurements were made at room temperature, and the flow rate was maintained at 75 ml/min. The quartz crystals were suspended from the top of the reaction chamber, and the coupons were mounted on a rack in the reaction chamber.

Exposure of the crystal surface to a reactive ambient results in the formation of a film on the surface and an increase in the mass of the crystal. The weight gain results in a decrease in the crystal frequency. The weight gain for a given frequency shift is obtained from the crystal constant (1.77×10^{-8}g cm^{-2} Hz^{-1}). A Sloan quartz crystal thickness monitor (DTM-3) was used as the power supply, and the crystal frequency was measured with an HP-5325A frequency counter. This frequency counter was interfaced with an HP-data acquisition system and the frequency was recorded by the computer every 10 min.

Due to the high vapor pressure of HCl, it is not possible to utilize the permeation tube apparatus for studying the HCl-Pd interactions. Therefore, another apparatus was constructed for HCl exposure and is schematically shown in Fig. 1. Dry air containing low levels of impurities is obtained from a commercial supplier. The pressure in the incoming air line is maintained at ~5 psig. Pressure fluctuations are minimized by using double pressure regulators. Part of the dry air flows through a bubbler and is fully saturated with water vapor (RH = 100%). Another part of the air from the incoming air line flows through a bubbler containing a 12% aqueous solution of HCl, maintained at 25°C in a constant temperature bath. This aqueous solution has an HCl partial pressure of 0.0145 mm and 19 mm of H_2O vapor pressure at 25°C in equilibrium state (8). The air flowing through this bubbler will be saturated with HCl and H_2O vapor corresponding to their respective partial pressures. By suitable mixing of the wet air (100% RH) with that of HCl containing air, the relative humidity (RH) and the concentration can be varied. Relative humidities of 84% RH and 90% RH and concentrations of 9 ppm and 10 ppm, respectively, were generated this way, and the samples were exposed in a similar way as in the Cl_2 gas environment. These are calculated concentration values. The actual values in the reaction chamber may be different. The computer controlled frequency counter measured the change in frequency, Δf, every 10 min.

The chemical composition of the corrosion films was analyzed on a Physical Electronics ESCA system. ESCA measurements were made using Mg K_α radiation at 400W input power. In order to correct for the instrumental drift and to obtain an accurate energy calibration, data were referenced to the Au $4f_{7/2}$ line at 84.0 eV using a gold standard.

Results

Figure 2 shows the kinetic growth rate data from the quartz crystal microbalance. The x-axis shows the time of exposure in minutes, and the y-axis is the frequency shift in Hertz. It will be shown later that the film which forms on Pd in chlorine environment at high relative humidity is hydrated palladium chloride. The thickness of the film can be calculated by knowing the density of $PdCl_2 \cdot 2H_2O$ (since $PdCl_2$ is hygroscopic), the area of the exposed material on the quartz crystal, and the total weight gain. The right side of the y-axis shows the film thickness calculated this way. Four curves are shown in this figure. These curves represent a combination of different relative humidities and concentrations of Cl_2 and HCl gas. It is seen that the rate of film growth is very small at 60% relative humidity for 1.8 ppm Cl_2. At 80% relative humidity, 1.8 ppm Cl_2, a very high linear corrosion growth rate was measured. For HCl, the growth rate at 84% relative humidity and 90% relative humidity at 9-10 ppm concentration is smaller than for 1.8 ppm Cl_2.

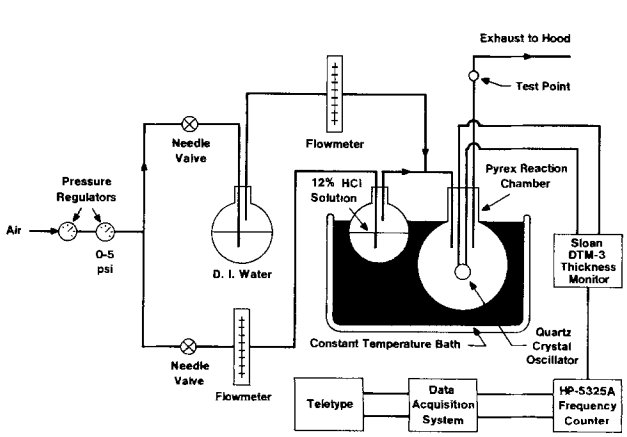

Fig. 1. Schematic of the apparatus for HCl exposure

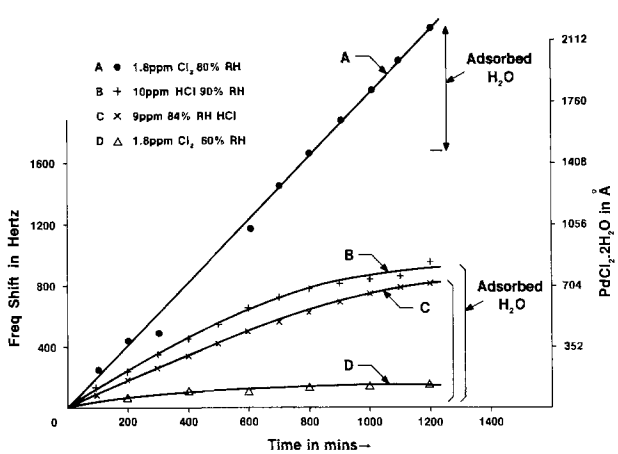

Fig. 2. Kinetic growth rate of $PdCl_2$ as a function of time at different relative humidities.

These curves should be modified somewhat to account for the fact that $PdCl_2 \cdot 2H_2O$ film may adsorb additional water at room temperature. In order to determine the amount of adsorbed water, the samples were exposed to dry air at the end of each experiment. These physically adsorbed species will desorb at low relative humidity. It was found that, on the average, a quantity of water and/or HCl vapors (in the HCl experiment) equivalent to ~700-800Å of $PdCl_2 \cdot 2H_2O$ were physically adsorbed on these films depending upon relative humidity. This adsorbed water is thought to be over and above the water of hydration in $PdCl_2 \cdot 2H_2O$. Thus, the true kinetics of growth is different than shown in Fig. 2. The final film thickness is lower than shown by the amount of adsorbed H_2O. Since the kinetics of water and/or HCl adsorption is hard to deconvolve from these figures, the true kinetics cannot be precisely determined. An approximation can be made, however, for the kinetic growth rate from these measurements. It should also be noted that in 1200 min, HCl has not reacted to an appreciable extent with Pd at 84% and 90% relative humidity, and most of the weight gain on the quartz crystal is due to the adsorption of water and HCl vapors. This is substantiated by the ESCA spectra taken on the Pd crystal which has been exposed to 1200 min to 10 ppm HCl at 90% relative humidity. This spectra is shown in Fig. 3. It is seen that the Pd $3d_{5/2}$ line occurs at ~335 eV. This line corresponds to metallic Pd. The Pd in $PdCl_2$ film occurs at ~338 eV. The absence of a line at 338 eV suggests that very little if any $PdCl_2$ formed at these conditions. The O 1s line is very broad partly due to the fact that the Pd 3p line also occurs in the same vicinity and also due to the presence of adsorbed water and adsorbed oxygen on Pd when exposed to the HCl vapors.

Figure 4 shows the ESCA spectra from Pd exposed to 1.8 ppm Cl_2 and 80% relative humidity for ~3 hr. There are two distinct Pd $3d_{5/2}$ peaks, one at 335 eV corresponding to metallic Pd and the other at ~338 eV corresponding to Pd^{+2}. The line at 338 eV corresponds to $PdCl_2$ (3). It is seen that the metallic Pd peak is higher than the Pd^{+2} peak. Since in 3 hr, films greater than the electron escape depth (~20Å) formed on the Pd surface (Fig. 2), it may be assumed that the films are patchy, and there are certain areas on the surface which have no $PdCl_2$ film in 3 hr. ESCA analyzes ~4 mm^2 area, and, therefore, this nonuniformity of the film can be seen in the spectra. This observation, that films form at discrete points and spread from these points over the entire surface, is consistent with the field grown films (3). The O 1s line shows the presence of at least two species, oxygen in H_2O and probably adsorbed oxygen. The $PdCl_2$ is known to have water of hydration associated with it. The composition of the film is $PdCl_2 \cdot 2H_2O$. This film is the same as that which grows in the field on Pd. The test utilizing Cl_2 at 80% relative humidity, therefore, duplicates the chemistry of the field grown film.

The behavior of Pd in the Cl_2 environment sharply contrasts with its behavior in the HCl environment. The rate of reaction of Pd with HCl is very slow as seen from Fig. 2. Very little if any $PdCl_2$ formed on Pd for 24 hr exposure in a flow environment at 90% relative humidity and 10 ppm HCl concentration. Ex-

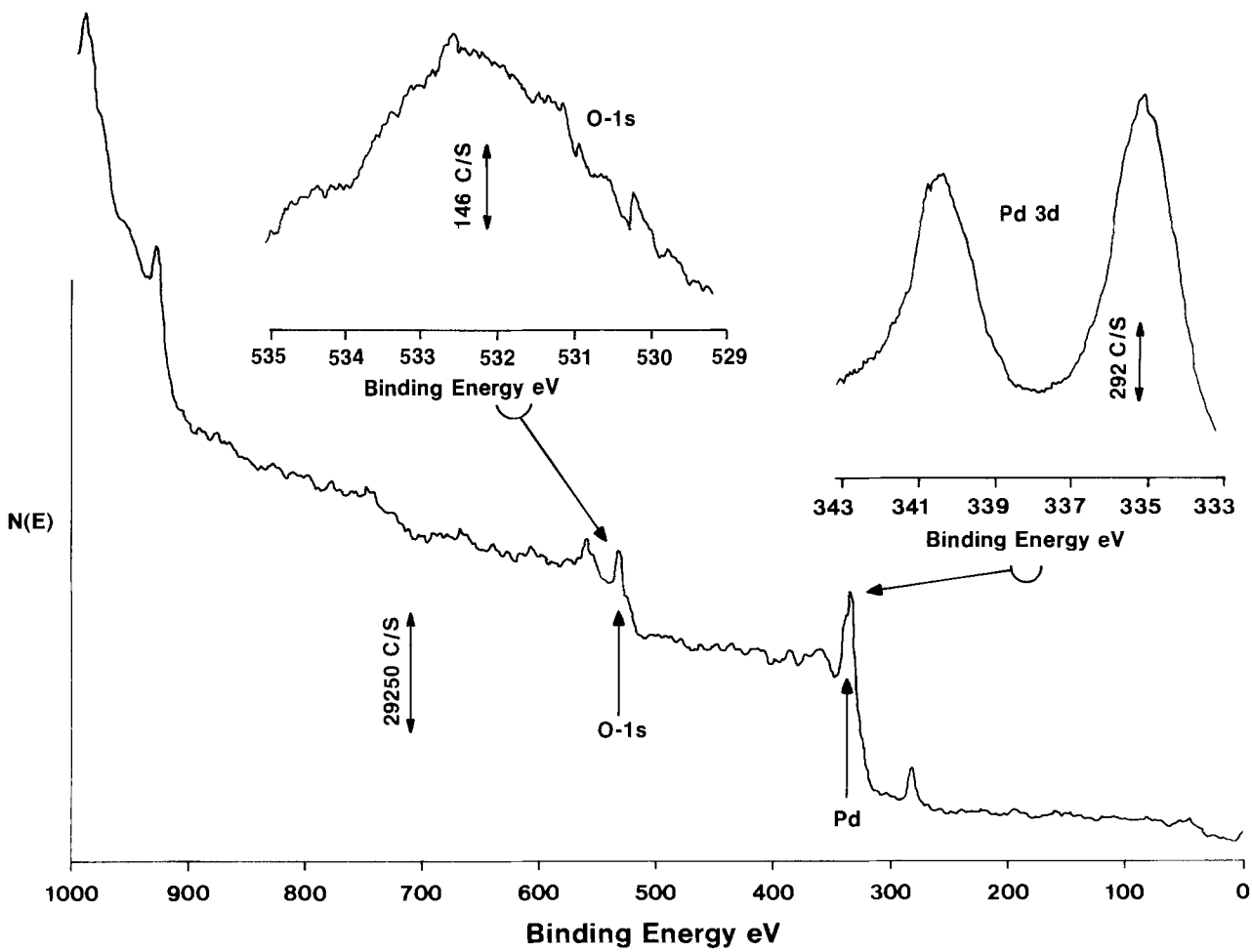

Fig. 3. Pd exposed to 10 ppm HCl, 90% relative humidity in a flow system, 24 hr

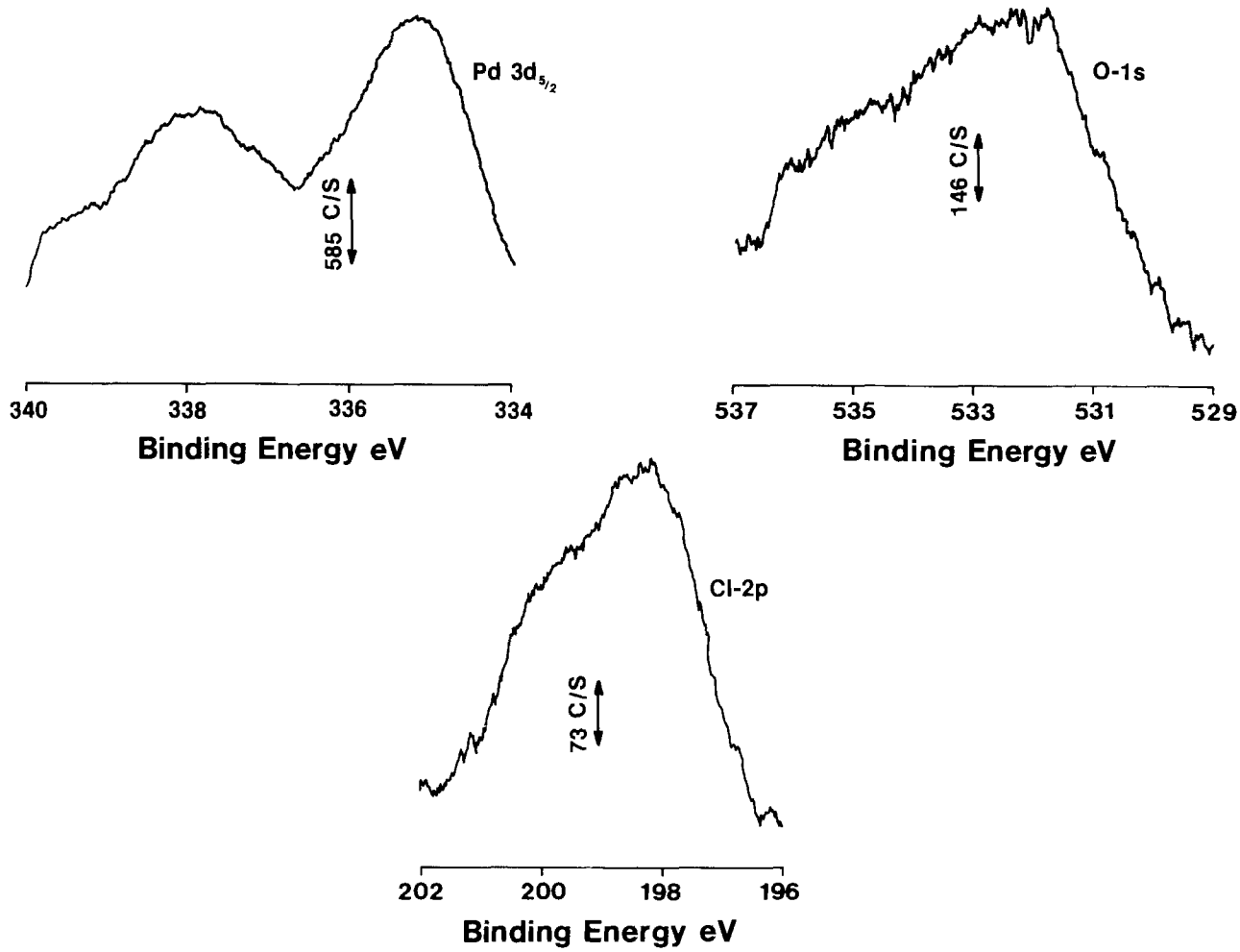

Fig. 4. Pd exposed to 1.8 ppm Cl_2, 80% relative humidity, 2 hr in a flow system

tended exposure in HCl vapors, however, does produce a chlorine containing film on Pd. Figure 5 shows the ESCA spectra obtained from a Pd sample which has been exposed to 10 ppm HCl at 90% relative humidity in a static environment for 21 days. There are two distinct Pd peaks, one corresponding to the metallic Pd (at 335 eV) and another Pd^{+2} at ~338 eV. Again, Pd^{+2} probably corresponds to $PdCl_2 \cdot 2H_2O$ as observed before.

Figure 6 shows the effect of relative humidity on the interaction of Pd with chlorine. This figure shows the weight gain on a Pd coated quartz crystal after 24 hr exposure in 1.8 ppm Cl_2 gas, plotted as a function of relative humidity. As in Fig. 2, the entire weight gain is not due to the film formation, but some of it is due to physically adsorbed water on the film, *i.e.*, water not chemically bound in the film. For example, the amount of adsorbed H_2O at 80% relative humidity is shown by the arrow on this figure. The actual curve is, therefore, somewhat lower than that shown in Fig. 6. However, it is clear that relative humidity $< 60\%$, the corrosion of Pd with Cl_2 is slow and insignificant. For relative humidity $> 60\%$, Pd is attacked very strongly by Cl_2. This relative humidity of 60% can be termed the critical relative humidity for $PdCl_2$ film formation on Pd.

Discussion

Pd does not react with Cl_2 at low relative humidities at room temperature. The reaction of dry Cl_2 with Pd does proceed but only at temperatures $> 300°C$ (9). It is, therefore, clear that water plays a key role in the observed reactions of Cl_2 with Pd at room temperature and high humidity. A model may be proposed where the Cl_2 gas dissolves in the adsorbed water layer on Pd and the reaction takes place between the dissolved Cl_2 and Pd. This would explain in part the dependence of the Pd corrosion on relative humidity, if more than a few monolayers of water are needed for the reaction to proceed. Work on the water adsorption isotherms on Pd is currently in progress and will be reported later. Thermodynamically, the standard enthalpy of formation of $PdCl_2$ is given by (9)

$$Pd + Cl_2 \rightarrow PdCl_2 \quad \Delta H° = -39 \text{ kcal/mol}$$

At a chlorine concentration of 1.8 ppm, the free energy of the reaction is −31 kcal/mol. The heat of formation provides important information about the overall thermodynamic stability of $PdCl_2$ film formation. It does not provide any information about the kinetics of this reaction. There is probably an activation energy associated with this reaction, and the role of water vapor may be to lower the activation energy for the reaction. However, it is clear that thermodynamically, this reaction should proceed to the right provided the energy barriers can be overcome.

Another important thermodynamic criterion is the standard oxidation potential (9)

$$Pd + Cl_2 \rightleftarrows Pd^{2+} + 2Cl^- \quad \Delta V° = 0.44$$

Thus, at the standard states, Cl_2 gas can easily oxidize Pd to Pd^{2+} and is itself reduced to Cl^- because $\Delta V°$ is positive. It is likely that even at 1.8 ppm Cl_2 concentration, the oxidation potential would remain positive, and the reaction would proceed to the right as written. The role of H_2O may be to support the oxidation of Pd by dissolving Cl_2 gas in the adsorbed H_2O film. This may explain in part why HCl reaction with Pd is small, because no such oxidation of Pd to Pd^{2+} may take place with HCl. Other strong oxidants, like O_3 in the atmosphere, may oxidize Pd, and the HCl reaction may proceed after this oxidation.

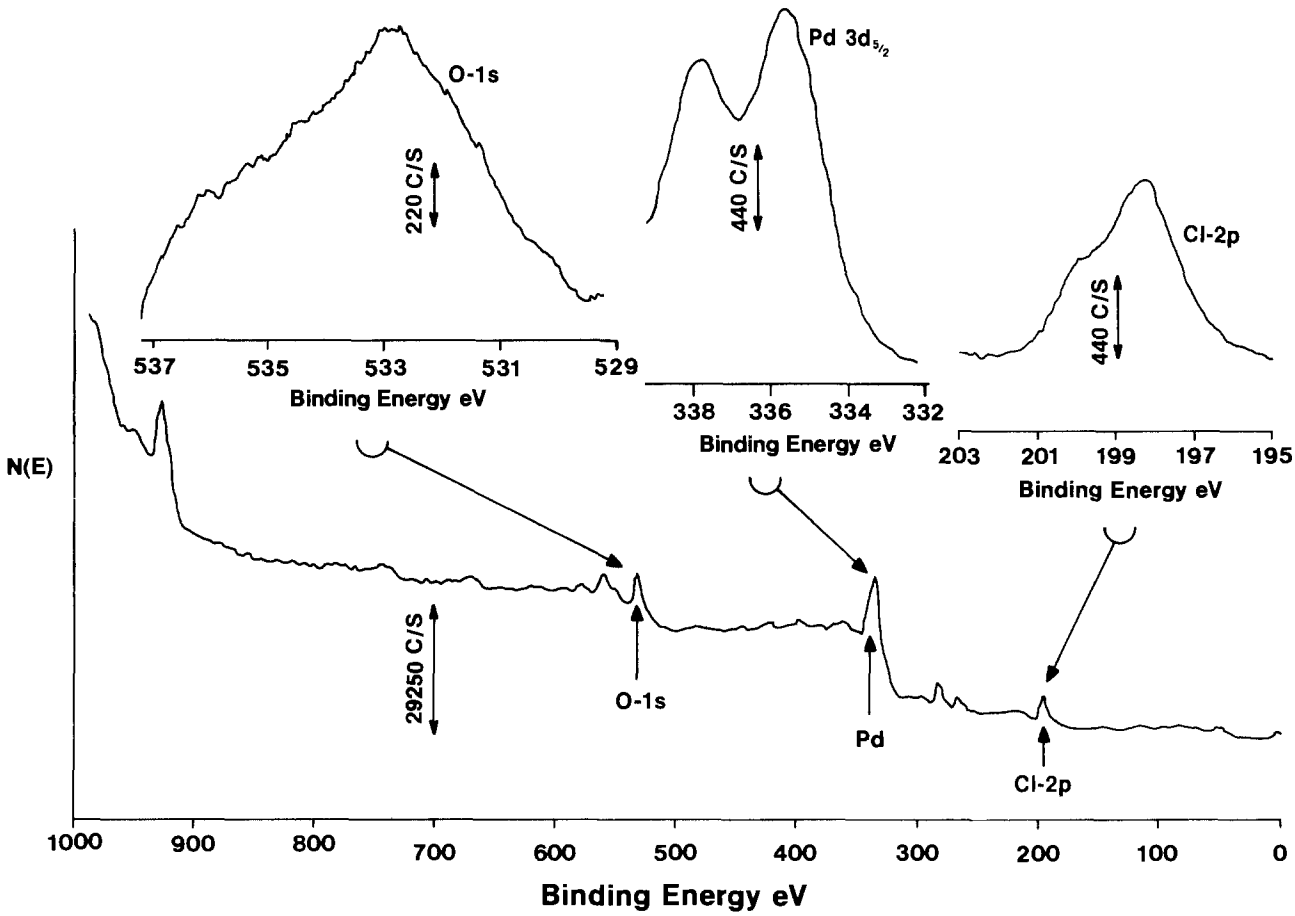

Fig. 5. Pd exposed to 10 ppm HCl vapors, 90% relative humidity, 21 days in static environment.

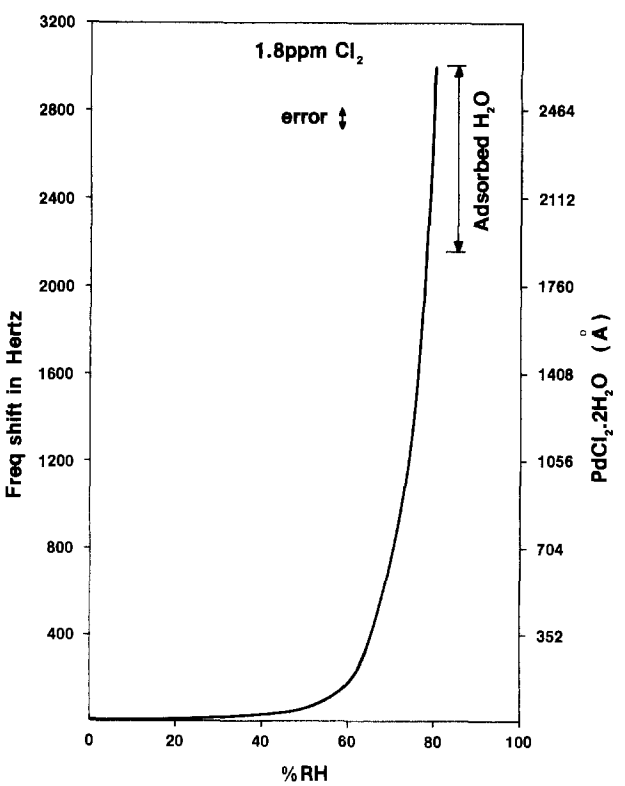

Fig. 6. Effect of relative humidity on the interaction of palladium with chlorine.

Palladium chloride is very hygroscopic. The dihydrate chloride, $PdCl_2 \cdot 2H_2O$ has a brown color. The anhydrous $PdCl_2$ obtained by heating $PdCl_2 \cdot 2H_2O$ is red-brown in color. Differential thermal analysis and x-ray diffraction studies indicate that there are at least two polymorphs of $PdCl_2$. The best known is α-$PdCl_2$ which is orthorhombic (a = 3.81Å, b = 3.34Å, and c = 11.0Å) with two formula units in the unit cell (9). Structure of α-$PdCl_2$ consists of infinite chains in which Pd is surrounded by four co-planar bridging Cl atoms at 2.31Å (9, 10). The angles between Pd Cl Pd

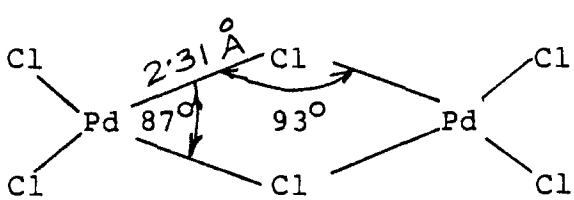

is 93°, and ClPdCl is 87°. The $PdCl_2$, therefore, resembles a polymer. The structure of $PdCl_2 \cdot 2H_2O$ is not known, but it appears likely that the chain structure of a $PdCl_2$ may be retained with the addition of 2 water molecules weakly bound to each palladium atom (10). A model of film formation based on the $PdCl_2$ structure may be proposed which accounts for the nonuniformity of the $PdCl_2$ film observed on Pd in early stages of formation. It is proposed that the polymer chain starts at few discrete points (defects, impurities, surface contaminants) which act as nucleation sites. Further growth takes place by adding bridging chlorine atoms on succeeding sites until the entire surface is covered. In the initial stages, there may be only

a few patches. This mechanism would account for the patchy character of the film observed in ESCA. The chemical shift of 3 eV suggests that there is a net decrease in the effective electronic charge on Pd atom, if we assume a simple charged sphere model where an atom is considered to be a sphere with a surface represented by the valence electrons. Utilizing Pauling's electronegativity principle and under the assumptions that only nearest neighbors and that only σ bonds contribute to the palladium charge, it is estimated that Pd in $PdCl_2$ has a net charge of 0.6. Thus, there is not strictly an ionic bond between Pd and chlorine in $PdCl_2$ but a partial ionic and a partial covalent bond.

It was mentioned earlier that $PdCl_2$ is very hygroscopic in nature. Once it is formed on the surface, it may adsorb water readily; this may increase the rate of corrosion at $< 60\%$ relative humidity. In the field, the presence of salts like $CaCl_2$ and NaCl (significant constituents of dust particulates present in the environment) may also cause the condensation of water at low relative humidity values (3). For example, 39% relative humidity will cause the condensation of water near a $CaCl_2$ particle. This may start the formation of $PdCl_2$ in real field environments. This point has been discussed further in another paper (3). The present results support the conclusion of Shimosato (11) that Cl_2 gas reacts strongly with Pd at high relative humidity. It also explains results of Long and Bradford (12) that Pd coupons developed high contact resistance when exposed to a chlorine containing environmental test.

Conclusion

A study has been conducted of Pd reactions in an ambient produced in the laboratory containing high concentrations of Cl_2 gas and HCl vapors at different relative humidities. A permeation tube apparatus was utilized for Cl_2 exposure, and a separate apparatus was constructed for exposing Pd to HCl vapors. The samples were prepared by electron beam evaporation of Pd on quartz crystal oscillators, and the weight gain was monitored by measuring the frequency change of the crystal when exposed to pollutant gases. The chemical analysis was done by ESCA. It has been found that the reaction of HCl with Pd proceeds very slowly at high relative humidity. The reaction of Cl_2 gas proceeds rapidly at relative humidity $> 60\%$. For relative humidity $< 60\%$, the reaction of Cl_2 does not proceed rapidly. The reaction of Cl_2 with Pd and an extended exposure of Pd to HCl vapors at high relative humidity ($> 80\%$) results in the formation of $PdCl_2 \cdot 2H_2O$ film on the surface. This film readily adsorbs more water and may increase the corrosion rate further. It has been found that the film which forms in the field can be duplicated in the lab by using high concentrations of Cl_2 at high relative humidity. These reactions suggest that for evaluating a connector product, using Pd as the material, an environmental test utilizing Cl_2 at high relative humidity should be employed. A high corrosion rate on exposed materials may not necessarily mean degradation of the electrical performance of mated connectors as the authors have shown in another study (13).

Acknowledgments

The authors wish to thank H. G. Tompkins for his help in the construction of HCl exposure apparatus. They also thank F. E. Bader for useful discussions.

Manuscript received Nov. 13, 1981.

Any discussion of this paper will appear in a Discussion Section to be published in the December 1983 JOURNAL. All discussions for the December 1983 Discussion Section should be submitted by Aug. 1, 1983.

Bell Laboratories assisted in meeting the publication costs of this article.

REFERENCES

1. M. Feder and F. E. Bader, Unpublished results.
2. M. Antler, C. A. Haque, and M. H. Drozdowicz, Paper presented at Electronic Components Conference, Atlanta, Georgia, April 1981.
3. S. P. Sharma, Paper presented at Holm Seminar on Electrical Contacts, Chicago, Illinois, September 21-23, 1981.
4. S. P. Sharma, *This Journal*, **125**, 2005 (1979).
5. C. A. Haque and M. Antler, Paper presented at Holm Seminar on Electrical Contacts, Chicago, Illinois, September 21-23, 1981.
6. S. P. Sharma, *This Journal*, **127**, 21 (1980).
7. A. E. O'Keeffe and G. C. Ortman, *Anal. Chem.*, **38**, 760 (1966).
8. National Research Council, "International Critical Tables," Vol. III, p. 301, McGraw-Hill, New York (1928).
9. F. R. Hartley, "The Chemistry of Platinum and Palladium," pp. 8-16 and pp. 230-240, John Wiley and Sons, New York (1973).
10. L. Pauling, "The Nature of the Chemical Bond," 3rd ed., pp. 257-259, Cornell University Press, Ithaca, NY (1966).
11. S. Shimosato, *Electron. Commun. Jpn.*, **55-C**, 90 (1972).
12. T. R. Long and K. F. Bradford, in 8th Int. Corp. on Electrical Contact Phenomena, p. 55, Tokyo, Japan, August 22-26, 1976.
13. E. S. Sproles, Jr. and S. P. Sharma, Paper presented at Annual Electronic Connector Study Group (ECSG) Conf., Philadelphia, Pennsylvania, November 11-12, 1981.

Pitting Mechanism of Aluminum in Hydrochloric Acid under Alternating Current

K. Vu Quang and F. Brindel

Centre d'Etudes de Chimie Métallurgique, C.N.R.S., 94400 Vitry, France

and G. Laslaz and R. Buttoudin

P.U.K. Aluminum Péchiney, 38340 Voreppe, France

ABSTRACT

The etching of high purity aluminum foils in hydrochloric acid under alternating current was investigated. Pit development and characteristics of etched foils were studied taking into account the a-c amplitude, the frequency, the etching time, and the electrolyte temperature, using light micrography and scanning electron micrography. A maximum of electrical capacitance C_M of etched and anodized foils is observed for certain frequency value ν_M; C_M and ν_M depend on the experimental conditions. The aluminum oxide formed on the metal etched surface exhibits minimum thickness for bath temperature near 60°C. Galvanodynamic voltammetry allows the determination of a pitting current and an induction time which depends on frequency. The pit density and the calculated anodic current efficiency for metal dissolution are found to decrease markedly with increasing frequency.

The etching of high purity aluminum foil in chemical or electrolytic processes is required to obtain, by a controlled pitting mechanism, a suitable surface porosity necessary for the production of electrolytic capacitors or of offset lithographic sheets (1-3).

The main advantage of the alternating current etching (6-9) consists in the resulting fine porosity and the remaining unattacked core part of the foil which preserves its pliability. Under alternating current, pitting and metal dissolution occur during the anodic half-cycle (10, 11), while reduction of protons in the cathodic half-cycle provokes local rise in *p*H, producing the repassivation of preexisting pits (2, 12). Therefore, in the next anodic half-cycle, the creation of new pits results in ramification of the attack. Many works have been devoted to pitting phenomena of aluminum in chloride solution (4, 5, 13, 14).

In this paper, pit development and characteristics of aluminum foils etched under alternating current are investigated, taking into account the influence of a-c frequency, a-c amplitude, etching time, and temperature (17).

Experimental

99.99% purity and 90 μm thick aluminum foils are used. The etched layer characteristics and the capacitance of etched and anodized foils are investigated in relation to a-c frequency ν (from 1 to 1000 Hz), a-c amplitude I, bath temperature T, and etching time t. The etching bath is based on 1.3N hydrochloric acid solution containing small amounts of nitric and phosphoric acids. The attack is performed on one side of the electrodes consisting of 38 mm diam disks cut out from the above foils. These disks are cleaned in trichlorethylene and in ethyl alcohol and are rinsed in deionized water. The disks are mounted on a Teflon support provided with electrical contact. The exposed surface (to be attacked) is 4 cm^2. In most experiments, the maximum current applied to electrode is 2A (for 4 cm^2). Two electrodes are placed face to face inside a 2.5 liter glass cell. A Teflon cylinder, provided with holes allowing the solution circulation, keeps constant the distance between electrodes (5 cm) and limits the side effect on etched samples. The sine alternating current utilized for etching is provided by a potentiostat Tacussel PRT 20-10X, monitored by a signal generator Tektronix 464. For experimental convenience, the potential of the working (aluminum) electrode is recorded with reference to the other aluminum electrode. The cell voltage is then recorded as a function of the current intensity (Fig. 8). Its values vary within the range +2 and −2V. The potential scale on the original voltammetric curves on the oscilloscope is 1 V/cm for 1 Hz and 0.5 V/cm for other frequencies. The anodization of etched foils is carried out in a boric acid solution at 90°C. The capacitance of etched and anodized aluminum foils is determined at 50 Hz frequency using a capacitance bridge HP 4282A. Capacitance values are referred to a unit of geometric surface area (dm^2).

Key words: aluminum, etching, pitting, capacitor, alternating current.

Results

Optical cross-sectional micrographs of etched foils in Fig. 1 show a coarse attack at 1 Hz frequency, resulting in an irregular surface topography. A regular fine porosity is obtained at 50 Hz. The etching at 100 Hz does not produce any noteworthy roughness in foil surface.

Scanning electron micrographs of etched foil in Fig. 2 exhibit etched pits at 1 Hz attack, developed in well-defined crystal directions. These pit shapes are similar to the ones formed in the direct current etching process. Pits created at 50 Hz have rounded outlines.

By an ellipsometry technique adapted to a rough surface, performed in the Research Center of Aluminium-Pechiney Voreppe, it has been found that the oxide thickness is minimum for the etching temperature range 55°-60°C (Fig. 3). This result was confirmed by the surface analysis data given by the glow discharge spectrometry (GDS) we carried out with the assistance of IRSID Institute (15). GDS data also indicate a maximum of oxygen and hydrogen content for a temperature around 50°C (Fig. 4). These two elements are associated to a hydrated oxide. The maximum of O and H contents is attributed to a maximum of total pore surface created at these temperatures.

Under the given experimental conditions, a maximum of electrical capacitance C_M is observed on each $C = f(\nu)$ plot relative to etched and anodized foils, at a given frequency ν_M. C_M and ν_M are found to depend on the a-c amplitude I, the bath temperature T, and the etching time (Fig. 5, 6, and 7).

The capacitance maximum decreases when the applied current amplitude I increases, whereas the ν_M value remains nearly unchanged. A temperature increase moves ν_M toward high frequency. It enhances the deterioration of the fine porosity structure of the etched foil. When etching time is decreased, the foil capacitance decreases and the capacitance peak is shifted toward low frequencies (Fig. 7). For an electric

Fig. 1. Cross-sectional micrographs of aluminum foils etched under alternating current at different frequencies: left, 1 Hz; center, 50 Hz; right, 100 Hz. (× 400) (c.d. = 0.5 A/cm^2, t = 4 mn 45 sec, T = 55°C.)

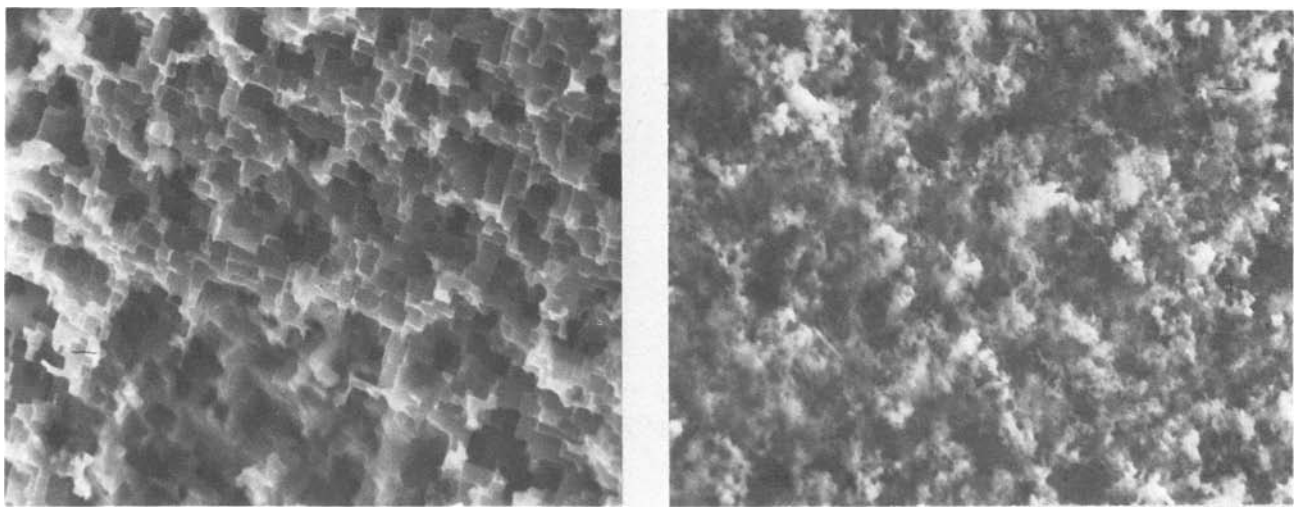

Fig. 2. Scanning electron micrographs of aluminum foils etched at 1 and 50 Hz, respectively. (× 1600.)

charge four times smaller (*i.e.*, for an etching time equal to 1 mn 11 sec instead of 4 mn 45 sec) the capacitance maximum C_M is only slightly reduced, about 15% smaller.

Galvanodynamic voltammetry curves relative to aluminum foils in the etching solution are recorded using an oscilloscope, for different frequencies (Fig. 8). On each curve, a small potential peak (maximum) is observed which corresponds to an intensity i_R and an induction time τ during which the current is mainly used for the electrical charging of the metal/solution interface. This peak would be related to the pit initiation (and corresponds to the pitting potential) that can be determined from a potentiodynamic voltammetry curve. During τ time, no dissolution of metal would occur. On the galvanodynamic curves, one can note the increase of i_R intensity as a function of increasing frequency.

From the equations relative to sine-shaped current, the expressions of τ and ρ were derived. i_o is the a-c maximum current amplitude, ρ is the anodic current efficiency for metal dissolution, defined by the ratio

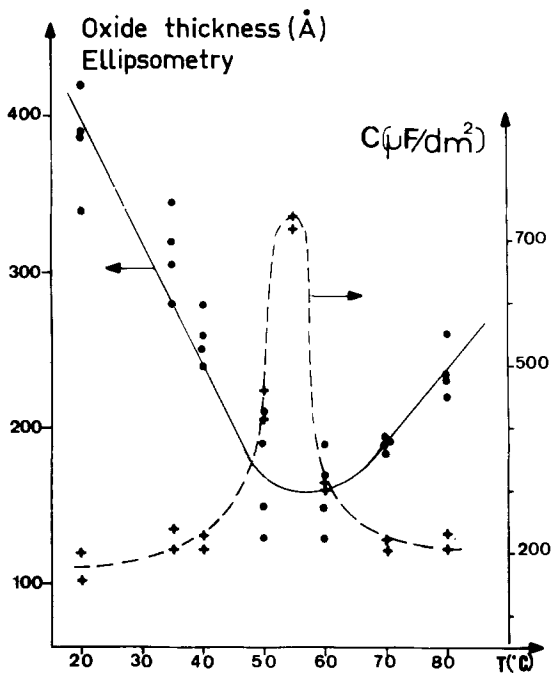

Fig. 3. Maximum of capacitance and minimum of oxide thickness observed for bath temperature range 55°-60°C (oxide thickness determined by an ellipsometry technique).

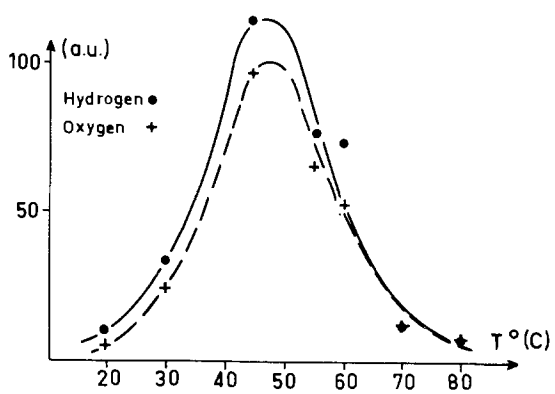

Fig. 4. Maximum of oxygen and hydrogen contents in porous part of aluminum etched foils observed for bath temperature near to 50°C (glow optical discharge spectrometry data).

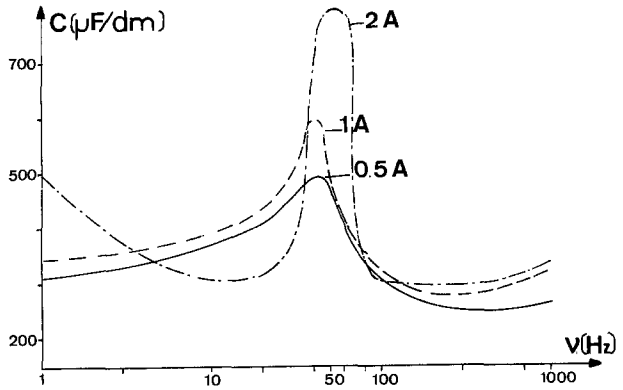

Fig. 5. Effect of the alternating current amplitude on the capacitance variation of etched and anodized aluminum foils.

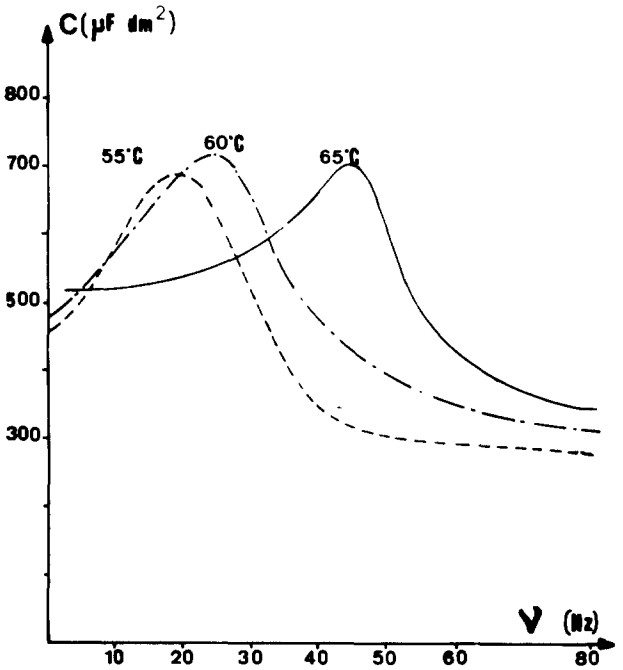

Fig. 6. Effect of the bath temperature on the capacitance variation of etched and anodized aluminum foils. (t = 1 mn 10 sec.)

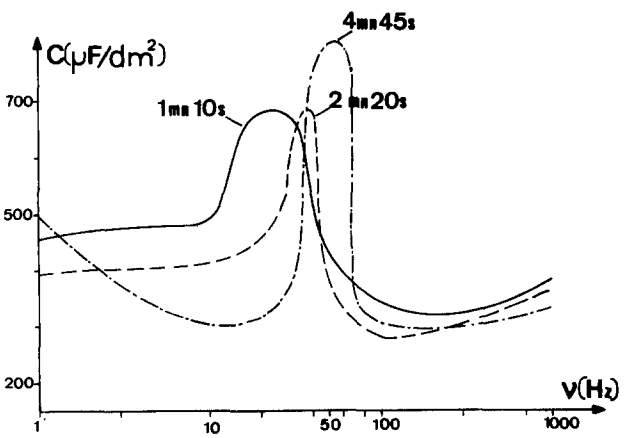

Fig. 7. Effect of etching time on capacitance variation of etched and anodized aluminum foils.

$Q_F/Q_{T/2}$, $Q_{T/2}$ is the total electrical charge corresponding to a half-cycle (area under the sine curve for a half-cycle, Fig. 9) and Q_F is the part of $Q_{T/2}$ used for the anodic dissolution of metal, after the induction time τ

$$\tau = \frac{1}{2\pi\nu} \arcsin\left(\frac{i_R}{i_o}\right)$$

$$Q_F = \int_{\tau}^{T/2} i_o \sin \omega t dt$$

$$Q_{T/2} = \frac{i_o}{\pi}$$

$$\rho\,(\%) = \frac{Q_F}{Q_{T/2}} \times 100 = \frac{1 + \cos 2\pi\nu\tau}{2} \times 100$$

The values of τ and ρ calculated from experimental ν and i_R values are reported in Table I which shows that the anodic current efficiency for metal dissolution ρ markedly decreases when a-c frequency increases.

Pit density is found to drop sharply as a function of frequency (Fig. 10). It is noted that the current density must be considerably reduced in this experiment otherwise the pit development was too quick and it was not possible to observe the phenomenon.

Discussion

The capacitance of the aluminum etched foils employed in the fabrication of electrolytic capacitors is known to be tightly bound to the etching conditions. The low capacitance values found for foils prepared in the laboratory results from two reasons: (*i*) in this study, the foils are etched on one side, instead of both sides of the foil as in an industrial plant, (*ii*) the difference in hydrodynamic condition of the bath near the foil surface: solution motion over the electrodes is rather limited in the laboratory cell. Nevertheless, the effect of different etching parameters has been clearly pointed out in this investigation.

The frequency of a-c etching is found to have a specific and great influence on etched and anodized foils: the existence of a capacitance peak for a given frequency value ν_M has been observed; furthermore, the peak amplitude decreases when the applied current increases, while the ν_M value remains nearly unchanged. However, the bath temperature affects the ν_M value: a temperature increase moves ν_M toward high frequency; micrographs of etched foils show that temperature enhances the fine structure deterioration. The aluminum oxide formed on the metal etched surface exhibits a minimum thickness for bath temperature near 55°-65°C.

The pit development influences the etching morphology and consequently the foil capacitance. It is controlled, among other factors, by the oxide formation on the metal surface and by the corrosion product concentration at the pit bottom. The oxide formation occurs in the cathodic half-cycle, probably because of a local pH rise provoked by the proton reduction (2). This oxide plays an important role since it passivates the previously created pits during the anodic half-cycle and promotes then the etching ramification.

The existence of a capacitance peak for certain frequency values could be connected to the etching development. As a matter of fact, it is found that frequency affects the pit morphology and the pit density. Furthermore, according to the voltammetry study, the anodic current efficiency for metal dissolution decreases with increasing frequency: the pit induction time is at the origin of the diminution of the proportion of the electric charge (used for the metal dissolution at each a-c cycle) as a function of frequency. In other words, the etching development is less important at high frequencies. Accordingly, for a given etching time and a

Table I.

ν, Hz	1	3	10	20	40
i_R, mA/dm²	62	175	300	375	500
τ, msec	19	18	10	6.7	6
ρ, %	99	97	90	83	53

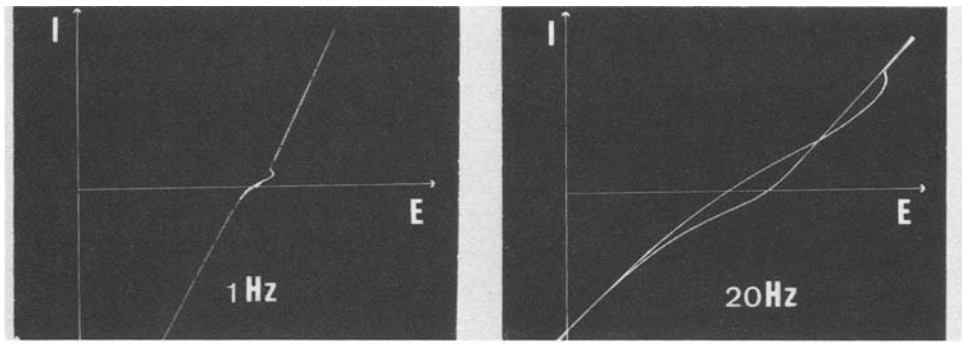

Fig. 8. Galvanodynamic voltammetry curves for different a-c frequencies. The maximum cathodic or anodic total current, for 4 cm^2 electrode, is 2A. Each curve is performed in one cycle, $t = 1/\nu$ (sec).

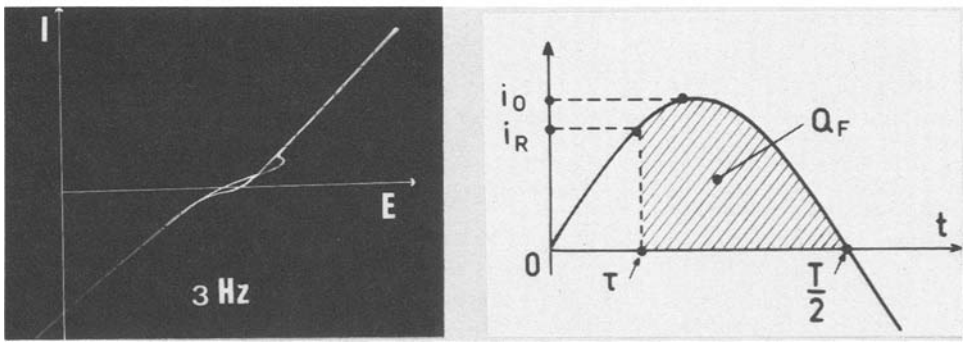

Fig. 9. Schematic representation of the induction time (τ) and the electric charge corresponding to anodic dissolution of metal (Q_F) in an a-c cycle.

given bath temperature, the capacitance maximum is obtained at an optimal frequency range, below which the fine structure of the porous layer is destroyed and above which the porous structure is not enough developed.

Previous data relative to pitting corrosion have been very useful for the comprehension of the aluminum etching mechanism. The pit formation depends mainly on chloride effect, based on a diffusion process and/or adsorption at the metal/solution interface. This process involves an induction time which depends on several parameters, in particular, the temperature and the level of electrochemical polarization. In the conditions of this study, the induction time, which controls the anodic current efficiency for metal dissolution, mainly consists of the time for electrical charging of the metal/solution interface. The low pit densities observed at high frequencies are due to high values of the pitting potential at these frequencies.

The influence of the main parameters and some steps in the a-c etching of aluminum in hydrochloric acid have been elucidated through these investigations.

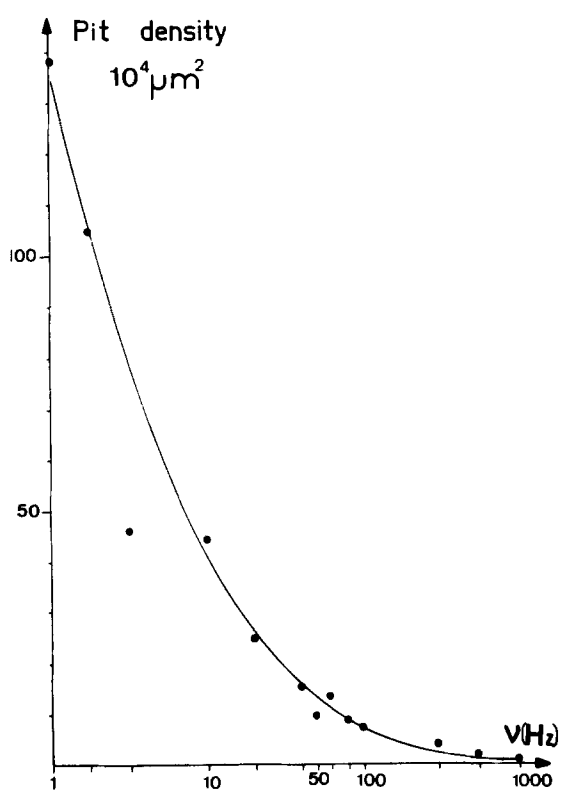

Fig. 10. Variation of the etched pit density on aluminum foil as a function of a-c frequency (c.d. = 0.05 A/cm^2, t = 20 sec).

Manuscript submitted Sept. 13, 1982; revised manuscript received Feb. 2, 1983. This was Paper 11 presented at the Montreal, Que., Canada, Meeting of the Society, May 9-14, 1982.

Any discussion of this paper will appear in a Discussion Section to be published in the December 1983 JOURNAL. All discussions for the December 1983 Discussion Section should be submitted by Aug. 1, 1983.

C.N.R.S. assisted in meeting the publication costs of this article.

REFERENCES

1. R. H. Broadbent, *Electrochem. Technol.*, **6**, 163 (1968).
2. G. E. Thompson and G. C. Wood, *Corros. Sci.*, **8**, 721 (1978).
3. A. J. Dowel, *Trans. Inst. Met. Fin.*, **57**, 138 (1979).
4. T. H. Nguyen and R. T. Foley, *This Journal*, **126**, 1855 (1979).
5. A. Ben Rais, F. Dalard, and J. Guitton, *Surf. Technol.*, **8**, 225 (1979); I.S.E. Meeting, Venice, Sept. 1980.
6. Der Tau Chin and S. Venkatesh, *J. Appl. Electrochem.*, **8**, 293 (1978).
7. U. Bertocci, *Corros. Sci.*, **35**, 211 (1979).
8. S. Kruger and C. E. Bird, *Br. Corros. J.*, **13**, 163 (1978).
9. W. K. Johnson, *ibid.*, **6**, 200 (1971).
10. C. Roth, *Metallob. Ang. Elek.*, **1**, 1 (1972).
11. C. Bargeron, *This Journal*, **124**, 1845 (1977).
12. K. Nisancioglu and H. Holtan, *Corros. Sci.*, **19**, 537 (1979).
13. B. N. Stirrup, N. A. Hampson, and I. S. Midgley, *J. Appl. Electrochem.*, **5**, 229 (1975).
14. E. Sato, M. Sato, and I. Uchiyama, *Jpn. Corros.*, **24**, 223 (1975).
15. R. Berneron, J. C. Charbonnier *et al.*, *Spectrochim.*

Acta., **33B**, 665 (1978); *Rev. Met.*, **78**, No. 1, 73 (1981).
16. F. Brindel and K. Vu Quang, *J. Electrochim., Brussels* (June 1981).
17. K. Vu Quang, F. Brindel, G. Laslaz, and R. Buttoudin, Paper 11 presented at The Electrochemical Society Meeting, Montreal, Que., Canada, May 9-14, 1982.

Formation of Salt Films during Anodic Metal Dissolution in the Presence of Fluid Flow

Richard Alkire* and Antonia Cangellari*

Department of Chemical Engineering, and Materials Research Laboratory, University of Illinois, Urbana, Illinois 61801

ABSTRACT

Anodic dissolution of a metal in the presence of flowing electrolytic solution was studied by both experimental and theoretical methods. A mathematical model was developed which included emphasis on the potential field distribution near the dissolving electrode, and on convective diffusion effects in both laminar and turbulent flow. Critical conditions were identified for saturation, by dissolved metal salt, of the solution adjacent to the anodic surface. Theoretical results were compared to measurements obtained in a channel flow system of the critical flow velocities above which pure iron would not repassivate in 0.5M H_2SO_4.

In a variety of electrochemical processes, dissolution of metal occurs at high rates from locally active anodic regions. Saturation of the electrolytic solution near the dissolving surface may occur, if the fluid is not too vigorously agitated, with the result that precipitation of a metal salt film takes place. The local accumulation of metal ions in the solution adjacent to the dissolving surface depends both upon the mass transfer and the potential field distribution. In general, the presence of a precipitated salt film can have either a beneficial or a detrimental effect upon the specific process involved. Determination of the range of flow velocities under which a dissolving metal may become coated with precipitated dissolution products was investigated in this study.

For example, to withstand severe corrosion environments, metals are often selected whose corrosion resistance depends upon a thin passive surface film which forms spontaneously and protects the metal. In the presence of fluid flow, the passive film may become locally damaged (1), as by impingement of particles, cavitation, or spontaneous depassivation. In such cases, sustained protection is maintained only if the small damaged region is capable of repassivation in the presence of fluid flow. Since some metals require, as a first stage of repassivation, the precipitation of a metal salt film (2-10), the presence of sufficiently high fluid velocities will impede recovery of passivity.

During pitting corrosion in many halide-containing mineral acids, early stages of pit growth have been postulated to occur in the presence of precipitated metal chloride salt which prevents pit repassivation and which controls the rate of metal dissolution (11-14). In such situations, the presence of sufficiently high fluid velocities would be expected to wash away the chloride salt, and would presumably assist recovery of passivity.

Additional examples of high rate electrodissolution are encountered in anodic electromachining (14) and in electropolishing (15) where the presence of precipitated dissolution products plays an important role on the morphology of the dissolving surface, as well as on influencing the rate at which the process occurs.

The literature cited above indicates clearly that salt films play a role in many electrochemical technologies. As a consequence, a general evaluation of the conditions under which salt films precipitate in the presence of fluid convection would contribute toward clarification of a variety of anodic dissolution processes.

The purpose of this investigation was to develop a mathematical model of steady-state anodic metal dissolution in the presence of fluid flow, and to predict the range of flow velocities under which metal salt films may occur on the dissolving surface (17). This study arose from observations on the effect of fluid flow on repassivation of iron in sulfuric acid (16), and on the appearance of metal salt films on such surfaces during the course of repassivation (7, 16). Since, for the Fe-H_2SO_4 system, the appearance of the salt film is thought to be a necessary precursor to repassivation, it is clearly important to investigate flow conditions under which salt film precipitation, and thus repassivation, is possible.

Theoretical Formulation

The geometry of the system studied in the present work is shown schematically in Fig. 1. Electrolytic solution flows between two parallel plates. On one of the plates, a small anodic region of bare metal is exposed to the solution while the other plate serves as (cathodic) counterelectrode. Active dissolution occurs at the metal surface, with a rate which varies with location along the anode owing to ohmic, mass transport, and charge-transfer processes.

The metal dissolution rate depends, for example, on the potential distribution between electrodes which varies according to the solution conductivity, electrode size, and charge-transfer resistance. In addition, concentration changes occur adjacent to the anode surface; for the conditions investigated here, these are

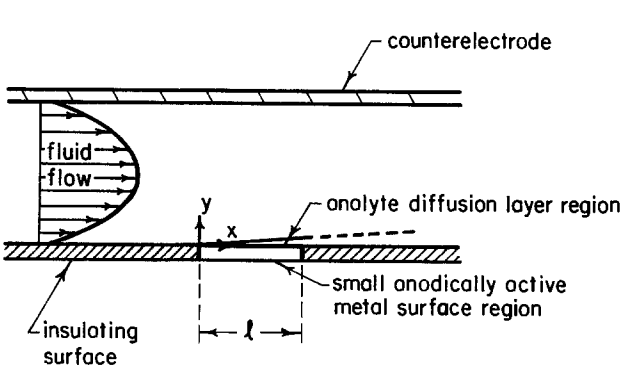

Fig. 1. Schematic diagram of the configuration studied

* Electrochemical Society Active Member.
Key words: corrosion, dissolution, metal, theory, transport.

confined to a mass transfer boundary layer which is very thin since the fluid flow acts to wash reaction products downstream rapidly. Two regions may, therefore, be identified in Fig. 1: a very thin diffusion layer where variation in concentration occurs, and a bulk region where the concentrations are uniform. In this work, mathematical solutions for the concentration and potential distribution in the two regions were obtained. Aspects of related and background interest are available in Ref. (18-20).

The particular geometry for which this work was originally intended corresponds to a small active site on an otherwise passive metal immersed in flowing corrosive solution. For this reason, simplifying assumptions will be introduced which deemphasize the influence of the counterelectrode geometry and the reactions occurring at the counterelectrode. Also, since most corrosion processes have large potential driving forces (on the order of 1V), additional important simplifications will be made on the form of the electrochemical dissolution reaction.

Assumptions.—Because rigorous calculations are cumbersome, various simplifications have been introduced into the physical picture described above. The particular application for which this work was originally intended corresponded to a small active site on an otherwise passive metal which was immersed in flowing acidic corrosive solution. The following assumptions retain the salient features of that application, but also avoid unwarranted numerical complications.

The fluid velocity profile in the smooth-walled channel is fully developed by virtue of an upstream entrance region of adequate length (not shown in Fig. 1). The distance between the opposing walls is large in comparison to the size of the electrode so that the behavior of the active metal site is not influenced by the size of the counterelectrode, nor by the reactions occurring upon it. The mass transfer boundary layer at the active surface is thin with respect to the channel width, and the Schmidt number (ν/D) is large. Diffusion along the direction of flow is negligible in comparison with convection in the same direction. The electrode dissolution reaction is assumed to operate under large potential driving forces typical of corrosion situations, and, therefore, is expressed by the Tafel form. In acidic solutions, the metal ions formed by dissolution are assumed not to undergo hydrolysis.

Migration of dissolved metal species was assumed to be negligible owing to the presence of supporting electrolyte, and the physical properties of the system were assumed to be constant. These last two assumptions may be questionable if the metal salt has a high solubility, since large metal ion concentrations can then arise within the diffusion layer. The effect of migration of, say, divalent metal ions and divalent anions serves to increase the mass flux by a factor of up to two, depending upon the ratio of supporting cations to total anion concentration (21). On the other hand, an increase in concentration also serves to decrease the diffusion coefficient. For the ferrous sulfate system used in experimental studies below, the diffusion coefficient Fe^{2+} in 0.5M H_2SO_4 saturated with ferrous sulfate is approximately one-half of the value in 0.5M H_2SO_4 containing negligible ferrous sulfate (22). Thus, for the system studied here, the two assumptions tend fortuitously to offset each other.

Dimensional equations.—The anodic dissolution reaction under study is

$$M^o \rightarrow M^{+n} + ne$$

The potential applied to the metal is consumed by ohmic resistance in the solution, charge-transfer overpotential at the dissolving surface, and concentration overpotential in the diffusion layer

$$\Phi_A = \Phi_o + \eta_s + \eta_c \qquad [1]$$

The potential Φ_A represents the potential of the working electrode with respect to a distant reference electrode of the same kind as the working electrode. The concentration overpotential, η_c, is

$$\eta_c(x) = \frac{RT}{n\mathbf{F}} \ln \frac{C_s(x)}{C_b} \qquad [2]$$

The surface overpotential, η_s, is expressed by the Tafel equation

$$i(x) = i_o e^{\frac{\alpha n \mathbf{F}}{RT} \eta_s(x)} \qquad [3]$$

The quantity Φ_o is the potential in the solution just outside the diffusion layer, and is obtained by solving Laplace's equation in the bulk electrolyte region

$$\frac{\partial^2 \Phi}{\partial x^2} + \frac{\partial^2 \Phi}{\partial y^2} = 0 \qquad [4]$$

Because the diffusion layer is so thin, the boundary conditions are written as though they applied at the electrode surface

$$i(x) = -\kappa \left.\frac{d\Phi}{dy}\right|_{y=0} \quad \text{at} \quad y = 0$$

$$\Phi = 0 \quad \text{as} \quad y \rightarrow \infty$$

$$\nabla \Phi = 0 \quad \text{at the insulator surfaces}$$

Wagner (23) obtained the solution of Eq. [4] from which the potential near the electrode surface is found to be

$$\Phi_o = -\frac{1}{2\pi\kappa} \int_o^l i(x') \ln (x - x')^2 dx' \qquad [5]$$

Equation [4] can also be solved with use of Green's function (20, 24). Although the method is more complicated, and requires more computer time for convergence, it is also more general and can be used for many other geometries.

For laminar flow in the very thin mass transfer boundary layer region, the steady-state convective diffusion equation is

$$U_x \frac{\partial C}{\partial x} = D \frac{\partial^2 C}{\partial y^2} \qquad [6]$$

with boundary conditions

$$C = C_b \simeq 0 \quad \text{at} \quad y \rightarrow \infty$$

$$C = C_b \simeq 0 \quad \text{at} \quad x = 0$$

$$\frac{i(x)}{n\mathbf{F}} = -D \left.\frac{dC}{dy}\right|_{y=0} \quad \text{at} \quad y = 0$$

Within the boundary layer, the fluid velocity varies linearly with distance from the wall, and is proportional to the shear stress at the wall

$$U_x = \frac{6\langle u \rangle}{h} y$$

A preliminary solution of Eq. [6] may be obtained for the simple case where the concentration along the dissolving electrode is constant and is equal to the saturation concentration

$$i_{sat} = \frac{n\mathbf{F}D(C_s - C_b)}{\Gamma(4/3)} \left(\frac{6\langle u \rangle}{9Dhx} \right)^{1/3} \qquad [7]$$

This preliminary result will find use in the discussion which follows. The more general result, obtained from Eq. [7] with use of Duhamel's superposition integral (25) is

$$i(x) = \frac{n\mathbf{F}D}{\Gamma(4/3)} \left(\frac{6\langle u \rangle}{9Dh} \right)^{1/3} \int_o^x \frac{dC_s(x')}{dx'} \frac{dx'}{(x - x')^{1/3}} \qquad [8]$$

where $\Gamma(4/3) = 0.89298$. For the laminar flow case, Eq. [1]-[3], [5], and [8] were solved simultaneously to obtain the current, potential, and concentration distributions along the dissolving surface.

For turbulent flow, the time-averaged equation of convective diffusion is

$$\bar{U}_x \frac{\partial \bar{C}}{\partial x} = \frac{\partial}{\partial y}\left[(D + \epsilon_D) \frac{\partial \bar{C}}{\partial y} \right] \quad [9]$$

in which the eddy diffusivity, ϵ_D, appears. In turbulent flow, the velocity profile in the thin boundary layer region (26) is

$$\bar{U}_x = \frac{\langle u \rangle^2}{\nu} 0.029\, \mathrm{Re}^{-1/4}$$

For large Schmidt numbers, ϵ_D varies as y^3 within the boundary layer (27)

$$\epsilon_D = Ay^3 \left(\frac{f}{2}\right)^{3/2} \langle u \rangle_b^3 \nu^{-3}$$

where f is the Fanning friction factor. The quantity "A" depends weakly upon the Reynolds number, but was set equal to the value of 4.25×10^{-4} in this study. The boundary conditions for Eq. [9] are the same as for Eq. [6]. For the turbulent flow calculations, Eq. [1]-[3], [5], and [9] were solved simultaneously.

Dimensionless equations.—The following dimensionless variables were used

$$x^* = \frac{x}{l}, \quad \eta^* = \frac{n\mathbf{F}}{RT}\eta, \quad i^* = i\frac{n\mathbf{F}l}{RT\kappa}, \quad C^* = \frac{C}{C_{sat}}$$

$$\Phi_A^* = \frac{n\mathbf{F}}{RT}\Phi_A, \quad \Phi_o^* = \frac{n\mathbf{F}}{RT}\Phi_o$$

The equations that define the model under laminar flow conditions are

$$V^* = \Phi_o^* + \eta_s^* + \eta_c^* \quad [10]$$

$$\eta_c^* = \ln \frac{C_s^*}{C_b^*} \quad [11]$$

$$i^* = f_{CT}\zeta e^{\alpha\eta_s^*} \quad [12]$$

$$i^* = \frac{2}{3} N_l \int_o^{x^*} \frac{dC_s^*}{dx^{*\prime}} \frac{dx^{*\prime}}{(x^* - x^{*\prime})^{1/3}} \quad [13]$$

$$\Phi_o^* = \frac{1}{2\pi}\int_0^1 i^*(x^{*\prime}) \ln (x^{*\prime} - x^*)^2\, dx^{*\prime} \quad [14]$$

In the case of turbulent flow, Eq. [9] was made dimensionless with the variables

$$x^+ = \frac{x}{\nu}\sqrt{\frac{\tau_w}{\rho}}, \quad y^+ = \frac{y}{\nu}\sqrt{\frac{\tau_w}{\rho}}$$

with the result

$$y^+ \frac{\partial C^*}{\partial x^+} = \frac{\partial}{\partial y^+}\left[\left(\frac{1}{Sc} + 0.000475 y^{+3} \right) \frac{\partial C^*}{\partial y^+} \right] \quad [15]$$

boundary conditions at

$$x^+ = 0 \quad C^* \simeq 0$$

$$y^+ \to \infty \quad C^* = 0$$

$$y^+ = 0, \quad x^+ = 0, \quad \frac{\partial C^*}{\partial y^+} = -i^*(x^*)$$

$$\frac{RT\kappa}{n^2\mathbf{F}^2 l\sqrt{\frac{\tau_w}{\rho}}} \frac{Sc}{(C_{sat} - C_b)} = -\frac{i^*}{N_t} \quad [16]$$

The parameters which appear in the foregoing dimensionless equations are

$$N_l = N_{ol}\left(\frac{l}{h}\right)^{1/3} \mathrm{Pe}^{1/3}$$

$$N_t = N_{ot}\left(\frac{l}{h}\right)^{1/8} \mathrm{Pe}^{0.875}$$

$$\zeta = \frac{n\mathbf{F}l}{RT\kappa}\langle i \rangle$$

In the presentation of results the dimensionless quantity

$$f_{sc} = \frac{\langle i \rangle}{\langle i_{sat} \rangle} = \frac{\zeta}{N} \quad [17]$$

was also used.

Parameters N_l and N_t represent, for laminar and turbulent flow, respectively, a dimensionless anodic current density for the special circumstance that the surface concentration everywhere along the surface is equal to the saturation concentration. Large flow velocities give large values of N_l and N_t, and correspond to conditions under which mass transfer does not tend to influence behavior. That is, mass transfer limitations predominate at low velocities.

The parameter ζ gives the relative magnitude of the ohmic resistance of the solution in comparison with the charge-transfer resistance of the dissolution reaction. The form of ζ is very similar to a Tafel polarization parameter. Thus, small values of ζ correspond to the situation where dissolution occurs under charge-transfer control, and with a rate which is uniform everywhere along the surface.

Method of solution.—For the case of laminar flow, Eq. [10]-[13] were combined to give

$$f_{CT}\zeta e^{\alpha(\Phi_A^* - \Phi_o^* - \ln (C_s^*/C_b^*))} = \frac{2}{3} N_l \int_o^{x^*} \frac{dC_s^*}{dx^*} \frac{dx^{*\prime}}{(x^* - x^{*\prime})} dx^{*\prime} \quad [18]$$

Equation [18] was solved simultaneously with Eq. [14] by an iterative procedure. A first guess of the current distribution along the electrode was made. Numerical integration of Eq. [14] with Simpson's method was used to obtain the potential distribution along the electrode surface. Equation [18] was discretized by the method suggested by Acrivos and Chambré (28) and was solved for the concentration distribution along the electrode. An improved guess of the current distribution along the electrode surface was then obtained from Eq. [18], and the procedure was repeated until two successive solutions for the current and concentration distribution differed less than 0.01% of the former value, at each point on the electrode surface. Details of the numerical procedure are given in Ref. (17).

For the case of turbulent flow, a different iteration procedure was used. A first guess of the current distribution along the electrode surface was made. Equation [15] was solved numerically in the boundary layer to obtain the concentration field; the equation was discretized in the six-point Crank-Nicolson form and the tridiagonal coefficient matrix was inverted by the method of Thomas (29). Equation [14] was integrated and the potential distribution along the electrode surface was obtained. Solutions of Eq. [10]-[12] then gave an improved guess for the current distribution, and the iterative procedure was repeated. Details of numerical procedure are available in Ref. (17).

Theoretical Results and Discussion

The foregoing model was used to predict behavior during steady-state metal dissolution under both laminar and turbulent flow conditions. The range of parameter values investigated is shown in Table 1. Some parameters were not varied as they were regarded as less important. The value of applied potential was

Table I. Parameters that appear in the model

	Parameter	Laminar flow	Turbulent flow
Held constant	α	0.5	0.5
	n	2.0	2.0
	Φ_A*	82	82
	C_b	10^{-9}	10^{-9}
	f_{OT}	10^{-10}	10^{-10}
Varied	ζ	0.6-130	100-300
	N	50-1000	5-200
	f_{SC}	0.02-2	1-30

selected to be 1.0V, a value typical of the experimental results which follow. The bulk concentration was set at 10^{-6}M so that the concentration overpotential, Eq. [2], was always well defined.

Potential distribution.—Figure 2 illustrates results calculated for the potential distribution along the dissolving surface for several sets of parameter values. It may be seen that the fluid flow has a relatively small influence even under conditions where the solution near the surface may be saturated ($N_l < \zeta$ or $N_t < \zeta$). This behavior is quite different from that observed at the cathodic mass transfer limiting current, where large concentration overvoltages appear when the surface concentration is driven toward zero.

Figure 2 also illustrates that the potential distribution depends upon the parameter ζ, which is similar in form to a polarization parameter. For large applied currents and small solution conductivity (large ζ), ohmic resistance of the solution controls the potential distribution, and thus favors the lateral edges of the electrode. For the experimental repassivation studies described below, ζ always exhibited a value larger than unity. The potential distribution does not depend upon the exchange current density (i_0) when the Tafel equation is used to describe charge-transfer kinetics. When the value of ζ is less than unity, the potential distribution along the electrode is essentially uniform.

Current distribution.—Consider now the special case when the concentration of metal ions on the dissolving surface is uniform everywhere and is equal to the saturation concentration. For laminar flow, Eq. [7] indicates that the local rate of dissolution (*i.e.*, the current distribution) would decrease with the cube root of distance from the leading edge of the dissolution region. For turbulent flow, a different dependence upon distance would be found. For either type of flow, the average value of this special case of current distribution will be denoted $\langle i_{sat} \rangle$ and will be used to normalize the current distributions shown in Fig. 3. The quantity $\langle i_{sat} \rangle$ is denoted the "anodic saturation current density" rather than a "limiting" current density, because it may be exceeded if the solution becomes

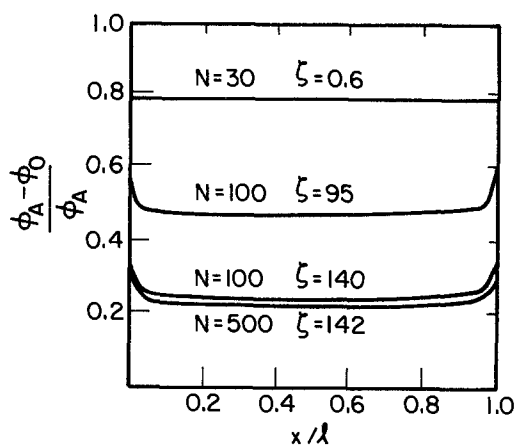

Fig. 2. Potential distribution at the electrode surface as a fraction of the applied potential.

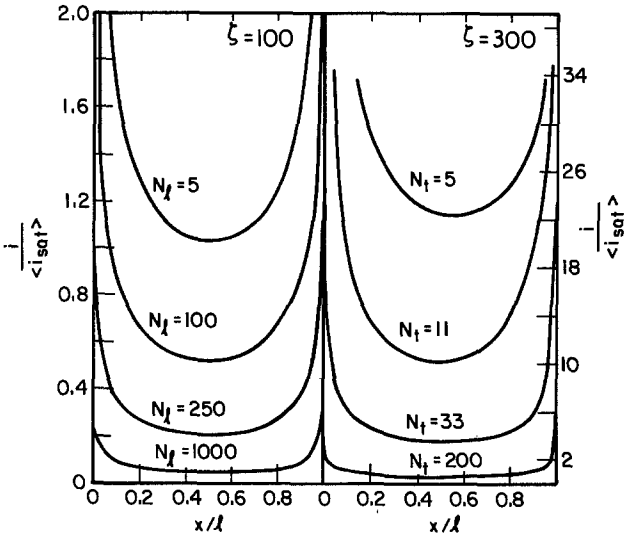

Fig. 3. Current distribution at the electrode surface under laminar (left) and turbulent (right) flow conditions.

supersaturated. In this respect, $\langle i_{sat} \rangle$ is distinctly different from a steady-state cathodic mass-transfer limiting current density, which can be exceeded only when additional cathodic reactions occur.

Figure 3 illustrates the effect of flow velocity N_l or N_t on the local rate of metal dissolution for both laminar (left-hand) and turbulent (right-hand) flow. The ratio $i/\langle i_{sat} \rangle$ represents a fraction of anodic saturation current density, f_{SC}, and may exceed unity if the solution becomes supersaturated with metal salt. Equation [17] indicates that when f_{SC} is unity, then $N = \zeta$, a point that will be exploited in the simplified theory discussed later.

The current distributions shown in Fig. 3 are nonuniform, and exhibit large current densities at both the leading ($x/l = 0$) and trailing ($x/l = 1$) edges, even when $i/\langle i_{sat} \rangle$ exceeds unity. In Fig. 3, the current distribution is nonuniform because of the ohmic resistance of the solution (ζ is large). Even though the anodic saturation current density may be reached, large increases in concentration overpotential do not arise. Therefore, the ohmic resistance essentially fixes the average current density at a constant value for all the curves shown in Fig. 3 because both ζ and the applied potential, Φ_A*, are held constant.

As a consequence, an increase in flow velocity (N_l or N_t) acts to decrease the fraction of anodic saturation current density ($i/\langle i_{sat} \rangle$). At sufficiently high velocities, the current density everywhere along the surface lies below the value needed to saturate the adjacent fluid.

It may also be seen in Fig. 3 that the current distributions are similar for both laminar and for turbulent flow, since concentration effects do not appreciably influence the potential distribution (see Fig. 2).

Concentration distribution.—Figure 4 illustrates the concentration adjacent to the dissolving surface for laminar (left-hand) and turbulent (right-hand) flow conditions, and at various velocities (N_l or N_t). The surface concentration can exceed the saturation value along portions of the dissolving surface.

Saturation of the solution occurs first at the trailing edge ($x/l = 1$) where the mass transfer boundary layer is thickest and where the current density is high (see Fig. 3). The surface concentration at the leading edge ($x/l = 0$) tends also to increase rapidly since the current density is high there. However, the mass transfer boundary is very thin at the leading edge so that the surface concentration does not attain as large a value as at the trailing edge, an effect that is more pronounced in laminar than in turbulent flow.

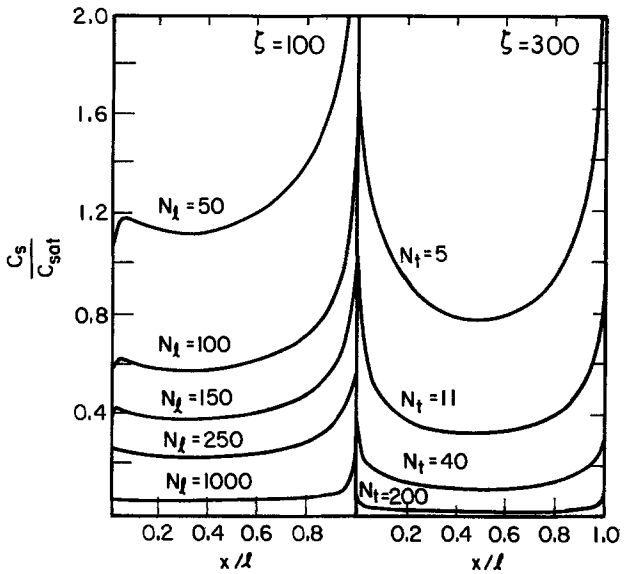

Fig. 4. Concentration distribution at the electrode surface under laminar (left) and turbulent (right) flow conditions.

Critical velocity for saturation.—It is clear from examination of Fig. 4 that for some conditions the surface concentration lies everywhere below the saturation concentration, while for other conditions it lies everywhere above. There is an intermediate region where a portion of the surface concentration lies above saturation, while other parts of the surface lie below saturation. This intermediate region exists because the current density distribution is nonuniform.

Figure 5 shows, for example, results for several different sets of parameter values; for each set, two diagonal lines appear in the figure. For any anode dissolving under fluid flow, values may be calculated for the quantities shown in the abscissa and the ordinate. If the coordinates of this point lie above and to the right of the upper diagonal line, then the fluid adjacent to the surface is below the saturation value everywhere. If the coordinates of this point lie below and to the left of the lower diagonal line, then the fluid is saturated everywhere along the surface.

Because the specific location of the diagonal lines in Fig. 5 depends upon the system parameters, it would be useful if a general result could be obtained which was simple to use for quick approximations. For this reason, the following simplifications have been developed.

Simplifications for quick estimates.—While the foregoing model is based on a fundamental treatment of concentration and potential distribution phenomena, less exact calculations may be useful for quick estimates. The following treatment, which uses simple algebra, can be employed for rough calculations. The particular geometry used in the development below corresponds to dissolution of a small circular disk embedded in the wall of the flow channel. A similar geometry was used in the experiments which follow.

There are four limiting cases which depend upon flow conditions (laminar or turbulent) and upon the value of ζ (larger or smaller than unity). In the first case, assume that dissolution from a small circular region occurs under laminar flow and ohmic resistance control (large ζ) either owing to poor solution conductivity or to small size of the dissolution site. Thus, $\Phi_A \approx \Phi_o$. By combining Ohm's law ($IR_d = \Phi_A$) with the resistance of flow to a circular disk (30)

$$R_d = \frac{1}{4\kappa r_o}$$

and with the area of the disk (πr_o^2), one finds the average current density

$$\langle i \rangle = \frac{4\kappa\Phi_A}{\pi r_o}$$

By denoting the length l as twice the radius r_o, one finds the dimensionless average dissolution current density to be

$$\zeta = \frac{8n\mathbf{F}\Phi_A}{\pi RT}$$

Thus since $N = \zeta/f_{SC}$, one may obtain from the definition of N_1 the following result

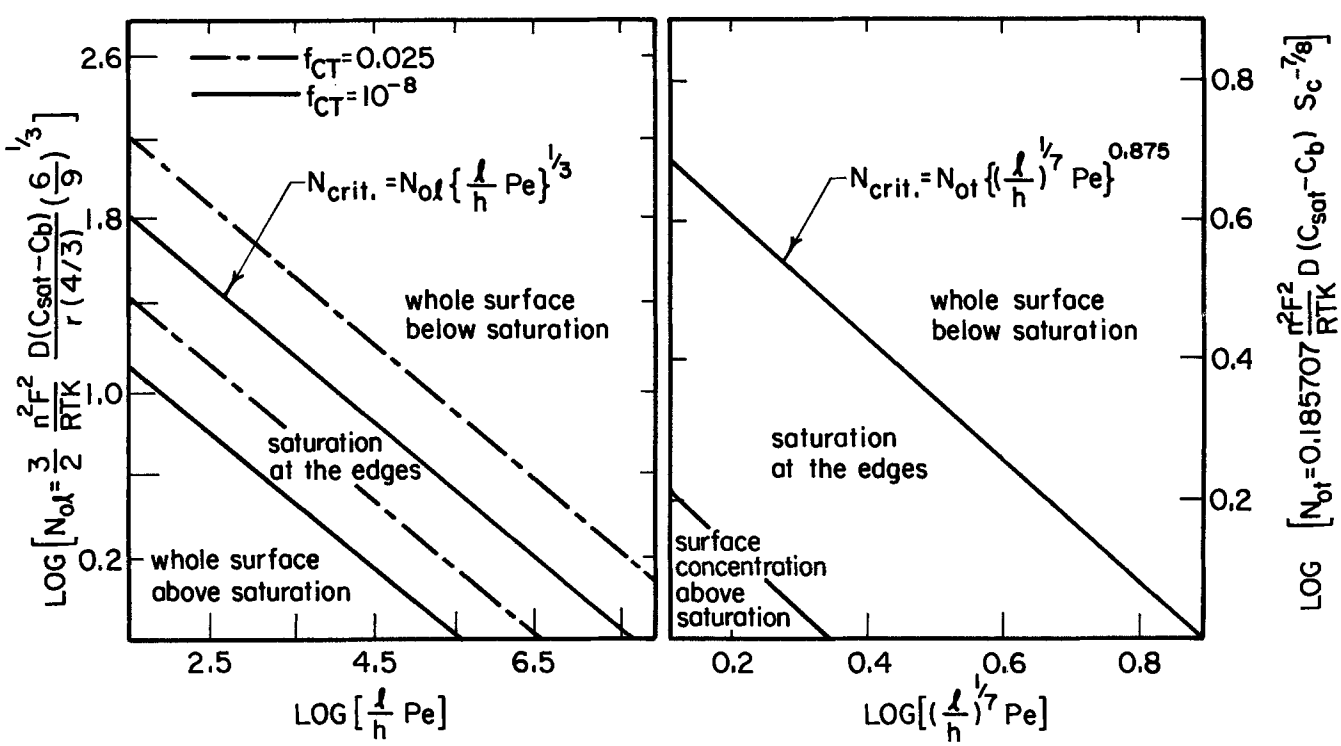

Fig. 5. Regions of parameter space where steady-state metal dissolution leads to saturation of flowing fluid in laminar (left) and turbulent (right) flow.

$$\langle Re_{crit} \rangle = \frac{9h^2D}{12\nu l^2}\left(\frac{16\Gamma(4/3)\kappa\Phi_A}{3\pi f_{SC} nFD(C_{sat} - C_b)}\right)^3 \quad [19]$$

which is valid for laminar flow when $\zeta > 1$.

In a similar manner, one may obtain estimates of the critical Reynolds number for cases when $\zeta < 1$ by using the Tafel expression, Eq. [3] instead of Ohm's law. That is, $\Phi_A \approx \eta_s$. Further estimates of behavior in turbulent flow may be made with the use of the definition of N_t instead of N_l. In this manner, the critical Reynolds numbers shown in Table II have been obtained for the four cases.

For any of the four cases reported, saturation of the fluid adjacent to the surface will not occur if the Reynolds number exceeds the critical value. If the Reynolds number is below the critical value, then precipitation is possible although supersaturation phenomena may impede its occurrence.

Experimental Apparatus

The schematic design shown in Fig. 6 describes the flow system which was fabricated from PVC piping. A magnetically driven pump was used (March MDX-MIT3) and was controlled with globe valves. The reservoir was fitted with a regulated heat exchanger for temperature control. The flow system contained 18 liters of solution. The flow cell, milled from PVC blocks, had a rectangular channel (0.3 × 0.4 cm) which was polished to a peak-to-valley roughness of less than 1 μm. The channel had an entrance region of 34 cm to provide well-developed hydrodynamic velocity profiles. Details of the flow channel were previously described (16).

The working electrodes were circular disks (0.32 cm diam) of iron (99.99%, Research Organic/Inorganic Chemical Corporation), mounted flush in the wall of the flow channel. The counterelectrode was a sheet of platinum mounted flush on the opposite wall. A backside reference electrode port (0.05 cm diam) was provided just downstream from the working electrode and was connected through polyethylene tubing to a mercurous sulfate (1M H_2SO_4) reference electrode. A potentiostatic power supply with function generator (PAR 173, 175) was used in conjunction with an X-Y recorder (Houston, 2000).

Experimental Procedure

Iron electrode surfaces were polished (Buehler Ecomet III) to a 0.3 μm alumina finish. The electrolyte (0.5M H_2SO_4) was prepared from reagent grade chemicals and distilled deionized water. Analysis of H_2SO_4 was by titration with NaOH to phenolphthalein endpoint. The procedure for experiments was to install the electrode, activate the flow system, and apply a slightly cathodic current (3 mA/cm²) for 2 min after which the potential was suddenly changed to an anodic value and held at that value for the duration of the experiment, while the current transient was recorded. After two such experiments, the electrode was removed and replaced with a freshly prepared electrode.

Experimental Results

Current transients obtained for different values of the fluid flow rate are illustrated in Fig. 7. For slow flow rates the current transient increased to large values (3 A/cm²) and then decreased within a second as repassivation occurred. At still higher flow rates, repassivation processes took longer. At still higher flow rates, repassivation did not occur; if, under such conditions, the pump was switched off then repassivation would occur within seconds. These results illustrate qualitatively that repassivation is adversely influenced by flow velocity, and that there is a critical flow velocity above which repassivation does not occur.

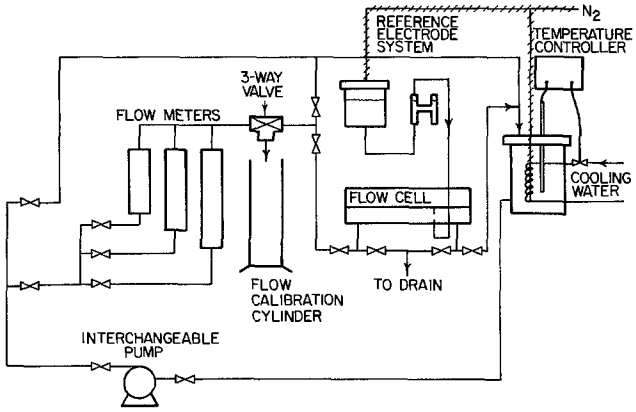

Fig. 6. Schematic diagram of the experimental apparatus

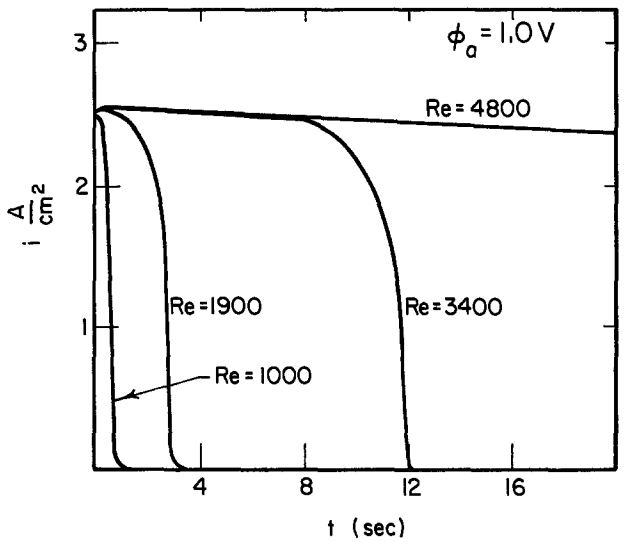

Fig. 7. Typical current transients observed under different flow rates.

Experiments were carried out by stepping the potential to 0.8, 1.0, and 1.2V *vs.* NHE at various flow velocities. Results are shown in Fig. 8. It is seen that, at each potential, repassivation occurred at low velocities but not at higher velocities. The surface geometry undoubtedly changed during the course of an experiment owing to the high rate of metal dissolution (2.5 A/cm² corresponds to surface retreat of 19 μm/sec). However, such slight changes are not expected to alter the configuration significantly over the range of variables reported here.

Table II. Critical Reynolds numbers above which saturation will not occur

	Laminar flow (Re < 4000)	Turbulent flow (Re > 10,000)
Ohmic control $\zeta > 1$	$\frac{9}{12}\frac{h^2}{l^2}\frac{D}{\nu}\left\{\frac{16\Gamma(4/3)\kappa\Phi_A}{3\pi f_{SC} nFD\,(C_{sat} - C_b)}\right\}^3$	$\left\{\frac{8h\ 2.936\Phi_A}{0.119\,\pi\, l\, F_{SC} nfD\,(C_{sat} - C_b)\,Sc^{1/3}}\right\}^{8/7}$
Charge transfer control $\zeta < 1$	$\frac{9}{12}\frac{h^2Dl}{\nu}\left\{\frac{2\Gamma(4/3)\,i_o\,e^{\frac{anF}{RT}\Phi_A}}{3D(C_{sat} - C_b)}\right\}^3$	$\left\{\frac{2.936\,h\,i_o\,e^{\frac{anF}{RT}\Phi_A}}{0.119\,nFD(C_{sat} - C_b)\,Sc^{1/3}}\right\}^{8/7}$

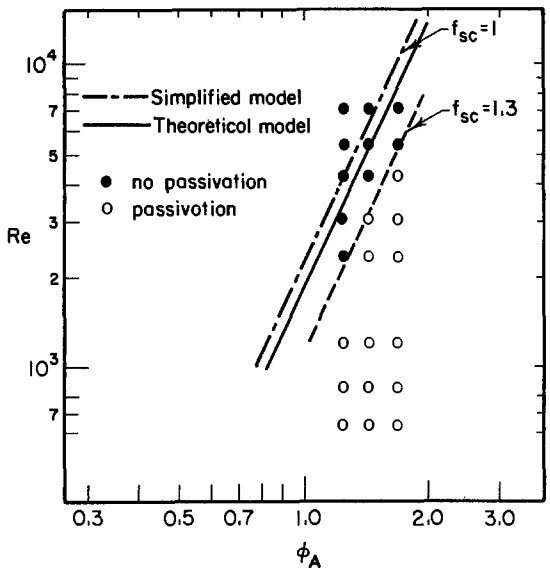

Fig. 8. Comparison of experimental observation of corrosion repassivation of iron in flowing H_2SO_4 with theoretical prediction of salt precipitation based on Eq. [19].

Also shown in Fig. 8 are theoretical results obtained with use of parameter values shown in Table III. The diagonal solid line corresponds to the right-hand line which appears in Fig. 5. The solid line in Fig. 8 denotes the velocity above which the entire surface lies below saturation. By comparison of experimental data with the solid line, it may be seen that the critical velocity for repassivation corresponds to conditions where salt film precipitation occurs. Calculations were also made for the experimental conditions for which the critical flow velocity was observed directly. It was found from these that the concentration at the trailing edge of the dissolving surface was predicted to be between 1.8-2.5 times larger than the saturation concentration.

Also shown in Fig. 8 are two dashed lines which correspond to the simple result given by Eq. [19] with use of two values of f_{SC}. It is seen that measured critical velocities are in agreement with the value of $f_{SC} = 1.3$. That is, the data would fit Eq. [19] if it would be assumed that the surface concentration is 1.3 times the saturation concentration when precipitation (repassivation) occurs. This empirical fit is in agreement with observations of others for the Fe/H_2SO_4 system (7, 10, 16, 31).

Table III. Experimental conditions and solution properties

Experimental conditions	
T	= 25°C
C_b	= 0.0
E_a	= 0.8-1.2V *vs.* NHE
N_{01}	= 0.9258746
Re	= 800-10,000
Pe	= 2.93×10^6-3.7×10^7
$f_{CT\zeta}$	= 1.21×10^{-3}
h	= 0.3 cm
l	= 0.3125 cm
i_o	= 10^{-5} A/cm² (35)
$\langle i \rangle$	= 1.4-4 A/cm²
Solution properties[1]	
0.5M H_2SO_4	
ν	= 0.011 cm²/sec
κ	= 0.2 $(\Omega\ cm)^{-1}$ (32)
Fe^{++} in 0.5M H_2SO_4	
$D_{Fe^{++}}$	= 5.6×10^{-6} cm²/sec (33)
C_{sat}	= 1.5M (34)

[1] The range of Reynolds numbers for these data was from 800 to 10,000. According to Son and Hanratty (36) the effect of turbulent mass transfer is insignificant at distances $x^+ < 700$. In this study: l = 0.3125 cm, ν = 0.011 cm²/sec, and for Re = 10,000, $L^+ = lU^*/\nu$ = 540, so the experimental results were correlated with laminar flow approximations.

Conclusions

Transport processes which accompany steady-state dissolution of metal into a flowing fluid have been modeled to predict conditions when saturation occurs by buildup of dissolution products along the surface. The method of theoretical analysis depends critically upon two assumptions which could be relaxed only with difficulty: the dissolved metal ions do not migrate, and the diffusion layer is thin with respect to the dimensions of the flow channel. Other less critical simplifications were introduced to direct attention to corrosion systems where repassivation of damaged sites occurs by formation of surface films. In particular, the repassivation of pure iron in 0.5M H_2SO_4 was studied. The general features of the model were also represented by simple equations (given in Table II) which predicted critical flow conditions for salt precipitation.

Experimental measurements of iron repassivation were carried out in the presence of fluid flow. By comparison of data with theoretical calculations, it was found that repassivation occurred at flow conditions which permitted formation of a ferrous sulfate salt film on at least a portion of the dissolving surface. At sufficiently high flow rates, precipitation of the metal salt film will be prevented and the dissolving region will not repassivate. Critical flow conditions for metal repassivation in such systems have been obtained in this work.

In order to apply these principles to other applications, modification of the approach could be made to account for rough surfaces, multiple electrode reactions, rapid homogeneous reactions, and thermal effects. More challenging would be incorporation of migration, precipitation of hydroxide or carbonate films from basic solutions, and simultaneous gas evolution.

It has been suggested that in systems containing chloride salts, the early stages of pit growth occur because of the existence of a salt layer on the corroding surface. If that is the case, then fluid flow should exert an influence on the salt layer and thus upon the course of pit evolution.

Development of hydrodynamic strategies for corrosion prevention has to date not been fully explored. The damage of materials by corrosion in the presence of impingement, erosion, cavitation, and other flow-related phenomena represents a research field of vital importance. Of special value would be improved understanding of flow conditions under which inexpensive materials of construction could be used with confidence in corrosive environments.

Acknowledgments

This research was supported by the Department of Energy, Division of Materials Science, through the Materials Research Laboratory, University of Illinois (DOE-1198-51).

Manuscript submitted Oct. 4, 1982; revised manuscript received Feb. 25, 1983.

Any discussion of this paper will appear in a Discussion Section to be published in the December 1983 JOURNAL. All discussions for the December 1983 Discussion Section should be submitted by Aug. 1, 1983.

The University of Illinois assisted in meeting the publication costs of this article.

LIST OF SYMBOLS

C	concentration, gmol/cm³
C_b	bulk concentration, gmol/cm³
C_s	concentration at dissolving surface, gmol/cm³
C_{sat}	saturation concentration, gmol/cm³
D	diffusion coefficient, cm²/sec
E_a	applied potential *vs.* NHE RE, V
$\mathbf{F}$	Faraday constant, (9.64846×10^4 C/equiv.)
f_{CT}	$i_o/\langle i \rangle$
f_{SC}	$\langle i \rangle/\langle i_{sat} \rangle$

h height of channel, cm
i current density, A/cm^2
i_o exchange current densitiy, A/cm^2
i_{sat} saturation current density, A/cm^2
$\langle i \rangle$ average current density, A/cm^2
$\langle i_{sat} \rangle$ average saturation current density, A/cm^2
l characteristic length of the active site, cm
M symbol for metal species
n number of electrons in dissolution reaction
N_l $\frac{3}{2}\frac{n^2\mathbf{F}^2}{RT\kappa}\frac{D(C_{sat}-C_b)}{\Gamma(4/3)}\frac{6^{1/3}}{9}\frac{l^{1/3}}{h}\mathrm{Pe}^{1/3}$, dimensionless average sauration current, laminar flow
N_{ol} $\frac{3}{2}\frac{n^2\mathbf{F}^2}{RT\kappa}\frac{D(C_{sat}-C_b)}{\Gamma(4/3)}\frac{6^{1/3}}{9}$
N_{ot} $0.185707\frac{n^2\mathbf{F}^2D}{RT\kappa}(C_{sat}-C_b)\,Sc^{-7/8}$
N_t $\frac{n^2\mathbf{F}^2l}{RT\kappa}\frac{D(C_{sat}-C_b)}{h\,5.385}\mathrm{Re}^{0.875}$
Pe Peclét number, $\langle u \rangle l/D$, dimensionless
r_o electrode radius, cm
Re Reynolds number, $\langle u \rangle h/2\nu$, dimensionless
Sc Schmidt number, ν/D
T temperature, °C
U_x velocity in x direction, cm/sec
$\langle u \rangle$ average velocity, cm/sec
x spatial coordinate
y spatial coordinate

Greek Letters
α kinetic parameter in Eq. [3]
$\Gamma(4/3)$ complete gamma function of 4/3, (0.89298)
$\Delta\phi$ potential difference, V
ϵ_D eddy diffusivity, cm^2/sec
ζ $n\mathbf{F}l\langle i \rangle/RT\kappa$ average current, dimensionless
η_c concentration overpotential, V
η_s surface overpotential, V
κ conductivity, 1/Ω cm
ν kinematic viscosity, cm^2/sec
ρ density, g/cm^3
τ_w shear stress at wall, g/cm^2
Φ_o ohmic drop, V
Φ_A applied potential, V

Superscripts
* symbol for dimensionless variable
$^+$ symbol for dimensionless variable, turbulent flow
$\overline{}$ symbol for time-averaged values, turbulent flow

REFERENCES

1. B. C. Syrett, *Corrosion*, **32**, 242 (1976).
2. W. J. Müller, "Die Bedeckungstheorie der Passivitat der Metalle und ihre Experimentelle Begrundung," Verlag Chemie, Berlin (1933).
3. M. Serra and S. Feliu, "Proceedings of the 6th C.I.T.C.E. Meeting," p. 360, Butterworths, London (1954).
4. H. S. Isaacs, *This Journal*, **120**, 1454 (1973).
5. H. H. Strehblow and J. Wenners, *Z. Phys. Chem. N.F.*, **98**, 199 (1975).
6. H. J. Engell, *Electrochim. Acta*, **22**, 987 (1977).
7. R. Alkire, D. Ernsberger, and T. R. Beck, *This Journal*, **125**, 458 (1978).
8. D. Landolt, R. F. Muller, and C. W. Tobias, *ibid.*, **116**, 1384 (1969).
9. Ya. M. Kolotyrkin and Yu. A. Popov, *Elektrokhimiya*, **12**, 406 (1976); *ibid.*, 527 (1976); *Russian Journal of Physical Chemistry*, **51**, 11, 12 (1977).
10. T. R. Beck, *This Journal*, **129**, 2412 (1982).
11. T. R. Beck and R. C. Alkire, *ibid.*, **126**, 1662 (1979).
12. N. Sato, *Electrochim. Acta*, **16**, 1683 (1971).
13. H. C. Kuo and D. Landolt, *ibid.*, **20**, 393 (1975).
14. M. Datta and D. Landolt, *This Journal*, **122**, 1466 (1975).
15. R. Kirchheim, K. Maier, and G. Tolg, *ibid.*, **125**, 1027 (1978).
16. K. R. Weisbrod, Ph.D. Thesis, University of Illinois, Urbana, IL (1981).
17. A. C. Cangellari, M.S. Thesis, University of Illinois, Urbana, IL (1982).
18. V. G. Levich, "Physicochemical Hydrodynamics," Prentice-Hall, Inc., Englewood Cliffs, NJ (1962).
19. J. Newman, in "Advances in Electrochemistry and Electrochemical Engineering," Vol. 5, C. W. Tobias and P. Delahay, Editors, Wiley Interscience, New York (1967).
20. R. Alkire and A. A. Mirarefi, *This Journal*, **120**, 1507 (1973).
21. J. Newman, "Electrochemical Systems," Prentice-Hall, Inc., Englewood Cliffs, NJ (1973).
22. K. R. Weisbrod, Ph.D. Thesis, p. 87, University of Illinois, Urbana, IL (1981).
23. C. Wagner, *This Journal*, **98**, 115 (1951).
24. M. D. Greenberg, "Applications of Green's Functions in Science and Engineering," Prentice Hall, Englewood Cliffs, NJ (1971).
25. H. S. Carslaw and J. C. Jaeger, "Conduction of Heat in Solids," 2nd ed., p. 31, Oxford University Press, Fair Lawn, NJ (1959).
26. H. Schlichting, "Boundary Layer Theory," p. 612, McGraw Hill Book Co., New York (1979).
27. T. Mizushina, F. Ogino, Y. Oka, and H. Fukuda, *Int. J. Heat and Mass Transfer*, **14**, 1705 (1970).
28. A. Acrivos and P. L. Chambré, *Ind. Eng. Chem.*, **49**, 1025 (1957).
29. G. H. Bruce, D. W. Peaceman, H. H. Rackford, and J. D. Rice, *Trans. AIME*, **198**, 79 (1953).
30. H. S. Carslaw and J. C. Jaeger, "Conduction of Heat in Solids," 2nd ed., p. 214, Oxford University Press, Fair Lawn, NJ (1959).
31. J. Salinas, M.S. Thesis, University of Illinois, Urbana, IL (1982).
32. T. W. Chapman and J. Newman, "A Compilation of Selected Thermodynamic and Transport Properties of Binary Electrolytes in Aqueous Solutions," Lawrence Radiation Lab., Berkeley, CA, May 1968.
33. A. M. Baticle, F. Perdu, and P. Vennereau, *C.R. Acad. Sci. Paris*, **264**, 12 (1967).
34. "Solubilities," 4th ed., p. 1049, C. Linke, A.C.S., Washington, DC (1958).
35. N. Tanaka and R. Tamamushi, *Electrochim. Acta*, **9**, 963 (1964).
36. J. S. Son and T. J. Hanratty, *AIChE J.*, **13**, 689 (1967).

Study of the Anodization of Niobium and Tantalum Superimposed Layers by ^{18}O Tracing Techniques and Nuclear Microanalysis

I. ^{18}O and Cation Depth Profiles

J. Perrière and J. Siejka

Groupe de Physique des Solides de l'Ecole Normale Supérieure, Université Paris VII, 75221 Paris Cedex 05, France

ABSTRACT

^{18}O tracing techniques and nuclear microanalysis were used to study oxygen and cation movements during the anodization of Nb on Ta (Ta/Nb) and Ta on Nb (Nb/Ta) superimposed layers. Analysis of ^{18}O depth distributions shows that the order of oxygen atoms is largely preserved for Ta/Nb systems, while it is partially inverted for Nb/Ta systems. The same dissymmetry holds for cations in these systems. For Nb/Ta, the fraction of the oxygen atoms taking part in the inversion of order depends on the formation conditions and on Ta layer thickness. Great similarities between Nb and these oxygen concentrations were observed in the various regions of oxide films. All the results are consistent with a short-range migration for oxygen, as well as for cation transport, and a strong correlation appears between oxygen and cation migration.

In previous papers (1-3), we reported results on migration studies of cations during anodization obtained by the use of what we called "substitute tracers" (2), *i.e.*, we studied the movements of metal atoms M_1 during the anodization of M_1 substrates covered with thin films of another metal M_2 (M_1/M_2 systems). The anodization of Nb and Ta superimposed layers showed that Nb and Ta cannot be considered as pure isotopic tracers (2), since we observed a dissymmetry of behavior for Ta and Nb cations during the anodization of Ta/Nb and Nb/Ta systems. In the first case, the order of cations is largely preserved, *i.e.*, a layer of pure Nb_2O_5 remains at the oxide-solution interface and pure Ta_2O_5 is formed underneath. However, in the second case, the order of cations is partially inverted, and the main results are the following:

1. Nb atoms migrate through the Ta_2O_5 layer, form a Ta and Nb oxide mixture, and reach the oxide-solution interface. A pure Nb_2O_5 layer appears at this interface at high potentials.

2. The fraction F_t of all oxidized Nb atoms which cross the inner edge of the Ta atom distribution is equal to 25%, in good agreement with the values of the transport number of cations. This means that Ta atoms can be used as a reference frame in order to measure transport numbers.

3. Part of the Ta atoms present in the surface region moves during oxide growth, but slower than Nb atoms. This leads to the burying of the Ta atoms in the oxide, and this burying is the same for Ta concentrations lying between 0.5 and 15%.

Similar studies were carried out for Al and Nb (3) and for Al and Ta (4) superimposed layers, leading either to the conservation or to a partial inversion of the order of cations. Two approaches have been developed in order to explain the partial inversion of the order of cations: (*i*) a microscopic treatment based on differences in movement probabilities of various cations (4) and (*ii*) a more macroscopic interpretation related to differences in ionic conductivities (5, 6). These are discussed in detail in the second part of this paper.

Following (*i*) the inversion of order is due to differences in movement probability P for various cations in mixed oxides. For example, if $P(M_1) < P(M_2)$ the order of cations must be preserved in M_1/M_2 systems, while it must be partially inverted if $P(M_1) > P(M_2)$. The important point is that this phenomenon does not lead to lateral macroscopic nonuniformities in the distribution of cations.

Following (*ii*) the inversion of the order of cations is due to the fact that the field E needed for the transport of a given ionic current i is different for each oxide (7). For example, in an M_1/M_2 system if, $E(M_1) > E(M_2)$ the order of cations will be preserved while it must be inverted if $E(M_2) > E(M_1)$. This will lead to a system described by Pringle (5, 6) as high ionic conductivity fingers (M_1 oxide) surrounded by low ionic conductivity regions (M_2 oxide). This means that lateral nonuniformities are associated with this approach.

In the case of Nb/Ta systems, we have shown that $P(Nb) > P(Ta)$ (2), while it is known that $E(Nb) < E(Ta)$. Moreover, it was not possible to find evidence for macroscopic nonuniformities in the Nb and Ta oxide mixture at a limit of resolution of 500 nm (4). Thus the following question arises: which phenomenon dominates, (*i*) or (*ii*)? A partial answer to this question can be obtained from the comparison of oxygen and cation movements. Following these two approaches it can be expected (4) that the order of oxygen atoms must be preserved for Ta/Nb, while it must be partially inverted for Nb/Ta. If we consider the movement probabilities, the difference between $P(Nb)$ and $P(Ta)$ must be related to differences in the nature of the bonds of Nb and Ta atoms with their surroundings. Thus, all the oxygen atoms would not be equivalent: oxygen atoms bound to Nb atoms must have a higher movement probability than the oxygen atoms bound to Ta atoms. Therefore, a partial inversion of the order of oxygen atoms might occur. If, on the contrary, we consider differences in ionic conductivities, since the ionic current does not pass through the Ta_2O_5 matrix, oxygen atoms in this matrix will not take part in ionic current. Hence, in this case also, a partial inversion of the order of oxygen atoms is expected. However, in the two cases the concentration of oxygen atoms that do not take part in ionic current will not be related in the same way to the Nb and Ta concentrations. Thus we can expect that it will be possible to find the determinant phenomenon (*i*) or (*ii*), and we have studied oxygen movements in these systems by means of ^{18}O tracing techniques (8).

Preliminary results have shown that differences exist for oxygen migration in Ta/Nb and Nb/Ta systems, and they have been briefly presented (9). In this paper, we report experimental results of systematic study of oxygen movements under a wide range of conditions. In order to compare oxygen and cation movements, we also present the Nb and Ta depth distributions in these films. The discussion of these results and of the possible microscopic transport mechanisms are presented separately in the second part of this paper. The possible correlation between the two approaches (*i*) and (*ii*) will be also analyzed.

Key words: anodization, ^{18}O tracing, niobium, tantalum.

Experimental

Film formation.—The Ta or Nb thin films were deposited by d-c triode sputtering (2). Anodic oxidations were carried out either in aqueous ammonium pentaborate solutions (0.5 weight percent (w/o), pH 9 maintained by ammonium hydroxide additions), or in ammonium citrate solutions (0.5 w/o, pH 6), at constant i and T. The water of the solutions had a natural isotopic composition (0.204% ^{18}O), or was enriched to concentrations that were always higher than 60% in ^{18}O. The ^{18}O labeled water was produced by the Weizmann Institute (Rehovot, Israel), In what follows, we call $^{16}O_{sol}$ solutions of natural isotopic composition and $^{18}O_{sol}$ solutions in which the ^{18}O concentration of water was enriched. As the same results were obtained with citrate or borate solutions, boron incorporations from borate solutions give no trouble for the analysis of the $^{18}O(p,\alpha)^{15}N$ resonant nuclear reaction (10). Thus in what follows, no distinctions are made between borate or citrate solutions.

Constituent analysis of the films.—Nuclear microanalysis by the direct observation of nuclear reactions and of backscattered particles was used to study samples before and after anodization. The experiments were performed using the 2 MeV Van de Graaff accelerator of the Ecole Normale Superieure.

The ^{16}O and ^{18}O contents of the films were measured, respectively, through the ^{16}O (d,p) $^{17}O^*$ and $^{18}O(p,\alpha)^{15}N$ nuclear reactions (11). Absolute values were obtained by comparison with ^{16}O and ^{18}O reference targets (12, 13). Absolute amounts of Nb and Ta in the films were obtained, using Rutherford backscattering techniques, by comparison with a Ta reference target (14). These measurements (overall content in oxygen and in cation in the layers) give independent measurments of oxide thickness and were found to agree within 5% which is the experimental uncertainty of the measurements. Oxide thicknesses were thus obtained in oxygen atoms (and cations)/cm^2. For convenience, oxide thicknesses are given in nanometers, because the oxygen and cation densities are practically the same for both Ta_2O_5 and Nb_2O_5, *i.e.*, 10^{15} oxygen atoms/cm^2 = 1.85 nm and 10^{15} cations/cm^2 = 4.6 nm, assuming the densities 8.04 and 4.74 for Ta_2O_5 and Nb_2O_5 (15).

Analysis of Nb and Ta distributions in the films.—$^4He^+$ Rutherford backscattering techniques were employed to analyze the depth distribution of cations in the films (16, 17). We have carried out a computer analysis of the backscattering spectra assuming lateral uniformity for the Nb and Ta oxide mixture. The Nb and Ta depth profiles are extracted by comparison of the experimental spectra with those calculated using trial profiles. These calculations are based on the work of l'Hoir (18) who has fully described such analysis. The straggling parameter and stopping power for $^4He^+$ in Nb_2O_5 or Ta_2O_5 were determined by fitting backscattering spectra registered on Al/Nb_2O_5 or Al/Ta_2O_5 for which the thickness of the Nb or Ta oxide was known (see previous section). Values of stopping power for $^4He^+$ in Nb_2O_5 and in Ta_2O_5 were found to be close and near those deduced from the values tabulated by Ziegler and Chu (19).

Figure 1 represents the result of such an analysis for an anodized Nb/Ta sample. The solid line represents the curve calculated using the profile (solid line) presented in Fig. 2. Region X corresponds (2) to the thickness of oxide formed by the anodization of the Ta film alone; the Nb concentration ([Nb]) (and also the Ta concentration ([Ta]) since [Nb] + [Ta] = 1) is uniform in this region. As [Nb] and [Ta] are important in the discussion of the results, we tested different values for [Nb] and [Ta] in this region. The two extreme values which give an acceptable fit are presented with dotted lines in Fig. 2, and this gives an idea of the sensitivity of the method: [Nb] and [Ta]

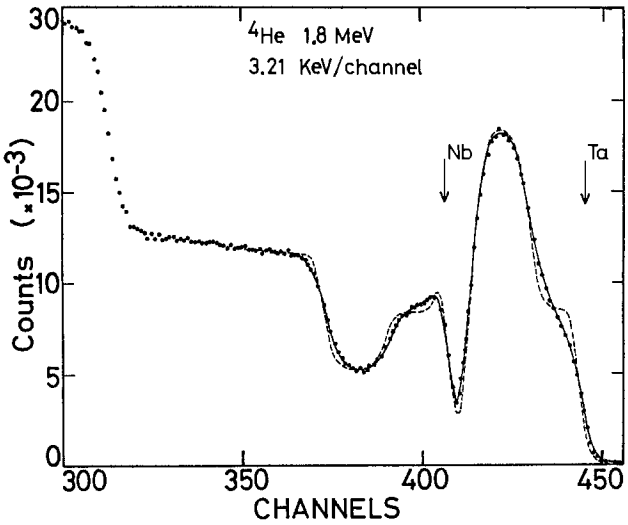

Fig. 1. Backscattering spectrum obtained on Nb/Ta (~23 nm) oxidized at 23°C and 180V. The solid line is the spectrum calculated with the profile (solid line) in Fig. 2; the dotted line corresponds to the profile (dotted line) in Fig. 2.

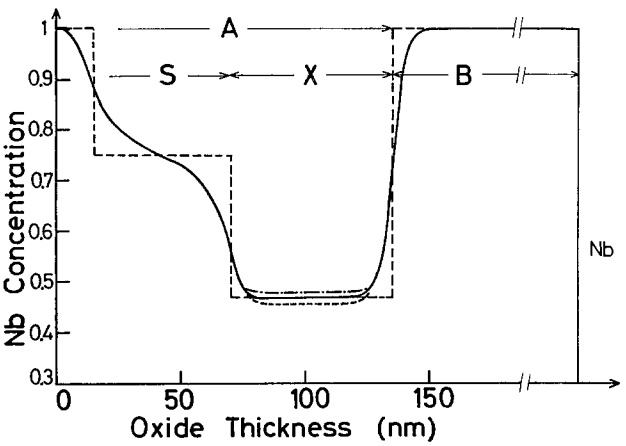

Fig. 2. Nb distribution in Nb/Ta samples oxidized at the conditions of Fig. 1; the dotted lines give an idea of the precision for Nb concentration in region X.

are known with a ±5% precision. The profile in Fig. 2 shows that the various interfaces are not sharp. For comparison purpose we present the spectrum calculated with sharp interfaces for the profile (dotted lines in Fig. 1 and 2). Ta atoms in the near-surface region of the oxide (region S) take part in oxide growth (2). This indicates that the ionic current is not fully confined in fingers in region S. Thus if nonuniformities exist, they are present solely in region X and can cause an error in the absolute values of [Nb] and [Ta] in this region. Since the backscattering yield is inversely proportional to the stopping power, this possible error is of the order of the precision that we find for [Nb] and [Ta] measurements.

Analysis of ^{18}O distribution in the films.—The ^{18}O depth profiles were obtained using the excitation curves of the $^{18}O(p,\alpha)^{15}N$ nuclear reaction near the 2 keV wide 629 keV resonance (10). The basic principles of such measurements and full theoretical calculations are given in detail in Ref. (10). Briefly, the yield $N(E_1)$ for an incident proton energy E_1 is given by

$$N(E_1) = \text{constant} \times \int_0^\infty \int_0^\infty C(x)\sigma_\theta(\eta)\, W(E_1, \eta, x)\, dx d\eta$$

where $C(x)$ is the ^{18}O concentration at a depth x; $\sigma_\theta(\eta)$ is the cross section at energy η; $W(E_1, \eta, x)$ is the probability that a proton of incident energy E_1

has at a depth x an energy in the vicinity of η. ($W(E_1, \eta, x)$ depends on two parameters, the straggling parameter and the stopping power for the protons, and these values have been experimentally determined for Ta_2O_5 and Nb_2O_5 (10). Knowledge of the stopping power for protons allows us to determine an energy-to-depth relationship, thus $C(x)$ may be determined if $C(E)$, *i.e.*, the ^{18}O concentration as a function of the energy of protons, is known. In this work (a Ta and Nb oxide mixture), a program permits computation of the excitation curve corresponding to a given ^{18}O profile $C(E)$. Such a procedure can be used since the straggling of protons for the same energy loss in Nb_2O_5 and in Ta_2O_5 is practically the same (less than 3% difference). Thus the $C(E)$ profiles are extracted by comparison of the experimental excitation curves with curves calculated using trial profiles. $C(E)$ is then transformed in $C(x)$ using the energy to depth relationship.

As an example, Fig. 3 shows an excitation curve recorded on an Nb/Ta sample anodized first in $^{18}O_{sol}$ (formation of $Ta_2O_5{}^{18}$) and then in $^{16}O_{sol}$ to a total oxide thickness of 330 nm. This curve exhibits two well-separated maxima. This means that one part of the ^{18}O atoms remains near the metal-oxide interface (high energy maximum) while a fraction of the ^{18}O atoms is located in the bulk of the oxide. The solid line represents the calculated best fit and corresponds to the ^{18}O depth profile presented as a solid line in Fig. 4. We will lay emphasis on the measurement of the ^{18}O concentration in region X ($[^{18}O]$). So, for comparison purposes, we present also in Fig. 3 two extreme curves (dashed lines) obtained with the other ^{18}O depth profiles of Fig. 4 (dashed lines). From these two curves we estimate the precision of this analysis at ±5%. As in the case of backscattering analysis, these profiles are obtained assuming lateral uniformity of the oxide. The possible presence of lateral nonuniformities in region X would introduce an error in the absolute value of $[^{18}O]$. However, the same considerations as for backscattering analysis lead to the conclusion that this error is the order of the precision that we find for $[^{18}O]$.

Results

Partial inversion of the order of oxygen atoms has been observed during Nb/Ta anodization (9). This is also obtained during Zr anodic oxidation (20), and this is generally related to the polycrystalline nature of anodic ZrO_2 (21). We examined the structure of anodic oxides formed on superimposed layers by transmission electron diffraction, using self-supporting oxide targets whose preparation is described elsewhere (22). Electron diffraction gives diffuse haloes similar to those observed on pure oxides, from which it is concluded that the mixed oxides are amorphous. Hence, we exclude the hypothesis of inversion of the order of oxygen atoms by preferential migration of oxygen along grain boundaries in a polycrystalline medium.

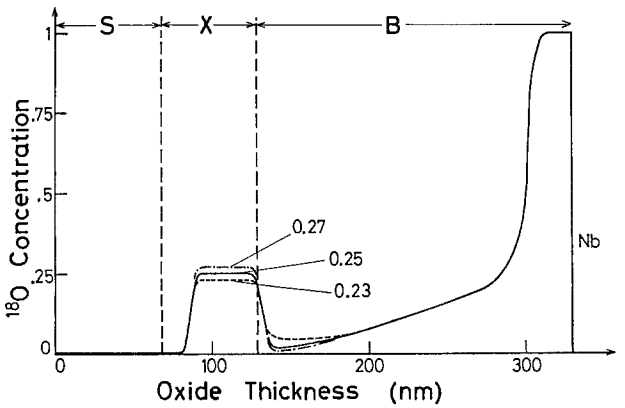

Fig. 4. ^{18}O profiles in oxides grown at conditions given in Fig. 3 The dotted lines give an idea of the precision for ^{18}O concentration in region X.

Anodization of Ta/Nb systems.—Samples with ~32 nm thick Nb deposits on Ta substrates were anodized at increasing potentials up to a total oxide thickness equal to 400 nm. Figure 5 represents some excitation curves of the $^{18}O(p, \alpha)^{15}N$ resonant nuclear reaction obtained for films grown on Ta/Nb in the following way: first, anodization to 40V in $^{18}O_{sol}$ (full oxidation of the Nb deposit: $Nb_2O_5{}^{18}$ formation) and then up to increasing potentials in $^{16}O_{sol}$. This figure shows that the maximum of the excitation curve is shifted toward higher energies with increasing Ta metal consumption. This shift can be interpreted as showing that the ^{18}O atoms remain at the metal-oxide interface during further growth in $^{16}O_{sol}$.

Figure 6 represents the ^{18}O distributions in the oxide giving the best fits. Since we have shown previously (1) that the order of cations is preserved during oxidation of Ta/Nb systems, we have also presented in this figure the Nb_2O_5 layer overlying the growing Ta_2O_5. In Fig. 6a (corresponding to curve a in Fig. 5), ^{18}O

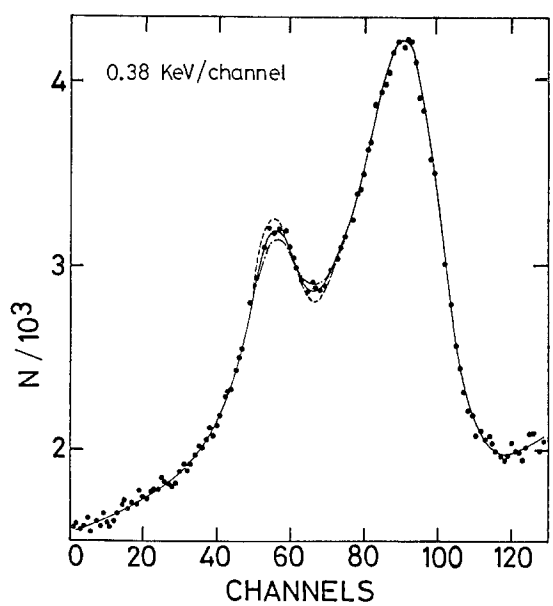

Fig. 3. Experimental (●) and computed excitation curves corresponding to Nb/Ta (~23 nm) oxidized first in $^{18}O_{sol}$ ($Ta_2O_5{}^{18}$ formation) and then in $^{16}O_{sol}$. The solid and dotted curves are calculated with the profiles presented in Fig. 4.

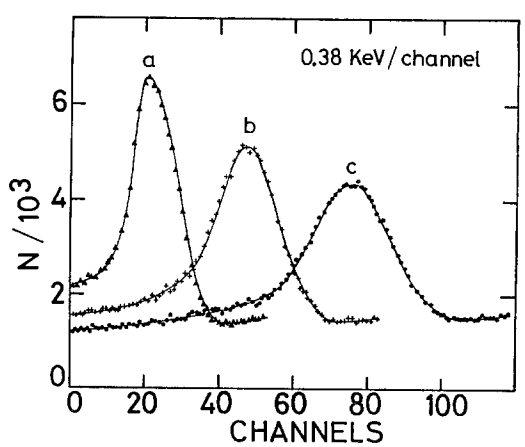

Fig. 5. Experimental and computed excitation curves obtained with Ta/Nb (~32 nm) oxidized first in $^{18}O_{sol}$ up to 80 nm (curve a) for $Nb_2O_5{}^{18}$ formation and then in $^{16}O_{sol}$ with additional oxide thicknesses equal to (b) 105 nm and (c) 260 nm.

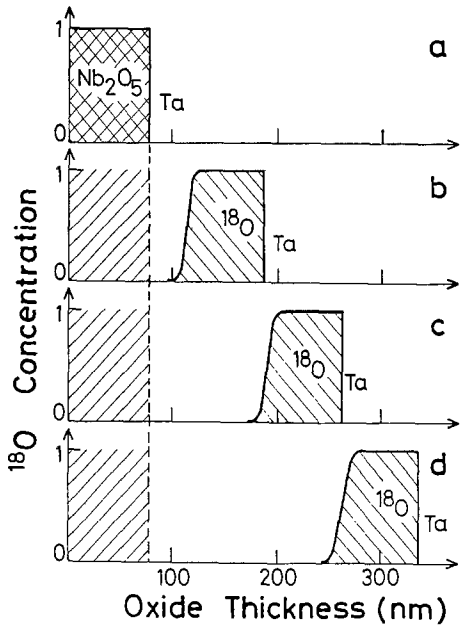

Fig. 6. ^{18}O profiles in oxides formed on Ta/Nb (~32 nm) samples oxidized first in $^{18}O_{sol}$ up to 80 nm (profile a) for $Nb_2O_5{}^{18}$ formation and then in $^{16}O_{sol}$ with additional oxide thicknesses equal to (b) 105 nm, (c) 180 nm, and (d) 260 nm. The schematic Nb distribution is also shown.

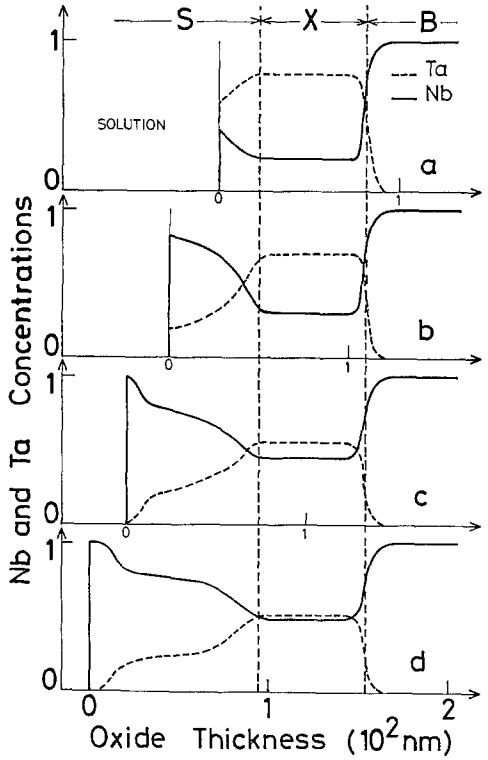

Fig. 7. Nb and Ta depth distributions in regions X and S of the oxide formed by anodization of Nb/Ta (~23 nm) samples at 5 mA/cm^2 and 23°C up to various thicknesses: (a) 150 nm, (b) 270 nm, (c) 368 nm, and (d) 420 nm.

atoms have formed $Nb_2O_5{}^{18}$. During reanodization in $^{16}O_{sol}$ (Fig. 6b-d), the ^{18}O atoms are found at the metal-oxide interface as $Ta_2O_5{}^{18}$. A slight broadening occurs at the ^{16}O-^{18}O oxide interface, but the width of this interface does not show a large increase with potential. Such a broadening is expected from a short-range migration of oxygen atoms. For example, if we assume a neighbor-to-neighbor jump process this would introduce some mixing between ^{16}O and ^{18}O atoms (8, 23). If the jump distance is the same for all oxygen atoms and equal to one interatomic distance, and if all jumps are in the field direction, this would cause the formation of an atomic mixture over a depth interval corresponding to the spread of a Poisson probability distribution. The derivative curve of the concentration profile would be nearly Gaussian with a width (FWHM) equal to about 9 nm when forming a 270 nm thick oxide in $^{16}O_{sol}$, with a site separation equal to 0.3 nm and a transport number of oxygen (t^-) equal to 0.75 (24). Such an explanation is consistent with the slight broadening at the ^{16}O-^{18}O oxide interface in Fig. 6. Therefore, we conclude from these results that during anodization of Ta/Nb systems there is both conservation of the order of cations (1) and of oxygen atoms. This excludes the hypothesis of ionic transport by interstitial oxygen through the oxide and the existence of pores in the Nb_2O_5 layers.

Anodization of Nb/Ta systems.—Samples with ~23 nm thick Ta deposits on Nb substrates were oxidized at increasing potentials and Rutherford backscattering spectra were registered for these samples. Figure 7 represents the Nb and Ta depth distributions in the oxides formed at various potentials. This figure shows that during oxidation of the Nb substrate a pure Nb_2O_5 region (part B) near the metal is covered with a layer in which both cations are present. This layer is due to the fact that Nb atoms migrate through the Ta_2O_5 layer (region X), form a Ta and Nb oxide mixture, and reach the oxide-solution interface. A pure Nb_2O_5 layer exists at this interface at higher potentials. The interface between part B and region X is not sharp; there is a slight broadening between the pure Nb_2O_5 oxide and the Ta and Nb oxide mixture that does not change as potential increases (Fig. 7b-d). These profiles show the difference between region X and region S (the near-surface region of the oxide). Region X is well defined at the beginning of the oxidation. It corresponds to the Ta_2O_5 formed by anodization of the Ta film. During the oxidation of Nb substrates, Nb atoms enter into the region X and "push" Ta atoms of this region. The Ta (or Nb) concentration profile is uniform in region X while it is varying in region S. Part of the Ta atoms present in region X does not take part in ionic current and can be used as a reference frame in order to measure transport numbers (4, 5). The formation of region S is due to the movements of cations (2) and its thickness increases with potential. In region S, part of the Ta atoms moves during oxide growth but slower than Nb atoms leading to their burying in the oxide and to the formation of the pure Nb_2O_5 layer at the oxide-solution interface.

Relative movements of both cations depend, thus, on the regions of the oxide mixture. In order to study the correlation between cations and oxygen movements in the various regions, we have carried out two kinds of experiments: experiments 1 and 2. In experiments 1 Nb/Ta systems were oxidized in the following way: oxidation in $^{18}O_{sol}$ (or $^{16}O_{sol}$) of the whole Ta deposit, and then in $^{16}O_{sol}$ (or $^{18}O_{sol}$). Thus, the Ta_2O_5 layer (region X) is labeled in ^{18}O (or ^{16}O), and the reoxidation gets insights into the oxygen movements in region X and in part B of the oxide. In experiments 2, Nb/Ta systems were oxidized first in $^{18}O_{sol}$ (or $^{16}O_{sol}$) up to potentials for which the region S has a thickness greater than 20 nm, and then the oxidation was pursued in $^{16}O_{sol}$ (or $^{18}O_{sol}$). These experiments 2 permit the studying of oxygen movements in region S. Let us notice that these last experiments get insights into the behavior of oxygen in region X and in part B and that the cation distributions do not depend on the kind of experiments for the same overall oxidation potential.

In all experiments cation dissolution and oxygen exchange were not evidenced. This means that the total content in Ta atoms in the deposited layers was preserved during the oxidation of the substrate; the same

conclusion holds for ^{18}O atoms fixed during the first oxidation.

Experiments 1.—Samples with ~23 nm thick Ta deposits on Nb substrates were oxidized at 40V in $^{18}O_{sol}$ (formation of $Ta_2O_5{}^{18}$) and then in $^{16}O_{sol}$ up to increasing potentials. Excitation curves of the $^{18}O(p, \alpha)^{15}N$ resonant nuclear reaction were registered for these samples. A typical result is shown in Fig. 3; other excitation curves are not presented, the ^{18}O concentration profiles are shown in Fig. 8 and 9. Figure 8 corresponds to potentials lower than 80V, *i.e.*, roughly to the transition regime previously found (2) in the potential-time relationship. Figure 9 is for potentials for which the growth laws of Nb substrate oxidation are the same as those found during pure Nb anodization (2).

By comparing Fig. 8a (formation of $Ta_2O_5{}^{18}$) and Fig. 8c (additional oxide thickness in $^{16}O_{sol}$ equal to 44 nm), one observes that ^{16}O atoms have deeply entered region X, leading to a partial inversion of the order of oxygen atoms. However, the majority of ^{16}O atoms are found in the oxide-surface region and correspond to an oxide thickness equal to ~20 nm in Fig. 8c. Practically all the oxide formed beneath region X (part B of the oxide) is an ^{18}O oxide.

In Fig. 8d a plateau appears in region X for the ^{18}O profile. A great similarity is thus found between the behavior of ^{16}O atoms and Nb cations in region X. There is a progressive penetration of ^{16}O atoms in region X, and at the same time there is also a progressive penetration of Nb cations into the same region. Moreover, in the two cases these movements lead to the formation of plateaus in the ^{18}O and Ta depth distributions in region X.

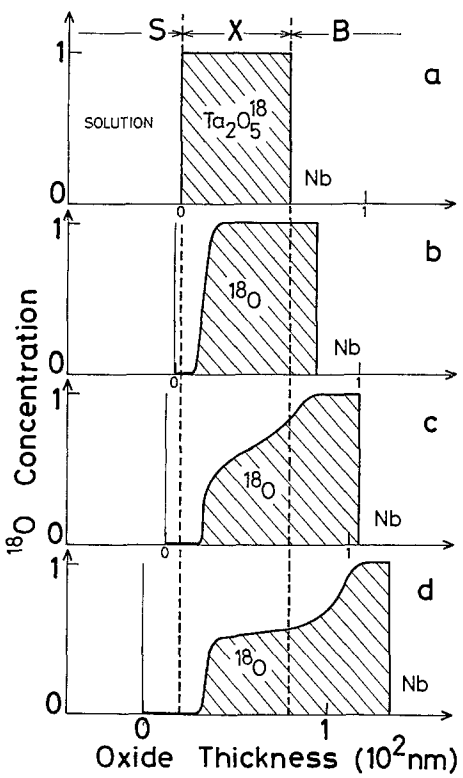

Fig. 8. ^{18}O profiles in oxides formed on Nb/Ta (~23 nm) samples oxidized first in $^{18}O_{sol}$ up to 60 nm (profile a) for $Ta_2O_5{}^{18}$ formation and then in $^{16}O_{sol}$ with additional oxide thicknesses equal to (b) 17 nm, (c) 44 nm, and (d) 80 nm.

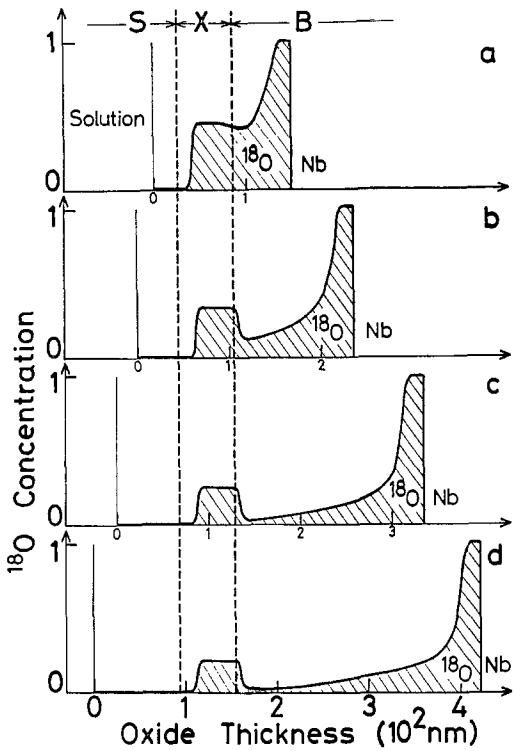

Fig. 9. ^{18}O profiles in oxides formed on Nb/Ta (~23 nm) samples oxidized first in $^{18}O_{sol}$ up to 60 nm ($Ta_2O_5{}^{18}$ formation) and then in $^{16}O_{sol}$ with additional oxide thicknesses equal to (a) 90 nm, (b) 210 nm, (c) 308 nm, and (d) 360 nm.

As the potential increases (Fig. 8d and Fig. 9), ^{16}O atoms reach part B of the oxide, *i.e.*, begin to form $Nb_2O_5{}^{16}$. The region S is continuously thickening and is a pure ^{16}O oxide. Thus, the near-surface region of oxide has the same isotopic label as the solution. The fact that ^{18}O atoms do not remain at the oxide-solution interface excludes any artifact such as flaws by which ^{16}O atoms would oxidize the Nb substrate.

During reanodization in $^{16}O_{sol}$, a fraction of region X (at the region X-region S interface) becomes a pure ^{16}O oxide. This fraction increases slightly and reaches about 20 nm for an additional oxide thickness equal to 210 nm (Fig. 9b). Within our experimental precision this thickness appears as constant during further growth. However, it may further increase about 5 nm between Fig. 9b and d. In the remainder of region X, [^{18}O] is represented as constant, although the experimental precision does not exclude a slight slope in [^{18}O]. However, this would be small; for example, in Fig. 9d the plateau at 21% can be replaced by a slope going from 19 to 23%. These profiles show that [^{18}O] in region X is at first rapidly decreasing (Fig. 8d to 9b) and then slowly (Fig. 9c and d). There is again a similarity between ^{18}O and Ta distributions in this region since [Ta] is also uniform (see Fig. 7) and decreases at first rapidly and then slowly when potential increases.

In the part B of the oxides (pure Nb_2O_5), ^{18}O atoms remain at the metal-oxide interface buried below an oxide formed with ^{16}O atoms passing through region X. Schematically the ^{18}O atoms are divided into two groups, those in region X and those at the metal-oxide interface. Between them, [^{18}O] varies with depth and with potential but is very small, for instance, less than 2% in Fig. 9d. These ^{18}O atoms represent a tail corresponding to the slight decrease of [^{18}O] in region X. The ^{18}O distribution near the metal is not noticeably broadening as potential increases. It can be well described by a shift of this part of the ^{18}O profile to greater depth when anodization in $^{16}O_{sol}$ is continued. As for Ta/Nb, the behavior of this part of the ^{18}O

distribution can be explained by the fact that oxygen movements in region B (pure Nb_2O_5) largely preserve the order for oxygen atoms, this is in agreement with results obtained during pure Nb oxidation (1).

The main conclusions that can be drawn are the following: the progressive penetration of ^{16}O atoms in region X eliminates a direct interstitial oxygen transport; a short range migration for oxygen is likely, if we take into account the evolution of the ^{18}O profile in part B. Some correlation seems to exist between cation and oxygen migration since [Ta] and [^{18}O] in region X show the same behavior whatever the potential.

When oxidation was performed in the reverse order, *i.e.*, first in $^{16}O_{sol}$ for full oxidation of the Ta deposit and then in $^{18}O_{sol}$, the ^{18}O profiles obtained were similar to the ^{16}O depth distributions deduced from Fig. 8 and 9.

Results of Fig. 8 and 9 were obtained on samples with an ~60 nm thick Ta_2O_5 layer. Similar experiments were carried out on samples with 37 nm thick Ta_2O_5. The ^{18}O profiles show the same essential features described above, but some quantitative differences appear. The value of [^{18}O] in region X was always lower in the latter case. For the same additional oxide thickness in $^{16}O_{sol}$ (for example 330 nm) [^{18}O] was 16% for 37 nm thick Ta_2O_5, while it is 22% for 60 nm thick Ta_2O_5. Here, too, a similarity appears between [Ta] and [^{18}O] in region X, since backscattering spectra show that [Ta] in region X decreases with Ta_2O_5 thickness for the same Nb substrate consumption.

We have previously shown (2) that cation movements depend on current density (i) and temperature (T) during anodization of Nb/Ta systems. In fact we have found that the fraction F_t of oxidized Nb atoms present in regions X and S increases with increasing i or decreasing T. This means that F_t increases with electric field, if we take into account the fact that at high i and low T the electric field will be higher than the one at low i and high T. Thus, experiments 1 were carried out at various i and T. Samples were ~15 nm thick Ta deposits (37 nm thick Ta_2O_5) on Nb substrates oxidized first in $^{18}O_{sol}$ and then in $^{16}O_{sol}$. The results of the computer analysis for two different typical cases are presented in Fig. 10. The formation conditions (see figure caption) are such that profile a corresponds to a low electric field, while profile b corresponds to a high one.

In Fig. 10, the overall thickness of the two profiles is the same, but due to the fact that F_t is different (2) (F_t ~27% for b and F_t ~21% for a), region S is larger in profile b than in profile a. These two profiles exhibit the same properties as those of Fig. 8 and 9, with uniform [^{18}O] in region X. However, these two values of [^{18}O] are different, 12% in a and 24% in b. This dependence of [^{18}O] in region X on the electric field was checked and it appears that the highest [^{18}O] corresponds to the highest field. For the same samples, backscattering analysis shows that [Ta] is a little lower for b than for a, by about 5%, Hence the lowest [Ta] in region X corresponds to the highest field, and a contradiction seems to appear between the Ta and ^{18}O behavior since [Ta] and [^{18}O] vary in opposite directions with the field. This can be qualitatively explained, if we take into consideration the fact that F_t (and the transport number of cations) increases with the field. This means that when the field increases more Nb cations will pass through region X, leading to a decrease of [Ta] in this region. At the same time, since the total ionic current is constant, fewer ^{16}O atoms will penetrate into region X, leading to an increase of [^{18}O]. This explanation qualitatively describes the respective variations of [Ta] and [^{18}O] in region X with the field.

Experiments 2.—Samples with ~23 nm thick Ta deposits on Nb substrates were oxidized at 120V in $^{16}O_{sol}$ and then in $^{18}O_{sol}$ up to increasing potentials. The anodization potential in $^{16}O_{sol}$ corresponds to the formation of a region S of ~40 nm. Figure 11 represents a typical excitation curve obtained on a sample oxidized at an overall potential equal to 200V. The large peak at the lower energies corresponds to ^{18}O atoms located at the oxide-solution interface, while the small high energy peak corresponds to ^{18}O atoms deeply buried in the oxide.

In Fig. 12 we present the calculated ^{18}O distributions for various additional oxide thicknesses in $^{18}O_{sol}$. The common feature of all these profiles is the presence at the oxide-solution interface of pure ^{18}O oxide, *i.e.*, the near-surface region of oxide has the isotopic label of the solution. The thickness of this pure ^{18}O oxide layer increases steadily with reoxidation potentials, going from 5 nm (Fig. 12a) to 25 nm (Fig. 12d). By comparison with the Nb depth distribution given in Fig. 7, it is seen that the thickness of this pure ^{18}O oxide layer is always greater than the thickness of the pure Nb_2O_5 layer which is present at the oxide-solution interface. For each profile, the thickness of this pure ^{18}O layer is also slightly greater than the thickness $d = F_t \times$ (additional oxide thickness in $^{18}O_{sol}$) which represents the oxide thickness grown by movements of cations (2). Another common feature of profiles b to d in Fig. 12 is the general shape of ^{18}O distributions. After the pure ^{18}O oxide layer,

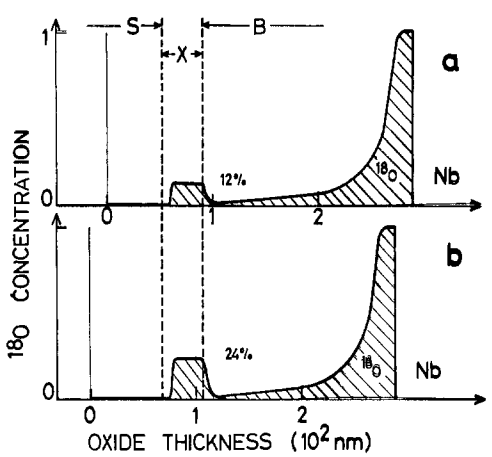

Fig. 10. ^{18}O profiles in oxides formed on Nb/Ta (~15 nm) samples oxidized first in $^{18}O_{sol}$ ($Ta_2O_5{}^{18}$ formation) and then in $^{16}O_{sol}$ up to an overall oxide thickness equal to 290 nm. (a) i = 0.1 mA/cm², T = 40°C; (b) i = 10 mA/cm², T = 20°C.

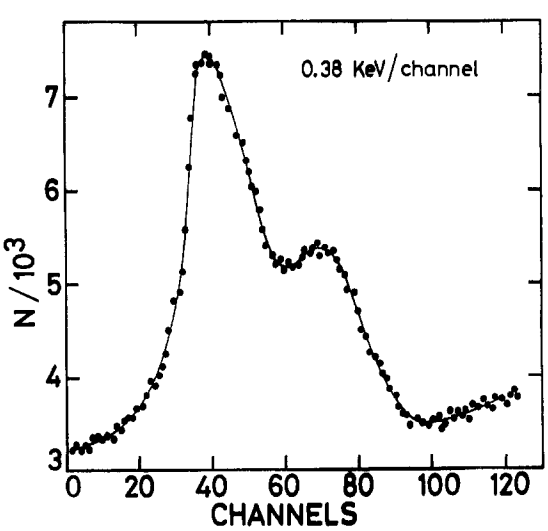

Fig. 11. Experimental (●) and computed excitation curves obtained with an Nb/Ta (~23 nm) sample oxidized first in $^{16}O_{sol}$ (226 nm) and then in $^{18}O_{sol}$ up to 347 nm.

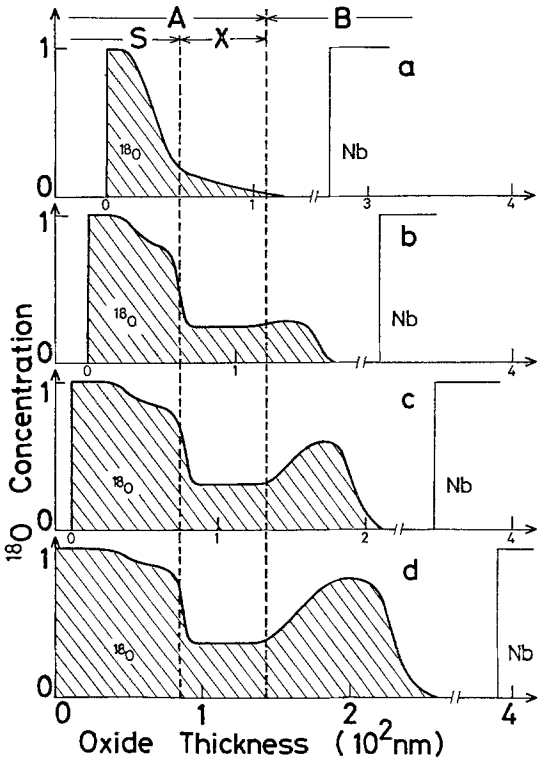

Fig. 12. ^{18}O profiles in oxides formed on Nb/Ta (~23 nm) samples oxidized first in $^{16}O_{sol}$ (226 nm) and then in $^{18}O_{sol}$ with additional oxide thicknesses equal to (a) 37 nm, (b) 81 nm, (c) 121 nm, and (d) 164 nm.

the ^{18}O concentration first slowly decreases and then a sharp drop is observed in the beginning of region X. The fact that [^{18}O] never reaches 100% in this part of region S demonstrates that the order of oxygen atoms is partially inverted in this region. This behavior of oxygen atoms is similar to the one for cations, since the order of cations is also partially inverted in region S.

In Fig. 12a (37 nm additional oxide thickness), ^{18}O atoms have penetrated regions S and X, but in this last region [^{18}O] does not exhibit a plateau. With further increase of oxide thickness ^{18}O atoms reach part B of the oxide, and for potentials higher than 150V (Fig. 12b-d) a plateau appears in region X for the ^{18}O concentration as in Fig. 9. This uniform [^{18}O] increases from 20 to 44% when additional oxide thickness increases from 81 to 164 nm. These ^{18}O atoms represent the oxygen atoms that take part in ionic current in region X, while this role is played by ^{16}O atoms in experiments 1. Thus we can compare [^{18}O] (in experiments 2) and 1 — [^{18}O] (obtained in experiments 1). It appears that for the same additional oxide thickness [^{18}O] in experiments 2 is always lower than 1 — [^{18}O] in experiments 1. This indicates that region X is not formed by two distinct phases (Nb_2O_5 and Ta_2O_5) which occupy two constant volumes, since, in this case, the two preceding quantities must be equal.

If we compare the ^{18}O distribution in regions X and S, we can conclude that in the two regions the order of oxygen atoms is partially inverted. However, the fractions of oxygen atoms which do not take part in ionic current are very different in the two regions (higher in region X than in region S). This behavior is similar to the one for cations, since Fig. 7 shows that Nb in region S changes with potential and is always higher than in region X. The comparison of cations and ^{18}O distributions (Fig. 7 and 12) shows the correlation between cation and oxygen movements in regions X and S: the general shape of Nb (or Ta) and ^{18}O (or ^{16}O) distribution is similar and the evolution with potential of these two distributions is also similar.

In part B of the oxide [^{18}O] increases with potential. The leading edge of the ^{18}O distribution does not show a large spread with further increase of oxide thickness. We conclude that the order of oxygen atoms is largely preserved in this part of the oxide (which is pure Nb_2O_5). For the maximum oxide thickness examined, shown in Fig. 12d, the ^{18}O concentration in part B increases from 44% near region X to almost 80% at a depth of 200 nm, then remains constant, while the interface with pure ^{16}O oxide is sharp. The fact that [^{18}O] never reaches 100% in this pure Nb_2O_5 region can be explained by the existence of a continuous ^{16}O flow in this region. This flow is due to ^{16}O atoms coming from region X and which are replaced by ^{18}O atoms during the reoxidation in $^{18}O_{sol}$. A fraction of this ^{16}O flow may also be due to ^{16}O atoms coming from region S and passing through region X, since the overall ^{16}O content decreases continuously in region S with increasing potentials.

The increase in [^{18}O] in part B of the oxide can be explained by the assumption that an angular aperture exists for the ionic movements (4, 25). This means that during anodic oxidation the ions can move in a direction which is not strictly the field lines. This angular aperture is related to the amorphous nature of these anodic oxides in which straight lines of atoms extending through the oxide appear very unlikely. The angular distribution of ionic movements in amorphous media has been examined in Ref. (4) in which the consequences of this phenomenon (inversion of order in mixed oxides, spread of the depth distributions of the constituents) have also been described. It is worth noting that this angular aperture permits an explanation of the slight broadening observed at the ^{16}O-^{18}O interface during isotopic tracing experiments (8, 23), and that this microscopic description can explain the macroscopic notion of confinement of the ionic current during anodic oxidation.

Experiments 2 were also carried out on samples oxidized at 80 or 160V in $^{16}O_{sol}$ and then in $^{18}O_{sol}$ up to increasing potentials. Similar results were obtained since the ^{18}O depth distributions show the presence of a pure ^{18}O oxide layer at the oxide-solution interface, the deep penetration of ^{18}O atoms in the bulk of the oxide, and the formation of a plateau in ^{18}O in region X as oxidation potential increases.

Experiments were carried out on samples oxidized in the reverse order (first oxidation in $^{18}O_{sol}$ and then in $^{16}O_{sol}$). Within our experimental precision, differences in the values of [^{18}O] and [^{16}O] in region X were not observed, and similar shapes for the profiles in region S were found.

Summary

The essential results found in this work can be summarized as follows:

Ta/Nb and Nb/Ta systems show a great dissymmetry of anodic behavior. The order of oxygen atoms is largely preserved in the first case, while it is partially inverted in the second case. The same dissymmetry holds for cations in these systems.

Partial inversion of the order of oxygen atoms has been evidenced in regions X and S of the oxides.

The oxygen atoms in region X can be schematically divided into two categories: those which take part in ionic current and those which do not. The fraction of oxygen atoms not taking part in oxide growth depends on the regime of oxidation and slowly decreases as the potential increases. Moreover, this fraction depends on the initial Ta thickness and on the electric field. The behavior of these oxygen atoms fixed in region X is very similar to that of Ta cations in the same region. It seems reasonable to conclude that these oxygen atoms and these Ta atoms are bound together in region X. It follows that the oxygen atoms taking part in ionic current and the Nb cations can also be considered as bound together.

In region S, near the surface, the order of oxygen atoms is preserved, while in the remainder of the region some oxygen atoms seem to be fixed, *i.e.*, do not take part in ionic current. While the depth distribution of these oxygen atoms is qualitatively comparable to the Ta depth distribution, the similarity is not as great as in region X.

In part B of the oxide (the pure Nb_2O_5 layer) oxygen movements lead to the conservation of the order of oxygen atoms. Moreover, the effects of the angular aperture of the ionic movements are observed in this region.

These results are fully compatible with a short-range migration for oxygen ion and cation transport processes. Thus vacancy or interstitialcy migration (26), network defects movement (27), or place exchange mechanism (28) can be envisaged for describing oxygen as well as cation migration.

Acknowledgments

The authors wish to thank G. Amsel for his numerous suggestions during this work and for enlightening discussions. The contribution of B. Maurel, A. L'Hoir, and C. Cohen in the analysis of excitation curves and backscattering spectra was appreciated. The authors are grateful to J. P. Enard and A. Laurent for technical assistance. This work was supported by the Centre National de la Recherche Scientifique (R.C.P. No. 157).

Manuscript submitted July 30, 1981; revised manuscript received Nov. 26, 1982. This was Paper 54 presented at the Minneapolis, Minnesota, Meeting of the Society, May 10-15, 1981.

Any discussion of this paper will appear in a Discussion Section to be published in the December 1983 JOURNAL. All discussions for the December 1983 Discussion Section should be submitted by Aug. 1, 1983.

REFERENCES

1. S. Rigo and J. Siejka, *Solid State Commun.*, **15**, 259 (1974).
2. J. Perrière, S. Rigo, and J. Siejka, *This Journal*, **125**, 1549 (1978).
3. J. Perrière, S. Rigo, and J. Siejka, Abs. 194, p. 462, The Electrochemical Society Extended Abstracts, Vol. 78-1, Seattle, Washington, May 21-26, 1978.
4. J. Perrière, Thesis, Université Paris VII, Paris (1981).
5. J. P. S. Pringle, *Electrochim. Acta*, **25**, 1403 (1980).
6. J. P. S. Pringle, *ibid.*, **25**, 1423 (1980).
7. L. Young, "Anodic Oxide Films," Academic Press, London and New York (1961).
8. G. Amsel and D. Samuel, *J. Phys. Chem. Solids*, **23**, 1707 (1962).
9. J. Perrière, S. Rigo, and J. Siejka, Abs. 196, p. 468, The Electrochemical Society Extended Abstracts, Vol. 78-1, Seattle, Washington, May 21-26, 1978.
10. B. Maurel, Thesis, Université Paris VII, Paris (1980).
11. G. Amsel, J. P. Nadai, E. D'Artemare, D. David, E. Girard, and J. Moulin, *Nucl. Instrum. Methods*, **92**, 481 (1971).
12. G. Amsel, J. P. Nadai, C. Ortega, S. Rigo, and J. Siejka, *ibid.*, **149**, 705 (1978).
13. G. Amsel, J. P. Nadai, C. Ortega, and J. Siejka, *ibid.*, **149**, 713 (1978).
14. S. Rigo, C. Cohen, A. L'Hoir, and E. Backelandt, *ibid.*, **149**, 721 (1978).
15. A. J. Schrijner and A. Middelhoek, *This Journal*, **111**, 1167 (1964).
16. W. K. Chu, J. W. Mayer, M. A. Nicolet, T. M. Buck, G. Amsel, and F. Eisen, *Thin Solid Films*, **17**, 1 (1973).
17. J. F. Ziegler, Editor, "New Uses of Ion Accelerator," p. 75, Plenum Press, New York and London (1975).
18. A. L'Hoir, Thesis, Université Paris VII, Paris (1975).
19. J. F. Ziegler and W. K. Chu, *Atom. Data Nucl. Atom Data Tables*, **13**, 463 (1974).
20. C. Ortega, Thesis, Université Paris VII, Paris (1981).
21. R. A. Ploc, *J. Nucl. Mater.*, **64**, 71 (1977).
22. G. Amsel, Thesis, Orsay (1963).
23. J. P. S. Pringle, *This Journal*, **120**, 1391 (1973).
24. J. P. S. Pringle, *ibid.*, **120**, 398 (1973).
25. G. Amsel, J. Siejka, M. Croset, and J. Perrière, Unpublished work.
26. P. Kofstad, "Nonstoichiometry, Diffusion and Electrical Conductivity in Binary Metal Oxides," p. 71, Wiley-Interscience, New York (1972).
27. M. J. Dignam, in "Oxides and Oxide Films," Vol. 1, J. W. Diggle, Editor, p. 192, Marcel Dekker, Inc., New York (1973).
28. A. T. Fromhold, Jr., *This Journal*, **127**, 411 (1980).

Study of the Anodization of Niobium and Tantalum Superimposed Layers by ^{18}O Tracing Techniques and Nuclear Microanalysis

II. Discussion

J. Perrière and J. Siejka

Groupe de Physique des Solides de l'Ecole Normale Supérieure, Université Paris VII, 75221 Paris Cedex 05, France

ABSTRACT

We have analyzed the cations (Nb and Ta) and oxygen profiles as a function of oxide growth conditions during the oxidation of Nb/Ta superimposed layers. Two approaches (*i*) and (*ii*) are considered which can explain the partial inversion of the order of cations and of oxygen atoms. These are based on the leading role of (*i*) differences in movement probabilities of Nb and Ta ions and between the oxygen ions bound to them, and (*ii*) differences in ionic conductivities between Nb_2O_5 and Ta_2O_5. It was shown that the evolution of ^{18}O and Nb profiles as a function of oxidation potential is different following (*i*) or (*ii*) mechanisms. Experimental data are in disagreement with (*ii*) and strongly suggest that (*i*) is valid, as it is possible to describe qualitatively our results despite the fact that, in this case, the analysis is based on an extreme assumption: the Ta oxide network is preserved and, moreover, a full random distribution of Nb and Ta cations in the oxide mixture is assumed.

The aim of this paper is to discuss the possible mechanisms which can explain the experimental results presented in the first part (1) of this work and which are summarized in Fig. 1. In order to discuss these results we use the notions of oxide network and oxide mixture, cation (or oxygen) transport event, probability of cation (or oxygen) movement, and ionic conductivity of the oxides.

Key words: anodization, transport mechanism, ionic conductivity.

The term "oxide network" is meant in the sense of the continuous random network theory of amorphous media, as the spatial distribution of the atomic sites and bonds, which is organized progressively as the

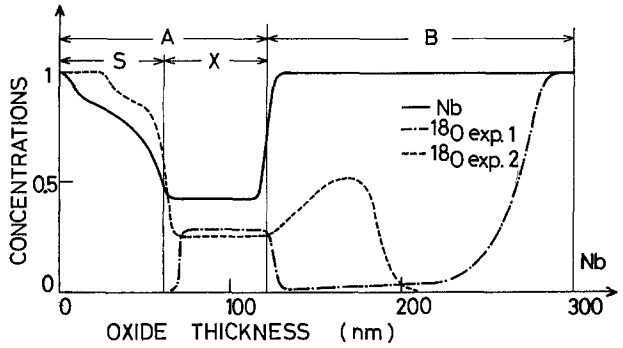

Fig. 1. Schematic Nb and ^{18}O distributions in an oxide formed on an Nb/Ta system. Experiments 1 correspond to oxidation first in $^{18}O_{sol}$ and then in $^{16}O_{sol}$, experiments 2 correspond to the reverse order. Part B is pure Nb_2O_5; region X corresponds to the initial Ta_2O_5 layer while region S is due to the movements of cations during oxidation (1).

oxides grow (2). The microscopic structure, *i.e.*, the valence state of cations, the coordination number of cation and oxygen, and the cation-oxygen bond length are very similar for Ta_2O_5 and Nb_2O_5. However, the ionicity of the cation-oxygen bond may be different in these two oxides, and we shall speak of a niobium or tantalum oxide network, meaning that these two oxides may be organized in two well-defined, possibly different, network types. The mixture of niobium and tantalum oxides in the region X (see Fig. 1) can thus be treated either as a perfect substitution of Ta atoms by Nb atoms, and this means that we assume that the Ta oxide network is preserved and keeps its nature despite the presence of 50% of Nb atoms; or assuming the destruction of the tantalum oxide network and the presence of two distinct phases (Nb_2O_5 and Ta_2O_5) having all macroscopic features of niobium and tantalum oxide networks.

By the term of transport event, one means the sequence of elementary jumps of one or more cations and/or oxygen ions which result, on the one hand, in a transport of charges from their creation point (interface) to that of their recombination (other interface) and, on the other hand, in oxide growth. The nature of the transport events seems to be determined by the oxide network since in Ta_2O_5 (3), Nb_2O_5 (4), or Al_2O_3 (5) it involves the movements of oxygen and cations, while only the oxygen atoms move in ZrO_2 (6) or HfO_2 (4). However, Hf atoms implanted in Ta_2O_5 move during the Ta substrate oxidation (7), while they do not during pure Hf oxidation.

During anodic oxidation a transport event involves the movement of one (or more) atoms in a very short period of time by comparison with the growth time. The propagation of such a transport event through the oxide raises the question of the probability for each atom of the oxide to take part in the transport event, *i.e.*, the probability of movement of the atoms. If we take the oxide network as a reference frame, each cation (or oxygen) moves during oxide growth a distance equal to $m \times l$, where m and l are the number of jumps and the jump distance, respectively. The number of jumps is related to the number of transport events and to the probability of each atom to take part in a transport event. In a homogeneous medium (pure oxide), this probability of movement is the same for each cation (or oxygen). However, in heterogeneous system in which two kinds of cation are present, different probabilities of movement may exist. This notion of probability of movement is well defined in an oxide mixture, such as a tantalum and niobium oxide mixture. According to the similarities between these two oxides, we assume that the jump distance is the same for Ta and Nb cations. We have observed (2) that Ta atoms introduced as traces in Nb_2O_5 are buried in the Nb_2O_5 during Nb substrate oxidation. This means that the Ta atoms present in niobium oxide take part in the transport events in a less important way than their Nb neighbors, *i.e.*, the probability of movement of Ta ($P(Ta)$) is lower than that of Nb ($P(Nb)$) (2).

The ionic conductivity of an oxide (σ) is related to the exponential-type relationship between ionic current i and electric field E obtained during anodic oxidation. Differences in σ are evidenced by the fact that the field needed for the transport of a given ionic current is different for each oxide (8). This means that Nb_2O_5 is a more conductive oxide than Ta_2O_5 since, for the same value of field, the ionic current in Nb_2O_5 is higher than the one in Ta_2O_5, for example, at $3 \cdot 10^6$ V/cm, $i(Nb_2O_5) \simeq 10^4\, i(Ta_2O_5)$ (8).

The following important point must be noticed: as the formation of many oxides (Nb_2O_5, Ta_2O_5, Al_2O_3, ...) involves oxygen and cation migration, the higher probability of movement of cation is not *a priori* related to the higher ionic conductivity. For example, we have found (9) that Al cations have a higher movement probability than Ta cations (in Ta_2O_5), although the ionic conductivity of Al_2O_3 is lower than that of Ta_2O_5.

The study of the anodic oxidation of M_1/M_2 superimposed layers (9) shows that the following distinct cases are found:

$P(M_1) > P(M_2)$ and $\sigma(M_1) > \sigma(M_2)$,

typical case: Nb/Ta

$P(M_1) < P(M_2)$ and $\sigma(M_1) < \sigma(M_2)$,

typical case: Ta/Nb

$P(M_1) > P(M_2)$ and $\sigma(M_1) < \sigma(M_2)$,

typical case: Al/Ta

$P(M_1) < P(M_2)$ and $\sigma(M_1) > \sigma(M_2)$,

typical case: Ta/Al

In what follows we discuss the partial inversion of order of cations and oxygen as a result of two extreme situations: (*i*) the leading phenomenon was the difference in movement probability of Nb and Ta cations and (*ii*) the leading phenomenon was the difference in ionic conductivity of Nb_2O_5 and Ta_2O_5.

For (*i*) the inversion of order is explained by a homogeneous microscopic transport mechanism related to a difference between the probabilities $P(Nb)$ and $P(Ta)$ and to a dependence of the probability of movement (P') of oxygen atoms on their cation surroundings. We have shown (2) that $P(Nb) > P(Ta)$, and we assume that P' of oxygen atoms bound to Nb atoms is higher than that of oxygen atoms bound to Ta atoms. With this assumption, the penetration of Nb atoms in the region X (see Fig. 1) taking place (1, 2) when the Nb substrate is oxidized would lead to a preferential movement of oxygen atoms bound to Nb atoms as compared to those bound to Ta atoms. The inversion of the order of cations would induce the inversion of the order of oxygen atoms. In this picture, the oxygen migration appears to be coupled to the cation migration via the cation surroundings of oxygen atoms. This means that the inversion of order of oxygen atoms is due to the presence of two different cationic species in the oxide. Thus, in pure Ta or Nb oxide, the order of oxygen atoms would be preserved, as was demonstrated (10, 11), and also in the Ta/Nb systems since the order of cations is preserved in this case.

We must associate this phenomenon (*i*) with a description of the Ta and Nb oxide mixture. We assume that the X region (the initial Ta_2O_5 layer) keeps its nature even if Ta atoms are replaced by Nb atoms. This hypothesis is based on the fact that the number of Nb or Ta atoms per unit oxide volume is practically the same in Nb or Ta oxides. Thus, to replace a Ta by an

Nb atom does not change *a priori* either the length or the orientation of the metal-oxygen bonds. We assume, thus, that macroscopic effects do not occur when Nb atoms penetrate region X. The description of this region is thus the following: Nb and Ta cations are fully randomly distributed in region X. This is an extreme hypothesis since we cannot exclude the existence of microscopic nonuniformities in the Nb and Ta oxide mixture (formation of Nb_2O_5 islands of small size due to the difference in the movement probabilities).

For (*ii*) the description of the Nb and Ta oxide mixture is quite different. We assume that the Ta oxide network is destroyed: macroscopic effects are associated with the penetration of Nb atoms in the Ta oxide. According to the proposals of Pringle (12, 13), fingers of Nb_2O_5 are formed through the Ta_2O_5 layer. We assume that the ionic current passes through high ionic conductivity fingers (Nb_2O_5) and passes around the low ionic conductivity matrix (Ta_2O_5). We can notice that such a description applies for region X, but is less appropriate in region S (see Fig. 1), since we have shown (1, 2) that some Ta atoms take part in oxide growth in this region. This means that the ionic current is not completely confined in the near-surface region of the oxide mixture. Restricting this description to region X, two important parameters exist and are related in this region, the size and the number of Nb_2O_5 fingers. These points will be a matter of discussion.

The effects of the difference of ionic conductivities on the anodic oxidation of M_1/M_2 superimposed layers have been analyzed by Pringle (12, 13) and will not be repeated here. However, for the creation of the Nb_2O_5 fingers, we can eliminate the roughness effect (12) at the Nb-Ta interface. In fact, experiments carried out either on polycrystalline Nb substrates or on Nb deposits on Si backing give exactly the same results, although in the last case the roughness effect must be minimum. The extreme description that we associate with phenomenon (*ii*) is the following: in region X two distinct phases (Nb_2O_5 and Ta_2O_5) exist, having all the macroscopic properties of the Nb and Ta oxide networks.

Cation and Oxygen Movements in Region X

The oxide network is preserved.—We assume that the inversion of the order of oxygen atoms is due to differences in movement probabilities P' of oxygen atoms. In order to establish a relationship between the experimental concentrations [Nb], [Ta], [^{18}O], and [^{16}O] (which are dimensionless quantities defined by [Nb] + [Ta] = 1 and [^{18}O] + [^{16}O] = 1), we must make some hypotheses on the structure of Ta and Nb anodic oxides.

First, we can consider these oxides as purely covalent, *i.e.*, the bonds of an oxygen atom involve only the two nearest metallic neighbors. We can distinguish three kinds of oxygen according to the nature of the neighbors to which the oxygen is bound: Nb—O—Nb (O1 type), Nb—O—Ta (O2 type), and Ta—O—Ta (O3 type). Moreover, the respective concentrations α_i of these three kinds of oxygen can be determined as a function of [Ta] and [Nb] with the hypothesis that Nb and Ta cations are randomly distributed in region X. Let us notice that this approach is in agreement with the treatment proposed by some authors (8, 14) (anodic oxides can be considered like glasses, the metal-oxygen bond being mainly covalent).

Another possibility is that the metal-oxygen bonds are partly ionic and partly covalent. In this case, oxygen atoms are bound with n cations where n is the coordinance of oxygen atoms. Therefore, $(n + 1)$ type of oxygen atoms can be defined according to the possible neighboring configurations and, in principle, $(n + 1)$ different movement probabilities can be envisaged. There are hence a great number of adjustable parameters and, obviously, it is possible to obtain a good fit of the experimental results.

However, following Pringle (15) or Cornish (16) it seems possible to admit that these M_2O_5 anodic oxides consist of a disordered variety of the Ta_2O_5 structure proposed by Stephenson and Roth (17): the metal atoms are arranged in sheets and are surrounded by oxygen atoms which form either octahedral or pentagonal bipyramidal coordination polyhedra. In this structure, two types of metal atoms appear: metal atoms of the first type are coordinated to six oxygen atoms in regular octahedron, while each metallic atom of the second type is coordinated to seven oxygen atoms in the form of a pentagonal bipyramid. Thus, if we admit that the, structure of these anodic oxides consists in a random network of six and seven coordinate metal-oxygen polyhedra (15), it follows that two kinds of oxygen atoms are present: those coordinated to two cations and those coordinated to three cations. Examination of the proposed structure (17) indicates that these two categories are in comparable proportions.

In this picture, neither all the cations nor the oxygen are equivalent. However, for pure Ta oxidation the order of atoms is preserved for the two species during isotropic tracing experiments. With this structure, this would mean that during ionic movements, oxygen and cations can occupy the various categories of sites and that these sites are equivalent from this point of view. From the above, the following types of oxygen atoms can be distinguished:

oxygen with a coordinance equal to 2

Nb—O—Nb (O1 type)

Nb—O—Ta (O2 type)

Ta—O—Ta (O3 type)

oxygen with a coordinance equal to 3

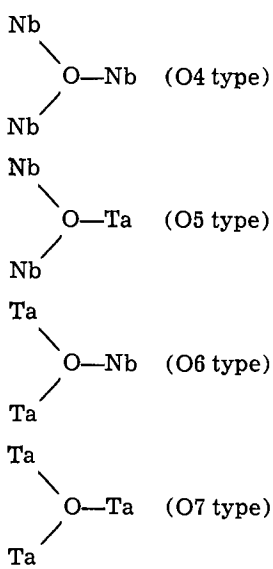

Assuming that $C2$ and $C3$ are the concentrations of oygen atoms coordinated to two and three metal atoms ($C2 + C3 = 1$), with a random distribution of Nb and Ta cations in the region X, the respective α_i concentrations are given by:

$$\alpha_1 = [Nb]^2C2$$

$$\alpha_2 = 2[Nb][Ta]C2$$

$$\alpha_3 = [Ta]^2C2$$

$$\alpha_4 = [Nb]^3C3$$

$$\alpha_5 = 3[Nb]^2[Ta]C3$$

$$\alpha_6 = 3[Nb][Ta]^2C3$$

$$\alpha_7 = [Ta]^3C3$$

We can notice that the case where the oxides are considered as purely covalent is obtained by considering that $C3 = 0$ in the α_i expressions.

In order to compare our experimental results ($[^{18}O]$) with the α_i values, additional hypotheses must be made on the P' probabilities. If we consider the oxides as purely covalent we can write

$$P'(O1) > P'(O2) > P'(O3) \quad [I]$$

while if we consider seven types of oxygen, we can write

$$P'(O1) = P'(O4);\ P'(O3) = P'(O7)$$

since it seems reasonable to assume that whatever the coordinance, an oxygen bound only with Nb (or Ta) will have the same movement probability. The exact relationship between $P'(O2)$, $P'(O5)$, and $P'(O6)$ is unknown, but let us assume as a working hypothesis that

$$P'(O1) = P'(O4) > P'(O2) \text{ or } P'(O5)$$
$$\text{or } P'(O6) > P'(O3) = P'(O7) \quad [II]$$

With the relationships [I] and [II] we can explain the partial inversion of the order of oxygen atoms and the great similarity of behavior of Nb atoms with ^{16}O atoms (for experiments 1) and ^{18}O atoms (for experiments 2). Moreover, at the beginning of the Nb substrate oxidation the O3 (or O3 and O7) atoms take part in oxide growth (1) (shift of the ^{18}O distribution with respect to region X for experiments 1). But for high potentials, these O3 (or O3 and O7) atoms do not seem to take part in oxide growth. Thus, we will first assume that $P'(O3)$ (or $P'(O3)$ and $P'(O7)$) equal zero, *i.e.*, oxygen atoms bound to Ta atoms never take part in ionic current. Studies of oxygen and cation depth profiles have been performed for relatively high additional oxide thicknesses which justify this assumption.

Experiments 1.—In these experiments since the oxidation is performed first in $^{18}O_{sol}$ and then in $^{16}O_{sol}$, the ^{18}O atoms in region X will be preferentially bound to Ta atoms according to the hypothesis that $P'(O3)$ [or $P'(O3)$ and $P'(O7)$] equal zero. We must compare $[^{18}O]$ in region X either with α_3 (covalent case) or with $\alpha_3 + \alpha_7$ (seven types of oxygen). One must notice that the α_3 value in the covalent case is higher than the one in the case of seven types of oxygen. In Fig. 2, curve 1 represents the $[^{18}O]$ values (measured in part I of this work), curve 2 the α_3 values, and curve 3 the $\alpha_3 + \alpha_7$ values as a function of additional oxide thickness in $^{16}O_{sol}$. Curve 3 was obtained by assuming that oxygen atoms with coordinance 2 and 3 are in equal proportion ($C2 = C3 = 0.5$). Figure 2 shows differences between the three curves which cannot be explained by measurement errors which are estimated to 5% (1), while an error higher than 20% is needed in order to admit that curves 1 and 2 fit. However, the variation of the three curves is similar. If we take into account the fact that the two hypotheses (Nb and Ta randomly distributed and $P' = 0$ for oxygen bound to Ta atoms) are very restrictive, the similar variation of the three curves indicates a qualitative agreement with the experimental results. In fact, if instead of taking $P' = 0$ for oxygen bound to Ta atoms we had assumed that these probabilities were functions of [Ta], we could have obtained a better adjustment.

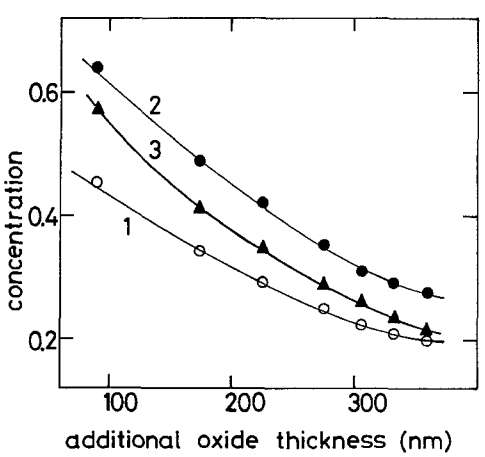

Fig. 2. Variations of the experimental values (curve 1) and of the calculated values (curves 2 and 3) of the ^{18}O concentration in region X as a function of additional oxide thickness in $^{16}O_{sol}$ for experiments 1.

Experiments 2.—In these experiments, as the oxidation is performed first in $^{16}O_{sol}$ and then in $^{18}O_{sol}$, the ^{18}O atoms will be preferentially bound to Nb atoms with the assumption that $P'(O1)$ [or $P'(O1)$ and $P'(O4)$] are the highest probabilities. We must compare $[^{18}O]$ in region X with α_1 or with $\alpha_1 + \alpha_4$. Figure 3 represents the values of $[^{18}O]$ (curve 1) of α_1 (curve 2) and $\alpha_1 + \alpha_4$ (curve 2') as a function of additional oxide thickness in $^{18}O_{sol}$ (the oxidation potential in $^{16}O_{sol}$ was 120V). Although α_1, $\alpha_1 + \alpha_4$, and $[^{18}O]$ are increasing functions of additional oxide thickness, a disagreement appears between absolute values, and this cannot be explained by measurement errors. Another assumption can be that O2 (or O2, O5, and O6) type atoms take part in a transport event with the same probability as O1 (or O1 and O4) type atoms. This means that all oxygen atoms move except those bound solely to Ta atoms and $[^{18}O]$ must be compared to $\alpha_1 + \alpha_2$ (covalent case) or $\alpha_1 + \alpha_2 + \alpha_4 + \alpha_5 + \alpha_6$ (seven types of oxygen). Figure 3 represents also the values of $\alpha_1 + \alpha_2$ (curve 3) and $\alpha_1 + \alpha_2 + \alpha_4 + \alpha_5 + \alpha_6$ (curve 3') which show a large disagreement with $[^{18}O]$. Thus, neither the hypothesis that solely oxygen bound to Nb moves nor that solely oxygen bound to Ta does not take part in ionic current can explain results of the experiments 2, since we have always

$$\alpha_1 < [^{18}O] < \alpha_1 + \alpha_2$$

and

$$\alpha_1 + \alpha_4 < [^{18}O] < \alpha_1 + \alpha_2 + \alpha_4 + \alpha_5 + \alpha_6$$

We can propose the following explanation: at the beginning of the reoxidation in $^{18}O_{sol}$ all the O1 (or O1 and O4) atoms will be labeled in ^{18}O, while pro-

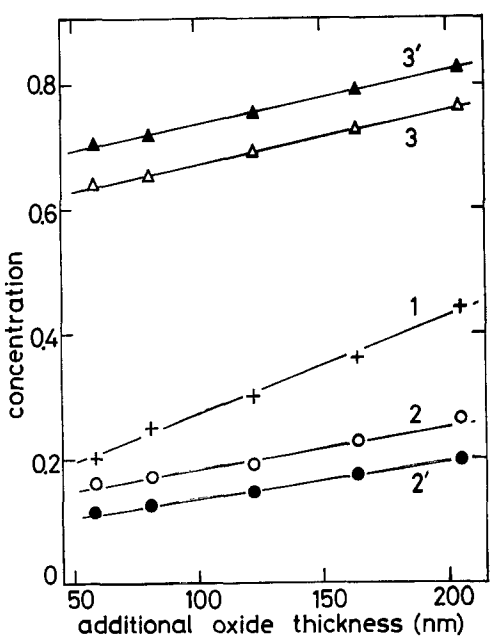

Fig. 3. Variations of the experimental values (curve 1) and of the calculated values (curves 2, 2' 3, and 3') of the ^{18}O concentration in region X as a function of additional oxide thickness in $^{18}O_{sol}$ for experiments 2.

gressively an increasing fraction of the O2 (or O2, O5, and O6) atoms will be also labeled. The concentration of these last atoms will be $[^{18}O] - \alpha_1$ or $[^{18}O] - (\alpha_1 + \alpha_4)$, and we can notice that these concentrations appear to be linearly increasing functions of additional oxide thickness. These results can be explained by assuming that $P'(O1) > P'(O2)$, but $P'(O2) > O$.

We can summarize this analysis by noting that qualitatively we can explain the results by a network-preserving mechanism (assuming the extreme case of a random distribution of cations in region X). Simple hypothesis for the various movement probabilities (P and P') leads to a qualitative agreement between experimental and predicted values of $[^{18}O]$ in region X, whatever the assumption on the metal-oxygen bond, *i.e.*, purely covalent or partly ionic and covalent.

The oxide network is destroyed.—In this case, we assume that the ionic current passes in high ionic conductivity fingers (Nb_2O_5 fingers) and passes around the low ionic conductivity matrix (Ta_2O_5 matrix). In order to describe such fingers, some hypotheses must be made and, according to Pringle (13), we make the following simplest assumption: as all the ionic current is confined in Nb_2O_5 regions for the stationary regime (2), we admit that for potentials higher than 100V [end of the transition regime in the $V = f(t)$ relationship (2)], the number of Nb_2O_5 fingers is constant and equal to n_o. Moreover we assume a cylindrical symmetry around the electric field. This means that all the directions perpendicular to the field are equivalent. So, in a perpendicular plane to the field in region X, an Nb_2O_5 finger can be schematically represented as in Fig. 4. The circle of radius a contains solely oxygen atoms bound to Nb atoms, while the zone border of thickness b corresponds to oxygen atoms bound to Ta and Nb atoms. Hence, from a geometrical standpoint, three kinds of oxygen atoms can be defined: oxygen atoms type 1 (O1), which are in the circle of radius a, *i.e.*, oxygen atoms bound to Nb cations; oxygen atoms type 2 (O2), which are in the zone of thickness b, *i.e.*, oxygen atoms bound to Nb and Ta cations; and oxygen atoms type 3 (O3), which are outside the circle of radius $(a + b)$, *i.e.*, oxygen atoms bound to Ta cations.

We can first assume that the radius a is the same for all the Nb_2O_5 fingers. However, in a more general approach, we assume that a distribution a_i exists for the radius of the fingers (in going from 1 to n_o); the thickness b being assumed the same for all fingers and equal roughly to the distance between cations in the oxides. If we consider a unit area (U), the respective concentrations α_1, α_2, and α_3 of the three oxygen types will be given by the various area ratios which are defined from Fig. 4 as

$$\alpha_1 = \left(\sum_{i=1}^{n_o} \pi a_i^2 \right) \Big/ U = S$$

$$\alpha_2 = \left(\sum_{i=1}^{n_o} (2\pi a_i b + \pi b^2) \right) \Big/ U = \Delta S$$

$$\alpha_3 = 1 - \alpha_1 - \alpha_2 = 1 - (S + \Delta S)$$

which can be also given as a function of $\bar{a}$ and $\overline{a^2}$ with

$$\bar{a} = \frac{1}{n_o} \sum_{i=1}^{n_o} a_i \text{ and } \overline{a^2} = \frac{1}{n_o} \sum_{i=1}^{n_o} a_i^2$$

$$\alpha_1 = (n_o \pi \overline{a^2})/U$$

$$\alpha_2 = (2n_o \pi b \bar{a} + n_o \pi b^2)/U$$

$$\alpha_3 = (1 - n_o \pi \overline{a^2} - 2n_o \pi b \bar{a} - n_o \pi b^2)/U$$

In the same way, we can relate the Nb and Ta concentrations with these quantities. There is a problem

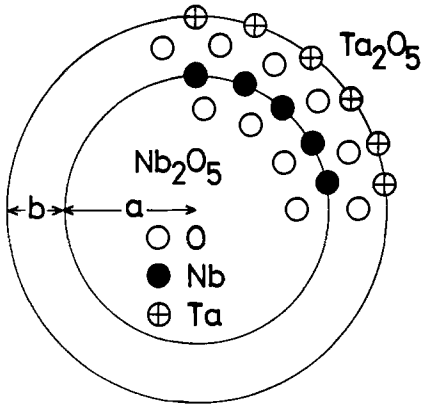

Fig. 4. Schematic representation of an Nb_2O_5 finger in a Ta_2O_5 matrix for a perpendicular plane to the field direction.

about the zone border and, as working hypothesis, we assume that

$$[Nb] = S + \frac{\Delta S}{2} \text{ and } [Ta] = 1 - S - \frac{\Delta S}{2}$$

and this leads to

$$[Nb] = \alpha_1 + \frac{\alpha_2}{2} \text{ and } [Ta] = 1 - \alpha_1 - \frac{\alpha_2}{2}$$

As we have shown previously (2) that [Nb] in region X is an increasing function of oxidation potentials, it follows that $\bar{a}$ must also be an increasing function of potentials. Moreover, we assume that the ionic current passes in Nb oxide fingers and passes around the Ta oxide matrix. Thus, O1 type oxygen atoms take part in ionic current while O3 type do not. A question arises about O2 type: Do these oxygen atoms behave like O1 or like O3 type oxygen atoms? This is the key question since following the mean value $\bar{a}$, α_2 could be lower, equal, or higher than α_1, according to the fact that α_1/α_2 decreases when $\bar{a}$ decreases. This question will be discussed in what follows.

Experiments 1.—We can assume either that only O1 type atoms take part in ionic current (case a) or that both O1 and O2 atoms do (case b). Since the oxidation is performed first in $^{18}O_{sol}$ and then in $^{16}O_{sol}$, the ^{18}O atoms will be found in the Ta_2O_5 matrix and thus, the experimental ^{18}O concentrations ($[^{18}O]$) are given by

$$[^{18}O] = 1 - \alpha_1 \quad \text{for case a}$$

$$[^{18}O] = 1 - (\alpha_1 + \alpha_2) \quad \text{for case b}$$

Moreover, as [Nb] is known, we obtain

$$\alpha_2 = 2([^{18}O] + [Nb] - 1) \quad \text{for case a}$$

$$\alpha_2 = 2(1 - [^{18}O] - [Nb]) \quad \text{for case b}$$

The values for α_2 are negative in case a for all additional oxide thickness. Possible errors on $[^{18}O]$ and [Nb] cannot explain this result since errors of about 50% must be assumed to obtain positive values for α_2. Hence, we can exclude case a, while case b (for which α_2 is positive) must be considered. Figure 5 represents the calculated α_2 values (curve 1) as a function of additional oxide thickness. Since [Nb] increases slowly with increasing thicknesses (1, 2) we may expect that each radius a_i must increase, leading to an increase of $\bar{a}$ and therefore of α_2 ($\alpha_2 = 2n_o \pi b \bar{a} + n_o \pi b^2$). Figure 5 shows that α_2 (in fact $\bar{a}$ since n_o and b are constant) decreases slowly by about 10% for the range of thickness studied. Taking into consideration the possible errors associated with nonuniformity effects, the absolute values of α_2 are not very precise. However, the relative precision from one point to another is sufficiently good to postulate that the decrease of α_2 is real.

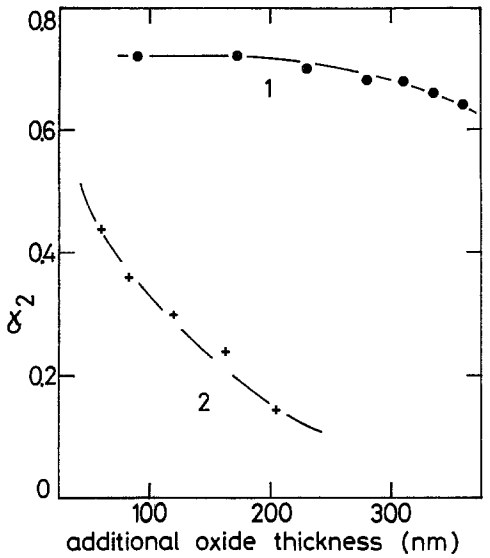

Fig. 5. Variations of $\alpha_2(\alpha_2 = 2n_o\pi b\bar{a} + n_o\pi b^2)$ with additional oxide thickness, respectively, in $^{16}O_{sol}$ for experiments 1 (curve 1) and in $^{18}O_{sol}$ for experiments 2 (curve 2).

Following the definition of α_2, a decrease of its value can only be due to a decrease of $\bar{a}$. This last effect is only possible if n_o is not constant. In fact, if the number of fingers increases, new fingers are created at each time with small values for their radii and this leads to a decrease in the value of $\bar{a}$. However, this conclusion is in full contradiction with the basic hypothesis of mechanism (*ii*): the ionic current flows only in the Nb_2O_5 fingers avoiding the Ta_2O_5 matrix.

Experiments 2.—In these experiments, as the oxidation is performed first in $^{16}O_{sol}$ and then in $^{18}O_{sol}$, the ^{18}O atoms will be found in the Nb_2O_5 fingers. Here also, two possibilities exist: $[^{18}O]$ in region X is either related only to O1 type atoms (case a) or both to O1 and O2 type atoms (case b). The ^{18}O concentrations are thus given by

$$[^{18}O] = \alpha_1 \quad \text{for case a}$$

$$[^{18}O] = \alpha_1 + \alpha_2 \quad \text{for case b}$$

and this leads to

$$\alpha_2 = 2([Nb] - [^{18}O]) \quad \text{for case a}$$

$$\alpha_2 = 2([^{18}O] - [Nb]) \quad \text{for case b}$$

The values for α_2 are negative in case b whatever the additional oxide thickness. Hence, only case a must be considered and Fig. 5 represents the calculated α_2 values (curve 2) as a function of additional oxide thickness. This figure shows that α_2 decreases and, as above, the experimental errors cannot explain such a decrease of α_2 with increasing oxide thickness. Therefore, the same conclusion can be inferred from this curve, $\bar{a}$ decreases when the oxide thickness increases. Note also the difference in the α_2 values for experiments 1 and 2 (curves 1 and 2) and that the variation of α_2 values with additional oxide thickness is different in the two cases.

Thus, it is not possible to explain the results of experiments 1 and 2 assuming an oxide network destroyed mechanism (existence of two distinct phases in region X) and a full confinement of the ionic current in Nb_2O_5 fingers. The following question arises: Is it possible to explain the results assuming a partial confinement of the ionic current in fingers, but with the creation of new Nb_2O_5 fingers at each time? In fact, $\alpha_2 = 2n_o\pi\bar{a}b + n_o\pi b^2$ decreases with increasing potential. If n_o is constant $\bar{a}$ must decrease and this has no physical meaning. If n_o increases, $\bar{a}$ can decrease according to the distribution of the a_i radii. Such an increase of n_o is possible if we assume that all the ionic current does not flow in the Nb_2O_5 fingers, and if we consider that new fingers are created at each time. In this case, the number of fingers will only depend on the potential and it will be the same in experiments 1 and 2 for the same overall potential. As the number of fingers increases, one can think that a potential must exist for which no further creation of fingers occurs since these fingers are close together. According to this hypothesis, experiments 1 show that $[^{18}O]$ in region X is roughly constant at high potentials and equal to 0.2. This would mean that the fraction of the area represented by the fingers is equal to 0.8. In this case, an estimation of $\bar{a}$ is possible. In fact, if we assume that the mean distance between fingers is given by $\bar{l} = 1/\sqrt{n}$ where n is the total number of fingers, and assuming also that $\bar{l}$ can be written as $\bar{l} = 2\bar{a}$ (the fingers are close), it leads to

$$4\bar{a}^2\alpha_2 - 2\bar{a}\pi b - \pi b^2 = 0$$

With experimental values this leads to $\bar{a} = 3b$. Assuming that b is of the order of 0.5 nm, the order of magnitude of $\bar{a}$ will be 1.5 nm (about three interatomic distances), while an estimation of the number of fingers will be $n \simeq 10^{13}$ cm^{-2}. Obviously, this is only a rough evaluation of these quantities, but these estimations indicate that the possible nonuniformities are not in a macroscopic scale and can explain the fact that such fingers were not experimentally observed (9). Moreover, if new fingers are created at each time, the evolution with potential of the concentration of oxygen taking part in oxide growth must be identical in experiments 1 and 2. The absolute values will be different, but the rate of increase must be the same. Examination of the results (1) shows that the variation of these oxygen concentrations is very different in the two experiments. Thus the hypothesis of two distinct phases (Nb_2O_5 and Ta_2O_5) in region X appears very questionable.

The main conclusion which can be drawn from this analysis is that a mechanism in which the oxide network is destroyed (lateral nonuniformities) cannot describe, even qualitatively, the results of experiments 1 and 2 in region X.

Cation and Oxygen Movements in Region S

The partial inversion of the order of oxygen atoms in region S (1) appears to be an intrinsic property of this region and is not due to the phenomena taking place in region X. This conclusion is drawn from the comparison of the ^{18}O profile in region S and in part B of the oxide (Fig. 1). In part B (pure Nb_2O_5), the order of oxygen atoms is largely preserved and the shape of the ^{18}O distribution is due to the inversion of the order in region X and to the angular aperture of the transport events (1, 9). If similar phenomena take place in region S, a similar ^{18}O profile should be observed. This is not the case, since the ^{18}O distribution (Fig. 1) shows a sharp drop at the region X-region S interface, while in part B, $[^{18}O]$ increases steadily and reaches a maximum about 40 nm after the region X interface. The inversion of the order of oxygen atoms in region S appears, thus, to be due to the presence of two different cationic species in this region. Nb and Ta depth profiles presented in part I (1) show that [Ta] and [Nb] change in region S, indicating that both Ta and Nb move in this region. However the burying of the Ta distribution (1, 2) does not exclude the fact that some Ta atoms in this region do not take part in ionic current. Thus, we can explain, at least qualitatively, the partial inversion of the order of oxygen atoms by the differences in P' which would induce a preferen-

tial movement of oxygen atoms bound to Nb atoms. This can explain the similarities between [Nb] and [^{18}O] observed in experiments 2 (1). Moreover, as stated previously, we can eliminate the possibility of the full confinement of the ionic current in region S. Therefore, it is not possible to explain the inversion of the order of oxygen atoms by the existence of two distinct phases (Nb_2O_5 and Ta_2O_5) in the near-surface region of the oxide.

Hence, as in region X, the presence of two distinct phases does not permit an acceptable interpretation of the results observed in region S, while the description associated with the difference in movement probabilities gives a qualitative interpretation of the experimental results.

Conclusions

We have associated two descriptions of the oxide mixture with the two leading phenomena that can explain a partial inversion of the order of cations and of oxygen atoms. The comparison between the ^{18}O experimental concentrations with those deduced from the two descriptions shows the following points:

There is a disagreement between the experimental data and the conclusions deduced from the mechanism based on differences in ionic conductivities of Nb_2O_5 and Ta_2O_5 (phenomenon *ii*), which leads to lateral nonuniformities in the oxide.

It appears possible to describe qualitatively the results by differences in movement probabilities of Nb and Ta cations and of oxygen atoms bound to them (phenomenon *i*).

This qualitative agreement appears despite the fact that the description of the oxide mixture is based on an extreme assumption: there is a random distribution of cations in the oxide mixture. This means that we consider the ionic current as laterally uniform. However, the differences in movement probabilities do not necessarily lead to such a description. In fact, the penetration of Nb atoms in the Ta oxide network (due to $P(Nb) > P(Ta)$) can lead to microscopic aggregations of Nb atoms, and we can call these microscopic islands or microscopic fingers. This can be due to the fact that as the oxidation is carried out the penetration of Nb cations will lead to the replacement of the original nearest neighboring Ta atoms of an Nb atom by Nb atoms. Thus, the Nb and Ta distributions can no longer be considered as fully random distributions. This can lead to a local destruction of the Ta oxide network and, thus, macroscopic effects can be envisaged. In this case, according to the difference in ionic conductivity of Nb_2O_5 and Ta_2O_5, the ionic current will flow preferentially in the microscopic Nb_2O_5 aggregations and pass around the Ta_2O_5 aggregations. However, taking into consideration the fact that a random distribution of cations gives a rather good explanation of the results, we can conclude that these aggregations do not involve the majority of the Nb atoms present in the oxide mixture (9).

Another way to describe this nonfully random distribution is to speak of microscopic nonuniformities in [Nb] and [Ta]. In a plane, [Nb] will change from place to place and the higher [Nb] is, the higher will be the current density, but there is no macroscopic finger in which [Ta] = O. Let us notice that in this approach phenomena (*i*) and (*ii*) appear to be coupled.

The comparison of cations and ^{18}O profiles in the oxide mixture shows that a correlation exists between oxygen and cation movements. This is not compatible with the simple model of independent movement of point defects (for cations and oxygen) through the oxide leading to the growth at both interfaces. This correlation can be explained in the frame of two distinct hypotheses on the transport events:

There is only one transport event involving the simultaneous movement of cations and anions. The example of such a process can be found in the place exchange mechanism suggested by Fromhold (18). However a question arises: How many cations and anions take part in the transport event? With this hypothesis, at a molecular scale, both cation and oxygen move in a ratio equal to the transport number which is a measure, at the macroscopic scale, of this movement and which appears as an intrinsic property of each oxide. As quoted by Fromhold (18), in order to explain the experimental values of transport number, one is forced to assume the simultaneous movement of a group of cations and of oxygen. If we admit the hypothesis of one transport event, ^{18}O distributions (1) indicate that these transport events are injected at the oxide-solution interface. In fact, ^{18}O profiles in part B of the oxide show an increase of [^{18}O] from the region X toward the oxide-metal interface which cannot be explained by the injection of the transport event at the metal-oxide interface.

Oxygen and cation transport events are distinct but not independent. In this assumption, the two transport events are only spatially correlated, *i.e.*, when an oxygen has taken part in ionic current, its nearest cationic neighbors will also take part in ionic current. This means that a transport event leads to a local disturbance of the oxide during its passage. In this approach, in order to explain the correlation of the movements, one must assume that each transport event marks its passage by a trace through the whole oxide and the opposite transport event follows this trace through the oxide.

New experiments have to be carried out to obtain insight into the physical nature of transport events.

Acknowledgment

This work was supported by the Centre National de la Recherche Scientifique (R.C.P. No. 157).

Manuscript submitted July 30, 1981; revised manuscript received Nov. 26, 1982. This was Paper 54 presented at the Minneapolis, Minnesota, Meeting of the Society, May 10-15, 1981.

Any discussion of this paper will appear in a Discussion Section to be published in the December 1983 JOURNAL. All discussions for the December 1983 Discussion Section should be submitted by Aug. 1, 1983.

REFERENCES

1. J. Perrière and J. Siejka, *This Journal*, **130**, 1260 (1983).
2. J. Perrière, S. Rigo, and J. Siejka, *ibid.*, **125**, 1549 (1978).
3. J. P. S. Pringle, *ibid.*, **121**, 865 (1974).
4. J. A. Davies, B. Domeij, J. P. S. Pringle, and F. Brown, *ibid.*, **112**, 675 (1965).
5. F. Brown and W. D. Mackintosh, *ibid.*, **120**, 1096 (1973).
6. J. L. Whitton, *ibid.*, **115**, 58 (1968).
7. J. P. S. Pringle, Abs. 59, p. 144, The Electrochemical Society Extended Abstracts, Vol. 78-1, Seattle, Washington, May 21-26, 1978.
8. L. Young, "Anodic Oxide Films," Academic Press, London and New York (1961).
9. J. Perrière, Thesis, University Paris VII, Paris (1981).
10. J. P. S. Pringle, *This Journal*, **120**, 1391 (1973).
11. S. Rigo and J. Siejka, *Solid State Commun.*, **15**, 259 (1974).
12. J. P. S. Pringle, *Electrochim. Acta*, **25**, 1403 (1980).
13. J. P. S. Pringle, *ibid.*, **25**, 1423 (1980).
14. M. J. Dignam, in "Oxides and Oxide Films," Vol. 1, J. W. Diggle, Editor, Marcel Dekker Inc., New York (1973).
15. J. P. S. Pringle, A.E.C.L. Report 5511 (March 1976).
16. W. D. Cornish, Thesis, The University of British Columbia, Vancouver (1972).
17. N. C. Stephenson and R. S. Roth, *Acta Crystallogr., Sect. B*, **27**, 1037 (1971).
18. A. T. Fromhold, Jr., *This Journal*, **127**, 411 (1980).

Mechanism for the Graphoepitaxy of Electrodeposited Tin

L. S. Darken*

Solid State Division, Oak Ridge National Laboratory, Oak Ridge, Tennessee 37830

ABSTRACT

Tin islands electrodeposited from basic cyanide solutions were grown graphoepitaxially on a substrate into which a square wave relief pattern had been reactively ion etched. The [100] axis of each island was normal to the substrate and the [001] axis was parallel to the relief structure in the plane of the substrate. Tin has a body-centered tetragonal crystal structure. At low cathodic polarizations ($|\eta| < 0.5$V), the islands nucleated at interior corners of the square wave pattern. Nucleation also occurred at the interior corners for all other electrodeposited metals studied (Cu, Pb, In, Zn). The tin islands grew with a highly faceted and linear morphology elongated in the [001] direction. Postdeposition and *in situ* observations suggested that the dominant mechanism for crystallographic orientation in the plane of the substrate was the physical confinement of the elongated islands in a single groove. The islands usually did not overgrow a step until they had grown as wide as the groove. This growth sequence suggests that the growing islands pushed away from the adjacent steps. Islands nucleated at random on the surface via a high cathodic polarization ($|\eta| > 0.5$V) pulse and subsequently grown at a lower polarization also possessed a strong degree of graphoepitaxy, thus demonstrating that the graphoepitaxial orientation can be induced after nucleation. Nucleation at interior corners may be helpful in starting the orientation process at an earlier growth stage and in placing the islands on the lower level of the square wave pattern where confinement can take place. This demonstration of graphoepitaxy in an electrocrystallization process broadens the range of potential applications for graphoepitaxy, and new information on the orienting mechanism provides guidance in selecting systems for which graphoepitaxy might be successful.

The use of substrate relief patterns to induce uniform crystallographic orientation of the individual nuclei or grains in a deposited or recrystallized film has been termed graphoepitaxy (1). The technique has been successfully applied to KCl islands grown from aqueous solution (2), liquid crystals (3), recrystallized silicon films heated near the melting point by incident radiation (1, 4), germanium grown from liquid solution (5), and tin islands electrodeposited at room temperature from a basic cyanide solution (6). The principal purpose of this article is to investigate the mechanism for the graphoepitaxial orientation of electrodeposited tin islands. It is proposed that the operating mechanism for graphoepitaxial alignment of the tin islands is the physical confinement of the islands by the surface relief structure.

Electrodeposited tin islands are an ideal system for an investigation of graphoepitaxy. The graphoepitaxial crystallographic alignment is fairly strong and the individual islands are so well faceted that the degree of alignment can be seen with an optical or electron microscope. A scanning electron microscope view of an individual island is shown in Fig. 1. Typically the [100] axis is aligned normal to the substrate within 0.2° FWHM (full width half maximum) and the [001] axis parallel to a square wave grid pattern within 5.0° FWHM (6). The morphology of growth is such that deposited islands are elongated in the [001] direction and the {100} and {001} faces are strongly faceted. Tin has a body-center tetragonal crystal structure. In electrodeposition nucleation and growth are potential-dependent rate processes, and the potential can be programmed to follow a variety of time-dependent functions. It is also convenient that, at least ideally, the rate of deposition is given by the cell current. The rest potential of the cell can be used to verify the presence of a deposit. Electrochemical cells can also be constructed to allow *in situ* observation of the cathode during deposition. Thus, the mechanism for graphoepitaxy should be easier to determine in an electrochemical cell than in other crystallization processes such as growth from the melt, solution, or the gas phase. A significant inference from this work is that the deposited islands have some rotational mobility even during later growth stages (length $\approx$ 1 μm) and that alignment can occur during this stage. Minimization of surface free energy in the electrodeposit/substrate system cannot adequately account for the azimuthal (in-plane) alignment of the tin islands reported here. All the cathodically deposited metals investigated including copper, lead, indium, and zinc as well as tin, normally nucleated at the interior corners of the square wave relief pattern. However, tin nucleated at random on the surface by means of a high ($|\eta| >$ 0.5V) cathodic polarization pulse also showed strong graphoepitaxial orientation. This indicates that the alignment occurs during growth rather than at the nucleation stage.

Graphoepitaxy is an innovative concept that is potentially useful in producing near-single crystalline films. The extent of its usefulness depends on the type and variety of systems to which it can be applied and on the degree of crystallographic perfection that can be achieved. Assessment of both of these factors would be helped by understanding the mechanism (or mechanisms) responsible for graphoepitaxy.

Graphoepitaxy depends on precisely defined surface-relief structures with edge acuity and, hence, borrows from fabrication technologies developed for microelectronics. The original idea was that surface relief structure appropriate for the surface energy anisotropy of the deposit/substrate system under consideration would significantly reduce the energy of a particular crystallographic orientation (7). Thus, films with an axial texture on a flat substrate might be

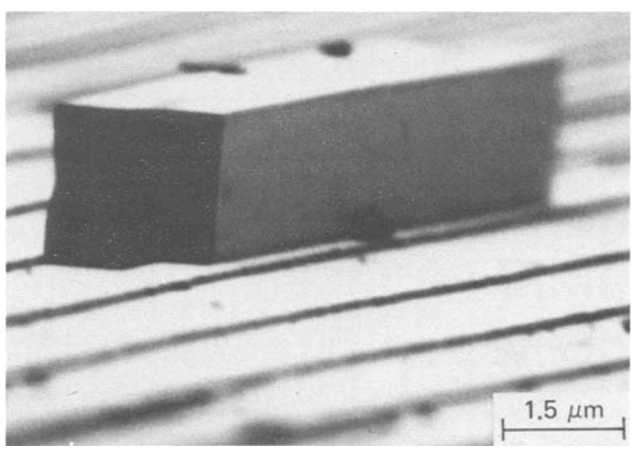

Fig. 1. Glancing incidence SEM view of tin island

* Electrochemical Society Active Member.
Key words: relief structure, textured substrates, crystallographic texture, nucleation enhancement.

deposited with only small angle grain boundaries on a substrate with the appropriate relief structure. Although barriers to achieving this equilibrium configuration may be formidable, it was encouraging that the interior corner radii of the square wave relief patterns produced by reactive ion etching (< 5 nm) might be less than the critical radius for nucleation in some crystal growth systems. Minimization of interfacial energy appears to be responsible for the graphoepitaxial alignment observed in liquid crystals (3) and has been incorporated into models to explain the graphoepitaxial recrystallization of silicon films (8). However, neither of these involves nucleation of the graphoepitaxially oriented phase from a parent phase.[1] The graphoepitaxy of solution-grown alkali halides has not yet been investigated in enough detail to confirm a mechanism. *In situ* UHV/TEM has been applied to the condensation of a variety of metals and alloys on topographically structured carbon substrates but only limited ordering was observed (9).

In the section entitled Experimental Techniques, the methods used for obtaining substrate relief on the cathode are presented. The details of the construction of the cell, including the modifications required for *in situ* observation (450×) of electrodepositions are also described. In the Results and Discussion section, the effects of the cathodic polarization on nucleation, growth, and graphoepitaxial alignment are presented and the results discussed.

Experimental Techniques

The electrochemical cell consisted of a covered Pyrex container for the electrolyte into which electrodes could be inserted.[2] The cell was purged with an inert gas prior to and during all depositions. The anode was fine mesh platinum screen spot-welded to a platinum wire. The saturated calomel electrode[2] (SCE) was connected to the electrolyte by a porous glass semipermeable plug. The construction of the cathodic substrate is shown in Fig. 2. The only materials of the cathode in contact with the electrolyte were chromium, fused quartz, and black wax.

Relief patterns were prepared by reactive ion etching (10) through photolithographically produced chromium masks on either SiO_2 thermally grown on silicon wafers or on fused SiO_2. The techniques employed were similar to those described by Geis *et al.* (1). Chromium was evaporated onto the SiO_2, and coated with photoresist. The photoresist was then exposed to a parallel grid pattern of light. This light pattern was obtained either by the interference pattern of an argon ion laser or by exposure through a mask in intimate contact with the photoresist. The exposed photoresist was developed away and the unprotected chromium underneath was removed in a liquid etch. The chromium grid pattern thus obtained was used as a mask during reactive ion etching of the uncoated SiO_2. Overexposure resulted in chromium strips narrower than the strips of uncoated SiO_2. The reactive ion etching was done on the cathode of an rf sputterer[3] in a 1 Pa rf plasma of CHF_3 at an incident power density of 1 W/cm^2. The etch rate was 33 Å/min. Corner radii on the order of 5 nm or less can be achieved by this reactive ion etching technique (7). Typically, the square wave had a depth of 0.1 μm and a periodicity of 2.7 μm. The etched patterns were then metallized for electrical continuity by evaporation of chromium. Two evaporations (7.5 nm each), with the substrate tilted in opposite directions, were necessary to ensure good coverage of the pattern. The substrates were then cleaved into smaller pieces and mounted in the manner shown in Fig. 2.

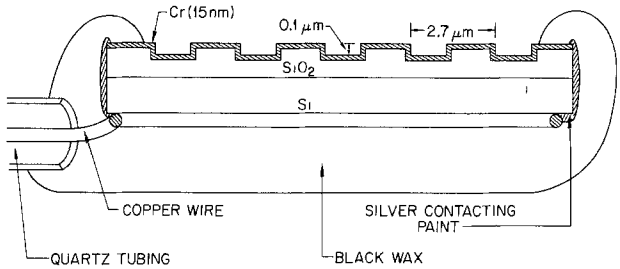

Fig. 2. Details of the construction of the cathodic substrate

An attempt was made to etch the relief pattern directly into a conductor. A layer of graphite was deposited on silicon wafers in a reaction tube by the pyrolysis of acetone at 900°C. Adherence of the pyrolytic films was improved by a titanium interlayer and slow cooling (2°/min). The rf reactive ion etching was done in 1 Pa of O_2. Both chromium and titanium were suitable mask materials. Adherence of the mask during the photolithographic processing steps was sometimes a problem. These structures, however, showed more small scale (0.1-1.0 μm) irregularities in the linearity of the relief pattern than did the structures etched into SiO_2. These irregularities are possibly related to the graphite grain size. It was difficult to obtain graphoepitaxial tin deposits on these pyrolytic graphite substrates and therefore the bulk of the experimental work was performed using the SiO_2 substrates coated with chromium.

A cell body was machined from polyethylene to allow *in situ* observation during electrodeposition. The cathode with the relief structure was sealed by black wax over a hole in the center of the cell bottom. Electrodeposition could also be observed in the transmission (illuminated from below) as well as reflection mode of the microscope. Fused quartz substrates were used to allow observation of the deposition in the transmission mode. The anode, SCE, and argon bubbler were held in place along the sides of the cell body. The apparatus was mounted on the stage of a microscope and the whole lower section of the microscope was enclosed in a shroud and purged with argon. The microscope objective (45×) was protected from the electrolyte by a thin (0.001 in.) Mylar sheet.

Results and Discussion

Nucleation.—The effect of substrate relief on nucleation will be presented first. In initial investigations a variety of metals were studied.[4] The deposition rates on patterned and on flat chromium-coated electrodes were compared. In the usual procedure the cathodes were immersed in a 5:1 chromic acid/sulfuric acid cleaning solution for 5 sec, thoroughly rinsed in flowing distilled and deionized water, and blown dry before use. That the chromium itself was inert to the acid cleaning solution was demonstrated by the lack of observable chemical attack after long (several days) immersions in this solution. Basic electrolytes were employed where convenient in order to minimize hydrogen reduction at the cathode. It should also be noted that basic electrolytes tend to passivate many metals including tin and chromium. The cathodic polarization with respect to the SCE was increased linearly with time and the cell current plotted. Deposition was confirmed by comparing the rest potential of the cathode to the rest potential of an electrode of the same metal also immersed in the electrolyte. The systems investigated are listed in Table I. The rest potentials given are all with respect

[1] This statement is probably less certain for the silicon case where more factors are involved. See Ref. (8) for details.
[2] Princeton Applied Research Corporation, Princeton, New Jersey.
[3] Vacuum Industries Incorporated, Somerville, Massachusetts.
[4] Most electrolytes used were taken from F. A. Lowenheim, "Modern Electroplating," Wiley Interscience, New York (1974).

to SCE. In each case enhanced deposition on the patterned cathode was observed.[5] The current *vs.* voltage plot at a scan rate of 0.5 mV/sec for a copper deposition is shown in Fig. 3. As the voltage increases, faster deposition at existing islands and the nucleation of new islands contribute to the increasing current. A scanning electron microscope picture of the deposited copper is shown in Fig. 4. The location of the smaller islands is consistent with nucleation at interior corners of the relief structure. X-ray diffraction indicated a [111] axial texture.

The textures observed in electrodeposits are frequently taken to be growth textures (11). That is, the texture arises after complete coverage of the substrate by unoriented grains when grains with certain favored orientations preferentially overgrow neighboring grains. The texture observed here is present before coalescence of the islands into a continuous film and is therefore demonstrably not of this type.

The nucleation of tin electrodeposited from a basic cyanide solution (12) was investigated in more detail. The tin deposited as poorly adherent isolated islands. These characteristics are consistent with an oxide or passive film on the chromium surface. Current density *vs.* voltage for a ramped potential is shown in Fig. 5 for patterned and flat substrates after various surface cleaning treatments. Immediately before electrodeposition the substrates were either rinsed in deionized water, chemically cleaned in a 5:1 sulfuric acid/chromic acid solution, or etched to remove 2.5 nm of chromium (Kodak etch). Tin coverage of about 1-5% was typical for the substrates at the conclusion of a deposition. The tin islands are evidently "heterogeneously" nucleated at defects or irregularities. This is an anticipated result as "homogeneous" nucleation on a flat substrate is unusual (13). Chemical cleaning or etching reduced the number or efficacy of these nucleation sites. For all surface preparations investigated, nucleation and growth of electrodeposited tin proceeded at lower cathodic polarizations on patterned substrates. Compared to rinsing in deionized water, chemical cleaning accentuated the difference in deposition rate between patterned and flat substrates. Etching 2.5 nm of chromium off the patterned substrate substantially eliminated the potency of the relief structure in inducing nucleation.

The nucleation at interior corners observed here during electrodeposition is similar to the decoration of cleavage steps during vapor deposition, which has been addressed by thermodynamic nucleation models (14). However, the critical nuclei for the electrodepositions described here are usually small compared to the acuity of the relief structure and are also smaller than can be estimated from classical nucleation theory. This issue is considered in more detail in an accompanying appendix.

[5] Preferential nucleation on macrosteps and scratches during copper electrodeposition was reported by V. Ueno, N. Kidokoro, and M. Tsuiki, *This Journal*, 121, 202 (1974).

Table I. Electrochemical cells investigated

Metal	Electrolyte	Comments
Sn	4.75 g/liter $SnCl_2$ $2H_2O$ 5.6 g/liter NaOH 50.0 g/liter NaCN	Enhanced nucleation on patterned substrates, box-like deposits; graphoepitaxy; V_{rest} = −1.03V
Cu	28.0 g/liter CuCN 93.0 g/liter NaCN 30.0 g/liter NaOH	Enhanced nucleation on patterned substrates; (111) texture; V_{rest} = −0.827V
Pb	3.6 g/liter $PbCO_3$ 37.0 g/liter KcN 16.8 g/liter KOH	Enhanced nucleation on patterned substrate V_{rest} = −0.741V
In	8.0 g/liter $InCl_3$	Enhanced nucleation on patterned substrate V_{rest} = −0.626V

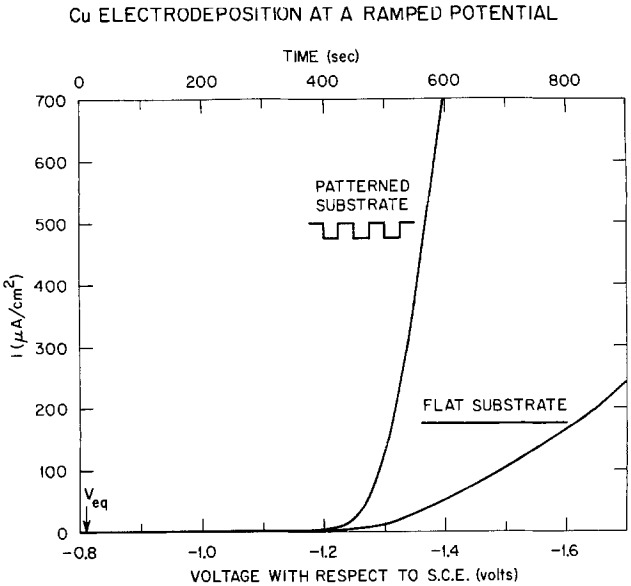

Fig. 3. Deposition rate of copper on patterned and on flat substrates. The cathode potential is ramped negatively at a constant rate.

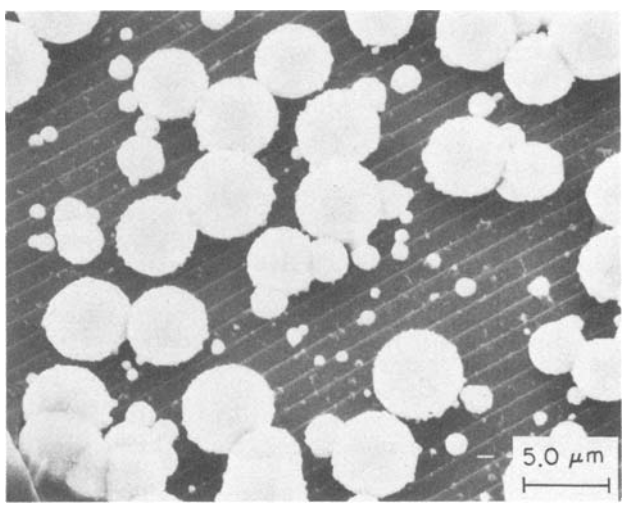

Fig. 4. SEM view of copper islands on patterned substrate of Fig. 3. The upper plateaus of the relief structure are the narrower, lighter bands.

The potency of the surface relief in inducing nucleation was confirmed by comparing current-time curves of substrates held at constant cathodic polarization. At −0.02V cathodic polarization, nucleation and growth proceeded immediately on a patterned substrate but not on a flat substrate (both chemically cleaned). It was also observed that the depositions on patterned substrates were strongly graphoepitaxial up to cathodic polarizations of roughly $|\eta|$ = 0.50V. At cathodic polarizations greater than $|\eta|$ = 0.50V examination of the deposit revealed no preferential nucleation at interior corners and internuclei spacing comparable to or less than the grating period. The issue as to what factors are crucial in suppressing graphoepitaxy was addressed by pulsed nucleation experiments to be described in the following section. The effect of cathodic polarization on nucleation at the interior corners is discussed in the appendix. Arguments are presented there which indicate that graphoepitaxy of electrodeposited tin has been observed when the critical radius for nucleation was smaller than the corner radius (~ 5 nm) of the interior corners of the relief structure. This is the first of several indications that the graphoepitaxial

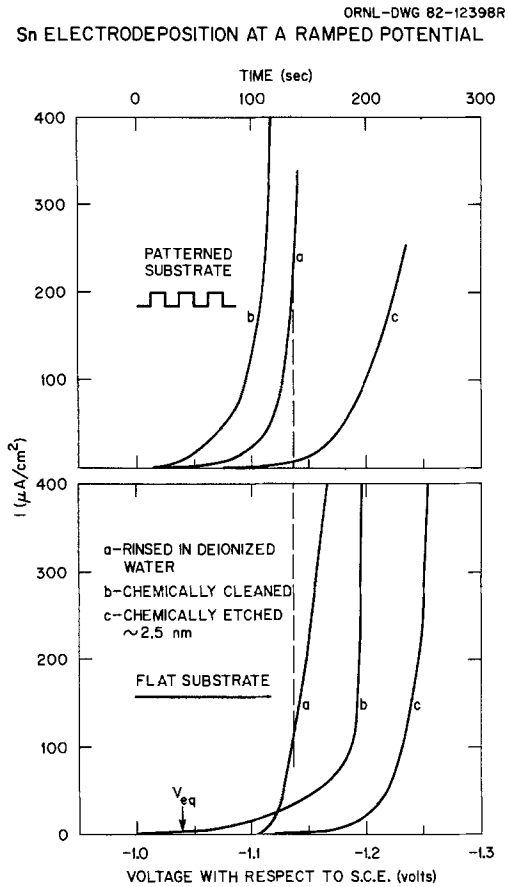

Fig. 5. Effect of substrate preparation tin deposition rates onto patterned and flat substrates.

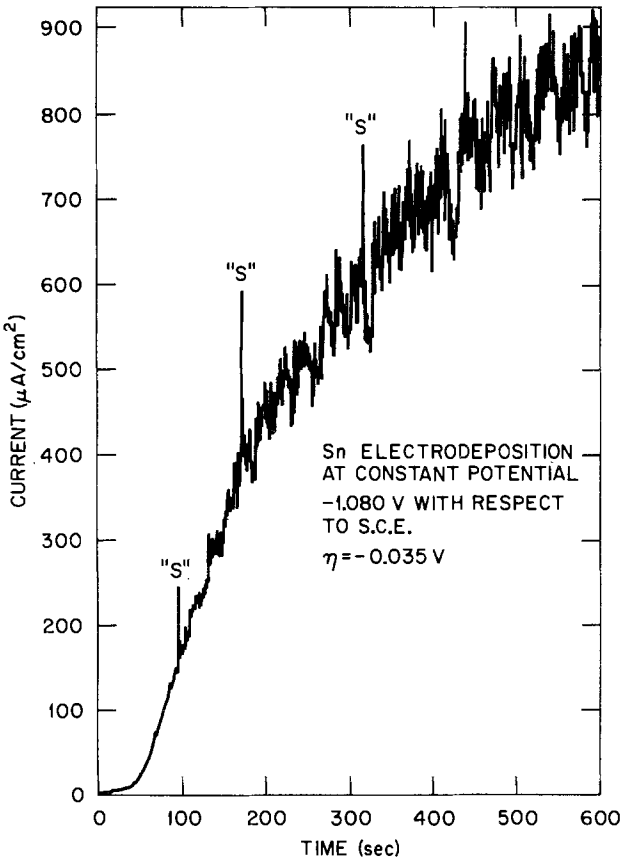

Fig. 6. Electrodeposition rate of tin at constant potential. "s" indicates cell was shaken.

orientation of the tin islands was not established by surface energy anisotropy at the nucleation stage. In fact, patterned substrates which had been etched so that nucleation did not preferentially occur at interior corners demonstrated definite, although incomplete, graphoepitaxy.

Growth of tin islands from $SnCl_2$/NaOH/NaCN electrolytes.—A current-time plot of a tin deposition at constant potential is shown in Fig. 6. The current spikes at locations labeled "s" were generated by shaking the cell. During the initial stages of deposition (current less than 100 μm/cm²), shaking the cell did not result in current spikes. Evidently mass transport in the electrolyte is important as a rate-limiting step only during the later deposition stages. Since the current was never limited for an extended current range by the charge transfer step, a Tafel equation analysis could not be used to test for a single or mixed reaction at the electrode.

Since the chromium overcoating the SiO_2 relief structure had been exposed to air, an initial surface oxide film was inevitable. Chromium could also passivate and have a surface adsorption layer in the cyanide electrolyte. The rest potential of the bare cathode was about −0.6V with respect to SCE. Immediately after immersion the cathode was routinely biased to −1.00V with respect to the SCE (slightly more positive than the rest potential for tin) to minimize oxidation. However, no current was observed until the cathodic polarization was negative enough for tin deposition, and the deposition current for either a constant or a ramped cathodic polarization did not depend on duration of immersion before deposition or on bias history.

The rest potentials of tin electrodes with respect to the SCE were measured in a series of electrolytes in which the NaOH and NaCN concentrations were held constant while the $SnCl_2$ concentration was varied from 1.6×10^{-2}M to 10^{-4}M. Nernst law behavior for a two-electron transfer process was qualitatively observed, but at the lower concentrations, it took several hours for the potential to stabilize and potentials did not get quite as negative as expected. It was also observed that when a cathode with a tin deposit was driven more positive than its rest potential, the anodic current over a period of a few minutes decayed markedly as if the surface was becoming passivated. *In situ* observations revealed that subsequent tin deposition proceeded largely through the nucleation of new islands. Pure tin electrodes immersed in the electrolyte overnight became tarnished. All these are indications that in addition to

$$Sn^{++} + 2e^- = Sn \quad [1]$$

the reaction

$$OH^- + Sn = SnO + \tfrac{1}{2} H_2 + e^- \quad [2]$$

or

$$Sn^{++} + 2\,OH^- = Sn(OH)_2 \quad [3]$$

may also be important.[6] Reactions like [2] or [3] will introduce a discrepancy between the equilibrium potential for reaction [1] and the observed rest potential of the cell, and may also have an effect on the growth morphology of the tin. Any surface passivation might contribute to growth rate anisotropy.

Postdeposition analysis.—A glancing incidence SEM micrograph of a tin deposition is shown in Fig. 7. The faceting and the orientation of the long axis of many islands with the grating direction is apparent. Also apparent is the notable fraction of the islands that are not aligned with the grating. Some deposits showed almost complete alignment, as in Fig. 8, and

[6] A review of the electrochemical reactions of tin in aqueous solution is given by B. N. Stirrup and N. A. Hampson, *Surf. Technol.*, 5, 429 (1977).

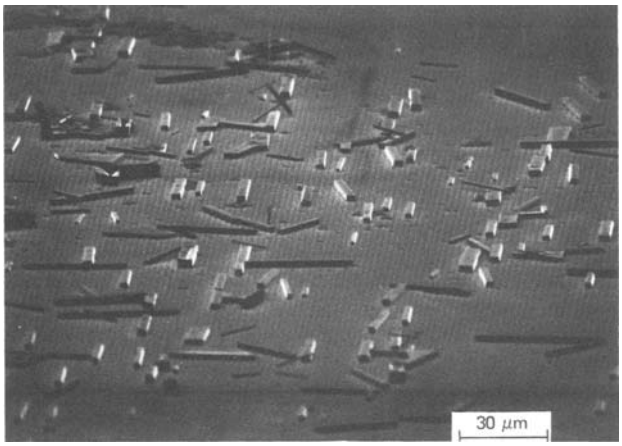

Fig. 7. Glancing incidence SEM view of a tin deposition

occasionally some depositions were completely random. The latter case was associated with severe edge ripple in the relief structure, such as occurred with the pyrolytic graphite substrates. Deposits on flat substrates also consisted of faceted linear islands but with random azimuthal orientation. Use of a silver rather than a chromium overlayer did not effect the morphology of island growth or the degree of graphoepitaxy.

The identification of the faceted surfaces and the crystallographic orientation of the tin islands with respect to the relief structure were determined by x-ray diffraction. The islands were shown to be bounded by {100} and {001} planes and elongated in the [001] direction (6). Pure [100] axial texture was found by x-ray diffractometry.[7] The angular distribution of the texture axis was less than the instrumental resolution of the diffractometer, 0.2° FWHM. The degree of azimuthal or in-plane alignment for a typical deposit is shown in Fig. 9. The FWHM of the distribution of the [001] axis about the grating direction is 5°. The degree of axial texture is superior to and the degree of azimuthal alignment is comparable to the best results reported for either silicon (1, 4) or germanium graphoepitaxy (5). Tin islands deposited on flat substrates also had pure [100] axial texture but showed no azimuthal ordering.

The extreme elongation of the islands indicates that their morphology is not due to minimization of surface energy. The shape of the islands is different

[7] J. F. Smith, *Trans. Inst. Metal Finish.*, **46**, 199 (1968) found [100] texture in tin films electrodeposited from an alkali sodium stannate bath and [110] texture in tin films electrodeposited from an acid stannous sulfate bath.

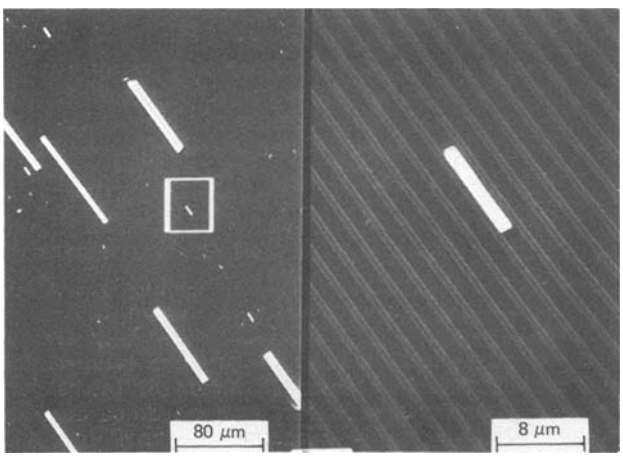

Fig. 8. SEM picture of tin deposition on a patterned substrate. Note the near complete alignment of the islands.

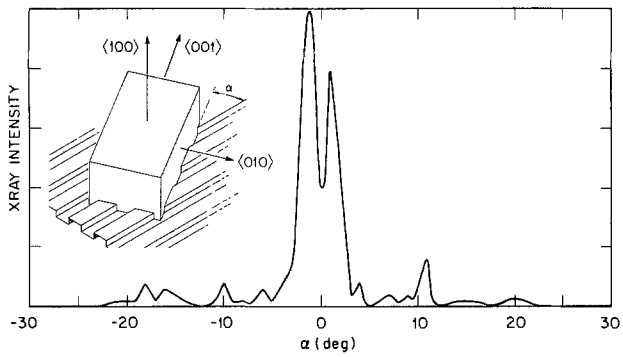

Fig. 9. Degree of azimuthal or in-plane alignment for a typical tin deposit.

than both the calculated equilibrium form (15, 16) and that obtained by condensation from the vapor (17). The observed shape of the islands is determined by kinetic rather than equilibrium considerations. Tin has a body-center tetragonal crystal structure in which the {100} are the most densely packed planes and the {001} planes are considerably rougher on the atomic scale. Easier nucleation of new atomic layers may result in a higher growth rate in the [001] direction.[8] Adsorption or passivation might also be more pronounced on {100} planes. This would also result in faster growth in the [100] direction. In either case the islands would be bounded by the slowest growing crystal planes. This is a common situation in crystal growth (18). Tin islands electrodeposited from simple $SnCl_2$ electrolytes or from acidic $Sn(BF_4)_2$ electrolytes were not elongated in the [001] direction. Thus anisotropic passivation in the basic cyanide electrolyte may be crucial in determining the island growth morphology observed.

Figure 10 illustrates a couple of frequently observed features of the growth morphology of the tin islands. In the upper right hand corner a smaller island growing from an interior corner of the relief structure is shown. Below it is a larger island which had grown to nearly fill the groove between two steps. Scanning electron microscopy examinations of dozens of depositions revealed this to be the typical placement for islands this size. The question arises, why do not the islands grow over the steps as well as across the grooves. Since the islands have a square cross section they become as high as the steps at an early stage. If the island were fixed to the substrate and

[8] Computer simulation of the effect of driving potential on nucleation rates on different fcc faces and the relationship to surface roughness has been reported by G. H. Gilmer, *J. Cryst. Growth*, **42**, 3 (1977).

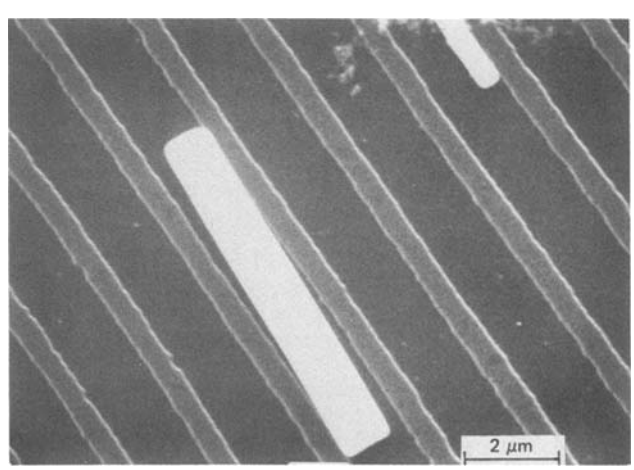

Fig. 10. SEM view of two electrodeposited tin islands. The view is not normal to surface so the larger island appears to overlap the step above it.

if electrodeposition occurred on all surfaces exposed to the electrolyte, islands nucleated at interior corners would grow over the adjacent steps and not remain entirely within a groove. The respective placement of a fixed and a mobile island nucleated at an interior corner are shown schematically in Fig. 11. An explanation for the growth morphology observed is that growth occurs on all sides exposed to the electrolyte, but the tendency toward faceting is so pronounced that the island physically pushes itself out into the groove toward the opposite step. This process would proceed until the island filled the breadth of a groove. It is proposed that this physical confinement of the growing islands by first one step and then the opposing step is responsible for the graphoepitaxial alignment observed. The details of how all this occurs are beyond the scope of this paper. Crucial microscopic and macroscopic aspects of the problem are uncertain. The microscopic mechanism for nucleation and growth in this system has not been investigated. The relative importance at various stages of diffusion of adions either across the cathodic substrate or across the growing crystal faces is not known. Also, the possibility of direct attachment of an ion in solution to a growth site cannot be excluded. Whether the angle of the interior corner is slightly greater than or less than 90° is not known. This information would be necessary in a more detailed model. Also, lateral potential and concentration gradients, as well as those normal to the substrate or to a crystal surface, would have to be considered. For all these reasons the details of the mechanism proposed could not be developed.

In Fig. 10 the misalignment of the large island with the grating is only 3°. Inspection will show that the nonlinearity of the relief structure on the submicron scale is considerably more than this. Apparently, some realignment occurred during growth. The model proposed requires some mobility of the islands and is consistent with the generally poor adhesion of the islands to the substrate. Sometimes a significant fraction of the islands were dislodged when the substrates were removed from the electrolyte and blown dry. To investigate further the role that the growth stage played in graphoepitaxial alignment, tin electrodepositions were observed *in situ*.

In situ analysis.—In situ observations were conducted using the apparatus and techniques described earlier. Observations based on postdeposition analysis were confirmed. There is a definite but not universal tendency for graphoepitaxial orientation and the graphoepitaxial islands generally undergo a period of confinement within a groove before overgrowing an adjacent step. New observations were also made. The only movement of the islands detected was that achieved by growth. When two islands coalesced, the merger was completed quickly. Usually nucleation only occurred immediately after the application of cathodic polarization.

Pulsed nucleation experiments were conducted to delineate further the roles of nucleation and growth in the graphoepitaxial alignment. This technique has been used to study nucleation rates (19). The idea is to nucleate during a brief pulse at a high cathodic polarization and to grow at a lower cathodic polarization, sufficient to ensure the growth of all the nucleated islands but not high enough to induce the nucleation of new islands. The experiment is outlined in Fig. 12. Tin islands deposited at cathodic polarizations greater than $|\eta| = 0.5$V nucleate randomly on the substrate, have a nearest neighbor distance less than the periodicity of the relief structure used in this work, and do not exhibit graphoepitaxy.

The results of the pulsed nucleation experiment are shown in Fig. 13. These photomicrographs were taken in the transmission mode. The substrate before deposition is shown in Fig. 13a. A defect in the substrate, visible near the center of the field of view, was located to ensure registration of successive photographs. During the nucleation pulse and most of the growth cycle, the microscope objective was raised above the solution to prevent interference with mass transport to the cathode surface. The substrate after a 70 msec nucleation pulse at $\eta_{nucl} = -0.67$V ($\eta_{grow} = -0.06$) is shown in Fig. 13b. A strong tendency toward graphoepitaxial alignment is apparent. Islands nucleated during an additional 100 msec nucleation pulse (Fig. 13c) were also largely graphoepitaxially aligned. The saturation nucleation site density is indicated in Fig. 13d on a different substrate for which $\eta_{nucl} = \eta_{grow} = -0.67$V. The graphoepitaxial alignment of the deposits in Fig. 13b and c is as complete as that frequently obtained at lower cathodic polarizations where $\eta_{nucl} = \eta_{grow} = -0.02$ to -0.40V. This strikingly emphasizes the role of the growth stage in achieving the graphoepitaxial orientation. The relationship between pulse duration and density of nucleation sites in Fig. 13b and c is linear (8×10^6 sec^{-1} cm^{-2}). This indicates that the duration of the nucleation pulses was long compared to the *RC* time constant of the cell. Nucleation was not observed to occur during the growth cycle. That nucleation occurred only during the nucleation pulse was confirmed when an inadvertent gas bubble shielded part of the substrate during a nucleation pulse. After the bubble was released, no islands were nucleated in that area during the growth cycle. It was found convenient to reduce the $SnCl_2$ concentration in the

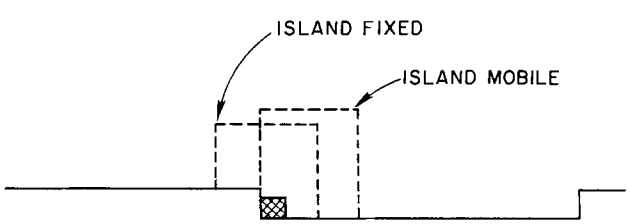

Fig. 11. Schematic indication of the growth habit of islands nucleated at an interior corner and which are subsequently either mobile or fixed to the substrate.

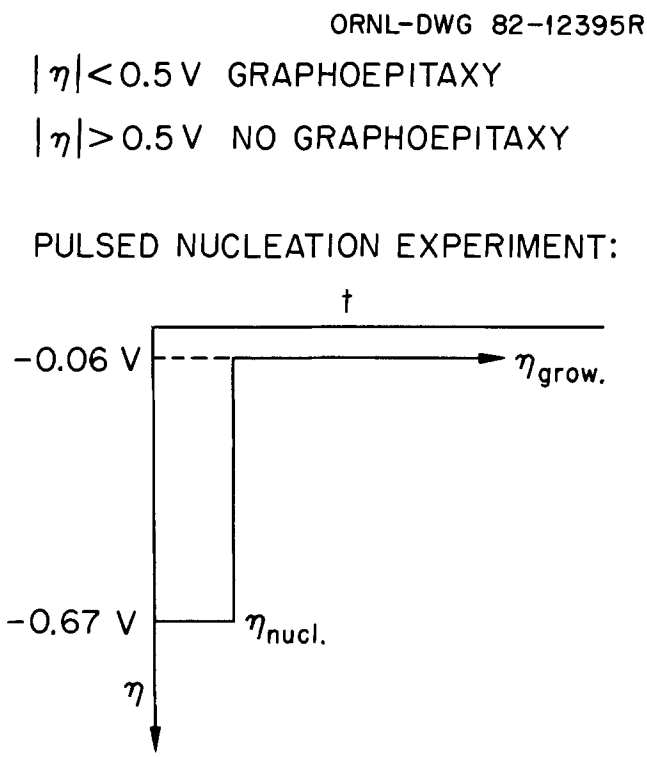

Fig. 12. Cathodic polarization vs. time for pulsed nucleation experiment.

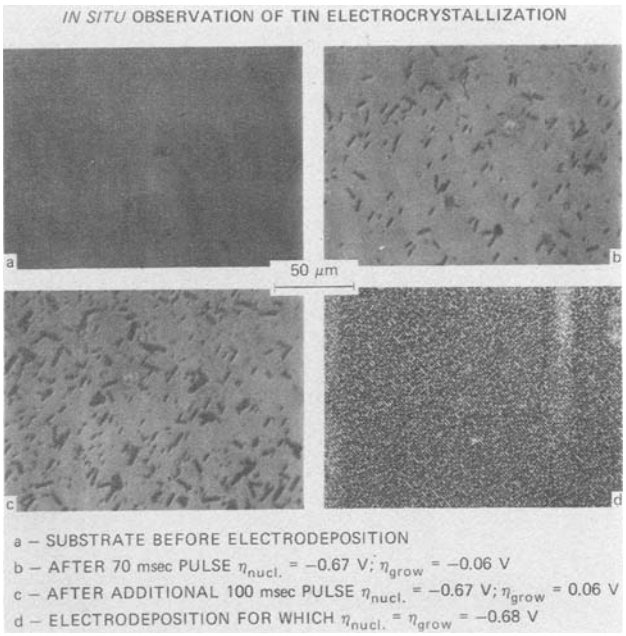

Fig. 13. *In situ* observation of pulsed nucleation experiment. a, Substrate before electrodeposition; b, after 70 msec pulse $\eta_{nucl} = -0.67$V, $\eta_{grow} = -0.06$V; c, after additional 100 msec pulse $\eta_{nucl} = -0.67$V, $\eta_{grow} = -0.06$V; d, electrodeposition on different substrate for which $\eta_{nucl} = \eta_{grow} = -0.68$V. A defect on the substrate (visible most clearly in the center of a was located before deposition to facilitate relocating the same area. b and c show 5 min of growth; d shows 45 sec of growth.

electrolyte by a factor of five in order to reduce the nucleation rate during the pulsed nucleation experiments. That the nucleation rate at the same overpotential was decreased at lower metal concentrations has been taken as indirect evidence for crystal growth by direct transfer of the metal ion from the electrolyte to the crystal lattice rather than by an intermediate surface diffusion process (19).

That graphoepitaxial orientation could occur during the growth stage was also confirmed by the graphoepitaxial alignment of seeded islands. Accidentally, a tear in the Mylar sheeting exposed a metallic part of the microscope objective to the electrolyte. Tin deposited in dendritic manner onto this surface. Turbulence broke up this structure and drove particulates of tin, smaller than the grating spacing, across the field of view of the microscope. Several of these particulates were observed to stick to the cathode and to grow in the graphoepitaxial orientation.

The physical confinement mechanism.—The results and observations reported here point to physical confinement as the mechanism for the graphoepitaxy of electrodeposited tin. The pronounced faceting of the tin islands and their linear growth morphology, are the decisive characteristics responsible for graphoepitaxial alignment. The role of the relief structure is principally to laterally confine laterally the islands. In this model the adhesion of the islands to the substrate must be weak enough to allow lateral motion of the islands away from surface steps before overgrowing these steps. Otherwise the island may overgrow the relief structure without reordering azimuthally.

Support for this model is drawn from several observations. In the first place, the fixing of the graphoepitaxial alignment at nucleation by anisotropy of surface energy appears questionable since the critical nucleus probably consists of only a few atoms. Furthermore, the unessential role of the nucleation and early growth stages was underscored by the pulsed nucleation experiments in which islands randomly nucleated on the surface showed a strong graphoepitaxial alignment. Similarly, graphoepitaxy was observed on patterned substrates whose potency in catalyzing nucleation had been largely lost after chemical etching of the substrate. The reluctance of the islands to overgrow a step and confined growth within a single groove were repeatedly observed both in postdeposition analysis and *in situ*. Nucleation at interior corners of the relief pattern, while possibly helpful in promoting island growth on the lower plateaus, is evidently not required for graphoepitaxy. It should be noted though that azimuthal ordering can start earlier via the pushing of the island against only one step if the island nucleates at an interior corner (see Fig. 10).

The axial texture may also be a result of the faceting. Any misalignment of the (100) plane with respect to the substrate would, in the extreme limit, provide only edge-like contact with the cathode surface. This configuration is unstable from the viewpoint of minimizing interfacial energy (including the electrostatic term) with respect to rotating the (100) facet flat against the substrate. The physical confinement mechanism proposed for the azimuthal or in-plane orientation is less exacting. Also the graphoepitaxial orientations may be lost either for individual islands or for whole areas by poor linearity of the relief structure or by insufficient island mobility. This would explain the superior completeness (essentially 100%) and acuity (<0.2°) of the axial texture, as opposed to the azimuthal or graphoepitaxial alignment.

While perhaps lacking the elegance of the mechanism invoking minimization of the anisotropic surface energy between a deposit and textured substrate (7), the mechanism proposed here retains a useful simplicity. It allows means of improving the quality of the deposits to be intelligently selected. The model proposed here indicates that efforts to improve the graphoepitaxial alignment should be directed at ensuring strong faceting and island mobility in addition to good linearity of the relief structure. It also provides guidance in determining which other materials may also be graphoepitaxially grown by this mechanism and what relief structure would be appropriate.

Graphoepitaxial tin films grown by this technique would not be continuous and hole free until an average thickness comparable to the distance between nucleated islands. For a graphoepitaxial deposit, internuclei spacing is limited by the periodicity of the relief structure. Obtainable periodicity was limited to more than 1.5 μm by the photolithographic techniques used in this work. However, square wave patterns with a periodicity of 0.16 μm have been reported using soft x-ray lithography (20).

The island mobility required for graphoepitaxy by the mechanism described here is a significant practical limitation as good adherence of deposited films to a substrate is usually desired. For some applications it might be possible to take advantage of the looseness of the deposit to remove the film and reuse the substrate. In any case, the poor adhesion requires serious consideration for any practical application.

Other systems.—Graphoepitaxial KCl islands grown from aqueous solution after the method described by Flanders and Smith (2) are shown in Fig. 14. The tendency of the islands to nucleate at interior corners and to remain confined within a groove are evident. These features were also noted by Flanders and Smith. This system has not been studied here in enough detail to distinguish between mechanisms. However, similarities to the growth morphology of electrodeposited graphoepitaxial tin are suggestive.

Faceted silicon and germanium (111) platelets grown by the VLS method on liquid metals by Klykov *et al.* (21) have been oriented with respect to microrelief structure by means of capillary forces between the microrelief and the crystallites. They have called

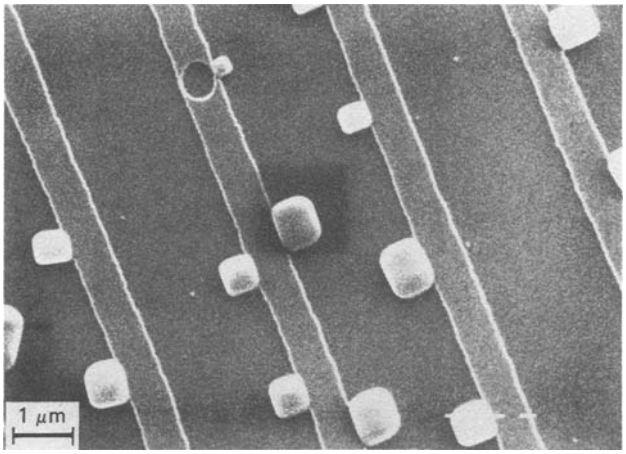

Fig. 14. Graphoepitaxial KCl islands grown from aqueous solution.

this effect diataxy. This is also an example of graphoepitaxial orientation achieved by confinement of faceted crystallites. Geis, Tsaur, and Flanders (5) have also graphoepitaxially grown germanium by the VLS method, but could not distinguish between mechanisms were not reported.

Mechanisms other than physical confinement of faceted crystals can also be effective in producing graphoepitaxy. For example, the role of minimization of surface energy is apparent in the graphoepitaxial alignment of liquid crystals (3). However, it has not been convincingly demonstrated in any system involving the nucleation of a new phase that surface energy anisotropy alone can align crystals with respect to a relief structure.

The mechanism for the graphoepitaxy of silicon films recrystallized using a CW laser or a strip heater is more involved. It has been proposed that the role of the relief structure is to lower the Gibbs free energy of the graphoepitaxially oriented grains via the interfacial energy term (8). These grains then preferentially survive a partially molten stage. Encapsulation and at least partial heating by radiation are necessary for the graphoepitaxial recrystallization of silicon films. Under these circumstances the dynamic melting and solidification generated by the higher reflectivity of the liquid phase produces "worms" of solid rather than faceted crystallites (22, 23). Physical confinement probably plays no role in this process. Less detailed work on the effect of relief structure on the growth of silicon by sputter deposition (24) and from liquid solution (25) has also been reported.

Summary

The major points of this paper are summarized as follows:

1. Reactive ion etched surface relief structure enhanced electrodeposition for all investigated metals (Sn, Cu, Pb, In, Zn). The observed placement of small tin and copper islands is consistent with nucleation at interior corners of the relief structure.

2. Graphoepitaxial electrodeposition of tin islands has been observed.

3. Graphoepitaxial orientation of the tin islands can occur after nucleation during growth.

4. It is proposed that the graphoepitaxy of the tin islands is due to the physical confinement of the linear, highly faceted deposits by the relief structure in the substrate.

As all crystal growth processes are necessarily nonequilibrium and faceting is commonly introduced by growth rate anisotropies, the possibility that the mechanism of physical confinement of faceted islands is responsible for graphoepitaxy in other reported systems has been discussed. It is frequently hard to distinguish on available evidence between this and other mechanisms.

Acknowledgments

The author is grateful to D. H. Lowndes for crucial support in the early phases of this project, to Burl Cavin for some of the x-ray diffraction characterization reported here, and to Milica Petek who generously provided the use of her electrochemical equipment and who also gave much useful advice on electrochemical techniques. The author would also like to thank Michael Geis and Henry Smith for useful conversations on graphoepitaxy and Eugene Kelly, F. W. Young, Jr., and Milica Petek for their suggestions on the manuscript.

This research was sponsored by the Division of Materials Science, U.S. Department of Energy under contract W-7405-eng-26 with the Union Carbide Corporation.

Manuscript submitted Aug. 6, 1982; revised manuscript received *ca.* Feb. 15, 1983. This was Paper 154 presented at the Montreal, Que., Canada, Meeting of the Society, May 9-14, 1982.

Any discussion of this paper will appear in a Discussion Section to be published in the December 1983 JOURNAL. All discussions for the December 1983 Discussion Section should be submitted by Aug. 1, 1983.

Oak Ridge National Laboratory assisted in meeting the publication costs of this article.

APPENDIX

Nucleation

By thermodynamics the critical radius for nucleation r^* is given by

$$r^* = \frac{-2\sigma}{\Delta G_v} \qquad [A\text{-}1]$$

where σ is the Gibbs free energy per unit interfacial area and ΔG_v is the Gibbs free energy difference per unit volume between the deposit in the condensed and nutrient phase. Equation [A-1] can only be applied to large nuclei (> 100 atoms or $r^* > 1$ nm) where bulk thermodynamic properties are relevant. There are also difficulties in obtaining σ and ΔG_v. Interfacial energies between metals and electrolytes are not well known, but interfacial energies in general fall in the range 10^2-10^3 erg/cm^2 (26). In addition to distinguishing between the observed rest potential and the equilibrium potential for tin electrodeposition, there are other problems in obtaining ΔG_v. Even immediately after application of a pulsed cathodic polarization, when resistance and concentration polarizations are not important, the microscopic interpretation of the polarization depends on the kinetics of nucleation. Nucleation is generally taken to proceed first by the transfer of metal ions across the double layer, then followed by diffusion of the adions over the surface of the electrode (27). In this case ΔG_v for Eq. [A-1] is that between the bulk condensed phase and the adions. It is not known in the tin electrodeposition considered here whether the rate-limiting step in nucleation is in the charge transfer process or in the formation of the critical nucleus from the adions. In other words, there is an unknown Gibbs free energy difference between the ions in electrolytic solution and the surface adions. If this difference were small so that one could take $\Delta G_v = 2e\eta/v$, (v = atomic volume) for the electrodeposition of stannous tin, Eq. [A-1] could be evaluated using the range of surface energies estimated above. For $\eta = -0.50$V, the highest continuous cathodic polarization for which graphoepitaxy was obtained, Eq. [A-1] implies $r^* = 0.04$-0.40 nm. Thus for r^* to be comparable to the corner radius of the interior corners (~ 5 nm), then $|\Delta G_v| << |2e\eta/v|$.

To obtain an upper limit on the size of the critical nucleus, additional information is required. This in-

sight is provided by the change in nucleation density and placement as cathodic polarization is increased. That the nucleation site density increases as $|\eta|$ increases is a direct qualitative indication that $|\Delta G_v|$ is also increasing. However, the change of nucleation site placement from interior corners to flat surfaces as $|\eta|$ is increased can be more directly compared to theory. It will be shown that for the tin electrodeposition reported here such a transition in nucleation morphology is inconsistent with a critical radius comparable to or larger than the acuity of the relief structure.

Nucleation at interior corners of relief structure is similar to nucleation at cleavage steps on single crystal substrates. Preferential nucleation at cleavage steps is a well-known phenomenon in vapor deposition. This effect was analyzed in the large critical nucleus limit by Chakraverty and Pound (14) using thermodynamic methods. They derived the expression

$$\frac{I_c}{I_F} = g \exp\left(4\pi\sigma^3/3\,\Delta G_v^2\, kT\right)\left[K(\theta) - F(\theta)\right] \quad \text{[A-2]}$$

for the ratio of the nucleation rates at interior corners I_c to that on the flat surface I_F. Here g is the fraction of surface sites occupied by the corners, while $K(\theta)$ and $F(\theta)$ are contact angle functions for a corner and for a flat surface, respectively. In applying Eq. [A-2] to etched surface relief structure, it must be kept in mind that the fabricated steps used here are not sharp on the atomic scale as are cleavage steps.

Equation [A-2] can be formally applied to the case of tin electrodeposition. The contact angle of the critical nucleus is taken to be 90°, that of the macroscopic islands. For $\theta = 90°$, $K(\theta) - F(\theta) = 1$ (14). The contact angle term in Eq. [A-2] will decrease for larger θ. For a periodicity of 2.7 μm, and a corner radius of 5 nm, g is taken to be 6×10^{-3}, the ratio of corner area to total surface area. The results obtained are fairly insensitive to the value of g chosen. Uncertainty in the value of σ is more important as this term appears in an exponential. Results will be calculated for the extreme values of σ expected, 10^2 erg/cm^2 and 10^3 erg/cm^2. That portion of the cathodic polarization occurring between the adions and a hypothetical bulk deposit shall be designated as η_n. The condition $I_c = I_F$ is met at $\eta_n = -0.05$V for $\sigma = 10^2$ erg/cm^2 and at $\eta_n = -1.59$V for $\sigma = 10^3$ erg/cm^2. This information is summarized in Table A-1. The corresponding critical radii for nucleation r^* are included. These r^* values are smaller than the corner radius of the relief structure. In fact, these values are smaller than can justifiably be derived from a thermodynamic expression such as Eq. [A-1]. However, this result does indicate that as cathodic polarization is increased (r^* decreased) the transition out of the thermodynamic regime ($r^* > 1$ nm) must occur before the transition to nucleation on the flat surface. This result suggests a different mechanism for the transition to nucleation on the flat surface than considered by Chakraverty and Pound. At some η_n the configuration critical for nucleation must become small enough compared to the acuity of the relief structure that the residual catalyzing effect of the interior corners on nucleation is counterbalanced by the statistical abundance of heterogeneous nucleation sites on the flat surface.

In summary, it appears that nucleation at interior corners of the relief structure and graphoepitaxial orientation of the deposited islands were obtained when the critical nucleus was significantly smaller than the acuity of the relief structure. Nucleation rate measurements in other electrodeposition systems ($|\eta| < 0.1$V) also indicate only a small integer number of atoms in the critical nucleus (19, 28). The small size of the critical nucleus indicates that graphoepitaxial alignment at nucleation is unlikely.

Table A-I. Table of corner decoration parameters

σ^a (erg/cm^2)	$\eta_n\left(\frac{I_c}{I_F} = 1\right)$(V)	r^* (mm)
10^2	−0.05	0.43
10^3	−1.59	0.14

[a] Interfacial energy between deposit and electrolyte.

REFERENCES

1. M. W. Geis, D. C. Flanders, and H. I. Smith, *Appl. Phys. Lett.*, **35**, 71 (1979).
2. H. I. Smith and D. C. Flanders, *ibid.*, **32**, 349 (1978).
3. D. C. Flanders, D. C. Shaver, and H. I. Smith, *ibid.*, **32**, 579 (1978).
4. M. W. Geis, D. A. Antoniadis, D. J. Silversmith, R. W. Mountain, and H. I. Smith, *ibid.*, **37**, 454 (1980).
5. M. W. Geis, B-Y. Tsaur, and D. C. Flanders, *ibid.*, **41**, 526 (1982).
6. L. S. Darken and D. H. Lowndes, *ibid.*, **40**, 954 (1982).
7. D. C. Flanders, Ph.D. Thesis, (MIT 1978); reprinted as MIT Laboratory Technical Report 533, 1978.
8. H. I. Smith, C. V. Thompson, M. W. Geis, R. A. Lemmons, and M. A. Bosch, Submitted to *This Journal;* H. I. Smith and M. W. Geis, Abs. 155, p. 249, The Electrochemical Society Extended Abstracts, Vol. 82-1, Montreal, Que., Canada, May 9-14, 1982.
9. R. Anton, H. Poppa, and D. C. Flanders, *J. Cryst. Growth*, **56**, 433 (1982).
10. H. W. Lehman and R. Widmer, *Appl. Phys. Lett.*, **32**, 163 (1978).
11. J. O'M. Bockris and G. A. Razumney, "Fundamental Aspects of Electrocrystallization," Plenum Press, New York (1967).
12. J. P. Sullivan and A. E. Pavlish, *Metals and Alloys*, **11**, 131 (1940).
13. F. L. Binsbergen, in "Progress in Solid State Chemistry," Vol. 8, J. O. McCaldin and G. Somorjai, Editors, p. 189, Pergamon Press, New York (1973).
14. R. K. Chakraverty and G. M. Pound, *Acta Metall.*, **12**, 851 (1964).
15. G. A. Wolf and J. G. Gualtieri, *Am. Mineral.*, **47**, 562 (1962).
16. R. Lachman, *J. Cryst. Growth*, **5**, 354 (1969).
17. K. Kimoto and I. Nishida, *Jpn. J. Appl. Phys.*, **6**, 1047 (1967).
18. See, for example, N. Cabrea and R. V. Coleman, in "The Art and Science of Crystal Growing," J. J. Gilman, Editor, p. 3, John Wiley and Sons, New York (1963).
19. A. Milchev, E. Vassileva, and V. Kertov, *J. Electroanal. Chem.*, **107**, 323 (1980); A. Milchev and E. Vassileva, *ibid.*, **107**, 337 (1980).
20. D. C. Flanders, H. I. Smith, H. W. Lehman, R. Widmer, and D. C. Shaves, *Appl. Phys. Lett.*, **32**, 112 (1978).
21. V. I. Klykov and N. N. Sheftal, *Acta Phys. Acad. Sci. Hung.*, **47**, 169 (1979); N. N. Sheftal, *ibid.*, **47**, 191 (1979); and V. I. Klykov and N. N. Sheftal, *J. Cryst. Growth*, **52**, 687 (1981).
22. M. A. Bosch and R. A. Lemmons, *Phys. Rev. Lett.*, **47**, 1151 (1981).
23. W. G. Hawkins, J. A. Black, and C. H. Griffiths, in Materials Research Society Proceedings, November 1981.
24. C. Weissmantel, *J. Vac. Sci. Technol.*, **18**, 179 (1981).
25. H. Mori, *Jpn. J. Appl. Phys.*, **20**, L905 (1981).
26. L. E. Murr, "Interfacial Phenomena in Metals and Alloys," Addison-Wesley Publishing Co., Reading, MA (1975).
27. J. O'M. Bockris and A. Damjanovic, in "Modern Aspects of Electrochemistry," No. 3, J. O'M. Bockris and B. E. Conway, Editors, p. 224, Butterworths, Washington (1964).
28. R. Lacman and H.-J. Randig, *J. Cryst. Growth*, **17**, 97 (1972).

Photoelectrochemical and Microprobe Laser Raman Studies of Lead Corrosion in Sulfuric Acid

Kathryn R. Bullock,* Glenn M. Trischan,* and Robert G. Burrow

Johnson Controls, Incorporated, Milwaukee, Wisconsin 53201

ABSTRACT

Microprobe laser Raman spectroscopy and photoelectrochemistry are two techniques which have recently been applied to the study of lead corrosion films. In this paper, we have used these techniques to study lead corrosion between 0.4 and 1.0V (*vs.* $Hg/Hg_2SO_4/1M\ H_2SO_4$) in $1M\ H_2SO_4$, where lead oxides form beneath a $PbSO_4$ film. Photoconductivity spectra were used to determine the bandgap energies of the lead oxides *in situ* during the constant-potential corrosion. Cross sections of the corrosion films were then analyzed by microprobe laser Raman spectroscopy. In addition, open-circuit potential decay curves of lead corrosion films were recorded. The results elucidate the mechanism of oxide film formation and explain discrepancies found in previous photoelectrochemical studies of lead corrosion.

The corrosion of the lead grid at the lead dioxide electrode is one of the major causes of failure of lead-acid batteries. Lead corrosion in lead-acid batteries is quite complex for several reasons. First, the acid concentration and voltage at the positive electrode can vary dramatically during battery operation. The electrolyte can drop from 30-40 weight percent (w/o) H_2SO_4 to nearly pure water under some conditions and the potential at the positive electrode can change by nearly a volt. Second, when a $PbSO_4$ film forms on the surface of the grid, it acts as a semipermeable, resistive membrane (1, 2) creating both a potential and a concentration gradient across the corrosion film. Changing conditions across the film favor different reactions, so that multiple corrosion products form (3). These products include lead sulfate, basic lead sulfates, and lead oxides. Third, the lead oxides form a complex series which can be represented by the general formula PbO_n, when $1 < n < 2$. Two polymorphs have been identified in lead corrosion films for both PbO (orthorhombic and tetragonal) and PbO_2 (α or rhombic and β or tetragonal). PbO_2 may also be amorphous. A variety of intermediate oxides, such as Pb_3O_4 and Pb_2O_3, have also been found. Burbank (4) suggests that these intermediate oxides are actually chemical combinations of PbO and PbO_2, which she designates $PbO_t \cdot xPbO_2$, and that an "infinitude of stoichiometries" may form.

Many authors have studied the mechanisms of lead corrosion in H_2SO_4, and reviews of the literature are available (5-7). Pavlov has separated lead corrosion films into 3 distinct composition regions related to oxidation potential, based on his x-ray diffraction and electrochemical studies of lead anodized in $1N\ H_2SO_4$ (8). From -950 to -300 mV *vs.* Hg/Hg_2SO_4, the corrosion film consists only of $PbSO_4$ crystals. From -300 to $+900$ mV, the corrosion film consists of $PbSO_4$ and an inner layer of tetragonal PbO. Pavlov has designated this the $Pb/PbO/PbSO_4$ electrode. He has also identified small amounts of $PbO \cdot PbSO_4$, $3PbO \cdot PbSO_4 \cdot H_2O$, $5PbO \cdot 2H_2O$ or orthorhombic PbO and α-PbO_2 in films formed in this potential range. Above 950 mV, α-PbO_2, t-PbO and β-PbO_2 become the predominant corrosion products.

The main techniques used in lead corrosion studies have been electrochemical measurements, x-ray diffraction, and electron microscopy. Excellent studies have been accomplished using these techniques. However, the development of greater knowledge about lead corrosion processes has been frustrated by the following limitations of these methods. First, it has been difficult to resolve the signals from the many chemical species which form in the corrosion film. Second, it has been difficult to analyze separately the distinct corrosion layers which are evident in microscopic examinations of film cross sections. Finally, it has been difficult to determine the time sequence of species formation because only electrochemical methods could be used *in situ* to monitor the corrosion process.

Recently, two new techniques have been used to overcome some of these limitations: laser Raman spectroscopy and photoelectrochemistry. In this paper, we have used both techniques to study the corrosion of lead at potentials between 400-1000 mV (*vs.* $Hg/Hg_2SO_4/1M\ H_2SO_4$), where the $Pb/PbO/PbSO_4$ electrode is formed. Our results show that these methods can be used to obtain new information about the corrosion process. Before presenting these results, however, we will give some background information about the methods themselves.

Laser Raman spectroscopy can be used either *in situ* or *ex situ* to identify lead corrosion products. In either approach, laser Raman spectroscopy has several advantages over x-ray diffraction for studying lead battery reactions. In x-ray diffraction, the pattern for $PbSO_4$ has many intense lines which coincide with those of other lead compounds. Furthermore, tetragonal PbO cannot be unambiguously identified because its strongest diffraction lines overlap with those of α- and β-PbO_2 (8). In contrast, the primary Raman signal for $PbSO_4$, at about 980 cm^{-1}, is a sharp intense singlet far downfield from the primary and secondary signals for the lead oxides at 150, 290, and 340 cm^{-1}. Secondary $PbSO_4$ peaks at 440, 455, 605, and 644 cm^{-1} do not pose serious interference problems with the important secondary spectrum of the lead oxides. PbO can be easily identified by the presence of an intense peak at about 150 cm^{-1}. Although this peak is not readily attributed to a specific crystal form, a secondary band at 340 cm^{-1} can be used to identify tetragonal PbO. Orthorhombic PbO can be identified, using the secondary peak at 290 cm^{-1}, with greater sensitivity than can tetragonal PbO. This is advantageous due to the relatively small quantities of o-PbO usually present in lead corrosion films. Although some differences in the spectra of the PbO compounds can be observed at frequencies below 100 cm^{-1}, low intensities and sloping baselines minimize the utility of such peaks. Similarly minor peaks observed above 300 cm^{-1} in the reference spectra of both PbO compounds are of insufficient intensity for use in Raman microprobe studies. One disadvantage of laser Raman spectroscopy is that it is not very sensitive to α- and β-PbO_2, since these are self-absorbing compounds. α- and β-PbO_2 are more easily identified by x-ray diffraction. It is, therefore, sometimes necessary to use both x-ray diffraction and laser Raman spectroscopy to fully characterize a sample.

Most of the laser Raman spectroscopic studies of lead corrosion have been done using the *in situ* approach (9, 10). This approach has two advantages. First, it

* Electrochemical Society Active Member.

Key words: semiconductor, battery, photoconductivity, oxidation.

eliminates the possibility of changes occurring in the corrosion product when the sample is removed from the cell and prepared for analysis. Second, it permits the study of progressive changes in the reaction products during an electrochemical experiment. Varma, Cook, and Yao recently demonstrated these advantages in their study of changes in lead-battery active materials during the formation process (11). A disadvantage of the *in situ* approach is that only a thin surface layer of the corrosion film can be analyzed. Another possible problem, which has not yet been discussed in the literature, is that the laser beam may affect the corrosion process. We shall discuss this problem later in relation to our photoelectrochemical studies.

In order to analyze subsurface corrosion films, it has traditionally been necessary either to cut the electrode into cross sections or to remove successive layers of material. However, material removal is difficult and cross-sectioned layers are generally too thin to analyze separately. Recently, we have used microprobe laser Raman spectroscopy on electrode cross sections to overcome this problem (12). The compositions of the multiple layers comprising the corrosion film can be resolved if the layers are at least 2 μm thick. This is possible because the laser beam has a diameter of only 1 μm. For comparison, we have been able to achieve a spatial resolution by micro x-ray diffraction techniques of only about 10 μm. Microprobe laser Raman spectroscopy has been described (13-17) and reviewed (18) in the literature.

Another new approach to studying subsurface lead corrosion films is photoelectrochemistry. Photoelectrochemical methods were first introduced by Pavlov and co-workers (19-21), who pointed out that the lead oxides which form underneath the lead sulfate film are photoactive semiconductors. Because sulfuric acid and lead sulfate are transparent, photocurrents are produced in the lead oxide layer when a corroded lead electrode is irradiated with visible light. Photoelectrochemistry can, thus, be used to study the growth of the lead oxide layers underneath the lead sulfate film *in situ* between -400 and 1200 mV *vs.* $Hg/Hg_2SO_4/H_2SO_4$. Pavlov has published data on the effects of potential, corrosion time, and amount of irradiation on photocurrents of lead electrodes corroded in 1*N* H_2SO_4 for 1 hr or more. Recently, Fletcher and Matthews (22) have measured both the corrosion current and photocurrent in potential sweep experiments on lead electrodes in 4.2m H_2SO_4, and Caldera *et al.* (23) have done similar experiments in 0.1*N* KOH. Peter (24) measured photocurrents of α-PbO_2 films as they were being reduced to lower oxides.

The bandgap energy of a photoactive semiconductor can be determined by measuring the photocurrent as a function of light wavelength. The longest wavelength at which the photocurrent appears is a measure of the light energy required to excite an electron from the valence to the conduction band, or bandgap energy. The plot obtained is generally called the photoconductivity spectrum.

Izvozchikov (25) has published photoconductivity spectra for both powder and ceramic forms of orthorhombic PbO, tetragonal PbO and $PbO_{1.34}$, and mixtures of these compounds. He also shows that the bandgap energy decreases with increasing O/Pb ratio for PbO_n where $1 \leq n \leq 2$. Others have also published photoconductivity spectra for orthorhombic and tetragonal PbO (26-29).

Based on these results, it seems reasonable that the composition of lead corrosion films could be determined from bandgap energies obtained by measuring the photocurrent as a function of light energy. Recently, Barradas *et al.* (30) have done some experiments of this type on lead corroded at 400 and 800 mV (*vs.* $Hg/Hg_2SO_4/0.5M\ H_2SO_4$) in 0.5M H_2SO_4 for 30 min. They measured a bandgap energy of 2.75 eV (450 nm) and concluded that the photoactive subsurface oxide layer is orthorhombic PbO.

This conclusion is in disagreement with Pavlov's results as well as much of the lead corrosion literature. Although he has not published data on the effect of light wavelength on photocurrent, Pavlov has stated that the photocurrents are produced with light of wavelengths shorter than 650 nm (19), which corresponds to a bandgap energy of 1.9 eV. On the basis of this result and his x-ray diffraction studies (8), Pavlov concluded that the lead oxide layer is tetragonal PbO. Peter (24) measured a bandgap energy of 1.8 eV on partially reduced α-PbO_2 films and noted the close correspondence of his results with those of Pavlov.

Experimental

Electrochemistry.—Lead electrodes approximately 1.3 cm^2 were made from 99.9% pure lead foil. Analysis of the foil by ICP emission spectroscopy showed that the main impurities were Sn and Cu with smaller quantities of Ag, Ni, and Cd. The electrodes were washed with acetone and deionized water and dried with a clean tissue. A three electrode potentiostat (Princeton Applied Research Model 173) was used to corrode the electrodes at constant potentials between 200 and 1000 mV *vs.* an $Hg/Hg_2SO_4/1M\ H_2SO_4$ reference electrode. The potential of our reference electrode is about 26 mV higher than Pavlov's electrode and 22 mV lower than Barradas' electrode (31). The counterelectrode was a cast lead-calcium-tin alloy grid, which was bent to encircle the working electrode. The electrolyte, 1.0M H_2SO_4, was made from reagent grade H_2SO_4 and distilled deionized H_2O. Unless otherwise specified, the experiments were done at room temperature (about 24°C). The cell was constructed with a quartz optical window on one side. It had a water jacket surrounding all portions, except the window, to allow temperature control at high temperatures. Currents were recorded using a Houston Instrument Model 2000 recorder. A Princeton Applied Research Model 175 Universal Programmer was used to provide a time base for the x-axis.

Photoelectrochemistry.—The light source, a 1 kW tungsten-halogen lamp, was operated at full intensity throughout the experiments. The position of the lead electrode was adjusted so that the light spot just covered the electrode surface. A McPherson Model 270 monochromator with a continuous scan attachment was used to scan the spectrum at a rate of 0.2 nm/sec. A continuous scan gives more information than a curve drawn from a few discrete points, as in Barradas' experiments (30). When an electrode held in the dark at constant potential is illuminated, the small d-c photocurrent produced is superimposed on a much larger d-c corrosion current, making the photocurrent difficult to detect. We increased the sensitivity of the measurement by placing a Princeton Applied Research Model 125A light chopper between the exit slit of the monochromator and the cell window. The light chopper converted the d-c photocurrent to an a-c signal of 169 Hz. A Princeton Applied Research Model 5101 lock-in amplifier, tuned to the same frequency, filtered the d-c corrosion current and amplified the photocurrent.

One limitation of this instrumentation was that we were unable to measure directly the intensity of the light coming from the monochromator. Since the photocurrent is a function of light intensity, the photoconductivity spectrum should be corrected for changes in light intensity with wavelength. This correction was done manually using the lamp spectrum specified by the manufacturer (Fig. 1). We are presently modifying our instrumentation to allow us to measure and automatically correct for the light intensity. This modification will increase the accuracy of the bandgap measurement.

Microprobe laser Raman spectroscopy and x-ray diffraction analysis.—Samples were prepared for laser

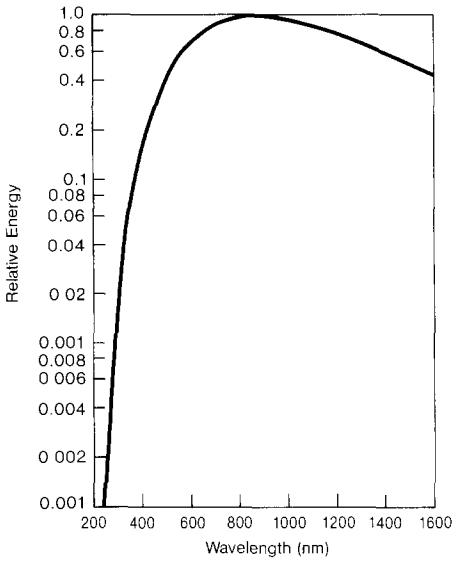

Fig. 1. Relative spectral distribution of tungsten-halogen lamp operated at full intensity.

Raman microprobe analysis by dividing each sample electrode laterally. One-half of the electrode was mounted in epoxy, cut, and polished as a typical metallographic sample for observation of corrosion layer cross sections. The remaining half of the electrode was preserved in its original condition for surface examination.

Laser Raman microprobe analyses were performed using an Instruments SA, Incorporated, MOLE at Walter C. McCrone Associates, Incorporated. For general observations, a 1 μm diam beam of radiation (514.5 nm) from a Spectra Physics Model 164 argon ion laser operated at 10 to 40 mW power output was employed. A 10Å half maximum band width (HBW) interference filter was used to remove plasma lines from the illumination beam. Control of the polarization orientation of the laser beam was accomplished by inclusion of a mica halfwave plate in the optical path of the illumination source. Samples were imaged at 1100× using a 100×, 0.90 numerical aperature Leitz objective. Vibrational frequencies in the range of 100-1200 cm^{-1} were scanned at 42 cm^{-1}/min. A Type R3F4 Hamamatsu photomultiplier cooled to −30°C was used to detect the scattered radiation passing through the instrument monochromator. Signal measurement was accomplished using a Princeton Applied Research Model 1140A Quantum Photometer.

Pertinent lead reference compounds were obtained from several sources and examined by x-ray powder diffraction to verify their identity prior to Raman analysis. Tetragonal (Code Number 2899-1) and orthorhombic (Code Number 2899-2) lead monoxide were obtained from the National Lead Company as reference compounds. Baker Analyzed Reagent (No. 5-2334) was used for the Pb_3O_4 source. Lead sulfate was procured as Fisher Certified Reagent (No. 75383). A General Electric XRD-6 x-ray powder diffractometer with a copper target radiation source was used in all cases. Authentication of compound identity was completed by comparison of peak positions and intensity ratios of the sample material patterns with reference patterns in the JCPDS powder diffraction file. Good agreement between the corresponding sample and reference diffraction patterns was found for all materials.

Initially the Raman activity of various lead compounds was studied using standard macro scale Raman techniques. Powders of reference compounds were pelletized with KBr for analysis. Pellets were spun during irradiation to minimize potential laser heating damage. The source of 488 nm radiation was a Spectra-Physics Model 164 argon-ion laser operating at 100 mW or less. Spectra were recorded using a Spex Model 1401 Raman spectrometer with a photon counting detection system. Comparable spectra of individual unmounted particles of reference compounds were collected using low power (≤100 mW) irradiation at 514.5 nm with the MOLE instrument previously described. The reference spectra generated during these experiments are summarized in Table I for the 100-1200 cm^{-1} range. Reasonable agreement for all strong and medium intensity bands was observed for all reference materials. Weak intensity bands, observed with varying degrees of success, were not used for this study.

The reference Raman spectra tabulation shows a significant advantage of Raman spectroscopy in the lead system as well as one of the serious general limitations of x-ray diffraction. Seemingly pure materials based on x-ray diffraction analyses are found to contain various impurities in three out of four materials examined using Raman spectroscopy. Raman spectroscopy appears to offer a significant improvement in sensitivity to mixtures of Raman active lead compounds compared to x-ray diffraction techniques.

Following the MOLE analysis, microscopic particles were picked from the corrosion film and prepared for micro x-ray powder diffraction analysis using standard procedures described by McCrone (32). The spatial resolution of particle picking techniques is approximately 10 μm. X-ray powder diffraction patterns were recorded for approximately 4 hr from samples under vacuum, irradiated at the spot focus of a fine-focus copper target x-ray tube. The diffraction patterns were identified by comparison with reference patterns in the JCPDS x-ray powder diffraction file.

Results and Discussion

Photoelectrochemistry.—Figure 2 shows photoconductivity spectra for an electrode corroded 0.5-6.5 hr at 800 mV. A significant increase in photocurrent occurs beginning at about 440 nm. This signal is even more pronounced when the photocurrent is normalized for constant light intensity by multiplying the photo-

Table I. Summary of Raman spectral features of selected lead compounds, 100-1200 cm^{-1}

Compound	Macro-Raman Spectra[a]		MOLE Raman Spectra[b]	
	ν (cm^{-1})	Intensity[c]	ν (cm^{-1})	Intensity[c]
Tetragonal PbO	148	VS	147	VS
	342	S	340	S
	—	—	478[d]	VW, B
	—	—	543[d]	W
Orthorhombic PbO	144	VS	143	VS
	288	S	288	VS
	341[e]	W	—	—
	385	M	386	M
	424	W	424	W
Pb_3O_4	—	—	120	W
	—	—	145	W
	—	—	167	W
	—	—	229	W
	310	W	317	W
	388	W	392	W
	478	M	479	M
	548	S	550	S
	1097	M-W, B	1097	M-W, B
$PbSO_4$	106	W	—	—
	138	VW, B	—	—
	157	VW, B	—	—
	191	VW, B	—	—
	443	M	440	M
	454	M	450	M
	608	MW	607	MW
	644	W	643	W
	981	VS	979	VS
	1065[f]	WB	1064[f]	W, B
	1158[f]	MB	1160[f]	M, B

[a] 488.0 nm argon ion laser excitation radiation, analysis of powder in KBr pellet.
[b] 514.5 nm argon ion laser excitation radiation, analysis of individual particles.
[c] VS = very strong, S = strong, M = medium, W = weak, and B = broad.
[d] Trace impurity of Pb_3O_4.
[e] Trace impurity of t-PbO suspected.
[f] Trace impurity of $Pb(HSO_4)_2$ suspected.

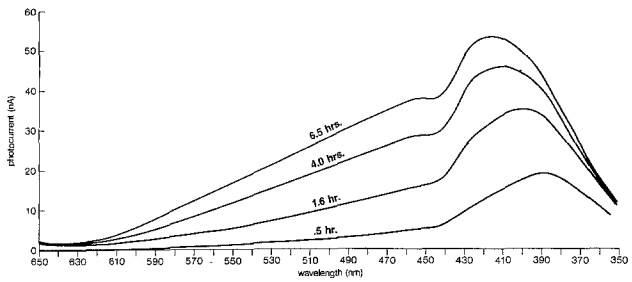

Fig. 2. Photoconductivity spectra of lead electrode corroded at 800 mV in 1M H_2SO_4 at room temperature.

current in Fig. 2 by the ratio of maximum light intensity to light intensity at a given wavelength, using the data in Fig. 1.

The normalized photoconductivity spectrum for 0.5 hr corrosion is shown in Fig. 3. This curve is very similar to data published by Barradas (30) for the same corrosion time. Extrapolation of the photocurrent to the baseline gives a wavelength of 444 nm, which corresponds to a bandgap energy of 2.8 eV. Barradas measured a bandgap energy of 2.75 eV (450 nm) and concluded that the corrosion product was orthorhombic PbO. The literature contains values of 2.6-2.9 eV (26-30) for orthorhombic PbO. The signal peaks at about 380 nm and then declines at shorter wavelengths. Keezer (26) attributes this decline to surface recombination.

Figure 2 shows that, in addition to the dominant signal, a long tail is also present which begins at around 600 nm. Barradas' curves also show some evidence of this signal, but since his curves are drawn from only 4-5 discrete points, the tail is not as obvious. This secondary signal grows as the corrosion time increases. After several days, it becomes dominant, as shown in Fig. 4.

After normalizing the photocurrents in Fig. 4 to account for the change in light intensity with wavelength, we obtained the curve in Fig. 5. Extrapolation of the signal to the baseline gives a bandgap energy of 621 nm or 2.0 eV. This is close to Pavlov's value of 650 nm or 1.9 eV (19), which was determined on samples

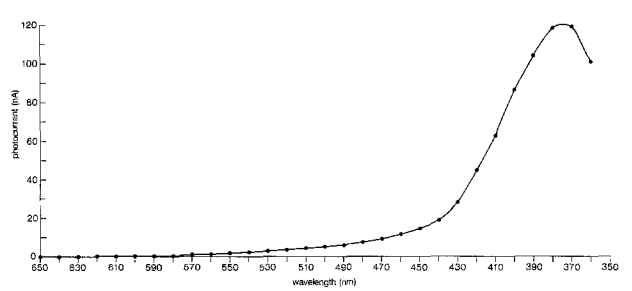

Fig. 3. Photoconductivity spectrum of lead electrode corroded at 800 mV for 0.5 hr, shown in Fig. 2, corrected for light intensity.

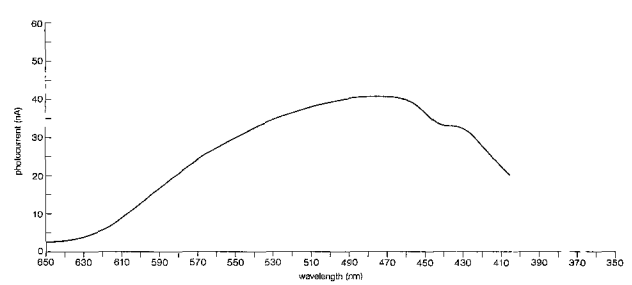

Fig. 4. Photoconductivity spectrum of lead electrode corroded at 800 mV for 72 hr in 1M H_2SO_4 at room temperature.

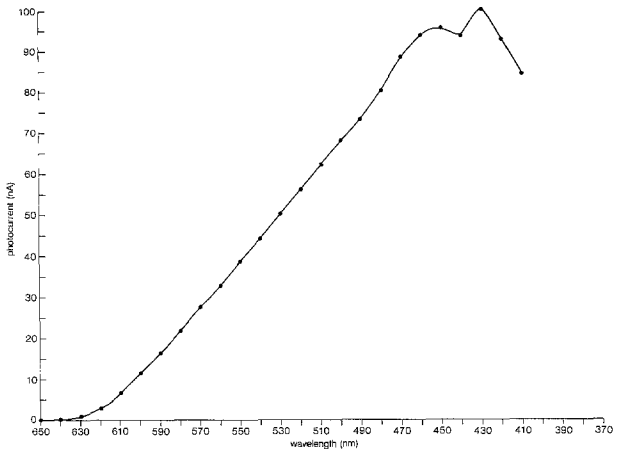

Fig. 5. Photoconductivity spectrum shown in Fig. 4, corrected for light intensity.

corroded for 1 hr or longer. Bandgap energies of 1.9-2.1 eV (19, 26, 29, 30, 33) are found in the literature for the indirect transition of tetragonal PbO and 2.75-2.84 eV (26, 33) for the direct transition. Thus, our results also support Pavlov's conclusion that tetragonal PbO forms at longer corrosion times. The gradual rather than sharp increase in photocurrent from 621 to 450 nm suggests that the tetragonal PbO film has multiple energy level transitions between 1.9 and 2.7 eV. A portion of the photocurrent under the peak which begins at 444 nm may thus be due to the direct transition in tetragonal PbO.

After the electrode had corroded for several hours, we were able to observe a third signal as well, which is shown in Fig. 6. This signal is so small that we first thought it might be a heating effect caused by a change in light intensity. However, Fig. 1 shows that the light intensity between 750-1000 nm does not track the signal in Fig. 6. In addition, we would have expected a signal from a heating effect to show hysteresis between forward and reverse scans. We looked for this but found that the forward and reverse scans overlaid one another.

The signal in Fig. 6 was not corrected for light intensity because the curve in Fig. 1 is nearly flat between 800 and 900 nm. The bandgap energy determined from this signal is about 910 nm or 1.4 eV. This indicates that it may be a signal from a higher valence lead oxide, PbO_n, where n is approaching 2. Bandgap energies of 1.4 (34) and 1.5 eV (35) have been published for PbO_2. Izvozchikov (25) has shown that the bandgap energies of lead oxide decrease as the O/PbO ratio increases.

The magnitude of the signal in Fig. 6 increases with corrosion time. However, the ratio of this signal to the others appears to remain constant with time. The signal magnitude is also affected by the corrosion potential. At 400 mV a readable signal was obtained in the same part of the spectrum, but the signal was weaker than at 800 mV. The photocurrents at shorter

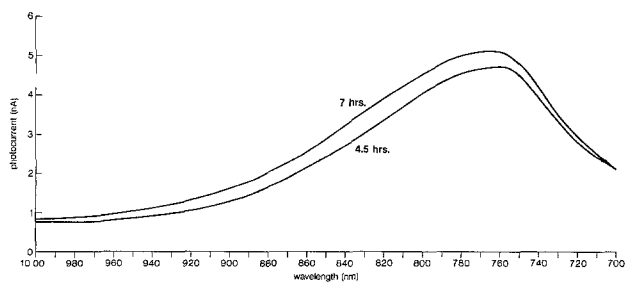

Fig. 6. Photoconductivity spectra of lead electrode corroded at 800 mV in 1M H_2SO_4 at room temperature.

wavelengths showed that the growth of orthorhombic and tetragonal PbO at 400 mV follows a pattern similar to that at 800 mV.

We also studied the photoconductivity of a lead electrode corroded at 1000 mV but were unable to detect a photocurrent. The noise at this voltage is much larger, for undetermined reasons, and the photocurrent is smaller (21). After corroding the sample at 1000 mV for 22 hr, we decreased the potential to 400 mV. Figure 7 shows the photocurrents observed 25 min after the potential was reduced. Two signals, corresponding to the previously observed signals at 444 and 621 nm are present. The shape of the curve is similar to curves from the electrodes corroded for long times at 400 and 800 mV. This may indicate that PbO forms at 1000 mV by a mechanism similar to that at lower voltages.

We have also carried out a few experiments at other temperatures. At 49°C, only the signal at 621 nm was observed. This may be because the noise was larger at high temperature and therefore the corrosion times required to observe a photocurrent were longer. At temperatures close to freezing, the photocurrent was not measurable.

Electrochemistry.—Studies of the open-circuit voltage decay of lead corrosion films in sulfuric acid can also give information about the corrosion products formed (1). A voltage plateau corresponds to the reduction of a specific corrosion product.

Figure 8 shows a series of voltage decay curves for lead electrodes corroded at 400 mV in the dark for 30, 60, and 90 min. In each case, the potential drops sharply to a plateau between −500 and −600 mV. A second plateau appears between −600 and −700 mV before the potential drops to the $Pb/PbSO_4$ potential at −940 mV. Both plateaus have a slight negative slope.

The length of the first plateau grows up to about 1 hr of corrosion time and then remains approximately constant. However, the length of the second plateau continues to increase during the corrosion process, indicating that more of the product is forming as corrosion proceeds. Similar curves are found for samples corroded at 800 mV.

Burbank (36), Pavlov (37), and Ruetschi (1), have attributed voltage plateaus in this voltage range to the reduction of lead (II) oxides and basic lead sulfates. Based on a comparison of the growth patterns of the two voltage plateaus and the two photocurrent signals at 444 and 621 nm, we attribute the first plateau to orthorhombic PbO and the second plateau to tetragonal PbO.

At higher voltages and longer times, evidence of higher valence lead oxides also appears. Figure 9 shows the first part of a voltage decay curve of a Pb electrode corroded at 800 mV for 16 hr in the dark. The potential decays slowly from the corrosion potential before dropping to a plateau at about −400 mV. In general when the higher oxides are present, the voltage plateaus for orthorhombic and tetragonal PbO are at a higher potential. This suggests that the potentials may be mixed values. This slow potential decay can be induced more quickly by illuminating the electrode. The appearance of this higher valence oxide corresponds to the appearance of the signal at 910 nm.

Microprobe Laser Raman Spectroscopy and Micro X-Ray Powder Diffraction

The lead samples used in the photoelectrochemical studies were removed from the cell, washed with distilled water, and dried. They were then analyzed using micro-laser Raman spectroscopy and micro x-ray diffraction.

Figure 10 is a photomicrograph of a cross section of the corrosion film from the study shown in Fig. 2. The sample was corroded for 72 hr at 800 mV. Three layers were visible under the microscope and were thick enough to be resolved with the microprobe laser Raman technique. The outer layer adjacent to the solution was 1-2 μm thick and contained primarily $PbSO_4$ along with a small amount of tetragonal PbO or basic lead sulfate. The middle layer, which was also 1-2 μm thick, contained a mixture of orthorhombic and tetragonal PbO with no $PbSO_4$. The inner layer, which was 2-3 μm thick, contained only tetragonal PbO with no trace of either orthorhombic PbO or $PbSO_4$. The position of the orthorhombic PbO in the middle layer verifies that it forms early in the corrosion process.

Based on the relative Raman peak heights for the two oxides, we can make a rough estimate that the

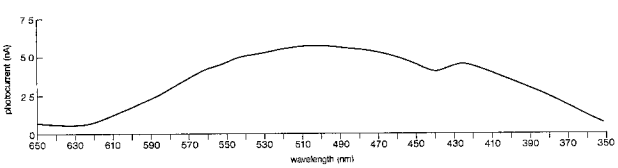

Fig. 7. Photoconductivity spectrum of lead electrode corroded at 1000 mV for 22 hr, then at 400 mV for 25 min.

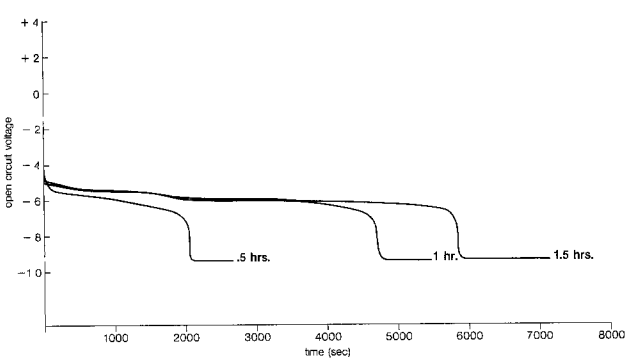

Fig. 8. Self-discharge of lead electrode corroded at 400 mV in 1M H_2SO_4 at room temperature in the dark. Voltage is given as V vs. $Hg/Hg_2SO_4/1M\ H_2SO_4$ reference electrode.

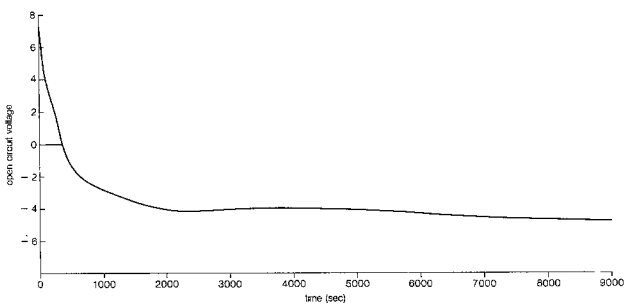

Fig. 9. Self-discharge curve of lead electrode corroded at 800 mV for 16 hr at room temperature in 1M H_2SO_4 in the dark. Voltage is given as V vs. $Hg/Hg_2SO_4/H_2SO_4$ reference electrode.

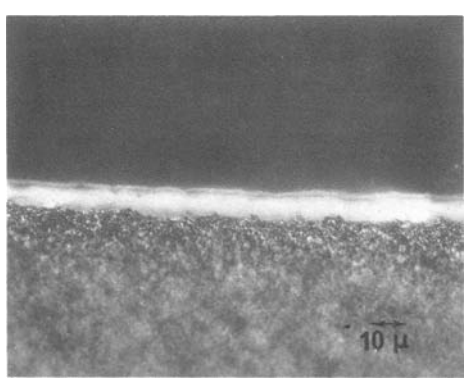

Fig. 10. Photomicrograph of cross section of lead electrode corroded at 800 mV for 72 hr.

middle layer of the sample in Fig. 10 contained <1% orthorhombic PbO. A more precise value cannot be determined without further study to determine whether preferred orientation of the crystals occurs and has an effect on peak ratios. This small quantity of orthorhombic PbO is surprising, considering the relative sizes of the photocurrents for orthorhombic and tetragonal PbO (see Fig. 2) and the fact that tetragonal PbO is several orders of magnitude more photosensitive than orthorhombic PbO (26, 29).

The small quantity of orthorhombic PbO in the center layer may indicate that the orthorhombic PbO converts to tetragonal PbO at the longer corrosion times. This is certainly possible, since tetragonal PbO is the stable form at room temperature (26) and since the change in free energy for the transition from orthorhombic PbO to tetragonal PbO is only 965 J/mol (38).

A second possibility is that some conversion of orthorhombic PbO to tetragonal PbO occurs *ex situ* during sample preparation. Clark and Rowan (39) have shown that grinding causes a transition from orthorhombic to tetragonal PbO and Keezer (26) induced the transition by cutting orthorhombic crystals with a scalpel. Bordovskij and Izvozchikov found that the surface of o-PbO crystals were converted to t-PbO after several hours exposure to air (40).

A third possibility is that only a small quantity of orthorhombic PbO forms early in the corrosion process right underneath the $PbSO_4$ film. In this case, the position of the orthorhombic PbO at the $PbSO_4$/PbO interface may account for the large photocurrent it produces at short corrosion times. The small amount found by laser Raman spectroscopy might then be due to the positioning of the laser beam in the center of the corrosion layer. We do not presently know what thickness of the lead oxide corrosion film is affected by light in the photoelectrochemical experiment, although Peter (24) has calculated a 7.5Å width for the space charge region in α-PbO_2 films. We do know that the photocurrent is a function of film thickness or corrosion time (see Fig. 2 and 6).

A fourth possibility is that a substantial portion of the photocurrent under the peak which begins at 444 nm is produced by the direct transition in tetragonal PbO. The manner in which the photoconductivity spectrum changes with time (see Fig. 2) would then suggest that additional energy levels are developing in the tetragonal PbO as the film grows. However, the open-circuit voltage decay curves in Fig. 8 do not, in our opinion, support this hypothesis since they show two voltage plateaus which become more distinct with increasing time. The real truth may be a combination of some or all of these hypotheses.

The sample illustrated in Fig. 9 was corroded for the longest time, and, therefore, had the thickest corrosion film. Separate layers were not evident in the other samples. However, in a sample corroded for 19 hr at 400 mV, laser Raman spectroscopy showed that the corrosion film was composed of tetragonal PbO and $PbSO_4$ with a small quantity of orthorhombic PbO. Both orthorhombic and tetragonal PbO were also found in a sample corroded first at 1000 mV for 22 hr and then at 400 mV for 20 hr (Fig. 7). Although Pb_3O_4 can be detected by laser Raman spectroscopy, we did not find any evidence of this oxide in any of the samples we analyzed.

Micro x-ray diffraction studies revealed $PbSO_4$, tetragonal PbO, and β-PbO_2 in the sample corroded first at 1000 mV for 22 hr and then at 400 mV for 20 hr. This method was not sensitive enough to detect the orthorhombic PbO. The presence of β-PbO_2 is consistent with previous studies at this voltage (21).

In micro x-ray diffraction studies on the 3 layer sample shown in Fig. 10, which was corroded for 72 hr at 800 mV, only tetragonal PbO and $PbSO_4$ were identified. Although the data in Fig. 6 and 9 suggest that a small quantity of a higher valence lead oxide is present in this sample, neither the x-ray diffraction nor the laser Raman spectroscopic techniques could detect it.

Why the orthorhombic form of PbO should be favored early in the corrosion process is not clear. Simple thermodynamic considerations indicate that tetragonal PbO should be more stable under these conditions. In the oxidation of lead to lead oxide, $Pb + H_2O = PbO + 2H^+ + 2e$, the tetragonal PbO form has a lower voltage than orthorhombic PbO. Furthermore, the tetragonal form has the lower solubility (38, 41). Phase diagrams also show that tetragonal PbO is the stable form at ordinary pressures and temperatures (26). Nevertheless, several authors have produced orthorhombic PbO at room temperature either by oxidizing thin lead films or by evaporating PbO onto a substrate (42, 43). The o-PbO films formed by oxidizing lead show a strong preferred (001) orientation parallel to the (111) preferred orientation in the evaporated Pb films.

Changes in *p*H should theoretically not influence the choice of polymorph, since the reactions would be the same for both forms. However, Burbank (4) found experimentally that the form of PbO produced by anodizing lead is dependent on the solution *p*H. Using x-ray diffraction, she identified orthorhombic PbO in corrosion films formed in solutions with *p*H <9.4 and tetragonal PbO at *p*H >9.4. This observation is consistent with our results, because the *p*H would be expected to increase as the corrosion film becomes thicker (1). This *p*H dependence suggests that the mechanisms of formation of the two polymorphs are different.

In our studies, we find that higher valence oxides begin to form at long corrosion times. Pavlov (21) has suggested that this process occurs at potentials above 900 mV in the dark and at potentials above 0 mV in the light. Our open-circuit voltage decay studies suggest that, although the process is favored as the potential increases, the formation of PbO_n, where n approaches 2, does take place slowly in the dark at potentials below 900 mV (see Fig. 9). However, the process is accelerated significantly by illumination.

The fact that light can influence the corrosion process would suggest that *in situ* laser Raman spectroscopy should be done with caution. The lasers generally used are at wavelengths in the visible region (9) where lead oxide films are photosensitive. A study is needed to define the effect of light wavelength on PbO_n formation. Such a study would help define how light enhances the rate of PbO_n formation and could also be used to define an appropriate laser for *in situ* Raman studies.

Summary

Lead corrosion has been studied between 0.4 and 1V (*vs.* Hg/Hg_2SO_4/1M H_2SO_4) in 1M H_2SO_4 using 4 techniques: photoelectrochemistry, open-circuit voltage decay curves, microprobe laser Raman spectroscopy, and micro x-ray diffraction. The results give the following information about the corrosion process.

Initially, a $PbSO_4$ film is produced which inhibits diffusion of acid to the underlying lead. As the environment underneath and within the $PbSO_4$ film becomes more basic, other divalent lead species such as the basic lead sulfates and lead oxides become thermodynamically stable (3). Orthorhombic PbO begins to form along with some tetragonal PbO. As the corrosion film becomes thicker, orthorhombic PbO ceases to form and tetragonal PbO becomes dominant. At longer times, a higher valence lead oxide, PbO_n, where n is approaching 2, also forms. This latter reaction occurs in the dark but is significantly accelerated by light. The exact nature of the PbO_n species and the reason for the preferential formation of orthorhombic PbO early in the corrosion process have not yet been determined.

Acknowledgments

The authors are grateful to Alan Attia for his help in setting up the photoelectrochemical apparatus and for his helpful discussions. The helpful discussions of William Tiedemann and Richard Johnson are also appreciated. Fred Graetz did the micro x-ray diffraction studies. Macro sample Raman spectra of reference materials were collected by Dr. Kazuo Nakamoto and his staff at Marquette University. MOLE Raman analyses were performed by Mr. Mark Anderson of Walter C. McCrone Associates, Incorporated. We gratefully acknowledge their contributions. The monochromator with scanner light source, light chopper, and lock-in amplifier used in the photoelectrochemistry were the property of the Solar Energy Research Institute. The research was supported entirely by Johnson Controls, Incorporated.

Manuscript submitted Nov. 15, 1982; revised manuscript received March 2, 1983. This was Paper 9 presented at the Detroit, Michigan, Meeting of the Society, Oct. 17-21, 1982.

Any discussion of this paper will appear in a Discussion Section to be published in the December 1983 JOURNAL. All discussions for the December 1983 Discussion Section should be submitted by Aug. 1, 1983.

Johnson Controls, Incorporated assisted in meeting the publication costs of this article.

REFERENCES

1. P. Ruetschi, *This Journal*, **120**, 331 (1973).
2. D. Pavlov and R. Popova, *Electrochim. Acta*, **15**, 1483 (1970).
3. K. R. Bullock, *This Journal*, **127**, 662 (1980).
4. J. Burbank, *ibid.*, **106**, 369 (1959).
5. J. Burbank, A. C. Simon, and E. Willihnganz, in "Advances in Electrochemistry and Electrochemical Engineering," Vol. 8, C. W. Tobias, Editor, p. 157, Wiley-Interscience, New York (1971).
6. J. L. Dawson, in "The Electrochemistry of Lead," A. T. Kuhn, Editor, p. 309, Academic Press, London (1979).
7. A. T. Kuhn, in "The Electrochemistry of Lead," A. T. Kuhn, Editor, p. 365, Academic Press, London (1979).
8. D. Pavlov, C. N. Poulieff, E. Klaja, and N. Iordanov, *This Journal*, **116**, 316 (1969).
9. R. J. Thibeau, C. W. Brown, A. Z. Goldfarb, and R. H. Heidersbach, *ibid.*, **127**, 1913 (1980).
10. R. Varma, C. A. Melendres, and N. P. Yao, *ibid.*, **127**, 1416 ((1980).
11. R. Varma, G. Cook, and N. P. Yao, *ibid.*, **128**, 1165 (1981).
12. K. R. Bullock and E. C. Laird, *ibid.*, **129**, 1393 (1982).
13. M. Delhaye and P. Dhamelincourt, *J. Raman Spectroscopy*, **3**, 33 (1975).
14. G. J. Rosasco and E. S. Etz, *Res./Dev.*, **28**, 20 (1977).
15. M. Delhaye, M. Leclercq, and D. Landon, *Ind. Res.*, **69** (1977).
16. McCrone Associates, "Insight," Vol. 8, W. C. McCrone Associates, Chicago (1978).
17. R. Z. Muggli, W. C. McCrone, J. G. Delly, and S. J. Palenik, in "The Particle Atlas," Vol. V, 2nd ed., Ann Arbor Science, Ann Arbor, MI (1979).
18. G. J. Rosasco, *Adv. Infrared Raman Spec.*, **7**, 223 (1980).
19. D. Pavlov, S. Zanova, and G. Papazov, *This Journal*, **124**, 1522 (1977).
20. D. Pavlov, *Electrochim. Acta*, **23**, 845 (1978).
21. D. Pavlov, *J. Electroanal. Chem.*, **118**, 167 (1981).
22. S. Fletcher and D. B. Matthews, *ibid.*, **126**, 131 (1981).
23. F. Caldara, A. Delmastro, G. Fracchia, and M. Maja, *This Journal*, **127**, 1869 (1980).
24. L. M. Peter, *Surf. Sci.*, **101**, 162 (1980).
25. V. A. Izvozchikov, *Phys. Status Solidi A*, **14**, 161 (1972).
26. R. C. Keezer, D. L. Bowman, and J. H. Becker, *J. Appl. Phys.*, **39**, 2062 (1968).
27. L. Heijne, *Philips Res. Rep. Suppl.*, 79 (1961); *J. Phys. Chem. Solids*, **22**, 207 (1961).
28. K. H. Gundlach and J. Kaldec, *Appl. Phys. Lett.*, **27**, 429 (1975).
29. J. C. Schottmiller, *J. Appl. Phys.*, **37**, 3503 (1966).
30. R. G. Barradas, D. S. Nadezhdin, J. B. Webb, A. B. Roth and D. F. Williams, *J. Electroanal. Chem.* **126**, 273 (1981).
31. H. S. Harned and W. J. Hamer, *J. Am. Chem. Soc.*, **57**, 27 (1938).
32. W. C. McCrone and J. G. Delly, "The Particle Atlas," Vol. 1, 2nd ed., pp. 119-129, Ann Arbor Science, Ann Arbor, MI (1973).
33. J. Van der Broek, *Philips Res. Rep.*, **22**, 36 (1967).
34. W. Mindt, *This Journal*, **116**, 1076 (1969).
35. F. Lappe, *J. Phys. Chem. Solids*, **23**, 1563 (1962).
36. J. Burbank, *This Journal*, **103**, 87 (1956).
37. D. Pavlov, *Ber. Bunsenges. Phys. Chem.*, **71**, 398 (1967).
38. Hans Bode, "Lead-Acid Batteries," R. J. Brodd and K. V. Kordesch, Translators, p. 14, John Wiley and Sons, Inc., New York (1977).
39. G. L. Clark and R. Rowan, *J. Am. Chem. Soc.*, **63**, 1302 (1941).
40. G. A. Bordovskij and V. A. Izvozchikov, *Krist. Tech.*, **3**, 219 (1968).
41. M. Pourbaix, "Atlas of Electrochemical Equilibria," Pergamon Press, Oxford (1966).
42. T. B. Light, J. M. Eldridge, J. W. Matthews, and J. H. Greiner, *J. Appl. Phys.*, **46**, 1489 (1975).
43. J. W. Matthews, C. J. Kircher, and R. E. Drake, *Thin Solid Films*, **42**, 69 (1977); *ibid.*, **47**, 95 (1977).

Corrosion of Magnesium at High Anodic Potentials

Theodore R. Beck* and Sandra G. Chan

Electrochemical Technology Corporation, Seattle, Washington 98107

ABSTRACT

During the pitting of magnesium in chloride solution a film of magnesium chloride forms on the corroding surface. This salt film is apparently a diffusion barrier for water and prevents repassivation by oxide. Properties of magnesium chloride layers were determined on corroding, high purity magnesium shielded electrodes (one-dimensional pits). Electrical transient experiments showed that the salt film thickness is proportional to applied anodic potential and that conduction is by the high field mechanism.

Corrosion of magnesium has been studied in relation to use as structural material in the atmospheric environment (1) as a cathodic protection anode (2) and as an anode in primary cells (3). Other studies have been made of associated thermodynamics (4) and kinetics and transport processes (5-9). Magnesium corrosion is highly hindered by surface hydroxide (8) and the mixed potential for dissolution is generally about 1V positive to the reversible potential of mag-

* Electrochemical Society Active Member.
Key words: films, mass transport, conductance, current efficiency.

nesium. The corroded surface is rough and the corrosion product film sometimes contains finely divided reactive magnesium particles (10). Hydrogen is simultaneously evolved so that the apparent valence of dissolution is about 1.4 rather than the standard valence of 2.

The pupose of the present paper is to describe and analyze corrosion of magnesium at high anodic potentials in magnesium chloride solutions in which a magnesium chloride film forms on the corroding surface. Mass transport effects and properties of the salt film are described. The results provide some illumination of corrosion mechanisms at lower anodic potentials.

Experimental

The experiments described in this paper were carried out with shielded (one-dimensional pit) electrodes, described previously (11). The working electrodes were 99.9% pure magnesium rods with 0.16 × 32 cm cross section cast in 0.6 cm diam epoxy resin insulating sheaths. Experiments were conducted with the anode facing up position for hydrodynamic stability, and the corroding surface was observed through a 60× binocular microscope above the cell. A flow cell that could be put under the microscope (12) was also used. The shielded pit electrodes faced up on the bottom of a 0.32 × 0.32 cm cross-sectional flow channel. All of the experiments were carried out in solutions of various concentrations of ACS specification reagent grade $MgCl_2 \cdot 6H_2O$ in distilled water.

Many different types of experiments were conducted with the shielded electrodes to characterize the transport mechanisms. Potentiodynamic polarization curves were measured under stagnant and forced convection conditions. The rate of evolution of hydrogen gas, produced simultaneously with corrosion, was measured in an inverted electrolyte-filled micro gas burette held over the pit. The effect of electrolyte velocity on the limiting current density was determined with a flow system (13) using a Teflon pump and a rotameter calibrated for each solution. Current density transients were measured under potentiostatic conditions in the early stages of development of the diffusion layer in various bulk $MgCl_2$ concentrations. Potential drop in the pit electrolyte was measured as a function of position with a vertically calibrated movable Luggin capillary (11).

Electrical transient methods were used to characterize the properties of the salt film on the metal surface. Step potentials were applied in the positive and negative direction to the magnesium anode corroding at steady-state conditions. Measured initial currents gave electrical conduction properties of the salt film. Integrated current density *vs.* time for a positive step potential gave the charge density of the incremental amount of salt film formed.

A Wenking Model 68T53 potentiostat and a PAR Model 173 potentiostat were used for the controlled potential experiments. For applied potentials greater than 10V, a well-filtered variable voltage d-c power supply was connected to the working and counter-electrodes; the working electrode potential was measured against a saturated calomel reference electrode. Fast electrical transients were measured on a Tektronix Model 564B storage oscilloscope and slow transients on a Hewlett-Packard Model 7046A X-Y plotter. A saturated calomel reference electrode was used in stagnant electrolyte experiments and a silver/silver chloride electrode in contact wth the solution in the flow experiments (13).

Electrolyte density, viscosity, and conductivity were also measured at 21° ± 1°C for a range of concentrations from 3 to 4.7M (saturation). These data are an extension of literature data (14) and were required in the mass transport analysis. Density was determined from weights of 10 ml pipetted volumes. Viscosity was determined with Gilmont falling-ball type viscometers and a Brookfield viscometer. Distilled water and glycerol were used as calibrating liquids. Conductivity was determined at 1000 Hz with a platinum electrode conductivity cell and an ESI Model 250 DA Impedance bridge.

Results and Discussion

Polarization curves.—A typical potentiodynamic polarization curve for magnesium in $MgCl_2$ solution is shown in Fig. 1. This curve was obtained in 0.94M $MgCl_2$ solution with a sweep rate of 1 V/min in the positive and negative directions. The current density in the approximately linear positive-sweep region from −1.3 to 2V is limited by ohmic resistance of the solution. In this region hydrogen bubbles evolve vigorously and cause increasingly unstable current with increase in potential. The corroding metal surface has a jet black appearance due to a microporous surface as observed for titanium in the ohmically limited region (11, 13).

At a potential above 2V, the current density deviates from the linear relationship and decays rapidly due to salt film passivation. The hydrogen evolution rate decreases significantly and the corroding surface becomes electropolished. In the salt film passivation region, agitation of the electrolyte in the pit causes the current density to increase. On the negative sweep from 10V, the current density remains small until the potential is below 0V. Then the hydrogen evolution increases significantly and the current density rises to the ohmic limit. The zero-current intercept is more negative on the negative sweep because the surface is completely active. On the initial positive sweep starting at −2V, the corrosion initiates at discrete small pits, and time is required for the whole surface to become active.

The polished surface of the metal is clearly visible in the salt layer region with no salt crystals obscuring the view. At a potential of about 20V, a flocculent salt precipitate occurs in the pit, even down to a solution pH of 1. The flocculent precipitate redissolves when the potential is decreased. This precipitate is presumed to be $MgCl_2 \cdot 6H_2O$, the stable solid phase in equilibrium with $MgCl_2$ solution.

The potential for salt film passivation, ϕ_p, and the corresponding current density, i_p, both decrease approximately linearly with increasing concentration. At saturation of $MgCl_2$, the salt passivation potential is about −1V and the passivation current density about 0.2 A/cm². Current density in the ohmic region can be described by (11)

$$i = \frac{\sigma \Delta \phi_e}{d + a\sqrt{lw}} \qquad [1]$$

although the hydrogen bubbles cause some error.

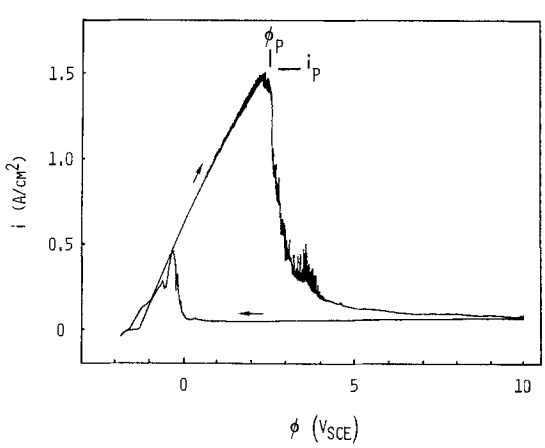

Fig. 1. Potentiodynamic polarization curve for magnesium in 0.94M $MgCl_2$; depth = 2 mm; sweep rate = 1 V/min.

The electrode reaction in the mass transport limited region is

$$Mg(c) + 2\,Cl^-(aq) \rightarrow MgCl_2(c) + 2\,e^- \qquad [2]$$

in which a layer of salt covers the metal. Magnesium chloride dissolves at the salt-solution interface and magnesium ions are transported away through the solution.

The standard reversible potential for reaction [2] is calculated from free energy data (15) to be -1.95 V_{SCE}. It is not possible to check this value on a polarization curve such as Fig. 1 because the salt film dissolves as the reversible potential is approached. An a-c technique was therefore used.

A sine wave was superimposed through the potentiostat on a pit at +3V d.c. in a 2.35M $MgCl_2$ solution. The current-voltage curve was displayed on the oscilloscope. At frequencies of 10-15 Hz the zero-current intercept occurred at -1.9 ± 0.1V. At lower frequencies the salt film dissolved and at higher frequencies capacitive charging and discharging of the salt film gave a hysteresis loop. There was a large hysteresis in the anodic current region at greater than 10 Hz, but essentially no hysteresis in the cathodic current region and in the region of the zero-current intercept. The metal surface remained bright under the salt layer in these tests. The zero-current (-1.9V) intercept is interpreted as the reversible potential for reaction [2] in this paper.

The valence of dissolution was determined in the mass transport limited region in 2.35M $MgCl_2$ solution at a potential of 5.0V. At this condition, the corroding metal surface is shiny and the hydrogen evolution rate is small. Four runs were made at 16 hr each starting from a condition of magnesium polished flush with the epoxy resin surface. The average depth at the end of the runs was measured with a machinist's dial gauge and compared to the integrated current from the strip chart recorder. The measured valence was 2.03 ± 0.03.

Hydrogen evolution.—The rate of hydrogen evolution was measured in 0.94M $MgCl_2$ solution at potentials from -1.5 to 19V. The volumetric rate (cm^3/sec) was converted to an equivalent cathodic hydrogen current density using the ideal gas law and Faraday's law

$$i_{H_2} = \frac{2Fv(273)(76 - p_w)}{22{,}400\,T(76)A} \qquad [3]$$

The ratio of the hydrogen current density to the actual anodic current density is plotted *vs.* potential in Fig. 2. The actual anodic current density is assumed to be the sum of the absolute values of the measured anodic current density and the hydrogen current density.

The ratio, i_{H_2}/i_a, is approximately constant at 0.3 for the ohmic limited region; both i_{H_2} and i_a increased with potential. This value corresponds to an apparent valence of 1.4, which is in general agreement with literature values (10). The ratio, i_{H_2}/i_a is about two orders of magnitude smaller at high potentials in the mass transport limited region. In each of these experiments between 0.5 and 19V in the mass transport limited region the hydrogen was collected over a period of time in which the average measured current was in the range 0.15 ± 0.07 A/cm^2. The ratio, i_{H_2}/i_a, decreases with increase in potential in this region.

The hypotheses is made here that the rate of hydrogen generation in the mass transport limited region is directly related to the rate of water diffusion through the salt layer. Because the metal/salt interface is at a very negative potential (-1.9V), it will be assumed that every water molecule arriving at the interface is reduced to hydrogen

$$H_2O + 2\,e^- \rightarrow H_2 + O^= \qquad [4]$$

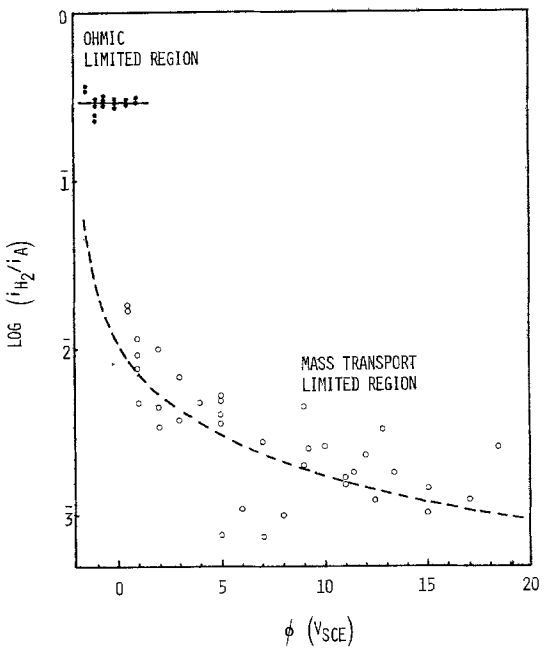

Fig. 2. Ratio of hydrogen current density to anodic current density in ohmic limited and mass transport limited regions for 0.94M $MgCl_2$.

Diffusion of hydrogen out is discussed further on. The small concentration of oxide ions simultaneously formed will be incorporated into the salt film as magnesium oxychloride.

The current density for hydrogen generation is, therefore

$$i_{H_2} = \frac{2FD_w\Delta C_w}{t} \qquad [5]$$

It will be assumed that the salt film thickness is directly proportional to the potential across the salt film

$$t = K_1(\phi + 1.9) \qquad [6]$$

(The value of K_1 is discussed further on.) Equations [5] and [6] may be combined to give the linear relation

$$1/i_{H_2} = K_2(\phi + 1.9) \qquad [7]$$

Experimental values of $1/i_{H_2}$ in the mass transport limited region were plotted *vs.* ϕ. The least squares line had a slope of 272 $(A/cm^2)^{-1}$ V^{-1}, an intercept of -4V, and a correlation coefficient of 0.66. A line was drawn through a zero-current intercept of -1.9V in accordance with Eq. [7], and gave a line

$$1/i_{H_2} = 325(\phi + 1.9) \qquad [8]$$

The data thus appear to be in reasonable accord with the hypothesis of water transport in the salt film. The dashed curve in Fig. 2 is

$$\frac{i_{H_2}}{i_a} = \frac{1}{(0.15)(325)(\phi + 1.9)} = \frac{0.0205}{(\phi + 1.9)} \qquad [9]$$

A curious side observation was made concerning the metal corrosion profile under small hydrogen bubbles on the surface. Bubbles with a diameter of $\sim$ 0.02 cm tended to collect on the metal surface in the corners next to the plastic walls. Instead of causing a hump on the metal due to shielding the metal by a high resistance current path through the solution, the metal became concave to fit the bubble curvature. Increased mass transfer to obtain a concave surface might be explained by electrokinetic motion of the bubble surface analogous to the well-known phenomenon with mercury drops in polarography. This bubble phenomenon remains to be examined in detail.

Effect of electrolyte velocity.—The effect of electrolyte velocity on current density in the mass transport limited region is shown in Fig. 3. These experiments were conducted in 2.35M $MgCl_2$. The depth of the recessed Mg electrode in the side of the flow channel was about 0.15 cm. The increase in current density with flow velocity shows that the current is mass transport limited, although the slope with potential at the higher flow rates indicates partial kinetic control.

An attempt was made to correlate current density *vs.* velocity from Fig. 3 with a prediction from a prior calibration of a flow cell (13). Agreement was within 20% at a velocity of 10 cm/sec, but the experimental current density from Fig. 3 was a factor of three higher than the prediction at 100 cm/sec. Hydrodynamic conditions in these corroding systems were not as well defined as desirable.

Conductivity of solution in pit.—Potential in the pit solution was measured as a function of depth with the position-calibrated small Luggin capillary (11) for bulk concentrations of 0.94, 2.35, and 4.7M. Pit depths were 0.2-0.3 cm. Solution conductivity calculated from the slope of the potential *vs.* depth curves varied smoothly from the saturation value at the bottom of the pit (0.063 *S*/cm) to the bulk concentration near the mouth. The pits with magnesium did not have the extremely viscous, low conductivity solutions near the bottom that were observed in pits with titanium (11). TiO^{++} tends to polymerize and apparently Mg^{++} does not.

Current density-time transients.—Experiments were conducted in which a step potential from the open-circuit value to +5.0V was applied for a range of bulk $MgCl_2$ concentrations. The pit depth averaged 0.09 ± 0.01 cm in these experiments. Current density-time transients are shown in Fig. 4. The initial current is ohmically limited. Salt passivation initiates in the time period, 0.01-0.1 sec. By 1 sec the salt film is fully developed and thereafter the current density decays as the diffusion layer thickness increases in the pit. At about 1000 sec the current density levels to the steady-state value for a diffusion layer thickness corresponding to the pit depth. The decrease in current density with bulk concentration of $MgCl_2$ in the unsteady-state and steady-state regions clearly indicates a mass transport limit for Mg^{++} ion.

In the unsteady-state region for a solution without supporting electrolyte the limiting current density can be described (16) by

$$i_L = \frac{zF(C_s - C_b)}{t_-}\sqrt{\frac{D}{\pi\tau}} \qquad [10]$$

and in the steady-state region it can be described by

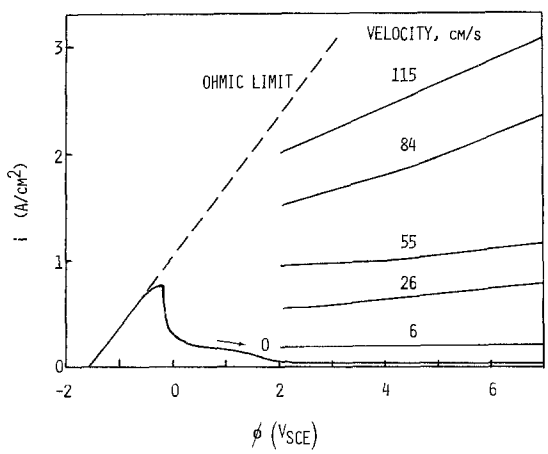

Fig. 3. Effect of electrolyte velocity on current density in mass transport limited region in 2.35M $MgCl_2$; depth = 1.5 mm.

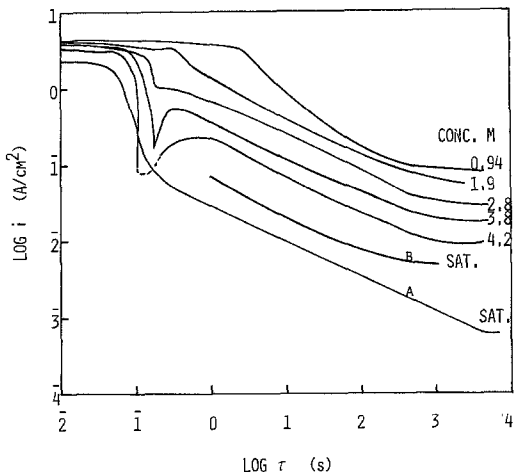

Fig. 4. Current-time transients for Mg in $MgCl_2$ solutions at ϕ = 5.0 V_{SCE}; depth = 0.9 mm; curve A = cooled from 30°C, curve B = cooled from 50° to 21°C.

$$i_L = \frac{zFD(C_s - C_b)}{t_-d} \qquad [11]$$

The chloride ion transference number has a value of about 0.79 (17) in concentrated $MgCl_2$ solution concentrations shown in Fig. 4. Values of D were calculated from Eq. [10] and [11] and Fig. 4 for bulk concentrations from 0.94 to 4.23M. The values were 1.1 ± 0.1 × 10^{-5} cm^2/sec for the unsteady-state curves and 1.8 ± 0.2 × 10^{-5} cm^2/sec for the steady-state curves, assuming d = 0.1 cm. These values are several times larger than would be expected in concentrated solution. A possible cause of the large apparent diffusivities is convective mixing by the hydrogen bubbles of the high concentration solution from the pit bottom to the lower concentration at the pit mouth. Quantitative calculations remain to be made.

A surprising result in Fig. 4 is that the current density did not go to zero in saturated solution, but also followed the same − ½ power law of Eq. [10]. The experiments were repeated a number of times with solution that was saturated with $MgCl_2$ at 30° or 50°C before pouring into the cell to insure saturation in the cell which was run at 21°C. Curve A is for initial 30°C saturated solution and curve B is for initial 50°C saturated solution. The pit was filled with solution-precipitated $MgCl_2 \cdot 6H_2O$ crystals for the 50°C solution, but only partly filled for the 30°C solution. The solution next to the salt film appears to be supersaturated so that the transport can be described by

$$i_L = \frac{zF(C^* - C_s)}{t_-}\sqrt{\frac{D}{\pi\tau}} \qquad [12]$$

The degree of supersaturation calculated from Eq. [12] and curve A, Fig. 4 for D = 1.1 × 10^{-5} cm^2/sec is 1.5 ± 0.3% above saturation. Supersaturation for curve B is calculated to be about 3% above saturation.

Supersaturation at the dissolving salt layer can be related to properties of small dissolving crystals by the Kelvin equation (18)

$$nRT \ln \frac{C^*}{C_s} = \frac{2\gamma V}{r} \qquad [13]$$

The dissolving particle radius is estimated from the following parameter values. C^*/C_s = 1.015-1.03 at 294 K and n is 3 ions per molecule. The molecular volume of anhydrous $MgCl_2$ is 41.0 cm^3/mol based on a density of 2.32 g/cm^3 (14). The surface energy of $MgCl_2$ crystals is based on Naumova *et al.* (19), who calculate values from bond energies. They give 1328 erg/cm^2 for cleavage along the interlayer plane and 850 erg/cm^2 for cleavage along the plane within the

layer. An average of 1090 erg/cm^2 was used. Naumova *et al.* (19) also give values of effective surface energy based on crystallization experiments and the Kelvin equation. Values for four compounds given averaged 0.17 times the calculated values. An effective value for $MgCl_2$ will therefore be assumed as (0.17) (1090) = 185 erg/cm^2. The value of r from these parameter values is 1370Å for the 1.5% supersaturation and 690Å for 3% supersaturation.

Experiments were conducted to determine if the apparent degree of supersaturation in saturated solution is a function of barrier layer thickness. An initial potential of 5V was applied in each case and the potential was switched to ϕ_2 at 5 sec from initiation. For values of ϕ_2 between 0 and 7V, there was no significant difference in the subsequent current density in the period from 5 to 1000 sec. The effective crystal radius in the barrier layer salt is thus independent of barrier film thickness in the range from 0 to 7V.

Step potential polarization curves.—Step potential experiments were conducted with Mg in 4.23M (90% saturated) $MgCl_2$ solutions in order to determine electrical properties of the $MgCl_2$ salt film over a wide range of potential. Potential was stepped up and down from an initial ϕ_1 to a value of ϕ_2 starting with the same initial current density of 0.02 A/cm^2. The potential range of ϕ_1 was from 1 to 10V. The initial current density, i_p, at each value of ϕ_2 was recorded on the storage oscilloscope. This initial current density is assumed to be determined by the sum of the solution resistance and the salt film thickness corresponding to ϕ_1. The data are plotted semilogarithmically in Fig. 5.

A linear relationship is obtained at current densities below 0.02 A/cm^2 in accordance with high field conduction (20)

$$i = i_o \exp\left(\frac{\beta\Delta\phi}{t_1}\right) \qquad [14]$$

At higher current densities the data deviate from the linear relationship due to an apparent series ohmic resistance. The value of t_1/β can be calculated from the linear region from the derivative of Eq. [14] assuming β and i_o are constant

$$t_1/\beta = \left(\frac{1}{2.30}\right)\left(\frac{d\phi}{d\log i}\right) \qquad [15]$$

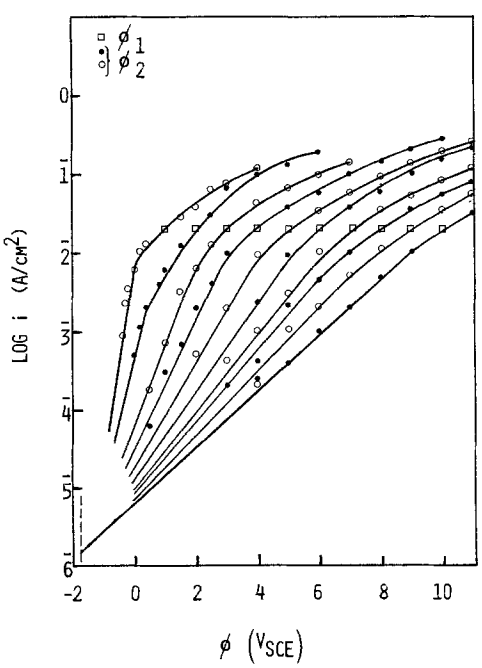

Fig. 5. Plots of initial current densities after step potential to ϕ_2 from ϕ_1 in 4.2M $MgCl_2$.

Values of $d\phi/d \log i$ determined from Fig. 5 are plotted *vs.* potential, ϕ_1, in Fig. 6. The data appear to be linear with potential, consistent with the salt film thickness being linear with potential and a constant β and i_o. The dashed line in Fig. 6 is drawn through the reversible potential

$$t_1/\beta = 0.098(\phi_1 + 1.9) \qquad [16]$$

The value of i_o in Eq. [14] is about 1×10^{-6} A/cm^2 from Fig. 5. This value is consistent with the coefficient of Eq. [16] which is 1/ln (i/i_o) from Eq. [14]; i_o = 0.02/exp (1/0.098) = 7.4×10^{-7} A/cm^2.

The difference between a curve at high current density and extrapolated linear region in Fig. 5 gives an apparent ohmic potential difference. Plots of these potential differences *vs.* current density are approximately linear and give generally increasing resistances from 270 to 770Ω (14 to 29 Ω-cm^2) for potentials from 1 to 10V. The solution resistance for an effective 0.2 cm deep pit is about 40Ω based on conductivity data. There is apparently a series ohmic resistance in the pit, perhaps a porous salt layer on top of the barrier salt layer.

Attempts were made to determine the incremental amount of barrier layer film growth for a step potential. In general, the current density increases at the step potential to a value above the mass transport limited current density, i_L, and decays in time back to i_L. It was assumed that the area under this curve would represent the charge for an incremental amount of barrier layer film. In practice there were complications that resulted in only a rough approximation; the poststep value of i_L was not always identical to the prestep value, and there was an overshoot in current density due to concentration changes in the solution side. Nevertheless, the average incremental thickness appeared to be about 15 Å/V, based on anhydrous $MgCl_2$, at limiting current densities of 0.1-1 mA/cm^2. The value of β can be estimated from this value of $dt_1/d\phi_1$ in the derivative of Eq. [16] assuming β and i_o are constant

$$\beta = \left(\frac{1}{0.098}\right)\frac{dt_1}{d\phi_1} \approx 1.5 \times 10^{-6}\ \text{cm/V} \qquad [17]$$

This value is about one-quarter to one-half the values obtained for oxide films (20) for titanium or aluminum. Values of $dt/d\phi$ appeared to decrease with i in accordance with the derivative of Eq. [14] for constant β and i_o

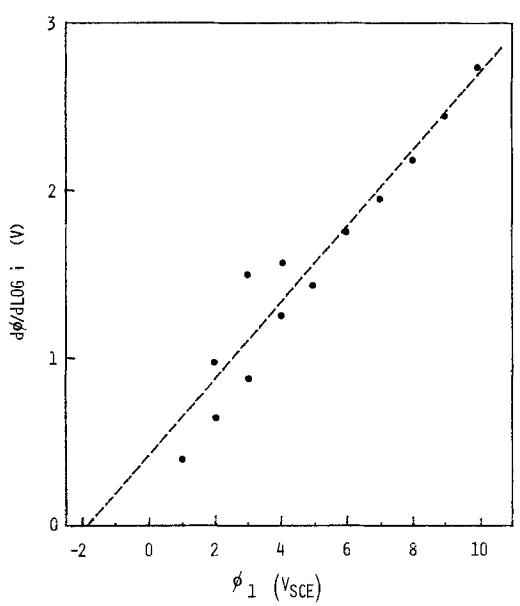

Fig. 6. Plot of slopes from Fig. 5 *vs.* ϕ_1

$$\frac{dt}{d\phi} = \frac{\beta}{\ln (i/i_o)} \quad [18]$$

but the correlation was not definitive because of considerable scatter in the data.

Open-circuit potential decay.—Potential decay transients were measured on the magnesium electrode when the connection to the counterelectrode was opened. The initial condition of the magnesium working electrode was a steady-state current under potentiostatic control. Current was interrupted to the counterelectrode with a mercury-wetted relay. The transient potentials from the saturated calomel reference electrode were recorded on the storage oscilloscope. Repeat traces were made at different sweep speeds in order to cover a wide range of time.

Data for initial potentials from 1 to 15.7V with a concentrated, 4.23M solution are given in Fig. 7. This concentrated solution was used in order to have a small initial current density and thus small ohmic drop in the pit. An average initial current density of 6×10^{-3} A/cm^2 and the highest ohmic resistance from the step potential experiments of 40 Ω-cm^2 gives 0.24V initial ohmic drop in the system. The remainder of the potential drop is assumed to be across the barrier layer salt film.

The decay of potential across a film having high field conduction can be described (see Appendix) by

$$\frac{d\phi}{d \ln \tau} = -\frac{t_1}{\beta} \quad [19]$$

In the time period, $3 \times 10^{-5} < \tau < 3 \times 10^{-3}$ sec, this relation is followed in Fig. 7. The slopes of these segments are plotted in Fig. 8 *vs.* the initial potential, ϕ_1. The least squares fit is

$$-\frac{d\phi}{d \log \tau} = 0.22 (\phi_1 + 1.7) \quad [20]$$

Assuming the intercept should be −1.9V

$$t_1/\beta = 0.096 (\phi_1 + 1.9) \quad [21]$$

This relationship is in apparent agreement with Eq. [16] for the step potential experiments. Equation [14] can be written

$$t_1/\beta = \frac{1}{\ln (i/i_o)} (\phi_1 + 1.9) \quad [22]$$

The initial current densities for the experiments of Fig. 5 and 7, respectively, were 0.02 and 0.006 A/cm^2. The ratios of the coefficients of potential in Eq. [21] should therefore be ln $(0.02/1 \times 10^{-6})$/ln $(0.006/1 \times 10^{-6}) = 1.14$. The actual ratio is $0.098/0.096 = 1.02$. Whether the difference between these numbers is due

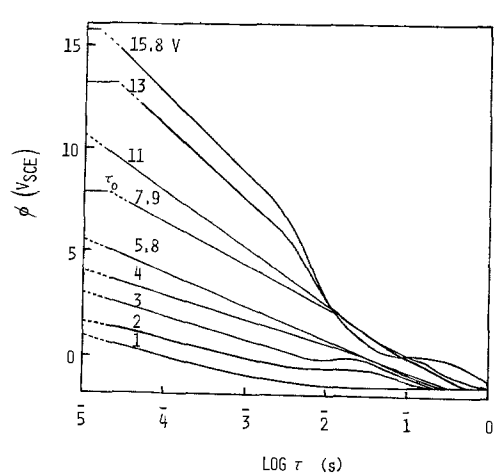

Fig. 7. Potential decay at open circuit in 4.23M $MgCl_2$; i(initial) $= 6 \times 10^{-3}$ A/cm^2; initial potential shown.

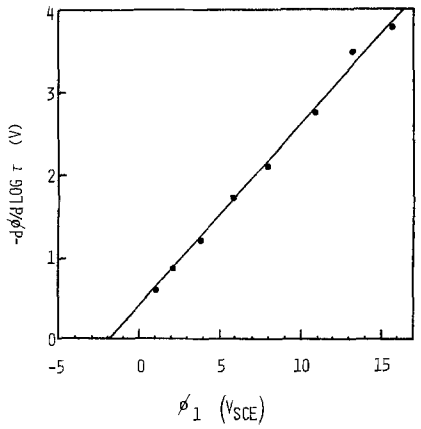

Fig. 8. Plot of slopes at $3 \times 10^{-5} < \tau < 3 \times 10^{-3}$ sec from Fig. 7 *vs.* ϕ_1.

to experimental error or whether i_o is a function of the initial current density remains to be determined.

The time to dissolve the barrier layer film after current interruption can be estimated from the initial current density and the film thickness

$$\tau_d = \frac{zFt_1}{Vi_1t_-} \quad [23]$$

Equation [21], with $t_1 \approx 1.4 \times 10^{-7} (\phi_1 + 1.9)$ for $\beta = 1.5 \times 10^{-6}$ in Eq. [20], $V = 41.0$ cm^3/mol, $i_1 = 6 \times 10^{-3}$ A/cm^2, and $t_- = 0.79$, gives values of dissolution times that are about twice the time at the −1.6V intercept in Fig. 7. The shorter actual time could be due to dissolution not being completely uniform; once patches of salt-film-free metal are formed these patches dominate in controlling the potential.

The dielectric constant of the barrier salt layer may be estimated (see Appendix) from the intercept time, τ_o, in Fig .7

$$\tau_o = \frac{\epsilon\epsilon_o}{\beta i_1} \quad [24]$$

For $\beta = 1.5 \times 10^{-6}$ cm/V and $i_1 \approx 6 \times 10^{-3}$ A/cm^2 and average $\tau_o \approx 1.5 \times 10^{-5}$ sec in Fig. 7, the average value of the dielectric constant, ϵ, is 1.5. Handbook values of dielectric constants for various chlorides range from 3 to 11 (14). The fraction of oxide in the salt layer, based on the hydrogen evolution experiments, should be negligible.

Permeability of water and hydrogen in barrier salt film.—A question to be faced is how to account for the observed hydrogen formation. Does the barrier salt film have sufficient electronic conductivity so that hydrogen is formed by water reduction on the solution side or does water diffuse through the film to the metal surface at a sufficient rate? The question cannot be answered definitively at this time, but evidence is in favor of diffusion of water and hydrogen.

Ohmic electronic current density could be described by

$$i_\theta = \frac{\sigma_\theta(\phi + 1.9)}{t} \quad [25]$$

The salt film thickness is proportional to potential by Eq. [6] so that the electronic conduction would be independent of potential

$$i_\theta = \frac{\sigma_\theta}{K_1} \quad [26]$$

This result is contrary to the experimental decrease in hydrogen rate with increase of potential shown in Fig. 2. Furthermore, the magnitude of the electronic conductivity required is considerably greater than extrapolated high temperature electronic conductivity data for salts. At a potential of $0V_{SCE}$, the hydrogen

current density from Fig. 2 is $\sim 1 \times 10^{-3}$ A/cm^2 and the value of K_1 is ~ 15 Å/V so that $\sigma_\theta \approx (1 \times 10^{-3})(15 \times 10^{-8})(1.9) \approx 3 \times 10^{-10}$ S/cm. This value is many orders of magnitude larger than extrapolations to 25°C from reported electronic conductivities of other salts in the 700°-900°C range (21).

Diffusion of water through a barrier salt film could be associated with imperfections. The supersaturation effect indicates a microcrystalline structure. Grain boundary water diffusion may therefore occur. The growth rate of the barrier salt film is fast and its lifetime is short so that the presence of imperfection is not surprising. At a current density of 0.1 A/cm^2, typical for nonflow conditions, the growth rate is $\sim 2 \times 10^{-5}$ cm/sec. At a potential of $0V_{SCE}$ the thickness is about 30Å so that the lifetime is about 0.015 sec.

The concept of lifetime of the barrier layer film is related to which ion, Mg^{++} or Cl^-, carries the current. If chloride ion carries the current the salt is formed at the metal/salt interface and is extruded from this interface. The salt dissolves at the salt/solution interface and thus has a lifetime as calculated. If magnesium ion carries all of the current the salt film could be considered to have infinite life. The stagnant salt film would have to conform to the changing metal microtopography as corrosion proceeded. As with oxide barrier layers (22) the real situation may be somewhere between the two limits.

The required diffusivity of water in the salt film can be estimated from the experimental data. Equations [5], [6], and [8] may be combined to give

$$D = \frac{K_1}{(325)(2)\mathbf{F}C} \qquad [27]$$

The value of K_1 is assumed to be 15×10^{-8} cm/V. The concentration of water found in barrier layer alumina films is ~ 1 mol percent (23). Using this value for $MgCl_2$, $C \approx 2.4 \times 10^{-4}$ mol/cm^3 and $D \approx 1 \times 10^{-11}$ cm^2/sec. The penetration time constant, $\tau_p \approx l^2/D$ for $\phi = 0V_{SCE}$ is $\approx (30 \times 10^{-8})^2/1 \times 10^{-11} = 0.009$ sec. This value is smaller than the lifetime of 0.015 sec so diffusion of water could occur for the case of chloride ion conduction. However, as the potential is increased to about 5V the penetration time could exceed the salt film lifetime and water diffusion would stop for the case of chloride ion conduction. This limitation would not apply to magnesium ion conduction.

Another question is whether hydrogen formed at the metal/salt interface could diffuse out fast enough. The answer is related to the relative limiting diffusion or permeability rates of hydrogen and water through the salt film. The calculation will be based on the relative permeability, $\bar{P} = DC$, because no information is available to estimate the solubility of hydrogen in $MgCl_2$. A common unit for permeability is cm^3 (STP) sec^{-1} cm^{-2} cm (cm Hg)$^{-1}$. The limiting current density for water reduction based on reaction [4] is then

$$i_w = \frac{2\mathbf{F}P_w\Delta p_w}{22{,}400t} \qquad [28]$$

The corresponding limiting current density for hydrogen is

$$i_{H2} = \frac{2\mathbf{F}P_{H_2}\Delta p_{H_2}}{22{,}400t} \qquad [29]$$

The ratio of H_2 to water flux is therefore

$$\frac{i_{H2}}{i_w} = \frac{P_{H_2}\Delta p_{H_2}}{P_w\Delta p_w} \qquad [30]$$

The value for p_{H_2} is 76 S cm Hg in which S is the supersaturation ratio, which may be very large for nucleation of H_2 bubbles in the salt film. The value of p_w above is ~ 0.8 cm Hg so that

$$\frac{i_{H2}}{i_w} \approx 100\,S\,\frac{p_{H2}}{p_w} \qquad [31]$$

Comparison of water and hydrogen permeabilities that are available for plastics (24) gives $\bar{p}_w \approx 100\,\bar{p}_{H_2}$. Assuming the same ratio in $MgCl_2$, the hydrogen permeability rate would appear to be adequate.

Conclusions

Corrosion experiments with a shielded, high purity magnesium anode in various concentrations of magnesium chloride showed the following. At high anodic potentials, magnesium ion transport in solution becomes limiting and a barrier layer salt film forms on the metal surface. Electrical conduction of the salt film is by the high field mechanism and the constants were determined. Thickness is proportional to applied potential. Water diffuses through the salt film leading to hydrogen evolution, with a rate inversely proportional to potential and film thickness.

Acknowledgment

This work was carried out under Office of Naval Research Contract No. N00014-76-C-0495.

Manuscript submitted June 17, 1982; revised manuscript received Oct. 22, 1982. This was Paper 179 presented at the Denver, Colorado, Meeting of the Society, Oct. 11-16, 1981.

Any discussion of this paper will appear in a Discussion Section to be published in the December 1983 JOURNAL. All discussions for the December 1983 Discussion Section should be submitted by Aug. 1, 1983.

The Electrochemical Technology Corporation assisted in meeting the publication costs of this article.

APPENDIX

Decay of Potential across Salt Film

Assume that charge stored in a capacitor with a salt film dielectric is discharged by high field conduction through the film. Therefore

$$i = i_o \exp\left[\frac{\beta\Delta\phi}{t_1}\right] \qquad [A\text{-}1]$$

and

$$i = -c\frac{d\Delta\phi}{d\tau} \quad \text{in which} \quad c = \frac{\epsilon\epsilon_0}{t_1} \qquad [A\text{-}2]$$

Assume t_1 is constant for time less than 10^{-3} sec based on potential transients (Fig. 7). Boundary conditions at $\tau = 0$ are

$$\Delta\phi = \Delta\phi_1 \quad \text{and} \quad i = i_L \qquad [A\text{-}3]$$

Eliminating i from Eq. [A-1] and [A-2] and rearranging gives

$$\frac{i_o}{c}d\tau = -\exp\left[-\frac{\beta\Delta\phi}{t_1}\right]d\Delta\phi \qquad [A\text{-}4]$$

which may be integrated using boundary conditions [A-3] to give

$$\frac{\beta i_o}{t_1 c}\tau = \exp\left[-\frac{\beta\Delta\phi}{t_1}\right] - \exp\left[-\frac{\beta\Delta\phi_1}{t_1}\right] \qquad [A\text{-}5]$$

Multiplying both sides by $\exp[\beta\Delta\phi_1/t_1]$, noting that $i_L/i_o = \exp[\beta\phi\Delta_1/t_1]$, and rearranging gives

$$-\exp\left[\frac{\beta}{t_1}(\Delta\phi - \Delta\phi_1)\right] = \frac{\beta i_L}{t_1 c}\tau - 1 = \frac{\beta i_L}{\epsilon\epsilon^o}\tau - 1 \qquad [A\text{-}6]$$

A limiting condition of interest is

$$\frac{\beta i_L}{\epsilon\epsilon^o}\tau >> 1 \qquad [A\text{-}7]$$

which gives

$$-\exp\left[\frac{\beta}{t_1}(\Delta\phi - \Delta\phi_1)\right] \approx \frac{\beta i_L}{\epsilon\epsilon^o}\tau \qquad [A\text{-}8]$$

or

$$\frac{\beta}{t_1}(\Delta\phi - \Delta\phi_1) \approx \ln\left[\frac{\beta i_L}{\epsilon\epsilon^o}\tau\right] \qquad [A\text{-}9]$$

Differentiating gives

$$\frac{d\phi}{d\ln\tau} \approx -\frac{t_1}{\beta} \qquad [A\text{-}10]$$

LIST OF SYMBOLS

a	constant
A	area, cm^2
c	capacitance, F/cm^2
C	concentration, mol/cm^3
d	depth, cm
D	diffusivity, cm^2/sec
$\mathbf{F}$	Faraday, 96,500 C/equiv.
i	current density, A/cm^2
i_o	exchange current density, A/cm^2
K	constant
l	length, cm
n	number of particles per mol
p	pressure, cm Hg
P	permeability, cm^3 (STP) sec^{-1} cm^{-1} cm (cm Hg)$^{-1}$
r	radius, cm
R	gas constant
S	supersaturation ratio
t	thickness, cm
t_-	transference number
T	absolute temperature, K
v	volumetric rate of H_2 evolution, cm^3/sec
V	molar volume, cm^3/mol
w	width, cm
z	valence, equiv./mol
β	exponential constant, cm/V
γ	surface energy, erg/cm^2
ϵ	dielectric constant
ϵ_0	permittivity of free space, 8.85×10^{-14} C/V · cm
σ	conductivity, S/cm
τ	time, sec
ϕ	potential, V

Subscripts

a	anodic
b	bulk
d	dissolution
e	electrolyte
H_2	hydrogen
L	limiting
p	peak
s	saturation
w	water
1	state 1
2	state 2
θ	electron

Superscripts

*	supersaturated

REFERENCES

1. G. D. Bengough and L. Whitby, *Trans. Inst. Chem. Eng.*, **11**, 176 (1933).
2. H. A. Robinson, *Trans. Electrochem. Soc.*, **96**, 485 (1946).
3. R. Glicksman and C. L. Morehouse, *This Journal*, **102**, 273 (1955).
4. G. E. Coates, *J. Chem. Soc.*, 478 (1945).
5. G. E. Coates, *ibid.*, 484 (1945).
6. C. V. King and W. H. Cathcart, *J. Am. Chem. Soc.*, **59**, 63 (1937).
7. G. R. Hoey and M. Cohen, *This Journal*, **105**, 249 (1948).
8. J. L. Robinson and P. F. King, *ibid.*, **108**, 36 (1961).
9. P. F. King, *ibid.*, **110**, 1113 (1963).
10. W. J. James, in "Advances in Corrosion Science and Technology," Vol. 4, M. G. Fontana and R. W. Staehle, Editors, pp. 128-133, Plenum Press, New York (1974).
11. T. R. Beck, *This Journal*, **120**, 1317 (1973).
12. T. R. Beck and S. G. Chan, *Corrosion*, **37**, 665 (1981).
13. T. R. Beck, *ibid.*, **33**, 9 (1977).
14. "C.R.C. Handbook of Chemistry and Physics," 58th ed., C.R.C. Press, Cleveland, Ohio (1978).
15. W. M. Latimer, "Oxidation Potentials," 2nd ed., Prentice Hall, Englewood Cliffs, NJ (1952).
16. G. Kortum, "Treatise on Electrochemistry," 2nd ed., Elsevier, New York (1965).
17. T. W. Chapman and J. Newman, Lawrence Radiation Laboratory Report, UC-4 Chemistry, TID-4500, May 1968.
18. R. T. Johnson, R. W. Rousseau, and W. L. McCabe, in "Crystallization from Solution: Nucleation Phenomena in Growing Crystal Systems," J. Estrin, Editor, p. 31, A.I.Ch.E. Symposium Series, No. 121, Vol. 68, New York (1972).
19. T. N. Naumova, Z. A. Starikova, L. S. Zhevina, L. I. Cklochina, and B. D. Stjepin, in "Industrial Crystallization," E. J. DeLong and S. J. Jancic, Editors, p. 37, Proc. 7th Symposium, Warsaw, Sept. 1978; North Holland Publishing Co., New York (1979).
20. L. Young, "Anodic Oxide Films," Academic Press, New York (1961).
21. *E.g.*, S. N. S. Reddy and R. A. Rapp, *This Journal*, **126**, 2023 (1979).
22. J. A. Davies, B. Domeij, J. P. S. Pringle, and F. Brown, *ibid.*, **112**, 675 (1965).
23. W. A. Lanford, R. S. Alwitt, and C. K. Dyer, *ibid.*, **127**, 405 (1980).
24. J. Brandrup and E. H. Immergut, Editors, "Polymer Handbook," III-229, John Wiley & Sons, Inc., New York (1975).

Conductance Measurements in an Electrolytic Membrane Cell at Elevated Temperatures and Pressures

A. Steck and H. L. Yeager*

Department of Chemistry, University of Calgary, Calgary, Alberta, Canada T2N 1N4

ABSTRACT

A Teflon test cell has been built to measure d-c membrane conductance in highly concentrated alkali metal hydroxide solutions at temperatures and pressures up to 200°C and 100 bar. The method allows these measurements to be conducted for membrane current densities up to 1.5 A-cm^{-2}. The membrane voltage drop is determined using reference electrodes which are placed on either side of the membrane. Conductance data were obtained for Nafion® perfluorinated sulfonate ionomer of 1150 equiv. wt in the temperature range of 100°-180°C. Results show a tenfold decrease in specific conductance when the solution concentration is increased from 5.0 to 10.0M sodium hydroxide solution.

Polymer ion exchange membranes must possess a combination of properties to enable their application in modern electrolytic industrial processes. These include good permselectivity, low electrical resistance, chemical and thermal stability, as well as sufficient mechanical strength at the operating conditions. Ion-exchange membranes have already found application in electrochemical cells (1), in solid polymer electrolyte (SPE) fuel cells (2), and in electrolysis cells for chlor-alkali and hydrogen production (3-4). In the latter process, significant gains in the efficiency of hydrogen production can be achieved by performing the electrolysis in highly concentrated alkaline hydroxide solutions at temperatures up to 200°C and pressures up to 40 bar (4). In recent years, chrysotile asbestos has been frequently used as a diaphragm separator in alkaline systems. However, this material is subject to chemical attack, especially at temperatures above 110°C (5). At present, no commercial separator exists that can withstand these extreme conditions for prolonged periods. Therefore, advancement in alkaline electrolyzer technology has to be accompanied by progress in synthetic membrane technology. At the same time, the electrochemical properties of newly developed membrane materials have to be studied and tested under the severe conditions described above. The measurement of separator resistance is of particular importance because of the direct relationship of membrane-related ohmic loss on the energy efficiency of the cell. In this paper, we describe a method to determine membrane conductance in highly concentrated potassium and sodium hydroxide solutions at temperatures and pressures up to 200°C and 100 bar. The method allows these measurements to be conducted for membrane current densities up to 1.5 A-cm^{-2}. The membrane voltage drop is determined using reference electrodes that are placed on either side of the membrane. Correction for solution resistance is made by performing a duplicate experiment with no membrane in place. The general method applied here is described by Lander and Weaver (6).

Several methods for measuring electrical conductance of ion-exchange membranes using mainly a-c techniques have been described by Steymans and others (7-10). A-c techniques are inappropriate since we wish to measure conductance under actual electrolysis conditions. In addition, the methods described in the literature are generally only suitable for measurements at temperatures below 100°C and ambient pressure.

Nafion® perfluorinated sulfonate ionomer of 1150 equiv. wt was used to test the method. This type of membrane shows promise in a number of electrochemical applications with corrosive environments because of its exceptional chemical inertness and thermal stability (11). The conductivities of Nafion membranes of various equivalent weights have been studied by several investigators. Coalson and Grot studied resistivities of Nafion having an equivalent weight of 1250 as a function of membrane water content (12). Resistivities were obtained by performing a-c conductance measurements for membranes which had been pre-equilibrated in 40% KOH solution. Kreja, Wodzki, and Grochowski described a device to measure a-c conductance of ion exchange membranes (8). Specific area resistance and specific conductance of 1200 equiv. wt Nafion membranes were measured at room temperatures in 0.1M NaCl solution. Hsu, Barkley, and Meakin determined room temperature conductivities of Nafion samples with equivalent weights ranging from 1050 to 1500 as a function of the volume fraction of the aqueous phase in the membrane (13). Sample conductivity was measured by an a-c technique at a current density of 1.25 mA-cm^{-2}. Berzins, as well as Yeo and co-workers, reports conductivity measurements of Nafion membranes in several industrially important electrolyte environments (14, 15). Berzins (14) describes an experimental apparatus for the determination of voltage drop across membranes in chlor-alkali cells under gas-free conditions. Voltage drops for Nafion samples were studied as a function of current density, temperature, sodium hydroxide concentration, and membrane equivalent weight. The experimental conditions used were similar to those encountered in chlor-alkali cells, in that concentrated sodium chloride and sodium hydroxide solutions were used at temperatures up to 90°C and current densities up to 0.5 A-cm^{-2}. Yeo and co-workers (15) studied d-c membrane conductivities as a function of hydrochloric acid in the temperature range of 25°-70°C. Cell resistance data for water electrolysis using Nafion 115 (1100 equiv. wt) as the separator at temperatures up to 95°C are reported elsewhere (16).

To date, no conductance results for ion exchange membranes at elevated pressures and temperatures over 100°C have been reported. Thus, the present work was initiated to explore these experimental conditions for applications such as the electrolytic production of hydrogen.

Experimental

Apparatus.—An electrolysis cell was designed and built for membrane conductance studies; components of the cell are shown in Fig. 1. Top and side sectional views of the cell are shown in Fig. 2. The cell is constructed of molded Teflon rod. Nickel oxide electrodes obtained from commercial nickel-cadmium batteries and circular platinum mesh electrodes (2.8 cm diam) are used as reference and working electrodes, respectively. The reference electrodes are 30 × 5 mm in size and are welded to nickel lead wires. New electrodes were used for each series of measurements to ensure reliability of operation.

* Electrochemical Society Active Member.
Key words: separator, resistivity, ion exchange.

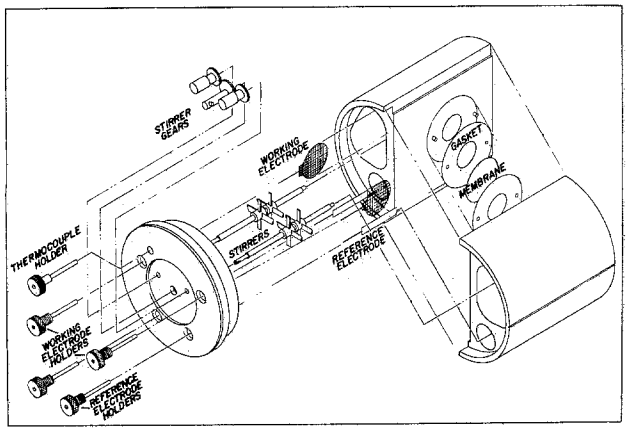

Fig. 1. Teflon test cell for the measurement of membrane conductance.

Two capillaries are used to connect each reference electrode chamber to one of the electrolysis chambers. A fine capillary, 0.3 mm diam, is used between the solution at the membrane face and the larger, 1.5 mm diam capillary. These capillaries are connected at an angle (Fig. 2, side view) to help prevent bubble blockage during electrolysis.

The shape of the electrolysis chambers was developed in order to maximize solution volumes without sacrificing structural integrity. The volume of each chamber is 130 ml. The membrane is placed between the half-cells using porous Teflon gaskets which are recessed and aligned by Teflon pins. The two cell compartments are clamped together with four spring-loaded bolts. The springs are essential to balance the cell expansion at higher temperatures. In a newer model, the bolts were replaced by two stainless steel straps. These straps are placed around the two half-cells into a recessed position where they are tightened with screws. With this improvement, a more uniform pressure at the gaskets was obtained.

Teflon stirring assemblies are connected to stainless steel stirring gears, as shown in Fig. 1. The electrolysis solutions are stirred at a speed of 500 rpm during electrolysis. A copper-constantan thermocouple in a Teflon sheath is employed to measure the temperature of the electrolyte in the cell.

A pressure vessel to house the conductance cell was built by the Parr Instrument Company. The vessel has a capacity of 1000 cm^3 and can withstand temperatures up to 350°C. It is fitted with a pressure gauge and rupture disk. Leads for working and reference electrodes, gas inlets and outlets, and sample valve have been designed specifically to fit the conductance cell. The sampling valve allows for liquid sample withdrawal from the test cell. Various connections are used to operate the cell inside the pressure vessel. The reference electrodes are connected by pressure-fit pins and inserts, while the working electrodes are attached with lock screws. All of the leads are coated with Teflon tubing. The pressure vessel is placed in an external heater for temperature regulation. Currents and voltages are measured with a Tektronix power module TM 501 and a Keithley Model 177 digital multimeter. The two quantities can be measured with an accuracy of ±0.1 mA and ±0.1 mV, respectively.

Procedure.—Nafion membrane samples of 3 cm diam were equilibrated at 100°C in the appropriate solutions for at least 12 hr. Such pretreatments are of importance and can greatly influence the chemical (17) and electrochemical (12, 15) properties of the membrane. In each case, the membrane was then blotted with paper tissue and carefully placed into the conductance test cell. The cell was slowly filled with degassed electrolyte solution. A light pressure with a Teflon piston was applied over the reference chambers to eliminate any adhering air bubbles in the capillary system. After insertion of the half-charged nickel

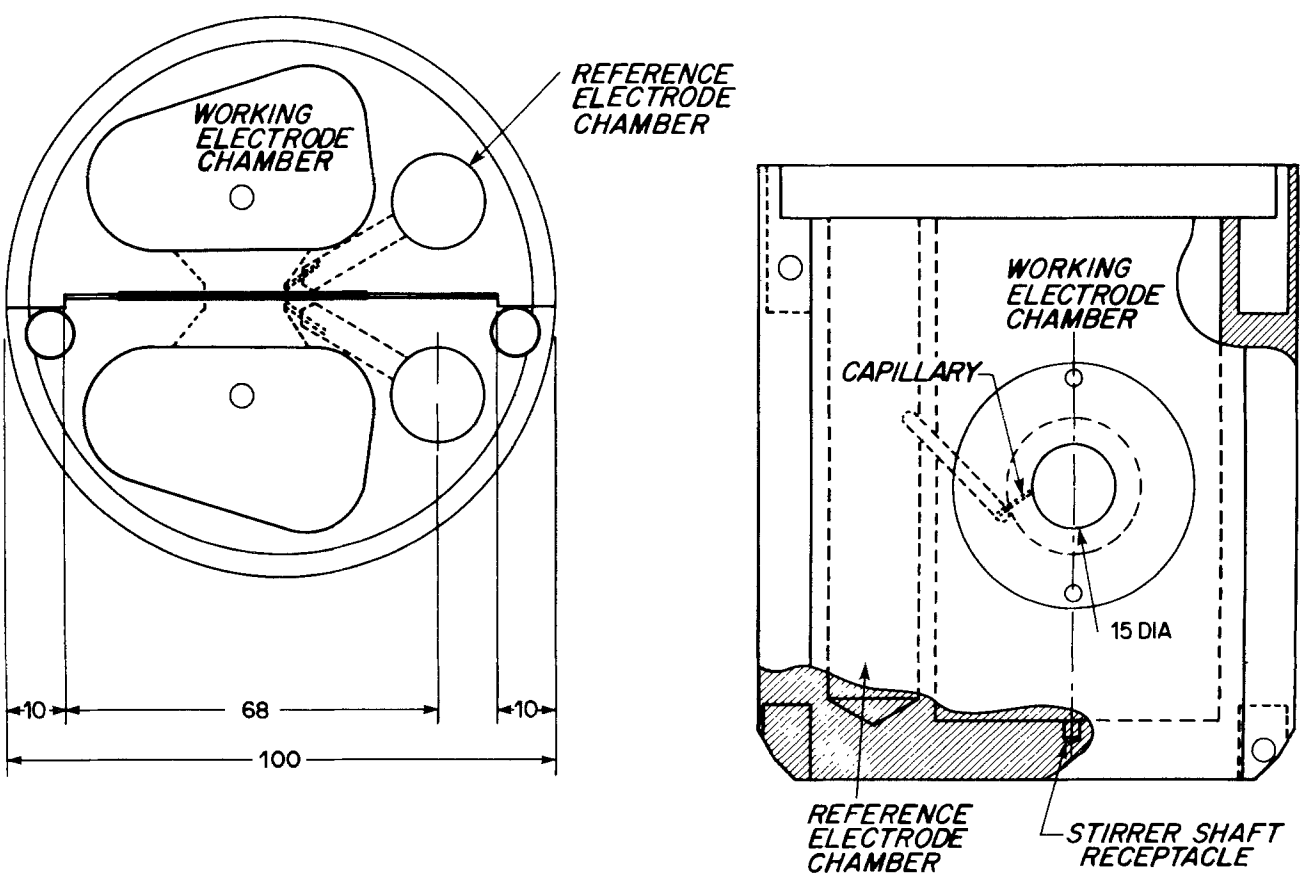

Fig. 2. Top and side cross-sectional views of the test cell, dimensions in mm

electrodes, the Teflon cell was placed into the pressure vessel. Voltage measurements were performed in the temperature range of 100°-180°C at intervals of 20°C. Slow heating rates of about 5°C/hr were chosen at the temperatures of interest to allow enough time for thermal equilibrium of the membrane. Once the desired temperature was reached, it was held constant for an additional 2-3 hr. Cell pressure was adjusted to 30 bar with pressurized nitrogen gas for all measurements. A small residual potential difference, on the order of 1-10 mV, was observed between the reference electrodes at zero electrolysis current. Measured voltages were corrected for this asymmetry potential; the corrections averaged about 1% for results reported here. Electrolysis was begun using the highest current density to be employed; the current was then decreased stepwise, and membrane voltage-drop was recorded at each current.

Voltage readings were taken as soon as a constant value was obtained, which was within 20 sec for a given current. The duration of an experiment covering the temperature and current density range of 100°-180°C and 0.05-1.0 A-cm^{-2}, respectively, is 36 hr. However, total electrolysis time is not more than 10 min. This causes an electrolyte concentration change of less than 1%. Experiments are performed both with and without the membrane to correct for the resistance of the electrolyte.

Materials.—A Nafion® perfluorosulfonate membrane (Plastics Department, du Pont and Company, Wilmington, Delaware) of 1150 equiv. wt was used in this work. The exchange capacity was determined to be 0.866 mequiv./g dry sodium ion form membrane by a radioisotope method (18). The thickness of the membrane determined at 140°C in 10.0M NaOH was 0.0190 cm.

Results and Discussion

The determination of membrane conductance data requires two series of experiments. The electrical potential gradient between the two reference electrodes is measured in the presence and in the absence of the membrane in the cell under otherwise identical conditions. The voltage drop due to the membrane alone is then the difference of the two values. Thus, the contribution of solution resistance is eliminated. This correction was 35% in the worst case and averaged approximately 10% for the data reported here. The method was checked in part for this cell design by measuring the solution conductance of a 20.0 weight percent (w/o) NaOH solution. The determined value of 0.32 Ω^{-1} cm^{-1} agrees well with the literature value of 0.33 Ω^{-1} cm^{-1} (19). Comparison of membrane conductance values with literature values is more difficult because of the strong influence of membrane pretreatment and equivalent weight on the conductance. The specific conductance of 1150 equiv. wt Nafion was measured in 0.10M NaOH solution at room temperature and low current densities. Our measured value of 7.0×10^{-3} Ω^{-1} cm^{-1} corresponds reasonably well with the literature value of 5.7×10^{-3} Ω^{-1} cm^{-1} found for 1200 equiv. wt Nafion (8). A higher value for 1150 equiv. wt Nafion would be expected because of its lower equivalent weight.

Membrane specific conductance is plotted *vs.* current density at various temperatures in 5.0 and 10.0M sodium hydroxide solutions in Fig. 3 and 4. Two major differences are seen between the results for the lower and higher solution concentrations. First, the membrane displays an approximate tenfold decrease in specific conductance when the solution concentration is increased from 5.0 to 10.0M NaOH. Second, there is a distinct difference in the functionality of specific conductance *vs.* current density for the two solution environments. The membrane essentially shows ohmic behavior in the less concentrated electrolyte, while in the more concentrated solution the specific conductance of the membrane increases with increasing current density. Solution specific conductances were found to be independent of current density in all cases here as expected.

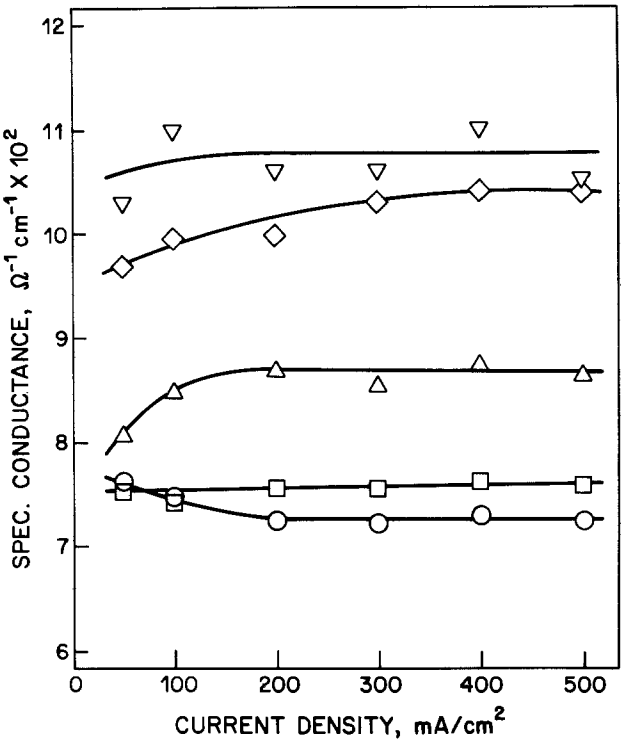

Fig. 3. Membrane specific conductance *vs.* current density in 5.0M NaOH solution, 30 bar. ○, 100°C; □, 120°C; △, 140°C; ◇, 160°C; ▽, 180°C.

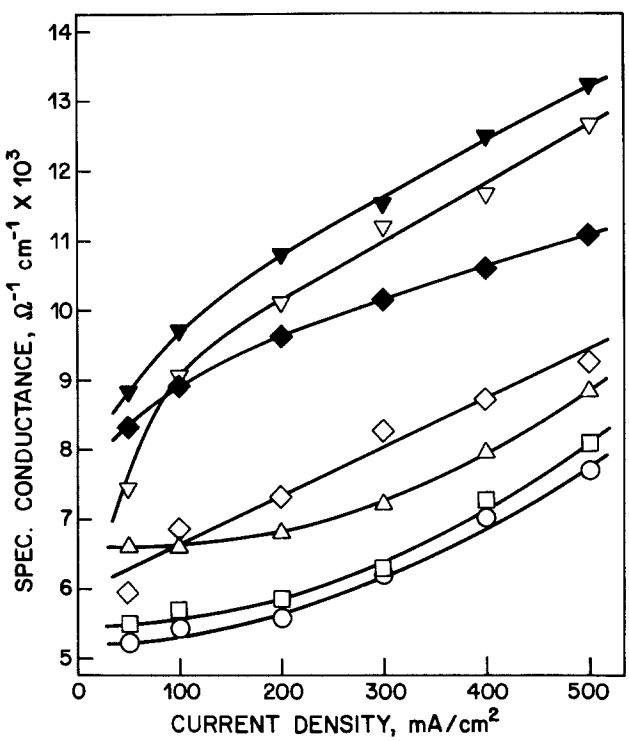

Fig. 4. Membrane specific conductance *vs.* current density in 10.0M NaOH solution, 30 bar. Closed symbols, repeated measurements after additional heating cycle. ○, 100°C; □, 120°C; △, 140°C; ◇, ◆, 160°C; ▽, ▼, 180°C.

The two curves with closed symbols in Fig. 4 were obtained by repeating the experiment after cooling the cell down to room temperature and reheating it to 180°C. Measurements then were taken beginning at the highest temperature. The change in conductance caused by the previous treatment of the membrane is evident;

this is probably due to morphological changes which are time and temperature dependent. Similar variations of specific conductance as a function of thermal cycling have been reported in the literature (15).

Membrane conductance and ionic diffusion coefficients are interrelated. The specific conductance is mainly governed by the concentration and mobility of the charge carriers in the membrane (20). In dilute solutions, the specific conductance of an ion exchanger increases with increasing solution concentration due to the onset of electrolyte sorption. However, this relationship may be inverted in highly concentrated solutions because of polymer dehydration. In order to interpret our results, it is useful to refer to available sorption and sodium ion diffusion results for this membrane. Results have been reported for the temperature range of 70°-90°C in 5.0-12.5M NaOH solutions (21-23). These studies indicate that the sorption properties of Nafion are generally characterized by relatively constant electrolyte uptake, but steadily decreasing water to ion ratios with increasing solution concentration. These features were also found at room temperature (24). The ratio of water to sodium ion at 80°C decreases by approximately 35% as the equilibrating solution concentrations are increased from 5.0 to 10.0M. This sorption behavior has a great impact on the ion diffusional properties of the membrane. Measured Na^+ self-diffusion coefficients decreased by a factor of 10 over the same concentration region (21). Membrane dehydration and the drop in the water to sodium ion ratio are seen as the major causes. This would be expected to be true even at the higher temperatures used here. Thus, the tenfold decrease in electrical conductance with increasing solution concentration correlates well with diffusion data. Interestingly, activation energies of 14 kJ mol^{-1} for diffusion (70°-90°C) and 10 kJ mol^{-1} for conductance (100°-180°C) are very close and were found to be similar in both solution environments.

The reason for nonohmic membrane behavior in 10M NaOH solution is not apparent. However, the effects of high current flow on a severely dehydrated membrane may produce morphological changes to alter the character of the ionic conduction path in the polymer.

In summary, a test cell for the measurement of membrane conductance at high current densities has been designed and built. The cell can be used at temperatures and pressures up to 200°C and 100 bar. Future work will include the use of this cell to study newly developed polymer membranes for use in high pressure high temperature alkaline water electrolyzers.

Acknowledgments

The authors wish to thank T. E. Mani, R. Keen, and J. D. Malinsky for their help in the construction of the conductance cell, and E. I. du Pont de Nemours and Company for samples of Nafion. Financial support was provided by the National Research Council of Canada.

Manuscript submitted July 21, 1982; revised manuscript received Feb. 16, 1983.

Any discussion of this paper will appear in a Discussion Section to be published in the December 1983 JOURNAL. All discussions for the December 1983 Discussion Section should be submitted by Aug. 1, 1983.

The University of Calgary assisted in meeting the publication costs of this article.

REFERENCES

1. J. S. Ling and J. Charleston, in "Ion Exchange," R. A. Yeo and R. P. Buck, Editors, p. 334, The Electrochemical Society Softbound Proceedings Series, Pennington, NJ (1981).
2. E. Gileadi, S. Srinivasan, F. J. Salzano, C. Braun, A. Beaufrere, S. Gottesfeld, L. J. Nuttal, and A. B. La Conti, *J. Power Sources*, **2**, 191 (1977).
3. "Perfluorinated Ionomer Membranes," A. Eisenberg and H. L. Yeager, Editors, Am. Chem. Soc. Symposium Series No. 180, American Chemical Society, Washington, DC (1982).
4. "Hydrogen Manufacture by Electrolysis, Thermal Decomposition and Unusual Techniques," M. S. Casper, Editor, pp. 111-205, Noyes Data Corp., Park Ridge, NJ (1978).
5. P. Godin, R. Graziotti, A. Damien, and P. Masniere, *Int. J. Hydrogen Energy*, **2**, 291 (1977).
6. J. J. Lander and R. D. Weaver, in "Characteristics of of Separators for Alkaline Silver Oxide Zinc Secondary Batteries," G. E. Cooper and A. Fleischer, Editors, pp. 53-68, Air Force Aero Space Propulsion Laboratory, Dayton, OH (1965).
7. Cl. Steymans, *Ber. Bunsenges. Phys. Chem.*, **71**, 818 (1967).
8. L. Kreja, R. Wodzki, and W. Grochowski, *Inzynieria Chemiczna IX*, 3, 663 (1979).
9. V. Subrahmanyan and N. Lakshminarayanaiah, *J. Phys. Chem.*, **72**, 4314 (1968).
10. R. Arnold and D. F. A. Koch, *Aust. J. Chem.*, **19**, 1299 (1966).
11. B. Kipling, in "Perfluorinated Ionomer Membranes," Chap. 19, Am. Chem. Soc. Symposium Series No. 180, American Chemical Society, Washington, DC (1982).
12. R. L. Coalson and W. G. Grot, U.S. Pat. 3,684,747 (1972).
13. W. Y. Hsu, J. R. Barkley, and P. Meakin, *Macromolecules*, **13**, 198 (1980).
14. T. Berzins, Paper 437 presented at The Electrochemical Society Meeting, Atlanta, GA, Oct. 9-14, 1977.
15. R. S. Yeo and J. McBreen, *This Journal*, **126**, 1682 (1979).
16. R. S. Yeo, J. McBreen, G. Kissel, F. Kulesa, and S. Srinivasan, *J. Appl. Electrochem.*, **10**, 741 (1980).
17. A. Steck and H. L. Yeager, *Anal. Chem.*, **52**, 1215 (1980).
18. H. L. Yeager and A. Steck, *ibid.*, **51**, 862 (1979).
19. P. L. Spedding, in "Proceedings of the First Australian Conference on Electrochemistry," J. A. Friend and F. Gutman, Editors, Sidney, 1963, Symposium Publications Division, Pergamon Press, Elmsford, NY (1965).
20. F. Helfferich, "Ion Exchange," Chap. 7, McGraw Hill Book Co., New York (1962).
21. Z. Twardowski, H. L. Yeager, and B. O'Dell, *This Journal*, **129**, 328 (1982).
22. H. L. Yeager, B. Kipling, and R. L. Dotson, *ibid.*, **127**, 303 (1980).
23. H. L. Yeager and J. D. Malinsky, in "Proceedings of the Symposium on Membranes and Electronic Conducting Polymers," Cleveland, OH, In press.
24. K. A. Mauritz, K. J. Branchick, C. I. Gray, and S. R. Lowry, *Polym. Prepr. Am. Chem. Soc. Div. Polym. Chem.*, **21**, 122 (1980).

Photoelectrochemical Behavior and Light-Induced Anodic Transformation of Zirconium Trisulfide

O. Gorochov, A. Katty, N. Le Nagard, and C. Levy-Clement*

Laboratoire de Physique des Solides, CNRS, Meudon, France

and A. Redon* and H. Tributsch[1]

Laboratoire d'Electrochimie Interfaciale, CNRS, Meudon, France

ABSTRACT

n-type ZrS_3, a semiconductor with a bandgap of approximately 2.1 eV turned out to be a photoelectrochemical material with large anodic photocurrents and low dark currents. In contrast to ZrS_2, CdS, and many other sulfides which derive their valence band mainly from sulfur p-states, ZrS_3 is interestingly not photo-oxidized to molecular sulfur and metal ions. Instead, there is a photoreaction involving water, and the originally bright red crystal is gradually converted into a white one containing oxygen without losing much of its original shape and consistency. The occurrence of sulfur in the form of S_2^{2-} in this material, as well as the possibility of intercalating oxidation products of water, is considered the reason for this particular photo-oxidation mechanism. It might open new ways for the understanding and control of photocorrosion.

Photoelectrochemical studies of semiconducting layer compounds have shown that the mechanism of light induced reactions depends on the electronic structure of the valence and conduction bands involved (1, 2). They have further demonstrated the possibility of light induced ion-transfer leading to intercalation or deintercalation of layer-type material (3, 4). Semiconductors of group IVA trichalcogenides crystallize in the monoclinic system (space group C_{2h}^2 — P $2_1/m$) (5). These structures have some one-dimensional characteristics due to the existence of trigonal prismatic MX_6 chains parallel to the b axis (Fig. 1). The chains form sheets of like units (parallel to the ab plane) and the sheets are bonded together by Van der Waals-like bonds. These crystallographic characteristics provide new possibilities for research concerning intercalation and photocorrosion properties.

First, the valence band of these trichalcogenides, which is essentially derived from sulfur and selenium orbitals, respectively, also contains electronic levels associated with $(S\text{-}S)^{2-}$ states according to the ionic formula $M^{4+}X^{2-}(X_2)^{2-}$ (Fig. 1). Second, these materials can be intercalated (6) and intercalation should also be possible utilizing light.

ZrS_3 has been characterized by x-ray techniques (7, 8), electronic and transport measurements (9), reflection data (10), and details on the electronic structure of the material have also been provided (11). There also exist studies on Raman spectroscopy (12-14). Energy gaps published in the literature are E_G = 2.2 eV (15) and E_G = 1.9 eV (16). However, there is also a higher value, E_G = 2.8 eV, obtained from optical absorption measurements (17). It is not clear whether this would be the same transition as in the preceding studies or a higher one. Perhaps the transition at 2.0 eV is the indirect gap and transition at 2.8 eV is the first direct transition. A schematic diagram for the electronic states in ZrS_3 has been elaborated by Khumalo and Hughes (10). We show in Fig. 2 a simplified diagram where we have further specified an energetic differentiation between sulfur p-states arising from S^{--} and S_2^{2-} orbitals, respectively. The electrons associated with S^{--} states are more firmly bound and, thus, lower in energy than electron belonging to S_2^{--}. Light induced holes, generated in the valence band, should therefore essentially be available on the latter states for photoelectrochemical reactions. It can be seen from Fig. 2 that the d-states of zirconium only contribute to the conduction band of ZrS_3.

Experimental and Materials

Preparation of samples.—ZrS_3 crystals were grown by chemical vapor transport using either chlorine or iodine as a transport agent. The charge compositions consisted either of stoichiometric mixtures of the elements, or prereacted polycrystalline ZrS_2. A concentration of 60 Torr Cl_2 or 5 mg/cm^3 I_2 was used in 10 mm ID × 200 mm silica tubes. A temperature gradient of 70°C over 100 mm was used. The temperature of the charge zone was 900°C and that of the growth zone 830°C. ZrS_3 crystals grown with Cl_2 from a stoichiometric charge were highly resistive ($\rho > 10^6$ Ωcm). Crystals grown with excess Zr (a charge composition of ZrS_2) with I_2 transport were n-type and had a resistivity on the order of 10^3 Ωcm at room temperature. All samples were characterized by x-ray diffraction, microprobe analysis, and electrical resistivity measurements. The carrier type was determined by qualitative Seebeck measurements. All samples studied were taken from the same batch of crystals grown by iodine transport.

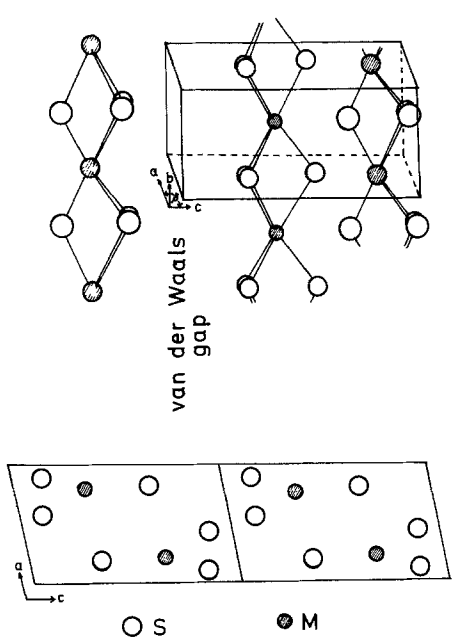

Fig. 1. Crystal structure of ZrS_3

* Electrochemical Society Active Member.

[1] Present address: Hahn Meitner Institut/Strahlenchemie, D-1000 Berlin 39, Gzienicker Strabe 100, Germany.

Key words: ZrS_3, photoelectrochemistry, corrosion mechanism, photopotential.

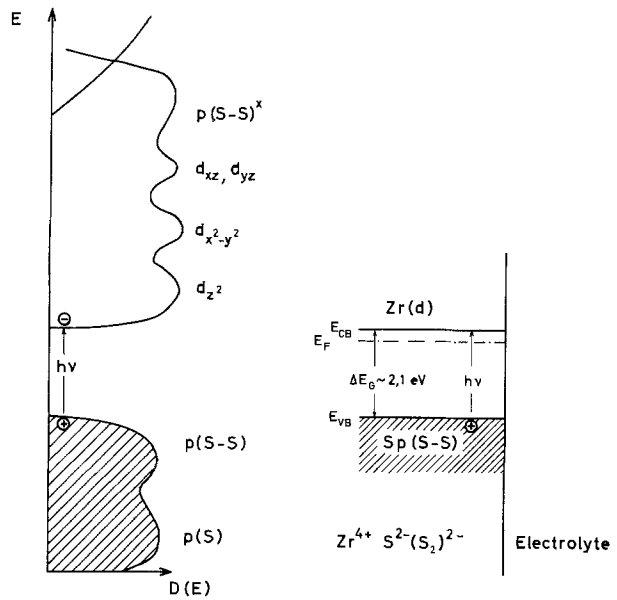

Fig. 2. Energy scheme (left) and band model (right) of ZrS_3

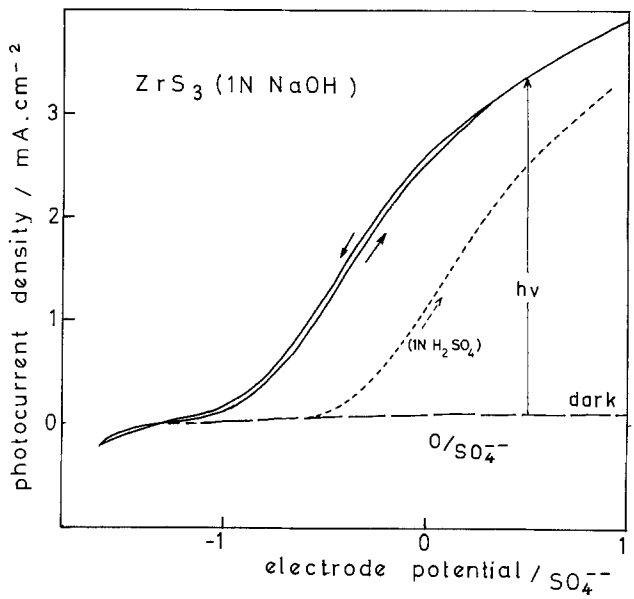

Fig. 3. Current-voltage characteristic of n-type ZrS_3 during and without illumination at $\lambda = 4358$Å.

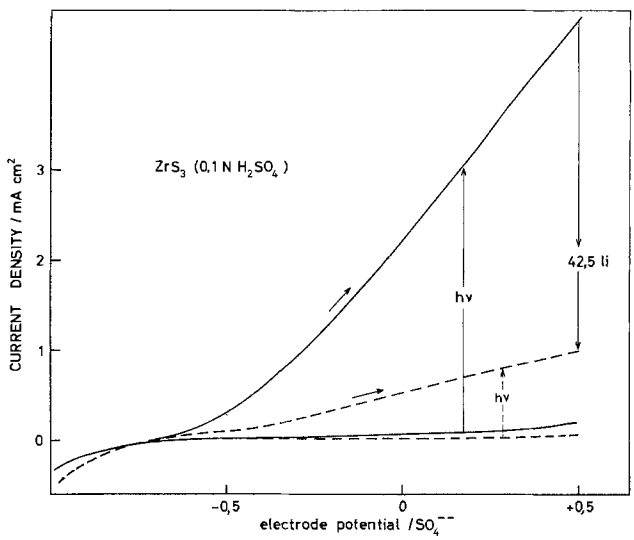

Fig. 4. Photocurrent, and dark current, voltage characteristic of ZrS_3 in contact with an acid electrolyte before and after passage of photocurrent for 42.5 hr at an electrode potential of 0.5V.

Electrochemical techniques.—The electrochemical experiments were performed in a standard photoelectrochemical apparatus. It consisted of a 900W xenon mercury lamp, a high intensity monochromator, an electrochemical cell with three electrodes, a potentiostat, a function generator, and a recorder. For some experiments, the lock-in technique was used. Typically, monochromatic light was used to excite photocurrents. ZrS_3 crystals were attached to a Teflon cylinder containing a copper contact using silver paste. The electrical contact was then isolated with an insulating epoxy resin (Scotch cast-3M) so that only the crystal was exposed.

Analysis of oxidation products.—During the photoanodic reaction, ZrS_3 crystals clearly change from a red transparent appearance into a white opaque product. This reaction preferentially affects some regions of the single crystal. Microprobe analysis has been used to determine the composition of the single crystal in each of its characteristic areas. Zirconium and sulfur have been found to be homogeneously distributed in all single crystals studied before the photoelectrochemical experiment. After an appropriately long time of photoanodic polarization, microprobe analysis has shown that the white regions of the single crystal have lost part of their sulfur content and oxygen was found in those regions.

Results

When an n-type ZrS_3 electrode is immersed in either acidic or basic aqueous electrolytes and illuminated, large anodic photocurrents are observed. Monochromatic light from a 900W mercury-xenon lamp ($\lambda = 4358$Å; 100 μW/cm²) induces photocurrents on the order of several mA/cm² in both acidic and basic solution as shown in Fig. 3. As compared with an electrode in contact with a 0.1*N* H_2SO_4 solution, the photocurrents of an electrode exposed to an alkaline electrolyte start at electrode potentials which are approximately 0.6V more negative. There is consequently a clear pH-effect in the electrochemical behavior of ZrS_3. When no redox systems besides the H_2O/O_2 couple are present in the electrolyte the photocurrents passing through the ZrS_3 sample gradually decrease. Figure 4 shows to what extent the photocurrent passing at 0.5V (against a sulfate reference) is dimishing in the course of 42.5 hr. Interestingly, the dark current across the ZrS_3-electrolyte interface is not increasing, but decreasing during this long-term exposure to light. There is also no pronounced change in the shape of the current-voltage characteristic of the semiconductor electrode. Figure 5 shows the spectral dependence of the ZrS_3-electrode interface. Two bandgap values published in the literature (13, 14) are indicated for comparison. A linear extrapolation of the main slope of the photocurrent edge yields approximately $E_G = 2.1$ eV which is a good average.

More optical experiments are needed to obtain a more accurate value for the bandgap and to understand the much higher value of $E_G = 2.8$ eV published in Ref. (17). When redox systems like $Ce^{3+/4+}$, Br^-/Br_2, $Fe^{2+/3+}$, I^-/I_3^- $Fe(CN)_6^{4-/3-}$, $Ti^{3+/4+}$, or S/S^{--} were added to the electrolyte in contact with ZrS_3 no significant displacement or modification of the photocurrent voltage characteristic was observed. Since a metal counterelectrode in contact with these redox agents would assume the corresponding redox potential, it should be expected that the photovoltage of ZrS_3 should increase with increasingly positive redox potential of the electrolyte. As Fig. 6 shows, this is not observed. The photopotentials observed stay almost constant between 0.32-0.37V regardless of whether I^-/I_2 (redox potential = 0.53V) or $Ce^{3+/4+}$ (redox potential = 1.44V) is present in the electrolyte.

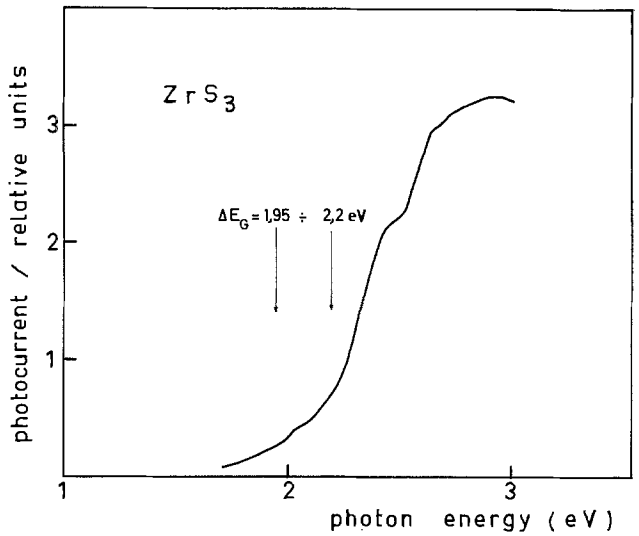

Fig. 5. Dependence of photocurrents across a ZrS_3 electrolyte interface on the energy of incident photons. Two values for the energy gap published in the literature (15, 16) are indicated.

A remarkable and entirely new type of photo-oxidation mechanism was detected with ZrS_3. The filamentary fibrous strands of ZrS_3 expose two entirely different interfaces to the electrolyte. One, // ab, is essentially a Van der Waals surface along which the crystal can be cleaved and where no dangling bonds are available. It forms the main surface areas of the flat, elastic ZrS_3 needles (Fig. 7). The other surface, // ac, forms only a smaller fraction of the ZrS_3 needles, as can readily be seen since the photoanodic attack of the crystals starts from this surface.

No molecular sulfur was found as a photo-oxidation product after long-term experiments in alkaline and acidic electrolytes. The total number of coulombs passing through the cell was 8 times higher than needed to completely convert all the sulfur ions to elemental sulfur. The white oxidation product found could not be identified as elemental sulfur by chemical means or by microprobe analysis techniques. It is clearly a Zr oxide or hydroxide. In addition, the photo-oxidation products are not an amorphous layer, as in the case of sulfur on CdS. Instead, the initially bright red and reddish transparent ZrS_3 crystals gradually become white. First, the rims turn white and, then, these white regions move in and entirely across the crystals. In most cases, the mechanical consistency

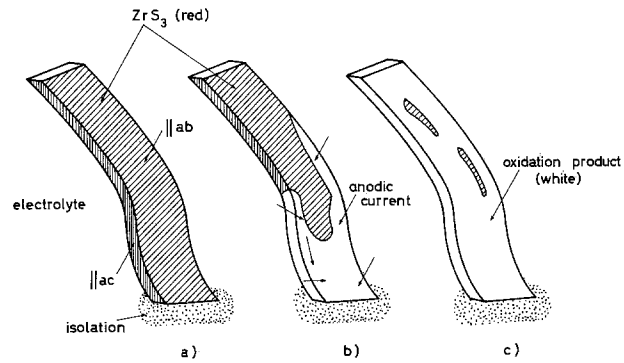

Fig. 7. Transformation of fibrous strand of ZrS_3 during photo-oxidation a) before experiment, b) during experiment, c) after nearly complete oxidation.

of the electrode was maintained and some samples were finally completely white while others still showed thin red filaments. They were apparently electrically disconnected from the bulk electrode. The white regions followed the current lines through the crystal as shown in Fig. 7.

They first penetrated the base of the crystals which attracted the highest current densities and subsequently expanded to the top. Experiments with the microprobe performed with these photo-oxidized ZrS_3 crystals showed that their content of sulfur had decreased and that oxygen had been taken up into the bulk material.

Discussion

Concerning the photoelectrical response, ZrS_3 appears to be an interesting system for photoelectrochemical studies. However, the photopotentials which have been produced with this system are far from being as high as theoretically possible. They also do not change with the redox potential of the electrolyte as would be expected theoretically. When redox couples are added, the flatband potential of the semiconductor is not noticeably affected. As a consequence, the mechanism responsible for the low value of photopotentials must involve a process which counteracts the flattening of the energy-bands during illumination. This might occur through an electron transfer process which enables excited electrons to pass over to oxidized surface states (Fig. 8). In order to explain a photopotential which is largely independent of the redox potential of the electrolyte, it has to be assumed that the position of these surface states change

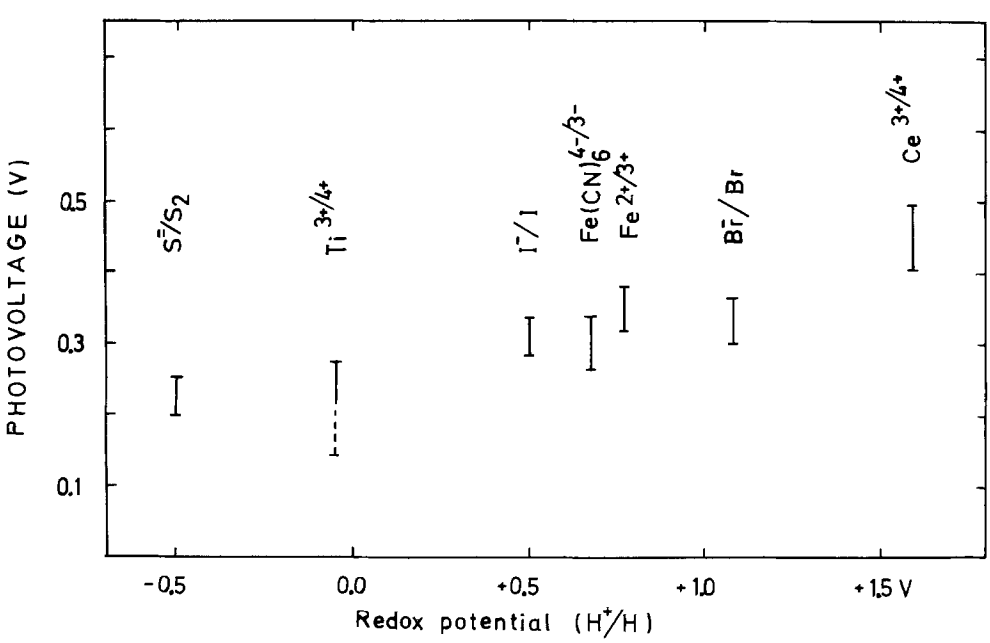

Fig. 6. Dependence of photopotentials of ZrS_3 (measured against a metal electrode) from the redox potential of the electrolyte.

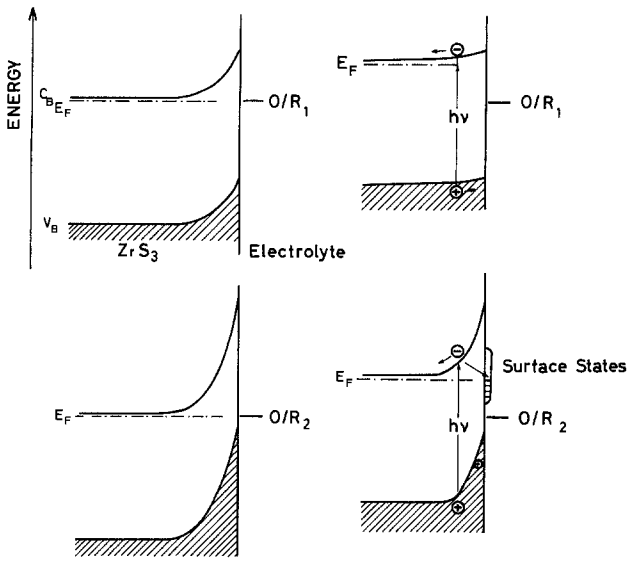

Fig. 8. Energy schemes showing the ZrS_3/electrolyte interfaces, without and during illumination in presence of two redox systems with very different redox potentials. The role of surface states in preventing flattening of the energy bands during illumination is indicated.

in a parallel way with the redox potential. It would seem to be reasonable to assume that these surface states are due to that interface which is chemically more reactive (// ac). However, it seems equally to be possible that these states originate from products which are intercalated into the ZrS_3 crystal. Thus, from the photoelectrochemical point of view, the ZrS_3 electrode is full of complications, which can only be resolved through more detailed experimental work.

The photoelectrochemical oxidation mechanism observed with ZrS_3 in contact with aqueous electrolytes is presently unique of its kind. Experience with metal sulfide electrodes has shown that molecular sulfur is a frequently obtained photo-oxidation product (*e.g.*, with CdS, ZrS_2). When a photoreaction with water is possible, sulfate may be obtained (*e.g.*, with MoS_2, WS_2). In the case of ZrS_3, however, oxygen is introduced into the crystal structure of the sulfide as a consequence of the anodic passage of photocurrents. A precondition for this is that sulfur bonds, which are essential for the stability of the crystal, are not broken and another one that water is photoreacting with the material, thus, releasing an oxygen containing intermediate which can be intercalated (the most probable candidate is intercalated OH). The fact that molecular sulfur is not released is important. It suggests that $(S\text{-}S)^{2-}$ groups are more favorable as hole mediators in photo-oxidation than S^{2-} states. The observation that an oxidation product of water is penetrating the solid electrode material is also interesting. This mechanism involves a kind of memory of photoelectrochemical processes which might have practical applications.

The fact that the photo-oxidation mechanism of ZrS_3 is entirely different from that of other sulfur containing electrodes suggests also the possibility of finding new ways of control of photocorrosion. What should, for example, be expected, when an organic electrolyte is used which cannot serve as an oxygen donor to illuminated ZrS_3? The mechanism of anodic phototransformation of ZrS_3 is presently under further study in our laboratory.

Acknowledgments

This work was supported by the European Community (project No. ESD-028-F). One of the authors thanks the Deutsche Forschungsgemeinchaft for Heisenberg fellowship. The authors wish to thank B. Fotouhi and K. Sieber for helpful discussions, and M. Rommeluere for the microprobe analysis.

Manuscript submitted March 4, 1982; revised manuscript received Feb. 2, 1983.

Any discussion of this paper will appear in a Discussion Section to be published in the December 1983 JOURNAL. All discussions for the December 1983 Discussion Section should be submitted by Aug. 1, 1983.

CNRS assisted in meeting the publication costs of this article.

REFERENCES

1. H. Tributsch, "Solar Energy Materials," Springer Verlag, Berlin (1981).
2. H. Tributsch, *This Journal*, **128**, 1261 (1981).
3. H. Tributsch, *Appl. Phys.*, **23**, 61 (1980).
4. M. Abramovich, O. Gorochov, and H. Tributsch, *J. Electroanal. Chem.*, To be published.
5. F. K. McTaggart and A. D. Wadsley, *Austr. J. Chem.*, **11**, 445 (1958).
6. R. R. Chianelli and M. B. Dines, *Inorg. Chem.*, **14**, 2427 (1975).
7. S. Furuseth, L. Brattas, and A. Kjekshus, *Acta Chem. Scand.*, **A29**, 623 (1975).
8. W. Kronert and K. Z. Plieth, *Anorg. Allg. Chem.*, **336**, 207 (1965).
9. G. Perluzzo, A. A. Lakhani, and S. Jandl, *Solid State Commun.*, **35**, 301 (1980).
10. G. Perluzzo, S. Jandl, and P. E. Girard, *Can. J. Phys.*, **58**, A3 (1980).
11. F. S. Khumalo and H. P. Hughes, *Phys. Rev.*, **B22**, 2078 (1980).
12. A. Zwick and M. A. Renucci, *Phys. Status Solidi B*, **96**, 756 (1979).
13. C. Sourisseau and Y. Mathey, *Chem. Phys. Lett.*, **74**, 128 (1980).
14. C. Deville Cavellin, G. Martinez, O. Gorochov, and A. Zwick, *J. Phys. C: Solid State Phys.*, **15**, 5371 (1982).
15. H. G. Grimmeiss, A. Rabenau, H. Hahn, and P. Neiss, *Z. Electrochem.*, **65**, 776 (1961).
16. L. Brattas and A. Kjekshus, *Acta Chem. Scand.*, **26**, 3441 (1972).
17. W. Schairer and M. W. Shafer, *Phys. Status Solidi A*, **17**, 181 (1973).

The Influence of Platinum Electrode Surface on the Electroadsorption and Electro-Oxidation of Methanol in Acid Solutions

E. P. M. Leiva and M. C. Giordano*

Departamento de Fisicoquímica, Facultad de Ciencias Químicas, Suc. 16, C.C. 61, Universidad Nacional de Córdoba, 5016 Córdoba, Argentina

ABSTRACT

The electro-oxidation of methanol in acid solutions on a platinum electrode modified by adatom adsorption (Ag, Cu, Pb, Sn, As, and Bi) is studied. The influence of different experimental variables (electrode pretreatment, methanol concentration, anion adsorption, and temperature) is reported. Inhibiting and activating effects of adatoms on the methanol oxidation mechanism is interpreted as a blocking effect at low methanol concentrations, and an increase of coverage by adsorbed water species on platinum when $\Theta_{org} \rightarrow 1$. The latter is traced to an induced heterogeneity which prevents organic adsorption in the surroundings of the adsorbed foreign atom.

It is well established that noble metals and their alloys are the best catalysts for methanol electro-oxidation in acid electrolytes (1-6) despite poisoning by organic residues (4, 7), a fact which requires further research in order to improve the catalyst performance. Different results obtained with several electrocatalysts and solution compositions (1-12) indicate that methanol electro-oxidation strongly depends on the surface activity, mainly through the number of sites required for the electrosorption of the molecule. In this case, the behavior of methanol is appreciably different from that of formic acid and formaldehyde (13, 14). Another remarkable difference between formic acid and methanol electrocatalytic oxidation is that the former adsorbs and oxidizes at relatively low positive potentials (15, 16), just within the hydrogen adatom potential region, while CO_2 production from methanol starts when the degree of surface coverage by hydrogen adatoms approaches zero (16). This indicates that the site requirements for the electroadsorption of both molecules and the availability of adsorbed water necessary to complete the electro-oxidation process are different for methanol and formic acid. Therefore, the electrocatalyst improvement for methanol electro-oxidation should be approached differently than that for formic acid.

This paper reports results for electrocatalytic oxidation of methanol at Pt electrodes in acid solutions, paying particular attention to the electrode pretreatment, the influence of methanol concentration, the anion adsorption, the influence of foreign adatoms (Ag, Cu, Pb, Sn, As, and Bi), and the temperature. From the analysis of data, a coherent interpretation of the complex process is attempted.

Experimental

Most of the experiments were carried out in a 120 ml conventional three electrode Pyrex glass cell. Some of the experiments were made in a flowing microcell of 5 ml total volume. The working electrodes were smooth Pt foils of about 2 and 0.9 cm^2 geometric area. Current density is reported in mA/cm^2 of real area determined from the current density/potential (i/V) profiles obtained in 0.5M H_2SO_4 background electrolyte, as described in the literature (15). Potentials were measured against a saturated hydrogen reference electrode in the same solution which was mounted with a Luggin capillary arrangement. Activation of the Pt surface was accomplished by applying successive potential steps between 1.4-1.6V (30 sec) and at 0.05V (30 sec) before the linear potential sweep. The electrode surface remained "active" for applied potentials lower than 0.6V.

Background electrolyte, 0.5M H_2SO_4 or xM $HClO_4$ (x = 1 and 0.05) were prepared from Analar H_2SO_4, Carlo Erba R.P. perchloric acid, and triply distilled water. Methanol concentration (Fluka P.A.) was varied from 10^{-3} to 5M. Solutions containing salts of different cations (Ag^+, Cu^{2+}, Pb^{2+}, Sn^{2+}, As^{3+}, and Bi^{3+}) prepared from analytical grade chemicals totaled 10^{-5}-10^{-4}M. Electrochemical measurements were made with a PAR 173 potentiostat and a PAR 175 programmer, and recorded with a Hewlett-Packard 7004B X-Y. Temperature was varied over −5°-30°C. Solutions were carefully degassed with purified nitrogen (99.999%) for half an hour before the experiments. Solutions were stirred with nitrogen.

Results

Potentiodynamic profiles at active platinum.—The potentiodynamic i/V profiles run for different methanol concentrations in 0.5M H_2SO_4 with an activated Pt electrode (Fig. 1) show either two or three anodic current peaks (paI, paII, and paIII) depending on the methanol concentration (17). There is a clear change of the i/V profiles on going from the first scan to the following ones. Some features of the repetitive i/V display appear only when the activation step applied to the electrode is made either less positive than 1.2V or more positive than 0.15V, (Fig. 2). The appearance of two peaks (paII′ and paII″) instead of a single one (paII), depends on the time the potential is held at 0.05V and also on the temperature. The optimum time for the splitting decreases as the temperature increases.

The electrode pretreatment becomes gradually more ineffective as the methanol concentration increases. Thus, when the methanol concentration is greater than 0.1M, a self-inhibition of the oxidation process in the 0.6-0.9V range is observed, in agreement with previous results (18-20). A similar effect is also found with methanol residue oxidation (Fig. 3) as the adsorption time at 0.5V is increased. The current peak height and its potential for methanol residue oxidation show a complex variation with the potential sweep rate (Fig. 4) and also depend on the degree of activation of the platinum surfaces.

Influence of anion adsorption.—The replacement of 0.5M H_2SO_4, where most of the experiments reported in the literature were performed (4, 5, 8-10, 21) by $HClO_4$ solutions (0.5 and 0.05M) where anion adsorption is almost absent (22), produces a considerable increase in the Pt electrode activity for methanol oxidation. The addition of *ca.* 10^{-3}M Na_2SO_4 to $HClO_4$ acid decreases considerably the methanol oxidation current (Fig. 5). The Pt activity towards methanol electrosorption depends also on the electrode pretreatment in $HClO_4$ background electrolyte, but then the organic

* Electrochemical Society Active Member.
Key words: catalysis, oxidation, adsorption, voltammetry, cations, activation, inhibition.

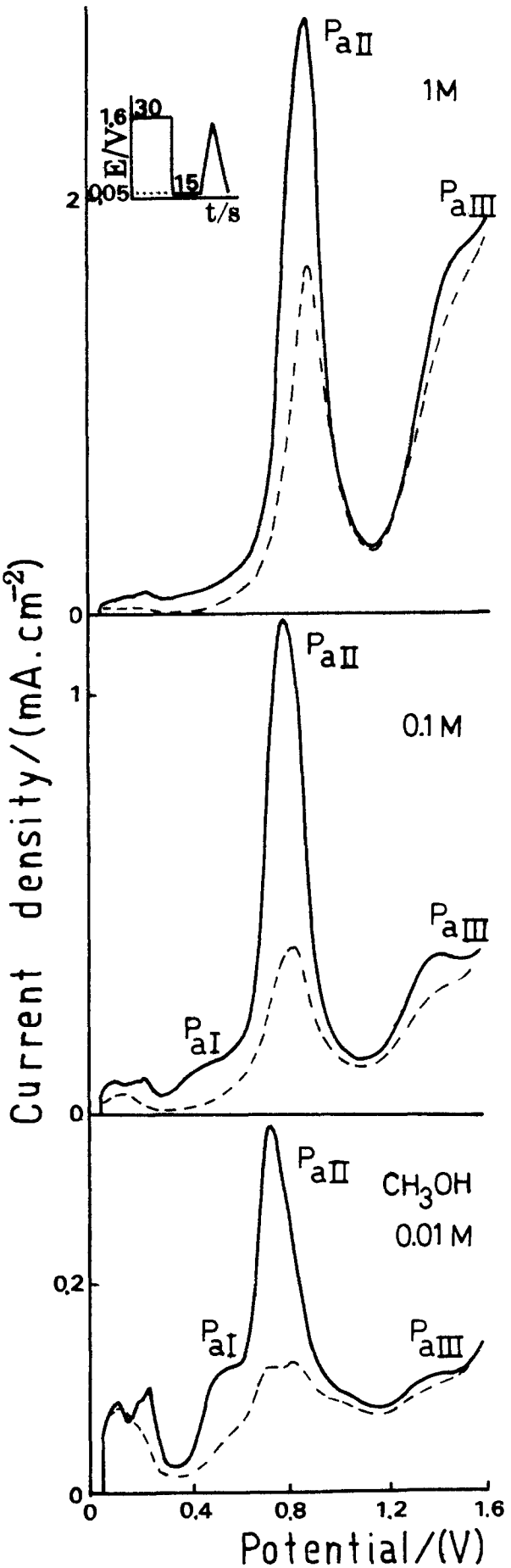

Fig. 1. Potentiodynamic *i/V* profiles for different CH_3OH concentrations in H_2SO_4 (0.5M) on an activated Pt electrode (——), and after several cyclic voltammograms (--), $v = 0.1$ Vsec^{-1}, $t = 20$°C.

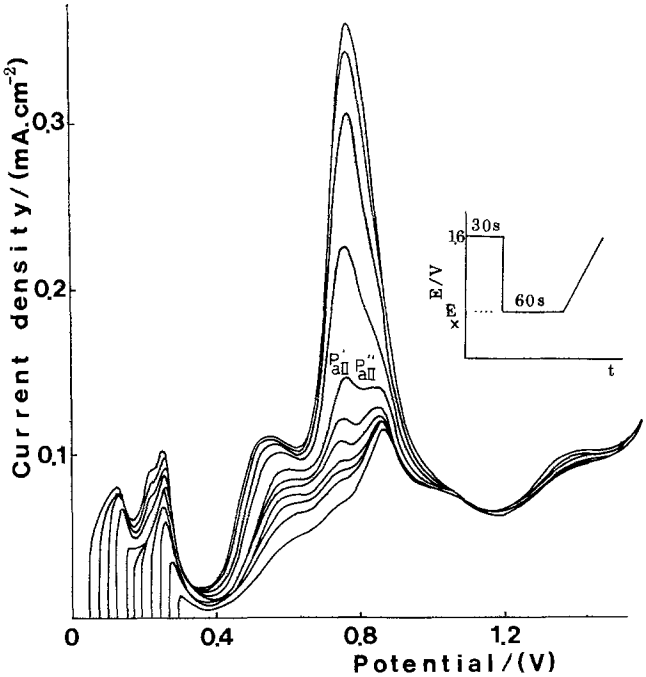

Fig. 2. Effect of holding potential (E_x) on the potentiodynamic *i/V* profiles. $H_2SO_4 = 0.5$M, $CH_3OH = 0.01$M, $v = 0.1$ Vsec^{-1}, $t = 15$°C.

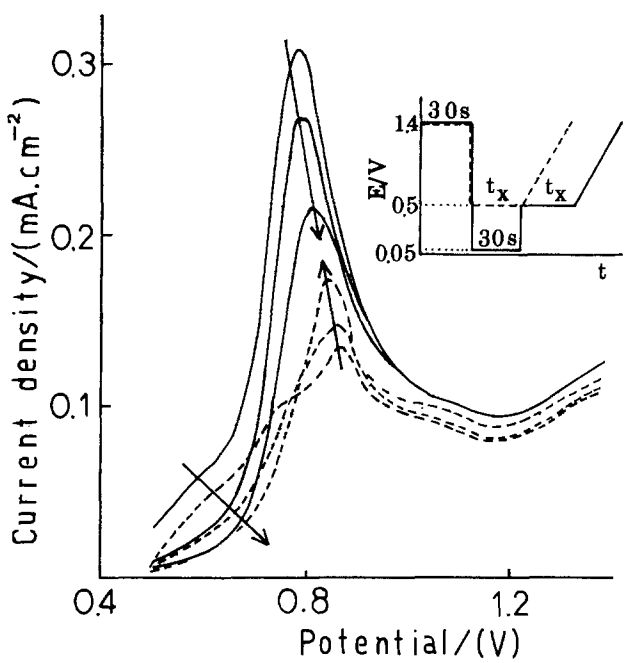

Fig. 3. Influence of potential holding time at 0.5V on methanol oxidation peak P_{AII}. With (——) and without (---) electrode pretreatment at 0.05V. $CH_3OH = 0.01$M, $v = 0.1$ Vsec^{-1}, $t = 15$°C, $t_x = 4$, 16, and 64 sec.

residue oxidation after methanol adsorption at 0.5V is less influenced than in 0.5M H_2SO_4.

Influence of foreign adatom adsorption.—Cyclic voltammograms for methanol electro-oxidation are modified by the presence of different cations in the solution (Fig. 6). Ag produces a very strong current inhibition on the whole potential range for methanol oxidation. Qualitatively similar effects are induced by As and Bi. Cu and Pb produce a slight decrease in current between 0.5-0.9V, while some increase is observed within the 0.5-0.7V potential range when Sn is added to the solution. Cd also produces some increase in the oxidation current between 0.6-0.9V. This current is enhanced by the activation potential step

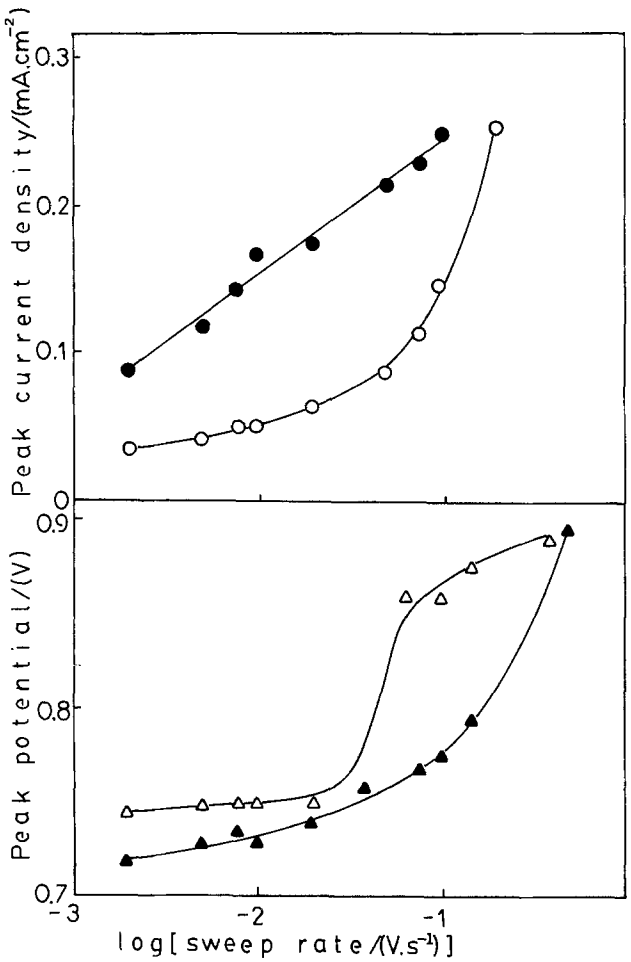

Fig. 4. Dependence of current and potential peak on potential sweep rate. Adsorption time for methanol at 0.4V = 60 sec. With (●, ▲) and without (○, △) activating pulse at 0.05V for 30 sec. CH_3OH = 0.01M, H_2SO_4 = 0.05M, t = 15°C.

program applied to the electrode before the potential sweep. The electrode pretreatment in the presence of foreign cations produces in general, a considerable decrease in methanol oxidation current since the potential step at 0.05V normally implies a greater surface coverage by foreign metal adatoms and, consequently, a decrease in the percentage of free Pt surface available for methanol electrosorption.

Qualitatively, the influence of foreign adatoms on the i/V profile for methanol residue oxidation is similar to that produced on the i/V profile for "reduced" CO_2 oxidation in the presence of adsorbed adatoms (17). Figure 7 shows oxidation profiles of adsorbed adatoms at 0.05V and methanol residue formed at 0.55V, both obtained in independent experiments. The oxidation profile obtained when the methanol residue is being formed on the Pt surface previously covered with a certain amount of foreign adatom is shown in full trace.

These runs show that Ag drastically decreases the total oxidation charge for the organic residue, while some increase is observed with Cu, mainly in the potential region where the metal desorbs (23-25). Pb and Cd behave like Cu. As and Sn strongly decrease the organic intermediate oxidation charge, although some increase in current is observed at lower potential.

Influence of an initial preset coverage of adsorbed foreign metals.—Initial preset coverages by adsorbed foreign metals were obtained either by polarizing the electrode at a constant potential in the presence of the metal ions in an auxiliary cell and then transferring it, after washing with background solution, to another cell filled with the methanol solution; or by using the

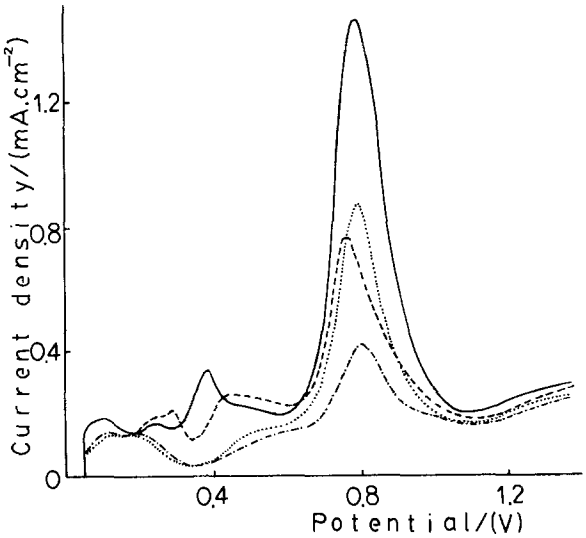

Fig. 5. Potentiodynamic i/V profiles for CH_3OH = 0.01M in $HClO_4$ 0.05M. (——) activated electrode, (·····) cycled electrode. Addition of Na_2SO_4 10^{-3}M, (----) activated electrode, (-·-·-·-) cycled electrode, v = 0.1 $Vsec^{-1}$, t = 15°C.

flowing microcell. The latter procedure in which the potential of the working electrode was kept at 0.05V during washing and refilling with methanol solution (*ca.* 60 sec) gave the most reproducible results.

Figure 8 shows cathodic and anodic i/V profiles obtained after applying the first procedure for Pb adsorption. A decrease in the Pt activity for methanol electrosorption is, then, observed since the charge for H-adatom adsorption is greater in the presence than in the absence of Pb. Simultaneously, the charge for the organic residue oxidation decreases.

Thus, the total surface coverage ($\theta_t = \theta_M + \theta'_{org}$) in the presence of both adsorbed foreign adatom (θ_M) and methanol (θ'_{org}) is lower than that obtained after methanol electrosorption in the absence of adsorbed Pb (θ_{org}), under the same experimental conditions. Nevertheless, the degree of surface coverage by organic residue referred to the Pt free surface ($Q_H^\circ - \Delta Q_H^{Pb}$), either in the absence ($\Delta Q_{org}^{Pb} = 0$, θ_{org}) or in the presence of adsorbed Pb (θ'_{org}) increases with methanol bulk concentration (Fig. 9). ($\theta'_{org} + \theta_M$) < θ_{org} at all methanol concentrations suggests that in the presence of adsorbed Pb there are sites excluded for methanol electrosorption.

Methanol oxidation current (corrected by metal adatom adsorption and background current) at 0.7 and 0.8V increases with methanol bulk concentration with and without adsorbed Pb (Fig. 10), but the slope of ln i *vs.* ln C_{org} is always larger with adsorbed Pb. Nevertheless, the great currents obtained in the presence of Pb are mainly observed when the methanol concentration is greater than 0.1M, just in the concentration range where the methanol self-inhibition starts.

Qualitatively, the same results are obtained for other foreign metals in 0.05M $HClO_4$ (Fig. 11), but the increase in methanol oxidation current starts at lower methanol concentrations in $HClO_4$ than in 0.5M H_2SO_4.

Discussion

General features.—To interpret the complex effects due to the presence of foreign metal atoms on the methanol electrocatalytic oxidation, it is convenient to refer first to the reaction occurring at activated Pt electrodes in acidic solutions. The main difference between potentiodynamic profiles run with activated Pt at different methanol bulk concentrations and repetitive cyclic voltammograms is the appearance of two extra peaks at low concentrations in the double layer

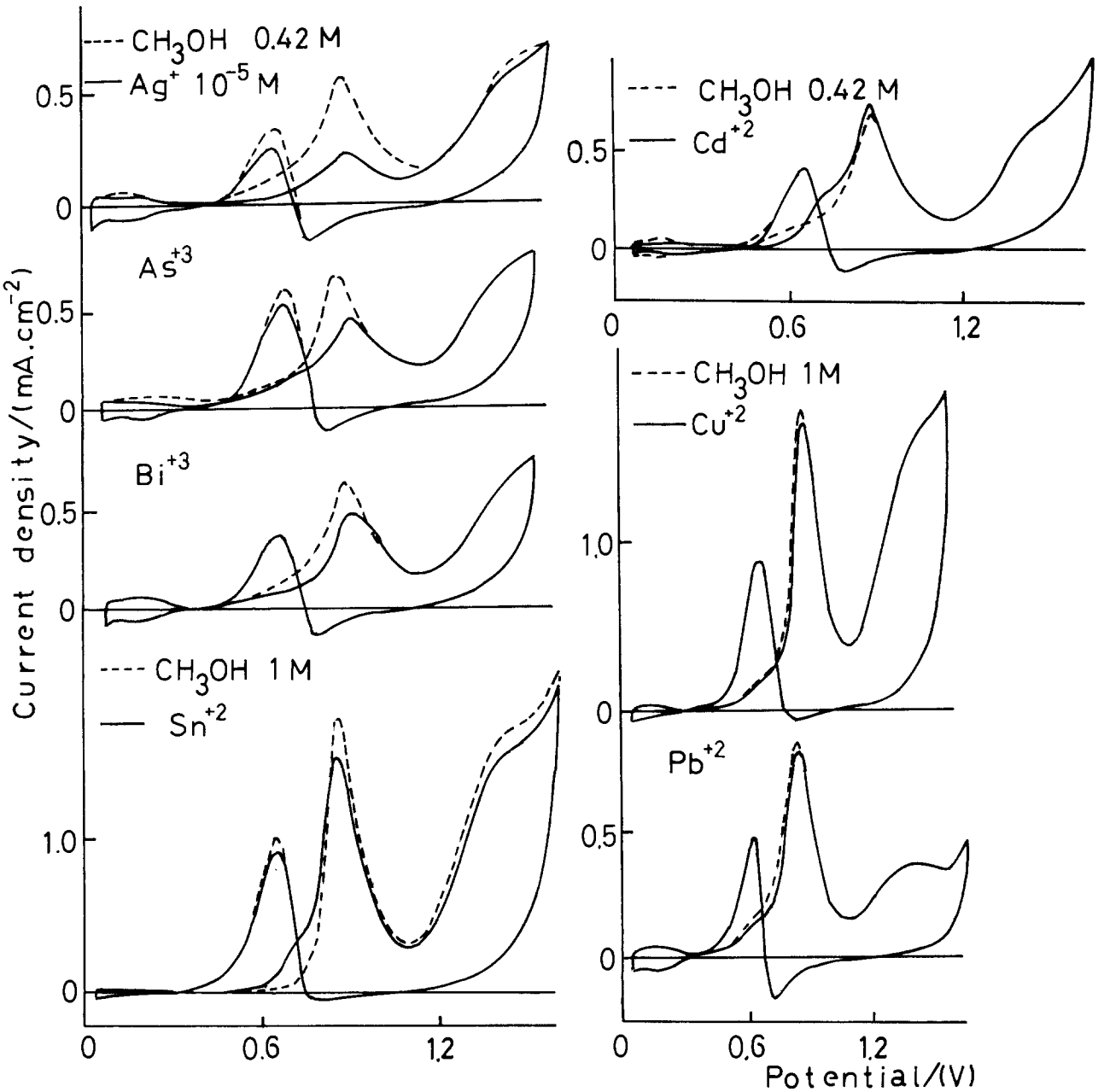

Fig. 6. Cyclic voltammograms for CH_3OH electro-oxidation in the absence (---) and in the presence (——) of foreign adatoms. H_2SO_4 = 0.5M, v = 0.1 Vsec^{-1}, t = 20°C. Pb^{+2} was added to CH_3OH = 0.042M in $HClO_4$ = 1M.

potential region. The first current peak, observed immediately after the hydrogen adatoms desorption is completed, is due to the electroadsorption of methanol (16). The increase in current at this potential cannot be attributed to methanol electrocombustion since no CO_2 production was detected by combined mass spectrometry-cyclic voltammetry experiments. Hence, in the 0.4-0.45V range, the current should be mainly related to the fast electro-oxidation of H-atoms produced by methanol dissociation on the electroadsorption process. As methanol oxidation to CO_2 starts at about 0.45V, a potential much lower than the electroformation potential of O-species at the Pt surface, it is clear that a fraction of adsorbed water is already available at this potential for the electro-oxidation of the methanol residue. Nevertheless, as the initial degree of coverage by organic residue, θ_{org}, decreases throughout the intermediate oxidation process, methanol readsorption on the bare electrode surface takes place continuously just before the O-electroadsorption initiates (26). From this standpoint, the electroadsorption of methanol should imply a competitive process between water and ion adsorption. The energy of the organic residue resulting from the primary electroadsorption process should depend on both the structural characteristics of the interface and the solution composition. Thus, the increase of Pt activity towards methanol electroadsorption by changing the base electrolyte from H_2SO_4 to $HClO_4$ can be related to an effect induced by the specific adsorption of HSO_4^-. The influence of anion adsorption in decreasing the Pt activity towards the electroadsorption and oxidation of methanol becomes evident when *ca.* 10^{-6}M NaCl is added to the electrolyte. Moreover, anion adsorption also influences the O-electroadsorption on Pt, rendering the whole process more irreversible (27-29).

The increase of the Pt activity through a potential step applied before the potential sweep becomes more remarkable in H_2SO_4 than in $HClO_4$. This suggests that some irreversible oxide is being completely removed during the potential holding at the lowest positive potential. The fact that the electrode activity towards H-adatom adsorption remains constant when

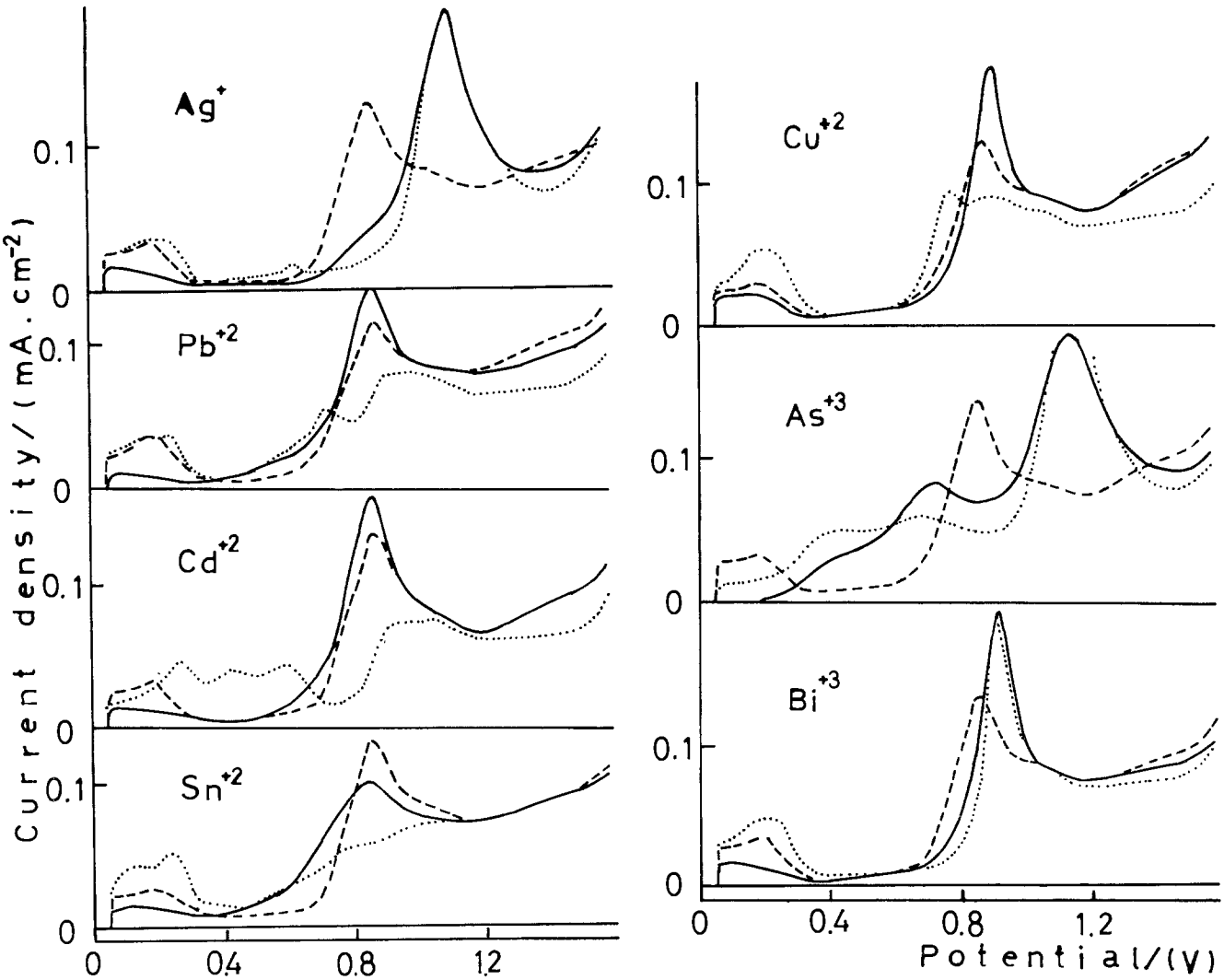

Fig. 7. Effect of several adatoms adsorption on CH_3OH residue oxidation. Adsorption time for methanol 0.01M in H_2SO_4 0.5M at 0.55V = 180 sec. Adsorption time for metals at 0.05V = 30 sec, (---) CH_3OH residue oxidation, (·····) adatom oxidation, (——) CH_3OH + adatom, $v = 0.1$ $Vsec^{-1}$, $t = 10°C$.

the oxide electroformation potential is avoided apparently agrees with the previous assumption.

Adsorption of foreign metal ions at either variable or low initial preset coverage influences in different ways both the methanol electroadsorpton and the oxidation process. This depends on the degree of coverage by adsorbed adatom, on the potential region, on the methanol concentration in the bulk of the solution, and on the electrolyte composition.

In principle, independently of the nature of the foreign metal ion, the foreign metal adatom inhibits the methanol electrosorption by producing a decrease of current in the 0.4-0.45V region on activated Pt electrodes, as was reported previously (17) in experiments performed by cyclic voltammetry with both

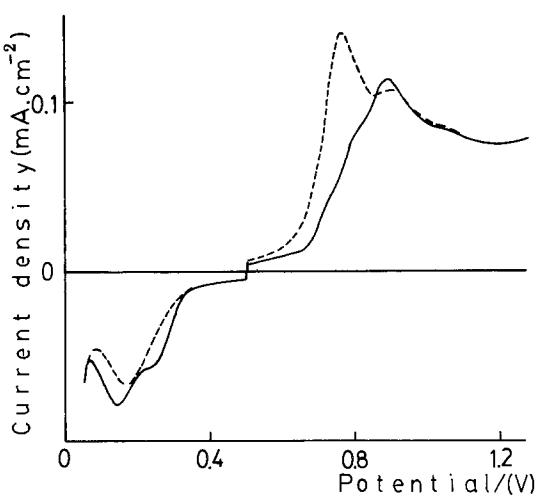

Fig. 8. Negative and positive potential sweeps in the presence (——) and in the absence (----) of adsorbed lead. ($\Theta_{Pb} = 0.15$.) Adsorption time for CH_3OH $3 \times 10^{-3}M$ = 30 sec, $v = 0.1$ $Vsec^{-1}$, $t = 15°C$.

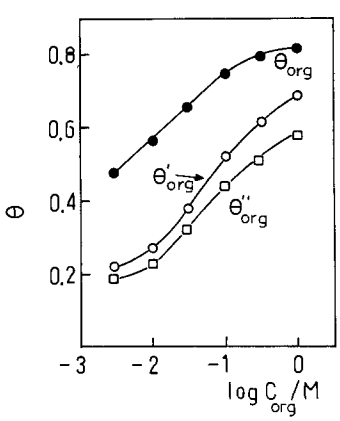

Fig. 9. Dependence of surface coverage on CH_3OH concentration. $\Theta_{Pb} = 0$ (●); $\Theta_{Pb} = 0.16$ (□), (○); $SO_4H_2 = 0.5M$, $t = 15°C$.

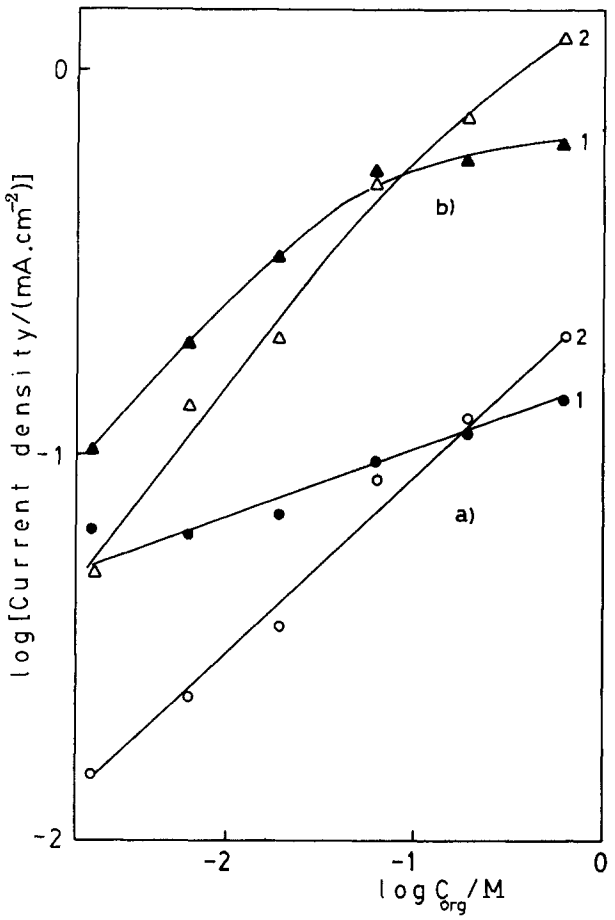

Fig. 10. Dependence of electro-oxidation rate on CH_3OH concentration. a) 0.7V; 1) without lead, 2) with lead; b) 0.8V, H_2SO_4 = 0.5M, t = 15°C.

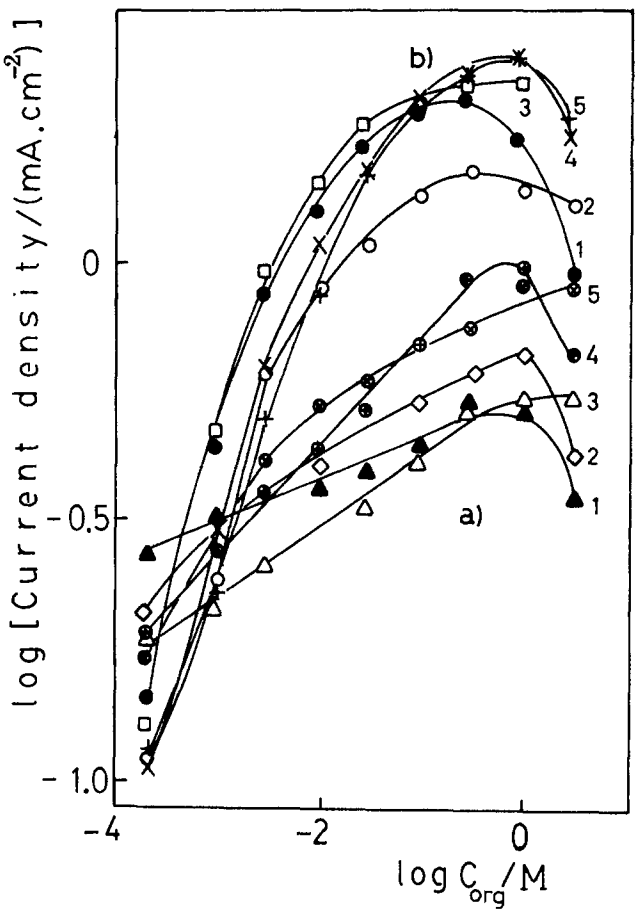

Fig. 11. Dependence of electro-oxidation rate on CH_3OH concentration in perchloric acid solutions. a) 0.7V, 1) without adatom, 2) Cd, 3) Cu, 4) Pb, 5) Sn. b) 0.8V, 1) without adatom, 2) Cu, 3) Cd, 4) Sn, 5) Pb $HClO_4$ = 0.05M, t = 15°C.

foreign cations and methanol present in the bulk of the solution. This effect is to some extent equivalent to that produced by anion adsorption.

The influence of foreign metal adatoms on the methanol residue oxidation in the 0.6-0.8V region also depends on the methanol bulk concentration and on the ionic composition of the solution. In this case, Cu seems to be the most inactive metal. Conversely, when either Sn, Cd, or Pb are used with methanol concentration over 0.1M, the methanol oxidation current is always greater than that observed on bare Pt.

Thus, foreign metal adsorption inhibits methanol electrosorption, while methanol residue oxidation is either inhibited or enhanced depending on methanol bulk concentration The concentration range where inhibition prevails is lower in $HClO_4$ than in H_2SO_4 solutions. Nevertheless, in all cases foreign metal adatoms are ineffective in overcoming the self-inhibition effect observed at high methanol concentration

Inhibition of methanol electrosorption by adsorbed Pb.—As $(\theta'_{org} + \theta_M) < \theta_{org}$ at low θ_M, a heterogeneous surface model induced by adatom adsorption is assumed to explain the effect produced by adsorbed Pb on methanol electrosorption. Thus, after adatom adsorption the number of active sites at the Pt surface (n_t) can be divided in the following way: (*i*) the number of sites occupied by Pb atoms (n_M); (*ii*) the number of sites around each adsorbed Pb atom where the methanol adsorption is energetically modified by the presence of adatom (n_M'), and (*iii*) the number of energetically unaltered Pt sites for organic adsorption ($n_t' = n_t - n_M - n_M'$) After organic adsorption, n_{org} and n'_{org} are the number of sites occupied by the organic residue in the absence and in the presence of Pb adatoms, respectively. Then, the following set of equations can be written for the degree of surface coverage by the organic species in the absence (θ_{org}) and in the presence (θ'_{org} and θ''_{org}) of adsorbed adatoms

$$\theta_{org} = n_{org}/n_t = n'_{org}/n_t' \quad [1]$$

$$\theta'_{org} = n'_{org}/(n_t - n_M) = n'_{org}/(n_t' + n_M') \quad [2]$$

and

$$\theta''_{org} = n'_{org}/n_t \quad [3]$$

These equations are set assuming that the number of sites for methanol electroadsorption in the presence of Pb, n_t', are equally available to the organic species as is the case for the total number of sites, n_t, in the absence of adatoms. The equations for metal coverage fraction and the coverage fraction of modified surface by metal adsorption are

$$\theta_M = n_M/n_t \quad [4]$$

and

$$\theta_{M'} = n_M'/n_t \quad [5]$$

The ratio between modified sites by adsorbed adatoms, n_M' and occupied sites by the adatoms themselves, n_M, is

$$\frac{n_M'}{n_M} = \frac{\theta_{org} - \theta''_{org} - \theta_{org}\,\theta_M}{\theta_{org}\,\theta_M} \quad [6]$$

Rearrangement of Eq. [6] gives

$$\theta_{M'} = 1 - \theta_M - \frac{\theta''_{org}}{\theta_{org}} \quad [7]$$

As both θ_{org} and θ''_{org} depend on methanol bulk concentration (Fig. 9), similar behavior should be expected for $\theta_{M'}$ provided that the initial θ_M remains

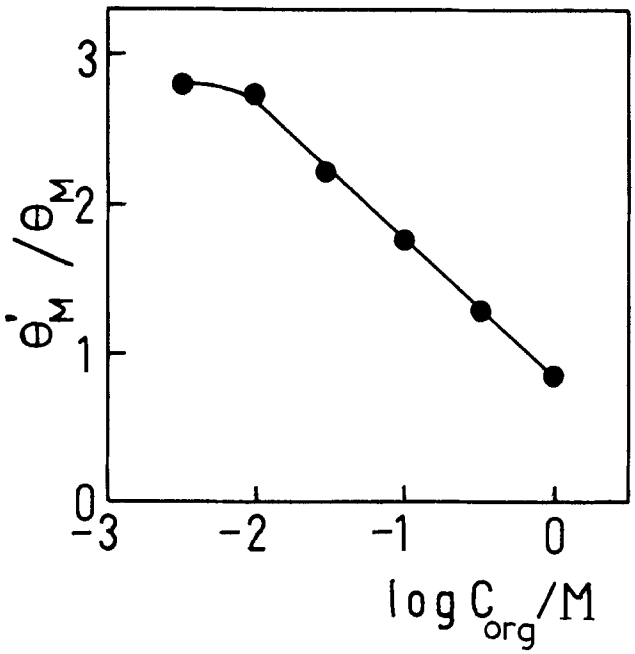

Fig. 12. Dependence of modified coverage (Θ_M') by adatom adsorption on methanol concentration. H_2SO_4 = 0.5M, t = 15°C, Θ_M = 0.16.

constant and independent of methanol bulk concentration. Experimental results fulfilled the predictions of Eq. [7], as seen by plotting θ_M'/θ_M as a function of methanol bulk concentration (Fig. 12).

The values found for θ_M' as methanol concentration is changed show that for $C_{CH_3OH} \to 0$, the number of modified Pt sites produced by Pb adsorption is close to three. As methanol concentration is raised, the site requirements for electroadsorption increase, producing a decrease of θ_M' which reaches a minimum value very close to the foreign adatom coverage fraction at high methanol concentrations. The minimum value for θ_M' can be taken as the excluded region for methanol adsorption around the adsorbed foreign adatom, θ_M''.

Effect of foreign metal adsorption on methanol electro-oxidation.—Methanol oxidation on Pt surface partially covered by foreign adatoms can be explained taking into account at least five complex stages: (*i*) the surface adsorption of methanol from the bulk of the solution, (*ii*) the dehydrogenation process involving simultaneously the H-atom oxidation and the formation of an adsorbed organic residue, (*iii*) the availability of adsorbed OH species at the surface for complete oxidation, (*iv*) the CO_2 production at the surface level with participation of adsorbed organic residue (θ'_{org}, θ_{org}) and adsorbed —OH-species, and (*v*) the diffusion of CO_2 from the surface to the bulk of the solution

The first stage depends on methanol bulk concentration through the corresponding adsorption isotherm. In this respect, any oxide remaining on the substrate as well as adsorbed anions or foreign metal adatoms should modify the quantity as well as the quality of surface sites available for the process. The rates of the second and third stages are potentially dependent, although in the double layer potential region where methanol oxidation starts, the rates of these processes can be also a function of the adsorbed water species at the interface. The fourth stage mainly depends on the relative coverage by the different adsorbed species.

Foreign metal adatoms have shown a double effect on the kinetics of methanol oxidation. At low methanol concentrations, a decrease in current is evident, while the opposite is observed for high methanol concentrations coincidently with the self-inhibition produced on bare Pt. Thus, the overall effect can be explained as follows: At low methanol concentrations, the foreign adatom adsorption decreases the substrate surface capability for methanol adsorption and dehydrogenation, which is rate determining. The inhibiting effect is given not only by the foreign adatom coverage fraction θ_M, but also by the modified region around it, θ_M'. As methanol bulk concentration is increased ($\theta'_{org} \to$ I), the coverage by metal adatoms should interfere with the organic residue close packing. The latter is probably responsible for the self-inhibition found at high methanol concentration at bare Pt. Hence, a decrease of residue coverage, θ''_{org} and simultaneously an increase of coverage for adsorbed water species on the modified region surrounding the foreign metal, θ_M'', is produced

Therefore, the influence of foreign adatoms at low coverages on methanol oxidation can be better understood in terms of an indirect action by decreasing the activity of the substrate around each metal adatom for the organic adsorption, and simultaneously promoting the electroadsorption of OH species.

In conclusion, the overall action of metal adatoms can be conceived to be like that of the effect of an induced heterogeneity at the surface, affecting various competitive processes, and the simultaneous decrease of the real electrocatalytic active area. The balance of the different contributions may result in either a decrease or an increase of the electrocatalyst activity and this strongly depends on the substrate, its history, the presence of metal adatoms, and its degree of surface coverage, and the composition of the electrolyte.

Acknowledgments

The authors acknowledge the support of part of this research by the Consejo Nacional de Investigaciones of Argentina. In addition, one of us thanks CONICET for the fellowship granted.

Manuscript submitted Sept. 14, 1982; revised manuscript received Jan. 31, 1983. This was Paper 526 presented at the Minneapolis, Minnesota, Meeting of the Society, May 10-15, 1981.

Any discussion of this paper will appear in a Discussion Section to be published in the December 1983 JOURNAL. All discussions for the December 1983 Discussion Section should be submitted by Aug. 1, 1983.

REFERENCES

1. M. W. Breiter and S. Gilman, *This Journal*, **109**, 622, 1100 (1962).
2. D. F. A. Koch, D. A. J. Rand, and R. Woods, *J. Electroanal. Chem.*, **70**, 73 (1976).
3. M. Watanabe and S. Motoo, *ibid.*, **60**, 259 (1975).
4. B. D. McNichol, in "Proceedings of the Workshop on the Electrocatalysis of Fuel Cell Reactions," W. E. O'Grady, S. Srinivasan, and R. F. Dudley, Editors, p. 93, The Electrochemical Society Softbound Proceedings Series, Princeton, NJ (1978)
5. V. S. Bagotzky, Yu. B. Vassiliev, O. A. Khazova, and S. S. Sedova, *Electrochim. Acta*, **16**, 913 (1971).
6. M. Watanabe and S. Motoo, *J. Electroanal. Chem.*, **60**, 267 (1975).
7. N. A. Hampson and M. J. Willars, *J. Power Sources*, **4**, 191 (1979).
8. M. M. P. Janssen and J. Moolhuysen, *Electrochim. Acta*, **21**, 869 (1976).
9. Yu. B. Vassiliev, V. S. Bagotzky, N. V. Osetrova, and A. A. Mikhailova, *J. Electroanal. Chem.*, **97**, 63 (1979).
10. B. Beden, F. Kadirgan, C. Lamy, and J. M. Leger, *ibid.*, **127**, 75 (1981).
11. R. R. Adzić, *J. Chem.* **18**, 166 (1979).
12. B. E. Conway, H. Angerstein-Kozlowska, and G. Czartoryska, *Z. Phys. Chem.*, **112**, 195 (1978).
13. R. R. Adzić, D. N. Simić, A. R. Despić, and D. M. Drazić, *J. Electroanal. Chem.*, **61**, 117 (1975); **65**, 587 (1975); **80**, 81 (1977).
14. M. D. Spasojević, R. R. Adzić, and A. R. Despić, *ibid.*, **109**, 261 (1980).

15. A. Capon and R. Parsons, *ibid.*, **45**, 205 (1973).
16. O. Wolter, C. Giordano, J. Heitbaum, and W. Vielstich, in "Proceedings of Symposium on Electrocatalysis," W. E. O'Grady, P. N. Ross, and F. G. Will, Editors, Vol. 82-2, p. 235, The Electrochemical Society, Softbound Proceedings Series, Pennington, NJ (1982).
17. E. P. M. Leiva and M. C. Giordano, in "Proceedings of Symposium on Electrocatalysis," W. E. O'Grady, P. N. Ross, and F. G. Will, Editors, Vol. 82-2, p. 347, The Electrochemical Society Softbound Proceedings Series, Pennington, NJ (1982).
18. V. S. Bagotzky and Yu. B. Vassiliev, *Electrochim. Acta*, **12**, 1323 (1967).
19. V. S. Bagotzky and Yu. B. Vassiliev, *ibid.*, **9**, 869 (1964).
20. T. Biegler and D. F. A. Koch, *This Journal*, **114**, 904 (1967).
21. M. W. Breiter, *J. Electroanal. Chem.*, **23**, 173 (1969).
22. P. N. Ross, Jr., *Surf. Sci.*, **102**, 463 (1981).
23. S. H. Cadle and S. Bruckenstein, *Anal. Chem.*, **43**, 1848 (1971).
24. N. Furuya and S. Motoo, *J. Electroanal. Chem.*, **72**, 165 (1976).
25. S. Stucki, *ibid.*, **80**, 375 (1977).
26. H. Angerstein-Kozlowska, B. E. Conway, and W. B. A. Sharp, *ibid.*, **43**, 9 (1973).
27. A. J. Arvía and M. C. Giordano, "Electrocatálisis, aspectos básicos y sus aplicaciones," FECYT, Buenos Aires, Argentina (1982).
28. R. O. Lezna, N. R. de Tacconi, and A. J. Arvía, *This Journal*, **126**, 2140 (1979).
29. N. W. Breiter, *Faraday Discuss. Chem. Soc.*, **45**, 79 (1968).

Electrochemical Studies of Cu(I) and Cu(II) in an Aluminum Chloride-N-(n-Butyl)Pyridinium Chloride Ionic Liquid

Chenniah Nanjundiah and R. A. Osteryoung*

Department of Chemistry, State University of New York at Buffalo, Buffalo, New York 14214

ABSTRACT

A study of the Cu-Cu(I)-Cu(II) redox systems has been carried out in a butylpyridinium chloride-aluminum chloride ionic liquid. Rotating disk (glassy carbon) and ring disk electrochemical studies were performed, as well as coulometric and potentiometric experiments. Cu(II) is reduced to both Cu(I) and Cu(0) in acidic (excess $AlCl_3$) melts and the process is quasi-reversible. Both Cu(I) and Cu(II) appear to adsorb at the glassy carbon electrodes in acidic melts. The reduction of Cu(II) appears reversible as determined by rotating disk voltammetry. In basic melts (excess butylpyridinium chloride), kinetic parameters for the slow electron transfer reduction of Cu(II) and oxidation of Cu(I) were evaluated. Both Cu(I) and Cu(II) appear to adhere to the Stokes-Einstein equation in both acidic and basic melts, although the constancy of the viscosity-diffusion coefficient product differs for each and changes as the melt is made either acidic or basic. Potentiometric measurements are interpreted as showing the presence of $CuCl_4^{-3}$ and $CuCl_6^{-4}$ in basic melts and perhaps $(Cu(AlCl_4)_3^{-2}$ and $Cu(AlCl_4)_4^{-2}$ in acidic melts. Standard potentials for the various redox couples in acidic and basic melts were determined.

Recently, interest has been shown in the development of high energy density low temperature thermal batteries which will supply high current density for short times (1, 2). Mixtures of $AlCl_3$ and NaCl were used as the battery electrolyte. These molten salt mixtures have also been used for electrodeposition of aluminum on various substrates (3, 4). Since the operating temperature of these molten salt mixtures are higher than ambient temperatures, investigations were directed towards decreasing the melting point of these electrolytes. At present, many low melting mixtures of $AlCl_3$ and RCl where R is N-alkyl pyridinium halides are known (5, 6, 7).

Gale, Gilbert, Robinson, and Osteryoung combined $AlCl_3$ with N-butyl pyridinium chloride (BuPyCl) and obtained room temperature ionic liquids at various mol ratios of these components (8, 9). Unlike other molten salt mixtures reported earlier, this system was a liquid in the vicinity of 27°C over the composition range of *ca.* 0.7:1 to 2:1 mol ratio of $AlCl_3$ to BuPyCl, and Raman spectral studies were carried out to characterize the melt species present (8). Their Lewis acid-base properties and the solvolysis equilibrium present have been investigated (10, 11). In addition, they have been employed extensively as media for fundamental electrochemical and spectroscopic studies of a variety of organic (8, 12, 13) and inorganic solutes (14, 15, 16, 17). Recently, we reported electrochemical studies of Fe(II)/Fe(III) at various melt acidities (18), and also determined the viscosity and density of the system as a function of the $AlCl_3$:BuPyCl mol ratio.

While details of the acid-base equilibrium in this system have been reported (10, 11), a brief summary may be helpful. The BuPyCl-$AlCl_3$ system is best characterized as $BuPy^+$ $AlCl_4^-$, with the acid-base equilibrium indicated as

$$2AlCl_4^- \rightleftarrows Al_2Cl_7^- + Cl^- \qquad [1]$$

The 1:1 mol ratio $AlCl_3$:BuPyCl system is "neutral"; excess BuPyCl renders it basic, while excess $AlCl_3$ renders it acidic. In the vicinity of a mol ratio of 1:1, the system acidity changes markedly.

To continue our study of various redox systems that may have applicability to ionic liquid battery systems, we here report on the study of Cu(I)/Cu(II) in the $AlCl_3$:BuPyCl system as a function of the system acidity. The electrochemical behavior of the Cu(I)/Cu(II) couple has been studied in $AlCl_3$ and NaCl mixtures (19). Hussey *et al.* (20) have investigated Cu(I)/Cu(II) couple in $AlCl_3$ and methyl pyridinium chloride (2:1) mixtures. Their results in this system, whose acidity could not be varied, indicated a reversible process for the Cu(II) + $e \leftrightarrows$ Cu(I) process as determined by rotating disk voltammetry.

Experimental

Purification of $AlCl_3$ and preparation and purification of BuPyCl have been described elsewhere (8). Cu(II) was added as $CuCl_2$ (Alfa Products) Cu(I) by anodizing a copper wire. Copper wire (Johnson-Matthey Chemicals, Limited) and aluminum wire (Alfa Products) were of 2 and 0.5 mm diam, respectively.

All voltammetric studies were performed at glassy carbon electrodes. Both disk and ring disk electrodes were employed. The glassy carbon disk electrode (RGCDE) was fabricated in this laboratory by sealing glassy carbon (Atomergics) into Pyrex glass and had an area of 0.196 cm^2. The rotating glassy carbon ring disk electrode (RGCRDE) was obtained from Pine

* Electrochemical Society Active Member.
Key words: fused salts, potential, voltammetry, diffusion.

Instrument Company and had electrode parameters: $r_1 = 0.3823$, $r_2 = 0.4097$, and $r_3 = 0.5563$ cm. A stationary glassy carbon electrode for cyclic voltammetry and potentiometry had an area of 0.057 cm^2. The glassy carbon electrodes were polished using 0.2 micron alumina on a wet polishing cloth, washed with water, and dried. A glassy carbon crucible was used as the working electrode to oxidize Cu(I) to Cu(II). Reference and counterelectrodes were Al wires dipped into the 2:1 $AlCl_3$:BuPyCl melt, and both were separated from the bulk electrolyte compartment by fine glass frits. Aluminum wire was cleaned in a 3:3:4 volume mixture of concentrated sulfuric, nitric, and phosphoric acid, washed with water and acetone, and dried. Copper wire was used as the working electrode either to introduce Cu(I) or to measure the Cu(O)/Cu(I) potential. The wire was cleaned with concentrated hydrochloric acid, and washed with water and acetone, and dried.

A PAR 174A Polarographic Analyzer was used for all voltammetric experiments, and voltammetric curves were recorded on an HP 7046-A X-Y-Y' recorder. A PAR 173 potentiostat with a Model 179 Coulometer was used in coulometric work. A Pine Instrument Company RDE 3 dual potentiostat and a Pine ASR rotator were used for rotating disk and ring disk experiments. Potential measurements were carried out with a digital voltmeter (Fluke 8000 A) in conjunction with a voltage follower. The electrochemical cell assembly was placed in a furnace whose temperature was controlled at 40° ± 1°C by a Thermo Electric 400 Temperature controller.

All electrochemical experiments were performed in a Vacuum Atmospheres Company (HE-193-2) dry box with a circulating, purified, argon atmosphere. A Metrohm glass cell (EA-875-20) was employed as an electrolytic cell. The cell was covered with a Teflon lid with several holes for reference and counterelectrode compartments, thermocouple well and the rotating disk or any other working electrode. Melts were prepared in the cell by mixing weighed amounts of purified $AlCl_3$ and BuPyCl (9, 14). Before every run, the electrode surface was conditioned by holding at an initial potential until a steady current was observed. Constant potential coulometric experiments were performed by changing the potential from a value where no current passed to one where the desired reaction would take place. The solution was stirred during coulometric experiments. In the potentiometric investigation of Cu/Cu(I), the total concentration of Cu(I) was maintained constant by coulometric oxidation of copper wire. During all potentiometric studies, the solutions were stirred.

Results and Discussion

Voltammetric studies in acidic melt.—Figure 1 shows cyclic voltammograms of Cu(II) as a function of melt acidity. Cu(II) in the acid melt undergoes a two-step reduction process, first to Cu(I) and then to Cu(O). Other aspects of this figure are discussed below.

A study of the oxidation of Cu(I) was performed. Table I shows anodic peak potentials (E_p^a), cathodic peak potentials (E_p^c), peak separations (ΔE_p), anodic peak currents (I_p^a), cathodic peak currents (I_p^c), and I_p^a/I_p^c for Cu(I) in a 2:1 melt as a function of sweep

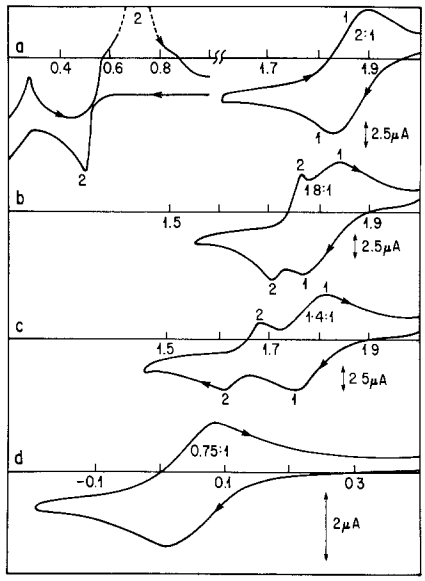

Fig. 1. Cyclic voltammograms for Cu(II) at 5 mV sec^{-1}, 40°C: Melt composition, concentration of Cu(II)/mol dm^{-3}. a. 2:1, 7.0 × 10^{-3}, b. 1.8:1, 6.7 × 10^{-3}, c. 1.4:1, 5.8 × 10^{-3}, d. 0.75:1, 4.9 × 10^{-3}.

rate (ν). Plots of I_p^a and I_p^c against $\nu^{1/2}$ are linear up to 20 mV/sec, but at higher sweep rates I_p^a and I_p^c deviate from linearity. I_p^a/I_p^c is nearly unity. E_p^a is nearly constant up to sweep rates of 20 mV/sec. At higher sweep rates, E_p^a shifts anodically. $E_p^a - E_{p/2}^a$ (difference between peak potential and potential at half the peak height) is 0.060 ± 0.005V (theoretical value is 0.060V for $n = 1$). Thus, the oxidation of Cu(I) is diffusion controlled and satisfies Nernstian conditions at lower sweep rates. E_p^c shifts cathodically with increasing sweep rate, which may be the result of irreversibility or a small amount of uncompensated resistance. Cyclic voltammograms of Cu(I) are distorted in the high temperature $AlCl_3$:NaCl system; this was attributed to the discharge of chlorine at the electrodes near the background limit (19). Hence, there is an uncertainty associated with the cathodic peak potentials.

Cu(I) can be reduced to Cu(O) and can be stripped in acidic melt compositions. A deposition and stripping voltammogram for a 2:1 melt is shown in Fig. 1a. (The small peak at *ca.* 0.2V may be due to Al stripping from the Cu covered surface.) As the melt composition is changed to 1.8:1, two cathodic and two anodic peaks were observed apart from the peak due to deposition of Cu(I) and stripping. $(E_p^c)_1$ peak 1, Fig. 1, is independent of sweep rate up to 100 mV sec^{-1} and $(I_p^c)_1$ *vs.* $\nu^{1/2}$ is linear passing through the origin. This indicates that Cu(II) reduction is diffusion controlled at the sweep rates employed. Table II shows E_p^c, E_p^a, ΔE_p, $E_p^c - E_{p/2}^c$, and $E_{1/2}$ for Cu(II) as a function of melt composition. $E_p^c - E_{p/2}^c$ is nearly 0.060 ± 0.005V at all sweep rates indicating that the reduction step involves one electron (theoretical value for $n = 1$ is 0.060V). An analysis of the anodic peak was not done since it is accompanied by a prewave.

Table I. Cyclic voltammetric results for oxidation of 9.0 × 10^{-3} mol dm^{-3} of Cu(I) in 2:1 melt composition

ν/V sec^{-1}	E_p^a/V	$(E_p^a - E_{p/2}^a)$/V	E_p^c/V	ΔE_p/V	$I_p^a/10^{-6}$A	$I_p^c/10^{-6}$A	I_p^c/I_p^a
0.002	1.880	0.060	1.820	0.060	6.5	6.5	1.0
0.005	1.880	0.060	1.815	0.065	10.0	10.0	1.0
0.010	1.885	0.060	1.810	0.075	17.5	17.0	1.0
0.020	1.885	0.060	1.800	0.085	24.0	24.0	1.0
0.100	1.905	0.060	1.780	0.125	54	54	1.0

ν - scan rate. E_p^a - anodic peak potential. E_p^c - cathodic peak potential. $\Delta E_p = E_p^a - E_p^c$. I_p^a - anodic peak current. I_p^c - cathodic peak current.

Table II. Cyclic voltammetric data for Cu(II) at different melt acidities

N_A/N_B	[Cu(II)] mol dm^{-3} × 10^{-3}	ν V sec^{-1}	$(E_p^c)_1$ V	$(E_{p/2}^c)$ V	$(E_p^c)_1 - (E_{p/2}^c)_1$ V	$E_{1/2}$ V	$(E_p^a)_1$ V	$(\Delta E_p)_1$ V	$(E_p^c)_2$ V	$(E_p^a)_2$ V	$(\Delta E_p)_2$ V
1.8	6.7	0.005	1.765	1.825	0.060	1.794	1.830	0.065	1.710	1.765	0.050
		0.010	1.760	1.820	0.060	1.789	1.825	0.065	1.705	1.775	0.070
		0.020	1.760	1.820	0.060	1.789	1.825	0.065	1.700	—	—
		0.050	1.760	1.820	0.060	1.789	1.825	0.065	1.685	—	—
		0.100	1.760	1.820	0.060	1.789	1.835	0.075	1.670	—	—
1.6	6.3	0.005	1.755	1.815	0.060	1.784	1.815	0.060	1.660	1.715	0.055
		0.010	1.755	1.815	0.060	1.784	1.815	0.060	1.655	1.720	0.065
		0.020	1.755	1.815	0.060	1.784	1.820	0.065	1.650	1.725	0.075
		0.050	1.755	1.815	0.060	1.784	1.820	0.065	1.635	1.735	0.100
		0.100	1.750	1.810	0.060	1.790	1.820	0.070	1.620	1.745	0.125
1.4	5.8	0.005	1.755	1.810	0.055	1.784	1.815	0.060	1.615	1.680	0.065
		0.010	1.750	1.805	0.055	1.779	1.815	0.065	1.615	1.690	0.075
		0.020	1.750	1.805	0.055	1.779	1.815	0.065	1.615	1.700	0.085
		0.050	1.750	1.805	0.055	1.779	1.815	0.065	1.595	1.710	0.115
		0.100	1.745	1.800	0.055	1.774	1.815	0.070	1.585	1.710	0.125
1.2	5.3	0.005	1.735	1.790	0.055	1.764	1.795	0.060	1.575	1.625	0.050
		0.010	1.735	1.790	0.055	1.764	1.795	0.060	1.575	1.630	0.055

N_A - Number of mols of $AlCl_3$.
N_B - Number of mols of BuPyCl.

Similar results were obtained in 1.6:1, 1.4:1, and 1.2:1 melts (Table II). The second cathodic and anodic peaks are at 1.710 and 1.765V, respectively, at 5 mV/sec. As the sweep rate is increased the anodic peak at 1.765V merges with the anodic peak at 1.825V, while the cathodic peak at 1.710V shifts cathodically. As the melt acidity is changed to 1.6:1, 1.4:1, and then to 1.2:1, the potential difference between Ep_a^1 (peak 1) and Ep_a^2 (peak 2) and that between Ep_c^2 and Ep_c^1 increases as can be seen in Table II. Both the second cathodic and anodic peaks disappear when tungsten is used as the working electrode. This suggests that the second peak is due to a surface process. This will be discussed below in connection with rotating disk electrode experiments.

Coulometric experiments in a 2:1 melt were carried out. Cu(I) was introduced by anodizing copper wire. The rest potential was measured (0.525 ± 0.005V), and then a potential anodic to the rest potential was applied while the current was integrated by a coulometer. This coulometry was stopped at various time intervals and the equilibrium potentials were measured. E_{eq} *vs.* ln[Cu(I)] was plotted and the slope of this line was 0.028 V/decade (theoretical value is 0.027V/decade for $n = 1$). Thus, Cu(I) is formed by anodizing copper wire. $E^{o'}$ for Cu/Cu(I) is reported in Table III.

Table III. Standard formal potential of Cu(I)/Cu(O), Cu(II)/Cu(I), and Cu(II)/Cu(O) in the melt

N_A/N_B	Redox couple	$E^{o'}$/V (*vs.* Al in 2:1 $AlCl_3$:BuPyCl)
2	Cu(I) + $e \rightleftarrows$ Cu(O)	0.784
2	Cu(II) + $e \rightleftarrows$ Cu(I)	1.825
2	Cu(II) + $2e \rightleftarrows$ Cu(O)	1.305 (Calculated)
0.75	Cu(I) + $e \rightleftarrows$ Cu(O)	−0.647
0.75	Cu(II) + $e \rightleftarrows$ Cu(I)	0.046
0.75	Cu(II) + $2e \rightleftarrows$ Cu(O)	−0.301 (Calculated)

Rotating ring disk voltammograms were also recorded (Fig. 2). A well-defined oxidation wave was observed at the disk and reduction currents at the ring. The nature of the limiting current was verified using the Levich equation

$$I_d = 6.2 \times 10^{-4} nFACD^{2/3} v^{-1/6} \omega^{1/2} \quad [2]$$

where C is the concentration in mol liter^{-1}, v is the kinematic viscosity, ω is the rotation rate in radians sec^{-1}, and all other symbols have their usual meaning. A plot of limiting current against $\omega^{1/2}$ is linear and passes close to the origin, showing that the limiting current is convective diffusion controlled (Fig. 3a). The mean of the collection efficiency at different rotation

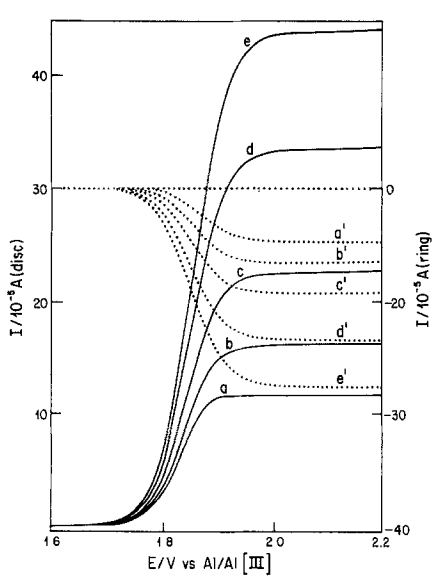

Fig. 2. Rotating ring disk voltammograms for 11 × 10^{-3} mol dm^{-3} Cu(I) at different rotation rates in 2:1 melt. Ring potential at 1.14V, disk current —, ring current ..., rotation rate in rpm a,a') 100, b,b') 200, c,c') 400, d,d') 900, and e,e') 1600.

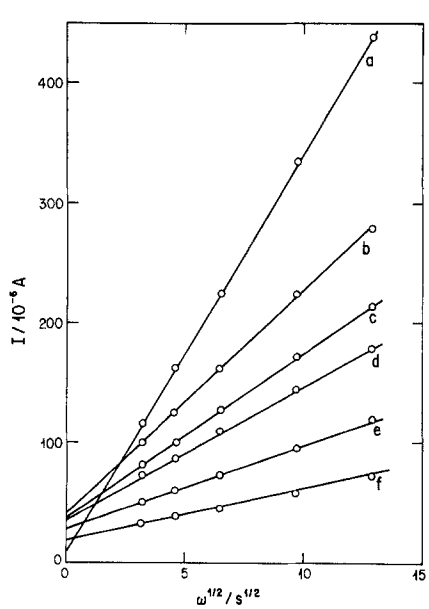

Fig. 3. Plot of I *vs.* $\omega^{1/2}$ for 11 × 10^{-3} mol dm^{-3} Cu(I) in 2:1 melt at different potentials a) 2.1V, b) 1.87V, c) 1.85V, d) 1.84V, e) 1.82V, and f) 1.80V.

rates is 0.41 ± 0.01 (theoretical value is 0.43), suggesting that the product is stable. To determine the number of electrons involved in the oxidation of Cu(I), constant potential coulometry was carried out on a glassy carbon electrode. Since the limiting current is convective diffusion controlled, the electrolysis potential of 2.0V was chosen to be on the limiting plateau of the voltammogram. The coulometry was stopped at various time intervals, and the voltammogram at the RGCDE was recorded in order to monitor the decrease in concentration of Cu(I). A plot of anodic limiting current as a function of Q is shown in Fig. 4. It is seen that the convective diffusion limited current decreases linearly up to 3C, but the points beyond 3C deviate and the limiting currents are greater than one would expect on the basis of a diffusion controlled coulometric reaction. One possible reason for this deviation may be due to a side reaction at the electrode at the potential of electrolysis, since 2.0V is near the oxidation limit of the melt. However, an extrapolation of points obtained up to 3C gave an intercept on the Q axis of 15.5C. The Cu(I) solution prior to coulometric oxidation of Cu(I) at the glassy carbon electrode was obtained by passing an anodic charge of 15.7C using a copper electrode. Thus, one electron is involved in the oxidation of Cu(I). During coulometric conversion of Cu(I) to Cu(II), the equilibrium potential of Cu(I)/Cu(II) system was measured at different ratios of Cu(I) to Cu(II) using a glassy carbon electrode. A plot of E_{eq} *vs.* ln [Cu(II)]/[Cu(I)] yields a linear plot with a slope of 0.029 V/decade indicating that the Cu(I)/Cu(II) couple obeys the Nernst equation. $E^{o'}$ for Cu(I)/Cu(II) is reported in Table III.

Analysis of rotating disk electrode voltammograms for the oxidation of Cu(I) was carried out. Plots of I against $\omega^{1/2}$ on the rising portion of the wave were linear (Fig. 3) in acidic melts from compositions ranging from 2.0:1 to 1.4:1 melt, but all these plots have an intercept. One possible reason may be the oxidation of an adsorbed Cu(I) species. However, a plot of the ln of the slopes of the plots in Fig. 3 *vs.* potential is linear with a slope of 29 mV, quite close to that expected for a reversible, one electron process.

Careful examination of the RGCDE voltammogram reveals that there is a small shoulder in the rising part of the voltammogram, presumed to arise from adsorption of Cu(II). As the melt composition approaches neutrality (1:1 mol ratio of $AlCl_3$:BuPyCl), the voltammogram gives a peak shape i-E plot; Cu(II) formed from the oxidation of Cu(I) precipitates at the electrode and passivates the electrode. Cu(II) added externally also precipitates near a neutral melt composition.

The reduction of Cu(II) in the acidic melt was also studied at an RGCDE. The reduction wave of Cu(II) at different rotation rates is shown in Fig. 5. It can be seen that the limiting current of the voltammogram is

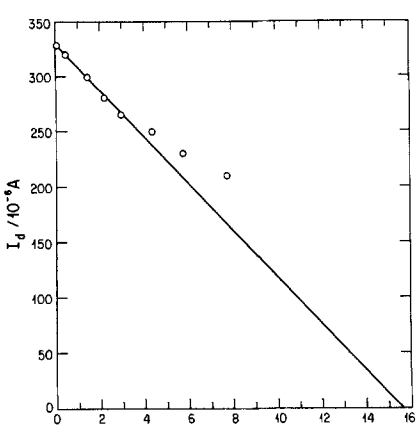

Fig. 4. Plot of I_d vs. Q in 2:1 melt at 900 rpm. Initial concentration of Cu(I) is 11 × 10^{-3} mol dm^{-3}.

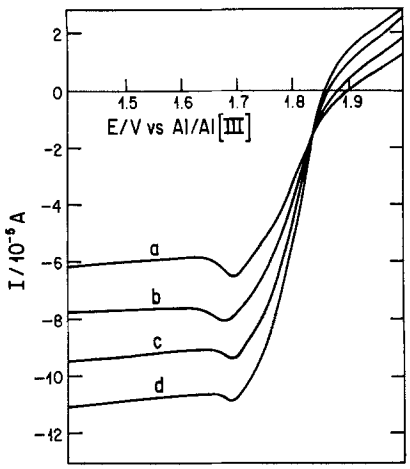

Fig. 5. Rotating disk voltammograms for 4.9 × 10^{-3} mol dm^{-3} Cu(II) in 1.8:1 melt at a) 100, b) 400, c) 900, and d) 1600 rpm.

preceded by a peak. Such peaks have been attributed to adsorption processes (21). A plot of limiting current against $\omega^{1/2}$ is linear and passes through the origin. Currents on the rising region of the voltammogram, except for the current at the peak, plotted against $\omega^{1/2}$ shows linear behavior and pass through the origin. This indicates that the current is convective diffusion limited at all points, except at the peak. A plot of E *vs.* $\ln[I_d - I)/I]$ is linear with a slope of 0.028 V/decade (theoretical value $n = 1$ is 0.027V) indicating a one electron reversible process. However, this line deviates from linearity as the potential approaches the limiting current in the region of the maximum as a result of adsorption of Cu(II). Half-wave potentials for the reduction of Cu(II) are shown in Table VI.

Voltammetric studies in the basic melt.—Cu(I) was introduced into the melt by anodizing copper wire. A potential positive to open-circuit potential (—0.85V) was applied and the current was integrated by a coulometer. Anodization was stopped at intervals, and the equilibrium potential was measured. Assuming Cu(I) is formed, a plot of ln Cu(I) against E was made and was linear with a slope of 0.028 V/decade, suggesting that Cu(I) is formed. $E^{o'}$ for Cu/Cu(I) was evaluated and is shown in Table III. Ring disk voltammograms at various rotation rates (Fig. 6) were recorded on the above solution containing Cu(I). A plot of limiting current against $\omega^{1/2}$ was linear and passed through the origin suggesting that the current is convective diffusion controlled (Fig. 7). Since the collection efficiency was 0.41 ± 0.01 (theoretical value 0.43), the product of the reaction is stable. Plots of I *vs.* $\omega^{1/2}$ at

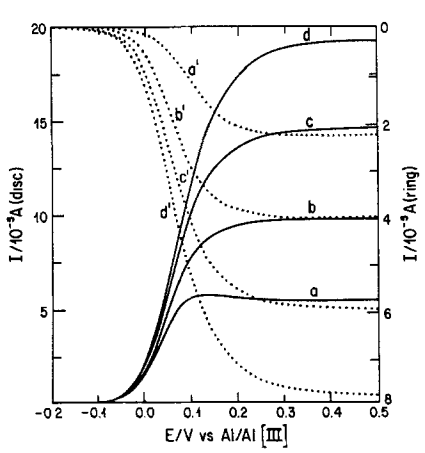

Fig. 6. Rotating ring disk voltammograms for 11 × 10^{-3} mol dm^{-3} Cu(I) at different rotation rate in 0.75:1 melt. Ring potential at —0.2V. Disk current —, ring current ..., rotation rate in rpm a,a') 100, b,b') 400, c,c') 900, and d,d') 1600.

Table IV. Kinetic parameters in the basic melt

N_A/N_B	[Cu(II)] mol dm^{-3}	[Cu(I)] mol dm^{-3}	$k_f^{o'}$ cm sec^{-1}	α	Technique
0.75	—	11.0×10^{-3}	1.6×10^{-4}	0.52	RDE
0.75	4.9×10^{-3}	—	4.2×10^{-4}	0.65	RDE
0.75	3.0×10^{-3}	3.0×10^{-3}	1.7×10^{-4}	0.50*	CV
0.95	—	5.0×10^{-3}	3.3×10^{-4}	0.50*	CV

* Assumed values.

potentials on the rising portion of the voltammogram were nonlinear, suggesting that the current is not convective diffusion controlled.

A Cu(I) solution was prepared by passing an anodic charge of 13.8C on a copper wire in a glassy carbon crucible. A potential corresponding to the limiting current of the oxidation of Cu(I) (+0.3V) was applied to the glassy carbon crucible. The decrease in concentration of Cu(I) was followed by recording voltammograms at an RGCDE at various intervals of coulometry. A plot of I_d against Q was made, and extrapolation of this line intercepts the Q axis at the charge necessary for complete oxidation (14C). Thus, Cu(I) is quantitatively oxidized to Cu(II). The same information was obtained by measuring the equilibrium potential using glassy carbon electrodes at various intervals of coulometry. A plot of $\ln[Cu(II)]/[Cu(I)]$ against E_{eq} is linear with a slope of 0.028 V/decade, corresponding to a one electron process. $E^{o'}$ values for the Cu(I)/Cu(II) couple are shown in Table III.

As pointed out earlier since plots of I against $\omega^{1/2}$ in the rising portion of the voltammogram are curved, the current is not controlled by diffusion. To determine if the current is controlled by a slow electron transfer step, plots of $1/I$ against $\omega^{-1/2}$ were made in accord with the following equation (22)

$$1/I = 1/I_k + (1.61\ v^{1/6})/(n\mathbf{F}ACD^{2/3}\omega^{1/2}) \quad [3]$$

where $I_k = n\mathbf{F}AC_0k$, and k is the electron transfer rate constant at a given potential. From the intercept, one can evaluate the rate constant at different potentials. A plot of ln k *vs.* E should be linear since (22)

$$k = k^{o'} \exp[-\alpha n\ \mathbf{F}(E - E^{o'})/RT] \quad [4]$$

where $k^{o'}$ is the rate constant at formal potential $E^{o'}$ and α is the charge transfer coefficient. A plot of ln k *vs.* E was linear suggesting that the electron transfer step is rate determining. Since $E^{o'}$ for the Cu(I)/Cu(II) couple is known from potentiometry, $k^{o'}$ was evaluated, and α was found from the slope. Data are tabulated in Table IV.

Reduction of Cu(II) in the basic melt was carried out at an RGCDE. A plot of limiting current *vs.* $\omega^{1/2}$ is linear and passes through the origin while such plots in the rising region of the voltammogram are nonlinear. This suggests that the limiting current is convective diffusion controlled. Plots of $1/I$ against $\omega^{-1/2}$ in the rising region of the voltammograms are linear and from these plots electron transfer rate constants were calculated as described earlier. Values of $k^{o'}$ and α are shown in Table IV.

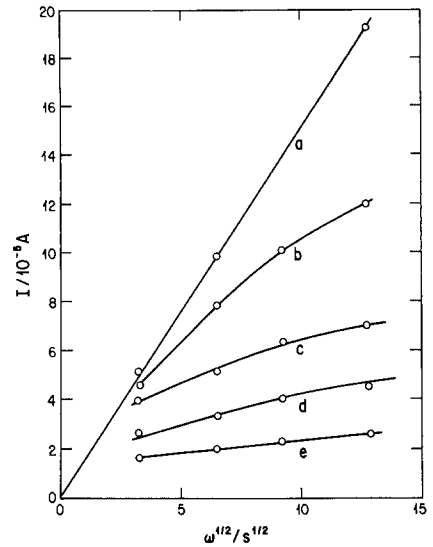

Fig. 7. Plot of I vs. $\omega^{1/2}$ for oxidation of Cu(I) at different potentials a) 0.60V, b) 0.10V, c) 0.05V, d) 0.025V, and e) 0.0V.

Cyclic voltammetric experiments were carried out in the basic melt for Cu(I) and Cu(II) as well. E_p^c, E_p^a, E_p, I_p^a, I_p^c, and I_p^c/I_p^a at two different melt acidities are shown in Table V. Plots of I_p^a and I_p^c against $v^{1/2}$ are nonlinear. E_p^a shifts anodically and E_p^c shifts cathodically as the sweep rate is increased. Because of this, ΔE_p increases with increasing scan rate. These results also suggest that the Cu(I)/Cu(II) system is quasi-reversible. Using Nicholson's method (23), k is evaluated assuming $\alpha = 0.5$: These values are shown in Table IV. The rate constant was in reasonable agreement with that evaluated using voltammograms at the RGCDE.

Evaluation of diffusion coefficients.—At all melt compositions, the limiting currents for the reduction of Cu(II) and Cu(I) are convective diffusion controlled. However, it is found that the limiting current increases as the melt acidity is varied. Changes in limiting currents were shown to be due to changes in viscosity (18), and using viscosity and density data previously reported (18), diffusion coefficients for Cu(I) and Cu(II) species were evaluated using the Levich equation. Table VI shows diffusion coefficients of Cu(I) and Cu(II) at various melt compositions. Changes in the diffusion coefficients are in agreement with that expected by the Stokes-Einstein relation

$$D = \frac{kT}{6\pi\eta\, r} \quad [5]$$

where r is the Stokes radius, η is the viscosity, and other symbols have their usual significance. It is seen that ηD differs for basic and acidic melts (Table VI). This suggests that the Stokes radii are different. Stokes radii were found to be 0.24 and 0.15 nm for Cu(I) and 0.46 and 0.34 nm for Cu(II) in the acidic and basic melt, respectively. The formation of chloro-complexes (see below) in the melts suggests that the values of r

Table V. Cyclic voltammetric data in the basic melt

N_A/N_B	[Cu(II)] mol dm^{-3}	[Cu(I)] mol dm^{-3}	v V sec^{-1}	E_p^a V	E_p^c V	ΔE_p V	I_p^a 10^{-6}A	I_p^c 10^{-6}A	I_p^c/I_p^a
0.75	$3.0\ 10^{-3}$	$3.0\ 10^{-3}$	0.005	0.135	0.040	0.095	15	15	1.0
			0.010	0.145	0.030	0.115	20	20	1.0
			0.020	0.155	0.020	0.135	28	26	0.9
			0.050	0.180	0.005	0.175	42	39	0.9
			0.100	0.205	0.005	0.210	57	52	0.9
0.95	—	$5.8\ 10^{-3}$	0.005	0.160	0.070	0.090	4.0	3.8	1.0
			0.010	0.165	0.065	0.100	5.8	5.0	0.9
			0.020	0.175	0.055	0.120	8.0	6.7	0.8
			0.050	0.200	0.040	0.160	11.5	8.8	0.8
			0.100	0.230	0.010	0.220	14.5	9.8	0.7

Table VI. Dependence of I_d, D, D, $E_{1/2}$, $E^{0\prime}$ on the melt composition

N_A/N_B	η g cm^{-1} sec^{-1}	[Cu(I)] 10^{-3} mol dm^{-3}	A cm^2	I_d 10^{-6}A	D cm^2 sec^{-1} 10^{-7}	ηD 10^{-7}g cm sec^{-2}	[Cu(II)] 10^{-3}M	A cm^2	I_d 10^{-6} A	D 10^{-7} cm^2 sec^{-1}	ηD 10^{-7}g cm sec^{-2}	$E_{1/2}$ V	$E^{0\prime(1)}$ V	$E^{0\prime(2)}$ V
0.75	0.514	11.0	0.459	147	2.88	1.48	4.9	0.196	17.0	1.37	0.70			0.046
0.75	0.514	6.7	0.196	38	2.86	1.47	—	—	—	—	—			
0.80	0.404	6.1	0.459	100	3.68	1.48	4.7	0.459	48.0	1.80	0.730			0.063
0.85	0.320	6.0	0.459	124	4.89	1.57	4.7	0.196	23.0	1.98	0.63			0.082
							4.6	0.459	52.0	1.95	0.63	1.770	1.756	1.755
1.4	0.180	7.4	0.196	64	4.02	0.72	5.8	0.196	35.0	2.36	0.43	1.775	1.762	1.768
1.6	0.170	8.0	0.196	78	4.69	0.80	6.3	0.196	44.0	2.89	0.49			
1.6	0.170	—	—	—	—	—	9.0	0.196	63.7	2.94	0.50			
1.8	0.160	8.5	0.196	93	5.50	0.88	6.7	0.196	55.0	3.62	0.58	1.800	1.784	1.787
1.8	0.160	9.0	0.196	113	6.68	0.97	—	—	—	—	—			
2.0	0.145	10.0	0.196	138	7.68	1.11	2.0	0.196	15.0	3.08	0.45	1.840	1.826	1.825
2.0	0.145	1.6	0.459	52	7.75	1.12	4.6	0.196	36.0	3.28	0.48			
2.0	0.145	3.1	0.459	88	6.32	0.92	7.0	0.196	59.0	3.67	0.53			
2.0	0.145	6.5	0.459	194	6.82	0.99								

[1] Values calculated from the half-wave potential at RDE using the relation $E^{0\prime} = E_{1/2} + 0.062 \log \left\{ \frac{D_{Cu(II)}}{D_{Cu(I)}} \right\}^{-2/3}$

[2] Calculated from Nernst plot.

reported here are too small. A modification of the Stokes-Einstein equation has been suggested when the particle whose radius is being calculated moves in a medium whose radii are similar in size (24); the modification results in replacement of the 6 in the Stokes-Einstein equation by a 4, thus, increasing the calculated value of the radii by 50%.

Potentiometry.—As described earlier, Cu/Cu(I) and Cu(I)/Cu(II) couples satisfy the Nernst criterion in both basic and acidic melts. The Cu/Cu(I) potential was measured as a function of composition of the melt acidity while keeping the total concentration of Cu(I) constant. A plot of the Cu/Cu(I) potential as a function of melt composition is shown in Fig. 8. In the basic melt, the Cu/Cu(I) potential shifts to cathodic potentials as the concentration of chloride (basicity) increases, suggesting that Cu(I) forms a chlorocomplex. A plot of E of the Cu/Cu(I) couple with respect to the Al/Al(III) (2:1 melt) *vs.* ln [Cl^-] is linear over a melt composition of 0.75:1 to 0.92:1, indicating only one chlorocomplex is formed (Fig. 9). The slope of the plot is 0.113 V/decade, which is nearly equal to a theoretically expected slope of 0.108V for a ligand number of four, suggesting the species is $CuCl_4^{-3}$. Near the neutral region, Cu(I) precipitates. The stability constant of this complex with respect to Cu/Cu(I) in the 2:1 melt is reported in Table VII. A plot of the Cu(II)/Cu(I) potential against the ln[Cl^-] is linear up to 0.95:1 melt composition (Fig. 10). The slope corresponds to 0.060 V/decade. This corresponds to a difference in ligand number between the Cu(I) and Cu(II) species of 2 (theoretical value is 0.054V). Thus, the ligand number of the Cu(II) species is six, *i.e.*, $CuCl_6^{-4}$. From the intercept of the plot the stability constant of the $CuCl_6^{-4}$ species is found and the value is reported in Table VII.

Table VII. Stability constants of copper complexes in acidic and basic melts

N_A/N_B	Metal ion	Ligand No.	Stability constant with respect to 2:1 melt	Complex species
0.75 to 0.92	Cu(I)	4	2.0×10^{23}/ mol^{-4} dm^{12}	$CuCl_4^{-3}$
0.75 to 0.90	Cu(II)	6	4.3×10^{31}/ mol^{-6} dm^{18}	$CuCl_6^{-4}$
1.05 to 1.84	Cu(I)	3		$Cu(AlCl_4)_3^{-2}$
1.4 to 1.8	Cu(II)	4		$Cu(AlCl_4)_4^{-2}$

The potential of the Cu/Cu(I) couple shifts positive in the acid region as the acidity increases. This suggests the presence of a Cu(I) complex whose stability decreases as the system becomes more acid. However, efforts to analyze the potentiometric data, as performed in the basic system, were rather perplexing. Figure 11 shows a plot of E for the Cu/Cu(I) couple in the acid melts against ln [Cl^-], ln [$Al_2Cl_7^-$], and ln [$AlCl_4^-$]. Similar measurements for the Fe(III)/Fe(II) couple in the acid melt (25) and the Sb/Sb(III) potential, against ln [Cl^-] (26) indicated the formation of $FeCl_2^+$ and $SbCl_2^+$. The linear portion of E for the Cu/Cu(I) couple *vs.* ln [Cl^-] yields a slope of 0.025V, suggesting a ligand number of unity; a similar analysis for the data *vs.* ln [$AlCl_4^-$] yields a slope of 0.074V, suggesting a ligand number of 3 ($RT/F = 0.027$V). Figure 12 shows similar data for the Cu(I)/Cu(II) couple in the acidic melt. One may interpret the small change in slope of the Cu(I)/Cu(II) couple *vs.* ln

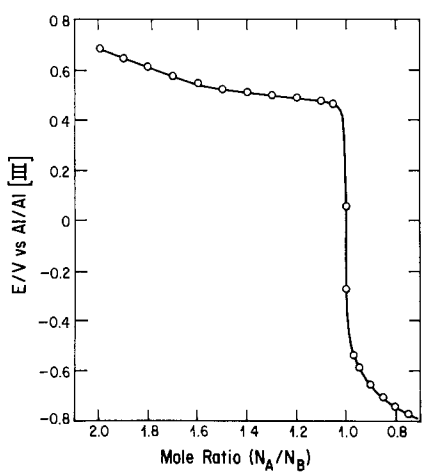

Fig. 8. Plot of potential of Cu/Cu(I) couple as a function of melt composition. N_A = Number of mols of $AlCl_3$. N_B = Number of mols of BuPyCl.

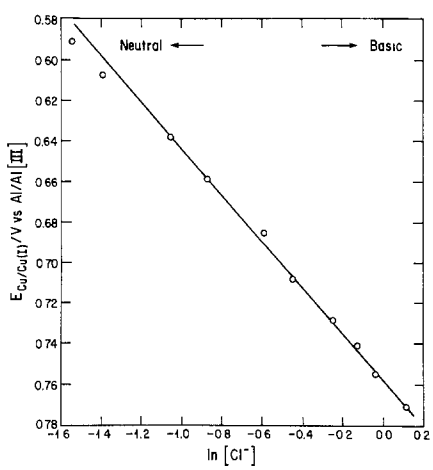

Fig. 9. Plot of E for Cu/Cu(I) couple *vs.* ln[Cl^-] in basic melt

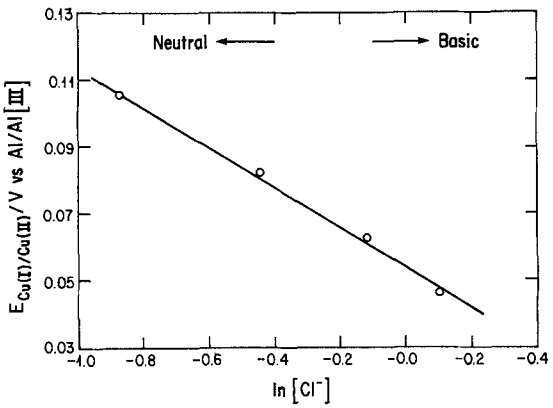

Fig. 10. Plot of E for Cu(I)/Cu(II) couple vs. ln[Cl⁻] in basic melt.

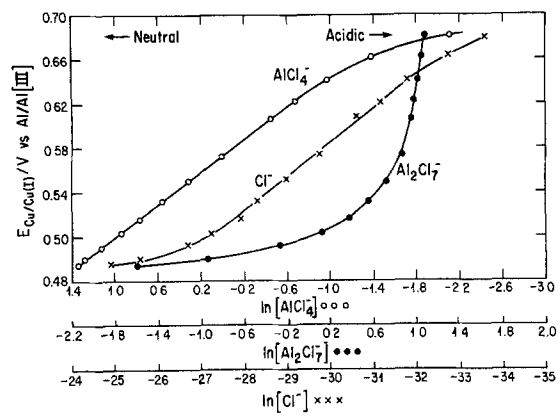

Fig. 11. E for Cu/Cu(I) vs. ln[Cl⁻], ln[$AlCl_4^-$] and ln[$Al_2Cl_7^-$] in acid melts.

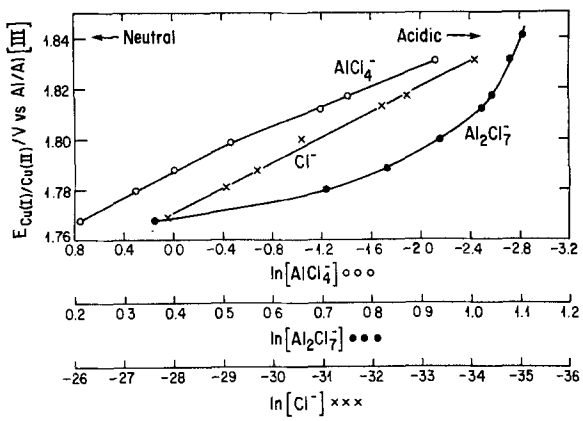

Fig. 12. E for Cu(I)/Cu(II) vs. ln[Cl⁻], ln[$AlCl_4^-$] and ln[$Al_2Cl_7^-$] in acid melts.

[Cl^-] as indicating no change in ligand number between the two species; the change in slope *vs.* ln [$AlCl_4^-$] corresponds to a ligand number change of one, *i.e.*, from 3 for Cu(I) (see above) to 4 for Cu(II). The data presented have at least been tentatively analyzed in terms of Cu(I) and Cu(II) forming $AlCl_4^-$ complexes (of ligand number 3 and 4), respectively. A large caveat should be attached to this interpretation. Finally, $E^{o\prime}$ values for the couples are shown in Table III, with respect to the Al reference in the 2:1 melt.

Acknowledgments

This work was supported by the Air Force Office of Scientific Research and, in part, by the Solar Energy Research Institute. A grant-in-aid from the Chevron Research Foundattion also contributed to this work.

Manuscript submitted July 29, 1982; revised manuscript received Jan. 24, 1983.

Any discussion of this paper will appear in a Discussion Section to be published in the December 1983 JOURNAL. All discussions for the December 1983 Discussion Section should be submitted by Aug. 1, 1983.

The State University of New York at Buffalo assisted in meeting the publication costs of this article.

REFERENCES

1. C. L. Hussey and L. A. King, Technical Report No. FJSRL-TR-77-0013, F. J. Seiler Research Laboratory, U.S. Air Force Academy (1977).
2. J. C. Nardi, J. K. Erbacher, C. L. Hussey, and L. A. King, Technical Report No. FJSRL-TR-77-0002, F. J. Seiler Research Laboratory, U.S. Air Force Academy (1977).
3. R. C. Howie and D. W. MacMillan, *J. Appl. Electrochem.*, **2**, 217 (1972).
4. B. Nayak and M. M. Misra, *ibid.*, **7**, 45 (1977).
5. F. H. Hurley and T. P. Wier, *This Journal*, **98**, 203 (1951).
6. F. H. Hurley and T. P. Wier, *ibid.*, **98**, 207 (1951).
7. R. A. Carpio, L. A. King, R. E. Lindstrom, J. C. Nardi, and C. L. Hussey, *ibid.*, **126**, 1644 (1979).
8. R. J. Gale, B. Gilbert, and R. A. Osteryoung *Inorg. Chem.*, **17**, 2728 (1978).
9. J. Robinson and R. A. Osteryoung, *J. Am. Chem. Soc.*, **101**, 323 (1979).
10. R. J. Gale and R. A. Osteryoung, *Inorg. Chem.*, **18**, 1603 (1979).
11. J. P. Schoebrechts and B. P. Gilbert, *This Journal*, **128**, 2679 (1981).
12. J. Robinson and R. A. Osteryoung, *J. Am. Chem. Soc.*, **102**, 4415 (1980).
13. C. P. Keszthelyi, *Electrochim. Acta*, **26**, 1261 (1981).
14. R. J. Gale, B. Gilbert, and R. A. Osteryoung, *Inorg. Chem.*, **18**, 2723 (1979).
15. C. L. Hussey and T. M. Laher, *ibid.*, **20**, 4201 (1981).
16. H. Linga, Z. Stojeck, and R. A. Osteryoung, *J. Am. Chem. Soc.*, **103**, 3754 (1980).
17. C. L. Hussey, L. A. King, and J. S. Wilkes, *J. Electroanal. Chem.*, **102**, 321 (1979).
18. C. Nanjundiah, K. Shimizu, and R. A. Osteryoung, *This Journal*, **129**, 2474 (1982).
19. L. G. Boxall, H. L. Jones, and R. A. Osteryoung, *ibid.*, **121**, 212 (1974).
20. C. L. Hussey, L. A. King, and R. A. Carpio, *ibid.*, **126**, 1029 (1979).
21. S. Bruckenstein and D. T. Napp, *J. Am. Chem. Soc.*, **90**, 6303 (1968).
22. Z. Galus, "Fundamentals of Electrochemical Analysis," p. 249, John Wiley and Sons, Inc., New York (1976).
23. R. S. Nicholson, *Anal. Chem.*, **37**, 1351 (1965).
24. E. McLaughlin, *Trans. Faraday Soc.*, **55**, 28 (1959).
25. C. L. Hussey, Private communication.
26. D. Habboush and R. A. Osteryoung, To be published.

Properties of Chemically Derivatized Nickel Electrodes: The Synthesis of an Electrocatalytic Interface

Andrew B. Bocarsly,* Sharon A. Galvin, and Sujit Sinha*

Frick Laboratory, Princeton University, Princeton, New Jersey 08544

ABSTRACT

Nickel electrodes yield poor charge transfer characteristics for the oxidation and reduction of the ferrocene couple, as well as for a number of other electrochemically interesting reactions. In this respect, nickel is typical of a variety of inexpensive metals which are potential electrode materials, however, which are not useful due to oxidative instability. In the case of nickel with the ferrocene redox couple, this problem can be overcome by chemical modification of the nickel electrode interface. Surface silylation techniques can be used to covalently bond various moieties to an anodized nickel electrode surface, although, these surfaces appear less reactive with respect to silylation than previously reported platinum or gold surfaces. Attachment of 1,1'ferrocendiyldichlorosilane or $[Fe(CN)_5(NC(CH_2)_3)]_2SiCl_2$ serves to stabilize the nickel interface and to electrocatalyze the ferrocene redox reaction. This effect is obtained by a combination of electron mediation by the surface attached material and inhibition of surface oxidation. The latter is in part due to a physical effect creating an environment in which oxidation is not favorable.

It would be extremely useful both for analytical and synthetic electrochemical purposes if one could change the relatively poor interfacial charge transfer properties of an inexpensive electrode material such as nickel into those of an electrocatalytic (and usually expensive) material such as platinum. The ability to carry out such a transformation would not only be of practical significance but would offer an opportunity to probe the details of interfacial charge transfer processes. Unfortunately, unlike platinum, the surface of nickel is extremely active with respect to oxidation and, thus, it is very difficult and often not possible to prepare nickel electrodes in a stable reproducible manner. Further, the chemical activity of the surface causes nickel to display unexpected behavior with respect to a number of common reversible (or quasi-reversible) redox couples. For example, both platinum and gold electrodes yield quasi-reversible electrochemistry for the oxidation of N,N-dimethylparaphenylenediamine in aqueous electrolyte or the oxidation of ferrocene in acetonitrile electrolyte. However, the same processes when carried out at a nickel electrode show a high degree of irreversibility. This is illustrated for the ferrocene couple in Fig. 1 a and b. Therefore, before one could consider the practical use of nickel as an analytic or synthetic electrode material, its surface has to be modified in such a manner as to make it act like a noble metal surface both with respect to electrocatalytic behavior and inertness.

We have attempted to carry out this transformation by using surface derivatization techniques (1-5) based on the formation of siloxane bonds between the surface and a charge transfer reagent, thus, endowing the interface with certain properties associated with the surface bound species. It has been demonstrated in a number of cases that an appropriately selected surface attached material can have a large influence on the mechanism and kinetics of interfacial charge transfer (6-13). The procedure employed involves the reaction of a hydrolytically unstable silane with a thin layer of an active surface oxide as illustrated in Scheme I. This technique has been previously used to modify a variety of metal and metal oxide surfaces (1, 5); although, it appears that nickel has not been previously treated in this manner

$$\text{Ni-Surface} \xrightarrow{\text{oxidized}} \text{Ni-Surface-O}_x\text{H}_y \quad [1]$$

$$\text{Ni-Surface O}_x\text{H}_y + \text{L}_3\text{SiR} \rightarrow \text{Ni-Surface-O}_x\text{-SiR} + 3\text{LH} \quad [2]$$

$$2\text{L}_4\text{Si} + \text{H}_2\text{O} \rightarrow \text{L}_3\text{Si-O-Si-L}_3 + \text{HCl} \quad [3]$$

Scheme I

where L = halide or alkoxide, and R = surface modification group. Note, Eq. [3] allows synthesis of multiple layers via siloxane polymer formation. Careful control of reaction conditions allows one to vary the surface coverage between submonolayer and multiple layers.

For the purposes of this study we have employed the ferrocene couple oxidation and reduction reaction both as a means of monitoring the heterogeneous charge transfer process and as the surface modification group. This reaction has been chosen because the readily available data on ferrocene with respect to both its electrochemistry and surface derivatization chemistry make it an ideal probe of the interface of interest (1, 5-7, 29).

Experimental

Electrochemistry.—Cyclic voltammetry was carried out with a PAR 174A potentiostat and a PAR 175 voltage programmer. Data was output using a Houston Instruments 2000 recorder. A standard three electrode cell with an SCE reference electrode and a Pt counter-electrode was employed. Reagent grade acetonitrile distilled over CaO and 0.1*M* (n-tetrabutylammonium) perchlorate (TBAP) (Southwestern Chemical) dried under vacuum at 80°C composed the electrolyte. The electrochemical cell was kept under an N_2 blanket. All experiments were run at room temperature.

Preparation of derivatized electrodes.—Nickel electrodes were made from 99% pure nickel wire (Alfa) having a 0.63 mm diam. Electrodes were abraded before use and in some cases potentiostated negative of the H_2 evolution potential in 1*M* NaOH for several minutes to remove any reducible surface oxides. Nickel electrode pretreatment involved repetitive scanning between H_2 and O_2 evolution potentials in 1*M* NaOH until a stable cyclic voltammogram (see text) was obtained (~2 hr). Pt/PtO electrodes were generated using standard literature procedures (1, 5). Pt electrodes were carried through the derivatization procedures along side Ni electrodes as a control (5). After pretreatment, electrodes were washed in H_2O and air dried.

Electrodes were derivatized at 25°C under an N_2 atmosphere in dry isooctane solvent containing ~10 m*M* of the silyl reagent. Reaction time varied from ~30 min up to ~48 hr. After derivatization, electrodes were repeatedly washed in isooctane followed by washing in acetonitrile and air drying. Electrodes treated with $[Fe(CN)_5H_2O]^{3-}$ were dipped for ~1 hr in an aqueous solution of the complex and sodium trifluoroacetate. Electrodes could be stored in air for several days without major deterioration.

Chemicals.—Ferrocene, $K_3Fe(CN)_6$, $K_4Fe(CN)_6$, $Na_2Fe(CN)_5NO$, and n-butyllithum (hexane) were

* Electrochemical Society Active Member.
** Electrochemical Society Student Member.
Key words: chemically modified surface, ferrocene, nickel electrode, corrosion.

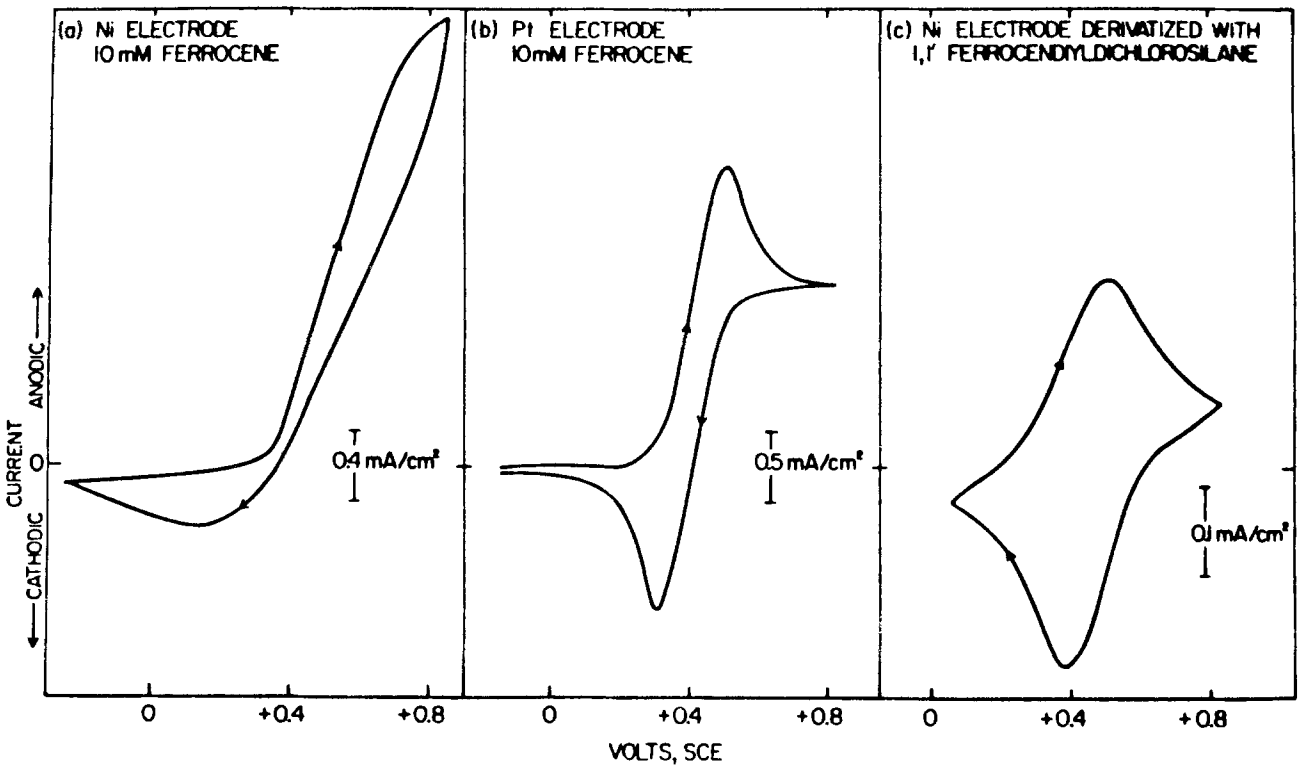

Fig. 1. Cyclic voltammograms in acetonitrile electrolyte with 0.1M TBAP supporting electrolyte. All scans are at 100 mV/sec. a) 10 mM ferrocene at a nickel electrode. Note lack of a well-defined oxidation peak indicating irreversibility; b) 10 mM ferrocene at platinum (reversible); c) nickel electrode derivatized with 1,1' ferrocenediyldichlorosilane.

reagent grade and used as received; $SiCl_4$ (Petrarch Research System, Incorporated) was distilled prior to use. $[Fe(CN)_5H_2O]^{3-}$ was either generated photochemically in slightly acidic (pH = 4) aqueous solution from $Fe(CN)_6^{3-}$ and used *in situ* or synthesized from nitropruside using a literature procedure (14). Ferrocendiyldichlorosilane was synthesized using standard literature procedures (5). All other silanes were reagent grade and used as received (Petrarch).

Results and Discussion

Preparation and characterization of silyl derivatized electrodes.—Surface pretreatment.—In order to evaluate various nickel oxides with respect to their ability to react with hydrolytically unstable silanes and form stable derivatized surfaces, the following procedure was employed. Electrodes were repeatedly cycled between the hydrogen evolution potential and the oxygen evolution potential in 1*M* NaOH until a fairly stable cyclic voltammogram was obtained. (A totally stable voltammogram was never observed.) During this process an anodic wave at ~ +0.37V *vs.* SCE was observed to form and grow, while a broad cathodic wave containing at least two peaks (~+0.31V *vs.* SCE and +0.24V *vs.* SCE) was noted as shown in Fig. 2. The exact potential and peak shape was strongly influenced by the cathodic switching potential. If excursions were made into the hydrogen evolution region, the potential and shape of the cathodic wave was found to change. Further, after prolonged cycling a dark, relatively thick, nonadhering coating was found on the electrode. The mechanical instability of this coating was undesirable, and it was found that its formation could be avoided by adjusting the cathodic switching potential such that hydrogen evolution was not visible on the electrode surface. Once the rate of change of the cyclic voltammogram had decreased significantly (~2 hr of cycling), the electrode was potentiostated for ~15 min at a final potential. This final potential was chosen to produce a specific surface oxide. Based on previous studies (15-20) potentials positive of the first anodic wave were chosen to produce a surface containing $Ni^{III}O(OH)$ species, while potentials negative of the cathodic wave were used to produce a $Ni^{II}(OH)_2$ surface species. The multiple waves associated with the reduction reaction have been correlated with different phases of these species (19). It has been suggested that, although no distinguishable cyclic voltammetric features are observable positive of +0.4V SCE, due to the onset of oxygen evolution, a Ni^{IV} oxide is generated in the region positive of +0.6V *vs.* SCE (21). We, therefore, also carried out pretreatment experiments in this region. All of the oxides generated were found to react with silicon chloride bonds. However, electrodes held positive of +0.40V *vs.* SCE were found to be much more reactive, forming reasonably stable derivatized surfaces. This suggests that it is the $Ni^{III}O(OH)$ species or possibly the Ni^{IV} oxide which is responsible for surface bonding. $Ni^{II}(OH)_2$ appears to only allow formation of very low coverage, unstable surfaces. In fact since not all nickel oxides are reversibly produced, it may be the presence of a Ni^{III} or Ni^{IV} species in the $Ni^{II}(OH)_2$ which is responsible for the observed chemistry. We also found that nickel wire which was simply exposed to air for ~24 hr had the capacity to pick up some of the chlorosilane reagent, suggesting that NiO, the native air oxide, is also reactive to some extent. Electrodes which were abraded just prior to reaction with a silyl reagent yielded no surface attached material. It was also found that electrodes reacted with the silyl derivatizing agent, if they were simply potentiostated at various anodic potentials. However, such electrodes were less stable and reproducible than those generated using the cycling procedure.

Derivatization procedure.—Pretreated electrodes were washed with water and allowed to air dry. Derivatization was effected by immersing the electrodes in dry isooctane solutions under Ar, containing one of the following three derivatization reagents: 1,1' ferrocendiyldichlorosilane (I), N-2 aminoethyl-3-aminopropyltrimethoxy silane (II), or bis(γ-cyanopropyl)dichlorosilane (III). Pt/PtO electrodes generated using stan-

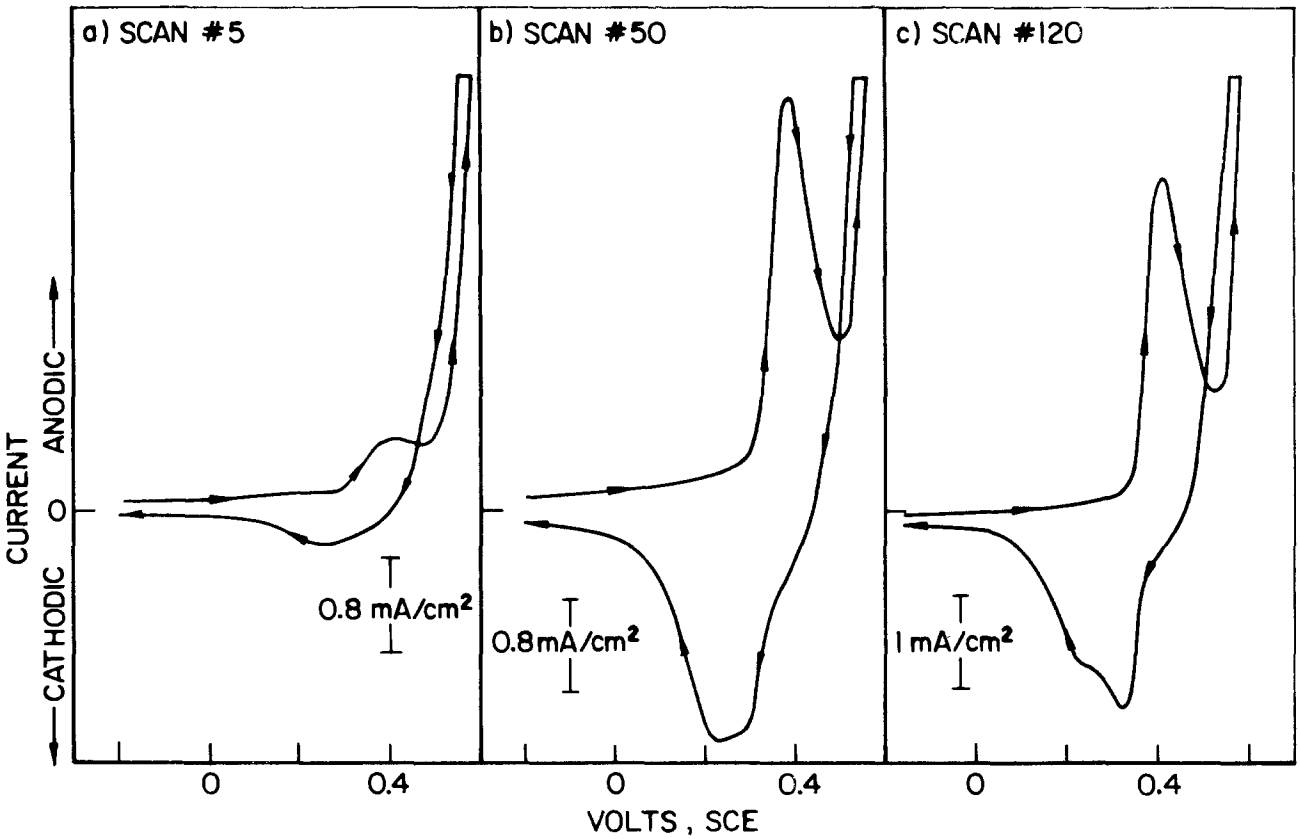

Fig. 2. Repetitive cyclic voltammograms of a freshly abraded nickel electrode in 1M NaOH. After 120 scans the cyclic voltammogram is essentially stable. The anodic peak at +0.37V vs. SCE is associated with $Ni^{III}(O)OH$ formation, while the cathode peaks are different $Ni^{II}(OH)_2$ phases. The off scale anodic current at +0.6V vs. SCE is concomitant with O_2 evolution. Scans are at 100 mV/sec; the cathodic limit of the scans is just positive of the H_2 evolution potential. No cyclic voltammetric features are observable at potentials negative of 0V vs. SCE.

dard literature procedures (1) were carried through the derivatization procedure with the Ni/NiO_x electrodes as a control. It has previously been demonstrated that all three of the derivatizing reagents react with the Pt/PtO substrate (1, 5). Reaction time, concentration of silane, and temperature were varied to control the amount of surface attached material obtained. However, as previously reported, a high degree of total reproducibility was not possible (5). Electrodes treated with either II or III were further reacted with $[Fe(CN)_5H_2O]^{2-}$ in aqueous solution. Ligand substitution of the surface bound amine for water generated an electrochemically active surface attached iron center.

The procedure outlined yielded similar results for Pt/PtO and Ni/NiO_x when compounds I and III were employed. Qualitatively the Pt/PtO surfaces appeared slightly more reactive than the Ni/NiO_x surfaces (higher coverage per unit reaction time). However, we could not generate a derivatized Ni electrode using compound II. Our Pt control did react with this reagent, however, the reaction rate was clearly slower than with the other compounds. Thus, the chemical reactivity of the anodized Ni surface appears significantly less than that obtained with oxidized Pt surfaces.

Characterization of derivatized surfaces.—1,1'ferrocenediyldichlorosilane derivatized surfaces were characterized by cyclic voltammetry in acetonitrile electrolyte which contained no deliberately added electroreactive material. A typical cyclic voltammogram is illustrated in Fig. 1c. Theory predicts (22) that an ideal reversible one electron surface immobilized species should yield a zero volts peak to peak separation, the peaks falling at the $E_{1/2}$ value. Further, a linear scan rate dependence of the peak current is expected along with a 90 mV full width at half height for the cyclic voltammogram.

As can be seen from Fig. 3 and Table I, the ferrocene derivatized electrodes yield a fairly reversible cyclic voltammogram with an $E_{1/2}$ of +0.43V *vs.* SCE in good agreement with similarly derivatized platinum electrodes (5) and with data for solution oxidation and reduction of ferrocene at a reversible electrode. The derivatized nickel electrodes were found to exhibit a linear scan rate dependence (Fig. 3) and no dependence upon solution stirring, suggesting further that the ferrocene was indeed surface attached. Etching the surface with HF removed the surface response as was expected. Electrochemical studies on oxide coated electrodes dipped in a ferrocene solution did not yield any evidence for a surface bound species. These data are strongly supportive of the chemistry outlined in Scheme I.

As can be seen in Table I, surface coverages obtained by integration of the area under the cyclic voltammogram with respect to time vary slightly from electrode to electrode. Coverages in general are $\sim 10^9$ mol/cm^2 suggesting formation of multiple layers (5). One also finds small variation in the exact peak potentials. Deviations from the theoretically predicted voltammogram are noted in terms of a slight peak to peak separation and a peak width which is significantly larger than the predicted 90 mV. It should be noted that the peak to peak separation at the slower scan rates in general is less than 60 mV, the theoretical value for a reversible one electron charge transfer reaction involving a dissolved species (23). From the data, it is clear that one can reproducibly attach 1,1' ferrocenediyldichlorosilane to a nickel surface. Further, although deviations from ideal behavior are observed, the surface bound species appears in general to behave very much like ferrocene in solution at a reversible electrode. Deviations from ideality can be accounted for by assuming there exists a number of different surface

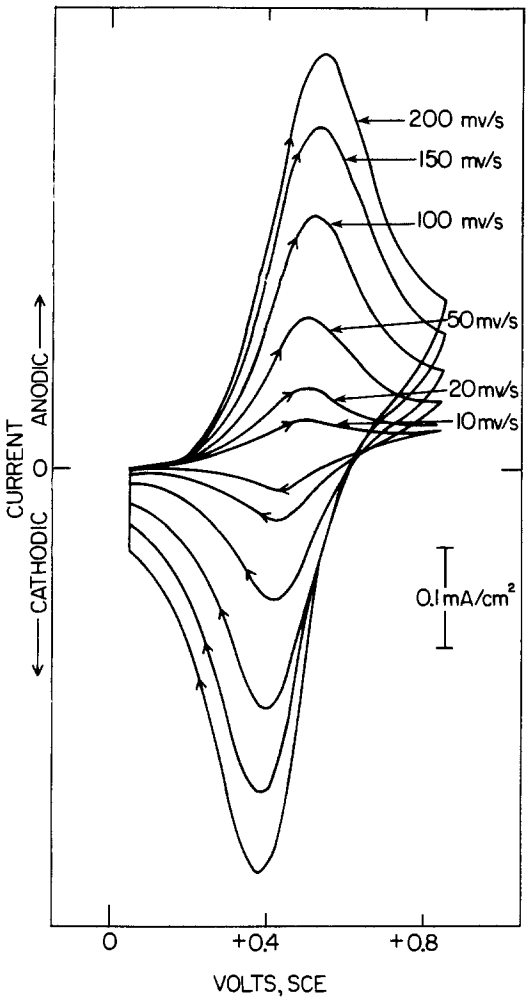

Fig. 3. Scan rate dependence for nickel derivatized with 1,1' ferrocenediyldichlorosilane in acetonitrile with 0.1M TBAP supporting electrolyte. Note that the peak current increases linearly with scan rate.

sites on the nickel surface. These sites produce a variety of redox couples each having a slightly different potential. In view of the heterogeneous chemical nature of the oxidized nickel surface this assumption appears fairly reasonable. Similar reasoning has been used to explain variations from ideality found for other derivatized metal surfaces (5, 24).

Bis(γcyanopropyl)dichlorosilane derivatized electrodes were analyzed in a manner similar to that carried out for the silylferrocene derivatized surfaces after having been electrochemically tagged as shown in Scheme II

$$\text{Ni-Surface oxide} + Cl_2Si[(CH_2)_3CN]_2 \rightarrow \quad [4]$$

$$\text{Ni-(Surface-O-)}_x SiCl_{2-x}[(CH_2)_3CN]_2$$

$$\text{Ni-(Surface-O-)}_x SiCl_{2-x}[(CH_2)_3CN]_2 + X[Fe(CN)_5H_2O]^{3-} \rightarrow \quad [5]$$

$$\text{Ni-(Surface-O-)}_x SiCl_{2-x}$$

$$[(CH_2)_3CNFe(CN_5]_x^{3-}[(CH_2)_3(CN)]_{2-x}$$

$X = 1, 2$

Scheme II

Cyclic voltammograms were carried out in an aqueous electrolyte containing 0.1*M* $NaClO_4$. As with the ferrocene surface, a linear scan rate and no dependence on solution stirring is observed (Fig. 4). However, the width and shape of the peaks suggest a relatively large deviation from ideality. Laviron has suggested that intermolecular interactions between bound surface species can account for these deviations in the cyclic voltammogram (27). Surface coverage (Table I) is similar to that observed for surface attached ferrocene. These numbers can only be used as a lower limit since it is not clear whether or not each surface silane molecule complexes a ferricyanide unit. The cyclic voltammetric peak positions yield an $E_{1/2}$ value of +0.34 in good agreement with solution data at a reversible electrode and recent reports by Anson and Murray on ferrocyanide electrostatically attached to a carbon electrode surface (25, 26).

Charge transfer behavior of derivatized nickel electrodes.—As noted earlier, nickel electrodes, in direct contrast to platinum and many other electrode materials, yield irreversible behavior for the oxidation of ferrocene in acetonitrile, and, therefore, it is quite surprising to observe that nickel derivatized with silylferrocene shows a reversible ferrocene surface wave (Fig. 1a, c). Based on this result, we attempted to use the ferrocene derivatized electrode to electrocatalyze the oxidation of solution ferrocene. A comparison of the cyclic voltammogram of solution ferrocene at platinum (Fig. 1b) with solution ferrocene at a silyferrocene derivatized nickel electrode (Fig. 5b) indicates that a reversible solution wave is obtained at the derivatized surface. Thus, surface attached ferrocene alters the behavior of the nickel electrode, turning an irreversible charge transfer reaction into a reversible charge transfer reaction. Scan rate analysis of solution ferrocene oxidation at the derivatized nickel electrode yields a $(\text{scan rate})^{1/2}$ dependence as seen in Fig. 6 for the anodic peak current confirming the reversible nature of this reaction (23). Similarly the peak to peak separation is found to be independent of scan rate.

Table I. Electrochemical data for derivatized Ni electrodes[a]

Derivatizing reagent	Expt.	Coverage[b] × 10^9 mols/cm²	E_{ox} V vs. SCE	E_{red} V vs. SCE	$E_{1/2}$[c] V vs. SCE
1,1'ferrocene-diyldichlorosilane	1	9.2	0.50	0.35	0.43
	2	2.3	0.48	0.38	0.43
	3	9.6	0.49	0.37	0.43
	4	2.2	0.50	0.36	0.43
	5	1.8	0.50	0.36	0.43
	6	2.8	0.47	0.34	0.41
	7	2.6	0.48	0.32	0.40
	8	3.6	0.47	0.34	0.40
Bis(γ-cyanopropyl)-dichlorosilane and $[Fe(CN)_5H_2O]^{3-}$	1	1.2	0.38	0.33	0.36
	2	1.4	0.36	0.29	0.32
	3	1.3	0.37	0.29	0.33
	4	1.1	0.38	0.32	0.36
	5	0.9	0.36	0.31	0.34

[a] All scans are at 100 mV/sec. Silylferrocene surfaces were characterized in acetonitrile/0.1*M* tetrabutylammonium perchlorate. Surface attached ferrocyanide was characterized in aqueous electrolyte containing 0.1*M* sodium perchlorate.
[b] Coverages were obtained by integration of the area under the anodic cyclic voltammogram wave.
[c] $E_{1/2} = E_{PC} + \frac{1}{2}(E_{PA} - E_{PC})$ where E_{PC} = cathodic peak potential and E_{PA} = anodic peak potential. The second term was used to correct for nonideality leading to a peak separation greater than zero.

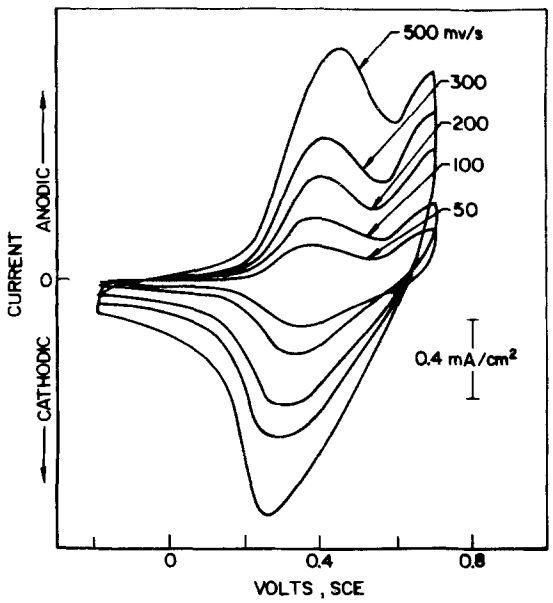

Fig. 4. Scan rate dependence for nickel derivatized with bis(γ-cyanopropyl)-dichlorosilane and $[(FeCCN)_5H_2O]^{3-}$ in aqueous electrolyte with 0.1M $NaClO_4$ supporting electrolyte. Peak current is a linear function of scan rate.

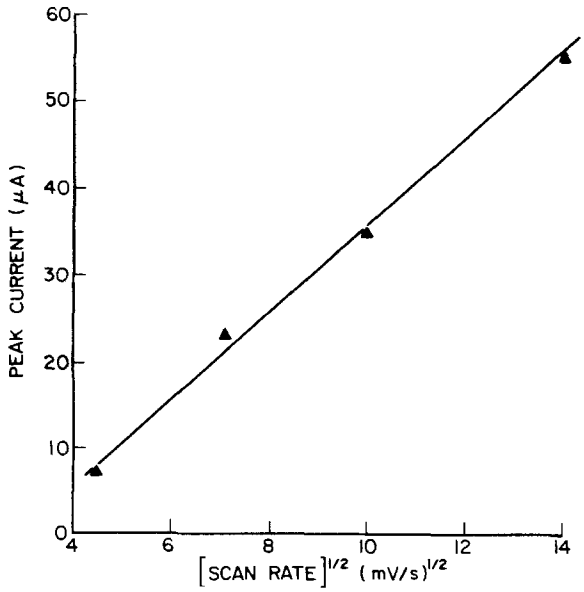

Fig. 6. Scan rate dependence of peak current from cyclic voltammetric data for a 10 mM ferrocene solution (0.1M TBAP/acetonitrile) at a silylferrocene derivatized nickel electrode. Solution concentration and current scale were chosen such that only the solution signal was observable.

Further as can be seen in Fig. 5b, repetitive cyclic voltammograms in ferrocene indicate the activity is fairly stable. Only a slight change in peak height is observed after 70 scans. This is to be compared with a pretreated (but not derivatized) electrode shown in Fig. 5a, which produces time dependent results upon repeated scanning. By scanning an untreated nickel electrode to fairly anodic potentials (+1.0V *vs.* SCE) a peak for the oxidation of solution ferrocene can be obtained. The exact position of this peak is variable. However, it usually occurs at 100-400 mV positive of the peak observed on derivatized nickel under the same conditions, suggesting that a barrier to ferrocene oxidation of ~2 kcal/mol is removed upon derivatizing the nickel surface.

We find that by abrading the nickel surface just prior to use and using dry acetonitrile electrolyte that the peak position for ferrocene oxidation at a nonderivatized nickel electrode can be brought significantly neg-

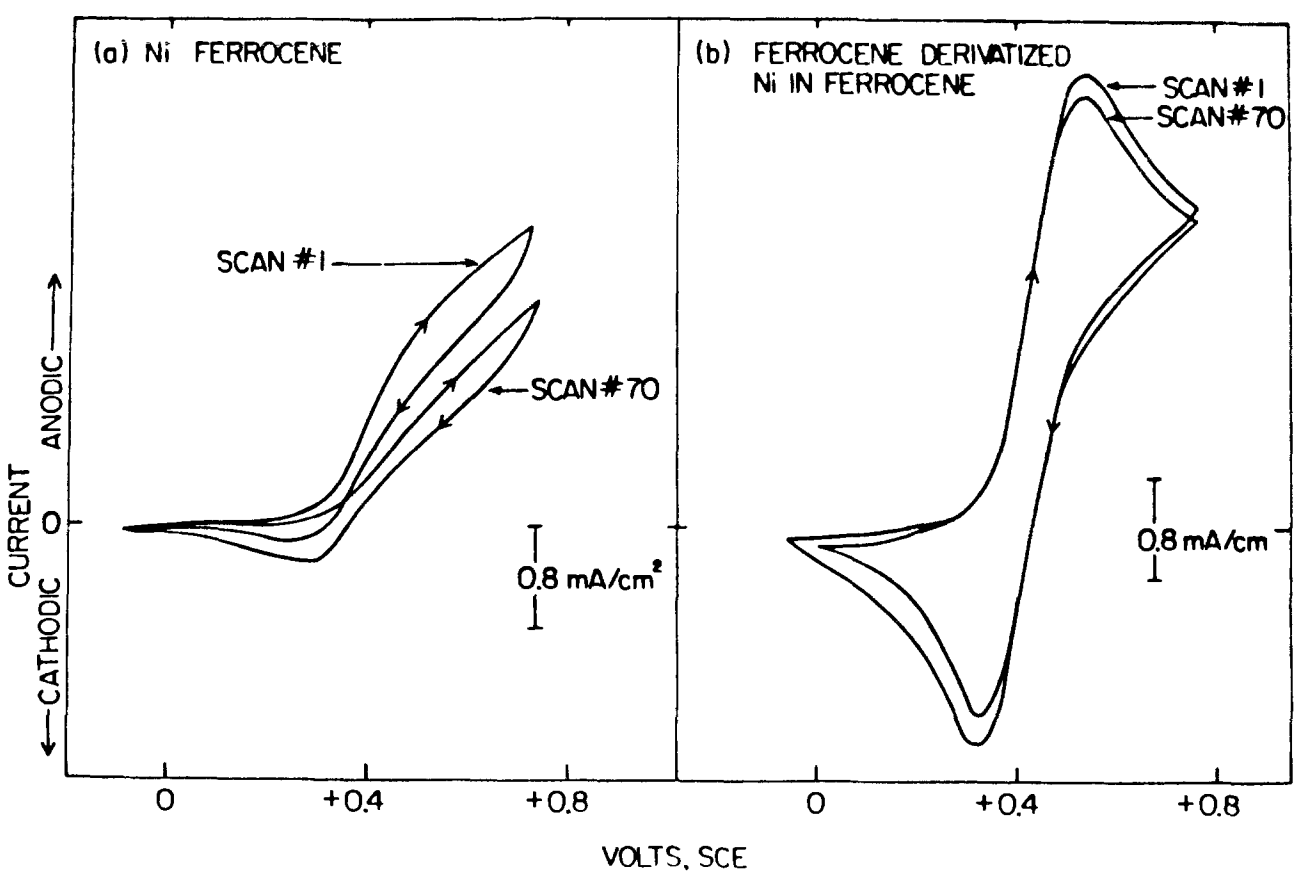

Fig. 5. a) Multiple cyclic voltammetric scans with a pretreated (anodized) nickel electrode in acetonitrile electrolyte containing 0.1M TBAP and 10 mM ferrocene; b) same as in a) using a silylferrocene derivatized nickel electrode. All scans are at 100 mV/sec.

ative of that found for a totally untreated nickel electrode; although, this treatment never produces an electrode which exhibits a cyclic voltammogram that is as reversible or stable as is observed using the derivatized electrode. This result suggests that the surface attached material may be blocking oxide formation while increasing the exchange current density for ferrocene and thus providing the catalytic conditions. To gain more insight into the mechanism by which catalysis is occurring a variety of derivatized nickel surfaces were characterized using cyclic voltammograms of solution ferrocene oxidation and reduction as a probe.

In order to ascertain whether or not the pretreatment used was responsible for generating the observed electrocatalytic behavior a pretreated electrode was cycled in the ferrocene electrolyte. As can be seen in Fig. 5a, no evidence for catalysis by the induced surface oxides is observed. Therefore, the actual derivatization process is responsible for the observed electrocatalysis.

One can envision two possible mechanisms by which surface modification can effect the charge transfer process. Either one or the other, or both, may be operating at the derivatized nickel interface. The observed effect may be due to establishment of a semipermeable physical barrier at the derivatized interface which separates the electrode surface from corrosive chemical reagents, thus, preventing the formation of insulating surface oxides, but allowing ferrocene to approach close enough to the nickel interface for charge transfer to occur. On the other hand, the surface attached ferrocene may be acting as a charge transfer mediator enhancing the rate of oxidation of solution ferrocene to such an extent that other charge transfer reactions (oxidation of the interface) cannot occur. To rule out that the first mechanism is the only mechanism operating, we derivatized the surface with a nonelectroactive silane, dimethyldichlorosilane. This material should have generated the same type of physical barrier as did the silylferrocene. The methylsilane derivatized electrode was tested by cyclic voltammetry in a ferrocene electrolyte. As Fig. 7 illustrates, no catalytic activity was noted. In fact, the electrode properties appear significantly worse than for the nonderivatized case. This result suggests but does not prove that simple physical protection is not enough to catalyze the ferrocene oxidation. Rather, it appears that placement of a silane on the surface of nickel may serve to insulate it from the electroactive species of interest.

Definitive proof that silylation of the surface is not sufficient to promote ferrocence oxidation is shown in Fig. 8. As can be seen in part a of this figure, derivatization of nickel with bis(γ-cyanopropyl)dichlorosilane, a nonelectroactive species, results in very poor

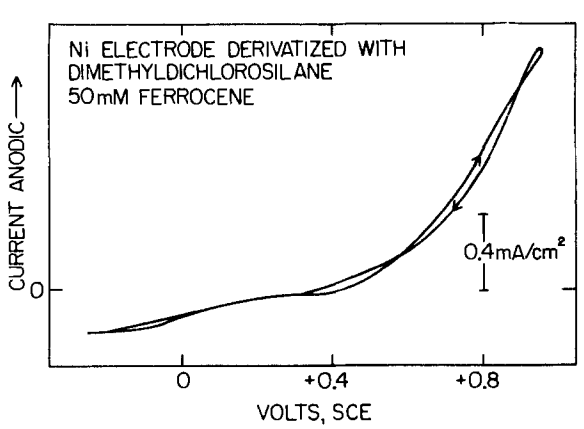

Fig. 7. Cyclic voltammograms of 50 mM ferrocene in acetonitrile/0.1M TBAP at 100 mV/sec at a nickel electrode derivatized with dimethyldichlorosilane. A scan rate of 100 mV/sec was used. Note some hysteresis is observed at the anodic limit.

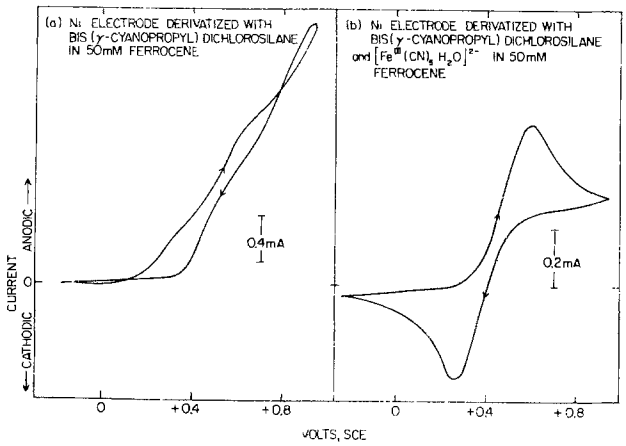

Fig. 8. Cyclic voltammograms of 50 mM ferrocene in acetonitrile/0.1M TBAP at 100 mV/sec. a) A nickel electrode derivatized with bis(γ-cyanopropyl)-dichlorosilane; b) a nickel electrode prepared as in Scheme II having $\sim 10^{-9}$ mols/cm² of surface attached ferrocyanide.

charge transfer characteristics for the oxidation of ferrocene. However, if this same electrode (part b of the figure) is reacted with $[Fe(CN)_5H_2O]^{3-}$ after derivatization so that an electroactive $[Fe(CN)_5]^{3-}$ is present on the surface, a reversible ferrocene oxidation is observed. This clearly indicates that it is the presence of an appropriate surface attached redox center on the nickel surface not the silane-surface interaction which catalyzes the charge transfer reaction. Further, since it is necessary to have a surface attached redox system, the second mechanism mentioned is implied, that is, the surface attached material is acting as an electron mediator thus enhancing the rate of charge transfer to solution ferrocene as shown in Scheme III

$$\text{Surface—Redox} \xrightarrow{e^-} \text{Surface—Redox}^+ \quad [6]$$

$$\text{Surface—Redox}^+ + \text{Ferrocene} \rightarrow \text{Surface—Redox} + \text{Ferricenium} \quad [7]$$

where: Redox indicates a surface attached redox couple.

Scheme III

However, the existence of this mechanism does not rule out the participation of a physical protection process; although, the experiments with nonelectroactive silanes indicate that physical protection itself is not sufficient to induce the observed electrocatalysis.

In fact, there exist data to suggest that some form of physical protection must be operational. For example, derivatized electrodes can be held at anodic potentials in wet acetonitrile electrolyte containing no deliberately added electroactive material for periods of time exceeding that necessary to totally oxidize all of the surface attached material without loss of electrocatalytic activity with respect to solution ferrocene. Yet, nonderivatized electrodes are further deteriorated with respect to ferrocene oxidation by this process. It is quite clear that electron mediation is incapable of protecting the surface against oxidation once the surface mediator is totally oxidized. Further, we find that certain solution species such as $Ru(NH_3)_6^{2+}$, which has E_{redox} significantly negative of surface ferrocene ($\sim$0.5V negative of surface ferrocene), can be reversibly oxidized at the derivatized electrode but not at an oxidized nickel surface. Under such conditions the rate constant for the reaction analogous to Eq. [7] must be slow according to Marcus theory, thus, mediated electrocatalysis cannot occur (28). This indirectly implicates the existence of physical protection. Such protection may consist of the formation of a hydrophobic

barrier at the electrode surface through which water cannot easily penetrate and, thus, surface oxidation cannot occur, or the binding and poisoning of potential corrosion sites by the formation of surface-siloxane bonds. The data available yields no specific details on the mechanism of protection.

Conclusion

Nickel electrode can be chemically derivatized to produce a stable electroactive interface using surface silylation techniques analogous to those previously employed on standard analytical electrode surfaces. Pretreated nickel electrodes are found to be less reactive than similarly treated platinum or gold surfaces and, thus, only very reactive silylating reagents can be employed. Once formed the surfaces show reasonable stability, although long-term stability is questionable.

Electrodes derivatized in the above manner, to yield a surface attached ferrocene or ferrocyanide, prove electrocatalytic for the oxidation and reduction of solution ferrocene, a reaction which is irreversible at the native nickel interface. The interfacial charge transfer to solution mechanism involves derivative mediated electron transfer; however, the total electrocatalysis mechanism is also dependent on the physical environment formed at the interface by the derivative. This yields an interface which selectively and rapidly oxidizes solution ferrocene while inhibiting other redox processes associated with oxide formation. It is apparently the formation of this oxide which gives nickel its irreversible charge transfer behavior with respect to ferrocene oxidation. That is, the ferrocene oxidation competes with oxide formation, the oxides formed inhibiting charge transfer. The surface derivative acts as a barrier to oxide formation while carrying out rapid surface to derivative charge transfer (Eq. [6]) and rapid derivative to electrolyte charge transfer (Eq. [7]), thus, causing the observed electrocatalysis. The first process may be rapid simply because a high concentration of electroactive material is present near the surface; while the second process is expected to be fast in the case of surface attached ferrocene since solution ferrocene has a very rapid self-exchange rate and it has previously been shown that surface attachment does not drastically affect this (6). Outer sphere electron transfer between $Fe(CN)_6^{4-/3-}$ and ferrocene$^{0/+1}$ is also known to be fast (6, 7). It is reasonable to assume the surface $Fe(CN)_5^{2-/3-}$ fragment behaves similarly.

Finally, we note that with respect to the oxidation and reduction of solution ferrocene the derivatized Ni electrode mimics the Pt electrode, supportive of the idea that surface modification techniques can be used to enhance the stability and electrocatalytic response of fairly inexpensive metals. In the case of Ni, the procedures reported herein are not sufficient to totally control the interfacial processes in that surface protection is lost at positive electrode potentials ($\geq$0.8V *vs.* SCE). However, it would appear that the appropriate combination of redox active surface species could produce a stable Ni interface having a quite large anodic working range. Currently, this possibility is under investigation.

Acknowledgments

Acknowledgment is made to the donors of the Petroleum Research Fund, administered by the American Chemical Society for support of this research. One of us also acknowledges the Dreyfus Foundation for a Newly Appointed Faculty Grant.

Manuscript submitted Aug. 4, 1982; revised manuscript received Jan. 10, 1983. This was Paper 26 presented at the Denver, Colorado, Meeting of the Society, Oct. 11-16, 1981.

Any discussion of this paper will appear in a Discussion Section to be published in the December 1983 JOURNAL. All discussions for the December 1983 Discussion Section should be submitted by Aug. 1, 1983.

Princeton University assisted in meeting the publication costs of this article.

REFERENCES

1. R. W. Murray, *Acc. Chem. Res.*, **13,** 135 (1980).
2. A. W. C. Lin, P. Yeh, A. M. Yacynych, and T. Kuwana, *J. Electroanal. Chem.*, **84,** (1977); A. M. Yacynych and T. Kuwana, *Anal. Chem.*, **50,** 640 (1978).
3. R. F. Lane and A. T. Hubbard, *J. Phys. Chem.*, **77,** 1401 (1973).
4. A. P. Brown and F. C. Anson, *J. Electroanal. Chem.*, **83,** 203 (1977); N. Oyama and F. C. Anson, *J. Am. Chem. Soc.*, **102,** 3450 (1979).
5. M. S. Wrighton, M. C. Palazzotto, A. B. Bocarsly, J. M. Bolts, A. B. Fischer, and L. Nadjo, *J. Am. Chem. Soc.*, **100,** 7264 (1978).
6. N. S. Lewis, A. B. Bocarsly, and M. S. Wrighton, *J. Phys. Chem.*, **84,** 2033 (1980).
7. A. B. Bocarsly, E. G. Walton, and M. S. Wrighton, *J. Am. Chem. Soc.*, **102,** 3390, (1980); J. M. Bolts, A. B. Bocarsly, M. C. Palazzotto, E. G. Walton, and M. S. Wrighton, *ibid.*, **101,** 1378 (1979).
8. J. P. Coleman, M. Marrocco, P. Denisevich, C. Koval, and F. C. Anson, *J. Electroanal. Chem.*, **101,** 117 (1979).
9. A. Bettelheim, R. J. H. Chan, and T. Kuwana, *ibid.*, **110,** 93 (1980).
10. J. B. Kerrard and L. L. Miller, *ibid.*, **101,** 263 (1979).
11. J. Zagal, *ibid.*, **109,** 389 (1980).
12. T. Matsue, M. Fujihara, and T. Osa, *Bull. Chem. Soc. Jpn.*, **52,** 3692 (1979).
13. A. Voulgaropoulos, R. Nowak, W. Kutner, and H. B. Mark, Jr., *Chem. Comm.*, **244,** (1978).
14. K. A. Hofmann and Justus Liebigs, *Ann. Chem.*, **312,** 1 (1900).
15. J. L. Weininger and M. W. Breiter, *This Journal*, **110,** 484 (1963).
16. J. L. Weininger and M. W. Breiter, *ibid.*, **111,** 707 (1964).
17. D. M. MacArthur, *ibid.*, **117,** 422 (1970).
18. M. A. Hopper and J. L. Ord, *ibid.*, **120,** 183 (1973).
19. R. S. Schrebler Guzmán, J. R. Vilche, and A. J. Arvía, *ibid.*, **125,** 1578 (1978).
20. J. F. Wolf, L. S. R. Yeh, and A. Damjanovic, *Electrochim. Acta*, **26,** 409 (1981); J. F. Wolf, L. S. R. Yeh, and A. Damjanovic, *ibid.*, **26,** 811 (1981).
21. L. D. Burke and T. A. M. Twomey, in "Proceedings of the Symposium on the Nickel Electrode," R. G. Gunther and S. Gross, Editors, Vol. 82-4, pp. 75-96, The Electrochemical Society Softbound Proceedings Series, Pennington, NJ (1982).
22. E. Laviron, *J. Electroanal. Chem.*, **39,** 1 (1972).
23. R. S. Nicholson and I. Shain, *Anal. Chem.*, **36,** 706 (1976), and references cited therein.
24. D. F. Smith, K. Willman, K. Kuo, and R. W. Murray, *J. Electroanal. Chem.*, **95,** 217 (1979).
25. N. Oyama and F. C. Anson, *This Journal*, **127,** 247 (1980).
26. K. N. Kuo and R. W. Murray, *J. Electroanal. Chem.*, **131,** 37 (1982).
27. E. Laviron, *ibid.*, **122,** 37 (1981).
28. F. C. Anson, *J. Phys. Chem.*, **84,** 3336 (1980).
29. J. M. Bolts and M. S. Wrighton, *J. Am. Chem. Soc.*, **101,** 6179 (1979).

High Reliability Drop-Fall Detector for Computerized Drop-Time Measurements

Marcello Carla', Giovanni Aloisi, Giorgio Papeschi, and Silvano Bordi*

Istituto di Chimica Fisica, Universita di Firenze, Via G. Capponi 9, Firenze, Italy I 50121

ABSTRACT

An electronic drop-fall detector for dropping mercury electrodes is described. The device has been conceived to work in a computer controlled apparatus. It offers an accuracy better than 500 μsec and a false triggering rate better than one error over 10^4 drops.

A fully computer controlled apparatus for electrocapillary measurements by the drop-time method has been assembled in our laboratory. It has been conceived to work continuously for several days unattended; thus, a drop-fall detector was needed with: (*i*) high accuracy, (*ii*) high noise immunity, and (*iii*) no need of trimming along a full run, even with solutions of different conductivity. A brief review of the available techniques, with a comparative analysis, can be found in Ref. (1-3).

We agree with Tyma (1) in considering the technique based upon a-c impedance measurements as being at present the most suitable one. Lawrence and Mohilner (4) have proved the absence of any perturbation due to the a-c signal on the interface, and various circuits have been described (1, 3, 5).

However, features (*ii*) (*i.e.*, the insensitivity to statics and to the electromagnetic disturbances generated by the other laboratory apparatus) and (*iii*) (*i.e.*, the ability to work properly for a long time without loss of performances even when solutions of very different conductivity are used) are hardly attainable with these devices. Several improvements have turned out to be necessary to meet the required degree of efficiency.

* Electrochemical Society Active Member.
Key words: drop-time, drop-fall, interfacial tension.

Description of the Circuit

The a-c signal, (Fig. 1) picked up on the working electrode, is amplified by a tuned amplifier, as in Ref. (1). The passband has been settled at 1.5 kHz to ensure best noise rejection, compatibly with the required response time (0.5 msec). Then, the signal, rectified by a full-wave circuit, instead of being compared with a fixed reference level as usual (1, 3-5), is split into two paths (Fig. 2): in one of them, the signal is integrated, and inverted, in the other, it is differentiated. Then, the differentiated pulse is compared with the integrated one. This makes the trigger behavior independent of the amplitude of the signal.

The 91 kHz signal is picked up by a tuned coil wound on a ferrite toroid slipped on the capillary. All other electromagnetic signals (noise) collected by the mercury column find a low impedance path to the ground, through the low output impedance of the 91 kHz generator. The current flowing through the

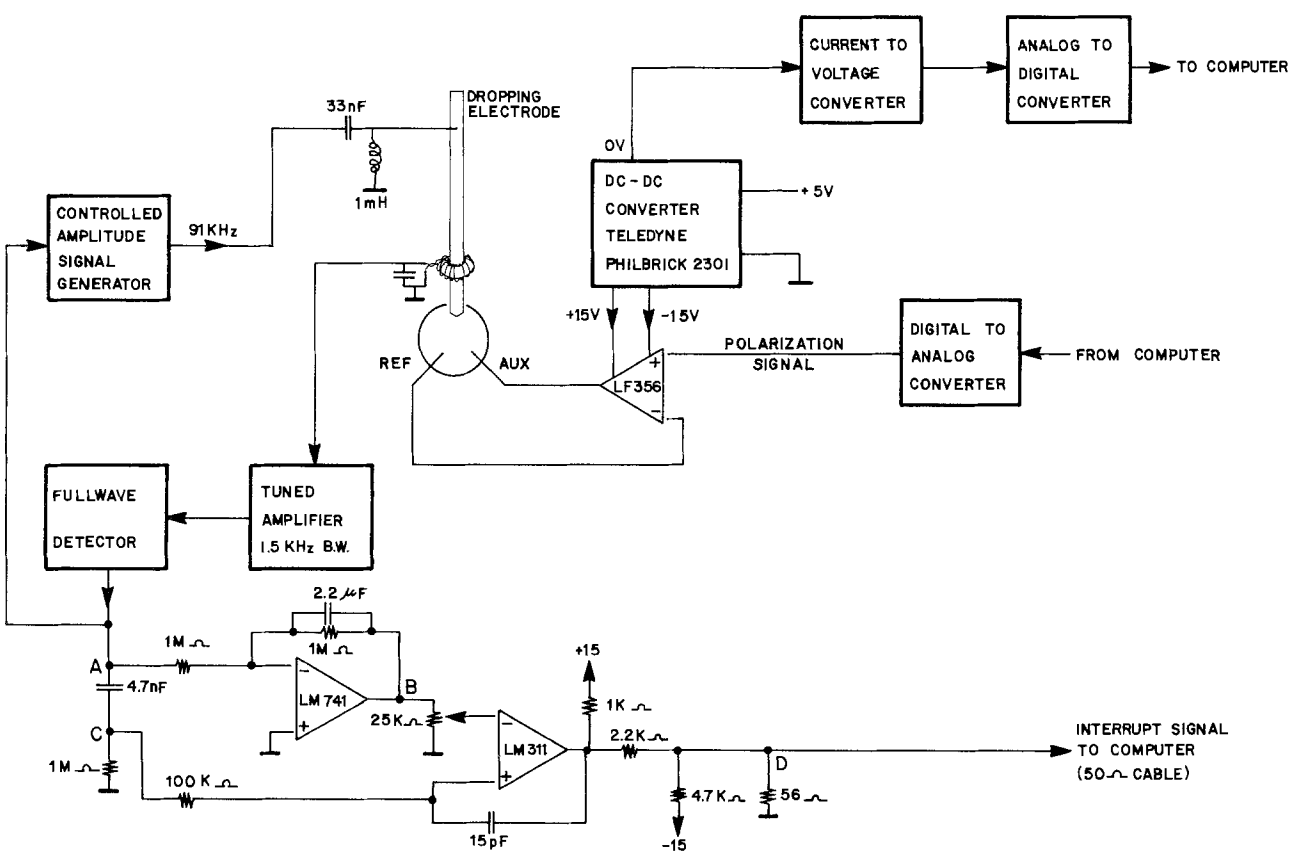

Fig. 1. Scheme of the drop detector

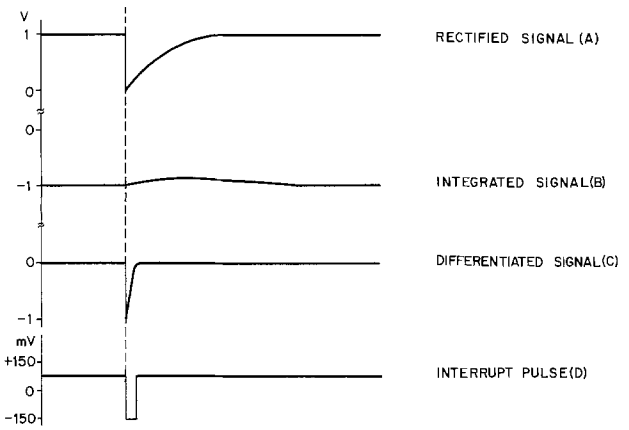

Fig. 2. Waveforms in the trigger circuit. (Integrated circuits: National Semiconductor or equivalents.)

working electrode is measured (inverted) at the ground return of the floating d-c power supply.

The amplitude of the signal of the 91 kHz signal generator is controlled through a negative feedback loop, to avoid the problems connected with very diluted ($< 10^{-3}$M) or very concentrated ($>$ 10M) solutions, *i.e.*, noise, instabilities, or amplifier saturation. With this arrangement, the (averaged) a-c current through the cell, rather than the voltage across it, is kept constant.

Applications and Results

This device has been used for over 2 years in our computer controlled apparatus for drop-time measures. The accuracy has been verified to be better than 500 μsec; the error rate due to false triggering is better than one error over a run of about 10^4 drops, despite the electromagnetic noise generated by other laboratory devices or atmospherics.

Manuscript received May 3, 1982; revised manuscript received *ca.* Oct. 1, 1982.

Any discussion of this paper will appear in a Discussion Section to be published in the December 1983 JOURNAL. All discussions for the December 1983 Discussion Section should be submitted by Aug. 1, 1983.

The Universite di Firenze assisted in meeting the publication costs of this article.

REFERENCES

1 P. D. Tyma, M. J. Weaver, and C. G. Enke, *Anal. Chem.*, **51**, 2300 (1979).
2. B. K. Hahn and C. G. Enke, *ibid.*, **46**, 802 (1974).
3. M. De Blasi, G. Giannelli, P. Papoff, and T. Rotunno, *Ann. Chim.*, **65**, 315 (1975).
4. J. Lawrence and D. M. Mohilner, *This Journal*, **118**, 259 (1971).
5. G. Papeschi, M. Costa, and S. Bordi, *Electrochim. Acta*, **15**, 2015 (1970).

A Thermodynamic Theory of Electric Potential Generated on Crystallization of Electrolytes

R. P. Rastogi and S. A. Khan[1]

Department of Chemistry, University of Gorakhpur, Gorakhpur 273001, India

ABSTRACT

A theory of precipitation potential based on thermodynamics of irreversible processes has been developed. In connection with the verification of theory, thermochemical experiments have been performed which suggest that during the development of precipitation potential associated with the crystallization from supersaturated solution, lattice energy is converted into electrical energy. The theory is found to explain qualitatively all the observed facts.

It has been fairly well established that potential differences are developed during (*i*) crystallization of electrolytes from their supersaturated solutions (1-4), (*ii*) dissolution of electrolytes in a solvent (1-4), (*iii*) freezing of water containing ionic impurities (5-9), and (*iv*) crystallization of electrolytes from their melts (10, 11).

The phenomenon of precipitation and dissolution potential was discovered[2] by Rastogi, Dass, and Batra (1). Comprehensive studies on these potentials have been reported by Rastogi *et al.* (1-4). It has been suggested by these workers that the sign and magnitude of these potentials depend on the unequal mobilities of cations and anions. They have postulated that the precipitation potential develops due to a difference in the rate of attachment of cations and anions during crystallization and that the dissolution potential develops due to a difference in the rate of detachment of cations and anions during dissolution.

Precipitation potential has been defined conceptually by Rastogi, Shukla, and Bhagat (3) as follows: "The precipitation potential is the potential difference arising from an electrical double layer developed at liquid/crystal interface by the ion migration from the liquid phase. The algebraic sign of the precipitation potential is the same as the electrostatic polarity (+) or (−) of the end of the dipolar double layer on the crystal side of the interface." However, the operational definition is as follows: "The precipitation potential is the potential of a platinum electrode coated with a layer of an electrolyte deposited by crystallization from a supersaturated solution at a temperature T less than the saturated temperature T_s. ($T_s - T$) is called the undercooling. The reference potential is a similar bare platinum electrode which is dipped in the above supersaturated solution once the crystallization has started. The observed precipitation potential is corrected for any asymmetry potential existing between the two platinum electrodes before the precipitation run. The potential difference is measured electrostatically by means of a Lindemann Electrometer."

[1] Present address: Chemistry Department, St. Andrew's College, Gorakhpur, India.

Key words: crystallization, electrolytes, thermodynamics, electric potential.

[2] Our attention has been drawn to the work of Jaenicke and coworkers by one of the referees. These workers [*Chem. Abst.*, 47, 10973d (1953); 48, 5612h (1954)] were concerned with the study of the development of potential changes during dissolution of sparingly soluble salts like AgBr used in reversible electrodes, and they interpreted the results on the basis of disturbed interface equilibrium on account of dissolution.

Recently Girdhar and Matta (12, 13) have studied the precipitation and dissolution potentials of a number of electrolytes in aqueous medium. Their results are in general agreement with those reported by Rastogi and co-workers. Ibl *et al.* (14, 15) have also recently reported careful experiments on crystallization and dissolution potentials using single crystals. In their experiments the crystal is always kept in contact with near-saturated solution so that the effect of diffusion is minimized. These workers have used a "corrosion" model based on the difference in the kinetics of dissolution of cations and anions to explain their results.

The experimental studies confirm that the precipitation and dissolution potentials depend on (*i*) temperature, (*ii*) concentration of the medium, (*iii*) nature of the electrolyte, (*iv*) time, and (*v*) $(U_+ - U_-)/(U_+ + U_-)$. Typical data obtained by different workers are summarized in Table I for the sake of comparison.

Quite recently, a thermodynamic theory of dissolution potential based on the thermodynamics of irreversible processes has been developed by Rastogi and Khan (16). In the present communication, an attempt has been made to develop a corresponding thermodynamic theory of precipitation potential. It is found that the theory gives a satisfactory explanation of the observed facts. In order to have a quantitative check, an inequality based on the theory has been tested for which calorimetric experiments had to be performed. These are described in the present communication. The thermochemical experiments suggest that it is the lattice energy that is converted into electrical energy during the development of precipitation potential.

Crystallization Process

The process of crystallization may be visualized as being made up of the following steps:

1. Formation of nuclei.
2. Transport of the cations and anions toward the nuclei.
3. Diffusion through a locally solute depleted zone at the growing interface.
4. Partial or complete desolvation of the moving ions. Complete desolvation would be required for the crystallization of NaCl and partial desolvation would be required for the crystallization of $BaCl_2 \cdot 2H_2O$.
5. Adsorption or chemisorption of ions on the surface of crystal nuclei.
6. Two-dimensional diffusion of the adsorbed or the chemisorbed species to a step.
7. Partial or complete desolvation of the moving ions toward the step.
8. Attachment to the step.
9. One-dimensional diffusion along the step to a kink.
10. Attachment to a kink.
11. Dissipation of the heat of crystallization which may occur stepwise after each of the attachments.

It is obvious that the precipitation potential would be generated at step 5. Further, on account of step 4, a higher temperature would develop in the solution layer near the crystal interface as compared to the bulk, so that a thermo-emf would also be generated. In addition, the diffusion potential would also develop on account of process 3. The equilibrium phase potential at the crystal/solution interface and the Nernst potential would also be included in the observed potential. Most of the experimental studies reported so far involve the observation of the net potential from which the value of the true precipitation potential can be easily estimated when the contributions due to other potentials are experimentally known. Rastogi and Shukla (2) have demonstrated that the values of thermo-emf and Nernst potential are negligible in most cases. Thus, under appropriate experimental conditions, the crystallization potential would largely consist of (*i*) precipitation potential and (*ii*) phase potential. The phase potential would include the unknown contact potential between metal electrodes and salts.

Irreversible Thermodynamics of Precipitation Potential

Theoretical

We may represent schematically the cell used for measuring the precipitation potential as follows

Pt	Solid electrolyte (α-phase)	Supersaturated solution of electrolyte (β-phase)	Pt

We represent the electrochemical system as made up of two subsystems α and β. We may consider, for example, the experimental conditions maintained by Ibl *et al.* (14) such that a uniform supersaturated solution is in contact with the α-phase. Further we may suppose that the temperatures of the two phase remain the same. This is a little simplification since phase transformation is always accompanied by enthalpy changes. We also assume that the crystal nuclei have similar surface energy and that they have average surface energy per unit area of the crystal face.

The total entropy change of the system dS would be given by

$$dS = dS^\alpha + dS^\beta \qquad [1]$$

where dS^α and dS^β are the entropy changes for the two subsystems. The Gibbs equation for the two subsystems is given by

Table I. Dissolution and precipitation potential of some electrolytes

Electrolyte	Medium	Observed dissolution potential (mV)	Observed precipitation potential (mV)	Diffusion potential (mV)	Phase potential (mV)	True dissolution potential (mV)	True precipitation potential (mV)	Reference
NaCl	Water	−170	− 78	− 73	−24	− 80	−54	(3, 2)
	Water	−120	− 90	− 40	− 8	− 72	−82	(4, 12, 13)
	D_2O	− 97	− 73	− 31	−24	− 42	−49	(3, 2)
	Acetone	+211	—	+ 69	−52	+194	—	(3, 2)
KCl	Water	−182	− 76	− 63	−21	− 97	−56	(3, 2)
	Water	−180	− 86	− 42	−20	− 18	−66	(4, 12, 13)
	D_2O	−105	− 66	− 33	−17	− 55	−49	(3, 2)
	Acetone	+268	—	+ 83	−73	+258	—	(3, 2)
	Formamide	+289	—	+ 83	+19	+187	—	(3, 2)
	DMF	+ 89	—	+ 56	−43	+ 76	—	(21, 28)
KBr	D_2O	−131	− 70	− 42	−21	− 68	−49	(3, 2)
	DMF	+124	—	+ 48	−26	+102	—	(21, 28)
$BaCl_2$	Water	−153	−123	+140	−10	−280	−11	(3, 2)
		−168	—	− 46	−12	−110	—	(4, 12, 13)

* Results for acetone reported by Rastogi and co-workers and by Girdhar and co-workers differ in sign as well as in magnitude due to different procedures adopted for purification in the two cases. Girdhar *et al.* report that when the procedure of purification adopted by Rastogi and co-workers is used, the observed value of the dissolution potential agrees in sign with that reported by Rastogi and co-workers.

$$TdS^{\alpha} = dU^{\alpha} + P^{\alpha}dV^{\alpha} - (\mu_1{}^{\alpha}dM_1{}^{\alpha} + \mu_2{}^{\alpha}dM_2{}^{\alpha}) - (e_1\phi^{\alpha}dM_1{}^{\alpha} + e_2\phi^{\alpha}dM_2{}^{\alpha}) - \gamma dA \quad [2]$$

$$TdS^{\beta} = dU^{\beta} + P^{\beta}dV^{\beta} - (\mu_1{}^{\beta}dM_1{}^{\beta} + \mu_2{}^{\beta}dM_2{}^{\beta}) - (e_1\phi^{\beta}dM_1{}^{\beta} + e_2\phi^{\beta}dM_2{}^{\beta}) \quad [3]$$

If we assume that the nuclei are spherical having radius r it can be easily shown that

$$dA = 8\pi r dr \quad [4]$$

and if ρ is the density, change in mass dM^{α} is related to dA by the equation

$$dA = 2dM^{\alpha}/r\rho \quad [5]$$

Hence, Eq. [2] can be rewritten as

$$TdS^{\alpha} = dU^{\alpha} + PdV^{\alpha} - (\mu_1{}^{\alpha} + e_1\phi^{\alpha})\,dM_1{}^{\alpha} - (\mu_2{}^{\alpha} + e_2\phi^{\alpha})\,dM_2{}^{\alpha} - \frac{2\gamma}{\rho r}dM^{\alpha} \quad [6]$$

Using Eq. [3] and [6] in Eq. [1] we obtain

$$TdS = dU^{\alpha} + dU^{\beta} + P^{\alpha}dV^{\alpha} + P^{\beta}dV^{\beta} - \sum_{i=1,2}(\mu_i{}^{\alpha} + e_i\phi^{\alpha})\,dM_i{}^{\alpha} - \sum_{i=1,2}(\mu_i{}^{\beta} + e_i\phi^{\beta})\,dM_i{}^{\beta} - \frac{2\gamma}{\rho r}dM^{\alpha} \quad [7]$$

If dQ is the heat supplied to the system as a whole, using first law of thermodynamics, Eq. [7] can be written as

$$TdS = dQ - \sum_{i=1,2}(\mu_i{}^{\alpha} + e_i\phi^{\alpha})\,dM_i{}^{\alpha} - \sum_{i=1,2}(\mu_i{}^{\beta} + e_i\phi^{\beta})\,dM_i{}^{\beta} - \frac{2\gamma}{\rho r}dM^{\alpha} \quad [8]$$

Now dS can be written as the sum of d_eS, the entropy exchange with the surroundings and d_iS, the change in entropy due to irreversible processes inside the system, so that

$$dS = d_eS + d_iS \quad [9]$$

where

$$d_eS = (dQ/T) \quad [10]$$

Hence

$$Td_iS = -\sum_{i=1,2}(\mu_i{}^{\alpha} + e_i\phi^{\alpha})\,dM_i{}^{\alpha} - \sum_{i=1,2}(\mu_i{}^{\beta} + e_i\phi^{\beta})\,dM_i{}^{\beta} - \frac{2\gamma}{\rho r}dM^{\alpha} \quad [11]$$

or

$$T = T\frac{d_iS}{dt} = -\sum_{i=1,2}(\mu_i{}^{\alpha} + e_i\phi^{\alpha})\frac{dM_i{}^{\alpha}}{dt} - \sum_{i=1,2}(\mu_i{}^{\beta} + e_i\phi^{\beta})\frac{dM_i{}^{\beta}}{dt} - \frac{2\gamma}{\rho r}\frac{dM^{\alpha}}{dt} \quad [12]$$

On account of the law of conservation of mass

$$J_i = dM_i{}^{\alpha}/dt = -dM_i{}^{\beta}/dt$$

So that Eq. [12] can be rewritten as

$$T\sigma = -\sum_{i=1,2}(\Delta\mu_i{}^{\alpha,\beta} + e_i\Delta\phi^{\alpha,B})\,J_i + \frac{2\gamma}{\rho r}J_c \quad [13]$$

where we have replaced $-dM^{\alpha}/dt$ by the crystallization rate J_c. Thus, Eq. [13] can be written as

$$T\sigma = \sum_{i=1,2}J_iX_i + J_cX_c \quad [14]$$

where

$$X_i = -(\Delta\mu_i{}^{\alpha,B} + e_i\Delta\phi^{\alpha,\beta}) \quad [15]$$

and

$$X_c = (2\gamma)/(\rho r) \quad [16]$$

J_i is defined with respect to the center of mass movement. Both J_i and X_i are vectorial in character but J_c and X_c are scalar in character. Hence, according to Curie's principle, we would have coupling between J_1 and J_2 only[3] so that we can write

$$J_1 = L_{11}X_1 + L_{12}X_2 \quad [17]$$

$$J_2 = L_{21}X_1 + L_{22}X_2 \quad [18]$$

$$J_c = L_{cc}X_c \quad [19]$$

where L_{11}, L_{12}, L_{21}, and L_{cc} are phenomenological coefficients and $L_{12} = L_{21}$ on account of the Onsager reciprocity relation.

It should be noted that at equilibrium, $J_c = 0$. Further, X_c is also zero since $r = \infty$. In some cases, r may not be equal to ∞ at equilibrium. If for such cases $r = r_e$ at equilibrium, then Eq. [16] would be written as (18)

$$X_c = (2\gamma)/\rho(1/r - 1/r_e) \quad [20]$$

according to which $X_c = 0$ when $r = r_e$ at equilibrium. For planar surfaces $r_e = \infty$.

The force X_i takes into account the whole transition region from the solid surface to the bulk of the solution and is associated with the change of electrochemical potential.

The current I flowing through the system would be given by

$$I = e_1J_1 + e_2J_2 \quad [21]$$

Since we measure the potential when $I = 0$, we have

$$e_1(L_{11}X_1 + L_{12}X_2) + e_2(L_{21}X_1 + L_{22}X_2) = 0 \quad [22]$$

Putting

$$e_1L_{11} + e_2L_{21} = l_1 \quad [23]$$

and

$$e_1L_{12} + e_2L_{22} = l_2 \quad [24]$$

We have

$$-\Delta\phi^{\alpha,\beta} = \frac{l_1}{e_1l_1 + e_2l_2}\Delta\mu_1{}^{\alpha,\beta} + \frac{l_2}{e_1l_1 + e_2l_2}\Delta\mu_2{}^{\alpha,\beta} \quad [25]$$

If $t_i{}^{o}$ denotes the transport number of unhydrated ith ion, its relation to the mass transfer from phase β to α would be given by

$$(t_1{}^{o})_{\Delta\mu1=0,\,\Delta\mu2=0} = \frac{e_1l_1}{e_1l_1 + e_2l_2} \quad [26]$$

and

$$(t_2{}^{o})_{\Delta\mu1=0,\,\Delta\mu2=0} = \frac{e_2l_2}{e_1l_1 + e_2l_2} \quad [27]$$

Hence, from Eq. [25], [26], and [27] we obtain

$$-(\Delta\phi)^{\alpha,\beta} = \frac{t_1{}^{o}}{e_1}\Delta\mu_1{}^{\alpha,\beta} + \frac{t_2{}^{o}}{e_2}\Delta\mu_2{}^{\alpha,\beta} \quad [28]$$

We now consider α to be the solid phase and β to be the liquid phase. Since $e_i = Z_i\mathbf{F}$, where Z_i is the valency of the ith ion which can be negative or positive, we obtain for a univalent electrolyte

$$-\mathbf{F}(\Delta\phi)^{\alpha,\beta} = t_1{}^{o}[\mu_1{}^{o(s)} - \mu_1{}^{o} - RT\ln a_1{}^{(ss)}] - t_2{}^{o}[\mu_2{}^{o(s)} - \mu_2{}^{o} - RT\ln a_2{}^{(ss)}] \quad [29]$$

where the superscript (ss) denotes the quantities in the supersaturated solution, $\mu_i{}^{o(s)}$ is the standard chemical potential in solid phase and $\mu_i{}^{o}$ is that in the liquid phase and

[3] It should be noted however, that the net change in mass fraction of the component (i = 1, 2) at a point is related to J_c and the divergence of J_i (17).

$$\ln a_1^{(s)} = \ln a_2^{(s)} = 0 \quad [30]$$

where $a_1^{(s)}$ and $a_2^{(s)}$ denote the activities of ions 1 and 2 in the solid state.

Equation [29] can be rewritten as

$$-\mathbf{F}(\Delta\phi)^{\alpha,\beta} = t_1^{o}[\mu_1^{o(s)} - \mu_1^{o} - RT\ln a_1^{(*)}] - t_2^{o}[\mu_2^{o(s)} - \mu_2^{o} - RT\ln a_2^{(*)}] + [t_1^{o}RT\ln a_1^{(*)}/a_1^{(ss)} - t_2^{o}RT\ln a_2^{(*)}/a_2^{(ss)}] \quad [31]$$

where $a_1^{(*)}$ is the activity of the ions at the crystal/solution interface.

There are three terms on right-hand side of Eq. [31]. Let us designate the first two terms as $(\Delta\phi)_{\mathrm{I}}$ and the third term as $(\Delta\phi)_{\mathrm{II}}$, respectively, for convenience. Thus we shall have

$$\mathbf{F}(\Delta\phi)_{\mathrm{I}} = t_1^{o}[\mu_1^{o(s)} - \mu_1^{o} - RT\ln a_1^{(*)}] - t_2^{o}[\mu_2^{o(s)} - \mu_2^{o} - RT\ln a_2^{(*)}] \quad [32]$$

$$\mathbf{F}(\Delta\phi)_{\mathrm{II}} = t_1^{o}RT\ln a_1^{(*)}/a_2^{(ss)} - t_2^{o}RT\ln a_2^{(*)}/a_2^{(ss)} \quad [33]$$

If $(\Delta\phi)_{\mathrm{Phase}}$ denotes the potential difference at the crystal/liquid interface, it is easy to show (19) that

$$\mu_1^{o(s)} - \mu_1^{o} - RT\ln a_1^{(*)} = -\mathbf{F}(\Delta\phi)_{\mathrm{Phase}} \quad [34]$$

$$\mu_2^{o(s)} - \mu_2^{o} - RT\ln a_2^{(*)} = +\mathbf{F}(\Delta\phi)_{\mathrm{Phase}} \quad [35]$$

where 1 denotes cation and 2 denotes anion. Thus from Eq. [32], [34], and [35] we obtain

$$\mathbf{F}(\Delta\phi)_{\mathrm{I}} = t_1^{o}[-\mathbf{F}(\Delta\phi)_{\mathrm{Phase}}] - t_2^{o}[+\mathbf{F}(\Delta\phi)_{\mathrm{Phase}}]$$

or

$$\mathbf{F}(\Delta\phi)_{\mathrm{I}} = -\mathbf{F}(\Delta\phi)_{\mathrm{Phase}} \quad [36]$$

since $t_1^{o} + t_2^{o} = 1$. From Eq. [33] we have

$$\mathbf{F}(\Delta\phi)_{\mathrm{II}} = (t_1^{o} - t_2^{o})\,RT\ln a^{(*)}/a^{(ss)} \quad [37]$$

where we have supposed that

$$a_1^{(*)}/a_1^{(ss)} = a_2^{(*)}/a_2^{(ss)} = a^{(*)}/a^{(ss)} \quad [38]$$

Thus from Eq. [31], [36], and [37] we find

$$-\mathbf{F}(\Delta\phi)^{\alpha,\beta} = -\mathbf{F}(\Delta\phi)_{\mathrm{Phase}} + (t_1^{o} - t_2^{o})\,RT\ln\frac{a^{(*)}}{a^{(ss)}} \quad [39]$$

The second term on the right-hand side of Eq. [39] denotes the precipitation potential and, therefore, if $(\Delta\phi)_{\mathrm{Pption}}$ is the potential difference arising from an electrical double layer developed at the liquid/crystal interface by the process of the migration of ions from solution phase to the crystal phase, we shall obtain

$$(\Delta\phi)_{\mathrm{Pption}} = -\frac{RT}{\mathbf{F}}\,\frac{U_+^{o} - U_-^{o}}{U_+^{o} + U_-^{o}}\ln\frac{a^{(*)}}{a^{(ss)}} \quad [40]$$

where U_+^{o} and U_-^{o} are the mobilities of bare unhydrated cation and anions, respectively.

Making use of usual thermodynamic arguments, it can be easily shown that

$$\ln\frac{a^{(*)}}{a^{(ss)}} \approx \frac{(\Delta H)^{\circ}}{R}\cdot\frac{(T_s - T)}{T_s T} \quad [41]$$

where $(\Delta H)^{\circ}$ is the enthalpy change associated with the development of the precipitation potential. Using Eq. [41], Eq. [40] can be rewritten as

$$(\Delta\phi)_{\mathrm{Pption}} = -\frac{1}{\mathbf{F}}\left(\frac{U_+^{o} - U_-^{o}}{U_+^{o} + U_-^{o}}\right)\frac{(\Delta H)^{\circ}(\Delta T)}{T_s} \quad [42]$$

Since the mobilities of bare ions are not known, Eq. [42] could not be tested quantitatively. However, since

$$\frac{U_+^{o} - U_-^{o}}{U_+^{o} + U_-^{o}} < 1 \quad [43]$$

it is obvious that

$$(\Delta\phi)_{\mathrm{Pption}} < \frac{1}{\mathbf{F}}\,\frac{(\Delta H)^{\circ}(\Delta T)}{T_s} \quad [44]$$

Test of the Theory

Inequality [44] is in a form which can be used for experimental verification. However, the question arises whether $(\Delta H)^{\circ}$ is equal to the heat of precipitation, which is equal in magnitude but opposite in sign to the heat of solution $(\Delta H)_s$, *i.e.*, whether

$$(\Delta H)^{\circ} = -(\Delta H)_s \quad [45]$$

or different?

The basic reaction that occurs during the attachment of ions in the crystal lattice is

$$A^+ + B^- = AB \quad [46]$$

where A^+ and B^- are bare unhydrated ions. If this is so $(\Delta H)^{\circ}$ should be equal to the lattice energy $(\Delta H)_L$, *i.e.*

$$(\Delta H)^{\circ} = (\Delta H)_L \quad [47]$$

For a quantitative check of the theory, the inequality [44] was tested. $(\Delta\phi)_{\mathrm{Pption}}$ was calculated both by substituting $(\Delta H)^{\circ}$ equal to $-(\Delta H)_s$ and $(\Delta H)_L$ in [44]. The results are given in Table II. The calculated values recorded in column 5 do not support the inequality [44]. However, the data presented in column 4 support the inequality. Hence, it follows that $(\Delta H)^{\circ}$ would be equal to $(\Delta H)_L$ rather than $-(\Delta H)_S$.

It is, therefore, obvious that Eq. [47] becomes crucial for the experimental test of inequality [44]. If [46] is the main controlling step for the development of the precipitation potential, the heat produced on crystallization of AB would be converted into electrical energy during crystallization and cooling instead of heating should be observed around the electrode at which crystallization is occurring. In order to test this point, thermochemical experiments were performed. These are described next.

Experiments on the Relationship of Lattice Energy and Precipitation Potential

In order to show that during the development of precipitation potential the lattice energy is converted into electrical energy, the following three types of experiments were performed.

The schematic diagram of the first type of experiments is shown in Fig. 1. The precipitation cell C was made of a double-walled Pyrex glass vessel (outer diameter 6 cm, height 12 cm; inner diameter 3 cm, height 10 cm). The annular space A of the cell was evacuated in order to minimize the heat losses. Two platinum electrodes E_1 and E_2, which were fused in Pyrex glass capillary tubes P_1 and P_2 of 1 mm diam, were used in the cell. Electrode E_1 was in the form of a coil through which a precision thermometer T could be inserted which could be read correctly to ± 0.2°C. Both the electrodes were connected to a Cambridge Lindemann Electrometer.

Table II. Comparison of experimental and the theoretically calculated values of $(\Delta\phi)_{\mathrm{Pption}}$ for some alkali halides using Eq. [44], [45], and [47] at T_s = 311 K and ΔT = 12°C

Electrolyte	$(\Delta H)_L$ (kcal/mol)	$-(\Delta H)_S$ (kcal/mol)	$(\Delta\phi)_{\mathrm{Pption}}$ Theoretical using Eq. [47] (mV)	$(\Delta\phi)_{\mathrm{Pption}}$ Theoretical using Eq. [45] (mV)	$(\Delta\phi)_{\mathrm{Pption}}$ Experimental [Ref. (2)] (mV)
KCl	169.9	4.1	−284	−5.74	−54
KBr	162.1	4.8	−272	−6.72	−52
NaCl	184.7	0.9	−310	−1.26	−56

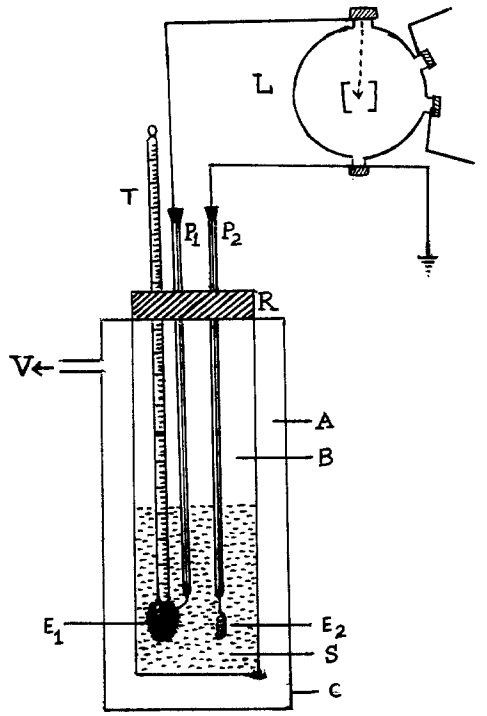

Fig. 1. Experimental setup for the measurement of cooling produced on the development of precipitation potential. (C = double walled calorimeter; S = saturated solution of KCl; E_1, E_2 = platinum electrodes; B = inner chamber of the cell; R = rubber stopper; P_1, P_2 = Corning glass capillary tubes of 1 mm diam; T = thermometer; V = vacuum pump; and L = Lindemann electrometer.)

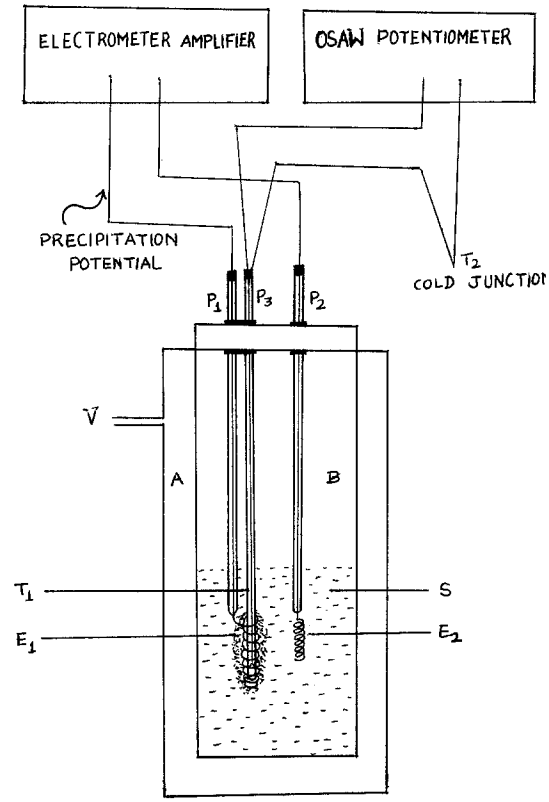

Fig. 2. Modified experimental setup for the measurement of cooling produced on the development of precipitation potential. (E_1 = platinum electrode wrapped around the capillary P_3 containing copper-constantan thermocouple junction T_1; E_2 = second platinum electrode; S = suppersaturated solution; T_2 = the junction of thermocouple kept at ice point.)

The following experimental procedure was adopted. 10 ml of KCl solution, saturated at 60°C, was placed in the precipitation cell. The electrode E_1 along with the thermometer T was inserted into the solution. Now the system was allowed to cool gradually. The second electrode E_2 was inserted into the solution as soon as a tiny crystal appeared on the first electrode. The development of the precipitation potential was indicated by the electrometer while the temperature of the calorimeter was recorded with the help of the thermometer as a function of time.

The second type of experiment was similar in principle except that a copper-constantan thermocouple was used for the measurement of temperature. The schematic diagram of the experimental setup is shown in Fig. 2. The same double-walled calorimeter C was used in this set of experiments also. Platinum electrodes E_1 and E_2 were fused in Pyrex glass capillary tubes P_1 and P_2 of 1 mm diam. The electrode E_1 was in the form of a coil through which the capillary tube P_3 containing the copper-constantan thermocouple junction T_1 (Omega International Corporation, Stanford, Connecticut) could be inserted. The other junction T_2, used as cold junction, was placed in molten ice kept in a Dewar flask. Thermocouple junctions were used in conjunction with an OSAW direct reading precision potentiometer with which the emf could be read correctly to ± 10 μV. Electrodes E_1 and E_2 were connected to an Electrometer Amplifier (Annadigi, Hyderabad, India) with which the voltage could be read correctly to ± 0.1 mV and which had a maximum input impedance of $10^{14}\Omega$.

The experimental procedure was similar to that adopted in the earlier experiment except in the following respects. The platinum electrodes E_1 and E_2 were kept a little above the aqueous solution of KCl saturated at 60°C. When the crystal started appearing in the bulk, the electrode E_1 was dipped into the solution and immediately raised up, so that on the evaporation of water, a few seed crystals were left on the electrode. Both electrodes E_1 and E_2 were now simultaneously inserted into the solution. The buildup and decay of precipitation potential and thermo-emf were simultaneously recorded.

In order to provide a more convincing proof, a third type of experiments was planned. An improved experimental setup was designed as shown schematically in Fig. 3. It consisted of twin cells R_1 and R_2 which were identical. These were in the form of two Corning glass tubes closed at one end. Both the tubes were 8 cm long and had a diameter of 1 cm. Each tube had a system of electrodes and temperature probe as shown in Fig. 3. The copper-constantan thermocouple junctions T_1 and T_2, kept in the cells R_1 and R_2, respectively, were connected to a PYE precision potentiometer with which the potential could be read correctly to ± 1 μV in conjunction with a sensitive Cambridge Spot Galvanometer. Further, the electrodes of cell R_1 were connected to an Electrometer Amplifier (Annadigi, Hyderabad) while this was not so for the electrodes of cell R_2 which acted as a dummy cell.

The following procedure was adopted. Both the cells were filled with the aqueous solution of KCl saturated at 60°C which was heated a little above the saturation temperature. The calorimeter was also filled with the same solution. Care was taken so that cells R_1 and R_2 and the liquid in the calorimeter were at the same temperature. Initially, the electrodes in both cells were kept a little above the surface of the solution. The assembly was allowed to cool gradually. When crystallization started, the electrodes E_1 of cell R_1 and E_2 of cell R_2 were lowered into the respective solutions and then raised up so that on evaporation of water seed crystals appeared on their surface. Now, electrode systems of both cells R_1 and R_2 were simultaneously inserted into the respective solutions. The buildup and decay of precipitation potential and thermo-emf were

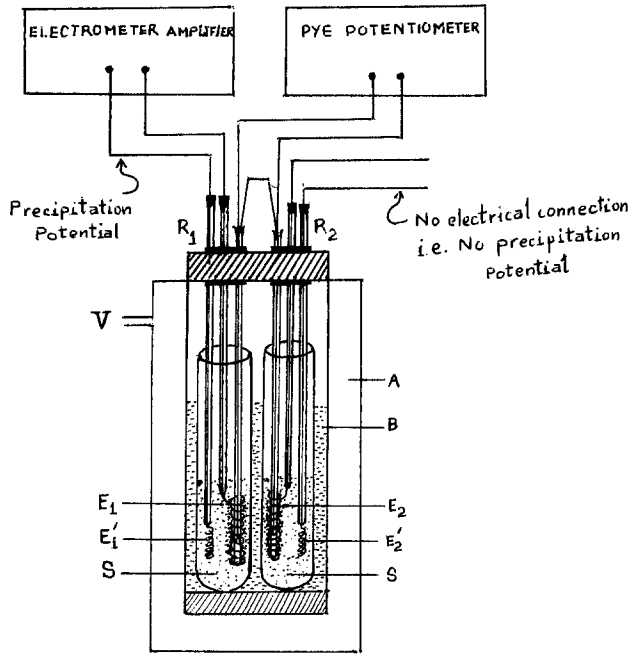

Fig. 3. Experimental setup for the simultaneous measurement of precipitation potential and thermo-emf during crystallization. (R_1, R_2 = twin precipitation cell; E_1, E_2 = platinum electrodes on which crystallization takes place; E_1', E_2' = bare platinum electrodes; T_1, T_2 = copper constantan thermocouple junctions; S = supersaturated solution of KCl; A = annular space of the vesssel C; and B = inner chamber of the vessel.)

simultaneously recorded with the help of the Electrometer Amplifier and PYE potentiometer, respectively.

Results and Discussion

Equation [40] shows how the precipitation potential depends on the mobility of the cations and anions. Further, it follows from Eq. [40] and [42] that, (*i*) the sign of $(\Delta\phi)_{\text{Pption}}$ would depend on the sign of $(U_+^\circ - U_-^\circ)$, (*ii*) the magnitude of $(\Delta\phi)_{\text{Pption}}$ would depend on the magnitude of ratio $(U_+^\circ - U_-^\circ)/(U_+^\circ + U_-^\circ)$, (*iii*) the magnitude of $(\Delta\phi)_{\text{Pption}}$ would also depend on the magnitude of undercooling $(T_s - T)$, and (*iv*) the decay of the observed precipitation potential would be related to the rate with which the concentration of the supersaturated solution approaches the saturation concentration. Thus, in the course of time, when crystallization stops and $a^{(s)}/a^{(ss)} \to 1$, $(\Delta\phi)_{\text{Pption}}$ would vanish and the observed precipitation potential would become equal to $(\Delta\phi)_{\text{Phase}}$.

Experimental data reported by Rastogi and coworkers (2, 3, 20, 21) show (Table III) that these conclusions are justified. However, it may be argued that the results on the precipitation potential of NaCl and KCl for water (Table III) and D_2O [Ref. (3)] do not support the theory, since one would expect the precipitation potential of NaCl to be greater than that of KCl owing to the fact that the mobility of Na^+ ion (hydrated) is lower than that of K^+ ion (hydrated). This argument is not sound since as suggested in Eq. [40] one has to take into account the mobilities of unhydrated ions rather than the mobilities of hydrated ions. Although such values are not available, some guess can be made about their relative magnitudes.

Table III. Sign and magnitude of $(U_+ - U_-)/(U_+ + U_-)$ and $(\Delta\phi)_{\text{Pption}}$

Electrolyte	$(U_+ - U_+)/(U_+ + U_-)$	$(\Delta\phi)_{\text{Pption}}$ (mV)
KCl	−0.0187	−54
KBr	−0.0303	−52
NaCl	−0.2072	−56

The transport number of hydrated and unhydrated ions will be related (22) by the equation

$$t_+^\circ = t_+ + C^\circ \Delta n_{H_2O} \quad [48]$$

$$t_-^\circ = t_- + C^\circ \Delta n_{H_2O} \quad [49]$$

where

$$\Delta n_{H2O} = n_{(h^+)} - n_{(h^-)} \quad [50]$$

Taking into account the appropriate values of hydration numbers (23, 24), Δn_{H2O} for KCl would be around unity and that for NaCl would be around 2. Hence, from Eq. [49] and [50] we observe that the transport numbers of unhydrated Na^+ and K^+ ions would be closer than that of their hydrated ions. It may also be noted that the transport numbers of Na^+ and K^+ ions are equal in molten NaCl and KCl (25).[4] Accordingly, it is not surprising that the magnitude of the precipitation potential in the case of NaCl and KCl are similar within the experimental error.

It is difficult at this stage to have a quantitative check of the theory developed in the section on Irreversible Thermodynamics and Precipitation Potentials. However, the inequality [44] is satisfied when $(\Delta H)^\circ$ is put equal to $(\Delta H)_L$ as Table II shows. The experiments described in the section on Experiments on the Relationship of Lattice Energy and Precipitation Potential show that such a substitution is justified. We discuss the thermochemical results further, in the following paragraphs.

In the first set of experiments a cooling of the order of 1°-2°C was observed in the vicinity of the electrode on which crystallization occurred when the development of the precipitation potential occurred, as was indicated by the electrometer. On the other hand, a blank experiment with the same cell without any electrical contact between the electrodes, gave evidence of heating of the order of 0.5°-1°C. Thus a cooling in the vicinity of electrodes on which crystallization occurs and the precipitation potential is developed indicates that the lattice energy is converted into electrical energy.

The data for a typical run in the second type of experiments on the simultaneous measurement of the precipitation potential and thermo-emf are shown in Fig. 4. It is clear from the figure that as soon as the precipitation potential is developed, as indicated by the sudden rise in curve a of Fig. 4, a sudden cooling occurs, as indicated by a corresponding sharp decrease in thermo-emf. The maximum in curve a and minimum in curve b, Fig. 4, coincide, confirming once again that cooling is produced in the vicinity of the electrode on which crystallization occurs and the buildup of the precipitation potential takes place. On the other hand, blank experiments without any electrical contact between the electrodes showed an increase of temperature of the order of 0.5°-1°C due to the liberation of the heat of precipitation.

The data for a typical run in the third type of experiments on the simultaneous measurement of the precipitation potential and thermo-emf are shown in Fig. 5. It is clear from curve a of Fig. 5 that at the instant of the development of the precipitation potential, the two cells show a thermo-emf equal to 48 ± 1 μV, which corresponds to a cooling of 1.24 ± 0.02°C in the cell R_1 which was the cold junction. It has to be noted that the electrodes in the other cell, R_2, were not in electrical contact and hence no precipitation potential could develop and its temperature was simply enhanced on account of the release of the heat of precipitation. In these experiments both the precipitation cells R_1 and R_2 were at thermal equilibrium initially. Simultaneous crystallization occurred in both of them.

[4] It is difficult to determine the transport number of unhydrated ions. However, efforts have been made to determine it by using a second solute such as sucrose as a reference for measuring the changes of salt concentration (26). This procedure has been questioned by Longsworth (27) since the added substance cannot be assumed to be motionless during the passage of the current.

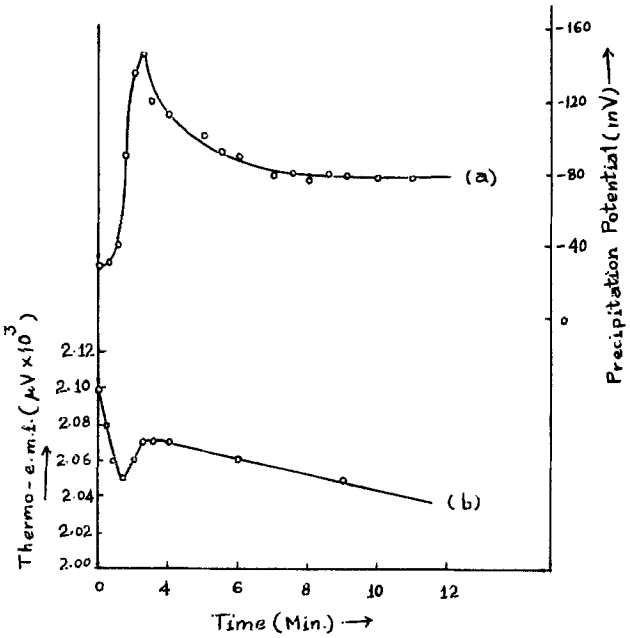

Fig. 4 Curve (a) buildup and decay of precipitation potential of KCl in water. Curve (b) thermo-emf corresponding to the cooling produced on the development of precipitation potential. The scale of the ordinate on the right-hand side refers to curve (a) while that on the left-hand side refers to curve (b).

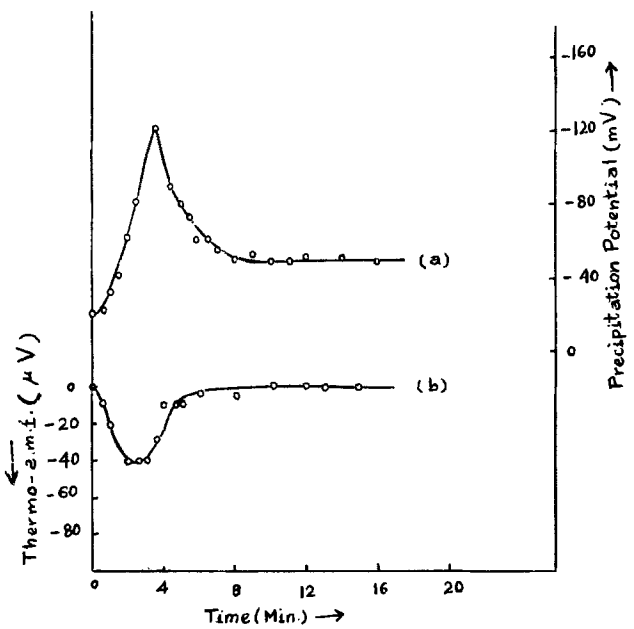

Fig. 5. Curve (a) buildup and decay of precipitation potential of KCl in water. Curve (b) thermo-emf corresponding to the cooling produced during the development of precipitation potential. The scale of the ordinate on the right-hand side refers to curve (a), while that on the left-hand side refers to curve (b).

One cell was involved in the development of the precipitation potential and the other was not. Therefore, a cooling in the former cell convincingly demonstrated that lattice energy is converted into electrical energy on account of the development of the precipitation potential.

The above discussion leads to a related question as to what is the source of electrical energy during the development of dissolution potential. Since

$$(\Delta H)_S = -(\Delta H)_h + (\Delta H)_L \qquad [51]$$

it was guessed that it is the hydration energy which is converted into electrical energy during the development of the dissolution potential because the key reaction in this case would be

$$A^+ + B^- + aq = A^+(aq) + B^-(aq) \qquad [52]$$

If this is so, much greater cooling than expected should occur on the electrode at which dissolution takes place. To test this point, experiments were performed with a twin calorimeter which confirmed this prediction (28). The principle of these experiments can be understood from Fig. 6.

The above experiments show that the energy released in the lattice formation is responsible for the generation of the precipitation potential and the hydration energy is converted into electrical energy during the development of the dissolution potential. Further, these show that the inequality [44] is justified and the thermodynamic theory of the precipitation potential developed in this paper is so far in qualitative agreement with the existing data.

Acknowledgments

The authore are extremely grateful to Professor Graham Hills, of Strathclyde University for helpful comments. The authors are also grateful to UGC and CSIR for providing financial assistance. S. A. Khan is thankful to Dr. John Patterson, Principal, St. Andrew's College, Gorakhpur, for providing the necessary facilities.

Manuscript submitted Feb. 24, 1982; revised manuscript received *ca.* Dec. 15, 1982.

Any discussion of this paper will appear in a Discussion Section to be published in the December 1983 JOURNAL. All discussions for the December 1983 Discussion Section should be submitted by Aug. 1, 1983.

LIST OF SYMBOLS

$a^{(*)}$	activity of electrolyte at the crystal/solution interface
$a^{(ss)}$	activity of electrolyte in supersaturated solution
$a_i^{(*)}$	activity of ith species at the crystal/solution interface
$a_i^{(ss)}$	activity of ith species in supersaturated solution
dA	change in area of solid surface

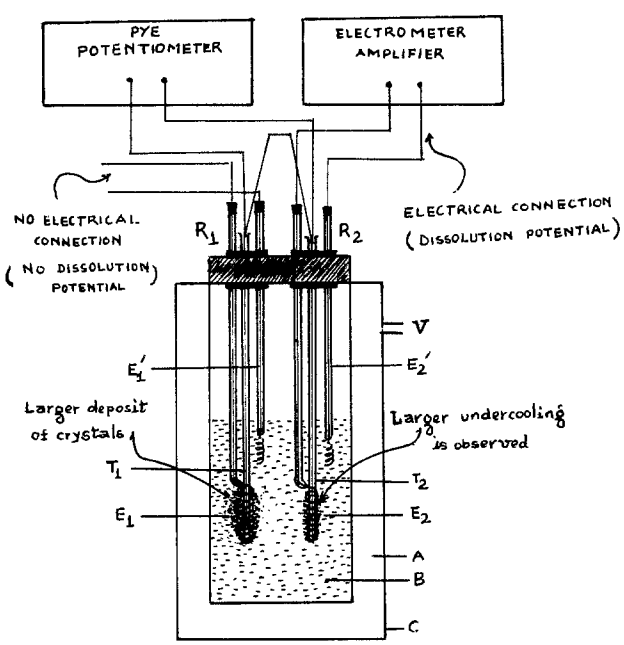

Fig. 6. Experimental setup for the simultaneous measurement of dissolution potential and thermo-emf produced during dissolution. (E_1, E_2 = platinum electrodes embedded with KCl crystals; E_1' E_2' = bare platinum electrodes; T_1, T_2 = copper-contantan thermocouple junction; R_1, R_2 = twin dissolution cells; and C = double walled vessels.)

C^o	initial concentration of the solution
e_i	charge per gram of ith species
F	Faraday of electricity
$(\Delta H)^\circ$	the enthalpy change associated with the development of precipitation potential
$(\Delta H)_h$	hydration energy
$(\Delta H)_L$	lattice energy
$(\Delta H)_S$	heat of solution
I	current
J_c	crystallization flux
J_i	mass flux of ith species
L_{ij}	phenomenological coefficients
M_i^α, M_i^β	masses of ith species in phases α and β, respectively
dM^α	change in total mass of phase α
h^i	hydration number of ith species
P^α, P^β	pressures of phases α and β, respectively
dQ	total heat supplied to the system
r	radius of crystal nuclei
r_e	radius of crystal nuclei at equilibrium
dS	total entropy change
d_eS	entropy exchanged with the surroundings
d_iS	entropy change due to irreversible processes inside the system
dS^α, dS^β	entropy changes in phases α and β, respectively
t	time
t_i^o	transport number of unhydrated ith species
t_i	transport number of hydrated ith species which is the conventional transport number
T	temperature of supersaturated solution
T_s	temperature of saturated solution
dU^α, dU^β	changes of internal energy in phases α and β, respectively
U_+, U_-	mobilities of hydrated cations and anions, respectively
U_+°, U_-°	mobilities of unhydrated cations and anion, respectively
dV^α, dV^β	changes in volume of phases α and β, respectively
X_c	force conjugate to the crystallization flux
X_i	force conjugate to the mass flux of ith species
Z_i	valency of ith species
α	solid phase
β	supersaturated solution of electrolyte
ν	surface tension at crystal/solution interface
$\mu_i^\alpha, \mu_i^\beta$	chemical potentials of ith species in phases α and β, respectively
μ_i°	standard chemical potential of ith species in liquid phase
$\mu_i^{\circ(S)}$	standard chemical potential of ith species in solid phase
ρ	density
σ	rate of entropy production
ϕ^α, ϕ^β	electric potentials of phases α and β, respectively
$(\Delta\phi)^{\alpha,\beta}$	electric potential generated on the crystallization of electrolyte
$(\Delta\phi)_{\text{Phase}}$	phase potential at the crystal/saturated solution interface
$(\Delta\phi)_{\text{Pption}}$	precipitation potential
i, j	components
1, 2	component 1 and component 2

REFERENCES

1. R. P. Rastogi, R. K. Dass, and B. P. Batra, *Nature*, **191**, 765 (1961).
2. R. P. Rastogi and R. D. Shukla, *J. Appl. Phys.*, **41**, 2787 (1970).
3. R. P. Rastogi, R. D. Shukla, and S. Bhagat, *This Journal*, **121**, 1564 (1974).
4. H. L. Girdhar and R. P. Matta, *Electrochim. Acta*, **22**, 173 (1976).
5. G. W. Gross, "Trace Inorganics in Water," Advances in Chemistry Series, No. 73, American Chemical Society (1968).
6. E. J. Workman and B. E. Reynolds, *Phys. Rev.*, **78**, 254 (1950).
7. E. J. Workman and B. E. Reynolds, *Nature*, **169**, 1108 (1952).
8. F. Heinmetes, *Trans. Faraday Soc.*, **58**, 788 (1962).
9. A. W. Cobb and G. W. Gross, *This Journal*, **116**, 611 (1969).
10. R. P. Rastogi and R. D. Shukla, *Indian J. Chem.*, **6**, 611 (1968).
11. K. Azuma and H. Kametani, *J. Phys. Soc. Jpn.*, **12**, 313 (1957).
12. H. L. Gridhar and R. P. Matta, *Indian J. Chem.*, **14A**, 160 (1976).
13. H. L. Girdhar and R. P. Matta, *J. Electroanal. Chem.*, **89**, 407 (1978).
14. N. Ibl, D. Richarz, and H. Federkehr, *Z. Phys. Chem. Neue Folge Bd.*, **988**, 123 (1975).
15. N. Ibl, *et al.*, "Topics in Pure and Applied Electrochemistry," Published by SAEST (1975).
16. R. P. Rastogi and S. A. Kahn, *This Journal*, **127**, 1989 (1980).
17. S. R. de Groot, "Thermodynamics of Irreversible Processes," p. 96, North-Holland Publishing Co., Amsterdam (1952).
18. R. A. Laudise, "The Growth of Single Crystals," p. 102, Prentice-Hall, Inc., Englewood Cliffs, NJ (1970).
19. J. V. Butler, "Electrical Phenomena at Interfaces," p. 14, Methuen & Co. Ltd., London (1951).
20. R. P. Rastogi, B. P. Batra, and R. K. Dass, *Bull. Natl. Inst. Sci. India*, **29**, 231 (1961).
21. Vishnu, S. A. Khan, and E. Jahan, *Electrochim. Acta*, **24**, 387 (1979).
22. L. I. Antropov, "Theoretical Electrochemistry," p. 74, (Translated from Russian by Artavaz Beknazarov), Mir Publishers, Moscow (1977).
23. J. Koryta, J. Dvorak, and V. Bohackova, "Electrochemistry," p. 14, Methuen & Co. Ltd., London (1970).
24. J. O'M. Bockris and A. K. N. Reddy, "Modern Electrochemistry," p. 125, A Plenum/Rosetta Edition, New York (1976).
25. H. Bloom, "The Chemistry of Molten Salts," p. 97, Benjamin Inc., New York (1967).
26. E. W. Washburn and E. B. Millard, *J. Am. Chem. Soc.*, **37**, 694 (1915).
27. L. G. Longsworth, *ibid.*, **69**, 1288 (1947).
28. S. A. Khan, Ph.D. Thesis, Gorakhpur University, Gorakhpur (1980).

Hole Injection and Electroluminescence of n-GaAs in the Presence of Aqueous Redox Electrolytes

F. Decker,*[1] B. Pettinger, and H. Gerischer*

Fritz-Haber-Institut der Max-Planck-Gesellschaft, D-1000 Berlin 33, Germany

ABSTRACT

The process of hole injection into the valence band of n-GaAs from the oxidized component of redox couples in aqueous solution has been studied by means of the rotating ring-disk system and by luminescence measurements as a function of electrode potential, mass transport, and electrolyte pH. It has been found that in all cases in which hole injection takes place, a luminescence signal is observed as a consequence of electron-hole recombination. The intensity of this signal depends on the electron density at the interface (therefore on potential) and on the chemical composition of the electrode surface. The luminescence signal at cathodic bias demonstrates that electron transfer from the valence band is still dominating if the electronic energy levels of the redox species match the energy levels of the valence band, although electron transfer from the conduction band is energetically more favorable.

The process of hole injection from redox electrolytes into small bandgap semiconductors is usually associated with that of corrosion (1, 2). In this case, the measurement of the electrode current alone is of little help in the quantitative evaluation of the hole injection current. For measuring the hole injection current the use of a rotating semiconductor disk-metal ring electrode is more appropriate. This technique has already been applied in analyzing the distribution between semiconductor corrosion and oxidation of redox species by photogenerated holes (3-6). Provided that the corrosion products do not interfere with the redox electrolyte, the ring electrode can suitably measure the amount of the redox species having holes injected into the semiconducting disk. In our work we employed an n-GaAs disk-Pt ring electrode, along with the one-electron redox couples $Fe^{2+/3+}$, $Fe(CN)_6^{3-/4-}$, $Ce^{3+/4+}$, deriving thereby the advantage from the fact that the corrosion products of GaAs are electrochemically inactive.

It is well known that minority carriers injected into semiconductors can recombine with majorities, emitting radiation during this process. Therefore, the occurrence of a hole injection process can be detected via electroluminescence. This has been observed with GaP by Beckmann and Memming (7). Luminescence from GaAs in electrolytes has been shown by Pettinger *et al.* (8) and Bernard *et al.* (9). In the first case, as in the experiments with GaP, the injection species was a highly active intermediate resulting from the reduction of peroxide or persulfate; in the second case, high cathodic voltages were necessary and resulted in a high concentration of the intermediates. In our experiments, we have studied luminescence due to the injection of holes into n-type GaAs by a simple redox species present in the electrolyte. Since the energy distribution of the injecting species used in the present work is reasonably well known, in contrast to that of radicals such as OH· and $SO_4^{-}\cdot$, the energetic conditions for hole injection into the valence band of GaAs can be carefully analyzed.

Experimental Techniques

We have developed a new ring-disk setup that is compact and easy to use. The complete electrode holder with bearings and silver-carbon contacts is 170 mm long and weighs only 120g (motor excluded). It fits to the standard NS 19/26 tapered electrode entrance of our cells. The interchangeable electrode tip is 30 mm long, 14 mm in diameter, and weighs about 15g. The rotation speed can be varied between 0 and 4000 rpm. Rotation speed controller and double potentiostat (independent potentiostatic control for ring and disk electrodes) have been built in the electronic workshop of the Fritz-Haber-Institut. The geometric parameters of our rotating ring-disk electrodes (RRDE) are $r_1 = 3$ mm, $r_2 = 3.5$ mm, and $r_3 = 4.5$ mm. From these values, using the definitions given by Albery and Hitchman (10), we can calculate a theoretical collection efficiency of 0.37, in excellent agreement with the experimental collection efficiency measured with the Pt-Pt RRDE (see, for example, Fig. 2). For the electroluminescence (EL) measurements an n-GaAs rotating disk electrode (radius ~ 3.5 mm) was used. The crystallographic (111) face of n-type GaAs, having a donor density of the order of 10^{17} cm^{-3}, was exposed to the solution in both RRDE and EL experiments.

The electrodes were polished, and before each run the semiconductor surfaces were etched in H_2SO_4:H_2O_2:H_2O (3:1:1 by volume). The optical setup for the electroluminescence measurements was similar to that described in a previous work (8); a photomultiplier (high responsivity RCA C31034) and a photon counter (SSR Institute, Model 1105) were used for light detection. All electrolytes were made with triply distilled water and high purity chemicals and then were deaerated with dry ultrapure nitrogen.

Experimental Results

Ring-disk measurements.—Ring-disk voltammograms with Fe^{3+} and Ce^{4+} in the same 0.1M H_2SO_4 supporting electrolyte are shown in Fig. 1 and 2. The

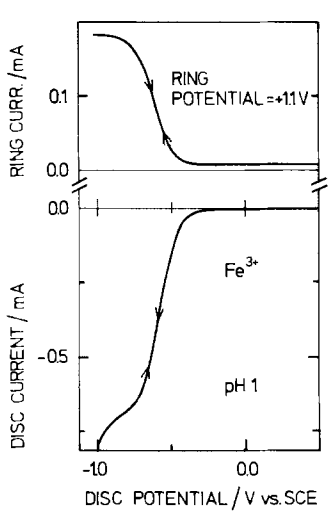

Fig. 1. Ring-disk voltammogram of an n-GaAs/Pt RRDE in 6×10^{-3}M $Fe_2(SO_4)_3$ + 0.1M H_2SO_4. Rotation frequency 9 Hz. Scan rate 10 mV/sec.

* Electrochemical Society Active Member.
[1] Permanent address: Instituto de Fisica, UNICAMP, 13100-Campinas (SP), Brazil.
Key words: photoelectrochemistry, semiconductor/electrolyte junctions, surface chemistry

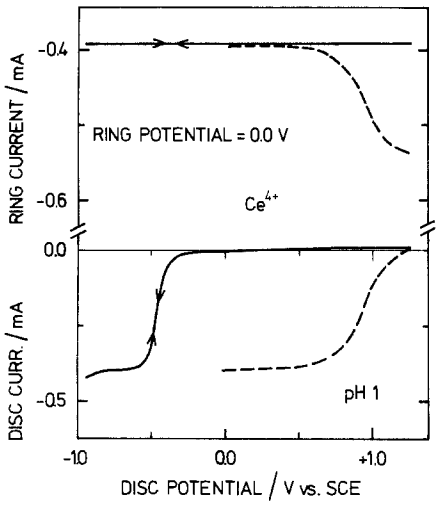

Fig. 2. Ring-disk voltammograms of an n-GaAs/Pt RRDE (solid lines) and of a Pt/Pt RRDE with the same geometry (dashed lines) in 6 × 10^{-3}M $Ce(SO_4)_2$ + 0.1M H_2SO_4. Rotation frequency 9 Hz. Scan rate 10 mV/sec.

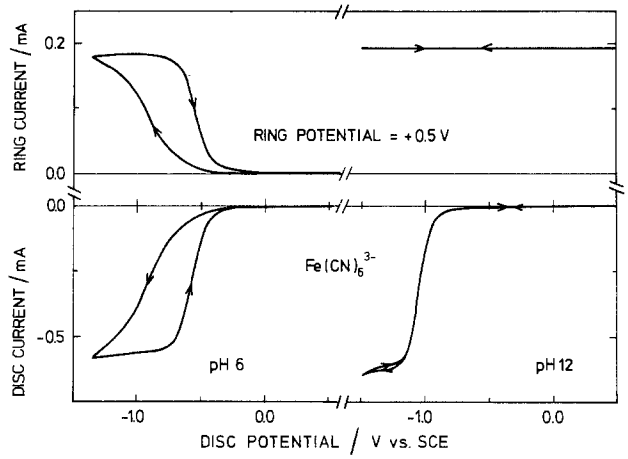

Fig. 3. Ring-disk voltammograms of an n-GaAs/Pt RRDE in 6 × 10^{-3}M $K_3[Fe(CN)_6]$ + 1M KCl. The pH was adjusted by addition of KOH. Rotation frequency 9 Hz. Scan rate 10 mV/sec.

ring collection current for Fe^{2+} is close to zero (actually ~ 7 μA) as long as the disk current is zero, then increases together with the disk current. With Ce^{4+}, however, the injection current detected by the ring electrode remains constant during the whole disk potential scan. Note here that the ring acts in the shielding mode at 0.0V, because to operate it in the collection mode requires excessively high positive potential and water oxidation would occur. In the shielding mode, lower cathodic currents at the ring mean higher injection currents at the disk. It is instructive to compare the curves of the GaAs-Pt RRDE (solid lines, Fig. 2) with those of a Pt-Pt RRDE with the same geometry and in the same conditions, *i.e.*, electrolyte, rotation speed, ring potential (dashed lines, Fig. 2). In contrast to GaAs-Pt, the Pt-Pt electrode configuration shows steps in the disk and ring current traces, which are symmetrical to each other, as expected. The ring current for the GaAs-Pt electrode remains constant over the whole range of the potential applied to the GaAs disk and has the same height as the ring current of the Pt-Pt electrode in the potential range where the disk current has reached its diffusion-limited value (cf. the dashed lines in Fig. 2). This indicates that Ce^{4+} is being reduced at the diffusion-limited rate in the region where the GaAs-disk current is zero, as well as in the region where the GaAs cathodic current reaches its maximum value. In the former region, the hole injection is followed by the anodic dissolution of the semiconductor, but its products are not detected at the ring. In the latter region, with increasing GaAs-disk current, the rate of GaAs corrosion decreases more and more, because of the recombination of electrons with injected holes. An additional conclusion that can be drawn from a comparison of Fig. 1 and 2 is that while Ce^{4+} is injecting holes at the highest possible rate, independently of the semiconductor potential, Fe^{3+} does not inject or injects at a very low rate, at anodic potentials.

Analogous observations can be made with respect to the $Fe(CN)_6^{3-}$ ion in two different electrolyte *p*H's (Fig. 3). Whereas $Fe(CN)_6^{3-}$ injects holes at the highest diffusion-limited rate only in alkaline environment, at *p*H 6 no injection is observed at anodic potentials. There is, however, a pronounced hysteresis in the disk voltammogram at neutral *p*H, which is likely to be caused by the progressive reduction of a passivating oxide layer on top of the GaAs surface. Because of this chemical transformation, the GaAs surface behaves quite differently in the passivated and nonpassivated state. Interestingly, the transition from the noninjection-case (*p*H 6) to the maximum-injection case (with the disk kept at open-circuit potential) is a smooth function of the OH^- concentration (Fig. 4). It can be seen that when the ratio between OH^- and $Fe(CN)_6^{3-}$ concentrations is lower than 1/3, the injection current is limited by the OH^- mass transport and its magnitude is linearly proportional to C_{OH^-}. For ratios larger than 1/3, the injection current saturates at a value slightly lower than that predicted from the diffusion limitation of the redox species (dashed line).

The open-circuit potential of the GaAs electrode varies with the OH^- concentration as can be seen in Fig. 5. Large displacements toward cathodic potentials are observed until C_{OH^-} and $C_{Fe(CN)_6^{3-}}$ are about the same; for larger C_{OH^-} a roughly Nernstian slope is approached (dashed line).

Electroluminescence measurements.—The ring-disk technique cannot distinguish between a hole injection into the valence band followed by a recombination process with a conduction band electron, and a direct capture of conduction band electrons by redox species

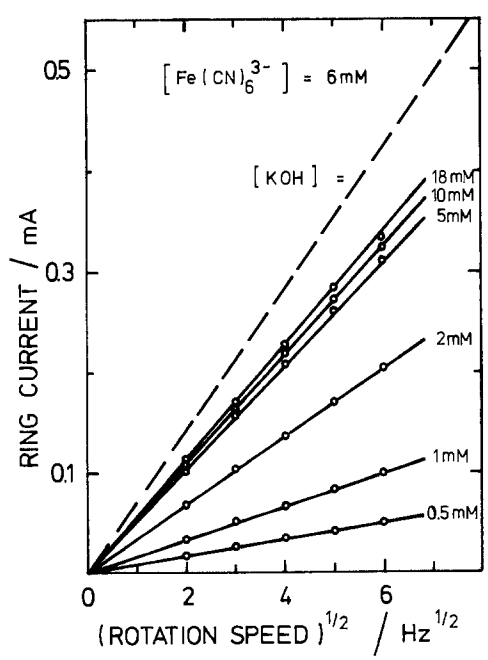

Fig. 4. Levich plots for the ring collection current (V_{RING} = +0.5V) of an n-GaAs/Pt RRDE in 6 × 10^{-3}M $K_3[Fe(CN)_6]$ + 1M KCl with additions of KOH. The disk potential was disconnected (open circuit).

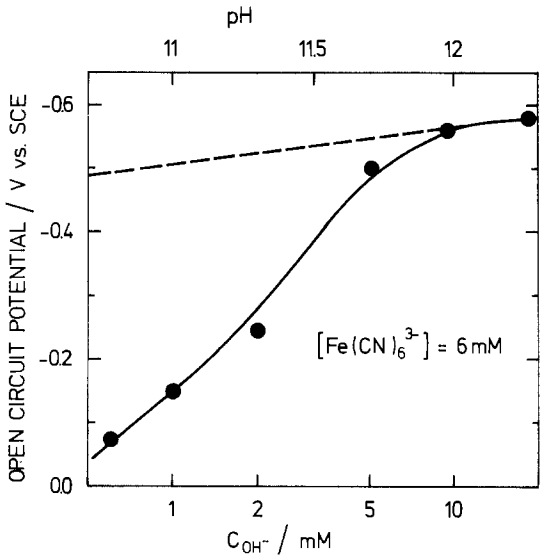

Fig. 5. Open-circuit potential of an n-GaAs RDE in the same electrolyte as in Fig. 4. Rotation frequency 9 Hz. The dashed line has a slope of 60 mV per pH unit.

when cathodic potentials are applied to the disk. Such distinction can only be made by means of an independent hole-sensitive measurement technique such as electroluminescence (EL). Therefore, EL has been measured in the same electrolyte as in the ring-disk experiments previously described, but with a simple rotating n-GaAs disk electrode. In the cases of Ce^{4+} at pH 1 (Fig. 6) and $Fe(CN)_6^{3-}$ at pH 12 (Fig. 7), the luminescence signals have a similar dependence on potential and comparable intensity. In contrast to the former situation, only a very weak (by about a factor of 500 lower) luminescence could be measured with Fe^{3+} at pH 1 in the potential range where the peaks appeared in the previous cases. However, the EL signal rose steeply at very negative potentials where hydrogen evolution occurs (Fig. 8).

The variations in the luminescence as a function of electrode potential indicate that the electron-hole radiative recombination follows a complex pattern (Fig. 6). First, the intensity increases as soon as the density of conduction band electrons increases, *i.e.*, at the same time as the disk cathodic current appears. The luminescence signal reaches its maximum in-

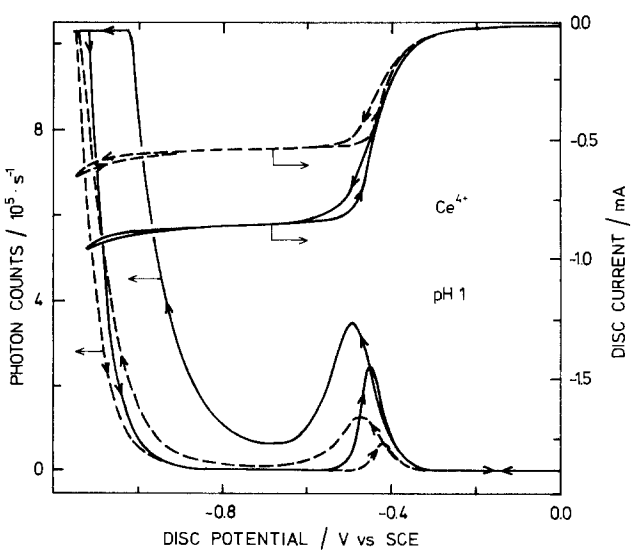

Fig. 6. Disk voltammograms and luminescence intensity vs. voltage curves of an n-GaAs RDE in the same electrolyte as in Fig. 2. Rotation frequency 9 Hz (dashed) and 25 Hz (solid lines). Scan rate 10 mV/sec.

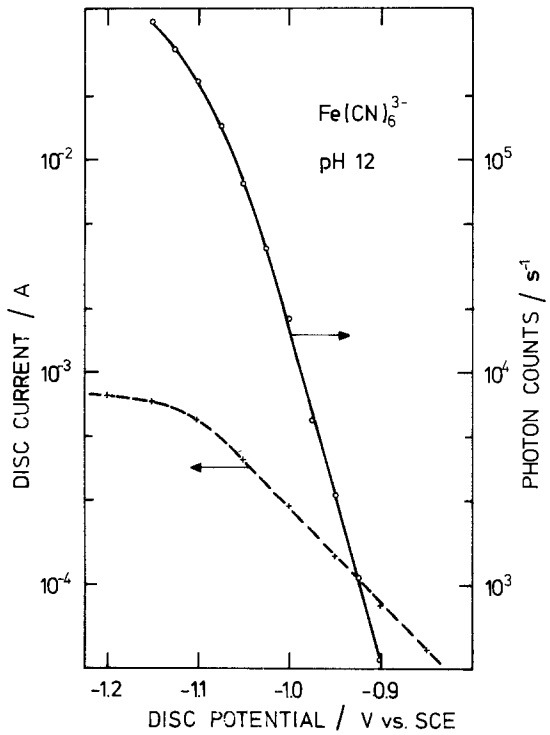

Fig. 7. Disk voltammograms and luminescence intensity vs. voltage curves for an n-GaAs RDE on logarithmic scale in 6 × 10^{-3}M $K_3[Fe(CN)_6]$ + 1M KCl, pH 12. Rotation frequency 9 Hz. Scan rate 10 mV/sec.

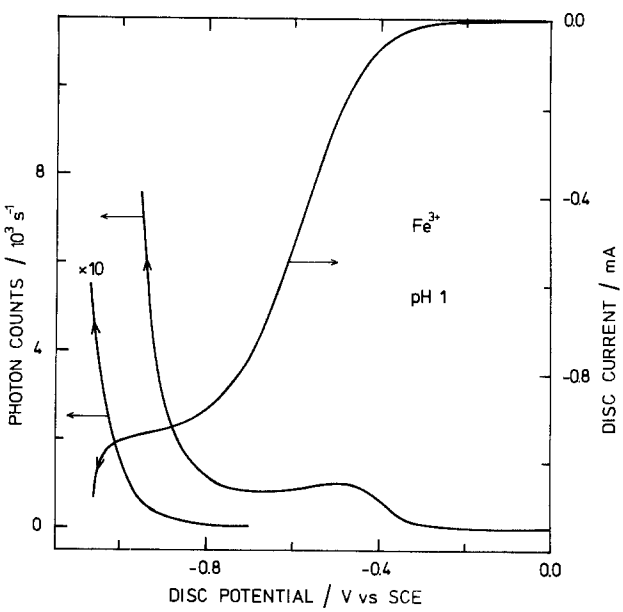

Fig. 8. Disk voltammogram and luminescence intensity vs. voltage curves of an n-GaAs RDE in the same electrolyte as in Fig. 1. Rotation frequency 9 Hz. Scan rate 10 mV/sec.

tensity at disk current values close to the diffusion-limited plateau. If we revert the scan at this point, both the current and the luminescence essentially retrace their respective curves. As the potential is scanned to more negative values, however, the luminescence first decreases, then increases again. In the reverse scan the luminescence intensity is much lower than that in the forward scan (Fig. 6). Furthermore, the luminescence signal is rotation-speed dependent, showing that in the whole potential range studied there is a mass transport control of the hole injecting species.

Noteworthy is that both cathodic current and luminescence rise exponentially (Fig. 7), however, the

luminescence increases with a much steeper slope than the current.

The spectral distribution of the electroluminescence was studied by means of long-pass filters. We found that no light was emitted with a wavelength below 780 nm. Since our photomultiplier has a cutoff near 860 nm, we could not decide how much light might have been emitted at longer wavelengths. It is probable that we may have lost a considerable part of the emitted light: this will be checked with an improved detection system in the near future. Within the accessible wavelength range of our present equipment, no difference in the spectral distribution of the EL could be seen for different redox systems. Assuming that the redox reaction occurs only by hole injection, the quantum yield of the EL can be calculated. This gives only the lower limit since our detection system recorded only photons in the visible range. The yield at the peak of the luminescence around −1.2V was about 10^{-7}. This small yield indicates that most of the recombination occurs radiationlessly.

Discussion

The observation of the ring currents when Fe^{3+} and Ce^{4+} are the species in the electrolyte (Fig. 1 and 2, both *p*H 1) helps us to distinguish whether hole injection is taking place (Ce^{4+}) or not (Fe^{3+}). This would not have been possible from the simple analysis of the disk currents alone. In fact, in both disk voltammograms the disk current is zero in the anodic potential range, where no conduction band electrons are present at the surface because a strong depletion layer is formed. Whereas, in one case, the consumption of the Ce^{4+} species via valence band electrons can be seen in the ring current, in the other case, the production of Fe^{2+} cannot be detected and, therefore, no hole injection occurs. The conclusion, drawn from this ring-disk experiment, is fully confirmed by the electroluminescence measurements because Ce^{4+} does in fact cause much higher EL than Fe^{3+}. Moreover, luminescence gives the additional information that at more negative potentials, where a cathodic current is observed at the disk, holes are still injected and not only conduction band electrons are extracted.

Simple energetic considerations can explain the differences in the hole injection process. The position of the valence bandedge of GaAs is such that at *p*H 1 electrons from this band can easily be injected into the Ce^{4+} acceptor levels, but not into the Fe^{3+} levels. The values for the valence and conduction bandedges of GaAs and for the standard redox potentials, shown in Fig. 9, were taken from the literature (11, 12) and are in good agreement with our results. The RRDE and EL results provide a relationship between hole injection, anodic dissolution of n-GaAs, and electron-hole recombination which is depicted in Fig. 10 for the case of n-GaAs in the presence of Ce^{4+} at *p*H 1. Holes are injected into the valence band of GaAs from the Ce^{4+} species at the same (diffusion-limited) rate independent of electrode potential. This potential does, however, determine how the injected holes will further react. At anodic potentials a depletion layer is formed in the n-GaAs and the injected holes cause the anodic dissolution of the semiconductor. At potentials approaching the flatband potential, conduction band electrons and injected holes are no longer spatially separated and can therefore recombine either through states within the bandgap, or directly. EL is the consequence of such radiative recombination processes. At sufficiently cathodic potentials the semiconductor dissolution is completely prevented, and EL has increased to its highest level before decreasing again because of changes in surface properties to be considered below. This proves that hole injection continues even in the presence of a large electron concentration at the surface and even though the electron capture from the conduction band has thermodynamically the far greater driving force. This result is in accordance with the kinetic model of electron transfer at electrodes where it is assumed that the highest rate is found at energies where the product of the initial and final state densities has the largest value (13-15). However, this result certainly does not exclude the possibility that part of the conduction band electrons are directly captured by the Ce^{4+} species with the excess energy transferred during the electron transfer into vibrational quantum states.

Although having a more negative standard redox potential than $Fe^{2+/3+}$, the species $Fe(CN)_6^{3-}$ can at *p*H 12 also inject holes into the valence band of n-GaAs, since this band has been shifted in the negative direction due to deprotonation of the semiconductor surface at higher *p*H's (Fig. 9) The mechanism of hole injection, anodic dissolution, and electroluminescence with $Fe(CN)_6^{3-}$ is analogous to that shown in Fig. 10.

The strong *p*H dependence of the voltammograms and luminescence is due to an oxide layer formation which modifies the injection current and the radiative and nonradiative recombination in a very complex pattern. To analyze these processes in more detail, further investigations would be required.

The formation of a passivating oxide layer affects the rate of corrosion as well as the rate of hole injection, but both reaction rates must match each other in the steady state of corrosion. If electronic equilibrium between the surface and the bulk of the semiconductor can be assumed, which is the case in the absence of a current, the difference between the Fermi level in the bulk of the semiconductor and position at flatbands, derived from the open-circuit voltage, should

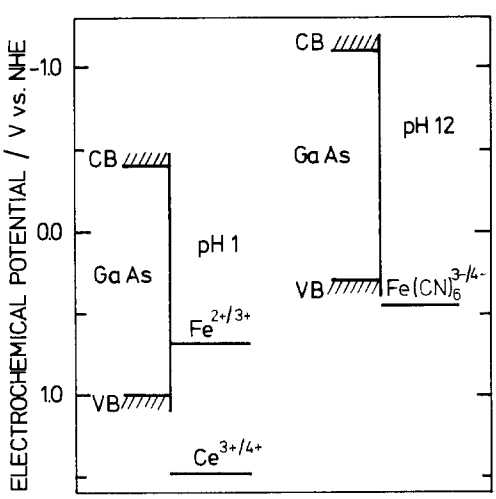

Fig. 9. Energy positions of GaAs bandedges [from Ref. (11)] and redox couple standard potentials [from Ref. (12)].

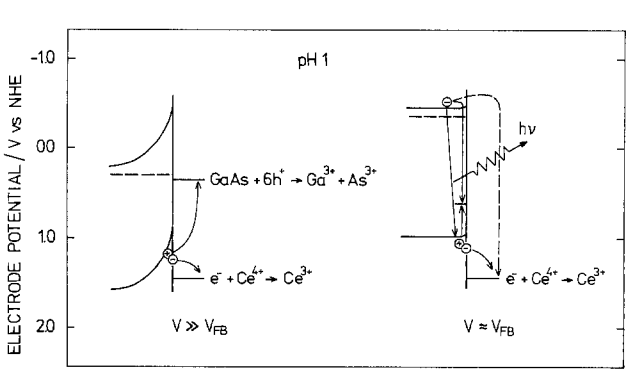

Fig. 10. Mechanism of hole injection, anodic dissolution, and electroluminescence of n-GaAs in a Ce^{4+} electrolyte. Further interaction of the corrosion products with water is not considered.

give a direct measure of the hole activity on the surface. However, the large shift of this potential to less negative values at low OH^- concentration, seen in Fig. 5, is mainly caused by the decrease of the pH at the semiconductor electrolyte interface since, according to Fig. 4, the transport of OH^- ions to the interface is rate determining under these conditions. The final products of the corrosion reaction are GaO_2^- and AsO_3^{3-} (16). The passivating oxide layer consists probably of Ga_2O_3 and the formation of the soluble GaO_2^- by the reaction $Ga_2O_3 + 2\ OH^- \rightarrow 2\ GaO_2^-$ might be the slow step.

The dependence of electroluminescence on potential is not only controlled by hole injection, but also by very complex surface properties which affect radiationless recombination. For the sake of simplicity we discuss only the cases of pH 1 and 12. In the case of Ce^{4+} in pH 1 it is evident that, although the hole injection process is potential independent (Fig. 2), the luminescence increases first, then is quenched, and finally increases again (Fig. 6). This observation is in apparent contradiction with the expectation that the more negative the electrode potential, the higher the electron density at the surface and, therefore, also the recombination probability. According to this model one would predict an electroluminescence intensity that should monotonically increase with negative potential. The unexpected quenching of luminescence could be ascribed to various causes: either to transition of the electron-transfer path from hole injection to a direct reaction of conduction band electrons with the redox species, or to an increase of the radiationless recombination rate. The first reason appears unlikely because the luminescence increases again at more negative potentials. More likely is that a compositional change of the semiconductor surface occurs and thereby creates new centers for radiationless recombination. The hysteresis in the *i-V* and EL curves provides some evidence for the latter case. It is well known that in the transition from anodic to cathodic bias a drastic change of the chemical composition occurs for germanium (17) and GaAs (18). The surface undergoes there a transformation between a stable oxidized (*i.e.*, oxygen covered) and reduced (*i.e.*, mainly hydrogen covered) state. During this transformation, unsaturated surface states (dangling bonds) are formed within the bandgap that can act as very efficient recombination centers. We cannot exclude the possibility that this recombination could also be connected with radiation since the wavelength would be beyond our detection system. The increase of surface recombination in this potential range has already been demonstrated for Ge-electrodes by Gobrecht *et al.* (19).

We suppose that the formation of such recombination centers, during the reduction of the oxygen coverage of the GaAs surface, is the reason for the decrease in EL during the cathodic potential sweeps shown in Fig. 6. If the surface is again stabilized by hydride formation, these recombination centers disappear and the EL can increase again with increasing electron concentration in the accumulation layer at the surface.

The formation of an accumulation layer also has another consequence. The potential drop now occurs increasingly in the Helmholtz double layer. Therefore, the position of the bandedges is shifted in the cathodic direction and consequently the matching of energy levels of the redox system with the electronic states of the valence band is improved. This increases the rate of hole injection, particularly for the redox systems having their energy levels above the valence bandedge in the anodic state of the semiconductor electrode. This shift will therefore be of minor importance for the $Ce^{4+/3+}$ redox system, but is important for the $Fe^{3+/2+}$ system as Fig. 8 has shown. In the latter case, EL appears only if the upward shift of the bandedges, via a cathodic bias, increases the rate of hole injection to such an extent that it can compete with the direct electron transfer from the conduction band. It is therefore clear that EL measurements can give very instructive insights into the mechanism of electron transfer reactions at semiconductor electrodes.

Conclusions

We can conclude that, with the exception of Fe^{3+}, electron transfer to the valence band of GaAs is the dominant process in all cases studied. We have shown that in these cases electron transfer from the conduction band is slower although having the greater driving force. This conclusion, therefore, supports the theory that electron transfer at the semiconductor-electrolyte interface occurs fast if the energy levels of the initial and final state are optimally matched. Luminescence due to minority carrier injection can give valuable information about surface properties and the mechanism for electron transfer reactions. For a more complete exploitation of the information available from such luminescence experiments, an extension of the measurements into the infrared range is necessary.

Acknowledgment

This work was partially supported by the European Communities, under Contract ESD-012-80 D (B).

Manuscript submitted Oct. 25, 1982; revised manuscript received Jan. 25, 1983.

Any discussion of this paper will appear in a Discussion Section to be published in the December 1983 JOURNAL. All discussions for the December 1983 Discussion Section should be submitted by Aug. 1, 1983.

The Fritz-Haber-Institut der Max-Planck-Gesellschaft assisted in meeting the publication costs of this article.

REFERENCES

1. H. Gerischer and F. Beck, *Z. Phys. Chem.*, **13,** 389 (1957).
2. H. Gerischer, *Ber. Bunsenges. Phys. Chem.*, **69,** 578 (1965).
3. T. Inoue, T. Watanabe, A. Fujishima, K. Honda, and K. Kohayakawa, *This Journal,* **124,** 719 (1977).
4. R. Memming, *Ber. Bunsenges. Phys. Chem.*, **81,** 732 (1977).
5. K. W. Frese, Jr., M. J. Madou, and S. R. Morrison, *J. Phys. Chem.*, **84,** 3172 (1980).
6. F. Cardon, W. P. Gomes, F. Vanden Kerchove, D. Vanmaekelbergh, and F. Van Overmeire, *Faraday Discuss.*, **70,** 153 (1980).
7. K. M. Beckmann and R. Memming, *This Journal,* **116,** 368 (1969).
8. B. Pettinger, H.-R. Schöppel, and H. Gerischer, *Ber. Bunsenges. Phys. Chem.*, **80,** 849 (1976).
9. J. Bernard and P. Handler, *Surf. Sci.*, **40,** 141 (1973).
10. W. J. Albery and M. L. Hitchman, "Ring-disc Electrodes," Clarendon Press, Oxford (1971).
11. R. Memming, *This Journal,* **125,** 117 (1978).
12. W. M. Latimer, "The Oxidation State of the Elements and Their Potentials in Aqueous Solutions," Prentice-Hall Chem. Series, Englewood Cliffs, NJ (1956).
13. R. Marcus, *Can. J. Chem.*, **37,** 155 (1959); *Ann. Rev. Phys. Chem.*, **15,** 155 (1964).
14. H. Gerischer, *Z. Phys. Chem. N. F.*, **26,** 223 (1960); **27,** 48 (1961).
15. R. R. Dogonadze and Yu. A. Chizmadzhev, *Dokl. Akad. Nauk USSR,* **144,** 1077 (1962); **145,** 848 (1962).
16. H. Gerischer, *Ber. Bunsenges. Phys. Chem.*, **69,** 578 (1965).
17. H. Gerischer, A. Mauerer, and W. Mindt, *Surf. Sci.*, **4,** 431 (1966).
18. H. Gerischer and I. Mattes, *Z. Phys. Chem. N. F.*, **49,** 112 (1966).
19. H. Gobrecht, O. Meinhardt, and M. Lerche, *Ber. Bunsenges. Phys. Chem.*, **67,** 486 (1963).

Diffusion-Controlled Multisweep Cyclic Voltammetry

I. Reversible Deposition on a Rotating Disk Electrode

P. C. Andricacos* and P. N. Ross, Jr.*

University of California, Lawrence Berkeley Laboratory, Materials and Molecular Research Division, Berkeley, California 94720

ABSTRACT

A model is proposed for the behavior of a diffusion-controlled reversible deposition reaction occurring on a rotating disk electrode at unit activity of deposit under conditions of multisweep cyclic voltammetry. Results are presented for dimensionless concentration, current density, and charge density functions, obtained by the application of the Nernst-Siver approximation for transient convective diffusion. The existence of a periodic state is demonstrated for cycle times of the order of the characteristic time for the rotating disk. Diagnostic criteria of potential electroanalytical use associated with the periodic state are developed in terms of dimensionless sweep rate, reversal time, and cathodic reversal overpotential. It is found that significant differences exist in the current and concentration functions as determined during the first and second, also periodic, cathodic sweeps. The potentiodynamic determination of diffusion-limiting current densities, as well as the applicability of a triangular periodic potential waveform, in plating are also briefly discussed.

It has been demonstrated (1, 2) that the application of periodic current pulses to a rotating disk electrode (RDE) gives rise to an output signal that also becomes periodic after a short time. In multisweep cyclic voltammetry (CV), a periodic triangular potential waveform is applied to the electrode and one might therefore expect the current response to become periodic[1] after the passage of relatively few cycles. The purpose of the present investigation is to define conditions for the rapid attainment of the periodic state and to describe the characteristics of the periodic state when electrodeposition reactions are studied by multisweep CV.

In the analyses to be presented, we examine the behavior of an electrodeposition reaction under conditions of pure diffusion control. Capacitive contributions to the current and electrolyte resistance effects are neglected. The deposition reaction is assumed to occur reversibly with the deposit at unit activity. Here in part I, we treat the problem of a rotating disk electrode (RDE) and employ the Nernst-Siver approximation (3) for transient convective diffusion.

Even with the foregoing assumptions and perhaps the simplest electrochemical reaction, the complexity of the computational problem is still considerable, especially when the reaction occurs on an RDE under multisweep CV conditions. However, these assumptions enable one to obtain analytical expressions for most quantities of interest. With respect to the more general use of multisweep CV in electrodeposition, analysis of reversible deposition behavior is expected to exhibit the characteristic features of a pure diffusion control and can thus serve as a guide for treatment of more realistic deposition problems. Such problems will have to be treated numerically, and the existence of a guide would be very helpful for the optimal manipulation of parameters.

It is shown from the analysis presented here that, besides currents, methods exist for the computation of both the concentration of the reacting ion and the integral charge associated with the deposition process. This is achieved by the introduction of dimensionless current density, charge density, and concentration functions. It is shown that if the electrode potential, initially at equilibrium, is changed linearly in the cathodic direction for a time greater than the RDE characteristic time, then, upon cyclic potential reversal, all three functions become periodic with respect to time. In other words, periodicity is attained immediately after the first cathodic sweep provided that it extends beyond the RDE characteristic time.

The first cathodic sweep in multisweep CV is equivalent to linear sweep voltammetry (LSV). The LSV current response for reversible deposition of an RDE has already been described in the literature (4). The periodic cyclic voltammogram is significantly different from the LSV. For instance, the height of the cathodic maximum is reduced, the extent of this reduction depending on the dimensionless sweep rate. In addition, its position on the potential axis is not fixed. Whereas the first sweep begins at zero current, the foot of the periodic CV current wave exhibits a dependence on dimensionless sweep rate which is of diagnostic importance. Concentration functions during single and multisweep CV are shown to be complex, *e.g.*, the existence of multiple concentration extrema into the electrolyte in the beginning of the periodic cathodic wave gives rise to local mass fluxes away from both the electrode surface and the bulk electrolyte toward a depleted region within the boundary layer. However, concentration profiles are shown to provide physical insight toward an understanding of the existence of a current maxima in multisweep CV. Finally, the charge density functions show that any complete CV sweep results in the formation of a net deposit on the electrode surface.

Definitions and Analysis

We begin our analysis by introducing dimensionless parameters. This is important not only because their number and range of variation is greatly systematized, but also because RDE behavior under CV conditions is described by a combination of dimensional sweep rate, v, and rotation speed, ω, rather than by each alone. This combination appears (4-7) in the definition of the dimensionless sweep rate

$$\sigma = n\mathbf{F}v\delta^2/RTD \qquad [1]$$

where δ is the thickness of the Levich diffusion layer and D is the diffusion coefficient of the reacting ion. n, $\mathbf{F}$, R, and T have their usual meaning. δ^2/D is the RDE characteristic time, defined once δ is fixed by the rotation speed. It should be noted that Eq. [1] becomes obvious once one realizes that it is the simplest way to reduce v. Also, it should be emphasized that σ increases with increasing dimensional sweep rate, but decreases with increasing rotation speed. For example, at 100 rpm, $\sigma \sim 10$ when $v = 100$ mV/sec^{-1} in an electrolyte with $\nu = 10^{-2}$ cm^2 · sec^{-1} and $D = 10^{-5}$ cm^2 · sec^{-1} ($n = 1$, $T = 25°$C). However at 1000 rpm, σ drops to $\sim$1 under the same conditions, and a sweep rate of 1 V · sec^{-1} is required to sustain its value at that rotation speed.

Dimensionless distance, time, and concentration are defined by the following equations

$$\xi = x/\delta; \quad \tau = Dt/\delta^2; \quad C = 1 - c/c^b \qquad [2]$$

* Electrochemical Society Active Member.

Key words: electrode, deposition, mass transport, voltammetry

[1] In the sense that the response to the $(l + 1)$ potential sweep is indistinguishable from the response to the lth sweep

where x is the distance away from the electrode surface, t is time, and c^b is the bulk (also initial) concentration of the reacting ion.

The dependence of the potential on dimensionless time is shown in Fig. 1a. The initial potential is the equilibrium, E_{eq}, computed from the Nernst equation on the basis of c^b. E_c is the cathodic reversal potential reached after a time of θ sec at a sweep rate of v V · sec^{-1}; θ' is then a dimensionless reversal time defined by

$$\theta' = D\theta/\delta^2 \qquad [3]$$

Since the initial potential is E_{eq}, the interval $E_c - E_{eq}$ is also one of cathodic overpotental varying from 0 to η_c, where η_c is the cathodic reversal overpotential. Figure 1b shows the dependence of the surface concentration on dimensionless time. When the potential is linearly dependent on time, the concentration is exponential through the Nernst equation. The list of dimensionless variables is extended by defining τ_c and τ_a. These are dimensionless times into a cathodic or anodic sweep, respectively. From Fig. 1a

$$\tau = 2l\theta' + \tau_c; \quad 0 \leq \tau_c \leq \theta'; \quad \tau \text{ during a cathodic sweep} \qquad [4a]$$

$$\tau = (2l+1)\theta' + \tau_a; \quad 0 \leq \tau_a \leq \theta'; \quad \tau \text{ during an anodic sweep} \qquad [4b]$$

Equations [4a] and [4b] are important in separating t in two components: the number of already applied complete cycles, l, and time into a cathodic or anodic sweep, τ_c or τ_a, respectively.

We now focus on the definition and methods of computation of the concentration, current density, and charge density functions. Let us assume for the moment that a step potential is applied to the RDE such that the surface concentration becomes 0 at $t = 0$ and remains at this value for all $t > 0$. The solution of this problem, $C_s(\xi,\tau)$, is related to $C(\xi,\tau)$ by means of Duhamel's (or superposition) theorem (4, 8, 9)

$$C(\xi,\tau) = \int_0^\tau \frac{\partial C}{\partial \tau}(0,\lambda) \cdot C_s(\xi,\tau-\lambda)\,d\lambda \qquad [5]$$

where $C(0,\tau)$ is the time dependence of the surface concentration (Fig. 1b). According to the Nernst-Siver approximation

$$C_s(\xi,\tau) = 1 - \xi + 2\sum_{j=1}^{\infty} (-1)^j (j\pi)^{-1} \sin[(1-\xi)j\pi] \exp(-j^2\pi^2\tau) \qquad [6]$$

By combining Eq. [4], [5], and [6], expressions for the concentrations during a sweep can be derived (see Appendix). Apart from ξ, the concentrations will depend either on τ_c or on τ_a, depending on the direction of the potential sweep, and also on the parameters σ and θ'. We can then write $C_c^l(\xi,\tau_c;\sigma,\theta')$ for the dimensionless concentration during the $(l+1)$ cathodic sweep as a function of dimensionless time into the sweep, τ_c, distance, ξ, away from the electrode surface, dimensionless sweep rate, σ, and reversal time, θ'. The corresponding symbol for the concentration during the $(l+1)$ anodic sweep is $C_a^l(\xi,\tau_a;\sigma,\theta')$.

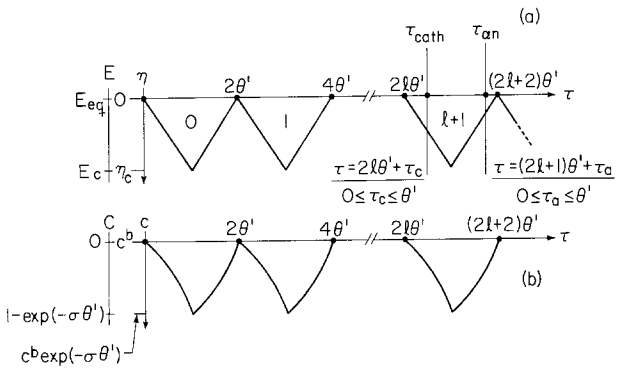

Fig. 1. Dependence of electrode potential and surface concentration on dimensionless time during multisweep cyclic voltammetry. (a) Electrode potential, (b) surface concentration for a reversible deposition reaction (Nernst equation).

Once concentrations are available, currents can be computed from their ξ-derivative on the electrode surface. We define a current density function, J, as the dimensionless ratio of the current density to the diffusion limiting current density, i_L. The current density function during the $(l+1)$ cathodic cycle will depend on τ_c and on the parameters σ and θ'. We can thus represent it by $J_c(\tau_c;\sigma,\theta')$; similarly, we can use $J_a^l(\tau_a;\sigma,\theta')$ for the $(l+1)$ anodic cycle. J's can be computed either from

$$J_c^l(\tau_c;\sigma,\theta') = -\frac{\partial C_c^l}{\partial \xi}(0,\tau_c;\sigma,\theta'); \quad J_a^l(\tau_a;\sigma,\theta') = -\frac{\partial C_a^l}{\partial \xi}(0,\tau_a;\sigma,\theta') \qquad [7]$$

or directly by Duhamel's theorem

$$J = -\int_0^\tau \frac{\partial C}{\partial \tau}(0,\lambda) \cdot \frac{\partial C_s}{\partial \xi}(0,\tau-\lambda)\,d\lambda = \int_0^\tau \frac{\partial C}{\partial \tau}(0,\lambda) \cdot \theta_3(0,\pi i(\tau-\lambda))\,d\lambda \qquad [8]$$

where the function θ_3 originates from differentiation with respect to ξ of Eq. [6].

Since detailed expressions are available for the dependence of current on time, the charge deposited during a time interval can be computed. We define a charge density function, R, as the dimensionless ratio of the charge density deposited during a sweep to a characteristic charge density. The latter quantity is $i_L\delta^2/D$, *i.e.*, the charge that would be deposited if the diffusion-limiting current was applied for δ^2/D.

By definition, R's do not represent charge accumulation during repeated cycling but are specific to a particular cycle. The symbol $R_c^l(\sigma,\theta')$ will be used to denote the value of the charge density during the $(l+1)$ cathodic sweep as a function of dimensionless sweep rate and reversal time; similarly, for $R_a^l(\sigma,\theta')$. Apart from R_c and R_a, a third charge function is of particular significance

$$R_n^l(\sigma,\theta') = R_c^l + R_a^l \qquad [9]$$

R_n^l represents the net cathodic ($R_n > 0$) charge deposited during the complete $(l+1)$ sweep. Expressions for the charge functions have been derived by integrating J's over time

$$R_c^l(\sigma,\theta') = \int_0^{\theta'} J_c^l(\tau_c;\sigma,\theta')\,d\tau_c; \quad R_a^l(\sigma,\theta') = \int_0^{\theta'} J_a^l(\tau_a;\sigma,\theta')\,d\tau_a \qquad [10]$$

Although $\theta' \geq 1$ is not a very important parameter in the computation of concentration and current density functions, its significance becomes decisive for R's. Since most electronic equipment available for electrochemical measurements control potential, it would be more useful to express R's as functions of reversal overpotential, η_c, rather than θ'. Expressing η_c as multiples of $RT/n\mathbf{F}$, we may introduce a dimensionless overpotential, H, by

$$H = \eta/(RT/n\mathbf{F}); \quad H_c = \eta_c/(RT/n\mathbf{F}) \qquad [11]$$

Expressions for $R_c^o(\sigma,H_c)$, $R_c(\sigma,H_c)$, $R_a(\sigma,H_c)$, and $R_n(\sigma,H_c)$ have been derived and are given in the Appendix.

Attainment of a Periodic State

It is shown in the Appendix that for

$$\theta' \geqq 1; \quad \theta \geqq \delta^2/D \qquad [12]$$

all functions C_c^l, C_a^l; J_c^l, J_a^l; R_c^l, R_a^l become independent of l for all practical purposes. In other words, if the first cathodic wave (LSV) lasts for a time greater than δ^2/D, then all subsequent anodic waves are identical. Furthermore, the second and all subsequent cathodic waves are also identical. This is true irrespective of the value of the dimensionless sweep rate. The restriction on the value of θ' is not very serious since δ^2/D is usually a small quantity. However, one should be careful in realizing that the criterion for periodicity is a time rather than a reversal overpotential. For example, at a rotation speed of 100 rpm, $\delta^2/D \sim 2.5$ sec. At a sweep rate of 1 V · sec^{-1}, the reversal overpotential should be at least 2.5V for the periodicity criterion, Eq. [12], to be met. Conceivably, if $\theta' < 1$, letting $l \to \infty$ will give rise to a periodic state that will be in general different than the one established when Eq. [12] is satisfied. In this paper, we analyze the periodic state arising from reversal times greater than the RDE characteristic time. Dimensionless periodic functions will be denoted by l-independent symbols, and by using $\geqq 1$ instead of θ' for emphasis. For example, the periodic cathodic current density function will be $J_c(\tau_c; \sigma, \geqq 1)$. It should be noted that periodic cathodic functions are independent of θ', so that its exact value is not of significance as long as it is $\geqq 1$.

Results and Discussion

We begin by discussing the periodic cathodic and anodic current density functions, $J_c(\tau_c; \sigma, \geqq 1)$ and $J_a(\tau_a; \sigma, \geqq 1)$. Contrary to stationary electrode behavior, RDE voltammetry gives results that are parametrized with respect to σ alone, rather than combinations of $\sigma\tau$ and $\sigma\theta'$, a fact which renders direct correlations with overpotential impractical. It has been shown (4) that $J_c^o(\tau_c; \sigma)$, LSV current function, is a monotonically increasing function of τ_c, when $\sigma \lesssim 3$; also $J_c^o(0; \sigma) = 0$ and $J_c^o(\infty; \sigma) = 1$. In other words, on the first sweep the initial value of the current is 0, in agreement with intuition, since the initial potential is the equilibrium potential, and for large τ_c values, the diffusion-limiting current, i_L, is reached. For $\sigma \gtrsim 3$, a maximum in J_c^o is observed. The reason for the existence of this maximum will be explained in the discussion of the concentration profiles. Although the position of the maximum on the dimensionless time axis changes to lower τ_c values as σ increases, when $\sigma \gtrsim 4$, the maximum appears at the same location on the overpotential axis, equal to 0.854 ($RT/n\mathbf{F}$) ($= 22/n$ at 25°C). This is true only for J_c^o for a reversible deposition; reactions with finite kinetics (6) show a markedly different behavior. For large values of σ ($\sigma \gtrsim 4$) achieved by fast dimensional sweep rates, v, or low rotation speeds (Eq. [1]), or both, the role of convection becomes insignificant and RDE behavior becomes indistinguishable from stationary electrode behavior. This is so because in this range of σ values, LSV peaks appear at very short times, in which the concentration disturbance is limited to a small distance into the diffusion layer. Lack of rotation speed dependence renders the value of the J_c^o maximum a linear function of $\sigma^{1/2}$ with a slope of 0.61. It should be noted that $\sigma^{1/2}$ is the only dependence which eliminates δ (thus ω) from the combination $i_L\sigma^{1/2}$.

Upon multiple sweeping, the behavior of the periodic currents is markedly different from those obtained by LSV (Fig. 2). This is expected since periodicity means relatively large times at which convective effects are fully operational. An important feature of the periodic cathodic current function is that a portion of it near its foot is anodic, *i.e.*, substrate dissolution rather than deposition occurs. The tail of the periodic current during the anodic sweep is also anodic. The periodic cathodic current does not exhibit a peak for $\sigma \lesssim 3$. For higher σ values, a maximum appears, which has the same physical origin as the LSV maximum; the origin of these maxima are discussed in the analysis of concentration profiles. As expected, the periodic anodic current function is always monotonic, since no conceivable limitation on the dissolution reaction exists. As will be seen later, the amount of deposit dissolved during a cycle in which the current is anodic never exceeds the amount deposited during the same cycle when the current is cathodic. By performing a multisweep experiment then, one does not run into the danger of dissolving the initial electrode substrate. However, this should initially be of the same materials as the reaction product to guarantee the definition of the equilibrium potential, as well as to satisfy the assumption of constant deposit activity.

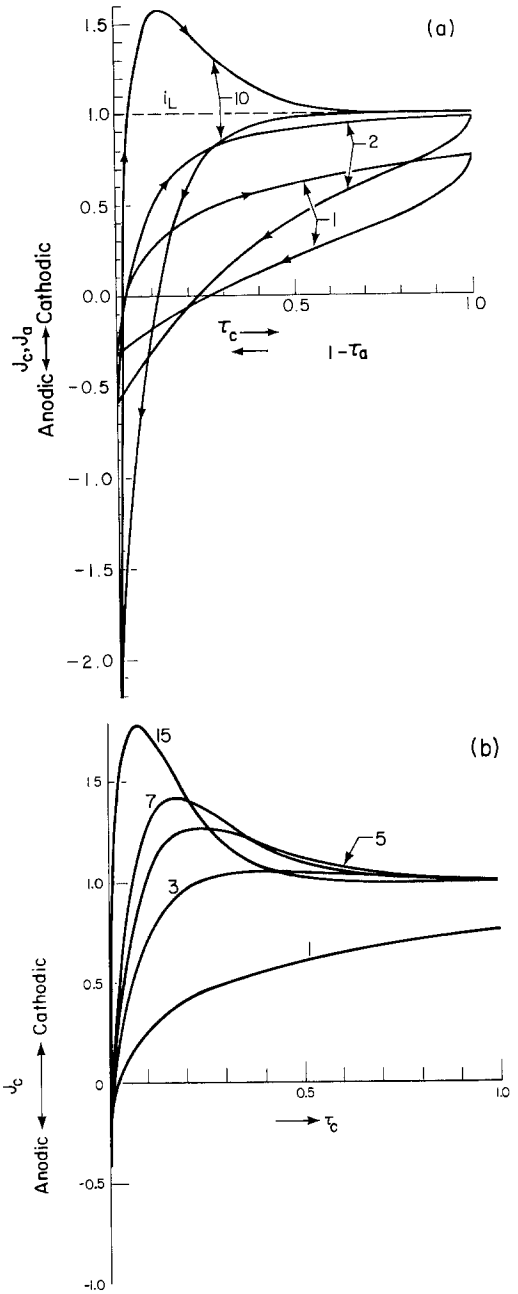

Fig. 2. (a and b) Periodic current density functions in terms of dimensionless time; numbers on curves are values of the dimensionless sweep rate; in Fig. 2b anodic current functions have been omitted.

The general shape of the periodic current density functions indicates that there are three criteria of diagnostic importance. These are: the dependence of the value of the foot of the cathodic sweep current (an anodic current) on σ; the dependence of the location and height of the cathodic current maxima on σ. Two properties of the current density functions should be emphasized. The absence of an extremum in the periodic anodic current renders such considerations as maxima separation on the time (or potential) axis inapplicable, and the expressions for J_c are independent of θ' provided that Eq. [12] is satisfied. That is why the quantities of diagnostic importance are defined only by σ and not by σ and θ'. Since the periodic anodic function assumes virtually the same values as the cathodic function at its foot and tail, it follows that it also exhibits an insignificant dependence on θ' at these points.

The dependence of J_c on σ at $\tau_c = 0$ is described by the following relation

$$J_c(0; \sigma, \geq 1) = J_a(\theta'; \sigma, \geq 1) = 1 - \sigma^{1/2} \coth (\sigma^{1/2})^{2} \quad [13]$$

This equation shows that $J_c(0)$ is always negative (anodic current) and that its value can become significantly higher than -1 depending on σ, *i.e.*, several multiples of i_L can be measured in the anodic current region (Fig. 2). For $\sigma \geq 9$, Eq. [13] can be simplified

$$J_c(0; \geq 9, \geq 1) = 1 - \sigma^{1/2} \quad [14]$$

The height of the maximum in the periodic current function ($\sigma \gtrsim 3$) is significantly lower than in LSV; whereas

$$J_{c,max}{}^{o} = 0.61\,\sigma^{1/2}; \quad \sigma \geq 4 \quad [15]$$

a numerical correlation indicates that

$$J_{c,max} = 0.881\,\sigma^{0.251} \sim 0.881\,\sigma^{1/4}; \quad \sigma \geq 9 \quad [16]$$

Values of $J_{c,max}$ in the range $3 < \sigma < 9$ are reported in Table I. It should be noted that as σ increases, the difference between $J_{c,max}{}^{o}$ and $J_{c,max}$ also increases. $J_{c,max}$ appears at generally higher cathodic overpotentials than $J_{c,max}{}^{o}$; whereas

$$H_{max}{}^{o} = 0.854; \quad \sigma \geq 4 \quad [17]$$

in the case of periodic current functions

$$H_{max} \cong 1.3\text{-}1.4; \quad \sigma \geq 9 \quad [18]$$

It should be pointed out that like Eq. [16], Eq. [18] is a numerical result, the validity of which has been investigated in the range $9 < \sigma < 50$.

We conclude our discussion on current density functions during LSV and multisweep CV by an analysis of their behavior in terms of dimensional times and potentials. To this effect, a single electron reversible deposition reaction is chosen ($n = 1$) occurring on an RDE with $\omega = 100$ rpm at 25°C from an electrolyte with $\nu = 10^{-2}$ cm^2 · sec^{-1}; the diffusion coefficient of the depositing ion is assumed to be equal to 10^{-5} cm^2 · sec^{-1}. With these data, the RDE characteristic time is ~2.5 sec. Figure 3a shows the dependence of $J_c{}^{o}$ (LSV current function) on dimensional time, for

[2] Application of de l'Hopital's rule shows that this expression has a finite limit as $\sigma \to 0$; *i.e.*, $\lim_{\sigma \to 0} J_c = 0$, despite $\lim_{\sigma \to 0} \coth (\sigma^{1/2}) = \infty$.

Table I. Values of $J_{c,max}$ in the interval $3 < \sigma < 9$

σ	$J_{c,max}$
3	1.059
4	1.176
5	1.274
6	1.354
7	1.421
8	1.478
9	1.528

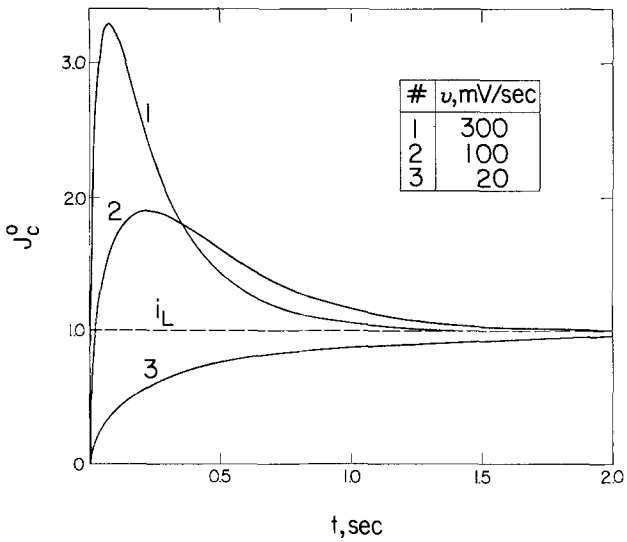

Fig. 3a. LSV current density function in terms of dimensional time for various values of the dimensional sweep rate.

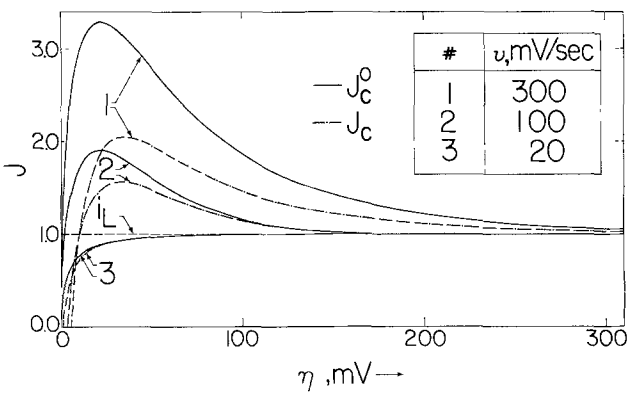

Fig. 3b. LSV (solid lines) and periodic (interrupted lines) cathodic current density functions in terms of cathodic overpotential for various values of the dimensional sweep rate. All solid lines begin at 0. Interrupted lines begin at some anodic value of the current which can be computed by Eq. [13].

various values of the dimensional sweep rate. At $v = 20$ mV · sec^{-1}, $\sigma \sim 1.9$ and no maximum appears. When $v = 100$ mV · sec^{-1} ($\sigma \sim 9.6$), the maximum appears at ~0.21 sec and its height is described by Eq. [15]. At 300 mV · sec^{-1} ($\sigma \sim 28.9$), the maximum appears at a much shorter time of ~0.07 sec. An interesting feature of Fig. 3a is that the time necessary for the attainment of the limiting current ($J_c{}^{o} = 1$) decreases with increasing sweep rate (10). It would thus seem advantageous to use as high a sweep rate as possible if the aim of the experiment is the measurement of i_L.

In order to attain periodic behavior in subsequent sweeps, the LSV sweep should last for at least 2.5 sec, in accordance with Eq. [12]. In terms of overpotential, one would have to apply at least 750 mV when $v = 300$ mV · sec^{-1}, as opposed to 50 mV if $v = 20$ mV · sec^{-1}.[3] Figure 3b shows the LSV and periodic cathodic current functions plotted *vs.* cathodic overpotential. It is clearly seen that as v increases, the difference in height between $J_{c,max}{}^{o}$ and $J_{c,max}$ also increases. When $v = 20$ mV · sec^{-1}, $J_c{}^{o}$ and J_c differ only around $\eta_c = 0$. The overpotential at the maximum for all LSV curves is 22 mV, whereas for the periodic curves it is ~35 mV; also, $J_{c,max}$ for 300 mV · sec^{-1} is slightly displaced toward more cathodic overpotentials as compared to the one at 100 mV · sec^{-1}. With respect to limiting currents, higher overpotentials

[3] The exact value of D may be very significant with respect to these considerations.

are required to attain i_L. It becomes obvious that although smaller times are required for the measurement of i_L, the combined time-sweep rate effect gives rise to the opposite behavior in terms of overpotential, *i.e.*, for faster sweeps, a higher overpotential must be applied for the current to reach the i_L value. Since in many situations undesirable reactions may occur concurrently with the deposition process, the choice of sweep rate in the potentiodynamic determination of i_L should result from a balance between times and overpotentials.

We now turn our attention to the concentration profiles that develop into the electrolyte during a multisweep CV experiment on an RDE. These are drawn in Fig. 4 and 5 from expressions for LSV and periodic CV concentrations developed in the Appendix. Two representative values of σ are used, 6 and 1, chosen by the presence or absence of a maximum in J_c^o and J_c. Figures 4a and 5a are the current functions for these values of σ. In all other figures, the function $1 - C(\xi,\tau;\sigma,\theta') = c/c^b$ instead of $C(\xi,\tau;\sigma,\theta') = 1 - c/c^b$ is plotted. Since the surface concentration ($\xi = 0$) decreases from c^b to $c^b \exp(-\sigma\theta')$ during a cathodic sweep and increases from $c^b \exp(-\sigma\theta')$ to σ^b during an anodic sweep, the function c/c^b changes from 1 to $\exp(-\sigma\theta')$ and from $\exp(-\sigma\theta')$ back to 1. For a given value of τ_c or τ_a, the derivative of the concentration curve evaluated at the surface ($\xi = 0$) yields the value of J at that time.

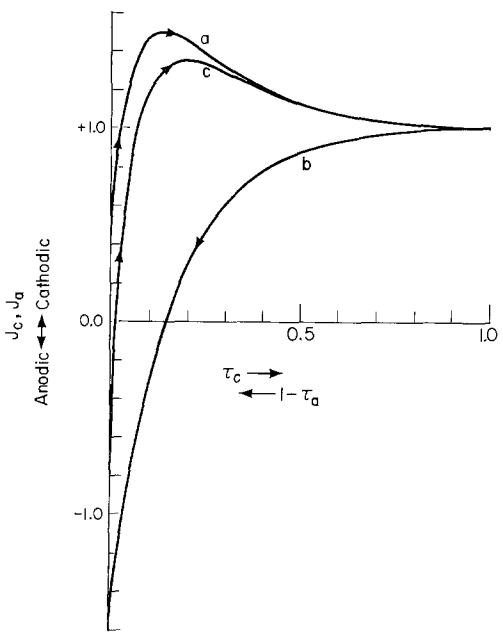

Fig. 4a. Current density functions for $\sigma = 6$. Curve a. $J_c^o(\tau_c; 6)$, LSV sweep (begins at zero); curve b. $J_a(\tau_a; 6, 1)$, periodic anodic; curve c. $J_c(\tau_c; 6, 1)$, periodic cathodic.

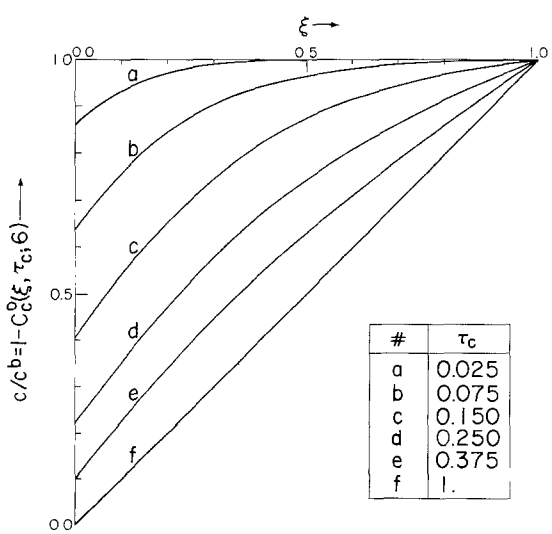

Fig. 4b. Dimensionless concentration profiles within the Levich diffusion layer during the LSV sweep for $\sigma = 6$. Corresponds to curve a of Fig. 4a.

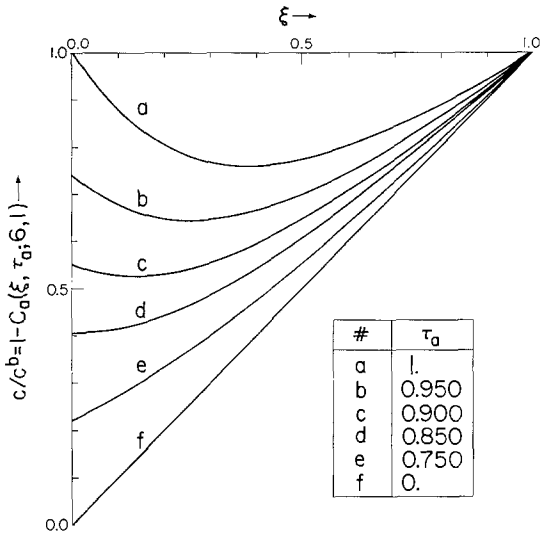

Fig. 4c. As in Fig. 4b, but during the first, also periodic, anodic sweep. Corresponds to curve b of Fig. 4a.

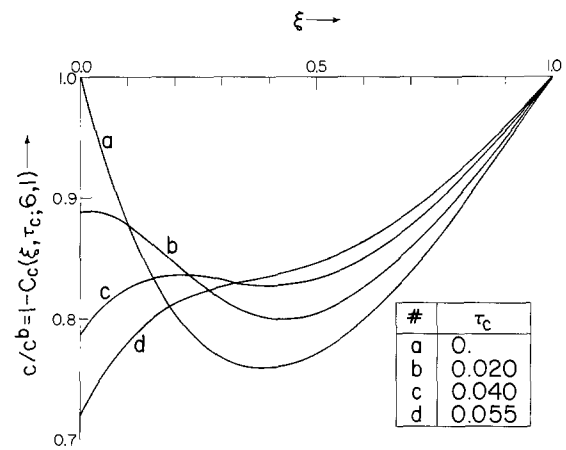

Fig. 4d. As in Fig. 4b, but during the initial stages of the second, also periodic, cathodic sweep. Corresponds to curve c of Fig. 4a.

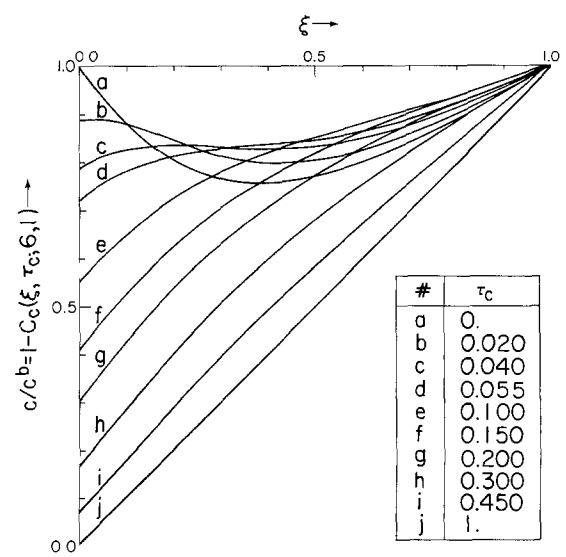

Fig. 4e. As in Fig. 4b, but during the second, also periodic, cathodic sweep. Corresponds to curve c of Fig. 4a.

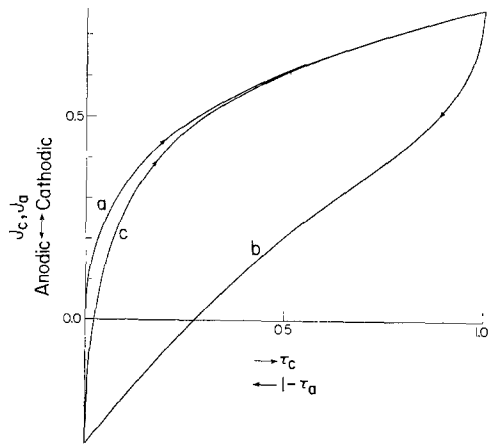

Fig. 5a. As in Fig. 4a, but for $\sigma = 1$. Curve a. $J_c^o(\tau_c; 1)$, curve b. $J_a(\tau_a; 1, 1)$, curve c. $J_c(\tau_c; 1, 1)$.

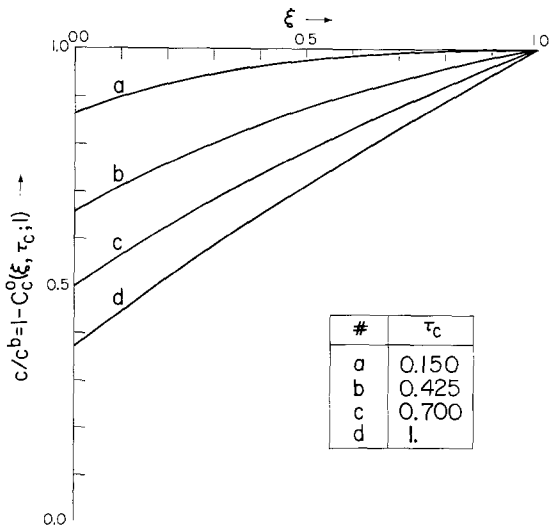

Fig. 5b. As in Fig. 4b, but for $\sigma = 1$

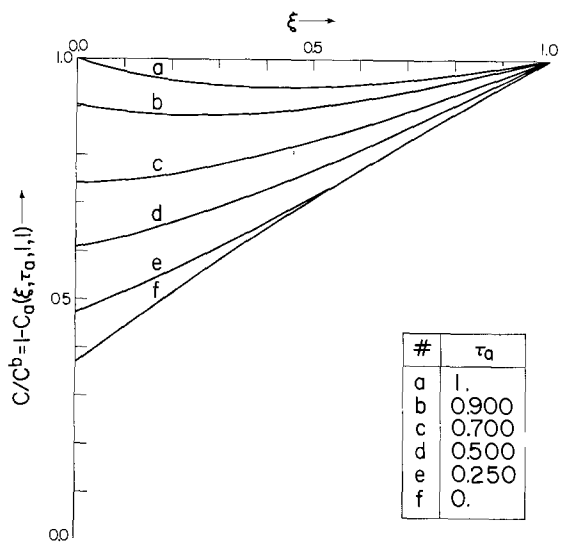

Fig. 5c. As in Fig. 4c. Corresponds to curve b of Fig. 5a

Figure 4b refers to curve a in Fig. 4a. Concentration curves bend continuously and their ξ-derivative at $\xi = 0$ is in the same direction, since the current is always cathodic. Curve c is nearest to the cathodic maximum. Comparison of curve c with b and d indicates that the appearance of a maximum in J_c^o is

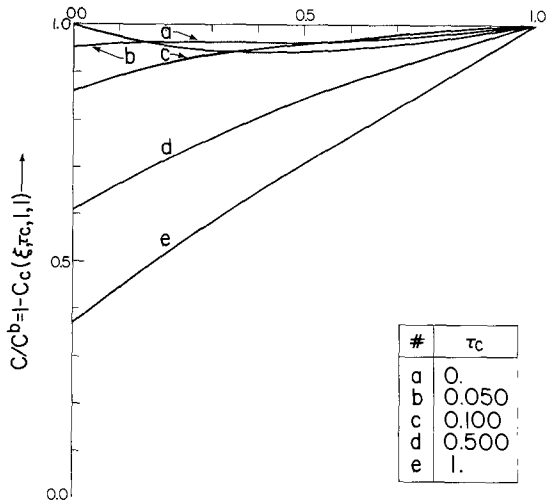

Fig. 5d. As in Fig. 4e. Corresponds to curve c of Fig. 5a

related to the curvature of the concentration profile into the electrolyte. It appears that the rate by which concentration changes at $\xi > 0$ cannot match the rate of variation at $\xi = 0$. This curvature gives rise to transient currents higher than i_L, despite the nonzero value of the concentration. When sufficient time passes, the whole profile comes closer to being linear, the curvature at $\xi = 0$ decreases and, consequently, the cathodic current also decreases. As shown by line f, Fig. 4b, the concentration profile is almost linear at $\tau_c = 1$.

When the first, also periodic, anodic cycle begins, Fig. 4a (curve c), the concentration profile is almost linear ($i \sim i_L$) (curve f in Fig. 4b and 4c) and the current is cathodic. The current remains cathodic for the time interval $0 < \tau_a < 0.85$. When $\tau_a = 0.85$, $J_a = 0$ as witnessed by a 0 derivative at $\xi = 0$ for curve d in Fig. 4c. For $\tau_a > 0.85$, the current is anodic and an inevitable concentration extremum is formed into the electrolyte, which is most pronounced when $\tau_a = 1$. The existence of this extremum can be predicted without a formal solution of the diffusion problem, since it is the only possibility that can simultaneously satisfy three requirements: that the current be anodic (surface derivative pointing downwards); that the concentration at $\xi = 0$ vary between c^b and $ca.$ 0 only; and that the concentration at $\xi = 1$ be fixed at c^b (according to the boundary condition imposed by the Nernst-Siver approximation).

In the beginning of the second, also periodic, cathodic sweep, the concentration profile has a complicated shape (curve a in Fig. 4c, d, and e). At the same time, the surface concentration changes rapidly. The inability of the concentration into the electrolyte to match the rapidity of the surface concentration change results in a complex regime of mass fluxes shown in Fig. 4e and d (exploded version of the early stages of 4e). Curvature readjustments can now explain both the existence of a maximum in the periodic cathodic current function and the fact that it is lower in height and delayed in time.

Apart from Fig. 4a and 5a, the differences between Fig. 4 and 5 are mostly of quantitative rather than qualitative nature. Curve d in Fig. 5b clearly shows that at the chosen low value of the dimensionless sweep rate, the value of the current is far from i_L when $\tau_c = 1$, despite the fact that the periodicity criterion, Eq. [12], is met. Finally, the concentration extremum is less intense during the periodic anodic sweep, resulting in faster readjustment during the following periodic cathodic sweep.

We conclude our discussion with an analysis of results pertaining to the charge density functions. These are drawn in Fig. 6a-c and Fig. 7a-b. Figure 6 il-

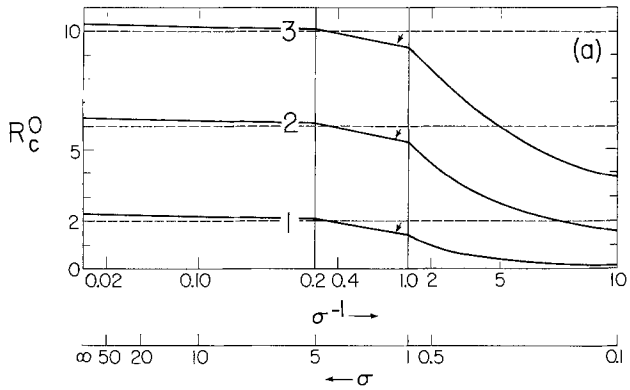

Fig. 6a. Charge density functions during the LSV sweep in terms of dimensionless sweep rate for various values of dimensionless reversal time. Curve 1. $R_c^o(\sigma, 2)$; curve 2. $R_c^o(\sigma, 6)$; curve 3. $R_c^o(\sigma, 10)$.

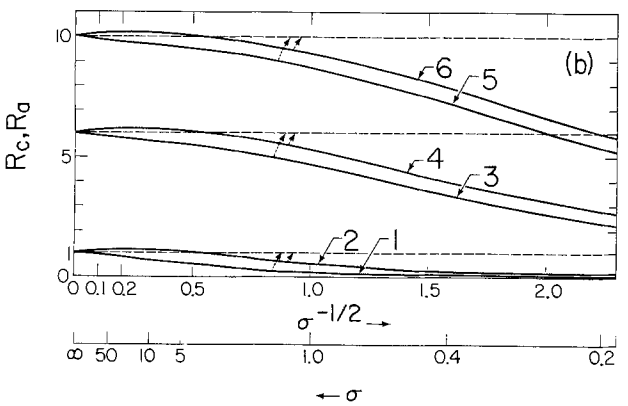

Fig. 6b. Charge density functions during the periodic cathodic and anodic sweeps. Curve 1. $R_a(\sigma, 1)$; curve 2. $R_c(\sigma, 1)$; curve 3. $R_a(\sigma, 6)$; curve 4. $R_c(\sigma, 6)$; curve 5. $R_a(\sigma, 10)$; curve 6. $R_c(\sigma, 10)$.

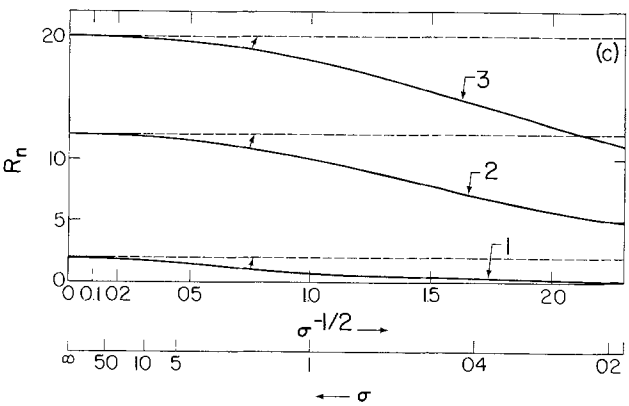

Fig. 6c. Net charge density functions. Curve 1. $R_n(\sigma, 1)$; curve 2. $R_n(\sigma, 6)$; curve 3. $R_n(\sigma, 10)$.

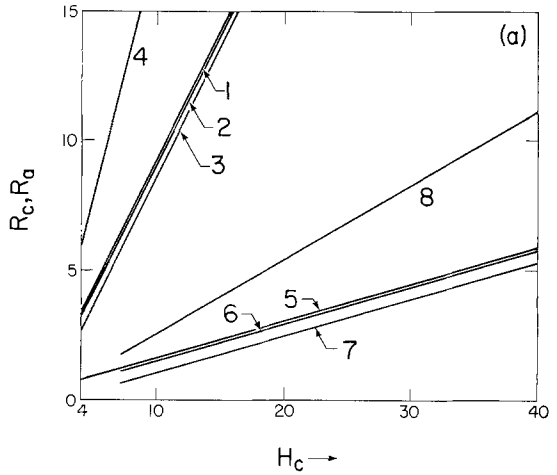

Fig. 7a. Charge density functions in terms of dimensionless cathodic overpotential. Curve 1. $R_c^o(1, H_c)$; curve 2. $R_c(1, H_c)$; curve 3. $R_a(1, H_c)$; curve 4. $R_n(1, H_c)$; curve 5. $R_c^o(7, H_c)$; curve 6. $R_c(7, H_c)$; curve 7. $R_a(7, H_c)$; curve 8. $R_n(7, H_c)$.

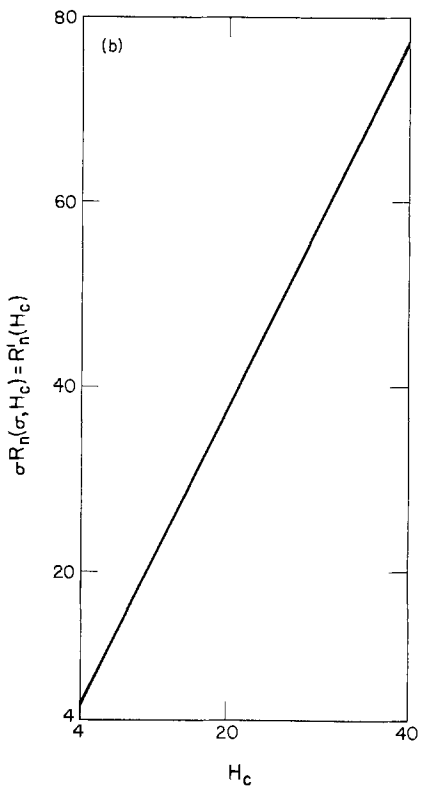

Fig. 7b. Dependence of the σ-independent combination $R_n' = \sigma R_n$ in terms of dimensionless cathodic overpotential.

lustrates the dependence of R's on σ and θ', whereas Fig. 7 on σ and H_c. The abscissa in Fig. 6 has been chosen with the purpose of contracting the scale of possible σ values. Apart from this, R_c^o depends linearly on σ^{-1} for large values of σ; the periodic charge functions are ultimately linear in $\sigma^{-1/2}$. Although both Fig. 6 and 7 describe the same functions, they differ in their potential experimental determination. In Fig. 6, each cycle has a fixed time duration; in Fig. 7, what is implicitly fixed is the reversal overpotential. In view of the paramount significance of θ' in determining the value of the charge density functions, this difference is extremely important: it accounts for the fact that the charge increases with increasing dimensionless sweep rate when θ' is fixed, whereas it decreases with increasing sweep rate when H_c is fixed. It is widely known from single sweep CV theory on stationary electrodes that charge is inversely proportional to dimensional sweep rate (usually its square root). Since charge functions for stationary electrodes usually depend on $(nF/RT)v\theta$, it is implied in this statement that during the experiment, the reversal overpotential, $v\theta$, is fixed and v is varied. It seems that emphasizing experimental conditions in RDE theory is necessary, mainly because of the dependence of relevant CV functions on both σ and $\sigma\theta'$. It is appropriate here to recall that σ increases as a result not only of increasing sweep rate but also of decreasing rotation speed. It is intuitively expected that when both reversal overpotential and dimensional sweep rate are fixed, less charge should be deposited as the rotation speed decreases.

For a fixed θ', it is interesting to compare the values of the charge density functions with the charge that would be obtained were the current constant and equal to i_L continuously during the performance of the experiment (interrupted lines, Fig. 6a-c). In the range of σ-values of electroanalytical significance ($\sigma \gtrsim 3$), it is seen that the values of the charge functions are primarily determined by θ'. This is expected since the dimensionless time interval during which the current is different than i_L is increasingly shorter as σ increases. It follows that the range of σ in which R's change significantly is below the value for which the cathodic current maximum appears.

Since the current density during an anodic cycle is always below the corresponding value for the cathodic cycle when both are cathodic and the opposite when they are anodic, it is expected that the periodic anodic charge density will always be lower than the periodic cathodic (Fig. 6b). It turns out that for $\theta' \geq 1$, it is also positive irrespective of σ, indicating that during any periodic anodic cycle a net deposit is added to the electrode. Obviously, the net charge density function, R_n (Fig. 6c) is also positive, indicating that a complete cycle always results in the formation of a net deposit. Similar conclusions can be drawn for the first sweep as well, since $R_c^o > R_c$ always. Interestingly, for very large values of σ, the interval over which the current is different from i_L is very narrow; in the limit of $\sigma \to \infty$, both periodic R_c and R_a tend to θ' and R_n to $2\theta'$. With respect to Fig. 6c, it is important to note that $R_n < 2\theta'$ for all finite σ. In other words, the amount of deposit obtained by plating with a non d-c potential, as in Fig. 1, can never exceed the amount obtained by d-c plating at the limiting current, i_L. This result is in agreement with conclusions drawn from the study of pulsed currents (1). The present results are rigorously valid only for deposition reactions with infinitely fast kinetics. Since the LSV currents do not have anodic portions, it is possible that R_c^o can exceed θ' as seen in Fig. 6a. Interestingly, the excess $R_c^o = \theta'$ is always less than one-third for finite σ and is independent of θ'.

Figure 7a is a plot of R *vs.* H_c for two representative σ values, 1 and 7. The range of H_c, $4 \leq H_c \leq 40$ for $n = 1$ corresponds to approximately 100-1000 mV. For $H_c \geq 4$, the dependence of R on H_c is linear to a good approximation. Note that for $\sigma = 7$, the periodic charge density functions are drawn for $H_c \geq 7$, to satisfy Eq. [12]. No such restriction exists for R_c^o, for all σ. For $\sigma = 1$, Eq. [1] is satisfied for all $H_c \geq 4$. Figure 7b emphasizes an interesting mathematical observation, namely, that the function, R_n'

$$R_n'(H_c) = \sigma R_n(\sigma,H_c) = 2[H_c + \exp(-H_c) - 1];$$
$$R_n(\sigma,H_c) = 2\sigma^{-1}[H_c + \exp(-H_c) - 1] \quad [19]$$

is a function of reversal overpotential alone. For $H_c \geq 4$, it is also linear in H_c. Alternatively, for a fixed H_c, R_n is inversely proportional to σ, indicating linear dependence on the rotation speed, ω, and on the inverse of the dimensional sweep rate, v. When both ω and v are varied so that σ is the same for each combination, R_n becomes independent of ω or v alone. This result emphasizes the fact that CV on an RDE is described by a combination of v and ω as it appears in σ, Eq. [1], rather than each alone. In connection with Fig. 7a one should note that for $\sigma = 1$, R_c^o, R_c, and R_a are close to each other; their separation increases with increasing σ but in each case there is a maximum for $\sigma \to \infty$.

Conclusions

It has been demonstrated that multisweep CV on an RDE leads to the establishment of a periodic response in concentrations, currents, and charges provided that the duration of each cycle is of the order of the RDE characteristic time. The first cathodic (LSV) sweep is the only one which is not periodic. Since this result originates from the study of reversible deposition reactions, its validity for other mechanisms can only be provisional.

The existence of a quickly attainable periodic state is significant in two respects. From the mathematical viewpoint, it indicates that the computational effort involved in the treatment of complicated reaction mechanisms need not be as great as one may originally think. From the electroanalytical viewpoint, the periodic currents and charges offer information of diagnostic importance, in addition to that obtained from LSV data. Experimentally, this is equivalent to the recording of two sweeps in each case, instead of only the first. However, one should be cautious in interpreting multisweep periodic data: the dependence of the current functions is not as strong as in LSV. In addition, the prolonged existence of the complicated mass flux regimes arising during CV experiments may lead to undesirable effects. Clearly more experimental and computational work must be done in order for the screening capabilities of the LSV-RDE and CV-RDE techniques to be ascertained on the quantitative level.

Acknowledgment

This work was supported by the Assistant Secretary for Conservation and Renewable Energy, Office of Advanced Conservation Technology, Division of Electrochemical Systems Research of the U.S. Department of Energy under Contract DE-AC03-76SF00098.

Manuscript submitted Sept. 13, 1982; revised manuscript received *ca.* Jan. 19, 1983. Portions of this paper were presented in Paper 322 at the Detroit, Michigan, Meeting of the Society, Oct. 17-21, 1982.

Any discussion of this paper will appear in a Discussion Section to be published in the December 1983 JOURNAL. All discussions for the December 1983 Discussion Section should be submitted by Aug. 1, 1983.

Lawrence Berkeley Laboratory assisted in meeting the publication costs of this article.

APPENDIX

Mathematical Derivation of Concentration, Current, and Charge Density Functions

Letting δ be the thickness of the Levich diffusion layer, dimensionless quantities are introduced by Eq. [A-1]

$$\xi = x/\delta;\ \tau = Dt/\delta^2;\ C(\xi,\tau) = 1 - c/c^b \quad [A\text{-}1]$$

where D is the diffusion coefficient of the ion being deposited and ξ, τ, C are dimensionless distance, time, and concentration, respectively. Figure 1a shows the dependence of applied potential on dimensionless time. The initial value of the potential is E_{eq}, the electrode equilibrium potential computed from the Nernst equation on the basis of c^b. At a constant rate of v V $\cdot$ sec^{-1}, the potential is changed in the cathodic direction for θ sec until it reaches E_c, the cathodic reversal potential. θ' is a dimensionless reversal time

$$\theta' = D\theta/\delta^2 \quad [A\text{-}2]$$

During the "anodic" cycle, the potential returns to its original value at the same rate. The first cathodic sweep refers to LSV, the first complete cycle is single sweep CV and several cycles to multisweep CV.

A combination of the RDE characteristic time, δ^2/D, characteristic voltage, $RT/n\mathbf{F}$, and v yield a dimensionless sweep rate, σ

$$\sigma = \frac{n\mathbf{F}}{RT} \cdot v \cdot \frac{\delta^2}{D} \quad [A\text{-}3]$$

where n, $\mathbf{F}$, R, and T have their usual meaning. As demonstrated in prior LSV-RDE theory (4-7), σ is a parameter of special significance. Since the initial potential has been assumed to be E_{eq}, the potential axis is also one of overpotential, beginning at 0 and ending at the cathodic reversal overpotential, η_c. Figure 1b shows the time dependence of the surface concentration obtained from the Nernst equation

$$C(0,\tau) = \begin{cases} 1 - \exp(2n\sigma\theta')\exp(-\sigma\tau); \\ \quad 2n\theta' \leq \tau \leq (2n+1)\theta'; \text{ cathodic cycle} \\ 1 - \exp[-(2n+2)\sigma\theta']\exp(\sigma\tau); \\ \quad (2n+1)\theta' \leq \tau \leq (2n+2)\theta'; \text{ anodic cycle} \end{cases} \quad [A\text{-}4]$$

Concentration functions.—In order to derive expressions for $C(\xi,\tau)$ we introduce another function, $C_s(\xi,\tau)$, which is the solution to the problem when an infinite overpotential is applied to the RDE. Then

$$C_s(0,\tau) = 1 \quad [A\text{-}5]$$

i.e., the surface concentration drops to 0 at the instant the infinite potential step is applied. The reason why $C_s(\xi,\tau)$ is introduced is that $C(\xi,\tau)$ can be obtained from $C_s(\xi,\tau)$ by an integral transform known as Duhamel's (or superposition) theorem (8, 9). Since the initial conditions for the dimensionless functions are 0, it holds that

$$\overline{C}(\xi,p) = p \cdot \overline{C}(0,p) \cdot \overline{C}_s(\xi,p) \quad [A\text{-}6]$$

where p is the Laplace parameter and $\overline{C}(0,p)$, $\overline{C}_s(\xi,p)$ are the Laplace transforms of $C(0,\tau)$ and $C_s(\xi,\tau)$, respectively; $\overline{C}(\xi,p)$ is the Laplace transform of $C(\xi,\tau)$, our unknown function. Equation [A-6] can be inverted by convolution in several ways. The most convenient turns out to result from associating p with $\overline{C}(0,p)$, to yield

$$C(\xi,\tau) = \int_0^\tau \frac{\partial C}{\partial \tau}(0,\lambda) \cdot C_s(\xi,\tau-\lambda)\, d\lambda \quad [A\text{-}7]$$

where λ is a dummy variable of integration. Note that

$$C_s(\xi,\tau) = 1 - \xi + 2\sum_{j=1}^{\infty} f_j(\xi) \cdot \exp(-j^2\pi^2\tau) \quad [A\text{-}8]$$

$$f_j(\xi) = (-1)^j (j\pi)^{-1} \sin[(1-\xi)j\pi] \quad [A\text{-}9]$$

While performing the integration indicated by Eq. [A-7], it is convenient to express time in terms of the number of cycles and time into a cathodic or anodic sweep. We can thus write (Fig. 1a)

$$\tau = 2l\theta' + \tau_c;\ 0 \leq \tau_c \leq \theta';\ \text{cathodic sweep} \quad [A\text{-}10a]$$

$$\tau = (2l+1)\theta' + \tau_a;\ 0 \leq \tau_a \leq \theta';\ \text{anodic sweep} \quad [A\text{-}10b]$$

where τ_c is dimensionless time into a cathodic sweep, τ_a is time into an anodic sweep, and l is the number of complete cycles which have already been applied. The outcome of the integration in Eq. [A-7] are two concentration functions, one for the cathodic sweep and one for the anodic sweep. Apart from ξ and τ_c (or τ_a), these will depend on l and on the two parameters, σ and θ'. We thus extend the symbol $C(\xi,\tau)$ to $C_c^l(\xi,\tau_c;\sigma,\theta')$ to describe the dimensionless concentration during the $(l+1)$ cathodic sweep (*i.e.*, after the passage of l complete cycles). The corresponding symbol for the concentration during the $(l+1)$ anodic sweep is $C_a^l(\xi,\tau_a;\sigma,\theta')$. For the special case of single sweep CV, $l = 0$, the cathodic (also LSV) function is independent of θ'. The notation for this case then is $C_c^o(\xi,\tau_c;\sigma)$ and $C_a^o(\xi,\tau_a;\sigma,\theta')$. The following results are obtained:

(*i*) single sweep CV; cathodic (also LSV)

$$C_c^o(\xi,\tau_c;\sigma) = (1-\xi)[1-\exp(-\sigma\tau_c)] + 2\sigma\exp(-\sigma\tau_c)\sum_{j=1}^{\infty} f_j(\xi)(j^2\pi^2-\sigma)^{-1} - 2\sigma\sum_{j=1}^{\infty} f_j(\xi)\exp(-j^2\pi^2\tau_c)(j^2\pi^2-\sigma)^{-1} \quad [A\text{-}11]$$

(*ii*) single sweep CV; anodic

$$C_a^o(\xi,\tau_a;\sigma,\theta') = (1-\xi)[1-\exp(-\sigma\theta')\exp(\sigma\tau_a)] + 2\sigma\exp(-\sigma\theta')\sum_{j=1}^{\infty} f_j(\xi)(j^2\pi^2-\sigma)^{-1} - 2\sigma\sum_{j=1}^{\infty} f_j(\xi)\exp(-j^2\pi^2\tau_a)\exp(-j^2\pi^2\theta')(j^2\pi^2-\sigma)^{-1} - 2\sigma\exp(-\sigma\theta')\exp(\sigma\tau_a)\sum_{j=1}^{\infty} f_j(\xi)(j^2\pi^2+\sigma)^{-1} + 2\sigma\exp(-\sigma\theta')\sum_{j=1}^{\infty} f_j(\xi)\exp(-j^2\pi^2\tau_a)(j^2\pi^2+\sigma)^{-1} \quad [A\text{-}12]$$

(*iii*) multisweep CV; cathodic

$$C_c^l(\xi,\tau_c;\sigma,\theta') = (1-\xi)[1-\exp(-\sigma\tau_c)] + 2\sigma\exp(-\sigma\tau_c)\sum_{j=1}^{\infty} f_j(\xi)(j^2\pi^2-\sigma)^{-1} - 2\sigma\sum_{j=1}^{\infty} f_j(\xi)\exp(-j^2\pi^2\tau_c)(j^2\pi^2-\sigma)^{-1} - 2\sigma\sum_{n=1}^{l}\sum_{j=1}^{\infty} f_j(\xi)\exp(-j^2\pi^2\tau_c)\exp(-2nj^2\pi^2\theta')(j^2\pi^2-\sigma)^{-1} + 2\sigma\exp(-\sigma\theta')\sum_{n=1}^{l}\sum_{j=1}^{\infty} f_j(\xi)\exp(-j^2\pi^2\tau_c)\exp[-(2n-1)j^2\pi^2\theta'](j^2\pi^2-\sigma)^{-1} + 2\sigma\exp(-\sigma\theta')\sum_{n=1}^{l}\sum_{j=1}^{\infty} f_j(\xi)\exp(-j^2\pi^2\tau_c)\exp[-(2n-1)j^2\pi^2\theta'](j^2\pi^2+\sigma)^{-1} - 2\sigma\sum_{n=1}^{l}\sum_{j=1}^{\infty} f_j(\xi)\exp(-j^2\pi^2\tau_c)\exp[-(2n-2)j^2\pi^2\theta'](j^2\pi^2+\sigma)^{-1} \quad [A\text{-}13]$$

(*iv*) multisweep CV; anodic

$$C_a^l(\xi,\tau_a;\sigma,\theta') = (1-\xi)[1-\exp(-\sigma\theta')\exp(\sigma\tau_a)] - 2\sigma\exp(-\sigma\theta')\exp(\sigma\tau_a)\sum_{j=1}^{\infty} f_j(\xi)(j^2\pi^2+\sigma)^{-1} + 2\sigma\exp(-\sigma\theta')\sum_{j=1}^{\infty} f_j(\xi)\exp(-j^2\pi^2\tau_a)(j^2\pi^2+\sigma)^{-1} - 2\sigma\sum_{n=0}^{l}\sum_{j=1}^{\infty} f_j(\xi)\exp(-j^2\pi^2\tau_a)\exp[-(2n+1)j^2\pi^2\theta'](j^2\pi^2-\sigma)^{-1} + 2\sigma\exp(-\sigma\theta')\sum_{n=0}^{l}\sum_{j=1}^{\infty} f_j(\xi)\exp(-j^2\pi^2\tau_a)\exp(-2nj^2\pi^2\theta')(j^2\pi^2-\sigma)^{-1} + 2\sigma\exp(-\sigma\theta')\sum_{n=1}^{l}\sum_{j=1}^{\infty} f_j(\xi)\exp(-j^2\pi^2\tau_a)\exp(-2nj^2\pi^2\theta')(j^2\pi^2+\sigma)^{-1} - 2\sigma\sum_{n=1}^{l}\sum_{j=1}^{\infty} f_j(\xi)\exp(-j^2\pi^2\tau_a)\exp([-(2n-1)j^2\pi^2\theta'](j^2\pi^2+\sigma)^{-1} \quad [A\text{-}14]$$

Several terms in Eq. [A-12]-[A-14] contain the expression $\exp(-kj^2\pi^2\theta')$ where k usually is a nonzero integer. Even when $k = 1$, the largest value that this term can take is $\exp(-j^2\pi^2\theta')$. For $\theta' \geq 1$, terms multiplied by $\exp(-kj^2\pi^2\theta')$ are very small and can be eliminated, rendering Eq. [A-12]-[A-14] much

simpler; furthermore, both C_c^l and C_a^l become independent of l. The physical interpretation of this is that the first anodic potential sweep and the second cathodic sweep yield concentrations that are periodic functions of time, irrespective of the value of σ, provided that $\theta' \geq 1$. The restriction on θ' is not limiting since when $\theta' = 1$, the dimensional reversal time is of the order of δ^2/D, which is a small number. In the elimination of terms containing $\exp(-kj^2\pi^2\theta')$, care should be taken to retain terms for which $k = 0$. The following results are obtained:

(v) multisweep CV; periodic cathodic

$$C_c(\xi, \tau_c; \sigma, \geq 1) = (1 - \xi)\,[1 - \exp(-\sigma\tau_c)] + 2\sigma \exp(-\sigma\tau_c) \sum_{j=1}^{\infty} f_j(\xi)\,(j^2\pi^2 - \sigma)^{-1} - 4\sigma \sum_{j=1}^{\infty} f_j(\xi)\, j^2\pi^2 \exp(-j^2\pi^2\tau_c)\,(j^4\pi^4 - \sigma^2)^{-1} \quad \text{[A-15]}$$

(vi) multisweep CV; periodic anodic

$$C_a(\xi, \tau_a; \sigma, \geq 1) = (1 - \xi)\,[1 - \exp(-\sigma\theta')\exp(\sigma\tau_a)] - 2\sigma \exp(-\sigma\theta')\exp(\sigma\tau_a) \sum_{j=1}^{\infty} f_j(\xi)\,(j^2\pi^2 + \sigma)^{-1} + 4\sigma \exp(-\sigma\theta') \sum_{j=1}^{\infty} f_j(\xi)\, j^2\pi^2 \exp(-j^2\pi^2\tau_a)\,(j^4\pi^4 - \sigma^2)^{-1} \quad \text{[A-16]}$$

One should note that the periodic concentration is independent of θ'. The notation chosen for the periodic functions does not include a dependence on l; also, we use the symbol ≥ 1 in place of θ', to emphasize the restriction on θ' for quick attainment of the periodic state.

Current density functions.—We define the current density functions, J, as ratios of the current density to the diffusion limiting current density, i_L. J is dimensionless and, in general, will depend on τ_c (or τ_a), the number of cycles, l, and the parameters σ and θ'. The notation for the current density function during a cathodic sweep is thus $J_c^l(\tau_c; \sigma, \theta')$, and $J_a^l(\tau_a; \sigma, \theta')$ for the subsequent anodic sweep. Expressions for J's can be derived either by application of Duhamel's transformation or by differentiation of the concentration functions at the surface. In essence, both methods are identical; however, if expressions for C's are not available, a suitable form of Duhamel's theorem yields J's directly. Since

$$\frac{i(\tau)}{i_L} = -\frac{\partial C}{\partial \xi}(0, \tau) \quad \text{[A-17]}$$

it follows from Eq. [A-7] that

$$\frac{i(\tau)}{i_L} = -\int_0^{\tau} \frac{\partial C}{\partial \tau}(0, \lambda) \cdot \frac{\partial C_s}{\partial \xi}(0, \tau - \lambda)\, d\lambda \quad \text{[A-18]}$$

$$\frac{\partial C}{\partial \xi}(0, \tau) = -\left[1 + 2\sum_{j=1}^{\infty} \exp(-j^2\pi^2\tau)\right] = -\theta_3(0, \pi i\tau) \quad \text{[A-19]}$$

θ_3 is one of the theta functions (11) whose relevance in RDE modeling under the Nernst-Siver approximation has been repeatedly demonstrated (4-6). We can then write

$$\frac{i(\tau)}{i_L} = \int_0^{\tau} \frac{\partial C}{\partial \tau}(0, \lambda) \cdot \theta_3(0, \pi i(\tau - \lambda))\, d\lambda \quad \text{[A-20]}$$

and compute J_c^l and J_a^l using Eq. [A-10]. Alternatively

$$J_c^l(\tau_c; \sigma, \theta') = -\frac{\partial C_c}{\partial \xi}(0, \tau_c; \sigma, \theta') \quad \text{[A-21a]}$$

$$J_a^l(\tau_a; \sigma, \theta') = -\frac{\partial C_a^l}{\partial \xi}(0, \tau_a; \sigma, \theta') \quad \text{[A-21b]}$$

where Eq. [A-13] and [A-14] can be used for the differentiations. Once expressions for J_c^l and J_a^l are available, the same elimination of terms containing $\exp(-kj^2\pi^2\theta')$, $k \geq 1$, can be done as previously, for $\theta' \geq 1$. Physically, this means that after the first cathodic (LSV) sweep, the current during the first anodic, second cathodic, and so on is in the periodic state, *i.e.*, does not change with further cycling. It turns out that when the value of the dimensionless sweep rate σ exceeds *ca.* 3, J_c^l exhibits a maximum both during the first and periodic sweeps; after the maximum, its value decreases to i_L. When $\sigma \lesssim 3$, J_c^l increases to i_L monotonically. In terms of dimensional time, attainment of i_L experimentally during the LSV sweep would guarantee that subsequent currents are periodic. However, this is not necessary since the criterion for periodicity is $\theta' \geq 1$, irrespective of whether i_L is reached within δ^2/D or not.

It should be noted here that when $\theta' < 1$, a periodic behavior of J_c^l and J_a^l is expected to be reached as $l \to \infty$; furthermore, the two periodic states may in general be different; *i.e.*, $J_c(\tau_c; \sigma, \geq 1) \neq J_c^{\infty}(\tau_c; \sigma, < 1)$ and $J_a(\tau_a; \sigma, \geq 1) \neq J_a^{\infty}(\tau_a; \sigma, < 1)$. The detailed behavior of J_c^{∞} and J_a^{∞} has not been investigated, since reversal times significantly less than δ^2/D are not expected to be of experimental importance. Expressions for the current density functions are as follows:

(i) single sweep CV; cathodic (LSV) (4)

$$J_c^0(\tau_c; \sigma) = 1 - \sigma^{1/2}\cot(\sigma^{1/2})\exp(-\sigma\tau_c) - 2\sigma \sum_{j=1}^{\infty} \exp(-j^2\pi^2\tau_c)\,(j^2\pi^2 - \sigma)^{-1} \quad \text{[A-22]}$$

(ii) single sweep CV; anodic

$$J_a^0(\tau_a; \sigma, \theta') = 1 - \sigma^{1/2}\coth(\sigma^{1/2})\exp(-\sigma\theta')\exp(\sigma\tau_a) - 2\sigma \sum_{j=1}^{\infty} \exp(-j^2\pi^2\theta')\exp(-j^2\pi^2\tau_a)\,(j^2\pi^2 - \sigma)^{-1} + 4\sigma \exp(-\sigma\theta') \sum_{j=1}^{\infty} j^2\pi^2 \exp(-j^2\pi^2\tau_a)\,(j^4\pi^4 - \sigma^2)^{-1} \quad \text{[A-23]}$$

(iii) multisweep CV; cathodic

$$J_c^l(\tau_c; \sigma, \theta') = 1 - \sigma^{1/2}\cot(\sigma^{1/2})\exp(-\sigma\tau) - 2\sigma \sum_{j=1}^{\infty} \exp(-j^2\pi^2\tau_c)\,(j^2\pi^2 - \sigma)^{-1} - 2\sigma \sum_{n=1}^{l} \sum_{j=1}^{\infty} \exp(-j^2\pi^2\tau_c)\exp(-2nj^2\pi^2\theta')\,(j^2\pi^2 - \sigma)^{-1} + 2\sigma \exp(-\sigma\theta') \sum_{n=1}^{l} \sum_{j=1}^{\infty} \exp(-j^2\pi^2\tau_c)\exp[-(2n-1)j^2\pi^2\theta']\,(j^2\pi^2 - \sigma)^{-1} + 2\sigma \exp(-\sigma\theta') \sum_{n=1}^{l} \sum_{j=1}^{\infty} \exp(-j^2\pi^2\tau_c)\exp[-(2n-1)j^2\pi^2\theta']\,(j^2\pi^2 + \sigma)^{-1} - 2\sigma \sum_{n=1}^{l} \sum_{j=1}^{\infty} \exp(-j^2\pi^2\tau_c)\exp[-(2n-2)j^2\pi^2\theta']\,(j^2\pi^2 + \sigma)^{-1} \quad \text{[A-24]}$$

(iv) multisweep CV; anodic

$$J_a^l(\tau_a;\sigma,\theta') = 1 - \sigma^{1/2}\coth(\sigma^{1/2})\exp(-\sigma\theta')\exp(\sigma\tau_a) + 2\sigma\exp(-\sigma\theta')\sum_{j=1}^{\infty}\exp(-j^2\pi^2\tau_a)(j^2\pi^2+\sigma)^{-1} - 2\sigma\sum_{n=0}^{l}\sum_{j=1}^{\infty}\exp(-j^2\pi^2\tau_a)\exp[-(2n+1)j^2\pi^2\theta'](j^2\pi^2-\sigma)^{-1} + 2\sigma\exp(-\sigma\theta')\sum_{n=1}^{l}\sum_{j=1}^{\infty}\exp(-j^2\pi^2\tau_a)\exp(-2nj^2\pi^2\theta')(j^2\pi^2+\sigma)^{-1} + 2\sigma\exp(-\sigma\theta')\sum_{n=0}^{l}\sum_{j=1}^{\infty}\exp(-j^2\pi^2\tau_a)\exp(-2nj^2\pi^2\theta')(j^2\pi^2-\sigma)^{-1} - 2\sigma\sum_{n=1}^{l}\sum_{j=1}^{\infty}\exp(-j^2\pi^2\tau_a)\exp[-(2n-1)j^2\pi^2\theta'](j^2\pi^2+\sigma)^{-1} \quad [A\text{-}25]$$

(*v*) multisweep CV; periodic cathodic

$$J_c(\tau_c;\sigma,\geq 1) = 1 - \sigma^{1/2}\cot(\sigma^{1/2})\exp(-\sigma\tau_c) - 4\sigma\sum_{j=1}^{\infty} j^2\pi^2\exp(-j^2\pi^2\tau_c)(j^4\pi^4-\sigma^2)^{-1} \quad [A\text{-}26]$$

(*vi*) multisweep CV; periodic anodic

$$J_a(\tau_a;\sigma,\geq 1) = 1 - \sigma^{1/2}\coth(\sigma^{1/2})\exp(-\sigma\theta')\exp(\sigma\tau_a) + 4\sigma\exp(-\sigma\theta')\sum_{j=1}^{\infty} j^2\pi^2\exp(-j^2\pi^2\tau_a)(j^4\pi^4-\sigma^2)^{-1} \quad [A\text{-}27]^4$$

Charge density functions.—We define charge density functions, R, as ratios of the charge density to a characteristic charge density. The latter quantity is the product of a characteristic current density, i_L, with a characteristic time, δ^2/D, and represents the charge per unit electrode area that would be deposited over a time δ^2/D were the current constant and equal to i_L. We choose R on a per cycle basis instead of a cumulative quantity which would describe deposit accumulation during a complete multisweep experiment. There are three types of such functions: R_c^l is the charge function associated with the $(l+1)$ cathodic sweep; R_a^l is associated with the $(l+1)$ anodic sweep; and R_n^l is the net charge deposited during the complete $(l+1)$ cycle; obviously

$$R_n^l = R_c^l + R_a^l \quad [A\text{-}28]$$

From their definition

$$R_c^l(\sigma,\theta') = \int_0^{\theta'} J_c^l(\tau_c;\sigma,\theta')\,d\tau_c; \qquad R_a^l(\sigma,\theta') = \int_0^{\theta'} J_a^l(\tau_a;\sigma,\theta')\,d\tau_a \quad [A\text{-}29]$$

note that R's are only functions of σ and θ' since they are integrals of J's over τ. By performing the integrations indicated in Eq. [A-29], the following expressions are obtained:

(*i*) multisweep CV; cathodic

$$R_c^l(\sigma,\theta') = \theta' - \sigma^{-1/2}\cot(\sigma^{1/2})[1-\exp(-\sigma\theta')] - 2\sigma\sum_{j=1}^{\infty}[1-\exp(-j^2\pi^2\theta')][j^2\pi^2(j^2\pi^2-\sigma)]^{-1} - 2\sigma\sum_{n=1}^{l}\sum_{j=1}^{\infty}\exp[-(2n-2)j^2\pi^2\theta'][j^2\pi^2(j^2\pi^2+\sigma)]^{-1} + \sum_{n=1}^{l}\sum_{j=1}^{\infty}\exp[-(2n-1)j^2\pi^2\theta'][4\sigma j^2\pi^2\exp(-\sigma\theta') + 2\sigma j^2\pi^2 + 2\sigma^2][j^2\pi^2(j^4\pi^4-\sigma^2)]^{-1} - \sum_{n=1}^{l}\sum_{j=1}^{\infty}\exp(-2nj^2\pi^2\theta')[4\sigma j^2\pi^2\exp(-\sigma\theta') + 2\sigma j^2\pi^2 + 2\sigma^2][j^2\pi^2(j^4\pi^4-\sigma^2)]^{-1} + 2\sigma\sum_{n=1}^{l}\sum_{j=1}^{\infty}\exp[-(2n+1)j^2\pi^2\theta'][j^2\pi^2(j^2\pi^2-\sigma)]^{-1} \quad [A\text{-}30]$$

(*ii*) multisweep CV; anodic

$$R_a^l(\sigma,\theta') = \theta' - \sigma^{-1/2}\coth(\sigma^{1/2})[1-\exp(-\sigma\theta')] + 2\sigma\exp(-\sigma\theta')\sum_{j=1}^{\infty}[1-\exp(-j^2\pi^2\theta')][j^2\pi^2(j^2\pi^2+\sigma)]^{-1} + 2\sigma\exp(-\sigma\theta')\sum_{j=1}^{\infty}[1-\exp(-j^2\pi^2\theta')][j^2\pi^2(j^2\pi^2-\sigma)]^{-1} - 2\sigma\sum_{j=1}^{\infty}\exp(-j^2\pi^2\theta')[j^2\pi^2(j^2\pi^2-\sigma)]^{-1} - 2\sigma\sum_{n=1}^{l}\sum_{j=1}^{\infty}\exp[-(2n-1)j^2\pi^2\theta'][j^2\pi^2(j^2\pi^2+\sigma)]^{-1} + \sum_{n=1}^{l}\sum_{j=1}^{\infty}\exp(-2nj^2\pi^2\theta')[4\sigma j^2\pi^2\exp(-\sigma\theta') + 2\sigma j^2\pi^2 - 2\sigma^2][j^2\pi^2(j^4\pi^4-\sigma^2)]^{-1} - \sum_{n=1}^{l}\sum_{j=1}^{\infty}\exp[-(2n+1)j^2\pi^2\theta'][4\sigma j^2\pi^2\exp(-\sigma\theta') + 2\sigma j^2\pi^2 + 2\sigma^2][j^2\pi^2(j^4\pi^4-\sigma^2)]^{-1} + 2\sigma\sum_{n=0}^{l}\sum_{j=1}^{\infty}\exp[-(2n+2)j^2\pi^2\theta'][j^2\pi^2(j^2\pi^2-\sigma)]^{-1} \quad [A\text{-}31]$$

Simplifications of Eq. [A-30] and [A-31] yield expressions for $R_c(\sigma,\geq 1)$ and $R_a(\sigma,\geq 1)$. The following are equations for the charge density function during the LSV sweep, $R_c^o(\sigma,\theta')$, and the periodic cathodic, anodic, and net charge density functions, $R_c(\sigma,\geq 1)$, $R_a(\sigma,\geq 1)$, and $R_n(\sigma,\geq 1)$, respectively

$$R_c^o(\sigma,\theta') = \theta' + 1/3 - \sigma^{-1} + \sigma^{-1/2}\cot(\sigma^{1/2})\exp(-\sigma\theta') \quad [A\text{-}32]$$

$$R_c(\sigma,\geq 1) = \theta' - 2\sigma^{-1} + \sigma^{-1/2}\cot(\sigma^{1/2})\exp(-\sigma\theta') + \sigma^{-1/2}\coth(\sigma^{1/2}) \quad [A\text{-}33]$$

$$R_a(\sigma,\geq 1) = \theta' + 2\sigma^{-1}\exp(-\sigma\theta') - \sigma^{-1/2}\cot(\sigma^{1/2})\exp(-\sigma\theta') - \sigma^{-1/2}\coth(\sigma^{1/2}) \quad [A\text{-}34]$$

$$R_n(\sigma,\geq 1) = 2\theta' - 2\sigma^{-1}[1-\exp(-\sigma\theta')] \quad [A\text{-}35]$$

Often repeated application of de l'Hôpital's rule yields

$$\lim_{\sigma\to 0} R = 0 \quad [A\text{-}36]$$

[4] The identities $\sum_{j=1}^{\infty} 2\sigma(j^2\pi^2-\sigma)^{-1} = 1 - \sigma^{1/2}\cot(\sigma^{1/2})$ and $\sum_{j=1}^{\infty} 2\sigma(j^2\pi^2+\sigma)^{-1} = \sigma^{1/2}\coth(\sigma^{1/2}) - 1$ have been used in the derivations (12).

which is in agreement with intuitive expectation but is not obvious in Eq. [A-32]-[A-35]. For large values of σ

$$R_c^o \sim \theta' + 1/3 - \sigma^{-1} \text{ (linear dependence on } \sigma^{-1}); \quad \sigma >> 1 \quad [A\text{-}37]$$

$$\lim_{\sigma \to \infty} R_c^o = \theta' + 1/3 \quad [A\text{-}38]$$

The periodic cathodic function exhibits a maximum at $\sigma = 16$

$$R_{c,max} = R_c(16, \geq 1) = \theta' + 1/8 \quad [A\text{-}39]$$

$$R_c \sim \theta' + \sigma^{-1/2} \text{ (linear dependence on } \sigma^{-1/2}); \quad \sigma >> 1 \quad [A\text{-}40]$$

$$\lim_{\sigma \to \infty} R_c = \theta' \quad [A\text{-}41]$$

Also

$$\lim_{\sigma \to \infty} R_n = 2\theta' \quad [A\text{-}42]$$

$$R_n > 0, \quad \sigma \neq 0 \quad [A\text{-}43]$$

Numerical investigation of charge densities indicates that they increase (except for R_c when $\sigma \geq 16$) with increasing σ, for a fixed value of θ'. However, this is the case when θ' is fixed. In usual experimental arrangements, the fixed parameter is the reversal overpotential, η_c. Expressing η_c as multiples of $RT/n\mathbf{F}$, we introduce a dimensionless cathodic overpotential, H_c

$$H_c = \eta_c/(RT/n\mathbf{F}) = \sigma\theta' \quad [A\text{-}44]$$

The charge density functions can then be expressed in terms of σ and H_c as follows ($\theta' \geq 1$)

$$R_c^o(\sigma, H_c) = 1/3 + \sigma^{-1}(H_c - 1) + \sigma^{-1/2} \cot(\sigma^{1/2}) \exp(-H_c) \quad [A\text{-}45]$$

$$R_c(\sigma, H_c) = \sigma^{-1}(H_c - 2) + \sigma^{-1/2} \cot(\sigma^{1/2}) \exp(-H_c) + \sigma^{-1/2} \coth(\sigma^{1/2}) \quad [A\text{-}46]$$

$$R_a(\sigma, H_c) = \sigma^{-1}[H_c + 2\exp(-H_c)] - \sigma^{-1/2} \cot(\sigma^{1/2}) \exp(-H_c) - \sigma^{-1/2} \coth(\sigma^{1/2}) \quad [A\text{-}47]$$

$$R_n(\sigma, H_c) = 2\sigma^{-1}[H_c + \exp(-H_c) - 1] \quad [A\text{-}48]$$

It should be noted that

$$\sigma R_n(\sigma, H_c) = R_n'(H_c) = 2[H_c + \exp(-H_c) - 1] \quad [A\text{-}49]$$

i.e., R' is independent of σ and depends only on H_c. Obviously, for a fixed H_c, all charge density functions decrease with increasing σ. This point is better illustrated in the discussion of the equations thus far derived on their relevance to electroanalytical investigations.

Applicability of RDE Models Other than the Nernst-Siver Approximation

Equation [A-18] can be rewritten as follows

$$\frac{i(\tau)}{i_L} = \int_0^\tau \frac{\partial C}{\partial \tau}(0, \lambda) \cdot \frac{i_s}{i_L}(0, \tau - \lambda)\, d\lambda \quad [A\text{-}50]$$

where i_s/i_L is the current density measured when a potential step is applied to an RDE such that the surface concentration is 0 for all $\tau \geq 0$. As already mentioned

$$\frac{i_s}{i_L}(\tau) = \theta_3(0, \pi i\tau) \quad [A\text{-}19]$$

when the Nernst-Siver approximation is used. Alternative expressions have been derived by Nisancioglu and Newman (8) and Viswanathan and Cheh (13). These are:

(Nisancioglu and Newman)

$$\frac{i_s(\tau)}{i_L} = 1 + \epsilon \sum_{j=0}^{\infty} B_j \exp(-\epsilon^2 \lambda_j \tau); \quad \epsilon = \Gamma(4/3)^{5} \quad [A\text{-}51]$$

(Viswanathan and Cheh)

$$\frac{i_s(\tau)}{i_L} = 1 + \sum_{j_1=1}^{\infty} C_{j_1} \exp(-\lambda_{j_1}^2 \tau) \quad [A\text{-}52]$$

Coefficients B_j, C_{j_1} and eigenvalues λ_j, λ_{j_1} have been computed numerically and reported in tabular form. Equations [A-51] and [A-52] are very similar. Equation [A-52] was independently proposed specifically to treat diffusion problems related to pulsed potentials. Equations [A-51] and [A-52] predict identical results (to four significant figures) over their range of applicability. Combination of Eq. [A-50] with each of Eq. [A-51] and [A-52] yields expressions for the l-dependent current density functions. For the $(l+1)$ cathodic sweep, these are as follows:

(Nisancioglu and Newman)

$$\begin{aligned} J_c^l(\tau_c; \sigma, \theta') = {} & 1 - \exp(-\sigma\tau_c) \\ & + \sigma\epsilon \exp(-\sigma\tau_c) \sum_{j=0}^{\infty} B_j(\epsilon^2\lambda_j - \sigma)^{-1} \\ & - \sigma\epsilon \sum_{j=0}^{\infty} B_j \exp(-\epsilon^2\lambda_j\tau_c)(\epsilon^2\lambda_j - \sigma)^{-1} \\ & - \sigma\epsilon \sum_{n=1}^{l} \sum_{j=0}^{\infty} B_j \exp[-(2n-2)\epsilon^2\lambda_j\theta'] \\ & \exp(-\epsilon^2\lambda_j\tau_c)(\epsilon^2\lambda_j + \sigma)^{-1} \\ & + \sigma\epsilon \exp(-\sigma\theta') \sum_{n=1}^{l} \sum_{j=0}^{\infty} B_j \exp[-(2n-1)\epsilon^2\lambda_j\theta'] \\ & \exp(-\epsilon^2\lambda_j\tau_c)(\epsilon^2\lambda_j - \sigma)^{-1} \\ & + \sigma\epsilon \exp(-\sigma\theta') \sum_{n=1}^{l} \sum_{j=0}^{\infty} B_j \exp[-(2n-1)\epsilon^2\lambda_j\theta'] \\ & \exp(-\epsilon^2\lambda_j\tau_c)(\epsilon^2\lambda_j + \sigma)^{-1} \\ & - \sigma\epsilon \sum_{n=1}^{l} \sum_{j=0}^{\infty} B_j \exp(-2n\epsilon^2\lambda_j\theta') \\ & \exp(-\epsilon^2\lambda_j\tau_c)(\epsilon^2\lambda_j - \sigma)^{-1} \end{aligned} \quad [A\text{-}53]$$

(Viswanathan and Cheh)

$$\begin{aligned} J_c^l(\tau_c; \sigma, \theta') = {} & 1 - \exp(-\sigma\tau_c) \\ & + \sigma \exp(-\sigma\tau_c) \sum_{j_1=1}^{\infty} C_{j_1}(\lambda_{j_1}^2 - \sigma)^{-1} \\ & - \sigma \sum_{j_1=1}^{\infty} C_{j_1} \exp(-\lambda_{j_1}^2\tau_c)(\lambda_{j_1}^2 - \sigma)^{-1} \\ & - \sigma \sum_{n=1}^{l} \sum_{j_1=1}^{\infty} C_{j_1} \exp[-(2n-2)\lambda_{j_1}^2\theta'] \\ & \exp(-\lambda_{j_1}^2\tau_c)(\lambda_{j_1}^2 + \sigma)^{-1} \\ & + \sigma \exp(-\sigma\theta') \sum_{n=1}^{l} \sum_{j_1=1}^{\infty} C_{j_1} \exp[-(2n-1)\lambda_{j_1}^2\theta'] \\ & \exp(-\lambda_{j_1}^2\tau_c)(\lambda_{j_1}^2 - \sigma)^{-1} \end{aligned}$$

(*Equation continued on next page*)

[5] The factor $\Gamma(4/3)$ arises because Nisancioglu and Newman use different dimensionless parameters; e.g., $\zeta = \Gamma(4/3)\xi$, where ζ is dimensionless distance according to these authors and ξ is defined in Eq. [A-1].

(Equation continued from page 1351)

$$+ \sigma \exp(-\sigma\theta') \sum_{n=1}^{l} \sum_{j_1=1}^{\infty} C_{j1} \exp[-(2n-1)\lambda_{j1}^2\theta'] \exp(-\lambda_{j1}^2\tau_c)(\lambda_{j1}^2+\sigma)^{-1} - \sigma \sum_{n=1}^{l} \sum_{j_1=1}^{\infty} C_{j1} \exp(-2n\lambda_{j1}^2\theta') \exp(-\lambda_{j1}^2\tau_c)(\lambda_{j1}^2-\sigma)^{-1} \quad [A\text{-}54]$$

Equations [A-53] and [A-54] could, in principle, be used to yield values for J_c^l. However, the number of published coefficients and eigenvalues is not sufficient to guarantee convergence of the series to the desired accuracy, even at large τ_c, due to the presence of terms such as $\Sigma B_j(\epsilon^2\lambda_j - \sigma)^{-1}$ and $\Sigma C_{j1}(\lambda_{j1}^2 - \sigma)^{-1}$. This constitutes an additional reason for applying the Nernst-Siver approximation.

LIST OF SYMBOLS

B_j coefficient, Ref. (8)
c concentration
c^b bulk concentration
C dimensionless concentration, Eq. [2]
$\overline{C}$ Laplace transform of C
C_s dimensionless concentration obtained when an infinite potential step is applied to an RDE for a reversible deposition reaction, Eq. [6]
$\overline{C}_s$ Laplace transform of C_s
C_a periodic dimensionless concentration during an anodic sweep, Eq. [A-16]
C_c periodic dimensionless concentration during a cathodic sweep, Eq. [A-15]
C_a^o dimensionless concentration during the first anodic sweep, Eq. [A-12]
C_c^o dimensionless concentration during LSV sweep, Eq. [A-11]
C_a^l dimensionless concentration during $(l+1)$ anodic sweep, Eq. [A-14]
C_c^l dimensionless concentration during $(l+1)$ cathodic sweep, Eq. [A-13]
C_{j1} coefficient, Ref. (13)
D diffusion coefficient
E_{eq} equilibrium potential
E_c reversal potential
H dimensionless overpotential, Eq. [11]
H_c dimensionless reversal overpotential, Eq. [11]
H_{max} value of H at the maximum of the periodic current density function
H_{max}^o value of H at the maximum of the LSV current density function
i current density
i_s current response of an RDE to which an infinite potential step is applied for a reversible deposition reaction, Eq. [A-19], [A-51], [A-52]
i_L diffusion limiting current density
j summation index
j_1 summation index
J_a periodic anodic current density function, Eq. [A-27]
J_c periodic cathodic current density function, Eq. [A-26]
J_a^o current density function during the first anodic sweep, Eq. [A-23]
J_c^o LSV current density function, Eq. [A-22]
J_a^l current density function during the $(l+1)$ anodic sweep, Eq. [A-25]
J_c^l current density function during the $(l+1)$ cathodic sweep, Eq. [A-24]
$J_{c,max}$ maximum value of J_c
$J_{c,max}^o$ maximum value of J_c^o
l number of applied complete potential cycles
p Laplace parameter
R_a periodic anodic charge density function, Eq. [A-34], [A-47]
R_c periodic cathodic charge density function, Eq. [A-33], [A-46]
R_n periodic net charge density function, Eq. [A-35], [A-48]
R_c^o charge density function during the LSV sweep, Eq. [A-32], [A-45]
R_a^l charge density function during the $(l+1)$ anodic sweep, Eq. [A-31]
R_c^l charge density function during the $(l+1)$ cathodic sweep, Eq. [A-30]
R_n^l net charge density function during the complete $(l+1)$ sweep, Eq. [9]
R_n' defined by Eq. [20], [A-49]
$R_{c,max}$ maximum value of R_c
t dimensional time
v dimensional sweep rate
x dimensional distance away from RDE surface
δ thickness of the Levich diffusion layer
ϵ $\Gamma(4/3)$, Eq. [A-51]
ζ dimensionless distance, Ref. (8)
η overpotential
η_c cathodic reversal overpotential
θ reversal time
θ' dimensionless reversal time, Eq. [3]
λ dummy variable of integration
λ_j eigenvalue, Ref. (8)
λ_{j1} eigenvalue, Ref. (13)
ν electrolyte kinematic viscosity
ξ dimensionless distance, Eq. [2]
σ dimensionless sweep rate, Eq. [1]
τ dimensionless time, Eq. [2]
τ_a dimensionless time into an anodic sweep, Eq. [4b]
τ_c dimensionless time into a cathodic sweep, Eq. [4a]
ω RDE rotation speed

REFERENCES

1. H. Y. Cheh, *This Journal*, **118**, 551 (1971).
2. T. R. Rosebrugh and W. L. Miller, *J. Phys. Chem.*, **14**, 816 (1910).
3. Yu. G. Siver, *Russ. J. Phys. Chem.*, **33**, 533 (1959); **34**, 273 (1960).
4. P. C. Andricacos and H. Y. Cheh, *This Journal*, **127**, 2153 (1980).
5. P. C. Andricacos and H. Y. Cheh, *ibid.*, **127**, 2385 (1980).
6. P. C. Andricacos and H. Y. Cheh, *J. Electroanal. Chem.*, **124**, 95 (1981).
7. G. P. Girina, V. Yu. Filinovskii, and L. G. Feoktistov, *Soviet Electrochem.*, **3**, 831 (1967).
8. K. Nisancioglu and J. Newman, *J. Electroanal. Chem.*, **50**, 23 (1974).
9. P. C. Andricacos and H. Y. Cheh, *ibid.*, **121**, 133 (1981).
10. J. R. Selman and C. W. Tobias, *ibid.*, **65**, 67 (1975).
11. E. T. Whittaker and G. N. Watson, "A Course of Modern Analysis," Cambridge University Press, London (1969).
12. L. S. Gradshteyn and I. M. Ryzhic, "Table of Integrals, Series and Products," Academic Press, New York (1980).
13. K. Viswanathan, M. A. Farrell-Epstein, and H. Y. Cheh, *This Journal*, **125**, 1772 (1978); K. Viswanathan and H. Y. Cheh, *J. Appl. Electrochem.*, **9**, 537 (1979).

Diffusion-Controlled Multisweep Cyclic Voltammetry

II. Reversible Deposition on a Stationary Planar Electrode

P. C. Andricacos* and P. N. Ross, Jr.*

University of California, Lawrence Berkeley Laboratory, Materials and Molecular Research Division, Berkeley, California 94720

ABSTRACT

Multisweep cyclic voltammetry applied to electrodeposition at a stationary planar electrode under conditions of semi-infinite linear diffusion is analyzed in terms of current and charge density functions. A hypothetical periodic state obtained at an infinite reversal overpotential serves as a lower bound for the values of the current function, which has as an upper bound the current measured on the first sweep. Another hypothetical periodic state reached by continuous cycling depends on the chosen finite value of the reversal overpotential. A quasi-periodic state is defined when current functions do not change significantly with further cycling. Whereas fewer cycles are necessary for quasi-periodic behavior in the current with increasing reversal overpotential, the opposite is true for the cathodic charge. It is found that the cathodic current always exhibits a maximum; multiple sweeping significantly reduces its height and shifts its position toward more cathodic overpotentials, but not by much. As in linear sweep voltammetry, the height of the cathodic maximum obtained by multiple sweeping depends linearly on the square root of the sweep rate, whereas the charge associated with each sweep depends linearly on its inverse. Each complete cycle results in a net accumulation of deposit, with the amount on each cycle decreasing with the total number of previous cycles. Whereas the first cathodic sweep starts from zero current, the current at the start of the second cathodic sweep is anodic; the value of this anodic current depends both on sweep rate and the reversal overpotential. Relative to linear sweep voltammetry, multisweep cyclic voltammetry generates characteristic currents that are unique to each sweep, thereby multiplying the criteria for reversibility manyfold. However, cyclic voltammetry also creates a substantial net deposit on each sweep, and any resulting surface area change with repeated cycling would make the multisweep diagnostics meaningless.

Whereas the application of single sweep potential cycles to stationary electrodes has become a technique with a long history in electrochemistry, multisweep methods have almost never been investigated. An exception is the paper by Matsuda (1) in which a reversible reaction with soluble product is examined under conditions of multisweep cyclic voltammetry (CV) occurring on a hanging drop electrode. In this investigation, we examine cyclic voltammograms obtained when multisweep CV is applied to a stationary planar electrode under conditions of semi-infinite linear diffusion. The reaction mechanism is that of a reversible deposition with the deposit at unit activity. Linear sweep voltammetry (LSV) results for this reaction have been reported previously by Berzins and Delahay (2). The first anodic sweep has been analyzed by White and Lawson (3) who also included the case of time-dependent deposit activity. A comparison is made where appropriate with the corresponding theory (4) for a rotating disk electrode (RDE). A complete description of the problem would require computation of concentration and current and charge density functions. Since the computation of concentration functions is a major task and it would add little information to that available from RDE theory (4), we have restricted ourselves to an analysis of current and charge density functions only.

By appropriately defining these functions, it has been possible to obtain expressions which depend only on the reversal overpotential. In this respect, they are different from the RDE functions, even if the latter were to be expressed in terms of dimensional quantities. To emphasize this point, different notation has been chosen for their representation. By analogy to RDE theory, a reversal overpotential has been sought which would guarantee periodic behavior immediately after the LSV sweep. It was found that this behavior is observed only with infinite overpotential. Both the mathematical and physical interpretation of the periodic current function at infinite reversal overpotential is difficult. It is thus being used only as a computational result, and the discussion will emphasize the quasi-periodic state. This is achieved when, for a given reversal overpotential, a sufficient number of cycles have been applied so that current density does not change significantly upon further cycling.

* Electrochemical Society Active Member.
Key words: electrode, deposition, mass transport, voltammetry.

Statement of the Problem and Definitions

The absence of a time-independent characteristic length associated with a stationary electrode does not allow the definition of dimensionless distance, time, and sweep rate. If 2θ is the duration of a complete cycle, the surface concentration during the cathodic sweep changes exponentially through the Nernst equation from c^b to $c^b \exp(-a\theta)$, where c^b is the bulk concentration; during an anodic sweep the variation is from $c^b \exp(-a\theta)$ back to c^b. For

$$a = (n\mathbf{F}/RT)v \qquad [1]$$

the parameter $a\theta$ is a dimensionless reversal overpotential; similarly, at, where t is dimensional time, is a dimensionless overpotential. In Eq. [1], v is the sweep rate, and n, $\mathbf{F}$, R, and T have their usual meaning. For reasons of consistency with previously published work (2), we retain the notation (at, $a\theta$) as opposed to (H, H_c) introduced in the RDE theory (4). If l is the number of already applied cycles, we can define dimensional time into a cathodic sweep, t_c, or into an anodic sweep, t_a, by the following equations

$$t = 2l\theta + t_c; \quad 0 \leq t_c \leq \theta; \quad t \text{ during a cathodic sweep} \qquad [2a]$$

$$t = (2l+1)\theta + t_a; \quad 0 \leq t_a \leq \theta; \quad t \text{ during an anodic sweep} \qquad [2b]$$

Since the surface concentration, $c(0,t)$ is a known function of time, current densities can be computed by the application of Duhamel's theorem (4, 5)

$$i(t) = -n\mathbf{F}(D/\pi)^{1/2} \int_0^t \frac{\partial c}{\partial t}(0,\lambda) \cdot (t-\lambda)^{-1/2}\, d\lambda \qquad [3]$$

For instance, combination of Eq. [2a] and [3] yields the current density during the $(l+1)$ cathodic cycle, i_c^l, as a function of l, v, and θ. As has been demonstrated by Berzins and Delahay (2) in the LSV case, the combination $i_c{}^o v^{-1/2}$ depends only on at_c. Since this property is retained in multisweep CV, the relevant current density functions are defined as follows

$$I_c^l(at_c; a\theta) = i_c^l/(n\mathbf{F}D^{1/2}a^{1/2}c^b) \quad [4]$$

$$I_c^l(at_a; a\theta) = i_a^l/(n\mathbf{F}D^{1/2}a^{1/2}c^b) \quad [5]$$

where I_c^l refers to the $(l+1)$ cathodic sweep and I_a^l to the $(l+1)$ anodic sweep. Note that I's are dimensionless and that the factor $n\mathbf{F}D^{1/2}a^{1/2}c^0$ is not related to a limiting current density, as is the case for J's in RDE theory; in addition, a transformation such as $J\sigma^{-1/2}$ for the RDE still depends on both σ and $\sigma\theta'$ rather than $\sigma\theta'$ $(= a\theta)$ alone.

The charge density during the $(l+1)$ cathodic or anodic sweep, q_c^l and q_a^l, respectively, can be obtained by integrating i_c^l and i_a^l over the time interval, 0 to θ. As for $i\nu^{-1/2}$, the quantity $q^l\nu^{1/2}$ depends only on $a\theta$. The charge density functions, Q_c^l and Q_a^l, can then be defined as follows

$$Q_c^l(a\theta) = q_c^l/(n\mathbf{F}D^{1/2}a^{-1/2}c^b) = \int_0^{a\theta} I_c^l(at_c; a\theta)\,d(at_c) \quad [6]$$

$$Q_a^l(a\theta) = q_a^l/(n\mathbf{F}D^{1/2}a^{-1/2}c^b) = \int_0^{a\theta} I_a^l(at_a; a\theta)\,d(at_a) \quad [7]$$

The net charge density function, $Q_n^l(a\theta)$, associated with the complete $(l+1)$ cycle is

$$Q_n^l(a\theta) = Q_c^l(a\theta) + Q_a^l(a\theta) \quad [8]$$

Expressions for I_c^l, I_a^l and Q_c^l, Q_a^l are derived in the Appendix.

Results and Discussion

In the limit $a\theta \to \infty$, both I_c^l and I_a^l become l-independent, indicating the existence of a hypothetical periodic state denoted by $I_c(at_c; \infty)$ and $I_a(at_a; \infty)$. Since an infinite amount of charge is consumed during the LSV sweep in the overpotential range 0 to ∞, this periodic state is unrealizable. From the mathematical viewpoint, the boundary condition an infinite distance away from the electrode surface dictates that the concentration should be retained at the bulk value, c^b, but over finite times. Indeed, concentration functions for the LSV sweep derived in the Appendix contain forms which cannot be determined when both distance away from the electrode surface and time are infinite.

Despite difficulties in the physical and mathematical interpretation of I_c and I_a, numerical evaluation of I_c^l and I_a^l over a large range of $a\theta$ and l values has indicated that

$$I_c^l > I_c \quad \text{and} \quad I_a^l > I_a \quad [9]$$

Since

$$I_c^0 > I_c^l \quad \text{and} \quad I_a^0 > I_a^l \quad [10]$$

we can write

$$I_c < I_c^l < I_c^0 \quad \text{and} \quad I_a < I_a^l < I_a^0 \quad [11]$$

indicating that the LSV current function and the periodic cathodic at infinite reversal overpotential are upper and lower bounds, respectively, for I_c^l irrespective of the value of l or $a\theta$. Similarly, I_a^l is bounded from the above by the current function during the first anodic sweep and from below by the periodic anodic at infinite reversal overpotential.

No closed form expressions have been derived for the periodic states obtained by letting $l \to \infty$. However, they can be shown to exist and are generally different from each other depending on the chosen finite value of $a\theta$. They also obey Eq. [11]. Since these periodic states involve infinite times, their physical and mathematical interpretation is under doubt.

Numerical investigations of current density functions have shown that for a given finite value of $a\theta$, a state is reached beyond which increasing the number of cycles does not effect significant changes in their value. This type of behavior can be termed quasi periodic and is attained within fewer cycles as the reversal overpotential is increased. This is expected since in the limit of infinite $a\theta$ the first cathodic sweep is sufficient for periodic behavior. The following discussion will focus on l-dependent functions and their relation to the hypothetical periodic state at infinite reversal overpotential.

Figures 1 and 2 are drawn for two different values of the dimensionless reversal overpotential, 6 and 24, respectively. As for the RDE, no extremum is expected to appear in the anodic sweeps, since no limitations have been imposed on the amount of material that can be stripped from the electrode surface. However, all cathodic curves exhibit a maximum. Thus, there are three criteria of diagnostic importance. These are: (*i*) the foot of the cathodic wave, $I_c^l(0; a\theta) = I_a^{l-1}(a\theta; a\theta)$; (*ii*) the position of the cathodic maximum on the potential axis, $(at_c)_{max}^l$; and (*iii*) the height of the cathodic peak, $I_{c,max}^l$. The values of these quantities for the two bounds, *i.e.*, the first cathodic wave (2) and the periodic wave at infinite overpotential are as follows

$$I_c^0(0) = 0; \quad (at_c)^0_{max} = 0.854; \quad I_{c,max}^0 = 0.610 \quad [12]$$

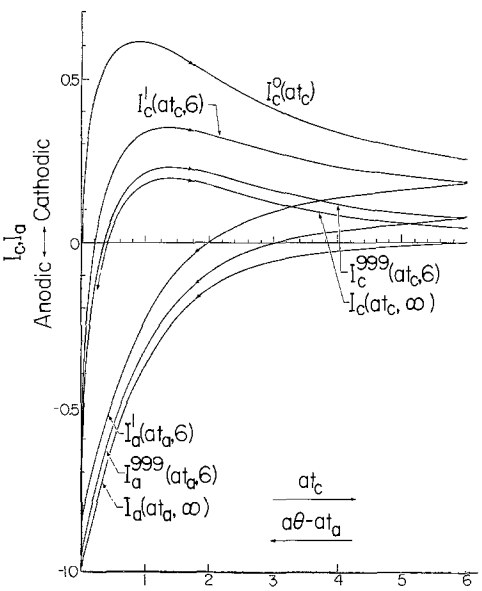

Fig. 1. Current density functions for a reversal overpotential of $6RT/nF$.

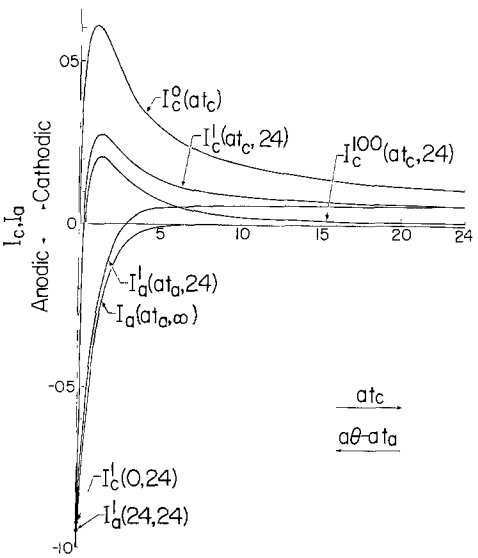

Fig. 2. As in Fig. 1, but for a reversal overpotential of $24RT/nF$; $I_c(at_c; \infty)$ is very close to I_c^{100} and is not included in the figure.

$$I_c(0, \infty) = -1; \quad (at_c)_{max} = 1.3; \quad I_{c,max} = 0.194 \quad [13]$$

As mentioned previously, these numbers define the total range of variation of the current functions. For instance, the cathodic maximum can never exceed 0.61 or be lower than 0.19, irrespective of l and $a\theta$. Furthermore, since $I_c(0. \infty) = -1$, a meaning can be assigned to the quantity $n\mathbf{F}D^{1/2}a^{1/2}c^b$ as that current density measured in the anodic direction at the foot of the periodic cathodic wave with infinite reversal overpotential.

A considerable reduction of the height of the cathodic peak during the second wave as compared to the first is one of the most important predictions of the present model. Its position is also shifted in the cathodic direction, but not by much, as can be inferred by a comparison of the $(at_c)_{max}$ values in Eq. [12] and [13]. The subsequent development of the current function profiles is mostly defined by the value of the reversal overpotential. For large such values, the height and position of the second cathodic wave maximum do not change significantly with further cycling. On the other hand, for values of the reversal overpotential which are near the maximum, current functions for different values of l show marked variations. This is a consequence of the slower approach to quasi-periodic behavior for smaller values of $a\theta$.

A summary of numerical results for the three diagnostic criteria is shown in Table I, over a range of $a\theta$ values of practical interest. For a single electron transfer reaction ($n = 1$), the reported range of $a\theta$ values corresponds to a cathodic reversal overpotential of approximately 0.16-0.62V. The way of using this table is as follows: let $i_c^l(0; a\theta)$ be the current density measured at the beginning of the $(l + 1)$ cathodic wave (or the end of the lth anodic) at a fixed reversal overpotential of $(RT/n\mathbf{F})a\theta$, and $i_{c,max}{}^l\,[(at_c)_{max}{}^l, a\theta]$ be the peak current density; then

$$i_c^l(0; a\theta) = Ac^b v^{1/2} I_c^l(0; a\theta) \quad [14]$$

$$i_{c,max}{}^l\,[(at_c)_{max}{}^l; a\theta] = Ac^b v^{1/2} I_{c,max}{}^l\,[(at_c)_{max}{}^l; a\theta] \quad [15]$$

$$A = (n\mathbf{F})^{3/2}\,(RT)^{-1/2}\,D^{1/2} \quad [16]$$

where $I_c(0; a\theta)$ and $I_{c,max}{}^l$ can be read off Table I (or computed from Eq. [A-16] of the Appendix). For example, if $a\theta = 24$, a plot of the peak current density measured during the fifth sweep ($l = 4$) *vs.* $v^{1/2}$ should be linear with a slope of 0.238 Ac^b. Similarly, a plot of the absolute value of the current density at the foot of the same wave should also be linear with a slope of 0.961 Ac^b. It should be remembered that these slopes also depend on the diffusion coefficient and the bulk concentration of the reacting ion; in addition, increasing l should not greatly affect these values (for instance, the maximum measurable slope for the current density at the foot of the wave *vs.* $v^{1/2}$ is Ac^b to be compared against 0.961 Ac^b for $l = 4$).

We now turn our attention to the charge density functions. In the hypothetical periodic states, these functions possess interesting properties; these can be summarized as follows

$$Q_c(\infty) = 1; \quad Q_a(\infty) = -1; \quad Q_n(\infty) = 0 \quad [17]$$

$$Q_n{}^\infty(a\theta) = 0 \quad [18]$$

Equation [18] indicates that, for any value of $a\theta$, no net deposit is formed or stripped from the electrode in the periodic state reached by letting $l \to \infty$; similarly, for the periodic state of $a\theta \to \infty$ (Eq. [17]). As in the case of $I_c(0; \infty)$, the limiting values of $Q_c(\infty)$ and $Q_a(\infty)$, Eq. [17], assign a meaning to the quantity $(\pm)\ n\mathbf{F}D^{1/2}a^{-1/2}c^b$, as the charge density obtained during a periodic cathodic (+) or anodic (−) sweep at infinite reversal overpotential.

Regarding quasi-periodic behavior of the charge functions, it should be noted that increasing number of cycles is required for increasing $a\theta$. This is contrary to the current function behavior, but should be expected since small variations in the current density acquire greater significance as $a\theta$ increases; this is a consequence of integrating currents over the entire $a\theta$ range.

Figures 3 and 4 are plots of cathodic, anodic, and net charge density functions with $a\theta$ as the variable and l as the parameter. As shown in Fig. 4, $Q_n{}^l$ is always positive indicating that a multisweep CV experiment for a reversible deposition reaction always results in the formation of a net deposit on the electrode surface, except in the hypothetical periodic state reached by $l \to \infty$ (Eq. [18]) when no net material is deposited (or stripped) irrespective of the reversal overpotential. Apart from the implications of this result on transient surface morphology, it also indicates that a thin film of deposit originally existing on the surface is sufficient for the performance of the experiment and is necessary

Table I. Numerical results for the current density function at the foot of the cathodic wave (a), the position of the cathodic maximum (b), and its height (c), in terms of the number of cycles, *l*, and the dimensionless reversal overpotential, $a\theta$. The range of values reported in columns (b) indicates that over this range the maximum value of the cathodic current density function was the same to four significant figures. Negative numbers refer to anodic currents.

	$a\theta = 6$			$a\theta = 8$			$a\theta = 10$			$a\theta = 12$			$a\theta = 14$		
l	a*	b	c	a	b	c	a	b	c	a	b	c	a	b	c
1	−0.868	1.324-8	0.355	−0.890	1.338-43	0.334	−0.903	1.345-51	0.319	−0.913	1.349-55	0.309	−0.920	1.355	0.300
2	−0.886	1.343-6	0.320	−0.906	1.351-5	0.301	−0.918	1.357-8	0.289	−0.926	1.359-61	0.280	−0.933	1.359-64	0.273
3	−0.896	1.346-52	0.304	−0.915	1.354-9	0.286	−0.927	1.359-61	0.275	−0.935	1.361-3	0.267	−0.941	1.361-6	0.261
4	−0.904	1.349-53	0.294	−0.922	1.357-9	0.277	−0.933	1.361-2	0.266	−0.940	1.362-5	0.259	−0.946	1.361-7	0.253
5	−0.909	1.351-4	0.287	−0.927	1.358-60	0.271	−0.937	1.360-4	0.260	−0.944	1.361-6	0.253	−0.950	1.363-6	0.248
10	−0.923	1.352-6	0.270	−0.940	1.359-62	0.255	−0.949	1.363	0.246	−0.956	1.361-7	0.240	−0.960	1.363-7	0.235
20	−0.935	1.354-6	0.257	−0.950	1.360-1	0.244	−0.959	1.360-6	0.235	−0.964	1.363-6	0.230	−0.968	1.363-7	0.226
30	−0.940	1.351-2	0.252	−0.955	1.359-63	0.239	−0.963	1.361-6	0.231	−0.969	1.362-8	0.226	−0.972	1.363-7	0.222
50	−0.945	1.354-7	0.246	−0.960	1.359-63	0.233	−0.968	1.361-6	0.226	−0.973	1.363-6	0.221	−0.976	1.365	0.218
	$a\theta = 16$			$a\theta = 18$			$a\theta = 20$			$a\theta = 22$			$a\theta = 24$		
l	a	b	c	a	b	c	a	b	c	a	b	c	a	b	c
1	−0.926	1.354-60	0.294	−0.930	1.357-61	0.288	−0.934	1.358-62	0.283	−0.938	1.359-63	0.279	−0.940	1.360-3	0.275
2	−0.938	1.360-6	0.268	−0.942	1.361-6	0.263	−0.945	1.363-5	0.259	−0.948	1.363-6	0.256	−0.951	1.362-8	0.253
3	−0.945	1.362-7	0.256	−0.949	1.362-7	0.252	−0.952	1.365	0.249	−0.954	1.363-8	0.246	−0.957	1.363-9	0.243
4	−0.950	1.363-7	0.249	−0.954	1.365-6	0.245	−0.956	1.363-7	0.242	−0.959	1.364-8	0.240	−0.961	1.364-8	0.238
5	−0.954	1.365	0.244	−0.957	1.362-7	0.241	−0.960	1.364-7	0.238	−0.962	1.363-9	0.235	−0.964	1.364-8	0.233
10	−0.964	1.363-8	0.232	−0.966	1.365-6	0.229	−0.969	1.365-8	0.227	−0.971	1.364-9	0.225	−0.972	1.364-9	0.223
20	−0.971	1.363-8	0.223	−0.974	1.364-8	0.221	−0.976	1.365-7	0.219	−0.977	1.365-8	0.217	−0.979	1.364-9	0.216
30	−0.975	1.364-8	0.219	−0.977	1.365-8	0.217	−0.979	1.365-8	0.215	−0.980	1.365-8	0.214	−0.982	1.365-8	0.213
50	−0.979	1.365-6	0.215	−0.981	1.365-7	0.213	−0.982	1.364-8	0.212	−0.984	1.365-8	0.211	−0.985	1.365-8	0.210

* a: $I_c{}^{l+1}(0, a\theta)$; b: $(at_c)_{max}{}^l$; c: $I_{c,max}{}^l$.

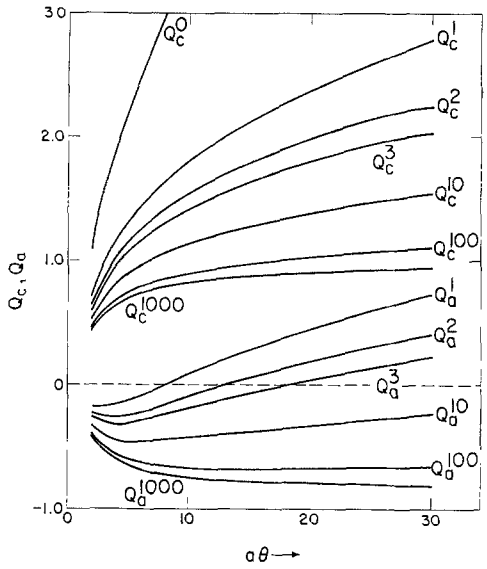

Fig. 3. Cathodic and anodic charge density functions in terms of dimensionless reversal overpotential, $a\theta$, and number of cycles.

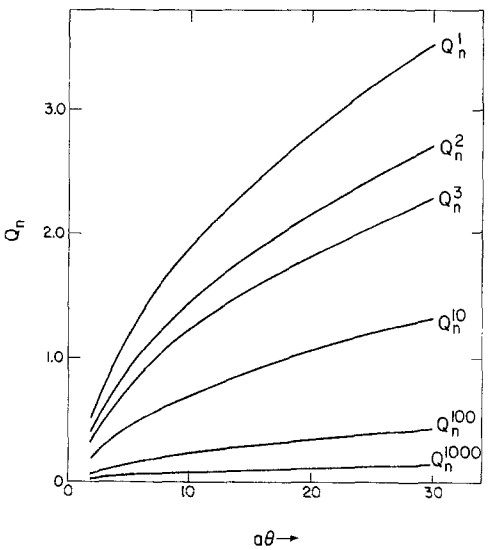

Fig. 4. Net charge density functions

for the electrode to have a well-defined equilibrium potential.

The definition of charge density functions shows that the actual charge density measured during a cathodic, anodic, or complete potential cycle should be correlated to the inverse of the square root of the sweep rate, $v^{-1/2}$, rather than $v^{1/2}$. If $q_n^l(a\theta)$ is the measured net charge density during the $(l+1)$ complete cycle, then

$$q_n^l(a\theta) = Bc^b v^{-1/2} Q_n^l(a\theta) \quad [19]$$

$$B = (n\mathbf{F}RTD)^{1/2} \quad [20]$$

where $Q_n^l(a\theta)$ values are read off Fig. 4. Similar expressions can be written down for q_c^l and q_a^l in terms of Q_c^l, Q_a^l, and $v^{-1/2}$. Figure 3 can be used to provide values for Q_c^l and Q_a^l.

Conclusions

Analysis of a reversible deposition reaction occurring on a stationary planar electrode under multisweep cyclic voltammetry conditions has demonstrated the absence of an experimentally realizable periodic state. Instead, all quantities of potential diagnostic use, such as the height of the cathodic current maximum, its position on the potential axis, and the magnitude of the anodic current at the equilibrium potential, vary continuously with the parameters of the method, such as the number of applied cycles and the reversal overpotential. These variations are most pronounced between the first and second sweeps and they diminish with continued cycling, eventually leading to quasi-periodic behavior. Relative to linear sweep voltammetry, multisweep cyclic voltammetry multiplies the characteristic criteria of reversibility manyfold.

Except in the hypothetical periodic states achieved by an infinite reversal overpotential or by an infinite number of applied cycles, in which no net deposit is formed during a complete potential sweep, all other states result in the formation of a net deposit on the electrode surface whose absolute amount depends on the concentration in the solution, the total number of applied cycles, and the nature of the material. The resulting changes in surface area may invalidate the detailed information that can be obtained in principle by multisweep measurements. Since the most important changes for diagnostic purposes occur on the first two sweeps, metal deposition studied by cyclic voltammetry should be limited to a few sweeps to avoid the roughness complication.

Acknowledgment

This work was supported by the Assistant Secretary for Conservation and Renewable Energy, Office of Advanced Conservation Technology, Division of Electrochemical Systems Research of the U.S. Department of Energy under Contract DE-AC03-76SF00098.

Manuscript submitted Sept. 13, 1982; revised manuscript received *ca.* Jan. 19, 1983. Portions of this paper were presented in Paper 322 at the Detroit, Michigan, Meeting of the Society, Oct. 17-21, 1982.

Any discussion of this paper will appear in a Discussion Section to be published in the December 1983 JOURNAL. All discussions for the December 1983 Discussion Section should be submitted by Aug. 1, 1983.

Lawrence Berkeley Laboratory assisted in meeting the publication costs of this article.

APPENDIX

Mathematical Derivation of Current and Charge Density Functions

Since no time independent characteristic length is associated with a stationary electrode, the diffusion problem is described in terms of dimensional quantities, such as distance, x, away from the electrode surface, time, t, and the concentration $c(x,t)$, of the reacting species. Assuming semi-infinite linear diffusion and excluding natural convection, double layer capacitance, pseudocapacitance, and electrolyte resistance effects, we can write

$$c(\infty, t) = c^b, \quad t \text{ positive and finite} \quad [A\text{-}1]$$

where c^b is the bulk, also initial, concentration of the reacting species, and

$$c(0,t) = \begin{cases} c^b \exp[-a(t-2n\theta)]; \\ \quad 2n\theta \leq t \leq (2n+1)\theta; \text{ cathodic cycle} \\ c^b \exp[-(2n+2)a\theta] \exp(at); \\ \quad (2n+1)\theta \leq t \leq (2n+2)\theta; \text{ anodic cycle} \end{cases} \quad [A\text{-}2]$$

$$a = (n\mathbf{F}/RT)v \quad [A\text{-}3]$$

where v is the dimensional sweep rate and n, $\mathbf{F}$, R, and T have their usual meaning. Equation [A-2] describes the dependence of the surface concentration on time; this is defined from the potential through the Nernst equation. It is assumed that the potential starts at the equilibrium value based on c^b, and changes linearly at a rate v for a time θ. The cycle is repeated in the opposite direction for the interval $(\theta, 2\theta)$ and so on [see Fig. 1 in Ref. (4)].

Expressions for the functions of interest are reported in terms of dimensional times, t_c and t_a, into a cathodic

and anodic cycle, respectively. These are defined as follows

$$t = 2l\theta + t_c;\ 0 \leq t_c \leq \theta;\ t \text{ during a cathodic sweep} \quad [A\text{-}4a]$$

$$t = (2l+1)\theta + t_a;\ 0 \leq t_a \leq \theta;\ t \text{ during an anodic sweep} \quad [A\text{-}4b]$$

Current Density Functions

For the purposes of the derivations in this work, we introduce two concentration functions, c' and c_s', defined as follows

$$c'(x,t) = 1 - c(x,t)/c^b \quad [A\text{-}5]$$

$$c_s'(x,t) = 1 - \text{erf}\left[\frac{1}{2} \times (DT)^{-1/2}\right] \quad [A\text{-}6]$$

where D is the diffusion coefficient of the reacting ion and "erf" is the error function (6)

$$\text{erf}\, x = 2\pi^{-1/2}\int_0^x \exp(-\zeta^2)\,d\zeta \quad [A\text{-}7]$$

Both Eq. [A-5] and [A-6] are related to the applicability of Duhamel's theorem. By Eq. [A-5], the initial condition on $c(x,t)$ changes from c^b to 0. Equation [A-6] is the solution to the infinite potential step problem. Transforming Eq. [A-2] according to Eq. [A-5], Duhamel's theorem yields

$$c'(x,t) = \int_0^t \frac{\partial c'}{\partial t}(0,\lambda) \cdot c_s'(x,t-\lambda)\,d\lambda \quad [A\text{-}8]$$

Since

$$i(t) = -n\mathbf{F}Dc^b\frac{\partial c'}{\partial x}(0,t) \quad [A\text{-}9]$$

we obtain

$$i(t) = -n\mathbf{F}Dc^b\int_0^t \frac{\partial c'}{\partial t}(0,\lambda) \cdot \frac{\partial c_s'}{\partial x}(0,t-\lambda)\,d\lambda$$

$$= -n\mathbf{F}(D/\pi)^{1/2}\int_0^t \frac{\partial c}{\partial t}(0,\lambda) \cdot (t-\lambda)^{-1/2}\,d\lambda \quad [A\text{-}10]$$

Equation [A-10] can be used directly for the computation of current density when combined with [A-2], [A-4a], or [A-4b].

As has been demonstrated for the case of LSV (2), the cathodic current i_c depends on $v^{1/2}$ and at. However, the quantity $i_c v^{-1/2}$ depends only on at. This property is the origin of the definition of current density functions for stationary electrodes. It should be noted that the corresponding quantity $(i_c/i_L)\sigma^{-1/2}$, for the RDE is still a function of the dimensionless sweep rate, σ, instead of $\sigma\tau$ or $\sigma\theta'$ alone (where τ and θ' are dimensionless t and θ, respectively). In order to emphasize that stationary electrode current density functions are defined differently than RDE functions, we represent them with the symbol I, instead of J (4). We can then write

$$I_c^l(at_c;a\theta) = i_c^l/(n\mathbf{F}D^{1/2}a^{1/2}c^b) \quad [A\text{-}11]$$

$$I_a^l(at_a;a\theta) = i_a^l/(n\mathbf{F}D^{1/2}a^{1/2}c^b) \quad [A\text{-}12]$$

where i_c^l is the current density measured during the $(l+1)$ cathodic sweep and i_a^l is the current density measured during the $(l+1)$ anodic sweep. Combination of Eq. [A-10] with [A-4a] or [A-4b] yields expressions for I_c^l and I_a^l in terms of the error function and Dawson's integral (6, 7) $F(x)$

$$F(x) = \exp(-x^2)\int_0^x \exp(\zeta^2)\,d\zeta \quad [A\text{-}13]$$

(i) single sweep CV; cathodic (also LSV) (2)

$$I_c^o(at_c) = 2\pi^{-1/2}F[(at_c)^{1/2}] \quad [A\text{-}14]$$

(ii) single sweep CV; anodic[1] (3)

$$I_a^o(at_a;a\theta) = 2\pi^{-1/2}\{F[(at_a+\theta)^{1/2}] - \exp(-a\theta)F[(at_a)^{1/2}]\} - \exp(-a\theta)\exp(at_a)\,\text{erf}\,[(at_a)^{1/2}] \quad [A\text{-}15]$$

(iii) multisweep CV; cathodic

$$I_c^l(at_c;a\theta) = 2\pi^{-1/2}F[(at_c)^{1/2}] - 2\pi^{-1/2}\sum_{n=1}^{l}\exp(-a\theta)\,F[(at_c+(2n-1)a\theta)^{1/2}] - F[(at_c+2na\theta)^{1/2}] + \sum_{n=1}^{l}\exp(at_c)\exp[(2n-2)a\theta]\{\text{erf}\,[(at_c+(2n-2)a\theta)^{1/2}] - \text{erf}\,[(at_c+(2n-1)a\theta)^{1/2}]\} \quad [A\text{-}16]$$

(iv) multisweep CV; anodic

$$I_a^l(at_a;a\theta) = -\exp(-a\theta)\exp(at_a)\,\text{erf}\,[(at_a)^{1/2}] - 2\pi^{-1/2}\sum_{n=0}^{l}\exp(-a\theta)F[(at_a+2na\theta)^{1/2}] - F[(at_a+(2n+1)a\theta)^{1/2}] + \sum_{n=1}^{l}\exp(at_a)\exp[(2n-1)a\theta]\{\text{erf}\,[(at_a+(2n-1)a\theta)^{1/2}] - \text{erf}\,[(at_a+2na\theta)^{1/2}]\} \quad [A\text{-}17]$$

Whereas Eq. [A-16] and [A-17] possess an l-independent limit as $a\theta \to \infty$, no closed form expression can be obtained for $l \to \infty$. The condition $a\theta \to \infty$ is similar to the condition $\theta' \to \infty$ in RDE theory, except that in the latter $\theta' \geq 1$ is sufficient to simulate infinity. Furthermore, $a\theta \to \infty$ is devoid of any physical sense because an infinite amount of charge would be consumed for the reversal overpotential to assume such high values. Mathematically, examining such a limiting behavior is not proper because the boundary condition, [A-1], is not satisfied. To demonstrate this, we examine the concentration profiles during the first cathodic sweep (LSV). Using Eq. [A-8] we obtain[2]

$$c_c^o(x,t)/c^b = \text{erf}\left[\frac{x}{2(Dt)^{1/2}}\right] + 1/2\exp\left(-\frac{x^2}{4Dt}\right)\left\{w\left[(at)^{1/2} + \frac{ix}{2(Dt)^{1/2}}\right] + w\left[-(at)^{1/2} + \frac{ix}{2(Dt)^{1/2}}\right]\right\} \quad [A\text{-}18]^3$$

from which it becomes obvious that expressions such as $x/(Dt)^{1/2}$ or x^2/Dt are indeterminate when both x and t tend to ∞. Similar arguments hold for $l \to \infty$

Letting $a\theta \to \infty$ in Eq. [A-16] and [A-17] we obtain

$$I_c(at_c;\infty) = 2\pi^{-1/2}F[(at_c)^{1/2}] - \exp(at_c)\{1 - \text{erf}\,[(at_c)^{1/2}]\} \quad [A\text{-}19]$$

$$I_a(at_a;\infty) = -\exp(-a\theta)\exp(at_a)\,\text{erf}\,[(at_a)^{1/2}] \quad [A\text{-}20]$$

Numerical evaluation of Eq. [16] and [17] has indicated that

$$I_c^l > I_c;\quad I_a^l > I_a \quad [A\text{-}21]$$

in other words, I_c and i_a are lower bounds for I_c^l and I_a^l, respectively. In addition

$$I_c^l < I_c^o \quad \text{and} \quad I_a^l < I_a^o \quad [A\text{-}22]$$

Since doubts exist about the physical interpretation of the limits of the current functions at infinite times (obtained by letting either $a\theta$ or l tend to ∞), it is more practical to investigate quasi-periodic behavior achieved when increasing l does not change the values of the current functions appreciably. Numerical in-

[1] This expression does not agree with the one reported in Ref. (3); in the latter, the multiplying factor for $F[(at_a)^{1/2}]$ is 1, rather than $\exp(-a\theta)$.

[2] For the definition of the function $w(z)$, see Ref. (6).

[3] $i = (-1)^{1/2}$ in this equation.

vestigations have shown that attainment of quasi-periodic behavior requires a larger number of cycles, l, as the reversal overpotential, $a\theta$, decreases.

One final point needs clarification: namely, that the hypothetical periodic state obtained by allowing $a\theta \to \infty$ is not identical to the one obtained for $l \to \infty$ but with finite $a\theta$. In the case of the cathodic current function, this can be demonstrated by examining the difference, ΔI_c^l, between I_c^l and I_c

$$\Delta I_c^l(at_c; a\theta) = I_c^l(at_c; a\theta) - I_c(at_c; \infty)$$
$$= \exp(at_c)\{1 - \text{erf}[(at_c + a\theta)^{1/2}]\}$$
$$+ \sum_{n=2}^{l} \exp(at_c) \exp[(2n-2)a\theta]\{\text{erf}[(at_c + (2n-2)a\theta)^{1/2}] - \text{erf}[(at_c + (2n-1)a\theta)^{1/2}]\}$$
$$- 2\pi^{-1/2} \sum_{n=1}^{l} \exp(-a\theta) F[(at_c + (2n-1)a\theta)^{1/2}] - F[(at_c + 2na\theta)^{1/2}]^4 \quad [A\text{-}23]$$

whereas $\Delta I_c^l(at_c; \infty) \to 0$ as expected, $\Delta I_c^{\infty}(at_c; a\theta) \neq 0$ in general and depends on the particular $a\theta$ value.

We end the section on current density functions by a discussion of some computational details. Expressions involving a dependence on l inside a series have been simplified by employing identities such as

$$\sum_{n=0}^{l} f(2l-2n-1)\, g(2l-2n) = \sum_{n=1}^{l} f(2n-1)\, g(2n) \quad [A\text{-}24]$$

where f and g are generally different functions of the argument. In several occasions, numerical evaluation of expressions such as

$$\exp(2na\theta)\{\text{erf}[(2na\theta)^{1/2}] - \text{erf}[((2n+1)a\theta)^{1/2}]\} \quad [A\text{-}25]$$

can be difficult, since it may involve multiplication of a very large with a very small number. This difficulty can be circumvented by using an asymptotic expansion (6, 8) of the error function for large arguments

$$\text{erf}\, x = 1 - \pi^{-1/2} \exp(-x^2)\left\{ x^{-1} + \sum_{j=1}^{\infty} (-1)^j [1.3\ldots(2j-1)]\, 2^{-j} x^{-2j-1} \right\} \quad [A\text{-}26]$$

The implications of the divergence of the series on the accuracy of the approximation are discussed in Ref. (8). It should be noted that Eq. [A-25] converges to 0 when either n or $a\theta$ tend to ∞. This can be shown by applying de l'Hôpital's rule.

Charge Density Functions

The charge q_c^l associated with the $(l+1)$ cathodic current wave (not a cumulative quantity) is

$$q_c^l = \int_0^{\theta} i_c^l\, dt_c \quad [A\text{-}27]$$

A similar expression can be written down for q_a^l. In view of Eq. [A-11] an obvious change of variable yields

$$Q_c^l(a\theta) = q_c^l/(n\mathbf{F}D^{1/2}a^{-1/2}c^b) = \int_0^{a\theta} I_c^l(atc; a\theta)\, d(at_c) \quad [A\text{-}28]$$

and, for anodic waves

$$Q_a^l(a\theta) = q_a^l/(n\mathbf{F}D^{1/2}a^{-1/2}c^b) = \int_0^{a\theta} I_a^l(at_a; a\theta)\, d(at_a) \quad [A\text{-}29]$$

[4] For $l = 1$, the series beginning with $n = 2$ is set equal to 0.

As in the case of $i^l v^{-1/2}$, the quantity $q^l v^{1/2}$ is independent of v and depends on $a\theta$ alone. It seems natural then to chose Q's as the charge density functions. Since charge densities in RDE models are defined differently, the symbol Q (rather than R) has been chosen to refer to stationary electrodes. The net charge contribution to the $(l+1)$ cycle, can be related to the net charge density function

$$Q_n^l(a\theta) = Q_c^l(a\theta) + Q_a^l(a\theta) \quad [A\text{-}30]$$

As noted previously, positive values for Q's indicate the net formation of a deposit. Expressions for the charge density functions are obtained from Eq. [A-28] and [A-29]:

(i) multisweep CV; cathodic

$$Q_c^l(a\theta) = -2\pi^{-1/2} F[(a\theta)^{1/2}] + 2\pi^{-1/2}(a\theta)^{1/2}[(2l+1)^{1/2} - (2l)^{1/2}]$$
$$- 2\pi^{-1/2} \sum_{n=1}^{l} F[((2n+1)a\theta)^{1/2}] - [1 + \exp(-a\theta)]\, F[(2na\theta)^{1/2}] + \exp(-a\theta)\, F[((2n-1)a\theta)^{1/2}]$$
$$+ \sum_{n=1}^{l} \exp[(2n-1)a\theta]\{\text{erf}[((2n-1)a\theta)^{1/2}] - \text{erf}[(2na\theta)^{1/2}]\} - \exp[(2n-2)a\theta]$$
$$\{\text{erf}[((2n-2)a\theta)^{1/2}] - \text{erf}[((2n-1)a\theta)^{1/2}]\} \quad [A\text{-}31]$$

(ii) multisweep CV; anodic

$$Q_a^l(a\theta) = -\text{erf}[(a\theta)^{1/2}] + 2\pi^{-1/2}(a\theta)^{1/2}[(2l+2)^{1/2} - (2l+1)^{1/2}]$$
$$- 2\pi^{-1/2} \sum_{n=0}^{l} F[((2n+2)a\theta)^{1/2}] - [1 + \exp(-a\theta)]\, F[((2n+1)a\theta)^{1/2}] + \exp(-a\theta)\, F[(2na\theta)^{1/2}]$$
$$+ \sum_{n=1}^{l} \exp(2na\theta)\{\text{erf}[(2na\theta)^{1/2}] - \text{erf}[((2n+1)a\theta)^{1/2}]\} + \exp[(2n-1)a\theta]$$
$$\{\text{erf}[((2n-1)a\theta)^{1/2}] - \text{erf}[(2na\theta)^{1/2}]\} \quad [A\text{-}32]$$

(iii) multisweep CV; net

$$Q_n^l(a\theta) = 2\pi^{-1/2}(a\theta)^{1/2}[(2l+2)^{1/2} - (2l)^{1/2}] - 2\pi^{-1/2}\{F[((2l+2)a\theta)^{1/2}] - \exp(-a\theta)\, F[((2l+1)a\theta)^{1/2}]\} + \exp(2la\theta)$$
$$\{\text{erf}[(2la\theta)^{1/2}] - \text{erf}[((2l+1)a\theta)^{1/2}]\} \quad [A\text{-}33]$$

For very large $a\theta$ values, the dependence of Q_c^l and Q_a^l on l and $a\theta$ is as follows

$$Q_c^l = 1 + 2\pi^{-1/2}(a\theta)^{1/2}[(2l+1)^{1/2} - (2l)^{1/2}] \quad [A\text{-}34]$$
$$Q_a^l = 1 + 2\pi^{-1/2}(a\theta)^{1/2}[(2l+2)^{1/2} - (2l+1)^{1/2}] \quad [A\text{-}35]$$

whereas integration of Eq. [A-19] and [A-20] yields

$$Q_c(\infty) = 1 \quad [A\text{-}36]$$
$$Q_a(\infty) = -1 \quad [A\text{-}37]$$

Since l and $a\theta$ can be varied independently, Eq. [A-34] and [A-35] can be made to converge to Eq. [A-36] and [A-37] irrespective of how high the value of $a\theta$ is. It is concluded then that for increasing values of $a\theta$, a larger number of cycles is necessary for the attainment of periodic behavior for the charge functions. This is contrary to the behavior of current functions and is probably due to the fact that small variations in the current cause greater variations in the charge with increasing $a\theta$, since the charge is the integral of the current over the total $a\theta$ range.

For the hypothetical periodic states, it should be noted that

$$Q_n(\infty) = 0; \quad Q_n{}^{\infty}(a\theta) = 0 \qquad [A\text{-}38]$$

indicating that for these cases, no net charge is dissolved or deposited during the passage of a complete cycle.

LIST OF SYMBOLS

a defined by Eq. [1]
$a\theta$ dimensionless reversal overpotential
at_a dimensionless overpotential into an anodic sweep
at_c dimensionless overpotential into a cathodic sweep
$(at_c)_{max}$ value of at_c at the maximum of the periodic current density function at infinite reversal overpotential, Eq. [13]
$(at_c)_{max}{}^{o}$ value of at_c at the maximum of the LSV current density function, Eq. [12]
A constant defined by Eq. [16]
B constant defined by Eq. [20]
c concentration
c′ dimensionless concentration defined by Eq. [A-5]
c^b bulk concentration
c_s' dimensionless concentration obtained when an infinite potential step is applied to a planar electrode, Eq. [A-6]
$c_c{}^{o}$ concentration during LSV sweep, Eq. [A-18]
D diffusion coefficient
i current density
I_a periodic anodic current density function at infinite reversal overpotential, Eq. [A-20]
I_c periodic cathodic current density function at infinite reversal overpotential, Eq. [A-19]
$I_a{}^{o}$ current density function during the first anodic sweep, Eq. [A-15]
$I_c{}^{o}$ LSV current density function, Eq. [A-14]
$I_a{}^{l}$ current density function during the $(l+1)$ anodic sweep, Eq. [A-17]
$I_c{}^{l}$ current density function during the $(l+1)$ cathodic sweep, Eq. [A-16]
$I_{c,max}$ maximum value of I_c
$I_{c,max}{}^{o}$ maximum value of $I_c{}^{o}$
l number of applied complete potential cycles
Q_a anodic charge density function at infinite reversal overpotential, Eq. [A-37]
Q_c cathodic charge density function at infinite reversal overpotential, Eq. [A-36]
Q_n net charge density function at infinite reversal overpotential, Eq. [A-38]
$Q_n{}^{\infty}$ net charge density function after an infinite number of cycles, Eq. [A-38]
$Q_a{}^{l}$ charge density function during the $(l+1)$ anodic sweep, Eq. [A-32]
$Q_c{}^{l}$ charge density function during the $(l+1)$ cathodic sweep, Eq. [A-31]
$Q_n{}^{l}$ net charge density function during the complete $(l+1)$ sweep, Eq. [A-33]
t time
t_a time into an anodic sweep, Eq. [2b]
t_c time into a cathodic sweep, Eq. [2a]
v sweep rate
θ reversal time
λ dummy variable of integration

REFERENCES

1. H. Matsuda, *Z. Elektrochem.*, **61,** 489 (1957).
2. T. Berzins and P. Delahay, *J. Am. Chem. Soc.*, **75,** 555 (1953).
3. N. White and F. Lawson, *J. Electroanal. Chem.*, **25,** 409 (1970).
4. P. C. Andricacos and P. N. Ross, Jr., *This Journal*, **130,** 1340 (1983).
5. W. H. Reinmuth, *Anal. Chem.*, **34,** 1446 (1962).
6. M. Abramowitz and I. A. Stegun, "Handbook of Mathematical Functions," NBS, Washington, DC (1964).
7. W. Lash Miller and A. R. Gordon, *J. Phys. Chem.*, **35,** 2785 (1931).
8. H. S. Carslaw and J. C. Jaeger, "Conduction of Heat in Solids," 2nd ed., Oxford, England (1959).

Molecular Oxygen Electroreduction at Pt and Au Electrodes in Acetonitrile Solutions

T. A. Lorenzola, B. A. López, and M. C. Giordano*

Departamento de Físico Química, Facultad de Ciencias Químicas, Universidad Nacional de Córdoba, Estafeta 32,5000 Córdoba, Argentina

ABSTRACT

Molecular oxygen electroreduction at both Pt and Au electrodes in acetonitrile solutions was studied by RDE and cyclic voltammetry techniques. Hydrogen peroxide was detected as the main reaction product on Pt as well as on Au electrodes. Molecular oxygen dissociative adsorption is inhibited by the organic solvent which produces a leveling effect of metal catalytic properties. Results obtained by cyclic voltammetry allowed the interpretation of the electrochemical process as a reversible single electron transfer to give O_2^-, followed by the disproportionation of superoxide ion that in the presence of residual water could account for hydrogen peroxide formation. The disproportionation constant was evaluated, its value being of the order of 10^5 M sec^{-1}. These results were further confirmed by the experiments performed at the RDE.

Molecular oxygen electroreduction is one of the classical problems in electrochemistry mainly in aqueous solutions. Much less is known about O_2 behavior in organic solvents, where most of the studies have been performed at mercury electrodes. Some of the early studies on O_2 electroreduction in organic solvents, acetonitrile, dimethylsulfoxide, and N-methylacetamide (1-3) have shown that the reduction process proceeds through two consecutive polarographic waves whose half-wave potentials occur at more cathodic values than in aqueous solutions. The first wave was attributed to the electroreduction of O_2 to H_2O_2 with further reduction of H_2O_2 to HO^- during the second wave.

Further work on the subject demonstrated that the first wave behaves in a quasi-reversible way while the second one as an irreversible process (4-9). Some authors agree that the redox couple O_2/O_2^- is reversible in some organic solvents (5), and the stability of O_2^- ion in the absence of hydrogen ions has been used for carrying many reactions with a variety of organic substrates in dimethylsulfoxide (10-13). Conversely, if hydrogen ions are present, the product at the first wave is HO_2^- ion or H_2O_2 produced by similar mechanisms as in aqueous solutions (14-18). Since most of the work on molecular oxygen electroreduction in

* Electrochemical Society Active Member.
Key words: chemisorption, reduction, solvents, voltammetry.

organic solvents has been performed in dimethylsulfoxide and dimethylformamide, it is interesting to compare the behavior of this electrochemical reaction in another inert aprotic solvent with a very low reactivity as acetonitrile in order to compare results with those in aqueous solutions.

Experimental

The solvent, acetonitrile (MeCN) Carlo Erba RP, was carefully purified as described elsewhere (19-21). Special precautions were taken in handling the solutions since molecular oxygen reduction at solid electrodes is strongly affected by soluble impurities and electrode surface state.

Ethylammonium perchlorate 0.1M was mainly used as the supporting electrolyte. Some experiments were performed with butylammonium iodide only for comparison. All chemicals were analytical grade reagents dried under vacuum for 48 hr before use.

Molecular oxygen was bubbled directly into the cell in order to obtain a saturated solution. Before entering the cell, oxygen (99.98%) was passed through a trap containing pure MeCN. The oxygen saturation value at 25°C in 0.1M Et_4NClO_4 in MeCN, determined by potentiometric titration (22), was 2.7 mM. Oxygen gas was flowed over the solution during cv and RDE experiments to keep constant its concentration on the solution.

Two different electrolysis cells were used. The electrolysis cell for cv and RDE experiments was a conventional one-compartment Pyrex glass container of about 100 ml capacity provided with standard glass joints for the working, the counter, and the reference electrodes and gas inlet and outlet. The second cell was a three-compartment glass container and it was used for constant potential electrolysis experiments. All joints were lubricated with high temperature Halocarbon grease and special precautions were taken to avoid solution or electrode contamination.

The working electrodes used in cv and RDE experiments were either Pt or Au (Koch-Light 99.999%) disks of 3 mm diam mounted in Teflon holders. The rotating disk electrode ensemble has been previously described (21, 23). Both Pt and Au electrodes were mirror polished with cerium oxide and then carefully rinsed with triply distilled water, acetone, and acetonitrile. Also an H_2SO_4:HNO_3 mixture was used mainly with Pt electrodes immediately after polishing. A Pt net of about 700 cm^2 was used for constant potential electrolysis experiments.

The auxiliary electrodes were Pt foils of about 4 and 6 cm^2, and the reference electrode was an aqueous saturated calomel electrode immersed in a glass tube provided at the bottom with a glass joint and filled with a solution of 0.1M Et_4NClO_4 in MeCN. The whole ensemble was placed in the cell through a Luggin capillary arrangement.

The reference electrode gave a pseudo ohmic resistance of about 90Ω. This value was electronically compensated all through the experiments. Measured potentials are referred to the SCE scale.

Current-potential curves were obtained either under steady-state conditions at the RDE or using transient techniques, as cyclic voltammetry and chronopotentiometry. Also constant potential coulometry was performed to study the number of electrons involved in the process and the final electrolysis product.

Results

Figure 1 shows polarization curves for oxygen electroreduction in 0.1M Et_4NClO_4 in MeCN solutions at Pt and Au electrodes. Only one limiting current (i_L) was observed in the potential range from 0 to −2.0V which increases with the electrode rotation speed (w), Fig. 2. The half-wave potentials at $w = 0$ were −1.08 and −0.945V for Pt and Au electrodes, respectively.

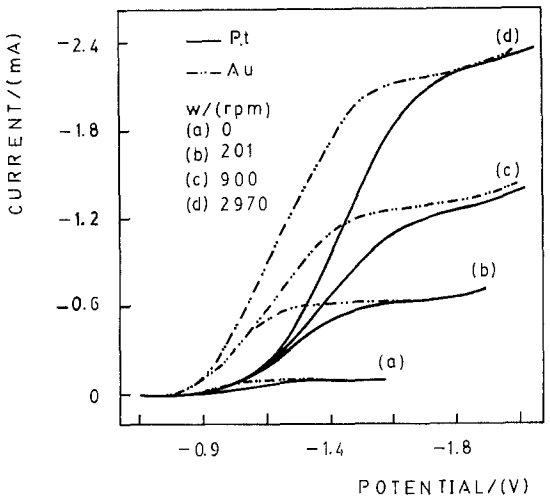

Fig. 1. Polarization curves for O_2 electroreduction at various rotation rates. Electrode area, 0.07 cm^2; temperature, 25.0°C.

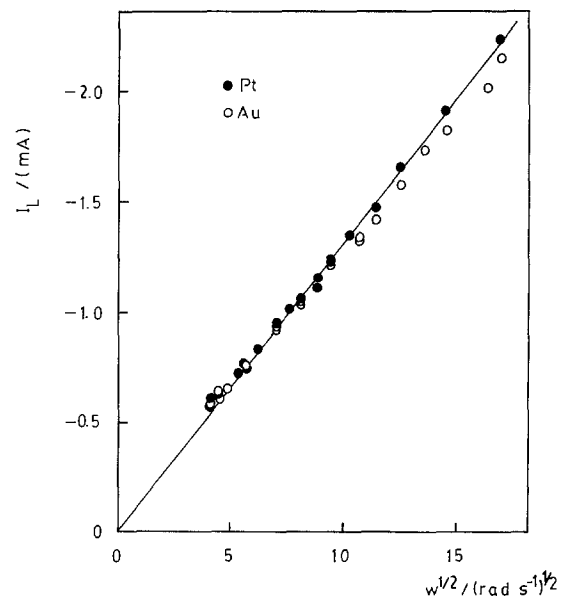

Fig. 2. Plot of I_L vs. $w^{1/2}$

The current observed after 3 hr under constant potential electrolysis at −1.0V at Pt electrodes showed only a 50% decay of its initial value. Thus the apparent number of electrons involved in the redox reaction could not be evaluated by this technique. Only hydrogen peroxide was detected by u.v. spectroscopy at 230 nm (24) and by chemical product analysis in the bulk of the solution. Even after 24 hr the electrolysis had been interrupted indicating the stability of the compound in MeCN solutions.

First cycle voltammograms performed at different potential sweep rates (v) on Pt electrodes, Fig. 3, showed a cathodic current peak around −1.2V in the negative going sweep and an anodic current peak near −0.6V on the positive sweep, depending on sweep rate values. This behavior was observed at sweep rates greater than 0.01V sec^{-1}; for slower sweeps, a cathodic limiting current was obtained as under steady-state conditions.

The potential difference between cathodic and anodic current peak (ΔE_p) of about 0.6V was considerably greater than the $0.058/n$ volt difference for a reversible reaction (25), this being an indication of some chemical process related to the product reoxidation.

Results obtained at Au electrodes, Fig. 4, showed the same general features as those reported for Pt, but

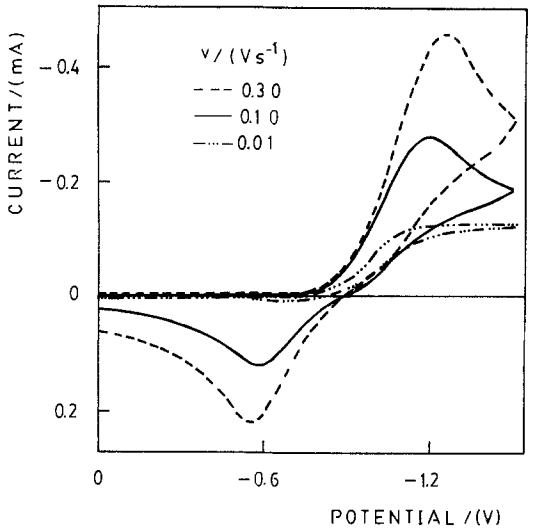

Fig. 3. Voltammograms for O_2 electroreduction at Pt at different sweep rates.

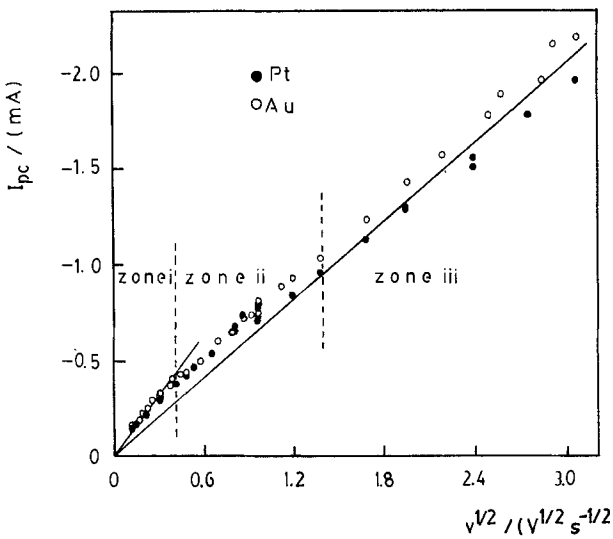

Fig. 5. Dependence of I_{pc} with $v^{1/2}$

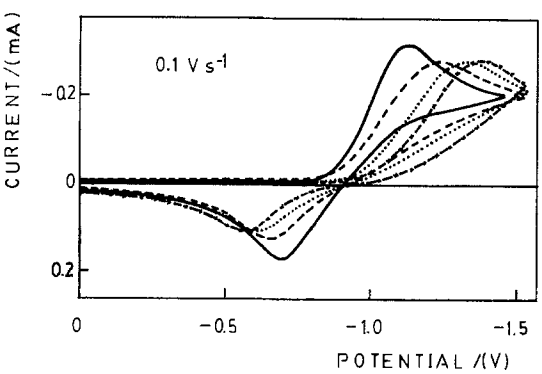

Fig. 4. Voltammograms for O_2 electroreduction at Au and Pt showing the electrode pretreatment effect. (a) —— Au; (b) Pt electrode pretreated with H_2SO_4 HNO_3: --- first cycle; ... repetitive cycles; —x— Pt electrode without H_2SO_4 HNO_3 pretreatment.

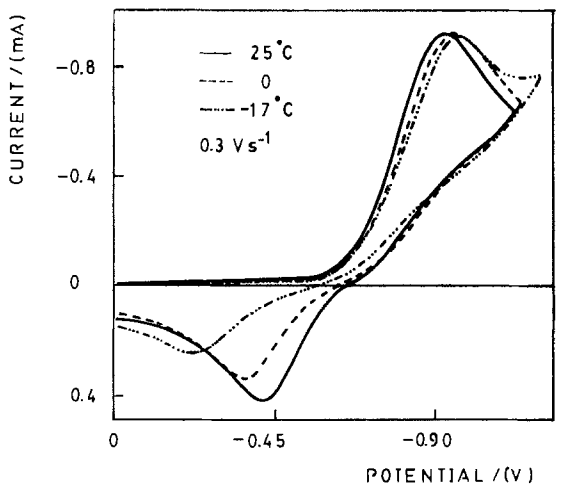

Fig. 6. Effect of temperature on the O_2 electroreduction at Pt

the cathodic peak potential was more positive and a smaller ΔE_p was observed.

Electrode pretreatment showed some effect on the *I/E* profiles mainly with Pt electrodes, Fig. 4. Voltammograms obtained after repetitive cycling at Pt resembled potentiodynamic profiles obtained with polished electrodes without chemical treatment with H_2SO_4:HNO_3 mixture, while repetitive cycling at Au electrodes gave coincident voltammograms. In any case oxygen electroreduction behaved more reversibly at Au than at Pt electrodes.

In Fig. 5 cathodic current peak values (I_{pc}) are plotted against the square root of potential sweep rate ($v^{1/2}$) for both electrodes. A departure from the linear behavior for a simple diffusion process is observed at intermediate v values.

The effect of the temperature on the cv is shown in Fig. 6. A decrease of about 40°C produced small modifications on the cathodic process while the anodic current was considerably diminished and its peak potential shifted toward more positive values.

Cyclic voltammograms performed with solutions previously electrolyzed for 3 hr at −1.0V showed a considerable decrease of the cathodic current but no appreciable change in the peak shape. Nevertheless, the most remarkable feature was obtained on the positive going sweep since no anodic current peak was evident irrespective of the sweep rate employed, indicating that hydrogen peroxide (the electrolysis product) is electrochemically inactive in this potential region.

The replacement of Et_4NClO_4 by Bu_4NI as supporting electrolyte only for comparison, Fig. 7, produced a better definition on the cathodic current peak but cleared away the anodic process probably through a chemical reaction between iodide and the anodic re-

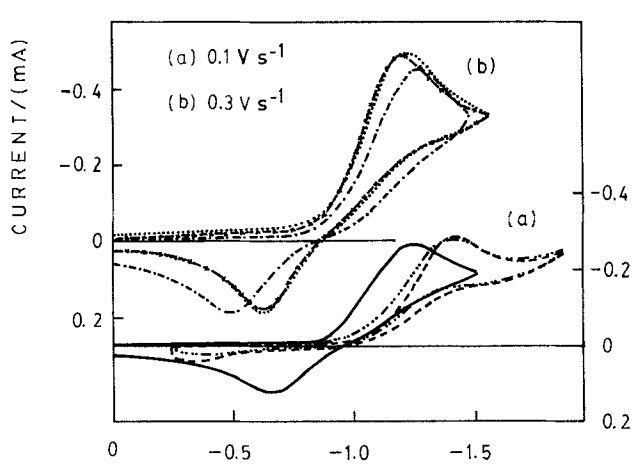

Fig. 7. Voltammograms showing the effect of the supporting electrolyte and basic substances on O_2 electroreduction at Pt. (a) Supporting electrolyte: —— Et_4NClO_4; --- B_4NI; — ··· — B_4NI + 0.16M collidine. (b) Supporting electrolyte, Et_4NClO_4: — · — without pyridine; ... 0.01M pyridine; —x— 0.1M pyridine.

actant. Addition of substances with basic properties, such as pyridine and collidine, produced a better definition on both cathodic and anodic current peaks and also a decrease on ΔE_p but they did not modify substantially the general features obtained in neutral solutions.

Addition of increasing amounts of water anodically shifted the cathodic peak potential and produced a considerable increase in current, almost doubling the value without water, but the anodic current peak was completely suppressed, Fig. 8. The increase of the acidity of the solution by $HClO_4$ acid produced qualitatively a similar effect.

Finally, galvanostatic E/t experiments were also performed. As with voltammetry, only one cathodic and one reverse transition time were obtained irrespective of constant current values employed.

Discussion

It is already well known that oxygen electroreduction in aqueous solutions is a rather complex multielectron reaction that may include a number of elementary steps forming various parallel-consecutive combinations (26-28). Intermediate H_2O_2 formation through a two-electron transfer reaction is the main pathway at mercury, pyrographite, other types of carbon materials, and gold (29, 30). The polarization curves are characterized by two waves, the first one corresponds to oxygen reduction to H_2O_2 and the second to hydrogen peroxide reduction at high overpotentials. In some cases the second wave is very difficult to detect because this process is extremely irreversible. On the other hand, on platinum family metals and silver (31, 32), oxygen electroreduction occurs both directly to water and to H_2O_2 through a parallel reaction, which decomposes by chemical or electrochemical mechanism. The polarization curves are characterized by a single wave with a limiting current closely related to a four-electron process. Electrode pretreatment, impurities, and different strongly adsorbed species inhibit the reduction of molecular oxygen directly to water while the reaction yielding intermediate formation of hydrogen peroxide is less affected. The different results reported in aqueous solutions allowed the distinction between two groups of electrode materials toward oxygen electroreduction. The simplest interpretation was the need for sites with high bonding energy for the dissociative chemiadsorption of molecular oxygen to give water (27, 31). Strongly bonded species could also interact with the same sites.

Representative materials of both groups, gold and platinum electrodes in acetonitrile solutions, were employed in this work and the main facts are the following: (*i*) The rest potential in oxygen-saturated solutions before electrolysis is close to 0.6V (SCE) and independent of electrode material. (*ii*) Only one limiting current appears at both platinum and gold electrodes.

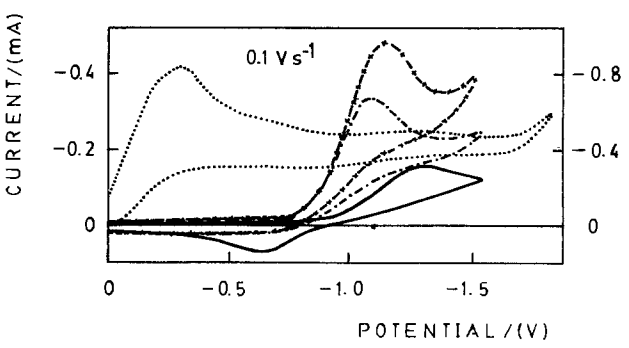

Fig. 8. Effect of H_2O and $HClO_4$ addition on the voltammograms for O_2 electroreduction at Pt in MeCN. —— Purified acetonitrile; — · — 0.1M H_2O; —x— 10^{-4}M $HClO_4$; ... 10^{-2}M $HClO_4$ (current scale on the right).

(*iii*) Half-wave potentials are similar. (*iv*) Hydrogen peroxide is detected in the bulk of the solution as the main reaction product in both cases. The similar results obtained with both types of material in MeCN solutions would indicate that the main factor responsible for the decrease of platinum electrode activity toward oxygen dissociative adsorption is the competition with the organic molecule adsorption on the metal surface (34, 35). This process would inhibit the oxygen to water pathway at Pt electrodes, producing a leveling effect between Pt and Au.

The kinetic analysis of the polarization curves at $w = 0$ gave Tafel slopes of 0.15 and 0.13 V/decade for Pt and Au electrodes, respectively. Higher values were obtained as electrode rotation speed was increased. Therefore an interpretation of reaction mechanism from these values was not pursued.

Taking into account the complexity of molecular oxygen electroreduction, the fact that $I_{pc}/v^{1/2}$ ratio at the fastest sweep rates is 1.5 times that at the lowest sweep rates and that the (I_{pc}/I_{pa}) ratio reaches a value around 1.7 at the highest sweep rates, first-order catalytic, ECE and parallel reaction mechanisms were analyzed (25). It was not possible to find a good coincidence between theoretical predictions and experimental results.

Assuming that the product for the first-electron transfer is O_2^- species, the chemical reaction that would come into play within the overall process to account for hydrogen peroxide final product could be a protonation or/and a dismutation, as has been postulated for oxygen electroreduction in organic solvents (18)

$$O_2 + 1e \rightleftharpoons O_2^- \qquad [1]$$

[I] [II]

$O_2^- + BH \rightarrow O_2H + B^-$ [2, I] $\quad 2\,O_2^- \rightarrow O_2 + O_2^=$ [2, II]

$O_2H + 1e \rightarrow HO_2^-$ [3, I] $\quad O_2^= + BH \rightarrow HO_2^- + B^-$ [3, II]

where BH is a proton donor in general terms. Mechanism [I] is an ECE mechanism with O_2H species more easily reducible than O_2, while mechanism [II] is a disproportionation providing a very fast [3, II] reaction as would be the case.

The route followed by O_2^- would strongly depend on its basic character toward different substances present in the solution. This property would also depend on the solvation energy provided by the aprotic solvent. Thus in the absence of a strong proton donor a mechanism such as [II] will be predominant in aprotic solvents with rather low solvation energy toward O_2^- ion.

Following this line a better interpretation of experimental results obtained from cv was attempted. In a first approximation the plot for the dependence of the cathodic current peak with $v^{1/2}$ could be divided in three different regions, Fig. 5: (*i*) a zone where the peak current is proportional to the square root of sweep rate, (*ii*) an intermediate zone where the peak current varies more slowly with sweep rate, and (*iii*) a third zone where I_{pc} varies again linearly with $v^{1/2}$.

Figure 9 shows the cathodic peak potential variation with sweep rate. A small dependence is found at low sweep rates, a greater variation is obtained for intermediate values, and finally over 3V sec^{-1} the peak potential remains almost independent of v.

From the dependence of I_{pc} on $v^{1/2}$ at low sweep rates [zone (*i*)], the diffusion coefficient of molecular oxygen in MeCN solution was evaluated by using the following equation for a disproportionation mechanism (36, 37)

$$I_{pc} = 0.634n^{3/2}D^{1/2}C^{\circ}v^{1/2} \qquad [4]$$

where n is the number of electrons exchanged; D is the

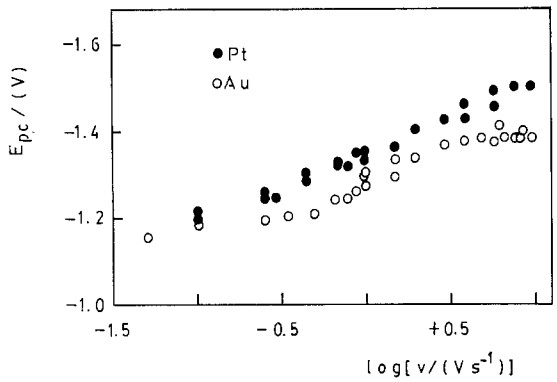

Fig. 9. Plot of E_{pc} vs. log v

diffusion coefficient in cm^2 sec^{-1}; C° is the molar concentration in the bulk of the solution, and v is the potential sweep rate in V sec^{-1}.

The value of D obtained for oxygen at 25°C was 5.74×10^{-5} cm^2 sec^{-1} in very good agreement with previous results (1, 17, 22, 38). With this figure a theoretical diffusional current peak for the single charge transfer reaction [I] was evaluated. From the ratio of experimental current peak values in zone (ii) and diffusional theoretical values the disproportionation rate constant k_D was evaluated (reaction [2, II]) or ([2, II] + [3, II]). Data for two different temperatures are compiled in Table I. The apparent activation energy calculated from these values averages 3.5 ± 1 kcal mol^{-1} and it is independent of the type of metal used. This rather low value is on the order of magnitude found for reactions in solution under chemical control. It seems reasonable to suppose that disproportionation reaction takes place on a reaction layer near by the electrode surface but probably with neither surface participation nor diffusion control of reacting species.

The same analysis performed for the ECE mechanism with catalytic complications (36, 37) gives current function values that were about half the values corresponding to the theoretical working curve.

A further test for the disproportionation mechanism can be made analyzing the variation of the cathodic peak potential and the wave shape function ($E_{pc} - E_{pc/2}$), with the kinetic parameter $\lambda_D = k_D C^\circ RT/nFv$ (36). Figure 10 shows the dependence of E_{pc} on log v^{-1} while in Fig. 11 the variation of ($E_{pc} - E_{pc/2}$) is shown. The experimental values of potential sweep rate and molecular oxygen concentration covered a log λ_D range from 0.8 to 3.8. A good agreement between the experimental and the theoretical curves are obtained within the kinetic parameter variation allowed by the conditions of a gas solution in an organic solvent.

The assumptions made in the analysis of cyclic voltammetry results in relation to the nature of the chemical reaction following the electron transfer reaction can be confirmed by the results under steady-state conditions at the RDE. In this case, the rate for disproportionation reaction is reflected as an increase on the experimental limiting current value over the theoretical one related to a simple two-electron diffusion-controlled reaction

$$O_2 + BH + 2e \rightleftharpoons HO_2^- + B^- \qquad [5]$$

The theoretical solution to the problem (39, 40) enabled the rate constant for the disproportionation reaction to be calculated from tabulated values of the parameter J vs. K. The parameter J is defined by

$$J = (I_L - I_d)/I_d \qquad [6]$$

where I_d is the theoretical diffusion-controlled current without molecular oxygen regeneration and I_L is the experimental limiting current. K is given by

Table I. Disproportionation rate constant values at Pt and Au electrodes obtained by cyclic voltammetry and rotating disk electrode experiments

v (V sec^{-1})	k_D Pt, 25.0°C × 10^{-5}* (M^{-1} sec^{-1})	k_D Au, 25.0°C × 10^{-5}† (M^{-1} sec^{-1})	k_D Pt, −17.0°C × 10^{-5} (M^{-1} sec^{-1})
0.25	5.8	—	—
0.30	5.8	7.88	0.84
0.45	2.26	—	—
0.65	—	3.17	—
0.70	3.96	—	1.49
0.80	—	4.39	0.84
0.90	3.68	2.16	—
1.0	3.25	5.34	0.62
2.0	1.71	2.49	0.70
3.0	1.55	3.15	0.93
4.0	—	5.02	1.05
6.0	2.96	5.72	—
8.0	3.70	5.57	—
10.0	4.06	5.49	—
$w^{1/2}$ (rad$^{1/2}$ sec$^{-1/2}$)			
4.6	0.85	0.85	
7.2	1.22	0.96	
7.7	1.16	—	
8.3	0.87	0.87	
9.7	1.19	1.02	
11.7	1.60	1.04	
16.8	—	1.08	

* k_D for Pt at 25.0°C by cv = 2.54×10^5 M^{-1} sec^{-1} by RDE 1.18×10^5 M^{-1} sec^{-1}.
† k_D for Au at 25.0°C by cv = 3.90×10^5 M^{-1} sec^{-1} by RDE 1.23×10^5 M^{-1} sec^{-1}.

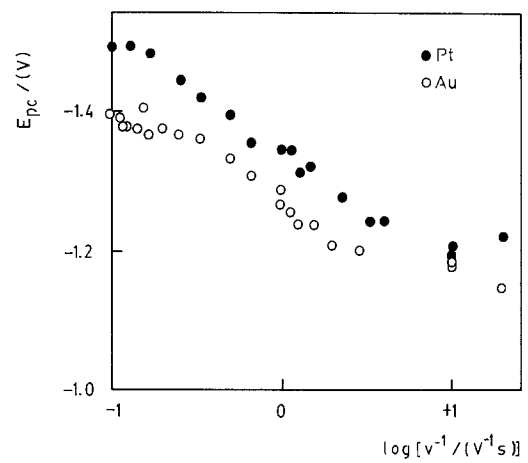

Fig. 10. Plot of E_{pc} vs. log v^{-1}

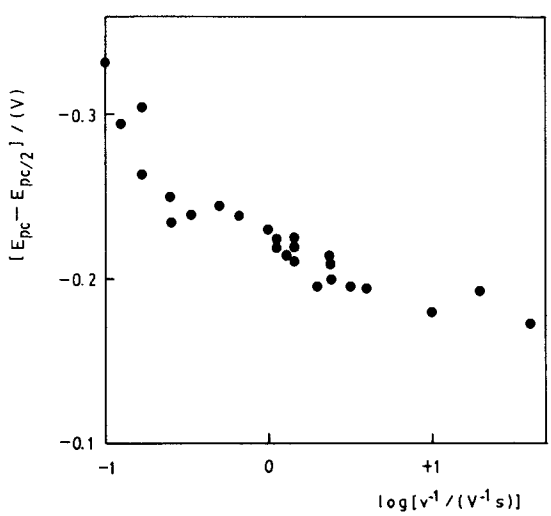

Fig. 11. Plot of [$E_{pc} - E_{pc/2}$] vs. log v^{-1}

$$K = 2k_D C^\circ (\nu/D)^{1/3}/(0.51)^{2/3} w \quad [7]$$

where k_D is the disproportionation rate constant, C° is the analytical concentration for O_2, ν is the kinematic viscosity, D is the diffusion coefficient for electroactive species, and w is the angular velocity of the RDE. The tabulated values of K are available up to $J = 0.560$. For higher values of J an approximate relation can ge used

$$K = 1.809\ (I + J)^2/(I - J)^3 \quad [8]$$

The figures obtained for the disproportionation rate constant with the RDE are included in Table I, showing good agreement with results obtained by cyclic voltammetry.

Experiments performed with the addition of increasing amounts of water showed that for a water content of about 10^{-2}M (ten times greater than the residual water) the modifications introduced in the voltammogram were not significant. For a water content of about 0.1M the cathodic peak current was doubled, the reduction peak potential was shifted anodically, and the O_2^- oxidation peak disappeared, being an indication that the initial one-electron reaction

$$O_2 + e \rightleftharpoons O_2^- \quad [9]$$

was changed to a two-electron reduction to peroxide as observed in aqueous solution

$$O_2 + H_2O + 2e \rightarrow HO_2^- + OH^- \quad [10]$$

Thus residual water content in the highly purified MeCN seems not to be enough as a proton donor mainly due to the lower basicity showed by the O_2^- ion in this aprotic solvent. The increase in basicity and stability of O_2^- ion by changing the aprotic solvent (41) would account for a greater stability of O_2^- ion and hence for a decrease on ΔE_p in going from MeCN > DMF > DMSO > HMPA (42). In this respect the physical chemical properties of the aprotic solvent, where residual water is very difficult to avoid, could change the route followed by the O_2^- solvated ion (43).

Proton addition as $HClO_4$ acid in the order of 10^{-4}M produced a still greater increase in reduction current (about three times) and the clearance of the oxidation peak. The lack of an O_2^- oxidation peak in the acidic medium would indicate that O_2^- is rapidly destroyed by a chemical reaction with protons, rendering O_2^- species quite unstable. In this case the reaction for oxygen electroreduction is likely to be replaced by

$$O_2 + 2H^+ + 2e \rightarrow O_2H_2 \quad [11]$$

Conclusion

Molecular oxygen electroreduction at Pt and Au electrodes in acetonitrile solutions resembles in principle the behavior observed in other organic solvents as dimethylsulfoxide and dimethylformamide. Differences in half-wave potential or half-peak potential between solvents could be related to differences in adsorption energy for the aprotic solvent at the metal surface and also to the different O_2^- ion solvation. The organic solvent molecule adsorption at the interface would produce a leveling effect toward catalytic activity of different metals in relation to molecular oxygen dissociative adsorption. These effects would be responsible for superoxide ion variable stability in organic solutions with low availability of protons.

Particularly in highly purified acetonitrile solutions without addition of water or acidic substances the results obtained by different experimental techniques would agree with a disproportionation mechanism with a reversible one-electron exchange in the first step to give O_2^-.

Addition of different amounts of water or protons to the aprotic solutions would change the route for the chemical reaction following the charge transfer reaction resembling the behavior observed for molecular oxygen electroreduction in alkali and acid aqueous solutions with metals of low activity for oxygen dissociation as gold (29).

Acknowledgment

This work was in part supported by the Consejo Nacional de Investigaciones Científicas y Técnicas of Argentina. The authors would like to acknowledge one of the reviewers of this paper because his concise report helped us considerably to improve it.

Manuscript submitted April 8, 1982; revised manuscript received *ca.* Sept. 20, 1982.

Any discussion of this paper will appear in a Discussion Section to be published in the December 1983 JOURNAL. All discussions for the December 1983 Discussion Section should be submitted by Aug. 1, 1983.

REFERENCES

1. J. F. Coetzee and J. M. Kolthoff, *J. Am. Chem. Soc.*, **79**, 6110 (1957).
2. J. M. Kolthoff and T. B. Reddy, *This Journal*, **108**, 980 (1961).
3. L. A. Knecht and I. M. Kolthoff, *Inorg. Chem.*, **1**, 195 (1962).
4. D. L. Maricle and W. G. Hodgson, *Anal. Chem.*, **37**, 1562 (1965).
5. M. E. Peover and B. S. White, *Electrochim. Acta*, **11**, 1061 (1966).
6. E. L. Johnson, K. H. Pool, and R. E. Hamm, *Anal. Chem.*, **38**, 183 (1966).
7. A. D. Goolsby and D. T. Sawyer, *ibid.*, **40**, 83 (1968).
8. L. N. Nekarasov, L. A. Dukhanova, N. I. Dubrovina, and L. N. Vykhodtseva, *Electrokhimiya*, **6**, 388 (1970).
9. T. Fujinaga and S. Sakura, *Bull. Chem. Soc. Jpn.*, **47**, 2781 (1974).
10. R. Dietz, A. E. J. Forno, B. E. Larcombe, and M. E. Peover, *J. Chem. Soc. (B)*, **5**, 816 (1970).
11. D. T. Sawyer, M. J. Gibian, M. M. Morrison, and E. T. Seo, *J. Am. Chem. Soc.*, **100**, 627 (1978).
12. F. Magno, G. Bontempelli, and M. M. Andreuzzi Sedea, *J. Electroanal. Chem. Interfacial Electrochem.*, **97**, 85 (1979).
13. C. L. Hussey, T. M. Laher, and J. M. Achord, *This Journal*, **127**, 1484 (1980).
14. F. Rallo and L. Rampazzo, *J. Electroanal. Chem. Interfacial Electrochem.*, **16**, 61 (1968).
15. J. A. Toni, *This Journal*, **116**, 212 (1969).
16. T. Fujinaga, K. Izutzu, and T. Adachi, *Bull. Chem. Soc. Jpn.*, **42**, 140 (1969).
17. H. J. James and R. F. Broman, *J. Phys. Chem.*, **75**, 4019 (1971).
18. G. Feroci and S. Roffia, *J. Electroanal. Chem. Interfacial Electrochem.*, **71**, 191 (1976).
19. J. F. Coetzee, G. P. Cunningham, D. K. McGuire, and G. R. Padmanabttan, *Anal. Chem.*, **34**, 1139 (1962).
20. M. Walter and L. Ramaley, *ibid.*, **45**, 165 (1973).
21. T. A. Lorenzola, Ph.D. Thesis, Fac. C. Químicas, Univ. Nac. de Córdoba (1981).
22. H. J. James and R. F. Broman, *Anal. Chim. Acta*, **48**, 411 (1969).
23. A. J. Arvía, S. L. Marchiano, and J. J. Podestá, *Electrochim. Acta*, **12**, 259 (1967).
24. C. Louis and R. L. Benoit, *ibid.*, **18**, 7 (1973).
25. R. S. Nicholson and I. Shain, *Anal. Chem.*, **36**, 706 (1964); **37**, 178 (1965).
26. H. S. Wroblowa, Y. D. Pan, and G. Razumney, *J. Electroanal. Chem. Interfacial Electrochem.*, **69**, 195 (1976).
27. A. J. Appleby and M. Savy, *ibid.*, **92**, 15 (1978).
28. J. O'M. Bockris, B. E. Conway, and E. Yeager, "Comprehensive Treatise of Electrochemistry," "Electrochemical Energy Conversion and Storage," Vol. 3, Plenum Ed. (1981).
29. E. Yeager, in "Proceedings of the Workshop on Electrocatalysis on Non-Metallic Surface," Nat. Bur. Stand., Dec. 9-12, 1975.
30. R. W. Zurilla, R. K. Sen, and E. Yeager, *This Journal*, **125**, 1103 (1978).
31. J. C. Huang, R. K. Sen, and E. Yeager, *ibid.*, **126**, 786 (1979).

32. P. Fischer and J. Heitbaum, *J. Electroanal. Chem. Interfacial Electrochem.*, **112**, 231 (1980).
33. E. Yeager, *This Journal*, **128**, 160C (1981).
34. R. Sereno, V. A. Macagno, and M. C. Giordano, *J. Electroanal. Chem. Interfacial Electrochem.*, **76**, 199 (1977).
35. G. A. Garwood, Jr. and A. T. Hubbard, *Surf. Sci.*, **118**, 223 (1982).
36. M. Mastragostino, L. Nadjo, and J. M. Saveant, *Electrochim. Acta*, **13**, 721 (1968).
37. M. Mastragostino and J. M. Saveant, *ibid.*, **13**, 751 (1968).
38. S. Lormeau and G. Calmar, *Bull. Soc. Chim. Fr.*, **3**, 794 (1971).
39. K. Holub, *J. Electroanal. Chem. Interfacial Electrochem.*, **30**, 71 (1971).
40. J. Kůta and E. Yeager, *ibid.*, **46**, 233 (1973).
41. S. W. Jacob, E. E. Rosenbaum, and D. C. Wood, "Dimethylsulfoxide," Vol. 1, Marcel Dekker Inc., New York (1971).
42. M. Tezuka, H. Hamada, Y. Ohkatsu, and T. Osa, *Denki Kagaku*, **44**, 17 (1976).
43. J. H. Chin, G. Chiericato, Jr., E. J. Nanni, Jr., and D. R. Sawyer, *J. Am. Chem. Soc.*, **104**, 1296 (1982).

Technical Note

Lithium Alloy-Thionyl Chloride Cells: Performance and Safety Aspects

E. Peled,*[1] A. Lombardi, and C. R. Schlaikjer*[2]

GTE Laboratories Incorporated, Waltham, Massachusetts 02254

The lithium-thionyl chloride cell has the highest energy density among all the commercially available batteries. The low rate, AA-bobbin cathode cell has been in the marketplace for several years while the wound or spiral electrode cell is still in the stage of development and not commercially available. The main reason for this is that the safety hazard problems of the high rate version have not yet been completely and satisfactorily understood and solved. The basic reasons for the safety hazard problems are the very high reactivity of lithium toward thionyl chloride and the rather low melting point of lithium (180.5°C). The practical stability of this system and the excellent storageability of this cell is due to an LiCl-passivating layer which forms spontaneously on the immersion of the lithium in the electrolyte. The part of this layer that is close to the lithium surface serves as a solid electrolyte interphase (SEI) through which only lithium can pass (1-5).

As the electronic conductivity of the SEI is very low it retards further corrosion of the anode. This SEI covers the lithium not only on OCV but also during plating and stripping (charging and discharging). As long as the lithium anode is fully covered by the LiCl-SEI, no hazardous conditions are created. This SEI can be momentarily damaged in several ways, such as plating, anodic stripping, or by mechanical deformation of the lithium. In most cases it will heal immediately by fast precipitation of LiCl (a corrosion product of lithium with thionyl chloride). However, in extreme conditions, such as hot spots, electric sparks, and a fast melting of lithium, the SEI cannot be fully healed due to either a fast streaming of molten lithium, or a fast local evaporation of lithium. As a result a very exothermic reaction of molten lithium with thionyl chloride occurs possibly resulting in an explosion of the cell.

Cells in which the electrode surface area is high have a very high short-circuit current. As a result an internal or external short leads to a fast heating of the cell, fast melting of lithium anode (above 180°C), and finally to explosion. A possible way to improve the safety performance of lithium cells, still under experimental development and testing, is to use lithium alloys instead of pure lithium. The compatibility of several lithium alloys with thionyl chloride was recently studied (5). No substantial difference was found between pure lithium and the four following alloys[3] (Li-6% Al, Li-5% Mg, Li-5% Ca, Li-4% Si) regarding the growth rate of the SEI, the resistivity of the SEI, and the overall corrosion rate. The discharge characteristics and storageability of several lithium alloys in thionyl chloride are described in a recently published technical report (6).

The purpose of this work was to study ways to reduce the short-circuit current and to improve the safety performance of the lithium-thionyl chloride cell by the use of lithium alloys which have been subsequently treated. This treatment includes: (*i*) predischarge at low rate in order to enrich the surface of the lithium anode with the alloying element and (*ii*) heating the predischarged cell for several days at 70°C (or by keeping it at room temperature) in order to sinter this lithium-depleted surface layer. As a result of this treatment, the lithium alloy anode is expected to be fully encapsulated by a thin film of less active barrier layer which is called an alloy barrier layer.

Experimental

As a test vehicle for the evaluation of several lithium alloy anodes, cells with stainless steel cases about the size of AA-cells were used (7). The surface area of the anode was 13 cm^2 and its thickness was 0.76 mm. The anode was pressed to the inside surface of the cell case, lined with 0.13 mm Crane nonwoven Pyrex fabric, and the cathode, a mixture of Shawinigan black and Teflon in the shape of a bobbin, was placed concentrically inside. Electrical contact to the cathode was through a twisted piece of 304 stainless steel foil welded to the feedthrough pin. The electrolyte was 1.8M $LiAlCl_4/SOCl_2$.

For electrochemical measurements an Li three-electrode glass envelope cell was used. This cell and other

* Electrochemical Society Active Member.
[1] Present address: Tel-Aviv University, Tel-Aviv, Israel. Work performed at GTE Laboratories while on sabbatical.
[2] Present address: Duracell, Incorporated, Burlington, Massachusetts.

[3] The content of the alloying element is given in atomic percent.

experimental techniques are described in Ref. (2 and 3). A Wavetek VCG Model 116 square wave generator with a sufficiently large resistor in series, typically 10 kΩ, was employed as a pulse galvanostat. The signal generator supplied a pulse up to about 10V. Since the series resistor was much larger than the cell impedance, the applied current could be held essentially constant up to 1 mA. A Tektronix Type 541 oscilloscope with camera was used to record the galvanostatic transients.

Several D-size spirally wound cells were assembled with an anode consisting of a lithium alloy. In these cells the cathode was longer and broader than the anode such that all anode surfaces faced cathode material directly across the separator material. The cathode dimensions were 380 × 44 × 0.84 mm and the anode dimensions were 305 × 38 × 0.38 mm.

Short-circuit experiments with AA-cells were done with loads between 0.1 and 1Ω. Short-circuit experiments with D-size cells were carried out using remotely activated relays, which connected the cells through welder cables to 5, 1, or 0.5 mΩ precision shunts. The potential was monitored and the current calculated as a function of time. The D-size cells, which contained no fuses or vents, were buried in a 20 liter barrel filled with vermiculite. The surface temperatures of the D-size cells were recorded with the use of iron constantan thermocouples which were attached to the cans by an adhesive tape.

Results

The effect of the pretreatment conditions on the short-circuit current (SCC) of AA-cells with Li alloy is summarized in Table I. The maximum SCC of a regular fresh AA-cell is 2-2.5A. It can be seen that the maximum SCC was reduced markedly in comparison with the regular AA-cell and values as low as 40 mA were recorded. The maximum SCC depends on the type of alloy, on the predischarge depth, and on the storage conditions of the predischarged cell. Upon increasing the predischarge from 4.8 to 19 mA-hr-cm^{-2}, the maximum SCC was reduced from 0.36 to 0.07A, for Li-5% Ca anode cells having the same heat-treatment. The increase of the heat-treatment temperature from room temperature to 70°C results in the decrease of the maximum SCC of Li-5% Ca cell from 0.36 to 0.05A. It appears that among all the alloys used, the Li-5% Ca and Li-5% Zn are the most effective in the reduction of the SCC, while the Li-2% Mg is the least effective. It should be emphasized that in most cases the SCC was almost constant or slowly declined (after passing the peak) during many hours of short circuit. The Li-5% Ca cells that were predischarged for only 2.4 mA-hr-cm^{-2} and stored for 14 days at 72°C, have a very high SCC (about 1A or more, Table I), however, the peak of the SCC was delayed for about half an hour. Cells having lithium alloy anodes that were predischarged but did not undergo heat-treatment or were not stored at room temperature have a comparable SCC to that of regular lithium cells.

The discharge characteristics of pretreated lithium alloy cells are summarized in Table II. The total capacity that can be drawn from the cells depends on the type of alloy: Li-5% Ca, Li-2% Mg, Li-5% Zn, Li-3% Mg-5% Ca, and Li-6% Al have about the same capacity as regular AA-cells. However, a capacity loss

Table I. Short-circuit current (SCC) of pretreated lithium alloy AA-cells

Alloy	Pretreatment		Short-circuit current, (A)**		
	Q_{pd}* (mA-hr-cm^{-2})	Storage conditions	$t = 0$	Maximum value	$t > t_{max}$
Li-5% Al	3.0	14 days at 72°C	0.3	0.47 (1000 sec)	
Li-20% Al	3.0	14 days at 72°C + 6 days at RT	0.21	0.31 (1200 sec)	
Li-4% Si	4.0	14 days at 72°C	0.07	0.115 (600 sec)	0.055 (5 hr)
Li-4% Si	4.0	14 days at 72°C + 6 days at RT	0.12	0.19 (400 sec)	0.055 (4 hr)
Li-5% Ca	4.8	4 days at RT	0.3	0.36 (2000 sec)	0.3 (3000 sec)
Li-5% Ca	4.8	3 days at RT + 2 days at 72°C	0.01	0.05 (2 hr)	0.05 (8 hr)
Li-5% Ca	9.6	4 days at RT	0.07	0.15 (2 hr)	
Li-5% Ca	19	4 days at RT		0.07 (3 hr)	
Li-5% Ca	2.4	14 days at 72°C	0.05	0.4 (1500 sec)	
Li-5% Ca	2.4	14 days at 72°C + 6 days at RT	0.025	0.9 (1800 sec)	
Li-10% Ca	4.4	6 days at 72°C	0.014	0.165 (1 hr)	0.130 (2 hr)
Li-2% Mg	10	6 days at 72°C	0.080	1.02 (1200 sec)	0.100 (2000 sec)
Li-3% Mg	10	3 days at RT		~0.5	
Li-3% Mg 5% Ca	5.2	6 days at 72°C	0.06	0.35 (900 sec)	0.22 (1 hr); 0.15 (2 hr)
Li-5% Zn	6.3	6 days at 72°C	0.02	0.04 (5 hr)	

* Q_{pd} = predischarge capacity per unit area of anode on 100Ω load.
** Values in parentheses are times measured after onset of discharge at which the current measurements were taken. Shunt resistance was 1Ω.

Table II. Discharge performances of pretreated Li-alloy AA-cells

Alloy	Pretreatment		Total capacity to 2V (A-hr) 100Ω load	Average working voltage (V)	Delay	
	Q_{pd} (mA-hr-cm^{-2})	Storage conditions			V_{min} (V)	Time to 2.5V (sec)
Li-6% Al	3.6	14 days at 72°C + 6 days at RT	1.6	2.5	2.63	0
Li-6% Al	3.6	14 days at 72°C + 6 days at RT	1.78	3.05	2.86	0
Li-5% Ca	2.4	14 days at 72°C + 6 days at RT	1.97	2.7	1.13	420
Li-4% Si	4.8	14 days at 72°C + 6 days at RT	1.38	2.8	2.6	0
Li-4% Si	4.8	14 days at 72°C + 6 days at RT	1.25	2.85	2.84	0
Li-4% Si	4.8	14 days at 72°C + 6 days at RT	1.16	3.2		
Li-5% Sn	6.3	6 days at 72°C	1.4	3.34		
Li-5% Ca	10	3 days at RT	1.6			
Li-10% Ca	4.4	6 days at 72°C	0.91	3.06		
Li-5% Zn	6.3	6 days at 72°C	1.82	3.29		
Li-3% Mg-5% Ca	5.2	6 days at 72°C	1.76	3.28		
Li-2% Mg	10	7 days at 72°C	1.6	3.26		

was found for Li-4% Si, Li-5% Sn, and Li-10% Ca. The discharge curves of Li-5% Zn, Li-5% Sn, and Li-10% Ca showed a very steep drop from 2 to 30 mV within 15 min at the end of discharge. The average working potential (on 100Ω load) of the pretreated lithium alloy cells is up to 0.7V lower than that of a regular lithium cell. Li-4% Si and Li-6% Al show no delay at all to 2.5V (on 100Ω load) after storage of 14 days at 72°C plus 6 days at room temperature, while the Li-5% Ca shows some voltage delay (Table II).

The electrochemical behavior of pretreated Li-5% Ca alloy in 1.8M $LiAlCl_4$-$SOCl_2$ was studied with the use of a three-electrode cell (2, 3). The working electrode (Li-5% Ca) was pretreated by a discharge of 6 mA-hr-cm^{-2} and three days of storage at room temperature. After this treatment the anodic overpotential at 2 mA cm^{-2} was 0.2V. However, at 15 mA cm^{-2} the overpotential exceeded 3.6V after 210 sec of discharge. This proves that the electrode was blocked. Immediately after this experiment, the interfacial capacity of the working electrode was measured with the use of the pulse galvanostatic technique discussed above, and it was found to be 0.9 μF cm^{-2}. The apparent thickness of the solid electrolyte interphase (SEI), which was calculated using this value, was only 80Å. This is a value that is characteristic of lithium freshly immersed in $LiAlCl_4$-$SOCl_2$ solution (2, 3, 5). The calculation was made assuming that the SEI was pure LiCl.

A few Li alloy spirally wound D-size cells were assembled, pretreated, and short-circuited as described above. The electrolyte in these cells was 1M $LiAlCl_4$. An Li-5% Ca anode cell was pretreated by a discharge of 12 mA-hr-cm^{-2} and storage at 70°C for 10 days. After this pretreatment the cell was shorted externally. The cell bulged, but did not explode or rupture. At the end of this experiment, the cell showed an open-circuit potential near zero. An Li-3% Mg anode spirally wound D-cell was pretreated by a discharge for 11 mA-hr-cm^{-2} at 0.5 mA cm^{-2} followed by storage for 12 days at 70°C. Then the cell was shorted externally. Its peak SCC was 16A. After 22 min, the cell cover violently flew off the can, however, the can itself did not rupture and kept its unity and original shape. The temperature of the can at this point was 197°C. An Li-5% Zn anode spirally wound D-cell was pretreated by a discharge for 11 mA-hr-cm^{-2} at 0.5 mA cm^{-2} followed by 12 days storage at 70°C. Then the cell was externally shorted. Its peak SCC was 9.6A. After 1 hr, the cover of the cell violently flew off the can. The weld area was broken but the can itself kept its integrity and original shape. The temperature of the can at this point was 184°C, some 23° higher than the melting point of this alloy. In all these experiments the SCC was very low (2-4A) during the first 5-10 min following shorting and then rose slowly to the peak value.

Discussion

Two different mechanisms can, in principle, be responsible for the reduction of SCC of the treated AA-cells. The first and trivial one is a possible passivation of the lithium alloy by a thick LiCl film, which was formed as a result of the pretreatment. We assume that lithium, being more electropositive than any of the alloying metals, predominates as the cation in the SEI. This mechanism can be ruled out because of the following findings:

1. The growth rate of the SEI and the overall corrosion and passivation rate of several Li alloys (Li-6% Al, Li-5% Mg, Li-5% Ca, Li-4% Si) were found to be similar to that of pure lithium (5).

2. A large decrease in the maximum SCC of AA-cells was measured for an Li-5% Ca anode cell which was predischarged for 4.8 mA-hr-cm^{-2} and stored for 4 days at room temperature while a very small decrease was measured for the same alloy when stored for 14 days at 72°C but predischarged for only 2.4 mA-hr-cm^{-2} (Table I). This indicates that in the case of Li-5% Ca alloy the predischarge depth is more efficient in the reduction of the SCC than is storage temperature.

3. In the case of Li-Mg alloys a higher Mg content of the alloy (3% instead of 2%) is more effective in reducing the SCC than storage at 72°C (Table I).

4. The apparent thickness of the SEI of pretreated Li-5% Ca alloy is only 80Å. This value is also characteristic of pure lithium.

5. Li-6% Al and Li-4% Si pretreated AA-cells which were stored for 14 days at 72°C followed by 6 days at room temperature reveal no delay to 2.5V on startup using 100Ω loads (Table II).

The second mechanism that can be responsible for the blocking of the pretreated lithium-alloy anode is the formation of an alloy barrier layer poor in pure lithium but rich in the alloying element that inhibits the mass transport of lithium atoms. As the emf of all the alloying elements used in this work is lower than that of pure lithium *vs.* C/$SOCl_2$, the discharge of the alloy will be expected to dissolve anodically only the lithium, while the alloying element will not be dissolved. As a result, the concentration of the alloying element near the surface of the alloy should increase and that of the pure lithium should decrease. All the alloys used (except Li-Mg) are heterogeneous and contain two phases: lithium saturated with the alloying element, and a second phase containing a lithium compound, such as Li_2Ca, Li_4Si, Li_2Zn_3, Li_2Al, or Li_4Sn. After predischarge, the surfaces of the anodes seem to be covered with these compounds, while in the case of Li-Mg alloy the surface is covered with a magnesium-rich alloy.

Storage of the predischarged cells, either at room temperature or at 72°C, probably causes the alloy particles to be sintered into a more compact and mechanically stable film. This film acts as an alloy barrier layer for the mass transport of lithium atoms from the bulk of the alloy to the solution. It can be seen that there is a correlation between the storage temperature needed for sintering and the melting point of the lithium compound. In the case of the Li-Ca system, the compound richest in lithium is Li_2Ca which melts at 230.9°C. Storage at room temperature was sufficient for the sintering of the alloy barrier layer. However, in the case of the predischarged Li-Al and Li-Si alloys, storage at room temperature was not effective enough and rather high short-circuit currents (0.5-1A) were measured. Therefore, a higher temperature (72°C) was needed in the sintering stage. The melting point of the Li_2Al and Li_4Si compounds are 522° and 752°C, respectively.

The capacity lost and the sharp decline in working potential at the end of the discharge of Li-5% Zn, Li-5% Sn, and Li-10% Ca cells seem to result from the separation of the anode from the can at the end of the discharge. During the discharge, the anode became increasingly rich in the alloying element and this made it very rigid and brittle until it lost electrical contact with the can. It is interesting to note that the alloy barrier layer does not dissolve even after 5-8 hr of continuous short circuit at about 4 mA cm^{-2} (Table I). During this time more than 0.1 mm of lithium was discharged, however, the alloy barrier layer was not damaged.

Some of the alloying elements used, such as magnesium and calcium can be discharged in thionyl chloride solutions. The working potential of a magnesium thionyl chloride cell is about 1.5V at 1 mA cm^{-2} (8) and that of a calcium cell is about 3V at 3.5 mA-cm^{-2} (9). A possible reason for the fact that the alloy barrier layer, at least in the case of magnesium or calcium, does not anodically dissolve under short-circuit conditions (although the pure metal is dischargeable) is that the alloy is covered with an LiCl SEI which is a good conductor of Li^+ cations, but may not be as good a conductor for Mg^{++} or Ca^{++}. This means that the transference numbers of Mg^{++} ($t_{Mg^{++}}$) or of Ca^{++} ($t_{Ca^{++}}$) in the SEI-covered lithium alloy,

is close to zero while that of Li^+ is about 1. The finding that the cationic conductivity of the SEI covering lithium in thionyl chloride is 2-3 orders of magnitude higher than of the SEI covering magnesium or calcium in thionyl chloride (2, 3, 8-10) support this hypothesis.

The current (i) during discharge of lithium atoms migrating through the alloy barrier layer should, as a first approximation, be given by

$$i = \frac{nFD(C^b - C^o)}{\delta} \quad [1]$$

where D is the diffusion coefficient of lithium atoms in the alloy barrier layer, C^b and C^o are the concentration of lithium atoms in the bulk of the alloy and in the SEI side of the alloy barrier layer, respectively, and δ is the thickness of the alloy barrier layer; n and $\mathbf{F}$ have their usual meanings. The maximum short circuit is limited by the mass transport of lithium atoms through the alloy barrier layer. Since C^b is constant and C^o is zero when $i = i_{lim}$, Eq. [1] can be written as

$$i_{sc}^{max} = i_{lim} = \frac{K}{\delta} \quad [2]$$

where K is a constant.

It was mentioned that δ should be a linear function of Q_{pd}. The following relation should, therefore, exist

$$i_{lim} = \frac{K'}{Q_{pd}}$$

where K' is a constant. In Fig. 1, the maximum short-circuit current for Li-5% Ca alloy AA-cells is plotted as a function of Q_{pd}^{-1}, using the data shown in Table I. These predischarged cells had been stored for 4 days at room temperature. The linearity of i_{lim} with Q_{pd}^{-1} supports the proposed model of an alloy barrier layer as the current limiting factor.

The few spirally wound D-cells show a much higher maximum short-circuit current density than the AA-cells. The reason for this is that the total current drawn from the D-cells is high enough to cause significant heating. As a result, the diffusion coefficient of the lithium in the alloy barrier layer increases, leading to further increase in the short-circuit current. Nevertheless, the maximum SCC of the pretreated cells is 2-3 times smaller than that of a regular pure lithium cell.

It seems that, although the safety hazard problem of spirally wound D-cells was not completely solved, it was at least alleviated. No D-cell disintegrated competely as the result of short circuit. The temperature of the can in which the cover was broken rose to a value much above the melting point of lithium. (The internal temperature may have been as high as 250°C or 70° higher than the melting point of lithium.) The time during short circuit needed to break the cover was extended by one order of magnitude in comparison with a regular cell. [A regular D-size spirally wound cell explodes on shorting after 1-3 min (11).] It is possible that the cover separated from the cell case as a result of the high pressure from sulfur dioxide which formed during the prolonged discharge. Since case rupture caused by high pressure is preferable to explosion caused by lithium ignition, the alloy anodes do provide at least some measure of safety. Another safety feature is that after the pretreatment, the lithium anode is completely covered by the alloy, which is less active than pure lithium and which may further protect the anode from other hazards, such as external heating or mechanical damage to the cell.

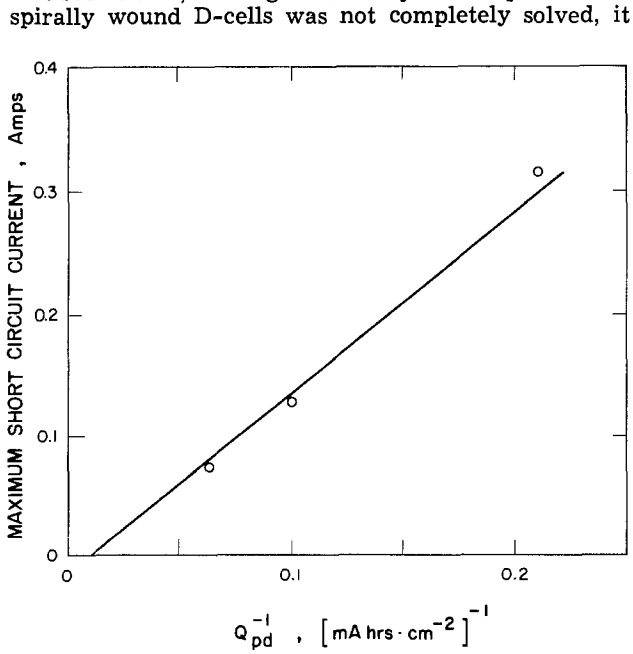

Fig. 1. A plot of the maximum short-circuit current (i_{lim}) of pretreated Li-5% Ca AA-cell as a function of the reciprocal of predischarge capacity for unit area of anode (Q_{pd}^{-1}). The cell was stored for 4 days at room temperature.

Summary

The maximum short-circuit current (SCC) of lithium alloy-thionyl chloride AA-cells was reduced by a factor of 20-50 in comparison with that of regular lithium cells. The maximum SCC of spirally wound D-size cells having a lithium alloy as an anode was reduced by a factor of 2-3. This was done by a pretreatment which includes discharge for 4-12 mA-hr-cm^{-2} (of anode) followed by storage at room temperature or 72°C for 3-14 days depending on the alloy type. It was concluded that as a result of this pretreatment an alloy-rich barrier layer is formed on the entire surface of the anode (beneath the LiCl passivating layer). Such a barrier layer may be formed in all the primary and secondary ambient temperature cells with lithium alloy anode. During intermittent use of any type of lithium alloy cells (not only Li/$SOCl_2$ cells) over long periods of time, an alloy barrier layer can be formed that, if allowed to grow in an uncontrolled manner, can decrease the rate capability of the cells below a useful value.

Manuscript submitted Sept. 30, 1981; revised manuscript received Feb. 8, 1983.

Any discussion of this paper will appear in a Discussion Section to be published in the December 1983 JOURNAL. All discussions for the December 1983 Discussion Section should be submitted by Aug. 1, 1983.

GTE Laboratories, Incorporated assisted in meeting the publication costs of this article.

REFERENCES

1. E. Peled, *This Journal*, **126**, 2047 (1979).
2. E. Peled and H. Yamin, in "Proceedings of the 28th Power Sources Symposium," Atlantic City, NJ, June 12-15, 1978, The Electrochemical Society, Inc., p. 237 (1979).
3. E. Peled and H. Yamin, *Israel J. Chem.*, **18**, 131 (1979).
4. C. R. Schlaikjer, C. A. Young, and M. Dobrusin, Report DELET-TR-78-0558.1F, ERADCOM, Ft. Monmouth, NJ (May 1980).
5. E. Peled, C. R. Schlaikjer, and N. Marincic, Abstract 553, p. 1380, The Electrochemical Society Extended Abstracts, Vol. 78-1, Seattle, Washington, May 21-26, 1978.
6. J. Driscoll *et al.*, ECOM Report No. 74-0030-8/9/10 (1976).
7. J. J. Auborn and N. Marincic, in "Power Sources 5," D. H. Collins, Editor, p. 683, Proceedings of the 9th International Symposium, Brighton, 1974, Academic Press, London (1975).
8. E. Peled and H. Straze, *This Journal*, **124**, 1030 (1977).
9. A. Meitav and E. Peled, in 31st ISE Meeting, Venice, Italy, Sept. (1980), Submitted.
10. A. Meitav and E. Peled, *This Journal*, **129**, 451 (1982).
11. A. N. Dey, ECOM 74-0109-6 (1975).

JOURNAL OF THE ELECTROCHEMICAL SOCIETY

SOLID-STATE SCIENCE AND TECHNOLOGY

JUNE 1983

High Rate Anisotropic Aluminum Etching

R. H. Bruce[1] and G. P. Malafsky

The Perkin-Elmer Corporation, Norwalk, Connecticut 06856

ABSTRACT

A high rate anisotropic etching process, suitable for plasma etching one wafer at a time, is discussed. Results indicate that the etch rate is overridingly dependent on the Cl_2 concentration and is independent of the rf power used to drive the discharge. Several additives are used to control the etching process. BCl_3 is added to initiate etching, and $CHCl_3$ is included to control the anisotropy. Large amounts of He assist photoresist preservation. Parametric studies supporting the roles of the additives have been made.

High rate anisotropic plasma etching processes are of considerable interest for increasing the efficiency of machines which process VLSI wafers devices. This paper describes such a process for etching aluminum with high rates (>5000 Å/min) and no undercutting, even with a 50% overetch. Previously processes for anisotropic etching of aluminum in parallel plate reactors have been reported using plasmas of many chlorine-containing compounds, including CCl_4, BCl_3, and Cl_2/BCl_3 mixtures (1-7). None of these etching processes, however, have been reported to have both high etch rates (>2500 Å/min) and no undercutting during overetching.

The etching of aluminum appears to involve two processes: the removal of the native aluminum oxide layer and the etching of the aluminum. The use of BCl_3 has been reported to facilitate the removal of the oxide layer, but alone it etches aluminum relatively slowly (1, 8). Mixtures of Cl_2 and BCl_3, however, were found to etch aluminum at high rates (1.2 μ/min) but isotropically. Anisotropic etching can be achieved with this mixture at high etch rates (4000 Å/min), however, in this case, undercutting typically results during overetching (1, 9). Anisotropic etching is possible with the addition of substances such as $CHCl_3$. This addition is thought to protect the side walls in a fashion similar to etching with CCl_4 where the anisotropic etching of Al was observed to correlate with the formation of a thin film on the etched aluminum edge (4, 5). Similar suggestions of a side wall protection promoting anisotropy have been made in other systems (10).

Experimental

The experiments were made in a small parallel plate etching chamber designed for single-wafer processing (Fig. 1). Gas was introduced uniformly through the rf electrode. For most of the results reported here, a porous stainless steel electrode was used; however, some experiments were done with a porous anodized aluminum electrode. The lower electrode was anodized aluminum with a 6 mm wide slightly raised outer ring which surrounded the wafer and held it in place during chamber evacuation. The base of the chamber, surrounding the lower electrode, was covered by a Teflon ring through which holes were drilled for evacuation. Both electrodes were 11.5 cm diam, and the electrode spacing was 2.5 cm. The discharge was confined between these electrodes. The lower electrode, on which the wafer rested, was cooled by circulating fluid. The fluid temperature was maintained at 15°C, but the electrode was observed by touch to warm to approximately 35°C during a 3 min, 2 W/cm² rf discharge. The chamber was not load locked, and to reduce adsorbed contaminants, a 0.5 W/cm² He discharge was applied for 30 sec prior to each experiment.

The wafers used in this work were 100 mm diam and patterned with AZ 1470 photoresist baked for 30 min at 120°C. The patterning mask was composed of blocks of equal lines and spaces (1.25-2.5μ wide). About 50% of the wafer surface was exposed 1μ thick aluminum which was deposited by magnetron sputtering. The wafers were not flat and, consequently, may not have had uniform contact to the lower electrode.

Etch times were determined by a combination of visual observation of aluminum on the wafer and blue emission from the discharge. This blue emission has been observed to coincide with emission from AlCl at 261 nm. This method allowed approximately a ±1 sec determination of etching initiation and ±2 sec determination of etching termination. Total etch times were typically 90 sec with approximately a 7 sec initiation time.

Measurements of the flow rate dependence were made by varying the flow rate of the particular gas being studied while keeping the flow rates of all other gases and the total pressure constant. Since the flow

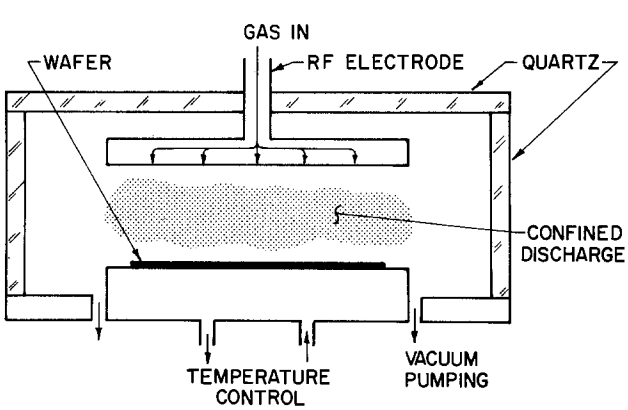

Fig. 1. Experimental apparatus

[1] Present address: Xerox Palo Alto Research Center, Palo Alto, California 94304.

Key words: plasma etching, plasma chemistry, chlorine discharges, semiconductor processing, dry processing.

rate of He, typically 200-250 sccm, was an order of magnitude larger than that of any of the gases whose flow rates were varied, the residence time was only slightly affected. The total pressure was normally 133-200 Pa, and the rf input 1.7 W/cm^2 at 13.56 MHz.

Anisotropy was determined from SEM's of line profiles after etching for a time 50% longer than that necessary to clear the pattern. Dies near the edge were chosen for examination as the edge generally finished etching first. The process was declared to be anisotropic if no undercutting could be detected on any of the small lines (1-2 microns). As the selectivity of aluminum etching to photoresist etching was at least 3:1, and several measurements were made on samples with nearly vertical photoresist sidewalls (from good contact printing), the measured absence of undercut was not thought to be due to resist erosion. Undercutting of about 200Å would have been observable.

Results

Measurements of Al etch rates were made as a function of Cl_2 flow rate with variations in several process parameters: the BCl_3 flow rate, $CHCl_3$ flow rate, and the power level. The etch rate was observed to be strongly dependent on the Cl_2 flow rate at lower flow rates and more weakly dependent at higher flow rates where saturation may be occurring. The etch rate dependence on the other process parameters was much weaker. The etch rate slightly decreased with increases in the $CHCl_3$ flow rates (Fig. 2) and was independent of the BCl_3 flow rate (Fig. 3). A strong dependence of the initiation time on BCl_3 at low flow rates was found (Fig. 4); however, at moderate flow rates, the initiation time was flow rate independent. No initiation of Al etching was observed after 5 min of exposure to the Cl_2 discharge with BCl_3 absent. There was essentially no dependence of the etch rate on rf power (Fig. 5) which is consistent with previous observations using CCl_4 (3). After initiation, the etching was observed to continue without the discharge over areas as large as one-half the wafer in nondiluted mixtures of BCl_3/Cl_2 at roughly the same etch rate as with the discharge. The entire wafer was never observed to clear without the discharge present. This effect was not studied in detail and will be discussed later in this paper. There was also no substantial difference in etch rate observed using steel or aluminum electrodes.

Anisotropy was measured as a function of Cl_2 flow rate as the $CHCl_3$ flow rate and rf power were varied

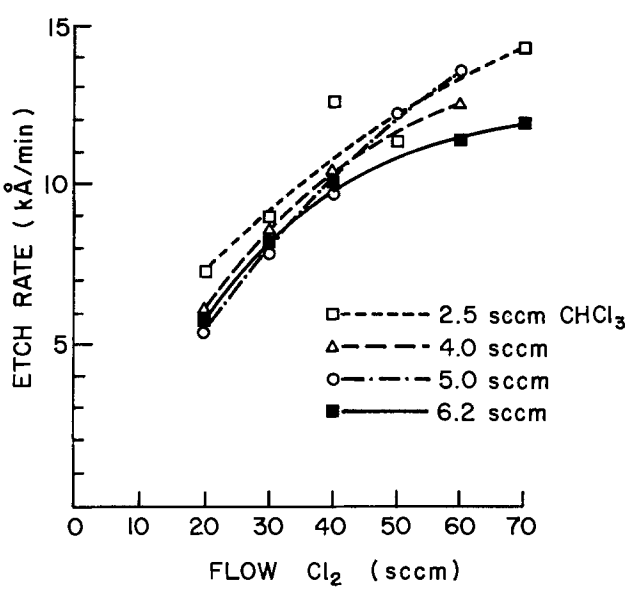

Fig. 2. Etch rate of Al vs. Cl_2 flow for different $CHCl_3$ flows. Other parameters include: 20 sccm BCl_3, 200 sccm He, 200 Pa total pressure, 1.75 W/cm^2 of 13.56 MHz rf power, and 2.5 cm electrode spacing.

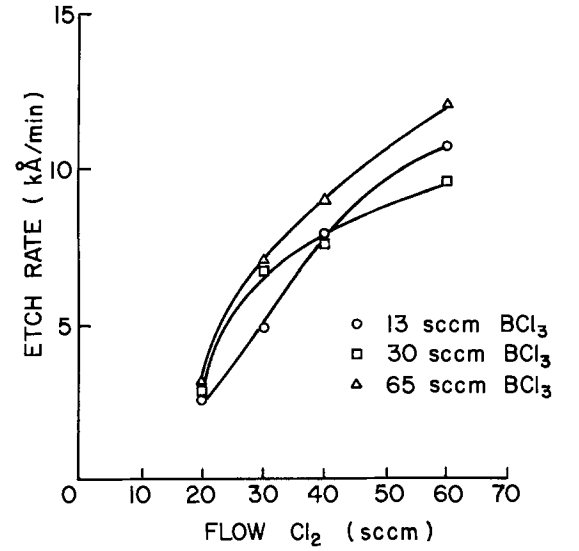

Fig. 3. Etch rate of Al vs. Cl_2 flow for different BCl_3 flows. Other parameters include: 250 sccm He, 9.4 sccm $CHCl_3$, 160 Pa total pressure, 1.7 W/cm^2.

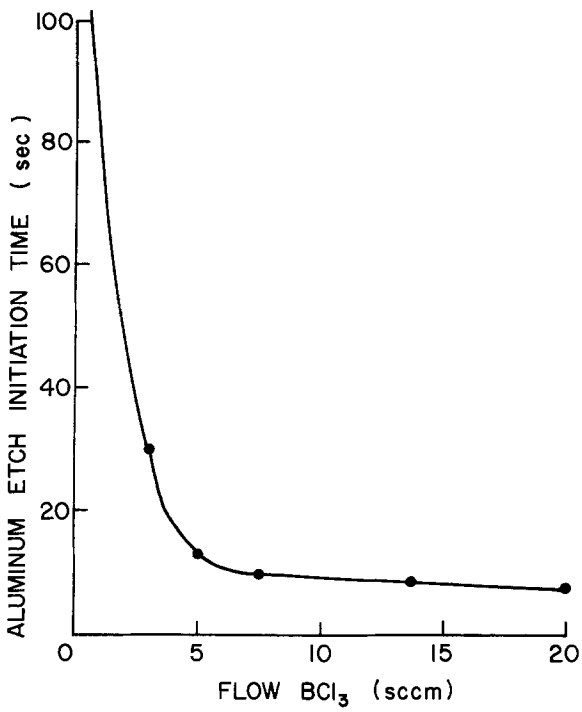

Fig. 4. Time necessary for initiation of aluminum etching vs. BCl_3 flow. Other parameters include: 20 sccm Cl_2, 200 sccm He, 200 Pa total pressure, 1.75 W/cm^2.

(Fig. 6, 7) with all other process parameters held constant. In each study, a threshold was observed in flow rate and power above which vertical profiles would be achieved but below which undercutting occurred. In addition, as the power and $CHCl_3$ flow rates were increased above this threshold, vertical profiles could be achieved at higher Cl_2 flow rates. The reduction of electrode spacing at constant power increased anisotropy in a way similar to that seen with increasing power (at constant electrode spacing); this indicates that the volume power density is important. With large amounts of $CHCl_3$, the discharge is unstable with localized regions of high intensity. These regions, extending from one electrode to the other, occupy approximately 1% of the electrode area and have emission intensities of a factor of ten in excess of surrounding plasma.

The etch rates of other materials (such as Si, SiO_2, and photoresist) were found to depend on several pro-

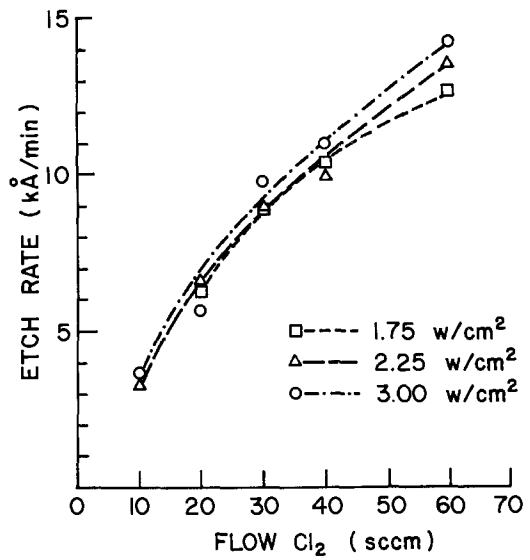

Fig. 5. Etch rate of Al vs. Cl_2 flow for different rf power levels. Other parameters include: 20 sccm BCl_3, 200 sccm He, 13.5 sccm $CHCl_3$, 200 Pa total pressure, 13.56 MHz rf excitation.

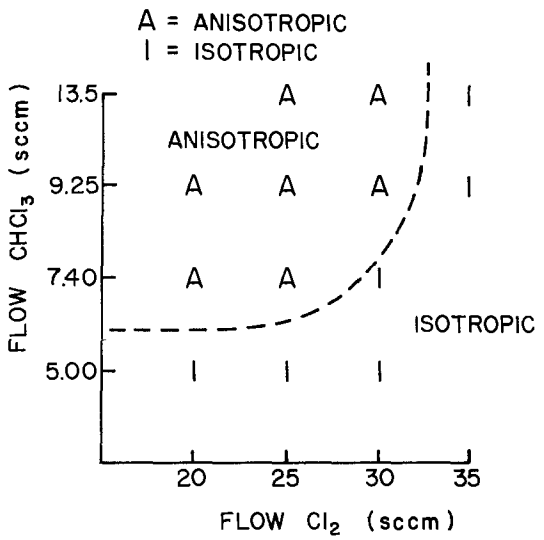

Fig. 6. Anisotropy with 50% overetch vs. Cl_2 flow for different $CHCl_3$ flows. Other parameters include: 30 sccm BCl_3 flow, 250 sccm He flow, 1.75 W/cm², 133 Pa pressure.

cess parameters. The most critical parameter was rf power which increased the etch rate of all three materials. Photoresist erosion was observed to be particularly sensitive to $CHCl_3$ concentration with better resist survival achieved at lower concentration. Also, the addition of He was observed to greatly reduce the resist erosion rate with very little effect of the aluminum etch rate. The oxide and resist etch rates were observed to increase with increases in BCl_3 concentration.

Uniformity depended on several factors: Cl_2 flow rate, electrode spacing, and exposed aluminum area. Generally, higher flow rates and larger spacing would provide more uniform etching while larger areas of exposed aluminum would make the etching less uniform. In nonuniform etching, the etch rate would generally be greater at the edge than the center; however, with higher Cl_2 flow rates wafers have been observed to etch fastest in the center as well as in a ring between the center and edge. For a specific resist pattern, conditions for uniform etching were found empirically and the effect was not studied in detail.

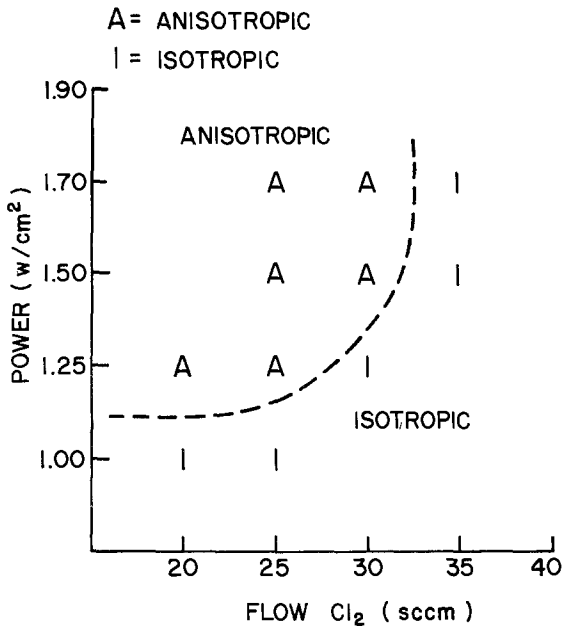

Fig. 7. Anisotropy with 50% overetch vs. Cl_2 flow for different rf powers. Other parameters include: 30 sccm BCl_3, 250 sccm He, 13.5 sccm $CHCl_3$, 133 Pa total pressure, 13.56 MHz rf excitation.

Discussion

The results presented in this paper support the concept that the etching of Al with a Cl_2 plasma is by a chemical reaction with no ion enhancement. Such a model would explain the insensitivity of the etch rate to rf power which affects both the ion energies and the ion flux. This concept of a purely chemical reaction is consistent with separate work done under ultrahigh vacuum conditions with a Cl_2 discharge beam (11). In that work, the etch rate was found not only to be independent of ion flux and energy but also independent of the presence of the discharge. The discharge is needed, however, to initiate etching presumably by removing the native aluminum oxide surface layer. No definitive identification of the chemical species responsible for the spontaneous reaction has been made in this work. However, the overriding dependence of the etch rate on Cl_2 flow and insensitivity to rf power, which would presumably affect the radical composition, suggests that the Cl_2 feed gas is no less reactive than any radical species formed in the discharge.

The large dependence of the initiation time on BCl_3, consistent with previous work (1, 8), indicates that the addition of BCl_3 is necessary for the removal of the aluminum oxide layer. The mechanism for this removal was not delineated in this work; however, the results here are consistent with either a direct reduction of the surface or a gettering of oxygen to prevent reoxidation of the surface after initial removal by sputtering (8). The suppression of the etch rate by increasing $CHCl_3$ flow rates could result from the recombination of fragments of $CHCl_3$ with chlorine (12) or the limiting of access to the Al surface to chlorine by passivating species.

In a system where the etching reaction is purely chemical, sidewall protection is necessary to prevent undercutting. The formation of a permanent surface protective layer has been reported (4, 5) in Al etching by CCl_4, suggesting a similar role in this work for $CHCl_3$, although no such layer has been observed here. For the process to be anisotropic, the adherence of these protective species must depend on the ion bombardment which, with parallel plate reactors, is normal to the surface. According to this model, those surfaces receiving sufficient ion bombardment to clear the passivant will etch, while those surfaces with insufficient ion bombardment will not.

The effect of such protective species on preventing undercutting is observed to depend on the flow rates of Cl_2 and $CHCl_3$ and the power (Fig. 6, 7). The dependence of the passivation on power suggests that a discharge product, not the $CHCl_3$, is the passivating species. This product could possibly contain photoresist decomposition species as well as $CHCl_3$ fragments. Other workers have observed a strong correlation between resist erosion and anisotropy (5, 13). Since the formation of these species is thought to start with fragmentation of $CHCl_3$, the amount of fragmentation products is expected to increase with increases in either the rf power of $CHCl_3$ concentration. Such increases in fragmentation have been observed in discharges of CCl_4 (6). The monomeric fragments could serve as passivants or participate in subsequent reactions to produce polymeric passivating species. The formation of polymer has been observed in this work under conditions of high power and $CHCl_3$ concentrations. The reduction of anisotropy with addition of Cl_2 could result from reactions with the fragments (possibly with the formation of CCl_4) which would reduce the concentration of fragments.

The decrease in selectivity of Al etching over other circuit material (SiO_2, Si, photoresist) with an increase in rf power may be due to additional ion bombardment. Although the Al etch rate is essentially unaffected by rf power, the etching of Si and SiO_2 in Cl_2 are ion enhanced reactions (11) and, consequently, the etch rates can increase with both ion flux and ion energy. The increase in photoresist erosion at higher power could be due to additional ion bombardment enhancing the erosion reaction by direct participation or thermal acceleration. Higher selectivities are possible at low rf power. As BCl_3 is thought to be a good reducing agent for aluminum oxide in a plasma, it is not unreasonable that the SiO_2 etch rate also depends on BCl_3 concentrations. The reduction of the resist erosion rate with the addition of He could be attributable to several factors, but the most likely is increased cooling of the wafer due to the high thermal conductivity of He (14). The thin He layer between the cooled electrode and the wafer can provide increased heat transfer.

A micrograph of 2.25μ wide features etched in a 1μ Al film using the gas mixture (Cl_2, BCl_3, $CHCl_3$, He) is shown in Fig. 8. The etching was completed in 135 sec after a 7 sec initiation period; however, the wafer was left in the reactive discharge an additional 30 sec to accentuate the absence of undercutting which is reflected in the vertical walls. A slight residue from the etched Al can sometimes be seen on the underlying SiO_2 layer. This residue appears intermittently with this process and has a pattern similar to the grain structure of the aluminum. Such a pattern suggests the residue is from the grain boundaries (possibly Al_2O_3). Residues with a similar appearance have been reported elsewhere for very different etching conditions (2).

Summary and Conclusions

The etching reaction of Al in Cl_2 appears to be fast and can be explained as a purely chemical effect without ion or discharge enhancement after the surface oxide layer has been removed. The native oxide layer can be very effectively removed by the addition of BCl_3 to the discharge making the mixture Cl_2/BCl_3 an attractive fast etchant but limited due to a lack of adequate means to control undercutting. Undercutting can be prevented with such a mixture by the addition of species to protect the sidewalls during etching. Under appropriate conditions, either CCl_4 or $CHCl_3$ will provide such protection. The erosion rate of the photoresist can be reduced by the addition of a large amount of He to the gas mixture.

Acknowledgments

The authors are grateful to R. Reed for his contributions to the work reported herein.

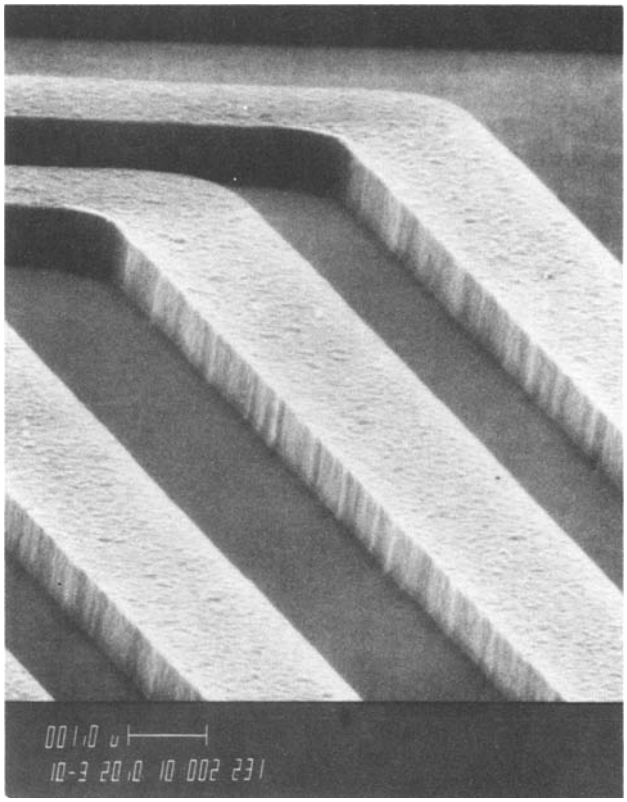

Fig. 8. Al features 2.25 μm wide etched with a mixture of Cl_2, BCl_3, $CHCl_3$, and He. The total pressure was 150 Pa (1.2 Torr) with 1.75 W/cm^2 13.56 MHz rf power. The aluminum cleared from the wafer after 135 sec of etching. The wafer was etched for 30 sec after the aluminum cleared.

Manuscript submitted April 5, 1982; revised manuscript received Feb. 28, 1983. This was Paper 288 presented at the Denver, Colorado, Meeting of the Society, Oct. 11-16, 1981.

Any discussion of this paper will appear in a Discussion Section to be published in the December 1983 JOURNAL. All discussions for the December 1983 Discussion Section should be submitted by Aug. 1, 1983.

The Perkin-Elmer Corporation assisted in meeting the publication costs of this article.

REFERENCES

1. R. B. Poulsen, H. Nentwich, and S. Ingrey, in "Proceedings of the IEDM Meeting," Washington, DC (1976).
2. P. M. Schaible, W. C. Metzger, and J. P. Anderson, *J. Vac. Sci. Technol.*, **15**, 334 (1978).
3. R. L. Bersin, *Solid State Technol.*, **21**, 117 (1978).
4. P. M. Schaible and G. C. Schwartz, *J. Vac. Sci. Technol.*, **16**, 377 (1979).
5. M. Oda and K. Hirata, *Jpn. J. Appl. Phys.*, **19**, 1405 (1980).
6. R. H. Bruce, in "Plasma Processing," R. G. Frieser and C. J. Mogab, Editors, p. 243, The Electrochemical Society Softbound Proceedings Series, Pennington, NJ (1981).
7. M. Nakamura, M. Itoga, and Y. Ban, in "Plasma Processing," R. G. Frieser and C. J. Mogab, Editors, p. 225, The Electrochemical Society Softbound Proceedings Series, Pennington, NJ (1981).
8. D. Hess, *Plasma Chem. and Processing*, **2**, 141 (1982).
9. R. A. Conrad and R. H. Bruce, Unpublished results.
10. C. J. Mogab and H. J. Levinstein, *J. Vac. Sci. Technol.*, **17**, 721 (1980).
11. D. L. Smith and R. H. Bruce, *This Journal*, **129**, 2045 (1982).

12. D. L. Smith and P. Saviano, *J. Vac. Sci. Technol.*, 21, 768 (1982).
13. R. A. M. Wolters, in "Plasma Processing," J. Dielman, R. G. Frieser, and G. S. Mathad, Editors, p. 293, The Electrochemical Society Softbound Proceedings Series, Pennington, NJ (1983).
14. E. J. Egerton, A. Nef, W. Millikin, W. Cook, and D. Baril, *Solid State Technol.*, 25 (8), 84 (1982).

Correlation of Solar Cell Electrical Properties with Material Characteristics of Silicon Cast by the Ubiquitous Crystallization Process

S. Hyland*
Jet Propulsion Laboratory, California Institute of Technology, Pasadena, California 91109

D. Leung
Applied Solar Energy Corporation, City of Industry, California 91746

A. Morrison* and K. Stika
Jet Propulsion Laboratory, California Institute of Technology, Pasadena, California 91109

and H. Yoo*,[1]
Applied Solar Energy Corporation, City of Industry, California 91746

ABSTRACT

Solar cells were fabricated using a conservative "baseline" process on 1-3 Ω-cm p-type silicon from ingots cast by the ubiquitous crystallization process. Conversion efficiencies of the cells were measured, as well as spectral response and minority carrier diffusion length. Adjacent slices from the same ingot were studied for their grain size, dislocation distribution, and impurity distribution. Cell performance was related to the observed structural features, as well as to the chemical structure of the ingot.

Polycrystalline silicon cast by the ubiquitous crystallization process, Semix, Incorporated (UCP) is a candidate sheet material for low-cost solar cell applications (1). The physical structure of the UCP material as it affects the solar cell performance has been widely reported (2-8).

In this paper, we describe the electrical characteristics of solar cells made from wafers taken throughout a single UCP ingot, and correlate these characteristics with the physical structure and elemental composition of the various portions of the ingot. The data obtained relate only to the specific UCP ingot under study, while some general conclusions are also drawn. Solar cell conversion efficiency (η) at AM1, spectral response, and minority carrier diffusion length (L_D) of the cells are discussed and correlated with grain size and impurity distribution. Spectral response and L_D were measured by a short-circuit current method (I_{sc}) using a filtered tungsten light as the source for carrier generation (9). Optical microscopy was used in parallel with electron beam induced current (EBIC) measurements to determine the structural characteristics of the material. Elemental composition was established by use of secondary ion mass spectroscopy (SIMS) and Zeeman atomic absorption (10, 11). A light spot scan was performed on selected cells using a light spot $\cong$ 40 μm diam that was filtered through a thin silicon sheet such that wavelengths $<$0.8 μm were not passed.

Experimental

For this work, one ingot, a 100 × 100 × 125 mm quarter of a full casting, was studied. The distribution of properties and structure of the whole casting are inferred from this ingot.

In order to map the material quality through the ingot, it was sliced horizontally in four sections; top (section 1), 1/3 down from the top (section 2), 2/3 down from the top (section 3), and bottom (section 4). Consecutive wafers were selected to represent each section. Continuity of the grain structure through all slices within each section was confirmed. In each section, two wafers were reserved for cell fabrication, one wafer for optical microscopy and SIMS, two wafers for EBIC, and one wafer for spreading resistance or other measurements. The wafer that had originally been "face-to-face" with the one on which solar cells were fabricated was marked and used for the optical microscopy.

It was observed that the grain size in the ingot varied from an average diameter of 0.4 cm at the bottom to an average of 0.8 cm at the top (Fig. 1).

Fig. 1. UCP 4 × 4 in. wafers from ingot 5848-13C; a, left) top, and b, right) bottom. Ingot center is at lower left.

* Electrochemical Society Active Member.
[1] Present address: ARCO Solar, Incorporated, Chatsworth, California 91311.
Key words: photovoltaic, gettering, impurity, defects.

Laue backreflection x-ray was used to obtain five 1 mm spots across each sample. The preponderant grain orientations measured were, at the bottom, (110) and (100), and at the top, (111). The range of grain sizes over each 10 × 10 cm wafer was small.[2]

Defects observed within the grains include large euhedral silicon carbide (SiC) crystal inclusions (>25 μm diam) and three distinct types of dislocation arrays. Although the SiC particles were dispersed throughout most of the ingot, their concentration increased from bottom to top (~1000/cm² at the top *vs.* ~500/cm² at a position 5 cm down from the top *vs.* none at the bottom). The SiC particles were much larger in the top of the ingot than in the center. Associated with each inclusion was a distinct spherical strain field extending to approximately twice the particle diameter (Fig. 3). Figure 3a shows a typical SiC particle with the dislocation strain field, while Fig. 3b shows the residual strain field left after removal of an SiC particle. Reduced light scan photoresponse in the vicinity of these precipitates, and generally reduced fill factor (FF) and open-circuit voltage (V_{oc}) in the top section of the ingot (see cell results below) can be interpreted as evidence of impurity accumulation around the SiC crystallites (12, 13). The dislocation arrays observed included lines emanating from sharp grain corners into the bulk of impacted grains (Fig. 4), sets of parallel lines apparently distributed around bending axes (14) (Fig. 4), and multiple subboundaries running parallel to the grain boundaries. These arrays are all artifacts of substantial intergranular stress, possibly generated during solidification, though more probably generated during cooldown after solidification.

Impurity distribution measurements were made using SIMS and Zeeman atomic absorption. Few impurities were observed within the limits of detection of the SIMS instrument, generally 10^{15}-10^{17}/cm³ for most elements. Specifically, the limit for Al is ~5 × 10^{15}/cm³ and for Cu is ~10^{17}/cm³. Low levels of Al were detected in the top of the ingot. No segregation of the Al to the grain boundaries was observed in this region. Using Zeeman atomic absorption measurements, single crystal areas of the ingot were observed to contain ~3 × 10^{15}/cm³ Cu at the bottom and ~10^{16}/cm³ Cu at the top. Cu was observed to have been segregated to the grain boundaries at the bottom, but not at the top of the ingot.

[2] This ingot is typical of one of two distinct ingot structures observed by the authors in the UCP ingots. The alternate structure shows evidence of a small-grained (~0.2 cm diam) core which appears to have grown from the center bottom of the ingot (~30% of the area) to the top (~80% of the area) in a shape resembling a "bouquet." The grains outside this "bouquet" are very large, ranging up to more than 2 cm (Fig. 2).

Fig. 2. UCP 4 × 4 in. wafers from a typical ingot showing bouquet; a, left) top, and b, right) bottom. Ingot center is at lower left.

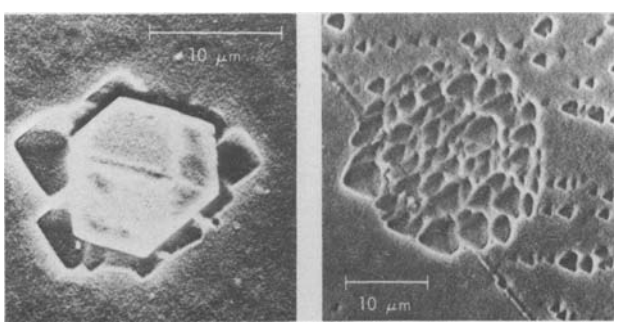

Fig. 3. Etched dislocation fields surrounding SiC particles

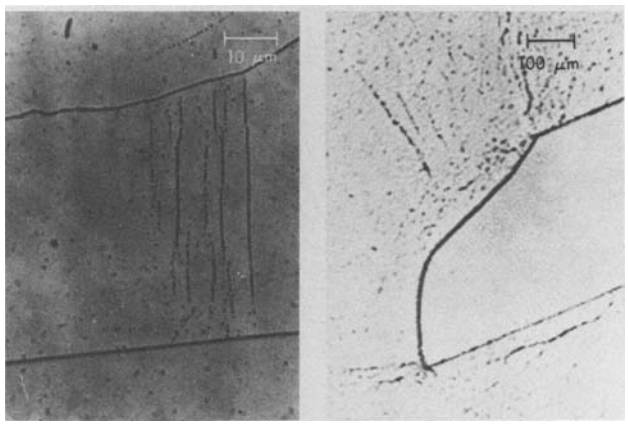

Fig. 4. Etched dislocation lines showing stress concentrations

One set of four wafers (one from each horizontal ingot section) was fabricated into 16 solar cells each using a simple "baseline" process (15) that did not include a back-surface field (BSF) or multilayer anti-reflective (AR) coating. The finished cells had a deep junction (~0.35 μm), Ti-Pd-Ag metallization and SiO AR. A matching set of four wafers was subjected to a diffusion glass gettering step and processed into solar cells along with the material that did not have the added gettering step. The gettering step consisted of $POCl_3$ diffusion and subsequent etching away of the glassy layers and the junction. A total of fifty-six 2 × 2 cm baseline process solar cells and 59 gettered cells was obtained.

Figure 5a shows efficiency as a function of position in the ingot. Over the entire ingot, the UCP cells made by the baseline process averaged 65% the efficiency of the controls. The gettered cells averaged 72% of the efficiency of control cells made from Czochralski (Cz) silicon. From Fig. 5b, it can be seen that the open-circuit voltage (V_{oc}) was low in the top of the ingot (section 1), but was higher in the center and bottom sections of the ingot (sections 2, 3, and 4). The V_{oc} at the bottom averaged 95% that of the Cz controls, while at the top it averaged only 81% that of the controls. The range of voltages was quite large for the UCP material, especially in the top section. These voltages were not appreciably affected by the additional gettering step. Low V_{oc} also seems to correlate with low *FF* (Fig. 5c).

In contrast to the behavior of V_{oc}, the short-circuit current (I_{sc}) (Fig. 5d) was low in the center two sections (2 and 3), but was higher in the top and bottom. Again, the variation in I_{sc} was very large in the UCP cells compared to that of the Cz controls. The top and bottom sections showed an I_{sc} approximately 90% that of the Cz controls, while the other two sections averaged approximately 75% of the controls. In addition, the center two sections improved an average of 20% with the added gettering step, while no appreciable improvement was seen in the I_{sc} of the top and bottom sections. After gettering, the I_{sc} of the center two sections was still lower than the I_{sc} of the top and bottom sections.

L_D (Fig. 6) was low in the center two sections and slightly higher in the top and bottom. (These data are supported by light spot scanning, see below). The L_D improved not only in the center sections with gettering,

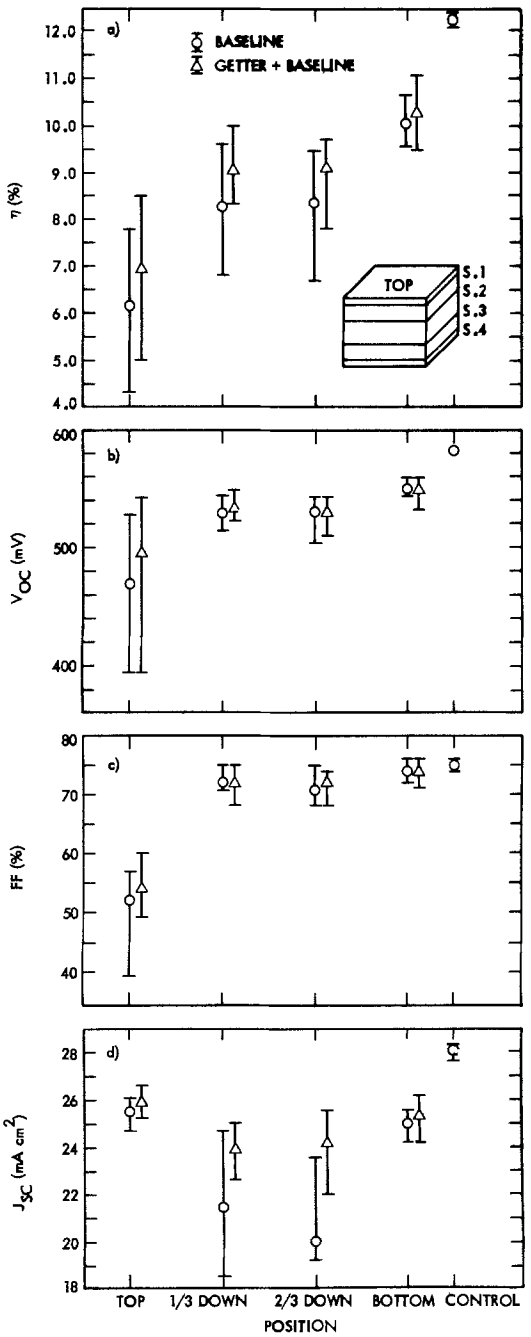

Fig. 5. Parameters of UCP and Cz control solar cells vs. wafer position; a) η, b) V_{OC}, c) FF, and d) J_{SC}.

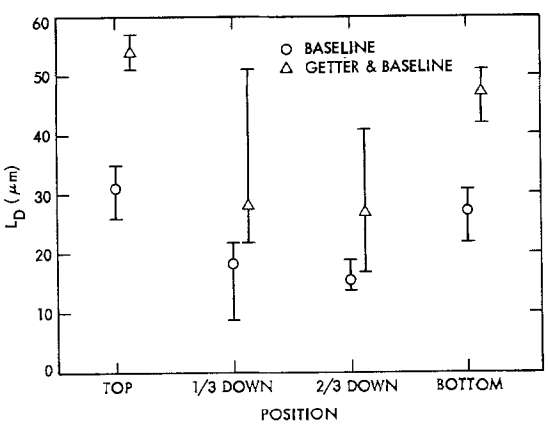

Fig. 6. L_D of UCP cells vs. wafer position in the ingot. Cz control cell measures $L_D \simeq 150$ μm.

but also improved in the top and bottom. The center sections improved approximately 95%, while the top and bottom improved on an average of 77%. This does not correspond to the improvements seen in I_{sc}.

Response of the center and top sections to light spot scanning (Fig. 7) reveals that the L_D is lower in the center section than in the top section, as indicated by the signal level within the grains. The top layer shows a great deal more variation in signal level probably as a result of the large number of SiC particles that act as recombination centers.

Discussion

Cell results indicate that this material did not produce as efficient solar cells as those produced from single-crystal Cz silicon. Using the EBIC technique, a loss of response corresponding to grain boundaries, as well as to "stress" regions of high dislocation density, was observed (Fig. 8). This loss of response is sufficient to cause the current of the polycrystalline cells to be lower than that of single-crystal Cz cells, but cannot explain the great variation in response throughout the ingot. Defects, including impurities, dislocations, and SiC particles, and their distribution within the individual grains of the UCP material are believed to be the controlling factor in the quality of solar cells from this material, and the nonhomogenous distribution of cell quality throughout the ingot. The impurity distribution leads us to believe that the ingot solidified directionally from the bottom to the top.

The higher L_D observed in the bottom section of the ingot is apparently due to segregation of impurities to the boundaries of the small grains in this region. This distribution was confirmed for Cu using Zeeman analysis (see above).

In the center two sections, low current corresponding to a low L_D was the main factor that degraded the cell performance. The light spot scan (Fig. 7) indicates that there was a loss of I_{sc} at the grain boundaries, but that lifetime within the grains was also limited. That

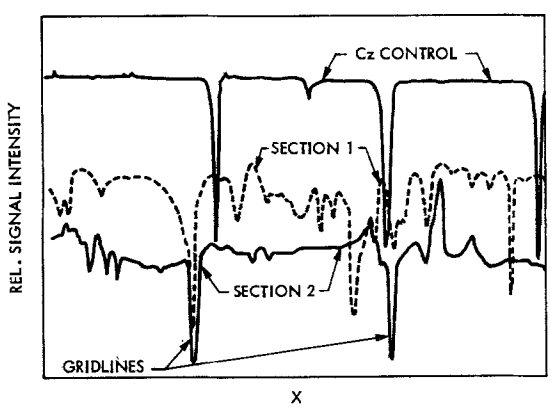

Fig. 7. Light spot scan of a Cz control compared to that of UCP cells from the top (S.1) and center (S.2). (Grid spacing is 2.5 mm.)

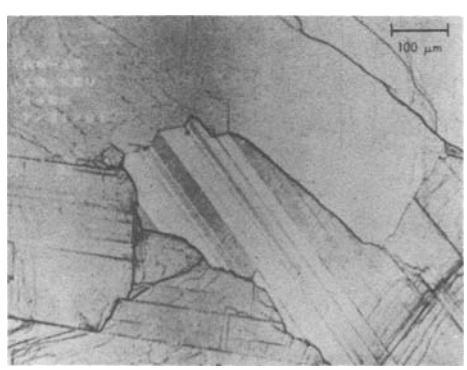

Fig. 8. EBIC image of response of UCP material

these two sections improved greatly with the addition of a phosphorus gettering step indicates that in this region there are mobile lifetime limiting impurities within the grains which degrade cell performance. In a separate experiment, blanks covered with a CVD layer of SiO_2 during the $POCl_3$ gettering step showed a smaller improvement in I_{sc}, indicating that part of the cell improvement is due to internal gettering by grain boundaries or defects, or to thermal annealing of defects; however, most of the improvement is due to the phosphorus gettering action.

The V_{oc} and *FF* were low in the cells from the top section, indicating that the junction was being shunted or that there was a high recombination current. The addition of an "external" gettering step had very little effect on the I_{sc} of these cells. From this evidence, we conclude that internal gettering of impurities, in part by SiC, is taking place in the top. Impurities "trapped" near SiC particles become electrically inactive and do not degrade lifetime (16), but will degrade V_{oc} and *FF*.

Conclusions

Impurities and defects, including grain boundaries, SiC particles, and dislocations, in the UCP ingot studied control the quality of solar cells made from this material. Their distribution causes a wide variation in the observed solar cell performance. In the bottom of the ingot, impurities are incorporated into the grain boundaries or are rejected into the melt during growth. This is supported by the fact that there is very little "cleaning" of the grain by gettering. The central sections of the ingot include a greater amount of these impurities within the grain bulk. These impurities are gettered and rendered ineffective by grain boundaries or defects during processing, or they can be gettered to the surface and etched away. At the top of the ingot where the grain sizes are large and a large number of SiC particles occur, the impurities remain in the bulk attached to these SiC particles. The SiC particles within the grain bulk act to decrease the quality of the junction of the solar cells even while they clean impurities from the grain bulk. There is no additional "cleaning" of the grains and improvement in I_{sc} in this section with the added gettering step, since the impurities are already immobilized by the strain field surrounding the SiC particles.

Acknowledgments

The authors wish to thank T. G. MacConnell for his valuable assistance in sample preparation and characterization. The work described was supported by the Flat-Plate Solar Array Project of the Jet Propulsion Laboratory, California Institute of Technology and was sponsored by the Department of Energy through an interagency agreement with NASA.

Manuscript submitted July 12, 1982; revised manuscript received Feb. 22, 1983. This was Paper 62 presented at the Montreal, Que., Canada, Meeting of the Society, May 9-14, 1982.

Any discussion of this paper will appear in a Discussion Section to be published in the December 1983 JOURNAL. All discussions for the December 1983 Discussion Section should be submitted by Aug. 1, 1983.

Jet Propulsion Laboratory assisted in meeting the publication costs of this article.

REFERENCES

1. "Semicrystalline Casting Process Development and Verification," Quarterly Progress Report No. 3, U.S. Department of Energy and Semix Incorporated Cooperative Agreement, DOE-FCO1-80ET 23197 (1980).
2. G. M. Storti, in 15th IEEE Photovoltaic Specialists Conference, Kissimmee, FL (1981).
3. J. Lindmayer, in 13th IEEE Photovoltaic Specialists Conference, Washington, D.C. (1978).
4. J. Lindmayer and Z. Putney, in 14th IEEE Photovoltaic Specialists Conference, San Diego, CA (1980).
5. R. G. Rosemeier, R. W. Armstrong, S. M. Johnson, G. M. Storti, and C. Cm. Wu, in 15th IEEE Photovoltaic Specialists Conference, Kissimmee, FL (1981).
6. S. M. Johnson, R. G. Rosemeier, C. D. Wang, R. W. Armstrong, H. C. Lin, and G. M. Storti, in IEEE Electron Devices Meeting, Washington, D.C. (1980).
7. G. M. Storti, S. M. Johnson, H. C. Lin, and C. D. Wang, 14th IEEE Photovoltaic Specialists Conference, San Diego, CA (1980).
8. A. D. Morrison, 13th IEEE Photovoltaic Specialists Conference, Washington, D.C. (1978).
9. H. I. Yoo, P. A. Iles, and D. P. Tanner, "Silicon Solar Cell Process Development Fabrication and Analysis," JPL Contract No. 955089, Annual Report (1979).
10. J. D. Miller and H. Koizumi, "Analytical Application of Zeeman Atomic Absorption," American Laboratory (1979).
11. T. Hadeishi and R. McLaughlin, "Zeeman Atomic Absorption Spectrometry," Lawrence Berkeley Laboratory Report, LBL-8031 (1978).
12. C. V. Hari Rao, H. E. Bates, and K. V. Ravi, *J. Appl. Phys.*, **47**, 2614 (1976).
13. H. Kressel, R. V. D'Aiello, E. R. Levin, P. H. Robinson, and S. H. MacFarlane, *J. Cryst. Growth*, **39**, (1977).
14. "Dislocations and Mechanical Properties of Crystals," J. C. Fisher, W. G. Johnson, R. Thomson, and T. Vreeland, Jr., Editors, Lake Placid Conference, Sept. 6-8, 1956, John Wiley and Sons, Inc., New York (1957).
15. H. I. Yoo, P. A. Iles, and D. P. Tanner, "Silicon Solar Cell Process Development Fabrication and Analysis," JPL Contract No. 955089, Annual Report (1979).
16. R. H. Hopkins, J. R. Davis, A. Rohatgi, M. H. Hanes, P. Rai-Choudhury, and H. C. Mollenkopf, "Effect of Impurities and Processing on Silicon Solar Cells," JPL Contract No. 954331, Final Report (1982).

Fabrication of Via Holes in 200 μm Thick GaAs Wafers

S. P. Yenigalla and C. L. Ghosh

ITT Electro-Optical Products Division, Roanoke, Virginia 24019

ABSTRACT

Etching of via holes from the back side of GaAs is an important processing step for fabrication of monolithic microwave integrated circuits. Normally, via holes are defined in wafers of 100 μm or smaller thickness. In this paper, we describe a process for fabrication of via holes in wafers of 200 μm thickness. A phosphoric acid-hydrogen peroxide based etch has been used. The etch rate decreases with time after the start of etching due to entrapment of etchant in the via hole.

Etching of via holes from the wafer back-side is an important processing step for fabrication of GaAs microwave IC's for low noise and high power applications (1-6). The via holes are used for source grounding in low noise and for reduction of parasitics (1), and for power dissipation (5) in high power applications. Since the via holes have to be plated with a material such as gold, they should have a funnel-shaped appearance with a wider opening at the back side of the wafer in order to obtain an electrically continuous film. The substrate on which integrated circuits are usually fabricated is semi-insulating GaAs. So far, the via holes have been fabricated in wafers of thicknesses of ~100 μm or less (1-5). GaAs wafers are extremely fragile which makes handling of wafers of this thickness very difficult. In this paper, we describe a method of reproducibly fabricating via holes in wafers of 200 μm thickness. This would have a significant impact on the process yield of GaAs IC's.

The GaAs starting wafers used in our experiments were undoped high resistivity with (100) orientation The wafers were first mechanically and then chemo-mechanically polished to a thickness of 200 $\pm$ 4 μm. Shipley AZ 1450J photoresist was used to define 3 mil diam holes on the wafer for etching. The wafer was postbaked to 135° for 45 min for hardening the photoresist so that it could withstand the etching process. To make funnel-shaped via holes, the etching solution should react almost isotropically with different faces of GaAs to avoid undercutting. We experimented with different etchants, such as: H_2SO_4:H_2O_2:H_2O, HCl:H_2O_2:H_2O, and NH_4OH:H_2O_2:H_2O. The problem encountered with these etchants was that to make these nearly isotropic, the ratio of oxidizing (H_2O_2) to oxide dissolving (acid or alkali) agent should be very high or very low, which makes the etch rate very low. The time required for good via holes made with these etchants was typically more than 3 hr. Additionally, the etch rate was not reproducible for these etchants, the worst case being the HCl-based ones. This is probably because of the reaction between H_2O_2 and HCl, resulting in reduction of H_2O_2 to H_2O.

Excellent reproducibility and a high etch rate were obtained by using a phosphoric acid based etch. The composition of the etching solution was 75 ml phosphoric acid, 100 ml H_2O_2, and 25 ml H_2O. To etch a 200 μm thickness takes about 35 min. A variation of less than 10% was observed in etch time. The end point was detected *in situ* with a microscope attached to the setup. In order to obtain uniformity of etching over a larger area, the following procedure was used: The substrate was attached to a glass plate by wax. The glass plate was held face down at a height of about 4 in. from the bottom of a beaker containing the etch solution. The solution was stirred by a magnetic stirrer at a constant speed. Figures 1a and b show the front and back surface of the wafer after the photoresist had been stripped. Figure 1c shows a section of the wafer with via holes.

Key words: gallium arsenide, gallium arsenide IC's, GaAs chemical etching, GaAs IC processing.

Figure 2 shows the section of the via holes at three different times during the etch while Fig. 3 shows the depth of the holes as a function of time. It can be seen that the vertical etch rate is higher at the beginning but it slows down toward the end. This is due to entrapment of the etching solution in the via holes and slow replenishment of the etchants from the bulk of the etching solution. The speed of stirring affects the etch rate which increases with an increase of the stirrer speed.

In conclusion, we have developed a process to fabricate via holes in semi-insulating GaAs wafers in thicknesses of 200 μm. The process is fast and reproducible and will be useful in improving the yield of monolithic microwave IC fabrication processing.

Acknowledgments

Thanks are due to Dr. Dennis Fisher and to ITT Electro-Optical Products Division for support in pursuing this work.

Manuscript submitted Sept. 29, 1982; revised manuscript received Dec. 17, 1982.

Any discussion of this paper will appear in a Discussion Section to be published in the December 1983

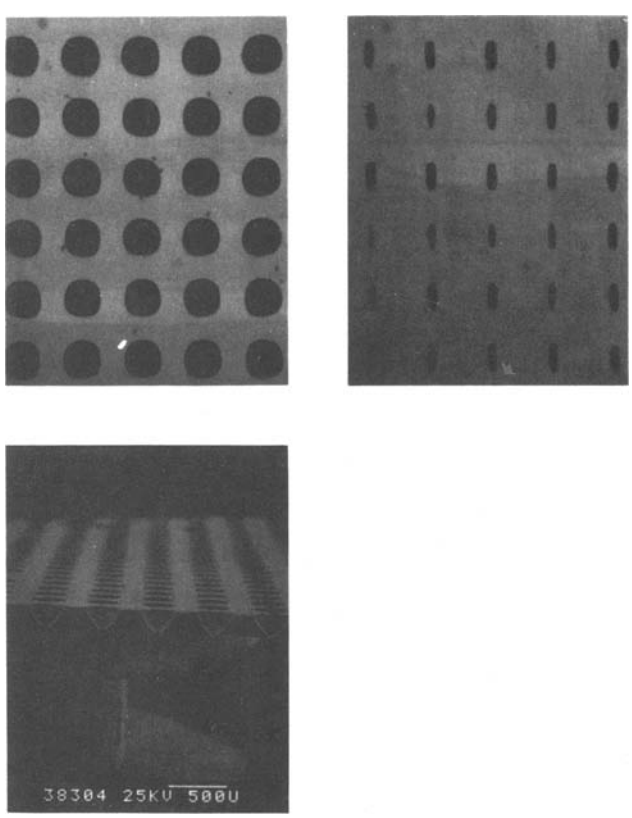

Fig. 1. GaAs wafer with via holes. (a) Back-side view, (b) top view, (c) section of via holes after cleaving of the wafer.

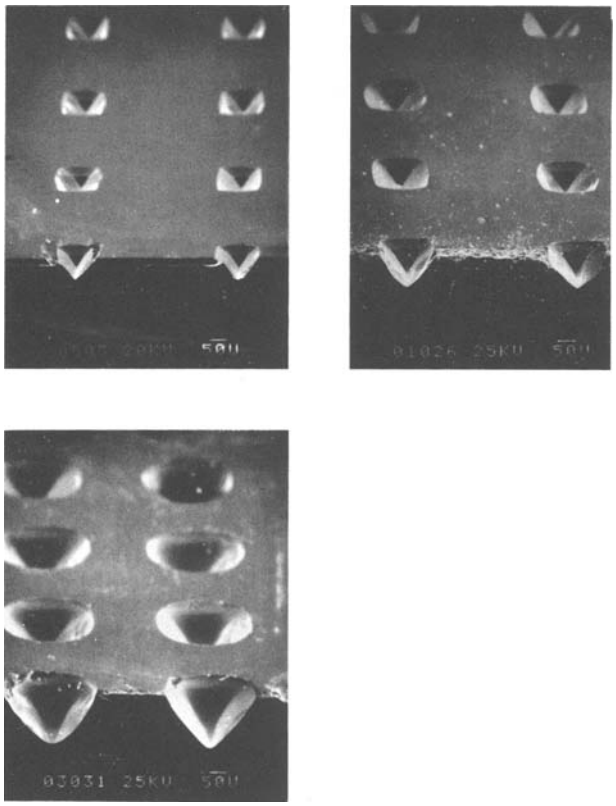

Fig. 2. Section of the wafer at different times during via hole etching. (a) 6 min, (b) 12 min, (c) 30 min.

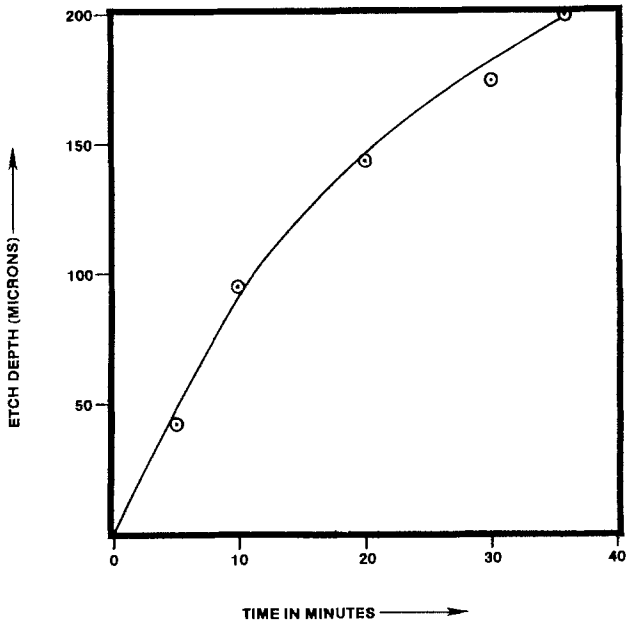

Fig. 3. Depth of etching for via holes vs. time during etching of the via holes.

JOURNAL. All discussions for the December 1983 Discussion Section should be submitted by Aug. 1, 1983.

ITT Electro-Optical Products Division assisted in meeting the publication costs of this article.

REFERENCES

1. Y. Hirachi, Y. Takeuchi, T. Matsumura, K. Ohta, K. Kosemura, and S. Yamamoto, Technical Digest, IEDM, p. 676, Washington, DC (1981).
2. J. L. Vorhaus, R. A. Pucel, and P. Ng, in "Proceedings of GaAs IC Symposium," p. 23, Lake Tahoe, Sept. 27-28, 1979.
3. R. E. Williams and V. Sokolov, in "Proceedings of GaAs IC Symposium," p. 24, Lake Tahoe, Sept. 27-28, 1979.
4. L. A. D'Asaro, J. V. DiLorenzo, and H. Fukui, Technical Digest, IEDM, p. 370, Washington, DC (1977).
5. F. Hasegawa, in "GaAs FET Principles and Technology," J. V. DiLorenzo and D. D. Khandelwal, Editors, p. 219, Artech House (1982).
6. R. M. Osgood, Jr., A. Sanchez Rubio, D. J. Ehrlich, and V. Danen, *Appl. Phys. Lett.*, **40**, 391 (1982).

Precise Evaluation of Oxygen Measurements on CZ-Silicon Wafers

K. Graff

Telefunken electronic GmbH, D-7100 Heilbronn, Germany

ABSTRACT

Intrinsic impurity gettering due to oxygen precipitates in the bulk of a silicon wafer has recently enhanced interest in precisely defined oxygen concentrations in Czochralski-silicon wafers. The determination of the oxygen content in as-received wafers by means of a common infrared absorption measurement has, however, proved to give systematic errors: The results depend on the applied evaluation method, based on single beam or multiple beam reflection, respectively, and on the residual damage on the reverse side of the wafer. A new method of evaluation is presented which is based on a corrected multiple beam reflection. For its application, an additional measurement is needed to determine the absolute transmission of the wafer. With the new method, unequivocal results were obtained, independent of the quality of the back side treatment of the wafer. By this means, the so far high measurement error was considerably reduced.

For standard measurements of the oxygen concentration in silicon crystals 2 mm thick slices which are polished on both sides are provided (1, 2). In order to calculate the absorption coefficient from the measured transmitted intensity, the expression for single reflection is usually applied. The difference between the application of single reflection and multiple reflection will be less than 10%. The deviations between these methods, however, depend on the thickness of the specimen and the total absorption due to lattice vibration, oxygen, free carriers, and surface damage.

The gettering effect of oxygen precipitates in the bulk of silicon wafers (intrinsic or internal gettering) which has recently been discovered and used to improve devices requires a well-defined oxygen content in every wafer. Therefore, silicon suppliers usually offer pulled crystals in three specifications: low, medium, and high oxygen content. The oxygen concentra-

Key words: oxygen, infrared absorption, back side damage.

tions in one specification vary only by about ±15% from the specified mean value. On the other hand, the measurement error using standard method (2) was estimated to slightly more than ±10%. If multiple reflection is neglected, this error will be enhanced by a systematic deviation of $\leqq +13\%$. So the oxygen concentrations of two neighboring specifications are practically within the measurement error. Furthermore, it would be desirable to measure the oxygen content on the as-received wafers, the thickness of which is between 350-600 μm in order to check the material quality and to control the effectiveness of processes for intrinsic gettering. This measurement, however, shows further deviations from the respective results which were obtained by means of the standard method on 2 mm thick slices.

This paper presents an improved method to evaluate infrared absorption measurements. With the aid of a first absorption spectrum using an air reference, the back side damage of the wafer to be measured is determined quantitatively. From a second common difference measurement, the oxygen concentration of this wafer is calculated by applying the expression for multiple reflection and taking into account the scattering of the radiation at the unpolished back side by assuming an enhanced lattice absorption. Corresponding to the height of the enhanced absorption, the results for the oxygen content of the wafer tend to approach those obtained for single reflection or those obtained for multiple reflection, thus, reducing the measurement error.

Experimental

From a 3 in. Czochralski-grown p-type silicon crystal (6.5 Ωcm), of medium oxygen content slices were cut in three different thicknesses: about 380 μm, 600 μm, and 2 mm. Every wafer was polished on the front side. The 2 mm thick specimens were polished on both sides in order to prepare specimens for the standard oxygen determination. These slices were taken from the front and tail of the selected area of the crystal rod to monitor the slope of the oxygen content with respect to the crystal axis. The back side of the thinner wafers were treated in different ways: polished, etched, sawed, ground, and sandblasted. Each treatment was carried out on wafers of 380 and 600 μm thickness. For difference measurements, reference specimens were prepared in the same way from a float-zoned n-type silicon crystal with a resistivity of 170 Ωcm[1]

The infrared absorption spectra were recorded from 1400 to 900 cm^{-1} by means of a Perkin-Elmer 684 microprocessor-assisted double beam grating spectrometer. Usually a medium slit width was used which enabled a spectral resolution of 2.5 cm^{-1}. In some experiments, a wide slit width was applied additionally to suppress interference effects. The scan velocity which is coupled to the suppression of noise was adapted to the respective signal height. All specimens were measured with air reference in an absolute scale (without sample = 100% transmission) and by the difference method using the respective reference specimen with the same back side treatment or other reference specimens which had only the same thickness.

Experimental Results

With the aid of the air reference spectra, the transmission at 1105 cm^{-1} was determined, where oxygen absorption was subtracted and phonon absorption was taken into account. This can be easily done if the spectrum of the respective reference specimen is recorded additionally. Transmissions were found to lie between 50 (both sides polished) and 12% (back side ground); the ground reference specimen exhibited a transmission of only 5.6%.

Results of the oxygen content obtained by the difference measurement are plotted in Fig. 1, showing values after applying the expression for single reflection, a, and multiple reflection, b, as function of the transmission from the air reference measurement. For the evaluation, the calibration factor of DIN was used which, indeed, is now the same as the factor presented in the new ASTM Standards F 121-81. The results of the linear regressions calculated from all measurement points and indicated in Fig. 1 (broken line) show a remarkable increase of the evaluated oxygen content with increasing transmissions, the gradients being equal for applying single and multiple reflections. This increase results in a deviation of the oxygen content of 18 and 19% between the transmissions of 10-50% in Fig. 1a and b, respectively. Furthermore, the linear regression is shifted to lower oxygen contents for applying multiple reflection. This shift amounts to 17%. The highest overall deviation between 50% transmission in Fig. 1a and 10% transmission in Fig. 1b amounts to 34%, even neglecting the scattering of measurement points which is enhanced for low transmission rates, mostly due to the noisy spectra.

Two widely separated specimens (380 μm thick both sides polished, and 380 μm thick back side ground) were measured by the difference method using reference specimens of various transmissions. The results are indicated in Fig. 1 at transmissions of 12.2 and 49.5%, respectively. They scatter within the common measurement error but do not show any dependence of the evaluated oxygen content on the specific properties of the respective reference specimen.

As deduced from the experimental results, an improved evaluation method should consider only the properties of the measurement specimen. Furthermore, it should compensate the dependence of the evaluated oxygen content on the transmission, the latter being determined mostly by the scattering of the radiation at the damaged back side.

Improved Evaluation Method

From the measured absolute transmission T at a wavelength of 1105 cm^{-1}, a corresponding absorption α^* (including the lattice absorption) or a reflection R^* can be calculated applying the expression for multiple reflection

$$T = \frac{(1-R)^2 e^{-\alpha^* x}}{1 - R^2 e^{-2\alpha^* x}} \quad [1]$$

or

$$T = \frac{(1-R^*)^2 e^{-\alpha x}}{1 - R^{*2} e^{-2\alpha x}} \quad [2]$$

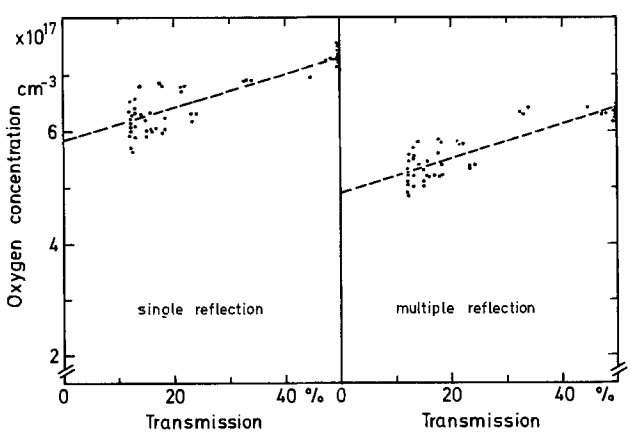

Fig. 1. Oxygen concentrations determined on specimens of different thicknesses and various back side treatments as function of their absolute transmissions at the wavelength of 1105 cm^{-1}. Evaluation based on the expression for single reflection (a, left) and multiple reflection (b, right).

[1] The wafer preparation was carried out by Dr. Ludsteck, Siemens AG, München, in order to perform a round robin within DIN committee NMP 221 to establish the influence of back side damage and wafer thickness on the determination of the oxygen content.

with x symbolizing the thickness of the specimen and a reflection $R = 0.3$. The lattice absorption α at this wavelength amounts to 0.8 (2) or 0.4 cm^{-1} (1), respectively. The value of 0.8 cm^{-1} was verified by a control measurement on a 2 mm thick float-zone Si specimen. Both methods for evaluating the absolute transmission are equivalent and yield finally the same equation.

For a reduced absolute transmission T due to back side damage, Eq. [1] and [2] yield increased values of the absorption α^* and the reflection R^*. As will be shown later in Eq. [9], α^* and R^* should move in an opposite direction in order to yield identical results for the oxygen content. Whereas an increased absorption α^* enables a reasonable correction, an increased reflection R^* does not. This can be explained by the fact that an increased absorption takes into account the intensity loss by scattering of the radiation at the damaged back side; whereas, an increased reflection does not reduce the intensity of the radiation with the exception of the transmitted beam. So only the application of the enhanced absorption coefficient α^* deduced from Eq. [1] yields the intended correction.

Evaluating the difference measurement the minimum of the oxygen absorption spectrum is calculated by solving the equation for

$$T_{cz}/T_{ref} \qquad [3]$$

cz = Czochralski-grown specimen, and ref = reference specimen. The baseline is usually determined graphically. For its calculation or measurement, two additional reference specimens would be needed to form the relative transmission

$$T_{ref\ 3}/T_{ref\ 2} \qquad [4]$$

This relative transmission must satisfy the following special condition to become the baseline for the oxygen band

$$T_{cz}\ (\text{neglecting oxygen})/T_{ref} = T_{ref\ 3}/T_{ref\ 2} \qquad [5]$$

The condition is satisfied if

$$R_i = R \qquad [6]$$

$$\alpha^*_{cz}x_{cz} = \alpha^*_{ref\ 3}x_{ref\ 3}\ (\text{neglecting } \alpha_0)$$

$$\alpha^*_{ref}x_{ref} = \alpha^*_{ref\ 2}x_{ref\ 2}$$

i = various indexes. Finally the oxygen concentration is calculated from the double quotient [3] and [4]

$$T_{cz}T_{ref\ 2}/T_{ref}T_{ref\ 3} \qquad [7]$$

Because of the conditions for the baseline [6], this expression depends only on the parameters of the Czochralski-grown measurement specimen: x_{cz} and α^*_{cz} for equal thicknesses of the reference specimen $x_{cz} = x_{ref}$. For simplicity the index, cz is now omitted

$$T_{cz}/T_{bl} = \frac{e^{-\alpha_0 x}\,(1 - R^2\,e^{-2\alpha^* x})}{1 - R^2\,e^{-2(\alpha^* + \alpha_0)x}} \qquad [8]$$

with T_{bl} symbolizing the transmission of the baseline at the wavelength of the minimum of the oxygen band. This is the usual equation for the evaluation based on multiple reflection (3) including an additional absorption due to the back side damage. α_0 is the absorption coefficient of the 9 μm oxygen band to be determined

$$e^{-\alpha_0 x} = A + \sqrt{A^2 + \frac{e^{2\alpha^* x}}{R^2}} \qquad [9]$$

$$A = \frac{T_{bl}}{2T_{cz}}\left(1 - \frac{e^{2\alpha^* x}}{R^2}\right)$$

Since A is negative for all $\alpha^* x$, the positive sign of the square root must be chosen. For high α^* (low transmission), A and the square root increase drastically. The result is the difference of two large quantities and scattering will increase. Finally, the oxygen concentration is calculated from α_0 by multiplying it with the calibration factor (1, 2).

The results obtained by applying this new method of corrected multiple reflection are indicated in Fig. 2a as function of the respective absolute transmission. The gradient of the linear regression (full line) is decreased by nearly one order of magnitude with respect to the gradients of Fig. 1 (broken lines). The residual gradient is far less than the scattering of the measurement points, and the deviation between the transmissions of 10 and 50% amounts to only 3%. The mean value of the oxygen content is nearly identical for several sets of measurement points and amounts to 6.25×10^{17} cm^{-3} with a standard deviation of about 4%.

As can be seen from Fig. 2a, the results applying single reflection (SR) are higher than those obtained by the new method with the exception of least transmissions observed on wafers with ground back sides. On the other hand, the results obtained by applying multiple reflection (MR) are lower than those by the new method with the exception of the highest transmissions observed on wafers which were well polished on both sides.

It is interesting to consider the results for the oxygen contents applying corrected multiple reflection with respect to the single reflection results as demonstrated in Fig. 2b. The difference between oxygen contents evaluated by corrected multiple reflection and multiple reflection divided by the difference between single and multiple reflection was plotted as function of the respective transmission. The results obtained on specimens with low transmissions tend to approach the single reflection boundary; whereas, the results obtained on highly reflecting specimens approach the multiple reflection side. Both boundaries, however, were not really touched. Because of an additional lattice absorption, the curves split for different thicknesses of the specimens indicated only for the two extremes. This splitting still depends on the lattice absorption coefficient. The curves are, however, independent of the oxygen concentration in that particular sample.

Conclusion

In order to get precise oxygen contents especially in as-received Czochralski silicon wafers, the traditional evaluation methods are not sufficient since the results depend on the respective back side damage of the wafer and on the evaluation method chosen (single reflection-multiple reflection). Wafers of different sup-

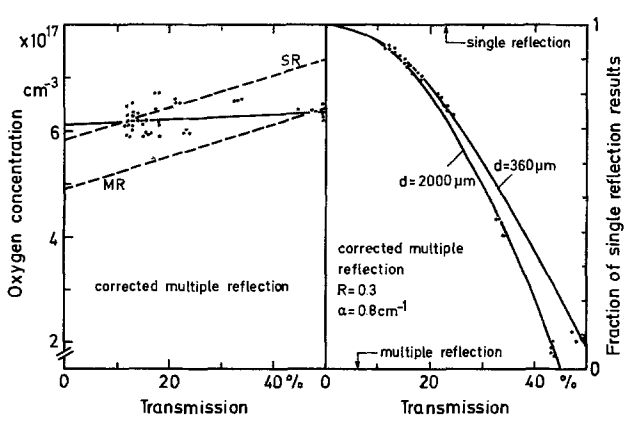

Fig. 2. (a, left) Oxygen concentrations measured on the same specimens as in Fig. 1, evaluation by the new method based on corrected multiple reflection. SR = single reflection, MR = multiple reflection from Fig. 1. (b, right) Results of Fig. 2a plotted in percentage of the results obtained by assuming single reflection as function of the transmission.

pliers vary considerably in the back side damage and absolute transmissions between 15 and 40% were measured. Therefore, high deviations from the true oxygen content can be expected when applying evaluation methods which hold only for boundary conditions.

Applying the new method based on a corrected multiple reflection, these difficulties can be overcome since the back side damage is taken into account. The overall deviation is practically reduced to the scattering of the measurement points; whereas, the traditional methods yield a maximum deviation of 34% neglecting the scattering of the measurement points.

The application of the new method requires an additional measurement of the absolute transmission of the specimen (air reference) and an expanded calculation which, however, is easily done with programmable calculators. To record the common difference spectrum, any reference specimen (float zone silicon) of about the same thickness can be used independent of the respective back side damage. The equality of thickness is not very critical since the phonon spectrum near the wavelength of 9 μm to be compensated by the reference specimen is relatively flat. For noncomputerized spectrometers, the transmissions of the reference specimen and the wafer to be measured should be comparable in order to get a relative transmission in the vicinity of 100% which can be adjusted to the desired height of 80-90%. Microprocessor-assisted spectrometers make this compensation possible over a very extended scale. The scattering of measurement points, however, is less for higher absolute transmissions of the measurement specimen for two reasons: (*i*) the difference absorption spectrum is less noisy, and (*ii*) low transmissions cause higher uncertainties in the evaluation of the oxygen absorption coefficient due to a difference of two large quantities.

We believe that the higher precision of the new method justifies the increased effort since differently treated specimens can be compared. The results are independent of a particular evaluation method. Therefore, the results obtained on the same specimen in different laboratories can be compared.

Manuscript received Nov. 12, 1982.

Any discussion of this paper will appear in a Discussion Section to be published in the December 1983 JOURNAL. All discussions for the December 1983 Discussion Section should be submitted by Aug. 1, 1983.

Telefunken Electronic assisted in meeting the publication costs of this article.

REFERENCES

1. ASTM F 121-81, "Annual Book of ASTM Standards," Part 43, Philadelphia, PA (1981).
2. DIN 50438, Teil 1, Beuth Verlag GmbH, Berlin (1978).
3. K. Graff, E. Grallath, S. Ades, G. Goldbach, and G. Tölg, *Solid-State Electron.*, **16**, 887 (1973).

Origin and Elimination of Crescent-Shaped Growth Defects in LPE Layers of InGaAs/InP Alloys

K. D. C. Trapp and F. Ermanis

Bell Laboratories, Murray Hill, New Jersey 07974

ABSTRACT

Crescent-shaped growth defects have been occasionally observed in InP/InGaAs liquid epitaxy layers grown on InP substrates. The source of these defects is traced to residual surface contamination involving S, adsorbed oxygen, and oxides of P and In from pregrowth etching of the substrate in $H_2SO_4/H_2O_2/H_2O$ solutions. Auger study of the cleaning procedure suggests that a thorough rinsing in DI water following the $H_2SO_4/H_2O_2/H_2O$ etch is essential to remove the S and reduce the O contamination to eliminate these crescent-shaped defects.

InGaAs/InP layers grown by liquid phase epitaxy (LPE) on <100> InP substrates are useful for photodetector applications. Generally, the substrate-epilayer interface is a source of defects that affects the quality of the epitaxial layer, the device yield, and the performance. These defects may be divided into two types: dislocations (initially present in substrates) that extend or multiply in the epilayers and defects that arise from nucleation problems at the substrate-epilayer interface. This communication reports the origin and elimination of crescent-shaped growth defects observed in InGaAs/InP LPE structures. The origin of these defects has been traced to residual contamination involving sulfur, adsorbed oxygen, and oxides formed on the InP substrate surface from etching in $H_2SO_4/H_2O_2/H_2O$ solutions.

The InP substrates used for LPE were polished with a 0.1% bromine-methanol solution and were degreased by boiling in acetone and methylene chloride. The substrates were then etched for 2 min in an H_2SO_4(10): H_2O_2(1):H_2O(1) solution to remove the polishing damage, rinsed in deionized water, and dried with N_2 gas before loading in the LPE boat. This cleaning procedure sometimes resulted in the crescent-shaped defects in the InP/InGaAs epilayers as shown in Fig. 1a. An enlarged view is shown in Fig. 1b. Figure 2a shows a cross-sectional view of a typical crescent-shaped defect taken on a cleaved edge. Figure 2b is a

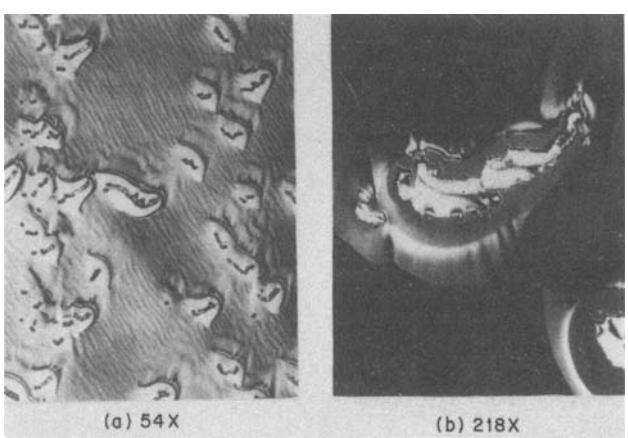

Fig. 1. (a) Optical micrograph showing typical crescent-shaped defects observed in InP/InGaAs LPE layers. (b) An enlarged view of one of the crescent defects.

Key words: III-V semiconductors, LPE, growth defects.

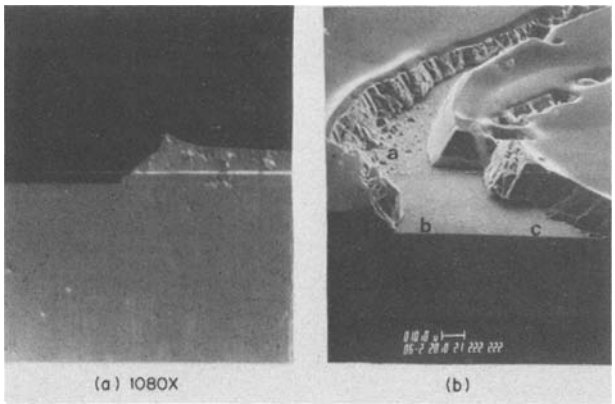

Fig. 2. (a) An optical micrograph of the crescent defect on a cleaved and etched <110> edge. (b) SEM micrograph showing the defect in a (See Fig. 3 for details of regions a, b, and c).

scanning electron micrograph of the same defect. Figure 3a, b, and c show details of the corresponding regions a, b, and c on Fig. 2b. It is apparent from Fig. 1, 2, and 3 that a crescent-shaped defect is an area where there is lack of continuous epilayer growth. The spherical sector-like pyramidal growth of the layers in Fig. 3b suggests poor nucleation. Moreover, Fig. 3c indicates complete lack of growth. The square pits illustrate the degree of InP substrate dissociation. These observations led us to conclude that these growth problems may be related to contamination on the InP substrate surface.

Auger analysis of several InP substrate surfaces was utilized to assess the nature of the residual contamination from the cleaning and etching procedures. Substrates of InP, with no intentional doping and with S and Sn doping, when etched in $H_2SO_4/H_2O_2/H_2O$ and rinsed with DI water all showed sulfur, adsorbed oxygen, and oxides of P and In. One should note that electron stimulated desorption makes the sulfur signal time dependent; however, the time dependency of the signal is constant for the two Auger spectra shown in Fig. 4. Figure 4a shows a typical spectrum. However, a thorough rinsing (5 min) in DI water removes the sulfur, and reduces the adsorbed oxygen and the oxides of P and In as shown in Fig. 4b. This can be seen by a qualitative comparison of the relative peak heights of the Auger spectra of the oxides of P and In with those of In, although the chemical constitution of the oxides is unknown. Auger spectra of InP substrates when etched directly in HF/H_2O (1:1) solutions and

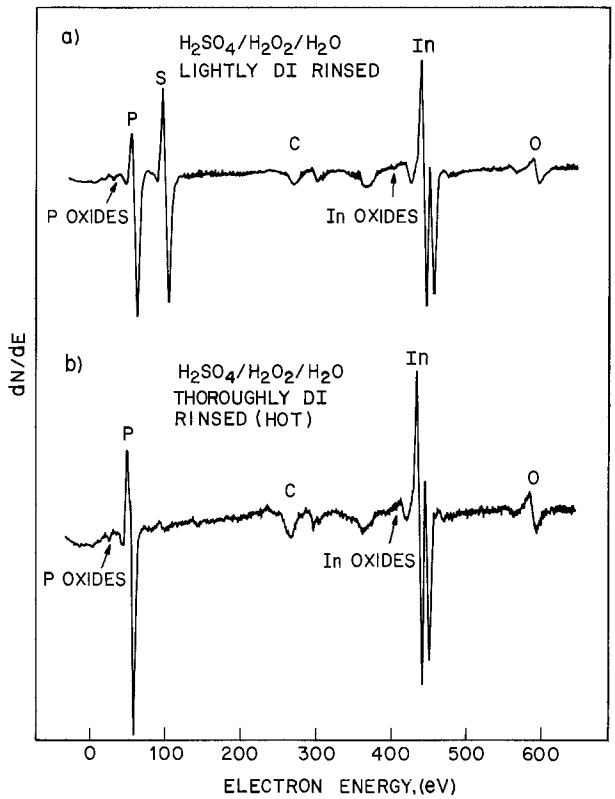

Fig. 4. Electron stimulated derivative Auger spectra of InP surfaces after etching with: (a) $H_2SO_4/H_2O_2/H_2O$ (10:1:1) for 2 min, followed by a light DI water rinse (30 sec) and (b) $H_2SO_4/H_2O_2/H_2O$ (10:1:1) for 2 min, followed by a thorough DI water rinse (5 min). (Spectra have been offset along the vertical axis for clarity of presentation.)

when etched with HF/H_2O and rinsed with isopropanol after $H_2SO_4/H_2O_2/H_2O$ are similar to the one in Fig. 4b.

In order to confirm that residual contamination is responsible for the origin of these defects, the following LPE experiment was performed. In order to rule out the possibility that the defects are not arising from defects present in the substrate, an InP:S substrate was selected from a neighboring section of the same boule that resulted in the formation of crescent-shaped defects in prior LPE experiments. It was cleaved into three pieces, labeled A, B, and C, to fit the substrate recess in the slider. All three pieces were

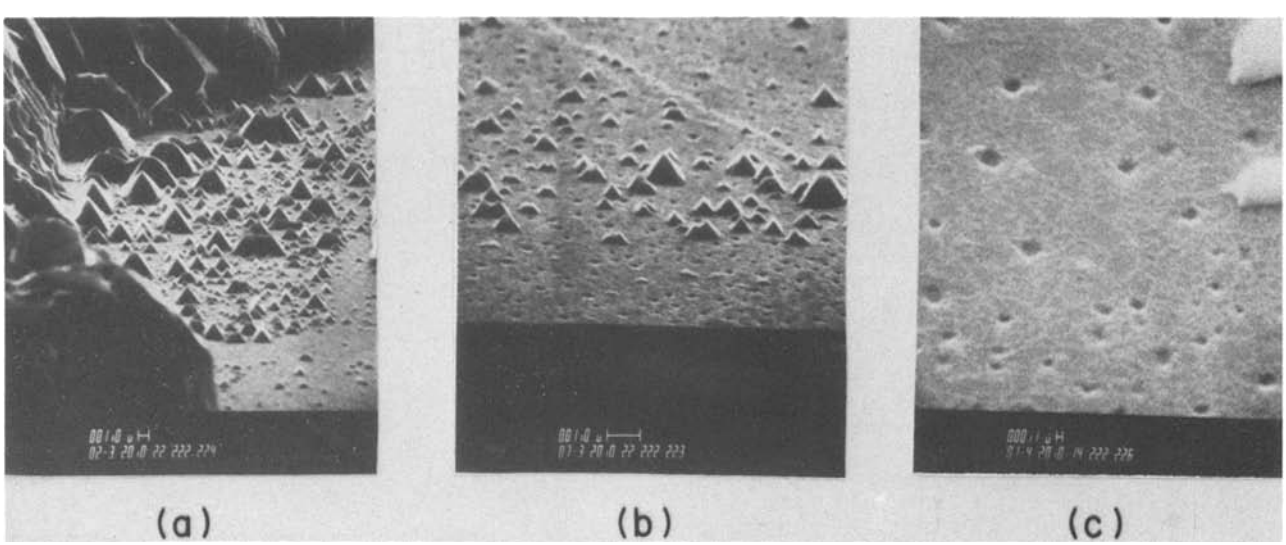

Fig. 3. (a) SEM micrograph showing spherical sector-like pyramidal epilayer growth in region a of Fig. 2b. b and c An enlarged view of the regions b and c of Fig. 2b.

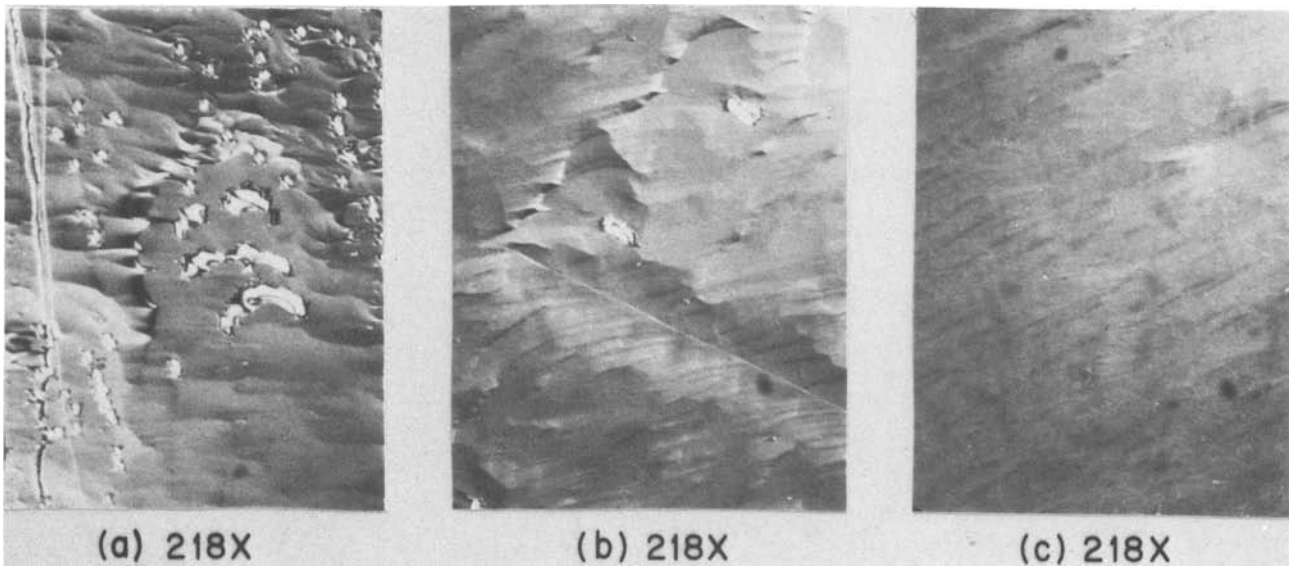

Fig. 5. Optical micrograph showing LPE growth of $InP/In_{0.53}Ga_{0.47}As$ on InP substrates etched in: (a) $H_2SO_4/H_2O_2/H_2O$ (3:1:1) for 2 min (no subsequent rinsing). (b) $H_2SO_4/H_2O_2/H_2O$ (10:1:1) for 2 min, followed by light rinsing in DI water (30 sec). (c) $H_2SO_4/H_2O_2/H_2O$ (10:1:1) for 2 min, followed by a thorough DI water rinse (5 min), etched for 2 min in HF/H_2O (1:1), rinsed again with DI water (2 min), and rinsed with isopropyl alcohol (2 min).

degreased by boiling in acetone and methylene chloride.

Piece A was etched in an $H_2SO_4(3):H_2O_2(1):H_2O(1)$ solution for 2 min and dried with N_2 gas. No rinsing in deionized water was employed in order to deliberately leave severe residual contamination on A's surface. Piece B was etched in an $H_2SO_4(10):H_2O_2(1):H_2O(1)$ solution for 2 min rinsed lightly (30 sec) with deionized H_2O, and dried with N_2 gas. The intent of light rinsing in deionized water was to leave some of the surface contamination on B. The third piece, C, of the wafer was etched in a $H_2SO_4(10):H_2O_2(1):H_2O(1)$ solution for 2 min, rinsed thoroughly (5 min) in deionized water, etched in an $HF(1):H_2O(1)$ solution for 1 min, rinsed (2 min) in deionized water, rinsed (2 min) in isopropyl alcohol, and dried. The HF etching and DI water rinse was used as a back-up to remove any inadvertent formation of oxide on the surface. In addition, HF was reported to be effective in removing S (1). The rinsing in isopropyl alcohol was based on results reported on GaAs surfaces (2) and on our own experience (3). The three pieces of the InP wafer were simultaneously loaded into a graphite slider boat for epitaxial growth from the same melts. Following growth-melt homogenization and a 15 sec melt back using an undersaturated In-melt, an InP buffer layer was deposited in the temperature interval of 649°-644°C. The buffer layer was followed by an InGaAs layer grown in the temperature interval of 644°-643°C. The cooling rate was 0.5°C/min.

Figure 5 shows the morphology of the epilayers on the three pieces A, B, and C. As can be seen in Fig. 5a, piece A showed a large density of crescent-shaped growth defects in the epitaxial layers. Piece B, shown in Fig. 5b, also showed similar defects, but the defect density is considerably reduced. However, the InP substrate, piece C, etched with 10:1:1, rinsed with deionized H_2O, 1:1 HF, and isopropyl alcohol showed no crescent-shaped defects in the epitaxial layers (see Fig. 5c).

One question that may arise is why the residual contamination on the InP substrate surface was not removed by the intentional meltback of the substrate. The chemical structure of the S-O contaminants is unclear, but is probably present in the form of SO_4 radicals chemisorbed onto the InP-surface, in addition to oxides of In and P. We suggest that the oxides do not readily dissolve in the melt and are therefore not removed by the meltback.

In conclusion, Auger analysis and the results of epitaxial growth discussed above suggest that the residual contamination of S, adsorbed oxygen, and oxide formation resulting from $H_2SO_4/H_2O_2/H_2O$ etching is responsible for wetting difficulties and poor nucleation that cause the observed crescent defects. A thorough cleaning of the surface to remove S and reduce O contamination is essential for growth of defect-free liquid epilayers of InP/InGaAs on InP.

Acknowledgments

We thank B. V. Dutt for several suggestions in this work and on the manuscript. We are indebted to W. A. Bonner for supplying the InP substrates and G. P. Schwartz for providing the Auger data of Fig. 4. We thank O. G. Lorimor for a critical reading of the manuscript.

Manuscript submitted June 24, 1982; revised manuscript received Dec. 15, 1982.

Any discussion of this paper will appear in a Discussion Section to be published in the December 1983 JOURNAL. All discussions for the December 1983 Discussion Section should be submitted by Aug. 1, 1983.

Bell Laboratories assisted in meeting the publication costs of this article.

REFERENCES

1. J. L. Zilko and R. S. Williams, *This Journal*, **129,** 406 (1982).
2. C. E. E. Stewart, *Solid-State Electron.*, **10,** 1199 (1967).
3. B. V. Dutt, Private communication.

The Effects of Pressure, Temperature, and Time on the Annealing of Ionizing Radiation Induced Insulator Damage in N-channel IGFET's

A. Reisman*,[1] and C. J. Merz

IBM T. J. Watson Research Center, Yorktown Heights, New York 10598

ABSTRACT

The effects of annealing pressure, temperature, and time (p,T,t) on residual levels of n-channel insulated gate field effect transistor (IGFET) process induced insulator radiation damage has been examined, and the behavior over the range p =1-5 atm H_2, T = 300°-450°C, and times up to 14 hr at 300°C have been defined for polysilicon gated devices. It has been found that higher temperatures, higher pressures, and longer times all lead to decreased residual neutral trap and positive charge densities levels, but that neutral traps are more difficult to remove. Removal of positive charge does not appear to depend on initial damage level while residual neutral trap level is sensitive to the initial damage level. It has been found also that with the specific damage technique employed, which involves electron beam (E-beam) metal evaporation, positive trap levels saturate at about 5×10^5 rads Si, while apparent negative charge and neutral traps appear to increase slowly with exposure of the gate insulator to this ionizing radiation. Adequate removal of all charged and neutral centers can be achieved in 50 atm of forming gas at 400°C for 30 min for doses as great as 5×10^7 rads SiO_2. If damage levels are not too high, 25 atm treatments are useful for the same temperature and time.

When subjected to ionizing radiation during fabrication, the insulators in insulated gate field effect transistor (IGFET's) exhibit damage in the form of fixed positive charge and neutral traps (1). This damage requires thermal annealing treatments in the 550°-600°C range for its complete removal. Metallized shallow junction devices cannot, however, be subjected to annealing temperatures much in excess of 400°C for perhaps 30 min because of the danger of junction penetration by the interconnection metal. Such an inadequate temperature-time cycle results in residual damage levels of 100-200 mV of equivalent net positive charge generally, and even larger levels of neutral traps which pose both yield and reliability problems in small dimension IGFET's (in the 1 μm ground-rule range).

Recently (2), first results were presented on the use of elevated pressure annealing cycles to remove such damage in polysilicon gated capacitors and n-channel IGFET's. The cited results were for a single damage level, *ca.* 10^7 rads Si, introduced in a specific way, and a single set of annealing conditions, 50 atm 10% H_2-90% Ar, 400°C, 30 min. Most of the preliminary data were in the form of capacitor flatband shifts, only a small number dealing directly with trapping of charge in insulator defects as a measure of damage. Commercially available elevated pressure systems have an upper operating pressure range of 20-25 atm, and it was of interest to learn how effective this pressure range might be in damage removal. In addition, FET threshold measurements are of greater practical significance than capacitor flatbands. Equally important is the observation that the annealing rate of FET gate insulators is different than that of the insulator of the much larger capacitor structure used in the first study (2). Consequently, only n-channel polysilicon gated FET's were employed in the present study, and all measurements were keyed to the hot electron injection technique reported by Ning *et al.* (3-5). The type of damage employed in the present study is that discussed by Ning in the 1978 report. This point is made, since the damage is created by aluminum x-rays, secondary electrons, and direct reflected electrons present in an electron-beam deposition of aluminum. The maximum energy of any of these species in our experiments was 10 keV, because of the technique employed. Furthermore, preliminary results obtained by us using pure x-ray sources with energies $\leq$ 10 keV on unbiased devices indicate that apparent negative charge observed in the present study is not generated to the same extent with low energy x-radiation alone. These differences are not of prime concern in the present paper. Here, we are mostly interested in demonstrating a technique for the removal of all process-induced radiation damage caused by dosages as high as 5×10^7 rads SiO_2. Such levels are quite possible using present day processing techniques.

* Electrochemical Society Active Member.
[1] Present address: Microelectronics Center of North Carolina, Research Triangle Park, North Carolina 27709, and North Carolina State University, Raleigh North Carolina 27650.
Key words: insulator damage annealing, elevated pressure.

Experimental Procedure

Elevated pressure system design and use.—Elevated pressure annealing was conducted in an oxidation-annealing system of our design, shown schematically in Fig. 1. Primary features of the system are that it is operable up to 100 atm, employs only a single pressurizing source, and enables system temperature equilibration at operating pressure prior to the wafer boat being introduced into the hot zone via a magnetic puller. The desired gas is introduced into the fused silica reactor, and exits through the retrograde closure into the outer chamber, thereby providing equalized pressures on both sides of the reactor. The gas finally exits from the system via a stainless steel tube radially concentric with the fused silica gas supply tube. Reactor gases are provided from ultra high purity preanalyzed cylinder banks whose moisture content is monitored continuously. 316 stainless steel was used throughout because of its corrosion resistance.

Because of severe convective effects in the system at pressures in excess of 20 atm, two radially concentric 3 zone furnaces were employed for heating. The outer furnace provides thermal biasing for the inner furnace, maintaining a small temperature differential between it and the inner furnaces to minimize convective effects. Even with this feature, it takes approximately 30 min for the system to equilibrate after pressurization. Silicon wafers to be annealed were mounted vertically in a fused silica boat capable of holding 55 wafers. In practice, only every second wafer position was filled, and experiments were run with a constant boat loading of 28 wafers even if only a few experimental wafers were treated at one time. These were put in the center region of the boat.

The annealing procedure employed was to position the loaded boat at the door, pressurize the system, and allow it to equilibrate for 3 hr with a flow of 1-5 liter/min at STp. After this equilibration cycle, the boat was drawn automatically into the hot zone in a 2 min cycle. For annealing studies, which were conducted at relatively low temperatures, the outer furnace was turned on after the boat was introduced into the system, and

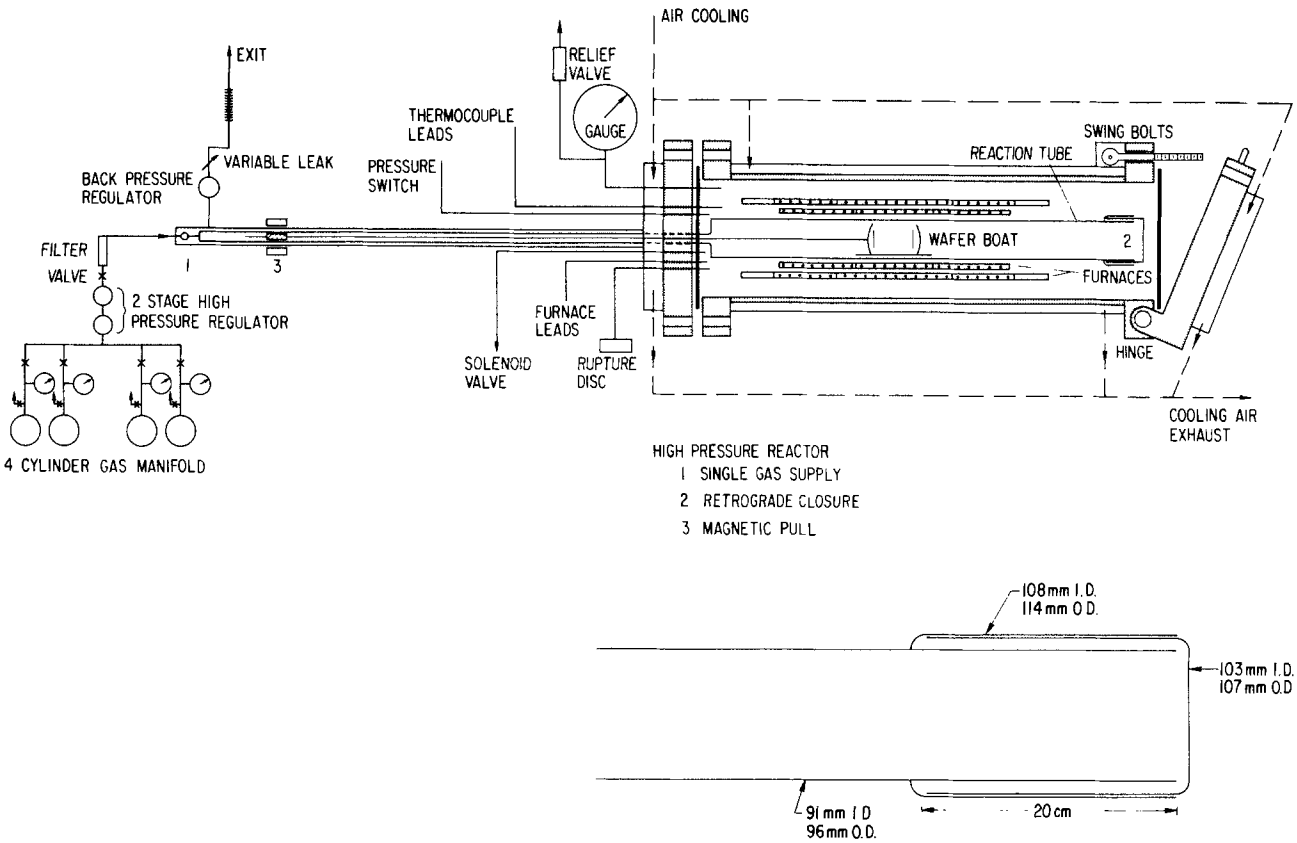

Fig. 1. Schematic diagram of elevated pressure system

the latter was pressurized. The outer furnace was turned off when the boat was returned to the door at the conclusion of the annealing cycle. When employed for oxidation studies, the outer and inner furnaces are left on at all times.

The retrograde reactor closure, that enables use of a single pressurizing source, is also depicted in Fig. 1. It functions as a high velocity nozzle, as can be seen from Fig. 2. Table I shows calculations for approximate drift and diffusion velocities in the reactor and the retrograde closure, as well as drift/diffusion velocity ratios in different parts of the system. The calculations were made for two system exit flow rates, referenced to STp. At the 5 liter/min flow rate, the drift/diffusion velocity ratio achieves a value of 5000/1 in the outer retrograde which provides the primary buffer to back diffusion. The inner retrograde ratio of 750/1 provides a second buffer, while the reactor length itself provides the third buffer zone.

Devices and radiation damage.—The polysilicon gated IGFET's were fabricated in p-type, 0.5 Ωcm 57 mm diam silicon wafers. Field oxides were 350 nm thick and were planar in order to simplify the fabrication process. These oxides were grown in a dry-wet-dry process at 950°C using 2% HCl. Gate oxides were 35 nm thick and were grown dry at 1000°C using 4.5% HCl. For the sake of process simplicity, no field or gate region threshold tailoring was employed. Junction depths were varied between 0.5-1.5 μm, depending on source-drain reoxidation conditions, and had no effect on the results. The polysilicon was deposited at 625°C via silane decomposition, and $POCl_3$ doped at 870°C followed by a 1000°C drive-in in O_2. Source-drains were formed in a similar fashion. Titanium formed via a lift-off process was employed as a contact-barrier metallurgy, and Al-3% Si was used as an

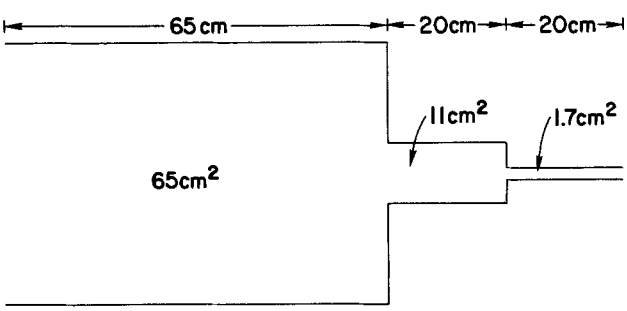

Fig. 2. Retrograde closure nozzle dimensions

Table I. Calculation of drift/diffusion velocity ratios referenced to STp[a] for oxygen

1) Flow rate *STp* (liter/min)	5	1
2) Flow rate *STp* (cm³/min)	83	17
3) Reactor cross sectional area (cm²)	65	65
4) Reactor entrance to 1st wafer distance (cm)	65	65
5) Inner retrograde cross sectional area (cm²)	11	11
6) Inner retrograde length (cm)	20	20
7) Outer retrograde cross sectional area (cm²)	1.7	1.7
8) Outer retrograde length (cm)	20	20
9) Mean velocity of gas, $\bar{c}$, *ST* (cm/sec)[b]	4×10^4	4×10^4
10) Mean free path of gas, *L*, (cm)[c]	1×10^{-5}	1×10^{-5}
11) Diffusion coefficient, *D*, (cm²/sec)[d]	0.2	0.2
12) Drift velocity in reactor, D_r, (cm/sec)[e]	1.3	0.26
13) Diffusion velocity in reactor, D_i, (cm/sec)[f]	0.006	0.006
14) D_r/D_i	220/1	43/1
15) Drift velocity in inner retrograde, D_{ir}, (cm/sec)	7.5	1.6
16) Diffusion velocity in inner retrograde, D_{vi}, (cm/sec)	0.01	0.01
17) D_{ir}/D_{vi}	750/1	160/1
18) Drift velocity in outer retrograde, D_{or}, (cm/sec)	50	10
19) Diffusion velocity in outer retrograde, D_{vo}, (cm/sec)	0.01	0.01
20) D_{or}/D_{vo}	5000/1	1000/1

[a] As $\bar{c}$, the mean velocity, increases with $\sqrt{T}$ and *L*, the mean free path, decreases as $1/p$, calculations were made only for *STp*.

[b] Mean velocity $\bar{c} = \sqrt{\frac{8}{3\pi}}\sqrt{\bar{c}^2} = 0.92\sqrt{\bar{c}^2}$ where $\sqrt{\bar{c}^2} = \sqrt{3RT/M}$, *M* = molecular weight, and $\sqrt{\bar{c}^2}$ = the root mean square velocity.

[c] Mean free path, $L = 1/\sqrt{2}\,\pi\, m\, \sigma^2$ where *m* = number of molecules in a unit volume of gas and σ = diameter of molecule.

[d] Diffusion coefficient *D* (273 K) = $\bar{c}\,L/2$.

[e] Drift velocity = flow rate/cross sectional area.

[f] Diffusion velocity = *D*/path length.

interconnection metallurgy. Except for control device evaluation, metallized wafers were not given post-metal annealing treatments at the conclusion of the fabrication steps, in order to simulate a real process sequence, *i.e.*, damage would be present prior to annealing. Such unannealed devices exhibited threshold voltages of 1.2 ± 0.2V using a −1V substrate bias. Control devices annealed for 30 min at 400°C in 10% H_2-90% N_2 (forming gas), or in pure H_2 exhibited thresholds of 1.2 ± 0.1V at −1V substrate bias. Based on the earlier referenced studies (1), the most useful devices for examining hot electron behavior were 20:1 width/length ratio structures with 50 μm channel lengths. These provided a gate area of 5×10^{-4} cm².

Wafers were radiation damaged at the conclusion of a complete fabrication cycle as follows. They were coated with 0.4 μm of photoresist, then subjected to aluminum evaporation in an E-beam metal evaporator. In the particular system employed, the reference deposition employed was 50 nm of aluminum deposition in 10 min from a scanned hearth at 10 keV and 0.5A. Based on a comparison of induced damage (specifically capacitor flatband shifts) from a calibrated Al Kα x-radiation source (6), this reference treatment provides 5×10^6-10^7 rads Si damage. This comparison is only an approximate one, since a flatband shift represents a net charge level. In the absence of injection data, such a shift cannot be attributed to a single charge sign. Furthermore, a flatband shift measurement tells us nothing about neutral traps. For the present study, a damage range between 5-150 nm of Al deposition was examined. Following aluminum evaporation, the photoresist-aluminum composite layer was lifted off leaving the damaged wafer ready for further study. The type of damage introduced is probably a good representation of what would result in a small dimension fabrication process in which the wafer surface would be exposed to electrons and x-rays with energies ≤ 10 keV. In the present instance, the electrons are secondaries and reflected electrons from the aluminum hearth, and the x-rays are of course the aluminum Kα and aluminum "white" radiation. Preliminary studies by us using "pure" x-radiation in this energy range indicate quantitative but not qualitative differences in the type of insulator damage generated.

A portion of each wafer was protected from ionizing radiation damage using a silicon wafer mask, and these undamaged regions were monitored during the course of the experiments. They showed no changes other than the small expected threshold shift following an initial annealing cycle.

Source-drain current, I_{SD}, *vs.* gate voltage, V_G, measurements were used to determine threshold voltages, V_T, at a −1V substrate bias, prior to and following thermal treatments and hot electron injections. These measurements served as reference values. The hot electron injections were conducted according to the method of Ning (3). First an $I_{SD} - V_G$ measurement was conducted at a 0.1V drain voltage, V_D, and a −1.0V substrate bias, V_{sx}, with the source grounded. Then electron-hole pairs were generated using visible light and 2.5×10^{13} electrons/cm² (2×10^{-9}C) were accelerated across the Si-SiO_2 interface with a gate voltage, V_G, of 2.5V and a substrate bias of −7.0V. This process, as described by Ning (5), results in the filling of positively charged traps with cross sections ≧ 10^{-13} cm². Following a second $I_{SD} - V_G$ measurement to determine the effect of this electron trapping, a second injection, this time of 1×10^{16} electrons/cm² (1×10^{-6}C) was conducted at a V_G of 2.5V and $V_{sx} = -16.0$V, and a final $I_{SD} - V_G$ trace was taken. This injection results in the filling of neutral traps with cross sections ≧ 10^{-15} cm². For practical purposes, traps with smaller cross sections are not of great interest. In fact, even traps in the 10^{-14}-10^{-15} cm² range are of somewhat marginal concern.

As a reference point, unirradiated 1 atm 400°C hydrogen annealed devices show positive trap levels of approximately 10 mV equivalent threshold shift following injection of 2.5×10^{13} electrons/cm², and neutral trap levels of approximately 60-80 mV equivalent threshold shift following injection of an additional 1×10^{16} electrons/cm². The 10 mV value is the smallest amount of charge that can be detected by the I-V method used.

Annealing studies.—A wide range of annealing conditions were examined which are discussed more appropriately in the results and discussion section. The temperature range studied was 300°-450°C, times were varied from 30 min to many hours, and pressures were varied from 1-50 atm. Since 10% H_2-90% Ar was employed as the annealing gas, the effective hydrogen pressure ranged from 0.1 to 5 atm.

Results and Discussion

Radiation induced defect levels.—At best, it is difficult to sort out what is actually taking place when IGFET insulators are subjected to ionizing radiation.[2] If one relies on threshold shift or flatband shift information alone, it is easy to arrive at erroneous conclusions as to the types and densities of generated defects, since one observes net effects or no effects at all if the generated defects are uncharged. For example, neutral defects have no effect on threshold at all. In addition, in the absence of injection measurements, it could also be concluded, in most instances, that only positive charge is generated, based on the normally encountered direction of threshold shifts in n-channel IGFET's. Even with injection measurements, some questions can remain unanswered. For example, in the present study where we are concerned only with trap cross sections ≧ 10^{-15} cm², it is implicit that we are concerned with defects of this size with a low reemission probability at room temperature. Further, it is possible that positively charged defects smaller than those we are concerned with are present. This latter type of trap would affect threshold, but not injection data in the injection range studied by us.

We have not seen evidence for the presence of significant quantities of small positively charged traps, *i.e.*, maximum observed negative threshold shifts correlate well with positive charge levels determined by injection within the 10 mV sensitivity of the injection measurement. If smaller cross section positive charge centers were present in any significant density, the maximum observed negative threshold shifts would have to be greater than the positive charge level determined by injection. The phrase maximum observed negative threshold shift is used advisedly, since it is only in the region of maximum threshold shift that this correlation can be made, for reasons which will be obvious shortly. In other threshold shift regions where the measured shift is less than expected, based on positive charge values determined by injection, the existence or absence of smaller cross section positive charge cannot be inferred. To simplify the discussion, we are assuming that trap densities in the different cross section regimes are the same, so that the probability of trapping is determined by the trap cross section.

As radiation doses are increased, measured thresholds were found to decrease to some minimum value, and to then increase monotonically. Coupled with measured positive charge levels, this behavior is indicative of negative charge. Such apparent negative charge levels were calculated using Eq. [1]

$$V_T - V_T^i + V_P = V_N \qquad [1]$$

where V_T is the measured threshold after irradiation,

[2] This problem is compounded by the fact that the details of the damage may be influenced by the rate of dosage, the photon or particle energy, and the mass of the species creating the damage. The data presented here are, therfore, representative of the specific damage method employed.

V_T^i is the measured threshold of unirradiated devices, V_P is the positive charge measured by injection, expressed in volts of threshold shift accompanying injection, and V_N is the calculated negative charge in volts of threshold shift also. This apparent negative charge could be in the form of surface states or bulk charge. It does not appear, based on preliminary studies, to be generated in significant quantities when SiO_2 is irradiated by 1-10 keV x-rays only. Electron bombardment appears to be necessary.

The measured values of V_T and V_P, and the calculated values of V_N as a function of nm of deposited Al (related to the dose in rads Si, where 10 nm of deposited Al is approximately equal to 1×10^6 rads Si) are plotted in Fig. 3. Also plotted is the variation of neutral trap levels under the same conditions. It is seen that V_T decreases from about 1.3 to approximately −0.15V after a dose of approximately 5 nm Al ($\sim 5 \times 10^5$ rads Si). After further irradiation, V_T increases to 1.84V at the highest damage level examined, 150 nm Al ($\sim 1.5 \times 10^7$ rads Si). This threshold is more than 0.5V higher than that of the unirradiated device. During this same sequence, the positive charge level increases from < 0.01V in the unirradiated device to approximately 1.4V after 5 nm of Al deposition, and then saturates rapidly at about 1.7V. Neutral traps do not appear to saturate, and their density exceeds that of the positive charge after 25 nm of Al ($\sim 2.5 \times 10^6$ rads Si) have been deposited, and exceeds 3V at a dose of 150 nm of Al ($\sim 1.5 \times 10^7$ rads Si). The calculated negative charge level rises monotonically at a relatively slow rate, and becomes equal to the positive charge level at about 115 nm of Al ($\sim 1.15 \times 10^7$ rads Si). At this crossover point where positive charge and apparent negative charge are equal, based on threshold shift data, the irradiated threshold value is exactly at its initially unirradiated value. Source-drain current, I_{SD} *vs.* gate voltage measurements, V_G, indicate a 10-20% transconductance degradation of the device at this crossover point at low drain voltages (0.1V). At 0.3V, this transconductance change is no longer detectable, and remains so up to the full value of the power supply voltage, V_{DD}. This is not a solid proof the interface charge level is low, but is an indication of this.

Since the positive charge has saturated by the time the crossover point is reached, and negative charge does not appear to generate at dosage levels much below 10^5 rads Si, even when electron bombardment is involved, this predamaged "titrated device" should now be "rad hard" to at least 10^5 rad additional dosages. Depending on the exact details of the fabrication process employed and the manner in which the "titration" damage is introduced, the absolute values of the required damage levels would be expected to vary from the values shown in Fig. 3, as would the crossover point. Using a given process, Fig. 3 shows the type of 1σ standard deviations obtained using two different irradiation experiments, separate wafers for each dose level and 5 device injections at each dose level. A calibration curve could possibly be established using an appropriate calibrated irradiation source and wafers to be made rad hard could be subjected to the required doses. Individual wafers could be probe checked to determine V_T and "touched up" if the value is too low, using intentionally low damage levels to insure that excess doses are not applied in the preliminary damaging. These "titration" thresholds appear stable. For example, after 3 hr at 300°C followed by 30 min at 400°C in pure Ar, little annealing is observed. Since the question of rad hardness was not of primary concern to us, the matter was not pursued further.

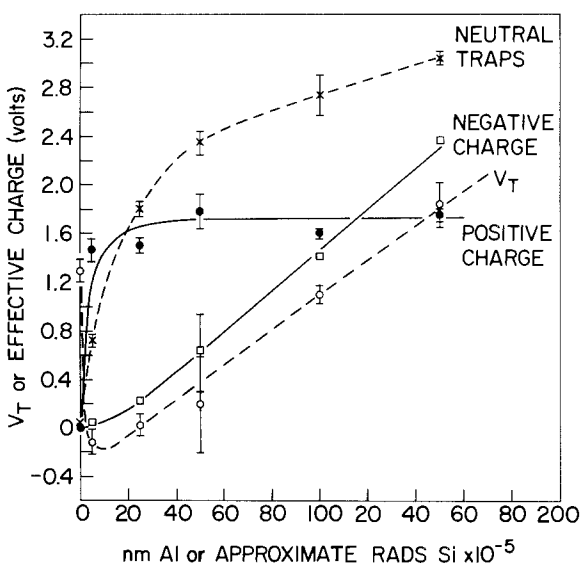

Fig. 3. Variation of threshold voltage, positive charge, apparent negative charge, and neutral traps with radiation dose.

Annealing as a function of temperature-time-pressure, T-t-p, and ambient atmosphere.—Effects of initial damage level on residual level.—Except where noted, a reference damage level of 50 nm Al was employed. This is in the range of 20 μC/cm^2 E-beam direct write dosages using E-beam exposure lithography. Several lots of wafers were utilized each having received similar, but not identical processing. Oxidation temperatures, for example, were not the same. Positive charge levels varied from a low of about 1.5V after irradiation to a high in one wafer, used for inert gas annealing, of approximately 2.5V. Neutral traps at this damage level varied somewhat less, from about 1.9 to about 2.3V. It was difficult, at the conclusion of an elevated pressure annealing cycle, to differentiate, based on residual positive charge levels between initially high or initially low damage level wafers. The bulk of the positive charge always appeared easy to remove, even with conventional annealing procedures. The residual charge removal is where the problem lays. This is not the case with neutral charge, however. Residual neutral levels were much more sensitive to starting damage levels. This can be seen with reference to Table II which shows residual positive charge and neutral trap levels after annealing devices, intentionally damaged to different starting levels, in either 50 or 25 atm 10% H_2-90% Ar mixtures for 30 min at 400°C following a 3 hr door equilibration.

From Table II, it can be seen that the residual positive charge level while quite sensitive to annealing pressure is relatively insensitive to initial damage level. This is not the case for neutral trap residual levels which are quite sensitive to both annealing pressure and starting damage level.

Table II. Residual damage levels as a function of starting damage levels at two annealing pressures

nm of E-beam evaporated Al	Anneal (T°C)	Anneal time	Anneal pressure (atm)	Positive charge (V)	Neutral traps (V)
0	400	30 min + 3 hr (door)	25	0.00 ± 0.00	0.05 ± 0.01
5	400	30 min + 3 hr (door)	25	0.08 ± 0.01	0.16 ± 0.01
25	400	30 min + 3 hr (door)	25	0.08 ± 0.00	0.34 ± 0.01
50	400	30 min + 3 hr (door)	25	0.09 ± 0.01	0.43 ± 0.02
0	400	30 min + 3 hr (door)	50	0.00 ± 0.00	0.05 ± 0.01
5	400	30 min + 3 hr (door)	50	0.01 ± 0.01	0.08 ± 0.00
25	400	30 min + 3 hr (door)	50	0.02 ± 0.02	0.16 ± 0.01
50	400	30 min + 3 hr (door)	50	0.02 ± 0.00	0.23 ± 0.00
150	400	30 min + 3 hr (door)	50	0.02 ± 0.00	0.32 ± 0.02

Pressure and time effects.—The reference treatments to which all others were compared are shown in Table III. These treatments were applied following reference deposition of 50 nm of Al ($\sim 5 \times 10^6$ rads Si). A variety of control anneals were conducted at the door of the elevated pressure system since this represented a part of every annealing cycle as we practiced it. When samples were loaded into the system with conditions set to achieve 400°C in the hot zone at whatever pressure was to be employed, the 3 hr equilibration at the door of the system was conducted at the same pressure. However, the temperature at the door of the system was approximately 100° lower at a 400°C hot zone temperature, 130° lower at a 450°C hot zone temperature, and 80° lower at a 350°C hot zone temperature. The specimens did not attain the door temperature for perhaps 20-30 min. This means that in Table III for example, lines 3 and 4 which compare H_2 at 1 atm for 3 hr at 300°C with 10% H_2-90% Ar at 10 atm (1 atm H_2 equivalent), respectively, are not exactly the same, since the time at 300°C was greater for the sample equilibrated in the 1 atm furnace. Since the total times involved are long, we are assuming that to a first approximation these types of experiments are equivalent. To a first approximation, lines 3 and 4 are the same, and the discrepancy is in the right direction since the 10 atm samples take longer to equilibrate than do the 1 atm samples.

From Table III, we see that none of the reference treatments serve to remove the damage sufficiently and that, as expected, hydrogen at 1 atm at 400°C is the most effective 1 atm treatment, albeit not a satisfactory one. It is also of interest that Ar at 50 atm is much more effective than Ar at 1 atm. This is believed due to the presence of water to the extent of several ppm in the high purity argon employed. At 50 atm, the partial pressure of H_2O increases from its initial value of approximately 3-150 mTorr. In a rate equation, it would be the latter partial pressure that would be effective if H_2O is involved in annealing. From recent work by Aitken, Irene, and Crowder (7), H_2O has been shown to be somewhat effective in removing ionizing radiation damage.

The reference treatment employed in our original study was 50 nm Al damage followed by a 50 atm anneal (in 10% H_2-90% Ar) for 30 min at 400°C, following a 3 hr equilibration in this gas mixture at this pressure at the door of the system. In order to compare this to a 1 atm treatment in pure H_2, one cannot use the results described on the second line of Table III since the door equilibration is not included in these data. Further, the question arises as to whether it is the hydrogen partial pressure that is important or the total pressure. In order to resolve these concerns, the experiments defined in Table IV were conducted. The Sequence A indicates that a 30 min anneal in 10% H_2-90% Ar at 50 atm (5 atm effective H_2 pressure) following a 3 hr door equilibration is more effective than a 30 min pure H_2 anneal at 1 atm following a 3 hr door experiment. The B sequence indicates that it is the effective H_2 pressure, not the total pressure that is important, everything else being the same. This B sequence compares annealing under two sets of conditions which subject the damaged sample to the same hydrogen partial pressure. The annealing results are seen to be essentially the same.

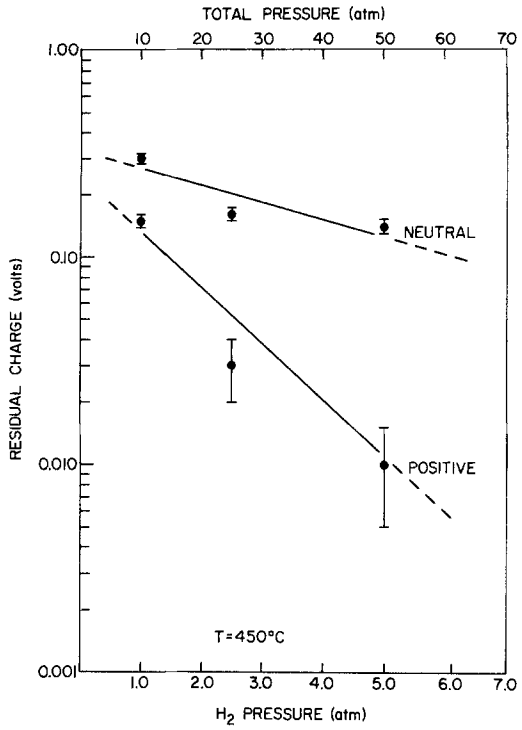

Fig. 4. Residual radiation damage as a function of atmospheres of H_2 pressure at 450°C.

Figure 4 shows the residual charge in volts for annealing conducted for 30 min at 450°C and 3 hr at the door in 10% H_2-90% Ar at different total pressures, expressed as atm of H_2 pressure. As might have been expected based on the results described in Table II, the neutral traps are more difficult to remove than positive charge. It is to be recalled that in undamaged devices, the neutral trap level lies in the range 0.06-0.08V. From Fig. 4, it is seen that even after a 50 atm anneal, there can exist as much as 0.13V of neutral

Table III. Reference annealing treatments

Gas	Temperature (°C)	Pressure (atm)	Time sequence	Positive charge (V)	Neutral traps (V)
N_2-H_2-N_2	450	1	5 min-30 min-5 min	0.15 ± 0.01	0.30 ± 0.01
N_2-H_2-N_2	400	1	5 min-30 min-5 min	0.19 ± 0.01	0.39 ± 0.07
N_2-H_2-N_2	300	1	5 min-180 min-5 min	0.29 ± 0.0	0.57 ± 0.01
10% H_2-90% Ar	300	10	180 min (door)	0.35 ± 0.01	0.87 ± 0.04
N_2	400	1	10 min	2.53 ± 0.08	2.33 ± 0.03
Ar	400	1	30 min + 180 min (door)	1.53 ± 0.03	1.65 ± 0.05
Ar	400	50	30 min + 180 min (door)	0.43 ± 0.02	0.76 ± 0.05

Table IV. Comparison of annealing cycles

Sequence	Initial damage levels (V) Positive	Neutral	Sequence	Residual damage levels (V) Positive	Neutral
A 1)	1.67 ± 0.07	2.24 ± 0.01	10% H_2-90% Ar 50 atm 30 min 400°C + 3 hr at door	0.02 ± 0.00	0.23 ± 0.00
2)	1.67 ± 0.07	2.24 ± 0.01	10% H_2-90% Ar 50 atm 3 hr at door	0.06 ± 0.01	0.41 ± 0.01
			+ 100% H_2 1 atm (5 min N_2-30 min H_2-5 min N_2) 400°C	0.05 ± 0.01	0.29 ± 0.02
B 1)	1.55 ± 0.07	2.24 ± 0.04	10% H_2-90% Ar 10 atm 30 min 400°C + 3 hr at door	0.12 ± 0.00	0.29 ± 0.01
2)	1.55 ± 0.07	2.24 ± 0.04	10% H_2-90% Ar 10 atm 3 hr at door	0.35 ± 0.01	0.87 ± 0.04
			+ 100% H_2 1 atm (5 min N_2-30 min H_2-5 min N_2) 400°C	0.10 ± 0.01	0.34 ± 0.02

traps when the damage level was of the order of 5×10^6 rads Si. At 400°C (from Table II), this neutral trap residual level can be as great as 0.23V for this damage level. At 450°C, the residual damage levels, R_{Nu}, R_p, neutral and positive, respectively, as a function of the effective H_2 pressure p_{H_2} are given by Eq. [2] and [3]

$$\log R_{Nu}^{450°C} = -8.34 \times 10^{-2} P_{H_2} - 0.48 \quad [2]$$

$$\log R_p^{450°C} = -2.71 \times 10^{-1} P_{H_2} - 0.61 \quad [3]$$

From Fig. 4, it would appear that effective H_2 pressures of 7-8 atm would be needed to decrease R_{Nu} to 0.08V. When the annealing cycles at 450°C were conducted for longer time periods at 50 atm, *e.g.*, 60 min + 6 hr at the door, and 90 min + 9 hr at the door, positive charge decreased first to 0.01V ± 0.00V then to 0.00V ± 0.0V. Neutral traps decreased to 0.11V ± 0.01V then to 0.10V ± 0.01V. For commonly employed barrier metallurgies, this is not considered by us to be a safe treatment. Figure 5 shows residual charge for annealing conducted at 400°C in 10% H_2-90% Ar for 30 min following a 3 hr door equilibration, as a function of effective H_2 pressure. In addition, the simulated 10 atm point discussed above is also plotted for comparison.

Equations [4] and [5] show the residual damage level dependencies on effective H_2 pressure at 400°C

$$\log R_{Nu}^{400°C} = -4.79 \times 10^{-2} p_{H_2} - 0.43 \quad [4]$$

$$\log R_p^{400°C} = -1.94 \times 10^{-1} p_{H_2} - 0.63 \quad [5]$$

It is seen at 400°C that the slopes of the positive charge and neutral trap curves are smaller than at 450°C. This is particularly the case for the neutral traps.

The 25 atm points in Fig. 4 and 5 are of particular interest since they are representative of what might be achievable in a commercially available elevated pressure system at 400°C, or, less desirably at 450°C, respectively.

At 400°C, as seen from Table II and Fig. 5, at a damage level of $\sim 5 \times 10^6$ rads Si, the residual positive charge and neutral traps following 25 atm annealing are marginally acceptable, but considerably better than annealing in pure H_2 at 1 atm and 400°C (Table III). Furthermore, as can be seen from Table II, at lower damage levels, the residual neutral trap levels are considerably smaller following annealing at 25 atm. If even lower residual neutral levels are required, 20% H_2-80% Ar might be used in the inner chamber of a commercial system, and pure Ar or N_2 could be

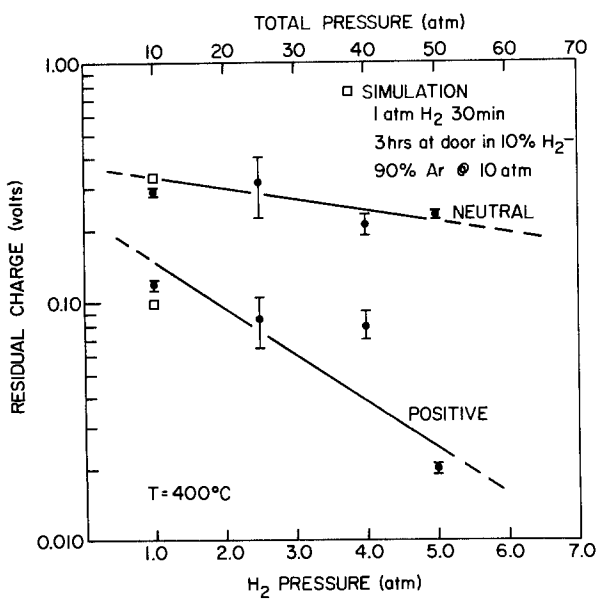

Fig. 5. Residual radiation damage as a function of atmospheres of H_2 pressure at 400°C.

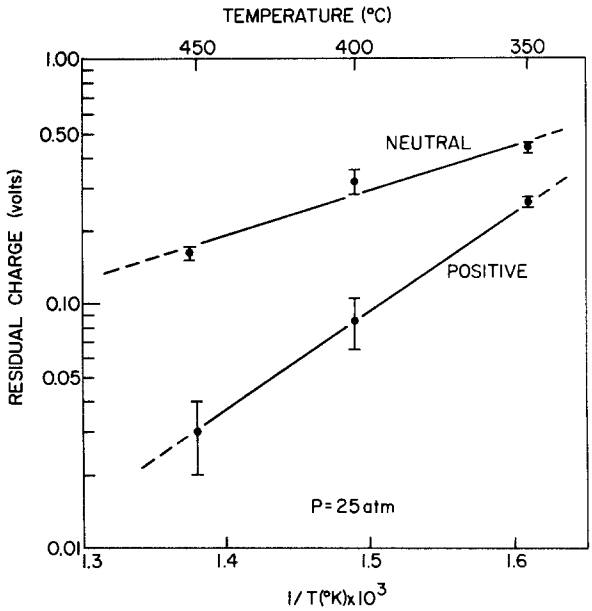

Fig. 6. Residual radiation damage as a function of temperature at 25 atm total pressure of 10% H_2-90% Ar.

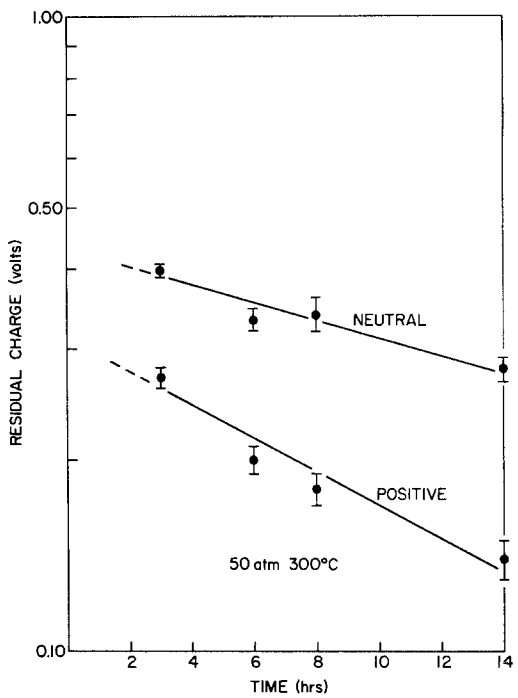

Fig. 7. Residual radiation damage as a function of time at 50 atm 10% H_2-90% Ar at 300°C.

used in the outer jacket. At 25 atm inner reactor pressure, this will be equivalent to our 50 atm experiments. In the event of an inner tube rupture, the outer reactor gas would dilute the 20% H_2-80% Ar to below its lower explosive limit of 10%.

Figure 6 shows the effect of temperature on annealing at 25 atm, while Fig. 7 plots residual charge as a function of time at 50 atm 10% H_2-90% Ar at 300°C. The data should be compared to those in Table III.

The dependencies of R_{Nu} and R_p on $1/T$ at 25 atm are given in Eq. [6] and [7]

$$\log R_{Nu}^{25\ atm} = 1.92 \times 10^3/T(K) - 3.42 \quad [6]$$

$$\log R_p^{25\ atm} = 4.08 \times 10^3/T(K) - 7.15 \quad [7]$$

The dependencies of R_{Nu} and R_p on time at 50 atm and 300°C are given by Eq. [8] and [9]

$$\log R_{Nu}^{300°C} = -1.39 \times 10^{-2} t - 0.37 \quad [8]$$

$$\log R_p^{300°C} = -2.63 \times 10^{-2} t - 0.51 \quad [9]$$

Conclusions

It has been found that high levels, *e.g.*, 10^7 rads SiO_2 of process induced radiation damage to the gate insulator of polygated IGFET's can be adequately removed by annealing treatments in 10% H_2-90% Ar mixtures at 50 atm and 400°C for 30 min. 25 atm annealing at 400°C is marginally adequate depending on initial damage level. The damage generated, based on threshold and charge injection-trapping measurements, takes the form of positive charge, neutral traps, and apparent negative charge. The positive charge generated by subjecting the devices to E-beam metal evaporation processes appears to saturate. The apparent negative charge and neutral traps appear to increase monotonically with increasing dose. The net result is that at total doses in excess of 10^7 rads SiO_2 the positive and negative charge levels appear to cancel out. Preliminary results indicate that such behavior requires electron damage, x-ray damage alone in the range 1-10 keV being ineffectual in creating high apparent negative charge levels. As expected, the efficiency of annealing in terms of residual damage is a strong function of temperature, T. The log residual damage appears to decrease linearly with $1/T$ K, *i.e.*, the residual damage level varies exponentially as a function of $1/T$.

Acknowledgments

The authors are indebted to A. K. Ray, C. M. Osburn, M. Berkenblit, J. M. Aitken, S. Lai, and T. H. Ning for their many helpful discussions. They are particularly indebted to C. J. Lucchese for conducting the E-beam damage runs, and to members of our processing facility for providing the device wafers used.

Manuscript submitted July 20, 1982; revised manuscript received Oct. 12, 1982. This was Paper 303 presented at the San Francisco, California, Meeting of the Society, May 9-13, 1983.

Any discussion of this paper will appear in a Discussion Section to be published in the December 1983 JOURNAL. All discussions for the December 1983 Discussion Section should be submitted by Aug. 1, 1983.

IBM T. J. Watson Research Center assisted in meeting the publication costs of this article.

REFERENCES

1. J. M. Aitken, *IEEE J. Solid State Circuits*, **sc-14,** 294 (1979).
2. A. Reisman, J. M. Aitken, A. K. Ray, M. Berkenblit, C. J. Merz, and R. P. Havreluk, *This Journal*, **128,** 1616 (1981).
3. T. H. Ning and H. N. Yu, *J. Appl. Phys.*, **45,** 5373 (1974).
4. T. H. Ning, C. M. Osburn, and H. N. Yu, *Appl. Phys. Lett.*, **26,** 248 (1975).
5. T. H. Ning, *J. Appl. Phys.*, **49,** 4077 (1978).
6. S. S. Iyer, Private communication.
7. J. M. Aitken, E. A. Irene, and B. L. Crowder, Private communication.

Computer Modeling of Infrared Curing of Photoresists

I. D. Calder, R. Sue, and H. M. Naguib*

Bell-Northern Research, Ottawa, Ontario, Canada K1Y 4H7

ABSTRACT

A computer model has been developed to simulate the baking of photoresist in an infrared oven. Account is taken of the spectral characteristics of the infrared emitter and the samples, the geometry of the oven, transport of the sample through the oven, and heat losses by radiation and convection. Excellent agreement is achieved in comparison with experimental measurements of the infrared curing of Shipley AZ1300 series photoresist on substrates of glass, Al-on-glass or silicon in a Zicon 1100 infrared oven. The model can be used to predict the conditions necessary for adequate baking of the photoresist (which occurs when the maximum temperature of the sample exceeds 80°C). Higher sample temperatures are achieved for higher emitter temperatures and slower conveyor speeds. The only adjustable parameter in the model is the speed of the air flow which produces forced convectional cooling.

One of the steps required for photolithographic processing of electronic devices is soft baking of the photoresist to remove excess solvents before the exposure and development stages. Conventional baking in forced hot air ovens gives rise to the formation of a surface skin, which inhibits evaporation of the solvents (1). This effect degrades the dimensional quality of the photoresist image and reduces the yield. To solve this problem, infrared curing of photoresists was introduced. It induces heating of the photoresist from the substrate interface outwards, thereby preventing skin formation and avoiding solvent retention. Although infrared curing is now commonly used in the electronics industry, only limited information is available on characterization of the infrared heating process (2). These authors investigated the infrared baking characteristics of photoresist deposited on Au and TaN coated substrates. However, only a qualitative description of the heating mechanism was presented. A model has also been presented by Nishimura *et al.* (3) for the infrared evaporation of liquid organic solvents, but the work has not been extended to thin films or photoresist baking. The main objective of the present investigation was to develop a computer model that affords a quantitative description of the infrared heating mechanism. The model can then be used to predict the effects of various processing parameters on the temperature-time profiles of arbitrary photoresist-coated substrates. Good agreement is obtained between model predictions and experimental results in a Zicon 1100 infrared oven under a wide range of operating conditions.

The Model

General concept.—In order to treat as many different sample structures as possible, the model should be very general. To this end, we allow an arbitrary number of films or layers to make up the sample (Fig. 1). For example, there might be a substrate, insulating films, semiconducting films, metallization, and photoresist. Each layer has an arbitrary thickness Δz_i, complex index of refraction $\hat{n}_i = n_i + j\alpha_i(k_o)/2k_o$, and magnetic permeability μ_i/μ_o. Each layer is considered to be homogeneous and of uniform thickness in the plane. The effects of solvent evaporation are ignored.

The calculation then proceeds by the use of the heat balance equation to calculate the temperature-time profile for one of these samples as it moves through the oven. The absorbed power is calculated by integrating the optical absorption of the sample structure over all wavelengths ($= 2\pi/k_o$) of the infrared radiation and over all angles of incidence inherent

* Electrochemical Society Active Member.
Key words: films, integrated circuits, infrared, polymerization.

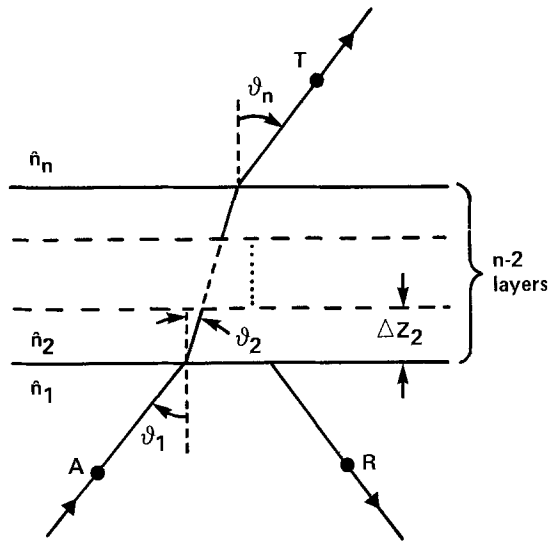

Fig. 1. Sample structure. There are n-2 layers (the air is layers 1 and n) with thickness ΔZ_i, index of refraction $\hat{n}_i = n_i + j\alpha_i(k_o)/2k_o$ and magnetic permeability μ_i/μ_o. A single infrared ray of wavelength λ ($= 2\pi/k_o$) incident at angle θ, is also shown.

in the oven geometry. This absorbed power is balanced by the various heat loss mechanisms. We now look at this model in more detail.

The heat balance equation.—In any heat flow situation, the principle of conservation of energy is expressed by the heat balance equation (4)

$$\rho C_p \frac{\partial T}{\partial t} = \nabla \cdot (\underline{\underline{K}} \cdot \nabla T) + G(r,t) \qquad [1]$$

which determines the temperature T as a function of time t and position r. The remaining quantities are the density ρ, specific heat C_p, thermal conductivity tensor $\underline{\underline{K}}$, and the heat generation (and loss) function $G(r,t)$. Because the time constant for evaporation is approximately L/G (L is the latent heat of the solvent), which is on the order of milliseconds, we ignore the thermal effects of evaporation. We assume that the entire sample is in equilibrium, so that the first term on the right side of Eq. [1] can be neglected. For example, if the ambient temperature $T_a = 300$ K, $T = 400$ K, and the thermal conductivity $K = 0.02$ W/cm-K, then the temperature differences across the sample (assuming radiative losses) is at most 0.5 K/mm. The problem now reduces to calculating $G(r,t)$. We assume that all the heat generation is due to the absorption of infrared radiation, while heat is lost because of radiation and convection. Conductive losses through the thermally insulating support structure are neglected.

Now consider the heat absorbed from a single beam of monochromatic radiation (wave vector k_o) incident at an angle θ_1, on our stack of $n - 2$ layers. Using standard techniques (5), we calculate the amplitude reflection and transmission coefficients R and T for a TE wave from

$$\begin{bmatrix} T \\ \dfrac{\hat{n}_n \cos\theta_n}{\mu_n/\mu_o} T \end{bmatrix} = \left[\prod_{i=2}^{n-1} \underline{\underline{N}}_i\right] \begin{bmatrix} 1+R \\ (1-R)\cos\theta_1 \end{bmatrix} \qquad [2]$$

where

$$\underline{\underline{N}}_i = \begin{bmatrix} \cos\beta_i & \dfrac{j\mu_i/\mu_o}{n_i\cos\theta_i}\sin\beta_i \\ \dfrac{\hat{n}_i\cos\theta_i}{\mu_i/\mu_o}\sin\beta_i & \cos\beta_i \end{bmatrix} \qquad [3]$$

$$\hat{n}_i \sin\theta_i = \sin\theta_1 \qquad [4]$$

and

$$\beta_i = k_o \hat{n}_i \Delta z_i \cos\theta_i \qquad [5]$$

[For the case of a TM wave (identical to TE for nonmagnetic materials), replace $n_i\mu_o/\mu_i$ by its inverse.] Then in terms of the incident power density P_o, the absorbed power density P_a is given by

$$P_a = P_o(1 - |R|^2 - |T|^2 n_n \cos\theta_n/\cos\theta_1) \qquad [6]$$

Layer n could be the air, if the substrate is optically polished, or the substrate, or the carrier (if it supports the substrate everywhere). This result must then be integrated over all wavelengths radiated by the infrared source and all angles of incidence occurring for a specific geometry (4). We ignore any changes in the optical properties of the photoresist due to solvent evaporation.

The radiative heat loss per unit area from a sample with upper and lower surface emissivities ϵ_1 and ϵ_2 is given by

$$\dot{Q}_r = (\epsilon_1 + \epsilon_2)\sigma(T^4 - T_a^4) \qquad [7]$$

where σ is the Stefan-Boltzmann constant.

For convective heat losses, we assume a uniform laminar flow of air at velocity v_a over the upper surface (forced convection) and no air flow (free convection) at the lower surface. We effectively consider v_a to be an adjustable parameter in the problem, since any detailed calculation of forced convective losses is prohibitively complicated. In general, the convective heat loss is given by (4)

$$\dot{Q}_c = (K_a/L)N_{Nu}(T - T_a) \qquad [8]$$

where K_a is the thermal conductivity of air, L is a characteristic length of the sample (typically the shortest dimension of a rectangular substrate), and N_{Nu} is the Nusselt number given by (4)

$$N_{Nu} = \begin{cases} 0.662(N_{Re})^{1/2}(N_{Pr})^{1/3} & \text{(forced)} \\ 0.055(T - T_a)^{1/4}L^{3/4}/K_a & \text{(free)} \end{cases} \qquad [9]$$

N_{Re} and N_{Pr} are the Reynolds and Prandtl numbers for a sample of length L in air. Then the total net heat generation function used in Eq. [1] is

$$G = P_a - \dot{Q}_r - \dot{Q}_c \qquad [10]$$

The total heat capacity ρC_p is the sum

$$\left(\sum_{i=2}^{n-1} \rho_i C_i \Delta z_i\right) \Big/ \left(\sum_{i=2}^{n-1} \Delta z_i\right)$$

All of the assumed heat generation and loss mechanisms are summarized in Fig. 2.

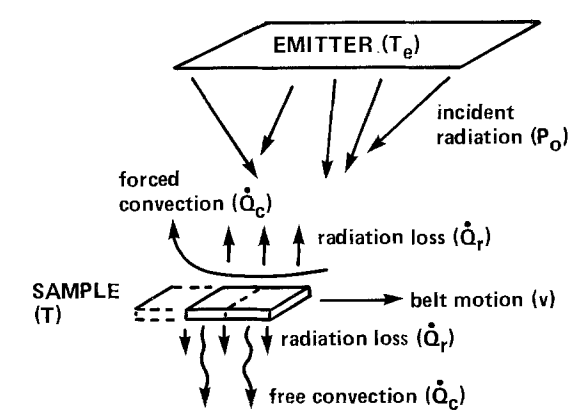

Fig. 2. Diagram of the principal components of the model. The infrared radiation (intensity P_o) from the emitter at temperature T_e is absorbed by the sample moving at velocity v. The sample is heated to a temperature T where the heat losses from radiation ($\dot{Q}_r$) and convection ($\dot{Q}_c$) balance the heat input.

Computational considerations.—We make the following assumptions about the physical parameters used in the model. (*i*) Assume $n(\lambda) = n_0\lambda^a$ and $\alpha(\lambda) = \alpha_0\lambda^b$. (*ii*) Assume emissivities are independent of temperature. (*iii*) For the properties of air, we use

$$K_a = 3.66 \times 10^{-5} + 3.76 \times 10^{-7}(T + T_a) \quad [11]$$

$$N_{Re} = v_a L[-1.36 \times 10^{-5} + 4.9 \times 10^{-8}(T + T_a)]^{-1} \quad [12]$$

and

$$N_{Pr} = 0.70 \quad [13]$$

where all quantities are in *MKS* units and the absolute temperature scale is used. (*iv*) The emitter (radiator) is assumed to be a black body at temperature T_e. Then, the spectral density of the radiation is given by Planck's radiation law

$$P_0(\lambda,T) = 2\pi hc^2\lambda^{-5}(e^{hc/\lambda kT} - 1)^{-1} \quad [14]$$

This expression is used in Eq. 6 and integrated over wavelength λ and angle θ to give the total power absorbed per unit area. We integrated numerically from $\lambda_M/2$ to $4\lambda_M$ where λ_M is the wavelength of the peak in the black body spectrum.

Comparison with Experiment

Our facility for infrared baking consists of two Gyrex 90 belt conveyors mounted beneath a Zicon 1100 infrared oven. The belt speed is adjustable from 4 to 37 mm/sec. The 60 × 60 cm planar infrared emitter is mounted parallel to the conveyor surface, at a height adjustable from 3.8 to 17.8 cm. The emitter temperature can be controlled to ±0.2°C over the range 50°-310°C. A class 100 air flow is maintained through the oven chamber.

Three different substrates (all 5.1 × 5.1 cm) were used in these experiments: glass 0.15 cm thick, glass with a 410 nm layer of evaporated Al, and 0.05 cm thick single crystal silicon. Each substrate had an individually calibrated (±0.2°C) Chromel-Alumel thermocouple evaporated onto the lower surface. Shipley AZ1300 series positive photoresists were then spun on with thicknesses of 1.0, 1.9, or 3.3 μm; control samples of each substrate type were baked without photoresist. Therefore, the important variables in our experiments were substrate type, photoresist thickness, emitter temperatures, belt speed, and emitter-sample separation.

The results of these experiments are shown in Fig. 3-6, along with the results of the computer modeling.

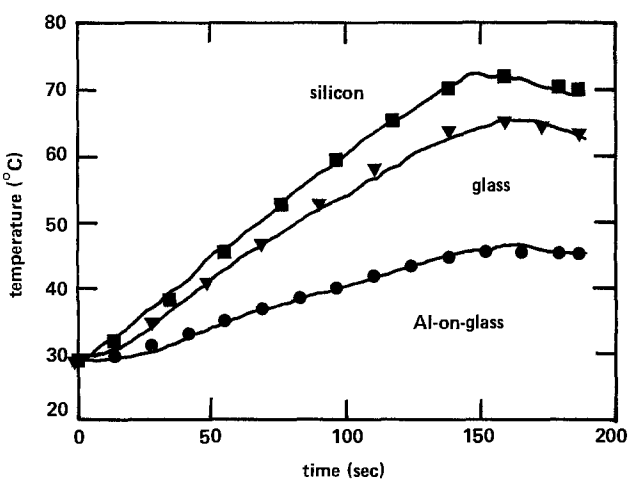

Fig. 3. Time-temperature profiles for the three control samples (no photoresist) moving at a speed of 4.3 mm/sec under an emitter at a temperature of 200°C and a height of 11.7 cm. The measured profiles are the solid lines while the model results are shown at discrete time intervals. The only adjustable parameter was the air flow speed.

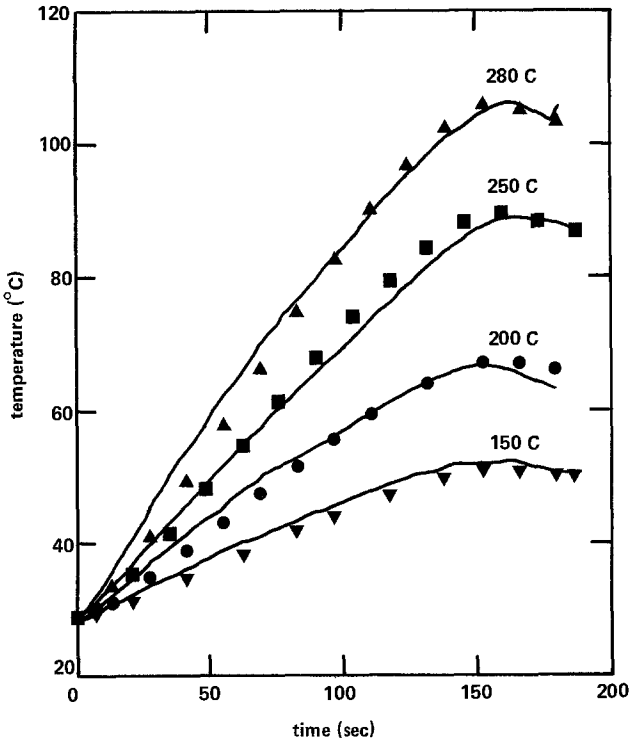

Fig. 4. Time-temperature profiles for glass substrates with 3.3 μm thick photoresist at four different emitter temperatures. The model results are shown at discrete time intervals while the solid lines are the equivalent experimental results. The belt speed was 4.3 mm/sec and the emitter-sample separation was 11.7 cm.

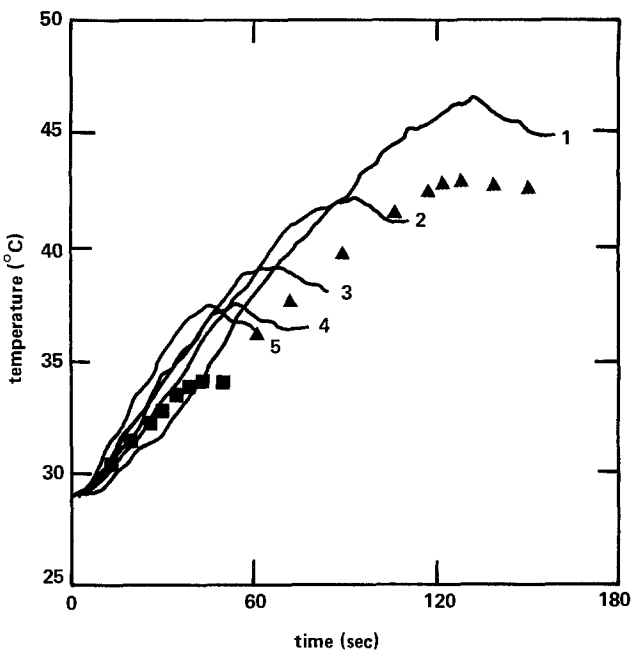

Fig. 5. Time-temperature profiles for Al-on-glass substrates without photoresist at a variety of conveyor speeds. The model calculations are shown at discrete time intervals for 5.1 and 15.3 mm/sec, while the solid lines are the equivalent experimental results for (1) 5.1, (2) 7.5, (3) 10.4 (4) 12.7, and (5) 15.3 mm/sec. The emitter temperature was 200°C, and the emitter-sample separation was 11.7 cm.

The only adjustable parameter in the model was the air speed, which was fixed at the value (20 cm/sec) that gave the best fit for a plain glass substrate. Otherwise, the major uncertainties lie in the values chosen for the optical properties of the various materials. Our values are listed in Table I. The results are most sensitive to material properties when there is a highly

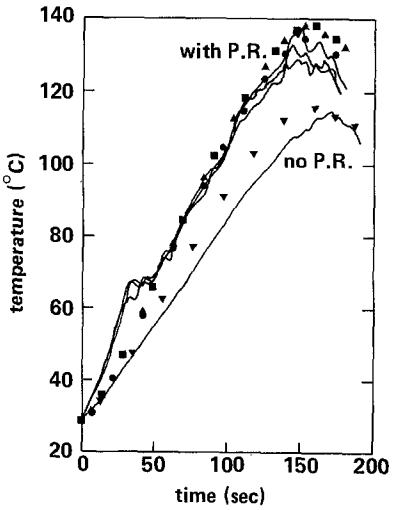

Fig. 6. Time-temperature profiles for silicon substrates with or without photoresist. The model calculations are for no photoresist (▼), 1.0 μm (●), 1.9 μm (▲), and 3.3 μm (■) while the solid lines are the equivalent experimental results. The emitter temperature was 280°C, the conveyor speed was 4.3 mm/sec, and the emitter-sample separation was 11.7 cm.

reflecting surface, or when neighboring films have markedly different complex indexes of refraction, that is, for the Al on glass substrates and to a lesser extent the Si substrates (Fig. 5-6). Slight adjustments in the $\hat{n}(\lambda)$ assumed for these materials will improve the predictive capability of the model under other conditions. The results are less sensitive to the emissivity, since convection makes a somewhat greater contribution to heat loss than radiation. This observation is contrary to the conclusions of Schantz and Pusch (2) who did not look at thin film effects or convective losses quantitatively.

Modeling becomes most useful when one can use it to predict the best baking conditions for a given sample structure. We have taken a first step in this direction by correlating the maximum temperature reached for a glass substrate during baking with the photoresist weight loss obtained, and then making a comparison with the weight loss resulting from oven baking under the manufacturer's recommended conditions. These results are shown in Fig. 7. There is a clear correlation between maximum temperature and weight loss, implying that maximum temperatures between 80°-110°C will provide optimum baking conditions, at least at the 4.3 mm/sec speed. From Fig. 4 and 5, we see that these higher temperatures are obtained at high emitter temperatures and slow belt speeds.

Higher emitter temperatures supply more energy ($\propto T_e^4$) and, therefore, heat the sample more. Higher speeds reduce the maximum temperature because the system never reaches a steady state. The thermal time constant is

$$\tau = \rho C_p d^2/K \qquad [16]$$

where ρ, C_p, d, and K are density, specific heat, thickness, and thermal conductivity of the sample. For a glass sample 5 mm thick (including a glass support) $\tau \simeq 40$ sec, comparable to the time spent in the chamber at the higher speeds.

Table I. Optical properties of various materials (glass, Shipley AZ1300 series photoresist, silicon, and aluminum)

	Glass	PR	Si	Al
n_o	1.45	1.7	3.45	0.19
a	−0.04	0	-3.5×10^{-3}	1.4
α_o	4.1×10^{-7}	8.2	0.252	2.38
b	4.97	0	0.37	0.4
ϵ	0.93	0.33	0.26	0.04

The first four lines define the complex index of refraction $n = n_o\lambda^a + j\alpha_o\lambda^{b+1}/4\pi$, where λ is expressed in μm. The last line lists emissivities.

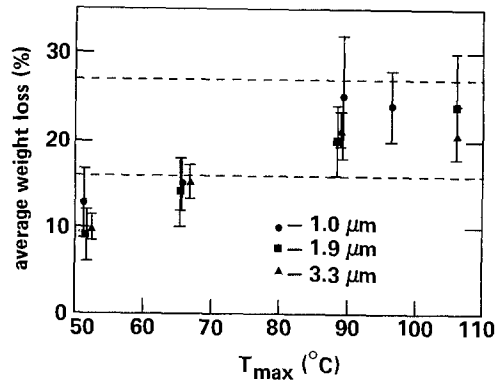

Fig. 7. Comparison between infrared oven and convection oven baking of photoresist. The hatched area between the dashed lines shows the approximate range of percentage weight loss obtained in a convection oven at 90°C for all the photoresist thicknesses used. The belt speed was 4.3 mm/sec.

Conclusions

The computer analysis successfully models the heating characteristics of a variety of substrates with or without photoresist in an infrared oven. The model can be used to predict the operating conditions required for complete baking of photoresist. This occurs for a maximum temperature in the range of 80°-110°C for Shipley AZ1300 resists on glass in a Zicon 1100 infrared oven on substrates moving at a conveyor speed of 4.3 mm/sec. The baking conditions necessary to achieve this result will be different for other sample structures, but they can now be calculated with the help of the present model. Higher maximum sample temperatures are obtained by using higher emitter temperatures and lower conveyor speeds.

Modeling of substrates with high reflectivity or several films of widely varying optical constants requires accurate values for the optical properties. In some cases, empirical adjustments to $\hat{n}(\lambda)$ may be necessary. The emissivities are less significant.

Acknowledgments

We wish to thank P. Hincke for his assistance at an early stage in the experiments. This work has been supported in part by the National Research Council of Canada through the Industrial Research Programme (IRAP PLASMA 1100).

Manuscript received Aug. 10, 1982. This was Paper 756RNP presented at the Montreal, Que., Canada, Meeting of the Society, May 9-14, 1982.

Any discussion of this paper will appear in a Discussion Section to be published in the December 1983 JOURNAL. All discussions for the December 1983 Discussion Section should be submitted by Aug. 1, 1983.

Bell-Northern Research, Limited assisted in meeting the publication costs of this article.

REFERENCES

1. W. S. DeForest, "Photoresist," McGraw-Hill Book Co., New York (1975).
2. L. Schantz and J. H. Pusch, "Infrared Baking of Positive Photoresist," Bendix Report BDX-613-1246 (1976).
3. M. Nishimura, K. Yamaguchi, M. Hirabayashi, Y. Hirabayashi, and S. Sugiyama, *Kagaku Kogaku Ronbunshu*, 3, 75 (1977).
4. H. S. Carlslaw and J. C. Jaeger, "Conduction of Heat in Solids," Oxford, New York (1954).
5. M. Born and E. Wolf, "Principles of Optics," Pergamon Press, New York (1959).

The Effect of a Constant Current Stress on the Oxides in MOS Capacitors

R. Radojcic

Burroughs Corporation, M.C.G., San Diego, California 92128

ABSTRACT

The effects of stressing high quality polysilicon—SiO_2-Si capacitors with a constant d-c current, are observed by use of C-V and I-V curve measurements. Short current stresses are found to produce positive charges, assumed to be holes, in the bulk of SiO_2. With prolonged stress, this charge is compensated by electron trapping in the oxide. With Si biased positively (polysilicon negative), effects attributed to direct tunneling of holes from the anode into SiO_2 are observed.

In a normal population of MOS devices, the usual distribution of dielectric breakdown voltages is Gaussian with an asymmetrical tail-off towards lower voltages. In the majority of cases, the measurement of dielectric breakdown, typically at 10 μA, is a destructive process resulting in oxide ruptures. This is a consequence of the nonuniformities in the distribution of the applied field (and, therefore, the Fowler-Nordheim current densities) caused by defects within the oxide.

In a portion of the population, however, these defects are minute or even absent, so that the field is uniformly distributed over the device area. In these samples, the destructive "hot spots" are not formed, so that it is possible to stress the devices at very high fields, thereby, forcing an appreciable oxide current but without causing physical destruction. This work summarizes a study of the effects of constant current stresses on MOS capacitors.

Experiment

The test structures used were 254 $\times$ 254 μm square polysilicon—SiO_2-(p)Si capacitors, surrounded by a thick field oxide and a p+ channel stop. The SiO_2 layers were grown in O_2/HCl ambient at 950°C to a typical thickness of 430 $\pm$30Å. The substrates were p^- wafers with a threshold adjust implant implanted through the gate oxide.

The devices were stressed with 1, 10, and 100 μA (1.55, 15.5, and 155 mA/cm^2) constant d-c current for varying time durations using a constant current source and a time controlled relay. With positive stress polarity (polysilicon positive), the voltage required to provide the desired current (critical voltage) was typically ~75V; whereas, negative stress polarity required approximately 45V.

The effects of the stress on the capacitors were evaluated by measuring C-V and I-V curves before and after each stress. C-V curves were measured by standard 1 MHz capacitance meter with a d-c bias sweep from -10 to $+4.0$V at approximately 1 V/sec sweep rate. I-V curves were measured with polysilicon biased negatively and with the maximum total current limited to less than 100 pA. In order to maximize the probability of finding a "good" device, the test population was screened for breakdown voltage better than 25V. Each individual capacitor was stressed only once, *i.e.*, the effects of repetitive stressing were not investigated.

Results

Positive bias stress (polysilicon positive).—The effect of $+10$ μA constant current stress of "short" duration ($t \simeq 1$ sec at critical voltage) on the C-V and I-V characteristics of MOS capacitors is illustrated by curve 2 in Fig. 1 and 2. Both curves shifted along the voltage axis, indicating the presence of a positive charge within the oxide. The effect of a prolonged ($t >> 2$ sec at critical voltage) stress on the C-V and I-V characteristics is illustrated by curve 3 in Fig. 1 and 2. The distortion in the C-V curve, as well as the decreased net shift along voltage axis in both the C-V and I-V curves, appears to be indicative of electron trapping in the surface states and in the bulk of the oxide.

Figure 3 is a plot of the net shift of the flatband voltage in the C-V curves and the shift in the I-V curves (at 50 pA) *vs.* stress time. Note that the x-coordinate corresponds to the total time the DUT was biased, a controlled instrument setting. The true time duration of the constant current stress is, in fact, lower. This discrepancy arises due to the instrument limitations: the output of the constant current source is smoothed by a capacitor which limited the rate at which the compliance voltage is reached. Consequently, compliance voltage is not achieved at "short" time settings. The first data point, in fact, corresponds to a constant current stress of ~1 sec. Correction of the x-axis to represent true time at constant current stress

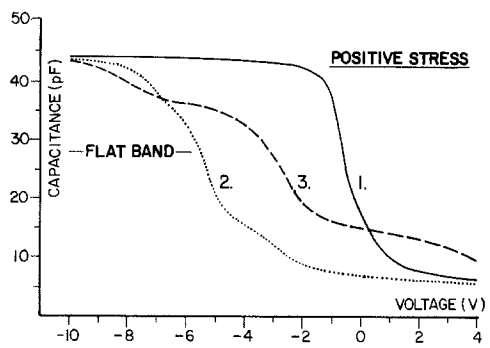

Fig. 1. C-V curves following constant positive ($+10$ μA) stress of differing durations. Curve 1—initial; curve 2—after ~1 sec stress; curve 3—after 100 sec stress.

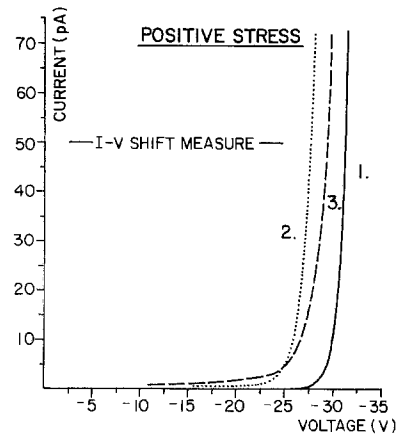

Fig. 2. I-V curves following constant positive ($+10$ μA) stress of differing durations. Curve 1—initial; curve 2—after ~1 sec stress; curve 3—after 100 sec stress.

Key words: dielectrics, capacitor, charge, trapping.

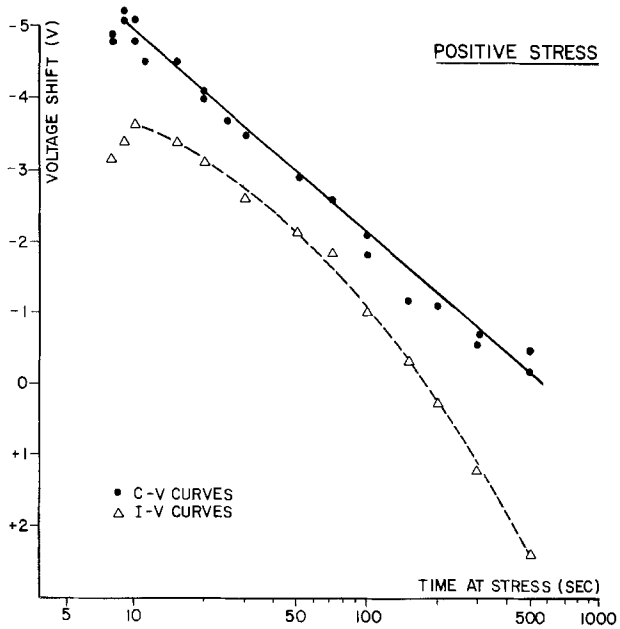

Fig. 3. Shift along the voltage axis of the flatband point of the C-V curves and the 50 pA point of the I-V curves with time at constant positive (+10 μA) stress relative to the initial unstressed curves.

would result in uncertainty in data points in the short stress region and would not alter the fundamental effects illustrated.

Negative bias stress (polysilicon negative).—With negative bias, the Fowler-Nordheim current is injected from polysilicon rather than from the substrate. The effects of "short" and "long" stress at −10 μA on the C-V and I-V characteristics of the devices is illustrated by curves 2 and 3 in Fig. 4 and 5, respectively. As can be seen, the initial behavior is similar to the one observed with positive stress but subsequent prolonged stress resulted in different trends. Figure 6 is a plot of the net shift of the flatband point of the C-V curves and the shift of the I-V curves (at 50 pA) *vs.* stress time. The contrast of the shifts in the C-V curves in this and in Fig. 3 is obvious in the sense that there appears to be no immediate build up of the negative charge.

Stress with various current densities.—The general behavior of the characteristics of the MOS capacitors stressed with ±1.0 and ±100 μA is similar to the one described above for ±10 μA, except that the magnitudes of the shifts differ. An experiment where the total charge forced through the devices is kept constant was performed by observing the C-V shifts under a constant current-time stress ($I \times t$) of 100 μA sec. In Fig. 7, the magnitude of the net shift of the flatband

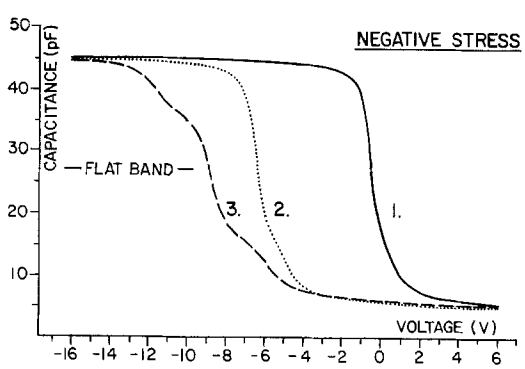

Fig. 4. C-V curves following constant negative (−10 μA) stress of differing durations. Curve 1—initial; curve 2—after ~1 sec stress; curve 3—after 100 sec stress.

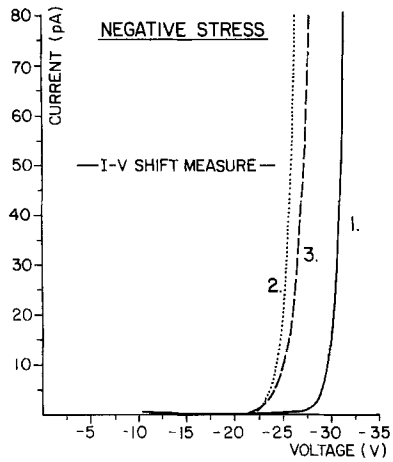

Fig. 5. I-V curves following constant negative (−10 μA) stress of differing durations. Curve 1—initial; curve 2—after ~1 sec stress; curve 3—after 100 sec stress.

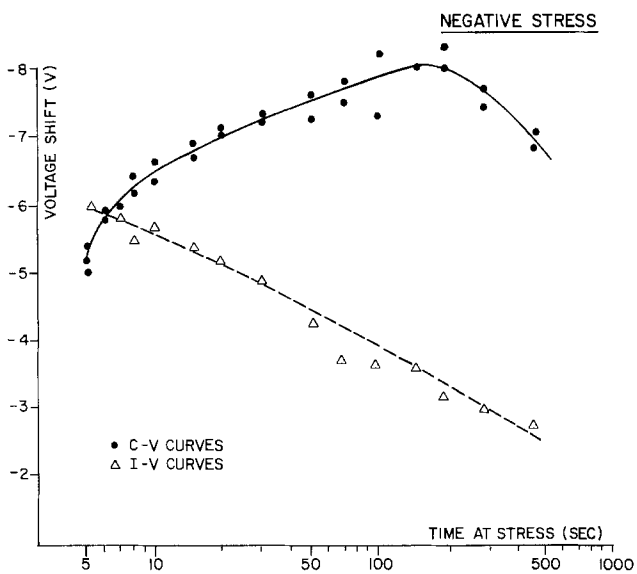

Fig. 6. Shift along the voltage axis of the flatband point of the C-V curves and the 50 pA point on the I-V curves with time at constant negative (−10 μA) stress relative to the initial, unstressed curves.

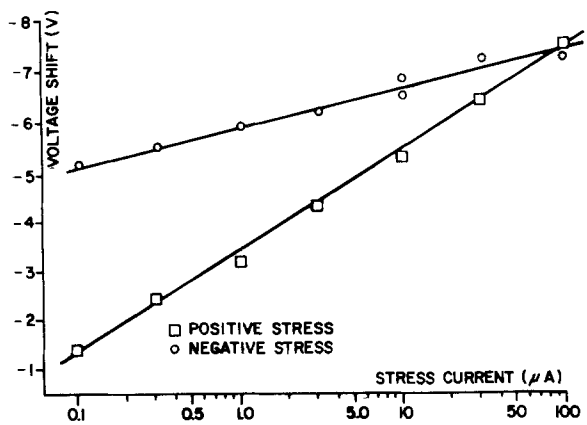

Fig. 7. Net observed shift in the flatband voltage of the C-V curves *vs.* current magnitude at constant current × stress time ($I \times t$) product of 100 μA sec.

point of the C-V curves is plotted against stress current under constant $I \times t$ conditions for positive and negative stress polarities. The slopes indicate that the mech-

anisms observed here do have some definite activation thresholds.

Relaxation and annealing properties.—It was found that all of the observed distortions in the C-V curves can be annealed. The surface-state effects (the smear in the slope and the kinks in the C-V curves) were the least stable, could be seen to relax even at room temperature, and could be annealed at 150°C. The curve shifts along the voltage axis were found to recover as well, particularly at elevated temperatures. In the samples stressed with positive bias for prolonged periods and then annealed, the C-V curve shifts first increased and only subsequently decreased towards the initial, unstressed position. This implied that at elevated temperatures, the rate of loss of the negative charge is higher than that of the positive charge.

Temperature alone (up to 300°C) was found to be insufficient in removing most of the charge from SiO_2, at least in reasonable time periods. A combination of temperature and relatively low bias (such that no measurable injection occurs), however, was found to be quite efficient at annealing out all the charges.

Discussion

It is obvious that whatever mechanism is responsible for the observed behavior, it must be consistent with stresses of either polarity. It is believed that the initial large positive charge observed in both positive and negative stresses is due to holes generated in the bulk of SiO_2 by impact ionization process. Since the mobility of the holes in SiO_2 is very small (1) (10^{-5} $cm^2V^{-1}sec^{-1}$), an avalanche-like process can be expected to leave behind a cloud of trapped positive charge (7, 8). Using the equation published by Jenq, *et al.* (3) and the magnitudes of the initial shifts in the I-V curves (most sensitive to the charge close to polysilicon/SiO_2 barrier) and the C-V curves (most sensitive to the charge close to Si/SiO_2 interface), it is calculated that the centroid of the initial positive charge is approximately 200 ± 30Å from the Si/SiO_2 interface, *i.e.*, the centroid is roughly in the middle of the oxide thickness rather than close to either interface indicating that bulk rather than surface effects are taking place. These conclusions are consistent with the work of Ishiuchi *et al.* (4). In Ref. (3) and (5), however, no evidence of bulk SiO_2 positive charge is observed. It is believed that the discrepancy arises from the fact that in those works very thin ($<<$400Å) SiO_2 films were used (perhaps too thin to support impact ionization and/or hole trapping?)

Continued positive stress, however, does not appear to generate further positive charge in the bulk of SiO_2 even though the field, albeit modified by the already generated holes, must be sufficiently large in at least a portion of the layer for impact ionization to occur. The number of residual holes seems to saturate quickly and is regulated by recombination process (8). With continued exposure to the positive stress, it is evident that a different mechanism becomes dominant: that of electron trapping (3, 5). It is believed that the electrons are continuously trapped in the existing or newly created traps and are, thus, compensating the charge due to the holes rather than that residual hole charge is being annihilated by recombination. Since the charge due to the electrons strongly affects both the C-V and the I-V curves, it is believed that the trapped electrons are uniformly distributed in the oxide (3) or at least, that this charge, too, is a bulk phenomenon. The electron trapping process is continuous and does not saturate like the mechanism that generated the holes, so that for long stress periods it becomes dominant and eventually produces a net positive shift along the voltage axis.

In the case of a stress with negative polarity, both mechanisms, *i.e*, the avalanche generation of holes and the continuous trapping of electrons, are believed to take place in the same manner as in the case of positive stress. The major differences in the behavior are attributed to a third mechanism, that of direct tunneling of positive charges from the anode into SiO_2 interface as proposed by Jenq *et al.* This tunneled positive charge resides only 20-50Å away from the silicon interface and, therefore, completely dominates the C-V curves, *i.e.*, it shields the silicon substrate from the influence of the charges deeper in the bulk of SiO_2. Eventually, this interface charge saturates and the effects of trapped electrons become apparent. The I-V curves controlled by the polysilicon/SiO_2 barrier are less sensitive to this charge and, thus, behave similarly with stresses of either polarity. Similar hole injection does not seem to occur from the polysilicon electrode (positive stress) due to the fact that polysilicon is a degenerate n+ material.

Other discrepancies in the behavior with positive and negative stresses could be attributed to the fact that with positive bias, Si surface is inverted and electron fluence through the structure (the controlled variable) is controlled by factors other than just the Si/SiO_2 barrier. Assuming that electron trapping occurs uniformly throughout the oxide, the slopes of the $\Delta V(I\text{-}V)$ *vs.* $ln\ (t)$ curves (Fig. 3 and 6) indicate that positive bias results in higher trapping rate. This implies that the positive stress leads to higher rate of generation of electron traps (3). Since electron current is the same with both stress polarities and since the field across the oxide itself is higher with positive bias, this could imply that trap generation is a field rather than current driven process (3).

The impact ionization generation of the bulk holes is a field-dependent mechanism, with a threshold related to the bandgap of SiO_2. Hole injection from the anode is expected to have a field threshold as well (albeit lower) but related to the Si/SiO_2 barrier height for the holes. The curves in Fig. 7 are indicative of these differing thresholds since the negative-stress curves are dominated by hole injection mechanism while the positive-stress curves are determined by bulk SiO_2 hole generation.

Summary and Conclusion

Three distinct mechanisms have been postulated to take place in MOS capacitors stressed at very high field strengths and current densities. The chain of events has been inferred from the charges in the I-V curves which, being controlled by the polysilicon/SiO_2 barrier height, are most sensitive to the charges nearest to that interface and, in the C-V curves, which are most sensitive to the charges nearest the Si/SiO_2 interface.

The results obtained provide experimental confirmation of, and deeper insight into, the mechanism of dielectric breakdown in MOS structures (6, 7, 8). The samples and methods used here allow measurements of the sequence of events that occur during the usual, destructive, dielectric breakdown. Thus, the generation of bulk holes and the consequent decrease in the cathode/SiO_2 barrier do confirm the "negative resistance" and "run-away" aspects of the dielectric breakdown which is normally evaluated under constant or ramped voltage conditions.

Furthermore, the experiment may prove to be a technique for evaluating some aspects of intrinsic oxide integrity, a technique not subject to the limitations imposed by avalanche electron injection or photoinjection types of measurements.

Manuscript submitted June 28, 1982; revised manuscript received March 7, 1983.

Any discussion of this paper will appear in a Discussion Section to be published in the December 1983 JOURNAL. All discussions for the December 1983 Discussion Section should be submitted by Aug. 1, 1983.

Burroughs Corporation assisted in meeting the publication costs of this article.

REFERENCES
1. D. J. DiMaria, in "The Physics of SiO_2 and Its Interfaces," S. T. Pantelidis, Editor, p. 160, Pergamon Press, New York (1978).
2. D. J. DiMaria, in "The Physics of MOS Insulator," G. Lucovsky, S. T. Pantelidis, and F. L. Geleener, Editors, p. 1, Pergamon Press, New York (1980).
3. C. S. Jenq, T. R. Ranganath, C. H. Huang, H. S. Jones, and T. L. Chang, in "International Electron Device Meeting," Washington, DC, p. 388, December 7-9, 1981.
4. H. Ishiuchi, Y. Matsumoto, T. Mochizuki, S. Sawada, and O. Ozawa, in "20th Annual Proceedings of Reliability Physics," San Diego, CA, p. 228, March 30-April 1, 1982.
5. E. Harari, *J. Appl. Phys.*, **49**, 2478 (1978).
6. T. H. DiStefano and M. Shatzkes, *J. Vac. Sci. Technol.*, **13**, 50 (1976).
7. P. Solomon, *ibid.*, **14**, 1122 (1977).
8. T. H. DiStefano and M. Shatzkes, *Appl. Phys. Lett.*, **25**, 685 (1976).

Two-Step Thermal Anneal and Its Application to a CCD Sensor and CMOS LSI

M. Ogino,[1] T. Usami, and M. Watanabe*

Toshiba Corporation, Research and Development Center, 72 Horikawacho, Saiwaiku, Kawasaki 210, Japan

and H. Sekine and T. Kawaguchi

Toshiba Corporation, Semiconductor Division, Kawasaki 210, Japan

ABSTRACT

The two-step thermal anneal has been investigated in detail for the control of oxygen precipitation. The correlations of interstitial oxygen reduction after the two-step thermal anneal, the interstitial oxygen in the as-grown wafer, and the microdefect density are made clear. There is a critical oxygen concentration for the oxygen precipitation. It depends on the first step annealing time and the substitutional carbon concentration. The two-step thermal anneal was applied successfully to a CCD image sensor and CMOS LSI to improve their performance.

Semiconductor technology has been looking for the purest material and the cleanest environment. However, in the manufacture of integrated circuits from single crystal silicon, complete elimination of contamination is not always possible. This forces us to develop an effective gettering technology to get rid of contaminants introduced during the manufacturing process. Among many gettering techniques (1-6), intrinsic gettering (IG), which was reported first by Tan *et al.* (7), has been most intensively studied recently (8-11), because of its high gettering capability. Since performance of IG depends upon the oxygen-related microdefects (MD) such as the oxygen precipitates, the dislocation loops and the stacking faults induced by oxygen precipitation (12-15), the control of the precipitation of oxygen, *i.e.*, the formation of MD, is necessary to control IG. It is well known that the formation of MD strongly depends on the oxygen concentration. Tan *et al.* used high oxygen concentration wafers as starting material to get effective IG, since a large number of precipitates are rapidly formed in them. Oxygen concentration in wafers commercially available is fairly variable so that it is better to control the precipitation to get reproducible IG.

In this paper, we will discuss control of MD formation by low temperature preheat-treatment which can enhance oxygen precipitation even in the low oxygen concentration wafers. Using preheat-treated wafers, microdefects grow during the LSI manufacturing processes. This is the two-step thermal anneal, *i.e.*, one step is a low temperature preheat-treatment to control the MD density, and the second step is the LSI processing to grow MD. In addition, the application of MD to a CMOS LSI and to a CCD image sensor will be shown. In both cases, the MD density was successfully controlled by the above two-step thermal anneal. Microdefects have been used as gettering sites in the previous works (7-11), but in the application to the CCD image sensor, we used them as reecombination sites for undesired carriers.

* Electrochemical Society Active Member.
[1] Present address: Toshiba Ceramics Corporation, 1-26-2 Nishi-shinjuku, Shinjuku, Tokyo, 160, Japan.
Key words: silicon, microdefects, oxygen concentration, intrinsic gettering.

Two-Step Thermal Anneal

Experiment.—Most of wafers used in the two-step thermal annealing experiments were p-type, 12-16 Ω-cm, 76 mm diam, CZ (100) polished wafers. Their carbon concentration was below $3 \times 10^{16}/cm^3$. In addition, high carbon ($>5 \times 10^{16}/cm^3$) wafers were used. These were p-type 2-6 Ω-cm, 62 mm diam, CZ (111) polished wafers. The wafers did not experience the so-called donor killer heat-treatment (around 600°C) which was expected to influence the density of nuclei of oxygen precipitation. First, the wafers were heat-treated at 800°C in nitrogen for 1-16 hr. Then, they were annealed at 1050°C in dry oxygen for 18 hr. The conditions for the second heat-treatment were chosen to simulate an actual LSI manufacturing process. The concentration of interstitial oxygen was measured before the first low temperature anneal and after the second high temperature anneal. A Fourier transform infrared spectrometer was used to measure absorption coefficients at 1108 cm^{-1} for interstitial oxygen and at 605 cm^{-1} for substitutional carbon. Interstitial oxygen and substitutional carbon concentrations were calculated from the absorption coefficients according to Kaiser and Keck (16) and Newman and Willis (17). After the second anneal, the microdefects were counted using Nomarski interference microscopy on (110) or (111) cleaved surfaces etched for 90 sec using Wright etch (18). Microdefects were also observed by x-ray section topography and transmission electron microscopy (TEM).

Results.—Interstitial oxygen concentration decreased after a two-step thermal anneal at 800° and 1050°C. The reduction of interstitial oxygen, O_{red}, depended on the initial oxygen concentration as shown in Fig. 1. The reduction of oxygen is defined as follows

$$O_{red} = O_i - O_f$$

where O_i is the oxygen concentration in the as-grown

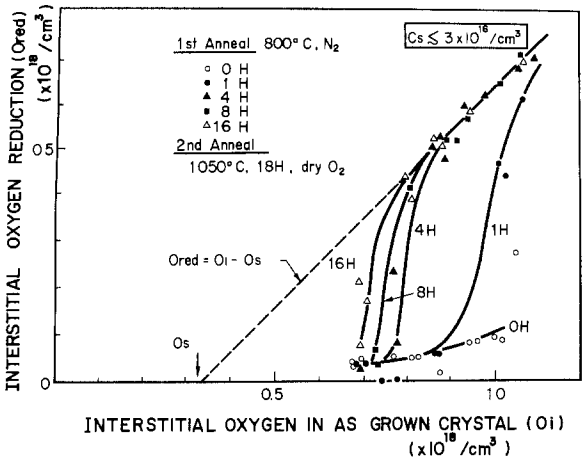

Fig. 1. Interstitial oxygen reduction after a two-step thermal anneal. Carbon concentration is below 3 × 10^{16}/cm³.

wafer, and O_f is the oxygen concentration after a two-step thermal anneal. For a certain two-step thermal annealing process, the reduction of oxygen took place only when the initial oxygen exceeded a certain critical concentration, O_{cri}. This is schematically shown in Fig. 2. The O_{red} was almost zero for O_i below O_{cri}. The critical value, O_{cri}, decreased with an increase in the first annealing time. The low temperature anneal at 800°C enhanced the precipitation. When O_i was sufficiently greater than O_{cri}, precipitation of oxygen was complete. Except for intermediate cases ($O_i \approx O_{cri}$), the amount of oxygen reduction had a definite correlation to the interstitial oxygen concentration in the as-grown wafer. This could be expressed as follows

$$O_{red} = O_i - O_s$$

for

$$O_i > O_{cri}$$

and

$$O_{red} = 0$$

for $O_i < O_{cri}$, where O_s is the oxygen concentration left unprecipitated. This corresponds to the solubility limit of interstitial oxygen at 1050°C. The O_s value obtained in this experiment was 3.4 × 10^{17}/cm³. It agrees well with Hrostowski's (19) solid solubility limit, 3.1 × 10^{17}/cm³. The above correlation was also confirmed by Wright etch and x-ray section topography as shown in Fig. 3 and Fig. 4. These are the results for the two-step thermal anneal, whose first step annealing time was 4 hr. In this case, O_{cri} was about 0.8 × 10^{18}/cm³. The etch pit density or the x-ray intensity for $O_i > O_{cri}$ was very high, while that for $O_i < O_{cri}$ was very low. The defect-free denuded zone was not clearly seen. The denuded zone for the dry oxygen ambient will be narrower than that for an inert gas ambient, because of small oxygen out-diffusion [according to Hu (20), it should be wider for the dry oxygen ambient.] Figure 5 shows TEM micrographs of microdefects shown as

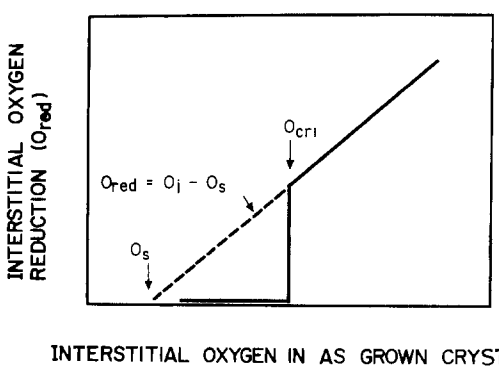

Fig. 2. Schematical figure of Fig. 1

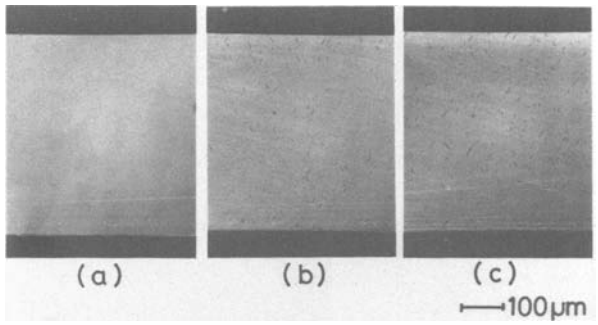

Fig. 3. (110) cleaved surfaces, Wright etched for 90 sec. The first step annealing time is 4 hr. (a) O_i = 0.77 × 10^{18}/cm³, (b) O_i = 0.86 × 10^{18}/cm³, (c) O_i = 1.05 × 10^{18}/cm³.

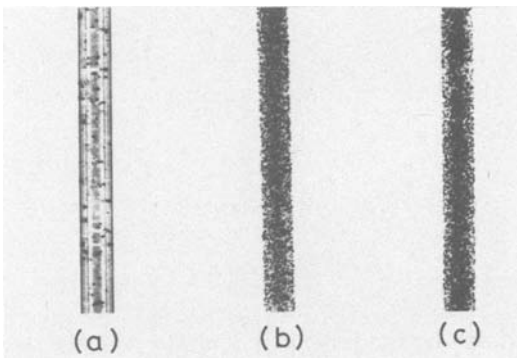

Fig. 4. X-ray section topographs corresponding to samples in Fig. 3. Ag $K\alpha_1$, 044 reflection.

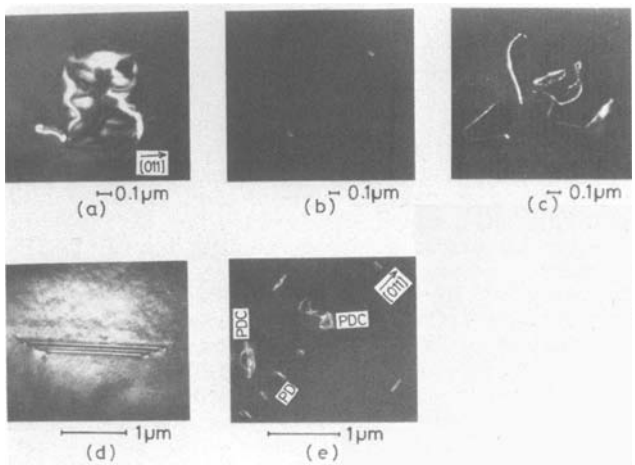

Fig. 5. TEM micrographs of microdefects observed in the two-step annealed wafers. (a) Platelike precipitate; dark field image, g = 022. (b) Tiny precipitates; weak beam image, g = 022, w = 3.3. (c) Precipitate oxygen complex (PDC); weak beam image, g = 022, W = 3.3. (d) Stacking fault; dark field image, g = 022. (e) Punch out dislocations (PD) and PDC; weak beam image, g = 022, W = 3.3.

etch pits in Fig. 3 or black spots in Fig. 4. They consisted of square shaped platelike precipitates whose surface normal was <100>, tiny precipitates whose shape was not clear, precipitate-dislocation complexes, stacking faults, and punched out dislocation loops. For a long first step annealing time, tiny precipitates were often observed.

The enhancement of oxygen precipitation by carbon which has been reported by Matsushita *et al.* (21) was also observed in the present experiment. Figure 6 shows the correlation between O_{red} and O_i for high carbon (>5 × 10^{16}/cm³) wafers. The O_{cri} was shifted to lower O_i. This is clearly shown in Fig. 7, in which the same annealing process was carried out for the low

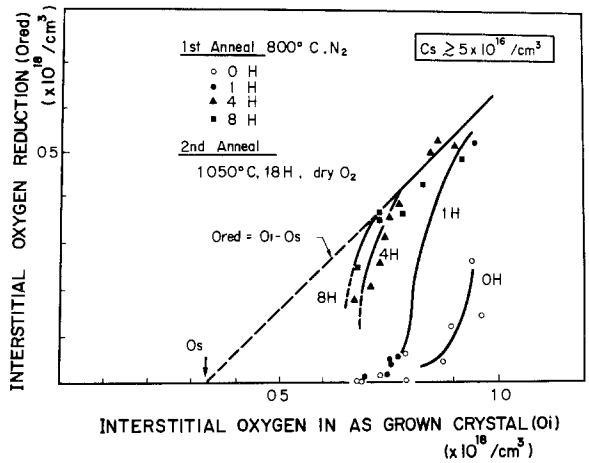

Fig. 6. Interstitial oxygen reduction after a two-step thermal anneal. Carbon concentration is above 5 × 10^{16}/cm³.

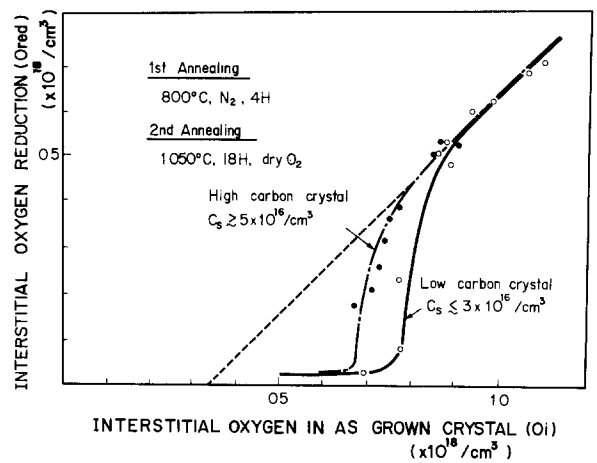

Fig. 7. Comparison of interstitial oxygen reduction between high carbon wafer and low carbon wafer.

and the high carbon wafer. The reduction in the substitutional carbon concentration after the two-step anneal, however, was below the detection limit, ~3 × 16^{16}/cm³, for all high carbon wafers.

Discussion.—The enhancement of oxygen precipitation by a two-step thermal anneal has been reported by several groups (9, 10, 22), but detailed correlations with the oxygen and the carbon concentrations in the as-grown wafer, or with the thermal annealing conditions have not been reported. Such a detailed investigation is indispensable for the application of IG technique to the device manufacturing process. Our results shown in Fig. 1 and 3 made clear those correlations and gave a possibility of controlling the oxygen precipitation even in fairly low oxygen wafers. That is, if we know the oxygen concentration in the as-grown wafer, we can choose an appropriate low temperature annealing time to enhance oxygen precipitation.

Of course, for actual semiconductor devices, we should have similar correlations to those in Fig. 1 for the manufacturing processes, in spite of the second anneal at 1050°C for 18 hr.

The density of microdefects is an important factor in their application to IG because the gettering is more effective in wafers with a high microdefect density. The simplest technique to evaluate MD density is counting etch pit density. However, this method generally has a large error because it does not take into account the defect size. In addition, etch pit density may depend on the person who counts it. Some objective parameter is needed for quantitative discussion on the microdefect density. The interstitial oxygen reduction O_{red} can be used as this parameter. Although the O_{red} is not directly correlated with some kinds of microdefects, such as the stacking fault and various dislocations, it can be indirectly correlated with them because they are induced by the oxygen precipitation.

Figure 8 shows the correlation of the etch pit density of MD with O_{red}. The O_{red} was fairly proportional to etch pit density. Using this figure and Fig. 1, the low temperature annealing time for sufficient microdefect density for IG could be predicted for a given O_i.

The nucleation of oxygen precipitates had been widely discussed by the use of the homogeneous model (23, 24), the heterogeneous model (15), or a combination of the two models (25, 26). Our result shown in Fig. 7 suggested the heterogeneous nucleation by substitutional carbon. In that case, the change in the substitutional carbon concentration was below the detection limit (3 × 10^{16}/cm³). From this fact and since the substitutional carbon concentration in CZ silicon is usually 1-10 × 10^{15}/cm³, the heterogeneous nucleation of the oxygen precipitates by substitutional carbon should take place in all CZ silicon wafers. However, the carbon effect can hardly be detected because the change in the substitutional carbon concentration is usually very small.

Besides the above classification by the homogeneous or the heterogeneous model for the oxygen precipitate nucleation, the oxygen precipitation can also be classified according to when the oxygen precipitates are nucleated.

Oxygen precipitates are nucleated not only during the thermal anneal after the crystal growth, but also during the crystal growth process. The two-step anneal was simulated from the above point of view. We could successfully explain O_{cri} and its dependence on the first step annealing time (27).

Application of Two-Step Thermal Anneal to CCD Image Sensor and CMOS LSI

The electrical properties of devices are sometimes degraded by microdefects (MD) in the bulk. This is due to the deep levels associated with the defects. This suggests that microdefects in the bulk can be recombination sites of excess carriers as well as gettering sites of heavy metals (IG). In this section, we will show the applications of MD as recombination sites in a CCD image sensor as well as gettering sites in CMOS LSI.

To generate sufficient MD, we used the two-step thermal annealing technique. Wafers used in both cases were heat-treated at 800°C for a suitable time be-

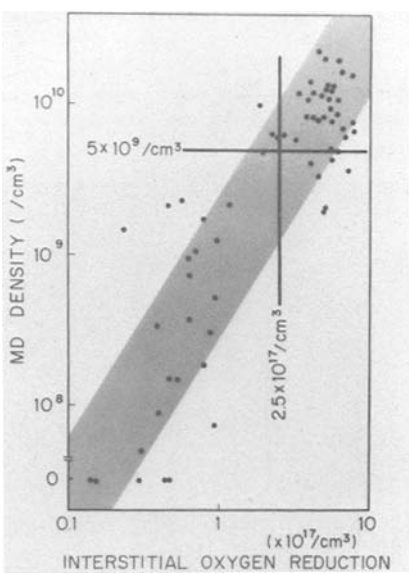

Fig. 8. MD density vs. interstitial oxygen reduction after a two-step thermal anneal.

fore putting them into the manufacturing processes. The second high temperature thermal anneal of a two-step anneal described in previous sections was automatically carried out in the manufacturing processes. That is, the high temperature anneal to grow precipitates is the manufacturing process itself.

Application to CCD.—In a CCD linear image sensor shown in Fig. 9, undesired carriers were excited by the infrared component of incident light in the region far from the light sensing area, for example at point X. These undesired minority carriers diffuse to the potential well under the photodiode and the transfer electrode. The extra signals resulted in nonuniform sensitivity of the sensor. Figure 10 shows the output of a linear CCD image sensor under uniform illumination. Nonuniform output was observed at edge elements made on the nonpreannealed wafer, while the output for the preannealed wafer was uniform. The (110) cleaved surface etched by Wright etchant is shown in Fig. 11. There were many MD in the preannealed wafer. The defect-free denuded zone was formed in the surface region of the preannealed wafer.

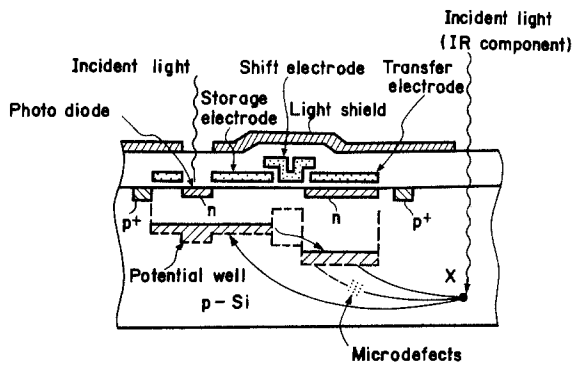

Fig. 9. Cross section of a CCD image sensor showing the recombination of excess carriers by microdefects.

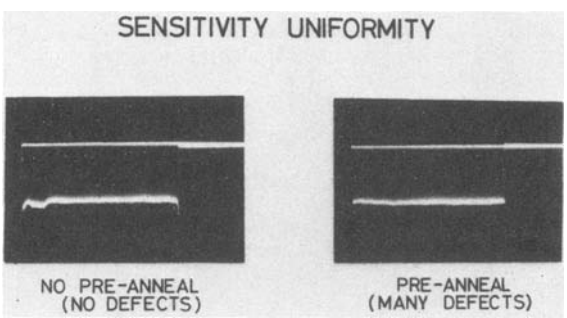

Fig. 10. Output of linear CCD image sensor. The upper line shows the nonilluminated level and the lower line shows the output under the uniform illumination.

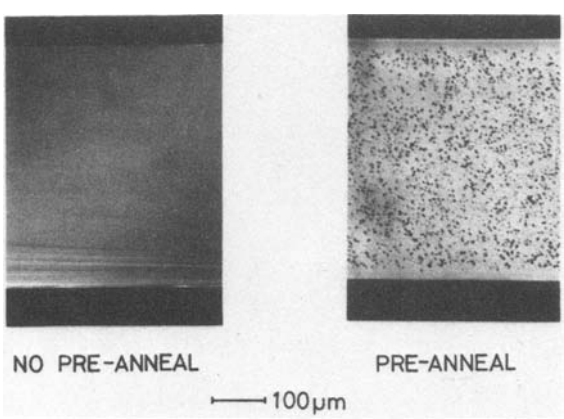

Fig. 11. (110) cleaved surfaces of nonpreannealed and preannealed wafers, Wright etched for 90 sec.

We also measured the minority carrier diffusion length L using a linear CCD sensor. Figure 12 shows the geometry of devices used in the measurement. Carriers were injected by a test transistor at some distance from the sensing CCD area. The output of the $2n$-th picture element $V(2n)$ is then approximately expressed by

$$V(2n) = V(0)\exp\{-(\sqrt{370^2 + (30n)^2} - 370)/L\} \quad [1]$$

where $V(0)$ is the output of the center picture element. Figure 13 shows the output of a CCD made on a nonpreannealed wafer (a) and on a preannealed wafer (b), when carriers were injected from the test transistor. From this figure, the diffusion length, L, was calculated by Eq. [1] to be 80 μm for the nonpreannealed wafer and 20 μm for the preannealed wafer. Other optical characteristics of CCD sensor, for example spectral response, spatial resolution, etc., were also improved by the use of the preannealed wafer. Any degradation of CCD response, such as an increase in the dark current due to the MD was not observed in the preannealed wafer. Details of these improvements will be published elsewhere.

The microdefects in the bulk could effectively stop the flow of injected excess carriers by acting as recombination sites. It has been reported that, while stacking faults are electrically inactive, they become active when decorated with metallic impurities (28, 29). Some microdefects, such as dislocations shown in Fig. 5, can act as recombination centers, because they are associated with deep levels (30).

Application to CMOS LSI.—The effect of high density MD caused by the preanneal on CMOS LSI was investigated by the effect on MOS generation lifetime. Three other kinds of wafers, besides the preannealed wafer, were used in this experiment for comparison. These were high ($\approx 1 \times 10^{18}$/cm^3) and low ($\approx 0.7 \times 10^{18}$/cm^3) oxygen content wafers without preannealing, and a wafer with back surface damage created by sandblasting. MOS capacitors were made on those wafers using a CMOS LSI process. After the lifetime

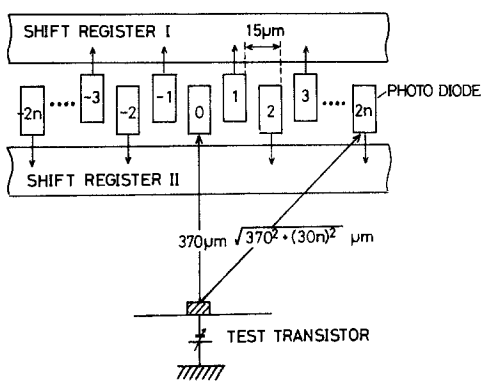

Fig. 12. Geometry of the linear CCD image sensor used in the measurement of diffusion length, L.

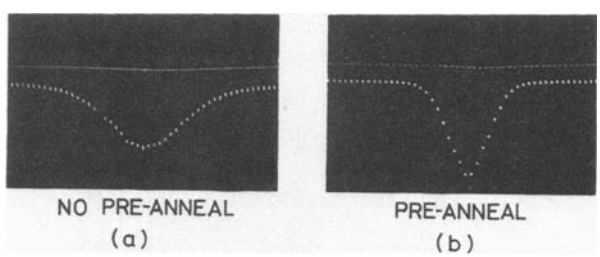

Fig. 13. Outputs of even number picture elements when carriers are injected from the test transistor. Upper dotted line shows the output without injection and the lower v-shaped dotted line shows the output with injection.

measurement, the wafers were cleaved and Wright etched.

Figure 14 shows the microdefect distribution at the center region on the (110) cleaved surface. Many microdefects were uniformly distributed in the preannealed wafer, sample B. Of course in the surface region, the denuded zone was formed and the depth was 10-20 μm. It was formed by the oxygen out-diffusion during the high temperature P-well diffusion. In the high oxygen wafer without preanneal, sample A, there were also many microdefects but the density distribution was not uniform and depended on oxygen concentration distribution as shown in Fig. 15. The density of microdefects was high at the wafer center and low at the wafer edge. However, in both the low oxygen wafer without the preanneal, sample C, and the damaged wafer, sample D, there were no microdefects (not shown in Fig. 14). The oxygen content in sample D was $\approx 0.7 \times 10^{18}/cm^3$. Figure 16 shows the lifetime distribution on the wafer. The lifetime distribution showed good agreement with the MD density distribution, shown in Fig. 14. The lifetimes of samples A and B were very high compared with samples C and D. The lifetime distribution of sample B was uniform, and that of sample A was high at wafer center and low at wafer edge. In spite of the back surface damage, the lifetime of sample D was very low. This means the gettering by back surface damage was ineffective. The damage on this wafer was damage that would generate

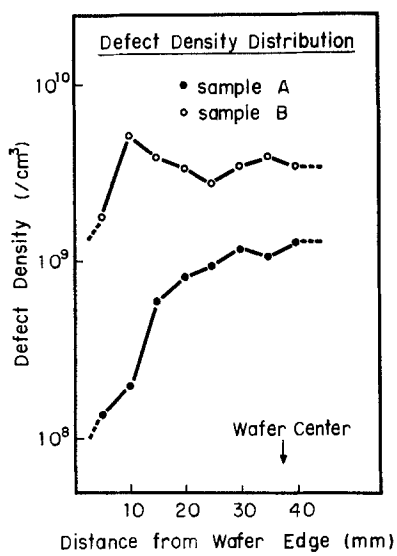

Fig. 14. MD density distributions of the preannealed wafer, sample B, and the high oxygen wafer, sample A. There were no MD in the low oxygen wafer, sample C, and the wafer with back surface damage.

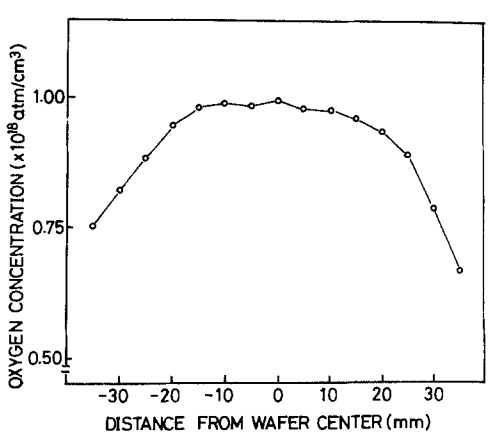

Fig. 15. Oxygen concentration distribution of the high oxygen wafer, sample A.

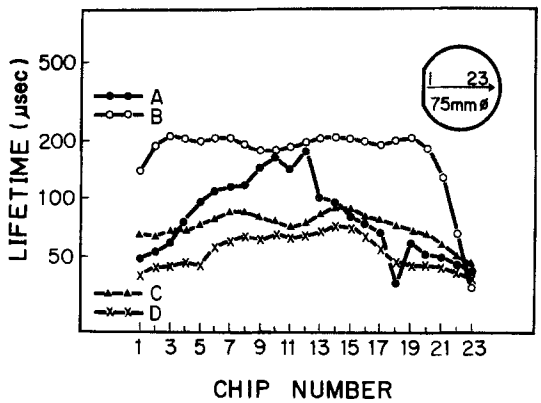

Fig. 16. The lifetime distribution, (A) high oxygen wafer, (B) preannealed wafer, (C) low oxygen wafer, and (D) damaged wafer.

stacking faults on the back surface during the oxidation in the manufacturing processes. However, no stacking faults were seen on the back surface of sample D after completing the manufacturing processes. Stacking faults shrink by high temperature heat-treatment above about 1200°C (31). Stacking faults which would be generated by the damage were annihilated in the high temperature P-well diffusion process. Figure 17 shows the shrinkage of stacking faults induced by sandblasting on the front polished surface. Stacking faults generated during the oxidation at 1000°C for 65 min in wet O_2 were shrunk by the subsequent high temperature anneal at 1190°C, which corresponded to the P-well diffusion temperature. The stacking faults had already shrunk after the 4 hr anneal. However, so-called hard damages which generate dislocations and are represented by D in Fig. 17 were not eliminated by the high heat-treatment. This hard damage is also effective for the gettering, however, they easily cause thermal slip or wafer warpage when a large number of hard damages are induced for effective gettering (32). Therefore, it is assumed that IG is a better technique than the back surface damage by sandblasting for the CMOS process. From Fig. 14 and 16, the correlation between the MD density and the lifetime was determined as shown in Fig. 18. It shows that more than about $5 \times 10^9/cm^3$ MD density was desirable to yield high lifetime. From the relation between the MD density and the oxygen reduction shown in Fig. 8, it was shown the oxygen reduction desirable for IG technique was more than $2.5 \times 10^{17}/cm^3$. Therefore, it became clear that a suitable low temperature thermal anneal to realize this value was necessary for conventional wafers as shown in Fig. 1.

Summary

The two-step thermal anneal and its application to CCD sensor and CMOS LSI were studied and had the following results: (i) Interstitial oxygen reduction after a two-step thermal anneal was $O_{red} = O_i - O_{sol}$ for $O_i > O_{cri}$ and zero for $O_i < O_{cri}$. O_{cri} decreased with

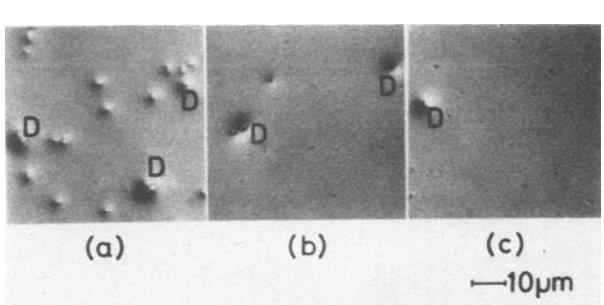

Fig. 17. Shrinkage of stacking faults. D shows the hard damage. Thermal anneals at 1190°C for (a) 0 hr, (b) 4 hr, and (c) 16 hr in $O_2/N_2 = 1/10$ were carried out after the anneal at 1000°C for 65 min in wet O_2.

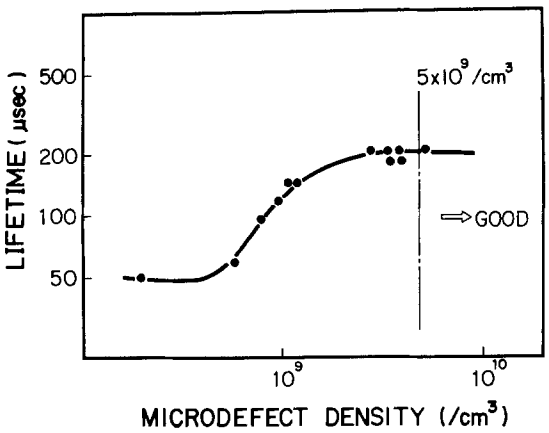

Fig. 18. Lifetime vs. MD density

first annealing time and with carbon concentration. Using the above results, it will be possible to control oxygen precipitation. (*ii*) In a CCD, MD as recombination sites improved the sensitivity uniformity. The MOS generation lifetime was greatly improved by MD in CMOS LSI. It was proved that IG using MD was better than the gettering using back surface damage created by sand blasting for a CMOS process, because the effect of the damage was annihilated in the high temperature P-well diffusion. Furthermore, it was shown that more than about $2.5 \times 10^{17}/cm^3$ oxygen concentration reduction was desirable for IG.

Acknowledgments

We wish to thank Mr. Y. Matsushita for many valuable discussions about this work, and Mr. M. Kohno and Mr. N. Akiyama of Komatsu Electronic Metals Company Limited for supplying the silicon wafers.

Manuscript submitted Jan. 28, 1982; revised manuscript received July 26, 1982. This was Paper 435 presented at the Hollywood, Florida, Meeting of the Society, Oct. 5-10, 1980.

Any discussion of this paper will appear in a Discussion Section to be published in the December 1983 JOURNAL. All discussions for the December 1983 Discussion Section should be submitted by Aug. 1, 1983.

The Toshiba Corporation assisted in meeting the publication costs of this article.

LIST OF SYMBOLS

- O_i interstitial oxygen concentration in the as grown wafer
- O_{red} interstitial oxygen concentration reduction after a two-step thermal anneal
- O_{cri} critical interstitial oxygen concentration in the as-grown wafer for oxygen precipitation
- O_s solid solubility limit of interstitial oxygen

REFERENCES

1. D. Pomerantz, *J. Appl. Phys.*, **38**, 5020 (1967).
2. T. E. Seidel, R. L. Meek, and A. G. Cullis, *ibid.*, **46**, 600 (1975).
3. G. A. Rozgonyi, P. M. Petroff, and M. H. Read, *This Journal*, **122**, 1725 (1975).
4. P. M. Petroff, G. A. Rozgonyi, and T. T. Sheng, *ibid.*, **123**, 565 (1976).
5. H. Shiraki, *Jpn. J. Appl. Phys.*, **15**, 83 (1976).
6. Y. Hayafuji, T. Yanada, and Y. Aoki, Abstract 485, p. 1232, The Electrochemical Society Extended Abstracts, Vol. 79-2, Los Angeles, CA, Oct. 14-19, 1979.
7. T. Y. Fan, E. E. Gardner, and W. K. Tice, *Appl. Phys. Lett.*, **30**, 175 (1977).
8. K. H. Yang, H. F. Kappert, and G. H. Schwuttke, *Phys. Status Solidi A*, **50**, 221 (1978).
9. M. Watanabe, M. Nakamura, and K. Homma, Abstract 490, p. 1244, The Electrochemical Society Extended Abstracts, Vol. 79-2, Los Angeles, CA, Oct. 14-19, 1979.
10. K. Yamamoto, S. Kishino, Y. Matsushita, and T. Iizuka *Appl. Phys. Lett.*, **36**, 195 (1980).
11. K. Nagasawa, Y. Matsushita, and S. Kishino, *ibid.*, **37**, 622 (1980).
12. D. M. Maher, A. Staudinger, and J. R. Patel, *J. Appl. Phys.*, **47**, 3813 (1976).
13. T. Y. Tan and W. K. Tice, *Philos. Mag.*, **34**, 615 (1976).
14. K. Tempelhoff and R. Spiegelberg, in "Semiconductor Silicon 1977," H. R. Huff and E. Sirtl, Editors, p. 585, The Electrochemical Society Softbound Proceedings Series, Princeton, NJ (1977).
15. Y. Matsushita, *J. Cryst. Growth*, **56**, 516 (1982).
16. K. Kaiser and P. H. Keck, *J. Appl. Phys.*, **28**, 882 (1957).
17. R. C. Newman and J. B. Willis, *J. Phys. Chem. Solids*, **26**, 373 (1965).
18. M. W. Jenkins, *This Journal*, **124**, 757 (1977).
19. H. J. Hrostowski and R. H. Kaiser, *Phys. Rev.*, **107**, 996 (1957).
20. S. M. Hu, *Appl. Phys. Lett.*, **36**, 561 (1980).
21. Y. Matsushita, S. Kishino, and M. Kanamori, *Jpn. J. Appl. Phys.*, **19**, L101 (1980).
22. J. R. Patel, K. A. Jackson, and H. Reiss, *J. Appl. Phys.*, **48**, 5279 (1977).
23. P. E. Freeland, K. A. Jackson, C. W. Lower, and J. R. Patel, *Appl. Phys. Lett.*, **30**, 31 (1977).
24. N. Inoue, K. Wada, and J. Osaka, in "Semiconductor Silicon 1981," H. R. Huff, R. J. Krieger, and Y. Takeishi, Editors, p. 282, The Electrochemical Society Softbound Proceedings Series, Pennington, NJ (1981).
25. R. A. Craven, in "Semiconductor Silicon 1981," H. R. Huff, R. J. Krieger, and Y. Takeishi, Editors, p. 254, The Electrochemical Society Softbound Proceedings Series, Pennington, NJ (1981).
26. R. F. Pinizzotto and H. F. Schaake, Abstract 450, p. 1127, The Electrochemical Society Extended Abstracts, Vol. 80-2, Hollywood, FL, Oct. 5-10, 1980.
27. M. Ogino and M. Watanabe, To be published.
28. R. B. Marcus, M. Robinson, T. T. Sheng, S. E. Haszko, S. P. Murarka, and L. E. Katz, *This Journal*, **124**, 425 (1977).
29. S. Kawado, *Jpn. J. Appl. Phys.*, **19**, 1591 (1980).
30. J. R. Patel and L. C. Kimerling, "Defects in Semiconductors," J. Narayan and T. Y. Tan, Editors, p. 273, Elsevier North Holland, Inc., New York (1981).
31. S. M. Hu, *Appl. Phys. Lett.*, **27**, 165 (1975).
32. D. Huber and E. Sirtl, *Jpn. J. Appl. Phys., Suppl.* **19-1**, 615 (1980).

Laser Annealing of Submicrometer NMOS Test Structures and Devices

G. Eckhardt and J. Y. Chen*

Hughes Research Laboratories, Malibu, California 90265

ABSTRACT

Properties of MOS gate oxides, as well as Al ohmic contacts on polysilicon, were studied as a function of annealing procedures and geometry down to submicron dimensions. Laser-annealed contacts were found to possess superior properties when compared to furnace-annealed Al contacts. Surface, as well as interface, morphology was markedly improved due to the elimination of interdiffusion, and contact resistance was significantly reduced. Likewise, laser annealing was shown to be much more effective than furnace annealing in removing process-induced damage in gate oxides under conditions that are compatible with Al contacts on Si. Since identical laser parameters were found to produce best results for Al contacts as well as for gate oxides, both can be annealed in a single operation.

Two important problems in submicrometer MOS technology have been addressed: the quality of ohmic contacts to polysilicon with Al metallization, and the damage introduced in gate oxides through high-energy electrons or x-rays.

Ohmic contacts to single crystal silicon, as well as polysilicon, are generally formed by Al metallization of highly doped substrates and subsequent furnace annealing to reduce the specific contact resistance. The annealing process was found to produce a significant drop in contact resistance only when temperatures of $\gtrsim$ 400°C for times of the order of tens of minutes are used (1). However, at these annealing temperatures for such long time periods, substantial interdiffusion of Si and Al takes place, and Si precipitates and/or a p-type Si layer may form at the interface (2-4). The nonuniform nature of the Si-Al interaction causes severe degradation in particular in submicron NMOS devices with small contact openings and/or shallow junctions (9) and, therefore, constitutes a significant limitation for all furnace-annealing procedures that must be carried out subsequent to contact metallization.

The necessity for high temperature processing steps arises not only from contact resistance requirements, but also from the use of electron-beam (E-beam) lithography, as well as from electron-gun (E-gun) evaporation and sputter-deposition of metals for the fabrication of MOS structures. It is well known that high-energy electrons and x-rays create positively charged and neutral traps in the gate oxides of MOSFET's. The positive charges manifest themselves by their effect on the threshold voltage (V_T) of these devices. They cannot only cause a reduction of V_T, but can also produce time-dependent shifts in V_T due to trapping and detrapping of hot electrons during device operation, thus creating a stability problem. The successful removal of this radiation damage requires annealing temperatures of $\gtrsim$ 550°C (5) or extended anneals (of the order of hours), *e.g.*, at 400°C (9). These annealing requirements for radiation damage removal are clearly incompatible with Al contacts without diffusion barriers, because they will result in high contact resistance or even Schottky barriers and the penetration of Al spikes into the junction area for shallow junction devices.

Several avenues have been pursued in the past to eliminate the restriction on processing temperatures following metal deposition. These are the introduction of diffusion barriers between Al and Si, as well as the use of Al:Si alloys, Al-silicide combinations, and refractory metals as contact materials (6-8). Recently, low-temperature annealing procedures for gate oxides, utilizing either an rf plasma, an H_2 atmosphere or elevated pressure, have also been developed (9-11). However, none of these measures, although some of them are used in device fabrication, has been found totally satisfactory, because either they are only partially effective, or they increase the complexity of the processing procedure, and/or they increase the specific contact resistance (12).

In recent years, furnace annealing in semiconductor processing has been substituted by laser annealing with very encouraging results. Using laser beams permits a heretofore unattainable control of parameters essential for annealing processes. In particular, the duration of the heating period can be varied over many orders of magnitude, from 10 nsec to times used for furnace annealing. Limiting the heating periods to very short times will, *e.g.*, minimize the interdiffusion of components even if considerably higher temperatures than those typically used for furnace annealing are applied (13). Thus, it appeared that, by using this novel technique, an improvement of Al ohmic contacts without a diffusion barrier and the elimination of radiation damage in gate oxides might be achievable simultaneously.

In the present study, we determined the effects of laser and furnace annealing on Al contacts to polysilicon resistors and on gate oxides of MOS capacitors and transistors. The properties of the contacts were studied as a function of contact dimensions and of the annealing method (furnace or laser). Contact resistance, metal surface morphology, and metal-polysilicon interface characteristics of samples were evaluated and compared for the two different metallizations and annealing procedures. The effect of laser and furnace annealing on process-induced damage in gate oxides was characterized by measurements of capacitance-voltage profiles of MOS capacitors and threshold voltages of MOS transistors with a range of gate length-to-width ratios. These measurements monitor the effect of the annealing procedures on positively charged traps only. They do not indicate changes in the neutral trap densities (5, 14).

Sample Preparation

Two types of test structures were used for this investigation. The samples fabricated for the ohmic contact study consisted of a Si substrate on which a 1000Å layer of SiO_2 was grown, followed by a 3000Å thick film of polysilicon formed by low pressure CVD. The polysilicon was doped by phosphorus diffusion to a level of $\gtrsim 10^{19}$ cm^{-3}, which resulted in a sheet resistance of 50 Ω/□. E-beam lithography was used to define submicron test structures, plasma etching with CF_4/O_2 was used to delineate the polysilicon resistors, and the lift-off technique was applied to define the metal patterns. The 3000Å thick Al metallization was applied by E-gun evaporation after cleaning the polysilicon with

* Electrochemical Society Active Member.

a 10:1 H_2O:HF etch. The test structures employed were the horizontal type Si resistors commonly used in integrated circuits (1) (Fig. 1), and the contacts were formed at the intersection of the metal leads and the polysilicon resistors as shown in Fig. 2. The contact width, W, which equals the resistor widths in this case, had a range from 2.0 to 0.4 μm (see Fig. 1). These self-aligned structures have several advantages over the standard contacts, because layout area and parasitic capacitance are reduced. Furthermore, no contact mask is needed to define the particular pattern used in this study.

Test chips containing MOS capacitors and a series of 6 MOS transistors with a range of gate length-to-width ratios were used for the gate oxide investigation. They were fabricated on <100> p-type, 10 Ω-cm, 0.38 mm thick Si wafers, using an E-beam NMOS process (15). The 4000Å thick field oxide was thermally grown and was patterned, using buffered HF, to define the channel regions. Deep B implantation provided the isolation structure for the transistor channels, which were then created by counterdoping a shallow region with a P implant. The 200Å gate oxide layer was grown by a wet oxidation process, followed by deposition of a 4000Å layer of polysilicon (using LPCVD) which was doped by P diffusion. Polysilicon gate patterns were defined and plasma etched, followed by a very shallow source and drain As implant to produce a junction with a depth of 2000Å. A third oxide layer (silox) was deposited on the polysilicon and contacts were patterned and etched.

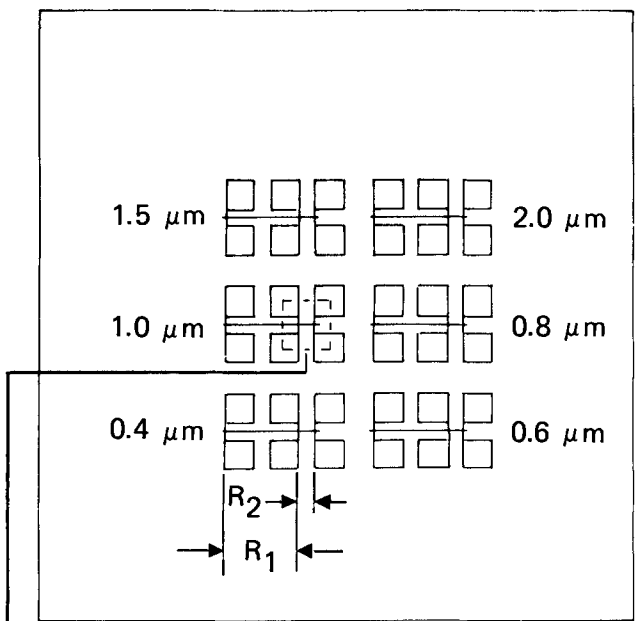

Fig. 1. Four-point probe test pattern for various contact widths

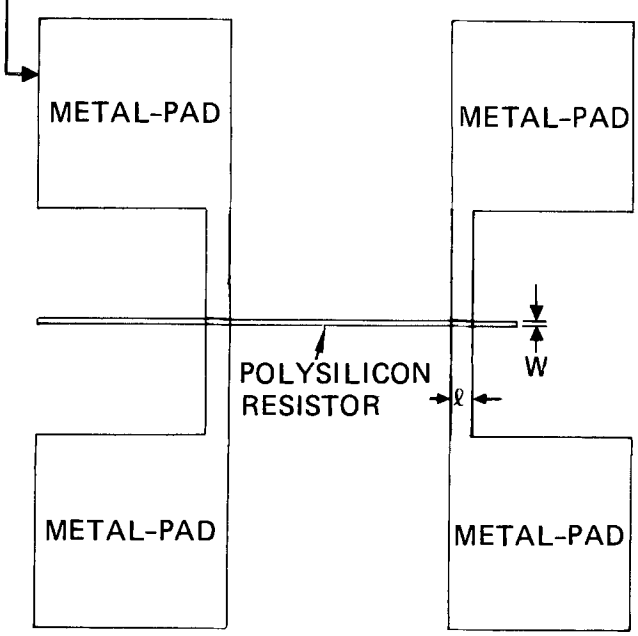

Fig. 2. Horizontal-type polysilicon resistors with self-aligned contacts.

An Al/W:Ti/n^+ polysilicon sandwich structure was used as the metallization system. Since the formation of the n^+ polysilicon buffer layer requires a high-temperature (900°C) process, this removed most of the damage created by previously applied processing steps at the same time. The 1000Å thick W:Ti layer, which served as a diffusion barrier between Al and Si, was deposited by Ar sputtering. Such a barrier layer is necessary when furnace-annealing procedures at temperatures $\gtrsim$ 400°C are planned subsequently to Al deposition, because the interaction of Al with n^+ polysilicon may produce a quasi Schottky barrier by forming a p-silicon layer on top of the n^+ silicon layer (4). Such a barrier is, however, superfluous when annealing is done by laser irradiation due to the very short heating times possible with this technique. In this case, it was applied to permit a comparison between laser and furnace annealing of oxide damage. The barrier layer was deposited by bombarding a W:Ti target with 2 keV Ar ions. This causes the emission of x-rays and secondary electrons, besides W and Ti particles, and some oxide damage may have been created by this processing step (16). The major damage, however, was probably produced during the definition of the metallization pattern by E-beam lithography, using a PMMA resist coating with a sensitivity of 10^{-4} C/cm^2 and 20 keV E-beam energy. Although the metal patterns were located at least 10 μm away from the gate oxides, they are still within reach of electrons back-scattered from the W:Ti substrate (9). A 3000Å thick Al layer was then deposited by E-gun evaporation. This process is known to create x-rays which can generate the same type of traps and charges in SiO_2 as electron beam lithography (5). After lift-off, the remaining Al served as a mask for etching the W:Ti and n^+ polysilicon layers using H_2O_2 and plasma techniques, respectively. The cross sections of the two devices (Fig. 3) show that substantial differences exist between their structures. In the transistors, the gate oxides were buried beneath two layers (n^+ polysilicon and silox) only, while in the capacitors the multilayer contact system was added.

Experimental Procedures

For furnace annealing, the samples were subjected to temperatures of 450° and 550°C for 15 min in an N_2 atmosphere. Laser annealing was performed with a scanning CW Ar ion laser (λ = 0.51 μm). The laser beam was focused with a 30 cm focal length lens on the samples held by vacuum to a metal plate. The focused beam diameter on the sample was 80 μm, defined as the diameter where the laser intensity was reduced to $1/e$ of its peak value. The beam was scanned across the samples in a raster pattern by means of orthogonally mounted galvanometer-driven mirrors, located between the lens and the sample holder. A scan velocity of 4 mm/sec and a range of laser beam power from 5 to 13W were used.

For the ohmic contact study, contact resistance values, R_c, were determined by four-point-probe measurements (17), and the contact metal surface and the

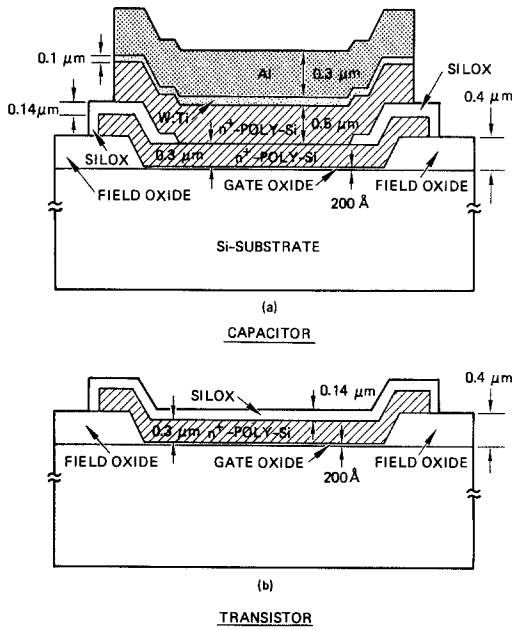

Fig. 3. Schematics of cross section for (a) MOS capacitor, and (b) MOS transistor.

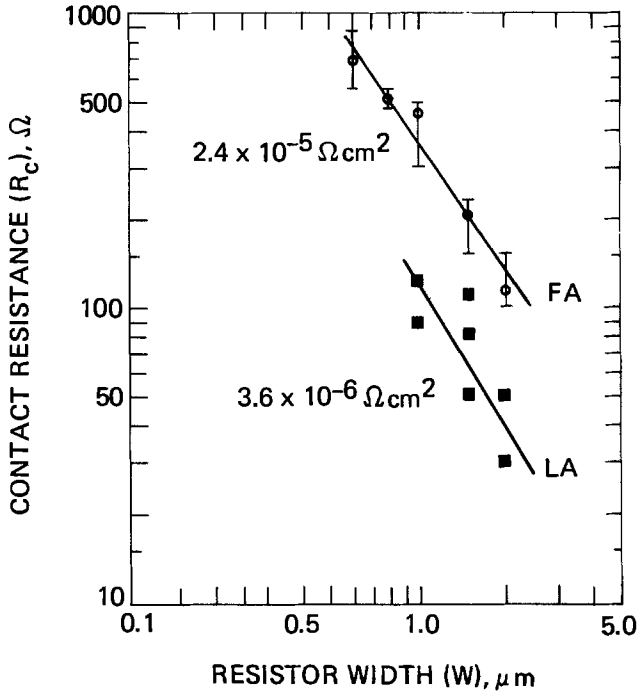

Fig. 4. Contact resistance as function of resistor width for furnace-annealed (FA) and laser-annealed (LA) Al contacts.

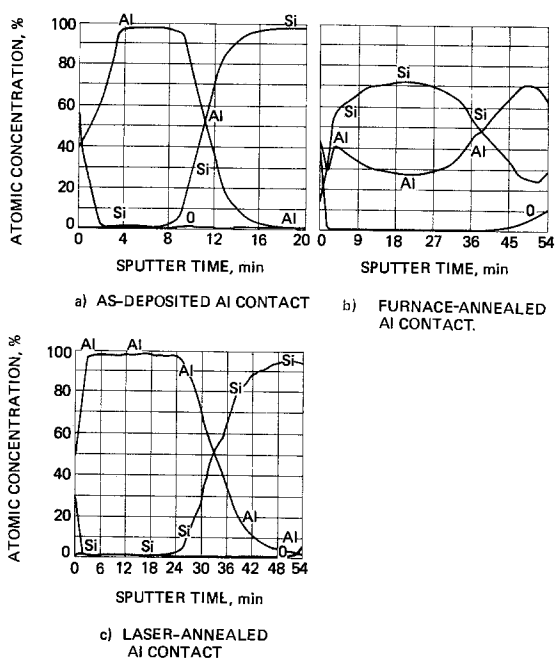

Fig. 5. Auger depth profiles of Al contacts on polysilicon

interface between metal and polysilicon were inspected using optical and electron microscopy. The interface was exposed by removing Al with H_3PO_4. The degree of interdiffusion of the contact materials for the two different annealing procedures was determined by Auger electron spectroscopy. For the gate-oxide annealing study, transistor threshold voltages were measured for different annealing conditions. The threshold voltage was defined as the gate voltage which generates 1 μA at 0.1V drain bias. The capacitance-voltage measurements were done at 1 MHz.

Results and Discussion

Laser annealing of Al contacts was found to lower the contact resistance by factors of 1.8-5.0 compared to the resistance of as-deposited contacts, while an improvement by a factor of about 1.2 was obtained by furnace annealing. A minimum contact resistance was obtained for laser beam powers of 8-10W. At the scan velocity of 4.0 mm/sec, this corresponds to a dwell time of 20 msec and a power density of 0.2 MW/cm². The results of the resistance measurements for the laser-annealed and the furnace-annealed Al contacts are given in Fig. 4, where the resistance is plotted as a function of the contact width. In the case of furnace annealing, temperatures of 450°C were used for 15 min. It can be seen that the resistance is approximately inversely proportional to the contact width (1) for both furnace- and laser-annealed contacts. The scatter of the resistance values is mainly caused by dimensional variations of the submicron structures. A calculation of the specific contact resistance (17) yields values of 2.4×10^{-5} Ω-cm² for the furnace-annealed contacts and 3.6×10^{-6} Ω-cm² for the laser-annealed contacts.

Auger depth profiles revealed significant differences between furnace and laser-annealed Al contacts (Fig. 5b and c). For reference, the Auger depth profiles for the as-deposited sample are shown in Fig. 5a. As can be seen from the data in Fig. 5b and c, furnace annealing had resulted in a thorough intermixing of Al and Si, while laser annealing had produced no detectable diffusion.

Figure 6 shows SEM pictures of two specimens after the contact metals were chemically removed. In the case of the furnace-annealed contact, the polysilicon dissolved along with the Al, while the polysilicon remained as-deposited for the laser-annealed contact. This result is understandable in view of the Auger depth profiles for these two cases, which showed a thorough intermixing of Al and Si for the furnace annealed contacts, but no or very little interdiffusion for the other case.

In order to compare the effects of the different annealing procedures on gate oxide damage, independent of contact problems, all devices used for this investigation had a W:Ti diffusion barrier. Threshold voltages measured for the FET's with the different gate length-to-width ratios are shown in Fig. 7 before and after annealing and for a variety of annealing conditions. They show a noticeable dependence on device geometry as expected for these dimensions due to short-channel and narrow-channel effects. Laser annealing produced almost identical threshold voltages as furnace annealing at 550°C, but considerably higher values than the standard furnace anneal at 450°C. This

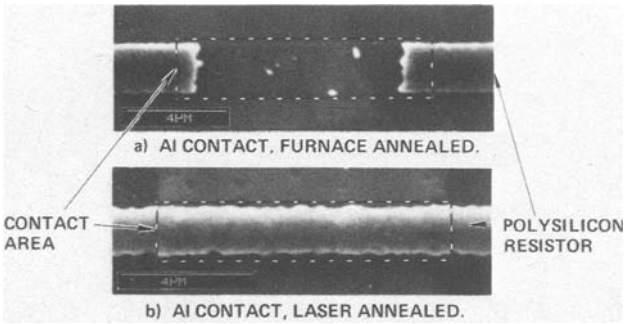

Fig. 6. SEM photographs of Al/polysilicon interfaces. Contact metal was removed by chemical etches.

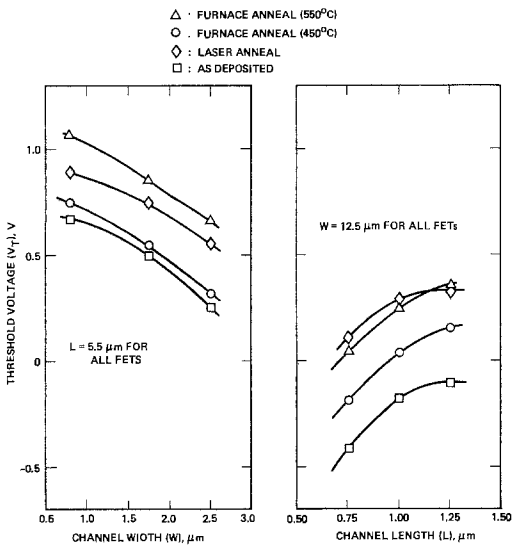

Fig. 7. Threshold voltage of MOS FET's as function of (a, left) channel width for a constant channel length, L, and (b, right) channel length for a constant channel width, W.

implies that the positive charges trapped in the FET gate oxide are removed effectively by laser annealing.

While the same laser power density successfully annealed ohmic contacts as well as gate oxides, this was not the case for the MOS capacitors. As described above, in these devices, the oxide was covered not only by several additional layers, but Al was their outermost layer instead of polysilicon. The large difference in reflectivity [$R(\mathrm{Si}) = 0.42$, at the laser energy densities used (18), $R(\mathrm{Al}) = 0.9$ (19)], between the two materials at the wavelength of the Ar-ion laser required a substantial increase in laser power density for successful oxide damage annealing. This is evident from the capacitance-voltage (C-V) curves shown in Fig. 8. Seven laser scans at a beam power up to 11.5W were used until the corresponding C-V curve became identical with the curve obtained after furnace annealing at 450°C. The hystereses of the C-V curves are omitted for clarity in Fig. 8. As-deposited capacitors exhibited a very large hysteresis (1.4V at flatband), but it became negligible (< 0.1V at flatband) after either laser annealing (7 and 8th laser scan) or furnace annealing (450° and 550°C).

The changes in the flatband voltage that were achieved after each of these laser scans are depicted in Fig 9, together with the results obtained by furnace annealing at 450° and 550°C. The number of charges/cm^2 that were removed during each annealing step can be deduced using the axis on the right-hand side of Fig. 9. Most likely, the flatband voltage shift obtained after eight laser scans could have been achieved with fewer scans with a different choice of annealing parameters. However, these experiments are described to

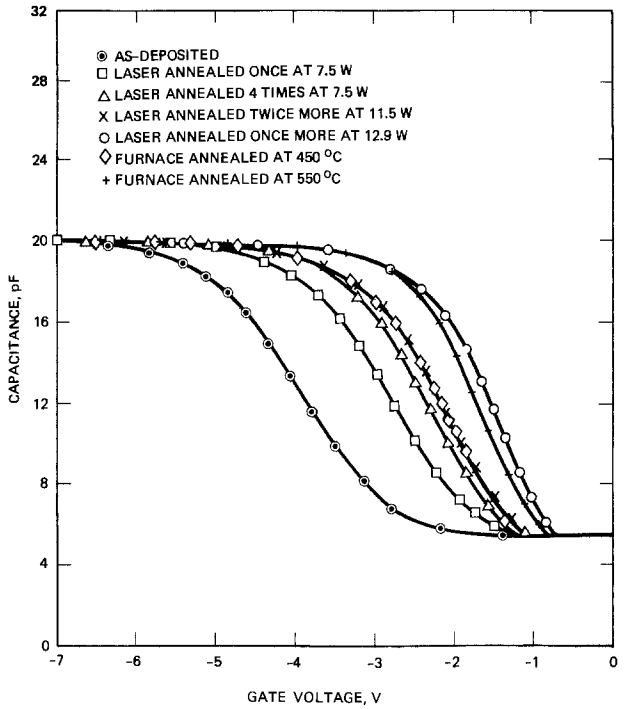

Fig. 8. Capacitance-voltage characteristics of MOS capacitors for a variety of annealing conditions.

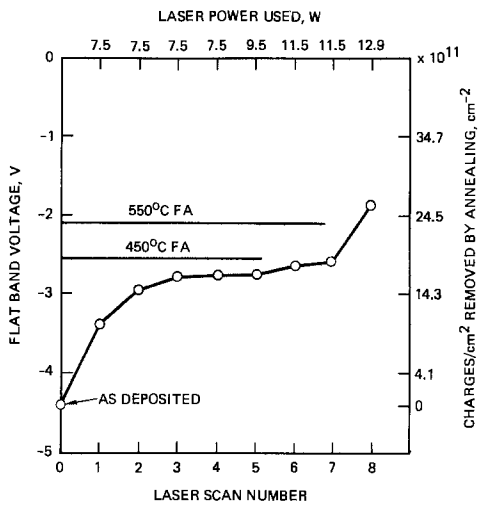

Fig. 9. Results of laser and furnace annealing: changes in flatband voltage and charge density for successive laser scans.

illustrate the importance of lateral heat flow when front-surface laser annealing of Si chips is used. The large differences in optical reflection coefficient between semiconductor and metal surfaces result in lateral temperature variations whose extent will depend on the particular topology of the circuit. Since Si is a reasonably good heat conductor, substantial lateral heat flow will take place and counteract the differences in surface reflectivity. If the dwell time of the laser is sufficient for extensive lateral heat flow to occur within the Si, and if the lateral dimensions of the metal layers are sufficiently small, the temperature differences within the IC structure will be negligible. In this case the capacitors had lateral dimensions of 152 × 81 μm. In spite of their large size it was only necessary to increase the laser power by a factor of 1.3 over what was used to anneal the gate oxides and not by a factor of 2.2 corresponding to the ratio of the two reflectivities, indicating that a sizable lateral heat flow had taken place.

An additional experiment was conducted to verify that laser annealing only removed positive charges and

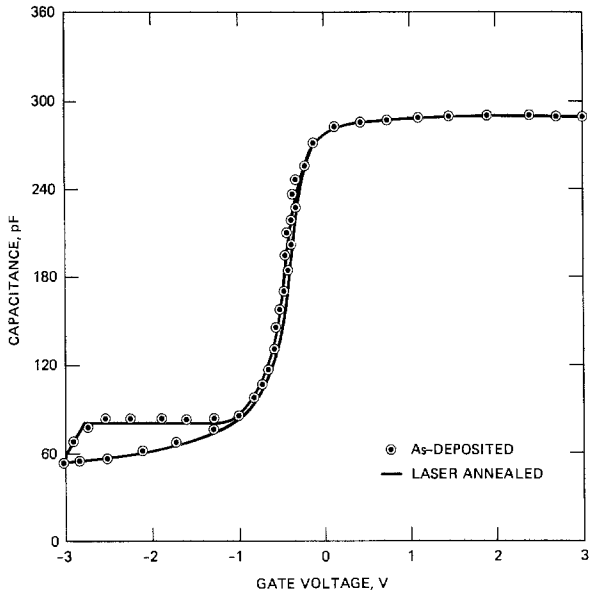

Fig. 10. Capacitance-voltage characteristics for polysilicon-gate capacitors after laser annealing at four different beam powers ranging from 8.1 to 13.1W. The four curves obtained after laser annealing are indistinguishable from each other.

did not create any compensating centers. This was accomplished by laser annealing polysilicon-gate capacitors. These capacitors were made by creating n^+ polysilicon dots on oxidized wafers using a photolithographic mask. Since neither W:Ti deposition nor E-beam lithography or E-gun evaporation were used, no oxide damage was created during processing before annealing. These undamaged capacitors were then laser-annealed with powers ranging from 8.0 to 13.1W, and their C-V curves are shown in Fig. 10. No differences were found in either hysteresis or flatband voltage before and after laser annealing up to the highest laser power used, indicating that no charges with reversed polarity were introduced during laser annealing.

Conclusions

The use of a scanning Ar-ion laser for the annealing of Al ohmic contacts and of process-induced damage in gate oxides was found to achieve superior results as compared to furnace annealing. Laser annealing permits the use of pure Al contacts on polysilicon without insertion of a diffusion barrier. Furthermore, it permits the annealing of Al contacts and gate oxides in a single operation. However, when front-surface irradiation is used, as was the case in the present study, the differences in optical reflectivity between metal and semiconductor surfaces result in local temperature variations whose extent will depend on the particular topology of the circuit. Lateral heat flow within the semiconductor will be sufficient for successful contact and gate-oxide annealing as long as none of the metal structures has more than one dimension in the tens-of-micrometers range. This potential problem can be avoided by using back-surface irradiation. More extensive testing of integrated circuits after laser processing must be done to determine whether any reliability and/or stability problems are created by the use of this method. In this study, the application of laser annealing has been shown to produce excellent results for the particular test structures and devices used, and to simplify the processing sequence for submicrometer MOS integrated circuits.

Acknowledgments

The authors would like to thank R. C. Henderson and L. D. Hess for their encouragement and continuous support.

Manuscript submitted June 11, 1982; revised manuscript received Feb. 15, 1983. This was Paper 237 presented at the Minneapolis, Minnesota, Meeting of the Society, May 10-15, 1981.

Any discussion of this paper will appear in a Discussion Section to be published in the December 1983 JOURNAL. All discussions for the December 1983 Discussion Section should be submitted by Aug. 1, 1983.

Hughes Research Laboratory assisted in meeting the publication costs of this article.

REFERENCES

1. H. M. Naguib and L. H. Hobbs, *This Journal*, **124**, 573 (1977).
2. J. O. McCaldin and H. Sankur, *Appl. Phys. Lett.*, **20**, 171 (1972).
3. K. Nakamura, J. O. Olowolafe, S. S. Lau, M-A. Nicolet, J. W. Mayer, and R. Shima, *J. Appl. Phys.*, **47**, 1278 (1976).
4. H. M. Naguib and L. H. Hobbs, *This Journal*, **125**, 169 (1978).
5. J. M. Aitken, *IEEE J. Solid-State Circuits*, **sc-14**, 294 (1979).
6. C. L. Kircher, *J. Appl. Phys.*, **47**, 5394 (1976).
7. M. Finetti, P. Ostoija, S. Solmi, and G. Soncini, *Solid-State Electron.*, **23**, 255 (1979).
8. R. W. Bower, *Appl. Phys. Lett.*, **23**, 99 (1973).
9. J. M. Aitken and C. Y. Ting, in "Int. Electron. Device Meeting," Washington, DC, Technical Digest (1981).
10. T. P. Ma, in "Semiconductor Silicon 1981," H. R. Huff, R. J. Kriegler, and Y. Takeishi, Editors, p. 427, The Electrochemical Society Softbound Proceedings Series, Pennington, NJ (1981).
11. A. Reisman, J. M. Aitken, A. K. Ray, M. Berkenblit, C. J. Merz, and R. P. Havreluk, *This Journal*, **128**, 1616 (1981).
12. H.-N. Yu, A. Reisman, C. M. Osburn, and D. L. Critchlow, *IEEE J. Solid-State Circuits*, **sc-14**, 240 (1979).
13. G. Eckhardt, in "Laser and Electron Beam Processing of Materials," C. W. White and P. S. Peercy, Editors, p. 467, Academic Press, New York (1980).
14. T. H. Ning, *J. Appl. Phys.*, **49**, 4077 (1978).
15. J. Y. Chen, R. C. Henderson, D. O. Patterson, and R. Martin, *IEEE Trans. Electron. Devices Lett.*, **edl-3**, 13 (1982).
16. T. Serikawa and T. Yachi, *IEEE Trans. Electron Devices*, **ed-28**, 882 (1981).
17. H. H. Berger, *This Journal*, **119**, 507 (1972).
18. S. A. Kokorowski and G. L. Olson, Private communication.
19. L. F. Drummeter, Jr. and G. Hass, in "Physics of Thin Films," G. Hass and R. E. Thun, Editors, Vol. II, p. 339, Academic Press, New York (1964).

Liquid Phase Epitaxial Growth of $ZnSnP_2$ on GaAs

G. A. Davis and C. M. Wolfe*

Semiconductor Research Laboratory, Washington University, St. Louis, Missouri 63130

ABSTRACT

$ZnSnP_2$ is a potentially useful semiconductor which can have either the sphalerite structure or the chalcopyrite structure with no tetragonal distortion (c = 2a). We have grown $ZnSnP_2$ on various orientations of GaAs by liquid phase epitaxy and found that the best growth occurs on {110} surfaces. Double-crystal x-ray diffraction measurements indicate that these {110} layers have a lattice constant of 5.6507Å, while {111} As layers grown under identical conditions have a lattice constant of 5.6532Å, which matches GaAs to within $\pm 2 \times 10^{-4}$Å. Back reflection Laue patterns show that the {110} layers are chalcopyrite, while the {111} As layers are sphalerite. The Laue patterns also indicate that the {110} epitaxy is mixed with the c-axis out of the growth plane. A possible explanation for these results is that the {110} GaAs surfaces in liquid phase epitaxy reconstruct into chalcopyrite-like chains in the [001] direction, while the {111} As surfaces do not. This would promote the formation of chalcopyrite $ZnSnP_2$ with antiphase boundaries on {110} surfaces.

$ZnSnP_2$ is an interesting semiconductor for the study of chalcopyrite growth on sphalerite GaAs. The primary reason for studying this system is the similarity between the structures of GaAs and $ZnSnP_2$ (1). The a to a mismatch of $ZnSnP_2$ on GaAs is small which allows for single crystal liquid phase growth. In addition, $ZnSnP_2$ exhibits no tetragonal distortion so the c to 2a mismatch is the same as the a to a mismatch. Thus, $ZnSnP_2$ grown on any substrate orientation will not incorporate any c to 2a mismatch. Since most chalcopyrites exhibit some tetragonal distortion, epitaxial growth is generally restricted to {100} oriented substrates to avoid c to 2a mismatch.

$ZnSnP_2$ is also of interest because solution-grown platelets exhibit both chalcopyrite and disordered sphalerite phases apparently having the same lattice constant (1, 2). The sphalerite phase dominates in platelets grown using large cooling rates ($\simeq$ 50°C/hr), while the chalcopyrite phase dominates for smaller cooling rates ($\simeq$ 5°C/hr). The existence of these two phases allows us to evaluate the growth conditions leading to chalcopyrite growth and provides insight for other chalcopyrite-on-sphalerite systems.

Growth Procedure

Liquid phase epitaxial growth of $ZnSnP_2$ on GaAs was performed in the open tube system shown schematically in Fig. 1. The starting materials used in this system were 99.999+% pure Zn and Sn and SnP_3 which was synthesized from 99.999+% pure Sn and red P_4 in a sealed tube process (3). The graphite boat shown in Fig. 1 was designed for growth of materials for which there is little phase diagram information. During homogenization of the growth melt, excess SnP_3 floats to the top and maintains a saturated solution as phosphorus evaporates into the gas stream. During growth, the homogeneous solution contained in the slider is positioned over the substrate and the temperature of the furnace is reduced linearly. Since little phosphorus loss to the gas stream was observed for the growth conditions used, the composition of the melt was adjusted so that there was little or no excess SnP_3 in the melt after saturation. The equivalent melt compositions used for various growth temperatures are shown in the partial phase diagram of Fig. 2. In all growth runs, the amounts of Zn, Sn, and SnP_3 were adjusted to give an equivalent $ZnSnP_2$ concentration in Sn with no excess Zn or P.

The cooling rates used in these growth experiments ranged from 1° to 5°C/hr. Cooling rates greater than 5°C/hr were not investigated due to the tendency of $ZnSnP_2$ to grow in the sphalerite phase at these rates. A homogenization period of 2 hr and growth periods of 6-18 hr were used. The homogenization or initial growth temperature ranged from 530° to 640°C. A hydrogen flow rate of 30 ml/min was maintained in the furnace tube during homogenization and growth for all experiments.

The GaAs substrates were carefully prepared by lapping and chemical-mechanical polishing both the front and back surfaces. After scribing and breaking the substrates to the proper dimensions for the boat (0.25 × 0.25 in.), they were cleaned in boiling trichloroethylene, acetone, and methyl alcohol. A 5:1:1 or 10:1:1 H_2SO_4:H_2O_2:H_2O chemical etch was used

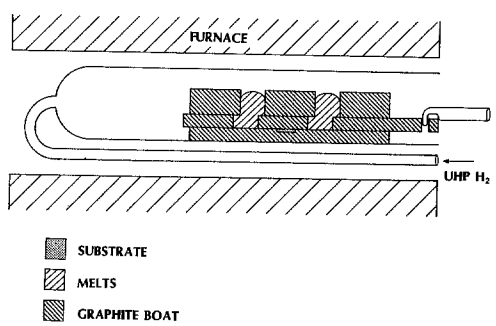

Fig. 1. Schematic illustration of the LPE boat used to grow $ZnSnP_2$ on GaAs.

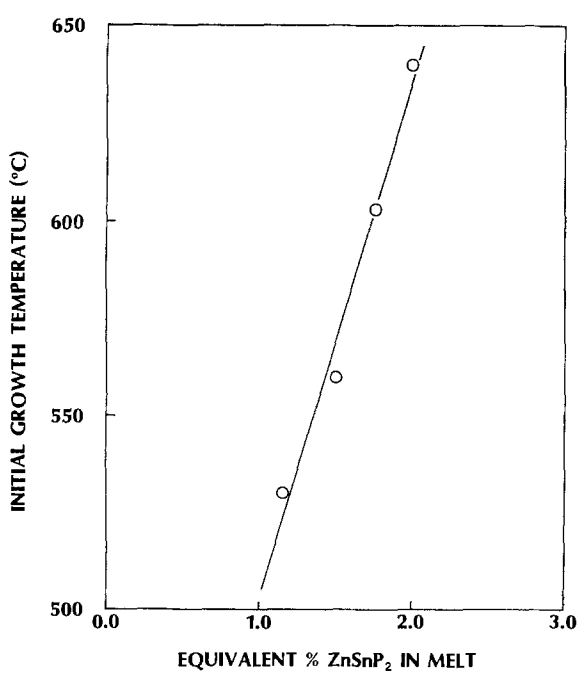

Fig. 2. Initial growth temperature as a function of $ZnSnP_2$ concentration for saturated or slightly supersaturated solutions.

* Electrochemical Society Active Member.

Key words: semiconductor, epitaxy, zinc tin phosphide, gallium arsenide.

prior to loading each substrate into the boat. This etch removed at least 10 μm of material from the growth surface. The 10:1:1 etch used in later experiments caused less rounding of the surface and produced more uniform growth.

Layer Morphology

Initial growth experiments were performed on {100}, {110}, {111}, and {211} oriented Cr-doped substrates to determine the optimum orientation for growth. Typical layers grown on some of these orientations are shown in Fig. 3, 4, and 5.

{100}, {211} Ga, {211} As, and {111} Ga oriented substrates produced growth which was quite rough and unsuitable for electrical measurements. Growth on {111} As oriented substrates had rough interfaces but uniform surfaces with very good morphologies. This is consistent with observations of predominant {111} facets in solution grown platelets (1) and with experiments in which we have observed low growth rates in the <111> directions. Layers grown on {110} oriented substrates revealed much smoother interfaces but had surfaces with more structure and tended to be of nonuniform thickness. Numerous growth experiments were performed on {111} As oriented substrates to reduce the amount of interfacial roughness, but little improvement was noted. In later experiments performed using {110} oriented substrates, we concentrated on improving the uniformity of the layers and eliminating large growth structures. By changing the final etch and adjusting the growth parameters, substantial improvements in the {110} oriented growth were noted.

For {111} As oriented substrates, the best growth was obtained using an initial growth temperature of 560°C with a cooling rate of 1°C/hr The melts for these growth runs had an equivalent $ZnSnP_2$ concentration of 1.4-1.5% with one gram of Sn used per run. For initial growth temperatures below 530°C, no layers could be grown, while for initial temperatures above 600°C, the morphologies and electrical characteristics of the layers degraded. The grown layers were generally 3-15 μm thick except for those grown at high temperatures, which were up to 30 μm thick.

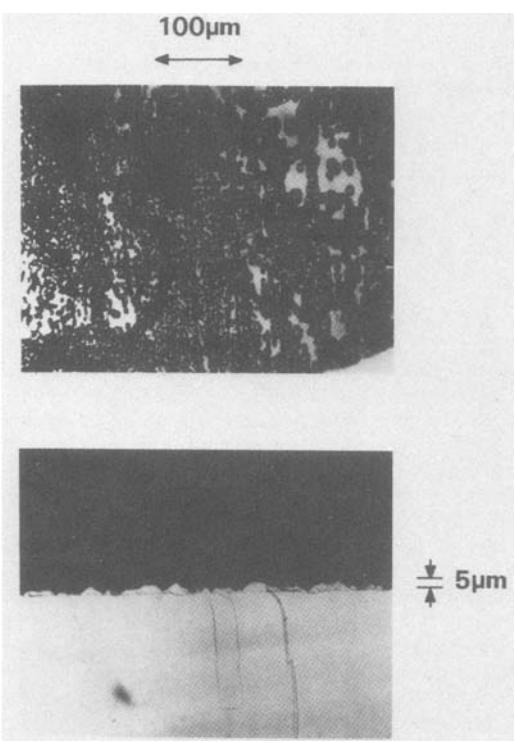

Fig. 3. (a, top) Surface and (b, bottom) cross-sectional views of typical $ZnSnP_2$ growth on {100} oriented GaAs.

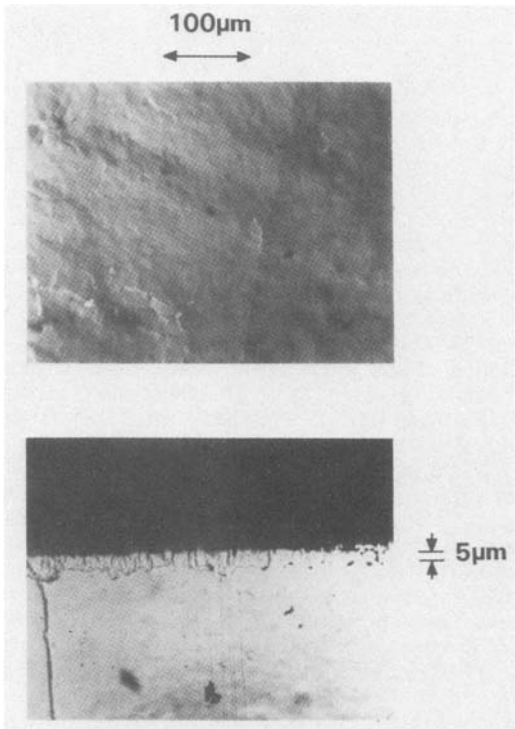

Fig. 4. (a, top) Surface and (b, bottom) cross-sectional views of typical $ZnSnP_2$ layers grown on {111} As oriented GaAs. The structure of the surface view was enhanced using a Nomarski interferometer.

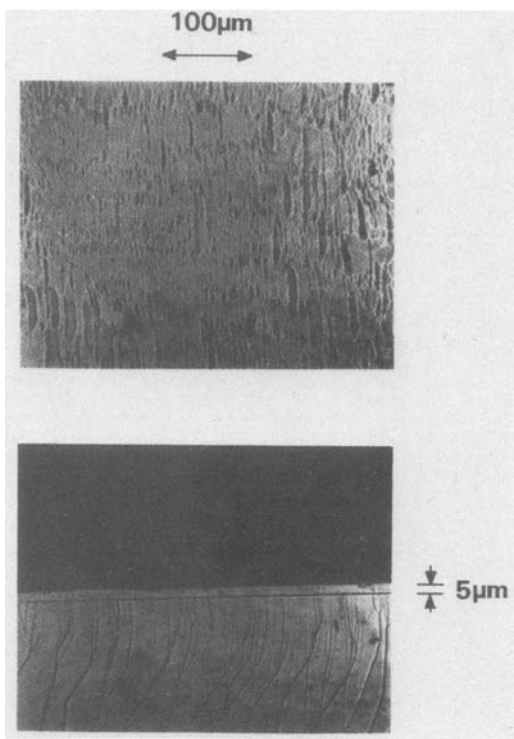

Fig. 5. (a, top) Surface and (b, bottom) cross-sectional views of a typical $ZnSnP_2$ layer grown on {110} oriented GaAs.

The conditions producing good growth on {110} oriented substrates are more restrictive than those for {111} As growth. For {110} oriented growth, the optimum initial growth temperature was 570°C. The layer quality degraded rapidly for initial growth temperatures less than 560° or greater than 580°C. The melt composition used was 1.4-1.5% $ZnSnP_2$ with one gram of Sn used per run. Good growth was obtained with cooling rates between 2.5°-5°C/hr. No layers were grown on {110} oriented substrates for cooling

rates less than 2.5°C/hr. All layers grown on {110} oriented substrates were less than 5 μm thick.

X-Ray Diffraction Measurements

X-ray diffraction measurements were made on the layers grown on {111} As and {110} oriented GaAs using a double crystal diffractometer aligned for the GaAs 333 reflection for Cu Kα radiation. Peak widths at half-peak intensity (FWHM) of 8.7 and 10.6 sec of arc were reproducibly obtained with the {111} and {110} GaAs used for growth substrates, respectively.[1] Some results of these measurements are shown in Fig. 6, 7, and 8.

Most of the {111} As samples revealed a single broadened GaAs peak with some slight background reflection as seen in Fig. 6. This suggests that this epitaxial material lattice matches GaAs to within 2×10^{-4}Å (4×10^{-3}%) based on an 8-7 sec resolution. The FWHM peak widths for these layers were 45 to 85 sec. The low intensity background reflection may be due to the rough interfaces of these layers or interfacial strain.

Some of the thinner {111} As layers revealed a secondary peak at about one tenth the intensity of the main peak separated by 4.9 min of arc as seen in Fig. 7. These layers were 3 μm thick and were grown using a 5°C/hr cooling rate. Typically, these {111} As layers had smoother interfaces than those grown with smaller cooling rates, and no broad background intensity was observed. The lattice constant associated with the secondary peak in Fig. 7 is 5.645Å which is 0.1% smaller than the 5.651Å lattice constant observed by other workers (1, 2) on solution-grown platelets. The FWHM widths of the main peaks were 20-30 sec, and those of the secondary peaks were around 2 min. The observation of secondary peaks from thin layers and broad background reflection from thick layers suggests that there is interfacial strain in these structures.[2]

A typical scan of the 333 reflection from a layer grown on {110} oriented GaAs is shown in Fig. 8. This scan shows two approximately equal intensity peaks, which are separated by 90 sec. All layers grown on {110} oriented material revealed these two peaks with the epitaxial layer peak intensity scaling with the layer thickness. The lattice constant of the layers calculated from these data is 5.6507Å ± 3×10^{-4}Å based on a 5.6532Å GaAs lattice constant (4) which is in excellent agreement with the platelet data.

[1] The 333 reflection from a {111} oriented Ge analyzer was used in all rocking curves presented. This causes some peak spreading due to the different lattice constants of the analyzer and sample crystals. The theoretical peak width for the 333 reflection using either Ge or GaAs {111} oriented analyzer and sample crystals is 4.7 sec of arc. [M. A. G. Halliwell, J. B. Childs, and S. O'Hara, in "Gallium Arsenide and Related Compound.," C. Hilsum, Editor, p. 98, The Institute of Physics, London (1973).]

[2] The existence of strain in these structures is evidenced by the broadening of the reflection peak. While strain in a layer can obscure the rocking curve analysis, the presence of primarily one peak indicates a lattice match. [W. J. Bartels and H. Veenvliet, in "Gallium Arsenide and Related Compounds." C. M. Wolfe, Editor, p. 229, The Institute of Physics, London (1979).]

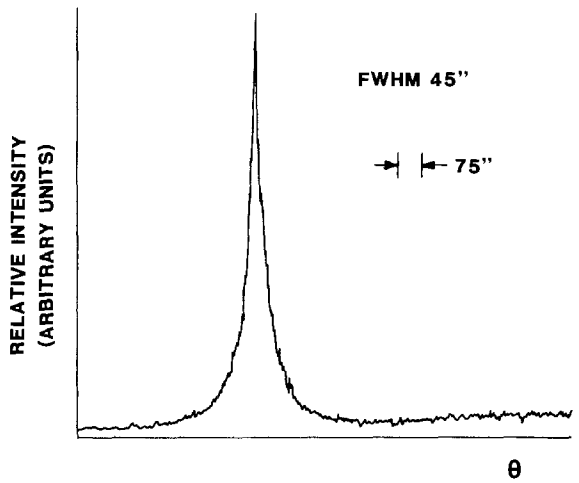

Fig. 6. A typical x-ray diffraction scan of the 333 reflection from $ZnSnP_2$ grown on {111} As oriented GaAs.

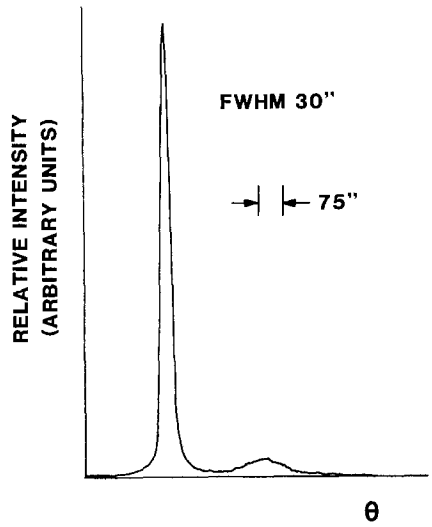

Fig. 7. A diffraction scan of the 333 reflection from $ZnSnP_2$ grown on {111} As oriented GaAs grown with a 5°C/hr cooling rate.

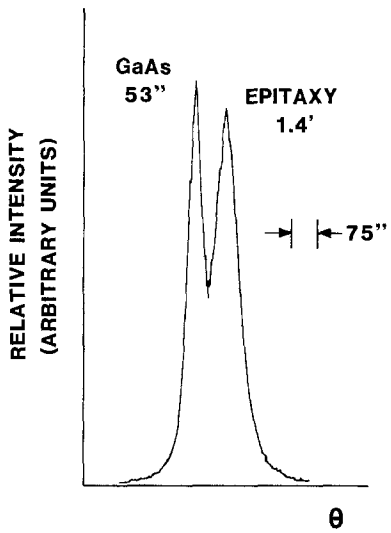

Fig. 8. A typical x-ray diffraction scan from $ZnSnP_2$ grown on {110} oriented GaAs.

Back Reflection Laue Patterns

Because of the differences between the diffraction measurements for {111} As and {110} oriented growth, back reflection Laue photographs of the layers were made to determine any differences in crystal structure. Typical photographs are shown in Fig. 9. In all photographs, the samples were aligned so that a <110> axis of the substrate was directed along the incident x-ray beam. A copper source was used for these exposures and the sample-to-film distance was approximately 4 cm.

Figure 9a is a photograph of an 8 μm $ZnSnP_2$ layer grown on {111} As oriented GaAs whose diffraction scan was similar to that shown in Fig. 6. Exposures of this layer contain no additional diffraction spots compared with exposures of GaAs. Hence, this $ZnSnP_2$ layer has grown with the sphalerite structure. A gnomonic projection of the sphalerite reflections observed in these photographs is shown in Fig. 10a. Figure 9b is a photograph of a 4 μm layer grown on

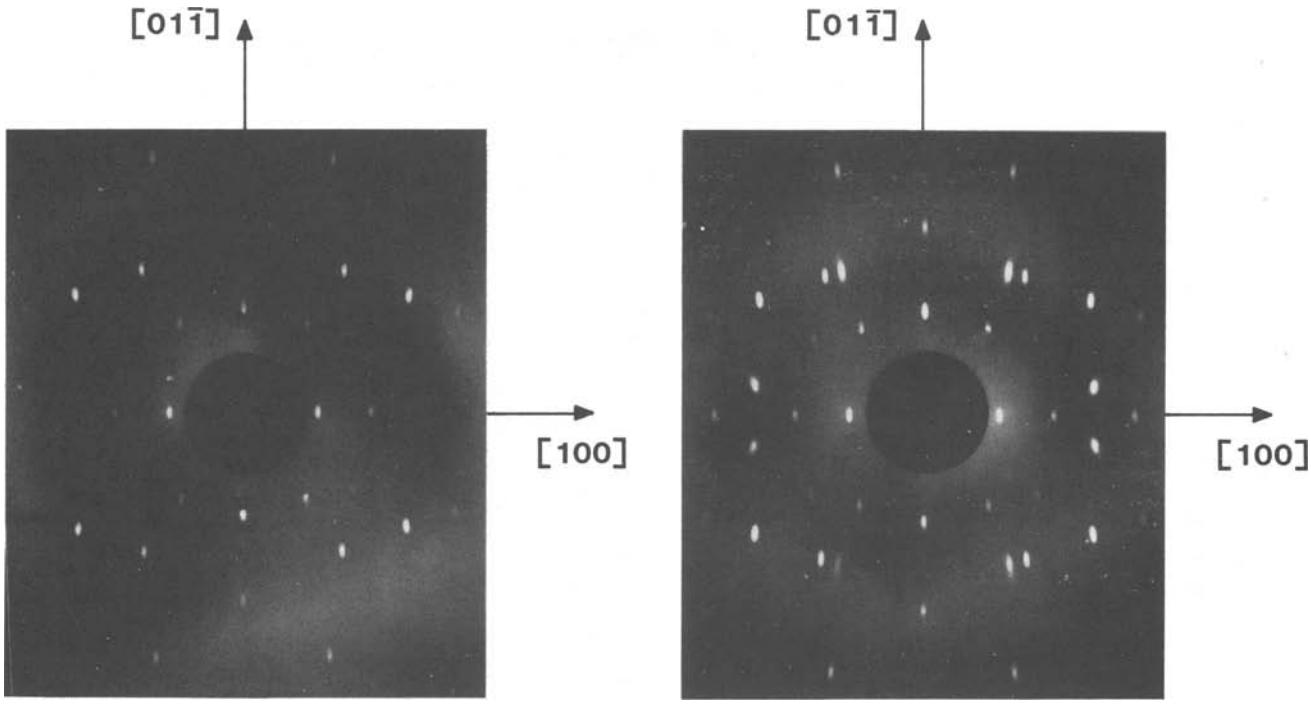

Fig. 9. Back reflection Laue photographs of $ZnSnP_2$ layers grown on (a, left) {111} As oriented GaAs and (b, right) {110} oriented GaAs.

{110} oriented GaAs. The diffraction scan for this $ZnSnP_2$ layer is shown in Fig. 8. The Laue photograph in Fig. 9b shows a number of diffraction spots which are not present in the GaAs exposure. These additional spots are due to a higher degree of ordering in the $ZnSnP_2$ layer and cannot be attributed to the slightly different lattice constant of the layer. The intense additional spots which are evident in this exposure are from high index chalcopyrite 167 and 259 planes, which are listed in catalogs of powder diffraction patterns. These diffraction spots are evident despite their small structure factor because they meet the first-order Bragg condition for a wavelength of 1.542Å, *i.e.*, at the high intensity Kα peak of the Cu x-ray spectrum. These observations indicate that the {110} oriented growth has the chalcopyrite structure. A gnomonic projection of the chalcopyrite reflections is shown in Fig. 10b.

Epitaxial Orientation

The manner in which the chalcopyrite structure of the $ZnSnP_2$ layer is oriented with respect to the sphalerite structure of the GaAs substrate is also of interest. Due to the tetragonal structure of the epitaxial layer, there are three ways in which it may orient relative to the substrate sphalerite structure. This is illustrated schematically in Fig. 11 where three chalcopyrite conventional (cubic) unit cells are shown at three different orientations on a {110} sphalerite surface. In this figure, the subscript "c" refers to chalcopyrite axes. The different relative orientations are with the [001]c axis oriented along the [100], [010], or [001] axes of the sphalerite structure. Other researchers (5) involved with chalcopyrite/sphalerite epitaxy have observed both unique epitaxy where only one relative orientation is present and

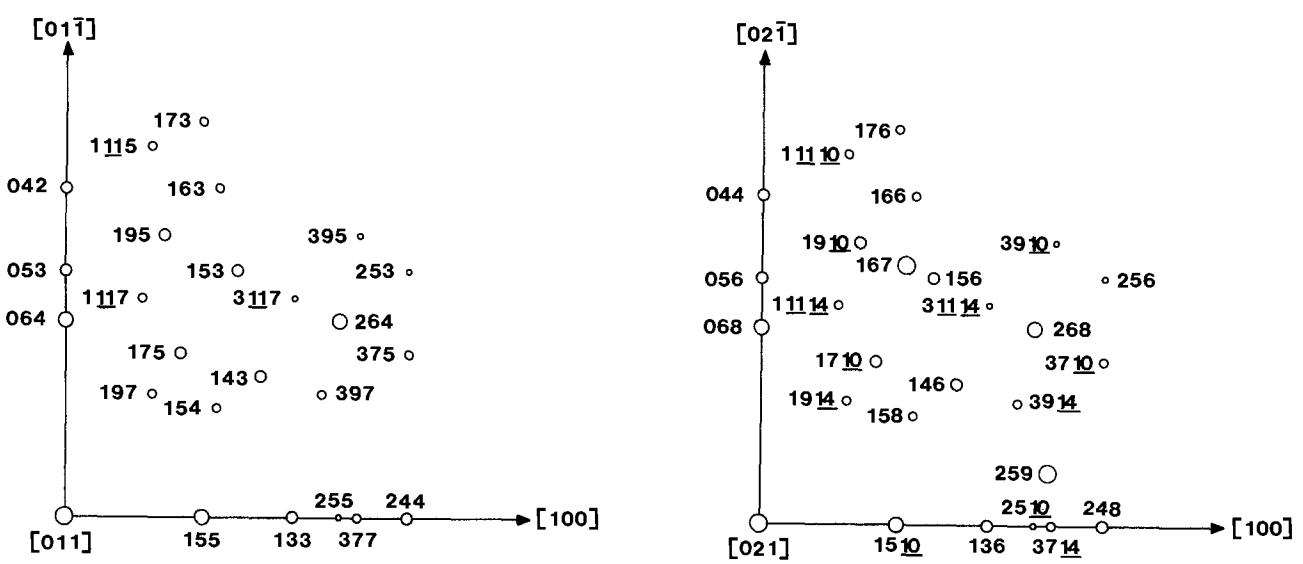

Fig. 10. Gnomonic projections of the (a) sphalerite reflections of Fig. 9(a) and (b) chalcopyrite reflections of Fig. 9(b). Larger circles represent larger reflected intensity.

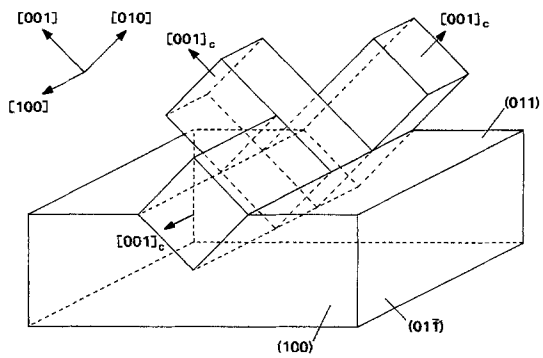

Fig. 11. Schematic illustration of the relative orientation of the chalcopyrite conventional unit cellls on a {110} sphalerite surface.

mixed epitaxy where more than one relative orientation is present.

Because $ZnSnP_2$ exhibits no tetragonal distortion, the uniqueness of the epitaxy cannot be determined from the diffraction scans of the 333/336c reflections. The chalcopyrite Laue spots, however, indicate that the epitaxy is mixed with the [001]c axis out of the growth surface.

Hall and Resistivity Measurements

Van Der Pauw resistivity and Hall measurements were made on the {111} As and {110} layers. All layers measured were found to be p-type. Layers grown on {111} As oriented substrates have carrier concentrations of 1×10^{18}-1×10^{21} cm^{-3} and calculated mobilities of 10-70 $cm^2/Vsec$. The resistivity of these layers ranged from 2.5×10^{-4}-1.2×10^{-1} Ωcm. Layers grown on {110} oriented substrates have carrier concentrations of 3×10^{19}-5×10^{19} cm^{-3} with calculated mobilities of 15-40 $cm^2/Vsec$ and resistivities of 4×10^{-3}-2×10^{-2} Ωcm. No strong correlations were observed between these data and the growth conditions of the layers.

Surface Effects

From the results discussed above, it is evident that the growth surface plays an important role in determining the crystal structure of $ZnSnP_2$ grown on GaAs substrates. A similar observation was made by Kroemer *et al.* (6) for GaAs grown on Ge substrates. For GaAs on Ge, the {110} orientation was found to be the optimum growth orientation for high quality GaAs layers. Kroemer *et al.* postulated that the {110} Ge surface is superior because of the formation of well structured As-like and Ga-like sites. They based this conclusion on Harrison's (7) model for the reconstruction of this nonpolar surface. Such a reconstructed Ge surface should suppress antiphase boundary formation in GaAs producing layers with superior properties.

An analogous effect may be responsible for the growth of the two $ZnSnP_2$ phases on different GaAs substrate orientations: The reconstructed {110} GaAs surfaces in liquid phase epitaxy may contain Ga sites which appear to be Zn-like or Sn-like, while the {111} As surfaces may not. In this manner, the {110} surfaces would promote chalcopyrite growth with antiphase boundaries. For instance, the {110} surfaces might reconstruct into linear chalcopyrite-like surface chains in the [001] direction which are out of phase with neighboring chains. This would promote the chalcopyrite phase with antiphase boundaries, and could explain the somewhat degraded electrical properties of our chalcopyrite layers in comparison to the sphalerite layers. If this is the case then growing on misoriented substrates could increase the lateral growth velocity and inhibit antiphase boundary formation. Another possibility is that misoriented substrates may produce a surface which reconstructs to give longer range chalcopyrite-like regions which are free of antiphase boundaries.

Although Harrison (7) considered the reconstruction of polar surfaces such as GaAs, he did not separate the metallic or nonmetallic sublattices into further sublattices of dissimilar sites since such considerations were secondary to the scope of his work. Considering the experimental results discussed in this paper, a study of such reconstruction may be warranted.

Conclusions

We have developed a procedure for growing $ZnSnP_2$ layers on GaAs in an open tube liquid phase epitaxial system. After a preliminary study of $ZnSnP_2$ growth on various GaAs substrate orientations, the growth procedures were refined for growth on {111} As and {110} oriented substrates. $ZnSnP_2$ grown on {111} As oriented substrates with cooling rates smaller than 5°C/hr was sphalerite and lattice matched GaAs. $ZnSnP_2$ grown on {110} oriented substrates with cooling rates between 2.5°-5°C/hr was mixed orientation chalcopyrite with a lattice constant of 5.6507Å, in agreement with data on solution-grown platelets. All layers grown were p-type with carrier concentrations of 1×10^{18}-1×10^{21} cm^{-3} and mobilities of 10-70 $cm^2/Vsec$. Antiphase boundaries, which are present in such mixed orientation epitaxy, may be responsible for the inferior electrical characteristics of the chalcopyrite layers.

Acknowledgments

This research was sponsored by the Air Force Office of Scientific Research, Air Force Systems Command, USAF under Grant No. AFOSR 79-0096 and AFOSR 82-0231.

Manuscript submitted Nov. 28, 1982; revised manuscript received Feb. 14, 1983.

Any discussion of this paper will appear in a Discussion Section to be published in the December 1983 JOURNAL. All discussions for the December 1983 Discussion Section should be submitted by Aug. 1, 1983.

Washington University assisted in meeting the publication costs of this article.

REFERENCES

1. J. L. Shay and J. H. Wernick, "Ternary Chalcopyrite Semiconductors: Growth, Electronic Properties, and Applications," Pergamon Press, Elmsford, NY (1975).
2. A. A. Vaipolin, N. A. Goryunova, L. I. Keschinskii, G. V. Loshakova, and E. O. Osmanov, *Phys. Status Solidi*, **29**, 435 (1968).
3. G. A. Davis, Master's Thesis, Washington University, St. Louis, MO (1981).
4. E. D. Pierron, D. L. Parker, and J. B. McNeely, *Acta Crystallogr.*, **21**, 290 (1966).
5. J. E. Andrews, H. H. Stadelmaier, M. A. Littlejohn, and J. Comas, *This Journal*, **128**, 1563 (1981).
6. H. Kroemer, K. J. Polasko, and S. C. Wright, *Appl. Phys. Lett.*, **36**, 763 (1980).
7. W. A. Harrison, *Surf. Sci.*, **55**, 1 (1976).

Study of the Orientation Dependent Etching and Initial Anodization of Si in Aqueous KOH

J. W. Faust, Jr.*,[1] and E. D. Palik

Naval Research Laboratory, Washington, DC 20375

ABSTRACT

A series of electrochemical measurements have been performed on a variety of n- and p-type Si wafers of {100} and {111} orientation in aqueous KOH. It has been determined that {100} surfaces have similar, systematic features regardless of carrier type and doping level below $10^{20}cm^{-3}$, while {111} surfaces have a different set of similar systematic features. These results suggest the presence of a different prepassive layer on each of these surfaces. In addition, ellipsometric measurements have been carried out in the voltage range beyond the passivation potential to clarify the anodization process.

The importance of orientation dependent (OD) etching in silicon technology has prompted us to study the etch mechanisms with the aim of improving the OD etching of silicon sufficiently to meet the needs of the microstructure electronics of the future and to devise similar type, equally reliable etchants for other materials (in particular the III-V intermetallic compounds) which show promise. There are several etchants that are orientation dependent not only for Si (1-6) but also for Ge (7-9), for many of the III-V intermetallic compounds (10), and for some other semiconductors and a few metals (11). At present most of these are not, or at least have not been shown to be strongly enough OD for uses similar to those of Si. The success of the OD etching in Si device technology is due to the strong orientation dependence of aqueous KOH (and of a few nonaqueous combinations of organic oxidizing and complexing agents).

Studies on the kinetics of chemical etching, in the absence of an electric field (open-circuit conditions in electrochemical studies), have been carried out on a number of materials (12-15). For Ge, it was shown (15) that the oxidizing agent controlled the type of attack while the complexing agent controlled the rate of attack; however, neither this study nor any of the other studies could explain why an etch was orientation dependent. Chemical etching has been referred to as a competition between the rate of oxidation by the oxidizing agent and the rate of dissolution of the oxide. In this respect, it is generally considered that there must be a "thick" layer of reaction products to obtain polishing. Attempts have been made to identify the chemical makeup of the reaction layer at the etching interface with little success. Izidinov *et al.* (16) reported that the gas evolved at the silicon surface during etching with aqueous KOH was hydrogen and suggested some form of silicate was produced (and presumably made up the layer) and went into solution. Neither the composition nor the structure of the reaction ("oxide") layer itself has been identified, although variations of SiO_x and/or other silicates have been suggested (1, 3, 17, 18). In our previous electrochemical studies on the action of aqueous KOH on silicon (19), we showed strong evidence to suggest that the "etch-stop" found at high carrier concentrations ($> 7 \times 10^{19}$ cm^{-3}) was due to the formation of a prepassive layer. At higher carrier concentrations, this prepassive layer is formed almost immediately upon immersion (*i.e.*, open-circuit potential conditions in electrochemistry). Furthermore, it was shown that the phenomenon was not unique to the p-type dopant, boron, but also occurred for the n-type dopant, phosphorous. In these studies, it was deemed necessary to study the anodic oxidation in order to clarify some of our findings. Several electrochemical studies of Si in a KOH electrolyte have been reported (16, 20-22); however, for the most part, they were not directed toward studying OD etching mechanisms. None of them had the range of information needed: various surface orientations, wide range of carrier concentration (both n- and p-type), temperature control, etc. Here, we give results for current-voltage curves and for ellipsometric measurement of anodic oxidation covering the range of voltage from open-circuit potential through the passivation potential where oxidation starts, to higher anodic potentials where oxide films thicken, to the point when breakdown, and/or anodic dissolution occurs.

Experimental

Current-voltage (I-V) curves.—Both n- and p-type silicon samples with surface orientations of {100} and {111} and covering a range of carrier concentrations from 10^{14} to 10^{20} cm^{-3} were used. The pertinent data on each sample studied are given in Table I. The samples were prepared in the manner previously described (19) with the exception that leads to most

Table I. Characterization parameters for Si

Sample no.	Type orientation	Resistivity (Ωcm)	Doping density (cm^{-3})	OCP (V)	PP (V)	Native oxide thickness (Å)	After HF (Å)
3-82	p{100}	19.3	7.0×10^{14}	−1.19	−0.69		
8-82		4.14	3.0×10^{15}	−1.25	−0.79		
21		1.25	1.2×10^{16}	−1.07	−0.85	29	
43		0.85	1.7×10^{16}	−1.06	−0.83		
7-82		0.84	1.7×10^{16}	−1.24	−0.76		
9-82		0.0081	1.1×10^{19}	−1.21	−0.93		
31		0.0072	1.5×10^{19}	−1.20	−0.92		
P2			2.8×10^{20}	−1.00	−0.86		
3		19.4	7.1×10^{14}	−0.87	−0.39	34	21
4-82	p{111}	12.4	1.1×10^{15}	−1.215	−0.775		
2		1.02	1.5×10^{16}	−1.225	−0.82		
10-82		0.15	1.3×10^{17}	−1.215	−0.835		
11-82		0.0094	9.0×10^{18}	−1.09	−0.87		
35		0.0069	1.7×10^{19}	−1.02	−0.78		
1			2.4×10^{20}	−1.00	−0.90	36	34
2-82	n{100}	15.5	3.0×10^{14}	−1.33	−0.68		
12		4.37	1.1×10^{15}	−1.32	−0.94	34	28
1-82		0.59	8.0×10^{15}	−1.36	−0.98		
22		0.44	1.5×10^{16}	−1.32	−0.66	30	
10		0.159	4.7×10^{16}	−1.32	−1.00		
5-82		0.0266	7.0×10^{17}	−1.32	−1.02		
30		0.0079	7.0×10^{18}	−1.30	−1.08		
23		0.0043	1.5×10^{19}	−1.28	−0.97		
P4			5.0×10^{20}	−1.34	−1.22		
12-82	n{111}	7.7	6.0×10^{14}	−1.17	−0.66		
6		6.9	6.8×10^{14}	−1.14	−0.77	34	
14-82		0.47	1.1×10^{16}	−1.175	−0.685		
39		0.102	9.0×10^{16}	−0.92	−0.50		
6-82		0.53	1.9×10^{17}	−1.17	−0.69		
38		0.0067	8.5×10^{18}	−1.13	−0.70		
15-82		0.0052	1.2×10^{19}	−1.175	−0.80		
P3			5.0×10^{20}	−1.29	−1.21		

The values of *OCP* and *PP* listed are averages of several runs and will not necessarily agree with values in the figures.

* Electrochemical Society Active Member.
[1] Permanent address: College of Engineering, University of South Carolina, Columbia, South Carolina 29208.
Key words: etching, anodization, Si, ellipsometry, current voltage.

of the samples were put on with In solder or In-Ga eutectic and a pressure contact rather than the conducting epoxy used previously. The edges of the samples were coated with black wax which had little effect upon the I-V curves. The experimental setup and procedures were also described in an earlier paper (19). For the present study, however, we used only a 2M KOH solution at (21° ± 0.5°C). The voltage sweep speed was usually 10 mV/min to ensure equilibrium. The potential of Si was measured with respect to a standard calomel electrode. Typical I-V curves are shown in Fig. 1 for a {100} n-type (No. 1-82) and a {100} p-type (No. 7-82) sample. The pertinent features are the open-circuit potential (OCP), the passivation potential (PP), and the Flade potential (FP) as pointed out in Fig. 1. The Flade potential is the potential at which the current is a minimum just beyond the PP. Data given in Table I and discussed here were obtained in-the-dark unless otherwise noted. The systematic differences in these parameters for the various samples of n, p, {100}, {111} Si are real and reproducible to better than 0.1V if the In or In-Ga contacts are used, especially on carrier concentrations below 10^{17} cm^{-3}. The poor reproducibility of the PP for samples below 10^{17} cm^{-3} reported in the previous paper (19) was due to sporadic high resistance in the epoxy contacts. Typically, lead resistance of <1500Ω did not shift either the OCP or PP values, while larger resistance did begin to shift the PP to more anodic values. Figures 2a and b show the much improved reproducibility in the PP at the lower concentrations while still showing the convergence of the OCP and the PP with increased carrier concentration, especially at concentrations above 10^{19} cm^{-3} as shown in Fig. 3a and b of Ref. (19). The OCP and PP points remain roughly parallel, separated by about 0.4-0.5V up to ~10^{19} cm^{-3}, then begin to converge quickly to ~0.1V. It is interesting to note that the etch rate remains constant also up to ~10^{19} cm^{-3}, then decreases rapidly as the etch stop occurs. The various portions of the I-V curves in Fig. 1 will be discussed in more detail in the Results Section. In connection with other experiments, we noticed that the In solder and In-Ga eutectic contacts on n-type substrates sometimes produced some rectification properties. The main results reported throughout this paper

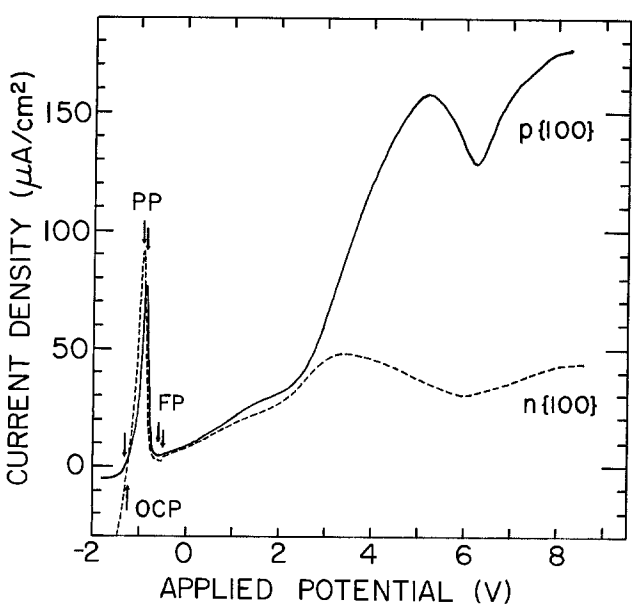

Fig. 1. I-V curves for samples 1-82 (dashed) and 7-82 (solid) showing the open-circuit potential (OCP) when $I = 0$, the passivation potential (PP) at the sharp peak in I, and the Flade potential (FP) at the current minimum. The curve for sample 1-82 above −0.05V was obtained with light.

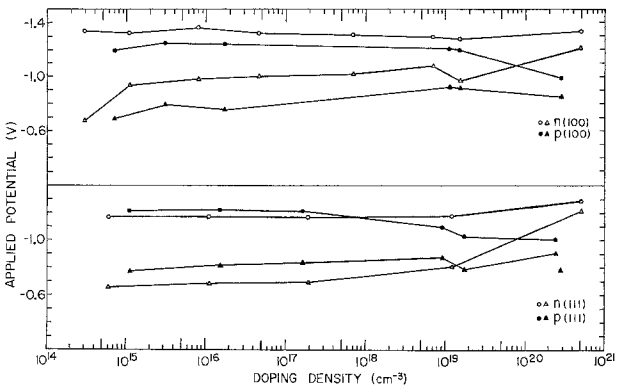

Fig. 2. (a) Values for OCP and PP for various n, p{100} samples as a function of doping density. (b). Value for OCP and PP for various n, p{111} samples, as a function of doping density.

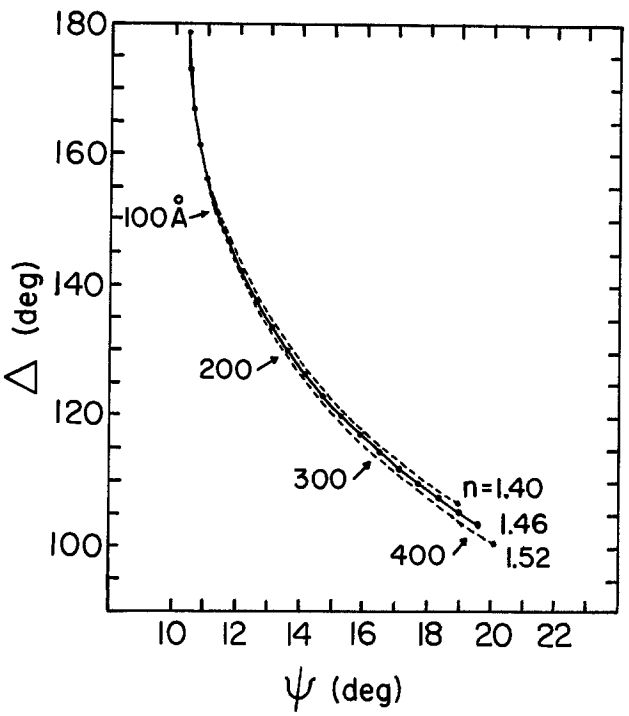

Fig. 3. Dependence of ellipsometric parameters ψ and Δ on the thickness d of an SiO_2 film on an Si substrate. Slight excursions of the refractive index from $n = 1.46$ are also noted by the dashed lines. The dots on the $n = 1.46$ curve specify 20Å intervals. The curves end at 400Å.

for such contacts and for low-resistance, conducting-epoxy contacts were similar, however.

Ellipsometry measurements.—The thickness of the anodic oxides formed under the various conditions were measured using a Rudolph Model 43702-200E, null ellipsometer, equipped with an He-Ne laser (6328Å). With this equipment, we were not able to make ellipsometric measurements *in situ;* thus, for each measurement of thickness, it was necessary to remove the sample from the electrolyte, wash it in deionized water, dry it, put it into the ellipsometer, and make the measurement. We were able to do this entire process within 15 min, thus, minimizing regrowth of oxide. The optical quality of the surfaces remained good throughout the various anodization runs for all samples except No. 22 (n-type {100}) which showed a slightly clouded surface after the first anodization and remained clouded throughout the rest of the runs. This slightly clouded surface may account for its apparent larger thickness compared to the other samples at voltages below 3V. The surface of the silicon is not optically flat but is "rough-

ened" by the etching action of the KOH prior to the first formation of the anodic oxide. The "roughness" is made up of {111} etch facets (planes), which appear as triangular arrays on {111} Si and square arrays on {100} Si. These pits are often truncated at the bottom (17, 23) with {111} or {100} planes, respectively. Williams and Aspnes (24) showed that such {111} sides formed on {111} Si in NaOH reflected the laser light out of the beam and did not contribute a rough-surface signal. Thus, the optical constants of Si determined from the specular {111} surfaces were reliable although the surface looked rough. Random interface roughness, however, would manifest itself as an apparent thicker film (25) as in the case of sample 22. Interface roughness contributes less and less of an error in the measured film thickness as the oxide thickness grows until a cycle is made on the Ψ-Δ curve.

We assumed the optical constants for Si to be $n = 3.86$, $k = 0.028$ at 6328Å (26), and $k = 0$ for SiO_2. The angle of incidence was 70°C. The analyzer and polarizer angles were measured in two quadrants and averaged. A McCracken-type computer program (27) was used to determine refractive index n and thickness d. For thick films > 100Å, we usually obtained consistent n and d values with $n = 1.46 \pm 0.2$. For $d = 200$Å, a variation of 0.1 in n corresponded to a variation of about 20Å in d. A graph of the ellipsometric parameters Ψ and Δ for the assumed constants of Si and SiO_2 is given in Fig. 3. The dots on the $n = 1.46$ curve indicate 20Å differences in d. The steepness of the curves for 0 to 100Å indicates that the Ψ must be measured to 0.1° or better to obtain reasonable solutions. Due to misalignment of the ellipsometer and/or the quality of the anodized films, the values of Ψ in the two quadrants were often as much as 0.3° apart. This margin of error in Ψ probably caused the computer program to fail to find a solution in thirty iterations with the restriction $1.2 < n < 1.7$. When this occurred, almost always below 100Å, we arbitrarily forced $n = 1.5$ to obtain a computer solution for d. Analysis of the dependence of Ψ and Δ on n and d suggested that a change of 0.1° in Ψ frequently produced a solution in thirty iterations with a value of d within ~20% of the value obtained with a forced value of $n = 1.5$. The refractive index might be significantly larger than 1.46 for a thin Si-rich transion layer which would make our calculated value of d too large. The transition layer from thermal SiO_2 to Si is reported ~7Å thick (26, 28) with a refractive index of about 3.26.

We did not include such a transition layer in the model since we do not know its properties for this particular anodic oxide. Since k is nonzero for Si-rich oxide, at 6238Å, this might cause some of the difficulty in the simpler model not giving reasonable results in thirty iterations for thicknesses considerably less than 100Å.

The wafers as received were typically Syton-polished with a native oxide. The first measurement prior to starting always gave a film thickness of ~30Å, somewhat larger than, but consistent with, a native oxide ~20Å thick (29). Removing of the native oxide in HF, two rinsings in deionized water, blowing dry, and remeasuring within 10 min always reduced these values by less than a factor of two. We assume this to be the limit set by the assumed n and k for Si, instrumental misalignment, adsorbed water and hydrocarbons (30), and partially regrown oxide. While the absolute values of thickness may be in question in the thin-film regime < 100Å, the relative increase in thickness as anodization takes place is easy to determine because Δ increases initially at about 0.35 deg/Å.

Results

Anodized film thickness.—The results of the thickness studies for four samples (No. 3, 6, 21, 22) over the range from zero volts (PP is taken as the zero of the anodization voltage scale) to 10V are shown in Fig. 4; two additional samples (No. 1, 12) were run to 15V to obtain more data points. All samples were stripped of native oxide by HF and then put into the KOH solution for ~10 min at OCP so that bubbling would indicate etching and removal of any vestige of oxide. Then, the potential was changed to produce passivation. The first four points near $V = 0$ are obtained at the respective FP's. The n-type samples were illuminated after the I-V curves had reached their current minimum (FP) to be sure that the measured thickness was voltage limited and not hole-concentration limited. The OCP and PP data listed for all samples in Table I, however, are for in-the-dark values. In addition, Table I contains the material characterization information, the thickness of the initial native oxide, and the thickness of the oxide after HF treatment. With the exception of sample 22 at low voltages (below 3V), all thickness values at a given voltage are equal within experimental error. The apparent increased thicknesses for sample 22 below 3V is attributed to a surface roughness.

There appear to be two regions of growth characterized fairly well by straight lines as shown in Fig. 4, namely, 0-4 and 6-15V with a curved section between. We have put straight lines through these extreme regions for emphasis. We assume there is an initial rapid growth to ~20Å at the onset of passivation (PP) and then the slower growth shown. *In situ* ellipsometry measurements now in progress bear this out. Once the initial ~20Å of oxide is established, the slope of the straight line at low voltage gives a growth rate of 6.8 Å/V, while for the higher voltage region, the slope gives a growth rate of 41.7 Å/V. Silicon

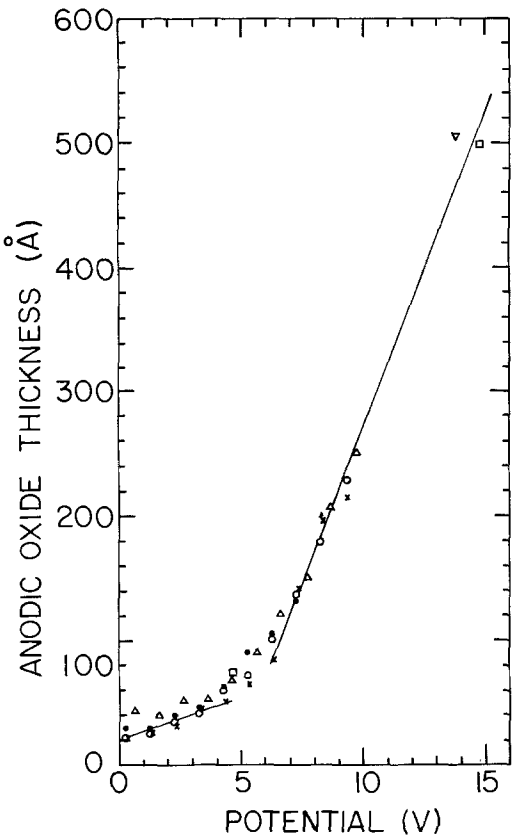

Fig. 4. Thickness of anodized oxide film determined ellipsometrically as a function of voltage above passivation potential for several samples described in Table I; 22 n{100} (△), 6 n{111} (○), 21 p{100} (×), 3 p{111} (●), 12 n{100} (□), 1 p{111} (▽). Straight lines have been drawn through the data points to emphasize two roughly linear ranges. The first point for each sample 22, 6, 21, 3, nearest to $V = 0$ was obtained at the FP.

anodized in a solution of KNO_3 in N-methylacetamide (31) gave results similar to our higher voltage region with the straight line extrapolating to intercept the voltage axis; however, anodization in KNO_3 in ethylene glycol (32) gave a curve extrapolating to intercept the thickness axis. In neither case were data reported at low voltages where initial growth occurs. While we are tempted to compare anodic oxidation with thermal oxidation, such comparison may be open to question.

At a given voltage (say 5V), we estimate from Fig. 4 for an oxide thickness of 70Å that the electric field across the oxide is at most 7×10^6 V/cm, while at 10V for an oxide thickness of 260Å, the electric field is 4×10^6 V/cm. The distribution of voltage across the Si space-charge layer, oxide film, and Helmholtz layer is not known but is probably less than 1V (33). At anodic potentials, n-type Si should have a depleted space-charge layer, while p-type Si should have an accumulated space-charge layer. This should affect the distribution of voltage drop across the interface to some extent lowering the above-mentioned fields. On the other hand, electric fields for oxide films grown in a nonaqueous electrolyte (31, 34) are $\sim 2.6 \times 10^7$ V/cm, considerably larger. This suggests that nonaqueous oxides have a better structure than aqueous oxides. Curiously, one finds that breakdown for "good" thermal oxide occurs at $\sim 8 \times 10^6$ V/cm. This suggests that nonaqueous anodic oxides are better in some respects than thermal oxides (35).

Above 10V, some bubbles appeared on the silicon. Typically, before 20V, some sort of anodic dissolution of the film occurred (36) resulting in the film becoming thinner and the current running away (not shown in the figures). This effect was a function of light intensity and of sample properties; however, both n- and p-type samples showed a thinning of the oxide film in this voltage range. Izidinov *et al.* (16) showed that 1Ω cm n-type Si (5×10^{15} cm^{-3}) in KOH exhibited current runaway at ~75V in the dark, but at ~20V in the light. They observed current runaway in comparable resistivity p-type samples at ~20V in the dark or light. While they attribute current runaway to breakdown of the oxide as the voltage is increased, our results indicate that current runaway occurs when anodic dissolution thins the film.

Etch-back experiments.—After anodizing to a given voltage, we reverted to open-circuit conditions and waited for the original OCP to be re-established. Results are shown in Fig. 5 for sample 2, where in a is shown the time to etch back a film grown to a given anodic voltage; in b, we used the results of Fig. 4 to replot thickness *vs.* time. The straight line is simply drawn through the origin. The etch-back rate is roughly constant at ~0.57 Å/min. In some cases, we also etched back monitoring the thick film ellipsometrically to determine the average etch rate. It was found to be ~0.67 Å/min. A wet-grown thermal oxide was measured to etch at ~0.11 Å/min in 2M KOH comparable to Kendall's value of 0.1 Å/min in 44 weight percent (w/o) KOH (11.2M) (3). The anodic oxide is evidently somewhat more porous than the thermal oxide, so that it etches faster. Anodic oxides grown in aqueous solutions are known to be less dense (34, 37).

The curve depicting the OCP as the film etches back contains steps as illustrated in Fig. 6, for sample 2. We show etch-back of the same sample after several anodizations to different voltages above PP. The ordinate is shifted for each case for clarity. When the bias is shut off, there is an immediate drop and then a slow decay with plateaus and dips. A characteristic of all but high-carrier-density ($> 10^{20}$ cm^{-3}) samples (19) is the last dip and slight rise and level off at OCP. Immediately after this, bubbling is observed with the etching of Si. Etch-back time is defined as

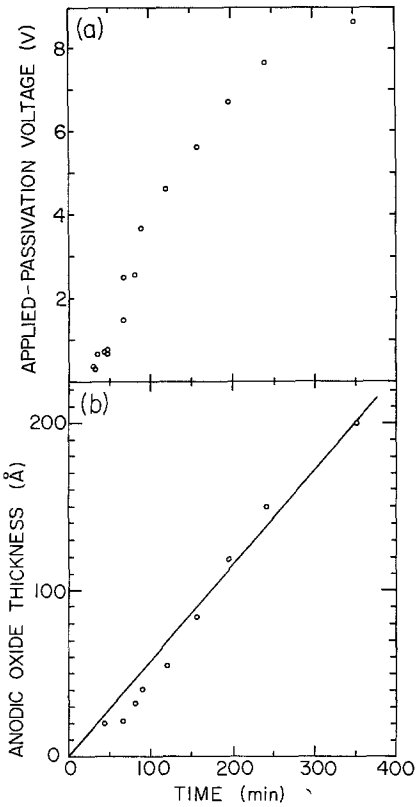

Fig. 5. (a) Etch-back time of an anodic-oxide film as a function of applied potential minus passivation potential for sample 2 described in Table I. (b). Etch-back time as a function of thickness as obtained using data of Fig. 4. A straight line has been drawn through the origin giving an etch-back rate of 0.57 Å/min.

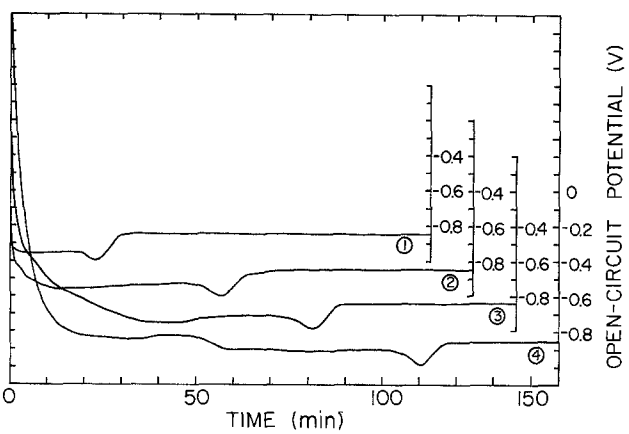

Fig. 6. Open-circuit potential as a function of time after initial growth of anodic oxide to 1) 0.28V, 2) 1.43V, 3) 3.66V, 4) 4.62V above PP for sample 2. The abscissa scale is displaced for clarity for each of the four voltages. Note the dip which occurs just before equilibrium OCP is attained presumably as the last of the oxide is etched off.

that point after the final dip when OCP is obtained. A discussion of possible origins of such plateaus has been given for GaAs (38) and Fe (39). The final dip might signify etching of the transition layer between Si and SiO_2. The properties of such a transition layer are not known for anodic oxides.

I-V curves.—The I-V curves expected for Si if no passivation were present should be similar to those of Ge (40). These are shown schematically in Fig. 7 for n- and p-type material. As discussed by Brattain and Garrett (40), and modeled by Gerischer (41) and Morrison (42), the current for p-type material saturates at cathodic potential and reverses sign and in-

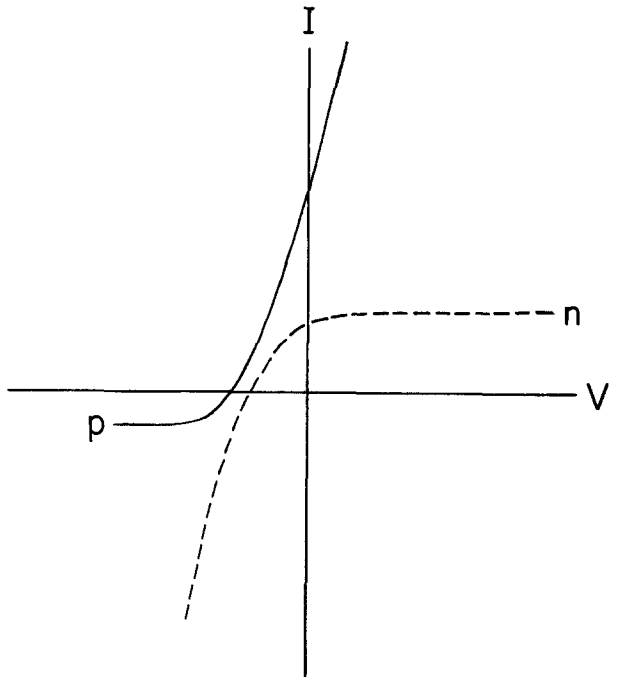

Fig. 7. Schematic I-V curves for an n- and p-type semiconductor such as Ge that does not passivate in KOH. Note that the current saturation regions are "reversed" for n- and p-type samples.

creases exponentially for anodic potential. This latter current is due to majority carriers (43). The saturation current depends on the number of thermally generated minority carriers and should be independent of carrier density. The I-V curve is "reversed" for n-type material. Since passivation occurs in Si, the I-V curves are altered somewhat as indicated in Fig. 1 with the appearance of a passivation peak near −0.8V. Upon passivation in the dark, the current at FP for many p-type samples is typically ~6 μA/cm^2, while it is ~3 μA/cm^2 for the n-type samples. As the p-type samples are further anodized, the current rises steadily to a peak or hump at 5V. The oxide thickness increases as shown in Fig. 4. The n-type sample, however, continues to have low current in the dark rising linearly to about ~14 μA/cm^2 at 5V (not shown), and the oxide film does not increase very much in thickness above its FP value. However, when light is used, the current at FP doubles or triples and as the voltage is increased, the current density is nearly the same as for the p-type sample in the dark or light. The increase in current presumably is due to holes needed at the interface to continue growing the oxide (42). The I-V curve for sample 1-82 n{100} was obtained in the dark from −1.5 to −0.5V, and then the sample was illuminated with a 25W high-intensity bulb placed 10 cm from the sample surface. Light had little effect on the I-V curves for p-type Si above the FP. Some shifting of the OCP and FP is observed with light (16), but these effects will be omitted except to say that for p-type material, OCP and PP are shifted anodic < 0.1V and for n-type samples OCP and PP are shifted slightly cathodic.

With light, the current for n-type samples is about the same magnitude as for the p-type sample (to within 20%) until about 3V (Fig. 1). Ellipsometry indicates that the films on the n- and p-type samples are about the same thickness for the same voltage above PP. However, above 3V, the currents diverge, the current rising more rapidly for the p-type sample. This is just about where the film growth rate begins to change rapidly in Fig. 4. The current for the p-type sample humps at about 5V, while the current for the n-type sample humps at about 3.5V. It is somewhat puzzling that the currents diverge, but the film thicknesses at higher voltages are the same. This implies that the growth rate (presumably determined by OH^- current) is the same but that additional current flows for p-type samples which does not lead to additional oxide growth. From Fig. 7, we see that without an oxide film, the current for n-type Si should saturate, while for p-type, Si it should rise exponentially. Perhaps these effects are beginning to appear without affecting the growth rate, since the anodic oxide is somewhat conducting at these voltages.

We also recorded I-V curves for sample 2, p{111}, 14-82, n{111}, 21, p{100}, and 22, n{100} of comparable doping density to those of Fig. 1 and obtained similar results.

I-V curves for many samples.—In Ref. (19), we noted that the shape of the PP peak seems to be systematic for {100} and {111} surfaces, *i.e.*, {100} surfaces showed single peaks predominantly, while {111} surfaces showed double peaks predominantly. After eliminating the high resistivity of the leads and waxing the edges of samples, we find that the {100} samples invariably show single PP peaks, and their shapes are characteristically different for n- and p-type material. On the other hand, the {111} samples invariably show double PP peaks of somewhat different shape for n- and p-type material. We summarize our results in Fig. 8a, where typical I-V curves for samples 1-82, n{100} and 8-82, p{100} are shown. The n-type peaks are wider and blunter than the p-type peaks. The p-type sample shows saturation at negative potential as has been demonstrated in p-type Ge (40). Interestingly, the current at PP is roughly independent of carrier density averaging (89 ± 15%) μA/cm^2 for n-type material and (93 ± 15%) μA/cm^2 for p-type material. The main error is in measuring the area of the sample under the liquid. For $> 10^{20}$ cm^{-3}, the peak currents tend to vary somewhat more.

For {111} samples 6-82 and 10-82 shown in Fig. 8b, the PP peak is more complicated showing two peaks. The peak currents average (13 ± 20%) μA/cm^2 for

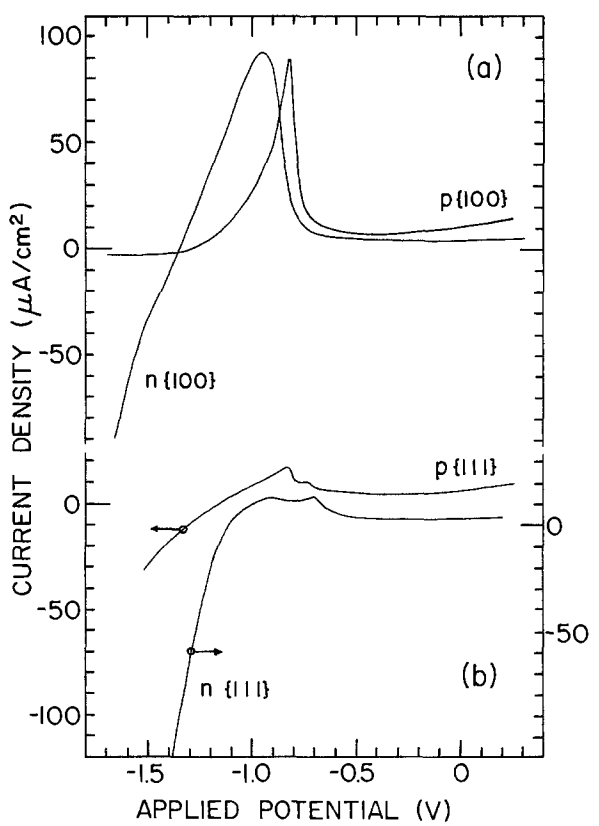

Fig. 8. (a) I-V curves for samples 1-82, n{100}, and 8-82, p{100}. (b). I-V curves for samples 6-82, n{111} and 10-82, p{111}.

n-type samples and (17 ± 15%) $\mu A/cm^2$ for p-type samples. For sample 10-82, we did not see the current saturation at cathodic potential. In general, about half the p-type samples showed saturation (44). This phenomenon is discussed by Green (45) and is dependent on surface preparation among other things.

It is not obvious where to define the PP for the {111} samples, but we have chosen the more anodic peak or shoulder. All samples showed the single- or double-peak structure for carrier densities $< 10^{20}$ cm^{-3}. Above this, the double peaks seem to smear out and only single peaks (or no peaks (19)) were observed. Double structure is seen in the passivation curves for some metals (46) and is attributed to formation of additional films. Since the commercial wafers can be misoriented, it is possible that the more anodic peak for nominal {111} surfaces is due to the {111} surface while the more cathodic peak is due to the misorientation steps which may be of other orientations.

The {111} surface (p or n) has about six times less current density than the {100} surface. This suggests that a resistive prepassive layer may be forming under the PP peak and determining the magnitude of the current. For Ge in KOH where etching only takes place at anodic potentials and no passivation occurs, the {111} anodic current is also about six times less than the {100} current (9).

I-V characteristics for sample 39.—Because of the observation that the {111} samples showed double peaks while the {100} samples showed single peaks and in view of the difference in etch rates on these two surfaces, we tried to investigate the voltage region between OCP and FP more carefully by a systematic repetition of V to repeat I-V curves. We attempted to exploit the sensitivity of the OCP and current to surface films to establish whether a prepassive film formed prior to the appearance of the oxide film between the PP and the FP. In general, we noticed that when abruptly changing the potential from OCP toward the cathodic direction by a 0.5V interval, and stopping, the current reached its equilibrium value within a minute or two. When shifting the voltage from OCP in the anodic direction by a similar amount, but not yet to PP, we noticed the current took several minutes to come to equilibrium. Once PP was passed, the current at any fixed voltage took considerably longer to come to equilibrium while anodic-oxide growth took place. In Fig. 9, results are shown for systematic sweeps of applied potential for sample 39. While this sample was an example of double peaks, the same kind of results was obtained for single-peak samples also. Curve 1 is the standard I-V curve run from −1.2 to −0.1V to produce an anodic oxide at a sweep rate of 0.025 V/min. Curve 2 (dashed line) is the immediate rerun of the sample, starting again at −1.2V. The oxide causes a large shift in OCP, and the passivation peak is gone. In the 0.7V interval from −1.2 to −0.5V taking 14 min until curves 1 and 2 coincided, the oxide did not etch back completely. The sequence of curves 3-8 have been shifted for clarity and represent systematic runs from −1.2V cathodic to anodic voltages in steps of 0.05-0.2V further each time. For example, at the end of curve 3, the voltage was moved to the beginning of curve 4, and the run was repeated a little further anodic this time. The results indicate that the cathodic current began to deviate from its initial value (−12.5 $\mu A/cm^2$) for curve 5 after curve 4 has been completed to the first current maximum. At the start of curve 6 after curve 5 had been completed to within 0.05V of the PP, the current had departed significantly. When passivation began at the end of curve 6, curve 7 showed drastic departure from the original shape of the I-V curve. During the course of a run, the curve would begin to retrace the curves previously run, if complete etch back occurred.

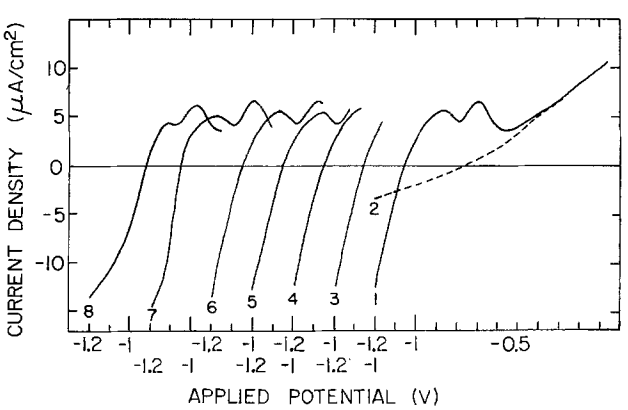

Fig. 9. A series of I-V curves for sample 39. Curve 1 is the full I-V curve; curve 2 is obtained immediately after completion of curve 1 showing that the passivation peak is gone. Curves 3-8 are partial sweeps of the I-V curves in sequence stopping at more anodic voltages each time. The initial current begins to deviate with the start of curve 5. This deviation is even more substantial at the beginning of curve 6 after curve 5 was stopped within 0.05V of the PP. The beginnings of curves 7 and 8 have deviated drastically from curve 1 since an anodic oxide has formed, but it etches off before the run is completed.

A similar approach was used by Turner (47) to study Ge in H_2SO_4. There, the voltage was monitored as a constant current was reversed from anodic to cathodic. The electrode potential increased as a function of time and leveled off after switching from anodic to cathodic. This behavior was attributed to the removal of a monolayer of hydride or oxide.

We interpret our results as the formation of an adsorbed layer prior to actual anodization. Since it is suggested (17, 18) that silicates are formed in etching, the adsorbed layer might consist of such silicates which are converted to silicon dioxide when the voltage passes PP. Such a sequence has been hypothesized by Harvey and Kruger (38) to explain ellipsometric data for the passivation of GaAs surfaces. In this case, a prepassive film was noted in the vicinity of PP ± 0.05V before rapid anodization took place between PP and FP. The sequence in the active-to-passive transition is suggested to be dissolution of the semiconductor, accumulation of the soluble products, nucleation on the surface, deposition from a super-saturated solution, stabilization of this film, and further growth as the applied potential is increased beyond the FP.

Discussion

In thermal oxidation, it is well established that initial linear growth rates for {111} surfaces are about a factor of two larger than for {100} surfaces (48). This is not understood in detail in light of the known number of unsatisfied dangling bonds on these surfaces, one for {111} and two {100}, or the corresponding number of back bonds (49) which need to be broken to grow an oxide, three for {111} and two for {100}. Growth proceeds by diffusion of oxygen species through the oxide to the $Si-SiO_2$ interface. At lower temperature, this difference in oxidation rates is even more striking, being as large as 10:1. It is this observation which prompted Kendall (3) to propose that in the etch solution an oxide film grows more rapidly on the {111} surface than on the {100} surface and is responsible for the difference in etch rates. We agree with this approach except to note that we may be dealing with a prepassive layer of monolayer thickness of still undetermined structure.

The anodization process has been shown to be more complicated than thermal oxidation. For example, by using tritium tagged hydroxyl groups in a "dry" (no H_2O) electrolyte, Schmidt and Ashner (34) have de-

termined that at low electric fields ($< 1.5 \times 10^7$ V/cm), growth takes place by diffusion of hydroxyl ions through the oxide to the Si-SiO_2 interface. By growing an anodic oxide in a phosphorus tagged electrolyte and in a nontagged electrolyte and tracing the phosphorus, Schmidt and Owen (50) showed that at high electric fields ($> 2 \times 10^7$ V/cm) oxide growth was by diffusion of Si cations through the oxide to the SiO_2-electrolyte interface. We are not aware of any similar study of an aqueous electrolyte, and detailed comparisons probably cannot be made between aqueous and nonaqueous electrolytes. The similarities between a prepassive film formed between OCP and PP and the transition layer between the Si and SiO_2 when an anodic oxide is formed are not obvious. In the former case, we expect some sort of silicate monolayer. The transition layer for a thermal oxide is an Si-rich oxide ~7Å thick (26, 28) of suggested structure SiO_x. The work of Revesz (51) indicates that the structure of thermal oxides does depend on the substrate orientation to thicknesses larger than the transition layer if water contamination during oxidation is kept very low. This suggests that the transition layers themselves may have different properties for different surfaces. Except for the obvious water contamination, taking this one step further implies that the prepassive films may have different properties on different surfaces which could account for the observed differences in current densities, for example.

The fact that the results are not dependent on free-carrier type suggests that the band-bending effects are small and do not exclusively determine the electrical conductivity of the surfaces. The trend is correct to suggest that the film is more protective for the {111} surface and, therefore, the etch rate near PP should be lower for {111} than for {100} surfaces. A useful experiment here would be a measurement of the bias-dependent etch rate for {111} and {100} surface from OCP to FP. We would expect the etch rate to drop as the voltage was varied from OCP to PP and once anodization started, to plummet toward 0.1 Å/min. A hint of this has been given by Hurd and Wrotenbery (20) for an n{111} Si surface in aqueous KOH, but not enough data points were obtained to show details.

Conclusions

A large number of n- and p-type Si wafers of {100} and {111} orientation ranging in doping density from 10^{14} to 10^{21} cm^{-3} have been used to determine I-V curves. All {100} surfaces regardless of doping density or type below 10^{20} cm^{-3} show single PP peaks, while all {111} surfaces regardless of carrier density or type below 10^{20} cm^{-3} show double peaks. The peak PP current is ~91 $\mu A/cm^2$ on all {100} surfaces, while it is ~15 $\mu A/cm^2$ on all {111} surfaces. We conclude that a prepassive layer forms on the {111} surface which limits the current and slows the etch rate in comparison to the {100} surface. Repetitive sweeping of the I-V curves from cathodic to the PP hint that a prepassive layer is forming in the vicinity of the PP −0.05V.

Ellipsometric measurements indicate that after etching at OCP and then sweeping the potential to PP, the oxide probably grows quickly to ~20Å between PP and FP. From this point, the growth rate is ~6.8 Å/V to 4V and then rapidly increases to ~41.7 Å/V in the range 6-15V. Beyond the PP, all surfaces n, p, {100}, {111} show the same thickness of oxide at the same potential from PP. All surfaces show the same magnitude of current at the same oxide thickness to about 4V. Above 4V, the current for p-type samples becomes larger than the current for n-type samples but the oxides still grow to the same thickness.

Etch-back of the anodic oxide at OCP conditions gives an etch-back rate of ~0.6 Å/min compared to an etch-back rate of ~0.1 Å/min for a thermal oxide, implying a less-dense structure.

Acknowledgments

We thank K. E. Bean of Texas Instruments, T. Digges of Virginia Semiconductor Corporation, and M. Rebbert of the Naval Research Laboratory for providing many of the samples. Assistance in the ellipsometric measurements was provided by M. Peckerar of NRL. We thank R. F. Greene and H. F. Gray of NRL, A. G. Revesz of Comsat Laboratories, and D. L. Kendall of the National Institute of Astrophysics, Optics and Electronics, Puebla, Mexico for fruitful discussions.

Manuscript submitted Sept. 9, 1982; revised manuscript received Jan. 24, 1983.

Any discussion of this paper will appear in a Discussion Section to be published in the December 1983 JOURNAL. All discussions for the December 1983 Discussion Section should be submitted by Aug. 1, 1983.

The Naval Research Laboratory assisted in meeting the publication cost of this article.

REFERENCES

1. J. B. Price, in "Semiconductor Silicon," H. R. Huff and R. R. Burgess, Editors, The Electrochemical Society Softbound Proceedings Series, Princeton, NJ (1973).
2. D. F. Weirauch, *J. Appl. Phys.*, **46**, 1478 (1975).
3. D. L. Kendall, *Ann. Rev. Mater. Sci.*, **9**, 373 (1979); *Appl. Phys. Lett.*, **26**, 195 (1975).
4. A. A. Epova, S. M. Repinskii, and T. P. Kirpinchnikova, *Inorg. Mater. USSR*, **12**, 144 (1976); *Izv. Akad. Nauk SSSR, Neorg. Mater.*, **12**, 166 (1976).
5. D. B. Lee, *J. Appl. Phys.*, **40**, 4569 (1969).
6. K. E. Bean, *IEEE Trans. Electron. Devices*, **ed-25**, 1185 (1978).
7. P. Wang, *Sylvania Technol.*, **11**, 50 (1958).
8. B. A. Irving, in "The Electrochemistry of Semiconductors," P. J. Holms, Editor, Chap. 6, Academic Press, London (1962).
9. H. Gerischer, in "Advances in Electrochemistry and Electrochemical Engineering," Vol. 2, P. Delahay and C. W. Tobias, Editors, p. 139, Wiley-Interscience, New York (1961).
10. J. W. Faust, Jr., in "Compound Semiconductors," Vol. 1, R. K. Willardson and H. L. Goering, Editors, p. 445, Reinhold, New York (1962).
11. C. S. Barrett and T. B. Massalski, "Structure of Metals," 3rd ed., p. 210, Pergamon Press, Oxford (1980).
12. P. R. Camp, *This Journal*, **102**, 586 (1955).
13. B. Schwartz and H. J. Robbins, *ibid.*, **106**, 505 (1959); **107**, 108 (1960); **108**, 365 (1961).
14. M. C. Cretella and H. C. Gatos, *ibid.*, **105**, 487 (1958).
15. J. W. Faust, Jr., in "International Conference on Reactivity of Solids," Vol. 63, p. 337, John Wiley and Sons, New York (1969).
16. S. O. Izidinov, T. I. Borisova, and V. I. Veselovskii, *Russ. J. Phys. Chem.*, **36**, 659 (1962); *Zh. Fiz. Khim.*, **36**, 1246 (1962).
17. J. W. Faust, Jr., in "The Surface Chemistry of Metals and Semiconductors," H. C. Gatos, J. W. Faust, Jr., and W. J. LaFleur, Editors, p. 151, John Wiley and Sons, New York (1960).
18. S. O. Izidinov, *J. Appl. Chem. USSR*, **44**, 1660 (1971); *Zh. Prik. Khim.*, **44**, 1642 (1971).
19. E. D. Palik, J. W. Faust, Jr., H. F. Gray, and R. F. Greene, *This Journal*, **129**, 2051 (1982).
20. M. Hurd and P. T. Wrotenbery, *Ann. NY Acad. Sci.*, **101**, 876 (1963).
21. H. A. Waggener, *Bell Syst. Tech. J.*, **49**, 473 (1970).
22. H. A. Waggener and J. V. Dalton, Abstract 183, p. 450, The Electrochemical Society Extended Abstracts, Vol. 70-2, Atlantic City, NJ, Oct. 4-8, 1970.
23. J. W. Faust, Jr., A. Sagar, and H. F. John, *This Journal*, **109**, 824 (1962).
24. M. D. Williams and D. E. Aspnes, *Phys. Rev. Lett.*, **41**, 1667 (1978).
25. R. M. A. Azzam and N. M. Bashara, in "Ellipsome-

try and Polarized Light," Chap. 4, North-Holland, Amsterdam (1977).
26. D. E. Aspnes and J. B. Theeten, *This Journal*, **127**, 1359 (1980); *Phys. Rev. Lett.*, **43**, 1046 (1979).
27. F. L. McCracken, Technical Note 479, National Bureau of Standards (1969).
28. E. Taft and L. Cordes, *This Journal*, **126**, 131 (1979).
29. R. J. Archer, *J. Opt. Soc. Am.*, **52**, 970 (1962).
30. E. D. Palik, J. W. Gibson, R. T. Holm, M. Hass, M. Braunstein, and B. Garcia, *Appl. Opt.*, **17**, 1776 (1978).
31. P. F. Schmidt and W. Michel, *This Journal*, **104**, 230 (1957).
32. J. D. E. Beynon, G. G. Bloodworth, and I. M. McLeod *Solid State Electron.*, **16**, 309 (1973).
33. S. R. Morrison, "Electrochemistry at Semiconductor and Oxidized Metal Electrodes," Chap. 2, Plenum Press, New York (1980).
34. P. F. Schmidt and J. D. Ashner, *This Journal*, **118**, 325 (1971).
35. A. G. Revesz, *J. Non-Cryst. Solids*, **11**, 309 (1973).
36. V. Brusic, in "The Anodic Behavior of Metals and Semiconductor Series; Oxides and Oxide Films," J. W. Diggle, Editor, p. 1 and references therein, Marcel Dekker, New York (1972).
37. W. A. Pliskin and H. S. Lehman, *This Journal*, **112**, 1013 (1965).
38. W. W. Harvey and J. Kruger, *Electrochim. Acta*, **16**, 2017 (1971).
39. B. MacDougall and M. Cohen, in "Passivity of Metals," R. P. Frankenthal and J. Kruger, Editors, p. 827, The Electrochemical Society Softbound Proceedings Series, Princeton, NJ (1978).
40. W. H. Brattain and C. G. B. Garrett, *Bell. Tel. Syst. J.*, **34**, 129 (1955).
41. H. Gerischer, *Surf. Sci.*, **18**, 97 (1969).
42. S. R. Morrison, "Electrochemistry at Semiconductor and Oxidized Metal Electrodes," Chap. 3, Plenum Press, New York (1980).
43. M. Seipt, *Z. Naturforsch.*, **14a**, 926 (1959).
44. J. F. Dewald, "Semiconductors," B. Hannay, Editor, p. 727, Reinhold, New York (1959).
45. M. Green, in "Modern Aspects of Electrochemistry," J. O'M. Bockris, Editor, p. 343, Butterworths, London (1959).
46. P. Lorbeer and W. J. Lorenz, *Corros. Sci.*, **21**, 79 (1981).
47. D. R. Turner, *This Journal*, **103**, 252 (1956).
48. Y. J. Van der Meuken, *ibid.*, **119**, 530 (1972).
49. J. R. Ligenza, *J. Phys. Chem.*, **65**, 2011 (1961).
50. P. F. Schmidt and A. E. Owen, *This Journal*, **111**, 682 (1964).
51. A. G. Revesz, *Phys. Status Solidi*, **57a**, 657 (1980); **58a**, 107 (1980).

Polycrystalline Silicon Micromechanical Beams

R. T. Howe and R. S. Muller

Department of Electrical Engineering and Computer Sciences, and the Electronics Research Laboratory, University of California, Berkeley, California 94720

ABSTRACT

Using the conventional MOS planar process, miniature cantilever and doubly supported mechanical beams are fabricated from polycrystalline silicon. Poly-Si micromechanical beams having thicknesses of 230 nm to 2.3 μm and separated by 550 nm to 3.5μm from the substrate are made in a wide range of lengths and widths. Two static mechanical properties are investigated: the dependences of maximum free-standing length and beam deflection on the thickness of the beam. By annealing the poly-Si prior to beam formation, both of these properties are improved. Nonuniform internal stress in the poly-Si is apparently responsible for the beam deflection.

A novel method is described for making cantilever and doubly supported micromechanical beams from polycrystalline silicon (poly-Si). Only two masking steps are needed, as illustrated in Fig. 1. The first step, Fig. 1a, opens windows in an oxide layer grown or deposited on the silicon wafer. Next, poly-Si is deposited and plasma-etched in a second masking step, leaving the cross-section of Fig. 1b. Immersing the wafer in buffered HF removes all oxide, undercutting the poly-Si layer and creating the cantilever beam, illustrated in Fig. 1c. Doubly supported beams, Fig. 1d, are made by including a second oxide window at the opposite end of the beam.

For several reasons, this technique for making poly-Si beams is a useful addition to silicon micromechanics technology. First, poly-Si is widely used in MOS integrated circuits and a well-developed technology exists for depositing it in thin films and controlling its electrical properties. Second, the piezoresistivity of poly-Si could be utilized in integrated sensors; a monolithic pressure transducer based on a poly-Si membrane has already exploited this property (1). Finally, the simple fabrication process outlined above uses only conventional MOS planar technology which greatly simplifies the integration of micromechanical beams and MOS circuitry. This compatibility with standard processing contrasts with beam fabrication techniques based on anisotropic etchants (2, 3). MOS transistors have been fabricated adjacent to miniature cantilever beams made by anisotropic etching of the epitaxial silicon underlying a patterned, etch-resistant layer (4). However, the use of an epitaxial layer and anisotropic etchants in this earlier work represents a substantial departure from the conventional MOS process.

To assess fully the potential of this new technique, both the static and dynamic mechanical properties of poly-Si beams should be determined. This study investigates the static properties by fabricating poly-Si beams having a wide range of dimensions. In particular, the dependences of maximum free-standing beam length and cantilever beam deflection on the thickness of the beam are determined. A more complex process,

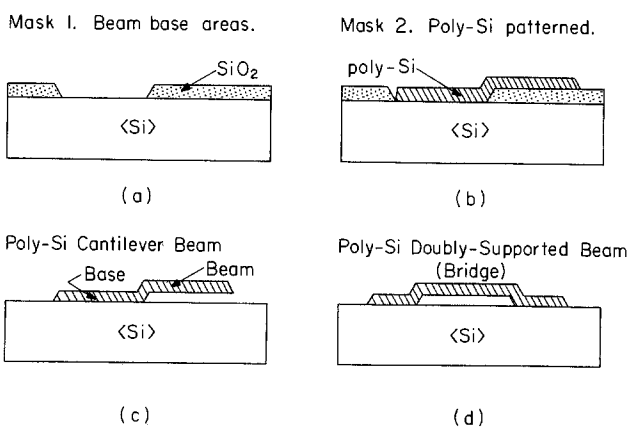

Fig. 1. Poly-Si microbeam fabrication

Key words: mechanics, membrane, integrated circuits.

including an MOS circuit for sensing the beam vibrations, is being developed to investigate the dynamic properties. Results for Young's modulus and fatigue characteristics of poly-Si micromechanical beams will be reported later.

Fabrication

We now describe poly-Si beam fabrication in more detail. In order to minimize stress concentration during flexing, the step in the poly-Si beam, shown in Fig. 1c, should be gradual. This consideration makes it desirable to have a tapered oxide-window edge. Two process runs with different oxide-layer compositions are made. Figure 2 illustrates the resulting oxide-window edges, as observed with a scanning-electron microscope. In the first run, the oxide layer is one-third wet thermal SiO_2 and two-thirds CVD SiO_2. The latter is densified at 975°C for 20 min after deposition. In the second run, a more gradual edge profile is obtained with an oxide layer consisting of 10% thermal SiO_2 and 90% phosphosilicate glass (about 8.75% phosphorus content). The thin, rapidly etching surface layer needed for a tapered oxide-window edge is created by a low-energy argon implant (5). The phosphosilicate glass is densified at 1100°C for 20 min prior to the argon implant.

The poly-Si thin film is deposited by pyrolysis of silane at a temperature of 640°C and a pressure of 600 mTorr, resulting in a deposition rate of approximately 10 nm min^{-1} and a grain size of 30-50 nm (6). No high temperature processing is done after poly-Si deposition, except for one sample having a 3.5 μm oxide layer and a 2.0 μm poly-Si layer. In this case, the wafer is annealed at 1100°C in N_2 for 20 min prior to immersion in buffered HF.

In order to establish the dimensional limitations on poly-Si beams, a wide variety of beams have been fabricated in the two process runs. Several combinations of oxide and poly-Si thicknesses, listed in Fig. 3, were used. The first-run cantilevers are T-shaped with the cross bar at the free end (cf. Fig. 5). They range in length from 25 to 200 μm, with various widths. Both simple cantilevers (without cross bars) and bridges are included on second-run masks. These cantilevers are 25-400 μm long, and the bridges range from 100 to 500 μm in length. Several series of beams are included in which length or width is varied with the other dimension being held constant. All cantilevers have bases as long as the beams (cf. Fig. 1c) except for one second-run series in which the base length has been progressively shortened.

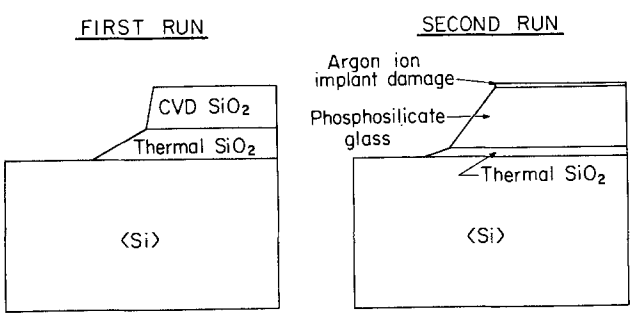

Fig. 2. Oxide-window edges for both process runs

Thickness of oxide supporting layer

Thickness of poly-Si beam	550 nm	1.7 μm	2.0 μm	3.5 μm
230 nm	○	○		○
800 nm	○	○		○
1.2μm			□	
2.0μm		○		○
2.3μm			□	

□: First run, Cantilevers.
○: Second run, Cantilevers & bridges.

Fig. 3. Poly-Si and oxide thicknesses used to fabricate beams

Results

All of the combinations of oxide and poly-Si thicknesses listed in Fig. 3 produce some free-standing poly-Si beams. No cracking is seen at the step in the poly-Si, even for first-run cantilevers, in which the oxide-window edge is very abrupt (cf. Fig. 2). Long bases for poly-Si cantilevers are not needed, as demonstrated by the series of cantilevers with shortened bases. For all the combinations enumerated in Fig. 3, a 5 μm long base is sufficient for a free-standing cantilever which is 45 μm long and 20 μm wide.

Scanning-electron micrographs of four representative cantilevers are shown in Fig. 4. These beams are 60 μm long, 800 nm thick, and are 3.5 μm above the silicon substrate. Widths range from 25 μm for the leftmost beam to 60 μm for the rightmost one. The bases are at the lower right, and the steps in the poly-Si are clearly visible. We will discuss later the upward deflection of these beams which can be seen in Fig. 4.

An apertured poly-Si beam is shown in Fig. 5. The T-shaped cantilever is 100 μm long, 40 μm wide, 2.3 μm thick, and has a 2 μm gap between beam and substrate. No special care in rinsing or drying the wafer after undercutting the beams is taken for the first process run, which produced this beam. An apertured cantilever is of interest for certain sensor applications (7) and the beam shown in Fig. 5 demonstrates the feasibility of this concept.

Very thin poly-Si layers can cover large oxide steps and form free-standing micromechanical beams, as can be seen in Fig. 6. The cantilever in Fig. 6 is 25 μm long and only 230 nm thick with a 3.5 μm separation be-

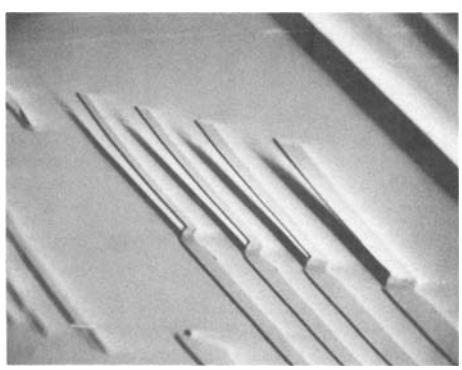

Fig. 4. Poly-Si cantilevers: 60 μm long, 800 nm thick, with a 3.5 μm beam-substrate gap.

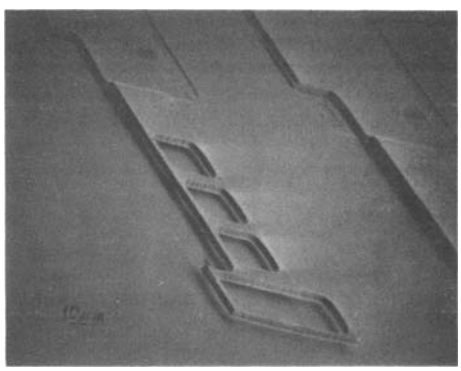

Fig. 5. Apertured poly-Si beam: 100 μm long, 2.3 μm thick, with a 2 μm beam-substrate gap.

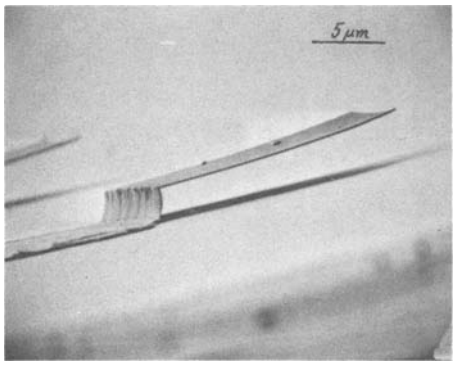

Fig. 6. Thin poly-Si cantilever: 25 μm long, 230 nm thick, with a 3.5 μm beam-substrate separation.

tween beam and substrate. Some debris from scribing is visible on top of the beam and variations in the oxide-window edge have been reproduced in the thin poly-Si layer. This beam is from a process run in which the wafers are dipped in water after etching in buffered HF and dried under an infrared lamp.

Beyond a certain length, both cantilevers and bridges are observed either to deflect downward and ultimately contact the substrate or to deflect upward severely. This limiting length, defined as the maximum free-standing length L_m, is repeatable from die to die within a wafer. It is observed that L_m depends strongly on the thickness of the beam. Width and beam-substrate gap do not have a repeatable influence on L_m in the first two process runs. However, the maximum free-standing length is probably sensitive to processing details, such as the poly-Si deposition conditions and the oxide etching procedure. The results obtained here are, nonetheless, useful as guidelines for evaluating poly-Si beam technology.

In order to determine L_m as a function of thickness for these poly-Si beams, a series of 15 μm wide cantilevers and bridges with increasing lengths were investigated. The average of the lengths of the longest repeatably free-standing beam and the next longer beam is an empirical estimate of L_m. This measurement is plotted against beam thickness for both cantilevers and bridges in Fig. 7. The curves in Fig. 7 are empirical fits to the data and are given by

$$L_m = \begin{cases} \sqrt{4500t} & \text{for cantilevers} \\ \sqrt{11{,}500t} & \text{for bridges} \end{cases} \quad [1]$$

where t(μm) is the beam thickness and L_m(μm) is the maximum free-standing beam length. Cantilevers or bridges located above the relevant curve in Fig. 7 cannot be used, since they will touch the substrate or be severely deflected. Note that the sample which is annealed before the beams are undercut shows substantial increases in maximum free-standing lengths for both cantilevers and bridges, as indicated by the filled symbols in Fig. 7. As mentioned above, these results are process-dependent and therefore should be considered as first-order guidelines.

Cantilever poly-Si beams with lengths less than L_m deflect upward, away from the substrate, as can be seen in Fig. 4 and 6. Scanning-electron micrographs indicate that the deflection curve is parabolic for small tip deflections (less than one-tenth of the beam length). In addition, the tip deflections of cantilevers of constant thickness are proportional to the squares of their lengths. These results suggest the presence of an internal bending-moment M_i in the poly-Si beams, since a tip deflection y given by

$$y = \frac{6M_i L^2}{E_Y t^3} \quad [2]$$

where L is the cantilever's length, t its thickness, and E_Y its Young's modulus, is predicted for this case (8). The physical origin for the bending moment M_i is discussed later.

It is convenient to use the quantity (y/L^2) to characterize beam deflection, since it is independent of beam length. The inset in Fig. 8 defines the tip deflection measurement, and the plot shows the variations of (y/L^2) with beam thickness for both first- and second-run cantilevers. According to Fig. 8, thicker beams deflect less at a given length, as one would expect. As before, annealing the sample affects the static mechanical properties of poly-Si beams. This is indicated by the filled circle in Fig. 8. In contrast to the unannealed sample of the same thickness no measurable deflection is observed for cantilevers shorter than L_m on the annealed wafer. These cantilever deflection results also are sensitive to processing details and should be interpreted accordingly.

Discussion

Micromechanical cantilever and doubly supported beams can be fabricated from poly-Si using a process that is compatible with MOS planar technology. This compatibility, the simple beam-fabrication process, and the piezoresistivity of poly-Si make these structures attractive for silicon micromechanics. In particular, an integrated sensor for organic vapors is being fabricated which incorporates a resonant poly-Si cantilever (7).

Two static properties of these beams have been investigated, the maximum length for a reliably free-standing beam, and the built-in deflection of cantilevers. The observed deflection is consistent with the presence of an internal bending moment which is plausible as the result of nonuniform internal stress across the poly-Si layer. Internal stress in a thin film arises from mismatches in thermal-expansion coefficients and from nucleation and growth phenomena (9). Annealing at 1100°C for 20 min before undercutting

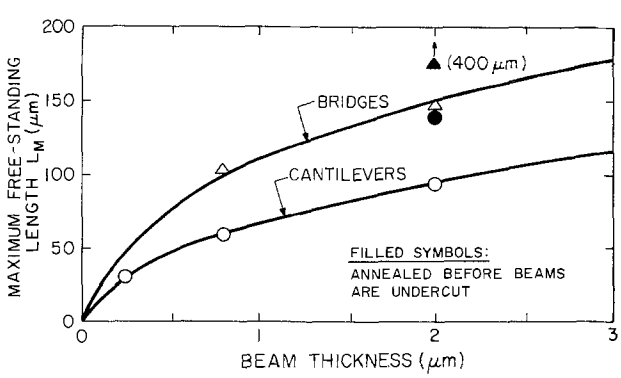

Fig. 7. Dependence of maximum free-standing length on beam thickness.

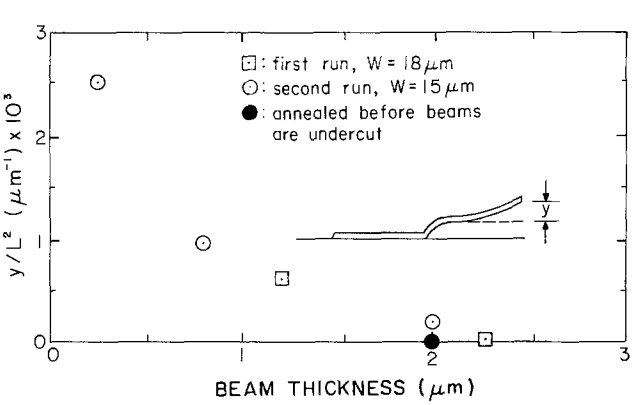

Fig. 8. Cantilever-tip deflection as a function of beam thickness

the beams with buffered HF increases the maximum free-standing length and eliminates the built-in deflection for beams shorter than L_m. This annealing procedure is sufficient to reflow the phosphosilicate glass layer underneath the poly-Si layer and cause recrystallization of the poly-Si, both of which may help to relax the nonuniform internal stress. Diffusion of phosphorus from the glass into the poly-Si will occur during this relatively severe anneal, which may be undesirable for certain applications. Additional research is needed to determine the minimum temperature and time required for stress relaxation in the poly-Si film. However, beams of useful sizes can be made without any post-deposition treatment of the poly-Si, as is demonstrated in Fig. 4-6. The dynamic properties of poly-Si micromechanical beams are currently being investigated, and the results will be reported later.

Acknowledgments

We would like to thank Mrs. D. McDaniel for valuable laboratory assistance, and Dr. J. Shott of Stanford Integrated-Circuits Laboratory for use of a CVD oxide reactor. This work was supported by the National Science Foundation under grants ENG78-21854 and ECS-81-20562.

Manuscript submitted Aug. 16, 1982; revised manuscript received Feb. 14, 1983. This was Paper 118 presented at the Montreal, Que., Canada, Meeting of the Society, May 9-14, 1982.

Any discussion of this paper will appear in a Discussion Section to be published in the December 1983 JOURNAL. All discussions for the December 1983 Discussion Section should be submitted by Aug. 1, 1983.

REFERENCES

1. J. M. Jaffe, *Electron Lett.*, **10,** 420 (1974).
2. K. E. Petersen, *IEEE Trans. Electron Devices,* **ed-25,** 1241 (1978).
3. R. D. Jolly and R. S. Muller, *This Journal,* **127,** 2750 (1980).
4. K. E. Petersen and A. Shartel, *Tech. Digest IEDM,* 673 (1980).
5. J. C. North *et al., IEEE Trans. Electron Devices,* **ed-25,** 809 (1978).
6. C. I. Drowley, Unpublished results.
7. R. T. Howe, M. S. Report, Dept. of Elect. Eng. and Comp. Sciences, Univ. of California, Berkeley, October 1981.
8. E. P. Popov, "Mechanics of Materials," 2nd ed., p. 361, Prentice-Hall, Englewood Cliffs, NJ (1976).
9. D. S. Campbell, in "Handbook of Thin Film Technology," L. I. Maissel and R. Glang, Editors, pp. 12-22, McGraw-Hill, New York (1970).

A Study of the Diffusion of Oxygen in α-Titanium Oxidized in the Temperature Range 460°-700°C

D. David and G. Beranger

Laboratoire de Métallurgie et de Physicochimie des Matériaux, Universite de Technologie de Compiegne, B.P. 233, 60206 Compiegne Cédex, France

and E. A. Garcia

Comision Nacional de Energia Atomica, Dpto Materiales, Avda del Libertador 8250, 1429 Buenos Aires, Argentina

ABSTRACT

The diffusion coefficient of oxygen in α-titanium was measured in the range 460°-700°C, by means of nuclear microanalysis from the reaction $^{16}O(d,p)^{17}O^*$. A new application of this method allows the determination of a complete diffusion profile, along about 2 μm, from a single proton spectrum. The results provide a value of diffusion coefficient consistent with a bulk diffusion process, with an activation energy of 48 kcal/mol, over the temperature range from 200° to 950°C.

The high temperature oxidation of α-titanium, with high current crystalline structure, gives a multilayered oxide film comprising several oxide species (1, 6). Moreover, a diffusion and dissolution of oxygen into the metal occurs under the oxide film, the oxygen atoms occupying the interstitial sites of the metal lattices. Thus, the oxygen concentration decreases continuously from the metal-oxide interface to the metal center. In order to understand the oxidation mechanism of titanium, it is necessary to analyze the two elementary mechanisms: growth of external oxides on one hand and formation of the oxygen-metal solid solution on the other hand.

Several investigations have been previously carried out on the oxygen diffusion phenomenon (2, 7-16). The values of the diffusion coefficient D published by other authors shows a considerable scatter and hence in those for the activation energy, but this dispersion is perhaps related to the corresponding diversity in the experimental methods. The value previously mentioned were all obtained for temperatures higher than 650°C. For temperatures ranging between 250° and 400°C, other values of the oxygen diffusion coefficient were calculated from stress strain aging experiments (17, 18). It can be noted that the corresponding plots fit quite well with those of Ref. (16), which were obtained on the same material from experimental diffusion profiles. These values were directly measured, point by point, thus increasing their accuracy. Between 400°-650°C, there remains a temperature range where the diffusion coefficient values are unknown. However, two D values for the temperatures of 420° and 490°C, have been obtained by Bertin (19) from calculations based upon internal friction measurements. Our results, and some others, are plotted in Fig. 1.

Thus, our purpose was to perform experiments in an intermediate temperature range, by means of a special application of nuclear microanalysis. The results obtained in this way cover the range from 460° to 700°C.

Key words: oxidation, diffusion, nuclear reactions, titanium.

Experimental

Specimens of rolled Kroll titanium, containing 930 ppm of oxygen, were supplied by Cezus (Pechiney-Ugine-Kuhlmann) under the trademark UT 40. In order to determine the diffusion profiles, they were previously anodically oxidized, then heated under vacuum to permit oxygen diffusion. In this case, the oxide layer acts as an inexhaustible oxygen source and the concentrations on each side of the metal-oxide interface remain constant.

In the temperature range studied here (460°-700°C), the diffusion treatment times were selected in such a manner that the oxygen diffusion profiles into the metallic matrix should not exceed 2 μm in depth. The nuclear microanaly-

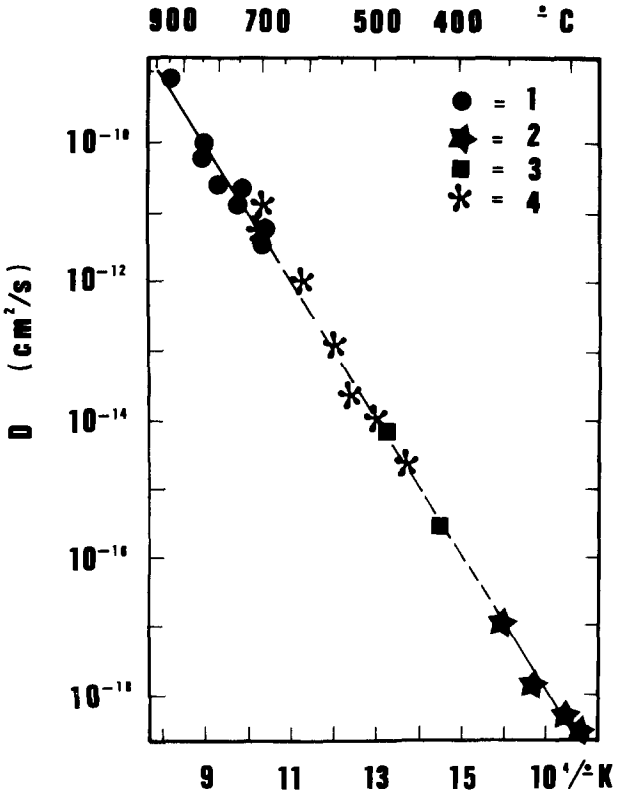

Fig. 1. Diffusion coefficient of oxygen in α-titanium vs. temperature, by several authors, in the range 250°-900°C. 1, (16); 2, (17,18); 3, (19); 4, this study.

sis data (energy-displacement relationships for charged particles penetrating the metal) are such that it is then possible to observe the complete profiles, without grinding the samples. Moreover, it is also possible to study in this manner the different rates of oxygen diffusion into the bulk and into the oxide film.

Specimen preparation.—The precise analysis of the impurities in the titanium used in this study is given in Table I. As the initial state of the metal surface has a considerable influence on its subsequent behavior, all the samples were prepared as follows: mechanical polishing with carborundum paper (grit 320), heating under vacuum (10^{-6} Torr); 2 hr/800°C, mechanical polishing (grit 1000), electrolytical polishing in a solution: 33% HF, 19% H_2SO_4, 48% lactic acid/10 min, 5°C, 16V, 0.2 A/cm². This preparation process yields an optimum surface microgeometry with minimum contamination by light elements such as oxygen, carbon, nitrogen, or fluorine (20).

The samples were then anodically oxidized up to 100V at room temperature, using an electrolyte made up of 100g borax ($Na_2B_4O_7$, 10 H_2O), dissolved at 80°C in 1 liter of diethyleneglycol (HO-C_2H_4-O-C_2H_4-OH) (21). The oxygen content of the resulting oxide layers was then determined by means of nuclear microanalysis, before performing the diffusion treatment. Interferential colors were observed. Finally, the samples were annealed under a vacuum of 10^{-6} Torr, in the previously indicated temperature range, for different times t giving values of $\sqrt{Dt}$ comprised between 0.3 and 2 μm, these values being ideal for the method employed here. It should be noticed that the temperature range studies was lower than the $\alpha \leftrightarrows \beta$ transition temperature for titanium.

Nuclear microanalysis.—Oxygen was analyzed by means of the nuclear reaction $^{16}O(d,p)^{17}O^*$, performed with a 900 keV deuteron beam. The energy spectra of the emitted protons were recorded at a 150° angle. The general features of the method, and its application to the measurement of diffusion profiles can be found in Ref. (22, 23). In the latter, this method was generally applied to the determination of diffusion profiles covering depths of several hundred microns, with the help of successive operations of mechanical grinding of the samples. In fact, the most convenient depth for each determination is less than 2 μm; if the concentration profile studied does not exceed this limit, it is possible to determine all its parameters by means of a single analysis (24, 25). To do this, we assume in fact that the profile is known, thus allowing us to calculate a particle energy spectrum, similar to the experimental one. This simulation involves principally two calculations of the energy loss for the charged particles through the matter (deuterons and protons), and the convolution of a theoretical ideal spectrum by a Gauss function (instrumental function). The calculated spectrum, then, has to be fitted to the experimental one, by adjusting the initially assumed concentration profile (26). To perform this work, a computer program has been used.

In fact, the depth of the profile may exceed the limits of each analysis to a small extent because fitting accuracy is only necessary in the range where the concentration decreases rapidly, which is not the case for the greatest depths.

Table I.

Impurities	O	Fe	N	H	C	Si
Rate (ppm weight)	930	650	150	50	170	250

Results and Discussion

Firstly, we have verified the validity of the method employed by studying a well-known sample with a homogeneous concentration of oxygen. The fit for a TA6V alloy, with a 2800 ppm oxygen content, is shown in Fig. 2. The experimental spectrum exhibits a narrow peak (A) typical of the surface oxide layer, and a plateau (B) which indicates the constant value of the bulk concentration.

The fitting treatments are performed on the experimental spectrum, after removing the surface layer peak. The good adjustment between the calculated curve and the experimental points is shown for the channel range 60-110.

In these conditions, the experimental spectra are fitted to a set of calculated curves obtained for different $\sqrt{Dt}$ values (Fig. 3). The apparatus parameters, such as the calibration (keV/channel), are easily integrated by the computer program.

Figure 4 gives an example of the fit obtained for the sample No. 6. The sample parameters and the results are given in Table II. All of the points, resulting from the four different methods, fall on a reasonably straight line which is the prolongation of the line obtained in the range 700°-950°C; its equation is

$$D = 0.45 \exp[-(200 \pm 30)\, 10^3/RT)] \quad \text{cm}^2/\text{sec}$$

It was assumed here, as a first approximation for calculating the D values, that the oxygen concentration profiles were erfc functions, and may be written

$$\frac{C - Co}{C_s - Co} = \frac{\operatorname{erfc} \dfrac{x + xo}{2\sqrt{Dt}}}{\operatorname{erfc} \dfrac{xo}{2\sqrt{Dt}}}$$

where C and C_s are, respectively, the concentration values as measured and at the metal-oxide interface; Co the initial oxygen concentration in the metal, and xo the distance between this interface and the initial surface of the sample. x is the experimental depth of analysis taken from the interface.

Table II.

Sample n^r	Temperature (°C)	Time	$\sqrt{Dt}$ (μm)	D (cm²/sec)
1	700	37 min	1.632	1.2×10^{-11}
2	700	2 hr 29 min	2.674	8.0×10^{-12}
3	648	4 hr 10 min	0.794	4.2×10^{-13}
4	616	20 hr 25 min	2.711	1.0×10^{-12}
5	562	87 hr 45 min	2.103	1.4×10^{-13}
6	540	70 hr 34 min	0.873	3.0×10^{-14}
7	502	50 hr 19 min	0.504	1.4×10^{-14}
8	459	71 hr 35 min	0.333	4.3×10^{-15}

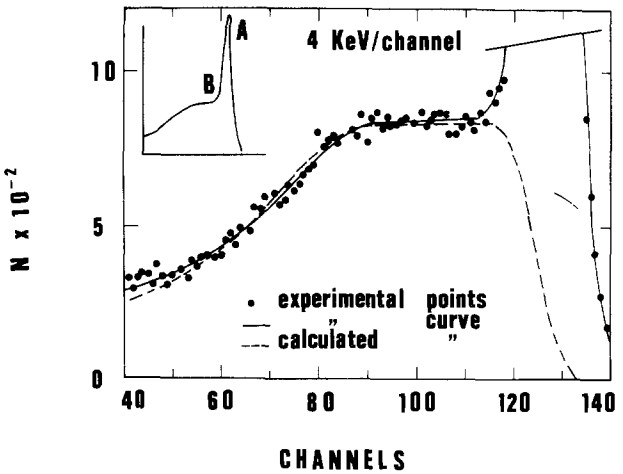

Fig. 2. Fit between a calculated spectrum and an experimental spectrum (homogeneous sample, containing 2800 ppm oxygen).

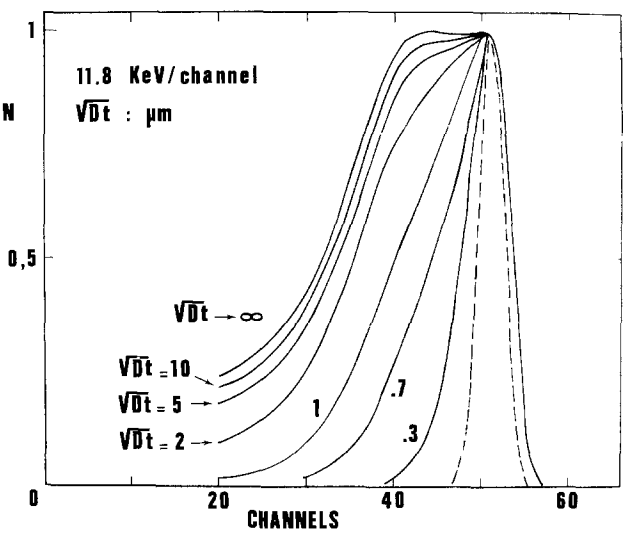

Fig. 3. Calculated spectra for some $\sqrt{Dt}$ values, and resolution curve

This relationship was found to be very convenient in our previous studies on oxygen diffusion in titanium and zirconium (16, 23, 27), under the following assumptions: constant diffusion coefficient D (independant of the oxygen content) and constant concentration at the interface metal-oxide. These studies were performed for diffusion times higher than the present ones, reaching 400 hr. We assume that the oxygen source strength is independent of time, and sufficient not to limit the diffusion process. This is valid here, because the anodic oxide film, partially dissolved into the metal, is still present after the thermal diffusion treatment (Fig. 5). The corresponding theory is further discussed in Ref. (23) and (27).

However, for some samples, the best fit results from a profile which is the sum of an erfc function and of an exponential function, the latter being necessary to take into account the spectrum range corresponding to the greatest depth. This particularity suggests perhaps two concomitant diffusion processes, including for example a grain boundary mechanism (24, 25). However, it is not easy to make a choice, because, as has been mentioned above, the fit using an exponential function is not very different from this obtained with an erfc function, for high depth values.

Finally, the understanding of the profiles by means of erfc functions is in agreement with our previous results obtained at higher temperatures and, especially, with those obtained by the strain aging method. As this latter technique is only related to bulk diffusion, our hypothesis is thus reinforced.

Conclusion

The particularity of the method described here is that by using mathematical treatment of the energy proton spectra

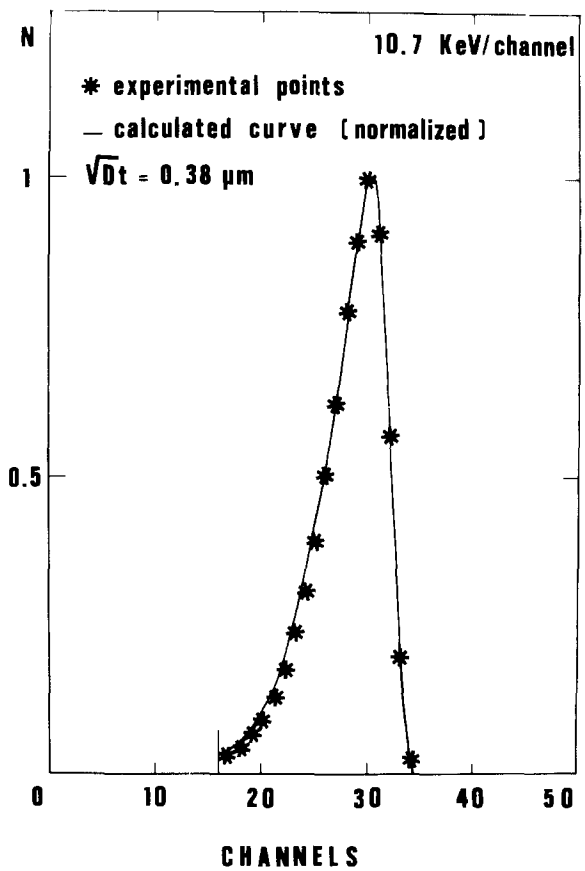

Fig. 4. Fit between a calculated and an experimental spectrum (variable oxygen rate vs. depth, $\sqrt{Dt}$ = 0.38 μm).

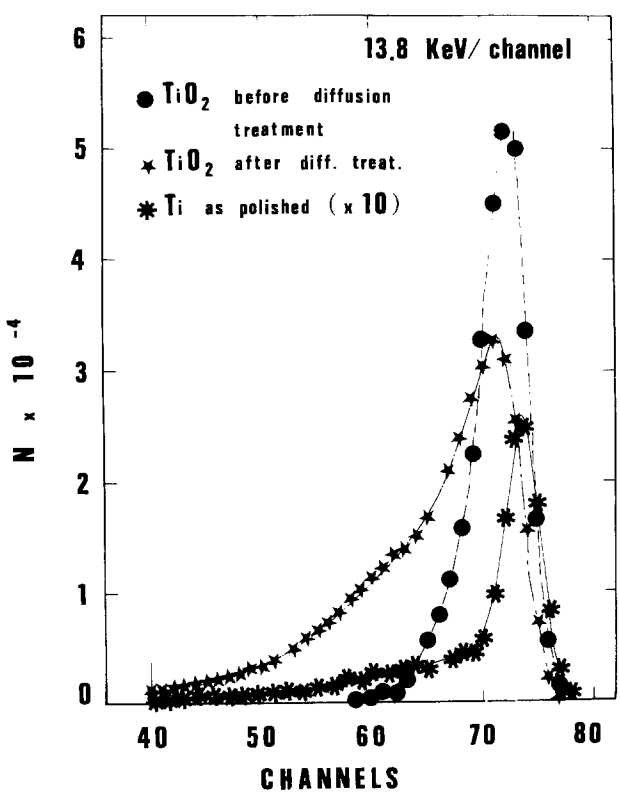

Fig. 5. Proton spectra at different specimen preparation times (treated sample: 650°C, 4 hr 10 min, $\sqrt{Dt}$ = 0.79 μm).

it is possible to calculate the diffusion profiles completely to a depth of 2 μm. It is thus a very convenient method for diffusion studies, where a low penetration occurs (low temperature or short diffusion time).

The diffusion coefficient values as calculated here are in good agreement with the one previously obtained, at lower

and higher temperatures. Thus, the collection of experimental plots is therefore nearly complete from 200° to 950°C. Taking into account the agreement between all these values, we can assume that the major diffusion process is a bulk one.

Acknowledgments

This work was supported by the Centre National de La Recherche Scientifique (ERA No. 910 and RCP No. 157). The authors wish to thank Dr. G. Amsel and the Groupe de Physique des Solides de L'Ecole Normale Supérieure (Paris) for performing the nuclear microanalyses.

Manuscript submited June 30, 1982; revised manuscript received *ca.* Feb. 23, 1983.

Any discussion of this paper will appear in a Discussion Section to be published in the December 1983 JOURNAL. All discussions for the December 1983 Discussion Section should be submitted by Aug. 1, 1983.

REFERENCES

1. E. A. Garcia, X. Lucas, G. Beranger, and P. Lacombe, *C. R. Acad. Sci., Ser. C*, **278,** 837 (1974).
2. P. Kofstad, "High Temperature Oxidation of Metals," John Wiley and Sons, Inc., London (1966).
3. G. Walwork and A. Jenkins, *This Journal*, **106,** 10 (1959).
4. J. Stringer, *Acta Metall.*, **8,** II (1960).
5. T. Hurlen, *J. Inst. Met.*, **89,** 128 (1960-61).
6. E. A. Garcia, *Met., Corros., Indus*, 638 (1978-79).
7. C. J. Rosa, *Metal. Trans.*, **1,** 2517 (1970).
8. W. P. Roe, H. R. Palmer, and W. R. Opie, *Trans. Am. Soc. Met.*, **52,** 191 (1960).
9. A. V. Revyakin, *Izv. Akad. Nauk, SSR*, **5,** 113 (1961).
10. L. Sokiryanskiy, D. Ignatov, and A. Shinyaev, *Fiz. Met. Metalloved.*, **28,** 287 (1969).
11. J. Com-Nougue, Thesis, Université of Paris XI, Paris, France (1972)
12. A. E. Jenkins, *J. Inst. Met.*, **82,** 213 (1954).
13. V. Tikhomirov and U. Dyachkov, *Zh. Prikl. Khim.*, **40,** 2405 (1967).
14. M. Dechamps and P. Lehr, *J. Less-Common Met.*, **56,** 193 (1977).
15. R. Feldman, M. Dechamps, and P. Lehr, *Met. Corros. Ind.*, **617,** 1 (1977); **619,** 105 (1977); **620,** 140 (1977).
16. D. David, E. A. Garcia, X. Lucas, and G. Beranger, *J. Less-Common Met.*, **65,** 51 (1979).
17. E. de Paula E. Silva, Thesis, Université of Paris XI, Paris, France (1972).
18. E. de Paula E. Silva, E. A. Garcia, and G. Beranger, "Journées d'Étude du Titane et de Ses Alliages," Nantes (1973).
19. Y. A. Bertin, Thesis, Poitiers (1979).
20. G. Beranger, D. David, E. A. Garcia, and X. Lucas, *Rev. Phys. Appl.*, **10,** 87 (1975).
21. F. Kover, Thesis, Fac. Sci. Paris, Paris, France (1967).
22. G. Amsel, J. P. Nadai, E. d'Artemare, D. David, E. Girard, and J. Moulin, Nucl. Inst. and Methods, **92,** 481 (1971).
23. D. David, G. Amsel, P. Boisot, and G. Beranger, *This Journal*, **22,** 388 (1975).
24. D. David, Thesis, Université Paris VII, Paris, France (1973).
25. G. Amsel and D. David, *Le Vide*, **177-178,** 130 (1975).
26. A. Choudhury, D. W. Palmer, G. Amsel, H. Curien, and P. Baruch, *Solid-State Commun.*, **3,** 119 (1965).
27. G. Amsel, G. Beranger, B. De Gelas, and P. Lacombe, *J. Appl. Phys.*, **39,** 2246 (1968).

Time-Resolved Optical Reflectivity and Emissivity during and after Chemical Vapor Deposition of Amorphous and Crystalline Silicon

A. M. Beers, H. T. J. M. Hintzen, and J. Bloem*

Research Institute of Materials, Department of Solid State Chemistry, University of Nijmegen, Toernooiveld N3096, 6525 ED Nijmegen, The Netherlands

ABSTRACT

In the temperature region 560°-800°C, the CVD of silicon from 2.3% SiH_4 in hydrogen at atmospheric pressure was investigated with optical techniques that were applied *in situ*. The crystallization of silicon layers, that grew amorphous, was studied during and immediately after growth with time-resolved optical reflectivity measurements. A new expression is derived which applies to the optical reflectivity of a layer, that at the same time both grows and undergoes a solid-state transformation process. Below $T' \approx 680$°C the crystallization rate of 1.6 μm thick CVD a-Si films was determined and found to depend on temperature with activation energy 2.9 eV. At higher temperatures, three-dimensional crystallization at nuclei, that were formed ($E_{act} = 9.0$ eV) at the surface of the growing material, is investigated. Application of the generalized Avrami equation for growth conditions leads to a new expression for the remaining amount of untransformed material at the end of growth. A limiting steady-state situation is described where this amount depends only on growth rate and nucleation/crystallization kinetics. Additional emissivity measurements allow the determination of the transition between amorphous and crystalline growth which was found to occur abruptly at $T^* \approx 766$°C. An expression is derived that describes the dependence of this transition temperature on growth rate.

In situ measurement of layer thicknesses by the detection of light that interfered with the layer is a widely used optical technique in scientific investigations as well as in industrial production control. In this paper, attention is especially focused on light from an external source that interferes after reflection by a layer of silicon during and after its growth from the gas phase. As a pendant to the technique that applies a continuous source with a range of wavelengths in order to determine a stationary thickness (1), here single-wavelength (laser) light is used in order to measure stationary growth velocities (2). Actually, in these experimental procedures, changes are measured in the optical pathlengths of the reflected rays upon change of wavelength or thickness in a given geometry. Therefore, in order to be able to determine layer thicknesses, the refractive index n of the material concerned should either be known or be determined in a separate experiment for the wavelength and temperature in question. It has been shown (3, 4), that with this knowledge the stationary growth velocity v_g of a stable deposit can be derived from the change of the intensity of the reflected light during growth according to

$$v_g = \Delta d \cdot \tau^{-1} \quad [1]$$

where during the duration τ of one oscillation in the recorded laser interference pattern the layer thickness increases with an amount $\Delta d = \lambda/2N$, with $N = (n^2 - n_0^2 \sin^2 \phi_0)^{\frac{1}{2}}$, n_0 is the refractive index of the gas atmosphere above the layer and ϕ_0 is the angle of incidence of light with wavelength λ.

In a recent paper (5), evidence was presented for the action of two different solid-state transitions which can take place during the deposition of silicon by chemical vapor deposition (CVD) from silane, namely, *(i)* the annealing

* Electrochemical Society Active Member.

Key words: semiconductor, reflectance, CVD, phase transformation.

(a-Si:H → a-Si) of a hydrogenated surface layer which was found (6) to be present during growth at temperatures below T' (~680°C) and *(ii)* the crystallization of amorphous silicon a-Si → c-Si. In this paper, we report on the findings of our investigations in connection with the latter transition *(ii)*.

Now, for stationary growth conditions, the constancy of τ in Eq. [1] cannot be taken for granted any longer and the conventional expression is in need of correction, when during deposition a second solid layer grows at the expense of the first one: If this second layer of material exhibits optical properties distinct from the first one, a more complicated situation arises. This is precisely what will occur during growth of amorphous silicon if crystallization in the freshly grown layer takes place at the same time. Such a process could to a certain extent explain the differences between various reports on the structure of silicon layers formed by CVD from silane. Some of these mention that the layers deposited are amorphous if grown below some definite temperature in the range 620°-700°C and crystalline at higher temperature (7, 8): whereas, others inform that these layers can be partially crystalline (9, 10). The technique of time-resolved reflectivity has lately been applied to follow laser-induced crystal growth kinetics in ion-implanted amorphous silicon (11). In this paper, the results are reported of *in situ* observations made during, as well as immediately after, depositions at systematically changed substrate temperatures in order to establish whether and, if so, to what extent crystallization takes place during deposition as an aftergrowth solid-state anneal process. To this end, a new model will be developed in order to analyze the laser interference pattern for the case of optical interference in a double growing layer system. In combination with the results of emissivity measurements, the transition between crystalline and amorphous growth is determined. Finally, a criterion will be formulated for the growth rate dependence of this transition.

Experimental Procedure

Silicon films were deposited at calibrated surface temperatures between 560°-800°C through pyrolytic decomposition of 2.3% SiH_4 in hydrogen at atmospheric pressure. This CVD process was carried out in a horizontal water-cooled reactor tube equipped with optical quartz windows, and the substrates were placed on an rf-heated, SiC-coated graphite susceptor. Using a ray of monochromatic light (He-Ne laser, $\lambda = 1.15$ μm) the intensity of the light that was reflected by the specimen during and after silicon growth on the Si_3N_4-coated silicon substrate was recorded. For maximum accuracy, the wavelength λ was chosen as low as possible, limited however by a sharply increasing absorption coefficient below $\lambda = 1.1$ μm. In addition, the thermal radiation emitted by the silicon layer on an adjacent silicon substrate was recorded for wavelengths between 1.9 and 2.6 μm.

In the appropriate temperature regions and for the wavelength considered, the refractive indexes of polycrystalline and amorphous silicon were found separately by determining the mean thickness increase per oscillation in the interference pattern as $\Delta d = D/p$. The total layer thickness D was measured at room temperature with a Tencor Alpha-step surface profiler, and the corresponding total number of oscillations p passed through in the time of growth was obtained from the recorded laser interference pattern. Growth was continued for 10.2 ± 0.1 oscillations in the interference pattern corresponding to approximately 1.6 μm layer thickness. After growth at temperatures below 650°C, the drawbacks of lengthy *in situ* anneals were evaded by annealing at a temporarily higher temperature. Further details of the experimental procedure have been published elsewhere (5, 6).

Experimental Results

Detailed measurements of oscillation duration τ by continuous monitoring of the deposition process at different growth temperatures resulted in the data which are compiled in the plots of Fig. 1. The determination of the refractive indexes resulted in $n_c = 3.69$, $N_c = 3.60$, and $\Delta d_c = 0.160$ μm/oscillation for polycrystalline layers grown around 800°C, and $n_a = 3.89$, $N_a = 3.81$, and $\Delta d_a = 0.151$ μm/oscillation for amorphous films around 600°C. As a first approximation, these values will be used throughout the temperature region investigated in view of the small temperature dependence of the refractive index of silicon single crystal in this region at the wavelength applied (12). In the calculation of the growth rates according to Eq. [1], two additional approximations were made: As the 6% difference between Δd_c and Δd_a would hardly show up in the semilog plot (Fig. 2) a value of 0.16 μm/oscillation was used for all experiments; as τ^{-1} changes during deposition, the value adopted was obtained as an average over the oscillations excepting the first one. Two further results are incorporated in the Arrhenius plot of the results of the growth rate measurements (Fig. 2), one connected with emissivity, the other with changes in optical pathlengths after deposition: *(i)* In contrast with growth experiments at lower temperatures, above $T^* = 766° \pm 7$°C the emissivity of the specimen was found to increase continuously during growth. Besides,

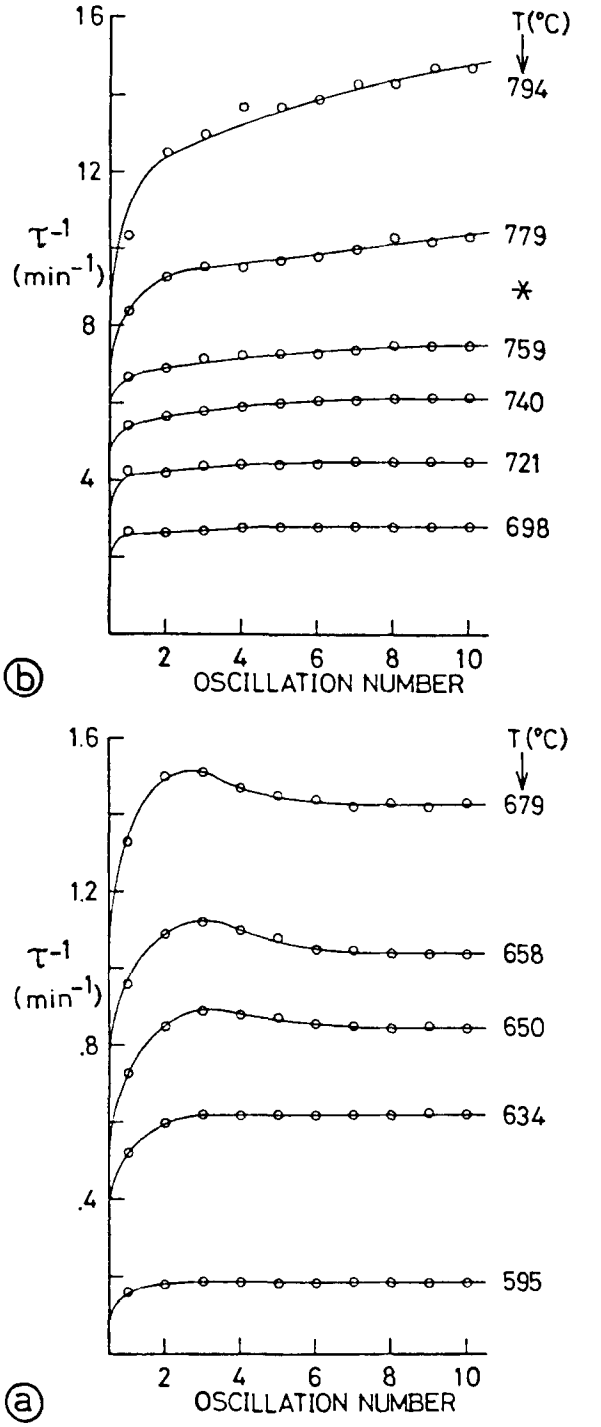

Fig. 1. The reciprocal of oscillation duration τ as a function of oscillation number showing the experimental points obtained from the laser interference potterns recorded during growth at different substrate temperatures.

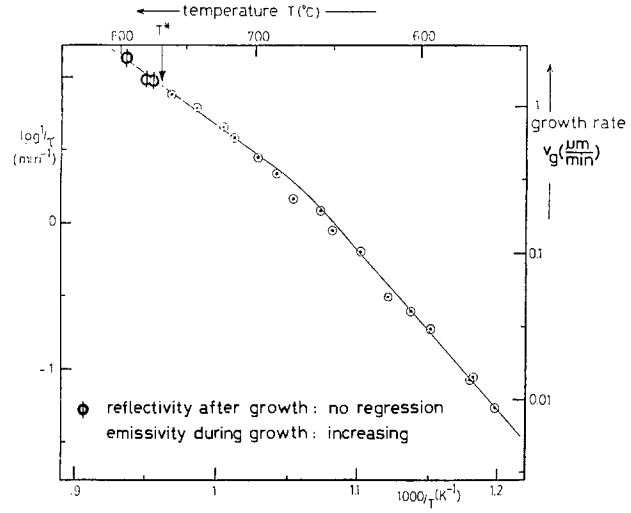

Fig. 2. Growth rate v_g logarithmically plotted as a function of the reciprocal of absolute surface temperature T. Above $T' \approx 680°C$, the slope of the curve corresponds to an apparent activation energy $E_{act} = 1.4$ eV, at lower temperatures $E_{act} = 2.2$ eV. The experimental points with deviating reflectivity and emissivity behavior (which are found to coincide) are separately indicated.

after the termination of growth effected by discontinuing the flow of silane, the increased emissivity remained constant at the same intensity as at the end of growth, if the specimen was kept at constant temperature in the same flow of hydrogen. *(ii)* Above the same temperature T^*, no changes were detected in the laser interference signal after the termination of growth. However, below this temperature, the recorded intensity signal appeared to double back its final trace after growth. The general shape of the interference pattern is represented in Fig. 3. Such a regression of the laser signal results from a decrease $r\lambda$ in optical pathlength difference of the reflected rays. In Fig. 3, it is shown that this difference is passed through in the corresponding time τ_r during growth. As over a full oscillation an additional optical pathlength difference λ is completed in time τ, it follows that regress ratio r is experimentally found as τ_r/τ. Figure 4 shows the result of the measurements of r as a function of growth temperature for the present growth/anneal experiments. The slope of this semilog plot corresponds to −3.9 eV. For experiments below about 620°C, no regression was detected immediately after the termination of growth. However, upon increasing the temperature, the regression was observed again.

Model for the Optical Reflectivity of a Double Growing Layer System

The intensity of the light that is reflected by a single layer system depends on thickness according to the well-known Airy formula for multiple-beam interference with a plane parallel plate (13). During growth, the time-dependence is given by the same formula if the growth rate and material

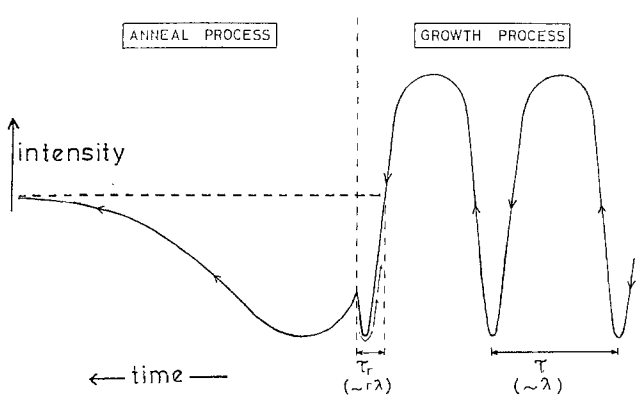

Fig. 3. General shape of a characteristic interference pattern showing the intensity of the reflected laser light as a function of time during as well as after growth.

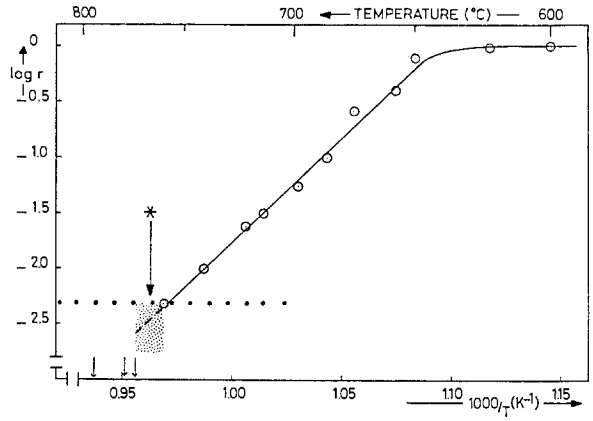

Fig. 4. Semilog plot of regress ratio r as a function of the reciprocal of absolute growth temperature (slope ~ −3.9eV). The dotted line represents the detection limit.

parameters are constant. The extinction condition is identical for both two-beam and multiple-beam interference and the minima, which, as opposed to transmission, are sharp in reflection, appear periodically. From Fig. 1, it follows, however, that oscillation duration τ is not constant at all in each of the present growth experiments. In order to understand this behavior, the concurrent action of a solid-state transformation process should be taken into account in addition to the growth process. As was already indicated at the beginning of this article, the crystallization of amorphous silicon is considered as an after-growth process (5). A simple model will be developed in order to obtain the expression for τ^{-1} for such a system, where the growth of a second (crystalline) layer at the expense of the original (amorphous) one is accounted for.

Consider a ray of monochromatic light (wavelength λ) that traverses a medium with refractive index n_o and hits a double-coated substrate at an angle of incidence ϕ_o (Fig. 5); the upper layer (thickness d_a) is assumed to represent amorphous silicon (refractive index n_a, density p_a), the lower layer (thickness d_c) crystalline silicon (refractive index $n_c < n_a$, density $\rho_c > \rho_a$). Considering the rays reflected at the outer surface and at the interface with the substrate, the intensity of the reflected light depends on their optical pathlength difference e (Fig. 5). Taking account of Snell's boundary conditions, it is found by application of standard theory that for the optical paths considered at time t

$$e(t) = 2N_a d_a(t) + 2N_c d_c(t) \qquad [2]$$

where for each layer (a, c) N is defined as indicated earlier. Changes of phase shift do not come into play for stationary growth conditions.

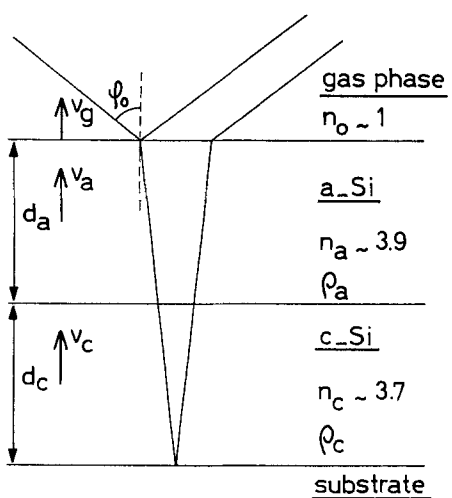

Fig. 5. Optical path in a simplified model for interference in a double growing layer system. The small refraction at the a-c interface is accounted for in the formulas but hardly shows up in this figure (experimentally: $\phi_o = 53°$).

Now the rate v_a of thickness increase of the amorphous layer is made up of two contributions, viz. *(i)* an increase v_g associated with the net particle flux across the gas-solid interface due to deposition from the gas phase, and *(ii)* a decrease $-\rho v_c$ associated with crystallization of the amorphous material, where v_c is the rate of thickness increase of the crystalline layer and the factor $\rho \equiv \rho_c/\rho_a$ (>1) is inserted to account for the difference in specific density (conservation of mass). For constant growth rate v_g it follows that

$$v_a(t) = v_g - \rho v_c(t) \quad [3]$$

and substitution into Eq. [2] leads with $v_c[t] \equiv \frac{d(d_c(t))}{dt}$ to

$$e(t) = 2N_a v_g t + (2N_c - 2N_a\rho)\int_0^t v_c(t)dt \quad [4]$$

For successive extinctions in the interference pattern, the optical pathlength difference changes by an amount equal to the wavelength

$$e(t + \tau) - e(t) = \lambda \quad [5]$$

An implicit expression for τ^{-1} is derived from Eq. [4] and [5]

$$\tau^{-1} = \left[1 + (\nu - \rho)\int_t^{t+\tau} v_c(t)dt/\tau v_g\right](2N_a/\lambda)v_g \quad [6]$$

where $\nu \equiv N_c/N_a$(<1). In this expression, the term $2N_a v_g/\lambda$ represents amorphous growth in the absence of crystallization; whereas, for $v_g = 0$, the remaining term accounts for the changes during annealing.

The significance of Eq. [6] extends beyond the material system investigated at present: It is equally valid for conversions such as solid-state segregation or decomposition processes, be it during deposition or not. Although Eq. [6] is specifically derived for a double growing layer system, the model developed is also valid for systems where the same total volumes of material are not arranged in such a layer-like fashion. In that case, however, rate v_c should be taken as the volume increase per unit area and unit time. For the special case of a time-independent crystallization rate v_c (which will be too naïve an approach if three-dimensional crystallization takes place in the bulk of the amorphous matrix), an explicit expression is obtained

$$\tau^{-1} = [1 + \eta v_c/v_g](2N_a/\lambda)v_g \quad [7]$$

where $\eta \equiv \nu - \rho$(<0).

Failing precise data regarding $v_c(t)$, Eq. [7] will be used as a first approximation in the evaluation of the τ^{-1}-plots instead of the more general Eq. [6]; application of the latter equation requires detailed knowledge of the mechanism of the particular nucleation and crystallization processes involved. Of course, for the special case that v_c equals zero the expression between square brackets becomes redundant and the conventional form (Eq. [1]) reappears. Observe also, that for the present case, where the value of η is negative, solid-state crystallization during amorphous deposition will result in a decrease of τ^{-1} as compared with the stationary growth of the amorphous deposit without solid-state transformation.

Analysis and Discussion

Refractive index.—As high-temperature values of the refractive index of polycrystalline and amorphous silicon films are not readily available from literature, a comparison with the presently-reported values is impeded. However, when the value of the polycrystalline films ($n = 3.69$) is compared with $n = 3.70$ as obtained after extra polation ($\lambda = 1.15$ μm; 1000 K) of the recommended data (12) for silicon single crystal, good correspondence is found. It has been observed (12) that the refractive indexes of pure silicon "thin" films tend to agree with those of bulk crystal if the films are deposited on substrates maintained at high temperatures during deposition or appropriately annealed after deposition. Nevertheless, for the thinnest films, a substantially lower (up to ~50%) value has been reported, and it was concluded from ellipsometry measurements at 620°C that the refractive index of growing layers gradually increases until the bulk value is reached at about 500Å layer thickness (14). Lacking high temperature data from literature, no direct comparison can be made for the amorphous films. However, a 5% higher value of the refractive index as compared to polycrystalline silicon films has also been reported (9, 15) for the room temperature values of CVD silicon films ($\lambda = 3$ μm).

τ^{-1}-plots.—In the temperature range of interest, the silane content of the gas phase was chosen such as to cover a large range of growth rates (Fig. 2). At the lowest temperatures (~560°C), the amorphous films grown did not crystallize; at the highest temperatures applied (~800°C), the films formed were crystalline, while gas-phase nucleation (14) was still prevented. The changes in the τ^{-1}-plots during each growth experiment, as given in Fig. 1, will be related to the deposition processes. It is found that τ^{-1} increases sharply before the second oscillation. This effect can be understood, Eq. [1], as the result of the increase of the refractive index, as well as the increase of the growth rate, in the first stages of growth. An initial increase of the growth rate results as a consequence of the particular way of nucleation of these layers (17); after the formation of a definite density of nuclei, these nuclei start to grow out and their surface area progressively increases. In this way, the growth rate, which is surface-controlled, increases until coalescence of the growing nuclei sets in. The optical layer model should be applied with caution to this very distinct physical situation; the growing, discontinuous layer of silicon clusters on Si_3N_4 can even cause an additional (small) phase shift as the nature of the interface changes. With the relatively high supersaturations used in the present study, however, the time needed to form a continuous silicon layer will be short compared to the value of τ.

For all but the first oscillation, τ^{-1} is found to remain constant for the growth experiments below about 620°C. This situation is covered by the conventional model for growth of stable deposits. Going to higher deposition temperatures, however, the plots in Fig. 1 show the development of a pronounced maximum. Such a maximum is not predicted either by the conventional model of optical interference, or by the model for a double growing layer system as derived above. This is not surprising as both do not account for the genesis of the second layer. For anneal experiments, it has been reported (18) that before crystallization of amorphous silicon takes place, an induction time ("delay time") is first passed through. It is only after this period in which stable crystalline nuclei are formed and $v_c = 0$, that crystallization takes place and $v_c > 0$. This behavior accounts for the maximum in the τ^{-1} plots as, in full agreement with the double growing layer model Eq. [7], the value of τ^{-1} decreases upon crystallization until it reaches a constant value for stationary growth/crystallization conditions. Observe (Fig. 1) that direct introduction of the Heaviside step function centered a definite induction time will not do to switch on v_c in Eq. [7] because of the different thermal histories at the successive heights in the growing layer. It follows, that under these circumstances, crystallization starts near the interface with the substrate and extends progressively into the amorphous layer; the optical model closely parallels the physical situation (interface-induced, unidirectional crystallization). It is also found (Fig. 1) that going towards higher temperatures the relative height of the maximum in the τ^{-1} plots increases, indicating, Eq. [7], that v_c/v_g increases. This corresponds to a higher activation energy for crystallization as compared to growth.

Going towards still higher temperatures, above $T' \approx$ 680°C, no such maximum as described above in the τ^{-1} plots is found anymore. In the light of the preceding discussion, this means that the delay time for the incubation of crystalline nuclei in the amorphous material falls within the first oscillation and become negligible. Above this temperature T', where the specimen grows without a hydrogenated layer near the surface (6), a contribution to the crystallization at nuclei originating from the surface of the growing material can no longer be excluded as, indeed, free surfaces are well-known to be the first among the places where the nucleation of a new phase will start (19).

Although growth is still amorphous, subsequent formation of crystalline nuclei at the surface of the unstable solid leads upon further deposition to buried nuclei which act as active growth centers for crystallization. In addition to the unidirectional crystallization discussed above, the contri-

bution of this type of three-dimensional crystallization increases for increasing temperatures.

In the absence of a maximum in the τ^{-1} plots, a gradual increase of τ^{-1} becomes apparent. This increase extends over a larger number of oscillations for higher temperatures and is observed below as well as above $T^* = 766°C$, which is the transition temperature for amorphous/crystalline growth (see below). In view of this and according to Eq. [1], this phenomenon is interpreted as a transient in the growth rate. After the initial increase, a stabilization is found after 1.3 ± 0.2 min for growth rates between 0.4-1.2 μm/min. Such transients associated with the deposition of silicon were recently reported (20); their existence was derived from a detailed examination of the dopant profiles in epitaxial films, but a deeper understanding as to their origin still awaits further investigation.

Anneal experiments.—From the results of the *in situ* anneals immediately after the termination of growth, the amount of amorphous material in the layer at the end of growth can be obtained. At the end of growth when p oscillations are passed through and the film is partly amorphous (~thickness d_a), partly crystalline (~thickness d_c) the optical path length difference between the reflected rays is given by

$$2 N_a d_a + 2 N_c d_c = p\lambda \quad [8]$$

Upon crystallization of the amorphous material, the optical pathlength difference decreases with an amount $r\lambda$ (Fig. 3) and becomes

$$2 N_c d'_c = (p - r)\lambda \quad [9]$$

where the final thickness

$$d'_c = d_c + \rho^{-1} d_a, \; \rho \equiv \rho_c/\rho_a \quad [10]$$

From Eq. [8]-[10], it follows that the amorphous layer thickness at the end of growth is directly proportional to regress ratio r

$$d_a = kr\lambda/2 \quad [11]$$

where

$$k \equiv (N_a - \rho^{-1} N_c)^{-1} \quad [12]$$

Also

$$d_c = (p - kN_a r)\lambda/2N_c \quad [13]$$

Experimentally, it is found (Fig. 4), that r is stationary for temperatures below about 620°C; no crystallization occurs during growth, the specimen is fully amorphous ($d_c = 0$), and d_a (and consequently r) will attain a maximum value. For growth at 600°C ($p = 10.19$; $r = 1.040$), k was evaluated according to Eq. [13]

$$k = p/N_a r = 2.57$$

and comparison with definition Eq. [12] then leads to $\rho^{-1} = 0.95$, which corresponds to a 5% difference in specific density in good agreement with the values known from literature (21). Going towards higher temperatures (Fig. 4), the decrease of regress ratio r is found to coincide with the development of a maximum in the τ^{-1}-plots (Fig. 1); crystallization takes place during growth. In view of Eq. [11], the region with constant slope in the Arrhenius plot of r corresponds to an exponentially decreasing amount of amorphous material with increasing temperature. This clearly illustrates the progressively increasing impact of crystallization during growth even though the growth times applied become continually shorter.

In order to analyze the observed temperature dependence, consider a slab of material with thickness $v_g dt$ at a height $v_g t$ in the layer. When growth terminates at time $t_g = D/v_g$, where D is the total thickness of material deposited, the thermal history of this layer is t_g-t and according to the general relation of Avrami (22), the volume fraction of uncrystallized material in this layer is given by

$$d(d_a)/v_g dt = \exp\{-A(t_g - t)^m\}$$

where $A = A_o \exp(-Q_A/RT)$ and $m(>0)$ are parameters directly related to the particular nucleation/growth mechanism which is operative in these layers. It follows, that at $t = t_g$ the total remaining amorphous layer thickness amounts to

$$d_a = v_g \int_{t=0}^{t=t_g} \exp\{-A(t_g - t)^m\} dt \quad [14]$$

Upon series expansion of the exponential and subsequent integration, the integral is evaluated as a convergent series

$$d_a = D \sum_{n=0}^{\infty} c_n X^n \quad [15]$$

where $c_n = (-1)^n/n!\,(mn + 1)$ ($\neq 0$) and $X = At_g^m$. The latter quantity depends on temperature with an activation energy $(Q_A - mQ_g)$, where Q_g is the activation energy for growth, and for a comparison with the experimentally found exponential temperature dependence of d_a (Fig. 4), the question is asked, whether the right-hand side of Eq. [15] can be expressed in the form aX^b. However, in view of the uniqueness of a power series expansion, this question must be answered in the negative. As an important consequence, it is concluded that within the model formulated, the observed anneal phenomena exclude the action of a single nucleation/growth mechanism. This result is in agreement with our findings in the discussion of the τ^{-1}-plots; at lower temperatures, interface-induced unidirectional crystallization with constant transformation rate predominates (mathematically: $m = 1$, $0 \leq At_g << 1$); whereas, going towards higher temperatures ($>T'$), the contribution of three-dimensional growth ($3 \leq m \leq 4$) in the bulk of the amorphous matrix becomes increasingly important. Of course, lack of knowledge of the separate contributions of the two nucleation/growth mechanisms in the crystallization of these layers during deposition prevents to account quantitatively for the slope of log r *vs.* $1/T$ that was found experimentally. However, these data can be used with confidence in an analysis of the limiting case of pure one-dimensional crystallization during growth at temperatures below $T' \approx 680°C$. According to the simple model valid for this special case, the rate of crystallization is given by

$$v_c = (D - d_a)/(t_g - t_o^c) \quad [16]$$

where d_a was calculated according to Eq. [11], and the induction time for crystallization t_o^c was estimated at the time that passed before the maximum in the τ^{-1} plot was reached. The results are presented in a semilog plot (Fig. 6) and compared with the results for unidirectional crystallization by Zellama *et al.* (23), who studied the crystallization kinetics of evaporated amorphous silicon layers through conductivity measurements. Excellent agreement is found upon comparison of the two sets of measurements above and below 620°C, respectively; the slope of the straight line through the points corresponds to an apparent activation energy of 2.9 ± 0.1 eV. This activation energy is higher than that for growth from the gas phase in the temperature region concerned (2.2 eV, see Fig. 2), which indeed conforms to the finding in the discussion of the τ^{-1}-plots. Exactly the same activation energy (and a curve shifted over approx. 15°C towards higher temperatures) has been reported in a study of the kinetics of crystallization of unsupported evaporated amorphous silicon films investigated through direct observation by hot stage transmission electron microscopy in the 550°-700°C temperature range (24). In accordance with the double-mechanism interpretation arrived at in the preceding discussion of both the τ^{-1}-plots and the temperature dependence of log r, systematic deviations from the straight line behavior are apparent above T', where the model does not apply. In this respect, it is of interest to compare the present crystallization kinetics also with reports on solid phase epitaxy (SPE) of Si-implanted amorphous silicon. There, an activation energy in the range 2.3-2.6 eV is generally reported (25, 26) for epitaxial regrowth (unidirectional crystallization) in the same temperature range as covered in Fig. 6. At much higher temperatures produced by cw laser annealing, however, three-dimensional growth on randomly distributed, crystalline nuclei in the bulk of the amorphous matrix was recently found (11) to constitute a process competitive to SPE and to give rise to a flattening of the log v_c *vs.* $1/T$ curve towards higher temperatures similar to Fig. 6. In the present straightforward approach, Eq. [16] represents the rate of crystallization accurately if crystallization occurs through a uniform translation of the crystallization front and crystalline fraction $x_c = d_c/D$ is linear in t. However, if x_c as a func-

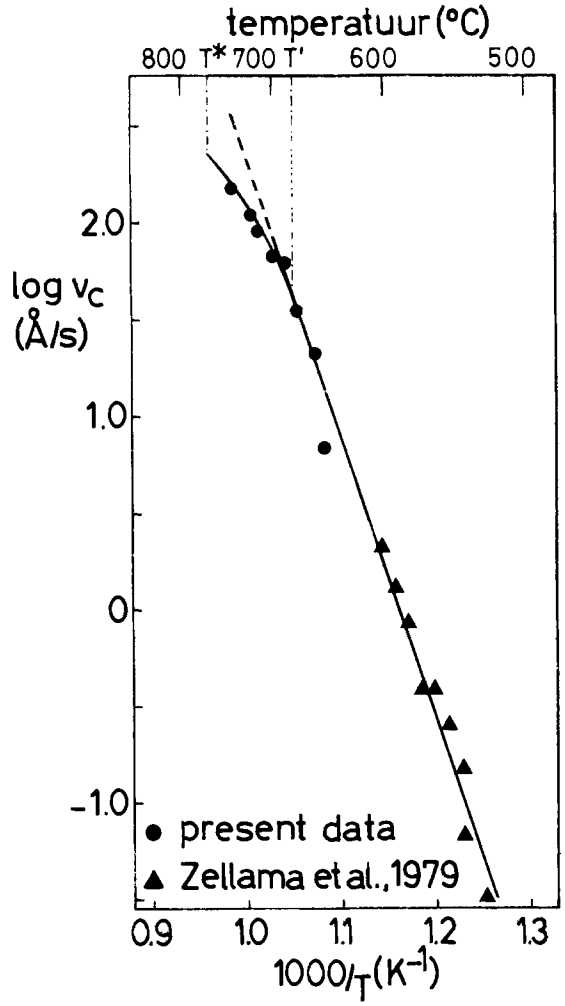

Fig. 6. Arrhenius plot of the rate of one-dimensional crystallization of amorphous silicon. The present data are compared with those from Ref. (23).

tion of anneal time is given by an S-shaped curve, such as occurs in the nucleation and growth of randomly distributed nuclei, the quantity $Dx_c/t_g - t_o^c$ cannot be interpreted meaningfully as a crystallization rate and, especially for the final anneal stages, too low a value will be obtained. Observe, that for $x_c \to 1 (d_a << D, t_c^0 << t_g)$, the v_c value obtained according to Eq. [16] eventually approaches v_g and so does its temperature dependence ($\downarrow$ 1.5eV see Fig. 2).

Of special interest is the limiting case of amorphous growth, where bulk three-dimensional crystallization eventually fully predominates. Upon a standard change of variable [$(\chi = A(t_g - t)^m$], Eq. [14] is transformed to

$$d_a = v_g A^{-1/m} \frac{1}{m} \lambda\left(\frac{1}{m}, X\right) \qquad [17]$$

with incomplete gamma function $\gamma\left(\frac{1}{m}, X\right) = \int_0^X e^{-\chi} \chi^{\frac{1}{m}-1} d\chi$. As for each growth/anneal experiment, A has a fixed value, the limiting value of d_a for increasing t_g is found for $X = At_g^m \to \infty$, where the resulting improper integral of the first kind is evaluated as the gamma function $\Gamma(1/m)$

$$\lim_{t_g \to \infty} d_a = \bar{d}_a = v_g A^{-1/m} \frac{1}{m} \Gamma\left(\frac{1}{m}\right) \qquad [18]$$

The physical significance of this equation is that during the unidirectional growth (growth rate v_g) of a solid, that undergoes a solid-state transformation with a nucleation/growth mechanism described by the generalized Avrami equation (A, m), the amount of untransformed material eventually reaches a finite limiting value; the magnitude of this steady-state value depends solely on v_g, A, and m according to Eq. [18]. Using a series expansion for $\gamma(1/m, X)$ (cf. Eq. [15] and [16]), we calculated the values $X_{0.95}$ of X for which the limiting values $\Gamma(1/m)$ are reached within 5%.

Table I.

m	$\frac{1}{m}\Gamma\left(\frac{1}{m}\right)$	$X_{0.95}$	$t_{g\,0.95}(A^{-1/m})$
1	1.00	3.0	3.0
2	0.89	2.0	1.4
3	0.89	1.7	1.2
4	0.91	1.3	1.1

These values are listed in Table I together with the corresponding growth times $t_{g,0.95}$ (in units $A^{-1/m}$) for a given nucleation/crystallization mechanism, *i.e.*, a given $A^{-1/m}$.

The steady state may not be reached in all experiments at temperatures above T': especially at the lower temperatures in this range unidirectional crystallization must be expected to occur to a large extent as compared to three-dimensional crystallization (see also the SPE experiments mentioned above). However, when the latter process predominates, it is not self-evident from Eq. [18] that going towards higher temperatures this condition remains fulfilled, not only because t_g decreases, but, even more important, A no longer has a fixed value. However, by transforming Eq. [17] into

$$d_a = DX^{-1/m} \frac{1}{m} \gamma\left(\frac{1}{m}, X\right) \qquad [19]$$

(see Eq. [15]), the temperature dependence of X which contains both t_g and A is easiest evaluated. It is found that at the same values of X for which $\gamma(1/m, X)$ is approximated by the limiting, constant value $\Gamma(1/m)$, d_a follows the temperature dependence of $X^{-1/m}$

$$\bar{d}_a = DX^{-1/m} \frac{1}{m} \Gamma\left(\frac{1}{m}\right) \qquad [20]$$

Conversely, in view of Eq. [11] X is found to increase indeed at increasing temperatures with activation energy 3.9 m (eV) ($m > 0$) indicating that the steady state is approached the better, the higher the temperature. This illustrates the increasing impact of three-dimensional crystallization going towards higher temperatures. In general, the limiting form Eq. [18] may be preferred as compared to Eq. [20] because of the absence of D and t_g. For a further analysis of our experimental data with Eq. [18], the particular nucleation growth mechanism, A and m, has to be assessed. These parameters cannot be learned from the present anneal data alone. However, in the discussion of the τ^{-1}-plots with respect to the crystallization mechanisms, the importance of surface-induced nucleation has been stressed for growth at temperatures above T'. On this basis, the meaning of A and m is evaluated.

Let the number of crystalline nuclei, which are formed at the surface per unit surface and unit time be given by the (time-independent) surface nucleation rate v_n, then the resulting nucleus density N_o is inversely proportional to v_g according to

$$N_o = v_n / v_g \qquad [21]$$

During growth, these nuclei are buried and subsequently these "pre-existing" nuclei start to grow out in three dimensions with isotropic growth rate v_c. For this case of site saturation, the quantities A and m are expressed (22) by

$$A = \frac{4\pi}{3} N_o v_c^3 \quad \text{and} \quad m = 3 \qquad [22]$$

Combining Eq [11], [18], [21], and [22], the surface nucleation rate is found according to

$$v_n = \left[\frac{3}{4\pi}\left(\frac{k\lambda}{2}\right)^{-3}\left\{\frac{1}{3}\Gamma\left(\frac{1}{3}\right)\right\}^3\right] v_g^4 r^{-3} v_c^{-3}$$

In the temperature range that r was obtained with $Q_r = -3.9$ eV, the activation energies of v_g and v_c were found resp. as an average value ($Q_g = 1.5$ eV) and upon extrapolation ($Q_c = 2.9$ eV). Substituting the temperature dependencies of v_g, r, and v_c, respectively, the surface nucleation rate is found to be thermally activated with apparent activation energy $Q_n = 4(1.5) - 3(-3.9) - 3(2.9) = 9.0$ eV. Exactly the same value was reported (23) by Zellama *et al.* for the bulk nucleation rate in amorphous silicon deposited at room temperature.

As bulk nucleation will preferentially occur along the internal surfaces of that slightly porous material, the two values are not necessarily mutually exclusive, but are probably in perfect agreement. However, failing knowledge of the internal surface area per unit volume, a direct comparison of the absolute values of the two nucleation rates is impeded.

Until sofar, the various processes of crystallization of amorphous silicon during chemical vapor deposition were qualitatively and quantitatively evaluated. We shall continue to consider the transition between the presently discussed limiting case of three-dimensional crystallization of silicon that grew amorphous and the situation at still higher temperatures, where silicon is known to grow in a crystalline fashion.

Emissivity measurements and the transition between amorphous and crystalline growth.—The increasing emissivity observed during growth at constant temperature ($>T^*$) indicates a continuing change of composition of the material near the surface or of the surface condition itself (27). Here, an increasing microscopic roughness of the surface is involved, which finds expression as an apparent increase of the absorption coefficient. This phenomenon is typically related to a (poly)crystalline growth mode and more specifically with the evolution of crystallographic texture during growth of silicon (7) at temperatures above T^*. It is judged that emissivity measurement proves to be a sensitive technique to distinguish between either crystalline or amorphous growth during deposition. According to these measurements, the transition between amorphous and crystalline growth is rather abrupt in the sense that the observed emissivity phenomenon was found to be either absent or present to a considerable degree.

It is of interest to connect these results with the findings of the anneal experiments (Fig. 4). Unfortunately, a direct comparison is not readily possible because the determination of regress ratio r at lower values is inhibited by a detection limit of approximately ½% in the present experiments. Aware of this complication, an extension of the present experimental results into the uncertain region leads upon a cautious extrapolation of the straight line (Fig. 4) to transition value $r^* = (3.6 \pm 0.8)\,10^{-3}$ at transition temperature $T^* = 766° \pm 7°C$. According to Eq. [11] and using the value of k derived for "bulk" material, this would correspond to a limiting amorphous layer thickness of $\bar{d}_a^* = 53 \pm 12$Å at the transition and we are led to conclude, just as indicated by the emissivity measurements, that according to the present experimental findings an abrupt, discontinuous transition exists between amorphous and crystalline growth of silicon by chemical vapor deposition. A discontinuous order-disorder phase transition was also recently reported (28, 29) for the microcrystalline/amorphous transition based on x-ray diffraction and Raman measurements after glow discharge deposition of silicon.

The value of $\bar{d}_a^*$ derived concerns the total amount of amorphous material irrespective of its layer geometry and may suffer from an inaccuracy due to a possibly inadequate value of k for the very thin layer involved. Besides, the theory used is of limited applicability on a nearly atomic scale. Furthermore, as questions can be raised as to the smoothness of the surface on an atomic scale during amorphous growth, the significance of this minimum value can not be ascertained at present. An attempt to relate this value to the existence of stable clusters of 25.4Å mean diam that were reported (30) to be involved in crystalline as well as in amorphous growth of silicon, could land us in the realm of sheer speculation. Instead, the transition will be treated as a kinetical phenomenon and, although the present results are pertinent to the experimental conditions applied, their significance will be extended beyond the limitations set by these in order to infer the temperature dependence of the growth rate for which the transition occurs. Such a dependence must be expected in view of the nature of the transition as discovered above. According to Eq. [18], a smaller $\bar{d}_a$ value and eventual crystalline growth can be obtained not only by increasing the temperature but also by decreasing the growth rate with roughly the same nucleation growth kinetics for crystallization at the same temperature. The anticipated decrease of the transition temperature on decreasing growth rate could also partly explain the lower transition temperatures reported in literature as compared to the present value.

At the transition

$$v_g(T) = v_g^* \qquad [23]$$

and according to Eq. [11], the transition temperature T^* was experimentally found for amorphous layer thickness

$$\bar{d}_a(T) = \bar{d}_a^* \qquad [24]$$

Combining Eq. [23] and [24], that determine the rate and thickness involved, the simultaneity of growth and crystallization at the transition is expressed by characteristic lifetime $\bar{d}_a^*/v_g^*$, and it follows that at the transition

$$v_g^* = \bar{d}_a^* \cdot v_g(T)/\bar{d}_a(T) \qquad [25]$$

Upon generalization and substitution of the values mentioned above, the growth rate at the transition is found to depend on temperature with activation energy 1.5 + 3.9 = 5.4 eV, which according to Eq. [18] is the activation energy of $A^{1/m}$. According to this result, a considerable shift of the transition temperature towards lower temperatures is to be expected for growth at smaller rates (<700°C below 0.2 μm/min). Still lower values reported (7, 8) for chemical vapor deposition of undoped silicon at normal pressure can be related to crystallization during and immediately after growth. It is noteworthy that in the present interpretation the transition between crystalline and amorphous growth is fully determined by the nucleation/growth kinetics of the crystallization of amorphous material. Work is in progress to verify this interpretation by an experimental investigation of the transition as a function of growth rate and temperature. Both kinetic and structural aspects will be subjects of a future paper (31).

Summary and Conclusions

In situ techniques are indispensable in the study of after-growth solid-state anneal processes, which occur during growth. Laser interference patterns obtained during growth of silicon were found to deviate significantly from those reported so far. The theory of time-resolved optical reflectivity during deposition of solid films is extended in order to cover the case of growth in combination with a solid-state transformation. Application to the combined effects which result from a 5% change in refractive index, as well as in specific density upon crystallization during and after chemical vapor deposition of amorphous silicon from SiH_4, not only leads to a fuller understanding of the laser interference pattern but also yields detailed information on the mechanism and extent of crystallization. Two crystallization mechanisms were discerned: *(i)* At lower temperatures unidirectional crystallization was found to predominate and was related to the different thermal histories at the various heights in the growing layer; the crystallization rate during growth was determined as a function of temperature ($E_{act} = 2.9$ eV). *(ii)* At higher temperatures, the crystallization at nuclei distributed throughout the amorphous layer becomes increasingly important; the rate of formation of these nuclei, which presumably originate from the surface of the material growing without hydrogenated surface layer, depends on temperature with $E_{act} = 9.0$ eV. The analysis of growth at constant rate in combination with a solid-state transformation process, which is described by the generalized Avrami equation, shows that eventually the layer of untransformed material takes a constant finite thickness. Such a finite thickness was also found for the borderline case where amorphous growth switches over to crystalline growth. This transition was detected at 766°C with both reflectivity and emissivity measurements and a criterion was derived that describes the temperature dependence of the growth rate at the transition ($E_{act} = 5.4$ eV).

In conclusion, it is remarked that the final structure of the deposited material evidently depends on the growth process as well as on the anneal process(es) that take place at the same time. Consequently, not simply just the deposition temperature but the kinetics and mechanism of growth and anneal process(es) have to be considered in order to understand the origin of the resulting structure.

Acknowledgments

The authors are especially indebted to Mr. T. Lemmens for his skilled craftsmanship in effectuating the required modifications with respect to the quartz reactor tube. The

investigations were supported in part by the Netherlands Foundation for Chemical Research (SON) with financial aid from the Netherlands Organization for the Advancement of Pure Research (ZWO).

Manuscript submitted Nov. 19, 1982; revised manuscript received Feb. 3, 1983.

Any discussion of this paper will appear in a Discussion Section to be published in the December JOURNAL. All discussions for the December 1983 Discussion Section should be submitted by Aug. 1, 1983.

The University of Nijmegen assisted in meeting the publication costs of this article.

REFERENCES

1. C. J. Dell'Oca, *This Journal*, **119**, 108 (1972).
2. K. Sugawara, T. Yoshimi, and H. Okuyama, *ibid.*, **121**, 1235 (1974).
3. W. R. Runyan, "Semiconductor Measurements and Instrumentation," p. 165, McGraw-Hill Book Co., New York (1975).
4. J. Bloem and L. J. Giling, in "Current Topics in Materials Science," Vol. I. E. Kaldis, Editor, p. 147, North-Holland Publishing Company, Amsterdam (1978).
5. A. M. Beers, H. T. J. M. Hintzen, and J. Bloem, in "Proceedings of the 2nd European Conference on Solid State Chemistry, Veldhoven, The Netherlands, June 1982.
6. A. M. Beers and J. Bloem, *Appl. Phys. Lett.*, **41**, 153 (1982).
7. T. I. Kamins and T. R. Cass, *Thin Solid Films*, **16**, 147 (1973).
8. R. M. Anderson, *This Journal*, **120**, 1540 (1973).
9. M. Janai, D. D. Allred, D. C. Booth, and B. O. Seraphin, *Sol. Energy Mater.*, **1**, 11 (1979).
10. F. Hottier and R. Cadoret, *J. Cryst. Growth*, **56**, 304 (1982).
11. S. A. Kokorowski and G. L. Olson, in "5th Int. Conf. on Vapor Growth and Epitaxy," p. 153, San Diego, July 19-24, 1981.
12. H. H. Li, *J. Phys. Chem. Ref. Data*, **9**, 561 (1980).
13. M. Born and E. Wolf, "Principles of Optics," p. 326, Pergamon Press, London (1959).
14. F. Hottier and J. B. Theeten, *J. Cryst. Growth*, **48**, 644 (1980).
15. F. Schwidewski, *Thin Solid Films*, **18**, 45 (1973).
16. T. U. M. S. Murthy, N. Miyamoto, M. Shimbo, and J. Nishizawa, *J. Cryst. Growth*, **33**, 1 (1976).
17. W. A. P. Claassen, Thesis, University of Nijmegen, The Netherlands (1981).
18. M. W. von Allmen, S. S. Lau, J. W. Mayer, and W. F. Tseng, *Appl. Phys. Lett.*, **35**, 280 (1979).
19. D. A. Porter and K. E. Easterling, "Phase Transformations in Metals and Alloys," p. 276, Van Nostrand Reinhold Company Ltd., New York (1981).
20. R. Reif and M. Vanzi, *This Journal*, **128**, 2187 (1981).
21. M. H. Brodsky, M. A. Frisch, and J. F. Ziegler, *Appl. Phys. Lett.*, **30**, 561 (1977).
22. J. W. Christian, "The Theory of Transformations in Metals and Alloys," p. 21, 472, Pergamon Press, Oxford (1965).
23. K. Zellama, P. Germain, S. Squelard, J. C. Bourgoin, and P. A. Thomas, *J. Appl. Phys.*, **50**, 6995 (1979).
24. U. Köster, *Phys. Status Solidi (a)*, **48**, 313 (1978).
25. L. Csepregi, J. W. Mayer, and T. W. Sigmon, *Phys. Lett.*, **54A**, 157 (1975).
26. L. Csepregi, E. F. Kennedy, and J. W. Mayer, *J. Appl. Phys.*, **49**, 3906 (1978).
27. J. L. Margrave, in "Physicochemical Measurements at High Temperatures," J. O'M Bockris *et al.*, Editors, Chap. 2, Butterworths, London (1959).
28. S. Veprek, Z. Iqbal, and F.-A. Sarott, *Philos. Mag.*, **B45**, 137 (1982).
29. Y. Mishima, S. Miyazaki, M. Hirose, and Y. Osaka, *ibid.*, **B46**, 1 (1982).
30. B. L. Mattes, in "Polycrystalline and Amorphous Thin Films and Devices", L. L. Kazmerski, Editor, Academic Press, New York (1980).
31. A. M. Beers, H. T. J. M. Hintzen, H. G. Schaeken, and J. Bloem, To be published.

The Effect of Substituents on the Photosensitivity of 2-Nitrobenzyl Ester Deep U.V. Resists

E. Reichmanis, C. W. Wilkins, Jr., D. A. Price, and E. A. Chandross

Bell Laboratories, Murray Hill, New Jersey 07974

ABSTRACT

2-Nitrobenzyl cholate/poly(methyl methacrylate-co-methacrylic acid) is a high contrast ($\gamma > 5$), high resolution photoresist which has a sensitivity of 150-200 mJ/cm^2 at 260 ± 20 nm. However, because of the low deep u.v. intensity of most conventional exposure "tools," it is desirable to improve this sensitivity. This may be accomplished by substitution on the o-nitrobenzyl chromophore. Appropriate substitution can be used to enhance the absorption characteristics of the ester and, thereby, improve the photochemical response of the system. A variety of o-nitrobenzyl esters have been prepared by standard synthetic techniques and examined for use in this two-component resist system. Improvements in sensitivity by a factor of ~2 have been obtained with the 2,6-dinitrobenzyl alcohol based inhibitor. Other resist characteristics remain unaffected by substitution. All materials examined exhibit contrast as high as the parent o-nitrobenzyl cholate system, and they retain its high resolution characteristics.

The 2-nitrobenzyl group has routinely been used as a photochemically removable protective group for carboxylic acids in organic synthesis (1, 2) and we have extended the usefulness of this chemistry to the development of a solution-inhibition deep u.v. photoresist (3, 4). 2-Nitrobenzyl cholate/poly(methyl methacrylate-co-methacrylic acid) exhibits high contrast, is capable of submicron resolution, and has a sensitivity of 150-200 mJ/cm^2 at 260 ± 20 nm. However, because of the low deep ultraviolet intensity ($\lambda <$ 280 nm) of most conventional exposure "tools," higher sensitivity is desirable.

Various substituted 2-nitrobenzyl esters, *e.g.*, methoxy and α-phenyl, have been employed as carboxylic acid protective groups (1, 2). While no information concerning their photosensitivity is available, substitution may be one means of improving resist sensitivity. Appropriate substitution can enhance the absorption characteristics of the ester and, thereby, improve the photochemical response of the system. Alternatively, a substituent induced change in the steric configuration of the inhibitor molecule may enhance the quantum yield of the rearrangement. A variety of 2-nitrobenzyl ester derivatives have been prepared and examined for use in this two-component resist system. The effects of substitution on resist sensitivity, contrast, and resolution are described.

Key words: photolithography, photodegradation, resists.

Experimental

Materials.—The substituted 2-nitrobenzyl cholate esters were prepared by standard synthetic techniques (3, 5, 6). Poly(methyl methacrylate-co-methacrylic acid) [P(MMA-MAA)] (7.5:2.5) was prepared as before (2). Poly(2-nitrobenzyl methacrylate) [P(NBMA)] was prepared in toluene at reflux temperature using benzoyl peroxide as

initiator. The polymer was isolated by consecutive precipitations from toluene solution into methanol and dried under vacuum.

Sensitivity, contrast, and resolution.—P(MMA-MAA) (7.5:2.5) (*MW* 67 × 10^3, *Mw/Mn*, 2.7) was dissolved in cyclopentanone [15 weight percent (w/o)] and the specified amount of inhibitor was added. P(NBMA) was dissolved in methoxyethyl acetate (15 w/o). The solutions were filtered (0.5 μm Millipore filter) prior to use and then applied to standard silicon substrates with a Headway Research spinner. Films were baked at 160°C for 60 min prior to exposure.

Sensitivity and contrast were determined by irradiating the coated substrates through a chrome on quartz step tablet with an Optical Associates Incorporated Deep u.v. Exposure System (Model 29 DH, 500W Hg-Xe lamp) optimized for exposure at 260 ± 20 or 310 ± 20 nm. Lamp intensity was controlled by an OAI Model 780 power supply and was kept at 10 and 30 mW/cm² for the 260 and 310 nm exposures, respectively. Exposure times, developer conditions, contrast, and resolution were determined as previously reported (2, 3). Developers and development times were chosen such that minimum thinning occurred in the unexposed regions of the film. When the 10% aqueous Na_2CO_3 or 0.4% aqueous NaOH soak were used as the sole development step, no loss of film thickness was observed.

Results and Discussion

The primary mechanism by which 2-nitrobenzyl cholate/P(MMA-MAA) works as a resist involves a photochemical reaction of the cholate ester solubility inhibitor (Fig. 1). Upon irradiation, the nitrobenzyl ester undergoes a rearrangement to generate o-nitrobenzaldehyde plus a carboxylic acid. In this manner, an alkali-insoluble ester is converted into a free acid which is chosen so as to be readily soluble in alkaline developers. The ease of rearrangement, and, thus, resist sensitivity, depends upon the extent of absorption of light by the 2-nitrobenzyl chromophore and the quantum yield of the photoreaction. Assuming that substitution causes no major change in the quantum yield, an increase in the absorbance of the inhibitor would be expected to enhance resist sensitivity.

Such changes in absorbance can be accomplished by substitution on the photoreactive chromophore, and a variety of 2-nitrobenzyl cholate derivatives were synthesized. The u.v. absorption spectra (in a P(MMA-MAA) matrix) of some of the esters prepared are shown in Fig. 2, and the absorption characteristics (in acetonitrile) of all the materials in question are given in Table I. A significant increase in the absorption coefficient at ~260 nm is observed only for the α-methyl and 6-cyano derivatives. While the methoxy substituted analogs exhibit a decrease in absorption intensity at ~260 nm, an additional band appears at longer wavelengths (~320 nm). Neither the 2,6-dinitro nor the 4-methoxycarbonyl-2-nitrobenzyl ester exhibits much change in absorbance at 260 nm *vs.* the unsubstituted parent.

Ring substitution appears to have little or no effect on the solubility of the irradiated ester/P(MMA-MAA) composite. The solubility difference between cholic acid and its esters is such that it overshadows the perturbations that result from phenyl ring substitution. The solubility of cholic acid in aqueous base is *ca.* 500 g/liter, while its simple aliphatic and aromatic esters are practically insoluble in such media.

Resist sensitivity.—The resist sensitivies of P(MMA-MAA)/20 w/o inhibitor are given in Table II. Only α-methyl-2-nitrobenzyl cholate exhibits both increased absorbance and improved sensitivity. The overall absorption of light by the chromophore, in the exposure range of 260 ± 20 nm, is

Table I. U.v. absorption spectral data for the substituted o-nitrobenzyl cholate esters

Cholate ester	λ_{max}(nm)(ε)[a]	Cholate ester	λ_{max}(nm)(ε)[a]
2-Nitrobenzyl	260(5450) 296(sh)(1850)	2-Cyano- 6-nitrobenzyl	261(8000) 295(2150)
2-Methoxy- 6-nitrobenzyl	259(2700) 320(1860)	4-Methoxycarbonyl- 2-nitrobenzyl	258(4950)
4-Methoxy- 2-nitrobenzyl	267(1730) 328(1000)	α-Methyl- 2-nitrobenzyl	253(7800) 320(sh)(1600)
2,6-Dinitrobenzyl	231(11800) 318(sh)(625)		

[a] In acetronitrile.

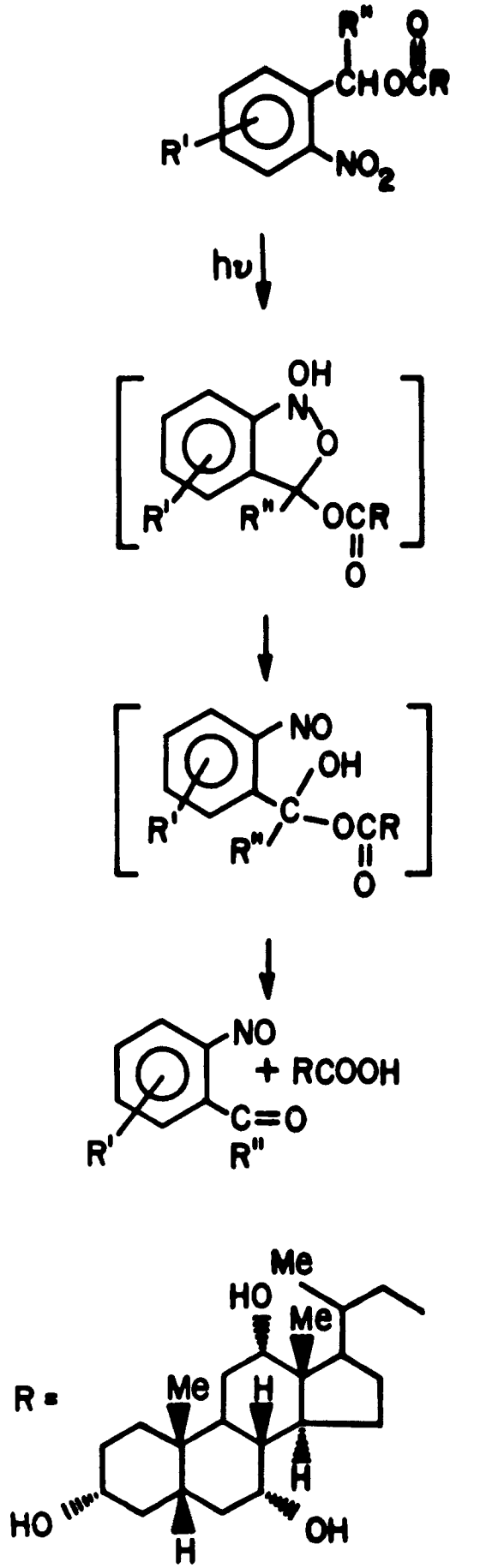

Fig. 1. Scheme depicting the photodegradation of the substituted 2-nitrobenzyl cholate esters.

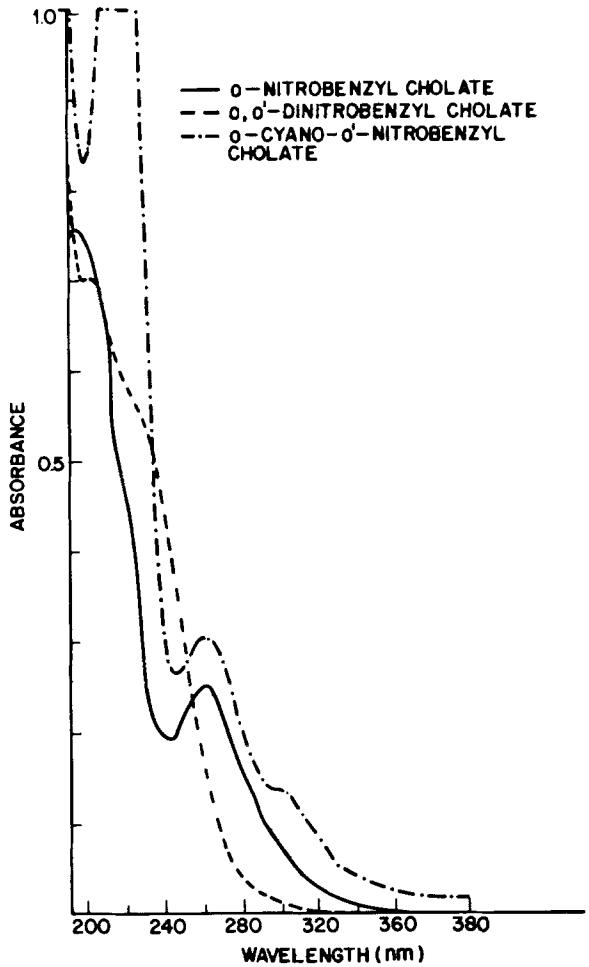

Fig. 2. U.v. absorption spectra of selected o-nitrobenzyl cholate esters in a P(MMA-MAA) matrix; o-nitrobenzyl cholate (—), o,o'-dinitrobenzyl cholate (— —), o-cyano-o'-nitrobenzyl cholate (—·—). Film thicknesses are nominally 1 μm.

significantly increased (see Table I for absorption characteristics) and resist sensitivity is improved by ~20%. Because of synthetic necessity, the α-methyl analog is a triformylcholate ester which changes the development characteristics of the system. [We have previously determined that esterification of the cholic acid hydroxyl appendages improves the resistance of the system to alkali, allowing one to use a more strongly alkaline developer (2)]. More extensive studies of the development of this resist system might then improve resist sensitivity still further. Presumably, the α-methyl substituent acts to change the configuration of the molecule, both improving its absorption characteristics and rendering the remaining benzylic proton more easily abstractable.

While the electron withdrawing o-cyano group enhances the optical absorption of the inhibitor by ~50%, it greatly decreases the efficiency of the photochemical rearrangement. Resist sensitivity is reduced by roughly a factor of three. While use of 2-methoxy-6-nitrobenzylcholate has a deleterious effect on resist sensitivity, the para isomer improves the photoreactivity of the system slightly.

The largest increase in sensitivity, a factor of nearly two, is obtained when 2,6-dinitrobenzyl cholate is the solution inhibitor for P(MMA-MAA). The improved photosensitivity must arise, in part, from a statistical increase in the probability of the reaction. The additional nitro group may also alter the steric configuration of the molecule such that the benzylic hydrogens are more accessible to attack. This result is consistent with the observed increase in quantum yield for the analogous 2-nitrobenzaldehyde to 2-nitrosobenzoic acid rearrangement when a 6-nitro group is added as a substituent (7).

The 2-nitrobenzyl chromophore has also been attached to a polymer chain, as in poly(2-nitrobenzyl methacrylate) (P(NBMA)), to determine whether this might be a more effective means of employing the same photochemistry to convert a hydrophobic material into one which is readily soluble in aqueous alkaline solutions. Copolymers of methyl methacrylate and o-nitrobenzyl methacrylate have been previously found to generate aqueous alkali soluble polymers upon irradiation (8). P(NBMA) was found to be substantially less sensitive than the two-component resist. Presumably the unphotolyzed o-nitrobenzyl ester moieties affect the wettability and solubility of the film, reducing its solubility in aqueous base. Even methanolic developers are unable to develop the resists effectively.

Table II. Effect of substitution on resist sensitivity and contrast at 260 ± 20 nm

Resist	Sensitivity (260 nm) (mJ/cm²)	Contrast
2-Nitrobenzyl cholate[a]	160	>5[b]
2,6-Dinitrobenzyl cholate[a]	90	>5[b]
2-Methoxy-6-nitrobenzyl cholate[a]	240	>5[b]
4-Methoxy-2-nitrobenzyl cholate[a]	130	>5[b]
2-Cyano-6-nitrobenzyl cholate[a]	500	>5[b]
4-Methoxycarbonyl-2-nitrobenzyl cholate[a]	200	>5[b]
α-Methyl-2-nitrobenzyl cholate[a]	120	>5[c]
Poly(2-nitrobenzyl methacrylate)	>500	—

[a] 20 w/o in P(MMA-MAA) (7.5:2.5) $MW = 67 \times 10^3$, film thickness ~1 μm.
[b] Developer: 10% aqueous Na_2CO_3 (3 min) followed by a 30 sec H_2O rinse.
[c] Developer: 0.4% NaOH (3 min) followed by a 30 sec H_2O rinse.

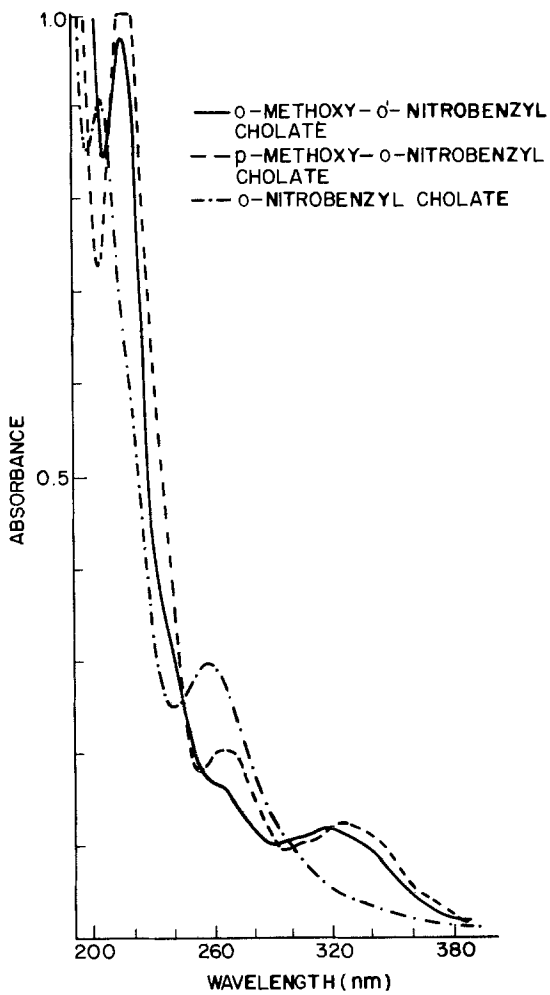

Fig. 3. U.v. absorption spectra of o-methoxy-o'-nitrobenzyl cholate (—), p-methoxy-o-nitrobenzyl cholote (— —), and o-nitrobenzyl cholate (—·—). Film thicknesses are nominally 1 μm.

As mentiond above, the methoxy substituted o-nitrobenzyl cholate esters possess an additional absorption band at 320 and 328 nm for the ortho and para isomers, respectively. Figure 3 compares the absorption spectra of these materials in a P(MMA-MAA) matrix. The existence of these absorptions led us to investigate the photochemical response of these solution inhibitors to 310 nm radiation. While the 310 nm sensitivity of both 4 and 6-methoxy-2-nitrobenzyl cholate/P(MMA-MAA) is enhanced over that of the parent, neither system exhibits sufficient sensitivity (Table III) for a practical resist. The most sensitive material, the 6-methoxy analog, requires an exposure dose of 960 mJ/cm². Significant improvements in the absorption characteristics of the inhibitor are required for 2-nitrobenzyl photochemistry to become practical for use in the 310 nm region. This might be accomplished through the use of photosensitizers (3).

Resist contrast.—Substituent effects can lead to significant improvements in resist sensitivity, but effects on other parameters such as contrast (γ), the rate at which a resist responds to incident light, must also be examined. The parent o-nitrobenzyl cholate/P(MMA-MAA) system is unusual for an organic resist system in that it has a very high contrast value; γ is > 5 when 10% aqueous Na_2CO_3 is used as the developer (2, 3). Typically, γ is < 3 for organic photoresists. These high values of γ are probably a result of the unusual dissolution characteristics of the new resist. The aqueous base developer appears to "swell" the exposed areas of the resist which are then dissolved on subsequent immersion in the water rinse. The ionized resin is apparently insoluble in the alkaline developer. This delicate solubility balance might easily be disturbed by changes in either the inhibitor or the base resin.

Fortunately, this proved not to be the case. When the developer is 10% aqueous Na_2CO_3, all of the substituted 2-nitrobenzyl cholate derivatives examined exhibit equally high contrast as the parent when incorporated into the P(MMA-MAA) base resin. As shown in Table II, γ is generally > 5, and Fig. 4 depicts a typical contrast curve, that for the 2,6-dinitro system.

The influence of the developer is illustrated by the results obtained with 2.5% aqueous diethanolamine followed by an aqueous rinse. Here, both contrast, and to a lesser extent, the amount of thinning of the film are dependent upon the substituent. The nitro and methoxycarbonyl derivatives are typical examples. As shown in Table IV, the latter undergoes 20% thinning on development, while the former loses only 5% of its original thickness. This compares with 10% loss of film thickness for the parent (3). As expected, contrast is best when less thinning is observed. Figure 4 also shows a contrast curve for the dinitro system when diethanolamine is the developer.

Resolution.—A critical test of a resist system is its ability to define a pattern. The high contrast we observe enables us to readily define features as small as 1 μm in all the materials studied here. A typical example is shown in Fig. 5. Here, nominal 1 μm lines and spaces are contact printed in 2,6-dinitrobenzyl cholate/P(MMA-MAA) using 260 ± 20 nm radiation and 10% aqueous Na_2CO_3 as the developer, followed by a 30 sec H_2O rinse. The lines are in fact less than 1 μm wide, while the spaces are somewhat larger.

High resolution is useless unless the defined features can be readily transferred to the substrate. Therefore, the reac-

Table III. Resist sensitivity and contrast at 310 ± 20 nm

Resist[a]	Sensitivity[b] 310 nm (mJ/cm²)	Contrast
2-Nitrobenzyl cholate	2500	>5
2-Methoxy-6-nitrobenzyl cholate	960	>5
4-Methoxy-2-nitrobenzyl cholate	1200	>5
2-Cyano-6-nitrobenzyl cholate	>>2500	—

[a] 20 w/o in P(MMA-MAA) (7.5:2.5) $MW = 67 \times 10^3$, $M_w/M_n = 2.7$, film thickness: ~1 μm.
[b] Using 10% aqueous Na_2CO_3 as the developer (3 min) followed by a 30 sec H_2O rinse.

Table IV. Resist sensitivity and contrast using diethanolamine as the developer

Inhibitor[a]	Resist[b] sensitivity (mJ/cm²)	γ	% Thickness remaining
2-Nitrobenzyl cholate	290	2.2	90
2,6-Dinitrobenzyl cholate	150	2.5	95
4-Methoxycarbonyl 2-nitrobenzyl cholate	300	~1.5	80

[a] 20 w/o in P(MMA-MAA) (7.5:2.5), $MW = 67 \times 10^3$, $M_w/M_n = 2.7$, initial thickness: 7×10^3 Å.
[b] 2.5% aqueous diethanolamine developer (3 min) followed by a 30 sec H_2O rinse.

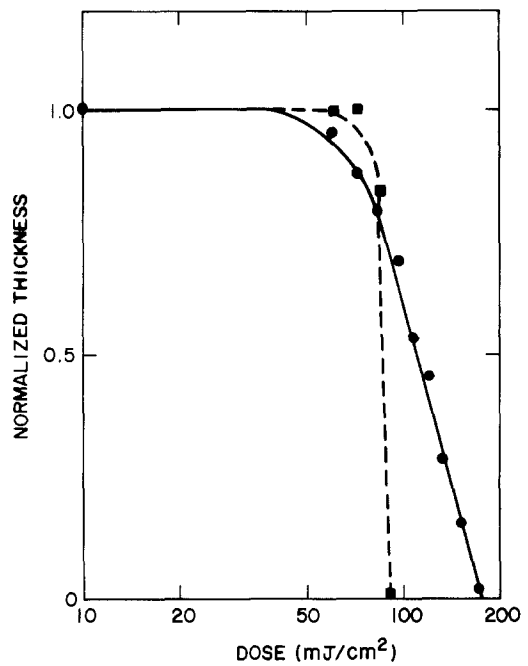

Fig. 4. Contrast as a function of developer for 2,6-dinitrobenzyl cholate; 10% aqueous Na_2CO_3 (— —), 2.5% aqueous diethanolamine (—).

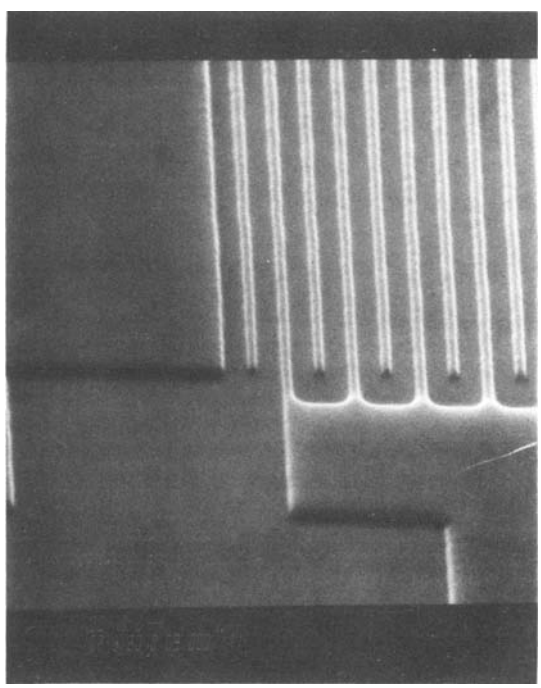

Fig. 5. SEM micrograph depicting nominal 1.0 μm lines and spaces printed in 2,6-dinitrobenzyl cholate/P(MMA-MAA).

tive ion etching characteristics of these resist systems were measured. They were found to be comparable to those of the parent 2-nitrobenzyl cholate resist (3), as was anticipated.

Conclusion

The sensitivity of o-nitrobenzyl ester based photoresists has been improved by substitution on the photoreactive chromophore. A 6-nitro or α-methyl substituent roughly doubles the sensitivity of 2-nitrobenzyl cholate/P(MMA-MAA) to 260 nm radiation. High contrast and resolution are retained with these analogs and no adverse effect on reactive ion etching resistance is observed.

Acknowledgment

The authors wish to thank L. M. Masakowski for SEM microscopy.

Manuscript submitted July 23, 1982; revised manuscript received Feb. 11, 1983.

Any discussion of this paper will appear in a Discussion Section to be published in the December 1983 JOURNAL. All discussions for the December 1983 Discussion Section should be submitted by Aug. 1. 1983.

Bell Laboratories assisted in meeting the publication costs of this article.

REFERENCES

1. V. N. Rajeskharan Pillai, *Synthesis*, 1 (1980).
2. B. Amit, U. Zehavi, and A. Patchornik, *Israel J. Chem.*, **12**, 103 (1974).
3. E. Reichmanis, C. W. Wilkins, Jr., and E. A. Chandross, *J. Vac. Sci. Technol*, **19**, 1338 (1981).
4. C. W. Wilkins, Jr., E. Reichmanis, and E. A. Chandross, Submitted for publication.
5. P. M. Kochergin and K. S. Bushueva, *Zh. Obshch. Khim.*, **32**, 3033 (1962).
6. F. Cortese and L. Bauman, *J. Am. Chem. Soc.*, **57**, 1393 (1935).
7. P. A. Leighton and F. A. Lucy, *J. Chem. Phys.*, **2**, 756 (1934).
8. H. Barzynski, M-J. Jun, D. Saenger, and O. Volkert, U.S. Pat. 3,849,137 (1974).

Technical Note

Comparison of Thermoluminescence and Phosphorescence between Electron-Excited and U.V.-Excited Zinc Silicate Phosphors

Takeshi Takamori* and Derek B. Dove*

IBM Thomas J. Watson Research Center, Yorktown Heights, New York 10598

The properties of a phosphor may be significantly affected by the presence of defects or impurities that give rise to intermediate trapping states for electrons. There is, therefore, considerable interest in investigating trap distributions produced by various means in phosphors in order to learn how to control efficiency, or modify persistence or other properties. To this end, many studies have been carried out on phosphorescence and thermoluminescence and on the correlation between these phenomena since they both reflect trap emptying processes. In almost all cases, this work has been carried out using u.v. excitation even in the case of phosphors intended for CRT applications. Although it has been known for a long time that the characteristics of phosphorescence after u.v. excitation and after electron excitation may be markedly different (1), thermoluminescence behavior of electron excited phosphors has rarely been reported (2). Correlation between thermoluminescence and phosphorescence has been discussed for u.v.-excited phosphors (3), but such correlation for electron-excited phosphors appears not to have been reported previously. Phosphorescence of electron-excited phosphors by itself has been studied by many workers, but its temperature dependency has not been well established. More extensive studies with electron excitation, however, should be of value in extending our knowledge of luminescence properties of CRT phosphors, their surface states, and their damage, if any, by electron bombardment. In this respect, the purpose of this communication is to present our first attempt to explore the thermoluminescence and phosphorescence behavior of electron-excited phosphors. As typical CRT phosphors, commercial P39 (U.S. Radium) and P1 (General Electric), which are Mn-activated zinc silicate phosphors with and without arsenic inclusion, are tested. The results are compared with those obtained with u.v. excitation. Many other aspects of these phosphors have recently been reported from this laboratory (4-10).

For measurements of thermoluminescence at a constant rate of temperature rise (hereafter referred to as a glow curve), sample powders were settled upon a copper block from ethanol suspension in the form of very thin layers. They were heated in a vacuum chamber with constant heating rates following electron excitation at liquid nitrogen temperature. For comparison, glow curves were also obtained on the same samples following excitation with 248 nm radiation from a high pressure mercury-xenon lamp at the same temperature. In estimating trap depths by the Hoogenstraaten plot (11), various heating rates in the range of 0.1°-0.8°C/sec were used. In comparison of thermoluminescence after different excitations, 0.5°C/sec was used. Measurements of phosphorescence decay were carried out at constant temperature over a wide temperature range, for time periods extending from one to hundreds of seconds, for both electron beam and u.v. excitation.

The electron beam was provided by a simple diode structure employing a tungsten filament source. The sample area was flooded with the unfocused beam and current was controlled by adjusting the source temperature.

In most of the electron excitation in the present work, the thermal electrons from the tungsten filament were accelerated to an energy of 10 keV. This is in contrast to the excitation energy of 248 nm (5 eV) of the u.v. radiation used for comparison. In spite of this large difference in excitation energies between the electron excitation and u.v. excitation, the thermoluminescence and phosphorescence in most cases were found to be qualitatively quite alike, once traps were filled. However, apparent difference in the behavior of trap filling was observed between electron excitation and u.v. excitation. For the measurement of phosphorescence as a function of temperature, the brightness of fluorescence during excitation at various temperatures

* Electrochemical Society Active Member.

Key words: inorganic, cathode luminescence, photoluminescence.

was adjusted to be approximately the same both in u.v. excitation and in electron excitation, so that the results obtained with different excitations could be compared directly.

Curves A in Fig. 1 and 2 show glow curves of P39 with electron excitation and with u.v. excitation, respectively. The two major peaks look alike in both cases, although the lower temperature peak of the u.v.-excited phosphor appears at a slightly higher temperature. The Hoogenstraaten plot for these two peaks indicated trap depth of 0.7 and 2.0 eV for lower and higher temperature peaks, respectively. On the glow curve of the electron excited P39, a significant third peak appeared at approximately 180°C as indicated by an arrow on the curve A in Fig. 1. This peak cannot clearly be recognized on the glow curve of the u.v.-excited P39; the Hoogenstraaten plot (11) for this peak indicated a trap depth of 1.6 eV. Since the electron penetration depth is much less than that of the u.v. radiation, this additional peak on the glow curve due to electron excitation may indicate a preferred location of certain traps near the surface of the powder particles. However, even when the accelerating potential was reduced to 80V, its height relative to the other peaks remained the same, indicating that such is not the case. Curve B in Fig. 1 shows the glow curve obtained by decreasing the length of excitation time and intensity in addition to reducing the accelerating potential. Comparison of curves A and B in Fig. 1 indicates that, of the deepest traps of approximately 2.0 eV, the shallower ones seem to be filled first. For this high temperature peak, the peak temperature on the curve B, for which the excitation condition of the sample was yet far from saturation, appeared at 20°C lower than that of the curve A, for which the excitation condition was near saturation. In contrast, however, when the same sample was excited with 248 nm u.v. for a shorter time, the peak temperature of this trap shifted slightly to higher temperature (curve B in Fig. 2) compared with that of near saturation (curve A).

The ratio of the larger peak height due to the 2.0 eV traps within the glow curves to that of the 0.7 eV traps (as seen in both Fig. 1 and 2), shows the higher population of the former traps in this phosphor. However, the relative height of this higher temperature peak becomes smaller when the phosphor is excited for a shorter time producing a highly unsaturated condition. This is shown by the curves B in Fig. 1 and 2. The observation here indicates that the traps of 0.7 eV are filled faster than those of 2.0 eV, the electron capture cross section of the former being greater.

A summary of the phosphorescence data, expressed here as the decay time to 1% brightness of the initial fluorescence, is plotted as a function of temperature for comparison in Fig. 1 and 2 (curves C). It is seen in Fig. 1, that with electron excitation, the phosphorescence curve of P39 very closely follows the glow curve in the whole temperature range studied. Such a close correlation of phosphorescence

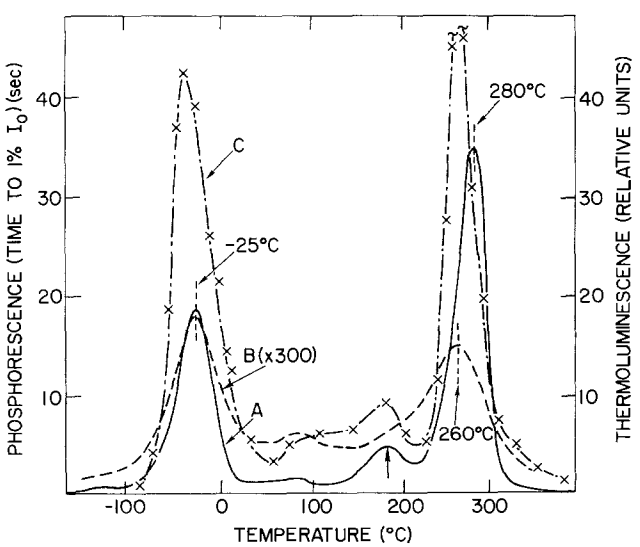

Fig. 1. Thermoluminescence (curves A and B) and phosphorescence (curve C) of P39 with electron excitation. Heating rate for the glow curves is 0.5°C/sec.

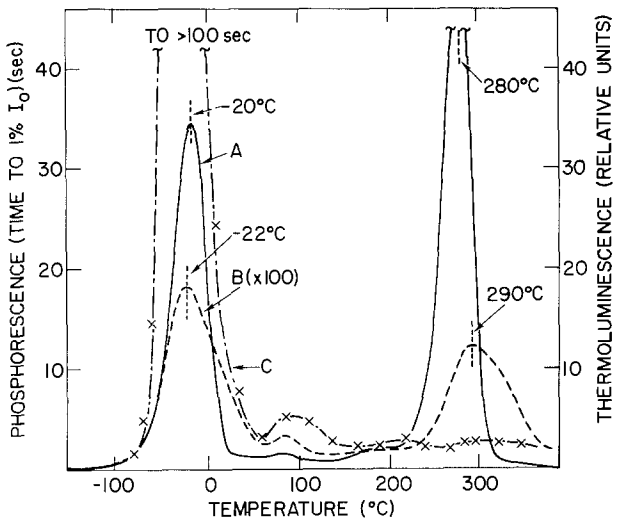

Fig. 2. Thermoluminescence (curves A and B) and phosphorescence (curve C) of P39 with u.v. excitation. Heating rate for the glow curves is 0.5°C/sec.

and thermoluminescence has been discussed for u.v.-excited phosphors in the literature (3). With u.v. excitation, however, the phosphorescence of P39 persists for extremely long times at temperatures near the glow curve peak due to the 0.7 eV traps, but shows no detectable indication of longer decay time at temperatures near the peak temperature of 2.0 eV traps as shown in Fig. 2.

The decay of phosphorescence after electron excitation is often much faster than after u.v. excitation. This difference is caused by the different densities of excitation per unit volume of phosphor in the two cases (1). The exciting electrons are absorbed in a relatively thin layer of the surface of the phosphor particles and so the excitation is relatively intense. The u.v. radiation excites a much larger volume of phosphor since the penetration depth of u.v. is much greater than that of the range of the 10 keV electrons, and, thus, a greater population of traps is filled, resulting in slower decay. This explains the longer phosphorescence near the glow peak of 0.7 eV in Fig. 2 compared with that in Fig. 1.

On the other hand, when P39 was excited at temperatures near the glow peak of 2.0 eV by u.v., the phosphorescent decay was much faster than the case when it was excited with electrons at temperatures in the same range, as seen by comparison of curves C in Fig. 1 and 2. Glow curves of P39 taken immediately after u.v. excitation at various temperatures showed that the peak height of the 2.0 eV peak became gradually lower with increasing temperature of excitation as shown in Fig. 3. Even when the excitation

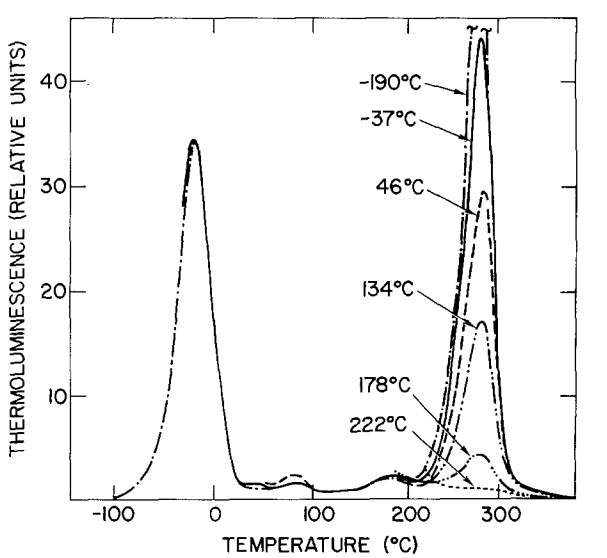

Fig. 3. Glow curves of P39 after u.v. excitation at various temperatures. Heating rate is 0.5°C/sec in all cases.

temperature was near room temperature, the peak height was still lower than that of the excitation at liquid nitrogen temperature. When the excitation temperature was beyond 200°C, effectively, no glow peak was observed. Apparently, no trap filling occurs due to u.v. radiation at the temperature of this glow peak. This is in contrast to the common observation in glow curve experiments in that some magnitude of glow peak is observed even if the sample phosphor is excited at the high temperature side of the glow peak, indicating the occurrence of trap filling under such a condition. It appears, therefore, that, in this particular case, trapping into shallower traps is a precursor state for electrons to be trapped into the deeper, 2.0 eV, traps. Electrons which fill shallow traps first may fall into deeper traps while time goes by during the trapping stage. Electrons are apparently not trapped into the deeper traps when the phosphor is irradiated by u.v. at temperatures at which the electron cannot stay in the shallower traps, even if the temperature is still well below that of the glow peak corresponding to this deeper trap. Only when the phosphor was excited within the temperature range which is at least covered by the high temperature side tail of the shallower glow peak was subsequent heating found to reveal a high temperature peak on the glow curve. The phosphorescence as a function of temperature (curve C in Fig. 2) did not follow the glow curve of this peak probably for this reason. Also, this interpretation is consistent with the observation on curve B in Fig. 2, where the relative height of the higher temperature peak due to the 2.0 eV traps becomes smaller when the phosphor is excited for a shorter time as described above.

Figure 4 shows glow curves taken immediately after electron excitation at various temperatures. In contrast to the results in Fig. 3, a glow peak was observed even after the excitation at temperatures close to the high temperature peak on curve A in Fig. 1. However, the height of this peak gradually decreased with increasing excitation temperature similarly to those in Fig. 3. It appears, therefore, that the decreasing trend of the trap filling as a function of excitation temperature is the same either with u.v. excitation or with electron excitation. Because of the high energy of the incident electrons and the complex behavior of the secondary electrons (1), however, the traps of 2.0 eV are partially filled with the electron excitation even at the temperatures at which the u.v. excitation cannot induce a detectable amount of trap filling. Thus, the close correlation between the glow curve and phosphorescence observed with electron excitation for the traps of 2.0 eV in Fig. 1 may be accidental rather than a rule. In contrast to the decrease of the peak height of the 2.0 eV traps, the peak heights of other traps such as of 1.6 eV increased slightly but detectably with increasing excitation temperature as seen both in Fig. 3 and 4. For example, in Fig. 3 even with the u.v. excitation the peak of 1.6 eV is now recognizable when excited at elevated temperatures.

All observations in the above indicate that the traps of 2.0 eV have small cross section for direct capture compared with other shallower traps. Although they exist in high density in this phosphor, most of the trap filling here proceeds through the help of electron capture by other coulombic traps of greater cross section.

In Fig. 5 and 6, glow curves with electron excitation and with u.v. excitation, respectively, of the P1 phosphor are shown together with the plot of phosphorescence, expressed as decay time to 0.1% brightness of the initial fluorescence. As indicated by the arrow on curve A in Fig. 5, a small shoulder appeared on the high temperature side of a major peak of the glow curve with electron excitation, indicating an additional peak which is not clearly observed with the u.v. excitation on the curve A in Fig. 6. When the power of the exciting electrons was reduced by an order of magnitude, this peak was not detectable even with higher sensitivity detection of the light output.

Extreme variations of the intensity of u.v. excitation to compare glow curves with saturated and unsaturated initial conditions did not result in any significant change in the relative heights between the two major peaks (curve B in Fig. 6). That is, the two kinds of major traps of this phosphor seem to be filled through similar kinetics. As shown by curve B in Fig. 5, however, when the accelerating potential

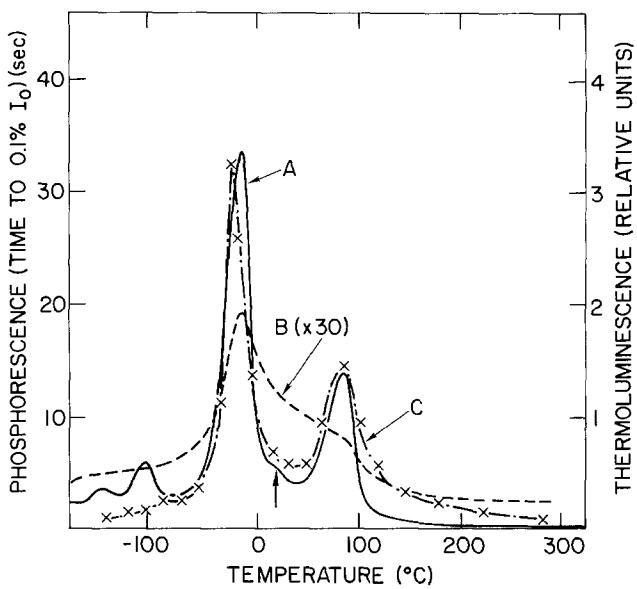

Fig. 5. Thermoluminescence (curves A and B) and phosphorescence (curve C) of P1 with electron excitation. Heating rate for the glow curves is 0.5°C/sec.

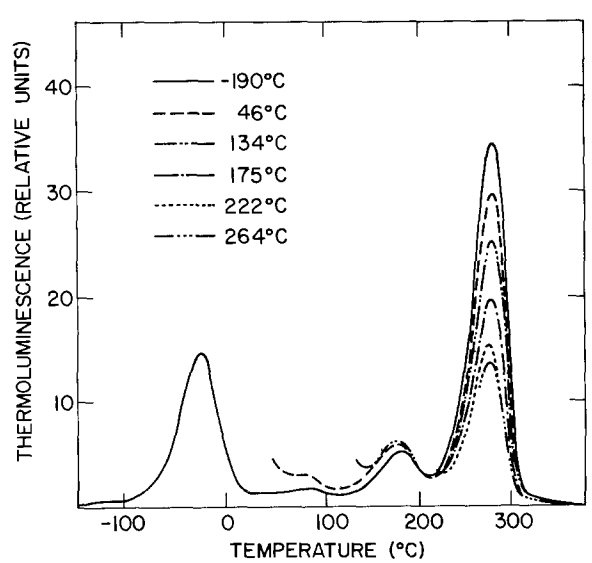

Fig. 4. Glow curves of P39 after electron excitation at various temperatures. Heating rate is 0.5°C/sec in all cases.

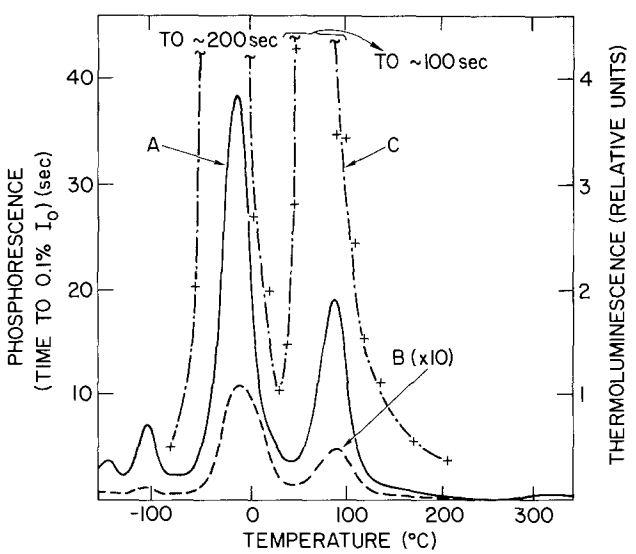

Fig. 6. Thermoluminescence (curves A and B) and phosphorescence (curve C) of P1 with u.v. excitation. Heating rate for the glow curves is 0.5°C/sec.

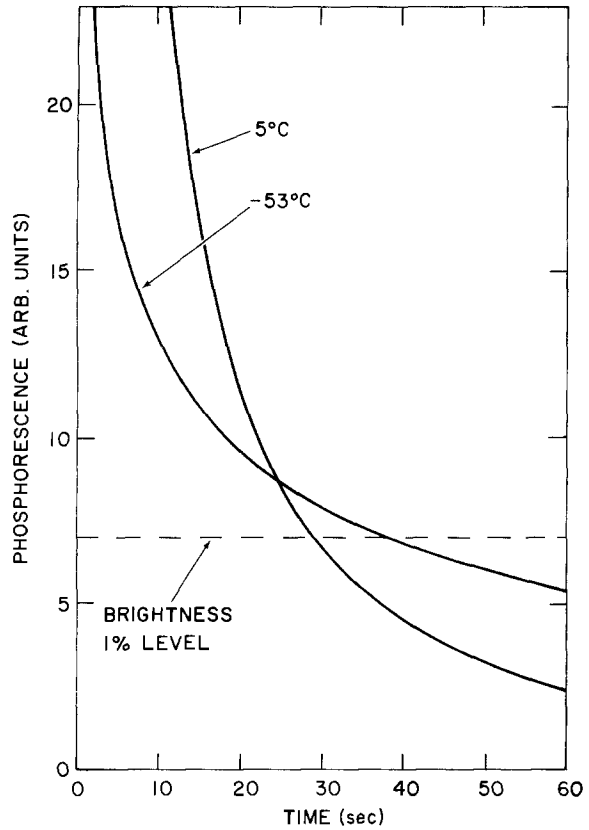

Fig. 7. Phosphorescent decay curves of P39 after u.v. excitation at temperatures below and above the glow peak. Level of brightness reaching 1% of the fluorescence is indicated by the dashed line.

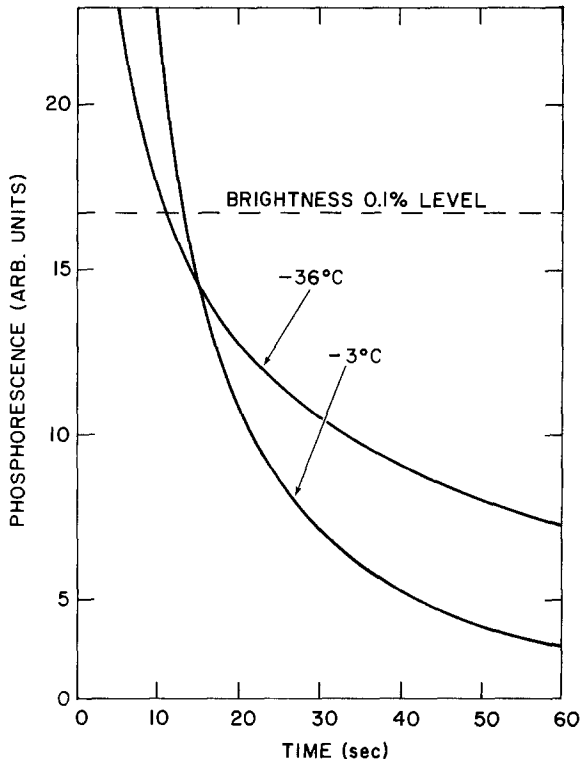

Fig. 8. Phosphorescent decay curves of P1 after electron excitation at temperatures below and above the glow peak. Level of brightness reaching 0.1% of the fluorescence is indicated by the dashed line.

of the electron excitation is decreased down to a few hundred volts to reduce the penetration depth of incident electrons, the relative height of the higher temperature one of the two major peaks decreased significantly. This observation may indicate preferred locations of certain traps in phosphor particles, although further studies are needed for more definitive discussion.

With both electron excitation and u.v. excitation, the phosphorescence of P1 closely follows the glow curves. By comparison of Fig. 5 and 6, it can be seen that the phosphorescent decay of P1 with the u.v. excitation is much longer than that with electron excitation in the entire range of temperature studied. This is different from the result for P39 discussed above. Although in Fig. 5 and 6 in the phosphorescence is represented by the decay time to 0.1% brightness instead of 1%, this does not change the overall picture too much. A small difference expected is that the temperatures of the maximum phosphorescence will shift to a slightly higher value than those in Fig. 5 and 6 when the phosphorescence is expressed by the decay time to 1%. This is because of the difference in decay characteristics between decays at lower and higher temperature sides of a glow peak. At the lower temperature side of a glow peak, phosphorescence always decays fast initially and more slowly later; whereas, at the higher temperature side, it decays more slowly initially but faster later. As typical examples, Fig. 7 and 8 show phosphorescence of P39 after u.v. excitation and that of P1 after electron excitation, respectively.

In summary, measurements have been made of the thermoluminescence and phosphorescence of zinc silicate phosphors, to compare particularly excitation by u.v. radiation and by electron beam. The results show both similarities and differences in properties and indicate the possibility of using the electron excitation technique for the exploration of surface states and for examining electron beam induced damage in phosphors. Further work is in progress in order to investigate the properties of phosphors for CRT applications.

Acknowledgments

Thanks are due to V. D. Beck for design advice of the electron gun, and to D. J. Robbins, N. S. Caswell, and I. F. Chang for useful discussions.

Manuscript received Jan. 17, 1983.

Any discussion of this paper will appear in a Discussion Section to be published in the December 1983 JOURNAL. All discussions for the December 1983 Discussion Section should be submitted by Aug. 1, 1983.

IBM T. J. Watson Research Center assisted in meeting the publication costs of this article.

REFERENCES

1. G. F. J. Garlick, "Luminescent Materials," Oxford University Press, London (1949).
2. J. J. Wei, Z. H. Wang, S. Y. Zhao, Y. Wu, S. H. Lu, and S. H. Xu, Abstract 148, p. 372, The Electrochemical Society Extended Abstracts, Minneapolis, Minnesota, May 10-15, 1981.
3. J. T. Randall and M. H. F. Wilkins, *Proc. Roy. Soc.*, **A184,** 366 (1945); *ibid.*, 390.
4. I. F. Chang, and G. A. Sai-Halasz, *This Journal*, **127,** 2458 (1980).
5. I. F. Chang, G. A. Sai-Halasz, and M. W. Shafer, *J. Lum.*, **21,** 323 (1980).
6. E. S. Yang, D. B. Dove, M. W. Shafer, and I. F. Chang, *J. Electron. Mater.*, **10,** 423 (1981).
7. I. F. Chang and M. W. Shafer, *Appl. Phys. Lett.*, **35,** 229 (1981).
8. P. Avouris and T. N. Morgan, *J. Chem. Phys.*, **74,** 4347 (1981).
9. I. F. Chang, P. Thioulouse, E. E. Mendez, E. A. Giess, D. B. Dove, and T. Takamori, *J. Lum.*, **24/25,** 313 (1981).
10. D. Dove, T. Takamori, I. F. Chang, P. Thioulouse, E. E. Mendez, and E. A. Giess, *ibid.*, **24/25,** 317 (1981).
11. W. Hoogenstraaten, *Philips Res. Repts.*, **13,** 515 (1958).

DISCUSSION SECTION

This portion of the Discussion Section contains discussion of papers in the Electrochemical Science and Technology Section of the *Journal of The Electrochemical Society*, Vol. 129, No. 7, 8, 9, and 10, July, August, September, and October 1982.

Vibrational Spectroscopic Determination of Structure and Ion Pairing in Complexes of Poly(ethylene oxide) with Lithium Salts

B. L. Papke, M. A. Ratner, and D. F. Shriver
(pp. 1434-1438, Vol. 129, No. 7)

J. Paul Devlin:[1] In this paper, the authors propose that the lithium ion in a polyethylene oxide (PEO) complex of $LiNO_3$ is interacting with the oxygens of the polymer and (in the case of some lithium ions) with a nitrate. We believe that application of some information obtained from studies of lithium nitrate contact ion pairs isolated in inert gases matrices as well as for ion pairs variably solvated in matrices spiked with controlled amounts of solvent,[2-4] adds to the understanding of this system.

In footnotes,[2-4] the data most useful in the present situation is that for the stepwise solvation of the lithium nitrate contact ion pair by tetrahydrofuran (THF) in an argon matrix. By varying the THF available to the lithium nitrate in the matrix, the splitting of the ν_3 mode for the solvated ion pairs can be seen to decrease in three discrete steps from a value of 262 to a value of 105 cm^{-1}. Since this latter splitting [directly attributable to (THF_3) $LiNO_3$] is close to the 92 cm^{-1} value observed for $(PEO)_x$ $LiNO_3$, one could draw the conclusion that there are at least three, and possibly four, oxygens of the PEO chain interacting with the lithium ion part of the contact ion pair $Li^+NO_3^-$.

On another point, Papke *et al.* base certain arguments on the published values for the ν_3 splitting in molten salts and concentrated aqueous solutions. This does not appear advisable since the splitting of ν_3 for these cases is significantly increased by transition dipole-transition dipole coupling of neighboring nitrates, as the ν_3 mode of the nitrate has an exceptionally large transition dipole.[5] In this respect, the increased ν_3 splitting (to values > 100 cm^{-1}) that accompanies increased salt concentration in aqueous solutions must have such an origin, as the splitting for the contact ion pair isolated in a glassy water matrix is only 65 cm^{-1}.[3]

Finally, we take exception to the authors following the lead of solution chemists in not assigning the two components in the ν_4 region of the nitrate ion to the doublet for the ion pair. The origin of these bands has not, to our knowledge, been conclusively demonstrated, but the simplest interpretation of two bands observed in this region (in a sample where the existence of the ion pair is suspected) is in terms of a split degeneracy, as the ν_4 degenerate mode must necessarily be split for an ion pair. The calculated ν_4 splitting using the Hester approach, for the case in which the ν_3 splitting is *ca.* 100 cm^{-1}, gives $\Delta\nu_3 \sim$ 10-50 cm^{-1}.[6] Although one of the ν_4 bands is more difficult to observe in matrix isolation than the other, results from this lab indicate a ν_4 splitting of 29 cm^{-1} for lithium nitrate isolated in an argon matrix.[7] Therefore, it seems more reasonable to say that all of the nitrate in this $(PEO)_x$ $LiNO_3$ compound is ion paired, as would be expected if the behavior of lithium nitrate in liquid THF is any guide.[8]

In an unrelated but opportune comment, it is also doubtful that the splitting of the ν_4 mode in molten lithium nitrate reflects two equilibrium forms of the nitrate ion (*i.e.*, place-exchange) rather than the doublet expected for the distorted ion. It has been our experience that the relative intensities of the doublet component bands are insensitive to a large temperature change of the sample (~450 K)[7,9] or to changes in the cation; a most unlikely behavior for bands produced by two species related through an equilibrium process.

[1] Department of Chemistry, Oklahoma State University, Stillwater, Oklahoma 74078.
[2] D. Smith, D. W. James, and J. P. Devlin, *J. Chem. Phys.*, **54**, 4437 (1971).
[3] G. Ritzhaupt and J. P. Devlin, *ibid.*, **79**, 2265 (1975).
[4] J. P. Toth, G. Ritzhaupt, and J. P. Devlin, *ibid.*, **85**, 1387 (1981).
[5] G. Ritzhaupt and J. P. Devlin, *ibid.*, **65**, 5246 (1976).
[6(a)] H. Brintzinger and R. E. Hester, *Inorg. Chem.*, **6**, 980 (1966).
[(b)] R. E. Hester and W. E. L. Grossman, *Inorg. Chem.*, **5**, 1308 (1966).
[7(a)] J. P. Devlin in "Advances in Infrared and Raman Spectroscopy," Vol. 2, Chap. 5, R. J. H. Clark and R. E. Hester, Editors, Heyden, London (1976). [(b)] Unpublished results from our laboratory.
[8] J. Toth, C. Thornton, and J. P. Devlin, *J. Soln. Chem.*, **7**, 783 (1978).
[9] A 450 K temperature variation is possible because a 10% $LiNO_3$ solution in molten $LiClO_3$ forms a supercooled liquid which has been studied down to 100 K, (G. Ritzhaupt and J. P. Devlin, *Chem. Phys. Lett*, **21**, 338 (1973).

Surface Structure of Ruthenium Dioxide Electrodes and Kinetics of Chlorine Evolution

S. Ardizzone, A. Carugati, G. Lodi, and S. Trasatti
(pp. 1689-1693, Vol. 129, No. 8)

L. D. Burke:[10] There is an important aspect of chlorine evolution at RuO_2-based anodes which does not appear to have received much attention in the present work. Unlike the oxygen gas electrode (which is highly irreversible), the chlorine/chloride electrode at an RuO_2 substrate behaves in a reversible manner, its use[11] as a reference electrode system in this area may be noted. Thus, the overall rate of reaction is probably strongly influenced by mass transfer reactions, in particular the slow transfer of the product (molecular chlorine) away from the interface. As pointed out previously,[11] the latter should strongly modify the potential-current density relationship. Such complications may account for the discrepancies in Tafel slope values, and their interpretation, in the chlorine gas evolution field (apart from the present paper, and its Addendum, see also footnotes[11] and [12] where some of these discrepancies are outlined).

The fact that increasing the true surface area does not improve the activity of RuO_2 for chlorine gas evolution has been pointed out previously;[11] it is of course understandable in view of the important role of mass transfer in this reaction. It is clear from recent work[13,14] on the reaction of organic material at this type of anode that, whatever about changes in bulk stoichiometry associated with residual hydration (p. 1693), one of the most important aspects of RuO_2 behavior in electrocatalytically demanding anodic reactions is the generation of higher oxidation state surface species, essentially surface-bonded strong oxidants (surface in the case of these porous anodes is assumed to include internal surface). Chlorine gas evolution in acid media[11] occurs at a potential just above 1.30V (RHE), a region where earlier investigation[13] indicates that the reactive (although not necessarily the sole) species present at the surface at low *p*H values is Ru(VI). Although it may not be a very demanding reaction in the electrocatalytic sense, chloride ion oxidation probably involves redox interaction with these surface species. Irrespective of the mechanism, which (due to the mass transfer limitations) does not appear to be unambiguously resolvable on the basis of Tafel slopes obtained by conventional means, it is not at all certain that high

[10] Chemistry Department, University College, Cork, Ireland.
[11] L. D. Burke and J. F. O'Neill, *J. Electroanal. Chem.*, **101**, 341 (1979).
[12] A. T. Kuhn and C. J. Mortimer, *This Journal*, **120**, 231 (1973).
[13] L. D. Burke and J. F. Healy, *J. Electroanal. Chem.*, **124**, 327 (1981).
[14] L. D. Burke and J. F. Healy, *J. Chem. Soc. Dalton Trans.*, 1091 (1982).

nonstoichiometry will improve the electrocatalytic behavior of RuO_2 films. Unlike normal semiconductor films, those of RuO_2 are generally highly conducting; the main resistance component is probably due to intergranular contact resistance in these microcrystalline layers.

S. Ardizzone,[15] A. Carugati,[15] G. Lodi,[15] and S. Trasatti:[15] The main point of Dr. Burke's remarks, as we understand it, is that there are no reasons to expect that the electrocatalytic activity of RuO_2 electrodes should be influenced by nonstoichiometry since the active surface sites at high anodic potentials are invariably Ru(VI) species. While we do not feel like agreeing on this concept in principle, we contend that Dr. Burke's criticism is not properly addressed. Figure 1 on p. 1690 and the related comment in our paper clearly point out that "cracked" and "compact" electrodes differ in the surface morphology rather than in the nonstoichiometry. Figure 3 shows that no appreciable difference is observed within each group of electrodes although the nonstoichiometry varies largely, yet a difference possibly exists between the two groups, which may, thus, be related to the surface morphology. Therefore, the message from this paper is that morphology rather than nonstoichiometry is the crucial factor in electrocatalysis at RuO_2 anodes.

That the surface morphology can affect the electrocatalytic properties of RuO_2 has been shown in our previous work[16] on O_2 evolution on some sets of electrodes. The effect in that case is admittedly more striking, and our conclusions have been confirmed in different laboratories.[17, 18] It has been neatly found[18] that the degree of crystallinity has a definite effect on the O_2 evolution mechanism. The point of zero charge of RuO_2 samples has been found [19, 20] to depend on the temperature of preparation and to be related, as expected from theories, with the crystal parameters of the oxide.[21] All of these observations emphasize the extreme sensitivity of the nature of the active sites to the morphology of the surface.

Dr. Burke contends that the degree of hydration is not expected to be important in imparting the electrocatalytic properties. It is well established, however, that a number of properties of RuO_2 are closely interrelated as a function of the temperature of preparation.[16, 22] Thus, the residual hydration decreases as T increases and at the same time the crystallinity increases. Hydration is presumably located in grain boundaries or at "inner" surfaces (pores, etc.). As the crystallites of RuO_2 grow, defect-rich regions will shrink. That is what Fig. 9 in our paper is devised to point out.

In Dr. Burke's opinion, we have not paid much attention to the above aspect apparently because we have not appreciated some points he touches upon in his comments. (*i*) Reversibility of the Cl_2 reaction: This is easily proved by the fact that we were able to measure the exchange current from equilibrium i-E curves [cf. footnote [23]]. The effect of mass transfer on the Tafel slope has been discussed by one of us in a previous paper[24] precisely in connection with the Cl_2 evolution reaction. We think that Losev's results[25] highlight this aspect at the best. We have also suggested that Losev's idea could account for the results in Fig. 3 but that we cannot offer any definite proof for this. In a chapter written by two of us,[26] the contrast between O_2 evolution as a "demanding," irreversible reaction and Cl_2 evolution as a reversible, possibly "facile" process has been exhaustively discussed. (*ii*) Relevance of surface redox behavior: We first suggested[27, 28] that the behavior of RuO_2 electrodes should be accounted for in terms of surface redox couples. The involvement of surface redox couples in electrocatalytic reactions has been recently rationalized by Krishtalik.[29] In any case, it is hard to think that the surface redox behavior is substantially unaffected by the solid phase composition. While the growth of a surface layer of more oxidized species might offset some of the expected differences, the features of the overlayer are still expected to depend on the characteristics of the underlying layers. Prolonged oxygen evolution may lead to a composition profile in the overlayer[30] which might smooth down initial differences between differently treated samples. However, in the case of Cl_2 evolution, the large specific adsorption of Cl^- ions[31] is to be taken into account when envisaging surface oxidation mechanisms. It is possible that some of the experiments cited by Burke are not sensitive enough to give evidence to surface effects. The free energy of a crystal is certainly affected by nonstoichiometry, and this is expected to be the case also for the surface where additional factors (morphology) have however to be taken into consideration. (*iii*) Nonstoichiometry and conductivity: Dr. Burke contends that, unlike semiconducting oxides, RuO_2 conduction properties are not affected by nonstoichiometry since it is a metallic conductor. Therefore, no improvement in the electrocatalytic properties are to be expected from this point of view. We certainly did not expect any effect of this sort since we drew attention to the metallic features of RuO_2 early in our work.[27] Dr. Burke's statement (with no reference) that the main resistance component in RuO_2 films is probably due to intergranular contact resistance has been experimentally substantiated in this laboratory and shown in a paper[33] where the main goal has been again to emphasize the role of morphology in imparting "apparent semiconducting properties" to RuO_2 films or pressed powders.

[15] Department of Physical Chemistry and Electrochemistry, University of Milan, Milan, Italy.
[16] G. Lodi, E. Sivieri, A. De Battisti, and S. Trasatti, *J. Appl. Electrochem.*, **8** 135 (1978).
[17] L. I. Krishtalik, Personal communication.
[18] R. Kötz and S. Stucki, Personal communication.
[19] S. Ardizzone, P. Siviglia, and S. Trasatti, *J. Electroanal. Chem.* **122,** 395 (1981).
[20] A. Daghetti, G. Lodi, and S. Trasatti, *Mat. Chem. Phys.*, **8,** 1 (1983).
[21] P. Siviglia, A. Daghetti, and S. Trasatti, *Coll. Surf.*, In press.
[22] S. Trasatti and G. Lodi, in "Electrodes of Conductive Metallic Oxides. Part A," S. Trasatti, Editor, p. 301, Elsevier, Amsterdam (1981).
[23] B. V. Tilak, *This Journal*, **126,** 343 (1979).
[24] S. Trasatti, *ibid.*, **120,** 1703 (1973).
[25] V. V. Losev, *Elektrokhimiya*, **17,** 733 (1981).
[26] S. Trasatti and G. Lodi, in "Electrodes of Conductive Metallic Oxides. Part B," S. Trasatti, Editor, p. 521, Elsevier, Amsterdam (1981).
[27] S. Trasatti and G. Buzzanca, *J. Electroanal. Chem.*, **29,** 1 (1971).
[28] D. Galizzioli, F. Tantardini, and S. Trasatti, *J. Appl. Electrochem.*, **4,** 57 (1974).
[29] L. I. Krishtalik, *Electrochim. Acta*, **26,** 329 (1981).
[30] T. Arikado, C. Iwakura, and H. Tamura, *Electrochim. Acta*, **22,** 513 (1977).
[31] R. G. Érenburg, L. I. Krishtalik, and I. P. Yarosherskaya, *Elektrokhimiya*, **11,** 1072 (1975).
[32] T. Arikado, C. Iwakura, and H. Tamura, *Electrochim. Acta*, **23,** 9 (1978).
[33] G. Lodi, C. De Asmundis, S. Ardizzone, E. Sivieri, and S. Trasatti, *Surf. Technol.*, **14,** 335 (1981).
[34] Chemistry Department A, The Technical University of Denmark, DK-2800 Lyngby, Denmark.
[35] R. W. Berg, S. von Winbush, and N. J. Bjerrum, *Inorg. Chem.*, **19,** 2688 (1980).

Complexing of Al^{+3} by S^{-2} Ions in Alkali Halide Melts

Z. Nagy, J. L. Settle, J. Padova, and M. Blander
(pp. 2034-2037, Vol. 129, No. 9)

R. W. Berg[34] and N. J. Bjerrum:[34] The experiments reported in the technical note by Nagy *et al.* are very interesting and complement our earlier results[35] in LiCl-CsCl melts. We would like to raise some general criticism regarding the interpretation of these new results in the light of our work, especially in relation to the proposed (and questionable) so-called "charge compensated coulomb complex" or "4C" model.

First, consider the question of the degree of complexation between Al^{+3} and Cl^- in sulfide-free chloride melts, either be it LiCl-KCl or LiCl-CsCl. Apparently, the authors of the note in their "4C" model treat the Al^{+3} and Cl^- as essentially uncomplexed. This is not in agreement with present commonly accepted knowledge, according to which $[AlCl_4]^-$ complex ions should be formed under such conditions.

We are sure that this formation of $[AlCl_4]^-$ takes place, because the Raman spectra of $AlCl_3$ dissolved in pure chloride melts show a strong polarized band at ca. 347 cm^{-1}. This

band has been repeatedly interpreted[35-38] as the characteristic strong ν_1 fundamental mode of vibration of the $[AlCl_4]^-$ tetrahedron. The solids $M[AlCl_4]$ with M = Li, Na, K, etc. definitely contain tetrahedral $[AlCl_4]^-$ ions (according to several definitive single crystal x-ray structure solutions,[39] and they also give the same ν_1 Raman band.[39] In this way, there can be no doubt that Al^{+3} predominantly exists as $[AlCl_4]^-$ ions in LiCl-KCl melts. This point has been neglected by the authors of the note; they merely mention as a possibility that the bonding between Al^{+3} and Cl^- could be not totally ionic.

Secondly, regarding mixed solutions of $AlCl_3$ and Li_2S in pure chloride melts such as LiCl-KCl or LiCl-CsCl eutectics, the situation is the same though not as clear-cut. Our Raman spectroscopic and other evidence[35] indicates the formation of polymeric species such as $[Al_nS_{n-1}Cl_{2n+2}]^{n-}$ with $n \geq 3$. We are sure, as are the authors of the note, that new complex species are indeed formed upon the addition of sulfides to the solutions of $AlCl_3$ in chloride melts; new Raman bands appear due to these new species (most notably near 325 cm^{-1}).[35] But, contrary to the authors of the note, we find no reason to postulate species devoid of chlorine, such as $[Al_mS_n]^{+(3m-2n)}$. Rather, we have presented evidence that the mixed solution contains $[Al_nS_nCl_{2n+2}]^{n-}$ (e.g. the preparation of the pure polymeric compound $CsAlSCl_2$ with a similar Raman spectrum).[35]

The so-called "4C" model, like other similar purely electrostatic models in physical chemistry, is simple and easy to use in calculations, but the results are of little or no value as long as chemical bonds are involved. The Raman evidence shows that this is the case in the considered system, and therefore the predictions obtained by the "4C" model are of little if any use. This conclusion takes nothing from the value of the experimental results obtained by the authors.

Z. Nagy,[40] J. L. Settle,[40] J. Padova,[40] and M. Blander:[40] The comments by Berg and Bjerrum are based on a misunderstanding of our use of the concept of complexing which may not have been clearly stated in our paper. We will attempt to clarify our view of this concept in this reply.

In binary systems of any two chlorides, the nearest neighbors of all cations are almost exclusively chloride ions, and all cations are, in a sense, complexed by anions. Thus, the difference between the "complexing" of Li^+, Al^{3+}, or even K^+ by chloride ions in a solution of LiCl, KCl, and $AlCl_3$ is one of degree not of kind. It is, of course, proper to define special complexes such as $AlCl_4^-$ in alkali halide melts where there is strong spectroscopic evidence for the existence of this species and where we believe the $AlCl_4^-$ is likely to be the major, if not exclusive, Al^{3+} containing species. Whether other species coexist depends on unknown factors related to the relative sensitivity of detecting these other species. Because there is always some uncertainty about the distribution of species (*e.g.*, there could be some Al^{3+} ions with coordination other than 4), it is more exact and safer to avoid defining the species in work such as is described in our paper. (This is even more important in other systems where the coordination species are more poorly understood or defined than in melts dilute in Al^{3+}.)

Contrary to Berg and Bjerrum's comment, we did not assume that Al^{3+} and Cl^- are not part of a complex nor that the $AlCl_4^-$ species does not exist. Thus, their second paragraph results from a misunderstanding of our paper and is not a point of contention. For the purposes of our paper, the definition of such species ($AlCl_4^-$) was irrelevant and unnecessary. The Al^{3+} ions have some average nearest neighbor environment and could be exclusively four coordinated or could have some distribution of coordination numbers. The S^{2-} ion will also have some average environment which need not be specified. When the Al^{+3} and S^{2-} ions associate, one can break down the process into two changes. The first is the replacement of a Cl^- in the first shell of an Al^{3+} by S^{2-} and the replacement of an alkali ion in the first shell of the S^{2-} by an Al^{3+} leading to a net energy change of about $-2e^2/d$. The second change is the rearrangement of the other neighboring alkali and halide ions which is related to the compensation or shielding of this interaction. Berg and Bjerrum make the unsupported claim that bonding of the AlS^+ and $AlCl_4^-$ species is "chemical" in nature. The word chemical is undefined in this context. In addition, there are no analyses of the energetics of these species to support any bonding type. Indeed, however unlikely it is, one can have $AlCl_4^-$ species in solution even if the bonds were purely ionic. If "chemical" is defined as non-coulombic interactions then, of course, noncoulomb forces are undoubtedly significant but they are likely to be smaller than the large coulomb forces involved (unless sulfide ions in solution have charges close to −1). To be important, the noncoulomb energy of interaction of Al^{3+} with a nearest neighbor chloride ion must be more negative than the noncoulomb energy of interaction of Al^{+3} with a nearest neighbor sulfide ion by an amount close in magnitude to the coulomb energy. This seems unlikely but, of course, is not impossible. Quantum mechanical calculations of the energetics of these species are underway.[41]

The average coulomb complex has an unknown and generally unspecified number of alkali and chloride ions of the solvent as near neighbors. To do as Berg and Bjerrum have done and single out a small number of solvating chlorides to be part of the complex is speculative and may not represent the real species, which could readily have a broad distribution of different ionic environments which could be extremely difficult, if not impossible to observe by any known structural measurement. From a thermodynamic point of view, the solvent ions in the environment are irrelevant if both Al^{3+} and S^{2-} are at low concentrations.

Berg and Bjerrum do bring out an important point concerning larger complexes. Although we felt that the evidence favored the simple AlS^+ complex (albeit solvated by solvent cations and anions), we could not rule out the importance of larger species as we stated in our paper.

It is unfortunate that Berg and Bjerrum contribute to the confusion concerning the differences between complexing in additive binary systems (*e.g.*, K^+, Al^{3+}/Cl^-) and in reciprocal systems (*e.g.*, K^+, Al^{3+}/Cl^-, S^{2-}). In the first case, all cations are "complexed" and one considers as "true" complexes those special and presumably tightly bound species where structural data are available to define the structure. Of all the binary chloride systems, those containing Al^{3+} ions are probably the clearest examples of systems with "true" complexes. For a major fraction of binary chloride systems, there is some uncertainty and there are many shades of gray. Even for the "true" complexes, the structural information by itself says nothing about the energetics and type of bonding which might even be largely ionic. Thus, evidence for the existence of a complex is of no value in understanding the energetics of reaction of Al^{3+} ions with sulfide or oxide ions. In reciprocal systems at low concentrations of solute cations and anions, a complex is formed between the solute ions when they are each others nearest neighbors with a greater than random probability. The configurations of the solvent ions about the separated solute ions and about the complex are usually not considered in defining such complexes. This type of complex is less subject to uncertainty in definition than the type in additive systems. Our point is that the coulomb attractions between S^{2-} (or any other polyvalent anion) with polyvalent cations in alkali halides (a reciprocal system) are very large and are likely to dominate the energetics of complex formation. Our 4C model provides a basis for predicting species which are likely to complex strongly. The accuracy of the model can be tested and improved in a well-defined manner with the use of molecular dynamics and quantum mechanical calculations under development for calculating the influence of shielding and of noncoulomb forces. If non-coulomb (*e.g.*, covalent) forces are important they could even enhance the effects we discussed. By contrast, Berg and Bjerrum do not offer any testable alternative.

[36] G. Torsi, G. Mamantov, and G. M. Begun, *Inorg. Nucl. Chem. Lett.*, **6**, 553 (1970).
[37] H. A. Øye, E. Rytter, P. Klaeboe, and S. J. Cyvin, *Acta Chem. Scand.*, **25**, 559 (1971).
[38] E. Rytter, H. A. Øye, S. J. Cyvin, B. N. Cyvin, and P. Klaeboe, *J. Inorg. Nucl. Chem.*, **35**, 1185 (1973).
[39] See e.g. F. Wallart, A. Lorriaux-Rubbens, G. Mairesse, P. Barbier, and J. P. Wignacourt, *J. Raman Spectrosc.*, **9**, 55 (1980) and references therein.
[40] Argonne National Laboratory Chemical Technology Division, Argonne, Illinois 60439.
[41] L. A. Curtiss, Personal communication.

The Affect of Arsenic on the Dealloying of α-Brass

M. J. Pryor and Kar-Kheng Giam
(pp. 2157-2163, Vol. 129, No. 10)

R. J. Jais[42] and S. M. M. de De Micheli:[43] In this paper and in the preceding one,[44] the authors present interesting information about the mechanism of the selective dissolution of Cu alloys. We have carried out a research on dealloying of β_i Cu-Al alloys in NaCl solutions at pH = 1 and pH = 6.5 at 0.7 and 1.25V_H. During polarization, there appeared insoluble corrosion products which were identified as atacamite ($Cu_2(OH)_3Cl$) and as CuCl. Thick layers (~100 μm) of Cu, similar in aspect to Fig. 3 (b) in the paper under discussion, were found on the substrate when corrosion products were not immediately removed from the attacked surface after the completion of each experiment. When this cleaning was performed, discontinuous thin films of Cu (~2 μm) were detected by means of SEM and EDAX observations in the cross section of the samples. Anodic currents of about 0.1 A/cm^2 were recorded during polarization, irrespective of the Cu layer characteristics. Metallographic studies of the cross sections of the thick layers showed that no relation existed between the substructure of the substrate and the substructure of the layer where Cu crystals quite smaller than the grains of the original alloy were observed. As it was pointed out by M. J. Pryor and Kar-Kheng Giam, cathodic deposition of Cu is not possible at high anodic potentials. Taking into account this consideration as well as the experimental results described above, the corrosion features of β_iCu-Al alloys in NaCl solutions at 0.7 and 1.25V_H could be explained by supposing that Cu crystals were formed after polarization, as a result of the reduction of Cu salts which were in contact with the surface of the samples at the corrosion potential in the presence of air. In this case, selective leaching of Al would not be the mechanism of dealloying. Could the authors give us their opinion about this interpretation?

M. J. Pryor[45] and Kar-Kheng Giam:[45] The authors thank Dr. Jais and Dr. de De Micheli for their interesting discussion. They are suggesting a mechanism for the formation of the dealloyed layer that has many elements in common to that proposed by Lucey.[46]

A metallic copper deposit could not arise from the presence of $Cu_2(OH)_3Cl$ as a corrosion product since this compound will dissolve in acid solutions without leaving a residue. It is a common component in the solution phase during the dealloying experiments at positive potentials and is completely soluble without residue upon acidification. Metallic copper could, as the writers suggest, result from the disproportionation of cuprous chloride. We do not believe that the copper layers reported in our paper result from the disproportionation of cuprous chloride on the specimen for the following reasons:

i. A specimen that has been treated in sodium chloride solution at either +0.25 or +0.5 V_{SHE} may be mechanically abraded under the solution without access to a high concentration of oxygen in which case the abrasion will expose a copper layer.

ii. It is possible to produce similar morphologies of dealloyed layers at active potentials of −0.25 and −0.5V_{SHE} if the dealloying experiments are conducted for a significantly longer period of time. In this case, the copper current is suppressed to a sufficient degree that no insoluble copper containing compounds are found on the surface of the specimen.

iii. A viable mechanism does not appear to exist for the suppression of dealloying at positive potentials due to the presence of very small amounts of arsenic either in the metal or in the solution as oxyanions.

For the foregoing reasons, we do not believe that the origin of the dealloyed layer at positive potentials in our study was related to the disproportionation of cuprous chloride.

[42] Comisión de Investigaciones Cientificas, Pcia. Bs. As., Argentina.
[43] División Corrosión, Departamento de Materiales, Comisión Nacional de Energía, Atómica, Arda del Libertador, 1429 Buenos Aires, Argentina.
[44] D. S. Keir and M. J. Pryor, *This Journal*, **127**, 2137, (1980).
[45] Olin Metals Research Laboratory, New Haven, Connecticut 06504.
[46] V. F. Lucey, *British Corrosion J.*, **1**, 9 (1965).

Interferometric Study of Combined Forced and Natural Convection

F. R. McLarnon, R. H. Muller, and C. W. Tobias
(pp. 2201-2206, Vol. 129, No. 10)

T. Z. Fahidy:[47] In this impressive and interesting paper, the authors show that the critical Rayleigh number of the onset of natural convection, obtained from interferograms of transient boundary layer growth, is about 1270 if the 90% boundary layer thickness is considered as characteristic length in the 500 ≤ Re ≤ 1500 region. A casual inspection of the variation of Ra with Re and z_c (location of transition) in their Table I would not reveal, however, that this variation has a discernible statistical trend. This trend is not evident from a simple scatter diagram but it may be ascertained by the averaging of z_c and Ra at the three Reynolds number levels shown below, and upon a lackness-of-fit test[48] of the numerical data. In the latter the ratio of the mean

Re	Average value of z_c, cm	Average value of the mid-point Ra
500	5.20	1,018
1,000	9.87	1,206[+]
1,500	14.17	1,226

[+]Ignoring the "outlier" Ra = 1820; otherwise this entry has the value of 1,360.

square due to lack of fit to the mean square due to pure error is about 0.87 if Re, and about 2.6 if z_c is considered to be the independent variable. Since this ratio of the mean squares is distributed as a Snedecor's F variable with (1;9) and (1;8) degrees of freedom, respectively, the test indicates failure to reject the assumption of lack of fit. Put otherwise, the scatter of the critical Ra is such that even a linear (Ra;Re) or (Ra;z_c) relationship cannot be ruled out in a statistical sense. This fact is not surprising; as shown *e.g.*, by Ross and Wragg[49] in a specific electrolytic system, and formulated by Acrivos[50] theoretically for heat transport, the presence of forced convection can effectively suppress natural convection. Hence, it appears reasonable to expect that the critical Rayleigh number is a function of the Reynolds number except at very low values of Re. The interferometric technique employed by the authors may prove very useful in determining this experimental relationship over a relatively wide range of forced flow conditions.

F. R. McLarnon,[51] R. H. Muller,[52] and C. W. Tobias:[52] T. Fahidy correctly points out that the critical Rayleigh number may indeed depend upon the Reynolds number. However, the data listed in Table I on our paper and retabulated above by T. Fahidy suggest that the critical Rayleigh number could vary with (up to) the one-sixth power of the Reynolds number. Unfortunately, the interferometric technique lacks the sensitivity necessary to securely establish such a weak functional dependence.

[47] Department of Chemical Engineering, University of Waterloo, Waterloo, Ontario, Canada N2L 3G1.
[48] N. Draper and H. Smith, "Applied Regression Analysis," Section 1.5, John Wiley and Sons, Inc. New York (1966).
[49] A. A. Wragg and T. K. Ross, *Electrochim. Acta.* **12**, 1421 (1967).
[50] A. Acrivos, *Chem. Eng. Sci.*, **21**, 343 (1966).
[51] Energy and Environment Division, Lawrence Berkeley Laboratory, Berkeley, California 94720.
[52] Materials and Molecular Research Division, Lawrence Berkeley Laboratory and Department of Chemical Engineering, University of California, Berkeley, California 94720.

This portion of the Discussion Section contains discussion of papers in the Solid-State Science and Technology Section of the *Journal of The Electrochemical Society*, Vol. 129, No. 7, 9, 10, and 11, July, September, October, and November 1982.

The Phase Relations in the Cu, In, S System and the Growth of $CuInS_2$ Crystals from the Melt

F. A. Thiel (pp. 1570-1571, Vol. 129, No. 7)

J. J. M. Binsma,[53] L. J. Giling,[54] and J. Bloem:[54] Thiel states that the Cu-In-S liquidus is not well documented. This is not the case, however, for the Cu_2S-In_2S_3 binary join as the complete T-x diagram for this system has been published by us.[55] The diagram which is presented by Thiel gives the liquidus temperature for the $Cu_{0.5}In_{0.5}$-S binary join. Some remarks can be made on Thiel's results in the light of our data obtained for the Cu-In-S system.[55] At first, the liquidus temperature as found by Thiel for $CuInS_2$ (1115°C) is well above the value quoted by Shay and Wernick[56] and the value of 1090°C obtained by us[55] and by other authors.[57] The difference possibly originates from the different experimental procedures (following of the solidification process by optical microscopy, and differential thermal analysis, respectively).

A very interesting phenomenon is the constant liquidus temperature of 740°C in the range 5-35 mol percent (m/o) S. This temperature coincides exactly with the additional heat effect which is observed when $CuInS_2$ is heated in an open ampul.[55] In an open system, the composition shifts from the $CuInS_2$ homogeneity region into the region bounded by $CuInS_2$, Cu_2S, βCuIn, and Cu by the evaporation of S and In_2S. The transition temperature of the additional heat effect remains unchanged also after prolonged heating and increased losses of S and In_2S.[55] Also in our case the transition at 740°C appears, thus, to be present for a wide range of compositions which are S and In_2S deficient. Actually, the relative peak areas vary from just above the detection limit to about twice the melting peak of $CuInS_2$ with increasing annealing time. When the heat effect at 740°C was relatively prominent, also a transition at 574°C could be observed, which most probably corresponds to the eutectoid decomposition of βCuIn.[58] So our data reveal the coexistence of $CuInS_2$, Cu_2S, and βCuIn at 740°C, whereas from Thiel's data it can be deduced, that $CuInS_2$, βCuIn, and the liquid coexist at 740°C. From this, it can be concluded, that a four phase point $CuInS_2$-Cu_2S-βCuIn-Liquid is situated at 740°C in the Cu-In-S system.

As far as the preparation of $CuInS_2$ single crystals is concerned, new and interesting possibilities are opened. Somewhat above 740°C $CuInS_2$ will be in equilibrium with the melt (CuIn) and because the solid-state transitions of $CuInS_2$ have been passed then already,[55] single crystals with the chalcopyrite structure may be grown directly from this melt. The formation of (native) defects might be limited in this case, moreover, because of the rather moderate growth temperature.

F. A. Thiel:[59] In differential thermal analysis, large effects are observed when the latent heat associated with a transition is released or absorbed by the sample under test within a relatively small period of time. Extremely slow heating ramps (cooling is not suitable because of extensive supercooling effects in pure compound semiconductor systems) are needed in liquidus measurements of complex ternary systems to maintain conditions close to equilibrium. With visual inspection methods, this is not a problem; nor is it a problem using DTA if the composition melts congruently. However, to the best of our knowledge, precise liquidus pressure *vs.* temperature data are unknown for the Cu, In, S system. Due to the existence of the free vapor volume, this creates a difficulty in hitting the congruently melting composition exactly. In fact, reports of both crystal growth and phase diagram experiments usually contain a list of the apparatus parameters which is too incomplete to allow calculation of the true liquidus composition even in retrospect once the required vapor pressure data become available. These may be some of the reasons leading to differences in the reported data. The comments concerning the two-liquid region reported in our paper are welcome and should lead to additional insight into the problems of $CuInS_2$ crystal growth.

[53] Interuniversity Reactor Institute, Mekelweg 15, 2629 JB Delft, The Netherlands.
[54] RIM Laboratory of Solid State Chemistry, Catholic University, Toernooiveld, 6525 ED Nijmegen, The Netherlands.
[55] J. J. M. Binsma, L. J. Giling, and J. Bloem, *J. Cryst. Growth*, **50**, 429 (1980).
[56] J. L. Shay and J. H. Wernick, "Ternary Chalcopyrite Semiconductors: Growth, Electronic Properties and Applications," Pergamon, Oxford (1975).
[57] T. V. Tyagunova, F. F. Kharakhorin, and E. N. Kholina, *Izv. Akad. Nauk. SSSR, Neorg. Mater.*, **13**, 46 (1977).
[58] M. Hansen, "Constitution of Binary Alloys," 2nd ed., p. 590, McGraw Hill, New York (1958).
[59] Bell Laboratories, Murray Hill, New Jersey 07974.

Deformation of Silicon Wafers by Thermal Oxidation

Y. Yoriume (pp. 2076-2081, Vol. 129, No. 9)

H.-U. Habermeier,[60] H. C. Alt,[60] and L. Tapfer:[60] One of the main experimental results of the paper under discussion can be deduced from a simple theoretical consideration presented in this comment. Yoriume concluded from his warpage measurements using Fizeau's interferometry that a homogeneous silicon wafer does not warp as a result of normal thermal oxidation.

We assume that the substrate is a dislocation-free monocrystalline silicon wafer of the orientation (100) with a homogeneous distribution of dopants and point defects like O, C, and N. The oxidation process is assumed to be carried out using slow insertion and withdrawing from the furnace in order to prevent plastic deformation induced by an inhomogeneous temperature distribution along the wafer radii. After such an oxidation procedure slip can occur only if the stress at the interface Si/SiO_2 introduced during the cooling process after oxidation, exceeds a critical value for the corresponding resolved shear stress, τ_c, in the glide system (111) [$\bar{1}$01].

Using Schmid's law, the critical stress, σ_c, in the (100) plane which is required to create dislocations in the (111) [$\bar{1}$01] glide system is calculated from the τ_c using data from Suezawa *et al.*[61] Suezawa's data for τ_c are adopted to realistic strain rates, $\dot{\epsilon}$, and temperatures for a MOS oxidation process by a relation given in Suezawa's paper

$$\tau = A\,\dot{\epsilon}^{1/n} \exp(U/kT) \qquad [1]$$

with $U = 1.24$ eV, $n = 2.4$, and $\dot{\epsilon} = 2 \cdot 10^{-7}$ sec^{-1}.

This strain rate corresponds to a cooling rate of 20 min/100°C. In Fig. 1, these data are plotted *vs.* the temperature, T_e, which is related to the oxidation temperature, T_o, by $T_e = (T_o - 100)$°C. A different set of values for σ_c in Fig. 1 is taken from Patel's data for wafers with different amounts of oxygen precipitated.[62]

The stress in the oxide films, σ_{SiO_2}, due to the different thermal expansion coefficients of silicon α_{Si}, and silicon dioxide, α_{SiO_2}, can be approximated by

$$\sigma_{SiO_2} = \int_T^{T_0} E'_{SiO_2}(T)\,[\alpha_{SiO_2}(T) - \alpha_{Si}(T)]\,dT \qquad [2]$$

$$E'_{SiO_2} = \frac{E_{SiO_2}}{1 - \nu_{SiO_2}}$$

(E_{SiO_2}: Young modulus ν_{SiO_2}: Poisson factor)

In the case of circular shaped samples with oxide on both sides, σ_{SiO_2} and the stress in the silicon substrate σ_{Si}, is related to one another by

[60] Max-Planck-Institut für Festkörperforschung, Stuttgart, Germany.
[61] M. Suezawa, K. Sumino, and I. Yonenaga, *Phys. Status Solide A*, **51**, 217 (1978).
[62] J. R. Patel and A. R. Chaudhury, *J. Appl. Phys.*, **34**, 2788 (1963).

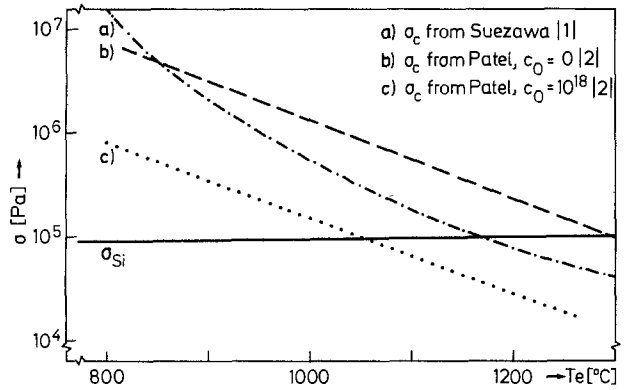

Fig. 1. Comparison of the stress in the plane of a (100) silicon wafer introduced by the mismatch of the thermal expansion coefficients of Si and SiO_2 with the critical stress in the plane corresponding to τ_c in the (111) [$\bar{1}$01] glide system.

$$\sigma_{Si} = \sigma_{SiO_2} \frac{2\, t_{SiO_2}}{t_{Si}} \qquad [3]$$

(t_{SiO_2}: thickness of the oxide, t_{Si}: substrate thickness.)

The stress in the silicon substrate due to the difference of thermal expansion coefficients is plotted in Fig. 1, too, using

$$\alpha_{Si} = 3.7 \cdot 10^{-6}\ \text{deg}^{-1},\ \alpha_{SiO_2} = 5 \cdot 10^{-7}\ \text{deg}^{-1},\ \nu_{SiO_2} = 0.17$$

The temperature dependence of Young's modulus in the range 800°C $\leq T \leq$ 1200°C was approximated by[63]

$$E_{SiO_2}(T) = (76 + 5 \cdot 10^{-3})\ \text{GPa} \qquad [4]$$

Plastic flow will occur, if

$$\sigma_{Si} \geq \sigma_c \qquad [5]$$

It can easily be deduced from Fig. 1 that homogeneous wafers with no oxygen precipitated will show no plastic deformation at realistic oxidation temperatures $T_0 \leq 1200$°C. Wafers with a concentration of oxygen precipitated c_0, in the order of 10^{18} atoms/cm^3 show the intersection of the lines for σ_{Si} and σ_c at $T_e \cong 1050$°C which corresponds to $T_0 = 1150$°C.

In conclusion, to prevent plastic deformation and thus warpage of homogeneous silicon wafers during cooling after the oxidation process, the oxidation temperature should not exceed a range 1150°-1250°C depending on c_0. From this point of view, it is obvious that the pattern misalignment observed by Yoriume is not due to intrinsic deformation of the wafer, but rather correlated to the process of contact printing the author was using.

Yutaka Yoriume:[64] The comments made by H.-U. Harbemeier *et al.* are noteworthy of consideration. Both the comments and my paper are saying the same thing from theoretical and experimental points of view, respectively.

From the pattern misalignment data, Ogawa *et al.* said that the misalignment originated from crystalline properties such as oxygen concentration or defects related to oxidation induced stacking faults.[65] I experimentally studied the deformation of silicon wafer due to thermal oxidation and put the pattern misalignment down to the process of contact printing. This is mentioned at the last part of results and discussion section and conclusion section in my paper. This is same as the conclusion of the comments. The comments should be appreciated for theoretically supplementing.

[63] E. Spinner, *ibid.*, **31**, 1409 (1960).

[64] Nippon Telegraph and Telephone Public Corporation, Ibaraki Electrical Communication Laboratory, Tokai, Ibaraki-ken 319-11 Japan.

[65] T. Ogawa, T. Yashiro, and E. Arai, *Oyo Butsuri*, (in Japanese) **47**, 402 (1979).

Application of the Regular Associated Solution Model to the Cd-Te and Hg-Te Binary Systems

J. D. Kelley, B. G. Martin, F. R. Szofran, and S. L. Lehoczky
(pp. 2360-2365, Vol. 129, No. 10)

Robert F. Brebrick:[66] In view of the analytical simplicity and widespread acceptance of Jordan's[67] simplification of the associated solution model (called the RAS model by him) the authors have made a valuable contribution in showing how much better the above system can be described by an unsimplified version of the model, *i.e.*, by a model in which the excess Gibbs energy of mixing for the liquid phase depends upon the mol fractions of the assumed liquid species. This note is written to bring together the literature on this subject. A preliminary report[67] in which an "unsimplified" associated solution model is used for the Hg-Cd-Te ternary liquid and a complete report[68, 69] have already appeared. Quantitative fits to the liquidus surface, partial pressures, pseudobinary section, and tielines are obtained with model parameters that are consistent with the enthalpy and entropy changes occurring at the congruent melting points of CdTe(s) and HgTe(s). In order to accomplish this under the assumption that HgTe and CdTe are the only molecular species in the liquid phase, it is necessary to write the excess Gibbs energy of mixing as a cubic polynomial in the species mol fractions with linearly temperature-dependent coefficients.

Electrical Properties of Al/Ti Contact Metallurgy for VLSI Applications

C. Y. Ting and B. L. Crowder (pp. 2590-2594, Vol. 129, No. 11)

Ronald S. Nowicki:[70] Ting and Crowder's paper on the Al/Ti metallization appears to be incomplete to the extent that although they conclude that Ti performs well as a diffusion barrier between Al and Si, they fail to discuss the possible reasons for this performance. In particular, they had not reported a thorough microanalysis of the Ti films used in the study, especially with regard to their O and N content. The significance of such data is obvious in light of the well-established correlation between impurity content and diffusion barrier properties found in refractory metals, which has been exhaustively studied and reported upon in the literature.[71-80]

C. Y. Ting[81] and B. L. Crowder:[81] Naturally, our emphasis was on the electrical performance of the devices fabricated with Al/Ti contact metallurgy. We proved that Ti is a good diffusion barrier between Al and Si at the device level on test chips and on VLSI chips with certain limitations on Ti thickness and the post Al anneal. We credited the originality to Patterson and the early physical studies to Bower (see references in the original paper). We appreciated that

[66] Materials Science and Metallurgy Program, College of Engineering, Marquette University, Milwaukee, Wisconsin 53233.

[67] T. Tung, C.-H. Su, P.-K. Liao, and R. F. Brebrick, Abstract 347, p. 345, The Electrochemical Society Extended Abstracts, Vol. 81-1, Minneapolis, Minnesota, May 10-15, 1981.

[68] T. Tung, C.-H. Su, P.-K. Liao, and R. F. Brebrick, *J. Vac. Sci. Technol.*, **21**, 117 (1982).

[69] C.-H. Su, P.-K. Liao, T. Tung, and R. F. Brebrick, *J. Electron. Mater.*, **11**, 931 (1982).

[70] Xerox Corporation, Palo Alto, California 94304.

[71] C. W. Nelson, in "Proceedings of International Symposium on Hybrid Microelectronics," Montgomery, Alabama, p. 413, (1969).

[72] P. H. Holloway and G. C. Nelson, *Thin Solid Films*, **35**, L13 (1976).

[73] W. J. Garceau and G. K. Herb, *ibid.*, **53**, 193 (1978).

[74] R. S. Nowicki, J. M. Harris, M.-A. Nicolet, and I. V. Mitchell, *ibid.*, **53**, 195 (1978).

[75] J. E. Baker, R. J. Blattner, S. Nadel, C. A. Evans, Jr., and R. S. Nowicki, *ibid.*, **69**, 53 (1980).

[76] H. M. Dalal, M. Ghafghaichi, L. A. Kasprzak, and H. Wimpfheimer, U.S. Pat. 4,214,256 (1980).

[77] S. Kanamori, *Thin Solid Films*, **75**, 19 (1981).

[78] C. Canali, G. Celotti, E. Fantini, and E. Zanoni, *ibid.*, **88**, 9 (1982).

[79] R. S. Nowicki, *Gold Bull.*, **15**, 21 (1982).

[80] M. Wittmer, *J. Appl. Phys.*, **53**, 1007 (1982).

[81] IBM T. J. Watson Research Center, Yorktown Heights, New York 10598.

Nowicki pointed out the significance regarding O and N in the Ti film in the light that perhaps it is the O and N incorporated with the films that makes the Ti a good diffusion barrier. He listed 10 footnotes regarding that subject. However, he overlooked one of the important ones by C. Y. Ting.[82] In that footnote, it deals with Ti by evaporation, the incorporation of N_2 in the film, and the use as a diffusion barrier between Al and Si.

Micrographic analysis with respect to oxygen was done but not reported. The oxygen depth profile inside has been analyzed[83] by using Auger electron spectroscopy. The Ti film prepared on silicon substrate is identical to that described in the paper; that is, using the same diffusion pump system evaporated at a base pressure of high 10^{-7} Torr. The oxygen inside the Ti film is about 1 atomic percent (a/o); however at the Ti-Si interface, the oxygen content can increase to a few percent depending on the surface cleaning prior to Ti deposition.

We also practiced the Ti deposition in a cryogenic pumping system which can ordinarily pump down to 2×10^{-7} Torr or less, sometimes in the 10^{-8} Torr range. We have not observed any degradation on the thermal stability due to the improvement of pumping. We have also tried Al evaporation either *in situ* with Ti or non *in situ* with Ti. In the case of non *in situ*, a thin layer of Ti oxide will no doubt exist at the interface. Again, we did not see any significant difference in thermal stability difference. We have exercised that contact technology for years without seeing exceptions or inconsistent results. Based on our experience and observations, we conclude that the good diffusion barrier behavior of Ti against Si diffusion has nothing to do with O and N impurities, although it will be enhanced by their presence as pointed out by Nowicki.

[82] C. Y. Ting, *J. Vac. Sci. Technol.*, **21**, 14 (1982).
[83] P. Ho, Analysis.

JOURNAL OF THE ELECTROCHEMICAL SOCIETY

ACCELERATED

—BRIEF COMMUNICATION—

JUNE 1983

Oxygen Evolution from Water Mediated by Infrared Light on Iron Doped RuS_2 Electrodes

H.-M. Kühne and H. Tributsch

Hahn-Meitner-Institut für Kernforschung Berlin, Bereich Strahlenchemie, D-1000 Berlin 39, Germany

ABC

With semiconducting n-type RuS_2 (ΔE_G = 1.85 eV) which derives the upper valence band from d-states of ruthenium it became possible to couple the absorption of short wavelength-visible light to the photoelectrochemical evolution of oxygen (1-3). This material which showed good stability catalyses in single crystalline form oxygen evolution with a quantum efficiency approaching 60% in the near UV region (3). Unfortunately, because of a kinetic inhibition of the reaction, a relatively large electrode potential has to be applied to liberate oxygen from water at a high rate (3).

We report here on a considerable improvement of the photoelectrochemical properties of the material: Through doping with Fe we succeeded in shifting the spectral sensitivity of RuS_2 by more than 0.7 eV towards the infrared while maintaining the oxygen evolution properties of the electrode and even improving them. The new electrode material is able to use photons of the entire visible and the near infrared spectral range to liberate oxygen and permits the electrolysis of water with partial use of solar energy.

As compared with the method of crystal growth used in ref. 3 and 4, (slow transport of Te from a RuS_2-Te melt in a small temperature gradient near 920°C during a period of 4 weeks), the following modifications were applied: $Ru_{1-y}Fe_yS_2$ powder was produced from a ruthenium sample which contained iron (Merck Art. No. 12316 LAB) and from sulphur. This sample was simply recrystallized in tellurium melt for 3 - 5 days between 900 and 1000°C (typically 100 mg in 2g Te). Subsequently, tellurium was dissolved in aqua regia to recover the $Ru_{1-x}Fe_xS_2$ crystals. 20 independent crystal growth experiments were performed which yielded single crystals with surfaces up to a size of approximately 2 mm^2. The average doping with Fe, measured with quantitative X-ray fluorescence analysis (SEMQ), varied from crystal to crystal in the range between 0 and 1.7% . (An inhomogeneous distribution of Fe has been observed in a smaller fraction of the crystals.) No mixed sulphide-telluride was found but under certain preparation conditions in addition ruthenium telluride crystals. The $Ru_{1-x}Fe_xS_2$ crystals (the concentrations of Fe and Ru were found to complement to 1 for x = 1.7% but not in other cases) were investigated by X-ray analysis (rotating crystal method) which showed crystal parameters identical to those of RuS_2 which crystallizes in the pyrite lattice.

The influence of iron doping on the spectral distribution of photocurrents of RuS_2 is shown in Fig.1. A clear shift of spectral sensitivity is observed towards the red. Interestingly the samples with the highest efficiency in the infrared showed an inhomogeneous distribution of Fe at an average Fe concentration of 1% or less. The inhomogeneous character of the samples could be confirmed with the electrochemical laser spot technique. Simple considerations, based on the difference of ionization energies for Fe and Ru which are supposed to be situated in identical sulfur environment, indicate that the red shift of the spectral sensitivity is caused by those d-states of Fe which contribute to the conduction band in isocrystalline pyrite (FeS_2). In iron doped RuS_2 these states would be placed up to 0.78 eV above the valence band of pure RuS_2. They are occupied by electrons in n-type $Ru_{1-x}Fe_xS_2$ (p-type material could also be obtained) and participate in the electrode's hole reactions. (The photoelectrochemistry of FeS_2 is discussed in ref. 5; no oxygen evolution from water is found.)

The photocurrent efficiency in the IR is not only controlled by the Fe concentration but also by recombination processes and the stoichiometry of the crystals. The quantum efficiencies of good crystals equaled and exceeded 60% at $h\nu$ = 3 eV and the best crystal reached 23% in the IR (1.4 eV).

A photocurrent voltage curve of $Ru_{1-x}Fe_xS_2$ obtained with white light is shown in Fig.2

where it is compared with the properties of three light-insensitive oxygen evolving RuO_2 based electrodes described in the literature. Above 1 V (NHE) light induced oxygen evolution from $Ru_{1-x}Fe_xS_2$ becomes clearly visible and is sustained when only infrared light ($h\nu < 1.5$ eV) is used for illumination. Oxygen evolution at this potential has analytically been confirmed with the help of gas chromatography. Photocurrent densities of oxygen evolution of up to 130 mA cm^{-2} have been observed and through electrode (3) (Fig.1) photo charges of 500 C cm^{-2} were passed without microscopic evidence for photo corrosion. At 5 mA cm^{-2} the potential saving as compared to the best presently existing oxygen evolving RuO_2 electrodes is 0.36 to 0.50 V (Fig.2). This is an encouraging result when considering that the photocurrent curve for our oxygen evolving material is far from being optimized and theoretically ideal. Traces of a ruthenium compound (apparently hydrated RuO_2) have been identified by X-ray fluorescence analysis on the epoxy insulation around the electrode. They were distributed in form of a convection pattern and appeared after polarization of the electrode at potentials larger than 1.5 V/NHE. They were found to be due to the formation of volatile RuO_4 at a quantum efficiency smaller than 1%. An alteration of a fresh $Ru_{1-x}Fe_xS_2$ electrode surface through electrochemical oxidation prior to the first onset of oxygen evolution has been clearly observed experimentally.

It has to be emphasized that light induced oxygen evolution has only been verified for electrode potentials equal or larger than 1 V (NHE). Due to the small size of the electrode surface, we have up to now no analytical evidence concerning the reaction products generated at very low potentials, where light induced oxygen evolution based on the participation of 4 photons per O_2 should become thermodynamically impossible.

The described system appears to be the first oxygen evolving photoelectrode which utilizes photons of the entire visible and near infrared solar spectrum under energy gain, while remaining reasonably stable and consisting of one interface only (although the inhomogeneity of the electrodes poses questions). It experimentally confirms the original proposal (6) that photoelectrolysis of water should be possible by developing a photoelectrochemistry based on transition metal d-states.

A detailed photoelectrochemical and solid state chemical study of the iron-ruthenium disulfide system will be published in a forthcoming paper (7).

Acknowledgements

The authors would like to thank Mr. Matiske, HMI, and Mrs. Siegmann, Free University Berlin for X-ray fluorescence measurements and Dr.H.J.Bleif, HMI, for the X-ray analysis.

REFERENCES

1. R.Guittard, R.Heindl, R.Parsons, A.M. Redon, and H.Tributsch, J.Electroanal. Chem. 111 (1980), 401

2. R.Heindl, R.Parsons, A.M.Redon, H.Tributsch, and J.Vigneron, Surface Science, 115 (1982) 91

3. H.Ezzaouia, R.Heindl, R.Parsons, and H.Tributsch, J.Electroanal.Chem., in press

4. H.Ezzaouia, PhD Thesis (1982)

5. W.Jaegermann and H.Tributsch, J.Appl. Electrochem., submitted

6. H.Tributsch, Z.Naturforsch. 32a (1977) 972

7. H.-M.Kühne and H.Tributsch, Ber.Bunsenges.Phys.Chem., in preparation

8. D.V.Kokaulina, Yu. I.Krasovitskaya, T. V.Ivanova, Elektrokhimiya, Vol.14, No.3 (1978) 470

9. G.Lodi, E.Sivieri, A.de Battisti, S.Trasatti, J.Appl.Electrochem. 8 (1978) 135

10. S.Trasatti and G.Lodi, in "Studies in Physical and Theoretical Chemistry (11), Electrodes of Conductive Metallic Oxides, Part B, S.Trasatti (ed.) (1981) 458.

Manuscipt submitted Jan. 26, 1983; revised manuscript received March 17, 1983.

Hahn-Meitner-Institute fur Kernforschung Berlin assisted in meeting the publication costs of this article.

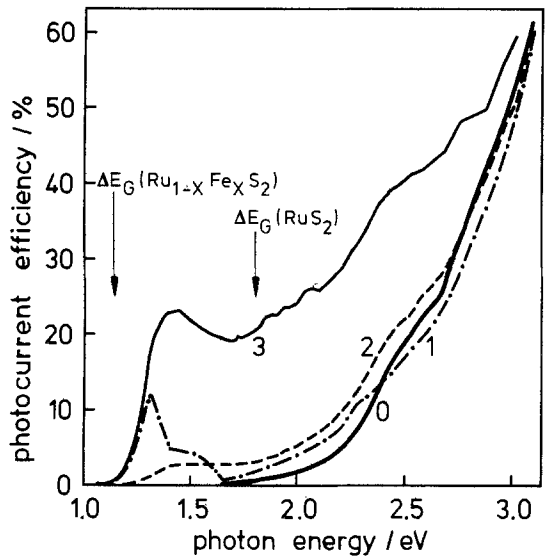

Figure 1. Spectral dependence of light-induced oxygen evolution of RuS_2 doped with various concentrations of iron
0: less than 0.02 % Fe
1: 99.5 % of the surface less than 0.02 % Fe, 0.5 %: 1-1.7 % Fe (islands)
2: 0.64 % Fe
3: average Fe content 1 % (inhomogeneous distribution, islands with up to 45 % Fe on 1 % of surface)
Electrode potential: 1 V (NHE), Electrolyte 1 N H_2SO_4, efficiency measured for sample 3, adapted at 3.1 V for samples 0, 1, 2.

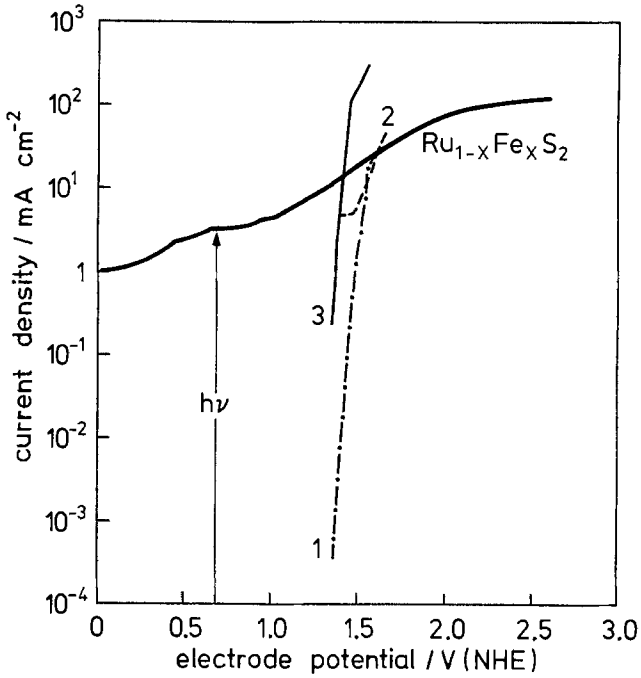

Figure 2. Semilogarithmic (Tafel) plot of photocurrent (white light, 890 mW cm^{-2} 250 W tungsten) of iron doped RuS_2 (3 of Fig.1) in 1 N H_2SO_4 compared with Tafel plots of RuO_2-based oxygen electrodes (in the dark) (1: Ref. 8; 2: Ref. 9; 3: Ref.10).

JOURNAL OF THE ELECTROCHEMICAL SOCIETY

ELECTROCHEMICAL SCIENCE AND TECHNOLOGY

JULY 1983

A Neutron Powder Diffraction Study of α- and β-PbO_2 in the Positive Electrode Material of Lead-Acid Batteries

A. Santoro

National Bureau of Standards, National Measurement Laboratory, Washington, DC 20234

P. D'Antonio

Naval Research Laboratory, Laboratory for the Structure of Matter, Washington, DC 20375

and S. M. Caulder*[1]

Naval Research Laboratory, Chemistry Division, Washington, DC 20375

ABSTRACT

A neutron powder diffraction study of α- and β-PbO_2, both chemically prepared and electrochemically formed in cycled battery plates, was carried out to correlate the electrochemical activity of the lead-acid battery with the atomic arrangement of the electrode constituents. Our results are consistent with the presence of hydrogen in the structure of β-PbO_2, but the departure of the occupancy factors from stoichiometric values are not large enough to unambiguously establish whether there are lead or oxygen deficiencies. If the Pb:O ratio corresponds to exact stoichiometry, any hydrogen which is present must be accompanied by a reduction of Pb^{+4}. There is a significant increase in the lattice parameter a of β-PbO_2 in cycled battery electrodes relative to the value found in chemically prepared β-PbO_2. No change in the c parameter, however, was detected. These dimensional changes are consistent with a configuration for hydrogen similar to that observed in the rutile-type structure of SnO_2, in which there are OH^- ions oriented perpendicular to the c axis. The profile parameters obtained in this analysis show that the crystallites of β-PbO_2 in the positive plate material of a battery cycled three times (Y3) are smaller than those in the chemically prepared compound (~450Å *vs.* 800Å), while there are no significant differences between the latter and β-PbO_2 in the positive plate material of a battery cycled 36 times (Y36). The average structure of α-PbO_2 cannot be accurately determined by profile analysis, at the present time. The difficulties encountered in the refinement may be due to extensive defects, nonspherical crystallites of small size, and/or small departures of the structure from orthorhombic symmetry.

The active materials of the lead-acid battery are formed electrochemically by charging a commercial paste made from a mixture of PbO and sulfuric acid. In the charging process, the α- and β-phases of PbO_2 are formed at the positive plate and spongy lead at the negative plate. During discharge, both forms of PbO_2 transform into $PbSO_4$. Positive battery plates cannot be fabricated by directly pasting the grids with chemically prepared α- and β-PbO_2, for these prove to be electrochemically inactive forms, *i.e.*, a battery made with these materials would not spontaneously generate a current when connected to an external circuit (1). The reason for this different behavior, resulting solely from the different methods of preparation of PbO_2, is not known at present.

Another phenomenon not yet understood is the loss of capacity of a battery after a number a charge-discharge cycles. Although mechanical factors may play a role in battery failures, chemical and structural changes must also be present (1). Caulder (2) has hypothesized that an inactive type of PbO_2 may form in increasing amounts during cycling. This hypothesis is consistent with differential thermal analysis (DTA), thermogravimetric analysis, high-temperature mass spectrometry, and pulsed nuclear magnetic resonance (NMR) measurements.

The origin of the electrochemical activity has also been linked with the presence of a hydrogen species in the crystal structures of α- and β-PbO_2. NMR relaxation studies show that the active materials contain small amounts of hydrogen in two configurations, while the inactive oxides, chemically or electrochemically prepared, showed that the bulk of the hydrogen is predominantly in only one configuration (3).

It has been suggested, from results of DTA measurements, that an electrochemically active amorphous form of PbO_2 exists in the positive plate materials in addition to the α- and β-phases (2). This amorphous oxide would undergo some structural reordering during cycling (with loss of hydrogen species) and would be converted to an electrochemically inactive PbO_2 with NMR, DTA, and mass spectroscopic characteristics similar to those obtained from the chemically prepared materials.

The studies mentioned above lead us to conclude that the oxide often labeled as "PbO_2" can in fact be one of the following materials: (*i*) α-PbO_2 and (*ii*) β-PbO_2, as they are present in the active material of the positive plate; (*iii*) α-PbO_2 and (*iv*) β-PbO_2 as present in the positive plate after loss of capacity; and, finally, (*v*) α-PbO_2, (*vi*) β-PbO_2, and (*vii*) amorphous PbO_2 chemically prepared.

In order to understand the nature of the electrochemical activity of the lead-acid battery, it is important to determine if there are detectable structural differences between the active and the inactive forms of each phase. This, of course, implies the determination of the detailed crystal structures of the materials listed above. Studies in this direction have been carried out by powder neutron diffraction on the chemi-

* Electrochemical Society Active Member.
[1] Present address: International Lead Zinc Research Association at the Naval Research Laboratory.
Key words: battery, crystallography, diffraction, electrode, failure.

cally prepared α- and β-PbO_2 (4, 5) and, more recently, on electrochemically active β-PbO_2 (6, 7) and on the lead dioxides obtained from the positive plate of the lead-acid battery (8). The results of these studies show that, while the structure of the β-phase is well determined, that of the α-phase has not yet been understood in detail. In addition, it seems that there is considerable disagreement about the presence of an "amorphous" phase in the plate materials.

As a part of a study of lead dioxides, we have decided to refine the structures of α- and β-PbO_2 as they exist at different stages of the battery life and compare these structures with those of the chemically prepared materials. Neutron diffraction has been used throughout this analysis to take advantage of the favorable values of the scattering lengths of oxygen and lead and to avoid the problems connected with high absorption and preferred orientation which impose severe limitations on the x-ray diffraction experiments. Since none of the materials of interest can be prepared as single crystals, the powder method has been used in all the experiments.

Experimental

Samples.—The material labeled Y-36 was obtained from a commercially available 12 A-hr (c/10 rate) battery. The battery contained acid with a specific gravity of 1.260. The cycling regime consisted of a 6.0A constant current discharge to a 10.50V cutoff (1.75 V/cell). The battery was then recharged at 4.0A constant current until a crossover constant voltage of 15.00V (2.50 V/cell) was reached. Charging at constant voltage was continued until 110% of the previous discharge capacity was obtained. The initial discharge capacity of the battery was 7.47 A-hr. After 6 cycles, the capacity had leveled off to 7.20 A-hr. The average capacity of these first 6 cycles was 7.35 A-hr. The final capacity measurements prior to disassembly, after 36 cycles, was 6.30 A-hr. This value represented a 15% decrease in capacity from the average of the first 6 cycles. After disassembly, the PbO_2 electrodes were washed in distilled water and vacuum dried. The samples used in the diffraction experiments were then ground and air dried at 135°C.

The Y3 material was obtained from another battery cycled in the same manner as above, and the PbO_2 electrode was disassembled after three cycles. The average capacity of the battery at this point was 7.53 A-hr.

The chemically prepared β-PbO_2 used in this study was Baker reagent grade (lot no. 4604) dried in air at 130°C. Chemically prepared α-PbO_2 was obtained by oxidizing ammoniacal lead acetate with ammonium persulfate, and the compound was dried in air at 130°C.

Neutron diffraction measurements.—The neutron diffraction intensities were measured at room temperature with the high-resolution five-detector diffractometer at the National Bureau of Standards Reactor (9), using the experimental conditions indicated in Table I. The data were analyzed with the Rietveld method (10), modified by Prince (11) to simultaneously process the intensities collected by the five counters of the diffractometer.

Refinements and Results

From the first stages of the structural analysis, it was apparent that the peaks of all samples examined had tails too broad to conform to a Gaussian distribution. This can be seen in Fig. 1a which shows a Gaussian least-squares fit of the reflection 002 of chemically prepared β-PbO_2. The discrepancy between observed and calculated intensities, especially evident in the tails and at the peak of the reflection, can be significantly reduced by using, for the fitting, the Pearson type VII function (12), as shown in Fig. 1b. A comparison of the two figures shows that the value of the goodness of fit χ, the background, and the full width at half maximum are higher for the Gaussian approximation than for the Pearson function. The differences in the background level and in the full width at half maximum, caused by the improper description of the peak shape, may result in an erroneous evaluation of the occupancy and temperature factors of the atoms in the structure and in underestimated values of the sizes of the crystallites in the sample. Because of these results, it was necessary to use the Pearson function in all refinements rather than the usual Gaussian distribution. At this stage, it was thought necessary to repeat the refinement of chemically prepared β-PbO_2 which had been previously analyzed (4) assuming that the profiles were Gaussian.

Table I. Experimental conditions used to collect the neutron powder intensity data for PbO_2

Monochromatic beam:	reflection 220 of a Cu monochromator
Wavelength:	1.5416(3) A
Horizontal divergences:	(a) in-pile collimator: 10 min. arc; (b) monochromatic beam collimator; 20 min. arc; (c) diffracted beam collimator: 10 min. arc
Monochromator mosaic spread:	~ 15 min. arc
Sample container:	vanadium can ~ 10 mm diam
Angular ranges scanned by each detector:	10-40, 30-60, 50-80, 70-100, 90-120
Angular step:	0.05°

The initial values of lattice, profile, and structural parameters were those obtained previously for β-PbO_2 (4), and the initial positional parameters of α-PbO_2 were those reported by Moseley *et al.* (5). The scattering amplitudes were $b(Pb) = 0.94$, $b(O) = 0.58 \times 10^{-12}$ cm (13).

The sample of chemically prepared β-PbO_2 was free from diffraction effects due to impurities, and therefore, the entire powder pattern was used in the refinement of the structure. The samples Y36 and Y3, however, contain both α- and β-PbO_2. The study of the β-phase in these samples could only be carried out by excluding, from the calculations, the angular regions containing the diffraction peaks of the α-phase and vice-versa.

In all cases, the background was assumed to be a straight line of finite slope and was refined for each of the five channels of the diffractometer, together with the profile and the structural parameters.

The value of the parameter m appearing in the Pearson equation (12) can be determined either by fitting isolated peaks or by carrying out a series of refinements with different values of the parameter m and selecting the refinement which gives the lowest R-factor and the most reasonable temperature parameters. Obviously, the first method is preferable, but it can only be used if the peaks selected for the determination of m are well isolated and permit an accurate evaluation of the background. This can be seen in Fig. 1c, which illustrates the Gaussian least-squares fit to the same 002 reflection of β-PbO_2, performed over an angular range too small for an accurate estimate of the background. The fit, which would be considered satisfactory without prior knowledge of the peak shape, would yield not only the wrong value of m but would also result in a background level so unreasonably high that it might affect even the atomic positional parameters calculated in the refinements. To avoid errors of this type, we have followed the second procedure, and the R-values *vs.* m obtained for β-PbO_2 are shown in Table II.

β-PbO_2.—The results of the refinements of β-PbO_2 in all the samples analyzed are given in Table III, where they are compared, where applicable, with those reported by previous authors. The calculated and observed profiles, with residuals, are shown in Fig. 2.

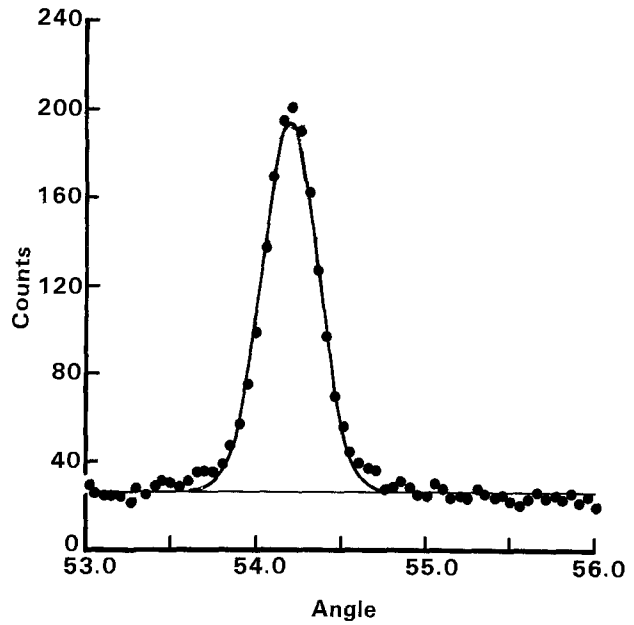

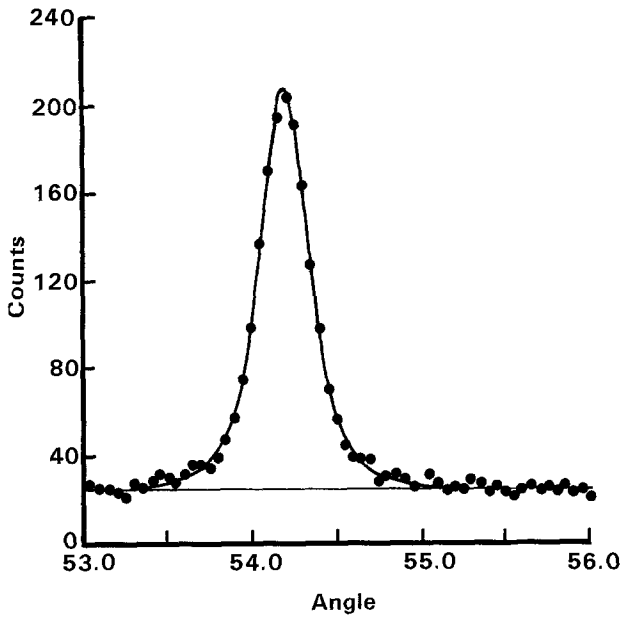

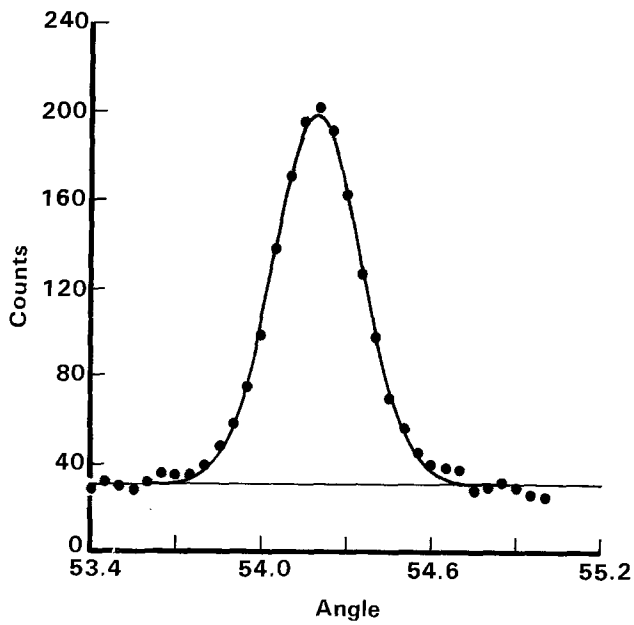

Fig. 1. Least-squares fits (continuous line) of the observed profile intensities (circles) for the reflection 002 of chemically prepared β-PbO_2: (a, top left) Gaussian fit (background = 268, peak height = 1675, 2θ = 54.20, m = 100, and χ = 2.11). (b, top right) Pearson fit (background = 247, peak height = 1834, 2θ = 54.20, m = 1.83, and χ = 1.36). (c, bottom) Gaussian fit over a limited angular range (background = 309, peak height = 1672, 2θ = 54.20, m = 100, and χ = 1.63). (The parameter m is the Pearson parameter and determines the profile shape, and χ is the goodness of fit.)

As shown in the table, the lattice parameter a of β-PbO_2 in Y3 and Y36 is significantly higher than that of chemically prepared β-PbO_2, with a shift/pooled error, Δ/Σ, of 30 and 24 for Y3 and Y36, respectively, [pooled error = $(\sigma_1^2 + \sigma_2^2)^{1/2}$]. On the other hand, the value of c does not vary significantly from sample to sample (maximum Δ/Σ = 7.6).

The positional parameter x of the oxygen atoms seems to decrease in the sequence β-PbO_2, Y36, Y3. The differences observed could indicate a trend, but they are too small to be considered significant (maximum Δ/Σ = 5.0). The interatomic distances and angles calculated for the samples analyzed are reported in Table IV, in which the labeling of the atoms is the same as that indicated in Fig. 3. As a result of the observed changes in the a and x parameters, the distance O(3)-O(4) increases and the distance Pb-O(1) decreases in the sequence β-PbO_2, Y36, Y3. The O(3)-O(5) distance, which is equal to the parameter c of the unit cell, remains unchanged, as does the distance O(2)-O(5). This situation corresponds to a stretching of the octahedral basal plane O(3)-O(4)-O(5)-O(6) along the direction [110] and to a compression of the octahedron along the direction [$\bar{1}$10]. The parameter x_m reported in Table III is given by

$$x_m = (1/8)[(c^2/a^2) + 2]$$

and represents the particular value of x for which all the Pb-O distances are equal. In all the samples studied, x_m is significantly larger than x, *i.e.*, the axial distances Pb-O (1, 2) are smaller than the equatorial distances Pb-O(3, 4, 5, 6). This result is of theoretical importance in the study of rutile-type AB_2 oxides (14), and it is in agreement with the conclusions of a previous analysis of chemically prepared β-PbO_2 (4).[2] The occupancy factor, n, of the lead atom differs from the theoretical value by 5σ or less.

The parameters U, V, and W shown in Table III appear in the equation

$$H^2 = U \tan^2\theta + V \tan\theta + W \qquad [1]$$

in which H is the full width at half maximum (*fwhm*) of the instrumental profile at the diffraction angle θ. In

[2] In the first study of chemically prepared β-PbO_2, a Gaussian peak shape was adopted, and subsequently it was found that the Pearson function should have been used instead. In spite of the use of the Gaussian approximation, the agreement between the results of the two determinations is very close for all structural parameters, and this may be partly due to the fact that in the first analysis the tails of the diffraction lines were excluded from the refinement.

Table II. R-factors vs. the Pearson parameter m obtained for β-PbO_2

β-PbO_2, chemically prepared

m	R_N	R_P	R_W	R_E
∞	6.61	8.55	10.86	4.66
4	5.62	7.44	9.36	4.66
3	5.25	7.14	9.02	4.66
2	5.00	6.83	8.77	4.66
1	5.78	9.23	12.07	4.66

β-PbO_2 in Y3

m	R_N	R_P	R_W	R_E
∞	8.43	4.90	6.23	3.51
2	4.48	4.18	5.29	3.51

β-PbO_2 in Y36

m	R_N	R_P	R_W	R_E
∞	6.09	6.62	8.38	6.22
3	5.62	6.10	7.70	6.22
2.5	5.48	6.07	7.66	6.22
2	5.37	6.08	7.67	6.22

The R-factors are defined in the following way

$$R_N = 100 \times \left\{ \frac{\Sigma|I(\text{obs}) - I(\text{calc})|}{\Sigma I(\text{obs})} \right\}$$

$$R_W = 100 \times \left\{ \frac{\Sigma w[y(\text{obs}) - y(\text{calc})]^2}{\Sigma w[y(\text{obs})]^2} \right\}^{1/2}$$

$$R_P = 100 \times \left\{ \frac{\Sigma|y(\text{obs}) - y(\text{calc})|}{\Sigma y(\text{obs})} \right\}$$

$$R_E = 100 \times \left\{ \frac{N - P + C}{\Sigma w[y(\text{obs})]^2} \right\}^{1/2}$$

In the above formulas N is the number of statistically independent observations, P the number of parameters refined, C the number of constraints, I the integrated intensities, and y the profile intensities of weight w.

Fig. 4, the values of H are plotted against θ for the three samples analyzed.

α-PbO_2.—The orthorhombic phase of PbO_2 is always present in the active material of the positive plate in varying quantities. In general, its proportion with respect to β-PbO_2 decreases as the number of battery cycles increases. It has been pointed out (5) that α-PbO_2 refines poorly, and it has been suggested that this behavior may be related to the defect structure of the compound.

The results of the structural and lattice parameter refinements obtained in this study are given in Table V, where they are compared with some of the results obtained by other authors. The calculated and observed profiles are shown in Fig. 5. It is evident from the table that the agreement between the various results is poor and that the determinations of both lattice and structural parameters are associated in all cases with unusually high standard deviations. Annealing the samples at 160°, 180°, and 200°C for 120 hr did not improve the quality of the powder patterns and the agreement between observed and calculated values of the parameters. Refinements of the lattice constants were also attempted by using the 2θ values reported in the literature (15, 16). In all cases, there were differences between observed and calculated values of 2θ, which cannot be attributed to experimental errors. Also the results given by Hill (8) on this phase of PbO_2 (Table V) show that the values of the lattice and structural parameters depend on the method of preparation of the compound. In addition, the large values of the standard deviation reported for the various samples are an indication that these parameters could not be determined as precisely as those of β-PbO_2.

The uncertainties in the peak positions and peak intensities make it impossible to subtract the contribution of α-PbO_2 from any pattern containing both the α- and β-phases, and this is the reason why the refinements of β-PbO_2 in Y36 and Y3 had to be done by excluding, from the calculations, quite large angular intervals.

Table IV. Interatomic distances (Å) and angles (deg) of β-PbO_2 in the samples analyzed

	Chemically prepared β-PbO_2	Y36	Y3
Pb-O (3, 4, 5, 6)	2.1679(3)	2.1712(6)	2.1758(9)
Pb-O (1, 2)	2.1501(5)	2.1475(10)	2.142(2)
O (3)-O (4) O (5)-O (6)	2.708(1)	2.721(2)	2.734(3)
O (1)-O (3, 4, 5, 6) O (2)-O (3, 4, 5, 6)	3.0532(2)	3.0538(4)	3.0531(5)
O (4)-O (6) O (3)-O (5)	3.3861(1)	3.3844(2)	3.3856(2)
O (3)-Pb-O (4) O (5)-Pb-O (6)	77.30(2)	77.59(4)	77.84(6)

Discussion

Stoichiometry.—Previous authors (18) have pointed out that both α- and β-PbO_2 are nonstoichiometric. At first, it was thought that these oxides had oxygen deficiency and that their electric conductivity could be, in some way, associated with the excess lead present in the structure. Subsequent neutron diffraction measurements by Jorgensen *et al.* (6, 7) showed that no oxygen vacancies were present in electrically active β-PbO_2 and that, instead, the structure seems to be lead deficient. These authors found that the refined occupation numbers of lead were 0.97(2) for β-PbO_2 cycled in H_2SO_4 and 0.95(1) for β-PbO_2 cycled in D_2SO_4. The values do agree with those obtained by Hill (8) for β-PbO_2 present in the positive plate materials. If, therefore, we assume that β-PbO_2 is lead-

Table III. Results of the refinements of the structure of β-PbO_2 in the samples analyzed. Space group: P4/mnm; $Z = 2$. The figures in parentheses are the standard deviations on the last decimal figure.

Parameter	Chemically prepared β-PbO_2	Y36	Y3	Jorgensen (7) β-PbO_2:D	Jorgensen (7) β-PbO_2:H	Naidu (14)	Hill (8) Chemically prepared	Hill (8) Fresh battery	Hill (8) Failed battery
x(O)	0.3068(1)	0.3061(2)	0.3052(3)	0.3070(2)	0.3070(2)		0.3066(2)	0.3054(5)	0.3072(2)
n(Pb)	0.493(2)	0.490(4)	0.477(4)	0.475(5)	0.485(10)		0.493(5)	0.475(8)	0.479(4)
a	4.9554(1)	4.9608(2)	4.9621(2)	4.9526(1)	4.9500(1)	4.9568(5)	4.9556(1)	4.9642(4)	4.9558(1)
c	3.3861(1)	3.3844(2)	3.3856(2)	3.3789(1)	3.3771(1)	3.3866(2)	3.3867(1)	3.3867(3)	3.3820(1)
x_m	0.3084	0.3082	0.3082	0.3082	0.3082	0.3083			
oxygen B			0.90(9)						
$\beta_{11} = \beta_{22}$*	87(3)	91(70)		103(9)	96(8)		113(6)	145(17)	127(5)
β_{33}	90(9)	103(20)		110(18)	86(17)		115(14)	207(66)	168(13)
β_{12}	−56(4)	−84(8)		−50(4)	−68(6)		−70(6)	−52(18)	−60(6)
Lead B			0.51(5)						
$\beta_{11} = \beta_{22}$	54(3)	70(6)		44(6)	53(7)		78(4)	99(16)	83(4)
β_{33}	32(7)	73(14)		38(14)	33(15)		44(11)	103(51)	74(10)
β_{12}	−2(3)	−32(7)		−7(3)	7(5)		−9(5)	−6(19)	−5(5)
U	3858(150)	4461(280)	3534(450)						
V	1979(55)	1579(105)	2079(190)						
W	1291(15)	1266(30)	1770(40)						

* The anisotropic temperature factors are $\beta_{ij} \times 10^4$. $\beta_{13} = \beta_{23} = 0$ for Pb and O atoms.

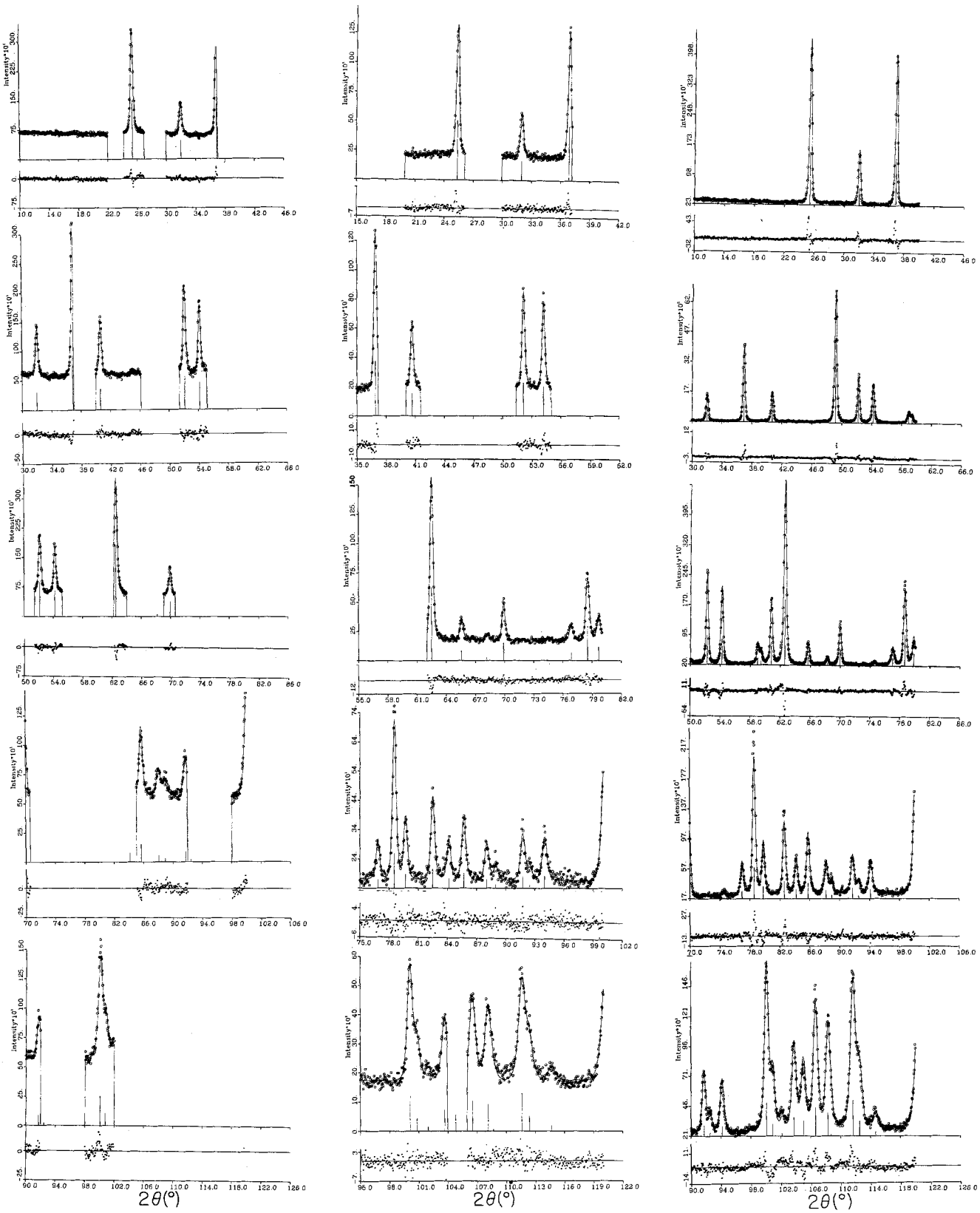

Fig. 2. Calculated (continuous line) and observed (circles) profiles, with residuals, over the five angular ranges for (a) β-PbO_2 in Y3 (b) β-PbO_2 in Y36 and (c) chemically prepared β-PbO_2.

deficient, the stoichiometry of the compound could be expressed by the formula

$$\beta\text{-}Pb^{+4}{}_{1-x}H^{+}{}_{4x}O_2$$

Our results support the view that the structure of β-PbO_2 is not oxygen deficient. In addition, the occupancy factors of lead obtained in our refinements do agree closely with those given by Jorgensen *et al.* (6, 7) and by Hill (8). We feel, however, that it is not possible to conclude that the structure is lead deficient. First of all, the departures from stoichiometry are only 5σ at the most, and second, the refined values of the occupation parameters may be affected by a number of factors which are difficult to account for. More specifically, an imprecise definition of the background level, especially at high values of 2θ, and/or uncer-

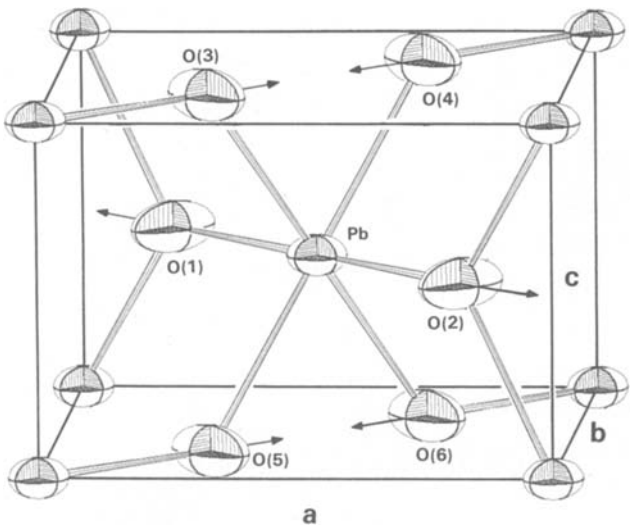

Fig. 3. Unit cell of β-PbO_2. Atoms are represented by their thermal ellipsoids. The labeling of the atoms is the same as that in Table IV. Arrows indicate the direction of oxygen displacements accompanying cycling.

tainties in the description of peak shapes may cause departures of the type observed for β-PbO_2. In addition, there are no chemical reasons which would require lead deficiency, not even if hydrogen must be accommodated in the structure (19). In fact, Moseley *et al.* have observed a close correlation between the quantity of hydrogen found from neutron transmission measurements and the difference between total Pb and Pb^{+4}, determined by analytical means. Consequently, they have proposed that the charge balance required by the incorporation of hydrogen in the structure is maintained by reduction of Pb^{+4} to, most probably, Pb^{+2} and have given for the compound the formula

$$\beta\text{-}Pb^{+4}{}_{1-x/2}Pb^{+2}{}_{x/2}H^{+}{}_{x}O_2$$

Oxygen or lead deficiencies are not necessary to explain the electric conductivity of PbO_2. In fact,

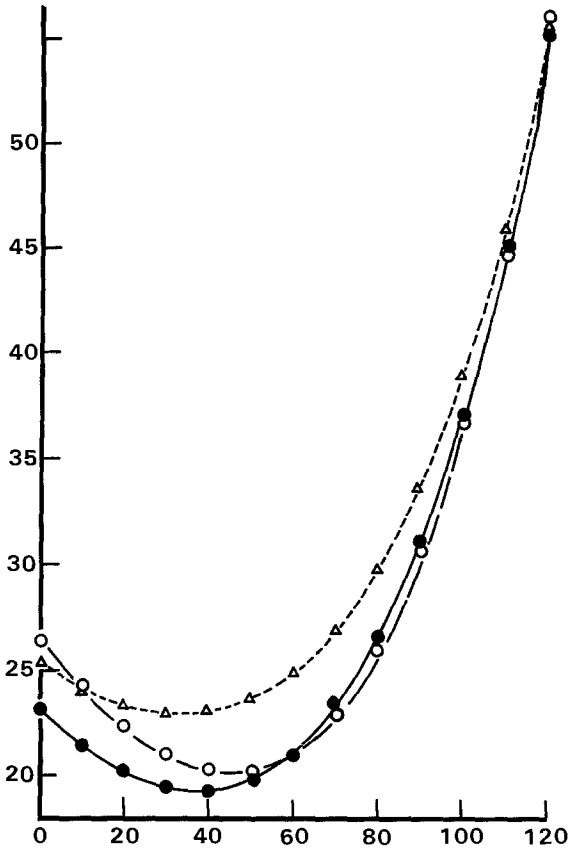

Fig. 4. The values of the full width at half maximum, H, calculated from the least-squares values of U, V, and W, using Eq. [1], are plotted *vs.* θ for β-PbO_2 (●), Y36 (○), and Y3 (△).

Ruetschi and Cahan (20) have pointed out that free electrons may be due to OH^- groups substituting for oxygen. This model is realistic because, as mentioned in the introduction, the presence of bound hydrogen in β-PbO_2 has been established beyond doubt by a number of workers [e.g., Ref. (3)]. Inelastic neutron

Table V. Results of the structural and lattice parameters refinements α-PbO_2 $R_N = 11.65$, $R_P = 5.59$, $R_W = 7.63$, $R_E = 3.46$, $m = 1$ space group Pbcn, $Z = 4$

A) Lattice parameters

	a	b	c	
From neutron profile refinement*	4.9627(10)	5.9588(13)	5.4812(8)	N
Y3 (202)**	4.980(9)	5.964(13)	5.473(6)	N
Y3 (130)***	4.986(10)	5.952(9)	5.472(6)	N
Annealed	4.967(10)	5.979(20)	5.482(8)	N
Hill (8): chem. prepared	4.9898(3)	5.9474(4)	5.4656(3)	N
Hill (8): acid electroformed	4.9947(11)	5.9614(15)	5.4707(11)	N
Bagshaw *et al.* (15)	4.993(3)	5.946(2)	5.459(3)	X(+)
Syono *et al.* (16)	4.998(1)	5.958(1)	5.465(1)	X
Moseley *et al.* (5)	4.998(1)	5.932(1)	5.441(1)	X
Zaslavskii *et al.* (17)	4.927	5.927	5.474	X

B) Structure

	Lead				
				Hill (8)	
	This study	Moseley *et al.* (5)	Zaslavskii *et al.* (17)	Chem. prep.	Acid el.
x	0	0	0	0	0
y	0.1596(8)	0.173(7)	0.178	0.1779(7)	0.1706(13)
z	1/4	1/4	1/4	1/4	1/4
B	0.13(9)	—	—	0.77(12)	0.23(22)
	Oxygen				
x	0.2546(12)	0.2(2)	0.276	0.2685(10)	0.2618(19)
y	0.4005(7)	0.35(8)	0.410	0.4010(7)	0.3977(15)
z	0.4225(7)	0.39(9)	0.425	0.4248(7)	0.4250(14)
B	0.07(9)	—	—	1.31(18)	2.58(33)

$U = 43300(4025)$, $V = 21850(1690)$, $W = 6185(230)$

* The structure was refined using the data obtained from chemically prepared α-PbO_2.

** Peak at $2\theta = 49.48°$ indexed as 202.

*** Peak at $2\theta = 49.48°$ indexed as 130.

(+) X and N indicate that the corresponding measurement was made with x-rays and neutrons, respectively.

studies on chemically prepared β-PbO_2, Y3, and Y36 have indicated that the hydrogen is incorporated in the structure and is not present in pockets of pure

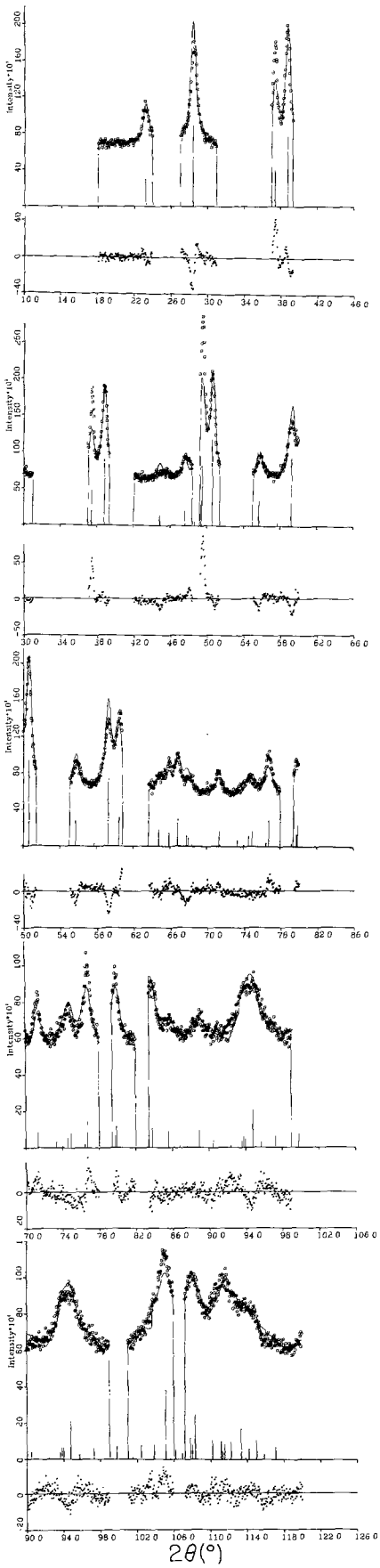

Fig. 5. Calculated (continuous line) and observed (circles) profiles, with residuals, over the five angular ranges for chemically prepared α-PbO_2.

or loosely bound water (21). The presence of hydroxyl ions, OH^-, has been established in other rutile-type oxides, such as SnO_2 (22) and TiO_2 (23). In SnO_2, for example, the substitution of doubly charged oxygen ions with OH^- ions is associated with the replacement of Sn^{+4} with Fe^{+3} or Cr^{+3}, which have similar sizes. It has also been observed, in polarized infrared studies on single crystals of SnO_2, that OH^- ions are formed with oxygen atoms of type 1 and 2 (Fig. 3) and are oriented perpendicular to the c axis of the tetragonal cell. A similar situation seems to also be present in TiO_2 (23). The same orientation of the OH^- ions in β-PbO_2 is very consistent with our results. In fact, both hydrogen content and length of the *a* axis are higher in Y36 and Y3 than in the chemically prepared compound, while the c axis remains practically unchanged in the two groups of samples. The above considerations, therefore, lead to the conclusion that our results, as well as those of Jorgensen *et al.* (6, 7) and of Hill (8) may be interpreted by saying that the β-phase is either stoichiometric or departs from stoichiometry to such an extent that the deviations cannot be detected with certainty with diffraction measurements of the type used in the reported experiments.

It has been impossible to meaningfully refine the occupation numbers of lead in α-PbO_2 and, therefore, no conclusions regarding the stoichiometry of this compound can be reached with our results.

Crystallite size.—The non-Gaussian shape of the reflections, observed in this study and in previous analyses (24), can be explained in a number of ways. The simplest and, probably, the most reasonable explanation is that the samples do contain crystallites with a distribution of sizes. If this is the case, then the pure profile (*i.e.*, the profile due solely to the sample) is nonGaussian, and therefore, its convolution with the Gaussian instrumental profile is also nonGaussian. If we assume that this interpretation is correct, we must conclude that the distribution of crystallite sizes of β-PbO_2 does not differ very much from sample to sample since the best refinements were obtained in all cases with a value of the Pearson parameter *m* of about 2.

The parameters *U*, *V*, and *W* of Eq. [1] depend on the experimental conditions and should be identical for identical geometric configurations of the diffractometer (25). Their variation from sample to sample, indicated in Table III and in Fig. 4, may be due to a number of factors, including crystallite size effects. This can be seen in the following way. If the crystallites are sufficiently small, there will be a broadening of the reflections according to Sherrer's equation

$$h = (K\lambda)/D \cos\theta \qquad [2]$$

where *h* is the *fwhm* of the pure profile, λ is the wavelength of the radiation, *D* is the linear dimension of the crystallites in the direction perpendicular to the reflecting planes, and *K* is a constant. The experimental intensity distribution is the convolution of the profiles due to the instrument and to the sample. If, for the sake of simplicity, we assume that the shape of both profiles is Gaussian, then the total *fwhm* H_{tot} is given by

$$H^2_{tot} = H^2 + h^2 = [(K^2\lambda^2/D^2) + U] \tan^2\theta + V \tan\theta + [(K^2\lambda^2/D^2) + W] \qquad [3]$$

If *D* is constant, *i.e.*, if the shape of the crystallites is spherical, or approximately spherical, Eq. [1] and [3] have the same form, although the numerical values of the coefficients are different. Thus, the curves of Fig. 4 can be interpreted as due to crystallite size effects. If we adopt this interpretation, we may conclude that the crystallites of β-PbO_2 in Y3 are smaller, on the average, than those in the chemically prepared compound, while there are no significant differences between the latter

and β-PbO_2 in Y36. A rough estimate of the crystallite size in our samples indicates that the average dimension in chemically prepared β-PbO_2 is about 800Å, while in Y3 it is around 450Å. These results are in broad agreement with those of Kordes (24), who found a mean size of 600-700Å for the β-phase of the positive plate. No estimates of sizes were attempted for α-PbO_2 in this study.

Lattice parameters of β-PbO_2.—As mentioned previously, the lattice parameter a of β-PbO_2 in Y3 and Y36 is significantly greater than that of the chemically prepared compound, while the c parameter remains unchanged. These results seem to be in disagreement with those obtained by Jorgensen *et al.* (7). These authors found that both parameters are smaller in the electrochemically prepared phase than those reported for the chemically prepared compound. However, if the Jorgensen parameters for PbO_2:H are mulitplied by a scale factor of 1.00248,[3] the new values agree to within one standard deviation with those obtained in this study for Y3. The constant factor relating the two determinations may be the result of errors in the calibration of the diffractometers used for the measurements in the two laboratories. It is interesting to note that Hill (8) observes the same variation of the parameter a as we do. His parameter c, however, is the same for chemically prepared β-PbO_2 and for β-PbO_2 present in the plate of a "fresh battery," but it is significantly lower for β-PbO_2 obtained from a "failed battery."

Refinements on α-PbO_2.—As mentioned previously, the difficulties encountered in the refinements of α-PbO_2 have been attributed to the presence of defects in the structure. This may certainly be true, since electron microscopy studies have shown that these defects are extensive (5, 19). Other factors, however, may also play a role. For example, the large discrepancies between calculated and observed 2θ values in lattice parameter refinements may be due to small departures of the structure from orthorhombic symmetry. The nature of the discrepancies in 2θ are also clearly shown in Fig. 5 for some reflections. A second possible cause for the poor profile refinements of α-PbO_2 may be due to the fact that some diffraction peaks do not follow the behavior indicated by Eq. [1]. This is an indication that the crystallites have nonspherical shape.

As the errors associated with the parameters are large, no differences between results can be established. We must, therefore, conclude that the data on the structure of α-PbO_2 are unreliable and that it is probably more useful to examine the detailed features of the compound with techniques other than diffraction, *e.g.*, by electron microscopy.

Amorphous PbO_2.—The presence of an amorphous form of PbO_2 has been proposed as a contributing active material of the positive plate (2) and to explain the nonGaussian profiles of the diffraction lines (24). The term "amorphous," however, has been used in a rather vague way to describe the lead-acid battery materials. In one case (26), it was meant to indicate the fraction of PbO_2 having crystallite sizes equal to, or less than, about 100Å.

Amorphous materials do not possess periodicity in one, two, or three dimensions and produce diffuse diffraction patterns characterized by broad halos. The first maximum would be evident in the 10°-40° angular range of the first detector. We have found no evidence of such diffuse scattering in any of our powder patterns. This result is in agreement with the observations of Jorgensen *et al.* (7) on electrochemically prepared β-PbO_2. On the other hand, Hill (8) has found "noncrystalline" material varying between 3 and 49 weight percent in the various samples analyzed. The disagreement between Hill's results and ours may be only apparent because it may depend simply on the definition of the term "amorphous" given in each case. If we define as "amorphous" a material without periodicity, as we have done previously, then we may conclude that amorphous PbO_2 is either not present in our samples or it is present in quantities nondetectable by diffraction methods of the type used in this study.

[3] The factor becomes 1.00195 for PbO_2:*D*, showing that the substitution of *H* with *D* is accompanied with expansion of both lattice parameters.

Conclusions

The results given in the previous sections can be summarized as follows: (*i*) The refined occupancy factor calculations indicate that the Pb:O ratio in β-PbO_2 is exactly or very near 1:2. Incorporation of hydrogen in the structure may be accompanied by reduction of Pb^{+4}. (*ii*) Dimensional changes in β-PbO_2 are consistent with the presence of OH^- ions in the structure, oriented along the [110] direction, as has been found in SnO_2 (22). (*iii*) The average structure of α-PbO_2 cannot be accurately determined by profile analysis at this time. The difficulties encountered in the refinement may be due to extensive defects, nonspherical crystallites, or small departures of the structure from orthorhombic symmetry. (*iv*) Based on the profile parameters, we may conclude that the crystallites of β-PbO_2 in Y3 ($\sim$ 450A) are smaller than those in the chemically prepared compound ($\sim$ 800A), while there are no significant differences between the latter and β-PbO_2 in Y36.

Acknowledgments

Thanks are due to Dr. J. J. Rush for many helpful discussions. This work was partly supported by the U.S. Department of Energy's Applied Battery and Electrochemical Research Project under interagency agreement EC-76-A-31-1003. Thanks are extended to the International Lead Zinc Research Organization, Incorporated, for their support of one of the authors and for permission to participate in this investigation. We also thank Dr. Jerome Karle for a critical reading of the manuscript.

Manuscript submitted Sept. 27, 1982; revised manuscript received March 7, 1983.

Any discussion of this paper will appear in a Discussion Section to be published in the June 1984 JOURNAL. All discussions for the June 1984 Discussion Section should be submitted by Feb. 1, 1984.

The International Lead Zinc Research Organization, Inc. assisted in meeting the publication costs of this article.

REFERENCES

1. J. Perkins, *Mater. Sci. Eng.*, **28**, 167 (1977).
2. S. M. Caulder and A. C. Simon, *This Journal*, **121**, 1546 (1974).
3. S. M. Caulder, J. S. Murday, and A. C. Simon, *ibid.*, **120**, 1515 (1973).
4. P. D'Antonio and A. Santoro, *Acta Cryst.*, **B36**, 2394 (1980).
5. P. T. Moseley, J. L. Hutchison, and M. A. M. Bourke, *This Journal*, **129**, 876 (1982).
6. J. D. Jorgensen, R. Varma, F. J. Rotella, G. Cook, and N. P. Yao, Paper 604 presented at The Electrochemical Society Meeting, Denver, CO, Oct. 11-16, 1981.
7. J. D. Jorgensen, R. Varma, F. J. Rotella, G. Cook, and N. P. Yao, *This Journal*, **129**, 1678 (1982).
8. R. J. Hill, *Mat. Res. Bull.*, **17**, 769 (1982).
9. E. Prince and A. Santoro, National Bureau of Standards, US Tech. Note 1117, pp. 11-12, F. Shorten, Editor, Washington, DC (1980).
10. H. M. Rietveld, *J. Appl. Cryst.*, **2**, 65 (1969).
11. E. Prince, National Bureau of Standards, US Tech. Note 1117, pp. 8-9, F. Shorten, Editor, Washington, DC (1980).
12. M. M. Hall, V. G. Veeraraghavan, H. Rubin, and P. C. Winchell, *J. Appl. Cryst.*, **10**, 66 (1977).
13. G. E. Bacon, *Acta Cryst.*, **A28**, 357 (1972).
14. W. H. Baur and A. A. Kahn, *Acta Cryst.*, **B27**, 2133 (1970).
15. N. E. Bagshaw, R. L. Clark, and B. Halliwell,

J. Appl. Chem., **16**, 180 (1966).
16. Y. Syono and S. Akimoto, *Mat. Res. Bull.*, **3**, 153 (1968).
17. A. I. Zaslavskii and S. S. Tolkachev, *Uch, Zap. Leningrad Gos. Univ. Ser. Khim. Nauk*, **12**, 186 (1953).
18. J. P. Carr and N. A. Hampson, *Chem. Rev.*, **72**, 679 (1972).
19. P. T. Moseley, J. L. Hutchison, C. J. Wright, M. A. M. Bourke, R. I. Hill, and V. S. Rainey, *This Journal*, To be published.
20. P. Reutschi and B. D. Cahan, *ibid.*, **104**, 406 (1957).
21. J. J. Rush, Private communication.
22. R. S. Katiyar, P. Dawson, M. M. Hargreave, and G. R. Wilkinson, *J. Phys. C.: Solid State Phys.*, **4**, 2421 (1971).
23. M. Primet, P. Pichat, and M. V. Mathieu, *J. Phys. Chem.*, **75**, 1216 (1971).
24. D. Kordes, *Chemie Ingenieur-Technik*, **38**, 638 (1966).
25. G. Caglioti, A. Paoletti, and F. P. Ricci, *Nucl. Instrum.*, **3**, 223 (1958).
26. M. T. Frost, J. R. Gardner, J. A. Hamilton, K. Harris, I. Harrowfield, R. J. Hill, J. F. Moresby, D. A. J. Rand, S. Swan, and L. B. Zalcman, International Lead Zinc Research Organization Project No. LE-290, Progress Report 5, July-December 1981.

Mathematical Analysis of a Zn/NiOOH Cell

H. Gu*

General Motors Research Laboratory, Electrochemistry Department, Warren, Michigan 48090

ABSTRACT

A mathematical model has been developed to predict the time dependent behavior of a Zn/NiOOH cell. The model uses experimentally determined polarization expressions to describe the losses between the positive and the negative electrodes. The electronic losses in the plane of the electrode are simulated by a network of resistors. The potential distribution, the current distribution, the cell voltage, the power capability, and the energy of a cell can be predicted. The mathematical model provides an analytical tool to evaluate, for example, the trade-offs between power capability and current collector mass, needed to design an electric vehicle battery.

An electrode current collector carries current from the battery terminal to active sites on the electrode where electrochemical reactions take place. With a large electrode, the electronic losses in the current collector can be appreciable such that an uneven distribution of reaction current and an uneven polarization exist on the electrode surface affecting both the specific power and the specific energy. Accelerated degradation and shorting of electrodes may result due to excessive localized gassing on the electrodes.

A current collector with high conductivity will give a uniform current distribution. Most often, a high conductivity current collector is synonymous with a heavy current collector. However, one can also improve the current distribution without increasing the overall weight of the current collector by strategically orienting the members of a current collector to evenly distribute the current. A mathematical model that can predict cell performance will facilitate the design of these strategic current collectors. Eventually, a computer program can be developed that will suggest an optimized current collector design for the specific application of a battery.

Tiedemann, Newman, and Desua (1) applied the resistive network model to bare lead-acid battery grids. The potential distribution on the grid was examined by assuming a uniform current density. Various grid designs were compared based on the magnitude of the maximum potential difference between the tab and the grid node. Using the same approach, Vaaler and Brooman (2) examined the current distribution of pasted positive lead-acid battery plates relative to an equipotential surface. Electrode kinetics were not included. Tiedemann and Newman (3) then expanded their earlier model to examine the transient behavior of a lead-acid cell. Cell polarization between the positive and the negative electrodes was expressed by using an empirical equation whose coefficients were determined based on the porous electrode model developed by Tiedemann and Newman (4). Recently, Sunu and Burrows (5) used a resistive model to examine the potential distributions of the positive plate and the negative plate of a lead-acid cell individually under uniform current density. They compared plates with different widths based on the tab-to-corner potential difference. The plate area was not kept constant in the comparison. Good agreement was shown between their mathematically predicted and experimentally measured potential distributions.

The present work describes the use of a resistive model to predict the transient behavior of a Zn/NiOOH cell with current collectors of different conductivities. The polarization characteristics of the Zn/NiOOH system was determined experimentally on small electrodes and the empirical equation obtained was used in the model to predict system behavior of cells with full size electrodes. The potential distribution, the current distribution, the cell voltage, the power capability, and the energy capability can be calculated to aid in the design of a Zn/NiOOH battery. Although the mathematical model can be applied to predict both charge and discharge behaviors, only the discharge behavior of a Zn/NiOOH cell will be discussed in this paper.

The Mathematical Model

The model simulates the electrode by a network of resistors where each model node is joined to adjacent nodes by resistors. For each node on the positive current collector, there is a node directly opposite to it on the negative current collector. Between opposite nodes, the reaction current is related to the potentials at the nodes by the empirical equation obtained experimentally on a cell with small electrodes approximately the size of the unit element (area) associated with a mathematical node. With reference to Fig. 1, the equation related to node j on an electrode was obtained by applying Kirchoff's law

$$\frac{\phi_n - \phi_j}{R_1} + \frac{\phi_k - \phi_j}{R_2} + \frac{\phi_l - \phi_j}{R_3} + \frac{\phi_m - \phi_j}{R_4} + i_j A_j = 0 \quad [1]$$

where ϕ's are the potentials (V), R's are the effective resistances (Ω) between nodes on the electrode, i_j is the reaction current density (A/cm^2), and A_j is the

* Electrochemical Society Active Member.

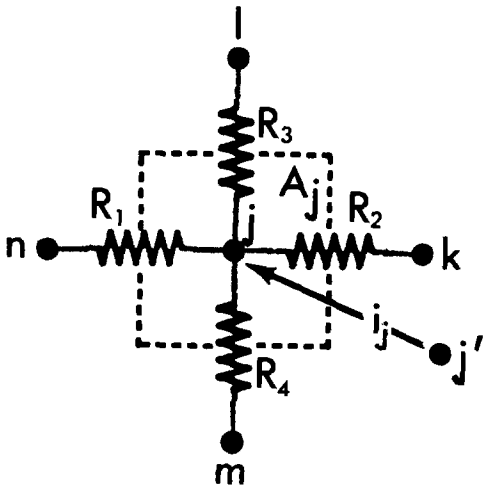

Fig. 1. Application of Kirchoff's law to a mathematical node on the current collector.

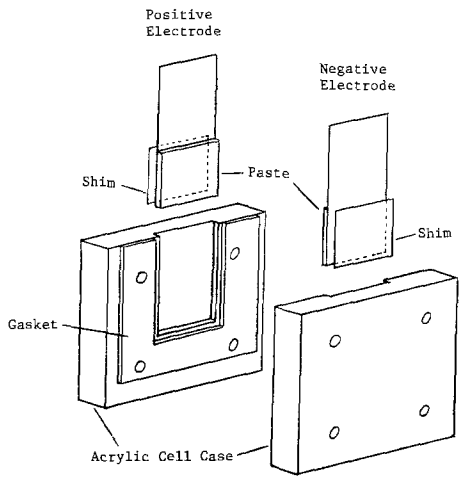

Fig. 2. The experimental cell. Separators and dielectric insulators above the paste are not shown.

unit element (cm^2) associated with node j. Node j' in Fig. 1 is the node on the counter electrode directly opposite to node j.

The mathematical model accepts the applied current as an input parameter. The applied current is defined to be positive for charge and negative for discharge. Other input parameters are: number of mathematical nodes used, time increment used in the transient calculation, maximum charge or discharge time, maximum charge cutoff voltage, minimum discharge cutoff voltage, electrode area, terminal locations, terminal resistances, theoretical capacity of the cell, initial cell capacity, positive electrode vertical and horizontal conductivities, and negative electrode vertical and horizontal conductivities.

The mathematical model calculates with respect to time the following parameters: cell voltage, power delivered, energy delivered, state of charge, potential distribution on the positive electrode with respect to the positive terminal, potential distribution on the negative electrode with respect to the negative terminal, active material distribution, reaction current distribution, and normalized average absolute deviation of reaction currents.

The normalized average absolute deviation (*NAAD*) is defined as the absolute difference between the reaction current density and the mean current density (the uniform current density), normalized by the mean current density, and averaged over the entire electrode as represented by the following equation

$$NAAD = \frac{\int_0^h \int_0^w |(i - im)/im| dxdy}{\int_0^h \int_0^w dxdy} \quad [2]$$

The *NAAD* serves as a measure of the uniformity of current distribution. A small *NAAD* indicates a uniform current distribution.

Determination of Polarization Characteristics

In the experimental determination of polarization between electrodes, small electrodes were used so that electronic losses in the current collector were negligible as compared to losses between electrodes. The construction of the experimental cell is shown in Fig. 2. The electrode dimensions were 2.54 × 2.85 cm. Expanded copper was used as current collectors.

The experimental cell was formed at a C/10 rate (17 mA) for 20 hr after a 24 hr soak-down period. The cell was then discharged at a C/3 rate to 0.4V. Following this formation cycle, the cell was cycled at a C/8 rate charge to the theoretical capacity and a C/3 rate discharge to a 1V cutoff. The cell polarization during discharge was determined in the 6th cycle. This was an arbitrary choice. The result obtained is only representative of the polarization characteristics in early life of the cell.

To determine the voltage-current characteristics, the cell was discharged at an apparent current density of 4.1 $mA\text{-}cm^{-2}$ and periodically ramped to 27 $ma\text{-}cm^{-2}$ at the rate of 0.27 $mA\text{-}cm^{-2}\text{-}sec^{-1}$. Discharge was terminated when the cell voltage fell below 1V.

The discharge cell voltage displayed a linear dependency on the apparent current density as shown in Fig. 3. An equation similar to that used by Tiedemann and Newman (3) was used to fit the data. The linear polarization expression is

$$i = Ya(\phi_p - \phi_n - U) \quad [3]$$

where i is the apparent current density (A/cm^2), U (V) is the intercept of the voltage-current curve (Fig. 3), Ya (S/cm^2) is the inverse of the slope of the voltage-current curve, and $\phi_p - \phi_n$ is the measured cell voltage. When Eq. [3] is applied in the model, ϕ_p corresponds to the potential at a node on the positive electrode and ϕ_n corresponds to the potential at the opposite node on the negative electrode. The current density i is equivalent to the i_j used in Eq. [1].

According to the data, both U and Ya varied with respect to the depth of discharge (DOD) defined relative to the theoretical capacity. Their dependencies

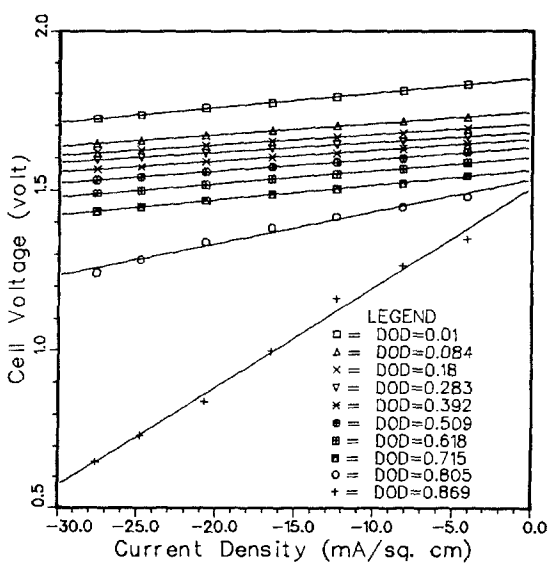

Fig. 3. The cell voltage as a function of applied current during discharge.

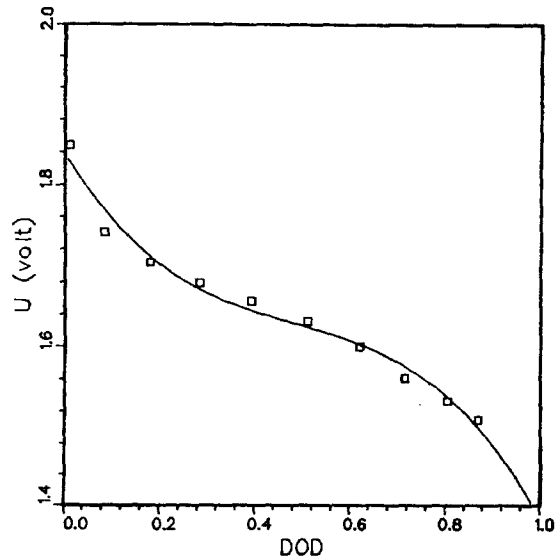

Fig. 4. The dependency of U on DOD

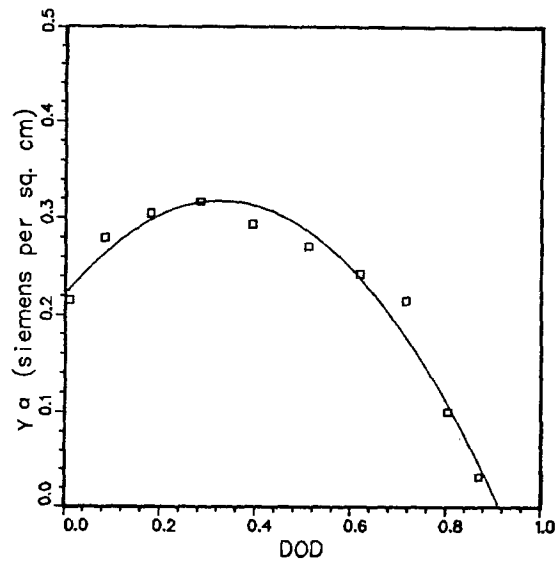

Fig. 5. The dependency of Ya on DOD

Fig. 4 and 5) can be expressed by the following equations

$$U = 1.838 - 0.966(\text{DOD}) + 1.649(\text{DOD})^2 - 1.136(\text{DOD})^3 \quad [4]$$

and

$$Ya = 0.220 + 0.598(\text{DOD}) - 0.919(\text{DOD})^2 \quad [5]$$

Predictions and Discussions

The mathematical model was used to analyze hypothetical full-size cells containing 16 × 16 cm electrodes. Five possible current collectors were examined with the expanded current collector used to determine the polarization characteristics as the standard and other four current collectors having conductivities 2, ½, ¼, and ⅛ times that of the standard in both the horizontal and the vertical directions. In this paper, these current collectors will be referred to as having relative conductances of 2, 1, ½, ¼, and ⅛. Identical current collectors were assumed to be used in both electrodes.

The current collectors were assumed to have the high conductivity in the vertical direction. The conductivity used for the vertical direction is 1279.56 S/cm and for the horizontal direction is 336.31 S/cm. Because of the relatively high conductivity of the copper current collector as compared to the paste conductivity, the current in the plane of the electrode was assumed to be carried solely by the current collector. This assumption, however, is not a necessary condition to apply the mathematical model.

For the calculations, nine nodes were used in each of the horizontal and vertical directions with a total of 162 nodes for both electrodes plus a node each for the positive terminal and the negative terminal. The negative terminal was assumed to be at zero volts. As mentioned earlier, the area associated with a node is relatively the same as that of the experimental electrodes used for the polarization determination.

Four discharge currents (15, 10, 5, and 2.5A) were used for the analysis. They are referred to as 3C, 2C, C, and C/2 rates respectively. The discharge behavior was analyzed based on a fully charged cell with a uniform distribution of active material on the electrodes at the beginning.

In Fig. 6, 7, and 8 are potential distributions and current distributions at time zero, 50% DOD, and 85% DOD, respectively, calculated for a cell containing the standard current collectors and discharging at the C rate. The potential distribution on the positive electrode is reported relative to the positive terminal excluding the terminal loss. The potential distribution on the negative electrode is reported relative to the negative terminal. Since the calculation was based on identical current collectors in both electrodes, potential distributions on the positive and the negative electrodes are similar. The current distribution is reported relative to the mean current density and normalized by the mean current density $((i - im)/im)$. If the current distribution is uniform, it will show a horizontal plane intersecting the $(i - im)/im$ axis at zero.

We can see from Fig. 6, 7, and 8 that the reaction current is concentrated near the terminals at the beginning of a discharge. At mid-way through the discharge, the current distribution becomes quite uniform. However, near the end of a discharge when the active material is depleted near the terminals, the reaction current is forced toward areas still containing the active material and thus resulting in higher reaction current near the bottom of the electrode.

To get a feel of actual magnitudes involved in the potential and the current deviations, the maximum potential difference on the electrodes and the maximum reaction current difference are listed in Table I for the

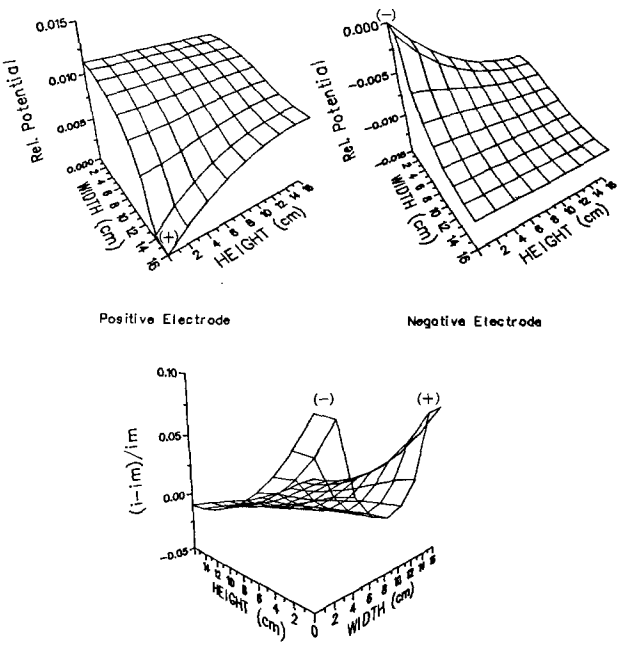

Fig. 6. Potential (V) and current distributions of a cell containing the standard current collectors during initial discharge. (+) represents positive terminal. (—) represents negative terminal.

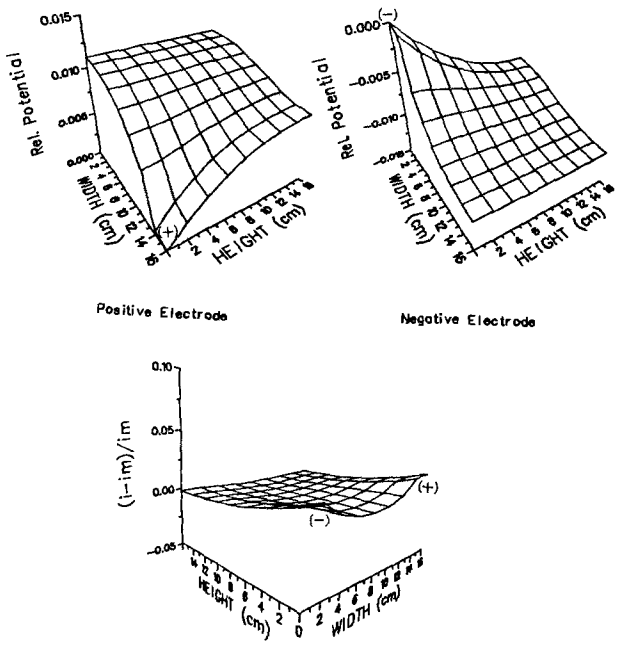

Fig. 7. Potential (V) and current distributions of a cell containing the standard current collectors at 0.50 DOD during discharge. (+) represents positive terminal. (—) represents negative terminal.

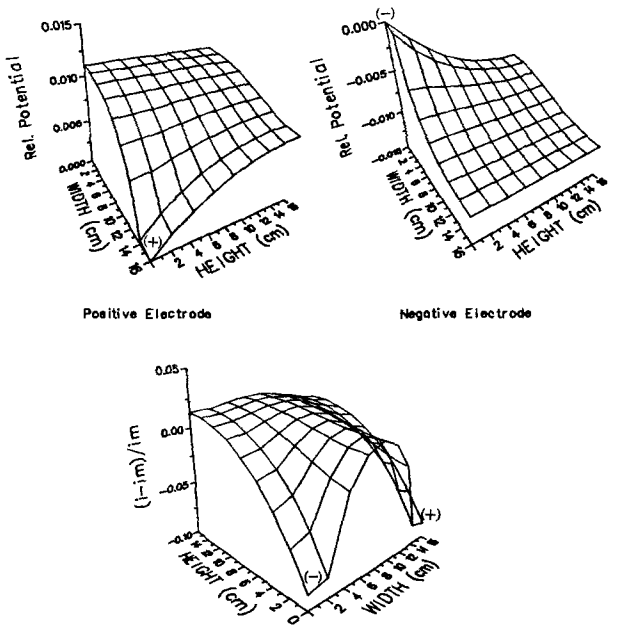

Fig. 8. Potential (V) and current distributions of a cell containing the standard current collectors at 0.85 DOD during discharge. (+) represents positive terminal. (—) represents negative terminal.

cells with current collectors of 1 and ⅛ relative conductances.

As we can see from Table I, the variation in potential on the electrodes is less than 0.1 mV and the variation in current distribution is in the mA-cm² range for the case with relative conductance of 1. These results seem to indicate that the current density is quite uniform for a cell with the standard current collectors discharging at the C rate. For the case with relative conductance of ⅛, however, the potential variation is now in the millivolt range and the current variation is ten times higher than the case with relative conductance of 1. At this level, we may have a current distribution problem. Results in Table I also reveal that the maximum potential difference on the electrode is not an indicator of the uniformity of current distribution. The maximum potential difference can be used as a guideline in comparing different current collectors only when the current distribution is uniform (such as near 0.5 DOD).

Table I. Maximum potential and current differences during discharge

Discharge rate	Current collector conductance	DOD	ϕ(max) − ϕ(min) (mV)	i(max) − i(min) (mA/cm²)
C	1	0	11.2	1.7
		0.50	11.2	0.5
		0.85	11.2	2.1
C	1/8	0	86.6	13.0
		0.50	86.7	2.6
		0.85	88.3	13.9

In Fig. 9, we have the *NAAD* for a cell with the standard current collectors at four discharge rates. As we can see, the current distribution is most uniform between 0.5-0.6 DOD.

In Fig. 10, we examine the cell voltage for a cell with the standard current collectors at four discharge rates. As one would expect, the average discharge voltage is lower at a higher rate of discharge. If 1V is

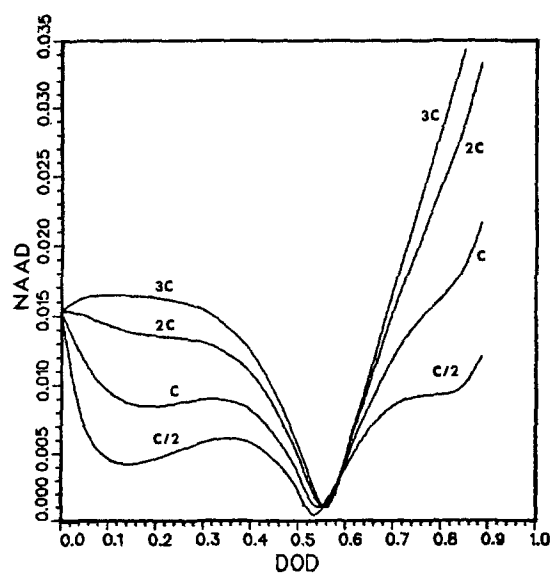

Fig. 9. The normalized absolute average deviation during discharge of a cell containing the standard current collectors.

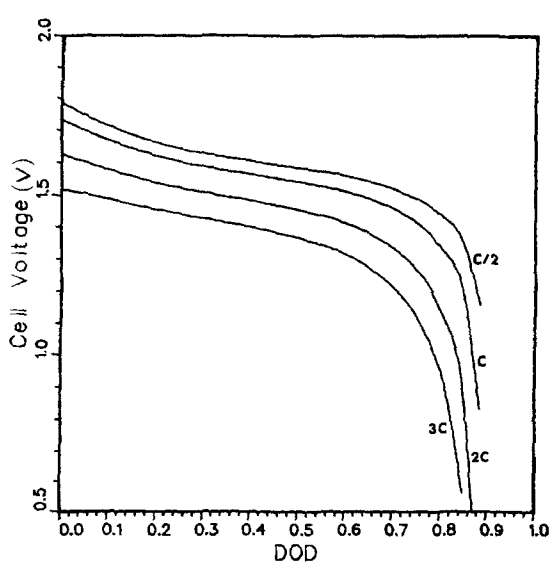

Fig. 10. The cell voltage during discharge of a cell containing the standard current collectors.

chosen as the cutoff voltage, one would get approximately 10% more capacity from the cell discharging at the C rate as opposed to the 3C rate, for example.

To estimate the maximum power capability at 0.5 DOD as a function of current collector relative conductance, we shall examine the voltage *vs.* current curves (Fig. 11). Slopes of the curves in Fig. 11 give us effective cell resistances at 0.5 DOD. The intercept (V_0) gives us the open-circuit cell voltage. The maximum available power is then calculated from the following equation

$$P = (V_0)^2/4R \qquad [6]$$

and is plotted in Fig. 12. As we can see, the maximum achievable power starts to level off with continuous increase in current collector conductance. This is because we are approaching the stage when the power capability is determined by kinetics and separator/electrolyte resistances and not by losses in the current collectors. In other words, improving the current collectors at this stage will not improve the power capability of the cell.

Using the same approach as described with Fig. 11, effective resistance of a cell at different stages of discharge can be obtained. Effective cell resistances determined for five cells with different current collectors are plotted in Fig. 13. The effective cell resistance approaches a lower limit as the current collector conductance increases. As mentioned earlier, this lower limit is determined by cell kinetics and separator/electrolyte resistances. The corresponding open-circuit cell voltage obtained from the intercept of the voltage *vs.* current curve as a function of DOD is the same as that shown in Fig. 4, *i.e.* $V_0 = U$.

The maximum power capability calculated using Eq. [6] is plotted in Fig. 14. As we can see, the power curve with relative conductance of 2 clearly indicates the cell being kinetics limiting. The shape of the curve corresponds very well with the *Ya* curve (Fig. 5) where the lowest polarization appeared approximately at DOD of 0.3. On the other hand, the effect of electronic losses in the electrodes has clearly shown up for the case with relative conductance of ⅛. As an example, if we need a minimum discharge capability up to 100 mA-cm² from a cell having the standard current collectors (relative conductance of 1), only 70% of the theoretical capacity can be utilized with a 1V cutoff. In other words, the cell should be rated at 70% of the theoretical capacity.

Available energies from five cells with different current collectors discharged to a cutoff voltage of 1V are shown in Fig. 15. The cell with the standard current

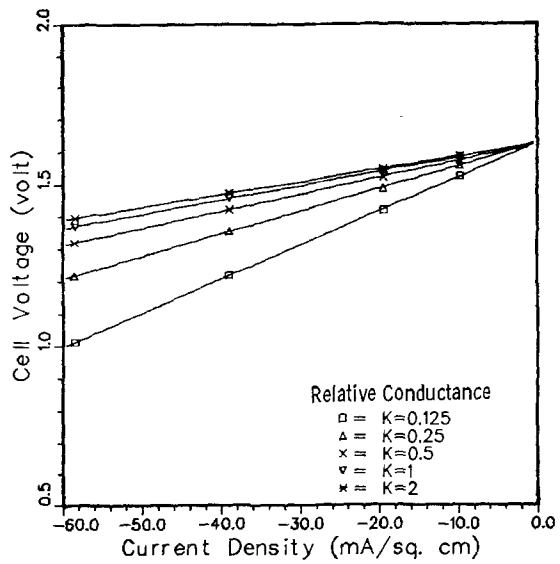

Fig. 11. The cell voltage as a function of the apparent current density at 0.5 DOD during discharge.

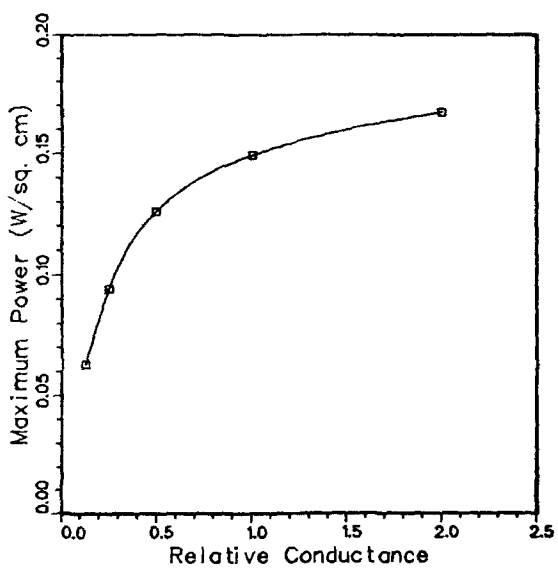

Fig. 12. The maximum power capability as a function of current collector conductance at 0.5 DOD.

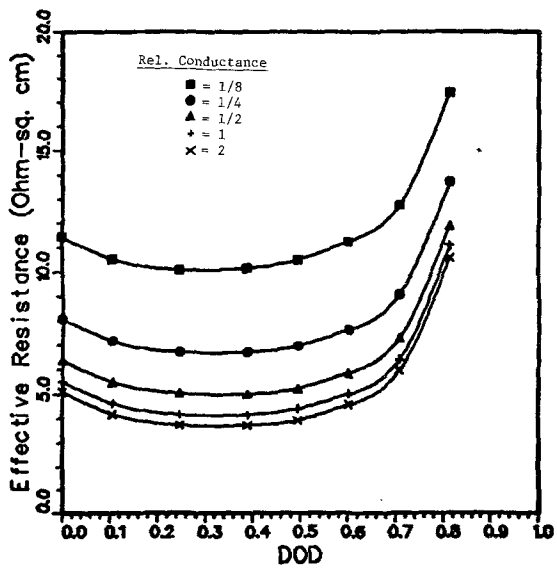

Fig. 13. Effective cell resistances of the five cells with different current collectors during discharge.

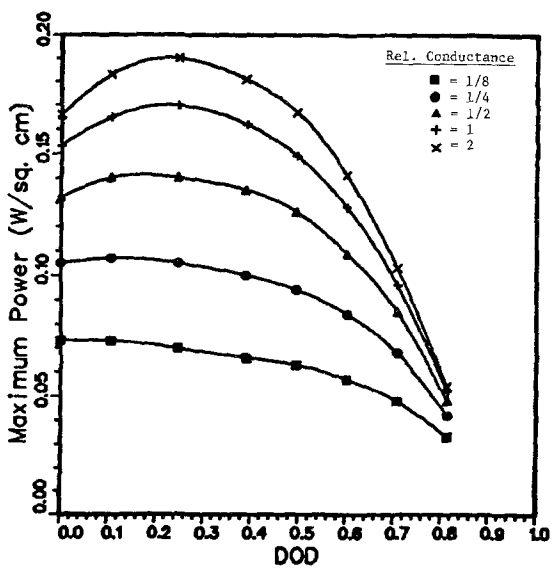

Fig. 14. Maximum power capabilities of the five cells with different current collectors.

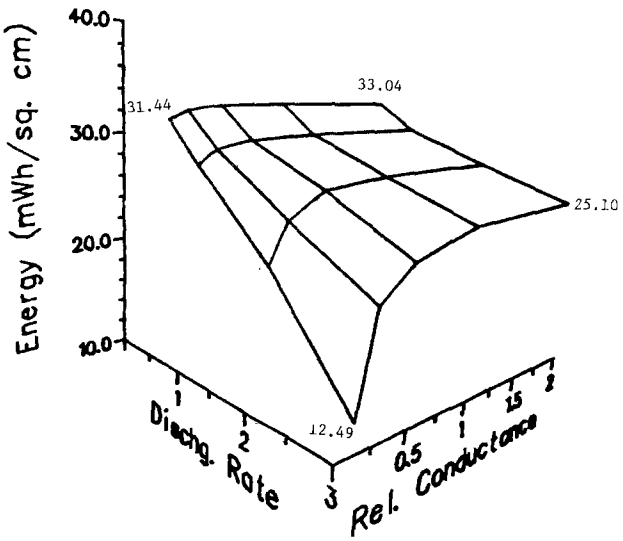

Fig. 15. Energy capabilities to 1V cutoff of the five cells with different current collectors.

collectors can deliver approximately 30 mW-hr/cm^2 at the four discharge rates. Higher conductivity current collectors will improve the energy only slightly.

The mathematical model is limited to calculate the current distribution and other related parameters as governed by the current collector resistances and electrode kinetics. Although the polarization due to kinetics was measured experimentally, losses due to parasitic reactions (such as gassing) were not considered. In other words, all the current is assumed to contribute to the capacity of the cell.

The model at this stage does not consider local concentration and thermal effects. These variables may play important roles in the behavior of the cell. When the concentration effect is included, the tertiary current distribution can be predicted.

Conclusions

The mathematical model will calculate the secondary current distribution of a Zn/NiOOH cell based on conductivities of the current collectors and experimentally determined polarization expressions. Without considering parasitic reactions, the model predicts quite uniform utilization of the active material. The reaction current is concentrated near the terminals at the beginning of a discharge, gradually becomes more uniform over the electrode surface, and becomes concentrated at the bottom of the electrode near the end of the discharge. The NAAD is a good indicator of the uniformity of current distribution.

When the current distribution is not uniform, the maximum potential difference on the electrode cannot be used to compare current collector designs. The variation in the maximum potential difference on the electrode is relatively small even with an appreciable change in the uniformity of current distribution.

The model can estimate the maximum power capability and the specific energy of a Zn/NiOOH cell. These calculated parameters can be used as guidelines to select current collectors for a particular application.

Manuscript received August 31, 1982.

Any discussion of this paper will appear in a Discussion Section to be published in the June 1984 JOURNAL. All discussions for the June 1984 Discussion Section should be submitted by Feb. 1, 1984.

General Motors Research Laboratories assisted in meeting the publication costs of this article.

REFERENCES

1. W. H. Tiedemann, J. Newman, and F. Desua, in "Power Sources 6," D. H. Collins, Editor, pp. 15-23, Academic Press, New York (1977).
2. L. E. Vaaler and E. W. Brooman, Paper 780221, SAE Congress and Exposition, Detroit, MI (1978).
3. W. H. Tiedemann and J. Newman, in "Battery Design and Optimization," S. Gross, Editor, Vol. 79-1, p. 39, The Electrochemical Society Softbound Proceedings Series, Princeton, NJ (1979).
4. W. H. Tiedemann and J. Newman, in "Battery Design and Optimization," S. Gross, Editor, Vol. 79-1, p. 23, The Electrochemical Society Softbound Proceedings Series, Princeton, NJ (1979).
5. W. G. Sunu and B. W. Burrows, *This Journal*, **129**, 688 (1982).

In Vivo Cyclic Voltammetry in Cotton Under Field Conditions

F. Silva-Diaz and W. Gensler

Department of Electrical Engineering, University of Arizona, Tucson, Arizona 85721

P. Sechaud

Laboratory for Bioenergetics and Bioelectrochemistry, University of Paris 14, Val de Marne, France

ABSTRACT

The method of cyclic voltammetry was applied to a bioelectrochemical system consisting of a palladium electrode inserted into a cotton plant and a reference electrode connected to the stem. Preliminary *in vitro* tests of the electrode system in a phosphate buffer established basic cyclic voltammograms and the presence of palladium oxides. Subsequent *in vivo* tests in a commercial cotton field yielded the same basic voltammogram. These results indicate the absence of an active redox couple in the plant apoplast electrolyte in the range of rest potentials normally encountered by the electrode system. Additional *in vitro* tests suggest the influence of oxygen on the rest potentials of cotton. The voltammograms from different anatomical regions of the plant were essentially the same.

During the last decade, an electrochemical technique has been developed which permits the measurement of electrical potentials of higher plants (1). The technique consist of placing a noble metal electrode into plant tissue and a silver chloride reference electrode in the soil to form a galvanic circuit. A high impedance amplifier measures the electrical potential

Key words: biological, electrode, voltammetry, metal.

at regular intervals of time. The potential has been found to vary coherently and reproducibly. This technique represents a passive measurement. No external excitation is applied to the bioelectrochemical system and the measuring amplifier has a high input impedance to avoid electrical loading of the biological system. This technique has been used to monitor cotton plants under field conditions on a day by day basis and the results show strong variations depending on plant water status.

Even though a correlation exists between the measured electrical potential and water status, little is known about the processes responsible for the resulting potential. A theoretical analysis indicates there are two prominent possibilities for the origin of the potential (2). The first possibility is based on the physical movement of the ion impregnated cell wall tissue contiguous to the probe under changes in plant water status. This tissue shift may cause a variation in image charge on the probe and a resulting change in probe potential. The probe is exceedingly close to normal plant cell walls (3). The second possibility centers on the presence of redox couples in the electrolyte contiguous to the probe surface. The basic objective of the present study was to determine the presence or absence of redox couples in the range of potential normally encountered under field measurements, namely, 0 to +400 mV relative to a silver/silver chloride reference.

In order to achieve this objective, the technique of cyclic voltammetry was applied to the probe circuit initially under *in vitro* conditions and then under *in vivo* field conditions in a commercial cotton field.

General Methods and Materials

Throughout the experiment, the working electrode consisted of a palladium wire approximately 8-10 mm long and 150 microns diam. The reference electrode consisted of a double Ag/AgCl cell. Each cell contained different concentrations of potassium chloride. This resulted in a potential difference between the cells and provides a means to check the stability of the reference electrode. This arrangement has been used successfully under field conditions. Its complete construction details have been described previously (1). The exchange current and equivalent resistance of the Ag/AgCl electrode have been found to be 100 μa/cm^2 and 2.5k Ω, respectively (4). This electrode was extensively tested prior to the field work to insure that its polarization was negligible under the current levels encountered.

The plant under investigation was cotton, *Gossypium hirsutum*, CV. Deltapine 61. The working electrode was inserted manually into the plant tissue. The penetration varied between 2-4 mm. Upon insertion of the metal probe, the plant forms a seal around the wound which does not allow the entrance of foreign substances from the external environment (3). In preliminary testing in July of 1981, probes were placed in the main apical meristem, in the mid trunk, in the leaf petioles and in peduncles of bolls of seven plants, approximately one meter in height. In further testing in August of 1981, seven more plants were tested at a 32 hectare commercial cotton field. Probes were placed in the main apical meristem, the petiole of the first or second axial leaf measured from the plant apex and the peduncle on fruiting branches at approximately the fifth node measured from the apex. Plant height was 1.0 $\pm$ 0.1 meters.

The experiments were divided into *in vitro* and *in vivo* tests. The *in vitro* tests refer to those performed with the palladium probe in potassium phosphate buffer, pH 7.0. The *in vivo* tests are those performed with the working electrode inserted in the plant tissue. Each procedure will now be discussed.

In vitro tests.—A palladium wire was immersed in a 1.0M potassium phosphate solution. In addition, the Ag/AgCl reference electrode and an aluminum foil counter electrode were in contact with the solution to complete the three electrode cell. The voltage excitation was provided by a Tacussel Signal Generator and a potentiostat. A Hewlett-Packard Model 7035 XY plotter was used to record the voltammograms. The Pd electrode was introduced into the solution, and the excition was applied until steady-state conditions were reached. Additional *in vitro* tests were performed following electrode preconditioning. Voltammograms were obtained after the electrode was oxidized for 10 min at +1.35V. A similar pretreatment was performed at −1.0V. Cyclic voltammograms under oxygen controlled conditions were also taken. A deaeration procedure was employed consisting of forcing a stream of nitrogen gas into the solution.

In vivo tests.—The experimental setup for the *in vivo* tests is depicted in Fig. 1. The palladium probe is placed in the plant tissue by hand to an approximate depth of 2-4 mm. This probe was connected to the electronic instrumentation, *i.e.*, the voltammetric apparatus. All potentials were measured relative to the Ag/AgCl reference electrode. The reference electrode was placed in a reservoir containing 1.0M potassium chloride. A long tygon tube also containing KCl was connected at the bottom of the reservoir. A polyacrylamide salt bridge was placed at the other end of the tube to prevent leakage of the KCl solution while providing a good conducting path. The salt bridge was in contact with the stem of the plant. A cotton wick saturated in KCl was placed between the stem and the salt bridge to maintain a moist interface. A piece of aluminum foil approximately 4 cm^2 was used as a counter electrode. The electronic instrumentation was either a laboratory constructed voltammetric analyzer or a commercial Tacussel unit. When the voltammetric analyzer was used, a two electrode system was employed as this device was specifically designed for this type of operation. Its construction details can be found in the references (4).

In the *in vivo* tests performed in the Avra Valley in Southern Arizona, it was necessary to use an ATR Model 53A d-c/a-c inverter to provide the electrical power to the Tacussel equipment. One major advantage of the voltammetric analyzer was that this device was completely portable in contrast to the commercial unit which was heavy and required a-c power.

In all the voltammograms shown a positive voltage indicates a measuring electrode at a potential algebraically positive with respect to the reference electrode. A positive current signifies a flow of positive ions from the measuring electrode into the plant tissue.

A major experimental problem arose due to the residual resistance in the path from the measuring electrode, through the stem of the plant, and then into the reference electrode. Total resistance of this path was typically 30k Ω. The reference electrode connection on the stem was about 100 mm from the measuring electrodes. It was not moved during the course of measurements on an individual plant.

Results and Discussion

In vitro tests.—Figure 2 shows the resulting voltammogram of a palladium probe in a potassium phosphate buffer. This test was done without previous conditioning of the working electrode. The potential was swept between −1.0 and +1.35V. Two limiting potentials are clearly visible. At −1.0V, the reduction of hydrogen proceeds through the reaction (5)

$$2H^+ + 2e \rightarrow H_2 \qquad [1]$$

This results in the discharge of large amounts of hydrogen gas. At the positive end of the voltammogram, a similar process occurs involving the evolution of oxygen. This process has been accepted to occur through the following reaction (6)

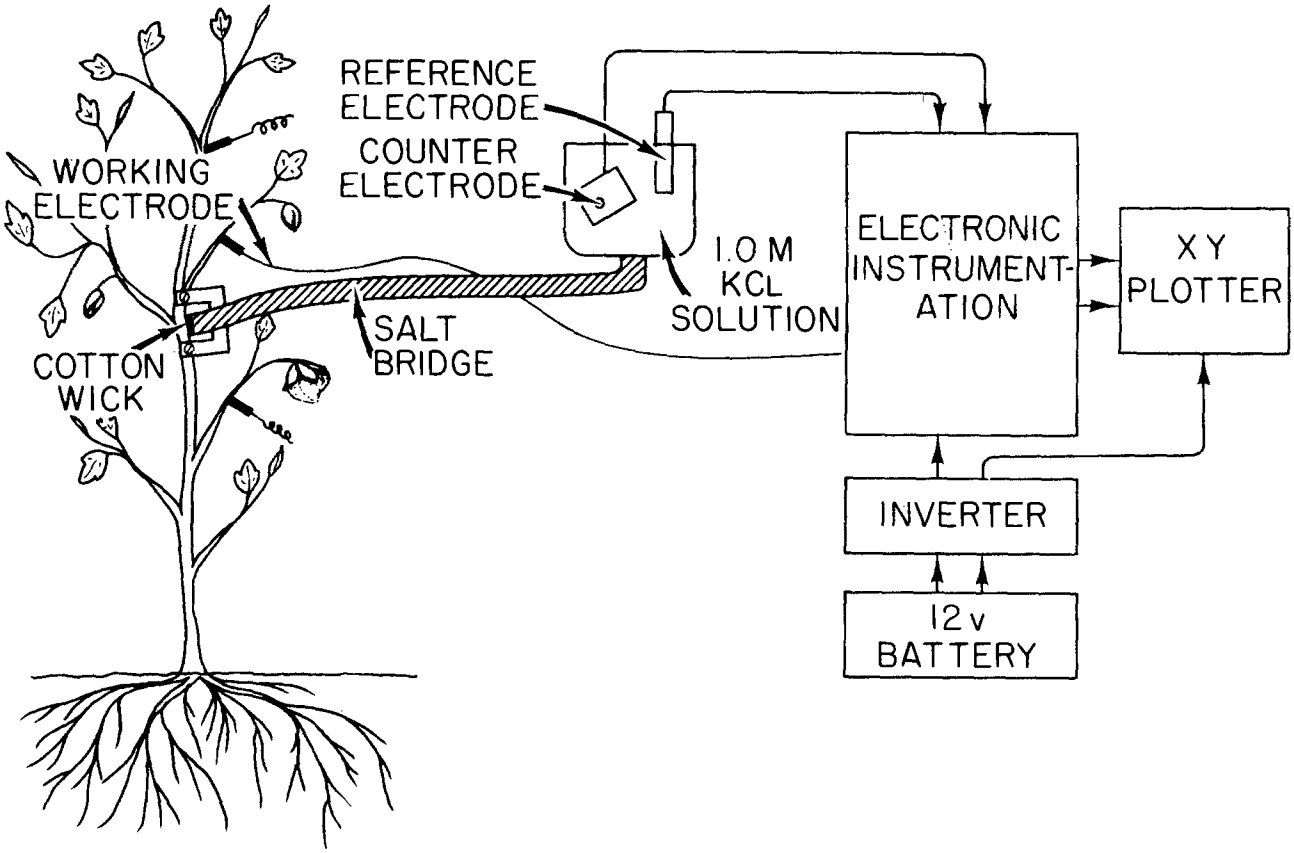

Fig. 1. Experimental set up for the *in vivo* test. The connection between the plant and the reference electrode is made through a polyacrylamide salt bridge. The voltammetric analyzer is used; the aluminum foil counter electrode is not employed, and the inverter drives only the plotter.

$$2H_2O \rightarrow O_2 + 4H^+ + 4e^- \quad [2]$$

However, Hoare (6) has suggested that the process of oxygen evolution may also proceed through the reaction

$$PdO_2 \rightarrow PdO + \tfrac{1}{2} O_2 \quad [3]$$

Four other reactions can be observed in the voltammograms. These reactions have been assigned four different regions labeled A through D in Fig. 2.

To gain a better understanding of these intermediate reactions, the working electrode was preconditioned prior to the voltammetric sweep. First, the palladium probe was maintained at −1.0V for 5 min. This preconditioning procedure caused large amounts of hydrogen gas to be maintained near the surface of the electrode. Equation [1] describes the process of hydrogen formation. Following the preconditioning period, the potential was cycled between the anodic and cathodic limits. The first cycle showed an increase in the wave in region A. As the potential continued cycling, the current in this region dropped and a steady-state curve was obtained after 10 cycles. The only difference observed between this test and the one presented in Fig. 2 was the transient wave at A. This region in the voltammogram must, therefore, be the result of the anodic dissolution current responsible for the oxidations of the sorbed hydrogen. A second preconditioning test was performed by maintaining the electrode at +1.35V for 5 min. This process produced large amounts of oxygen according to Eq. [2] and/or [3]. The voltammograms obtained following this preconditioning procedure showed a marked increase in the resulting current at regions C and D. These two regions are therefore related to oxygen concentration. A more detailed description of these two regions was obtained by performing the voltammetric analysis under oxygen controlled conditions. Figure 3 shows the resulting voltammograms for palladium in aerated and deaerated potassium phosphate solutions. By bubbling nitrogen gas into the solution dissolved oxygen is removed and is no longer available for reduction. The voltammogram for the deaerated solution only showed wave C. The process taking place in region D was not observed in the voltammetric sweep. This suggests that wave D is responsible for the reduction of oxygen. The reduction has been described as a two step process in neutral solutions (8)

$$O_2 + 2H_2O + 2e^- \rightarrow H_2O + 2\,OH^- \quad [4]$$

followed by

$$H_2O_2 + 2e^- \rightarrow 2\,OH^-$$

The ongoing reactions at points B and C still need to be explained. Rand and Woods (9) showed that palladium is oxidized in the anodic region as

$$Pd + H_2O \rightarrow PdO + 2H^+ + 2e^- \quad [6]$$

It is presumed that this is the reaction which occurs at point B. This is a logical assumption because there must be PdO available at the electrode before PdO_2 can be formed at the anodic limit as described by Eq. [3].

A better picture of the anodic regions is presented in Fig. 4. In this case, the electrode was maintained at −0.2V for 5 min. The voltammogram was cycled between −0.2 and +1.35V. This range eliminated the effects due to the formation of hydrogen at more negative potentials. Another two regions were clearly shown in the resulting voltammogram, these are labeled E and F. The reaction taking place at E may be result of converting PdO to PdO_2 possibly through the reaction

$$PdO + H_2O \rightarrow PdO_2 + 2H^+ + 2e^- \quad [7]$$

This reaction forms the necessary PdO_2 to maintain the process of oxygen evolution at the anodic limit

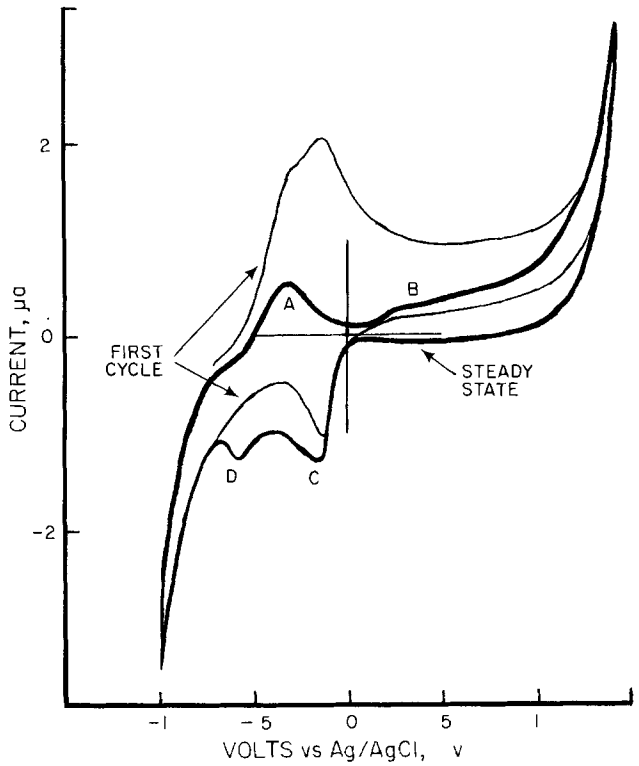

Fig. 2. *In vitro* voltammogram at a palladium electrode. The palladium electrode is immersed in 1.0M potassium phosphate solution. A three electrode cell is used. The excitation was provided by the Tacussel equipment. The anodic and cathodic limits are clearly shown. The first cycle and steady-state curves are shown. Voltage sweep rate = 100 mV/sec.

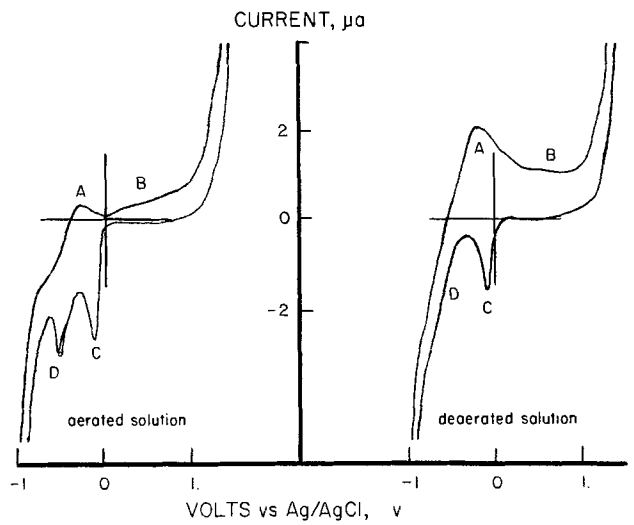

Fig. 3. *In vitro* voltammogram at a palladium electrode in an oxygen controlled solution. The electrode is immersed in potassium phosphate solution. The amount of oxygen is controlled by bubbling nitrogen gas. The Tacussel equipment was used. Voltage sweep rate = 100 mV/sec.

(10). The other wave at region F is probably the reverse reaction due to either the voltage reversal or the unstable characteristic of PdO_2. Finally, wave C is the result of the reduction of the available PdO to Pd. Cadle (11) obtained a reduction peak at +0.29V relative to a standard calomel electrode in 0.2M H_2SO_4.

In vivo tests.—Similar voltammograms of the *in vivo* system were obtained using the experimental set up previously discussed. Figure 5 shows a typical *in vivo* voltammogram. The excitation was applied through several cycles until steady state conditions were

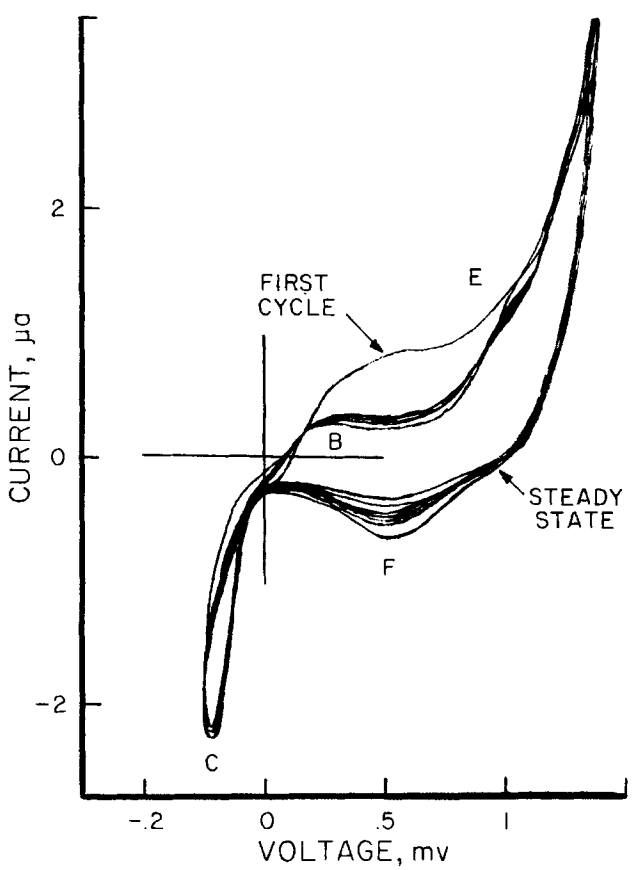

Fig. 4. *In vitro* voltammogram at a palladium electrode in the anodic region. The potential is initially maintained at −0.2V for 5 min. Four distinctive regions are clearly visible. The first cycle and steady-state curves are shown. The Tacussel equipment was used. Voltage sweep rate = 100 mV/sec.

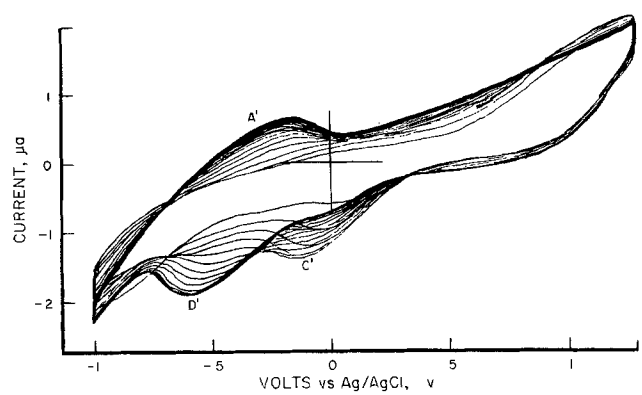

Fig. 5. *In vivo* voltammogram at a palladium electrode in cotton. The electrode is placed in the stem. The excitation is provided by the voltammetric analyzer. There are three distinctive waves in the voltammogram. Notice the similarities with the *in vitro* test at points A', C', and D'. Voltage sweep rate = 100 mV/sec.

reached. The voltammograms showed three distinctive waves which are labeled A', C', and D' corresponding to similar reactions in the *in vitro* tests. The waves maintained their relative positions but they were shifted toward more positive potentials. Also, the background limits were less defined than in the *in vitro* tests. These two characteristics of the *in vivo* voltammograms can be attributed to the large series resistance which separates the working electrode and the Ag/AgCl reference electrode. This series resistance was minimized by the special arrangement depicted in Fig. 1 which permits placing the reference electrode very close to the palladium probe. It is important to mention that whenever the voltammetric analysis was

attempted with the reference electrode buried in the soil, the response was completely incoherent, characterized by excessive noise at the current output.

Even though the high series resistance obscured the available information from the voltammograms, the results were highly reproducible regardless of which equipment was used. It was also observed that the plant returned to its stable pretest potential region immediately after the external excitation was removed. This characteristic allowed one to apply cyclic voltammetry at the same probe several times without causing permanent damage to the tissue.

When the excitation was applied at different part of the plant, very little difference was observed. The peak current for the voltammogram at the stem were somewhat larger than those corresponding to the petiole and the peduncle. This is due to a larger series resistance between the latter probes and the reference electrode. Figures 6a and b shows voltammograms at a petiole and a peduncle, respectively.

In general, the voltammograms of the *in vitro* system were very similar to those obtained *in vivo*. This similarity allows one to extrapolate the resulting processes of the palladium probe *in vitro* to those *in vivo*.

The results suggest a lack of electroactive species in the *in vivo* plant apoplast solution. Even if there are redox couples in this extracellular fluid, they could go undetected due to their low concentrations, or the high series impedance present in the system masks their detection, or simply because the species is electrochemically inactive at palladium.

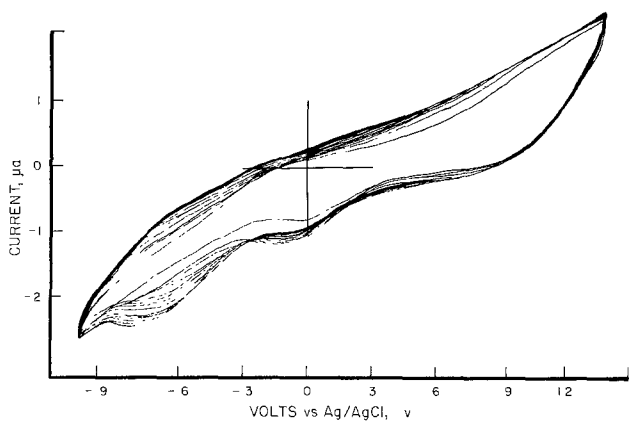

Fig. 6a. Voltammogram at the peduncle, the voltammetric analyzer provided the excitation. Voltage sweep rate = 100 mV/sec.

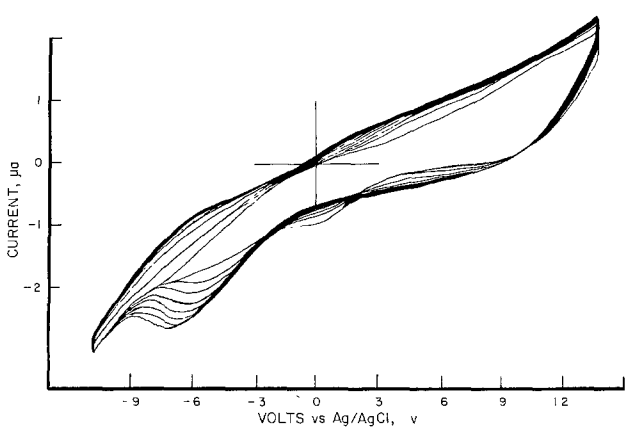

Fig. 6b. Voltammogram at the petiole, the voltammetric analyzer provided the excitation. Voltage sweep rate = 100 mV/sec.

If there are no redox couples originally in the apoplast electrolyte to account for the potential values encountered in the plant, then the only possible explanation for redox activity is the presence of palladium oxides. These oxides can be formed through contact with the fluid adjacent to the palladium probe. The concentration of the oxides can vary depending on the volume of fluid which in turn must depend on the amount of water available in the plant.

At this point, it is very difficult to affirm which oxide is responsible for the rest *in vivo* potential. Furthermore, the rest potential of the *in vivo* system may not necessarily be limited to a single oxide. Hoare has suggested (7) that the rest potential of palladium in an acid medium is the result of a mixed potential determined by the reactions

$$Pd \rightarrow Pd^{++} + 2e^- \quad [8]$$

and

$$O_2 + Pd^{++} + 2e^- \rightarrow PdO_2 \quad [9]$$

where the resulting potential is modulated by the concentration of PdO_2 and O_2. Therefore, a similar mechanism may be responsible for the equilibrium potential of the plant. This argument is supported by the fact that the potential of the palladium probe in the potassium phosphate solution was found to drop sharply when the solution was deaerated with nitrogen. This drop is very similar to the change of potential of the plant following irrigation.

In summary, the *in vitro* and *in vivo* voltammograms were basically the same shape. This indicates the absence of active redox couples in the plant apoplast electrolyte. The *in vitro* tests indicate the presence of palladium oxides. The presence or absence of oxygen influences the *in vitro* rest potential. This suggest that the *in vivo* rest potential could be a result of a mixed potential whose value is influenced by the presence of oxygen.

Manuscript submitted May 3, 1982; revised manuscript received *ca.* Oct. 28, 1982.

Any discussion of this paper will appear in a Discussion Section to be published in the June 1984 JOURNAL. All discussions for the June 1984 Discussion Section should be submitted by Feb. 1, 1984.

The University of Arizona, Cotton Inc. and the Office of Water Policy, DOI, Grant AZB091 assisted in meeting the publications costs of this article.

REFERENCES

1. W. Gensler, *This Journal*, **127**, 2365 (1980).
2. A. Goldstein and W. Gensler, "Bioelectrochemistry and Bioenergetics," Vol. 8, 645 (1981).
3. A. Goldstein, *Am. J. Bot.*, **69**, 513 (1982).
4. F. A. Silva-Diaz, M.S. Thesis, University of Arizona, Tucson, AZ (1982).
5. J. Heyrovsky, "Principles of Polarography," p. 225, Academic Press, New York and London (1969).
6. R. N. Adams, "Electrochemistry at Solid Electrodes," p. 19, Marcel Dekker, Inc., New York (1969).
7. J. Hoare, *This Journal*, **111**, 610 (1964).
8. A. Bard and L. Faulkner, "Electrochemical Methods," p. 175, John Wiley and Sons, New York (1980).
9. D. Rand and R. Woods, *J. Electrochem. Anal. Chem.*, **35**, 209 (1972).
10. J. Hoare, *This Journal*, **112**, 1120 (1965).
11. S. Cadle, *Anal. Chem.*, **46**, 587 (1974).

Anodic Oxide Films on $Pb_{1-x}Sn_xSe$

S. C. Gupta[1] and H. J. Richter*,[2]

Fraunhofer-Institut fur Physikalische Messtechnik, Heidenhofstrasse 8, D-7800 Freiburg, Germany

ABSTRACT

The process for forming the anodic oxide on $Pb_{1-x}Sn_xSe$ ($x \sim 0.068$) using a constant current source is studied. The electrolyte is composed of N-methyl acetamide, water, and propylene glycol. Reproducible films are obtained with the electrolyte when adjusted to $pH = 6.6 \pm 0.2$ by using oxalic acid and ammonium hydroxide. Surface analysis using x-ray photoelectron spectroscopy has been made. All the three components Pb, Sn, and Se participate in the oxidation. The anodic oxide is composed of PbO, SnO_2, and an oxide of Se.

The ternary alloy $Pb_{1-x}Sn_xSe$ is a narrow gap semiconductor material. Its energy gap can be varied continuously from 0 to 0.17 eV at 77 K by changing the lead to tin ratio (1). It finds applications in infrared emitting and detecting devices (2-5). Their performance is closely related to the surface properties. In order to get stable devices, it is necessary to passivate the $Pb_{1-x}Sn_xSe$ surface. Up to now very little work has been done in this direction. One way to passivate the surface is to form a native oxide. This can be accomplished by either anodic oxidation, plasma oxidation, or thermal oxidation. In III-V group compounds and $Hg_{1-x}Cd_xTe$, anodic oxidation has proved to be a promising technique (6-10). We have applied this method to $Pb_{1-x}Sn_xSe$. In this paper, we describe the procedure for the film growth similar to the method described in Ref. (11) for $Pb_{1-x}Sn_xTe$. The chemical behavior of the anodic films to various organic and inorganic solvents, and their chemical composition using x-ray photoelectron spectroscopy (XPS) were examined. To the authors knowledge, this is the first work on anodic oxidation of $Pb_{1-x}Sn_xSe$.

Anodization Procedure

The $Pb_{1-x}Sn_xSe$ ($x \sim 0.068$) wafers used were both n and p type vapor phase grown single crystals. The carrier concentration was in the range 10^{18}-10^{19} cm^{-3}. The surface was prepared first by lapping with 3.5 μm Al_2O_3 powder. The lapped surface was chemomechanically polished first with HBr/Br_2 and then with KOH/H_2O_2.

The setup used for anodic oxidation is as shown in Fig. 1. A platinum foil or wire was used as the cathode. The electrolyte consisted of a mixture of water, N-methyl acetamide (NMA), and propylene glycol. The pH-value of the solution was adjusted by oxalic acid and ammonium hydroxide. The anodic oxidation was carried out under normal light condition at room temperature using a constant current d-c source. The cell voltage with time was measured by a voltmeter as shown in Fig. 1. After anodization, the samples were rinsed in deionized water for a few seconds and then dried in pure nitrogen gas flow.

For optimizing film growth conditions, the water to NMA ratio and the pH-value were varied in order to obtain maximum cell voltage which is a measure of the insulating quality of the film.

Figure 2 shows the variation of the maximum cell voltage and pH-value by varying the volume ratio of water to NMA. The current density was kept constant at $J = 2$ mA/cm^2. It was observed that with time the cell voltage first increased, reached a maximum (as shown in Fig. 2) and then decreased. The cell voltage had the largest value when the volume ratio of water to NMA was 0.2. Yet the films thus obtained were non-uniform. Good, uniform and reproducible films were obtained when the pH-value was adjusted to 6.6 ± 0.2 by oxalic acid and ammonium hydroxide.

Figure 3 shows the variation of cell voltage with time at various current densities ranging from 0.5 to 2 mA/cm^2 for an electrolyte consisting of one part water to five parts NMA and a constant pH-value of 6.6. The cell voltage first increased with time and then saturated for all chosen current densities. The saturation voltage is almost linear to the current density (curve A in Fig. 3). For further experiments, the current density was kept constant at 1 mA/cm^2.

If propylene glycol was added to the electrolyte, the cell voltage was not saturated for times up to 14 min and much higher cell voltages could be obtained (Fig. 4). For comparison, the 1 mA/cm^2 curve of Fig. 3 is

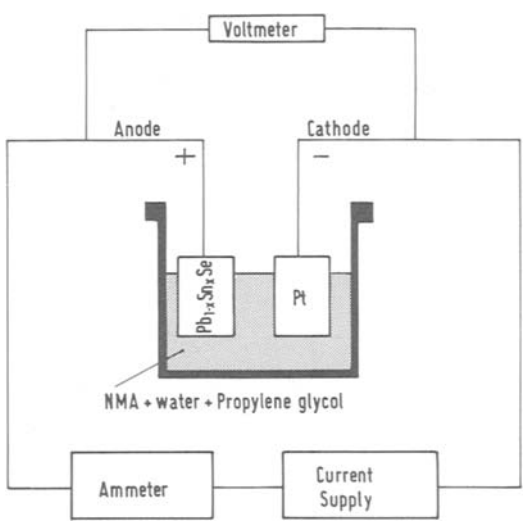

Fig. 1. Systematic arrangement for anodizing $Pb_{1-x}Sn_xSe$

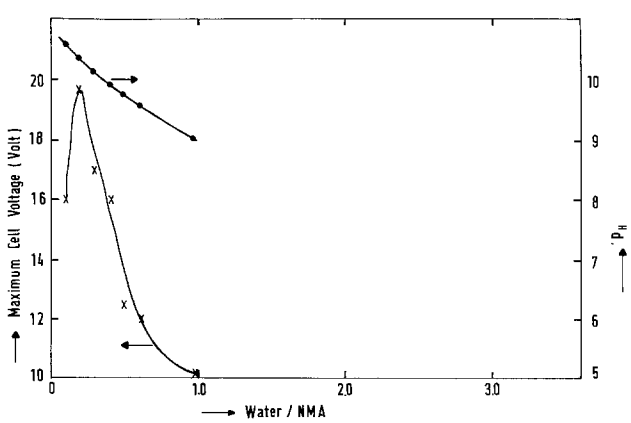

Fig. 2. Maximum cell voltage *vs.* volume ratio of water and NMA at a current density 2 mA/cm^2 and the variation of the pH-value with the electrolyte composition.

* Electrochemical Society Active Member.

[1] Permanent address: Solid State Physics Laboratory, Lucknow Road, Delhi-7, India.

[2] Permanent address: Fraunhofer-Institut fur Angewandte Festkorperphysik, Eckerstr. 4, D-7800 Freiburg, Germany.

Key words: anodic oxide, lead tin selenide, pH value, chemical composition.

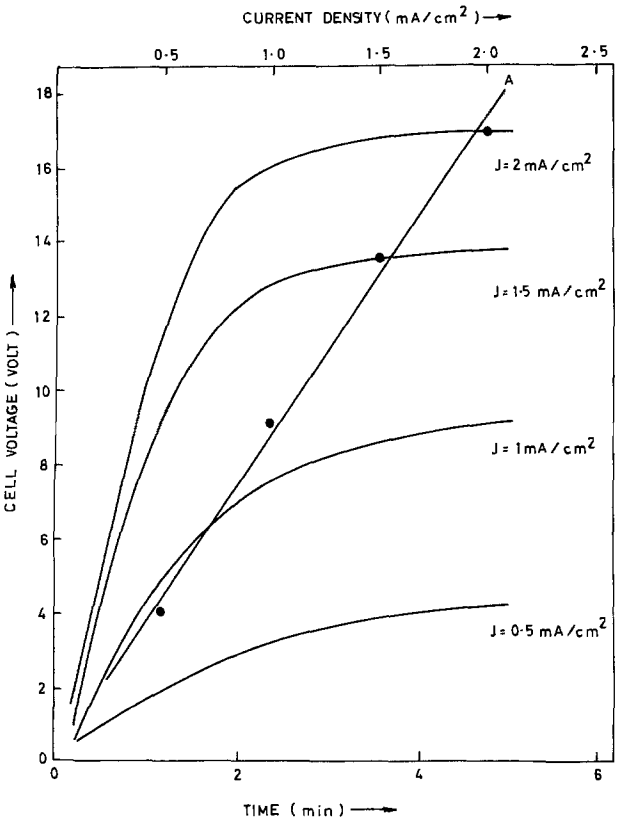

Fig. 3. Cell voltage vs. anodic oxidation time at various current densities and saturated cell voltage vs. current densities (curve A) for the electrolyte composition: volume ratio of water to NMA 1:5 and pH ≃ 6.6.

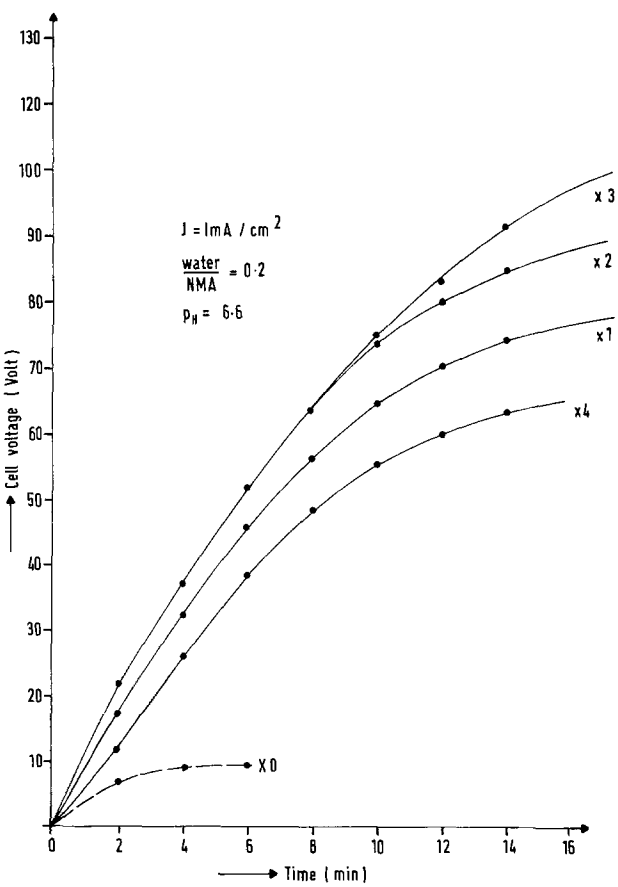

Fig. 4. Effect of adding glycol: (× 2 etc.) means adding twice as much propylene glycol as the volume content of water and NMA.

shown in Fig. 4 as broken line. The optimum ratio of electrolyte to propylene glycol is about 1:3. Figure 5 shows the cell voltage as a function of time at a current density of 1 mA/cm² for various compositions of water and NMA with equal content of propylene glycol as the mixture of water and NMA and pH ≃ 6.6. The cell voltage was the largest when the volume ratio of water and NMA in the electrolyte was 0.2, consistent with the earlier finding. Since the curves of Fig. 4 and 5 are similar one can expect this optimum ratio water: NMA independent of the propylene glycol content.

Film Properties

The oxide films were transparent for cell voltages up to 50V. Films obtained above 50V were opaque. Figure 6 shows the microphotographs of the film grown up to 45V. Though the films have a homogeneous appearance to the naked eye, some black spots appear, which seem to be a crystalline phase (Fig. 6b). The size of these spots increases with the cell voltage. The origin of crystalline phase is not clear. Similar spots have appeared in the anodic oxidation of $Pb_{1-x}Sn_xTe$ (11). There they have been considered to depend on the surface treatment with HBr/Br_2. However, we find that the black spots always appear independent of the surface preparation with or without propylene glycol added to the electrolyte. The additional surface treatments tested were: polishing with Al_2O_3 (grain size 3.5 μm) only, iodine plus KOH and also as grown facets.

The thickness of the oxide film as a function of cell voltage was determined by interferometry. Figure 7 gives a relation between the cell voltage and the thickness of the film. The colors of the film obtained at these cell voltages were as indicated in the same figure. It is an important result that the film thickness increases linearly with cell voltage in the range 20-50V.

It was easy to etch the transparent films in acidic or alkaline solution. The solubility properties are summarized in Table I. The anodic oxides were not chemically attacked by organic solvents such as acetone,

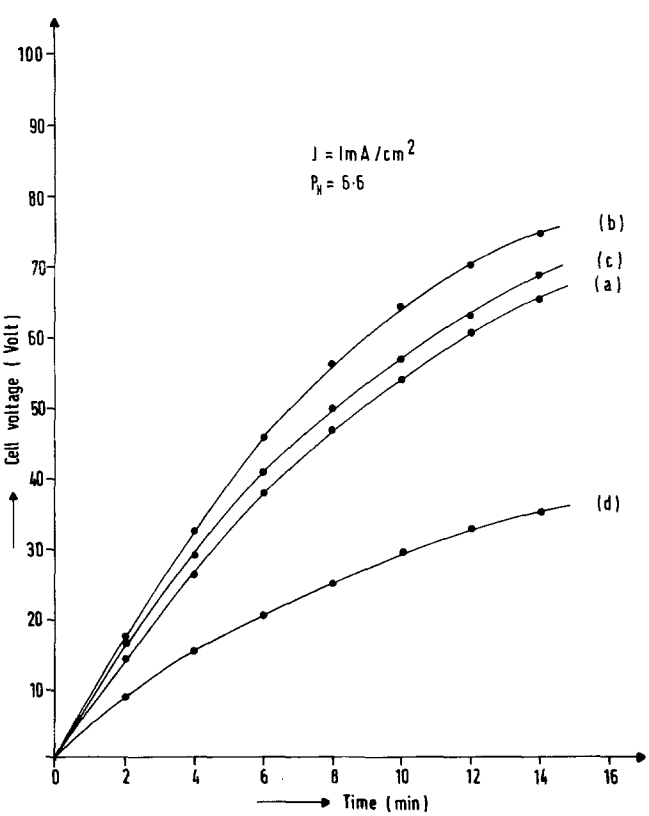

Fig. 5. Cell voltage vs. oxidation time for various compositions of water and NMA (a) 0.1 (b) 0.2 (c) 0.4 and (d) 0.7. The propylene glycol to the water + NMA ratio is 1:1.

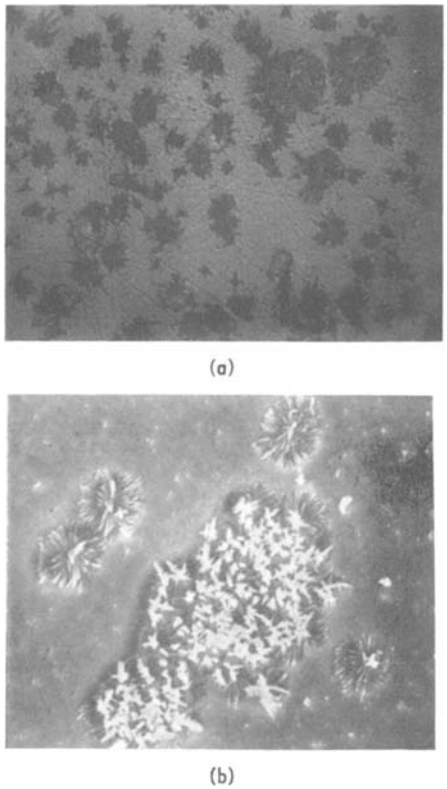

Fig. 6. Microphotographs of an anodic oxide film grown for the electrolyte: water, NMA and propylene glycol 1:5:18, pH = 6.6, J = 1 mA/cm^2, cell voltage = 45, magnification (a) 500 and (b) 1300.

benzene, trichloroethylene, xylene, glycol, methanol, carbon tetrachloride, and thiourea. The XPS measurements were carried out with a *p*H1 system of Physical Electronics Industries. The x-ray photoelectrons were excited by the Mg Kα line (1253.6 eV) and analyzed by a double pass cylindrical mirror analyzer with an accuracy ± 0.3 eV. Figure 8 shows the overall (of both crystalline and amorphous phases) XPS spectrum of an unoxidized $Pb_{1-x}Sn_xSe$ (x = 0.068) surface, of a 950Å thick anodic oxide layer on $Pb_{1-x}Sn_xSe$ surface and an argon sputtered (at 4 keV for 15 min) anodic oxide $Pb_{1-x}Sn_xSe$ surface. The principal XPS structures consist of Pb 4f doublets, Sn 3d doublets, and Se 3d lines. The XPS spectrum for oxygen is not shown. In the unoxidized $Pb_{1-x}Sn_xSe$ sample Sn $3d_{5/2}$ peaks at 485.8 eV corresponding to Sn^{2+}, Pb $4f_{7/2}$ peaks at 137.8 eV corresponding to Pb^{2+} and Se 3d peaks at 53.7 eV corresponding to Se^{2-} in $Pb_{1-x}Sn_xSe$. These Sn, Pb, and Se signals shifted to higher energy in an oxidized surface. These changes in the binding energies are due to chemical shifts caused by changes in chemical bonds.

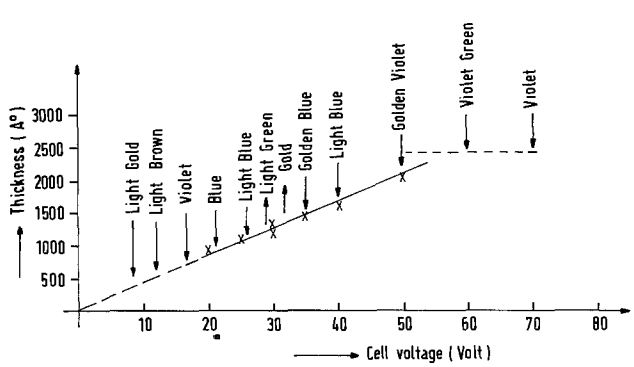

Fig. 7. Oxide film thickness and its color *vs.* cell voltage at a current density of 1 mA/cm^2 for the electrolyte: water, NMA, propylene glycol as 1:5:18, pH = 6.6.

Table I. Solubility of the anodic oxide film in acid and alkaline solutions

Solution	Solubility
HCl	Soluble
HNO_3	Soluble
H_2SO_4	Soluble
HF	Soluble
CH_3COOH	Insoluble
NaOH	Soluble
KOH	Soluble
NH_4OH	Soluble

The chemical shift of Sn $3d_{5/2}$ from 485.8 to 486.7 eV corresponds to a change in the oxidation state from Sn^{2+} to Sn^{4+} in SnO_2 (12), and a shift in Pb $4f_{7/2}$ from 137.8 eV to 138.8 eV corresponds to the position of Pb in PbO (13, 14). The observed chemical shift of the Se 3d was from 53.7 to 59 eV. It is impossible to assign an oxidation state to Se. This is because the data on various oxidation states of Se vary in a certain range, *e.g.*, the binding energy for Se^{4+} in SeO_2 varies from 59.2 to 59.7 eV, in Na_2SeO_3 from 58.3 to 59 eV and in H_2SeO_3 it is 59.3 eV (15). However the shift in the Se signal gives a strong indication that Se was indeed oxidized. We may conclude that the anodic oxide is a component containing of PbO, SnO_2 and an oxide of Se.

The results of Fig. 8 show that the oxide of Se is decomposed by sputtering with argon ions. Besides the oxide peak a second peak appears which is most likely due to elemental selenium (Se°). The slight shifts of the PbO and SnO_2 peaks are in the resolution limit of the experiment. The effect of the argon sputtering is probably due to the increased temperature of the oxide film. It is known from Ref. (17) that TeO_2 decomposes at temperatures above 400°C.

The relative concentration of the elements Pb, Sn, Se, and O within the detection depth of 5-10Å was determined from the intensities of their respective XPS peaks. Table II shows the atomic ratio of Pb, Sn, Se and O in the anodic oxide for two samples S1 and S2 grown at cell voltages 16 and 21V, respectively. These results show that the oxidized surface is enriched in Sn compared to the unoxidized surface. This might be due to migration of Sn during oxidation because Sn diffuses faster (16). Similar results have been obtained in case of thermal oxidation of PbSnTe (17).

Conclusions

Conditions for growing anodic oxide films on $Pb_{1-x}Sn_xSe$ ($x \sim 0.068$) have been established. The electrolyte composed of one part of water, 5 parts of NMA, and 18 parts of propylene glycol when adjusted to pH = 6.6 ± 0.2 gives good transparent films for cell voltage up to 50V. These films are composed of two phases, an amorphous and a crystalline one. The proportion of the crystalline phase increases with the cell voltage. The films can be grown in spite of the fact that one of the oxide components SeO_2, is soluble in water. The transparent films can probably be delineated into any shape by masking with a photoresist, since they are soluble in common acid or alkaline solution. The results of XPS measurements indicate that all the three elements Pb, Sn, and Se are oxidized. The oxide of Se was found to be less stable to bombardment with Ar ions than the oxides of Pb and Sn. These films may find applications for passivation of laser and detector devices as in the case of PbSnTe (18, 19).

Table II. Atomic ratio of Pb, Sn, Se, and O in the oxide as obtained by XPS measurements

	Pb	Sn	Se	O
Sample	at	at	at	at
S1	3.6	1	4.2	20
S2	3.8	1	4	18

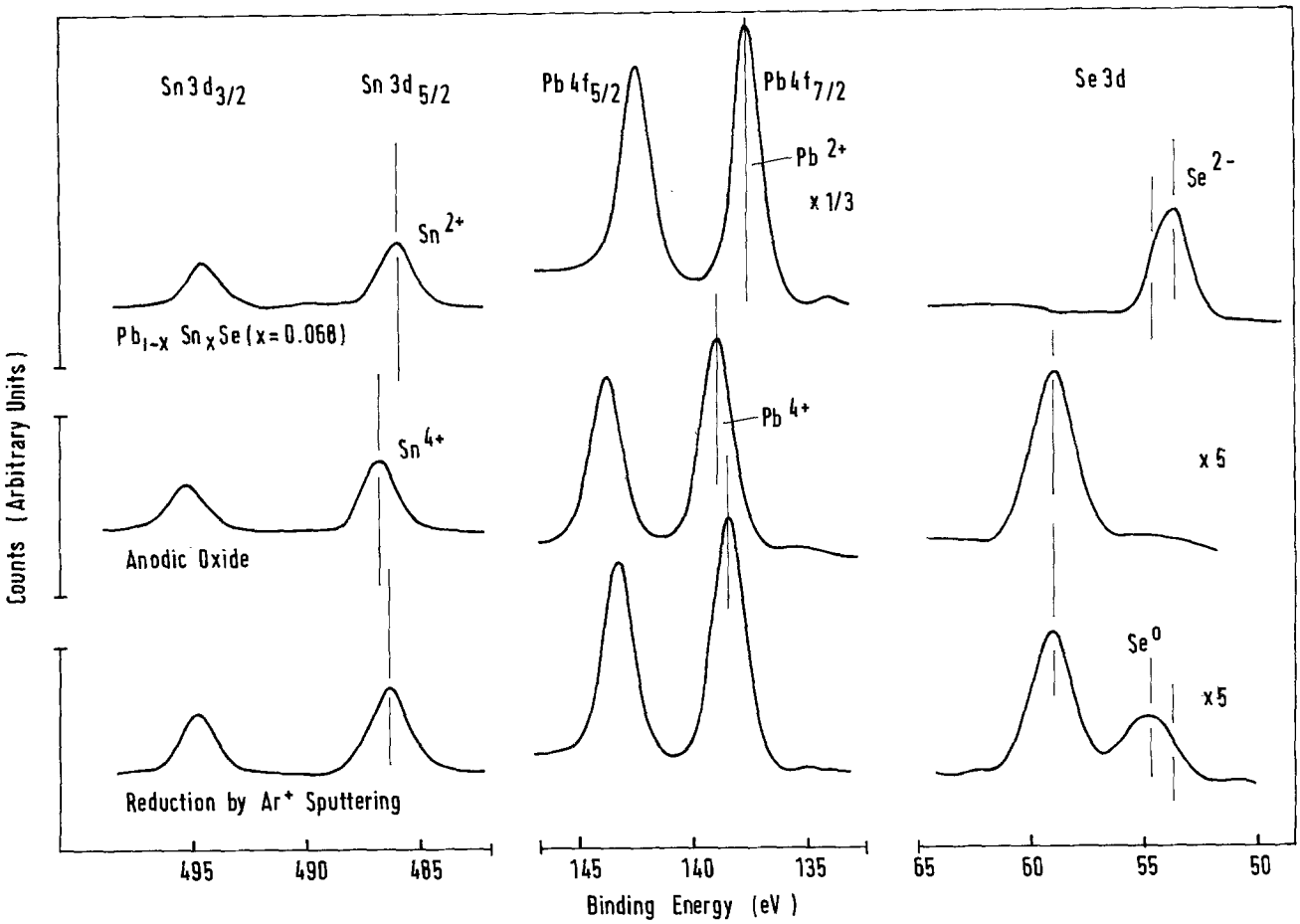

Fig. 8. XPS spectra of a $Pb_{1-x}Sn_xSe$ ($x = 0.068$) surface, anodic oxide surface, and argon sputtered anodic oxide surface

Acknowledgments

One of the authors (S.C.G.) is grateful to Dr. H. Preier for providing the facilities, suggesting the problem, and critically reviewing the manuscript, and thanks Dr. Boettner and Dr. Bachem of this Institute for the help during the course of this work. S. C. Gupta would also like to acknowledge the financial support from the Alexander von Humboldt Foundation during his stay at the Fraunhofer Institute.

Manuscript submitted Oct. 25, 1982; revised manuscript received Jan. 28, 1983.

Any discussion of this paper will appear in a Discussion Section to be published in the June 1984 JOURNAL. All discussions for the June 1984 Discussion Section should be submitted by Feb. 1, 1984.

REFERENCES

1. J. O. Dimmock, I. Melngailis, and A. J. Strauss, *Phys. Rev. Lett.*, **16**, 1193 (1966).
2. H. Preier, *Appl. Phys.*, **20**, 189 (1979).
3. J. Hesse, *Jpn. J. Appl. Phys.*, **16/1**, 297 (1977).
4. I. Melngailis and T. C. Harman, in "Semiconductors and Semimetals," Vol. 5, R. K. Willardson and A. C. Beer, Editors, p. 111, Academic Press, New York (1970).
5. D. K. Hohnke, H. Holloway, K. F. Yeung, and M. Hurley, *Appl. Phys. Lett.*, **29**, 98 (1976).
6. H. Müller, F. H. Eisen, and J. W. Mayer, *This Journal*, **122**, 653 (1975).
7. K. P. Pande, *IEEE Trans. Electron Devices*, **ed-27**, 631 (1980).
8. A. Yamamoto and C. Uemura, *Electron Lett.*, **18**, 63 (1982).
9. P. C. Catagnus and C. T. Baker, U.S. Pat. 3,977,018 (1979).
10. J. Shirafuji, M. Amono, M. Inoue, and Y. Inuishi, *Electron Lett.*, **18**, 653 (1982).
11. T. Jimbo, M. Umeno, H. Shimizu, and Y. Amemiya, *Surf. Sci.*, **86**, 389 (1979).
12. W. E. Morgan and J. R. van Wazer, *Phys. Chem.*, **77**, 964 (1973).
13. St. Evans and J. M. Thomas, *J. Chem. Soc. Faraday Trans. II*, **71**, 313 (1975).
14. J. M. Thomas and M. J. Tricker, *J. Chem. Soc. Faraday Trans. II*, **71**, 329 (1975).
15. "Handbook of X-Ray Photoelectron Spectroscopy," G. E. Muilenberg, Editor, Perkin Elmer Corporation, Physical Electronics Div. (1979).
16. T. S. Sun, S. P. Buchner, N. E. Byer, and J. M. Chen, *J. Vac. Sci. Technol.*, **13**, 940 (1976).
17. M. Bettini and H. J. Richter, *Surf. Sci.*, **80**, 334 (1979).
18. M. Yoshikawa, M. Koseto, and R. Ueda, IEE/OSA Conference on Laser and Electro-Optical Systems, San Diego, CA (1978).
19. S. Rotter, D. Kasemset, and C. G. Fonstad, *IEEE Electron Dev. Lett.*, **edl-3**, 66 (1982).

TEM Observations of Laser-Induced Pt and Au Deposition on InP

D. Brasen, R. F. Karlicek, and V. M. Donnelly

Bell Laboratories, Murray Hill, New Jersey 07974

ABSTRACT

Laser-induced deposits of Au or Pt on (001) InP surfaces have been examined by transmission electron microscopy. It is found that Pt deposition results in the formation of Pt (P, $In)_2$; whereas, in the case of Au, Au and Au_4In are observed. A description of the general morphology, together with a discussion as to why the compound and alloy might form is presented.

Currently, several techniques are used to metalize the surface of III-V compound semiconductors for electronic device fabrication (1-4). These electrical contacts are usually fabricated by depositing metals through a mask, onto the semiconductor surface. Metals may be deposited by electrochemical plating (1), evaporation (2), or by plasma sputtering (3). Production of ohmic contacts frequently requires an alloyed interfacial region between the metal and semiconductor surface to improve adhesion and reduce contact resistance. This alloyed region may be produced by annealing, and/or by the use of reactive metals [such as Pd (1) or Be (2)] to promote physical and electrical bonding to the semiconductor surface.

Recently, there has been considerable interest in developing single-step laser-induced metal deposition for producing ohmic contacts on III-V compounds. In this process, a metal pattern is "written" directly onto the surface by rastering the focused laser beam. The most widely reported technique (4) involves laser photolysis of gas-phase metal compounds on or near the surface. We have recently reported an alternative procedure in which metals are deposited on semiconductor substrates via pulsed laser irradiation of a metal salt solution in contact with the semiconductor surface. In this way, it has been shown that Pt and Au can be deposited on both n and p-type <100> InP substrates, with good adhesion, at pulsed laser intensities sufficient to initiate thermal decomposition of the InP surface, yet below the threshold intensity at which gross surface damage occurs (5).

This paper reports the use of transmission electron microscopy (TEM), to investigate the general morphology and different alloyed interfaces formed during laser induced deposition of Au or Pt on InP. In addition, an attempt is made to understand and rationalize the formation of the resulting deposits.

Experimental

Platinum and gold were deposited on InP as previously reported (5). Basically, Pt was deposited by immersing InP substrates into an aqueous solution of chloroplatinic (H_2PtCl_6) acid. However, a methanolic solution of chloroauric ($HAuCl_4$) acid was used to produce the Au deposits examined in this study, since this solution (as opposed to aqueous $HAuCl_4$ solutions) was found to yield smoother films. A Lambda Physik model F12000 dye laser, with model EMG102 excimer laser pumping, producing ~10 nsec pulses at 10 Hz repetition rates, was then directed to irradiate the semiconductor surface at normal incidence. Several thousand pulses at incident energy densities of ~0.2-0.5 J/cm^2 were used to produce Pt deposits on {100} InP, while Au deposits were produced on {100} InP using ~100 pulses at incident energy densities below ~0.2 J/cm^3.

Samples were prepared for transmission electron microscopy by polishing and thinning down from the backside of the wafers to ~10 mils using a mechanical chemical technique. Next, 3 μm diam disks were ultrasonically cut out of the wafers. The disks were then thinned down for microscopy from the back, while protecting the metalized side, by polishing them in a solution of 1.5% Br in methanol. The foils were then examined in a JEM200 transmission electron microscope operating at 200 keV.

Results

Figures 1a, b, and c shows, respectively, bright field micrograph, dark field micrograph, and corresponding

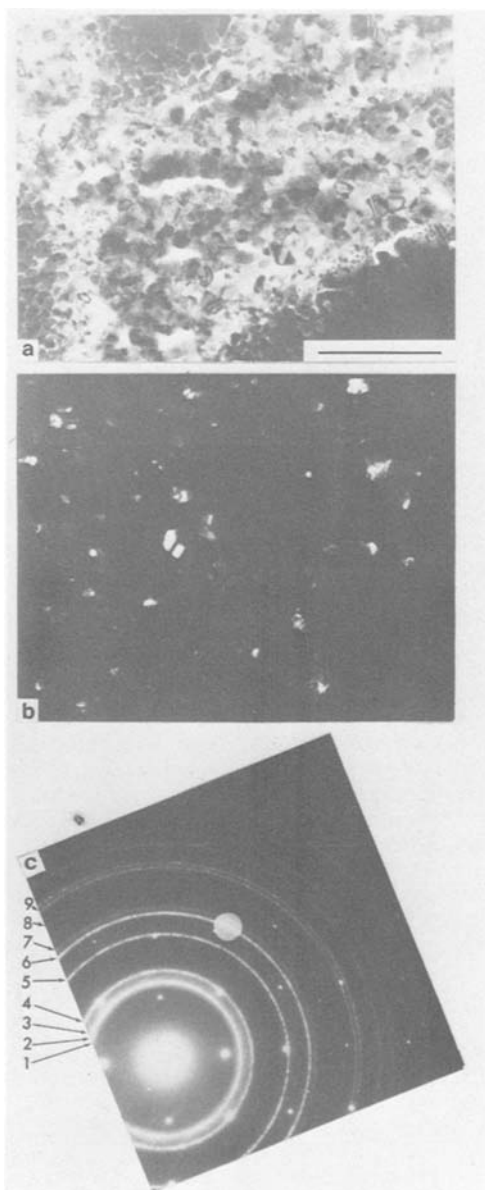

Fig. 1. A) TEM micrograph of an area of InP which is coated with Au and Au_4In particles. Marker = 2000Å. B) Dark field micrograph of same area at same magnification. C) Corresponding diffraction pattern. The rings are caused by Au or Au_4In while the discrete spots are due to the InP substrate.

diffraction pattern of an area in which Au was laser deposited. It is apparent from Fig. 1a that the gold is deposited in polycrystalline form. The diffraction pattern, Fig. 1c, shows that most of the deposition results in crystallites being randomly oriented on the surface of the InP. In addition, Fig. 1b shows that these crystallites also appear to be fairly uniformly distributed, varying in size from ~50 to ~500Å. The diffraction pattern of Fig. 1c shows the discrete spots caused by the InP matrix and rings which are produced by the deposited crystallites. In order to identify the phases formed on the InP surface, the d-spacings of the rings were measured from the diffraction pattern and are tabulated in Table I. As can be seen from the table, most of the rings are due to the deposition of Au. Further, if the diffraction pattern is carefully studied and indexed, as in Table I, it is possible to see that the inner most Au ring is actually a triplet consisting of the (111) Au/(002) Au_4In diffraction rings plus the (100) and (101) diffraction rings of Au_4In, *i.e.*, the ζ phase. Several such areas, on different specimens, were examined, and all of them yielded essentially the same results.

TEM examination of the Pt deposits on the other hand, did not show any elemental Pt. Instead, crystallites were formed which were also randomly oriented similar to the Au deposition, as seen in Fig. 2a and b. Further, the crystals varied in size from ~50 to ~400Å. The d-spacings which were measured from the diffraction rings of Fig. 2c are tabulated in Table II. By comparing these measured values with the d-spacings of the known binary In-Pt alloys and In-P compounds, it was found that PtP_2 (CaF_2 type, a = 5.695) gave the best fit. However, as the results of Table II show, a better fit would occur if the lattice constant was assumed to be 5.84Å.

Discussion

The diffusion of In into Au with the resultant formation of Au_4In appears to be the primary reason for the adhesion of the deposited layer to the substrate. It is interesting to note that by evaporating Au onto InP to form ohmic contacts, Keramidas *et al.* (2) observed that after alloying their samples at 420°C for 7 min, a TEM analysis of the spreading of the contacts shows the formation of the intermetallic Au_9In_4. As an outgrowth of this work, Vandenberg *et al.* (8) have used x-ray analysis to show that an InP substrate on which Au contacts were evaporated, exhibits multiple Au-In alloy phase changes upon continuous heating. Up to 335°C only Au is found. However, between 335°-355°C, Au_4In is formed and remains stable up to 390°C where it begins to transform into Au_9In_4. Hence, one may infer from this that the formation of Au_4In by laser deposition occurs during the heating of the surface of the InP to temperatures between 335°-390°C. In addition, it should be noted that since the irradiation pulses were only ~10 nsec in duration, kinetics reasons may also be responsible for the failure to form the more complex Au_9In_4 phase at the interface. However, this temperature range is consistent with the observation of minimal InP surface decomposition at the laser power densities used to initiate decomposition (5). Minimal surface damage is expected at temperatures only slightly in excess of the InP decomposition temperature (360°C).

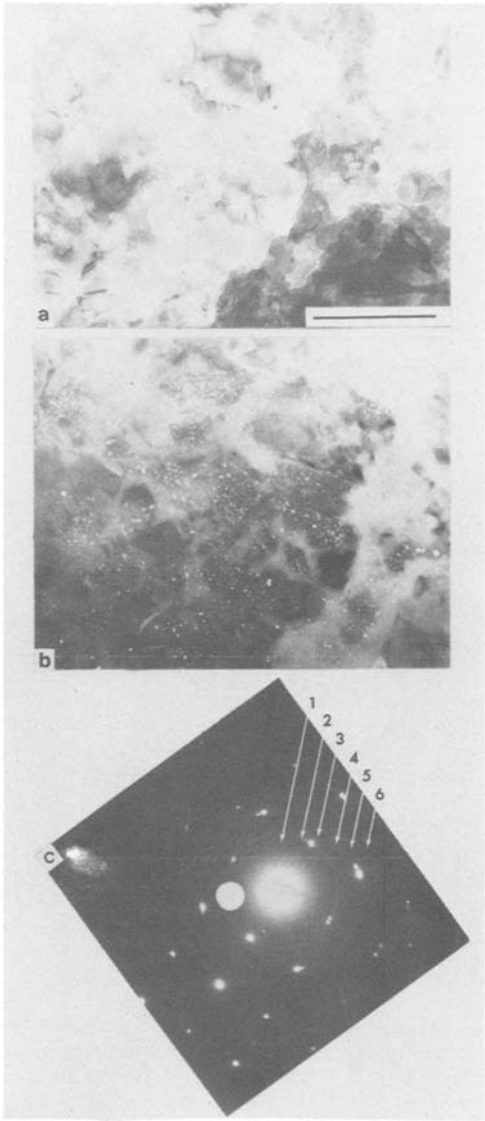

Fig. 2. A) TEM micrograph of an area of InP after Pt has been laser deposited. Marker = 5000Å. B) Dark field micrograph of same area at same magnification. C) Corresponding diffraction pattern. The rings are due to the $Pt(P,In)_2$, while the discrete spots are due to the InP substrate.

The fact that no Au-P compounds were observed is not too surprising, since the observed behavior for Au is consistent with results obtained by alloying evaporated Au layers on InP (2, 8). Further, it is known that P is insoluble with Au at room temperature and that, in fact, Au is known to form only one binary compound with P, *i.e.*, Au_2P_3 (6, 9). However, since the heat of reaction to form Au_2P_3 from Au + InP is very endothermic (+1.73 eV/metal atom) (10), the formation of a gold phosphide compound would not be expected.

Table I. Comparison of measured d-spacings of diffraction rings with known d-spacings of Au and Au_4In

Ring #	Measured d-space	ASTM file of Au d-spacing	plane	ASTM file Au_4In d-spacing	plane
1	2.52			2.52	(100)
2	2.37	2.36	(111)	2.397	(002)
3	2.23			2.20	(101)
4	2.08	2.04	(200)		
5	1.43	1.44	(220)		
6	1.23	1.23	(311)		
7	1.18	1.18	(222)		
8	1.02	1.02	(400)		
9	0.93	0.94	(331)		

Table II. Comparison of measured d-spacings of diffraction rings with calculated d-spacings of PtP_2 assuming $a = 5.695$Å (7) and $a = 5.84$Å

Ring #	Measured d-spacings	Calc d-spacings assuming $a = 5.695$Å	plane	Calc d-spacings assuming $a = 5.84$Å
1	3.37	3.29	111	3.37
2	2.93	2.85	200	2.92
3	2.63	2.55	210	2.61
4	2.39	2.32	211	2.38
5	2.09	2.01	220	2.06
6	1.76	1.72	311	1.76

A possible explanation which could account for the lattice parameter discrepancy, in the case of Pt deposition (Table II), is that there is indium as well as phosphorus in this phase. Since both PtP_2 and $PtIn_2$ have the same crystal structure (CaF_2 type), it is reasonable to assume that replacement of P-P pairs with In-In or In-P pairs could occur. Assuming that Vegard's law is applicable in this case, replacing ~20% of the phosphorus with indium would lead to a lattice parameter close to that observed.

The reduction of Au or Pt ions to their neutral state for deposition of Au/(Au_4In) or Pt/($Pt[P,In]_2$) requires the oxidation of P from InP (possibly forming soluble PCl_3) in the case of Au deposition, and the oxidation of In and some P from InP (possibly forming soluble $InCl_3/PCl_3$) for Pt deposition. This would then leave the interface region rich in In (for Au deposition) or P (for Pt deposition), as observed. In addition, metal deposition may also occur without oxidation of the InP surface atoms, *i.e.*

$$2HAuCl_4 \xrightarrow{\Delta} 2Au_{(s)} + 2HCl + 3Cl_2 \quad [1]$$

$$H_2PtCl_6 \xrightarrow{\Delta} 2Pt_{(s)} + 2HCl + 2Cl_2 \quad [2]$$

However, since elemental Pt is not seen in the deposits used in this study, it may be assumed that, at least in the initial stages, Pt deposition occurs primarily by the oxidation of In. Au deposition, on the other hand, could be accomplished by a combination of oxidation of P and decomposition of the metal salt. In later stages of growth, the deposited film covers the substrate, and metal deposition occurs according to reactions [1] and [2] (5).

Conclusion

TEM observations have shown that laser induced depositions of Pt or Au from solution results in the formation of $Pt(P,In)_2$ or Au + Au_4In on InP, similar to observations of thermally annealed, evaporated metal films (2, 8, 10). In the initial stages of growth these deposits appear to consist of a fairly uniform distribution of randomly oriented crystals ranging in size from ~50 to ~500Å.

The Au + Au_4In is probably formed through a combination of oxidation of P and decomposition of the metal salt. Since the competing reaction to form Au_3P_2 is known to be endothermic (10), this compound would not be expected to form. On the other hand, Pt deposition, in the initial stages, apparently does require only the oxidation of In and some P.

Acknowledgments

The authors wish to thank S. Mahajan for his many helpful discussions and constructive comments.

Manuscript submitted June 2, 1982; revised manuscript received Jan. 17, 1983.

Any discussion of this paper will appear in a Discussion Section to be published in the June 1984 JOURNAL. All discussions for the June 1984 Discussion Section should be submitted by Feb. 1, 1984.

Bell Laboratories assisted in meeting the publication costs of this article.

REFERENCES

1. L. A. D'Asaro, S. Nakahara, and Y. Okinaka, *This Journal*, **127**, 1935 (1980).
2. V. G. Keramidas, H. Temkin, and S. Mahajan, Inst. Phys. Conf. Ser. No. 56, Chap. 5 (1980).
3. J. L. Vossan and W. Kern, "Thin Film Processes," Academic Press, New York (1978).
4. D. J. Ehrlich, R. M. Osgood, Jr., and T. F. Deutsch, *J. Quantum Electron.*, **qe-16**, 1233 (1980).
5. R. F. Karlicek, V. M. Donnelly, and G. J. Collins, *J. Appl. Phys.*, **53**, 1084 (1982).
6. M. Hansen, "Constitution of Binary Alloys," p. 210, McGraw-Hill, New York (1958).
7. A. Baghdadi, A. Finley, P. Russo, R. J. Arnott, and A. Wold, *J. Less Common Metals*, **34**, 31 (1974).
8. J. Vandenberg, S. Nakahara, and H. Temkin, Unpublished work.
9. R. P. Elliot, "Constitution of Binary Alloys—First Supplement," p. 77, McGraw-Hill Book Co., New York (1965).
10. R. H. Williams, V. Montgomery, and R. R. Varma, *J. Phys. C.: Solid State Phys.*, **5**, 11 (1978).

A Voltammetric Study of the Reduction of Chromic Acid on Bright Platinum

J. P. Hoare*

General Motors Research Laboratories, Electrochemistry Department, Warren, Michigan 48090

ABSTRACT

The reduction of chromic acid catalyzed and uncatalyzed with H_2SO_4 was studied on Pt microelectrodes by steady-state (galvanostatic and potentiostatic voltammetry) and nonsteady-state (cyclic voltammetry) polarization techniques. The rest potential of Pt in chromic acid is a mixed potential. Although the reduction of hexavalent Cr to trivalent occurs readily at Pt cathodes, the reverse process does not take place at Pt anodes due to the high overvoltage for $[Cr(H_2O_6]^{+3}$ ion oxidation. It is for this reason that PbO_2 anodes are used in commercial Cr plating practice since the overvoltage for O_2 evolution is much higher on PbO_2 than on Pt, thus allowing the current to be used in the oxidation of $[Cr(H_2O)_6]^{+3}$ ion instead of O_2 evolution. The reduction of an oxidized Pt surface occurs with more difficulty in chromic acid than in H_2SO_4. Metallic Cr is deposited in catalyzed chromic acid at the expense of the reduction of Cr VI to Cr III and H_2 evolution.

It is known (1-3) that metallic deposits of chromium can be obtained from the electroreduction of solutions of chromic acid containing H_2SO_4 or HF as a catalyst but not from simple solutions of trivalent chromium such as solutions of $Cr_2(SO_4)_3$ or $CrCl_3$. This behavior is traced to the fact that Cr III in aqueous solution forms a hexa-aquo complex, $[Cr(H_2O)_6]^{+3}$, (4) whose inner coordination sphere is so strongly bound that Cr cannot be separated from the complex.

A working model of the mechanism of the electrodeposition of metallic Cr from sulfate-catalyzed chromic acid solutions has been proposed (5, 6) in which the HSO_4^- ion acts both as a catalyst and as a blocking agent and the Cr in solution exists chiefly as the trichromate ion, $HCr_3O_{10}^-$. Because of the highly oxi-

* Electrochemical Society Active Member.
Key words: anion adsorption, surface films, electron spectroscopy, anode material.

dizing nature of chromic acid, an oxide layer is formed on the basis metal surface which must be removed before metallic Cr can be deposited. In addition, Cr is electrodeposited from a viscous cathodic film. To help understand the behavior of these surface films, an investigation of the reduction of chromic acid on bright Pt cathodes was undertaken using steady-state and nonsteady-state voltammetric techniques. The results of this work are presented in this report.

Experimental

All measurements were obtained on bright Pt bead microelectrodes (0.035-0.04 cm^2 in area) melted at the end of Pt wires (99.99% pure) in an oxygen torch. The Pt beads were cleaned in a burning H_2-jet and sealed in Teflon spaghetti as described earlier (5). Three Pt beads (for duplicate runs) were mounted in the Teflon cell, depicted before (5). The cell was filled with 2.5M chromic acid (250g CrO_3/L) made with triply distilled water from an all quartz still. The solution was stirred with purified N_2 (~150 cm^3/min) and all potential measurements were made against a saturated calomel reference electrode (SCE) at ambient temperatures (~24°C).

When the rest potential had reached a steady state, the cyclic voltammograms were obtained between −200-1500 mV at sweep rates ranging from 100 to 17 mV/sec. It required about 10 cycles of polarization before a steady-state voltammogram was obtained. A family of voltammograms were recorded by reducing the potential range of the sweep in steps of 100 mV beginning at the cathodic end until the final sweep extended from 1000 to 1500 mV. By reducing the potential range from the anodic end in steps of 100 mV until the potential was finally scanned between −200-500 mV, a second family of voltammograms was generated. After the voltammograms had been recorded, the steady-state galvanostatic and potentiostatic polarization curves were determined as before (5). Steady-state voltammetry studies provide knowledge of the potential-determining processes in certain ranges of current density. In the constant current density case, identification of these electrode processes is aided by an understanding of the chemistry (colorimetry, AES, XPS, etc.) and the electrochemistry (rest potential, Tafel slope, etc.) of the system under consideration. From constant potential studies, electrode surface area changes produced by the formation or reduction of deposited films (such as oxides or metallic deposits) are clearly observed. Armed with such knowledge, an intelligent interpretation of the current peaks present on the cyclic voltammograms can be offered.

Finally, just enough concentrated H_2SO_4 was added through the gas exit port with a hypodermic syringe to bring the chromic acid solution to 0.25M in H_2SO_4. As before, the cyclic voltammograms were determined as well as the steady-state polarization curves.

Results and Discussion

In Fig. 1, the steady-state galvanostatic polarization curve for Pt in uncatalyzed 2.5M chromic acid is plotted (circles). At open circuit, the rest potential has a value of 1140 ± 10 mV (at least 6 determinations) and is considered (5) to be a mixed potential resulting from the local cell composed of the anodic oxidation of Pt and the cathodic reduction of $HCr_3O_{10}^-$ ion

$$Pt + H_2O \rightarrow Pt\text{-}O + 2H^+ + 2e \quad [1]$$

and a reaction such as

$$HCr_3O_{10}^- + 6H^+ + 6e \rightarrow Cr_2O_3 + HCrO_4^- + 3H_2O \quad [2]$$

giving the overall local cell reaction

$$3Pt + HCr_3O_{10}^- \rightarrow 3Pt\text{-}O + Cr_2O_3 + HCrO_4^- \quad [3]$$

A steady rest potential is observed because the oxygen at a Pt-O site can dissolve into the bulk Pt leaving another bare Pt site to support the local cell current (7, 8). Any Cr_2O_3 formed in these highly acid conditions ($pH = -7$) would dissolve

$$Cr_2O_3 + 6H^+ \rightarrow 2Cr^{+3} + 3H_2O \quad [4]$$

and the Cr^{+3} in aqueous media would complex to the stable hexa-aquo complex, $[Cr(H_2O)_6]^{+3}$.

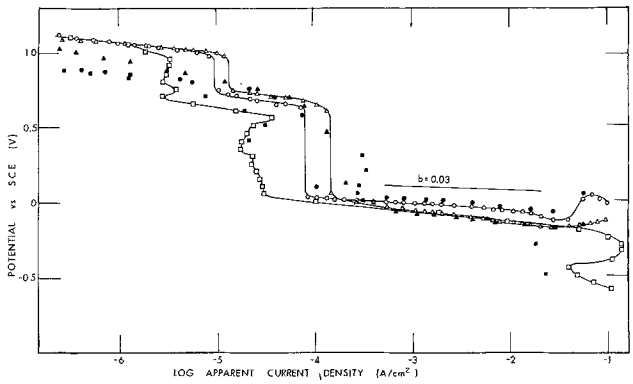

Fig. 1. Steady-state galvanostatic polarization curves obtained on Pt cathodes in uncatalyzed (circles) and sulfate catalyzed (triangles) 2.5M chromic acid; potentiostatic (squares) curve on Pt in sulfate-catalyzed chromic acid; open symbols, increasing current and filled symbols, decreasing current.

As the local cell is driven by the application of an external cathodic current, the potential is shifted from the mixed potential, where the local anodic and local cathodic current are equal and the external current is zero, to a less noble value. At this point, the external current is equal to the difference between the absolute values of the local anodic and cathodic currents according to the analysis of local cell polarization (9). With increasingly applied cathodic current, the anodic current contribution becomes less and less and generates the top linear region of the polarization curve in Fig. 1 between 1100-950 mV. When the potential has been shifted below the reversible potential of the local anodic reaction, the local anodic contribution is reduced to zero, and the external current is determined solely by the local cathodic reaction. The second linear region between 750-650 mV in Fig. 1 is due to the reduction of Cr VI to Cr III according to Eq. [2] and [4].

At still higher applied cathodic current, the rate of Cr VI reduction is not high enough to support the demanded current and the potential shifts at a limiting current density to values near zero volts where hydrogen is evolved by the reduction of H^+ ion. The Tafel slope of the third linear section of Fig. 1 is consistent with a slope of 0.03 (compare to 0.03 slope drawn on the plot) which is the value obtained for hydrogen overvoltage on Pt (10). Although the current in the third section is consumed chiefly in H_2 evolution, considerable current is consumed in the reduction of Cr VI to Cr III (11) producing deviations from 0.03 at higher currents.

Above 5×10^{-2} A/cm^2, the polarization curve bends back on itself as a negative resistance region. This behavior results from a change in surface area due to the laying down of a deposit (5). Visual inspection of a Pt sample removed from the cell at this high current density shows that the bead is black or brownish black. Analysis with Auger spectroscopy (AES) shows the deposit to consist of Cr and O in about equal amounts and ESCA analysis indicates a high concentration of oxides of Cr. Uncatalyzed chromic acids solutions are known to give black chromium deposits (12, 13) which were analyzed (14, 15) as 75% Cr and 25% chromium oxides.

After reaching the highest current density studied, the current is reversed and the data for decreasing cur-

rent are denoted by the filled circles in Fig. 1. In the high current density region the data are quite reproducible for increasing and decreasing current. Apparently, the Cr black film is removed as the current is made less cathodic. Since Pt is a good catalyst for the H_2 reaction, one would expect the data to be reproducible in the H_2 region.

With continued decreasing current, a point is reached where the rate of surface oxidation by chromate ions becomes greater than the rate of H_2 evolution and the potential rises along a limiting current to high anodic values. A hysteresis in the limiting current is observed probably because hydrogen can be dissolved in the Pt metal (16). This dissolved hydrogen can diffuse to the surface and the depolarizing effect of this hydrogen requires a lower current density to be reached before oxidation of the surface can take place. Once the open circuit is reached, the potential slowly (over a period of several hours) drifts to the recorded rest potential again.

When H_2SO_4 was added ($CrO_3/H_2SO_4 = 100/1$), a steady-state galvanostatic polarization curve was obtained as the triangles in Fig. 1. In this case, the rest potential and the shape of the polarization curve for the catalyzed system is very similar to that for the uncatalyzed system except at the highest current densities. Here the negative resistance region is not as prominent and visual inspection of the bead removed at the high current shows that the Pt surface is covered with a gray deposit of metallic Cr. Analysis by AES indicated that the oxygen content of the deposit was about half that of the Cr content. Since the surface roughness of the gray deposit is much less than that of the black deposit, the change in area at high current densities, and hence the magnitude of the negative resistance region, should be much less for the catalyzed system, in agreement with the data of Fig. 1.

Also shown in Fig. 1 is the steady-state potentiostatic polarization curve obtained for the catalyzed system. The uncatalyzed curve is not shown because it is so similar to the catalyzed case that it would clutter Fig. 1. As in the constant current case, the constant potential curve exhibits three linear sections separated by two limiting current regions. At the very high current densities, the large swing in current (negative resistance region) testifies to the change in area produced by the deposition of the Cr layer.

In Fig. 2, the family of cyclic voltammograms (between −200-1500 mV) for a Pt bead electrode in uncatalyzed 2.5M chromic acid is presented as a function of the potential sweep speed from 100 (outside curve) to 17 mV/sec (innermost curve) in steps of 17 mV/sec. Since the peak currents for each peak on the potential scan is a linear function of the sweep speed, the electrochemical processes responsible for the current peaks occur at the electrode surface and are not due to the diffusion of impurities from the bulk solution (17).

The main peaks on the anodic-going sweep are identified by the Roman numerals with the subscript H in the hydrogen region and O in the oxygen region. A similar notation is used for the cathodic-going sweep with a distinguishing prime added.

Figure 3 contains the family of cyclic voltammograms obtained by shortening the potential scan range in steps of 100 mV beginning at the cathodic end. Consider now the changes in the voltammogram pattern as the sweep range is shortened. By starting at 100 mV, both I_H and II_H disappear and so one can associate I_H and II_H with I_H'. For those traces beginning at potentials cathodic to IV_O', little change takes place in the shape of II_O, III_O, and IV_O but with potentials anodic to IV_O', II_O, and IV_O rapidly decrease while III_O becomes more distinct. The peak III_O disappears on traces begun at very anodic potentials (above 1000 mV). Consequently, peaks II_O and IV_O are associated with IV_O' and III_O is associated with peaks I_O', II_O', and III_O'.

When one shortens the potential range scanned from the anodic end in 100 mV steps, the family of cyclic voltammograms pictured in Fig. 4 is obtained. As one progesses from traces scanned up to 1500 mV to those scanned to 1300 mV, IV_O', becomes less and shifts to the right. The trace at 1200 mV exhibits only IV_O' shifted far to the right on the cathodic scan since I_O', II_O', and III_O', disappear. But two hydrogen adsorption peaks, I_H' and II_H' appear. Under these conditions enough oxide-free Pt sites are available so that the two hydrogen adsorption sties on Pt (17-20) can be observed. When the potential was scanned to only 1000 mV, the cathodic-going trace fell abruptly to very

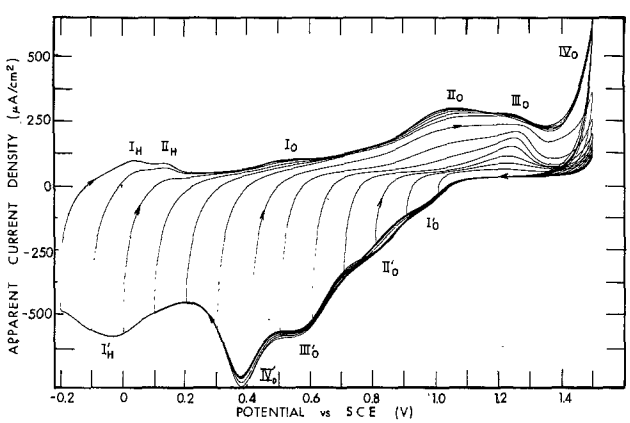

Fig. 3. Family of cyclic voltammograms obtained on Pt in uncatalyzed 2.5M chromic acid by decreasing the potential range scanned from the cathodic end in steps of 100 mV.

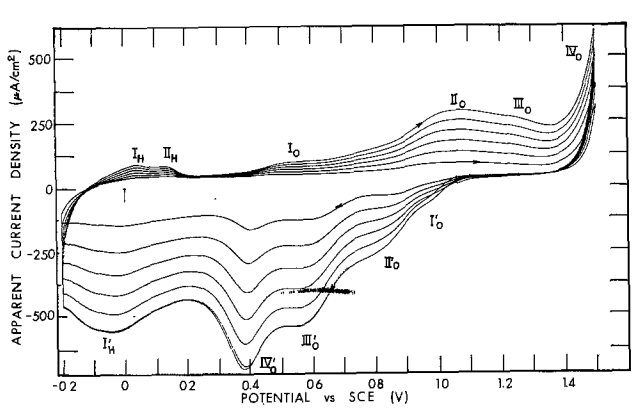

Fig. 2. Family of cyclic voltammograms obtained on Pt in uncatalyzed 2.5M chromic acid as a function of the sweep speed (100, 83, 67, 50, 33, and 17 mV/sec); 100 mV/sec curve is outside curve; Roman numerals identify major peaks.

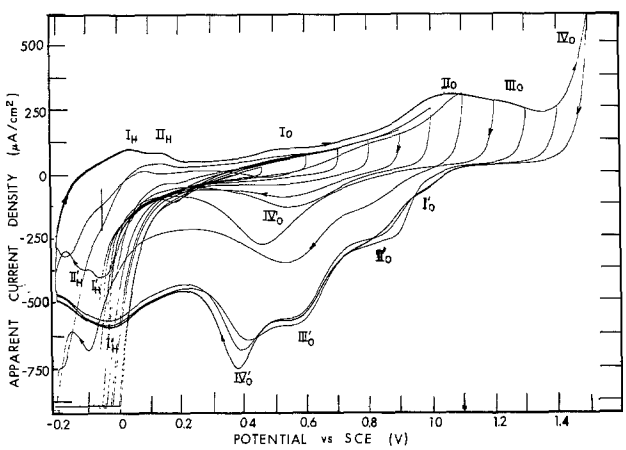

Fig. 4. Family of cyclic voltammograms obtained on Pt in uncatalyzed 2.5M chromic acid obtained by decreasing the potential range scanned from the anodic end in steps of 100 mV.

large cathodic currents in the hydrogen region. Since the Pt surface remains reduced in this potential range, H_2 gas is vigorously evolved accounting for this high cathodic current. Voltammograms swept between −200 mV and potentials below 900 mV show little or no structure since the main electrochemical reaction is the reduction of H^+ ion or the oxidation of H_2.

From a consideration of the data in Fig. 1-4, the following account of the behavior of Pt in pure chromic acid may be proposed. As Pt is anodized in Fig. 2 from −200 mV, one observes the desorption of hydrogen from two adsorption sites on Pt indicated by peak I_H and II_H in agreement with the literature (18). At more anodic potentials, polychromate species become absorbed on the Pt surface with the appearance of I_O on the voltammogram, and with further increasing anodic potential, the Pt surface becomes oxidized with a layer of Pt-O (21) producing the peak II_O. Polychromatic species may complex with this absorbed oxygen layer (5, 6) producing the diffuse peak III_O. Above 1300 mV, Pt-O sites may be oxidized to PtO_2 and oxygen is evolved on the PtO_2 layer giving rise to peak IV_O.

At 1500 mV, the potential is reversed and the cathodic trace is obtained. Below 1100 mV, the oxygen adsorbed during the anodic-going sweep is reduced and the reduction or desorption of the various components of the oxide layer generate a series of peaks I_O', II_O', III_O' and IV_O'. Guided by the data in Fig. 4, I_O', II_O' and III_O' are associated with the reduction or desorption of the polychromate complexes since such structure is not observed on voltammograms obtained on Pt in H_2SO_4 or HF (17-20). The IV_O' peak may be generated by the reduction of Pt oxides and any oxygen dissolved in the Pt metal produced by anodization above 1000 mV (7, 8). Because the overvoltage for the reduction of the oxygen layers on Pt in chromic acid is so high (large shift between anodic oxidation peaks and the corresponding cathodic reduction peaks), the oxygen desorption region overlaps into the hydrogen adsorption region and only one broad hydrogen adsorption peak, I_H', appears. It is noted that these oxygen desorption and hydrogen adsorption peaks ride on a relatively large background current on the cathodic-going sweep. This background current is the result of the reduction of Cr VI to Cr III (Eq. [2] and [4]). Such a background current is not observed on the anodic-going sweep because it is not possible on Pt to oxidize the $[Cr(H_2O)_6]^{+3}$ ion back to Cr VI.

The family of cyclic voltammograms obtained by varying the sweep speed (from 100 to 17 mV/sec) on a Pt-bead electrode in sulfate catalyzed chromic acid (CrO_3/H_2SO_4 = 100/1) is recoded in Fig. 5. As before the linear dependence of the peak current on the sweep speed for the various peaks indicates that the electrochemical reactions involved occur at the Pt surface and are not the result of diffusion of impurities from the bulk solution. One observes that the anodic-going scan contains only a single peak at 1100 mV besides the oxygen evolution peak IV_O. It is designated as V_O. On the cathodic-going trace, however, all four of the oxygen desorption peaks are evident. Below 300 mV, the current shifts abruptly to very large cathodic values where metallic Cr is deposited along with large amounts of hydrogen (current efficiency for Cr deposition (1, 11) is less than 15%). When −200 mV is reached, the potential is reversed to the anodic-going sweep, not on a Pt surface but on a Cr-plated Pt surface. Consequently, in the hydrogen region, there is not any structure to the trace, which may indicate that specific sites for hydrogen adsorption or desorption do not exist on the Cr-plated surface as on a pure Pt surface (17-19).

The family of curves obtained by shortening the sweep-range of potential from the cathodic end in 100 mV steps is presented in Fig. 6. As long as the potential sweep is initiated below 300 mV where Cr deposition takes place, peak V_O remains prominent. On the scan initiated at 300 mV, V_O disappears and in its place appears II_O and III_O as in Fig. 3. Accordingly, V_O may be associated with removal or dissolution of the Cr deposit laid down on the Pt surface during the cathodic sweep. For this reason, peaks I_O' to IV_O' appear on the cathodic-going sweep in Fig. 5, because the Cr deposit is removed at potentials above 1200 mV and O_2 is evolved on the oxidized Pt surface. If the electrode of Fig. 5 is cycled no lower than 300 mV, the anodic-going trace exhibits the expected oxidation of the Pt surface leading to O_2 evolution as observed in Fig. 3. Cyclic voltammograms initiated at potentials above 300 mV have the same structure as the corresponding ones recorded in Fig. 3, and so, the same interpretation.

In Fig. 7 is displayed the family of cyclic voltammograms obtained when the scanning range is shortened from the anodic end in 100 mV steps. When the electrode is cycled to potentials above 1200 mV where the Cr deposit is removed, one observes the same behavior of the four oxygen desorption peaks on the cathodic-going trace as that in Fig. 4, but when cycled to potentials below 1000 mV where the Cr deposit is not removed, the voltammograms exhibit little structure. Cycling between 300-1000 mV, the main electrochemical process is the reduction of Cr VI to Cr III.

In both catalyzed and uncatalyzed chromic acid a major portion of the current is consumed in H_2 evolution and the reduction of $HCr_3O_{10}^-$ ion to trivalent Cr at Pt cathodes. In the catalyzed case, however, hexavalent Cr is reduced to metallic Cr at the expense of H_2 evolution and reduction of Cr VI to Cr III since the background current is less in Fig. 5 than in Fig. 2 in

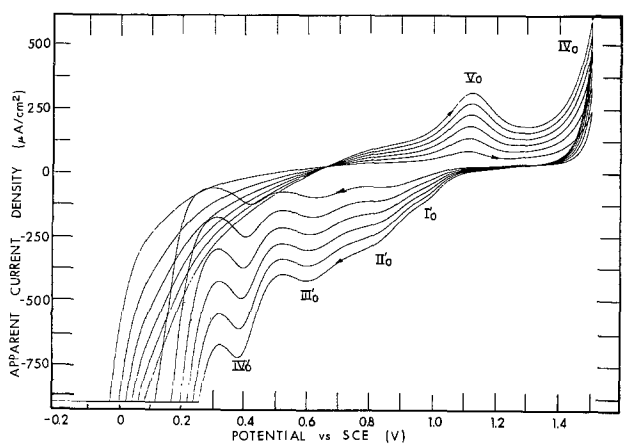

Fig. 5. Family of cyclic voltammograms obtained on Pt in sulfate-catalyzed 2.5M chromic acid; notation and sweep rates are same as in Fig. 2.

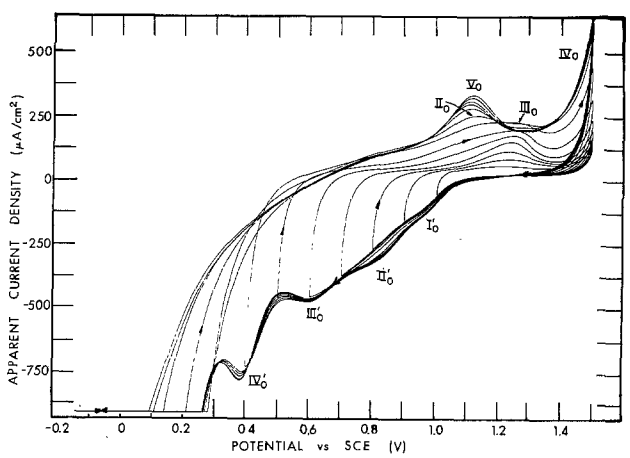

Fig. 6. Family of cyclic voltammograms obtained on Pt in sulfate-catalyzed 2.5M chromic acid; notation same as in Fig. 3.

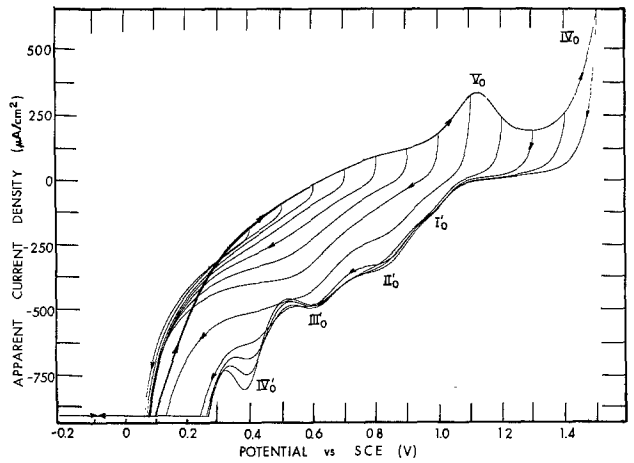

Fig. 7. Family of cyclic voltammograms obtained on Pt in sulfate-catalyzed 2.5M chromic acid; notation same as in Fig. 4.

agreement with mass balance measurements carried out by Griffin (11).

It is concluded from this work that the rest potential at a Pt electrode in N_2-saturated chromic acid solutions (with or without H_2SO_4 additions) is a mixed potential arising from a local cell composed of the anodic oxidation of Pt and the cathodic reduction of the trichromate ion ($HCr_3O_{10}^-$). In the absence of sulfate, the main products of the reduction of chromic acid at a Pt cathode are the evolution H_2 and the generation of trivalent Cr (Fig. 2). At high enough current densities, a deposit of brown Cr smut or black Cr may be obtained (Fig. 1). With sulfate present, reduction of chromic acid leads to metallic Cr at the expense of the reduction to trivalent Cr and H_2 evolution. The reduction of an oxidized Pt surface is more difficult (higher overvoltage) in chromic acid than in H_2SO_4 or HF. Apparently, polychromates can complex with the oxidized Pt surface. Although the reduction of hexavalent Cr to trivalent occurs readily at a Pt cathode, the reverse does not at a Pt anode because the overvoltage for the oxidation of $[Cr(H_2O)_6]^{+3}$ ion is greater than that for O_2 evolution. For this reason in commercial Cr plating practice, a PbO_2 anode is used to control the Cr^{+3}-content of the bath by oxidizing trivalent Cr to hexavalent at a surface (PbO_2) having a very high O_2 overvoltage.

Acknowledgments

The author is indebted to J. D. Thomas, assistant head of the Electrochemistry Department of GMR, for his faithful support and guiding suggestions and to M. A. LaBoda for many stimulating and profitable discussions.

Manuscript submitted Dec. 6, 1982; revised manuscript received *ca.* March 31, 1983.

Any discussion of this paper will appear in a Discussion Section to be published in the June 1984 JOURNAL. All discussions for the June 1984 Discussion Section should be submitted by Feb. 1, 1984.

General Motors Research Laboratory assisted in meeting the publication costs of this article.

REFERENCES

1. G. Dupernell, "Modern Electroplating," 2nd ed., F. Lowenheim, Editor, p. 80, John Wiley and Sons, New York (1963).
2. A. T. Vagramigan and N. T. Kudryavtsev, "Theory and Practice of Chromium Plating," (English Translation), Academy Sciences USSR, Moscow (1965).
3. P. Morisset, "Chromium Plating," R. Draper Ltd., England (1954).
4. J. P. Hunt and H. Taube, *J. Chem. Phys.*, **19,** 602 (1951); **18,** 757 (1950).
5. J. P. Hoare, *This Journal*, **126,** 190 (1979).
6. J. P. Hoare, A. H. Holden, and M. A. LaBoda, *Plating and Surf. Fin.*, **67,** 42 (1980).
7. J. P. Hoare, *J. Phys. Chem.*, **79,** 2175 (1975).
8. J. P. Hoare, *Electrochim. Acta*, **26,** 225 (1981).
9. J. P. Hoare, *This Journal*, **112,** 602 (1965).
10. S. Schuldiner, *ibid.*, 99, 488 (1952); **101,** 426 (1954); **106,** 891 (1959).
11. J. L. Griffin, *Plating*, **53,** 196 (1966).
12. M. F. Quaely, *ibid.*, **40,** 982 (1953).
13. K. Arndt and H. Endrass, *Z. Metallkd.*, **30,** 21 (1938).
14. E. A. Ollard, *J. Electrodepositers Tech. Soc.*, **12,** 33 (1936).
15. A. K. Graham, *Proc. Am. Electroplaters Soc.*, **46,** 61 (1959).
16. S. Schuldiner and T. B. Warner, *This Journal*, **112,** 212 (1965).
17. H. Angerstein-Kozlowska, W. B. A. Sharp, and B. E. Conway, *J. Electroanal. Chem.*, **43,** 9 (1973); in "Proceedings of the Symposium on Electrocatalysis," M. Breiter, Editor, p. 94, The Electrochemical Society Softbound Proceedings Series, Princeton, NJ (1974).
18. F. G. Will, *This Journal*, **112,** 481 (1965).
19. J. P. Hoare, *Electrochim. Acta*, **27,** 1751 (1982).
20. H. Angerstein-Kozlowska, B. E. Conway, and W. B. A. Sharp, *J. Electroanal. Chem.*, **43,** 9 (1973).
21. J. P. Hoare, "The Electrochemistry of Oxygen," p. 39, John Wiley and Sons, New York (1968).

Electrodeposition of Niobium-Germanium Alloys from Molten Fluorides

U. Cohen*,[1]

Department of Materials Science and Engineering, Stanford University, Stanford, California 94305

ABSTRACT

Niobium-germanium alloys were obtained by electrodeposition from molten fluoride solutions containing 5 mol percent of K_2NbF_7, and various concentrations of K_2GeF_6 in the KF-LiF eutectic solvent. The molten bath temperature was typically about 750°C. Cathodes (or substrates) were made of Mo and W foils, and a Ge sheet was used as a dissolving anode. Stable growth deposits were obtained of the intermetallic compounds $NbGe_2$, Nb_3Ge_2, Nb_5Ge_3, and their phase-mixtures by varying the germanium ion concentration in the molten bath. Germanium was found to be more noble than niobium in the molten fluoride bath, thus facilitating the deposition of germanium rich alloys. The superconducting compound, Nb_3Ge, however, could not be obtained as a single-phase deposit. It was obtained only as a minor constituent in certain phase-mixtures when operating under extreme conditions.

The Nb-Ge system received much attention, since the intermetallic compound Nb_3Ge was shown (1, 2) to possess the highest known superconducting transition temperature, $T_c \simeq 23.2$ K. This compound (as well as the other A-15 superconductors) is highly brittle and nonmachinable. Conventional metallurgical techniques such as melting and casting, rolling and extrusion, and wire-drawing are, therefore, inadequate for its fabrication. Electroplating of the Nb_3Ge compound and other A-15 superconductors might be of great technological significance.

The so-called "stoichiometric" A-15 superconductors Nb_3Sn, V_3Si, and V_3Ga, which are stable at their stoichiometric composition [75:25 mol percent (m/o)], can be produced by several techniques such as chemical vapor deposition (3, 4), dipping-diffusion (5), and diffusion through a copper-matrix medium (6-8). The "nonstoichiometric" superconductors such as Nb_3Al, Nb_3Ge, and Nb_3Si, appear to be more difficult to produce with homogeneous and reproducible properties. Several studies suggest that the stoichiometric composition Nb_3Ge is thermodynamically unstable below about 800°-1,000°C, when in the pure state (9, 10). The thin films of the stoichiometric compound with high T_c, obtained at lower temperatures, are believed to be stabilized by impurities, crystal defects, and interfacial energy.

Molten alkali fluorides, due to their high decomposition potentials (>3V) (11, 12), provide inert media suitable for electrodeposition of many metals and alloys that cannot be obtained from aqueous electrolytes. This, and other attractive features of the alkali fluoride solvents, have been discussed previously (11, 13). A general method of electroplating coherent and dense coatings of the refractory metals from all-fluoride electrolytes was developed by Senderoff and Mellors (14-18). In particular, they studied niobium (14, 15), which was further investigated by Cohen (11, 19). An all-fluoride bath was also used by Cohen to obtain coherent coatings of high purity Si (11, 20-23). Intermetallic compounds were also electrodeposited from molten fluorides. Senderoff and Mellors (18) mentioned obtaining the compound V_3Si from an all-fluoride electrolyte, but gave no details. Several binary, ternary, and quaternary alloys were obtained by Cohen (11). They included V-Si, Nb-Sn, Nb-Ge, Ge-Ni, Nb-Sn-Ni(substrate), Nb-Ge-Ni(subst.), Nb-Ge-Cu(subst.), Ge-Fe-Ni(subst.), and Nb-Ge-Fe-Ni(substrate).

The present paper describes the conditions found suitable to obtain stable growth deposits of the Nb-Ge compounds and their phase mixtures.

Experimental

The experimental setup has been described in detail elsewhere (11, 22). Solutions of either 5 or 80 m/o K_2NbF_7 in the KF-LiF eutectic solvent were prepared in the manner previously described (11, 19). A salt mixture containing 47.5 m/o LiF, 37.5 m/o KF, 5 m/o K_2NbF_7, and 10 m/o KHF_2 was first melted under vacuum. This was followed by purging the melt with purified helium, the equilibration of the niobium valences with a niobium sheet (11, 19), and purification by prolonged electrolysis onto a sacrificial cathode. The electrodes were then removed, and the melt was cooled to room temperature. A weighed amount of K_2GeF_6 salt was then introduced into the crucible through a long funnel. Remelting under vacuum and admitting helium completed the procedure for solution preparation.

Experiments were performed with various metal substrates as cathodes, but best results were obtained with a Mo foil. A Ge sheet was used as a dissolving anode, and the redox electrode Mo/Nb(IV),Nb(V) was used as a quasi-reference electrode.[2] Transient techniques such as cyclic voltammetry and chronopotentiometry, were utilized for the electrochemical investigation of the solutions. A typical electrodeposition run was preceded by obtaining several cyclic voltammograms to reveal the potential regions of interest. Electrodeposition runs were mostly of the steady-state potential (potentiostatic) type, but other modes such as steady-state current, cyclic sweeping (current or potential controlled), as well as cyclic pulsating (current or potential controlled) were also used.

The samples deposited were subject to analyses by x-ray diffraction (XRD), x-ray fluorescence (XRF), metallography, electron microprobe (EM), scanning electron microscopy (SEM), and superconducting measurements. Rough estimates were also made of the deposit adherence and morphology.

Results and Discussion

Germanium was found to be more noble than niobium in the fluoride melts. Immersion of Nb metal in melts containing K_2GeF_6 salt yielded spontaneous displacement of germanium from the solutions to virtually zero concentration. Subsequent electrolysis from such solutions yielded Nb exclusively. The displacement reaction is believed to be

$$Nb^\circ + Ge(IV) \rightarrow Nb(IV) + Ge^\circ \qquad [1]$$

The immersed Nb metal lost weight and was typically

* Electrochemical Society Active Member.
[1] Present address: MPI, Santa Clara, California 95051.
Key words: alloy electrodeposition, fused salts, superconductivity.

[2] The potential of this electrode is not well defined [cf. Footnote 2 in Ref. (19)]. However, the potential of this electrode reaches a steady-state value after a few minutes of immersion, and is stable (within ± 1 mV) over periods of several days.

covered with some alloy containing Ge. Utilization of Nb metal as a dissolving anode in such melts was thus excluded. However, Ge metal was found suitable for this purpose.

The dependence of the deposited Nb-Ge alloy composition on the bath composition, temperature, and the individual electrode potentials is given (11, 24) by

$$\left(\frac{a_{Ge}}{a_{Nb}}\right) = \left(\frac{a_{Ge(IV)}}{a_{Nb(IV)}}\right) \cdot \exp\left[\frac{4\mathbf{F}}{RT}\left(E^{\circ}_{Ge} + \eta_{Ge} - E^{\circ}_{Nb} - \eta_{Nb}\right)\right] \quad [2]$$

Here a_{Ge} and a_{Nb} are the alloy activities of germanium and niobium, respectively, in the deposited alloy, and $a_{Ge(IV)}$ and $a_{Nb(IV)}$ are the activities of the respective ions in the bulk of the solution. R and $\mathbf{F}$ are the gas and Faraday's constants, respectively. E°_{Ge} and E°_{Nb} are the standard electrode potentials defined for the standard states (pure substances), for which $a_{Ge} = a_{Ge(IV)} = 1$ and $a_{Nb} = a_{Nb(IV)} = 1$, respectively. η_{Ge} and η_{Nb} are the total individual polarizations (including activation and concentration polarization terms) of germanium and niobium, respectively. Note that for all cathodic processes, the polarization terms must be negative: $\eta_{Ge}, \eta_{Nb} \leq 0$. Also, since Ge was found to be more noble than Nb, $E^{\circ}_{Ge} - E^{\circ}_{Nb} > 0$. Thus Eq. [2] indicates that the ratio Ge/Nb in the deposited alloy is larger than the ion concentration ratio Ge(IV)/Nb(IV) in the solution, when operating under conditions close to equilibrium ($\eta_{Ge} \simeq \eta_{Nb} \simeq 0$). In order to obtain alloys richer in niobium, one may consider the following routes: (*i*) decrease the ion concentration ratio in the solution, (*ii*) raise the operating temperature and, (*iii*) increase cathodic polarization in hope that it will affect η_{Ge} more than η_{Nb} (through concentration polarization).

Locating the potential regions of interest.—Figure 1a shows a typical cyclic voltammogram obtained from an equilibrated solution of niobium alone. In comparison, Fig. 1b shows the effect of adding 0.18 m/o of K_2GeF_6 salt. Obviously, the redox potential of the quasi-reference electrode shifted by about 260 mV towards a more positive (anodic) value. This shift is probably due to the establishment of a new equilibrium with the dissolving anode

$$Ge^{\circ} + Ge(IV) = 2Ge(II) \quad [3]$$

The shift magnitude increased with the increase of the germanium salt concentration. Note also that while a Cu-foil was used for the redox electrode of Fig. 1a, an Mo-foil was used in Fig. 1b. Cu was found to be

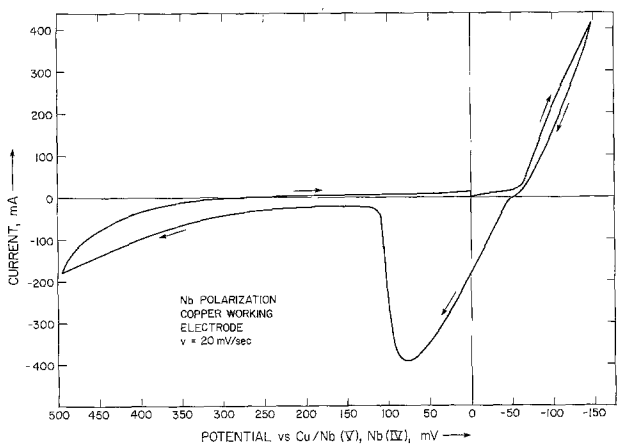

Fig. 1a. Cyclic voltammogram of 6 m/o solution of K_2NbF_7. Cu-working electrode (2 cm²), Nb-counter electrode, and Cu/Nb(V), Nb(IV) quasi-reference electrode. $T = 750°C$.

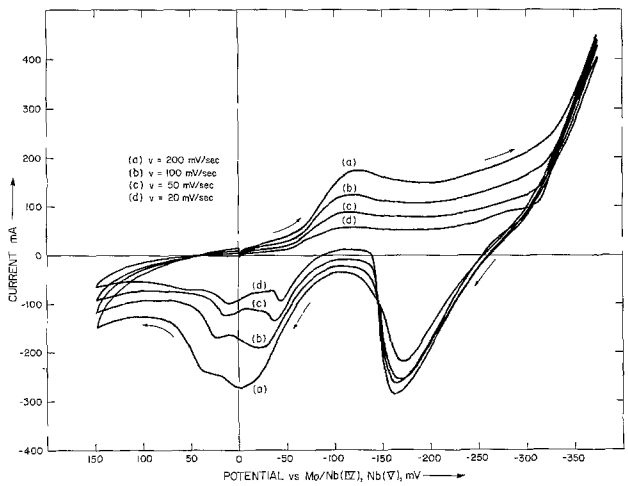

Fig. 1b. Cyclic voltammogram of a solution containing 5 m/o K_2NbF_7 and 0.18 m/o K_2GeF_6. Mo-working electrode (2 cm²), Ge-counter electrode, and Mo/Nb(V),Nb(IV) quasi-reference electrode. $T = 753°C$.

incompatible in germanium-containing solutions, due to its slow alloying with Ge.

Two distinct waves are seen in Fig. 1b. The first starts at about −60 mV, and the second at about −300 mV. The anodic peak at −165 mV, in Fig. 1b, completely disappeared when the scanned potential range did not cover the second cathodic wave (*i.e.*, beyond about −300 mV). Similarly, the other anodic peaks (located around zero mV) also disappeared when the scanned potential range did not reach the first cathodic wave (at about −60 mV). Electrolysis under constant cathodic potential (potentiostatic control at potentials corresponding to the first cathodic wave (at about −60 mV yielded deposits of various Nb-Ge compounds; the particular compound(s) being a function of the concentration and temperature. Electrolysis at potentials corresponding to the second wave (at about −300 mV) yielded a very thin transient layer of Nb-Ge alloy, followed by a niobium layer. Electrolysis at potentials corresponding to the plateau between the two cathodic waves resulted in very thin adherent layers (less than 1 μm thick), and loose powders or dendrites of the same compound(s) obtained at the edge of the first wave.

It is concluded that, the first cathodic wave (at about −60 mV) is due to the simultaneous codeposition of Nb-Ge compound(s), and that its corresponding anodic peaks (at about zero mV) are due to the stepwise anodic stripping of the Nb-Ge deposit. The second cathodic wave (at about −300 mV) and its corresponding anodic peak (at about −165 mV) are attributed to the electrodeposition and electrostripping, respectively, of Nb metal.

Relatively rich germanium solutions revealed more than one step (peak) on the first cathodic wave (cf. Fig. 1c). It was found that each step corresponded to the deposition of a certain Nb-Ge alloy: The more cathodic the step, the richer the alloy in Nb. Cyclic voltammograms of lower germanium concentrations revealed only one step on the first cathodic wave (cf. Fig. 1d). Potentiostatic electrolysis at this step yielded the alloys richer in Nb (Nb_3Ge_2, Nb_5Ge_3, or Nb_5Ge_3 + Nb_3Ge mixture). At least two anodic peaks corresponding to the first cathodic wave were always observed. The relative magnitude, separation, and location of the peaks were dependent upon the scanning rate, temperature, and solution concentration.

Nb-Ge deposits with a stable growth interface were only obtained when the operating cathodic potential corresponded to the base of the first step (peak). Electrolysis at potentials more cathodic than about $E_{p/2}$ yielded deposits of a thickness-limited nature, even-

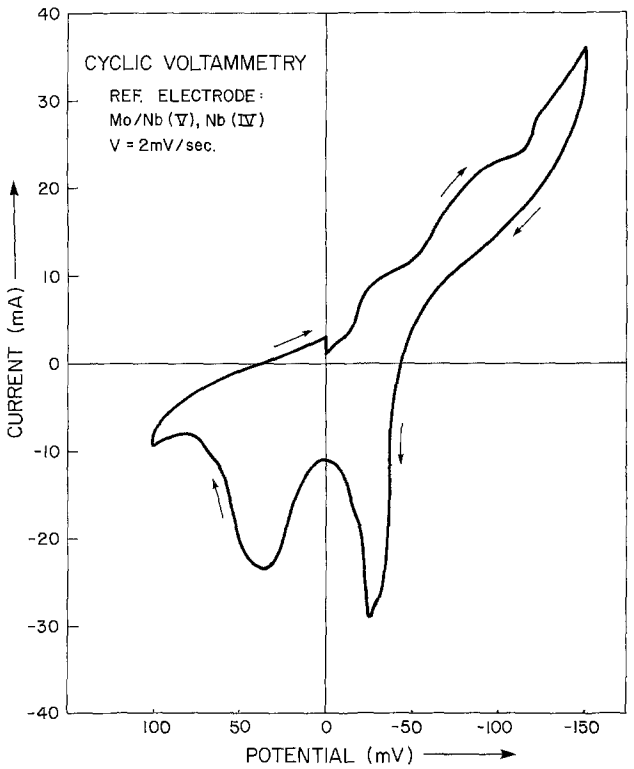

Fig. 1c. Cyclic voltammogram of the first cathodic wave. Solution containing 5 m/o K_2NbF_7 and 0.16 m/o K_2GeF_6. Electrodes as in Fig. 2. $T = 707°C$.

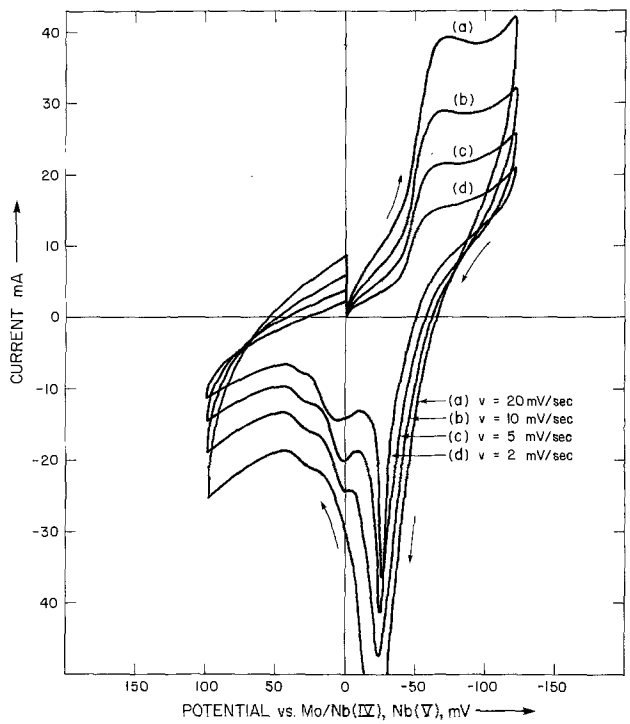

Fig. 1d. Cyclic voltammograms showing the first cathodic wave composed of one step (peak) only. Solution containing 5 m/o K_2NbF_7 and 0.08 m/o K_2GeF_6. Electrodes as in Fig. 2. $T = 756°C$.

tually developing into dendrites and powders. The exact potential region at which to operate was determined by taking several cyclic voltammograms prior to each electrolysis run.

Typical conditions for the stable growth of the various Nb-Ge phases are summarized in Table I. This table is not an exhaustive list of the bulk of the data, and is only given for the purpose of demonstration. In most of these experiments, Mo strips of 1 cm width and 0.5 mm thickness were used as substrates. They were exposed on both sides and were usually immersed to about 1 cm depth in the melt, thus exposing a total surface area of about 2 cm^2. Coatings with a thickness of more than 100 μm were obtained.

$NbGe_2$.—This compound was deposited from the relatively rich germanium solutions. Figure 2 shows the coating surface. Note the growth of individual crystallites. This suggests a small nucleation frequency and therefore easy single-crystal growth. The compound was obtained by electrolysis with a constant cathodic potential corresponding to the base (−18 mV) of the first step on the first cathodic wave shown in Fig. 1c (see also Table I).

Nb_3Ge_2.—This compound was obtained from the relatively rich germanium solutions when electrolyzing with constant cathodic potentials corresponding to the second step (−54 to −90 mV) of Fig. 1c. This procedure, however, resulted in thickness-limited coatings which began to deteriorate after a thickness of several microns. $NbGe_2$ crystallites were occasionally observed in these coatings. A better procedure was to utilize an intermediate germanium concentration and electrolyze at the base of the single-step first cathodic

Table I. Stable Nb-Ge compound codeposition

	Bath composition (m/o)	Temperature (°C)	Electrical[a] signal	Alloy[b, c] composition (m/o)	X-ray diffraction analysis	T_c (°K)	Remarks
$NbGe_2$	Nb 5.000 Ge 0.161	707 ± 2	Constant $\eta = -18$ mV	Nb 34.0-34.5 Ge 66.0-65.5	$NbGe_2$	—	Individual crystallites
$NbGe_2/Nb_3Ge_2$	Nb 5.000 Ge 0.053	703 ± 2	Constant $\eta = -30$ mV	Nb 57.8-63.5 Ge 42.2-36.5 Nb 36.7 Ge 63.3	$NbGe_2$ Nb_3Ge_2	—	Separate microprobe analysis of the two phase regions
Nb_3Ge_2	Nb 5.000 Ge 0.050	758 ± 2	Constant $\eta = -35$ mV	Nb 60.8-61.2 Ge 39.2-38.8	Nb_3Ge_2	—	
Nb_3Ge_2/Nb_5Ge_3	Nb 5.000 Ge 0.077	867 ± 2	Constant $\eta = -39$ mV	Nb 59.4-65.7 Ge 40.6-34.3	Nb_3Ge_2 Nb_5Ge_3	—	Very common mixture
Nb_5Ge_3	Nb 5.000 Ge 0.042	707 ± 2	Constant $\eta = -45$ mV	Nb 63.5-65.4 Ge 36.5-34.6	Nb_5Ge_3	—	
Nb_5Ge_3/Nb_3Ge	Nb 5.000 Ge 0.059	816 ± 2	Constant $\eta = -42$ mV	Nb 65.2-68.8 Ge 34.8-31.2	Nb_5Ge_3 and minor Nb_3Ge	—	
Nb_3Ge/Nb	Nb 5.000 Ge 0.150	760	Constant $\eta = -350$ mV	Nb > 95 Ge < 5	Nb and minor Nb_3Ge	8.8-9.2 9.2-9.3	Very short run. Conditions of operation very remote from equilibrium
Nb	Nb 5.000 Ge 0.000	751 ± 2	Constant $i = 5$ mA/cm^2	Nb ≃ 100.0 Ge ≃ 0.0	Nb	8.8-9.2	

[a] Constant cathodic potential versus the reference electrode Mo/Nb(V), Nb(IV).
[b] Electron microprobe chemical analysis with spot resolution up to 1 μm, and precision of ± 5% of the cited concentration.
[c] Stoichiometric composition of the various compounds: $NbGe_2$(33.3-66.7%); Nb_3Ge_2(60-40%); Nb_5Ge_3(62.5-37.5%); Nb_3Ge(75-25%).

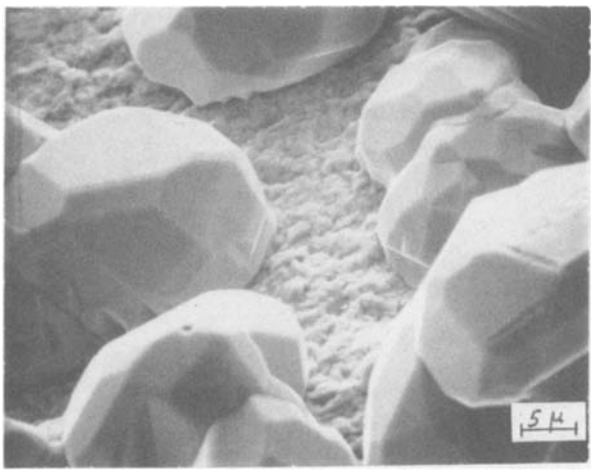

Fig. 2. SEM showing individual crystallites of $NbGe_2$

wave (such as shown in Fig. 1d). Figure 3 shows the coating surface of the single-phase Nb_3Ge_2, which was obtained by electrolyzing at −35 mV with the latter procedure (cf. Table I).

Nb_5Ge_3.—This compound was prepared from the low germanium concentration solutions by electrolyzing under a constant potential corresponding to the base of a single-step first cathodic wave. Figure 4 shows the coating surface of this compound obtained at −45 mV (cf. Table I).

Phase-mixtures.—The following phase-mixtures were obtained under various operating conditions as summarized in Table I. Notice that often in such mixtures the crystallites appear to be more rounded and lack the sharp angles and flat facets of the single-phase coating surfaces.

$NbGe_2$ + Nb_3Ge_2.—A coating surface of this mixture is shown in Fig. 5. The large individual crystallites are the $NbGe_2$ compound, and the flat uniform coating is Nb_3Ge_2. This was confirmed by electron microprobe and XRD analyses.

Nb_3Ge_2 + Nb_5Ge_3.—A coating surface of this mixture is shown in Fig. 6. Notice the rounded appearance of the crystallites and the spreading of small pimple-like particles on the larger crystallites. It is not known whether these are a secondary nucleation or the second phase.

Nb_5Ge_3 + Nb_3Ge.—A mixture with Nb_3Ge as the minor constituent was deposited under similar conditions to those of Nb_5Ge_3 (cf. Table I). A higher temperature, however, was used (T = 815°C). Figure 7 shows the coating surface of this mixture. It is not yet clear whether the small particles which are spread about on the larger crystallites are secondary nuclei or the second phase (Nb_3Ge).

Nb_3Ge + Nb.—Mixtures with the Nb_3Ge as the minor constituent could be obtained under extreme conditions of polarization. Electrolysis under constant cathodic potentials corresponding to the base of the

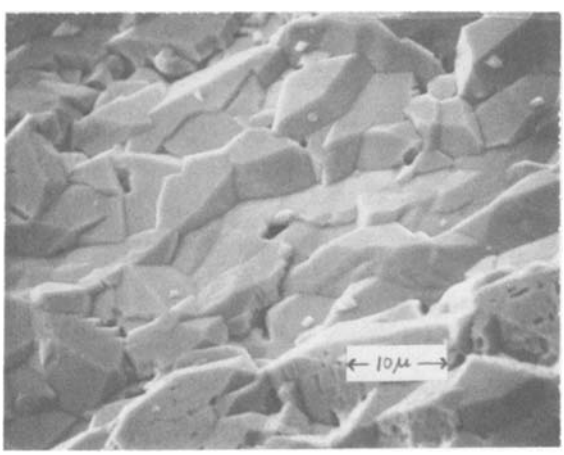

Fig. 3. SEM of Nb_3Ge_2 coating surface

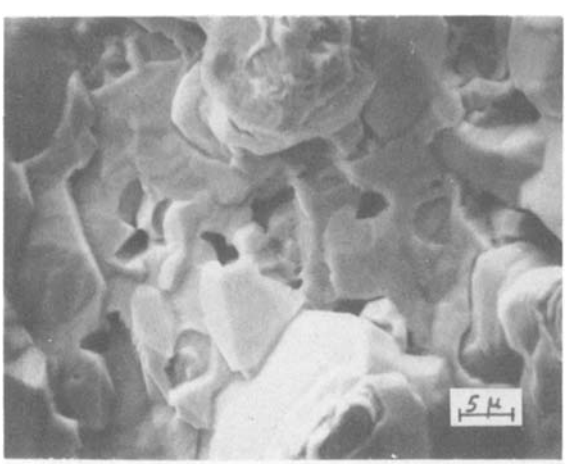

Fig. 4. SEM of Nb_5Ge_3 coating surface

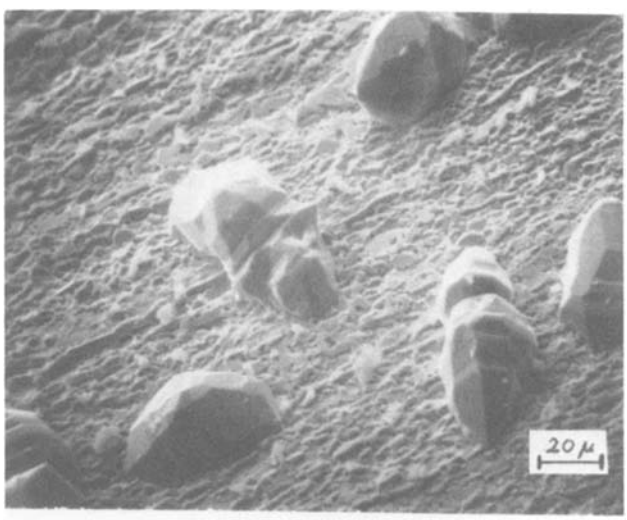

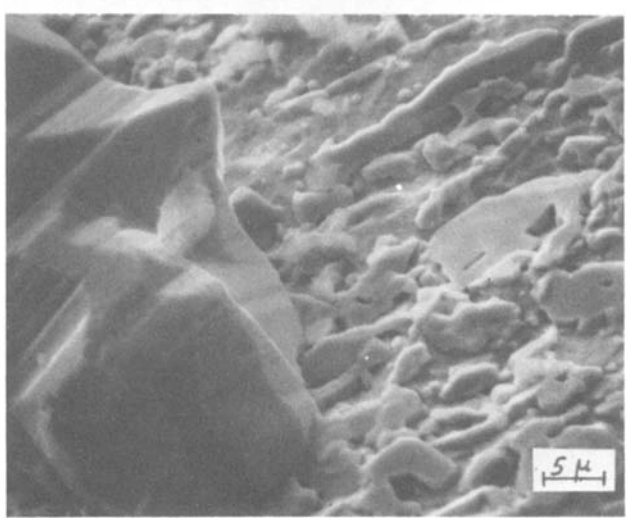

Fig. 5. SEM of the mixture $NbGe_2$ + Nb_3Ge_2 coating surface. The large crystallites are the $NbGe_2$ compound. The rest of the surface is composed of the Nb_3Ge_2 compound.

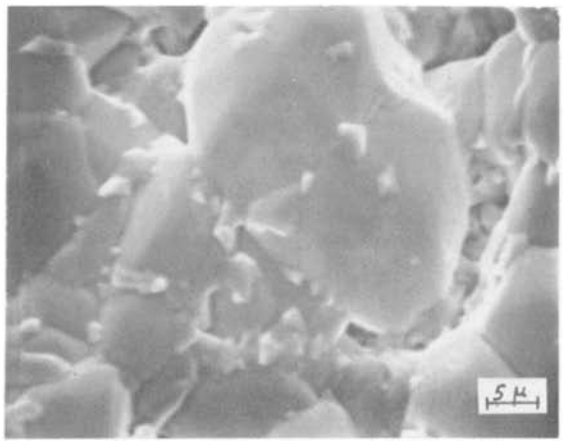

Fig. 6. SEM of the mixture Nb_3Ge_2 + Nb_5Ge_3 coating surface

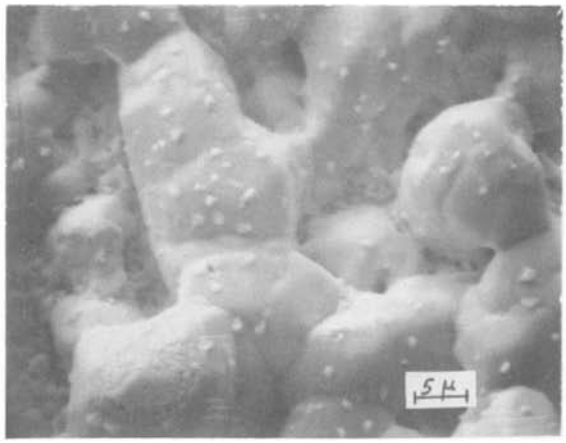

Fig. 7. SEM of the mixture Nb_5Ge_3 + Nb_3Ge (minor) coating surface.

second cathodic wave, or slightly to its left, yielded a very thin transient layer underlying a niobium deposit layer. The transient layer, as verified by XRD, contained the phase Nb_3Ge. A superconducting transition temperature was observed for these coatings at about 9.3 K, just above the regular Nb transition at 9.2 K.

The deposited Nb-Ge compounds were characterized by XRD for their lattice parameters, and by electron microprobe for their composition. A least-square computer program was used to optimize the calculation of the lattice parameters. Table II compares the present results with values reported in the ASTM-Powder-XRD file. The differences in the values are believed to be due to the different compositions obtained at the lower temperatures and more internal defects in the electrodeposited samples. The ASTM values are reported for bulk samples, typically prepared at much higher temperatures.

Attempts to obtain the Nb_3Ge compound.—A substantial effort was devoted in attempts to obtain single-phase Nb_3Ge coatings. Altogether about 130 experiments were performed towards this goal. Quite disappointingly, they were always unsuccessful.

Most of these experiments were characterized by large cathodic polarization, corresponding to the vicinity of the second cathodic wave (Nb) of Fig. 1b. The purpose was to increase the ratio of Nb/Ge in the deposit by raising the concentration polarization of germanium (cf. Eq. [2]). The effect, however, was always to produce unstable growth of powders and dendrites, on top of a thin adherent layer.

Following the significant improvement of Nb plating rate and deposit morphology (11, 19), a periodic reversal (PR) technique was attempted in hope to improve the Nb-Ge deposit morphology while still utilizing large cathodic polarization. The results were not conclusive. Typically a thin uniform and adherent film (of less than 1 μm) was found on the substrate surface, and a massive deposit ("umbrella") grew perpendicular to the substrate, on top of the electrolyte. The difficulties encountered are believed to be due to the separate stripping potentials of the various Nb-Ge alloys (cf. Fig. 1c and d). A few experiments were attempted with a new cyclic multilayered alloy (CMA) technique. Here the idea was to cyclically sweep or step the potential between the two limits corresponding to the deposition of the Nb-Ge phase(s) and the Nb phase, respectively. It was hoped that a thin intermediate (transient) layer of Nb_3Ge would be formed on each cycle between the alternating layers. Again the results were inconclusive; the deposits being essentially similar to those obtained by the PR technique.

Table II. Lattice parameters of Nb-Ge compounds

	ASTM reported (bulk prepared)	Present work (electrochemically prepared)
Nb_3Ge	Cubic (A) a_o = 5.168	Cubic (A) a_o = 5.14-5.17
Nb_5Ge_3	Tetragonal a_o = 10.148 c_o = 5.152	Tetragonal a_o = 10.149 ± 0.005 c_o = 5.085 ± 0.010
Nb_5Ge_3	Hexagonal a_o = 7.718 c_o = 5.370	Hexagonal a_o = 7.774 ± 0.002 c_o = 5.380 ± 0.002
$NbGe_2$	Hexagonal a_o = 4.966 c_o = 6.781	Hexagonal a_o = 4.964 ± 0.006 c_o = 6.786 ± 0.009

According to Eq. [2], the ratio Nb/Ge in the deposited alloy might also be increased by raising the operating temperature and by the decrease of the ion concentration ratio Ge(IV)/Nb(IV) in the solution. However practical limits are imposed on these two routes. Rapid volatilization and bath depletion become substantial at temperatures above about 850°C. Attempts to operate at 815°C yielded the phase-mixture Nb_5Ge_3 + Nb_3Ge, but not the single-phase Nb_3Ge (cf. Table I). A lower limit is imposed (11, 24) on the ion concentration ratio due to either a lower limit of Ge(IV) concentration or to a higher limit of Nb(IV) concentration. As the bulk concentration of Ge(IV) is reduced, its fluctuations near the cathode interface become significant. Also, the available deposition rate soon decreases to below a practical value. Attempts to start deposition from solutions containing no Ge(IV), and continuously increase it by the anodic dissolution of a Ge sheet, yielded the phase Nb_5Ge_3 as the first deposit to form. The other remedy, that of increasing the Nb(IV) concentration to its higher limit, was also tried. Experiments with 80 m/o of K_2NbF_7 yielded essentially identical results to the 5 m/o solution, with inferior quality coatings as a rule. Other problems encountered with the highly concentrated solution are the high vapor pressure and bath depletion, and the high viscosity. The latter is associated with low ionic mobilities and slow deposition rates. Several experiments with 80 m/o K_2NbF_7 solutions, starting from zero Ge(IV) concentration and continuously increasing it by anodic dissolution of a Ge sheet, again failed to yield the single-phase Nb_3Ge deposit. The first deposit to form was always too rich in germanium.

It is now the author's opinion that, electrodeposition of single-phase Nb_3Ge coatings is not feasible from the present fluoride system. The main hindrance is attributed to the thermodynamic instability of the Nb_3Ge phase, when in its pure state (9, 10). One might speculate that, if not for the extensive purification of the fluoride electrolytes, particularly with regard to moisture and oxide-containing traces, one could have had a better chance to achieve this goal. However, one must also consider the fact that germanium is more noble

than niobium in the fluoride melts and tends to deposit preferentially. Plating Nb-rich alloys, therefore, becomes more difficult as the ratio Nb/Ge increases. Moreover, electrodeposited alloys, in general, may differ considerably from those of thermally prepared alloys (*i.e.*, cast alloys) in their phase-composition-ranges. Metastable supersaturated phases are quite common, and the range of existence of other phases may be smaller, or the phase may not exist at all (25). Kinetic effects are usually of paramount significance in alloy plating and may influence the electrodeposited phase(s) considerably.

Conclusions

Electrodeposition of Nb-Ge alloys from molten fluoride electrolytes was demonstrated. Stable growth deposits were obtained of the intermetallic compounds $NbGe_2$, Nb_3Ge_2, Nb_5Ge_3, and their phase-mixtures. However, the superconducting compound Nb_3Ge could not be obtained as a single-phase deposit. It was obtained only as a minor constituent in certain phase-mixtures when operating under extreme conditions. Germanium was found to be more noble than niobium in the molten fluoride system, thus facilitating the deposition of Ge-rich alloys.

Acknowledgments

The author would like to thank Professor T. H. Geballe and his Cryogenic Group for suggestions, discussions, and help with the superconductivity measurements. The technical assistance of R. Koch, L. J. Anderson, C. R. Zercher, and M. K. Pyzyna from Stanford-CMR is gratefully acknowledged. The research was supported, in part, by the Center for Materials Research (CMR) at Stanford University under the NSF-MRL Program. This paper is based on the author's Ph.D. thesis [Ref. (11)].

Manuscript submitted April 26, 1982; revised manuscript received April 4, 1983. This was Paper 148 presented at the Dallas, Texas, Meeting of the Society, Oct. 5-10, 1975.

Any discussion of this paper will appear in a Discussion Section to be published in the June 1984 JOURNAL. All discussions for the June 1984 Discussion Section should be submitted by Feb. 1, 1984.

MPI assisted in meeting the publication costs of this article.

REFERENCES

1. J. E. Gavaler, *Appl. Phys. Lett.*, **23**, 480 (1973).
2. L. R. Testardi, J. H. Wernick, and W. A. Royer, *Solid State Commun.*, **15**, 1 (1974).
3. J. J. Hanak, "Metallurgy of Advanced Electronic Materials," G. E. Brock, Editor, Wiley Interscience Inc., New York (1963).
4. R. E. Enstrom, J. J. Hanak, and G. W. Cullen, *RCA Rev.*, **31**, 702 (1970).
5. A. Echarri and M. Spadoni, *Cryogenics*, **11**, 274 (1971).
6. A. R. Kaufmann and J. J. Pickett, *J. Appl. Phys.*, **42**, 58 (1971).
7. M. Suenga and W. B. Sampson, *Appl. Phys. Lett.*, **18**, 584 (1971).
8. K. Tachikawa, Y. Yoshida, and L. Rinderer, *J. Mat. Sci.*, **7**, 1154 (1972).
9. A. B. Hallak, Ph.D. Dissertation, Stanford University, Stanford, CA (1976).
10. T. H. Geballe and M. R. Beasly in "Energy and Materials," G. C. Libowitz and M. S. Wittingham, Editors, Academic Press, New York (1976).
11. U. Cohen, Ph.D. Dissertation, Stanford University, Stanford, CA (1977).
12. U. Cohen, Paper 346 presented at The Electrochemical Society Meeting, Pittsburgh, PA, Oct. 15-20, 1978.
13. N. C. Cook, J. D. Evans, and B. A. Fosnocht, in "Proceedings of the International Conference on Protection Against Corrosion by Metal Finishing," Basel (1966).
14. G. W. Mellors and S. Senderoff, *This Journal*, **112**, 266 (1965).
15. G. W Mellors and S. Senderoff, Can. Pat. 688,546 (1964).
16. S. Senderoff and G. W. Mellors, *This Journal*, **112**, 840 (1965); **113**, 60 (1966); **114**, 586 (1967).
17. G. W. Mellors and S. Senderoff, *Plating*, **51**, 972 (1964).
18. S. Senderoff, *Met. Rev.*, **11**, 97 (1966).
19. U Cohen, *This Journal*, **128**, 731 (1981).
20. U. Cohen, U.S. Pat. 3,983,012 (1976).
21. U. Cohen and R. A. Huggins, *This Journal*, **123**, 381 (1976).
22. U. Cohen, *J. Electronic Mater.*, **6**, 607 (1977).
23. U. Cohen, U.S. Pat. 4,142,947 (1979).
24. U. Cohen and W. A. Tiller, Paper 154 presented at The Electrochemical Society Meeting, Pittsburgh, PA, Oct. 15-20, 1978.
25. A. Brenner, "Electrodeposition of Alloys," Vol. I, Academic Press, New York (1963).

Measurement of Electroless Plating Rate by Coulostatic Method

N. Sato,* M. Suzuki, and Y. Sato

Toshiba Corporation, Toshiba Research and Development Center, 1, Komukai Toshiba-cho, Saiwai-ku, Kawasaki-city Kanagawa, 210, Japan

ABSTRACT

The copper deposition rate in a production electroless copper plating bath was measured by the coulostatic method. The effects of the substrate material and the degree of bath aging on the measured parameters were investigated. The deposition current density i_{ELP}, obtained from weight gain data of the specimen, the double layer capacity C_d, and the polarization resistance R_p measured by this method depended on the substrate material, while the proportionality constant K for conversion from R_p to i_{ELP} was almost constant. The dependence of i_{ELP}, C_d, and R_p on the substrate material was interpreted in terms of the surface roughness of the substrate. The possibility of using this method for real time monitoring of electroless deposition rates was demonstrated by these results.

In electroless deposition of metals, the deposition rate is thought to be one of the most important parameters for controlling plate quality and plating bath, as well as for understanding the deposition process. So far, not many studies on deposition rate measurements have been reported (1-8).

In the previous paper (9), the coulostatic method was successfully applied in *in situ* measurements of copper and nickel plating rates. The results indicated that the coulostatic method has the advantage that the

* Electrochemical Society Active Member.
Key words: deposition, plastics, transients, SEM.

measurement is very rapid (within a few tens of milliseconds) and needs no correction for solution resistance, which is essential in the usual linear polarization method (5). It was found that the polarization resistance measured by the coulostatic method is inversely proportional to the deposition current density calculated from weight gain data and that the proportionality constant K varies with the kind of bath used. In the previous study, no attention was paid to influences of additives and byproducts accumulation because plating baths used were composed of only basic components, namely, metal ion to be plated, reducing agent and complexing agent, and also because the period of each experimental run was relatively short. In production electroless baths, however, it is impossible to avoid the changes in the concentration of additives and the accumulation of reaction byproducts, which bring about a change in solution property (10).

This work was undertaken to determine whether the quantitative relationship found with the coulostatic method can be applied under such practical conditions. Furthermore, studies were also made on effects of substrate material on the deposition rate.

Experimental

The method of coulostatic measurements for determining polarization resistance R_p and double layer capacity C_d was the same as that described previously (9).

Cuposit Coppermix 328 A, L (Shipley Far East, Limited) was employed as a practical electroless copper plating bath. Besides the freshly prepared bath, a few aged plating solutions taken from a production installation were used.

An all-glass, single compartment cell with three electrodes was used. It contained 200 ml of the plating solution. All experiments were carried out without removing dissolved oxygen from the bath. The temperature range for measurements was 20°-30°C.

Three kinds of substrates were employed as working and reference electrodes: epoxy glass base copper clad laminated sheet (copper clad laminate), epoxy glass base laminated sheet (epoxy-glass laminate), and rolled copper sheet. Two specimens of the same material and size (1 × 2 cm in size, with 0.3 mm diam copper lead wire, respectively) served as working and reference electrodes, alternately. Activation of the electrodes was carried out using Catalyst 6F and Accelerator 19 (Shipley Far East, Limited) in the usual way. A platinum sheet of 4 cm^2 was used as a counter electrode for these experiments.

Electrodes were dried in nitrogen atmosphere and weighed before and after coulostatic measurements in order to obtain weight gain data. By dissolving the deposited copper from two arbitrary samples with 5% ammonium persulfate solution and determining the mass of copper by atomic absorption spectroscopy, the reliability of weight gain measurements was evaluated. For these samples, both results agreed with each other within 1%. Deposition current density, i_{ELP}, was calculated from weight gain data; i_{ELP} of 1 $\mu A/cm^2$ corresponds to the deposition rate of 2.85 $mg/dm^2/day$ for copper.

For the various substrates the proportionality constant K for conversion from R_p to i_{ELP} was examined using Eq. [1]

$$i_{ELP} = K/R_p \qquad [1]$$

The apparatus and method used were the same as those described previously (9). The immersion time of each test piece was about 1 hr.

Results

Results on the freshly prepared bath.—A typical overvoltage decay curve for the electroless copper deposition on the rolled copper sheet electrode is shown in Fig. 1. For almost all the experiments, the overvoltage

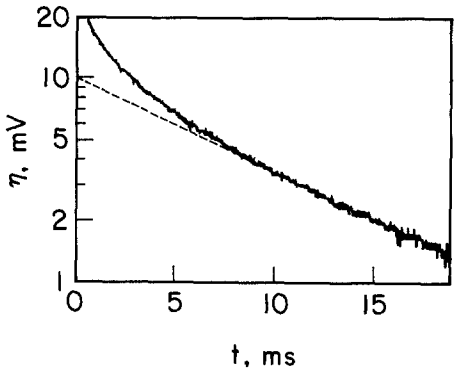

Fig. 1. Example of the potential decay curve for rolled copper sheet electrode at 20°C.

decayed within a few tens of milliseconds. In the case of the epoxy-glass laminate electrode, it was difficult to obtain meaningful decay curves immediately after immersion. As the metal deposition proceeded, it became possible to obtain decay curves similar to that shown in Fig. 1.

As seen in Fig. 1, the measured log η_t *vs.* t relations were not completely linear for all electrodes, particularly in the early part of the decay, which suggests the presence of pseudocapacity on the electrode surface as pointed out previously (9). Determination of the C_d and R_p values was carried out by analyzing a straight line which was fitted to the linear part of the log $\eta_t - t$ curve (the dotted line in Fig. 1). R_p values did not change noticeably during immersion in each experimental run.

Table I lists the parameters measured for epoxy-glass laminate, copper clad laminate, and rolled copper sheet electrodes as substrates at 20°C. The R_p values in Table I are the averages obtained from graphic integration of the $R_p^{-1} \sim t$ relation during the entire immersion period. C_d's are the range of the measured values. The deposition current density, i_{ELP}, was obtained from the weight gain data of the electrode. It is seen from the table that both C_d and R_p depended on the substrate material in spite of the bath condition being the same, while the K values, the proportionality constant in Eq. [1], were essentially identical. In Fig. 2, the i_{ELP} values calculated from weight gain data are plotted *vs.* the average R_p values on a log-log scale. These plots fell on a single line having a slope of −1, showing that the measured R_p values are inversely related to the deposition rates regardless of the substrate material and/or temperature. The K value obtained by the least squares method was 27.3 mV.

Results on aged baths.—In the production electroless copper bath, consumed ingredients are replenished so that the level of copper ion, formaldehyde, and pH is kept almost constant. However, the deposition rate changes as plating proceeds because of the byproducts accumulation during the plating reaction. This aging phenomenon cannot be avoided even if the concentrations of main components are kept constant.

From the practical standpoint, the coulostatic method should be applicable throughout the entire bath life. In order to ascertain this, coulostatic measurements were

Table I. Measured parameters for various substrates (20°C)

Substrate	C_d ($\mu F\ cm^{-2}$)[1]	R_p ($\Omega\ cm^2$)[2]	i_{ELP} ($mA\ cm^{-2}$)[3]	K (mV)
Rolled copper sheet	250 ~ 350	32.3	0.834	26.9
Copper clad laminate	350 ~ 500	28.2	0.933	26.3
Epoxy-glass laminate	500 ~ 700	16.2	1.690	27.4

[1] Range of values measured during immersion.
[2] Average value during immersion.
[3] From weight gain data.

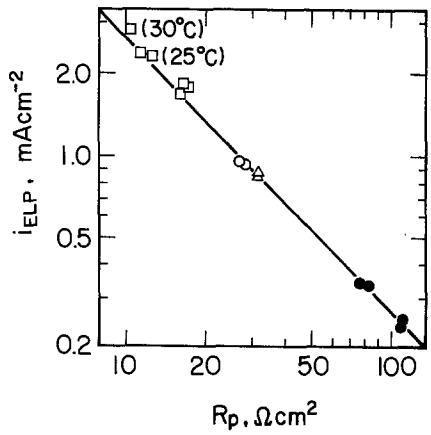

Fig. 2. $R_p \sim i_{ELP}$ relation at 20°C for various substrates in freshly prepared bath, □: epoxy-glass laminate, ○: copper clad laminate (● in aged bath), and △: rolled copper sheet.

carried out using aged Cuposit Coppermix 328 solutions sampled from an extensively used production bath. Results are shown in Fig. 3, where the deposition current density i_{ELP} obtained from weight gain data of the specimen (solid circles) and the measured R_p (open circles) are plotted against the total plating area of the printed wiring boards (PWB). It is seen that the deposition rate decreased with the aging of the bath while the obtained R_p value increased. This relation was compared with that of the fresh bath, and i_{ELP} was plotted *vs.* R_p (Fig. 2, solid circles). These data fell on the same straight line as those obtained in the fresh bath. This result proves that the deposition rate can be measured quantitatively by the coulostatic method throughout the entire bath life. Furthermore, the degree of bath degradation can be estimated from the increase in the R_p value.

Discussion

Even when a nonconducting substrate such as the epoxy-glass laminate is used as electrodes, coulostatic measurements become possible after several minutes from the initiation of the plating reaction. Sard's work on carbon substrates using electron microscopic techniques revealed that the electroless deposition of copper initially occurred by three-dimensional nucleation only at catalytic sites on the surface and that these nuclei formed aggregates of randomly oriented copper crystallites (11). He concluded that continuous copper films were obtained from the repeated three-dimensional nucleation and recrystallization process. Dumesic *et al.* found that the copper deposition on glass substrates started at silver-tin activated sites and grew through an open network structure into a fairly rough and porous, polycrystalline copper film (2). From these investigations, copper deposition onto the epoxy-glass laminate is thought to occur only at catalytic sites, namely onto palladium particles adsorbed during the activation process (12, 13). It appears that coulostatic measurements become possible when the surface was covered with continuous copper film. Dumesic and coworkers have investigated copper deposition rates onto silver-activated glass substrates at relatively early stages (2). Their results indicate that the deposition rate onto copper differs from that onto silver probably due to the difference in the nature of the catalytic surface. Although the authors could not measure deposition rates at the initial stage before continuous copper films were formed, it seems likely that the deposition rate on palladium nuclei differs from that on copper. However, this difference cannot lead to a significant error in results because the period of copper deposition taking place on palladium nuclei should be negligible as compared with the total plating period.

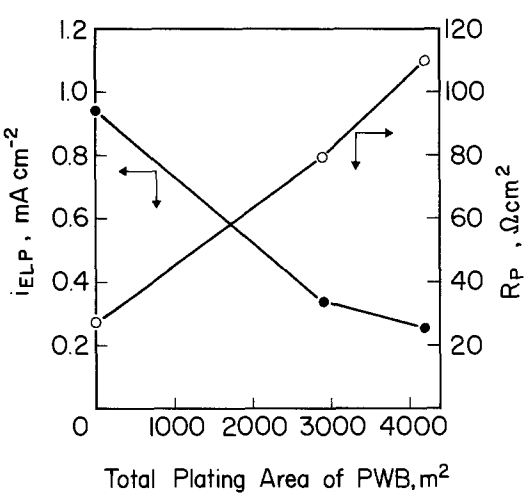

Fig. 3. Variations in i_{ELP} and R_p during the bath life at 20°C (epoxy-glass laminate electrode).

It can be seen from Table I that the deposition rate itself and C_d values varied with the substrate material. Differences in plating rate on copper and on plastic substrates are well known (14, 15). However, the $R_p \sim i_{ELP}$ relation was independent of the substrate material as seen in Fig. 2. In order to clarify this phenomenon in some detail, scanning electron microscopic (SEM) observations were performed.

Figures 4a, b, and c are SEM's of the substrate surfaces of the epoxy-glass laminate, the copper clad laminate, and the rolled copper sheet, respectively, prior to electroless plating. The surface of the epoxy-glass laminate proved to be considerably rougher than copper surfaces in b and c. Figures 4d, e, and f show the corresponding surfaces after copper deposition (about 1 μm film thickness). An x-ray diffraction study elucidated that the deposits on the epoxy-glass laminate consist of aggregates of small copper crystallites with a face-centered cubic structure. It appears that electroless deposition of copper occurred along the surface roughness, so that the deposited copper film reflected

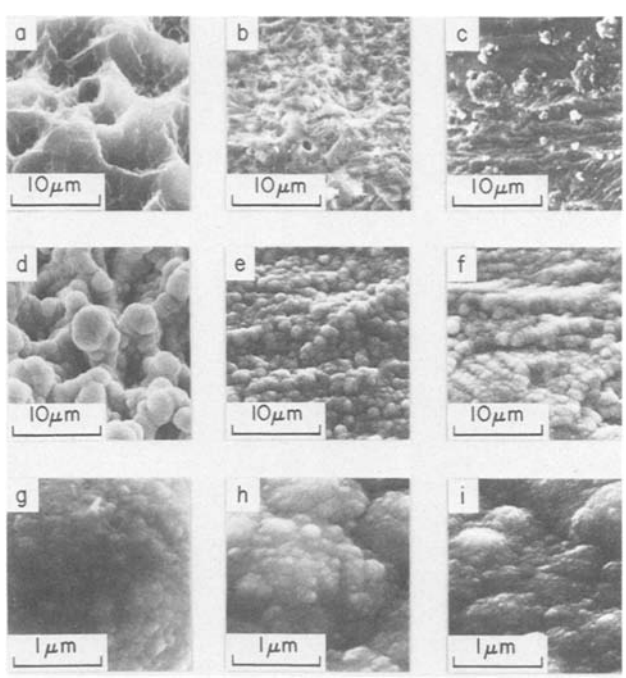

Fig. 4. SEM's of substrates (a ~ c) and films (1 μm thick) deposited on each substrate (d ~ i). (a): bare epoxy-glass laminate, (b): bare copper clad laminate, (c): bare rolled copper sheet, (d, g): deposits on epoxy-glass laminate, (e, h): deposits on copper clad laminate, and (f, i): deposits on rolled copper sheet.

the roughness of the substrate surface. However, from a comparison of the micrographs taken with a higher magnification (Fig. 4g, h, and i), it can be concluded that the microstructural characteristics are essentially independent of the substrate material. This result suggests that once a continuous copper film is formed, copper deposition on an insulator such as the epoxy-glass laminate proceeds by the same autocatalytic mechanism as the deposition on copper substrate. Therefore, an identical relation between i_{ELP} and R_p is considered to be valid for various substrates. From Table I and Fig. 4, it is seen that the larger the surface roughness, the smaller the measured R_p. On the basis of the above observation, the measured large C_d and small R_p values can be interpreted in terms of the difference in surface roughness. In fact, the time constant, $C_d \times R_p$, was approximately constant for all substrates. If both values of C_d and R_p were normalized not by apparent area but by true area, they should not depend on the substrate material.

The identity of the deposition characteristics for various substrate materials must be the reason for the identical relationship observed between R_p and i_{ELP}, which makes this method effective and practical for deposition rate measurements.

Conclusions

From coulostatic measurements and microstructural observations, the following results were obtained. (*i*) A nonconducting substrate such as the epoxy-glass laminate could be used as the electrode for the coulostatic measurements. (*ii*) The deposition rate i_{ELP}, obtained from weight gain data, and the apparent C_d and R_p values, obtained from the present method, depended on the substrate material used. (*iii*) The K value, which is the proportionality constant in the relation $i_{ELP} = K/R_p$, was constant independent of the substrate material, and the K value was 27.3 mV. (*iv*) The deposition rate fell with the aging of the bath. However, the proportionality constant K did not change. (*v*) Microscopic observations revealed that the dependence of i_{ELP}, C_d, and R_p on the substrate material was due to the surface roughness of the substrate. This method is suitable for monitoring the electroless deposition rate.

Manuscript submitted Dec. 20, 1982; revised manuscript received March 23, 1983.

Any discussion of this paper will appear in a Discussion Section to be published in the June 1984 JOURNAL. All discussions for the June 1984 Discussion Section should be submitted by Feb. 1, 1984.

The Toshiba Corporation assisted in meeting the publication costs of this article.

REFERENCES

1. M. Paunovic, *Plating*, **55**, 1161 (1968).
2. J. Dumesic, J. A. Koutsky, and T. W. Chapman, *This Journal*, **121**, 1405 (1974).
3. F. L. Shippey, C. U. Yu, and F. M. Donahue, *Plating*, **59**, 762 (1972).
4. M. J. Brown, *Insulation/Circuits*, **21**, 17 (1975).
5. C. Gabrielli and F. Raulin, *J. Appl. Electrochem.*, **1**, 167 (1971).
6. I. Ohno, *J. Metal Finishing Soc. Jpn.*, **29**, 600 (1978).
7. S. Haruyama, A. Yoshizawa, and I. Ohno, *ibid.*, **30**, 289 (1979).
8. G. Hermann, *Galvanotechnik*, **65**, 462 (1974).
9. M. Suzuki, N. Sato, K. Kanno, and Y. Sato, *This Journal*, **129**, 2183 (1982).
10. C. I. Courduvelis and G. Sutcliffe, *Plating*, **67**, 71 (1980).
11. R. Sard, *This Journal*, **117**, 864 (1970).
12. T. Osaka, H. Takematsu, and K. Nihei, *ibid.*, **127**, 1021 (1980).
13. A. T. El-Mallah, S. M. El-Raghy, E. A. Abou-Saif, M. Y. Saada, and A. E. El-Mehoiry, *Plating*, **67**, 61 (1980).
14. A. M. Poskanzer and S. C. Davis, *ibid.*, **69**, 94 (1982).
15. R. A. Nesbitt and C. Courduvelis, "Proceedings of the 8th Symposium on Plating in the Electronics Industry," American Electroplaters' Society, Phoenix, AZ, January 20-21, 1981.

Semiconductor Electrodes

52. Photoelectron Spectroscopic Determination of the Structure of Thin Platinum Silicide Layers Formed on Si(100) and Si(111) for Use as Electrodes

G. A. Hope, F.-R. F. Fan, and A. J. Bard*

Department of Chemistry, The University of Texas at Austin, Austin, Texas 78712

ABSTRACT

Platinum silicide was grown on (100) and (111) silicon by vacuum annealing an evaporated layer (0-15 nm thick) at 400°C, immediately following deposition. The element distribution in the product layer was measured using electron spectroscopy (XPS and AES) in conjunction with argon ion sputtering of the sample. The silicide thus produced was covered by a thin surface layer of SiO_2. The decrease in platinum concentration with increasing penetration into the sample was characteristic of a reaction mechanism in which a platinum species diffuses into the Si.

Among the methods for protecting the surface of n-type silicon from photocorrosion when employed as an electrode for generating highly oxidizing species, such as chlorine and oxygen in photoelectrochemical (PEC) cells, the use of thin noble metal silicide films has been particularly beneficial (1, 2). Such films, sometimes suitably modified with metal oxides or other catalysts, can also promote the interfacial electron transfer reactions of photogenerated carriers. Moreover, several silicide systems have been investigated because of their application in the electronics industry (3). The silicides formed from Pd(4), Pt(5), and Ni(6) have been particularly well studied. There is, however, only limited information available on the structure and properties of the very thin layers (<50 nm) which are of primary interest in electrochemical studies. In this paper, we report the results of x-ray photoelectron spectroscopy (XPS or ESCA) and Auger electron spectroscopy (AES) studies of the Pt-Si films formed on single crystal surfaces of Si.

* Electrochemical Society Active Member.

Experimental

Substrates for silicide growth were n-Si(100) and p-Si(111) (0.4-0.6 Ω cm) donated by Texas Instruments. The crystals were polished with 0.6 μm alumina and etched with HNO_3:HF:HOAc (3:3:1) containing 0.03% Br_2 for 10-15 sec, followed by concentrated HF for 10-15 sec, and then washed with distilled water and methanol immediately prior to insertion into the evaporation chamber. A known mass of platinum (Alfa Ventron, 99.9%) was evaporated from a tungsten filament in an Edwards E306A vacuum coating system. The source to substrate distance was 8 cm and base pressure during evaporation did not exceed 1×10^{-6} Torr. The silicon crystals were supported by a mica plate resting on a molybdenum heating stage. Following Pt deposition, the temperature of the heating stage was raised to 400°C and held to within ±10° for a few minutes up to 1 hr. The temperature was measured with a chromel-alumel thermocouple in contact with the mica. After heat-treatment, the samples were allowed to cool and removed from the vacuum system for study by XPS, AES, and scanning electron microscopy. XPS measurements were made of the Pt 4f, Si 2p, and O 1s peaks with a Physical Electronics 548 instrument using a Mg Kα source (2 mm spot diam) on the as-prepared sample surface and following varying periods of 5 keV argon ion bombardment at a current density of 6 μA-cm^{-2}. The AES data were obtained on a Physical Electronics 590 system, the exciting radiation being 5 keV electrons with a sample current of 240 μA over a spot diameter of 3 μm. The sample spectra were measured from 25 to 2000 eV for the as-prepared specimens and between sputtering periods. During sputtering (at 40 μA-cm^{-2} with 3 keV argon ions, rastered over 6 mm^2) the intensities of the Si KL_2L_2 C KL_2L_2 O KL_2L_2 and Pt $N_5N_7O_4$ peaks were monitored. The sample topography was investigated with a JEOL JSM 35C electron microprobe analyzer (EMP).

Results and Discussion

When the cleaned unannealed silicon surface was inspected in the EMP, it was found to be smooth and slightly pitted, the pits having been generated in the cleaning process. Reaction of this surface with platinum to form the silicide altered the topography only slightly, generating no detectable surface structure at magnifications up to 100,000 times. Reacted samples were also investigated by scanning mode AES, where the surfaces resembled those observed in the EMP. AES spectra of the surface both before sputtering and after having been sputtered until approximately 9 nm of the sample had been removed are shown in Fig. 1. The unsputtered surface was contaminated with carbon and oxygen and, although the Si peak at 92 eV was small, it had a shape that resembled that found for SiO_2. There were only very weak peaks which could be attributed to Pt. The sample spectrum after sputtering contained only small signals for carbon and oxygen, the major peaks were those of silicon and platinum. On further sputtering of the sample, the platinum peaks decreased in intensity and eventually only the silicon signals were obtained.

Samples were also depth-profiled while monitoring the Si KL_2L_2, C KL_2L_2, O KL_2L_2, and Pt $N_5N_7O_4$ Auger peaks to determine the elemental distribution. A typical depth profile is presented in Fig. 2. The original surface of the sample was characterized by a region approximately 5 nm thick, which was enriched in oxygen and carbon and deficient in platinum. Beneath this surface region the maximum platinum signal was obtained and, as sputtering removed more of the sample, the platinum signal decreased and the silicon signal increased. This was observed for samples with annealing times as short as 5 min at this temperature. The intensity of the Si peak reached a maximum when approximately 21 nm had been sputtered from the surface; however, the

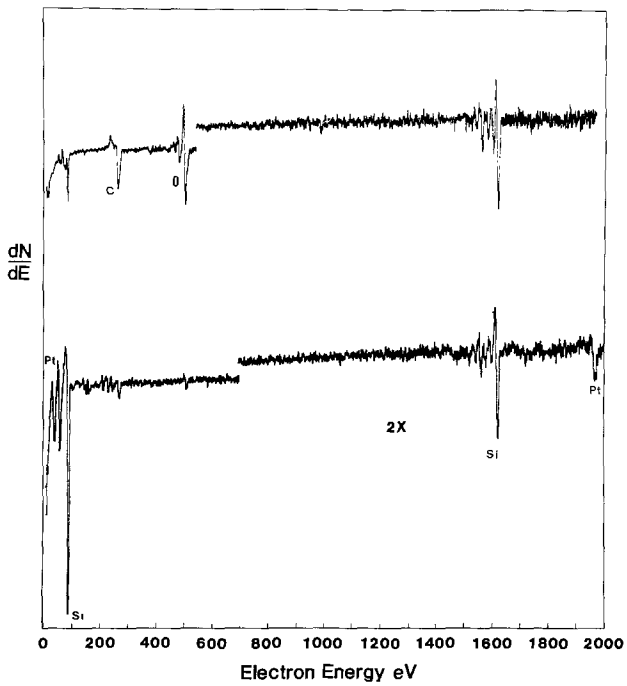

Fig. 1. The Auger electron spectrum of a platinum silicide sample prepared by annealing an evaporated Pt film on (100) n-Si at 400°C for 30 min. For the upper spectrum, the sample had not been sputtered, and the lower spectrum was taken after approximately 9 nm of the sample had been removed.

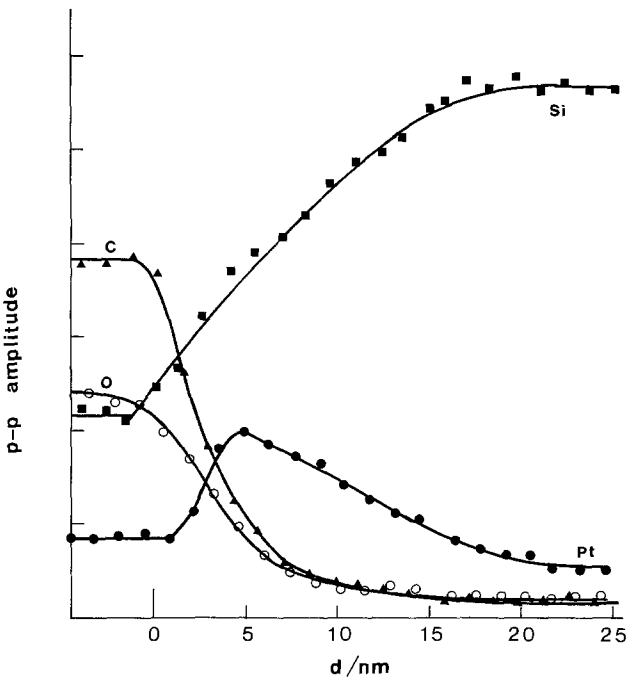

Fig. 2. The elemental depth profile of the sample of Fig. 1. This profile shape is typical of all annealed samples.

platinum signal was still present and continued to decrease with sputtering—it was present even after 30 nm of sample had been removed.

The information provided by depth-profiling the silicide layer and monitoring the surface composition with AES gives strong support for a model of silicide formation in which platinum is the mobile species, since it is the platinum which penetrates the silicon. This mechanism is in agreement with that proposed from tracer studies using ^{31}Si (7), but contrary to that proposed on the basis of Rutherford backscattering (RBS) using thicker silicide layers (8, 9). It is possible that the sputtering of the silicide does not remove the platinum

fully; however, Poate *et al* (10), have studied the sputtering process in the argon ion energy range which we have used and found almost stoichiometric sputtering of PtSi. For the pure materials, Pt sputters 2.4 times as fast as Si. Additional information on the chemical nature of the silicide layer and the extent of platinum penetration into the silicon was obtained with high resolution XPS. In Fig. 3, the changes in the silicon 2p peak are shown for various depths of sample sputtering. The initial peak is significantly broadened and consists of a higher energy component, located where the Si 2p peak in SiO_2 is found as well as a sharper peak closer to the elemental Si peak location. The Si 2p peak narrows, shifts to lower energy, and increases in strength after approximately 2 nm of sample had been sputtered away; this result indicates that the thin surface layer of SiO_2 present on the sample was removed. The energy of the silicide Si 2p peak was 99.3 ± 0.3 eV determined by reference to the silicon substrate after the Pt $4f_{7/2}$ signal was no longer detected. O 1s peak intensities were only significant in the initial 3 nm of the sample. The Pt 4f peaks were also measured after each sputtering, and the energy of the Pt $4f_{7/2}$ peak was measured relative to Pt $4f_{7/2}$ peak obtained from a platinum foil mounted next to the silicon. Typical scans of the Pt 4f peaks for varying degrees of sputtering are shown in Fig. 4. The energy of the silicide Pt $4f_{7/2}$ peak is approximately 1.6 eV higher in energy than for the metal, Pt° has a value of 72.5 ± 0.2 eV. This is most probably the value for PtSi which must be intergrown with silicon. Note that atomic ratios of Pt/Si > 1, with a stoichiometry of PtSi near the electrode surface, have also been found (2); the composition of the surface layer depends upon the amount of Pt deposited and the annealing time. From the intensity data obtained with the XPS measurements, a depth profile can be drawn, derived from the stronger platinum signal, and obtained using higher energy argon ions operated at a lower ion current density to give a slower sputtering rate than that used to obtain the AES profile. The XPS derived Pt-Si depth profile is presented in Fig. 5. This profile resembles the AES depth profile in elemental distribution, and provides additional information on the composition of the platinum containing layer.

Several important conclusions can be drawn from the depth profiles and the AES and XPS spectra. First, the depth resolution obtained with XPS and AES show

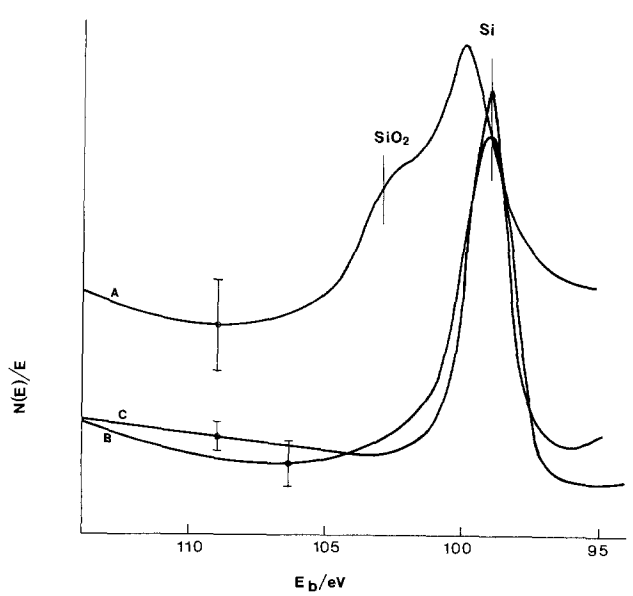

Fig. 3. Variation in the Si 2p peak shape with extent of sputtering (A) lightly (1 nm) sputtered with Si 2p peak shape characteristic of the presence of SiO_2, (B) Si 2p peak after approximately 5 nm of the sample have been removed, (C) after 15 nm removed.

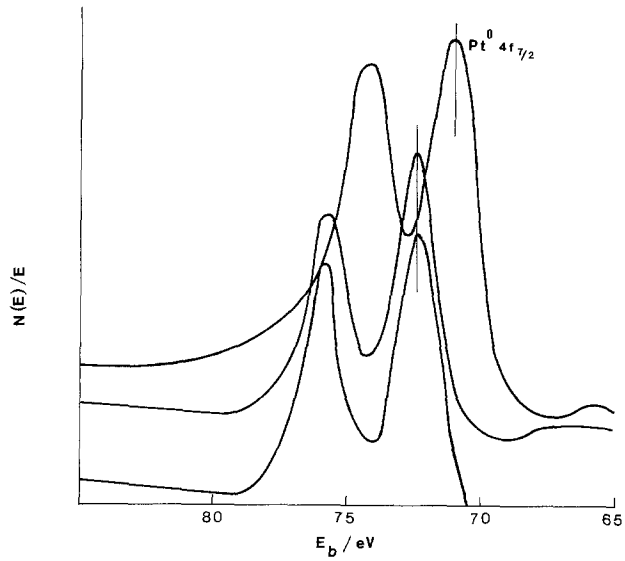

Fig. 4. The Pt 4f peak shape and location in the silicide layer compared to a platinum foil standard (upper curve) (A). The spectra were recorded after 10 (B) and 18 (C) nm (lower curve) were sputtered away.

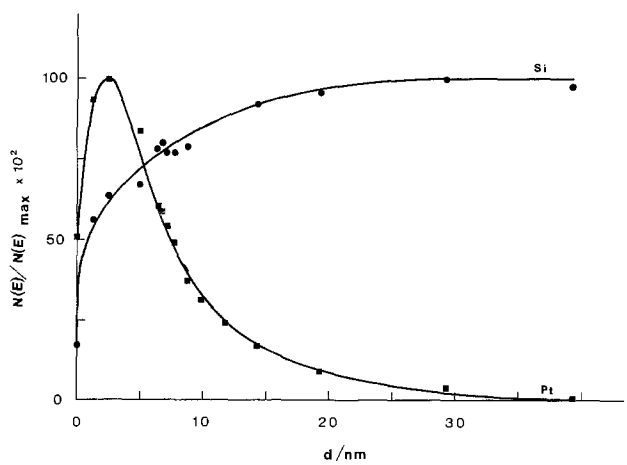

Fig. 5. The XPS depth profile showing the variation in element peak intensity as a function of sputtering depth.

that the thin Pt° films are converted into silicide containing layers which are approximately 4 times thicker than the original metal film. This layer does not achieve a uniform PtSi stoichiometry, and under the conditions here was richer in silicon, supporting a model which involves diffusion of platinum into the silicon substrate. Under these conditions of preparation, there was also no discrete PtSi/Si interface, and the only oxygen or carbon contamination is located close to the sample/vacuum interface. The XPS result presented in Fig. 3 shows that SiO_2 is present at the vacuum/sample surface, although some oxygen is detected at greater depths into the sample using AES. Since these signals are also associated with carbon, the source of the oxygen is probably related to oxidation of Si, prior to platinum film deposition. There is no evidence to support the intergrowth of Pt-Si and SiO_2 throughout the film. The diffuse nature of the silicide layer on silicon probably strongly influences the properties of any Schottky barrier between this layer and the silicon substrate.

Acknowledgments

We gratefully acknowledge the generous assistance of Dr. M. Schmerling, Mr. D. Finello, and Mr. D. Belton. The support of this work by the SERI and NSF (CHE 800682) is gratefully acknowledged.

Manuscript received Dec. 27, 1982.

Any discussion of this paper will appear in a Discussion Section to be published in the June 1984 JOURNAL. All discussions for the June 1984 Discussion Section should be submitted by Feb. 1, 1984.

The University of Texas at Austin assisted in meeting the publication costs of this article.

REFERENCES

1. F-R. F. Fan, G. Hope, and A. J. Bard, *This Journal*, **129**, 1647 (1982).
2. F-R. F. Fan, R. Keil, and A. J. Bard, *J. Am. Chem. Soc.*, **105**, 220 (1983).
3. K. N. Tu and J. W. Mayer, in "Thin Films, Interdiffusion and Reactions," J. M. Poate, K. N. Tu, and J. W. Mayer, Editors, John Wiley and Sons, New York (1978).
4. G. Majni, F. Nava, G. Ottaviani, E. Dana, G. Leggieri, A. Luches, and G. Celotti, *J. Appl. Phys.*, **52**, 4055 (1981).
5. C. A. Crider, J. M. Poate, J. E. Rowe, and T. T. Sheng, *ibid.*, **52**, 2860 (1981).
6. K. N. Tu, E. I. Allessandrini, W. K. Chu, H. Krautle, and J. W. Mayer, *Jpn. J. Appl. Phys.*, **13**, Suppl. 2, Pt. 1, 669 (1974).
7. R. Pretorius, *Proc. Electrochem. Soc.*, 80-2, 481 (1980).
8. A. Hiraki, M-A. Nicolet, and J. W. Mayer, *Appl. Phys. Lett.*, **18**, 178 (1971).
9. J. M. Poate and T. C. Tisone, *ibid.*, **24**, 391 (1974).
10. J. M. Poate, W. L. Browne, R. Homer, W. M. Augustyniak, J. W. Mayer, K. N. Tu, and W. F. Van der Weg, *Nucl. Instrum. Methods*, **132**, 345 (1976).

A New (W, Mo)C Electrocatalyst Synthesized by a Carbonyl Process: Its Activity in Relation to H_2, HCHO, and CH_3OH Electro-Oxidation

T. Kudo, G. Kawamura, and H. Okamoto

Central Research Laboratory, Hitachi, Limited, 1-280 Higashi-koigakubo, Kokubunji, Tokyo, 185 Japan

ABSTRACT

Tungsten and molybdenum mixed carbide electrocatalysts are formed on a carbon fiber substrate using a novel technique, in which metallic film given by CVD at 450°C using $W(CO)_6$ and/or $Mo(CO)_6$ is then carburized with CO at 820°C. The catalyst thus obtained has a hexagonal WC structure (a_0:2.89, c_0:2.85Å), and there is little contamination by carbon in elemental forms, on its surface, according to observation by Auger electron spectroscopy. Activity tests in relation to electro-oxidation of H_2, HCHO, and CH_3OH, are conducted in 1M H_2SO_4, revealing that the potentiostatic current produced by each reactant per real surface area of the catalyst is 0.12 A/m² (at 0.2V *vs.* RHE), 0.04 (at 0.3V) and 0.00082 (at 0.5V), at 50°C. No stationary current due to methanol oxidation is observed in the molybdenum-free catalyst.

Since Levy and Boudart (1) reported that tungsten carbide (WC) exhibited platinum-like properties, owing to its surface electronic structure being similar to that of platinum, a number of studies have been carried out to determine the nature of catalytic activity in WC. To date, however, no definite conclusion has been obtained, mainly because WC with identical surface properties was not used in each of these studies: *i.e.*, the catalytic behavior of WC is highly influenced by the method of preparation.

Whether the surface of WC is platinum-like or not, it exhibits remarkable activity to chemical or electrochemical reactions that are catalyzed by platinum. Therefore, WC is attracting attention as a catalyst to replace the more expensive platinum. This is especially true for electrocatalysts used in acidic solutions because WC is not easily corroded by acids.

Ross *et al.* (2) investigated the electrocatalytic activity of WC from several different origins. His studies centered on hydrogen oxidation in an aqueous solution of sulfuric acid, and he concluded, on the basis of measurement using Auger electron spectroscopy (AES), that activity depends on surface composition, *i.e.*, the ratio of tungsten to carbon. Only carbon deficient WC showed good activity. It was so active that the current density based on real surface area amounted to 0.02 A/m² at a potential of 0.2V *vs.* RHE and 22°C. More recently, Miles (3) investigated WC catalysts in an attempt to utilize such catalysts in methanol fuel cells using acidic solutions. However, the result was negative, not only because his catalyst, prepared by carburization of WO_3 with CO, exhibited no significant activity for electro-oxidation of methanol, but also because the catalyst corroded at potentials above 0.4V (*vs.* RHE). Nevertheless, it is noteworthy that his catalyst, containing about 20 atomic % (a/o) molybdenum, seemed to have some activity in relation to methanol electro-oxidation.

In the present work, mixed carbide electrocatalysts of tungsten and molybdenum are synthesized using a novel technique involving CVD from carbonyls. These electrocatalysts exhibit notable activity in regard to the electro-oxidation of hydrogen, formaldehyde, and methanol in acidic solution. The relationship between electrocatalytic activity and surface composition of the catalyst thus obtained is also investigated using Auger electron spectroscopy and other techniques.

Key words: electrocatalyst, tungsten carbide, chemical vapor deposition, fuel cell.

Experimental

Preparation of catalyst-deposited electrodes.—A schematic drawing of the apparatus used for preparation of catalyst-deposited electrodes is shown in Fig. 1. Two carbon paper substrates (Kureha Chemical Company, E-715) (characteristics of which are summarized in Table I) were hung in a double-walled quartz reaction tube and heated under evacuation by an image furnace powered by infrared light sources. Cooling air was introduced between the walls, so that only the substrates were heated. The temperature of the substrates was measured using a thermocouple installed in a quartz tube put between them. When the substrate temperature reached 450°C, the valve was opened, allowing the CVD source, a mixture of $W(CO)_6$ (Mitsuwa Chemical), and $Mo(CO)_6$ (Aldrich), to evaporate. During the process, the system was pumped by a vacuum pump having a capacity of 100 liter/min. Carbonyl compounds decomposed on the heated substrates to give metallic W and Mo. (This deposit contained a notable amount of carbon also.) After evaporation was completed, or stopped after the desired duration by closing the valve, the substrates were again heated up to 700 ~ 820°C. At this temperature, CO was introduced

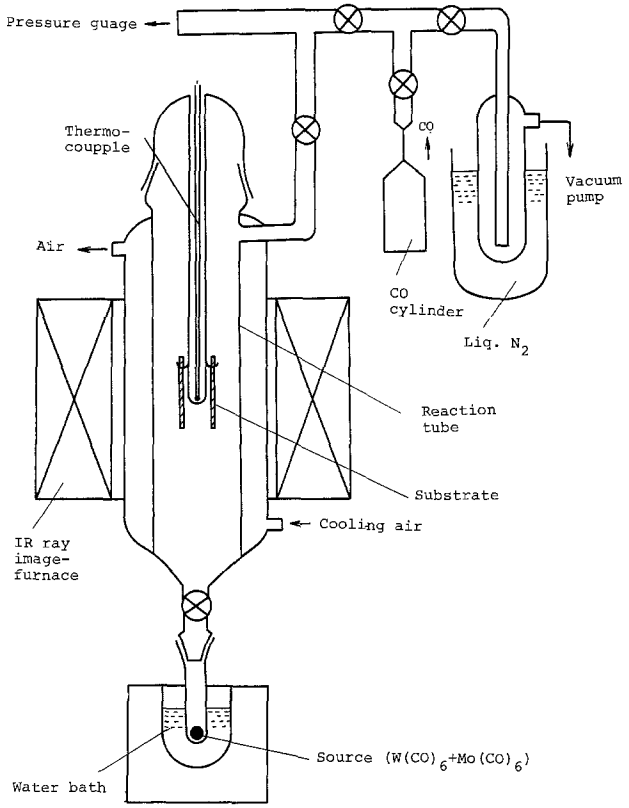

Fig. 1. Apparatus for preparing (W, Mo)-deposited electrodes. Wall of reaction tube is kept cold during CVD process.

into the reaction tube to carburize the deposited W and Mo. The pressure of the CO just after introduction was about 500 Torr and did not change notably for temperatures higher than 800°C, but a considerable decrease was observed when the temperature was as low as 700°C, presumably as a result of the disproportionation reaction

$$2CO = C + CO_2 \quad [1]$$

The catalyst-deposited electrodes thus obtained were stored in distilled water or 1M H_2SO_4 to prevent direct contact with air.

Analytical techniques.—To obtain x-ray data, a normal scanning diffractometer (Rigaku Denki) was used with Ni-filtered CuK_α. The as-obtained sample, a piece of catalyst-deposited carbon fiber, or Au, was directly set into a goniometer.

Bulk composition of the catalyst was measured using an inductively coupled plasma spectrometer (ICPS). The solution for this analysis was prepared by heating the catalyst in oxygen at 700°C. The resultant mixture of WO_3 and MoO_3 was then dissolved in an ammoniac solution.

The surfaces of the catalysts were investigated by AES and x-ray photoelectron spectroscopy (XPS). For AES, a spectrometer equipped with a titanium-coated tungsten cathode (electron probe diam: 0.03-0.5 μm) was employed. This instrument was recently developed at the Central Research Laboratory, Hitachi, Limited; XPS was carried out using a Vacuum Generator ESCA 3, Mark 2. Further details of analysis will be given later in this work.

Electrochemical measurements.—The electrocatalytic activity of the catalyst-deposited electrodes was investigated using a potentiostatic method. For measurement of the real surface area of the electrode, a linear sweep voltammetric technique was employed. All electrochemical experiments described here were conducted using a glass cell, kept at a constant temperature, in which the sample electrode was immersed in a

Table I. Specifications of carbon paper*

Items	Specifics
Material	fiberous carbon from pitch coal
Apparent density (g/m²)	150
Resistance (ohm · cm²)	0.5
Thickness (mm)	0.4
Surface area (m²/g)	0.11
Impurities	Ca, Al (trace)

* Carbon paper, E-715, produced by Kureha Chemical Company (Japan).

1M H_2SO_4 solution. The electrode was connected to the outer circuit through an Au lead wire, because Au proved to be negligibly active to the reactants, *i.e.*, H_2, HCHO, and CH_3OH. A bubbling hydrogen reference electrode was connected via a capillary to the solution containing the sample electrode. A counter electrode made of Au was separated by a porous glass filter from the solution to avoid possible contamination of the evolving gases. Pure N_2, containing less than 1 ppm O_2, was bubbled through the solution, except when H_2 was bubbled.

Electrocatalytic activity was tested in the following sequence: Bubbling of N_2 was continued until the sample electrode showed a constant potential (typically 0.4 ~ 0.5V *vs.* RHE). Then, the N_2 was replaced by H_2 and the change in potential recorded. After the open circuit potential became constant, potentiostatic measurements were conducted in the range of potentials between 0 and 0.5V *vs.* RHE. In the next stage, N_2 was again introduced to purge the H_2. The oxidation current through the sample electrode, which was kept at a potential of 0.5V, diminished as the H_2 was purged, and became almost null (typically, in the order of 0.1 μA). Depending on synthesizing conditions, however, some samples showed a notable background current due to corrosion of the electrode. When the background current became constant, CH_3OH (Kanto Chemical Company, ultra GR grade) was introduced using a syringe. The current generated by the CH_3OH was determined by the current difference between the actual and background levels at the corresponding electrode potentials. Activity for HCHO oxidation was tested in the same manner.

Results and Discussion

Characterization of deposited catalysts.—Substrate carbon paper consists of intertwined smooth-surface carbon fibers. A scanning electron micrograph (SEM) of such a paper is shown in Fig. 2(a). X-ray diffraction shows that the as-deposited film formed on this carbon surface at 450°C is amorphous. It consists of W and Mo, as well as some carbon probably derived from carbonyls, according to the AES data. This result presents a contrast to that reported by Miyake *et al.* (4), in which Mo films formed on graphite at 400°C using a similar CVD from $Mo(CO)_6$ were in a crystallized phase.

Figure 2(b) is a SEM picture of a typical sample (No. 271), obtained by carburizing the deposit at 820°C. This SEM shows that every carbon fiber is almost completely covered with the film thus formed. Ripples in the film surface are shown in the picture. In order to observe the film surface in more detail, such film was also formed on smooth Au under exactly the same conditions. A SEM of this sample magnified fifty thousand times (originally) is shown in Fig. 2(c). It shows grains with diameters of about 500Å.

An x-ray diffraction pattern from the same sample (No. 271) as that in Fig. 2(b), is shown in Fig. 3. It indicates that the film formed on the carbon substrate is in a single phase having a hexagonal WC-like structure, in which the lattice parameters for a_0 and c_0, are

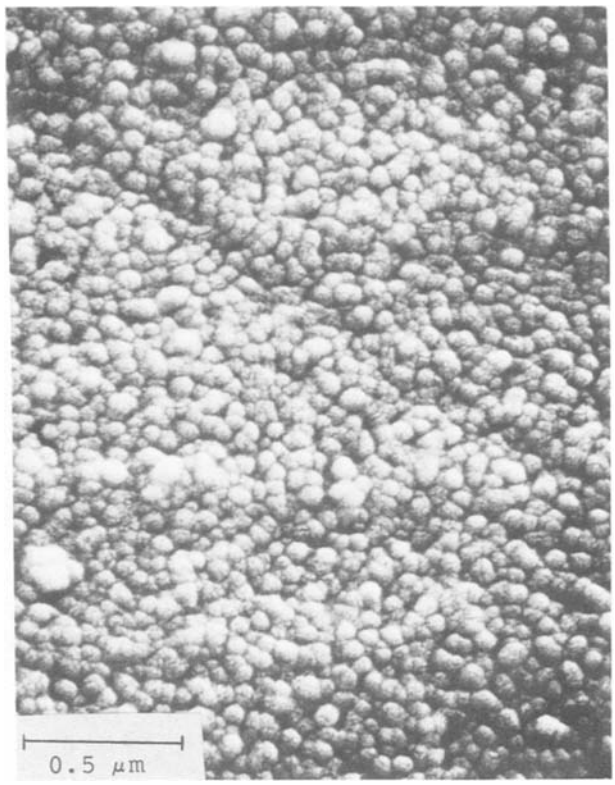

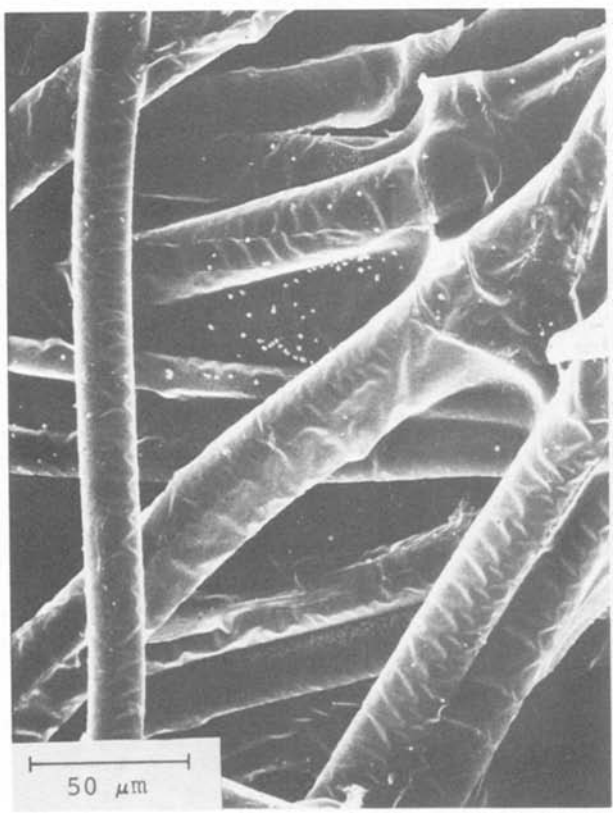

Fig. 2. Scanning electron microscope (SEM) pictures, (a): substrate (carbon fiber paper), (b): (W, Mo)C-deposited electrode (#271), (c): (W, Mo)C film formed on a smooth Au piece by the same manner as in (b). Samples in (b) and (c) were prepared under conditions as follows: CVD at 450°C with source ($W(CO)_6$ 10mg + $Mo(CO)_6$ 2mg) at 20°C, carburization at 820°C with 500 Torr CO for 1 hr.

2.89 and 2.85Å, respectively. The broad peak at 26.4° (2θ) is assigned to the carbon paper substrate. Hexagonal parameters of the sample deviate from the usually accepted values (a_o: 2.906, c_o: 2.836Å) (1). This deviation may arise from carbon deficiencies in the bulk lattice, as suggested by Ross (2) for his sample WC, or from the partial substitution of Mo at W sites. It should be noted that the film formed on Au gives the same x-ray pattern as that in Fig. 3, except that weak peaks derived from the W_2C-like phase are seen. This phase seems to be formed in the deeper part of the deposited films.

The surface of the sample (No. 271), shown in Fig. 2(b) gives the AES pattern shown in Fig. 4. A 10 keV electron beam with a diam of 0.3 μm was used as the excitation source. Weak Ar ion bombardment (5 keV, 5×10^{-5} Torr) was done for 2 min before recording the spectra to eliminate contaminants from the storage atmospheres and/or the analyzing chamber. Figure 4 shows that the surface is composed mainly of W and C, including Mo and oxygen as minor components. A peak derived from the Mo LMN transition can be seen at about 2000 eV. The surface Mo concentration is estimated to be in the range between 1 and 5 a/o,

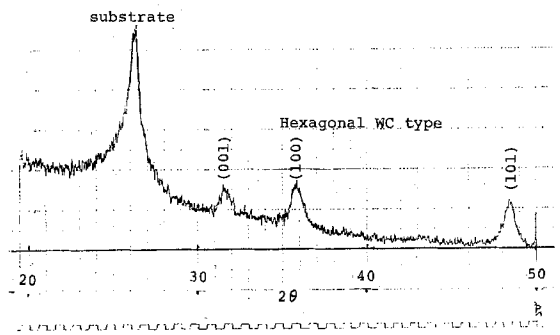

Fig. 3. X-ray diffraction pattern obtained with (W, Mo)C-deposited electrode (#271), the same sample as (b) of Fig. 2.

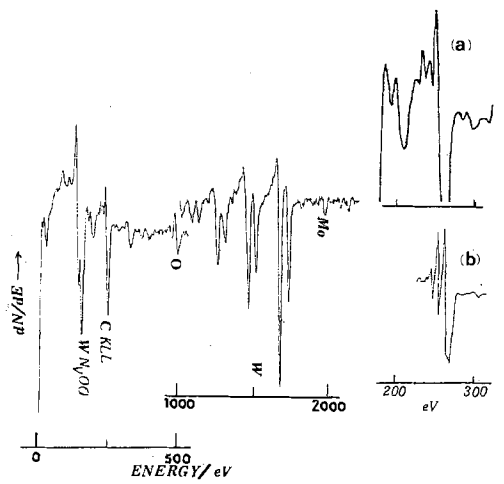

Fig. 4. Auger electron spectrum given by (W, Mo)C-deposited electrode (#271). (a) shows details of spectrum from C KLL transitions at 200-300 eV. (b) shows carbon spectrum of WC reported by Chang [taken from Ref. (6)].

which is much smaller than that expected from the source composition. (The mol ratio of Mo to W is 1:4, in the source used here.) This result is reasonable because $Mo(CO)_6$, having higher vapor pressure than $W(CO)_6$ (5), may be consumed faster, resulting in a Mo-deficient vapor composition in the final stage of CVD. The overall ratio in the deposited film, however, proved to be 1:4, identical with the source composition. This was determined by chemical analysis using ICPS.

Figure 4 also shows that the main peak of the KLL transition in C at 260 eV is followed by two smaller, but significant, subpeaks on the low-energy side. The shape of this C KLL transition is characteristic of carbons in a binding state with metals. The reported carbon spectra (6), also shown in the figure, is, for the most parts identical with these results. It should be noted that the sample using an Au substrate gave almost the same results.

However, samples carburized at temperatures lower than 700°C, or prepared under a CVD condition in which the source was kept at a high temperature (*i.e.*, the vapor pressure of the carbonyls was high), present a different AES pattern, as shown in Fig. 5. This sample was prepared in the same way, except that the CVD source was heated to 70°C. The main peak of the carbon spectrum at 260 eV is greatly intensified, but conversely, the subpeaks disappear. This shape is characteristic of graphitic, nonbinding, *i.e.*, free, carbon. The fact that a remarkable amount of free-carbon remains on the surface even after having been ion-bombarded suggests that the origin of the free-carbon does not arise from a simple contamination, but from the carburization process. Carbon accumulates on the surface through the disproportionation reaction of CO represented in Eq. [1]. It should also be noted in Fig. 5 that the intensity of the N_VOO transition in W at 165

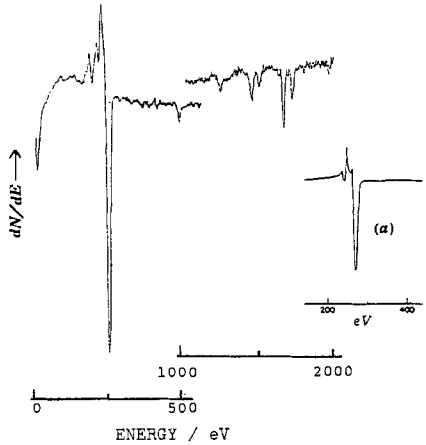

Fig. 5. Auger electron spectrum given by sample (#258) severely contaminated with free carbon. (a) shows carbon spectrum of graphite [taken from Ref. (6)].

eV is much smaller than that in Fig. 4, suggesting that the surface of the catalyst is covered with a thick (~ 100Å) free carbon layer. The amount of carbon accumulating on the surface during carburization may depend on the catalytic activity of the surface itself toward the disproportionation reaction of CO, if the temperature is the same. If the Mo or Mo-rich carbide is active, the severe contamination in this sample could easily be explained: its surface contains a large amount of Mo because CVD was stopped while the vapor pressure of the $Mo(CO)_6$ was still high.

XPS measurement was also carried out to investigate the surface chemistry involving oxygen, which is likely to play a considerable role in the catalytic oxidation of H_2 (2, 7). The results obtained for the sample using the Au substrate in Fig. 2(c) are shown in Fig. 6 and 6(a), the latter showing details in the binding energy range between 30-40 eV. The measurement using Al-K_α irradiation (13 kV-20 mA) was done with V_c, vacuum level and angle of irradiation at 1.7 kV, 10^{-10} Torr, and 45°, respectively. As shown in Fig. 6(a), the peaks of the spectrum derived from W(4f) are at binding energy levels identical with those of metallic W, which is very close to the binding energy of W in WC (8). In the sample obtained here, therefore, the amount of W binding with oxygen is considered to be much smaller than that observed by Ross *et al.* (2) for AEG-Telefunken WC, although very weak peaks resulting from W^{6+} are observable around 37 eV. The peak intensity of O (1s) at 530 eV in Fig. 6 also suggests that the surface of the catalyst is only slightly oxidized. It is noteworthy that the C (1s)

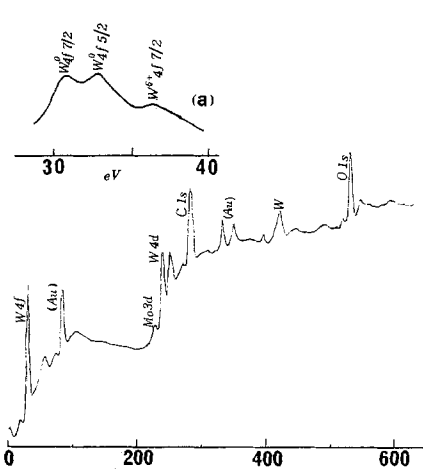

Fig. 6. X-ray photoelectron spectrum of (W, Mo)C film formed on a smooth Au piece, the same sample as (c) of Fig. 2.

spectrum has a very sharp peak at 280 eV, suggesting that almost all the carbon is in a binding state with the W. This presents a clear contrast to Miles' (3) results in which the surface carbon state was either carbonyl or carbonate. The shoulder seen at 230 eV is derived from Mo (3d) emission, indicating that the surface Mo concentration might be 1 ~ 5 a/o, a value identical with that obtained from AES.

Real surface area of the electrodes.—Figure 7 is a linear sweep voltammogram of a (W, Mo) C/Au electrode (1 × 3 cm^2) prepared under the same conditions as were used when the sample giving the SEM picture in Fig. 2(c) was prepared. The conditions are shown in Fig. 2. Since the voltammogram in 1M H_2SO_4 was reproducible and reversible during repeated cycles, the current observed in Fig. 7 is reasonably considered to be generated by double layer capacitance and adsorption-desorption of hydrogen on the electrode. The capacitance of the electrode can be given by

$$C = i/(dE/dt) \qquad [2]$$

where i is the current and (dE/dt) is the sweep rate. A capacitance of 750 μF was estimated from a plateau current of 7.5 μA and a sweep rate of 10 mV/S. Almost the same value of capacitance was obtained even though the sweep rates were changed in the range from 1-50 mV/S. Therefore, the process on the electrode is considered to be reversible in this experimental conditions. From the micrograph in Fig. 2(c), it might be assumed that the roughness factor of the electrode be unity. Then, the capacity per unit real surface area would be 1.25 F/m^2.

Voltammetry was also conducted on the (W, Mo)C/carbon paper electrode under the same conditions as above. The result showed that this electrode gives substantially the same shape voltammogram, as shown in Fig. 7, although the current is much higher. In this case, the capacitance was estimated to be 0.012F. Consequently, the real surface area of the (W, Mo)C/carbon paper electrode (No. 271) may be calculated to be about 100 cm^2.

Electrocatalytic activity in (W, Mo)C/carbon paper electrodes.—The open circuit potential of the electrode (No. 271) under continual bubbling of N_2 reached about 0.5V (*vs.* RHE) at 50°C. It decreased rapidly and reached the same potential as RHE about 10 min after the introduction of H_2 in place of the N_2. The results of potentiostatic current measurements conducted thereafter are shown in Fig. 8, in which the current is normalized by the real surface area determined above. The plot of H_2 oxidation current is linear in the potential range between 0.05-0.12V. It becomes nonlinear at higher potentials due to the onset of diffusion control. The exchange current estimated by extrapolation of the linear part of the plot is about 10^{-2} A/m^2, which is two or three orders of magnitude lower than that of Pt reported by Vetter *et al.* (9). Nevertheless, the

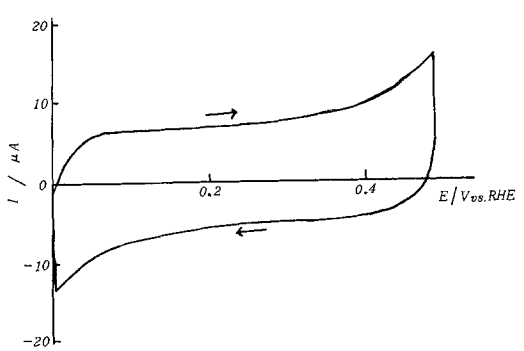

Fig. 7. Linear sweep voltammogram of (W, Mo)C/Au electrode (prepared by the same method as in sample (c) of Fig. 2), 1M H_2SO_4. 10 MV/s.

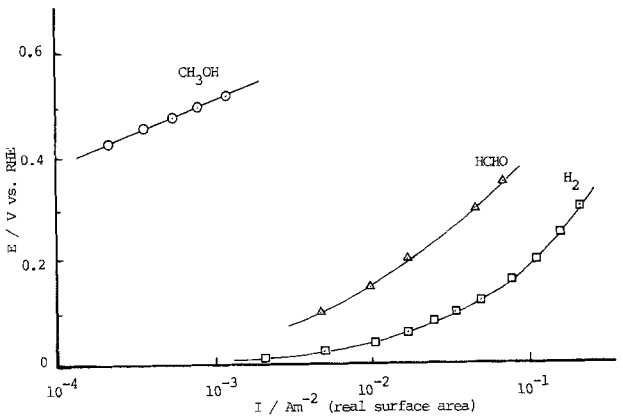

Fig. 8. Potentiostatic currents obtained from (W, Mo)C-deposited electrode (#271). Currents are normalized by real surface area of the electrode. Temperature: 50°C. Concentration of H_2, HCHO, and CH_3OH: saturated H_2 at 50°C, 1.25M, and 5M, respectively.

present (W, Mo) C/carbon paper electrode is more active toward H_2 electro-oxidation than any other WC reported. The best catalyst among them may be AEG-Telefunken's WC (not containing Mo), which was reported to exhibit current density of 2 × 10^{-2} A/m^2 (real surface area) at 0.2V (*vs.* RHE) and 22°C (2). Under the same conditions, the current of the electrode in the present study is estimated to be 3 × 10^{-2} A/m^2.

The open circuit potential observed when the electrolyte was fueled with CH_3OH (5 mol/liter) was about 0.35V (*vs.* RHE), which is considerably higher than the reversible potential, 0.04V. The currents generated by the electro-oxidation of methanol

$$CH_3OH + H_2O + 6e^- = CO_2 + 6H^+ \qquad [3]$$

are plotted *vs.* potentials in Fig. 8. The potentiostatic current at 0.5V is 8 × 10^{-4} A/m^2 at 50°C, which is about one or two orders of magnitude smaller than pure Pt, and three orders smaller than for a Pt-Sn alloy (10, 11).

Miles (3) reported that molybdenum-treated WC (containing 20 a/o Mo) exhibited catalytic activity for the electro-oxidation of methanol. This material was prepared using a method in which a mixture of ammonium molybdate and ammonium paratungstate was heated in air at 400°C and then carburized in CO at 700°C. Because data on the surface area is not available and a significant corrosion current was observed at potentials higher than 0.4V (*vs.* RHE), it is hard to estimate precise current density for methanol electro-oxidation of this catalyst. To estimate very roughly, however, the current due to electro-oxidation of methanol per real surface area might be, at most, in the order of 10^{-7} A/m^2. It should be noted that the corrosion current reported by Miles was not observed at all in the electrode (No. 271) of the present study at 0.4V, and even at 0.5V the background current probably due to corrosion decreased rapidly.

Formaldehyde, a possible intermediate in the methanol oxidation process, underwent electro-oxidation more easily on the electrode (No. 271) than methanol did. The open circuit potential for HCHO (1.25 mol/liter) was about 0.0V (*vs.* RHE), which is close to the reversible potential, 0.08V. Potentiostatic current at various potentials is also shown in Fig. 8.

The temperature dependence of the electro-oxidation current corresponding to H_2, HCHO and CH_3OH is shown in Fig. 9. The activation energies are given as 47.6, 50.2, and 75.2 kJ/mol for H_2, HCHO, and CH_3OH, respectively. The activation energy for H_2 agrees well with that reported for pure WC. 48.1 kJ/mol (12). It is, therefore, not likely that Mo plays an essential role in the electro-oxidation of H_2. The value obtained with methanol is similar to those usually reported for Pt-based catalysts, such as Pt-Sn alloys.

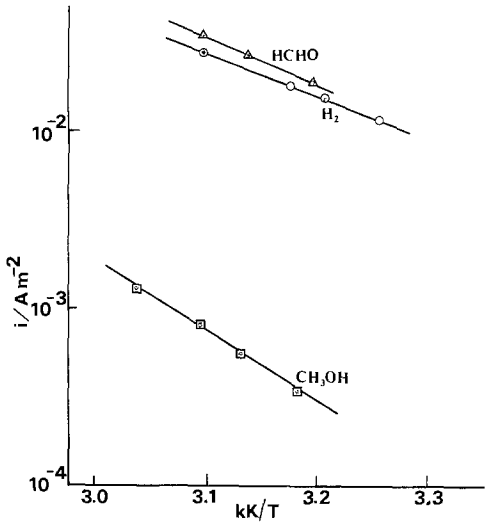

Fig. 9. Arrhenius plots of potentiostatic anodic current of (W, Mo) C-deposited electrode (#271). Electrode potential is 0.1, 0.3, and 0.5V vs. RHE, respectively.

Influence of surface free-carbon.—It has often been mentioned that surface contamination by carbon generally brings about degradation in the activity of WC catalysts, including the electrocatalytic oxidation of H_2 (2). This kind of degradation, probably arising from surface contamination by carbon in elemental (or graphitic) form, was observed in the present study. Since the contaminant is considered to be derived from the disproportionation reaction of CO during the carburization process, the degree of contamination may be dependent on synthesis conditions.

In Table II, the electrocatalytic activities of electrodes prepared under different conditions are compared to show the relationship between their activity and degree of contamination. The ratio of the peak-to-peak value of the C KLL transition at about 270 eV to that of the W N_VOO transition at 163 eV, is used as a measure and is represented by (C/W) in the table. The activity changes dramatically with degree of contamination. The difference between the cleanest electrode, No. 271, and the least clean one, No. 258, is more than four orders of magnitude in the activity to H_2, even though the bulk composition of both electrodes is almost the same. The AES patterns recorded for these two electrodes were in Fig. 4 and 5, respectively. The severe contamination in electrode, No. 258, was explained in previous section.

Comparing sample No. 242 with No. 253, it is obvious that the electrode carburized at 820°C has a cleaner surface than that at the lower temperature, 695°C. This result is reasonable because the thermodynamics of the CO disproportionation reaction suggests that carbon is more easily created at low temperatures. Thus, the higher the carburization temperatures, the more active the catalysts. In addition, it should be noted that sample No. 240, which has undergone exposure to CO at lower temperatures, shows very little activity. Its surface has probably been contaminated to a great extent during heating from 450-700°C, because, as in this case, CO was introduced immediately after the CVD process at 450°C. Duration of exposure to CO also influences the activities of electrodes. If too short, high activity does not result, because carburization is not completed. Also, prolonged carburization, exceeding 2 hr, as seen in sample No. 262, causes degradation, probably because free-carbon formation proceeds even at a temperature as high as 820°C, though very slowly. The free energy change of the disproportionation reaction (*e.g.* [1]) is about +42 kJ/mol at 800°C, but a great excess of CO was included in the carburization atmosphere.

Effect of Mo.—To investigate the effect of Mo, Mo-free electrode, (No. 261), was prepared in the same manner and its activities were compared with those of electrode (No. 271), which contains 1 ~ 5 a/o of Mo on its surface. The results shown in Table III suggest that, in relation to H_2 electro-oxidation, activities of both electrodes are almost the same, leading to the conclusion that Mo does not play an essential part on H_2 oxidation. This has also been suggested by the discussion involving activation energy in the previous section.

Conversely, the current produced by methanol oxidation is observable only in the electrode containing Mo. Although stationary current in the table is null for the Mo-free electrode, transient current was detectable for a few minutes after methanol was introduced into the electrolyte. A similar decay in transient current was also observable in the electrode containing Mo, but became stationary within several min. Suzui *et al.* (13) have recently reported that the potentiostatic methanol current in a Pt electrode in acidic solution decays rapidly (*i.e.*, about one order in 1 min), and that this decay results from the catalyst being poisoned by an intermediate generated by the oxidation of methanol. It is therefore, reasonable to consider that Mo in the electrodes obtained here acts to remove poisonous intermediates, or it leads the electrochemical reaction to another path in which poisons are not produced.

Conclusion

An electrocatalyst has been obtained using a novel method involving CVD from $W(CO)_6$ and/or $Mo(CO)_6$. Catalytic activity is greatly influenced by surface contamination from carbon in elemental forms produced by the disproportionation reaction of CO. The most active catalyst obtained here gives H_2-oxidation current density of 0.12 A/m^2 (based on real surface area) in an acidic solution at 0.2V (*vs.* RHE) and 50°C. The exchange current density, estimated to be 3×10^{-2} A/m^2, is larger than that of any other WC known to date. Oxidation current in methanol as large as 8.2×10^{-4} A/m^2 is observed with catalyst containing Mo at

Table II. Activities of electrodes prepared by various conditions

Electrode No.	Synthesizing conditions: Source temp. (°C)	Synthesizing conditions: Carb. temp. (°C)	Duration of carb. (hr)	(C/W)*	i_{H_2} at 0.2V (10^{-2} A/m^2)	i_{HCHO} at 0.3V (10^{-2} A/m^2)	i_{CH_3OH} at 0.5V (10^{-4} A/m^2)
240†	70	700	2	(—)	0.35	<0.03	~0
242	70	695	2	2.1	1.9	0.20	~0
245	70	818	2	(—)	5.0	0.90	2.7
253‡	70	824	2	1.4	5.2	1.60	1.7
258§	70	823	2	30.0	<0.002	~0	~0
262	20	819	2	1.2	8.1	1.50	1.3
271	20	820	1	0.6	11.5	4.00	8.2

* The p-p intensity ratio, C KLL/W N_VOO transition, determined by AES.
† CO was introduced at 450°C. In other samples, at the carburization temperature.
‡ Source composition: $W(CO)_6$ 20 mg + $MO(CO)_6$ 4 mg. In others, 10 mg + 2 mg, respectively.
§ Evaporation of source [$W(CO)_6$ 21 mg + $MO(CO)_6$ 4 mg] was stopped at 2 min.

Table III. Effect of Mo on electrocatalytic activities

Electrode No.	CVD source	Surface Mo conc. (a/o)	i_{H_2} (10^{-2} A/m²)	i_{HCHO} (10^{-2} A/m²)	i_{CH_3OH} (10^{-4} A/m²)
271	$W(CO)_6$ + $Mo(CO)_6$	1 ~ 5	11.5	4.0	8.2
261	$W(CO)_6$	0	9.3	1.2	0

* Currents in the Table are stationary ones.
* Potential for H_2, HCHO, and CH_3OH is 0.2, 0.3, and 0.5V (vs. RHE).

0.5V and 50°C. Molybdenum seems to act as a center to remove poison intermediates or to lead the electrochemical reaction to another path in which poisons are not formed.

Acknowledgment

The authors wish to express their gratitude for the technical contributions and useful advice given by S. Kawase of the Materials Analysis Center, Central Research Laboratory, Hitachi, Limited.

Manuscript submitted June 30, 1982; revised manuscript received Nov. 10, 1982.

Any discussion of this paper will appear in a Discussion Section to be published in the June 1984 JOURNAL. All discussions for the June 1984 Discussion Section should be submitted by Feb. 1, 1984.

Hitachi, Limited assisted in meeting the publication costs of this article.

REFERENCES

1. R. B. Levy and M. Boudart, *Science*, **181**, 547 (1973).
2. P. N. Ross, Jr., J. McDonald, and P. Stonehart, *J. Electroanal. Chem.*, **63**, 450 (1975).
3. R. Miles, *J. Chem. Tech. Biotechnol.*, **30**, 35 (1980).
4. M. Miyake, Y. Hirooka, T. Imoto, and T. Sano, *Thin Solid Films*, **79**, (1981).
5. J. J. Lander and L. H. Germer, *AIME Trans., Inst. Metal. Div.*, **175**, 648 (1948).
6. C. C. Chang, in "Characterization of Solid Surfaces," P. F. Kane and G. B. Larrabee, Editors, p. 536, Plenum Press, New York (1974).
7. P. N. Ross, Jr. and P. Stonehart, *J. Catal.*, **39**, 298 (1975).
8. L. Ramquist, K. Hamrin, G. Johansson, A. Fahlman, and C. Nordling, *J. Phys. Chem. Solids*, **30**, 1835 (1969).
9. K. J. Vetter and D. Otto, *Z. Electrochem.*, **60**, 1072 (1956).
10. M. R. Andrew, J. S. Drury, B. D. McNicol, C. Pinnington, and R. T. Short, *J. Appl. Electrochem.*, **6**, 99 (1976).
11. M. M. P. Janssen and J. Moolhuysen, *Electrochim. Acta*, **21**, 861 (1976).
12. P. Stonehart, NBS Special Publication **455**, p. 167 (1976).
13. Y. Suzuki, K. Ota, and M. Takahashi, Proc. Fall Meet. of The Electrochemical Society of Japan, p. 129, Urawa (1981).

A Voltammetric Investigation of Oxygen Reduction in a Trickle Bed Cell Using Graphite Chip and RVC Cathodes

J. B. Davison,[1] J. M. Kacsir,[2] P. J. Peerce-Landers,[3] and R. Jasinski*

Occidental Research Corporation, Irvine, California 92714

ABSTRACT

Steady-state voltammetry measurements were used to assess the uniformity of reaction conditions along the length of the packed bed electrode in a two-compartment trickle bed cell. The model reaction was the cathodic reduction of oxygen in 2M caustic under various conditions of O_2 pressure, cell temperature, and catholyte flow rate. Two kinds of carbon cathodes were employed: small chips of high purity graphite and a piece of reticulated vitreous carbon foam. Oxygen reduction was shown to occur at these carbons in two steps, $O_2 \rightarrow HO_2^-$; $HO_2^- \rightarrow OH^-$. Generally, an increase in current density produced an increase in the potential gradient along the cathode bed, favoring the reduction of HO_2^- to OH^-. This nonuniform potential distribution is attributed to local differences in the oxygen supply. We conclude that mass transfer in the trickle bed cell is not efficient enough to replace all the oxygen consumed by electrolysis at current densities above *ca.* 200 A/m².

The trickle bed cell (1) uses a three-dimensional packed bed electrode to electrolyze gaseous reactants (2-5). Mass transfer of reactant gas into the fluid phase is facilitated by the trickling flow of the electrolyte layer over each particle in the electrode bed.

Previous work with the trickle bed cell suggested that the potential distribution in the cathode bed was nonuniform in the direction of current flow and, thus, the particle bed thickness was limited to *ca.* 3-6 mm (3). Reaction conditions along the length of the cathode bed, in the direction of gas/electrolyte flow, can also be nonuniform by virtue of the nonuniform distribution of reactants. This could impose a maximum size or current density limitation on the cell. In order to assess this latter nonuniformity, we experimentally determined the potential difference between two points along the length of the cathode bed for a two-step electrolysis. This was accomplished by steady state voltammetry measurements during the electroreduction of oxygen in 2M caustic. The variables were gas pressure, cell temperature, and catholyte flow.

It was anticipated that the cell performance could also be a function of the configuration of the carbon bed, since this factor could also affect the contact of gas and electrolyte. Accordingly, we compared the performance of two different types of carbon cathodes: a packed bed of graphite chips and a single piece of reticulated vitreous carbon foam (RVC).

Experimental

An exploded view of the trickle bed cell used in these experiments is shown in Fig. 1. This design is a slight modification of that described in the literature (1). The 5 × 50 × 1 cm anode and cathode plates were made of #316 stainless steel and had channeled interiors to permit the circulation of heating or cooling water. It is presumed that the ohmic drop down this plate is minimal so that the back side of the bed is effectively an equipotential surface. The 5 × 50 × 0.3 cm cathode

* Electrochemical Society Active Member.
[1] Present address: J. C. Schumacher Company, Oceanside, California 92054.
[2] Present address: Beckman Instruments Incorporated, Analytical Instrument Sales & Service Division, Anaheim, California.
Key words: carbon, electrode, electrolysis, particles.
[3] Present address: Betz Laboratory, The Woodlands, TX 77380.

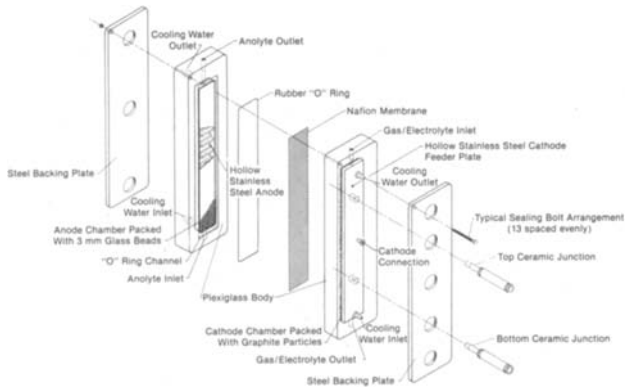

Fig. 1. Exploded view of the two-compartment trickle bed cell

bed was filled with either −10 to +16 mesh Ultra F graphite chips (Ultra Carbon Company) or a piece of RVC-100S foam (The Fluorocarbon Company). This thickness (0.3 cm) is that required to minimize nonuniform potential drop across the thickness of the bed (3). The membrane between anode and cathode was Nafion #425 (E. I. du Pont de Nemours & Company). It was physically supported by glass beads on the anode side. These elements were sandwiched between two 2 in. plexiglass plates. For safe operation at pressures up to 1750 kPa, the cell was enclosed between two ¼ in. stainless steel backing plates.

The steel backing plates, the plexiglass cell body, and the steel cathode plate were drilled to permit the introduction of two specially constructed ceramic junctions (Broadley-James Corporation). These junctions were inserted nominally 0.5 mm into the cathode bed 30 cm apart, one 10 cm from the top and the other 10 cm from the bottom. Outside the cell, the junctions were connected to electrolyte wells in which saturated calomel reference electrodes were immersed. Cathode potentials were measured with a Keithley 616 Digital Electrometer.

The anode chamber was flooded with 2*M* NaOH flowing at a rate of *ca.* 40 ml/min. The flow of catholyte (2*M* NaOH) trickling through the graphite bed was controlled by a metering pump. Catholyte and oxygen gas were premixed prior to entering the cathode chamber by passing through a 50 ml mixing column filled with glass beads. Oxygen flow into the cell was regulated by a high pressure rotometer.

The oxygen pressure is given in the data Tables. The flow rates were in the range of 500-1000 cc/min STP (depending on the pressure head and the pressure drop within the bed). This flow rate is equivalent to a current of 80-160A. The maximum current used in these experiments was 50A. The temperature of the catholyte stream was measured by thermocouples located in the plumbing immediately outside the cell. Cell voltages were applied with a Hewlett Packard 6269 B 50A power supply. Cell current was measured with a Keithley 177 Digital Multimeter. Current densities were calculated by dividing the measured cell current by the area of the cathode feeder plate, 0.025 m^2. Peroxide concentrations were determined by titrating 1 ml aliquots from the catholyte stream with a standard ceric ammonium sulfate solution (6).

For the steady-state voltammetry experiments, the cell pressure, electrolyte exit temperature, and electrolyte flow rate were maintained within the following tolerances: cell pressure = ±2 psi; electrolyte exit temperature = ±1.5°C with graphite cathode and ±4.0°C with RVC cathode; electrolyte flow rate = ±1.5 ml/min. The applied cell voltage was adjusted to maintain the top cathode potential at a predetermined value. The bottom cathode potential, the cell current, and the peroxide concentration were measured every 5 min. A steady state was assumed when these values stayed within the following limit for at least 20 min: bottom cathode potential at 0-0.9V = ±2 mV graphite cathode, ±10 mV RVC; bottom cathode potential at −1.2V = ±110 mV graphite cathode, ±30 mV RVC; cell current = ±1.0A graphite cathode, ±0.25A RVC; $[HO_2^-]$ = ±0.03 weight percent (w/o). Generally, all the variables were well within the quoted tolerance limits. However, at higher current densities a variable could fluctuate to these limits.

The extent of thermal decomposition for caustic peroxide solutions as a function of temperature was determined by circulating a 1.4 w/o peroxide/2M caustic solution through the graphite chip trickle bed at open circuit.

Results

The first experiments were intended to establish the potential at which peroxide is reduced under well controlled and well defined mass transport conditions, on the specific carbon used in the trickle bed. As shown in Fig. 2, curve A, the reduction of oxygen in 2M NaOH at an Ultra F graphite paste rotating disk electrode (RDE) occurs in two steps, the first wave beginning at *ca.* −0.2V, the reduction of oxygen to peroxide

$$O_2 + H_2O + 2e \rightarrow HO_2^- \quad [1]$$

and a second wave beginning at *ca.* −0.7V, due at least in part, to the reduction of peroxide to hydroxide

$$HO_2^- + H_2O + 2e \rightarrow 3\ OH^- \quad [2]$$

A similar polarization curve is obtained on a commercially available vitreous carbon RDE.

The next objective of the voltammetry experiments was to show that oxygen was indeed electrochemically reduced by the same two-step process at a trickle bed graphite cathode as at a graphite RDE. Steady-state potential measurements were made on a graphite bed at the following six cathode potentials: −0.25 (at the foot of the oxygen reduction wave), −0.35, −0.50, −0.70 (at the foot of the RDE HO_2^- reduction wave), −0.90 (where both reaction (I) and reaction (II) occur), and at −1.2V (which is almost the potential at which water is electrolyzed). To prevent HO_2^- from reaching the anode where it would be oxidized via

$$HO_2^- + OH^- \rightarrow O_2 + H_2O + 2e \quad [3]$$

a peroxide-stable cation exchange membrane (Nafion) separated the anode from the cathode. The data so obtained (Table I) is consistent with this two-step reduction in the trickle bed, in that 100% current efficiencies were obtained when the cathode potential was less negative than −0.7V, and a decrease in current efficiency was observed at cathode potentials negative

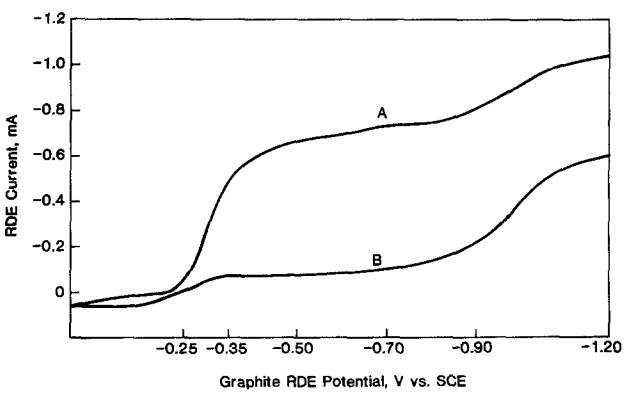

Fig. 2. Curve A: The reduction of oxygen in 2M NaOH occurs in two steps at an Ultra F graphite paste rotating disk electrode. Curve B: The reduction of $5 \cdot 10^{-3}$M H_2O_2 in oxygen-free 2M NaOH at the same electrode. Rotation speed = 3000 rpm; scan rate = 100 mV/sec.

Table I. Steady state voltammetry data using the graphite bed cathode

Run number	Cell pressure, kPa	Electrolyte temperature, °C	Electrolyte flow, ml/min	Cathode potential, −V			Cell current A	Current density, A/m²	Conc H_2O_2 w/o	Current efficiency, %
				Top	Bottom	ΔV				
1	1725	31	10.4	0.250	0.250	0	0.34	13.6	0.05	100
		31	9.3	0.354	0.352	0.002	2.00	80.0	0.22	100
		31	10.1	0.504	0.552	0.048	4.95	198.0	0.48	100
		32	9.8	0.714	0.831	0.117	8.43	337.3	0.69	81
		29	10.7	0.916	1.028	0.112	15.0	600.0	0.75	55
		31	8.6	1.18	1.59	0.41	49.9	1996.0	0.10	2
2	1725	45	9.3	0.251	0.253	0.002	0.38	15.2	0.05	100
		45	9.7	0.360	0.339	0.021	1.93	77.2	0.20	100
		45	9.4	0.504	0.536	0.032	5.37	214.8	0.55	99
		45	10.0	0.713	0.801	0.088	12.0	480.0	0.89	76
		45	9.4	0.891	0.979	0.088	22.8	912.0	1.25	53
3	1725	61	10.1	0.252	0.252	0	0.41	16.4	0.03	82
		61	10.7	0.350	0.343	0.007	2.57	102.8	0.17	74
		60	9.6	0.505	0.511	0.006	6.90	276.0	0.53	75
		60	10.1	0.701	0.779	0.078	17.7	708.0	1.04	61
		61	10.3	0.914	1.107	0.193	42.2	1688.0	1.17	29
4	1725	29	28.3	0.252	0.247	0.005	0.28	11.2	—	—
		29	30.2	0.350	0.345	0.005	1.70	68.0	0.07	100
		29	28.8	0.502	0.516	0.014	3.65	146.0	0.12	100
		29	28.8	0.706	0.765	0.059	6.00	240.0	0.20	97
		29	29.0	0.901	0.974	0.073	11.2	448.0	0.24	64
		29	28.6	1.188	1.418	0.230	36.0	1440.0	0.10	8
5	345	30	9.9	0.250	0.254	0.004	0.12	4.8	—	—
		30	10.5	0.350	0.362	0.012	1.03	41.2	0.10	100
		30	9.6	0.509	0.514	0.005	1.87	74.8	0.17	92
		31	10.2	0.709	0.725	0.016	4.18	167.2	0.32	80
		32	11.1	0.925	0.960	0.035	13.5	540.0	0.20	17
		33	8.1	1.20	1.57	0.37	44.5	1780.0	0	0

of −0.7V. Exceptions, *i.e.*, runs 3 and 5, are explained below. That reaction [2] indeed occurs in the trickle bed cell at potentials more negative than −0.7V was also shown by an experiment in which a solution containing HO_2^-, but no oxygen (1725 kPa argon) began to electrolyze at *ca.* −0.7V. We determined in separate experiments that H_2O electrolysis begins in the trickle bed cell at *ca.* −1.4V. So in those cases where the bottom cathode potential exceeds this value (runs 1, 4, and 5), H_2O is being reduced along with O_2 and HO_2^-.

The effect of pressure.—An increase in reactant oxygen gas pressure resulted in an increase in HO_2^- concentration, as long as the cathode potential was kept positive of −0.7V. This can be seen by comparing runs 1 and 5 in Table I and in Fig. 3. Under identical conditions of temperature and catholyte flow, significantly higher concentrations of peroxide were produced at a given cathode potential at the higher pressure of oxygen (1725 kPa *vs.* 345 kPa). At both pressures, the differences in the solution potential between the bottom and the top of the cathode bed, increased with increasing applied cell voltage (current). (With a few exceptions occurring only at low applied cathode potentials, this was true for all five runs: see Table I.)

The effect of temperature.—Resistive heating is likely to be an important consideration in any large-scale electrosynthesis using a stack of trickle bed cells. To determine the effect of temperature on the performance of the trickle bed cell, voltametric measurements were made under identical conditions of pressure and flow at 30°, 45°, and 60°C. (These temperatures were attained by circulating water from a constant temperature bath through the hollow anode and cathode plates.) The results are presented in Table I, runs 1-3, and in Fig. 4.

At 60°C, the current efficiency for HO_2^- production is well below 100% even at potentials well positive of −0.7V. Experiments outside the cell demonstrated that thermal decomposition of caustic peroxide solutions is substantial above 50° (Table II).

However, the data also suggest that a certain amount of resistive heating may be beneficial in terms of increased synthesis. For example, 1.25 w/o HO_2^- is produced at 45°C compared with 0.75 w/o at 30°C at nearly identical potentials and current efficiencies. The increase in current density can result from an increase in the rate constants for the electrode reactions and an increase in the diffusion coefficient for O_2. Opposing these effects is the decrease in O_2 solubility at higher temperatures (7). However, the net overall effect in the case of O_2 reduction is an increase in rate and product yield with an increase in temperature (until the onset of thermal decomposition).

The effect of catholyte flow rate.—Because of its potentially major impact on mass transfer conditions, the catholyte flow rate is an important process variable in a trickle bed cell (3, 5). Voltametric data was obtained at a catholyte flow rate of 29 ml/min in run 4 of Table I. These data may be compared with those from run 1 at 10 ml/min under identical conditions of temperature and pressure (see Fig. 5).

Substantially higher HO_2^- concentrations were obtained at the slower flow rate. This is likely due to the

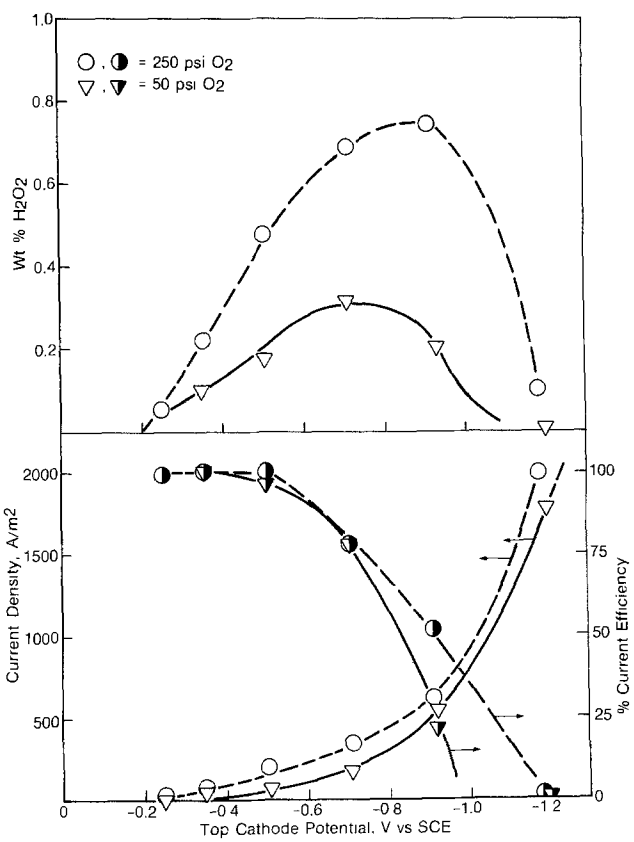

Fig. 3. The effect of O_2 pressure at various cathode potentials on peroxide concentration, current efficiency, and current density at the graphite chip cathode.

Table II. Thermal decomposition of H_2O_2* in the graphite chip trickle bed cell at open circuit

Outlet temperature °C	% Change
26	
41	4
48	4
54	11
60	26

* 1.4% H_2O_2 in 2M NaOH at 35 ml/min.

increased residence time of the catholyte in the cell. The current efficiency at both rates is 100% at potentials below −0.7V. At cathode potentials more negative than −0.7V, the current efficiency is *ca.* 10-15% less at 10 ml/min than at 29 ml/min. The voltammetry data suggest why peroxide production is more inefficient at the lower flow rate. For example, when the top cathode potential is −0.7V, the bottom potential at 10 and 29 ml/min are more negative by 117 and 59 mV, respectively. Thus at 10 ml/min, the bottom of the cathode is well into the potential region where HO_2^- is reduced (*cf.* Fig. 2).

The use of a reticulated vitreous carbon cathode.—A piece of reticulated vitreous carbon (RVC) foam was cut to fit the cathode compartment of the trickle bed cell. Voltametric data obtained at 1725 kPa and ambient temperature, 29 ± 3°C, appear in Table III. These conditions correspond approximately to those of run 1 in Table I using the graphite bed cathode. A comparison of the two runs is shown in Fig. 6.

As with the graphite chips, the current efficiency for HO_2^- production is *ca.* 100% at potentials more positive than −0.7V. At potentials beyond this value, less current was sustained than with the graphite bed, but more peroxide was obtained using the RVC cathode.

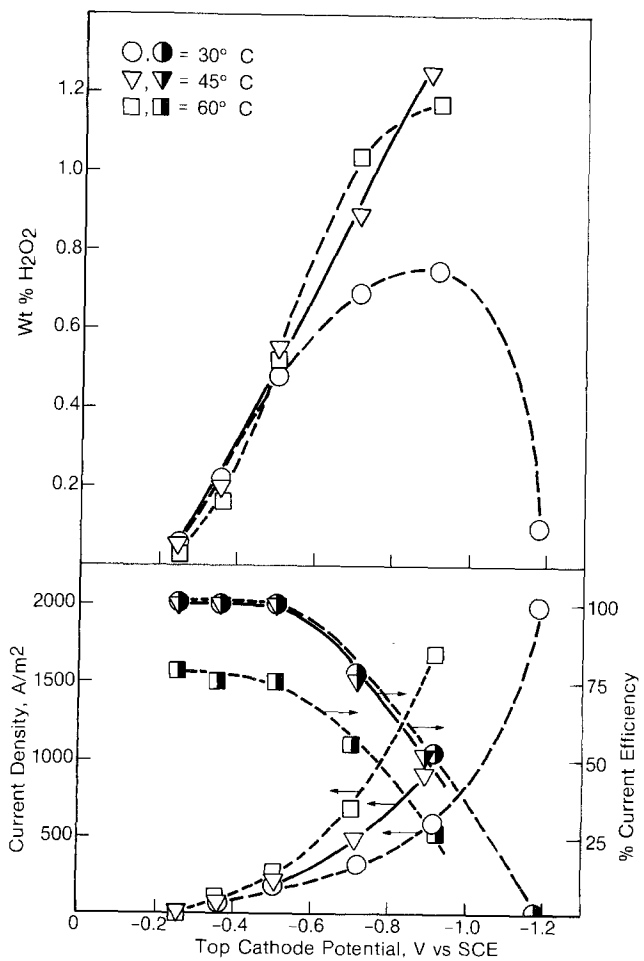

Fig. 4. The effect of cell temperature at various cathode potentials on peroxide concentration, current efficiency, and current density at the graphite chip cathode.

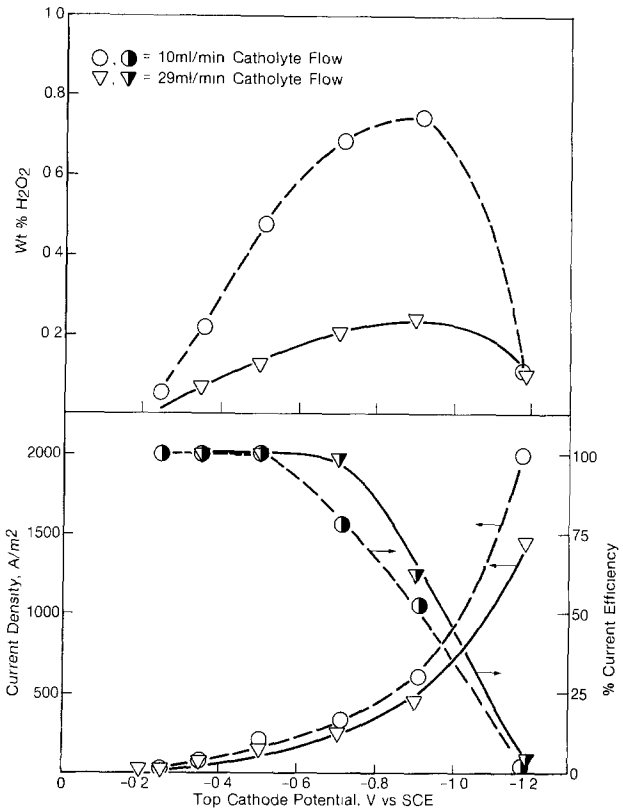

Fig. 5. The effect of catholyte flow rate at various cathode potentials on peroxide concentration, current efficiency, and current density at the graphite chip cathode.

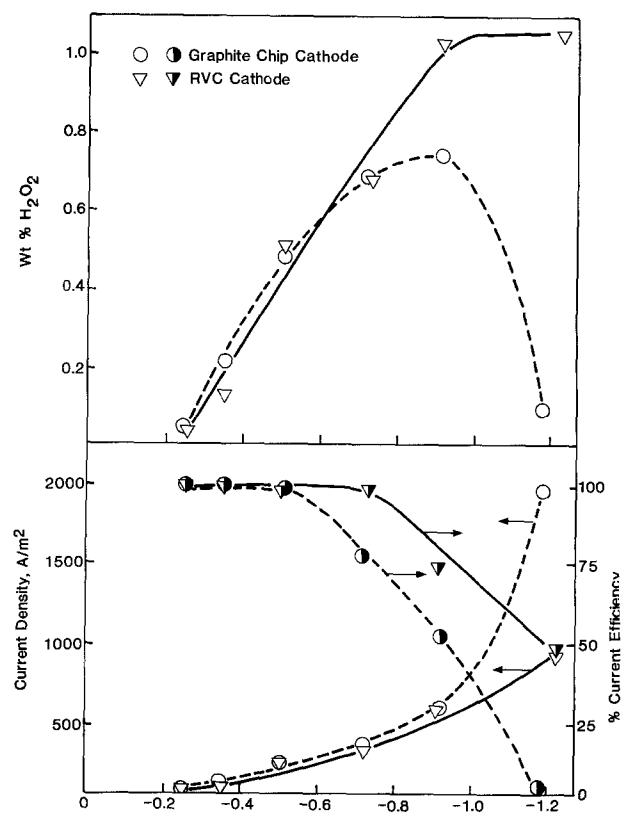

Fig. 6. The effect of cathode material on peroxide concentration, current efficiency, and current density. Cell pressure = 1725 kPa, catholyte flow rate ≈ 10 ml/min, cell temperature ≈ 29°C.

Table III. Steady state voltammetry data at 1725 kPa using the RVC cathode

Electrol temperature, °C	Electrol flow, ml/min	Cathode potential −V Top	Bottom	ΔV	Cell current,A	Current density, A/m²	Conc H_2O_2, w/o	Current efficiency, %
26	9.2	0.252	0.311	0.059	0.13	5.2	0.03	100
29	9.5	0.351	0.379	0.028	0.89	35.6	0.12	100
30	9.5	0.500	0.597	0.097	5.1	204.0	0.52	97
25	9.3	0.724	0.776	0.052	6.5	260.0	0.67	97
33	9.4	1.22	1.34	0.12	21.9	876.0	1.05	46

The potential variation along the length of the bed at high current, *e.g.* 876 A/m², is also less with the RVC than with the graphite (run 1).

At slower electrolyte flow rates, the performance of the RVC cathode is significantly better than that of the graphite chips. For example, at a flow rate of 7 ml/min and a current density of 800 A/m², the RVC cathode produces 2.32 w/o HO_2^- at 85% current efficiency compared to 0.64 w/o HO_2^- at 23% current efficiency for the graphite chips.

Discussion

Our voltammetry indicates that the cathodic reduction of oxygen in the trickle bed cell follows the same two-step mechanism observed at a graphite RDE, *i.e.*, $O_2 \rightarrow HO_2^- \rightarrow OH^-$. Furthermore, the two reduction steps initiate at essentially the same potentials in the beds as on the RDE, *i.e.*, −0.2 and −0.7V. At potentials more positive than *ca.* −0.7V, HO_2^- is produced at nominally 100% current efficiency at current densities up to *ca.* 200 A/m² at both a graphite bed and a RVC bed. At more negative potentials, peroxide synthesis efficiency falls. The physical mechanism accounting for most of these potential changes with operating variables is likely mass transport of oxygen to the surface of the bed particles. In both cell systems, more positive half cell potentials and higher concentrations of peroxide at high currents were favored by high oxygen pressures and low catholyte flow rates. Increasing current densities increased the potential gradient along the length of the bed.

These specific effects are in the directions expected in terms of the current depleting the oxygen content by the $O_2 \rightarrow HO_2^-$ process faster than the rate of replacement of oxygen by dissolution from the gas phase. With the cells studied, the quantity of oxygen present in the gas phase was always greater than that required to sustain the observed currents by the process: $O_2 \rightarrow HO_2^-$. The effects of these operating variables are all consistent with: (*i*) more effective mixing of gas and electrolyte occurring before the mixture enters the cell than on the bed and (*ii*) more effective mixing of oxygen and electrolyte occurring on the RVC bed than on the graphite chip bed.

The higher net yields of peroxide observed with the RVC bed are a consequence of a more uniform voltage distribution down the length of the bed. Less peroxide is reduced down the bed when the half cell potential at the entrance of the bed is nominally −0.7V. This more uniform current-potential distribution must be related to the physical structure of the RVC relative to that of the graphite chip bed, rather than a variation in ohmic drop along the bed (the current collector also runs the length of the bed). The RVC is a more open structure containing less total surface than the graphite chip bed, and as would be expected, the net current flow for a given half cell potential (at the top of the bed) is less with the RVC than the graphite. Presumably, the RVC bed is less flooded than the graphite chips. It would be necessary to study this factor in more detail. Regardless of the exact explanation, the RVC bed is more effective in producing HO_2^- than is the graphite chip bed.

REFERENCES

1. C. W. Oloman and A. P. Watkinson, U.S. Pat. 4,118,-305 (1978).
2. C. W. Oloman and A. P. Watkinson, U.S. Pat. 3,969,-201 (1976).
3. C. W. Oloman and A. P. Watkinson, *J. Appl. Electrochem.*, **9**, 117 (1979).
4. C. W. Oloman, *This Journal*, **126**, 1885 (1979).
5. M. L. Bathia and A. P. Watkinson, *Can. J. Chem. Eng.*, **57**, 631 (1979).
6. D. A. Skoog and D. M. West, "Fundamentals of Analytical Chemistry," 2nd ed., Holt, Rinehart and Winston, Inc., New York (1969).
7. A. Broden and R. Simonson, *Svens. Pap. T.*, **16**, 487 (1979).

Jet Impingement Systems for Electroplating Applications: Mass Transfer Correlations

A. A. Sonin[1]

NAPCO, Division of Thermo Electron Corporation, Terryville, Connecticut 06786

ABSTRACT

A study is presented of mass transfer rates in some jet impingement systems which are suitable for electrochemical processes where high transfer rates are required. Experimental data are presented and an empirical correlating equation is proposed. An application to high speed electroplating of printed circuit boards is described.

Jet impingement systems are used in many industrial processes which require high heat or mass transfer rates of surfaces. These systems consist of arrays of jets which are directed at the surface where the transfer process is to take place. In most applications, the carrier fluid is a gas. A significant literature is available on the performance of gaseous jet impingement systems, which have applications in the paper-making industry (1, 2).

Jet impingement systems also have applications in electrochemical systems. Electroplating is an obvious example. Here, the maximum current at which the

[1]Present address: Professor, Mechanical Engineering, Massachusetts Institute of Technology, Cambridge, Massachusetts 02139.

plating can take place without sacrifices in plate quality is less than the limiting current, the latter being the maximum rate at which the plated metal ions can reach the surface by convection and diffusion. To the extent that jet impingement devices can be used to increase the limiting current, they will allow an increase in plating speed.

Electrochemical applications use liquids as the carrier fluid, however, and relatively little systematic information is available on the mass transfer characteristics of liquid jet impingement systems. There are several important differences between gaseous and liquid systems. Liquids typically have very high Schmidt numbers, and their Sherwood number correlations will be different in form from those of gases, which have Schmidt numbers of order unity. Liquids also have a much higher density, and their use in jet impingement systems will require excessive pumping power unless the system has lower open areas than typical gaseous systems ("open area" refers to the ratio of the exit area of one of the jets to the transfer area associated with one jet).

This paper presents data on the mass transfer characteristics of some jet impingement systems suitable for electrochemical applications. A correlating equation is proposed, and an application to high speed plating of printed circuit boards is described.

Jet Impingement Systems

Some dozen different jet impingement systems were built, each consisting of an array of parallel manifold pipes with orifices distributed on the side facing the mass transfer surface (Fig. 1). All systems had pipes with the same outer diameter of 1.3 in. (3.3 cm) and the same centerline to centerline spacing of 4.0 in. (10.2 cm). They were distinguished by the size, shape, and distribution of their orifices. Depending on the system, the pipes would have one to five rows of orifices along axial lines. Some systems had orifices with contoured shapes so as to minimize frictional losses. The open area f ranged from about 10^{-3} to 10^{-2}.

Figure 1 shows an example of a system with good mass transfer characteristics, B-1, which had two rows of holes with a 45 degree included angle between the rows. The holes had a diameter of 0.099 in. (0.25 cm) and an axial center-to-center separation of 1.0 in. (2.5 cm), giving the system an open area $f = 0.00385$. Another good system, B-2, had three rows of holes

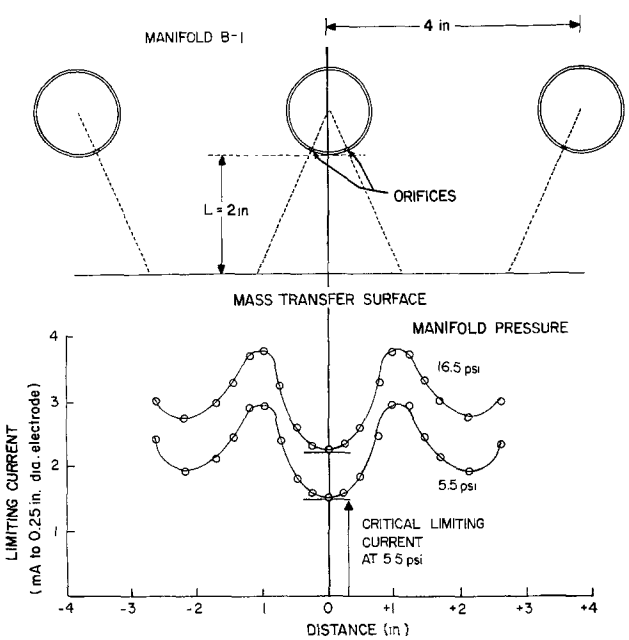

Fig. 1. Limiting current distribution for B-1 manifold system at a separation of 2 in. (5.1 cm).

with 45° between adjacent rows. The holes had a diameter of 0.059 in. (0.15 cm) and an axial center-to-center separation of 1.0 in. (2.5 cm), giving an open area $f = 0.00205$. The systems were completely submerged in the working fluid and tested over a range of manifold pressures (flow rates). Several separations between the manifold pipes and mass transfer surface were tried, usually 1.5 and 2.0 in. (3.8 and 5.1 cm). Volume flow rates and manifold pressures were recorded independently, and the hydraulic loss coefficients of the various systems determined (see Table I).

Mass Transfer Measurements

Diffusion-limited mass transfer rates were determined by measuring the limiting current due to the reduction of ferricyanide ions at a nickel cathode (3, 4). The working fluid was an aqueous solution of 0.01M potassium ferricyanide, 0.01M potassium ferrocyanide, and 2M sodium hydroxide. Limiting current density was measured at a circular 0.25 in. (0.635 cm) diam nickel cathode imbedded flush in the surface of a nonconducting epoxy-resin/fiberglass board. A large stainless steel sheet mounted on the other side of the manifold pipes served as the anode. The cathode diameter was large compared with the diffusion layer thickness, but small enough to resolve the changes in mass transfer conditions over the board. The current associated with the ferricyanide ion reduction reached a limiting plateau at a cathode voltage of about 0.2V, and remained constant to about 1V. The limiting current was typically measured at a fixed voltage of 0.5V. Limiting current distributions were measured by moving the board relative to the manifold pipes (Fig. 1).

For purposes of data reduction, the diffusion coefficient of the ferricyanide ion at the typical 20°C operating temperature was taken as 4.70×10^{-10} m^2/sec (5), and the solution density and viscosity were taken as 1080 kg/m^3 and 1.56×10^{-3} kg/msec, respectively (6).

Figure 1 shows limiting current distributions in the B-1 system at two manifold pressures, 5.5 and 16.5 psig (0.38 and 1.07 bar). As expected, mass transfer is highest where the jets impact directly on the surface, and lowest, in this case, directly under each manifold pipe, between jet impact points. The minimum transfer rate is some 30% lower than the average across the board.

The nonuniform distribution of limiting current under the jets has some relevance in electroplating applications. The local limiting current represents the maximum current that can in principle be sustained locally by the deposited ions alone. In electroplating applications, plating quality deteriorates ("burning" occurs) when the applied current reaches a certain fraction of the limiting current of the plated metal ions (what that fraction is must be determined experimentally). Hence, to avoid "burning" at any point, the applied current density must be less than the critical fraction of the limiting current at every point on the plated surface.

When we refer to a system's limiting current in what follows, we mean the lowest limiting current in that system (the value labeled the "critical" limiting current in Fig. 1).

Figure 2 shows the limiting current in the B-1 system as a function of manifold pressure for two different manifold-to-board separations. The one-third power law relations between limiting current and manifold pressure was typical of all our data. The coefficient in

Table I. Sherwood number coefficient a

System	L, in. (cm)	f	C_e	C_v	a
B-1	1.5 (3.8)	0.00385	1.0	0.816	0.96
B-1	2.0 (5.1)	0.00385	1.0	0.816	0.87
B-2	1.5 (3.8)	0.00205	1.0	0.620	0.97
B.2	2.0 (5.1)	0.00205	1.0	0.620	0.97

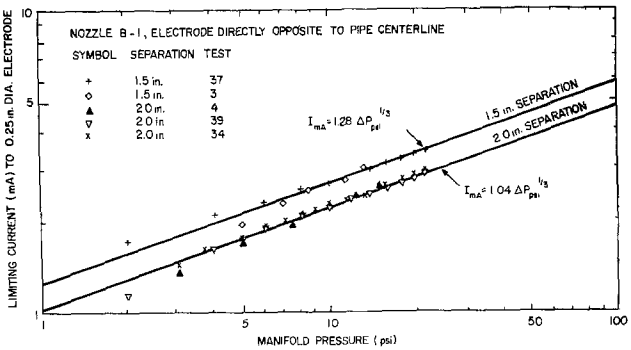

Fig. 2. Minimum limiting current density for B-1 manifold as a function of manifold pressure.

that relationship depended on system configuration (*i.e.*, distribution, size and shape of orifices, manifold-to-board separation).

Scoping tests were run with some dozen different manifold configurations to establish those which showed the most promise of providing the highest limiting current for the least pumping power input. Systems B-1 and B-2 were among this latter group, and the mass transfer characteristics of these systems were determined with some care (e.g., Fig. 2).

Mass Transfer Correlations

Dimensionless correlations.—Consider a set of geometrically similar arrays of circular nozzles exhausting onto a flat mass transfer surface. The systems are of effectively infinite extent, with a repeating pattern of nozzles. "Geometrically similar" in this context implies that the center to center distribution pattern of the nozzles is the same, when measured in units of the distance L of the nozzles from the mass transfer surface. The systems may differ via their characteristic size L, via their nozzle diameter (which is a "free" parameter not related to the scale L) and via their fluid properties and flow conditions.

We restrict our attention to systems where the nozzle diameter is small compared with L, so that the mass transfer surface is in the far field of the jets; to fluids with very large Schmidt number; and to flow conditions whert the jets are fully turbulent. These restrictions are very often satisfied in practice; they also simplify the mass transfer scaling laws considerably.

The mass transfer surface being in the far field of the jets, we can be assured (7) that the jets will affect the transfer rate at the surface only via the magnitude of the momentum flux on unit surface area

$$J = \rho V^2 C_c f \qquad [1]$$

where

$$V = C_v (2\Delta p/\rho)^{1/2} \qquad [2]$$

is the jet velocity at the vena contracta. It follows from dimensional considerations that, at least for dilute solutions, the mass transfer data for a geometrically similar set of systems should correlate in the form

$$\mathrm{Sh} = \mathrm{Sh}(\mathrm{Sc}, \mathrm{Re}) \qquad [3]$$

where

$$\mathrm{Sh} = NL/D(c - c_w) = j_{lim} L/n\mathbf{F}Dc \qquad [4]$$

is the Sherwood number

$$\mathrm{Sc} = \mu/\rho D \qquad [5]$$

is the Schmidt number, and

$$\mathrm{Re} = (\rho L/\mu)(J/\rho)^{1/2} \qquad [5a]$$

$$= (\rho V L/\mu)(C_c f)^{1/2} \qquad [5b]$$

$$= (L/\mu)(2fC_cC_v^2\Delta p)^{1/2} \qquad [5c]$$

is a Reynolds number based on the momentum flux from the jets per unit area of mass transfer surface.

For fully turbulent flow conditions, we may approximate Eq. [3] with a power-law form. The dependence $\mathrm{Sh} \sim \mathrm{Sc}^{1/3}$ has been demonstrated (8, 9) and widely accepted for various Schmidt number, turbulent flows [see also the study of a single jet impingement system by Chin and Tsang (10)]. As for the dependence on Re, both our own experiments with liquids and the extensive correlations of Martin (1) for gases suggest that $\mathrm{Sh} \sim \mathrm{Re}^{2/3}$ (see Fig. 2). These facts imply a correlation of the form

$$\mathrm{Sh} = a\,\mathrm{Sc}^{1/3}\,\mathrm{Re}^{2/3} \qquad [6]$$

The coefficient "a" depends on the nozzle distribution geometry, in the sense defined earlier. In concentrated solutions, it may also be affected by the mass fractions of the species in the solution. Table I shows that for systems B-1 and B-2, which were the best among the manifolds tested

$$a = 0.9\text{-}1.0 \qquad [7]$$

Note that the Sherwood number referred to in these correlations is based on the lowest limiting current measured on the transfer surface, not the average. The average was typically a factor of about 1.5 higher (see Fig. 1).

Limiting current.—Based on Eq. [6], the limiting current (or mass transfer coefficient) can be expressed in terms of either the jet velocity or the manifold pressure as

$$j_{lim}/n\mathbf{F}c = a(C_c f\rho/\mu L)^{1/3}(VD)^{2/3} \qquad [8a]$$

$$= a(C_v D)^{2/3}(2C_c f\Delta p)/\mu L)^{1/3} \qquad [8b]$$

Consider how j_{lim} depends on pumping power. The pumping power W_p/A consumed by the jets per unit transfer area is the manifold pressure Δp times the volume flow rate per unit area, $VC_c f$. With Eq. [2], this can be written

$$W_p/A = C_v C_c f(2/\rho)^{1/2}\Delta p^{3/2} \qquad [9]$$

The power in the jets can be changed either via the open area f or the manifold pressure Δp or both. Note that every doubling of the power by the increase of Δp alone will increase the limiting current by only 17%, while every doubling of power by the increase of f alone will increase the limiting current by 26%, a somewhat larger, but still low figure. The limiting current for jet impingement systems is thus very insensitive to the pumping power input. Little headway can be made by brute force increase in pumping power. It is important to use optimized systems with the highest possible "a" and with contoured nozzles with minimum friction.

Temperature dependence.—Finally, Eq. [8] predicts the temperature dependence of the mass transfer coefficient. If the subscript (o) denotes conditions at a reference temperature, 20°C, say, we can write for liquids

$$\mu D/T = \mu_o D_o/T_o \qquad [10]$$

$$\rho = \rho_o \qquad [11]$$

where T is the absolute temperature. The temperature dependence of the viscosity can be approximated with (11)

$$\mu = \mu_o \exp\frac{\Delta G}{R}\left(\frac{1}{T} - \frac{1}{T_o}\right) \qquad [12]$$

where ΔG is the free energy associated with the viscosity. Based on Eq. [10]-[12], and [8], we find

$$\frac{j_{lim}}{(j_{lim})_o} = \left(\frac{T}{T_o}\right)^{2/3} \exp\frac{\Delta G}{R}\left(\frac{1}{T_o} - \frac{1}{T}\right) \qquad [13]$$

where $(j_{lim})_o$ is the limiting current at the reference temperature T_o and j_{lim} is the limiting current at temperature T at the same concentration and same jet velocity (or same manifold pressure, or same pumping

power). The temperature dependence is quite strong. For example, in the temperature range 20°-50°C, the viscosity of water can be fitted with $\Delta G/R = 2000$ K [12] and based on this, a bath temperature rise from 20° to 40°C, say, would raise the mass transfer coefficient by 62%.

Application to Electroplating of Printed Circuit Boards

Figure 3 shows how the jet impingement systems of this study can be set up for electroplating printed circuit boards. Note the staggered distribution of manifold pipes on the two sides of the board. This insures good agitation in the holes which pass through the board.

A bench-scale electroplating system was set up using the B-1 manifold design with $L = 1.5$ in. (3.8 cm). Typical two-sided printed circuit boards (type IPC B-25 test panels) were pattern plated with copper in acid copper solutions, using a delivered pumping power $W_p/A = 2$ kW/m^2. Two different acid copper plating baths were tested. Bath A was a conventional high-throw acid copper bath (0.3M Cu, 1.8M H_2SO_4, plus small concentrations of proprietary additives and chloride). Bath B was an experimental bath designed specifically for high speed plating (0.6M Cu, 2.2M H_2SO_4, plus additives and chloride) at a higher-than-normal operating temperature.

A practical limiting current for the plating applications was determined by increasing the average current density (the current divided by the actual copper area being plated) in steps and noting the value at which a deterioration in plate quality ("burning") first appeared anywhere on the board. Plating tests were carried out over a range of current densities and bath temperatures. Burning was invariably first observed on certain isolated lines or pads.

The average current densities where burning first occurred in Bath A can be deduced from Fig. 4; the dark points indicate burning at some point on the board, and the white points none. The solid line on Fig. 4 represents 0.15 j_{lim}, where j_{lim} is computed from Eq. [16] and [13] with $a = 0.95$, with the bath properties quoted previously, and with $\Delta G/R = 2000$ K (appropriate for water). The data suggests that the practical

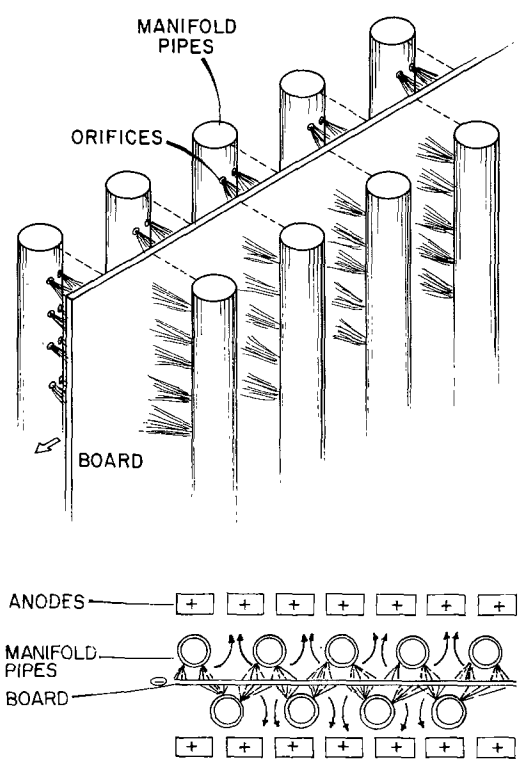

Fig. 3. Jet impingement system for high speed electroplating of printed circuit boards.

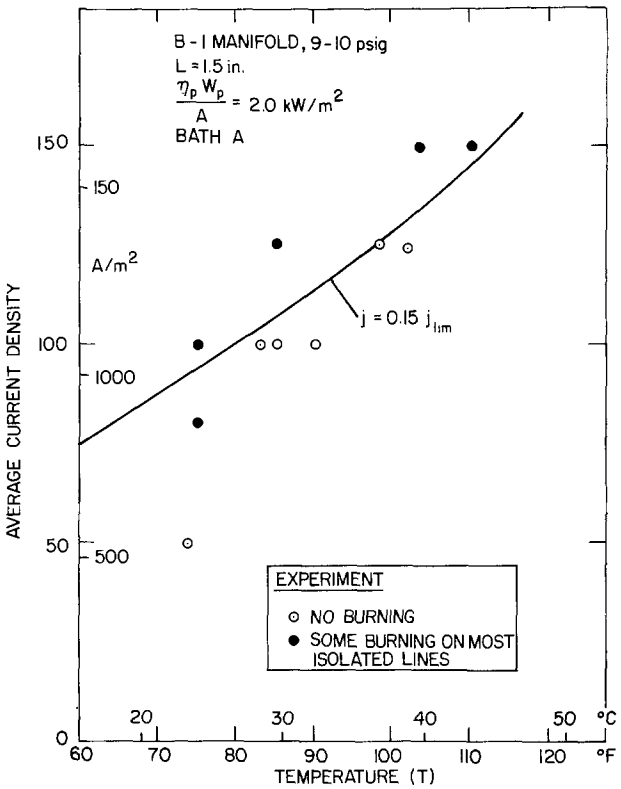

Fig. 4. Practical limiting current as a function of bath temperature for IPC B-25 test panels (B-1 manifold, 2kW/m^2 pumping power input).

limiting current for this board was about 15% of the limiting current deduced from our mass transfer correlation.

Tests were also conducted with a manifold which had the same orifice distribution as B-1, but with smaller holes, so that the open area was only $f = 0.00137$. For these data also the practical limiting current correlated well with 0.15 j_{lim}.

When manifold B-1 was used with Bath B at a pumping power of 2 kW/m^2 and a temperature of 40°C (103°F), burning occurred above 225 ASF (2420 A/m^2). The gain was due entirely to the higher copper concentration in Bath B. When reduced to dimensionless form, the data gain correlated approximately with 0.15 j_{lim}.

Clearly, the data suggests that for these boards, the practical limiting current, that is the maximum current which can be used without compromising the plate quality anywhere on the board, was only about 15% of the copper limiting current based on our mass transfer correlation. This is not entirely surprising. Plate quality deteriorates before the full copper limiting current is reached. Kessler & Alkire (13), for example, observed a practical limiting current of the order of 25% of the actual mass transfer limited value.

Secondly, burning always occurs first on a printed circuit board at isolated points or lines, where the local current density is higher than the average value on the board. At the isolated point where burning usually began on the IPC B-25 test board, the local current density (as measured by plate thickness prior to burning) was over twice as high as the average. The local burning current was therefore actually more than 30% of the full copper limiting current.

Although these data for plating are rather limited, they do suggest that the practical limiting current is controlled largely by the limiting current for the metal ions and by the pattern on the board.

Conclusion

A mass transfer correlation has been derived for jet impingement system suitable for electrochemical appli-

cations. With such systems, high transfer rates (limiting currents) can be attained over large surfaces. Although the limiting current can in principle be continuously increased by increasing the pumping power, only 17-26% increase in rate results from every doubling of the power, depending on whether the power is increased by boosting manifold pressure or opening jet area. This rule applies to jet impingement systems in general. For this reason, it is important that systems be well designed so that the maximum fraction of the hydraulic power input is used for promoting mass transfer. Other factors affecting the limiting current are ion concentration and bath temperature.

An application of a jet impingement system for increasing production rates in acid copper electroplating of printed circuit boards showed that average operating current densities over 100 ASF (1080 A/m^2) can be employed using a conventional high-throw acid copper bath (0.3M Cu, or 10 oz/gal copper sulfate), a typical printed board and moderate pumping power inputs. This working current was more than doubled to 225 ASF, or 2430 A/m by using a bath with twice the conventional copper concentration (0.6M) and higher operating temperature (40°C, or 103°F), without any increase in pumping power.

Acknowledgments

Dr. Thomas Martin, David Russell, and other members of NAPCO's R&D Center contributed to this research. Special thanks are due to Gary Parent, who performed most of the tests.

Manuscript submitted July 12, 1982; revised manuscript received *ca.* March 1, 1983.

Any discussion of this paper will appear in a Discussion Section to be published in the June 1984 JOURNAL. All discussions for the June 1984 Discussion Section should be submitted by Feb. 1, 1984.

Thermo Electron Corporation assisted in meeting the publication costs of this article.

LIST OF SYMBOLS

- a coefficient in Sherwood number correlation, Eq. [6]
- A total area of mass transfer surface (m^2)
- c bulk concentration of surface-reacting species (mol/m^3)
- c_w concentration of surface-reacting species at wall (mol/m^3)
- C_c contraction coefficient: area of jet at vena contracta divided by jet exit area
- C_v velocity coefficient, Eq. [2]
- D diffusion coefficient of surface-reacting species (m^2/sec)
- f exit area of single jet/mass transfer area per jet
- $\mathbf{F}$ Faraday's constant
- ΔG Gibbs free energy of activation (J/mol K)
- j_{lim} limiting current density (A/m^2)
- L separation between mass transfer surface and face of manifold pipe; a characteristic length (m)
- n number of electrons transferred in reaction of one molecule of surface-reacting species at wall
- N flux of surface-reacting species to surface (mol/sec m^2)
- Δp manifold gage pressure (N/m^2)
- R universal gas constant
- Re Reynolds number, Eq. [5]
- Sc $\mu/\rho D$, Schmidt number
- Sh Sherwood number, Eq. [4]
- T absolute temperature (K)
- V jet velocity at vena contracta (m/sec)
- W_p pumping power input into jets (W)
- μ viscosity (kg/m sec)
- ν μ/ρ, kinematic viscosity (m^2/sec)
- ρ density (kg/m^3)

Subscripts

- (o) conditions at a reference temperature

REFERENCES

1. H. Martin, in "Advances in Heat Transfer," J. P. Hartnett and T. F. Irvine, Editors, Vol. 13, pp. 1-60, Academic Press, New York (1977).
2. N. T. Obot, A. S. Mujumbdar, and W. J. M. Douglas, in "Drying '80," A. S. Mujumbdar, Editor, Vol. 1, pp. 388-402, Hemisphere Press, New York (1980).
3. L. P. Reiss and T. J. Hanratty, *A.I.Ch.E. J.*, **8,** 245 (1962).
4. T. J. Hanratty and J. A. Campbell, in "Fluid Mechanics Measurements," R. J. Goldstein, Editor, Hemisphere Press, New York (1982).
5. J. C. Bazan and A. J. Arvira, *Electrochim. Acta,* **10,** 1025 (1965).
6. "Handbook of Chemistry and Physics," R. C. Weast and M. J. Astle, Editors, 61st ed., CRC Press, Boca Raton, FL (1980).
7. G. N. Abramovich, "The Theory of Turbulent Jets," MIT Press, Cambridge MA (1963).
8. A. S. Monin and A. M. Yaglom, "Statistical Fluid Mechanics," Volume 1, MIT Press, Cambridge, MA (1975).
9. B. S. Petukhov, in "Advances in Heat Transfer," J. P. Hartnett and T. F. Irvine, Editors, Vol. 6, pp. 503-564, Academic Press, New York (1970).
10. D. T. Chin and C. H. Tsang, *This Journal,* **125,** 1461 (1978).
11. J. O. Hirschfelder, C. F. Curtiss, and R. B. Bird, "Molecular Theory of Gases and Liquids," p. 625, John Wiley and Sons, Inc., New York (1964).
12. "Handbook of Applied Engineering Science," 2nd ed., R. E. Bolz and G. L. Tuve, Editors, p. 89, CRC Press, Cleveland (1973).
13. T. Kessler and R. Alkire, *This Journal,* **123,** 990 (1976).

Electrochemistry of Polyphenylene Films Deposited Anodically on Platinum or Glassy Carbon Electrodes in HF-Benzene System

I. Rubinstein*,[1]

General Electric Corporate Research and Development, Schenectady, New York 12301

ABSTRACT

Polyphenylene films were deposited on Pt or glassy carbon electrodes by anodically oxidizing benzene in liquid hydrogen fluoride. The polymer is electroactive in liquid HF, with a remarkably low oxidation potential. It can also undergo electrochemical oxidation-reduction in dry propylene carbonate containing $LiAsF_6$, and charging/discharging curves of the system are presented. The polymer film is shown to be suitable for electrode surface modification by means of simple chemical reactions performed on the coated electrodes.

Two different areas of research which have attracted much attention in recent years include modified electrodes (1) and conducting polymers (2). In some cases, however, the two are strongly linked, as some polymer films deposited electrochemically (or otherwise) on electrodes become electrically conductive under certain conditions. This is the case, for example, with polypyrrole and its derivative (3), polyaniline (4), and polyacetylene (5). These polymers are, in addition, electrochemically reactive, showing reversible oxidation-reduction waves for the polymer (3-5).

Among the known conducting polymers, chemically synthesized polyacetylene films (6) and poly-p-phenylene powder (7) are probably the most widely investigated. Both polymers become highly conductive upon either vapor-phase or liquid-phase doping with strong electron acceptors (*e.g.*, AsF_5) or electron donors (*e.g.*, Li) (2). Both can also be electrochemically oxidized or reduced (*i.e.*, doped) in a reversible manner in nonaqueous solvents under inert atmosphere (8, 9), a property which has been used to demonstrate their applicability as active materials for energy storage (9, 10).

The possibility of obtaining polyphenylene deposits via the anodic oxidation of benzene has been demonstrated previously, in HF-benzene bi-phasic system (11) and in mesitylene:HCl:$2AlCl_3$ solutions (12). More recently, polyphenylene films on electrodes were obtained by electrochemically oxidizing benzene in liquid SO_2 (13) or in HF/SbF_5 super acid (14). In a recent publication (15), we investigated the properties of polyphenylene films grown anodically in HF-benzene system. The films become electrically conductive ($\leq 10^{-2}$ Ω^{-1} cm^{-1}) upon vapor-phase doping with AsF_5; the measured conductivities were, however, lower than those obtained with doped chemically synthesized poly-p-phenylene ($\sim 10^{2}$ Ω^{-1} cm^{-1}) (16). This was explained on the basis of the polymer structure being amorphous, in contrast with the crystalline nature of poly-p-phenylene.

In the present publication, different aspects of the electrochemistry of polyphenylene deposition in this system and of the resultant polymer are examined in a preliminary manner. Some possible applications of polyphenylene films on electrodes are also presented, along with experimental results demonstrating the principles.

Experimental

Materials.—Hydrogen fluoride (Air Products) and arsenic pentafluoride (Ozark-Mahoning) gases, 49% hydrofluoric acid (Fisher, Reagent A.C.S.) and benzene (Mallinckrodt, A.R.) were used as received. NaI (BDH, Reagent) was dried under vacuum before use. Dimethyl formamide (DMF) (Baker, Analyzed Reagent) was dried over 4A molecular sieves (Alfa-Ventron) before and during the experiments. $Ru(bpy)_3(ClO_4)_2$ (where bpy = 2,2'-bipyridine) was prepared from the chloride (Strem Chemicals) (17). Propylene carbonate (PC) (Burdick and Jackson, glass distilled) was further purified by passing through a 4A molecular sieve column in a dry box. $LiAsF_6$ (Alfa-Ventron) was dried under vacuum overnight and kept in the dry box.

Cell and instrumentation.—Simple 50 ml disposable polypropylene cells were used for experiments involving HF, with a Teflon cover, through which holes were drilled to accommodate the electrodes. Pt disks (area, 0.02 cm^2) or glassy carbon (GC) (Atomergic Chemetals) disks (area, 0.04 cm^2) were used as working electrodes, with a Pt coil counterelectrode. A Pd/H_2 reference electrode (18) was used in HF solutions (+0.145 and −0.060V *vs.* SCE in 93% HF and 49% HF, respectively). For experiments below room temperature, the cell was immersed in a methanol-water bath, held at the desired temperatures using a Lauda Model RC3 circulator. For current-voltage curves in aqueous H_2SO_4, a standard three-electrode glass cell was used, with a K_2SO_4-saturated mercurous sulfate reference electrode (MSE). In DMF solutions, a silver wire quasi-reference electrode (19) was employed. The same type of cell was used for electrochemical measurements in PC/$LiAsF_6$, which were carried out in a dry box under Ar atmosphere, using an Li wire reference.

Procedures for HF solutions.—Experiments with 49% HF were carried out at room temperature, using commercially available hydrofluoric acid. For experiments in 93% HF, the following procedure was undertaken: 1 ml of water was placed in the cell, which was then immersed in the cooling bath at −5°C. 13 ml of pure HF were then condensed from the gas cylinder into the cell, using a copper coil-type condenser, also kept at −5°C. When condensation was completed, the temperature was raised to +7°C, and kept constant throughout the experiments. At that point, if necessary, a layer of 10 ml benzene was added on top of the HF phase.

Results and Discussion

Polyphenylene deposition.—Current-potential curves for a Pt electrode in 49% HF and in the two-phase system, 49% HF-benzene (electrode immersed in the HF phase) are shown in Fig. 1. It is conceivable that in the two-phase system a small amount of benzene is dissolved in the HF. The increase in anodic current in the Pt-oxide region in the presence of benzene is attributed to electro-oxidation of benzene adsorbed on the Pt surface, a behavior similar to that reported by Gileadi *et al.* (20) for platinized Pt in aqueous H_2SO_4 containing a small amount of dissolved benzene. It seems, however, that soluble species rather than polyphenylene, are the oxidation products in this case, since no film was detected on the electrode surface upon repetitive cycling.

A totally different behavior is observed in 93% HF-benzene two-phase system (electrode immersed in the

* Electrochemical Society Active Member.
[1] Present address: Department of Plastics Research, Weizmann Institute of Science, Rehovot 76100, Israel.

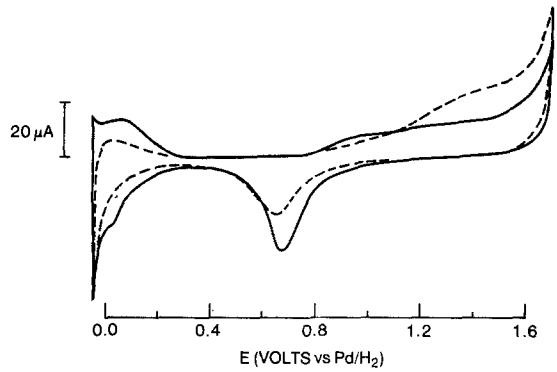

Fig. 1. Current-potential curves for a Pt electrode in 49% HF (——) and in 49% HF-benzene (---) (scan rate = 0.1 V/sec).

HF phase), as shown in Fig. 2A. Upon scanning the potential of a Pt electrode in the positive direction, no current is observed prior to the sharp rise at *ca.* +1.1V On the reverse scan, a small cathodic peak is already observed at +0.35V. When scanning positively again, an anodic peak develops at +0.55V, which continuously grows upon repetitive cycling, along with the corresponding cathodic peak. (Note that on this current scale, the background current for Pt in 93% HF with no benzene coincides with the base line.) At the same time, a film, which thickens and becomes darker with cycling, is observed on the electrode surface.

If at some point the positive potential limit is lowered to +0.85V, the reversible wave remains unchanged for numerous cycles, as shown in Fig. 2B. If the electrode is then transferred to 93% HF solution (no benzene), the waves are still evident at steady-state cycling (Fig. 2C). The same type of behavior is also observed with GC electrodes.

It is clear from these observations that benzene, dissolved to some degree in the 93% HF, is anodically oxidized at *ca.* 1.1V, to form the polyphenylene deposit on the electrode surface. The sharp rise in current attributed to benzene oxidation is continuously shifted to less positive potentials upon cycling, as the irregularly shaped, conductive polymer is deposited on the surface (15), providing an increasing surface area for further deposition (14). The outstanding properties of liquid HF as a catalyst for different organic reactions, including alkylation of benzene and various polymerizations, are well known (21). It is not surprising, therefore, that liquid HF also provides an excellent medium for electrochemical polymerization of benzene. Furthermore, the unique properties of liquid HF as a solvent in electrochemical reactions are demonstrated by the chemically reversible oxidation of polyphenylene in this medium at *ca.* 0.55V. This is approximately 1V less anodic than in nonaqueous medium (see below), and is not observed at all in liquid SO_2 (13). It indicates a considerable stabilization of the polymer radical cation in this system, probably by association with fluoride ions, some of which are reversibly incorporated in the polymer upon oxidation. If this is indeed the case, it might be a rare example of polyphenylene doping with a halogen ion.

Note that in cases where the amount of electrical charge passed during the deposition is specified, the polymer was deposited galvanostatically at 1.0 mA cm^{-2}, for the desired length of time.

Properties.—Physical and chemical properties of electrochemically deposited polyphenylene are discussed elsewhere (11, 15). It was shown that the polymer thus produced, though largely para-linked, is actually composed of mixed types of linkages, and is amorphous in nature (15). The film appears dendritic, with varying degrees of porosity, depending on the deposition conditions (15). The porous nature of a galvanostatically deposited film is demonstrated in Fig. 3, where current-potential curves for a polyphenylene-coated Pt electrode (denoted Pt/PP) in 0.1*M* H_2SO_4 are presented. Although smaller, the Pt oxygen and hydrogen adsorption/desorption peaks are apparent, indicating that part of the surface is exposed to the solution. The amount of exposed Pt surface is not very reproducible, and some films show a markedly different porosity than others, grown under similar conditions. This may be related to an "aging" effect of the deposition solution, and requires further investigation.

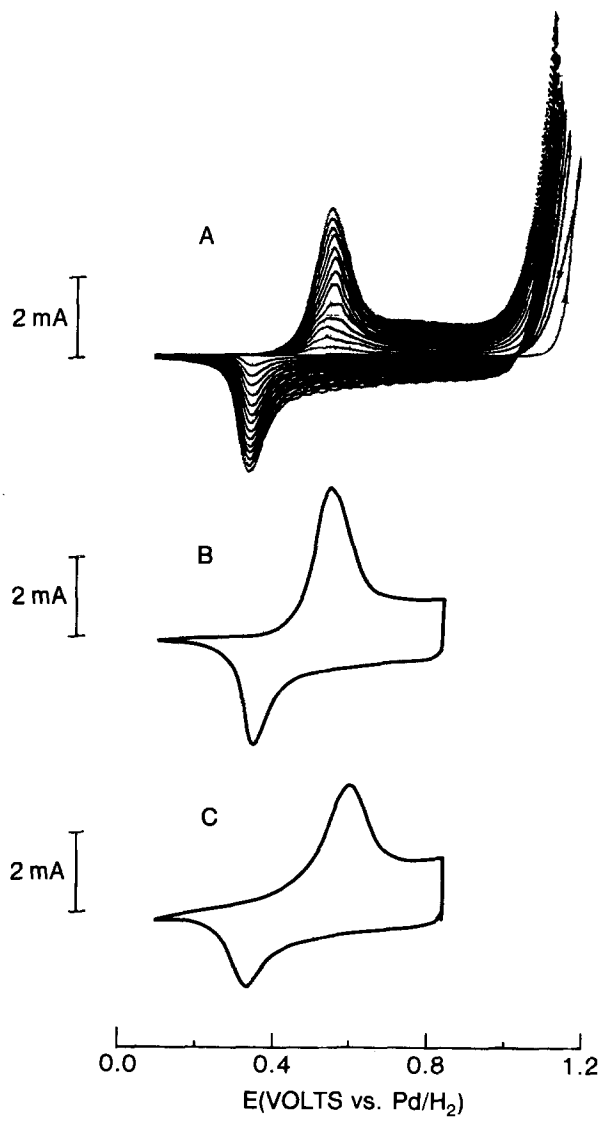

Fig. 2. Current-potential curves for a Pt electrode, in consecutive steps: (A) repetitive cycling in 93% HF-benzene, (B) steady-state cycling in the same solution, (C) steady-state cycling in 93% HF (scan rate = 0.1 V/sec).

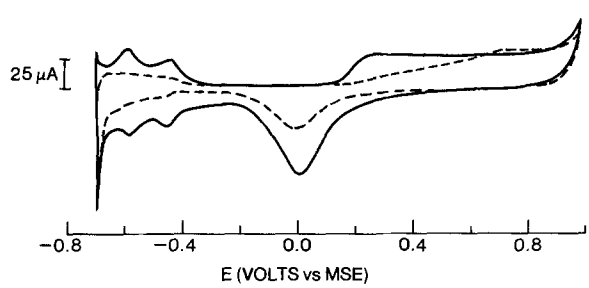

Fig. 3. Current-potential curves in 1.0*M* H_2SO_4 for a bare Pt electrode (——) and for Pt/PP, prepared by passing 8.6 × 10^{-3} C (---) (scan rate = 0.1 V/sec).

Electrochemistry in nonaqueous medium.—In Fig. 4 are presented current-potential curves for a bare Pt electrode (4A) and a Pt electrode electrochemically coated with polyphenylene (4B), in a propylene carbonate solution containing 0.2*M* $LiAsF_6$. The polyphenylene film appears to be anodically oxidized under these conditions, with two oxidation peaks, at +4.73 and +5.18V, and two reduction peaks, at +4.30 and +2.82V. Electrochemical oxidation-reduction of chemically synthesized poly-p-phenylene has been previously observed under similar conditions, accompanied by incorporation of AsF_6^- ions into the polymer lattice (9). From the two plots in Fig. 4B, it appears that the anodic oxidation of the polymer occurs in two stages, with the second (at 5.18V) considerably less reversible than the first. This might be related to the reported two-stage chemical oxidation of poly-p-phenylene in the vapor-phase doping with AsF_5 (16, 22). Upon repetitive cycling, the height of the oxidation and reduction peaks constantly decreases, apparently due to poor chemical reversibility of the second oxidation. If the cycled electrode is left at open circuit for several minutes, a considerable increase in the peaks' amplitude is observed, indicating that the reduced state of the polyphenylene is regenerated via a slow chemical reaction. This will be further stressed in connection with charging curves of the polymer. By integrating the charge under the oxidation curve in Fig. 4B, one can estimate that in the first cycle 8% of the phenylene groups are oxidized, *i.e.*, 8 mol percent (m/o) AsF_6^- is incorporated into the polymer. This is considerably higher than in the vapor-phase doping of the same polymer (15).

On the cathodic side in Fig. 4, one only observes the deposition-dissolution of Li, rather than reduction of the polymer. The Li/Li^+ waves are smaller than those obtained with the bare Pt electrode, probably because Li is deposited on the exposed part of the Pt surface, rather than on the undoped, poorly conducting polyphenylene. It has been reported (9) that chemically synthesized poly-p-phenylene is cathodically reduced in a reversible manner at potentials more positive with respect to Li deposition, in contrast with the behavior of polyphenylene films. It appears that on this time scale (and down to 2 mV/sec) the polymer film reduction is too slow to be noticeable; the reason for this behavior is not clear at this point.

Figure 5 presents a typical charging-discharging curve for a GC/PP electrode, charged for 5 min at constant current to a level of 2 m/o. The results are close to those obtained with poly-p-phenylene pellets (9), and demonstrate the possible application for energy storage. One also notices that the transition time for the discharge is shorter than the charging time, an effect which becomes more pronounced with longer charging times. This indicates a slow self-discharge

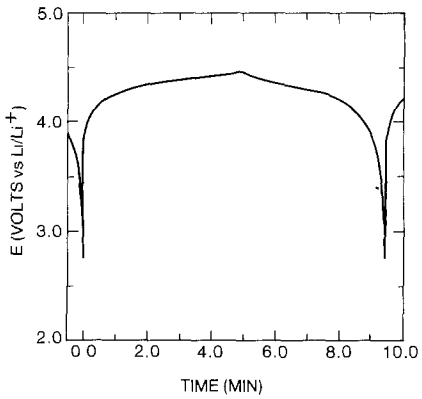

Fig. 5. Charge-discharge curve in PC containing 0.2M $LiAsF_6$ for a GC/PP electrode prepared by passing 0.3C, performed at a constant current of ±10 μA to a level of 2 m/o doping.

process in this system, as already mentioned above, most likely by reaction of oxidized polymer with the solvent or with traces of water.

Application to electrode surface modification.—The electrochemically deposited polyphenylene coating is highly chemically stable, insoluble in all common solvents, adherent to Pt or carbon surfaces, and can be grown to a desired thickness, with a very high surface area and variable porosity. These properties make the system very attractive as means for modifying electrode surfaces. In normal working potential range (excluding the oxidation at high positive potentials in strictly nonaqueous medium) and particularly in aqueous solutions, the polymer is electrochemically inert. However, since polyphenylene is composed of simple phenylene units, highly susceptible to various substitution reactions, it can rather simply be modified to contain electrochemically reactive groups or species. Two examples of this approach are presented below, employing nitration and sulfonation of the polymer (23). In the first, polyphenylene films on Pt were nitrated by dipping coated electrodes in a solution of H_2SO_4(conc):HNO_3(conc):H_2O(5:3:1) for 30 min at 58°C. As shown in Fig. 6A, the partially nitrated polymer is electroactive, though the reduction of the nitro groups is not as reversible as that of nitrobenzene (Fig. 6B). Upon repetitive cycling the peaks continuously diminish, apparently due to irreversible reductive conversion of nitro groups (24).

In the second case, polyphenylene films on Pt were sulfonated by dipping the coated electrode in concentrated H_2SO_4 for 5 hr at 155°C. Note that longer reaction times result in separation of the polymer layer from the surface. The resultant sulfonated polyphenyl-

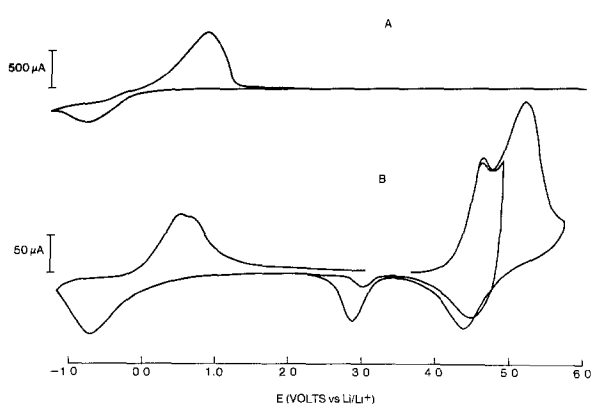

Fig. 4. Current-potential curves in PC containing 0.2M $LiAsF_6$ for a bare Pt electrode (A) and for Pt/PP, prepared by passing 2.6×10^{-2} C (B) (scan rate = 0.2 V/sec).

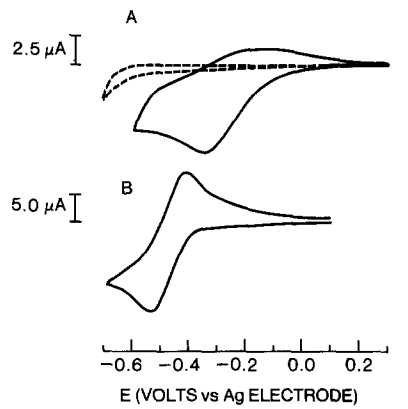

Fig. 6. Current-potential curves for (A) Pt/PP prepared by passing 8.6×10^{-3}C, before (---) and after (——) nitration, in DMF containing 0.1M NaI, (B) bare Pt electrode in DMF and 0.1M NaI containing 3.0 mM nitrobenzene (scan rate = 0.1 V/sec).

ene is an ion-exchange polymer, and is capable of binding electroactive cations by ion-exchange action (1C). A current-potential curve for the sulfonated Pt/PP and for a bare Pt electrode in aqueous solution containing 0.5 m*M* $Ru(bpy)_3(ClO_4)_2$ is shown in Fig. 7A. It is evident from the two curves that the sulfonated polymer incorporates a high concentration of reactive complex ions. No such effect is observed with unsulfonated Pt/PP. If the modified electrode is then transferred to background solution, the oxidation-reduction waves persist (Fig. 7B), indicating actual binding of the complex to the electrode surface. Upon repetitive cycling, however, slow loss of active material from the surface is observed, by ion-exchange with protons in solution.

Conclusions

Benzene is readily oxidized electrochemically in liquid hydrogen fluoride to form a layer of polyphenylene on Pt or GC electrodes. The deposited polyphenylene exhibits oxidation-reduction peaks in the same solvent at remarkably low potentials (*ca.* +0.45V *vs.* Pd/H_2). This demonstrates the unique properties of liquid HF as a solvent in electrochemical systems, in this case by stabilizing aromatic radical cations. Polyphenylene films are anodically oxidized in dry PC/$LiAsF_6$, and can be repetitively charged and discharged, with some loss of oxidized material by a slow chemical process. This slow process is probably either reaction with traces of water or with the solvent, in which case the system will be inherently unstable in PC. In a clear deviation from the behavior of chemically synthesized poly-p-phenylene, no reduction of the polymer is observed on the time scale of the cyclic voltammograms, positive to Li deposition. This and some other aspects of the electrochemical behavior of polyphenylene films are not fully understood at this point, and require further investigation.

The polymer film, which is very stable, adherent, and has a high surface area, can be employed for electrode surface modifications. By carrying out simple chemical substitution reactions on coated electrodes, electroactive or catalytic groups can be bound to the electrode surface. Although nitration and sulfonation did not produce highly stable modifications, it should in principle be possible to obtain well-behaved modified electrodes from polyphenylene films, particularly by covalent attachment of stable electroactive groups to the phenylene units.

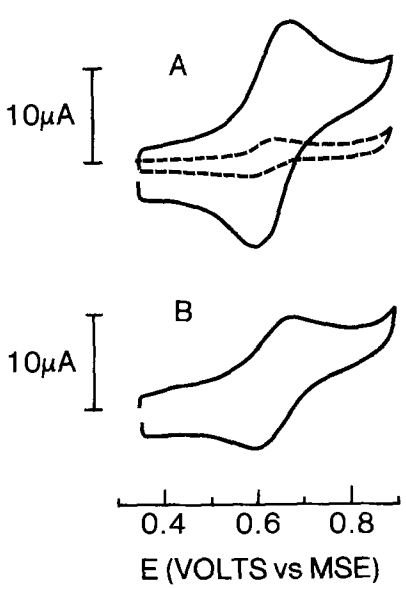

Fig. 7. Current-potential curves for (A) bare Pt electrode (---) and sulfonated Pt/PP prepared by passing 2.1 × 10^{-2}C (——), in 0.1M H_2SO_4 containing 0.5 mM $Ru(bpy)_3(ClO_4)_2$, (B) sulfonated Pt/PP electrode of (A), rinsed and transferred to 0.1M H_2SO_4.

Manuscript submitted Nov. 15, 1982; revised manuscript received March 11, 1983.

Any discussion of this paper will appear in a Discussion Section to be published in the June 1984 JOURNAL. All discussions for the June 1984 Discussion Section should be submitted by Feb. 1, 1984.

General Electric Corporate Research and Development Center assisted in meeting the publication costs of this article.

REFERENCES

1. K. D. Snell and A. G. Keenan, *Chem. Soc. Rev.*, **8**, 259 (1979); R. W. Murray, *Acc. Chem. Res.*, **13**, 135 (1980); I. Rubinstein and A. J. Bard, *J. Am. Chem. Soc.*, **103**, 5007 (1981), and references therein.
2. "Conductive Polymers," R. B. Seymour, Editor, Plenum Press, New York (1981); *Chem. Scr.*, **17** (1981); *Mol. Cryst. Liq. Cryst.*, **77** (1981).
3. A. F. Diaz and J. I. Castillo, *J. Chem. Soc. Chem. Commun.*, 397 (1980); A. F. Diaz, J. I. Castillo, J. A. Logan, and W.-Y. Lee, *J. Electroanal. Chem.*, **129**, 115 (1981); K. K. Kanazawa, A. F. Diaz, M. T. Krounbi, and G. B. Street, *Synth. Met.*, **4**, 119 (1981).
4. A. F. Diaz and J. A. Logan, *J. Electroanal. Chem.*, **111**, 111 (1980).
5. A. F. Diaz and T. C. Clarke, *ibid.*, **111**, 115 (1980).
6. T. Ito, H. Shirakawa, and S. Ikeda, *J. Polym. Sci. Poly. Chem. Ed.*, **12**, 11 (1974).
7. P. Kovacic and A. Kyriakis, *J. Am. Chem. Soc.*, **85**, 454 (1963); P. Kovacic and J. Oziomek, *J. Org. Chem.*, **29**, 100 (1964).
8. P. J. Nigrey, A. G. MacDiarmid, and A. J. Heeger, *J. Chem. Soc. Chem. Commun.*, 594 (1979).
9. L. W. Shacklette, R. L. Elsenbaumer, R. R. Chance, J. M. Sowa, D. M. Ivory, G. G. Miller, and R. H. Baughman, *ibid.*, 361 (1982).
10. P. J. Nigrey, D. MacInnes, Jr., D. P. Nairns, and A. G. MacDiarmid, *This Journal*, **128**, 1651 (1981).
11. A. F. Shepard and B. F. Dannels, *J. Polym. Sci., A-1*, **4**, 511 (1966).
12. D. G. Walker and N. E. Wisdom, Jr., U.S. Pat. 3,437,569 (1969); N. E. Wisdom, Jr., U.S. Pat. 3,437,570 (1969).
13. M. Delamar, P.-C. Lacaze, J.-Y. Dumousseau, and J.-E. Dubois, *Electrochim. Acta*, **27**, 61 (1982).
14. G. Brilmyer and R. Jasinski, *This Journal*, **129**, 1950 (1982).
15. I. Rubinstein, *J. Polym. Sci. Polym. Chem. Ed.*, In press.
16. L. W. Shacklette, R. R. Chance, D. M. Ivory, G. G. Miller, and R. H. Baughman, *Synth. Met.*, **1**, 307 (1979).
17. N. E. Tokel-Takvoryan, R. E. Hemingway, and A. J. Bard, *J. Am. Chem. Soc.*, **95**, 6582 (1973).
18. E. Gileadi, E. Kirowa-Eisner, and J. Penciner, "Interfacial Electrochemistry," p. 220, Addison-Wesley, Reading, MA (1975).
19. C. P. Keszthelyi, H. Tachikawa, and A. J. Bard, *J. Am. Chem. Soc.*, **94**, 1522 (1972).
20. E. Gileadi, L. Duic, and J. O'M. Bockris, *Electrochim. Acta*, **13**, 1915 (1968).
21. J. H. Simons, in "Fluorine Chemistry," Vol. 1, J. H. Simons, Editor, p. 261, Academic Press, New York (1950).
22. D. M. Ivory, G. G. Miller, J. M. Sowa, L. W. Shacklette, R. R. Chance, and R. H. Baughman, *J. Chem. Phys.*, **71**, 1506 (1979).
23. P. Kovacic, V. J. Marchionna, F. W. Koch, and J. Oziomek, *J. Org. Chem.*, **31**, 2467 (1966).
24. A. F. Diaz, W-Y. Lee, A. Logan, and D. C. Green, *J. Electroanal. Chem.*, **108**, 377 (1980).

Photomodulated and One-Beam and Two-Beam Potential Modulated Photoelectrochemical Spectroscopies

J. F. McCann

School of Physics, The University of New South Wales, Kensington, N.S.W. 2033 Australia

M. Skyllas-Kazacos

School of Chemical Engineering and Industrial Chemistry, The University of New South Wales, Kensington, N.S.W. 2033 Australia

ABSTRACT

Three techniques for measuring interband transitions in semiconductor electrodes in electrolytes are described. These are photomodulated and one-beam and two-beam potential modulated spectroscopies. The usefulness of the techniques is demonstrated by using each technique to measure the direct band gap transition for a single crystal n-CdSe electrode in a 1M S-1M Na_2S-1M NaOH electrolyte. The difference between a two-beam potential modulated photoelectrochemical spectrum and a corresponding one-beam spectrum is interpreted to be a measure of minority carrier recombination inside and at the surface of the semiconductor electrode. Peaks in the modulated photocurrent spectra at the direct bandedge of CdSe are attributed to field induced absorption effects.

Interband transitions in semiconductor electrodes *in situ* have been measured by electroreflectance (1), photoelectrochemical (2), two-beam (3), and more recently by stress modulated photoelectrochemical spectroscopies (4). Each of these techniques has advantages and disadvantages. For example, electroreflectance spectroscopy requires a fairly complex instrument arrangement (5). In photoelectrochemical spectroscopy, the slopes of the photoresponse-wavelength curves are subject to change due to wavelength dependent surface and depletion layer recombination effects (4). Stress modulated photoelectrochemical spectroscopy requires a piezoelectric disk to be attached to the semiconductor electrode (4). In addition, the ratio of the amplitude of the stress modulated signal to the noise level is often small and is consequently sometimes difficult to detect in practice.

The techniques described in this paper are based on the effect of an electric field on the optical properties of space-charge regions. Franz (6) and Keldysch (7) discussed the effect of a strong electric field on the absorption of light by crystals of insulators and semiconductors. They predicted that the electric field will cause the bandedge for fundamental absorption to shift toward longer wavelengths. This effect was demonstrated by a number of workers who measured the changes in the light transmitted through crystals of various materials, as a function of wavelength, on application of electric fields within the crystal of 10^5 V/cm or larger (8-10).

This electric field induced light absorption was explained in terms of the model shown in Fig. 1. The slope of the bands arises from the external application of a high electric field to the insulator or semiconductor. This has the result that electrons with a given total energy exist in states which lie in the valence band at one point (A) in the space, and in the conduction band at another point (E). A barrier to the free motion of electrons is set up, but this may be traversed by quantum mechanical tunnelling under certain conditions. This can give rise to a finite electron density at points in the forbidden zone such as C. Light absorbed by such an electron will raise it to state D where it may then move through the conduction band as shown.

The need to externally apply a high electric field of over 10^5 V/cm to enable these effects to be observed in semiconductor crystals, was eliminated when it was realized that such field strengths may be obtained in the space charge regions of p-n junctions, metal-semiconductor contacts, metal electrolyte, and semiconductor-electrolyte interfaces (11, 12). In a study of electroabsorption effects in the space-charge region of a germanium p-n junction, Frova and Handler (13) measured changes in the absorption edge for various values of electric field, and showed a peak in the field induced absorption at a wavelength corresponding to the direct bandgap of the semiconductor.

A differential photocurrent response method (14) has also been used to study electroabsorption in GaAs, Ge and Si p-n junctions. This technique employed a small-signal ac voltage in series with the biasing voltage to produce a differential photocurrent, and an oscillatory dependence of the absorption coefficient on the field for photon energies greater than the absorption edge, was observed for the direct transition region of Ge and GaAs.

In this paper, three techniques are described, which make use of electro-absorption effects to measure strong interband transitions in semiconductors *in situ*.

In the one-beam and two-beam potential modulated photoelectrochemical spectroscopies (OBPMP and TBPMP, respectively), a small a-c potential is superimposed on the d-c potential applied to the semiconductor. The d-c voltage determines the maximum value of the electric field in the space charge region, while the a-c voltage, by altering the field, modulates the light absorbed at the interface. This results in a modulated component of the photocurrent which can be electronically separated and amplified by means of a lock-in amplifier.

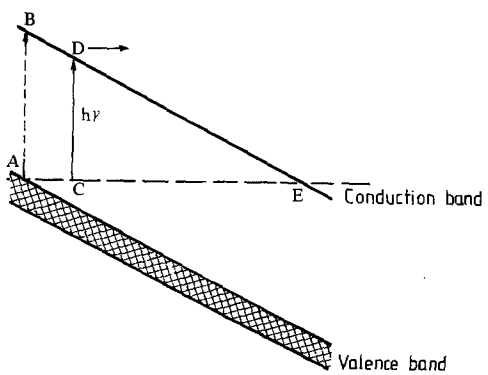

Fig. 1. Energy levels of an insulator or a semiconductor in an electric field.

In photomodulated photoelectrochemical (PhMP) spectroscopy, a constant potential is applied to the semiconductor which is simultaneously illuminated with chopped laser light and unchopped monochromatic light. The intense laser light excites electrons from sub bandgap states into the conduction band in a manner similar to that proposed in a previous study (15). A modulated photocurrent can thus be obtained as a function of wavelength of the unchopped monochromatic light.

As will be shown, the above techniques do not require complex instrument assemblies, nor special attachments to the semiconductor electrode. Furthermore, the potential modulated techniques yield large signal to noise ratios in comparison to stress modulated photoelectrochemical spectra.

Experimental

An ohmic contact was made to a single crystal of n-CdSe (Cleveland Crystals) by soldering In onto the back of the sample. A tin coated copper wire was soldered onto the In contact and an electrode was fabricated by mounting the sample in an epoxy resin (Epirez Australia). A CoS counter electrode was used and 1M Na_2S-1M S-1M NaOH was the electrolyte. The n-CdSe single crystal was etched in conc. aqua regia for 20 sec, dipped in 1M KCN, and rinsed in distilled water before use. A schematic of the experimental arrangement used for measuring PhMP spectra is shown in Fig. 2.

Experimental arrangements for measuring OBPMP and TBPMP spectra are shown in Fig. 3. In each case, the semiconductor electrode potential was maintained at a constant value (positive of the flatband potential for n-type semiconductors and vice versa for p-type semiconductors) with a potentiostat (PAR model 173 fitted with a PAR model 176 current to voltage converter).

To measure photomodulated photoelectrochemical spectra, the semiconductor was illuminated with laser light chopped at 33 Hz (He-Ne laser 2mW; Laser Electronics Pty. Limited, Gold Coast, Queensland, Australia) and simultaneously illuminated with unchopped monochromatic light emerging from a scanning monochromator (Spex Minimate; Spex Industries, Incorporated, New Jersey). The source of the polychromatic light entering the monochromator was a 300W quartz-halogen lamp (Phillips). The modulated laser light results in a modulated photocurrent which is detected with a lock-in amplifier and is offset to zero with a zero offset.

OBPMP and TBPMP spectra were measured by superimposing a 10 mV a-c potential of frequency

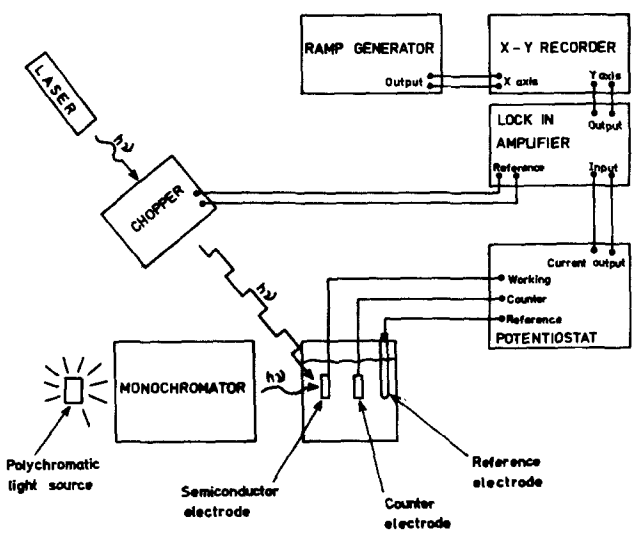

Fig. 2. Schematic diagram of the experimental arrangement for photomodulated photoelectrochemical spectroscopy.

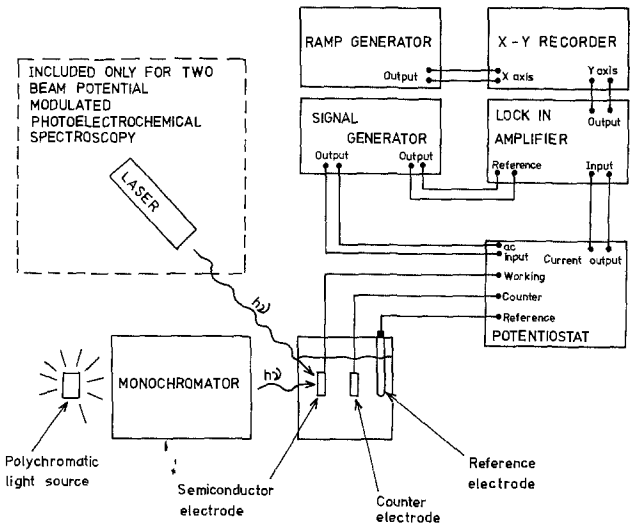

Fig. 3. Schematic diagram of the experimental arrangements for one-beam and two-beam potential modulated photoelectrochemical spectroscopies.

392 Hz on the d-c potential applied to a single crystal CdSe electrode. In OBPMP spectroscopy, the semiconductor electrode (in this case n-CdSe) is illuminated with unchopped monochromatic light as a function of wavelength from a scanning monochromator. A modulated photocurrent within certain wavelength limits can be measured at the same frequency as the frequency of the a-c signal. The photomodulated signal which is superimposed on the dark a-c signal is readily measured by using the zero offset on the lock-in amplifier to offset the dark a-c signal.

The experimental arrangement in TBPMP spectroscopy is identical to that of OBPMP spectroscopy except that a source of intense illumination, a He-Ne laser is used to simultaneously illuminate the semiconductor electrode as well as the scanning monochromatic light. The intense illumination causes an additional photocurrent signal to be superimposed on the dark a-c signal. Both these signals are offset with the lock-in amplifier and the modulated signal due to the scanning monochromatic light is recorded only. One and two-beam photoelectrochemical spectra of an n-CdSe single crystal in 1M S-1M Na_2S-1M NaOH were also recorded in the usual manner (3) for comparison. In one-beam photoelectrochemical spectroscopy the potential of the n-CdSe single crystal was maintained constant with a potentiostat while the semiconductor was illuminated with chopped monochromatic light and the resultant modulated photocurrent detected with a lock-in amplifier and recorded as a function of wavelength. In two-beam photoelectrochemical spectroscopy light from an unchopped helium-neon laser was simultaneously used to illuminate the n-CdSe surface and the modulated photocurrent resulting from the chopped monochromatic light was detected and recorded in an identical manner to the one-beam photoelectrochemical spectroscopic technique.

Results and Discussion

For the purpose of comparison, typical one and two-beam photoelectrochemical spectra as described by Heller, Chang, and Miller (3) for an etched n-CdSe single crystal at −0.7V (vs. SCE) are shown in Fig. 4. As can be seen, the amplitude of the photocurrent-wavelength response of the two-beam spectrum is slightly less than the one-beam spectrum. This drop off is attributed to the presence of imperfections, even in the etched single crystal, which act as recombination centres (3). When the laser is on, more electrons are excited into the conduction band and a proportion of these can recombine with the holes produced by the

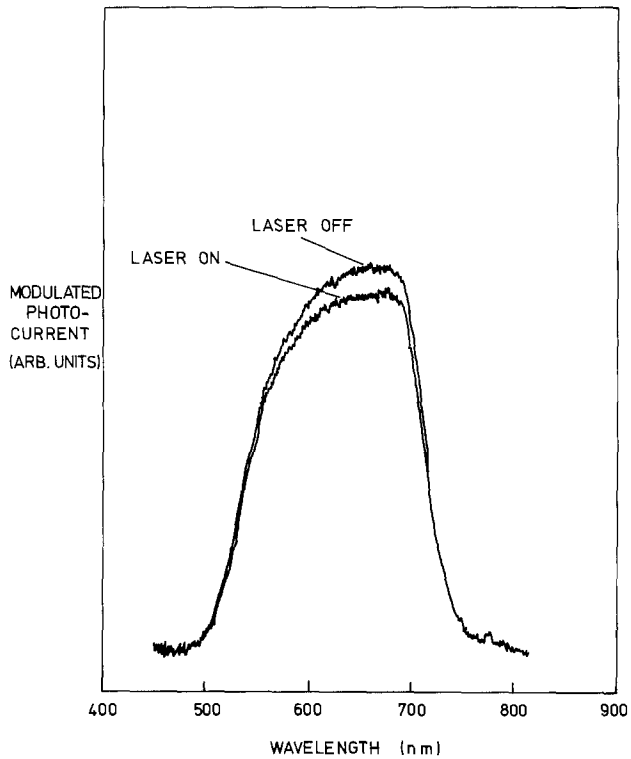

Fig. 4. One and two-beam photoelectrochemical spectra for a single crystal n-CdSe electrode at −0.7V (*vs.* SCE) in 1M S/1M Na_2S/1M NaOH.

chopped monochromatic light resulting in a lowering of the modulated photocurrent.

A PhMP spectrum is shown in Fig. 5 for an etched n-CdSe single crystal at −1.07V (*vs.* SCE). The spectrum is fairly ill defined due to the unfavourable signal to noise ratio but the photocurrent response commences at about 475 nm and finishes at approximately 850 nm with a band gap transition peak centered around 720 nm. Such a peak is not present in the conventional photocurrent spectra shown in Fig. 4 indicating that it is not due to filtering of the higher energy light by the polysulphide solution. As mentioned earlier, the modulated photocurrent results from the excitation of electrons by the chopped laser light, from subband-gap states into the conduction band.

OBPMP and TBPMP spectra for an etched single crystal n-CdSe electrode are presented in Fig. 6 for an n-CdSe potential of −0.7V and in Fig. 7 for an n-CdSe potential of −1.4V (*vs.* SCE). The shapes of the OBPM

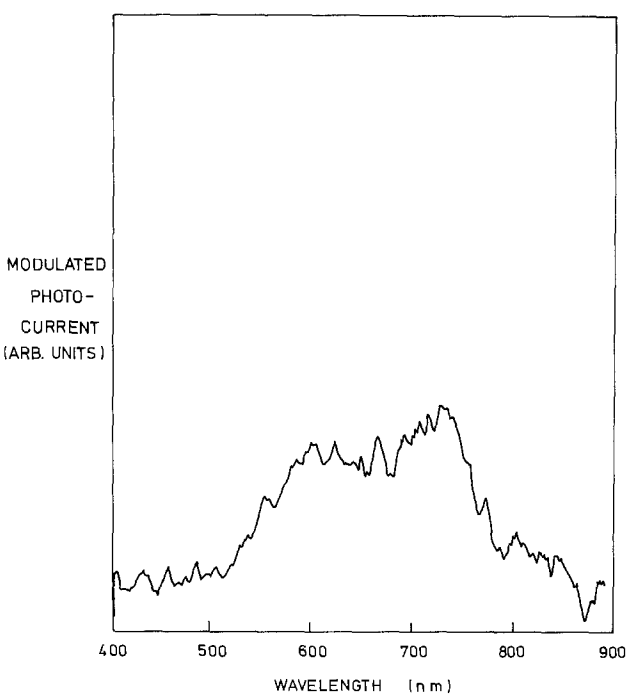

Fig. 5. Photomodulated photoelectrochemical spectrum for an etched single crystal n-CdSe electrode at −1.07V (*vs.* SCE) in 1M S/1M Na_2/1M NaOH.

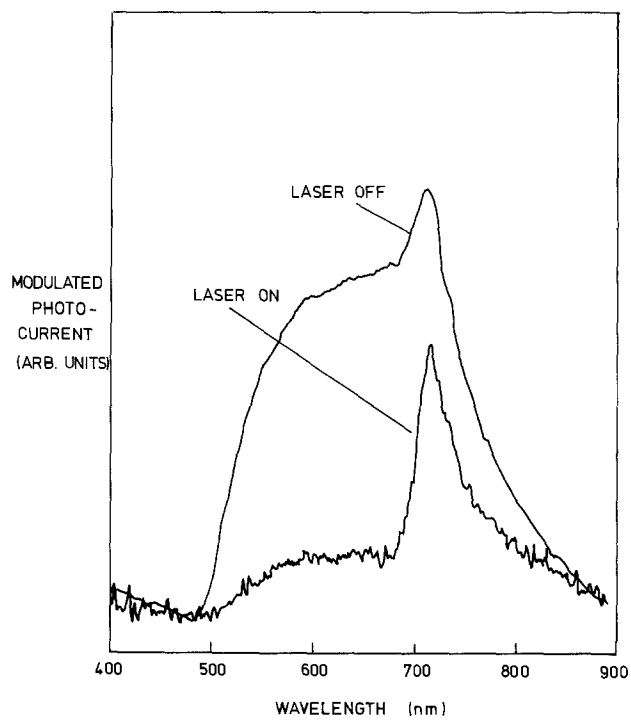

Fig. 6. One-beam and two-beam potential modulated spectra for an etched single crystal n-CdSe electrode at −0.7V (*vs.* SCE) in 1M S/1M Na_2S/1M NaOH.

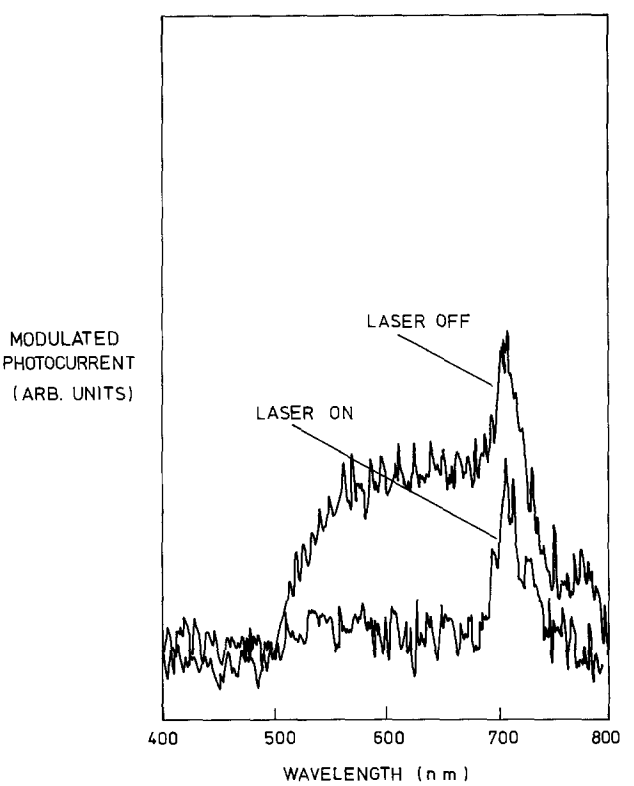

Fig. 7. One-beam and two-beam potential modulated spectra for an etched single crystal n-CdSe electrode at −1.4V (*vs.* SCE) in 1M S/1M Na_2S/1M NaOH. Intensity of laser illumination same as for Fig. 6.

spectra at −0.7 and −1.4V are similar to each other although the magnitude of the response at −1.4V is much smaller than that at −0.7V. The shapes of the OBPM spectra are also similar to that of the PhPM spectrum but are more clearly defined in the former cases due to the more favorable signal-to-noise ratios. At −0.7V, the TBPMP spectrum is different from the OBPMP spectrum at this potential in one main respect. While the shape of the TBPMP spectrum is similar to the corresponding OBPMP spectrum the amplitude has decreased significantly. At more negative potentials the photoresponse in the OBPMP spectrum other than the band gap transition peak at 720 nm decreased to a negligible value in the TBPMP spectrum as shown in Fig. 7 for n-CdSe at −1.4V (*vs.* SCE). The decrease in the amplitude of the response of an OBPMP spectrum when a laser is used to simultaneously illuminate an electrode is presumably due to the same reason a decrease is observed in a photoelectrochemical spectrum when subjected to intense illumination (3). That is, it is a result of an increase in the recombination rate due to the larger number of electrons excited into the conduction band by the illumination. Thus, in each of the spectra shown in Fig. 6 and 7, a peak is observed at an energy corresponding to the bandgap of the semiconductor. This can be attributed to the changes in the field-induced absorption which have been reported to occur around the band edge of insulator and semiconductor materials (6-14).

Another significant feature of the PhMP, OBPMP, and TBPMP is the presence of a large photocurrent response in the sub-band gap regions. Unlike the results of conventional photocurrent spectra, this sub-band gap response is observed even for the etched single crystal n-CdSe electrode. As described at the beginning of this paper, this sub-band gap photocurrent response in OBPMP and TBPMP results from the field induced absorption which causes the band edge to shift towards longer wavelengths. The increase in this field-induced absorption with increasing field strength is also exemplified here in the differences between the spectra obtained at −0.7 (Fig. 6) and −1.4V (Fig. 7). The electric field strength in the space charge region is much greater at −0.7 than at −1.4V *vs.* SCE. As expected, therefore, the field induced sub-band gap response is considerably greater in Fig. 6 where the electric field strength is the higher.

One final point is that the effect of the laser is much greater on the one-beam potential modulated spectra than it is on the photoelectrochemical spectra for the etched n-CdSe. This suggests that the combination of OBPMP and TBPMP spectroscopies can be used as a suitable and a sensitive alternative for monitoring defects in semiconductor electrodes, to the combination of one and two-beam photoelectrochemical spectroscopies introduced by Heller, Chang, and Miller (3).

Conclusions

It has been demonstrated that the band gap transition for a single crystal n-CdSe electrode can be measured *in situ* using photomodulated, OBPMP and TBPMP spectroscopies. In addition, it has been shown that OBPMP and TBPMP spectroscopies can be compared with each other to give a measure of recombination in a semiconductor *in situ*.

Acknowledgments

This work was supported by the National Energy Research Development and Demonstration Council.

Manuscript submitted Jan. 14, 1982; revised manuscript received March 8, 1983.

Any discussion of this paper will appear in a Discussion Section to be published in the June 1984 JOURNAL. All discussions for the June 1984 Discussion Section should be submitted by Feb. 1, 1984.

REFERENCES

1. M. Cardona, K. L. Shaklee, and F. H. Pollak, *Phys. Rev.*, **154**, 154 (1967).
2. F. P. Koffyberg, K. Dwight, and A. Wold, *Sol. Stat. Comm.*, **30**, 433 (1979).
3. A. Heller, K. C. Chang, and B. Miller, *This Journal*, **124**, 697 (1977).
4. L. J. Handley, J. F. McCann, and D. Haneman, *J. Appl. Phys.*, In press.
5. S. A. Mack and P. Handler, *Phys. Rev. B.*, **9**, 3415 (1974).
6. W. Franz, *Z. Naturforsch*, **13a**, 484 (1958).
7. L. W. Keldysch, *J. Exptl. Theoret. Phys., (USSR)*, **34**, 1138 (1958); translation: *Soviet Phys. JETP*, **7**, 788 (1958).
8. K. W. Boer, H. J. Hansch, and U. Kummel, *Z. Physik*, **155**, 170 (1959).
9. K. W. Boer, *ibid.*, **155**, 184 (1959).
10. R. Williams, *Phys. Rev.*, **126**, 442 (1962).
11. R. Williams, *ibid.*, **117**, 1487 (1960).
12. P. Handler, *ibid.*, **137**, A1862 (1965).
13. A. Frova and P. Handler, *ibid.*, **137**, A1857 (1965).
14. K. G. Ashar and R. L. Anderson, *ibid.*, **154**, 721 (1967).
15. M. Skyllas-Kazacos, J. F. McCann, and D. Haneman, *J. Electroanal. Chem.*, **143**, 205 (1983).

The Potential of Zero Charge of Oriented Single-Crystal RuO_2 in Aqueous Electrolytes

M. Tomkiewicz,* Y. S. Huang,[1] and F. H. Pollak

Department of Physics, Brooklyn College of the City University of New York, Brooklyn, New York 11210

ABSTRACT

The impedance of 5 virgin faces of single crystal RuO_2 was measured over the frequency range of 1-10^6Hz, in three electrolytes—10^{-3}M and 1M Na_2SO_4 and 10^{-3}M KF. The fastest relaxing capacitive element was identified, and its values measured as a function of the electrode potential. A major contribution to this capacitance is due to the double layer capacitance. The potential of zero charge in 10^{-3}M Na_2SO_4 was measured for the five crystalline faces. The variations of the potential of zero charge with the crystalline faces are small. "Average" value is (-0.09 ± 0.1) V *vs.* SCE. The potential of zero charge correlates well with the reported work functions of RuO_2 and Ru metal.

Ruthenium dioxide (RuO_2) belongs to the family of transition metal dioxide compounds with rutile type structure which possess an interesting variety of electric and magnetic properties; distinctive among them is the high intrinsic metalic conductivity of the material. RuO_2 is well known as a corrosion resistant, dimensionally stable, low overpotential electrode for chlorine and oxygen evolutions (1-7). It has been recently reported that RuO_2 is also an effective catalyst for oxygen evolution in water photolysis on powders or solid photoelectrodes (8). A considerable amount of work was done on the electrochemistry of thin films of RuO_2 (9). Recently, we have succeeded in growing single crystals of RuO_2 large enough so that the fundamental electrochemical properties can be investigated as a function of crystal face.

The technique of relaxation spectrum analysis in which the impedance of a junction is monitored over a wide frequency range and the results are portrayed in terms of a set of parallel frequency independent R-C elements was used in the past to describe the potential distribution at the semiconductor electrolyte interface (10). In this paper, we make the first attempt at extending the applicability of the concepts that were introduced there, to analyze the potential distribution at the metal aqueous solution interface.

RuO_2 is of particular interest for this purpose because its crystal structure is similar to that of TiO_2 (rutile) which was the system most thoroughly analyzed by relaxation spectrum analysis (11). The cyclic voltammetry of single crystal RuO_2 has been reported earlier (12). The voltammogram was interpreted in terms of field induced structure changes at the surface which are superimposed on the charging curve of the "double layer." It is clear from these results that RuO_2 does not behave in any potential region as an ideally polarizable electrode. The technique of relaxation spectrum analysis is advantageous in such a system because it can differentiate between processes with various relaxation times. The pseudocapacitance effects which are associated with oxidation-reduction of the surface are usually considerably slower than the charging and discharging of the "double layer." In this paper, we report on the behavior of the fastest relaxing charge accumulation modes. The identification of slower modes will be discussed in future publications.

Experimental

RuO_2 single crystals of typical dimensions $10 \times 5 \times 5$ mm^3 where grown (13) by the method of chemical transport in the flowing oxygen system. The gaseous oxide RuO_3 is formed by the following mechanisms

$$RuO_2 \text{ (solid)} + \tfrac{1}{2} O_2 \rightarrow RuO_3 \qquad [1]$$

$$Ru \text{ (solid)} + 3/2\, O_2 \rightarrow RuO_3 \qquad [2]$$

when oxygen at atmospheric pressure is passed over a mixture of polycrystalline RuO_2 and purified Ru metal powder at a temperature of about 1350°C with a flow rate of approximately 60 ml/min. The volatile RuO_3 gas decomposes and crystallizes into highly ordered single crystals of RuO_2 in a cooler region where the temperature is approximately 1100°C.

The crystal orientation were determined by the Laue backscattering x-ray diffraction method. The measurements were made on RuO_2 (100), (101), (001), (110), and (111) "as-grown" crystal surfaces.

The electrodes were prepared in the following way: The crystals were mounted on a copper plate and glued with conducting silver paint. One end of the copper plate was soldered to a copper wire which passed through a pyrex tube. The wires and plate were insulated with microstop, leaving only the desired face exposed to the electrolyte. The geometric surface areas in the five different orientations (100), (101), (001), (110), and (111) were 3.6, 8, 3.8, 6.4, and 3.5 mm^2, respectively. The counter electrode was a Pt plate with surface area of 4 cm^2 exposed on both sides. A saturated calomel electrode was used as reference. Measurements were made in a standard, Teflon made, single compartment electrochemical cell, under nitrogen atmosphere.

An IBM Model EC/225 voltammetric analyzer was used for cyclic voltammetry. For the impedance measurements, a HP network analyzer was used, following a procedure that was previously described (10). Before each experiment the electrode was scanned repetitively between −0.4-1.0V *vs.* SCE at a rate of 50 mV/sec till a reproducible cyclic voltammogram emerged (typically 20 scans). Each complete set of impedance measurements took about 3 hr. After completion of each experiment, the voltammogram was again traced and proved to be identical to the one that we have started with. All chemicals were analytical grade and were used without further purification.

Results

Figure 1 shows the impedance spectrum of the (111) face of single crystal RuO_2 in contact with a 1M Na_2SO_4 solution. Under the conditions in which relaxation spectrum analysis can be performed, there exists a frequency region in which the equivalent circuit can be reduced to a single R-C element (10). In this frequency range, the impedance is given by

$$Z_{HF} = R - \frac{J}{\omega C_f}$$

In this regime, the real part of the impedance, R, is frequency independent and equal to R_s the series resistance, while the imaginary part is given by

* Electrochemical Society Active Member.
[1] Present address: Department of Electronic Engineering and Technology, National Taiwan Institute of Technology, Taipei, Taiwan.

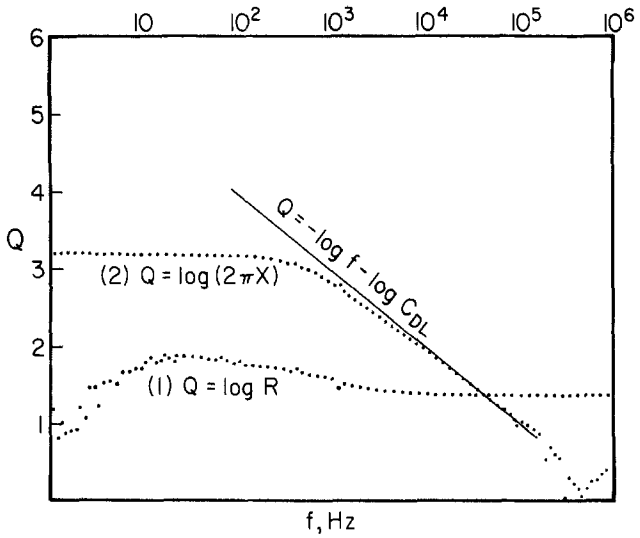

Fig. 1. Impedance response curves for the RuO_2 (111) virgin surface in 1M Na_2SO_4 at $U = +0.2V$ vs. SCE. Area: 0.035 cm^2.

$$X = 1/\omega C_f$$

where $\omega = 2\pi f$ is the angular frequency, f the frequency, and C_f the capacitance which is associated with the fastest relaxing R-C element. In the case of metal-solution interface, this is associated with the charging of the double layer.

Under these conditions

$$\log (2\pi X) = -\log f - \log C_f$$

and log $(2\pi X)$ should be linear with log f with a slope of -1 and an intercept from which C_f can be extracted. From Fig. 1, the frequency range of 20,000-200,000 Hz satisfy these criteria. The exact frequency regime in which these criteria are met varies with the conditions in which the experiment was carried out. For each experiment, the entire frequency dispersion of the impedance was measured, the frequency regime in which only the fastest relaxing R-C element was identified and the resistance and capacitance values in this regime measured. The resistive element, R_s, measures the series resistance of the system. In all cases referred to in this paper, the series resistance is controlled by the resistivity of the electrolyte, and is potential independent. The parameter which is of prime interest in this work is the capacitive element associated with the fastest relaxing R-C element.

Figure 2 shows the C_f as a function of electrode potential for the five crystal faces of RuO_2 in 10^{-3}M Na_2SO_4. On the negative bias side, the $C(U)$ curves of all faces show a well defined minima at potentials summarized in Table I. The capacitance increases on both sides of the minima with considerable amount of structure emerging at the more positive potentials.

Figure 3 shows the cyclic voltammograms of the various crystal faces, taken under the same conditions

Table I. Position of the minima in $C(U)$ and PZC vs. SCE of the various crystalline faces of RuO_2

Face	(100)	(101)	(001)	(110)	(111)
Minimum V vs. SCE	−0.07	−0.18	−0.04	−0.11	−0.13
PZC V vs. SCE	−0.05	−0.16	−0.02	−0.09	−0.11
Average composition[a]	1 Ru	2 Ru	1 Ru 2 O	2 Ru 2 O	½ Ru
Atomic density (atoms/cm²)	7.1×10^{14}	8.2×10^{14}	5.0×10^{14}	10×10^{14}	3.5×10^{14}

[a] Per projection of the unit cell onto the given crystal face.

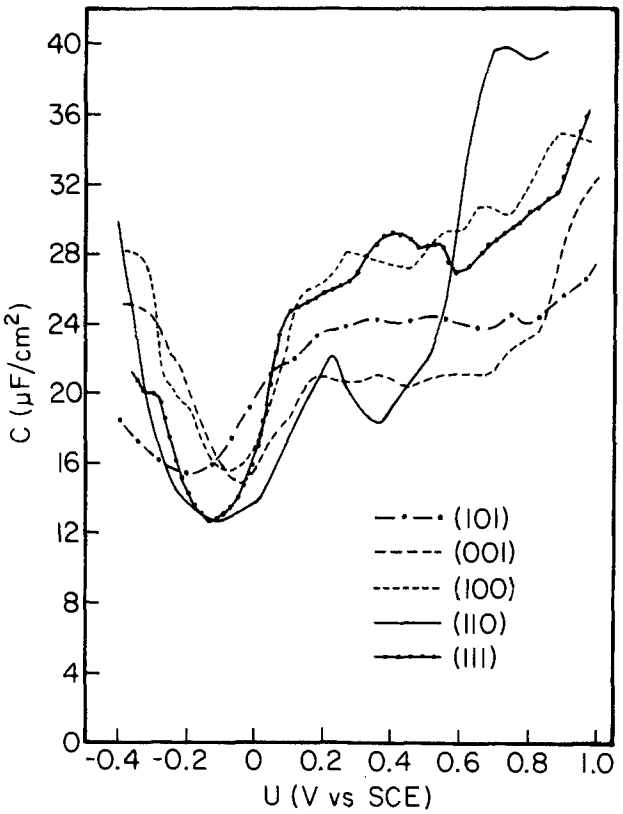

Fig. 2. C(U) curves for the five RuO_2 crystalline faces in 10^{-3}M Na_2SO_4.

as the $C(U)$ data. There is considerable amount of structure on these voltammograms which is superimposed on the charging of the double layer. Similar voltammograms were measured in acidic electrolyte and analyzed in terms of charge transfer to and from intermediate of the oxygen and hydrogen evolution reactions, or to use a different terminology, with oxidation and reduction at the surface of RuO_2.

Figure 4 shows the $C(U)$ curves of the (111) face of RuO_2 in two different electrolyte concentrations. The distinctive minimum in the $C(U)$ curve disappears in the high electrolyte concentration. A broad potential range can be identified in which the capacitance is approximately potential independent with values of 17 ± 1 $\mu F/cm^2$. At more positive potentials, the capacitance increases also in 1M Na_2SO_4, but throughout the potential regions, except in the area of the minimum, the capacitance in the concentrated electrolyte is lower than the capacitance in the more dilute electrolyte. In an effort to distinguish between effects of solvent and

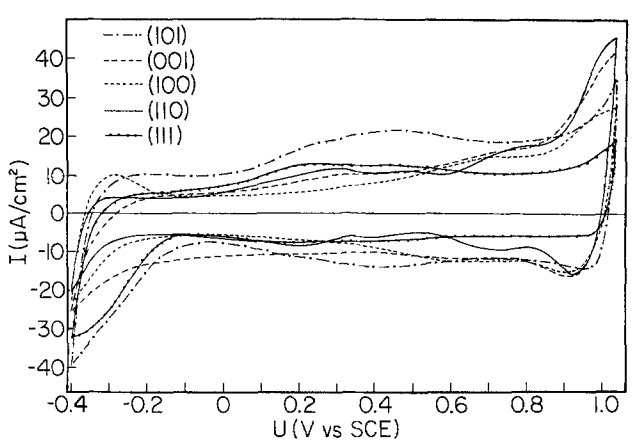

Fig. 3. Cyclic voltammetry curves for the five RuO_2 crystalline faces in 10^{-3}M Na_2SO_4 scan speed: 50 mV/sec.

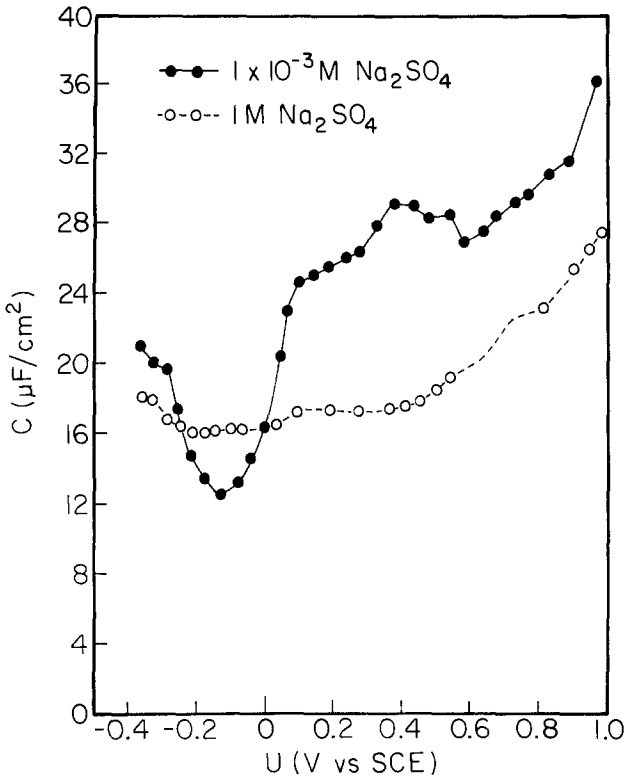

Fig. 4. C(U) curves for RuO_2 (111) virgin surface in 10^{-3} and 1M Na_2SO_4.

solute on the C(U) curves, we have taken measurements, also in 10^{-3}M KF.

Figure 5 shows the C(U) curve of the (110) face in 10^{-3}M KF. The capacitance remain approximately constant till $U \approx 0.3$V *vs.* SCE, with only very shallow minimum visible at -0.2V *vs.* SCE. The capacitance value in the region, which is independent of potential, is approximately the same as the one found for the (111) face in 1M Na_2SO_4. At potentials more positive than 0.3V *vs.* SCE, a sharp increase in capacitance is observed. Comparison of the C(U) of the (110) face in 10^{-3}M KF and in 10^{-3}M Na_2SO_4 reveals that there are qualitative similarities at the most positive potential region.

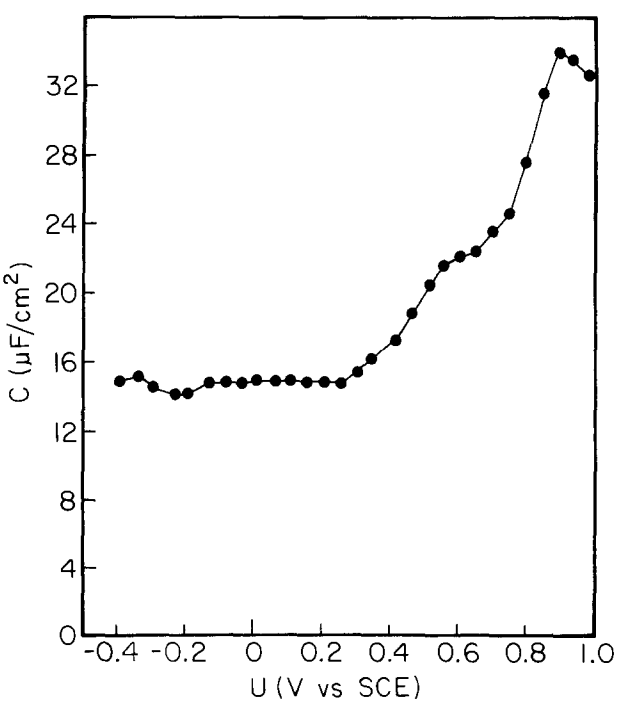

Fig. 5. C(U) curve for RuO_2 (110) virgin surface in 10^{-3}M KF

Figure 6 shows the cyclic voltammogram of the (110) face in 10^{-3}M KF. In agreement with the C(U) data, it is structureless till about 0.5V *vs.* SCE where it reflects only the charging of the double layer, while at more positive potentials, strong pseudocapacitance peaks due to the intermediates of the oxygen evolution reaction are evident.

Discussion

The first and most important question that we must address is whether the distinct minima in the C(U) curves in all five faces in the dilute electrolyte are associated with the diffuse double layer. It is obvious from the correlation between the cyclic voltammograms and the C(U) curves that even at these high frequencies, in which the equivalent circuit of the interface can be represented in terms of a single R-C elements, there are surface reactions which are fast enough to contribute to pseudocapacitance on both the cathodic and the anodic side of the C(U) curves. The minima can result from compensation between the pseudocapacitive branches (14). The strongest evidence in favor of associating the capacitive minima with the diffuse double layer comes from Fig. 4. As expected from the diffuse double layer theory, as we increase the concentration from 10^{-3}M to 1M Na_2SO_4, the capacitance due to the diffuse double layer increases and the capacitance will be dominated by the compact inner layer, which is expected to be potential independent as long as anions will not penetrate through this layer. The numerical value of the capacitance due to the compact inner layer agrees well with the one that was found for the inner layer on the surface of mercury electrode and is believed to be due to dielectrically saturated solvent layer (15, 16). This agreement requires assignment of roughness factor equal to 1 to the surface of RuO_2 which is reasonable with native crystal faces of a good single crystal. For a 1:2 valance type electrolyte, the diffuse layer capacitance is expected to obey the following equation (17)

$$Cd = -3.46 \times 10^{13} \left(\frac{\epsilon\epsilon_0 e^2}{kT}\right)^{1/2} \sqrt{C} \frac{[\exp(-y) - \exp(2y)]}{[\exp(y) - 1][1 + 2\exp(-y)]} \quad [3]$$

where ϵ is the dielectric constant, ϵ_0 the permittivity of free space, k the Boltzmann constant, e, the electronic charge, and T, the absolute temperature, C the

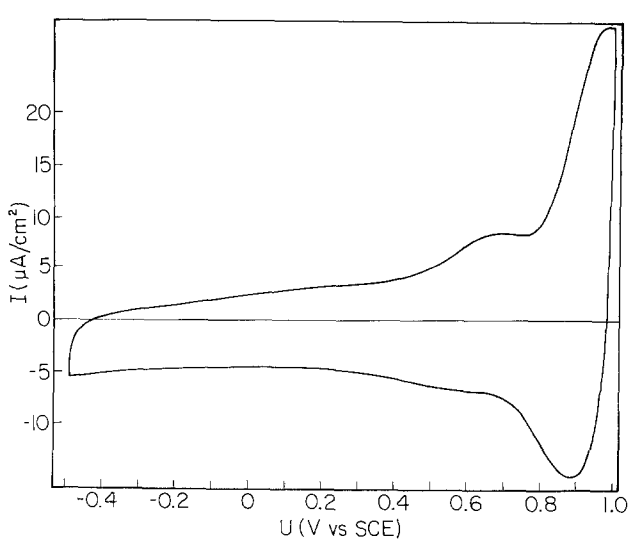

Fig. 6. Cyclic voltammetry curve for RuO_2 (110) virgin surface in 10^{-3} KF scan speed: 50 mV/sec.

molar concentration, and

$$y = e\psi/kT \quad [4]$$

where ψ is the potential, relative to the solution of the outer Helmholtz layer which relates to the electrode potential through

$$\psi = U - U_{\sigma=0} \quad [5]$$

where $U_{\sigma=0}$ is the potential of zero charge (PZC). All the parameters in Eq. [3] are expressed in SI units except the concentration of the electrolyte which is expressed in mols/liter. The resulting capacitance is expressed in F/m^2. All the data in the paper will be expressed in $\mu F/cm^2$. It can be easily seen by differentiation of Eq. [3] that the minimum in the $C(U)$ curve is not at the potential of zero charge but is shifted by 16 mV negative to this potential. Using Eq. [3], the capacitance at the minimum can be calculated and for $10^{-3}M$ of Na_2SO_4, it should be 11.2 $\mu F/cm^2$. Taking the inner layer capacitance to be 17 $\mu F/cm^2$, the total expected capacitance at the minimum should be 6.75 $\mu F/cm^2$. The total observed capacitance at the minimum varies from face to face, but in all cases it is higher than the expected value. This might well be due to distortion of the real minima by the anodic and cathodic pseudocapacitive branches. We can estimate the uncertainty in positioning the minima by solving Eq. [3], to give us the potential range which will result in the observed total capacitance. For 12 $\mu F/cm^2$ at the minimum, a shift of 0.106V in the negative direction or 0.044V in the positive direction is required. We estimate that the accuracy of the determination of the potential of zero charge on RuO_2 is within this range of potentials.

The results in $10^{-3}M$ KF that are shown in Fig. 5 and 6 are not fully consistent with our interpretation of the data with Na_2SO_4. KF was chosen, following the published work on metal electrode (15, 16) to distinguish between effects of anions like $SO_4^=$ that do adsorb on the surface of the electrode and F^- which due to relatively large negative hydration energy, do not adsorb. It was expected that in the region of the potential of zero charge, the behavior in $10^{-3}M$ KF will be similar to that of $10^{-3}M$ Na_2SO_4 and that at more positive potentials the data with F^- will enable us to differentiate between contributions due to pseudocapacitance of the intermediates of the oxygen evolution reaction and adsorption due to $SO_4^=$. The data as shown in Fig. 5 and 6 do not follow these predictions. The minimum in the $C(U)$ curve, although it appears in the same potential range as in Na_2SO_4, is hardly visible in $10^{-3}M$ KF. The general features of the $C(U)$ curve in KF more nearly resemble the behavior in the concentrated solution of Na_2SO_4, as shown in Fig. 4, than in the dilute one. The cyclic voltammetry in KF, as shown in Fig. 6, is also different from the one observed in Na_2SO_4 or for that matter, the one previously observed in H_2SO_4 and NaOH (12). The cathodic region seem to be completely devoid of surface reactions and dominated by the charging of the double layer. While the anodic region is dominated by the underpotential charging and discharging of intermediates of the oxygen evolution reaction. Although additional data are needed to understand this system, the explanation might reside in the observations on powders of transition metal oxides that F^- is chemisorbed on the surface of these oxides and that the strength of adsorption within the halogen series is reversed on this class of materials, compared to the situation on the surface of mercury electrode (18).

At positive potentals, the $C(U)$ curves in dilute Na_2SO_4 show an increase with considerable amount of structure while the $C(U)$ curves in 1M Na_2SO_4 and $10^{-3}M$ KF show a potential independent capacitive value up to $U = +0.3V$ *vs.* SCE with an increase in the capacitance values at more positive potentials.

It is also worth noticing that throughout the entire range, except for the potential range in which the minima in the $C(U)$ curves appear, the capacitance values at the more concentrated electrolyte are lower than those obtained in the more dilute electrolyte. This behavior is distinctly different from the expected shift in the maxima in the $C(U)$ curve that was interpreted in terms of specific adsorption (19, 20). It suggests that the major contributions to the $C(U)$ curves at more positive potentials result from pseudocapacitance due to formation of intermediates in the oxidation of the solvent. This explanation is consistent with cyclic voltammograms, but the reduction in the activity of the solvent at high electrolyte concentrations is insufficient to account for a factor of two reduction in capacitance. Considerable amount of additional information is needed before the $C(U)$ curves in this region can be completely deciphered. Returning now to Table I, we will attempt, in spite of the uncertainties mentioned, to correlate the PZC with the crystalline structure of the interface. The most striking result that emerges out of Table I, is the insensitivity of the PZC to the crystalline face. We have included in Table I also the average composition for the projection of the unit cell onto that crystal face and the atomic densities at each "ideal" face. Both parameters vary considerably from one face to the next, while the variations in the PZC are almost the same as the uncertainty imposed by the concomitant presence of the pseudocapacitance. This result is in sharp contrast to the reported variations of the PZC with the crystallographic face in elemental metals such as Ag, Au, and Cu (21). This relative insensitivity to crystalline face allows us to calculate an "average" PZC as $PZC_{avg} = 1/N \sum_N PZC = -0.09 \pm 0.1V$ *vs.* SCE when the summation is over all the measured crystal faces, and the error margin covers the individual values and the uncertainty due to the pseudocapacitance. It was shown that the PZC varies linearly with the electron work function of a metal — ϕ according to the following relation (22)

$$U_{\sigma=0}\ (\text{NHE}) = \phi - 4.72 \quad [5]$$

while for transition metals similar relation, but with somewhat different intercept, was proposed (23)

$$U_{\sigma=0}\ (\text{NHE}) = \phi - 5.01 \quad [6]$$

The two formulas are only marginally outside our error margin and will be treated here as equivalent. Our "average" PZC will translate to $U_{\sigma=0}$ (NHE) = 0.15V *vs.* NHE. From Eq. [5], ϕ for RuO_2 should be 4.87 eV. In a preliminary report (24), the work function of single crystal RuO_2 grown by the Brooklyn College group, was measured by photoemission, to be $\phi = 4.8$ eV. But as yet to be explained, coincidentally, the work function of Ru metal in polycrystalline foil was reported as 4.73 eV (25) and in films on tungsten as 4.86 eV (25). If we interpret all these results literally, we will be forced to conclude that not only the work function of RuO_2, through its linear dependence with the PZC, is independent of the crystalline face, but there is also no difference between the work functions of Ru metal and RuO_2. This might be in conflict with Riviera's result (25) that reported that during measurements of average work function of polycrystalline ruthenium foil, he found a progressive lowering of ϕ during electron bombardment as long as there was an evolution of gas, but no further change, once gas evolution ceased. The conflict arises if we interpret the untreated sample as coated with oxide. Comparison of the scarce literature data which are available for the work function of metals and their oxides (25) also reveal that there should be a difference in their work functions. It should be pointed out that all these oxides are insulators or semiconductors and none of them is metallic like RuO_2.

A possible alternative explanation, that will account for all the available data is that the work function and the PZC were not measured on intrinsic surfaces of the respected materials; that in spite of the precautions taken, the work functions of Ru metals were measured on slightly oxidized surfaces while the measurements on RuO_2, on slightly reduced surfaces. In our case, since PZC is in the potential range of the hydrogen evolution reaction, this is a distinct possibility.

An alternative source for comparing the PZC data is to measurements of the point of Zero Zeta Potential (PZZP). Colloidal chemists refer to this as point zero charge (PZC) not to be confused here with the potential of zero charge which is also abbreviated as PZC (26). The PZZP is the *p*H at which the concentration of adsorbed OH^- and H^+ ions is equal. Ardizzone *et al.* (27) have measured the PZZP of suspensions of RuO_2 prepared by thermal decomposition of $RuCl_3 \cdot nH_2O$ in two different temperatures, 400° and 700°C. They have reported that the PZZP of the sample prepared at 400°C is 5.1 ± 0.05 while the one prepared at 700°C is 6.1 ± 0.05. They have argued that these differences might be due to possible different stoichiometries in the two samples. Trasatti *et al.* (9) have reported that the rest potential of RuO_2 changes with *p*H according to

$$U(\text{SCE}) = 0.71 - 0.059\,p\text{H} \qquad [7]$$

and substituting the PZZC values in this equation, Ardizzone *et al.* (27), obtained $U_{\sigma=0} = +0.41$V *vs.* SCE for the sample treated at 400°C and +0.35V *vs.* SCE for sample treated at 700°C. While these results lie at more positive potentials than the PZC reported in this work, these differences should be viewed in terms of the different parameters that were measured and large differences in the properties of the samples. For example, Ref. (27) states that "the presence of Cl^- ions in the first formed suspension of RuO_2 can be minimized but not eliminated." Also, it has been noted that Cl^- is generally found in material made by the thermal decomposition of $RuCl_3 \cdot nH_2O$ (9). While PZZC measurements are extremely sensitive to traces of adsorption by foreign ions, they are not effected by charge transfer across the interface. These results should not be viewed as in conflict, but rather should point out to the complexity of the interface of this important system and to additional work that is required before a consistent understanding of this interface will emerge.

Conclusions

The potential of zero charge of single crystal RuO_2 was measured in aqueous electrolytes at five different crystalline faces. It was found that within the accuracy of the measurements, estimated here to be ±0.1V, the PZC is independent of the crystalline face. The average PZC in 10^{-3}M Na_2SO_4 was found to be −0.09V *vs.* SCE.

Based on the linear relation between PZC and the work function, the work function of RuO_2 was found to be 4.9 eV which corresponds to direct measurements of the work function of RuO_2 by photoemission. The same work function was also reported for polycrystalline Ru metal. These results were also compared to PZZP measurements on powders of RuO_2 from which the PZC was estimated to be at more positive potentials and to vary with sample preparation.

Acknowledgments

This work was supported by the Department of Energy under contract DE-AC02-80ER-10654 and by the Office of Naval Research under contract N00014-81-K-0339.

Manuscript submitted Nov. 19, 1982; revised manuscript received March 26, 1983.

Any discussion of this paper will appear in a Discussion Section to be published in the June 1984 JOURNAL. All discussions for the June 1984 Discussion Section should be submitted by Feb. 1, 1984.

The Brooklyn College of the City University of New York assisted in meeting the publication costs of this article.

REFERENCES

1. A. T. Kuhn and C. J. Mortimer, *This Journal*, **120**, 231 (1973).
2. S. Puschaver, *Chem. Ind.*, 236 (1975).
3. H. V. K. Udupa, R. Thangappan, B. R. Yadev, and P. Subbiah, *Chem. Age India*, **23**, 545 (1975).
4. R. R. Dukes and R. G. Milner, *This Journal*, **117**, 9C (1970).
5. S. Trasatti and G. Buzzanca, *J. Electroanal. Chem.*, **29**, A1 (1971).
6. W. O'Grady, C. Iwakura, J. Huang, and E. Yeager, in "Electrocatalysis," p. 286, The Electrochemical Society Softbound Proceedings Series, Princeton, NJ (1974).
7. L. D. Burke, O. J. Murphy, J. F. O'Neill, and S. Venkatesan, *J. Chem. Soc. Faraday Trans. 1*, **73**, 1659 (1977).
8. M. Gratzel, *Acc. Chem. Res.*, **14**, 376 (1981).
9. S. Trasatti and G. Lodi, in "Electrodes of Conductive Metallic Oxides," S. Trasatti, Editor, p. 301, part A, Elsevier, Amsterdam (1980); S. Trasatti and W. E. O'Grady, in "Electrochemistry and Electrochemical Engineering," H. Gerischer and C. W. Tobias, Editors, John Wiley and Sons, New York (1981).
10. M. Tomkiewicz, *This Journal*, **126**, 2220 (1979).
11. M. Tomkiewicz, *ibid.*, **126**, 1505 (1979).
12. W. E. O'Grady, A. K. Goel, F. H. Pollak, H. L. Park, and Y. S. Huang, Submitted for publication.
13. Y. S. Huang, H. L. Park, and F. H. Pollak, *Mat. Res. Bull.*, To be published.
14. E. Gileadi and B. E. Conway, in "Modern Aspects of Electrochemistry," J. O'M. Bockris and B. E. Conway, Editors, Vol. 3, p. 347, Butterworths, London (1964).
15. R. Parsons, in "Modern Aspects of Electrochemistry," J. O'M. Bockris and B. E. Conway, Editors, Vol. 1, p. 103, Butterworths, London (1954).
16. J. O'M. Bockris and A. K. N. Reddy, "Modern Electrochemistry," p. 757, Plenum/Rosetta Edition, New York (1977).
17. D. Grahame, *J. Chem. Phys.*, **21**, 1054 (1953).
18. D. E. Yates and T. W. Healy, *J. Chem. Soc. Faraday I*, **76**, 9 (1980).
19. G. Valette, A. Hamelin and R. Parsons, *Z. Physikal. Chem.*, **113**, 71 (1978).
20. R. Payne, *This Journal*, **113**, 999 (1966).
21. R. Parsons, *J. Electroanal. Chem.*, **118**, 3 (1981).
22. A. N. Frumkin, *Svensk Kem. Tidskr.*, **77**, 300 (1965).
23. S. Trasatti, *J. Electroanal. Chem.*, **33**, 351 (1971).
24. M. Honorez, Master Thesis, Universite De L'Etat a Mon, France (1980); L. Laude and F. H. Pollak, Private communication.
25. J. C. Riviere, in "Solid State Surface Science," M. Green, Editor, Vol. 1, p. 719, Marcel Dekker, New York (1969).
26. M. A. Butler and D. S. Ginley, *This Journal*, **125**, 228 (1978); S. H. Maron and S. F. Prutton, "Principles of Physical Chemistry," p. 848, MacMillan Co., London (1965).
27. S. Ardizzone, P. Siviglia, and S. Trasatti, *J. Electroanal. Chem.*, **122**, 395 (1981).

Evidence for the Growth Mechanism of Cr_2O_3 at Low Oxygen Potentials

H. Hindam[1]

Materials and Molecular Research Division, Lawrence Berkeley Laboratory, University of California, Berkeley, California 94720

D. P. Whittle*

Department of Materials Science and Mineral Engineering, University of California, Berkeley, California 94720

ABSTRACT

The growth rate of Cr_2O_3 on pure Cr, Ni-25, and 50% Cr and Co-25% Cr in flowing CO-CO_2 mixtures of effective oxygen pressures in the range 8.4×10^{-15}-8.3×10^{-9} atm at 1000°C has been measured. The parabolic growth constant is virtually independent of oxygen potential for both pure Cr and the alloys; for the alloys, it is about an order of magnitude smaller than for pure Cr. These results provide supportive evidence for Cr interstitials being the predominating mobile defect species in Cr_2O_3 under these conditions.

Cr_2O_3 is an important oxide; it provides the protective scale on many technologically important alloys. Nevertheless, neither its defect and transport properties, nor its growth mechanism are well understood. This is the case in spite of the many investigations of Cr_2O_3 formation on both pure Cr and many Cr_2O_3-forming alloys. Most of these have been summarized recently (1, 2).

With some justifiable reservations, the growth kinetics of Cr_2O_3 are generally diffusion-controlled (parabolic), at least at some stage of the reaction. However, apparent rate constants at 1000°C, for example, can differ by as much as a factor of 10^4. Indeed, the largest scatter in rate constants is obtained with growth on pure Cr, rather than with alloys (2).

Considerable effort has been expended in attempts to explain these large differences, but little consensus has been achieved. Nevertheless, one of the major contributory factors is the development of nonuniform growth of Cr_2O_3 in the form of oxide nodules, blisters, convoluted, and multilayered scales; the detailed metallographic observations of several authors (1, 3, 4) provide excellent examples. Detachment of the Cr_2O_3 scale from the substrate as a result of poor adhesion, or stress development during growth supposedly does not stifle its growth since the vapor pressure and transport rate of Cr from the metal to the underside of the oxide are high enough to sustain continued growth. Cracking of the detached oxide and formation of a second or more layer of Cr_2O_3 is a common occurrence. There is seemingly little correlation with experimental variables, such as surface condition, sample purity, temperature, oxygen pressure, etc.

Nevertheless, although not definable *a priori*, under certain conditions, Cr_2O_3 does grow as a protective layer which may or may not be adherent to the substrate, and it is possible to rationalize the parabolic growth constant by comparing its magnitude with that calculated from independent diffusion measurements of the transport rate of the predominantly mobile species in the oxide. In doing this, Lillerud and Kofstad (1) were only able to rationalize their results by assuming that the important cation lattice defects were Cr interstitials and not vacancies, as seems to have been commonly accepted in literature discussions, although the basis for this seems rather obscure, or at least tentative. Kröger (5) has comprehensively reviewed all the evidence and is unable to differentiate between $V_{Cr}^{\alpha'}$ or $Cr_i^{\alpha\cdot}$ as the predominating defect.

An important implication of Cr interstitials being the predominant defects is that the parabolic growth constant is independent of oxygen pressure, as observed (1), and that Cr diffusivity in Cr_2O_3 increases with decreasing oxygen pressure. According to Lillerud and Kofstad (1), this explains the observation that the Cr diffusion coefficient was approximately 10 times higher in hot pressed than in sintered Cr_2O_3 compacts (6). The original authors (6) reported that the hot pressed samples contained free Cr, suggesting (1) that the effective oxygen pressure within the samples was close to the Cr/Cr_2O_3 dissociation pressure and lower than that existing within sintered samples which were annealed in nitrogen (residual oxygen being 10^{-7}-10^{-6} atm). As pointed out (1), enhanced sintering of Cr_2O_3 as the oxygen partial pressure is decreased is also consistent with n-type defect model, oxygen vacancies being the minority defect.

The present paper reports additional data which support the proposed (1) defect model. It is not meant to be a comprehensive study, but represents data obtained for the growth kinetics of Cr_2O_3 on Cr and Cr-rich alloys as part of a research program on alloy behavior in sulfur-containing atmospheres of low oxygen potential (7).

Experimental

Samples of pure Cr, NiCr, and CoCr alloys were cut from induction melted and vacuum cast ingots to dimensions approximately $12 \times 12 \times 1$ mm and their surfaces prepared by grinding through 600 grit SiC papers. After cleaning, the samples were suspended by quartz fiber in a Cahn 1000 microbalance assembly, for which, under the present operating conditions, the sensitivity of the thermogravimetric measurements was better than 30 μg. The sample hung in the center of the inner of two concentric mullite tubes. These had diameters of approximately 1 and 2.5 cm, respectively. The gas flow passed down the outer tube and up the inner one, and so was preheated before coming into contact with the sample. The mullite tubes were heated by a quartz lamp furnace, controllable within $\pm$ 1°C. A purified argon gas flow passed through the balance head chamber, and was exhausted with the reactive gas above the furnace tube.

Control of the reactive gas composition was achieved by mixing metered flows of certified grade CO_2 and CO_2-CO mixtures. Prior to mixing, the flow rates of the individual supplies were controlled through motorized needle valves actuated through calibrated mass flow meters. The flow rate of the final gas mixture was also monitored with a calibrated mass flow meter and was kept constant throughout all the experiments. The

* Electrochemical Society Active Member.
[1] Present address: Physical Metallurgy Research Laboratory, CANMET Ottawa, Ontario, Canada K1A0G1; on leave to: Industrial Materials Research Institute, NRC, Bel-Air, Montreal, Quebec, Canada H4C2K3

linear gas velocity was 0.3 cm/sec. However, few runs were carried out to determine the effect, if any, of this variable on the reaction rate.

The kinetic data were recorded on a chart recorder, the experimental data points marked on accompanying figures indicating the values taken from the original chart recordings. Samples were examined after exposure by standard metallographic techniques including SEM and EPMA.

Results

Figure 1 presents weight change data plotted as a function of square root of time for pure Cr exposed at 1000°C to a number of CO/CO_2 mixtures. The effective oxygen partial pressure is listed in Table I. Protective behavior was always observed up to maximum periods of exposure. All the lines deviate slightly from linearity; however, as discussed later, this was related to slight grain coarsening during scale growth and does not invalidate the determination of a meaningful parabolic rate constant. Indeed, linear correlation coefficients were always better than 0.999. The rate constants are included in Table I.

There was no systematic variation of the parabolic rate constants with oxygen partial pressure. The slight differences were almost certainly related to subtle changes in the grain size of the Cr_2O_3, which may be dependent on the exposure conditions, although this was not studied in detail. For a particular set of conditions, the kinetic curves were reproducible. Figure 2 shows an example of three independent weight gain/time curves in CO_2-0.3 volume percent (v/o) CO at 1000°C, at linear gas velocities of 0.03, 0.33, and 0.66 cm/sec. The weight changes at the longest exposure time (15 hr) were within ± 50 $\mu g/cm^2$; the standard deviation of the parabolic rate constants for the three runs is $\pm 0.05 \times 10^{-10}$ $g^2\ cm^{-4}\ sec^{-1}$.

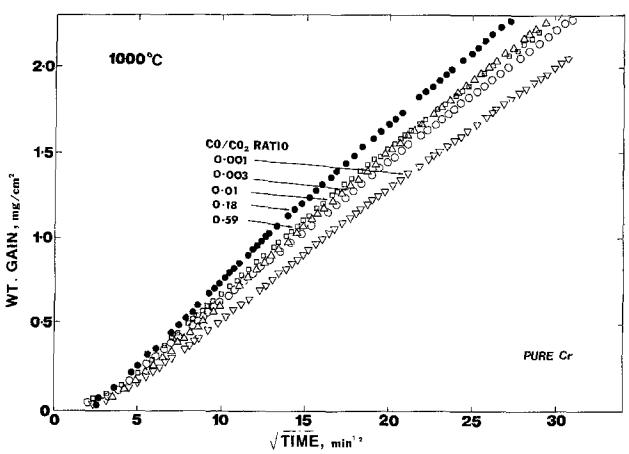

Fig. 1. Parabolic growth kinetics of Cr_2O_3 on pure Cr at 1000°C in CO_2/CO mixtures.

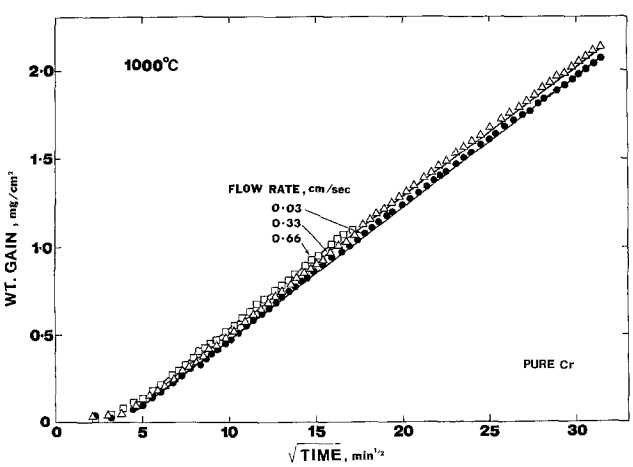

Fig. 2. Parabolic growth kinetics of Cr_2O_3 on pure Cr at 1000°C in CO_2-0.3 v/o CO at linear gas flow velocities of 0.03, 0.33, and 0.66 cm/sec.

Table I. Parabolic growth constants for Cr_2O_3 growth on pure Cr at 1000°C

Gas mixture	Oxygen potential, (atm)	K_g ($g^2\ cm^{-4}\ sec^{-1}$)
CO_2-0.1% CO	8.3×10^{-9}	9.21×10^{-11}
CO_2-0.3% CO	9.2×10^{-10}	9.50×10^{-11}
CO_2-0.3% CO	9.2×10^{-10}	1.00×10^{-10}
CO_2-0.3% CO	9.2×10^{-10}	1.07×10^{-10}
CO_2-1% CO	8.2×10^{-11}	1.18×10^{-10}
CO_2-15% CO	2.7×10^{-13}	1.33×10^{-10}
CO_2-37% CO	2.4×10^{-14}	1.03×10^{-10}
		mean—1.07×10^{-10}

In addition, volatilization of Cr_2O_3 to CrO_3 (3) is not expected at the low oxygen pressures. This was confirmed by recording the weight change of a large flake of Cr_2O_3 (scale spalled from one of the samples) exposed to the CO_2-0.1% CO mixture (highest P_{O_2}). Within the sensitivity of the microbalance, no weight change was observed over a time period corresponding to that of a typical experiment.

In all cases, only uniform single layer scales of Cr_2O_3 were ever observed, although in most cases, these spalled from the surface as large rectangular flakes when cooled rapidly from the reaction temperature. They exhibited a macroscopic wrinkled appearance, inferring plastic deformation without fracture at these reduced oxygen potentials. Presumably, they were not totally adherent to the substrate; however, they evidently did not crack open. Figure 3 shows a typical fracture section through spalled flake. Equiaxed grains with uniform submicron size are evident, although not easily measurable. Some whiskers protrude out of the outer surface of the scale, but would not contribute any significant amount to the total weight gain.

Figure 4 shows weight change data for Co-25 weight percent (w/o) Cr and Ni-25 and 50 w/o Cr at 1000°C in different gas mixtures as detailed in Table II. Again, the rates are substantially parabolic, decreasing very slightly with extended exposure, but not sufficiently that a meaningful average parabolic rate constant cannot be defined. The rates, given in Table II, are virtually independent of gas composition and alloy chromium content (at least in Ni alloys for the range 25-50 w/o Cr), slightly greater for Ni alloys compared with the Co alloys, and considerably lower than the corresponding rates for pure Cr. Examination of the scales showed no apparent differences in grain morphology to those formed on pure Cr and no detectable Ni or Co contents.

Discussion and Conclusions

Based on the present observations and data available in the literature, it is now possible to formulate a

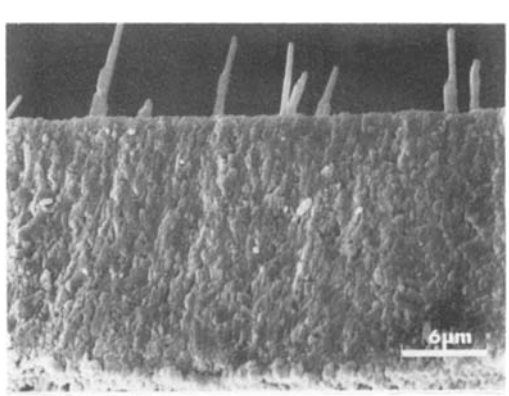

Fig. 3. Fracture section through a spalled flake of Cr_2O_3 formed on pure Cr.

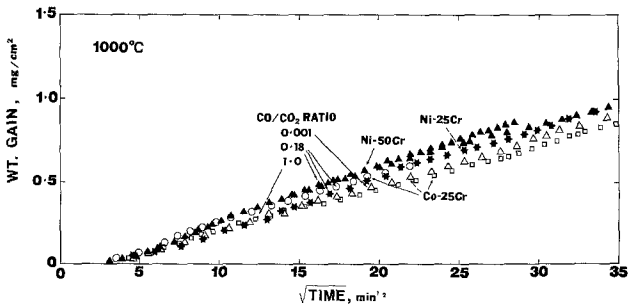

Fig. 4. Parabolic growth kinetics for Cr_2O_3 on Co-25 Cr and Ni-25 and 50 Cr at 1000°C in CO_2/CO mixtures.

growth model for Cr_2O_3. The present measurements provide strong support for recent suggestions by Lillerud and Kofstad (1).

Firstly, the parabolic growth constant is virtually independent of oxygen fugacity. According to the abbreviated version of Wagner's parabolic equation (8), if Cr_2O_3 grows by bulk diffusion of interstitial Cr ions of effective charge α, then

$$K_P\ [(\text{oxide thickness})^2/\text{time}] = (\alpha + 1) D_{Cr}{}^{o} \{(P_{O_2}{}^{i})^{-3/4(\alpha+1)} - (P_{O_2}{}^{a})^{-3/4(\alpha+1)}\} \quad [1]$$

where K_P is the parabolic rate constant in terms of oxide thickness, $D_{Cr}{}^{o}$ is the self diffusion coefficient of Cr in Cr_2O_3 in equilibrium with oxygen at unit activity, and $P_{O_2}{}^{i}$ and $P_{O_2}{}^{a}$ are the effective oxygen partial pressures at the inner and outer scale interfaces, respectively. In the case of pure Cr, $P_{O_2}{}^{i}$ is of course the dissociation pressure of Cr_2O_3 in contact with Cr, which is $10^{-21.57}$ atm at 1000°C, and hence even at the lowest ambient oxygen potential used (2.4×10^{-10} atm)

$$P_{O_2}{}^{a} >> P_{O_2}{}^{i}$$

and Eq. [1] reduces to

$$K_p\ [(\text{oxide thickness})^2/\text{time}] \simeq (\alpha + 1) D_{Cr}{}^{o} (P_{O_2}{}^{i})^{-3/4(\alpha+1)} \simeq (\alpha + 1) D_{Cr}{}^{i} \quad [2]$$

where $D_{Cr}{}^{i}$ is the self-diffusion coefficient of Cr in Cr_2O_3 in equilibrium with Cr (*i.e.*, at $a_{Cr} = 1$). Thus, the rate is independent of the external oxygen pressure. Assuming a value of $\alpha = 3$ (fully ionized interstitials) and converting the measured gravimetric rate constant, K_g, to K_p

$$K_p = \left(\frac{1}{y\rho_{Ox}}\right)^2 K_g \quad [3]$$

where y is the average weight fraction of oxygen in the oxide (for Cr_2O_3 = 48/152) and ρ_{Ox} is the density of the oxide ($\rho_{Cr_2O_3}$ = 5.21 g/cm³), gives an average value of $D_{Cr}{}^{i}$ of 4.93×10^{-12} cm²/sec. This is very close to the value extrapolated (their measurements were in the range 1030°-1500°C, so this is only a small extrapolation) from the diffusion experiments of Hagel and Seybolt (6) in hot-pressed compacts of Cr_2O_3: 5.57×10^{-12} cm²/sec. As referred to earlier, because of the presence of unreacted Cr in the compacts, the effective oxygen potential of the measurements was thought (1) to be equivalent to the dissociation pressure of Cr_2O_3 in contact with Cr.

An alternative view of the growth mechanism would involve Cr transport through the oxide via cation vacancies, when

$$K_p\ [(\text{oxide thickness})^2/\text{time}] = (\alpha + 1) D_{Cr}{}^{o} \{(P_{O_2}{}^{a})^{3/4(1+\alpha)} - (P_{O_2}{}^{i})^{3/4(1+\alpha)}\} \quad [4]$$

Again, with $P_{O_2}{}^{a} >> P_{O_2}{}^{i}$, the rate constant depends on the 3/4 $(1 + \alpha)$th power of the ambient oxygen pressure. This means that over the range of oxygen potentials examined in the present study, 2.4×10^{-14} to 8.3×10^{-9} atm, the rate constant should have increased by a factor of 11 ($\alpha = 3$, fully dissociated vacancies) or much greater than that if $\alpha < 3$ (120 if $\alpha = 1$), and would have been easily detected with the present experimental arrangement. The dependence of the gravimetric constant K_g (Eq. [3]) on $P_{O_2}{}^{a}$ for the assumed defect models (Eq. [2] and [4]) along with the experimental values are plotted in Fig. 5. Evidently, the data substantiate the interstitial model.

The second piece of evidence presented here is the lower growth constant observed for Cr_2O_3 growth on the alloys. Again, this is a direct consequence of the interstitial model. For alloys, the Cr activity at the alloy/oxide interface is less than unity, and hence, the effective oxygen pressure there is higher than when pure Cr is the substrate. In terms of a vacancy model, this would make virtually no difference to the expected growth rate ($P_{O_2}{}^{a} >> P_{O_2}{}^{i}$), except at low alloy Cr contents when the diffusion of Cr from the bulk alloy to the scale became rate-controlling (11). Furthermore, this difference in reaction rate, which is approximately an order of magnitude, cannot be accounted for by a variation in oxide grain size. As indicated earlier, no attempts were made for detailed grain size measurements since no significant difference was observable as a function of time or oxygen potential, or between scales formed on pure Cr or the alloys. Nonetheless, based on the grain boundary "short cir-

Table II. Parabolic growth constants for Cr_2O_3 growth on alloys at 1000°C

Alloy	Gas mixture	Oxygen potential, (atm)	K_g (g² cm⁻⁴ sec⁻¹)
Ni-25 w/o Cr	CO_2-15% CO	2.7×10^{-13}	1.54×10^{-11}
Ni-50 w/o Cr	CO_2-15% CO	2.7×10^{-13}	1.79×10^{-11}
Co-25 w/o Cr	CO_2-0.1% CO	8.3×10^{-9}	1.28×10^{-11}
Co-25 w/o Cr	CO_2-15% CO	2.7×10^{-13}	1.47×10^{-11}
Co-25 w/o Cr	CO_2-50% CO	8.4×10^{-15}	1.15×10^{-11}

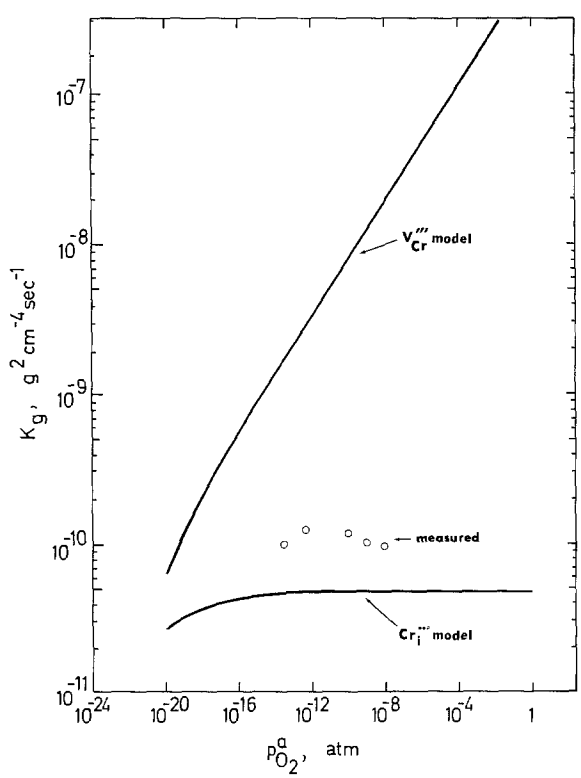

Fig. 5. Dependence of the gravimetric parabolic rate constant for Cr_2O_3 growth on Cr on ambient oxygen potential according to an interstitial (Eq. [2]) and vacancy (Eq. [4]) model, and experimental data.

cuit" model (9, 10), it can be shown that if this were the case, the grain size would have been different by at least an order of magnitude since the "apparent" rate constant is roughly inversely proportional to the average grain diameter.

As the reaction is diffusion controlled, the Cr concentration (activity) at the alloy/scale interface is uniquely defined and is less than that in the bulk alloy by an amount depending on the ratio of the scale growth constant to the alloy interdiffusion coefficient. In order to estimate this parameter, it is necessary to balance the fluxes of Cr into the scale and from the bulk alloy. Following the usual analysis (11, 12), for the case where the alloy is single-phase, has a concentration-independent interdiffusion coefficient, and where selective oxidation is complete, gives

$$X_{Cr^i} = \frac{X_{Cr^b} - \mathbf{F}(\eta)}{1 - \mathbf{F}(\eta)} \quad [5]$$

where X_{Cr^i} and X_{Cr^b} are the atomic fractions of Cr at the interface and in the bulk alloy, and

$$\eta = \sqrt{\frac{K_c}{2\tilde{D}_{all}}} \quad \text{and} \quad \mathbf{F}(\eta) = \sqrt{\pi}\exp\eta^2\operatorname{erfc}\eta \quad [6]$$

where K_c is the so-called "corrosion constant," and represents a parabolic rate constant in terms of the displacement of the alloy/oxide interface, Δx_{metal}, due to scale growth as defined by

$$\Delta x_{metal} = \sqrt{2\,K_c\,t} \quad [7]$$

K_c is, thus, related to the gravimetric rate constant by

$$K_c = \frac{1}{2}K_g\left[\frac{1}{\rho_{metal}}\,\frac{1-y}{y}\right]^2 \quad [8]$$

where ρ_{metal} is the density of the metal substrate and y, as defined earlier, is the average weight fraction of oxygen in the oxide [$y_{Cr_2O_3} = 0.3158$]. $\tilde{D}_{all}$ is the alloy interdiffusion coefficient.

For the Ni-Cr system, the alloy interdiffusion coefficient is approximately independent of composition in the range 0-40 w/o Cr (13) and at 1000°C has a value of 2.2×10^{-11} cm²/sec. Combining this with the measured gravimetric rate constants for Cr_2O_3 growth on Ni-25 and Ni-50% Cr alloy, 1.54×10^{-11} and 1.79×10^{-11} g² cm^{-4} sec^{-1}, respectively, and using Eq. [5], [6], and [8] give an atomic fraction of Cr at the alloy/scale interface of 0.1 and 0.35 for the two alloys, respectively. The 50% Cr alloy actually contains two phases, the γ-Ni solid solution and an α Cr-rich bcc phase. The solubility limit of Cr is approximately 44% at this temperature. However, this would not significantly alter the calculated Cr-content at the interface.

The effective P_{O_2} at the alloy scale interface is now obtained by considering the equilibrium relationship between Cr_2O_3 and Cr in the alloy. Thus,

$$P_{O_2{}^i} = \frac{1}{(a_{Cr^i})^{4/3}}\exp\left[\frac{2\Delta G^\circ_{Cr_2O_3}}{3RT}\right] \quad [9]$$

where $\Delta G^\circ_{Cr_2O_3}$ is the Gibbs standard free energy of formation of Cr_2O_3 and a_{Cr^i} the activity of Cr at the alloy/scale interface. On pure Cr, $a_{Cr^i} = 1$ and $P_{O_2{}^i} = \pi_{Cr_2O_3}$, the dissociation pressure of Cr_2O_3 in contact with pure Cr. Thus, combining Eq. [2] and [9], the ratio ψ, of parabolic growth constants for Cr_2O_3 on an alloy to that on pure Cr is given by

$$\psi = (a_{Cr^i})^{1/(\alpha+1)} \quad [10]$$

for the case where interstitials are the major defect.

This result is in contrast to that if vacancies were the dominant diffusion species, when ψ is given by a combination of Eq. [4] and [9]

$$\psi = \frac{1 - (a_{Cr^i})^{-1/(\alpha+1)}\,(\pi_{Cr_2O_3}/P_{O_2{}^a})^{3/4(1+\alpha)}}{1 - (\pi_{Cr_2O_3}/P_{O_2{}^a})^{3/4(1+\alpha)}} \quad [11]$$

In the present case, since $P_{O_2{}^a} >> \pi_{Cr_2O_3}$, and unless a_{Cr^i} is very small, ψ is little different from unity

Thus, it is argued that since experimentally, $\psi \approx 0.15$, and although this is not entirely consistent with Eq. [10], that fact that is considerably less than unity favors the interstitial model.

Similar calculations for the Co-Cr system, in which D_{all} appears (14-16) to fall in the range (3.3-5.5) $\times 10^{-12}$ cm²/sec suggest that a_{Cr^i} is somewhat smaller than in the Ni-Cr system. However, diffusion coefficients [Cr tracer in Co-21 w/o Cr, 2 v/o y_2O_3 (17)] as high as 10^{-11} cm²/sec have been measured, and this would give Cr concentration at the interface of similar magnitudes to those in the Ni-Cr system. Again, the measured ratio of growth constants is ~0.12, and there is no evidence that the oxide growth rate is being controlled by Cr diffusion in the underlying alloy, for example a tendency to develop a nonplanar alloy/scale interface.

Although the growth constants for Cr_2O_3 on the alloys are not quantitatively consistent, they do qualitatively agree with the general behavior observed at higher oxygen potentials (1 atm): parabolic rate constants for Cr_2O_3 growth on Fe, Ni, and Co-Cr all increase with increasing alloy Cr content (18). However, under these conditions, it has usually been speculated that this is related to a decrease in the noble metal (Fe, Ni, or Co) content of the oxide modifying the defect concentrations. With the present experiments, significant solubility of Ni or Co in the Cr_2O_3 is not anticipated since the P_{O_2} is either below, or only slightly above the dissociation pressures of NiO or CoO. Nevertheless, the apparent independence of the growth constant on the alloy Cr content, and by implication the content at the alloy/scale interface, is puzzling.

Acknowledgments

This work was supported by the Director, Office of Energy Research, Office of Basic Energy Sciences, Materials Sciences Division of the U.S. Department of Energy under Contract No. DE-AC03-76SF00098.

Manuscript submitted Aug. 27, 1982; revised manuscript received Jan. 19, 1983.

Any discussion of this paper will appear in a Discussion Section to be published in the June 1984 JOURNAL. All discussions for the June 1984 Discussion Section should be submitted by Feb. 1, 1984.

The Industrial Materials Research Institute assisted in meeting the publication costs of this article.

REFERENCES

1. K. P. Lillerud and P. Kofstad, *This Journal*, **127**, 2397, 2410 (1980).
2. D. P. Whittle and H. Hindam, "Proceedings of NACE Conference on Corrosion/Erosion of Coal Conversion System Materials," Berkeley, CA (1982).
3. D. Caplan, A. Harvey, and M. Cohen, *Corros. Sci.*, **3**, 161 (1963).
4. D. Caplan and G. I. Sproule, *Oxid. Met.*, **9**, 459 (1975).
5. F. A. Kröger, in "Proceedings of NACE Conference on High Temperature Corrosion," San Diego, CA (1981).
6. W. C. Hagel and A. U. Seybolt, *This Journal*, **108**, 1146 (1961).
7. H. Hindam and D. P. Whittle, To be published.
8. P. Kofstad, "High Temperature Oxidation of Metals," John Wiley and Sons, New York (1966).
9. J. M. Perrow, W. W. Smeltzer, and R. K. Ham, *Acta Met.*, **15**, 577 (1967).
10. J. M. Perrow, W. W. Smeltzer, and J. D. Embury, *ibid.*, **16**, 1209 (1968).

11. C. Wagner, *This Journal*, **99**, 369 (1952).
12. B. D. Bastow, D. P. Whittle, and G. C. Wood, *Oxid. Met.*, **12**, 413 (1978).
13. Y. E. Ugaste, *Fiz. Metal. Metallored.*, **24**, 442 (1967).
14. J. M. Weeton, *Trans. ASM*, **44**, 436 (1952).
15. A. Davin, V. Leroy, D. Coutsouradis, and L. Habraken, *Cobalt*, **14**, 51 (1963).
16. A. Green, D. P. Whittle, J. Stringer, and N. Swindells, *Scripta Met.*, **7**, 1079 (1973).
17. M. S. Seltzer and B. A. Wilcox, *Met. Trans.*,
18. G. C. Wood, I. G. Wright, T. Hodgkiess, and D. P. Whittle, *Werk, u. Korr.*, **21**, 900 (1970).

Cyclic Voltammetry and *In Situ* Laser Raman Spectroscopy Studies of Electrogenerated Methyl Viologen Radical Cation

C. A. Melendres*

Argonne National Laboratory, Materials Science and Technology Division, Argonne, Illinois 60439

P. C. Lee and D. Meisel

Argonne National Laboratory, Chemistry Division, Argonne, Illinois 60439

ABSTRACT

The electrogeneration of methyl viologen radical cation (MV^+) at a silver electrode in chloride solution has been studied. Evidences for the adsorption of MV^+ or a related species have been obtained by cyclic voltammetry and *in situ* laser Raman spectroscopy measurements. It was observed that electrode cycling and high chloride ion concentration stabilize the adsorbed state of MV^+ at the electrode. It appeared possible to distinguish between Raman signal due to surface species and to species dissolved in the solution. Characteristic spectra are presented. The Raman technique also seems capable of detecting submonolayer quantities of MV^+ and to be useful for monitoring concentration changes of the radical cation.

Considerable interest presently exists in the use of methylviologen (N,N'-dimethyl-4,4'-bipyridine, MV^{+2}) as an electron relay in various schemes for hydrogen generation through the photochemical splitting of water (1). Various derivatives of pyridinium salts are also well-known potent herbicides; they are often considered as model systems for NAD^+ (nicotinamide dinucleotide) and other components of biological electron transfer chains (2). A common scheme for the photocleavage of water would involve production of MV^+ by electron transfer from an excited sensitizer to MV^{+2}. This radical would then transfer an electron to a noble metal catalyst usually present in the system in the colloidal state (3). The interaction of MV^+ with noble metals such as Pt, Au, and Ag is of much interest. Thus, for example, the question of adsorption of MV^+ on the metal surface prior to the electron transfer act is of crucial importance in evaluating the performance of the catalyst. This question was previously addressed in attempts to observe surface enhanced Raman scattering (SERS) from MV^+, possibly adsorbed on colloidal Ag catalysts (3). Although resonance Raman scattering (RRS) was easily obtained from MV^+ in solution, no SERS was observed in the colloidal system (3). Very recently, however, a SERS spectrum of MV^+ on Ag electrodes has been observed (4). An analysis of the Raman spectrum of MV^+ in solution was also reported (5). Our spectroelectrochemical investigations were in progress when these works appeared. We were interested in further clarifying the question of radical adsorption and determining the origin of the Raman spectrum of the electrogenerated species, *i.e.*, whether from species dissolved in the solution or adsorbed on the electrode surface. Moreover, this system also appeared very well suited to test the sensitivity of the Raman spectroscopic technique for *in situ* interfacial studies since coulometric generation of the radical cation allows accurate surface coverage to be determined. We report here the results of our study.

Experimental

The N,N'-dimethyl-4-4'-bipyridinium dichloride ($MVCl_2$) was obtained as a hydrated salt (Aldrich Chemical Company, Milwaukee, Wisconsin) and was used without further purification. Solutions were prepared using 4-times distilled water and were deaerated by bubbling with research grade He. The cell for electrochemical measurements was of a conventional H-type design with 3 compartments. Rubber stoppers (provided with holes for insertion of the electrodes) were used as covers to exclude atmospheric oxygen. The Ag electrodes were fabricated from 0.010 in. thick Marz grade (99.99% purity) foil (Materials Research Corporation, Orangeburg, New York). The working electrode was cleaned and roughened by abraiding with size 600 grit emery cloth and then washed with acetone and distilled water. A saturated calomel reference electrode was used in this study, and all potentials quoted here are referred to it. A Princeton Applied Research Model 173 Potentiostat and a Model 179 Universal Programmer were employed for cyclic voltammetry studies. Raman spectral measurements were carried out in a 3-compartment cell fitted with a quartz optical window (6). A SPEX model 1400-II double monochromator fitted with 1200 groove/mm gratings and a photomultiplier tube detector was used. Slit widths of 200-250 μm were employed. Signal processing was done through a SPEX model DPC-2 Digital Photometer operated in the photon-counting (PC) mode. Sample excitation was by Kr^+ (Coherent model CR 750 K) and Ar^+ (model CR 6) lasers at power levels between 50-120 mW.

Results and Discussion

Electrochemical measurements.—Figure 1 shows a typical cyclic voltammogram on a Ag electrode in deaerated 5×10^{-3}M methyl viologen chloride ($MVCl_2$) solution. The general shape of the voltammogram is in good agreement with that reported by Steckham and Kuwana (7). The oxidation-reduction waves have been interpreted in terms of the reactions

$$MV^{++} + e^- \underset{Ia}{\overset{Ic}{\rightleftarrows}} MV^+ \qquad [1]$$

$$MV^+ + e^- \underset{IIa}{\overset{IIc}{\rightleftarrows}} MV \qquad [2]$$

* Electrochemical Society Active Member.
Key words: methyl viologen radical cation, Raman spectra, cyclic voltammetry.

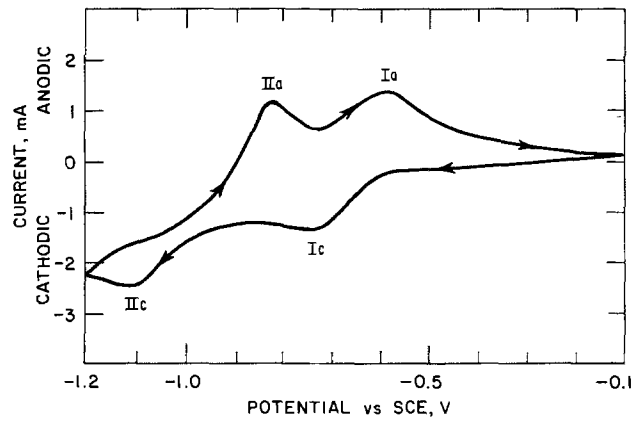

Fig. 1. Cyclic voltammogram of 5 × 10^{-3}M MV^{+2} solution on Ag electrode. Scan rate = 20 mV/sec.

In this paper, we will confine ourselves to a detailed study of the first wave, *i.e.*, the electrogeneration of the methyl viologen radical cation (MV^+) and its possible interaction with the silver electrode. Figure 1 shows that reaction (1) proceeds fairly reversibly at the Ag electrode. The separation between anodic and cathodic peaks in Fig. 1 is, however, greater than the 60 mV required for a truly reversible reaction because of high solution resistance in the absence of a supporting electrolyte. In the presence of a supporting electrolyte, *e.g.*, 0.1M KCl or LiCl, the peak separation is close to the theoretical value of 60 mV as shown in Fig. 2. The increased Cl^- concentration, however, gives rise to new waves (IIIa and IIIc, Va, and Vc, Fig. 2). Following the treatment of Wopschall and Shain (8), the waves IIIa and IIIc are attributed to the adsorption of the product of the cathodic reduction of MV^{++}, *i.e.*, the radical cation MV^+ or a related species. We will discuss the interpretation of Va and Vc later on. A plot of the ratio of anodic to cathodic peak currents in 5 × 10^{-3}M $MVCl_2$ solution against the square root of the scan rate (Fig. 3) shows a deviation from the value of 1.0 that is characteristic of an uncomplicated and reversible charge transfer process (9). While this deviation could be partly attributed to solution resistance, it is also probably due to adsorption occurring at the electrode surface. Evidence of an adsorbed state in the pure MV^{+2} solution (no KCl or LiCl supporting electrolyte) is observed more prominently (Fig. 4) when the electrode is cycled between the potential for anodic dissolution of Ag (greater than 0.2V *vs.* SCE) and its subsequent redeposition (less than or equal to about −0.5V). Adsorption prepeaks IIIa and IIIc appear following even one anodic dissolution and cathodic reduction cycle of Ag (corresponding to waves IVa and IVc in Fig. 4, respectively). These adsorption waves are not observed even if the electrode potential is taken to rather negative values (*e.g.*, −1.2V as in Fig. 1) so long as massive Ag dissolution and deposition do not occur. While it has been found that a film of methyl viologen polymer is formed at Au and Ni electrodes in buffered solutions (10, 11) as well as on tin oxide electrodes (7) at rather negative potentials (*i.e.*, about −1.0), it is not apparent from Fig. 1 that such is the case in the present system nor that the presence of a polymer film gives rise to adsorption prewaves. The waves IIIa and IIIc in Fig. 4 could, therefore, not be attributed *a priori* to the same type of film that Landrum (10), Bowden (11), and Steckham (7) have found on their electrodes. The waves found here have all the characteristics of adsorption prepeaks treated by Wopschall and Shain (8); they appear more likely to be due to adsorption of the product of the cathodic reduction of MV^{+2}, which is MV^+. It is not unlikely, however, that such an adsorbed species as discovered here may be the precursor of the film formed in the studies by Landrum and others.

Figure 5 shows cyclic voltammograms in 10^{-5}M MV^{+2} and 0.1M KCl solution taken with various switching potentials. (The numbers in parenthesis indicate the nth consecutive scan.) Two effects are immediately apparent. One is the increased prominence of waves Va and Vc. Secondly, extending the cathodic switching potential to −1.0V does not give any stronger indication of the formation of a polymeric film on the electrode surface. On repeating the same experiment after cycling the electrode between +0.3 and −0.9V, for one to three cycles, the results shown in Fig. 6 are obtained. The appearance of the adsorption-desorption waves, IIIa and IIIc, is certainly fascinating.

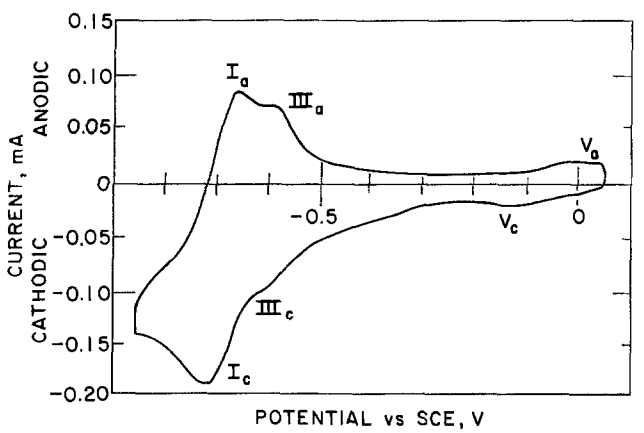

Fig. 2. Cyclic voltammogram in 10^{-3}M MV^{+2} and 0.1M KCl solution. Scan rate = 100 mV/sec.

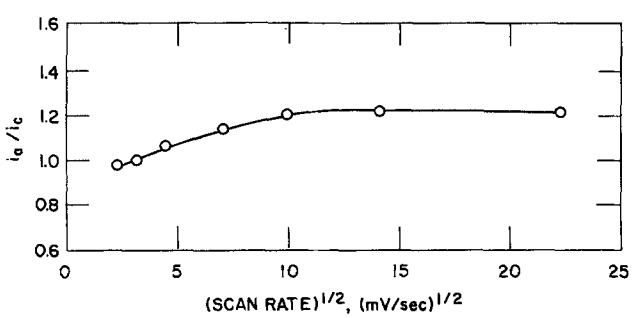

Fig. 3. Peak current ratios for MV^+ as function of scan rate

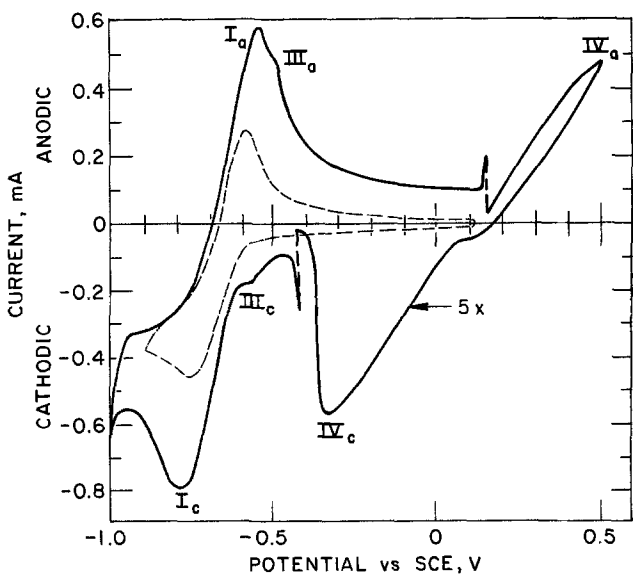

Fig. 4. Cyclic voltammogram of 5 × 10^{-3}M MV^{+2} solution on Ag electrode. ------- second scan before cycling electrode to anodic potentials; scan rate = 50 mV/sec. ——— fifth cyclic scan between 0.5 and −1.0V; scan rate = 100 mV/sec.

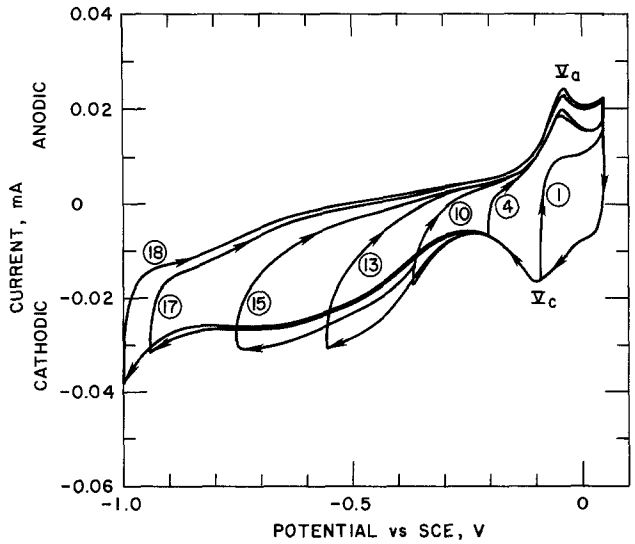

Fig. 5. Cyclic voltammograms in 10^{-5}M MV^{+2} and 0.1M KCl solution before cycling electrode to anodic potentials; scan rate = 50 mV/sec.

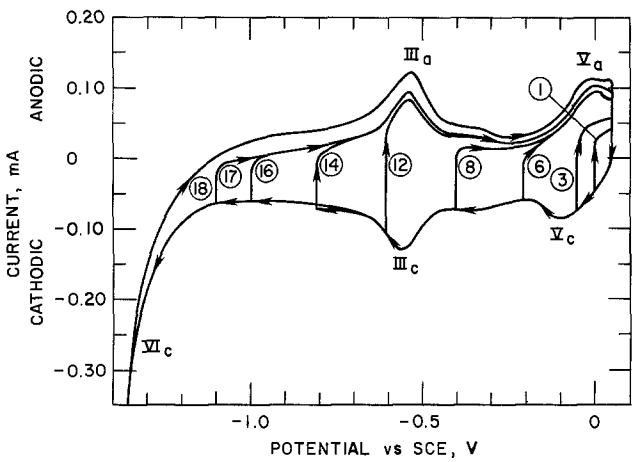

Fig. 6. Cyclic voltammograms in 10^{-5}M MV^{+2} and 0.1M KCl solution after cycling to anodic potentials; scan rate = 50 mV/sec.

It is clear from the figure that it is not necessary to scan the electrode to hydrogen evolution (wave VIc) in order to form the surface species. It is also obvious that a Ag dissolution-deposition cycle indeed stabilizes the state of the adsorbed species on the electrode. It is not clear to us at the moment how this effect comes about. The increase in interaction of MV^+ with the Ag surface on cycling may be due to an increase in "cleanliness" of the surface, a roughening of the surface, the generation of Ag adatoms, or some related species which interact more strongly with the MV^+, or a combination of these factors. The fact that electrode cycling can enhance adsorption has, to our knowledge, not been demonstrated electrochemically and may be of considerable significance in the interpretation of other physical phenomena, *e.g.*, the surface enhanced Raman effect (SERS). We shall show in the next section that indeed the stabilization of the adsorbed state appears to correlate with our obtaining a better signal in our Raman spectroscopy experiments. Moreover, since an increase in the Cl^- concentration (as brought about by the addition of KCl or LiCl supporting electrolyte) appears also to stabilize the adsorbed state at about −0.5V even without prior cycling, it is probable that the cycling process may be leading to an increase in concentration of a chlorosilver complex on the electrode surface or the double layer region.

Finally, we consider the interpretation of waves Va and Vc. These waves become more prominent with decreasing MV^{+2} concentration and with addition of KCl or LiCl. The variation of peak current with scan rate for these waves is shown in Fig. 7. The linear behavior suggests that these correspond also to a set of adsorption-desorption waves, although somewhat irreversible compared to IIIa and IIIc. The identity of the surface species involved in the process needs to be further elucidated.

In situ laser Raman spectroscopy studies.—These studies were undertaken in conjunction with the electrochemical measurements in order to determine the structure of the species in the interphase region and to further elucidate the nature of the processes occurring at the electrode. Figure 8a shows the Raman spectrum of MV^+ electrogenerated at a Ag electrode in 10^{-5}M MV^{+2} solution using Kr^+ laser excitation with the 6471Å line. The spectrum was obtained with the electrode potentiostated at −0.8V *vs.* SCE. (The spectra reported here have been retraced and reduced from actual chart recorder outputs; hence, they have been smoothed out in the process.) The measured band positions are in good agreement with the solution spectrum previously obtained by others (3, 4, 5). Essentially the same spectrum is obtained with excitation using the 5471Å line of the Ar^+ laser. The quantity of charge integrated during the time the spectrum was obtained corresponded to many layers of material reduced so that it is reasonable to conclude that the spectrum is due principally to species on the solution side of the double layer region. The relatively good intensity of the signals observed is presumably mainly

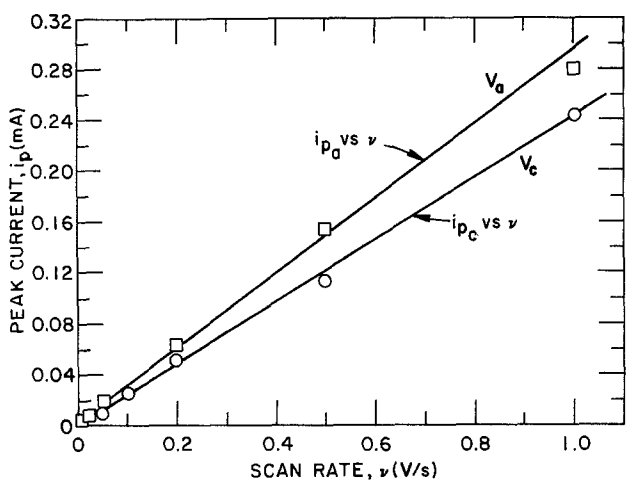

Fig. 7. Variation of peak currents with scan rate for waves V_a and V_c. 10^{-5} MV^{2+} and 0.1M KCl solution.

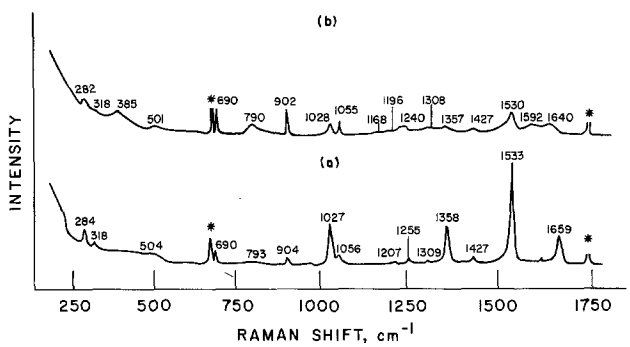

Fig. 8. (a) *In situ* Raman spectrum of electrogenerated MV^+ dissolved in 10^{-5}M MV^{+2} solution. E = −0.8V *vs.* SCE. (b) *In situ* Raman spectrum of MV^+ adsorbed on a Ag electrode in 10^{-5}M MV^{+2} and 0.1M KCl solution. E = −0.6V *vs.* SCE. Kr^+ laser, P = 100 mW, and * = ghost bands (artifacts due to grating imperfections).

due to the resonance Raman effect, since the laser excitation is within the electronic absorption band (3) of MV^+. To see if we could detect a monolayer quantity of MV^+, spectral scans were made as a function of charge passed. We were unable to observe the whole spectrum of a monolayer equivalent of MV^+. However, by monitoring the intensity of the strongest band of MV^+ at 1530 cm^{-1}, it appeared possible to detect about one-half of a monolayer of the radical cation with a signal-to-noise ratio of 1:1 for this band. We found no significant difference between spectra taken at −0.80 and −0.90V *vs.* SCE. We did not see the spectrum of MV^{+2} (even in 5×10^{-3} MV^{+2} solution) nor that of the species responsible for the voltammetric waves V_a and V_c as Regis and Corset (4) claim to have observed. Moreover, our spectra showed no bands that can be attributed to MV^+ dimers which are likely to be formed with increasing MV^+ and MV^{+2} concentrations.

A special effort was made to detect the presence of MV^+ adsorption using Raman spectroscopy and to distinguish the Raman signal of the adsorbed species from that dissolved in the solution. Regis and Corset have reported observing the Raman spectrum of MV^+ adsorbed on a Ag electrode. They did not, however, observe the same on Pt implying that the difference may be due to a surface enhancement of the spectrum on the Ag. Ohsawa *et al.* (12) obtained only the spectrum of the solution species produced at a Pt electrode. Comparing the vibrational bands attributed by Regis (4) to adsorbed MV^+ with the solution spectra obtained by Ohsawa (12) and Forster (5), one finds no major differences in the band positions that these authors have observed except for the band at 1650 cm^{-1} for the adsorbed MV^+ being shifted to higher frequency (~1660 cm^{-1}) in the solution case. Our spectra for electrogenerated MV^+ at −0.80 and −0.90V are essentially the same as that obtained by Forster for chemically prepared material (Fig. 8a). This supports our initial claim that the spectra obtained at these potentials are due to solution species. We normally could only observe a band at 1530 cm^{-1} when potentiostating the electrode at −0.60V and this at a signal to noise ratio of about 1:1. However, on cycling the electrode between anodic Ag dissolution and cathodic redeposition potentials in the presence of added KCl, we find a significant increase in intensity of the Raman signal (~25 times) which allows us to obtain the complete spectrum at −0.60V. Figure 8b illustrates what we observed. From correlation of the spectrum with the electrochemical data presented in Fig. 6 and 7, it is logical to attribute this spectrum with that of MV^+ adsorbed at the electrode. Our spectrum for adsorbed MV^+ shows a shift of the 1659 cm^{-1} (for the solution species) to 1640 cm^{-1} and the band at 1255 to 1240 cm^{-1}. Three new bands at 1168, 1196, and 1592 cm^{-1} appear for the surface species (Fig. 8b) compared to the solution one.

Further evidence for our assignment of the spectra at −0.8 and −0.90V as being mainly due to the solution species comes from measurements of the relaxation of the Raman signal for the 1530 cm^{-1} band following a return to open-circuit conditions. In this experiment, the Ag electrode is potentiostated at the desired potential while the monochromator is set to detect the 1530 cm^{-1} band. The decay of the Raman signal intensity (I) is followed as the circuit is opened and equilibrium allowed to be established. Figure 9a shows the result of such an experiment. The decay of the electrode potential is also monitored for comparison. The linear plot of log I *vs.* time, t, is consistent with that predicted theoretically for a diffusional process (13) occurring in the solution. At −0.80V, it is sometimes possible to observe a break in the initial portion of the log I *vs.* t curve (Fig. 10) followed by the usual linear behavior. This faster decaying process is probably due to the injection of charge by adsorbed MV^+ to the Ag electrode resulting in its reoxidation to

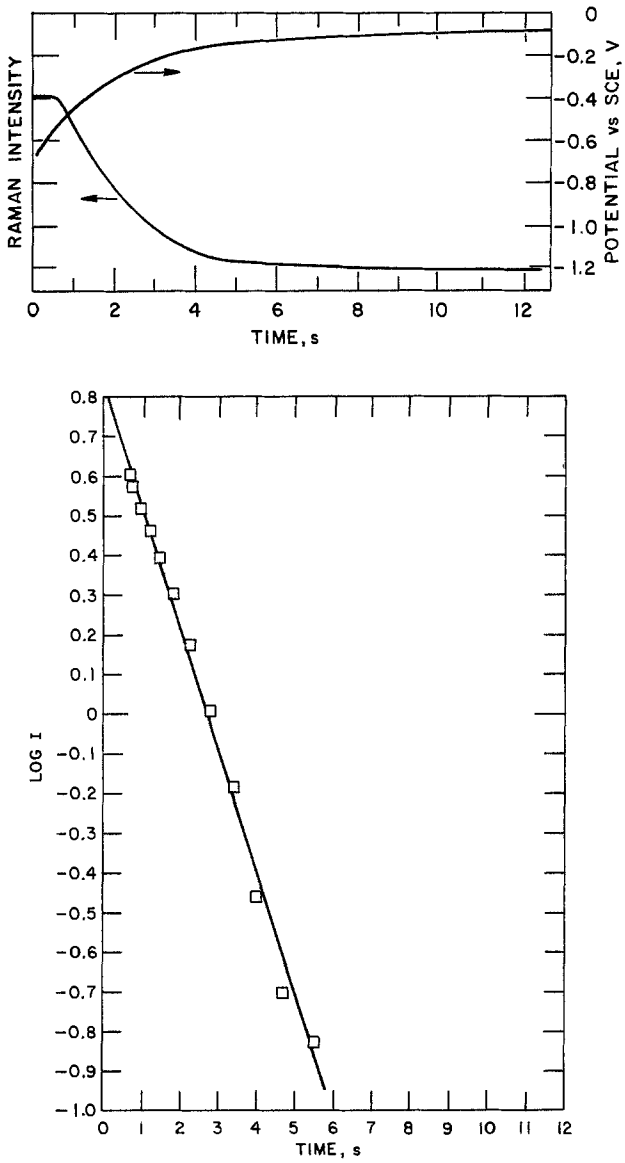

Fig. 9. (a) Relaxation of open-circuit potential and Raman signal at 1530 cm^{-1}. (b) Logarithmic plot of the decay of Raman signal after potentiostating at $E = -0.90$V *vs.* SCE.

MV^{+2}. It is not unreasonable to expect that the Raman spectra of MV^+ at a Ag electrode would be a superposition of spectra attributable to both adsorbed species and species dissolved in the solution, with one dominating over the other depending on the potentiostating voltage.

Finally, we illustrate the utility of the Raman spectroscopic technique for monitoring the changes in concentration of MV^+. Figure 11a shows the Raman signal for the 1530 cm^{-1} band as the potential is swept cyclically at the rate of 5 mV/sec. The corresponding voltammogram is illustrated in Fig. 11b. It can be seen that while the formation of MV^+ and its reoxidation back to MV^{+2} are hardly discernible from the voltammogram, these are clearly detectable by the Raman spectroscopic technique. It is also worthwhile to note the presence of a shoulder at about −0.8V in the second half of the intensity-potential curve. From a correlation of this curve with the voltammograms in Fig. 6 and 7, it is reasonable to interpret the intensity variation during the positive scan to be due to a superposition of signals both from solution species and adsorbed material on the electrode. Thus, at −1.15V (point A, Fig. 11a), the electrode is presumably covered with a film (7) of neutral MV^o. As the potential becomes more positive, the MV^o is converted to MV^+ resulting in the observed increase in Raman signal (due to the solution

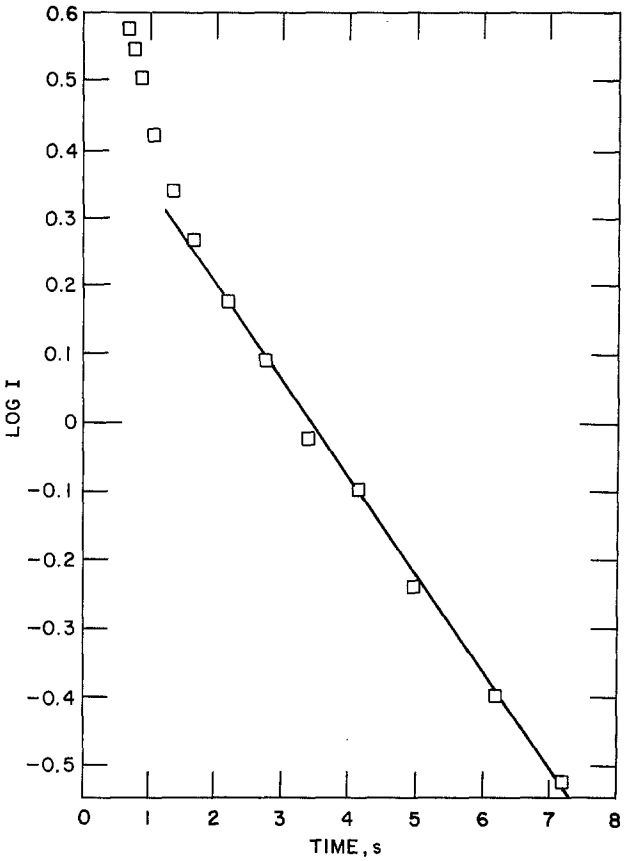

Fig. 10. Relaxation of Raman signal at 1530 cm^{-1} after potentiostating at $E = -0.80V$ vs. SCE.

species). As the MV^{o} is exhausted, adsorption of the MV^{+} occurs resulting in an enhancement of the Raman signal due to the adsorbed species (point B). Both components of the Raman signal decrease as the MV^{+} is converted to MV^{+2} at potentials more positive than $-0.6V$.

Acknowledgments

The authors acknowledge the financial support by the divisions of Materials Science and Chemical Science, Office of Basic Energy Sciences, Department of Energy.

Manuscript submitted July 27, 1982; revised manuscript received Jan. 28, 1983.

Any discussion of this paper will appear in a Discussion Section to be published in the June 1984 JOURNAL. All discussions for the June 1984 Discussion Section should be submitted by Feb. 1, 1984.

Argonne National Laboratory assisted in meeting the publication costs of this article.

REFERENCES

1. J. Kiwi, K. Kalyanasundaram, and M. Grätzel, in "Structure and Bonding," Vol. 49, M. J. Clarke *et al.*, Editors, p. 37, Springer Verlag, Berlin (1982).
2. E. M. Kosower, in "Free Radicals in Biology," Vol. 2, W. A. Pryor, Editor, p. 1, Academic Press, New York (1976).

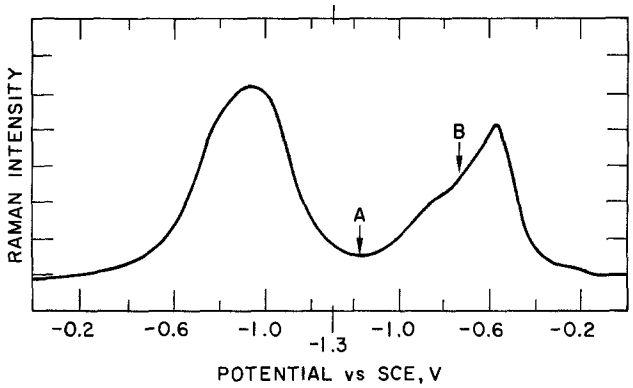

Fig. 11a. Variation in intensity of the 1530 cm^{-1} band as a function of potential.

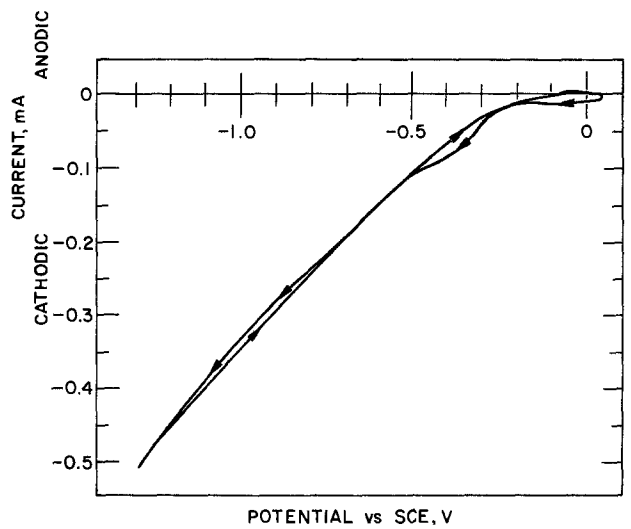

Fig. 11b. Cyclic voltammogram in $10^{-5}M$ MV^{+2} and 0.1M KCl solution. Scan rate = 5 mV/sec.

3. D. Meisel, W. A. Muloc, and M. S. Matheson, *J. Phys. Chem.*, **85**, 179 (1981); P. C. Lee, K. Schmidt, S. Gordon, and D. Meisel, *Chem. Phys. Lett.*, **80**, 242 (1981).
4. A. Regis and J. Croset, *J. de Chim. Phys.*, **78**, 687 (1981).
5. M. Forster, R. B. Girling, and R. E. Hester, *J. Raman Spec.*, **12**, 36 (1982).
6. C. A. Melendres and F. A. Cafasso, *This Journal*, **128**, 755 (1981).
7. E. Steckham and T. Kuwana, *Ber. Bunsenges. Phys. Chem.*, **78**, 253 (1974).
8. R. H. Wopschall and I. Shain, *Anal. Chem.*, **39**, 1514 (1967).
9. R. S. Nicholson and I. Shain, *ibid.*, **36**, 706 (1964).
10. H. Lynn Landrum, R. T. Salmon, and F. M. Hawkridge, *J. Amer. Chem. Soc.*, **99**, 3154 (1977).
11. E. F. Bowden and F. M. Hawkridge, *J. Electroanal. Chem.*, **125**, 367 (1981).
12. M. Ohsawa, K. Nishijima, and W. Suëtaka, *Surf. Sci.*, **104**, 270 (1981).
13. J. S. Clarke, A. T. Kuhn, and W. J. Orville-Thomas, *J. Electroanal. Chem. Interfacial Electrochem.*, **54**, 253 (1974).

Two-Plateau Rechargeable Sodium/Sulfur(IV) Molten Chloroaluminate Cell

G. Mamantov,* K. Tanemoto, and Y. Ogata

Department of Chemistry, University of Tennessee, Knoxville, Tennessee 37996

ABSTRACT

The behavior of the rechargeable cell

Na/β''-alumina/SCl_3^+ in molten $AlCl_3$-NaCl

under conditions in which S(IV) is reduced to S(−2) is described. It is shown that the use of reticulated vitreous carbon as the positive current collector and high concentrations of active material result in cells which operate at temperatures ≤220°C and have very high energy densities (>450 W-hr/kg).

Previous studies have described the use of tetravalent sulfur in molten chloroaluminate secondary batteries (1-3). It has been shown in this laboratory that the rechargeable cell

Na/β''-alumina/SCl_3^+ in $AlCl_3$-NaCl

has an open-circuit voltage of 4.2V and can be operated at 180°-250°C. Long cycle life [1370 cycles for one of the cells (4)] and high energy densities (~280 W-hr/kg) have been demonstrated for cells in which S(IV) is reduced to elemental sulfur in accordance with the overall reaction

$$4Na + SCl_3AlCl_4 + 3AlCl_3 = S + 4NaAlCl_4 \quad [1]$$

Although our early studies (5) demonstrated the presence of the second discharge plateau in which sulfur is reduced further to sulfide, only preliminary results (3) have been reported to date. In this paper, we present the results of additional studies on the two-plateau Na/S(IV) chloroaluminate cell. It is shown that a significant gain in energy density and lower operating temperatures have been obtained through these studies.

* Electrochemical Society Active Member.
Key words: battery, rechargeable, chloroaluminate sulfur, Beta-alumina.

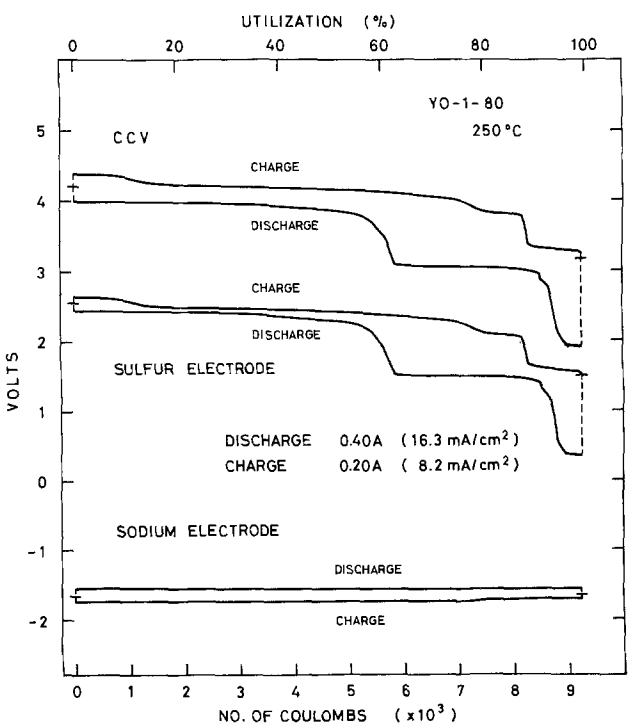

Fig. 1. Galvanostatic charge-discharge curve and potentials of sulfur and sodium electrodes *vs.* Al(III)/Al (in $NaCl_{sat}$ melt) reference electrode at 250°C. Discharge time 6.4 hr. Percent utilization is calculated for the $6e^-$ process. Initial positive electrode mix: 0.52g of sulfur and 50.0g $AlCl_3$-NaCl (57-43 m/o ≅ 57/43).

Experimental

Melt preparation, laboratory procedures, and a description of the laboratory cell used for charge/discharge studies have been reported previously (2, 6, 7).

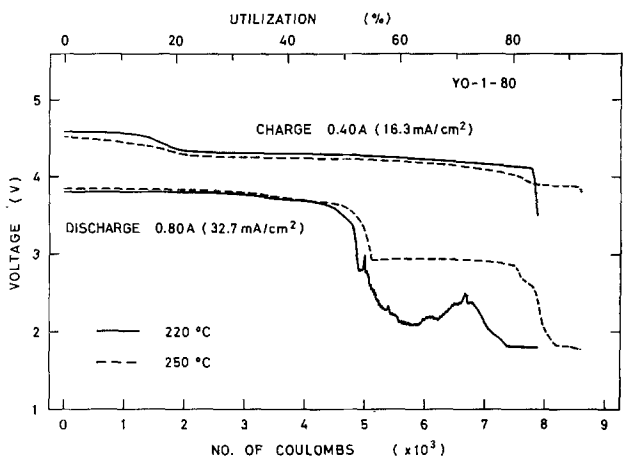

Fig. 2. Galvanostatic charge-discharge curves at 220° and 250°C

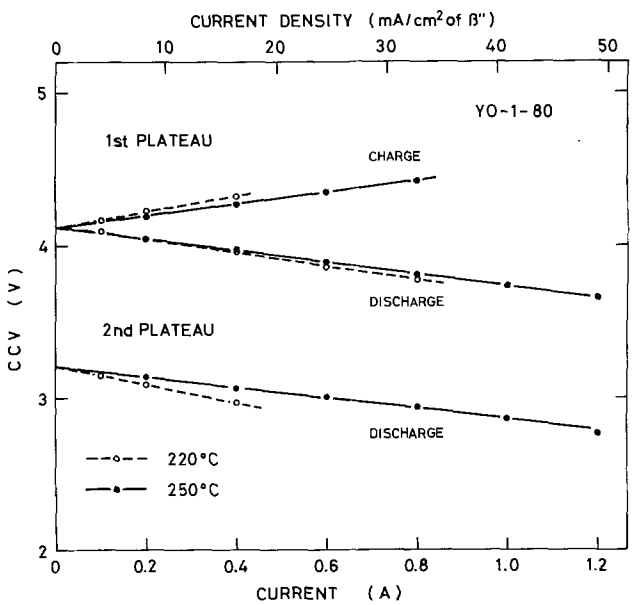

Fig. 3. Current dependence of the closed circuit voltage (CCV) measured at the midpoint of discharge for each plateau at 220° and 250°C.

In some of the cells, reticulated vitreous carbon (RVC 6 × 1 — 45S from Fluorocarbon Company) was used as the positive electrode current collector in place of a tungsten spiral. Sulfur (t5N5 grade from Alfa) was used as received; S(IV) was added as SCl_3AlCl_4 (8). An ECO Model 545 galvanostat and electrometer (ECO Instruments) and a Mark II automatic cycler (Argonne National Laboratory) were used for cycling of the laboratory cells.

Results and Discussion

Preliminary studies have shown (9) that pronounced voltage oscillations occur at the end of the first discharge plateau (corresponding to the formation of elemental sulfur) when the melt composition at that point corresponds to an Al(III)/Na(I) ratio of ~1 (neutral melt) and when a tungsten spiral is used as the positive current collector. Our initial approach to correct this problem was to use lower sulfur concentrations (~0.3*m*), which result in smaller acidity changes during the discharge. In this way, the melt remains acidic (Al(III)/Na(I) ratio > 1) at the end of the second discharge plateau. A galvanostatic charge/discharge curve and the variation of sulfur and sodium electrode potential *vs.* an Al(III)/Al reference electrode for a 2.6 A-hr cell are shown in Fig. 1. As expected from the ratio of the *n*-values, the ratio of the number of coulombs in the first to the second plateau was found to be ~2, indicating the formation of sulfur in the −2 state. Recent Raman spectroscopic studies (10, 11) have shown that sulfide in acidic melts is present as oligomeric AlSCl. The overall reaction corresponding to the second discharge plateau can be written in simplified form as

$$2Na + S + AlCl_3 = AlSCl + 2NaCl \qquad [2]$$

Thus, the melt chloroacidity continues to decrease during the second discharge plateau. Further discharge after the second plateau results in the formation of a black product (presumably aluminum) on the tungsten current collector. It may be seen from Fig. 1 that charging of the cell results in much greater overall irreversibility for the second plateau as compared to the first one. This behavior is at least partially due to the low solubility of sulfide and sulfur in melts that are not strongly acidic (10, 12). The second plateau was poorly defined at lower temperatures and higher applied current densities using tungsten spiral as current collector (Fig. 2). Good definition of the second discharge plateau was obtained at higher temperatures (Fig. 2). The dependence of the cell voltage on current density is illustrated in Fig. 3. The behavior for the first plateau is similar to that reported previously (2, 3); because of the large irreversibility of the second charge plateau, the CCV dependence on the current density for the second charge plateau is not shown. The energy densities obtained in this cell were low (<200 W-hr/kg) because of the low concentration of the active material. Much better results for the second plateau were obtained with an RVC current collector. This spongy material provides a much larger surface area; it also minimizes problems related to the low solubilities of sulfur and sulfide in neutral and basic melts. The results obtained with an RVC current collector are shown in Fig. 4. No voltage oscillations are observed although the melt composition becomes basic (melt is saturated with NaCl) during the second plateau. It should also be noted that the irreversibility of the second charge plateau is considerably less as compared to the cell which uses a tungsten spiral (Fig. 1).

A very significant increase in the energy density resulted by using very high concentrations of the active material (1.17*m*) and an RVC current collector. Charge-discharge curves for such a cell, as well as the variations of the potentials of the sulfur and sodium electrodes, are shown in Fig. 5. The comparison of the parameters between a "sulfur-rich" and a "normal" RVC cell is shown in Table I. The energy density achieved (457 W-hr/kg) is significantly higher than the values obtained previously (2, 3). Because the reduction of one SCl_3^+ ion is accompanied by the conversion of 3 $AlCl_3$ molecules to $AlCl_4^-$ (see Eq. [1]), it is necessary to use very acidic melts for experiments involving "sulfur-rich" positive mixes. Such melts have

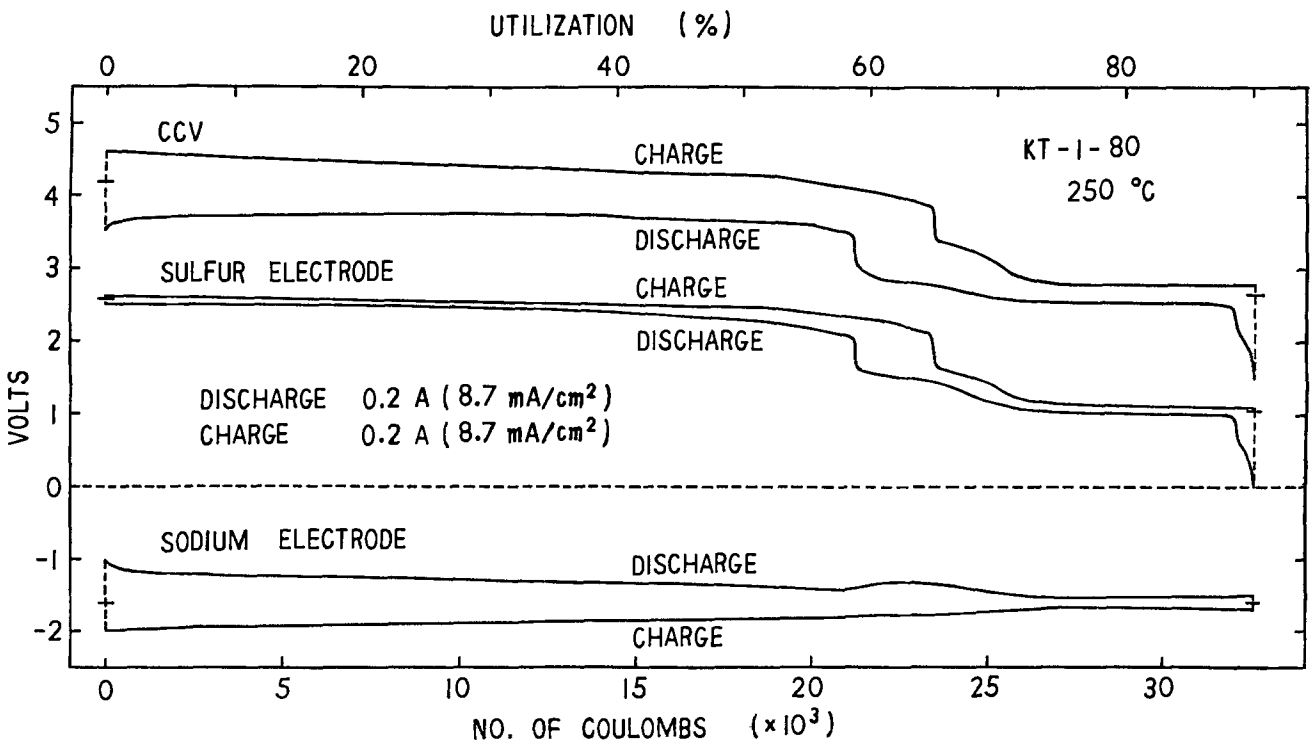

Fig. 4. Galvanostatic charge-discharge curve and potentials of sulfur and sodium electrodes *vs.* Al(III)/Al (in $NaCl_{sat}$ melt) reference electrode at 250°C. Discharge time 45.2 hr. Percent utilization is calculated for the $6e^-$ process. Reticulated vitreous carbon used as positive current collector. Concentration of SCl_3AlCl_4 0.701*m*

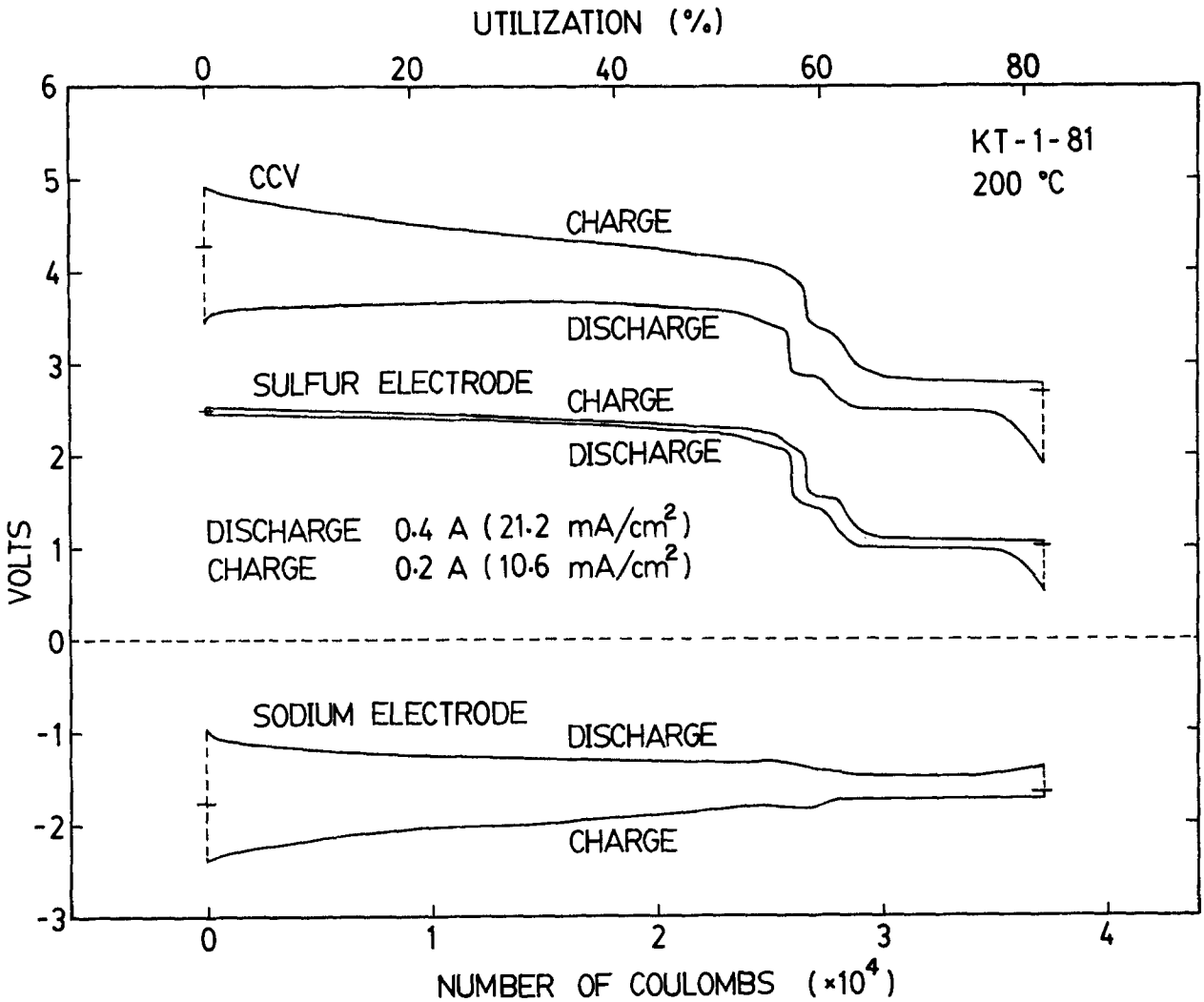

Fig. 5. Galvanostatic charge-discharge curve and potentials of sulfur and sodium electrodes vs. Al(III)/Al (in $NaCl_{sat}$ melt) reference electrode at 200°C. Reticulated vitreous carbon used as positive current collector.

low conductivities and high vapor pressures. Therefore, "sulfur-rich" cells are usually operated at lower current densities (≤25 mA/cm²) and lower temperatures (≤220°C); in addition, the charging is restricted to <90% of full charge compared to the complete conversion to S(IV). The cell described in Table I underwent 108 deep charge/discharge cycles and was in continuous operation for ~8 months. Some degradation in performance was observed at ~90th cycle. Post mortem examination of the RVC used in this two-plateau cell indicated some attack of the material by the positive mix. On the other hand, RVC used as the current col-

Table I. Typical parameters of two-plateau cells using RVC current collectors

			1st Plateau					2nd Plateau					Overall	
Temperature °C	Current density[a] mA/cm² DC	CH	Average cell voltage V DC	CH	Energy efficiency %	Energy density W-hr/kg	Utilization, %	Average cell voltage, V DC	CH	Energy efficiency %	Energy density W-hr/kg	Utilization, %	Energy density W-hr/kg	Utilization, %
						"Normal" RVC-Cell[b]								
220	17.4	8.7	3.32	4.61	72.1	206[d]	87.6[j]	2.24	3.21	69.7	72[o]	90.8	278[f]	88.7
						"Sulfur-rich" RVC-Cell[c]								
180	10.6	5.3	3.61	4.78	75.5	348[g]	84.5[k]	2.49	2.95	84.3	107[h]	77.8	455	82.3
200	21.2	10.6	3.62	4.43	81.6	354	85.7[l]	2.50	2.98	83.9	103	74.6	457	82.0
220	21.2	10.6	3.73	4.31	86.4	306	72.3[m]	2.51	2.99	83.9	111	80.8	417	75.1
250	21.2	10.6	—	—	—	—	—	2.58	2.89	89.2	126	89.6	—	—

[a] Current density based on the inner surface area of β″-alumina.
[b] Initial positive electrode mix: 19.2g SCl_3AlCl_4 in 69.8g $AlCl_3$-NaCl (66.0-34.0 m/o) melt. Theoretical Capacity 10.0 A-hr.
[c] Initial positive electrode mix: 24.1g SCl_3AlCl_4 in 42.6g $AlCl_3$-NaCl (83.4-16.6 m/o) melt. Theoretical Capacity 12.6 A-hr.
[d] Maximum energy density 288 W-hr/kg. [The required weight of sodium is included.]
[e] Maximum energy density 129 W-hr/kg.
[f] Maximum energy density 417 W-hr/kg.
[g] Maximum energy density 458 W-hr/kg.
[h] Maximum energy density 208 W-hr/kg.
[i] Maximum energy density 666 W-hr/kg.
[j] Prior charge 100%.
[k] Prior charge 89.8%.
[l] Prior charge 91.4%.
[m] Prior charge 77.6%.

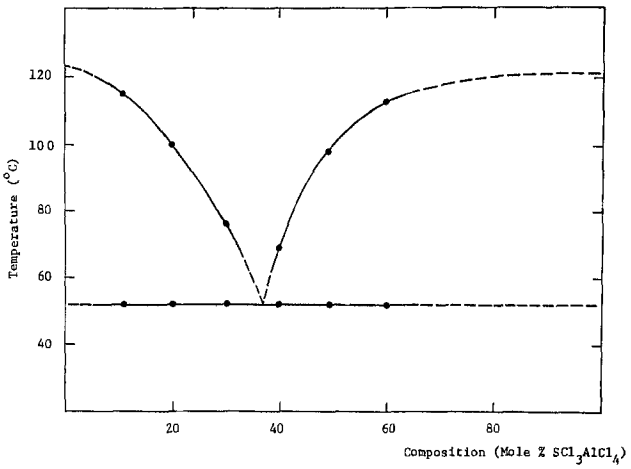

Fig. 6. Phase diagram of SCl_3AlCl_4-(63-37 m/o $AlCl_3$-NaCl) section of SCl_3AlCl_4-$AlCl_3$-NaCl system (phase compositions were not determined).

lector for cells in which charge/discharge involved only the first plateau, did not exhibit similar deterioration.

Finally, much lower operating temperatures are possible with "sulfur-rich" cells as indicated by the partial phase diagram for the system SCl_3AlCl_4-(63/37 $AlCl_3$-NaCl) shown in Fig. 6. The lowest liquidus temperature obtained was 52°C. Thus, cell operation over a relatively narrow composition region should be possible a few degrees above the melting point of sodium (105°C). However, at such temperatures the resistivity of β''-alumina may be too high for a satisfactory performance.

Acknowledgments

This research has been supported by the Department of Energy, University of California Subcontract 4502810. We would like to thank Dr. C. Petrovic of this Laboratory for providing the partial phase diagram for the system SCl_3AlCl_4-(63/37 $AlCl_3$-NaCl).

Manuscript submitted Sept. 7, 1982; revised manuscript received *ca.* March 4, 1983.

Any discussion of this paper will appear in a Discussion Section to be published in the June 1984 JOURNAL. All discussions for the June 1984 Discussion Section should be submitted by Feb. 1, 1984.

The University of Tennessee assisted in meeting the publication costs of this article.

REFERENCES

1. G. Mamantov and R. Marassi, U.S. Pat. 4,063,005 (1977).
2. G. Mamantov, R. Marassi, M. Matsunaga, Y. Ogata, J. P. Wiaux, and E. J. Frazer, *This Journal*, **127**, 2319 (1980).
3. G. Mamantov, R. Marassi, Y. Ogata, M. Matsunaga, and J. P. Wiaux, in "Proceedings of the 15th Intersociety Energy Conversion Engineering Conference," Vol. 1, 809107, American Institute of Aeronautics and Astronautics, Seattle, WA, August 18-22, 1980.
4. A. Katagiri and G. Mamantov, Unpublished work.
5. G. Mamantov, R. Marassi, J. P. Wiaux, S. E. Springer, and E. J. Frazer, in "Proceedings of the Symposium on Load Leveling," N. P. Yao and J. R. Selman, Editors, pp. 379-383, The Electrochemical Society Softbound Proceedings Series, Princeton, NJ (1977).
6. G. Torsi, K. W. Fung, G. M. Begun, and G. Mamantov, *Inorg. Chem.*, **10**, 2285 (1971).
7. R. Marassi, J. Q. Chambers, and G. Mamantov, *J. Electroanal. Chem. Interfacial Electrochem.*, **69**, 345 (1976).
8. G. Mamantov, R. Marassi, F. W. Poulsen, S. E. Springer, J. P. Wiaux, R. Huglen, and N. R. Smyrl, *J. Inorg. Nucl. Chem.*, **41**, 260 (1979).
9. Y. Ogata and G. Mamantov, Unpublished work.
10. R. W. Berg, S. von Winbush, and N. J. Bjerrum, *Inorg. Chem.*, **19**, 2688 (1980).
11. K. Tanemoto, A. Katagiri, and G. Mamantov, *This Journal*, **130**, 890 (1983).
12. R. Marassi, G. Mamantov, M. Matsunaga, S. E. Springer, and J. P. Wiaux, *This Journal*, **126**, 231 (1979).

Analysis of The Flow-Through Porous Trielectrode Reactor

R. Pollard*

Department of Chemical Engineering, University of Houston, Houston, Texas 77004

and J. A. Trainham*

E.I. du Pont de Nemours and Company Incorporated, Polymer Products Department, Wilmington, Delaware 19898

ABSTRACT

The limiting current analysis has been applied to a flow-through porous electrode with two counterelectrodes. The electric driving force variation through the working electrode can be minimized by adjusting the fraction of the total current that passes through each counterelectrode. For applications with a maximum acceptable ohmic potential drop in the reactor, the use of two counterelectrodes can substantially increase the maximum processing rate for a flow-through reactor and hence make it more competitive with the flow-by electrode configuration.

Flow-through porous electrodes (current flow parallel to the fluid flow) have been studied to a great extent both experimentally and theoretically, and they have the potential for numerous industrial applications (1-3). Electrode performance has been shown to be dictated by the distribution of the electric driving force within the electrode (4-8). For flow-through porous electrodes of industrial interest, the current must traverse a significant distance through the bed. This can result in highly nonuniform current and potential distributions and, hence, in poor reaction selectivity.

Two types of flow-by electrode geometries (current flow perpendicular to the fluid flow) have been suggested to improve the system behavior: (*i*) spirally wrapped sandwich construction (9-12) suitable for a mixed anolyte-catholyte electrochemical system [also referred to as the "Swiss Roll Cell" (13)] and (*ii*) separate anolyte-catholyte configuration (14, 15).

Trainham and Newman (16), with an approximate model for a redox battery (operation below the limit-

* Electrochemical Society Active Member.
Key words: limiting current, mass transfer, potential distributions.

ing current), have shown that the flow-by geometry [(*ii*) above] is superior to the flow-through configuration. Fedkiw (17) has shown that, at the limiting current, the flow-by geometry [(*ii*) above] with an aspect ratio $L/d > 5$ allows a higher processing rate than a flow-through porous electrode with an upstream counterelectrode.

Trainham and Wu (8) have suggested the use of multiple current collectors to improve the performance of the flow-through configuration. Their analysis indicates that electric driving force variations are significantly smaller for a working electrode with two current collectors rather than one. Also, Ng (18) has shown experimentally that with two counterelectrodes ("the porous trielectrode reactor"), the electric driving force distribution is more uniform and higher processing rates are possible than with the standard bielectrode system.

In this paper, a theoretical analysis of the porous trielectrode system suggested by Ng (18) is presented. The analysis is restricted to the limiting current and, consequently, only the overpotential variations within the electrode can be minimized. Results are compared with the analysis for multiple current collectors (11), with available experimental data (18), and with results for the flow-by geometry (17).

Analysis

The one-dimensional model is based on the macroscopic theory of porous electrodes in which the solution and matrix phases are treated as superposed continua (19). At the limiting current, and with the assumption that axial diffusion and dispersion can be neglected, a material balance within the porous electrode becomes (3)

$$\frac{dc_R}{dx} = -\frac{ak_m}{v} c_R \qquad [1]$$

Integration of Eq. [1] yields

$$c_R = c_{Rf} e^{-\alpha x} \qquad [2]$$

where $\alpha = ak_m/v$ and c_{Rf} is the upstream feed concentration of reactant. The parameter α is assumed to be independent of position in the packed bed.

The movement of electrons in the matrix phase is governed by Ohm's law

$$i_1 = -\sigma \frac{d\Phi_1}{dx} \qquad [3]$$

where σ is the effective matrix conductivity. Ohm's law can also be used to represent the variation of potential in the pore solution

$$i_2 = -\kappa \frac{d\Phi_2}{dx} \qquad [4]$$

provided that the concentration of the limiting reactant is small compared to that of the supporting electrolyte.

The effective conductivity κ of the solution within the pores can be related to the bulk conductivity κ_∞ by (20)

$$\kappa = \kappa_\infty \epsilon^{1.5} \qquad [5]$$

As a consequence of the condition of electrical neutrality, the divergence of the total current density is zero

$$\nabla \cdot i_1 + \nabla \cdot i_2 = 0 \qquad [6]$$

For a single electrode reaction, represented as

$$\sum_i s_i M_i^{z_i} \rightarrow ne^- \qquad [7]$$

(with $s_R < 0$ for reductions and $s_R > 0$ for oxidations), Faraday's law is expressed as

$$aj_{in} = -\frac{s_i}{nF} \frac{di_2}{dx} \qquad [8]$$

if double-layer charging at the electrode surface can be ignored. The pore-wall flux j_{Rn} of reactant at the limiting current is related to the mass transfer coefficient k_m by

$$j_{Rn} = k_m (c_{Rw} - c_R) = -k_m c_R \qquad [9]$$

Combination of Eq. [2], [8], and [9] yields

$$\frac{di_2}{dx} = \frac{nF}{s_R} ak_m c_{Rf} e^{-\alpha x} \qquad [10]$$

The current distribution in the working electrode can be obtained by integration of Eq. [10], subject to the appropriate boundary conditions. For an electrode with finite matrix conductivity, these boundary conditions depend on the location of the current collector relative to the direction of fluid flow. If the matrix conductivities of the counterelectrodes can be regarded as infinite, there are two electrode configurations, as illustrated in Fig. 1. The corresponding boundary conditions are given in Table I. The parameter f represents the fraction of the total current i that passes through the downstream counterelectrode. In both cases, the superficial current density i_2 in the pore phase is, from Eq. [10]

$$i_2(x) = fi - B(e^{-\alpha x} - e^{-\alpha L}) \qquad [11]$$

where

$$B = \frac{nFvc_{Rf}}{s_R} = \frac{i}{1 - e^{-\alpha L}} \qquad [12]$$

The distribution of local overpotential $\eta (= \Phi_1 - \Phi_2)$ is derived by combination of Eq. [3], [4], [6], and [10] and integration

$$\eta(0) - \eta(x) = A[(1 + R_o)(1 - e^{-\alpha x} - \alpha x e^{-\alpha L}) - f'\alpha x(1 - e^{-\alpha L})] \qquad [13]$$

where A and R_o are assumed to be constants and are defined as

$$A = B/\alpha\kappa, \quad R_o = \kappa/\sigma \qquad [14]$$

The current factor f' in Eq. [13] is equal to f for an upstream current collector and to $f + R_o$ for a downstream current collector. In the limiting case of infinite matrix conductivity in the working electrode, $R_o = 0$, and the results are independent of current collector location.

Results and Discussion

Equation [13] can be used to calculate the distribution of electric driving force in a flow-through porous

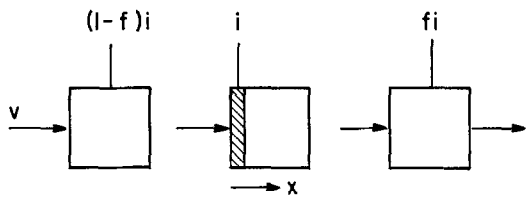

a) Upstream current collector

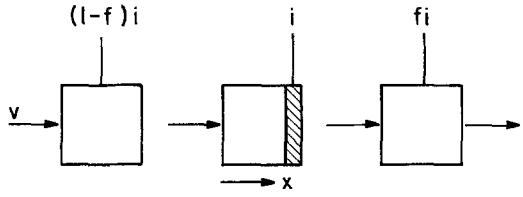

b) Downstream current collector

Fig. 1. Electrode configurations

Table I. Boundary conditions for electrode configurations in Fig. 1

	$i_1(x=0)$	$i_2(x=0)$	$i_1(x=L)$	$i_2(x=L)$
Fig. 1a	i	(f − 1)i	0	fi
Fig. 1b	0	(f − 1)i	−i	fi

electrode with two counterelectrodes. The equation applies to a system operated at the limiting current where the reactant is transported through the electrode by convection alone. In practice, it may be desirable to choose the parameter f to minimize potential variations across the bed because the variations can govern the specificity of the reactor (2).

For the configurations shown in Fig. 1, there are two modes of behavior of physical interest. When

$$0 < f' < (1 + R_o)(1 - f_u) \quad [15]$$

where (8)

$$f_u = \frac{\alpha L + e^{-\alpha L} - 1}{\alpha L(1 - e^{-\alpha L})}$$

the electric driving force $\eta(0) - \eta(x)$ is smallest at the fluid inlet and largest at some intermediate point x_u. When

$$(1 + R_o) > f' > (1 + R_o)(1 - f_u) \quad [16]$$

the driving force is also largest at a point within the electrode but it is smallest at the fluid outlet.

Figure 2 shows the relationship between $\eta_{max} - \eta_{min}$ (the difference between the largest and smallest overpotentials in the electrode) and the current factor f', for one set of bed characteristics. In this example, the driving force varies least when $f' = f'_{min} = 0.154$. This is the current factor associated with the discontinuity in Fig. 2, and it represents the condition for the location of the smallest electric driving force to switch between the fluid inlet and the fluid outlet. It corresponds to $f = 0.154$ with an upstream current collector and $f = 0.144$ with a downstream current collector.

Comparison of Eq. [15] and [16] indicates that, in general, f'_{min} is given by

$$f'_{min} = (1 + R_o)(1 - f_u) \quad [17]$$

With this value of f', the electric driving force is the same at the front and the back of the electrode. Substitution of Eq. [17] into [13] shows that the potential variation associated with f'_{min} is

$$\frac{\eta_{max} - \eta_{min}}{A(1 + R_o)} = 1 - w + w \ln w \quad [18]$$

where

$$w = e^{-\alpha x_u} = \frac{1 - e^{-\alpha L}}{\alpha L} \quad [19]$$

The value of the minimum electric driving force variation obtained from Eq. [18] is identical to that predicted for a flow-through porous electrode with multiple current collectors [see Eq. [37], [39], [53], and [58] of Ref. (8)]. However, the corresponding optimum division of current between the two counterelectrodes is not the same as that between the two current collectors [compare Eq. [17] with [47] and [68] of Ref. 8)]. This indicates that, under optimum conditions, the improvements obtained with the porous trielectrode reactor are equivalent to those achieved with multiple current collectors, but that the nature of the corresponding operating conditions is different.

Changes in $\eta_{max} - \eta_{min}$ with κ/σ are presented in Fig. 3, for one particular value of αL. For the special case of $R_o = 0$, the minimum variation in electric driving force is with $f = f'_{min} = 0.152$. At larger values of R_o, f_{min} is larger for the upstream current collector configuration, in accordance with Eq. [17] and with the definition of f'. It should be noted that, for $\alpha L = 6.5$, values of f'_{min} greater than approximately 0.3 (*i.e.*, $\kappa/\sigma \simeq 1$) are unlikely to be encountered in practice. For a downstream current collector, the fraction f of the total current that passes through the downstream counterelectrode must be less than 0.152 with $R_o > 0$, if the minimum overpotential variation is to be attained.

Figure 4 shows the dependence of f'_{min} and $\eta_{max} - \eta_{min}$ on the dimensionless streamwise bed depth αL. As the magnitude of αL is increased, the minimum electric driving force variation becomes larger and, to operate at f'_{min}, more current must be collected from the upstream counterelectrode.

In Fig. 5, predicted overpotential distributions are compared with previously published experimental data (18). For each αL, the experimental value of $\eta(0) - \eta(L)$ is used to calculate the fraction f of current in the downstream counterelectrode. This parameter, together with Eq. [13], is used to obtain each theoretical curve. In the three examples, there is a discrepancy of approximately 60 mV between the calculated and the observed values of $\eta(0) - \eta(x)$ at $x/L = 0.5$. This might result from side reactions, such as reduction of oxygen in the cathode, although parasitic reactions generally reduce the magnitude of potential variations (3). It should also be noted that the discrepancies are not

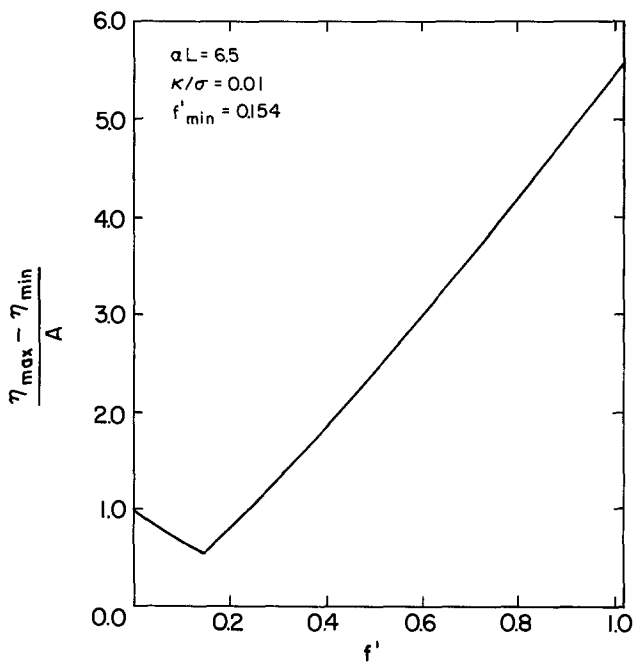

Fig. 2. Dependence of the variation in the electric driving force on the current factor, at the limiting current.

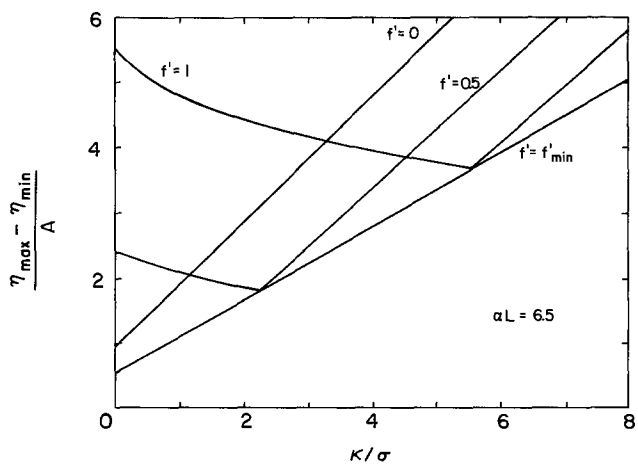

Fig. 3. Dependence of the variation in the electric driving force on the conductivity ratio of the solution phase to the matrix phase, at the limiting current.

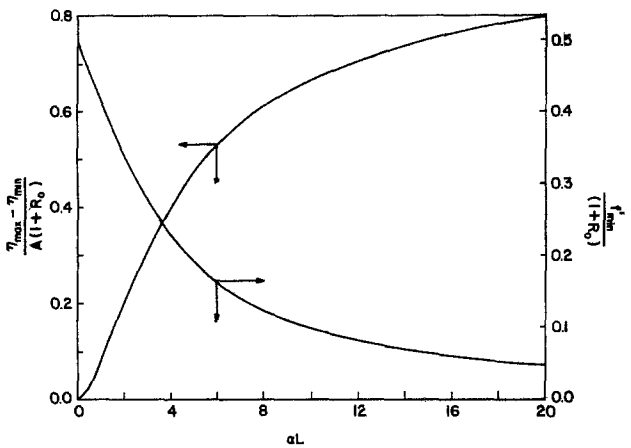

Fig. 4. Dependence of the variation in the electric driving force and of the current factor on the dimensionless streamwise bed depth, at the limiting current.

particularly sensitive to the choice for $\eta(0) - \eta(L)$. For $\alpha L = 0.48$, $\eta(0) - \eta(L)$ would need to be approximately 0.17V to give $\eta_{max} - \eta_{min}$ close to the observed value of 0.18V and, even then, the maximum would be at $x_u/L = 0.78$, rather than at the center of the electrode. The predicted minimum variations in electric driving force are listed in Table II, together with the corresponding values of f_{min} and x_u/L. The results indicate that, in the absence of side reactions and with the limiting current condition across the whole bed, the potential variations could be even smaller than those obtained experimentally. With adjustment of the current flow through each counterelectrode, reduction in potential changes through the electrode and improvements in reaction specificity should be attainable.

Table III compares calculated solution phase ohmic potential drops for the trielectrode reactor with previously published calculations (17) for flow-by and standard flow-through electrodes. Results are presented at three values of the conversion, each at two Péclet numbers. For the flow-through system, addition of a second counterelectrode reduces the potential variation substantially in each case. The effect is largest at low processing rates (low Pe) and small fractional conversions (large θ).

Table II. Predicted minimum variation of electric driving force for trielectrode reactor. Parameters as in Fig. 5

αL	f_{min}	$\frac{x_u}{L}$	$\eta_{max} - \eta_{min}$ (V)
0.480	0.460	0.480	0.075
0.285	0.476	0.488	0.132
0.142	0.488	0.494	0.270

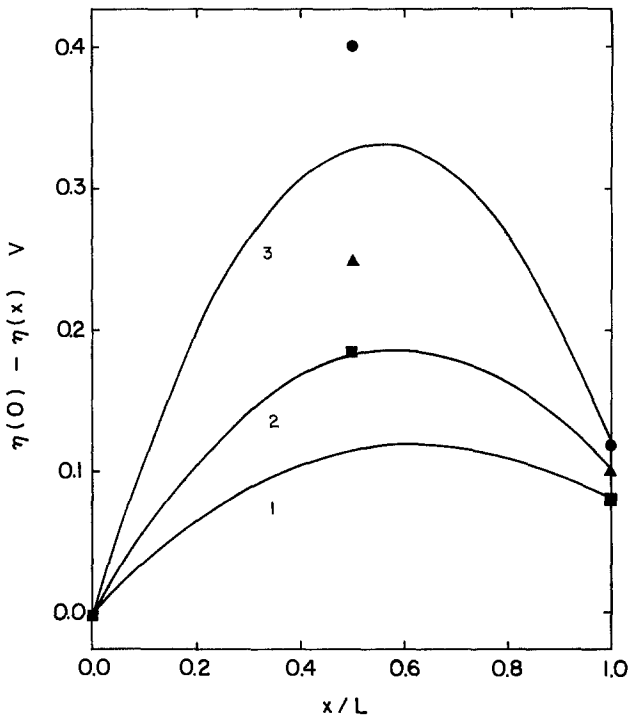

Fig. 5. Overpotential distributions for a trielectrode reactor. Curves represent theoretical predictions. Data points are for reduction of a silver plating bath solution (18). Experimental conditions: $\kappa = 0.017\ \Omega^{-1}cm^{-1}$; $\sigma \simeq 10^5\ \Omega^{-1}cm^{-1}$; $a = 8.05\ cm^{-1}$; $L = 5$ cm; $c_{Rf} = 1.08 \times 10^{-6}$ mol/cm^3; $n = 1$; $s_R = -1$. ■ (curve 1): $v = 0.051$ cm/sec; $k_m = 6.12 \times 10^{-4}$ cm/sec. ▲ (curve 2): $v = 0.140$ cm/sec; $k_m = 9.90 \times 10^{-4}$ cm/sec. ● (curve 3): $v = 0.537$ cm/sec; $k_m = 1.89 \times 10^{-3}$ cm/sec.

The trielectrode reactor also compares favorably with the flow-by porous electrode, especially at high conversions. Consider an example with 99% conversion at a fluid flow rate corresponding to Pe = 10. At the limiting current, the flow-through trielectrode system has a maximum dimensionless potential drop of 73 whereas the flow-by electrode would need an aspect ratio greater than 3.5 to achieve a smaller potential variation. For 99.9% conversion, the flow-by electrode would need to be even longer ($L/d \geq 4.8$) to give a smaller ohmic potential drop than the flow-through reactor with two counterelectrodes.

Conclusions

A limiting current analysis has been used to predict the variation of electric driving force within a flow-through porous trielectrode reactor. The potential variation through the bed can be minimized by controlling the fraction of the total current that passes through each counterelectrode. The optimum value of this fraction depends on the dimensionless streamwise bed depth and the conductivity ratio of the solution to

Table III. Comparison of maximum dimensionless ohmic potential drop in a flow-through porous trielectrode with corresponding values (17) for flow-by porous electrodes with different aspect ratios and for a porous electrode with one counterelectrode

		$\frac{\Delta\Phi_2}{(anFD_oc_{Rf}/\kappa s_R)}$					
		Flow-through		Flow-by			
θ	Pe = v/aD_o	Trielectrode	Bielectrode	$L/d = 2$	$L/d = 3$	$L/d = 4$	$L/d = 5$
10^{-0}	10	131	245	445	256	170	122
	10^2	5,876	10,200	18,700	10,800	7,130	5,100
10^{-1}	10	73	157	170	94	61	42
	10^2	2,912	6,130	6,810	3,760	2,420	1,690
10^{-1}	10	32	96	51	26	16	11
	10^2	1,250	3,360	1,980	1,020	622	421

matrix phases. The analysis shows that, for applications where conversion and maximum electric driving force variation are specified, the maximum processing rate that can be obtained in flow-through electrodes with two counterelectrodes is always greater than that with one counterelectrode and, under some circumstances, can be greater than that for flow-by porous electrodes.

Manuscript submitted Nov. 8, 1982; revised manuscript received April 1, 1983.

Any discussion of this paper will appear in a Discussion Section to be published in the June 1984 JOURNAL. All discussions for the June 1984 Discussion Section should be submitted by Feb. 1, 1984.

LIST OF SYMBOLS

a interfacial area per unit electrode volume (cm^{-1})
A parameter defined by Eq. [14] (V)
B maximum possible superficial current density as defined by Eq. [12] (A/cm^2)
c_R reactant concentration per unit volume of solution (mol/cm^3)
c_{Rf} feed concentration of reactant (mol/cm^3)
c_{RL} outlet concentration of reactant (mol/cm^3)
c_{Rw} concentration of reactant at electrode wall (mol/cm^3)
d bed depth perpendicular to fluid flow direction (cm)
D_o free stream diffusion coefficient (cm^2/sec)
f fraction of total superficial current density that passes through downstream counterelectrode
f_{min} value of f that corresponds to the minimum variation in electric driving force through working electrode
f' current factor (see below Eq. [13])
f'_{min} value of f' that corresponds to the minimum variation in electric driving force through working electrode
f_u parameter in Eq. [15]
$\mathbf{F}$ Faraday's constant (96,487 C/equiv.)
i superficial current density to working electrode ($i < 0$ for reductions and $i > 0$ for oxidations) (A/cm^2)
i_1 superficial current density in matrix phase (A/cm^2)
i_2 superficial current density in pore phase (A/cm^2)
j_{in} pore-wall flux of species i from the solid phase to the solution (mol/cm^2 sec)
k_m average mass transfer coefficient between flowing solution and electrode surface (cm/sec)
L thickness of porous electrode (cm)
M_i symbol for the chemical formula of species i
n number of electrons transferred in electrode reaction
Pe Péclet number, v/aD_o
R_o κ/σ, ratio of solution conductivity to matrix conductivity
s_i stoichiometric coefficient of species i in electrode reaction
v superficial fluid velocity (cm/sec)
x distance through working electrode measured from the fluid inlet (cm)
x_u value of x for which the electric driving force is a minimum (see Eq. [19])
z_i valence or charge number of species i

Greek Letters

α $= ak_m/v$, reciprocal of penetration depth at limiting current (cm^{-1})
ϵ porosity or void volume fraction
η $= \Phi_1 - \Phi_2$, local overpotential (V)
θ conversion, c_{RL}/c_{Rf}
κ effective solution conductivity (mho/cm)
σ effective matrix conductivity (mho/cm)
Φ_1 electric potential in the matrix (V)
Φ_2 electric potential in the solution (V)

Subscripts

R reactant
∞ bulk solution property

REFERENCES

1. J. Newman and W. Tiedemann, *AIChE J.*, **21**, 25 (1975).
2. J. Newman and W. Tiedemann, in "Advances in Electrochemistry and Electrochemical Engineering," Vol. 11, H. Gerischer and C. W. Tobias, Editors, Wiley-Interscience, New York (1977).
3. D. N. Bennion and J. Newman, *J. Applied Electrochem.*, **2**, 113 (1972).
4. R. C. Alkire and B. E. Gracon, *This Journal*, **122**, 1594 (1975).
5. R. C. Alkire and R. Gould, *ibid.*, **123**, 1842 (1976).
6. J. A. Trainham and J. Newman, *ibid.*, **124**, 1528 (1977).
7. J. A. Trainham and J. Newman, *ibid.*, **125**, 58 (1978).
8. J. A. Trainham and J.-J. Wu, *ibid.*, **129**, 991 (1982).
9. J. M. Williams, U.S. Pat. 3,859,195 (1975).
10. K. B. Keating and J. M. Williams, *Resource Recovery Conserv.*, **2**, 39 (1975).
11. J. M. Williams and M. C. Olson, *AIChE Symp. Series*, **73**, 119 (1976).
12. J. M. Williams and K. B. Keating, *Dupont Innovation*, **6**, 6 (1975).
13. P. M. Robertson and N. Ibl, *J. Applied Electrochem.*, **7**, 323 (1977).
14. R. C. Alkire and P. K. Ng, *This Journal*, **121**, 95 (1974).
15. L. H. Thaller, U.S. Pat. 3,996,064 (1976).
16. J. A. Trainham and J. Newman, *Electrochim. Acta*, **26**, 455 (1981).
17. P. S. Fedkiw, *This Journal*, **128**, 831 (1981).
18. P. K. Ng, *ibid.*, **128**, 792 (1981).
19. J. Newman and C. W. Tobias, *ibid.*, **109**, 1183 (1962).
20. R. E. de la Rue and C. W. Tobias, *ibid.*, **106**, 827 (1959).

Electrochemical Synthesis of Photoactive MoS_2

L. F. Schneemeyer* and U. Cohen*,[1]

Bell Laboratories, Murray Hill, NJ 07974

ABSTRACT

The growth of polycrystalline films and single crystals of molybdenum disulfide by electrolytic reduction of a sodium tetraborate-sodium fluoride melt containing molybdenum trioxide and sodium sulfate has been examined and physical properties of those deposits studied. Polycrystalline n-type MoS_2 is readily obtained from a melt at 800°C while larger single-crystals are obtained if the melt temperature is raised to 900°C. MoS_2 is a semiconductor with bandgap well matched to the solar spectrum and with unusual resistance to photoelectrochemical corrosion. Electrochemically-grown single crystals and polycrystalline films were employed as photoanodes in aqueous iodide-triiodide electrolytes under ~40 mW/cm² tungsten-halogen illumination. Open-circuit photopotentials of ~150 mV were observed for polycrystalline MoS_2. For single crystal electrolytic MoS_2 an open-circuit photopotential of 210 mV and ~2 mA/cm² short circuit current were reached. The use of electrochemical methods to prepare these materials offers the advantages of relatively low growth temperatures, controlled thickness, and excellent adaptability to producing large-area films inexpensively.

In the search for new materials for solar energy conversion, the layered transition metal dichalcogenides such as MoS_2 have attracted much interest (1). Favorable characteristics of this family of materials include bandgaps well-matched to the solar spectrum, and inherent corrosion resistance. Solar to electrical power conversion efficiencies as high as 10, 9, and ~5% have been reported for single crystals as WSe_2, $MoSe_2$, and MoS_2, respectively (2-4). However, efficiencies are extremely dependent on crystal quality and are lowered by defects and steps which have been shown to act as recombination centers or sites at which back-reaction or corrosion occurs (5-7). Efforts to develop edge plane passivation techniques applicable to these materials are aimed at reducing such losses (8-10). Further, the usual crystal growth technique, halogen vapor phase transport, is difficult in the case of MoS_2 and in general, is not well suited to the preparation of large area samples. MoS_2 is transported from a hot zone at 1100°C (2), a temperature at which quartz ampules used for sample containment rapidly devitrify.

Conventional thin-film preparation techniques such as sputtering have failed to yield photoelectrodes of MoS_2 or other layered dichalcogenides with any significant activity even when subjected to post-treatments such as annealing (11, 12). The use of well-crystallized MoS_2 to fabricate flux-pasted electrodes and electrodes using a PMMA polymer binder has improved the performance of such thin-film electrodes (12). Polycrystalline p-WSe_2 films prepared by a transport technique have yielded ~1% efficient regenerative photoelectrochemical (PEC) cells using red light (11). Using various hot-pressing techniques combined with a post-treatment of the surface, light to electricity conversion efficiencies of 2.3% have been obtained with polycrystalline n-WSe_2 in 1M NaI/0.1M I_2 electrolytes (13). Attempts to prepare MoS_2 films by electrocrystallization from room temperature aqueous solutions have yielded deposits of poor crystal quality and no detectable photoresponse (14).

The preparation of MoS_2 as well as WS_2 by an electrolytic reduction of fused salts was first reported by Weiss (15). Small hexagonal blue-grey platelets were obtained by electrolysis under drastic conditions, 7.5V and 15A. However, only chemical analysis of the products was reported. An alternative molten salt system yielding MoS_2 as the product has been patented (16), but again, little characterization of the product material is included.

We are interested in the electrocrystallization of MoS_2 as a method which could be extended to the preparation of large area photoelectrodes. We report the growth of molybdenum disulfide single crystals and polycrystalline films by electrodeposition from a sodium tetraborate melt at $T > 800$°C. The physical properties of these deposits and their application as photoanodes for photoelectrochemical cells is discussed.

Experimental

The apparatus used for the electrochemical crystal growth is shown in Fig. 1. The melt was contained in a vitreous carbon crucible (Nomar Industries, Anaheim, California) which served as the anode. The crucible was seated into a graphite support which was contacted by a molybdenum wire. This assembly was contained within a quartz vessel, in which a N_2 atmosphere was maintained, inside a Lindberg crucible furnace. The MoS_2 was obtained from a melt of composition 1 $Na_2B_4O_7$ + 0.5 NaF + 0.14 MoO_3 + 0.1 Na_2SO_4, similar to one developed by Weiss (15). WS_2 was obtained from the melt developed by Weiss (1$Na_2B_4O_7$ + 0.5 NaF + 0.26 WO_3 + 0.17 Na_2SO_4) (15). Analytical grade reagents which were dried before use were used. High-density high purity pyrolytic graphite rod, Mo wire (Alfa, 99.97%), Ta wire (Alfa, 99.9%), and Pt wire were employed as cathode materials. Deposition was carried out under galvanostatic control in a two-electrode configuration. Following deposition, traces of salt were removed by immersing the sample in HF (24%) for a few minutes. For cyclic voltammetry, a gold wire served as a pseudo-reference electrode.

Scanning electron micrographs (SEM) of MoS_2 deposits were taken with an ETEC Corporation Autoscan Scanning Electron Microscope operated at 20 kV. Samples were examined by x-ray diffraction on a

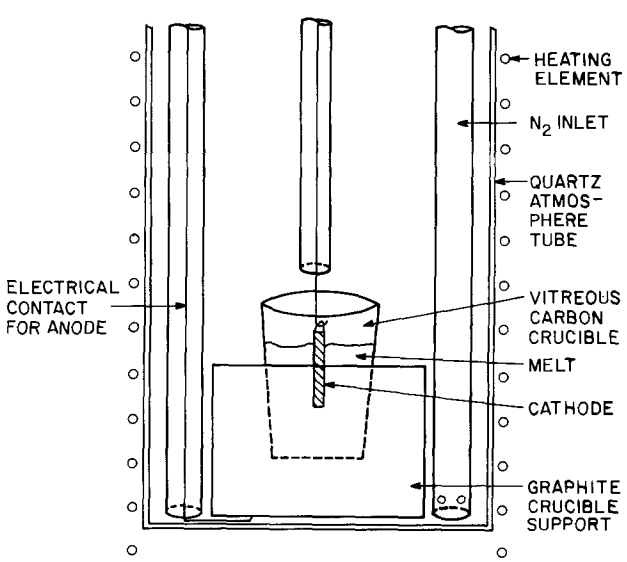

Fig. 1. Schematic representation of molten salt electrolysis system

* Electrochemical Society Active Member.
[1] Present address: Sperry Univac, Santa Clara, California 95051.

Rigaku Powder Diffractometer using CuKα radiation and a scan speed of 2° min^{-1}.

Electrodes for photoelectrochemical experiments were fabricated from selected electrochemically grown single crystals as follows. Satisfactory electrical contacts were made by rubbing Ga/In eutectic on one side of a crystal which was mounted (with conducting silver epoxy) onto a flattened copper wire. With 4 mm Pyrex tubing shielding the Cu wire lead, and ordinary epoxy insulating the assembly, only the MoS_2 (001) face (~0.02-0.05 cm^2 exposed area) makes contact with the electrolyte.

A Princeton Applied Research Corporation (PAR) Model 173 potentiostat/galvanostat equipped with a Model 179 digital coulometer was used for crystal growth experiments. For cyclic voltammetry on the melt, the above was used in conjunction with a PAR Model 175 programmer. Current-voltage behavior in aqueous electrolytes was monitored using a Pine Instruments RDE3 dual-potentiostat and an HP Model 7046A X, Y, Y' recorder. Electrochemical experiments were performed in a one-compartment cell with carbon rod counterelectrode and a saturated calomel reference electrode. Electrolytes were prepared using reagent grade chemicals and triply distilled water. The cell was equipped with an optical flat window to permit semiconductor illumination with a 100W Oriel tungsten-halogen lamp operated to yield ~40 mW/cm^2 incident intensity. For measurements of the spectral response of this material, the lamp output was passed through an Oriel scanning monochromator. The output of the electrode operated at short circuit was corrected for lamp spectrum and monochromator throughput and normalized by the light frequency to obtain a measure of the relative quantum efficiency. Open-circuit photopotential, V_{oc}, and short-circuit current, i_{sc}, measurements as a function of incident power were made by passing a 632.8 nM He-Ne laser (1.0 mm beam) through a calibrated a KLC crossed polarizer attenuator. The photopotential was monitored on a DVM and the short current was approximated by placing a 10Ω resistor across the cell in otherwise the same configuration. The transmission spectrum of the electrolyte was recorded on a Perkin-Elmer Model 330 Spectrophotometer.

Results and Discussion

The electrolytic reduction of a tetraborate melt containing MoO_3 and Na_2SO_4 produces crystalline deposits of molybdenum disulfide. Figure 2 shows a SEM of a sample deposited on a Mo cathode at a current density of 10 mA/cm^2 at a melt temperature of 800°C. Typical platelet crystallites are ~0.1 mm diam and very thin. Figure 3 shows the same sample at higher magnification (500×). The porosity of this film is evident, with much intergrowth of crystallites. Samples examined by x-ray diffraction were generally found to be the 3R rhombohedral polytype of MoS_2, although one sample grown from a melt at 900°C was found to be a mixture of 2H and 3R phases. Current density seems to have little effect on crystallite size at a given melt temperature. Beyond a limiting current density which depends on melt composition, a different phase, $Na_{0.6}MoS_2$, results from the electrolysis (17). This phase is produced more readily from melts containing lower sodium sulfate concentration.

Several materials, including graphite, molybdenum, tantalum, and platinum, were tried as cathode materials on which MoS_2 deposition was attempted. Molybdenum appeared to be the most suitable substrate for the preparation of polycrystalline MoS_2 in terms of the adhesion of the deposit. Tantalum was of interest as a substrate which could later be passivated to reduce back-reaction through the substrate when immersed in the electrolyte. However, a layer of metallic TaS_2 which forms during the deposition eliminates the usefulness of tantalum as a substrate material.

Larger crystals were obtained by raising the melt temperature to 900°C. Graphite and molybdenum were typically used as cathode materials at this temperature. The obtained crystals were very thin and large as 1 cm diam. Their thinness made it difficult to avoid introducing tears or wrinkles during handling, but we were still able to select and mount several as described.

The spectral response of an electrolytic MoS_2 crystal at short circuit in 0.1M NaI + 0.01M I_2 solution is shown in Fig. 4. The apparent bandgap as judged from the wavelength at which photocurrent begins to increase rapidly is 1.7 eV as expected for MoS_2 which has a 1.7 eV direct gap and 1.2 eV indirect gap (18). Features of the spectral response are similar to those reported for both natural and vapor phase transport synthesized MoS_2 (19, 20). The transmission spectrum of the electrolyte, which contributes to the short-wavelength cut-off in the photoresponse, is provided for comparison.

A steady-state photocurrent-voltage curve for a single MoS_2 crystal in the more concentrated electrolyte, 1.0M KI + 0.1M I_2, illuminated by a tungsten-halogen lamp is shown in Fig. 5. The solution potential, E_{redox}, indicated by the arrow, is 0.266V *vs.* SCE. The

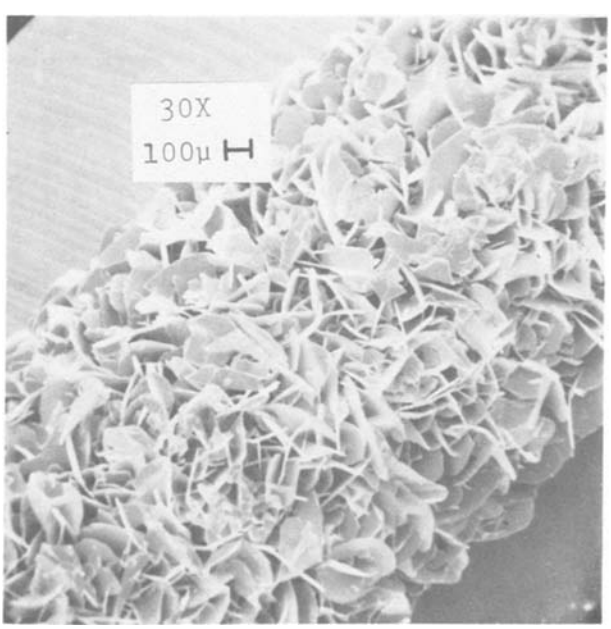

Fig. 2. SEM of MoS_2 deposited on Mo wire at 10mA/cm^2 under galvanostatic control. T_{Melt} = 800°C. Magnification 30×.

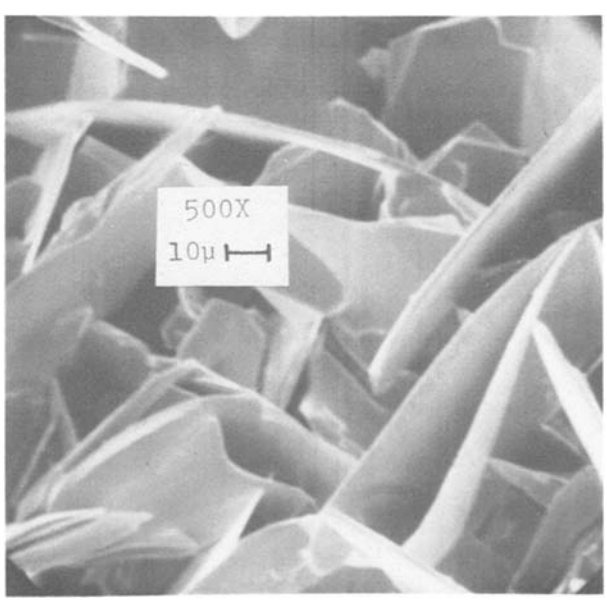

Fig. 3. SEM of MoS_2 sample of Fig. 2 at 500× magnification

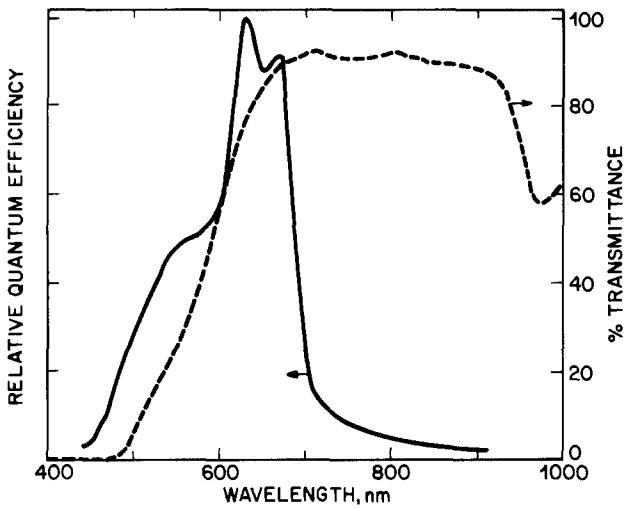

Fig. 4. Solid line shows the wavelength dependence of the photoresponse of a single MoS_2 crystal in 0.1M KI + 0.01M I_2 under short-circuit conditions. The dotted line is the transmission spectrum for this solution.

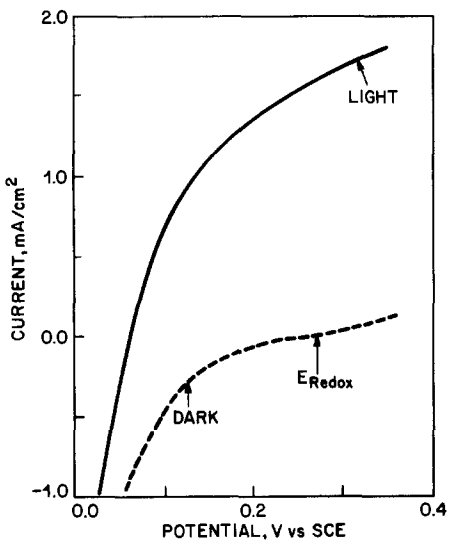

Fig. 5. Steady-state photocurrent-voltage curve for a single MoS_2 crystal in 1.0M KI + 0.1M I_2 illuminated by a 100W tungsten-halogen lamp (solid line) and in the dark (dashed line). The solution potential, E_{Redox}, is indicated by the arrow.

open-circuit photopotential, V_{oc}, under illumination intensity of ~40 mW/cm² was 210 mV for this crystal. Representative data for electrolytic MoS_2 crystals examined under conditions similar to those above are given in Table I.

Table I. Data from steady-state photocurrent—voltage curves for I^- oxidation at illuminated MoS_2[a]

MoS_2 sample	i_{sc}[b] (mA/cm²)	V_{oc}[c] (mV)	Fill factor[d]
1	2.6	270	0.42
2	1.17	330	0.30
3	1.51	185	0.31
4	0.90	280	0.29

[a] All data are for 1.0*M* KI/0.1*M* I_2 solutions at 25°C. Samples are electrochemically-grown single crystals illuminated by a tungsten-halogen lamp with a beam intensity of 50 mW/cm² uncorrected for solution absorption.
[b] Short circuit current.
[c] Open circuit voltage.
[d] Fill factor is a measure of the rectangularity of the output photovoltage-photocurrent curve and is defined to be (max power out)/($V_{oc} \times i_{sc}$).

The open-circuit photopotential, V_{oc}, and the short circuit current, i_{sc}, for an MoS_2 single crystal immersed in 1M KI + 0.1M I_2 are shown as a function of incident intensity, $I_{h\nu}$, in Fig. 6. The slope of log $I_{h\nu}$ *vs.* V_{oc} is 95 mV/decade (ideal Schottky junction value 59 mV/decade) for a quality factor of 1.61. The logarithmic rate of change of i_{sc} with $I_{h\nu}$ is slightly less (0.9) than the unity slope expected ideally. This result likely arises from slope in the current-voltage curve for this crystal near zero output voltage which makes the determination of the light limited current have a kinetic dependence.

Several polycrystalline films on Mo and graphite substrates were also examined in the 1.0M KI + 0.1M I_2 electrolyte with tungsten-halogen illumination. Open-circuit photopotentials of ~150 mV were observed initially. However, the response dropped to ~50 mV within a few moments, presumably as the electrolyte penetrated to the Mo substrate thus leading to an increased back-reaction. All samples, both single and polycrystalline, had n-type conductivity as determined from their photoresponse.

While photoactive MoS_2 polycrystalline films and single crystals have been prepared by the electrolytic reduction of a sodium tetraborate-sodium fluoride melt containing molybdenum trioxide and sodium sulfate, the mechanism for the electrochemical formation of MoS_2 in this medium is not known. However, the reaction may be written formally as

$$MoO_3 + 2\,Na_2SO_4 \rightarrow \begin{matrix} 2\,Na_2O + MoS_2 \text{ (cathode)} \\ +9/2\,O_2 \text{ (anode)} \end{matrix}$$

which implies that the number of electrons required to deposit one molecular unit of MoS_2 is 18. Indeed, bubbles, presumably from oxygen evolution, were observed on the pyrolytic graphite crucible anode. At a melt temperature of 800°C, polycrystalline films of MoS_2 such as those shown can be formed on graphite or molybdenum substrates. The photoactivity of the electrodeposited polycrystalline MoS_2 samples is noteworthy since thin film samples of layered dichalcogenides have generally failed to show any significant photoresponse (11, 12). Djemal *et al.* (12) have shown film crystallinity to be of major importance to the preparation of their flux-pasted and polymer binder treated MoS_2 electrodes which show significant photoresponse. Exposure of crystal surfaces other than the Van der Waals ($\perp c$) plane to the electrolyte has deleterious effects on PEC cell performance.

A serious difficulty with polycrystalline MoS_2 photoanodes prepared by electrolysis is the problem of pas-

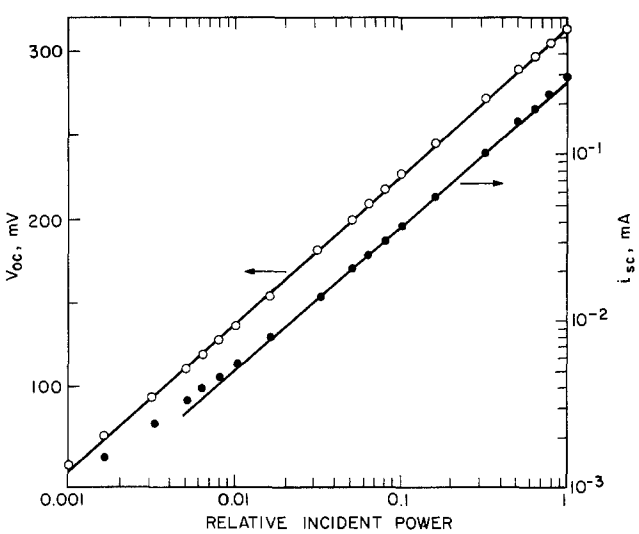

Fig. 6. Open-circuit photopotential *vs.* relative incident power and short circuit current *vs.* relative incident power for a single MoS_2 crystal in 1.0M KI + 0.1M I_2. Unity relative intensity corresponds to 2.58 mW in a 1 mm diam spot.

sivation of the substrate. Because of the porosity of the films, electrolyte can penetrate to the metallic substrate where back-reactions can occur. Methods to passivate the Mo substrate following film formation are under study. The use of a polymer binder to isolate the substrate may represent another approach to this problem.

Larger single crystals of MoS_2 (~1 cm diam) have been prepared by raising the melt temperature to 900°C. Under the conditions of these experiments, crystals produced are very thin. It is thus difficult to handle them without introducing damage which reduces their performance as photoanode materials in photoelectrochemical cells. Still, such a crystal yielded an open-circuit photopotential of 210 mV and 2 mA/cm^2 short-circuit current in aqueous iodide/triiodide electrolyte illuminated by a tungsten/halogen lamp at ~40 mW/cm^2.

The electrodeposition of WS_2 was also attempted. The deposition carried out under potentiostatic control at −0.7V *vs.* the counterelectrode yielding a current density of ~17 mA/cm^2 on a graphite cathode. The melt temperature was 800°C. WS_2 deposits were not examined further.

In principle, the technique of electrochemical crystallization of MoS_2 is applicable to a continuous growth process yielding large single crystals (21). The design of efficient photoelectrochemical systems employing layered dichalcogenides such as the polycrystalline MoS_2 films which are readily prepared as described awaits development of techniques for passivating the substrate and for edge plane passivation. While not yet fully competitive with halogen vapor phase transport for the production of large, defect-free MoS_2 single crystals, the encouraging properties of electrolytically-grown MoS_2 films suggests that the electrolytic reduction of a molten salt is an interesting alternative growth technique for MoS_2.

Manuscript submitted Oct. 8, 1982; revised manuscript received March 23, 1983.

Any discussion of this paper will appear in a Discussion Section to be published in the June 1984 JOURNAL. All discussions for the June 1984 Discussion Section should be submitted by Feb. 1, 1984.

Bell Laboratories assisted in meeting the publication costs of this article.

REFERENCES

1. H. Tributsch, *Faraday Discuss.*, **70**, 190 (1981).
2. G. Kline, K. K. Kam, D. Canfield, and B. A. Parkinson, *Sol. Energy Mater.*, **4**, 301 (1981).
3. G. Kline, K. K. Kam, R. Ziegler, and B. A. Parkinson, *ibid.*, **6**, 337 (1982).
4. L. F. Schneemeyer and M. S. Wrighton, *J. Am. Chem. Soc.*, **102**, 6964 (1980).
5. W. Kautek, H. Gerischer, and H. Tributsch, *Ber. Bunsenges. Phys. Chem.*, **83**, 1000 (1979).
6. H. J. Lewerenz, A. Heller, and F. J. DiSalvo, *J. Am. Chem. Soc.*, **102**, 1877 (1980).
7. S. M. Ahmed and H. Gerischer, *Electrochim. Acta*, **24**, 705 (1979).
8. B. A. Parkinson, T. E. Furtak, D. Canfield, K. Kam, and G. Kline, *Faraday Discuss.*, **70**, 234 (1981); D. Canfield and B. Parkinson, *J. Am. Chem. Soc.*, **103**, 1279 (1981).
9. G. Razzini, L. Peraldo Bicelli, G. Pini, and B. Scrosati, *This Journal*, **128**, 2134 (1981).
10. H. S. White, H. D. Abruna, and A. J. Bard, *ibid.*, **129**, 265 (1982).
11. H. D. Abruna and A. J. Bard, *ibid.*, **129**, 673 (1982).
12. G. Djemal, N. Muller, U. Lachish, and D. Cahen, *Sol. Energy Mater.*, **5**, 403 (1981).
13. D. S. Ginley, R. M. Biefeld, B. A. Parkinson, and K. Keung-Kam, *This Journal*, **129**, 145 (1982).
14. H. J. Byker and A. E. Austin, Paper 536 presented at The Electrochemical Society Meeting, Denver, CO, Oct. 11-16, 1981.
15. G. Weiss, *Ann. Chim.*, **1**, 446 (1946).
16. H. J. Heinen, D. H. Baker, Jr., and J. M. Gomes, U.S. Pat. 3,375,180 (1968).
17. J. M. Tarascon and L. F. Schneemeyer, To be published.
18. J. A. Wilson and A. D. Yoffe, *Adv. Phys.*, **18**, 193 (1969).
19. H. Tributsch and J. C. Bennett, *J. Electroanal. Chem.*, **81**, 97 (1977); H. Tributsch, H. Gerischer, C. Clemen, and E. Bucher, *Ber. Bunsenges. Phys. Chem.*, **83**, 655 (1979).
20. W. Kautek, J. Gobrecht, and H. Gerischer, *Ber. Bunsenges. Phys. Chem.*, **84**, 1034 (1980).
21. R. C. DeMattei, R. A. Huggins, and R. S. Feigelson, *J. Cryst. Growth*, **34**, 1 (1976).

Technical Note

Electrochemistry of Coal Slurries III. FTIR Studies of Electrolysis of Coal

Patrick M. Dhooge and Su-Moon Park*

Department of Chemistry, The University of New Mexico, Albuquerque, New Mexico 87131

In our previous papers (1, 2), we described the mechanism of what was originally reported by Coughlin et al. (3-5) as the "electrochemical coal gasification" reaction. As a result of our detailed studies on this reaction, employing various electrochemical techniques, we established the reaction mechanism of the oxidation. The mechanism can be described as a catalytic oxidation of coal in acidic solution by iron ions possessing a sufficiently high standard electrode potential according to the half-cell reaction

$$C + 4Fe^{3+} + 2H_2O \rightarrow CO_2 + 4Fe^{2+} + 4H^+ + \text{other products}$$

at the anode and

$$4H^+ + 4e \rightarrow 2H_2$$

* Electrochemical Society Active Member.
Key words: coal slurry oxidation, FTIR, electrochemical coal gasification, ^{18}O enriched water.

at the cathode. Here coal is simplified as elemental carbon (C) and the iron ions were shown to come from coal by us (1) and other investigators (6, 7). The Fe^{2+} thus produced from the reaction with coal is then oxidized back to Fe^{3+} at the electrode forming a complete catalytic cycle. The order of the reaction was shown to be approximately 1.0 with respect to both reactants, *i.e.*, Fe^{3+} and coal (2). This indicates that the overall oxidation reaction consists of a series of one-electron transfer reactions. Further, we postulated (2) from several experimental results that the formation of oxides may precede CO_2 evolution.

In our current communication, we address two questions, (*i*) whether surface oxides are indeed formed when coal slurry is oxidized and (*ii*) whether the oxygen atoms in the product CO_2 are derived from the solvent water as implied by the above stoichiometry. We used the Fourier transform infrared (FTIR) spectroscopic technique for these studies.

The electrochemical cell used has been described elsewhere (1, 2). Electrochemical oxidations were carried out under the nitrogen atmosphere by bubbling water vapor saturated nitrogen gas (2). All the infrared spectrum recordings and analyses were conducted with a Nicolet Model 6000 computerized FTIR system. Gas samples were taken in a 10.0 cm gas cell with KBr windows. Solid samples (1.5 mg) of coal mixed with 300 mg KBr were pressed into disks for infrared analysis. Alfa Products' ^{18}O enriched water (10% $H_2{}^{18}O$) was used for the isotope tracing experiments. Coal samples from San Juan Basin of northwestern New Mexico and Pittsburgh Seam No. 8 (PSOC-1099) were used for this study.

Since we found that acid-washed coals showed some slight changes in their infrared spectra compared with those of unwashed ones, we compared infrared spectra of Fe^{3+} or Ce^{4+} treated, and electrolyzed, coals with acid washed ones. Figure 1 shows the difference spectrum of electrolyzed minus acid-washed San Juan coal, Ce^{4+}-treated minus acid-washed San Juan coal, and the spectra of Ce^{4+} treated and acid-washed Pennsylvania coal, respectively. San Juan coal (< 60 mesh, 20.0g) had been electrolyzed at 70°C in 150 ml of 1.0*M* H_2SO_4 solution containing 0.10*M* Fe^{3+} at an applied potential of 1.0V *vs.* NHE until about 10,000C of charges had been passed. "Acid-washed" coal samples were washed with 1:1 sulfuric acid at room temperature for 48 hr. These samples were filtered, washed and dried.

In Fig. 1a, one can see obvious differences between electrolyzed and washed coals, notably the increase in absorption peaks at ~1700, ~1650, and 1100-1000 cm^{-1} region. These peaks have been assigned by previous investigators (8-11) to —COOH, quinoids, and aliphatic ethers and alcohols, respectively. One also sees an increase in hydroxyl stretch at about 3400 cm^{-1}. The peak at ~1260 cm^{-1} is characteristic of the C-O stretch of phenolic groups. We may conclude from this result that oxygen containing compounds are being formed on the coal surface during reaction with Fe^{3+}. Surprisingly, aliphatic-type acids, ethers, and alcohols are seen, as well as evidence of conjugated C = O (*i.e.*, quinoids) and phenolic C-OH (*i.e.*, phenols and/or hydroquinoids).

As a method for comparison, 2.0g of San Juan coal were placed in 70°C 1*M* H_2SO_4 plus 0.50*M* Ce^{4+} for 48 hr, and Pennsylvania coal was treated similarly in solutions containing 0.50*M* Fe^{3+} and 0.50*M* Ce^{4+}. Admittedly, these are not as rigorous oxidative conditions as the electrolysis, but we believed they would be sufficient for oxidative changes to be seen in the coals.

Figure 1b shows the difference spectrum between the Ce^{4+}-oxidized San Juan coal and acid-washed San Juan coal. The differences are not nearly as great as with the electrolyzed coal, but are somewhat similar to those seen with Fe^{3+}. Figure 1c shows the spectrum of acid-washed Pennsylvania coal with the spectrum of Ce^{4+} oxidized Pennsylvania coal. Similar results

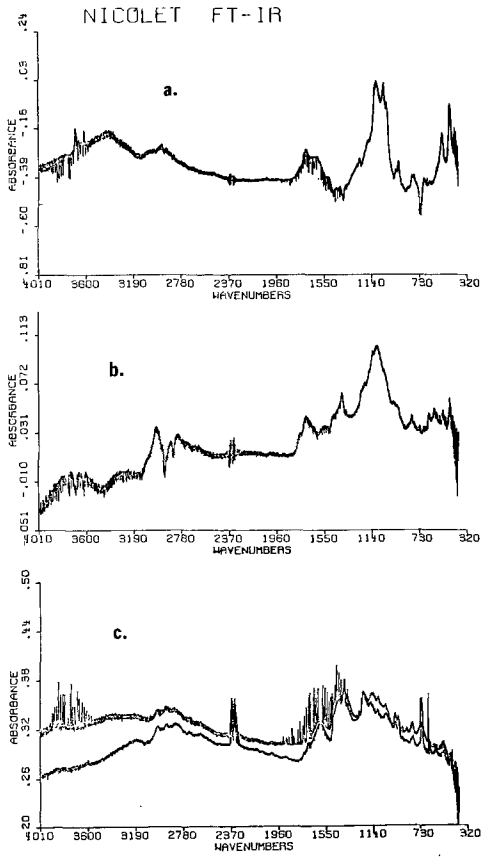

Fig. 1. (a) Difference spectrum obtained from electrolyzed coal and washed coal (San Juan). (b) Difference spectrum obtained from Ce^{4+} treated and washed coals. (c) Spectra obtained from Pennsylvania coal washed with 1:1 H_2SO_4 (lower curve) and the same coal subjected to Ce^{4+} in 1.0*M* H_2SO_4 at 70°C (upper curve).

were obtained for Ce^{3+} treated Pennsylvania coal. Neither of these oxidized coals has much variation from the parent coal.

This fact is fairly significant in view of the CO_2 production efficiency values reported earlier (2). Pennsylvania coal had high current efficiency values indicating little formation of partially oxidized functionalities, while current efficiencies for San Juan coal indicated that much of the oxidation current was being used (indirectly) to produce compounds other than CO_2. This is confirmed by the spectral data showing the formation of oxygen compounds on San Juan coal but not as much on Pennsylvania coal. There is some evidence of partial oxidation on Pennsylvania coal using Fe^{3+} as the oxidant, as well as enhancement of compounds containing C-H. This can be interpreted to be due to the lower redox potential of the Fe^{3+}/Fe^{2+} pair, which is not able to completely oxidize many sites, therefore leaving partially oxidized functionalities.

In order to determine whether the CO_2 produced in coal oxidation was from water or from oxygen already existing in the coal, we studied the products of the coal oxidation reaction in 10% $H_2{}^{18}O$. Figure 2a shows a 0.5 cm^{-1} resolution FTIR spectrum at the CO_2 bending region of a standard gas mixture having 270 ppm CO_2 and 31 ppm CO in nitrogen. Fig. 2b shows a typical spectrum obtained from the gaseous coal oxidation product in the purge gas N_2-stream using 10% $H_2{}^{18}O$ as solvents. When an isotopic substitution is made in a simple molecule, the equilibrium bond length and the force constant are unchanged, since they depend only on the behavior of the bonding electrons. However, the reduced mass does change and this will affect the vibration and rotation of the molecule, resulting in a shift in transition to lower wavenumbers. Since the force constant and symmetry remains the same despite

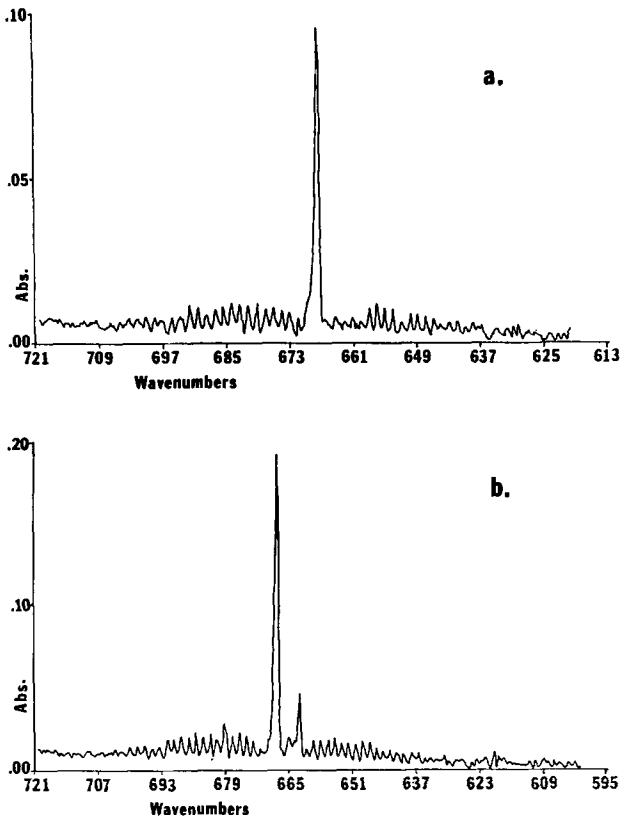

Fig. 2. FTIR spectrum of CO_2 bending region from 10 cm gas cell containing: (a) standard gas, 270 ppm CO_2 in nitrogen. and (b) effluent gas from ~10% $H_2{}^{18}O$ coal oxidation experiment.

this isotopic substitution, the simple ratio of the two peaks can be used to determine the percentage of $C^{18}O^{16}O$ as long as two transition peaks are resolved. As can be seen in Fig. 2b, there is now a second large peak due to the transition for $C^{18}O^{16}O$, shifted to lower wavenumbers. The small peak at about 665 cm^{-1} is consistent with that of $C^{17}O^{16}O$ from the reduced mass calculation and the composition of the solvent (3.80% $H_2{}^{17}O$).

Figure 3 presents the ratios of $C^{18}O^{16}O$ found in the product gas with the electrolysis time for San Juan coal with Fe^{3+} or Ce^{4+} as an oxidation catalyst. The ratio of $C^{18}O^{16}O$ stays reasonably constant and represents the amount which would be found if both oxygens in the CO_2 produced come from the water, since

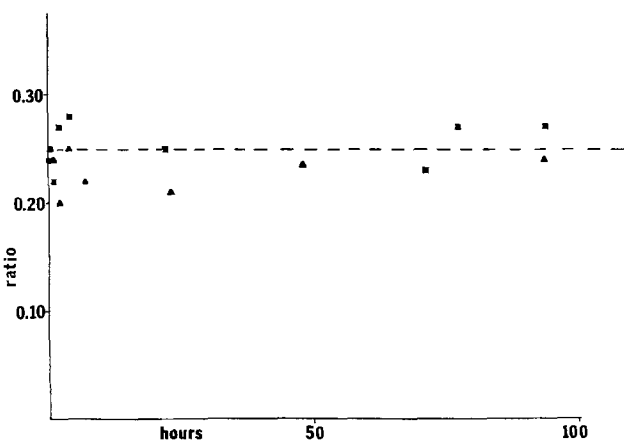

Fig. 3. Ratio of $C^{16}O^{18}O$ peak height to $C^{16}O_2$ peak height vs. time for oxidation of coal using 10.65% $H_2{}^{18}O$ as a solvent: △—0.50M Fe^{3+} + 5.0g San Juan coal in 150 ml 1.0M H_2SO_4 at 70°C and +1.0V anodic potential, and □—0.50M Ce^{4+} + 5.0g San Juan Coal in 150 ml 1.0M H_2SO_4 at 70°C and +1.50V anodic potential. The dotted line is the calculated value from the $H_2{}^{18}O$ content.

First oxidation:

$$C + 10\%\ H_2{}^{18}O \Longrightarrow 10\%\ C^{18}O + 90\%\ C^{16}O + 2H^+ + 2e$$

Second oxidation:

$$CO + 10\%\ H_2{}^{18}O \Longrightarrow 1\%\ C^{18}O_2 + 9\%\ C^{16}O^{18}O + 9\%\ C^{18}O^{16}O + 81\%\ C^{16}O_2 + 2H^+ + 2e$$

With the isotopically enriched water used here, which was 10.65% $H_2{}^{18}O$, and 3.8% $H_2{}^{17}O$, one would obtain 6.5% $C^{17}O^{16}O$, 73.12% $C^{16}O_2$ and 18.22% $C^{16}O^{18}O$, if the two oxygens are added to the coal from water. This gives a ratio, $C^{18}O^{16}O/C^{16}O_2$, of 0.249. This value, indicated by a dotted line in Fig. 3, is within the experimental error.

These studies are significant in that they establish for the first time the role of water in the coal oxidation reaction. Water is intimately involved in the oxidation mechanism, supplying the source of oxygen for production of carbon oxides, much as in the coal gas reaction for the production of H_2 + CO. In fact, this electrochemical process is remarkably similar to the coal gas reaction. Both oxygens are supplied independently in the electrocatalytic oxidation of coal, and are irreversibly bonded in the final step as verified by the fraction of $C^{16}O^{18}O$ produced in the reaction. Along with other evidence presented earlier (2), it can be concluded that the oxygens are added in two separate steps. The first step may be the formation of a quinoid group and follows the second step where oxygen is added would be conversion of the quinone to CO_2.

These experiments have demonstrated the exocarbonaceous source of the oxygen in CO_2 produced from coal under these conditions. This fact disputes the contention which has been put forward by some investigators (7) that the carbon dioxide produced in this reaction is from carbonates or other carbon-oxygen compounds extant in the coal. The source of CO_2 is a rather straightforward oxidation of carbon sites in the presence of an oxygen source (H_2O).

In conclusion, we have shown by FTIR spectroscopy and isotope experiments that the anodic electrolysis of coal proceeds in two steps: the formation of surface oxides and the evolution of CO_2. The oxygen in CO_2 is shown to be derived from the solvent, water.

Acknowledgments

Grateful acknowledgment is made to the U.S. Department of Energy, Fossil Fuel Program for supporting this research through contract, DE-AC21-81MC16377. The Nicolet 6000 FTIR spectrometer was purchased through an instrumentation grant from the National Science Foundation to the University of New Mexico, Department of Chemistry (Grant No. CHE 8007979).

Manuscript submitted Aug. 2, 1982; revised manuscript received March 18, 1983.

Any discussion of this paper will appear in a Discussion Section to be published in the June 1984 JOURNAL. All discussions for the June 1984 Discussion Section should be submitted by Feb. 1, 1984.

The University of New Mexico assisted in meeting the Publication costs of this article.

REFERENCES

1. P. M. Dhooge, D. E. Stilwell, and S.-M. Park, *This Journal*, **129**, 1719 (1982).
2. P. M. Dhooge and S.-M. Park, *This Journal*, **130**, 1029 (1983).
3. R. W. Coughlin and M. Farooque, *Nature (London)*, **279**, 301 (1979).
4. M. Farooque and R. W. Coughlin, *ibid.*, **280**, 666 (1979).
5. M. Farooque and R. W. Coughlin, *Fuel*, **58**, 705 (1979).
6. R. P. Baldwin, K. F. Jones, J. T. Joseph, and J. L.

Wong, *ibid.*, **60,** 739 (1981).
7. G. Okada, V. Guruswamy, and J. O'M. Bockris, *This Journal*, **128,** 2097 (1981).
8. P. C. Painter, R. W. Snyder, D. E. Pearson, and J. Kwong, *Fuel*, **59,** 282 (1980).
9. P. C. Painter, M. M. Coleman, R. W. Snyder, O. Mahajan, M. Kamatsu, and P. L. Walker, Jr., *Appl. Spectrosc.*, **35,** 106 (1981).
10. J. B. Speight, *Appl. Spectrosc. Rev.*, **5,** 211 (1971).
11. P. C. Painter, R. W. Snyder, M. Starsinic, M. M. Coleman, D. W. Koehn, and A. Davis, *Appl. Spectrosc.*, **35,** 475 (1981).

JOURNAL OF THE ELECTROCHEMICAL SOCIETY

SOLID-STATE SCIENCE AND TECHNOLOGY

JULY 1983

Planarization Properties of Resist and Polyimide Coatings

L. K. White*

RCA Laboratories, David Sarnoff Research Center, Princeton, NJ 08540

ABSTRACT

The planarization properties or thickness changes on topographical features are examined in detail for several types of spun-on polymer films. A profilometer is used to measure the step height changes of isolated line features of various dimensions. The viscosity of the solution appears to give a reasonable indication of the spun-on planarization properties. However, in many cases, the thermal flow of the polymer during a subsequent curing procedure is the dominant planarization mechanism. Methods for producing highly planarized surfaces with positive resist materials are described along with the effects of feature size on the planarization properties.

The use of spun-on polymer coatings is of widespread importance in semiconductor manufacture. Resists used for optical, E-beam, x-ray, and ion-beam lithographic processes are for the most part spun-on polymer coatings. When these coatings are applied to substrates with topographical features, changes in the coating thickness occur at and around the features. Since the whole coating receives the same dose during most lithographic exposures, any influence the resist thickness exerts on the effective exposure can introduce dimensional control deviations (1-4).

Spun-on dielectric polymer films are also becoming increasingly important (5-7). For these applications, the thickness changes in the spun-on coating influences the electrical characteristics of the insulator (8, 9). More recently spun-on polymer coatings have been proposed to planarize device topography in multilevel resist processing schemes (10-13) and in surface smoothing procedures that employ dry etching techniques (14). In the multilevel approach, one of the functions of the sublayer is to smooth topographical features so that a subsequent spun-on resist coating exhibits smaller thickness variations. This procedure is by no means trivial and in some cases there is no marked improvement in the resist thickness variations with the sublayer coating. Proper planarization techniques are necessary to gain the maximum benefit from a multilevel resist processing scheme (15). Conversely, for conventional single-layer resist processing, the planarization properties should be minimized so that resist thickness changes do not produce significant linewidth deviations.

In this work, quantitative information is presented for the planarization properties or the film thickness changes on topographical features for several spun-on polymer materials. These properties are related to the polymer solution properties. Other properties, mainly the thermal flow properties during a subsequent cure step, are shown to strongly influence the planarization properties. Methods for producing highly-planarized diazoquinone, novolac-resin based positive resist films, are presented.

Experimental

Table I lists the materials evaluated in this study and their relevant solution properties. Most of these materials are industry standards, familiar to most workers. These materials were spin-coated onto 3 in. silicon wafer substrates with known topography. All solutions were equilibrated to room temperature prior to spin-coating. The spin time was 30 sec and spin speeds ranged from 4000 to 7000 rpm. The spun-on coating thickness was measured with a Rudolph film thickness monitor on unpatterned bare silicon wafers for every polymer solution and spin speed. The resist thickness variations across these control wafers were less than 100Å. Substrates with topographical features were prepared in this manner: A thermal oxide was grown onto the bulk silicon wafer to the thickness of the desired step height. In this work, 0.5 and 1.0 μm step heights were examined. The substrate was patterned in positive resist with a mask having isolated line features of various widths. The isolated linewidths were 50, 20, 9, 7, 5, and 3 microns, and the lengths of the lines were nominally 500 μm. The thermal oxide was etched in a plasma system, anisotropically, to produce near-vertical walls and to maintain an accurate linewidth dimensions. Following the removal of the resist, the substrates were then coated with 0.5 μm of polysilicon deposited by LPCD or 1.0 μm of In-source Al. This procedure was followed to duplicate polymer planarization properties as they might occur during lithographic processing of an IC device.

The polysilicon coated substrates were used for most experiments because they provided the most near-vertical wall profiles and less surface roughness for the substrate. Polymer films coated onto polysilicon

Table I. Solution properties of spun-on polymer films*

	% Solids	Viscosity	Specific gravity	Solvent system
HPR204	27.8%	18.5 cps	1.036	Cellosolve acetate
HPR206	33.0%	43 cps	1.055	Cellosolve acetate
HNR120	13.5%	31 cps	0.870	Xylene
Kodak 809	32%	23 cSt	1.045	Cellosolve acetate
KTI PMMA 496k	9%	90 cSt	—	Chloro-benzene
PI2555 Dupont polyimide	20%	1,000 cps	1.060	n-methyl-2-pyrroli-done

* From manufacturer data sheets.

* Electrochemical Society Active Member.

Key words: polymers, topography, films, surfaces.

substrates planarized topographical features slightly better than those coated onto aluminum substrates. This is attributed to slight differences in the measured feature size and the wall profile; however, it is conceivable that interface properties may account for these differences.

Planarization profiles were measured with a Tencor Alpha-Step Profilometer operating with a 12 μm radius stylus and a 15 mg stylus tracking force. Step heights were measured before and after the polymer coating procedure. Only isolated lines were analyzed with this technique, since the radius of the stylus prohibits an accurate analysis of similarly dimensioned spaces.

Measurements were made of isolated lines at several orientations with respect to the center of the wafer. In general, no dependence in the spun-on planarization properties was detected for the various orientations of the isolated lines. Flood exposures of positive resist films for the planarization studies were done with a high pressure mercury lamp on a Canon PLA 500F aligner. A 100 mJ/cm^2 exposure was used as determined by an OAI 310-125 intensity meter with an P400-3 probe. Batch oven bakes of various materials were done in mechanical convection ovens for 30 min in room air ambients. Hot plate bakes were for 30 min in room air ambients.

Spun-On Polymer Planarization Properties

The spun-on planarization properties or film thickness changes on topographic features for any polymer film are exceedingly complex. It is often difficult to isolate the effects of all the variables involved. In this work, we deal with relatively isolated line features. Figure 1 displays a schematic of a spun-on polymer film going over an isolated line topographical feature. Four different thicknesses are shown. T_{BOT} is the thickness at the bottom of the step on the flat expanse. This is usually the spun-on coating thickness if the isolated feature is far away from other topographical features. T_{MAX} is the maximum polymer film thickness and usually is associated with the bottom of the step. T_{MIN} is the minimum polymer film thickness and is associated with the top corner of the step. T_{TOP} is the maximum polymer film thickness on top of the step. It is generally less than T_{BOT} provided that the line feature is small. T_{TOP} depends on numerous parameters that include: step height, polymer film thickness, isolated line feature size, step edge profile, surrounding topographical features, the nature of the spun-on polymer solution, and the processing of the resultant spun-on layer.

We will only be considering the difference in polymer film thickness at the top of the step, T_{TOP}, and at the bottom of the step, T_{BOT}. It should be realized, though, that greater changes in polymer film thickness are possible at the edge of a step. The difference between the measured original step height and the final step height (H_1 and H_2, respectively, in Fig. 1) gives the change in polymer film thickness ($T_{BOT} - T_{TOP}$). Figure 2 displays spun-on planarization results for the materials listed in Table II. The fraction of the step height after applying the polymer, H_2/H_1, is plotted against the polymer film thickness. An isolated

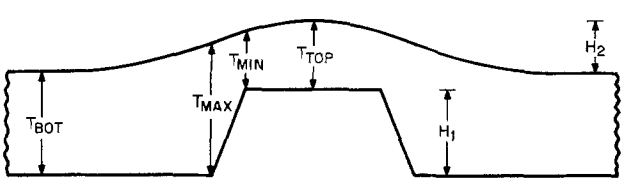

$$H_1 - H_2 = T_{BOT} - T_{TOP}$$

Fig. 1. Schematic of spun-on polymer coating over an isolated line feature.

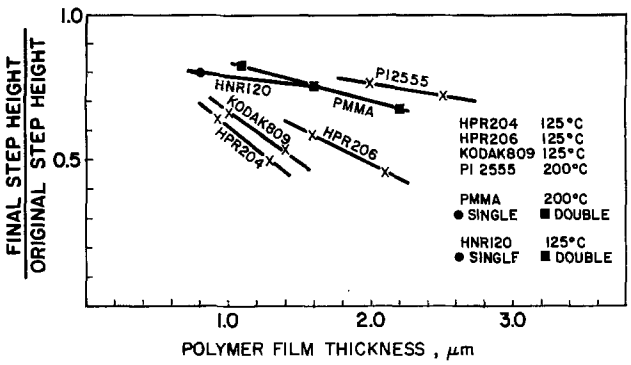

Fig. 2. Spun-on planarization properties vs. polymer film thickness for 20 μm isolated line feature and a one micron polysilicon step height.

20 μm line feature is used for this initial evaluation. Materials that fall on the lower left portion of the graph are the best planarization materials. These materials yield the maximum step height reduction at the lowest spun-on polymer film thickness. The polyimide film cured at 200°C has the worst planarization properties, followed by PMMA, and then most of the resist materials. HPR204 resist material had best spun-on planarization properties of all the materials evaluated. Lui (16) has reported a similar planarization ranking of polyimide, PMMA, and HPR204 resist.

Other aspects of this data are noteworthy. For the HPR204, HPR206, Kodak 809, and PI2555 materials, where the polymer film thickness was varied by using different spin speeds, 4000 and 7000 rpm, extrapolation of the line back to a zero film thickness yields a number close to one. This suggests that, at least for the spun-on films displayed here, a planarization characterization scheme independent of the polymer film thickness may be possible. Hirata (17) has also plotted planarization data versus a spun-on planarization thickness in a linear fashion that also extrapolates to the appropriate intercept at a zero polymer film thickness. The slope of this extrapolated line is used to compare the planarization properties to the spun-on polymer solution properties. This planarization constant represents the percent reduction in step height for an one micron change in polymer film thickness. The greater the absolute value of the slope, the better are the planarization properties of the material. The constant is defined for a particular feature size and step height and is meant to factor out the effects of the polymer film thickness.

It is somewhat surprising that only slight improvement in the spun-on planarization properties results through the use of this multiple coating technique. The second coating sees a reduced step height and with all other things being equal, a similar percent reduction in step height for a subsequent coating might be expected. Obviously, all other things are not equal, the wall profile is less steep and the top corner of the step is no longer sharp. In addition, the feature size has effectively changed. Generally, the isolated feature size dimension is somewhat larger for the coated feature. Another effect may also contribute to the reduced planarizing capability of multiple coating techniques. Usually, the second coating tends to mix or dissolve a

Table II. Planarization constants of various materials

	1.0 μm step	0.5 μm step
HPR204	0.38	0.43
HPR206	0.26	0.20
Kodak 809 (32%)	0.31	0.35
HNR120	0.21	0.25
KTI PMMA 496k	0.16	~0.10
PT2555	0.12	~0.10

portion of the initial coating, this phenomena increases the viscosity and percent solids composition of the polymer solution at the interface between the coatings. This change in solution properties could adversely effect the spun-on planarization properties of the subsequent coating. Using spin speeds below 4000 rpm to increase coating thickness is not practical because they do not produce uniform coatings across substrates (18).

The relative positions of HPR204 and HPR206 data are also significant. Although HPR206 gives a thicker coating at the same spin speed, no marked improvement in the spun-on planarization properties is observed. Apparently, the change in polymer solution properties for these quite similar materials has affected the spun-on planarization properties.

In view of these observations, an attempt was undertaken to correlate the planarization properties with the polymer solution properties shown in Table I. The best correlation was found with the viscosity of the solution. Figure 3 displays this correlation. The log of viscosity is plotted against the planarization constant (*i.e.*, the slope from Fig. 2) for a 1.0 micron step (see Table II). The planarization properties of all the materials in Table I can be ranked correctly according to their viscosity with the exception of HNR120. The lower viscosity solution produces the better spun-on planarization properties. A number of other solution properties undoubtably contribute to the planarization properties. The evaporation of solvent during spinning changes the solution viscosity. The solvent, percent solids composition, and the spin speed influence the evaporation rate (19, 20). However, considering the diversity of the materials studied here, the solution viscosity gives a reasonable indication of the spun-on planarization properties of a polymer solution.

Although the definition of the planarization constant used here was intended to factor out the effects of polymer film thickness relative to the step height, the data displayed in Table II shows that changes do occur in the planarization constant for different step heights. These changes are not fully understood. Most materials show an increase in the planarization constant for the smaller step height. The films that are deposited in relatively thick layers, PI2555 and HPR-206, show decreases in their planarization constant. It appears that the linear correction for polymer film thickness is not entirely valid and that different realms of behavior in the planarization characteristics may be present in regard to the polymer film thickness relative to the step height. However, for spun-on film thicknesses approximately equal to and somewhat greater than the step height, this definition of the planarization constant appears to produce consistent results. Applying the same constant to polymer films with spun-on thicknesses less than or much different than the step height may not be valid. A different correlation between viscosity and planarization properties may also exist under these conditions.

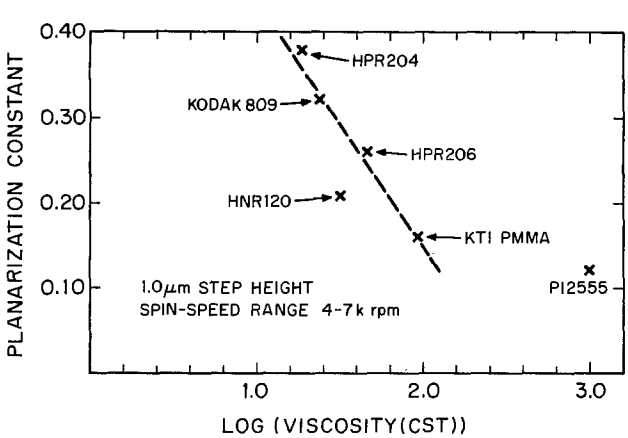

Fig. 3. Correlation between viscosity and planarization

Rothman (21) has reported a different correlation between the planarization and solution properties for cured polyimide coatings. The best planarization properties were related to a high percent solids composition, which generally would produce high viscosities. As Rothman points out, planarization properties are not just confined to the spun-on properties, film shrinkage and thermal flow during subsequent curing steps also affect these properties. Rothman studied cured polyimide films, so that data are a reflection of the thermal flow properties of polyimide films as well as the spun-on planarization properties of the polyimide solution. A following section in this work addresses the effects of thermal flow on planarization properties. These results show that polyimide films do flow to a considerable degree when they are cured.

The data displayed in Fig. 1 only reflects spun-on planarization properties. The cure conditions for the various polymer films, we believe, do not appreciably alter the spun-on planarization properties.

Feature Size Dependence

Figure 4 shows profilometer traces of PMMA and Kodak 809 spun-on coatings. Although the thickness of the PMMA coating is greater than that of Kodak 809 material, the planarization properties of the Kodak 809 material are better than the double coating of PMMA. The change in feature size affects the degree of planarization obtained from both coatings. Small features are planarized to a greater degree than the larger features.

For large features ($\geq$ 50 μm) only a small degree of planarization occurs, although all the polymer coatings do produce a shallower smoother wall profile for the step. For some feature sizes, a slight increase in step height has actually been observed. Presumably, there

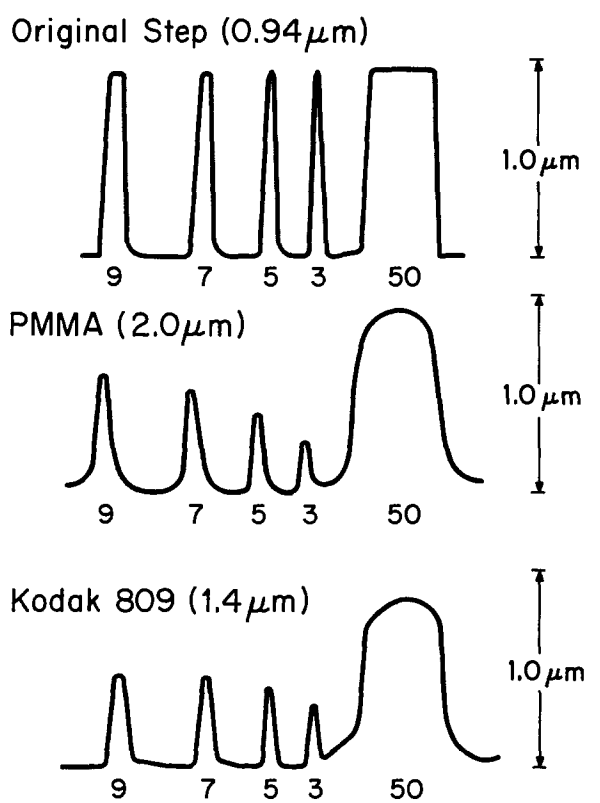

Fig. 4. Profilometer traces of PMMA and Kodak 809 coatings. The substrate is LPCVD polysilicon. The PMMA is a double coating of a 9% solids solution curing at 200°C. The Kodak 809 coating is a single layer spun-on at a 4k spin-speed. Linewidth, 3-50 μm is indicated for each feature.

is a tendency for the polymer solution to puddle on certain size features.

Figure 5 plots the degree of planarization obtained for various feature sizes as a function of the polymer film thickness. As expected, smaller feature sizes show greater step height reductions. Smaller features also have a somewhat greater change in step height as the polymer film thickness is increased. Planarization constants tend to be greater for the smaller feature sizes.

Surrounding topographical features also influence the planarization properties. The complexity of the effects make a quantitative description difficult, but some qualitative statements can be made. As feature sizes become finer and the complexity of the pattern increases, the degree of planarization and polymer film thickness variations increase. The closer one feature is to another the more influence it has on the degree of planarization obtained for the adjacent feature. Features next to each other help planarize both features with the greatest effect being incurred on the smaller feature.

In this work, data are presented only for isolated line features. Applying these data to complex patterns requires caution. To predict the maximum polymer film thickness variation within a complex pattern, the smallest dimensioned line or space feature within the pattern should be considered. The polymer film thickness variations are usually no less than that encountered for the isolated line. If the dimension between small features is of similar magnitude as the small feature itself, greater polymer film thickness variations can be expected. The isolated line planarization only represents a first approximation of the polymer film thickness variations encountered on real device structures. For example, the step heights are more reduced and resist thickness variations larger for 10 × 10 μm gratings than they are for 10 μm isolated line features.

Coating Considerations for Resist Processing

Although it is well known that thicker resist coatings cover steps better than thinner coatings, the details of this observation deserve further attention, particularly for design rules below three microns. Resist thickness variations on topography become extremely important in regard to linewidth dimensional control. Figure 6a shows the absolute resist thickness change on 1.0 μm topography for softbaked HPR204 and HPR-206 resist materials. The minimum resist thickness change is observed for HPR206 spun at 7000 rpm. Even though the resulting thickness of the coating is significantly greater than the HPR204 coating thickness, the resist thickness change on topography is diminished. These results suggest that to minimize resist thickness

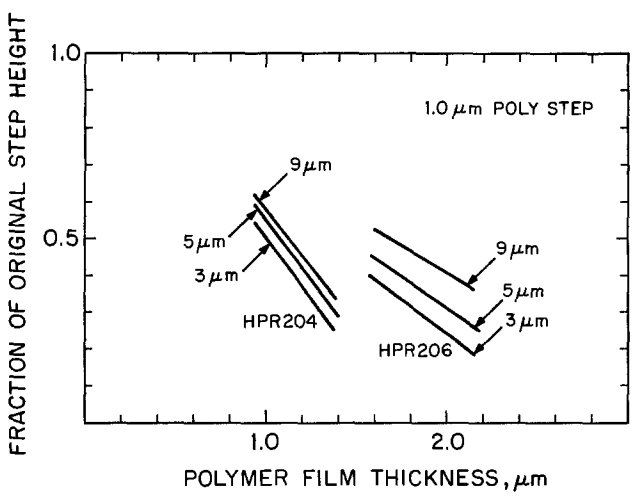

Fig. 5. Planarization data for various feature sizes. Both HPR 204 and HPR 206 are spin-coated in the 4-7 krpm spin-speed range.

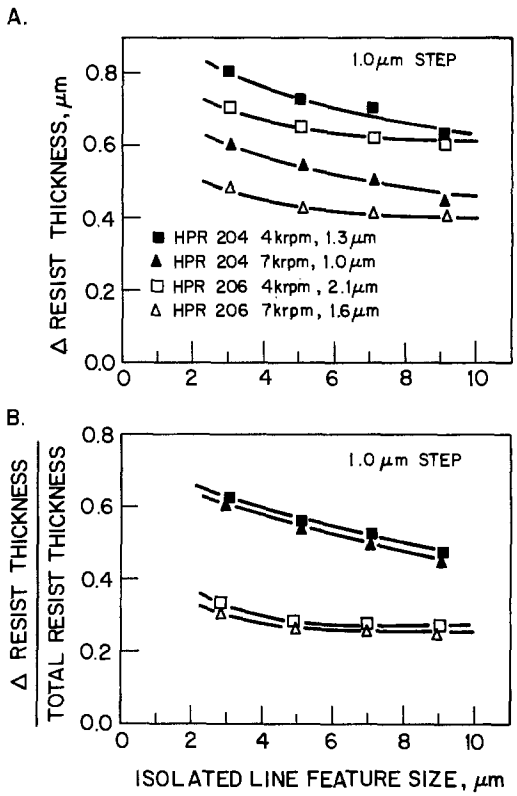

Fig. 6. (a) Absolute resist thickness changes vs. feature size. (b) Fractional resist thickness change vs. feature size.

changes, the higher viscosity resist formulation at high spin speed should be used. Note that this advantage becomes more significant as the feature size decreases.

Although Fig. 6a does not show any advantages in terms of the absolute resist thickness changes using the lower spin speeds, benefits are possible over the whole spin speed range for the higher viscosity materials. Since the exposure dose of the resist is usually adjusted to pattern the thickest portion coating, the fractional resist thickness change is a more important measure of linewidth control than the absolute resist thickness change. Figure 6b displays the same data in terms of the fractional resist thickness change. Thicker resist coatings produced by spin speed variations offer little or no advantage in reducing the functional resist thickness change. Significant differences in the fractional resist thickness deviations do exist for different viscosity resist formulations. At the 10 μm feature size range, the fractional resist thickness change on 1.0 μm topography for the HPR204 and HPR206 materials are 0.45 and 0.25, respectively.

The monotonic linewidth dimensional variation due to the resist thickness variation can be expected to be nearly halved using the higher viscosity resist material. This advantage must be balanced against possible reductions in resolution accompanying the use of thicker resist coatings. Resist wall profiles, however, tend to be steeper for the thicker resist films, particularly, if high resolution direct wafer stepper imaging is being employed. The increased exposure energy for the generally thicker resist coatings are presently of minor importance for 10-X reduction stepper thruput considerations.

It should be pointed out that other factors also contribute to dimensional variations. Reflective substrates and more monochromatic light sources tend to enhance standing wave interferometric phenomena and differences in exposure due to sidewall reflections. If dimensional control problems exist on topography that are primarily due to resist thickness variations, turning to higher viscosity resist formulations at high spin

speeds appears to offer a way to minimize resist thickness variations and reduce the fractional resist thickness change. These slight changes in conventional single level resist processing should be attempted before resorting to multilevel resist processing schemes.

Effects of Thermal Flow on Planarization Properties

Frequently, the spun-on polymer film undergoes a heat-treatment to remove residual solvent or to cure the film in some fashion. During this procedure, both film shrinkage and polymer flow can occur. In many cases, polymer flow during a subsequent heat-treatment can be the dominant planarization mechanism. An example of the effects of polymer flow on the planarization properties is shown in Fig. 7. The profilometer traces of a polyimide film show a significant improvement in the planarization properties when polymer flow occurs. The measured step heights for small features are reduced by almost 50% with the 400°C cure. Although the step-height is not reduced for the 50 μm feature size with polymer flow, the trace does indicate a substantial change in the wall profile. The wall profile is more sloped and a greater degree of thinning of the polymer film at the top corner of the step appears to occur. The types of wall on large feature size profiles are almost diagnostic for the occurrence of thermal flow of the polymer material. These results indicate that if polymer film thickness changes are undesirable, thermal flow of the polymer film should be minimized; if planarization is desired, polymer flow should be maximized. Polyimide films that are used as a dielectric should be processed so that thinning of the films on topography is minimized. Polyimide materials that have diminished thermal flow properties during curing and cure cycles that minimize thermal flow should be an important consideration when this material is used as a dielectric.

The thermal flow properties of a particular polymer film are dependent upon several parameters. Among them are: the temperature, rise to temperature, nature of thermal source, ambient, polymer film thickness, substrate thermal properties, substrate step height, and in some cases changes in the polymer film molecular structure. Figure 8 illustrates the effects of the nature of the heat source and changes in polymer molecular structure on the flow properties of a diazoquinone novolac resin positive resist. The profilometer traces show the planarization properties for batch oven baked and hot-plate (backside bake of substrate) baked 0.6 μm topography. Both unexposed and exposed resist films were examined. The batch oven bake shows no difference between unexposed and exposed samples. The hot plate bake shows an improvement for both the unexposed and exposed resist samples. The exposed resist film, however, shows dramatically improved planarization properties. Feature sizes below 10 μm are planarized to within 0.1 μm. The large feature (50 μm) still is not planarized appreciably, although considerable polymer flow is evident from the profilometer trace of the wall profile.

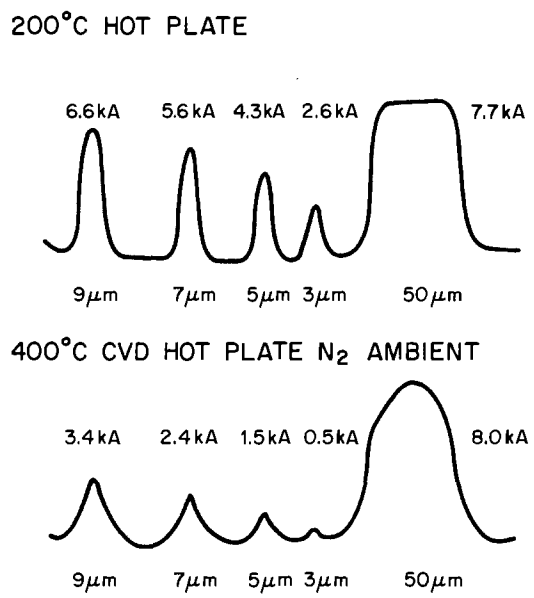

Fig. 7. Profilometer traces of polyimide films at two cure temperatures.

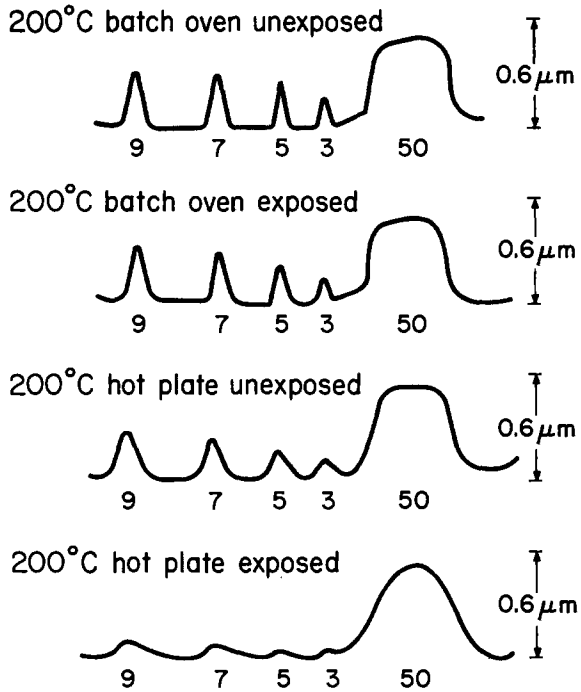

Fig. 8. Profilometer traces for HPR 204 on 0.58 μm topography. Linewidth, 3-50 μm, is indicated for each feature.

The same experiment was also conducted with the same HPR204 resist material on 1.0 μm topography. Figure 9 shows a schematic of these results. In this case, although some polymer flow occurs at the 200°C baking temperature, no marked difference between the unexposed and exposed materials is observed. The 10 μm features are only planarized to within 0.4 μm. Apparently, the polymer flow that does occur does not planarize topography features as well for the larger step heights. Since the polymer film thickness is less on top of the step, it is conceivable that a certain thickness of polymer is necessary to induce a sufficient amount of flow to planarize topography. To test this hypothesis, the experiment was repeated with HPR206 resist on the 1.0 μm topography. Figure 10 shows the results. In this case, the improved planarization prop-

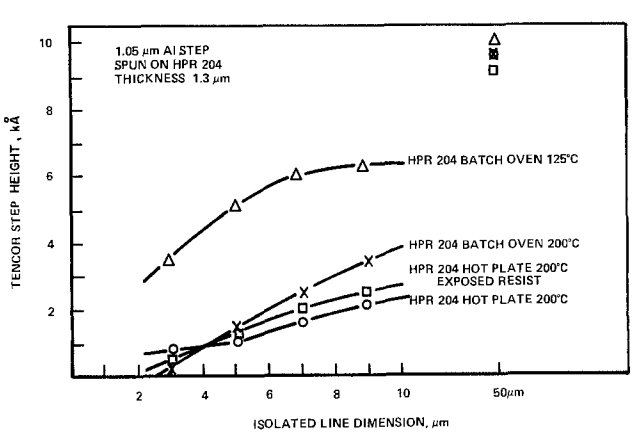

Fig. 9. Step heights vs. feature size for HPR 204 on 1.0 μm topography.

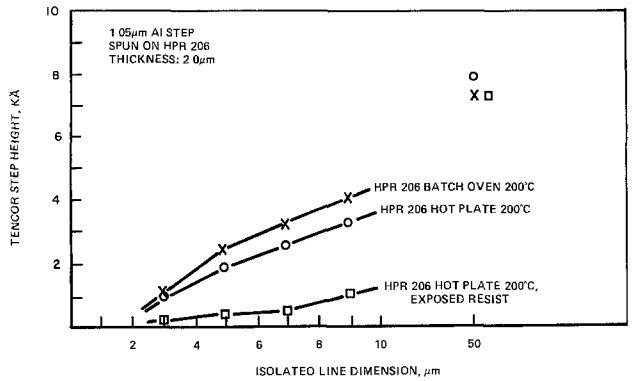

Fig. 10 Step heights vs. feature size for HPR 206 on 1.0 μm topography.

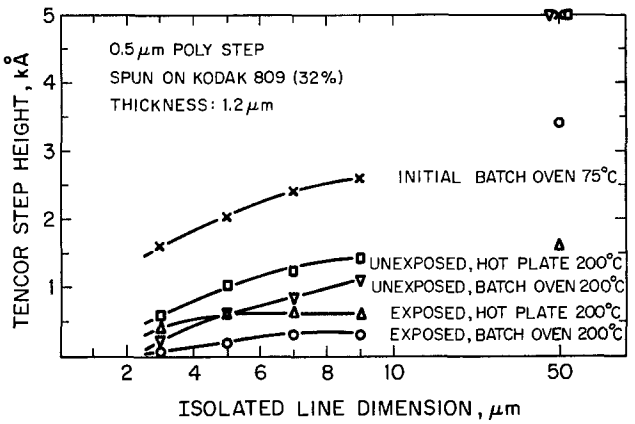

Fig. 11. Step heights vs. feature size for Kodak 809 on 0.5 μm topography.

erties for the exposed, hot-plate cured resist is observed. The thicker coating has promoted the improved flow properties of the polymer from the top of the step. Presumably, the improved thermal flow properties of exposed resist material is related to the functional group modification of the sensitizer portion of the resist. This modification prior to baking may prevent polymer crosslinking reactions from occurring during a subsequent bake. Using a 125°C hot plate or batch oven bake to destroy the sensitizer does not improve the thermal flow characteristics.

Our studies also evaluated another diazoquinone resist material with reportedly greater thermal flow properties (22). Figure 11 displays experimental results for Kodak 809 (32% solids) spun-on to a soft-baked thickness of 1.4 μm on 0.5 μm topographical features. In this case, the 10 μm features were planarized to within 0.05 μm for exposed resist film in both the batch and hot-plate bake ovens. More significantly, large features (50 μm) are planarized to a substantial degree, unlike the HPR204 results. Crust formation for this resist material may not be as prevalent as that in other diazoquinone resist materials, or, a lower glass transition temperature may allow polymer flow to occur before a crust is formed. This Kodak 809 material has produced the most planarized surfaces to date. To produce highly planarized surfaces for features size up to 10 μm, it appears that thermal flow of the applied polymer coating is essential. The use of resist materials for this purpose is attractive because of their high purity, widespread use, and well-characterized properties.

Summary

The planarizing properties or the thickness variations on topographical features have been examined for several spun-on polymer thin-film materials. The viscosity of the spun-on polymer solution appears to be a reasonable indicator of the spun-on planarization characteristics. Diazoquinone novolac resin resist solutions had the best spun-on planarization properties followed by polymethylmethacrylate (PMMA) and polyimide solutions. To obtain the minimum absolute resist thickness change on topographical features with positive resist materials, high viscosity materials at high spin speeds should be used. The fractional resist thickness change is improved over the entire spin speed range using higher viscosity materials.

In many cases, thermal flow of the polymer film during a subsequent cure step is a dominant planarization mechanism. Backside (hot plate) bakes appear to promote thermal flow to a greater degree than batch oven bakes. Fully exposed (bleached) diazoquinone novolac-resin resist materials have produced the greatest degree of planarization to date. With processing conditions that promote thermal flow, an isolated 10 μm line feature with a 0.5 μm step height can be planarized to within 0.1 μm or less with a polymer coating less than 1.5 μm thickness. Of the positive resist materials studied, Kodak 809 resist clearly exhibits the superior planarization properties primarily due to its improved thermal flow properties during the high temperature postbake process.

Manuscript submitted Jan. 13, 1983; revised manuscript received March 29, 1983.

Any discussion of this paper will appear in a Discussion Section to be published in the June 1984 JOURNAL. All discussions for the June 1984 Discussion Section should be submitted by Feb. 1, 1984.

RCA Laboratories assisted in meeting the publication costs of this article.

REFERENCES

1. D. W. Widimar and H. Binder, *IEEE Trans. Electron Devices*, **ed-22,** 467 (1975).
2. A. R. Neurether, P. K. Jain, and W. G. Oldham, *SPIE Proceedings*, **275,** 110 (1981).
3. J. LaRue and C. Ting, *ibid.*, **275,** 17 (1981).
4. J. D. Cuthbert, *Solid State Technol.*, **20**(8), 59 (1977).
5. K. Mukai, A. Saiki, K. Yamanaha, S. Harado, and S. Shoje, *IEEE J. Solid State Circ.*, **sc-13,** 462 (1978).
6. P. Shak, D. Laks, and A. Wilson, in "Proceedings of International Electron Devices Meeting," p. 465 Washington, DC, Dec. 3-5, 1979.
7. H. Katto, H. Kawamoto, K. Misusada, and K. Itoh, *Electron.*, **53,** 103 (1980).
8. S. J. Rhodes, "Semiconductor International," pp. 65-70, March, 1981.
9. A. J. Gregoritsch, in "Proceedings of 14th Annual Reliability Physics Conference," pp. 228-231, Las Vegas (1976).
10. B. J. Lin and T. H. P. Chang, *J. Vac. Sci. Technol.*, **16,** 1669 (1979).
11. M. Hatzakis, *ibid.*, **16,** 1984 (1979).
12. J. Moran and D. Maydan, *ibid.*, **16,** 1620 (1979).
13. R. E. Howard, E. L. Hu, L. D. Jackel, P. Grabbe, and D. M. Tennant, *Appl. Phys. Lett.*, **36,** 592 (1980).
14. A. C. Adams and C. D. Capo, *This Journal*, **128,** 423 (1981).
15. L. K. White, Preprints for Proceedings of Kodak Microelectronics Seminar, Interface '82, San Diego, CA, October 21-22, 1982.
16. E. D. Lui, M. M. O'Toole, and M. S. Chang, 1981 Workshop on Micrometer and Submicrometer Lithography, Lake Placid, NY, July 28-30, 1981.
17. K. Hirata, Y. Ozaki, M. Oda, and M. Kimizuka, *IEEE Trans. Electron Devices*, **ed-28,** 1323 (1981).
18. W. J. Daughton and F. L. Givens, *This Journal*, **129,** 173 (1982).
19. D. Meyerhofer, *J. Appl. Phys.*, **49,** 3993 (1978).
20. G. F. Damon, in "Proceedings of the Second Kodak Seminar on Microminiaturization," p. 36, Eastman Kodak Co., Rochester, NY (1967).
21. L. B. Rothman, *This Journal*, **127,** 2216 (1980).
22. D. W. Frey, J. R. Guild, and E. B. Hryhorenko, in "Proceedings of Kodak Microelectronics Seminar, Interface '81," Dallas, TX, p. 40, October 15-16, 1981.

Study of Breakdown Fields of Oxides Grown on Reactive Ion Etched Silicon Surface: Improvement of Breakdown Limits by Oxidation of the Surface

N. Lifshitz

Bell Laboratories, Murray Hill, New Jersey 07974

ABSTRACT

The oxide breakdown field is known to be low if the silicon surface prior to oxidation was treated by reactive ion etching (RIE) in Cl_2 or other ambient with high Si etching rate. It is believed that the early breakdown is due to poor morphology of Si surface, viz. pores and spikes caused by RIE and associated inhomogeneities of the electric field in the oxides grown on such surface. In the present work, a method to upgrade the oxide to a device quality is suggested. The method consists in growth of a thin sacrificial oxide and its chemical removal prior to gate oxidation. For example, with the sacrificial oxide as thin as 180Å, this process results in improving the breakdown field from 4 to approximately 6 MV/cm. Growth of sacrificial oxide about 600Å thick yields a breakdown field as high as that of oxides grown on virgin silicon wafers.

Reactive ion etching (RIE) of silicon and polysilicon in Cl ambient yields high etching rates and good selectivity relative to SiO_2. Nevertheless, silicon surfaces subjected to RIE can not be used for device fabrication. Breakdown fields of oxides grown on such surfaces are low, and incidence of low field failure is high (1, 2).

It is believed that the early breakdown of oxides grown on Si surfaces etched in chlorine atmosphere is due to poor morphology of the surface, viz. pores and spikes and associated inhomogeneities of the electric field in the oxide (1, 3, 4).

Schwartz and Schaible studied reactive ion etching of silicon in a plasma containing chlorinated species (5). They report roughening of the etched surface in CCl_4 and Cl_2 plasmas. The effect was particularly pronounced in Cl_2 plasma when the formation of black silicon (black plague) was observed.

There are at least two plausible mechanisms of formation of surface inhomogeneities during RIE in Cl_2 ambient. For example it can be: (*i*) high density of defects and dislocations (local etching rate is higher near the defects), or (*ii*) high selectivity of etching Si over SiO_2. If the etching rate ratio in chlorine medium is high (typically 20 ÷ 30), local variations in the native oxide thickness can be transformed into sizable spikes and craters. It has been noticed that at very high ratios microroughness of etched silicon becomes severe (black plague) (4).

In the present work, a method is suggested to upgrade breakdown properties of oxides grown on RIE exposed surface to a device quality by improving morphology of the surface. In this methed, thin layers of sacrificial oxides are grown and chemically removed prior to gate oxidation.

Experimental

Sample preparation.—Si wafers (p-type Wacker <100> oriented, 6-8 Ω cm) were thermally oxidized to grow 4000Å of SiO_2, and the oxide was removed in buffered hydrofluoric acid. The exposed silicon surface was then reactive ion etched to remove about 5,000Å of Si. Chlorine was used as the reactive ion medium in these experiments. In Table I, some parameters of RIE process are gathered.

After RIE, sacrificial oxides of different thicknesses were thermally grown at 950°C and removed in BHF. After a standard preoxidation clean, the gate oxide 250Å thick was grown at 1000°C in dry O_2/HCl. A polysilicon layer 3500Å thick was deposited, doped with phosphorus at 950°C, patterned in 30 mil dots, and plasma etched to form MOS capacitors.

To determine the oxide breakdown field a 10 × 10 array of 30 mil diam capacitors were probed. The field was incremented in 0.5 MV/cm steps until a current of 2 μA was reached. This current was chosen as a criterion for breakdown. The voltage was recorded, reset to zero, and the next capacitor was probed.

High frequency (1 MHz) capacitance-voltage and conductance-voltage measurements were made on a PAR Model 410 C-V plotter to determine the effect of Cl_2 reactive ambient exposure on MOS properties of the Si/SiO_2 interface. A heated chuck was used to perform bias-temperature stress experiments. All measurements were made in a dark box.

Table I.

Reactor type	Flow (cc/min)	Pressure (μm)	Power density (w/cm²)	Si etching Rate (Å/min)	Selectivity over SiO_2
Parallel Plate	20	5	0.22	500	20:1

Results

Results of the measurements are gathered in Fig. 1 and 2 and Table II. In Fig. 1, the log-normal probability distribution of the breakdown fields is plotted for the oxides grown on Si surface etched in Cl_2 medium. For comparison, the data for a control sample (oxide grown on virgin Si) is also plotted (filled triangles). It is

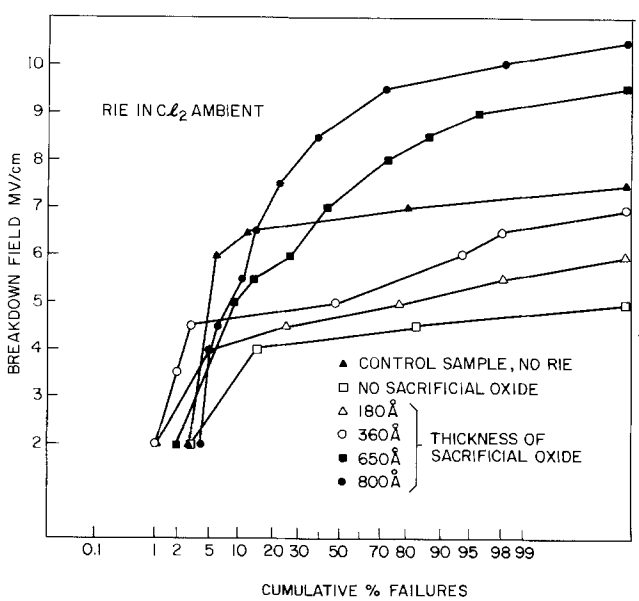

Fig. 1. Breakdown field vs. cumulative percent failure for RIE in Cl_2 ambient.

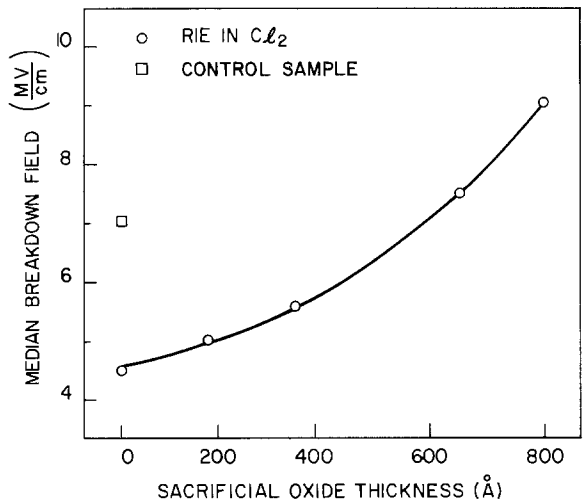

Fig. 2. Breakdown field as a function of sacrificial oxide thickness

easy to see that the reactive ion exposure caused degradation of the oxide breakdown properties. Median breakdown field of oxides grown directly on the exposed Si surface (open squares) is only 4.5 MV/cm, while for the control sample this field is 7 MV/cm (see Table II). The breakdown fields begin to improve as soon as the sacrificial oxide growth and chemical removal procedure is introduced. As the sacrificial oxide thickness d_s increases, the distribution plots move to higher fields. Median breakdown field grow steadily as shown in Fig. 2 and exceeds that of the control sample at $d_s = 600$Å.

At the same time, sacrificial oxide procedure leads to increasing the spread of breakdown fields. Figure 3 illustrates the observation. Here the histograms of breakdown fields from Fig. 1 are plotted for different d_s. While moving to higher fields the distributions spread over wider and wider range and lose their sharpness.

The occurrence of a low-field ($\leq$ 2 MV/cm) breakdown shown in the last column of Table II does not seem to correlate either with d_s or median breakdown fields. Table II also presents values of the fixed charge density at Si/SiO_2 interface obtained from C-V and G-V measurements. Exposure of Si surface to RIE in Cl_2 atmosphere does not seem to affect the MOS properties, though a slight increase in the charge density is observed on samples with thicker sacrificial oxides. Bias-temperature stress measurements conducted at 250°C with electrical fields of 2 MV/cm showed no changed or shift of C-V characteristics after 15 min with either positive or negative bias. This indicates the absence of traps at the Si/SiO_2 interface and mobile ionic charges in the gate oxide.

Conclusions

A method to improve the morphology of a Si surface exposed to RIE in chlorine environment is suggested.

Table II.

Reactive ambient	Sacrificial oxide thickness d_s (Å)	Median breakdown field (MV/cm)	Low field breakdown (%)	Interface charge density (10^{10} cm^{-2})
Control (no RIE)	0	7.0	3	2
RIE in Cl_2 ambient	0	4.5	3	2
	180	5	1	4
	360	5.5	1	9.5
	650	7.5	5	4
	800	9.0	4	10

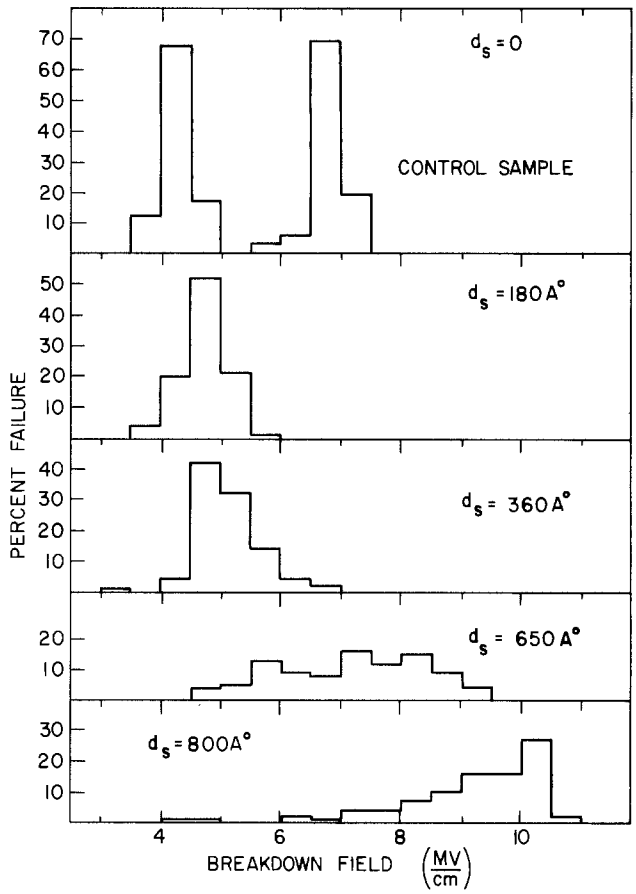

Fig. 3. Breakdown field hystogram (RIE in chlorine ambient)

The method consists of slight oxidation of the surface with subsequent removal of the oxide. It is believed that the process moderates violent nonuniformities generated during reactive ion etching of the surface. The method allows one to upgrade breakdown properties of oxides grown on the etched surfaces to a device quality.

Acknowledgments

I wish to thank E. N. Fuls and H. J. Levinstein for helpful discussions. I would like to extend my thanks to W. E. Willenbrock for his help with reactive ion etching.

Manuscript submitted Jan. 19, 1983; revised manuscript received April 6, 1983.

Any discussion of this paper will appear in a Discussion Section to be published in the June 1984 JOURNAL. All discussions for the June 1984 Discussion Section should be submitted by Feb. 1, 1984.

Bell Laboratories assisted in meeting the publication costs of this article.

REFERENCES

1. L. M. Ephrath, *IEEE Trans. Electron Devices*, **ed-28,** 1315 (1981).
2. W. W. Weick, Unpublished.
3. L. M. Ephrath and R. S. Bennett, *This Journal*, **129,** 1822 (1982).
4. C. M. Horwitz, *IEEE Trans. Electron Devices*, **ed-28,** 1320 (1981).
5. G. C. Schwartz and P. M. Shaible, *J. Vac. Sci. Technol.*, **16,** 410 (1979).

Some Observations on Oxygen Precipitation/Gettering in Device Processed Czochralski Silicon

H. R. Huff,*[1] H. F. Schaake,* J. T. Robinson,* S. C. Baber,* and D. Wong*[2]

Texas Instruments, Incorporated, Dallas, Texas 75265

ABSTRACT

Several results of our experimental program studying the relationship between the properties of the silicon starting material and N-channel MOS dynamic RAM circuit performance is described. The thermal history and oxygen and carbon concentrations control the silicon material properties and much of the subsequent circuit performance. The beneficial effect of intrinsic gettering due to precipitation of oxygen in the bulk on MOS dynamic RAM refresh performance will be shown. Equivalent thermal processes will result in similar circuit performance only when the silicon material is equivalent. Some circumstantial evidence is also presented for a degrading effect of high concentrations of carbon in the starting material.

The correlation of integrated circuit performance with silicon material and IC process parameters is an active area of current research. In particular, the use of gettering procedures affords greater control over IC product performance and consequently has attracted much attention (1-5). The present paper details several results of our experimental program studying the relationship between the properties of the silicon starting material and N-channel MOS dynamic RAM circuit performance. Our approach has been to use the MOS dynamic RAM as a diagnostic probe to assess the role of several starting material variables and thereby identify the critical material parameter(s). We have correlated the circuit refresh time with the MOS minority carrier generation lifetime and with the amount of oxygen precipitation which occurs in the bulk of the wafer, as determined from x-ray topography. The results show a significant beneficial effect of the intrinsic gettering provided by the oxygen precipitation.

In this work, three different sets of experiments were conducted: (*i*) an evaluation of material from several different sources on yield loss due to refresh failure of a 16K dynamic RAM, (*ii*) an evaluation of wafers produced from a single crystal as a function of position in the crystal and as a function of the temperature of a single low-temperature anneal before the wafers are committed to processing, and (*iii*) calibration of the intensity of x-rays which are diffracted during an x-ray topography scan with the amount of oxygen which has precipitated in the wafer.

Experimental Procedures

Wafer selection and preparation.—All wafers used in these investigations were 76 mm diam, <100> oriented, 10-15 Ω-cm boron-doped, dislocation-free, non back-surface damaged, Czochralski-grown wafers. For the first set of experiments, a total of 23 wafers from three vendors was selected for processing in five split lots. These wafers were used "as is," and consequently both the surface preparation and the low-temperature anneal to annihilate the oxygen donors and stabilize the resistivity were uncontrolled and a function of the vendor.

For the second set of experiments, a single crystal was selected after growth, sectioned as shown in Fig. 1, and processed in two split lots. The crystal had received no heat-treatment, other than that which it received during the Czochralski growth process. Slabs, 2 mm in thickness, were taken between each of the sections for room temperature measurements of the oxygen and carbon concentrations by FTIR techniques (6, 7). Each of these sections was then subjected to a single four hour low-temperature anneal as indicated in Fig. 1. Non back-surface damaged wafers were then prepared from each section by conventional production techniques and the wafers were committed to the fabrication of 16K dynamic RAMS.

For the third set of experiments, a single section taken from the top of a Czochralski crystal was selected. This particular crystal was grown such that there was a large radial variation in the oxygen concentration. This section had received no anneal subsequent to its growth. Slabs, 2 mm in thickness, were taken from either end of the section for determination of the carbon and oxygen concentrations using an FTIR spectrometer. These measurements were made as a function of position across the slabs. The oxygen concentration showed a variation of nearly a factor of 2 from edge to center, while the carbon concentration was below the limits of detection, *i.e.*, $<2 \times 10^{16}$ cm^{-3}. Both top and bottom slabs yielded the same results, indicating that all wafers which were prepared from the section between the two slabs had identical oxygen and carbon concentrations. The wafers which were prepared from this section were polished on both sides to enable FTIR measurements to be made of the oxygen and carbon concentrations.

Circuit fabrication test procedure.—N-channel 16K dynamic RAM circuits were fabricated on the as-received wafers using a double level polysilicon gate structure (8). In addition to the specific experimental wafers described above, a number of control wafers, drawn from the front-end inventory, were included in each lot of wafers which was processed. The identical process and process facility were used for the wafers processed for experiments reported here. A series of functional and parametric tests were performed on completed wafers to identify good devices prior to a detailed series of circuit refresh measurements using

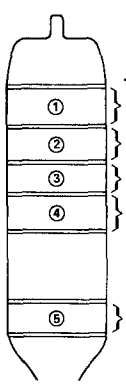

	G FACTOR	LOW-TEMPERATURE ANNEAL (°C)	OXYGEN (10^{18}/CM^3)	CARBON (10^{16}/CM^3)
①	.04-.12	600	2.16	ND
②	.12-.20	700		ND
③	.20-.29	650	1.87	ND
④	.29-.40	600	1.70	ND
⑤	.83-.91	700	1.46	<5.6

Fig. 1. Summary of oxygen, carbon, and low-temperature thermal anneal data for particular Czochralski-grown crystal.

* Electrochemical Society Active Member.
[1] Present address: Philips Research Laboratories Sunnyvale, Signetics Corporation, Sunnyvale, California 94086.
[2] Present address: Arco Solar, Inc., Chatsworth, California.
Key words: integrated circuits, gettering, semiconductor, x-rays.

conventional industrial automated test probe procedures.

The importance of these refresh measurements is because information in a dynamic RAM MOS memory cell is retained on a small capacitance, typically much less than 1 picofarad. Such volatile charge is subject to the destruction of information due to leakage currents. Consequently, a mechanism is required to return the capacitor to its original charge state. The terminology "circuit refresh time" refers to this mechanism and is the maximum allowable time interval to both sense and restore sufficient charge on the capacitor to discriminate the original information content. A pass/fail criterion based on a circuit refresh time of 50 msec at 25°C is used in this paper. The terminology "time for the first bit to fail" refers to the length of time when one can no longer reliably sense the charge on the capacitor and, therefore, the information is irretrievably lost. Not surprisingly, reduced wafer refresh loss was found to correlate with increased time for the first bit to fail when averaged over the good devices on a wafer.

Lifetime and x-ray topography measurements.—The minority carrier generation lifetime was measured by the pulsed capacitance-time (C-t) technique (9) on the process control monitors located on each of the completed circuit wafers.

Transmission x-ray topographs were made of all wafers after processing using a (220) reflection and Mo $K\alpha_1$ radiation, in a microcomputer automated topography camera with automatic alignment and Bragg angle control. Wafers on which dynamic RAMS had been fabricated were stripped to the bare silicon substrate prior to this topographic examination. As the wafer was scanned, the intensity corresponding to the peak in the Bragg reflection was recorded as a function of position. Since the crystal growth procedure results in nearly radially symmetric wafers, the single scan across a wafer diameter yields information on the entire wafer.

To calibrate the diffracted x-ray intensity to the amount of oxygen precipitation, each of the third set of wafers was subjected to a single low-temperature anneal followed by a 16 hr anneal at 1000°C in dry oxygen. The low-temperature anneals were performed in nitrogen at 550°, 600°, 650°, 700°, or 750°C for times ranging from 0.5 to 128 hr. After removal of the surface oxide, the diffracted x-ray intensity from each wafer was recorded as a function of position along the diameter of the wafer as the transmission topograph was made. The oxygen concentration after precipitation was then measured as a function of position on the wafer in the FTIR, the difference between this measurement and the initial concentration yielding the amount of precipitated oxygen. Since the wafers had a large radial variation in the oxygen concentration, the results for a single wafer yielded information on the precipitation kinetics for a wide variation of oxygen concentrations.

Results and Analysis

The results of the x-ray topography calibration experiments are shown in Fig. 2 and 3. In Fig. 2, the change in the relative diffracted x-ray intensity is plotted against the amount of oxygen which had precipitated, as determined from the IR measurements. With some scatter, it can be seen that the change in the x-ray intensity is exactly proportional to the amount of oxygen which had precipitated, regardless of the low-temperature anneal conditions. This leads us to propose that for a fixed high-temperature anneal, the diffracted x-ray intensity will be a measure of the total amount of precipitated oxygen, regardless of an initial low-temperature process. (In work subsequent to this, we have found that this statement is not true if the wafer contains large amounts of carbon, *e.g.*, $\geq 10^{17}$ cm^{-3} or if the wafer is subjected to a prolonged anneal at $\simeq$450°C

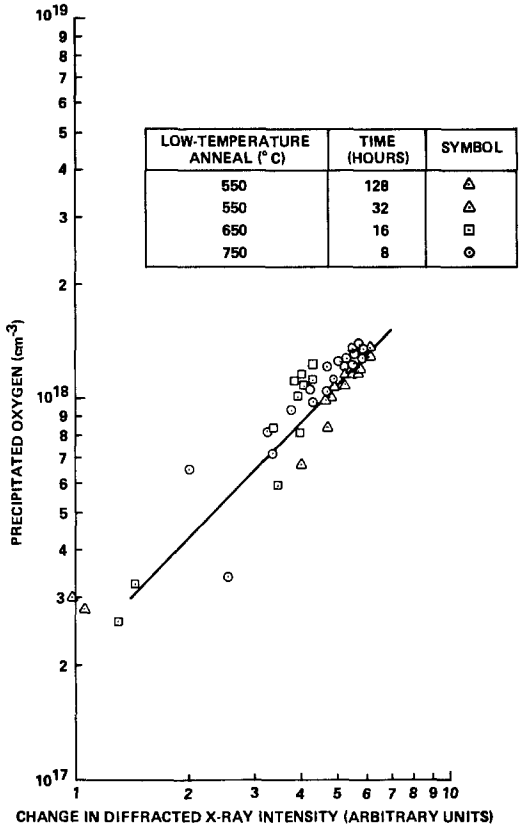

Fig. 2. Correlation of precipitated oxygen with change in diffracted x-ray intensity.

prior to the subsequent low-temperature anneal. It is also not true for the earliest stages of precipitation, which result in a decrease in the diffracted intensity.) Figure 3 is a plot of the initial oxygen concentration *vs.* the diffracted x-ray intensity, which by the foregoing is proportional to the amount of precipitated oxygen. In the linear regions of this log-log plot, the amount of precipitated oxygen is found to be proportional to the eighth power of the initial oxygen concentration. This extreme sensitivity to oxygen concentration is a manifestation of the nucleation kinetics and has been noted before (10). The data for the 1 hr 650°C anneal is identical with that which was found if no low-temperature anneal were performed prior to the 1000°C anneal. This is a result of the nucleation of oxygen precipitates which had occurred during the crystal growth process.

The results of the experiments on the 23 wafers from various vendors processed in 5 split lots is summarized in Fig. 4-6. Figure 4 illustrates the relative wafer refresh loss *vs.* the corresponding MOS generation lifetime. The blackened data points in this figure denote wafers in which at least some oxygen precipitation was detected by the x-ray intensity measurements. A quantitative examination of the dependence of the relative wafer refresh loss at room temperature with the degree of precipitation for the same processed wafers is illustrated in Fig. 5. The general absence of data in the upper right hand portion of this figure is significant and shows that high refresh losses are associated with minimum precipitation of oxygen in the bulk. Increased oxygen precipitation correlates with reduced wafer refresh loss. Figure 6 dramatically illustrates this. This figure shows transmission topographs for four different completed wafers from two vendors processed in a single split lot. Each vendor's material exhibits significantly different refresh yield losses. The letters A-D correspond to the similarly labeled data points in Fig. 5. The two topographs on the right show significant precipitation while the two on the left do not.

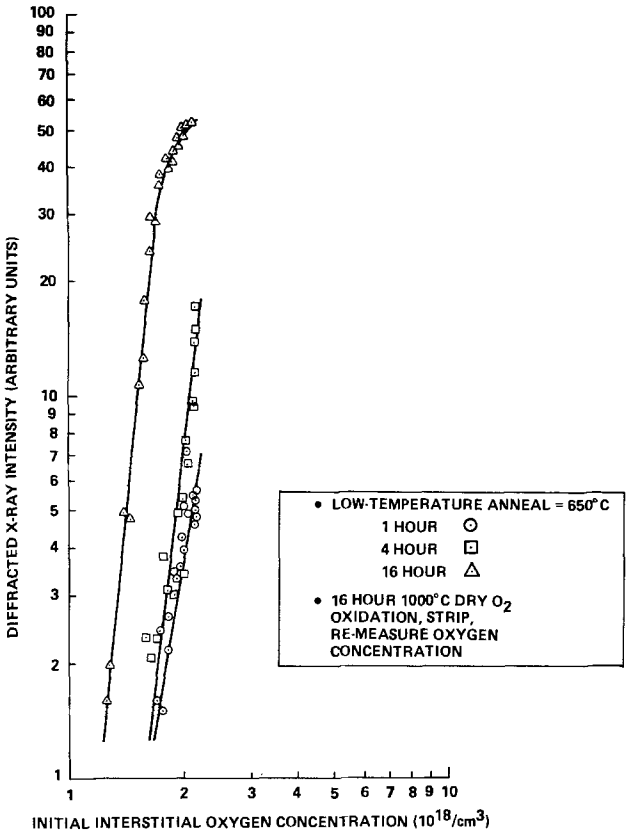

Fig. 3. Correlation of diffracted x-ray intensity with initial interstitial oxygen concentration.

Refresh loss results on wafers made from the crystal shown in Fig. 1 and processed in two split lots are shown in Fig. 7. While there is considerably more scatter in this data than in Fig. 5, it will be noted that again there is a correlation between the amount of oxygen precipitation and reduced refresh loss. Several additional points are illustrated in these results: (*i*) Precipitation alone does not insure minimal refresh loss and the lack of precipitation does not guarantee high refresh loss. (*ii*) Material from the top of the crystal (high oxygen, low carbon) generally performs better than material from the bottom of the crystal (low oxygen, high carbon). (*iii*) Even though precipitation occurred in material from the bottom of the crystal, refresh losses were comparatively large for these wafers. (*iv*) The 4 hr 650°C anneal appears to be somewhat superior to other anneals, although the small amount of data limits this generalization.

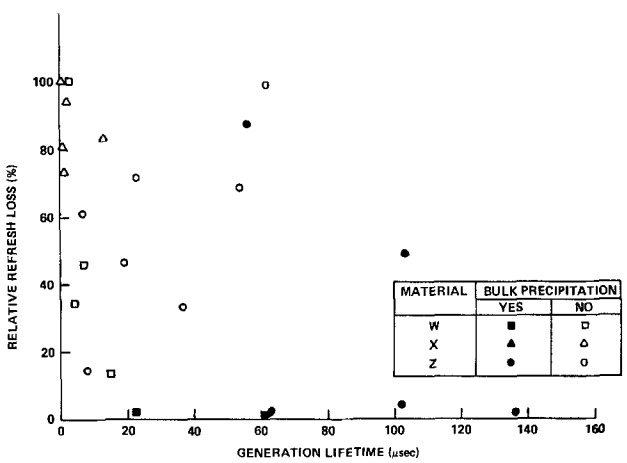

Fig. 4. Correlation of completed wafer relative refresh loss with MOS generation lifetime.

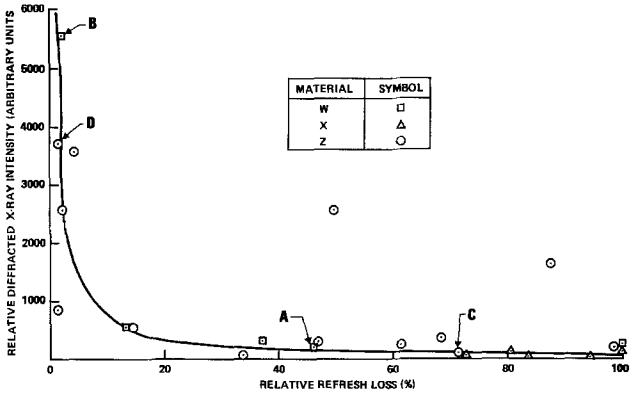

Fig. 5. Correlation of completed wafer diffracted x-ray intensity with wafer relative refresh loss (letters A-D correspond to similarly labeled transmission topographs in Fig. 6).

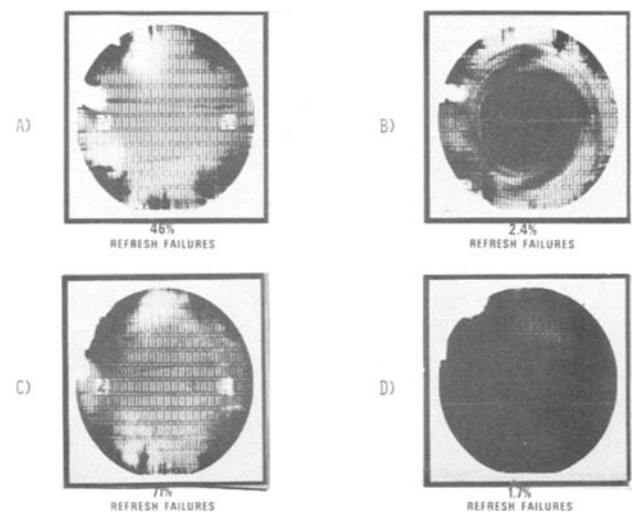

Fig. 6. Transmission topographs illustrating the wafer relative refresh loss for four different completed wafers from two vendors processed in a single split lot. Each vendor's material exhibits significantly different refresh yield losses. (Letters A-D correspond to similarly labeled data points in Fig. 5.)

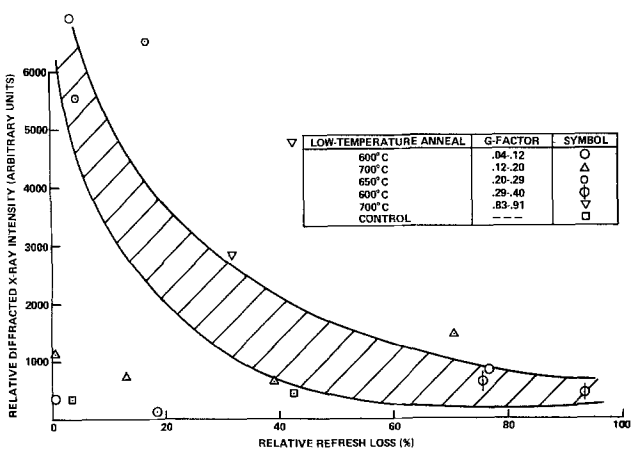

Fig. 7. Correlation of completed wafer diffracted x-ray intensity with wafer relative refresh loss for wafers from crystal noted in Fig. 1.

Discussion

The beneficial effect of intrinsic gettering from precipitation of oxygen in the bulk has been reported by several authors. Reduced p-n junction leakage current (3), controlled epitaxial stacking faults (11), reduced s-pit formation (12), slip retardation (13-15), and improved MOS generation lifetime (16, 17) have been

observed. The importance of sample thermal history has been noted (18) and the magnitude of the generation current has been shown to depend on both the sample location within the grown crystal and on the subsequent thermal processing (19).

In the present work, Fig. 5 and 7 clearly indicate a correlation between improved MOS dynamic RAM circuit refresh performance and increased oxygen precipitation. This work also clearly shows that good refresh performance is possible in wafers in which no detectable precipitation has occurred. The role of intrinsic gettering by the precipitation of oxygen may therefore be said to widen the process window in which low refresh losses are to be expected.

The role of low-temperature anneals and oxygen concentration on the nucleation kinetics of oxygen precipitation is well established (10, 20, 21). In this work, the nucleation kinetics and subsequent precipitation were highly repeatable in well-characterized material (*e.g.*, the material used in the x-ray topography calibration experiments, Fig. 2 and 3). The variation in the material used in the experiments summarized in Fig. 1 and 7, however, was sufficient to make precipitation somewhat unpredictable. Figure 3 provides an explanation for this behavior. Since the amount of precipitated oxygen depends on the eighth power of the initial oxygen concentration, in order to control the amount of precipitation to within ±50%, it is necessary to control the oxygen concentration to within ±5%. The material used, even within a given G-factor range, did not fully meet these requirements. This also demonstrates the usefulness of recent work aimed at growing radially and axially uniform crystals containing controlled amounts of oxygen (21-24).

In the present work, a surface zone denuded of oxygen precipitates was not intentionally introduced by the out-diffusion of oxygen before processing (25, 26). Clearly, such a denuded zone did form, however, as a large amount of precipitation within the depletion depth of the MOS capacitors in the memory cells ($\simeq$5 μm for the device) would lead to catastrophic refresh failures. Presumably the denuded zone formed both during the initial oxidation due to the suppression effect of the ambient on the precipitation of oxygen (27, 28) and during the subsequent processing due to the dissolution of precipitates during the processing cycle.

It was noted in the previous section that material from the bottom of the crystal had higher refresh failure, even though oxygen precipitation was present. This correlates well with increased carbon concentration in the material, and may demonstrate a degrading effect of large amounts of carbon. which is known to affect the precipitation of oxygen (29).

Summary and Conclusions

It has been shown that internal gettering by oxygen precipitation in the bulk of a silicon wafer can significantly reduce yield losses due to refresh failures in dynamic memory devices. The high sensitivity of the precipitation kinetics on oxygen concentration, nucleation time and temperatures, and carbon necessitates stringent control on the starting material, if internal gettering is to be predictable during the IC processing cycle. Some circumstantial evidence for the harmful role of high concentrations of carbon on refresh losses has also been found. In this work, the lowest refresh losses were consistently found on material containing oxygen precipitation and having low carbon concentrations. Certainly, continued work aimed at control of the precipitation of oxygen and the formation of the denuded zone in the active region of the device is warranted.

Acknowledgments

We appreciate the facilities and support of Gary Heerssen and Dale Harbison for the fabrication of the MOS integrated circuits and Bill Loftin for the refresh time measurements.

Manuscript submitted April 19, 1982; revised manuscript received Feb. 7, 1983. This was Paper 498 presented at the Los Angeles, California, Meeting of the Society, Oct. 14-19, 1979.

Any discussion of this paper will appear in a Discussion Section to be published in the June 1984 JOURNAL. All discussions for the June 1984 Discussion Section should be submitted by Feb. 1, 1984.

Texas Instruments, Incorporated assisted in meeting the publication costs of this article.

REFERENCES

1. Abstracts 483-500 in the International Symposium on Gettering in Semiconductors, pp. 1224-1269, The Electrochemical Society Extended Abstracts, Vol. 79-2, Los Angeles, California, Oct. 14-19, 1979.
2. "Semiconductor Silicon 1981," H. R. Huff, R. J. Kriegler, and Y. Takeishi, Editors, The Electrochemical Society Softbound Proceedings Series, Pennington, NJ (1981).
3. T. Y. Tan, E. E. Gardner, and W. K. Tice, *Appl. Phys. Lett.*, **30**, 175 (1977).
4. J. R. Monkowski, *Solid State Technol.*, 44 (1981).
5. J. E. Lawrence and H. R. Huff, in "VLSI Electronics-Microstructure Science," N. G. Einspruch, Editor, Vol. 5, pp. 51-102, Academic Press, New York (1982).
6. American Society for Testing and Materials, 1977 Annual Book of Standards, 43, F121-76.
7. American Society for Testing and Materials, 1977 Annual Book of Standards, 43, F123-74.
8. V. L. Rideout, *IEEE Trans. Electron Devices*, **ed-26**, 839 (1979).
9. H. R. Huff and T. L. Chiu, *This Journal*, **126**, 1142 (1979).
10. N. Inoue, K. Wada, and J. Osaka, "Semiconductor Silicon/1981," H. R. Huff, R. J. Kriegler, and Y. Takeishi, Editors, p. 282, The Electrochemical Society Softbound Proceedings Series, Pennington, NJ (1981).
11. L. E. Katz and D. W. Hill, *This Journal*, **125**, 1151 (1978).
12. W. Lin and C. W. Pearce, *J. Appl. Phys.*, **51**, 5540 (1980).
13. "Semiconductor Silicon 1981," H. R. Huff, R. J. Kriegler, and Y. Takeishi, Editors, pp. 208-231, The Electrochemical Society Softbound Proceedings Series, Pennington, NJ (1981).
14. S. M. Hu, *J. Vac. Sci. Technol.*, **14**, 17 (1977).
15. K. Yasutake, M. Umeno, and H. Kawabe, *Appl. Phys. Lett.*, **37**, 789 (1980).
16. G. A. Rozgonyi and C. W. Pearce, *ibid.*, **32**, 747 (1978).
17. K. H. Yang, H. F. Kappert, and G. H. Schwuttke, *Phys. Status Solidi (A)*, **50**, 221 (1978).
18. P. E. Freeland, K. A. Jackson, C. W. Lowe, and J. R. Patel, *Appl. Phys. Lett.*, **30**, 31 (1977).
19. W. J. Patrick, S. M. Hu, and W. A. Westdorp, *J. Appl. Phys.*, **50**, 1399 (1979).
20. J. Osaka, N. Inoue, and K. Wada, *Appl. Phys. Lett.*, **36**, 288 (1980).
21. R. A. Craven, in "Semiconductor Silicon/1981," H. R. Huff, R. J. Kriegler, and Y. Takeishi, Editors, pp. 254-271, The Electrochemical Society Softbound Proceedings Series, Pennington, NJ (1981).
22. K. E. Benson, W. Lin, and E. P. Martin, in "Semiconductor Silicon/1981," H. R. Huff, R. J. Kriegler, and Y. Takeishi, Editors, pp. 33-48, The Electrochemical Society Softbound Proceedings Series, Pennington, NJ (1981).
23. F. Shimura, in "VLSI Science and Technology/1982," C. J. Dell'Oca and W. Murray Bullis, Editors, pp. 17-32, The Electrochemical Society Softbound Proceedings Series, Pennington, NJ (1982).
24. A. Murgai. W. J. Patrick, J. Combronda, and J. C. Felixe, *IBM J. Res. Dev.*, **26**, 546 (1982).
25. H. J. Ruiz and G. P. Pollack, *This Journal*, **125**, 128 (1978).

26. K. Nagasawa, Y. Matsushita, and S. Kishino, *Appl. Phys. Lett.*, **32**, 622 (1980).
27. H. F. Schaake, S. C. Baber, and R. F. Pinizzotto, in "Semiconductor Silicon/1981," H. R. Huff, R. J. Kriegler, and Y. Takeishi, Editors, pp. 273-279, The Electrochemical Society Softbound Proceedings Series, Pennington, NJ (1981).
28. R. A. Craven and H. W. Korb, *Solid State Technol.*, 55 (1981).
29. R. F. Pinizzotto and H. F. Schaake, "Defects in Semiconductors," T. Y. Tan and J. Narayan, Editors, p. 387, North-Holland, New York (1982).

Oxidation of Arsenic Implanted Polycrystalline Silicon

E. Kinsbron,* S. P. Murarka,* T. T. Sheng, and W. T. Lynch

Bell Laboratories, Murray Hill, New Jersey 07974

ABSTRACT

The techniques of Rutherford backscattering spectrometry, neutron activation, and transmission electron microscopy were employed in this extensive study of the thermal oxidation of arsenic implanted polycrystalline silicon (polysilicon) films. Some evidence for slower oxidation rates were found for polysilicon layers lying over silicon dioxide substrate as compared to the oxidation rates of films lying directly over bare silicon. Complete oxidation of films lying over silicon dioxide substrates left scattered arsenic-silicon-oxygen inclusions trapped at the original polysilicon/silicon dioxide interface. Significant arsenic diffusion through the underlying silicon dioxide layer, into the silicon substrate, was measured after the complete oxidation of thick polysilicon films over thin silicon dioxide substrates.

Polycrystalline silicon (polysilicon) films are widely used in MOS integrated circuits technology. Phosphorus doped polysilicon films are often used as MOS gates and as interconnections and several studies have reported on the thermal oxidation of these films (1-5). With the recent use of silicide films at gate interconnections and with the development of polysilicon films doped with arsenic during the film deposition, the use of arsenic doped films has become more attractive. In spite of the usefulness of arsenic doped polysilicon, it was found during this study that there is practically no information about thermal oxidation of arsenic doped polysilicon.

In this work, the thermal oxidation of arsenic implanted polysilicon films was extensively investigated. The effects of parameters such as: doping doses, oxidation ambient, oxidation temperature, and substrate structure were tested and characterized. The techniques of Rutherford backscattering spectrometry (RBS), neutron activation, and transmission electron microscopy (TEM) were applied during this study to obtain maximum information about the oxidation process.

Arsenic is known to preferentially segregate in silicon during oxidation (6) and therefore arsenic atoms are "piled-up" at the oxide/polysilicon interface. Due to grain boundary diffusion and grain boundary segregation arsenic in polysilicon also piles up at the interface of the polysilicon film and the substrate (7). If an arsenic doped polysilicon film lying over an oxidized substrate is thermally oxidized the polysilicon layer remaining between the grown oxide and the buried substrate oxide will become richer and richer in arsenic. The question of what will happen to the last tens of angstroms of the polysilicon layer, very rich in arsenic, if it is forced to be completely oxidized, was never addressed in the past and is answered in this paper.

The results are presented in three main sections. The first summarizes the oxidation rates for the various oxidation conditions. The second examines the behavior of the oxidation of thin polysilicon films over thick oxide substrates. The third section presents the results of oxidizing thick polysilicon films over thin oxide or bare silicon substrates.

Experimental

Silicon wafers of <100> orientation boron doped to 6-8 Ωcm, both with and without thermal oxide, were used as substrates for the polysilicon deposition. The polysilicon films were deposited by the thermal decomposition of silane at 625°C in a standard low pressure (150 mTorr) chemical vapor deposition reactor. Four main groups of sample structures were tested during this work: (A) thin polysilicon (500Å) deposited over a thick oxide layer (2500Å), (B) thick polysilicon (2500-6000Å) deposited over a thin oxide layer (300-1000Å), (C) polysilicon films deposited directly over single crystal silicon substrates, and (D) bare single crystal samples without polysilicon film (see Table I and Fig. 1). Arsenic ions were implanted into the polysilicon films at 30 keV with doses of 0.7-7 × 10^{15} cm^{-2}. No annealing treatment was given to the implanted samples prior to the oxidation. This will leave the top surface of the film amorphous and not electrically activated. The thermal oxidation was performed either in a wet ambient at 900° and 1050°C or in a dry ambient at 1000° and 1100°C. Oxide thicknesses were determined by ellipsometer for oxides on single crystal silicon or by a Talystep step height reader for those on polysilicon films. In some cases, the oxide thickness was also determined from measurements conducted on scanning electron microscope (SEM) cross-section samples or from the RBS measurements. Good agreement was found between these different methods.

The arsenic distribution and location after the oxidation were determined by RBS or by neutron activation techniques. The backscattering spectra were taken with

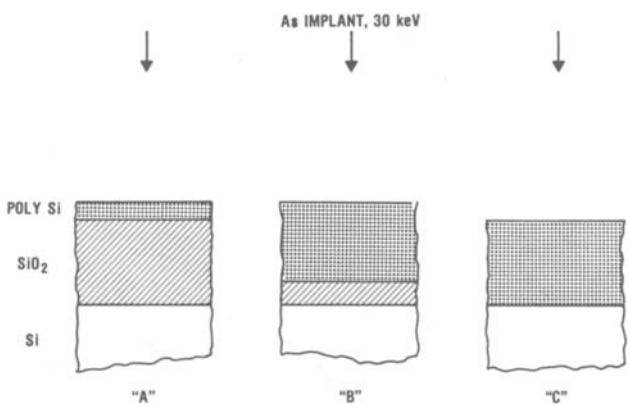

Fig. 1. Schematic cross-section views of three of the four different group of samples used in this work.

* Electrochemical Society Active Member.

Table I.

Sample group	Initial structure		As implantation		Oxidation	
	Oxide thickness (A)	Polysilicon thickness (Å)	Energy (KeV)	Dose 1×10^{15} (cm^{-2})	Wet (°C)	Dry (°C)
A	2500	500	30	1	900	1000
B	300	6000	30 and 90	1	900 and 1050	—
B	1000	5000	30	0.7 and 7	900 and 1050	1000 and 1100
B	1000	2500	30	1	900 and 1050	—
C	—	2500	30	1	900 and 1050	—
D	—	—	30	1	900 and 1050	—

2 MeV He^+ ions and a system energy calibrated to 4.00 KeV/channel: depth determination was done using published (8) values of stopping cross sections.

For the detection of small arsenic concentrations, trapped in the grown oxide, the neutron activation technique was applied. The samples were activated by a thermal neutron flux of 2×10^{13} per cm^2 per second, and the total gamma ray activity of arsenic at 560 KeV was measured approximately 40 hr later for a fixed time of 100 sec by use of a Ge(Si) detector and a computerized pulse height analyzer. The depth profiles of the arsenic distribution were obtained by successively etching a thin layer of oxide and recounting the (cumulative) remaining arsenic activity, $N(x)$. The oxide thinning was done by chemical etching using BHF mixtures containing a few drops of 1000 ppm inactive arsenic solution to reduce redeposition of activated arsenic during the etching and rinsing.

The TEM study was conducted at 200 KeV on thin film vertical cross-section samples which were prepared according to an established technique (9). These studies were performed in order to reveal the presence of arsenic inclusions (if any) at the original polysilicon/oxide interface and for characterization of the oxide/polysilicon interface morphology.

Results and Discussion

Oxidation rate.—The oxide thicknesses of thermal oxide grown from arsenic implanted polysilicon films in wet and dry oxygen ambient at various temperatures and times are given in Fig. 2. From the comparison of the oxidation rates of a reference undoped (111) silicon single crystal (dashed lines), it is concluded that at the lower temperatures the wet oxidation of the doped polysilicon films is faster. This result is similar to what was reported for the oxidation of phosphorus doped films (10). The doping affects the chemical surface reaction and is more significant at the lower temperatures. The oxidation in the dry ambient also occurred at a higher rate for the doped polysilicon films than for the reference undoped (111) silicon single crystal.

No significant difference was found between the oxidation rate of the low dose (7×10^{14} cm^{-2}) and the high dose (7×10^{15} cm^{-2}) implanted samples. The reason can be because the top 500Å of the polysilicon films were amorphized during the implantation process. The samples were not annealed prior to the oxidation and faster oxidation rates and As segregation could take place during the initial oxidation. The high segregation coefficient of As in Si, the fast grain boundary diffusion and the As accumulation at the polysilicon/buried oxide interface leave the polysilicon grains at a relatively low arsenic concentration independent of the implanted dose. The difference in the sample structure can explain why our results of the oxidation rate are different from Ohkawa (11) results on oxidizing As-implanted silicon single crystal substrates, at relatively low temperatures (650°-850°C). The oxidation rate is faster than the As diffusion rate, and there is a continuous increase in the As concentration at the oxidized surface of the single crystal substrate. This As segregation depends on the initial implanted dose and affects the oxidation rate.

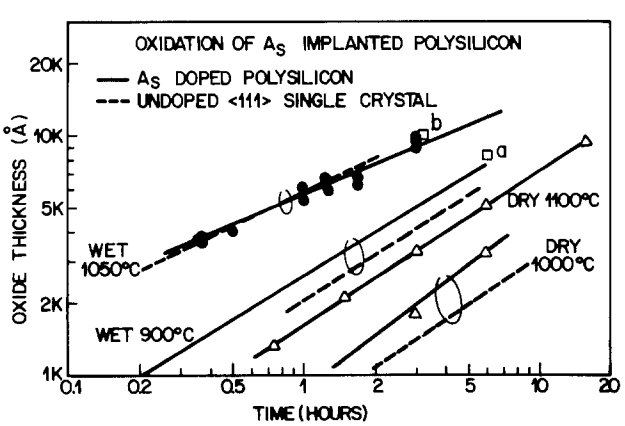

Fig. 2. Oxide thickness as a function of time for thermal oxidation of arsenic implanted polycrystalline silicon films lying over silicon dioxide substrate. Points a and b are for polysilicon films on bare silicon substrate.

The oxide thickness of oxidized polysilicon lying on bare silicon substrate (group "C" samples) are also shown on Fig. 2 by the a and b data points. As can be seen on Fig. 2, only small differences in the oxidation rate have been found between samples of this group and samples of group "B", with the buried oxide under the polysilicon film. The result probably reflects the fact that at the grown SiO_2/polysilicon interface the buried oxide layer does not affect the arsenic concentration until the very end of the polysilicon oxidation. At this point, the polysilicon layer becomes very rich in arsenic and the oxidation rate can be affected but could not always be determined in our experiments where the average oxidation rate was obtained by dividing the total oxide thickness by the oxidation time. Some evidence for slower oxidation rate in samples from group "B" were observed in the RBS spectra and will be discussed later.

During the etching of the oxide films, it was found that the 1050°C wet oxidized films are etched about 7% faster than the 900°C wet oxidized films. This result is related to the different amount of arsenic which had been trapped in the oxide film and will be discussed later.

Oxidizing thin polysilicon films.—Samples from group "A" (Table I) were oxidized at 900°C in a wet ambient for 10, 20, and 60 min, or at 1000°C in a dry ambient for 200 min. The energy spectra of He^+ ions backscattered from these 900°C wet oxidized samples are shown in Fig. 3. It is clear from this figure that the arsenic is pushed ahead from the top surface towards the buried SiO_2/polysilicon interface during the short oxidation. The "bump" near the Si edge of the He^+ spectra (see Fig. 3) indicates that the polysilicon was not completely oxidized after 10 min of oxidation, and a thin polysilicon layer is still trapped between the original buried oxide and the new grown oxide. The same result was obtained also from the TEM cross-sectioned samples. When the oxidation is completed (after ~20 min), all the arsenic is located at the original buried oxide/polysilicon interface (Fig. 3). The arsenic or the arsenic compound is trapped in the form of small inclusions (as will be demonstrated later) at the original polysilicon/buried SiO_2 interface. After longer oxidation (60 min), the arsenic does not change its location and remains at the same position as after

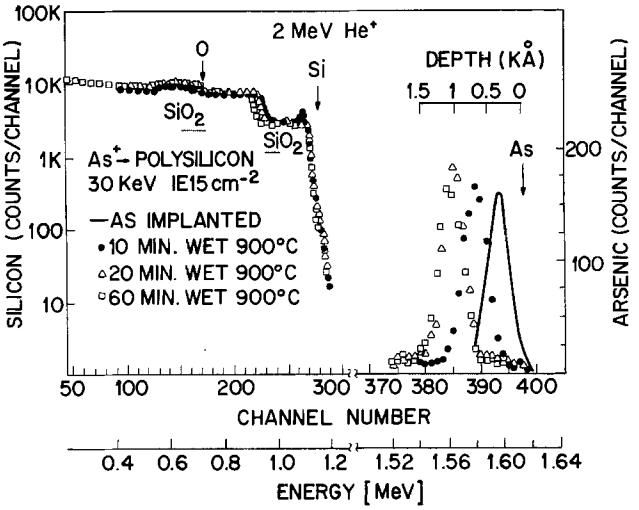

Fig. 3. Energy spectra of 2.0 MeV He^+ ions backscattered from samples of thin polysilicon over thick oxide (see insert) after being wet oxidized at 900°C for 10 min (●), 20 min (△), and 60 min (□). Notice the same location of the arsenic peak after the 20 and 60 min oxidation.

the 20 min oxidation (see the As spectra in Fig. 3). The arsenic rich layer imbedded in the oxide does not influence the oxidation of the Si substrate below as is seen in the SiO_2 part of the spectra in Fig. 3.

The RBS technique was not sensitive enough to detect the arsenic distribution in the oxide, during the oxidation of the thin polysilicon layers over thick oxide substrates and the measurements were done by the neutron activation technique. Figure 4 demonstrates the results of the neutron activation measurements obtained from a wet oxidized sample (900°C, 60 min). The arsenic activity, $N(x)$ (normalized to the initial activity $N(0)$), as a function of depth is given in part c of this figure. A measure related to the arsenic concentration C_{As} (Fig. 4d) is obtained by dividing the difference in the arsenic activity of two successive layers, $N(x - \Delta x) - N(x)$, by the thickness, Δx, of the layer removed between the two measurements. As was expected, due to the high segregation coefficient of arsenic in silicon, a very small quantity of arsenic is trapped in the top oxide layer and most of the arsenic is present at the original polysilicon/buried oxide interface. Figure 5 summarizes the neutron activation data for the partially oxidized film at 900°C (steam) and the completely oxidized films at 900°C (steam) and 1000°C (dry). In the partially oxidized sample, most of the arsenic remains in the unoxidized polysilicon layer. The sharp drop in the arsenic content at the oxide/polysilicon interface is probably caused by the etching of a thin surface layer of silicon after the top oxide removal. The apparent spread in the arsenic distribution near the polysilicon/buried oxide interface for the completely oxidized samples in Fig. 4 and 5 could be caused by the variations in the thickness of the polysilicon films across the wafer or by variations in the oxide etching.

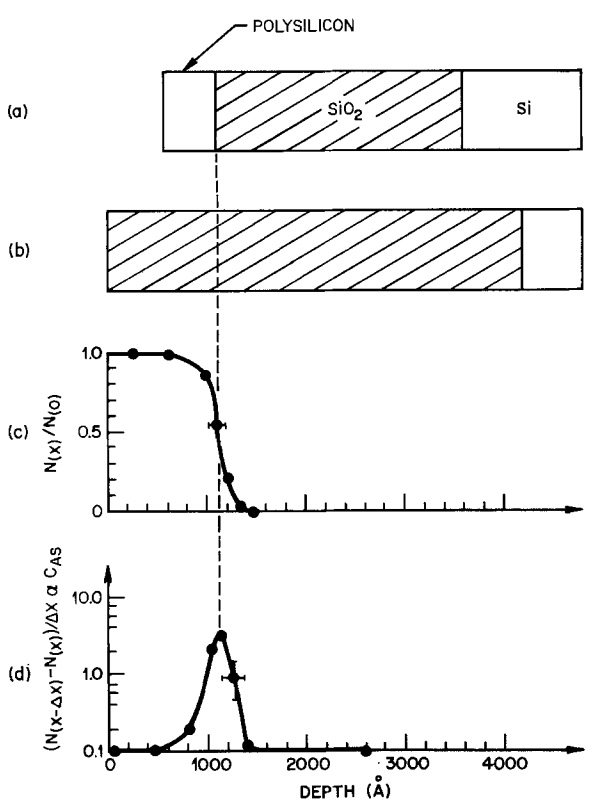

Fig. 4. (a) Thin polysilicon layer over thick buried oxide, (b) after wet oxidation at 900°C for 60 min, (c) the arsenic activity (normalized to the initial activity) as a function of depth, (d) arsenic concentration profile (in arbitrary units) as obtained from the neutron activation measurements.

Note that there is no detectable arsenic diffusion into the buried oxide layer in the 900°C wet oxidized samples. On the other hand, there was substantial arsenic diffusion into the buried oxide during the longer 1000°C dry oxidation (Fig. 5). For the 900°C wet oxidation, the temperature is too low and the time is too short for any detectable arsenic diffusion into the underlying oxide. A rough estimate of the arsenic diffusivity can be obtained by assuming that the arsenic front displacement in the 1000°C dry oxidized sample compared to that of the 900°C wet oxidized sample is about $\sqrt{Dt}$, where D is the arsenic diffusivity in SiO_2 at 1000°C and t is the dry oxidation time. The value of $D \approx 1 \times 10^{-15}$ cm²/sec, obtained by this approximation, is slightly higher than some previous results obtained for arsenic diffusion in silicon dioxide (12, 13) but is in very good agreement with the data of Tsukamoto *et al.* (14). The Tsukamoto experiments showed that the arsenic diffusivity in silicon dioxide is enhanced by introducing extra oxygen into the silicon dioxide from an oxidizing atmosphere. Arsenic interacts with the extra oxygen, and an arsenic-oxygen compound is formed which has a much higher diffusivity than elemental arsenic.

Oxidizing thick polysilicon films.—Samples of group "B" or "C" (see Table I) were used for evaluating the long oxidation runs and the arsenic diffusion through the thin buried oxide substrate (see Fig. 6a). The backscattering spectra, taken with 2.0 MeV He^+ ions from samples that were partially oxidized at 900°C are given in Fig. 7. The SiO_2 edges and the arsenic location in this spectrum indicate that thinner oxides were grown on samples of group "B". This slowing down of

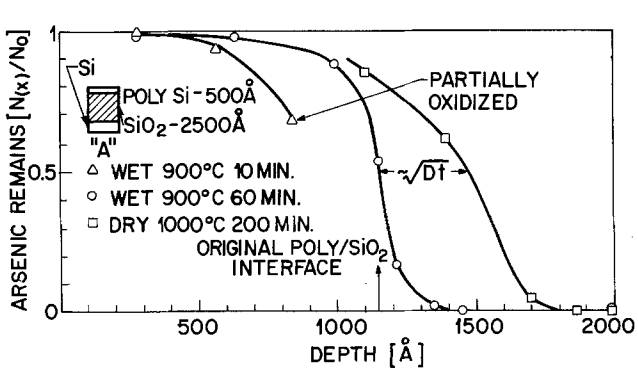

Fig. 5. Arsenic losses in the grown oxide as measured by the neutron activation technique on thin polysilicon films oxidized over a thick silicon dioxide substrate, after successive etching of SiO_2.

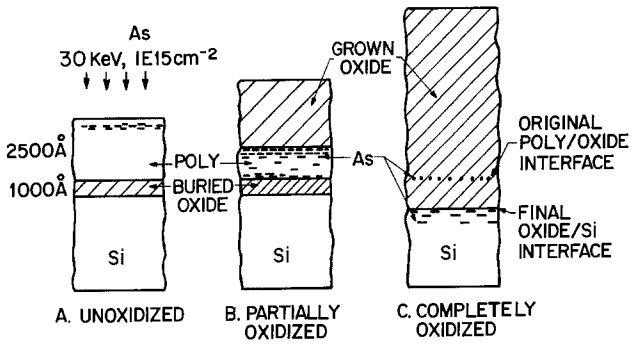

Fig. 6. Schematic cross-section views of different stages in the oxidation of thick polysilicon films laying over thin silicon dioxide substrate. Notice the arsenic distribution at the different stages.

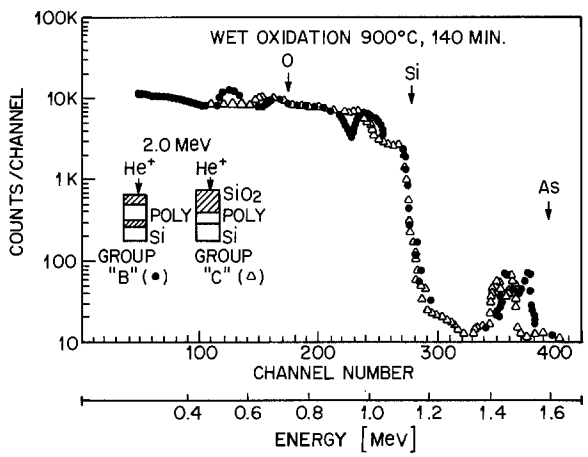

Fig. 7. Backscattering spectrum using 2.0 MeV He^+ ions from samples of thick polysilicon deposited on thin oxide or bare silicon substrates, arsenic implanted (30 keV, $1 \times 10^{-15}cm^{-2}$) and partially oxidized at 900°C. Notice the arsenic pile-up at the top and bottom interfaces of the deposited layer.

the oxidation is due to the presence of the buried oxide under the polysilicon film which affects the arsenic concentration in the remaining polysilicon layer. Arsenic forced to concentration above the solubility limit in silicon could form an intermetallic compound which may oxidize slower than pure silicon. Both samples of Fig. 7 shows the arsenic pile up at the top and bottom edges of the remaining polysilicon (see also Fig. 6b). The arsenic pile up at the grown oxide/polysilicon interface is as expected. The arsenic accumulation at the polysilicon/substrate interface can be explained (7) in terms of diffusion and segregation of arsenic in the grain boundaries and by considering the interface between the polysilicon and the substrate (single crystal or oxide film) to be analogous to the interface between grains in a polycrystalline material. When the polysilicon is completely oxidized, most of the arsenic remains at the original polysilicon/oxide interface (Fig. 6c), but some of the arsenic diffuses through the thin oxide and is smoothly distributed below the new oxide/silicon interface. It was not determined if the arsenic diffused into the silicon substrate was in an elemental form or as As_2O_x.

Figure 8a is a TEM micrograph of a vertical cross-sectional sample of group "B" after being completely oxidized in steam at 900°C. The scattered dark dots along the original polysilicon/buried oxide interface were analyzed by an energy dispersive x-ray of an EDAX spectrometer in a Philips EM 400 STEM, and found to be a compound of arsenic-oxygen-silicon. The size of these inclusions were too small for a definite identification of their composition and structure. Since the arsenic is exposed, during the oxidation, to an oxygen environment and since the arsenic had shown

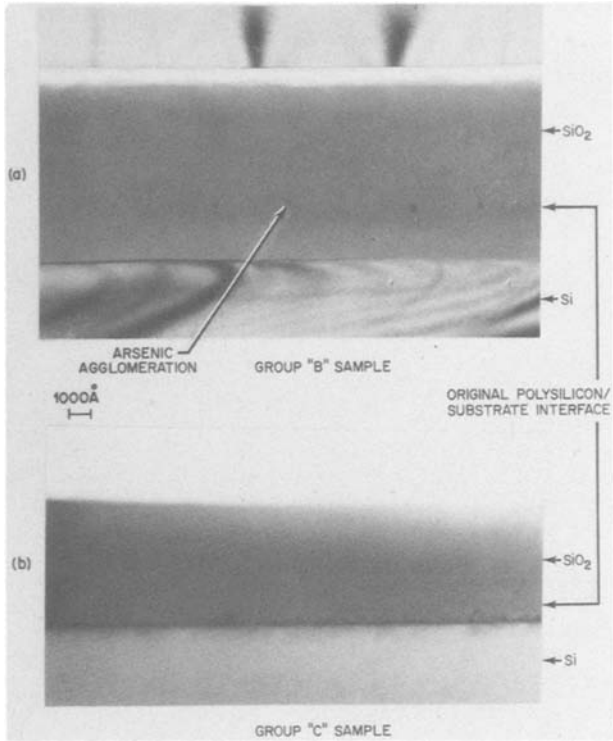

Fig. 8. Transmission electron microscope, cross-section micrographs after a complete oxidation at 900°C in steam of thick polysilicon film (2500Å) deposited over (a) thin oxide (1000Å) or (b) bare silicon substrates.

a significant diffusion into the buried oxide, we believe that the arsenic inclusions are in the form of arsenic oxide. An unsuccessful attempt was made to analyze the arsenic compound in this sample by Auger spectroscopy (15). The Auger measurements failed to detect the arsenic either due to the average low concentration of the scattered arsenic inclusions or due to the fact that the arsenic-oxygen compounds have a high vapor pressure [10^{-5} Torr (16)] at room temperature and were volatilized during the ion beam milling used to obtain the Auger depth profile. More experiments are required to better analyze the chemical state of the arsenic oxygen complex. The distribution of these arsenic agglomerations at distances comparable to the polysilicon grain size strengthen the assumption that the arsenic segregates at the grain boundaries of the polycrystalline material.

The neutron activation analysis of the oxidation of samples from group "B" and "C" are given in Fig. 9. These results are different from the results obtained after oxidizing thin polysilicon over thick oxide (Fig. 4). Even after etching the oxide behind the original polysilica/buried oxide interface, the arsenic concentration is still high. The arsenic activity remains strong even after the complete removal of the oxide indicating that arsenic must have diffused into the silicon substrate through the 1000Å of the buried oxide. This large amount of arsenic diffused into the substrate is probably due to the relatively long time of oxidation that was required for completing the oxidation of the 2500Å polysilicon and due to the fact that arsenic diffusion in SiO_2 is enhanced in a wet oxygen ambient (14). By further etching of the silicon after the oxide removal, it was found that in most cases the diffused arsenic into the silicon substrate is located at the first 500Å below the oxide interface. Figure 10 summarizes the normalized activity of the remaining arsenic as a function of depth, for samples wet oxidized at 1050°C. In this figure, three regions of sharp drop in the amount of the remaining arsenic are observed. Those at the right hand of the figure are caused by the arsenic accumulation near the SiO_2/Si interface. The drop in

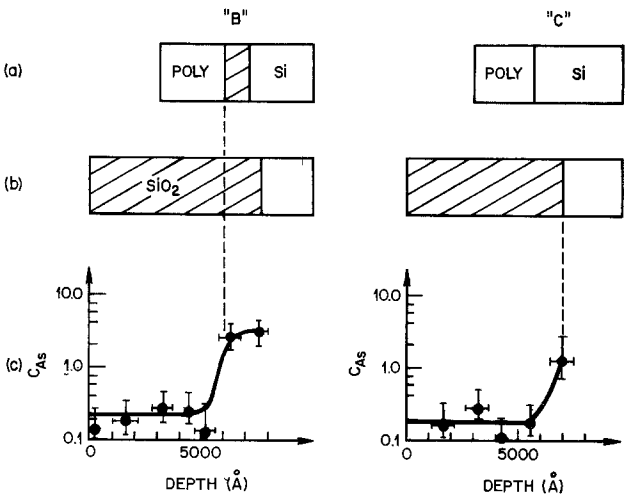

Fig. 9. (a) Thick polysilicon layer over buried oxide or bare silicon substrate. (b) Samples after wet oxidation at 1050°C for 200 min. (c) Arsenic concentration profiles (in arbitrary units) as obtained from the neutron activation measurements.

the arsenic content of samples c and d, around the depth of 5700Å (~2500/0.45), is due to loss of the arsenic accumulated at the original polysilicon/SiO_2 interface as it was observed also by the TEM and the RBS. Sample b with the polysilicon deposited directly on the silicon substrate does not show, as expected, this arsenic loss. It is still not fully understood what caused the changes of the arsenic absorbed in the oxide around the depth of 3000Å.

Neutron activation measurements were conducted also on the steam 900°C steam oxidized samples and an example for these results in comparison with the 1050°C oxidation are shown in Fig. 11. The arsenic remaining in the silicon substrate, after the oxide removal, is slightly lower (~5%) as compared to the 10% which remains in the 1050°C samples. This difference is due to the faster diffusivity of the arsenic through the buried oxide at the higher temperature. These results can be compared with the results of group "A" samples, with the thick oxide substrates, (shown also in Fig. 11) where no arsenic was detected in the silicon substrate after the oxide removal.

Figure 11 also shows that more arsenic is trapped in the oxide grown at the 900°C than in the 1050°C oxide films. This variation in the arsenic concentration in the grown oxide could be the reason for the different etching rate which was reported earlier.

The morphology of the final oxide/silicon interface of group "B" samples is different from that of group "C" samples as is shown in Fig. 8b. In the group "C" samples (2500Å polysilicon/Si), small protuberances

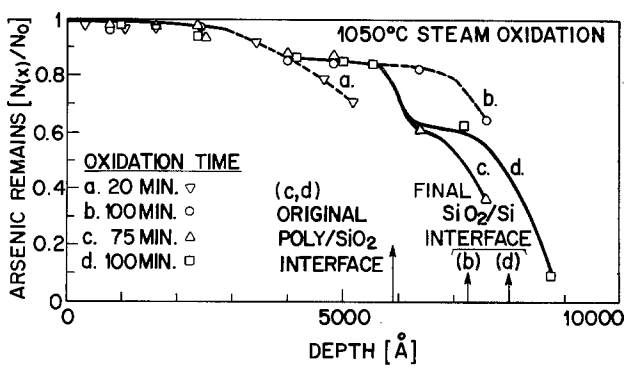

Fig. 10. Neutron activation measurements of the arsenic distribution in thick polysilicon films implanted with arsenic (30 keV, 1×10^{-15}cm^{-2}) and oxidized at 1050°C in steam. The solid lines are for group "B" samples (2500Å polysilicon over 1000Å SiO_2) and the dashed lines are for group "C" samples (2500Å polysilicon over bare silicon substrate).

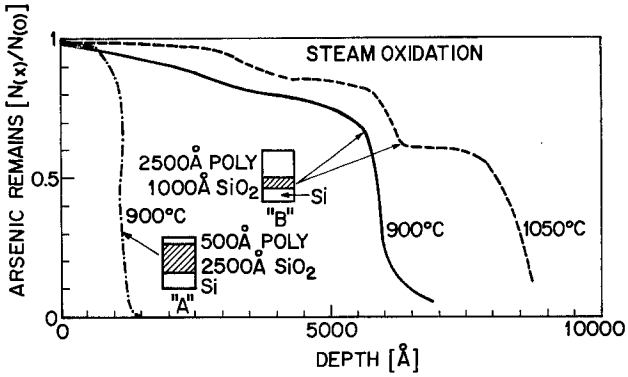

Fig. 11. Comparison of the arsenic distribution after wet oxidation of samples from group "A" and "B" at 900° and 1050°C.

in the oxide near the substrate interface were observed. The nonuniform distribution of arsenic at the interface is again due to the grain boundary segregation. Silicon inclusion in the polysilicon oxide as found by Anderson and Kerr (17) or Marcus and Sheng (5) could not be detected in this work in any group of samples or oxidation temperatures. It should be mentioned that whenever thin polysilicon films (~500Å) were completely oxidized over bare single crystal substrates the oxide/silicon interface was always smooth and uniform as for normal thermal oxidation of silicon single crystal. This is probably because of the complete amorphization of the polysilicon layer during the implantation process.

Conclusions

The complete oxidation of arsenic implanted polycrystalline films over oxidized substrates can be achieved with the following features: (*i*) The oxidation rate of polysilicon is slightly reduced by the presence of a buried oxide layer under the polysilicon. (*ii*) Arsenic, probably in the form of an arsenic-oxygen compound, is trapped at the original polysilicon/buried SiO_2 interface. (*iii*) The diffusion of arsenic through the buried oxide is enhanced in dry or wet oxygen ambient. With long oxidation time and with a thin buried oxide a significant amount of arsenic can diffuse through the oxide into the silicon substrate.

Oxidation of the doped arsenic films over bare silicon substrate resulted in the following conclusions: (*i*) Arsenic accumulated at both oxide/polysilicon and polysilicon/silicon interfaces when the films were only partially oxidized. (*ii*) The oxide/silicon interface, after the oxide reaches the silicon substrate, was rough when thick polysilicon layers (2500Å) were oxidized and smooth in the case of oxidizing thin polysilicon layers (500Å). (*iii*) No inclusions or protuberances were found in any of the oxide films grown from the implanted polysilicon films. Further analysis to identify the arsenic-oxygen compound is necessary.

Acknowledgments

The authors would like to thank H. J. Levinstein for his continued interest, encouragement, and fruitful discussions. Thanks are given to D. C. Jacobson and W. M. Augustyniak for their help with the RBS and to C. C. Chang and E. Lane for their Auger analysis, to R. Knoell for the EDAX measurements, to E. I. Povilonis for carrying out the oxidation, and to E. Lloyd for his help with the neutron activation measurements.

Manuscript submitted Dec. 15, 1982; revised manuscript received April 5, 1983.

Any discussion of this paper will appear in a Discussion Section to be published in the June 1984 JOURNAL. All discussions for the June 1984 Discussion Section should be submitted by Feb. 1, 1984.

Bell Laboratories assisted in meeting the publication costs of this article.

REFERENCES
1. H. Sunami, *This Journal*, **125**, 892 (1978).
2. T. I. Kamins, *ibid.*, **126**, 838 (1979).
3. E. A. Irene, E. Tierney, and D. W. Dong, *ibid.*, **127**, 705 (1980).
4. C. C. Chang, T. A. Shankoff, T. T. Sheng, and W. S. Lindenberger, Bell Laboratories internal memorandum, Murray Hill, NJ.
5. R. B. Marcus and T. T. Sheng, Paper 278 presented at The Electrochemical Society Meeting, Minneapolis, MN, May 10-15, 1981.
6. R. B. Fair and J. C. C. Tsai, *This Journal*, **122**, 1689 (1975).
7. B. Swaminathan, E. Demoulin, T. W. Sigmon, R. W. Dutton, and R. Reif, *ibid.*, **127**, 2227 (1980).
8. W. K. Chu, J. W. Mayer, and M. A. Nicolet, "Backscattering Spectroscopy," Academic Press, New York (1978).
9. T. T. Sheng and R. B. Marcus, *This Journal*, **127**, 737 (1980).
10. H. Sunami, M. Koyanagi, and N. Hashimoto, *ibid.*, **127**, 2499 (1980).
11. S. Ohkawa and Y. Nakagima, *ibid.*, **125**, 1997 (1978).
12. S. N. Shabde and K. Helliwell, *ibid.*, **126**, 2279 (1979).
13. M. Ghezzo and D. M. Brown, *ibid.*, **120**, 110 (1973).
14. K. Tsukamoto, Y. Akasaka, and K. Horie, *Appl. Phys. Lett.*, **32**, 117 (1978).
15. C. C. Chang and E. Lane, Private communication.
16. I. Barin and O. Knacke, "Thermochemical Properties of Inorganic Substances," Springer-Verlag, Berlin (1973).
17. R. M. Anderson and D. R. Kerr, *J. Appl. Phys.*, **48**, 4834 (1977).

Infrared Characterization of α- and β-Crystalline Silicon Nitride

J. P. Luongo

Bell Laboratories, Murray Hill, New Jersey 07974

ABSTRACT

Silicon nitride, Si_3N_4, used as a passivating layer in microelectronics, exists in the crystalline forms, α-Si_3N_4 and β-Si_3N_4, and as amorphous material. Although the two crystalline modifications differ only slightly in their structure, it has been found that each modification can be distinguished by infrared spectroscopy. The spectral characteristics of α- and β-Si_3N_4 are described and a method for determining the concentration of one phase in the presence of the other has been developed.

The current interest in the highly desirable properties of Si_3N_4 for use in microelectronics has prompted a need for an improved characterization of crystalline Si_3N_4. The purpose of this work is to describe how the α- and β-modifications of crystalline Si_3N_4 can be quantitatively characterized by infrared spectroscopy.

The formation of bulk silicon nitride was first noted by early workers (1, 2) who heated several metal-silicon alloys in nitrogen at approximately 1400°C and then extracted the unreacted metal phase from the reaction mixture. Preliminary evidence of two different nitrides was first reported by Turkdogan and Ignatowicz (3). Although other workers attempted to characterize the two modifications as orthorhombic, rhombohedral, etc., it was the experiments of Turkdogan *et al.* (4) and Hardie and Jack (5) that established the actual identity of the two forms which were designated "α-" and "β-." Turkdogan *et al.* (4) found that the α- and β-forms could be prepared by first heating pure amorphous silica to 1450°C in a stream of extremely pure nitrogen. Samples from this "master batch" were then heated to 1450°C in a stream of 2% hydrogen plus 98% nitrogen over a period of 2-8 days in a temperature range of 1450°-1600°C. Periodic x-ray diffraction analyses of the samples during the nitriding process showed progressive changes occurred in the diffraction pattern over the 2-8 day period even though there was no change in the chemical composition or density of the samples.

The initial crystalline phase of Si_3N_4 that formed at the lower temperature (1450°C) he called "α" and the crystalline phase that formed at the higher temperature (1600°C) and prolonged nitriding was called "β." X-ray analysis of specimens formed between the initial and final stages showed they contained various ratios of α- and β-Si_3N_4. Further experiments confirmed that the α-phase formed in the presence of excess elemental silicon and the β-phase formed in the absence of silicon. Hardie and Jack (5) in collaboration with Turkdogan have shown that the crystalline structure of both α- and β-Si_3N_4 is hexagonal and that the basic unit is a tetrahedron. They established that the difference between the two modifications is that the β-form is a slightly distorted tetrahedron relative to the α-form.

The infrared spectrum of crystalline α-Si_3N_4 has been reported by Prochazka and Greskovich (7) and Taft (8) has compared the infrared spectra of crystalline β-Si_3N_4 and amorphous Si_3N_4. Additionally, a group theoretical analysis of the crystalline Si_3N_4 infrared spectra has been reported by Wada *et al.* (9) and Wild *et al.* (10) have suggested that atomic substitutional changes in crystalline β-Si_3N_4 are reflected in spectral changes.

In the current manufacture of crystalline Si_3N_4, the ratio of the α- and β-Si_3N_4 modifications can vary considerably depending on the starting materials and conditions of the nitriding process.

In this work, the quantitative infrared determination of the α- and β-modifications in commercially available samples of crystalline Si_3N_4 will be described.

Experimental

The spectra (as KBr pellets) were recorded using a Perkin-Elmer Model 283B infrared spectrometer interfaced with a Model 3500 Data Station Computer. In Table I, the frequency location (cm^{-1}) of the absorption bands are correlated with the corresponding numbers shown on the absorption bands in Fig. 1 and 2.

Figure 1 shows the spectra of α-Si_3N_4 and β-Si_3N_4 in the 1300 to 320 cm^{-1} region. The main strong absorption band near 950 cm^{-1} is a fundamental vibration due to the Si-N-Si antisymmetrical stretching mode

Table I.

Band	cm^{-1}	Band	cm^{-1}	Band	cm^{-1}
1	1040	7	854	13	443
2	957	8	684/675	14	406
3	941	9	600	15	378
4	906	10	578	16	371
5	893	11	509/495	17	352
6	871	12	460		

Key words: spectroscopy, analytical, silicon.

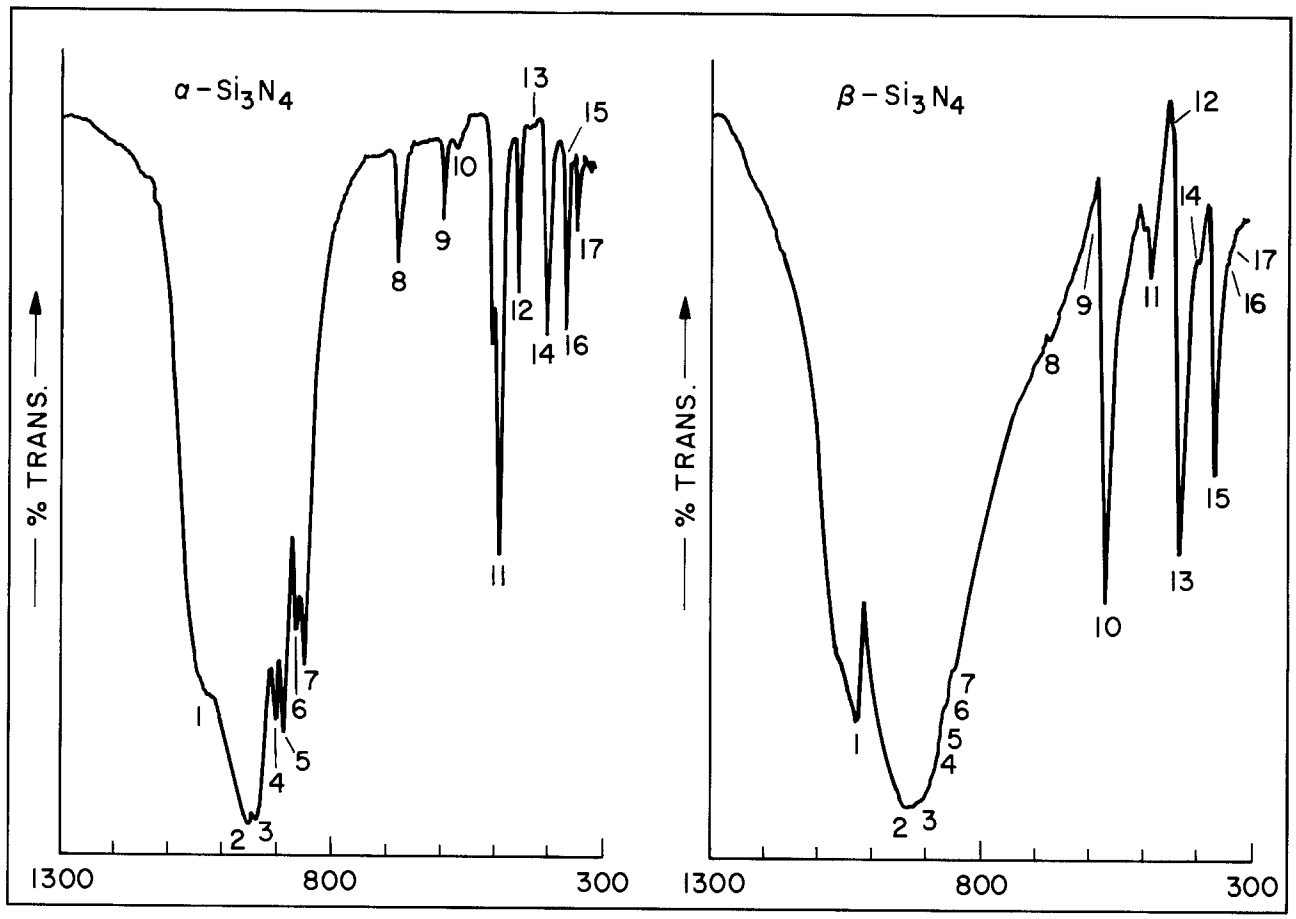

Fig. 1. Infrared spectra of α- and β-Si_3N_4 in the 1300 cm^{-1} to 300 cm^{-1} region

and the absorption at 495 cm^{-1} is the symmetrical stretching mode for the Si-N-Si molecular group (6). The considerable variation in the intensities of the α- and β-phase absorption bands reflect the subtle difference in the distorted tetrahedron of the β-phase relative to the α-phase.

In the α-phase (Fig. 1), the bands at 957, 941, 906, 893, 871, and 854 cm^{-1} appear as distinct absorptions whereas in the β-phase these absorptions form a band envelope with the main absorption minima at 941 cm^{-1}. The most significant difference can be seen at 684/675, 600, 495, 460, 406, and 352 cm^{-1}. In the α-phase, these absorptions appear as strong sharp bands when compared to the β-phase at the same frequencies. In the β-phase, the bands at 578, 443, and 378 cm^{-1} are strong and distinct when compared to the α-phase. In Fig. 2

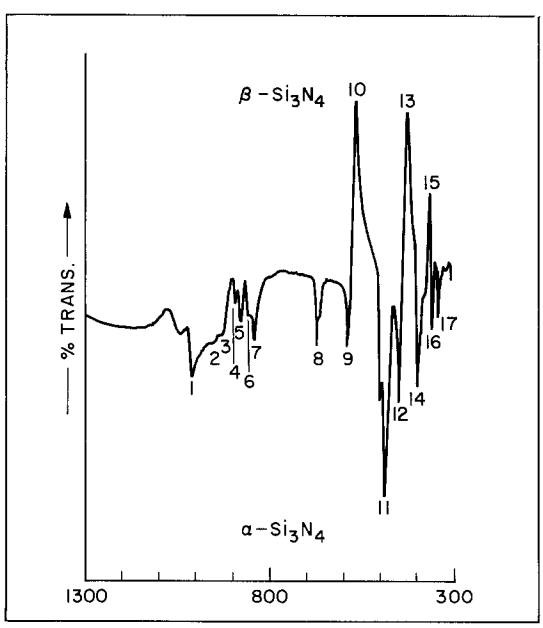

Fig. 2. Difference spectra of α- and β-Si_3N_4

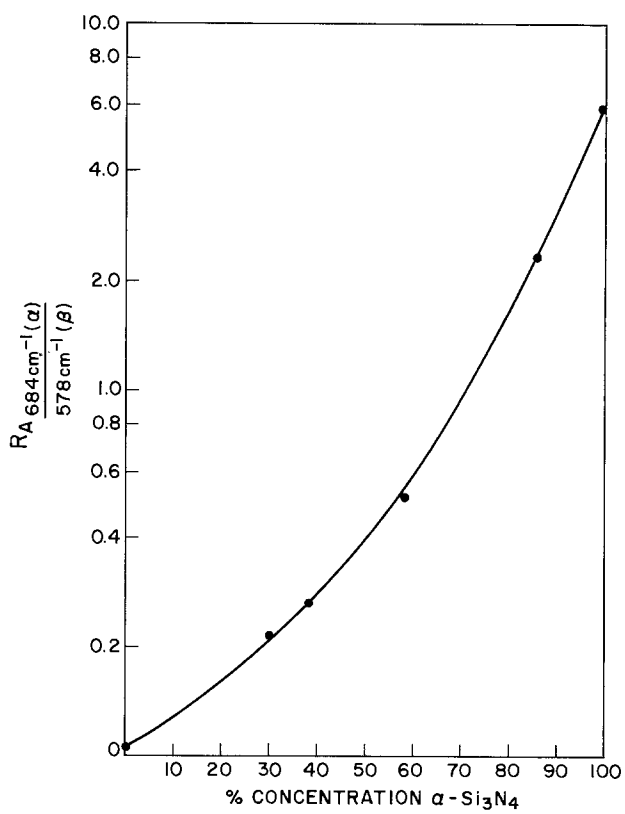

Fig. 3. 684 cm^{-1}/578 cm^{-1} absorption ratio vs. % w/w α-Si_3N_4

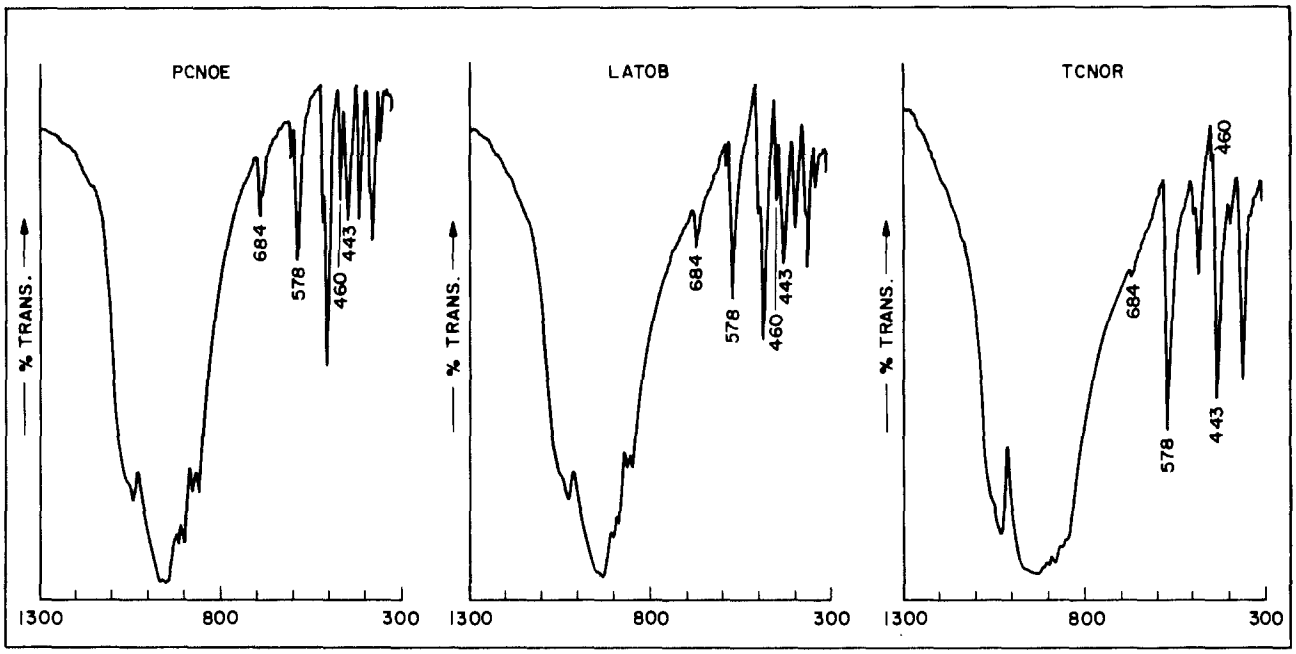

Fig. 4. Infrared spectra of three samples of commercial grade crystalline Si_3N_4

is shown the computer-assisted difference spectrum of the α- and β-modifications. The absorptions above the baseline at 578, 443, and 378 cm^{-1} are due to the β-modification and the absorption below the baseline are due to the α-modification.

Since the 684/675, 600, 509/495, 460, 406, 371, and 352 cm^{-1} absorptions are assignable to the α-phase and the 578, 443, and 378 cm^{-1} absorptions are attributable to the intramolecular interactions of the β-phase, the ratio of the absorbances at 684 and 578 cm^{-1} can be used to quantitatively determine the amount of α- and β-Si_3N_4 in unknown mixtures.

The absorbance ratios, $R = \dfrac{A_{684\ cm^{-1}(\alpha)}}{A_{578\ cm^{-1}(\beta)}}$ from the spectra of known mixtures were plotted *vs.* % concentration α-Si_3N_4 and are shown in Fig. 3.

In Fig. 4, are shown the spectra of three commercially available samples of crystalline Si_3N_4 to illustrate the α/β variations encountered. The $R = \dfrac{A_{684\ cm^{-1}(\alpha)}}{A_{578\ cm^{-1}(\beta)}}$ ratio of the three samples was calculated and the concentrations of the α- and β-phases determined from Fig. 3. Table II shows the concentrations of the α- and β-modifications found in the three commercial samples.

The minimum concentration of either the α- or β-modification that can be detected in the presence of the other was found to be $\pm 1\%$ (w/w). For example, in the spectrum of the "TCNOR" sample, Fig. 4, the 684 cm^{-1} absorption represents 3% α-Si_3N_4. Using computer generated scale expansion of the α- or β-absorptions, it is estimated that the detection limits can be reduced to $\pm 0.5\%$ (w/w) of either the α- or β-modifications.

Table II.

Sample	% α-Si_3N_4 (w/w)	% β-Si_3N_4 (w/w) (100% -%α)
PCNOE	54	46
LATOB	49	61
TCNOR	3	97

Conclusion

The absorption spectra of the α- and β-phases of Si_3N_4 can be used to distinguish the two crystalline modifications. The absorption bands due to each phase have been assigned and the absorbance ratios of the respective bands can be used for the quantitative determination of crystalline α- and β-silicon nitride.

Manuscript submitted Dec. 10, 1982; revised manuscript received March 15, 1983.

Any discussion of this paper will appear in a Discussion Section to be published in the June 1984 JOURNAL. All discussions for the June 1984 Discussion Section should be submitted by Feb. 1, 1984.

Bell Laboratories assisted in meeting the publication costs of this article.

REFERENCES

1. L. Weiss and T. Engelhardt, *Z. Anorg. Chem.*, **65**, 38 (1910).
2. H. Funk, *Z. Anorg. Chem.*, **133**, 67 (1924).
3. E. T. Turkdogan and S. Ignatowicz, *J. Iron Steel*, **185**, 200 (1957).
4. E. T. Turkdogan, P. M. Bills, and V. A. Tippett, *J. Appl. Chem.*, **8**, 296 (1958).
5. D. Hardie and K. H. Jack, *Nature*, **332**, 180 (1957).
6. U. Wannagat, "Advances in Inorganic Chemistry and Radiochemistry," p. 232, Academic Press, New York and London (1964).
7. S. Prochazka and Greskovich, *Ceramic Bull.*, **57**, 6 (1978).
8. E. A. Taft, *This Journal*, **118**, 1341 (1971).
9. N. Wada, S. A. Solin, J. Wong, and S. Prochazka, *J. Non-Cryst. Solids*, **43**, 7 (1981).
10. S. Wild, H. Elliott, and D. P. Thompson, *J. Mater. Sci.*, **13**, 1739 (1978).

The Influence of the LOCOS Processing Parameters on the Shape of the Bird's Beak Structure

T.-C. Wu,* W. T. Stacy,* and K. N. Ritz*

Philips Research Laboratories Sunnyvale, Signetics Corporation, Sunnyvale, California 94086

ABSTRACT

A qualitative model to explain the influence of processing parameters on the shape of the "bird's beak" structure, the transition region from field oxide to pad oxide, has been developed. The parameters included are (*i*) pad oxide thickness, (*ii*) field oxidation temperature, (*iii*) wafer orientation, (*iv*) thickness of the field oxide grown, and (*v*) field oxidation pressure. The strength of the influence of each parameter is also discussed. Experimental results are also presented that verify the model.

The local oxidation process (LOCOS) has been widely applied as a device isolation technique to improve the performance and to increase the packing density of integrated circuits (1). In a typical LOCOS process, there is a layer of SiO_2 (the pad oxide layer) under the Si_3N_4 oxidation mask. The pad oxide layer serves two major purposes: (*i*) as a buffer layer to reduce the stress from Si_3N_4 which causes defects in silicon during the LOCOS step, and (*ii*) as an etch step layer during the nitride etching step. Lateral diffusion of the oxidant through the pad oxide layer during the LOCOS step creates a region which is called the bird's beak (BB) near the edge of the masking nitride layer.

The length of the BB (L_{bb}) is comparable to the thickness of the field oxide which is typically of the order of 1 μm. Therefore, the magnitude of L_{bb} makes it an important factor in VLSI technology. Not only does the BB region reduce the area of the active devices, but also the edge effect due to the BB has to be taken into account for small geometry devices. For two-dimensional device modeling, it is important to know the shape of the BB in detail. Furthermore, it is desirable to use the oxide wall as a self-aligned edge for the contact opening to improve the density of the circuit. The contact etching step then is critical so that a good contact can be made without exposing the p-n junction under the BB region. All of these require an understanding of the influence of the LOCOS processing parameters on the shape of the BB.

In this paper, a qualitative model is presented to describe the relationship between the processing conditions and the shape of the BB. The processing parameters included in this paper are (*i*) pad oxide thickness (*ii*) oxidation temperature, (*iii*) wafer orientation, (*iv*) thickness of the field oxide grown, and (*v*) oxidation pressure. The shape of the BB is obtained by transmission electron microscope (TEM) or scanning electron microscope (SEM) cross-sectional techniques. The data agree very well with the proposed model.

The Mechanism of the Bird's Beak Formation

The growth mechanism of the BB can be illustrated by the schematic drawing of Fig. 1a. At a particular time during the LOCOS process, the point $S(t)$, $y = 0$, is the end of the BB. At the same time, some amount of the field oxide, $T_{ox}(t)$, has grown in areas without Si_3N_4. As the oxidation reaction continues, the oxidant diffuses through $T_{ox}(t)$ to increase the thickness of the field oxide and through the existing BB region to extend the length of the BB. By comparing the oxidation rate under the nitride mask and the oxidation rate under the existing field oxide, the influence of parameters on the shape of the BB can be obtained.

The oxidation rate in the region $y > 0$ of Fig. 1b can be obtained by solving a simple diffusion equation together with the oxidant consumption rate. The flux of the oxidant $I(y, t)$ at any point $y > 0$ for time $t > 0$ can be expressed as

$$I(y,t) = T_{pd} \cdot J(y,t) = -T_{pd} D \frac{dC(y,t)}{dy} \quad [1]$$

where $J(y, t)$ is the flux density of the oxidant, T_{pd} is thickness of the pad oxide layer, D is the diffusivity of the oxidant in SiO_2, and $C(y, t)$ is the concentration of the oxident. Meanwhile, the consumption rate of the oxidant between y and $y + dy$ is

$$-\frac{dI(y,t)}{dy} = T_{pd} D \frac{d^2C(y,t)}{dy^2} = k_s C_i(y,t) \quad [2]$$

where $C_i(y, t)$ is the concentration of the oxidant at the Si/SiO_2 interface corresponding to position y, and k_s is the surface reaction rate of oxidation. For a typical pad oxide of 200-500Å, the profile of the oxidant along the z-direction can be assumed to be linear. Therefore

$$D \frac{C(y,t) - C_i(y,t)}{T_{pd}/2} = k_s C_i(y,t)$$

or

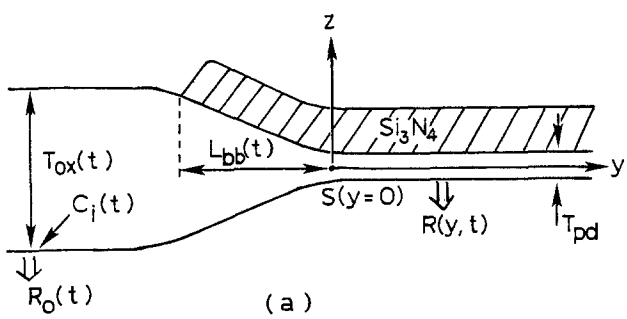

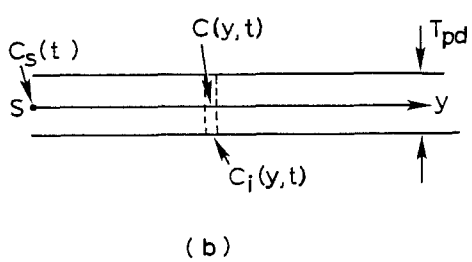

Fig. 1. (a) Schematic drawing for the growth mechanism of the bird's beak, (b) detail drawing of the region $y > 0$ in (a).

* Electrochemical Society Active Member.
Key words: local oxidation, field oxidation, LOCOS process, bird's beak structure.

$$C_i(y,t) = \left(\frac{1}{1+\frac{T_{pd}k_s}{2D}}\right) C(y,t) \quad [3]$$

Substituting Eq. [3] into Eq. [2]

$$\frac{d^2C(y,t)}{dy^2} = \left[\frac{k_s}{T_{pd}D}\left(\frac{1}{1+\frac{T_{pd}k_s}{2D}}\right)\right] C(y,t) \quad [4]$$

solving Eq. [4] with the proper boundary conditions, we find

$$C(y,t) = C_s(t)\exp(-\gamma y) \quad [5]$$

where $C_s(t)$ is concentration of the oxidant of point S ($y = 0$) at time t; and

$$\gamma = \left[\frac{k_s}{T_{pd}D}\left(\frac{1}{1+\frac{T_{pd}k_s}{2D}}\right)\right]^{1/2} \quad [6]$$

Therefore, the oxidation rate at the Si/SiO_2 interface under the masking nitride is

$$R(y,t) = k_sC_i(y,t) = k_sC_s(t)\left(\frac{1}{1+\frac{T_{pd}k_s}{2D}}\right)\exp(-\gamma y) \quad [7]$$

At the same time, the oxidation rate under the existing field oxide is

$$R_o(t) = k_sC_i(t) \quad [8]$$

where $C_i(t)$ is the concentration of the oxidant at the Si/SiO_2 interface under $T_{ox}(t)$. Combining Eq. [7] and [8]

$$\frac{R(y,t)}{R_o(t)} = \frac{C_s(t)}{C_i(t)}\left(\frac{1}{1+\frac{T_{pd}k_s}{2D}}\right)\exp(-\gamma y) \quad [9]$$

This relationship holds throughout the entire LOCOS step, so that it correlates the ratio of L_{bb} to T_{ox} (thickness of the field oxide grown). By analyzing Eq. [9], the influence of the processing parameters on the shape of the BB can be obtained. Even though Eq. [9] is illustrated for the case of a typical MOS process (Fig. 3b), it works for the recessed oxide case (Fig. 3a), also.

The right-hand side of Eq. [9] consists of an exponential decay term and a pre-exponential factor. The exponential decay term shows the decrease of the oxidation rate with the distance away from the nitride edge, which is the dominating mechanism of the BB formation. The larger the decay coefficient γ is, the smaller the value of L_{bb}/T_{ox} will be. It can be seen from Eq. [6] that γ is a function of k_s (surface reaction rate of oxidation), D (diffusivity of the oxidant in SiO_2), and T_{pd} (thickness of the pad oxide layer). For steam oxidation at around 1000°C and pad oxide thickness of around 500Å, the value of $T_{pd}k_s/2D$ is of the order of 0.1 which makes the $(1 + T_{pd}k_s/2D)^{-1}$ term of γ much less important,.

Table I lists the effects of varying processing parameters on the values of γ and L_{bb}/T_{ox}. The smaller arrow indicates the less influential effect which is about an order of magnitude smaller than the long arrow. The major conclusions are as follow:

(*i*) Decreasing the thickness of the pad oxide layer causes both term, $k_s/T_{pd}D$, and the second term, $(1 + T_{pd}k_s/2D)^{-1}$, in γ to increase which results in a drastic decrease of L_{bb}/T_{ox}. This is the most common method of reducing the length of BB. However, the purposes of the pad oxide layer impose a limit on the pad oxide thickness.

(*ii*) Increasing the value of k_s will give a net reduction in the value of $L_{bb}T_{ox}$. This can be done by using wafers with different orientation, such as using <111> wafer instead of <100>. This effect explains the results reported in the literature (2) where the p-channel process, using <111> wafers, has a shorter BB than the n-channel process, using <100> wafers.

(*iii*) Increasing the processing temperature: Both k_s and D increase as the temperature increases. Since k_s is more temperature dependent than D is, the value of k_s/D increases as the temperature increases. It results in a net decrease of L_{bb}/T_{ox}. Therefore, higher processing temperature provides a shorter BB in the LOCOS step.

As the values of T_{pd}, k_s, and D remain constant, secondary effects due to the variation of the pre-exponential factor in Eq. [9] can be detected. The value of L_{bb}/T_{ox} is determined by the cumulative effect of $C_s(t)/C_i(t)$, where both terms are time dependent. In the beginning of the LOCOS process, the oxidation reaction is in the linear regime. The ratio of $C_s(t)/C_i(t)$ is very close to 1. As the reaction progresses, both the Si/SiO_2 interface under the field oxide and point S move away from the source of the oxidant (gas stream). In addition, the development of the BB limits the solid angle of the oxidant supply to point S. Therefore, the ratio of $C_s(t)/C_i(t)$ decreases. With these arguments, qualitative variations of L_{bb}/T_{ox} due to the effect of $C_s(t)/C_i(t)$ can be obtained.

(*iv*) The value of L_{bb}/T_{ox} depends on the thickness of the field oxide grown. For thinner field oxide, a larger value of L_{bb}/T_{ox} is expected, because a greater portion of the reaction is in the initial regime. As the field oxide gets thicker, the portion in the initial regime becomes less important, so that the value of L_{bb}/T_{ox} gradually approaches a constant number.

(*v*) High pressure oxidation results in a slightly longer BB. Both the linear rate and the parabolic rate constants have been observed to have a linear pressure dependence (3) for steam oxidation. This indicates that both k_s and D are pressure independent. The effect of high pressure oxidation on L_{bb}/T_{ox} is mainly due to the effect of $C_s(t)/C_i(t)$. For a fixed thickness of the field oxide, more of the reaction is in the initial regime in the case of high pressure oxidation. This results in a slightly larger value of L_{bb}/T_{ox}.

Table I. The influence of varying the processing parameters on the values of γ and L_{bb}/T_{ox}

$$\gamma = \left[\frac{k_s}{T_{pd}D}\left\{\frac{1}{1+\frac{T_{pd}k_s}{2D}}\right\}\right]^{1/2}$$

	$\frac{k_s}{T_{pd}D}$	$\frac{1}{1+\frac{T_{pd}k_s}{2D}}$	γ	$\frac{L_{bb}}{T_{ox}}$
T_{pd} ↓	↑	↑	↑ ↑	↓ ↓
k_s ↑	↑	↓	↑ ↓	↓ ↑
Processing temperature ↑	↑	↓	↑ ↓	↓ ↑

Experimental Results

The processing sequence for the experiments are listed in Table II. The field oxidation steps were car-

Table II. Processing sequence of the experiments

(1)	starting material: p-type <100> 5-7 Ω-cm p-type <111> 7-21 Ω-cm
(2)	pad oxide growth: 950°C in O_2, 300-600Å
(3)	LPCVD Si_3N_4 deposition: 800°C, SiH_2Cl_2, 1000-2000Å
(4)	photolithography
(5)	plasma etch of Si_3N_4
(6)	strip photoresist
(7)	pad oxide etch
(8)	field oxidation under various conditions
(9)	LPCVD poly-Si deposition: 650°C SiH_4, 2500-5000Å
(10)	TEM and SEM cross section

ried out in pyrogenic steam at pressures of 1 or 10 atm with temperature between 920°-1000°C. Two groups of samples were prepared: (*i*) Type 1 samples have field oxide thickness of 1 μm. The thickness of the field oxide grown was controlled to be as close to 1.0 μm as possible. This is to eliminate the effect listed in item (*iv*) of the last section. (*ii*) Type 2 samples were used to study the influence of varying the thickness of the field oxide. Wafers of the same orientation and pad oxide thickness were oxidized in pyrogenic steam at 1000°C for various times. This gives the dependence of L_{bb}/T_{ox} on T_{ox}.

After the local oxidation step, a layer of LPCVD poly-Si was deposited on the wafer to protect the top surface so that a better cross-sectional profile can be obtained. Figure 2 is a typical TEM cross-sectional photograph of the BB immediately after the LOCOS step. The high resolution of the TEM technique allows us to investigate the BB structure in fine detail. For some studies, the SEM cross-sectional technique was applied to simplify the step of the sample preparation. It can be seen from Fig. 3a and b that the poly-Si layers make the top boundaries of the SiO_2 very sharp. The length of the BB (L_{bb}) is defined as the horizontal distance between the Si_3N_4 edge to the place where the pad oxide is 5% thicker than the original value.

The results of the measurements are summarized in Fig. 4 and 5. Figure 5 is the plot of the values of L_{bb}/T_{ox} *vs.* the processing temperature. All the data points are for field oxide thickness of about 1.0 μm. The following trends can be clearly seen in Fig. 4: (*i*) Reducing the pad oxide layer from 500 to 330Å decreases the value of the L_{bb}/T_{ox} dramatically. (*ii*) The value of L_{bb}/T_{ox} decreases as the temperature of the field oxidation increases. (*iii*) For any given temperature, <111> wafer has smaller L_{bb}/T_{ox} than <100> wafer. (*iv*) Field oxides grown at 10 atm pressure have a slightly larger value of L_{bb}/T_{ox} than the comparable 1 atm oxidation. These four results confirm the predictions obtained from Eq. [9].

Figure 5 is the plot of L_{bb}/T_{ox} *vs.* T_{ox} for <100> wafers with 500Å of pad oxide and <111> wafers with 550Å of pad oxide. The oxidation step was done in 1 atm pyrogenic steam at 1000°C .The decreasing trend of L_{bb}/T_{ox} *vs.* T_{ox} agrees very well with the prediction (*iv*) of the last section.

For further analysis, the data points which correspond to samples with <100> wafer and field oxidation in 1 atm steam are plotted in Fig. 6. From this plot, the comparison between the effect of reducing pad oxide thickness and the influence of increasing oxidation temperature can be made, and the activation energy of the term k_s/D can be roughly estimated. It can be seen from Fig. 6 that the LOCOS step at 920°C

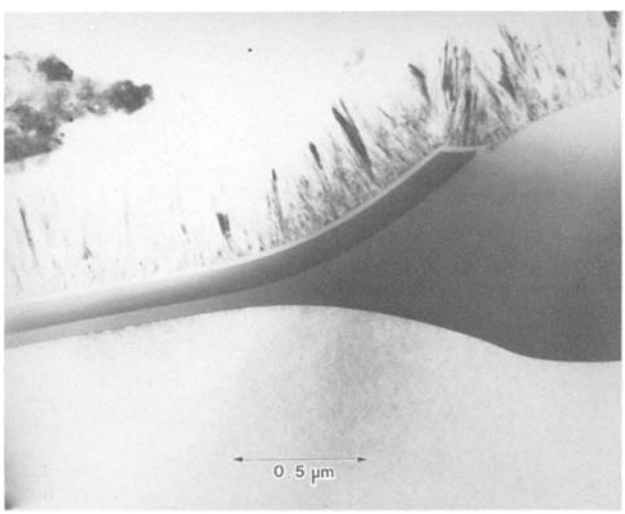

Fig. 2. A TEM cross-sectional photograph of the bird's beak

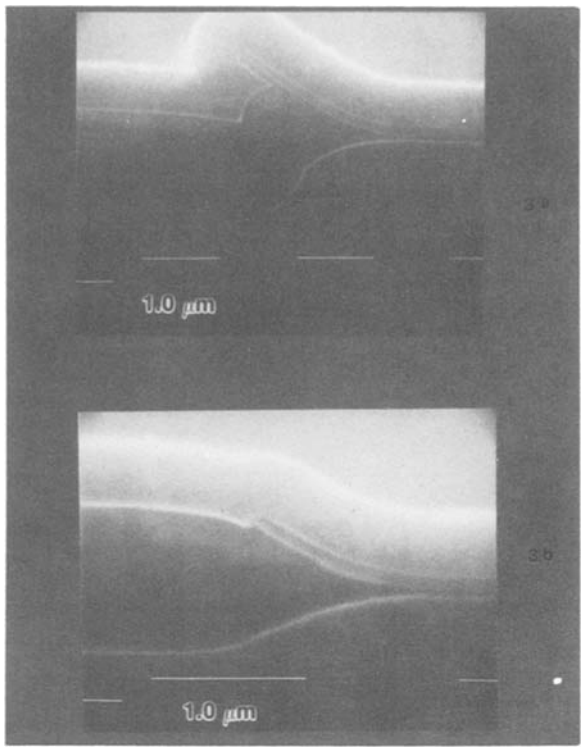

Fig. 3. SEM cross-sectional photographs of the bird's beak, where (a) typical bipolar process and (b) typical MOS process.

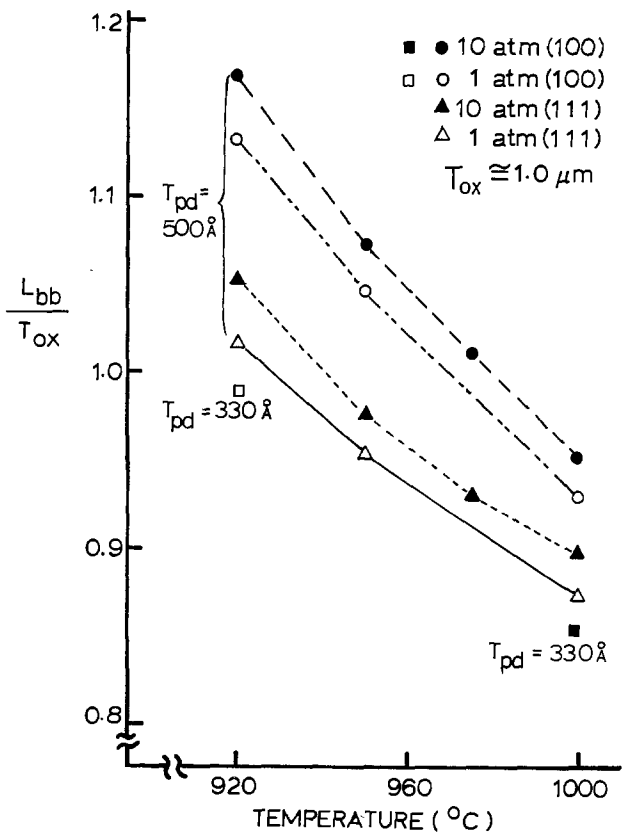

Fig. 4. Experimental results of L_{bb}/T_{ox} vs. the processing temperature.

with 330Å of pad oxide has the same value of L_{bb}/T_{ox} as the LOCOS step at around 972°C with 500Å of pad oxide. Since the dominating factor of L_{bb}/T_{ox} has been shown to be the decay coefficient γ in Eq. [9], all the influence is assumed to be caused by γ only. Therefore

$$\frac{(k_s/D) \text{ at } 972°C}{(k_s/D) \text{ at } 920°C} \simeq 1.6 \qquad [10]$$

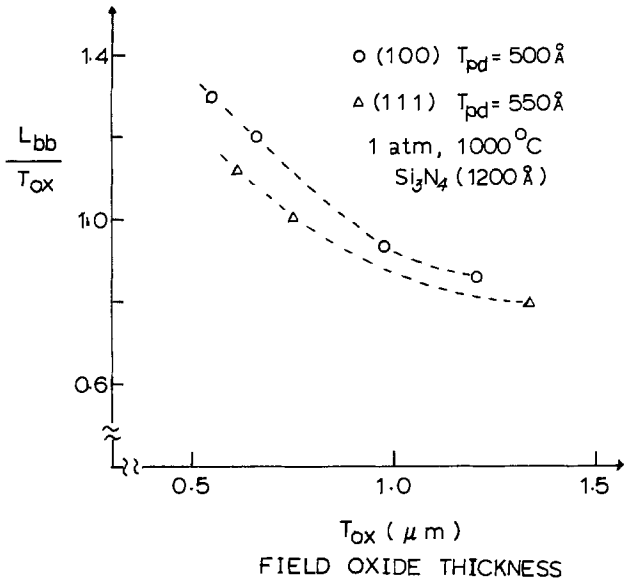

Fig. 5. Experimental results of L_{bb}/T_{ox} vs. T_{ox}

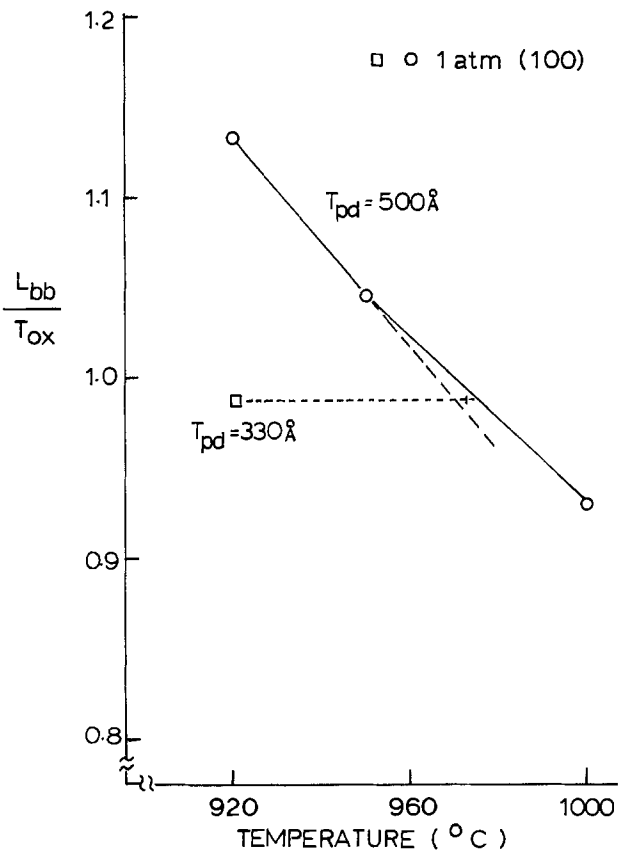

Fig. 6. Experimental data for the comparison between the effects due to temperature and the pad oxide layer.

This lead to an activation energy of 1.2 eV for the terms k_s/D. The reaction kinetics of oxidation is usually described by the linear-parabolic model (4) where the linear rate constant, B/A, and the parabolic rate constant, B, are

$$B/A \equiv \frac{k_s h}{k_s + h} \frac{C^*}{N_1} \quad [11]$$

$$B \equiv 2D \frac{C^*}{N_1} \quad [12]$$

where C^* is the concentration of the oxidant at the gas phase, N is the number of the oxidant molecules incorporated into a unit volume of oxide, and h is the gas-phase mass-transfer coefficient in terms of concentration in solid.

It has been shown that h is typically much larger than k_s (5), so that Eq. [11] can be simplified as

$$B/A \simeq k_s \frac{C^*}{N_1} \quad [13]$$

From Eq. [12] and [13], we obtain

$$\frac{k_s}{D} \propto \frac{\text{Linear Rate Constant } (B/A)}{\text{Parabolic Rate Constant } (B)} \quad [14]$$

The activation energies of B/A and B for steam oxidation are 2.05 and 0.78 eV (6), respectively. From Eq. [14], the activation energy for k_s/D should be 1.27 eV which is consistent with the value (1.2 eV) estimated from Eq. [10].

Conclusions

A qualitative model to explain the influence of the processing parameters in the LOCOS process has been developed, and it agrees very well with the experimental results. The model can be applied to both the MOS LOCOS process, Fig. 3b, or the Bipolar process, Fig. 3a. Besides the well understood effect of the pad oxide thickness, the variation of the length of the BB due to the wafer orientation is correlated with the difference in the surface reaction rate of the oxidation (k_s). This effect has to be taken into account if the oxide isolated bipolar process is to be converted from the traditional <111> wafer to the <100> wafer. Since the oxidation temperature has a larger influence than the oxidation pressure, the combination of both effects has to be considered as high pressure oxidation is introduced into the processing sequence. To shorten the length of the BB, it is better to operate at higher temperature and shorter oxidation period than to operate at lower temperature. Finally, the dependence of the value of L_{bb}/T_{ox} on the thickness of the field oxide grown has to be included when scaling down to smaller dimensions.

Acknowledgments

The authors would like to thank Dr. D. W. Greve for reviewing the manuscript and G. DeGroot for help in processing wafers.

Manuscript submitted March 3, 1982; revised manuscript received May 18, 1982.

Any discussion of this paper will appear in a Discussion Section to be published in the June 1984 JOURNAL. All discussions for the June 1984 Discussion Section should be submitted by Feb. 1, 1984.

Signetics Corporation assisted in meeting the publication costs of this article.

REFERENCES

1. E. Kooi and J. A. Appels, in "Semiconductor Silicon," H. R. Huff and R. R. Burgess, Editors, p. 860, The Electrochemical Society Softbound Proceedings Series, Princeton, NJ (1973).
2. T. A. Shankoff, T. T. Sheng, S. E. Haszko, R. B. Marcus, and T. E. Smith, *This Journal*, **127**, 216 (1980).
3. R. R. Razouk, L. N. Lie, and B. E. Deal, *ibid.*, **128**, 2214 (1981).
4. B. E. Deal and A. S. Grove, *J. Appl. Phys.*, **36**, 3770 (1965).
5. A. S. Grove, "Physics and Technology of Semiconductor Devices," John Wiley and Sons Inc., New York (1967).
6. B. E. Deal, *This Journal*, **125**, 578 (1978).

Profile Control of Polysilicon Lines with an SF_6/O_2 Plasma Etch Process

R. W. Light* and H. B. Bell

Sandia National Laboratories, Albuquerque, New Mexico 87185

ABSTRACT

Typical plasma etching techniques used in integrated circuit fabrication can generate steep topographies that cannot be covered adequately by subsequent deposition steps. An SF_6/O_2 plasma etching process for polysilicon using controlled photoresist erosion produces tapered edge profiles compatible with step coverage requirements. The degree of taper is a function of the photoresist profile, the photoresist to polysilicon etch rate ratio, and the extent of overetch. The photoresist and the polysilicon appear to etch predominantly anisotropically with the isotropic component of the polysilicon etch rate increasing during the overetch period.

High resolution photolithographic techniques and plasma etching processes are required for the manufacture of fine line semiconductor devices. Typical anisotropic or isotropic plasma etching processes can produce vertical profiles or profiles approaching 90° at the top of the step that cannot be covered adequately by subsequent deposition steps. Examples of this problem are metal coverage of contact windows etched through silicon dioxide by an anisotropic technique or metal lines crossing conformal SiO_2 layers covering anisotropically etched polysilicon lines. A thermal reflow of the SiO_2 layer is often applied to minimize these problems but can result in undesired dopant diffusion or degradation of radiation hardness in MOS devices. By eroding the edges of the photoresist mask during a plasma etch, a coverable tapered profile can be formed on the etched feature. In this fashion, the photoresist profile can be transferred to the film being etched if the thicknesses and etch rates of the film and the photoresist are similar. Controlled photoresist erosion (1-5) and flexible diode (6) methods have been employed to obtain tapered profiles on plasma etched patterns. Reports on these techniques have generally given qualitative results.

This work describes the plasma etching of tapered polysilicon lines with an SF_6/O_2 process and details the relationship among the photoresist profile, photoresist etching behavior, polysilicon etching characteristics, and the final polysilicon profiles. The effects of feed gas composition, loading, and etch time on the silicon, photoresist, and silicon dioxide etch rates are discussed, and the polysilicon profile is examined as a function of the photoresist to silicon (PR/Si) etch rate ratio and the initial photoresist profile.

Experimental

Photolithography.—KTI 1470J positive photoresist was dispensed onto the wafer, accelerated to the necessary spin speed, and prebaked at 90°C for 7.5 min in an infrared oven. The photoresist was exposed with Kasper Instruments Model 2001 contact aligners and dip developed using KTI 351 developer (3.5 parts water: 1 part developer) at 21°C for 60 sec. The photoresist coated wafers were baked at 90°C for 30 min in a convection oven and used either without further baking or with an additional bake at a higher temperature for a 30 min period.

Samples.—One hundred mm diameter wafers of <100>, 3-6 Ω-cm silicon were oxidized, patterned, and wet etched to leave one-half of the wafer bare silicon and the other half silicon dioxide. A grid pattern of KTI 1470J photoresist was applied over the wafer. These half and half wafers were used in the initial characterization of the silicon, silicon dioxide, and photoresist etch rates. Characterization of the loading effects and the etching profiles was performed using thermally oxidized 100 mm silicon wafers coated with 0.60 microns of LPCVD polysilicon. The polysilicon was phosphorus doped to give a sheet resistivity of 20 Ω/□. Some of the wafers were then coated with 0.50 μm of aluminum. Both types of wafers were coated with KTI 1470J positive photoresist and patterned with 2, 3, 4, and 5 μm lines and spaces. The aluminum coated wafers were wet etched and the photoresist removed, providing a noneroding etch mask for the polysilicon.

Etching.—A Plasma Therm Incorporated PK-2440, dual plasma/reactive ion etching system with a 3000W, 13.56 MHz rf power supply was used for this study. The rf power was applied to the upper electrode, and the lower wafer-containing electrode was grounded. The 24 in. diam aluminum electrodes have a separation of 2.0 in. and were temperature regulated at 30°C, lower, and 25°C, upper. Sulfur hexafluoride and oxygen were introduced using calibrated automatic mass flow controllers. The pressure was set up without wafers in the reactor and was not throttle valve controlled during the etch. The half and half samples described above were etched for 3.0 min, and the patterned polysilicon profile wafers were etched either by time or until endpoint as indicated by monitoring the 704 nm fluorine emission line. The polysilicon profile wafers were arranged symmetrically around the outside of the electrode. Eleven wafers can be accommodated per run with an etch time of 2-4 min.

Measurements.—Etch rates were determined using either a Tencor Alpha-Step Profilometer or by scanning electron microscopy (SEM) of transversely sectioned wafer samples. Photoresist and polysilicon profile data were obtained by SEM. The accuracy of the SEM measurements based upon comparison of the pattern pitch (4, 6, 8, and 10 μm) with the indicated magnification was within ±5% of nominal among the three SEM instruments used and the repeatability for each instrument was ±2%, relative ±σ. Samples were taken from the center of the wafer and 15-20 mm in from the edge of the wafer.

Results and Discussion

Etch rates.—The Si, SiO_2, and photoresist etch rates and the uniformities of the etch rates across the reactor and within the wafer were optimized using the half and half wafers described above over a range of pressure, power, total flow, and percent oxygen values. The total flow, pressure, and power were fixed at 450 sccm, 150 mTorr, and 1500W, respectively. Rf discharges of SF_6 and SF_6/O_2 mixtures are particularly attractive for polysilicon etching because of the high Si etch rate and Si to SiO_2 selectivity displayed (7, 8). As shown in Fig. 1, the Si etch rate determined from 3.0 min runs with two half and half samples per run is reduced as the percent O_2 is increased. This effect has been attributed to competition between oxygen atoms and fluorine atoms for chemisorption on the silicon surface (5). The etch rate data replotted in Fig. 2 as etch rate ratios demonstrate that the Si to SiO_2 selectivity can be maintained above 10-1 while bringing the PR/Si etch rate ratio to approximately one to one.

* Electrochemical Society Active Member.
Key words: semiconductor, plasmas, etching.

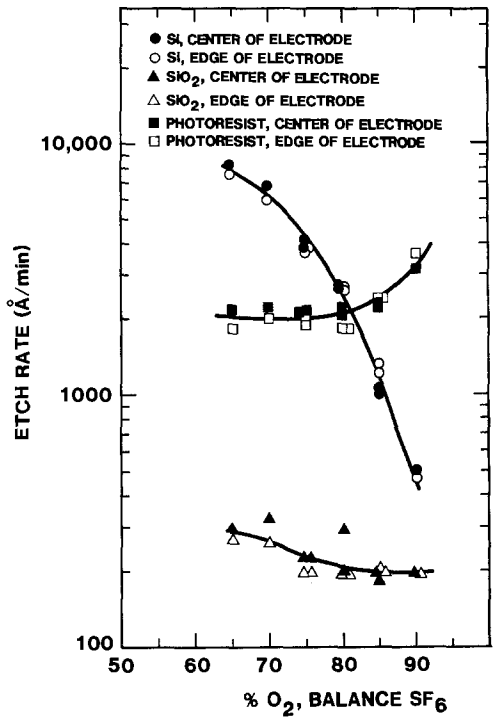

Fig. 1. The effect of percent O_2 in SF_6 on the etch rates of <100> Si, SiO_2, and AZ 1470J photoresist.

A typical loading effect using the patterned polysilicon wafer samples is observed for this system with the inverse of the polysilicon etch rate proportional to the number of wafers in the reactor (9). These data are plotted in Fig. 3 as the photoresist to silicon etch rate ratio *vs.* the number of wafers, since the photoresist erosion rate is relatively constant under these conditions. By adjusting the percent O_2 in the etchant mixture, the loading curve can be shifted to accommodate varying numbers of wafers at a given PR/Si etch rate ratio. Silicon dioxide does not exhibit a significant loading effect in this system.

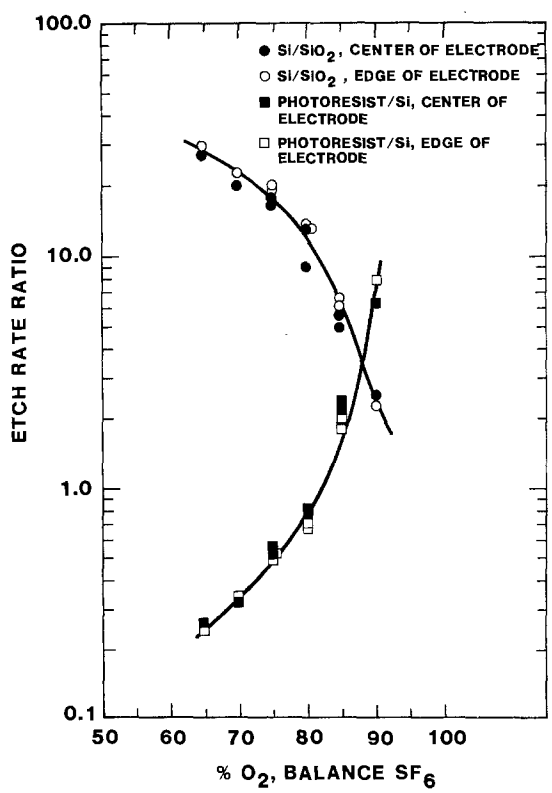

Fig. 2. The effect of percent O_2 in SF_6 on the <100> Si/SiO_2 and photoresist/Si etch rate ratios.

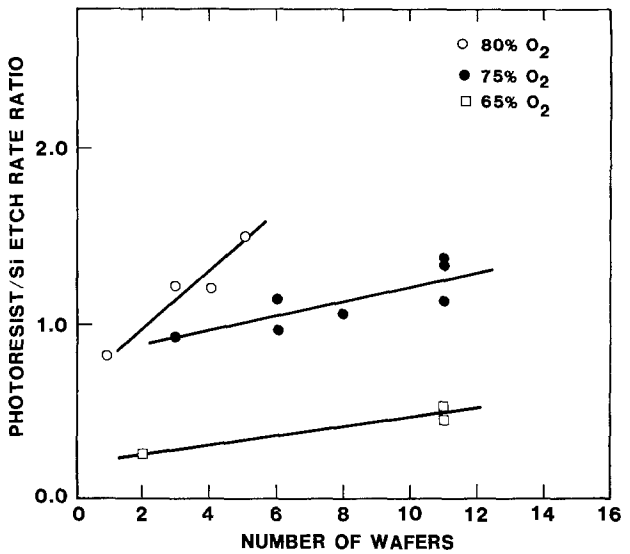

Fig. 3. The effect of loading on the photoresist/polysilicon etch rate ratio.

The PR/Si etch rate ratios derived with the patterned polysilicon sample are based on etching the wafers to completion using the 704 nm fluorine emission line to detect the endpoint. These etch ratios are, in fact, averages, since the polysilicon etch rate is proportional to the etch time. This effect is illustrated in Fig. 4 for a six wafer load and a 75% O_2/25% SF_6 mixture. Separate runs are used to obtain data for each etch time. Similar effects have been observed in barrel etching and were attributed to heating of the wafers during the etch (10). Although the electrodes are temperature controlled, the wafers may be thermally isolated since they are not in hard contact with the electrode surface. Inspection of the wafers in various stages of the etch demonstrates that the etching is nonuniform with the wafers etching radially inward on the electrode and radially inward on the wafer. This gives a lopsided bull's-eye appearance to partially etched wafers. An interesting feature of the etch rate *vs.* etch time data is that the deviation in the etch rate uniformity, wafer center to wafer edge, becomes more severe as the etch progresses.

Photoresist profiles.—The shape and the etching characteristics of KTI 1470J photoresist can be altered by the temperature of the postdevelopment bake. Examination of photoresist lines after a 90°C, 30 min bake reveals a steep wall profile. Photoresist lines baked at 90°C for 30 min, then at 140°C for 30 min, show a dome shape, the profile of which can be closely

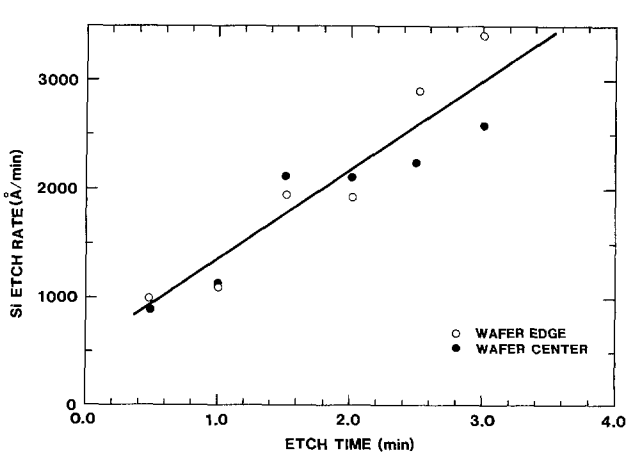

Fig. 4. The time dependence of the polysilicon etch rate

approximated by a segment of a circle. The two stage bake appears to increase the reproducibility of this process. The doming of the photoresist lines thins the edges of the line, enhancing the etching at the base. This may occur through a densification of the edges of the line by release of volatile components. While the width of the photoresist line at the base does not change upon baking at 140°C, the thickness of the line does change and is a function of the linewidth. Two, three, four, and five micron wide photoresist lines of 1.1-1.2 μm thickness after baking at 90°C will yield thicknesses of 1.0-1.1, 1.1-1.2, 1.2-1.3, and 1.3-1.4 μm, respectively, after baking at 140°C. At 165°C and above, melting of the film will occur, causing severe distortion of the pattern.

Polysilicon profiles.—Under the conditions employed for polysilicon etching outlined in this work, the photoresist appears to etch anisotropically. The curves in Fig. 5 illustrate the side loss expected for photoresist lines of 3, 4, and 5 μm (thicknesses 1.2, 1.3, and 1.4 μm, respectively) baked at 90°C for 30 min and 140°C for 30 min as a function of the thickness lost for isotropic etching and anisotropic etching, assuming a circular segment profile. The anisotropic etching mechanism is more consistent with the experimental data, although these data show a lot of spread. The photoresist etch rate shows little dependence upon gas composition from 65 to 80% O_2, wafer load in the reactor, or bake temperature, and averages 2200 ± 250 Å/min (±σ) on patterned polysilicon test samples. It is evident from Fig. 5 that a 5 μm photoresist line will give a greater side loss than a 3 μm photoresist line for a given thickness loss. The profiles of the etched polysilicon lines are, therefore, linewidth dependent, with the smaller lines steeper than the larger lines. This effect is illustrated in Fig. 6 for 140°C baked photoresist lines at three PR/Si etch rate ratios. The angle, θ, is defined in the inset to Fig. 6. Although the polysilicon profiles observed in this study may appear slightly convex or concave, an overall angle can easily be assigned and

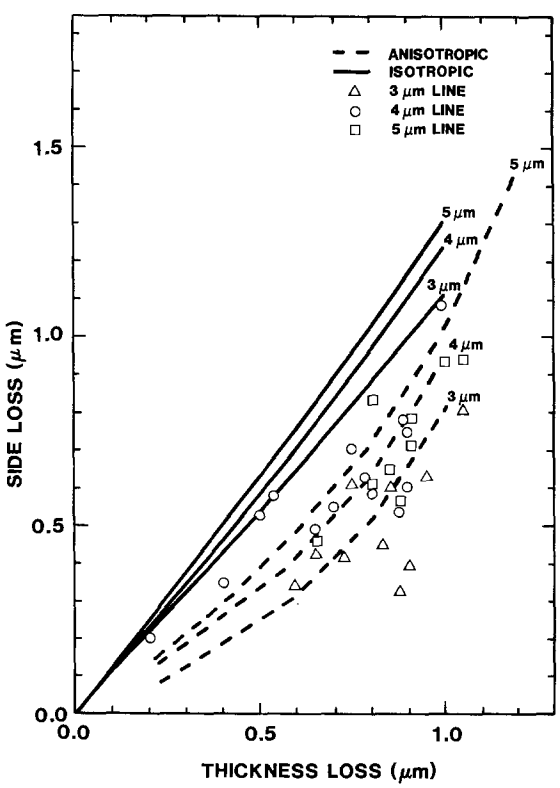

Fig. 5. The effect of thickness loss on the side loss for AZ 1470J photoresist lines baked at 90°C for 30 min and at 140°C for 30 min. The dashed lines and the solid lines illustrate the side loss expected for anisotropic and isotropic photoresist etching, respectively.

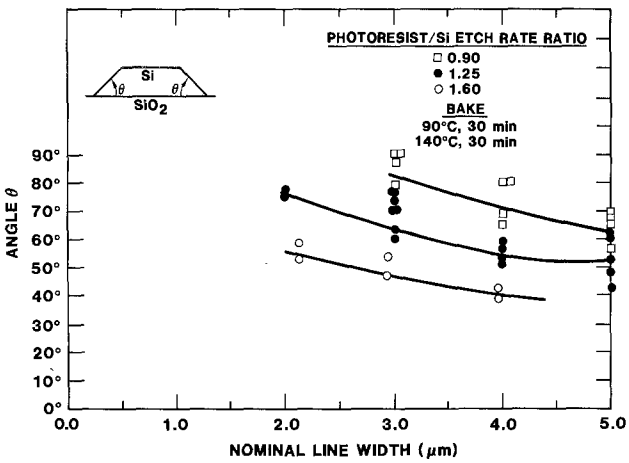

Fig. 6. The influence of the photoresist linewidth and the photoresist/polysilicon etch rate ratio on the polysilicon line taper for photoresist baked at 90°C for 30 min and 140°C for 30 min.

provides a useful first-order approximation to the line shape. When significant curvature was present, the steepest assignable angle characterized the profile. A typical polysilicon profile with the photoresist on the line is shown in Fig. 7. The angles formed are a function of the PR/Si etch rate ratio indicating that photoresist edge erosion is controlling the polysilicon line profile. In general, the more photoresist removed during the etch, the smaller the polysilicon slope angle produced. Photoresist lines baked at 90°C erode more slowly at the edge, producing steep (large θ) polysilicon line profiles that are not dependent upon linewidth and PR/Si etch rate ratio. These data appear in Fig. 8.

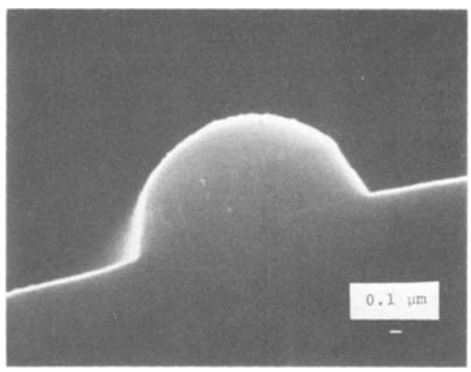

Fig. 7. SEM photograph of a 2 μm wide polysilicon line with photoresist.

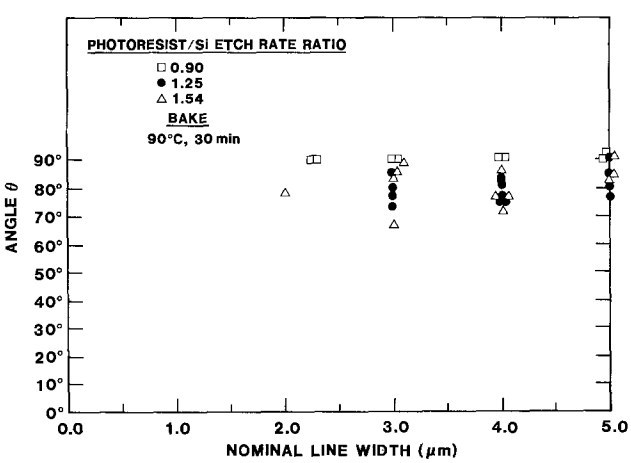

Fig. 8. The effect of the photoresist linewidth and the photoresist/polysilicon etch rate ratio on the polysilicon line taper for photoresist baked at 90°C for 30 min.

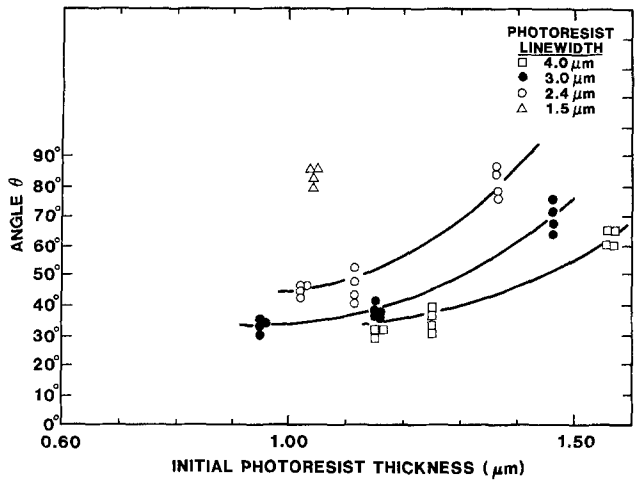

Fig. 9. The influence of initial photoresist thickness on the polysilicon line taper.

An alternative to manipulating the PR/Si etch rate ratio for obtaining sloped lines is variation of the photoresist thickness. The natural thinning of the photoresist over steps forms the practical limit for this sloping technique in device production. Figure 9 demonstrates the effect of initial photoresist thickness (140°C bake) on line slope for several linewidths at a PR/Si etch rate ratio of 1.6. The linewidth dependence discussed above is clearly evident in these data.

SEM data of lines etched with either aluminum masking or with photoresist baked at 90°C indicate a substantial anisotropic component with the vertical etch rate at least twice the lateral etch rate. The detailed dependence of the anisotropic component on the plasma parameters is currently being investigated. The profile data suggest that a change in the degree of anisotropy occurs as the polysilicon lines begin to overetch. As mentioned above, the polysilicon etch rate is nonuniform across the wafer resulting in a bull's-eye effect. The extreme outside of a wafer may receive as much as a 50% overetch during a typical run. The overetch tends to steepen the slopes and reduce the linewidths. A completely anisotropic overetch at etch rates typically observed during overetch period does not account for either the amount of linewidth loss at the base of the line, or the angles observed. However, an isotropic overetch is consistent with the linewidth loss and the steepening of the angles. Figure 10 illustrates the change in step angle and linewidth at the base of the polysilicon line as a function of the PR/Si etch rate ratio for a 4 μm wide, 1.2 μm thick photoresist line baked at 140°C. The dashed lines indicate the range of slopes and linewidths predicted using simple geometric considerations and an anisotropic photoresist and silicon etching mechanism with no overetch, with an isotropic overetch, and with an anisotropic overetch at (3000 Å/min overetch rate, beginning 1.0 min before the endpoint). While this model is consistent with the data, the exact roles of time dependent phenomena such as wafer temperature and the change in local loading during the approach of the endpoint remain undefined. Further work will be necessary to fully characterize this complex etching mechanism.

Conclusion

The profiles of plasma etched polysilicon lines are determined by the relative rates of photoresist and polysilicon etching and the photoresist profile. The average silicon etch rate can be adjusted by varying the percent O_2 in SF_6 and the number of silicon wafers in the reactor while the photoresist and SiO_2 etch rates remain relatively constant. In this manner, the PR/Si etch rate ratio can be set independent of reactor loading. The photoresist line profile is a function of post-development bake temperature and assumes a semicircular profile after baking at 90°C for 30 min followed by a 140°C 30 min bake. The semicircular profile results in more rapid edge erosion of the photoresist line during the polysilicon etch than possible with photoresist lines baked only at 90°C and produces tapered polysilicon line profiles. The polysilicon and photoresist appear to etch anisotropically with the isotropic polysilicon etching component becoming dominant during the overetch period.

Production processes for 3 and 2 μm design rule technologies based on this work have been established. The 2 μm process uses a PR/Si etch rate ratio of 0.5 and yields a steep polysilicon profile, while the 3 μm process

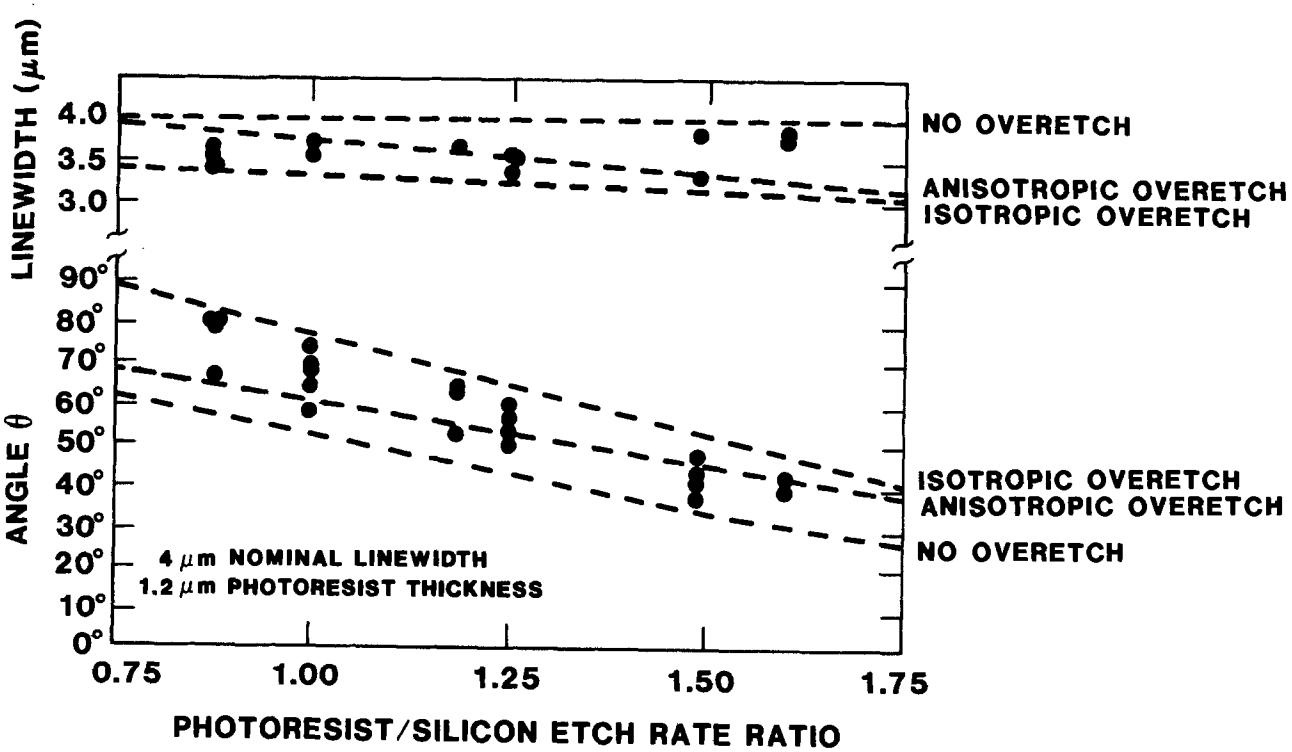

Fig. 10. The effect of the photoresist/polysilicon etch rate ratio on the polysilicon line taper and linewidth at the base

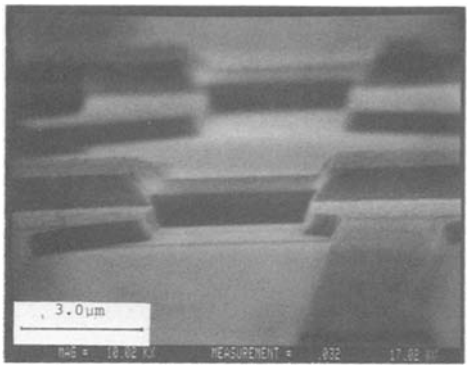

Fig. 11. An SEM photograph of an etch polysilicon pattern with the photoresist removed.

uses a PR/Si etch rate ratio of 1.2 and gives both tapered and steep polysilicon profiles. Linewidth variations of the minimum geometry polysilicon gates within the wafer and wafer to wafer are typically ±5-7%, relative $\pm\sigma$. An SEM photograph at 20° tilt of an etched polysilicon pattern in the 3 μm technology is shown in Fig. 11. The topographic and linewidth dependences of the polysilicon profile are evident in this photograph with the wide features on top of the SiO_2 step (middle of photograph) appearing tapered and the narrow lines in the lower, active regions (foreground of the photograph) displaying a steep profile. Step coverage of Al/Si lines crossing over underlying tapered polysilicon lines is significantly better than those crossing over underlying vertical polysilicon lines. Since a linewidth loss of 0.5-0.7 μm at the base of the polysilicon line is produced and mask biasing is necessary, this process is limited to reproducing a 4 μm pitch with 1.5 μm minimum resolution in the photoresist.

Acknowledgments

The authors wish to thank M. E. Puckett for the sample preparation, L. F. Tafoya, F. P. Ganyard, Kathy Rogers, and Jake Young for the SEM data, J. J. Clement for useful suggestions, and J. L. Reynolds for helpful discussions and SAMPLE program simulations. This work performed at Sandia National Laboratories was supported by the U.S. Department of Energy under Contract number DE-AC04-76DP00789.

Manuscript submitted Nov. 28, 1982; revised manuscript received April 5, 1983.

Any discussion of this paper will appear in a Discussion Section to be published in the June 1984 JOURNAL. All discussions for the June 1984 Discussion Section should be submitted by Feb. 1, 1984.

Sandia National Laboratories assisted in meeting the publication costs of this article.

REFERENCES

1. J. A. Bondur, *J. Vac. Sci. Technol.*, **13,** 1023 (1976).
2. H. W. Lehmann and R. Widmer, *ibid.*, **15,** 319 (1978).
3. C. M. Melliar-Smith, *ibid.*, **13,** (1976).
4. J. A. Bondur and R. G. Frieser, in "Plasma Processing," R. G. Frieser and C. J. Mogab, Editors, The Electrochemical Society Softbound Proceedings Series, Pennington, NJ (1981).
5. L. B. Rothman, J. L. Mauer, IV, G. C. Schwartz, and J. S. Logan, in "Plasma Processing," R. G. Frieser and C. J. Mogab, Editors, The Electrochemical Society Softbound Proceedings Series, Pennington, NJ (1981).
6. L. M. Ephrath, *This Journal*, **129,** 62C (1982).
7. R. d'Agostino and D. L. Flamm, *J. Appl. Phys.*, **52,** 1962 (1981).
8. K. M. Eisele, *This Journal*, **128,** 123 (1981).
9. C. J. Mogab, *ibid.*, **124,** 1262 (1977).
10. R. G. Poulsen and M. Brocher in "Etching for Pattern Definition," H. L. Hughes and M. J. Rand, Editors. The Electrochemical Society Softbound Proceedings Series, Princeton, NJ (1976).

Growth Process of Silicon Over SiO_2 by CVD: Epitaxial Lateral Overgrowth Technique

L. Jastrzebski,* J. F. Corboy, J. T. McGinn, and R. Pagliaro, Jr.

RCA Laboratories, Princeton, New Jersey 08540

ABSTRACT

The epitaxial lateral overgrowth (ELO) process of depositing single crystal silicon over a SiO_2 mask is described. A CVD technique has been developed which consists of depositing silicon in openings in a SiO_2 mask and then growing the silicon laterally over the SiO_2 film. By optimizing the HCl concentration in the gas, growth temperature, and the use of a growth procedure based on a series of growth/etch steps the nucleation of polysilicon over SiO_2 has been eliminated and monocrystalline ELO films have been grown. Low defect density ELO films have been achieved by orientating the oxide islands along the [010] direction on (100) substrates. The growth kinetics, overgrowth morphology, and defect formation in ELO films are described as a function of the growth conditions. One can conclude that optimization of the growth process has allowed us to grow monocrystalline, low defect density ELO films with smooth mirrorlike surfaces.

A significant amount of interest has been generated in the last few years in SOI (silicon over SiO_2) (1). The dielectric isolation process for bipolar circuits (2) could be significantly simplified by using SOI layers if their thickness and minority carrier lifetime were sufficiently high. Also, stress enhancement of the carrier mobility observed in SOI structures (3) obtained by strip heater recrystallization of silicon films on quartz or sapphire substrates (4) could provide significant improvement in device performance. SOI structures would give an additional degree of freedom to the circuit designer in designing conventional CMOS circuits (5) and in the future could allow the achievement of three dimensional vertically integrated IC's (6).

To make state-of-the-art LSI or VLSI circuits, silicon films with a low defect density are required (7). To date graphoepitaxy (8), seeded or unseeded electron beam, laser recrystallization (1) or strip heater methods (4) have been used to obtain continuous SOI films. To improve the surface morphology of the recrystallized films, SiO_2 or Si_3N_4 caping usually has to be used to contain recrystallizing silicon during annealing. To obtain good quality films, contact with the single crystal substrate to provide a seed for solidification is required. Laser annealing is a low temperature

* Electrochemical Society Active Member.

technology which has a significant advantage when making three dimensional circuits, but unfortunately the time required to recrystallize a four inch wafer is long and the recrystallized film contains large polysilicon grains (1). The strip heater technique has yielded good quality films which have been recrystallized at the rate of a few mm/sec (4). During strip heater recrystallization, a silicon film, sandwiched between dielectric layers, is melted by a strip heater and resolidified. Monocrystalline solidification is induced by seeds which are in intimate contact with the recrystallizing film. The major disadvantages of this technique are the high temperatures (around 1420°C) to which the substrate surface region is heated during recrystallization and the large horizontal and vertical temperature gradients across the wafer. The high temperature can destroy any circuits already present in the substrate and the large temperature gradients may generate slip and warpage in the wafer (9), adversely affecting the yield of IC circuits manufactured on these wafers (7). Graphoepitaxy uses CVD silicon techniques and relies upon inducing the crystallographic orientation of the deposited film by forcing nucleation and growth along a pattern present on the surface of an amorphous substrate (8). Practical problems with grid preparation have hampered development of this method so far.

Another approach is a CVD epitaxial lateral overgrowth technique (ELO) in which an epilayer is seeded through openings in the mask and from these openings grows laterally over the mask (10-19). The technique has been applied with excellent results to the growth of GaAs (12). This method takes advantage of the well developed silicon epitaxial technology. The major problem encountered during the ELO deposition process has been the formation of polysilicon nuclei over the SiO_2 surface (16-19). When incorporated into the overgrowing ELO layer, these nuclei have introduced defects into the silicon film (17-19). Growth conditions which prevent the formation of poly or amorphous silicon and give only homoepitaxial growth are required to obtain good quality ELO layers.

Attempts to obtain monocrystalline silicon growth over SiO_2 using a CVD technique has been previously reported (14-19). Because nucleation of polysilicon on SiO_2 requires a certain amount of time ($t_{critical}$) (20, 21), monocrystalline layers of silicon overgrowing thin oxides have been obtained only when the growth time was shorter than $t_{critical}$ (16, 17). If all the silicon atoms deposited on the SiO_2 surface were to diffuse to the growing interface of the monocrystalline silicon, no nucleation of polysilicon would take place. Therefore, close spacing of seeds (approximately equal to the diffusion distance of silicon atoms on SiO_2) could also give monocrystalline ELO films (14, 15). These restrictions on the growth time or on seed spacing have provided a serious limitation for any practical application. A significant increase in $t_{critical}$ (suppression of nucleation) has been observed when chlorine was introduced into the gas during the growth process (17-19, 22-24). By optimizing the concentration of HCl and the growth temperature a decrease in the nuclei density on the SiO_2 surface from 10^7-10^8 cm^{-2} to 10^3-10^2 cm^{-2} has been achieved (19). To decrease their density even further, growth/etch procedures have been proposed (6, 19).

In the present work, we report on a growth procedure which totally suppresses the nucleation of silicon over SiO_2. We discuss how growth parameters affect surface morphology and defect formation in the ELO films, and show how by optimizing temperature, gas composition, and seeding procedure high quality monocrystalline ELO films can be grown.

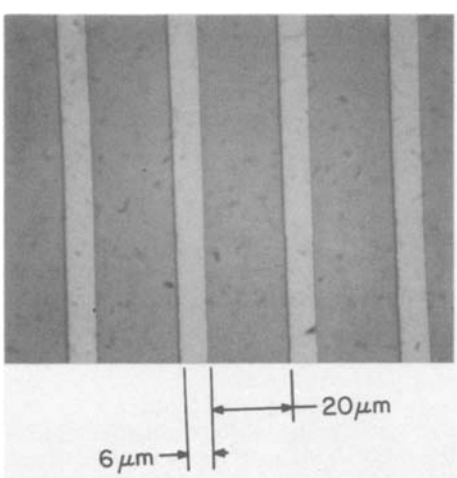

Fig. 1. Pattern used during the ELO growth: 6 μm wide Si and 20 μm wide SiO_2 strips or vice versa.

Experimental Procedure

Epitaxial films have been prepared on (100) three inch diameter silicon wafers in the radiant heated barrel reactor. Film characteristics were studied as a function of deposition temperature, concentration of HCl in the gas phase, time of the growth/etch cycle, orientation of the openings in SiO_2 mask, geometry of the SiO_2 strips, and thickness of the epilayer. Samples were prepared by thermally oxidizing the silicon wafers at 1100°C in steam for 90 min (~8000Å SiO_2). Parallel periodic channels or squares were etched through the oxide exposing the underlying Si surface. The repeat distance of the remaining strips of SiO_2 was 26 μm. Samples with an oxide strip width of either 6 or 20 μm have been prepared (see Fig. 1). The channels in SiO_2 were etched along either [011] or [001] directions. The silicon films were deposited in a series of growth steps using a mixture of SiH_2Cl_2, H_2, and HCl. Each growth step was followed by an etching step using a HCl, H_2 mixture. Prior to growth the samples were *in situ* etched for two minutes in HCl at 1100°-1200°C. Subsequently, the susceptor temperature was decreased to the growth temperature, 1000°-1200°C, and the deposition was started. During growth, the silicon epilayer grows up through the channel openings and then proceeds to expand laterally across the surface of the SiO_2 island while continuing to grow vertically. The surface morphology of as-grown layers was analyzed using Nomarski microscopy, and the surface topology was measured using a Teledyn profilometer. To study growth kinetics, (100) samples have been cleaved along the (110) direction and cross sections have been analyzed using SEM and Nomarski microscopy. The crystallographic defect structure in ELO films was studied by wet chemical etching and TEM. For wet chemical etch experiments, samples were angle lapped and polished (about 1°) using Syton and subsequently Dash etched. TEM samples were prepared for planar and cross section topographs.

Experimental Results

Nucleation of silicon over SiO_2.—Formation of polysilicon nuclei over the SiO_2 has been studied as a function of growth temperature, HCl concentration in the gas phase and length of the growth and etch steps. Figure 2 shows the surface morphology of epilayers grown at 1100° and 1150°C, with all other deposition conditions being the same (specified in the caption of Fig. 2). The observed stripe pattern on the surface reflects the pattern of the SiO_2 islands which were covered by a 12 μm thick ELO layer (for the relationship between surface morphology and epi thickness see below). The irregularities present on the epilayer surface were most likely generated by polysilicon nuclei formed on the SiO_2 and then incorporated into the epilayer. The density of the surface defects in the

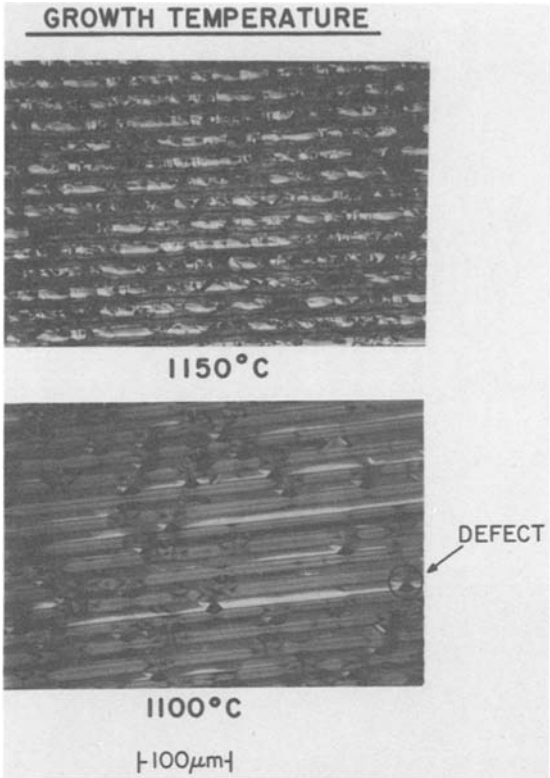

Fig. 2. Comparison of the surface morphology of 17.5 μm thick ELO films grown at 1150° and 1100°C. Other growth parameters kept the same: 0.75 l/min SiH_2Cl_2 + 0.5 l/min HCl + 82 l/min H_2, 25 cycles, 2 min deposition + 1 min etch, SiO_2 width 20 μm oriented along [010].

ELO films was found to be similar to the density of polysilicon nuclei observed on the surface of large areas of SiO_2 which the ELO film had not overgrown (see Fig. 3). It was observed that the defect density is dramatically reduced by decreasing the growth temperature. In addition, increasing the HCl concentration in the gas phase during the growth cycle also resulted in a decrease in the defect density as shown in Fig. 4. On the basis of the presented results, it can be concluded that the defect density, caused by polysilicon nuclei formed over the SiO_2, decreases with decreasing growth temperature and increasing HCl concentration. By combining low deposition temperature and high HCl concentration, the density of polysilicon nuclei on SiO_2 has been reduced to about 10^2-10^3 cm^{-2}. It has to be emphasized that even for optimized growth temperature and HCl concentration we were not able to completely eliminate these nuclei dur-

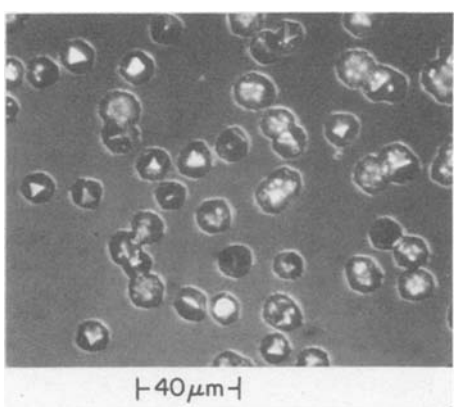

Fig. 3. Polysilicon precipitates observed on the surface of SiO_2 which was not covered by silicon. Deposition: 1100°C, 0.75 l/min SiH_2Cl_2 + 0.55 l/min HCl + 82 l/min H_2, 25 cycles, 2 min deposition + 1 min etch.

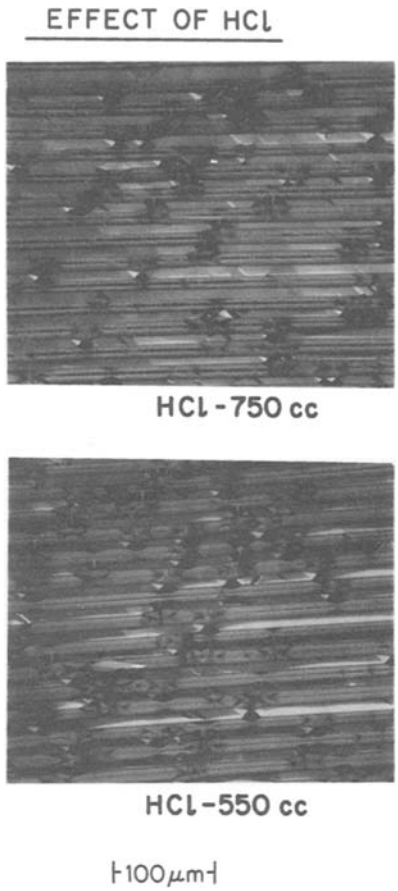

Fig. 4. Comparison of the surface morphology of 17.5 μm thick ELO layers grown with different concentrations of HCl (0.75 l/min and 0.55 l/min). Growth conditions: 1100°C, 0.75 l/min SiH_2Cl_2 + 82 l/min H_2, 25 cycles, 2 min deposition + 1 min etch, 20 μm wide SiO_2 oriented along [010].

ing the two minute growth cycle. It has been established that these nuclei were usually found after the initial few minutes of the ELO process. To further reduce the density of polysilicon nuclei, additional adjustments of the length of the growth and etch periods have been required.

As is shown in Fig. 5, by increasing the etch time from one to two minutes and by reducing the growth time from two to one minute, the density of polysilicon nuclei was significantly reduced. Optimization of the deposition variables: low deposition temperature, high HCl concentration during deposition, and short growth/long etch time during the growth/etch cycle, resulted in the complete elimination of the polysilicon nuclei (below 1 per cm^2) on SiO_2 surfaces (see Fig. 9).

Effect of substrate parameters.—The orientation of the edge of the oxide mask had a dramatic effect on the surface morphology of the ELO layers that were grown under conditions where nucleation on the SiO_2 was totally suppressed. Figure 6 shows a comparison of the surface morphology in ELO layers grown on (100) substrates that were seeded along the [010] direction and the [011] direction. It is clearly seen in Fig. 6 that layers seeded along the [010] direction do not exhibit any surface irregularities, whereas irregularities were observed in layers seeded along the [011] direction. The surface roughness of layers seeded along the [011] direction was most likely caused by twins or low angle grain boundaries intersecting the surface of the ELO layers. A significant difference in the defect density of layers seeded along the [010] *vs.* the [011] direction is seen in the TEM cross sectional micrographs of Fig. 7a and b. The ELO film seeded along the [011] direction (Fig. 7a) shows a high den-

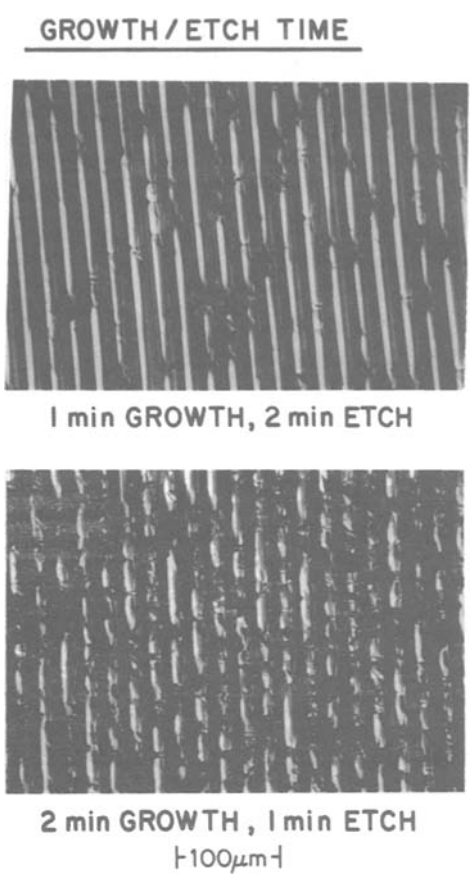

Fig. 5. Comparison of the surface morphology of ELO films grown with 1 min growth, 2 min etch cycle and 2 min growth, 1 min etch cycle. Other growth parameters: 1150°C, 82 l/min H_2 + 0.75 l/min SiH_2Cl_2 + 0.55 l/min HCl, 50 cycles, 20 μm wide SiO_2 oriented along [010].

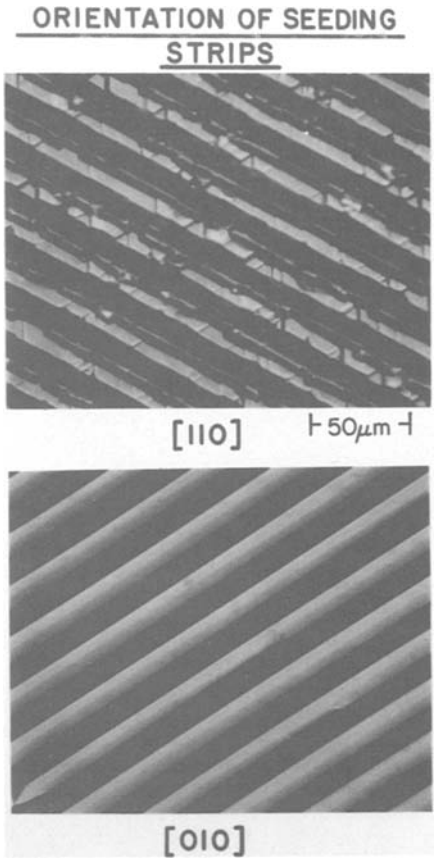

Fig. 6. Comparison of the surface morphology of 18 μm thick ELO films grown on (100) substrates with different orientation of oxide islands: [110] and [100]. Growth conditions: 1050°C, 0.75 l/min SiH_2Cl_2 + 2 l/min HCl + 140 l/min H_2 35 cycles, 1 min deposition + 2 min etch, 20 μm wide SiO_2 oriented along <010>.

sity of twins, stacking faults and a single low angle grain boundary above the middle of the SiO_2 island. In the epilayer seeded along the [010] direction shown in Fig. 7b, only one line dislocation and a void was observable above the oxide strip imaged. The void was located above the center of the SiO_2 island where the two growth fronts, seeded from opposite sides of the SiO_2 island, would have met.

Overgrowth Process

Cross-sectional views of ELO layers which had been grown to various thicknesses over a 6 μm wide SiO_2 island are presented in Fig. 8. The deposition conditions used to prepare these films are given in the caption of Fig. 8. When the epilayer reached a vertical height of approximately 4.5 μm, it completely covered the 6 μm wide SiO_2 island (Fig. 8b). The approximate ratio between horizontal and vertical growth rates was one. When the two growth fronts, seeded on opposite ends of the SiO_2 strip, initially joined together a surface flatness perturbation (dip) of about 4 μm was formed above the center of the SiO_2 island (Fig. 8b). Increasing the epilayer thickness by 2.0 μm (Fig. 8c) decreased the depth of the dip to about 0.1 μm, increasing it by another 1.5 μm completely eliminated the dip. The presence of the dip was reflected in the surface morphology. Figure 9 shows a top view of 13, 17, and 18.5 μm thick silicon layers grown over 20 μm wide SiO_2 strips. The location of the SiO_2 strip and the topology of ELO films is also shown in Fig. 9. In the 17 μm thick epi film, the depth of the groove (dip) was much less than 1 μm, whereas in the 13 μm thick film it exceeded 3 μm. Increasing the film thickness to 18.5 μm completely eliminated the dip, resulting in a flat surface. Decreasing the SiO_2 island width gives the same effect on surface morphology of ELO layers as increasing the epilayer thickness (Fig. 10). Thinner layers overgrowing narrower SiO_2 islands will give smooth and flat surfaces.

The lateral growth rate varied during deposition with time. Etching of the silicon layer during the

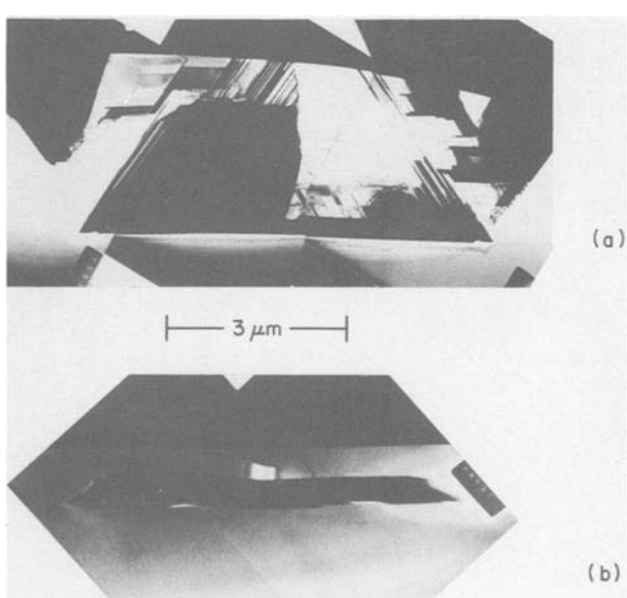

Fig. 7. Comparison of the defect structure observed by cross section TEM in ELO films grown on (100) substrates over 6 μm wide SiO_2 islands oriented along [110] and [010] (Fig. 7a and b, respectively). All other growth conditions same as in Fig. 6.

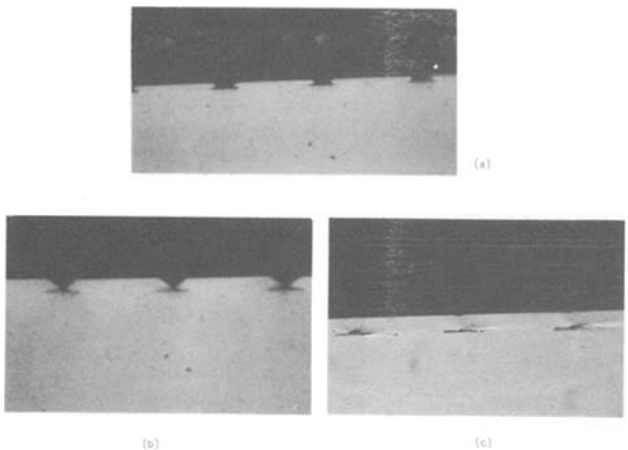

Fig. 8. Different steps of the overgrowth process. ELO films are: 2.5 μm (a), 4.5 μm (b) and 6.5 μm (c) thick. Growth conditions: 1050°C, 0.75 l/min SiH_2Cl_2 + 2.0 l/min HCl + 82 l/min H_2, 4 cycles (a), 11 cycles (b) and 16 cycles (c), 1 min deposition + 2 min etch, 6 μm wide SiO_2 oriented along [010]. Wafers have been cleaved along [110] direction.

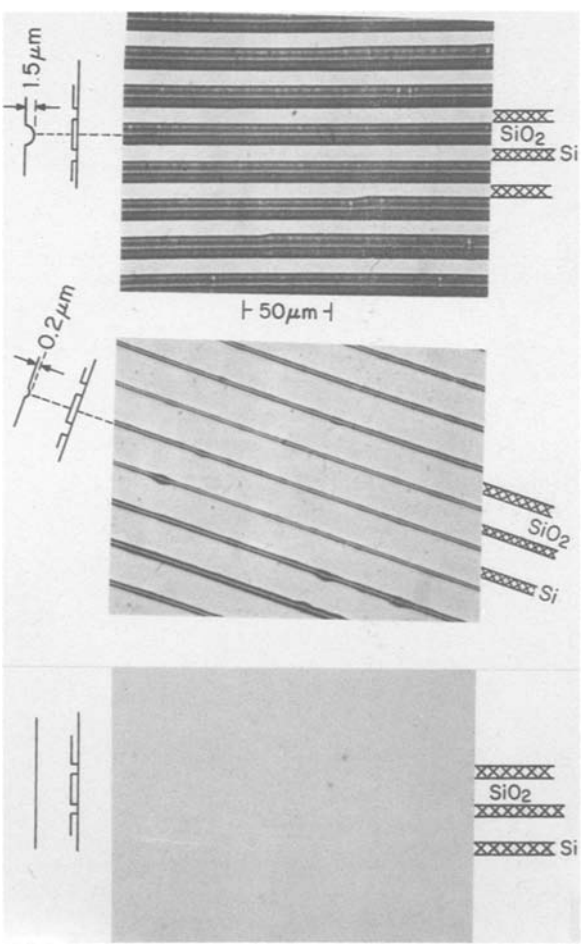

Fig. 9. Surface morphology vs. film thickness of ELO films. Thickness = 13 μm (a), 18 μm (b) and 19.5 μm (c). Growth conditions: temperature 1050°C, 0.75 l/min SiH_2Cl_2 + 2.0 l/min HCl + 82 l/min H_2. Growth cycle 1 min deposition + 2 min etch, SiO_2 width 20 μm, orientation along [010]. Location of SiO_2 islands and surface topology of ELO are schematically marked in the figure.

etch portion of the deposition/etch cycle delineated the interface between growth steps. These interfaces are observed as lines in the planar TEM micrographs of the ELO films shown in Fig. 11. From these interface demarcation lines the microscopic lateral growth rate during the ELO process has been calculated. The

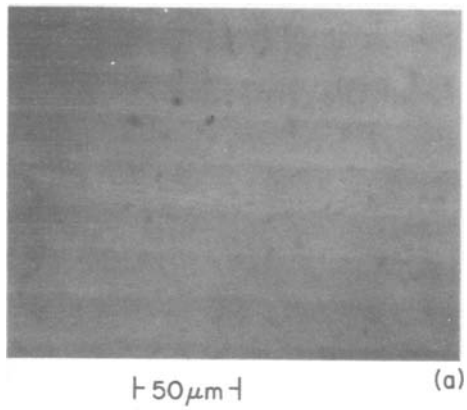

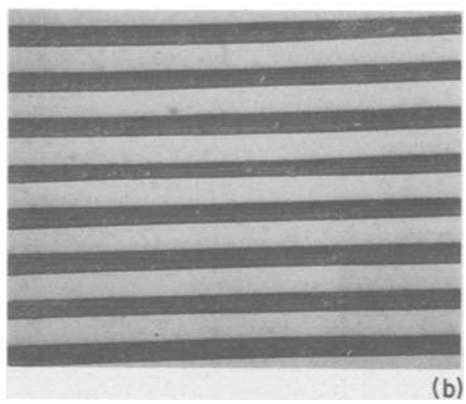

Fig. 10. Comparison of the surface morphology of 13 μm thick ELO films grown over (a) 6 μm wide SiO_2 islands and (b) 20 μm wide SiO_2 islands. Growth temperature: 1100°C, 0.75 l/min SiH_2Cl_2 + 2.0 l/min HCl + 82 l/min H_2, 50 cycles, growth cycle: 1 min growth + 2 min etch.

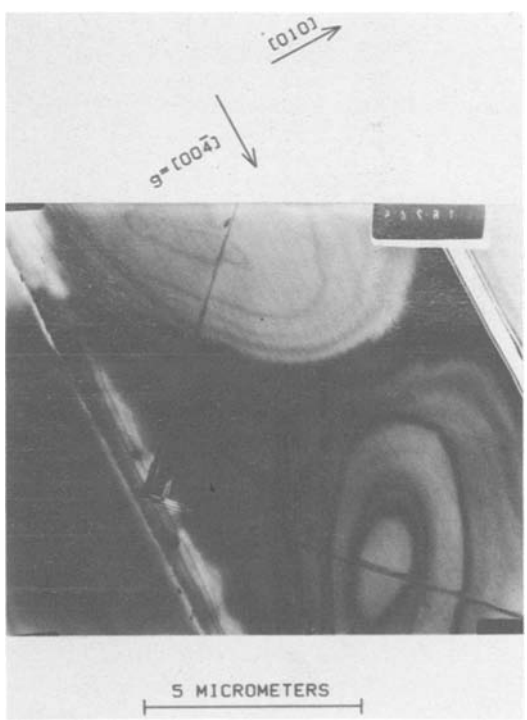

Fig. 11. Planar TEM micrograph of an ELO film grown over a 20 μm wide SiO_2 island oriented along the [010] on a (100) substrate. Growth conditions were chosen to suppress nucleation of the SiO_2. TEM contrast conditions chosen to reveal interface demarcation lines caused by etch cycles.

lateral growth rate as a function of the number of growth/etch cycles is presented in Fig. 12. Complete coverage of the 20 μm wide SiO_2 strip was obtained after about thirty cycles when the two growth fronts seeded from opposite sides of the oxide strip joined. It is evident that as the two growth fronts approached each other lateral growth rate dropped to about 50% of the initial value.

The shape of the growing interface was found to be a function of the concentration of HCl present in the gas phase during the etch and growth cycles. Figure 13 presents a cross-sectional view of epilayers grown with and without HCl present during the growth cycle while all other growth conditions were held constant (growth conditions were chosen to suppress nucleation on SiO_2). It is quite clear that the shape of the growing interface is different in the two cases. When HCl was present during deposition, it reduces the vertical growth rate by approximately 20% and the horizontal growth rate by approximately 35%. The HCl concentration also influenced the physical extent of the (001) and (101) planes. With increased HCl concentration the size of the (001) plane increased at the expense of the (101) plane.

The effect of the duration of the HCl etching cycle on the shape of the growing interface is shown schematically in Fig. 14 (data obtained from cross-section photographs). An increase in the HCl etching period from 20 to 40 sec decreased the vertical layer thickness by about 0.6 μm and reduced the width of the layer in the horizontal (100) plane by about 1.0 μm. Therefore, it can be concluded that the effect of having HCl present during the growth and/or the etch cycle is greater on the horizontally growing (001) (101) planes than on the vertically growing (100) plane.

Growth Model

To understand the influence of the growth parameters on ELO films, one has to consider the mechanisms involved in epitaxial overgrowth. When a supersaturation exists in the gas phase, the absorption and desorption of silicon atoms from the growth surface takes place simultaneously over the silicon and SiO_2 surfaces. Nucleation and growth occurs almost instantaneously on the silicon surfaces. However, there is a certain amount of time, t_D, required to deposit silicon on the SiO_2 surfaces and an additional amount of time, t_C to coalesce these atoms and form polysilicon nuclei. The critical time ($t_{critical} = t_D + t_C$) required to form nuclei on the SiO_2 is a strong function of the growth conditions (20, 21). An increase in the growth temperature will increase the diffusion constant of silicon over the SiO_2 which will reduce t_C and increase the rate of nuclei formation (Fig. 2). When HCl is added

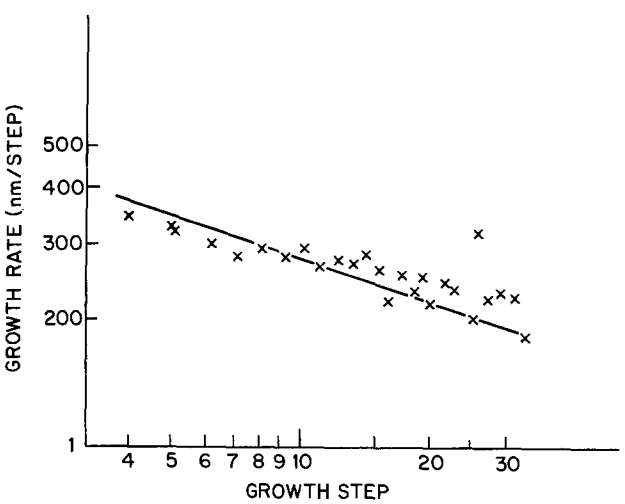

Fig. 12. Lateral growth rate as a function of the number of growth steps (growth time) for the ELO film from Fig. 12.

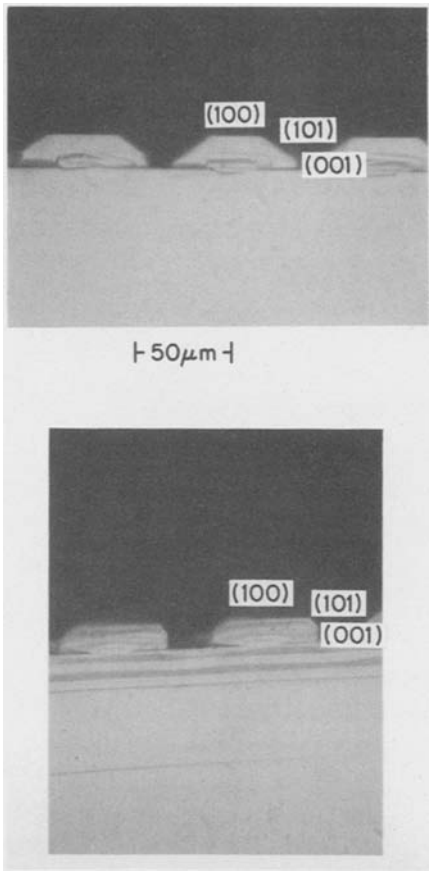

Fig. 13. Cross sectional views of ELO films grown with different concentration of HCl in the gas during the growth step: 2 l/min HCl (a), no HCl (b). Growth conditions: 1050°C, 0.75 l/min SiH_2Cl_2 + 180 l/min H_2, 12 cycles: 40 sec growth + 60 sec etch, 20 μm SiO_2 islands along [010]. Notice the difference in the shape of the horizontally growing interface (contribution from (100) and (110) planes).

to the gas stream, silicon is etched from the SiO_2 surfaces via the following reaction (24, 25)

$$2Si + 2HCl \rightarrow SiCl_2 + H_2$$

Therefore, an increase in times t_D and t_C can be expected when the HCl concentration increases (26) which is in agreement with data presented in Fig. 4. The presence of contaminants or topological defects on SiO_2 surface could significantly reduce t_D and t_C and, therefore, these defects will act as nucleation sites for polysilicon (heterogeneous nucleation). We believe that a distinct difference in $t_{critical}$ exists between spontaneous nucleation over SiO_2 and heterogeneous nucleations on a SiO_2 surface. For the spontaneous nucleation $t_{critical}$ is longer than the time of growth experiments (10^2 min) for the optimum temperature and HCl concentration. For the heterogeneous nucleation, $t_{critical}$ is on the order of minutes (this also depends on

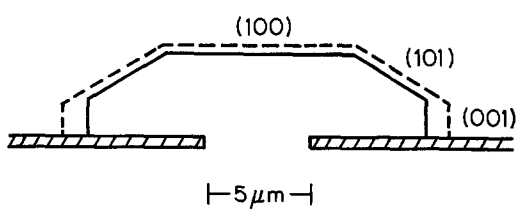

Fig. 14. Schematic representation of the effect of the duration of the etch cycle on the overgrowing films. Growth conditions: 0.75 l/min SiH_2Cl_2 + 2 l/min HCl + 180 l/min H_2. 12 cycles; 20 sec growth + 10 sec etch (dashed line) or 40 sec etch (solid line). Notice the difference between the etch rate of the horizontal and vertical (100) plane.

type of heterogeneous nucleation site). Therefore, it is not surprising that for a growth process that exceeds a few minutes, even a process that has been optimized for HCl concentration and temperature, polysilicon nuclei densities of 10^2-10^3 cm^2 were observed on SiO_2 surfaces. For practical reasons, the growth time very often exceeds the shortest $t_{critical}$ time for heterogeneous nucleation, therefore, the following procedure is proposed to obtain defect free epilayers. Growth should be stopped after a time equal to or less than the shortest $t_{critical}$ and should be followed by an etch cycle. During the etch cycle, silicon atoms and small nuclei which have formed around the heterogeneous nucleation sites on the SiO_2 surfaces are removed with only a slight etching of the homoepitaxially grown silicon. As is shown in Fig. 5, a decrease of the growth time and an increase of the etch time has dramatically reduced the density of polysilicon precipitates incorporated into the overgrowing layers. Following the etch period, the SiO_2 surface is free of unwanted silicon and the growth/etch cycle can be repeated as often as required until the desired thickness of the epilayer or SiO_2 coverage is achieved. The value of $t_{critical}$ and, therefore, the length of the growth/etch periods are a function of the growth temperature, gas composition, concentration of SiH_2Cl_2 and HCl, and the preparation of the SiO_2 surface. All of these variables affect absorption and the nucleation process of silicon over SiO_2. Optimization of these parameters have resulted in the growth of defect free epilayers over SiO_2 as is shown in Fig. 9c.

The atoms depositing on the silicon surface will contribute to homoepitaxial growth, which in the initial stages of growth is 100% vertical and only in the SiO_2 mask openings. When the epi growth is level with the surface of the oxide layers, it also grows horizontally over the SiO_2. For (100) substrates and [010] oxide edges, the horizontal and vertical growth planes are crystallographically identical and of the {100} type. In addition to these two growth planes, the growing interface also contains {101} planes (see Fig. 13). The shape of the growing interface will be a function of the growth rate of the horizontal and vertical {100} planes and the {101} plane. When the horizontal (001) plane grows faster than the vertical (100) plane, the contribution of the {101} plane to the growing interface will increase with growth time as is shown schematically in Fig. 15. Under extreme conditions, the horizontal (001) plane almost disappears and the {101} planes becomes the predominant horizontally growing plane (Fig. 13a). When two growth fronts, seeded from opposite sides of the oxide, join together a surface perturbation is formed. The depth and dimensions of surface perturbations will depend on the shape of this interface. Interfaces with small contributions from the {101} will have a small, shallow dip (Fig. 16a) while interfaces containing no {101} plane will have no dip. When the interfaces are formed with the major contribution coming from the {101} planes, the surface perturbation will be wide and deep (Fig. 16b). Growth rate differences between the horizontal growing and the vertical growing {100} interfaces are attributable to differences in the silicon flux from the gas phase to the growing interfaces which could be related to: (*i*) a sharper horizontal than vertical concentration gradients in the gas phase due to a higher supersaturation over the SiO_2 than silicon (27), (*ii*) an addtional flux of silicon atoms deposited on the SiO_2 and diffusing to the growing interface from a distance shorter than the diffusion length (14). It is impossible from the available experimental data to assess quantitative contribution from each of these mechanisms, but one can find some experimental evidence which indicates that both of them play an important role in ELO processing. Surface diffusion, the second mechanism, explains the different shapes of the growing interface in the presence and absence of HCl during the growth cycle (Fig. 13). When HCl is not present in the gas, more of the silicon atoms are deposited on SiO_2, which results in a higher diffusion flux along the oxide to the growth interface. The higher flux of silicon to the laterally expanding (001) plane will increase its growth rate and thus result in a decrease in its contribution to the growing interface. On the other hand, a decrease in the lateral growth rate as a function of time can be explained by differences between the horizontal and vertical concentration gradients in the gas phase, the first mechanism (Fig. 13). The lateral concentration gradient in the gas phase would decrease as the two growth fronts seeding on opposite sites of the oxide strip come together, which would result in the observed decrease in the lateral growth velocity. This phenomena cannot be explained by a decrease in diffusion flux of silicon atoms deposited on SiO_2, because the diffusion distance of silicon atoms estimated from the spacing of homogeneous nucleus does not exceed a few micrometers in the 1050°-1100°C temperature range.

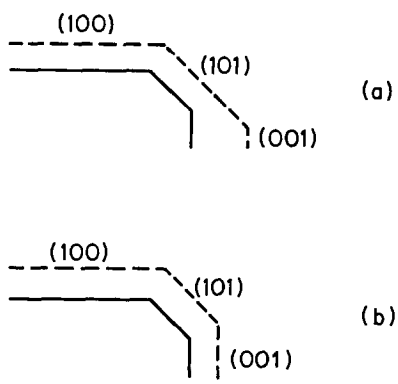

Fig. 15. Schematic representation of the effect that the growth rate of the laterally moving (001) growth front has on the shape of the overgrowing interface. When the two {001} growth fronts and the (101) plane advance at the same rate, the shape of the interface is preserved (b). When the lateral moving (001) growth front advances more rapidly than the vertically moving (100) front the contribution to the growing interface from the (101) plane increases (a).

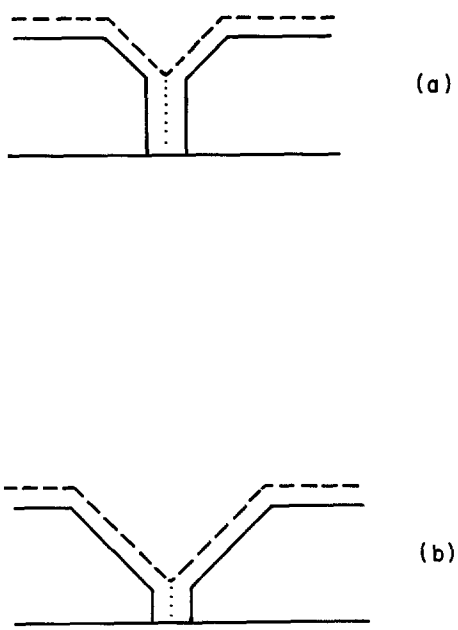

Fig. 16. Schematic representation of the relationship between the shape of the growing interface and the depth of the surface perturbation formed upon completion of the overgrowth. The larger contribution from the (101) plane to the growing interface results in a deeper surface perturbation.

Defect Structure of ELO Films on (100) Si Wafers

The nature of the defect structure of the silicon overgrowth was found to be strongly dependent upon the orientation of the edge of the oxide strips (Fig. 6 and 7). It is suggested that this dependence is directly related to the ease with which the internal stresses generated during growth and subsequent cooling are relieved through deformation. A mechanism for fault formation which is consistent with our observations is proposed for the configuration in which the edge of the oxide strip runs along a [001] direction.

For oxide strips aligned along the [011] direction, the silicon which overgrew the SiO_2 was highly defective (Fig. 7a). This defect region was bounded below by the oxide strip, above by the free surface and laterally by the $(1\bar{1}1)$ and $(\bar{1}11)$ planes. The predominant defect features observed within this volume were microtwins. Commonly 70-90% of the volume of the defective region was twin related to the substrate. Above the center of the oxide strip, an incoherent grain boundary extended from the sample's surface to the base of the overgrowth. This boundary was presumably formed when the silicon growth fronts emanating from the two edges of the SiO_2 joined above the center of the oxide strip. Along this boundary, irregularly shaped grains which were commonly twin related to the substrate have been observed.

When channels in the SiO_2 layer were etched along [001] direction, a dramatic improvement in the quality of the overgrowth was achieved. Above 6 μm wide oxide strips, high quality silicon was grown as shown in Fig. 7b. A void at the base of the overgrowth and above the center of the oxide strip was the only consistent defect. Occasionally, isolated stacking faults or microtwins were found but the grain boundary above the center of the overgrowth where the growth fronts joined was not observed.

Silicon overgrowths above 20 μm wide [001] oriented oxide strips displayed a wide variation in the defect structures. These variations seem to be random in nature. In low defect density samples, only scattered dislocations and the central void were observed (similar to the defects presented in Fig. 7b). In highly defective samples, stacking faults, dislocation networks eminating from the edges of the oxide strip, as well as a central void and grain boundary were all present (Fig. 17). To one side of the central boundary, stacking faults were active on two of the four {111} planes. While across the boundary, the remaining {111} stacking fault planes were active. That is, on a given side of the central grain boundary, only that pair of {111} planes which form a closed tetrahedron with the central grain boundary and the overgrowth oxide interface was found to contain stacking faults (28). It was determined from TEM contrast conditions that the bounding dislocations and therefore the stacking faults were of the a/6 <211> Shockley type (29). Figure 18 is a planar view of the overgrowth-SiO_2 interface. The stacking faults are seen to have formed in pairs along two intersecting {111} planes. The line of intersection extended from the edge of the oxide through the remaining overgrowth. Each of the stacking faults extended from this line of intersection to the central void along its respective {111} plane. The walls of the central void were deformed where the intersection with the stacking fault occurred, as seen in the insert in Fig. 18. These observations suggest that the stacking faults were nucleated at the edge of the oxide film after the central void had been formed.

Shear stress measurements (30) were taken along the overgrowth-oxide interface in both high and low defect density samples. Selected area transmission electron diffraction patterns were obtained from the ELO film in such a manner that the incident electron beam was coincident with the [001] direction. Shear strain was measured by finding the deviation from orthagonality of the 400 and 040 spots in the electron diffraction pattern. In the high defect density samples, the shear stress was below the detectable levels. In the low defect density samples, shear stresses of 3.6×10^9 dyne/cm^2 which changed sign symmetrically across the center of the oxide strips were measured. The specific nature of the defect generation in the overgrowth film has been shown to be highly sensitive to the crystallographic orientation of the edge of the oxide strip. This may be understood if these orientations are considered relative to the slip planes in silicon. These planes are the planes along which dislocations can most easily glide, and thus deformation can most readily occur.

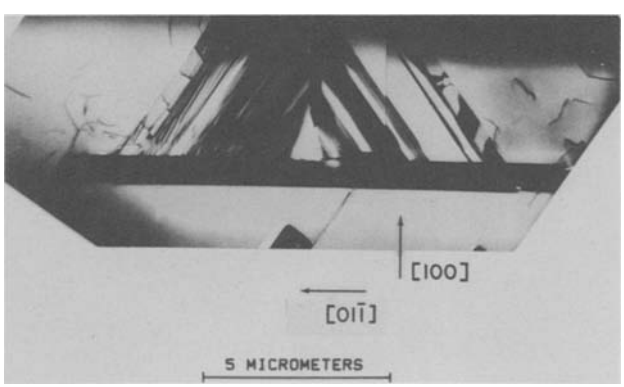

Fig. 17. A TEM cross sectional micrograph of an ELO film with high defect density grown over 20 μm wide SiO_2 strips oriented along the [010] on a (100) substrate. The overgrowth contains a high density of stacking faults, a grain boundary and a central void. Growth performed under conditions of suppressed nucleation on SiO_2.

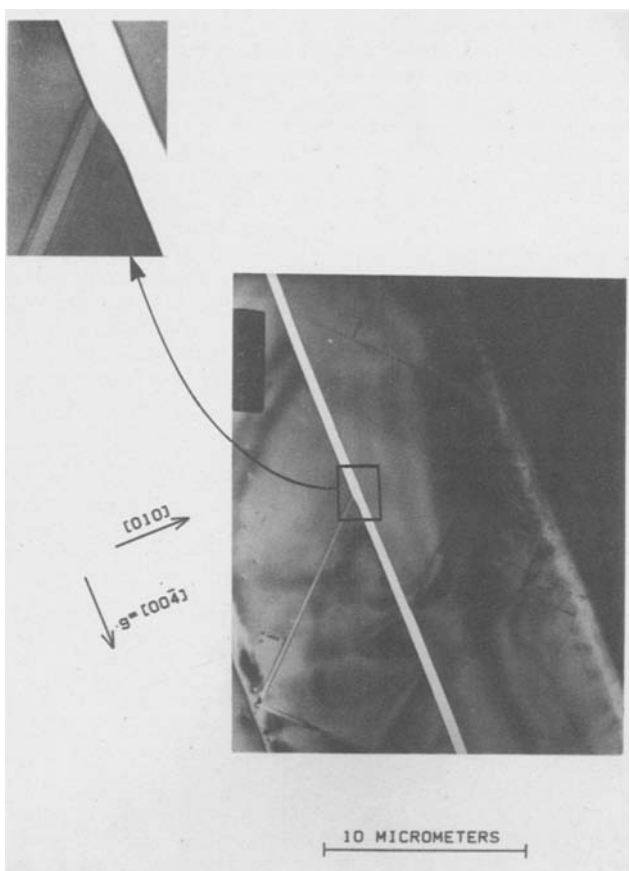

Fig. 18. A planar TEM micrograph of an ELO film with low defect density grown over 20 μm wide SiO_2 strip oriented along the [010] on a (100) substrate. Growth performed under conditions of suppressed nucleation on SiO_2. Notice the stacking faults originating at the oxide edge and central void.

They are the {111} family of planes in silicon. Only those dislocations for which the line of the dislocation and the Burgers vector are contained on a slip plane are free to move by glide through the crystal. Internal stresses can thus most easily be relieved if a large component of that stress can be resolved onto one of these planes. Internal stresses probably occur due to differences in the thermal coefficients of expansion between silicon and SiO_2. The disposition of these internal stresses relative to the {111} slip planes and the <110> directions will strongly influence the deformation mechanisms available for the relaxation of the crystal. If the oxide strip is aligned along the [011] direction, internal stresses which occur during growth or subsequent cooling are ideally situated to nucleate dislocations. Internal stress risers, such as the edges of the oxide strip (28), the central grain boundary, and associated void, all run along the [011] direction and are possible sites for nucleation of perfect, low-energy dislocations. Once nucleated, these dislocations would be free to glide along either the $(11\bar{1})$ or $(1\bar{1}1)$ planes creating a large number of defects.

If the oxide strip runs along the [001] direction on a (100) substrate, the lines of high internal stress do not coincide with a direction along which easy nucleation of dislocations would occur. Any dislocation lying along the [001] direction would be in a high-energy state and thus would require a high internal stress for nucleation to occur. In cases where sufficient internal stress exists for a dislocation to nucleate, movement of the dislocation could only occur by climb and not by glide since the dislocation is not contained in a slip plane. If such a dislocation were nucleated along the [001] edge of the oxide strip, it could climb to a low energy position along <110> directions. Once in its new configuration, the now segmented dislocation could dissociate into Schockley particles on the (111) and $(1\bar{1}\bar{1})$ planes. As these particles expand, they leave behind a pair of stacking faults (Fig. 18). The suggested mechanism is very similar to, and largely adopted from, the mechanism proposed for the formation of stacking fault tetrahedra in gold (31).

The proposed model for stacking fault generation is consistent with the nature of the stacking faults observed above oxide strips aligned along the [001] direction. The shear strain measurements made in the overgrowth indicated that samples with low stacking fault densities had large shear strains while the shear strain in highly faulted samples was below detectable limits. This suggests that the stacking faults were generated as a strain relief mechanism rather than as growth defects due to nucleation errors.

Summary

The growth of silicon over SiO_2 using a CVD epitaxial overgrowth technique has been discussed. Epilayers were seeded through openings in the SiO_2 mask and from these openings grow over the SiO_2 surface. Growth has been carried out using a mixture of SiH_2Cl_2, H_2, and HCl in the temperature range of 1050°-1200°C. To avoid previously encountered problems with the formation of polysilicon nucleations over SiO_2, which introduce defects into the overgrowing silicon epilayer, the growth process had to be carried out in a series of growth/etch steps. Growth temperature and HCl concentration were also optimized. The time of the growth step has been adjusted so as not to exceed the critical time required to form polysilicon nuclei over SiO_2. During the HCl etch step the silicon atoms deposited on the SiO_2 surface were removed with minimal etching of the homoepitaxially grown silicon. The growth/etch was repeated until the desired film thickness was achieved. The length of the growth and etch periods was found to be a function of the gas composition, the growth temperature and the quality of the SiO_2 surface. A typical cycle consisted of a one minute growth followed by two minutes of etching at 1050°C with a gas composition of $\sim 7.0 \times 10^{-3}$% volume of SiH_2Cl_2 and 2×10^{-2}% volume of HCl.

The defect structure of ELO films grown under conditions of suppressed silicon nucleation over SiO_2 has been found to be critically sensitive to the orientation of the SiO_2 islands on (100) substrates. The lowest defect density (10^2-10^3 cm^{-2}) is achieved in layers grown over SiO_2 islands oriented along the [010] direction. For the same growth conditions ELO films overgrowing SiO_2 islands oriented along the [110] direction have orders of magnitude higher defect densities. This difference has been attributed to differences in the nucleation energy of stacking faults and dislocations along stress risers such as the edge of the oxide strip. The difference in the nucleation energy between [001] and [011] oriented oxide strips has been attributed to the differences in the angular arrangement of the stress risers relative to the {111} slip planes and the <110>, low energy dislocation directions in these two type samples.

The overgrowth process has been shown to be controlled by the aspect ratio between the vertical and horizontal growth rates which depends on the growth conditions and, in our experiments, varied between one and two. The growth rate of the horizontal interface is controlled by: (*i*) the diffusion flux of silicon atoms in the gas, which is in turn controlled by the horizontal concentration gradient and, (*ii*) the diffusion flux of the silicon atoms deposited on the oxide at a distance shorter than the diffusion length. The growth rate of the horizontal interface controls the shape of the horizontally growing interface (contribution from (100) and (101) planes) and also the surface morphology of ELO films when SiO_2 coverage becomes complete.

One can conclude that the optimization of the growth parameters: deposition temperature, gas composition, and length of the growth/etch cycle, results in the reduction of polysilicon nuclei on SiO_2 to below 1 cm^{-2}. Under these conditions, an ELO film seeded from a silicon substrate and grown by CVD over an SiO_2 mask has the orientation of the substrate and is monocrystalline. Epilayers about 18 μm thick were grown over 20 μm wide SiO_2 islands at a growth rate of approximately 0.25 μm/min in a radiant heated reactor. Smooth mirrorlike surfaces were obtained. It has been found that when growth conditions that suppress the nucleation of polysilicon over SiO_2 are used the ELO films are practically defect free if the SiO_2 islands have been properly oriented (along the [010] on a (100) substrate).

Manuscript submitted Oct. 27, 1982; revised manuscript received April 4, 1983.

Any discussion of this paper will appear in a Discussion Section to be published in the June 1984 JOURNAL. All discussions for the June 1984 Discussion Section should be submitted by Feb. 1, 1984.

RCA Laboratories assisted in meeting the publication costs of this article.

REFERENCES

1. L. Jastrzebski, J. F. Corboy, and R. H. Pagliaro, Jr., Paper 149 presented at The Electrochemical Society Meeting, Montreal, Que., Canada, May 9-14, 1982; J. J. McGinn, L. L. Jastrzebski, and J. F. Corboy, Paper 152 presented at the Electrochemical Society Meeting, Montreal, Que., Canada, May 9-14, 1982.
2. T. Suzuki, A. Mimura, T. Kamei, and T. Ogawa, *This Journal*, **127**, 1537 (1980).
3. B. Y. Tsaur, J. C. C. Fan, M. W. Geis, D. Silverman, and R. W. Mountain, 1981 Int. Electron. Device Meeting, Dec. 1981, Washington, DC, IEDM Technical Digest, p. 232 (1981).
4. B. Y. Tsaur, J. C. C. Fan, M. W. Geis, D. Silverman, and R. W. Mountain, *Appl. Phys. Lett.*, **39**, 561 (1981).
5. L. Jastrzebski, A. C. Ipri, and A. Kokkas, Unpublished.

6. L. Jastrzebski, J. F. Corboy, J. McGinn, and R. Pagliaro, Jr., Electronic Materials Conference, Fort Collins, CO, June 1982.
7. L. Jastrzebski, *IEEE Trans. Electron. Devices*, **ed-29**, 475 (1982).
8. H. I. Smith and M. W. Geis, Paper 155 presented at The Electrochemical Society Meeting, Montreal, Que., Canada, May 9-14, 1982.
9. D. Thebault and L. Jastrzebski, *RCA Rev.*, **41**, 592 (1980).
10. F. W. Tausch, Jr. and A. G. Lapierre, *This Journal*, **112**, 706 (1965).
11. M. Michelitsch, *ibid.*, **112**, 747 (1965).
12. A. Mellend, C. Bozeler, and J. C. C. Fan, *Appl. Phys. Lett.*, **37**, 560 (1980).
13. H. M. Manasevit, A. Miller, F. L. Morritz, and D. H. Forbes, AIME Meeting, October 1966.
14. S. M. Blumenfeld, G. W. Ellis, R. W. Redington, and R. H. Wilson, *IEEE Trans.*, **ed-18**, 1036 (1971).
15. W. E. Engeler, S. M. Blumenfeld, and E. A. Taft, *Appl. Phys. Lett.*, **16**, 202 (1970); W. E. Engeler, U.S. Pat. 3,746,908 (1973).
16. D. D. Rathman, D. J. Silverman, J. A. Burns, and C. O. Bozler, RNP 699 presented at The Electrochemical Society Meeting, Hollywood, FL, Oct. 5-10, 1980; D. D. Rathman, D. J. Silverman, and J. A. Burns, 5th International Conference on Vapor Growth and Epitaxy, July 1981, Coronado, CA.
17. D. D. Rathman, D. J. Silverman, and J. A. Burns, *This Journal*, **129**, 2303 (1982).
18. L. Jastrzebski, J. F. Corboy, and R. Pagliaro, Jr., *ibid.*, **129**, 2645 (1982).
19. L. Jastrzebski, J. F. Corboy, and R. Pagliaro, Jr., Paper 152 presented at The Electrochemical Society Meeting, Montreal, Que., Canada, May 9-14, 1982.
20. J. Bloem and W. A. P. Claassen, *This Journal*, **127**, 194 (1980).
21. T. Kamins and T. R. Cass, *Thin Solid Films*, **16**, 147 (1973).
22. B. D. Joyce and J. A. Baldrey, *Nature*, **195**, 485 (1962).
23. E. G. Alexander and W. R. Runyan, Trans. Meet. Soc., AIME, **236**, 284 (1966).
24. D. M. Jackson, Jr., *ibid.*, **233**, 596 (1965).
25. W. A. P. Claassen and J. Bloem, "Semiconductor Silicon 1981," H. R. Huff and R. J. Kriegler, Editors, p. 365, The Electrochemical Society Softbound Proceedings Series, Pennington, NJ (1981).
26. J. Bloem and L. J. Giling, in "Current Topics in Materials Science," Vol. 1, E. I. Caldis, Editor, p. 303, North Holland, Amsterdam (1978).
27. W. G. Oldham and R. Holmstrom, *This Journal*, **114**, 381 (1967).
28. J. T. McGinn, L. Jastrzebski, and J. F. Corboy, Paper 152 presented at The Electrochemical Society Meeting, Montreal, Que., Canada, May 9-14, 1982.
29. P. B. Hirsch, A. Howie, R. B. Nicholson, D. W. Pashley, and M. J. Whelan, "Electron Microscopy of Thin Crystals," p. 234, Butterworths, London (1965).
30. M. S. Abrahams, J. Blanc, C. J. Buiocchi, and W. E. Ham, *J. Appl. Phys.*, **49**, 652 (1978).
31. J. Silox and P. B. Hirsch, *Philos. Mag.*, **4**, 72 (1959).

Multizone Modeling of Impurity Redistribution in Ion-Implanted Materials

R. Kwor and C. Paz de Araujo*†

Department of Electrical Engineering, University of Notre Dame, Notre Dame, Indiana 46556

ABSTRACT

Implanted impurity redistribution has been observed during annealing of many ion-implanted materials. Experimental evidence suggests some position dependence in the redistribution process. The tail region of ion-implanted impurity profiles usually exhibits faster diffusion than the near-surface region. In this paper, a multizone model for the redistribution of implanted impurities is presented. The implanted substrate is considered as a stratified medium with zones where a local diffusion equation is obeyed, and an effective diffusion coefficient is defined within each zone. The basic formulation of the model and its mathematical background are discussed. The multizone equations are solved using the Crank-Nicolson method. A computer program is used to generate a plot of the post-annealing redistributed impurity profile. The model is applied to the case of sulfur-implanted GaAs for dose range of 4×10^{13} to 4×10^{15} cm^{-2}, with energies of 120 and 300 keV. Good agreement is obtained between the computer generated profile and the SIMS experimental profile.

Ion implantation offers a number of advantages in the fabrication of semiconductor devices and is now an established technology for production. Its attractiveness comes from the ability to achieve doping profiles which are controllable, reproducible, and sometimes not easily obtained by other techniques. In the designing and characterization of ion implanted devices, it is therefore very important to know or to be able to predict the doping profile. In most cases, the final carrier concentration profile is closely related to the implanted impurity distribution and the post-implantation annealing. High-temperature annealing is necessary for the removal of radiation damage and the activation of implanted atoms. However, the diffusion of the impurity atoms during annealing often results in substantial movement of these atoms, altering the impurity distribution. The preannealing impurity distribution is usually described by the profiles of LSS (1), joined half-Gaussian (2), and more recently, the Pearson IV (3, 4). Depending on the implantation conditions, these profiles have various degrees of success. For post-annealing profiles, however, the effect of diffusion must generally be included. The commonly used model for impurity diffusion during annealing assumes an initial Gaussian distribution and a constant diffusion coefficient (5, 6). In the case of capped substrate such as Si_3N_4 on GaAs, the encapsulant is sometimes considered a continuation of the substrate. According to this model, annealing will result in a broader and lower Gaussian distribution. This type of diffusion can only be regarded as an approximation, whereas the actual diffusion of implanted species is, in general, far more complex. Factors such as lattice defects may play an important role in the diffusion mechanics of impurity atoms. During implantation different types of defect occur in damage clusters around the path of the implanted particle (7). The nature and spatial distribution of radiation damage is extremely complicated. The exact class of defect or defect complex depends on many factors, in-

* Electrochemical Society Active Member.
† Present address: Dept. of Electrical Engineering, University of Colorado at Colorado Springs.
Key words: ion implantation, diffusion, multizone, sulfur.

cluding the mass and energy of the incident particles and the mass of the target atom. Generally, the damage profile does not coincide with the implanted ion profile; the degree of disparity between these two being a function of the mass difference between the bombarding ion and the lattice atoms. Moreover, when the solid solubility of the implanted species in the substrate is exceeded, as in the case of high dose implantation, precipitates sometimes occur, thus changing the local characteristics of the medium. Clearly, the preannealing substrate cannot be considered as a homogeneous medium for diffusion of the implanted impurity atoms. Another important parameter which may also have a considerable influence on the final distribution of implanted ions is the substrate-encapsulant boundary condition. Most encapsulants behave as barriers to outdiffusion, leading to a build-up of impurity atoms at the substrate surface, but it is also possible for some to act as sinks. The strain at the substrate-encapsulant interface also has an effect on the diffusion of the implanted impurities (8). This complexity is supported by the experimental evidence that many post-annealing impurity profiles cannot be accurately described by the simple diffusion theory. Examples of long diffusion tails are numerous (9-11). They suggest that the implanted medium may be characterized by two or possibly more zones with different diffusion constants. This results in a multizone modeling scheme for the ion implanted medium. The medium is divided into zones where a local diffusion equation is obeyed with an effective diffusion coefficient which lumps the effects of the defects and possible precipitates. With appropriate boundary and interface conditions, this model can be used to more accurately describe the post-annealing impurity profiles. In its extended form it can be used to model outdiffusion of implanted species into the encapsulant. In this paper, the basic formulation of the model and its mathematical background are discussed. A computer program is then used to generate a plot of the post-annealing redistributed impurity profile. Reasonable agreement is obtained between the computer generated profile and the SIMS atomic profile of sulfur-implanted Cr-doped GaAs for dose range of 4×10^{13} to 4×10^{15} cm^{-2} with energies of 120 and 300 keV. This provides a simple and yet more accurate way of estimating the diffusion coefficients of an ion implanted medium. The advanced matrix formulation of the model allows the computer program to be independent of the initial profile and also virtuallv independent of constrictions in the boundary conditions. The method is thus very suitable for profile analysis in ion implantation when the initial profiles cannot be defined by analytical forms as in the case of non-Gaussian profiles or multiple implantations.

Basic Formulation of Multizone Model

The basic concepts of a double-zone model will first be discussed. In later sections, these basic concepts are generalized for the multizone case. Figure 1 shows the geometry of a double-zone model. The general continuity equation for the position dependent diffusion coefficient is

$$\frac{\partial C}{\partial t} = \frac{\partial}{\partial x}\left[D(x) \frac{\partial c}{\partial x} \right] \qquad [1]$$

where $C(x, t)$ is the concentration of the implanted impurity atoms, $D(x)$ is the position dependent diffusion coefficient, t is the time, and x is the depth. For a double-zone model, each of the two zones is assumed to have a constant diffusion coefficient

$$D(x) = \begin{cases} D_1 & \text{for } 0 \leq x \leq a^- \\ D_2 & \text{for } a^+ \leq x \leq l \end{cases} \qquad [2]$$

where D_1 and D_2 are the effective diffusion coefficients

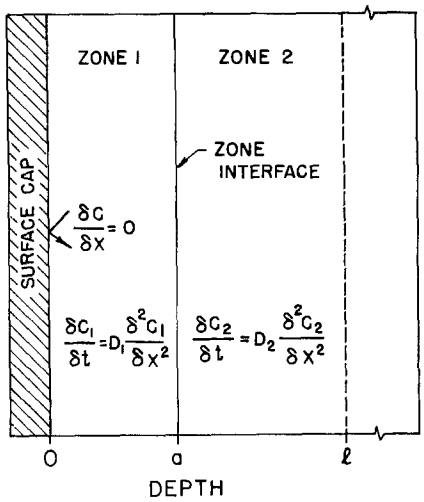

Fig. 1. Configuration of a double-zone model for impurity redistribution.

for zone 1 and zone 2 respectively, a is the location of the zone interface and l is the location of the second zone boundary. Thus, Eq. [1] becomes the familiar Fick's second law inside each zone

$$\frac{\partial C_1}{\partial t} = D_1 \frac{\partial^2 C_1}{\partial x^2} \quad \text{for} \quad 0 < x < a \qquad [3a]$$

$$\frac{\partial C_2}{\partial t} = D_2 \frac{\partial^2 C_2}{\partial x^2} \quad \text{for} \quad a < x < l \qquad [3b]$$

where C_1 and C_2 are the concentrations in their respective zones. If the initial condition, *i.e.* the as-implanted impurity profile is $F(x)$, then

$$C_1(x) = F(x) \quad \text{for} \quad 0 \leq x \leq a \qquad [4a]$$

$$C_2(x) = F(x) \quad \text{for} \quad a \leq x \leq l \qquad [4b]$$

In our simple double-zone model, three boundary conditions will be assumed. A perfectly reflective cap is assumed to exist at the surface. Thus

$$\left.\frac{\partial C_1}{\partial x}\right|_{x=0} = 0 \qquad [5]$$

For large l, it is assumed that no diffusing impurity will cross the boundary at $x = l$ for the short annealing time used in ion implantation. Then

$$\left.\frac{\partial C_2}{\partial x}\right|_{x=l} = 0 \qquad [6]$$

And at the zone interface of $x = a$, the flux in zone 1 equals that in zone 2. Hence

$$D_1 \frac{\partial C_1}{\partial x} = D_2 \frac{\partial C_2}{\partial x} \quad \text{at} \quad x = a \qquad [7]$$

Physically, this means that the interzone boundary is nonabsorbing and does not segregate impurities. Also in this model, the locations of the zone boundaries are assumed to be time-independent. Then, given an initial condition $C(x, 0) = F(x)$, and with the boundary conditions specified by the Eq. [5]-[7], Eq. [3] can be solved to yield the functions C_1 and C_2 for a specific combination of annealing time and the effective diffusion coefficients in the two zones. The mathematical method is outlined in the next section.

Discretization of the Diffusion Equations for Double-Zone Model

To solve Eq. [3a] and [3b] for the double-zone case, the continuous set of space-time points $\{(x, t)\}$ pairs is substituted with a grid of discrete points $\{x_m =$

$m\Delta x$; $t_n = n\Delta t\}$, where Δx and Δt are small intervals of distance and time respectively, m and n are non-negative integers, $m = 0, 1, 2, ..., L$; $n = 0, 1, 2, ..., T$. At the beginning of first zone, $x_m = 0$, $m = 0$; and at the end of second zone, $x_m = l$, $m = L$. The total annealing time is equal to $T\Delta t$. The function $C(x, t)$ at the grid point (m, n) is approximately represented by the point C_m^n. Using the Crank-Nicholson method (12), Eq. [3] can be transformed to

$$\mathcal{D}_t^+ C_m^n = D_i \mathcal{D}_x^+ \mathcal{D}_x^- \left(\frac{C_m^n + C_m^{n+1}}{2} \right) \quad [8]$$

where D_i is the diffusion coefficient of the ith zone.

$\mathcal{D}_t^+ =$ the finite difference operator for the forward time step

$$\mathcal{D}_t^+ C_m^n = \frac{C_m^{n+1} - C_m^n}{\Delta t}$$

$\mathcal{D}_x^+ =$ the finite difference operator for the forward distance step

$$\mathcal{D}_x^+ C_m^n = \frac{C_{m+1}^n - C_m^n}{\Delta x}$$

$\mathcal{D}_x^- =$ the finite difference operator for the backward distance step.

$$\mathcal{D}_x^- C_m^n = \frac{C_m^n - C_{m-1}^n}{\Delta x}$$

The Crank-Nicholson method is chosen because of its convergence and unconditional stability. Equation [8] can be expanded to a set of equations

$$(1 + \lambda_i) C_m^{n+1} - \frac{\lambda_i}{2} (C_{m+1}^{n+1} + C_{m-1}^{n+1}) = (1 - \lambda_i) C_m^n + \frac{\lambda_i}{2} (C_{m+1}^n + C_{m-1}^n) \quad [9]$$

where $\lambda_i = D_i \Delta t / (\Delta x)^2$, the normalized diffusion coefficient for the ith zone. The initial condition $(n = 0)$ is readily incorporated in this system, and the boundary conditions in the discrete space-grid are: (*i*) At the beginning of the first zone, $x_m = 0$, $m = 0$, $i = 1$. Equation [9] thus becomes

$$(1 + \lambda_1) C_o^{n+1} - \frac{\lambda_1}{2} (C_1^{n+1} + C_{-1}^{n+1}) = (1 - \lambda_1) C_o^n + \frac{\lambda_1}{2} (C_1^n + C_{-1}^n) \quad [10]$$

If we assume a perfectly reflecting surface, then Eq. [10] becomes

$$(1 + \lambda_1) C_o^{n+1} - \lambda_1 C_1^{n+1} = (1 - \lambda_1) C_o^n + \lambda_1 C_1^n \quad [11]$$

(*ii*) At the end of the second zone, $x_m = l$, $m = L$, $i = 2$

$$\mathcal{D}_x^o C_o^n = 0$$

Eq. [9] beomes

$$(1 + \lambda_2) C_L^{n+1} - \lambda_2 C_{L-1}^{n+1} = (1 - \lambda_2) C_L^n + \lambda_2 C_{L-1}^n \quad [12]$$

(*iii*) At the zone interface, $x_m = a$, $m = A$, and

$$D_1 \mathcal{D}_x^- C_A^n = D_2 \mathcal{D}_x^+ C_A^n$$

then the interzone equation can be shown to be

$$\left(1 + \frac{\lambda_1}{2} + \frac{\lambda_2}{2}\right) C_A^{n+1} - \frac{\lambda_1}{2} C_{A-1}^{n+1} - \frac{\lambda_2}{2} C_{A+1}^{n+1} = \left(1 - \frac{\lambda_1}{2} - \frac{\lambda_2}{2}\right) C_A^n + \frac{\lambda_1}{2} C_{A-1}^n + \frac{\lambda_2}{2} C_{A+1}^n \quad [13]$$

For $m = 0, 1, 2, ..., L$, the system of equations Eq. [9] can be represented by a matrix equation

$$\mathbf{A}\, \mathbf{C}^{n+1} = \mathbf{B}\, \mathbf{C}^n \quad [14]$$

where

$$\mathbf{C}^{n+1} = \begin{bmatrix} C_o^{n+1} \\ C_1^{n+1} \\ \cdot \\ \cdot \\ \cdot \\ \cdot \\ \cdot \\ C_L^{n+1} \end{bmatrix} \quad \text{and} \quad \mathbf{C}^n = \begin{bmatrix} C_o^n \\ C_1^n \\ \cdot \\ \cdot \\ \cdot \\ \cdot \\ \cdot \\ C_L^n \end{bmatrix}$$

Depending on the surface condition (at $x_m = 0$), the interzone conditions and the last zone boundary condition (at $x_m = l$), the **A** and **B** matrices will take different forms. A computer program is then used to solve the matrix equation Eq. [14] and calculate the values of C_m^n at different grid points (m, n). The Crout-Doolittle algorithm is used to perform the necessary matrix inversion. The redistributed profile after a certain annealing time can then be plotted.

The Multizone Model with General Boundary Conditions

The multizone model follows the same arguments as the double-zone model. Inside the ith zone, where $i = 1, 2, 3, ..., I$, Fick's law is assumed to be obeyed

$$\frac{\partial C_i}{\partial t} = D_i \frac{\partial^2 C_i}{\partial x^2} \quad \text{inside ith zone} \quad [15]$$

Assume the boundary condition at the surface to be

$$\frac{\partial C_1}{\partial x} + p_1 C_1 = \phi_1(t) \quad \text{at} \quad x = 0 \quad [16]$$

And at $x = l$ the boundary condition is

$$\frac{\partial C_I}{\partial t} + p_I C_I = \phi_I(t) \quad [17]$$

Here $\phi_1(t)$ and $\phi_I(t)$ are time dependent sources (or sinks) at the first and last boundaries. The functions p_1 and p_I are related to the permeability of the boundaries. These boundary conditions are now discretized

$$D_x{}^o C_o^s + p_1 C_o^s = \phi_1^s \quad x_m = 0 \quad [18]$$

$$D_x{}^o C_L^s + p_I C_L^s = \phi_I^s \quad x_m = l \quad [19]$$

where $s = n, n + 1$

The first and last equations in Eq. [14] then become

$$[1 + (1 - \Delta x p_1)\lambda_1] C_o^{n+1} - \lambda_1 C_1^{n+1} + \lambda_1 \Delta x \phi_1^{n+1} = [1 - (1 - \Delta x p_1)\lambda_1] C_o^n + \lambda_1 C_1^n - \lambda_1 \Delta x \phi_1^n \quad [20]$$

$$[1 + (1 + \Delta x p_I)\lambda_I] C_L^{n+1} - \lambda_I C_{L-1}^{n+1} - \lambda_I \Delta x \phi_I^{n+1} = [1 - (1 + \Delta x p_1)\lambda_1] C_L^n + \lambda_I C_{L-1}^n + \lambda_I \Delta x \phi_I^n \quad [21]$$

Equations [20] and [21] are seen to reduce to Eq. [11] and [12] for the double-zone case if $I = 2$, $p_1 = p_I = 0$ and $\phi_1 = \phi_I = 0$ for all $t > 0$. For the multizone case, another matrix equation can be obtained

$$\mathbf{A}\, \mathbf{C}^{n+1} + \boldsymbol{\Phi}^{n+1} = \mathbf{B}\, \mathbf{C}^n + \boldsymbol{\Phi}^n \quad [22]$$

where

$$\boldsymbol{\Phi}^s = [\lambda_1 \Delta x \phi_1^s \quad 0 \quad 0 ..... \lambda_I \Delta x \phi_I^s]^T \quad s = n, \quad n + 1$$

If the interzone conditions are kept the same as that for the double-zone case, *i.e.*, assuming no interface resistance or enhancement to particle flow, approaches similar to that for the double-zone model can be used to find the matrices **A** and **B**. And again the redistributed profiles can be calculated given the annealing time and the set of diffusion coefficients for the I zones.

Application of the Model to the Redistribution of Sulfur in Ion-Implanted GaAs

In this section, the multizone model described in the previous sections is applied to some profiles of sulfur implanted in <100> oriented Cr-doped semi-insulating GaAs substrate. The implantations were done at room temperature and in a nonchanneling direction to doses ranging from 4×10^{13} to 4×10^{15} cm^{-2}. After implantation, the samples were capped with either Si_3N_4 or SiO_2 and then annealed. There is a significant redistribution of sulfur as a result of diffusion during annealing. As indicated by the SIMS profiles (Fig. 2-5), the as-implanted profile cannot be adequately described using LSS. Pearson IV distribution was therefore used as the initial condition for the multizone model. Using the same approach as that in Ref. (4), the four moments for the Pearson IV distribution were found. These four moments were then fed to the computer which generates the initial condition for the model. Attempts to match the post-annealing profiles for these sulfur implants with Pearson IV distribution have been unsuccessful because of the long diffusion tails involved. However, as will be seen later, the triple-zone model can be used to adequately describe these profiles. Double-zone model has also been tried, but it does not give as good results. As discussed earlier, the model accepts initial condition of any distribution. Pearson IV has been used throughout because it gives satisfactory results for these particular applications. From the SIMS data shown in Fig. 2-5 the different zones in the redistributed profiles are apparent. Depending on the annealing time, temperature, implantation energy, and dose, the effective diffusion coefficients in different zones are different. In Fig. 2-4, the impurity concentrations near the surface exceed the solid solubility due to high dose implantation. Precipitation and/or a large amount of unannealed disorder in this region results in a very small effective diffusion coefficient. Deeper in the substrate, the sulfur atoms diffuse with a larger effective diffusion coefficient. Under such circumstances, significant redistribution of sulfur only occurs in the tail region of the profile. In lower dose implants, there is a much smaller

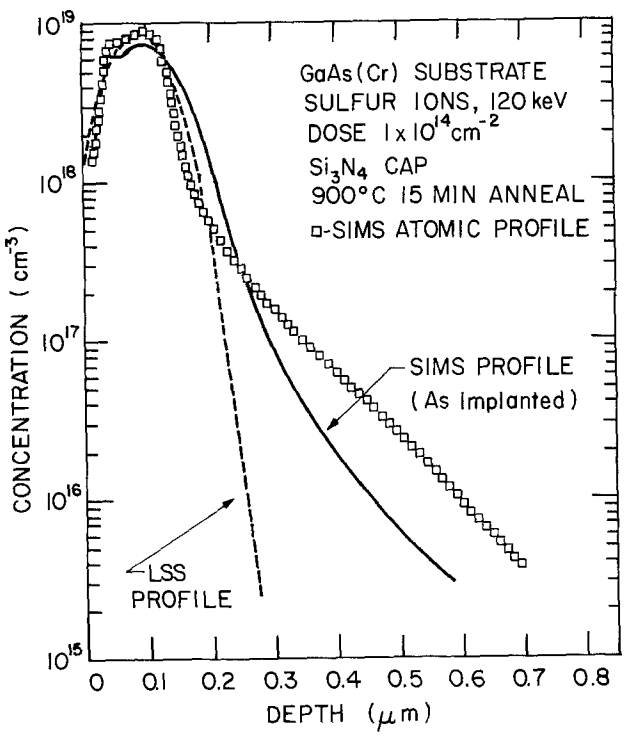

Fig. 2. SIMS unannealed and annealed profiles of Cr-doped GaAs implanted with 120 keV, 10^{14} cm^{-2} ^{32}S. 15 min anneal was performed with an Si_3N_4 encapsulant.

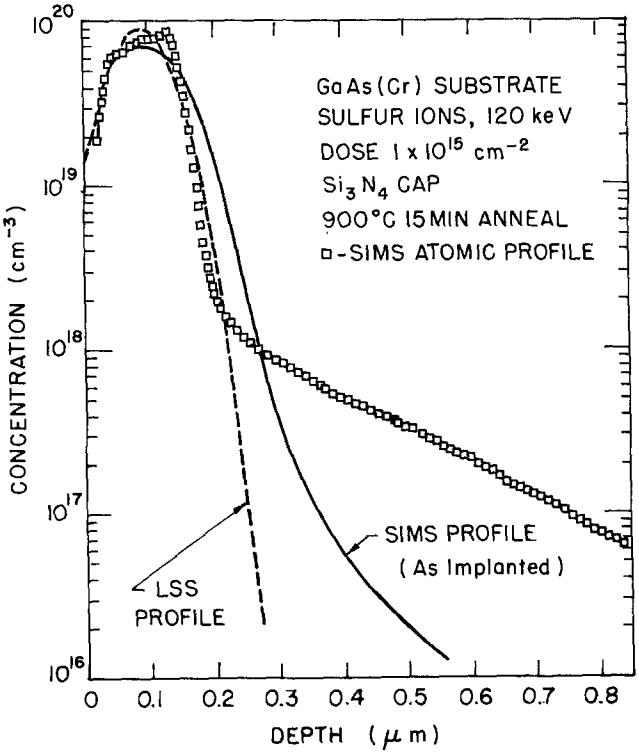

Fig. 3. SIMS unannealed and annealed profiles of Cr-doped GaAs implanted with 120 keV, 10^{15} cm^{-2} ^{32}S. 15 min anneal was performed with an Si_3N_4 encapsulant.

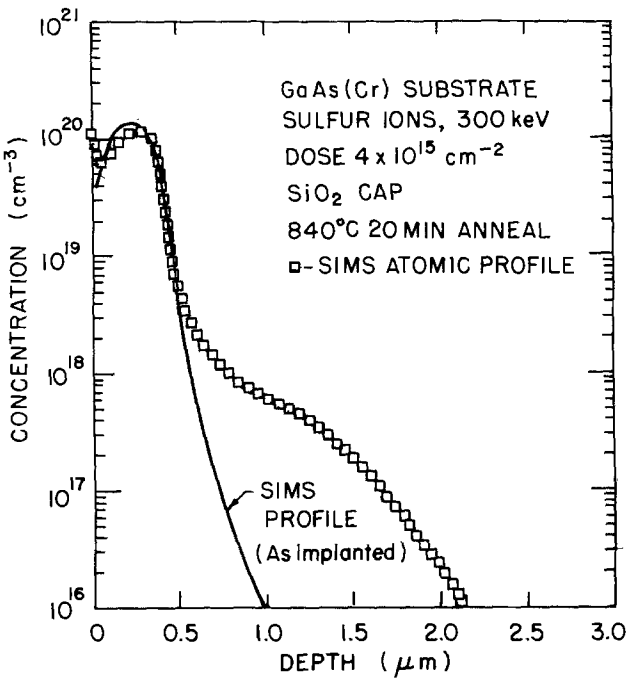

Fig. 4. SIMS unannealed and annealed profiles of Cr-doped GaAs implanted with 300 keV, 4×10^{15} cm^{-2} ^{32}S. 20 min anneal was performed with an SiO_2 encapsulant. [After C. A. Evans *et al.*, Ref. (10)].

difference in the effective diffusion coefficients of different zones, except in the lower temperature annealing. Figure 5 gives such an example.

The multizone model was applied to four cases. In each case, the Pearson IV moments for the as-implanted profile were found from the SIMS data and used to generate the initial profile. The redistributed profile after annealing was then calculated using a computer. The time and spatial steps used were $\Delta t = 1$ sec and $\Delta x = 0.01$ μm. The program required approx-

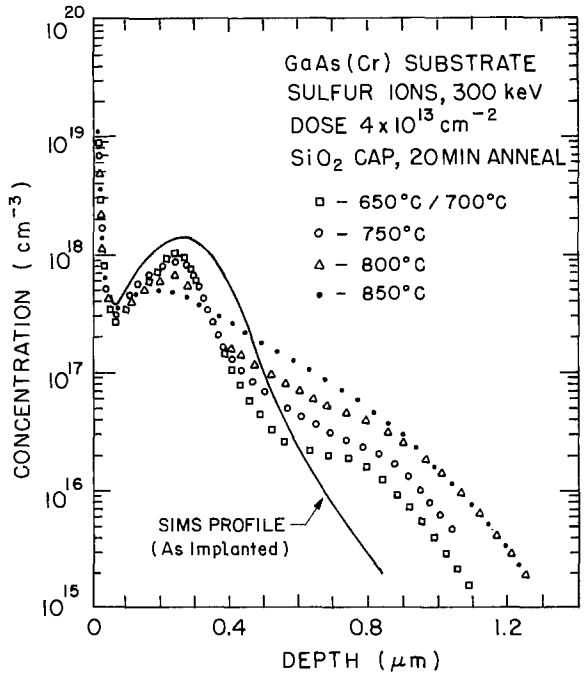

Fig. 5. SIMS unannealed and annealed profiles of Cr-doped GaAs implanted with 300 keV, 4 × 10^{13} cm^{-2} ^{32}S. 20 min anneal was performed with an SiO_2 encapsulant. [After R. G. Wilson, Ref. (11)].

imately 2 sec CPU time. The four cases are discussed below.

The SIMS unannealed and annealed profiles of Cr-doped GaAs implanted with 120 keV, 10^{14} cm^{-2} ^{32}S are shown in Fig. 2. These profiles were reported earlier in Ref. (9). The annealed profile shows a very distinct multizone characteristics. Pearson IV distribution was used to describe the as-implanted profile which is seen to deviate substantially from LSS. With the choice of four moments of $R_p = 0.1$ μm, $\sigma = 0.08$ μm, $\gamma = -1.7$ and $\beta = 40$, a good fit was obtained except near the tail region where the Pearson IV distribution has a slightly shallower penetration. After a 15 min anneal at 900°C, performed with an Si_3N_4 encapsulant, a pronounced tail appeared in the annealed profile. The tail is seen to start at about 2 × 10^{18} cm^{-3}, which is commonly accepted as the solid solubility of implanted sulfur in GaAs. To model this annealed profile, a triple-zone scheme was used. The Pearson IV distribution with the above mentioned four moments was used as the initial condition. The triple-zone profile with interfaces at 0.2 and 0.22 μm, and three effective diffusion coefficients of $D_1 = 4 \times 10^{-16}$ cm^2/sec, $D_2 = 8 \times 10^{-15}$ cm^2/sec, $D_3 = 1.36 \times 10^{-13}$ cm^2/sec, is shown in Fig. 6.

In Fig. 3, the SIMS unannealed and annealed profiles of Cr-doped GaAs implanted with 120 keV, 10^{15} cm^{-2} ^{32}S are shown. The four moments used in the Pearson IV distribution for the as-implanted profile were $R_p = 0.11$ μm, $\sigma = 0.097$ μm, $\gamma = -2.5$ and $\beta = 40$. Again, a good fit was obtained except near the tail region where the Pearson IV has a shallower penetration, which is common in all the cases reported in this work. After 15 min anneal at 900°C, performed with an Si_3N_4 encapsulant, a pronounced tail similar to the above-discussed 10^{14} cm^{-2} dose case appeared. The triple-zone profile for the annealed curve is shown in Fig. 7. The interfaces used were at 0.21 and 0.23 μm. The three effective diffusion coefficients were $D_1 = 4 \times 10^{-16}$ cm^2/sec, $D_2 = 8 \times 10^{-15}$ cm^2/sec, and $D_3 = 5.6 = 10^{-13}$ cm^2/sec.

The SIMS data studied in the last case here were also from Ref. (11). Several annealed curves for different temperatures are shown in Fig. 5. Multizone characteristics of the profile are more apparent in the lower temperature annealed curves. Triple-zone modeling was performed for the 700°C annealed profile. The SIMS as-implanted profile from Fig. 8 was first calibrated in terms of concentration by integrating the area under the curve and setting it equal to the area under the 700°C annealed curve. The four moments of the Pearson IV were then found: $R_p = 0.24$ μm, $\sigma = 0.12$ μm, $\gamma = -1$ and $\beta = 40$. This initial condition was then used for the triple-zone model. (Fig. 9). The interfaces used were at 0.42 and 0.60 μm. The effective diffusion coefficients were $D_1 = 9 \times 10^{-16}$ cm^2/sec, $D_2 = 2.07 \times 10^{-13}$ cm^2/sec, and $D_3 = 2.7 \times 10^{-13}$ cm^2/sec.

The above results indicate that for high dose implants, there is very little diffusion in the first two zones, while the effective diffusion coefficient in the third zone is between 10^{-13} and 10^{-12} cm^2/sec, near the values of sulfur diffusion coefficient reported by other researchers (6, 14, 15, 16). For lower dose and high energy implants, there is also a significant difference in diffusion coefficients of different zones. At annealing temperatures below 700°C, there is little diffusion in the first zone where there is still a significant density of unannealed disorder, but the rate of diffusion in the third zone is near that of a single crystal. This is attributed to faster crystalline regrowth near

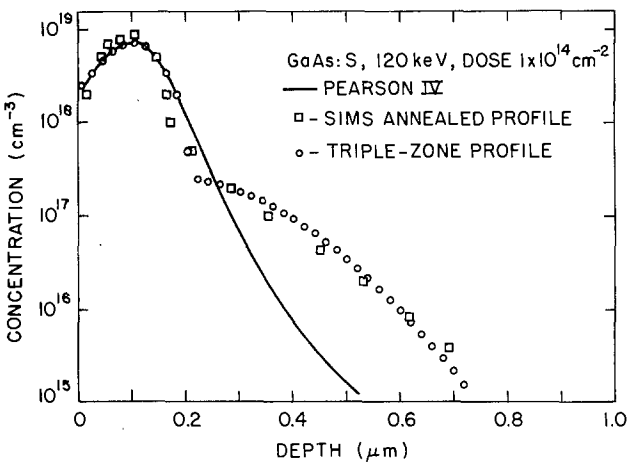

Fig. 6. SIMS profile of 120 keV, 10^{14} cm^{-2} ^{32}S implant annealed at 900°C for 15 min; Pearson IV profile initial condition; and triple-zone profile with interfaces at 0.2, 0.22 μm and D_1, D_2, D_3 equal 4 × 10^{-16}, 8 × 10^{-15}, 1.36 × 10^{-13} cm^2/sec, respectively.

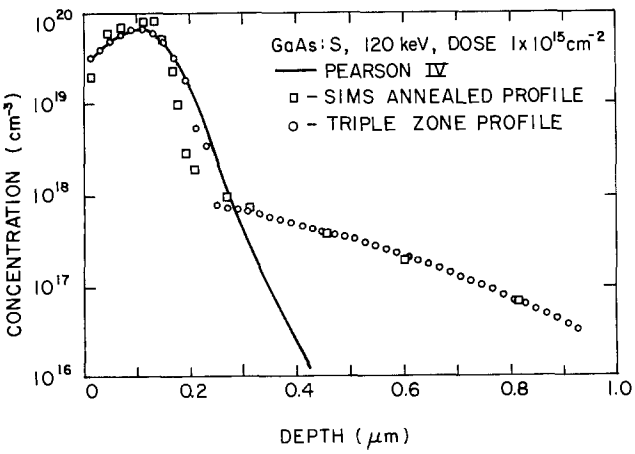

Fig. 7. SIMS profile of 120 keV, 10^{15} cm^{-2} ^{32}S implant annealed at 900°C for 15 min; Pearson IV profile initial condition; and triple-zone profile with interfaces at 0.21, 0.23 μm and D_1, D_2, D_3 equal 4 × 10^{-16}, 8 × 10^{-15}, 5.6 × 10^{-13} cm^2/sec, respectively.

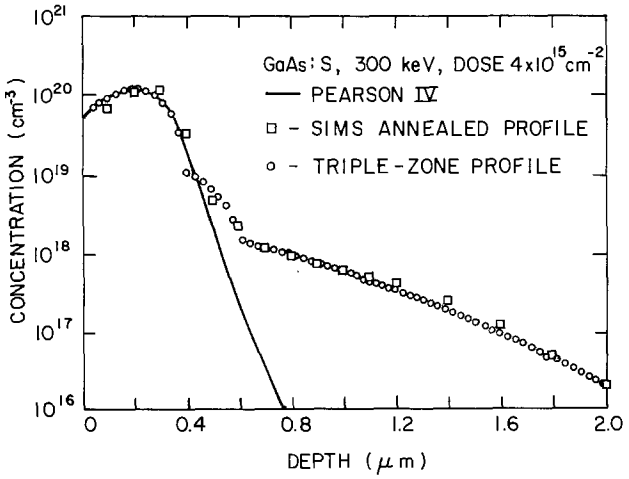

Fig. 8. SIMS profile of 300 keV, 4 × 10^{15} cm^{-2} ^{32}S implant annealed at 840°C for 20 min; Pearson IV profile initial condition; and triple-zone profile with interfaces at 0.39, 0.60 μm and D_1, D_2, D_3 equal 9 × 10^{-15}, 1.44 × 10^{-13}, 1.98 × 10^{-12} cm²/sec, respectively.

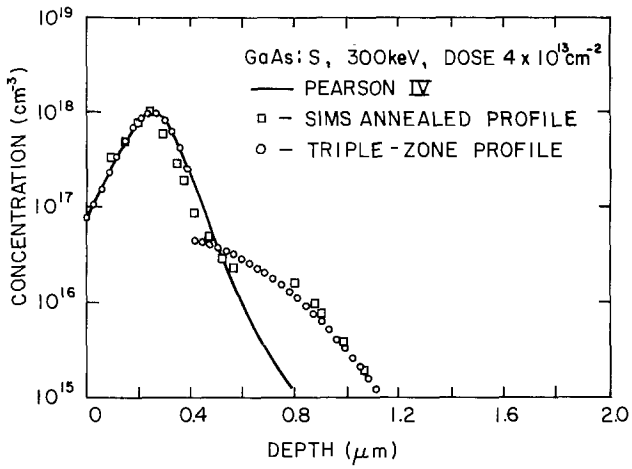

Fig. 9. SIMS profile of 300 keV, 4 × 10^{13} cm^{-2} ^{32}S implant annealed at 700°C for 20 min; Pearson IV profile initial condition; and triple-zone profile with interfaces at 0.42, 0.60 μm and D_1, D_2, D_3 equal 9 × 10^{-16}, 2.07 × 10^{-13}, 2.7 × 10^{-13} cm²/sec, respectively.

the boundary between the implanted (damaged) medium and the undamaged bulk crystal. It is believed that the third zone quickly attains higher crystalline order than the other zones and since the impurity distribution in that zone is well below the solubility limit, single crystal type of diffusion behavior is expected.

Summary and Discussion

In all cases studied, reasonable fit was obtained between the triple-zone profile and the corresponding SIMS annealed curve, with best fit obtained in the first and third zones. The assumption of a perfectly reflecting interface between the encapsulant and the medium is valid here for S-implanted GaAs since experimental evidence has shown that there is negligible outdiffusion of sulfur (9). As there is a change of as much as several orders of magnitude in the effective diffusion coefficients from the first to the third zones, the second zone is in reality a transition zone in which there is a continuous change of diffusion coefficient. Because of the piece-wise linear nature of the triple-zone model, only one effective diffusion coefficient is chosen for the second zone. Thus the greater the difference between the diffusion coefficients in the first and third zones, the more difficult it is to have an accurate fit of the profile in the second zone. The results from the multizone modeling show that the impurity diffusion is related to implantation energy, dose and annealing temperature. This model implies that heavier damage in the first two zones leads to lower diffusion coefficients; whereas the diffusion coefficient in the third zone seems to have been enhanced. Faster crystalline regrowth in the third zone coupled with increased vacancy density diffusing from the other defect saturated zones provides a reasonable picture to this complex system. Figure 5 gives a good indication of the influence of annealing temperature on the difference in effective diffusion coefficients of different zones. In this case, when the implantation energy is high and annealing temperature is low (around 700°C), not much of the implantation damages near the surface are removed during annealing, and there is a great difference in the effective diffusion coefficients of the different zones. At higher annealing temperatures, the implantation damages are removed, the difference in diffusion coefficients in different zones is reduced. At 850°C annealing temperature, the annealed profile has almost lost its multizone characteristics.

In summary, the multizone model gives a reasonably accurate description of the post-annealing atomic profile for ion-implanted impurities. It also gives some insight of the physical process occurring during the post-implantation annealing, yielding some information of the position dependence of the diffusion. Using the model, effective diffusion coefficients in different zones of the implanted material can be more accurately calculated. A table of effective diffusion coefficients can be compiled for different implant and anneal conditions once enough experimental data are available. They shall have some predictive value for profile analysis. This model accepts any profiles as initial condition, and is thus very suitable for those ion implantations when the initial profiles are non-Gaussian and cannot be defined by analytical forms.

Acknowledgments

This work was supported by the Air Force Office of Scientific Research under contract No. AFOSR-82-0161. The authors would like to thank Dr. Y. S. Park at Air Force Wright Aeronautical Laboratories for providing some of the SIMS data used in this research.

Manuscript submitted July 23, 1982; revised manuscript received April 4, 1983. This was Paper 330 presented at the Denver, Colorado, Meeting of the Society, Oct. 11-16, 1981.

Any discussion of this paper will appear in a Discussion Section to be published in the June 1984 JOURNAL. All discussions for the June 1984 Discussion Section should be submitted by Feb. 1, 1984.

The University of Notre Dame assisted in meeting the publication costs of this article.

REFERENCES

1. J. Lindhard, M. Scharff, and H. E. Schiott, *Matt. Fys. Medd.*, **33**, 39 (1963).
2. J. F. Gibbons and S. Mylroie, *Appl. Phys. Lett.*, **22**, 568 (1973).
3. W. K. Hofker, *Phillips Res. Reports*, **8**, 41 (1975).
4. R. G. Wilson, *Radiation Effects*, **46**, 141 (1980).
5. T. E. Seidel and A. U. MacRae, *Trans. Met. Soc. AIME*, **245**, 491 (1969).
6. M. Fujimoto, H. Yamazaki, and T. Honda, in "Ion Implantation in Semiconductors," F. Chernow, J. A. Borders, and D. K. Brice, Editors, p. 89, Plenum Press, New York (1977).
7. J. F. Gibbons, *Proc. IEEE*, **60**, 1062 (1972).
8. C. P. Lee, R. Zucca, and B. M. Welch, *Appl. Phys. Lett.*, **37**, 311 (1980).
9. Y. K. Yeo, Y. S. Park, and R. Kwor, *J. Appl. Phys.*, **53**, 1815 (1982).
10. C. A. Evans, Jr., C. G. Hopkins, J. C. Norberg, V. R. Deline, R. J. Blattner, R. G. Wilson, D. M. Jamba, and Y. S. Park, Paper presented at the Semi-Insulating III-V Materials Conf., Nottingham, En-

gland, April 14-16, 1980.
11. R. G. Wilson, Unpublished data.
12. L. Vescan, J. Seders, H. Krautle, W. Kutt, and H. Beneking, *Electron. Lett.*, **18**, 533 (1982).
13. A. R. Mitchell and D. F. Griffiths, in "The Finite Difference Method in Partial Differential Equation," John Wiley and Sons, New York (1980).
14. S. G. Liu, E. C. Douglas, C. P. Wu, C. W. Magee, S. Y. Narayan, S. T. Jolly, F. Kolondra, and S. Jain, *RCA Rev.*, **41**, 227 (1980).
15. H. Matino, *Solid-State Electron.*, **17**, 35 (1974).
16. R. G. Frieser, *This Journal*, **112**, 697 (1965).

Influence of Carbon Addition on the Electrical and Structural Properties of Phosphorus and Boron Doped Silicon Layers

W. A. P. Claassen, J. Bloem,* and F. H. P. M. Habraken[1]

Philips Research Laboratories, 5600 JA Eindhoven, The Netherlands

ABSTRACT

Phosphorus and boron doped polycrystalline silicon layers grown by chemical vapor deposition were additionally doped with carbon via the introduction of C_2H_2 in the gas phase. Addition of carbon to n-type and p-type polycrystalline silicon gives rise to characteristic differences in resistivity *vs.* $P_{C_2H_2}$ input pressures, at least at small input pressures of C_2H_2. The difference in resistivity can be explained by a donor activity of carbon or silicon-carbon complexes or by an asymmetrical energy distribution of grain boundary traps, both at the grain boundaries. It is also shown that the addition of carbon has a strong influence on the morphology of the growing silicon layer. With increasing values of $P_{C_2H_2}$, the size of the grains in the layer decreases, under certain circumstances even amorphous silicon is formed, and this effect is stronger at the lowest temperatures. The decomposition kinetics of C_2H_2 has also been discussed. It is concluded that at high input pressures of C_2H_2 the deposition rate of carbon is gas phase diffusion controlled. At lower $P_{C_2H_2}$ values and temperatures above 850°C, the formation of Si-C nuclei is rate-limiting as far as the introduction of carbon is concerned.

Polycrystalline silicon layers are used extensively for the fabrication of integrated circuits (1), *e.g.*, gate material in MOS field effect transistors and lateral diodes (2). The electrical properties of chemically deposited polycrystalline silicon layers strongly depend on the size of the polysilicon grains in the layers (3). Due to the presence of grain boundaries, there is a large difference in the resistivity-dope characteristics between polycrystalline silicon and monocrystalline silicon. The impurity segregation model (4), the carrier trapping model (5), or a combined mechanism of dopant segregation, carrier trapping, and carrier tunneling through grain boundaries (6) are proposed to explain the electrical properties of polycrystalline silicon. The grain size of the polycrystalline silicon layers can be influenced by the addition of small concentrations of impurities like carbon or oxygen. In this way, the electrical behavior of the silicon layers can be changed (7).

This paper describes a study of the influence of carbon addition on the electrical properties of polycrystalline silicon for the SiH_4-H_2-B_2H_6 system and the SiH_4-H_2-PH_3 system via the introduction of C_2H_2 during the growth of the silicon layers.

Experimental

The deposition experiments were performed in a horizontal rf heated CVD reactor at atmospheric pressure by adding small concentrations of C_2H_2 and PH_3 or B_2H_6 to hydrogen loaded with silane. Experimental details have been described in an earlier paper (8), where we used the same system for studying nucleation and growth of silicon from silane. Additional information is given below. The gases PH_3, B_2H_6, SiH_4, and C_2H_2 were of electronic grade. The substrates used were silicon slices covered with an amorphous 150 nm thick LPCVD layer of Si_3N_4, while in the same run n- or p-type (2-5 Ωm), silicon slices were exposed to the reaction mixture in the reactor.

The electrical properties of the grown layers were determined by resistivity (four-point) and Hall effect measurements. As it is possible to deposit monocrystalline silicon on monocrystalline silicon wafers at 1000°C, Irvin's curves (9) can be used to estimate the dopant concentration in the epitaxial film. According to Monkowski *et al.* (10), the dopant concentration of polycrystalline silicon and similarly grown monocrystalline silicon films are equal at a deposition temperature of 1225°C. Although there could be some dopant segregation at the grain boundaries, we assume that at a deposition temperature of 1000°C, the dopant concentration of the films deposited on Si_3N_4 are in a first approximation equal to the dopant concentrations in the epitaxial films (other things being equal).

The layer morphology was studied via transmission electron microscopy (TEM) and the presence of carbon and silicon carbide was detected by infrared absorption spectroscopy. The carbon content of the layers was measured by AES spectrometry, after removal of several surface layers by Ar^+ bombardment. The hydrogen content in the layer was measured with a katharometer while heating the wafer at 1150°C. Thickness measurements were performed in the middle of the wafer by infrared and Talystep measurements.

Experimental Results

Chemical and structural analysis.—The carbon concentration in the silicon layers was determined by means of Auger electron spectroscopy using the AES sensitivity factors of Ref. (11). Figures 1 and 2 give the amount of carbon in the films as a function of the C_2H_2 pressure and the substrate temperature. The carbon concentration varies between 0 and 12 atomic percent (a/o) in the temperature and C_2H_2-pressure range under investigation. In Fig. 1, it is shown that at 700°C the carbon concentration increases linearly with the C_2H_2-pressure, both for H_2 and a 96% N_2/4% H_2 gas mixture as carrier gas. At 1000° and 1080°C, the carbon concentration is lower than at 700°C and increases more than linearly with the C_2H_2 pressure, while at 850°C an intermediate curve is observed (Fig. 2). The value of the PH_3 partial pressure and the substrate used [Si_3N_4 or Si(111)] have no influence on the amount of carbon incorporated. However, at C_2H_2 pressures less than 3×10^{-5} bar boron doped layers were found to contain a slightly larger amount of

* Electrochemical Society Active Member.
[1] Present address: University of Utrecht, Utrecht, The Netherlands.
Key words: polycrystalline, amorphous monocrystalline, silicon.

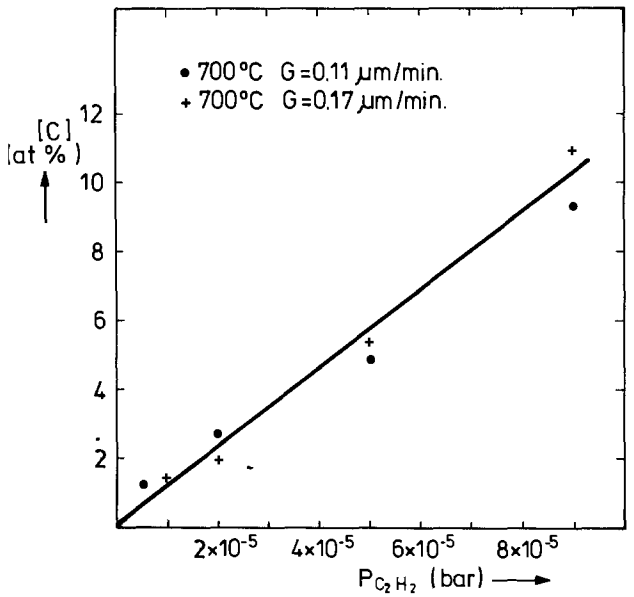

Fig. 1. Carbon content of silicon layers deposited at 700°C as a function of the C_2H_2 partial pressure (+0.2 v/o SiH_4 in a 96% N_2-4% H_2 gas mixture, ● 0.4% v/o SiH_4 in H_2).

carbon. The deposition rate of silicon was found to be independent of the C_2H_2, PH_3, and B_2H_6 input concentrations in the experimental regime under discussion. Infrared transmission spectra of the layers grown at temperatures below 850°C show a broad absorption band with a maximum at 740 cm^{-1} indicative of the formation of Si-C bonds (12). At temperatures above 850°C and at C_2H_2 pressures larger than 3×10^{-5} bar, the band shifts to shorter wavelengths; the maximum is found at 800 cm^{-1}, which value is characteristic for crystalline silicon-carbide (SiC) (12). According to TEM data of Hendriks *et al.* (13), precipitation of β-SiC particles at the grain boundaries was found at $P_{C_2H_2}$ pressures higher than 3×10^{-5} bar. The SiC band is not observed at C_2H_2 pressures below 3×10^{-5} bar at any temperature. The film also contains hydrogen. Its concentration was determined by heating the wafers at 1150°C and measuring the amount of hydrogen given off to the gas phase. The hydrogen

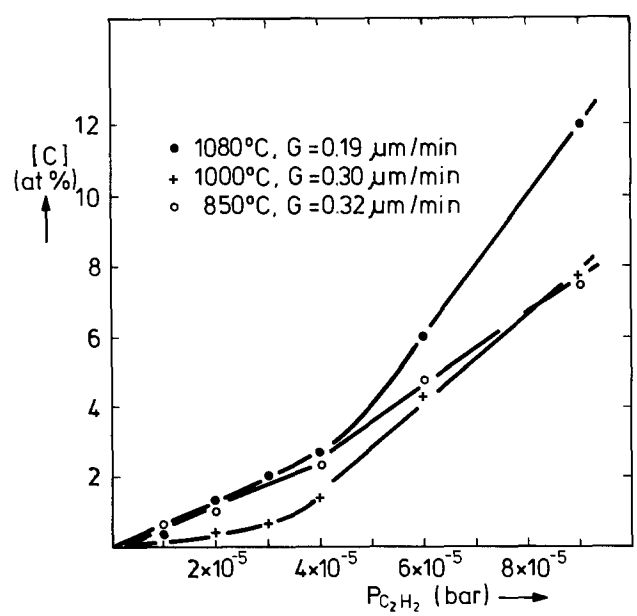

Fig. 2. The amount of incorporated carbon as a function of $P_{C_2H_2}$ for CVD silicon layers deposited at 850°, 1000°, and 1080°C (○ 0.2 v/o SiH_4 in H_2, + 0.1 v/o SiH_4 in H_2, ● 0.05 v/o SiH_4 in H_2.)

Table I. Hydrogen and carbon concentrations for layers deposited at 700°, 850°, 1000°, and 1080°C (deposition rates are given in Fig. 1 and 2)

Deposition temperatures (°C)	$P_{C_2H_2}$ (bar)	P_{dope} (bar)	[H] (at/cm³)	[C] (at/cm³)
700°C	9×10^{-5}	1.9×10^{-7} (PH_3)	4×10^{21}	5×10^{21}
850°C	9×10^{-5}	8.4×10^{-9} (PH_3)	2.4×10^{21}	3.5×10^{21}
1000°C	6×10^{-5}	1.9×19^{-8} (PH_3)	1.3×10^{21}	3.5×10^{21}
1000°C	6×10^{-5}	1.2×10^{-8} (B_2H_6)	1.9×10^{21}	4.5×10^{21}
1000°C	9×10^{-5}	1.9×10^{-7} (PH_3)	1.2×10^{21}	3.5×10^{21}
1000°C	9×10^{-5}	1.9×10^{-8} (PH_3)	1.5×10^{21}	3.5×10^{21}
1000°C	9×10^{-5}	1.2×10^{-8} (B_2H_6)	3.2×10^{21}	4.5×10^{21}
1080°C	9×10^{-5}	1.7×10^{-9} (PH_3)	2.5×10^{21}	6×10^{21}

concentrations are given in Table I. It appears that the hydrogen content decreases with increasing deposition temperature and is nearly independent of the PH_3 input pressure.

The boron doped layers appear to contain somewhat more hydrogen. The grain size as a function of C_2H_2 pressure was studied by means of TEM for the samples deposited at 850°C. Up to C_2H_2 pressures of 2×10^{-5} bar, the average grain diameter is almost constant and amounts to approximately 0.1 μm. At C_2H_2 pressures above 2×10^{-5} bar, the grain size becomes smaller and the material is amorphous at high C_2H_2 pressures as detected by x-ray diffraction.

From x-ray diffraction line broadening measurements and analysis of layers deposited at 900° and 1000°C, Hendriks *et al.* (13) also found the same tendency with respect to the grain size. Furthermore, they deduced that the microstrain in the layers becomes larger as a result of the introduction of carbon.

In Fig. 3, SEM photomicrographs are given of an SiO_2 substrate, with silicon clusters (8) obtained in the early stage of growth in a SiH_4-H_2-HCl gas mixture at 1000°C with and without addition of C_2H_2. In these experiments, HCl is added in order to reduce the supersaturation in the gas phase, and it appears from TEM analysis that all silicon clusters are monocrystal-

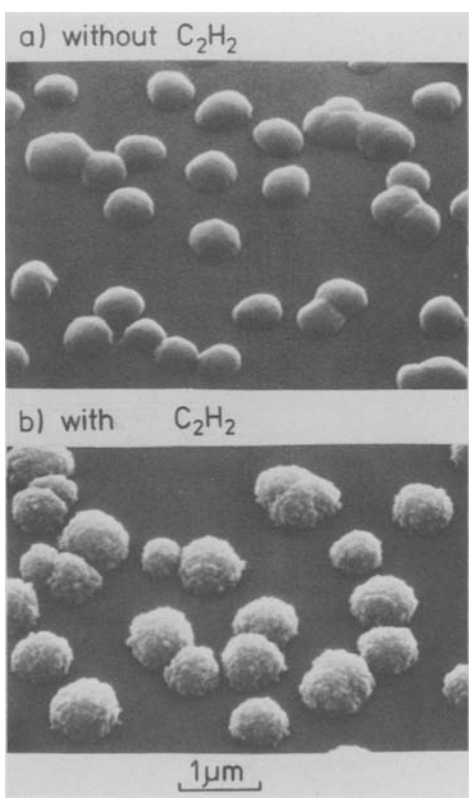

Fig. 3. SEM pictures of the Si nucleus density at 1000°C on an SiO_2 substrate for $P_{SiH_4} = 10^{-3}$ bar and $P_{HCl} = 4 \times 10^{-3}$ bar (a) without C_2H_2 addition, (b) with $P_{C_2H_2} = 6 \times 10^{-5}$ bar.

line. Introduction of C_2H_2 in the system has no influence on the number density of silicon clusters as can be seen on the SEM picture (Fig. 3); however, the clusters are no longer monocrystalline as found from TEM analysis.

Electrical results.—Figures 4, 5, and 6 give plots of the room temperature resistivity of the silicon layers, measured in the dark as a function of the C_2H_2 input pressure. The silicon films were deposited at 700° (Fig. 4), 850° (Fig. 5), and 1000°C (Fig. 6), while varying the PH_3 pressure, and hence the phosphorus-dopant concentration. The figures also give the activation energy for the resistivity ($E\rho$) in the temperature region 20°-70°C.

In the resistivity values of the samples deposited at 850°C, three regions can be distinguished, as schematically shown in Fig. 7. In region I, the resistivity of the layer decreases with increasing C_2H_2 input pressure notably at the lowest PH_3 concentrations. In region II, the resistivity increases while in region III the resistivity is seen to decrease again with increasing C_2H_2 values. Comparison of Fig. 4, 5, and 6 shows that at a growth temperature of 700°C region I and at 1000°C region III is absent. The minimum in the resistivity, observed in the 850° and 1000°C experiments, tends to shift to lower C_2H_2 pressures, when the dopant concentration is increased. At all temperatures considered, the resistivity tends to become independent of the PH_3 input pressure at high C_2H_2 input concentrations. For the activation energy of resistivity a qualitatively similar behavior is measured.

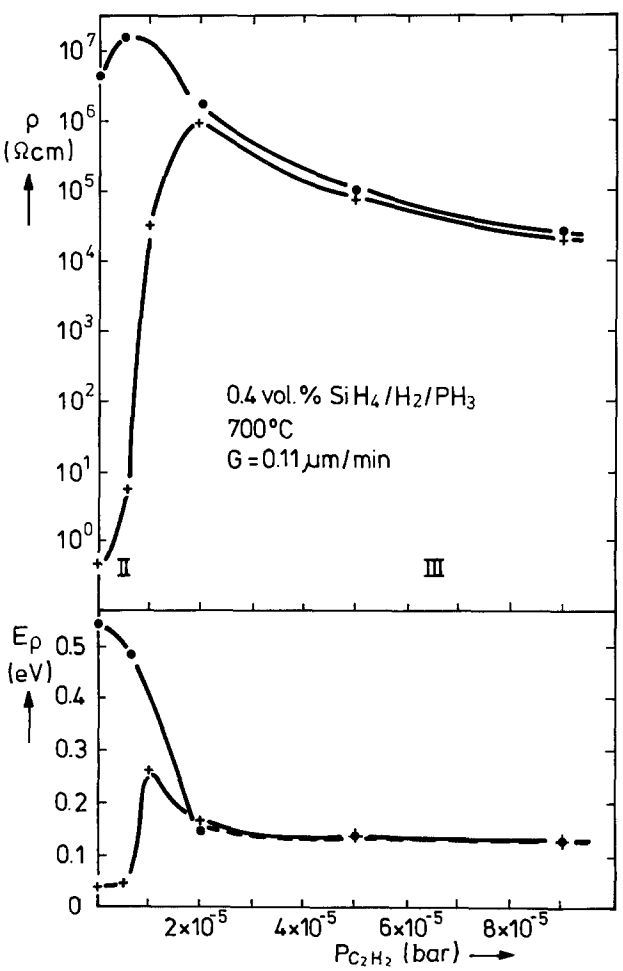

Fig. 4. Resistivity (ρ) and temperature dependence of the resistivity $E\rho$ (between 20° and 70°C) as a function of $P_{C_2H_2}$ for layers deposited at 700°C. (● $P_{PH_3} = 1.7 \times 10^{-9}$ bar, + $P_{PH_3} = 1.9 \times 10^{-7}$ bar.)

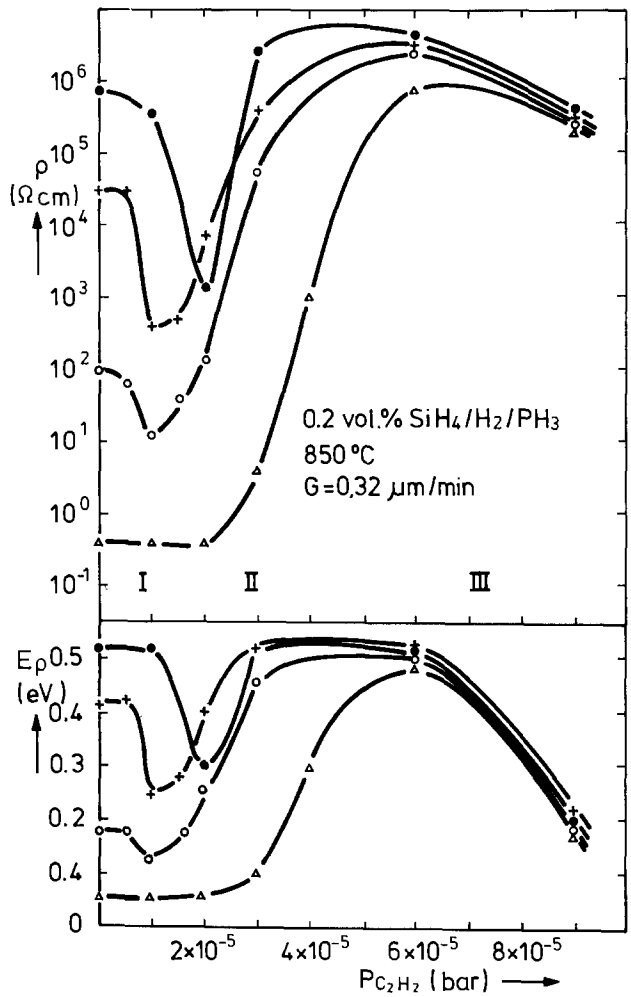

Fig. 5. ρ and $E\rho$ measurements as a function of the C_2H_2 input pressure for layers deposited at 850°C. (● $P_{PH_3} = 1.7 \times 10^{-9}$ bar, + $P_{PH_3} = 8.4 \times 10^{-9}$ bar, ○ $P_{PH_3} = 1.9 \times 10^{-8}$ bar, △ $P_{PH_3} = 1.9 \times 10^{-7}$ bar.)

In order to compare the n-type silicon films with p-type silicon layers, a series of deposits were made at 1000°C, by adding B_2H_6 to the SiH_4-H_2-C_2H_2 gas mixtures. Figure 8 shows the resistivity of these films and the activation energy for the resistivity ($E\rho$) as a function of the C_2H_2 input pressure with the diborane pressure as parameter. Contrary to the n-type films, the resistivity of the B-doped layers goes through a maximum at the lower C_2H_2 pressures, whereas the maximum shifts to larger $P_{C_2H_2}$ values with increasing B_2H_6 input pressure. Figure 8 also gives the resistivity and $E\rho$ of undoped silicon films. After an initial constant region ($\sim 10^6$ Ωcm), the resistivity and $E\rho$ decrease when $P_{C_2H_2} > 2 \times 10^{-5}$ bar. Simultaneously with the deposition on Si_3N_4, monocrystalline silicon substrates were covered at 1000°C with carbon containing deposits in the same run. The resistivity of these films as a function of $P_{C_2H_2}$ is shown in Fig. 9, with the PH_3 and B_2H_6 partial pressures as parameter. At small input pressures of C_2H_2, the resistivity of the n- and p-doped silicon layers remains almost constant although the layers contain a large amount of carbon (Fig. 2) which greatly exceeds the solubility of carbon in silicon. At higher C_2H_2 input pressures, the resistivity increases due to the fact that the deposited layer becomes polycrystalline. It also appears that the beginning of the increase of resistivity depends on the doping level, and shifts to smaller $P_{C_2H_2}$ values at lower dopant input pressures.

Figure 10 gives the results of Hall measurements, showing the mobility (μ) and the free carrier con-

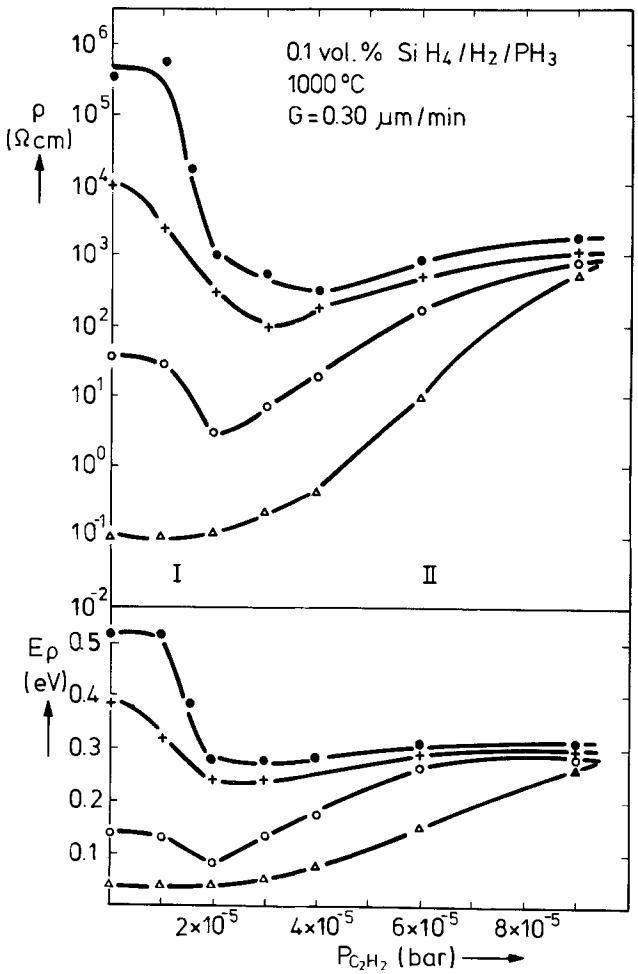

Fig. 6. As Fig. 4, with a deposition temperature of 1000°C

centration (n) at 20°C as a function of $P_{C_2H_2}$ for heavily doped n-type and p-type layers ($PH_3 = 1.9 \times 10^{-7}$ bar, $P_{B_2H_6} = 1.1 \times 10^{-7}$ bar). The corresponding resistivity of these layers is given in Fig. 6 and 8. It can be observed that the free carrier concentration (n) is almost constant up to $P_{C_2H_2} = 2 \times 10^{-5}$ bar followed by a strong decrease in the concentration of free carrier at higher $P_{C_2H_2}$ values, notably in boron doped silicon layers. It can also be observed that the mobility

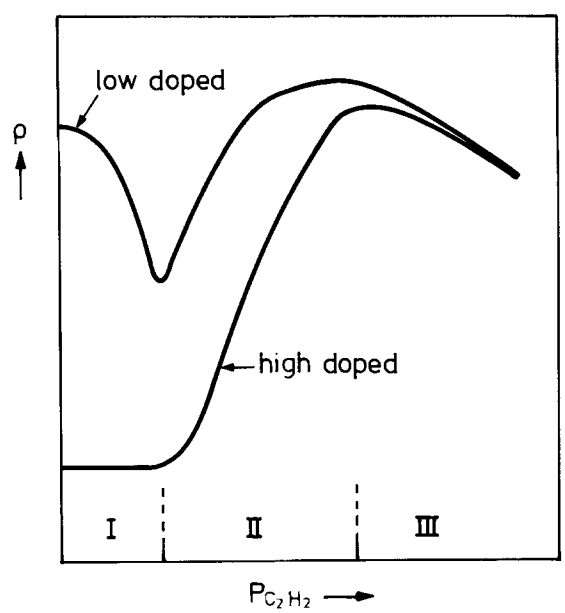

Fig. 7. A schematic picture of ρ vs. $P_{C_2H_2}$

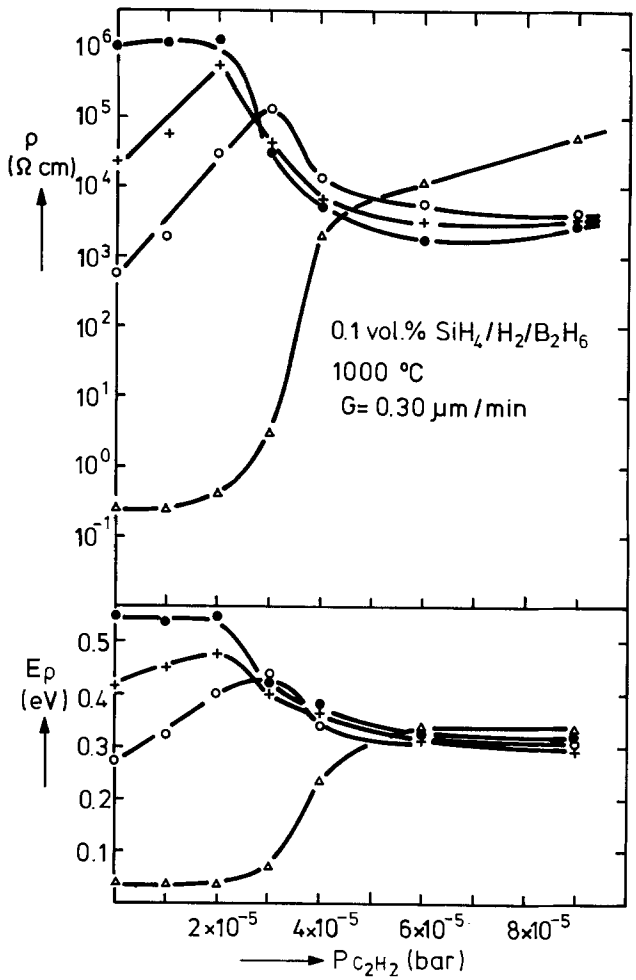

Fig. 8. ρ and $E\rho$ vs. $P_{C_2H_2}$ measurements for boron doped silicon deposited at 1000°C (● undoped. + $P_{B_2H_6} = 1.1 \times 10^{-9}$ bar, ○ $P_{B_2H_6} = 1.2 \times 10^{-8}$ bar, △ $P_{B_2H_6} = 1.1 \times 10^{-7}$ bar).

of free carriers (μ) is hampered with increasing $P_{C_2H_2}$ values.

Discussion

First we want to spend a few words on the kinetics of the carbon incorporate. To be able to make a better comparison of the rate of carbon incorporate at different temperatures and silicon growth rates, we have calculated the carbon deposition rate (atoms/cm² min) (Table II). This table also gives experimental data of Booth *et al.* (14). According to Table II, the carbon deposition rate depends slightly on temperature; at the same time as much as 10% of the C_2H_2 input contributes to the carbon incorporate.

These data point to a gas phase diffusion controlled kinetics. Calculation shows that if the carbon deposition rate is gas phase diffusion controlled the deposition rate at 1080°C is about 1.8 times higher than at 630°C using a diffusion coefficient which is proportional to $T^{3/2}$. According to Table II, this is the right order of magnitude, at least at $P_{C_2H_2} = 9 \times 10^{-5}$ bar. However, not all experimental data can be explained by a gas phase controlled deposition rate of carbon. In order to understand this, Tables I and II can be used together with Fig. 1 and 2.

At temperatures above 850°C, the shape of the curves is characteristic of a nucleation and growth mechanism; a more than linear increase in the rate of carbon uptake is observed around $P_{C_2H_2}$ 4 $\times 10^{-5}$ bar (Fig. 2). Acording to the JANAF tables (15), the growth of silicon carbide is thermodynamically feasible under all growth conditions of this study. Whether it really occurs is of course a matter of kinetics, which includes the breaking of C—H and C≡C bonds. As dis-

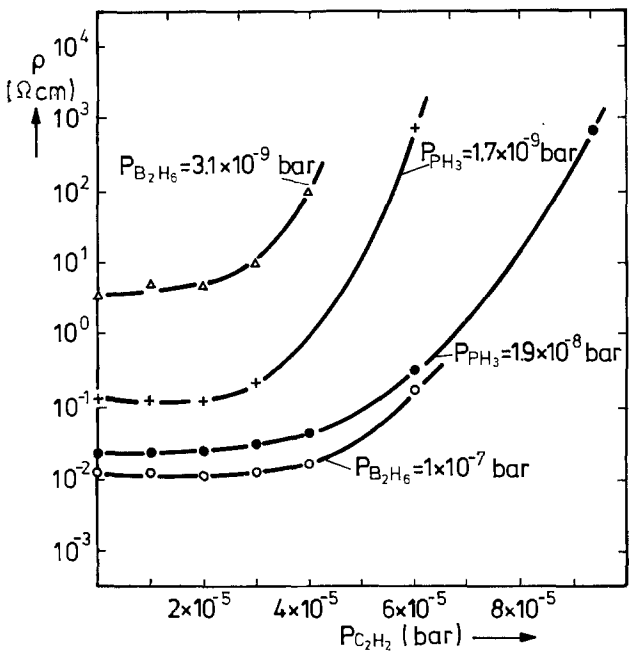

Fig. 9. ρ as a function of $P_{C_2H_2}$ for silicon layers deposited on monocrystalline silicon at 1000°C. (Substrate 2-5 Ωcm p-doped for n-doped layers and 2-5 Ωcm n-doped for p-doped layers.)

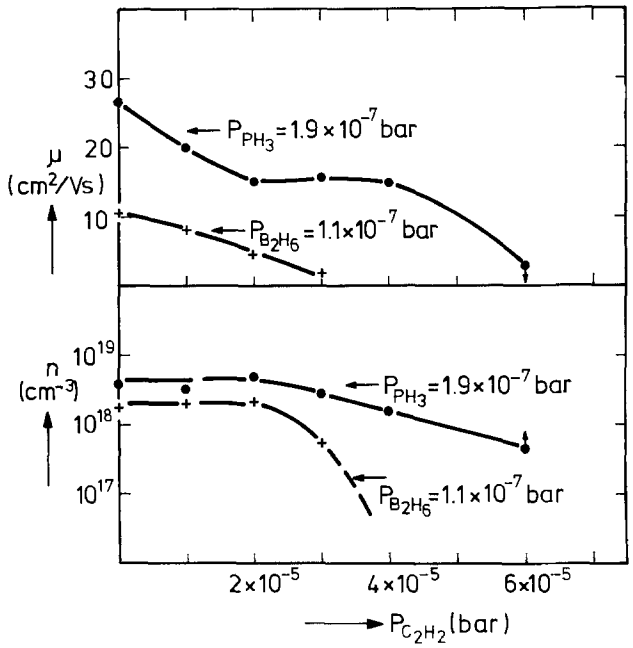

Fig. 10. Hall measurements for layer deposited at 1000°C. (↕ is the detection limit.)

cussed before, infrared spectra reveal bands that are characteristic of silicon carbide at temperatures higher than 850°C and for C_2H_2 pressures above 3×10^{-5} bar. Therefore, we suggest the following model. For $T \geq$ 850°C and low input pressures of C_2H_2, the reaction step that determines the carbon concentration has to be found in a surface-controlled process. In such a process adsorption, decomposition of C_2H_2, surface diffusion, and deposition of C_2H_2, surface diffusion and deposition of carbon (formation of Si—C bonds) has to be taken into account. According to Chung *et al.* (16), who studied adsorption of C_2H_2 on Si(111), C_2H_2 desorbs easily at temperatures above 700°C indicating that the rate-limiting step is not likely to be in the adsorption of C_2H_2. It should be noted that, as the silicon layer is growing, adsorbed C_2H_2 molecules can be buried before desorption or decomposition which would explain the large uptake rate of carbon and hydrogen (Tables I and II). At $P_{C_2H_2} > 3 \times 10^{-5}$ bar, SiC nuclei are formed, which have a higher reactivity for the decomposition of C_2H_2 leading to a second phase of silicon carbide. As discussed before, TEM analysis of Hendriks *et al.* (13) reveals the presence of βSiC precipitates at the grain boundaries at C_2H_2 input pressures above 3×10^{-5} bar. At still higher uptake rates, the uptake rate of carbon can be expected to become gas-phase diffusion controlled (Table II). According to Table I, the silicon layers doped with carbon contain a large amount of hydrogen notably at the lowest temperatures. The hydrogen is assumed to be present in C—H bonds, because Si—H bonds decompose around 550°C (17). At 700°C (Fig. 1), the decomposition of C_2H_2 does not proceed fast enough for the formation of carbide islands, as discussed before, while at the same time the carbon deposition rate is proportional to $P_{C_2H_2}$. As desorption of C_2H_2 becomes less important with decreasing temperatures and due to the high growth rate of silicon, Si—H—C complexes (Table I) are incorporated in the film at a rate which is determined by gas phase diffusion of C_2H_2 towards the growing film.

Discussion of the Electrical Data

It is commonly accepted now that the conductivity in polysilicon is determined by trapping of carriers in grain boundary traps (18) and also in the case of doping with phosphorus and arsenic, by segregation of these dopants at lower temperatures to the grain boundaries, where they are electrically inactive (19). We shall assume that the models also hold for the carbon-containing film and furthermore that the grain boundary segregation of phosphorus is not influenced by the uptake of carbonaceous species. Firstly we shall consider the region where little reduction in grain size occurs (roughly speaking at $P_{C_2H_2} \leq 2 \times 10^{-5}$ bar at temperatures $\geq$ 850°C). Secondly we shall treat the region where a strong reduction in grain size is found ($P_{C_2H_2} > 2 \times 10^{-5}$ bar at 850°C) and at all $P_{C_2H_2}$ values at 700°C.

Low carbon contents.—The curves, representing the resistivity of the polysilicon films, and its temperature dependence, as a function of the C_2H_2 input pressure at $T \geq$ 850°C, show a minimum in the phosphorus-doped film and a maximum in the boron-doped films. This minimum and maximum is most pronounced in the lower dope regions (Fig. 5, 6, and 8). With

Table II. The deposition rate of carbon atoms (cm^{-2} min^{-1}) at different temperatures and C_2H_2 input pressures

Temperature Carrier gas	1080°C H_2	1000°C H_2	850°C H_2	700°C H_2	700°C 4% H_2 in N_2	700°C He*	630°C He*
Deposition rate (Si) μm/min	0.1g	0.30	0.32	0.11	0.17	0.13	0.09
$P_{C_2H_2} = 2 \times 10^{-5}$ bar	1.3×10^{16}	0.6×10^{16}	1.6×10^{16}	1.5×10^{16}	1.3×10^{16}	—	2×10^{16}
$P_{C_2H_2} = 5 \times 10^{-5}$ bar	3.8×10^{16}	4.2×10^{16}	5.2×10^{16}	3.2×10^{16}	4.5×10^{16}	—	4×10^{16}
$P_{C_2H_2} = 9 \times 10^{-5}$ bar	11.4×10^{16}	11.5×10^{16}	12.0×10^{16}	5.3×10^{16}	8.3×10^{16}	5×10^{16}	6×10^{16}

* Experimental data of Booth *et al.* (14).

larger phosphorus doped concentration, the minimum shifts to lower C_2H_2 input pressures, *i.e.*, to lower [C] contents in the film, while the maximum in the boron doped layers shows an opposite behavior. The undoped film (Fig. 8) shows a resistivity which is almost constant up to $P_{C_2H_2} = 2 \times 10^{-5}$ bar, followed by a decrease in resistivity at higher P values of $P_{C_2H_2}$.

A simple explanation for these phenomena can be found in donor activities of carbon or with an asymmetrical energy distribution of grain boundary traps around midgap. According to de Graaff *et al.* (2), the energy distribution of grain boundary traps in polycrystalline silicon is symmetrical (U-shaped) around midgap. de Graaff *et al.* calculated this U-shaped trap energy distribution from the shape of the curve of the barrier height (E°) *vs.* the donor concentration. (E° is the barrier height at $T = 0$ K.) In Fig. 11, we have plotted E values ($E \approx E^\circ$) as a function of acceptor (boron) and donor (phosphorus) concentration using E values as given in Fig. 6 and 8 (without C_2H_2 addition and with $P_{C_2H_2} = 2 \times 10^{-5}$ bar). It can be observed that for n-type silicon, the E values for carbon doped silicon are smaller than the E values without carbon addition, while for p-type doped silicon the opposite is the case. It can therefore be concluded that, if the trap energy distribution function of polysilicon layers without carbon doping is U-shaped, the trap energy density of the carbon doped silicon layers is asymmetrical around midgap. This leads to an increase in the free carrier concentration as the capturing of electrons is hampered and consequently to a reduction in resistivity with increasing $P_{C_2H_2}$ values in the n-type regime where the grain size is constant. In p-type layers the opposite occurs leading to an increase in resistivity at low input pressures of C_2H_2.

Hall effect measurements (Fig. 10), which could only be performed on the highly doped samples, give support for this model. First, at $P_{C_2H_2} \leq 2 \times 10^{-5}$ bar, the free carrier concentration is almost constant while the activation energy for the resistivity (E_ρ) increases with carbon addition for p-type doped silicon, while for n-type doped silicon the opposite is the case (Fig. 11). Second, at $P_{C_2H_2} > 2 \times 10^{-5}$ bar, the free carrier concentration and the mobility in the boron doped layers decrease faster with increasing carbon content than in the phosphorus doped films. The mobility already shows a decrease at low carbon content in both n-type and p-type films which indicates that some reduction in grain size already occurs in that region. Films grown on monocrystalline substrates (Fig. 9) exhibit little or no change in resistivity upon the introduction of C_2H_2 in the reactor with $P_{C_2H_2} \leq 3 \times 10^{-5}$ bar. This indicates that the suggested asymmetric energy distribution of grain boundary traps is restricted to the carbon atoms present at grain boundaries.

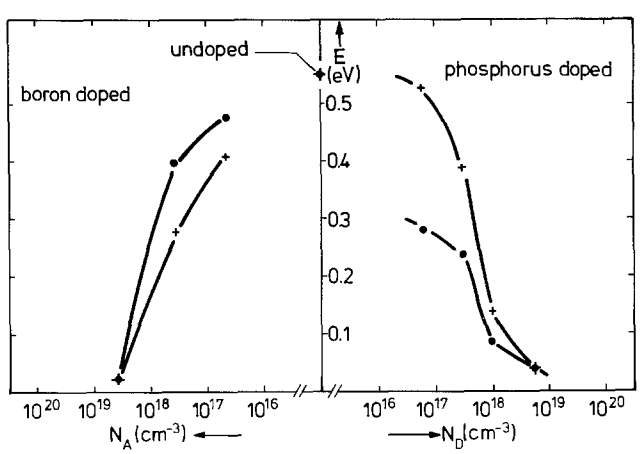

Fig. 11. The temperature dependence of the resistivity *vs.* the donor and acceptor concentration (+ without C_2H_2 addition, ● $P_{C_2H_2} = 2 \times 10^{-5}$ bar).

The minimum in the resistivity observed in the phosphorus doped films at $T \geq 850$°C and at low carbon contents is not observed at the growth temperature of 700°C. This is because the slightest C_2H_2 concentration in the gas phase is already sufficient to give nearly amorphous growth at this temperature.

High carbon contents.—At the onset of this region ($P_{C_2H_2} > 2 \times 10^{-5}$ bar at $T \geq 850$°C), the resistivity and its temperature dependence of the phosphorus doped layers grown both at 850° and 1000°C increases with increasing $P_{C_2H_2}$ pressures (Fig. 5 and 6). The resistivity of the highly doped boron films and its temperature dependence increases also, but in the low doped boron films the resistivity decreases (Fig. 8). The resistivity of the samples on monocrystalline substrates (Fig. 9) also increases. This increase is ascribed to a strong reduction of the grain size as is deduced from TEM and x-ray data (the "epitaxial" films become polycrystalline).

At the highest carbon uptake, the resistivity is independent of the dopant concentration as is expected for amorphous material. At $P_{C_2H_2} = 9 \times 10^{-5}$ bar, the resistivity of the films grown at 1000°C is smaller than at 850°C, whereas the carbon concentration is about equal. At that point, the grain size is smaller at 850°C than at 1000°C according to the x-ray data of Hendriks *et al.* (13). At 850°C, the resistivity decreases for $P_{C_2H_2}$ above 6×10^{-5} bar, whereas the resistivity becomes only weakly dependent on temperature. At 700°C, the same effect is observed at $P_{C_2H_2} = 2 \times 10^{-5}$ bar. This indicates that another type of conduction is operating in that region, which may be due to a parallel conduction path via precipitated carbon or silicon carbide.

Conclusions

The results of a study on the influence of the addition of carbon via C_2H_2 on the electrical properties of silicon layers doped with phosphorus and boron show that addition of carbon to n-type and p-type silicon layers gives rise to different characteristics of resistivity *vs.* $P_{C_2H_2}$. The curves representing resistivity as a function of $P_{C_2H_2}$ show a minimum for n-type layers, which minimum shifts to lower C_2H_2 input pressures with larger phosphorus doped concentrations. On the other hand, the p-type films show a maximum in the resistivity *vs.* $P_{C_2H_2}$ curve, a maximum which shifts to larger $P_{C_2H_2}$ values with larger boron concentrations in the gas phase. A model is postulated in which the differences in the resistivity *vs.* $P_{C_2H_2}$ curves between n- and p-type doped layers can be explained by donor activities of carbon or by an asymmetrical energy distribution of the grain boundary traps.

A parallel study of the influence of carbon addition on the morphology of the silicon films and the decomposition kinetics of carbon shows that at temperatures above 850°C the addition of small amounts of carbon gives rise to only a slight reduction in grain size, while at higher input pressures of C_2H_2, the grain size is strongly reduced and even amorphous layers can be formed. At 700°C, amorphous silicon layers can already be formed when small amounts of C_2H_2 are added to the gas phase.

It is concluded that at low input pressures of C_2H_2 and at temperatures above 850°C, the rate of incorporation of carbon is surface-controlled. In this regime, the formation of SiC nuclei is rate-limiting. At higher input pressures of C_2H_2, the formation of SiC nuclei is no longer rate-limiting and the carbon uptake rate is determined by gas phase diffusion of C_2H_2 towards the growing film surface. At 700°C, the incorporation of carbon is also gas phase diffusion controlled but no silicon carbide is formed. Due to the high silicon growth rate, adsorbed C—H complexes are trapped into the film, notably at the lowest temperatures.

Acknowledgments

The authors wish to thank Prof. S. Radelaar and Mr. M. Hendriks for discussions on the structure of the deposited layers and for performing x-ray diffraction line broadening measurements.

Manuscript submitted Oct. 22, 1983; revised manuscript received March 7, 1983.

Any discussion of this paper will appear in a Discussion Section to be published in the June 1984 JOURNAL. All discussions for the June 1984 Discussion Section should be submitted by Feb. 1, 1984.

Philips Research Laboratories assisted in meeting the publication costs of this article.

REFERENCES

1. T. I. Kamins, M. M. Mandurah, and K. C. Saraswat, *This Journal*, **125**, 927 (1978).
2. H. C. de Graaff and M. Huybers, *Solid-State Electron.*, **25**, 67 (1982).
3. M. W. M. Graef, Thesis, University of Nijmegen, Nijmegen, The Netherlands, (1980); J. J. Yang, W. I. Simpson, and R. P. Ruth, *J. Electron. Mater.*, **10**, 1011 (1981).
4. M. E. Cowher and T. O. Sedgwick, *This Journal*, **119**, 1565 (1972).
5. T. I. Kamins, *IEEE Trans. Parts Hybrids Packag.*, **php-10**, 221 (1974).
6. M. M. Mandurah, K. C. Saraswat, and T. I. Kamins, *IEEE Trans. Electron Devices*, **ed-28**, 1171 (1981).
7. J. Bloem and W. A. P. Claassen, *Appl. Phys. Lett.*, **40**, 725 (1982).
8. W. A. P. Claassen and J. Bloem, *This Journal*, **127**, 194 (1980).
9. J. C. Irvin, *BSTJ*, **41**, 387 (1982).
10. J. R. Monkowski, J. Bloem, L. J. Giling, and M. W. M. Graef, *Appl. Phys. Lett.*, **35**, 410 (1979).
11. L. E. Davis, N. C. MacDonald, P. W. Palmberg, G. E. Riach, and R. E. Weber, "Handbook of Auger Electron Spectroscopy," Physical Electronics, Eden Prairie, MN (1976).
12. I. P. Akimchenko, Kh. R. Kazdaev, I. A. Kamenskikh, and V. V. Krasnopevtsev, *Sov. Phys. Semicond.*, **13**, 219 (1979).
13. M. Hendriks, R. Delhez, Th. H. de Keijser, and S. Radelaar, Abstract AII7, 2nd European Conference on Solid State Chemistry, Veldhoven, Netherlands, June 6-9, 1982.
14. D. C. Booth, D. P. Allred, and B. O. Seraphin, *Sol. Energy Mater.*, **2**, 107 (1979).
15. JANAF Thermochemical Tables, 2nd ed., NSRDS-NBS-37, June 1971.
16. Y. W. Chung, W. Siekhaus, and G. A. Somorjai, *Surf. Sci.*, **58**, 341 (1976).
17. J. A. McMillan and E. M. Peterson, *J. Appl. Phys.*, **50**, 5238 (1979).
18. J. Y. W. Seto, *ibid.*, **46**, 5247 (1975).
19. M. M. Mandurah, K. C. Saraswat, C. R. Helms, and T. I. Kamins, *ibid.*, **51**, 5755 (1980).

Reactive Ion Etching of Silicon with Cl_2/Ar(1)

H. B. Pogge,* J. A. Bondur,* and P. J. Burkhardt

IBM Corporation General Technology Division, East Fishkill Facility, Hopewell Junction, New York 12533

ABSTRACT

A study of the use of reactive chlorine species for etching silicon and silicon dioxide in a plasma etching process has been made with a Cl_2-Ar gas mixture in a cathode-coupled diode system. A key advantage of the Cl_2-Ar gas mixture is the ability to achieve high etch rate ratios between silicon and silicon dioxide ($\geq$ 20:1) coupled with no mask undercutting, which tends to be prevalent with fluorinated gas systems. Etching characteristics of Si as a function of process parameters (Cl_2 concentration, pressure, system loading) and material parameters (*e.g.*, Si conductivity, edge shape of SiO_2 mask) have been evaluated. These parameters can influence the silicon etch rate, the Si/SiO_2 etch rate ratio, as well as the etched edge shape.

Much of the progress reported recently for plasma etching has related to processes which use fluorinated hydrocarbon gases, in particular CF_4, for etching semiconductor materials. The results obtained with CF_4 have been varied, and this can be attributed to differences in the techniques for generating the plasma, or in the coupling of the rf field to the wafer. For example, etching processes using high pressure CF_4 plasmas (0.2-1.0 Torr) have resulted in silicon etch rates that range from 0.05-0.6 μm/min (2). The etch rates, produced under these processing conditions, are sensitive to wafer temperature, gas flow, and pressure, as well as to the wafer load present in the system. Furthermore, the resultant etched regions are typically isotropic or nondirectional; that is, the silicon is etched laterally as well as vertically, and the final silicon pattern is, therefore, wider than the mask pattern. Isotropic etching also results in the loss of image resolution caused by a significant etch bias.

Besides high pressure CF_4 plasma etching, the gas has also been evaluated for etching silicon in the reaction ion etching (RIE) mode. Schwartz *et al.* (3) have reported on operating conditions with which they could achieve either directional or isotropic silicon etching. The change-over from one type of etching to the other was predominantly dictated by the system load; that is, as the load was increased for a fixed set of plasma conditions, the silicon etch profile became more vertical. Concurrently, this was accompanied by a decrease in the overall etch rate for the fixed set of operating conditions, although, in the case of the high pressure CF_4 plasma system, this effect was not as dominant. This reduced etch rate sensitivity could be attributable to the wafers having been placed in contact with a cooled cathode and, consequently, to a lower wafer temperature. Alternatively, it could also be due to a reduced supply of radicals when the system is fully loaded. A further demonstration, which indicates that the control of the etched geometry of a material (in this case insulators) can be impacted by the loading effect, was reported by Bondur (4) when etching with CF_4 in an RIE system and employing photoresist as a mask.

The referenced work (4) demonstrated that the photoresist etch rate was also load sensitive. Under full load conditions, the photoresist etch rate was less than that of SiO_2. Thus, it is possible to change the SiO_2 patterned image by varying the resist/SiO_2 etch rate ratio through system load variations.

In summary, the experimental data with CF_4 thus indicate that the control over image shapes and pattern

* Electrochemical Society Active Member.

resolution has been achievable only with conditions in which relatively low silicon etch rates were used; that is, rates less than 0.05 μm/min. Such low etch rates tend to be impractical for applications in which as much as 3-4 μm of silicon are to be etched, since it would imply the need for very stable mask materials that must be able to withstand long exposures to the etchant plasmas. These material choices are very limited.

An alternative gas system, which overcomes the shortcomings mentioned above, would have a significant impact on extending silicon processing techniques. This could be accompanied by the possibilities of enhanced and unique device fabrication capabilities. A Cl_2/Ar gas mixture was found to fit the basic process requirements when used in a water-cooled cathode RIE system. The results have indeed shown that in most instances deep vertical silicon trenches can be etched at high etch rates with high Si/SiO_2 etch rate ratios. Some restrictions of silicon etch rates were, however, required for highly doped silicon, in which case a greater tendency for lateral etching was observed for higher etch rates.

Experimental

The reactive ion etching was performed in a parallel plate diode system (2-4) with a water-cooled silica plate (bonded to copper cathode) on which the samples were placed. The general operating ranges were

Pressure	10-100 μm
Gas mixture	3-10% Cl_2 in argon
Gas flow (total)	10-50 cc/min
Power density	0.16 watts/cm^2
rf frequency	13.56 MHz
Cathode diameter	18 cm

The silicon wafers were of <100> orientation, normally p-type (boron ~10^{15} atoms/cm^3), and patterned with SiO_2 films. In several experiments, wafers containing heavily doped arsenic- or boron-diffused regions were used either directly or after an epitaxial n-type film (arsenic 2×10^{16} atoms/cm^3) was deposited over those regions. The SiO_2 film pattern was etched either by standard wet etching techniques or by reactive ion etching with CF_4.

The etch rates of SiO_2 were determined either *in situ* by means of a laser etch rate monitoring technique (5-6) or indirectly by differential film thickness measurements before and after the etch process .The latter measurements were made by either a step gauge or with the use of an IBM Thin Film Analyzer. The silicon etch rates were calculated by measuring groove depths via a Talystep or from optical or SEM photomicrographs of 90° cross-sections.

To assure the absence of any possible geometric distortions in the vertical and horizontal directions when measuring the silicon groove shapes, all such evaluations were made on 90° beveled cross-sections by SEM at nominally 10,000X.

Results

Our early work with Cl_2 etching resulted in inconsistent etch rate data. Certain runs exhibited very little etching, and this was usually accompanied with the etch areas being blackened. Figure 1 provides an example of such a surface. The high magnification micrograph shows a dense array of needle-like structures. This columnar material was readily removable with standard silicon wet etches. The height of the columnar silicon, or the depth of the crevices between the columnar pedestals, was inconsistent from run to run, even though the same etch times were employed.

The primary cause of the black silicon formation was found to be residual moisture in the vacuum system. The conclusion is based on two observations. Firstly, the prevalence of black silicon was greater on days of high humidity, and this tended also to be associated with more difficulties in efficient system pump-downs.

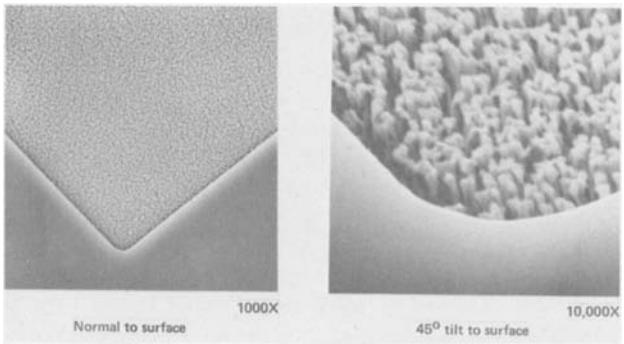

Fig. 1. RIE of silicon with Cl_2/Ar using poor etch conditions, residual system pressure $\leq 10^{-6}$ atm.

Secondly, extensive system pump-downs resulting in background pressures of 5×10^{-7} Torr (or lower), before back filling with Cl_2/Ar gas mixtures, effectively eliminated the occurrence of black silicon. The exact nature of the apparent nonuniform masking film, which permitted the columnar structure formation, has not been identified. However, we suspect it to be some form of SiO_2.

Once we recognized that good pump-down conditions influenced etch characteristics, etch repeatability was found to be very consistent. An indication of pattern replication capability with good etch conditions is shown in Fig. 2. The sample consisted of a substrate with an epitaxial layer, the latter containing epitaxial stacking faults. Stacking faults have a nominal height difference with respect to the wafer's surface of about 20 nm. As can be seen in Fig. 2, this height difference is sufficiently well retained throughout a 4 μm deep etching process to remain visible at the bottom of the groove.

Some system-to-system process sensitivity was observed, and this is given in Fig. 3. The silicon etch rate increases linearly with increasing operating pressure; one system is somewhat less sensitive to pressure changes than the other. This may be due to slight variations in gas flow for the two systems involved. In the lower etch rate region, however, the systems behave similarly, not only in terms of etch rates of silicon but also with respect to etch rate ratios between silicon and silicon dioxide. Notice should be taken of the fact that relatively high etch rate ratios can be achieved at high silicon etch rates. In several instances, we have observed ratios greater than 20:1. The etch rate for SiO_2 tends to remain relatively constant at about 5-8 nm/min for the range of etch conditions evaluated so far. In these experiments, the gas flow rate varied as pressure conditions were changed.

Figure 4 gives an example of the influence of operating pressure on pattern groove geometries. The samples were all etched with the same gas composition and for equal times; the difference in depth is, therefore, at-

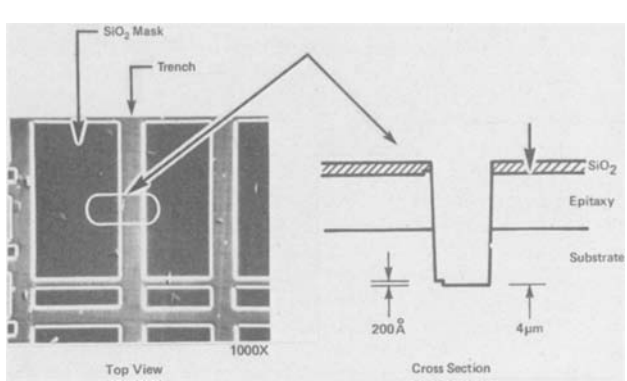

Fig. 2. RIE of silicon with Cl_2/Ar with optimum etch conditions

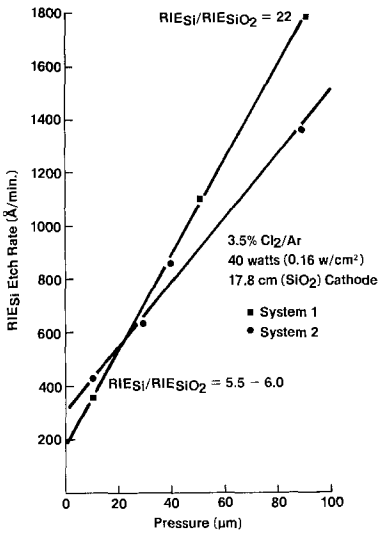

Fig. 3. Silicon etch rate changes with system pressure in two different reactors.

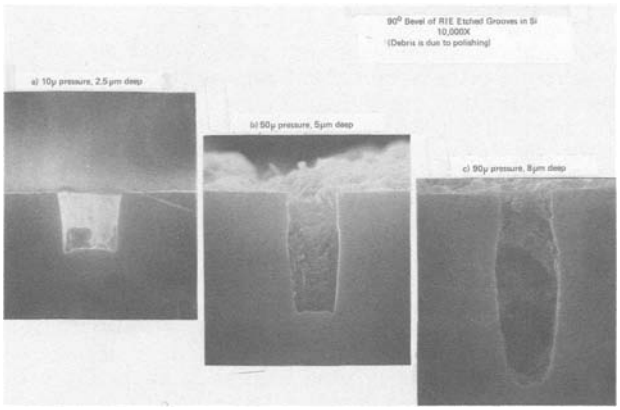

Fig. 4. Silicon groove etching into P⁻ substrates under different pressures.

tributable to etch rate changes as the system pressure was varied. As can be seen in Fig. 4, the groove geometry is also influenced by this parameter change. The tapering in the sample, etched under 10 μm pressure conditions, is partly due to the low Si/SiO_2 etch rate ratio, which causes a partial translation of the existing SiO_2 taper into the silicon groove. However, the tendency of some lateral etching in samples etched at higher pressures was more directly related to factors that are associated with accompanying higher silicon etch rates.

The lateral silicon etching can become a dominant feature for highly doped silicon. Figure 5 indicates excessive lateral etching of this type for a buried, highly doped arsenic diffused region covered with an epitaxial layer. Appropriate adjustments of etch conditions can result in very uniformly etched grooves, as shown in Fig. 6 and 7. The samples in Fig. 5 and 6 had common process history up to the silicon etching step so that all samples had the same starting SiO_2 pattern window geometry. Three of the four cross-sections in Fig. 6 have been preferentially etched with standard staining techniques to delineate the N^+ diffused region. As indicated, the taper angle varies from near vertical to about 21° away from vertical. Thus, the process flexibility available to achieve different groove geometries with the Cl_2/Ar gas system is suggested by Fig. 6, and these data are summarized in Fig. 8.

Additional process parameter data are given in Fig. 9-11. Proper use of these data allow the fabrication of predetermined silicon taper angles in the silicon groove,

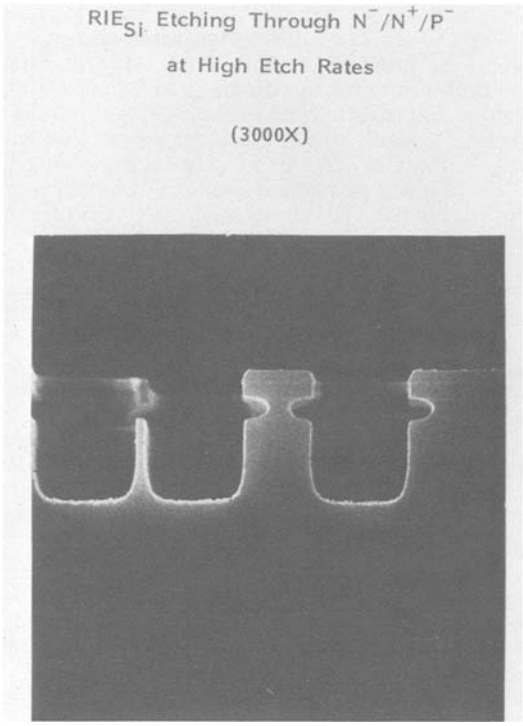

Fig. 5. Silicon underetching in N^+ diffused regions

provided the SiO_2 taper angle of the SiO_2 mask pattern is controlled.

Discussion

As indicated by the experimental results, Cl_2/Ar gas mixtures in an RIE environment can be used effectively for silicon groove pattern formation in the presence of an SiO_2 mask. Its extension for use in etching polysilicon is implied, provided appropriate etch conditions are determined to accommodate doping and crystallinity effects. Appropriate control over process parameters permits either fabrication of silicon grooves with predetermined depth and geometries or selective removal of silicon to create patterned islands, pedestals, and ridges of various shapes.

It is long known that chlorine chemisorbs onto silicon at room temperature to form stable surface structure (7). At elevated temperatures (300°C), it reacts spontaneously with silicon to form volatile species, very much in the same manner as fluorine atoms react with silicon at room temperature to form volatile species. Consequently, different etching results could very well be expected with the use of chlorine or fluorine chemistries for RIE of silicon. Furthermore, in the case

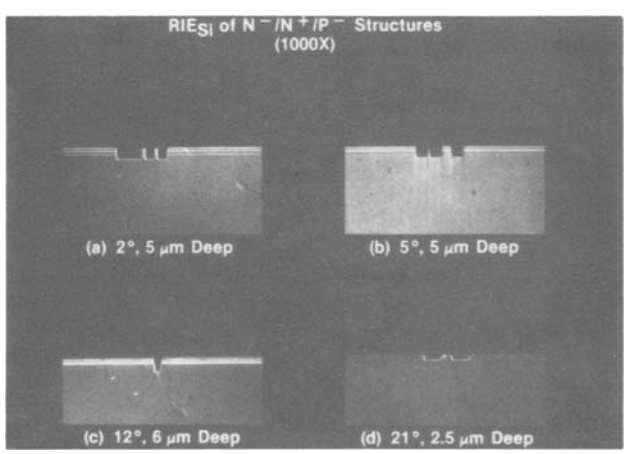

Fig. 6. Silicon groove etching of $N^-/N^+/P^-$ structures under controlled etch conditions (Mag. 1000×).

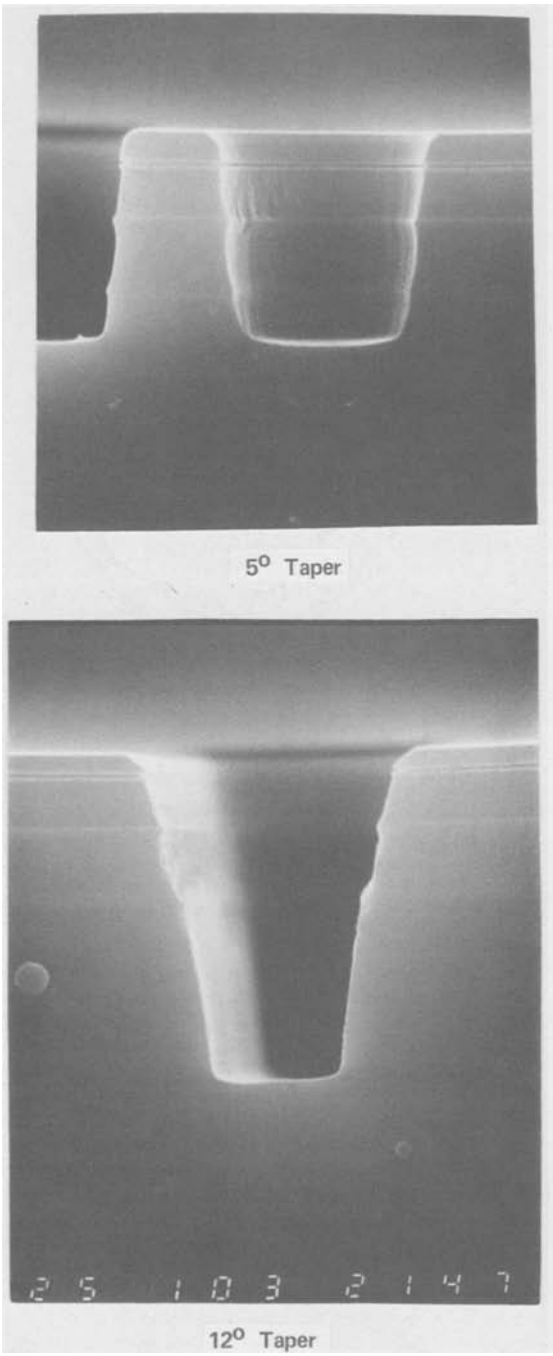

Fig. 7. Silicon groove etching of $N^-/N^+/P^-$ structures. Samples are the same as Fig. 6b and c. The scalloping is caused by the Si decorating etch for SEM delineation purposes (Mag. 10,000×).

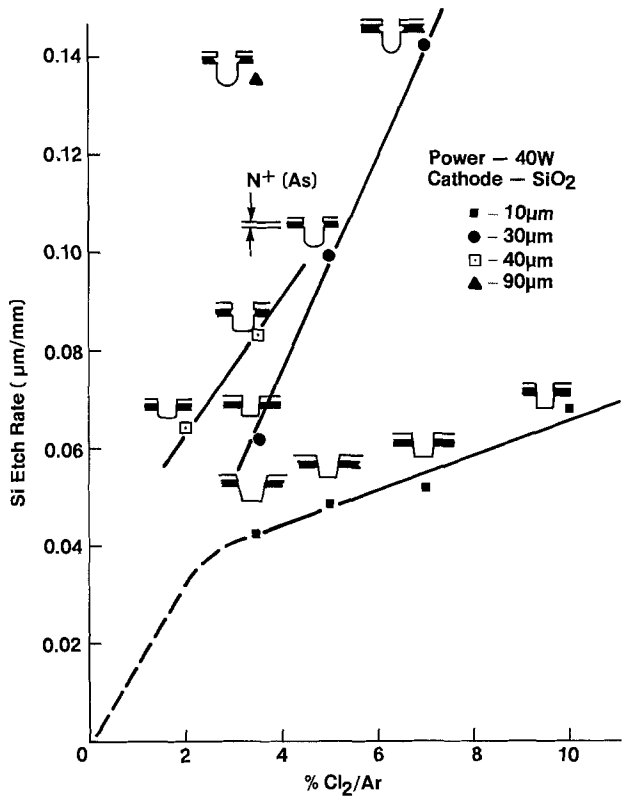

Fig. 8. Silicon etch rates and groove shape as a function of Cl_2/Ar concentration and system pressure.

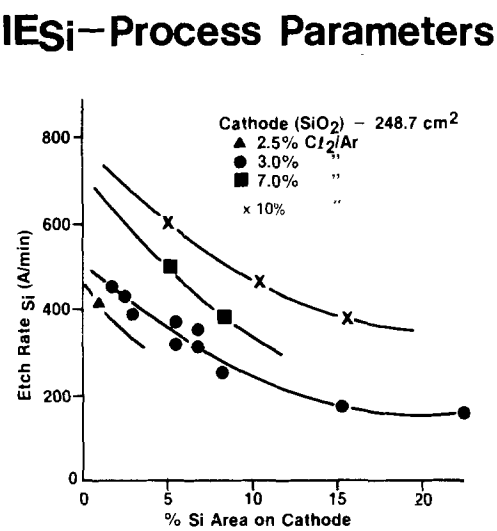

Fig. 9. Loading effect on silicon etch rates for different Cl_2/Ar concentrations.

of the chlorine species, a change in etching characteristics could be expected to result from variations in the substrate temperatures. The spontaneous reaction of the halogen with silicon and its resultant volatile species will cause isotropic etching, whereas stable surface compound formation could result in anisotropic etching.

Winters' studies (8) indeed have shown that silicon is etched by "F" radicals at room temperature in the absence of high energy radiation, thereby causing isotropic etching. In contrast to the "F" radicals, the "Cl" species was found to chemisorb onto the silicon surface rather than to react spontaneously with silicon at room temperature and cause Si etching. The strength of interaction between the chlorine species and silicon is apparently sufficient to form a chlorine-silicon complex which, with the bombardment energy supplied by the argon plasma, can be dislodged to cause silicon etching (8-10). Since the energy supplied by the RIE plasma would be imparted predominantly in a directional manner, the effective etching of silcon would only occur in the vertical direction. On the other hand, the chemisorbed "Cl" remains on the sidewalls and is unaffected by the plama, thus preventing or "protecting" the sidewalls from any significant etching.

These general effects appear to be operative in the Cl_2/Ar system. However, some qualifications must be considered to account for the significant lateral etching of samples containing highly doped diffused regions. The data in Fig. 8 indicate lateral etching of diffused regions occurs when the etch rates of silicon exceed the 0.06 μm/min. The effect is sensitive to the "Cl_2" concentration in the gas plasma, as observed in Fig. 8, which indicates the relationship between the "Cl_2" partial pressure and silicon etch rates. This lateral under-etching of N^+ regions can be reduced signifi-

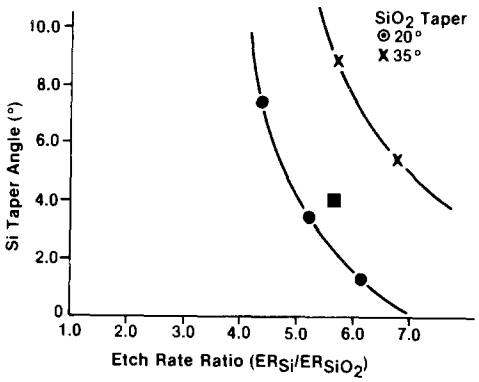

Fig. 10. Relationship between the silicon etch rate and the Si/SiO_2 etch rate ratio.

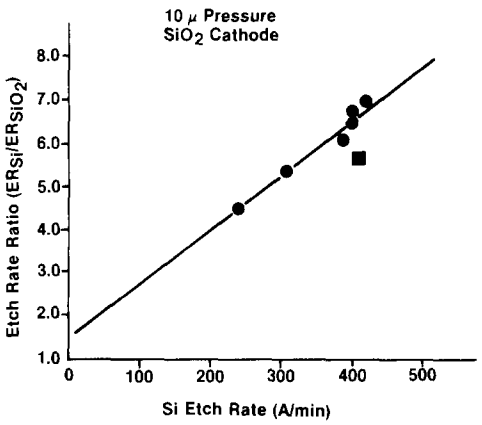

Fig. 11. Final silicon groove taper angle as a function of the Si/SiO_2 etch rate ratio.

cantly for samples being etched under high etch rate conditions, provided the etching cycle is interrupted rather than continuous. The etching interruption would allow the wafer to be cooled and thus possibly change the "Cl_2" interaction with silicon from a spontaneous reaction (causing isotropic etching) to a stable chlorine-silicon complex formation (causing vertical etching). This heating sensitivity has been further confirmed by experiments as reported by Schwartz and Schaible (11). The heating effect is also apparent in the data in Fig. 4 for sample etching at 90 μm pressure under conditions of high etch rates. The lateral etching is, however, significantly less for the p-type substrate (Fig. 4) as opposed to N^+ diffused regions (Fig. 5 and 8). Several experiments with P^+ diffused regions also exhibited strong lateral etching in those regions similar to that observed in N^+ diffused regions.

An alternative argument for the excessive lateral underetching of highly doped silicon could be based on differences in the chemical reactivities of "Cl_2" and the diffused regions as opposed to lowly doped silicon. It is known that chlorine reacts spontaneously with either arsenic and boron to form volatile species. Thus, isotropic etching of highly doped regions could be expected. However, the atomic impurity concentration levels in the diffused regions are at best ~1%, and this makes it somewhat difficult to explain, on this basis alone, the significantly higher isotropic etching of these regions.

It may turn out that actually both factors (*i.e.* thermal heating and enhanced chemical reactivities) together contribute to the lateral etching of highly doped silicon regions. For one, the thermal conductivity of highly doped n-type and p-type silicon is lower than for undoped silicon (see Fig. 12). Consequently, such regions would experience a faster heat rise during the RIE etch process than undoped silicon. This in turn would enhance the isotropic etching characteristics in the highly doped regions. The effect would be further enhanced, if one considers the real possibility that the critical temperature for the onset of isotropic etching in arsenic- and boron-rich silicon regions could well be expected at lower temperatures than for undoped silicon. This would primarily be due to the ease of volatile chlorine-arsenic (or boron) species formation at lower temperature. Although the combination of these two effects could explain the currently available experimental data, more work is required to more clearly identify and quantize the individual effects.

The other significant observation, that of black silicon, also lacks clear understandings, although this form of surface texturing has been observed and reported in the literature (12). Based on the present results, it appears that its formation may be due to the presence of a thin nonuniform oxide film in the window areas prior to the etch process. Alternatively, instead of a nonuniform film, the silicon surface in the window area may have been very preferentially oxidized to form small oxide islands. In either case, the oxide was most probably formed by the residual moisture present in the etching chamber. The presence of the moisture has been verified with the use of a residual mass analyzer. However, a particular moisture level below which the black silicon was absent was not clearly established. It was found easier and more convenient to insist that the system pressure be below 5×10^{-7} Torr before starting an etch run. This was typically achieved much faster whenever the relative humidity was low.

The presence of the nonuniform oxide film on the silicon surface would permit the formation of the columnar type growth, because of differences in etch rates between silicon and SiO_2. Furthermore, the silicon etch rate becomes enhanced in the case when a very low silicon surface area is exposed (see Fig. 9), whereas the SiO_2 etch rate remains relatively constant. The resultant high etch rate ratio will favor the columnar growth until the masking SiO_2 film has been etched away. Further etching will then recess the columnar structure below the original silicon substrate surface. This has typically been observed. The fact that the depth (or height) of the columnar structure varied from run to run may very well be associated with different thicknesses of nonuniform SiO_2 films due to different moisture conditions in the chamber prior to those runs.

It is somewhat more difficult to explain that, in association with the occurrence of black silicon formation, the effective silicon etch rate tends to be reduced to zero after a certain etch time. However, it is known that silicon etching by gaseous HCl can be hindered in the presence of an oxide layer (formed by residual oxygen in the reaction chamber), especially in an argon environment (13). It seems that argon

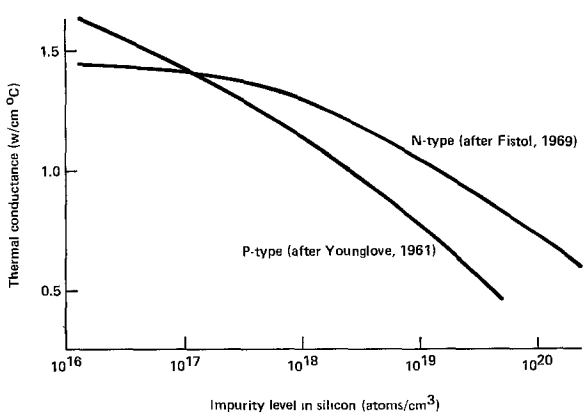

Fig. 12. Thermal conductance of silicon with different doping levels.

aids in the formation of a "closed structured" oxide layer, which is less penetrable to the HCl, than an oxide formed in a hydrogen environment. In an RIE system, the chamber and pumping line are coated with deposited reaction product materials, most probably containing a high proportion of chlorine-containing species. The deposits can represent a very large surface area and are prone to rapid moisture adsorption. Such absorbed moisture can be difficult to remove during the pump-down cycle and, in fact, could be misinterpreted as a "virtual leak" in the system.

It is speculated that for an incomplete pump down, the retained moisture in the chamber and on the target (cooled cathode) can be gradually released as the etching process proceeds, due to a general temperature rise in the system. The moisture, if at sufficient levels, could poison the silicon surface, including the surfaces of the columnar structures, and thereby effectively stop further etching. The onset of the moisture release and its efficiency to poison the silicon surface could again be variable due to specific etch conditions and moisture content in the system.

The other process parameters tend to exhibit normal behavior and are similar to those found in other etchant systems. In order to offset variations in etch rates due to changes in wafer loads (loading effect because of different pattern densities), it has been found useful to add to the RIE system an appropriate amount of silicon to increase the exposed silicon surface to about 10% rather than adjusting the Cl_2/Ar concentrations, system pressure and/or gas flow rates. This is especially true for very low percentages of silicon surface areas to be etched. The final groove taper angles can also be adjusted at will, provided a good reliable photolithographic process and a controlled SiO_2 window pattern taper formation are in use.

Summary

The Cl_2/Ar gas system was found to be an excellent candidate to preferentially etch silicon when using SiO_2 as a masking material. Etch rate ratios for Si/SiO_2 $\geq$ 20:1 have been achieved. The etched profiles can be either evenly tapered or vertical, provided proper etch conditions are utilized. Enhanced lateral etching can occur, especially for highly doped silicon, and this was found to be substrate temperature sensitive. Etch bias was missing for this process. System moisture was found to dramatically influence the etch characteristics of silicon and must be kept to a minimum for good process control.

Acknowledgments

The authors thank Mr. R. Gray and Mr. T. Hansen for their technical assistance in the experimental phases of this work.

Manuscript submitted Nov. 19, 1982; revised manuscript received April 15, 1983.

Any discussion of this paper will appear in a Discussion Section to be published in the June 1984 JOURNAL. All discussions for the June 1984 Discussion Section should be submitted by Feb. 1, 1984.

IBM East Fishkill Facility assisted in meeting the publication costs of this article.

REFERENCES

1. H. B. Pogge, J. A. Bondur, and P. J. Burkhardt, RNP 387 presented at The Electrochemical Society Meeting, Pittsburgh, PA, Oct. 15-20, 1978.
2. J. A. Bondur, *J. Vac. Sci. Technol.*, **13**, 1023 (1976).
3. G. C. Schwartz, L. B. Zielinski, and T. S. Schopen, Abstract 52, p. 146, The Electrochemical Society Extended Abstracts, Vol. 76-1, Washington, DC, May 2-7, 1976.
4. J. A. Bondur, *This Journal*, **126**, 226 (1976).
5. J. A. Bondur, W. R. Case, and H. A. Clark, Abstract 303, p. 760, The Electrochemical Society Extended Abstracts, Vol. 78-1, Seattle, WA, May 21-26, 1978.
6. J. A. Bondur and H. A. Clark, Abstract 304, p. 762, The Electrochemical Society Extended Abstracts, Vol. 78-1, Seattle, WA, May 21-26, 1978.
7. W. Latimer and J. Hildebrand, "Reference Book of Inorganic Chemistry, Macmillan Co., New York (1951).
8. H. F. Winters, *J. Appl. Phys.*, **49**, 5165 (1978).
9. C. J. Mogab, H. L. Levinstein, *J. Vac. Sci. Technol.*, **17**, 721 (1980).
10. J. S. Lechaton and J. L. Mauer, "Plasma Processing," R. G. Frieser and C. J. Mogab, Editors, p. 75, The Electrochemical Society Softbound Proceedings Series, Pennington, NJ (1981).
11. G. C. Schwartz and P. M. Schaible, *J. Vac. Sci. Technol.*, **16**, 410 (1979).
12. R. S. Robinson and S. M. Rossnagel, *ibid.*, **21**, 790 (1982).
13. H. J. Rijks, J. Bloem, and L. J. Giling, *J. Cryst. Growth*, **47**, 397 (1979).

Ramp Breakdown Study of Double Polysilicon RAM's as a Function of Fabrication Parameters

D. K. Brown* and C. A. Barile*

IBM General Technology Division, East Fishkill Hopewell Junction, New York 12533

ABSTRACT

Interelectrode ramp breakdowns have been studied on double- polysilicon RAM's as a function of five fabrication parameters: (*i*) the polysilicon thickness, (*ii*) the polysilicon doping, (*iii*) the removal of the first-gate oxide, (*iv*) the oxidation of the second gate, and (*v*) the post second-gate thermal annealing. For the particular case using an 800°C wet/HCl second-gate oxidation, a 1000°C 15 min post gate 2 anneal significantly improved the breakdown yield. Without the anneal, the breakdown yield was found to be extremely dependent on the poly 1 phosphorus concentration between 1.41×10^{20} to 7.0×10^{20} atoms/cm^3. The breakdown dependence on all five parameters has been explained in terms of a previously reported stress model.

Polysilicon gate technology is rapidly becoming the industry-wide standard for 64-k RAM fabrication. Single-, double-, and even triple-level polysilicon gate products are available in the market place today. Though the technology has many positive attributes, it is not without problems (1-3).

Certainly, one of the major concerns in the multilevel technology is interelectrode reliability. A number of technical papers have been published on this

* Electrochemical Society Active Member.

subject, offering a variety of solutions to the problem (4-6). Very few solutions, however, are without consequence.

In this paper, the results of 5 changes made in the fabrication process of a double-polysilicon RAM are presented. The interelectrode integrity was monitored by ramped voltage breakdown measurements on 8-k RAM chains. The results may be explained in terms of a stress model, which was published in an earlier paper (2).

Experimental

The double-polysilicon gate RAM chains (7) were fabricated in split- and single-process lots, making variations from a standard process in: (*i*) polysilicon thickness, (*ii*) the first polysilicon doping, (*iii*) the removal of the first-gate oxide, (*iv*) the second-gate oxide's oxidation temperature, and (*v*) a post second-gate anneal.

The polysilicon electrodes (also referred to as poly 1 and poly 2) were deposited in a low pressure (~0.3 Torr), chemical vapor deposition system at about 625°C, using an anhydrous HCl gas preclean and a 100% silane gas deposition process. The films were grown to a nominal thickness of 420 nm for the standard case (the first polysilicon was deposited over a 45 nm gate oxide/640 nm field oxide structure).

The polysilicon deposition was followed by a 900°C $POCl_3$ diffusion to dope the electrode with phosphorus. The flow conditions for the standard process were 3.72 liter/m of N_2 plus 0.73 liter/m of O_2 injected directly into the furnace, while 0.35 liter of N_2 was bubbled through the liquid $POCl_3$ source (held at 24°C ± 1°C) prior to injection. The duration of the doping step was 20 min. It was immediately followed by a 45 min N_2 anneal, also at 900°C, with the PSG still on the polysilicon. Upon cooling, the PSG film was stripped off in a buffered hydrofluoric acid solution.

The next step in the standard process was a 105 nm plasma-enhanced CVD oxide deposition. This step was carried out in a parallel plate reactor. This oxide was not densified prior to gate 2 oxidation in order to retain a favorable etch rate ratio to the gate 1 oxide.

After the plasma oxide was deposited, the poly 1 was defined. Photoresist was applied, exposed, developed, and then both the plasma oxide, and the polysilicon were etched in a parallel plate plasma reactor. Upon completion of the dry etching, the first-gate oxide was wet etched in a buffered hydrofluoric acid solution. The resist was then stripped. and the wafers were prepared for the second-gate oxidation.

For the standard process, the second-gate oxidation was an 800°C steam/HCl reaction, which was designed to grow 65 nm on a p-type (100) substrate. The oxidation rate on the standard doped polysilicon was approximately 3 times higher on the top of the electrode than on the substrate.

The post second-gate anneal was performed *in situ*, immediately following the oxidation, for the standard process. The conditions of annealing were 15 min at 1000°C in N_2. The ramp time from 800° to 1000°C was 30 min, and the ramp down was also 30 min.

The second polysilicon was deposited, doped, and defined in a similar manner as for the first polysilicon. The wafers were then fully processed through first metal and ramp tested.

The experimental matrices and process variations are listed by the corresponding figure numbers in Table 1. Polysilicon thickness increases (Fig. 6) were obtained by increasing the deposition times while doping increases (Fig. 4 and 7) were obtained by increasing the N_2 flow through the $POCl_3$ bubbler. An overetch of the first gate (Fig. 7a, b, and c) was prepared by increasing the standard etch time by a factor of three. An anisotropic dry etch of the first-gate oxide (Fig. 8) was performed in the same reactor as the dry etch of the plasma oxide. A 900°C, 65 nm second gate was grown in a steam and HCl environment and annealed *in situ* at 1000°C for 15 min (Fig. 9).

Table I. Experimental matrix by figure number

Fabrication step								
Field oxide	640 nm	Std	4a, b, c, d	5	6	7a, b, c	8	9
Gate 1 oxide	45 nm	Std	4a, b, c, d	5	6	7a, b, c	8	9
Poly 1	420 nm	Std	4a, b, c, d	5	6	7a, b, c	8	9
(LPCVD)	470 nm				6			
	520 nm				6			
Poly 1 doping	Lightly		4c, d			7c		
(N_2-O_2-$POCl_3$)	Transition	Std	4b	5	6	7b	8	
	Heavily		4a			7a		9
Plasma oxide	105 nm	Std	4a, b, c, d	5	6	7a, b, c	8	9
Poly 1 etch	Dry	Std	4a, b, c, d	5	6	7a, b, c	8	9
Gate 1 removal	Wet 1X	Std	4a, b, c, d	5	6	7a, b, c	8	9
	Wet 3X					7a, b, c		
	Dry 1X						8	
Gate 2 oxide	65 nm 800°C	Std	4a, b, c, d	5	6	7a, b, c	8	9
(Wet/HCl)	65 nm 900°C							9
Gate 2 anneal	*In situ*	Std	4a, b, c, d	5	6	7a, b, c		9
(N_2-1000°C-15')	Separate			5			8	
	No anneal		4a, b, c, d	5				
Poly 2	420 nm	Std	4a, b, c, d	5	6	7a, b, c	8	9
(LPCVD)	470 nm				6			
	520 nm				6			
Poly 2 doping	Transition	Std	4a, b, c, d	5	6	7a, b, c	8	9

A separate post gate 2 anneal (Fig. 5) was performed in a different furnace than the oxidation furnace. The wafers were cooled to room temperature before insertion into the anneal furnace. The time/temperature cycle from 800° to 1000°C was the same as for the *in situ* anneal.

Film thicknesses were measured using an IBM Film Thickness Analyzer and/or an SEM. The phosphorus content in the polysilicon was measured by x-ray fluorescence.

Ramp breakdowns on the 8-k chains were measured on a logarithmic picoammeter (1 V/sec) and recorded on an x-y chart recorder. This method insured that the true destructive breakdown was measured and was not simply high leakage. Since the reliability of the structure was the primary concern, dead shorts were eliminated from the data. The substrate potential was maintained at half of the poly 1's potential, while the poly 2 was grounded. An electrode-to-substrate test was made after each breakdown in order to verify that an interelectrode breakdown had occurred.

Results

The phosphorus concentration in the polysilicon prior to the second-gate oxidation is given as a function of the $POCl_3$ doping concentration in Fig. 1. Also presented are the single-crystal sheet resistance values of the furnace monitor wafers which correspond to

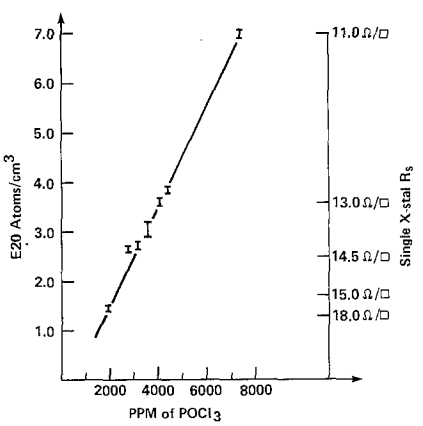

Fig. 1. The phosphorus concentration in the polysilicon as a function of $POCl_3$ concentration in the furnace (left hand y-axis). The right hand y-axis shows the approximate corresponding single-crystal silicon sheet resistance on the furnace monitor wafers. (The initial polysilicon thickness was 420 nm.)

each condition. The concentration of phosphorus in the polysilicon varies linearly with the $POCl_3$ concentration in the furnace. The single-crystal values (R_s in $\Omega/\square$) increase as the phosphorus concentration decreases. Typically, from run to run, the single-crystal R_s values correspond only roughly to the polysilicon's phosphorus concentration.

Figure 2 gives the poly 1 to poly 2 ramp yield for breakdowns exceeding 30V as a function of poly 1 doping. Each data point signifies one lot of wafers tested. The lot size varied from 5 to 18 wafers and six 8-k RAM gate chains were ramped per wafer. The yield for each lot is the percentage of gate chains which had exceeded a 30V breakdown over the total number of gate chains tested in that lot. Circled data points indicate that the lot received a 1000°C post gate 2 anneal, while noncircled data points indicate that there was no post gate 2 anneal.

The lots that were processed without the 1000°C post gate 2 anneal exhibit a strong breakdown dependence on the poly 1 doping level. The dependence curve has been divided into three regions: the "heavily doped" region, the "transition" region, and the "lightly doped" region. The "heavily doped" region is characterized by the unannealed lot having a ramp yield of 0%. In the "transition" region, the ramp yield on unannealed lots varied from 0 to 95%. In the "lightly doped" region, the yields were greater than 80%.

In contrast to the unannealed lots were the lots that received the 1000°C post gate 2 anneal. The ramp yield by lot shows a striking improvement with the anneal, particularly for the "heavily doped" and "transition" regions. Further evidence on the effect of the post gate 2 anneal is offered in Fig. 3. The 30V ramp yield is given as a function of when the lot was processed through the second-gate oxidation. Before the anneal was added to the process, the ramp yields varied from 0 to 95%. After the institution of the anneal, the ramp yield settled at above 80%.

Figure 4 gives the fractional cumulative failures as a function of voltage for a within-a-lot split of poly 1 doping and post gate 2 anneal *vs.* no anneal. In every case, the annealed samples were superior to the unannealed samples. The difference becomes dramatic in the "transition" and "heavily doped" regions. The optimum condition, from a breakdown point of view, appears to be the annealed "transition" region sampled. This condition consistently produces a high breakdown voltage. The singular high breakdown for the annealed samples increases with poly 1 doping.

Figure 5 gives the poly 1 to poly 2 breakdown results of a within-a-lot split, comparing the *in situ* post gate 2 anneal, the separate post gate 2 anneal, and an unannealed gate 2. For this case, the poly 1 was doped in the "transition" region. There is a significant

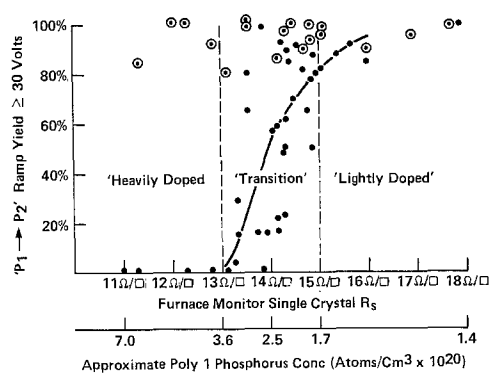

Fig. 2. The poly 1 to poly 2 ramp breakdown voltage yield (percentage ≧ 30V) as a function of the poly 1 dopniq. The circled data represents wafer lots which received the 1000°C 15 min post gate 2 anneal. Noncircled data represents wafer lots which received no post gate 2 anneal. (All samples had wet/HCl 800°C second gates.)

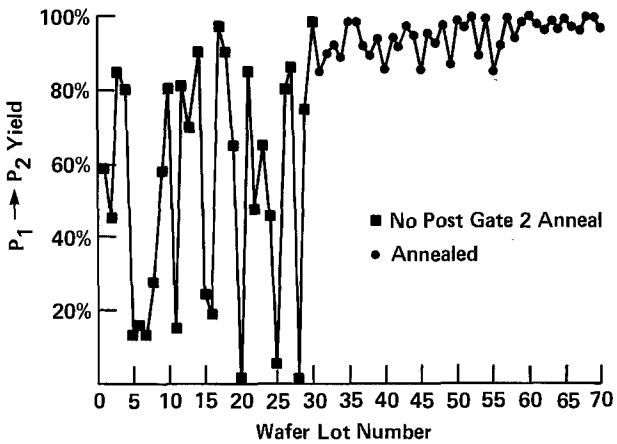

Fig. 3. The poly 1 to poly 2 ramp breakdown yield (percentage ≧ 30V) before and after the institution of the 1000°C 15 min post gate 2 anneal. (All samples had wet/HCl 800°C second gates.)

difference between the unannealed wafers and those that were annealed. However, there is very little difference between the *in situ* and the separate post gate 2 anneals.

The results from using a constant $POCl_3$ doping process and varying the poly 1 thickness are given in Fig. 6 for annealed samples. The early fails are decreased by increasing the thickness of the poly 1.

Figure 7 gives the results of an experiment where the gate 1 oxide etch time was increased by a factor of three in each of the poly 1 doping regions on annealed samples. In all cases, the median breakdown voltage was reduced by undercutting of the first polysilicon. A dramatic shift occurs in the "heavily doped" region.

Figure 8 shows the difference in breakdown distributions between a wet isotropic etch and a dry anisotropic etch of the gate 1 oxide for unannealed samples in the "heavily doped" region. There is an overall improvement in the distribution for the anisotropic gate oxide etch.

The results of increasing the oxidation temperature of the gate oxide from 800° to 900°C in the "heavily doped" region (for annealed samples) is given in Fig. 9. The 900°C process is significantly better than the 800°C process for this particular doping condition.

Discussion

The material problems that may develop during the low-temperature oxidation of a heavily doped polysilicon electrode have been discussed by Brown, Hu, and Morrissey (2). The origin of the problems is twofold and interdependent. Firstly, when one volume of silicon oxidizes, 2.27 volumes of SiO_2 are formed. The newly formed volume must be accommodated for in some manner. On a planar surface, the oxide is simply displaced normally to the plane. However, on a concave or convex surface the oxide will exhibit an additional lateral displacement, *i.e.*, grow either into itself on a concave surface or grow away from itself on a convex surface. Secondly, at low temperatures (*e.g.*, 800°C) and high oxidation rates, the viscoelastic flow of the SiO_2 cannot readily occur in response to the rapid straining generated by the oxidation. Under these conditions, stress will build up in the SiO_2 and the surrounding polysilicon until a point is reached where one of the materials must yield.

On convex polysilicon corners, the oxide grows into tension. As the oxide thickness increases, the lateral stress increases. If the oxide stress exceeds a critical value, the oxide will crack. The oxide's critical value may be determined by physical defects, such as pinholes, or by the chemical environment which could initiate Si-O bond breaking (8).

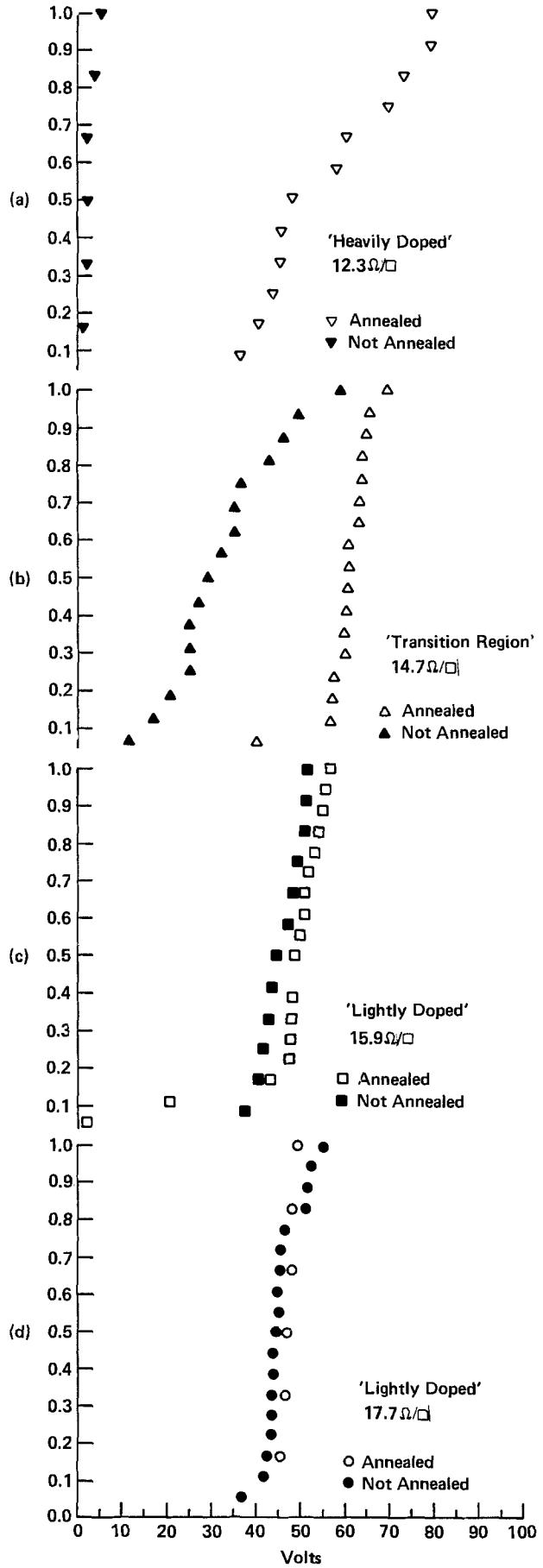

Fig. 4. The fractional cumulative failures as a function of voltage for a within-a-lot split of poly 1 doping and post gate 2 anneal vs. no anneal. (All samples had wet/HCl 800°C second gates.)

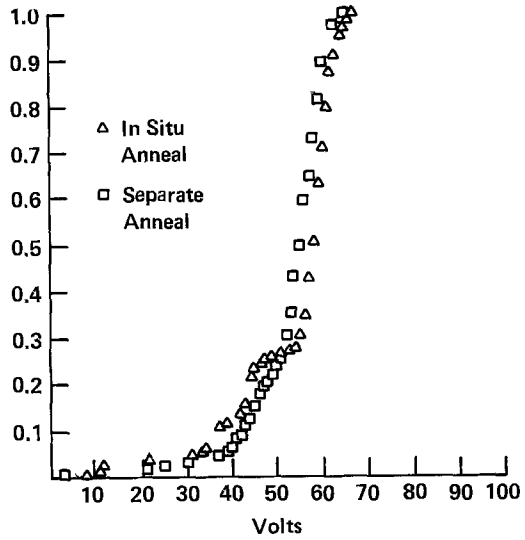

Fig. 5. The poly 1 to poly 2 fractional cumulative failures as a function of voltage for a within-a-lot split, comparing the *in situ* post gate 2 anneal, the separate post gate 2 anneal, and an unannealed gate 2. (All samples had wet/HCl 800°C second gates and a 15 Ω/□ single-crystal poly 1 doping monitor.)

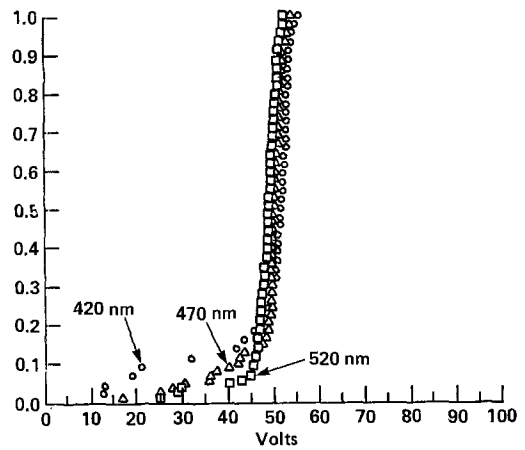

Fig. 6. The poly 1 to poly 2 fractional cumulative failures as a function of the initial polysilicon thickness. The $POCl_3$ doping was identical for all samples. (All second gates were 800°C wet HCl oxides annealed at 1000°C for 15 min.)

In confined regions (such as under the edge of the polysilicon electrode) the oxide grows into itself, generating enormous compressive stress. The excess volume in this case must be accommodated for in one of several ways. If the viscosity of the oxide was low, the excess SiO_2 volume would flow out from underneath the polysilicon land. This, however, has been found not to be the case at 800°C. Rather, the polysilicon itself yields plastically to the ever increasing SiO_2 volume.

The yielding of the polysilicon occurs in two ways. Primarily, there is sliding of the polysilicon grains. This vertical movement may occur abruptly and be accompanied by a crack in the sidewall oxide. Secondarily, the polysilicon can yield to the enormous compressive stress through diffusion creep and/or transgrain sliding. In this case, the movement of the polysilicon is lateral rather than vertical. The lateral movement deforms the polysilicon/oxide sidewall continuously through the oxidation, generating poly 1 protrusions and thin oxide regions.

The breakdown dependence on poly 1 doping can be explained by using the aforementioned model. As the doping is increased, the oxidation rate of the poly 1 rises. This increased oxidation rate of the poly 1 has the end result of generating more SiO_2, which must be displaced and accommodated. Hence, the stress in-

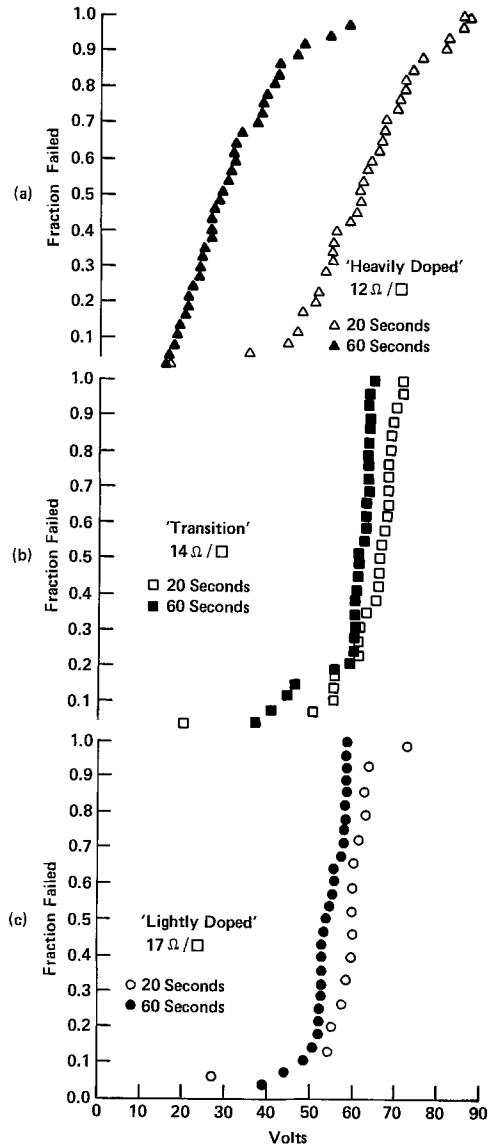

Fig. 7. The poly 1 to poly 2 fractional cumulative failures as a function of voltage for a within-a-lot split of poly 1 doping and gate 1 etch times. (All samples had wet/HCl 800°C second gate oxides which were annealed at 1000°C for 15 min.)

creases, as does the polysilicon deformation. The final state of the sidewall oxide after gate 2 oxidation is therefore very doping dependent.

The residual stress in the structure can be relaxed by a 1000°C post gate 2 anneal of the structure for 15 min. The end result of the anneal is to eliminate any

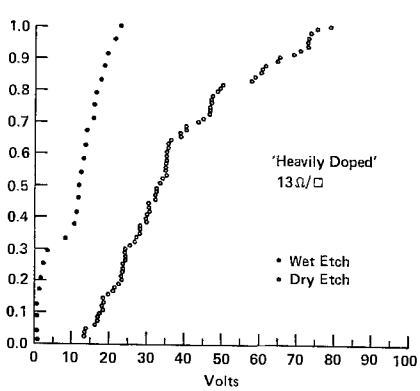

Fig. 8. The fractional cumulative failures as a function of voltage for a within-a-lot split comparing a wet isotropic vs. a dry anisotropic gate 1 etch. (All samples had wet/HCl 800°C gate 2 oxides which were not annealed.)

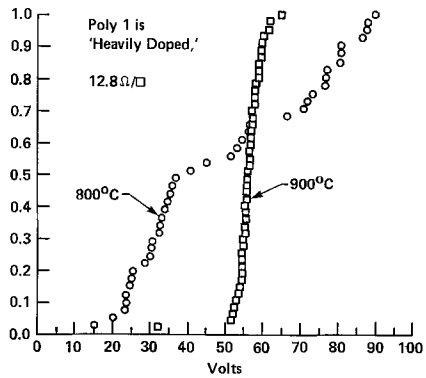

Fig. 9. The fractional cumulative failures as a function of voltage for a within-a-lot split comparing wet/HCl 800° and a 900°C second gate. (All samples had the 1000°C 15 min post gate 2 anneal and had "heavily doped" poly 1.)

post oxidation cracking. The benefit of the anneal is shown in Fig. 4. It is believed that the 1000°C anneal will cause flow only in the oxide which is under stress. That is to say that if the oxide stress has been relieved by cracking, the cracked oxide will not self heal (at least not at 1000°C). From the projection of the oxide's viscosity at 1000°C, it is orders of magnitude too high for this to occur (2).

A significant clue to the question of when the oxide cracks can be drawn from the *in situ vs.* the separate 1000°C anneal data. Since the breakdown results of the *in situ* and the separate anneals are basically equivalent (Fig. 5) and accepting the hypothesis that cracks in the oxide will not self heal at 1000°C, the conclusion must be reached that the oxide does not readily crack during the gate 2 oxidation or the thermal cycling (at least not at these doping concentrations). The reader is reminded that for the separate anneal the wafers are pulled from the furnace after the 800°C oxidation, cooled to room temperature, and placed in another furnace for the 1000°C anneal. For the *in situ* anneal, the furnace simply is ramped up to 1000°C after the oxidation is completed. The cracking must therefore be induced after the oxidation and thermal processing is complete. This was alluded to earlier in the discussion when the oxide's critical stress (the level of tensile stress at which the oxide can sustain before fracture) was stated to be a function of the chemical environment. The exact post oxidation process step to which this phenomenon can be attributed has not yet been determined. However, it must occur prior to the second polysilicon deposition since all cracks are filled in with the second polysilicon. Both the wet chemical preclean and the dry HCl clean prior to poly 2 deposition are likely suspects.

The dependency of poly 1 to poly 2 breakdown voltage on the poly 1 doping, even on the annealed samples, is quite remarkable (*e.g.*, Fig. 2 and 4). The strength of the relationship is further substantiated by the results from the experiment varying the poly 1 thickness (see Fig. 6). For a constant $POCl_3$ doping process, the phosphorus concentration in the polysilicon must decrease linearly as the poly thickness increases. This is a consequence of the polysilicon phosphorus concentration having a linear dependence on the $POCl_3$ concentration (see Fig. 1). As the doping concentration in the poly is diminished by the thicker poly film, the early failures are reduced. This is despite the fact that the sidewall oxide's surface area is increasing linearly with poly 1 thickness. Thus, the surface area of the wall and the area-related defects are of far less importance than the polysilicon doping level and the doping-related flaws. A comment which is apropos at this time is that while thickness control is critical in that it affects the final doping, one may avoid this problem altogether by adapting an *in situ* doped poly-

silicon, where the doping remains constant during deposition.

The effect that undercutting the poly 1 land has on interlevel breakdowns (Fig. 7) also may be explained in terms of the aforementioned model. Over thin oxide regions, the lateral depth of the undercut is proportional to the lateral depth of the wedge oxide formed. This is in turn proportional to the volume of polysilicon that must be displaced. The volume of polysilicon displaced determines, in part, the magnitude of the poly 1 protrusion and/or the vertical rise of the grains if grain boundary sliding occurs. Figure 10 is a schematic depiction based on observations (2) of the undercutting over a thin oxide region.

Over the thick oxide region, the vertical separation between the leading edge of the polysilicon and the surface of the oxide below is increased with undercutting (as is the lateral depth of the undercut). One result of the undercut over thick oxide is that an extra polysilicon convex corner is exposed, *i.e.*, the lower corner. When oxidized, the additional corner increases the area of tensile stressed oxide. Figure 11 depicts the proposed undercut phenomena over the thick oxide region. Referring back to Fig. 7, it is apparent that the undercut effect is exacerbated by increasing the poly 1 doping level.

The deleterious effect of exposing the poly 1 lower corner over thick and thin oxide regions is further verified by the results of the anisotropic gate oxide etch given in Fig. 8. Since a vertical etch eliminates any possible undercutting, the aforementioned mechanisms are minimized. Figure 12 is a depiction of vertical etching of the gate oxide over thin and thick oxide regions.

A primary advantage of oxidizing at low temperatures (*e.g.*, 800°C) is that the oxidation rate of heavily phosphorus-doped silicon is substantially enhanced (9-11). The differential oxidation rates between the heavily doped polysilicon and an intrinsic or low-doped substrate in this case are as high as 4:1. It is clear from the stress model that thicker oxides, which grow on the heavily doped polysilicon at low temperatures, can lead to substantial material problems. These problems should intensify if the second-gate oxidation temperature is lowered, if the second-gate thickness is increased, or if the first-polysilicon doping is increased. Each of these changes would increase the thickness of the oxide grown on the polysilicon and raise the propensity to flaw. Conversely, if a change were made in the opposite direction (*e.g.*, raising the temperatures of the second-gate oxidation), a less flawed structure would be formed. This prediction is corroborated by the 900°C data given in Fig. 9 (for poly 1 from the "heavily doped" region). As the temperature is raised, the differential oxidation rate is decreased and less oxide is grown on the heavily doped polysilicon. It is, therefore, not surprising that the 900°C "heavily doped" data compares quite well with the 800°C "transition" region data in Fig. 4c. Should higher doped electrodes be desired, raising the oxidation temperature can be used to offset oxidation enhancement effects. Higher temperatures, however, do enhance autodoping phenomena; and proper precautions, such as oxygen preheats, are advisable.

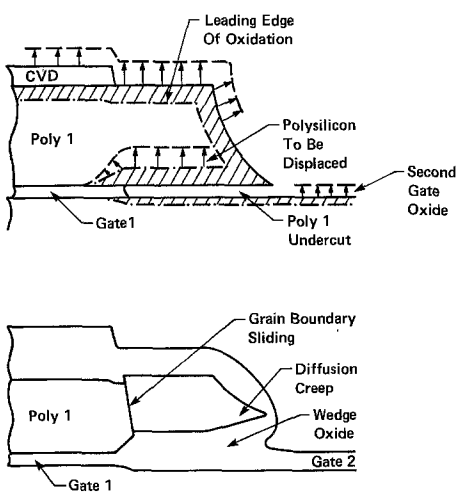

Fig. 10. The undercut of poly 1 during the gate 1 oxide wet etch—shown over a thin oxide region before and after the second gate is oxidized. The volume of polysilicon which is displaced is proportional to the undercut and determines, in part, the magnitude of the poly 1 protrusion, and/or the vertical rise of the grains when grain boundary sliding occurs.

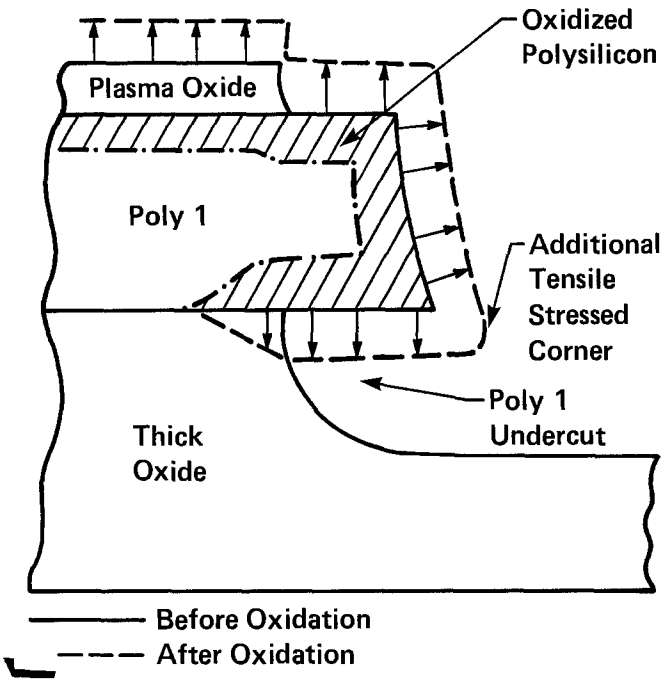

Fig. 11. The undercut of poly 1 during the gate 1 oxide wet etch—shown over a thick oxide region. The additional exposure of the lower poly 1 corner increases the area of tensile-stressed oxide.

A thicker sidewall oxide, if flawless, will result in a higher breakdown voltage. The anneal prevents certain flaws from being generated. This accounts for the wider distribution of breakdown voltages found on "heavily doped" post gate 2 annealed samples (*e.g.*, Fig. 4d). The early fails are created by flaws such as poly 1 protrusions and sidewall oxide thin spots, while the late fails are a result of the ultimately thicker oxide on the less flawed sidewalls.

Summary

Interelectrode ramp breakdowns have been studied on double polysilicon RAM's as a function of fabrication parameters. For the particular case using an 800°C

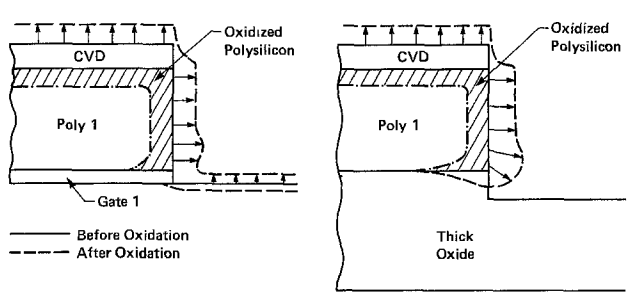

Fig. 12. The results of an anisotropic gate 1 etch over thick and thin oxide regions. Comparatively less deformation and stress should be achieved with this structure.

wet/HCl second-gate oxidation, a 1000°C post gate 2 N_2 anneal significantly improved the breakdown yield. The improvement is attributed to the relief of stress in the structure, which prevents further flawing (induced after the oxidation and thermal cycling).

The poly 1 to poly 2 breakdown dependence on poly 1 doping was also studied and partitioned into three regions: "heavily doped," "transition," and "lightly doped." The breakdown results in each of these regions are dependent not only on the poly 1 doping concentration, but also on the second-gate oxidation temperature, the poly 1 undercut prior to the oxidation, and the post gate 2 anneal step.

In the "heavily doped" region (for an 800°C wet gate 2), the poly 1 undergoes severe deformation and the encapsulating oxide approaches critical stress levels on convex corners. The 1000°C post gate 2 anneal can remove the stresses; however, poly 1 protrusions and oxide thin spots will remain as artifacts. In the "transition" region, these artifacts lessen in magnitude. When annealed, the "transition" region samples are superior in integrity to the "heavily doped" region samples. In the "lightly doped" region, both stress and the artifacts are of a noncritical nature and the post gate 2 anneal adds little benefit.

The undercutting of the poly 1 land was found to have the most deleterious effect when the poly 1 is heavily doped. This holds true even for annealed samples (since the poly 1 protrusions and oxide thin spots are not removed by the post gate 2 anneal). There is significant improvement on "heavily doped" unannealed samples if the poly 1 land is not undercut (by anisotropic removal of the gate 1 oxide). Oxidizing the second gate at higher temperatures (*e.g.*, 900°C) reduces the concentration-dependent oxidation rate and therefore decreases the stress build-up due to the displacement of oxide generated. If heavily doped electrodes are required, it would be prudent to raise all post process oxidation temperatures as well as include anneals. However, one must guard against autodoping effects if these measures are to be taken (3). Few changes in this system are without consequence.

Acknowledgments

The authors gratefully acknowledge the assistance of L. K. Martin in the process experiments, R. Smallwood, T. Andreozzi, and N. Kohlmaier in the ramped breakdown measurements, and B. Fitzgibbons in the data collection. Our special thanks are given to J. M. Morrissey for his interest and support in this subject and to M. Shatzkes and M. AvRon for their development of an accurate breakdown measurement test.

Manuscript submitted May 3, 1982; revised manuscript received Jan. 20, 1983.

Any discussion of this paper will appear in a Discussion Section to be published in the June 1984 JOURNAL. All discussions for the June 1984 Discussion Section should be submitted by Feb. 1, 1984.

IBM Corporation assisted in meeting the publication costs of this article.

REFERENCES

1. A. K. Sinha, T. T. Sheng, T. A. Shankoff, W. S. Linderberger, E. N. Fuls, and C. C. Chang, in "Reliability Physics Symposium, Technical Digest," pp. 35-38, San Francisco, April 24-26, 1979.
2. D. K. Brown, S. M. Hu, and J. M. Morrissey, *This Journal*, **129**, 1084 (1982).
3. H. Sunami, M. Koyanagi, and N. Hashimoto, *ibid.*, **127**, 2499 (1980).
4. M. Koyanagi, T. Kamiyama, H. Sunami, and N. Hashimoto, Abstract 87, p. 225, The Electrochemical Society Extended Abstracts, Vol. 79-1, Boston, MA, May 6-11, 1979.
5. H. Sunami and M. Koyanagi, *Supplement Jpn. J. Appl. Phys.*, **18-1**, 255 (1979).
6. W. G. Oldham, N. Chau, and N. Rovedo, Abstract 165, p. 439, The Electrochemical Society Extended Abstracts, Vol. 79-1, Boston, MA, May 6-11, 1979.
7. T. C. Lo, R. E. Scheurlein, and R. Tamlyn, *IBM J. Res. Dev.*, **24**, 318 (1980).
8. P. G. Fox, *Phys. Chem. Glasses*, **21**, 161 (1980).
9. B. E. Deal and M. Sklar, *This Journal*, **112**, 430 (1965).
10. W. A. Pliskin, *IBM J. Res. Dev.*, **10**, 198 (1966).
11. C. P. Ho, J. D. Plummer, J. D. Meindl, and B. E. Deal, *This Journal*, **125**, 665 (1978).

Properties of Molybdenum Silicide Film Deposited by Chemical Vapor Deposition

S. Inoue,* N. Toyokura, and T. Nakamura

Fujitsu Laboratories, Limited, 1015 Kamikodanaka, Nakahara-ku, Kawasaki, Japan 211

M. Maeda and M. Takagi*

Fujitsu Limited, 1015 Kamikodanaka, Nakahara-ku, Kawasaki, Japan 211

ABSTRACT

$MoSi_2$ films used as gate electrodes and interconnects were deposited on oxidized Si substrates via reactions between $MoCl_5$ and SiH_4. At high temperatures, HCl generated by reactions involving $MoCl_5$, H_2, and SiH_4 reacts with Si to form volatile SiH_3Cl, SiH_2Cl, $SiHCl_3$, and $SiCl_4$; thus Si is etched away and is not available to form $MoSi_2$, resulting in deposited film consisting of only metallic Mo. At low temperatures, the deposited film consists of $MoSi_2$ which is thermodynamically stable. The deposited films show characteristics (resistivity, crystal structure, and so forth) similar to those of $MoSi_2$ films deposited by sputtering. Chlorine in the deposited films has a gettering effect for mobile ions such as Na^+.

In very large-scale integrated circuits, the relatively high electrical resistivity of polycrystalline silicon used for interconnections and gate electrodes is a major limitation on circuit performance. The high resistivity of polycrystalline silicon lowers the speed of the circuits. Refractory metal silicides, such as WSi_2, $TaSi_2$, and $MoSi_2$, are being studied as highly conductive interconnect materials for very large-scale integrated circuits to replace polycrystalline silicon (1-6).

* Electrochemical Society Active Member.
Key words: CVD, $MoSi_2$, interconnect, gate electrode.

Several techniques have been used to form the silicides: (*i*) sputtering from the stoichiometric compounds (1, 4), (*ii*) co-evaporation of the metal and silicon (2), (*iii*) cosputtering of metal and silicon (3, 5), (*iv*) sequential deposition of individual components followed by annealing (3), and (*v*) chemical vapor deposition (CVD) (7-9). The second and third techniques are widely used; however there are some problems associated with these techniques, such as poor step coverage and irradiation damage caused by electron beams or sputtering. These problems can be avoided if CVD is used for deposition of the silicides; however, CVD silicides have columnar or rough surfaces. If fluoride, such as WF_6 and MoF_6, is used, fluorine or hydrofluoride generated in the reaction etches the SiO_2 film.

To solve these problems, we studied a CVD technique using $MoCl_5$ and SiH_4. This paper presents the CVD technique and film properties such as the resistivity, crystal structure, and MOS characteristics.

Experimental Procedure

Figure 1 shows a schematic diagram of the CVD system. SiH_4 was used as the silicon source, and $MoCl_5$ was used as the metal source. The $MoCl_5$ was first heated to 160°C, then supplied to the reaction furnace using H_2 as carrier gas. Ar, H_2, or N_2 was used as the diluent gas. The deposition was carried out at a pressure of 0.6-2.0 Torr, and at 520°-800°C. Gases in the furnace were analyzed by quadrupole mass spectrograph before and during the depositions.

In the experiments, a 4 in. diam p-type Si wafer was used and the molybdenum silicide film was deposited onto the oxidized Si substrates. After deposition, the wafers were annealed in N_2 for 20 min at temperatures between 700°-1000°C. The deposited films were evaluated as follows: crystal structure by x-ray diffraction, composition by Rutherford backscattering spectroscopy (RBS), impurities in the film by ion microprobe mass analysis, and resistivity by 4-point probe.

MOS capacitors were made on (100) p-type Si. The 1000Å thick oxides were grown at 1000°C in dry O_2, and then the 3000Å thick silicide films were deposited onto oxide and patterned into 400 μm diam dots with photoresist and etched in reactive ion etching with CF_4/O_2. A final annealing step in H_2/N_2 at 450°C completed the process.

Figure 2 shows the deposition rate dependence on the deposition temperature. The depositions were carried out using $MoCl_5$ with H_2 carrier gas at 190 cm^3/min, SiH_4 at 210 cm^3/min, and N_2 as a diluent gas. Deposition rate is limited by reaction in this condition and the deposition rate increases with deposition temperature at pressure of 0.6-2.0 Torr.

Film Properties

Figure 3 shows the film resistivity dependence on deposition and annealing temperatures after deposition. Annealing was carried out in N_2 for 20 min. The resistivity of the film deposited at 800°C was 7×10^{-6} Ωcm and did not change after annealing. Film deposited at 800°C was found to be a Mo film as analyzed by x-ray diffraction traces and RBS. The resistivity of the film deposited at 700°C was 2×10^{-5} Ωcm, several percent of silicon as determined by Auger electron spectroscopy. The resistivity of the film as-deposited at 670°C was 1×10^{-3} Ωcm, and decreased to about 1.2×10^{-4} Ωcm after annealing at 1000°C. This film was evaluated by RBS and x-ray diffraction as follows. Figure 4 shows the RBS results on the film deposited at 670°C. This composition was Mo:Si = 1:2, as determined by calculating the Mo and Si peak heights. There are several forms of molybdenum silicide, namely Mo_3Si, Mo_5Si_3, and $MoSi_2$. However, in the present study, only $MoSi_2$ was obtained because it is the stable form for the deposition condition used.

The crystal structure was determined by x-ray diffraction, as shown in Fig. 5. The crystal structure

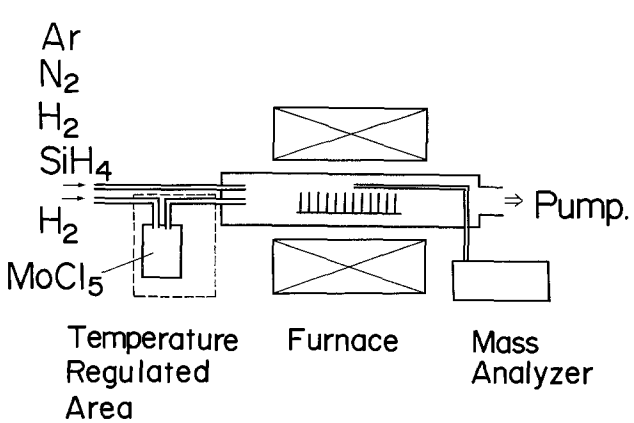

Fig. 1. Conceptual diagram of reactor

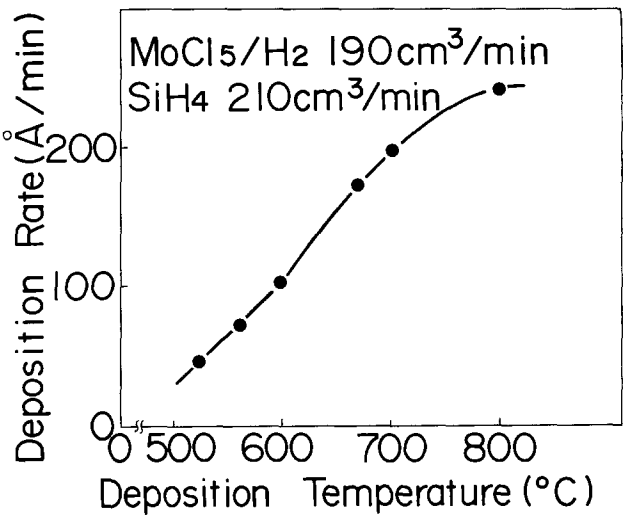

Fig. 2. Deposition rate dependence on deposition temperature

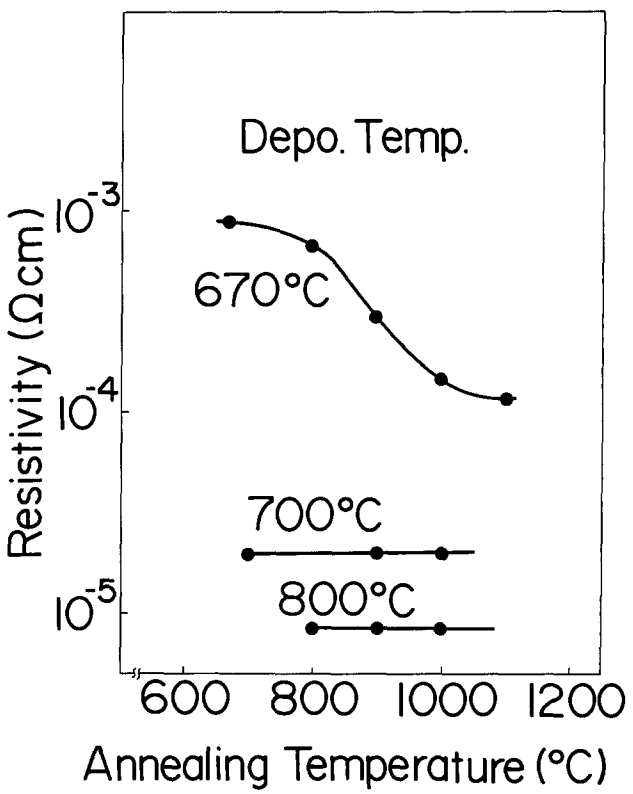

Fig. 3. Film resistivity dependence on annealing temperature

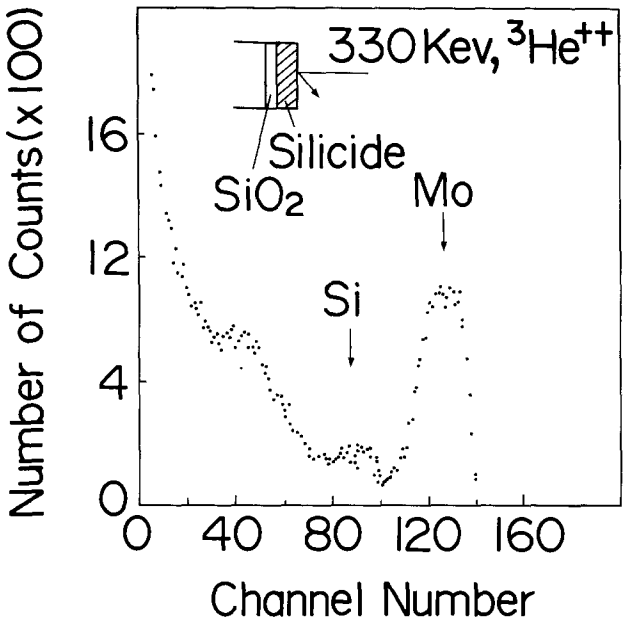

Fig. 4. Rutherford backscattering spectroscopy results on film deposited at 670°C.

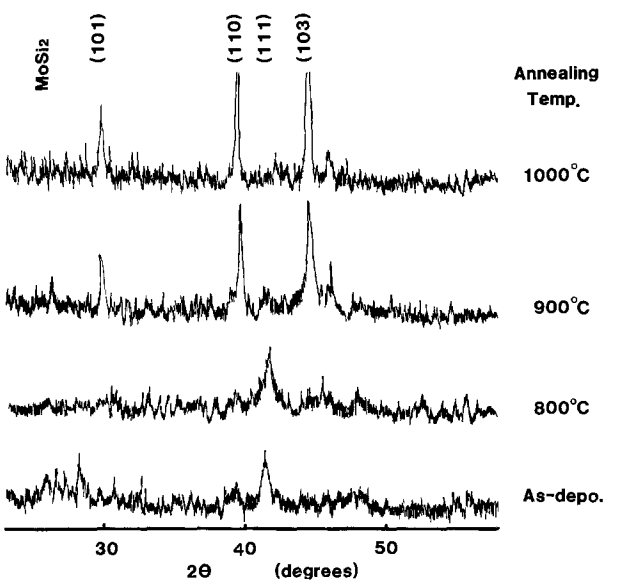

Fig. 5. X-ray diffraction spectra of annealed film

of the as-deposited film was hexagonal $MoSi_2$ (ASTM cards 17-917) and changed to tetragonal $MoSi_2$ (ASTM cards 6-681) when annealed at 900°C or higher. By contrast, the structure of sputtered films changed at lower temperatures, ≧800°C (5, 6).

In the CVD method, the as-deposited $MoSi_2$ films were in the crystalline form, as opposed to the amorphous structure obtained by sputtering (5, 6); therefore, impurities such as chlorine to be shown later in Fig. 10, tend to segregate along the grain boundaries and might make difficult the crystal structure change upon annealing.

We studied the gases in the reaction furnace to analyze the above results. Figure 6 shows the mass spectrograph when $MoCl_5$ and SiH_4 were supplied together in the reaction furnace at 625°C at a pressure of 0.8 Torr. Mass peaks of HCl, SiH_3Cl, SiH_2Cl_2, $SiHCl_3$, and $SiCl_4$ appeared as soon as the $MoCl_5$ and SiH_4 were supplied to the furnace. During the deposition, the mass peaks of SiH_3Cl, SiH_2Cl_2, $SiHCl_3$, and $SiCl_4$ were almost constant and disappeared when the $MoCl_5$ gas flow was stopped, as shown in Fig. 7. These results show that the following reactions occurred in the reaction furnace

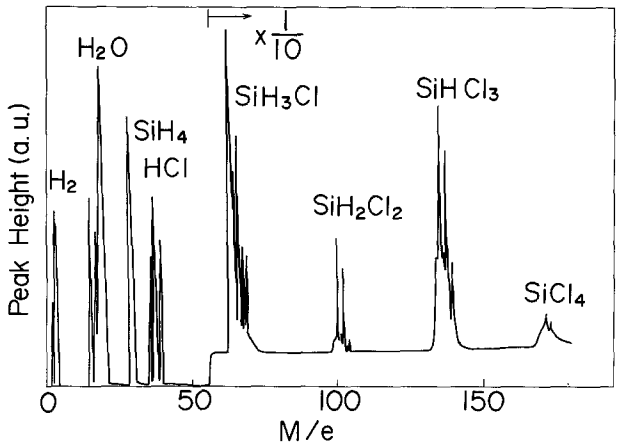

Fig. 6. Mass peaks of gases in reaction furnace

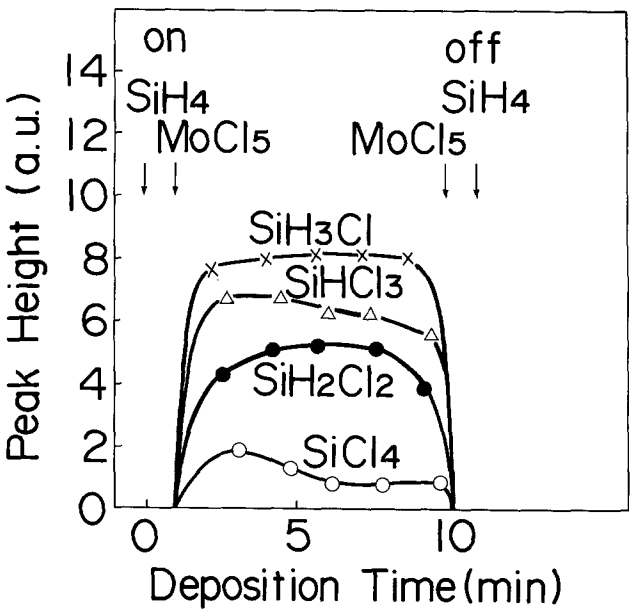

Fig. 7. Change of reaction gas mass peaks

$$MoCl_5 + \frac{5}{2}H_2 \rightarrow Mo + 5HCl \quad [1]$$

$$SiH_4 \rightarrow Si + 2H_2 \quad [2]$$

$$Mo + 2Si \rightarrow MoSi_2 \quad [3]$$

$$Si + HCl + H_2 \rightarrow SiH_3Cl \quad [4]$$

$$Si + 2HCl \rightarrow SiH_2Cl_2 \quad [5]$$

$$Si + 3HCl \rightarrow SiHCl_3 + H_2 \quad [6]$$

$$Si + 4HCl \rightarrow SiCl_4 + 2H_2 \quad [7]$$

In general, $MoCl_5$ and SiH_4 decompose to Mo and Si, respectively, to form molybdenum silicide films. However, Si from decomposed SiH_4 and HCl of decomposed $MoCl_5/H_2$ react and form SiH_xCl_y. At high temperatures, the reaction between HCl, H_2, and SiH_4 changes to volatile SiH_3Cl, SiH_2Cl_2, $SiHCl_3$, and $SiCl_4$. Si is etched away and not available to form $MoSi_2$, resulting in only metallic Mo film deposits. The film was deposited either as Mo or $MoSi_2$ film depending on the etching or depositing of Si. We have not yet established the kinetics of the deposition reaction.

MOS Properties

To study the effects of material properties on device characteristics, MOS capacitors were fabricated and tested. The flatband voltage was studied with com-

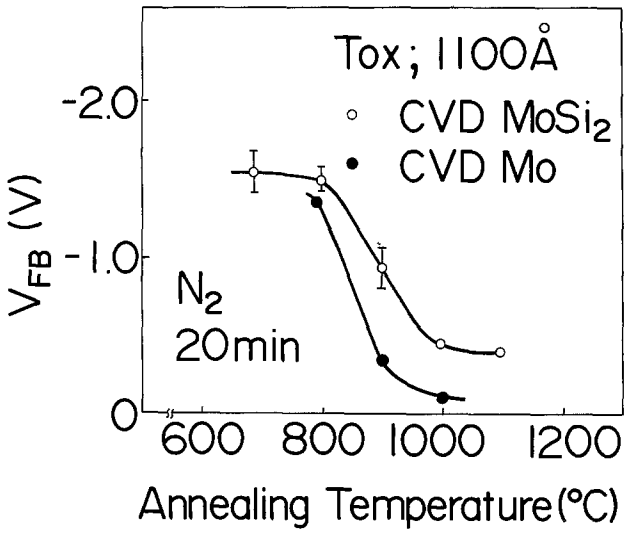

Fig. 8. V_{FB} dependence on annealing temperature

parative C-V measurements. Figure 8 shows the flat-band voltages determined from C-V measurements for Mo and $MoSi_2$ gates. When the film was annealed at above 1000°C, the surface state and fixed charge of the Mo and $MoSi_2$ gates were less than 3×10^{10} cm^{-2}. So the value of the V_{FB} difference between $MoSi_2$ and Mo is caused by the work function difference as shown in previous work (5, 6).

The film must be stable if it is to be used as a gate electrode. It is known that mobile ions such as Na^+ are the stability degradation factor. The mobile ion density in the CVD films was measured using the triangular voltage seep (TVS) method at 230°C and a voltage seep rate of 33 mV/sec (10). Figure 9 shows the measurement results. The mobile ion density for the as-deposited films was on the order of 1×10^{11} cm^{-2}, which is quite large. When annealed at above 900°C for 20 min, the mobile ion density decreased, and when annealed at 1000°C the density fell below the measurement limit, that is less than 1×10^9 cm^{-2}.

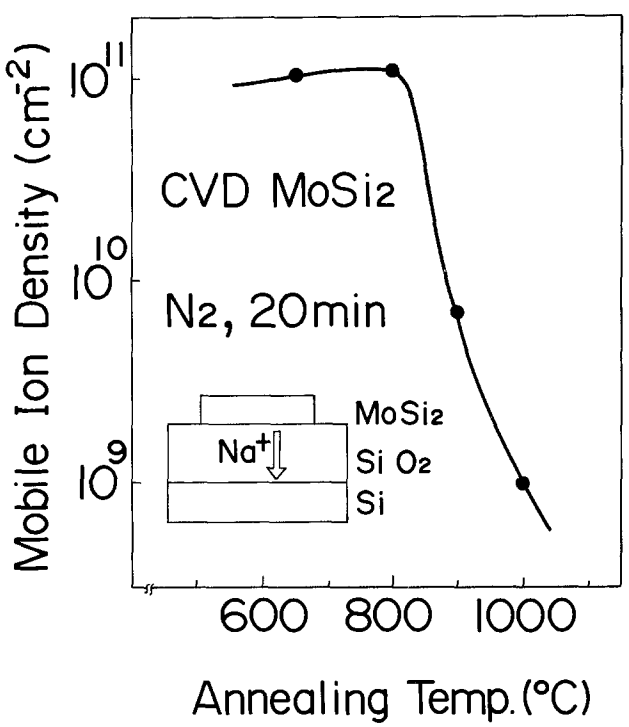

Fig. 9. Mobile ion density dependence on annealing temperature

These values are less than or equal to those of polycrystalline silicon gates and provide sufficient stability.

By ion microprobe mass analysis, it was determined that the CVD film contained Cl^- as shown in Fig. 10, where the data for both sputtered and CVD films are presented for comparison. It can be considered that mobile ions are reduced because Cl^- in the silicide films deposited using $MoCl_5$ acts as a getter for Na^+, as in HCl-processed gate oxide films.

Step Coverage

Figure 11 shows an SEM photograph of the $MoSi_2$ deposited on the Si substrate with patterning. The step height is 0.8 μm and the film thickness is 0.3 μm. The side wall thickness is almost the same as that of the flat plateau. The CVD is therefore an attractive method for depositing $MoSi_2$ films with good step coverage.

Conclusions

We have demonstrated that $MoSi_2$ can be deposited by CVD via reactions between $MoCl_5$ and SiH_4. At high temperatures, HCl generated by reactions involving $MoCl_5$, H_2, and SiH_4 changes Si to volatile $SiHCl_3$, SiH_2Cl_2, SiH_3Cl, and $SiCl_4$. Thus, Si is etched away and is not present to form $MoSi_2$, resulting in only metallic Mo film deposits. $MoSi_2$ can be deposited in a low-temperature reaction region, but sufficient SiH_4 must be supplied to produce $MoSi_2$.

The deposited films show characteristics similar to those of silicide films deposited by sputtering. Chlorine in the deposited films has sufficient gettering effect for mobile ions such as Na^+. The step coverage of the CVD-deposited films is excellent compared with the sputtered $MoSi_2$ film.

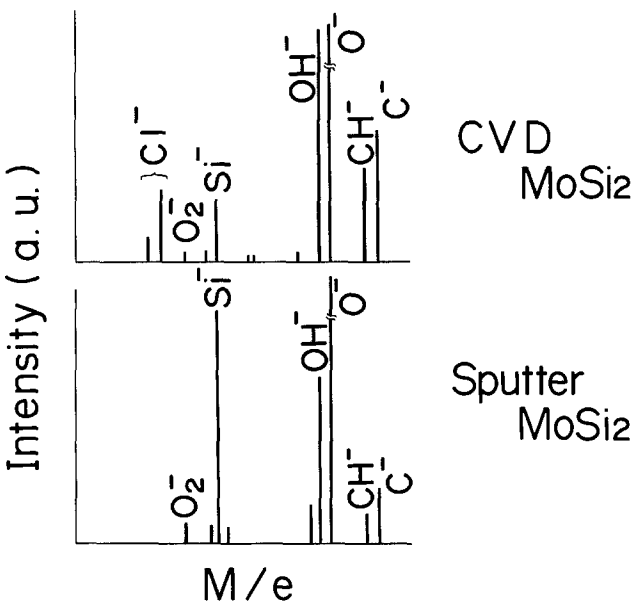

Fig. 10. Ion microprobe mass analysis spectra on CVD and sputtered $MoSi_2$

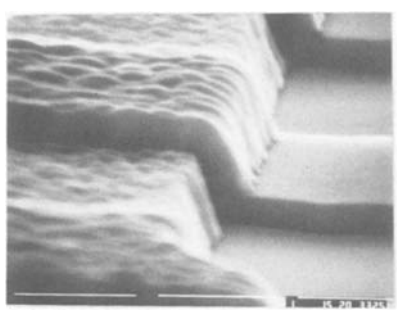

Fig. 11. SEM photograph of CVD $MoSi_2$ film

As previously explained, silicide films deposited in the CVD method can be used as gate electrode and interconnect materials. We believe that this technique must be improved for greater reliability in the future.

Acknowledgments

The authors are grateful to Dr. T. Misugi and H. Ishikawa for their encouragement and discussions and to H. Horie and H. Miyamoto for their helpful contributions to the work.

Manuscript submitted June 7, 1982; revised manuscript received April 7, 1983.

Any discussion of this paper will appear in a Discussion Section to be published in the June 1984 JOURNAL. All discussions for the June 1984 Discussion Section should be submitted by Feb. 1, 1984.

Fujitsu Laboratories, Limited assisted in meeting the publication costs of this article.

REFERENCES

1. T. Mochizuki, K. Shibata, T. Inoue, and K. Ohuchi, *Jpn. J. Appl. Phys.*, **17-1**, 37 (1978).
2. B. L. Crowder and S. Zirinsky, *IEEE J. Solid-State Circuits*, **sc-14**, 291 (1979).
3. S. P. Murarka, D. B. Fraser, A. K. Sinha, and H. J. Levinstein, *IEEE Trans. Electron Devices*, **ed-27**, 1409 (1980).
4. T. P. Chow and A. J. Steckl, *Appl. Phys. Lett.*, **36**, 297 (1980).
5. S. Inoue, N. Toyokura, T. Nakamura, and H. Ishikawa, in "Semiconductor Silicon 1981," H. R. Huff, R. J. Kriegler, and Y. Takeishi, Editors, p. 596, The Electrochemical Society Softbound Proceedings Series, Pennington, NJ (1981).
6. S. Inoue, N. Toyokura, T. Nakamura, and H. Ishikawa, *This Journal*, **128**, 2402 (1981).
7. K. C. Saraswat and F. Mohammadi, Abstract 159, p. 419, The Electrochemical Society Extended Abstracts, Vol. 80-1, St. Louis, MO, May 11-16, 1980.
8. D. E. R. Kehr, "6th International Conference on CVD," L. F. Donaghey and P. Rai-Choudhury, Editors, p. 511, The Electrochemical Society Softbound Proceedings Series, Princeton, NJ (1977).
9. K. Akimoto and K. Watanabe, *Appl. Phys. Lett.*, **39**, 445 (1981).
10. M. Yamin, *IEEE Trans. Electron Devices*, **ed-13**, 79 (1966).

Crystallographic Orientation and Surface Morphology of Chemical Vapor Deposited Al_2O_3

C.-S. Park, J.-G. Kim, and J. S. Chun

Department of Materials Science and Engineering, Korea Advanced Institute of Science and Technology, Seoul, Korea

ABSTRACT

Deposits of aluminum oxides (Al_2O_3) have been formed by a chemical vapor deposition technique involving the application of gaseous mixtures of $AlCl_3$, CO_2, and H_2 onto TiN-coated cemented carbide substrates. Reaction parameters (deposition temperature, system pressure, and composition of reactant gases) and their effects on the crystalline structure, crystallographic orientation, and surface morphology of the Al_2O_3 deposit have been studied. Al_2O_3 crystals maintain a corundum structure throughout the entire range of deposition conditions. Crystals of Al_2O_3 appear to nucleate in random orientations on the TiN layer, and further growth proceeds with $(10\bar{1}4)$ and $(11\bar{2}6)$ preferred orientations. The effects of reaction parameters on the final surface morphology of the Al_2O_3 deposit can be described by considering the supersaturations of the reactants and the growth rate. The crystals of the Al_2O_3 deposit become finer and more uniform as the supersaturation of the reactant controlling the Al_2O_3 nucleation increases.

The chemical and physical properties of a solid are determined mainly by its crystal structure, crystallographic orientation, and morphology. In chemical vapor deposition (CVD), the crystal structure, crystallographic orientation, and morphology vary widely according to the deposition condition. Because CVD involves the repetition of nucleation and growth of the nucleus, the crystal morphology of a deposit is affected by their characteristics.

Classical nucleation theory indicates that the nucleation rate is a function of the deposit formation flux and the statistical probability of embryo's growth over the critical nucleus size. The critical parameters which determine the above statistical probability, and likewise affect the nucleation rate, are the temperature and supersaturation of the reactants (1, 2). Recently, attempts have been made to investigate the influence of supersaturation on the nucleation (3, 4) and final crystal morphology (5) of the deposit in the CVD process. Since CVD is generally accompanied by multiple chemical reactions, and the nucleation characteristics are concealed by the growth behavior, the quantitative analysis of crystal morphology with supersaturation becomes very complex.

In this work, a wide range of deposition conditions have been evaluated with respect to the resulting crystal structure, crystallographic orientation, and surface morphology of CVD Al_2O_3 employing gaseous mixtures of $AlCl_3$, CO_2, and H_2. The effect of the deposition conditions on the crystal morphology is described as a function of the supersaturation of the reactants and the growth rate of the Al_2O_3 deposit.

Key words: CVD, crystallography, coatings.

Calculation of Supersaturation

The supersaturation of a reactant, Σ_i, is defined as

$$\Sigma_i = \frac{P_{in}(i)}{P_{eq}(i)} \quad [1]$$

where $P_{in}(i)$ and $P_{eq}(i)$ are the inlet partial pressure and the equilibrium partial pressure, respectively, of the i species. Since CVD generally involves many chemical species, a total supersaturation can be defined only after considering all the chemical species. Due to the lack of detailed information on the kinetics of each chemical reaction involved in Al_2O_3 CVD, the inlet composition on the substrate surface cannot be obtained; therefore, the total supersaturation cannot be specified. In this work, the reactants were divided into two groups (Al-donor and O-donor), and the supersaturations of both the Al-donor and the O-donor were calculated in place of the total supersaturation.

Calculations for the equilibrium partial pressure of each chemical species are based on the minimization of total free energy, and are carried out by a simple

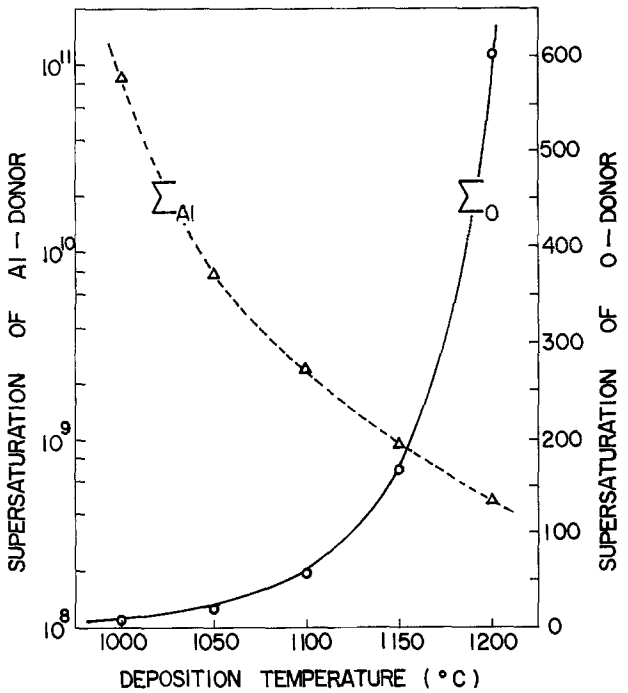

Fig. 1. Calculated supersaturation as a function of the deposition temperature. (System pressure: 100 Torr, $AlCl_3$ mol fraction: 2.0×10^{-3}, mol ratio of CO_2 to H_2: 1.)

iteration method on a computer (6, 7). The calculation results give both the vapor phase and deposit equilibrium compositions when the initial composition is known for each deposition condition.

Even though the only inlet reactant containing aluminum is $AlCl_3$, the equilibrium partial pressure of the Al-donor is calculated by considering all aluminum chlorides such as AlCl, $AlCl_2$, $AlCl_3$, and Al_2Cl_6, since any of these can be converted into Al_2O_3 by reacting with the O-donor

$$\Sigma_{Al} = \frac{P_{in}(AlCl_3)}{P_{eq}(AlCl) + P_{eq}(AlCl_2) + P_{eq}(AlCl_3) + 2P_{eq}(Al_2Cl_6)} \quad [2]$$

H_2O vapor formed by the reaction of CO_2 and H_2 is considered as an O-donor (8, 9), (and the inlet value is calculated from the empirical equation of Tingey (10) (10)

$$\Sigma_O = \frac{P_{in}(H_2O)}{P_{eq}(H_2O)} \quad [3]$$

The supersaturations obtained from Eq. [2] and [3]

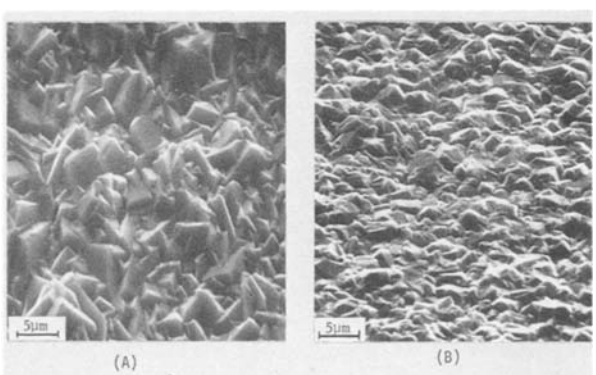

Fig. 2. Scanning electron micrographs of the surface of Al_2O_3 crystals deposited at different temperatures for 1 hr. (System pressure: 100 Torr, $AlCl_3$ mol fraction: 2.0×10^{-3}, mol ratio of CO_2 to H_2: 1, gas flow rate: 1 liter/min.) (A) 1050°C, (B) 1150°C.

Table I. Measured x-ray intensities and texture coefficients of Al_2O_3 crystals deposited at different temperatures for 1 hr

		T = 1000°C		T = 1050°C		T = 1100°C		T = 1150°C	
(hkil)	I_o	I_m	TC	I_m	TC	I_m	TC	I_m	TC
$10\bar{1}2$	71	60	1.06	63	0.99	30	0.75	21	0.64
$10\bar{1}4$	98	73	0.94	100	1.14	100	1.82	100	2.18
$11\bar{2}0$	41	27	0.83	25	0.68	10	0.43	7	0.36
$11\bar{2}3$	100	100	1.25	94	1.05	40	0.71	42	0.90
$02\bar{2}4$	43	33	0.96	38	0.99	23	0.94	14	0.71
$11\bar{2}6$	81	60	0.93	88	1.22	73	1.60	68	1.80
$12\bar{3}4$	30	27	1.13	31	1.15	14	0.84	14	1.01
$30\bar{3}0$	45	33	0.91	31	0.77	23	0.91	7	0.43

System pressure: 100 Torr, $AlCl_3$ mol fraction: 2.0×10^{-3}, mol ratio of CO_2 to H_2: 1, gas flow rate: 1 liter/min.

are shown in Fig. 1, 3, 5, and 7 as functions of each reaction parameter.

Experimental

The deposition experiments have been conducted in an open flow-type reactor using gaseous mixtures of $AlCl_3$, CO_2, and H_2. The substrates used in this experiment were TiN coated cemented carbides [WC-6 weight percent (w/o) Co], with the dimensions of 10 × 6 × 3 mm. The detailed deposition procedure was described in a previous work (9).

In order to study their crystalline structures and crystallographic orientations, a series of deposits was investigated through x-ray diffraction analysis Cu Kα radiation with an Ni filter. The measured intensities of given (hkil) planes were substituted in Eq. [4] to get the texture coefficients, T.C. (hkil)

$$T.C.(hkil) = \frac{I_m(hkil)/I_o(hkil)}{\frac{1}{N}\sum_N I_m(hkil)/I_o(hkil)} \quad [4]$$

where I_m is measured intensity, I_o is the ASTM standard intensity, and N is the number of reflections. The texture coefficients of various diffracting planes are shown in Table I, II, III, and IV as functions of each re-

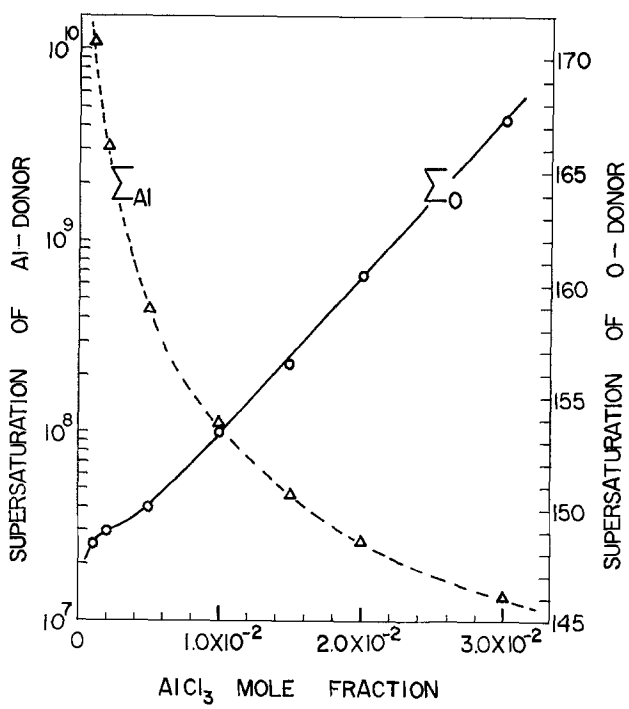

Fig. 3. Calculated supersaturation as a function of the $AlCl_3$ mol fraction. (Temperature: 1150°C, system pressure: 100 Torr, mol ratio of CO_2 to H_2: 1.)

Table II. X-ray diffraction intensities and texture coefficients of Al_2O_3 crystals deposited at different $AlCl_3$ mol fractions for 1 hr

(hkil)	I_o	$X_{AlCl_3} = 1.0 \times 10^{-3}$		$X_{AlCl_3} = 2.0 \times 10^{-3}$		$X_{AlCl_3} = 1.0 \times 10^{-2}$		$X_{AlCl_3} = 3.0 \times 10^{-2}$	
		I_m	TC	I_m	TC	I_m	TC	I_m	TC
$10\bar{1}2$	71	39	0.80	21	0.64	6	0.27	8	0.32
$10\bar{1}4$	98	100	1.49	100	2.18	100	3.39	100	3.01
$11\bar{2}0$	41	9	0.32	7	0.36	4	0.33	4	0.30
$11\bar{2}3$	100	49	0.63	42	0.90	15	0.50	26	0.77
$20\bar{2}4$	43	32	1.08	14	0.71	5	0.40	7	0.47
$11\bar{2}6$	81	78	1.40	68	1.80	47	1.93	52	1.89
$12\bar{3}4$	30	18	0.88	14	1.01	8	0.90	10	0.97
$30\bar{3}0$	45	43	1.40	9	0.43	4	0.30	4	0.27

Deposition temperature: 1150°C, system pressure: 100 Torr, mol ratio of CO_2 to H_2: 1, gas flow rate: 1 liter/min.

action parameter. Scanning electron microscopy has been used to observe the crystal morphology of the Al_2O_3 deposit.

Results and Discussion

The effect of deposition temperature.—Figure 1 shows the calculated supersaturations of the Al-donor and the O-donor as functions of the deposition temperature. Since the Al_2O_3-producing reaction is exothermic, the supersaturation of the Al-donor decreases as the deposition temperature increases. In contrast, the O-donor supersaturation increases with the deposition temperature because the H_2O inlet concentration is more sensitive to temperature than the H_2O equilibrium concentration. Figure 2 shows the final surface morphology of the Al_2O_3 crystals which were deposited at different temperatures. The crystals of the Al_2O_3 show faceted structures which become coarser as the deposition temperature increases. Although the O-donor supersaturation increases with the deposition temperature, the exponentially increased growth rate shows the coarser crystals to exist at the higher deposition temperature.

X-ray diffraction analysis reveals the Al_2O_3 crystals deposited at temperatures between 1000°-1200°C to have a corundum structure. The texture coefficient of each diffracting crystal plane is shown as a function of deposition temperature in Table I. The crystals deposited at 1000°C are randomly oriented, however, the Al_2O_3 crystals deposited at higher temperatures show the evident preferred orientations of $(10\bar{1}4)$ and $(11\bar{2}6)$, and are accompanied by an increased growth rate.

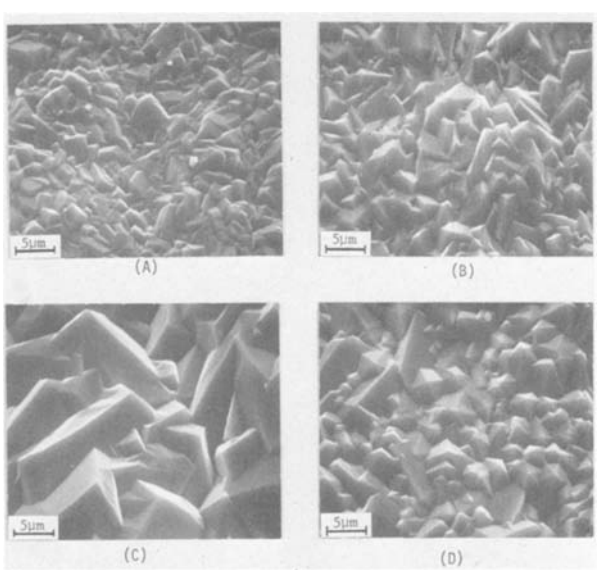

Fig. 4. Scanning electron micrographs of the surface of Al_2O_3 crystals deposited at different $AlCl_3$ mol fractions for 1 hr. (Deposition temperature: 1150°C, system pressure: 100 Torr, mol ratio of CO_2 to H_2: 1, gas flow rate: 1 liter/min.) (A) 1.0×10^{-3}, (B) 2.0×10^{-3}, (C) 1.0×10^{-2}, and (D) 3.0×10^{-2}.

From these results, it can be concluded that the Al_2O_3 crystals nucleate on the TiN layer without a preferred orientation, and proceed with stable growth at $(10\bar{1}4)$ and $(11\bar{2}6)$ preferred orientations.

The effect of $AlCl_3$ mol fraction.—Figure 3 shows the dependence of the supersaturations of the Al-donor and the O-donor on the $AlCl_3$ mol fraction. With an increase of the $AlCl_3$ mol fraction, the supersaturation of the Al-donor decreases, while that of the O-donor increases. The surface appearance and texture coefficients of Al_2O_3 crystals deposited at different $AlCl_3$ mol fractions are shown in Fig. 4 and Table II, respectively. When the $AlCl_3$ mol fraction is increased to 1.0×10^{-2}, the Al_2O_3 crystals become coarser and clearly exhibit the preferred orientations of $(10\bar{1}4)$ and $(11\bar{2}6)$. From the experimental results in Fig. 4 and the calculated supersaturations in Fig. 3, it can be concluded that crystal morphology is controlled by the Al-donor supersaturation up to the $AlCl_3$ mol fraction of 1.0×10^{-2}. Above 1.0×10^{-2}, the nucleation of the Al_2O_3 crystals seem to be limited by the O-donor supersaturation, hence the crystals become finer and the preferred orientations are reduced with a further increase of the $AlCl_3$ mol fraction.

The effect of CO_2 mol fraction.—Figure 5 shows the supersaturations of the Al-donor and the O-donor as functions of the CO_2 mol fraction at the $AlCl_3$ mol

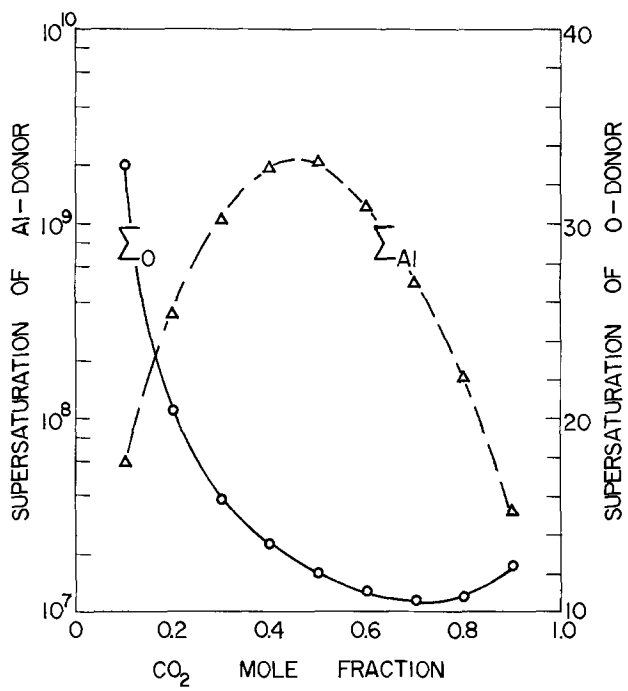

Fig. 5. Calculated supersaturation as a function of the CO_2 mol fraction. (Temperature: 1027°C, system pressure: 100 Torr, ACl_3 mol fraction: 1.0×10^{-2}.)

Table III. Measured x-ray diffraction intensities and texture coefficients of Al_2O_3 crystals deposited at different CO_2 mol fractions for 1 hr

		$X_{CO_2} = 0.10$		$X_{CO_2} = 0.35$		$X_{CO_2} = 0.65$		$X_{CO_2} = 0.90$	
(khil)	I_o	I_m	TC	I_m	TC	I_m	TC	I_m	TC
$10\bar{1}2$	71	29	0.73	29	0.70	17	0.40	38	0.83
$10\bar{1}4$	98	100	1.83	100	1.90	100	1.98	100	1.58
$11\bar{2}0$	41	—	—	9	0.51	—	—	18	0.68
$11\bar{2}3$	100	39	0.69	43	0.84	32	0.60	55	0.86
$20\bar{2}4$	43	20	0.83	15	0.64	16	0.44	20	0.82
$11\bar{2}6$	81	55	1.22	66	1.51	63	1.52	62	1.19
$12\bar{3}4$	30	16	0.96	17	1.20	20	1.20	20	1.0
$30\bar{3}0$	45	19	0.77	16	0.71	19	0.76	21	0.74

Deposition temperature: 1027°C, system pressure: 100 Torr, $AlCl_3$ mol fraction: 1.0×10^{-2}, gas flow rate: 2 liter/min.

Table IV. Measured x-ray diffraction intensities and texture coefficients of Al_2O_3 crystals deposited at different system pressures for 1 hr

		50 Torr		100 Torr		200 Torr		400 Torr	
(hkil)	I_o	I_m	TC	I_m	TC	I_m	TC	I_m	TC
$10\bar{1}2$	71	30	0.59	23	0.65	27	0.62	23	0.48
$10\bar{1}4$	98	100	1.44	100	2.07	100	1.66	100	1.54
$11\bar{2}0$	41	23	0.77	9	0.45	13	0.49	15	0.56
$11\bar{2}3$	100	70	0.79	41	0.83	59	0.96	65	0.97
$20\bar{2}4$	43	25	0.82	14	0.67	25	0.94	22	0.77
$11\bar{2}6$	81	75	1.31	74	1.85	86	1.72	80	1.49
$12\bar{3}4$	30	28	1.30	16	1.08	19	1.02	26	1.31
$30\bar{3}0$	45	25	0.79	9	0.4	16	0.59	26	0.87

Deposition temperature: 1125°C, $AlCl_3$ mol fraction: 2.0×10^{-3}, mol ratio of CO_2 to H_2: 1, gas flow rate: 1 liter/min.

fraction of 1.0×10^{-2}. The Al-donor supersaturation reaches its maximum value at the CO_2 mol fraction of 0.5, and the O-donor supersaturation has a minimum value at 0.7. The surface morphology and the texture coefficients of the Al_2O_3 crystals deposited at different CO_2 mol fractions are shown in Fig. 6 and Table III, respectively. The Al_2O_3 crystals deposited at the CO_2 mol fraction of 0.65 are coarser and show the $(10\bar{1}4)$ and $(11\bar{2}6)$ preferred orientations more distinctly than in any other condition. This is consistent with the calculated supersaturation of the O-donor.

The effect of system pressure.—Figure 7 shows the variations of the supersaturations of the Al-donor and the O-donor with the system pressure at a constant mol fraction of each reactant. The supersaturation of the Al-donor is nearly constant, while that of the O-donor is raised with the system pressure by a power of about ½. Figure 8 shows the surface appearance of Al_2O_3 crystals deposited at different system pressures. Even though the growth rate at 100 Torr is much greater than that at 50 Torr (9), Fig. 8 shows that the crystal size at 100 Torr is comparable with that at 50 Torr, consistent with the supersaturations in Fig. 7. In addition to the increase in the O-donor supersaturation, the vapor phase intermolecular collision frequencies also increase with the system pressure, thereby permitting the homogeneous nucleation of Al_2O_3 at the higher system pressure. The soots of Al_2O_3 were observed on the surface of the Al_2O_3 crystals deposited at 200 Torr and 400 Torr. At the higher system pressure, the preferred orientations of $(10\bar{1}4)$ and $(11\bar{2}6)$ were reduced by the increased O-donor supersaturation and by the attachment of the randomly oriented Al_2O_3 soots to the crystal surface (Table IV).

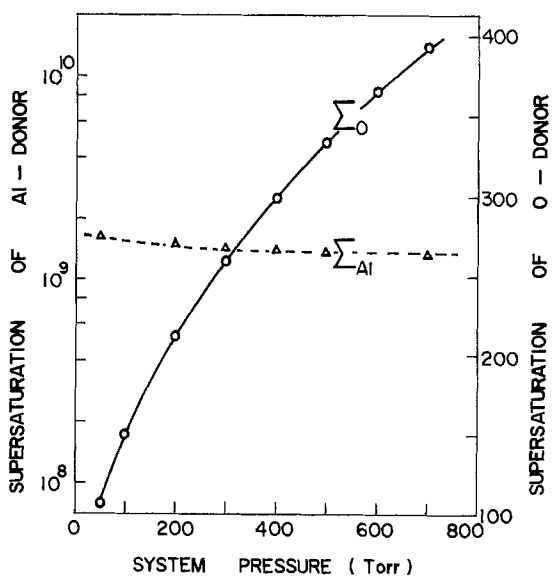

Fig. 7. Calculated supersaturation as a function of the system pressure. (Temperature: 1125°C, $AlCl_3$ mol fraction: 2.0×10^{-3}, mol ratio of CO_2 to H_2: 1.)

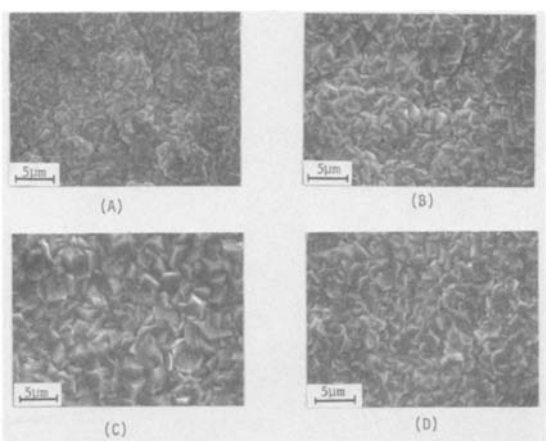

Fig. 6. Scanning electron micrographs of the surface of Al_2O_3 crystals deposited at different CO_2 mol fractions for 1 hr. (Deposition temperature: 1027°C, system pressure: 100 Torr, $AlCl_3$ mol fraction: 1.0×10^{-2}, gas flow rate: 2 liter/min.) (A) 0.1, (B) 0.35, (C) 0.65, and (D) 0.9.

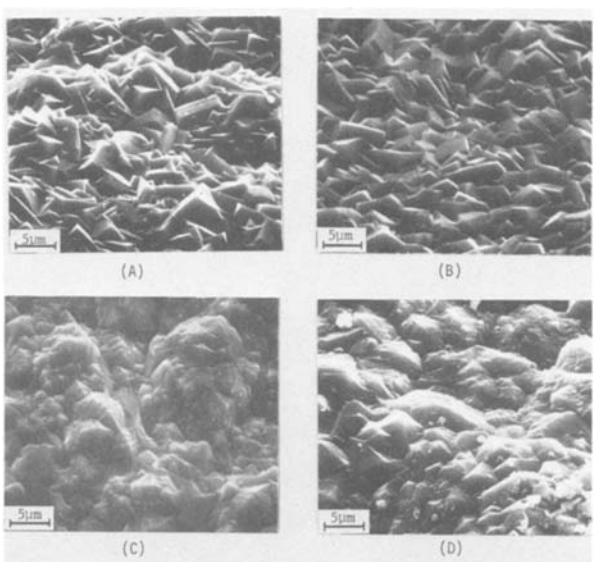

Fig. 8. Scanning electron micrographs of the surface of Al_2O_3 crystals deposited at different system pressures for 1 hr. (Deposition temperature: 1125°C, $AlCl_3$ mol fraction, 2.0×10^{-3}, mol ratio of CO_2 to H_2: 1, gas flow rate: 1 liter/min.) (A) 50 Torr, (B) 100 Torr, (C) 200 Torr, and (D) 400 Torr.

Conclusion

The Al_2O_3 crystals maintain a corundum structure throughout the entire range of deposition conditions. The Al_2O_3 crystals appear to nucleate on the TiN layer with random orientation, and proceed with stable growth at $(10\bar{1}4)$ and $(11\bar{2}6)$ preferred orientations. The surface morphology of the Al_2O_3 deposit is shown to be mainly affected by the oxygen-donor supersaturation and the growth rate, however, at the low $AlCl_3$ mol fraction below 1.0×10^{-2} the surface morphology is controlled by the aluminum-donor supersaturation.

Manuscript received Feb. 9, 1983.

Any discussion of this paper will appear in a Discussion Section to be published in the June 1984 JOURNAL. All discussions for the June 1984 Discussion Section should be submitted by Feb. 1, 1984.

The Korea Advanced Institute of Science and Technology assisted in meeting the publication costs of this article.

REFERENCES

1. J. P. Hirth, in "Vapor Deposition," C. F. Powell, J. H. Oxley, and J. M. Blocher, Jr., Editors, p. 126, John Wiley and Sons, New York (1966).
2. J. M. Blocher, Jr., *J. Vac. Sci. Technol.*, **11**, 680 (1974).
3. R. T. Johannesson and J. N. Lindström, *ibid.*, **12**, 854 (1975).
4. J. N. Lindström and R. T. Johannesson, *This Journal*, **123**, 555 (1976).
5. L. Vandenbulcke and G. Vuillard, *ibid.*, **124**, 1937 (1976).
6. C. Bernard, Y. Deniel, A. Jacquot, P. Vay, and M. Ducarrior, *J. Less-Common Met.*, **40**, 165 (1975).
7. L. P. Hunt and E. Sirtl, *This Journal*, **119**, 1741 (1972).
8. P. Wong and M. Robinson, *J. Am. Ceram. Soc.*, **53**, 617 (1970).
9. C.-S. Park, J.-G. Kim, and J. S. Chun, To be presented at the Fourth European conference on CVD (1983).
10. G. L. Tingey, *J. Phys. Chem.*, **70**, 1406 (1968).

Pore Size Distribution in Porous Silicon Studied by Adsorption Isotherms

G. Bomchil,* R. Herino,[1] K. Barla, and J. C. Pfister

Centre National d'Etudes des Télécommunications de Grenoble, BP. 42, 38240 Meylan, France

ABSTRACT

Porous silicon was obtained by anodic attack of single crystal silicon substrates in 25% hydrofluoric acid solutions. Specific surface area, total porous volume, and pore size distribution of porous silicon have been determined. The experimental technique used is based on the measurement of the volume of gas adsorbed at low constant temperature by the porous silicon. The adsorption isotherms show the general behavior found for porous materials, but at the same time, they show clear differences following different preparation conditions of porous layers. Quantitative analysis using models extensively used in the catalysis field lead to large values for the porous silicon specific surface area and sharp pore size distribution. Mean pore radii are found to vary in the range 20-100Å when forming current density varies from 10 to 240 mA/cm^2.

Porous silicon films were first obtained by Uhlir (1) and Turner (2) while studying the electropolishing of silicon in dilute hydrofluoric acid solutions. Since then, this new porous material has been investigated particularly because of its potential use in integrated circuit technology (3-6). Porous silicon layers of any desired thickness up to several microns can be obtained by anodization of silicon wafers in hydrofluoric acid (HF) solutions. According with the experimental conditions of porous silicon preparation, *e.g.*, current density, electrolyte concentration, films of different densities have been obtained and the mean porous silicon density has been found to decrease when increasing the forming current density during the anodic reaction (7). This density variation could be related to changes in pore diameter. Nevertheless, no accurate determination of the pore sizes has been obtaind yet. Scanning electron microscopy of the porous surface only shows some pits on the entire anodized area and even after partial etching in NaOH, it is not possible to identify the pore structure. Transmission electron microscopy (TEM) reveals the existence of an extremely fine structure of pores, with a predominant orientation normal to the surface and limits in size lower than 200Å (8). Accurate measurements are difficult mainly because of the S-shape of pores in the thickness direction, which complicate the analysis of the obtained microphotographs.

The purpose of the work was to obtain a better knowledge of the porous structure. We show in this paper that the pore size distribution on porous silicon can be determined by the analysis of adsorption isotherms of gases at low temperatures and that this technique is appropriate to give a quantitative measure of changes in the mean pore size of porous silicon prepared in different electrochemical conditions.

Experimental

Uniform porous silicon layers were obtained by anodic reaction in H_2O 25%, HF 25%, C_2H_5OH 50%. The silicon crystals were p-type (boron doped), 10^{-2} Ω cm resistivity, <111> oriented. The wafers were mounted at the bottom of the electrochemical cell and a well-delimitated part of the front surface was exposed to the electrolyte. The cathode was a platinum grid facing the silicon substrate at a distance of 3 cm. A constant current source was used. Forming current densities were varied from 10 to 240 mA/cm^2 in different experiments. The anodic reaction time was varied to obtain porous layers of about 80 microns thickness for each current density. Exact thickness of the porous layer and geometrical profiles were measured by optical microscopy on cleaved samples for each different experimental condition.

Usually porous silicon films are prepared by anodic attack of crystalline silicon in aqueous hydrofluoric acid solutions. Hydrogen evolution is observed during the reaction, bubbles stick at the silicon surface, and in general prevent the formation of a homogeneous

* Electrochemical Society Active Member.
[1] Universite Scientifique et Medicale de Grenoble, 38240 Meylan, France.

layer of porous silicon. Improvements in the quality of the porous silicon layers can be obtained using mechanical means to remove bubbles, *e.g.*, ultrasonic agitation associated with gas sweeping of the electrode surface or forced electrolyte circulation during the anodic attack. However, we have found that in all these cases x-ray topographies of the samples reveal the existence of strains induced by the presence of the hydrogen bubbles.

The use of ethanol-aqueous hydrofluoric solutions results in a large decrease in the size of hydrogen bubbles and in a much easier removal from the surface. A much better homogeneity in the porous silicon layer is obtained. Quite similar results in homogeneity can be obtained using galvanostatic pulses of current instead of continuous current during the anodic reaction.

The x-ray topography technique is an appropriate tool to illustrate the effect even in cases where optical microscopy reveals few differences between samples prepared in aqueous and in alcoholic solutions. The x-ray topography of the $2\bar{2}0$ reflection in the sample prepared by the usual technique reveals large strains resulting from the presence of hydrogen bubbles during the electrochemical reaction (Fig. 1a) (9). Figure 1b shows the same topography but in a sample prepared in the alcoholic solution; in this case, there is a marked improvement and only small defects are present in the whole volume of the layer. In addition to the good homogeneity of the layer the use of the alcoholic solution leads to a better reproducibility in all the physical measurements of the porous silicon layer, in particular in the pore size distributions obtained from the gas adsorption experiments.

The gas adsorption experiments are based on the measure of the volume of gas adsorbed by the sample as a function of the equilibrium pressure (10). The minimum volume that can be detected with this experimental procedure fixes a lower limit in quantity of porous material in the sample container. To obtain good accuracy in the adsorption measurements the geometrical volume of porous silicon should be at least 0.05 cm^3. This was obtained by preparing porous silicon samples 80 μm thick and 10 cm^2 of geometrical surface area.

Wafers with the porous silicon layer were introduced in a sample container for adsorption measurement constructed in Pyrex glass and specially flat-designed to minimize the dead volume. Prior to determination of an isotherm, all physisorbed material was removed from the surface of the porous silicon by outgassing 6-10 hr until the residual pressure was reduced to values lower than 10^{-5} Torr.

Nitrogen adsorption isotherms were measured using precision manometric techniques. The gas volume adsorbed by the sample was measured as a function of the equilibrium pressure. Constant values of the equilibrium pressure were obtained within 1-3 min after the introduction of the gas dose. Sample temperature during the experiment was kept constant at 77.2 K. Both adsorption and desorption isotherms were obtained during the same run; several runs were made for each sample showing excellent reproducibility.

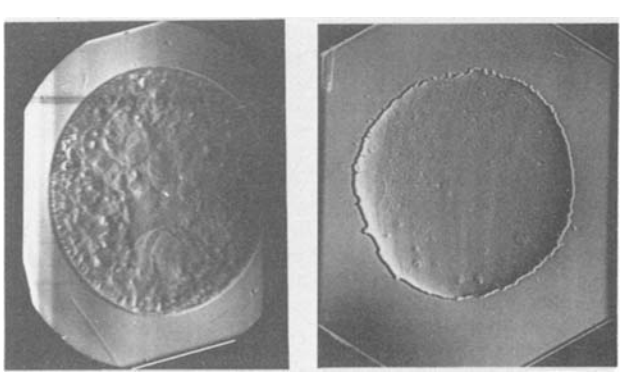

Fig. 1. (a, left) 220 x-ray topography of porous silicon samples prepared in HF-H_2O solutions. (b, right) idem in HF-H_2O-C_2H_5OH solutions.

Results

The adsorption isotherm of gas by a porous solid presents a definite particular shape. In the presence of pores, the physical adsorption of gases by a surface is increased relative to a nonporous surface by capillary condensation in pores, which starts at values of relative pressure where the smallest pores begin to be filled.

Two examples of adsorption isotherms obtained for porous silicon samples prepared at two different current densities are shown in Fig. 2. They present the typical shape of isotherms obtained in mesoporous solids (pores between 20-500Å). Similar results are obtained for other preparation conditions of the porous layers. The experimental results are presented as the ratio of the adsorbed gas volume V_{N2} reduced to normal conditions of temperature and pressure (273 K, 760 Torr) over the total geometrical volume of porous material V_p (obtained from the thickness and geometrical surface of the porous film) *vs.* the relative pressure P/P^o, P^o being the saturated vapor pressure of nitrogen at 77.2 K.

The first part of the curves, for P/P^o lower than 0.4 can be used for the determination of the specific surface area of samples by using the conventional BET method. BET plots have proved to be quite successful in evaluation of the specific surface area of heterogeneous substrates presenting isotherms like the ones shown in Fig. 2 (10). In Table I are shown the specific surface area obtained from the BET plots of the experimental isotherms for samples prepared at different current densities.

Results indicate that within the accuracy of the method; the specific surface is independent of the forming current density. The average value 200 m^2/cm^3 is quite large and in the order of those obtained for materials used as adsorbents and catalysts (11).

The rising part of the curves for P/P^o greater than 0.6 corresponds to capillary condensation of the adsorbate in the pores; then a plateau is observed which

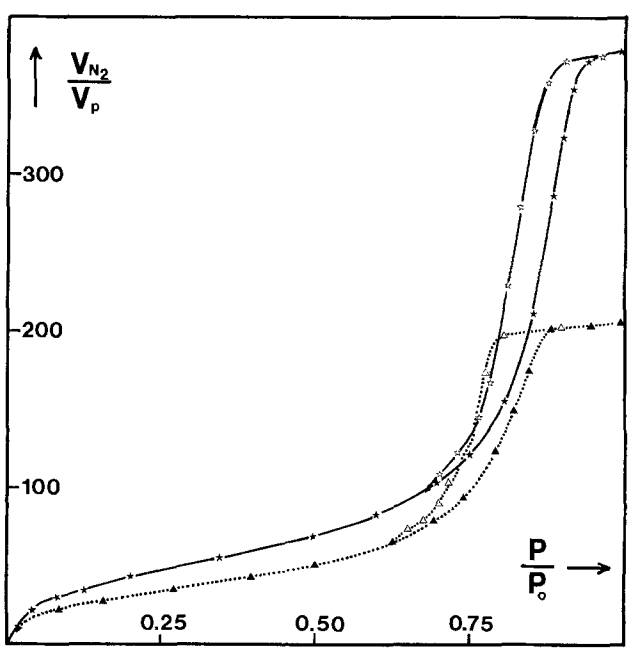

Fig. 2. Adsorption isotherms of two porous silicon samples, corresponding to a forming current density of V_{N2} (cm^3) 240 mA/cm^2 (full line) and 80 mA/cm^2 (dotted line). Adsorbed gas volumes are plotted relative to the geometrical volume of porous material V_p (cm^3).

Table I.

Forming current density (mA/cm²)	Specific surface area (m²/cm³)
10	180
80	225
240	205

represents the filling of all the pores with liquid adsorbate. When the amount of gas adsorbed along the plateau is expressed as a volume of liquid, we obtain the void volume in the porous material. The ratio void/geometrical volume and the corresponding apparent density are calculated and the results, shown in Table II, indicate a strong dependence with the forming current density.

Values of the apparent density have been checked using an independent gravimetric method. Samples were weighed before anodic reaction (m_1), after anodic reaction (m_2), and after removal of the porous silicon layer (m_3). Porous silicon is removed by dissolution in dilute NaOH solutions. We have verified that during the time necessary to dissolve porous silicon, there was no measurable change in weight of the silicon substrate. The apparent density was obtained from

$$\rho_{ps} = \rho_{Si}\ (m_2 - m_3/m_1 - m_3)$$

Results shown in Fig. 3 and comparison with results shown in Table II indicate an excellent agreement between the apparent density obtained from the adsorption isotherms and that obtained by the gravimetric method.

The hysteresis loops observed for P/P^o greater than 0.6 which correspond to capillary condensation in the adsorption branch and evaporation in the desorption branch are different, due to different pore size distributions. The pore size distribution can be computed from the experimental isotherms using various different methods. We have used a procedure developed by Barret-Joyner-Halenda known as the BJH method (12).

Figure 4 shows the pore size distributions obtained for three different forming current densities. The pore size distribution appears quite sharp for the lower current density, and rather broad for the highest. It is clear that when current density increases, the mean values of pore radii increase. Using other procedures to calculate the pore size distribution, we have obtained the same relative results although there are slight differences in the absolute values of mean pore radii.

As the smallest pore radius which can be determined using the gas adsorption techniques is in the order of 20Å, a peak in the pore size distribution for this value represents the contribution of all pore sizes up to 20Å. This means that for low current densities (10 mA/cm²) as shown in Fig. 3, a large number of very small pores is present.

The area under a pore distribution peak is equal to the total adsorbed gas volume which as shown before increases with the increase in the current density. As the geometrical porous volume V_p was nearly the same for each of the samples, there was a large difference in the anodic reaction time between the samples prepared at different current densities, *e.g.*, the anodic reaction time at 10 mA/cm² is 25 times larger than at 240 mA/cm². However the pore distribution at 10 mA/cm² is sharp compared to the pore distribution at 240

Table II.

Forming current density (mA/cm²)	Void volume/geometrical volume	Apparent density (g/cm²)
10	0.3	1.63
80	0.6	0.93
240	0.7	0.69

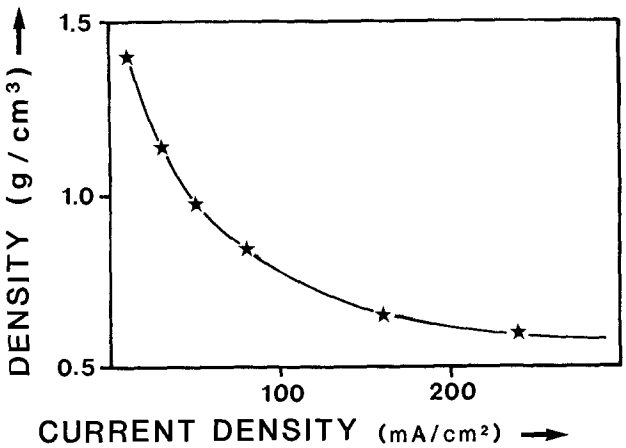

Fig. 3. Apparent density of porous silicon layers as a function of the anodic current density.

mA/cm². When high current density samples are left in the electrolyte on open circuit during an equivalent time to the lower current density samples, no noticeable change can be detected in the pore size distribution. These results indicate that the broadening in the pore size distribution is due to a specific effect of the current density, and is neither related to the anodic reaction time, nor affected by chemical reaction with the electrolyte on open circuit.

All these results were obtained with porous silicon samples at about 80 microns thick. However, gravi-

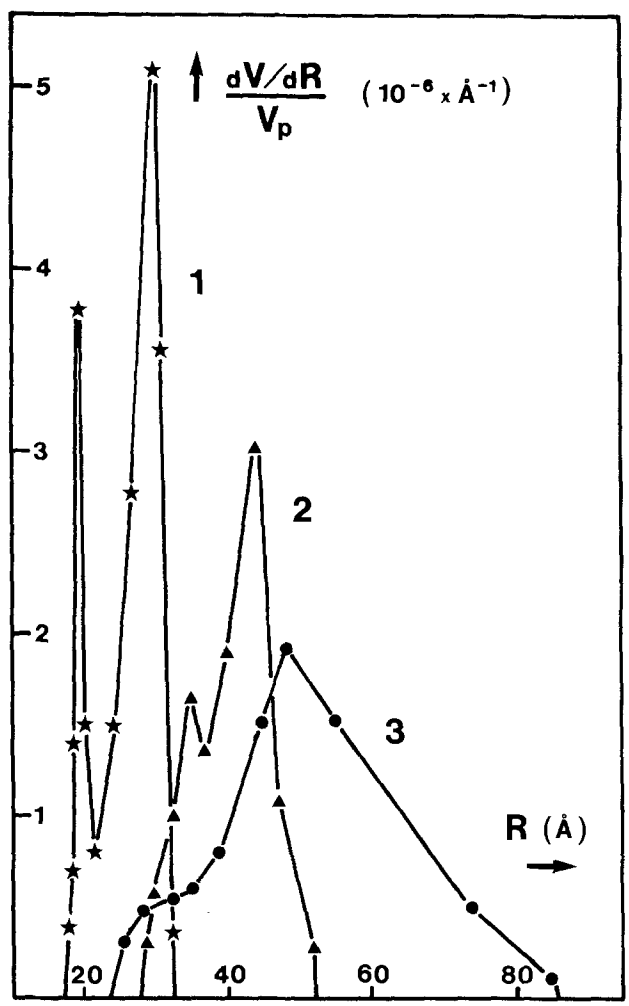

Fig. 4. Distributions of pore of three samples corresponding to different current densities: 1—10 mA/cm², 2—80 mA/cm², 3—240 mA/cm². The pore volume per group of pores of radius R, dV/dR (cm³ × Å⁻¹) is plotted relative to the geometrical volume of porous material V_p (cm³), as a function of R.

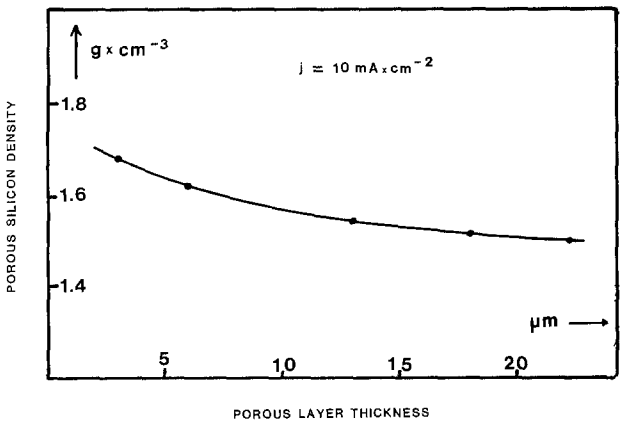

Fig. 5. Apparent density of porous silicon layers as a function of thickness for anodic current density $j = 10$ mA/cm^2.

metric measurements indicate that the apparent porous silicon density is nearly independent of the porous layer thickness, except for the lowest values of the current density, where a slight decrease in porous density is observed in the first 15 microns, as shown in Fig. 5. It will be interesting now to follow the evolution of the pore size distribution as a function of thickness, especially for thin layers of porous silicon. Work in this direction is in progress, although we have observed some scatter in the results, due to the very small porous volume which is analyzed in these cases.

Conclusion

We have shown that the gas adsorption technique is an appropriate tool to measure the pore sizes in porous silicon layers, and to investigate the evolution of the pore size distribution as a function of the formation conditions. The results demonstrate the determining role played by the forming current density in the pore formation. Further work should be oriented towards the study of pore size distribution as a function of other parameters, like electrolyte composition and substrate resistivity. This would probably lead to a better understanding of the pore formation mechanisms.

Acknowledgments

The authors are much indebted to Mr. Ginoux from the Ecole d'Electrochimie de USMG (Université Scientifique et Médical de Grenoble) for gas adsorption measurements.

Manuscript submitted Dec. 27, 1982; revised manuscript received April 3, 1983. This was paper 223 presented at the Detroit, Michigan, Meeting of the Society, Oct. 17-21, 1982.

Any discussion of this paper will appear in a Discussion Section to be published in the June 1984 JOURNAL. All discussions for the June 1984 Discussion Section should be submitted by Feb. 1, 1984.

The Centre National d'Etudes des Télécommunications de Grenoble assisted in meeting the publication costs of this article.

REFERENCES

1. A. Uhlir, *Bell Syst. Tech. J.*, **35**, 333 (1956).
2. D. R. Turner, *This Journal*, **105**, 402 (1958).
3. Y. Arita and Y. Sunohara, *ibid.*, **124**, 285 (1977).
4. Y. Arita, K. Kato, and T. Sudo, *IEEE Trans. Electron Devices*, **ed-24**, 756 (1977).
5. Y. Arita, T. Sakai, and T. Sudo, *Rev. Elect. Comm. Lab.*, **27**, 41 (1979).
6. K. Imai and S. Nakajima, *IEDM*, 81 376.
7. T. Unagami, *This Journal*, **127**, 476 (1980).
8. H. Baumgart, R. C. Frye, L. E. Trimble, H. J. Leamy, and G. K. Celler, "Laser and Electron Beam Interactions with Solids," B. R. Appleton and G. K. Celler, Editors, p. 609, North Holland, New York (1982).
9. K. Barla, J. Baruchel, G. Bomchil, R. Herino, and J. C. Pfister, Paper 193 presented at The Electrochemical Society Meeting, Montreal, Que., Canada, May 9-14, 1982.
10. S. J. Gregg and K. S. Sing, in "Surface and Colloid Science," E. Matijeirc, Editor, Vol. 9, pp. 231-359, John Wiley and Sons, New York (1976).
11. S. J. Gregg and K. S. Sing, "Adsorption, Surface Area and Porosity," pp. 104-105, Academic Press, New York (1982).
12. E. P. Barret, L. G. Joyner, and P. H. Halenda, *J. Am. Chem. Soc.*, 73, 373 (1951).

Technical Notes

Electroepitaxial Growth of HgCdTe from Te-Rich Solution

L. Jedral, H. Ruda, P. Becla, J. Lagowski,* and H. C. Gatos*

Massachusetts Institute of Technology, Cambridge, Massachusetts 02139

HgCdTe is ideally suited for advanced infrared detection and imaging. However, due to inherent problems associated with the growth of bulk material, epitaxial techniques are now widely pursued. Liquid phase electroepitaxy (LPEE) has been employed for the growth of multicomponent III-V compounds and has been found to have a number of advantages over conventional LPE techniques (1). Thus, the growth velocity and doping are readily controlled by the current density; in addition, it leads to improved surface morphology and defect structure (2). It was also shown most recently that LPEE offers enhanced interface stability compared to conventional LPE (3).

LPEE layers of HgCdTe have been grown from Hg-rich solutions at temperatures as low as 290°C (4). In the present communication, we present results on LPEE growth of HgCdTe from Te-rich solution at 501°C.

Growth experiments were performed in a two-zone furnace. A graphite boat with BN slider of a design similar to that described elsewhere (5) was placed in the high temperature zone. The lower temperature

* Electrochemical Society Active Member.
Key words: mercury cadmium telluride, electroepitaxy, tellurium-rich solution.

zone contained a pure Hg reservoir. The mercury pressure over the growth system was controlled by selecting the temperature of this zone and the flow rate of H_2. A Te-rich solution with the composition $Hg_{0.188}Cd_{0.012}Te_{0.800}$ was used. The experimentally determined liquidus temperature for this solution was 501°C, with a mercury reservoir temperature of 294°C at a H_2 flow rate of about 50 cm³/min.

LPEE requires low resistivity substrates to avoid excessive Joule heating due to current flow through the substrate-solution system. Commercially available CdTe of high or medium resistivity (commonly used in LPE) was found to be unsuitable as a substrate material for electroepitaxy. To overcome this problem, we grew a low resistivity HgCdTe layer about 200 μm thick on CdTe (111) wafers (B-surface) by isothermal VPE (6); the CdTe wafer was subsequently thinned down to less than 100 μm by mechanical polishing. Thus, the substrates used for LPEE consisted of a 200 μm thick HgCdTe layer on a 100 μm thick CdTe; the CdTe A-surface was used for LPEE growth.

A low resistivity and uniform back-side electrical contact between the HgCdTe surface of the substrate and the graphite boat was made with a mixture of graphite and Te powders. The substrate (1 cm²) resistivity at 500°C was less than 20 mΩ. As established experimentally, the Joule heating interference was negligible up to a current density of 10 A/cm².

Prior to growth the solution was melted under mercury pressure smaller than the equilibrium one. Subsequently, the temperature of the Hg reservoir was raised, and the system was equilibrated for a period of about one hour, close to the liquidus temperature. Growth was then initiated and sustained by passing a constant electric current across the substrate-solution interface. (The polarity of the substrate was positive.) The duration of growth was varied from 15 to 90 min. The current densities were between 2-10 A/cm².

Uniform single crystalline layers of $Hg_{(1-x)}Cd_xTe$ were grown with thickness up to 50 μm of a composition of $x = 0.23$. The electrical characteristics of the layers were comparable to those obtained by other epitaxial techniques. As-grown, they were p-type; after standard annealing in a Hg atmosphere, they exhibited typical carrier concentrations of the order of 10^{16} cm^{-3} and carrier mobilities of the order of 10^5 cm^2 V^{-1} sec^{-1}.

The electroepitaxial growth behavior of HgCdTe was found to be similar to that of the III-V compounds, previously reported. As shown in Fig. 1, the electroepitaxial growth velocity increased linearly with the current density. For 10 A/cm⁻², the growth velocity was about 0.8 μm/min, *i.e.*, appreciably higher than that reported for III-V compounds at typical LPE growth temperatures 700°-800°C; [for GaAs a rate of ~0.4 μm/min has been reported for 800°C (7)]. In Fig. 2, the thicknesses of electroepitaxial layers are presented as a function of growth time for three values of current density. It is seen that the layer thickness can be very well approximated by a linear dependence on the growth time.

The results of Fig. 1 and 2 can be quantitatively accounted for by the multicomponent theory of LPEE, presented in Ref. (1); the overall electroepitaxial growth velocity can be expressed as

$$v = \frac{-\Delta T_o}{(\pi t)^{1/2}} \left[\sum_{i=1}^{2} \frac{\alpha_i (C_i^{so} - C_i^{o})}{(D_i)^{1/2}} \right]^{-1} + E \sum_{i=1}^{2} \frac{\mu_i C_i^{o} \alpha_i}{(D_i)^{1/2}} \left[\sum_{i=1}^{2} \frac{\alpha_i (C_i^{so} - C_i^{o})}{(D_i)^{1/2}} \right]^{-1} \quad [1]$$

where i refers to components Hg and Cd; ΔT_o is the current-induced change of the interface temperature due to the Peltier effect); μ_i is the solute mobility; E is the electric field in the solution (which is proportional to the current density); $\alpha_i \equiv \partial T/\partial C_i|_{C_i=C_i^o, T_o}$ are the liquidus slope components; D_i is the diffusion coefficient of the solute in the solution; t is the growth time and C_i^{so} and C_i^{o} are the solid and liquid concentrations, respectively.

The first term on the right-hand side of Eq. [1] represents the Peltier effect contribution to the growth velocity. This term is time dependent and plays a role only at the initial stages of electroepitaxial growth. After the initial transient, the second term becomes dominant, and the growth proceeds with a constant growth velocity controlled by solute electromigration. It is important to note that the results of Fig. 1 and those of Fig. 2 indicate that electromigration is the dominant contribution to growth, as there is no appreciable deviation of the growth velocity from a linear dependence on time (the thickness increases linearly with time over a growth period of 10-90 min). Using expression [1], no contribution from the Peltier effect, the phase diagram and transport data in Ref. (8, 9) and the results of Fig. 1 and 2, we have estimated the electromigration velocities $E\mu_{Hg}$ and $E\mu_{Cd}$ (assumed to be equal) to be of about 1.3×10^{-6} cm/sec for a current density of 10 A/cm².

These values were used to calculate the electroepitaxial growth velocity for other solid compositions (x values) and growth temperatures. The theoretically calculated dependences of the electroepitaxial growth velocity on x are shown in Fig. 3. It is seen that there is a general tendency for the growth velocity to increase with decreasing x and with increasing growth

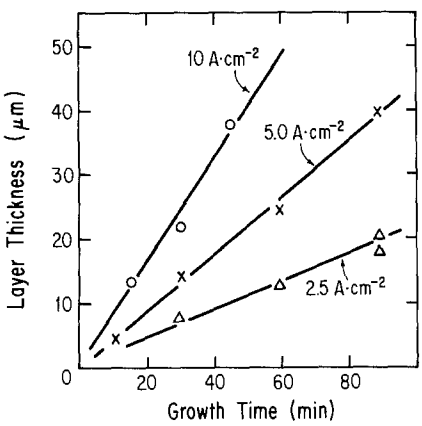

Fig. 1. Average electroepitaxial growth velocity as a function of current density. Growth was carried out at 501°C from $Hg_{0.188}Cd_{0.012}Te_{0.800}$ solution. Individual points correspond to growth times ranging from 15 to 90 min.

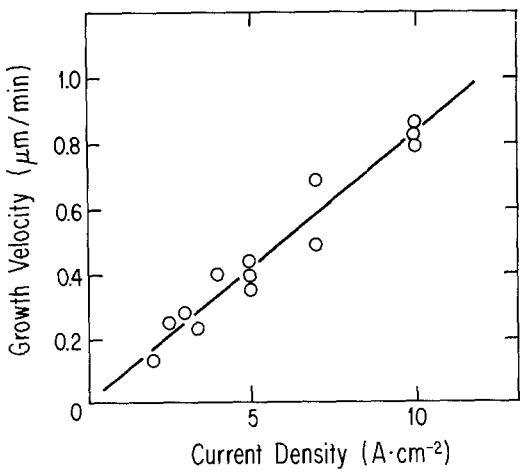

Fig. 2. Layer thickness vs. growth time for three values of current density. Growth conditions as in Fig. 1.

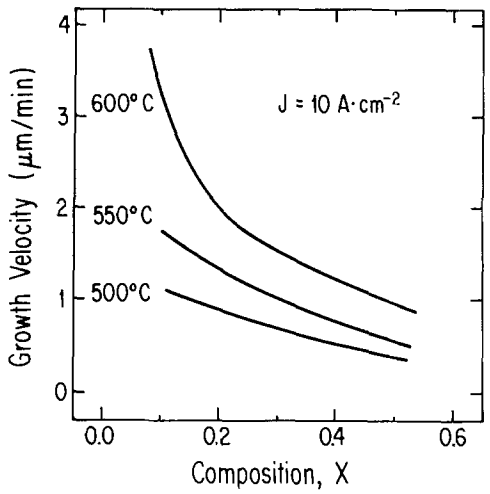

Fig. 3. Electroepitaxial growth velocity of $Hg_{1-x}Cd_xTe$ as a function of x calculated from electroepitaxial model in Ref. (1). See text.

temperature. In the region of low x values (*e.g.*, $x = 0.2$ which is of greatest interest for practical applications), the growth velocities exceeding 2 μm/min can be realized between 550°-600°C using a rather low current density of 10 A/cm². Such high growth rates can be of considerable practical importance since they minimize interfering effects of solid state diffusion within the epilayer and outdiffusion of defects from the substrate (10, 11).

In summary, we have demonstrated the feasibility of electroepitaxial growth of HgCdTe from Te-rich solution in an open-tube slider system. Problems of Joule heating were essentially eliminated by using substrates consisting of a low resistivity HgCdTe layer and a very thin CdTe layer and employing a low resistivity back contact. The thickness of electroepitaxial layers with $x \simeq 0.23$ was found linearly dependent on the current density and on the growth time. For a current density of 10 A/cm², the average growth velocity was about 0.8 μm/min. Electromigration was found to be the dominant growth mechanism.

Acknowledgments

The authors are grateful to the Defense Advanced Research Projects Agency for financial support.

Manuscript submitted Dec. 3, 1982; revised manuscript received *ca.* March 30, 1983.

Any discussion of this paper will appear in a Discussion Section to be published in the June 1984 JOURNAL. All discussions for the June 1984 Discussion Section should be submitted by Feb. 1, 1984.

The Massachusetts Institute of Technology assisted in meeting the publication costs of this article.

REFERENCES

1. T. Bryskiewicz, J. Lagowski, and H. C. Gatos, *J. Appl. Phys.*, **51**, 988 (1980).
2. Y. Imamura, L. Jastrzebski, and H. C. Gatos, *This Journal*, **125**, 1561 (1978).
3. A. Okamoto, J. Lagowski, and H. C. Gatos, *J. Appl. Phys.*, **53**, 1706 (1982).
4. P. E. Vanier, F. H. Pollak, and P. M. Raccah, *J. Electron. Mat.*, **9**, 153 (1980).
5. L. Jastrzebski, Y. Imamura, and H. C. Gatos, *This Journal*, **125**, 1141 (1978).
6. P. Becla, J. Lagowski, and H. C. Gatos, *ibid.*, **128**, 1171 (1981).
7. L. Jastrzebski, J. Lagowski, H. C. Gatos, and A. F. Witt, *J. Appl. Phys.*, **49**, 5909 (1979).
8. T. C. Harman, *J. Electron. Mat.*, **9**, 945 (1980).
9. V. N. Ambrosimov, A. V. Vanyukov, T. N. Saburova, and A. S. Tomson, *Izv. Akad. Nauk. SSSR, Neorgan. Mat.*, **12**, 1676 (1976).
10. L. Svob, Y. Marfaing, R. Triboulet, F. Bailly, and G. Cohen-Solal, *J. Appl. Phys.*, **46**, 4251 (1975).
11. L. Jastrzebski, J. Lagowski, and H. C. Gatos, *This Journal*, **126**, 223 (1979).

Absence of Oxidation in Polysilicon Fuse Links

D. W. Greve

Carnegie-Mellon University, Pittsburgh, Pennsylvania 15213

Polysilicon links are presently being used in large MOS memories to deselect defective rows and/or columns and therefore enhance yield. Both electrical and laser programming of the polysilicon links have been demonstrated (1). Electrical programming is probably the most desirable, but the high programming currents required are a major difficulty.

Some previous reports (1, 2) have suggested that oxidation of the polysilicon link plays some role during programming. On the other hand, we have reported that the most important mechanism was migration of molten silicon in the applied electric field (3, 4). Because the resistivity of silicon decreases on melting, we found that very large currents were required. It is possible, of course, that both mechanisms may occur depending on programming conditions. If this were the case, it might be possible to choose programming conditions so that only oxidation occurred and lower programming currents could be used. We have, therefore, conducted some experiments to look specifically for an oxidation mechanism in polysilicon fuse programming.

The fuses we studied had a notch of width 2 and length 4 μm with wider ends for contacts. The polysilicon thickness was ≃0.3 μm and the underlying SiO_2 layer ≃1.5 μm; there was no passivation layer on top of the fuses. The fuses were programmed as previously reported (4) with a source resistance $R_s = 50\Omega$ and pulse length 45 μsec. Current and voltage waveforms were recorded during programming.

Consistent with our earlier results (3, 4), we found essentially no change in fuse resistance unless a second breakdown transition (evidenced by a rise in current and a drop in voltage) was observed. We previously showed that this transition results from formation of a molten silicon filament extending lengthwise through the fuse. Of the fuses showing this type of transient, some opened while others remained continuous.

Figure 1 shows a fuse which did not open; the maximum current during programming was 47 mA and the fuse resistance decreased to 90 from 100Ω. A fuse which opened is shown in Fig. 2; an open circuit was observed after programming and the maximum current was 48 mA. In these photographs, it is clear that the fuse in Fig. 2 is discontinuous. However, when viewed from a direction nearer to the normal, the original outline of the fuse is still visible. From such photographs, one might conclude that there was no gap and that the fuse had opened by oxidation. This interpretation is supported to some extent by the apparent increase in thickness.

Key words: SEM, fuses, semiconductor, melting.

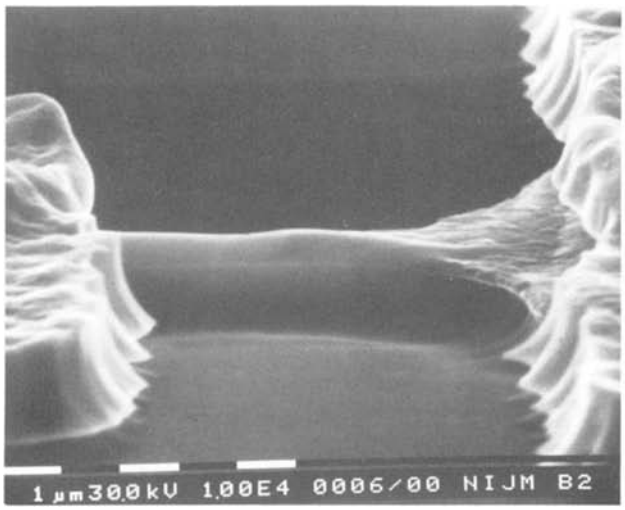

Fig. 1. SEM photograph of programmed polysilicon fuse. A second breakdown transition was observed but the fuse remained continuous.

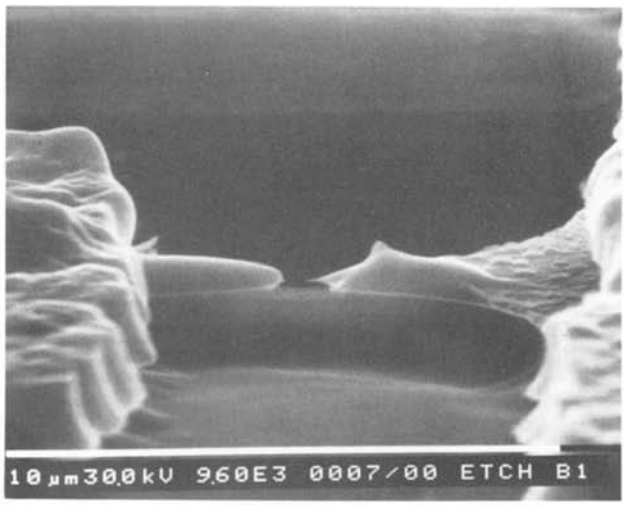

Fig. 3. Programmed polysilicon fuse of Fig. 2 after etching with hydrofluoric acid. The fuse material is not removed so a negligible amount of SiO_2 was formed during programming.

Our photographs show clearly that there is a gap in the polysilicon and that the outline of the fuse which remains after programming is due to etching of the underlying oxide during fabrication. We can check this by etching the programmed sample in oxide etch and reexamining the fuse. The result is shown in Fig. 3; approximately 0.2 μm of oxide has been removed under the fuse leaving polysilicon suspended over the gap. The appearance of the fuse material is unchanged indicating that none of it is silicon dioxide. The apparent increase in thickness near the gap is due to transport of silicon away from the righthand (positive) contact. Some thinning of the polysilicon layer near the positive contact is visible in Fig. 1.

We noted one difference between these notched fuses and the bar fuses we studied previously. Notched fuses which showed the second breakdown transition but did not open showed a small decrease in resistance, in contrast to the increase observed in bar fuses. This is because transport of silicon in a bar fuse must result in a thinner region somewhere and therefore an increase in resistance. In a notched fuse, the material can come from the wider end regions. The fuse resistance in this case is mostly determined by the notch region which increases in thickness.

Finally, we explored the possibility that oxidation could occur during long pulses below the threshold for second breakdown. For this experiment, we used the bar fuses previously studied (3, 4) with the top passivation layer removed. We used a pulse length of 12 msec and adjusted the amplitude so that some of the fuses would just go into second breakdown. Those that did not go into second breakdown would then reach a temperature near, but below the silicon melting point. All of the fuses not showing second breakdown decreased in resistance. Oxidation would be expected to cause an increase in resistance. We note that the pulse length we used is several times the length of all pulses added together in a commercial programming procedure (5).

In conclusion, then, we find that under all practical programming conditions oxidation of polysilicon fuses is negligible. The fuses open by field-induced migration of silicon ions in a molten filament. We find no evidence for a mechanism which does not require formation of a molten filament. It appears, then, that high programming currents are unavoidable.

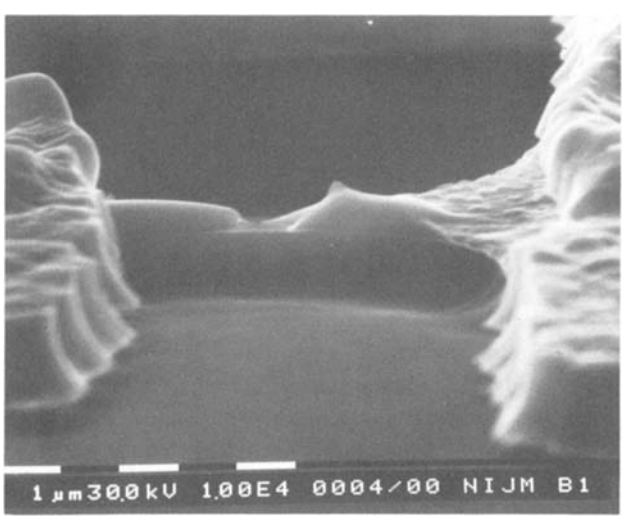

Fig. 2. Polysilicon fuse programmed at slightly higher current. The fuse is an open circuit.

Manuscript received March 9, 1983.

Any discussion of this paper will appear in a Discussion Section to be published in the June 1984 JOURNAL. All discussions for the June 1984 Discussion Section should be submitted by Feb. 1, 1984.

Carnegie-Mellon University assisted in meeting the publication costs of this article.

REFERENCES

1. R. C. Smith *et al.*, in "14th Annual Proceedings on Reliability Physics," p. 193, Las Vegas, NV (1976).
2. R. J. Smith, IEDM Digest of Technical Papers, p. 608, Dec. 1982.
3. D. W. Greve, IEDM Digest of Technical Papers, p. 70, Dec. 1981.
4. D. W. Greve, *IEEE Trans. Electron Devices*, **ed-29**, 719 (1982).
5. "Intel 1981 Component Data Catalog," p. 2-72, Santa Clara, CA (1981).

JOURNAL OF THE ELECTROCHEMICAL SOCIETY

ACCELERATED

—BRIEF COMMUNICATIONS—

JULY 1983

Reactions at the Anode during Storage of Partially Discharged Li/SO_2 Cells

K. M. Abraham* and L. Pitts

EIC Laboratories, Inc., Newton, Massachusetts 02158

Although the Li/LiBr, CH_3CN/SO_2 cell is one of the most advanced among the non-aqueous Li cells, concerns of safety have precluded it from being widely accepted. In a recent study (1) involving a literature and user survey of the safety hazards in Li/SO_2 cells, we have shown that partially discharged and stored Li/SO_2 cells and batteries have a greater propensity for safety hazards, especially in use under harsh conditions such as high current pulses, temporary short-circuits and overdischarges. In an effort to understand the underlying chemistry we have analyzed cells which had been stored for about one year at room temperature after a partial discharge corresponding to ~50% of their rated capacity. Because of the great concern in the user community for the safety of partially discharged and stored Li/SO_2 cells, we wish to communicate some of our preliminary analytical results obtained from these cells. We believe that the results have considerable practical relevance.

The Li/SO_2 cells used in these studies were commercial C-size cells procured from two different manufacturers. We found the same analytical results with both types of cell. The cells, having a rated capacity of ~3 Ahr, were discharged at a constant current of 100 mA to a depth of ~50% or 1.5 Ahr. The 100 mA current corresponds to current densities of 0.6 and 0.8 mA/cm^2 respectively for the two kinds of cells. The cells were then stored at laboratory temperature for 11 months and 2 weeks prior to the analysis. Several undischarged cells were similarly stored for comparative analysis. The stored cells were opened and analyzed for gaseous, liquid and solid products. Our technique which permits cell analysis without atmospheric contamination has been described elsewhere (2,3). Infrared (IR) spectrometry, ESCA, gas chromatography (GC) and mass spectrometry were the principal analytical tools (2,3). Qualitative identification of some of the sulfur-oxy compounds were also made using standard analytical procedures (4).

Vapor phase IR spectra and GC data did not reveal any materials other than SO_2 and CH_3CN in the gas phase. Our GC analysis conditions were suitable for detecting, among others, H_2 and CH_4. The IR spectrum of the cathode (Fig. 1) shows only the absorptions at 1085(s), 1020(s), 900(s), 550(m) and 500(m) cm^{-1} due to $Li_2S_2O_4$ (3).

Evidence for a considerable amount of reaction products (several milligrams) on the anodes of partially discharged cells was obtained when their Li-anodes were compared with those of the undischarged cells stored for the same period. The SEM micrograph in Fig. 2 indicates that there are several components in the anode product. The anodes of undischarged cells had so little material on them it could not be separated for analysis.

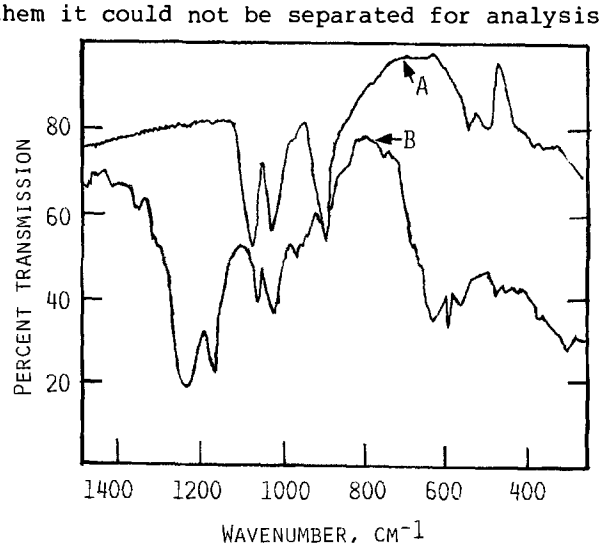

Fig. 1. Infrared spectra of the cathode (curve A), and the product(s) formed on the Li anode (curve B) from a partially discharged (~50% DOD) and stored (~1 year at 25°C) Li/SO_2 C-cell.

*Electrochemical Society active member.

Key words: SO_2 battery, anode, cathode, $Li_2S_4O_6$.

An IR spectrum (KBr pellet) of the product from the anode of a partially discharged cell is shown in Figure 1. The spectrum indicates that $Li_2S_2O_4$ is one of the components. This was confirmed by qualitative analysis with Naphthol Yellow-S (4). Of course, $Li_2S_2O_4$ is believed to be the protective film on Li. The spectrum showed no absorptions due to the organic compounds, β-aminocrotononitrile and 3,5-diamino-2,4-hexenenitrile which are products of the reaction between Li and CH_3CN (2,3). The absence of these and other organic compounds was also confirmed by mass spectral data (2) with the anode product.

A striking feature of the IR spectrum is the absorptions at 1240 (broad s), 1170(s) and 570(m) cm^{-1}. A few inorganic sulfur-oxy compounds which give rise to IR absorptions in the 1200-1250 cm^{-1} region are the alkali metal thionates, $S_nO_6^{-2}$, n = 2-6 (5). The latter compounds also show absorptions around 1000-1050 cm^{-1} and 600 cm^{-1} (5). Alkali metal sulfates show characteristic absorptions at ~1100-1150 cm^{-1} (5). Thus, the IR absorptions strongly suggest that the anode film includes, in addition to $Li_2S_2O_4$, Li-thionate(s), and possibly Li_2SO_4. An ESCA spectrum of the sample had peaks due to three types of S with the S(2p) binding energies at 163.6, 166.8 and 168.3 eV. The peak at 166.8 eV is most probably due to the S in $Li_2S_2O_4$ (3). The peak at 163.6 eV is in the range expected for "-S-" type sulfur and the broad peak at 168.3 eV is in the range expected for S^V or S^{VI} or both. The IR spectrum and ESCA data strongly support our contention that one of the components in the anode product is a thionate. Since none of these except $Li_2S_2O_4$ is found on the cathode, it seems that reactions involving Li are necessary for the formation of the anode products. We suggest the following reactions would satisfactorily account for the various observed products.

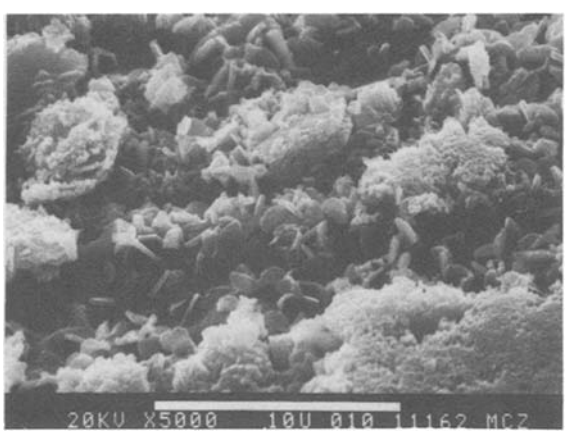

Fig. 2. The SEM of the Li anode from a partially discharged and stored Li/SO_2 cell. Magnification, 5000X.

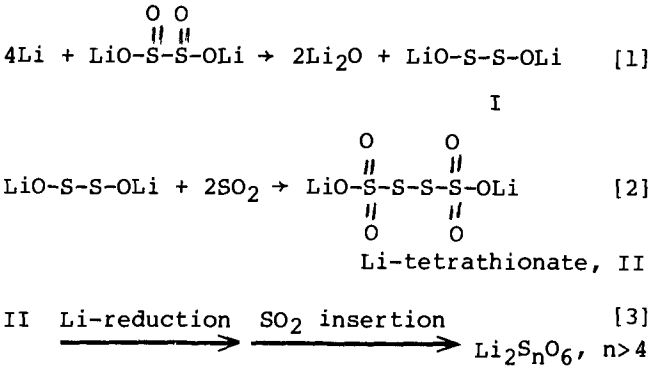

I is analogous to $H_2S_2O_2$, an intermediate proposed in the synthesis of thionic acids from sulfurous acid and H_2S (6). The proposed mechanism is also consistent with the synthesis of $K_2S_4O_6$ from S_2Cl_2 and sulfurous acid followed by neutralization with KOH (7). In the latter synthesis, the first step apparently involves the insertion of SO_2 into the S-OH bonds of HO-S-S-OH, formed first by hydrolysis of S_2Cl_2 (7).

Dithionate can be ruled out since it is formed under oxidizing conditions (6) and we do not find it on the cathode. It is possible to conceive of SO_4^{-2} formation via reactions of the type in equation 4.

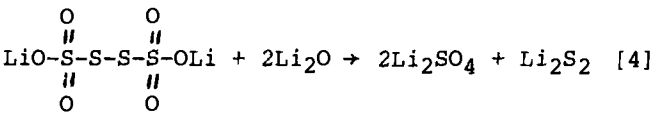

Such redistribution reactions are well known in solution chemistry (8), but they are unusual in the solid state. It should be noted Li_2SO_4 was previously identified, from ESCA spectra, on the anodes of discharged cells (9), although the storage history of those cells after the discharge was not reported.

We note that polythionates have a tendency to decompose with heating to give off S which has been shown to sustain exothermic runaway reactions. Another implication of our findings is that given the opportunity, sulfur species ranging from S^{VI} to S^{-2} could be expected as reaction products in the Li/SO_2 cell.

The observed reduction of SO_2 mostly to $S_2O_4^{-2}$ in the normal discharge is simply

because of the kinetic restrictions of the reaction. In this connection the recent report of Li_2S as a reaction product of Li and SO_2 is interesting (10).

The presence of larger amounts of reaction products on partially discharged as opposed to undischarged anodes may be attributed to the differences in the nature of the Li films in the two cases. Our evidence suggests that very small quantities of $S_nO_6^{-2}$ are also formed on the anodes of undischarged stored cells. The implication of our findings on the safety and performance of Li/SO_2 cells is being studied further.

ACKNOWLEDGEMENT

This work was supported by Naval Surface Weapons Center, White Oak, Maryland, under Contract No. N60921-82-C-0178.

REFERENCES

1. K. M. Abraham, M. W. Rupich and L. Pitts, in "Proc. 30th Power Sources Symposium," Atlantic City, NJ (1982).

2. K. M. Abraham, M. W. Rupich and L. Pitts, Final Report on NSWC Contract N60921-81-C-0084, Report No. NSWC TR-82-148, April 1982.

3. M. W. Rupich, L. Pitts and K. M. Abraham, J. Electrochem. Soc., 129, 1857 (1982).

4. J. H. Karchmer, Editor, "The Analytical Chemistry of Sulfur and Its Compounds, Part 1," Vol. 29, Wiley Interscience, NY (1970).

5. G. Nickless, Editor, "Inorganic Sulfur Chemistry", Elsevier, NY (1968) pp. 162.

6. See Ref. 4, pp. 238.

7. W. A. Hart and O. F. Beumel, Jr. in "Comprehensive Inorganic Chemistry", Vol. 1," J. C. Bailar, Jr. et al., Editor, Pergamon Press, NY (1973).

8. J. C. Lockhart in "Redistribution Reactions", Academic Press, NY (1970).

9. W. P. Kilroy and C. R. Anderson, paper presented at the fall meeting of the Electrochemical Society, Detroit, MI (1982); Extended Abstract No. 317.

10. K. W. Nebesny, R. Kaller, N. R. Armstrong and R. K. Quinn, J. Electrochem. Soc., 129, 2861 (1982).

Manuscript submitted Feb. 22, 1983; revised manuscript received April 11, 1983.

Diffusion-Coupled Active Dissolution in the Localized Corrosion of Stainless Steels

R. C. Newman* and H. S. Isaacs*

Corrosion Science Group, Brookhaven National Laboratory, Upton, New York 11973

We have examined the anodic dissolution of stainless steels in environments relevant to localized corrosion in neutral chloride solutions. There is a maximum active dissolution rate, for a given potential, which is not associated with the most concentrated localized environment. This observation seems to be significant with respect to the stability of localized corrosion in these alloys. Results of this kind are capable of explaining the existence of a critical pit solution, a protection potential against pitting, multiple steady states, low frequency electrochemical noise and differences between open circuit and potentiostatic behavior.

An artificial pit technique was used to examine two materials in 1 mm wire form: type 304L stainless steel (18.50Cr, 8.99Ni, 0.013C, 1.61Mn, 0.33Cu, 0.62Si, 0.32Mo, 0.021S, 0.17Co, 0.136N) and a high purity iron-19Cr-10Ni alloy (18.7Cr, 10.3Ni, others <0.01). The high purity alloy was homogenized for 16 hours at 1150°C in an evacuated silica tube and cooled by immersing the intact tube in mineral oil; the stainless steel was used as received. Both alloys were fully austenitic. The wires were abraded lightly with 600 grit paper, washed with methanol and mounted in rods of epoxy resin. After abrading to expose the end of the wire, each specimen was mounted in a 150 ml glass cell containing a saturated calomel electrode (SCE) and a perforated stainless steel tube which served both as counter electrode and as an inlet for high purity nitrogen. The electrolyte was deoxygenated 1M NaCl, pH 6, at 25 ± 1°C. The metal surface, facing upwards, was first polarized at +400 mV (SCE) to induce a general breakdown of passivity by coalescence of pits. Diffusion-controlled dissolution was allowed to continue until a cavity 0.8 mm deep was produced. The cell was then flushed with distilled water and fresh electrolyte added. The metal surface was flat and bright. After deoxygenation, polarization was repeated at +200 mV, for just long enough to establish a steady state in the cavity. This time is about $2\delta^2/D$, where δ is the depth of the cavity and D the ionic diffusivity ($\sim 10^{-5}$ cm^2/s). Generally, 20 minutes was allowed to elapse before beginning the next stage; this involved the dissolution of about 50 μm of metal. The diffusion controlled current density of ~100 mA/cm^2 at a pit depth of 0.85 mm indicated that the interfacial concentrations of Fe^{2+}, Cr^{3+} and Ni^{2+} were about 2.8, 0.7 and 0.35 molar, respectively (1,2).

Open circuit behavior in pit environments

The first attempt to understand the behavior of the alloys in solutions of their corrosion products involved simply switching off the potentiostat. In these experiments the salt film present during diffusion-controlled dissolution (1) is dissolved within about one second. The alloy surface is then exposed to a decreasing concentration of its dissolution products, and may eventually passivate. Assuming constant diffusivity, and that the new dissolution rate of the alloy is negligible, the interfacial concentration C_o of, for instance, Cr^{3+} is given by:

$$C_o = 8C_s/\pi^2 \sum_{n=1}^{\infty} \frac{1}{(2n-1)^2} \exp\left\{-\left[\frac{(2n-1)\pi}{2\delta}\right]^2 Dt\right\} \quad 1)$$

where C_s is the saturation concentration. For practical purposes, this fortuitously reduces to the useful form:

$$\log_{10} (C_o/C_s) \approx -t/\tau \quad 2)$$

where $\tau = \delta^2/D$.

The alloys behaved differently in the open circuit experiment (Fig. 1). Whereas the potential of the high purity alloy immediately fell

---

* Electrochemical Society Active Member.

Key words: stainless steel, localized corrosion, anodic dissolution.

to below -400 mV, that of the steel remained close to -250 mV for about 10 minutes. This clearly results from the presence of an oxidizing agent (other than H^+) in the pit solution. Copper ions could be present as a result of dissolution of the 0.33% copper from the steel; this could give an interfacial concentration close to 0.01M, and -250 mV is a reasonable potential for plating of copper from a solution of relevant species such as $CuCl_2^-$ (3,4). In another paper we will report microelectrode studies of the dissolution and plating of copper in artificial pits on type 304L stainless steel.

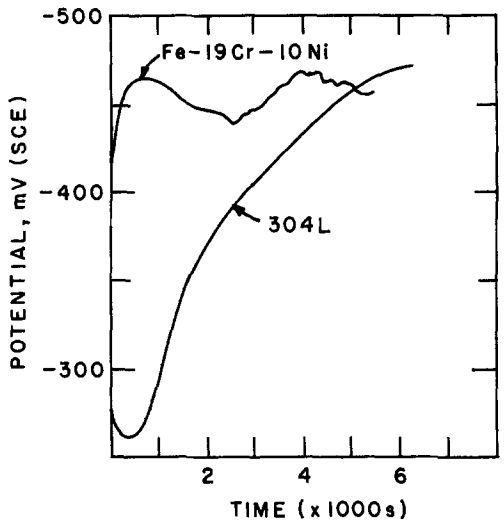

Fig. 1 Variation of open circuit potential for 0.85 mm deep artificial pits, following diffusion-controlled dissolution at +200 mV.

Potentiostatic behavior in pit environments

The impurity effects preclude the use of the artificial pit technique to examine the dissolution of the stainless steel below -250 mV. This limits information on crevice corrosion, which often propagates at potentials between -400 and -300 mV (5). However, there were no difficulties in making measurements down to about -400 mV on the high purity alloy. Fig. 2 shows a set of potentiostatic current-time curves for the high purity alloy following treatment at +200 mV; δ was 0.85 $\pm$ 0.05 mm throughout. Above -300 mV the curves showed an initial increase in current, followed by a decrease. At some potentials rapid passivation occurred; at others a more prolonged active state was maintained. The stainless steel showed a more complex behavior with a second levelling out of the current prior to passivation. Fig. 3 shows current density-potential curves constructed for both alloys at the

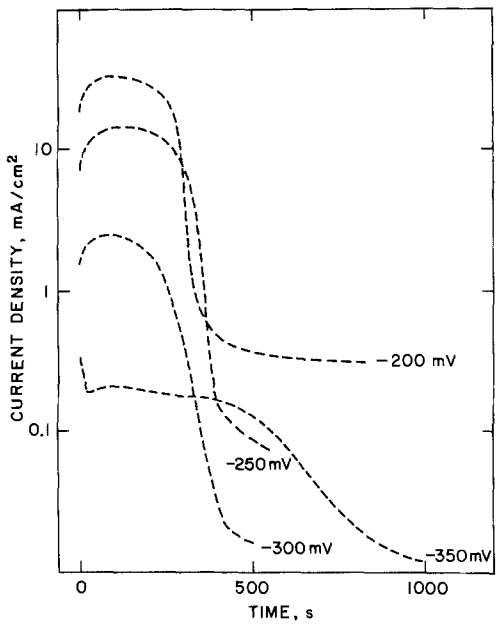

Fig. 2 Current density variation for 0.85 mm artificial pits of the iron-19Cr-10Ni alloy, following diffusion controlled dissolution at +200 mV. $\delta^2/D \simeq 700$ s. Initial c.d. $\simeq 100$ mA/cm^2.

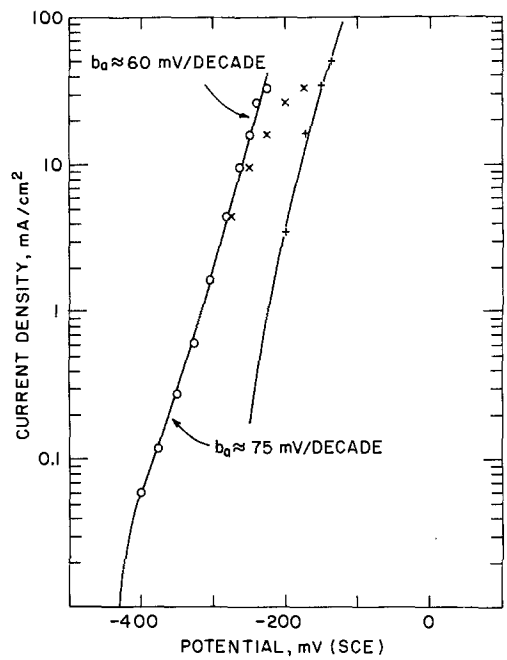

Fig. 3 Anodic dissolution kinetics for 95% saturated solutions of corrosion products. o,x: iron-19Cr-10Ni, with and without IR correction respectively; + : 304L, IR corrected. For iron-19Cr-10Ni a possible change in Tafel slope at about -300 mV is indicated.

near-saturation level. We have indicated a possible change in Tafel slope for the high purity alloy at around -300 mV; this has a precedent in the behavior of iron in similar solutions (6). The stainless steel has a parallel but much displaced Tafel line for potentials above -200 mV.

To ensure that the increasing portions of the current-time (I-t) curves were not due to surface roughening, the dependence on pit depth was examined. When the pit depth was doubled, the duration of the current rise increased by a factor of about four. As a further check, the concentration range of the measurements was extended by supersaturating the solution (2). This involved switching off the potentiostat for 5 seconds during diffusion-controlled dissolution, then polarizing again at +200 mV until the salt film was about to precipitate. On pulsing to -275 mV this gave an extended region of positive dI/dt, and also showed that the shape of the current-time curve is the same whether the prior high potential dissolution is resistance or diffusion controlled.

Mechanism of dissolution and consequences for localized corrosion

The occurrence of a region of negative dI/dC_o indicates acceleration by OH^-, as in iron (6). Water and chloride ion activities also undoubtedly influence the kinetics. The subsequent region of positive dI/dC_o is due to an increasing coverage by chromium-oxygen species, finally leading to passivation. The occurrence of a maximum suggests a significant coupling between dissolution and diffusion.

Consider a localized corrosion site with a one dimensional diffusion path length δ. Possible steady state current densities i_s are given by (2):

$$i_s = zDFC_o/\delta = kC_o \qquad 3)$$

At constant potential and geometry, therefore, steady states are given by the intersection of equation 3 with an $i\text{-}C_o$ curve such as those implicit in Figure 2 and shown schematically in Fig. 4. The stability of these steady states can be analyzed by considering the effect of fluctuations in i or C_o. For small fluctuations, a steady state is stable if $k > di/dC_o$. States in the region of negative di/dC_o are therefore particularly stable (e.g. B', Fig. 4), but states such as B are also stable. States such as A and A' are unstable or metastable depending on the frequency and size of the fluctuations; for small δ (pitting) such states will generally be unstable, and the

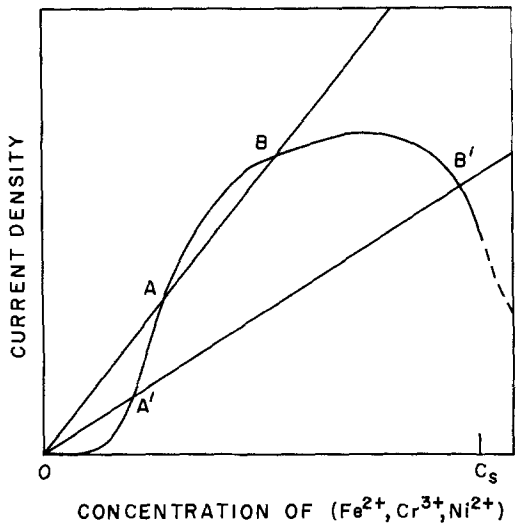

Fig. 4 Schematic variation of current density with concentration of dissolution products at constant potential (curved line), with superimposed straight lines representing Fick's first law for two values of δ at a one-dimensional steady state.

metal will either repassivate (that is, pass to another steady state close to the origin) or increase its dissolution rate to B or B'. For large δ (crevice corrosion), a single fluctuation is generally not catastrophic and a random variation in i without repassivation is expected. This may be a component of the electrochemical "noise" during crevice corrosion. There are generally two or more diffusion-coupled steady states; usually only one of these is a stable active state. There are indications that the stainless steel may have more stable states than the high purity alloy. For crevice corrosion, Tromans and Frederick (7) have obtained results which may be analyzable in terms of multiple steady states. A different type of multiple steady state behavior, involving passivation which requires salt precipitation, is described by Epelboin et al. (8). Because of the stringent requirements for pit stability in neutral chloride solutions, actively dissolving pits in stainless steel are probably stable over a range of potential corresponding to a factor of only about two in current density. This gives a simple interpretation of the protection potential against pitting. At constant bulk chloride concentration, increased stability can be attained by adding a supporting strong acid (9), by applying a potential or restricting diffusion sufficiently to precipitate a salt film (1), or by

adding sulfur compounds to stabilize the active state (10). Some stabilization (smaller di/dC_o) can also be attained by relaxing control of the potential. We should also note that the complexity of the $i-C_o$ curve is reduced as the solution ohmic drop (which is a function of i and δ) increases, finally becoming virtually a step function.

Further consequences

Several further possibilities are suggested by the form of the $i-C_o$ curve. First, smooth pit surfaces may be expected if di/dC_o is negative, since the onset of facetting will be hindered by more rapid dissolution of the asperities which are exposed to a less concentrated solution. Second, we note that the relevant $i-C_o$ curve for a very small pit is not the approximately steady state relationship determined using the present technique. At short times following a very rapid change in C_o, the value of di/dC_o is decreased. In effect, this defines a form of electrode impedance relating the current density to the concentration of dissolution products at constant potential. Finally, the hydrolysis of Cr^{3+} ions to $Cr(OH)_3$ is slow at ambient temperature, taking 1-3 days to reach equilibrium (11); this involves a pH change of up to one unit and is another possible stabilizing factor. More detailed results are in press (12).

Acknowledgements

This work was supported by the U.S. Department of Energy under contract no. DE-AC02-CH00016. Discussions with J. B. Sanborn are gratefully acknowledged.

References

1. J. W. Tester and H. S. Isaacs, J. Electrochem. Soc. 122, 1438 (1975).
2. H. S. Isaacs and R. C. Newman, "Corrosion and Corrosion Protection", p. 120. The Electrochemical Society, 1981.
3. M. Pourbaix, "Atlas of Electrochemical Equilibria in Aqueous Solutions", p. 384. Pergamon Press, 1966.
4. "Stability Constants Supplement Number 1", p. 276. Chemical Society Special Publication 25, London, 1971.
5. J. W. Oldfield and W. H. Sutton, Brit. Corros. J. 13, 104 (1978).
6. H. C. Kuo and K. Nobe, J. Electrochem. Soc. 125, 853 (1978).
7. D. Tromans and L. Frederick, Corrosion, in press (1983).
8. I. Epelboin, C. Gabrielli, M. Keddam and H. Takenouti, Z. Phys. Chem. 98, 215 (1975).
9. N. Sato, T. Nakagawa, K. Kudo and M. Sakashita, "Localized Corrosion", p. 447. NACE (1974).
10. R. C. Newman, H. S. Isaacs and B. Alman, Corrosion 38, 261 (1982).
11. J. Mankowski and Z. Szklarska-Smialowska, Corros. Sci. 15, 493 (1975).
12. R. C. Newman and H. S. Isaacs, Proceedings of 5th International Symposium on Passivity, Bombannes, France, 1983 (in press).

Manuscript submitted Dec. 12, 1982.

Brookhaven National Laboratory assisted in meeting publication costs of this article.

The Dealloying of a Cu-8.9% Al Solid Solution

M. J. Pryor*

Metals Research Laboratories, Olin Corporation, New Haven, Connecticut 06511

The author had proposed earlier that the kinetics of dealloying in Cu-Mn[1], Cu-Zn[2] and Cu-Ni[3] solid solutions appeared to be better related to the difference between the test potential and the reversible potential of the solute element than to the relative diffusion kinetics in the solid solutions.[1] Cu-Al solid solutions may provide a test of this hypothesis since the reversible potential of Al (-1.66 V_{SHE}) is more active than that of Mn (-1.16 V_{SHE}). Furthermore, the diffusion coefficient at 27°C is over four orders of magnitude lower for the Cu-18.7 a/o Al alloy than for a Cu-27.8 a/o Mn alloy.[10] A Cu-18.7 a/o Al solid solution grows a thin film of Cu_2O at room temperature following mechanical surface preparation. The Cu_2O film evidently includes some aluminum ions since it exhibits relatively high electronic resistance virtually identical to that reported earlier for a Cu-10 a/o Ni alloy and much higher than that of Cu_2O grown on Cu as judged by its cathodic polarization characteristics in sodium chloride solution[4]. Aluminum oxide does not exist as a separate phase in the room temperature oxide film and thus, is not capable of generating the highly irreversible and much more noble corrosion potentials exhibited by aluminum itself. Previous work on Cu-Al alloys suggests that this system is inherently more resistant to dealloying than Cu-Zn alloys.[5] Most references refer to dealloying of β' and γ phases[6-8] with the α Cu-Al solid solutions being reported to be relatively free from severe dealloying.[9]

A Cu-18.7 a/o Al alloy was induction melted and chill cast in a 2x10x20 cm water cooled copper mold. The casting was heated for two hours at 850°C and hot rolled to a thickness of 1.0 cm. Cu-18.7 a/o Al is a hypereutectic alloy that can be transformed to a homogeneous α solid solution by extended soaking around the eutectoid temperature of 565°C. Accordingly, the hot rolled plate was heated at 570°C for 16 hours followed by heating at 540°C for 24 hours. The homogenized plate was milled to remove around 0.07 cm from each surface. It was then cold rolled to a final thickness of 0.075 cm with intermediate anneals at thicknesses of 0.35 and 0.175 cm and a final anneal. Intermediate and final annealing was conducted in a 96% nitrogen-4% hydrogen atmosphere at 500°C for 4 hours. Metallographic evaluation of the annealed Cu-18.7 a/o Al alloy showed that it exhibited a fine grained (0.030 mm) equiaxed structure and contained no residual β' or γ phase.

Mass balance experiments on the dealloying of this solid solution were carried out in 0.5 M NaCl solution at 25°C at potentials ranging from +0.50 to -0.50 V_{SHE} in the fashion described in an earlier publication[2]. One difference in experimental technique compared with the previous work was the preparation of the surface by mechanical means rather than by etching. This was achieved by light unlubricated end milling of the specimen surface followed by careful degreasing in benzene. The second difference was that larger specimen areas (12 sq cm) were used at potentials of 0, -0.25 and -0.50 V because of the lower corrosion rates of the Cu-Al solid solution in this potential region.

Figure 1 shows the weights of Cu plus Al dissolved from the specimens at different potentials in 20 hours. The relationship of total weight loss to potential is basically similar to that reported earlier for a Cu-29.4 a/o Zn alloy[2] except that the weight losses of the Cu-Al solid solution are lower at potentials of -0.25 and -0.50 V. The specimens held at +0.50 and +0.25 V exhibited surface dealloying very similar to that reported earlier for a Cu-29.4 a/o Zn alloy. Figure 2 shows the surface of a Cu-18.7 a/o Al alloy held at +0.50 V for 20

hours. The surface is extensively faceted and there is extensive porosity very similar to that observed earlier on Cu-29.4 a/o Zn. The thickness of the dealloyed surface layer is also similar to that found earlier on Cu-29.4 a/o Zn. Figure 3 shows the percent of Al removed from the Cu-Al alloy as a function of potential. On a mass balance basis, it is clear that there is substantial and effective dealloying of the Cu-Al alloy solid solution starting at a potential of 0.00 V with the selectivity of dealloying, (i.e. the enhancement of solute concentration found in the total corrosion product) increasing as the potential is depressed to -0.50 V. Dealloying of Cu-18.7 a/o Al is somewhat more selective than that of a Cu-29.4 a/o Zn alloy[2] but less selective than that of a Cu-27.8 a/o Mn alloy[1].

Table I compares at a fixed potential of -0.25 V_{SHE} the excess solute removed* in 20 hours from 1 sq cm of the Cu-Mn, Cu-Zn and Cu-Al solid solutions. Due to the very low overall corrosion rates of Cu-Al solid solutions at potentials of 0.00 V and more active, the kinetics of dealloying fall in the order of Cu-Mn > Cu-Zn > Cu-Al. This is despite the fact that the aluminum is enriched in the total corrosion product to a greater degree than zinc.

The foregoing experiments confirm the widely held view that Cu-Al solid solutions are somewhat more resistant to dealloying than Cu-Zn solid solutions. This is despite the fact that the electrochemistry of the system would appear to favor more rapid removal of aluminum. Superficially, this work would tend to favor solid state diffusion as the controlling factor in dealloying kinetics since it places Al and Zn in the correct kinetic order. Diffusion considerations however, fail to place Mn in the correct order as pointed out earlier[1]. One of the limiting features is the low limit of solubility of Al in the α solid state solution (19.6 a/o) which to date has prevented direct comparison of the three solute elements at equal atomic concentrations. This comparison is being made in continuing work.

*over and above the Cu:solute ratio in the alloy.

Acknowledgements

The author wishes to acknowledge support of this work by the Brass Group, Olin Corporation. The experimental help provided by Mr. S. Roth and Mr. A. F. Beck is also acknowledged.

Table I.

Alloy	Excess Wt. of Solute Removed 20 Hrs. at -0.25 V_{SHE} (mg/cm^2)
Cu-27.8 a/o Mn	0.009
Cu-29.4 a/o Zn	0.003
Cu-18.7 a/o Al	0.0002

REFERENCES

1. D. S. Keir & M. J. Pryor, J Electrochem Soc 127 2138 (1980)
2. M. J. Pryor & K. K. Giam, J Electrochem Soc 129 2157 (1982)
3. R. G. Blundy & M. J. Pryor, Corrosion Science 12 65 (1972)
4. R. F. North & M. J. Pryor, Corrosion Science 10 297 (1970)
5. A. A. Read & R. H. Greaves, J. Inst. Metals 11 197 (1914)
6. R. Lange, H. Kaiser & J. Kaesche, Werkestoffe u. Korrosion 29 404 (1978)
7. B. Upton, Corrosion 19 204t (1963)
8. R. E. Maersch & J. M. Cieslewicz, Matl Prot. 3 54 (1964)
9. R. Heidersback, Corrosion 24 38 (1968)
10. M. J. Pryor & J. C. Fister - unpublished work.

Manuscript submitted Sept. 27, 1982.
Revised manuscript received April 20, 1983.

Olin Corporation assisted in meeting publication costs of this article.

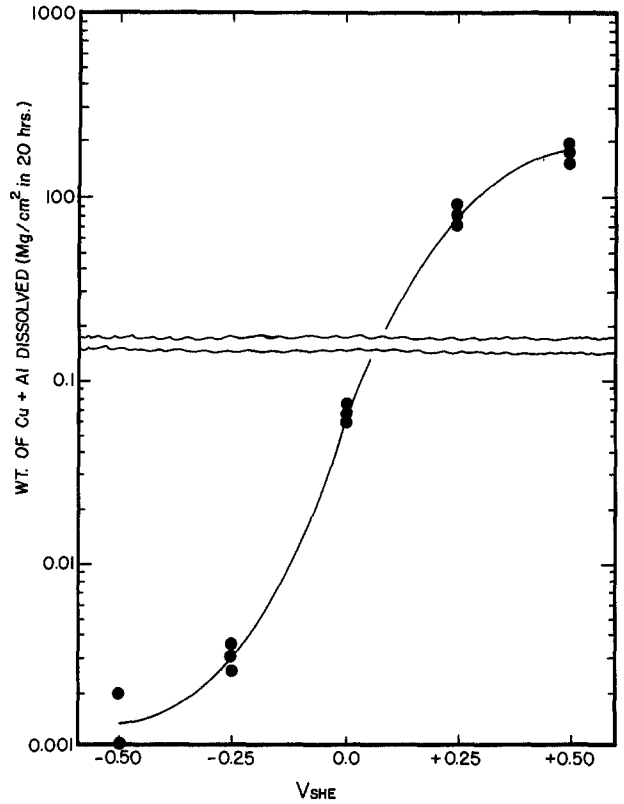

Fig. 1. Relationship between the weights of Cu plus Al dissolved in 0.5M NaCl at 25°C in 20 hr and potential.

Fig. 2. Dealloyed surface of a Cu-18.7 a/o Al alloy held at +0.50 V_{SHE} in 0.5M NaCl for 20 hr (x200).

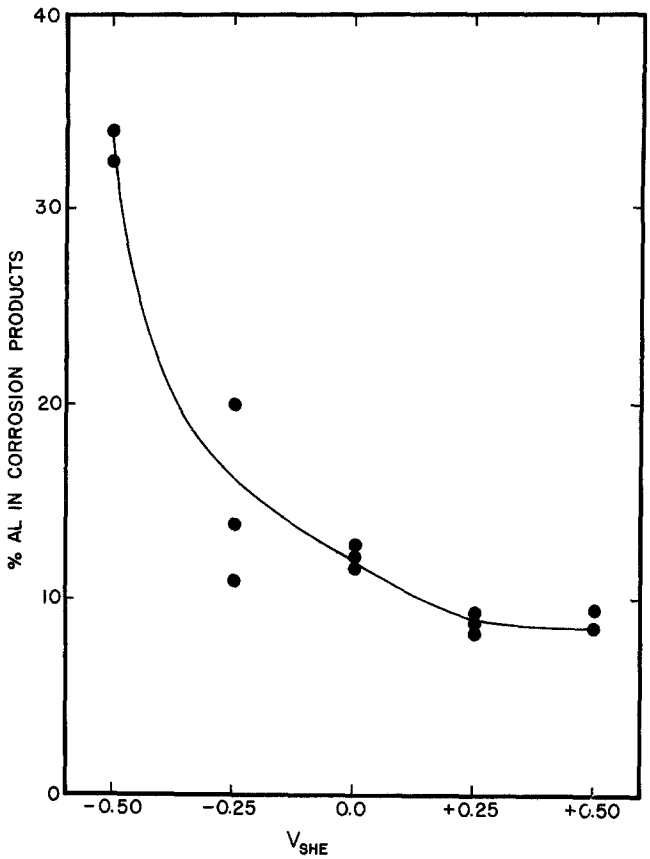

Fig. 3. W/o Al dissolved from a Cu-18.7 a/o Al alloy in 0.5M NaCl at 25°C in 20 hr as a function of potential.

Orientation of (100) InGaAsP/InP Wafers By HCl Chemical Etching

L. W. Stulz

Crawford Hill Laboratory, Bell Laboratories, Holmdel, New Jersey 07733

L. A. Coldren

Bell Laboratories, Holmdel, New Jersey 07733

A wide variety of optical, electronic, and optoelectronic devices are currently being developed on InP or InP-substrate based systems.[1] Many of these devices require a special orientation of the substrate to achieve the desired device structure. Injection lasers fabricated from the InGaAsP/InP material system provide one example. These are currently of interest for application in optical fiber communication systems operating at $\lambda = 1.3\ \mu m$ and 1.55 μm. Laser structures that utilize a real refractive index waveguide, such as the buried heterostructure (BH), channel substrate or ridge waveguide lasers, have been shown to have advantages with respect to current threshold, output spectra, and freedom from pulsations or light jump behavior.[2] For most refractive index - guided laser structures, the fabrication sequence usually requires a chemical etching step to form either a mesa or channel which ultimately defines the optical cavity of the laser.

We find that, similar to the case of GaAs,[3] preferentially etched mesas or channels on (100) InP wafers have different side wall geometries depending on the orientation of the etching mask with respect to the [011] or [01$\bar{1}$] crystal directions.

Fig. 1 illustrates the result with HCl etching and mask edges aligned along either the [011] or [01$\bar{1}$] direction on (100) InP.[4] Note that the (01$\bar{1}$) plane is exposed for the orientation in Fig. 1(a) but the corresponding (011) plane is not defined when the mask is rotated 90° as in Fig. 1(b). As is generally the case for III-V compounds with the zinc-blend crystal structure, the relative orientation of the polar generic {111} planes are the major contributing factors to this kind of selective etching anisotropy.[3–7] As detailed by Tuck,[5] one set of {111} planes contain a layer of *In* at the surface and is conventionally labeled *A* (even number of bars, e.g., (111)); the opposite set of planes contain a layer of *P* at the surface and is conventionally labeled *B* (odd number of bars, e.g., ($\bar{1}\bar{1}\bar{1}$)). The {111}A planes etch slowly compared with the {111}B planes.

Thus, in distinguishing the (011) from the (01$\bar{1}$) for the important purpose of device fabrication, one is really determining whether the {111}A or the {111}B, respectively, separates the "top" or "working" surface (100) from the perpendicular edge surface. There is no real chemical difference between the (011) and the (01$\bar{1}$). They appear to behave differently only because of the different relative position of the difficult to etch {111}A plane with respect to the working surface. Figure 2 illustrates this common convention that results from defining the working surface as (100) on a {100} wafer. (Note that if the working surface had been labeled ($\bar{1}$00), the new (011) and (01$\bar{1}$) planes would interchange properties, since then the {11$\bar{1}$}*B* and {111}A, respectively, would fall in between. That is, rotation about [100] by 90° is equivalent to inversion of the substrate axis.[4])

The orientation procedure consists of etching a small portion of the InP or InGaAsP/InP wafer in HCl (for 20 sec at 20°C) followed by inspection of the edges in an optical microscope. For best results, the test piece should be cleaved in both perpendicular directions to allow comparison of the

Manuscript submitted Nov. 5, 1982; revised manuscript received April 26, 1983.

Bell Laboratories assisted in meeting publication costs of this article.

Keywords: Orientation, HCl Chemical Etching, InP.

two {011} edges. The cleaved edges of the test piece might turn out to be either smooth or severely terraced depending on the quality of the cleave. In the latter case, longer etching is required to produce the triangular etch pits. Figure 3 illustrates results starting from either smooth (a) or rough (b) cleaves. If the substrate is already masked, the edges of the entire wafer can be used so that no material is lost. Also in this case, there is no danger of mixing-up the orientation of the test piece relative to the wafer.

Triangular pits (i.e., depressions) pointing away from the (100) work surface indicate the (011) edge. Sometimes it is easier to focus on the triangular mesas left behind between large pits when they coalesce. Then, triangular mesas (i.e., protrusions) pointing away from (or hanging down from) the (100) work surface designate the $(01\bar{1})$ edge. Another characteristic of the (011) edge is the appearance of "blackish", fine-textured areas after prolonged etching; see Fig. 3(b).

Again, we point out that a (100) surface must first be chosen (if not already decided by the existence of epi-layers, masking films, etc.), for we are really determining the relative location of the {111} planes. The side from which the triangular etch pits point away is where the [111]A falls between the surface and edge normals (see Fig. 2).

In summary, we have presented a very simple method for orienting (100) InP wafers. It does not require x-rays, photomasking or the loss of a significant amount of material. The technique is superior to other orientation techniques, which generally require masking the surface.[5,8–10] The most reliable prior technique necessitated a photolithographic mask, etching and then careful inspection of the etched wall profile.[10] Other techniques, which utilize etch pits that occur randomly at a defect[8,9], have proven difficult to use and somewhat unreliable. In our case, the edge-to-surface juncture provides a natural nucleation site, and most desirably, it is best to have a mediocre cleave that provides edge striations for a distinctive result as shown in Fig. 3. Such results are obtained consistently. Little or no wafer area need be sacrificed, and virtually no additional processing time is spent in this orienting procedure.

REFERENCES

1. See for example, "Special issue on quaternary compound semiconductor materials and devices - sources and detectors", *IEEE J. Quantum Electron.* Vol. QE-17, February 1981.
2. R. J. Nelson and N. K. Dutta, "Self-sustained pulsations and negative-resistance in InGaAsP (λ=1.30 μm) double heterostructure lasers", *Appl. Phys Letts.*, Vol. 37, pp. 769-771, November 1980.
3. R. P. Tijburg and T. VanDonger, "Selective Etching of III-V Compounds with Redox Systems", *J. Electrochem. Soc.*, Vol. 123, p. 689-691, May 1976.
4. L. A. Coldren, K. Furuya, and B. I. Miller, "Combined dry and wet etching techniques to form planar (011) facets in GaInAsP/InP double heterostructures", *Electron. Lett.*, Vol. 18, pp. 235-237, March 1982.
5. B. Tuck and A. J. Baker, "Chemical etching of {111} and {100} surfaces on InP", *J. Mat. Sci*, Vol. 8, pp. 1559-1566, 1973.
6. S. Adachi and H. Kawaguchi, "Chemical etching characteristics of (001) InP", *J. Electrochem. Soc.*, Vol. 128, pp. 1342-1349, June, 1981.
7. L. A. Coldren, K. Furuya, and B. I. Miller, "On the formation of planar etched facets in GaInAsP/InP double heterostructures", Submitted to *J. Electrochem. Soc.*
8. A. Huber and N. T. Linh, "Révélation métallographique des défauts cristallins dans InP", *J. Cryst. Growth*, Vol. 29, pp. 80-84, 1975.
9. S. B. Phatak and G. Kelner, "Material-selective chemical etching in the system InGaAsP/InP", *J. Electrochem. Soc.*, Vol. 126, pp. 287-292, February 1979.
10. K. Iga and B. I. Miller, "Chemically etched-mirror GaInAsP/InP lasers-review", *J. Quant. Elec.*, Vol. QE-18, pp. 22-29, January 1982.

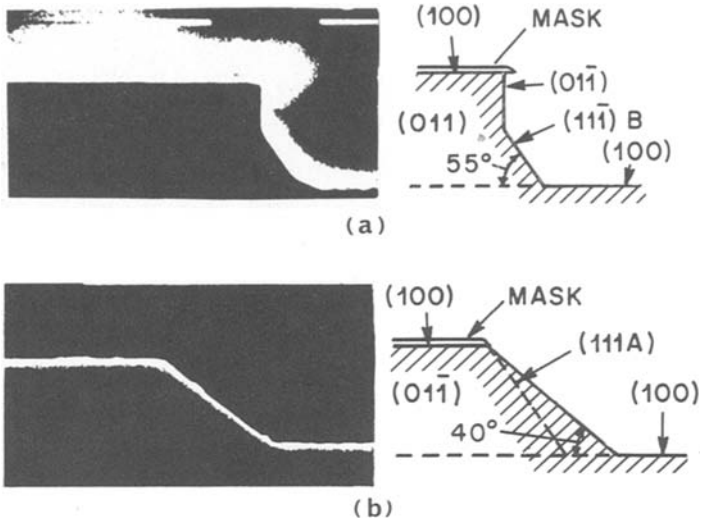

Fig. 1 - SEM and schematic cross sectional cuts, illustrating HCl etched wall profiles for mask edges in the (a)-(01$\bar{1}$) and (b)-(011) planes. For the photos markers = 10μm; etching time = 1 min.

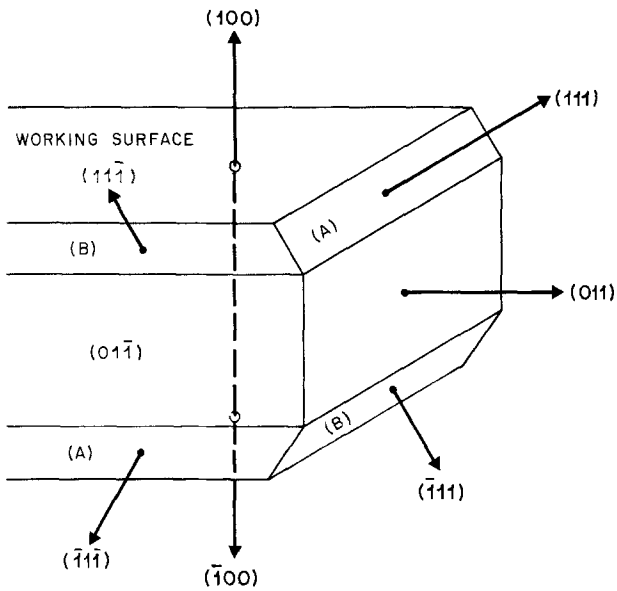

Fig. 2 - Crystal plane diagram showing relative location of polar [111] A and B planes in a III-V compound.

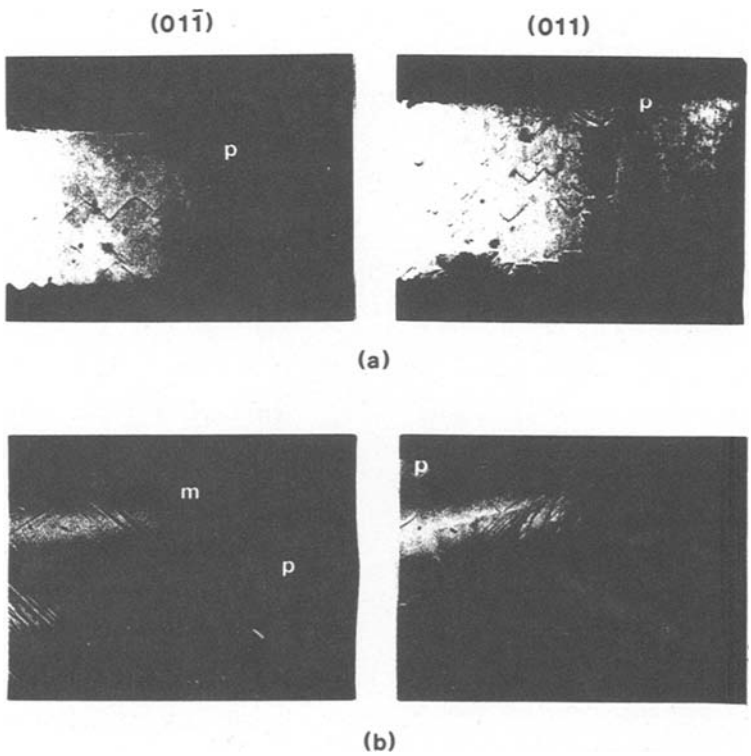

Fig. 3 - InP edge facets after HCl etching for (a) 20 sec on a "smooth" cleave, and (b) 2 min on a "rough" cleave. Both illustrate the characteristic triangular etch pits. $p \equiv pit$; $m \equiv mesa$. Labeling assumes (100) is the top surface.

A New Electrodeposited Oxide Film Containing Lead and Thallium with the Cubic Fluorite-Type Structure

M. Sakai, T. Sekine,* and Y. Yamazaki

Department of Electronic Chemistry, Graduate School at Nagatsuta, Tokyo Institute of Technology, Yokohama, Japan

In the previous papers, the comparative investigation on the anodic oxidation of Tl(I) to Tl_2O_3 with that of Pb(II) to PbO_2 was carried out in alkaline solutions (1,2). As a result of these analyses, the possibility of the anodic co-deposition of PbO_2 and Tl_2O_3 was suggested on the basis of the similarity of both anodic reactions to produce the corresponding oxides. On the way of this extention, a new compound having the cubic fluorite-type structure was obtained by means of the anodic oxidation of the mixture of Pb(II) and Tl(I) under a certain electrolytic condition.

The electrodeposited oxide, $Pb_8Tl_5O_{24}$, was prepared in the following manner: the electrolytic solution was prepared with 1.0M NaOH solution containing 60mM Pb(II) and 30mM Tl(I); anodic potential was controlled at 0.200 volts *vs.*SCE by using a potentiostat; a platinum plate(3x2cm) was used as an electrode substrate; the total quantity of electricity consumed in the electrolysis was 500 coulombs; the anolyte was kept at 25°C under moderate agitation. The electrolytic cell consists of a cylindrical anode chamber ($440cm^3$) and a couple of cathode chambers($200x2cm^3$) connected with the salt bridges having sintered glass diaphrams to prevent the diffusion of the electrolytes during the electrolysis. The compositions of the catholyte and the solution in the salt bridges were the same as that of the anolyte.

The obtained electrodeposited oxide on the platinum substrate was black with metallic luster and had a good electric conductivity.

The composition of the electrodeposited oxide was determined as $Pb_8Tl_5O_{24}$ through the following procedure. After measuring the weight of the dried electrodeposited oxide on the platinum substrate, the oxide was cathodically treated with the constant current(300mA) till Tl(III) was completely reduced to Tl(I) in 6.0M HNO_3 solution. Before the simultaneous determination of Pb(II) and Tl(I) by polarography, the pH of the above solution containing Pb(II) and Tl(I) was controlled to be a strongly alkaline solution by the addition of NaOH solution. The amount of oxygen in the electrodeposited oxide was calculated by subtracting the obtained weight of lead and thallium from the weight of the oxide.

In order to obtain the accurate results of the chemical analysis, the polarographic measurement was repeated twelve times for each specimen of the electrodeposited oxide, where five specimens were prepared under the same electrochemical conditions. The significant figures and the errors listed in Table I were calculated through the error analyses on the determination processes for lead, thallium, and oxygen.

Table I shows the most probable values of the stoichiometric coefficients for the prepared oxide and their relative errors in percent. From the data in Table I, the composition of lead, thallium, and oxygen in the oxide was determined as $Pb_8Tl_5O_{24}$.

The crystal structure of the oxide was investigated with an X-ray powder diffractmeter equipped with a graphite monochromator. The CuKα radiation was used for the measurement and the goniometer was calibrated with

*Electrochemical Society Active Member.

Key words: $Pb_8Tl_5O_{24}$, fluorite-type oxide, X-ray analysis, electrodeposition

Table I. Analytical values of lead, thallium, and oxygen

	M.P.V.[a)]	E.M.S.[b)]	R.E.(%)[c)]
Lead (x)	7.94	±0.06	0.8
Thallium (y)	5.00	±0.03	0.6
Oxygen (z)	24	±1	4

a): Most probable values of the stoichiometric coefficients of the prepared oxide($Pb_xTl_yO_z$).
b): Errors mean square for M.P.V..
c): Relative errors.

Table II. X-ray powder diffraction data for $Pb_8Tl_5O_{24}$

hkl	d_{obsd}	d_{calcd}[a)]	I/I_1
111	3.0778	3.0791	100
200	2.6649	2.6666	28
220	1.8855	1.8855	30
311	1.6084	1.6080	25
222	1.5398	1.5395	8
400	1.3333	1.3333	3
331	1.2235	1.2235	8
420	1.1925	1.1925	5
422	1.0887	1.0886	5
511,333	1.0264	1.0264	5
440	0.9429	0.9428	1
531	0.9016	0.9015	5
600,442	0.8890	0.8889	3
620	0.8435	0.8432	2

a): Calculated on the basis of the lattice constant a=5.3331Å.

standard silicon powder(NBS-SRM640).

Table II shows the X-ray powder diffraction data of the electrodeposited oxide $Pb_8Tl_5O_{24}$. The Miller-indices of the lattice planes of this oxide were determined completely by assuming that the crystal system of $Pb_8Tl_5O_{24}$ had the fcc structure, since all diffraction lines were well-defined and were not including any unidentified ones. The values of the relative integration intensity of the diffraction lines listed in Table II were calculated on the basis of the values obtained with the scaler. From the above X-ray data, the crystal structure of $Pb_8Tl_5O_{24}$ was considered to be the cubic fluorite-type structure and the lattice constant of this oxide was determined as 5.3331±0.0003Å.

As a result, $Pb_8Tl_5O_{24}$ having the cubic fluorite-type structure was in-

dubitably determined to be a single phase being diverse from PbO_2 or Tl_2O_3 by considering the data in Table II and the X-ray diffraction data of α-PbO_2 (orthorhombic)(3), β-PbO_2(tetragonal) (4),and Tl_2O_3(scandium oxide structure) (5).

The $Pb_8Tl_5O_{24}$ is quite stable under atmospheric pressure at room temperature, and the X-ray diffraction lines of this oxide have never changed for five months since the fresh $Pb_8Tl_5O_{24}$ was prepared by electrolysis.

The synthesis of PbO_2 having the cubic fluorite-type structure under high pressure more than 50Kb from α-PbO_2 was reported by Syono *et al.*(6). However, the oxide was unstable and was not a single phase, and undergo a retrogressive transition to α-PbO_2 even at room temperature (6).

REFERENCES

1. M.Sakai, N.Sato, and T.Sekine, *Denki Kagaku.*, 50, 485 (1982)

2. S.Obara and T.Sekine, *Denki Kagaku.*, 43, 44 (1975)

3. JCPDS Index Card 11-549.

4. JCPDS Index Card 25-447.

5. JCPDS Index Card 30-1351.

6. Y.Syono and S.Akimoto, *Mater.Res. Bull.*, 3, 153 (1968)

Manuscript submitted Nov. 29, 1982; revised manuscript received April 28, 1983.

Stabilization of Glassy Carbon Electrodes

R. Jasinski,* G. Brilmyer,*,[1] and L. Helland

Occidental Research Corporation, Irvine, California 92713

INTRODUCTION

A need exists for low cost, stable anode materials in the electrolytic synthesis of laboratory and industrial chemicals. Platinum and the DSA class of materials are expensive. Platinum and stainless steels corrode in halide-containing media. Lead dioxide is subject to chemical decomposition, depending on electrolyte composition. Carbons (graphite and glassy carbon) are cheaper but are dimensionally unstable anodes for the evolution of oxygen in aqueous electrolytes.

We have found that the addition of fluoride ion to aqueous acid electrolytes of sulphate, phosphate and chloride significantly represses the physical deterioration of glassy carbon anodes. There is precedence for this effect. It has been known for some time that the addition of fluoride, thiocyanate and chloride ions delay the evolution of oxygen on platinum from sulfate electrolyte, favoring the generation of $S_2O_8^-$(1,2).

This stabilization is not found on graphite.

RESULTS AND DISCUSSION

Glassy carbon anodes 3mm in diameter and 10mm long were immersed in the appropriate electrolyte using an undivided cell and a platinum cathode 1cm square. Half cell potentials vs. an Ag/AgCl reference electrode were monitored as a function of time at a constant current of 300 ma. As the electrolysis proceeded in the absence of fluoride ion, the glassy carbon electrode slowly deteriorated. Particles of carbon sloughed off the surface. Eventually the structure had disintegrated to the point that little surface was left immersed in solution and the electrode potential increased exponentially. Shown in Table 1 are the times required to reach these potentials, the solution compositions with and without fluoride present, and the initial steady state half cell potentials. The "Deterioration Time" value for the chloride solutions and the H_2SO_4, H_3PO_4 solution fluoride-free represent major, visible deterioration of the glassy carbon.

Obviously, fluoride ion significantly extends the lifetime of the glassy carbon rods in all solutions. This effect was not found for graphite or pyrolitic graphite. The effect was also not permanent. Glassy carbon rods, anodized in sulfuric acid/F^- solutions without deterioration, were then placed into fluoride-free sulfuric acid. Disintegration of the electrode took place upon electrolysis of the solution.

The mechanistic role of the fluoride ion is not at all clear. However, it is involved with the evolution of oxygen. In sulfuric acid, synthesis of persulfuric acid is favored with respect to the evolution of oxygen. It was observed that the rate of gas evolution had decreased from the addition of fluoride ion and that a strong soluble oxidant was formed. Phosphoric acid containing fluoride ion also exhibited both phenomena upon electrolysis. The half cell potentials in Table 1 do indicate a shift to more positive potentials with fluoride ion present in the electrolyte. However, disintegration of the glassy carbon was also suppressed in the chloride-containing medium. Gas evolution was not dramatically retarded in the HCl solution. However, green chlorine gas was observed coming off the electrode surface when fluoride was present but not when fluoride was absent. Detailed gas chromatographic analyses and mass balances were not done to quantify this effect.

---

*Electrochemical Society Active Member.
[1]Present address: Johnson Controls, Inc., Milwaukee, Wisconsin.
Key Words: glassy carbon, anodes, dimensionally stable anodes.

Table I. Effect of NaF on the stability of glassy carbon electrodes

Electrolyte	NaF Concentration	E 1/2* vs Ag/AgCl	Deterioration Time (hr.)
3M H_2SO_4	0	3.6V	5
	1.2 M	4.0	>24
2M H_3PO_4	0	3.8	2.5
	1.2	4.3	>24
3M HCl	0	3.2	32
	1.2	3.2	363

*at 300 ma initial current.

REFERENCES

1. A. Bard, ed. "Encyclopedia of Electrochemistry of the Elements" 4, 342, 1975; M. Dekker Ed.

2. O. Jyurikova, N. Miller, E. Kasatkin, Elektrokhimiya, 14 1078 (1978).

Manuscript submitted Aug. 30, 1982; revised manuscript received April 6, 1983.

Occidental Research Corporation assisted in meeting publication costs of this article.

Polymer Films on Electrodes

13. Incorporation of Catalysts into Electronically Conductive Polymers: Iron Phthalocyanine in Polypyrrole

R. A. Bull, F.-R. Fan, and A. J. Bard*

Department of Chemistry, University of Texas at Austin, Austin, Texas 78722

Abstract

Tetrasulfonated iron phthalocyanines (FePcS) can be incorporated into electronically conducting polypyrrole by electrochemical polymerization of pyrrole in the presence of FePcS. The FePcS modified glassy carbon electrodes catalyzed the reduction of O_2 at potentials 250 to 800 mV less negative than at bare glassy carbon or at polypyrrole-coated glassy carbon not containing FePcS. Rotating ring-disk experiments indicated some hydrogen peroxide formation at most pH's. However, at high pH essentially exclusive reduction of O_2 to H_2O was observed at potentials 250 mV less negative than at a non-catalyzed electrode.

(end of abstract)

One of the main motivations for the preparation of modified electrodes, including those covered with polymer films, is the incorporation of electrocatalysts onto the electrode surface. For example, catalysts have been covalently attached to the substrate, irreversibly adsorbed, and introduced into polymer films via electrostatic binding (1). Of particular interest have been electrocatalysts for the reduction of oxygen (2-5); these often are based on metal porphyrins and phthalocyanines. Among the problems arising in the utilization of catalytic modified electrodes are the limited effectiveness on monolayers (6), instability of the attached or adsorbed materials, and low rate of charge transport through non-electronically conductive films. We suggest here the incorporation of a catalyst into a conductive polymer layer by electrochemical polymerization in the presence of catalyst and briefly describe the characteristics of such an electrode for the reduction of oxygen.

Electrochemical Society Active Member *

Key Words: catalysis, polymers, voltammetry, electrodes

Manuscript submitted Feb. 22, 1983.

The conductive polymer chosen was polypyrrole (PP); a number of electrochemical studies of this material have demonstrated that this can be readily deposited by electrochemical oxidation of pyrrole from nonaqueous or aqueous solutions (7-10). The catalyst was tetrasulfonated phthalocyanine incorporating iron (FePcS) and the substrate was glassy carbon (GC). The advantages of this system include ease of preparation, and both high conductivity and high porosity of the PP film (11), leading to rapid transport of both charge and solution substrate within the electrode structure.

Polypyrrole films were deposited from aqueous 0.05 M sodium trifluoroacetate solutions (NaTFA) (pH 1-7) that were 0.1 M in pyrrole by anodic oxidation at +0.7 V vs. SCE at GC. Polymer film thicknesses were estimated by taking 24 mC/cm^2 of charge to be equivalent to a 1 μm film (8c). GC/PP/FePcS films were prepared by an identical procedure except that the solution contained only 1 mM FePcS and 0.1 M pyrrole. Oxidation of pyrrole in the presence of FePcS was necessary for catalyst incorporation. Control experiments in which a GC electrode was held at +0.7 V vs. SCE in a FePcS solution not containing pyrrole showed no O_2 - reduction catalysis. PP films deposited in the absence FePcS and then cycled through the PP redox waves in a solution containing FePcS also showed no catalytic activity.

CV Experiments.--A typical cyclic voltammogram (CV) of a FePcS/PP film (0.1 μm thick) is shown in Fig. 1a for a 0.1 M NaTFA electrolyte (pH 1.7) saturated with N_2. The small waves for FePcS reduction and re-oxidation are superimposed on the large PP background; the large background currents have been ascribed to capacitive charging of the highly porous PP film (11). An estimate of the amount of electroactive FePcS in the polymer from the CV, assuming n=1 for Fe(III)/Fe(II) couple

is 2 to 6 x 10^{-11} moles/cm^2 geometric area. The FePcS redox waves were stable to cycling within the potential limits imposed by PP. Scanning to potentials sufficiently negative for PP reduction (i.e. out to -0.3 to -0.5 V vs. SSCE) resulted in a decrease in the peak currents (i_p) for the FePcS waves. Potentials positive enough for irreversible PP oxidation (+0.8 V vs. SSCE at pH 1 to +0.4 V at pH 13) also decreased i_p for the FePcS redox waves, although the film still remained on the electrode surface.

In O_2-saturated solutions the current at the FePcS wave was greatly increased (Fig. 1b); this is attributed to the catalyzed reduction of O_2. In all cases significantly higher reduction currents were found at more positive potentials at GC/PP/FePcS than at GC/PP or bare GC electrodes. For example, under the conditions of Fig. 1b, O_2 reduction at GC/PP occurs at about -0.8 V vs. SSCE. The effect of pH on the potentials for catalyzed O_2-reduction was similar to that found for the FePcS waves themselves. At pH < 3, the shift of E_p was 45 mV/pH unit. As with the FePcS redox waves themselves, the waves attributed to O_2 reduction disappeared upon irreversible PP oxidation.

RRDE Experiments.--Reduction of O_2 at bare and modified GC disk electrodes with detection of products (e.g. H_2O_2) via oxidation at a Pt ring electrode provided additional information about catalysis by incorporated FePcS (Fig. 2). At a bare GC electrode O_2-reduction occurred to produce a mass transfer controlled wave, with the limiting current, i_L, increasing with angular rotation velocity, ω. For GC/PP electrodes a wave at similar potentials was observed, but i_L reached a limiting value at about 1000 rpm. The collection efficiencies, N, found for GC and GC/PP electrodes (for O_2 reduction at the disk and H_2O_2 oxidation at the ring) were generally 0.26 - 0.30; this is less than the collection efficiency found with this electrode and a soluble redox couple such as $Fe(CN)_6^{3-/4-}$, where N = 0.39. For a GC/PP/FePcS disk electrode, the reduction of O_2 essentially conincided with the FePcS reduction wave and occurred at less negative potentials compared to GC and GC/PP electrodes, similar to the CV results. At most pH's anodic ring currents were observed when O_2 was reduced at the disk (e.g. at pH = 6.5, E_d = -0.6 V; E_r = +1.0 V vs. SSCE), demonstrating that some H_2O_2 is produced. Typical results for a 0.1 μm PP/FePcS film in O_2-saturated 0.1M NaTFA (pH 6.5) are given in Fig. 2a. Strict correspondence to the Levich equation (i_L vs. $\omega^{1/2}$) was not found with this electrode, perhaps because of interference from the background processes of PP. The reduction of O_2 at GC/PP/FePcS in 0.1 M NaOH did not lead to anodic ring currents until the disk potential attained values where direct O_2 reduction of GC/PP occurs. Typical RRDE voltammograms are given in Fig. 2b. After an initial "break-in period" during which the reduction current decreased, the current between -0.1 and -0.3 V was independent of ω. No ring currents were observed at these values of E_d. When E_d reached -0.35 V, the onset potential for O_2 reduction at bare GC, anodic current became apparent. Note, however, that even at these potentials the anodic currents were very small, so that N-values in this region were two orders-of-magnitude smaller than for catalyzed O_2 reduction at lower pH. These results suggest that FePcS catalyzes the decomposition of H_2O_2 in 0.1 M NaOH solution.

In general, over the pH range of 1.7 to 13, N-values for GC/PP/FePcS electrodes were always smaller than those for bare GC electrodes at the same pH. However, at lower pH, N was nearly the same as that for the bare electrode. At pH 13, N was two orders of magnitude less than at a bare GC electrode, even at potentials where peroxide is produced at GC.

The stability of FePcS-PP films depended on the pH and the cathodic scan limits. If the PP films were reduced, O_2-reduction activity decreased. As a result, limiting currents and i_L vs. $\omega^{1/2}$ data could not be obtained. This was particularly so at low pH, where PP reduction began at only slightly negative potentials. The stability of the catalyst-film during O_2 reduction and in the presence of reduction products, e.g. H_2O_2, is also of interest. Successive O_2-reduction scans, especially at low pH, resulted in a gradual decrease in the disk current. After prolonged O_2 reduction the initially shiny blue-black FePcS-PP film changed to a gray particulate deposit that was easily removed from the electrode. At this point, little O_2 reduction activity was observed and, after N_2 saturation, no FePcS redox activity was found. The addition of H_2O_2 to the electrolyte also brought about rapid delay of catalytic activity.

In conclusion, this method of incorporation of catalysts via conductive polymers onto an electrode surface appears to be a promising one. For the GC/PP/FePcS electrodes we have observed significant

catalytic activity for O_2 reduction at potentials 250 to 800 mV less negative (depending on pH) than at bare GC or GC/PP electrodes. Moreoever, the observed current densities for O_2 reduction based on the geometric area of the electrode appear to be larger than those reported for similar catalysts adsorbed on electrodes (2,5). This can probably be attributed to the high conductivity and porosity of the PP matrix, making a larger number of catalyst centers accessible per unit area of electrode to dissolved O_2.

The PP background often hindered the collection of precise peak and limiting current data for quantitative kinetic analysis. As a result, only qualitative aspects of O_2 reduction mechanisms can be discussed. The similarity of the FePcS and catalyzed O_2 reduction potentials suggests a redox-type mechanism (12). However, the voltammetric behavior and the change of N with pH suggest at least two simultaneous O_2 reduction processes. At low pH the reduction is predominantly to peroxide and N is nearly that found for an unmodified GC electrode. As the pH is raised the Tafel slopes increased and N decreased from that at an unmodified electrode. At intermediate pH, the 2e and 4e processes are competitive, but at high pH no peroxide was detected at potentials positive of O_2 reduction at GC, suggesting a direct 4e reduction to H_2O. The 4 electron process probably involves the dismutation of H_2O_2 by FePcS, as suggested for iron porphyrins in methylacrylate polymers (13). Direct reduction of H_2O_2 is also possible; however, H_2O_2 contributes to instability of PP and loss of catalytic activity. The stability of PP/FePcS catalyst increased at higher pH.

The catalytic behavior found here is qualitatively similar to those observed by Zagel et. al. (2) and perhaps involve similar mechanisms. This suggests that incorporation of FePcS into PP has essentially no effect on the mechanism or catalytic behavior. However, the conductive support enhances the effectiveness of the catalyst by providing more surface area and a larger percentage of active centers than are present in adsorbed films or catalysts in non-conducting polymers and provides a convenient method of attaching the catalyst to the substrate (14).

References

1. R. W. Murray in "Electroanalytical Chemistry," A. J. Bard, ed., Marcel Dekker, Inc., New York, Vol. 13, 1983 (in press).

2. J. Zagel, P. Bindra, E. Yeager, This Journal, 127, 1506 (1980).

3. J. P. Collman, M. Marrullo, P. Denisevich, C. Koval, F. C. Ansoh, J. Electroanal. Chem., 101 117 (1978).

4. R. R. Durand, Jr., F. C. Anson, J. Electroanal. Chem. (in press).

5. A. Bettelheim, R. J. H. Chan, T. Kuwana, J. Electroanal. Chem., 99, 391 (1979).

6. C. R. Andrieux, J. M. Dumas-Bouchiat and J. M. Saveant, J. Electroanal. Chem., 123, 171-178 (1981).

7. A. Dall'Olio, G. Dascola, V. Varacca and V. Bocchi, Comp. Rend., 433, 267c (1968).

8. (a) A. F. Diaz and K. K. Kanazawa, J. Chem. Soc., Chem. Commun. 635 (1979); (b) K. K. Kanazawa, A. F. Diaz, R. H. Geiss, W. D. Gill, J. F. Kwak, J. A. Logan, J. F. Rabolt and G. B. Street, ibid, 854 (1979); (c) A. F. Diaz and J. I. Castillo, ibid., 397 (1980); (d) K. K. Kanazawa, A. F. Diaz, W. D. Gill, P. M. Grant, G. B. Street and G. P. Gardini, Synthetic Metals, 1, 329 (1979/80); (e) A. Diaz, J. M. Vasquez Vallejo and A. Martinez Duran, IBM J. Res. Develop., 25, 42 (1981).

9. (a) R. Noufi, A. J. Frank and A. J. Nozik, J. Am. Chem. Soc., 103, 1849 (1981); (b) R. Noufi, D. Tench and L. F. Warren, This Journal, 127, 2310 (1980); (c) T. Skotheim, I. Lundstrom, and J. Prejza, This Journal, 128, 1625 (1981).

10. F.-R. F. Fan, B. Wheeler, A. J. Bard and R. Noufi, ibid., 128, 2042 (1981).

11. R. A. Bull, F.-R. F. Fan, A. J. Bard, ibid, 129, 1009 (1982).

12. F. Beck, J. Appl. Electrochem., 7, 239 (1977).

13. A. Bettelheim, R. J. H. Chan, T. Kuwana, J. Electroanal. Chem., 110, 93 (1980).

14. Support of this research, a joint project with Prof. A. B. Lever, by the Office of Naval Research and by the National Science Foundation (CHE 7903729) is gratefully acknowledged.

Thermal Modulation Voltammetry

B. Miller*

Bell Laboratories, Murray Hill, New Jersey 07974

The temperature dependence of current through an electrode/solution interface under a controlled potential scan arises from a number of possible sources. These include equilibrium potentials, electron transfer rate constants, chemical kinetics, and mass transport factors which will contribute according to their respective temperature coefficients and influence in the overall electrochemical sequence involved at the particular potential, E. If the electrode mass is subjected to a periodic temperature perturbation by means of an external heat pulse, there will be a corresponding modulation component, Δi_T, about the average (isothermal) current, i. Such a process yielding Δi_T-E curves along with conventional i-E plots is the subject of this communication and will be referred to as Thermal Modulation Voltammetry (TMV).

The current response to thermal modulation will be the net of the interaction of the aforementioned temperature coefficients and the fluctuating thermal gradients. The changing contribution to current control by factors such as reaction kinetics and transport will be determining of the $\Delta i_T/i$ ratios at any given potential. Initial experiments are described here in which such heat pulses are applied to the rigorously controllable mass transport system of the rotating disk electrode (RDE) and Δi_T and i are measured as a function of E.

A schematic of the electrode and heating mode part of the experiment is shown in Figure 1. The electrode is a very thin disk ($\approx 10\mu$) of gold backed by somewhat thicker copper whose surface was converted to a black, absorptive oxide film. This copper remains after sequential etching of a machined dish shape upon which the gold shell and disk were electrodeposited. The structure provides an electrode of low thermal mass, high thermal conductivity, and a highly heat absorptive rear surface. Heat is provided through an argon ion laser beam (power to 1.5 w) incident on the electrode back. The RDE stirring generates the solution flow past the electrode to provide the major dissipation of the heat pulses.

The light is chopped and the cell current response obtained by band pass filter-rectification or synchronous detection as described for the parallel requirements of hydrodynamic modulation experiments (1).

The results of an experiment with a 5 mM Fe^{+3}-1.1 M $HClO_4$ solution and the gold disk are shown in Figure 2 in the form of Δi_T versus E and i versus E plots. The example was chosen to illustrate a variety of reaction types. There are six labeled regions of interest (*a-f*) starting from +0.6 v versus SCE, scanning positive to 1.8 v, then negative to −0.6 v. They represent, respectively

a - gold oxidation
b - oxygen evolution
c - gold oxide reduction
d - rising portion of Fe^{+3} wave
e - mass transfer limited Fe^{+3} reduction
f - hydrogen evolution

Comparison of the traces indicates that Δi_T and i have different response to these various features, perhaps better seen from the potential scans in a Δi_T versus i and E versus i format as in Figure 3. Results from the latter are interpreted in Table I as the $\Delta i_T/i$ response in relative scale units for the given feature, either as a constant slope (*b,f*), plateau height ratio (*a,e*), or peak ratio (*c,d*).

The center values of i traced in the Figure 2 or 3 scans are about 10% higher than i without the 50% laser duty cycle (at 5 Hz) heating. This represents the equivalent to steady state thermal rise.

Characterization of the actual electrode temperature rise and spatial profiling of the solution phase await elucidation — the present efforts are designed to document the attainability of the TMV effect under easily accessible conditions and some of its relative properties. In the same vein TMV responsivity is a function of heat pulse factors related to beam cross-section, chopper frequency, rotation speed, and beam power by relationships not treated here.

Other survey experiments of the type in Figure 2 reinforce the expectation that diagnostic discrimination by thermal sensitivity for mechanism and current controlling elements may be developed into a valuable addition to the repertoire of the electrochemist. The electrode design could be adapted to many materials by appropriate attachment modifications. A particular area of interest would be to semiconductor electrodes (with and without front illumination) and the possible discrimination of solid state and surface recombination from electrochemical kinetics.

---

* Electrochemical Society Active Member

Key Words: Electrode, Energy Transfer, Mass Transfer

Manuscript submitted April 13, 1983; revised manuscript received *ca.* April 25, 1983.

Bell Laboratories assisted in meeting publication costs of this article.

ACKNOWLEDGMENTS

The author is grateful to T. D. Harris for generously contributing laser, optics, and expertise and to S. S. DeBala for mechanical design assistance.

REFERENCES

1. B. Miller and S. Bruckenstein, Anal. Chem. *46*, 2026 (1974).

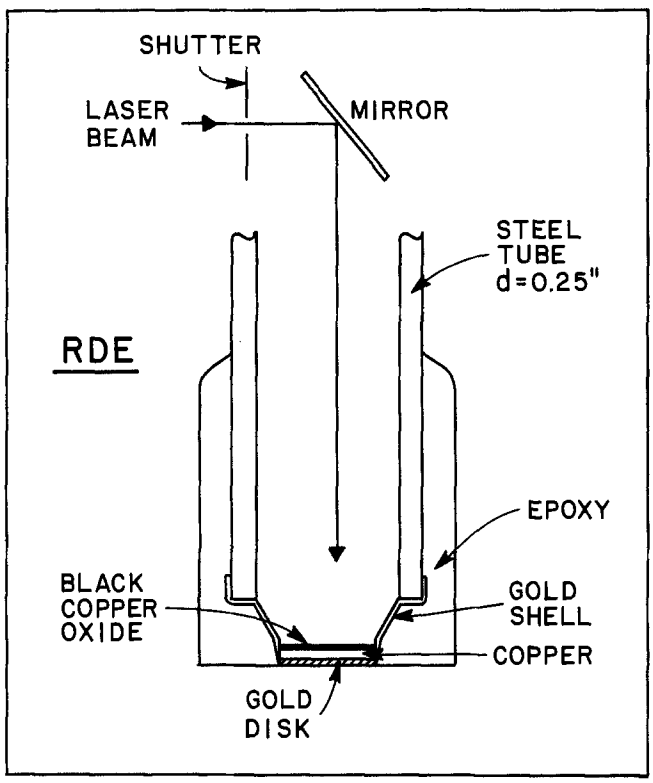

Figure 1. Schematic of RDE for TMV.

TABLE I. Relative Thermal Response

	Region					
$\Delta i_T/i$	*a*	*b*	*c*	*d*	*e*	*f*
slope		1.5-2				0.8
plateau ratio	0.4				0.4	
peak ratio			1	1.2		

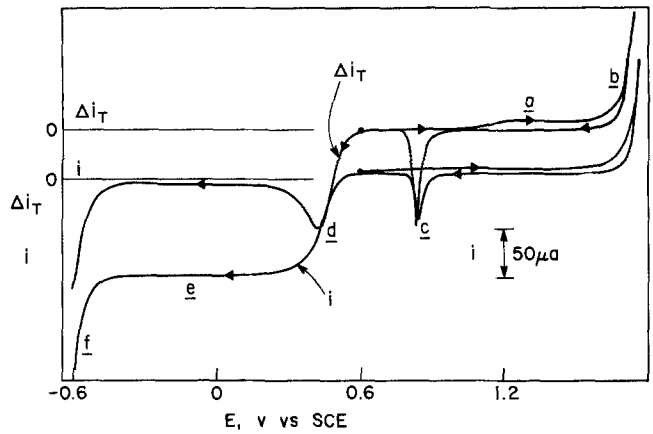

Figure 2. Gold disk E scan at 10 mv/s, 900 RPM, 1 w beam chopped at 5 Hz, lock-in detection after 10x bandpass amplification. 5mM Fe^{+3}, 1.1 M $HClO_4$.

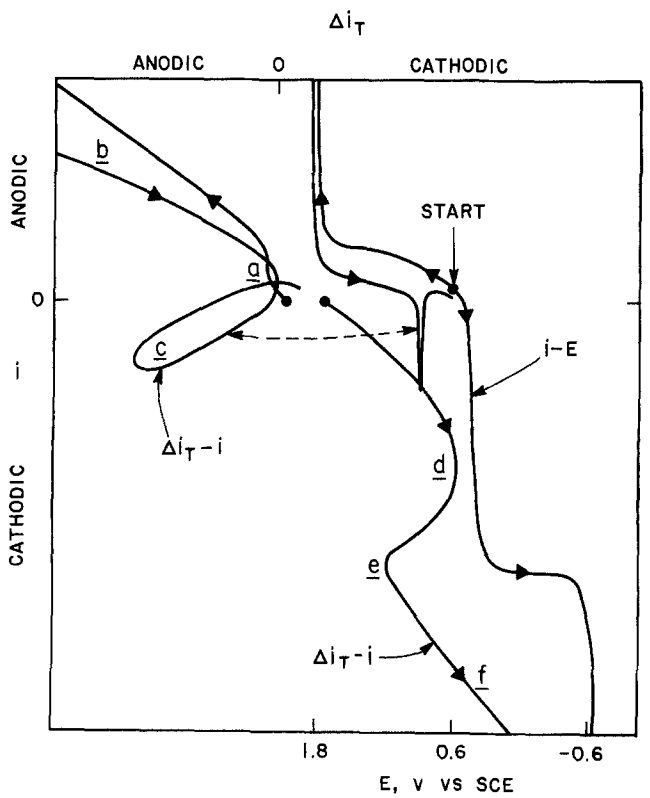

Figure 3. E scan at 5 mv/s and bandpass-rectifier Δi_T display with current sign restored. Others as Figure 2. Scan +0.6 to 1.8 and return (anodic Δi_T branch); scan +0.6 to negative (cathodic Δi_T branch).

JOURNAL OF THE ELECTROCHEMICAL SOCIETY

ELECTROCHEMICAL SCIENCE AND TECHNOLOGY

AUGUST 1983

Zinc Electrode Morphology in Alkaline Solutions

II. Study of Alternating Charging Current Modulation on Pasted Zinc Battery Electrodes

J. McBreen* and E. Gannon

Department of Energy and Environment, Brookhaven National Laboratory, Upton, New York 11973

D-T. Chin* and R. Sethi*

Department of Chemical Engineering, Clarkson College of Technology, Potsdam, New York 13676

ABSTRACT

The dependence of the faradaic conductance and the morphology of pasted zinc electrodes on the charging method has been investigated. The charging methods included d.c. (3-125 mA-cm^2) and d.c. (3-125 mA-cm^2) with superimposed square waves of a.c. of various amplitudes and frequencies (0.1-5000 Hz). In the case of d-c charging, the faradaic conductance goes through a maximum at ~75 mA-cm^2. The decrease in the faradaic conductance at higher current densities (100 mA-cm^2) is related to the formation of dense zinc deposits on the electrode surface. At low d.c. (<30 mA-cm^2), superimposition of a.c. promotes growth of zinc close to the current collector and results in small amounts of dispersed hexagonal zinc deposits on the current collector. Except where dense deposits are formed at high current density, the remainder of the zinc deposit has a very fine structure. Pulsed charging at low current densities (<30 mA-cm^2) is beneficial in that it increases the electrode faradaic conductance and promotes growth of the zinc deposit close to the current collector. The relaxation time for the double layer in pasted zinc electrodes is ~50 msec. This indicates that the optimum frequency for pulsed charging is between 1 and 10 Hz.

Alkaline zinc batteries can be designed to ensure complete dissolution of the discharge product in the electrolyte, or provisions can be made to cause precipitation of the discharge product in the electrode structure. In the case of the former, operational problems can occur because of the formation of nonadherent mossy deposits and the growth of nodules and dendritic zinc. The problems with second type of electrode are related to zinc electrode shape change, densification of zinc, and penetration of zinc through the separator (1).

In the past, approaches for stabilizing soluble electrodes were careful control of the hydrodynamic conditions and the use of additives. Promising results have been obtained using modified charging methods (2-6). There is general agreement that pulsed charging methods suppress formation of mossy zinc and yield a smoother deposit. In the case of insoluble zinc electrodes, improvement in cycle life has been obtained by several electrode and cell design modifications. These are modification of cell geometry (1), use of additives, improved separators, sealed cell operation, and use of a pressure switch cutoff to prevent overcharge (7). There have been several reports on the effect of modified charging methods on the capacity and life of alkaline zinc batteries. Romanov (8) found that asymmetric current charging of zinc-silver oxide cells improved the cell capacity by as much as 20%. This was correlated with a change in the distribution of monovalent and divalent silver in the positive electrode (9). In the case of zinc-nickel oxide cells, it was found that asymmetric current charging suppressed the tendency for zinc dendrites to grow into the separator (10). More recently, Smithrick (11) investigated the effect of various charging wave forms of 120 and 1000 Hz on the performance and cycle life of zinc nickel oxide cells. He found little or no effect. Wagner (7), on the other hand, has reported significant gains in cycle life using pulsed charging current with frequencies 10 Hz or less.

This paper reports a study of the effect of superimposed square wave pulses on the charging current for pasted zinc electrodes. The study included an investigation of the effect of the charging method on the faradaic conductance, potential relaxation phenomena, and the morphology of the electrode.

Experimental

Cell.—Experiments were carried out in a small two-electrode zinc-nickel oxide cell with a reference electrode. A schematic of the cell is shown in Fig. 1. The cell design was very similar to that described previously (12) except the electrodes were circular (diameter = 1.27 cm^2) and the reference electrode consisted of a zinc wire masked with heat shrinkable tubing to below the level of the electrolyte. The zinc electrodes were 0.063 cm thick and were made by pressing 200 mg of a PTFE-bonded ZnO mixture (98% ZnO + 2% PTFE) onto an expanded silver screen (Exmet Corporation 5 Ag 12.5-2/0). Preparation of the ZnO/PTFE mixture is described in detail elsewhere (12). The separator system consisted of a 0.127 mm nonwoven polyamide felt (Pellon Corporation 2504K4) in abuttal with the nickel electrode. The main separator was two layers of 0.025 mm microporous polypropylene (Celanese Corporation Celgard 3501).

Instrumentation.—Most of the experiments were done using a Stonehart BC-1200 potentiostat in the galvanostatic mode. The current profile could be varied by inputs of square wave pulses to the poten-

* Electrochemical Society Active Member.
Key words: battery, SEM, electrodeposition.

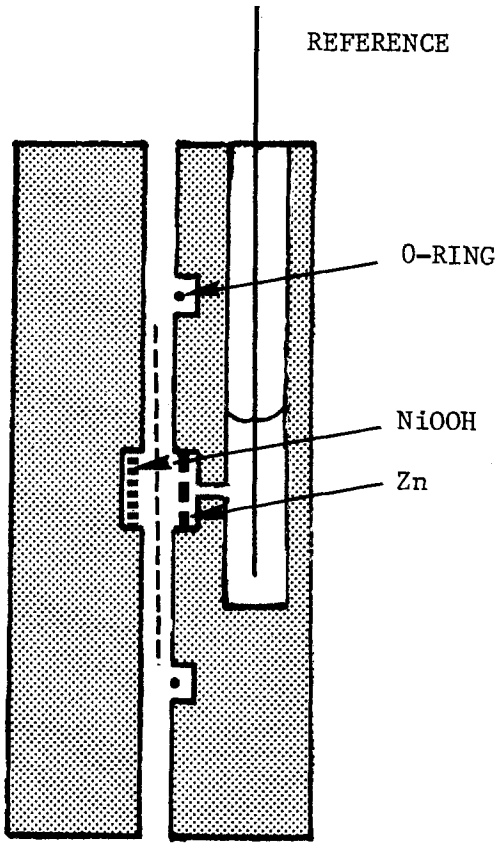

Fig. 1. Schematic of experimental zinc-nickel oxide cell

tiostat from a Hewlett-Packard 3325A function generator. Cyclic voltammetry measurements were made by using the potentiostat in conjunction with a Princeton Applied Research PAR-175 programmer and a Soltec 6432 X-Y_1-Y_2 recorder. The potential and current wave forms were periodically monitored on a Tektronix 7634 oscilloscope.

Procedures.—The cells were wetted down with electrolyte (8.4M KOH + 0.5M LiOH + 0.74M ZnO) and allowed to soak for at least 2 hr. The cells were then vacuumed in a bell jar, using a mechanical pump, and backfilled with nitrogen. Cells were then charged to a capacity of 100 mA-hr using various current regimes. After charging, cells either were used for cyclic voltammetry measurements or were dissected for examination by scanning electron microscopy (SEM). The cells for the cyclic voltammetry measurements were evacuated at the end of charge to remove gas bubbles and were backfilled with nitrogen. Cyclic voltammetry measurements were made by scanning the zinc electrode potential in a narrow potential envelope (±25 mV), at 10 mV/sec, about the open-circuit potential. The preparation of zinc samples for scanning electron microscopy is described in detail elsewhere (12).

Results

Charging mode and faradaic conductance of zinc electrodes.—The cyclic voltammograms showed a small constant hysteresis. The data presented here give the average between the anodic and cathodic sweeps. Figure 2 shows a family of cyclic voltammograms for electrodes that were charged to 100 mA-hr at various current densities. The slope of these curves is a measure of the faradaic conductance of the electrode. Figure 3 shows that the faradaic conductance of the electrode goes through a maximum at a charging current density of about 75 mA-cm^2. The effect of superimposed 60 Hz square wave current is dependent on the d-c and a-c component of the current. At the normal low current densities <30 mA-cm^2, used to

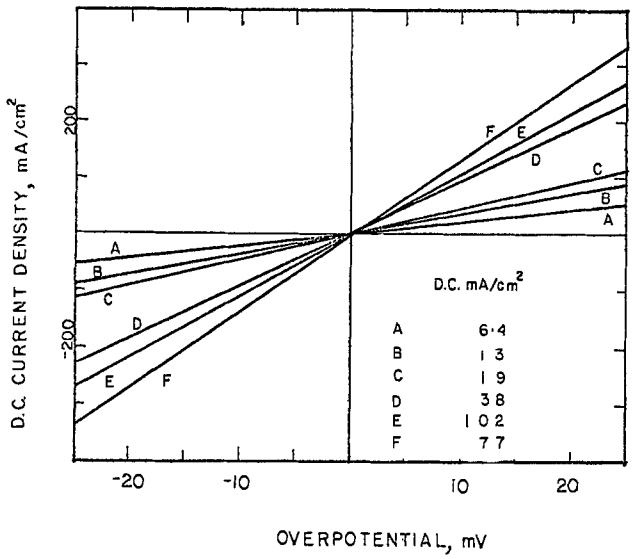

Fig. 2. Cyclic voltammetry for pasted zinc electrodes charged to 100 mA-hr at various current densities. Current densities are indicated on the figure; sweep rate 10 mV/sec.

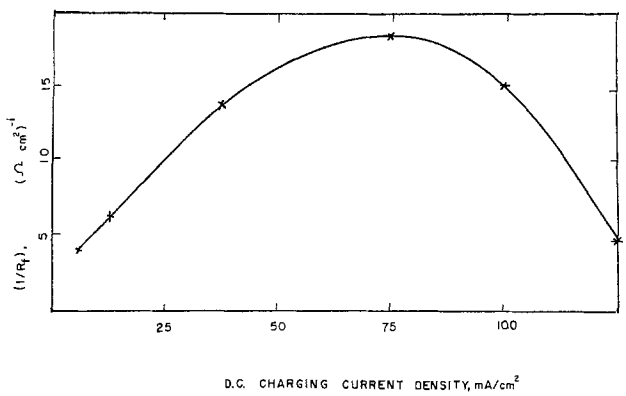

Fig. 3. Faradaic conductance of pasted zinc electrodes vs. charging current.

charge batteries, superimposition of a.c. tends to increases the faradaic conductance of the electrode. At higher current densities, superimposition of a.c. decreases the faradaic conductance. These trends are shown in Fig. 4. Figure 5 is a set of cyclic voltammograms on electrodes charged at 76.8 mA-cm^2 with an a-c current of 19.1 mA-cm^2 of various frequencies superimposed on it. The faradaic conductance is dependent on frequency and goes through a maximum in

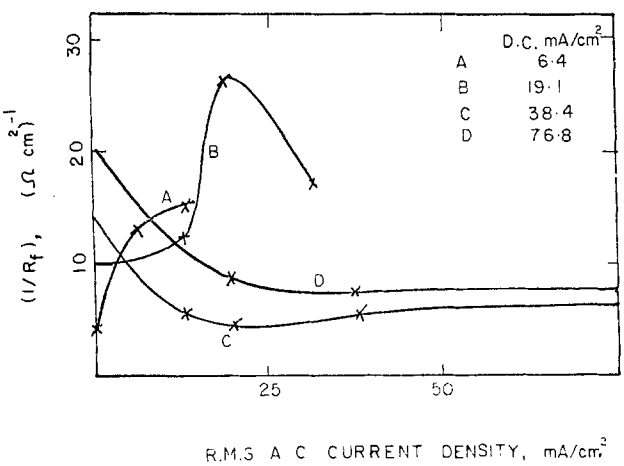

Fig. 4. Dependence of faradaic conductance on the a-c component of the charge for various d-c charging current densities. The a.c. was a square wave of 60 Hz.

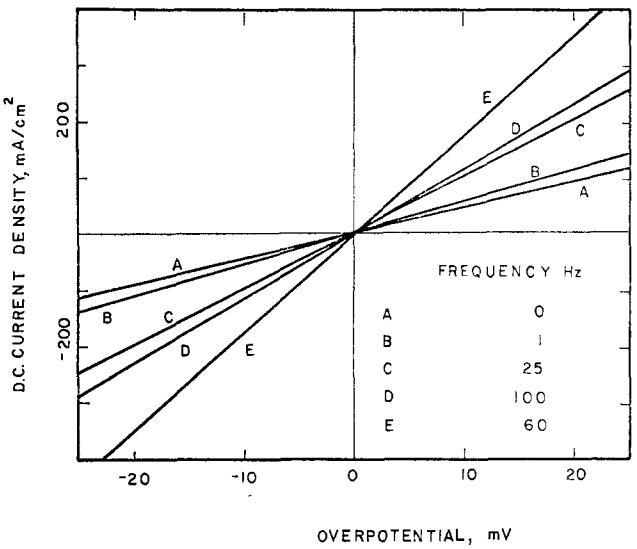

Fig. 5. Effect of frequency of the a-c component of charge on the electrode polarization. The d-c current was 76.8 mA-cm², and the a-c current was 19.1 mA-cm². Frequency of the current square wave is shown on the figure.

the vicinity of 60 Hz. At 1000 Hz, the effect of superimposed a.c. disappears completely.

Relaxation phenomena in zinc electrodes.—Figure 6 shows potential relaxation phenomena in a zinc electrode that was charged to a capaciy of 50 mA-hr at a current density of 5.0 mA-cm². In the relaxation studies, a 5.0 mA-cm² square wave of various frequencies was applied to the d-c component. Both potential and current were recorded on oscillograph traces. The results in Fig. 6 show that the current trace was an undistorted square wave. Significant potential relaxation was observed only at low frequencies (<15 Hz). At frequencies of 200 Hz or greater, the potential relaxation phenomenon disappeared completely.

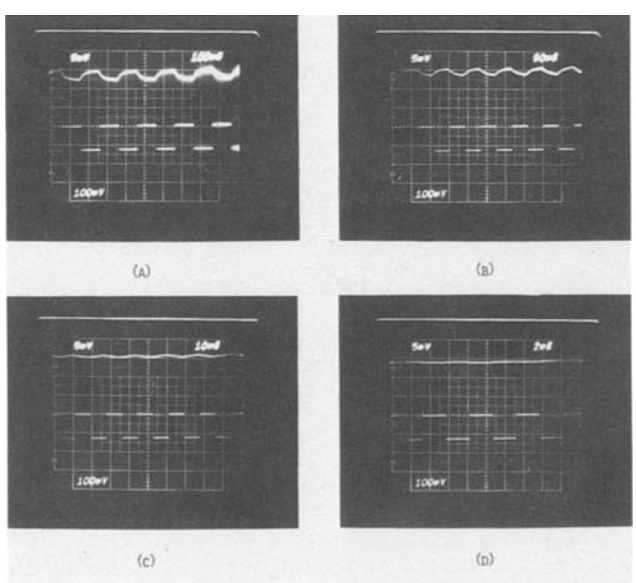

Fig. 6. Oscilloscope traces of the current (square wave) and potential on a pasted zinc electrode that had been charged to 50 mA-hr at 5 mA-cm². The center horizontal line of the oscillograph was zero for both current and potential. Potential is displayed on top curve (5 mV/division) and current is displayed on the bottom square wave (10 mA/division). Tests were at 5 mA-cm² d.c./5 mA-cm² a.c.; (A) 5 Hz, (B) 12 Hz, (C) 60 Hz, (D) 200 Hz.

Charging mode and zinc electrode morphology.—For d-c charging currents of <75 mA-cm², the zinc had a very finely divided morphology like that shown in Fig. 7. At higher current densities (~60 mA-cm²), the only difference observed was some open areas in the deposit, such as those shown in Fig. 8. At very high current densities (~100 mA-cm²), the zinc tended to form a metallic skin on the electrode surface in abuttal with the separator. Some areas on the electrode surface were dense, as shown in Fig. 9.

Superimposition of a-c square waves produced a number of differences in the zinc distribution in the electrode and in the morphology. When a-c square waves were superimposed on low d-c charging cur-

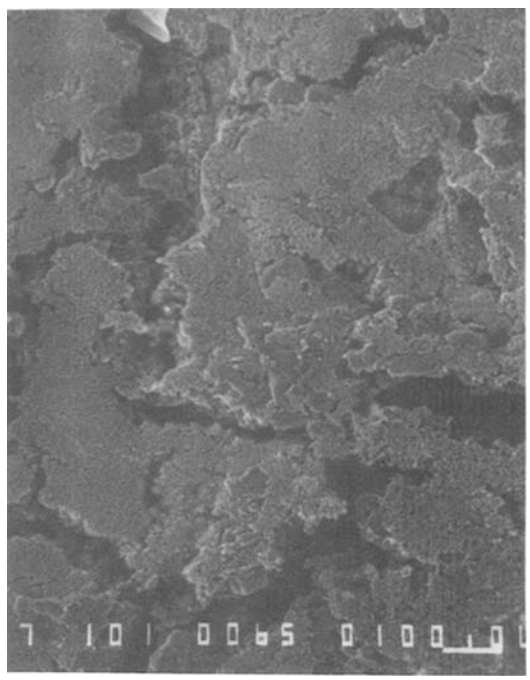

Fig. 7. Electrode charged at 6.4 mA-cm² to a capacity of 100 mA-hr.

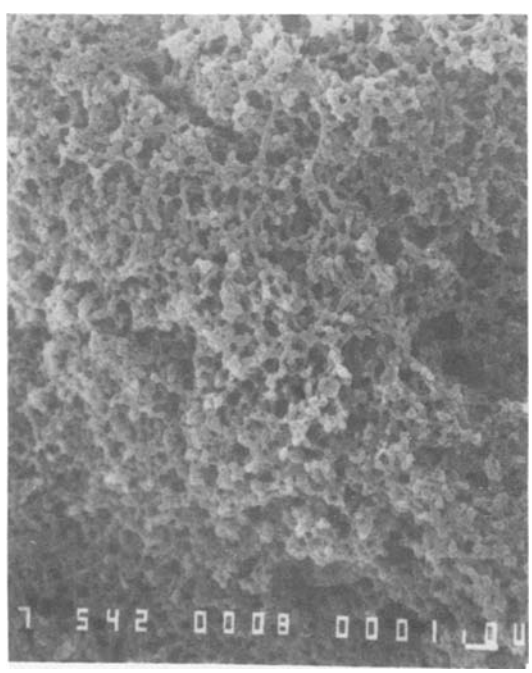

Fig. 8. Sconning electron micrograph of the zinc deposit in a pasted zinc electrode charged at 60 mA-cm² to a capacity of 100 mA-hr.

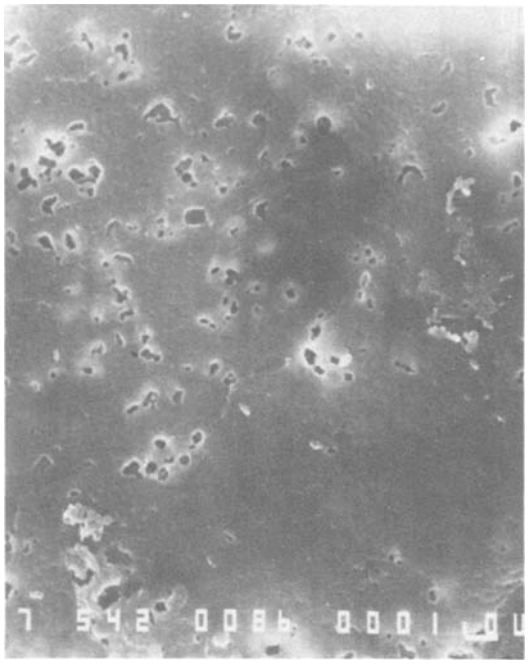

Fig. 9. Scanning electron micrograph of a dense portion of the zinc deposit on the surface of a pasted zinc electrode charged at 100 mA-cm^2 to a capacity of 100 mA-hr.

rents (<30 mA-cm^2), most of the zinc deposit was in the vicinity of the current collector. At the end of charge, the electrode surface in contact with the separator was still mostly white zinc oxide. The bulk of the zinc deposit was of a finely divided nature and appeared identical to that shown in Fig. 6. When a-c square waves were superimposed, additional small amounts of dispersed crystalline zinc deposits were formed on the silver current collector. These had a well defined hexagonal crystalline morphology as shown in Fig. 10. Extensive investigations were made on electrodes charged at 6.4 mA-cm^2 d.c. with a 6.4 mA-cm^2 a-c square wave superimposed on it. Crystalline deposits were observed on the current collector at frequencies between 1 and 1000 Hz. No crystalline deposits were found at 0.1 and 5000 Hz. Charging regimes of 60 Hz, for which these localized crystalline deposits on the current collector were found, were 3.1 mA-cm^2 d.c./3.1, mA-cm^2 a.c., 6.4 mA-cm^2 d.c./6.4 mA-cm^2 a.c., 15 mA-cm^2 d.c./15 mA-cm^2 a.c., 30 mA-cm^2 d.c./15 mA-cm^2 a.c., 60 mA-cm^2 d.c./20 mA-cm^2 a.c. At high d-c current densities (100 mA-cm^2), superimposition of a.c. did not produce these crystalline deposits or any other detectable change in zinc morphology.

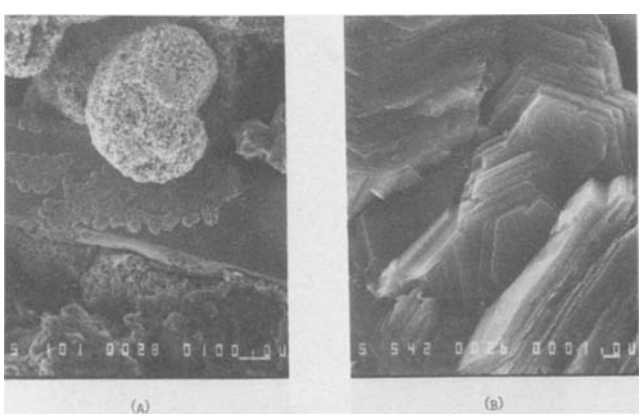

Fig. 10. Scanning electron micrograph of the zinc deposit in a pasted zinc electrode charged at 6.4 mA-cm^2 d.c. and 6.4 mA-cm^2 a.c. to a capacity of 100 mA-hr. (A) The crystalline deposit on the horizontal silver strand can be seen at the center of the micrograph; (B) is the same deposit at higher magnification.

Discussion

Charging processes in pasted zinc electrodes.—The mechanism of charging pasted zinc electrodes is still a moot point. Hladik and Schwabe (13) concluded that reduction occurred predominantly by the direct reduction of zinc oxide. These results were disputed by Drazic and Nagy (15) on the basis of investigations of single-crystal zinc oxide in zincate electrolytes. They concluded that direct reduction contributes only about 2% to the overall reduction and that the remainder of the deposition was via the soluble zincate intermediate. Direct reduction of ZnO has been reported in perchlorate electrolytes (15, 16). More recent results indicate that the reduction of zinc oxide films on zinc occurs via a solid-state mechanism in dilute KOH (0.1M) and via the zincate intermediate in more concentrated KOH (2.5M) (17). It was also found that the ratio of the amount reduced via the solid-state reaction or via the soluble intermediate could be altered by the addition of organic additives (18). Cyclic voltammetry studies (12) indicate that some cathodic process occurs on the first charge of a pasted zinc electrode, at about 400 mV positive to the reversible zinc potential. This process is not seen when cyclic voltammetry is carried out on the silver current collector in zincate electrolyte with no zinc oxide paste present. It would appear then that the reaction process in pasted zinc electrodes is quite different from that found in a zincate solution. Direct reduction of zinc oxide must somehow be involved. Pulsed charging could affect the degree of direct reduction of zinc oxide and, as has been shown (6), the morphology of zinc formed by the reduction of zincate.

Faradaic conductance and electrode morphology.—One salient aspect of the zinc morphology in zinc electrodes charged with d-c current is the very fine structure of the zinc deposit. The structure is even finer than that found for mossy deposits in zincate electrolyes at low overvoltages (6). The results in Fig. 2, 3, and 7-9 indicate that the charging current density effects both the faradaic conductance and the zinc morphology. Below a charging current of 75 mA-cm^2, there was no detectable change in the microstructure of the deposit. The increase in faradaic conductance on going from a charging current of 6.4-75 mA-cm^2 could only be attributed to the open spaces (Fig. 8) which impart some macroporosity to the electrode structure. The decrease in the faradaic conductance at very high current densities (>75 mA-cm^2) is due to the formation of dense low surface area zinc on the electrode surface (Fig. 9).

Effect of a.c. on faradaic conductance and electrode morphology.—No apparent affect of a.c. on the fine structure of the bulk of the deposit could be detected. However, visual observations indicated that superimposition of a.c. on low d-c current densities (<30 mA-cm^2) resulted in growth of most of the deposit close to the current collector. This may be due to the increase in nucleation rate of zinc that is expected on superimposition of a-c square waves (19). The concentration of zinc close to the current collector furnishes extra space and reducible material in front of the zinc deposit and reduces the polarizability of the electrode.

The isolated hexagonal crystalline deposits (Fig. 10) that are found on the superimposition of a.c. are only found as adherent deposits on the strands of the expanded metal current collector. These deposits are very similar to those found on imposition of an alternating potential square wave at low overvoltages in zincate electrolytes (6). This would indicate that these

crystalline deposits are due to the reduction of zincate onto the current collector.

Deposit morphology at high current density.—The dense deposit morphology on the electrode surface at high current densities (~100 mA-cm^2) is probably due to the reduction of zincate that migrates in from the pores of the separator. High overvoltages are known to promote a more dense deposit from zincate electrolyte (6). Superimposition of a.c. has little effect. This is also the case in zincate electrolyte at high overvoltages. Actually, one analysis predicts a decrease in the nucleation rate at high overvoltages for superimposition of a.c. of large amplitude (19). Thus, in such a case, superimposition of a.c. might even lead to more dense deposits.

Effect of frequency.—It is known that the smearing effect of the double layer on the potential can eliminate the effects of pulsating current on metal deposition (20, 21). The results in Fig. 6 indicate that it takes ~50 msec for discharge of the double layer in a half-charged zinc electrode. Thus, the most beneficial effects are expected at frequencies of 10 Hz or less. This is in agreement with the findings of Wagner (7) who uses a pulsating current regime of about 5 Hz to achieve long cycle life in zinc-nickel oxide cells. The beneficial effect of pulse charging disappears at low frequency (0.1 Hz) because one approaches the d-c case. At high frequencies, the smearing effect of the double layer capacitance prevails. This would explain the absence of any major effects in the work of Smithrick (11) at high frequencies.

Pulsed charging and the mechanism of zinc deposition.—In previous work on zinc deposition from zincate electrolyte, it was found that pulsed charging could result in compact hexagonal zinc deposits, even on stationary zinc electrodes in quiescent electrolyte. If deposition in pasted electrodes was via a zincate mechanism one would expect some pulse charging regime to yield a completely hexagonal crystalline deposit. However, only scattered localized crystalline deposits were found on the current collector. This would indicate that the direct reduction of ZnO is dominant. With d-c charging, the mossy zinc deposited via reduction of zincate is indistinguishable from the fine deposit from ZnO reduction. Application of a.c. converts the mossy deposit to hexagonal platelets and leaves the direct reduction of ZnO unaffected except for the tendency of most of the deposit to be formed adjacent to the current collector.

Pulse charging and battery cycle life.—The works of Wagner (7) and Romanov (10) indicate that some pulse charging regimes inhibit the growth of zinc dendrites into the separator and improve cycle life. This effect is most probably due to the redistribution of zinc that occurs on superimposition of pulses. The zinc deposit is adjacent to the current collector, and the part of the electrode in contact with the separator is largely zinc oxide. This furnishes a reservoir of reducible material that prevents concentration polarization and the concomitant formation of dendritic deposits in the separator (22). In addition, at low current densities, superimposition of a.c. increases the faradaic conductance. This improves the electrode performance, particularly at high rates of discharge, and also improves the useful life of the cell by mitigating capacity fading effects due to densification.

This work shows that superimposition of a-c. can induce many effects during the first charge of pasted zinc electrodes in a zinc-nickel oxide cell. Further work is necessary to elucidate the effect of such charging during prolonged cycling of cells.

Acknowledgments

The authors acknowledge helpful discussions with O. C. Wagner of the U.S. Army Electronics Research Development Command, Fort Monmouth, New Jersey. The authors wish to thank R. L. Sabatini (BNL) for the scanning electron microscopy. One of us (R.S.) gratefully acknowledges the financial support of the National Science Foundation Grant ENG-25153. This work was performed under the auspices of the U.S. Department of Energy Contract No. DE-AC02-76CH-00016.

Manuscript submitted Feb. 3, 1983; revised manuscript received April 20, 1983. This was Paper 5 presented at the Minneapolis, Minnesota, Meeting of the Society, May 10-15, 1981.

Any discussion of this paper will appear in a Discussion Section to be published in the June 1984 JOURNAL. All discussions for the June 1984 Discussion Section should be submitted by Feb. 1, 1984.

Brookhaven National Laboratory assisted in meeting the publication costs of this article.

REFERENCES

1. J. McBreen and E. J. Cairns, in "Advances in Electrochemistry and Electrochemical Engineering," H. Gerischer and C. W. Tobias, Editors, pp. 273-352, John Wiley and Sons, New York (1978).
2. R. Yu. Bek and N. T. Kudryavtsev, *Zh. Prikl. Khim.*, **34**, 2013 (1961).
3. R. Yu. Bek and N. T. Kudryavtsev, *ibid.*, **34**, 2020 (1961).
4. S. Arouette, K. F. Blurton, and H. G. Oswin, *This Journal*, **116**, 166 (1969).
5. M. Knaster, Abstract 92, p. 250, The Electrochemical Society Extended Abstracts, Vol. 80-2, Hollywood, FL, Oct. 5-10, 1980.
6. D-T. Chin, R. Sethi, and J. McBreen, *This Journal*, **129**, 2677 (1982).
7. O. C. Wagner, A. Almerine, and R. Smith, in "Proceedings of the 29th Power Sources Conference," Atlantic City, NJ, June 9-12, 1980, The Electrochemical Society Inc., p. 237, (1981).
8. V. V. Romanov, *Vestnik Electroprom.* **31**, 26 (1960).
9. V. V. Romanov, *Zh. Prikl. Khim.*, **34**, 1313 (1961).
10. V. V. Romanov, P. D. Lukovtsev, G. N. Kharchenko, and P. I. Sandler, *ibid.*, **33**, 1556 (1960). 1556 (1960).
11. J. J. Smithrick, in "Proceedings of 15th IECEC Meeting," p. 1203, American Institute of Aeronautics and Astronautics, New York (1980).
12. J. McBreen and E. Gannon, *Electrochim. Acta*, **26**, 1439 (1981).
13. O. Hladik and K. Schwabe, *Electrochim. Acta*, **15**, 635 (1970).
14. D. Drazic and Z. Nagy, *This Journal*, **118**, 255 (1971).
15. H. Gerischer and W. Mindt, *Electrochim. Acta*, **13**, 265 (1968).
16. H. Gerischer, *Surf. Sci.*, **13**, 265 (1969).
17. E. F. Zavgorodnaya, V. I. Lubyanova, and Yu. P. Rodak, *Elektrokhimiya*, **16**, 1025 (1980).
18. E. F. Zavgorodnaya, V. I. Lubyanova, and Z. E. Degtyarnova, *ibid.*, **16**, 1019 (1980).
19. D-T. Chin and S. Venkatesh, *This Journal*, **128**, 1439 (1981).
20. K. I. Popov, M. D. Maksimovic, B. M. Ocokoljic, and B. J. Lazarevic, *Surf. Technol.*, **11**, 99 (1980).
21. M. D. Maksimovic, S. K. Zecovic, and B. M. Ocokoljic, *Glas. Hem. Drus. Beograd*, **45**, 289 (1980).
22. J. O'M. Bockris, Z. Nagy, and D. Drazic, *This Journal*, **129**, 30 (1973).

Statistical Analysis of Lithium Iron Sulfide Status Cell Cycle Life and Failure Mode

E. C. Gay,* J. E. Battles, and W. E. Miller

Argonne National Laboratory, Chemical Technology Division, Argonne, Illinois 60439

ABSTRACT

Groups of 12 or more identical Li-alloy/FeS cells fabricated by Eagle-Picher Industries, Incorporated and Gould Incorporated were operated at Argonne National Laboratory in the status cell test program to obtain data for statistical analysis of cell cycle life and failure modes. The cells were full-size electric vehicle battery cells (150-350 A-hr capacity) and were cycled at the 4 hr discharge rate and 8 hr charge rate. The end of life was defined as a 20% loss of capacity or a decrease in the coulombic efficiency to less than 95%. Seventy-four cells (6 groups of identical cells) were cycle life tested, and the results were analyzed statistically. The ultimate goal of this analysis was to predict cell and battery reliability. Testing of groups of identical cells also provided a means of identifying common failure modes which were eliminated by cell design changes. Mean time to failure for the cells based on the Weibull distribution is presented. Post-test examinations determined the causes of failure in each cell group, and corrective actions are discussed.

For the past several years, Li-Al/FeS cells for electric vehicles have been developed at Argonne National Laboratory (ANL) and its industrial subcontractors (Eagle-Picher Industries, Incorporated and Gould Incorporated). The performance goals of these cells are (*i*) high reliability, (*ii*) a specific energy of 125 W-hr/kg at the 3 hr rate, and (*iii*) peak specific power of 185 W/kg at 50% charge. Progress in the fabrication and development of cells toward achieving these goals was determined by life tests at ANL for groups of 12 or more identical state-of-the-art cells ("status" cells) supplied by each contractor. These cells were operated to obtain data for statistical analysis of cell cycle life, performance, and failure modes.

The major task confronted in the cycle life study was to assess the applicability of a selected statistical model on the basis of the given data. This was accomplished using two approaches: probability plotting and analysis of the data using the W-test and the Kolmogorov-Smirnov statistical test for goodness of fit (1, 2). Based on these tests, the Weibull distribution provided an adequate representation of the data. The Weibull distribution is widely used in engineering practice because of its versatility. The probability density function for the Weibull distribution has a variety of shapes (1). In particular, when the Weibull slope, b, is greater than one, the Weibull probability density function is single-peaked; for $b < 1$, the probability density function is reverse J-shaped; for $b = 1$, the Weibull distribution is equivalent to the exponential distribution. The principal use of the Weibull distribution is in the field of life phenomena. The end of life for the status cells was defined as a 20% loss of the initial stabilized capacity or a decrease to less than 95% coulombic efficiency. Attempts to develop separate statistics for these two end-of-life events showed that they reflected common life factors. In all but one case (Gould Group I cells shown in Table I), a single Weibull slope provided the best correlation of the cycle life data. Analysis of the cycle life data also indicated that the mean time to failure (MTTF) for the status cell groups would be increased substantially if the end-of-life criteria were changed to 30% loss of initial stabilized capacity or a decrease to 90% coulombic efficiency.

The cells fabricated by Eagle-Picher contained Li-Al negative electrodes and BN-felt separators and were filled with electrolyte by a vacuum infiltration technique; cells fabricated by Gould contained Li-Al-Si negatives and MgO powder separators, and emphasis was placed on the starved electrolyte cell design. The starved electrolyte cell design contained insufficient electrolyte to fill the voids in the as-fabricated electrodes and separators. Electrolyte powder was mixed with powdered active materials for the electrodes or with MgO powder for the separators and pressed to form plaques for assembly into the cells. The initial volume percent gas in the cell components for the solid state of the electrolyte was 12% for the positive electrodes, 14% for the negative electrodes, and 5% for the separators. The construction of the status cells was described in a previous report (3).

* Electrochemical Society Active Member.
Key words: reliability, cell, failure, fused salts.

Statistical Analysis of Cycle Life

In early 1980, Eagle-Picher fabricated 14 Li-Al/FeS multiplate cells (Group I) which had a specific energy of 71 W-hr/kg at the 4 hr discharge rate and peak power at 50% discharge of 55 W/kg. These somewhat low values were the result of the use of very heavy components in the electrode structures; these components have since been significantly reduced in weight. The Group I cells showed very stable capacity (Fig. 1) with an average decline rate of 0.03% per cycle and an MTTF of 410 cycles. The Weibull slope for these cells was 2.9.

Subsequently, three additional status cell groups (Group III, VI, and IX cells) were fabricated by Eagle-Picher and tested at ANL. As shown in Table I, the average specific energy for all cell groups was 71-94 W-hr/kg at the 4 hr discharge rate with an average decline rate of 0.03% per cycle. The average peak specific power was 55-80 W/kg at 50% charge. The Weibull slope was 1.4-3.2 and the MTTF was 138-410 cycles. The Group IX cells showed no cell failures until about 200 cycles (Fig. 2) as did the earlier Group I cells. The Group IX cells, however, showed an improvement in the specific energy and specific power to 90 W-hr/kg at the 4 hr rate and 80 W/kg at 50% charge. Within the range tested, 460°-490°C, the performance of the Eagle-Picher cells was independent of temperature.

The MTTF for the second group of Gould status cells with MgO powder separators is shown in Fig. 3 for different operating temperatures. The MTTF at 455°C (the operating temperature recommended by Gould) was 268 cycles. Subsequent operation at higher temperatures increased the MTTF to 330 cycles before the loss of initial stable capacity exceeded 20%. The Weibull slopes for these cells were 3.1 at 455°C and 2.9 at the higher temperature. The specific energy of these cells was 80 W-hr/kg at the 4 hr rate. The capacity decline was 0.08% per cycle at 455°C and 0.06% per cycle over the range 455°-475°C. A +5° temperature increase from the base temperature

Table I. Summary of Li/FeS cell performance tests at ANL

	Gould MK II status cells		Eagle-Picher MK II status cells			
	I	II	Group I	Group III	Group VI	Group IX
No. of cells in group	12	12	14	12	12	12
Theo capacity, A/hr	194	194	360	394	394	394
Avg operating temperature, °C	465	see below	465-475	475-490	470-480	465
Avg peak capacity, A/hr	158	157	288	294	347	340
Std deviation in peak capacity, ± %	4.5	3.2	5.2	6.6	0.9	2.1
Avg specific energy, W-hr/kg	74	80	71	81	94	90
Peak specific power, W/kg	70	70	55	55	74	80
		Temperature[c]				
		455	455-475			
Cycle life[a]						
High/low, cycles	307/14	467/121	542/158	1031/238	908/23	201/100	517/193
Mean time to failure, cycles	218[b]/26[b]	268	330	410	362	138	345
Weibull slope	2.0/3.4	3.1	2.9	2.9	1.4	2.1	3.2
Avg capacity loss rate, % per cycle		0.08	0.06	0.032	0.027	0.045	0.024

[a] End of life defined as 20% capacity loss or decrease in coulombic efficiency to < 95%.
[b] Correlated as five and seven cell groups single group correlation not possible.
[c] Cells run initially at 455°C to 20% capacity loss, temp then increased in 5° steps.

(455°C) was just as effective in restoring cell capacity as a +10°C increase, and when capacity again declined after the initial temperature change, subsequent temperature change had little effect. The temperature sensitivity of these cells may be attributed to the use of 22 mol percent (m/o) LiF-31% LiCl-47% LiBr electrolyte in the cells. This salt has a liquidus temperature of 445°C compared to the 425°C mp of the LiCl-KCl salt used in the Eagle-Picher cells. These cells showed a large improvement over the first group of status cells with MgO powder separators (Table I). Figure 3 basically shows that the Gould cells failed by capacity loss; in fact at 455°C, all of the failures were by this route.

Testing of all of the status cells shown in Table I has been completed. The statistical significance of the status cell tests is shown in Table II and was determined by comparing the Weibull distribution mean lives for the cells. At confidence levels between 90-99%, it was concluded that, with respect to longer cycle life, Gould Group II was better than Group I, Eagle-Picher Group I was better than Groups VI and IX, and Group IX was better than Group VI.

Uniformity in cell performance for all cell groups was also assessed. The standard deviation in peak capacity among cells in the groups is shown in Table I. For both contractors, this has decreased with time, showing an improving control of the cell manufacturing process.

One objective of the status cell program was to forecast the reliability of Li-alloy/FeS cells in batteries. It was assumed in the statistical analysis that no new factors are brought to bear on the cycle life of cells operated in a battery compared to the operation of single cells. This assumption appeared valid in the testing of these cells based on the manner in which the cells are clamped between constraining plates to prevent volume increase during cycling. The constraining techniques are nearly identical for single-cell and multiple-cell testing in a battery. Forecasts of cell failures in 10-cell modules are shown in Table III. Based on the two 10-cell modules tested to date which contained cells identical to status cells tested in the program, it was concluded that at a 95% confidence level, the projected number of cell failures shows good agreement with the measured number of cell failures.

Cell Failure Modes

Post-test examinations, which have been an important part of the Li-alloy/FeS battery development program, have provided valuable information for

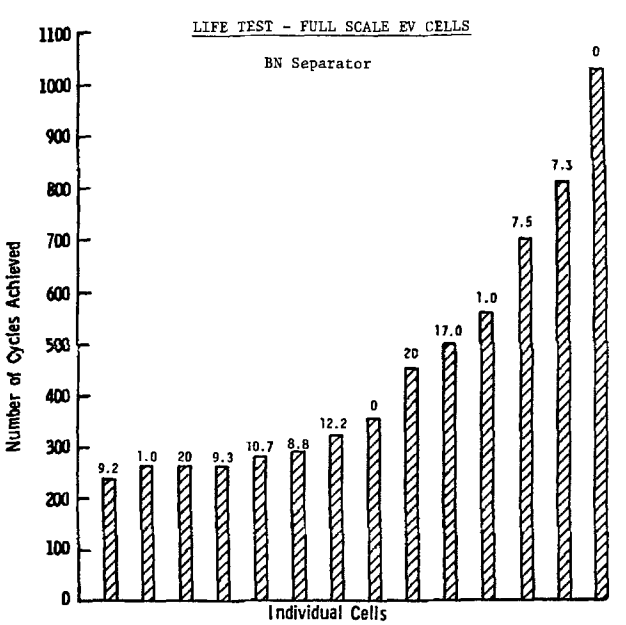

End of life defined by 20% loss of capacity or 5% loss of coulombic efficiency.
Numbers above bar show percent capacity loss.

Fig. 1. Life test for Eagle-Picher Mark II Group I cells

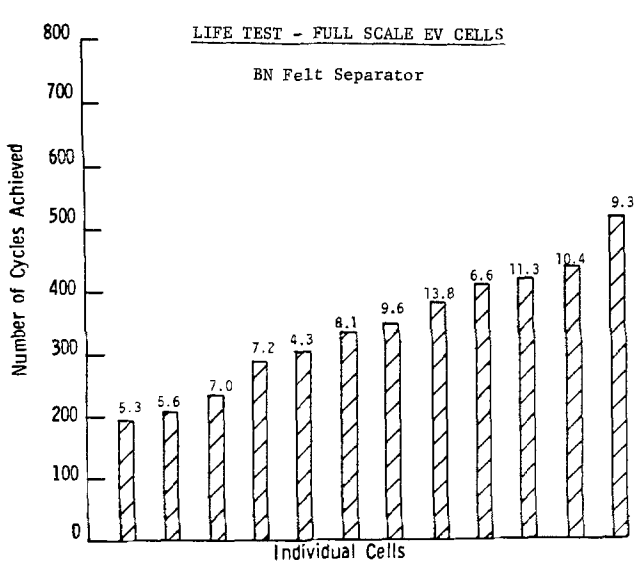

End of life defined by 20% loss of capacity or 5% loss of coulombic efficiency.

Numbers above bar show percent capacity loss.

Fig. 2. Life test for Eagle-Picher Mark II Group IX cells

Table II. Statistical significance of status cell tests

	Groups[b]	Gould[a] II/I[c]	Eagle-Picher[a] I/III	I/VI	I/IX	IX/VI	III/IX
Combined degrees of freedom		44	143	143	143	122	122
Mean-life ratio		1.5	1.1	3.0	1.2	2.6	1.02
Weibull slope		2.9/1.6	2.9/1.4	2.9/2.1	2.9/3.2	3.2/2.1	1.4/3.2
Confidence level, %		95	—[d]	> 99	> 90	> 99	—[d]
Best cell group in comparison test		II	—[d]	I	I	IX	—[d]

[a] Gould cells have MgO powder separators; Eagle-Picher cells have BN-felt separators.
[b] Significance test was based on mean-life ratio of indicated groups of status cells.
[c] Based on five MgO powder separator cells with mean time to failure of 218 cycles.
[d] Undetermined; statistical tables needed for this analysis were not generated.

Table III. Forecasts of Li-alloy/FeS battery cycle life

Designation of status cells	Sample mean life to failure, cycles	Weibull slope	Projected number of cell failures[a] Cycles	Low	High	Measured number of cell failures[b] Cycles	No.
EPI Group IX	345	3.2	200	0	3		
			300	1	7		
			400	4	10		
Gould Group II	330	2.9	200	0	4		
			300	1	8		
			400	4	10		
EPI Group III	362	1.4	200	0	7	225	1
			300	2	10		
			400	4	10		
EPI Group VI	138	2.1	100	0	7	90	1
			150	3	10	110	2
			200	6	10	130	3

[a] Cycle life data were analyzed using the Weibull distribution, and calculations were based on the 95% confidence level for 10-cell modules.
[b] 10-cell modules with cells similar to the indicated status cells.

recommendation on designs to achieve improved cell performance and reliability and for the selection of materials (4, 5). The major objective of the post-test examinations has been the determination of cell failure mechanisms. Other objectives are the determination of the electrode microstructure, the distribution, uniformity, and utilization of active materials, and the in-cell corrosion of current collector materials. These post-test examinations include metallography, chemical analysis, x-ray diffraction, ion and electron microprobe analysis, and scanning electron microscopy. Because the cell materials (LiCl-KCl, LiAl, and Li_2S) react rapidly with the ambient atmosphere, a unique helium atmosphere facility was constructed for the post-test examination of cells (5). The results presented in this paper pertain to the failure analysis of Eagle-Picher and Gould status cells.

The failure analysis has been completed for the Eagle-Picher Groups I, III, VI and IX status cells, and the failure modes are summarized in Table IV. In all cases, failure has been by an electrical short circuit between opposing electrodes, which is indicated by a decline in the coulombic efficiency.

Table IV. Failure analysis of Eagle-Picher status cells Groups I, III, VI, and IX

Failure mechanisms	Number
Li-Al protrusions across BN-felt separator	26
Extrusion of active material from ruptures in the electrode edge retainers	9
Short circuit in feedthrough	1
Assembly difficulty	3
Other	3
Not identified	3
Not examined	5
TOTAL	50

Two major failures have been identified for the Eagle-Picher status cells. The first is the formation of Li-Al protrusions that penetrate the BN-felt separator and contact the positive electrode. A typical example of a protrusion, with the porous structure typical of the negative electrode, is shown in Fig. 4. This failure mode was most prevalent in Groups III, VI, and IX cells (23 of 36 cells failed by this mode), and it coincided with changes in methods of cell assembly and pretreatment of BN-felt separators, *i.e.*, present BN felts are saturated with magnesium acetate or nitrate, compressed, and then pyrolyzed before assembly; previous felts were untreated and compressed during cell assembly. Although the mechanism for the formation of Li-Al protrusions has not been completely elucidated, recent studies have shown they can be prevented by simple mechanical design changes. The MTTF for Group IX cells was significantly extended over that of Group VI cells, MTTF of 345 cycles compared to 138 cycles; this was accomplished by reducing the size of the openings in the photoetched retainer screens, *i.e.*, from 0.33 to 0.23 mm diam. Post-test examination of Group IX cells showed that although the failures were caused by protrusions, the number of protrusions was considerably less than that observed in Group VI cells. Additional cell tests have shown that protrusion formation can be completely prevented by incorporat-

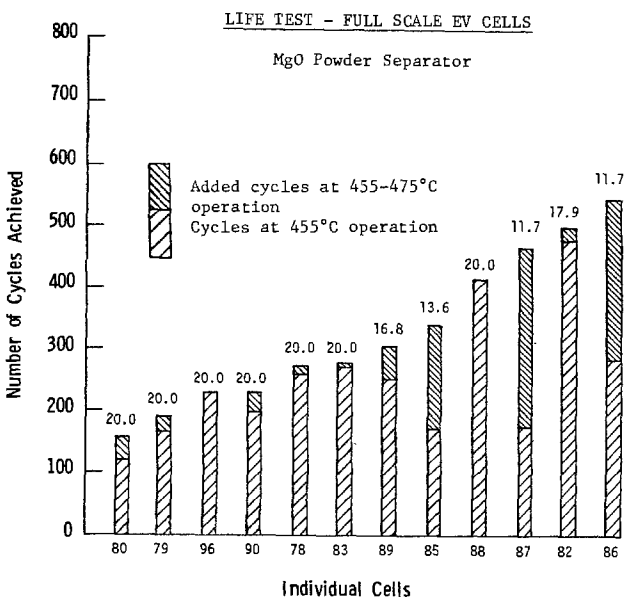

End of life defined by 20% loss of capacity or 5% loss of coulombic efficiency. Numbers above bar show percent capacity loss.

Fig. 3. Life test for Gould second MgO powder separator status cells.

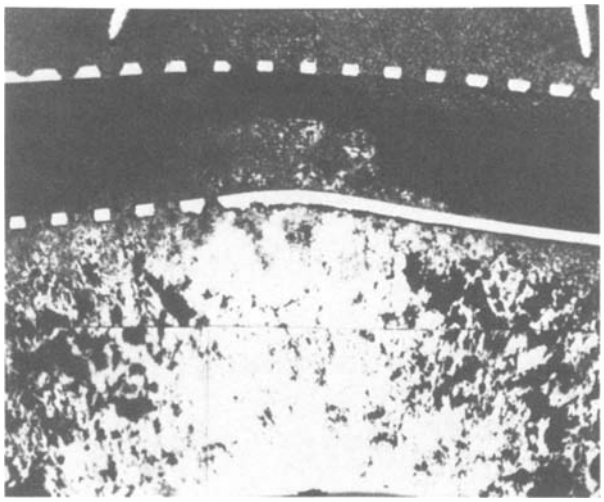

Fig. 4. Penetration of BN-felt separator by an Li-Al protrusion

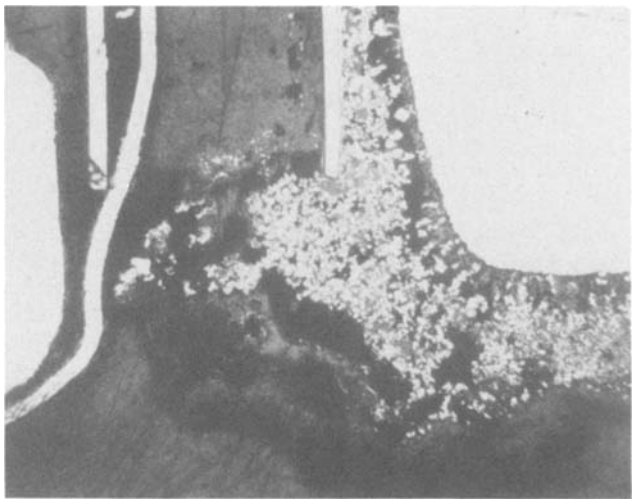

Fig. 5. Cell failure caused by extrusion of positive material

ing a fine mesh screen (200 mesh) inside the normal photoetched retainer screen.

The second major cause of short-circuit failures in Eagle-Picher status cells was the extrusion of active material at the edge of the electrodes. An example of this failure mode is shown in Fig. 5 where the positive electrode material has extruded through a rupture in the edge retainer and contacted the negative electrode. This failure mode, which was caused by inadequate mechanical restraint at the electrode edges, was the predominant cause of short-circuit failures in Group I cells (9 of 14 cells in this group failed by this mode). No additional extrusion failures have occurred since a U-shaped channel was added to reinforce the mechanical restraint at the edges of both electrodes. The formation of Li-Al protrusions was

Table V. Failure analysis of Gould status cells
Groups 1 and 2—MgO powder separators

Failure mechanisms	Number
Separator penetrated by positive electrode material	9
Short circuit in feedthrough	2
Capacity decline	2
Not examined	11
TOTAL	24

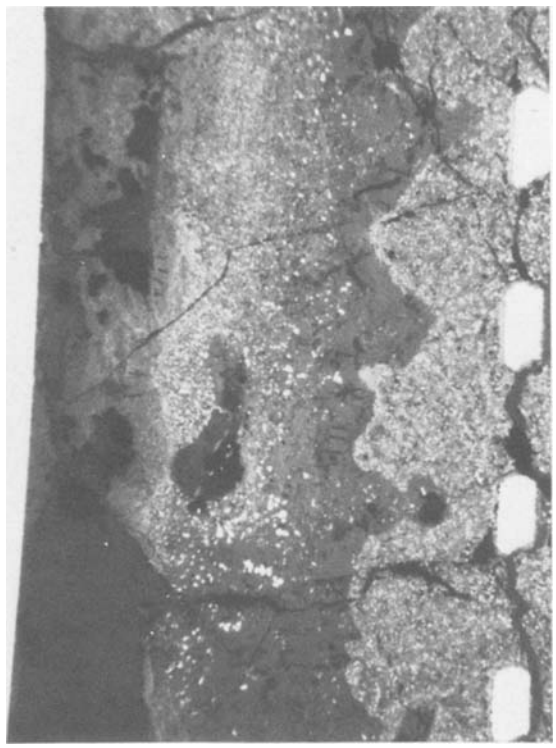

Fig. 6. Penetration of MgO powder separator by active material from the positive electrode.

observed in Group I cells, and three cell failures were caused by these protrusions.

Post-test examination of the two groups of Gould status cells showed only a single mechanism for the internal short-circuit failures. The failure modes are summarized in Table V. Two cell failures were caused by short circuits in the electrical feedthroughs. Although all of the cells in the first group and most of the cells in the second group failed because of capacity loss, cell operation was continued to the point of short-circuit failure (coulombic efficiency decline) except for two cells in the first group. In these cells, the predominant failure mode was short circuits caused by complete penetration of the MgO powder separator by active material from the positive electrode as shown in Fig. 6. The material from the positive electrode compressed the MgO powder, and its irregular advance resulted in numerous localized penetrations which eventually contacted the negative electrode (~300-500 cycles). This failure mode occurs because the mechanical properties of the present MgO powder separators are inadequate for the containment of the positive electrode material. Elimination of this failure mechanism requires substantial improvements in the mechanical properties of the powder separator/retainer system.

Conclusions

The statistical model for evaluating cell performance has been verified and found applicable on the basis of experimental results. The failure mechanisms, which result in short circuits, have been identified for Li-Al/FeS cells that use both BN-felt and MgO powder separators.

Acknowledgments

The authors would like to express their gratitude to J. Arntzen for the status cell tests, F. Mrazek for the cell post-test examinations, and to D. L. Barney and R. K. Steunenberg for their support during this work. This work was conducted under the auspices of the Department of Energy.

Manuscript submitted Nov. 16, 1982; revised manuscript received March 3, 1983. This was Paper 44 presented at the Detroit, Michigan, Meeting of the Society, Oct. 17-21, 1982.

Any discussion of this paper will appear in a Discussion Section to be published in the June 1984 JOURNAL. All discussions for the June 1984 Discussion Section should be submitted by Feb. 1, 1984.

Argonne National Laboratory assisted in meeting the publication costs of this article.

REFERENCES

1. G. J. Hahn and S. Shapiro, "Statistical Models in Engineering", John Wiley and Sons, Inc., New York (1967).
2. F. J. Massey, Jr., *Am. Stat. Assoc. J.*, **46**, 68 (1951).
3. D. L. Barney, *et al.*, Progress Report, ANL-81-65 (1981).
4. J. E. Battles and F. C. Mrazek, Abstract 59, p. 161, The Electrochemical Society Extended Abstracts, Vol. 77-2, Atlanta, GA, Oct. 9-14, 1977.
5. J. E. Battles, F. C. Mrazek, and N. E. Otto, Argonne National Laboratory Report ANL-80-130 (1981).

The Influence of Smoke and Isobutane on Corrosion in Sulfur Dioxide-Polluted Environment

J. B. Johnson, B. S. Skerry, and G. C. Wood

Corrosion and Protection Centre, University of Manchester Institute of Science and Technology, Manchester, England

ABSTRACT

Specimens of iron, zinc, and aluminum were exposed to an air atmosphere containing 3000 ± 500 ppm CO_2, at 298 ± 0.5 K and 97 ± 2% relative humidity for times up to 200 hr. To this atmosphere could be added separately or in combination 3.5 ppm SO_2, 60 vpm isobutane, and smoke at 160 or 360 $\mu g\ m^{-3}$. Corrosion was enhanced by SO_2 or smoke in all cases, and by isobutane plus SO_2 in the case of aluminum and zinc. In contrast, isobutane as a single pollutant slightly inhibited the corrosion of each metal, and the corrosivity of SO_2 in the case of iron. Possible mechanisms concerning the observed effects of smoke and isobutane are suggested. These include corrosion promotion by smoke via an enhancement of the microclimate activity of water and sulfur dioxide, and corrosion inhibition by isobutane via competitive reactions with water molecules.

Industrial highly polluted atmospheres contain many substances, the sources of which include the combustion of fossil fuels. Such combustion produces sulfur dioxide and smoke and, while the corrosion associated with the presence of sulfur dioxide has been, and still is, extensively studied (1-7), in comparison less research has been carried out on the corrosivity of smoke particles. This situation exists in spite of the fact that the research carried out on carbon particles has shown that such material has an adsorption capacity for both water and sulfur dioxide, strongly catalyzes the cathodic reduction of oxygen and has an enhancing effect on the corrosivity of sulfur dioxide (2, 8-10).

However, industrially produced smoke particles will differ from carbon particles both physically and chemically. Smoke particles are generally less than 10^{-7}m diam and will be associated with sorbed materials, such as moisture, sulfur dioxide, and hydrocarbons (11). Clearly then, in order to study the corrosivity of industrial smoke particles, the action of moisture, sulfur dioxide, and laboratory produced "clean" smoke should be assessed as individual pollutants and in various combinations. The overall action of industrial smoke particles may then be interpreted by recourse to knowledge of the actions and possible interactions of the particle components. This paper addresses itself to a preliminary investigation using this approach, with the high concentrations of carbon dioxide, sulfur dioxide and smoke that can be found in the proximity of fossil fuel combustion emissions. Many hydrocarbons are present in the atmosphere, (12, 13), the sources of which include combustion processes, biological, and geothermal activities. Isobutane is a relatively abundant trace pollutant, up to 35 ppb, (14), and was chosen to be studied because of possible reactivity due to its polar character, (15).

Experimental Procedure

An atmospheric test chamber (16, 17) was used in which the environmental temperature and humidity were controlled at 298.3 ± 0.5 K and 97 ± 2%, respectively, while the air environment included 3000 ± 500 ppm of carbon dioxide. Further, when required, 3.5 ± 0.5 ppm of sulfur dioxide, laboratory produced smoke at concentrations of 160 and 360 $\mu g\ m^{-3}$, and 60 ± 10 vpm (volumes per million volumes of air) isobutane could be introduced into the chamber.

The test chamber environment was an atmosphere produced by the controlled combustion of natural gas (analysis: 93 ± 2% CH_4, 3.5 ± 0.5% C_2H_6, and 1.5 ± 0.5% N_2). Prior to combustion, the controlled flow of natural gas was passed over analytical reagent quality carbon disulfide, maintained at 271 K. The flow rate and temperature controlled the resultant concentrations of CS_2 in the natural gas, and thus (after combustion) the concentration of SO_2 in the test chamber. Smoke was produced by the controlled combustion of high quality paraffin (18) using a simple wick burner lamp (flame temperature maximum 757 K) beneath an inverted funnel. The smoke then passed into the chamber close to a small distributing fan. The isobutane (analysis: 99.4% isobutane, 0.55% n-butane, and 0.05% propane) was passed into the test chamber at a controlled rate of flow (19). Table I summarizes the various atmospheres used.

Checks on the composition within the test chamber included wet and dry bulb temperature observation for relative humidities, Drager tube sampling for carbon dioxide (20), and standard test methods for sulfur dioxide and for smoke (21). With reference to sulfur dioxide, the technique consisted of drawing a known volume of chamber atmosphere through a 0.3%

Table I. Experimental exposure conditions

Exposure	Test atmosphere
(a)	Control air
(b)	Control air including 60 ± vpm isobutane
(c)	Control air including 3.5 ± 0.5 ppm sulfur dioxide
(d)	Control air including 60 ± 10 vpm isobutane and 3.5 ± 0.5 ppm sulfur dioxide
(e)	Control air including smoke (360 $\mu g\ m^{-3}$)
(f)	Control air including 3.5 ± 0.5 ppm sulfur dioxide and smoke (160 $\mu g\ m^{-3}$)

Key words: metals, particles, mobility, atmosphere.

v/v solution of hydrogen peroxide at pH 4.5. This solution oxidized sulfur dioxide to sulfuric acid. The acid produced was then back-titrated to pH 4.5 with a standard solution of sodium borate. The amount of alkali required related directly to the amount of sulfur dioxide absorbed. The measurement of smoke also involved sampling a known volume of chamber atmosphere which, in this case, was drawn through a Whatman No. 1 filter paper, such that a stain of 25 mm diam was produced. The decrease in reflection caused by the stain, compared with nonstained filter paper and with standard white and gray plates, was measured by a Diffusion System Limited Model 43 Smoke Stain Reflectometer Meter. This decrease was then related to the weight of smoke, and so to the atmospheric concentration, using standard charts. It was important that further analysis was also carried out. Thus, although the specification for the paraffin permitted the presence of a maximum of 0.2% sulfur, gas chromatographic inspection (22, 23) of the atmosphere within the test chamber produced by the combustion of natural gas and of the paraffin (using a Pye 104 Chromatograph) did not detect the presence of sulfur dioxide, or the presence of either organo-sulfides of hydrogen sulfide when natural gas was burned with the carbon disulfide. The instrumental detectability limits were 10^{-5}, 10^{-4} and 10^{-6} μg sec^{-1}, respectively.

The metals studied were iron, zinc, and aluminum, being representative of commonly exposed material. Their compositions are given in Table II. Specimens were cut from 0.025 mm foils into strips 50 × 10 mm. They were then twice ultrasonically degreased in analytical reagent quality acetone, dried in warm air, and stored in a desiccator until required. Specimens of the 99.99% purity aluminum were treated differently in that they were electropolished in a solution of 80% ethanol 10% perchloric acid, using an aluminum cathode for 5 min at 100 mA cm^{-2} and 263 K. They were then rinsed in distilled water followed by analytical quality acetone, and finally dried and stored in a desiccator until required.

After careful weighing, specimens of each of the metals were suspended from a slowly rotating carousel within the test cabinet, and were subjected in separate experiments to each test environment shown in Table I for periods up to 220 hr. After exposure, the specimens were dried in a desiccator and reweighed. They were then treated to the appropriate corrosion product removing method (24), as given in Table III, then rinsed in flowing water, washed in acetone, air dried, and reweighed. Specimens of unexposed metals were also treated with the appropriate solutions, as shown in Table III, such that weight loss measurements could be corrected for any metal (as opposed to corrosion product) removal due to these solutions. However, no correction was found necessary.

A sufficient number of specimens were exposed at the same time so that morphological examinations could be carried out. Such examinations used both optical microscopy and scanning electron microscopy with an energy dispersive analysis by x-rays facility.

Smoke particle characterization was carried out using a Philips 301 transmission electron microscope, a Corning PT1-8 conductivity meter and a pH meter. Samples for the TEM were obtained by exposing standard copper grid foils for 30 min in the exposure chamber and then submitting the specimens to examination. The conductivity work was carried out on the exposure chamber atmosphere by drawing it through 200 ml of deionized water and measuring the conductivity at various times up to 54 hr. In order to assess the effect of the smoke particles, measurements were carried out on the combustion gases alone by filtering out the smoke particles themselves using Whatman No. 1 filter papers, and on the combustion gases plus the smoke particles. The initial pH of the deionized water, and the final pH after passage of the smoke, was measured using an Electronic Instruments Limited Model 7050 pH meter.

Table II. Test metal compositions

Metal	Purity	Composition (ppm)
Iron	99.5%	Mn 3000, Si 1000, C 800, P 400, S 500
Zinc	99.5%	Ca 1, Cd 20, Cu 15, Fe 10, In 10, Mg 1, Na 2, Ni 1, Pb 100, Si 2, Sn 8
Aluminum	99.0%	Cu 1000, Fe 7000, Mn 1000, Si 5000, Zn 1000
Aluminum	99.99%	Ag 1, Ca 2, Cu 5, Fe 8, Ga 2, Mg 20, Na 1, Ni 2, Pb 2, Si 7

Table III. Methods used for chemical cleaning after exposure testing

Metal	Solution	Temperature (K)	Time (min)
Aluminum	70% nitric acid in water	293	5
Iron	2% antimony trioxide 5% stannous chloride in hydrochloric acid	283	12
Zinc	10% ammonium chloride in water, then washed in water and dipped into 5% chromic acid plus 1% silver nitrate in water	293 Boiling	5 0.33

Results

Weight changes.—While weight gains are indicative of the extent and nature of corrosion products and their retention on the metal surface, weight losses after chemical cleaning of the corroded surfaces represent a true measure of the metal losses by corrosion.

Figures 1 to 6 display the weight changes of the metals caused by the various environments. The data shown consist of either results from duplicate specimens when the values are shown as the two values

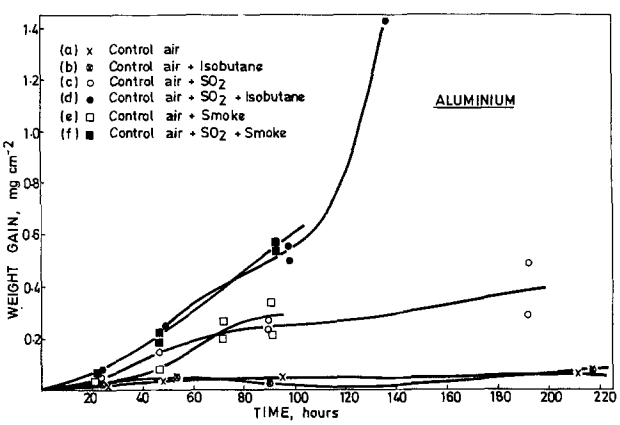

Fig. 1. Weight gains for aluminum in the various atmospheres

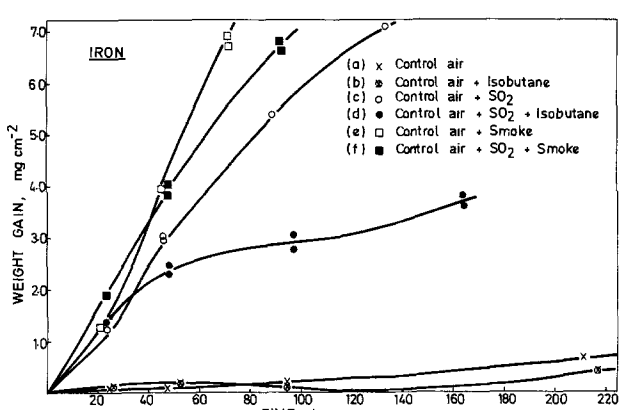

Fig. 2. Weight gains for iron in the various atmospheres

obtained, or as single points which are the average of triplicate test specimens. The variation between any given set of triplicate results was never more than ±7% of the average value. Figures 1-3 show the weight gain with time, and Fig. 4-6 present the weight loss with time. These latter figures will be commented upon as the more direct indication of corrosion, while the former figures will be considered later with reference to the possible corrosion products formed.

The influence of isobutane on the action of the control air, *i.e.*, comparing the effects of environments (b) with (a), is inhibition of corrosion. Figures 5 and 6 show that with respect to iron and zinc, the control air at 200 hr caused losses of 0.9 and 0.3 mg cm^{-2}, respectively, while when isobutane was also present the respective changes were reduced to 0.4 and 0.07 mg cm^{-2}.

The action of smoke particles, in contrast to the above, is to enhance the corrosion effect of the control

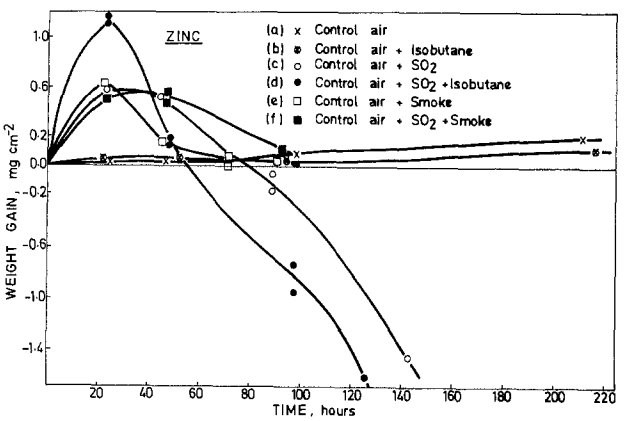

Fig. 3. Weight gains for zinc in the various atmospheres

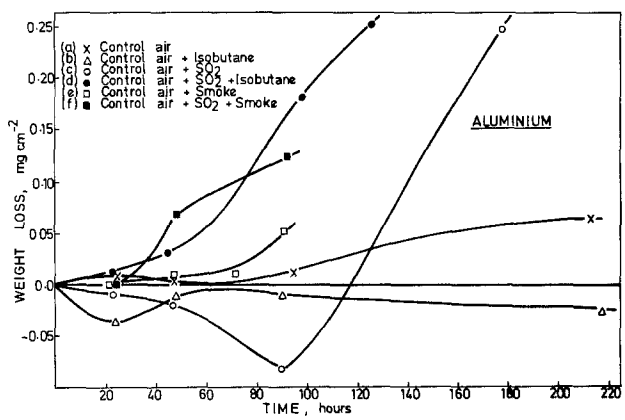

Fig. 4. Weight losses for aluminum in the various atmospheres

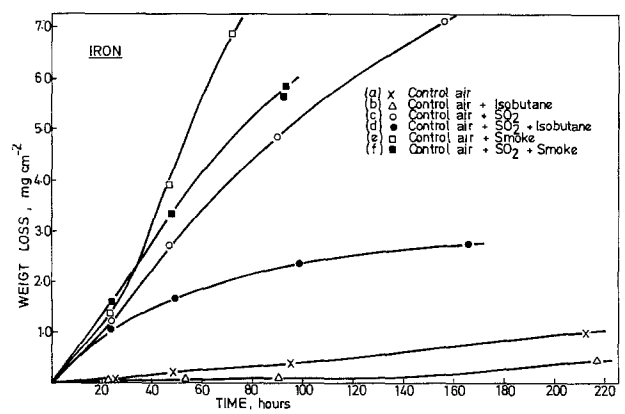

Fig. 5. Weight losses for iron in the various atmospheres

air. Thus, comparing the environments (e) and (a), Fig. 4 and 6 show that at 100 hr, while control air produced losses of aluminum and zinc of 0.015 and 0.2 mg cm^{-2}, respectively, the smoke addition increased losses to 0.065 and 1.1 mg cm^{-2}. This corrosion enhancement effect is shown to be particularly dramatic in the case of iron, as shown in Fig. 5, which at 70 hr showed an increase in metal loss from 0.25 to 7 mg cm^{-2}.

The expected increase in corrosion due to the presence of sulfur dioxide is also clearly shown in Fig. 4, 5, and 6. Comparing the influence of environments (c) and (a), the metal losses at 180 hr of aluminum, iron, and zinc in control air (a) were 0.063, 0.85, and 0.25 mg cm^{-2}, while the addition of sulfur dioxide (c) produced losses of 0.25, 7.5, and 4.75 mg cm^{-2}, respectively.

The effects of the various combinations of the contaminants isobutane, sulfur dioxide, and smoke are complex. Figures 4 and 6 show that, for aluminum and zinc, the additional presence of isobutane (d), or smoke (f), enhance the corrosivity of sulfur dioxide (c). The highest environmental corrosivity is shown by isobutane plus sulfur dioxide (d), followed by smoke plus sulfur dioxide (f). While the additional action of smoke is consistent with its effect as a sole contaminant (e), the corrosion promotion effect of isobutane in combination with sulfur dioxide contrasts with its inhibiting action when alone (b).

Iron was affected differently. Figure 5 shows that the dominant contaminant was smoke (e), followed by smoke plus sulfur dioxide (f), and that the effect of isobutane was to inhibit the action of sulfur dioxide (d) compared to (a).

In addition to the results shown in Fig. 4 and 5 that demonstrate the much better corrosion resistance of aluminum compared with that of iron, and in Fig. 5 that emphasize the high corrosivity of sulfur dioxide to zinc, a more general comparison of weight gains against weight losses is also instructive. This comparison gives a tentative indication of the nature of the corrosion products formed. Ideally, for example, a corrosion product M_aX_b would give a weight gain to weight loss ratio equal to the ratio of "b" times atomic weight of anion X to 'a' times atomic weight of metal M. Thus for aluminum, comparing the weight gains shown in Fig. 1 with the weight losses in Fig. 4, the similar values of weight gain and loss in the control air (a) atmosphere indicates the presence of Al_2O_3 (ratio of 3×16 to $2 \times 26.98 = 1.12$). In contrast, both the sulfur dioxide plus isobutane (d) and the sulfur dioxide plus smoke (f) atmospheres produce high ratios of weight gain to weight loss of approximately 4:1. These results indicate the joint presence of both $Al(OH)_3$ and $Al_2(SO_4)_3$, (ratio of 4.18:1) suggesting by implication, that both smoke and isobutane promote the production of $Al_2(SO_4)_3$ by sulfur dioxide. In contrast to the weight changes found for the 99% aluminum, the electropolished 99.99% pure aluminum showed no corrosion effects in any of the test atmospheres.

In the case of iron, as shown in Fig. 2 and 5, the ratio of weight gain to weight loss (0.6) suggests that in the case of control air (a) the corrosion product is likely to be FeOOH (ratio of 33 to 55.85 = 0.59). In each of the remaining environments the corrosion product is probably better represented by $FeOOH \cdot H_2O$ or $Fe(OH)_3$, with a ratio of approximately 1.

Finally, with reference to zinc, Fig. 3 and 6 show approximately equal ratios of 1:1 for weight gain to weight loss in both the control air (a) and control air plus isobutane (b) environments. This suggests that the corrosion products include a high proportion of $ZnCO_3$, probably as the basic carbonate. However, while at the 20 hr point the higher gain to loss ratio caused by environment (d) suggests the presence of some $ZnSO_4$, the decreasing weight gain shown in Fig.

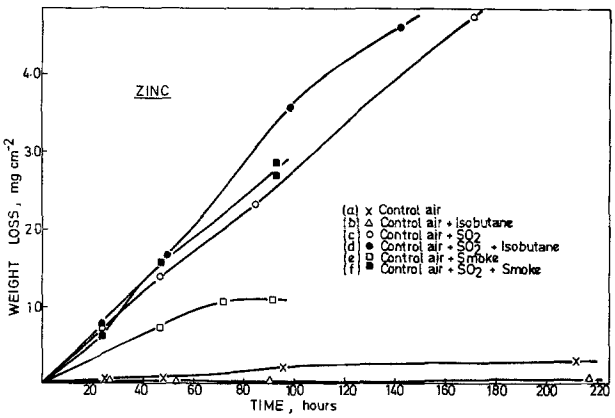

Fig. 6. Weight losses for zinc in the various atmospheres

3 (due to soluble corrosion product dripping from specimens) invalidates any further comparisons.

Topography.—The corrosion products formed on the aluminum (99% purity) specimens were very similar irrespective of the test environment. Thus, a whitish-gray colored tarnish layer developed on the surface, becoming visible after approximately 24 hr. This layer thickened with time and with severity of environment and often then displayed a generalized cracking as shown in Fig. 7. The electropolished high purity (99.99%) aluminum specimens developed only a very slight tarnish film after approximately 96 hr, and this occurred only in the control air plus SO_2 and isobutane environment (d).

Two general types of corrosion products were observed upon zinc. Those environments not containing SO_2 produced a smooth and even grayish-white colored tarnish layer. Those environments containing SO_2 also demonstrated a grayish tarnish layer but developed an overlying even distribution of a white powdery crystalline material, which transformed with time to a more transparent corrosion product.

The overall appearance of iron specimens exposed to the control air (a), and to the control air plus isobutane (b), was that of a shiny metal covered with an even distribution of discrete rust particles. In the case of environment (a) the particles of rust were orange-red in color, while in the case of environment (b), they appeared reddish-brown. The typical morphology of these corrosion locations is shown in Fig. 8 and 9. The presence of SO_2 produced a much different corrosion appearance. Thus, control air plus SO_2 (c), and control air plus SO_2 and isobutane (d), caused the

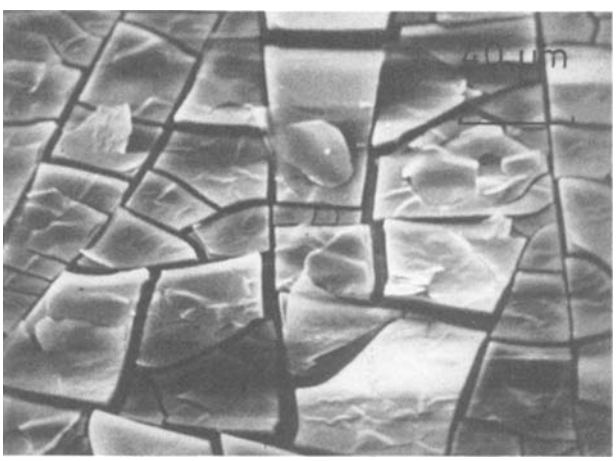

Fig. 7. Scanning electron micrograph of surface of aluminum (99% purity) after exposure for 93 hr to control air plus 3.5 ppm SO_2 and 160 μg m^{-3} smoke, showing the general surface cracking of corrosion products.

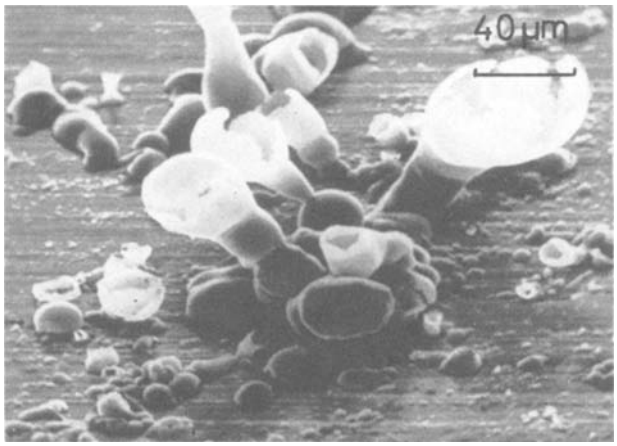

Fig. 8. Scanning electron micrograph of surface of iron after exposure for 96 hr to control air, showing localized corrosion postules amid relatively nonaffected areas.

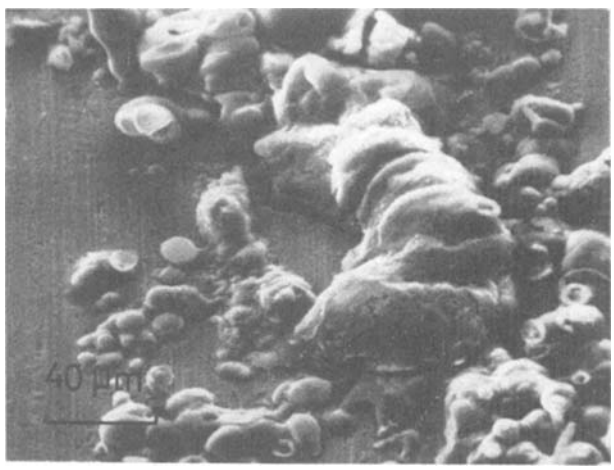

Fig. 9. Scanning electron micrograph of surface of iron after exposure for 283 hr to control air plus 60 ± 10 vpm isobutane, showing laterally developed corrosion amid relatively nonaffected areas.

corrosion to cover within 24 hr practically the entire surface of the test specimens with a rust layer. As the exposure time increased, the color of this rust layer changed from reddish-brown to brownish-black and back to reddish-brown. Cracking of the reddish-brown corrosion layers was often associated with the presence of an orange-red colored crystalline material. Figure 10 illustrates the appearance of the cracked corrosion layer. A much different corrosion product topography was observed upon those specimens exposed to the control air plus smoke (e) atmosphere. The corrosion product appeared as a very even, bright russet colored layer, which was very fragile and consisted of densely packed minute tubular globules of rust growing vertically from the surface of the metal.

The environment including both smoke and SO_2 (f), produced an appearance similar to that of environment (e), except that the general color was a darker brown and that the corrosion globules were much less uniform in both distribution and size.

Energy dispersive analysis by x-rays.—Sulfur peaks were detected in corrosion products from four of the six test environments. These included environments (c), (d), and (f) as expected, but also the control air and smoke atmosphere (e). However, in this latter case, the sulfur Kα peak height was only slightly greater than the background level, thus indicating a trace only of sulfur contamination in the corrosion

Fig. 10. Scanning electron micrograph of iron after exposure for 47 hr to control air plus 3.5 ± 0.5 ppm SO_2, showing complete surface coverage by corrosion products with general cracking of such products.

products. The corrosion products associated with a rapid and continuing decrease in weight gains (c) and (d) noted for zinc all contained much sulfur. This contrasts with its absence in the corrosion products produced by environments of control air (a) and control air plus isobutane (b) which caused continuing gain of weight, as seen in Fig. 3. This result suggests that initially formed hydroxides and basic carbonates of zinc, (stable in environments (a) and (b)), react to produce water soluble sulfates in the presence of SO_2.

The chlorine $K\alpha$ peak was found in the corrosion products on aluminum and iron produced in the atmosphere of control air plus isobutane (b), and in the environments of control air plus SO_2 and isobutane (d) and control air plus smoke (e) in the case of aluminum. Again the peak heights were very slightly above the background levels indicating only trace amounts.

The other trace contaminants found among the corrosion products upon the three metals were sodium and silicon. It can only be assumed that the presence of the trace contaminants is due to, and occurred during, the carrying and manipulation of the specimens, in spite of much care being taken at all stages.

Smoke particle characterization.—The physical characterization of the smoke particles indicated that they were in the form of aggregated graphite-like individual platelets, approximately 13 × 10^{-9}m diam, joined in long chains with a certain amount of platelet clumping. The stereoscopic view (Fig. 11) suggests that the structure of particle agglomerations was three dimensional. Thus, instead of simply having an essentially planar structure, *i.e.*, threads of joined particles lying flat in one place, they appeared to consist of strands of joined particles twisted in all directions.

The conductivity measurements, Table IV, showed that smoke particles themselves had a significant conduction increasing effect. Thus, while passing the combustion gases for 54 hr increased the conductance to 91.4 μS cm^{-1}, smoke particles increased the conduction by 319.2 μS cm^{-1}. Over the same period a *p*H fall from 7.2 to 4.6 was observed due to the passage of smoke.

Discussion

General considerations.—Physicochemical processes such as the relative adsorption of water, sulfur dioxide, and isobutane molecules on the different metal surfaces, and on smoke particles, are clearly important. Other associated processes include condensation and concentration, the specific and competitive adsorption of chemical species, and catalysis. Further, while electrochemical reactions provide the basis of the mechanisms of corrosion, nevertheless the extent of the reactions depends upon the transport to and from reaction sites of chemical species.

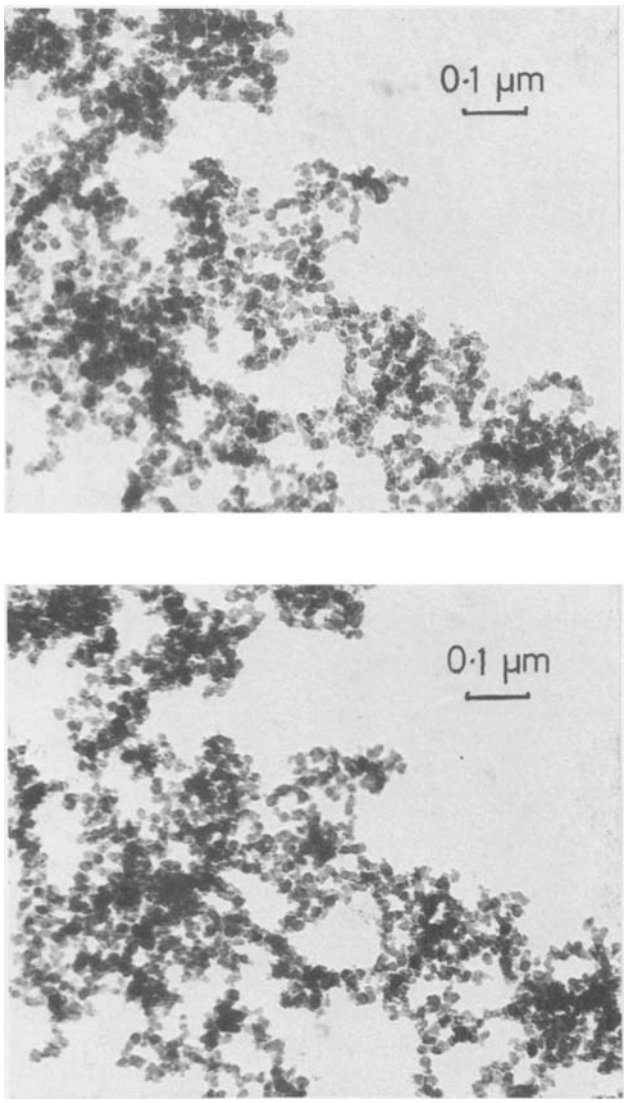

Fig. 11. Stereoscopic electron micrographs of smoke particles showing relative displacement appearance. Top micrograph for a −6° specimen stage tilt. Bottom micrograph for a +6° specimen stage tilt.

Considering the control air (a) environment, the two reactive chemical species present are water and carbon dioxide molecules. The amount of corrosion is a function of the nature of the surface, *e.g.*, oxide/hydroxide/carbonate film produced, and weak spots or active sites within it. However, the corrosion rate of iron increases rapidly with increase of water activity. In contrast, both zinc and aluminum have only first order corrosion rates with respect to water, and are therefore less affected by water activity than iron in their corrosion behavior (7). Thus, the presentation of an entity which enhanced water activity would increase the corrosion of iron by a greater factor than it increased the corrosion of zinc or aluminum. Considering carbon dioxide, its high concentration in this work has much relevance to the corrosion of zinc. The corrosion product produced in a clean damp air atmosphere is basic carbonate (7), so in this work the development of this product may reasonably be expected to be accelerated.

Influence of sulfur dioxide.—While each of the metals responded to the presence of sulfur dioxide by yielding a large increase in corrosion, the mechanisms responsible are different. Various authors have shown

Table IV. Conductivity change due to passage of smoke particles into deionized water

Passage time (hr)	Conductivity (μS cm^{-1}) Combustion gas (filtered)	Smoke particles (+ gas)	Passage time (hr)	Conductivity (μS cm^{-1}) Combustion gas (filtered)	Smoke particles (+ gas)
1	2.9	8.2	27	60.4	215.6
2	5.2	16.3	28	63.5	227.7
3	7.8	25.9	29	64.2	240.7
4	10.3	32.8	30	66.9	252.0
5	12.7	40.5	48	85.6	384.8
6	15.4	49.5	49	85.0	390.2
7	17.3	57.3	50	86.5	397.9
8	20.6	66.0	51	88.3	402.1
24	54.1	180.4	52	89.6	409.8
25	56.0	192.1	53	90.5	415.3
26	58.2	204.8	54	91.4	420.6

that sulfur dioxide adsorption varies from metal to metal (3, 6, 25), both in amount and distribution. In the case of iron, the adsorption occurs in discrete locations, while on aluminum and zinc it is considered to be a more uniform coverage. Further factors with reference to iron should be noted. The electrical conductivity of γ-FeO(OH) is increased by chemisorption of sulfur dioxide, so accelerating corrosion (26). Sulfur dioxide takes part directly in the electrochemical reactions (4, 5, 7), after metal ions have catalyzed the oxidation to sulfates (27-29). Homogeneous catalysis is suggested since, at the high relative humidities used in this work, a distinct liquid phase, *i.e.*, an electrolyte, would be present (30-34). With zinc, however, the primary corrosion products are the oxide and hydroxide, and basic carbonate (7), and sulfur dioxide reacts with these products to form soluble sulfates which can drip-wash at high humidities. The lesser corrosion effects upon aluminum are due to the more protective nature of the aluminum oxide/hydroxide surface layer which, upon development, may also reduce the rate of sulfur dioxide adsorption and thus subsequent reaction (35).

Influence of isobutane.—The effects produced in the presence of isobutane are probably the result of sorption causing changes in surface tension (36, 37), and competitive adsorption with water molecules for metal atoms and ions. Thus, adsorption at incipient corrosion reaction sites could interfere with anodic electrochemical reactions.

A direct interference with the anodic reaction may arise by the polarization of the isobutane molecules $H^{\delta-}$ - $C^{\delta+}(CH_3)_3$ (38, 39), and their association with metal atoms and metal hydrates at the anodic site interface. The association with metal atoms at anodic sites is a suggested competitive action against water molecules, which otherwise would assist the release of metal atoms as charged hydrated ions. The reaction of isobutane with hydrated ions would retard the motion of such ions away from the anodic sites. Both processes would therefore inhibit the anodic process (40).

With sulfur dioxide added, competitive adsorption and reaction may interfere with the catalytic conversion of sulfur dioxide to sulfates, and so reduce the effective corrosivity of sulfur dioxide. This consideration would apply in the case of iron where the production of ferrous ions is known to catalyze the conversion of SO_2 to sulfate (4, 28). In contrast, the corrosion promotion of sulfur dioxide by isobutane in the case of aluminum (Fig. 4) and zinc (Fig. 5) may be due to an interference with the development and repair of a protective film of surface oxides/hydroxides, via competitive adsorption with water molecules.

The effects of isobutane observed in this study are therefore primarily an inhibition of oxidation by competition against the reactions of water, and are similar to other research (40), in which it was demonstrated that the presence of isobutane inhibited the corrosivity of noncontaminated air to iron, zinc, and aluminum. It was also shown that while isobutane inhibited the corrosivity to iron of a sulfur dioxide contaminated air, it enhanced the corrosion of such contaminated air to zinc and aluminum.

Future papers will discuss the effects on metal corrosion of low molecular weight gases representing the alkyl, olefin, and acetylenic group of organic chemicals in the presence and absence of smoke and/or sulfur dioxide.

Influence of smoke particles.—The conductivity experiments showed that smoke increased the conductivity of deionized water, while the pH fell from 7.2 to 4.6. There are two types of surface active complex which form on graphite surfaces, and the principal functional groups formed are carbonyl, hydroxyl, and carboxylic (41, 42).

One type of surface complex is acid adsorbing. Such adsorption sites occur at, for example, a C_XO surface site which is quinolic in nature. The equilibrium with water is as follows

$$(C_xO) + H_2O \rightleftarrows (C_xOH)^+ + OH^-$$

This would lead to alkalinity in the surrounding solution. The second type of surface active complexes is base adsorbing. Such a complex would be C_ZO having the nature of an acid anhydride. In this case the reaction equilibrium with water is as follows

$$C_ZO + H_2O \leftrightarrows (C_ZO_2H)^- + H^+$$

This would lead to acidity in the surrounding solution (43, 44). The adsorption characterization of graphite relates to the predominance of one or the other of these two types of surface oxygen active complexes, which depends mainly upon the combustion flame temperature (lower than approximately 820 K for base absorbing sites, higher temperatures for acid absorbing sites), and on the amount of oxygen present (45). The maximum flame temperature measured in this work was 757 K. Thus the increase in conductivity and decrease in pH are considered to be a result of the increasing quantity of hydrogen ions produced at the active sites. Since atmospheric corrosion proceeds by electrochemical mechanisms, any increase in conductivity must play an important role in enhancing corrosion. In addition to an increase in ionic conductivity, as shown above, the joined strings of graphite-like smoke particles implies the presence of electronic conduction (45, 46).

The influence of the presence of smoke particles depends upon their capacity to adsorb, concentrate, and react with chemical species, and the finely divided nature of smoke being an important factor. It is considered that a population of minute deposits of smoke particles establishes microcells of increased water activity and cathodic reactivity (8). This consideration would apply for iron in the presence of smoke contamination alone. In the cases of aluminum and zinc, similar considerations also apply, but here the increased water activity and the different nature of the electrochemical reactions would largely promote a thickening of the oxide and hydroxide layers (7).

In the case of the additional presence of sulfur dioxide, the particular behavior of a metal depends upon the specific manner in which sulfur dioxide takes part in the corrosion reactions. The first action is considered to be that of the smoke particles adsorbing, concentrating, and converting the sulfur dioxide in solution as sulfite and bisulfite ions to sulfate (47-50). The necessary presence of a liquid phase is supported by the high relative humidity used in this work (34).

Then, for iron, the reactions involve further catalytic oxidation of sulfur dioxide to sulfate (27-29) due to the presence of metal ions in an electrolyte, with direct participation in the anodic reactions, and corrosion is promoted (4-7). In the case of aluminum and

zinc, corrosion enhancement is due to sulfur dioxide indirect reactions with the primary corrosion products of oxide and hydroxide, interfering with protective film formation in the case of aluminum, and producing soluble corrosion products as for zinc.

Manuscript submitted June 14, 1982; revised manuscript received April 22, 1983.

Any discussion of this paper will appear in a Discussion Section to be published in the June 1984 JOURNAL. All discussions for the June 1984 Discussion Section should be submitted by Feb. 1, 1984.

REFERENCES

1. W. H. J. Vernon, *Trans. Faraday Soc.*, **27**, 255 (1931).
2. W. H. J. Vernon, *ibid.*, **31**, 1668 (1935).
3. N-G. Vannerberg and T. Sydberger, *Corros. Sci.*, **10**, 43 (1970).
4. U. R. Evans and C. A. J. Taylor, *ibid.*, **12**, 227 (1972).
5. J. R. Duncan, *Werkst. Korros.*, **25**, 420 (1974).
6. J. R. Duncan and D. J. Spedding, *Corros. Sci.*, **14**, 241 (1974).
7. K. Barton, "Protection Against Atmospheric Corrosion," J. R. Duncan, Editor, John Wiley and Sons Ltd., London (1976).
8. G. Agabio and A. Tamba, *Br. Corros. J.*, **5**, 112 (1970).
9. R. Ericsson, B. Heimler, and N-G. Vannerberg, *Werkst. Korros.*, **24**, 207 (1973).
10. A. C. Baldwin, *Int. J. Chem. Kinetics*, **14**, 269 (1982).
11. "Combustion Generated Pollution," The Science Research Council, High Holborn, London, Bournehall Press, Welwyn Garden City, Herts, England (1976).
12. D. J. Spedding, "Air Pollution," p. 65, Oxford University Press, Oxford, (1974).
13. T. E. Graedel, "Chemical Compounds in the Atmosphere," p. 55, Academic Press, New York (1978).
14. A. P. Altshuller and J. J. Bufalini, *Environ. Sci. Technol.*, **5**, 39 (1971).
15. "Handbook of Chemistry and Physics," R. C. Weast, Editor, p. E65, CRC Press, Cleveland (1974-1975).
16. P. F. Preston, *Trans. Inst. Metal Finishing*, **50**, 125 (1972).
17. Industrial Atmospheric Test Cabinet E. W. 1978, Manufactured by W. Canning and Co., Ltd., Birmingham, United Kingdom.
18. Specification NATO F-35 Aviation Turbine Fuel.
19. B. S. Skerry, M.Sc. Thesis, University of Manchester Institute of Science and Technology, England (1977).
20. Draeger Safety Ltd., Blyth, Northumberland, England.
21. BS 1747: Parts 2 and 3: 1969. The British Standards Institute, 2 Park Street, London W1A 2BS, England.
22. R. M. Bethea and M. C. Meador, *J. Chromatog. Sci.*, **7**, 655 (1969).
23. F. Bruner, P. Ciccioli, and F. Di Nardo, *Anal. Chem.*, **47**, 141 (1975).
24. W. H. Ailor, "Handbook on Corrosion Testing and Evaluation," John Wiley and Sons, Inc., New York (1971).
25. N-G. Vannerberg and T. Sydberger, *Corros. Sci.*, **12**, 775 (1972).
26. K. Kanelio and K. Inovye, *ibid.*, **21**, 639 (1981).
27. B. Heimler and N-G. Vannerberg, *ibid.*, **12**, 579 (1972).
28. S. Beilke and G. Gravenhurst, *Atmos. Environ.*, **12**, 231 (1978).
29. D. A. Hegg and P. V. Hobbs, *ibid.*, **12**, 241 (1978).
30. P. J. Sereda, *Mater. Res. Standards*, 719 (1961).
31. H. Guttman, *ASTM Special Technical Publication*, **435**, 223 (1968).
32. V. Kucera and E. Mattson, *ibid.*, **558**, 239 (1974).
33. F. Mansfeld and J. V. Kenkel, *Corrosion*, **33**, 13 (1977).
34. Y. N. Mikhailovsky, "Atmospheric Corrosion," W. H. Ailor, Editor, p. 85, John Wiley and Sons, Inc., New York (1982).
35. G. Schikorr, *Aluminium (BRD)*, **43**, 108 (1967).
36. W. A. Zisman and H. W. Fox, *J. Colloid Int. Sci.*, **5**, 514 (1950).
37. E. Hauxwell and R. H. Ottewill, *ibid.*, **34**, 473 (1970).
38. M. Maryott and T. Birnbaum, *J. Chem. Phys.*, **24**, 1022 (1954).
39. L. Lide and G. Mann, *ibid.*, **29**, 914 (1959).
40. M. R. Arshadi, J. B. Johnson, and G. C. Wood, *Corros. Sci.*, In press.
41. J. C. Studebaker, R. Hoffman, F. Wolfe, and N. Nabors, *Ind. Eng. Chem.*, **48**, 162 (1956).
42. V. Blom, P. R. Edelhausen, and B. Van Krevelen, *Fuel*, **36**, 135 (1957).
43. M. O. Davies, M. Clark, E. Yeager, and F. Hovorka, *This Journal*, **106**, 56 (1959).
44. C. Clau, E. Plas, P. L. Boehm, and V. Hofman, *Z. Anorg. Chem.*, **291**, 295 (1957).
45. R. N. Smith, *Quart. Rev. Chem. Soc.*, **13**, 287 (1959).
46. S. R. Forrest and T. A. Witten, *J. Phys. A: Maths. Gen.*, **12**, L109 (1979).
47. T. Novakov, S. G. Chang, and A. B. Harker, *Science*, **186**, 259 (1974).
48. R. Brodzinsky, S. G. Chang, S. S. Markowitz, and T. Novakov, *J. Phys. Chem.*, **84**, 3354 (1980).
49. S. G. Chang, R. Toossi, and T. Novakov, *Atmos. Environ.*, **15**, 1287 (1981).
50. T. Tartarelli, P. Davini, F. Morelli, and P. Corsi, *ibid.*, **12**, 289 (1978).

Mass Transfer and Current-Potential Relation in Pulse Electrolysis

D-T. Chin*,[1]

Technisch Chemisches Laboratorium, Eidgenossische Technische Hochschule (ETHZ), CH8092 Zurich, Switzerland

and

Department of Chemical Engineering, National University of Singapore, Kent Ridge, Singapore 0511

ABSTRACT

A generalized theory is presented for pulse electrolysis with rectangular current pulses, periodical pulse reverse, and double rectangular pulses with relaxations. It is shown that very high instantaneous mass transfer rates corresponding to a current density of 100-1000 A/cm² can be attained by short current pulses at high pulse frequencies. Numerical results for the concentration fluctuations and potential responses have also been calculated for the deposition/dissolution of copper on a rotating disk electrode in acid copper sulfate solution. The results indicate that the current pulses can profoundly change the current-potential relationships and thus the current distribution and the morphology of electrodeposits on the electrode surface.

Electrolysis with a pulsating current (PC) has been extensively used in pulse plating, electrodissolution, anodizing, and a-c corrosion processes (1). In particular, the pulse current can cause a profound change in the morphology of electrodeposits (2-5); it gives a softer, more uniform, and compact deposit with better adherence to the substrate. This can be attributed to the fact that PC modifies the mass transport processes, enhances the rate of nucleations, and improves the kinetics of electrode reaction. It produces a pulsating diffusion layer (6-10) wherein the concentrations of the ionic species fluctuate periodically with time near the electrode surface. The resulting concentration and surface overpotentials depend not only on the magnitude of pulsating current density but also on the frequency of pulses.

There are several waveforms available for the laboratory and industrial applications of pulse electrolysis. These include the sinusoidal wave, the triangular wave, and the rectangular wave. In the electroplating industry, the symmetrical and asymmetrical rectangular waves have been traditionally used in pulse plating. Small sinusoidal and triangular waves are used for electroanalytical applications; whereas a 50 $\sim$ 60 Hz sinusoidal current of large amplitudes is encountered in the a-c corrosion process. A theoretical study of pulse electrolysis was first made by Warburg (11, 12) who considered a redox process when a sinusoidal PC was applied to the electrode. He recognized that PC produced periodic concentration changes of the oxidized and the reduced species at the electrode surface. Using these as the boundary conditions, he solved Fick's diffusion equation and obtained concentration changes with an amplitude that decreased rapidly with the distance from the electrode. The concentration overpotential from these concentration fluctuations was then expressed in terms of a polarization capacity and a polarization resistance called the Warburg impedance. Kruger (3) modified Warburg's analysis by taking into account the supporting electrolyte which contributed to the structure of electric double layer. These investigations which have led to a good understanding of the electrical double layer are treated in great detail in Grahame's review (14, 15). Levart and Schumann (16-18) and Newman *et al.* (19, 20) have calculated the Warburg impedance of a rotating disk electrode. Venkatesh, Sethi, Meyyappan, and Chin (7-10) have made an analysis for the sinusoidal potential and current modulation of the rotating disk and hemispherical electrodes. They calculated the current-potential relationship for the dissolution and deposition of copper in an acid copper sulfate solution. Mass transfer with rectangular current pulses, periodical pulse reverse, and a ramp current has been treated by Viswanathan and Cheh (21-24). Popov *et al.* (5) calculated the current-potential curves for pulse electrolysis with rectangular waves. A review of the pulsating electrode processes was given by Venkatesh and Chin (1).

This paper describes a theory of pulse electrolysis with a generalized double rectangular wave consisting of (*i*) a cathodic current pulse, (*ii*) a low current or relaxation period, and (*iii*) a short anodic current pulse as shown in Fig. 1a. The waveform is of particular interest to electroplaters. The cathodic pulse of a suitably high magnitude would activate numerous nucleation sites and cause metal deposition to proceed at a rate several orders of magnitude higher than the limiting current density. The relaxation period of a small or zero current would allow the metal ions to diffuse to the electrode surface and be available for further deposition; it would also allow the absorption of certain additives or the desorption of codeposited atomic hydrogen from the electrodeposits. A reverse pulse of high anodic current would enable the metal to dissolve into the electrolyte from high points such as burrs and dendrites. The waveform can be reduced to the special cases of (*i*) regular pulse plating if $i_2 = 0$ and $t_3 = 0$ (Fig. 1b), and (*ii*) periodical pulse reverse if $t_2 = 0$ (Fig. 1c). The present mathematical model is similar to a previous analysis for the sinusoidal current and potential pulses (7-9). The model considers the mass transport process during the pulse electrolysis as a linear combination of a steady-state time-averaged concentration component and a fluctuating (or pulsating) concentration component caused by the current fluctuations at the electrode surface. The convective diffusion equation for the time-averaged concentration component can be solved by conventional methods whereas a Silve-Hale approximation (25, 26) is used for the solution of the fluctuating concentration component. The results for the concentration changes are then substituted into the electrokinetic equations for the solution of the surface, the concentration, and the ohmic overpotential losses in pulse electrolysis. The analysis can be used for all pulse waveforms as well as for the superimposition of pulsating current onto a direct current (d.c.).

Theoretical Analysis

Convective mass transfer.—Mass transfer in pulse electrolysis is a nonsteady-state process. The concentration of a diffusing ion at any given location in the electrolyte would periodically fluctuate with the time. To simplify the analysis, we shall assume that (*i*) the solution has sufficient inert salt so that the migrational flux of the diffusing ion in the electric field can be neglected; (*ii*) the physical properties of the electro-

* Electrochemical Society Active Member.
[1] Present address: Department of Chemical Engineering, Clarkson College of Technology, Potsdam, New York 13676.
Key words: electrodeposition, dissolution, mass transport, polarization.

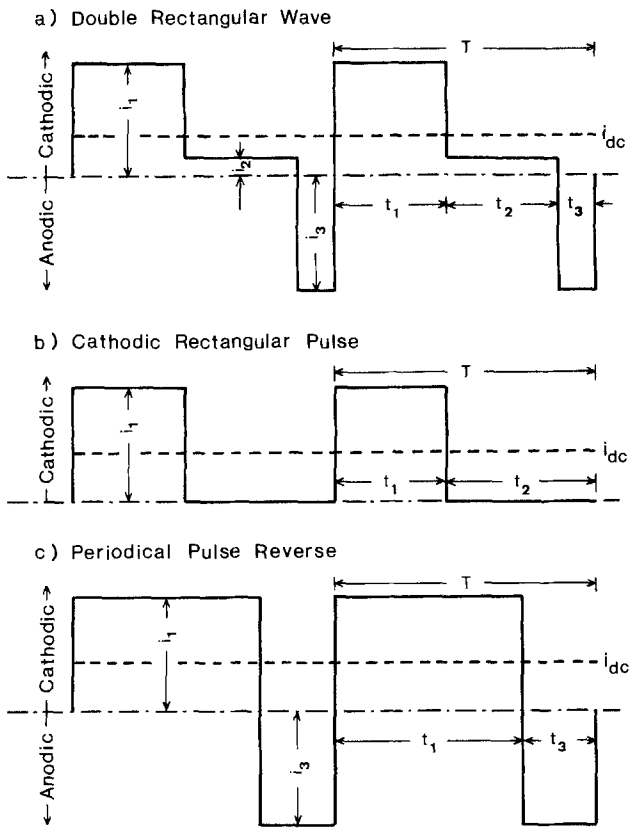

Fig. 1. Schematic representation of a generalized double rectangular pulsating current wave consisting of *(i)* a cathodic current pulse, *(ii)* a low current or relaxation period, and *(iii)* a short anodic current pulse, (a). The waveform can be reduced to the special cases of rectangular cathodic current pulses (b), and periodical pulse reverse (c).

lyte are constant; (*iii*) the effect of gravitational force on the diffusion field is negligible; (*iv*) there is no homogeneous chemical reaction in the electrolyte; and (*v*) the effect of an electric double layer on the concentration and potential responses can be neglected. The last assumption is reasonable as long as the pulsating period of current pulses is much greater than the double layer charge/discharge time which is on the order of a few microseconds. Under these circumstances, the convective diffusion equation and the associated boundary conditions may be given as

$$\frac{\partial C}{\partial t} + \vec{V} \cdot \vec{\nabla} C = D\nabla^2 C \qquad [1]$$

boundary conditions

$$\left.\begin{aligned} &C = C_\infty \quad \text{at} \quad t = 0 \\ &C = C_\infty \quad \text{at} \quad t = \infty \\ &-D\frac{\partial C}{\partial y} = \frac{i(t)}{n\mathbf{F}} \quad \text{at} \quad y = 0 \end{aligned}\right\} \qquad [2]$$

where C is the concentration of the diffusing ion, t is the time, y is the vertical distance from the electrode surface, and the subscript ∞ denotes the bulk properties.

During the pulse electrolysis, one may consider the current flowing across the electrode/electrolyte interface to be composed of a time-averaged d-c component, $i_{d.c.}$, and a fluctuating alternating current (a-c) component, $i_{a.c.}$

$$i(t) = i_{d.c.} + i_{a.c.}(t) \qquad [3]$$

For the generalized double rectangular wave shown in Fig. 1a, the time-averaged d-c component may be obtained from the following expression

$$i_{d.c.} = \frac{1}{T}\int_o^T i(t)\,dt = \frac{1}{T}\,(i_1 t_1 + i_2 t_2 + i_3 t_3) \qquad [4]$$

where i_1, i_2, and i_3 are the instantaneous current densities at the electrode surface during the cathodic pulse, the relaxation, and the anodic pulse periods, respectively. Likewise, one may also split the concentration C into a time-invariant steady-state component, $\overline{C}$, and a fluctuating component, $\tilde{C}$

$$C(y,t) = \overline{C}(y) + \tilde{C}(y,t) \qquad [5]$$

Substituting Eq. [5] into Eq. [1]-[2], one obtains two sets of differential equations and associated boundary conditions, one for the steady-state concentration $\overline{C}$ and the other for the fluctuating concentration $\tilde{C}$. The equations for the steady-state concentration are

$$\vec{V} \cdot \vec{\nabla}\overline{C} = D\nabla^2\overline{C} \qquad [6]$$

$$\left.\begin{aligned} &\overline{C} = C_\infty \quad \text{at} \quad y = \infty \\ &-D\frac{\partial \overline{C}}{\partial y} = \frac{i_{d.c.}}{n\mathbf{F}} \quad \text{at} \quad y = 0 \end{aligned}\right\} \qquad [7]$$

The solution to the above equation would give a surface concentration component $\overline{C}_s$ in the form

$$\frac{\overline{C}_s}{C_\infty} = 1 - \frac{i_{d.c.}}{i_{lim}} \qquad [8]$$

where i_{lim} is the d-c limiting current density for a given convective condition. The thickness of the steady-state Nernst diffusion layer, δ, may be evaluated from the concentration gradient at the electrode surface by

$$\delta = -\frac{D}{C_\infty - \overline{C}_s}\left(\frac{\partial \overline{C}}{\partial y}\right)_{y=0} \qquad [9]$$

The equations for the fluctuating concentrations are

$$\frac{\partial C}{\partial t} + \vec{V} \cdot \vec{\nabla}\tilde{C} = D\nabla^2\tilde{C} \qquad [10]$$

$$\left.\begin{aligned} &\tilde{C} = 0 \quad \text{at} \quad t = 0 \\ &\tilde{C} = 0 \quad \text{at} \quad y = \infty \\ &-D\frac{\partial \tilde{C}}{\partial y} = \frac{i_{a.c.}(t)}{n\mathbf{F}} \quad \text{at} \quad y = 0 \end{aligned}\right\} \qquad [11]$$

It has often been assumed that the concentration fluctuations occur essentially within a thin region of the steady-state Nernst diffusion layer where the contribution of the convective flux term, $\vec{V} \cdot \vec{\nabla}\tilde{C}$ may be assumed to be negligibly small. This approximation was first introduced by Silver (25). Hale (26) has shown that the approximation gave a surface concentration only 4% higher than the exact solution over a wide range of the time domain. Several other literature evidences (8-10, 19, 20) have suggested that this is a reasonable assumption for pulse electrolysis at high frequencies. Accordingly, one may drop the convective flux term $\vec{V} \cdot \vec{\nabla}\tilde{C}$ in Eq. [10] and replace the boundary condition at $y = \infty$ with a condition at $y = \delta$

$$\frac{\partial \tilde{C}}{\partial t} = D\nabla^2\tilde{C} \qquad [12]$$

$$\left.\begin{aligned} &\tilde{C} = 0 \quad \text{at} \quad t = 0 \\ &\tilde{C} = 0 \quad \text{at} \quad y = \delta \\ &-D\frac{\partial \tilde{C}}{\partial y} = \frac{i_{a.c.}(t)}{n\mathbf{F}} \quad \text{at} \quad y = 0 \end{aligned}\right\} \qquad [13]$$

One dimensional mass transfer processes.—For one-dimensional problems, Eq. [12]-[13] can be solved with the Laplace transform method (8, 9), and the fluctuating surface concentration can be expressed as

$$\frac{\tilde{C}_s}{C_\infty} = \frac{1}{n\mathbf{F}C}\int_o^t Y(t-u)\cdot i_{a.c.}(u)\,du \qquad [14]$$

where

$$Y(t) = \frac{2}{\delta}\sum_{m=1}^{\infty}\exp\left[-\frac{\pi^2 D}{\delta^2}(m-\tfrac{1}{2})^2 t\right] \qquad [15]$$

The total surface concentration may be obtained by substituting Eq. [8] and [14] into Eq. [5]

$$\frac{C_s}{C_\infty} = \frac{\bar{C}_s + \tilde{C}_s}{C_\infty} = \left(1 - \frac{i_{d.c.}}{i_{lim}}\right) + \frac{1}{n\mathbf{F}C_\infty}\int_o^t Y(t-u)i_{a.c.}(u)\,du \qquad [16]$$

For pulse electrolysis with the generalized double rectangular current wave shown in Fig 1a, Eq. [14]-[16] can be analytically integrated. The resulting surface concentration change during the pth ($p = 1, 2, 3 \ldots$) period may be expressed by the following dimensionless equations

(*i*) during the cathodic pulse time ($p - 1 < t^* < p - 1 + \theta_1$)

$$C^*_s = \bar{C}^*_s + \tilde{C}^*_s = (1 + i^*_{d.c.}) + 2T^*\sum_{m=1}^{\infty}\frac{1}{\lambda_m}\exp(-\lambda_m t^*)\left\{\sum_{k=0}^{p-2}\sum_{j=1}^{3}(i^*_j - i^*_{d.c.})[\exp(\lambda_m(k+d_j)) - \exp(\lambda_m(k+d_{j-1}))] + (i^*_1 - i^*_{d.c.})[\exp(\lambda_m t^*) - \exp(\lambda_m(p-1))]\right\} \qquad [17]$$

(*ii*) during the low current or relaxation time ($p - 1 + \theta_1 < t^* < p - 1 + \theta_1 + \theta_2$)

$$C^*_s = \bar{C}^*_s + \tilde{C}^*_s = (1 + i^*_{d.c.}) + 2T^*\sum_{m=1}^{\infty}\frac{1}{\lambda_m}\exp(-\lambda_m t^*)\left\{\sum_{k=0}^{p-2}\sum_{j=1}^{3}(i^*_j - i^*_{d.c.})[\exp(\lambda_m(k+d_j)) - \exp(\lambda_m(k+d_{j-1}))] + (i^*_1 - i^*_{d.c.})[\exp(\lambda_m(p-1+\theta_1)) - \exp(\lambda_m(p-1))] + (i^*_2 - i^*_{d.c.})[\exp(\lambda_m t^*) - \exp(\lambda_m(p-1+\theta_1))]\right\} \qquad [18]$$

(*iii*) during the anodic pulse time ($p - 1 + \theta_1 + \theta_2 < t^* < p$)

$$C^*_s = \bar{C}^*_s + \tilde{C}^*_s = (1 + i^*_{d.c.}) + 2T^*\sum_{m=1}^{\infty}\frac{1}{\lambda_m}\exp(-\lambda_m t^*)\left\{\sum_{k=0}^{p-2}\sum_{j=1}^{3}(i^*_j - i^*_{d.c.})[\exp(\lambda_m(k+d_j)) - \exp(\lambda_m(k+d_{j-1}))] + (i^*_1 - i^*_{d.c.})[\exp(\lambda_m(p-1+\theta_1)) - \exp(\lambda_m(p-1))] + (i^*_2 - i^*_{d.c.})[\exp(\lambda_m(p-1+\theta_1+\theta_2)) - \exp(\lambda_m(p-1+\theta_1))] + (i^*_3 - i^*_{d.c.})[\exp(\lambda_m t^*) - \exp(\lambda_m(p-1+\theta_1+\theta_2))]\right\} \qquad [19]$$

Here the eigenvalues λ_m are given as

$$\lambda_m = \pi^2 T^*(m - \tfrac{1}{2})^2, \quad m = 1, 2, 3, \ldots \qquad [20]$$

and the dummy variables d_j ($j = 0, 1, 2, 3$) are

$$\left.\begin{aligned} d_0 &= 0 \\ d_1 &= \theta_1 \\ d_2 &= \theta_1 + \theta_2 \\ d_3 &= \theta_1 + \theta_2 + \theta_3 \end{aligned}\right\} \qquad [21]$$

The other dimensionless variables and parameters in the above equations are defined as

dimensionless time	$t^* = t/T$	[22a]
dimensionless surface concentration	$C^*_s = C_s/C_\infty$	[22b]
dimensionless pulse period	$T^* = DT/\delta^2$	[22c]
dimensionless cathodic pulse time (or cathodic duty cycle)	$\theta_1 = t_1/T$	[22d]
dimensionless relaxation time	$\theta_2 = t_2/T$	[22e]
dimensionless anodic pulse time (or anodic duty cycle)	$\theta_3 = t_3/T$	[22f]
dimensionless cathodic pulse current density	$i^*_1 = i_1/\lvert i_{lim}\rvert$	[22g]
dimensionless current density during the low current or relaxation time	$i^*_2 = i_2/\lvert i_{lim}\rvert$	[22h]
dimensionless anodic pulse current density	$i^*_3 = i_3/\lvert i_{lim}\rvert$	[22i]

Limiting pulse current density.—An important quantity in the analysis of pulsating mass transfer problem is the determination of the limiting pulse current density, i_{PL}, which is defined as the current density at which the surface concentration of the reacting species becomes zero at the end of the cathodic pulse time

$$i_{PL} = i \Big|_{\substack{@\,\bar{C}_s + \tilde{C}_s = 0 \\ @\,t = (p-1)T + t_1}} \qquad [23]$$

This quantity can be evaluated by letting Eq. [17] equal to zero and solving for i^*_1 at the end of a cathodic duty cycle $t^* = p - 1 + \theta_1$. The result may be expressed as

i^*_{PL} (dimensionless limiting pulse current density) $= i_{PL}/\lvert i_{lim}\rvert$

$$= -\frac{1 + i^*_2[(1 - f_1 - f_2 - f_3)\theta_2 + f_2] + i^*_3[(1 - f_1 - f_2 - f_3)\theta_3 + f_3]}{(1 - f_1 - f_2 - f_3)\theta_1 + f_1} \qquad [24]$$

with

$$f_1 = 2T^*\sum_{k=0}^{p-1}\sum_{m=1}^{\infty}\frac{1}{\lambda_m}\exp(-\lambda_m(p-1+\theta_1))[\exp(\lambda_m(k+\theta_1)) - \exp(\lambda_m k)] \qquad [25]$$

$$f_2 = 2T^* \sum_{k=0}^{p-2} \sum_{m=1}^{\infty} \frac{1}{\lambda_m} \exp(-\lambda_m (p - 1 + \theta_1)) [\exp(\lambda_m (k + \theta_1 + \theta_2)) - \exp(\lambda_m (k + \theta_1))] \quad [26]$$

$$f_3 = 2T^* \sum_{k=0}^{p-2} \sum_{m=1}^{\infty} \frac{1}{\lambda_m} \exp(-\lambda_m (p - 1 + \theta_1)) [\exp(\lambda_m (k + 1)) - \exp(\lambda_m (k + \theta_1 + \theta_2))] \quad [27]$$

For the steady-state pulsating electrolysis, $p \to \infty$, $f_1 + f_2 + f_3 = 1$, and Eq. [24]-[27] can be simplified to

$$i^*_{PL} (\text{as } p \to \infty) = -\frac{1 + i^*_2 f_2 + i^*_3 f_3}{f_1} \quad [24a]$$

$$f_1 (\text{as } p \to \infty) = 2T^* \sum_{m=1}^{\infty} \frac{1 - \exp(-\lambda_m \theta_1)}{\lambda_m [1 - \exp(-\lambda_m)]} \quad [25a]$$

$$f_2 (\text{as } p \to \infty) = 2T^* \sum_{m=1}^{\infty} \frac{\exp[-\lambda_m (1 - \theta_2)] - \exp(-\lambda_m)}{\lambda_m [1 - \exp(-\lambda_m)]} \quad [26a]$$

$$f_3 (\text{as } p \to \infty) = 2T^* \sum_{m=1}^{\infty} \frac{\exp[-\lambda_m (\theta_1 + \theta_3)] - \exp(-\lambda_m)}{\lambda_m [1 - \exp(-\lambda_m)]} \quad [27a]$$

The magnitude of the limiting pulse current density as seen from the above equations, depends upon the bulk concentration, the convective condition, the transport properties of the diffusing ion, and the conditions of current pulses. The physical significance of i_{PL} is similar to the limiting current density, i_{lim}, in d-c electrolysis. It represents a maximum current limit caused by the mass transfer limitation of the electrode reaction. To operate the cell at the current densities beyond i_{PL} would generally result in poor quality electrodeposits or loss of the coulombic efficiency because of depletion of the reacting ions at the electrode surface.

Potential-current relations.—The surface concentrations obtained in the foregoing analysis can be used to evaluate the potential-current relations in pulse electrolysis. For the simplicity of the analysis, we shall consider only the one-dimensional problem, *i.e.*, the current distribution is uniform across the electrode surface.

The total overpotential of an electrode during the electrolysis consists of three components. They are (*i*) the surface overpotential η_s, (*ii*) the concentration overpotential η_{conc}, and (*iii*) the ohmic overpotential η_{ohm}

$$\eta = \eta_s + \eta_{conc} + \eta_{ohm} \quad [28]$$

For an electrochemical reaction consisting of a metal electrode and an ion of the metal

$$M^{n+} + ne^- = M \quad [29]$$

the surface overpotential may be related to the current density at the electrode surface by the Butler-Volmer equation of the type

$$i(t) = i_o \left(\frac{C_s(t)}{C_\infty}\right)^\gamma \left[\exp\left(\frac{\alpha n \mathbf{F}}{RT} \eta_s(t)\right) - \exp\left(-\frac{\beta n \mathbf{F}}{RT} \eta_s(t)\right)\right] \quad [30]$$

where i_o is the exchange current density based upon the bulk concentration C_∞, of M^{n+} ion, α and β are the anodic and the cathodic charge transfer coefficients, respectively, and γ is a kinetic parameter relating to the order of the electrochemical reaction.

The concentration overpotential is caused by a difference in concentration between the electrode surface and the bulk solution. For the metal/metal-ion system, it may be given by the Nernst equation as

$$\eta_{conc}(t) = \frac{RT}{n\mathbf{F}} \ln \frac{C_s(t)}{C_\infty} \quad [31]$$

The ohmic overpotential is caused by the electric resistance of the electrolyte. If ρ is the electrolyte resistivity, and l is the distance between the working and the reference electrodes, the ohmic overpotential may be expressed in terms of one-dimensional Ohm's law as

$$\eta_{ohm}(t) = \rho l\, i(t) \quad [32]$$

Equations [28]-[32] describe the potential responses of an electrode during the pulse electrolysis. The potential will be periodically fluctuating with time, and it can be considered to consist of a time-averaged d-c component, $\eta_{d.c.}$, and a fluctuating a-c component $\tilde{\eta}$

$$\eta(t) = \eta_{d.c.} + \tilde{\eta}(t) \quad [33]$$

The d-c overpotential component may be obtained by carrying out the time averaging of the total overpotential profile over one pulse period

$$\eta_{d.c.} = \frac{1}{T} \int_{(p-1)T}^{pT} \eta(t)\, dt \quad [34]$$

Introducing the following dimensionless variables and parameters

dimensionless overpotential $$\eta^* = \frac{n\mathbf{F}}{RT} \eta \quad [35a]$$

dimensionless exchange current density $$i^*_0 = i_0/|i_{lim}| \quad [35b]$$

dimensionless ohmic resistance $$(\rho l)^* = \frac{n\mathbf{F}}{RT} \rho l |i_{lim}| \quad [35c]$$

the governing equations for the potential responses may be expressed in the dimensionless form as

surface overpotential $$i^* = i^*_0 C_s^{*\gamma} [\exp(\alpha \eta^*_s) - \exp(-\beta \eta^*_s)] \quad [36]$$

concentration overpotential $$\eta^*_{conc} = \ln C^*_s \quad [37]$$

ohmic overpotential $$\eta^*_{ohm} = (\rho l)^* i^* \quad [38]$$

total overpotential $$\eta^* = \eta^*_s + \eta^*_{conc} + \eta^*_{ohm} \quad [39]$$

d-c overpotential $$\eta^*_{d.c.} = \int_{p-1}^{p} \eta^* dt^* \quad [40]$$

Equations [36]-[38] permit one to calculate the instantaneous overpotential components, η^*_s, η^*_{conc}, and η^*_{ohm}, once the surface concentration of the diffusing ion is obtained from Eq. [17]-[19]. The total overpotential wave, η^*, and the d-c overpotential component, $\eta^*_{d.c.}$ are then obtained from Eq. [39] and [40], respectively. For a given PC waveform, the calculation can be made at various d-c current densities to generate a d-c polarization curve in the form of $\eta^*_{d.c.}$ *vs.* log $i^*_{d.c.}$. The apparent electrokinetic parameters for pulse electrolysis can be then evaluated from the d-c polarization curves.

Results and Discussion

The limiting pulse current density.—In this work, numerical calculations have been made on a digital computer for (*i*) the rectangular cathodic current

pulses ($i_2 = 0$ and $t_3 = 0$), (*ii*) the periodical pulse reverse ($t_2 = 0$), and (*iii*) the double rectangular current pulses with relaxation ($i_2 = 0$) and reverse pulses (Fig. 1). Using Eq. [24]-[27] and [24a]-[27a], the limiting pulse current density was first evaluated for these waveforms. Since the equations represent a generalized solution for one-dimensional mass transfer problems, the numerical results were generated without specifying the electrode geometry and the convective conditions at the electrode surface. Only the results obtained with the steady-state periodical concentration and potential oscillations will be reported in this paper. The typical transient time was less than two pulse periods for $T^* = 10$ and less than 10 pulse periods for $T^* = 0.001$.

Figures 2, 3, and 4 show the dimensionless limiting pulse current density as a function of the dimensionless pulse period $T^* = DT/\delta^2$ for (*i*) the rectangular cathodic pulses, (*ii*) a rectangular pulse reverse ($i^*_3 = 5.0$), and (*iii*) a double rectangular pulse with $i^*_2 = 0$, $i^*_3 = 10$, and $\theta_3 = 0.1$, respectively. The parameters in the figures are the cathodic duty cycle $\theta_1 = t_1/T$. The results cover a wide range of T^* from 0.001 to 10 and θ_1 from 0.001 to 1.0. The value of i^*_{PL} increases with decreasing T^* and θ_1. At very small pulse periods and cathodic duty cycles, a very high limiting pulse current density corresponding to 100 ~ 1000 times of the d-c limiting current density is obtained.

To illustrate the practical applications of the results, let us consider the deposition of copper from a typical acid copper sulfate bath containing 188 g/liter $CuSO_4 \cdot 5H_2O$ (0.75M) with the rectangular cathodic pulse current. If one uses a value of 0.001 cm for the thickness of the steady-state Nernst diffusion layer δ and a value of 7.6×10^{-6} cm²/sec for the diffusivity of Cu^{2+} ion (8, 9), then the d-c limiting current density can be estimated as

$$i_{lim} = -\frac{nFDC_\infty}{\delta} = -1.1 \text{ A/cm}^2$$

Using this i_{lim} value and the curves shown in Fig. 2, the limiting pulse current density for the pulse plating of copper can be estimated for various pulse periods and duty cycles (32). For the small duty cycles $\theta_1 = 0.001 \sim 0.01$, the values of i_{PL} are

(*i*) at $T = 0.13$ msec $-i_{PL} = 790 \sim 88$ A/cm²

(*ii*) at $T = 1.3$ msec $-i_{PL} = 210 \sim 56$ A/cm²

It is seen that the values of i_{PL} can be as high as several hundred amperes per square centimeter. The result is rather interesting for it demonstrates that in pulse plating, one may apply an extremely high cathodic current density of a duration of 0.1 ~ 100 μsec without depleting the metallic ion at the electrode surface. This provides the electroplaters an additional option to improve the properties of electrodeposits. The present calculation agrees with the works of Ibl *et al.* (3, 4, 6, 27, 28) who performed the pulse plating of several metals at the pulse current density up to 200 A/cm² and obtained good quality electrodeposits.

For electrolysis with rectangular cathodic pulses, Viswanathan, Farrel Epstein, and Cheh (22-24) have used a different approach and calculated the limiting pulse current density for moderately high duty cycles ($\theta_1 = 0.2$ to 0.8). Their numerical results are shown in Fig. 2 as ○; the agreement between the two solutions was within 1%.

Figures 3 and 4 show the effect of anodic pulses on the limiting pulse current densities. The average (or d-c) current density when the electrode is being operated at i_{PL} can be calculated from the following equation

$$i^*_{d.c.} = i^*_{PL}\theta_1 + i^*_3\theta_3 \quad (\text{for } i^*_2 = 0) \qquad [41]$$

It should be noted that i^*_{PL} represents a cathodic process; it has a negative value. The quantity i^*_3 represents an anodic current density; it has a positive

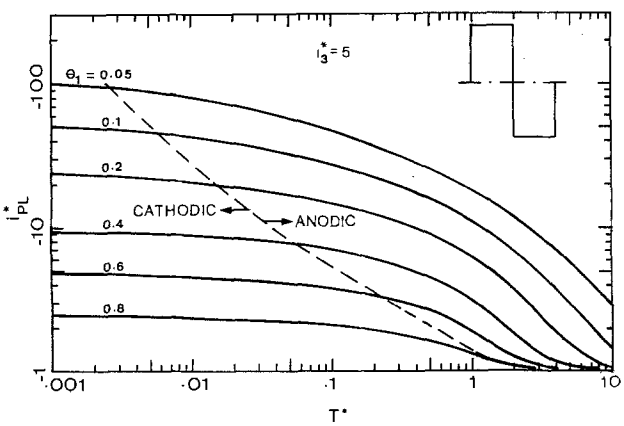

Fig. 3. Dimensionless limiting pulse current density as a function of a dimensionless pulse period. The results are given for a rectangular periodical pulse reverse with $i^*_3 = 5.0$.

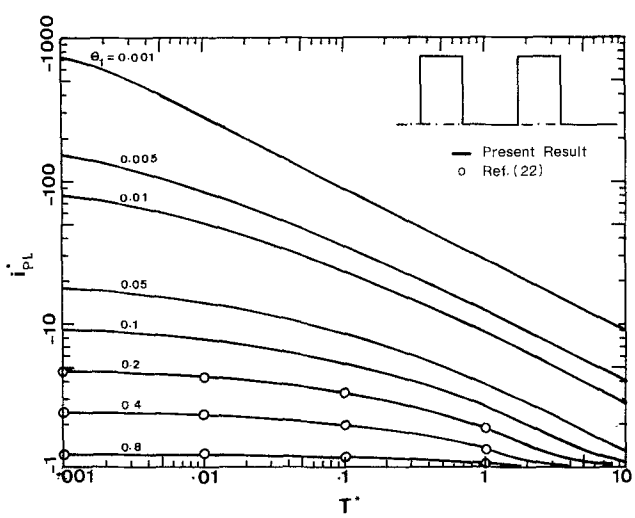

Fig. 2. Dimensionless limiting pulse current density as a function of a dimensionless pulse period. The results are given for a rectangular cathodic pulsating current. The numerical results obtained from Ref. (22) are shown by the symbol ○.

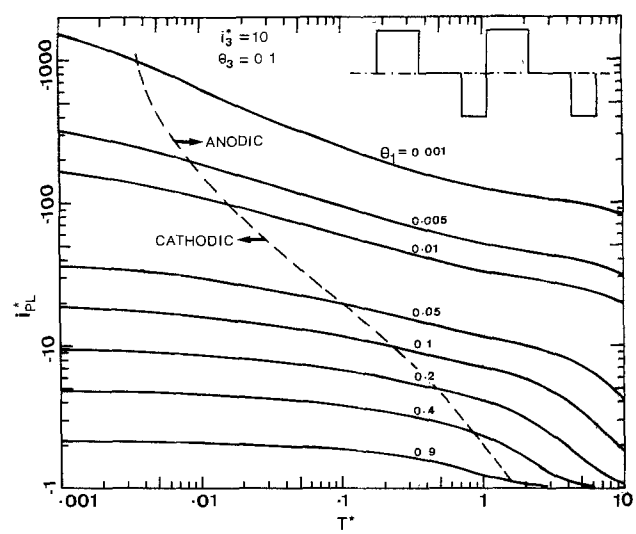

Fig. 4. Dimensionless limiting pulse current density as a function of a dimensionless pulse period. The results are given for double rectangular current pulses with $i^*_2 = 0$, $i^*_3 = 10$, and $\theta_3 = 0.1$.

value. The value of $i^*_{d.c.}$ represents the net rate of an electrode reaction in pulse electrolysis. If $i^*_{d.c.}$ is negative, the net reaction is cathodic. If $i^*_{d.c.}$ is positive, the net reaction is anodic. The net reaction rate becomes zero if

$$i^*_{d.c.} = i^*_{PL}\theta_1 + i^*_3\theta_3 = 0 \quad (\text{for } i^*_2 = 0) \qquad [42]$$

This equation has been numerically solved for the pulse wave shown in Fig. 3 and 4 and is plotted in the figures as a dashed curve. This curve represents a condition for the change in the direction of an electrochemical reaction in pulse electrolysis. The region to the left of the dashed curve is cathodic and the region to the right of the curve is anodic. The curve can serve as a guideline for the electroplaters to determine the proper values of i^*_1 and i^*_3 in pulse plating. It should be noted that the limiting pulse current density i^*_{PL} represents a maximum cathodic pulse limit for the onset of a mass transfer-controlled condition. Since the anodic current pulses cause an increase in the surface concentration of the reactive ion during the anodic duty cycle, the value of i^*_{PL} for the pulse waves with a pulse reverse is generally greater than that with the rectangular cathodic pulses.

Surface concentration and potential fluctuations.— The calculations for the concentration and the potential responses were performed for the deposition/dissolution of a copper rotating disk electrode in 0.05M $CuSO_4$ and 0.5M H_2SO_4. This electrolyte system was chosen because the electrokinetic parameters of the Cu^{2+}/Cu reaction and the thermodynamic and transport properties of the solution have been well-documented in the literature. In addition, mass flux of the diffusing ion to the rotating disk electrode is one-dimensional; the steady-state d-c limiting current density, i_{lim}, and the thickness of the Nernst diffusion layer, δ, have been obtained by Levich (31) as

$$i_{lim} = -0.62045\, nFC_x D^{1/3}\nu^{-1/6}\Omega^{1/2} \qquad [43]$$

$$\delta = 1.61173\, D^{1/3}\nu^{1/6}\Omega^{-1/2} \qquad [44]$$

These two equations together with Eq. [17]-[22] and [36]-[40] permit one to determine the fluctuations in the surface concentration of Cu^{2+} ion and the overpotential changes of the Cu^{2+}/Cu reaction on the rotating disk electrode for the pulsating current waveforms shown in Fig. 1. A base calculation was made for various pulse conditions at an electrode rotational speed of 300 rpm and a pulse period of 100 msec. The input parameters for the numerical computations are listed in Table I.

Figure 5b shows a set of steady-state surface concentration oscillations when the electrode is polarized with rectangular cathodic current pulses having a dimensionless pulse period $T^* = 0.1103$ and a cathodic duty cycle $\theta_1 = 0.4$. Three sets of surface concentrations corresponding to the pulse current densities of $i^*_1 = -0.179$, -1.07, and -1.96 are given. It is seen that during the current pulse period, the surface concentration of Cu^{2+} ion diminishes with time and reaches a minimum value at the end of the duty cycle (or the current-on period). During the relaxation (or current-off) period, the surface concentration recovers quickly to the original value. In this way, the surface concentration fluctuates between a high and a low value; the time average of the concentration fluctuations is shown as a dashed line in the figure. The time-averaged dimensionless surface concentration, $\bar{C}^*_s$, is related to the time-averaged d-c current density, $i_{d.c.}$, by Eq. [8]; for a given pulse period and duty cycle, its value decreases with increasing cathodic current pulses, i^*_1. On the other hand, the magnitude of the fluctuating concentration component, $\tilde{C}^*_s$, becomes larger as i^*_1 increases, and the total surface

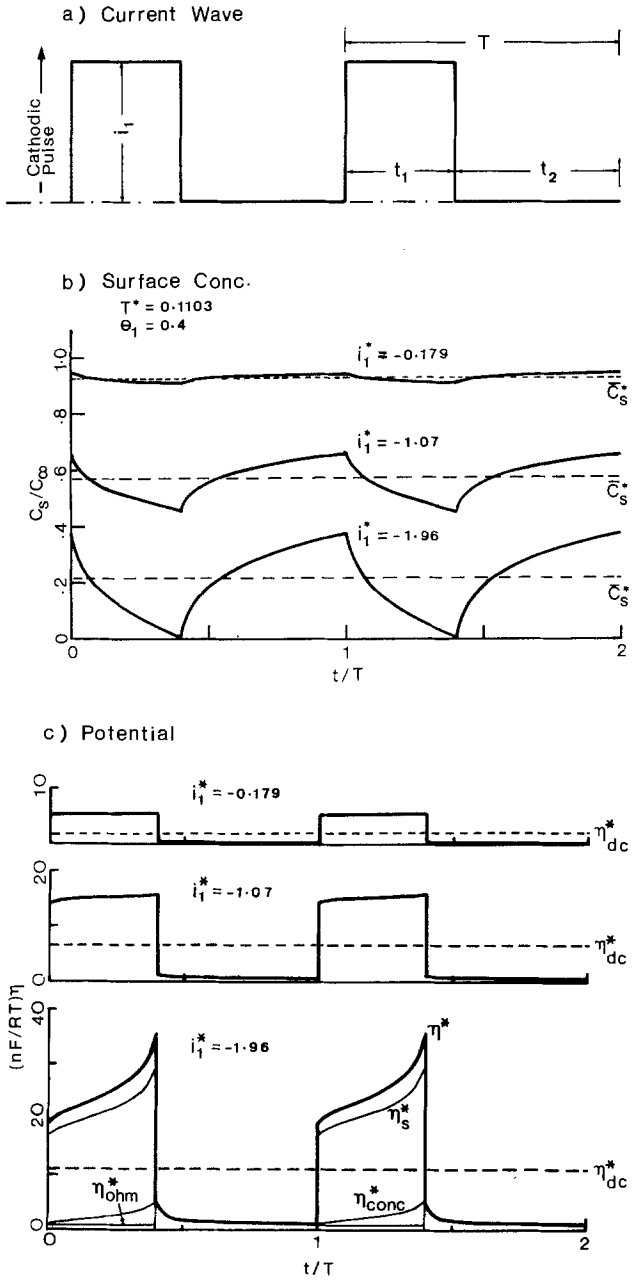

Fig. 5. Surface concentration and overpotential responses for the rectangular cathodic current pulses. The calculation was made for a copper rotating disk electrode in an acid copper sulfate solution at 300 rpm with the following pulse conditions: T = 100 msec (or $T^* = 0.1103$); and $\theta_1 = 0.4$.

Table I. Input parameters for the numerical computation of the potential-current relation of a copper rotating disk electrode (RDE) in 0.05M $CuSO_4$ and 0.5M H_2SO_4 at 298 K

Parameter	Value	Reference
Exchange current density, i_0	1.5 mA-cm^2	(9)
Anodic charge-transfer coefficient, α	0.75	(29)
Cathodic charge-transfer coefficient, β	0.25	(29)
Kinetic parameter, γ	0.75	(29)
Diffusivity of Cu^{2+} ion, D	7.6×10^{-6} cm^2/sec	(8)
Kinematic viscosity of electrolyte, ν	0.01 cm^2/sec	(8)
Resistivity of electrolyte, ρ	1 $\Omega \cdot$ cm	(30)
Distance of reference probe, l	0.2 cm	
Base calculations at 300 rpm and T = 100 msec:		
D-C limiting current density, i_{lim}	-27.95 mA/cm^2	
Thickness of the Nernst diffusion layer, δ	2.924×10^{-3} cm	
Dimensionless pulse period, T^*	0.1103	

concentration, $C^*_s = \bar{C}^*_s + \tilde{C}^*_s$, at the end of a duty cycle decreases with increasing i^*_1. At a sufficiently large $i^*_1 = -1.96$, the total surface concentration at the end of the cathodic duty cycle becomes zero as shown in Fig. 5b. Accordingly, this current pulse value of $i^*_{PL} = -1.96$ may be taken as the limiting pulse current density, i^*_{PL}, which signifies the beginning of a mass transfer-controlled process.

The corresponding steady-state potential oscillations of the Cu^{2+}/Cu reaction for the above rectangular cathodic current pulses are shown in Fig. 5c. The potential wave is rectangular at the small pulse current density of $i^*_1 = -0.179$. At an intermediately high $i^*_1 = -1.07$, the potential wave is distorted from the rectangular shape. The overpotential of the copper rotating disk electrode increases with time toward the negative direction during the cathodic duty cycle; this is primarily due to a decrease in the surface concentration of Cu^{2+} ion during the same period as shown in Fig. 5b. When the pulse current reaches the limiting pulse current density, $i^*_1 = i^*_{PL} = -1.96$, the electrode potential becomes a very large value at the end of the cathodic duty cycle because of the depletion of Cu^{2+} ion on the electrode surface. This property is useful to experimentally determine the values of i_{PL} for various flow and pulse conditions. The three overpotential components, η^*_s, η^*_{conc}, and η^*_{ohm}, for $i^*_1 = -1.96$ are also plotted in the figure. It is seen that contrary to the common judgment, the contributions of the ohmic overpotential, η^*_{ohm}, and the concentration overpotential, η^*_{conc}, to the total overpotential, η^*, are rather small (η^*_{ohm} less than 4% and η^*_{conc} less than 14%). The surface ovepotential, η^*_s, on the other hand, constitutes more than 80% of the total overpotential losses.

For electrolysis with a current wave having an anodic pulse reverse, the surface concentration generally undergoes a rapid increase during the current reversal period. This is clearly shown in Fig. 6b and d, where the calculated surface concentration is plotted for a generalized double rectangular wave with a cathodic pulse ($i^*_1 = -1.79$ and -2.85, and $\theta_1 = 0.4$), a relaxation period ($i^*_2 = 0$ and $\theta_2 = 0.5$) and an anodic pulse ($i^*_3 = 5.0$ and $\theta_3 = 0.1$). The surface concentration, C^*_s, undergoes a decrease during the cathodic duty cycle, a slow recovery during the relaxation cycle, and a fast rise during the anodic pulse cycle. The results also indicate that under certain pulse conditions, the surface concentration of the reactive ion can become greater than the bulk concentration, even though the overall process (as represented by $\bar{C}^*_s < 1$) is cathodic and there is a net consumption of the reactive ion at the electrode surface. Figures 6c and e show the calculated overpotential responses for this particular current waveform. During the cathodic duty cycle, the potential response is similar to the curves shown in Fig. 5c. During the anodic duty cycle, the potential change is relatively flat and independent of the time. This is because the anodic current pulse causes an increase in the surface concentration of Cu^{2+} ion. Consequently, the concentration overpotential, η^*_{conc}, shifts toward the positive direction, and the surface overpotential, η^*_s, shifts toward the negative direction. The two overpotential components cancel each other giving a flat anodic potential response as shown in Fig. 6e.

Time-averaged d-c potential-current relations.— The steady-state potential oscillation waves shown in Fig. 5 and 6 can be numerically integrated over one pulse period to yield the d-c overpotential component, $\eta^*_{d.c.}$. For a given current pulse wave, one can obtain a d-c polarization curve by plotting $\eta^*_{d.c.}$ *vs.* $i^*_{d.c.}$ on a semilogarithmic scale. For the purpose of evaluating the effect of pulsating current on the electrokinetic parameters of the Cu^{2+}/Cu reaction, all the d-c polarization curves depicted herewith will be compensated for the ohmic overpotential in the electrolyte (*i.e.*, by letting $\eta^*_{ohm} = 0$). Except as noted,

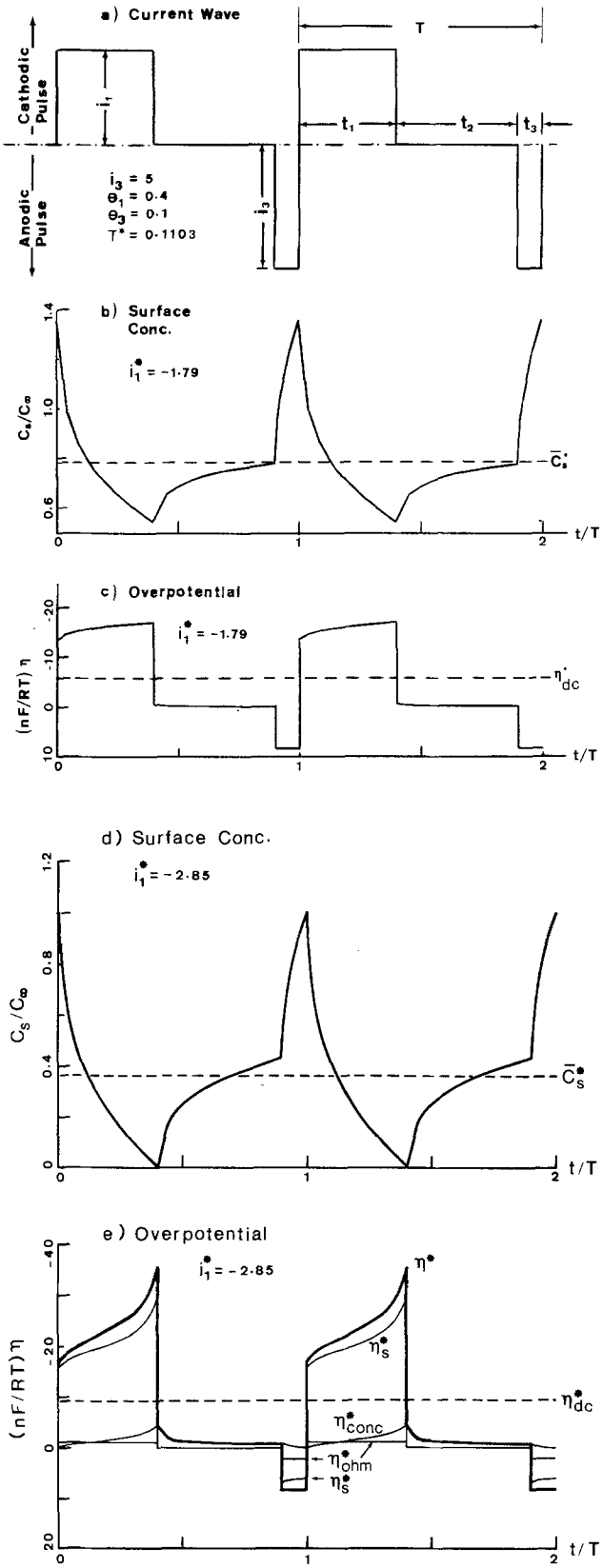

Fig. 6. Surface concentration and overpotential responses for a double rectangular pulsating current with $i_2 = 0$. The calculation was made for a copper rotating disk electrode in an acid copper sulfate solution at 300 rpm for the following common pulse conditions: $T = 100$ msec (or $T^* = 0.1103$); $\theta_1 = 0.4$; $\theta_3 = 0.1$; $i^*_1 = 5.0$. The cathodic pulse current densities in the figures are (b) and (c), $i^*_1 = -1.79$ and (d) and (e), $i^*_1 = -2.85$.

all the calculations were made for the base case of 300 rpm and $T = 100$ msec.

Figure 7 shows a set of d-c polarization curves for the rectangular cathodic current pulses having a dimensionless pulse period $T^* = 0.1103$. The parameters in the figure are the cathodic duty cycle θ_1 (0.01 ~ 1.0). For each curve, the calculation was made by gradually increasing the values of i^*_1 until it reaches 99.9% of the limiting pulse current density, i_{PL}. For comparison, the anodic and cathodic polarization curves for d-c electrolysis are also plotted in the figure as the thin curves. It is seen that PC strongly modifies the shape of the polarization curves. It behaves as a depolarizer, *i.e.*, for a given d-c current density, PC reduces the d-c overpotential required for the copper deposition reaction. The extent of reduction in polarization increases with decreasing cathodic duty cycle θ_1. At $\theta_1 = 0.01$, the cathodic polarization curve is seen to become a near horizontal line. It should be noted that although the theory allows very high cathodic current pulses at several hundred times greater than the d-c limiting current density, the time-averaged cathodic d-c current density can never exceed the d-c limiting current density. This picture is clearly shown in Fig. 7 where each polarization curve with PC is terminated at i^*_{PL} with an $|i^*_{d.c.}| < 1$.

The effect of anodic current pulses on the d-c polarization curves is shown in Fig. 8 and 9, respectively, for a rectangular periodical pulse reverse ($\theta_2 = 0$ and $\theta_3 = 0.2$), and a double rectangular wave with relaxation and pulse reverse ($\theta_1 = 0.4$, $\theta_3 = 0.1$, and $i_2 = 0$). The parameters in the two figures are the magnitudes of anodic pulse current density, i^*_3 (from 1 to 19). For the double rectangular wave, the effect of the cathodic duty cycle, θ_1, is given in Fig. 10, where the d-c polarization curves are plotted for $\theta_3 = 0.1$ and $i^*_3 = 5.0$. It is seen that for the PC with both anodic and cathodic current pulses, not only is there a change in the shape of the polarization curves, but also there is a shift in the apparent rest potential (the electrode potential at $i_{d.c.} = 0$) toward the negative direction. This is caused by the nonsymmetrical anodic and cathodic polarization behavior of the Cu^{2+}/Cu reaction system as described in Ref. (8, 9). The magnitude of the rest potential shift increases with increasing anodic pulse current density, i^*_3, as well as the cathodic duty cycle, θ_1. No Tafel regimes can be observed for all the curves with PC. Although

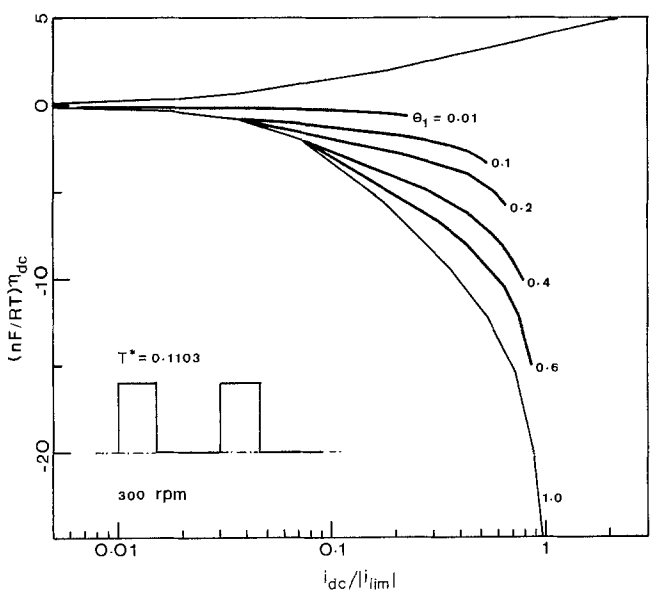

Fig. 7. Dimensionless d-c polarization curves for pulse electrolysis with rectangular cathodic current pulses. The calculations were made for a copper rotating disk electrode in an acid copper sulfate solution at 300 rpm for $T = 100$ msec.

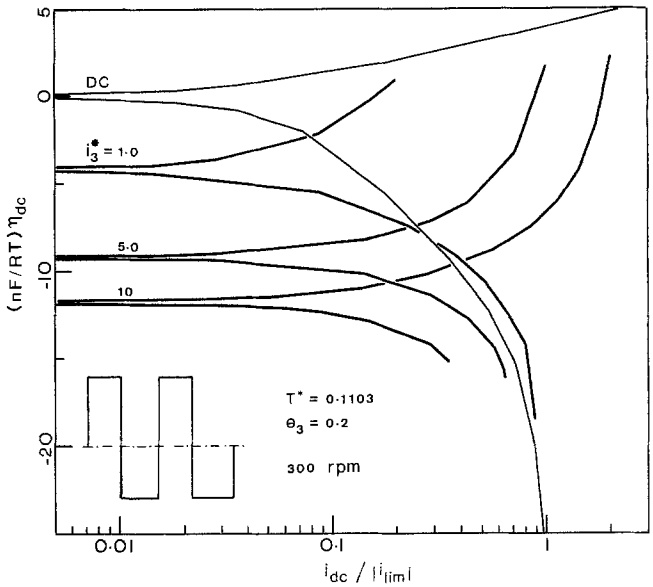

Fig. 8. Dimensionless d-c polarization curves for the rectangular periodical pulse reverse. The calculations were made for a copper rotating disk electrode in an acid copper sulfate solution at 300 rpm for $T = 100$ msec, $\theta_1 = 0.8$, and $\theta_3 = 0.2$.

PC reduces the overpotential for the cathodic deposition reaction, this is not always true for the anodic dissolution reaction. The anodic polarization curves with PC appear to reach a current plateau at high anodic d-c current densities.

Effect of pulse period.—A particular set of computations was performed to determine the effect of pulse period (or pulse frequency) on the d-c polarization curves. In these calculations, the rotational speed of the copper disk electrode was kept at 300 rpm, and the period of PC waves varied from 1 to 1000 msec (or 1000-1 Hz). The results are plotted in Fig. 11 for the rectangular cathodic current pulses with θ_1 varying from 0.1 to 1.0. The PC with smaller pulse period (or high frequency) extends the polarization curves to higher values of the d-c current densities. The

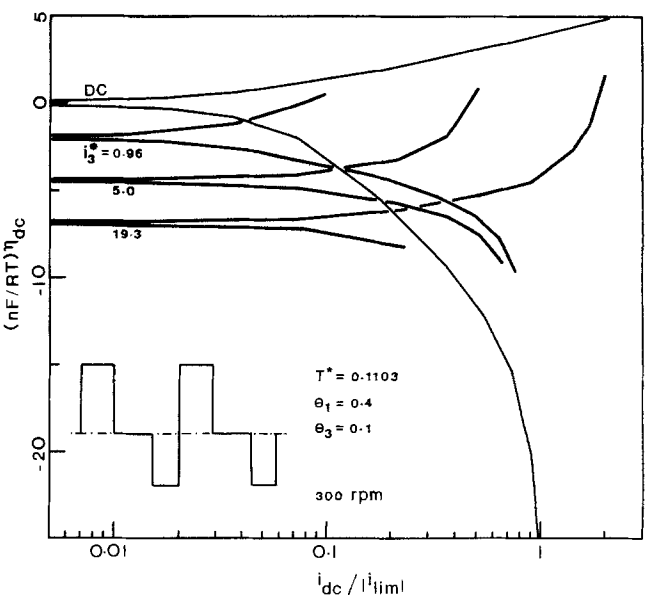

Fig. 9. Dimensionless d-c polarization curves for the double rectangular current pulses with relaxations ($i_2 = 0$). The calculations were made for a copper rotating disk electrode in an acid copper sulfate solution at 300 rpm for $T = 100$ msec, $\theta_1 = 0.4$, $\theta_2 = 0.5$, and $\theta_3 = 0.1$. The parameters in the figure are the anodic pulse current densities, i^*_3.

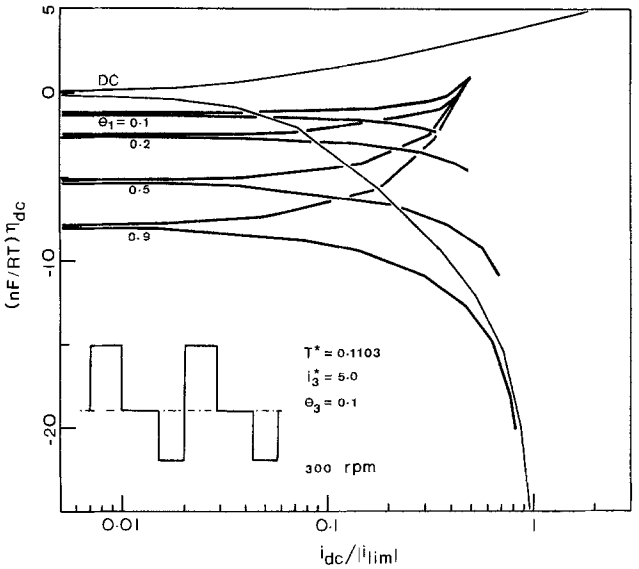

Fig. 10. Dimensionless d-c polarization curves for the double rectangular current pulses with relaxations ($i_2 = 0$). The calculations were made for a copper rotating disk electrode in an acid copper sulfate solution at 300 rpm for $T = 100$ msec, $\theta_3 = 0.1$, and $i^*_3 = 5.0$. The parameters in the figure are the cathodic duty cycles θ_1.

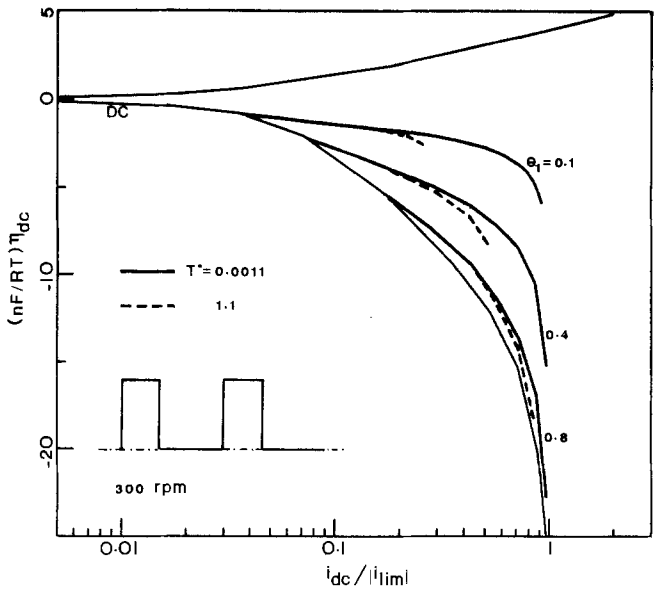

Fig. 11. Effect of pulsating period (or pulse frequency) on the dimensionless d-c polarization curves for the rectangular cathodic current pulses. The calculations were made for a copper rotating disk electrode in an acid copper sulfate solution. The electrode rotational speed was kept at 300 rpm; whereas the pulsating period varied from 1 to 1000 msec for various duty cycles θ_1.

effect is particularly apparent for the curves with a small cathodic duty cycle $\theta_1 = 0.1$. At small d-c current densities and large duty cycles, the difference between the high and low pulse periods becomes less significant. It should be noted that the present calculation did not account for the charge/discharge of an electric double layer at the electrode surface. This assumption greatly simplifies the mathematical complications and gives a good approximation if the current pulse time is much greater than the double layer charge/discharge time. The effect of the double layer capacitance on the shape of polarization curves in pulse electrolysis has been discussed in Ref. (8, 9).

Implication to the secondary current distribution.— Since the current density during the pulse is usually higher than that in the d-c electrolysis, it has been thought that the primary current distribution would prevail and the current distribution would be less uniform during the pulse electrolysis (6, 33). However, there have been numerous contradicting results reported in the literature. Sheshadri (34) examined the copper deposits obtained with PC, and concluded that PC reduced grain size and produced more leveled and smoother deposits. Enchev (35) used PC in the electrowinning of nonferrous alloys; he obtained higher quality deposit and higher current efficiency. Chin *et al.* (2, 36) have found that PC greatly enhanced the nucleation rate and produced more uniform zinc deposits in acid zinc chloride and alkaline zincate solutions. With a pasted zinc electrode in a nickel-zinc battery, they found that the use of PC during the charge period caused a deeper penetration of current into the porous electrode matrix and more zinc deposits were obtained at the silver grid located on the back side of the electrode. PC has been used commercially in the color anodizing of aluminum (37-39). The color of anodized aluminum alloys appeared to be brighter with pulse electrolysis because of deeper penetration of metallic dye ions into the micropores of the oxide film on the aluminum surface. These evidences imply that more uniform current distributions can be achieved with pulse electrolysis.

The present calculation can be used to obtain an insight into the secondary current distribution in pulse electrolysis. For a moderately fast electrochemical reaction, such as the Cu^{2+}/Cu reaction, the contributions of the ohmic overpotential and concentration overpotential to the total overpotential losses are small as cmpared with that of the surface overpotential (Fig. 5 and 6), and the secondary current distribution would prevail at moderately high pulse current densities. An important quantity in the uniformity of the secondary current distribution is the value of a dimensionless group called Wagner number (40)

$$\mathrm{Wa} = K(d\eta_{\mathrm{d.c.}}/di_{\mathrm{d.c.}})/L$$
$$= 2.3K(d\eta_{\mathrm{d.c.}}/d\log i_{\mathrm{d.c.}})/i_{\mathrm{d.c.}}L \qquad [45]$$

where K is the conductivity of the electrolyte, L is a characteristic length depending upon the electrode geometry (*e.g.*, radius of the disk electrode), and $d\eta_{\mathrm{d.c.}}/d\log i_{\mathrm{d.c.}}$ is the slope of the d-c polarization curve of the electrode reaction. This number represents the ratio of the activation (or charge-transfer) resistance to the ohmic resistance of the electrolyte. The current distribution is generally more uniform at large Wagner numbers. Since PC strongly modifies the shape of d-c polarization curves as shown in Fig. 7-11, the apparent Wagner numbers evaluated from these figures will be rather different from those of d-c electrolysis. For small d-c current densities, the slope of the polarization curves with PC is generally smaller than those of the d-c electrolysis. Consequently, the Wagner number with PC is smaller and the current distribution will be less uniform with PC at small d-c current densities. However, the slope with PC is seen to increase with increasing $i_{\mathrm{d.c.}}$ and eventually becomes larger than that of the polarization curves of d-c electrolysis at high $i_{\mathrm{d.c.}}$ values. The phenomenon is particularly obvious for the anodic polarization curves in Fig. 8-10. Consequently, one would expect to have a more uniform current distribution with PC at high d-c current densities. Thus, PC can improve or worsen the current distribution depending upon the pulse conditions. The polarization curves presented in Fig. 7-11 can serve as a guidance in the estimate of the secondary current distribution during the pulse operation.

Conclusions

A mathematical model has been presented for the analysis of convective mass transfer and potential-current relations in pulse electrolysis. Numerical re-

sults for the limiting pulse current densities were generated for the rectangular cathodic current pulses, the periodical pulse reverse, and the double rectangular wave with relaxation and pulse reverse. It was shown that an instantaneous mass transfer rate 100 ~ 1000 times greater than the steady-state d-c limiting current density could be obtained with short pulses and small pulse period. The concentration fluctuations and the potential-current responses were subsequently calculated for the deposition/dissolution of copper on a rotating disk electrode in acid copper sulfate solution. The PC caused a profound change in the current-potential relationships. PC reduced the overpotential required for the electrode reaction and eliminated the Tafel regime from the polarization curves. For the pulse waveforms having both anodic and cathodic current pulses, PC shifted the apparent rest potential toward the negative direction. The implication of the results to the secondary current distributions and the pulse plating processes was discussed.

Acknowledgments

This paper is dedicated to the late Prof. N. Ibl. The author would like to thank the Eidgenossche Technische Hochschule, Zurich, Switzerland, and the National University of Singapore for a Visiting Professorship during the course of this work. Acknowledgment is also made to the U.S. National Science Foundation Grant ENG 77-25153 and to the donors of the Petroleum Research Fund, administered by the American Chemical Society, for partial support of this research.

Manuscript submitted Aug. 12, 1982; revised manuscript received Feb. 15, 1983.

Any discussion of this paper will appear in a Discussion Section to be published in the June 1984 JOURNAL. All discussions for the June 1984 Discussion Section should be submitted by Feb. 1, 1984.

LIST OF SYMBOLS

C	concentration of ionic species, kg-mol/m^3
C_s	surface concentration, kg-mol/m^3
C_∞	bulk concentration, kg-mol/m^3
$\bar{C}$	steady-state concentration component, kg-mol/m^3
$\tilde{C}$	fluctuating concentration component, kg-mol/m^3
C^*	dimensionless concentration defined as C/C_∞
D	diffusivity of ionic species, m^2/sec
d_j	a dummy variable, Eq. [21], dimensionless
$\mathbf{F}$	Faraday constant, 9.65 $\times$ 10^{-7} C/kg-equivalent
f_1, f_2, f_3	infinite series defined by Eq. [25]-[27]
i	current density at the electrode surface, A/m^2
$i_{a.c.}$	fluctuating a-c current density, A/m^2
$i_{d.c.}$	d-c current density, A/m^2
i_{lim}	d-c limiting current density, A/m^2
i_{PL}	limiting pulse current density, A/m^2
i_0	exchange current density, A/m^2
i_1	cathodic pulse current density, A/m^2
i_2	current density during the relaxation time, A/m^2
i_3	anodic pulse current density, A/m^2
i^*	dimensionless current density defined as $i/\lvert i_{lim}\rvert$
j	a dummy index, dimensionless
K	conductivity of electrolyte, Ω^{-1} m^{-1}
k	a dummy integer, Eq. [17]-[19] and [25]-[27], dimensionless
L	characteristic length, m
l	distance between the working electrode and the reference probe, m
m	a dummy integer, Eq. [17]-[19] and [25]-[27], dimensionless
n	number of electrons transferred in the electrode reaction, kg-equivalent/kg-mol
p	period number, dimensionless
R	universal gas constant, 8.314 J/kg-mol $\cdot$ K
T	pulse period, sec; also absolute temperature in Eq. [30], K
T^*	dimensionless period defined as DT/δ^2
t	time, sec
t_1	cathodic pulse time, sec
t_2	relaxation time, sec
t_3	anodic pulse time, sec
t^*	dimensionless time defined as t/T
V	velocity of electrolyte, m/sec
Wa	Wagner number defined as $K(d\eta_{d.c.}/di_{d.c.})/L$
Y	infinite series given by Eq. [15]
y	vertical distance from the electrode surface, m

Greek Letters

α	anodic charge transfer coefficient, dimensionless
β	cathodic charge transfer coefficient, dimensionless
γ	a kinetic parameter in Eq. [30]
δ	thickness of the steady-state Nernst diffusion layer, m
η	overpotential, V
η_{conc}	concentration overpotential, V
$\eta_{d.c.}$	d-c overpotential component, V
η_{ohm}	ohmic overpotential, V
η_s	surface overpotential, V
η^*	dimensionless overpotential defined as $(n\mathbf{F}/RT)\eta$
θ_1	cathodic duty cycle defined as t_1/T, dimensionless
θ_2	dimensionless relaxation time defined as t_2/T
θ_3	anodic duty cycle defined as t_3/T, dimensionless
λ_m	an eigenvalue defined by Eq. [20], dimensionless
ν	kinematic viscosity, m^2/sec
ρ	resistivity of electrolyte, $\Omega \cdot$ m
(ρl)	product of ρ and l, $\Omega \cdot$ m^2
Ω	speed of electrode rotation, rad/sec

Subscripts

s	surface value
∞	bulk value

Superscript

*	representing a dimensionless parameter or variable, see Eq. [22] and [35] for various definitions

Other Symbols

—	time-averaged steady-state value
~	fluctuating value
→	vector notation

REFERENCES

1. S. Venkatesh and D-T. Chin, *Isr. J. Chem.*, **18**, 56 (1979).
2. D-T. Chin, R. Sethi, and J. McBreen, *This Journal*, **129**, 2677 (1982).
3. N. Ibl, J. Cl. Puippe, and H. Angerer, *Surf. Tech.*, **6**, 287 (1978).
4. J. Cl. Puippe and N. Ibl, *Plating Surf. Finish*, **67**, 68 (1980).
5. M. G. Pavlovic, M. D. Maksimovic, and K. I. Popov, *J. Appl. Electrochem.*, **8**, 61 (1978).
6. N. Ibl, *Surf. Tech.*, **10**, 8 (1980).
7. S. Venkatesh and D-T. Chin, *This Journal*, **128**, 2588 (1981).
8. S. Venkatesh, M. Meyyappan, and D-T. Chin, *J. Colloid Interfacial Sci.*, **85**, 216 (1982).
9. R. Sethi and D-T. Chin, Submitted to *J. Electroanal. Chem.*
10. D-T. Chin, *This Journal*, **127**, 2162 (1980).
11. E. Warburg, *Ann. Physik*, **67**, 493 (1899).
12. E. Warburg, *ibid.*, **6**, 125 (1901).
13. F. Kruger, *Z. Phys. Chem.*, **45**, 1 (1903).
14. D. C. Grahame, *Chem. Rev.*, **41**, 441 (1947).
15. D. C. Grahame, *Ann. Rev. Phys. Chem.*, **6**, 337 (1955).
16. E. Levart and D. Schumann, *J. Electroanal. Chem.*, **28**, 45 (1970).
17. E. Levart and D. Schumann, *ibid.*, **53**, 77 (1974).
18. E. Levart and D. Schumann, *This Journal*, **122**, 1082 (1975).
19. R. V. Homsy and J. Newman, *ibid.*, **121**, 421 (1974).
20. P. Appel and J. Newman, *ibid.*, **124**, 1964 (1977).
21. K. Viswanathan and H. Y. Cheh, *ibid.*, **126**, 398 (1979).
22. K. Viswanathan, M. A. Farrel Epstein, and H. Y.

Cheh, *ibid.*, **125**, 1772 (1978).
23. H. Y. Cheh, *ibid.*, **118**, 1132 (1971).
24. H. Y. Cheh, *ibid.*, **118**, 551 (1971).
25. Yu G. Silver, *Zh. Fiz. Khim.*, **34**, 577 (1960).
26. J. M. Hale, *J. Electroanal. Chem.*, **6**, 187 (1963).
27. J. Cl. Puippe and N. Ibl, *Plating Surf. Finish*, **67**, 68 (1980).
28. K. Hosokawa, H. Angerer, J. Cl. Puippe, and N. Ibl, *ibid.*, **67**, 52 (1980).
29. J. O'M. Bockris and H. Kita, *This Journal*, **109**, 928 (1962).
30. A. Numanoglu, Eidgenossische Technische Hochschule (ETH), Zurich, Switzerland, Private communication.
31. V. G. Levich, "Physicochemical Hydrodynamics," Prentice-Hall, Englewood Cliffs, NJ (1962).
32. D-T. Chin, in "Proceedings of the Symposium on Transport Processes in Electrochemical Systems," R. S. Yeo, T. Katan, and D-T. Chin, Editors, The Electrochemical Society Softbound Proceedings Series, Pennington, NJ (1982).
33. N. Ibl, in "Proceedings of the 2nd International Pulse Plating Symposium," Chicago, IL (1981).
34. B. S. Sheshadri, *Plating Surf. Finish*, **65**, 43 (1978).
35. I. Enchev, *Hutn. Listy*, **26**, 820 (1971).
36. D-T. Chin and S. Venkatesh, *This Journal*, **128**, 1439 (1981).
37. N. Baba, *Metal Finish Soc. J.*, **24**, 34 (1973).
38. N. Baba, M. Nakamura, and T. Yoshino, *ibid.*, **26**, 224 (1975).
39. T. Asada, *ibid.*, **21**, 490 (1970).
40. N. Ibl, in "Comprehensive Treatise on Electrochemistry," Vol. 6, J. O'M. Bockris, E. Yeager, B. Conway, and S. Sarangapani, Editors, Plenum, New York (1980).

Electrodeposition of Zinc on Glassy Carbon from $ZnCl_2$ and $ZnBr_2$ Electrolytes

J. McBreen* and E. Gannon

Brookhaven National Laboratory, Department of Energy and Environment, Upton, New York 11973

ABSTRACT

The initial stages of the electrocrystallization of zinc from 3M $ZnCl_2$ and 3M $ZnBr_2$ on glassy carbon has been investigated using cyclic voltammetry, the potential step method, and scanning electron microscopy. Particular care was taken to ensure electrolyte purity and to eliminate resistance effects in the measurements. The nucleation overvoltage in 3M $ZnCl_2$ was ~ 17 and ~ 12 mV in 3M $ZnBr_2$. In 3M $ZnCl_2$, the current transients from the potential step measurements could be fitted to a simple model that assumes instantaneous nucleation followed by growth of three dimensional centers under kinetic control. A similar mechanism is operative for 3M $ZnBr_2$ at low overvoltages. At higher overvoltages, the current transient is governed by mixed kinetic and diffusion control and cannot be fitted to a simple model. The lower nucleation overvoltage and the faster kinetics in 3M $ZnBr_2$ is correlated with the lower stability constants for the zinc bromide complexes. Erroneous results are obtained when resistance effects are not accounted for.

The zinc electrode is common to both zinc/chlorine and zinc/bromine batteries. Although considerable progress has been made in engineering these batteries, there are still problems with the zinc electrode (1-8). These are related to changes in zinc electrode morphology which result in dendritic growth and nonadherent deposits. These problems are more severe under conditions of random shallow cycling.

There have been several publications on the kinetics of zinc deposition from zinc chloride electrolytes (9-16). There have been reports on the dependence of zinc morphology on additives (17) and a-c modulation of the charging current (18). The kinetics of dendrite growth in zinc chloride electrolytes has been reported recently (19). Except for brief references in a few publications (2, 6), there is no information in the open literature on the electrodeposition of zinc from zinc bromide electrolytes. In the case of zinc chloride, the publications deal mainly with the electrodic reactions (10-16) and the electrode morphology after prolonged deposition (17-19). There are no publications on the processes involved in the initial stages of nucleation and growth of zinc on foreign substrates.

In zinc halogen batteries, zinc is deposited on an inert current collector. Materials that have been used are plastic bonded carbon (5), dense graphite (7), vitreous carbon (6), or silver plated titanium. In the present study, the initial stages of zinc deposition on glassy carbon were investigated using the potential step technique (20). This included studies in both 3M $ZnCl_2$ and 3M $ZnBr_2$ electrolytes.

* Electrochemical Society Active Member.
Key words: battery, SEM, nucleation.

Experimental

Reproducible results, which fitted reasonable nucleation and growth models, could only be obtained after careful attention was given to current distribution, resistance effects, and electrolyte purity.

Cell design.—The cell used in these studies was a modification of the design of Cahan *et al.* (21). The cell, which was machined from PTFE, is shown in Fig. 1. The three PTFE parts were held together by aluminum flanges and tiebolts. The bottom two parts were sealed with a CTFE O-ring and a 0.25 mm PTFE spacer. The counter and reference electrodes were 1 mm diam zinc wires (99.9999% pure). These were covered with heat shrinkable PTFE tubing to a level below the top of the electrolyte. This cell design ensured uniform current distribution over the electrode surface. The working electrode was a 7.5 mm diam glassy carbon electrode with a PTFE collar (Pine Instrument Company). The collar formed a tight leak free slip fit with the bottom part of the cell.

Electrolyte preparation.—High purity 3M $ZnCl_2$ was prepared by reacting high purity zinc (99.9999%) with the distilled azeotrope of HCl. Concentration adjustments were made by additions of triply distilled water. High purity 3M $ZnBr_2$ was prepared by reacting high purity zinc with high purity bromine under triply distilled water. The reaction was carried out in an Erlenmeyer flask immersed in an ice bath.

Electric circuitry.—Cyclic voltammetry measurements were made using a Stonehart BC-1200 potentiostat in conjunction with a PAR 175 programmer and a Soltec 3316 X-Y recorder. Resistance correction was

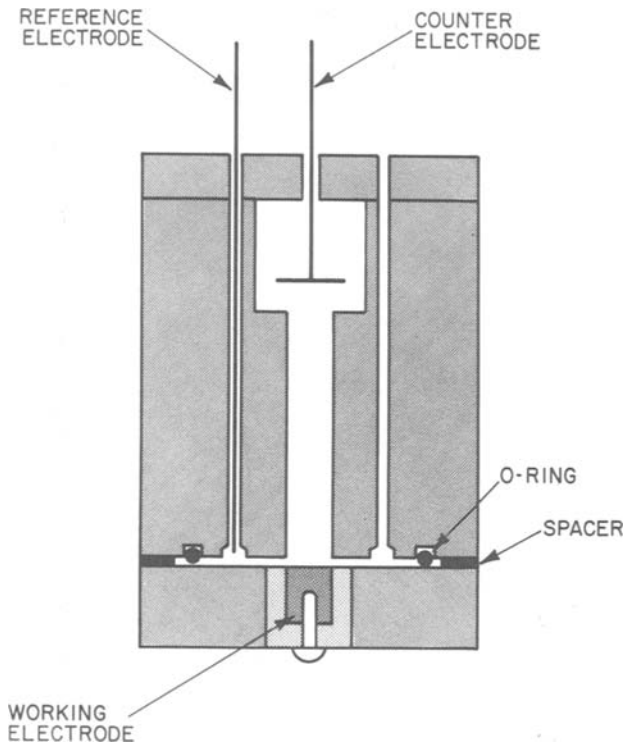

Fig. 1. Schematic of cell for zinc deposition studies

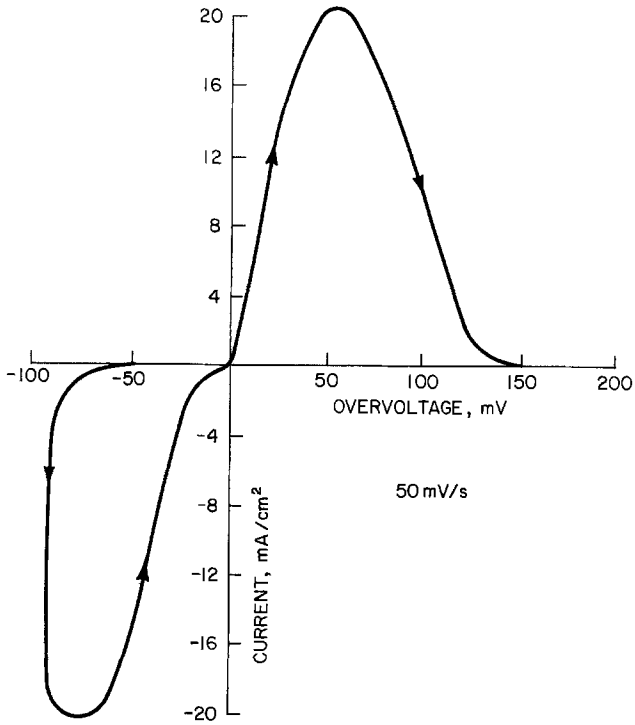

Fig. 2. Cyclic voltammogram for zinc deposition on glassy carbon in 3M $ZnCl_2$, pH = 2.8, sweep rate 50 mV/sec.

made using the potentiostat in conjunction with a Hewlett-Packard 3325A function generator and a Tektronix 7634 oscilloscope. Potential step measurements were made using the potentiostat in conjunction with the X-Y recorder.

Experimental procedure.—The electrodes were successively polished with 320 and 600 grit sandpaper, 3 and 1μ diamond polish. The electrodes were then rinsed with triply distilled water and assembled in the cell. Particular care was taken to ensure that the electrode surface was flush with the top surface of the bottom part of the cell. The cell was filled with 20 ml of deaerated electrolyte, and the electrochemical measurements were immediately carried out. When samples were prepared for scanning electron microscopy, the cell was quickly disassembled and the electrode was rinsed with water and methanol. Samples were stored under deaerated methanol prior to carrying out the electron microscopy. In some cases, the electrodes were weighed so as to determine the current efficiency for zinc deposition.

Results

Figure 2 is a cyclic voltammogram for zinc deposition from 3M $ZnCl_2$ on glassy carbon. The cyclic voltammogram exhibits a nucleation loop in that cathodic current on reversal of the sweep is higher than that found on going in the cathodic direction. Qualitatively, the results, in zinc bromide, were similar. There was no evidence of underpotential deposition of zinc.

Figures 3 and 4 show the results of the potential step measurements in 3M $ZnCl_2$ and 3M $ZnBr_2$, respectively. The current transients show a small induction time followed by a smooth rise to a current plateau. The potential step measurements indicate that the critical overvoltage for zinc deposition is ~17 mV in 3M $ZnCl_2$ and ~12 mV in 3M $ZnBr_2$. For the same overvoltage, the current is much higher in 3M $ZnBr_2$. At the higher overvoltages in 3M $ZnBr_2$, the shape of the current transients change. When the resistance correction is not made the currents are much lower. As the current increases, the iR component increases and the real applied potential decreases with

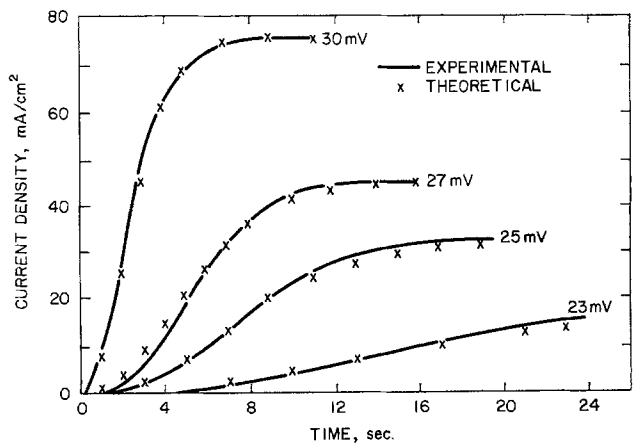

Fig. 3. Current transients (solid lines) for zinc deposition on glassy carbon in 3M $ZnCl_2$, pH = 2.8. Overvoltages are indicated on the figure. Calculated values for the current based on Eq. [2] in the discussion and the constants in Table I are also shown (×).

time. This tends to level off the current transient.

Figure 5 shows scanning electron micrographs (SEM) of the deposit in 3M $ZnBr_2$ and 3M $ZnCl_2$. The SEM data indicate that the growth pattern may be described by the growth of equally sized zinc particles dispersed at random over the zinc surface. The number of particles per cm^2 increases with the applied overvoltage. When deposition was carried out for a long time the deposit morphology was essentially identical to that found by Oren and Landau (19). Weight measurements indicated that the current efficiency for zinc deposition was ~100%.

Discussion

Models for electrocrystallization.—Several models have been developed for describing the nucleation and growth of metals during electrodeposition at constant potential (20, 22-25). These models include various assumptions regarding nucleation and growth of three dimensional centers. Nucleation can be instantaneous or can occur over a period of time, governed by a first order kinetic law. Growth can occur under

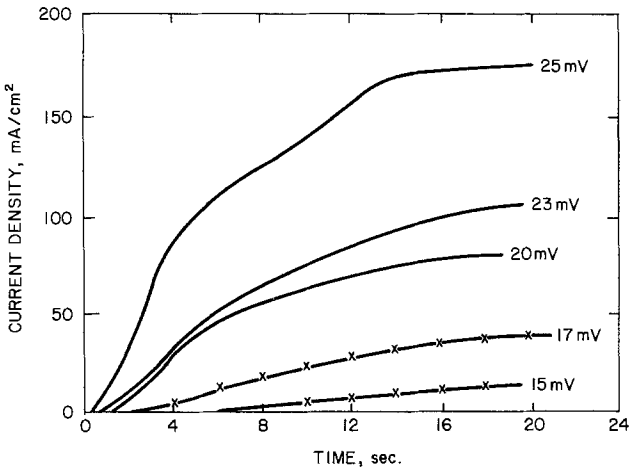

Fig. 4. Current transient (solid lines) for zinc deposition on glassy carbon in 3M $ZnBr_2$, pH = 3.0. Overvoltages are indicated on the figure. Calculated values for the current at 15 and 17 mV (×) are also shown. These are based on Eq. [2] in the discussion. At 15 mV $k^2N_0 = 2.13 \times 10^{-5}$ mol² cm^{-6} sec^{-2}, and at 17 mV, $k^2N_0 = 3.66 \times 10^{-5}$ mol² cm^{-6} sec^{-2}.

either kinetic or diffusion control. In the kinetic control growth models, provisions can be made to account for overlap of growth centers using the Avrami theorem (26). More complicated models have been developed which take into account such things as the death of growth centers (24, 25) and simultaneous layer growth along with the nucleation and growth of three dimensional centers (27-29).

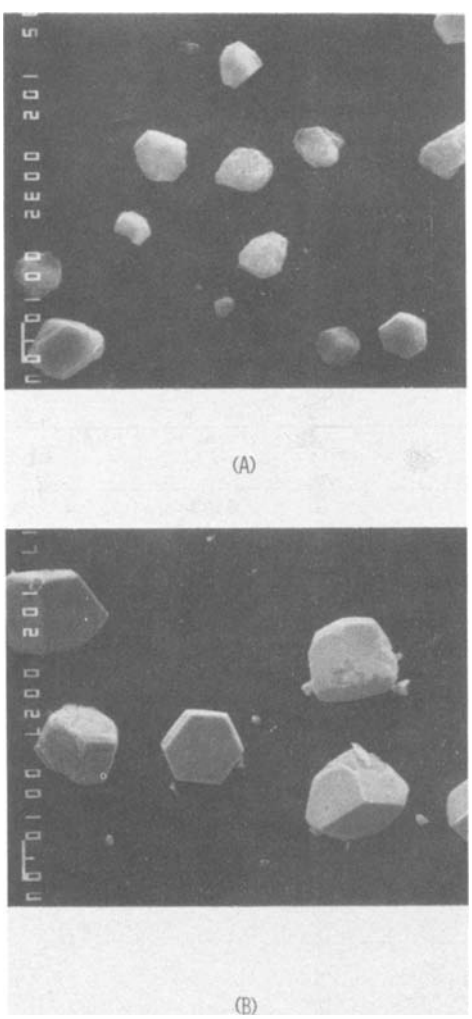

Fig. 5. Scanning electron micrograph of the deposit on glassy carbon after 10 sec of electrodeposition, (A) $ZnCl_2$ at 25 mV, (B) $ZnBr_2$ at 18 mV.

For the simpler models, rising current transients are predicted. For short times the relationship between the current, i, and time, t is

$$i \propto t^n \qquad [1]$$

The exponent n depends on the geometry, the type of nucleation, and the growth conditions. For instantaneous nucleation and growth under diffusion control, $n = 0.5$, and for progressive nucleation and growth under diffusion control, $n = 1.5$. For instantaneous nucleation and growth under kinetic control, $n = 2$, and for progressive nucleation and growth under kinetic control $n = 3$.

Electrodeposition in 3M $ZnCl_2$.—In the case of electrodeposition in 3M $ZnCl_2$, the following conclusions can be drawn from the experimental facts. The results from cyclic voltammetry, potential step measurements, and current efficiency determinations indicate that the contribution of hydrogen evolution to the overall current is negligible. Thus, the data can be treated without considering the contribution from hydrogen evolution. For short times $i \propto t^2$. This would indicate a mechanism involving instantaneous nucleation and growth under kinetic control. The scanning electron microscopy observations indicate that the zinc growths are approximately of equal size. This implies that the nucleation is instantaneous. The current time relationship for the growth of right circular cones under conditions of instantaneous nucleation and growth under kinetic control is

$$i = z\mathbf{F}k^1\left[1 - \exp - \left(\frac{\pi M^2 k^2 N_0 t^2}{\rho^2}\right)\right] \qquad [2]$$

where k^1 and k are the respective rates (mol cm^{-2} sec^{-1}) of crystal growth in the direction perpendicular and parallel to the substrate, M is the molecular weight of zinc (65.38 g/mol), ρ is the zinc density (7.14 g cm^{-3}), and N_0 the instantaneous nucleation rate; $z = 2$ and $\mathbf{F}$ is the faraday constant.

Theoretical values of i, calculated according to Eq. [2] are shown in Fig. 3. The values of $z\mathbf{F}k^1$ and k^2N_0 for various overvoltages are given in Table I. The agreement between theory and experiment for the current transients is quite good. This, together with the microscopic observations, indicates that a simple mechanism based on instantaneous nucleation followed by growth of three dimensional centers under kinetic control, is operative.

Electrodeposition in 3M $ZnBr_2$.—In the case of zinc deposition from $ZnBr_2$ electrolyte, the contribution of hydrogen evolution can also be neglected. The microscopic observations and the dependence of the current on the square of the time for short times indicates that the mechanism is similar to that found in $ZnCl_2$ electrolyte. However, only the current transients at 15 and 17 mV could be fitted to Eq. [2]. The data at higher overvoltages could not be fitted to any simple theoretical model. Close fits could be obtained for models that assumed the onset of a second set of nuclei after a few seconds. However, the microscopic observations indicated that all the zinc growths were identical in size, and no nuclei beyond those instantaneously formed by the potential step were observed.

Table I. Values of $z\mathbf{F}k^1$ and k^2N_0 for zinc deposition from 3M $ZnCl_2$ electrolyte

Overvoltage (mV)	$z\mathbf{F}k^1$ (mA/cm²)	k^2N_0 (mol² cm^{-6} sec^{-2})
23	15.84	1.42×10^{-5}
25	32.59	4.13×10^{-5}
27	45.27	9.75×10^{-5}
30	75.14	4.04×10^{-4}

The divergence from the simple theoretical model is most likely due to the onset of diffusion limitations at high current densities.

Comparison of electrodeposition in 3M $ZnCl_2$ and 3M $ZnBr_2$.—The nucleation overvoltage is lower (~12 *vs.* ~17 mV) in $ZnBr_2$ than in $ZnCl_2$ electrolytes and the electrode kinetics are faster in $ZnBr_2$. It is known that the complexing halide ions can effect the exchange current density for molybdenum deposition from molten salts (30). A similar effect apparently occurs in the case of zinc in aqueous electrolytes. The stability constants for zinc chloride complexes are much higher than those for zinc bromide complexes (31). This would explain the lower nucleation overvoltage and the faster kinetics in $ZnBr_2$ electrolytes.

Effect of resistance corrections.—When no resistance corrections are made, the potential step measurements yield erroneous results particularly at high current densities. The nucleation rate is not greatly affected since the initial current is very low. However, as the current transient rises the real applied potential at the electrode falls and the current transient rises with a lower time exponent. At high current densities, the current *vs.* the square root of time yields linear plots. Thus, without resistance correction the data could be erroneously interpreted as having growth under diffusion control conditions. These results, and those of Cahan *et al.* in alkaline electrolyte (21), indicate that it is imperative to eliminate resistance effects in zinc electrode kinetic measurements. Otherwise, erroneous conclusions on mechanisms can be easily made.

Acknowledgment

This work was supported by Lawrence Berkeley Laboratory under subcontract No. 4516210. The authors wish to thank R. L. Sabatini (BNL) for the scanning electron microscopy. This work was performed under the auspices of the U.S. Department of Energy, Contract No. DE-AC02-76CH00016.

Manuscript submitted Nov. 12, 1982; revised manuscript received April 19, 1983.

Any discussion of this paper will appear in a Discussion Section to be published in the June 1984 JOURNAL. All discussions for the June 1984 Discussion Section should be submitted by Feb. 1, 1984.

Brookhaven National Laboratory assisted in meeting the publication costs of this article.

REFERENCES

1. S. Barnartt and D. A. Forejt, *This Journal*, **111**, 1202 (1964).
2. G. Clerici, M. deRossi, and M. Marchetto, "Power Sources 5," D. H. Collins, Editor, pp. 167-181, Academic Press, London (1975).
3. R. Zito, U.S. Pat. 3,328,202 (1972).
4. J. E. Oxley, R. A. Putt, M. J. Montgommery, A. Sammels, and F. M. Walsh, Abstract 63, p. 166, The Electrochemical Society Extended Abstracts, Vol. 72-2, Miami Beach, FL, Oct. 8-13, 1972.
5. R. J. Bellows, D. J. Eustace, P. Grimes, J. A. Shropshire, H. C. Tsien, and A. F. Venero, "Power Sources 7," J. Thompson, Editor, pp. 301-312, Academic Press, London (1979).
6. F. G. Will, *ibid.*, J. Thompson, Editor, pp. 313-328, Academic Press, London (1979).
7. P. C. Symons, SAE Trans. paper No. 730253 (1973).
8. J. McBreen and E. J. Cairns, "Advances in Electrochemistry and Electrochemical Engineering," Vol. II, H. Gerischer and C. W. Tobias, Editors, pp. 273-352, John Wiley and Sons, New York (1978).
9. L. Gaiser and K. E. Heusler, *Electrochim. Acta*, **15**, 161 (1970).
10. T. Hurlen and E. Eriksard, *J. Electroanal. Chem.*, **45**, 205 (1973).
11. T. Hurlen and K. P. Fischer, *ibid.*, **61**, 165 (1975).
12. E. Eriksurd, *ibid.*, **76**, 27 (1977).
13. H. B. Sierra Alcazar and J. A. Harrison, *Electrochim. Acta*, **22**, 627 (1977).
14. I. Epelboin, M. Ksouri, E. Lejay, and R. Wiart, *ibid.*, **20**, 603 (1975).
15. I. Epelboin, M. Ksouri, and R. Wiart, *This Journal*, **122**, 1206 (1975).
16. J. T. Kim and J. Jorne, *ibid.*, **127**, 8 (1980).
17. D. J. McKinnon, J. M. Brannen, and V. I. Lakshmann, *J. Appl. Electrochem.*, **9**, 603 (1979).
18. D-T. Chin and S. Venkatesch, *This Journal*, **128**, 1439 (1981).
19. Y. Oren and V. Landau, *Electrochim. Acta*, **27**, 739 (1982).
20. M. Fleischman and H. R. Thirsk, "Advances in Electrochemistry and Electrochemical Engineering," P. Delahay, Editor, p. 123, Wiley Interscience, New York (1963).
21. B. D. Cahan, Z. Nagy, and M. A. Genshaw, *This Journal*, **119**, 64 (1972).
22. D. J. Astley, J. A. Harrison, and H. R. Thirsk, *Trans. Faraday Soc.*, **64**, 192 (1968).
23. G. A. Gunawardena, G. J. Hills, and I. Montenegro, *Electrochim. Acta*, **23**, 693 (1978).
24. M. Y. Abyaneh and M. Fleischman, *J. Electroanal. Chem.*, **119**, 187 (1981).
25. M. Y. Abyaneh, M. Fleischman, and M. Labram, in "Proceedings of the Symposium on Electrocrystallization," R. Weil and R. G. Barradas, Editors, pp. 1-26, The Electrochemical Society Softbound Symposium Series, Pennington, NJ (1981).
26. M. Avrami, *J. Chem. Phys.*, **7**, 1103 (1939); **8**, 212 (1940); **9**, 177 (1941).
27. J. A. Harrison and H. R. Thirsk, "Electroanalytical Chemistry," Vol. 5, A. G. Bard, Editor, pp. 67-148, Marcel Dekker, New York (1971).
28. A. Harrison, H. B. Sierra Alcazar, and J. Thompson, *J. Electroanal. Chem.*, **53**, 145 (1974).
29. I. R. Burrows, J. A. Harrison, and J. Thompson, *ibid.*, **58**, 241 (1975).
30. S. M. Selis, *J. Phys. Chem.*, **72**, 1442 (1968).
31. E. L. Short and D. F. C. Morris, *J. Inorg. Nucl. Chem.*, **18**, 192 (1961).

Mathematical Modeling of High-Current Chromium Plating with Application of a Rotating Disk Electrode

I. Drela, W. Popytak, and J. Kubicki

Instytut Technologii Nieorganicznej, 1 Nawozow Mineralnych, Politechniki Wroclawskiej, ul. M. Smoluchowskiego 25, 50-372 Wroclaw, Poland

ABSTRACT

Based on a mathematical design of experiments, the effect of temperature, current density, H_2SO_4, and K_2SiF_6 concentrations, and hydrodynamic conditions on the current efficiency, electrical energy consumption, speed of deposition, gloss, and the microhardness of chromium coatings obtained at current densities of 200-400 A/dm² was investigated. The results are presented by means of regression equations in the form of quadratic polynomials.

Traditional electrolytic plating of chromium is characterized by low deposition speed of chromium and low current efficiency. In recent years, a number of papers were published which describe chromium plating processes at high current densities whose rate of deposition may be higher by an order of magnitude as compared with standard processes (1-6). High-current densities up to 20 A/cm² may be applied if a suitable flow rate of electrolyte with respect to the cathode is ensured. In order to maintain the electrolyte flow, gear pumps are used (1-3, 6) and, if the components to be chromium plated are of rotational symmetry, the workpieces are rotated (3-5). It is convenient to investigate the chromium plating process under variable hydrodynamic conditions on a rotating disk electrode (3). One does not need then an expensive and complicated installation for forcing the electrolyte flow and the bath is not contaminated with corrosion products of the system. In addition, in a cell equipped with a rotating disk electrode one can readily determine and monitor the hydrodynamic conditions (7).

Experimental Procedure

A priori information contained in the literature and obtained in our studies enables us to distinguish four (Table II) or five (Table I) factors affecting the properties either of the chromium deposit or of process conditions. In order to carry out a full factorial experiment, it would be necessary to perform $2^4 = 16$ experiments for four factors and, for five factors, 32 experiments at levels -1, 0, $+1$. Taking into account replicates of experiments one should perform 32 and 64 experiments. In order to reduce the number of experiments, fractional replicates of the 2^{5-2} and 2^{4-1} type suggested for the first time by Finney in 1945 were carried out; they required 8 experiments repeated twice each. As a defining contrast (16) or in other words a basis of the design (17) of the 2^{5-2} type, the relations $I = -x_1x_2x_5 = -x_3x_4x_5 = +x_1x_2x_3x_4$ were assumed. For the 2^{4-1} design the defining contrast was taken according to the formula $I = x_1x_2x_3x_4$. The defining contrasts selected this way affected the entire design in such a way that they enabled the minimization of the necessary number of experiments. It also determined the combined estimates, aliases, and mutual relations of the design matrix columns. The more complicated design 2^{5-2} will be discussed here in a detailed way. Table I describes the factors, ranges of their changes, and code symbols.

The following symbols are used (Table I): $\tilde{x}_i$, value of the dimension related factor, x_i, dimensionless (coded) value of the factor. $\tilde{x}_{oi}$ and x_{oi}, values of factors in the design center, related and unrelated to dimension, respectively, z_i, is the range of factor variations, $i = 1, 2, \ldots, 5$.

Factor coding and the inverse operation are according to the formulas

$$x_i = \frac{\tilde{x}_i - \tilde{x}_{oi}}{z_i} \qquad \tilde{x}_i = x_i z_i + \tilde{x}_{oi} \qquad [1]$$

The design matrix of the 2^{5-2} type was prepared on the basis of the 2^3 matrix. According to our defining contrast, in the 2^3 design the column of the three-factor interaction $x_1x_2x_3$ (column 5 in Table II) was substituted with factor x_4. Meanwhile column 7 in Table II of the two-factor interaction $-x_1x_2$ was substituted with factor x_5, the signs of coded values having been changed to the opposite ones, according to the defining contrast $I = x_1x_2x_5$. Table II shows the structure of the design matrix 2^{5-2} where the current efficiency (y_1) was the optimization parameter. Taking into account the defining contrast or keeping track of mutual relations of signs in the design matrix columns, one finds

Table I.

Factor 1	Dimension 2	$\tilde{x}_i$ 3	$\tilde{x}_i$ 4	$\tilde{x}_{oi}$ 5	$\tilde{x}_i$ 6	z_i 7
K_2SiF_6 concentration	kg/m³	$\tilde{x}_1$	2	4	6	2
Temperature	°C	$\tilde{x}_2$	30	40	50	10
H_2SO_4 concentration	kg/m³	$\tilde{x}_3$	1	2	3	1
Cathodic current density	A/dm²	$\tilde{x}_4$	200	300	400	100
Disk electrode speed	1/sec	$\tilde{x}_5$	30	45	60	15
Coded factor values			$x_i = (-1) = (-)$	$x_{oi} = 0$	$x_i = (+1) = (+)$	

The basic electrolyte: CrO_3—250 g/liter, Cr_2O_3—7 g/liter.
Before the measurements, analytical determinations of the CrO_3, Cr_2O_3, H_2SO_4, and K_2SiF_6 concentrations were made.

Table II.

u	x_0 1	x_1 2	x_2 3	x_3 4	x_4 5	x_5 6	x_1x_2 7	x_1x_3 8	x_2x_3 9	$\bar{y}_{iu}$ 10
1	+	−	−	−	−	−	+	+	+	40.20
2	+	+	+	−	−	−	+	−	−	32.16
3	+	−	−	+	+	−	+	−	−	48.47
4	+	+	−	+	−	+	−	+	−	49.43
5	+	−	+	+	−	+	−	−	+	36.87
6	+	+	−	−	+	+	−	−	+	34.36
7	+	−	+	−	+	+	−	+	−	38.00
N = 8	+	+	+	+	+	−	+	+	+	45.85
					$x_1x_2x_3$	$-x_1x_2$				

$x_1x_2 = x_3x_4 = -x_5$; $x_1x_3 = x_2x_4$;

$x_2x_3 = x_1x_4$; $x_1 = -x_2x_5$; etc.

Such an arrangement of the entire design by means of the defining contrast has two aspects. The one is the fact that the estimated regression coefficients b_i and b_{ij} where $i \neq j$ and $i, j \in \{1, 2, \ldots, 5\}$ are biased with higher order interactions and the combined estimate system has the form

$$\begin{aligned} b_0 &\rightarrow B_0 + \Sigma B_{ij} \\ b_1 &\rightarrow B_1 - B_{25} + B_{234} + B_{1345} \\ b_2 &\rightarrow B_2 - B_{15} + B_{134} - B_{2345} \\ b_3 &\rightarrow B_3 - B_{45} + B_{124} - B_{1235} \\ b_4 &\rightarrow B_4 - B_{35} + B_{123} - B_{1245} \\ b_5 &\rightarrow B_5 - B_{12} - B_{34} + B_{12345} \\ b_{13} &\rightarrow B_{13} - B_{25} + B_{24} - B_{145} \\ b_{23} &\rightarrow B_{23} + B_{14} - B_{135} - B_{245} \end{aligned} \quad [2]$$

This means that the calculated regression coefficients b_0, b_i, b_{ij} are estimates of their expected values B_0, B_i, B_{ij} in the parent population of all the possible experiments for the process under investigation. In general, it is assumed that three-factor and higher order interactions are insignificant. Therefore, the terms B_{ijk}, B_{ijkl}, and B_{ijklm} in [2] may be neglected. The system of estimates determines also the sign relations between particular columns. For instance, the second relation shows that the x_2x_5 column will have symmetrically opposite signs with respect to the x_1 column, whereas the $x_2x_3x_4$ column will have consistent signs.

The other aspect which results from the defining contrast is that using the regression equation

$$\hat{y} = b_0 + \sum_{i=1}^{5} b_i x_i + \sum_{i<j}^{5} b_{ij} x_i x_j = b_0 + b_1x_1 + b_2x_2 + b_3x_3 + b_4x_4 + b_5x_5 + b_{13}x_1x_3 + b_{23}x_2x_3$$

it is possible, remembering the equalities $x_1x_3 = x_2x_4$ and $x_2x_3 = x_1x_4$, to analyze them in an interesting fashion.

The regression coefficients were calculated from the expression

$$b_i = 1/N \sum_{u=1}^{N} x_{iu} y_u, \quad \text{where} \quad i = 0, 1, \ldots, k, \quad [3a]$$

$k + 1$ = number of regression coefficients to be determined.

The significance of the regression coefficients was determined through an F-test. Since all coefficients in the 2^{5-2} design are determined with the same error, hence

$$\sigma^2\{b_i\} \rightarrow S^2\{b_i\} = \frac{1}{N} S^2\{y\} \quad [4]$$

Each experiment was repeated twice, so

$$S^2\{y\} = \frac{2 \sum_{u=1}^{N} (y_u - \bar{y})^2}{N} \quad [5]$$

where $\bar{y}$ is the mean of the two experimental results. Next the $F_{calc,0} = \frac{b_0}{S^2(b_0)}$; $F_{calc,i} = \frac{b_i}{S^2(b_i)}$; $F_{calc,ij} = \frac{b_{ij}}{S^2(b_{ij})}$ ratio was calculated and compared with F_{crit} for $f_1 = 1$, $f_2 = N$, $\alpha = 0.05$, from the tables. When $F_{calc} < F_{crit}$ the zero hypothesis of the significance of a given coefficient was rejected. That meant that the coefficient is considered insignificant in comparison with the error of its determination. The adequacy of presenting the measured results by means of the regression equation was also defined by means of the F-test. To this end the sum of squares for the remainder was calculated from the equation

$$S_R = \sum_{u=1}^{N} \bar{y}_u^2 - N \sum_{i=0}^{K} b_i^2 \quad [6]$$

and the residual variance

$$S_R^2 = \frac{S_R}{f_R}$$

where f_R is the number of degrees of freedom

$$f_R = N - k - 1$$

$k + 1$ is the number of regression coefficients to be determined. The F ratio was determined from the equation

$$F_{calc} = \frac{S_R^2}{S^2(y)} \quad [7]$$

and compared with F_{crit} from the tables for $f_1 = f_R$, $f_2 = N$, $\alpha = 0.05$. Again, for $F_{calc} > F_{crit}$, the zero hypothesis of adequacy of presenting the results by the polynomial obtained was rejected.

In the 2^{5-2} design, y_1, y_2, y_3, y_4 defined below were selected as response functions. Another design performed in order to investigate the silicofluoride-sulfate bath was the 2^{4-1} design. Table III describes the factorial space for that design, using symbols as in Table I. The design matrix was constructed such that in the 2^3 design the $x_1x_2x_3$ column was replaced by the x_4 factor column. This is tantamount to the assumption that $B_{123} = 0$. The combined estimate system has the form

$$\begin{aligned} b_0 &\rightarrow B_0 + \Sigma b_{ii} \quad & b_3 &\rightarrow B_3 + B_{124} \quad & b_{12} &\rightarrow B_{12} + B_{34} \\ b_1 &\rightarrow B_1 + B_{234} \quad & b_4 &\rightarrow B_4 + B_{123} \quad & b_{13} &\rightarrow B_{13} + B_{24} \\ b_2 &\rightarrow B_2 + B_{134} & & & b_{23} &\rightarrow B_{23} + B_{14} \end{aligned} \quad [8]$$

Application of the main defining contrast enabled us to considerably improve the resolution of the design. The basic regression coefficients b_i are biased only with three-factor interactions. In general, it is assumed that these interactions are insignificant. Two-factor interactions are estimated jointly in twos (aliases). Transformations of the defining contrast enable us to find the following important relations

$$x_1x_2 = x_3x_4, \quad x_1x_3 = x_2x_4, \quad x_2x_3 = x_1x_4$$

These relations, as in the case of the 2^{5-2} design, may be used for more extensive interpretation of the regression equations obtained. In this case, the response surface may be described by the following equation

$$\hat{y} = b_0 + b_1x_1 + b_2x_2 + b_3x_3 + b_4x_4 + b_{12}x_1x_2 + b_{13}x_1x_3 + b_{23}x_2x_3 \quad [9]$$

Table III.

Factor 1	Dimension 2	$\tilde{x}_i$ 3	$\tilde{x}_i$ 4	$\tilde{x}_{oi}$ 5	$\tilde{x}_i$ 6	z_i 7
H_2SO_4 concentration	kg/m³	$\tilde{x}_1$	2	3	4	1
Temperature	°C	$\tilde{x}_2$	30	37	44	7
Cathodic current density	A/dm²	$\tilde{x}_3$	200	300	400	100
Disk electrode speed	1/sec	$\tilde{x}_4$	30	60	90	30
Coded factor values			$x_i = (-1) = (-)$	$x_{oi} = 0$	$x_i = (+1) = (+)$	

Calculations of the regression coefficients, statistical calculations, and the method of testing the statistical hypotheses were the same as those for the 2^{5-2} design.

Favorable results obtained based on the 2^{5-2} and 2^{4-1} designs encouraged us to make an attempt at a more detailed description of the quasi-stationary response surface by means of partial fourth degree polynomial of the type

$$\hat{y} = b_0 + \sum_{i=1}^{N} b_i x_i + \sum_{i<j}^{N} b_{ij} x_i x_j + \sum_{i<j<k}^{N} b_{ijk} x_i x_j x_k + b_{1234} x_1 x_2 x_3 x_4 + \sum_{i=1}^{N} b_{ii} x_i^2$$

Due to economic considerations (number of experiments) and the level of calculation difficulties, the 3^n and rotatable designs were abandoned. The central composite orthogonal design (CCOD) was selected whose mathematical principles were worked out by Box and Wilson in 1951 (14). In our case, this design is a composite of the 2^4 design, stars of design, and one central point. In the CCOD, the results of the reduced 2^{4-1} design were utilized.

The basic matrix of the CCOD contains 25 lines and 4 columns. The full matrix used for calculations contains 20 columns, *i.e.*, 500 elements, and for this reason it is not mentioned in the present paper [cf. (15), page 92]. The possibility of constructing 20 columns makes it possible to calculate 20 coefficients of the partial fourth-degree polynomial. The factorial space in the CCOD is, of course, identical to that in 2^{4-1} design (Table III). Contrary to the 2^{5-2} and 2^{4-1} designs, the estimated coefficients are not biased with interactions, for instance

$$b_0 \rightarrow B_0,\ b_1 \rightarrow B_1,\ b_1b_2 \rightarrow B_{12},\ b_2b_3b_4 \rightarrow B_{234},\ b_{11} \rightarrow B_{11} \text{ etc.}$$

Introduction of the columns obtained by squaring the values of linear factors into the design matrix causes inorthogonalities in these columns. In order to maintain the design orthogonal, the following transformation should be introduced.

$$x_i' = x_i^2 - \frac{1}{N}\sum_{u=1}^{N} x_{iu}^2 = x_i^2 - \overline{x_i^2} \qquad [11]$$

and the "star arm" length, α, should be determined which for the 2^4 CCOD is: $\alpha = \pm 1.4142$. The transformation introduced is used for calculation of b_0, b_{ii} and for construction of the x_i^2 columns.

The regression coefficients of the CCOD design are caluculated according to the formulas

$$b_0' = \frac{1}{N}\sum_{u=1}^{N} x_{ou} \cdot y_u; \quad b_0 = b_0' - b_{11}\overline{x_1^2} - \ldots - b_{ii}\overline{x_i^2}$$

$$b_i = \frac{\sum_{u=1}^{N} x_{iu} \cdot y_u}{\sum_{u=1}^{N} x_{iu}^2}; \quad b_{ii} = \frac{\sum_{u=1}^{N} x_{iu}' \cdot y_u}{\sum_{u=1}^{N} (x_i')^2} \qquad [11a]$$

The regression equations were tested by an F-test in the case of the designs discussed earlier.

Testing Set

The main part of the testing set was a disk electrode with an electrolytic cell. The set consisted also of a d-c supply unit and measuring instruments, and is shown schematically in Fig. 1. A special gloss-meter was designed for measuring the gloss of chromium coatings. Its diagram is shown in Fig. 2.

Preparation of surface for deposition.—Before each measurement, the platinum disk surface was ground with abrasive paper No. 800 and degreased in trichloroethylene. After degreasing and drying, the disk was immediately chromium plated, without additional treatment.

Results and Discussion

In most papers dealing with high-current chromium plating (1, 2, 4-6), a standard sulfate electrolyte was used. In the present paper, studies have been performed with the silicofluoride-sulfate electrolyte which is more efficient, under stationary conditions, than the sulfate electrolyte. Using the 2^{5-2} design previously discussed (Tables I and II), the following regression equations were obtained

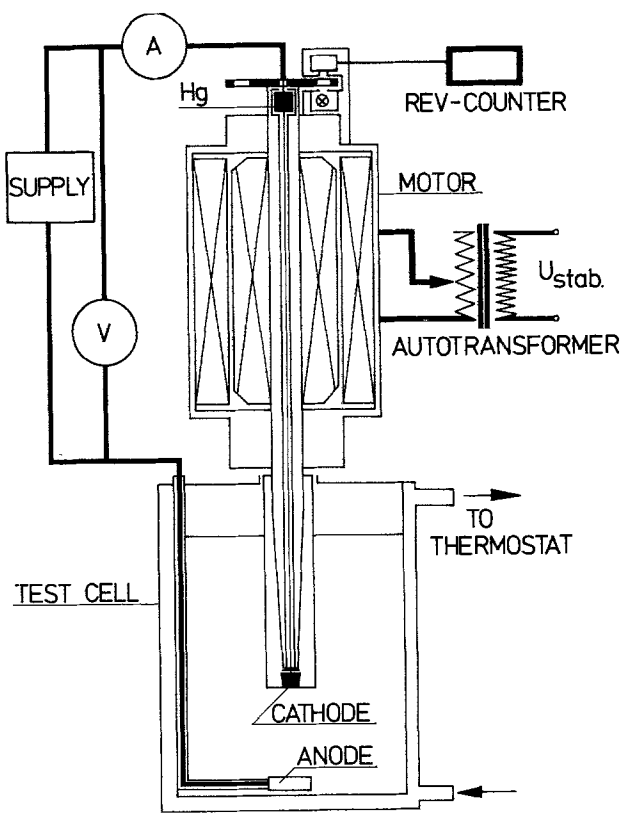

Fig. 1. Schematic diagram of experimental setup

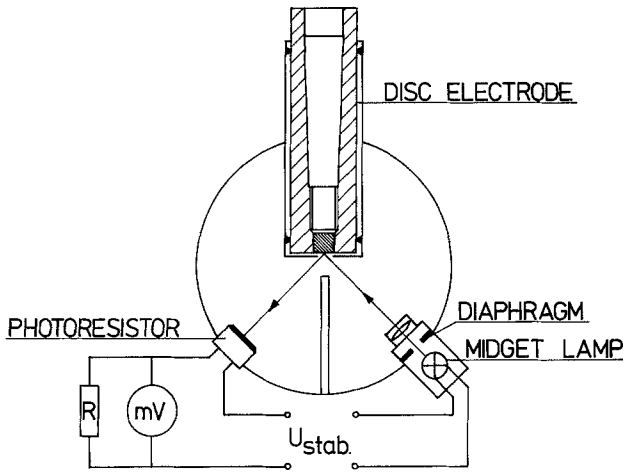

Fig. 2. Schematic diagram of gloss-meter

$y_1 = \dfrac{m_r \cdot \mathbf{F} \cdot n \cdot 100}{M \cdot i \cdot t}$ (%) is the current efficiency

$y_2 = \dfrac{u \cdot i \cdot t}{m_r}$ (kJ/kg) is the electric energy consumption

$y_3 = \dfrac{m_r}{A \cdot d \cdot t}$ (μm/sec) is the deposition rate

y_4 (%) is the gloss

(Prior to measurements, the gloss-meter (Fig. 2) was calibrated by setting the diaphragm to 100% for a standard chromium coating, obtained from a sulfate bath and wet ground with abrasive paper No. 600), where: m_r is the mass of chromium deposited on the cathode, **F**, is Faraday's constant, n is the number of electrons exchanged in the reaction $Cr^{6+} \rightarrow Cr^0$, M is the molecular mass of Cr, i is the current density, t is electrolysis time, u is the mean voltage between the anode and cathode, d is the chromium density, A is the disk surface area, equals 16 mm^2.

$$\hat{y}_1 = 40.67 - 0.2175x_1 - 2.4475x_2 + 4.4875x_3 + 1.0025x_4 - 1.0025x_5 + 2.7025x_1x_3 - 1.3475x_2x_3 \quad [12]$$

$$\hat{y}_2 = 112129 + 2534x_1 + 1635x_2 - 12628x_3 + 6917x_4 + 3526x_5 - 8717x_1x_3 + 3268x_2x_3 \quad [13]$$

$$\hat{y}_3 = (154.64 - 2.512x_1 - 5.837x_2 + 18.162x_3 + 54.887x_4 - 9.412x_5 + 7.112x_1x_3 - 5.362x_2x_3) \cdot 10^{-3} \quad [14]$$

$$\hat{y}_4 = 13.237 - 1.462x_1 - 8.525x_2 - 0.288x_3 - 1.15x_4 - 2.95x_5 + 0.587x_1x_3 - 0.9x_2x_3 \quad [15]$$

The b_1 coefficients in the $\hat{y}_1$ equation and b_1, b_3, b_4, b_{13}, and b_{23} in the $\hat{y}_4$ equation appeared to be statistically insignificant. All estimates of the regression coefficients for functions $\hat{y}_2$ and $\hat{y}_3$ appeared to be significant, so, due to the absence of any degrees of freedom, the adequacy of these equations was not tested. After rejecting the insignificant coefficients in Eq. [12] and [15], other coefficients describe the response space adequately. In spite of initial suppositions, the silicofluoride content of the bath (from 2 to 6 g/liter) appeared to have an insignificant effect on the current efficiency of chromium and on the gloss coating. The effect of the silicofluorides on the electrical energy consumption and rate of covering is unfavorable. However, a relatively high value of the b_{13} coefficient, which is a combined estimate of interactions of the silicofluoride concentration and sulfate concentration as well as of the temperature and current density, may indicate a favorable effect of the silicofluorides together with the sulfates on y_1, y_2, and y_3.

An influence similar to that of the silicofluorides is exerted on the investigated values by the bath temperature. Its increase affects adversely y_1, y_3, and y_4 and also increases the energy consumption y_2. In all equations, the effect of temperature appeared to be significant. The temperature range from 30° to 50°C is found to have an extremely negative effect on the gloss of the coating y_4. A similar negative effect of temperature in this range on the smoothness of coating obtained at the current density of 370 A/dm^2 at the sulfate electrolyte flow was found by Suzuki *et al.* (4). The highest roughness was exhibited by the coatings prepared over the temperature range from 50° to 65°C. Contrary to the effect of the temperature and silicofluoride concentration, the sulfuric acid concentration has a favorable effect on the optimization parameters. An increase of the concentration of H_2SO_4 increases considerably y_1 and y_3 and decreases y^2. The effect of the concentration of H_2SO_4 on y_4 appeared to be insignificant.

The assumed current density range exerts the strongest influence on the plating rate y_3 resulting in a high asymmetry of the equation. Certain significant coefficients are lower by one order of magnitude than the b_4 coefficient at the current density. Therefore, the coefficients in the equation for $\hat{y}_3$ should be treated with caution. An increase in current density from 200 to 400 A/dm^2 increases slightly y_1 but, at the same time, increases y_2, mainly as a result of the increased voltage between the cathode and anode. The effect of current density on y_4 appeared to be insignificant. An increase in the disk electrode speed from 30 to 60 rps was found to exert a slightly negative effect on y_1, y_3, and y_4 and a favorable effect on y_2. In spite of the negative effect of increasing the electrode speed over the assumed range on all optimization parameters, it was not possible to obtain satisfactory coatings of uniform thickness at the same other parameters under stationary conditions. Chromium coatings deposited on the platinum disk at 300 A/dm^2, 40°C, K_2SiF_6 concentration of 4 g/liter and H_2SO_4 concentration of 2 g/liter (2^{5-2} design center) but without rotating the electrode, were gray, brittle, and had no adhesion to the base. The bottom limit of the electrode speed, 30 rps, was assumed because at lower speeds the disk electrode was blocked by hydrogen bubbles, particularly at higher current densities.

Application of a high fractionality design (which is highly saturated), such as the 2^{5-2} design, provides, a rapid response in the form of assumed functions at a small number of points (8 points for 5 factors) but, at the same time, such a design has a low resolving power. The linear coefficients are estimated here in conjunction with the two-factor interactions which appeared to be significant. Therefore, in this design, one should take into consideration a considerable adulteration of the effect of particular factors on the optimization parameters. Since the effect of the K_2SiF_6 concentration on the optimized parameters did not appear to be very significant and for technological reasons it is advantageous to introduce excess silicofluorides to saturate the bath, in further studies a bath containing 20 g/liter K_2SiF_6 was used.

In light of the results obtained in the next design, we decided to lower the basic level, to decrease the level of temperature variations, and to increase the basic level with the same interval of H_2SO_4 variations. In order to emphasize the effect of the electrode speed on the optimized parameters, we decided to increase their basic level and to enlarge the interval of variations. Although the favorable effect of increased current density on the

plating rate and current efficiency suggests that it should be increased, the formation of dendrites and lower adhesion of coating at current densities exceeding 400 A/dm² suggested keeping constant both the basic level and interval of variations in the subsequent design.

This time the 2^{4-1} design was accomplished for four factors. The factorial space for this design, together with the values of levels and intervals of variations, is given in Table III. Apart from the same optimization parameters $y_1 - y_4$ as in the previous design, an additional parameter y_5 (microhardness) was adopted for this design. The following regression coefficients were obtained [y_5 (kg/mm²) is the microhardness. It was determined by Vickers' method under the load of 0.1 kg.]

$$\hat{y}_1' = 43.50 + 1.487x_1 + 0.612x_2 + 1.975x_3 - 3.825x_4 + 0.325x_1x_2 + 2.337x_1x_3 + 0.537x_2x_3 \quad [16]$$

$$\hat{y}_2' = (107.28 - 4.23x_1 - 5.78x_2 + 5.360x_3 + 9.7x_4 + 1.21x_1x_2 - 6.42x_1x_3 - 2.76x_2x_3) \cdot 10^3 \quad [17]$$

$$\hat{y}_3' = (166.68 + 8.47x_1 + 2.98x_2 + 62.17x_3 - 14.87x_4 - 6.01x_1x_2 + 10.63x_1x_3 + 2.79x_2x_3) \cdot 10^{-3} \quad [18]$$

$$\hat{y}_4' = 19.38 - 2.17x_1 + 7.96x_2 - 4.67x_3 - 3.52x_4 + 1.21x_1x_2 - 2.27x_1x_3 - 3.02x_2x_3 \quad [19]$$

$$\hat{y}_5' = 1127.56 + 17.56x_1 - 82.68x_2 + 14.83x_3 - 19.56x_4 - 3.18x_1x_2 - 0.31x_1x_3 - 29.31x_2x_3 \quad [20]$$

On rejecting the insignificant coefficients, the equations assumed the following form

$$\hat{y}_1' = 43.50 + 1.487x_1 + 1.975x_3 - 3.825x_4 + 2.337x_1x_3 \quad [21]$$

$$\hat{y}_2' = (107.28 - 4.23x_1 - 5.78x_2 + 5.36x_3 + 9.70x_4 - 6.42x_1x_3) \cdot 10^3 \quad [22]$$

$$\hat{y}_3' = (166.68 + 8.47x_1 - 62.17x_3 - 14.87x_4 - 6.01x_1x_2 + 10.63x_1x_3) \cdot 10^{-3} \quad [23]$$

$$\hat{y}_4' = 19.38 - 2.17x_1 - 7.96x_2 - 4.67x_3 - 3.52x_4 - 2.27x_1x_3 - 3.02x_2x_3 \quad [24]$$

$$\hat{y}_5' = 1127.56 + 17.56x_1 - 82.68x_2 + 14.93x_3 - 19.56x_4 - 29.31x_2x_3 \quad [25]$$

These equations adequately describe the experimental results. A comparison of the 2^{5-2} and 2^{4-1} designs shows that all optimization parameters were considerably improved. First of all, the absolute values of the free b_0 terms which in these designs are mean values of measurements, were increased. This profit results mainly from a decrease in temperature and increase in the concentration of H_2SO_4 in the bath. Unexpectedly, in the 2^{4-1} design for equations $\hat{y}_1'$ and $\hat{y}_3'$ the estimate of the coefficient changed its sign at temperature (b_2) from (−) to (+) in the 2^{5-2} design and for the $\hat{y}_2'$ equation from (+) to (−). This fact might be explained by a positive interaction of temperature with the concentration of K_2SiF_6 in the bath. As mentioned previously in the 2^{4-1} design K_2SiF_6 was added to saturation and, as is well known, its concentration in solution increases with temperature. The values of estimates for the b_1 coefficients in the 2^{4-1} design decreased considerably for $\hat{y}_1'$, $\hat{y}_2'$, and $\hat{y}_3'$, which might indicate that the plot of these parameters *vs.* the concentration of H_2SO_4 is flattened on increasing this concentration. In the second design, the estimate of the b_1 coefficient in the equation for $\hat{y}_4'$ appeared to be significant. The nature of the relationship of optimized parameters with current density was unchanged, in principle, for both designs.

An increase in the interval of variations and increase in the basic level of electrode speed resulted in an increase of absolute values and regression coefficients in the 2^{4-1} design without changing their signs. In the second design, an additional optimization parameter was microhardness (y_5). Its mean value of 1127 kg/mm² is, in principle, consistent with the values reported by other investigators for this type of bath. From the analysis of the estimates of regression coefficients it is seen that microhardness of coatings decreases considerably with increasing temperature and less rapidly with increasing rotational speed in the intervals assumed. On the other hand, microhardness increases with increasing H_2SO_4 concentration and current density. A considerable value in the equation for $\hat{y}_5'$ was reached by the combined estimate of interactions (aliases) of the concentration of H_2SO_4 and rotational speed as well as of temperature and current density. A comparison of microhardness values for these interactions, for the case when both the factors are at the lower level as well as when both are at the higher level, shows that the main contribution is the interaction of temperature and current density.

Based on the analysis of the results of both designs a decision was made to describe, in a detailed way, the response surface in the factorial space of the 2^{4-1} design. To this end the CCOD discussed earlier was accomplished. Its estimates of the regression coefficients are summarized in Table IV. After rejection of insignificant estimates, other estimates describe adequately the experimental data for the $\hat{y}_1''$, $\hat{y}_2''$, and $\hat{y}_4''$ models, but the $\hat{y}_3''$ model appeared to be inadequate. This may be explained as a result of a too-large asymmetry of the regression coefficient estimates caused by a too-large interval of variations assumed for the current density.

Because of high labor consumption involved in the determination of microhardness, this parameter was not determined in this design. The difference in estimates of the free b_0 terms in the CCOD with respect to the

Table IV.

	Current efficiency (%) $\hat{y}_1''$	Electrical energy consumption (kJ/kg) $\hat{y}_2'' \times 10^{-3}$	Plating speed (μm/sec) $\hat{y}_3'' \times 10^3$	Gloss (%) $\hat{y}_4''$
b_0	49.773	90.4400	186.324	15.93
b_1	1.7512	−4.3319	12.709	−2.63
b_2	0.6303	−5.0003	5.872	6.39
b_3	1.2360	6.8480	43.670	−4.38
b_4	−1.7394	3.8396	−2.080	(0.37)
b_{12}	(−0.3250)	1.1969	−2.750	0.84
b_{13}	1.2812	−3.7781	3.000	−1.98
b_{14}	−0.9750	1.6531	−3.937	−0.98
b_{23}	1.5125	−4.4344	6.125	−2.04
b_{24}	1.0562	−2.7531	(1.062)	(−0.29)
b_{34}	(0.0000)	(0.0281)	−2.187	(0.36)
b_{123}	−1.8125	5.1719	(−1.250)	−3.95
b_{124}	0.7437	−1.7594	−17.690	−0.77
b_{134}	(0.0500)	(−0.6969)	(1.187)	1.52
b_{234}	(0.0562)	(−0.1156)	8.063	(0.06)
b_{1234}	(0.3812)	1.4656	2.937	(0.36)
b_{11}	−1.0645	3.0812	−3.140	(0.31)
b_{22}	−1.7020	4.6437	−5.515	2.16
b_{33}	−1.4520	3.0562	−3.040	1.48
b_{44}	−1.6220	4.4562	−5.265	−0.84

(. . .) — statistically insignificant estimates were determined.

estimates from the 2^{4-1} design is mainly due to a large value of the quadratic terms (see the method of calculating b_0 in the CCOD). At the same time, this confirms the advisability of the second order design for description of the selected response surfaces. The estimates of linear coefficients were also changed, which was caused by separation of the linear effects from the second order interactions in the CCOD with respect to the 2^{4-1} design. The estimates of the two-factor interactions and also some of the three-factor interactions in all four mathematical models appeared to be very significant and comparable with the estimates of linear effects. This is indicative of the complex effects of the selected factors on the electrolytic chromium plating process.

In discussing regression equations, we have focused on the remarks and conclusions essential for our further studies. The reader interested in optimum (extremal) values of the given model functions may find an answer to his questions by solving differential equations. By applying the method of steepest ascent, one may also obtain information about directions of changes of particular model functions. The application of extrapolation with respect to the functions given makes it possible to get the answer concerning the values of a given parameter beyond the sphere presented in the paper. To sum up, one should note that the chromium plating speed is affected to the greatest extent by current density whose increase also increases the current efficiency but at the same time the electrical energy consumption rises and the coating gloss decreases. The second factor which affects the assumed parameters is H_2SO_4.

With its increasing concentration in the bath the current efficiency, plating speed, and microhardness increase, whereas the electrical energy consumption and gloss decrease. Temperature has the greatest influence on microhardness and gloss of the coatings. With increasing temperature, the microhardness is lowered and the gloss is increased. Although an increase in the electrode speed reduces all the optimized parameters over the interval of variations under investigation, at the same time the electrolyte flow through the cathode compartment is necessary to prepare technically useful coatings at high current densities.

Summary

The object of the paper is to detect cooperation of parameters of chromium plating at high current densities, which studied with electrochemical methods would allow us to determine the mechanism of the process. It was found that the addition of fluorosilicate ions to the bath containing chromic acid anhydride and sulfate ions, which considerably increases current efficiency and quality of the chromium coating under stationary conditions, has a much smaller effect at higher current densities of 200-400 A/dm^2 when the flowing electrolyte is applied. The current efficiency of chromium obtained under such conditions was equal to about 50%, and it increased with increasing concentration of sulfate ions in the electrolyte and increasing current density. By the application of mathematical methods, it was found that at least the same effect as that of the above-mentioned factors is exerted on the current efficiency by cooperation of two or more factors, *e.g.*, temperature and current density or concentration of sulfate ions, temperature, and current density. Additional parameters introduced during our investigations, such as unitary energy consumption, chromium deposition rate, gloss, and microhardness of chromium coatings, confirm the thesis of a complex effect of temperature, current density, electrolyte composition, and hydrodynamic conditions on the process parameters and quality of the coatings obtained.

Since the criteria of the optimum process are always to a great extent arbitrary, no optimum process conditions are given. They may easily be found by formulating the demanded criteria and making use of the regression equations given in our paper.

Manuscript submitted Jan. 11, 1982; revised manuscript received Feb. 16, 1983.

Any discussion of this paper will appear in a Discussion Section to be published in the June 1984 JOURNAL. All discussions for the June 1984 Discussion Section should be submitted by Feb. 1, 1984.

REFERENCES

1. J. P. Hoare, A. H. Holden, and M. A. LaBoda, *Plating Surf. Finishing*, **67**, 42 (1980).
2. D-T. Chin, *ibid.*, **64**, 57 (1977).
3. A. D. Davydov, A. Ya. Ryaboi, and V. D. Kascheev, *Soviet Electrochem.*, **9**, 1299 (1973); USSR Pat. 264094 (1977).
4. S. Suzuki *et al.*, U.S. Pat. 4,080,268 (1978).
5. N. P. Koval, G. M. Galperin, A. B. Bernstein, Yu. N. Petrov, and G. N. Zaidman, *Elektron. Obrab. Mater.*, **2**, 42 (1972).
6. M. A. LaBoda, *Plating Surf. Finishing*, **66**, 50 (1979).
7. Yu. V. Pleskov and V. Yu. Filinovskiy, "Vrashchayushchiysya Diskoviy," pp. 222-247, Elektrod, Nauka, Moscow (1972).
8. E. Müller, *Z. F. Elektrochem.*, **32**, 399 (1926).
9. G. J. Sargent, *Trans. Electrochem. Soc.*, **37**, 479 (1920).
10. J. P. Hoare, *This Journal*, **126**, 190 (1979).
11. C. G. Fink, U.S. Pat. 1,581,188 (1926); 1,802,463 (1931).
12. R. Bilfinger, "Das Hartverchromungs," 2nd ed., p. 43, Verfahren, Leipzig (1942).
13. R. A. Fisher, "The Design of Experiments," Oliver and Boyd, Edinburgh (1935).
14. G. E. Box and K. B. Wilson, *J. Royal Statistical Society*, **B13**, 1 (1951).
15. V. V. Nalimov and N. A. Chernova, "Statystychne Metody Planovania," pp. 7-92, Dosviadchen Ekstremalnych, WNT Warsaw (1967).
16. P. W. M. John, "Statistical Design and Analysis of Experiments," p. 157, Canada (1971).
17. "Experimental Designs in Industry," V. Chow, Editor, p. 80, J. Wiley and Sons, Canada (1958).

Compositions of Electroless Nickel Plating Baths by ^{31}P NMR Spectroscopy

D. J. Eustace* and K. D. Rose

Exxon Research and Engineering Company, Solar Energy Conversion Unit and Analytical and Information Division, Linden, New Jersey 07036

ABSTRACT

Phosphorus-31 nuclear magnetic resonance spectroscopy has been used to determine the $H_2PO_2^-$ and HPO_3^- concentrations of electroless Ni plating baths. The ^{31}P NMR resonances of $H_2PO_2^-$ and HPO_3^{2-} are narrow and resolvable in alkaline solution, appearing at +8.0 and +4.7 ppm with respect to neat phosphoric acid, and are the only resonances detected in fresh and spent plating bath solutions. In the presence of proton coupling, these resonances appear as multiplets due to direct proton coupling, with characteristic coupling constants: $^1J(^{31}P\text{-}^1H)$ = 517.6 Hz for $H_2PO_2^-$ and = 566.4 Hz for HPO_3^{2-}. Although the compositions of alkaline baths can be monitored without additional sample treatment, the phosphorus resonances in acid baths are broad and overlapped indicating that the phosphite anions can compete and exchange with solvent molecules for solvation positions about the paramagnetic Ni^{2+}. Strong Ni^{2+}- complexing agents, like $EDTA^{2-}$ and NH_3, are effective in displacing the phosphorus-containing ligands from the Ni^{2+} coordination sphere, thus permitting species determination by ^{31}P NMR. Compositions of the phosphorus species of Ni plating baths obtained by this method are reported and compared to results obtained by the traditional titration method. Monitoring of the $H_2PO_2^-$ and HPO_3^{2-} levels as a function of bath use is demonstrated using this approach.

The concentrations of hypophosphite ($H_2PO_2^-$) and orthophosphite (HPO_3^{2-}) must be strictly monitored for optimum operation of electroless nickel plating baths. For the deposition of nickel on silicon, the $H_2PO_2^-$ interacts with the surface which has been sensitized with a hydrogenation-dehydrogenation catalyst, such as Ni, Pd, Au, and Co. The reactive intermediate, which forms (1) subsequently, reduces Ni^{2+} to form the nickel deposit. It also reacts with itself to produce H_2 gas, which is evolved from the bath, and elemental phosphorus, which becomes incorporated into the plated nickel layer. In all cases, more mols of $H_2PO_2^-$ than Ni^{2+} are consumed.

During normal plating bath operation, the concentration of HPO_3^{2-} increases with the number of wafers plated. Although $Ni(H_2PO_2)_2$ is readily soluble in the aqueous plating solution, the nickel orthophosphite and phosphite have low solubility [for example, $NiHPO_3$ solubility: 0.29g/100 cm^3 at 50°C (2)] and can precipitate under typical bath operating conditions. In addition to reducing the total nickel concentration in solution, these insoluble salts provide nucleation sites for spontaneous bath decomposition. Commercial nickel plating baths contain nickel ion complexing reagents, such as lactate, that help delay the onset of precipitation and bath decomposition. Bath life can be extended by regular monitoring and replenishment of plating bath components.

The $H_2PO_2^-$ concentration in an electroless plating bath can be monitored by an indirect iodometric titration (3). Alternatively, an indirect cerimetric titration method (4), where $H_2PO_2^-$ is oxidized by iron (III) giving iron (II), which in turn is oxidized by cerium (IV), can be used. Quantitative hydrogen evolution, polarography, and kinetic colorimetry have also been reported (3). None of these techniques, however, can quantitatively measure the $H_2PO_2^-$ and HPO_3^{2-} concentrations simultaneously and nondestructively. For this reason an NMR spectroscopic technique has been developed, which can be used to characterize electroless nickel baths.

Phosphorus-31 NMR spectroscopy is a convenient and nondestructive method which can be used to identify phosphorus-containing species. Several properties of the NMR experiment make this technique particularly attractive for routine plating bath analysis. Under typical measurement conditions, ^{31}P NMR studies can be performed at phosphorus levels higher than about 1 mM, generally using less than 2 ml of solution. The ^{31}P resonances associated with phosphate and phosphite bath components are narrow (less than 0.1 ppm), yet span roughly 50 ppm in chemical shift values about the reference signal of H_3PO_4. The correlation of chemical shift values with subtle molecular structure changes are well documented for phosphorus species (5). In addition to relative intensities of phosphorus resonances and their characteristic chemical shift values, the phosphorus nuclei are sensitive to neighboring (covalently bonded) magnetic nuclei, such as ^1H, and certain paramagnetic metal cations, such as Ni^{2+}. Nuclear interactions are manifested by multiplet splitting patterns of characteristic magnitudes; paramagnetic interactions are indicated by a broadening and shifting of the phosphorus resonances which sample the paramagnetic environment. Thus, each of the phosphorus-containing species present in the original bath or generated by metal deposition can be simultaneously identified and quantitatively measured using ^{31}P NMR. In order to avoid ambiguity in the NMR experiment, the resonances of phosphate, hypophosphite, and orthophosphite species have been assigned by evaluating the characteristic hydrogen-phosphorus interactions or couplings as well as the chemical shift values. We report here the application of ^{31}P NMR to plating bath technology for monitoring the consumption of $H_2PO_2^-$ in alkaline and acid nickel plating baths. The results obtained by this technique are compared to those obtained using traditional analytical methods.

Experimental

^{31}P NMR.—The NMR measurements were made using a JEOL-FX-900 spectrometer operating at 36.27 MHz for ^{31}P. The magnetic field was externally locked to deuterium oxide. Acquisition conditions used in these experiments included a 10 μsec rf pulse (about 45° flip angle) a 2.0 sec delay between acquisitions, and gated proton decoupling. Other spectra obtained using longer repetition delays gave identical peak ratios. About 30 min of data collection per spectrum was required. The plating bath solutions were examined as received using 10 mm NMR tubes. Chemical shift values are referenced to neat phosphoric acid.

Optical spectroscopy.—Optical spectra were taken on solutions contained in 1 cm path length cuvettes using a Cary 17 spectrophotometer operating over the spectral range 350-1300 nm at ambient temperature.

* Electrochemical Society Active Member.

Key words: electroless deposition, ^{31}P NMR, semiconductor, solar.

Alkaline nickel plating bath.—The initial bath was composed of a stock solution comprising the following reagent grade chemicals: 65 g · liter^{-1} ammonium citrate, 60 g · liter^{-1} ammonium chloride, 30 g · liter^{-1} nickel chloride, and 12 g · liter^{-1} sodium hypophosphite, adjusted to pH ~ 9.5 by ammonium hydroxide. The total volume of the bath was 1.8 liter. Properly sensitized, 100 cm^2 silicon solar cells were processed individually through the bath at 88°C for 10 min. Aliquots were withdrawn at intervals after the bath had cooled to 25°C and had been adjusted in volume and pH. Samples were studied by energy dispersive x-ray fluorescence, iodometry, and ^{31}P NMR spectroscopy.

Acid nickel plating baths.—Experiments were performed on a 1.8 liter Enthone® NI-410 (Enthone Incorporated, New Haven, Connecticut) plating bath and an 11 liter Niklad 1000 (Allied Kelite Division of the Richardson Company, Des Plaines, Illinois) plating bath. ^{31}P NMR and optical spectra were obtained on 2-5 cm^3 aliquots taken at selected stages during use. Reagent grade di-sodium ethylenediaminetetraacetate was used to make an EDTA solution for the nickel complexation studies. It was determined to be 0.25*M* based on titration with a standard zinc bromide solution.

Results and Discussion

Alkaline nickel bath studies.—Aliquots of the alkaline nickel bath described in the experimental section were taken at intervals as silicon wafers were processed through the bath. These aliquots were subjected to several analytical tests including elemental Ni and P analyses, iodometric titration, optical spectroscopy, and ^{31}P NMR. The ^{31}P NMR spectrum of the fresh plating solution showed a single sharp resonance at +8.0 ppm with respect to neat phosphoric acid. The aliquot, sampled after 22 wafers had been processed, showed resonances at +8.0 and +4.7 ppm (Fig. 1a), which were assigned to the $H_2PO_2^-$ starting reagent and HPO_3^{2-} oxidation product, respectively. No additional resonances were detected in this or other aliquots. To confirm these resonance assignments, the ^{1}H-coupled ^{31}P spectrum (Fig. 1b) was obtained and compared to the ^{1}H-decoupled result. The large one-bond, phosphorus-hydrogen couplings and characteristic triplet and doublet coupling patterns are consistent with the $H_2PO_2^-$ and HPO_3^{2-} assignments. The chemical shift values and coupling constants are also consistent with literature values for the sodium salts of these anions in aqueous solution (6). The spectra, obtained for aliquots sampled through 66 wafers processed, are compared in Fig. 2. The peak intensity

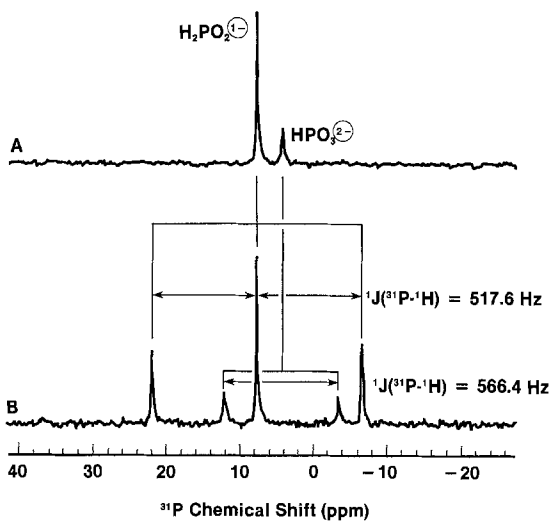

Fig. 1. (A) ^{1}H-decoupled and (B) ^{1}H-coupled ^{31}P NMR spectra of the electroless nickel plating solution after processing 22 wafers.

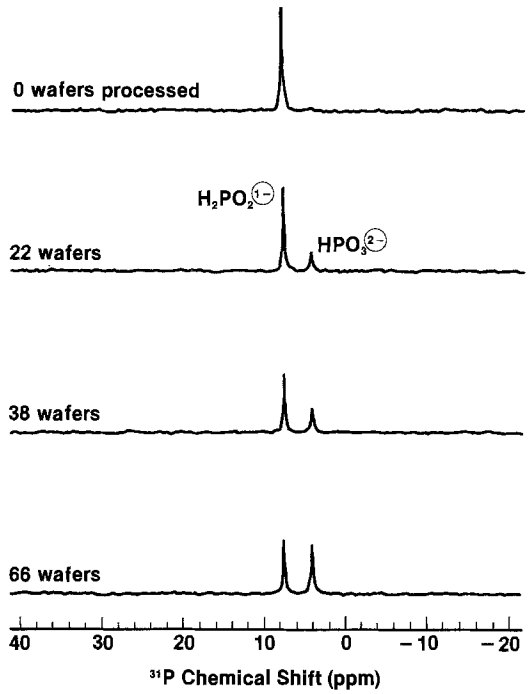

Fig. 2. ^{1}H-decoupled ^{31}P NMR spectra of electroless nickel plating solutions.

data were used to obtain the distribution of $H_2PO_2^-$ and HPO_3^{2-}.

Table I summarizes bath compositions for these same samples using the solution density (1.14 g/cm^3) and elemental analyses. Hypophosphite and orthophosphite concentrations, obtained by combining XRF determinations and ^{31}P NMR peak ratios, are compared to results from iodometric titration measurements of the hypophosphite concentration. The $H_2PO_2^-$ results determined by NMR and elemental analyses agree very well with iodometric titration.[1]

No conclusive statement can be made about the relative rates of the nickel deposition and the two side reactions based on the data presented. It can be observed that different amounts of $H_2PO_2^-$ were consumed per wafer in each interval and different amounts of phosphorus were lost from the plating bath by incorporation into the nickel deposit as the bath was used. A comprehensive study which would yield a detailed mass balance might include nickel metal composition determinations (Ni/P) and hydrogen gas analyses.

Acid nickel bath studies.—Aliquots of the acid nickel plating baths, described in the experimental section, were taken at intervals as silicon wafers were processed through the baths. The ^{31}P NMR spectrum of the freshly prepared Enthone 410 solution showed a single, broad resonance at 12.0 ppm with respect to neat phosphoric acid (Fig. 3a). The downfield shift and broadening of the phosphorus resonance in this spectrum are due to paramagnetic ion interactions between phosphorus-containing ions and Ni^{2+} in solution. Addi-

[1] Absolute concentrations of hypophosphite and orthophosphite could also be determined by ^{31}P NMR using weighed additions of sample and a suitable phosphorus-containing reference material. This approach was not used here but would eliminate the need for the quantitative XRF results.

Table I. Determinations of nickel and phosphorus species concentrations in an alkaline plating bath

Number of wafers processed	[Ni^{2+}]	XRF [P_{total}] (M)	XRF and [$H_2PO_2^-$]	^{31}P NMR [HPO_3^{2-}] (M)	Iodometry [$H_2PO_2^-$] (M)
0	0.11	0.101	0.101		0.09 ± 0.02
22	0.10	0.091	0.067	0.024	0.06 ± 0.02
38	0.091	0.088	0.054	0.034	0.05 ± 0.02
66	0.086	0.085	0.033	0.052	< 0.03

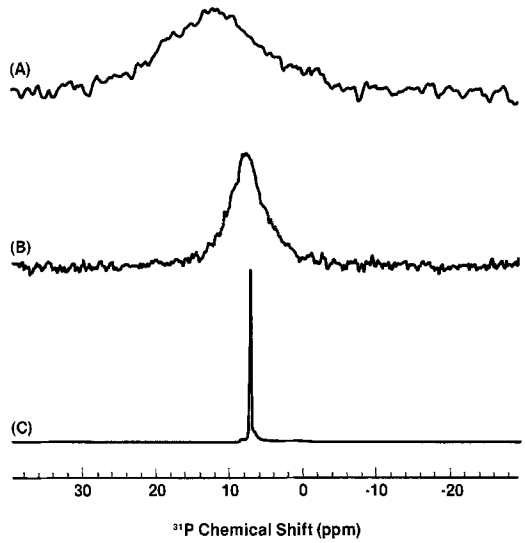

Fig. 3. Effect of $EDTA^{2-}$ addition on an unused acid nickel plating bath (Enthone 410). (A) 1.1 meq Ni^{2+}, (B) 1.1 meq Ni^{2+} and 0.5 meq EDTA, and (C) 1.1 meq Ni^{2+} and 2.5 meq EDTA.

tion of $EDTA^{2-}$ (equivalent ratio 2.5:1.1::$meq_{EDTA^{2-}}$:$meq_{Ni^{2+}}$) sharpens and shifts upfield the resonance signal (Fig. 3c). This result could be caused by two effects. The Ni^{2+} ions could be converted from octahedral and paramagnetic to four-coordinate and diamagnetic by $EDTA^{2-}$ coordination. Alternatively, the nickel ions could become fully coordinated by the $EDTA^{2-}$ ligands. The strength of the nickel $-EDTA^{2+}$ interaction (log K = 17.5) and steric factors would prevent the phosphite anions from entering the nickel first coordination sphere. Either mechanism would prevent phosphite anions from interacting with paramagnetic nickel ions and result in sharp phosphorus resonances which appear at the chemical shift positions observed in alkaline solutions.

Optical spectra of the solutions (Fig. 4) confirms that the resonance line narrowing is due to displacement of the phosphite anion by $EDTA^{2-}$ ligands. Most octahedral nickel complexes are paramagnetic, appearing yellow, green, or blue with different ligands depending on the ligand position in the spectrochemical series. These complexes give rise to absorption spectra with three bands at 7.-13. $\times 10^3$, 11.-20. $\times 10^3$, and 20.-28. $\times 10^3$ cm^{-1} (9). The freshly prepared, acid nickel solution is green and has three absorption bands at 8.7 $\times 10^3$, 14. $\times 10^3$, and 25. $\times 10^3$ cm^{-1}. The Ni^{2+} solution to which $EDTA^{2-}$ has been added shifts to blue with absorption bands at 10. $\times 10^3$, 16. $\times 10^3$, and 26. $\times 10^3$ cm^{-1}. Since diamagnetic nickel complexes are red or orange and have two absorptions at 15.-23. $\times 10^3$ and 23.-27. $\times 10^3$ cm^{-1}, the optical absorption spectra support the conclusion that the nickel-$EDTA^{2-}$ complex is octahedral under these conditions.

The importance of this result is that the phosphite anions can be prevented from interacting with the paramagnetic nickel ion, without adjusting the solution pH, giving rise to ^{31}P NMR spectra equivalent to those observed in alkaline plating baths. This makes possible analysis of both $H_2PO_2^-$ and HPO_3^{2-} in a plating bath. Practical application of ^{31}P NMR and nickel complexation to partially processed and spent Enthone nickel plating solutions is shown in Fig. 5. Both solutions were treated with the $EDTA^{2-}$ solution as described above before the spectra were taken. The figure shows that in these acid nickel plating baths, HPO_3^{2-} is the only oxidation product detected and its concentration can be monitored in the presence of unoxidized $H_2PO_2^-$ anion.

Conclusions

It has been shown that ^{31}P NMR spectroscopy can detect $H_2PO_2^-$ and HPO_3^{2-} and be used to analyze their concentrations in alkaline electroless nickel plating baths nondestructively. In acid nickel baths, however, the phosphorus resonances are broadened and overlapping due to interaction of the phosphite ligands with the Ni^{2+} coordination sphere positions. This result demonstrates that the phosphite ligands which occupy Ni^{2+} coordination positions in acid solution are prevented from doing so by NH_3 in alkaline solutions. To perform the NMR analyses for acid solutions, the phosphite ligands must first be displaced from the Ni^{2+} environment by complexing the metal ion with reagents, such as $EDTA^{2-}$. The ^{31}P NMR spectra can then be interpreted in the same way as alkaline bath results.

Hypophosphite concentrations obtained by ^{31}P NMR and elemental analyses compare well to results obtained by iodometry. Thus, ^{31}P NMR is a useful approach for investigating the phosphorus species distribution resulting from plating bath use.

^{31}P NMR analysis should be useful for determining replenishment schedules for the addition of hypophosphite and for monitoring the performance of electroless nickel baths. It also makes possible correlations between plating quality and the state of the plating bath. The ^{31}P NMR approach for determining $H_2PO_2^-$ and HPO_3^{2-} should be useful for all hypophosphite-driven, electroless metal reduction systems. ^{11}B NMR analysis of boron-containing, reducing-reagent baths should provide the same kind of information for electroless plating baths.

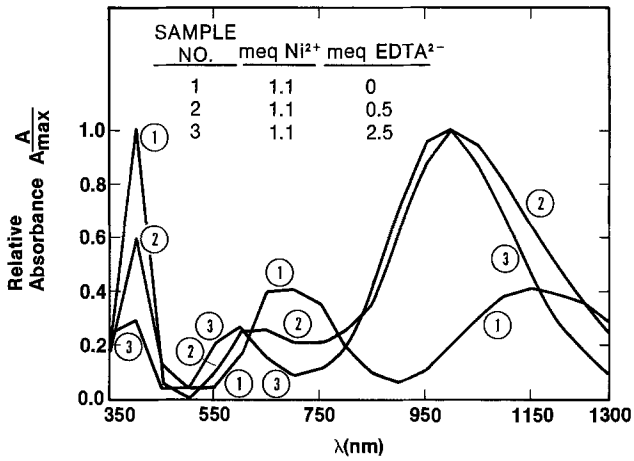

Fig. 4. Relative absorbance of electroless nickel plating solutions as a function of amount of $EDTA^{2+}$ added.

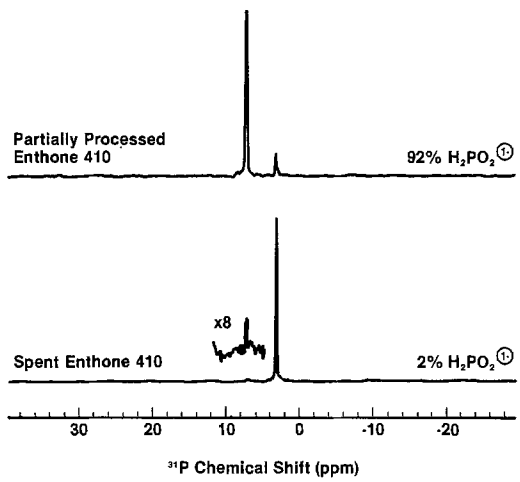

Fig. 5. ^{31}P NMR of an acid nickel plating bath at different stages of bath use after addition of $EDTA^{2-}$.

This paper is dedicated to Professor E. Grunwald on the occasion of his 60th birthday.

Acknowledgments

The authors wish to acknowledge the capable experimental assistance of J. V. Vieira and R. J. Lusher.

The samples resulted from constructive interactions with Mr. M. Schneider, E. Bucker, and Dr. R. W. Francis. We wish to express our thanks to Dr. J. A. Amick for his encouragement during the course of this work.

Manuscript received March 7, 1983.

Any discussion of this paper will appear in a Discussion Section to be published in the June 1984 JOURNAL. All discussions for the June 1984 Discussion Section should be submitted by Feb. 1, 1984.

Exxon Research and Engineering Company assisted in meeting the publication costs of this article.

REFERENCES

1. M. V. Sullivan and J. H. Eigler, *This Journal*, **104**, 226 (1956); H. Iwasa, M. Yokozawa, and I. Teramoto, *ibid.*, **115**, 485 (1968).
2. G. Gutzeit, *Plating*, **46**, 1158, 1275, 1377 (1959); **49**, 63 (1960).
3. J. P. McCloskey, *ibid.*, **51**, 689 (1964).
4. Reviewed in K. M. Gorbunova, A. A. Nikiforova, and G. A. Sadakov, "Achievements of Science: Chemistry, Electrochemistry, 1965," S. S. Kruglikov, Editor (1965).
5. M. M. Critchfield, C. H. Dungan, J. H. Letchev, V. Mark, and J. R. Von Water, "^{31}P Nuclear Magnetic Resonance," John Wiley and Sons, New York (1967).
6. M. M. Critchfield, C. H. Dungan, J. H. Letchev, V. Mark, and J. R. Von Water, "^{31}P Nuclear Magnetic Resonance," pp. 289-290, John Wiley and Sons, New York (1967).

Semiconductor Electrodes

XLIX. Evidence for Fermi Level Pinning and Surface-State Distributions from Impedance Measurements in Acetonitrile Solutions with Various Redox Couples

G. Nagasubramanian, B. L. Wheeler, and A. J. Bard*

Department of Chemistry, University of Texas, Austin, Texas 78712

ABSTRACT

Capacitance-voltage (C-V) measurements were made for the single crystal semiconductors n-TiO_2, n-CdS, n-InP, p-Si, p-GaAs, n- and p-WSe_2, and n-$MoSe_2$ in acetonitrile containing a number of redox couples whose potentials (V_{redox}) spanned a potential regime much wider than the bandgaps. The flatband potential (V_{FB}) evaluated from capacitance-potential (C-V) measurements (Mott-Schottky plots) exhibited three types of behavior with varying solution redox potentials: (*i*) V_{FB} varied monotonically with V_{redox} for p-Si, p-GaAs, and n-InP; (*ii*) for n-TiO_2 and n-CdS, V_{FB} did not shift for couples located negative of the midgap potential, but varied monotonically for couples positive of this value; (*iii*) for the layer-type, compounds ($MoSe_2$, WSe_2), V_{FB} was almost independent of V_{redox}. These differences were ascribed to differences in surface-state densities. For n-TiO_2 crystals, (001) face etched with molten $KHSO_4$ and reduced, evidence for surface states at two different potentials was obtained from the in-phase component of the total admittance. Tentative assignment of these states is to lattice defects. The states closer to the conduction band are assigned to oxygen vacancies and the deeper states to Ti (III). The densities of surface states (N_{ss}) evaluated from G_p/ω *vs.* ω plots for TiO_2 and p-Si are around 10^{10} and 10^{13} cm^{-2}, respectively. These two values represent different situations, *i.e.*, while the former value of N_{ss} is not sufficient for pinning the Fermi level, the latter value is sufficiently high for the occurrence of Fermi level pinning.

There has been increasing evidence, based on measurements of open-circuit photopotentials (V_{oc}) developed by semiconductor electrodes, that the model for the semiconductor/liquid interface (1), in which the bandedges remain fixed in the presence of different redox couples, often does not hold. The observed effect is that V_{oc} is relatively independent of V_{redox}, the potential of the redox couple in solution. This has been ascribed to Fermi level pinning (FLP) (2) in the presence of a high density of interface or surface states. Under these conditions, a change in potential across the semiconductor/solution interface is largely absorbed by a change in the potential drop across the Helmholtz layer rather than across the space charge layer within the semiconductor (Fig. 1). Thus, in the presence of FLP, the flatband potential, V_{FB}, changes with V_{redox} so that $V_{oc} \approx |V_{FB} - V_{redox}|$ remains relatively constant. This shift of V_{FB} with V_{redox} has not been the subject of many investigations. Previously, we have shown by capacitance measurements that V_{FB} shifts for p-Si in MeCN solutions (3). In this paper, we extend these studies to several other semiconductor materials. We might note that FLP is also well known for semiconductor/metal junctions where the barrier height across the junction for a given semiconductor, *e.g.*, GaAs, is found to be independent of the metal work functions (4).

Even with large bandgap materials, surface states may mediate interfacial electron transfer processes in PEC cells (5-10). Surface states can also affect the efficiency of PEC cells, *e.g.*, by acting as recombination centers or by abetting dark backreactions. For example, the shape of the photocurrent *vs.* applied bias curve can be used as a measure of efficiency of a PEC cell; the precipitous increase in photocurrent near V_{FB} for n-TiO_2 etched in a special way with simmering H_2SO_4 was taken as a sign of improvement (11). Such a sharp rise to the saturation value has been attributed to an absence of recombination sites and surface states (12). The dependency of the Schottky barrier heights on metal work function with large bandgap materials, such as TiO_2 and $SrTiO_3$ solid-state devices

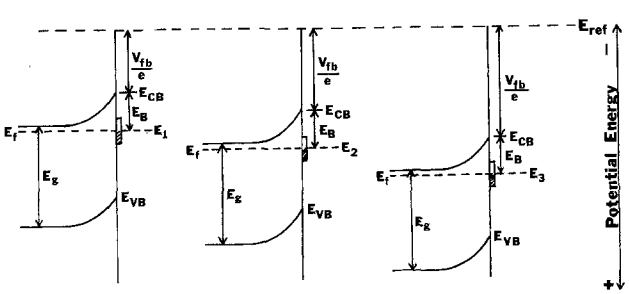

Fig. 1. Scheme 1. Position of bandedges upon variation of the redox energy level of the contacting medium (E_1, E_2, E_3) for a Fermi level pinned n-type semiconductor. E_B is invariant with E_i, while V_{FB} varies with respect to the energy level of a reference electrode, E_{ref}.

* Electrochemical Society Active Member.
Key words: capacitance, flatband potential, conductance.

(13), has been attributed to the absence of a high density of surface states. Further, the absence of surface states is sometimes assumed when frequency independent Schottky-Mott (S-M) plots (plots of C^{-2} *vs.* V, where C is capacitance) are found. However, we (14) and others (15-17) have shown that with small bandgap semiconductors, the in-phase (0°, conductance) component of the total admittance is more sensitive to the presence of surface states than the quadrature (90°, capacitance) component (see Appendix).

We report here a-c impedance studies of several single-crystal semiconductors in MeCN and show that V_{FB} shifts with V_{redox} occur with several of these. The effect of pretreatment of TiO_2 on its impedance behavior and investigation of surface states by conductance measurements are also discussed.

Experimental

The single crystals employed were n-TiO_2, n-InP, n-CdS, n- and p-WSe_2, n-$MoSe_2$, p-Si, and p-GaAs. The procedures for polishing and mounting the semiconductor electrodes have been described elsewhere (18-24) and the etching procedures are given in Table I. Two different types of TiO_2 crystals were employed. The undoped TiO_2 single crystal (Nakazumi Earth Crystals, Japan) is denoted crystal A and the Nb-doped TiO_2 crystal, obtained from H. S. Jarrett, du Pont, is denoted crystal B. Both were oriented with the (001) face exposed to solution, as ascertained by x-ray diffraction (ASTM Card No. 23-1486). Some crystals were treated by a procedure recommended by Jarrett to produce a smooth surface (treatment 1). These were polished in succession with 0.3 μm alumina and 1 μm diamond paste to produce a mirror-like surface. This surface was then etched with molten $KHSO_4$ in a Pt crucible (625°C) for 2 hr. An SEM photograph (Fig. 2) shows a very smooth surface. Since the crystals had a straw-colored appearance after the molten $KHSO_4$ etch, implying that they were oxidized, they were subjected to a reduction pretreatment before use. The Nb-doped crystals were reduced in flowing CO at 700°C for 1 hr, the undoped crystals were reduced in an H_2 atmosphere at 625°C for 20 min. These were mounted as electrodes and used without further treatment. In treatment 2, the undoped TiO_2 crystals were not etched with $KHSO_4$, but instead were only reduced in H_2 (625°C for 20 min) directly after polishing with Al_2O_3 and diamond paste. The methods of purification of the solvent acetonitrile (MeCN) and sources of redox couples are given elsewhere (18). Abbreviations of the various redox couples employed are given in Table II. Their concentrations varied from 0.1 to 30 mM. With perylene, rubrene, chrysene, and $MV(PF_6)_2$ (where MV = methyl viologen) the concentrations were about 0.1 m*M*; for $Ru(bpy)_3^{2+/+}$, and $AQ^{0/-}$ (where bpy = bipyridine and AQ = anthraquinone) they were about 0.5 and 2 m*M*, respec-

Table I. Doping density and etching procedures for different semiconductors

SC	$N_{D(A)}$/cm³	Etching procedures
TiO_2	~10^{19}	Conc HNO_3 for 1 min followed by conc HF for 10 sec, then rinsed with distilled water. This procedure was repeated twice.
CdS	~10^{17}	Conc HCl for 40 sec, then rinsed with distilled water.
n-WSe_2, n-$MoSe_2$, p-WSe_2	~10^{15}	6*M* HCl for 30 sec, then rinsed with distilled water. This procedure was repeated twice.
n-InP	~10^{16}	6*M* HCl for 30 sec, then rinsed with distilled water.
p-GaAs	~10^{15}	H_2SO_4:H_2O_2(30%):H_2O (3:1:1 by volume) solution for 5 sec, then rinsed with distilled water.
p-Si	~10^{15}	HNO_3:CH_3COOH:HF, (3:1:3 by volume) containing a drop of Br_2 per 50 ml for 30 sec followed by conc HF for 5 sec, then rinsed with distilled water.

Table II. V_{FB} of various semiconductors in MeCN containing different redox couples. The values in the parentheses represent V_{redox} vs. SCE

SC	Blank	1 $CHR^{0/+}$ (1.56)	2 $Th^{0/+}$ (1.26)	3 $Per^{0/+}$ (1.14)	4 $Rub^{0/+}$ (0.94)	5 10-$MP^{0/+}$ (0.79)	6 $Fe(Cp)_2^{0/+}$ (0.53)	7 $TMPD^{0/+}$ (0.27)	8 $Fe(\eta^5\text{-}C_5Me_5)_2$ (−0.12)	9 $OX^{0/+}$ (−0.2)	10 $MV^{2+/+}$ (−0.43)	11 $BQ^{0/-}$ (−0.56)	12 $AQ^{0/-}$ (−0.96)	13 $Ru(bpy)_3^{2+/+}$ (−1.27)	14 $PhNO_2^{0/-}$ (−1.33)	15 $Ph(CN)_2^{0/-}$ (−1.72)
TiO_2	~−1.0	−0.13		−0.18	−0.42	−0.7	−0.82	−1.0	−1.0							
n-CdS	−0.9		−0.2			−0.4	−0.7	−0.8								
n-WSe_2	−0.3		−0.4			−0.4		−0.4								
n-$MoSe_2$	+0.1		−0.1			0.0		−0.12								
p-WSe_2	0.78										0.75	0.62			0.75	
n-InP	−0.75	−0.2	0.05				−0.31				−0.5			0.8		
p-GaAs	0.06											−0.06	−0.14		−0.33	−0.46
p-Si	+0.15									−0.02		−0.12	−0.44	−0.52	−0.53	

1, CHR = Chrysene; 2, Th = Thianthrene; 3, Per = Perylene; 4, Rub = Rubrene; 5, 10-MP = 10-Methylphenothiazine; 6, $Fe(Cp)_2$ = Ferrocene; 7, TMPD = N, N, N', N'-Tetramethyl-p-phenylenediamine; 8, $Fe(\eta^5\text{-}C_5Me_5)_2$ = Decamethyl Ferrocene; 9 OX-1 = Oxazine-1; 10, MV = Methyl Viologen; 11, BQ = p-Benzoquinone; 12, AQ = 9,10-Anthraquinone; 13, Ru(bpy)₃ = Ruthenium (tris-bipyridine); 14, $PhNO_2$ = Nitrobenzene; 15, $Ph(CN)_2$ = Phthalonitrile.

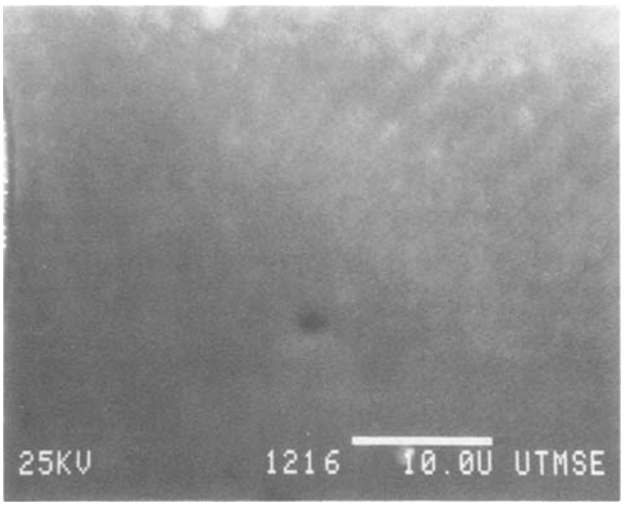

Fig. 2. Scanning electron micrograph of TiO_2 after etching with $KHSO_4$ for 2 hr in Pt crucible.

tively. Nitrobenzene used with p-Si was about 30 m*M*. All other couples were 10 m*M*. The concentrations of the electrochemically generated forms were about 20-30% of the starting material. The supporting electrolyte was electrometric grade tetra-n-butylammonium perchlorate (TBAP) (Southwestern Analytical Chemicals, Austin, Texas). This was purified by dissolving it in a minimum quantity of acetone, filtering the solution, and then recrystallizing with ether. This procedure was repeated twice. The recrystallized TBAP was dried for two days at 80°C under vacuum ($<10^{-5}$ Torr). All chemicals were stored in a helium-filled glove box (Vacuum Atmosphere Corporation, Hawthorne, California).

A conventional two-compartment electrochemical cell of ~25 ml capacity was used for electrochemical studies. For impedance measurements, a large area (~40 cm^2) Pt-gauze immersed in the same compartment as the working electrode was used as a counter-electrode. A Pt-gauze (~10 cm^2), separated from the main compartment by a medium porosity glass frit, was used as a counterelectrode for electrochemically generating radicals. An aqueous SCE with a KCl-saturated agar plug, directly introduced into the main compartment, was used as the reference electrode. All the potentials are expressed against this aqueous SCE unless otherwise specified.

A PAR Model 173 potentiostat and a PAR 175 universal programmer (Princeton Applied Research Corporation, Princeton, New Jersey) equipped with a Model 2000 X-Y recorder (Houston Instruments, Austin, Texas) were used to obtain the cyclic voltammograms as well as for capacitance-voltage measurements. A Soltec (Sun Valley, California) Model 6432, X-Y_1Y_2 recorder was used for recording both the 0° and 90° components simultaneously. In these latter experiments, a lock-in amplifier technique, which yields the in-phase and the out-of-phase components of an a-c signal superimposed on a linear sweep, was used. The a-c signal (~12 mV peak-to-peak) at different frequencies was obtained for input into the potentiostat from a Model 200CD wide range oscillator (Hewlett-Packard, Palo Alto, California). Its components at 0° and 90° were obtained by using either a PAR Model HR-8 or a PAR Model 5204 lock-in amplifier. An MINC-11 (Digital Equipment Corporation, Marlboro, Massachusetts) computer could also be used for continuous data acquisition from the lock-in amplifier, and a Houston Instruments digital plotter (Model DMP-5) was used for the data output. The experimental apparatus and procedures are similar to those previously described (3) and will be described in more detail in a separate paper. All solutions were prepared and sealed inside the glove box prior to removal for experimentation.

Results

C-V data.—Capacitance values were obtained for a number of single-crystal semiconductors in 0.1*M* TBAP MeCN solutions as a function of frequency and applied potential in the absence and presence of various redox couples spanning a wide range of V_{redox}. The flatband potential *vs.* an aqueous SCE, V_{FB}, was then determined from a Schottky-Mott (S-M) plot of $1/C^2$ *vs.* V

$$\frac{1}{C^2} = \frac{2}{e\epsilon\epsilon_0 N}(V - V_{FB} - 0.025) \qquad [1]$$

where C is the capacitance per unit area; e, the electronic charge (1.6×10^{-19} C); ϵ, the semiconductor dielectric constant; ϵ_0, the permittivity of free space (8.85×10^{-14} F/cm); and N, the acceptor (p-type) or donor (n-type) density. Although in some cases determination of V_{FB} from the intercept of S-M plots involves some ambiguity (25), V_{FB} can generally be determined to within 0.1V, and shifts in V_{FB} can quite readily be determined from the C-V plots themselves. As shown previously (3), linear S-M plots which yield V_{FB} can be obtained in the presence of surface states when the frequency used to obtain the capacitance is such that the surface-state capacitance does not make an appreciable contribution. In Fig. 3 are given the S-M plots for unetched TiO_2 (crystal A, treatment 2) in supporting electrolyte alone at three different frequencies; in Fig. 4a, b, the C-V and the corresponding S-M plots, respectively, are shown for a solution containing the $TMPD^{0/+}$ couple (abbreviations used are given in Table II). Although the V_{FB} for n-TiO_2 in the absence and presence of the $TMPD^{0/+}$ couple is the same, addition of other redox couples, such as $10\text{-}MP^{0/+}$ or $Per^{0/+}$, causes an appreciable shift of V_{FB} to more positive values. The results are summarized in Table II. Similar shifts in V_{FB} with V_{redox} are found with n-CdS and n-InP (Fig. 5 and 6). In Fig. 7, the plots of variation of V_{FB} with V_{redox} are given for p-Si, p-GaAs, p-WSe_2, and n-InP along with n-TiO_2 and n-CdS. Note however, that for the layer-type compounds n-WSe_2, n-$MoSe_2$, and p-WSe_2, V_{FB} is essentially invariant with V_{redox}. This finding agrees with a previous study of the C-V behavior of another layer-type compound, α-$MoTe_2$, where V_{FB} was independent of V_{redox} (14).

The behavior of the semiconductors which show shifts of V_{FB} with V_{redox} is consistent with FLP and the presence of surface states on the electrode surface. The density and distribution of these states can be

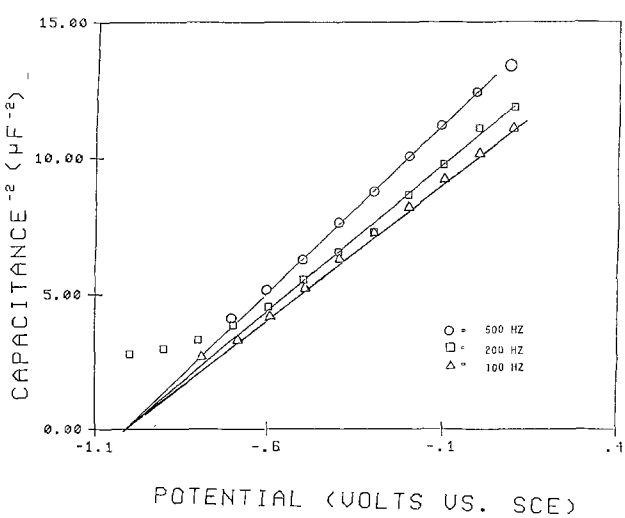

Fig. 3. Schottky-Mott (S-M) plots for TiO_2 contacting MeCN, containing 0.1*M* TBAP only.

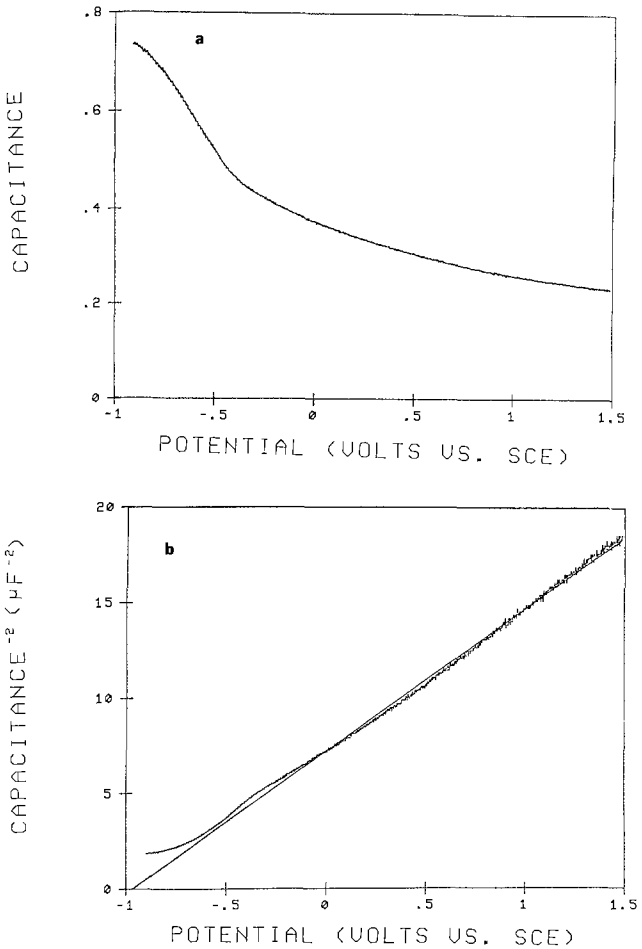

Fig. 4. (a) Capacitance (C) *vs.* potential of TiO_2/MeCN containing 10 mM TMPD and 2 mM $TMPD^+$ in 0.1M TBAP; f = 200 Hz; (b) S-M plot for the C-V curve in (a).

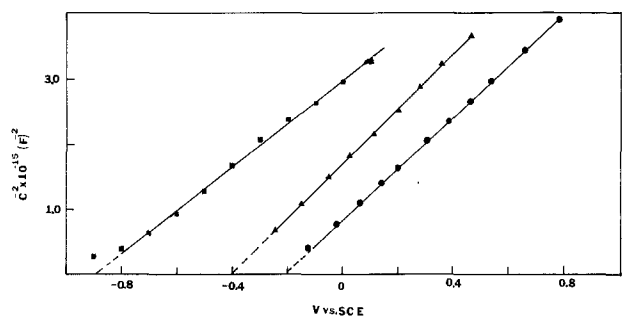

Fig. 5. S-M plot for n-CdS contacting MeCN, 0.1M TBAP, containing various redox couples; f = 2 kHz blank (■); 10-$MP^{0/+}$ (▲); $Th^{0/+}$ (●) (For abbreviations, see Table II).

probed by conductance measurements (14). If a surface-state level is assumed with a time constant, τ, independent of potential, the measured overall in-phase (0°) component, G_p, of a semiconductor in contact with a liquid electrolyte can be related, under certain conditions (see Appendix), to the surface-state capacitance, C_{ss}, and its time constant (τ) by the following equation (14)

$$\frac{G_p}{\omega} = \frac{G_{ss}}{\omega} + \frac{G_D}{\omega} = \frac{C_{ss}\omega\tau}{1 + \omega^2\tau^2} + \frac{G_D}{\omega} \qquad [2]$$

where G_D is the depletion layer conductance, G_{ss} is the surface-state conductance, and ω is the angular frequency. Then a plot of G_p/ω *vs.* ω at a given potential will go through a maximum when $\omega\tau = 1$. The reciprocal of this peak angular frequency will yield a time constant which represents a weighted average of the

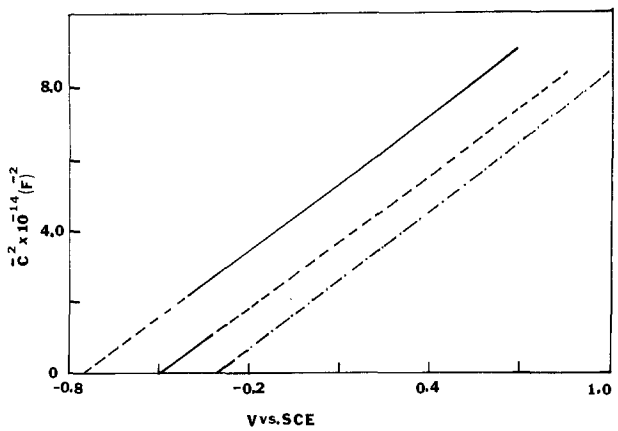

Fig. 6. S-M plots for n-InP/contacting MeCN, 0.1M TBAP containing various redox couples f = 5 kHz. Blank (——); $MV^{2+/+}$ (---); $Fe(CP)_2^{0/+}$ (—·—·). (For abbreviations, see Table II).

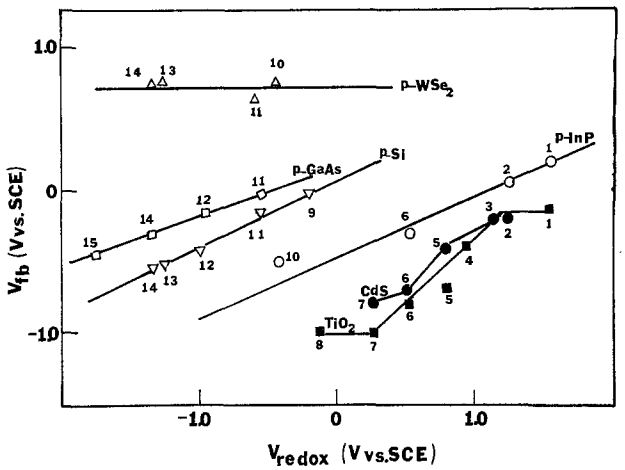

Fig. 7. Plots of variation of V_{FB} with V_{redox} for different semiconductor electrodes in MeCN, 0.1M TBAP containing various redox couples. The numbers on the figure represent different redox couples; see Table II.

time constants associated with the surface states located around that potential. For the layer-type compound, n-$MoSe_2$, a plot of G_p/ω *vs.* ω at +0.25V *vs.* SCE, in MeCN, 0.1M TBAP, containing 10-MP is given in Fig. 8a. The time constant, τ, corresponding to the peak frequency evaluated from this plot, is around 1.14×10^{-4} sec. This value of τ is in good agreement with that obtained by Kautek and Gerischer for $MoSe_2$ (26). Notice also that the peaks of the G_p/ω *vs.* ω plots (Fig. 8a) occur at about the same frequency for different applied potentials in the region where the peak is observed in the G_p *vs.* V plots; this suggests that τ is relatively independent of potential. With this value of τ, the surface-state density as a function of potential (N_{ss}, in cm^{-2} eV^{-1}) can be calculated from the equation

$$N_{ss} = \frac{2G_{ss}}{e} \cdot \tau \qquad [3]$$

where e is the electronic charge. The procedure used to determine G_{ss} is given in the Appendix. A typical plot of N_{ss} (cm^{-2} eV^{-1}) *vs.* V is shown for n-$MoSe_2$ over the potential range +0.1-0.45V *vs.* SCE in Fig. 8b. The integrated value of the curve in Fig. 8b when multiplied by τ/e yields the value of N_{ss} (cm^{-2}). Thus for n-$MoSe_2$, the surface-state density in the +0.1-0.45V regime is estimated as about 1.4×10^{10} cm^{-2}. This value of the density of surface states is comparable to that obtained with α-$MoTe_2$ (14) which is 10^{10} cm^{-2}. Similar values for τ and N_{ss} were obtained for n- and p-WSe_2. In Fig. 9a, b are shown the plots of G_p/ω *vs.* ω at −0.1V and N_{ss} *vs.* V, respectively, for p-Si.

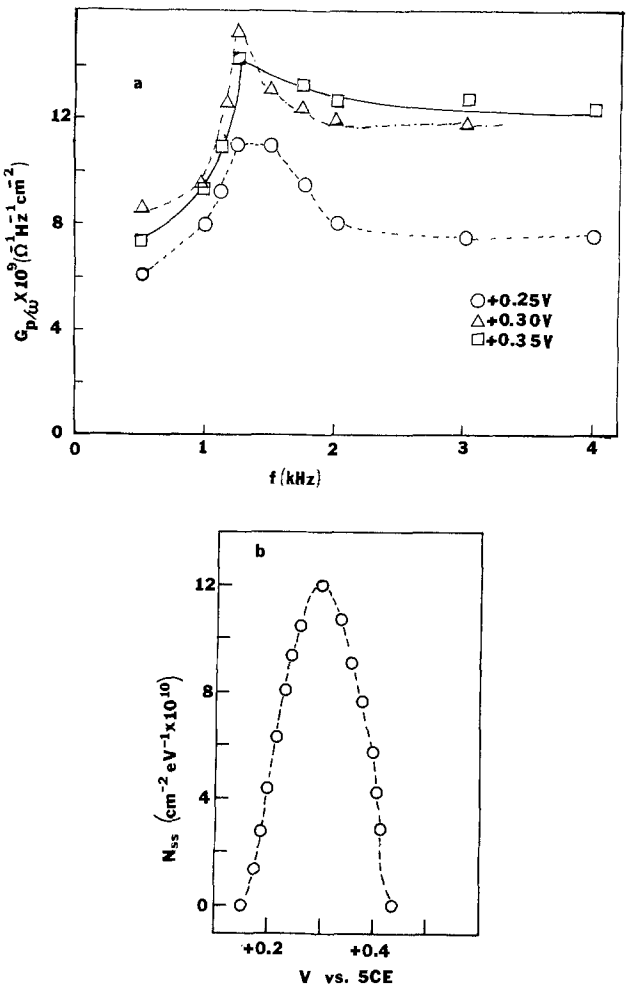

Fig. 8. (a) G_p/ω vs. f (where G_p is the measured equivalent parallel conductance and f is the frequency) for n-$MoSe_2$ in MeCN, 0.1M TBAP, 18 mM 10-MP at different potentials; (b) N_{SS} vs. V for n-$MoSe_2$ in MeCN, 0.1M TBAP containing 18 mM 10-MP.

Following the method described above for n-$MoSe_2$, the τ and N_{ss} are about 4×10^{-5} sec and 10^{13} cm^{-2}, respectively.

Effect of pretreatment on TiO_2 behavior.—For TiO_2, the etching procedures documented in literature span a wide regime of chemical activity—from such caustic mixtures as $H_2SO_4/(NH_4)_2SO_4$ (1:1) (27) and molten NaOH (28, 29) to solutions that probably only clean the surface, such as dilute acids (30-32). Molten bisulfates have been shown to dissolve TiO_2 at high temperatures, and $KHSO_4$ as an etchant has been shown to be specific for the TiO_2 (001) face (33). We report below the effects of two different pretreatment procedures (treatment 1 and 2, see Experimental) on the properties of surface states on n-TiO_2 (001). To probe the effects of these two different treatments on the properties of surface states such as time constant, energy, and density distribution, the 0° component was measured both as a function of potential and frequency for two undoped (crystal A) and Nb-doped (crystal B) TiO_2 crystals. In Fig. 10 are shown the G_p *vs.* V curves in MeCN, 0.1*M* TBAP containing 10 m*M* 10-$MP^{0/+}$ for crystal A (treatment 1). For crystal A (treatment 2) such plots are shown in Fig. 11. For Nb-doped TiO_2

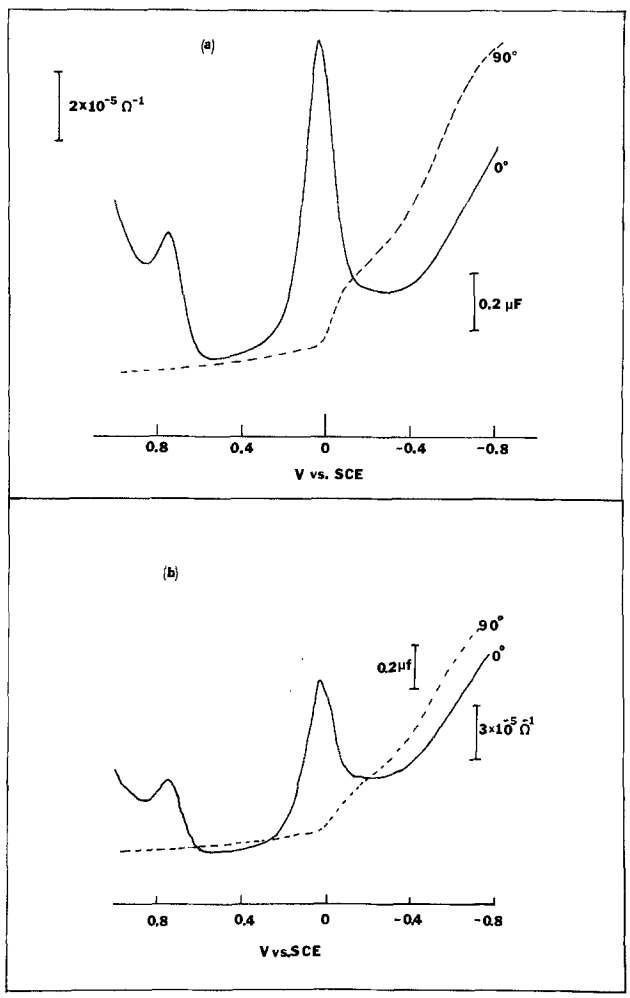

Fig. 10. G_p and C_p vs. V for TiO_2 (crystal A, treatment 1) in MeCN, 0.1M TBAP containing 10 mM 10-$MP^{0/+}$; (a) $f = 25$ Hz; (b) $f = 50$ Hz.

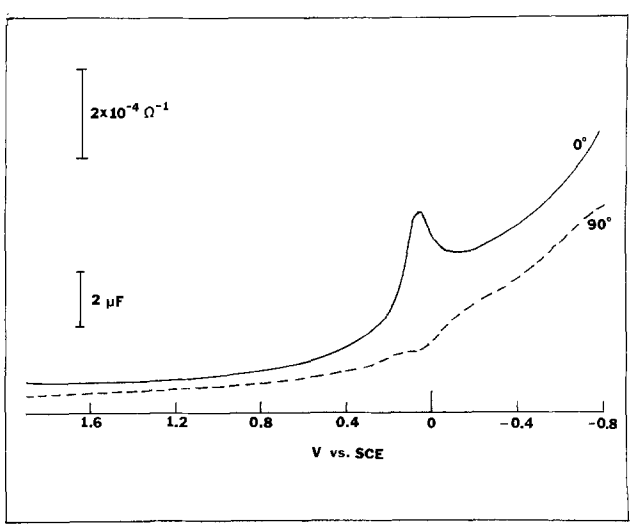

Fig. 11. G_p and C_p vs. V for TiO_2 (crystal A, treatment 2) in MeCN, 0.1M TBAP, containing 10 mM 10-$MP^{0/+}$; $f = 25$ Hz.

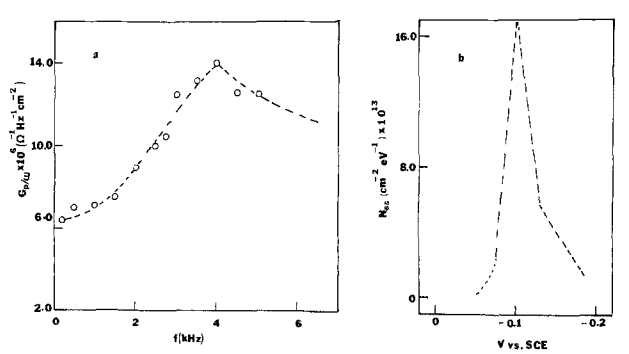

Fig. 9. (a) G_p/ω vs. f for p-Si in MeCN, 0.1M TBAP at a potential of 0.1V *vs.* SCE; (b) N_{SS} vs. V for p-Si in MeCN, 0.1M TBAP.

crystals (treatment 1), G_p *vs.* V plots are given in Fig. 12. The frequencies employed and the concentrations of the redox couples used are given in the respective figure captions. For crystal B, the S-M plots in the presence of different redox couples are shown in Fig. 13. A typical G_p/ω *vs.* ω plot is given for crystal B in Fig. 14. Following the arguments given for n-$MoSe_2$, the time constant, τ, and the density of surface states located around 0V *vs.* SCE are around 8×10^{-5} sec and 10^{10} cm^{-2}, respectively. Similar values of τ and N_{ss} were obtained for crystal A.

Discussion

Not many studies have been reported in literature pertaining to the a-c impedance measurements of semiconductors in nonaqueous solvents (34). Dutoit *et al.* (25) and Tyagai and Kolbasov (35) have made a systematic investigation of the C-V behavior of single crystal TiO_2 and CdS in aqueous solutions. Essentially both of these studies indicate that surface states located within the bandgap influence the mechanism of the overall charge transfer occurring at the interface. For n-TiO_2 (crystal A, treatment 2), the V_{FB} was found to be frequency independent, although there was a marginal variation in the slope (Fig. 3). A similar observation was made by Kabir-ud-Din *et al.* (36), although the V_{FB} values in MeCN reported by them were more negative by about 0.3V than our values; values of V_{FB} closer to ours were reported earlier (8, 37). In the presence of $Fe(\eta^5\text{-}C_5Me_5)_2^{0/+}$ and $TMPD^{0/+}$, which are located above half of the gap, there is little variation in the V_{FB} from the blank solution. However, for couples such as $Fe(Cp)_2^{0/+}$ and $10\text{-}MP^{0/+}$, located below half the gap, the V_{FB} varies monotonically as

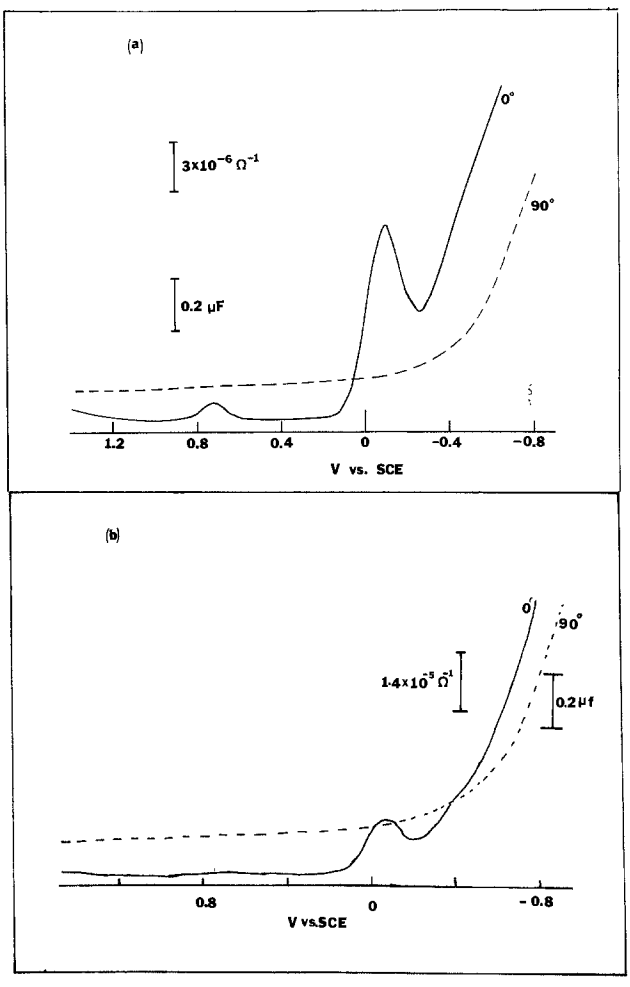

Fig. 12. G_p and C_p *vs.* V for TiO_2 (crystal B) in MeCN, 0.1M TBAP containing 10 mM $10\text{-}MP^{0/+}$; (a) $f = 10$ Hz; (b) $f = 25$ Hz.

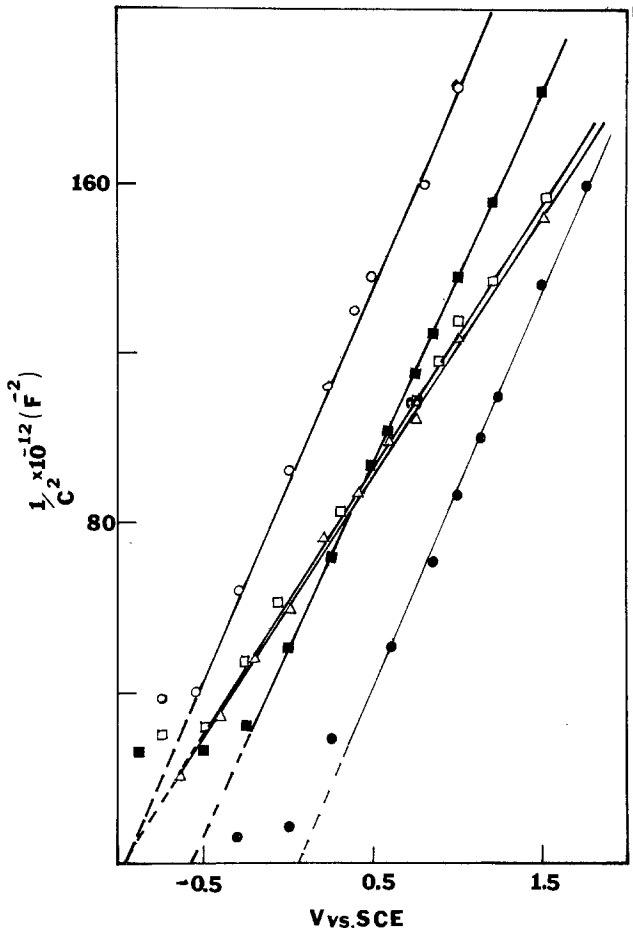

Fig. 13. S-M plots for n-TiO_2 (crystal B) contacting MeCN, 0.1M TBAP containing different redox couples; $f = 200$ Hz; (○) I^-/I_2; (●) $Th^{0/+}$; (△) $[Fe(\eta^5 - C_5Me_5)_2]^{0/+}$; (□) Blank; (■) $10\text{-}MP^{0/+}$.

shown in Fig. 7. In the case of n-CdS, the variation in V_{FB} with V_{redox} is similar to that of n-TiO_2 (see Fig. 7). A similar observation was made by Frese (38) for n-CdSe in aqueous solutions. With p-Si, p-GaAs, and n-InP, the V_{FB} varies montonically with V_{redox} (Fig. 7). In the case of n-InP, the S-M plot is linear for the entire bandgap (Fig. 6); similar observations with n-InP were made by Van Wezemall *et al.* (39) in aqueous solutions and by Tuck *et al.* (40) for solid-state Al/n-InP Schottky barriers. They observed that the S-M plot is linear over a range of 0.8V and deviates slightly thereafter implying the presence of deep donor levels about 0.8V below the conduction band. The layer-type compounds represent a different situation where there is no significant shift in V_{FB} with V_{redox} from that observed in blank solutions for couples with $E^{o'}$s located within or outside of the bandgap (Fig. 7). This probably indicates that while for many large and small bandgap semiconductors the role of bandgap surface states is important, for layer-type compounds the surface states have only marginal effects. The time constant associated with surface states on p-Si is around 4×10^{-5} sec, and this falls in the domain of fast surface states. The N_{ss} is around 10^{13} cm^{-2}, and this is high enough for Fermi level pinning to occur.

The surface states on TiO_2 made conductive by reduction are due in part to oxygen vacancies and Ti^{3+}. Several investigators have used different techniques to deduce the presence of these states. These include (*i*) thermal and photoelectronic properties (41), (*ii*) electron spectroscopy (42), (*iii*) catalytic decomposition of N_2O supplemented with EPR studies (43), and (*iv*) low frequency capacitance-voltage method (44). However, in all the methods, the evidence for surface states was not obtained with TiO_2 in contact with an

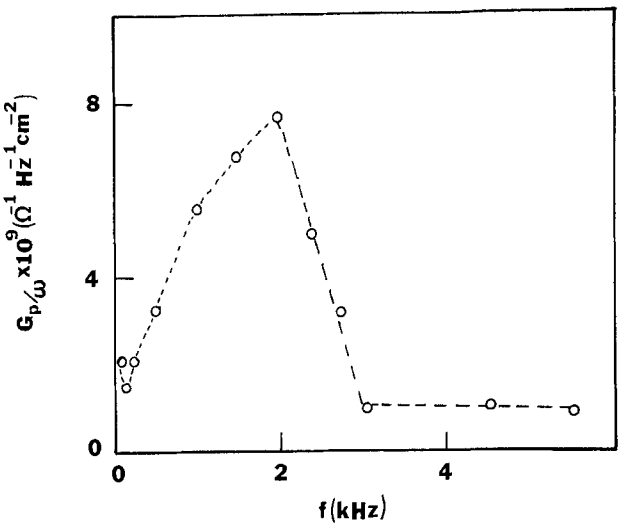

Fig. 14. G_p/ω vs. f for TiO_2 (crystal B) contacting MeCN, 01M TBAP. G_p value was extracted at a potential 0.0V vs. SCE.

electrolyte. Since the properties of the electrode surface dramatically change upon immersion in electrolyte (because of the large electric field in the interfacial region and interaction with solvent and electrolyte), a study of surface states *in situ* produces more meaningful information about the electrode surface. The low frequency C-V method, which employs the quadrature component of the a-c impedance, can be employed to study the properties of the surface states, but it suffers from the limitation (15) that the spread in the space charge capacitance values, even when the frequency is increased by one order of magnitude, is only 14%. This means large errors will be introduced in the calculation of the surface-state properties as we discussed in more detail in a recent paper (14). The conductance technique is more useful in extracting surface-state properties. In our studies on the a-c admittance characteristics of n-TiO_2 (crystals A and B, treatment 1), the in-phase component yields evidence for the presence of states at two energies (Fig. 10, 12). However, in the case of TiO_2, crystal A, treatment 2, only one peak in the G_p *vs.* V plot at 0.1V *vs.* SCE is observed (Fig. 11). Based on the evidence obtained by other investigators, we tentatively assign those closer to V_{FB} (shallow level) to oxygen vacancies and those around the middle of the gap (deep levels) to Ti^{3+}, The peak heights are frequency dependent as shown in Fig. 10-12. The shift in V_{FB}'s of the $KHSO_4$-etched TiO_2 crystals to positive values when V_{redox} is below half the gap (Fig. 13) is similar to that observed with crystal A (treatment 2) (see Fig. 7). In all the S-M plots, the deviation from linearity near the V_{FB} is due to the constancy of the capacitance around V_{FB} since at potentials negative of V_{FB} an n-type semiconductor behaves like a metal. For both crystals etched with $KHSO_4$, the peak potentials of the surface states due to Ti^{3+} are located at the same potential (0.72V *vs.* SCE), but those due to oxygen vacancies (shallow levels) are offset by 0.1V (crystal B 0.1V more negative than crystal A). Note that surface states due to Ti^{3+} and oxygen vacancies are present in both the crystals subjected to treatment 1. Thus it appears that in TiO_2 crystals etched with $KHSO_4$, with the reduction by either CO or H_2, two sets of surface states occur. The time constant evaluated from the G_p/ω *vs.* ω plot (Fig. 14) is $\sim 8 \times 10^{-5}$ sec, and the surface-state density for oxygen vacancy is $\sim 10^{10}$ cm^{-2}. This value of N_{ss} is too small for Fermi level pinning to occur (2). The absence of the Ti^{3+} surface-state peak for crystal A, treatment 2 (Fig. 11) is difficult to explain. Perhaps the surface Ti^{3+} ions are oxidized in this crystal or a surface layer forms to block these sites.

Conclusions

Based on the results reported here, we can assign the semiconductors studied here into three categories: (*i*) Small bandgap compound and elemental semiconductors (GaAs, InP, Si) represent a situation where V_{FB} tracks V_{redox} monotonically; (*ii*) Large bandgap semiconductors (TiO_2, CdS) where V_{FB} remains fairly constant for couples located above half of the gap and varies monotonically for couples located below half of the gap; and (*iii*) Layer-type compounds (WSe_2) where V_{FB} does not vary with V_{redox}. Evidence for two sets of surface states on a TiO_2 surface contacting MeCN has been obtained by a-c impedance measurements of the in-phase component of the total admittance. The time constant associated with surface states on TiO_2 surfaces is equal to 8×10^{-5} sec, and the N_{ss} for the level at 0V *vs.* SCE was found to be $\sim 10^{10}$ cm^{-2}. The time constant and the N_{ss} for p-Si are 4×10^{-5} sec and 10^{13} cm^{-2}, respectively. This value of N_{ss} is sufficient for pinning the Fermi level.

Acknowledgment

The support of this work by the Solar Energy Research Institute is gratefully acknowledged. The authors wish to thank Dr. H. S. Jarrett of du Pont and Dr. Y. Nakazumi of Nakazumi Earth Crystals Corporation, Japan, for generously donating the TiO_2 single crystals. We also would like to thank G. Garcia for his help with computer programming.

Manuscript submitted Oct. 25, 1982; revised manuscript received Jan. 21, 1983.

Any discussion of this paper will appear in a Discussion Section to be published in the June 1984 JOURNAL. All discussions for the June 1984 Discussion Section should be submitted by Feb. 1, 1984.

The University of Texas at Austin assisted in meeting the publication costs of this article.

APPENDIX

Figure A-1 is the equivalent circuit of the semiconductor/liquid interface (45), neglecting the contribution from the Helmholtz layer and counterelectrode capacitance as well as the bulk resistance of the semiconductor, resistance of the electrolyte, and the Faradaic impedance. The net equivalent circuit comprises a series combination of surface-state resistance (R_{ss}) and capacitance (C_{ss}) connected in parallel to a parallel combination of space charge layer capacitance (C_D) and resistance (R_D) respectively; these are frequency independent but voltage dependent. The total admittance of the equivalent circuit is $Y_p = G_p + j\omega C_p$ where the in-phase component

$$G_p = \frac{\omega^2 C_{ss}^2 R_{ss}}{1 + R_{ss}^2 \omega^2 C_{ss}^2} + \frac{1}{R_D} \qquad [A\text{-}1]$$

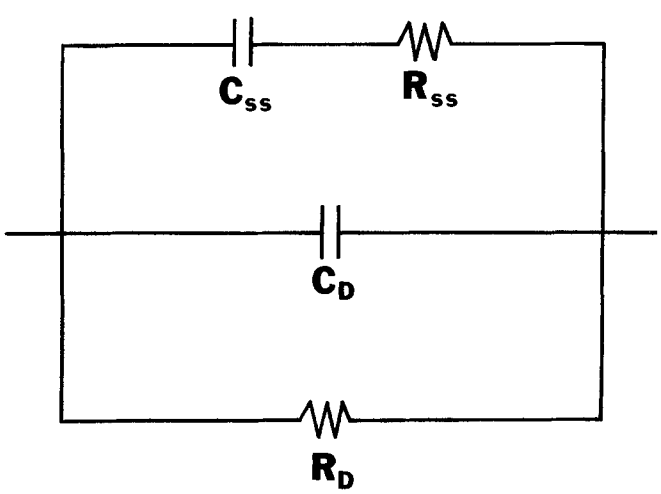

Fig. A-1. Equivalent circuit of the semiconductor/electrolyte interface in the presence of surface states.

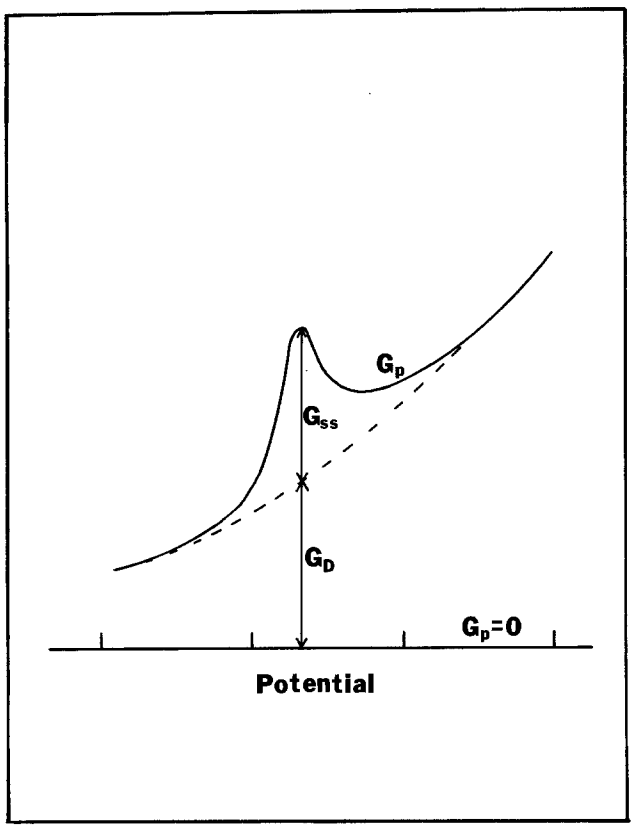

Fig. A-2. Illustration of the method used to extract G_{ss}

and the out-of-phase component

$$C_p = \frac{C_{ss}}{1 + R_{ss}^2 \omega^2 C_{ss}^2} + C_D \qquad [A-2]$$

Equations [A-1] and [A-2] can be written as

$$G_p = \frac{\omega^2 \tau C_{ss}}{1 + \omega^2\tau^2} + G_D = G_{ss} + G_D \qquad [A-3]$$

and

$$C_p = \frac{C_{ss}}{1 + \omega^2\tau^2} + C_D \qquad [A-4]$$

where $G_{ss} = C_{ss}\omega^2\tau/(1 + \omega^2\tau^2)$, $\tau = R_{ss}C_{ss}$, and $G_D = 1/R_D$. G_p can be equated with C_{ss} and hence N_{ss}, only after considering G_D (Eq. [A-3]). Therefore, Eq. [2] holds only when G_D is small compared to G_{ss}. Since G_D (and C_D) are frequency independent, a change in the value of G_D would be manifested in the G_p/ω *vs.* ω plot by a shift parallel to the G_p/ω axis. The ω value corresponding to the peak would not be affected by such a change. Hence, the G_p/ω *vs.* ω plot will always be valid for finding the value of τ independent of the relative values of G_{ss} and G_D.

To determine N_{ss}, Eq. [2] can be written

$$\frac{G_p - G_D}{\omega} = \frac{C_{ss}\omega\tau}{1 + \omega^2\tau^2} \qquad [A-5]$$

Theoretically, the G_p/ω *vs.* ω plot should yield values of G_D from the baseline of the plots. However, these plots do not always have flat baselines, and obtaining reliable values of G_D becomes difficult. In these situations, the G_p *vs.* V curves can be more helpful. Values of G_D at a particular potential can be obtained by extrapolating a smooth parabolic baseline in the regime of the peak due to surface states (Fig. A-2). This value can then be subtracted from the measured value of G_p to obtain C_{ss}.

REFERENCES

1. H. Gerischer, in "Physical Chemistry: An Advanced Treatise," Vol. 9A, H. Eyring, D. Henderson, and W. Jost, Editors, p. 463, Academic Press, New York (1970).
2. A. J. Bard, A. B. Bocarsly, F. R. Fan, E. G. Walton, and M. S. Wrighton, *J. Am. Chem. Soc.*, **102**, 3671 (1980).
3. G. Nagasubramanian, B. L. Wheeler, F. R. Fan, and A. J. Bard, *This Journal*, **129**, 1742 (1982).
4. C. A. Mead and W. G. Spitzer, *Phys. Rev.*, **134**, A713 (1964).
5. J. M. Bolts and M. S. Wrighton, *J. Phys. Chem.*, **80**, 2641 (1976); H. Morisaki, M. Hariya, and K. Yazawa, *Appl. Phys. Lett.*, **30** (1977).
6. J. G. Mavroides, V. E. Henrich, H. Zeiger, G. Dresselhaus, J. A. Kafalas, and D. F. Kolesar, in "Electrode Materials and Processes for Energy Conversion and Storage," J. D. E. McIntyre, S. Srinivasan, and F. G. Will, Editors, p. 45, The Electrochemical Society Softbound Proceedings Series, Princeton, NJ (1978).
7. B. Parkinson, F. Decker, J. F. Juliao, M. Abramovich, and H. C. Chagas, *Electrochim. Acta*, **25**, 521 (1980).
8. S. N. Frank and A. J. Bard, *J. Am. Chem. Soc.*, **97**, 7427 (1975); R. N. Noufi, P. A. Kohl, S. N. Frank, and A. J. Bard, *This Journal*, **125**, 246 (1978).
9. E. C. Dutoit, F. Cardon, and W. P. Gomes, *Ber. Bunsenges. Phys. Chem.*, **76**, 81 (1972).
10. J. Vandermolen, W. P. Gomes, and F. Cardon, *This Journal*, **127**, 324 (1980).
11. M. P. Dare-Edwards and A. Hamnett, *J. Electroanal. Chem. Interfacial Electrochem.*, **105**, 283 (1979).
12. J. Gobrecht and H. Gerischer, *Solar Energy Mater.*, **2**, 131 (1979); D. Laser and A. J. Bard, *This Journal*, **123**, 1828 (1976).
13. T. C. McGill, *J. Vac. Sci. Technol.*, **11**, 935 (1974); S. Kurtin, T. C. McGill, and C. A. Mead, *Phys. Rev. Lett.*, **22**, 1433 (1969).
14. G. Nagasubramanian, B. L. Wheeler, G. A. Hope, and A. J. Bard, *This Journal*, **130**, 385 (1983).
15. E. H. Nicollian and A. Goetzberger, *Bell Syst. Tech. J.*, **46**, 1055 (1967).
16. P. R. Barabash and R. S. C. Cobbold, *IEEE Trans. Electron Devices*, **ed-29**, 102 (1982).
17. J. Dubow and K. Rajeshwar, Final Report, Oct. 1981, Submitted to SERI Div., Golden, CO 80401; M. Abe, H. Morisaki, and K. Yazawa, *Jpn. J. Appl. Phys.*, **19**, 1421 (1980).
18. G. Nagasubramanian and A. J. Bard, *This Journal*, **128**, 1055 (1981).
19. H. S. White, F. R. Fan, and A. J. Bard, *ibid.*, **128**, 1045 (1981).
20. F. Di Quarto and A. J. Bard, *J. Electroanal. Chem. Interfacial Electrochem.*, **127**, 43 (1981).
21. P. A. Kohl and A. J. Bard, *This Journal*, **126**, 598 (1979).
22. L. F. Schneemeyer and M. S. Wrighton, *J. Am. Chem. Soc.*, **102**, 6964 (1980).
23. F. R. Fan and A. J. Bard, *This Journal*, **128**, 945 (1981).
24. F. R. Fan and A. J. Bard, *J. Am. Chem. Soc.*, **102**, 3677 (1980).
25. E. C. Dutoit, R. L. Van Meirhaeghe, F. Cardon, and W. P. Gomes, *Ber. Bunsenges. Phys. Chem.*, **79**, 1206 (1975).
26. W. Kautek and H. Gerischer, *Electrochim. Acta*, **27**, 1035 (1982).
27. H. Tamura, H. Yoneyama, C. Iwakura, H. Sakamoto, and S. Murakami, *J. Electroanal. Chem. Interfacial Electrochem.*, **80**, 357 (1977).
28. E. C. Dutoit, F. Cardon, and W. P. Gomes, *Ber. Bunsenges. Phys. Chem.*, **80**, 475 (1976).
29. R. H. Wilson, *J. Appl. Phys.*, **48**, 4292 (1977).
30. T. Ohnishi, Y. Nakato, and H. Tsubomura, *Ber. Bunsenges. Phys. Chem.*, **79**, 523 (1975).
31. M. S. Wrighton, D. S. Ginley, P. T. Wolczanski, A. B. Ellis, D. L. Morse, and A. Linz, *Proc. Natl. Acad. Sci. USA*, **72**, 1518 (1975).
32. D. M. Shub, A. A. Remnev, and V. I. Veselovskii, *Elektrokhimiya*, **9**, 676 (1973).
33. H. S. Jarrett, E. I. du Pont de Nemours and Co., DE, Personal communication.
34. G. Nagasubramanian, B. L. Wheeler, F. R. Fan, and A. J. Bard, in "Photoelectrochemistry: Fundamental Processes and Measurement Techniques," W. L. Wallace, A. J. Nozik, and S. K. Deb, Edi-

tors p. 372, The Electrochemical Society Softbound Proceedings Series, Vol. 82-3, Pennington, NJ (1982).
35. V. A. Tyagai and G. Ya. Kolbasov, *Surf. Sci.*, **28**, 423 (1971).
36. Kabir-ud-Din, R. C. Owen, and M. A. Fox, *J. Phys. Chem.*, **85**, 1679 (1981).
37. M-S. Lin, N. Hung, and M. S. Wrighton, *J. Electroanal. Chem. Interfacial Electrochem.*, **135**, 121 (1982).
38. K. W. Frese, Jr., *J. Appl. Phys.*, **53**, 1571 (1982).
39. A. M. Van Wezemael, W. H. Laflere, F. Cardon, and W. P. Gomes, *J. Electroanal. Chem. Interfacial Electrochem.*, **87**, 105 (1978).
40. B. Tuck, G. Eftekhari, and D. M. de Cogan, *J. Phys. D: Appl. Phys.*, **15**, 457 (1982).
41. A. K. Ghosh, F. G. Wakim, and R. R. Addiss, Jr., *Phys. Rev.*, **184**, 979 (1969).
42. V. E. Henrich, G. Dresselhaus, and H. J. Zeiger, *Phys. Rev. Lett.*, **36**, 1335 (1976).
43. J. Cunningham and A. L. Penny, *J. Phys. Chem.*, **78**, 870 (1974).
44. K. Kobayashi, Y. Aikawa, and M. Sukigara, *Chem. Lett.*, 679 (1981).
45. W. P. Gomes and F. Cardon, *Ber. Bunsenges. Phys. Chem.*, **74**, 431 (1970).

A Study of the Transition from Oxide Growth to O_2 Evolution at Pt Electrodes in Acid Solutions

V. I. Birss*

Department of Chemistry, University of Ottawa, Ottawa, Ontario, Canada

A. Damjanovic*

Corporate Research and Development, Allied Corporation, Morristown, New Jersey 07960

ABSTRACT

A Pt ring disk electrode was used in acid solutions to study the transition from Pt oxide growth to oxygen evolution and to distinguish the rates of these two processes. When a constant current is applied to the disk electrode, the disk potential, V, initially increases linearly with time, and hence with the charge density, while a negligible current is observed at the ring. In this potential region, essentially all of the applied current is used for the growth of a Pt oxide film. Following the linear V/t region, V continues to increase but now more slowly and nonlinearly with time, while the ring current initially increases sharply and then slowly approaches the value expected for 100% oxygen evolution at the disk electrode. Thus, the Pt oxide film continues to grow in the nonlinear V/t region even when oxygen evolution becomes the major reaction. In the nonlinear V/t region, V again increases nearly linearly with the integrated charge density for oxide film formation or with the oxide film thickness. This V/q relationship in the nonlinear V/t region is different from the V/q relationship in the linear V/t region. However, the mechanism of Pt oxide growth and the properties of the film when the O_2 evolution reaction is the dominant reaction remain the same as in the initial Pt oxide growth region where O_2 evolution is not significant. The distribution of potentials in the oxide film and in the inner and outer Helmholtz layers is discussed.

When a constant anodic current is applied to a prereduced oxide-free Pt electrode starting from the rest potential in O_2-saturated acid or alkaline solutions, $V_R = 0.98$V *vs.* RHE (1), three distinct potential regions can be seen in a V/t transient (2-5). Initially, the potential increases rapidly and nonlinearly with time as the first monolayer of an oxide film is formed (5-7). Following this region, the electrode potential increases fairly linearly with time (Fig. 1) with the current being used for further growth of the oxide film (8). Eventually at higher potentials, oxygen evolution begins and soon becomes the major electrode reaction.

In Fig. 1, potential/time curves are shown for three constant current densities in a 0.2*N* H_2SO_4 solution. In this figure, the time axis has been scaled for each current density to represent charge density, $q = it$. At a particular potential, which depends on the applied current density and the pH, the linear increase of the potential with time, or charge density, ceases. Now, the potential increases at a rate which decreases with time while O_2 evolution continues to increase and soon becomes the predominant electrode reaction (9). Previous work has shown that at long times the potential changes nearly linearly with the logarithm of time of polarization and the oxide film continues to grow at a very slow rate (3, 9, 10).

In this study, a Pt ring disk electrode has been used to separate the reactions of Pt oxide growth and O_2 evolution. A comparative analysis of their individual rates and their dependence on the electrode potential is expected to yield information on the nature of the changes in the kinetics of oxide growth and on the potential distribution across the complex interface, comprised of the oxide film and the inner and outer Helmholtz layers, during the transition from the oxide growth to O_2 evolution. Such an analysis is also expected to aid in the overall understanding of the mechanism of the O_2 evolution reaction at oxide-covered electrodes.

* Electrochemical Society Active Member.
Key words: metal, kinetics, chemisorption.

Experimental

A commercially designed Pt disk-Pt ring electrode (Pine Instrument Company, disk radius 0.383 cm, ring inner radius 0.399 cm, and ring outside radius 0.422 cm) was utilized in an all-glass cell similar to that described in (11). The ring-disk electrode was polished to a mirror finish with alumina paste. In some experiments, a thin layer of gold (~1000Å) was electrodeposited over the ring electrode. A saturated calomel electrode in a separate compartment served as the reference electrode, and a Luggin capillary extended upwards toward the center of the disk electrode. A Pt counterelectrode was placed in the same compartment as the ring disk electrode.

Solutions were prepared from reagent grade sulfuric acid and conductivity water. No extensive purification of solutions was carried out, *e.g.*, by preelectrolysis. In all experiments, solutions were first purged of O_2 with high purity Ar. During electrochemical measurements, Ar was passed over the solution.

Prior to each series of experiments, the disk electrode was anodically oxidized and cathodically re-

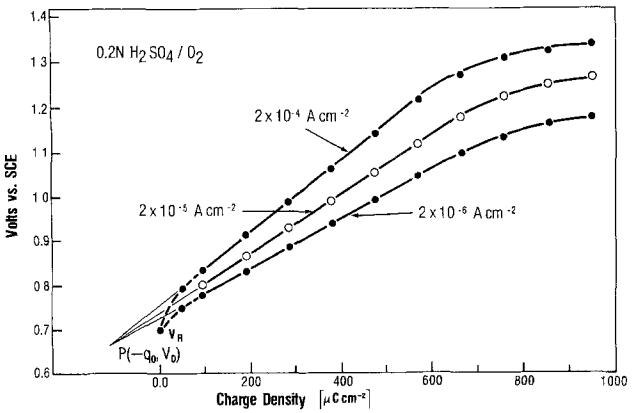

Fig. 1. *V-q* relationships at three constant current densities. Current and charge densities are corrected for surface roughness (wire electrode, RF = 1.6).

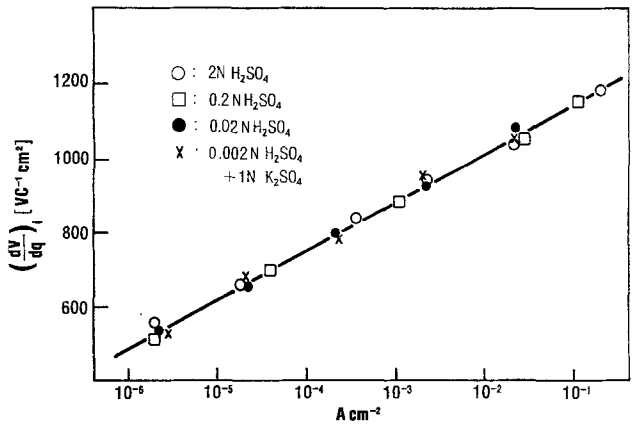

Fig. 2. Slopes of the *V-q* traces, such as those in Fig. 1, plotted against the applied current density. Data are corrected for surface roughness.

duced several times after which the solution was replaced. Then, a constant anodic current was applied to the disk electrode from a high voltage battery pack (~190V) and precision resistors in series with the disk electrode. The ring potential was kept constant at 0.4V *vs.* RHE using a commercial potentiostat so that oxygen evolved at the disk electrode could be detected at the ring electrode. The ring current observed at the longest time of polarization of the disk electrode was scaled to be equal to the current applied at the disk as essentially 100% oxygen evolution occurs at long times. In the potential region of O_2 evolution, all other currents are much smaller than that for O_2 evolution. For instance, Pt dissolution current density is about 10^{-9} A-cm^{-2} (12). The ring currents at shorter times could then be readily converted, by reference to this scale, to give the fraction of the applied disk current utilized in the O_2 evolution. For this scaling, it does not matter whether O_2 is reduced to H_2O or to H_2O_2, providing the ratio of the currents for these partial processes is constant during measurements. With the gold ring electrode in acid solutions, H_2O_2 is the predominent product in the reduction (11, 13), and this is reflected in lower ring currents than calculated. This is discussed below.

Both the potential at the Pt disk and the current at the Pt ring electrode were monitored with time on an X-Y-Y recorder.

Results and Discussion

Rates of the individual processes of oxide growth and oxygen evolution.—Growth of oxide film in the linear V/t region.—The relationships between V and q in the linear V/t region are given in Fig. 1 with the slopes, $\partial V/\partial q$, increasing with increasing constant current density, i, applied to the disk electrode. These slopes are found to increase linearly with log i over a few decades of current density (Fig. 2) with the same dependence being observed in acid solutions of different pH (7).

In Fig. 1, it can also be seen that the linear V/q traces intercept in extrapolation to a common point, $P(-q_o, V_o)$. The parameter q_o can be considered as the charge density equivalent to the oxygen species adsorbed at the Pt surface prior to the application of a constant current (5, 7). The parameter V_o has been found to depend on pH, decreasing 60 mV *vs.* a pH independent reference electrode as the pH increases one unit

$$V_o = V_{oo} - \frac{2.3RT}{F}\text{pH} \qquad [1]$$

This pH dependence of V_o is the cause of the shift along the V axis of the V/q traces with pH. V_o can also be seen to be independent of the applied current density (Fig. 1). V_{oo} is a constant that depends on the choice of the reference electrode (V_{oo} = 0.94V *vs.* NHE).

In the linear V/t region, the following relationships hold

$$\frac{\partial V}{\partial q} = \frac{1}{\alpha}\ln\frac{i}{i_o} = f(i_{disk}) \qquad [2]$$

and

$$\frac{\partial V}{\partial \ln i_{disk}} = \frac{q}{\alpha} = f(q) \qquad [3]$$

Here, i_o is the current density at which $\partial V/\partial q = 0$ (Fig. 2) and can be considered to be the exchange current density (7).

Therefore, the kinetics of Pt oxide growth in the linear V/t region can be described by the rate equation (7, 14)

$$i_{og} = i_{o,og}\exp\left[\frac{\alpha(V - V_o)}{q + q_o}\right] \qquad [4]$$

where α can be evaluated from

$$\frac{\partial^2 V}{\partial q \partial \ln i_{og}} = \alpha^{-1} \qquad [5]$$

From Fig. 2, α = 0.018 CV^{-1}-cm^{-2} and i_o is equal to 2×10^{-10} A-cm^{-2} independent of the pH. The values of i_o, q_o, and α are given with respect to the true area of the Pt electrode surface (7). In the linear V/t region, almost all the applied current density at the disk, i_{disk}, is used for oxide formation and hence $i_{disk} \simeq i_{og} \simeq i$.

The observed rate, Eq. [4], can be derived from the Cabrera and Mott model (15) of the high field-assisted growth of anodic oxide films (7, 14)

$$i_{og} = i_{o,og}\exp\left[\frac{ze\lambda(V - V_o)}{dkT}\right] \qquad [6]$$

Here, ze is the charge of ions migrating in the field and participating in the rate determining step, and λ is the half-jump distance of the ions. An analysis has shown that $(V - V_o)$ is the potential difference across the growing oxide film and the inner Helmholtz layer (16). Accordingly, V_o is the potential of the inner Helmholtz plane with respect to a pH independent reference electrode. Therefore, V_o gives a measure of the potential difference across the outer Helmholtz layer (16).

A model of the complex interface, comprised of the oxide film and the inner and outer Helmholtz layers, is suggested in Fig. 3 for two constant current densities. During oxide growth, the potential difference across the outer Helmholtz layer (OHL) remains constant (V_o = const) at all current densities. Potential difference across the inner Helmholtz layer (IHL) is also

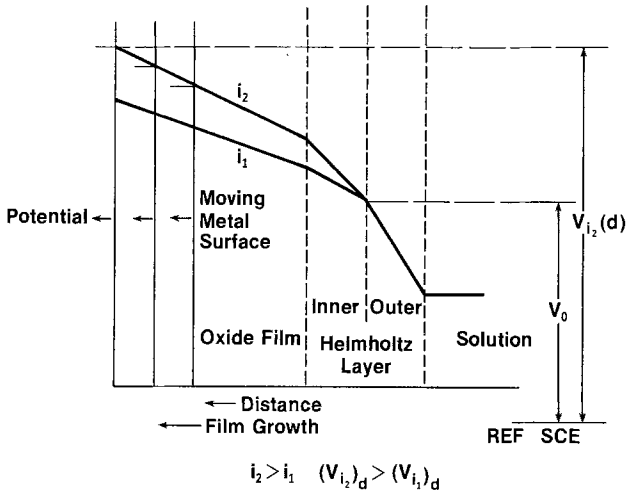

Fig. 3. A model of the interface of the oxide film and inner and outer Helmholtz layers during the oxide growth at a constant current density. Note that the potential difference across the outer Helmholtz layer is independent of applied current density.

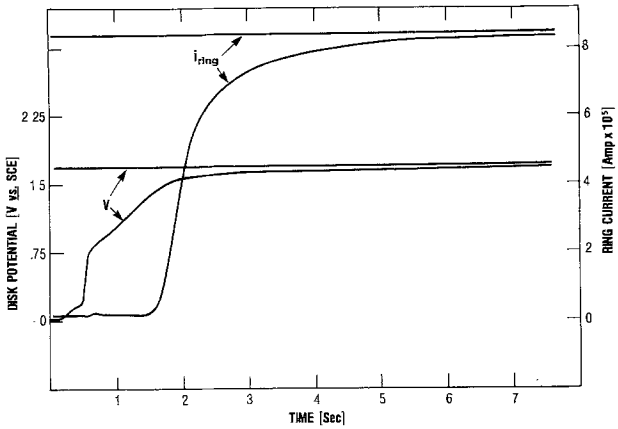

Fig. 4. Rotating ring disk electrode experiment. The ring current and the disk potential change with time. Disk current is 10^{-3} A-cm^{-2}; solution is 2*N* H_2SO_4. The ring electrode is electroplated with Au.

constant during the oxide growth at a constant current density. It decreases, however, as the current density of oxide growth increases. As the film grows at a constant current density and the metal-oxide interface propagates to the left, only the potential difference across the oxide film increases with time (and hence film thickness). However, the fields within the oxide film and the IHL remain constant during oxide growth at a given current density (16). As the current density for oxide growth decreases, these fields decrease too.

The dependence of the field in the film on the applied current density and the strength of the fields at different current densities can readily be obtained from Fig. 2 (7). For example, at 10^{-3} A-cm^{-2}, the field is about 7×10^6 V-cm^{-1}. This field is of the same magnitude as those observed for insulating anodic oxide films at valve metals (17) which shows clearly that Pt oxide films are also very poor electronic conductors.

At a constant current density, the field at any point of the complex interface (Fig. 3) should be invariant with time and thickness of the film. Therefore, it could be anticipated that the process of oxide growth would be uninterrupted and that the films would continue to thicken indefinitely as they do at valve metal electrodes. Instead, at a critical potential or a critical oxide film thickness (Fig. 1), the electrode potential ceases to increase linearly with time and O_2 begins to evolve and soon becomes the predominant reaction. In the following section, this transition from the linear *V/t* region, where oxide growth is the major reaction, to the nonlinear *V/t* region of O_2, evolution predominance is analyzed and discussed.

Growth of Pt oxide film in the transition region.— The individual rates of the oxide growth and the O_2 evolution reactions can be obtained from ring disk experiments, such as that shown in Fig. 4 for $i_{disk} = 10^{-3}$ A-cm^{-2}. The potential of the Pt disk electrode and the ring current are followed with time. The ring current is converted to give the fraction of the applied current at the disk which is utilized in the O_2 evolution reaction, i_{O_2}. Then, $i_{disk} - i_{O_2}$ gives the current due to the oxide growth reaction, i_{og}

$$i_{og} = i_{disk} - i_{O_2} \qquad [7]$$

In the linear *V/t* region (Fig. 4), no O_2 is measured at the ring electrode and essentially all of the current applied to the disk is used for oxide film formation. At the point where the linearity ceases and a charge density of about 1000 μC-cm^{-2} has passed, O_2 begins to evolve and the ring current commences to increase sharply with time (Fig. 4). However, the current at the ring electrode soon levels off and then very slowly approaches the value corresponding to 100% O_2 evolution at the disk electrode. It follows, therefore, that the current due to oxide growth is still quite significant in the transition region. In fact, after the linear *V/t* region, the film still grows an additional 30-35% for the same period of time that it grew in the linear region. Only after longer times, such as 100 sec at 1 mA-cm^{-2}, is the current at the disk due almost entirely to the O_2 evolution reaction (>99%).

It can be seen from Fig. 4 that after 15 sec, the ring current is already 8.6% of i_{disk}. After about 100 sec, the ring current reaches 9.2% of i_{disk} and remains practically unchanged with further time of polarization. At this stage, i_{disk} is used almost entirely for O_2 evolution and then i_{ring} divided by i_{disk} gives the collection efficiency of the ring electrode. In the experiment shown in Fig. 4, the ring electrode was Au-plated. Au electrodes were found to be less sensitive to residual impurities in solutions than Pt electrodes (11), and more stable ring currents were observed with these electrodes. In view of the fact that at gold electrodes O_2 is reduced mainly to H_2O_2 (11, 13), the collection efficiency is 18.4%. This value is close to the efficiency (18.2) calculated and tabulated in (18). The experimentally obtained efficiency is used to scale the ring current and calculate i_{og} according to [7].

In the nonlinear *V/t* region, the potential is again seen to increase nearly linearly with the integrated charge density for oxide film growth, $q = \int_0^t i_{og}\, dt$. This is shown in Fig. 5 for two constant current densities applied to the disk electrode. To minimize errors due to stepwise integration of small currents, the integration was carried out only up to the time when i_{ring} corresponded to about 95% i_{disk}. The dependence of *V* on *q* calculated in this way in the nonlinear *V/t* region is quite different from that in the initial linear *V/t* region and can be represented by Eq. [8], rather than by Eq. [2]

$$\frac{\partial V}{\partial q} = m = 270\ \text{VC}^{-1}\text{-cm}^2 \neq f(i_{disk}, q) \qquad [8]$$

It is shown below that this relationship is an approximate one and that $\partial V/\partial q$ is equal to *m* only at large values of *q*. As can be determined from the four current densities used in these experiments (10^{-4}, 3×10^{-4}, 10^{-3}, and 3×10^{-3} A-cm^{-2}), the following relationship holds at any *q* in the nonlinear *V/t* region (Eq. [3])

$$\frac{\partial V}{\partial \ln i_{disk}} = \frac{2RT}{F} \neq f(i_{disk}, q) \qquad [9]$$

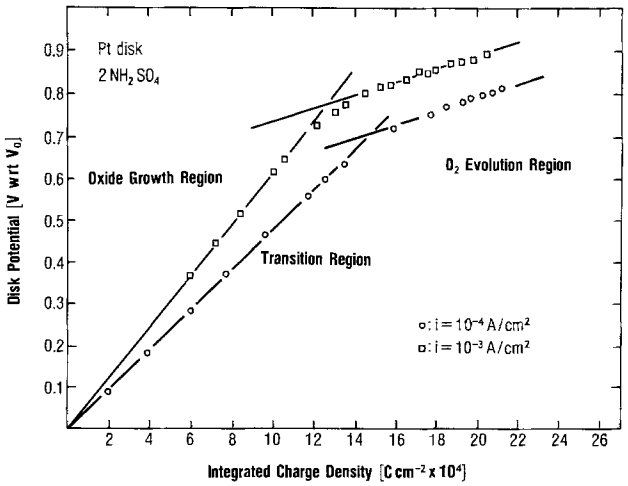

Fig. 5. Potential at the disk electrode vs. integrated charge density for oxide film growth at two current densities. Note that the V-q relationships at high q's change from those at low q's. Current and charge densities are not corrected for surface roughness (disk electrode RF = 1.4).

These relationships in the nonlinear V/t region are quite different from the corresponding relationships in the linear V/t region (Eq. [2], [3]).

To determine whether these differences in the V/q relationships in the oxide growth region and in the O_2 evolution region indicate a change in the oxide growth mechanism and/or a change in the physical properties of the film, *e.g.*, film aging and/or increasing conductivity (3), the following calculations were carried out. By using the experimentally determined values for i_{og} and q, $V - V_o$ ($=V_{calc}$) was calculated for all q by using Eq. [4] and was then compared to the observed value of $V - V_o$ ($=V_{obs}$) at each q. For this calculation, $i_{o,og}$, α, and V_o were determined from the linear V/t region for which Eq. [4] holds. The results of this comparison are shown in Fig. 6 for two applied constant current densities. It can clearly be seen that V_{calc} closely overlaps V_{obs} in all regions of the V/q curve.

It was possible to conclude from this analysis that the Pt oxide film continues to grow with the same mechanism in the transition region and in the predominantly O_2 evolution region as in the linear V/t or oxide growth region. The physical properties of the film do not change in going from the oxide growth region to the case where O_2 evolution is the major reaction. It follows then that in the O_2 evolution region, the films must still be poor electronic conductors. Furthermore, the structure of the double layer in the transition and the O_2 evolution region is basically the same as in the oxide growth region. In particular, ΔV_{OHL} remains constant, independent of the applied current density and the oxide film thickness, and has the same value as in the linear V/t region. In the nonlinear V/t region, at any constant applied current density, the fields in the film and in the IHL, however, decrease with increasing film thickness because the current density for oxide film growth continuously decreases with time or increasing film thickness. In spite of this decrease in the fields, the potential difference across the oxide film and the IHL, $(V - V_o)$, still increases with time. This is because the thickness of the film increases at a faster rate than the rate at which the field increases. This is illustrated in Fig 7. It may be noted that although the potential difference across the film and the IHL, $(V - V_o)$, increases with time, the potential difference across the IHL itself slowly decreases with time (since field decreases with time). This is discussed further below.

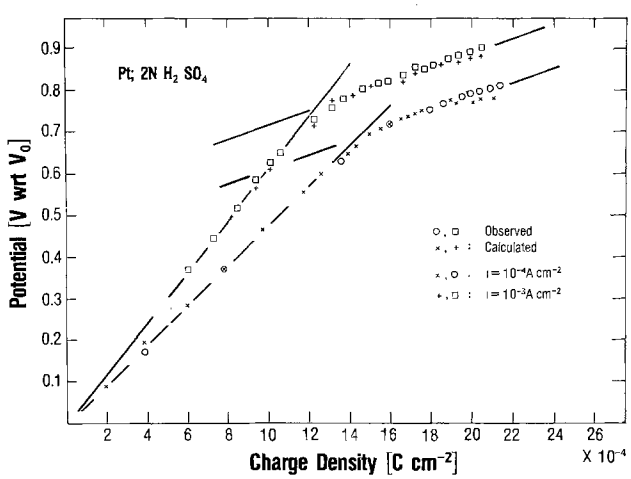

Fig. 6. Calculated and observed potentials vs. integrated charge density.

Oxygen evolution reaction in the transition region.— Once O_2 evolution becomes the predominant reaction, its rate as a function of q and V can be derived from the V/q relationships represented by Eq [8] and [9] and shown in Fig. 5 and 6. By integration of Eq. [8] and [9], the following rate equation is obtained

$$i_{O_2} = i_{o,O_2} \exp\left[-\frac{m\mathbf{F}}{2RT} q\right] \exp\left[\frac{\mathbf{F}(V - V_R)}{2RT}\right]$$

$$= i_{o,O_2} \exp\left[-\delta d\right] \exp\left[\frac{\mathbf{F}(V - V_R)}{2RT}\right] \qquad [10]$$

Here, d, the thickness of the oxide film, is equal to rq, where r ($= 9 \times 10^3$ ÅC^{-1}-cm^2) (9) converts charge density into film thickness.[1] The parameter δ is then equal to $m\mathbf{F}/(2RTr) = 0.6$ Å^{-1}. The integration constant, V_R, is chosen to be the reversible potential for the oxygen evolution reaction. The electrode potential, V, increases with time in the same way as does the potential difference, $V - V_o$, across the oxide film and the IHL. Irrespective that at a constant applied current density the potential difference across the IHL decreases gradually and ever so slowly with time, as discussed above, the current density for O_2 evolution still increases with time. This is because the current density for O_2 evolution depends on the potential difference across the oxide film and the IHL,

[1] For the $Pt(OH)_2$ structure, a monolayer of the oxide film corresponds to about 170 μC-cm^{-2}. If it is assumed that a monolayer is 2Å thick, the r factor would be somewhat higher (11.8×10^3 AC^{-1}-cm^2) than calculated from the density of $Pt(OH)_2$ (2, 9).

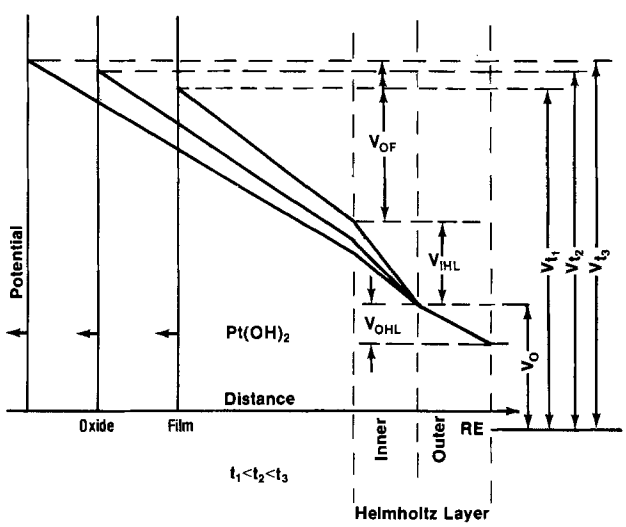

Fig. 7. A simple model of potential distribution across the oxide film and inner and outer Helmholtz layers when O_2 evolution becomes significant. Though field in the film decreases, overall potential still increases with time.

$V - V_0$, and not only on the potential difference across the IHL. This dependence on the potential difference across the oxide film and the IHL can be explained by a mechanism in which the first electrochemical step involving electron tunneling through the oxide films and IHL is rate determining. Both q and V increase with time, but the first exponential term in Eq. [10] increases at a faster rate than the second exponential term decreases, and hence the current for O_2 evolution increases with time.

An equation identical to Eq. [10] has been obtained previously from steady-state Tafel line measurements which were obtained after the initial polarization of an electrode at a constant potential or current density higher than the potentials at which the Tafel relationships were subsequently obtained (9, 19, 20). In this way, the films became fairly thick but their thickness, as determined by ellipsometry (9), remained constant during the Tafel measurements. From the ellipsometric measurements, the parameter δ was determined to be 1.4 $Å^{-1}$. The discrepancy between δ obtained in this study and that obtained by ellipsometry is not clear. No special significance is, however, given here to this difference in δ's.

The pre-exponential factor, i_{o,O_2}, is the exchange current density which would be expected at zero film thickness at the reversible potential. It can be evaluated by extrapolation to $q = 0$ of the linear V/q lines from the nonlinear V/t region. Such an extrapolation for a disk current of 10^{-3} A-cm^{-2} (Fig. 6) gives $V_{q=0} = 0.545$V *vs.* V_o, where V_o is 0.94V *vs.* RHE (7). Similarly, for a disk current of 10^{-4} A-cm^{-2}, $V_{q=0} = 0.430$V *vs.* V_o. The exchange current density at zero film thickness can now be calculated by determining the current density, i_{O_2}, expected at the reversible potential for oxygen evolution, $V_R = 1.23$V *vs.* RHE. Since this potential is 0.29V positive to V_o, it follows that, at 10^{-4} A-cm^{-2}, for instance, the overpotential for the oxygen evolution reaction is 0.14V (0.43-0.29V). Since for each decade of the applied current density, the potential changes about 115 mV, i_{o,O_2} at the reversible potential is equal to 6×10^{-6} A-cm^{-2}.

The above analysis shows that the same rate equation applies to the O_2 evolution reaction in the transition region at short times of polarization (2-10 sec at 10^{-3} A-cm^{-2}), as well as at long times (10^2-10^4 sec at 10^{-3} A-cm^{-2}). The mechanism of O_2 evolution does not change with changes in the thickness of the oxide film and with the time of polarization, and the films do not age or change their conductive properties with film thickening. However, Eq. [10] does show that the rate of O_2 evolution depends exponentially on the thickness of the oxide film. In fact, a substantial part of the overpotential for the oxygen evolution reaction arises from the effect of the barrier to charge transfer which these insulating films exert.

Oxygen evolution and oxide growth as parallel processes.—The transition from the oxide growth region to the O_2 evolution region at different current densities, such as those shown in Fig. 5, can now be understood in the following way. At any applied current density and at any q, the two processes of oxide growth and O_2 evolution, with respective partial current densities i_{og} and i_{O_2}, occur in parallel, and Eq. [7] is obeyed. These two processes depend differently on q and V (Eq. [4] and [10]). Thus for oxide growth, the V-q lines at different current densities originate at V_o and diverge linearly to infinite thicknesses and potentials. For O_2 evolution, the V-q lines are parallel and equally spaced along the potential axis for equal increments of current density. In Fig. 8, a family of diverging V/q lines, representing oxide growth at different current densities, intercept a family of parallel V/q lines, representing O_2 evolution at different current densities. When the lines for the same current density intercept, the rate of both reactions is equal.

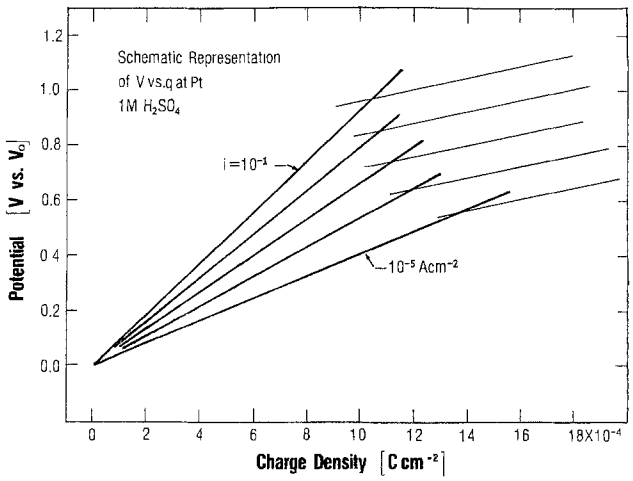

Fig. 8. Schematic representation of V-q relationships for oxide growth and O_2 evolution. At the intercepts of V-q lines for any given current density, the major process changes from oxide growth to O_2 evolution.

Quite generally, when two processes occur in parallel, the process which occurs at the lower potential, at any q, will predominate. Thus at low q, the oxide films grow with nearly 100% current efficiency. At high q, much higher potentials would be required to maintain the uninterrupted growth of the oxide films than for the evolution of oxygen. Consequently, O_2 begins to evolve and soon becomes the predominate reaction.

Figure 8 indicates that the potential of the transition points should increase while the charge density at this point should decrease with increasing applied current density. In Fig. 9, the potentials of the transition points, obtained experimentally, are plotted *vs.* the applied current density. In this figure, data of previous workers (7, 9) are included. It can be seen that the potential at the transition point does indeed increase with increasing applied current density.

Combining oxide growth and O_2 evolution in a single expression.—In the preceding discussion, it was shown that the growth of an anodic Pt oxide film obeys the same growth law (Eq. [4]) in the transition and O_2 evolution region as in the initial linear V/t region in which Pt oxide film growth is the predominant electrode reaction. Also, O_2 evolution is described by the same rate (Eq. [10]) in all regions. These equations provide the basis for the analysis of the entire V/q relationship.

The question remains as to whether the two apparently linear regions in Fig. 5 and 6 would be antici-

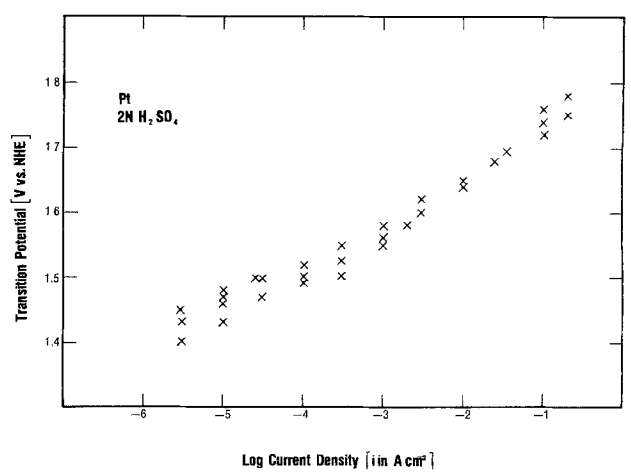

Fig. 9. Transition potentials from oxide growth to O_2 evolution in 2N H_2SO_4 as a function of applied current density.

pated to be linear by Eq. [4] and [10] when both processes occur in parallel. At any film thickness, Eq. [7] holds, and with the elimination of i_{O_2} and i_{og} from Eq. [10] and [4] by using Eq. [7], the dependence of V on q at any applied current density is readily obtained in an implicit form

$$i_{o,og} \exp\left[\frac{\alpha V}{q_T}\right] + i_{V_o,O_2} \exp\left[-\frac{mFq_T}{2RT} + FV/(2RT)\right] - i = 0 \quad [11]$$

In this equation, V is given *vs.* V_o for both the oxide growth and the oxygen evolution reaction. For this reason, i_{o,O_2} in [10] is replaced by i_{V_o,O_2} which is the current density for oxygen evolution at V_o and zero film thickness and is equal to 2×10^{-8} A-cm^{-2}. q_T represents the total charge density for oxide growth. By differentiation and by using the relationship $di_{og} = -di_{O_2}$, the following dependence of dV/dq on i_{og}, i_{O_2}, and q_T can be obtained

$$\frac{dV}{dq_T} = \frac{2RTi_{og} \ln (i_{og}/i_{o,og}) + mFq_Ti_{O_2}}{2RT\alpha i_{og} + Fq_Ti_{O_2}} \quad [12]$$

dV/dq_T continuously decreases with q_T and, therefore, neither the first nor the second V-q region should truly be linear. However, when $i_{og} >> i_{O_2}$, as in the first apparently linear V/q region, dV/dq is virtually constant for a constant current density and is given by Eq. [2]. Also, when $i_{O_2} >> i_{og}$, as in the second apparently linear V/q region, dV/dq must also become virtually constant and equal to m (Eq. [8]).

In order to estimate more accurately the degree of the linearity in both regions of the V/q plots, Eq. [11] has been calculated by computer using the experimentally determined parameters. The parameter m was determined in two ways with the first being from the slopes of the V/q traces, as discussed above. This procedure may be subject to error due to the fact that V/q traces are not expected to be quite linear. The second method for determining the value of m was by using the median value of the ring current where $i_{og} = i_{O_2}$ and where q and V are known. Then, from Eq. [10]

$$\frac{i_{disk}}{2} = i_{o,O_2} \exp\left[-\frac{mF}{2RT} q_{T,1/2} + \frac{FV_{1/2}}{2RT}\right] \quad [13]$$

where $q_{T,1/2}$, and $V_{1/2}$ are the values of q and V at $i_{og} = i_{O_2} = \frac{1}{2} i_{disk}$. With the first procedure, $m = 270$ VC^{-1}-cm^2, and with the second, $m = 330$ VC^{-1}-cm^2.

The computer-calculated V/q curve is shown in Fig. 10 and can be compared to the experimentally obtained V/q relationship as in Fig. 5. It is clear that the change of $\partial V/\partial q$ with q is negligible everywhere but near the transition point. It can therefore be concluded that a virtually linear V/q relationship exists for oxide film growth, both when the oxide growth is the predominant reaction and when the oxygen evolution is the major reaction.

Summary and Conclusions

The individual rates of Pt oxide growth and O_2 evolution at a Pt electrode in acid solutions were separated using rotating ring-disk electrode experiments. When a constant anodic current is applied to the disk electrode, the potential of the electrode is initially observed to increase linearly with time. In this linear V/t region, essentially all of the current is utilized in the formation of an insulating Pt oxide film.

Following the linear V/t region, V increases nonlinearly with time, and current at the ring electrode now commences to flow. This ring current increases sharply at first and then more slowly approaches the value expected for essentially 100% oxygen evolution. In the nonlinear V/t region, the potential is also seen to increase nearly linearly with the integrated charge density for oxide film growth.

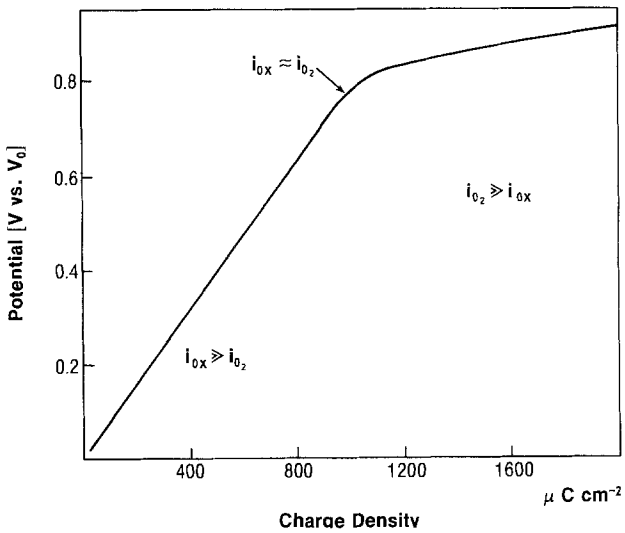

Fig. 10. Computer calculation (Eq. [11]) of V w.r.t. V_o as a function of total charge density. Note that both V/q regions are virtually linear.

In order to test the high field model for Pt oxide film growth when O_2 evolution is the major reaction, a calculation of the potential for the Pt disk electrode was made with the assumption that the mechanism of oxide growth is the same in the nonlinear V/t region as it was in the oxide growth region. It was found that the observed and the calculated potentials match closely at all values of q. Therefore, it was concluded that Pt oxide films continue to grow beyond the linear V/t region according to the same mechanism as in the linear V/t region. Consequently, the physical properties of the film, such as the electronic conductivity, do not change in going from the oxide growth region to the predominantly O_2 evolution region.

The close match between the calculated and the observed V/q curves also implies that the structure of the oxide film/solution interface remains unchanged throughout the V/q curves. In particular, the potential difference across the OHL remains constant, independent of the applied current density, and has the same value in the nonlinear V/t as in the linear V/t region.

The mechanism of the O_2 evolution reaction does not change with increasing oxide film thickness although the rate of the O_2 evolution reaction depends exponentially on the film thickness. The exchange current density for oxygen evolution at zero oxide film thickness is as high as 6×10^{-6} A-cm^{-2} compared to about 10^{-10} A-cm^{-2} at oxide-covered electrodes (19).

At any applied current, the two processes of oxide growth and O_2 evolution occur in parallel. The process which occurs at the lower potential for the same current density and oxide thickness predominates. A computer calculation of the entire V/q curve shows that virtually linear V/q relationships exist both when oxide growth is the predominant reaction and when oxygen evolution is the major reaction.

Manuscript submitted Jan. 15, 1982; revised manuscript received Jan. 11, 1983.

Any discussion of this paper will appear in a Discussion Section to be published in the June 1984 JOURNAL. All discussions for the June 1984 Discussion Section should be submitted by Feb. 1, 1984.

Allied Corporation assisted in meeting the publication costs of this article.

REFERENCES

1. M. L. B. Rao, A. Damjanovic, and J. O'M. Bockris, *J. Phys. Chem.*, **67**, 2508 (1963).
2. A. Damjanovic, A. T. Ward, B. Ulrick, and M.

O'Jea, *This Journal*, **122**, 471 (1975).
3. K. J. Vetter and J. W. Schultze, *J. Electroanal. Chem.*, **34**, 131, 141 (1972).
4. J. L. Ord and F. C. Ho, *This Journal*, **118**, 46 (1971).
5. A. Damjanovic, L-S. R. Yeh, and J. F. Wolf, *ibid.*, **127**, 1945 (1980).
6. H. Angerstein-Kozlowska, B. E. Conway, and W. B. A. Sharp, *J. Electroanal. Chem.*, **43**, 9 (1973).
7. A. Damjanovic and L-S. R. Yeh, *This Journal*, **126**, 555 (1979).
8. L. B. Harris and A. Damjanovic, *ibid.*, **122**, 593 (1975).
9. A. T. Ward, A. Damjanovic, E. Gray, and M. O'Jea, *ibid.*, **123**, 1599 (1976).
10. B. E. Conway and S. Gottesfeld, *J. Chem. Soc. Faraday Trans. I*, **69**, 1090 (1973).
11. A. Damjanovic, M. A. Genshaw, and J. O'M. Bockris, *This Journal*, **114**, 466, 1108 (1967).
12. A. N. Chemodanov, Y. M. Kolotyrkin, M. A. Dembrovskii, and T. V. Kudryavina, *Dokl. Akad. Nauk. SSSR*, **171**, 1384 (1966).
13. M. A. Genshaw, A. Damjanovic, and J. O'M. Bockris, *J. Electroanal. Chem.*, **15**, 163 (1967).
14. A. Damjanovic and A. T. Ward, in "International Review of Science; Physical Chemistry," Series II, Vol. 8, Butterworths, London (1976).
15. N. Cabrera and N. F. Mott, *Rept. Prog. Phys.*, **12**, 163 (1949).
16. A. Damjanovic, L-S. R. Yeh, and J. F. Wolf, *This Journal*, **129**, 55 (1982).
17. L. Young, "Anodic Oxide Films," Academic Press, New York (1961).
18. W. J. Albery and M. L. Hitchman, in "Ring-Disc Electrodes," pp. 22, 156, and 157, Oxford University Press, Oxford, England (1971).
19. A. Damjanovic and B. Jovanovic, *This Journal*, **123**, 374 (1976).
20. A. Damjanovic, A. T. Ward, and M. O'Jea, *ibid.*, **121**, 1186 (1974).

A Study of the Anomalous *p*H Dependence of the Oxygen Evolution Reaction at Platinum Electrodes in Acid Solutions

V. I. Birss[1]

Department of Chemistry, University of Ottawa, Ottawa, Ontario, Canada

A. Damjanovic*

Corporate Research and Development, Allied Corporaton, Morristown, New Jersey 07960

ABSTRACT

Steady-state V-log i relationships have been determined for the oxygen evolution reaction at platinum electrodes in acid solutions of various pH's. At all pH's, Tafel slopes close to $2RT/\mathbf{F}$ have been obtained after initially cathodically pretreating the electrode, polarizing it at a high anodic current density for a particular length of time, and then measuring the V-log i relationships at current densities lower than that used in the initial anodic electrode pretreatment. The order of the reaction with respect to hydrogen ions is then found to be one-half.

In other experiments, a rotating Pt ring disk electrode was used in solutions of various pH's in order to separate the currents due to Pt oxide film growth and those due to the oxygen evolution reaction and to accurately determine the charge density utilized for film growth. From this, it could be seen that the potential, at any constant charge density and pH, increases 120 mV for a tenfold increase of the current density, and that at a given current density and charge density, the potential decreases 60 mV as the pH increases one unit. These results confirm that the unusual fractional reaction order with respect to hydrogen ions is still obtained when the thickness of the oxide film remains constant. Further, it is reported here that the dependence of the oxygen evolution rates on pH can be attributed entirely to the dependence on the pH of the potential difference across the outer Helmholtz layer at the oxide film/solution interface. This simultaneous study of oxide film growth and the oxygen evolution reaction has led to a model for the potential distribution across the metal/oxide film/IHL/OHL/solution interface during the oxygen evolution reaction and to the conclusion that a fast quasi-equilibrium process exists across the outer Helmholtz layer.

The oxygen evolution reaction (OER) at platinum electrodes, in both acid and alkaline solutions, is a complex process that is still not satisfactorily understood. Evidence of this is shown by the great variance in the kinetic data of previous workers, even when apparently the same experimental conditions have been used, thus making any analysis of the reaction mechanism rather difficult. For example, in an early work, Hickling and Hill (1) reported a Tafel slope of $2RT/\mathbf{F}$ (130 mV/decade) for the OER in 1N H_2SO_4 solutions at current densities from 10^{-5} to 10^{-3} A-cm^{-2}. On the other hand, Pushnograeva *et al.* reported two different Tafel slopes for the OER in this same solution (2). For current densities of about 10^{-5}-10^{-3} A-cm^{-2}, the slope was close to $2RT/\mathbf{F}$, while for current densities from about 10^{-3}-5×10^{-2} A-cm^{-2}, the slope was close to $3RT/\mathbf{F}$ (175-190 mV/decade). Shultze and Vetter, however, reported V-log i relationships with a slope of about 120 mV/decade at low current densities but a slope of only 95 mV/decade at high current densities (3). Most other workers (4-11) have reported Tafel slopes close to $2RT/\mathbf{F}$ in acid solutions, frequently for over five decades of current density (4, 6, 7).

Part of this variance in Tafel slope determinations can be related to the lack of control of electrode pretreatment and of the procedure of V-log i measurements. It is now well documented that a thin insulating oxide film, presumably $Pt(OH)_2$ (12), grows at a platinum surface at potentials more positive than about 1.0 V/RHE (13-16). The rate of growth depends on the potential and film thickness (13-16). It is also well known that the rate of the OER depends critically on the thickness of these films (3, 9, 17) so that the current density at a given potential decreases exponentially with increasing thickness of the oxide film (3, 17).

Due to the effect of the film thickness on the kinetics of the OER, it is essential that the determination of the Tafel lines, required for a mechanistic analysis of the OER, is carried out under strictly controlled conditions of film growth or film thickness. For example, meaningful Tafel lines have been obtained when the

* Electrochemical Society Active Member.
[1] Present address: Department of Chemistry, University of Calgary, Alberta, Canada.

electrode was first anodically pretreated for a specified length of time at a higher current density, i_p, than those at which subsequent Tafel measurements were made (6, 9, 10). At current densities lower than i_p, and hence at the lower potentials, the field within the film that is the driving force for film growth (13-16) sufficiently decreases to render any further film growth negligible, as experimentally observed (12, 17-19). The Tafel lines can then be determined at an essentially constant film thickness. The film thickness itself will depend on the potential or the current density as well as the duration of electrode pretreatment. Irrespective of the film thickness, the Tafel lines obtained after this type of electrode pretreatment have a slope close to $2RT/\mathbf{F}$ over a few decades of current density (6, 8-10, 17). However, they are shifted parallel to each other when different electrode pretreatment is used, *i.e.*, the exchange current density changes (3, 9, 17).

It has also been recently demonstrated, with the use of a rotating ring disk electrode which can separate the two processes of oxygen evolution and oxide growth, that even when the oxide film is very thin and still growing, the V-log i relationships for oxygen evolution at any constant charge density representing the oxide film growth have a slope of 120 mV/decade (20).

As is customary in electrode kinetics, these slopes of 120 mV/decade have been associated with a mechanism in which a first charge transfer step is rate determining (4, 8, 10). A serious difficulty with this simple interpretation is that it cannot account for the observation that for the same electrode pretreatment (*e.g.*, i_p = cont., t = cont.) at any constant current density in the Tafel region, the potential decreases 60 mV as pH increases one unit (3, 9, 21). This leads to a fractional reaction order of one-half with respect to hydrogen ions (cf., Ref. 3 and 9).

The question can then be raised as to whether the observed fractional reaction order is related to different oxide film thicknesses existing in solutions of different pH's. In order to answer this, experiments have been carried out in which a solution of a given pH was rapidly replaced with a solution of a lower pH without interrupting the current flow during the Tafel measurements. These experiments showed that the fractional reaction order is real (9).

One explanation for this fractional reaction order has been that these thin oxide films are electronic insulators so that instead of having only a single barrier for charge transfer across the double layer at the oxide film/solution interface, a dual barrier comprised of both the oxide film and the oxide film/solution interface exists. If a chemical step following the first charge transfer step is then considered to be the rate-determining step, a Tafel slope of 120 mV/decade and a fractional reaction order of one-half with respect to hydrogen ions can be accounted for (9).

In recent studies of the growth of anodic oxide films at platinum, it has been suggested that the potential distribution across the metal/oxide film/solution interface is even more complex than suggested by the dual barrier model (14, 22) and is actually a distribution across three barriers, namely, the oxide film and the inner and outer Helmholtz layers. Under constant current conditions, the film initially grows without any significant oxygen evolution occurring, and the potential difference across the film increases linearly with increasing film thickness. The potential difference across the inner Helmholtz layer is considered to remain constant at a constant current density and increases as the current density for oxide growth increases. In contrast, the potential difference across the outer Helmholtz layer has been found to remain constant at all rates of oxide growth (22). Also, at any given film thickness and current density, the potential distribution across the film and the inner Helmholtz layer is independent of pH [in acid solutions only (22, 23)] while the potential difference across the outer Helmholtz layer decreases 60 mV as pH increases one unit. Even when both the OER and oxide growth occur concurrently, or when the OER is the major reaction, it has been shown by rotating ring disk experiments that oxide film growth continues according to the same rate equation as when only oxide film growth occurs (20). This indicates that when either oxide growth or oxygen evolution is the primary reaction, the potential distribution across the metal/oxide film/solution interface remains essentially unchanged. In particular, the potential difference across the outer Helmholtz layer remains independent of the rate of either oxide growth or of oxygen evolution and dependent on pH.

With the progress made in the studies of oxide growth at platinum anodes and with the development of a rational model for the potential distribution across the various interfaces, as well as with the success of the ring disk experiments in separating the rates of the individual processes, it has become warranted to examine the pH dependence of the OER and to analyze the fractional reaction order with respect to hydrogen ions by the rotating ring disk methods.

Experimental

Two types of experiments have been carried out. In the first, the steady-state V-log i relationships were determined for the OER in acid solutions of various pH's. A prereduced electrode was first subjected to an anodic current density of 3×10^{-3} A-cm^{-2} for 1 hr, and then the V-log i relationships were determined at current densities less than this value.

In the second series of experiments, a Pt ring disk electrode was used in acid solutions of various pH's to separate and to follow individually the rates of oxide growth and the OER with time. The cell, electrode pretreatment, experimental procedures, and analysis of data were the same as described in a previous paper (20), and all measurements were made at room temperature.

Results and Discussion

Steady-state V-log i determination for the oxygen evolution reaction on Pt at a given pH.—As discussed above, steady-state V-log i relationships have been determined after first cathodically reducing the Pt electrode and then subjecting it to a constant anodic current density, i_p, in a $2N$ H_2SO_4 solution for various periods of time. Some typical Tafel lines, which were obtained by the stepwise decrease of current density after the electrodes were charged at $i_p = 10^{-3}$ A-cm^{-2} for 10^2, 10^3, and 10^4 sec, are shown in Fig. 1. After recording the potentials at the lowest current density, the V-log i relationships could be retraced by increas-

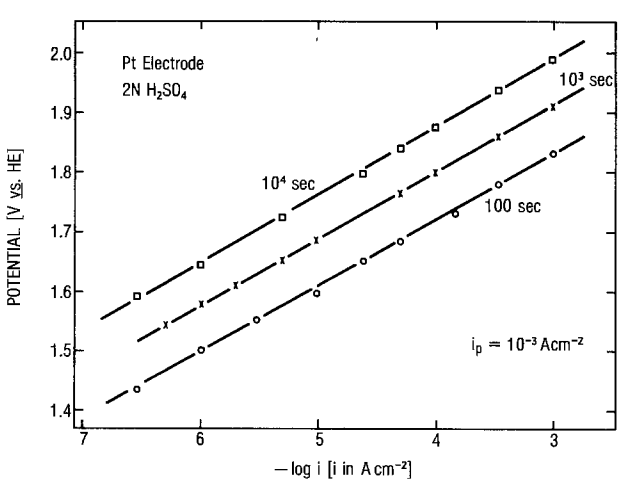

Fig. 1. V-log i relationships at Pt electrodes after various times at 10^{-3} A-cm^{-2} in $2N$ H_2SO_4. Note a decrease in the catalytic activity of the electrodes with time of pretreatment at 10^{-3} A-cm^{-2}.

ing current densities up to the current density of the initial anodic pretreatment. The electrode could remain at this current density for only a short time, such as 20-50 sec for the initial polarization time of 10^3 sec, as otherwise the potential would slowly increase further with time as the film thickness begins to increase again.

It can be seen in Fig. 1 that the Tafel lines for 3.5 decades of current density all have a slope close to 120 mV, independent of the length of time of anodic pretreatment at 10^{-3} A-cm^{-2}, as given in Eq. [1]

$$\frac{\partial V}{\partial \ln i} = \frac{2RT}{\mathbf{F}} \neq f(d, V) \qquad [1]$$

where d is the oxide film thickness, which is known to increase with time of polarization at the current density of electrode pretreatment (9, 16, 24).

It can also be seen in Fig. 1 that a tenfold increase of the polarization time at any particular current density increases the potential by about 75 mV

$$\frac{\partial V}{\partial \log t} = d \approx 75 \text{ mV} \qquad [2]$$

This increase of the potential with time is indicative of the increasing oxide film thickness with time.

It is clear that a linear V-log i relationship would not have been observed if the electrode had been brought from a potential of about 1.0 V/RHE to a higher potential by gradually increasing either the potential or the anodic current density. This has been well documented by various workers (4, 6, 7, 10). Also, a linear V-log i relationship would not have been obtained if the measurements had been made first at low current densities, or potentials, and then at higher current densities, or potentials, as the films would have thickened during the course of these measurements.

It is clear, therefore, that linear Tafel lines with the slope of 120 mV can be obtained only when the thickness of the oxide film remains constant during Tafel line determinations[2] and that for a meaningful mechanistic analysis, the thickness of the oxide film should be known.

The pH dependence of the OER from steady-state measurements.—In order to determine the pH dependence of the OER under these steady-state conditions, a constant current density of $i_p = 3 \times 10^{-3}$ A-cm^{-2} was applied to a prereduced electrode for 1 hr in all of the solutions studied. The Tafel lines were then determined by decreasing the current density in steps. Figure 2 shows that at any constant current density in the Tafel region, the potential has decreased 60 mV as the pH increased one unit. This potential-pH relationship is also shown in Fig. 3 for all of the solutions studied in this work. Significantly, it can be seen that an addition of neutral salts does not affect the kinetics of oxygen evolution. Further, it is seen that the same V-log i relationship is obtained in both H_2SO_4 and $HClO_4$ solutions of the same pH.

The data in Fig. 2 and 3 result in the following rate equation for oxygen evolution, where the reaction order with respect to hydrogen ions is one-half

$$i_{O_2} = K\,[H_3O^+]^{1/2} \exp\left[\frac{\mathbf{F}V}{2RT}\right] \qquad [3]$$

This fractional reaction order has been previously obtained from measurements in sulfuric acid solutions of two pH's in the absence of a neutral salt (9). It is now confirmed over a wide pH range in both H_2SO_4 and $HClO_4$ solutions, with and without salt.

The separation of the rates of oxide growth and oxygen evolution in solutions of different pH's with a ring disk electrode.—Rotating ring disk electrode experiments simultaneously provide the electrode potential, V, the current due to oxide growth, i_{og}, the current due to oxygen evolution, i_{O_2}, and the charge density, q, which is equivalent to the thickness of the oxide film, at all times of polarization by a constant anodic current, where q can be obtained by Eq. [4]

$$q = \int_0^t i_{og}\, dt \qquad [4]$$

Thus, as has been shown previously (20), when a constant current is applied to a prereduced disk electrode, the potential initially increases linearly with time, starting at about 1.0 V/RHE. In this linear potential region, essentially all of the current is utilized for oxide film growth, and the ring current is essentially zero. This oxide film grows by the high field mechanism (13, 15) according to the following rate equation (25, 26)

$$i_{og} = i_{og,o} \exp\left[\frac{V - V_o}{cq}\right] \qquad [5]$$

where c is a constant ($= 57$ VC^{-1} cm^2) independent of pH, and V_o is a parameter which depends on pH. The field within the oxide film is proportional to $(V - V_o)/q$.

After some time of constant current polarization, the linear V/t behavior ceases and the potential increases

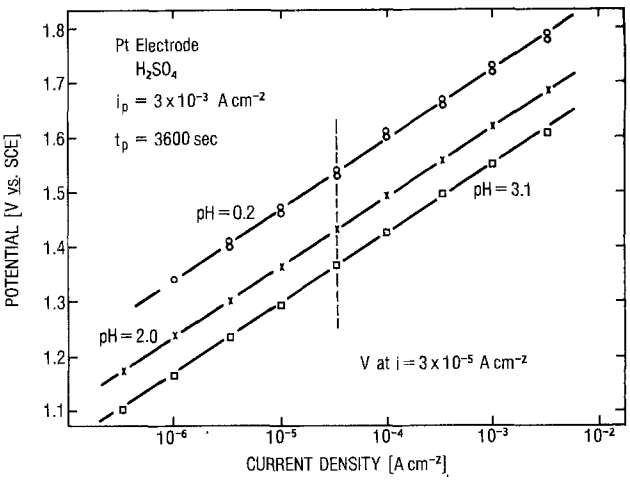

Fig. 2. V-log i relationships at electrodes after 1 hr at 3×10^{-3} A-cm^{-2} prior to measurements in solutions of various pH's.

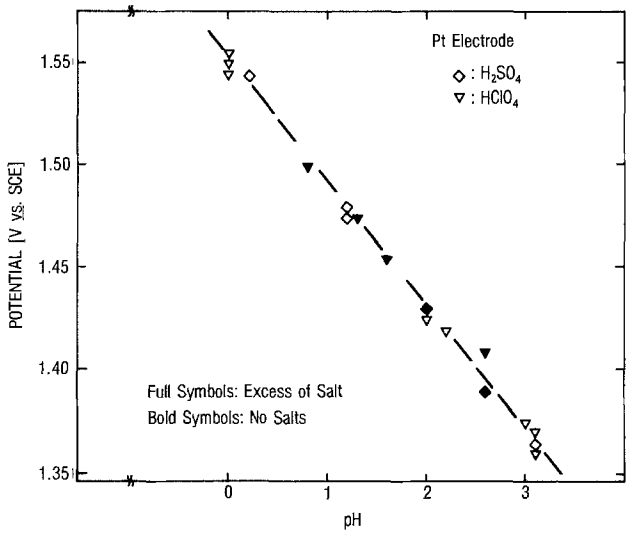

Fig. 3. Potentials at 3×10^{-5} A-cm^{-2} at electrodes after 1 hr at 3×10^{-3} A-cm^{-2} prior to V-log i measurements at $i < 3 \times 10^{-3}$ A-cm^{-2}. Potentials are recorded vs. SCE. Full symbols: an addition of the corresponding K^+ salt up to 1M.

[a] In the older data showing the slope of 120 mV/decade, the pretreatments of electrodes, which were frequently very extensive, appear to have led to the required condition for the constant slope.

more slowly and nonlinearly at a rate which decreases with time. The current at the ring electrode then increases due to the reduction of oxygen which is being evolved at the disk electrode, but the current soon levels off and rather slowly approaches the current expected for essentially 100% oxygen evolution at the disk electrode (20).

When the current at the ring electrode, i_{ring}, is scaled to the current at the disk electrode, i_{disk}, the current due to Pt oxide growth can be obtained as in Eq. [6] (20)

$$i_{og} = i_{disk} - i_{ring} \quad [6]$$

These ring disk data show that the oxide film continues to grow even when oxygen evolution is the main reaction at the disk electrode. This has previously been observed by coulometry (24) and ellipsometry (16).

It can be seen in Fig. 4 that, as in the case when only oxide growth occurs and Eq. [5] is obeyed, the observed V/q relationship is also linear even when the OER is the primary reaction at the disk. Further, when V is calculated from Eq. [5] by utilizing the integrated value of q (Eq. [4]) and the current due to oxide growth (Eq. [6]) and is then compared to the observed potential at the disk electrode, these two V/q relationships match very closely as shown in Fig. 4 for two pH's. Consequently, the oxide films continue to grow at all pH's in acid solutions with the same mechanism even during vigorous oxygen evolution as when no significant oxygen evolution occurs.

At any constant charge density and a given pH, the potential increases 120 mV for a tenfold increase of the current density (not shown in Fig. 4). It follows that the rate of the OER in a solution of a given pH can be expressed by the following equation (20)

$$i_{O_2} = k' \exp\left[\frac{-m\mathbf{F}q}{2RT}\right] \exp\left[\frac{\mathbf{F}V}{2RT}\right] \quad [7]$$

where m ($= \partial V/\partial q$) is a constant which has been determined to be 270-330 VC^{-1} cm^2 (20), and where other symbols have their usual significance. Equation [7] shows that the rate of the OER depends critically on the thickness of the oxide film.

It is also seen in Fig. 4 that in both linear V-q regions, the potential at any constant thickness of the oxide film has decreased 60 mV as the pH has increased by one unit. As essentially all of the current in the second linear V/q region is utilized for the OER, the following relationships can be established for the OER

$$\frac{\partial V}{\partial \mathrm{pH}} = -\frac{2.3RT}{\mathbf{F}} \neq \mathbf{F}(q, i_p) \quad [8]$$

and

$$\frac{\partial V}{\partial q} = m \neq f(\mathrm{pH}, i_p) \quad [9]$$

By combining these equations with Eq. [7], the following rate equation for the OER is obtained

$$i_{O_2} = K[H_3O^+]^{1/2} \exp\left[\frac{-m\mathbf{F}q}{2RT}\right] \exp\left[\frac{\mathbf{F}V}{2RT}\right] \quad [10]$$

Since Eq. [10] is determined from simultaneous measurements of V, i, and q in solutions of different pH's, the fractional reaction order with respect to H_3O^+ is confirmed at all thicknesses of the oxide film, even at the earliest stages of oxygen evolution when the films are very thin and still growing. This fractional reaction order cannot be ignored and must be considered in any mechanistic analysis.

Model of the metal oxide film solution interface and dependence on pH.—The growth of the anodic oxide film at Pt electrodes has been found to obey Eq. [5], which also expresses the rate of the high field migration of ions through an insulating film (25). In this equation, V_0 is the only pH dependent parameter, decreasing 60 mV as pH increases one unit (15, 23). V_0 is considered to be the potential in the inner Helmholtz plane with respect to a pH independent reference electrode, and therefore, it gives a measure of the potential difference across the outer Helmholtz layer, ΔV_{OHL}. $(V - V_0)$ is then the potential difference across the growing oxide film and the inner Helmholtz layer (22). A simple model suggested for the potential distribution across the complex interface, comprised of the oxide film and the inner and outer Helmholtz layers, is shown in Fig. 5, for two current densities and two pH's.

The close match between the calculated and observed potentials (Fig. 4) in the ring disk experiments has shown that even when oxygen evolution becomes the major reaction, the potential difference across the outer Helmholtz layer, ΔV_{OHL}, remains constant at a given pH, irrespective of the rate at which the oxide is still growing (22). In other words, ΔV_{OHL} has the same value in the predominantly oxygen evolution region as in the predominantly oxide growth region. This implies that as the rate of oxide growth decreases and the OER becomes more predominant, the observed increasing potential must be a result of an increased potential difference across the oxide film and the IHL, rather than across the OHL. Since Eq. [5] also holds in the oxygen evolution region, and since i_{og} continuously decreases with the thickness of the oxide film,

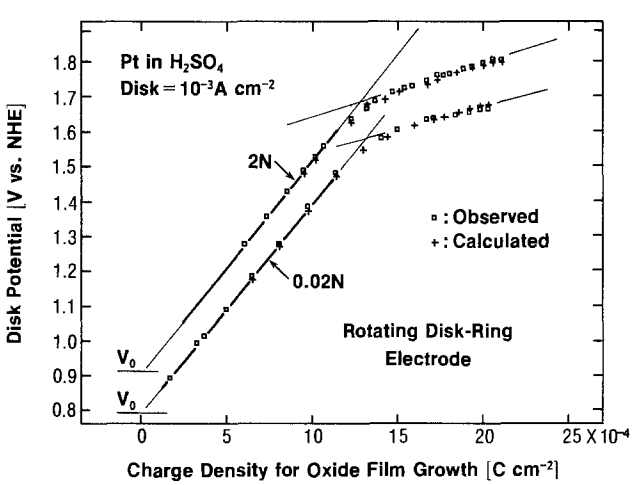

Fig. 4. V-q relationships at two pH's. Note two regions in which V-q lines in solutions of different pH's are parallel. Note also the close match of the calculated and observed potentials.

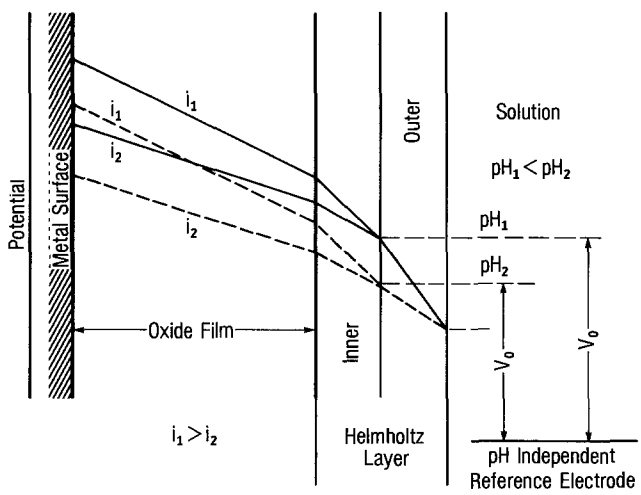

Fig. 5. Model of the potential distribution across the oxide film and the inner and outer Helmholtz layer at two current densities and two pH's. The same model holds both when oxide growth process and the oxygen evolution reaction predominate. Note that potential difference across the OHL is independent of the applied current density but decreases as pH increases.

the field within the film and the IHL must also decrease. This is possible only because the thickness of the film increases at a faster rate than the potential difference across the oxide film (Fig. 6).

When the solution pH increases one unit, V_o decreases 60 mV and the potential of the inner Helmholtz plane, with respect to a pH independent reference electrode, also decreases 60 mV (22, 23). Therefore, in solutions of different pH's, the potential difference across the film and the inner Helmholtz layer is the same for the same current density of oxide growth and the thickness of the oxide film, independent of pH, as is illustrated in Fig. 5. As a consequence, the V-q lines in the first linear V-q region, when essentially only oxide growth occurs, and in the second V-q region, when oxygen evolution is the major reaction, are parallel but shifted along the V axis by 60 mV per pH unit (cf. Fig. 4). The shift is due entirely to the dependence of ΔV_{OHL} on pH.

Because ΔV_{OHL} does not change with a change in current density when a Tafel line is determined by decreasing current density over a range of current densities, it is the potential difference across the oxide film and the inner Helmholtz layers which changes 120 mV for each decade of current density (Fig. 7). It follows that it is the potential difference across the oxide film and the inner Helmholtz layer which controls the rate of the OER. The observed 60 mV dependence of the rate of the OER on pH and the observed fractional reaction order with respect to hydrogen ions reflects only the change of ΔV_{OHL} with pH, while the potential differences across the oxide film and the inner Helmholtz layer at a given current density, $(V - V_o)$, do not change, *i.e.*, $(V - V_o)$ at any constant current density is independent of pH. The explanation of the observed pH dependence of the OER and the fractional reaction order with respect to hydrogen ions is, therefore, an explanation of the pH dependence of ΔV_{OHL}.

The fact that ΔV_{OHL} remains constant over a large range of current densities must mean that the charge transfer process occurring across the outer Helmholtz layer is fast and in quasi equilibrium. The most likely process for this would be the rapid transfer of a proton from a water molecule at the inner Helmholtz plane across the outer Helmholtz layer to a water molecule in the outer Helmholtz plane, according to

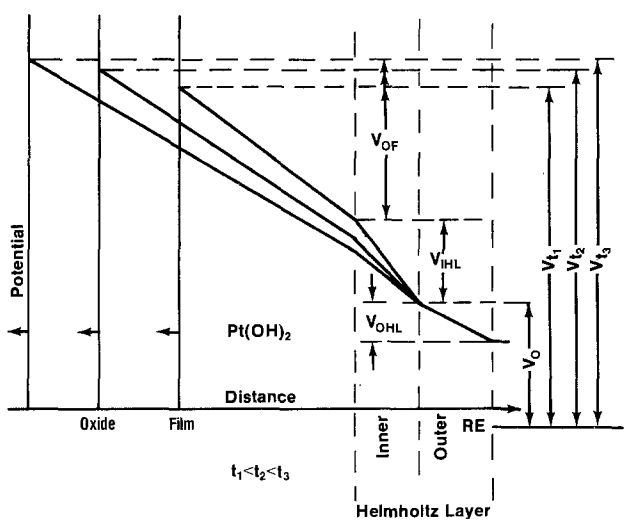

Fig. 6. Model for the potential distribution across the oxide film and the inner and outer Helmholtz layer in the transition from predominantly oxide growth to predominantly oxygen evolution. As current density for oxide growth and the fields in the oxide film and IHL decrease, the potential still increases because the film thickness increases faster than the field decreases. Note that ΔV_{OHL} is not affected in the transition.

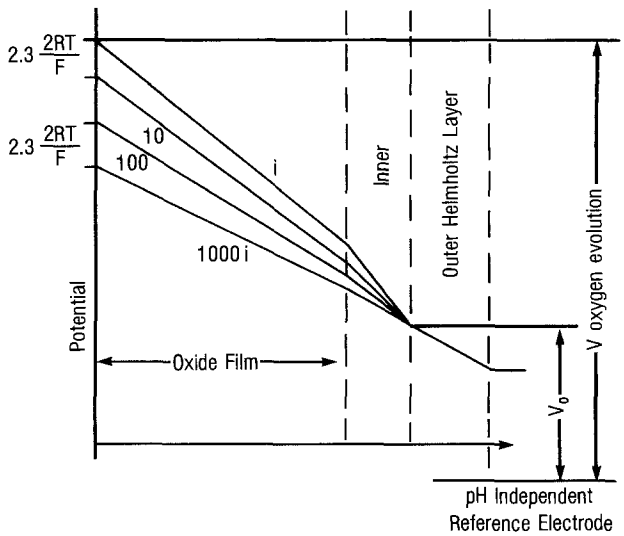

Fig. 7. When the Tafel lines are determined by decreasing the current density incrementally, the potential distribution across the oxide film and the inner and outer Helmholtz layer adjusts so that ΔV across the oxide film and the IHL decreases 120 mV for a tenfold decrease of current density. Note that ΔV_{OHL} remains constant.

$$H_2O)_{IHP} + H_2O)_{OHP} \rightleftarrows OH^-)_{IHP} + H_3O^+)_{OHP} \quad [11]$$

Alternatively, during oxygen evolution, a water molecule in the inner Helmholtz plane may discharge, ejecting a proton across the outer Helmholtz layer

$$2H_2O)_{IHP} \rightarrow OH)_{IHP} + e^-_m + H_3O^+)_{IHP} \quad [12]$$

$$H_3O^+)_{IHP} + H_2O)_{OHP} \rightleftarrows H_2O)_{IHP} + H_3O^+)_{OHP} \quad [13]$$

Therefore, while the rate of proton transfer across the outer Helmholtz layer is fast and independent of ΔV_{OHL}, the slower electron transfer step across the anodic film and the inner Helmholtz layer are potential dependent and rate limiting. The mechanism of the electron transfer is another subject and will be dealt with in a subsequent paper.

The actual value of ΔV_{OHL} is not known. If it is assumed that at Pt the zero electrode potential coincides with the potential of zero charge (pzc) and that the pzc decreases 60 mV per unit of pH *vs.* a pH independent reference electrode, as reported (27), then ΔV_{OHL} can be considered to be constant at every pH. The rate of the OER could then be expressed with respect to the pzc as follows

$$i = C \exp\left[\frac{-m\mathbf{F}q}{2RT}\right] \exp\left[\frac{V_{pzc}}{2RT}\right] \quad [14]$$

where V_{pzc} is the electrode potential against the pzc and C is a constant independent of the pH.

It is evident from this work and a previous paper (20) that the OER and the oxide growth reaction at a Pt electrode are closely interrelated. Substantial progress has been made in understanding the anomalous pH dependence of the OER and its fractional reaction order with respect to hydrogen ions by understanding the potential distribution at the metal/oxide film/solution interface. Further progress in the understanding of the OER and of the dependence of ΔV_{OHL} on pH is expected by extending these types of studies to alkaline solutions where the pH dependence of the oxide growth reaction (22) and of the OER (28) are more complex than in acid solutions.

Manuscript submitted March 2, 1982; revised manuscript received Feb. 7, 1983.

Any discussion of this paper will appear in a Discussion Section to be published in the June 1984 JOURNAL. All discussions for the June 1984 Discussion Section should be submitted by Feb. 1, 1984.

Allied Corporation assisted in meeting the publication costs of this article.

REFERENCES

1. A. Hickling and S. Hill, *Trans. Faraday Soc.*, **46**, 550 (1950).
2. I. I. Pushnograeva, A. M. Skundin, Yu. B. Vasil'ev, and V. S. Bagotskii, *Soviet Electrochem.*, **6**, 134 (1970).
3. J. W. Schultze nd K. J. Vetter, *Electrochim. Acta*, **18**, 889 (1973).
4. J. O'M. Bockris and A. K. M. Shamshul Huq, *Proc. R. Soc. London, Ser. A*, **237**, 277 (1956).
5. W. Visscher and M. A. V. Devanathan, *J. Electroanal. Chem.*, **8**, 127 (1964).
6. A. Damjanovic, A. Dey, and J. O'M. Bockris, *Electrochim. Acta*, **11**, 791 (1966).
7. D. V. Kokoulina, Yu. I. Krasovitskaya, and L. I. Krishtalik, *Soviet Electrochem.*, **7**, 1172 (1971).
8. G. N. Afon'shin, G. F. Volodin, and Yu. M. Tyurin, *Soviet Electrochem.*, **7**, 1295 (1971).
9. A. Damjanovic and B. Jovanovic, *This Journal*, **123**, 374 (1976).
10. J. P. Hoare, *ibid.*, **112**, 602 (1965).
11. E. I. Krushcheva, O. V. Morovskaya, N. A. Shumilova, and V. S. Bagotskii, *Elektrokhimiya*, **8**, 205 (1972).
12. S. H. Kim, W.-K. Paik, and J. O'M. Bockris, *Surf. Sci.*, **33**, 617 (1972).
13. J. L. Ord and F. C. Ho, *This Journal*, **118**, 46 (1971).
14. K. J. Vetter and J. W. Schultze, *J. Electroanal. Chem.*, **34**, 131, 141 (1972).
15. A. Damjanovic, A. T. Ward, B. Ulrick, and M. O'Jea, *This Journal*, **122**, 471 (1975).
16. A. Ward, A. Damjanovic, E. Gray, and M. O'Jea, *ibid.*, **123**, 1599 (1975).
17. A. Damjanovic, A. T. Ward, and M. O'Jea, *ibid.*, **121**, 1186 (1974).
18. H. E. Laitinen and C. G. Enke, *ibid.*, **107**, 773 (1966).
19. S. Gilman, *J. Electroanal. Chem.*, **2**, 111 (1967).
20. V. I. Birss and A. Damjanovic, *This Journal*, **130**, 1688 (1983).
21. T. Erdey-Gruz, M. Gallyas, and E. Szetey, *Acta Chim. (Budapest)*, **69**, 43 (1971).
22. A. Damjanovic, L-S. R. Yeh, and J. F. Wolf, *This Journal*, **129**, 55 (1982).
23. A. Damjanovic and L-S. R. Yeh, *ibid.*, **126**, 555 (1979).
24. D. Gilroy and B. E. Conway, *Can. J. Chem.*, **46**, 875 (1968).
25. N. Cabrera and N. F. Mott, *Rep. Prog. Phys.*, **12**, 163 (1949).
26. A. Damjanovic and A. T. Ward, in "International Review of Science: Physical Chemistry," Series II, Vol. 6, p. 103, Butterworths, London (1976).
27. E. Gileadi, S. D. Argade, and J. O'M. Bockris, *J. Phys. Chem.*, **70**, 2044 (1966).
28. A. Damjanovic, A. Dey, and J. O'M. Bockris, *This Journal*, **113**, 739 (1966).

The Recombination of Photogenerated Minority Carriers in the Depletion Layer of Semiconductor Electrodes

W. J. Albery* and P. N. Bartlett*

Department of Chemistry, Imperial College, London SW7 2AY, England

ABSTRACT

The problem of depletion layer recombination in illuminated semiconductor electrolyte systems, as used for solar energy conversion, is considered. It is shown that there can be four different kinetic cases. The conditions for the existence of these different cases as a function of the potential drop across the depletion layer, the irradiance, and the photocurrent are derived. Analytical solutions for current voltage curves for the different cases are derived and criteria for distinguishing between the different cases are given. The effects of concentration polarization of the majority carriers are considered and shown to be negligible for typical semiconductors.

In a previous paper (1), we extended the treatment by Gartner (2) and by Wilson (3) of the problem of the transport and kinetics of photogenerated minority carriers in semiconductor electrolyte cells to include the effect of the recombination of minority carriers in the depletion layer. In Ref. (1), we assumed that the kinetics of the recombination were first order throughout the depletion layer. This assumption may be contrasted with that made by Reichman (4) in his treatment of depletion layer recombination. He followed Sah, Noyce, and Shockley (5) and assumed that because of the repulsion of majority carriers from the surface, the recombination kinetics changed somewhere in the depletion layer from being first order in minority carriers to being first order in majority carriers. In this paper, we present a unified treatment of these two cases. We also consider two other new cases which can arise where the recombination kinetics are first order in both majority and minority carriers. We describe and discuss the conditions under which these four different cases are found. We present a simple general diagram which shows how the zones of dominance of the different cases depend upon experimental variables such as irradiance and applied potential. We derive simple analytical expressions for the current-voltage curves and show how the different cases may be distinguished. Hitherto it has been assumed that the concentration of majority carriers is given by a Boltzmann distribution in the field of the depletion layer. Laser and Bard's simulation (6) showed that there could be a buildup of photogenerated majority carriers, while they are waiting to be transported out of the depletion layer. In our treatment, we consider the effect of transport on the concentration of majority carriers. We show that although there can indeed be a buildup, it is unlikely to effect the recombination kinetics of typical semiconductors. Throughout this paper, we will consider the case of a p-type semiconductor.

The Rate Limiting Step in Recombination

We assume that the recombination process is the same as that of Shockley and Read (7), but we will use the normal notation of chemical kinetics. With the following rate constants

	k_1		k_2	
e	$\rightleftarrows$	e	$\rightleftarrows$	e
conduction band	k_{-1}	trap	k_{-2}	valence band

* Electrochemical Society Active Member.

Key words: photoelectrochemistry, semiconductor kinetics, semiconductor/liquid electrolyte.

the expression for the rate of recombination, r, is

$$\frac{1}{r} = \underset{\text{I}}{\frac{1}{k_1 n}} + \underset{\text{II, 1}}{\frac{k_{-1}}{k_1 k_2 np}} + \underset{\text{II, 2}}{\frac{k_{-2}}{k_1 k_2 np}} + \underset{\text{III}}{\frac{1}{k_2 p}} \qquad [1]$$

where n is the concentration of electrons (the minority carriers), p is the concentration of holes (the majority carriers), k_1 and k_2 are first-order rate constants, and k_{-1} and k_{-2} are zero-order rate constants.

The zero-order rate constants k_{-1} and k_{-2} describe the rate of thermal excitation of electrons from the full traps to the conduction band (k_{-1}) and from the valence band to the empty traps (k_{-2}). As depicted in Fig. 1 each of the terms in [1] relates to a different situation with respect to first the rate-limiting step and second whether the traps are full or empty. The relative sizes of II, 1 and II, 2, depend upon k_{-1} and k_{-2} and in Fig. 1, we have shown the location of the traps within the bandgap which leads to either II, 1 or II, 2 being found.

We assume that in the field-free region the recombination kinetics are first order in the photogenerated minority carriers (n) and that the rate is given by term I in [1]. This is because term I is the only term that does not contain the concentration of majority carriers (p) which in the field-free region will be close to the unperturbed value. Now in the depletion layer n increases and p decreases so that in [1] one of the other terms labeled II or III may become the dominant term. Combining II, 1 and II, 2, Fig. 2 shows a contour diagram for the recombination rate r and the three zones of dominance for the different terms. Hence, the first-order kinetics in n (I) may give way to second-order kinetics (II), I → II. If $k_{-1} > k_{-2}$ (case II, 1) then this change occurs when, because of the repulsion of holes from the surface, an electron falling into the traps, which are empty, is more likely to return to the conduction band than to find a scarce hole in the valence band. If $k_{-2} > k_{-1}$ (case II, 2), the change occurs when the Fermi level fills the traps, so that an electron in the conduction band now has to find a scarce hole in the trap (see Fig. 1). Secondly, the first-order kinetics in n may give way to the first-order kinetics in p, I → III. An even more complicated case is possible where close to the electrolyte surface as n rises and p drops the system passes through the sequence I → II → III. If both n and p obey a Boltzmann distribution in the field of the depletion layer then the locus of any system in Fig. 2 is a line of slope −1. In

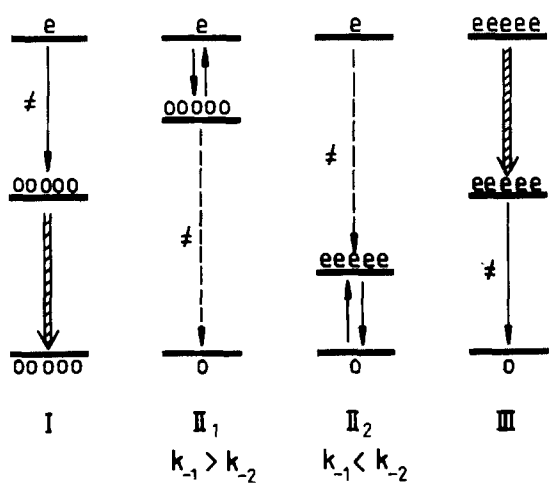

Fig. 1. The kinetics of recombination of minority carriers (e for a p-type semiconductor) as described by the 4 terms in Eq. [1]. The transition state symbol ≠ shows the rate limiting step. The symbols e and o show whether the trap is full or empty; in the sequence of dominant terms I through to III, n increases and p decreases.

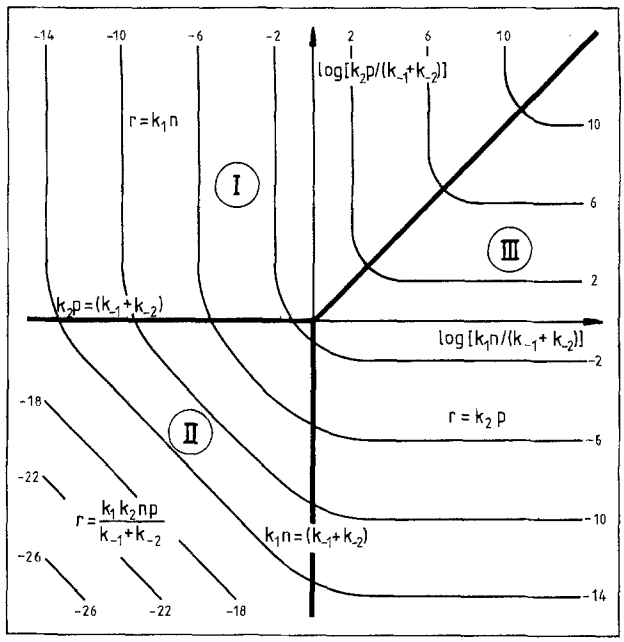

Fig. 2. The zones of dominance of terms I, II, and III in Eq. [1] as a function of the concentrations of electrons and holes. The value of log $(r/(k_{-1} + k_{-2}))$ is shown by the contours and approximate expressions for r are given in each zone. As n rises and p falls, a system moves from zone I towards the bottom right corner. If n and p both obey a Boltzmann distribution then the locus has a gradient of −1.

Table I, we collect together the different cases and using Fig. 2, we describe the region in the depletion layer where the rate of recombination is largest. Which sequence is found and where the kinetic boundaries are depends on the distributions of n and p in the depletion layer.

Distribution of Minority Carriers

From Eq. [15], [22], and [23] of Ref. (1), a good approximation for the concentration of minority carriers in the depletion layer is

$$n = n_o \exp(\theta - \theta_o) - \frac{2^{1/2} L_D}{D_n}\left[I_o(1 - \beta - N) - \frac{k_1 n_o L_D}{(2\theta_o)^{1/2}} \right] \exp(\theta) \int_{\theta^{1/2}}^{\theta_o^{1/2}} \exp(-\lambda^2)\, d\lambda \qquad [2]$$

where

$$n_o = NI_o/k_\Sigma' \qquad [3]$$

In these equations, $\theta = \mathbf{F}V/RT$ and is a dimensionless potential measured with respect to the bulk of semiconductor; n_o is the concentration of electrons at the electrolyte interface; N is the collection efficiency which is the flux of electrons through the electrolyte interface divided by I_o; I_o is the irradiance at the electrolyte interface; k_Σ' is the sum of the heterogeneous rate constants for removing minority carriers at the electrolyte interface; D_n is the diffusion coefficient of the electrons; $\beta = \exp(-W/L_\epsilon)$ where W is the width of the depletion layer, L_ϵ, the absorption length, is the reciprocal of the absorption coefficient, and β describes the fraction of light that penetrates to the field-

Table I. Location of maximum rate of recombination for different kinetic cases

Case	Location
I	Sharp maximum at electrolyte surface
I → II	Constant rate between electrolyte surface and I, II boundary
I → II → III	Constant rate between I, II and II, III boundaries
I → III	Sharp maximum on I, III boundary

free region; $W = (2\theta_0)^{1/2}L_D$ where L_D is the Debye length. In Ref. (1), we showed that the second term on the right-hand side of [2] which describes concentration polarization is dominant at the inner boundary of the depletion layer while the n_0 term is dominant through most of the rest of the layer. Since any switch in kinetics is unlikely to take place near the inner edge of the depletion layer, we can neglect the second term and write

$$n \simeq (NI_0/k_\Sigma') \exp(\theta - \theta_0) \quad [4]$$

Distribution of Majority Carriers

The differential equation describing transport and kinetics for the majority carriers is

$$D_p\left(\frac{\partial p}{\partial x} + p\frac{\partial \theta}{\partial x}\right) = -I_0\left[1 - \exp\left(-\frac{x}{L_\epsilon}\right)\right] + \int_0^x kp\,dx + \rho N I_0 \quad [5]$$

In this equation, D_p is the diffusion coefficient of the holes, x is the distance from the electrolyte interface, and k is a first-order rate "constant" for the recombination of the majority carriers; k will vary with x depending on the different kinetic regimes. At the electrolyte interface, the total flux of minority carriers passing through the interface is NI_0. Of this flux, we assume a fraction ρNI_0 undergo surface recombination while the remainder $(1 - \rho)NI_0$ take part in faradaic reactions. The flux of holes consumed at the electrolyte interface by surface recombination is then given by ρNI_0.

In Table I, we listed where the zone of maximum recombination is to be found for each kinetic case. Because of the exponential terms in the concentration profiles, one can show that recombination in the space between this zone ending at a distance x_{RZ} and the inside edge of the depletion layer at $x = W$ is negligible. We now define κ which describes the total loss due to recombination in the depletion layer

$$\kappa = \int_0^{x_{RZ}} kp\,dx \quad [6]$$

Then for $x_{RZ} < x < W$, we substitute Eq. [6] in [5] and treat κ as a constant. Equation [5] then has the same form as [19] of our previous treatment where in that equation $k = 0$. We can solve Eq. [5] by the same method to obtain for p in the region $x_{RZ} < x < W$ a similar equation to Eq. [2]

$$p = p_w \exp(-\theta) + \frac{2^{1/2}L_D}{D_p}\left[I_0\left(1 - \beta\exp\left\{\frac{\sqrt{2\theta}L_D}{L_\epsilon}\right\} - \rho N\right) - \kappa\right]\exp(-\theta)\int_0^{\theta^{1/2}} \exp(\lambda^2)\,d\lambda \quad [7]$$

where p_w is the concentration of majority carriers in the field-free region.

Differentiation of Eq. [7] and use of the relation $dx/d\theta = -(2\theta)^{1/2}L_D$ shows that (providing $L_D << L_\epsilon$ which is almost certain to be true)

$$-D_p(dp/dx)_{x=W} = I_0[1 - \beta - \rho N] - \kappa \quad [8]$$

Equation [8] shows that, as with the minority carriers, the second term in Eq. [7] describes the concentration polarization necessary to carry the photogenerated majority carriers out of the depletion layer. They are generated by $I_0(1 - \beta)$ — the fraction of light absorbed in the depletion layer. They are destroyed firstly at the electrolyte interface by surface recombination, ρNI_0 and secondly by homogeneous recombination in the reaction zone κ. As found in the simulation of Laser and Bard (6) when the right-hand side of Eq. [8] is positive, the concentration of majority carriers will pass through a maximum somewhere in the depletion layer. Similarly from Eq. [2], we find that the flux of minority carriers at $x = W$ is given by

$$-D_n(dn/dx)_{x=W} = I_0(1 - \beta - N) - \kappa \quad [9]$$

where for the first-order case (1)

$$\kappa = n_0L_Dk_1/(2\theta_0)^{1/2} \quad [10]$$

Subtraction of Eq. [8] and [9] shows that the net current at $x = W$ is $I_0N(1 - \rho)$, and it is satisfactory that this equals the faradaic current at the electrolyte interface.

Returning to Eq. [7], we can now find the concentration of majority carriers p_{RZ} at the potential θ_{RZ} in the reaction zone

$$p_{RZ} = p_w \exp(-\theta_{RZ}) + \frac{L_D}{D(2\theta_{RZ})^{1/2}}[I_0(1 - \beta' - \rho n) - \kappa] \quad [11]$$

Boltzmann Transport

where

$$\beta' = \exp(-x_{RZ}/L_\epsilon) \quad [12]$$

The square bracket in Eq. [11] describes the flux of majority carriers passing from the reaction zone to the relative safety of the inner part of the depletion layer where there are very few minority carriers to destroy them. The analysis of the terms is similar to that in Eq. [7].

As in our previous treatment of the minority carriers (1), p_{RZ} can be determined either by the classical Boltzmann term or by the transport term describing the concentration polarization required to move the majority carriers. However, whereas for the minority carriers, the Boltzmann term dominates near the electrolyte interface and the transport term near the internal interface, for the majority carriers the situation is reversed. If the transport term in Eq. [7] is to dominate, it must be in a region near the electrolyte interface where the first term has been reduced to insignificance by $\exp(-\theta_{RZ})$.

The Collection Efficiency

Equation [29] of Ref. (1) was shown to be a good approximation for the collection efficiency

$$N \simeq \frac{1 - \beta + \beta L_K/(L_K + L_\epsilon)}{1 + \frac{k_1}{k'_\Sigma}\left[\frac{L_D}{(2\theta_0)^{1/2}} + \frac{L_K}{\exp(\theta_0)}\right]} \quad [13]$$

where L_K is the diffusion length for minority carriers in the field-free region; $L_K = (D_n/k_1)^{1/2}$. The three terms in the denominator of Eq. [13] (the "kinetic term") describe the three fates of minority carriers at the electrolyte interface, passage through the interface, first-order recombination in the depletion layer and recombination in the field-free region. Now the exact location and type of kinetics for maximum recombination does not effect the form of Eq. [13]. Hence substituting from Eq. [10], we can write a general expression for N

$$N = \frac{1 - \beta + \beta L_K/(L_K + L_\epsilon)}{1 + \frac{\kappa}{k'_\Sigma n_0} + \frac{k_1L_K}{k'_\Sigma \exp(\theta_0)}} \quad [14]$$

In the kinetic term, the third term describes minority carriers which reach the electrolyte interface but even so return against the field described by θ_0 and are destroyed in the field-free region. Figure 8 of Ref. (1) shows that the zone of dominance of this term is limited to small values of θ_0 and so for simplicity we will henceforward ignore it.

The Boltzmann Case

Next, we consider the case where we can neglect the transport term in Eq. [11] and the distribution of the

majority carriers is given by the Boltzmann term. Consideration of Eq. [1] together with [4], and [11] allows us to construct Fig. 3 which shows how the four cases in Table I depend on the potential difference across the depletion layer (θ_o) and the irradiance or photocurrent (NI_o). We now consider each boundary line in turn.

The line OA is fixed by the potential difference, $\theta_o = \theta_{I,II}$, at which the electrolyte interface, the surface concentration of majority carriers, p, is so reduced that term II becomes equal to term I. From Eq. [1] and [11]

$$\theta_{I,II} = \ln [k_2 p_w/(k_{-1} + k_{-2})] \quad [15]$$

The line OB is fixed by the value of $NI_o = (NI)_{II,III}$ which so increases n that at the surface term II is so reduced that it becomes equal to term III. From Eq. [1] and [4]

$$\ln (NI)_{II,III} = \ln [k'_\Sigma (k_{-1} + k_{-2})/k_1] \quad [16]$$

The line OD is fixed by the values of NI_o and of θ_o which make term III equal to term I at the electrolyte interface. From Eq. [1], [4], and [11]

$$\ln (NI_o) + \theta_o = \ln [k'_\Sigma k_2 p_w/k_1] \quad [17]$$

The point O is the unique point for any semiconductor electrolyte system where the three terms I, II, and III in Eq. [1] are all equal at the electrolyte interface. The line OC describes the values of NI_o and θ_o where the three terms I, II, and III are all equal at some point inside the depletion layer. This line shows where term II is squeezed between terms I and III, and hence marks the limit of its region of dominance. The equality of terms I and II means that the value of θ when the triple equality occurs is always $\theta = \theta_{I,II}$. From Eq. [1], [4], and [11], we find that OC is given by

$$\ln (NI_o) - \theta_o = \ln (NI)_{II,III} - \theta_{I,II} \quad [18]$$

Hence, the case diagram is divided into the four different regions shown.

In deriving Eq. [1], we assume (7) that $k_1 k_2 np$ is much larger than $k_{-1}k_{-2}$; the recombination of photogenerated carriers is much larger than recombination in the dark. The line EF in Fig. 3 shows the locus of the condition for thermal equilibrium $k_1 k_2 np = k_{-1}k_{-2}$. The equation is

$$\ln (NI_o) - \theta_o = \ln (NI)_{II,III} - \theta_{I,II} - 2 \ln \left[\left(\frac{k_{-1}}{k_{-2}} \right)^{1/2} + \left(\frac{k_{-2}}{k_{-1}} \right)^{1/2} \right] \quad [19]$$

Comparison of Eq. [19] and [18] for the line OC shows that the lines are parallel with the separation given by the last term in Eq. [19]. The systems we are considering must lie significantly above the line EF since they are irreversible ($k_1 k_2 np >> k_{-1}k_{-2}$). When $k_{-1} = k_{-2}$, the separation is only 2 ln 2 so for systems with this equality the lines EF and OC are so close that the cases with term II dominant can be neglected. For the term II cases to exist, we require $k_{-1} >> k_{-2}$ or $k_{-2} >> k_{-1}$ (see Fig. 1). Either condition depresses EF below OC and therefore allows the existence of regions where term II may be dominant.

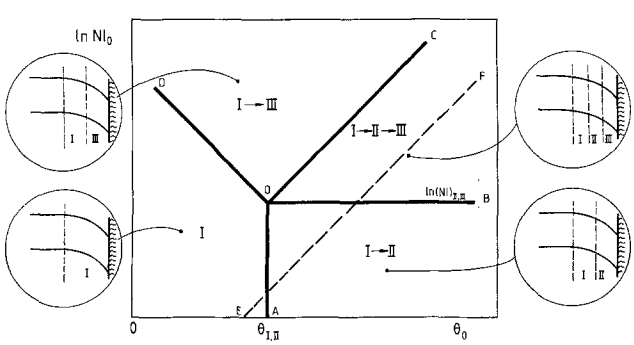

Fig. 3. Case diagram showing how the existence of the four cases in Table I depends upon the band bending, θ_o, and the irradiance or photocurrent, NI_o. The line EF represents a typical locus for the system at thermal equilibrium in the dark. Equation [1] assumes that the illuminated systems are displaced upwards by at least an order magnitude from EF. For each case, the insets show schematically the typical locations of the dominant kinetic terms within the space charge layer.

Cases I and I → III

We now consider the different cases in Table I and Fig. 3. We have to find expressions for κ and then use [14] for N. For case I, we already have Eq. [10] for κ. However in the Appendix, we present a unified treatment of case I previously considered by us (1) and case I → III previously considered by Reichman (4). Starting with

$$\kappa = \int_o^w \frac{k_1 k_2 np}{k_1 n + k_2 p} dx$$

we obtain

$$\frac{GT}{N} - 1 = \frac{\frac{1}{2} k_1 L_D \exp(\theta_{RZ} - \theta_o) [\frac{1}{2}\pi + \tan^{-1} \sinh (\theta_o - \theta_{RZ})]}{k'_\Sigma [(2\theta_o)^{1/2} + \{(2\theta_{RZ})^{1/2} - (2\theta_o)^{1/2}\} S(\theta_o - \theta_{RZ})]} \quad [20]$$

In Eq. [20], GT is the "generating term" and is given by the numerator of Eq. [14]. It describes the supply of photogenerated minority carriers to the depletion layer; $S(\lambda)$ is the unit step function where if $\lambda < 0$ $S = 0$ and if $\lambda > 0$ $S = 1$; for case III systems θ_{RZ} describes the value of θ where there is maximum recombination in the depletion layer, and is given by

$$\theta_{RZ} = \frac{1}{2}\theta_o + \frac{1}{2} \ln [k_2 p_w k'_\Sigma / k_1 NI_o] \quad [21]$$

For simple case I systems, $\theta_o - \theta_{RZ}$ will be less than -3 and

$$\tan^{-1} \sinh (\theta_o - \theta_{RZ}) \simeq -\frac{1}{2}\pi + 2 \exp (\theta_o - \theta_{RZ}) \quad [22]$$

It is satisfactory that substitution of Eq. [22] in [20] recovers our previous results for this case

$$\frac{GT}{N} = 1 + \frac{k_1 L_D}{k'_\Sigma (2\theta_o)^{1/2}} \quad [23]$$

For borderline and I → III systems, we have Eq. [20] and [21] to determine the two unknowns, N and θ_{RZ}. To solve these equations, we introduce an approximate solution for θ_{RZ}, θ^*_{RZ}, where

$$\exp (\theta^*_{RZ} - \theta_{RZ}) = 1 - N/GT \quad [24]$$

When N is much smaller than GT, $\theta_{RZ} \to \theta^*_{RZ}$. Multiplication of $(GT/N - 1)$ from Eq. [20] by (N/GT) from [21] gives an expression for $(1 - N/GT)$. Substitution in Eq. [24] yields the following expression for θ^*_{RZ}

$$\theta^*_{RZ} + \frac{\ln (2\theta^*_{RZ})}{2} - \ln \left[\frac{1}{2} + \frac{\tan^{-1} \sinh (\theta_o - \theta^*_{RZ})}{\pi} \right] \simeq \ln \left[\frac{\frac{1}{2}\pi k_2 p_w L_D}{I_o (GT)} \right] \quad [25]$$

Since θ^*_{RZ} will usually be much larger than unity, the ln terms on the left-hand side of Eq. [25] are fairly insignificant and in these terms we can replace θ_{RZ} with the approximate value, θ^*_{RZ}. We can similarly replace θ_{RZ} with θ^*_{RZ} in the nonexponential terms in Eq. [20]. Multiplication of Eq. [20] by [24] then gives

$$\frac{GT}{N} \left(1 - \frac{N}{GT} \right)^2 = \frac{\frac{1}{2} k_1 L_D \exp(\theta^*_{RZ} - \theta_o) [\frac{1}{2}\pi + \tan^{-1} \sinh (\theta_o - \theta^*_{RZ})]}{k'_\Sigma [(2\theta_o)^{1/2} + \{(2\theta^*_{RZ})^{1/2} - (2\theta_o)^{1/2}\} S(\theta_o - \theta^*_{RZ})]} \quad [26]$$

This equation holds for borderline and I → III cases. When $\theta_0 - \theta^*_{RZ}$ is larger than 3, then the system is a simple I → III case and Eq. [25] and [26] can be simplified. The second ln term on the left-hand side of Eq. [25] is zero. Substitution from Eq. [25] in [26] then gives

$$\frac{GT}{N}\left(1 - \frac{N}{GT}\right)^2 = \frac{\pi^2 k_1 k_2 p_w L_D^2}{8k'_\Sigma I_0(GT)\theta^*_{RZ}} \exp(-\theta_0) \quad [27]$$

with

$$\theta^*_{RZ} \simeq \ln\left[\frac{\frac{1}{2}\pi k_2 p_w L_D}{I_0(GT)}\right] \quad [28]$$

The quadratic form of Eq. [27] is the same as that found by Reichman for the I → III case (4). There are, however, two differences. First of all in following Sah, Noyce, and Shockley (5), Reichman assumed $k_1 = k_2$; we have not made this assumption. Secondly, we have derived Eq. [28] for θ^*_{RZ}.

An important result that emerges from our analysis, Eq. [24], [27], and [28] is that when N is much smaller than GT, θ_{RZ}, the value of θ where the maximum recombination takes place, has a constant value of θ^*_{RZ} (providing that I_0 and GT remain constant). The reason for this is that with only a small fraction of the minority carriers reacting at the surface ($N << GT$) the depletion layer recombination must have a constant flux equal to $I_0(GT)$. At a constant value of the potential θ^*_{RZ}, the concentration of majority carriers is fixed by the Boltzmann distribution and is always the same. The concentration of minority carriers also remains the same being fixed by the condition $k_1 n = k_2 p$ which maximizes the integrand for κ. The rate under these conditions matches the supply of minority carriers and so does not change even though the location of the reaction zone within the depletion layer may well alter. For instance as θ_0 increases the location of $\theta = \theta^*_{RZ}$ will shift further into the semiconductor. Meanwhile back at the surface the concentration of minority carriers is increasing and so the k'_Σ pathway is becoming more and more likely. Inspection of the right-hand side of Eq. [26] shows that it describes the partition of the minority carriers between the reaction at the surface, k'_Σ, and the drift back into the semiconductor against the field, $\exp(\theta^*_{RZ} - \theta_0)$, followed by the recombination, $k_1 L_D/(2\theta^*_{RZ})^{1/2}$. When N approaches GT, there will be less depletion layer recombination; the removal of carriers at the surface lowers n so that p is also lower at θ_{RZ} leading to less recombination and θ_{RZ} is closer to the surface than θ^*_{RZ}. This is described by Eq. [24]. Figure 4 illustrates the behavior of Eq. [27] and shows how N increases with θ (assuming GT is constant). The insets show typical concentration profiles.

It is also interesting to consider the effect of the more complicated expression in Eq. [27] on an observed Tafel plot. Given a limiting current i_L, it is customary to plot ln $[i/(i_L - i)]$ against potential. Figure 5 is calculated from Eq. [27] and shows the appearance of such a plot near the half-wave potential. At potentials below the half-wave potential the "transfer coefficient" α, approaches unity while at potentials above the half-wave potential it approaches a limiting value of ½. From Eq. [22], the half-wave potential itself is given by

$$\theta_{1/2} = \ln\left\{\frac{k_1 k_2 p_w L_D^2 \pi^2}{4k'_\Sigma I_0 GT\theta^*_{RZ}}\right\} \quad [29]$$

In this expression as one might expect the half-wave potential is larger, the faster are the kinetics of the depletion layer recombination, k_1 and k_2 the more majority carriers there are p_w or the fatter is the depletion layer, L_D. The half-wave potential is reduced by fast surface reaction k'_Σ, or by increased irradiance, I_0. The reason for the latter, is that increasing I_0 increases n_0. The matching of n and p must now take place at a larger value of p or further into the semiconductor at a lower value of θ_{RZ}. This is shown by the line OD in Fig. 3. At this lower value of θ_{RZ}, there are in proportion less minority carriers and hence the depletion layer recombination is less effective. Finally, it is interesting that, when N is less than GT, $\ln(NI_0)$ varies linearly with θ_0. This means that the locus of a system in Fig. 3 in the I → III region runs parallel to the line OC. We may conclude that systems which are in the I → III zone do not cross the OC line into the I → II → III zone as θ increases.

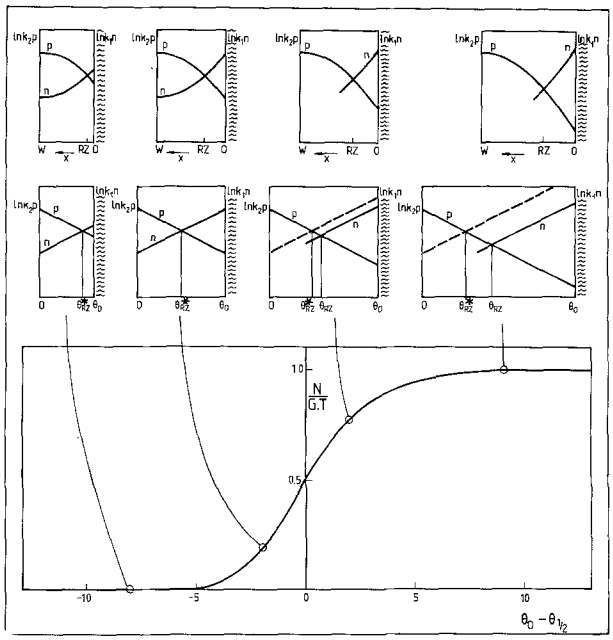

Fig. 4. Photocurrent voltage curve calculated from Eq. [27]. The insets show the concentration profiles for majority (p) and minority (n) carriers in the depletion layer, together with the location of the reaction zone at θ_{RZ}. The approximate location, θ_{RZ}* from Eq. [28] is also shown. The broken lines show the profile of the minority carriers that would be observed if there was no significant flux at the interface. On the limiting plateau, the main pathway is reaction at the interface and the recombination at θ_{RZ} is much less than that at θ^*_{RZ}. In the top row of insets, the profiles are plotted against distance from the interface; in the bottom row of insets, they are plotted against potential.

The I → II and I → II → III Zones

Next we consider the I → II and I → II → III cases in Table I and Fig. 3, again assuming a Boltzmann

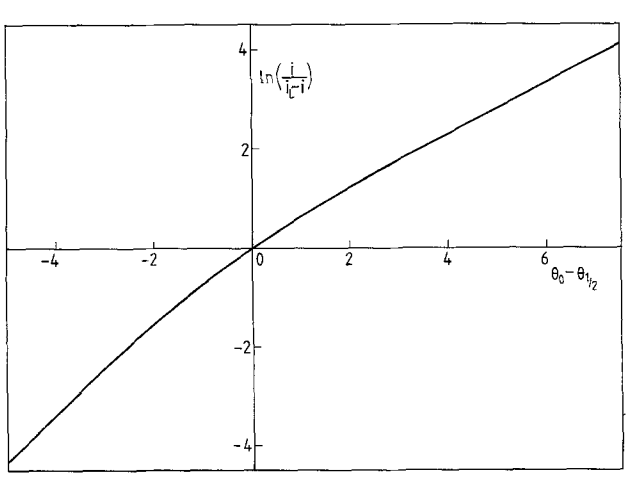

Fig. 5. Appearance of Tafel plot for a system in the I → II case calculated from Eq. [27]. The currents are plotted according to the conventional correction for a limiting current i_L:—ln $[i/(i_L - i)]$.

distribution for the majority carriers. In these zones, the maximum rate of reaction is found in zone II. The Boltzmann factors in θ for the holes and electrons cancel and so the integration is simple. We find

$$\kappa = \frac{k_1 k_2 p_w n_o \exp(-\theta_o) L_{II}}{k_{-1} + k_{-2}} \quad [30]$$

where L_{II} is the width of zone II in the depletion layer. For the I → II case this width is given by

$$L_{II} = L_D [(2\theta_o)^{1/2} - (2\theta_{I,II})^{1/2}] \quad [31]$$

For the I → II → III case, we find from Eq. [1] and [16] that

$$\theta_{II,III} = \theta_o + \ln (NI)_{II,III} - \ln NI_o \quad [32]$$

and hence

$$L_{II} = L_D [(2\theta_o - \ln \{NI_o/(NI)_{II,III}\})^{1/2} - (2\theta_{I,II})^{1/2}] \quad [33]$$

where $\theta_{I,II}$ and $(NI)_{II,III}$ are given in [15] and [16]. The expression for N is

$$\frac{GT}{N} = 1 + \frac{k_1 k_2 p_w \exp(-\theta_o) L_{II}}{k'_\Sigma (k_{-1} + k_{-2})} \quad [34]$$

where L_{II} is given by Eq. [31] or [33].

Although Eq. [31] and [33] show that L_{II} increases with θ_o this effect on N is small compared with the effect of the exponential term in $(-\theta_o)$. Differentiation shows that when N is smaller than GT

$$\partial \ln N/\partial \theta_o \simeq 1 - \tfrac{1}{2}\theta_o^{-1} \simeq 1$$

Thus, the locus of a system in zones I → II and I → II → III in Fig. 3 runs parallel to the line OC, and Tafel plots should have $\alpha \simeq 1.0$. As in the previous case, changing the potential cannot make a system cross the line OC into the I → III zone. Thus for any particular light intensity, systems are divided into those above the line OC, the I → III systems, and those below, the II systems. Since for both types of system N varies with $\exp(\theta_o)$ one cannot use the dependence of photocurrent on potential to distinguish between the two different types. However from Eq. [34], we find that the half-wave potential for type II systems is given by

$$\theta_{1/2} = \ln \left\{ \frac{k_1 k_2 p_w L_{II}}{k'_\Sigma (k_{-1} + k_{-2})} \right\} \quad [35]$$

As above, the half-wave potential is larger the more efficient is the recombination ($k_1 k_2 p_w L_{II}$) and is smaller for larger k'_Σ or for more efficient back reaction ($k_{-1} + k_{-2}$). However, apart from the ln I_o term in Eq. [33], Eq. [35] shows that $\theta_{1/2}$ is roughly constant and will not be changed much by varying the irradiance. Equation [29] for the I → III systems shows that $\theta_{1/2}$ varies with − ln I_o. In Fig. 6, we show two typical current voltage curves for the same system in the I → III zone and in the II zones; we also show the lines of the half-wave potential as I_o is varied. If this pattern of behavior is found, then the line OC can be fixed from the point C' and the line OD from D' or the line OA from A'; hence Fig. 3 can in principal be constructed.

Variation of Zones with Irradiance

So far we have concentrated on the loci of current voltage curves across the zones of Fig. 3. It is however instructive also to consider the different types of behavior that can be found as the irradiance I_o is varied at a constant value of θ_o. Under these conditions, the depletion layer does not change its dimensions and therefore the θ_o scale can also be considered as measuring the distance through the depletion layer. As shown in Fig. 7a and b, one can then plot the zones of dominance of the different kinetic terms in Eq. [1]. One can also see in Fig. 7a how for $\theta_o < \theta_{I,II}$, the system will start for low I_o in case I and for higher I_o will become case I → III. For $\theta_o > \theta_{I,II}$, we have Fig. 7b. Here with increasing I_o, the system will go through the sequence of cases I → II, I → II → III; I → III. Note how in Fig. 7b that $\theta_{I,III}$ is still equal to θ_o on the ex-

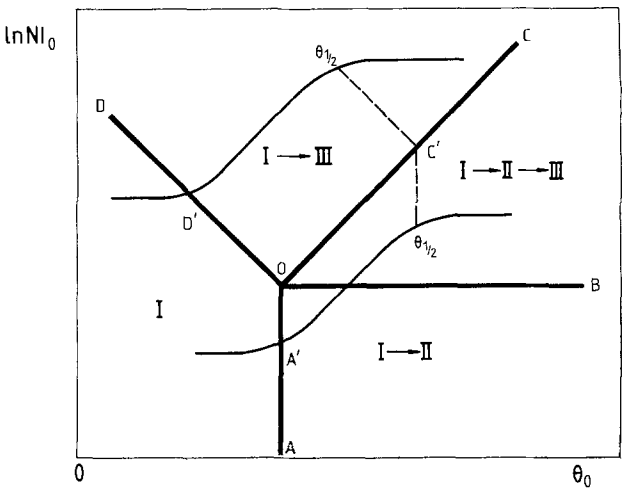

Fig. 6. Typical current voltage curves from Eq. [23], [27], and [34]. The broken line shows the locus of the half-wave potential as I_o is varied From the breaks in the lines one can in principle identify the points A', C', and D' and hence construct the diagram from experimental results.

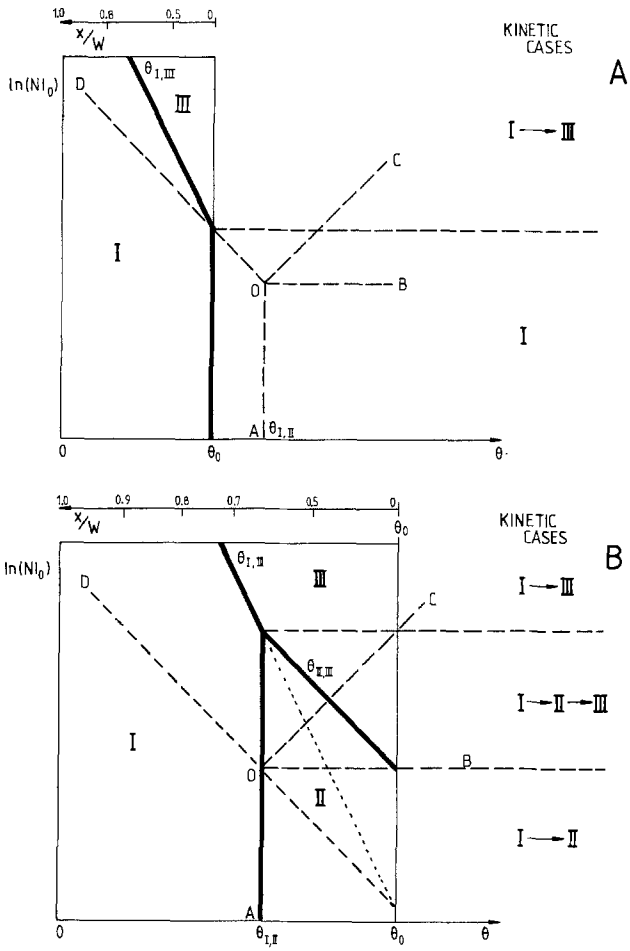

Fig. 7. A and B show the effect of increasing NI_o at constant θ_o with $\theta_o < \theta_{I,II}$ for A and $\theta_o > \theta_{I,II}$ for B. The θ_o scale can also be regarded as describing distance into the depletion layer, see the scales (x/W). The zones of dominance of the different terms in Eq. [1] and the different kinetic cases in Table I are shown. The reaction zone lies along the boundary between I and III, at the interface for case I and across the plateau of zone II.

tension of the line DO. These diagrams also show where the reaction zone is and confirm the conclusions in Table I. In Fig. 7a, the zone is along the I/III boundary and then at the interface. In Fig. 7b, the zone is along the I/III boundary and then a plateau in region II.

Effect of Transport Terms

We now return to Eq. [11] to examine whether the transport term can ever be larger than the Boltzmann term. This possibility might arise when the Boltzmann exponential factor has greatly reduced the concentration of majority carriers near the electrolyte interface. However for the photogenerated majority carriers to be trapped and destroyed while waiting to be transported out of the depletion layer, they have to be generated between the electrolyte interface and the reaction zone. Concentration polarization of photogenerated majority carriers further into the semiconductor will not lead to their destruction since they will be repelled by the field and expelled from the depletion layer.

In Eq. [11], substitution of the relation

$$\kappa = I_0(GT - N)$$

and assuming that there is no surface recombination ($\rho = 0$), gives

$$I_0\,(1 - \beta \exp(\sqrt{2\theta}\,L_D/L_\epsilon) - \rho N) - \kappa$$

$$= I_0\left(N - \beta \exp\left[\sqrt{2\theta_{RZ}}\,L_D/L_\epsilon\right] + \beta\frac{L_\epsilon}{L_\epsilon + L_\kappa}\right) \quad [36]$$

This expression is negative or very small if β is close to unity, where β describes the fraction of light that penetrates into the field-free region.

Under these conditions, there is little photogeneration of carriers in the depletion layer, and so instead of a buildup, the negative value implies a reduction caused by recombination. In order to have as large a buildup as possible, we will assume therefore that β is small and that most of the light is absorbed in the depletion layer. So we will ignore the β terms in Eq. [36]. We can now write down a relation between θ_{RZ} and NI_0 which describes when the Boltzmann term and the transport term in Eq. [11] are equal

$$\theta_{RZ} \simeq \ln\left[D\,(2\theta_{RZ})^{1/2}\,p_w/L_D\right] - \ln NI_0 \quad [37]$$

In the I → III zone, we combine Eq. [37] with [21] to find the locus of the value of θ_0, $(\theta_0)_{BT}$, for which the Boltzmann and transport terms are equal

$$(\theta_0)_{BT} = \ln\left\{\frac{D^2k_1p_w\,(2\theta^*_{RZ})}{k'_\Sigma k_2 L_D^2}\right\} - \ln NI_0 \quad [38]$$

For the I → II → III case, we take θ_{RZ} in Eq. [37] to be $\theta_{II,III}$ since it is here that the Boltzmann term will be smallest. Combining Eq. [32] and [37], we find

$$(\theta_0)_{BT} = \ln\left[\frac{Dp_w\,(2\theta_{II,III})^{1/2}}{L_D(NI)_{II,III}}\right] \quad [39]$$

In this zone $(\theta_0)_{BT}$ does not depend on NI_0. It is satisfactory that evaluation of the different constants shows that Eq. [38] and [39] intersect on the line OC in Fig. 3. Finally in zone I → II, we take θ_{RZ} to be θ_0, and Eq. [37] defines the locus of $(\theta_0)_{BT}$: Eq. [37] and [39] clearly intersect on the line OB with $\theta_{II,III} = \theta_0$. Hence as shown in Fig. 8, a line of the shape PQRS will describe where the transport term in Eq. [11] may become larger than the Boltzmann term. We now use Eq. [29], [35], [38], and [39] to find the difference between $(\theta_0)_{BT}$ and $(\theta_0)_{1/2}$. In the I → III zone, we find

$$[(\theta_0)_{BT} - (\theta_0)_{1/2}]_{NI_0} = 2\ln\left[\frac{D2\theta^*_{RZ}}{L_D^2k_2}\right] \quad [40]$$

and in the I → II → III zone

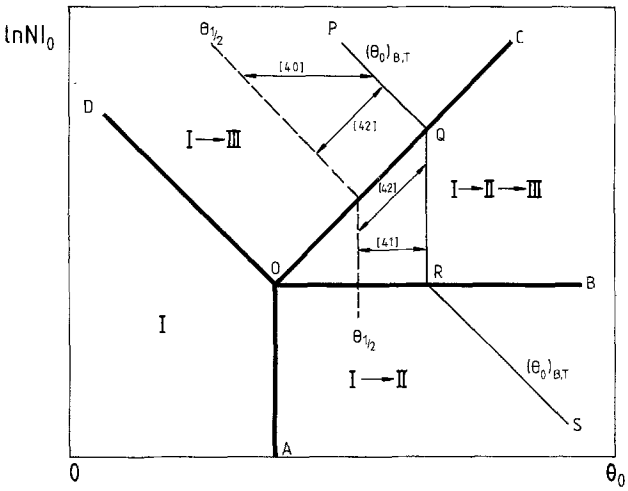

Fig. 8. The locus of $(\theta_0)_{BT}$, which describes the value of θ_0 where the Boltzmann and transport terms in Eq. [11] are equal, is shown from Eq. [37] [38], and [39] to be the line PQRS. The locus of typical half-wave potentials is shown from Eq. [29] and [35] by the broken line. The separation between the two lines is given by Eq. [40] for case I → III and Eq. [41] for case I → II → III. At constant NI_0, the separation in Eq. [40] is twice that in [41]. Since with increasing θ_0 systems travel parallel to the line OC, the separation between $\theta_{1/2}$ and $(\theta_0)_{BT}$ is the same along these lines and is given by Eq. [42].

$$(\theta_0)_{BT} - (\theta_0)_{1/2} = \ln\left[\frac{D}{L_D^2k_2\,[1 - (\theta_{I,II}/\theta_{II,III})^{1/2}]}\right] \quad [41]$$

It can be seen that apart from the θ terms the separation is given by the same group $D/L_D^2k_2$. The term D/L_D^2 describes the characteristic time for transport of holes in the depletion layer while the rate constant k_2 describes the lifetime of the holes given by term III in Eq. [1]; this term is partially rate limiting for the cases considered. The factor of 2 in Eq. [40] arises, because, as shown in Fig. 8, the difference is θ's has been calculated for a constant value of NI_0. As discussed above in both zones for a particular system ln NI_0 varies with θ_0 and therefore along lines parallel to OC we may write that the separation between $(\theta_0)_{BT}$ and $(\theta_0)_{1/2}$ (for both zones) obeys the condition

$$[(\theta_0)_{BT} - (\theta_0)_{1/2}]_{OC} \geqq 2^{1/2}\ln\,(D/L_D^2k_2) \quad [42]$$

Now a typical value of D/L_D^2 is 10^{12} sec^{-1}, and we consider it is likely that for nearly all systems k_2 will not be as large as this value. Hence, we conclude that the half-wave potential will be reached before the system crosses the line PQRS and that when depletion layer recombination is significant the concentration of majority carriers is given by the simple Boltzmann distribution. The assumptions that we made in reaching this conclusion were all in the direction which favored the transport term so any breakdown in the assumptions renders our conclusion even more secure.

Summary and Conclusions

We now collect together the main conclusions and expressions found in this work.

1. Depletion layer recombination can be divided into four different cases as given in Table I.

2. Term II of the rate law, Eq. [1], cannot be dominant if $k_{-1} = k_{-2}$ which is likely to arise for traps situated midway between the valence and conduction bands. When the traps are unsymmetrically placed, term II can be dominant.

3. From Eq. [23], systems which remain in case I of Fig. 3 will show current voltage curves where i varies with $\theta^{1/2}$ providing that the generation term is constant.

4. Current voltage curves for other systems divide into two classes: I → III above the line OC in Fig. 3 and II below the line OC.

5. For both classes (I → III and II), ln NI_0 will vary with θ_0 for low values of N giving a sharp rising current voltage curve, with a well-defined half-wave potential.

6. For the (I → III) case, the half-wave potential will decrease with ln NI_0 (Eq. [29]) but will be constant for the II case (Eq. [35]).

7. Concentration polarization of the majority carriers is unlikely to be significant.

8. Analytical equations for the current voltage curves have been derived as follows: I, [23]; I → II, [34] with [31]; I → II → III [34] with [33]; I → III, [27] with [28].

Acknowledgments

We thank the 1851 Commissioners for a Research Fellowship for P.N.B. This is a contribution from the Oxford Imperial Energy Group.

Manuscript submitted Nov. 5, 1982; revised manuscript received Feb. 24, 1983.

Any discussion of this paper will appear in a Discussion Section to be published in the June 1984 JOURNAL. All discussions for the June 1984 Discussion Section should be submitted by Feb. 1, 1984.

APPENDIX

In this Appendix, we obtain an expression for N for cases I and I → III assuming a Boltzmann distribution of the majority carriers. We start with

$$\kappa = \int_0^W \frac{k_1 k_2 np}{k_1 n + k_2 p}\, dx$$

where $p = p_w \exp(-\theta)$ and $n = n_0 \exp(\theta - \theta_0)$. Let θ_{RZ} be the value of θ where $k_1 n = k_2 p$ and the integrand for κ passes through its maximum; for case I, θ_{RZ} will be larger than θ_0. Then

$$\theta_{RZ} = \tfrac{1}{2}\theta_0 + \tfrac{1}{2}\ln[k_2 p_w/k_1 n_0] \qquad [A\text{-}1]$$

and

$$\kappa = \tfrac{1}{2} L_D [k_1 k_2 n_0 p_w \exp(-\theta_0)]^{1/2} \int_{-\theta_{RZ}}^{\theta_0-\theta_{RZ}} \frac{d\theta'}{(2\theta)^{1/2}\cosh(\theta')}$$

where $\theta = \theta' + \theta_{RZ}$. Now $\cosh(\theta')$ varies much more strongly with θ' than $(2\theta)^{1/2}$ and so following Sah, Noyce, and Shockley (5) for case I → III, we can replace $(2\theta)^{1/2}$ with $(2\theta_{RZ})^{1/2}$ and then integrate.

Similarly for case I, we can replace $(2\theta)^{1/2}$ with $(2\theta_0)^{1/2}$ since the integrand has its maximum value at $\theta' = \theta_0 - \theta_{RZ}$ or $\theta = \theta_0$. We also assume that θ_{RZ} is sufficiently negative (< -5) so that there is negligible error in replacing the integration limit of $-\theta_{RZ}$ with $-\infty$.

We then obtain after integration and using [A-1]

$$\kappa \simeq \frac{\tfrac{1}{2} L_D k_1 n_0 \exp(\theta_{RZ} - \theta_0)[\tfrac{1}{2}\pi + \tan^{-1}\sinh(\theta_0 - \theta_{RZ})]}{(2\theta_0)^{1/2} \text{ for } \theta_0 < \theta_{RZ} \quad \text{or} \quad (2\theta_{RZ})^{1/2} \text{ for } \theta_0 > \theta_{RZ}} \qquad [A\text{-}2]$$

Now from Eq. [14]

$$GT/N \simeq 1 + \kappa/k_\Sigma' n_0 \qquad [A\text{-}3]$$

where the generating term GT is the numerator of Eq. [14], and we have neglected the third term in the kinetic term. Substitution of Eq. [3] in [A-1] gives

$$2\theta_{RZ} + \ln NI_0 + \ln[k_1/k_2 k'_\Sigma p_w] = \theta_0 \qquad [A\text{-}4]$$

It is satisfactory that comparison of Eq. [A-4] with [17] shows that $\theta_0 = \theta_{RZ}$ on the line OD in Fig. 3. We now have three equations [A-2]-[A-4] for three unknowns, θ_{RZ}, κ, and N. Elimination of κ between [A-2]-[A-3] leads to [20] and rearrangement of [A-4] gives [21].

REFERENCES

1. W. J. Albery, P. N. Bartlett, A. Hamnett, and M. P. Dare-Edwards, *This Journal*, **128**, 1492 (1981).
2. W. W. Gärtner, *Phys. Rev.*, **116**, 84 (1959).
3. R. H. Wilson, *J. Appl. Phys.*, **48**, 4292 (1977).
4. J. Reichman, *Appl. Phys. Lett.*, **36**, 574 (1980).
5. C-T. Sah, R. N. Noyce, and W. Shockley, *Proc. IRE*, **45**, 1228 (1957).
6. D. Laser and A. J. Bard, *This Journal*, **123**, 1828 (1976).
7. W. Shockley and W. T. Read, *Phys. Rev.*, **87**, 835 (1952).

Role of Pt Overlayers on TiO_2 Electrodes in Enhancement of the Rate of Cathodic Processes

T. Kobayashi, H. Yoneyama,* and H. Tamura

Department of Applied Chemistry, Faculty of Engineering, Osaka University, Osaka 565, Japan

ABSTRACT

The decrease in cathodic overpotentials by platinization of TiO_2 single crystals was studied for dark reductions of Ce^{4+}, Fe^{3+}, O_2, and H^+ as a function of the thickness of the Pt overlayers both for a well-etched TiO_2 substrate and for a mechanically damaged one. Improvements in the cathodic properties of TiO_2 electrodes by platinization occur in two different modes. One is related to high electrocatalytic activities of Pt and is observed for reduction of O_2 and evolution of H_2 when both etched and damaged TiO_2 electrodes are loaded with a Pt layer having only 3Å thickness. The other results from enhancement of probabilities of electron exchange between the electrode and electrolyte species caused by platinization and is observed for reductions of Ce^{4+}, Fe^{3+}, and O_2 when the Pt thickness exceeds 100Å for the etched TiO_2 and 10Å for the damaged one. Action spectra of anodic photocurrents suggest that new electronic levels are created by platinization.

Photocatalytic activities of TiO_2 powder for a variety of heterogeneous reactions can be improved by loading Pt on its surfaces. It is usually believed that the improvement is brought about by high electrocatalytic activities of Pt for cathodic processes involved in the heterogeneous reactions (1-5). However, the electrocatalytic activity may not necessarily explain all the functions of the loaded Pt. As suggested for ZnO electrodes (6), for example, the loading of Pt may create new electronic states in TiO_2 which facilitate electron transfer from the conduction bands to solution species. Thus, it is important to clarify in detail how Pt loaded on TiO_2 enhances the rates of cathodic processes. For

* Electrochemical Society Active Member.
Key words: semiconductor electrodes, platinized TiO_2, dark cathode, overpotentials.

this purpose, cathodic properties of TiO_2 must be studied both in reaction systems for which Pt has high electrocatalytic activities and in those for which no remarkable effects of Pt substrate is usually observed. The amount of Pt deposited on TiO_2 will be an important variable (3, 7).

As the method of the Pt loading, the photodeposition technique (1) has often been employed (2, 3, 8, 9). Previous reports concerning the photodeposition of noble metals such as Pt and Pd on n-type semiconductor single crystals show that the metal deposition selectively occurs at flaws existing in the semiconductor surfaces (10, 11). Therefore, in order to have more knowledge on the role of the deposited Pt in light-induced heterogeneous reactions, investigations on surface conditions will be important. However, photodeposition does not always give the Pt layers of a homogeneous thickness. Thus, the arc plasma spraying method was chosen to prepare the electrodes. Effects of surface conditions of the TiO_2 substrate on cathodic properties of the platinized electrodes were then investigated by using two kinds of TiO_2 single crystals: well etched TiO_2 and mechanically damaged crystals. In this paper, it is shown how overpotentials for several cathodic reactions are decreased by the platinization, and discussion on the results obtained are given based on the energetic point of view of the deposited Pt.

Experimental

The preparation of the well etched surfaces of TiO_2 single crystals was previously reported (11, 12). The surface exposed to electrolytes was the (001) face. The damaged surfaces were prepared by lapping the well etched surfaces with No. 500 SiC abrasives. The deposition of Pt with use of the arc plasma spraying technique was carried out under a fixed condition (application of 1 kV between the Pt target and TiO_2 substrate under 10^{-2} Torr). A deposition rate of 0.46Å sec^{-1} was obtained as determined by measuring the thickness of the Pt layers as a function of the spraying time by using a multiple beam interferometer (Model 2, Mizojiri Kogaku). Since the present method of platinization of TiO_2 might cause oxidation of the deposited Pt, the platinized TiO_2 electrodes prepared were usually polarized cathodically in 0.5M H_2SO_4 at -0.2V *vs.* SCE for more than 10 min before use in electrochemical measurements.

The base electrolyte used was 0.5M H_2SO_4 into which an oxidizing agent of either one of $Ce(SO_4)_2$, $Fe_2(SO_4)_3$, or O_2 was dissolved. The concentration of the former two oxidizing agents was 10^{-2}M, while saturated solutions were used for the case of O_2. The electrolytes were prepared by using twice-distilled water and reagent grade chemicals, and all measurements were carried out under N_2 atmospheres except for the case of reduction of O_2. A potentio-galvanostat (DPGS-1, Nikko Keisoku) was used for electrochemical measurements. An SCE served as a reference electrode, and all potentials cited in this paper are referred to this electrode.

Amounts of H_2O_2 produced in the course of O_2 reduction were determined by means of a rotating ring-disk electrode (RRDE) as previously reported (13). A Pt ring electrode with 7.0 mm inner diameter and 9.0 mm outer diameter was mounted in a concentric position to the TiO_2 disk electrode with 5.8 mm diameter in the RRDE. The rotation rate of the RRDE was fixed at 2000 rpm.

Spectral response of anodic photocurrents was measured by an auto phase lock-in amplifier (LI-574A, NF Circuit Block) joined to the potentio-galvanostat with chopped monochromatic light which was obtained from a 500W xenon lamp (UXL-500D, Ushio Electric) with series combination of a monochrometer (CT-25N, JASCO), a cutoff glass filter (UV-39, Toshiba Glass), and a 30 Hz light chopper (M-250, Nikon). The number of incident photons was measured by a thermopile (E-6, Eppley Laboratory).

Results

Current-potential curves for O_2 reduction at TiO_2 electrodes with and without the Pt overlayers are shown in Fig. 1. As expected, the Pt loading decreases the overpotentials for the reduction reaction by positively shifting electrode potentials. However, the positive shift of potentials is not simple. There are two kinds of modes in shifting the potential. One is parallel shifts of Tafel lines which are brought about by the Pt loading of 3Å for both the damaged TiO_2 (D-electrode) and the well etched one (E-electrode). The other is seen when the thickness of the Pt overlayers increases from 30 to 300Å for the E-electrode and from 3 to 30Å for the D-electrode. In these cases, the parallel shifts of the electrode potentials towards positive direction are observed in a region of low current densities, but the degree of the positive shift of the electrode potentials become less marked with an increase in the current density, resulting in deformation of the Tafel lines into "inverted S shapes." Further increase in the Pt thickness from 30 to 300Å for the D-electrode seems to have effects in shifting an inflection point in the "inverted S curves" towards high current densities.

When the electrode potentials at 10^{-4} A-cm^{-2} are plotted as a function of the Pt loading, Fig. 2 is obtained. The following is clearly shown in this figure. The Pt deposition of 3Å thickness caused a marked positive shift of electrode potentials or a marked decrease in overpotentials for oxygen reduction, but further increase in the thickness of the Pt overlayers did not bring about any remarkable decrease in the overpotentials up to a critical thickness which was *ca.* 10Å for the D-electrode and *ca.* 100Å for the E-electrode. Beyond the critical thickness, however, an appreciable decrease in the overpotentials appeared again. It is noticed in Fig. 1 that the electrodes having Pt greater than the critical thickness give current-potential curves of the "inverted S-type."

For the case of evolution of H_2, a Pt loading of 3Å thickness is found to be enough to decrease the overpotentials to those achieved at Pt electrodes for both D- and E-electrodes. Since the Pt loading of 3Å thickness causes similar positive shifts of electrode potentials for both evolution of H_2 and reduction of O_2, the nature of the shift in these cases must be the same. Indeed, parallel shifts in the Tafel lines similar to those observed for O_2 reduction were seen in current-potential curves for evolution of H_2 (not shown).

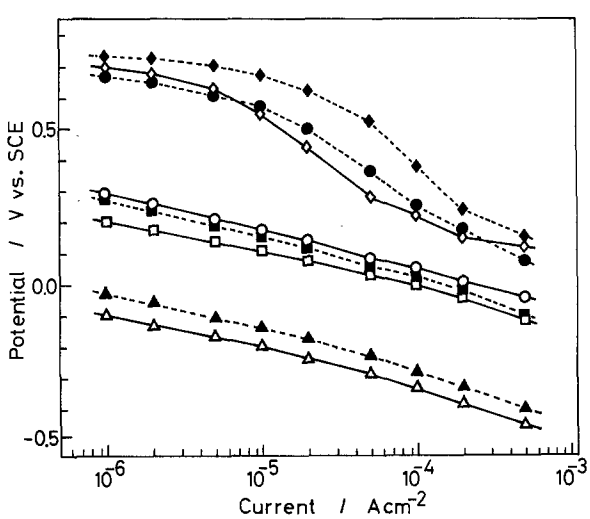

Fig. 1. Current-potential curves for reduction of O_2 at TiO_2 electrodes with and without Pt overlayers having various thickness. Open symbol; well etched TiO_2 substrate, closed symbol; mechanically damaged one. Thickness of Pt layer/Å: (—△—, —▲—); 0, (—□—, —■—); 3, (—○—, —●—); 30, (—◇—, —◆—); 300.

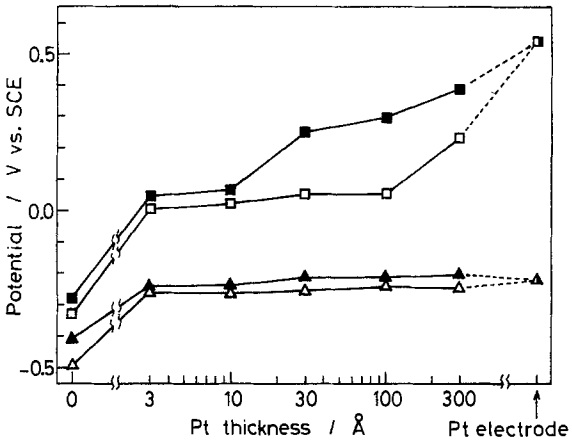

Fig. 2. Variation of electrode potentials at the cathodic current of 10^{-4} A-cm^{-2} for reduction of O_2 and evolution of H_2 with Pt overlayers having various thickness. (—□—, —■—, —◨—); in O_2 saturated 0.5M H_2SO_4, (—△—, —▲—, —◬—); in N_2 saturated 0.5M H_2SO_4, (—□—, —△—); well etched TiO_2, (—■—, —▲—); mechanically damaged TiO_2, (—◨—, —◬—); Pt electrode.

Effects of the Pt loading on reduction of Ce^{4+} and Fe^{3+} are shown in Fig. 3. For both reactions on the E-electrode, the potentials varied negligibly with increasing thickness of the Pt overlayers up to 100Å, but beyond that, effects of platinization become marked to make the electrode potentials finally approach those of Pt electrodes. In cases of the D-electrode, effects of platinization appear at smaller thickness (>10Å). Except for the Pt thickness less than 3Å, the electrode potentials *vs.* the amount of Pt loading relations shown in this figure have patterns similar to those shown in Fig. 2 for reduction of O_2 in that the Pt loading does not markedly change the electrode potentials up to the critical amount of the Pt loading beyond which marked positive shifts appeared. When the Pt loading was enough to cause appreciable positive shifts of the electrode potentials, current-potential curves of the resulting electrode had "inverted S curves" similar to those shown in Fig. 2. The marked parallel shifts of the Tafel lines of the current-potential curves as observed for reduction of O_2 and evolution of H_2 in the Pt loading of 3Å thickness was not seen in these reactions.

It was reported that O_2 is reduced to H_2O_2 on TiO_2 electrodes (14) but to H_2O on Pt electrodes (15). In order to obtain information on how much the Pt loaded on TiO_2 influences the reduction behavior of O_2, current efficiencies of the formation of H_2O_2 were measured by means of the RRDE technique as a function of the thickness of the Pt layers. The potential of the Pt ring electrode was kept at 1.15V *vs.* SCE (15) in order to oxidize all of H_2O_2 formed on the TiO_2 disk electrode. The current efficiency (Φ/%) was determined by using Eq. [1]

$$\Phi = (100/N)\ (I_r/I_d) \qquad [1]$$

where N denotes an inherent collection efficiency of the RRDE (= 0.35) (12), I_r an increment of the anodic ring current due to the oxidation of H_2O_2, and I_d the reduction current at the disk electrode which was fixed at 10^{-4} A-cm^{-2} in the present study.

The current efficiency of the formation of H_2O_2 on the bare well etched TiO_2 electrode was *ca.* 70% as shown in Fig. 4, and it was dropped to *ca.* 15% by the Pt loading of only 3Å thickness. From these results, it is clear that the main reaction of O_2 reduction at the bare TiO_2 electrode is the expected one

$$O_2 + 2H^+ + 2e^- \rightarrow H_2O_2 \qquad [2]$$

and that for Pt-loaded TiO_2 electrodes is

$$O_2 + 4H^+ + 4e^- \rightarrow 2H_2O \qquad [3]$$

In order to obtain information on energy levels of the deposited Pt, measurements of anodic photocurrents were carried out for the E-electrodes with and without 30Å Pt layers at 1.5V *vs.* SCE in 0.5M H_2SO_4. As shown in Fig. 5, a photoresponse appeared for the platinized electrode at photon energies lower than 3.0 eV. This photoresponse must be caused by the deposited Pt and not by some surface states inherent to TiO_2 because the appearance and disappearance of this photoresponse were reproducible by attaching and eliminating the deposited Pt, as shown in the figure.

The apparent electrical conductivity of the deposited Pt layers was measured by means of the four-probe method. In this case, the Pt layers were prepared on glass plates by employing the same method as used in the preparation of the Pt layers on TiO_2 substrates. As shown in Fig. 6, remarkable changes in the surface conductivity occur in a thickness region covering from *ca.* 20Å to *ca.* 200Å.

Discussion

It is clear from the results shown in Fig. 5 that Pt layers form new electronic states in the TiO_2 electrodes. Figure 7 represents two kinds of conceivable energy diagrams for the explanation of the new photoresponse observed. In the model I, the photoexcitation occurs in the Pt layer at the semiconductor/Pt boundaries, while in the model II, electrons are photoexcited from the semiconductor to the Pt layer and then from the Pt

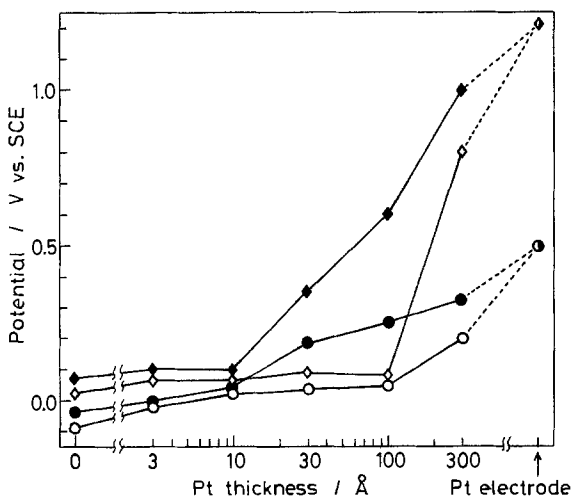

Fig. 3. As in Fig. 2, but for reduction of Ce^{4+} and Fe^{3+}. (—◇—, —◆—, —◈—); in 0.5M H_2SO_4 with 10^{-2}M Ce^{4+}, (—○—, —●—, —◑—); in 0.5M H_2SO_4 with 10^{-2}M Fe^{3+}, (—◇—, —○—); well etched TiO_2, (—◆—, —●—); mechanically damaged TiO_2, (—◈—, —◑—); Pt electrode.

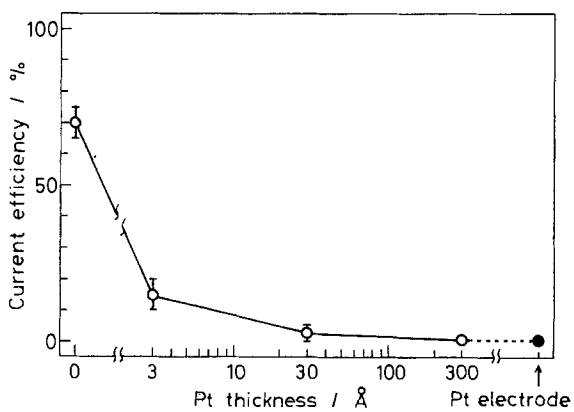

Fig. 4. Current efficiency of H_2O_2 formation in the course of reduction of O_2 at well etched TiO_2 electrodes with and without Pt overlayer and at Pt electrode. Open symbol; TiO_2 substrate, closed symbol; Pt electrode.

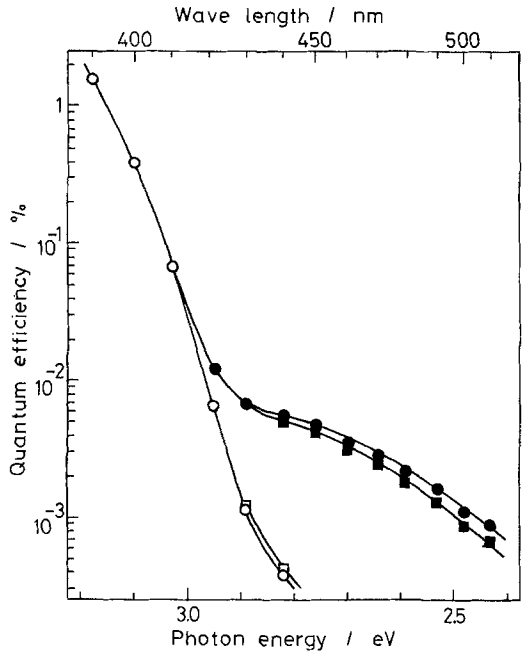

Fig. 5. Spectral response of anodic photocurrents in 0.5M H_2SO_4 at a well etched TiO_2 electrode with and without a 30Å Pt layer. Measurements were successively carried out for the same TiO_2 sample: (—○—); bare electrode, (—●—); after deposition of 30Å Pt layer, (—□—); after rinsing in aqua regia for 30 min to remove Pt layer, (—■—); after redeposition of 30Å Pt.

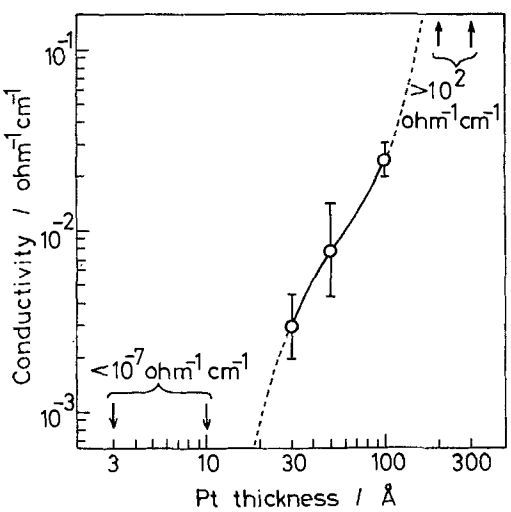

Fig. 6. Surface conductivity of Pt layers with various thickness deposited on glass plates.

layer into the conduction band by the quantum-mechanical tunneling processes. However, the model II seems less likely because photoexcitation of electrons from the semiconductor to deposited metal does not easily occur (16).

The modes of enhancement of cathodic reactions by introducing Pt overlayers are classified into two types, as described in the previous section. One is the parallel shift of the Tafel lines towards a direction of positive potentials and is observed in cases of evolution of H_2 and reduction of O_2 when the electrodes are loaded with 3Å Pt. Although the deposited Pt on the TiO_2 surfaces forms new electronic states, this is not responsible for the parallel shift observed because the Pt layers of 3Å thickness did not cause any appreciable effect on the reductions of Ce^{4+} and Fe^{3+}. On the other hand, it is well known that Pt serves as a good electrocatalyst for reduction of O_2 and evolution of H_2 but not so for reduction of Ce^{4+} or Fe^{3+} (17). The results obtained by loading with 3Å Pt seem then to reflect the effects of electrocatalysis of Pt (compare Fig. 2 with Fig. 4).

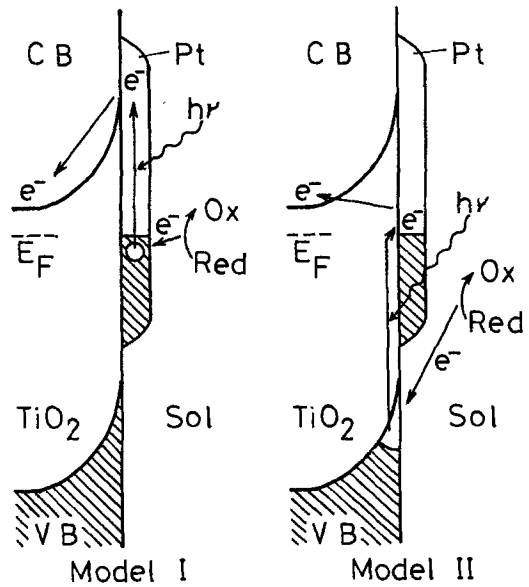

Fig. 7. Schematic representation for explanation of the additional anodic photoresponse observed at TiO_2 electrodes having Pt overlayers of 30Å thickness. Model I; excitation in the Pt layer, model II; excitation from the valence bands to the Pt layer.

The other type of the enhancement of the rate of cathodic reactions by depositing Pt, in which Tafel lines in current-potential curves are deformed into "inverted S curves," requires a thicker layer of Pt, but the amount is influenced by surface conditions of TiO_2 substrate and is smaller for damaged surfaces than for well etched surfaces. Judging from the results shown in Fig. 2 and 3, the amount required will be roughly 30 ~ 300Å with which apparent two-dimensional electrical conduction appears in the Pt layer (Fig. 6).

The abrasion of the crystals introduces lattice defects into their surfaces to a depth comparable to the particle size of the abrasive, and these defects work as electron traps in the forbidden zone of the semiconductors (18-20). The electron traps can facilitate electron transfer from the semiconductor to solution species by providing a pathway for electrons in the Schottky barrier layer formed at the surface (21); this permits cathodic processes to occur easily as noticed from comparison of the results shown in Fig. 1 to 3 for the Pt-free D- and E-electrodes. However, the enhancement in the rate of the cathodic processes in this case is not so large as that achieved by platinization of TiO_2. The electron traps are localized energetically and positionally, and hence the effective area of the electrode surfaces for the cathodic reactions via such electron traps must be restricted.

In the cases where the surface of TiO_2 is loaded with Pt, however, a different situation can occur. An increase in the amount of Pt loaded on the surface can bring about an increase in electrical conduction in the two-dimensional plane, and furthermore, an increase in the probability of contact between the deposited Pt and electron trap sites on the surfaces. This results in delocalization of electrons which reach the electrode surface from the bulk via such electron traps (Fig. 8). Thus, the Pt layers thick enough to show appreciable conduction on the surface can give a large cross section for cathodic reactions. The enhancement of the rate of cathodic reactions by platinization will depend in this case on the number of electron traps existing in the surface region of the TiO_2 electrodes. Since the concentration of lattice defects in well etched TiO_2 surfaces is much lower than that in mechanically damaged surfaces, a thicker layer of Pt, which shows higher two-dimensional conductivity and brings about higher probability of contact with the electron trap site, is

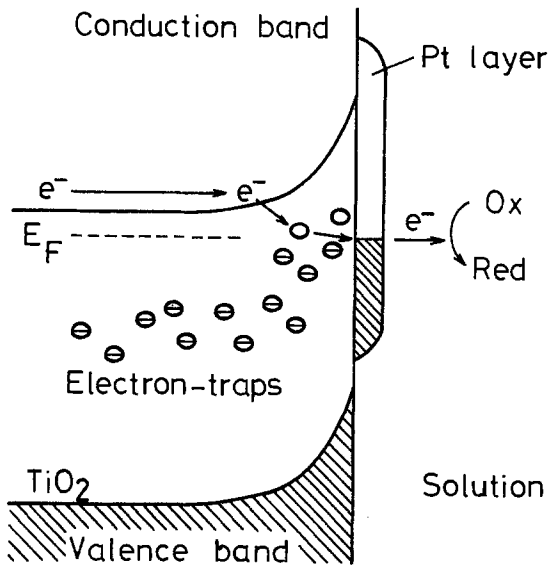

Fig. 8. Schematic representation for electron transfer from the conduction bands to solution species through Pt overlayers via electron traps in the semiconductor.

needed for appearance of this type of improvement in the cathodic processes.

The validity of our view proposed here can be checked by calculating current-voltage curves of a Schottky barrier diode with leak resistance. One can easily recognize that log (forward current) *vs.* forward bias relations of ideal diodes satisfy linear relations similar to the Tafel lines shown in Fig. 1. However, the linear relations are distorted if a leak resistance is introduced parallel to the ideal diode. The resulting relations in this case are similar to those given in Fig. 1 for reduction of O_2 with a relatively high number of the Pt loadings, which will be shown below.

Let us consider an equivalent circuit presented in Fig. 9a. In this figure, D_{sc} denotes the Schottky barrier diode which is applicable to an ideal contact of TiO_2/electrolyte and/or to that of TiO_2/Pt/electrolyte. According to our model of electron transfer from the conduction band to the electrolyte, electrons first fall into the electron traps in the Schottky barrier layer and then move to the Pt overlayers under assistance of electric fields, as shown in Fig. 8. Such a situation will be reasonably shown by inserting a series combination of two different leak resistances in parallel with D_{sc}. R_1 represents a leak resistance originating from electron traps in the Schottky barrier. Its value is varied by the number of the electron traps existing in the space charge layer of TiO_2 and must be much larger in the etched TiO_2 than in the damaged one. R_2 is a resistance characterizing effects of platinization, the magnitude of which is governed both by the probability of contacts between the deposited Pt and electron trap sites on the surface and by the electrical conductivity of the Pt layer in the two-dimensional plane, as discussed above. Therefore, the value of R_2 decreases with increasing amounts of the deposited Pt. In order to construct a complete equivalent circuit, an additional resistance characterizing electrochemical reactions has to be incorporated, but it is omitted here to avoid too much complication. Effects of damaged TiO_2 substrate and of platinization on physical properties of Schottky barriers formed at the electrode/electrolyte interface can be explained with use of the simple circuit presented here.

The current-voltage relation characterizing the diode, D_{sc}, is given by Eq. [4] (22, 23)

$$I_f^D = I_o\,[\exp(qV_f/kT) - 1] \qquad [4]$$

where I_f^D denotes the forward current in ampere, I_o the exchange current of D_{sc} under equilibrium, *i.e.*, at zero bias, and V_f the forward bias to the diode in volt.

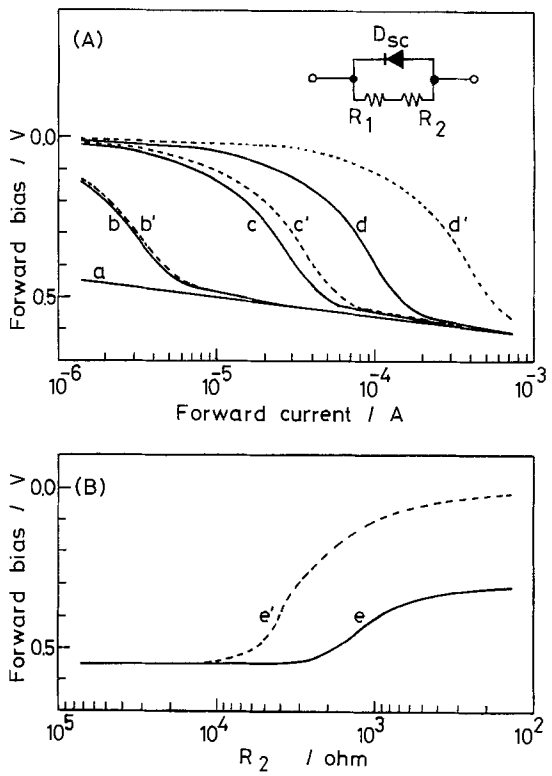

Fig. 9. Calculated current-voltage curves of Schottky barrier diode, D_{sc}, with two kinds of leak resistances of different nature, R_1 and R_2, (a), and bias voltages required to flow a constant current of 10^{-4}A for two different values of R_1 as a function of R_2 (b). Solid lines and dashed lines concern the curves with a fixed R_1 of 3 kΩ and 30 Ω, respectively, with R_2 values given below: (a); ∞, (b,b'); 100 kΩ, (c,c'); 10 kΩ, (d,d'); 1 kΩ, and (e,e'); variable. The solid lines correspond to the etched TiO_2 substrate while the dashed lines correspond to the damaged one. (For details, see text.)

The forward current, I_f^R, in the leak resistances is given by Eq. [5]

$$I_f^R = (R_1 + R_2)/V_f \qquad [5]$$

The total forward current, I_f, can then be given by Eq. [6]

$$I_f = I_f^D + I_f^R = I_o\,[\exp(qV_f/kT) - 1] + (R_1 + R_2)/V_f \qquad [6]$$

In order to fit Eq. [6] to the experimentally obtained current-potential relations, shown in Fig. 1, numerical definitions of I_o, R_1, and R_2 are needed. In cases of Schottky diodes, a condition of $V_f = 0$ can be applied to the open-circuit condition where there is a band bending in the semiconductor at the metal/semiconductor junction the magnitude of which is in principle equal to the difference in the work function between the metal and the semiconductor. Thus, when Eq. [6] is applied to the semiconductor/electrolyte junction, V_f should be measured from the open-circuit condition where *ca.* 0.7V *vs.* SCE was achieved at the platinized TiO_2 electrodes in the O_2-saturated solution. Note that an increase in V_f corresponds to an increase in the cathodic polarization of the semiconductor electrodes.

As described in the previous section, the Pt loading of only 3Å thickness gives a marked change in the apparent activities for reduction of O_2 as well as for evolution of H_2. High electrocatalytic activities of Pt for these reactions rather than any leakage of the conduction band electrons to the surface through the space charge layer seem to have an intimate relation to the observed phenomena, especially for the case of the etched electrode. Thus, I_o was evaluated by extrapolating the Tafel-like relations obtained at the Pt(3Å)/

etched TiO_2 to the open-circuit potentials, and the value determined was 2×10^{-14}A.

In order to evaluate the sum of the values of R_1 and R_2 in the equivalent circuit used, current-voltage curves of Pt(1000Å)/TiO_2 diode were measured in the solid state for both etched and damaged TiO_2 substrates in a bias voltage region from -0.3 to 0.3V. The results obtained were $3 \sim 5$ kΩ for the etched substrate and $70 \sim 150$Ω for the damaged one. The Pt layers having 1000Å thickness in the Pt/TiO_2 diodes will make a contribution of R_2 to the total resistance values relatively small. By this reason, two different values of 3 kΩ and 30Ω are assumed for R_1 for the E- and D-electrodes, respectively, and current-voltage relations were calculated with variation of R_2.

Figure 9a shows the current-voltage relations obtained by using Eq. [6] for R_2 values of ∞, 100, 10, and 1 kΩ. The bias voltages required for the forward currents of 10^{-4}A are also plotted in Fig. 9b as a function of R_2 values.

By taking into account that R_2 gives a relative measure of the amount of the Pt overlayers, one can recognize from Fig. 9a that "inverted S curves" in current-potential relations appear depending on the Pt loading, as observed in Fig. 1. The amount of electron traps in the semiconductor surfaces, a relative measure of which is given by the value of R_1, influences on the current-voltage relations if the Pt loading is rather high, as observed also experimentally.

Furthermore, it is noticed that the calculated V_f *vs.* R_2 relations shown in Fig. 9b have patterns similar to those given in Fig. 2 for reduction of O_2. According to this figure, the bias voltages required to flow a constant current of 10^{-4}A decrease with a decrease in the value of R_2 if R_2 is smaller than the critical value which depends on the magnitude of R_1. Thus, one can understand how the thickness of the Pt overlayers influences the decrease in the overpotentials, as shown in Fig. 2, and it is believed that similar situations are valid also for the case of Fig. 3.

In summary, the good matching of the experimentally obtained results with those obtained with the use of the equivalent circuit not only clarifies the observed complicated behaviors of the Pt-loaded TiO_2 electrodes but also supports the validity of our proposed view on the role of Pt overlayers on TiO_2 electrodes in electrochemical reactions in the dark.

Acknowledgment

This research was carried out under a Japanese-U.S. cooperative science program on "Metal Oxide Electrodes with Noble Functions." The financial support by the Japan Society for the Promotion of Science is gratefully acknowledged.

Manuscript submitted Oct. 18, 1982; revised manuscript received *ca.* Feb. 4, 1983.

Any discussion of this paper will appear in a Discussion Section to be published in the June 1984 JOURNAL. All discussions for the June 1984 Discussion Section should be submitted by Feb. 1, 1984.

REFERENCES

1. B. Kraeutler and A. J. Bard, *J. Am. Chem. Soc.*, **100,** 4317 (1978).
2. H. Reiche and A. J. Bard, *ibid.*, **101,** 3127 (1979).
3. K. Kogo, H. Yoneyama, and H. Tamura, *J. Phys. Chem.*, **84,** 1705 (1980).
4. T. Kawai and T. Sakata, *Nature*, **286,** 474 (1980).
5. A. J. Bard, *J. Photochem.*, **10,** 59 (1979); *Science*, **207,** 139 (1980), and references cited therein.
6. H. Gerischer, B. Pettinger, and M. Lübke, in "Electrocatalysis," M. W. Breiter, Editor, p. 162, The Electrochemical Society Softbound Proceedings Series, Princeton, NJ (1974).
7. T. Sakata, T. Kawai, and K. Hashimoto, *Chem. Phys. Lett.*, **88,** 50 (1982).
8. I. Izumi, W. W. Dunn, K. Wilbourn, F.-R. F. Fan, and A. J. Bard, *J. Phys. Chem.*, **84,** 3207 (1980).
9. W. W. Dunn and A. J. Bard, *Nouv. J. Chim.*, **5,** 651 (1982).
10. H. Yoneyama, H. Shiotani, N. Nishimura, and H. Tamura, *Chem. Lett.*, 157 (1981).
11. T. Kobayashi, Y. Taniguchi, H. Yoneyama, and H. Tamura, *J. Phys. Chem.*, **87,** 768 (1983).
12. T. Kobayashi, H. Yoneyama, and H. Tamura, *J. Electroanal. Chem.*, **138,** 105 (1982).
13. H. Tamura, H. Yoneyama, and T. Kobayashi, in "Photoeffects at Semiconductor/Electrolyte Interfaces," A. J. Nozik, Editor, p. 131, ACS Symposium Series 146, American Chemical Society, Washington, DC (1981).
14. P. Clechet, C. Martelet, J. R. Martin, and R. Olier, *Electrochim. Acta*, **24,** 457 (1979).
15. A. Damjanovic, M. A. Genshaw, and J. O'M. Bockris, *This Journal*, **114,** 467 (1967).
16. D. M. Kolb, M. Przanyski, and H. Gerischer, *Z. Phys. Chem. Neue Folge*, **93,** 1 (1974).
17. R. A. Marcus, *J. Chem. Phys.*, **43,** 679 (1965).
18. H. Gerischer, F. Fein, M. Lübke, E. Meyer, B. Pettinger, and H. R. Schöppel, *Ber. Bunsenges. Phys. Chem.*, **77,** 284 (1973).
19. S. R. Morrison and T. Freund, "Electrocatalysis on Non-Metallic Surfaces," A. D. Franklin, Editor, p. 139, NBS Spec. Publ. 455, National Bureau of Standards, Washington, DC (1976).
20. D. M. Tench and H. Gerischer, *This Journal*, **124,** 1612 (1977).
21. S. R. Morrison, "Electrochemistry at Semiconductor and Oxidized Metal Electrodes," p. 164, Plenum Press, New York (1980).
22. H. Gerischer, in "Physical Chemistry, An Advanced Treatise," Vol. IX A, H. Eyring, Editor, p. 492, Academic Press, New York (1970).
23. P. Singh and K. Rajeshwar, *This Journal*, **128,** 1724 (1981).

Technical Notes

Voltammetric Reduction of Sulfuryl Chloride in the Presence of Calcium Tetrachloroaluminate

W. K. Behl *

U. S. Army Electronics Technology and Devices Laboratory (ERADCOM), Power Sources Division, Fort Monmouth, New Jersey 07703

Recently, it has been suggested (1-6) that the safety of the thionyl chloride and sulfuryl chloride cells can be significantly improved by replacing the low melting lithium anode (mp 180.7°C) with a high melting calcium anode (mp 839°C). Thus, both the calcium-thionyl chloride (1-4) and calcium-sulfuryl chloride (5, 6) cells have been investigated during the past three years. For both these cells, solutions of lithium tetrachloroaluminate or calcium tetrachloroaluminate have been used as electrolytes. However, the cathode capacities in calcium cells using lithium tetrachloroaluminate solutions as electrolytes were found (5, 6) to be smaller than the cathode capacities in corresponding lithium cells. The cathode capacities in calcium cells were even smaller if solutions of calcium tetrachloroaluminate were used as electrolytes (2, 5, 6). Therefore, in order to gain an insight into the cathodic process in calcium cells, we have studied the voltammetric reduction of sulfur oxychloride solvents at smooth glassy carbon electrodes in solutions containing calcium tetrachloroaluminate. This paper summarizes our results in sulfuryl chloride solutions.

Experimental

Anhydrous lithium tetrachloroaluminate (7, 8) and anhydrous calcium chloride (9) were prepared by fusion under a flowing atmosphere of hydrogen chloride gas according to the procedures previously described. The fused salts were then treated with chlorine gas in order to oxidize any organic matter. The excess of any hydrogen chloride and chlorine gases were then removed by purging with pure dry argon gas. The anhydrous salts so prepared were solidified and stored under an argon atmosphere. Aluminum chloride (iron and water free; Fluka AG) was used as received. Sulfuryl chloride (Matheson, Coleman, and Bell Company) was refluxed over lithium metal and distilled as colorless liquid. 0.4 molar $Ca(AlCl_4)_2$-SO_2Cl_2 and 1.0 molar $LiAlCl_4$-SO_2Cl_2 solutions were prepared by dissolving requisite amounts of anhydrous salts in freshly distilled sulfuryl chloride. The $LiAlCl_4$-SO_2Cl_2 and $Ca(AlCl_4)_2$-SO_2Cl_2 solutions were then equilibrated with a small crystal of lithium chloride and calcium chloride, respectively, in order to neutralize traces of excess aluminum chloride, if any, in the solutions. The choice of the concentration of $Ca(AlCl_4)_2$-SO_2Cl_2 solutions used in the present study was dictated by the solubility limit (~0.5 mol/liter) of calcium tetrachloroaluminate in sulfuryl chloride (6).

A three-electrode system was used for all measurements. The reference (1 × 5 cm) and counter (3.5 × 6 cm) electrodes were both made by pressing lithium or calcium onto a nickel screen. Both electrodes were mechanically abraded and thoroughly washed with carbon tetrachloride before use. The lithium electrodes were used in 1.0 molar $LiAlCl_4$-SO_2Cl_2 as well as in lithium tetrachloroaluminate solutions containing small amounts of calcium tetrachloroaluminate whereas the calcium electrodes were used in 0.4 molar $Ca(AlCl_4)_2$-SO_2Cl_2 solutions. The reference electrode was separated from the other electrodes by the use of a Pyrex tube with a coarse porosity fritted glass bottom. The working electrode consisted of a 3.18 mm diam glassy carbon rod (Beckwith Carbon Company), heat-sealed in a shrinkable Teflon tubing and polished as previously described (10). The cross-section area of the working electrodes was 0.079 cm^2.

The cyclic voltammetric scans were performed using an EG&G PAR potentiostat/galvanostat (Model 173) coupled with the EG&G PAR universal programmer (Model 175) and recorded on Hewlett-Packard X-Y recorder (Model 7047A).

Results and Discussion

Cyclic voltammograms obtained at glassy carbon electrodes in 0.4 molar $Ca(AlCl_4)_2$-SO_2Cl_2 solutions were similar to those obtained in 1.0 molar $LiAlCl_4$-SO_2Cl_2 solutions (10). Thus, at a scan rate of 0.1 V/sec, a typical cyclic voltammogram (Fig. 1) exhibited a broad reduction peak at ~2.1V[1] with a shoulder at ~2.55V. The shoulder in these voltammograms was distinguishable only at scan rates below ~0.5 V/sec and at higher scan rates only one broad reduction peak was obtained. In solutions containing chlorine or aged solutions, only one broad reduction peak was obtained as was also observed in $LiAlCl_4$-SO_2Cl_2 solutions (10). The peak potentials in $Ca(AlCl_4)_2$-SO_2Cl_2 solutions are close to the peak po-

[1] All potentials are referred with respect to the calcium reference electrode.

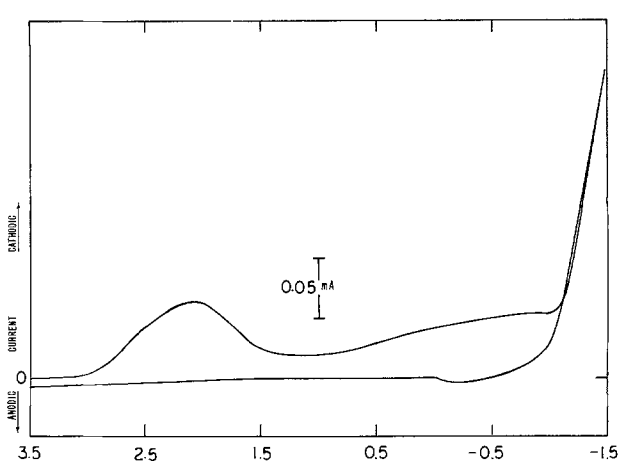

Fig. 1. Typical cyclic voltammogram at glassy carbon electrode in 0.4M $Ca(AlCl_4)_2$-SO_2Cl_2 solutions at a scan rate of 0.1 V/sec.

* Electrochemical Society Active Member.
Key words: electrolyte, battery voltammetry.

tentials observed in $LiAlCl_4$-SO_2Cl_2 solutions (10) considering that the potential of the calcium metal electrode in 1.0M $LiAlCl_4$-SO_2Cl_2 solutions was found to be ~0.7V *vs.* the lithium reference electrode. The peak heights increased with increasing scan rates and the peak potentials shifted to less positive potentials. At all scan rates, the cyclic voltammograms did not show any oxidation peaks corresponding to these reduction peaks during the reverse scan.

Since, sulfuryl chloride is known (11) to decompose to chlorine and sulfur dioxide, the shoulder at ~2.55V and peak at ~2.1V in the cyclic voltammograms (Fig. 1) may be, analogous to $LiAlCl_4$-SO_2Cl_2 solutions, attributed to the reduction of chlorine and sulfuryl chloride, respectively

$$Cl_2 + Ca^{++} + 2e \rightarrow CaCl_2 \quad [1]$$

$$SO_2Cl_2 + Ca^{++} + 2e \rightarrow CaCl_2 + SO_2 \quad [2]$$

Since, calcium chloride was found to be insoluble in sulfuryl chloride solutions, the deposition of calcium chloride at the glassy carbon electrode surface results in its passivation. The total charge required to passivate the electrode surface was measured by integrating the area under the cathodic reduction peaks at each scan rate and is plotted in Fig. 2 as a function of the scan rate. From the total charge passed, the thickness of the calcium chloride film on the glassy carbon electrode surface was calculated using a value of 2.154 g/cm³ for the density of calcium chloride at 25°C. As in $LiAlCl_4$-SO_2Cl_2 solutions (10), the total charge required to passivate the glassy carbon electrode surface as well as the thickness of the calcium chloride film were found to decrease with increasing scan rate. However, at all scan rates, both the charge passed under the cathodic reduction peaks as well as the thickness of the passivating film on glassy carbon electrode were found to be much smaller in calcium tetrachloroaluminate solutions than those obtained in lithium tetrachloroaluminate solutions (10). This large decrease in the charge required to passivate the glassy carbon electrode is not simply accounted for by the relatively small increase in the equivalent volume (equiv. vol) as the electrode film changes from lithium chloride (equiv. vol 20.5 cm³) in $LiAlCl_4$-SO_2Cl_2 solutions to calcium chloride (equiv. vol 25.8 cm³) in $Ca(AlCl_4)_2$-SO_2Cl_2 solutions. Therefore, it appears that the morphology of the calcium chloride deposits is such that it results in thinner, less porous, and more passivating film on the electrode surface than the passivating film obtained with lithium chloride deposits. Thus, Gilman and co-workers (6) have found that the cathode capacities in Ca/$Ca(AlCl_4)_2$-SO_2Cl_2/C cells were only one-tenth of the cathode capacities in Li/$LiAlCl_4$-SO_2Cl_2/C cells.

At more negative potentials (~ −1.1V), the cyclic voltammograms in $Ca(AlCl_4)_2$-SO_2Cl_2 solutions (Fig. 1) show a large increase in the cathodic current which may be regarded as due to some deposition of calcium metal. On the reverse scan, the cyclic voltammograms (Fig. 1) exhibit a small anodic peak at ~ −0.17V. Since this anodic peak is not observed if the direction of voltage scan is reversed prior to the onset of increasing cathodic current at ~ −1.1V, it may be ascribed to the dissolution of the deposited calcium metal.

The deposition of some calcium metal at glassy carbon electrodes in $Ca(AlCl_4)_2$-SO_2Cl_2 solutions was also indicated by the cathode potential-time plots obtained on constant current electrolysis of these solutions. Thus, at a current density of 1 mA/cm², the cathode potential-time plot (Fig. 3) first shows the reduction of sulfuryl chloride beginning at ~2.2V and as the glassy carbon electrode is passivated by the deposition of calcium chloride, the cathode potential quickly decreases to ~ −1.17V and remains at this potential until the current is turned off after 10 min of electrolysis. Similar voltage plateaus were observed at current densities up to ~5 mA/cm² though the plateau potential decreased to more negative potentials as the current density was increased (*e.g.*, −1.63V at a current density of 5 mA/cm²). At higher current densities, cathode potential-time plots showed slightly sloping voltage plateaus. After the electrolysis is terminated, the cathode potential-time plot (Fig. 3) shows an arrest at ~ −0.7V indicating some deposition of calcium metal. The freshly deposited calcium metal quickly corrodes in $Ca(AlCl_4)_2$-SO_2Cl_2 solutions and the glassy carbon electrode potential increases to more positive values. As in $Ca(AlCl_4)_2$-$SOCl_2$ solutions (2, 4), the deposition of calcium metal in sulfuryl chloride solutions was not found to be very efficient. Thus, upon current reversal after 10 min of electrolysis at a current density of 1 mA/cm², the number of coulombs recovered was only a tiny fraction of the number of coulombs consumed during the electrolysis.

In 1.0 molar $LiAlCl_4$-SO_2Cl_2 solutions containing small amounts of calcium tetrachloroaluminate, the cyclic voltammograms at glassy carbon electrodes showed a decrease in peak heights as well as a decrease in the charge passed under the cathodic peaks. The total charge under the cathodic peaks, at a fixed scan rate of 0.1 V/sec, is plotted in Fig. 4 as a function of the concentration of calcium tetrachloroaluminate. It is seen that the addition of even small amounts of calcium tetrachloroaluminate in 1.0 molar $LiAlCl_4$-SO_2Cl_2 solutions results in a relatively large decrease in the quantity of charge passed under the cathodic peaks. These results are also in agreement with the results of Gilman and co-workers (6) who found that, at similar discharge rates, the capacities of the carbon black cathodes in Ca/$LiAlCl_4$-SO_2Cl_2/C cells were

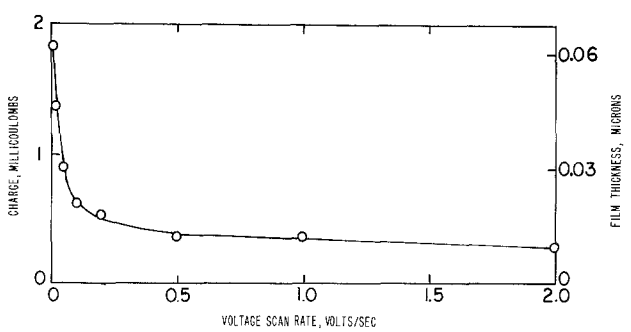

Fig. 2. Total charge passed under the cathodic reduction peaks and the calcium chloride film thickness as a function of scan rate.

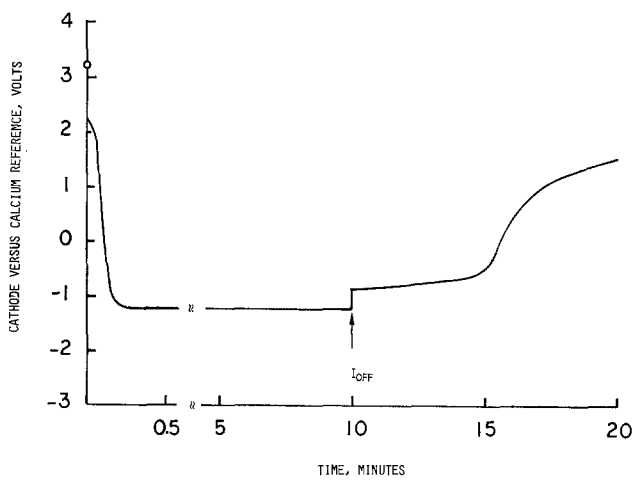

Fig. 3. Cathode potential-time plot obtained at glassy carbon electrode in 0.4M $Ca(AlCl_4)_2$-SO_2Cl_2 solution at a current density of 1 mA/cm². Open circle on the ordinate represents the open-circuit potential.

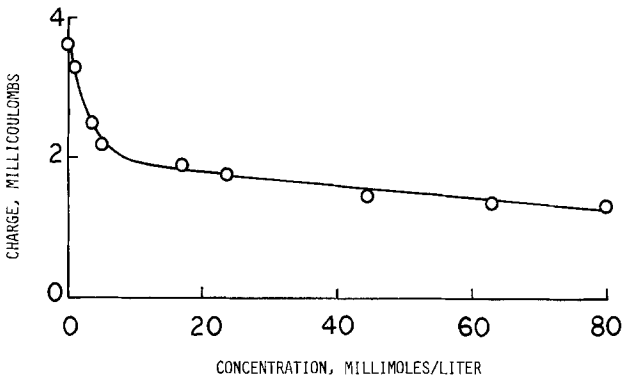

Fig. 4. Total charge passed under the cathodic reduction peaks at a scan rate of 0.1 V/sec in 1.0M $LiAlCl_4$-SO_2Cl_2 solution as a function of calcium tetrachloroaluminate concentration.

only one-third of the cathode capacities in Li/$LiAlCl_4$-SO_2Cl_2/C cells. Therefore, it appears that the formation (5) of calcium tetrachloroaluminate in solution in the early stages of discharge of the Ca/$LiAlCl_4$-SO_2Cl_2/C cell and the subsequent coprecipitation of calcium chloride and lithium chloride seems to "poison" the carbon black cathodes resulting in reduced cathode capacities in calcium-sulfuryl chloride cells.

Manuscript submitted Jan. 28, 1983; revised manuscript received *ca.* April 26, 1983.

Any discussion of this paper will appear in a Discussion Section to be published in the June 1984 JOURNAL. All discussions for the June 1984 Discussion Section should be submitted by Feb. 1, 1984.

U.S. Army Electronics Technology and Devices Laboratory assisted in meeting the publication costs of this article.

REFERENCES

1. R. L. Higgins and J. S. Cloyd, in "Proceedings of the 29th Power Sources Conference," Atlantic City, NJ, June 9-12, 1980, The Electrochemical Society, Inc., p. 147 (1981).
2. R. J. Staniewicz, *This Journal*, **127**, 782 (1980).
3. E. Peled, A. Meitav, and M. Brand, *ibid.*, **128**, 1936 (1981).
4. A. Meitav and E. Peled, *ibid.*, **129**, 451 (1982).
5. M. Binder, S. Gilman, and W. Wade, Jr., *ibid.*, **129**, 897 (1982).
6. M. Binder, W. Wade, Jr., and S. Gilman, in "Proceedings of the 30th Power Sources Conference," Atlantic City, NJ, June 7-10, 1982, The Electrochemical Society, Inc., In press.
7. W. K. Behl, J. A. Christopulos, M. Ramirez, and S. Gilman, *This Journal*, **120**, 1619 (1973).
8. W. K. Behl, in "Proceedings of the 27th Power Sources Conference," Atlantic City, NJ, June 24-26, 1976, The Electrochemical Society, Inc., p. 30 (1977).
9. W. K. Behl and J. J. Egan, *J. Phys. Chem.*, **71**, 1764 (1967).
10. W. K. Behl, *This Journal*, **127**, 1444 (1980).
11. J. W. Mellor, "A Comprehensive Treatise of Inorganic and Theoretical Chemistry," Vol. 10, Longmans, Green and Co., London (1930).

Corrosion by Alternating Current: Polarization of Mild Steel in Neutral Electrolytes

D-T. Chin* and P. Sachdev

Department of Chemical Engineering, Clarkson College of Technology, Potsdam, New York 13676

This laboratory has undertaken a series of investigations of the effect of a.c. on the corrosion of metals. Sixty cycles sinusoidal a.c. was superimposed onto an oxygen diffusion cell, and the measurement of corrosion current was compared to the actual weight loss of the specimens in soil (1-2). It was found that sinusoidal a.c. enhanced the corrosion of aluminum, copper, mild steel, and a 50-50% tin-lead alloy. At high a-c levels, severe pitting corrosion occurred on copper and mild steel specimens. Subsequent polarization measurements for mild steel in a neutral sodium sulfate solution (3-4) revealed that sinusoidal a.c. enhanced the corrosion current, shifted the corrosion potential toward the negative direction, and destroyed the passivity of mild steel at the passive potentials. The effect was similar to the addition of chloride ions to sulfate solutions.

In the present work, the polarization measurement has been extended to neutral sodium chlorate, sodium nitrate, and sodium perchlorate solutions. Anions can exert profound influence on the passivation mechanism. In sulfate and perchlorate solutions, the passivity of iron is initiated by a dissolution and precipitation mechanism (5). In nitrate solution, the literature evidences (6-7) suggest that the passivity of iron is caused by the anodic deposition of ferric oxide from the electrolyte; whereas in neutral chlorate solution (8), the passivity is attributed to a direct oxidation of iron by absorbed chlorate ions. It is the objective of the present work to investigate the interaction of a.c. with these anions on the passivation of mild steel in aqueous solutions. Also there are three forms of a.c. available for laboratory investigations. They are: (*i*) sinusoidal wave, (*ii*) square wave, and (*iii*) triangular wave. The second objective of this study is to investigate the effect of a-c waveforms on the polarization behavior of mild steel. A simple model is used to account for the changes in the potential-current relations with these a-c waveforms.

* Electrochemical Society Active Member.
Key words: passivity, voltammetry, dissolution.

Experimental

There are two ways to investigate the effect of a.c. on the electrode processes. The first method is called alternating current (a-c) modulation. This method uses a constant alternating current passing through the electrode-electrolyte interface, and the resulting time-averaged (or d-c) electrode potential is measured as a function of d-c current densities. The second method is the alternating voltage (AV) modulation. In this method, an alternating voltage rather an alternating current is applied across the reference and the working electrodes; the resulting d-c current density is then measured as a function of d-c electrode potentials. Both methods would yield the same results concerning the effect of a.c. on the electrode processes (3-4). In the present work, the method of AV modulation has been used. The advantage of AV modulation is that the measurement is potentiostatically controlled. For the metals, such as iron, which exhibit an active-passive transitional property, it is easier to analyze the experimental results with the AV modulation method.

The details of the experimental setup and the electrical circuit for the AV modulation measurement have been described in a previous publication (4), and will not be repeated here. The electrolytes used were: (*i*) 0.5M Na_2SO_4, (*ii*) 1.0M $NaClO_4$, (*iii*) 1.0M $NaNO_3$, and (*iv*) 1.0M $NaClO_3$. All the solutions were prepared by dissolving reagent grade chemicals in distilled water and were deaerated with high purity nitrogen before and during the experiment. A stationary mild steel[1] circular disk electrode having a surface area of 0.079 cm^2 was used for the measurement. The electrode was placed in a 3 liter Plexiglas cell equipped with a platinum-screen counterelectrode and a saturated calomel reference electrode. For each run, the mild steel electrode was polished with 600 grit emery paper, degreased with methanol, cleaned in dilute sulfuric acid, and rinsed with distilled water; after that, the electrode was transferred to the cell. The steady-state polarization measurements were carried out in each electrolyte for three different types of AV superimpositions, *i.e.*, (*i*) sinusoidal, (*ii*) square, and (*iii*) triangular waves. The magnitude of AV varied from 0 to 2000 mV rms. Except as noted, the frequency of AV was kept at 60 Hz. All the runs were made at a constant room temperature of 22° ± 1°C.

Results

Effect of AV waveforms for mild steel in sulfate solution.—Figure 1 shows the anodic polarization of mild steel in 0.5M Na_2SO_4 solution when the electrode was superimposed with 60 Hz sinusoidal, square, and triangular AV at 750 mV rms. The curves are designated by the symbols: —○— for sinusoidal wave, —□— for square wave, and —△— for triangular wave. For comparison, the polarization curve without any superimposed AV is also plotted in the figure as the filled dots, —●—. Figure 2 shows the oscilloscope traces of the resulting a-c current at various d-c potentials. It is seen that the effect of AV was characterized by: (*i*) a shift in the corrosion potential toward the negative direction, (*ii*) an increase in d-c current densities in the active and the transpassive regions, and (*iii*) the disappearance of passivity at the passive potentials.

In the passive region, the increase in the passivity current was the highest for triangular wave, and the effect diminished according to the order

[1] Composition of mild steel was: Fe, 97.5-97.9%; C, 0.085%; Co, 0.05%; Cr, 0.1-0.2%; Mn, 1.0%, Ni, 0.1-0.2%; Si, 0.1-0.2%.

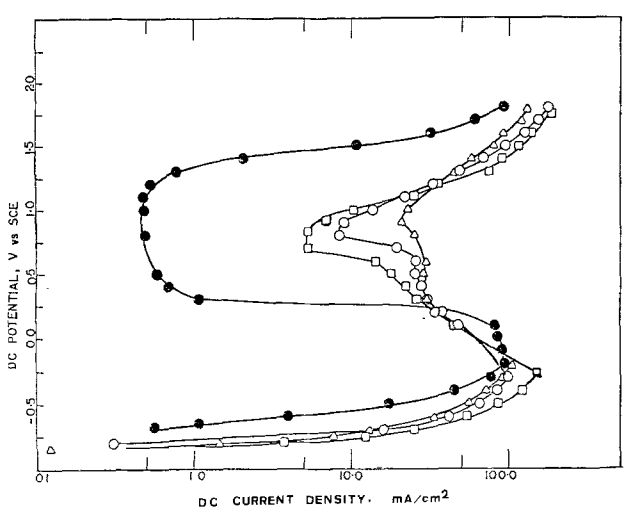

Fig. 1. Effect of AV waveforms on the polarization of mild steel in 0.5M sodium sulfate solution. The curves are designated by the symbols: —○— for sinusoidal wave, —□— for square wave, —△— for triangular wave, and —●— for without AV superimposition. All the AV had a magnitude of 750 mV rms and a frequency of 60 Hz.

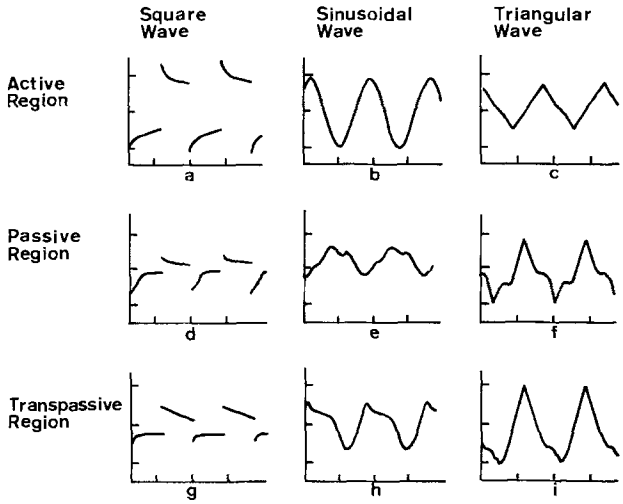

Fig. 2. The oscilloscope traces of a-c currents for AV modulation of mild steel in 0.5M sodium sulfate solution. The magnitude of 60 Hz AV was 1000 mV rms. The values of controlled d-c potentials are: —0.5V *vs.* SCE for a, b, c, 0.5V *vs.* SCE for d,e, 1.0V *vs.* SCE for f, 1.5V *vs.* SCE for g, h, and 2.0V *vs.* SCE for i. Vertical scale: 20 mA/div; horizontal scale: 5 msec/div.

$$\text{Triangular} > \text{Sinusoidal} > \text{Square} \qquad [1]$$

This sequence is in accordance with the instantaneous peak voltage of the applied AV. For a given root-mean square (rms), the peak voltage, V_p, of various waveforms can be calculated by the correlations

$$\left.\begin{array}{ll} \text{Triangular wave} & V_p = 1.73 \text{ rms} \\ \text{Sinusoidal wave} & V_p = 1.41 \text{ rms} \\ \text{Square wave} & V_p = \text{rms} \end{array}\right\} \qquad [2]$$

Apparently, the influence on the passivity is related to the peak voltage. A triangular wave had the highest peak voltage and accounted for the severest destruction of passivity. For the same reason, the passivity current for sinusoidal wave was between those of triangular and square waves as shown in Fig. 1.

In the active and the transpassive regions, the effect of AV waveforms was in the reverse order of Eq. [1], although the difference was not as large as that in the passive region

$$\text{Square} > \text{Sinusoidal} > \text{Triangular} \qquad [3]$$

the exact nature of this reverse order is not clear. It is likely that abrupt current reversal in the square-wave mode played an important role in the current-potential relationship.

Figure 3 shows the shift in the corrosion potential of mild steel in 0.5M Na_2SO_4 as a function of the rms of AV for three different waveforms. The natural corrosion potential of mild steel in the system was —0.7V *vs.* SCE. The corrosion potential was first shifted by AV toward the negative direction, and reached a minimum value of —0.82 to —0.83V *vs.* SCE at 750-1000 mV rms AV. Then, the corrosion potential was shifted back toward the positive direction with further increase in AV and approached asymptotically to —0.76V *vs.* SCE at very high AV values. Figure 3 further indicates that square wave had the greatest effect; sinusoidal wave was the next, and triangular wave had the least effect on the shift of corrosion potentials. The trend was similar to the effect of AV waveforms on d-c current densities in the active and the transpassive regions. However, the differences among various waveforms were not significantly large. Judging from the shape of the curves shown in Fig. 1 and 3, one may conclude that the effect of different AV waveforms were qualitatively similar. The same results were also observed for mild steel in neutral

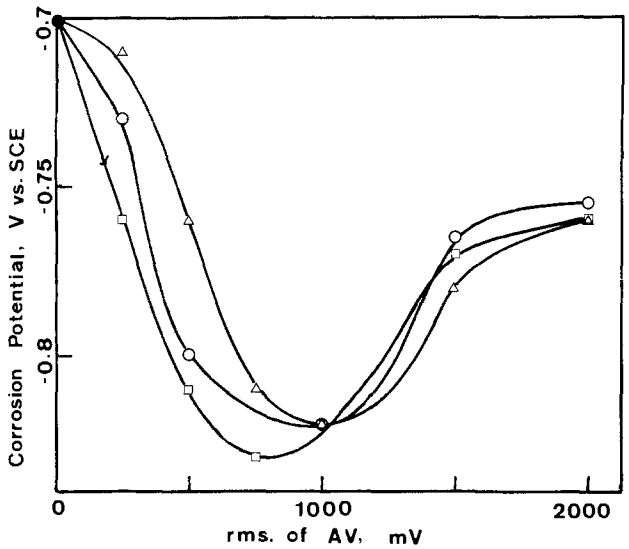

Fig. 3. Corrosion potential of mild steel in 0.5M sodium sulfate solution as a function of the rms of superimposed AV (60 Hz). The various notations are: —○— for sinusoidal wave, —□— for square wave, and —△— for triangular wave.

nitrate, perchlorate, and chlorate solutions. For this reason, only the results obtained with the square wave AV modulation will be presented in the subsequent sections.

Polarization of mild steel in nitrate and perchlorate solutions.—The results for the square-wave AV modulations of mild steel in 1.0M $NaNO_3$ and 1.0M $NaClO_4$ solutions are given in Fig. 4 and 5, respectively. Again, 60 Hz AV was used in the polarization measurements. The magnitude of AV varied from 0 to 2000 mV rms for nitrate solution, and from 0 to 1000 mV rms for perchlorate solution. In the active and the transpassive regions, the effect of AV was similar to that in sulfate solution: AV increased d-c current densities and shifted the corrosion potential toward the negative direction. The magnitude of the potential shift increased with increasing AV values.

In the passive region, AV destroyed the passivity and increased the passivity current densities by one to two orders of magnitude. At large AV values, two distinct passive regions were observed. For nitrate solution, this occurred at the AV values greater than 500 mV rms. The phenomenon was more predominant with the square-wave AV modulation than with the sinusoidal and the triangular waves. The first active-to-passive transitional potential occurred near the natural Flade potential of 0V *vs.* SCE, and the second active-to-passive transitional potential occurred approximately at 0.75V *vs.* SCE.

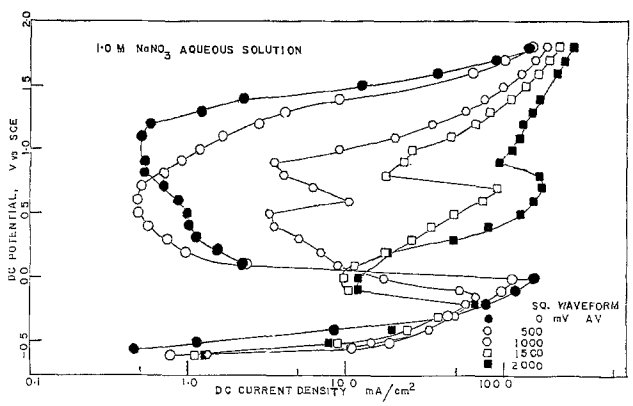

Fig. 4. Effect of 60 Hz square wave AV on the polarization of mild steel in 1.0M sodium nitrate solution. The magnitude of AV varied from 0 to 2000 mV rms as indicated in the figure.

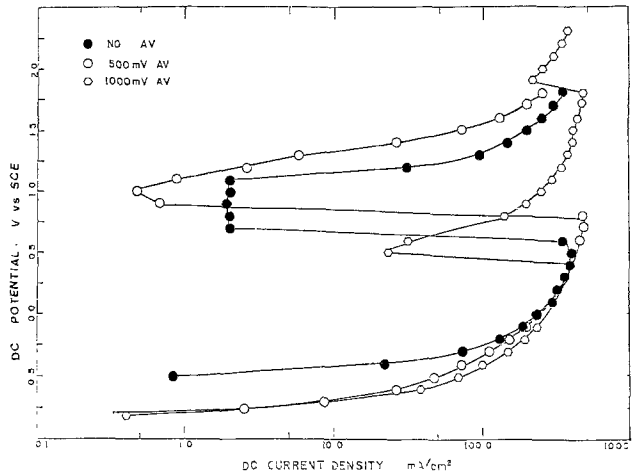

Fig. 5. Effect of 60 Hz square wave AV on the polarization of mild steel in 1.0M sodium perchlorate solution. The magnitude of AV varied from 0 to 1000 mV rms as indicated in the figure.

For perchlorate solution, the occurrence of the active-to-passive transitional potentials was less reproducible. This was because the oxide film on mild steel was initiated by a dissolution-precipitation mechanism, and the value of the active-to-passive transitional potential depended heavily on the electrolyte convective conditions (5). The oxide film in perchlorate solution was less stable, and the electrode possessed an active region larger than that in sulfate and nitrate solutions. Also at the transpassive potentials, the oxygen evolution at the electrode was less vigorous than in the other solutions. Figure 5 indicates that when 500 mV rms AV was superimposed onto the electrode, the potential range of the passive region was considerably reduced. At 1000 mV rms AV, two active-to-passive transitional potentials were observed: the first occurred near the natural Flade potential of 0.5V *vs.* SCE, and the second one occurred at a large noble value of 1.75V *vs.* SCE.

AV modulation of mild steel in chlorate solution.—The behavior of mild steel in neutral sodium chlorate solution was rather different from those in the other electrolytes. The natural corrosior potential in this solution was —0.3V *vs.* SCE as compared to —0.6 to —0.8V *vs.* SCE for sulfate, nitrate, and perchlorate solutions. Figure 6 shows the effect of 60 Hz square-wave AV on the polarization of mild steel in 1.0M $NaClO_3$ solution. It is seen that the corrosion potential was shifted toward the positive direction rather than the negative direction. AV also eliminated the passive region in chlorate solution. For AV greater than 500 mV rms, no passive region was observed, and the active dissolution region was extended to 1.8V *vs.* SCE as shown in the figure. It seems that AV had the ability

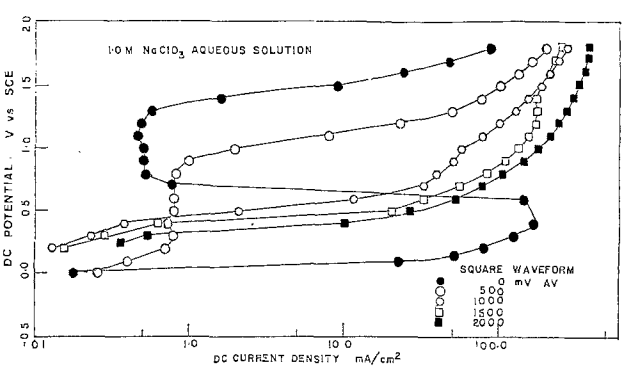

Fig. 6. Effect of 60 Hz square wave AV on the polarization of mild steel in 1.0M sodium chlorate solution. The magnitude of AV varied from 0 to 2000 mV rms as indicated in the figure.

to prevent the formation of oxide film in chlorate solution.

Discussion

The shift in the corrosion potential could be explained by the faradaic rectification due to a nonsymmetrical behavior between the cathodic and the anodic polarizations. The calculations made by Chin *et al.* (3-4) indicate that the corrosion potential will be shifted toward the negative direction if the anodic Tafel slope is smaller than the cathodic Tafel slope. Conversely, if the anodic Tafel slope is greater than the cathodic Tafel slope, then the shift in the corrosion potential will be in the positive direction. For small AV, the potential of the mild steel electrode was fluctuating between a cathodic value and a value in the active region of the anodic polarization curve. The Tafel slope of the anodic polarization curve in the active region was smaller than that of the cathodic polarization curve (4), and consequently, the corrosion potential was shifted toward the negative direction. As the superimposed AV increased, the potential of the mild steel electrode would fluctuate over a wider potential range. When the electrode was superimposed with an AV greater than 750-1000 mV rms, the instantaneous peak voltage could easily extend into the passive region, where the polarization curve possessed an infinitely large Tafel slope. It is believed that this interaction with the passive region caused the eventual shift back of the corrosion potential toward the positive direction at high AV values.

An attempt has been made to explain the foregoing phenomena with a simple mathematical model based on the polarization behavior without any superimposed AV. It was thought that the increase in the passivity current density was caused by the instantaneous potential variations along the S-shaped polarization curve when an AV of a sufficient magnitude was superimposed onto the electrode. At large AV values, the electrode potential could easily change from a cathodic value, through the active region on the anodic polarization curve, to a value in the passive or the transpassive region, and then back through the same path to the cathodic region. This instantaneous potential variation caused a complex current fluctuation at the electrode, and the enhancement of d-c current was the result of the time-averaging of the current fluctuations. Mathematically, the current density-potential relationship at the mild steel electrode may be represented by a function, $f(\phi)$

$$i = f(\phi) \qquad [4]$$

This function can be obtained with the polarization measurement without any superimposed AV. It should be noted that Eq. [4] covers both anodic and cathodic regions of the polarization curves. When the electrode potential, ϕ, is more negative than the corrosion potential, ϕ_{corr}, the net reaction of the electrode is cathodic, and according to the electrochemical convention, i should have a negative value. Conversely, if ϕ is on the positive side of ϕ_{corr}, the net reaction is anodic, and i is positive. When the electrode is polarized with a d-c potential, ϕ_{DC}, superimposed with an AV, ϕ_{AC}, the instantaneous current can be calculated by

$$i(\omega t) = f[\phi_{DC} + \phi_{AC}(\omega t)] \qquad [5]$$

where t is the time and ω is the frequency of superimposed AV. The quantity ϕ_{AC} for sinusoidal, triangular, and square-wave AV may be given as

sinusoidal wave

$$\phi_{AC} = V_p \sin \omega t \qquad [6]$$

triangular wave

$$\phi_{AC} = \begin{cases} (2/\pi)V_p[\omega t - 2(m-1)\pi], \\ \qquad 2(m-1)\pi < \omega t < (2m - 3/2)\pi \\ (2/\pi)V_p[(2m-1)\pi - \omega t], \\ \qquad 2(m - 2/3)\pi < \omega t < (2m - 1/2)\pi \\ (2/\pi)V_p[\omega t - 2m\pi], \\ \qquad (2m - 1/2)\pi < \omega t < 2m\pi \end{cases} \qquad [7]$$

square wave

$$\phi_{AC} = \begin{cases} V_p, & 2(m-1)\pi < \omega t < (2m-1)\pi \\ -V_p, & (2m-1)\pi < \omega t < 2m\pi \end{cases} \qquad [8]$$

where V_p is the peak voltage, and m denotes the cycle number ($m = 1, 2, 3, \ldots$) of superimposed AV. The d-c current is equal to the time-average of the instantaneous current over the mth period fluctuations

$$i_{DC} = (1/2\pi) \int_{2(m-1)\pi}^{2m\pi} f[\phi_{DC} + \phi_{AC}(\omega t)]d(\omega t) \qquad [9]$$

It should be noted that the concentration polarization and the effect of charging and discharging the electric double layer have been neglected in the analysis for the sake of simplicity of calculation. The above equations have been used by Chin and Venkatesh (4) to simulate the sinusoidal AV modulation of mild steel in sodium sulfate solutions.

In the present study, a series of experimental runs were made to determine the anodic and the cathodic polarization curves without any superimposed AV for mild steel in 0.5M Na_2SO_4, 1.0M $NaNO_3$, 1.0M $NaClO_4$, and 1.0M $NaClO_3$ solutions. These data were then used as the function $f(\phi)$ in Eq. [4]-[9], and the numerical results were generated on a digital computer to simulate the square-wave AV modulations. Figure 7 shows the typical computer-simulated polarization curves for mild steel in sodium perchlorate solution. It is seen that in spite of the simplicity of the model, the simulated curves clearly demonstrate that (*i*) there is a shift in the corrosion potential by AV toward the negative direction, (*ii*) AV increases d-c current densities in the cathodic region and in the active region of the anodic polarization curve, (*iii*) AV destroys the passive region and increases the passivity current densities, and (*iv*) at high AV values, there are two distinct active-to-passive transitional potentials. These results qualitatively agree with the experimental curves shown in Fig. 5 and present a good explanation of the behavior of the mild steel electrode under the superimposed AV conditions, in sodium sulfate, sodium nitrate, and sodium perchlorate solutions. For sodium chlorate solution, the computer-simulated polarization curves showed the characteristics similar to those in the other solutions, but contrary to the trend of the experimental curves shown in Fig. 6. This discrepancy implies that the change in the shape of the polarization curves in chlorate solution was not caused by the electrical interference of AV on nonsymmetrical

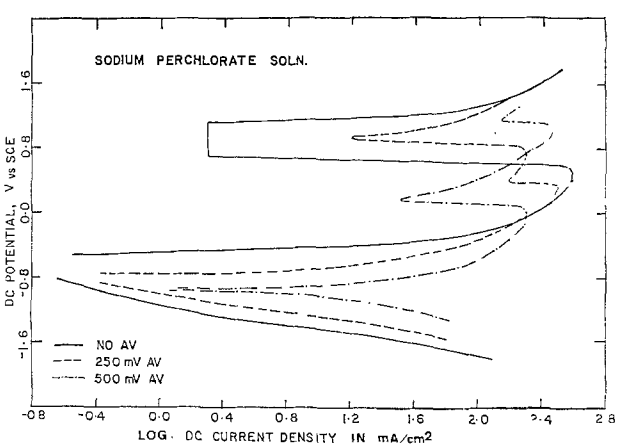

Fig. 7. Computer-simulated polarization curves for the square-wave AV modulation of mild steel in sodium perchlorate solution.

polarization behavior of the anodic and cathodic reactions. Rather, the effect was of a chemical nature, and AV caused a profound change in the mechanism of iron dissolution and film formation processes in chlorate solution. It is suggested that further studies be undertaken to resolve the problem.

Conclusions

A study has been made of the effect of alternating voltage (AV) on the polarization of mild steel in neutral sodium sulfate, nitrate, perchlorate, and chlorate solutions. The types of AV used were 60 Hz sinusoidal, square, and triangular waves, and the measurements were carried out for a range of AV from 0 to 2000 mV rms. Based upon the experimental results, the following conclusions could be made:

1. AV caused a shift in the corrosion potential toward the negative direction for mild steel in sulfate, nitrate, and perchlorate solutions. In chlorate solution, the corrosion potential was shifted toward the positive direction.
2. AV behaved as a depolarizer and substantially increased d-c current densities in the active and the transpassive regions of the polarization curves.
3. In the passive region, AV destroyed the passivity and increased the passivity current density by one to two orders of magnitude for mild steel in sulfate, nitrate, and perchlorate solutions. In chlorate solution, AV prevented the formation of oxide film on the electrode, and completely eliminated the passive region in the polarization measurements.
4. At high AV values, two distinct active-to-passive transitional potentials were observed for mild steel in nitrate and perchlorate solutions.
5. The effects of various AV waveforms were qualitatively similar for all the solutions investigated. Triangular wave caused the severest destruction of passivity in the passive region; whereas square wave caused the highest increase in d-c current in the active and the transpassive regions.
6. A simple mathematical model was used for the computer simulation of the polarization behavior of the mild steel electrode under the superimposed AV conditions. The simulated curves agreed qualitatively with the experimental curves for sulfate, nitrate, and perchlorate solutions.

Acknowledgment

Acknowledgment is made to the Donors of the Petroleum Research Fund, administrated by the American Chemical Society for support of this research.

Manuscript submitted Sept. 23, 1982; revised manuscript received Jan. 7, 1983.

Any discussion of this paper will appear in a Discussion Section to be published in the June 1984 JOURNAL. All discussions for the June 1984 Discussion Section should be submitted by Feb. 1, 1984.

The Petroleum Research Fund assisted in meeting the publication costs of this article.

REFERENCES

1. S. R. Pookote and D-T. Chin, *Materials Performance*, **17**, 9 (1978).
2. S. Venkatesh and D-T. Chin, *Isr. J. Chem.*, **18**, 56 (1979).
3. D-T. Chin and T. W. Fu, *Corrosion*, **35**, 514 (1979).
4. D-T. Chin and S. Venkatesh, *This Journal*, **126**, 1908 (1979).
5. D-T. Chin, *ibid.*, **119**, 1043 (1972).
6. D-T. Chin, *ibid.*, **119**, 1181 (1972).
7. D-T. Chin, *ibid.*, **121**, 527 (1974).
8. D-T. Chin, *ibid.*, **118**, 174 (1971).

Galvanostaircase Polarization

S. T. Hirozawa

BASF Wyandotte Corporation, Wyandotte, Michigan 48192

Cyclic potentiodynamic polarization is used most often to study the localized corrosion of metals. There are two critical potentials that are generally believed to be relevant to localized corrosion. The first of these is the potential at which the current begins to rise above the passive current—it has been referred to by various names (and symbols): breakdown potential (E_b), breakthrough potential (E_b), critical breakdown potential (E_c), transpassivation potential, pitting potential (E_p, E_{pit}), protection potential against pitting (E_{pp}), critical pitting potential (E_c, E_{cp}), and pit nucleation potential (E_{np}) (1-4). The second critical potential is the potential at which the current on the reverse voltage scan reaches the passive current; it has been referred to as the protection potential (E_p, E_{prot}) (2, 3) and repassivation potential (E_{repass}). In this paper, the two critical potentials will be represented by the breakdown (E_b) and protection (E_{prot}) potentials. E_p was purposely avoided because it is used sometimes to stand for the pitting potential.

The electrochemical techniques used to study localized corrosion can be divided into two general groups: potential (E)-controlled and current (i)-controlled polarization. The E-controlled group includes potentiodynamic or potentiokinetic polarization (PDP), stationary potentiostatic polarization, quasi-stationary potentiostatic polarization (QSP), scratch or scrape potentiostatic method, chronocoulometry (record i-*vs.* t-curve at constant potential) (1) and the pit propagation rate (PPR) method (3). The i-controlled methods include galvanokinetic polarization, stationary galvanostatic polarization [galvanostep (5)], quasi-stationary galvanostatic polarization, and chronopotentiometry (record E- *vs.* t-curves at constant current) (4, 9).

The electrochemical method used to study localized corrosion must be selected carefully because it will have a large influence on induction time, hysteresis, scan rate effect, and charge effect, all of which affect the values of E_b and E_{prot}. The classical E-controlled polarization techniques such as PDP and QSP are extremely prone to induction time effects which shift E_b in the noble direction and cause the reproducibility to be very poor. The reason for this tendency is that the classical E-controlled methods are passive in nature, *i.e.*, one raises the voltage across the passive layer and waits for the breakthrough of charge or breakdown of the passive layer. The i-controlled methods are active in nature; one does not wait for the breakdown but actually programs it on any desired schedule (6). Therefore, i-controlled techniques are not affected by induction time effects.

In a PDP or QSP curve, a high induction time can lead to excessive, uncontrollable current hysteresis (6, 7); hence the charge density or the extent of pit propagation cannot be reproduced. Wilde (2) has found that the value of E_p varies linearly with the log of the coulombs passed. Syrett (3) tried to avoid the

passage of excessive charge (which is probably related to pit propagation) by raising E above E_b to the breakthrough, then quickly reducing E to a constant level between E_b and E_{prot} and holding at the selected potential for 10 min. The pit propagation rate was obtained by dividing the average pit propagating current by the pit area, then plotting the pit propagation current density against potential to obtain E_{prot}. By minimizing the extent of pit propagation, the E_{prot} value should relate closely to the conditions of the metal surface existing in service. He found the E_{prot} values of stainless steels in Tyrode's solution much more noble than the values found by potentiodynamic polarization.

Pesall and Liu (8) used the potentiostatic approach but avoided the induction time by forcing a breakdown by scratching the surface. The scratch method approaches the minimal pit propagation recommended by Syrett, but it has the disadvantage in that the scratch location may not involve any of the most vulnerable pitting sites. In the PPR (3) method, the most vulnerable sites are involved.

Because current is under control in i-controlled techniques, it is not possible to have current hysteresis. Hence the charge density (coulombs/cm^2) in a given test is under complete control. However, i-controlled techniques are subject to voltage hysteresis due to slow kinetics in the precipitation and possible recrystallization of insoluble salts. The galvanokinetic method has the same disadvantage as the PDP method in that the kinetics of the electrode process is not evident. The stationary and quasi-stationary galvanostatic methods can virtually eliminate the hysteresis effect by judicious adjustment of the time allowed for each step to reach steady state. Broli *et al.* (4, 9) found that the quasi-stationary galvanostatic method gave the most reproducible results and concluded that there was only one characteristic protection potential for pitting, E_{pp}.

The present paper introduces the galvanostaircase polarization (GSCP) method which is an adaptation of the quasi-stationary galvanostatic method. Instead of plotting the steady-state potential against current, the voltage transients, which are responses to the current staircase signal, are recorded. The GSCP method not only combines the advantages of the scratch potentiostatic method, the PPR curve method, and the quasi-stationary galvanostatic method, but also provides additional advantages.

Experimental

A programmable timer was used to control a Princeton Applied Research Company (PAR) Model 175 universal programmer to create a voltage staircase signal. This voltage staircase signal was fed to the PAR Model 73 potentiostat/galvanostat, and under the "CONTROL I" mode the resulting current staircase signal was applied to the aluminum working electrode. The potential transients resulting from the applied current staircase were recorded. The steady-state potentials at the end of the up-steps were extrapolated to zero time or current to obtain the breakdown potential (E_b) and the steady potentials at the end of the down-steps were extrapolated to zero current to obtain the protection potential (E_p, E_{prot}). (6).

The preparation of the aluminum test specimens and the test media were described earlier (5).

Results and Discussion

Figure 1 shows the GSCP curves for 3003 Al in 100 ppm Cl^- and in 1% NO_3^- in 25% glycol using the fast scan rate (20 μA/cm^2: 1 min steps). Note that there is a slight separation between E_b and E_{prot} ($\Delta E > 0$) for both cases. Figure 2 shows that slowing down the scan rate by one-half causes ΔE to drop to a virtual zero for both Cl^- and NO_3^-. This appears to support the view of some (4, 9) that there is only one critical potential. However, the GSCP curve of a well inhibited antifreeze coolant shows a very wide separation of E_b and

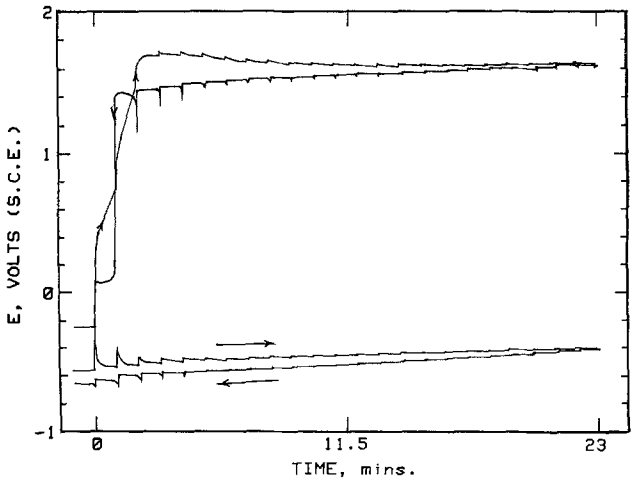

Fig. 1. GSCP curves of 3003 Al in 100 ppm Cl^- and 1% $NaNO_3$ in 25% reference antifreeze (1% borax in glycol) using fast scan rate (20 μA/cm^2: 1 min steps). Lower curve is Cl^-.

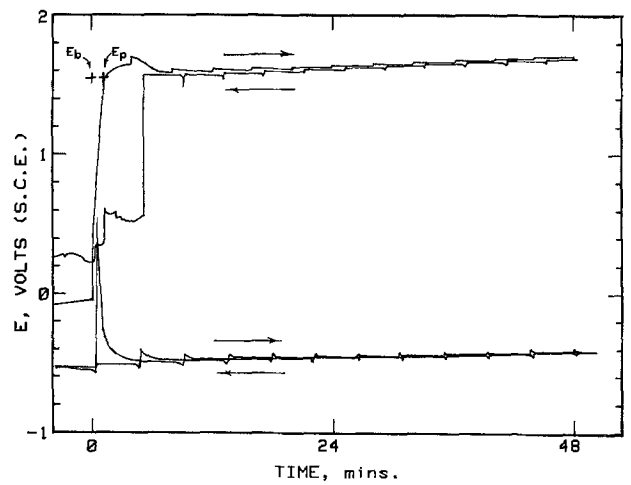

Fig. 2. GSCP curves of 3003 Al in 100 ppm Cl^- and 1% $NaNO_3$ in 25% reference antifreeze using medium scan rate (40 μA/cm^2: 4 min steps). Lower curve is Cl^-.

E_p at the fast scan rate (Fig. 3). Figure 4 shows that slowing the scan rate down 2/15 times diminished ΔE somewhat but failed to eliminate it completely. The "loop" formed by the up-step and down-step sections of the GSCP curve (Fig. 4) is not the result of hysteresis. In an i-controlled mode, only voltage hysteresis is allowed. *i.e.*, voltage would be lagging current and the

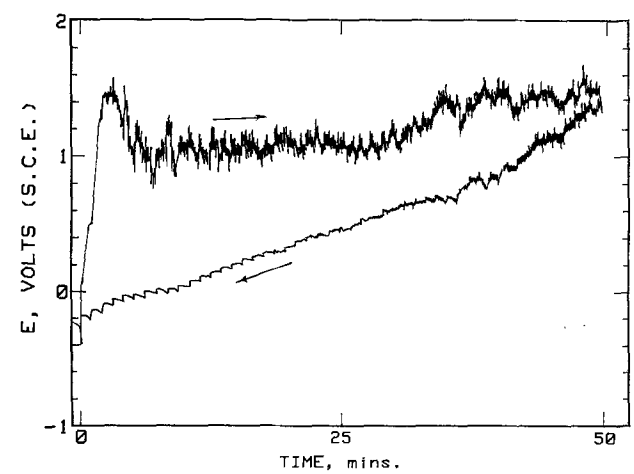

Fig. 3. GSCP curve of 3003 Al 25% experimental antifreeze 363-1. 20 μA/cm^2: 1 min steps.

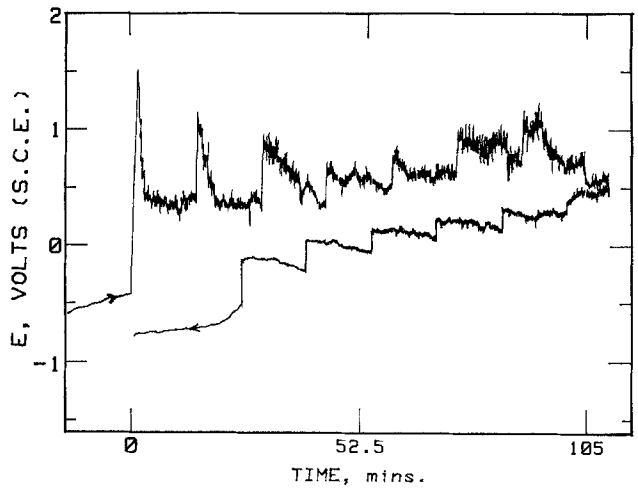

Fig. 4. GSCP curve of 3003 Al 25% experimental antifreeze 363-1. 40 μA/cm^2: 15 min steps.

loop should have swung upward instead of downward if hysteresis occurred. The raising of E_b relative to E_{prot} probably means that an outer passive film was formed which resists the flow of ions, thereby decreasing the general corrosion rate. It is then quite understandable why E_b is affected by the previous history of the metal which affects the thickness and permeability of the passive film to ions. E_b is rather nonreproducible in an inhibited environment, while in a noninhibited or slightly aggressive medium where the metals do not passivate, it is quite reproducible. The single critical potential, E_{pp}, proposed by Broli *et al.* (4) and the E_{pit} obtained by Wiggle *et al.* (10) (both obtained by *i*-controlled methods) probably correspond to E_b. In media such as chloride or nitrate, both of these potentials would be equivalent to E_{prot}; however, in highly inhibited medium, *e.g.*, experimental coolant No. 363-1 in Fig. 3 and 4, the agreement will not hold true.

E_{prot} obtained by GSCP was shown to be the true pitting potential (5, 6). E_{prot} of Al in 3000 ppm Cl^- agreed very well with the repassivation potential obtained by Rudd and Scully (7) by the scrape potentiostatic method. When the applied potential was below E_{prot}, the localized corrosion of Al was prevented. When the applied potential was between E_b and E_{prot}, both pitting and crevice corrosion occurred. E_b appears to have no direct relevance to localized corrosion; however, it seems to have indirect relevance. For example, we found that the greater the ΔE, the more severe was the crevice corrosion of Al (5, 6).

There are two phenomena observed in polarization curves which are dependent on the method of polarization. In *E*-controlled polarization, a current maximum may be observed which corresponds to the active/passive transition of certain metals in certain media; this maximum cannot be observed in *i*-controlled polarization curves. Meanwhile, in *i*-controlled polarization, a voltage maximum is observed occasionally; this voltage maximum is not detectable by *E*-controlled methods (5). The voltage maximum appears at the early stages of polarization at low current and it could be noisy (pitting) or noise free. At higher currents past the maximum, the curve can remain noise free, or noise could appear indicating that pitting has commenced. The availability of this noise information is one of the advantages of GSCP. The voltage maximum is probably due to slow passivation/depassivation processes—this phenomenon is probably the cause of the negative shift of E_b with slower scan rate in potentiodynamic polarization. The problem posed by the voltage maximum can be easily avoided by increasing the current step interval in the GSCP method.

The voltage maximum discussed above is often referred to as the pit nucleation potential (E_{pn}) (1, 4). E_{pn} should not be considered as one of the critical potentials because it is highly dependent on the kinetics of the electrode processes and scan rate, and if given sufficient time, it should drop down to E_b.

Aluminum is the ideal metal to show the big difference between *E*-controlled and *i*-controlled polarization. The reason for this is that Al has a very strong tendency to passivate in neutral media and forms a very thick (2000-5000Å) passive layer. Figure 5 shows the QSP curves obtained by Rudd and Scully (7) for Al in 0.08M benzoate in 3000 ppm Cl^- after 1/2 and 16 hr immersion time. To facilitate comparison, the corresponding GSCP curves are overlaid on the QSP curves. Note the very large positive shift in E_b obtained by QSP due to the induction effect. The severe hysteresis in the QSP curves makes it difficult to determine E_{prot}. The total charges passed are about 0.08 and 15.2 coulombs/cm^2 for the QSP curves for the 1/2 and 16 hr immersion times, respectively, while the charge density for the two GSCP curves was exactly 0.086 coulombs/cm^2. GSCP allows the total charge to be kept at a minimum predetermined constant.

The PPR curve method (3) is an *E*-controlled method, and therefore the actual charge passed per test is not under absolute control although the author tried to keep it to a minimum. The lowest charge density used was 1.12 coulombs/cm^2, and the charge density was as high as 17.4 coulombs/cm^2. Fortunately, the data points, other than those derived from zero pit propagation current density, appear irrelevant. Perhaps the main weakness of the PPR method is that E_b and E_{prot} must be known and they are obtained by *E*-controlled methods which make the value of E_b

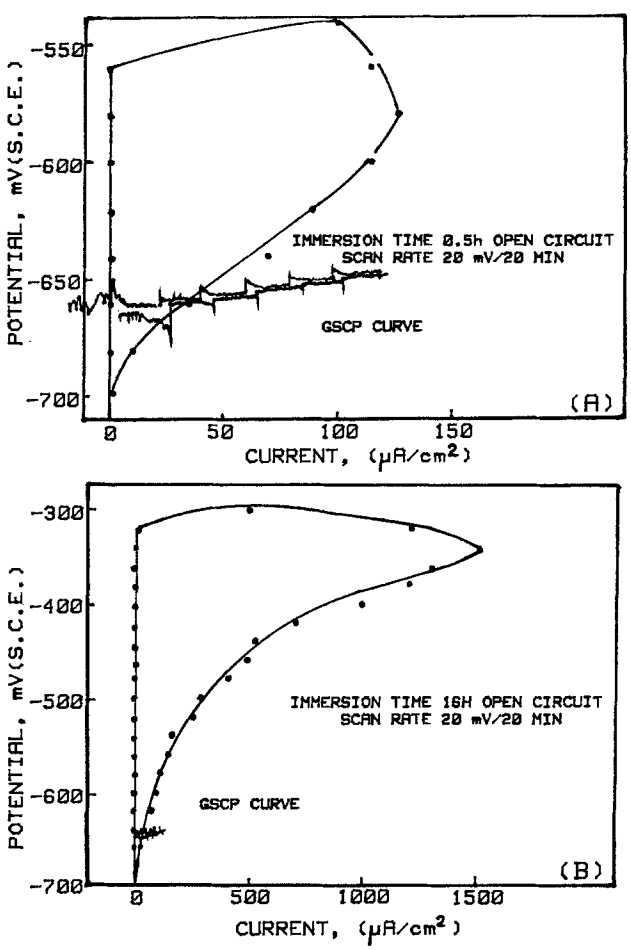

Fig. 5. Potential/current density curves (of Al) obtained in 0.08M benzoate solutions (a) after 0.5 hr pre-exposure and (b) 16 hr pre-exposure. Different values of E_{pit} (E_b) were attained as a result of the different times of exposure. [Courtesy of W. J. Rudd and J. C. Scully, Pergamon Press. See Ref. (7).] GSCP curves obtained under identical conditions are overlaid on their QSP curves.

doubtful especially when applied to Al in neutral medium.

Conclusion

A GSCP method was developed which combines the advantages of the quasi-stationary galvanostatic method [Broli, *et al.* (4)], the scratch potentiostatic method [Pessall and Liu (8)], and the PPR curve method [Syrett (3)]. The advantages of the GSCP method are summarized:

1. Rapid, accurate and precise.
2. Eliminates induction time.
3. Eliminates hysteresis.
4. Charge flow is programmed precisely—kept at minimum.
5. Noise information in voltage transients signals commencement of pitting (if it occurs).
6. Corrosion is localized at the most susceptible sites.
7. Two critical potentials are obtained: (*i*) E_{prot} is reproducible and related directly to localized corrosion, and (*ii*) E_b is not reproducible because it is related to the degree of passivation. The higher the E_b (relative to E_{prot}) the greater the inhibition against general corrosion but the greater the tendency towards crevice corrosion.

Manuscript submitted Nov. 16, 1982; revised manuscript received *ca.* May 5, 1983. This was Paper 48 presented at the Detroit, Michigan, Meeting of the Society, Oct. 17-21, 1982.

Any discussion of this paper will appear in a Discussion Section to be published in the June 1984 JOURNAL. All discussions for the June 1984 Discussion Section should be submitted by Feb. 1, 1984.

BASF Wyandotte Corporation assisted in meeting the publication costs of this article.

REFERENCES

1. S. Smialowska and M. Czachor, in "Localized Corrosion," R. W. Staehle, B. F. Brown, J. Kruger, and A. Agrawal, Editors, p. 353, NACE-3, Houston (1974).
2. B. E. Wilde, *ibid.*, p. 283.
3. B. C. Syrett, *Corrosion*, **33**, 221 (1977).
4. A. Broli, H. Holtan, and K. L. Prestud, *Corrosion*, **30**, 427 (1974).
5. S. T. Hirozawa, "Corrosion/82," Submitted for publication.
6. S. T. Hirozawa, Paper 48 presented at The Electrochemical Society Meeting, Detroit, MI, Oct. 17-21, 1982.
7. W. J. Rudd and J. C. Scully, *Corrosion Sci.*, **20**, 611 (1980).
8. H. Pessall and C. Liu, *Electrochim. Acta*, **16**, 1987 (1971).
9. A. Broli and H. Holtan, *Corrosion Sci.*, **13**, 237 (1973).
10. R. R. Wiggle, V. Hospadaruk, and E. A. Styloglou, *Materials Performance*, **20**, 13 (1981).

JOURNAL OF THE ELECTROCHEMICAL SOCIETY

SOLID-STATE SCIENCE AND TECHNOLOGY

AUGUST 1983

Centrifugal Etching: A Promising New Tool to Achieve Deep Etching Results

H. K. Kuiken and R. P. Tijburg

Philips Research Laboratories, 5600 JA Eindhoven, The Netherlands

ABSTRACT

This paper presents some theoretical considerations to show that by etching in an enhanced acceleration field, such as can be obtained in a centrifuge, it is possible to circumvent many of the typical objectionable features of some of the traditional etching techniques. The theory is corroborated by a small series of experiments. These clearly indicate that centrifugal etching may yield very low undercutting, large etch rates, and, if proper care is taken, an extremely smooth surface finish.

In many etching processes, the diffusional transport of the active components of the etchant to the surface or of the etched materials away from the surface, is a factor that severely limits the etch rate. The reason is that the diffusion coefficient of species dissolved in liquids is very small. D is of the order of 10^{-9} m^2/sec (1), but it may be greater than that number depending upon the temperature. To increase the etch rate, various methods, such as jet, spray, or film etching, are used. The common feature of these methods is that the etchant is forced to flow along the surface, thus adding the effect of convectional transport. If the purpose of the etching procedure is to produce small holes or slits in an otherwise smooth surface, the flow will almost never directly penetrate into the holes (2). Except when the cavity is shallow, the etchant moves along the hole, the flow in the cavity being characterized by one or more trapped eddies. It has been shown before (3) that the transport of reactants or of reaction products often occurs in a thin boundary layer that exists along the rim of the vortex. The exchange of etching products occurs by means of diffusion across the streamline that separates the eddies from one another or from the outer flow (Fig. 1).

Although adding convection will certainly increase the etch rate, etching methods that involve the forcing of the etchant along the hole pattern have one inherent drawback. It has, in fact, been shown experimentally (4) and explained theoretically (3) that the emergence of every new vortex leads to a drastic reduction of the etch rate (Fig. 2). This results in strong undercutting effects. In any case, it is doubtful whether, in the end, the etch depth will ever be much larger than the final hole width. Therefore, deep etching using forced flow outside the holes is probably impossible. This is also borne out by the experiments performed by Allen *et al.* (5-8). When convection effects are excluded, *i.e.*, in purely diffusional processes, deep etching with respect to hole diameter in isotropic materials is equally impossible. Indeed, in such materials a diffusion process does not have a characteristic direction, and eventually etching will result in almost spherically shaped cavity walls.

The purpose of this paper is to propose an alternative method of etching that does involve convection but circumvents the deleterious side effects mentioned above. This method makes use of the fact that in an actual etching process, the density of the liquid certainly is not uniform throughout the system. In many instances, the fluid will become more dense if reaction products are added to it. This means that in such cases the fluid close to the wall of the cavity is more dense than the remaining pure etchant. When the complete system is put in an acceleration field, *e.g.*, inside a centrifuge or in the ordinary gravity field, and care is taken to ensure that the acceleration vector is pointing out of the hole, the more dense "polluted" fluid will be drawn out, thus creating a natural convection pattern inside the cavity. Now there will be no trapped vortex within the cavity of the kind sketched in Fig. 1, as the fluid flows outward along the wall and, by the requirement of continuity, inward through the center (Fig. 3). It should be realized that pure etchant now first encounters the bottom of the cavity, thereby creating the largest etch rate exactly where it is needed. The impurity level grows along the side walls in the upward direction which results in lower etch rates closer to the orifice. It would seem that, by using this method, deep levels of penetration can be reached and that undercutting can be kept to a minimum.

It is obvious that the acceleration vector should point inward when addition of dissolution products to the etchant leads to lower densities. This is equally true if the removal of active species leads to an etchant of lower density. The acceleration vector should also point inward when the heat produced during the etching process is so large that thermal expansion exceeds the density enhancement due to the addition of etching products. If it is difficult to assess the relative magnitude of these two effects by theoretical means, suitable experiments will be needed in order to decide how to apply the acceleration field.

In the remaining part of this paper, we discuss some of the theoretical ideas that explain how natural convection can be an effective means of transporting reactants into and reaction products out of a cavity. Several experiments were carried out using a centrifuge, and we present some of the results in this paper. To simplify the presentation, we assume an etching process in which the "polluted" etchant has a higher density than pure etchant. As was explained above, the other cases can be dealt with similarly.

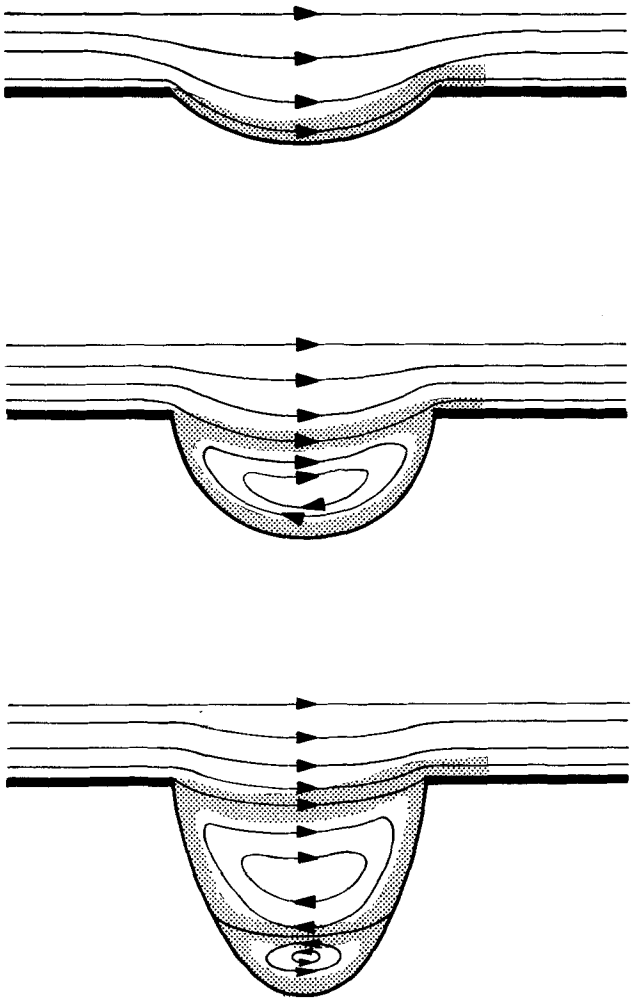

Fig. 1. Qualitative picture of mass transfer from an open cavity as a function of cavity depth in jet etching. Arrows denote flow direction. Reaction products occupy the dotted regions.

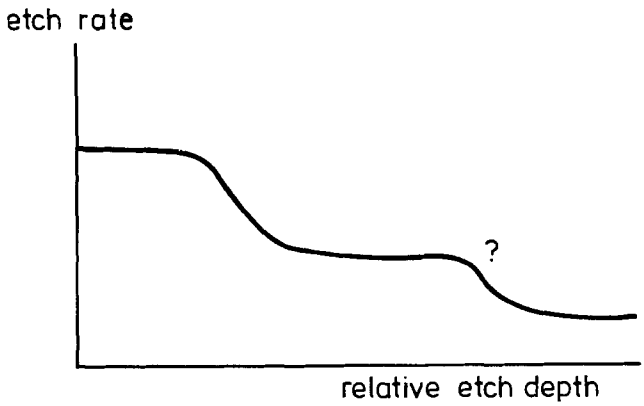

Fig. 2. Qualitative picture of etch rate as a function of etch depth in jet etching. Dips are caused by the emergence of new cells in the flow pattern. The question mark signifies that due to undercutting the two-cell pattern may never arise in practice.

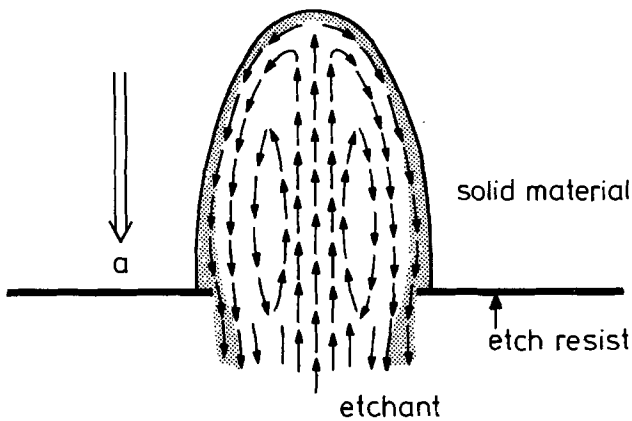

Fig. 3. Mass transfer from a cavity with free convective stirring. Arrows denote the direction of flow. Reaction products occupy the dotted region. The acceleration field is denoted by a. Case depicted assumes that reaction products are heavier than pure etchant.

Theoretical Considerations

In order that we may decide whether natural convection of the type described in the above section can really contribute to the transport of etched materials in an actual situation, we must have an estimate of the relative magnitudes of convectional and diffusional transport. In a standing etchant, *i.e.*, when stirring is absent, the transport of reaction products is due solely to diffusion down a concentration gradient. Therefore, the convective transport due to free convective stirring should at least be as large as the diffusional transport component, if it is to be noticeable at all.

Clearly, free convective stirring will be useful only if it dominates convection. In a system that is characterized by a large Schmidt number

$$\mathrm{Sc} = \nu/D \qquad [1]$$

where ν is the kinematic viscosity of the etchant ($\sim 10^{-6}$ m^2/sec) and D is the diffusion coefficient ($\sim 10^{-9}$ m^2/sec), it is essentially the Rayleigh number (Ra)

$$\mathrm{Ra} = a\beta(\Delta c)l^3/(\nu D) \qquad [2]$$

that determines the relative importance of convection and diffusion (9). In Eq. [2], a denotes the acceleration field (m/sec^2) and l is a length (m) that is characteristic for the size of the system. At the start of the etching process, l may be taken as the half-width of the etchable area. When a deep hole has been etched, the depth may be taken as the characteristic length. Further, Δc is a measure of the concentration difference (mol/m^3) of the reaction products, and β is the coefficient of volumetric expansion. In actual fact, if the density variations are not too large, the density of the polluted etching fluid can be given by the linear relationship

$$\rho = \rho_0(1 + \beta\Delta c) \qquad [3]$$

where ρ_0 is the density of pure etchant. Should thermal effects be important (reaction heat), Eq. [3] will have to be extended to include these

$$\rho = \rho_0(1 + \beta\Delta c - \beta_H\Delta T) \qquad [4]$$

where T is the temperature and β_H signifies the coefficient of thermal expansion.

Convection effects are dominant if the Ra number is considerably larger than unity. It is known, from both the heat and the mass transfer literature (10, 11), that Ra should at least be on the order of one hundred for convection really to dominate over diffusion. To obtain an idea of the values Ra may assume, consider what happens in an ordinary gravity field ($a = 10$ m/sec^2), using the values of D and ν already given. If the cavity to be etched has an original width of 100 μm, we have $l \sim \frac{1}{2} \cdot 10^{-4}$m (half-width). A reasonable value of $\beta\Delta c$ would seem to be 0.01, which means a density change on the order of one percent. Ra for this case is about 10, which seems to be too small for convection to have a significant influence on the etching process.

To obtain large etching rates in the example cited above, we might employ what may be called an artificial gravity field that can be created inside a centri-

fuge. Values of a up to 10^4 m/sec^2 can be created even in a simple centrifuge. Using such an apparatus, we may induce an intense natural-convective stirring right from the start of the process. In the example given above, the Ra number would be on the order of 10^4 at least, ensuring the dominance of natural convection over pure diffusion.

When the holes to be etched become smaller, the Ra number decreases in proportion to the third power of the characteristic length. Therefore, when etching smaller holes, leaving all other parameters in the system unchanged, we eventually have to use a more powerful ultracentrifuge (larger a) to keep the Ra number at high levels.

Further, it should be remarked that in Ra-number-determined flows, cellular flow patterns may emerge. These are called Bénard cells, which emerge when the fluid density gradient and the external field are parallel but directed oppositely. An array of such cells is sketched in Fig. 4, together with the etching pattern that may be expected on account of these cells. Later in this paper, we consider this phenomenon in more detail to explain certain experimental results.

To conclude this section, we devote some attention to the possible Sherwood numbers (Sh) that can be obtained through centrifugal etching. Here the Sh number is defined by

$$\mathrm{Sh} = \phi L/(D\Delta c) \qquad [5]$$

where ϕ is the flux of dissolved product and L is a length that characterizes the size of the active surface, *e.g.*, the hydraulic radius. To get an insight into the possible values Sh may attain, we appeal to the results obtained for free-convective mass transfer at horizontal electrodes (12). If Ra is in the range $3 \times 10^4 < \mathrm{Ra} < 2.5 \times 10^7$, we have

$$\mathrm{Sh} = 0.64\,\mathrm{Ra}^{1/4} \qquad [6]$$

Although it is not explicitly stated in (12), it would seem that both Ra and Sh in Eq. [6] are based on the width L of the mass transfer area.

The Ra range of validity of Eq. [6] is restricted by the transition to turbulent flow (upper bound) and the inaccuracies of laminar boundary-layer theory at smaller Ra numbers (lower bound). The results of Goldstein *et al.* (13) are very useful to determine the Sh number in the lower Ra range. The correlations established by these authors are

$$\mathrm{Sh} = 0.59\,\mathrm{Ra}^{1/4} \quad (\mathrm{Ra} > 200) \qquad [7a]$$

$$\mathrm{Sh} = 0.96\,\mathrm{Ra}^{1/6} \quad (\mathrm{Ra} < 200) \qquad [7b]$$

It should be noted that the characteristic length used in Eq. [7a] and [7b] is determined by dividing the area of the mass transfer region by its perimeter. For long stripes, this means that the half-width should be taken. On the other hand, for circular or square regions the quarter-diameter and the quarter-width should be used respectively.

It is tempting to compare the Sh-Ra correlations of Eq. [6] and [7] with those referring to forced convection flows that prevail in jet etching. The appropriate Sh-Sc-Re correlation depends strongly upon the way in which the etchant is forced onto and along the surface. Reference (9) presents some of these correlations which show that for $\mathrm{Ra} = 10^4$, the Sh numbers that follow from Eq. [6] or [7] are an order of magnitude smaller than the corresponding forced convection ones. However, as the holes become deeper, the forced convection Sh numbers will rapidly drop to lower values for reasons discussed before (see discussion of Fig. 1). The natural-convective correlations, on the other hand, will remain valid. Since free convection along vertical surfaces is more effective in terms of mass transfer rates, the free-convective Sh numbers may even go up a little bit as soon as a vertical sidewall of a length comparable to the hole width has been developed during the etching process.

Experimental

A beaker containing the etchant was placed in a centrifuge with a maximum rotation rate of 30 rps, which gave an artificial gravity of + or − 500g at the location of the test samples. The apparatus we used was a simple table centrifuge that was originally designed for the spin drying of silicon wafers.

The samples were mounted on the top or the bottom surface of a glass holder along which the etchant could flow freely. During spinning, samples mounted on the top of the holder experienced a positive, *i.e.*, inward directed artificial gravity with respect to the test pattern surface, whereas samples fixed to the bottom surface were subject to a negative (outward directed) gravity at the test pattern surface. A schematic picture of the experimental setup is given in Fig. 5.

A single experiment (±25,000g) was carried out in an ultracentrifuge. In the latter experiment, we used a Teflon sample holder, the shape and the size of which

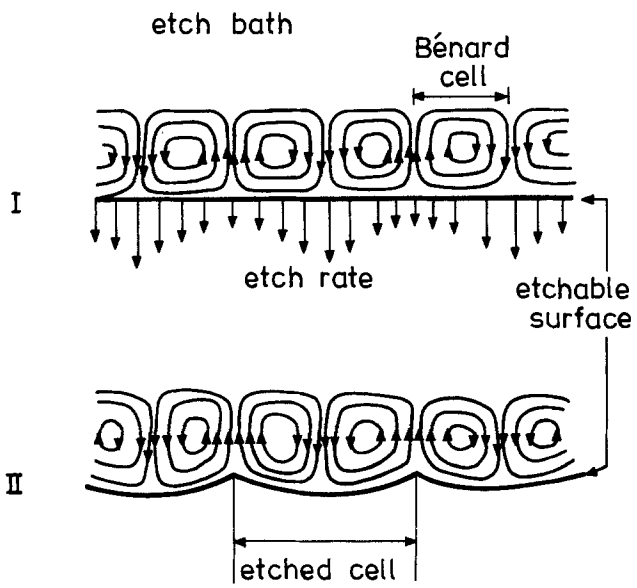

Fig. 4. Bénard cell flow pattern and resulting etching structure. (I) Initial flow pattern and etch rate distribution. (II) Sketch typifying a later stage of the etching process.

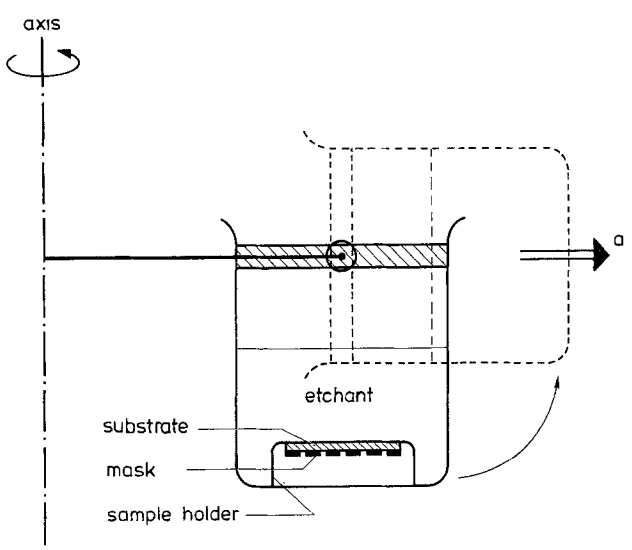

Fig. 5. Apparatus used in centrifugal etching. Case depicted refers to negative artificial gravity. The acceleration field is denoted by a.

were adapted to the special elongated beakers employed in an ultracentrifuge of the swing-out type. Again, this kind of centrifuge was not specially designed for etching purposes, as it is used extensively for biological sedimentation experiments.

In order to investigate whether the theoretical considerations presented earlier in this paper are valid, we took as test samples monocrystalline (1,0,0) oriented n-type GaAs slices as well as magnesium-bronze sheets both with thicknesses of 200 and 400 μm. We used a test pattern of circles with diameters ranging from 80 to 5000 μm. The etch resistant layer on GaAs was pyrolitic SiO_2 and on bronze the so-called C lacquer.[1]

The GaAs slices were etched either with a preferential or a nonpreferential etchant. The former is very sensitive to crystallographic orientation, and the etchant used (3,1,1) exhibits the lowest etch rate on (1,1,1) surfaces.

3 vol parts CH_3OH (methanol)
1 vol part H_3PO_4 (conc)
1 vol part H_2O_2 (30%)

The nonpreferential etchant (5,5,2) had the following composition

5 vol parts H_3PO_4 (conc)
5 vol parts H_2SO_4 (conc)
2 vol parts H_2O_2 (30%)

At the start of the experiment, the temperature of the etchant was 20°C.

Results

In Table I, results with GaAs pertaining to the etched depths have been summarized. The circular areas had large diameters compared to the etched depths. It should be noted that the nonpreferential etchant yields an extremely smooth surface finish (Fig. 6).

Sheets of bronze were etched in a centrifuge in aqueous solutions of $FeCl_3$ with s.w. 1.40 g/cm^3 and with an artificial gravity ranging from + 500 to −25,000g. Results obtained from experiments in which the artificial gravity was directed away from the test pattern surface, as well as those where the artificial gravity was directed inward, seem to confirm some of the theoretical expectations.

When the gravity field was directed toward the test pattern, the etched holes, with diameters ranging from 80 to 5000 μm have perpendicular sidewalls and flat bottom surfaces. There is no evidence of Bénard cell structures which are characteristic for the negative gravity case (see below). The undercutting amounted to about one-half of the etched depth for etching times of up to 15 min. For longer etching times, it tends to become equal to the etched depth. With the conditions described in Table II for the − 350g experiment, the + 350g experiment showed etching depths of approximately 40 and 50 μm for etching times of 15 and 30 min, respectively. After 90 min of etching, the holes were rather deformed with a maximum depth of about 100 μm.

With the gravity field directed away from the test pattern surface, we used accelerations of − 140, − 350, −500, and −25,000g. To achieve the largest of these values, we used an ultracentrifuge in a single experiment. Apart from the etching time, the depths of the holes obtained depend on the artificial gravity and on original hole diameter. Since the thickness of the bronze sheet used was not more than 400 μm, holes which otherwise would have been deeper could not be measured. The lower values given in Table II refer to holes with a diameter of 100 μm.

The 5000 μm hole shows an exception to this rule, as the average etch rate drops continually; we attribute this unusual behavior to a temperature effect. In Table III, results are given for various etching times and hole diameters. Starting at a rather high value, the etch rate remains virtually constant for times lasting up to 90 min. The etch rate of $FeCl_3$ in a standing etchant is 1 μm/min for hole diameters $\geq$ 100 μm. The etch rate produced in the ultracentrifuge (−25,000g) was $\geq$ 40 μm/min for a hole diameter of 250 μm and 13 μm/min for a hole diameter of 100 μm.

With artificial gravity directed outward, we observed Bénard cell structures. Figure 7, which refers to a short etching time and therefore shallow etching, clearly shows the hexagonal structure characteristic of Bénard cells. This particular experiment was carried out in − 350g. The average size of the cell is about 100-200 μm. Smaller diameter holes etched under the same experimental conditions showed a similar cell pattern, the average cell size being again approxi-

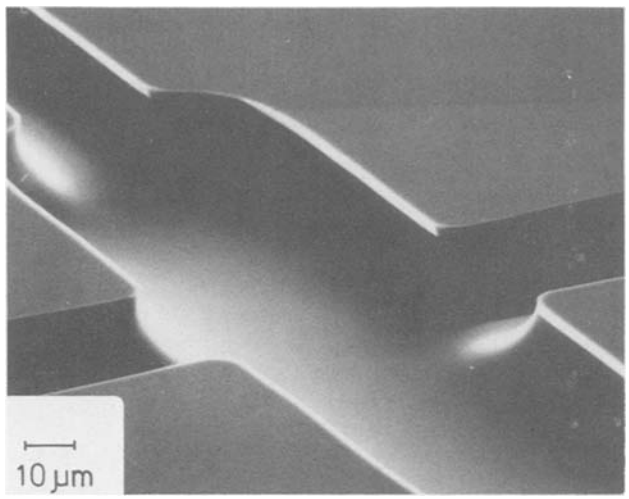

Fig. 6. Smooth surface finish in GaAs (+350g); 70°C; 30 sec; etch bath 3:1:1 (H_2SO_4:H_2O_2:H_2O).

[1] A polyvinylbutyral-based negative lacquer (made by Philips for internal use).

Table I. Effect of gravity field on etched depth (μm) after 6 min etching of GaAs; hole diameter: 250 μm.

Etching time: 6 min	Etchant 5,5,2	Etchant 3,3,1
Standing etchant	6 μm	11 μm
+ 350g	25 μm	25 μm
− 350g	55 μm	50 μm

Table II. Effect of gravity field and etching time on the etched depth (μm) of bronze; hole diameters: 100-1000 μm.

Artificial gravity	Etching time 7.5 min	15 min	60 min
+ 1g		20	
− 140g		100	100-300
− 350g	50	100	120-400
− 500g		125	160-400
−25,000g		200-400	

Table III. Average etch rate (μm/min). Etch depth (μm) per min for an artificial gravity of −350g; bronze.

Etching time used for averaging (in min)	Initial hole diameter (μm) 5000	500	250	100
7.5	17	7	6	8
30	13	3.5	3.5	2
60	7	3.5	3.5	2
90	4.5	3.5	3.5	2

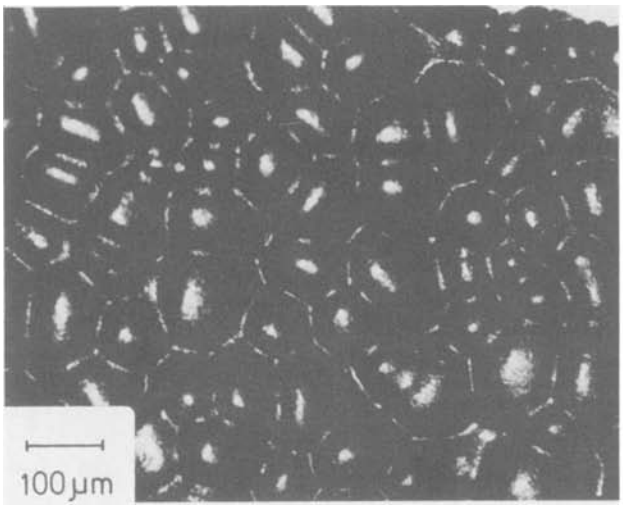

Fig. 7. Bénard cell structure (bronze, —350g); etching time, 15 min; etchant, $FeCl_3$; s.w., 1.35.

mately 100 µm, indicating that this is a length characteristic for the prevailing etching conditions. Although the hexagonal structure disappears as larger depths are reached, the cells remain, their appearance becoming more rounded. Smaller holes, with a diameter only a few times the characteristic length, exhibit a ring-like series of deep holes showing a pillar-like structure in the middle (Fig. 8-10). Below hole diameters of 150 µm, the multicell phenomenon disappears for reasons that should be obvious. Figure 11 shows a cylindrical hole of 100 µm diameter etched through a sheet that was 200 µm thick.

A simplified picture of the type of fluid flow that can be expected due to the Bénard phenomenon is shown in Fig. 4, where a linear array of Bénard cells is shown. Typically, the width and the height of a particular cell are of the same order of magnitude. The etch rate will be largest where downward directed fluid reaches the etchable surface. It will be lowest where the streamlines are directed away from the surface. Clearly, the etched cells will be approximately twice as large as the Bénard fluid cells. The ideal picture sketched in Fig. 3 refers to the case when exactly two Bénard cells fit into the cavity.

In the single experiment carried out at —25,000g, a similar cellular structure could be observed, although the phenomenon was not very distinctive. The cells appeared to have a diameter that was about one-quarter of those resulting from the — 350g experiment. Figure 12 shows a hole with a diameter slightly larger than 100 µm. The bottom contains a great many cells; however the cells are rather vague. At — 350g, the same hole shows only a single cell

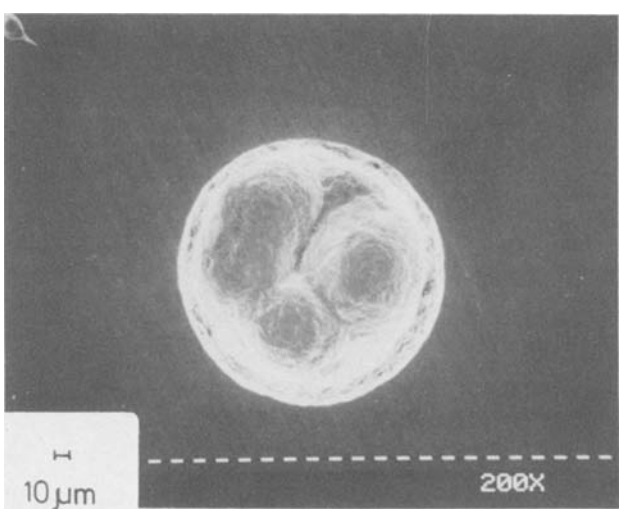

Fig. 8. Cellular pattern. Original hole width (OHW): 200 µm. (Bronze, —350g.) Etching time: 1 hr; etchant: $FeCl_3$; s.w.: 1.39.

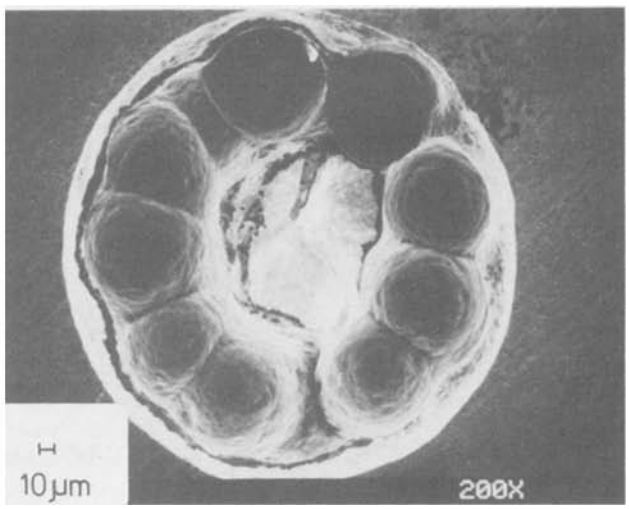

Fig. 9. Cellular pattern (OHW 350 µm. Bronze, —350g). Etching time: 1 hr; etchant: $FeCl_3$; s.w.: 1.39.

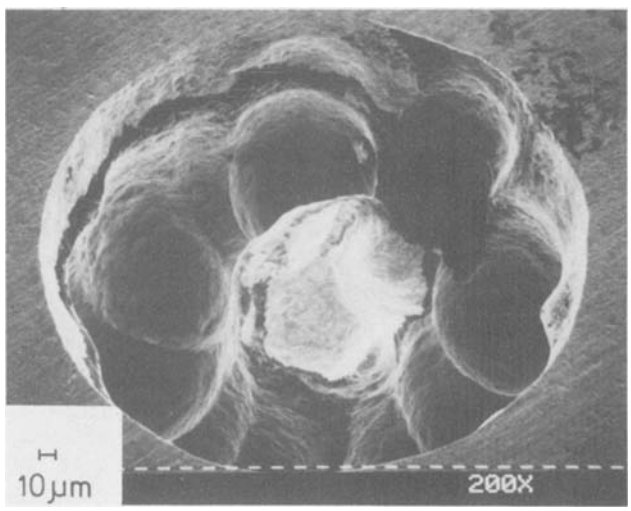

Fig. 10. Side view showing central pillar. Hole same as that of Fig. 9. (Bronze, —350g.)

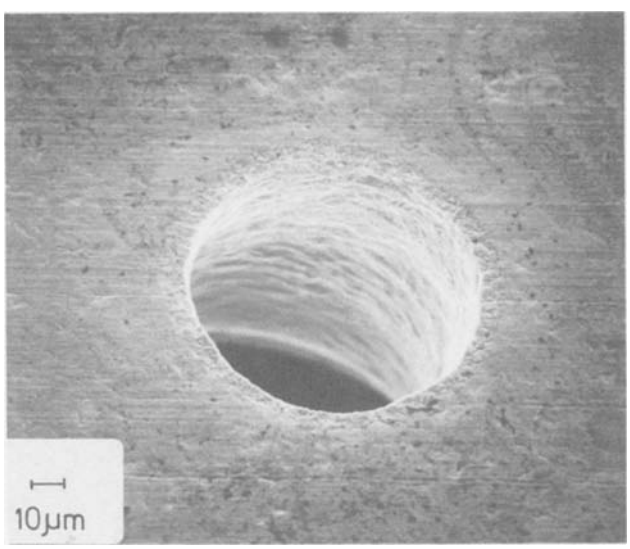

Fig 11. Cylindrical hole in bronze (width: 100 µm, depth: 200 µm, —350g). Etching time: 15 min; etchant: $FeCl_3$; s.w.: 1.35.

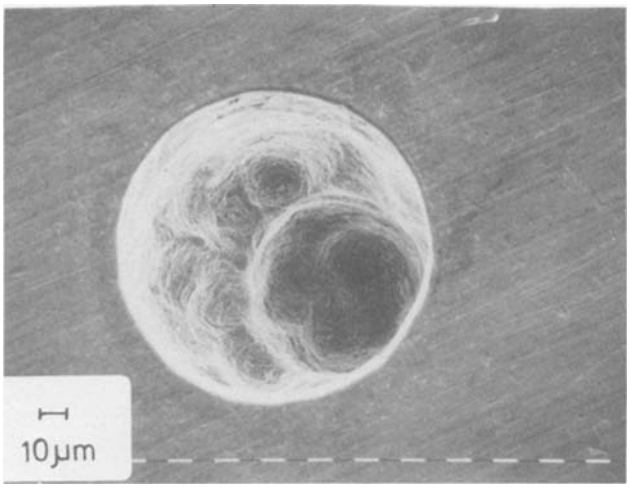

Fig. 12. Cellular pattern at −25,000g (OHW 120 μm, bronze). Etching time: 15 min; etchant: $FeCl_3$.

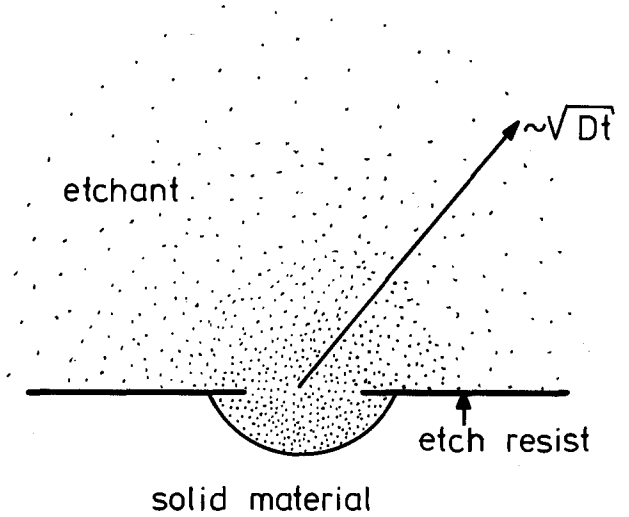

Fig. 13. Diffusion field in a standing etchant. The density of the dots denotes the concentration level of reaction products. *D* is the diffusion coefficient and *t* is the time.

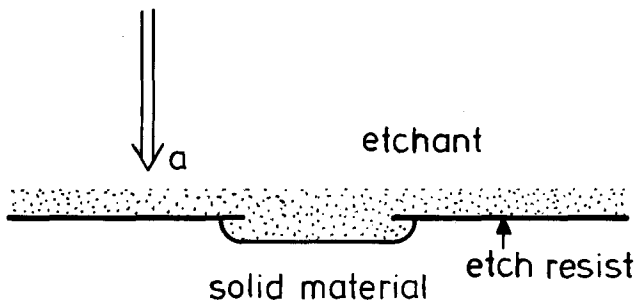

Fig. 14. The squeezing of reaction products against the substrate by means of an applied acceleration field *a*. It is assumed that reaction products are heavier than pure etchant.

and that would have filled the entire cavity. Pillar formation evidently depends upon the characteristic cell size; the larger the artificial gravity applied, the smaller the hole diameter is that reveals the phenomenon.

Despite these cells, the undercutting of the photoresist was very slight. When the sheets were etched through, no evidence of the cell structures was left, as the walls were smooth. Table IV gives a summary of the ratio of underetching to etched depth for various artificial gravities. This ratio appears to be independent of hole diameter. From the single experiment carried out in the ultracentrifuge, we tentatively conclude that the etch factor can even be much smaller under extreme acceleration conditions. At −25,000g, the etch factor appeared to be on the order of 0.05.

Although etch rate and undercutting seem to have a more or less regular behavior as a function of hole diameter and other parameters mentioned, it simply occurred too often to be considered accidental that, for hole diameters in the range 100-160 μm, the etch rate was clearly higher than that of both smaller and larger holes. In 15 min, we etched a hole 200 μm deep with a diameter of 100 μm holes. Holes of 400 μm deep with a diameter of 140-160 μm were etched in 30 min. The walls of these holes were as perfect as all the other holes obtained during the same experiments.

When holes had been etched through completely before etching stopped, an increase of the hole diameter occurred in the lower part of the holes. Figures 15 and 16, which refer to results obtained in the ultracentrifuge, clearly show this phenomenon.

Discussion

The experimental results presented in this exploratory paper clearly indicate that some remarkable results may be obtained by centrifugal etching. It would seem that relative etching depths can be reached that are simply not obtainable by the traditional methods of jet, spray, and film etching. The degree of undercutting is extremely low by ordinary standards. In many instances, our centrifugal etching procedure gave holes that were almost cylindrical, the etched depth being considerably larger than the final hole diameter. In an ultracentrifuge, etch rates may be achieved that are even larger than those obtained by ordinary jet etching methods. All these remarkable results were obtained when the artificial gravity was pointing away from the surface being etched.

Table IV. Underetching—depth etching ratio for various artificial gravities and etching times: bronze.

Artificial gravity	Etching time		
	15 min	60 min	90 min
− 140g	0.13	0.13	
− 350g	0.13	0.12	0.10
− 500g	0.12	0.08	

Inward-directed artificial gravity.—On the other hand, when the acceleration field was pointing inward, extremely smooth surface finishes were seen. The etched bottoms were very flat, but now undercutting was not negligible. Still, the etch rate proved to be a fair bit higher than that obtained in a standing etchant. As an explanation, we might venture the following.

With inward directed artificial gravity, the reaction products are squeezed against the surface, the polluted layer becoming almost one-dimensionally stratified (Fig. 14). In the absence of the acceleration field, the etching products would have assembled in a semispherical slowly expanding diffusion region (Fig. 13), the thickness of which would be on the order of the diffusion length $(Dt)^{1/2}$. Since polluted etchant was assumed to be more dense than pure etchant, this semispherical region cannot be maintained in a force field that acts on the mass of a substance. Therefore, the polluted etchant will spread out over the surface which is "lowest" in the field, much as a layer of cold air would spread out over the surface of the earth. The one-dimensional stratification of the former case (with inward directed force field applied) leads to an effective diffusion length that is much smaller, where the diffusion length could be defined as the distance over which the concentration drops to 50% of its

highest value. As the etch rate is inversely proportional to the effective diffusion length, we may understand that etching will then proceed more rapidly. Evidence for this can be found in Table I where the application of a positive field led to an etch rate that was at least two times larger than that observed in a stationary etchant.

The smoothness of the surface finish observed in the positive, inward directed gravity case could be explained as follows. During etching, gaseous products may be created at the surface. In case these products are not dissolved completely, tiny gas bubbles will appear. If these remain attached to the wall, a coarse etched surface will be obtained. A strong positive field will pull these bubbles away from the surface the moment they appear, and a smoother etching process is obtained.

Bénard cells.—Returning now to the negative gravity case, it would seem that the most favorable conditions for fast deep etching exist when the hole diameter is just a little over the characteristic length given by the Bénard cell size. As we said before, for a given etching system, the cell size is fully determined by the magnitude of the artificial gravity. From the experiments on bronze in an $FeCl_3$ environment, performed at -350 and $-25{,}000$g, respectively, we found a reduction of the cell size from ~ 120 to ~ 30 μm. Since the etching systems were the same in the two cases, this means that the Ra number based on cell size (Eq. [2]) was the same in both experiments. Referring to the classical theories of Rayleigh-Bénard instability (14), we conclude that there is a critical Ra number at which convection sets in in a horizontally stratified fluid. This value of Ra is in the neighborhood of 1000. If this theory applies to the present case, we have a means of determining the correct acceleration needed to etch a given hole in an optimal sense. The required acceleration is

$$a = a_r(l_r/l)^3 \qquad [8]$$

where a_r and l_r are values obtained from an experiment that was carried out for reference purposes, and l is the given hole diameter. If Eq. [8] is applied to the two experiments mentioned earlier in this paragraph, we readily find that the values $a_r = 350$g, $a = 25{,}000$g, $l_r = 120$ μm, and $l = 30$ μm do satisfy Eq. [8] to a remarkable extent. Here it should be realized that the values of l_r and l were read directly from the photographs of Fig. 7 and 12 and are only correct in an approximate sense.

Etch rates: a comparison between theory and experiment.—We shall now investigate how the etch rates as shown in Table II can be explained with a view to the theoretical etch rates as expressed by Eq. [7]. In using Eq. [7], one should take into consideration that this equation is applicable only when the etching process has not yet proceeded to depths that are larger than the original width of the cavity. Indeed the experiments that led to Eq. [7] (13) were done on nonetchable stationary surfaces. When etching has proceeded to greater depths, the motive force attributable to free convection along vertical surfaces will dominate the etching process and a different (probably larger) Sh number will be obtained.

Another complicating factor that may hamper a correct judgment of the relative etch rates is to be found in the heat production that will occur during many etching processes. If the etchable area is much larger than the thickness of the sheet, the main part of the produced heat has to be carried off to the fluid, conduction through the sheet being only of minor importance. On the other hand, if the holes are relatively small, conduction may well be the main cooling factor, especially if the sheet material is a good heat conductor such as bronze. In the former case, only one mode of heat transfer is present, and we may expect higher temperatures and consequently higher etch rates. Table III presents some evidence for this phenomenon, as the etch rate observed for the 5000 μm hole is significantly above that for the smaller holes.

With the provisos of the previous paragraph in mind, we may still attempt to explain the etch-depth variations presented in Table II. Since the Sh number is a measure of the ratio of the actual overall mass transport on the one hand and mass transport solely due to diffusion on the other, it will have a value of about one when stirring is absent or only very moderate. In Eq. [7a], we see that Sh is in the range of 3.5 to 6 when the Ra number varies in the range of 10^3-10^4. The etched depths given in Table II (15 min column) for the standing etchant and centrifugal ones of down to -500g do seem to confirm this range of values. An estimate of the true value of the Ra number may be obtained as follows. As postulated above, in each centrifugal case, the value of Ra based on the width of the Bénard cell (half the width of the etched cell) is around 10^3. In the case of -500g, this size is $l_b \sim 60$ μm. For round holes, the Ra number of Eq. [7a] was based on the quarter-diameter (13). The Ra number can therefore be estimated as follows

$$\mathrm{Ra} = 10^3(l/4l_b)^3 \qquad [9]$$

where l is the diameter of the hole.

When comparing the etch rates obtained under different centrifugal conditions, one should be careful always to use holes of the same original diameter, since a rule such as Eq. [7a] gives the overall mass transfer from the hole. In actual fact, it is the mass-flow density (see Eq. [5]) that determines the etch rate. If we enter $L = l/4$ in [5], which is in accord with the conditions of Ref. (13), we may obtain from Eq. [7a] and [9]

$$\phi = 4.7\, D(\Delta c) l^{-1/4} l_b^{-3/4} \qquad [10]$$

which shows a rather weak dependence upon the size of the cavity. The dependence upon l_b, the size of the Bénard cell, however, is rather strong. If two holes of the same size are etched with different centrifugal accelerations, the etch rate can be compared with the following rule

$$\phi_1/\phi_2 = [(l_b)_2/(l_b)_1)]^{3/4} = (a_1/a_2)^{1/4} \qquad [11]$$

where the last equality follows upon an application of Eq. [8]. If we apply Eq. [11] to the results presented in the 15-min column of Table II, taking the result for -500g as a reference, we find an etched depth of 91 μm for -140g, 114 μm for -350g, and 330 μm for $-25{,}000$g. The observed values cannot be overly accurate, as it is impossible to define the exact depth of a cavity when the bottom is quite uneven. Nevertheless, there is a good correspondence between theory and experiment. In particular, it is satisfying to find that the depth predicted by Eq. [11] for $-25{,}000$g is in the range of the observed values.

That the etch rate as expressed by Eq. [10] is only weakly dependent upon the width of the cavity, [*i.e.*, as long as the cavity is wider than $2l_b$] is an added advantage of the centrifugal etching technique over pure diffusion etching. In a standing etchant, the etch rate is dependent upon the initial size of the cavity, *i.e.*, the area of the etchable region. When the etched depth has become much larger than the initial hole diameter, the etch rate will have dropped to values that are much lower than those prevalent in the initial stages of the etching process. Obviously, this phenomenon will occur earlier when etching smaller holes. Therefore, a simultaneous etching of holes of different sizes may present problems if equal depths are required in the end. Jet etching, as we mentioned in

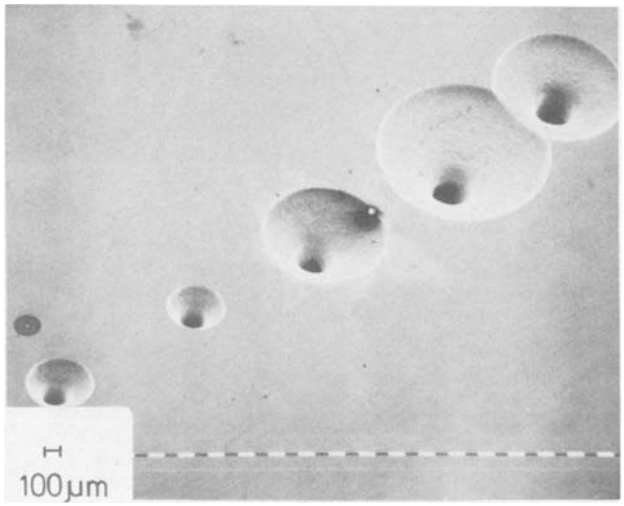

Fig. 15. Abnormal etching at the underside after complete etch-through has occurred (bronze, —25,000g).

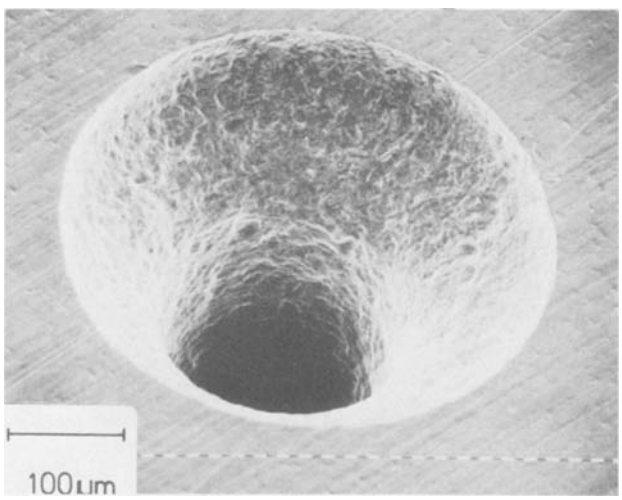

Fig. 16. Blow up of second cavity from the left in Fig. 15 (width: 400 µm; bronze, —25,000g).

the first section will also present problems here, as the etch rate will drop drastically when a depth comparable to the hole width has been reached. Centrifugal etching may offer a way out when care is taken that at least two Bénard flow cells fit into the smallest of the holes.

Abnormal etching after etch-through.—To explain the phenomenon shown by Fig. 15 and 16, we should realize the following. As soon as etch-through occurs, the concentration boundary layer acquires a definite leading edge. From the literature on boundary layers (1), we know that the largest normal gradients (for instance, that relating to mass transfer) occur at and close to the leading edge. In our case, this must necessarily lead to a rapid sideways etching. This process clearly does not stop when the bottom has been etched away. Eventually, the shape of the sidewall will reflect the distribution of the mass transfer coefficient at the wall. Due to the special nature of this phenomenon, its occurrence is independent of the fact whether or not a photoresist layer covers the other side of the substrate. The only cause for its existence is that fresh etchant now hits the lower edge of the sidewall first. If the bottom is open, fresh etchant will be pulled in from behind the substrate. If a photoresist provides a permanent cover of the other side of the substrate, fresh etchant will be brought in through the orifice, then down through the center and along the photoresist cover toward the sidewall.

In conclusion, it is clear that our preliminary etching results do not give a complete picture of the capabilities of the centrifugal etching technique. Nevertheless, they do indicate that centrifugal etching can be a new and powerful tool in material technology.

Acknowledgment

The authors acknowledge with thanks the help of Ing. C. G. I. van der Staak, who put at their disposal all the metal sheets with photoresist patterns on which the etching experiments were carried out.

Manuscript submitted Nov. 9, 1982; revised manuscript received April 28, 1983.

Any discussion of this paper will appear in a Discussion Section to be published in the June 1984 JOURNAL. All discussions for the June 1984 Discussion Section should be submitted by Feb. 1, 1984.

Philips Research Laboratories assisted in meeting the publication costs of this article.

REFERENCES

1. A. H. P. Skelland, "Diffusional Mass Transfer," Wiley-Interscience, New York (1974).
2. S. A. Trogdon and D. D. Joseph, *J. Non-Newt. Fluid Mech.*, **10**, 185 (1982).
3. H. K. Kuiken, *J. Eng. Math.*, **12**, 129 (1978).
4. G. Goosen and J. van Ruler, in "Proceedings of the World Conference on Metal Finishing," Interfinish, Amsterdam (1976).
5. D. M. Allen, D. F. Horne, and G. W. W. Stevens, *J. Photogr. Sci.*, **25**, 254 (1977).
6. D. M. Allen, D. F. Horne, and G. W. W. Stevens, *ibid.*, **26**, 72 (1978).
7. D. M. Allen, D. F. Horne, and G. W. W. Stevens, *ibid.*, **26**, 242 (1978).
8. D. M. Allen, D. F. Horne, and G. W. W. Stevens, *ibid.*, **27**, 181 (1979).
9. J. R. Selman and C. W. Tobias, *Adv. Chem. Eng.*, **10**, 212 (1978).
10. R. B. Bird, W. E. Stewart, and E. N. Lightfoot, "Transport Phenomena," Wiley, New York (1960).
11. V. G. Levich, "Physicochemical Hydrodynamics," Prentice Hall, Englewood Cliffs, NJ (1962).
12. A. A. Wragg, *Electrochim. Acta*, **13**, 2159 (1968).
13. R. J. Goldstein, E. M. Sparrow, and D. C. Jones, *Int. J. Heat Mass Transfer*, **16**, 1025 (1973).
14. S. Chandrasekhar, "Hydrodynamic and Hydromagnetic Stability," Clarendon Press, Oxford (1961).

Studies of Chemistry at the Ta/Si Interface as a Function of Thermal Processing

P. W. Lew[1] and C. R. Helms*

Department of Electrical Engineering, Stanford University, Stanford, California 94305

T. M. Reith[2]

IBM Data Systems Division, East Fishkill Facility, Hopewell Junction, New York 12533

ABSTRACT

Ta and Ta-oxide Schottky barrier diodes structures on n-type (100) Si substrates were prepared under various standard processing conditions using either sputter deposition or electron beam (E-beam) evaporation, and these samples were analyzed for their oxygen and carbon content using high resolution Auger sputter profiling. We found that the bulk Ta of the sputter-deposited and E-beam-deposited Ta films contain 3 atomic percent (a/o) oxygen. In addition, E-beam-deposited Ta films contain approximately 0.3 a/o carbon in the bulk and 1-3 a/o carbon at the interface. Photoresist use prior to deposition left residual carbon at the Ta-Si interface, and this carbon remained intact after an anneal of 400°C for 1 hr in vacuum. Oxygen present in Ta-oxides at the Ta-Si interface diffused away from the interface and tended to redistribute itself uniformly throughout the Ta layer for anneals of 400°C for 1 hr. Greater redistribution occurred for annealing at 450°C for 3 hr.

As VLSI processes continue to evolve, the need for new materials and their control has increased. In particular, many new circuit applications are optimized by use of a low barrier height (0.5-0.6 eV) Schottky barrier diode (SBD) component. Common materials usually used in SBD fabrication such as Al or PtSi are not suitable because their barrier heights to n-type Si are too high (0.7 eV for Al, 0.85 eV for PtSi). There are, nevertheless, a number of materials with appropriate barrier heights (0.5-0.6 eV) such as Ti, W, and Ta. At present, however, the reproducibility of many Schottky barriers using these materials is not sufficient ($\pm$ 0.1 eV). This poor reproducibility appears to be related to the cleanliness of the metal/silicon interface. Indeed, the scatter in the values of barrier heights is usually attributed, in part, to the variation in the surface treatment of the Si prior to metal deposition (1).

In order to overcome the effects of interfacial contamination, low temperature anneals are usually performed after metal deposition. These anneals which usually do not exceed 500°C due to circuit fabrication constraints, may remove interfacial impurities by chemical reduction or silicide formation. For example, for Al/Si contacts, it is believed that annealing causes Al to chemically reduce any interfacial SiO_2 and, hence, form a more intimate and reproducible contact to the Si (2). Another method of removing interfacial contaminants is to consume the outer layers of the Si by forming a metal-silicon compound, that is, a silicide. In this case, the silicide/silicon interface advances into the bulk of the Si, away from the region of residual contaminants (3). This technique of forming Schottky barrier diodes has been utilized successfully for high barrier Schottky barrier diodes such as the PtSi/Si system (3).

In this work, we report an investigation of how various deposition conditions affect bulk Ta and Ta-Si interfacial impurity content (oxygen and carbon) and how low temperature (400°-500°C) anneals cause redistribution of the impurities. Since Ta does not form a silicide below 650°C (4), the consumption of the interfacial impurities by a silicide was not possible and only impurity dissolution was possible. Characterization of the impurity distribution was performed using high resolution high sensitivity Auger sputter profiling.

Sample Preparation

The Ta was deposited onto silicon substrates either by sputtering or evaporation. Sputtering was also used to prepare the samples which had intentional oxygen contamination; evaporation was used for those with intentional carbon, present as photoresist residue or deposited from a charge not previously outgassed.

The sputtered Ta films were deposited in a Materials Research Corporation Model 822 sputtersphere in the rf diode mode using 500W forward power and 8 μm Ar pressure with no sputter cleaning prior to deposition. Oxygen contamination was introduced, via an ultrathin layer of Ta_xO_y at the Ta/Si interface, by nonreactively sputtering from a Ta target which had been preoxidized by reactively sputtering in an Ar/10% O_2 ambient. The details of this sample preparation technique have been described elsewhere (5).

The evaporated Ta films were deposited from an E-gun source using a Temescal FC-1800 evaporation tool. Intentional carbon contamination was introduced in some films by using new, nonoutgassed Ta source material. Carbon was also introduced by depositing a layer of AZ 1350 H photoresist material prior to the deposition. A blanket exposure and development was subsequently used to remove all but a thin residue of carbon-bearing contamination, as observed in these studies.

Sample annealing was performed in a Linde induction-heated furnace. The sputter-deposited $Ta/Ta_xO_y/Si$ sample was chosen for study because it contains an oxide layer between the Ta and Si thick enough so that it could be easily followed in detail after annealing. Similarly, the E-beam Ta/Si sample processed with photoresist and with a used charge was chosen since it has a large amount of interfacial carbon which could be followed after annealing. The $Ta/Ta_xO_y/Si$ sample was annealed by sealing it in a quartz tube and then placing the tube into the furnace. The tube was outgassed and then pumped to a pressure of 10^{-6} Torr using sorption and ion pumps. The Ta/Si sample was annealed in a similar tube pumped to a pressure of about 10^{-6} Torr using a mechanical and diffusion pump. The annealing was performed in vacuum to minimize effects due to chemical reactions with residual gases, since Ta is an excellent getter.

Auger Sputter Profiling System Parameters

A Varian Auger microprobe (Model 2738) was used to obtain the Auger sputter profiles. Electrons from the integral gun of the cylindrical mirror analyzer

* Electrochemical Society Active Member.
[1] Present address: IBM Data Systems Division, Hopewell Junction, New York 12533.
[2] Present address: IBM General Products Division, Tucson, Arizona 85744.

(CMA) struck the sample at an angle of incidence of 30°. The E-beam had an energy of 4.5 keV and a current of 18 μA focused into a 10 μm diam beam. This beam was then rastered over a 200 × 200 μm area to minimize E-beam damage (*e.g.*, Ref. 6). Routinely, the CMA was operated at an energy resolution of 0.3%. To allow detection of low concentrations of the element of interest, the CMA was operated at an energy resolution of 1.2% to increase transmission without excessive broadening of the transitions of interest. The sputtering gun was typically operated with 1.5 keV Ne^+ ions with a current density of 48 $\mu A/cm^2$ broadened by scanning to a full width at half maximum of a few millimeters. The Si_{KLL} (1619 eV), O_{KLL} (502 eV), C_{KLL} (272 eV), and the Ta_{MNN} (1680 eV) transitions were monitored during the experiment.

Concentrations are usually estimated using the peak-to-peak height of the derivative Auger spectrum, $dN(E)/dE$ [where $N(E)$ is the number of Auger electrons at energy E]. A more accurate method is to use the areas of the peaks of the $N(E)$ spectrum. These areas were obtained by integrating the derivative spectrum twice using a Tracor Northern TN-1710 data processor. Since the concentration of oxygen in Ta_2O_5 is known, a comparison of the ratio of the oxygen Auger peak area [$N(E)$ spectrum] in the Ta_2O_5/Si and Ta/Ta_xO_y/Si samples yields the concentration of oxygen in the Ta layer. A similar comparison of the ratio of the oxygen Auger peak-to-peak height to the Ta Auger peak-to-peak height [$dN(E)/dE$ spectrum] also gives an oxygen concentration, although not the same value obtained using peak areas. The ratio of oxygen concentrations calculated from the two methods give a calibration factor to convert from Auger peak-to-peak heights to concentration assuming no changes in lineshape are occurring.

Calibration of the carbon concentration could not be achieved in a similar manner as the oxygen concentration due to the lack of a carbon standard. Instead, the carbon concentration was estimated using the published derivative Auger spectrum of TaC (7). Comparing the ratio of the carbon peak-to-peak height to the Ta peak-to-peak height in the published data and the Ta/Si sample gives the concentration of carbon in the Ta layer.

The sputter time (minutes) was converted to depth by using the sputter rate (Å/min) as a calibration factor. The sputter rate was calculated by combining thickness measurements with total sputtering time, where the thickness was measured by at least one of the three following methods: ellipsometry, Rutherford backscattering, and Dektak stylus. For the operating parameters used (see above), the sputter rate was 15 Å/min for Ta and 50 Å/min for Si. These values are accurate to ±15% giving that level of confidence in the depth calibration. The metallurgical interface is taken to be the position where the Ta concentration is 50% of the bulk concentration. The Ta-Si interface widths were measured from these profiles by taking the difference in depths of the positions where the concentration of Ta was 10% and 90% of the bulk concentration. These measured widths represent upper values of the actual width due to possible broadening by knock-on mixing, sample roughness, and other effects (6).

Care was taken to prevent adsorption of background gases on the sample being analyzed. The standard procedure was to start with the base pressure in the 10^{-10} Torr range; the profiling was performed with the ion pump turned off but with fresh Ti in the sublimation pump; finally, the chamber was backfilled with the sputtering gas. After the ion pump is turned off, the total pressure rose about one order of magnitude. This is due primarily to noble gases which are released by the ion pumps when turned off. In order to detect low concentrations of oxygen, as in the present studies, additional precautions had to be taken to minimize the contribution of background gases to the oxygen Auger signal. A liquid nitrogen cryoshroud around the Ti sublimation pump is found to be effective in this respect and can be used with Ne^+ for sputtering while cryopumping gases which will interfere with the oxygen Auger signal. A differentially pumped ion gun would also provide acceptable results but was not necessary for these studies.

Results

A typical Auger sputter profile is shown in Fig. 1. This profile of the Ta/Ta_xO_y/Si sample clearly shows oxygen at the interface. Unexpectedly, there is also carbon (peak concentration 4.0 a/o) at the interface. Since the measured widths of these peaks are < 70Å, they could only be reliably detected by carefully choosing the operating conditions of the high resolution Auger microprobe (see previous section). The importance of choosing appropriate operating parameters is exemplified by a comparison with an Auger sputter profile of a similar sample obtained under different conditions (5). In this previous profile, the oxygen peak is not so evident. Compared to the present study, this oxygen peak is lower in concentration, broader in width, and shifted away from the interface towards the surface of the sample. The difference between the profiles is probably due to artifacts of the Auger sputter profiling technique (6). Attempts have been made to minimize these effects in this work.

In the present study, the oxygen in the Ta/Ta_xO_y/Si sample has been examined even more carefully in order to follow the oxygen after annealing (Fig. 2a). This profile has been reduced from the raw Auger signal *vs.* sputtering time spectrum to a concentration *vs.* depth profile by the method described in the previous section. It can be seen that, not only is the interfacial oxygen peak apparent in detail, but the low level of bulk oxygen in the Ta is also quantitatively detected and determined to be 2.0 a/o (relative to the atomic concentration of Ta). The peak concentration of the oxygen is 20 a/o and the peak width is 67Å. This measured value represents an upper limit of the width. The actual width is less than 67Å but broadened due to artifacts of the Auger sputter profiling technique (6). For comparison, the integrated amount of oxygen represented by the 67Å layer of "Ta_xO_y" is the same as the amount of oxygen in a 15Å layer of Ta_2O_5.

The various Ta/Si samples analyzed in this study differ only in their interfacial composition. The impurity content in the bulk Ta layer appears rather independent of processing and deposition procedures.

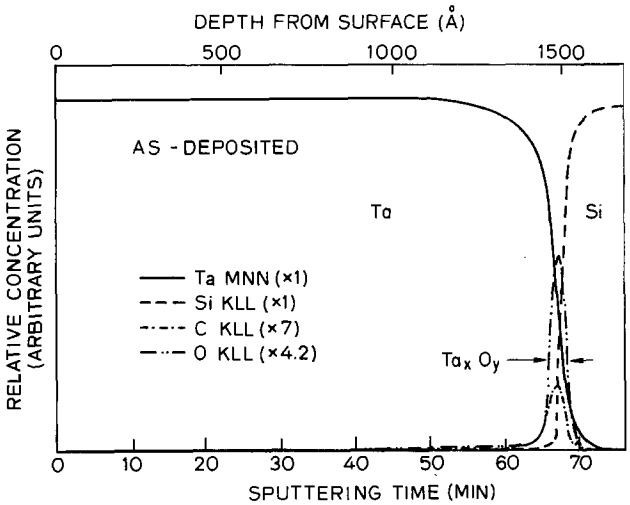

Fig. 1. Auger sputter profile of the sputter-deposited Ta/Ta_xO_y/Si sample. As-deposited.

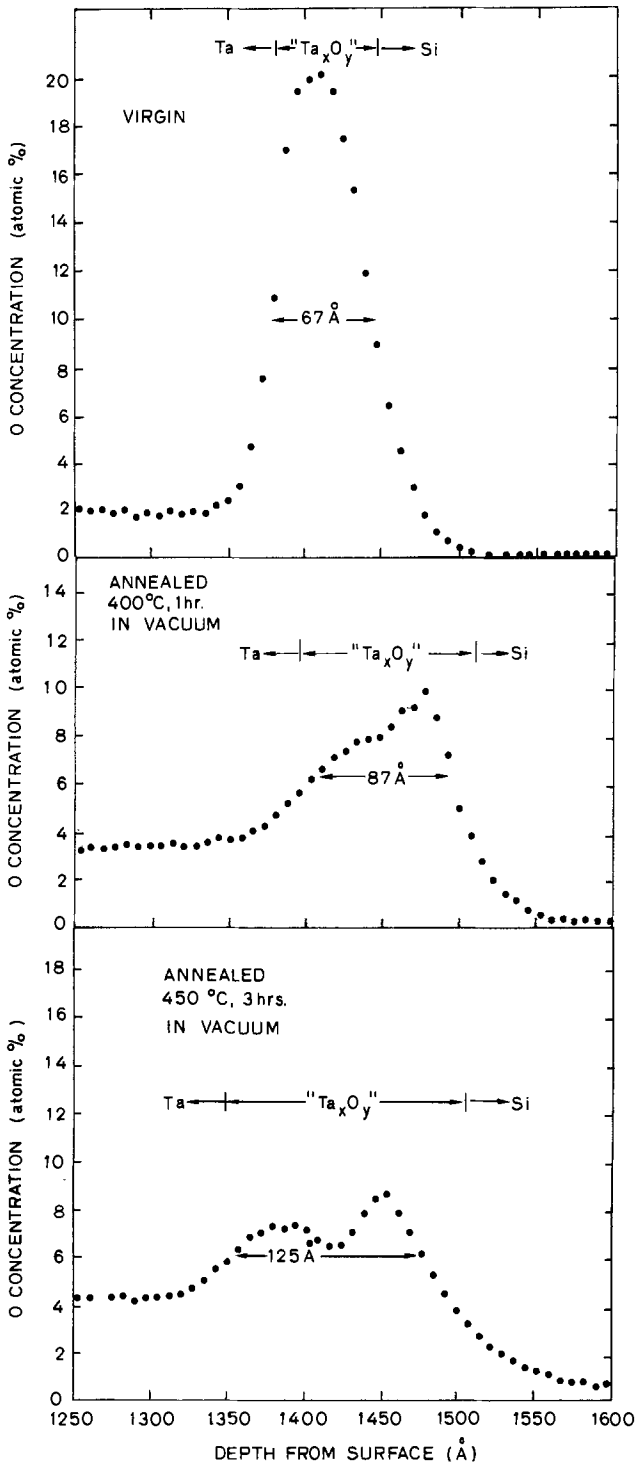

Fig. 2. Auger sputter profiles of the Ta/Ta_xO_y/Si sample displaying only the oxygen profile: (a) as-deposited, (b) annealed 400°C, 1 hr in vacuum, (c) annealed 450°C, 3 hr in vacuum.

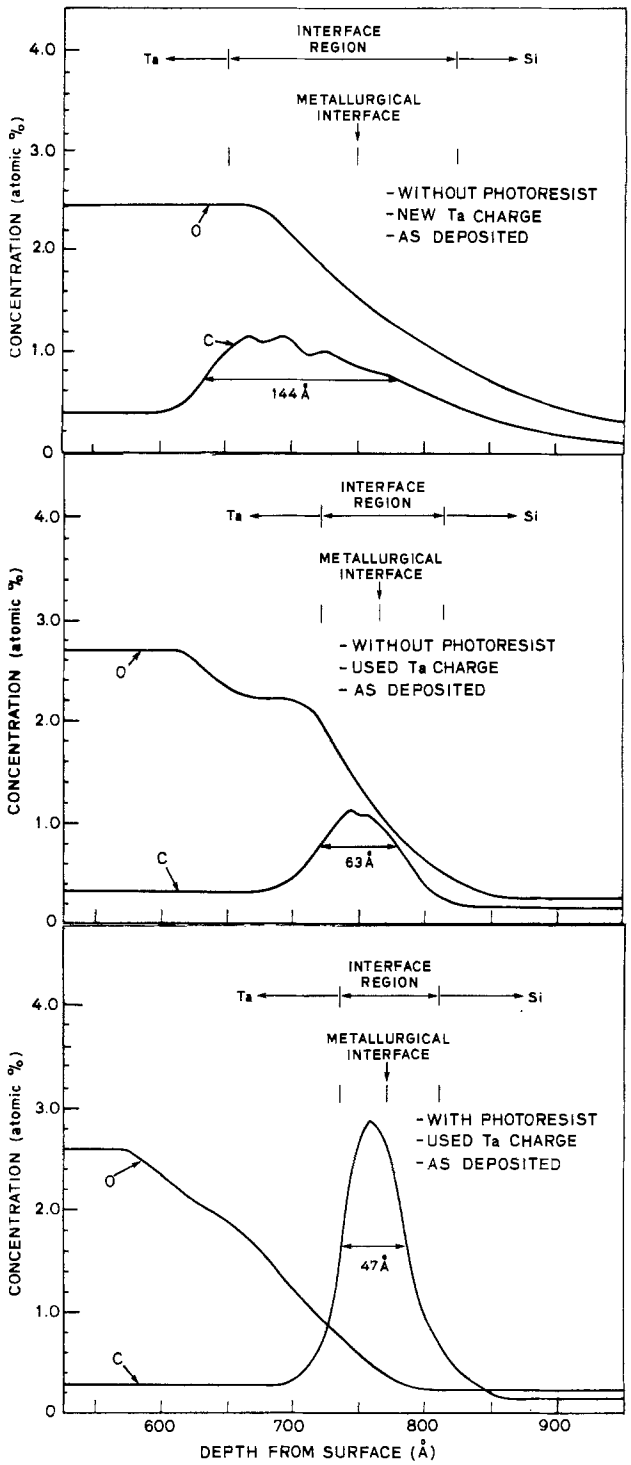

Fig. 3. Auger sputter profiles of the E-beam-deposited Ta/Si samples displaying only the oxygen and carbon profiles in the as-deposited condition: (a) processed without photoresist and with a new Ta charge, (b) processed without photoresist and with a used Ta charge, (c) processed with photoresist and with used Ta charge.

Oxygen levels are roughly 2.6 a/o and carbon levels are about 0.35% for E-beam Ta/Si samples, regardless of whether or not photoresist processing was used and whether a new or used charge was used in the evaporator (Fig. 3a-c). In addition, the sputter-deposited Ta/Ta_xO_y/Si sample (Fig. 1) and Ta/Si sample (Fig. 4) also contain about the same amount of oxygen in the bulk Ta as the E-beam samples (see Table I for a detailed summary of the processing procedure and impurity content of the E-beam samples).

Profiles of the E-beam-deposited samples are shown in Fig. 3a, c. The interface region of the E-beam Ta/Si samples have similar oxygen profiles but quite distinct carbon profiles. The oxygen begins at a minimum in the Si (about 0.2 a/o due to background contamination), rises monotonically over 200Å, then levels off at the oxygen concentration of the bulk Ta (about 2.6 a/o). These are the primary features of the oxygen profiles of each sample. The sample processed without photoresist and with a used charge has an additional feature: additional oxygen over a region 25Å wide (Fig. 3b at a depth of 700Å). There is some evidence of a similar feature in the sample processed with photoresist and with a used charge (Fig. 3c at a depth of 650Å). The possible origin of this region is discussed in the discussion section of this article.

Table I. Processing procedure and impurity content

Sample	Deposition method	Figure	Bulk oxygen (a/o)	Bulk carbon (a/o)	Peak carbon (a/o)	Carbon peak width (Å)	Total interfacial carbon (No. atoms/cm²)
Ta/Si	E-beam without photoresist new charge	3a	2.5	0.40	1.2	144	9×10^{14}
Ta/Si	E-beam without photoresist used charge	3b	2.7	0.33	1.1	63	3×10^{14}
Ta/Si	E-beam with photoresist used charge	3c	2.6	0.28	2.9	47	7×10^{14}

The oxygen profile for the sputter-deposited Ta/Si sample (Fig. 4) is also graded, as in the E-beam samples. However, the grading occurs over 100Å instead of 200Å. Furthermore, the sputter-deposited sample contains a small peak at the interface with a half-width of 40Å and a peak concentration of 3.2 a/o. This is only a small increase over the bulk concentration of 3.0 a/o but still corresponds to a total level of interface oxygen of 4×10^{14} cm^{-2}.

The three types of E-beam samples have similar amounts of carbon but have distinct distributions. The sample processed without photoresist and with a new charge contains 9×10^{14} carbon atoms/cm² in the interface region (Fig. 3a), distributed in a low and broad peak (1.2 a/o high, 144Å wide). At the Si side of the interface, the carbon profile parallels the oxygen profile. At the Ta edge of the interface, however, the oxygen concentration levels off at its maximum value, whereas the carbon reaches a maximum value and then falls to the concentration of bulk Ta (0.40 a/o). The entire carbon peak is not symmetric and is skewed towards the Ta side of the interface. The interface region itself is quite broad (175Å), suggesting that some of the features of this profile are artificially broadened by the profiling technique. Such broadening is discussed further in the discussion section of this article.

The sample processed without photoresist and with a used charge has the least amount of carbon (3×10^{14} cm^{-2})—about one-half the amount in either of the other two E-beam samples. The carbon in the sample (Fig. 3b) is distributed in a low and narrow peak (1.1 a/o high, 63Å wide). Again, the carbon profile parallels the oxygen profile within the interface region, peaks near the Ta edge of the interface, and then falls to the bulk level (0.33 a/o). The peak in this sample is symmetric and is only slightly skewed towards the Ta side of the interface. The interface width in this case is 95Å, whereas the oxygen still takes 200Å to change from its minimum to its maximum value. This means that on top of the interface region is a Ta layer with a graded oxygen content (to be discussed further in the discussion section of this article).

The sample processed with photoresist and with a used charge (Fig. 3c) has 7×10^{14} carbon atoms/cm² distributed in a high and narrow peak (2.9 a/o high, 47Å wide). The carbon concentration still peaks within the interface region and falls to its bulk value just outside (to 0.28 a/o), however, the carbon profile does not parallel the oxygen profile. Indeed, the carbon profile rises at the Si side of the interface before the oxygen rises. The carbon peak is symmetric and slightly skewed towards the Ta side of the interface. The width of the interface is 75Å.

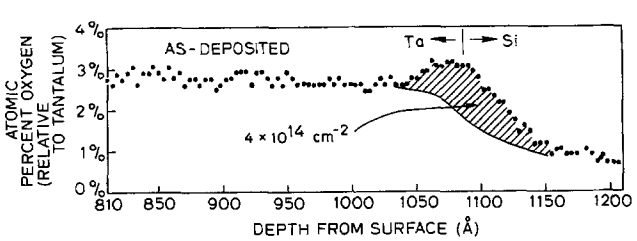

Fig. 4. Auger sputter profile of the sputter-deposited Ta/Si sample displaying only the oxygen profile. As-deposited.

To study the effects of annealing on interfacial carbon, the E-beam-deposited Ta/Si sample processed with photoresist and with a used charge was chosen since it has a carbon-containing layer that could be followed in detail after annealing. The carbon profile after annealing at 450°C for 1 hr was essentially the same as for the as-deposited sample (Fig. 3c).

To study the effects of annealing on interfacial oxygen, the Ta/Ta_xO_y/Si sample was chosen since it contained an oxide layer between the Ta and Si that could be easily followed in detail after annealing. It was found that a low temperature anneal causes oxygen in the thin oxide layer to redistribute into the Ta layer. The profiles show (Fig. 2a, b) that, upon annealing in vacuum at 400°C for 1 hr, the peak oxygen concentration decreased from 20 to 10% and the width increased from 67 to 87Å. In addition, the oxygen level in the Ta bulk increased from 2 to 3.5%. Furthermore, there was an indication of a second peak appearing in the profile after annealing. The oxygen peaks in the profiles for the as-deposited and the annealed samples are located within 50Å of each other. This is less than 5% of the total depth which is well within the reproducibility of the profiling technique and the depth calibration.

Annealing at 450°C for 3 hr (Fig. 2c) caused even more oxygen redistribution than for annealing at 400°C for 1 hr. The peak concentration has fallen to 9%, the width has risen to 125Å, and the concentration in the bulk Ta has increased to 4.3%. These experiments show that low temperature annealing causes oxygen to leave the interface region to enter the bulk Ta layer. Also, two peaks are clearly formed in the "oxide" region.

The chemical state of the "oxide" region is not at all certain. Compounds such as TaO_2, Ta_2O_5, or SiO_2 may be present, as well as Ta and Si. Another possibility for the composition is two different layers of oxides, such as two layers of Ta oxides or one layer of Ta oxide and one layer of Si oxide. Because of the uncertainty in the makeup of the "oxide" region, it has been labeled "Ta_xO_y" in the profiles. (It should also be noted that, since the actual interfaces are not abrupt, the labeling of the Ta/"Ta_xO_y"/Si interfaces is only approximate.)

Discussion

It is interesting to note that the bulk impurity levels are quite close to reported high temperature equilibrium solid solubilities in Ta: oxygen solubility is 1-3 a/o for temperatures 700°-1000°C, and carbon solubility is 0.1-0.3 a/o for temperatures 338°-2800°C (8). The samples prepared for this study did not reach such high temperatures during deposition and are therefore likely not at thermodynamic equilibrium. However, the similarities between the measured oxygen and carbon levels and the reported solubilities suggest that the properties of the Ta film itself limits the amount

of oxygen and carbon incorporated. This is consistent with the observation that the bulk oxygen and carbon contents are rather independent of processing and deposition procedures.

The profiles of the E-beam Ta/Si samples can be described by dividing the profiles into four regions: (*i*) the Si substrate, (*ii*) a thin layer of contaminants (including carbon and oxygen), (*iii*) a layer of Ta containing carbon and oxygen of varying concentrations, and (*iv*) the layer of bulk Ta which contains constant concentrations of carbon and oxygen. This is shown in Fig. 5. The layer of contaminants is considered to have been present before deposition of Ta and would include any residue from the photoresist. Also included in this layer is any carbon and oxygen which was adsorbed by the Si substrate during its exposure to air following the last chemical cleaning step.

Carbon and oxygen are also deposited during evaporation of the Ta. This carbon and oxygen may come from the Ta charge itself or from the residual gas in the evaporation chamber. In the first stages of the deposition, there will be a transient during which the deposition rates must approach steady state. Until such a steady-state condition is reached, the carbon and oxygen content of the deposited Ta layer will vary. This is the origin of the third region described above, which can be of the order of up to 100Å thick.

The two samples evaporated from a used charge, without and with photoresist (Fig. 3b, c, respectively), show the four regions of the model clearly. The carbon peak at the interface is mainly the surface contamination layer (Region 2) and partly the deposited carbon (the beginning of Region 3). The surface oxygen appears to have been broadened and shifted in position due to artifacts of the sputtering process. This can explain the bump in the oxygen profiles (at 700Å in Fig. 3b and 650Å in Fig. 3c). The rising oxygen level outside the interface region corresponds to non-steady-state deposition (Region 3).

The only difference between the two samples evaporated from a used Ta charge is that one was processed with photoresist and the other was not. Therefore, the difference in the carbon profiles is due to carbon from the residual photoresist. The carbon in the profile of the sample with photoresist (Fig. 3c) also rises before the oxygen does. This indicates that the additional carbon is located adjacent to the Si surface. This lends further support to the interpretation of the extra carbon as residual photoresist.

The sample processed with a new charge is quite different from the samples processed with a used charge. This sample (Fig. 3a) has an asymmetric and broad carbon peak and the interface width is very broad also (175Å)—about twice as broad as the other two samples. These three features of the profile suggest that the true profile has been experimentally broadened. This broadening could be due to lateral nonuniformity of the area studied (about 200 × 200 μm). For example, small islands (say 10-30 μm diam) of carbon or TaC deposited from the Ta charge could alter the profiling process.

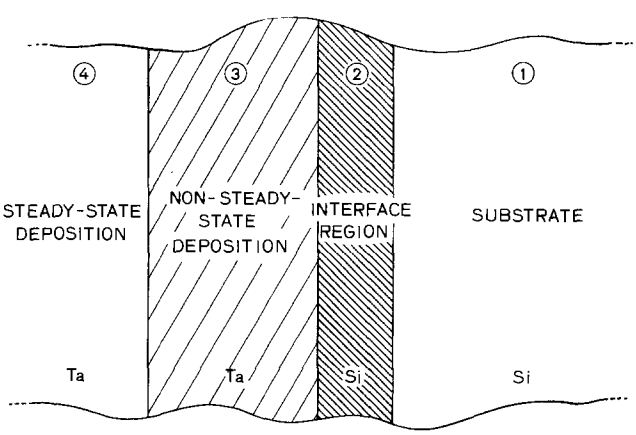

Fig. 5. Physical description of the E-beam deposited Ta/Si samples.

Annealing Schottky barrier diode structures apparently produces more reproducible barrier heights. In this work, we found that oxygen present in Ta-oxides at the Ta-Si interface diffused away from the interface for anneals of 400°C for 1 hr. Greater redistribution occurred for an extended anneal at 450°C for 3 hr. If the variation of barrier height is due to a thin oxide layer introduced during the cleaning of the silicon substrate, then perhaps annealing dissolves the oxide layer to produce a more intimate contact and more reproducible electrical characteristics.

It has been shown above that photoresist processing prior to Ta deposition left residual carbon at the Ta-Si interface. Furthermore, this carbon remained intact after an anneal of 400°C for 1 hr in vacuum. It is not known whether the carbon is in a polymer form characteristic of processed photoresist or if the carbon is in a conducting graphitic form. It is possible that polymerized photoresist adheres more strongly to silicon than other carbon containing contaminants. Hence, in principle, it is possible that some types of carbon contaminants may diffuse away from the Ta-Si interface in a manner similar to interfacial oxygen. It is uncertain whether the interfacial carbon is insulating or conducting. The effects of a thin insulating interfacial layer on the electrical characteristics of Schottky barrier diodes is well documented and understood (9). The effects of a conducting carbon are still unclear.

Conclusions

For device applications, reproducible and low barrier Schottky barrier diodes are required. Reproducibility appears to be related to the ability of the contact metal to dissolve or to consume interfacial contaminants upon low temperature annealing. Tantalum has been shown to dissolve oxygen for anneals of 400°C for 1 hr, but Ta is not able to dissolve carbon. Also, Ta does not form a silicide below 500°C, which is the temperature limit for postmetallization anneals. For these reasons, Ta may not be a good choice for reproducible Schottky barrier diodes.

Acknowledgments

The authors gratefully acknowledge W. Schweiger for the sputtered Ta/Ta_xO_y/Si sample preparation, D. Grose for coordination of the evaporated Ta/Si samples, and L. Berenbaum and P. Totta for helpful discussions. They are all at IBM, East Fishkill. Work supported by Army Research Office Contract No. DAAG 29-80-K-0059 and IBM Contract No. BK-584372Z. In addition, this work has benefited from facilities (equipment) made available to Stanford University by the NSF-MRL Program through the Center for Materials Research at Stanford University.

Manuscript received Jan. 28, 1983.

Any discussion of this paper will appear in a Discussion Section to be published in the June 1984 JOURNAL. All discussions for the June 1984 Discussion Section should be submitted by Feb. 1, 1984.

Stanford University assisted in meeting the publication costs of this article.

REFERENCES

1. E. H. Rhoderick, "Metal-Semiconductor Contacts," p. 55, Oxford University Press, Oxford (1978).
2. H. Sello, in "Ohmic Contacts to Semiconductors," B. Schwartz, Editor, p. 277, The Electrochemical Society Softbound Proceedings Series, New York (1969).
3. M. P. Lepselter and J. M. Andrews, in "Ohmic Contacts to Semiconductors," B. Schwartz, Editor, p. 159, The Electrochemical Society Softbound Proceedings Series, New York (1969).

4. K. N. Tu and J. W. Mayer, in "Thin Films—Interdiffusion and Reactions," J. M. Poate, K. N. Tu, and J. W. Mayer, Editors, p. 359, The Electrochemical Society Softbound Proceedings Series, New York (1978).
5. T. M. Reith and P. J. Ficalora, *J. Vac. Sci. Technol.*, **16**, 303 (1979).
6. J. S. Johannessen, W. E. Spicer, and Y. E. Strausser, *J. Appl. Phys.*, **47**, 3028 (1976).
7. L. E. Davis, N. C. MacDonald, P. W. Palmberg, G. E. Riach, and R. E. Weber, "Handbook of Auger Electron Spectroscopy," 2nd ed., Physical Electronics Industries, Inc., MN (1976).
8. (a) M. Hansen, "Constitution of Binary Alloys," pp. 1067-8, McGraw-Hill, New York (1959); (b) R. P. Elliott, "Constitution of Binary Alloys, First Supplement," p. 694, McGraw-Hill, New York (1965); (c) F. A. Shunk, "Constitution of Binary Alloys, Second Supplement," p. 575, McGraw-Hill, New York (1969).
9. E. H. Rhoderick, "Metal-Semiconductor Contacts," pp. 121, 136, Oxford University Press, Oxford (1978).

Properties of Thermal Oxides Grown on Phosphorus *In Situ* Doped Polysilicon

M. Sternheim,[1] E. Kinsbron*, J. Alspector, and P. A. Heimann*

Bell Laboratories, Murray Hill, New Jersey 07974

ABSTRACT

The oxidation characteristics and the electrical conductivity and breakdown of thin oxides grown on phosphorus *in situ* doped polysilicon are reported. Breakdown fields of 8 mV/cm and leakage currents as low as 5×10^{-8} A/cm^2 at 3.5 MV/cm were measured for 400-to 1200Å oxides grown thermally at 1000°C in dry O_2 on phosphorus *in situ* doped films deposited at 600°C. The oxides grown on the 600°C polysilicon films are superior to the oxides grown on the 640°C polysilicon films. The high breakdown fields and low leakage currents are related to the film structure and surface morphology as revealed by SEM and TEM micrographs.

Oxides grown on polycrystalline silicon films play an important role in the fabrication of MOS devices. Thermal oxides grown on polysilicon, referred to as polyoxides, are used as insulating materials in double polysilicon structures of RAM's (1) and various PROM's (2). The properties of polyoxides grown on films doped by diffusion from PBr_3 or $POCl_3$ sources have been extensively studied and reported in the literature. Oxidation characteristics of undoped and heavily doped polysilicon (3-5) and the electrical conduction and breakdown fields of the polyoxides (6-9) and techniques to improve those properties (10, 11) were of major concern.

The availability of *in situ* doped polycrystalline silicon films (12-14) led to the investigation of their oxidation rates and of the electrical properties of the thermal oxides grown on these films. In this paper, we report results of studies of the oxidation rates of phosphorus *in situ* doped films in wet and dry ambients, the electrical activatiion of the dopant during the oxidation process, and the breakdown fields and the leakage currents through the oxides. The properties of oxides grown on films deposited at 600°C are compared with those grown on films deposited at 640°C and are correlated to the film structure as revealed by TEM studies.

Experimental Procedure and Results

Film deposition.—Thermally oxidized (1000Å) 3 in. silicon wafers were used as substrates for the study of the properties of polyoxides grown on phosphorus *in situ* doped polysilicon. The phosphorus *in situ* doped films were deposited by pyrolysis of SiH_4 and PH_3 diluted in N_2 in an LPCVD system. The films were deposited in the temperature range of 600°-640°C and had thicknesses between 6000-7000Å.

Oxidation of phosphorus in situ *doped polysilicon.*—Samples were oxidized in steam at 800° and 950°C and, in a dry ambient, at 1000°C. The oxide thickness was measured using a Taylor-Hobson stylus instrument or by measuring the capacitance between 20 mil Al dots patterned on top of the polyoxide and the phosphorus *in situ* doped polysilicon film. The oxidation rates for the different processes are presented in Fig. 1. Oxide uniformity was measured on 25 capacitors spread on an area of 1000×500 mil^2 and found to have a standard deviation of about 0.7%.

In three cases, the change in the thickness of the polysilicon film as a result of the oxidation step was measured. The initial and final thicknesses of the polysilicon films were measured using the stylus instrument. The amount of polysilicon consumed during the oxidation is approximately half of the oxide thickness.

Resistivities of the phosphorus *in situ* doped films as deposited and after oxidation were measured using a four-point probe. For the 600°C phosphorus *in situ* doped polysilicon $\bar{\rho} = (6.5 \pm 1) \times 10^{-4}$ Ω-cm (after oxidation) and $\bar{\rho}/\bar{\rho}_0 \simeq 0.3$ where ρ_0 is the resistivity of

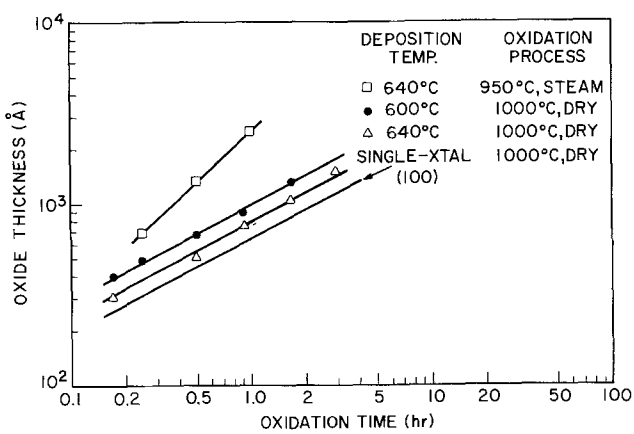

Fig. 1. Oxidation rate of phosphorus *in situ* doped polysilicon deposited at 600° and 640°C.

* Electrochemical Society Active Member.
[1] Present address: Intel, Livermore, California 94550.

the as-deposited film. For the 640°C phosphorus *in situ* doped films, the final resistivity is 1.5×10^{-3} Ω-cm and $\bar{\rho}/\rho_0 \simeq 0.1$.

The etching rate of the polyoxides either in 30:1 BHF at room temperature or in a reactive sputter etching (RSE) system utilizing CHF_3/4% NH_3 gas mixture (15) is the same as that of thermal oxides grown on single-crystal silicon. The polyoxide etch rate is 300 Å/min in 30:1 BHF and 280 Å/min for the conditions used in the RSE reactor. The etch rate of the polyoxide is independent of the oxidation process.

Electrical conduction and breakdown fields of 400Å-1200Å thick polyoxides.—Electrical conduction through thin polyoxides grown on phosphorus *in situ* doped polysilicon and the electrical breakdown fields (BF) of these oxides were measured on capacitors. The phosphorus *in situ* doped polysilicon film served as a common plate for all the capacitors, and the field plates were patterned using lithographic techniques and etched to form 20 mil Al dots on top of the polyoxides. The electrical currents were measured using a logarithmic picoammeter and a ramped voltage source. The BF were measured using a minicomputer-controlled system (16).

The breakdown test is done as follows: each capacitor is stressed by a sequence of increasing electric fields. At each field value the capacitor is stressed for about 60 msec and then the field is reduced to 2 MV/cm to measure the current through the capacitor at the low field. If the current at 2 MV/cm is more than 2 μA, the capacitor is considered broken. Otherwise the stressing electric field is increased and the test continues. No capacitors were found to pass 2 μA without suffering irreversible breakdown.

The electrical breakdown fields (BF) were measured on 100 capacitors for each of the oxide thicknesses varying between 400 and 1200Å grown on 600° and 640°C phosphorus *in situ* doped polysilicon at 1000°C in dry ambient. The cumulative failure in (%) at different stressing fields is shown in Fig. 2. Two thicknesses (400 and 900Å) of polyoxides grown in a dry ambient on 600°C polysilicon films are compared with 700Å of polyoxide grown on 640°C polysilicon film. The median BF for the oxide grown on the 600°C poly is 8.0 ± 0.25 MV/cm and for the oxide grown on the 640°C poly is only 5.0 ± 0.25 MV/cm. The stressing field was applied with positive polarity to the top Al plate. At this polarity, enhanced electron emission from the polysilicon into the oxide occurs (6-9) due to asperities at this interface. No capacitors broke down at fields below 6 MV/cm for the 600°C poly. The median BF is higher for capacitors having thinner oxides as the dielectric layer. Figure 3 describes the dependence of the BF on the oxide thickness as it varies from 300 to 1200Å. The BF of the oxides grown on the 600°C-deposited films increases approximately 10% as the oxide thickness is reduced from 1000 to 400Å. The improvement of the BF is more dramatic on the oxides grown on 640°C poly. As the oxide thickness is reduced from 500 to 300Å, the BF increases from 5 to 7 MV/cm, and there are no low field failures (freaks).

Typical current field curves (16, 17), comparing the leakage currents through polyoxides grown on 600° and 640°C polysilicon for the positive polarity applied to the field plate, are shown in Fig. 4. The field was ramped at a rate of 0.1-0.2 (MV/cm)/sec. The leakage current through the oxide grown on the 640°C polysilicon is four orders of magnitude higher than the

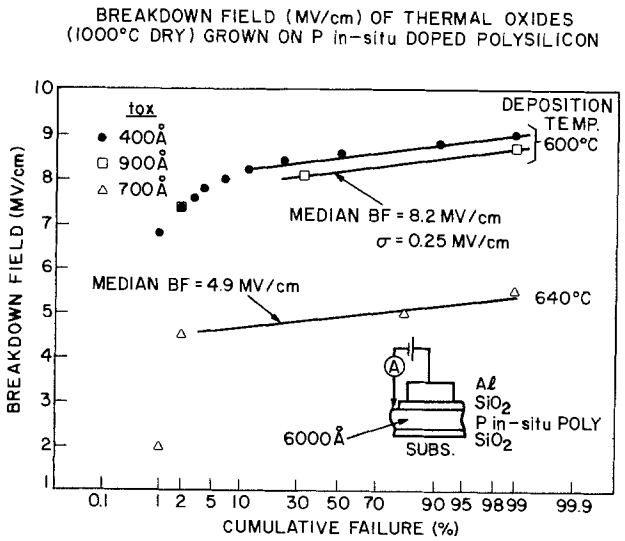

Fig. 2. The electrical breakdown field *vs.* cumulative failure % of the phosphorus *in situ* doped polysilicon deposited at 600° and 640°C for a positive polarity field (*insert*).

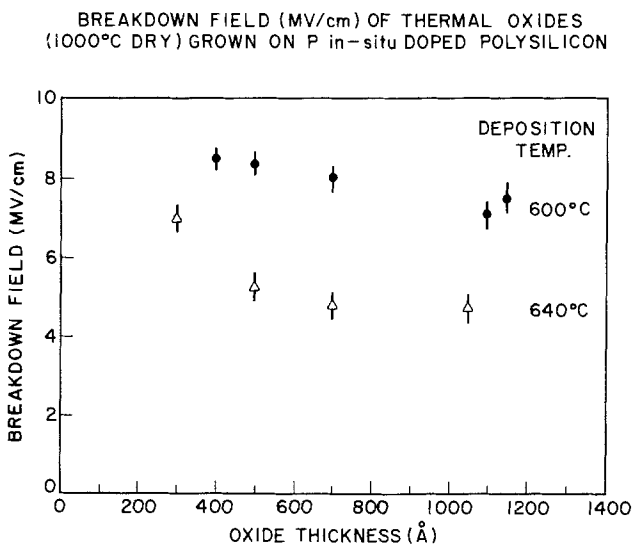

Fig. 3. Median breakdown field for the phosphorus *in situ* doped polysilicon deposited at 600° and 640°C as a function of the oxide thickness.

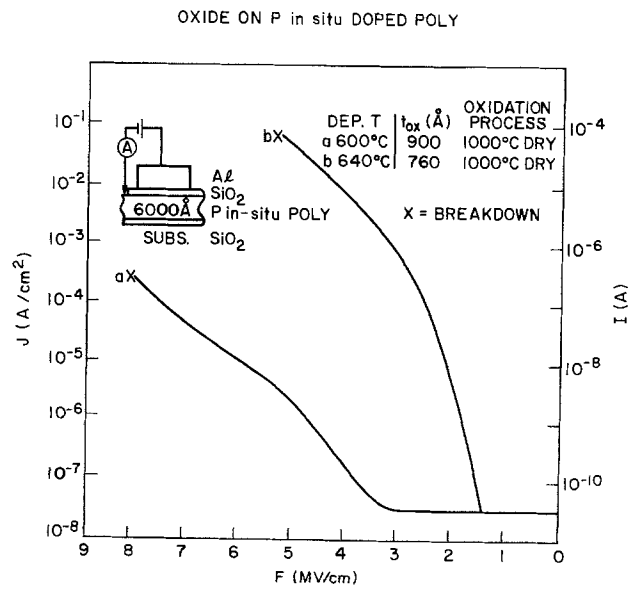

Fig. 4. The current density through a polyoxide grown at 1000°C in dry O_2 on the 600°C (a) and 640°C (b) phosphorus *in situ* doped polysilicon as the stressing field applied at a positive polarity is varied at a rate of 0.1 (MV/cm)/sec. The capacitors were stressed up to breakdown. Notice the low leakage current through polyoxide grown on the 600°C phosphorus *in situ* doped polysilicon.

current through the oxide grown on 600°C polysilicon at the same field and is lower for a negative polarity applied to the field plate, independent of the deposition temperature.

The current density through the polyoxide has a time dependence of $J \sim t^{-n}$ (9), $n \simeq 0.6$-0.7 (Fig. 5). The current through a 500Å polyoxide was measured using a logarithmic picoammeter stressing the capacitors at various constant electric field values between 4.0-7.5 MV/cm at a positive polarity. The dependence of the current density on a stressing field was also measured using the computer-controlled probing station. For each field value, 25 capacitors were stressed for 10 sec before measuring the current densities. The data for 400 and 500Å polyoxides are presented in Fig. 6 in the form of (J/E^2) *vs.* $1/E$, where J is the measured current density and E is the stressing electric field (9).

The electrical conduction and breakdown fields for dry (1000°C) and steam (950°C) oxidation on *P in situ* doped polysilicon films deposited at 600° and 640°C are summarized in Table I.

Discussion

Resistivity.—The low specific resistivity ($\rho_0 \simeq 3 \times 10^{-3}$ Ω-cm) of the phosphorus *in situ* doped films as deposited at 600°C indicates that the films are polycrystalline. The structure of the films was found to be predominantly (111), whereas the structure of the undoped films deposited at the same temperature was found to be amorphous (18). The resistivity of the as-deposited films at 640°C is about four times higher than the resistivity of the 600°C as-deposited films (Table I). This difference in resistivity is due to the difference in the film grain size (Fig. 7) and the phosphorus content. Figure 7 shows TEM micrographs (taken by T. T. Sheng). The thin film vertical sections were made according to established procedures (19) after coating the unoxidized films with a 1200Å protecting layer of plasma-deposited SiO_2. Figure 7a shows the relatively large grains of the 600°C as-deposited film as compared to the columnar grains, 50-100Å wide, of the 640°C as-deposited film (Fig. 7b). Although the grain structure after oxidation of these two films is similar (Fig. 7c, 7d), the final resistivity of the 600°C film is lower. This result indicates the higher phosphorus content in the film deposited at lower temperature. By comparing our data to Sunami's (4) values for the resistivity of phosphorus-doped films as a function of the phosphorus concentration, one can estimate the concentration in our films to be about 2-4 $\times 10^{20}$ cm^{-3}. The phosphorus content of the 600°C and the 640°C phosphorus *in situ* poly was measured using SIMS analysis (18) and neutron activation techniques (20) to be 4×10^{20} cm^{-3} and about 2×10^{20} cm^{-3}, respectively, in good agreement to Sunami's predicted values. During the dry oxidation at relatively high temperatures, the phosphorus diffuses ahead into the remaining unoxidized polysilicon film and increases the phosphorus concentration of the film. For steam oxidation (and especially at the low temperatures), the oxidation rate is faster than the phosphorus diffusion rate, so phosphorus is trapped in the grown oxide and the final resistivity does not reach as small a value and, in some cases (800°C steam), results in a resistivity higher than that of the as-deposited film ($\bar{\rho}/\bar{\rho}_0 = 1.3$).

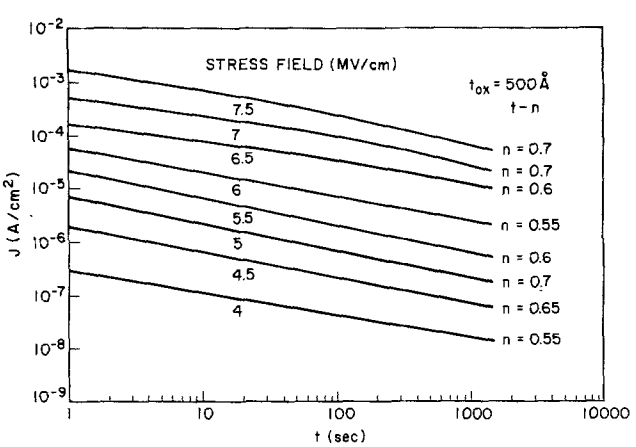

Fig. 5. The current density as a function of time through 400Å polyoxide grown on 600°C phosphorus *in situ* doped polysilicon.

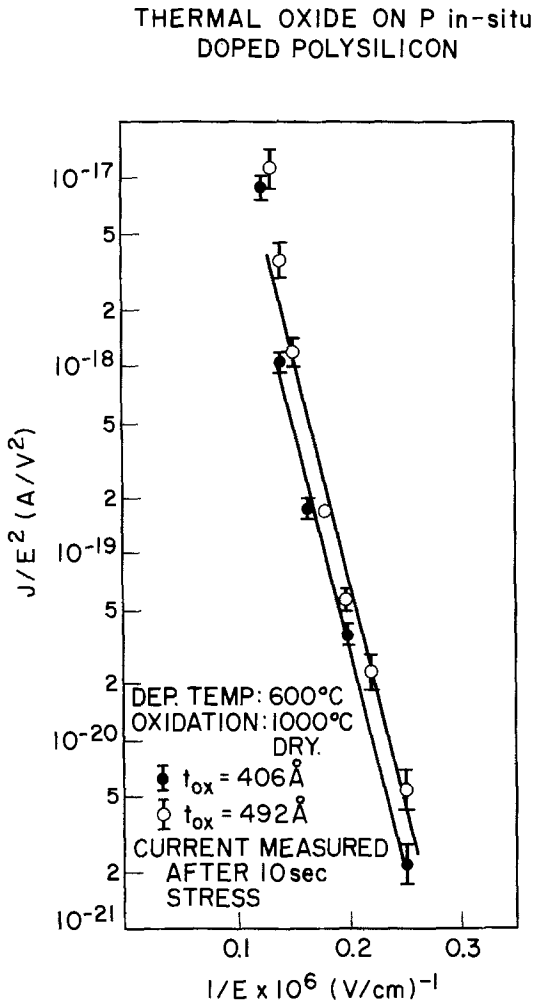

Fig. 6. J/E^2 as a function of $1/E$ for 400 and 500Å polyoxides grown on 600°C phosphorus *in situ* doped polysilicon. The functional dependence follows the Fowler-Nordheim tunneling behavior.

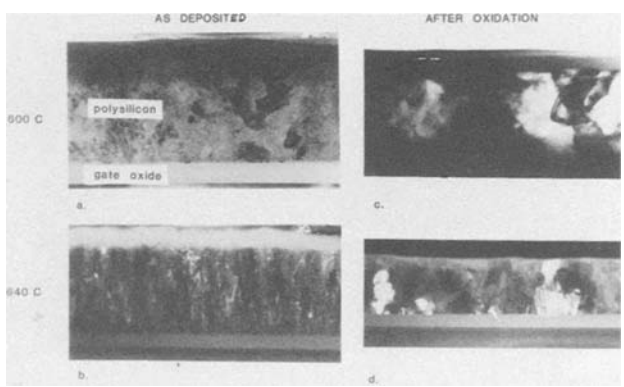

Fig. 7. TEM cross sections of the 600° and 640°C phosphorus *in situ* doped polysilicon film taken by T. T. Sheng. The micrographs compare the films as deposited (a,b) and after oxidation at 1000°C in dry O_2 (c, d). The gate oxide is 1000Å thick. Notice the different structure of the films as deposited at 600° and 640°C.

Table I. Electrical leakage and breakdown results

Deposition temperature (°C)	Oxidation process	Oxide thickness (Å)	Leakage current (A/cm²) at positive* electric field (MV/cm)	Breakdown field (MV/cm) Positive +	Negative −
600	1000°C dry	400	2×10^{-9} at 3.3 10^{-4} at 7.8	8.5 ± 0.5	8.5 ± 0.25
600	1000°C dry	900	2×10^{-8} at 3.0 10^{-4} at 7.5	8.0 ± 0.5	8.0 ± 0.5
600	950°C steam	1900	2×10^{-8} at 0.8 10^{-4} at 5.0	5.25 ± 0.5	5.5 ± 0.5
640	1000°C dry	700	2×10^{-9} at 1.3 3×10^{-3} at 4.3	5.0 ± 0.5	7.0 ± 0.5
640	1000°C dry	1050	2×10^{-8} at 1.15 1.4×10^{-2} at 4.3	4.75 ± 0.5	6.5 ± 0.5
640	950°C steam	1700	2×10^{-8} at 0.88 10^{-3} at 4.4	4.5 ± 0.5	5.0 ± 0.5

* Polarity applied to aluminum top electrode.

Oxidation.—Figure 1 shows that the dry oxidation rate is about 30% higher for the polysilicon films deposited at 600°C than the oxidation rate of the film deposited at 640°C. This enhancement of the oxidation rate is probably due to the higher phosphorus concentration and the strong (111) preferred oriented texture (18) of the polysilicon films deposited at 600°C. For the same reason, the oxidation rate of the *in situ* doped polysilicon films is faster than that of the single-crystal silicon with the (100) orientation.

Figure 8 shows three pair of SEM micrographs, comparing the top surfaces of the 600° and 640°C polysilicon films as deposited (Fig. 8a, b), the surfaces of the oxides grown on these films (1000°C dry ambient) (Fig. 8c, d), and the surfaces of the polysilicon films after stripping the oxides (Fig. 8e, f). Two important conclusions are drawn from these micrographs: the surface of the 640°C poly is rougher than the surface of the 600°C poly at all the processing steps, including the high temperature step of oxidation, and the oxidation process causes the surface to become rougher (compare the 600°C poly surface as deposited and after oxide strip) (5).

After oxidation in steam, even the polysilicon film deposited at 600°C with its original smooth surface (Fig. 9a) resulted in an oxide-polysilicon interface full of asperities (Fig. 9c) (21). Since there is evidence for the increase of conductivity in oxide grown on polysilicon due to asperities (7), a dry oxidation is preferable for good insulators and capacitors.

Oxide breakdown.—It is clear from the data of Table I and from Fig. 2 that the breakdown field of the oxide grown on the 600°C-deposited polysilicon film is much higher than that of the oxide grown on the

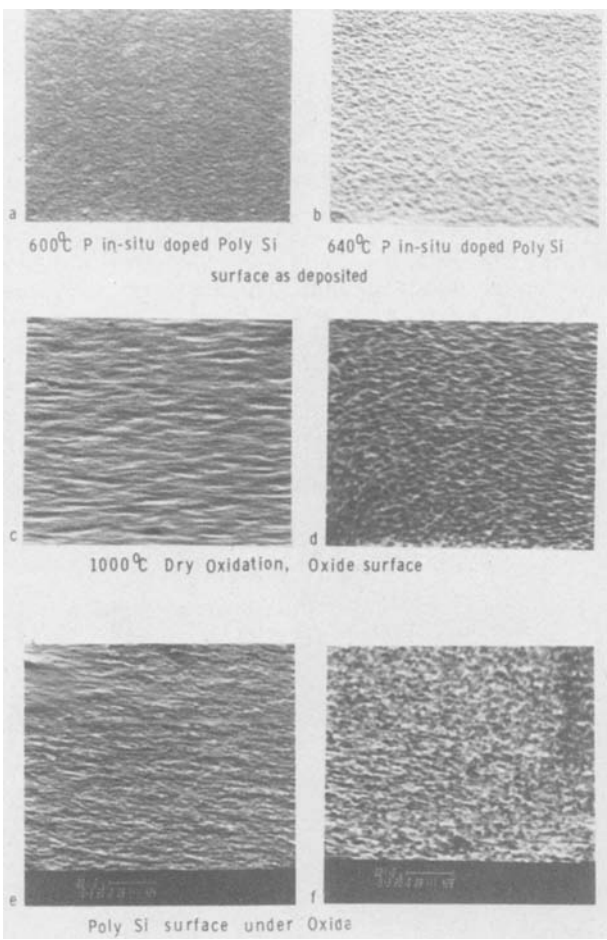

Fig. 8. SEM micrographs of the surface of the 600° and 640°C phosphorus *in situ* doped polysilicon film as deposited (a, b), of the surface of the polyoxide grown at 1000° C in dry O_2 (c, d), and of the surfaces of the polysilicon after polyoxide was stripped in BHF (e, f). See text for discussion.

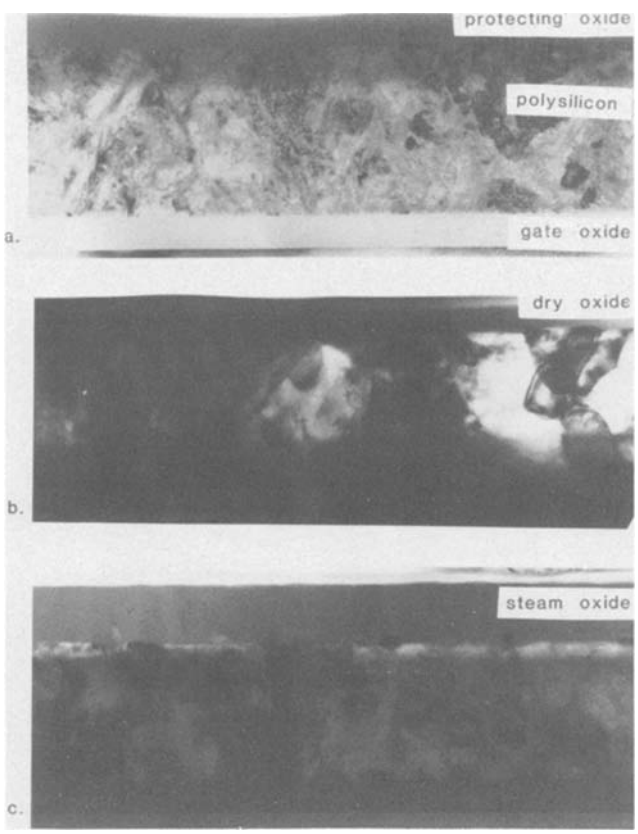

Fig. 9. TEM cross section of the 600°C phosphorus *in situ* doped polysilicon film as deposited (a), after oxidation at 1000°C in dry O_2 (b), and after oxidation in steam at 950°C (c). TEM micrograph was taken by T .T. Sheng.

640°C-deposited films. This difference in the breakdown field is due to the differences in the size and quantity of protuberances and bumps at the oxide-polysilicon interface, which are expected to lower the electric strength by increasing the local electric field (22). The initial surface morphology and the grain structure of the as-deposited films affect the size and density of the final protuberances and bumps (19). Therefore, the 600°C-deposited film with the smoother surface and fewer grain boundaries behaves more like the single-crystal substrate which yields oxides with a high breakdown field. The variance in the breakdown field is tight and almost the same for the different oxide thicknesses. Figure 2 shows also that there are no freaks in the oxide grown on the low temperature-deposited films. Contrary to what is found for oxides grown on polysilicon films doped by PBr_3 (23), the breakdown field (BF) for thinner oxides is higher than the BF for the thicker oxides grown on the *in situ* doped films (Fig. 3). The effect is emphasized on the 640°C-deposited films. The *in situ* doped films are relatively flat and smooth, and during the short period of oxidation (for the thin oxide) there is no buildup of bumps or protuberances which lower the breakdown field. As the oxides grown on the phosphorus *in situ* doped films become thicker, intergranular oxidation enhances the surface roughness of the polysilicon film, and the oxide breakdown field is reduced.

As is summarized in Table I, the breakdown fields for the negative polarity of the 640°C-deposited polysilicon films are about 30-40% higher than the fields measured with a positive polarity. The fact that there is no polarity dependence in the breakdown field of the 600°C-deposited films indicates that the top surface of the oxide is as smooth as its bottom surface.

Electrical conduction.—The electrical conduction of the polyoxides, as seen from Fig. 4, 5, and 6, is controlled by traps in the polyoxide (9, 16, 24, 25). Most of the electrons are trapped close to the polyoxide-polysilicon interface (16).

The much higher leakage current of the polyoxides grown on the 640°C *P in situ* poly compared to those through the oxides grown on the 600°C poly can be correlated to the surface morphology as revealed in the SEM micrographs (Fig. 8). The roughness of the polysilicon/polyoxide interface causes enhanced local electric fields which increase the injection of electrons into the polyoxide, yielding high leakage currents (22).

The data presented in Fig. 5 for the time dependence of the current density J show that $J \sim t^{-n}$ and $n \sim 0.55$-0.7. These results agree with results reported previously for 1000°C dry oxidation (9). The currents are controlled by electron traps which lower the effective local fields at asperities as they fill. No attempt was made to pursue a detailed model to explain the results. The dependence of J/E^2 on $1/E$, as given in Fig. 6 (E is the stressing field), follows approximately a functional dependence $J = aE^2 \exp(-b/E)$ expected for the Fowler-Nordheim tunneling (26). However, the two numerical factors a and b cannot be given a simple physical interpretation, as in the case of oxide on single-crystal silicon, since local field enhancement occurs over a portion of the area.

Conclusions

The electrical properties of thin oxides thermally grown on phosphorus *in situ* doped polysilicon films in a dry ambient at 1000°C have been studied. High breakdown fields (~8 MV/cm) and low leakage currents (5×10^{-8} A/cm^2 at 3.5 MV/cm) through the oxide (thickness varying from 400 to 1200Å) have been obtained. Thermal oxides grown on phosphorus *in situ* doped polysilicon deposited at 600°C are superior to those grown on the phosphorus *in situ* polysilicon deposited at 640°C. The sheet resistance of the 600°C-deposited films is reduced from 35 to 10-13 Ω/□ after 10 min of dry oxidation at 1000°C for films that are 6000Å thick. Under the same condition, the sheet resistance of the 640°C-deposited films is decreased only by a factor of 8 to a final value of 20-25 Ω/□. The electrical characteristics of the polyoxides are related to the smoothness of the interface between the phosphorus *in situ* doped polysilicon, deposited at 600°C, and the oxide.

The use of polyoxide grown on polysilicon doped *in situ* with phosphorus at the optimal conditions has two major advantages for IC technology: (*i*) the breakdown fields are 25% higher, and the leakage currents are more than an order of magnitude lower than polyoxides fabricated on PBr_3-diffused polysilicon films, and (*ii*) a high temperature processing step of doping the polysilicon films by PBr_3 diffusion can be eliminated.

Acknowledgments

We would like to thank H. J. Levinstein, A. C. Adams, J. T. Clemens, and W. J. Bertram for emphasizing the importance of the project; R. M. Levin, S. Vaidya, V. Starov, and W. T. Lynch for many valuable discussions; T. T. Sheng for the most important TEM work; W. E. Willenbrook for SEM work; and C. W. van Hise and D. V. Speeney for their technical assistance.

Manuscript submitted Oct. 19, 1982; revised manuscript received Jan. 15, 1983.

Any discussion of this paper will appear in a Discussion Section to be published in the June 1984 JOURNAL. All discussions for the June 1984 Discussion Section should be submitted by Feb. 1, 1984.

Bell Laboratories assisted in meeting the publication costs of this article.

REFERENCES

1. V. L. Rideout, *IEEE Trans. Electron Devices* **ed-26,** 839 (1979).
2. S. Sze, "Physics of Semiconductor Devices," 2nd ed., p. 501, John Wiley & Sons, New York (1981).
3. T. I. Kamins and E. L. Mackenna, *Metall. Trans.*, **2,** 2242 (1971).
4. H. Sunami, *This Journal*, **125,** 892 (1978).
5. E. A. Irene, E. Tierney, and D. W. Dong, *ibid.*, **127,** 705 (1980).
6. D. J. DiMaria and D. R. Kerr, *Appl. Phys. Lett.*, **27,** 505 (1975).
7. R. M. Anderson and D. R. Kerr, *J. Appl. Phys.*, **48,** 4834 (1977).
8. S. A. Abbas, C. A. Barile, and R. C. Dockerty, Abstract 327, p. 842, The Electrochemical Society Extended Abstracts, Vol. 76-2, Las Vegas, NV, Oct. 17-22, 1976.
9. H. R. Huff, R. D. Halverson, T. L. Chiu, and D. Guterman, *This Journal*, **127,** 2482 (1980).
10. G. Yaron and L. D. Hess, *Appl. Phys. Lett.*, **36,** 284 (1980).
11. H. Sunami, M. Koyanagi, and K. Hashimoto, *This Journal*, **127,** 2499 (1980).
12. T. W. Hickmott and R. D. Isaac, *J. Appl. Phys.*, **52,** 3464 (1981).
13. J. Murota, E. Arai, and K. Kudo, *This Journal*, **127,** 1188 (1980).
14. M. Sternheim, Private communication.
15. G. Smolinsky, D. N. K. Wang, and D. Maydan, Abstract 281, p. 686, The Electrochemical Society Extended Abstracts, Vol. 81-2, Denver, CO, Oct. 11-16, 1981.
16. P. A. Heimann, S. P. Murarka, and T. T. Sheng, Submitted to the *J. of Appl. Phys.*
17. C. Hu, Y. Shum, T. Klein, and E. Lucero, *Appl. Phys. Lett.*, **35,** 189 (1979).
18. E. Kinsbron, M. Sternheim, S. Vaidya, and T. T. Sheng, To be published.
19. T. T. Sheng and R. B. Marcus, *This Journal*, **127,** 737 (1980).
20. S. P. Murarka, Private communication.
21. R. B. Marcus, T. T. Sheng, and P. Lin, Submitted

to This Journal.
22. B. K. Pidley, J. Appl. Phys., 46, 998 (1975).
23. J. Alspector, M. Sternheim, E. Kinsbron, R. M. Levin, P. A. Heimann, and D. V. Speeney, Private communication.
24. H. S. Lee and C. H. Feng, Appl. Phys. Lett., 37, 1080 (1980).
25. M. Itsumi, J. Appl. Phys., 52, 3491 (1981).
26. M. Lenzlinger and E. H. Snow, J. Appl. Phys, 40, 278 (1969).

Cation and Anion Transport Numbers in Anodic GaAs Oxides

C. W. Fischer and J. D. Canaday*

Department of Physics, University of Guelph, Guelph, Ontario N1G 2W1 Canada

ABSTRACT

An Xe^{134} marker atom layer of concentration 2×10^{15} cm^{-2} has been implanted into GaAs to a depth of 20 nm. The GaAs containing the Xe^{134} was anodized to various thicknesses, and Rutherford backscattering was used to measure the change in the Xe^{134} marker atom depth relative to the change in oxide thickness. These measurements are used to calculate the cation and anion transport numbers which are 0.18 and 0.82, respectively. A secondary result from backscattering measurements is the oxide bulk stoichiometry and oxide density. The results show a bulk oxide composition of (Ga + As): O = 2:3, and an oxide density of 4.64 g/cm^3.

The exceptional electronic and optical properties of GaAs has resulted in extensive materials research, much of it aimed at the development of devices on this semiconductor. Not surprisingly the oxide of GaAs has also received considerable attention. Many studies have characterized the oxidation kinetics in a variety of electrolytes (1-3) and have measured the oxide composition profile (4-6). The electrical properties of the oxide and the oxide-semiconductor interface have also been reported in the literature (3, 5, 7, 8). Unfortunately these studies have shown that the native GaAs oxide is inferior to that of SiO_2. Subsequent research was aimed at understanding the oxidation mechanism of GaAs and in the ways in which it differed from that of Si and valve metals.

The oxygen distribution in GaAs anodic oxides grown from electrolytes prepared with H_2O^{16} and H_2O^{18} has been analyzed by Coleman *et al.* (9). The data showed that as the oxide thickens, additional oxygen is incorporated into the film at the oxide-electrolyte interface. This result and the hypothesis that mass transport occurs through the interstices of the thickening oxide lead to the conclusion that Ga and As were mobile during anodization. A result similar to that of Coleman *et al.* (9) was reported by Koshiga and Sugano (10), and Yamasaki and Sugano (11) for anodic GaAs films grown by plasma oxidation. Composition profiles showed that oxygen initially incorporated in the film was located near the GaAs-oxide interface, whereas subsequent oxygen incorporation remained near the oxide-vacuum interface. Thus, the oxygen order was seen to be preserved, and interstitial oxygen migration could be ruled out, as this process would have reversed the oxygen order.

The mechanism of cation transport in anodic GaAs has also been considered. Wilmsen *et al.* (12) have proposed that oxide growth occurs primarily by the migration of Ga and As towards the oxide-electrolyte interface. Breeze and Hartnagel (13) hypothesize that Ga and As are ionized at the GaAs-oxide interface and then migrate interstitially under the influence of the anodic field. Thus, there is strong evidence that both cation and anion transport occurs during anodic oxidation.

The magnitude of the cation and anion migration in anodic GaAs oxides has, heretofore, not been measured. The main purpose of this paper is to report the results of a direct measurement of the relative fraction of the oxide formed by cation and anion migration. In this work we will adopt the terminology which has been used in the study of valve metal oxides, namely: the fraction of the oxide formed by metal ion transport is defined to be the cation transport number. Similarly, the complement of this fraction is the anion transport number, it represents the fraction of oxide formed by oxygen transport. The reader may refer to Pringle (14) for a concise summary of the transport number measurements reported on many valve metals and several semiconductors, as well as parameters characterizing the oxidation kinetics. It is of particular interest to note that in Si, the cation transport number is virtually zero (15, 16) whereas for Al it is approximately 0.4 (17). An interesting correlation between the cation transport number and cation radius was made by Hartnagel (18). He showed that the cation contribution to oxide thickening approaches zero linearly with increasing ionic radii. In fact for ionic radii greater than 0.8Å this correlation showed that the metal ion contribution to oxide thickening is approximately zero. Applying this correlation to tripositive Ga and As ions, we would expect a cation transport number of approximately 0.3. Furthermore, since the Ga and As ions are of different size, we might expect one element to drift more rapidly than the other and result in nonuniform oxides. These nonuniform oxides have in fact been observed for GaP (19), GaAs (4, 6), and InSb (20), and furthermore, the composition profile has been shown to be sensitive to the pH of the electrolyte (19, 21).

The experimental technique, described in the next section, which is used to measure the transport number, is based on an implanted Xe^{134} marker atom layer through which the migrating ions can pass. Our choice of marker was based on a number of considerations, many of which have been discussed by Pringle (22). First of all, the marker should be a nonreactive neutral atom which is not easily ionized by the anodic field. Secondly the marker concentration must be low so that its presence will not interfere with the movement of cations and anions. And finally, if the concentration is to be low and Rutherford backscattering is to be used for location of the marker position then the marker must have a mass exceeding that of Ga and As. Pringle (22) showed that the noble gases were essentially inert and immobile and provided reliable transport number measurements.

Experimental

The material used in this study was (100) oriented undoped GaAs with a net donor density of approximately 8×10^{16} cm^{-3}. The surfaces were prepared by

* Electrochemical Society Active Member.
Key words: semiconductor, electrode, mass transport.

successive polishing and lapping steps, the final one employing ¼ μm diamond. This step was followed by etching the water for 10 sec in a 2% by volume Br: CH_3OH solution followed by hot methanol and trichloroethylene rinses. Approximately 1 cm^2 of the surface of each wafer was then implanted with Xe^{134} at an energy of 40 keV. By use of backscattering spectrometry, the Xe^{134} was found to have a maximum concentration of approximately 3 parts per thousand located 20 nm below the surface and a full width at half maximum of 12 nm. Attempts to implant the marker in a preformed oxide were unsuccessful because of oxide sputtering during exposure to the Xe^{134} beam.

Anodization

Anodization was performed at 25°C using the previously described (6) cell. By repeatedly masking the wafer, oxides of different thickness, each layer approximately 0.25 cm^2 in area, were grown on a single wafer. Growth was performed at a constant current of 1.0 mA/cm^2 in an aqueous solution of 2% tartaric acid in ethylene glycol in the ratio of 1:2 by volume. The measured pH of the electrolyte was 2.5. Application of the current resulted in a linear anode voltage rise measured relative to a saturated calomel electrode (SCE). The measured voltage-time graphs and the oxide interference colors were identical with those observed on unimplanted wafers. The resulting oxide thickness was measured by first masking the oxide, except for a small area which was exposed to an HF etchant ($HF:H_2O = 1:10^3$). The masking was washed off and the resulting step between the oxide and the substrate was measured using a Dectak stylus instrument. Figure 1 illustrates the results of these thickness measurements plotted as a function of the final oxide voltage. We define the final oxide voltage to be the difference between the GaAs anodic potential relative to the SCE at the termination of anodization and the breakdown voltage of the Schottky barrier formed between the electrolyte and the n type GaAs. The solid line on Fig. 1 is a linear least squares fit to the data and has a slope of 1.86 nm/V. This value is nearly midway between 1.98 nm/V reported by Hartnagel (7) using a similar electrolyte and the value of 1.78 measured by the authors (3) in a 0.2*N* methanolic potassium hydroxide electrolyte.

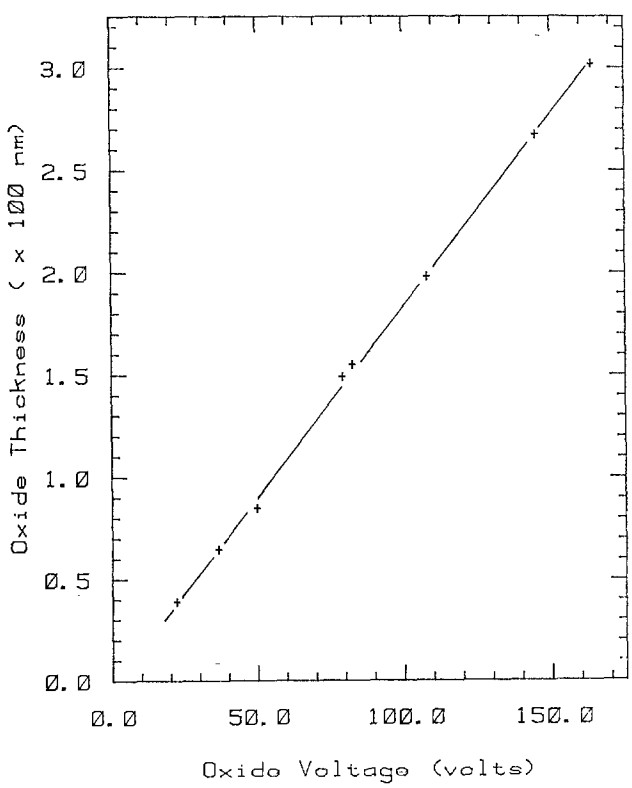

Fig. 1. Oxide thickness vs. oxide voltage measured relative to a saturated calomel electrode.

Backscattering Spectrometry

The bulk stoichiometry and the position of the Xe^{134} within the oxide were measured using backscattering spectroscopy with He^4 ions at normal incidence and with an incident energy of 1.60 MeV. The backscattered ions were detected at approximately 180° using an annular silicon surface barrier detector with a resolution of approximately 15 keV. Typical incident ion currents and total flux were 0.5 nA and 1.0 μC, respectively. The GaAs wafers were mounted on a multiple target holder along with samples of C, Al, V, Nb, and Ta which were used for energy calibration. A typical backscattering spectrum is shown in Fig. 2. The gross features of interest in this spectrum are the yields from the O, and the Ga and As in the oxide, as well as the Xe^{134} yield and its position on the energy axis. All measured backscattering spectra were similar to Fig. 2 except that, for the thinner oxides, the maximum yield from the Xe^{134} was shifted toward higher energies and the energy width for scattering from the O, and the GaAs in the oxide, was reduced. Detailed examination of the spectra showed that the plateau region corresponding to scattering from the Ga and As in the oxide was flat, thereby indicating a homogenous oxide structure with no gross deficiencies of excesses at the interfaces or within the bulk. Further, the half-height yield of the leading edge of the spectra corresponded to an energy consistent with scattering from an element of mass equal to the mean of the Ga and As masses.

Results and Discussion

The energy axis of the backscattering spectrum of Fig. 2 may be converted to a depth scale using the relation (24)

$$KE_0 - E = Nt[\epsilon] \qquad [1]$$

where K is the kinematic scattering factor, E_0 the incident ion energy, and E is the detected energy after scattering from a similar atom at depth t. The concentration of scattering elements is N and ϵ is the stopping cross section factor given by $[\epsilon] = K\epsilon(E_0) + \epsilon(KE_0)$ where ϵ is the stopping cross section which is evaluated at energies E_0 and KE_0. In each case, we assume Bragg's law to evaluate the stopping cross section. As pointed out by Chu *et al.* (24), the use of Eq. [1] to convert from an energy scale to a depth scale assumes that the oxide density is known. The required information on oxide bulk stoichiometry and density was obtained by the use of backscattering, as follows.

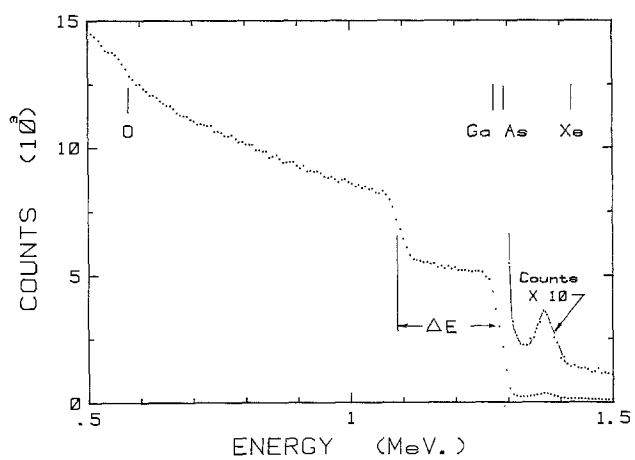

Fig. 2. Backscattered spectrum of an anodic GaAs film of 267.4 nm thickness measured at 1.60 MeV. The vertical lines above the elements O, Ga, As, and Xe^{134} indicate the detected He ion energies for these atoms on the surface.

Because of the small mass difference between Ga and As, backscattering spectroscopy cannot be used to measure composition profiles. However the bulk stoichiometry, that is, the Ga plus As concentration relative to the oxygen atom concentration is easily measured from the backscattered yields using the relation (24)

$$\frac{N_O}{N_{GA}} = \frac{H_O}{H_{GA}} \frac{\sigma_{GA}}{\sigma_O} \frac{[\epsilon]_{GA}^{ox}}{[\epsilon]_O^{ox}} \quad [2]$$

where H_O and H_{GA} are the heights of the scattering yields from the oxygen and Ga and As in the oxide, respectively, and σ_{GA} and σ_O are the Rutherford scattering cross-sections for Ga and As (mean value assumed) and the oxygen, respectively. The terms $[\epsilon]_{Ga}^{ox}$ and $[\epsilon]_O^{ox}$ are the stopping cross-sectional factors for scattering from Ga and As atoms and oxygen atoms in the oxide, respectively. Table I summarizes the results of the use of Eq. [2] to evaluate the bulk stoichiometry for oxides of thicknesses ranging from 35 to 302 nm. The two thinnest oxides were not analyzed because the oxygen yield was insufficient to obtain a meaningful measure of the stoichiometry. The results show that the oxide is composed of Ga plus As and O in the ratio of 2:3. This formulation is consistent with that reported by Mizokawa *et al.* (25) and also Ishii and Jeppson (26) who used an electrolyte similar to ours. The bulk Ga to As ratio in anodic oxides has been measured using Auger spectroscopy (4, 6). These measurements generally show a Ga and As composition variation near the interfaces, however, the bulk Ga to As ratio is approximately 1:1.

The third column of Table I is a tabulation of the energy width of the oxide. That is the difference in energy between the measured yields at the half-heights for He^4 ions scattering from Ga and As atoms on the surface and scattering from the oxide-GaAs interface. This quantity is identified in Fig. 2. Using the measured stoichiometry, we calculate the stopping cross-sectional factor $[\epsilon]_{GA}^{ox}$ appearing in Eq. [1], and defined in [2] ($[\epsilon]_{GA}^{ox} = 5.12 \times 10^{-13}$ eV cm^{-2}) and then calculate the number of scattering centers, Nt per cm^2 in the oxide (column 4, Table I). The number of scattering centers/cm^3 is given by Nt/t_{ox} where t_{ox} is the physical oxide thickness. These calculations are summarized in column 5. Finally, the oxide density (column 6, Table I) is evaluated by use of the calculated density of scattering centers and a weighted average molecular weight based on the bulk stoichiometry.

The average oxide density of 4.64 g/cm^3 with a standard deviation of 0.17 is within 5% of 4.81 g/cm^3 which is the value that would be calculated assunming the oxide was composed of equal fractions of Ga_2O_3 and As_2O_3 of density 5.88 and 3.74 g/cm^3 (23), respectively. This value of 4.64 g/cm^3 is also very close to 4.78 g/cm^3 measured by the authors (3) using a weighing and stripping technique and also similar to the value 4.7 g/cm^3 reported by Hasegawa and Hartnagel (2).

The technique we have applied in this section is an important and necessary step whenever the energy scale of backscattered spectra has to be converted to a depth scale. It is particularly important with thin films where the film density may be dependent on the formation process, as is the case when Al is anodized in some electrolytes.

Table I.

Oxide thickness (nm)	Stoichiometry (Ga+As):O	Energy width (ΔE) (keV)	Molecules (10^{17}/cm^2)	Molecules (10^{22}/cm^3)	Oxide density (g/cm^3)
39.1	—	30	0.586	1.50	4.79
65.0	—	49	0.957	1.47	4.71
85.0	0.636	65	1.269	1.49	4.78
149.2	0.607	110	2.148	1.44	4.61
155.2	0.686	117	2.284	1.47	4.71
198.1	0.661	150	2.928	1.48	4.73
267.4	0.656	185	3.612	1.35	4.32
301.9	0.719	215	4.197	1.39	4.45
Mean	0.66 + 0.04			1.45 + 0.05	4.64 + 0.17

Transport Numbers

As previously described the oxides were grown to a range of thicknesses as given in Table I. The location of the Xe^{134} below the oxide vacuum interface was calculated from the backscattered spectra using Eq. [1]. In using Eq. [1], t was considered to be the depth of the Xe^{134}, E represents the energy of the maximum Xe^{134} yield, and K_{Xe} is the kinematic factor for scattering from Xe^{134}. The stopping cross-sectional factor $[\epsilon]_{Xe}^{ox} = K_{Xe}\epsilon(E_o) + \epsilon(K_{Xe}E_o)$ is evaluated assuming Bragg's law and the mean oxide stoichiometry as listed in Table I. We use the surface energy approximation for $[\epsilon]$ and calculate its value to be 5.265×10^{-13} eV cm^{-2}. The average value of N in Eq. [1] is taken from Table I. Before presenting the results of the Xe^{134} position as a function of oxide thickness, we will discuss the model which we use for our analysis.

The quantity of importance to us is the change in the Xe^{134} marker depth as a function of the change in oxide thickness. Figure 3 schematically illustrates the effect of the initial anodization, which we assume incorporates the Xe^{134} in the oxide. Although the Xe^{134} is shown to be distributed near the midpoint of this thin oxide, its exact location is not known. However, this aspect is not important for the discussion which follows. Subsequent anodization of this thin oxide to higher potentials results in oxide thickening by one of the mechanisms illustrated in Fig. 3a-d. In a, we assume that Ga and As ions move through an existing oxide to react at the oxide-electrolyte interface, forming new oxide at this interface. Here the Ga and As transport mechanism could be interstitial or substitial via anion vacancies. Either transport mechanism will result in oxide thickening and the Xe^{134} marker would be located at the GaAs-oxide interface. In this case, a plot of the change in marker depth *vs.* the change in oxide thickness would have a slope of unity. This slope is defined to be the metal or cation transport number.

In Fig. 3b, we assume that all oxide thickening is due to oxygen ion transport and that new oxide is formed at the GaAs-oxide interface. In this case, the

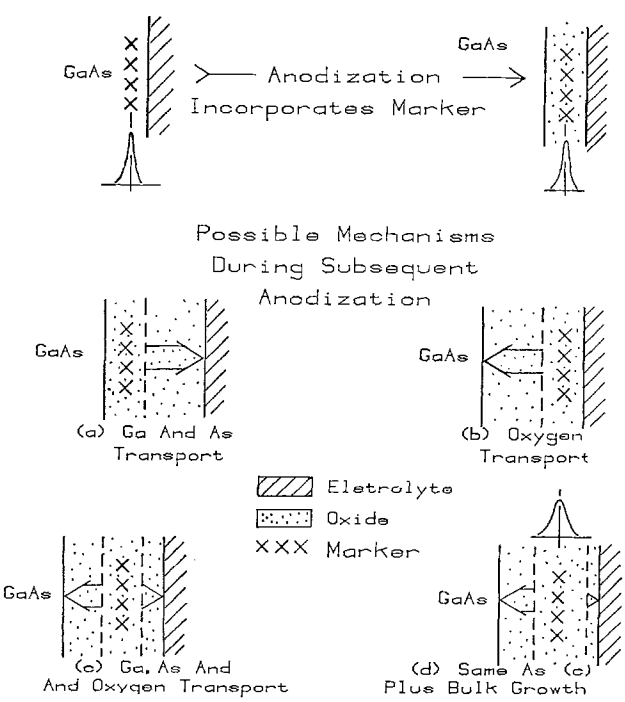

Fig. 3. Change in Xe^{134} position measured relative to the oxide-electrolyte interface (+) and measured relative to the GaAs-oxide interface (○) as a function of the change in oxide thickness.

initial anodization would incorporate the marker atoms at a depth below the oxide-electrolyte interface given by its initial depth below the GaAs surface multiplied by the Pilling-Bedworth ratio, that is, the volume of oxide formed divided by the volume of metal consumed (1.5 for GaAs) (2). Following this initial anodization, any further anodization would result in a zero change in marker depth for increasing oxide thickness. In this case, a plot of the change in marker depth *vs.* the change in oxide thickness would have zero slope. The cation transport number would be zero and the anion transport number would be unity.

Part c of Fig. 3 combines the effects of parts a and b, namely: oxide formation at the oxide-electrolyte interface due to Ga and As migration, and also oxide formation at the GaAs-oxide interface due to oxygen ion transport. In this case, as the oxide thickness increases, the Xe^{134} would be found at an increasing depth below the oxide-electrolyte interface, however, a graph of the change in marker depth *vs.* the change in oxide thickness would have a slope between zero and unity. In this case, the transport numbers would sum to unity.

Finally in Fig. 3d, we allow for the mechanism in c plus the possibility of oxygen reacting with Ga and As within the bulk of the existing oxide. This mechanism would result in a broadening of the marker distribution. The broadening should increase with increasing oxide thickness. Therefore by measuring the change in marker atom position relative to the oxide-electrolyte interface and its distribution, it should be possible to differentiate between the mechanisms described. The analysis of the data is based on the model just presented. A crucial aspect of this model is the chemical inertness and stability of the marker atom layer. Pringle (22) has discussed the necessary properties of markers and has examined the behavior of radioactive noble gas markers in Ta_2O_5. Pringle (22) found that the transport number of Ta in Ta_2O_5 was independent of the marker type and that the effect of the marker atoms on anodization was negligible. As the previous section has shown, the anodic properties of the GaAs implanted with Xe is essentially identical with the unimplanted wafers. Furthermore, since both the GaAs anodic oxides and the tantalum oxides are amorphous, the Ga, As, and Ta ions are nearly identical in size, and since similar oxidation fields are measured in the two oxides, we will assume that the Xe^{134} in the GaAs anodic oxide will not drift and will therefore behave in a manner similar to that reported by Pringle (22).

Figure 4 illustrates the results of our measurements of the change in depth of the Xe^{134} *vs.* the change in oxide thickness. We also show the change in the Xe^{134} marker position measured relative to the GaAs-oxide interface. Both sets of data show that the distance of the Xe^{134} from the interfaces increases as the oxide thickens. Thus new oxide is formed on top of and below the marker layer. By definition the cation and anion transport numbers are simply the slopes of the data shown in Fig. 4. A linear least squares fit to the data gives the cation and anion transport numbers of 0.176 and 0.824 $\pm$ 0.005, respectively. These results clearly rule out mechanisms a and b illustrated in Fig. 3. It is of interest to note that the magnitude of the cation transport number is considerably less than would be expected on the basis of Hartnagel's (18) correlation assuming similar sizes of interstitial sites and tripositive Ga and As ions of radii 0.62 and 0.58Å, respectively. The fact that our measured transport number is substantially less than expected suggests that the Ga and As may drift via an anion vacancy exchange mechanism rather than through the interstices of the oxide. Silicon is another example of an element which does not drift interstitially during anodization (16). Our measured cation transport number of approximately 0.18 does not distinguish between Ga and As transport. As pointed out earlier a Rutherford back-

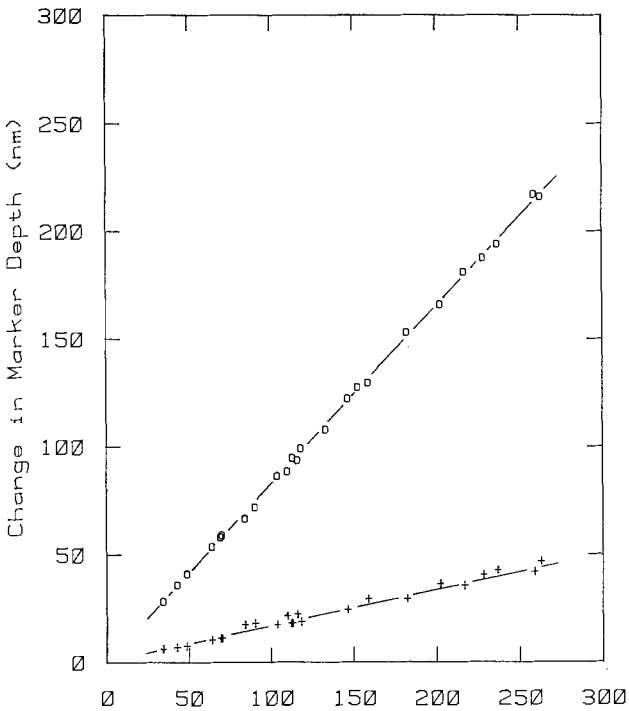

Fig. 4. The effects of O, Ga, and As transport on the Xe^{134} marker position in thickening oxides. (a) Oxide thickening at the oxide electrolyte interface due to Ga and As ion transport. (b) Oxide thickening at the GaAs-oxide interface due to O transport. (c) Oxide thickening at both interfaces plus (d) thickening within the bulk.

scattering composition profile does not permit differentiation between Ga and As in the oxide. When the entire oxide is considered backscattering shows that we have a uniform mixture of the form $Ga_2O_3 + As_2O_3$. It is very likely that Ga and As will drift at slightly different rates. The results are consistent with nonuniform composition profiles which have been reported (4-6). An indirect measurement of Ga transport of 0.13 (14) in GaP anodic oxides (19) is very similar to our composite measurement.

The previous discussion has ruled out mechanisms a and b, as illustrated in Fig. 3, for oxide thickening, we must now consider the evidence for oxide formation within the bulk. If bulk growth occurs then as discussed earlier we would expect to observe an increase in the width of the marker atom distribution. Following the method of Chu *et al.* (24), the full-width-at-half maximum (FWHM) values of the approximately gaussian Xe^{134} distribution were determined by subtracting in quadrature the detector resolution and energy straggling terms from the measured profiles. These results show the FWHM increases from approximately 12 to 16 nm for oxide thickness increases ranging from 65 to 267 nm. This increase would suggest bulk oxide formation of up to 2%. However, during a study of the behavior of Ar^{41}, Kr^{79}, Xe^{125}, and Rn^{222} markers in Ta_2O_5, Pringle (22) also observed a broadening of a magnitude similar to that measured here. Pringle (22) attributed this broadening to collisions between the marker species and the migrating ions. If collisions are responsible for the broadening then because of differing ion fluxes, masses, and directions of motion, we might expect to observe an asymmetry in the marker atom distribution. Unfortunately, the low Xe concentration does not permit a meaningful measure of the change in asymmetry of the marker atom distribution. However, our results show that bulk growth is insignificant compared with that occurring

at the interfaces. We conclude that in the case of anodic GaAs, the oxide thickening is due to both the transport of cations to oxide-electrolyte interface and anions to the GaAs-oxide interface with bulk growth accounting for less than 2%.

Summary and Conclusions

Implanted Xe^{134} marker atoms and backscattering spectrometry has been used to show that during the anodic oxidation of GaAs the oxide thickens at both the oxide semiconductor and the oxide electrolyte interface. In particular, it is found that at 25°C at a current density of 1 mA/cm^2 that 82% of the oxide thickening occurs at the GaAs oxide interface by the inward migration of oxygen. The complementary fraction or 18% of the oxide is formed at the oxide-electrolyte interface by the outward migration of Ga and As ions.

Backscattering spectrometry was also used to measure the oxide stoichiometry in the presence of the Xe^{134} marker atoms. It was found that the Xe^{134} marker atoms in the oxide did not have any significant effect on either the anodization kinetics or the bulk oxide stoichiometry. The anodization constant was measured and found to have a value of 1.86 nm/V at a current density of 1 mA/cm^2. The oxide bulk stoichiometry was measured and within the resolution of backscattering spectrometry, we find (Ga + As):O = 2:3. The oxide density was measured to be 4.64 g/cm^3.

Acknowledgments

We would like to thank J. A. Davies and Atomic Energy Canada Limited, Ontario for the ion implantation and the National Sciences and Engineering Research Council for their financial support.

Manuscript submitted Sept. 15, 1982; revised manuscript received March 7, 1983. This was Paper 240 presented at the Montreal, Quebec, Canada, Meeting of the Society, May 9-14, 1982.

Any discussion of this paper will appear in a Discussion Section to be published in the June 1984 JOURNAL. All discussions for the June 1984 Discussion Section should be submitted by Feb. 1, 1984.

REFERENCES

1. B. Schwartz, F. Ermanis, and M. H. Brastod, *This Journal*, **123**, 1089 (1976).
2. H. Hasegawa and H. L. Hartnagel, *ibid.*, **123**, 719 (1976).
3. C. W. Fischer and J. D. Canaday, *ibid.*, **129**, 1016 (1982).
4. C. C. Chang, B. Schwartz, and S. P. Murarka, *ibid.*, **124**, 922 (1977).
5. J. Stannard, *J. Vac. Sci. Technol.*, **15**, 1508 (1978).
6. K. M. Geib and C. W. Wilmsen, *ibid.*, **17**, 952 (1980).
7. H. Hasegawa, K. E. Forward, and H. L. Hartnagel, *Appl. Phys. Lett.*, **26**, 567 (1975).
8. R. L. Ahrenkiel, R. S. Wagner, S. Pattillo, D. Dunlavy, and T. Jarvis, *ibid.*, **40**, 700 (1982).
9. D. J. Coleman, Jr., D. W. Shaw, and R. D. Dobrott, *This Journal*, **124**, 239 (1977).
10. F. Koshiga and T. Sugano, *Thin Solid Films*, **56**, 39 (1979).
11. K. Yamasaki and T. Sugano, *J. Vac. Sci. Technol.*, **17**, 959 (1980).
12. C. W. Wilmsen, R. W. Kee, and K. M. Glib, *ibid.*, **16**, 1434 (1979) and references therein.
13. P. A. Breeze and H. L. Hartnagel, *Thin Solid Films*, **56**, 51 (1979).
14. J. S. Pringle, *Electrochim. Acta*, **25**, 1423 (1980).
15. W. D. Mackintosh and H. H. Plattner, *This Journal*, **124**, 396 (1977).
16. S. S. Christy and J. B. Condon, *ibid.*, **128**, 2170 (1981).
17. F. Brown and W. D. Mackintosh, *ibid.*, **120**, 1096 (1973).
18. H. L. Hartnagel, "Oxides and Oxide Films," Vol. 6, Ashok and Vijh, Editors, Marcel Dekker Inc., New York (1981).
19. J. M. Poate, P. J. Silverman, and J. Yahalom, *This Journal*, **120**, 844 (1973).
20. D. J. Dewald, *ibid.*, **104**, 244 (1957).
21. J. C. Verplanke and R. P. Tijburg, *ibid.*, **124**, 802 (1977).
22. J. P. S. Pringle, *ibid.*, **120**, 398 (1973).
23. "Handbook of Chemistry and Physics," 49th ed., Chemical Rubber Company, Cleveland, Ohio, 1968.
24. W. K. Chu, J. W. Mayer, and M. A. Nicolet, "Backscattering Spectroscopy," Academic Press, New York (1978).
25. Y. Mizokawa, H. Iwasaki, R. Nishitani, and S. Nakamura, *This Journal*, **126**, 1370 (1979).
26. T. Ishii and B. Jeppson, *ibid.*, **124**, 1784 (1977).

Optical Probing of Silicon-Sapphire Interface of Heteroepitaxial SOS Films

J. Lagowski,*,[1] L. Jastrzebski,* and G. W. Cullen*

RCA Laboratories, Princeton, New Jersey 08540

ABSTRACT

The reflectivity of silicon-on-sapphire in the visible and near infrared spectral range is found to be dependent on the crystalline quality and on the film processing such as thermal annealing and hydrogenation. These findings are quantitatively explained taking into account an amorphous-like character of the silicon-sapphire interface. It is also shown that reflectivity for $h\nu > 2$ eV can be used as a means for probing the crystalline quality of the silicon-sapphire interface.

Silicon-on-sapphire plays an important role as a material especially suited for radiation-hard integrated circuits. The SOS technology has also been considered as a potential contributor to high performance VLSI and VHSI applications. Recent work on silicon-on-sapphire/MOS devices has clearly demonstrated a direct relationship between the crystalline perfection of SOS films and device parameters (1). It has also been shown that crystalline imperfections have a detrimental effect on electronic properties of SOS films, such as excess carrier lifetime, trapping centers, degree of amorphization, and microscopic electrical inhomogeneities (1-3).

It has been our experience that the pace of the optimization of materials properties in the heteroepitaxial silicon technology is closely related to the ability to characterize the quality of the deposits. The entire thickness of the film can be observed by cross-

* Electrochemical Society Active Member.
[1] Present address: Massachusetts Institute of Technology, Cambridge, Massachusetts 02139.

section transmission microscopy, but this method is laborious and time consuming, and therefore cannot serve as rapid feed-back for materials optimization efforts. u.v. reflectometry (1, 4) now serves as a rapid method to characterize the crystalline quality of the heteroepitaxial silicon most remote from the silicon/substrate interface. No fast method is currently available, however, for the characterization of the crystalline nature of the silicon near the silicon/substrate interface. Specific aspects of device performance (for instance, leakage current) are associated with the properties of the silicon near the substrate interface. In this study, we describe a method of characterization which may prove to be useful in the rapid and nondestructive characterization of the near-interface silicon.

In the commonly utilized u.v. reflection technique (1, 4), the concentration of (221) twins is taken as the measure of the crystalline quality of the SOS films. For practical purposes, the commercially available films have been divided into six categories (A to F). The best films, belonging to category A, contain $\leq 3\%$ by volume (221) twins. The inferior quality films of F category show the presence of 15-17% by volume (221) twinning planes. The u.v. reflection technique relies on an empirically established correlation between the reflection coefficient of Si at $\lambda = 0.28$ μm ($h\nu \simeq 4.4$ eV) and the concentration of (221) twin planes as measured by x-ray topography. In the photon energy range employed in this technique, the absorption coefficient, α, of Si exceeds 10^6 cm^{-1}. The Si film is not transparent and the reflection from the Si/sapphire interface is of no importance (note that for a film of a typical thickness $d \simeq 0.6$ μm, the factor $\alpha d \simeq 60$). Thus, the u.v. technique probes the quality of SOS film in the vicinity of the outside surface.

In the present work, we analyze the reflectance in a lower photon energy range, $h\nu < 2$ eV, in which the epitaxial film is not absorbing the incident light ($\alpha d << 1$). Accordingly, the intensity of reflected light probes not only the outside surface, but also the Si/sapphire interface. The Si/sapphire interface region contains a high density of crystalline imperfections generated during heteroepitaxial growth (1, 5). In view of the importance of this region, new means (Si^+ and O^+ implantations combined with subsequent annealing) have recently been proposed for improving the crystalline quality of Si near the Si/sapphire interface (6-8).

In the present work, we identify the optical effects related to the Si/sapphire interface and the influence of thermal annealing and hydrogenation on imperfections located near this interface.

Experimental Results

Silicon-on-sapphire can be represented as a silicon film of thickness d confined between two interfaces, Si/air and Si/sapphire, characterized by reflection coefficients R_1 and R_2, respectively, (see Fig. 1a). In reflection measurements, this film is illuminated with a monochromatic light at close to normal incidence. As shown schematically in Fig. 1b, the intensity of reflected light measured as a function of photon energy exhibits a sequence of interference maxima-minima. Energy positions of maxima-minima can be used to determine the film thickness d and the value and energy dependence of refractive index n. In a low photon energy range ($\alpha d << 1$), the reflectivity values at maxima and minima provide a measure of R_1 and R_2 (9). In a higher photon energy range, the amplitude of reflectivity oscillations decreases due to absorption and the oscillations rapidly vanish when αd exceeds 1. For a perfect interface, the reflectivity is determined by values of refractive indexes between two media. Thus, a comparison between measurements of the energy position of interference extrema (which determine n) (9) and of the amplitude of oscillations (which depend on R_2) (9) can be used to draw conclusions on the quality of interfaces.

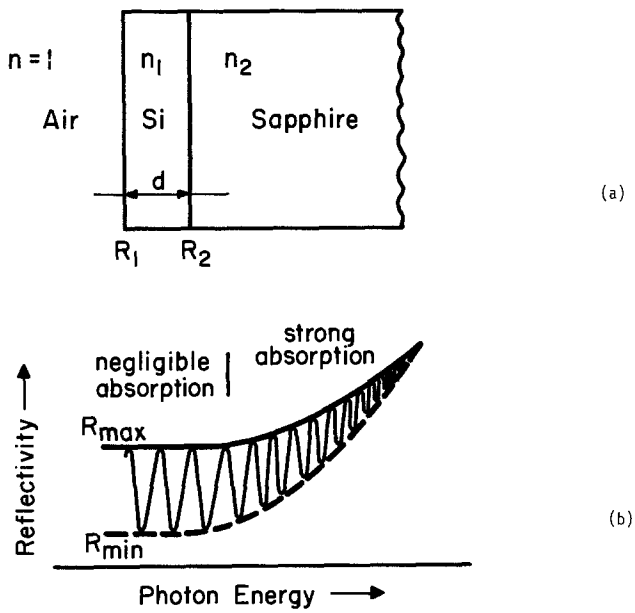

Fig. 1. (a) Optical representation of silicon-on-sapphire film. (b) Reflectivity oscillations vs. photon energy and definitions of R_{max} and R_{min}.

In the experimental procedure used in this work the intensity of reflected light, I_R, was recorded (in arbitrary units) as a function of the photon energy. This experimental dependence enabled the determination of $I_{R_{max}}$ and $I_{R_{min}}$ (see Fig. 1b) in arbitrary units and also the ratio $I_{R_{max}}/I_{R_{min}}$ which measured directly the ratio of the maximum to minimum reflectivity R_{max}/R_{min}. It should be emphasized that the ratio R_{max}/R_{min} is accurately determined without any additional measurements required for the determination of absolute values of reflectivities R_{max} and/or R_{min} and correcting I_R ($h\nu$) according to the spectral distribution of the incident light intensity and the sensitivity of the detector.

The present studies were carried out using the samples of heteroepitaxial silicon-on-sapphire listed in Table I. Three inch diameter SOS-wafers often exhibit Si-film thickness variations which exceed $\pm 5\%$. In order to minimize the error resulting from thickness variations, we found it necessary to reduce the diameter of an incident beam to about 1 mm. SOS wafers contain a rather homogeneous central portion and a highly inhomogeneous peripheral region (within 1 cm from wafer edges) which is of inferior crystalline and electronic quality. Unless explicitly stated, the results reported further on refer to the central portion of the wafers.

Table I. Characteristics of SOS films

No.	Crystallinity according to u.v. method	Processing	Comments
1	A	as-grown	different vendors
2	A	as-grown	
3a	F	as-grown	sections of the same wafer
3b	F	hydrogenated (1^h; 300°C)	
4a	B	as-grown	sections of the same wafer
4b	B	hydrogenated (1^h; 300°C)	
5a	B	as-grown	sections of the same wafer
5b	B	heat-treated (1100°C; 3^h)	

Refractive Index

Figure 2 presents the position, λ^{-1}, of reflectivity extrema *vs.* a consecutive number of extremum, l, for films listed in Table I. The position of extreme is related to the wavelength λ_l, maxima 2 and minima 2, respectively, of the reflectance occur at $nd = (2l + 1)\lambda/4$ and $nd = (2l + 2)\lambda/4$ [E_l (eV) $= 1.24/\lambda_l$ (μm)]. For low energy, E_l increases linearly with l due to a constant value of the refractive index. In this region, different slopes in various films results from small differences in the film thickness αd, which was about 6000Å. For higher energy, the separation between extreme decreases due to increasing value of the refractive index $n(E)$. In Fig. 3a, we show the energy dispersion of the refractive index calculated from the data in Fig. 2. It is of importance to note that there is no measurable difference between as-grown, heat-treated, and hydrogenated films. Such behavior is similar to single-crystalline Si and quite different from that encountered in amorphous silicon. In this latter case, the refractive index significantly decreases upon annealing (10). Most recent results have also shown that the value of n in amorphous silicon is highly sensitive to the presence of hydrogen (11).

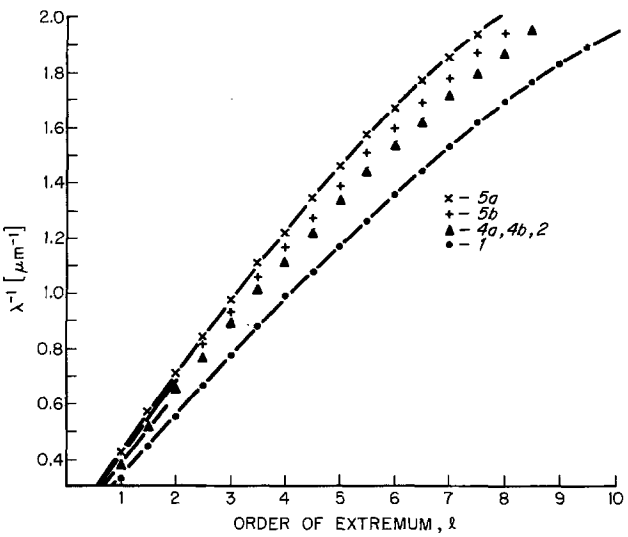

Fig. 2. Energy position of reflectivity extrema vs. the consecutive number of extremum; measurements done on SOS films listed in Table II.

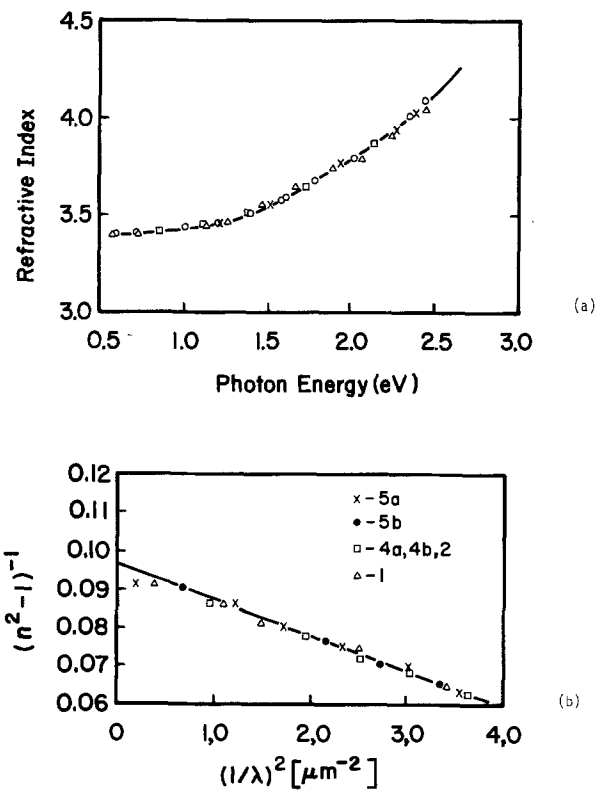

Fig. 3. (a) Summary of results on the energy dependence of the refractive index of silicon-on-sapphire films subjected to a different processing treatment (b) $(n^2 - 1)^{-1}$ vs. λ^{-2} for the SOS films of Table I (see text).

For a comparison between crystalline-noncrystalline materials and/or the effects of processing, the index of refraction is compared with a phenomenological dependence, $1/(n^2 - 1)$ *vs.* $1/\lambda^2$, which defines the long-wavelength limit of the refractive index $n(\lambda = \infty) = n_0$ (12). The results obtained for SOS films satisfy a linear dependence of $1/(n^2 - 1)$ *vs.* $1/\lambda^2$ (see Fig. 3b). The value of $n_0 = 3.37 \pm 0.05$ determined in this manner is very similar to n_0 of single crystalline silicon (13) and is independent of film processing, in agreement with recent studies (14). Therefore, one can conclude that the long wavelength refractive index of silicon films is the same in all films and equal to this of bulk silicon.

Amplitude of Interference Extrema

The magnitude of interference extreme in different SOS wafers was found to exhibit small but definite differences. We will present these results using two quantities, *i.e.*, R_{max} ($h\nu$) and R_{max} ($h\nu$)/R_{min} ($h\nu$), where R_{max} and R_{min} are the maximum and minimum values of reflectivities.

As shown in Fig. 4, R_{max} ($h\nu$) exhibits two specific features: (*i*) it increases with increasing photon energy and (*ii*) its value in a higher photon energy range slightly decreases upon thermal annealing and hydrogenation. It is also seen in Fig. 4 that R_{max} ($h\nu$) has definitely higher value at the edges of the wafer than in the middle. Changes of R_{max} can be caused by two factors: (*i*) changes in reflectivities of two interfaces (air-silicon and silicon-sapphire) and (*ii*) changes in optical absorption. Increase in optical absorption will tend to decrease R_{max}, especially in a higher photon energy range $h\nu = 1.8$ eV whereby αd becomes noticeable (for $h\nu = 1.8$ eV $\alpha d \simeq 0.18$). This effect is probably responsible for the leveling of the R_{max} seen in Fig. 4. The increase of R_{max} clearly observed for lower energy cannot be related to optical absorption. In this low energy range, d is negligible ($d\alpha = 6 \times 10^{-3}$ and 3×10^{-2} for $h\nu = 1.2$ eV and 1.4 eV, respectively). Furthermore, the increase of R_{max} would require a decrease of the absorption coefficient with increasing $h\nu$ which is opposite to the well established behavior. Thus, we believe that an explanation of results of Fig. 4 should involve changes in reflectivity. In further estimates, the changes in optical absorption

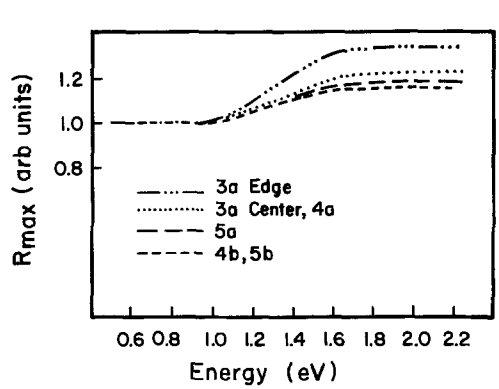

Fig. 4. Energy dependence of the reflectivity maxima R_{max} of SOS films. Note small but definite change upon hydrogenation and thermal annealing, and a difference between the center and the edge of the SOS wafer. (The value of 1 on reflectivity scale corresponds to the absolute value of R_{max} of about 0.55.)

Table II. Reflectivity of silicon-on-sapphire

	SOS Films								
			3a						
	1	2	Center	Edge	3b	4a	4b	5a	5b
$K_1 = R_{max}/R_{min}$ (1 eV)	6.1	6.1	6.1	6.1	6.0	6.3	6.1	6.3	5.9
$K_2 = R_{max}/R_{min}$ (1.8 eV)	6.5	6.5	7.0	7.2	6.3	6.7	6.3	7.7	6.3
K_2/K_1*	1.07	1.07	1.15	1.18	1.05	1.06	1.03	1.22	1.07

* Theoretical limit of K_2/K_1 calculated using R_2-values of crystalline Si [Ref. (13-16)] is 1.06 while the limit calculated using R_2 for a-Si/sapphire [after Ref. (10)] is 1.25.

will be neglected in order to avoid numerical calculations. As summarized in Table II, the quantity R_{max}/R_{min} exhibited a similar but quantitatively more pronounced tendency of decreasing upon thermal treatment and hydrogenation. The value of R_{max}/R_{min} was also higher in samples of inferior crystalline quality than in the best wafers of category A. (In further analysis, we will discuss a ratio R_{max}/R_{min} because in our experimental procedure this ratio is determined more accurately than absolute values of R.)

Discussion

Results presented in Fig. 4 and in Table II clearly demonstrate that, in a spectral region of negligible absorption, the reflectivity of SOS films is sensitive to the processing of films and to their crystalline quality. As discussed in the previous section, none of these factors affected in any detectable way the average refractive index of epitaxial SOS films. It is also of importance to note that extensive u.v. reflection studies have not revealed any measurable changes of u.v. reflectivity as a function of film processing such as thermal annealing and hydrogenation (15). These u.v. reflection measurements were carried out at a photon energy range of $\alpha d >> 1$, *i.e.*, they probed only the front surface of SOS films. Furthermore, the u.v. reflection coefficient was found to increase with improvement of the film quality (1, 4), while the presently studied amplitude of reflectivity is higher in films of inferior crystalline quality.

The following optical characteristics of SOS films have been experimentally observed: (*i*) insensitivity of the average refractive index, n, of silicon films to processing and crystalline perfection, (*ii*) insensitivity of u.v. reflection to processing, but sensitivity to crystalline perfection, (*iii*) sensitivity of lower energy reflection to processing and crystalline perfection. These observations can consistently be explained assuming the presence of an interface region, near the Si/sapphire interface, of different optical properties than the rest of the Si-film. Such a region of thickness much lower than the film thickness, d, would not affect the average refractive index, n, consistent with result (*i*); it would also play no role in u.v. reflection, consistent with result (b); however, it would evidently affect the reflection coefficient, R_2, of the Si/sapphire interface, leading to anomalous characteristics of reflectivity in the lower photon energy range.

The required characteristics of R_2 can be derived from quantitative interpretation of the present reflectivity results. For a negligible adsorption ($\alpha d << 1$) and a normal incidence the thin film interference extrema of reflectivity are given by the following expressions (9)

$$R_{max} = \left(\frac{\sqrt{R_1} + \sqrt{R_2}}{1 + \sqrt{R_1 R_2}}\right)^2 \qquad [1]$$

and

$$R_{min} = \left(\frac{\sqrt{R_1} - \sqrt{R_2}}{1 - \sqrt{R_1 R_2}}\right)^2 \qquad [2]$$

Calculated values of R_{max}, R_{min} and R_{max}/R_{min} as a function of R_2 are shown in Fig. 5 for R_1 = constant and $\alpha d << 1$. It is seen that R_{max} and R_{max}/R_{min} increase with increasing R_2. Accordingly, the experimental results of Fig. 4 and Table II can be explained as due to (*i*) increase of R_2 with decreasing crystalline quality (note the highest value of $R_{max}/R_{min} = 7.7$ in the as-grown wafer 5a, of poor crystallinity), (*ii*) decreasing of R_2 as a result of heat-treatment (note the low value of R_{max}/R_{min} for heat-treated film 5b), and (*iii*) decreasing of R_2 as a result of hydrogenation (note low values of R_{max}/R_{min} in a hydrogenated film, 3b and 4b). The increase of R_{max} in a spectral region (1.4-1.7 eV) would require (*iv*) a strong increase of R_2 in this range.

It is of significance to note that characteristics (*i*)-(*iv*) of R_2 are in fact consistent with the behavior which can be expected from the interface between amorphous or partially amorphized Si and the sapphire. The reflection coefficient between two media of the refractive index, n_1 and n_2, is given as

$$R_2 = \left(\frac{n_1 - n_2}{n_1 + n_2}\right)^2 \qquad [3]$$

Between 1-1.8 eV, the refractive index, n_2, of sapphire changes insignificantly (from 1.75 to 1.76) (16). Thus, the behavior of R_2 is determined by n_1 (interfacial silicon). The refractive index of a-Si exhibits the following characteristics (10-12): (*i*) Its value is higher than the value of crystalline Si; this would lead to a higher R_2 value than for crystalline Si and thus higher amplitude of oscillations, R_{max}/R_{min}; (*ii*) The value decreases upon thermal annealing; this would lead to a lower R_2 value in annealed samples and thus lower R_{max}/R_{min}; (*iii*) The value increases more rapidly with photon energy (due to proximity of the optical energy gap of a-Si) than in crystalline silicon; this would account for the fast increasing of R_{max}/R_{min} with photon energy (Fig. 5). Optical properties of a-Si are also known to be affected by hydrogen (12), which

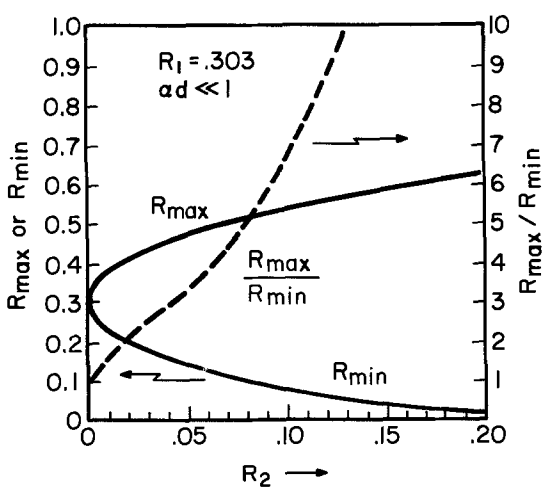

Fig. 5. R_{max}, R_{min}, and R_{max}/R_{min} as a function of R_2

may explain the sensitivity of reflectivity oscillations to hydrogen.

For a comparison, we have also indicated in Table II the values of K_2/K_1 calculated according to the expressions (*i*)-(*iii*), using the following approximations of the interfaces: R_1 for crystalline silicon/air and R_2 for crystalline silicon/sapphire; and R_1 for crystalline silicon/air and R_2 for amorphous Si/sapphire. The following values of parameters were used

$$h\nu = 1.0\text{ eV}: \quad n_{Si} = 3.48 \qquad h\nu = 1.8\text{ eV}: \quad n_{Si} = 3.7$$

$$n_{a\text{-}Si} = 3.8 \qquad n_{a\text{-}Si} \approx 4.5$$

It is seen that experimental values fall in between two approximations, which would indicate only partial amorphization of SOS in the vicinity of the sapphire interface rather than a completely amorphous character of this highly defected region.

Silicon has essentially the same short-range order[2] in crystalline and amorphous form and thus the different optical properties of a-Si are interpreted as due to a large number of dangling bonds on internal surfaces, large strain, and different density (10, 12, 17). In the vicinity of sapphire, epitaxial silicon obviously contains a large number of dangling bonds associated with surface atoms of the walls of small-size crystallites.

The number of dangling bonds in silicon decreases upon annealing and also upon hydrogenation. Thus, for annealed or hydrogenated SOS films, the properties of the Si/sapphire interface tend to approach theoretical values for an ideal crystalline Si/sapphire interface. A large strain in an interfacial region of SOS films can be expected as a result of the lattice mismatch between sapphire and silicon. It is of interest to note that changes of dangling bonds and strain are considered to be responsible for the annealing-induced changes of optical properties of amorphous Si-films (10). In this case, a decrease of n_1 upon annealing was attributed to an increase of the size of crystalline grains rather than to amorphous-crystalline transition.

Interpretation of the present findings in terms of a high concentration of dangling bonds is consistent with the most recent studies of electrical properties of hydrogenated (18) and annealed silicon-on-sapphire (19). These studies were addressed to average properties of SOS films rather than to the Si/sapphire interface. However, they also revealed the effects related to dangling bonds and the reduction of dangling bonds upon hydrogenation and thermal annealing. As a result of hydrogenation, we have also observed (using a test-device structure) a drastic increase in electrical conductivity in the vicinity of the Si/sapphire interface (20). In a-Si, the reduction of dangling bonds is well known to lead to increased conductivity. Accordingly, the above observations can be considered as additional indirect evidence supporting the model of an amorphous-like Si/sapphire interface containing a large number of dangling bonds.

Summary

It is found that the reflectivity of heteroepitaxial silicon-on-sapphire in the energy range of negligible absorption ($h\nu < 2$ eV) is sensitive to the crystalline quality of the film and to the film processing. The value of reflectivity decreased as a result of thermal annealing and hydrogenation. None of these factors was found to affect the refractive index of the silicon films in any measurable way. This apparent inconsistency of two interrelated optical properties was explained in terms of a model which takes into account a partial amorphization of the silicon film in the vicinity of sapphire. This amorphization was attributed to a large number of dangling bonds on the internal surfaces of small size crystallites and to the interfacial strain. Reflectivity characteristics calculated from such a model, considering the known optical properties of a-Si, are in agreement with experimental data. It should be emphasized that presently revealed effects of epitaxial layer/sapphire interface are not observed in the higher photon energy range employed in the u.v. reflection technique for characterization of SOS-films, whereby only reflection from the front surface is probed due to very high optical absorption. As shown in this work, an extension of reflectivity measurements to lower photon energy range offers a new means for probing the quality of silicon film in the vicinity of sapphire substrates.

[2] Short-range order is generally considered as a major factor in determining the optical properties (refractive index).

Acknowledgments

The authors would like to thank M. Duffy and J. Corboy for providing SOS films with u.v. data, J. Pankove for hydrogenation of SOS films, and R. Soydan for assistance in carrying out our experiments.

Manuscript submitted July 22, 1982; revised manuscript received March 16, 1983.

Any discussion of this paper will appear in a Discussion Section to be published in the June 1984 JOURNAL. All discussions for the June 1984 Discussion Section should be submitted by Feb. 1, 1984.

RCA David Sarnoff Research Center assisted in meeting the publication costs of this article.

REFERENCES

1. G. W. Cullen *et al.*, *J. Cryst. Growth*, **56**, 281 (1982).
2. L. Jastrzebski, G. W. Cullen, M. T. Duffy, J. F. Corboy, and J. Lagowski, *ibid.*, **58**, 37 (1982).
3. L. Jastrzebski, G. W. Cullen, and J. Lagowski, *This Journal*, In press.
4. M. T. Duffy, J. F. Corboy, R.. T. Smith, G. W. Cullen, G. Harbeke, J. R. Sandercock, and M. Blumenfeld, *J. Cryst. Growth*, **58**, 10 (1982).
5. M. S. Abrahams, C. J. Buiocchi, R. T. Smith, J. F. Corboy, J. Blanc, and G. W. Cullen, *J. Appl. Phys.*, **47**, 5139 (1976); M. S. Abrahams, C. J. Buiocchi, J. F. Corboy, and G. W. Cullen, *Appl. Phys. Lett.*, **28**, 275 (1976).
6. S. S. Lau, S. Matteson, J. W. Mayer, P. Reversz, G. Gyulat, J. Roth, T. W. Sigmon, and T. Cass, *ibid.*, **34**, 76 (1979).
7. Y. Yamamoto, T. M. Wilson, and T. Itoh, *ibid.*, **34**, 403 (1979); T. Inoue and T. Yashii, *ibid.*, **36**, 64 (1980).
8. Y. Yamamoto, T. Sugiyama, A. Hara, and T. Inada, *J. Appl. Phys.*, **53**, 793 (1982).
9. O. S. Heavens, "Optical Properties of Thin Solid Films," Dover Publications, Inc., New York (1965).
10. M. M. Brodsky, R. S. Title, K. Weiser, and G. D. Pettit, *Phys. Rev.*, **B1**, 2632 (1970).
11. A. V. Zherzdev, A. I. Koszrev, A. A. Andreev, A. A. Rodiua, and D. P. Utkin-Edin, *Sov. Phys. Semicond.*, **15**, 811 (1981).
12. See for example: J. Tauc, in "Amorphous and Liquid Semiconductors, T. Tauc, Editor, Chap. 5, Plenum Press, New York (1974).
13. H. R. Phillips and E. A. Taft, *Phys. Rev.*, **129**, 37 (1960).
14. J. Lagowski, L. Jastrzebski, and G. W. Cullen, *This Journal*, **128**, 2666 (1981).
15. M. T. Duffy, Private conversation.
16. L. H. Malitson *et al.*, *J. Opt. Soc. Am.*, **48**, 72 (1958).
17. M. M. Brodsky and P. J. Stiles, *Phys. Rev. Lett.*, **25**, 798 (1970).
18. L. Jastrzebski, J. Lagowski, G. W. Cullen, and J. I. Pankove, *Appl. Phys. Lett.*, **40**, 713 (1982).
19. L. Jastrzebski, J. Lagowski, R. Smeltzer, and G. W. Cullen, Submitted to *This Journal*.
20. A. Kokkas, Private conversation.

Dark Conductivity Peak in P-Type Glow-Discharged a-SiC:H Films

O. Kuboi

Komatsu Electronic Metals Company, Hiratsuka, Kanagawa, Japan

ABSTRACT

Here we report the doping characteristics of a-SiC:H, specifically the dark conductivity peak of P-type a-SiC:H. When the CH_4 concentration in the gas mixture of SiH_4, CH_4 and B_2H_6 was varied under constant B_2H_6 concentration, a clear dark-conductivity peak was observed for glow-discharged a-SiC:H film at nearly 20% of CH_4. The peak becomes clearer below 0.5% of B_2H_6 in the gas mixture. We have not yet seen this feature reported in the literature. No peak is observed for undoped and phosphorus-doped a-SiC:H.

Efforts to develop the high efficiency photovoltaic a-Si solar cells are being made at many laboratories. a-SiC:H (1, 2) is used on the light incident side as a wide bandgap material for a high efficiency a-Si solar cells. Recently, efficiencies above 8% have been obtained by using this material (3, 4). We are also studying the material. The glow-discharge method is used to prepare a-SiC:H and CH_4 is used as the carbon source.

In this paper, we discuss impurity doping characteristics of a-SiC:H, specifically our new finding about the dark conductivity peak of the boron doped one. A. Tawada *et al.* (3) reported the doping characteristics, but did not discuss that the P-type a-SiC:H has a peak in the dark conductivity. The shoulder of the photoconductivity of P-type a-SiC:H reported by A. Tawada *et al.* (3) seems to be located right above the dark conductivity peak, and the recovery of the photoconductivity by boron doping, as reported in the literature, seems to be related to the dark conductivity peak.

Experimental

The glow-discharge system used in the experiments is as follows: The reaction chamber was made of quartz. Diameter of quartz tube was 150 mm. Width of ring-shaped electrode made of copper plate was 20 mm. Distance between two electrodes was 30 mm. Distance between the center of two electrodes and substrate was 110 mm. Ring-shaped copper electrodes are set on it. The rf frequency was fixed at 8 MHz. rf power was 30W in all experiments. Gases used for the experiments were SiH_4, CH_4, H_2, B_2H_6 (1 volume percent (v/o): diluted with H_2) and PH_3 (1 v/o: diluted with H_2). The total gas flow was fixed at 50 sccm including H_2. Tylan Model FC260 mass flow controllers were used to control the flow rates. The total pressure in the reaction chamber was fixed at about 1 Torr for all experiments.

The substrate for the a-SiC:H film was Corning 7059 glass. The temperature of the substrate was set at 250°C. The samples for conductivity measurements were prepared by evaporating two Al electrodes onto a-SiC:H films. The electrodes were 10.0 mm wide with 1.0 mm gap. Lead wires were attached with conductive Ag paste, and then the samples were annealed at 150°C for 1 hr in the air to form the ohmic contacts. The conductivity measurements were performed with two-probe configuration.

For measurements of σ_D (dark conductivity) and σ_{ph} (photoconductivity), a YHP 4140B pA meter/d-c voltage source, and a Wacom R & D Corp. WXS-180H solar simulator were used in combination with HP 9845B desk-top computer. σ_{ph} was measured under AM-1 illumination. Eg(opt) (optical bandgap) of a-SiC:H was graphically determined by using the following empirical relation

$$\sqrt{\alpha h\nu} \propto h\nu - Eg \qquad [1]$$

where α is absorption coefficient and $h\nu$ is photon energy. All of the samples were measured at room temperature. The carbon concentrations in a-SiC:H were determined by x-ray photoelectron spectroscopy (XPS) measurements using a VG Scientific Limited ESCA LAB-5.

Results

Carbon concentration in a-SiC:H.—The carbon concentrations in the a-SiC:H were determined by XPS measurement (5). Before the measurements, the a-SiC:H were sputtered off by argon ions by 80-100Å in thickness. The XPS signals of Si_{2p} and C_{1s} were deconvoluted into gaussian type line shapes by setting the appropriate binding energy and full width at half maximum of the shapes.

Following Katayama *et al.* (5), the gaussian type line shapes around 102 and around 284 eV were neglected. The carbon concentrations were calculated from the atomic sensitivity factors (area) of Si_{2p} and C_{1s} signals. The factors of Si_{2p} and C_{1s} were set at 0.17 and 0.20, respectively, in accordance with the VG Scientific Limited text book.

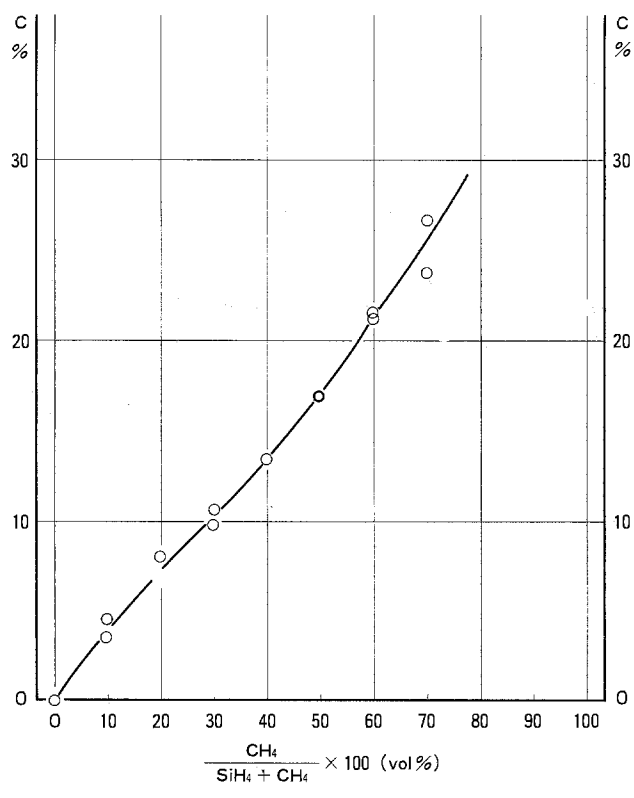

Fig. 1. C% (atomic concentration of carbon in a-SiC) vs. CH_4% (volume concentration of CH_4 in the gas mixture). The data shown in Fig. 1 and 2 were obtained from the samples of the same batch.

Key words: semiconductor, amorphous, cell, photovoltaic, energy conversion.

The results obtained are shown in Fig. 1, in which the relationship between the carbon concentration in a-SiC:H and CH_4 concentration in the gas mixture are plotted.

σ_D peak in P-type a-SiC:H film.—Curves of σ_D *vs.* CH_4% are shown in Fig. 2 where the concentration of B_2H_6 was varied. The gas flow rate of $SiH_4 + CH_4$ was fixed at 8 sccm. The concentration of B_2H_6 is given by the following equation

$$B_2H_6\% = \frac{B_2H_6}{SiH_4 + CH_4} \times 100 \qquad [2]$$

Every curve has a conductivity peak, and all the peaks are located at nearly 20% of CH_4. The peaks for 0.25 and 0.50% of B_2H_6 are shaper, compared with 1.00% of B_2H_6. The absolute values of σ_D, however, becomes larger as the concentration of B_2H_6 increases. A similar peak was not observed for undoped and phosphorus-doped a-SiC:H film.

In the case of fixed flow rate of $SiH_4 + CH_4$, as the flow rate of CH_4 increases, the rate of SiH_4 must be decreased inversely resulting in increase in the ratio of B_2H_6 to SiH_4. If it is assumed that the growth of the a-SiC:H depends mainly on the gas flow rate of SiH_4 not on the rate of CH_4, the σ_D of the film is expected to become larger with increase in the gas flow rate of CH_4, for the above reason.

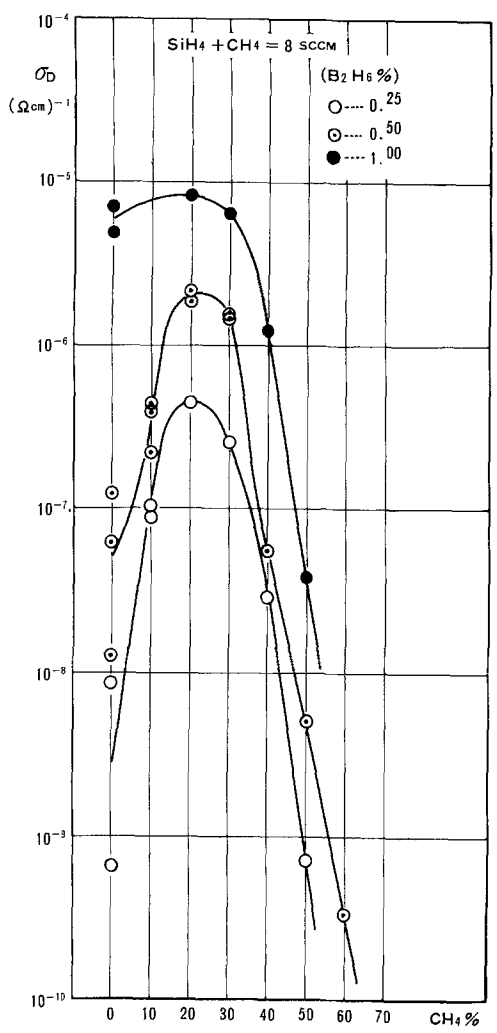

σ_D VS CH_4%

Fig. 2. Dark conductivity vs. CH_4 concentration in the gas mixture of SiH_4, CH_4, and B_2H_6. Gas flow of $SiH_4 + CH_4$ was fixed to 8 sccm.

To check this possibility, experiments with fixed SiH_4 flow rate were performed. In the experiments, the concentration of B_2H_6 is presented by the following equation

$$B_2H_6\% = \frac{B_2H_6}{SiH_4} \times 100 \qquad [3]$$

Then, the ratio of B_2H_6 to SiH_4 was held constant through the experiments.

CH_4 was mixed only for the purpose of changing the ratio of SiH_4 to CH_4. The results are shown in Fig. 3 compared with the results of fixed flow rate of $SiH_4 + CH_4$.

From the figure, it can be seen that the discrepancy between the two data is negligible and there is also a clear peak at nearly 20% of CH_4. Then, it can be concluded that the increase in σ_D in the curves of the area below 20% of CH_4 in the Fig. 2 is not due to the increase in the ratio of B_2H_6 to SiH_4.

Other doping characteristics.—The σ_D, σ_{ph} *vs.* CH_4% for the P-type and N-type a-SiC:H are shown in Fig. 4. The flow rate of $SiH_4 + CH_4$ and the doping concentration, defined by

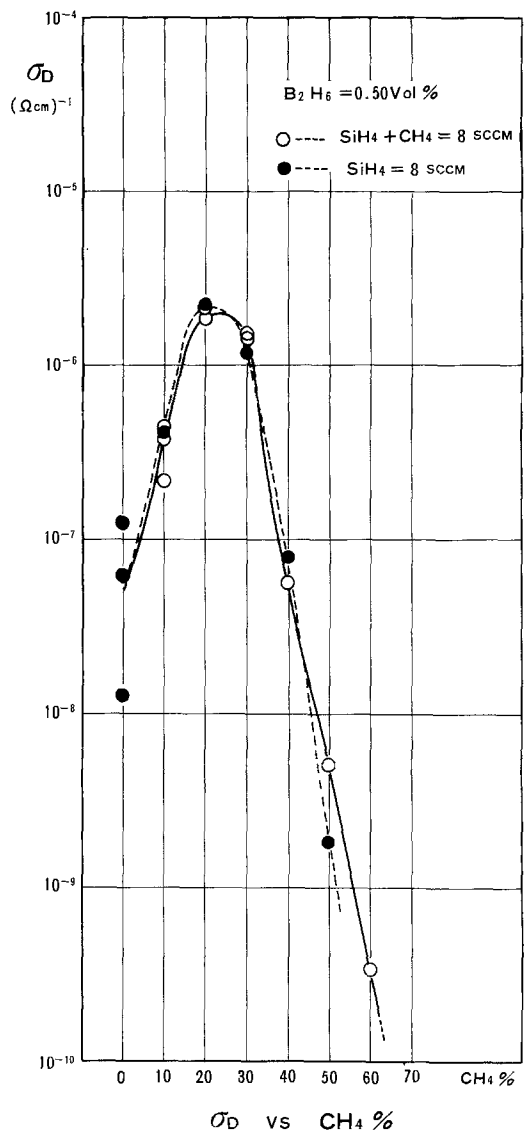

σ_D VS CH_4 %

Fig. 3. Dark conductivity vs. CH_4 concentration in the gas mixture of SiH_4, CH_4, and B_2H_6. B_2H_6 concentration of open circle is equal to $\frac{B_2H_6}{SiH_4 + CH_4} \times 100$ and that of solid circle, $\frac{B_2H_6}{SiH_4} \times 100$.

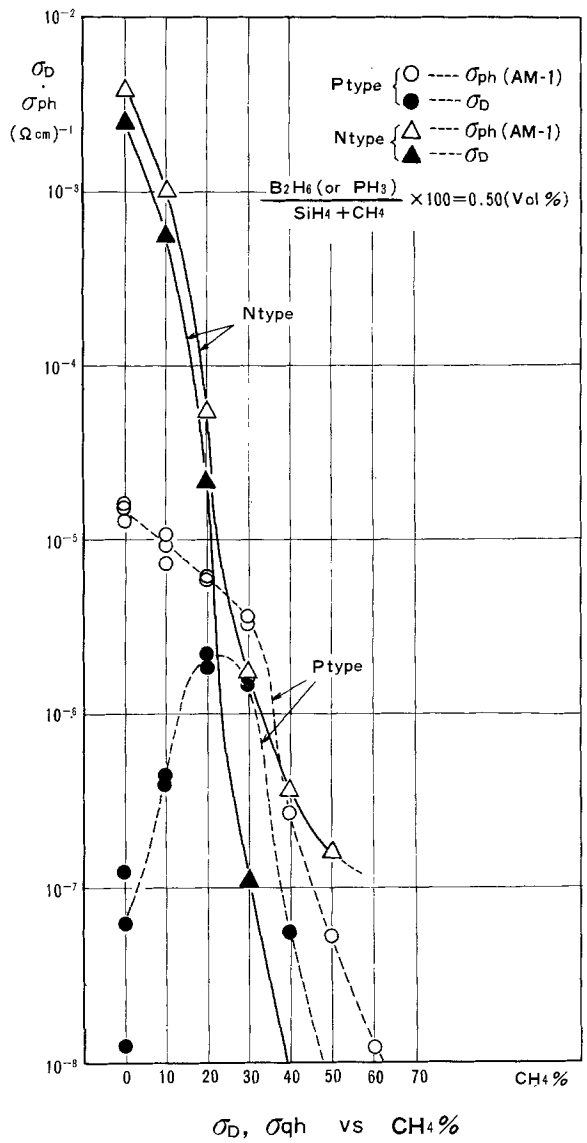

Fig. 4. Dark conductivity and photoconductivity vs. CH_4 concentration in the gas mixture of SiH_4, CH_4, and B_2H_6 or SiH_4, CH_4, and PH_3.

$$\frac{B_2H_6 \text{ (or } PH_3)}{SiH_4 + CH_4} \times 100 = 0.50 \text{ v/o} \qquad [4]$$

were fixed.

σ_D values of P-type a-SiC:H are the same one as shown in Fig. 2 and 3. There is no peak in σ_{ph} for both P-type and N-type a-SiC:H, but the shoulder is seen at nearly 30% of CH_4 for the P type.

This shoulder has already been reported (3). σ_{ph} values of the P-type a-SiC:H which contain different concentration of B_2H_6 (0.25, 0.50, 1.00%) did not vary as in the case of σ_D. The σ_D, σ_{ph} *vs.* B_2H_6% and PH_3% are shown in Fig. 5. The flow rate of $SiH_4 + CH_4$ and CH_4%, defined by

$$\frac{CH_4}{SiH_4 + CH_4} \times 100 = 30 \text{ v/o} \qquad [5]$$

were fixed.

σ_D depends largely on the doping concentration. It shows about six orders of magnitude in the range from 0.05 to 1.00% of the doping concentration for both the P-type and N-type. On the other hand, σ_{ph} is nearly constant in the range between 0.025-0.25% of the dopant concentrations. These facts are worthy of note from the view point of application of the material to an efficient a-Si solar cell, since Eg (opt) decreases when the B_2H_6 concentration is increased.

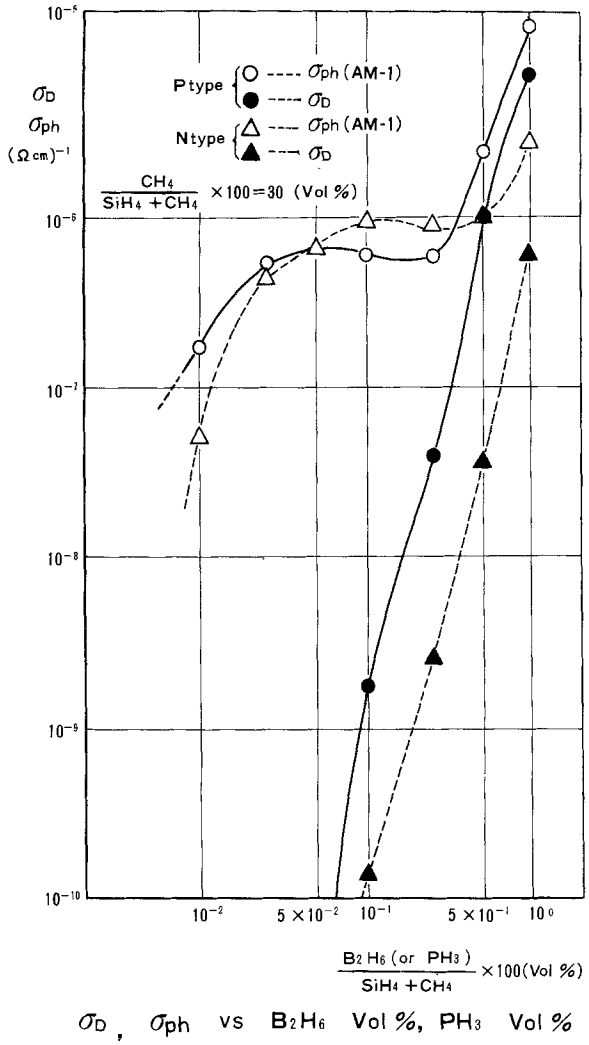

Fig. 5. Dark conductivity and photoconductivity vs. doping concentration of B_2H_6 or PH_3.

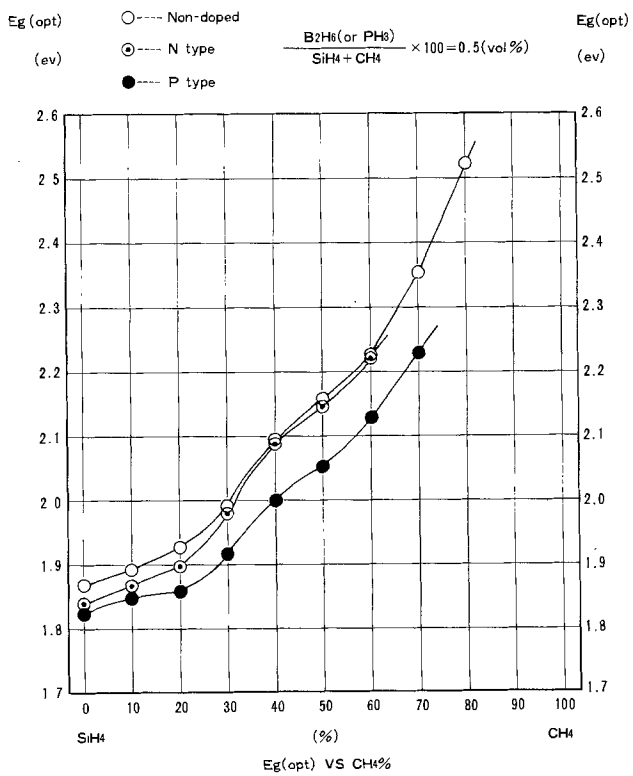

Fig. 6. Optical bandgap vs. CH_4 concentration for undoped, P type, and N type a-SiC:H.

In Fig. 6, Eg (opt) *vs.* CH_4% are shown for undoped, P-type and N-type a-SiC:H. The Eg (opt) increases monotonically with increasing CH_4% in all cases. But the rates of increase in Eg (opt) with increasing CH_4% are different. The order of the rate is as follows: Undoped is the first, N-type the second, and P-type the third. The rate of undoped and N-type are nearly the same. It seems that there is a small shoulder in the curves of Eg (opt) of all the a-SiC:H at nearly 40% of CH_4. The Eg (opt) shrinkage was observed only for P-type a-SiC:H with increasing dopant concentration.

Summary and Discussion

We found the clear maxima in σ_D in the P-type glow-discharged a-Si:H films. The origin of this peak has not yet been clarified. But it is worthy of note that the dopant and hydrogen form dopant-hydrogen complexes (6). The shoulder of the σ_{ph} of P-type a-SiC:H reported by Tawada *et al.* (3) seems to be located right above the σ_D peak, and the recovery of the σ_{ph} by boron doping, as reported in the literature, seems to be related to th σ_D peak. The peak appears to result from the two curves. One is the up slope curve and the other is the down slope one. It is inferred that the increase in σ_D in the up slope curve is caused by more incorporation of boron which becomes electrically active in accordance with the increase in the flow rate of CH_4, while the decrease in σ_D in the range over 30% of the flow rate of CH_4 is concerned with the degradation of quality of the a-SiC:H and increase in Eg (opt) by the higher concentration of carbon. Studies on the origin of the peak in σ_D for the P-type a-SiC:H is presently being planned.

Acknowledgments

Author would like to thank Dr. E. Nakanishi, the director of Energy Laboratory of Komatsu Limited, for encouragement of this work and Y. Yatsurugi, the director of R & D of Komatsu Electronic Metals Company, Limited, for helpful discussions. Author also thanks Mr. I. Uchino for the XPS measurements.

Manuscript submitted Nov. 30, 1982; revised manuscript received April 7, 1983.

Any discussion of this paper will appear in a Discussion Section to be published in the June 1984 JOURNAL. All discussions for the June 1984 Discussion Section should be submitted by Feb. 1, 1984.

Komatsu Electronic Metals Company assisted in meeting the publication costs of this article.

REFERENCES

1. D. A. Anderson and W. E. Spear, *Philos. Mag.*, **35**, 1 (1977).
2. Y. Katayama, T. Shimada, K. Usami, and S. Ishioka, Proc. 1st. Photovoltaic Science & Engineering Conf. Japan, Tokyo (1979), *Jpn. J. Appl. Phys.*, **19-2**, 115 (1980).
3. Y. Tawada, K. Tsuge, M. Kondo, H. Okamoto, and Y. Hamakawa, *J. Appl. Phys.*, **53**, 5273 (1982).
4. A. Catalano, R. V. D'Aiello, J. Dresner, B. Faughnan, A. Firester, J. Kane, H. Schade, Z. E. Smith, G. Swartz, and A. Triano, 16th IEEE Photovoltaic Specialists Conference, San Diego, CA (1982).
5. Y. Katayama, K. Usami, and T. Shimada, *Philos. Mag.*, **43**, 283 (1981).
6. D. E. Carlson, R. W. Smith, C. W. Magee, and P. J. Zanzucchi, *ibid.*, **45**, 51 (1982).

Si on Cubic Zirconia

H. M. Manasevit,*[,1] I. Golecki,*[,2] L. A. Moudy, J. J. Yang,[3] and J. E. Mee

Rockwell International, Microelectronics Research and Development Center, Anaheim, California 92803

ABSTRACT

Epitaxial growth of single-crystal Si films has been realized on the (100), (110), and (111) crystallographic planes of yttria-stabilized, cubic zirconia single crystals. The Si films were grown by chemical vapor deposition, using the pyrolysis of SiH_4 at temperatures in the range 950°-1075°C and at deposition rates of 0.08-1.2 μm/min. A predeposition annealing procedure has been developed, resulting in a quasi-stable, oxygen-deficient zirconia surface. A model is presented to explain the dependence of oxygen kinetics in cubic zirconia on temperature and yttria content. The heteroepitaxial Si films have been characterized by optical and scanning electron microscopies, reflection electron diffraction, x-ray diffraction, Rutherford backscattering and channeling, and surface electrical conductivity and Hall effect measurements. Several 0.4-0.5 μm thick (100)- and (110)-oriented Si films on cubic zirconia were found to be of higher crystal quality than commercial (100) Si on sapphire films of similar thickness.

High quality submicron-thick, single-crystal Si films on insulating substrates are highly desirable for use in fabricating high speed, high density, radiation hard integrated circuits. The current state-of-the-art material is chemically vapor-deposited (CVD) silicon-on-sapphire (SOS), first demonstrated in our laboratories over 18 years ago (1). This early success was subsequently expanded in our laboratories to include epitaxial Si grown by CVD on other insulating substrates such as spinel (2), beryllium oxide (3), and chrysoberyl (3), and the growth of a host of different compound semiconductors and alloys by metalorganic-CVD (MOCVD) on this same kind of insulators (4). The only film insulator combination that has been put to a practical use to date seems to be SOS, and specifically (100) Si on $(01\bar{1}2)$ sapphire. For device purposes, 0.5-0.6 μm thick SOS films are routinely used in fabricating large scale integrated circuits with device dimensions down to and sometimes below 2 μm, but the quality of these thin films is inferior to that of bulk Si. This has been attributed to the thermal and lattice mismatches between film and substrate. Successful efforts have been made in recent years to improve films for device applications (5-7). Ideally, however, the use of the as-grown Si films without regrowth steps would be preferred.

In this paper, we present the initial results of a CVD study on a new heteroepitaxial system, Si on single-crystal yttria-stabilized cubic zirconia (YSZ) substrates. YSZ is a defect solid solution, the defects being oxygen vacancies created to preserve lattice neutrality when Y^{+3} ions are substituted for Zr^{+4} ions in the fluorite-type structure. These vacancies give rise to high oxygen ion mobilities (8). From a prac-

* Electrochemical Society Active Member.
[1] Present address: TRW, Technology Research Center, El Segundo, California 90245.
[2] Also Visiting Associate, California Institute of Technology, Pasadena, California 91125.
[3] Present address: TRW, Redondo Beach, California 90278.
Key words: semiconductor, CVD, heteroepitaxy, ceramic, insulator.

tical standpoint, YSZ presently is commercially available as large single crystals with linear dimensions up to ~5 cm. In this form, it has been used mainly as a diamond substitute in the jewel industry. In the past, the use of zirconia containing yttria, calcia, or other additives to stabilize the cubic phase was limited mostly to polycrystalline material and to its high temperature ionic oxygen conducting properties (9, 10). The Y_2O_3-ZrO_2 system has been studied by several investigators (11-13). It was determined that YSZ containing ~8 to ~40 mol percent (m/o) yttria possesses the cubic (CaF_2) structure and, depending upon its Y_2O_3 content, can vary in lattice parameter from 5.14Å to 5.23Å as compared to 5.43Å for Si. Thus, it is better lattice-matched to Si than is sapphire (see below). Its average expansion coefficient between room temperature and 1000°C (for ~9 m/o Y_2O_3) is 11.4 × 10^{-6}/°C (14), ~30% greater than that of sapphire. We show here that single crystal epitaxial growth of Si on YSZ has been achieved with film orientations that parallel those of the substrate. In addition, the crystal quality of 0.4-0.5 μm thick (100)-oriented films has been found to be better than that of commercially available SOS of similar thickness.

Experimental

Single-crystal $(Y_2O_3)_m$ $(ZrO_2)_{1-m}$ boules, having nominal yttria mol fractions, m, of 0.09, 0.12, 0.18, and 0.33, grown by the skull melting technique (15) at ≈2700°C in air, were obtained from Ceres Corporation (16) and Singh Industries (17). The skull melting technique (15) uses a specially shaped radio frequency apparatus for melting the source powders and employs solidification of the melt and crystal formation in a skull of its own composition. These boules have been in most cases large enough in size to cut substrates of 1.2 × 1.2-2.5 × 2.5 cm dimensions in any orientation, although much larger crystals can be grown by this technique. Figure 1 is a photograph of one of the largest substrates grown upon to date in this study. Boules were oriented by means of x-ray back-reflection Laue techniques, sliced and polished at Rockwell into 0.75 mm thick wafers having the (100), (110), and (111) crystallographic orientations (within 0.3°). Wafers were lapped with a series of Al_2O_3 powders/colloidal silica mixtures and then chemically mechanically polished in colloidal silica at pH = 3-4 to obtain an "epitaxial quality" surface finish. Reflection electron diffraction (RED) using 50-100 keV electrons and MeV $^4He^+$ Rutherford backscattering (RBS) and channeling measurements (see below) indicated that the as-polished YSZ surfaces were of relatively high crystal quality.

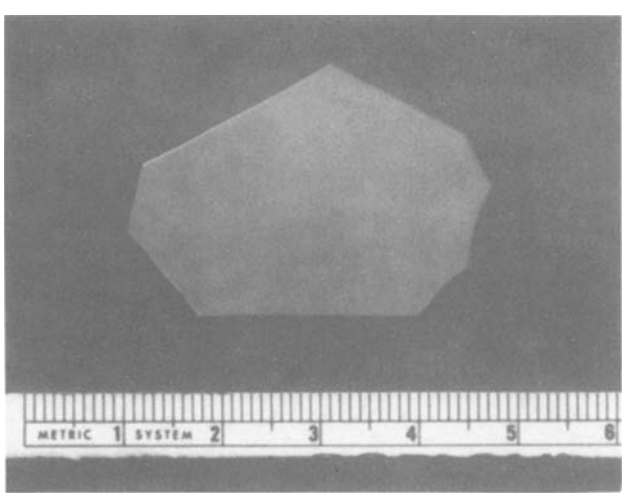

Fig. 1. One of the largest yttria-stabilized cubic zirconia substrates used in the present study.

Si films were grown at 1 atm pressure via the pyrolysis of SiH_4 in a vertical cold-wall quartz reactor. The gases and flow rates generally used were as follows: Pd-purified H_2 as the carrier, 3000 cm³/min, and 5% SiH_4-in-He, 10-100 cm³/min. The substrates were cleaned in organic solvents and then heated in the reactor on a rotating, rf-coupled, SiC-coated graphite susceptor, ~57 mm in diameter. Before each growth experiment, the reactor portion of the system was evacuated to at least 10^{-3} Torr pressure and then filled with purified flowing H_2 prior to heating the susceptor. Temperature measurements were made with an optical pyrometer on the side of the susceptor. Values given here are uncorrected readings; previous calibrations (18) had shown that the actual wafer temperature on the top of the susceptor was 33°-50°C lower at 950°-1075°C, respectively. After deposition, selected films were characterized by Nomarski optical and scanning electron microscopies (SEM), RED, x-ray diffraction (XRD), RBS/channeling, transmission electron microscopy (TEM) (19), and electrical measurements.

Results and Discussion

Substrate purity and composition.—A preliminary analysis of the chemical composition of as-received and sliced YSZ substrate material was carried out by spectrochemical means at a specialized laboratory (20) where samples of the four Y_2O_3-content levels were analyzed. Qualitatively, the measured amount of the two main metallic constituents, Zr and Y, followed the nominal compositions. Trace amounts (200-700 ppm) of SiO_2, MgO, and TiO_2 were detected in a sample which had nominally a 33% mol Y_2O_3 content. RBS/channeling measurements using 0.8-2.0 MeV $^4He^+$ ions were revealed in as-polished YSZ 2-4% mol HfO_2, where the Hf occupied substitutional positions in the metal sublattice (21). The mass resolution of the RBS system was insufficient, however, to provide a quantitative measure of the Y and Zr content in YSZ.

The bulk composition of as-polished, single-crystal YSZ substrates from most boules was also indirectly determined by measuring their lattice parameters, a, using the x-ray Bond technique. Comparison to values reported in the literature (13) for Hf-free YSZ, shown in Fig. 2, indicates that the present values of a are lower by (6-12) × 10^{-2}%. This small systematic difference could be due to the HfO_2 in our samples (22) and possibly to an actual Y_2O_3 content 0.4-1.5% mol lower than the nominal value.

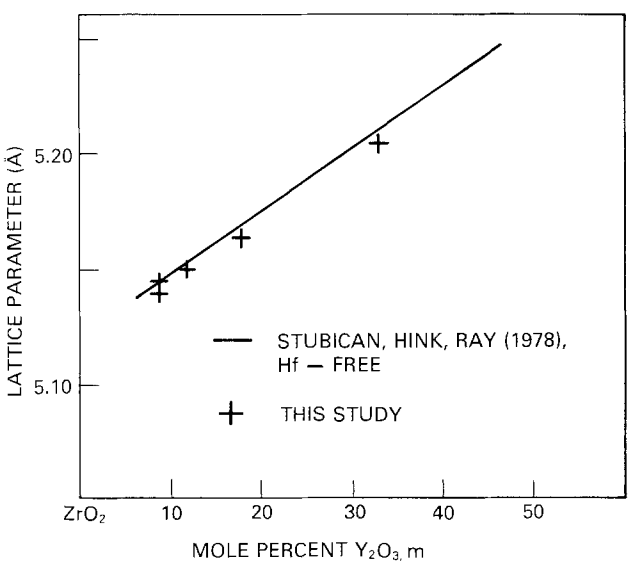

Fig. 2. Variation of the lattice parameter of yttria-stabilized cubic zirconia with yttria content. The solid line is for Hf-free material from Ref. (13); the crosses are for the present material, having 2-4% mol HfO_2.

Substrate crystal quality.—The crystal quality of the as-polished YSZ substrates was found to be high by (*i*) the presence of diffraction spots and Kikuchi lines in RED patterns, and (*ii*) the presence of a surface peak and surface oscillations in RBS/channeling spectra (21). The value of the axial surface channeling yield, $\chi_0 = 0.07$ (at 0.8 MeV $^4He^+$ incident energy) for the Y + Zr sublattice in (100) YSZ could be lowered even further by high temperature annealing as described in the next section.

Thermal stability study of substrates.—Early in the investigation, it was found that the substrates cnanged color during the process of being heated in H_2 to the temperature prepared for Si growth. The color range (from colorless to yellow to orange to brown to black) was found to begin at ~475°C and to continue progressively with temperature increase, the final color being a function of the time of exposure to H_2, the maximum temperature of exposure, and the composition of the substrate. In the latter case, the lower the Y_2O_3 content, the more quickly did the substrate darken and the darker was the final color. Heating under somewhat poor vacuum conditions ($\approx 10^{-3}$ Torr) or in flowing 99.9999% pure liquid-nitrogen-trapped He gas caused only slight changes in substrate color. For example, 90 min in flowing He at ~1250°C turned an 18% mol Y_2O_3-containing substrate light yellow; in H_2, under the same thermal conditions, it became dark brown. The darkening of YSZ substrates in oxygen-poor ambients is related to the loss of oxygen from the substrates.

It was also observed that a substrate which was blackened at ~1250°C, in this case with a Y_2O_3 composition of ~12 m/o, would on prolonged exposure in H_2 at a lower temperature (~3 hr at 1000°C) revert to a yellow-brown color. This change was probably caused by reabsorption of trace amounts of O_2 from the gaseous atmosphere. A substrate so treated did not readily lend itself to epitaxial growth of Si from SiH_4 (see below).

This "blackening" phenomenon of YSZ has been reported previously (23), but there is only a limited number of studies (24, 25) of the quantitative variation of the oxygen deficiency, x, in $Y_{2m}Zr_{1-m}O_{2+m-x}$ as function of m, T, and $p(O_2)$, the oxygen partial pressure in equilibrium with YSZ. The latter quantity is given by $p(O_2) = [\exp(-\Delta G/RT)]\ [p(H_2O)/(p(H_2)]^2$, where ΔG is the Gibbs free energy of the reaction $2H_2 + O_2 \rightleftharpoons 2H_2O + \Delta G$, $p(H_2) = 1$ atm, and $p(H_2O)$ is determined by trace amounts of residual water vapor in the system. Qualitatively, x increases with increasing temperature and decreasing $p(O_2)$, while $p(O_2)$ also decreases with increasing temperature (at constant partial pressures of water vapor and hydrogen) (26). Under our experimental conditions, we estimate the order of magnitude of x in "blackened" YSZ to be 1% mol.

Although the quantitative thermodynamics, *i.e.*, $x[m, T, p(O_2)]$ of the YSZ system has not been fully investigated, the kinetics of oxygen loss or absorption can be readily calculated from the measured electrical conductivity data (9). We have performed such calculations, using the Nernst-Einstein equation to calculate the oxygen diffusion coefficient, D, in YSZ as function of m and T

$$D = \sigma_i kT/n_i q_i^2$$

where $\sigma_i = \sigma_o(m) \exp[-\Delta E(m)/kT]$ is the ionic conductivity of YSZ from Ref. (9), $n_i = 7.1 \times 10^{27}\ [4m/(1+m)]$ is the number of oxygen vacancies in YSZ per m^3 (15), and $q_i = 2e$ is the charge per oxygen vacancy. The assumptions used in this procedure are (*i*) oxygen is the only conducting ionic species in YSZ, verified in Ref. (9), and (*ii*) the "blackening" (*i.e.*, reduction) of YSZ does not appreciably alter its ionic conductivity. This will be true if the vacancy concentration produced by the reduction is small compared to the initial concentration, determined by the yttria content, m. Extrapolations of published (24a) ionic conductivity data as a function of x for $x = 0$-0.014 and $m = 0.09$ to the temperature range of interest here (950°-1250°C) show that this is indeed the case (see Fig. 10 in Ref. 24a). Similar electrical-nonstoichiometry data for reduced YSZ with higher m are not available, but since the initial oxygen vacancy concentration increases with m, this approximation is expected to hold possibly even better for higher m.

Using these calculated values for the oxygen diffusion coefficients in a standard solution of the one-dimensional diffusion equation in a thin plate (27), we obtained an expression for a characteristic equilibration time, t_{eq}, of YSZ, with the surrounding $p(O_2)$ as a function of m and T: $t_{eq} = b^2/2D(m, T)$. Here $b = 0.75$ mm is the thickness of the YSZ wafers, and t_{eq} is the time necessary to reach 0.991 of the final oxygen concentration midway between the two faces of the YSZ wafer. We assumed symmetric diffusion from both polished and unpolished faces of the YSZ, *i.e.*, the absence of surface effects. The results of our calculation are given in Fig. 3. As expected, t_{eq} increases with increasing yttria content, m, in the YSZ, and with decreasing temperature. These calculated values are in agreement with our visual observations of color changes and with limited thermogravimetric measurements (25) considering the experimental uncertainties in the determination of the wafer temperature and in the thermodynamics of YSZ.

X-ray diffraction measurements were also performed in our laboratories on a limited number of YSZ samples as a function of high temperature treatment in H_2 in our CVD reactor. No significant systematic change in lattice parameter could be detected within the experimental accuracy in agreement with Ref. (28).

Finally, as noted above, RBS/channeling measurements indicated that the "blackened" YSZ substrates had a significantly better surface and near-surface crystal quality compared to the already satisfactory as-polished condition. In fact, the surface channeling yield of 0.034, measured (21) for the Y + Zr sublattice in a

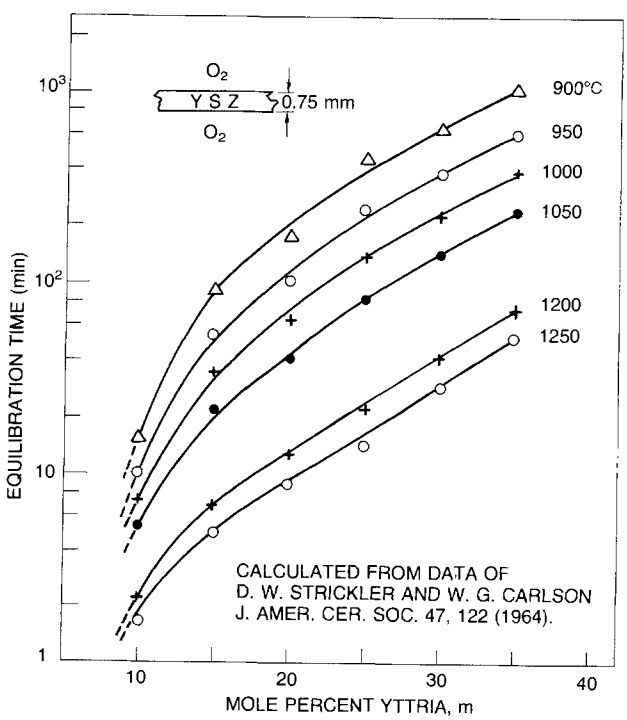

Fig. 3. Calculated equilibration time for the oxygen content in a 0.75 mm thick, yttria-stabilized cubic zirconia wafer, as function of yttria content and temperature; the lateral dimensions of the wafer were assumed to be much larger than its thickness. The solid lines are intended as an aid to the eye.

$(Y_2O_3)_{0.12}(ZrO_2)_{0.88}$ sample after a 30 min annealing in H_2 at 1250°C, corresponds to an essentially perfect single crystal.

As indicated below, some of the above observations had a significant influence on the experimental growth procedures used to effect epitaxial growth of Si on YSZ of different compositions.

Si growth studies.—Most studies were performed with substrates having $m = 0.12$ and 0.18 from which polished slices of all three orientations, (100), (110), and (111), were obtained, with the emphasis, however, put on (100) YSZ substrates. It was found in the early stages of this study that in order to obtain epitaxial Si growth, a stable oxygen-deficient YSZ surface was necessary. For example, annealing of the YSZ substrates in H_2 at ≈1000°C for 10 min prior to Si deposition at the same temperature resulted in either continuous polycrystalline Si films or sometimes discontinuous islands. However, preheating of the substrates at more elevated temperatures caused a change in the nature of Si growth that was obtained at ≈1000°C. For example, it was observed that films grown at 1000°C on substrates with $m = 0.12$ and 0.18 after heat-treatment at 1150° and 1225°C, respectively, for about 15 min, consisted of nonuniform island growth and partial coverage but with crystallites now displaying a high degree of order. Single-crystal, epitaxial, continuous Si growth was obtained only after the YSZ substrates had been first annealed in H_2 at ≈1250°C for 30-180 min (the annealing times corresponding to $m = 0.12$-0.33, respectively) before Si deposition at 950°-1075°C. As explained above, the two major effects of this predeposition, high temperature annealing in H_2 are (*i*) stabilization of an oxygen-deficient composition in the YSZ. The length of time required to reach equilibrium throughout the thickness of the YSZ substrate increases with yttria content, *m*, as shown in Fig. 3, due to the lower oxygen diffusion coefficient. When the substrate temperature is subsequently lowered by 200°-300°C, and during the Si deposition (lasting only several minutes), the previously stabilized, oxygen-deficient composition remains approximately "quenched-in" because of the slower kinetics at this lower deposition temperature. Therefore, this procedure avoids the presence of oxygen near the substrate, which might otherwise evolve out of the YSZ, react with the SiH_4 and H_2 to generate SiO_2 at the surface, and impede epitaxy; and (*ii*) significant improvement in the crystalline perfection of the polished YSZ surface. It is not known whether this improvement is due only to thermal annealing of residual polishing damage or also to material removal by the H_2 as is the case for Al_2O_3 (29).

Table I lists the set of predeposition annealing parameters and deposition temperatures which were found sufficient for epitaxial Si growth on YSZ. Most of the films were grown at deposition rates of 0.08-0.8 μm/min, with a few grown at 1.2 μm/min. The thickness range of epitaxial Si/YSZ films was 0.25-10 μm. No systematic growth studies were performed outside this set of parameters. Properties of the epitaxial Si/YSZ films are described in the next section.

Table I. Sufficient conditions for epitaxial Si growth on $(Y_2O_3)_m(ZrO_2)_{1-m}$ by the pyrolysis of SiH_4

Composition *m*	Orientation	H_2 annealing temperature (°C)/ time (min)	Approximate growth temperature (°C)
0.09	(100)	1250/45	1000-1025
0.12	(100)	1250/60	950-1025
	(110)		975-1025
	(111)		1000-1075
0.18	(100)	1250/90	1000-1025
	(110)		975-1025
	(111)		1000-1045
0.33	(100)	1250/180	1000
	(110)		1000

Si film characterization: morphology, crystalline structure, and perfection.—Optical microscopy with a Nomarski interference attachment showed the epitaxial Si/YSZ films to have a "grainy" surface topography similar to commercial SOS films. XRD analysis on a full-circle goniometer showed that the crystallographic orientations of the films were the same as those of the substrates; in addition, the in-plane film/substrate orientations were also found to be parallel, *i.e.*, Si(*hkl*)//YSZ(*hkl*) and Si[*hkl*]//YSZ[*hkl*]. An example of the measured epitaxial relationships for a (100) Si film on a (100) YSZ substrate ($m = 0.12$) is given in Fig. 4. This parallelism was found to hold for all samples analyzed by this technique, having $m = 0.12$ and 0.18, and for all three principal cubic orientations: (100), (110), and (111).

The surface crystal quality of the Si films was evaluated qualitatively by means of RED. Figures 5a and 5b show such RED patterns of 0.4 μm and 0.45 μm thick, (100) and (110) Si/YSZ films grown at 977° and 1002°C, respectively, on YSZ substrates having $m = 0.12$. The presence of Kikuchi lines in the patterns attests to the high surface crystal quality of these films.

Quantitative measurements of the crystalline perfection of the Si/YSZ films as a function of depth were obtained by means of RBS/channeling, using 0.8-2.0 MeV $^4He^+$ ions with a variable scattering angle detection system. The Si films were first aligned and measured in the glancing exit mode (scattering angle $\theta = 95°$-108°), which enabled the top half of submicron thick Si/YSZ films to be measured without the higher intensity interfering background from the heavy elements Y and Zr in the substrate and with high depth resolution (30). The surface barrier detector was then positioned at a larger scattering angle ($\theta = 151°$-168°), and the channeling spectra were remeasured. This latter geometry provided useful information on the crystal quality of the Si films throughout their thickness, and especially near the Si/YSZ interface. Figures 6a and 6b and Table II illustrate the results obtained for a 0.45 μm thick (100)Si/(100)$(Y_2O_3)_{0.18}(ZrO_2)_{0.82}$ film in comparison to a (100) state-of-the-art commercial CVD SOS film of similar thickness and to (100) bulk Si. The SOS samples selected for comparison are the best that we have measured out of a large number of commercial wafers grown under various conditions

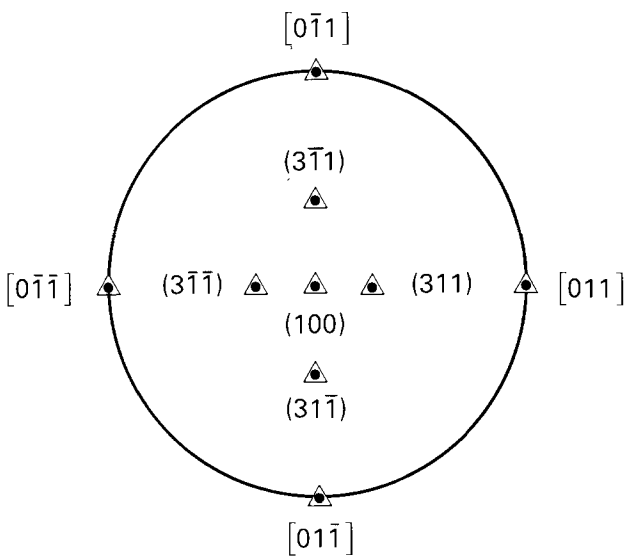

Fig. 4. Stereographic projection of the crystallographic planes of a 0.9 μm thick, epitaxial Si film (solid circles) grown at 1005°C on a $(Y_2O_3)_{0.12}(ZrO_2)_{0.88}$, (100)-oriented, single-crystal substrate (open triangles). These data were obtained by means of x-ray diffraction, using a full-circle goniometer, and demonstrate the epitaxial relationships between film and substrate, (100) Si // (100) YSZ, [011] Si // [011] YSZ.

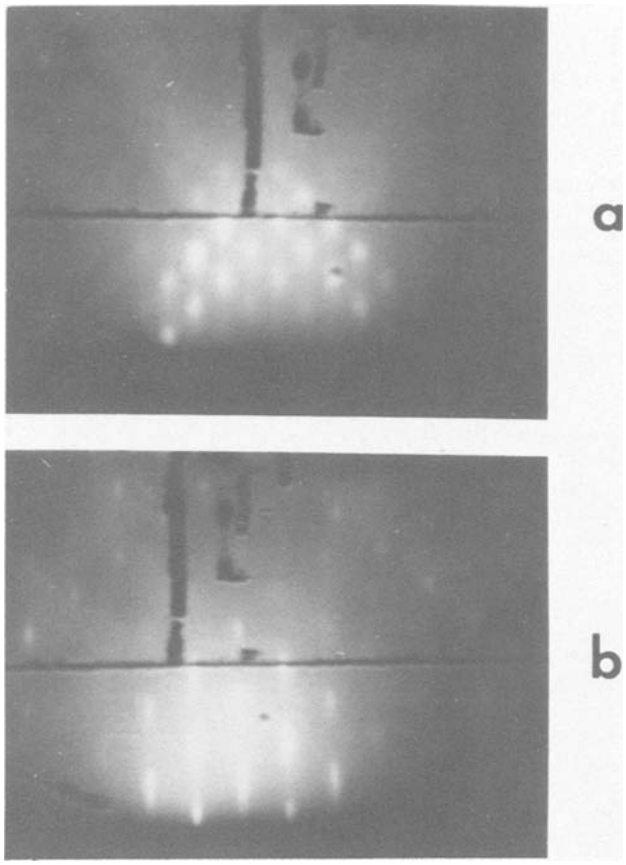

Fig. 5. Reflection electron diffraction patterns obtained with 100 keV electrons on (a) a 0.4 μm thick (100) Si single-crystal film grown at 977°C, and (b) a 0.45 μm thick (110) Si single-crystal film grown at 1002°C on $(Y_2O_3)_{0.12}$ $(ZrO_2)_{0.88}$ single-crystal substrates of the respective orientations.

in the last five years. The following conclusions can be drawn from these and similar measurements on a large number of samples:

1. The surface and near-surface crystal quality of 0.4-0.5 μm thick (100)- and (110)-oriented (19) Si/YSZ films grown in our laboratories is superior to that of state-of-the-art commercial CVD (100) SOS films of similar thickness. This conclusion was supported by XRD measurements of the width of the Si rocking curve, $\Delta\omega$, which is an inverse measure of the depth-averaged crystal quality of the film. For example, $\Delta\omega$(Si/YSZ) = 17 min of arc and $\Delta\omega$(SOS) = 29 min of arc for the samples in Fig. 6 and Table II. TEM analyses (19) also supported this conclusion.

2. The crystal quality of (111) Si/YSZ films was significantly poorer than that of (100)- and (110)-oriented films. Channeling yields in (111) films were generally at least twice the values found for the other orientations, and XRD measurements revealed the presence of relatively high twin densities.

3. The concentration of the dechanneling defects in the Si/YSZ films, shown by TEM (19) to consist of stacking faults, twins, and dislocations, increased rapidly with depth and was highest at the Si/YSZ interface. A similar situation has been known to exist in SOS films. We believe that it is the relatively high difference in thermal expansion coefficients (14) between Si ($\bar{\alpha}_{25°\text{-}1000°C} = 3.8 \times 10^{-6}$/°C) and either cubic zirconia ($\bar{\alpha} = 11.4 \times 10^{-6}$/°C) or sapphire ($\bar{\alpha} = 9 \times 10^{-6}$/°C) which is mainly responsible for the defective interface. This thermal mismatch results in a severe compressive strain in the plane of the Si film which develops during cooling from the deposition temperature to room temperature. Part of this compressive strain is relieved into crystallographic defects. We have

Table II. Surface channeling yields, χ_0, and average dechanneling rates, $\overline{d\chi/dz}$, for a 0.45 μm thick, (100) Si / (100) $(Y_2O_3)_{0.18}(ZrO_2)_{0.82}$ film, a commercial CVD (100) Si / $(01\bar{1}2)$ Al_2O_3 film of similar thickness, and bulk, (100) Si. E_0 is the incident energy of the $^4He^+$ analyzing beam, and θ is the scattering angle.

	E_0 = 0.8 MeV, θ = 108°		E_0 = 1.5 MeV, θ = 102°, 156°/158°	
Sample	χ_0	$\overline{d\chi/dz}$ (μm)$^{-1}$ 0-0.2 μm	χ_0	$\overline{d\chi/dz}$ (μm)$^{-1}$ 0-0.4 μm
Si/YSZ	0.067	0.56	0.10	1.2
SOS	0.125	0.75	0.13	1.3
Bulk Si	0.034	0.13	0.035	0.08

measured the depth-averaged macrostrain in both Si/YSZ and SOS (31) by determining the peak position of the Si rocking curve. We have found that at room temperature the in-plane strain, $\epsilon_{\parallel}$, in as-deposited Si/YSZ films was systematically higher than in SOS films. For example, $\epsilon_{\parallel}$(Si/YSZ) = -5.4×10^{-3} (corresponding to an in-plane stress $\sigma_{\parallel} = -9.7 \times 10^9$ dyne/cm^2) and $\epsilon_{\parallel}$(SOS) = -4.1×10^{-3} ($\sigma_{\parallel} = -7.4 \times 10^9$ dyne/cm^2) for the samples in Fig. 6 and Table II. This difference is due to the higher expansion coefficient of YSZ as compared to sapphire. It is noteworthy that in spite of the higher strain, the defect level is lower in the Si/YSZ films, possibly due to the smaller lattice mismatch between Si and YSZ (4.1-5.3% for m = 0.33-0.09, respectively) as compared to Si and Al_2O_3 (≈10%).

Si film characterization: electrical properties.—The electrical properties of the epitaxial Si layers were found to be dependent upon the composition and orientation of the substrate and the predeposition substrate preparation. Unintentionally doped, (100)-oriented films grown on substrates with m = 0.09 tended to be p-type; for m = 0.12, they were n-type with depth-averaged carrier concentration generally in the 5×10^{16}-10^{18} cm^{-3} range; and for m = 0.18, they were also n-type with carriers in the 10^{14}-10^{17} cm^{-3} range. Depth-averaged Hall mobilities for several of the as-grown films were measured using the Van der Pauw technique, with the four contacts being placed around the rims of the samples, thus resulting also in lateral averaging over the entire areas (3-5 cm^2) of the Si films. The Hall mobilities of these unintentionally doped films were in the same range as those we have measured in commercial, intentionally doped, n-type CVD SOS films of the same carrier concentration and thickness. Representative values for the Si/YSZ films were as follows: the 0.45 μm thick (100) Si/YSZ film characterized by RBS/channeling in Fig. 6 had μ_e = 200 cm^2/Vsec (at $n_e = 7 \times 10^{16}$ e/cm^3), and a 2.2 μm, (100) film had μ_e = 310 cm^2/Vsec (at $n_e = 1.2 \times 10^{17}$ e/cm^3). These mobility values were typical for the respective Si film thicknesses. They are lower than some values reported in the literature (32) for intentionally arsenic-doped SOS films of similar thickness, *e.g.*, μ_e = 330 cm^2/Vsec in a 0.5 μm thick film (at $n_e = 6 \times 10^{16}$ e/cm^3). Due to the rapidly increasing defect level in these films as the Si/YSZ interface is approached, the surface mobility is expected to be higher than the Hall mobility (32); it is the former quantity which determines the speed of an enhancement-mode, n-channel, metal oxide semiconductor, field effect transistor, for instance. Additional information on the electrical properties of Si/YSZ films must await the systematic growth of intentionally doped films.

Summary

1. Yttria-stabilized cubic zirconia (YSZ) has been found to be an adequate substrate for the epitaxial growth of Si layers.

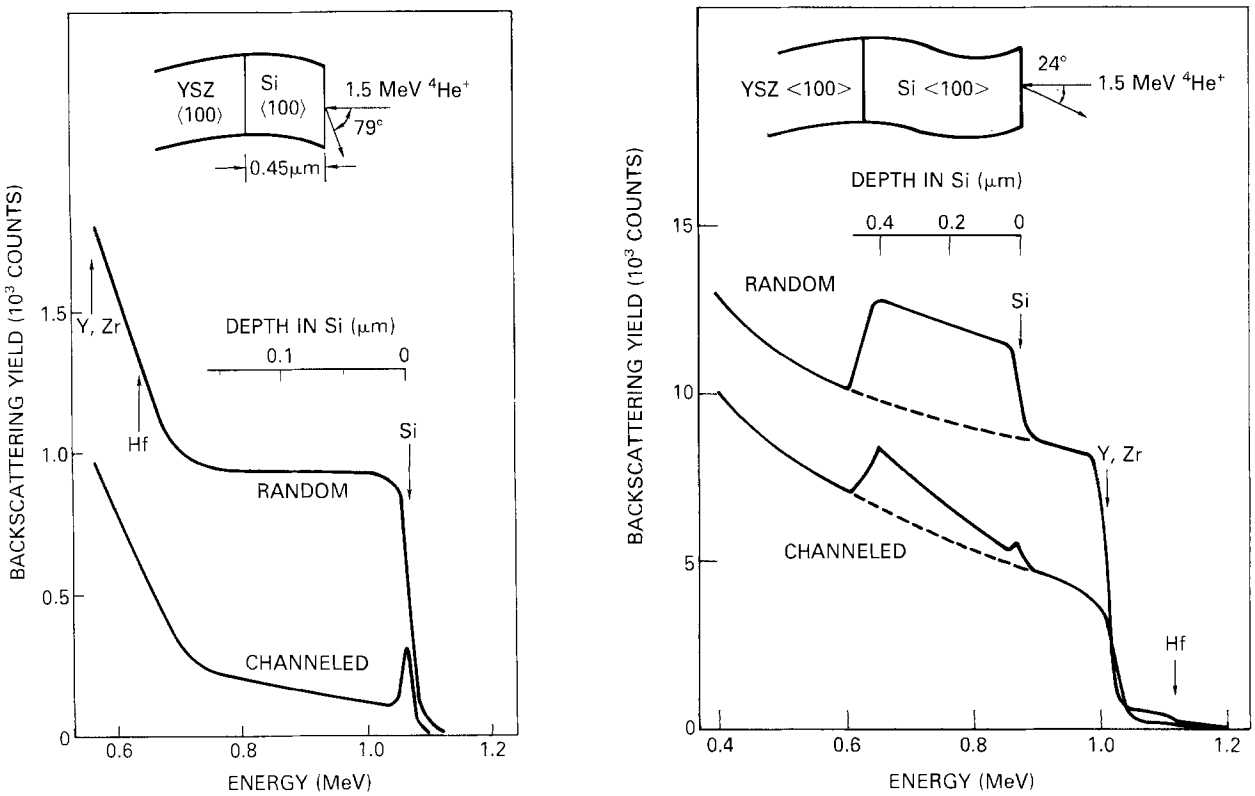

Fig 6 a(left), b (right). Energy spectra of 1.5MeV $^4He^+$ ions, backscattered at (a) 101° and (b) 156° from a 0.45 μm thick epitaxial (100) Si/ (100) $(Y_2O_3)_{0.18}(ZrO_2)_{0.82}$ film grown at 1002°C. In these spectra, lines were passed through the raw data points from the multichannel analyzer in order to bring out the salient features. The substrate contains ≈3.5% mol. HfO_2 in substitutional lattice positions. The dashed lines indicate the background which must be subtracted in order to calculate the channeling yield in the Si films. (See Table II for χ_0 and $d\chi/dz$ values.)

2. A high temperature exposure to hydrogen prior to Si film growth at a lower temperature has been found essential for achieving epitaxial growth. This predeposition treatment assures the necessary absence of oxygen near the YSZ during Si epitaxy and improves the YSZ crystalline perfection.

3. The orientations and directions of the epitaxial layers are parallel to those of the substrate, *i.e.*, Si(*hkl*)//YSZ(*hkl*) and Si[*hkl*]//YSZ[*hkl*].

4. Preferred growth temperatures have been determined for the growth of (100)-, (110)-, and (111)-oriented Si films by the pyrolysis of SiH_4.

5. RBS/channeling, XRD, and TEM (19) data indicate that the crystal quality of 0.4-0.5 μm thick (100)- and (110)-oriented films is better than that of commercially available (100) SOS films of similar thickness. However, the Si/YSZ interface is a source of planar lattice defects as in SOS.

6. The electrical properties of unintentionally doped films are dependent upon the substrate composition and orientation and the predeposition surface preparation of the substrates.

Acknowledgments

The authors wish to acknowledge the significant technical assistance of A. Crouse for slicing the YSZ boules, D. Medellin for polishing, R. E. Johnson for RED and SEM measurements, and M. D. Lind for lattice parameter measurements of the substrates. This research was supported by the Materials Laboratory, AFWAL, Wright-Patterson Air Force Base, Ohio 45433, under contract No. F33615-81-C-5041 (J. O. Crist and M. C. Ohmer).

Manuscript submitted Oct. 28, 1982; revised manuscript received March 22, 1983. This was Paper 207 presented in part at the Montreal, Que., Canada, Meeting of the Society, May 9-14, 1982.

Any discussion of this paper will appear in a Discussion Section to be published in the June 1984 JOURNAL. All discussions for the June 1984 Discussion Section should be submitted by Feb. 1, 1984.

Rockwell International Corporation assisted in meeting the publication costs of this article.

REFERENCES

1. H. M. Manasevit and W. I. Simpson, *J. Appl. Phys.*, **35,** 1349 (1964).
2. H. M. Manasevit and D. H. Forbes, *ibid.*, **37,** 734 (1966).
3. H. M. Manasevit, D. H. Forbes, and I. B. Cadoff, *Trans. AIME*, **236,** 275 (1966).
4. H. M. Manasevit, *J. Cryst. Growth*, **22,** 125 (1974).
5. I. Golecki, G. Kinoshita, A. Gat, and B. M. Paine, *Appl. Phys. Lett.*, **37,** 919 (1980); **38,** 648 (1981).
6. M. E. Roulet, P. Schwob, I. Golecki, and M-A. Nicolet, *Electron. Lett.*, **15,** 527 (1979).
7. I. Golecki, H. L. Glass, and G. Kinoshita, *Appl. Phys. Lett.*, **40,** 670 (1982).
8. C. Wagner, *Naturwissenschaften*, **31,** 265 (1943).
9. D. W. Strickler and W. G. Carlson, *J. Am. Ceram. Soc.*, **47,** 122 (1964).
10. W. D. Kingery, J. Pappis, M. E. Doty, and D. C. Hill, *ibid.*, **42,** 393 (1959).
11. P. Duwez, F. H. Brown, Jr., and F. Odell, *This Journal*, **98,** 356 (1951).
12. H. G. Scott, *J. Mater. Sci.*, **10,** 1527 (1975).
13. V. S. Stubican, R. C. Hink, and S. P. Ray, *J. Am. Ceram. Soc.*, **61,** 17 (1978).
14. Y. S. Touloukian, "Thermophysical Properties of High-Temperature Solid Materials," Vol. 4, MacMillan Co., New York, (1967); T. H. Nielsen and M. H. Leipold, *J. Am. Ceram. Soc.*, **47,** 155 (1964); V. A. Osipova and V. A. Andrianova, *Tr. Mosk. Energ. Inst.*, **313,** 24 (1976).
15. V. I. Aleksandrov, V. V. Osiko, A. M. Prokhorov, and V. M. Tatarintsev, in "Current Topics in Materials Science," Vol. 1, E. Kaldis, Editor, p. 421, North Holland, Amsterdam (1978).
16. Ceres Corp., Waltham, MA 02154.
17. Singh Industries, Inc., Randolph Park West, Randolph, NJ 07801.
18. W. I. Simpson, Unpublished.

19. I. Golecki, H. M. Manasevit, L. A. Moudy, J. J. Yang, J. E. Mee, and T. J. Magee, To be published.
20. Pacific Spectrochemical Laboratory, Inc., Los Angeles, CA 90064.
21. I. Golecki, H. M. Manasevit, L. A. Moudy, J. J. Yang, and J. E. Mee, *Appl. Phys. Lett.*, **42**, 501 (1983).
22. M. Duclot, J. Vicat, and C. Déportes, *J. Solid State Chem.*, **2**, 236 (1970).
23. For 'blackening' induced by current passage through YSZ, see: D. A. Wright, J. S. Thorp, A. Aypar, and H. P. Buckley, *J. Mater. Sci.*, **8**, 876 (1973); J. M. Farley, J. S. Thorp, J. S. Ross, and G. A. Saunders, *ibid.*, **7**, 475 (1972); J. S. Thorp, A. Aypar, and J. S. Ross, *ibid.*, **7**, 729 (1972).
24. (a) M. Kleitz, M. Lévy, J. Fouletier, and P. Fabry, in "Advances in Ceramics," Vol. 3, p. 337, American Ceramic Society (1981); (b) J. Fouletier and M. Kleitz, *This Journal*, **125**, 751 (1978).
25. I. Golecki, Unpublished thermogravimetric measurements performed at West Coast Technical Services, Inc., Cerritos, CA.
26. T. B. Reed, "Free Energy of Formation of Binary Compounds," MIT Press, Cambridge, MA (1971).
27. R. M. Barrer, "Diffusion In and Through Solids," pp. 14-15, Cambridge University Press, Cambridge, England (1941).
28. J. S. Thorp and H. P. Buckley, *J. Mater. Sci.*, **8**, 1401 (1973).
29. D. W. Readey and G. C. Kuczynski, *J. Am. Ceram. Soc.*, **49**, 26 (1966).
30. J. S. Williams, *Nucl. Instrum. Methods*, **126**, 205 (1975).
31. I. Golecki, H. L. Glass, G. Kinoshita, and T. J. Magee, *Appl. Surf. Sci.*, **9**, 299 (1981).
32. G. W. Cullen and J. F. Corboy, *This Journal*, **121**, 1345 (1974).

Oxidation of Cu_3Sn and Cu_6Sn_5 Films in Room Air from 175° to 250°C

H. G. Tompkins,[1] J. E. Bennett,* J. A. Augis, and T. M. Paskowski

Bell Laboratories, Columbus, Ohio 43213

ABSTRACT

Stoichiometric single-phase samples of Cu_3Sn and Cu_6Sn_5 were fabricated by sputter deposition. These were subsequently heated in air for various times and temperatures. For most of the time-temperature combinations, the resulting film was tens of angstroms thick and primarily an Sn oxide containing some copper. The film growth can be described kinetically with a logarithmic rate law. For the higher temperatures for longer times, when the Cu-to-Sn ratio in the center of the oxide film reached about 1:1, the film growth mechanism changed. This resulted in films several hundreds of angstroms thick which were primarily copper oxide.

One of the most common and oldest means of joining metallic components in the electrical/electronic technologies is soft soldering. From older systems incorporating discrete components to modern integrated circuit systems, there are likely to be many soldered connections. Many such connections are copper or copper base alloy terminations joined with lead-tin solders. It has been extensively documented (1-6) that at the time of solder coating or joining such electrical connectors the tin of the solder reacts readily with the copper of the substrate to form the intermetallic compounds Cu_3Sn and Cu_6Sn_5 and that subsequent thermal treatment will cause continued growth of the compounds. Influence of these compound layers on the mechanical and electrical behavior of the joined region has also been the subject of numerous investigations (7-14).

Conversely, the present work deals with a subtle and unstudied aspect of these intermetallics. Previous work by two of the authors (15) demonstrated that subsequent thermal treatments of thin solder coatings on copper base substrates can result in marked changes in the surface character of the solder. The actual surface may have regions of Cu_6Sn_5 and/or Cu_3Sn exposed to the environment. Obviously, the reactivity of the exposed intermetallics with the environment could have an important bearing on shelf life with regard to solderability of components having such surfaces. This paper reports on the oxidation characteristics of the pure intermetallic compounds. Additional work is in progress comparing solderability of the oxidized *vs.* the unoxidized compounds and will be reported elsewhere.

Experimental

Sample preparation.—Initially, several attempts to prepare the pure compounds were made by conventional induction melting procedures in a protective atmosphere followed by long homogenizing anneals. The Cu_3Sn compound could be prepared in this manner, but the Cu_6Sn_5 compound could not be prepared as a homogeneous single phase. Ingots of the latter were always multiphased, containing Cu_3Sn and/or Sn, even after remelting and high temperature (200°-400°C), long-time anneals (up to 680 hr). This difficulty is attributed to the uncertainty of the composition temperature limits of this phase field in the equilibrium diagram (16); the phase field is narrow and slanting, thus requiring accurate knowledge of actual melt composition and precise control of homogenizing temperatures. Reichenecker (17) had similar difficulty preparing this compound but chose to ignore the minor amounts of the second phases for his thermal expansion measurements. As a consequence of this problem, an alternative procedure was developed for preparing both of the compounds for use in our investigation.

The samples were ultimately prepared by sputter deposition (18) of the compounds onto quartz crystals which are routinely used for thin film deposition thickness monitoring. The equipment used for the deposition was a Sloan S-300 sputtering gun which uses magnetron-enhanced sputtering (where a toroidal magnetic field confines the plasma at the cathode). The sputtering parameters were

Cu_3Sn	445V	0.9A	Substrate temp, 112°-120°C
Cu_6Sn_5	495V	0.9A	Substrate not heated

in 8 mTorr of argon, and metallic films about 3 μm thick were deposited.

The sputter deposition equipment uses a ring cathode, a cylinder 2 cm tall and 8 cm in diameter. In order to employ this equipment, special ring cathode targets had to be developed. They were fabricated by spot welding regions of Sn onto a copper cylinder, as shown in Fig. 1. Because of different sputtering yields, the stoichiometry of the remaining film was not simply

* Electrochemical Society Active Member.
[1] Present address: EG&G Idaho, Incorporated, Idaho Falls, Idaho 83415.
Key words: sputter deposition, corrosion, intermetallics, thin films.

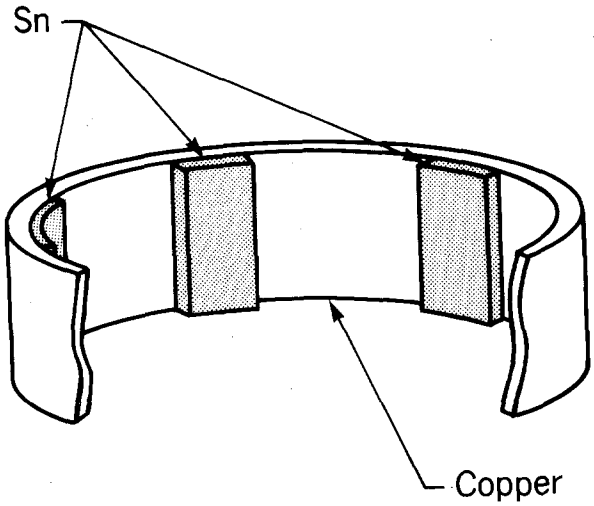

Fig. 1. Ring cathode for sputter deposition shown schematically

the ratio of the areas of the two materials. This is shown in the initial deposition values shown in Table I. If 55% of the exposed area of the cathode is Cu, then the deposited film contains 79% Cu. After some trial and error and guided by energy dispersive x-ray analysis measurements of the film stoichiometry, the required area ratio was determined and this is shown in Table I for each compound. At this point, intermetallic deposits were prepared with the proper stoichiometry using no special sample temperature control. The analysis of the deposits was done by energy dispersive x-ray analysis using pure elements and the Cu_3Sn ingot sample for calibration. They were further analyzed by x-ray diffraction and metallography. The Cu_6Sn_5 samples were found to be single-phase and to exhibit only the Cu_6Sn_5 diffraction lines. The samples deposited with the Cu_3Sn stoichiometry, however, were found to be multiphase, having Cu_6Sn_5 and Cu-Sn B-phase diffraction lines in addition to the Cu_3Sn diffraction lines. By experimentation, it was determined that if the sample temperature was held at temperatures between 110°-120°C during deposition and then quenched to room temperature, the Cu_3Sn samples were single-phase and exhibited only Cu_3Sn diffraction lines.

Heat-treatment.—For the oxidation, the heat-treatments were done in glass tube furnaces which were fabricated by wrapping a 15 mm diam glass tube with a heating tape. The temperature was held constant with a thermistor probe temperature controller and was quite stable for the required times. The tube furnace was constructed with a hot zone which remained within ±3°C over a distance of several inches hence several samples could be heated at the same time. The environment was normal laboratory air with a room temperature relative humidity of about 50%. Temperatures of 175°, 200°, 225°, and 250°C, and heating times varying from 2 to 1000 hr were used. The samples were stored in a desiccator between deposition and heat-treatment and prior to analysis.

Analysis of oxide film characteristics.—The atomic composition and thickness of the oxide films were analyzed using Auger electron spectroscopy (AES) along with argon ion sputter etching. A Physical Electronics Industries instrument was used. Electron beam parameters were 3 kV, 2 μA, and a spot diameter of about 10 μm. Derivative spectra were taken with a modulation voltage of 3V. Ion beam parameters for the sputter etching were 1 kV, 11.7 ± 0.2 $\mu A/cm^2$ average current density (rastering). The sputtering yield is not known for the oxide which forms on these compounds, so the thickness is reported in sputtering time. For illustration purposes, the sputtering rates (measured in the same instrument) for Sn, Cu, and Cu_2O, using the same ion beam parameters, are 35, 14, and 11 Å/min, respectively. A typical spectrum and profile are shown in Fig. 2 and 3, respectively.

Table I. Stoichiometry* vs. relative area of sputter cathode

	Compound	Theoretical %		% area on cathode		% element in deposited film	
		Cu	Sn	Cu	Sn	Cu	Sn
Initial deposition	Cu_6Sn_5	55	45	55	45	79	21
	Cu_3Sn	75	25	75	25	87	13
Final deposition	Cu_6Sn_5	55	45	26	74	52	48
	Cu_3Sn	75	25	47	53	74	26

* As determined by energy dispersive x-ray analysis.

Results

Film composition.—After heating, the resulting films were normally several tens of angstroms thick and composed of Sn, O, Cu, and the usual carbonaceous contamination which occurs on most samples which have been in the air for any length of time. In the typical spectrum shown in Fig. 2, the primary components in the film are Sn and O. All of the films formed did contain some Cu, however. As indicated in the typical profile shown in Fig. 3, the Sn signal rises rapidly as the carbonaceous layer is removed, reaches a maximum, and then decreases to the equilibrium value in the bulk of the metal after the film has been removed. The O signal parallels the Sn signal to some

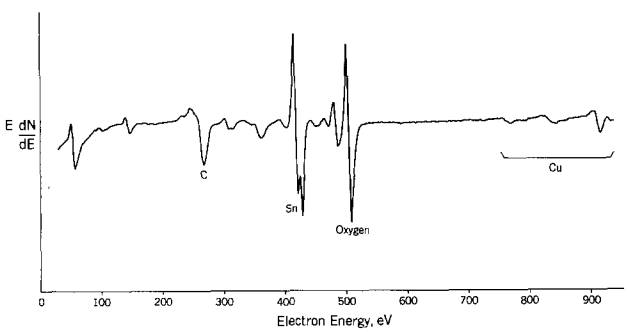

Fig. 2. Typical Auger electron spectrum. Cu_3Sn heated at 200°C for 20 hr.

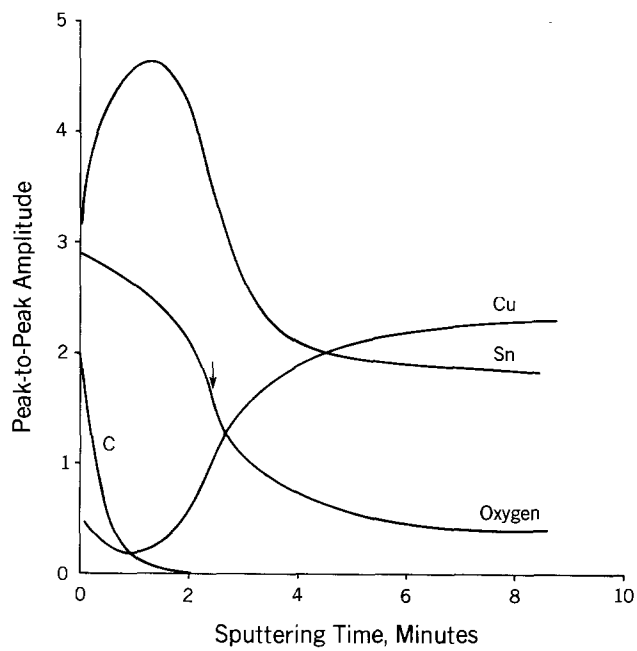

Fig. 3. Depth profile, typical for the films which were essentially tin oxide containing some copper. This was a Cu_3Sn sample heated at 200°C for 20 hr.

extent until the film has been removed. The Cu signal decreases initially, levels out, and then increases to its bulk equilibrium value. Using elemental sensitivity factors from Ref. (19), rough estimates can be made of the concentration of copper in the center of the film. For the lower times and temperatures, the ratio of Cu to Sn is of the order of 1 to 4 for Cu_6Sn_5 and 1 to 2 for Cu_3Sn. For higher temperatures and longer times, the amount of Cu in the film increases. As long as the ratio of Cu to Sn is below about 1 to 1, the O signal parallels the Sn signal and the thickness is several tens of angstroms. When the ratio of Cu to Sn becomes greater than 1 to 1, the situation changes rather abruptly. This is shown in Fig. 4 where the O signal parallels the Cu signal and the thickness is several hundreds of angstroms thick. The film changes from being several tens of angstroms thick to being several hundreds of angstroms thick when it changes from being essentially a "tin oxide" film containing Cu to being a "copper oxide" containing some or no tin. X-ray photoelectron spectroscopy (XPS) measurements suggest that, with the exception of the short time-175°C Cu_6Sn_5 samples, the Sn and Cu are in the Sn(IV) and Cu(II) states, suggesting SnO_2 and CuO. For the short time 175°C Cu_6Sn_5 samples, Sn(II) is a possibility. This tends to be confirmed using quantitative AES analysis where sensitivity factors from Ref. (19) or the values in Ref. (20) are used.

Film thickness.—Let us take the "thickness" of the film, measured in sputtering time, to be that time where the O signal is half of the maximum value, as indicated in Fig. 3 with an arrow. The times to half maximum, measured for all of the heating times and temperatures, are shown in Tables II and III and Fig. 5. The lines in Fig. 5 are intended to show which points go with which temperatures and should not be taken to suggest any particular rate law. As indicated previously, for the higher temperatures and the longer times, the film changes from being essentially a tin oxide to being a copper oxide. These conditions are noted in the tables. Although not observed experimentally, we would expect this changeover to occur for all of the temperatures at times somewhat greater than 1000 hr. No changeover time predictions can be made due to insufficient data.

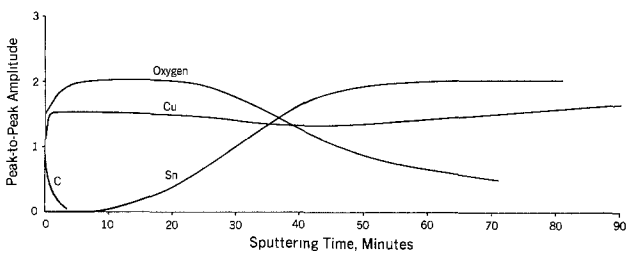

Fig. 4. Depth profile, typical for the higher temperatures at longer times. This is essentially copper oxide containing a little tin. This sample was Cu_6Sn_5 heated at 225°C for 1000 hr.

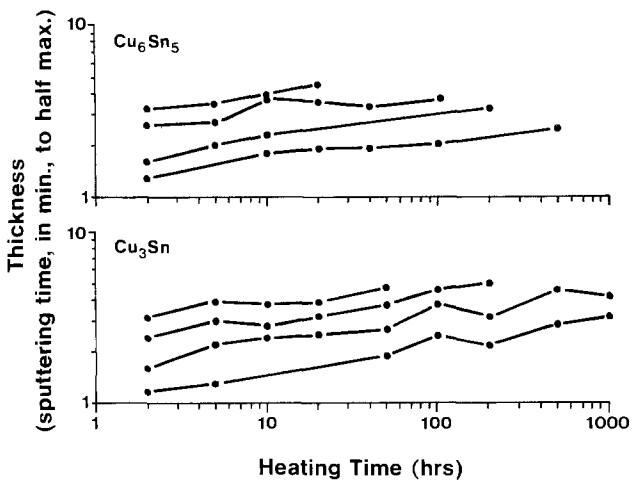

Fig. 5. "Thickness" of the oxide film vs. heating time for various temperatures. The circles refer to Cu_6Sn_5 and the triangles refer to Cu_3Sn. The straight lines are plots of the logarithmic rate law, Eq. [2], with the indicated rate constant *b*.

Table II. Oxide "thickness" for Cu_3Sn for various temperatures (expressed in sputter etch time to half max)

Heating time (Hr)	175°C	200°C	225°C	250°C
	(Min)			
2	1.2	1.6	2.4	3.1
5	1.3	2.2	3.0	3.9
10		2.4	2.8	3.7
20		2.5	3.2	3.8
50	1.9	2.7	3.8	4.7
102	2.5	3.8	4.6	4.6
200	2.2	3.2	5.0	•
506	2.9	4.3	5.3	•
1000	3.2	4.1	6.5	•

* Primarily copper oxide.
Note: With the same sputter etching parameters, the sputtering rates of Sn, Cu, and Cu_2 are 35, 14, and 11 A/min, respectively.

Table III. Oxide "thickness" for Cu_6Sn_5 for various temperatures (expressed in sputter etch time to half max)

Heating time (Hr)	175°C	200°C	225°C	250°C
	(Min)			
2	1.3	1.6	2.6	3.2
5		2.0	2.7	3.4
10	1.8	2.3	3.7	3.8
20	1.9		3.5	4.5
50	1.9		3.3	•
102	2.0		3.6	•
200		3.2	5.4	•
506	2.4		•	•
1000		4.5	•	•

* Primarily copper oxide.
Note: With the same sputter etching parameters, the sputtering rates of Sn, Cu, and Cu_2O are 35, 14, and 11 A/min, respectively.

Discussion and Conclusions

Film growth rate law considerations.—Since we have "thickness" *vs.* time for three orders of magnitude of time, it is reasonable to attempt to draw conclusions about a possible rate law for the film growth for the "tin oxide" films. The data shown in Fig. 5 are plotted on a log-log plot and it is easy to test for a power law such as

$$x^n = kt \qquad [1]$$

A slope of 1/2 on the plot would give the familiar quadratic rate law with $n = 2$. From the figure, it can be seen that if a power law were appropriate, the value of n would be roughly 6. Although rate laws with $n = 2$, 3, or 4 have been demonstrated, values of n as high as 6 are not usually encountered. No first principle model predicts a value this high. Another rate law which is sometimes proposed is the logarithmic rate law

$$x = a \ln(bt + 1) \qquad [2]$$

When this is derived from a first principle model, the rate constant b contains an activation energy term E

$$b = b_0 e^{-E/RT} \qquad [3]$$

where R is the gas constant and T is the absolute temperature.

The value of b can be plotted on an Arrhenius plot to obtain the activation energy E. The data for both Cu_3Sn and Cu_6Sn_5 fit the logarithmic rate law rather well. Figure 6 shows the data plotted on semilog plots. The solid line represents Eq. [2] above. The values of b for the different temperatures are shown in this

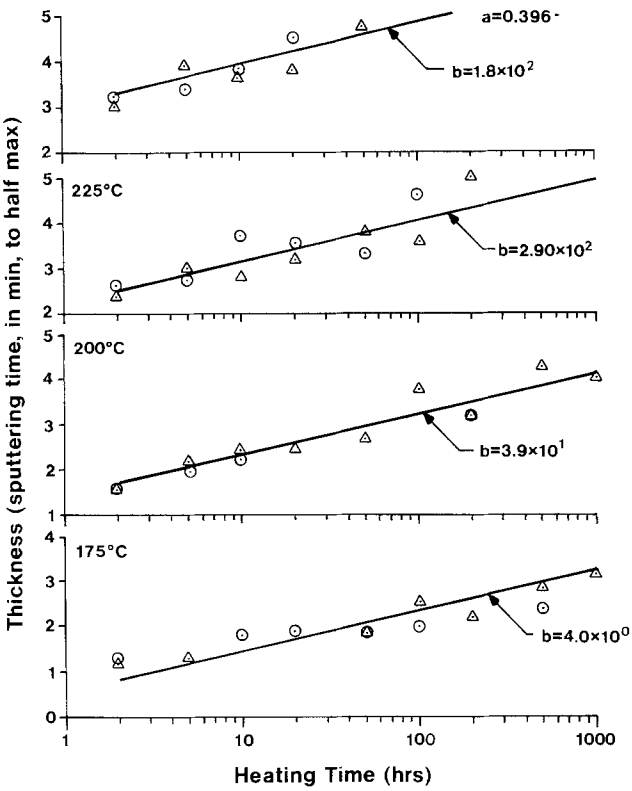

Fig. 6. Data plotted on semilog plots

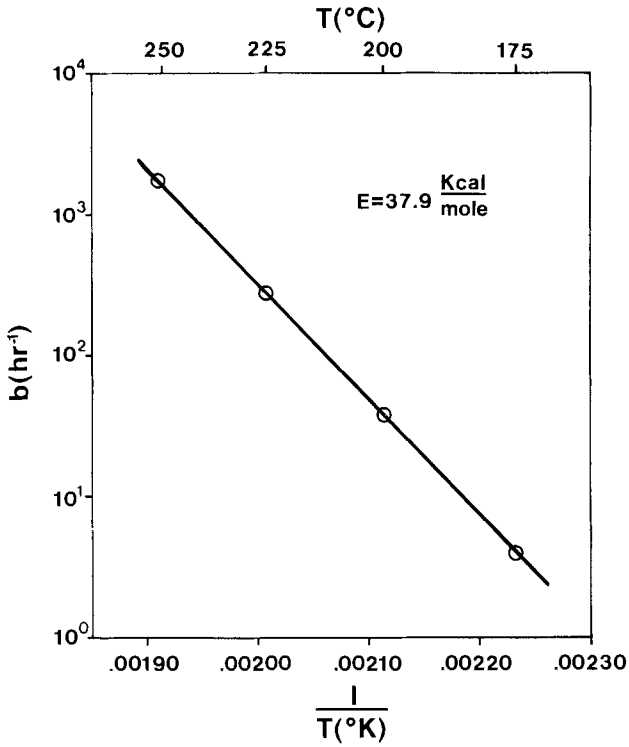

Fig. 7. Arrhenius plot of rate constant *b* from Fig. 6 plotted *vs.* inverse temperature.

figure and are also plotted on an Arrhenius plot in Fig. 7.

Comparisons with Pure Elements

Oxidation of copper and of tin has been studied rather extensively (20-28). Oxidation of pure copper gives films much greater than those obtained with the intermetallic compounds. Pinnel et al. (26) found that a temperature of 150°C (less than the temperatures used herein) produced films hundreds of angstroms thick for times of 5-1000 hr (*e.g.*, about 500Å for 20 hr).

A few samples of pure tin were given the same treatments as the intermetallic compounds. The samples which were heated at 200°C for 20 and 50 hr had films with sputter "depths" of 10 and 20 min (*i.e.*, 100-300Å). Reference (28), using cathodic reduction, suggests that 200-400Å films result from heating Sn at 180° and 210°C for 20 hr.

The key point here is that the film which forms on the intermetallic compounds is much thinner than the film which forms on either of the pure elements alone. This film, particularly while it is still primarily tin oxide, gives significant protection from additional oxidation.

Summary

Using the sputter deposition technique, we have fabricated homogeneous single-phase samples of Cu_3Sn and Cu_6Sn_5. These samples were then heated in room air at temperatures from 175° to 250°C for times varying from 2 to 1000 hr.

For the lower temperatures and the shorter times, the resulting films were primarily Sn oxide containing some Cu. Under these conditions, the films were tens of angstroms thick and grow with a logarithmic rate law. When the copper-to-tin ratio in the film exceeds about 1:1, the film growth mechanism changes and the resulting films are hundreds of angstroms thick and are primarily copper oxide containing very little or no tin.

Manuscript submitted Feb. 11, 1983; revised manuscript received April 22, 1983.

Any discussion of this paper will appear in a Discussion Section to be published in the June 1984 JOURNAL. All discussions for the June 1984 Discussion Section should be submitted by Feb. 1, 1984.

Bell Laboratories assisted in meeting the publication costs of this article.

REFERENCES

1. C. J. Thwaites, *Trans. Inst. Met. Fin.*, **36**, 203 (1959).
2. M. Creydt and R. Fichter, *Metall.*, **25**, 1124 (1971).
3. D. A. Unsworth and C. A. Mackay, *Trans. Inst. Met. Fin.*, **51**, 85 (1973).
4. P. J. Kay and C. A. Mackay, *ibid.*, **54**, 68 (1976).
5. K. N. Tu, *Acta. Met.*, **21**, 347 (1973).
6. K. Kumar, A. Moscaritolo, and M. Brownawell, *This Journal*, 128, 2165 (1981).
7. R. Chadwick, *J. Inst. Metals*, **62**, 277 (1938).
8. G. Faber, *Brown Boveri Review*, **49**, 640 (1962).
9. R. N. Wild, *Welding Research*, **51**, 521s (1972).
10. D. Olsen, R. Wright, and H. Berg, "13th Annual Proc. Reliability Physics," IEEE, 80 (April, 1975).
11. U. Lindborg, *et al.*, *IEEE Trans.*, **php-12**, 33 (1976).
12. C. J. Thwaites and W. B. Hampshire, *Welding Journal*, **55**, 323s (1976).
13. B. T. Lampe, *ibid.*, **55**, 330s (1976).
14. K. Kumar and A. Moscaritolo, *This Journal*, **128**, 379 (1981).
15. J. E. Bennett, T. M. Paskowski, and H. E. Bair, in "Proceedings of 10th North American Thermal Analysis Society Conference," p. 185 (October, 1980).
16. "Metals Handbook," Vol. 8, 8th ed., p. 299, American Society for Metals, Metals Park, OH (1973).
17. W. J. Reichenecker, *Insulation/Circuits*, **27**, 109 (1981).
18. L. Maissel, "Handbook of Thin Film Technology," McGraw-Hill Company, New York (1970).
19. L. E. Davis, N. C. MacDonald, P. W. Palmberg, G. E. Riach, and R. E. Weber, "Handbook of Auger Electron Spectroscopy," 2nd ed., Physical Electronics Ind. Inc., Eden Prairie, MN (1976).
20. A. W. C. Lin, N. R. Armstrong, and T. Kuwana, *Anal. Chem.*, **49**, 1228 (1977).
21. R. O. Ansell, T. Dickinson, A. F. Povey, and P. M. A. Sherwood, *J. Electron Spectrosc. Relat. Phenom.*, **11**, 301 (1977); *This Journal*, **124**, 1360 (1977).
22. T. Farrell, *Metal Sci.*, **10**, 87 (1976).
23. T. L. Barr, *J. Vac. Sci. Technol.*, **14**, 660 (1977).
24. C. L. Lau and G. K. Wertheim, *ibid.*, **15**, 622 (1978).

25. A. Ronnquist and H. Fischmeister, *J. Inst. Metals*, **89**, 65 (1960).
26. M. R. Pinnel, H. G. Tompkins, and D. E. Heath, *J. Vac. Sci. Technol.*, **16**, 161 (1979); *Appl. Surface Sci.*, **2**, 558 (1979).
27. H. Leidheiser, Jr., "The Corrosion of Copper, Tin, and Their Alloys," Krieger Publishing Co., Huntington, NY (1979).
28. S. C. Britton and K. Bright, *Metallurgia*, **56**, 163 (1957).

Changes in Adhesion Forces during Picture Tube Screen Production

E. Scharrer, L. Grimm, H. Mayatepek, and W. Ritsert

Valvo Bildröhrenfabrik der Philips GmbH, 5100 Aachen-Rothe Erde, Germany

ABSTRACT

When luminescent screens are manufactured for color TV tubes, various layers are applied successively to the glass screen. The bonding of the layers to the screen glass and to each other is caused by various forces. These interaction forces affect the adhesion of the different interfaces. The adhesion mechanism of the precoating, phosphor, and lacquer layers and the aluminum backing before and after baking out the luminescent screen are discussed.

Manufacturing the phosphor picture tube screen is, as regards surface chemistry, the most interesting part of picture tube production. Modern color TV tubes have screens with a pattern of some 700 triads of green, blue, and red stripes, each stripe approximately one-quarter of a millimeter wide. To manufacture these screens, adhesion layers are applied one after the other and, during the process, partly or wholly removed again. From the sequenced process involved in producing the picture tube screens, it is obvious how necessary it is to have an optimum and reproducible process control to be able to manufacture at an economic yield. Precise knowledge of the physical and chemical process taking place is therefore very important.

The PVAL Precoat Layer on the Glass Faceplate

The production of phosphor screens starts with precoating the glass faceplate. In order to create a reproducible surface, the inside of the faceplate is washed with hydrofluoric acid and rinsed with an ample quantity of demineralized water. This creates (*i*) a new surface by dissolving the topmost layer of glass, (*ii*) reactive silanole groups from the siloxane groups of the glass surface, and (*iii*) the exchange of cations on the surface of the glass for H^+ ions. Scharrer (1) and Dünewald (2) confirmed this mechanism by experiments with powdered TV screen glass (Fig. 1).

The glass surface, which is still wet, is then covered with a precoat layer of polyvinyl alcohol (PVAL). During the subsequent drying process, covalent bonds are formed with the surface of the glass by an esterification reaction. The OH groups in the PVAL react with the hydrogen in the silanole groups on the surface of the glass (Fig. 2).

Tests on the solubility of the PVAL layer showed that even after treating with water several times, an approximately 0.003 μm thick PVAL layer (more or less monomolecular) remained on the surface of the glass and could only be completely removed with hydrofluoric acid (Fig. 3).

According to Jenkel and Rumbach (4) and Fleer, Koopal, and Lyklema (5), only about 30% of the PVAL chain on the surface of the solid lies flat on it, the rest projecting from the surface in the form of loops or bristles. This projecting PVAL bonds further PVAL molecules via H-bridges (Fig. 4).

The Phosphor Layer

The phosphor suspension for coating the faceplate contains phosphor, PVAL and ammonium dichromate (ADC). The PVAL layer formed in the suspension on the grains of phosphor behaves in the same manner as on the glass surface, forming loops and bristles (4, 5). Probably, a covalent bond of the PVAL with the surface of the phosphor does not exist. It is assumed that H-bridges are developed between the PVAL and the hydration layer of the phosphor surface or the hydrated ions adsorbed on the surface.

ADC and PVAL form the photosensitive system. After flow coating the phosphor suspension (green first) onto the glass surface and drying, the phosphor screen is exposed to ultraviolet light through the slots in the shadow mask. During this exposure, a redox reaction takes place in which the PVAL is oxidized and the $Cr_2O_7^{2-}$-anions are reduced (6).

Key words: phosphor screen, adhesion forces, baking-out changes.

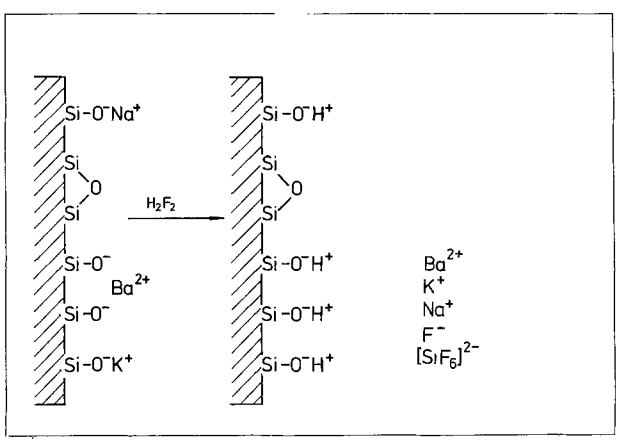

Fig. 1. Surface of glass before and after treatment with hydrofluoric acid.

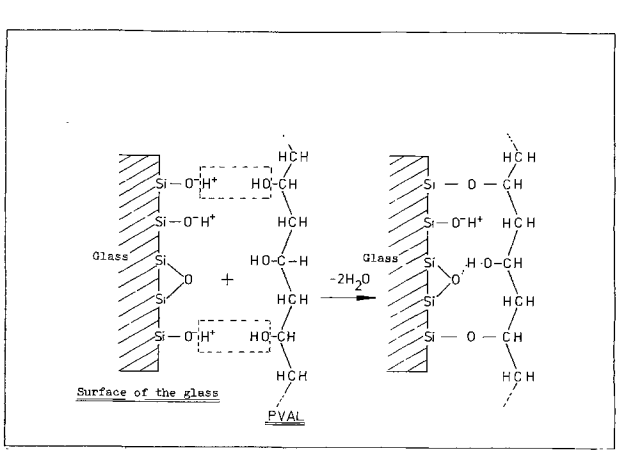

Fig. 2. Glass/PVAL reaction schematic diagram

Drying temperature °C	Solubility mg PVAL in 300 ml demineralized water exposure time 1 min	5 min	10 min	Solubility mg PVAL/screen in H_2F_2 after treatment with 300 ml demineralized water 5 min	Total amount mg PVAL/screen
25	10,7	11,5	11,0	0,9	11,9
38	8,7	9,5	10,7	0,9	11,6
50	7,3	8,6	10,5	0,9 - 1,2	11,4 - 11,7
	soluble in water			insoluble in water	

The figures given are mean values from 3 to 5 measurements.

Determination of PVAL according to Horacek, Zeitschrift fur Analytische Chemie 199 (1964), page 220.

The proportion of PVAL insoluble in water falls, if the screen is put aside for a period of time (0,5 and 24 hours) between washing (H_2F_2) and rinsing with H_2O, thus permitting the silanole groups to decrease. Unwashed screens have the same low values as they would have if put aside for 24 hours after washing.

Fig. 3. Solubility of the PVAL precoat layer

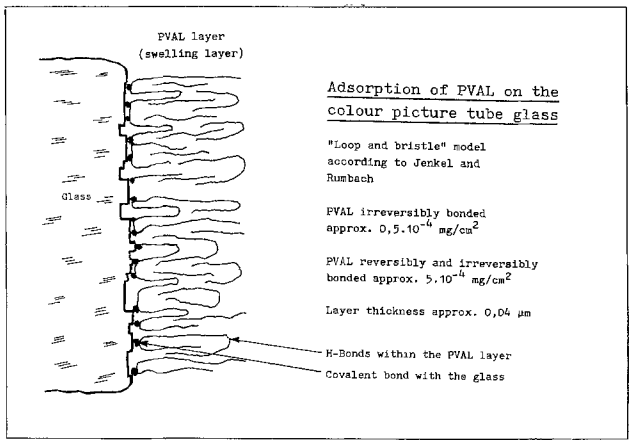

Fig. 4. Adsorption of PVAL on the color picture tube glass

The PVAL oxidation products form complex compounds with the Cr^{3+} cations reduced from the $Cr_2O_7^{2-}$-anion. Complex bonding prevents swelling up and thus removal of the PVAL (Fig. 5) (7).

It is assumed that the thickness of the hardened PVAL layer on the phosphor surface is of the same magnitude as on the glass surface (0.04 µm). The reasons for this statement are as follows: the loss of weight in flow-coated u.v.-hardened and developed phosphor particles under baking-out conditions (heating up 10°/min to 450°C, 1 hr holding time and cooling down) is 3g PVAL/100g. This is less than half of the PVAL content in the phosphor suspension (7.6g PVAL/100g solid matter).

As one can see from microphotographs made with an electronmicroscope (magnification 4,600×), there is a lot of PVAL in the angles and the pores of the phosphor particles. Along the contact points between the phosphor particles, the PVAL layer thickness must be smaller than 0.1 µm, which was calculated from the loss of weight (3 g/100g) and the surface area of the phosphor powder (average surface area 0.2 m^2/g). Assuming that the thickness of the PVAL layer on the phosphor particles at the contact points is about the same as on the glass surface and that 2-3 phosphor particles (average grain size 5-8 µm) make up the thickness of the phosphor layer, then all the PVAL layers between the phosphor particles and the glass surface together have a thickness of about 0.20 µm.

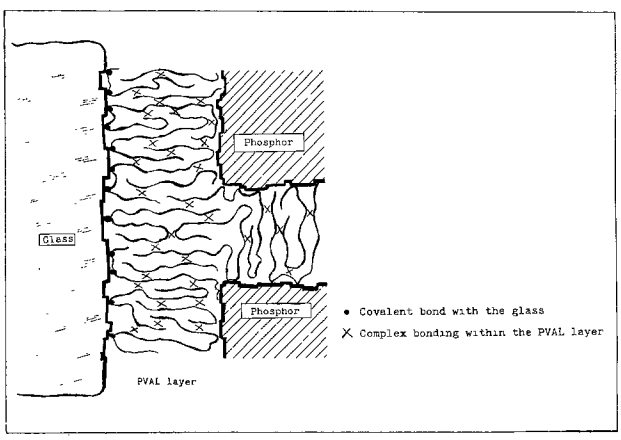

Fig. 5. "Loop and bristle" model after the PVAL/ADC u.v.-photoreaction.

Development with demineralized water at about 30°C which then follows, causes the unexposed portions of the phosphor to swell up again. In other words, these portions are washed off. The exposed portions form the desired pattern (stripes) of the first phosphor layer. After subsequently drying this layer, phosphor stripes of the other two colors (blue and red) are applied in turn in identical process sequences (flow-coating, drying, exposure, development, and drying).

It is concluded that the phosphor particles are bonded to the glass faceplate via the PVAL layers around the phosphor surface and the glass surface. The PVAL loops and bristles of the glass surface and the phosphor particles are fixed together via the complex bonding system.

The Lacquer and Aluminum Layer

To reflect the light excited in the phosphor by the electron beam in the direction of the viewer and thus to enhance the screen brightness, aluminum is evaporated onto the rear of the luminescent screen. To prevent the aluminum from penetrating into the porous layer of phosphor when evaporation of the aluminum onto the phosphor under high vacuum is taking place, it is necessary to provide a foundation layer for the aluminum. The most suitable foundation for use in picture tube production is usually a film of lacquer made up from a mixture of polymethacrylate and polyacrylate. The lacquer film can be produced in various ways: (*i*) by spraying on the lacquering substance dissolved in an organic solvent and (*ii*) by flow coating on a stabilized dispersion.

In both lacquering processes, the phosphor layer is wetted again. This means that the pores between the particles of phosphor are filled by the aqueous phase. Due to their size, the lacquer droplets which form the dispersion do not penetrate into the interstices but rather remain on the surface of the phosphor coating. In the spraying process, lacquer droplets are formed on the surface. If a solution of PVAL is used as a wetting agent, a relatively stable emulsion of lacquer droplets of the "oil-in-water" type is created during spraying (8).

In Fig. 6, the various stages of lacquer film creation are shown. While drying, the lacquer droplets coalesce and form a continuous film of lacquer, adhering to the phosphor particles via the H-bridges of the PVAL layers (Fig. 7, 8).

The thickness of the lacquer layer which has been determined by dissolving and weighing the lacquer is 1.5 µm. Aluminum is then evaporated onto this lacquer coating under high vacuum, approximately 10^{-7} bar. The process is designed to provide a layer approximately 0.25 µm thick in the middle of the luminescent screen. After evaporation, this extremely thin layer of aluminum follows the contours of the lacquer film exactly. It adheres to the layer of lacquer due to dispersion forces (Fig. 9).

Baking Out the Screen

Since organic substances are not stable in a high vacuum and organic polymers also have a certain vapor pressure coming from residual monomers and from decomposition or depolymerization which would upset the functioning of the color picture tube and shorten

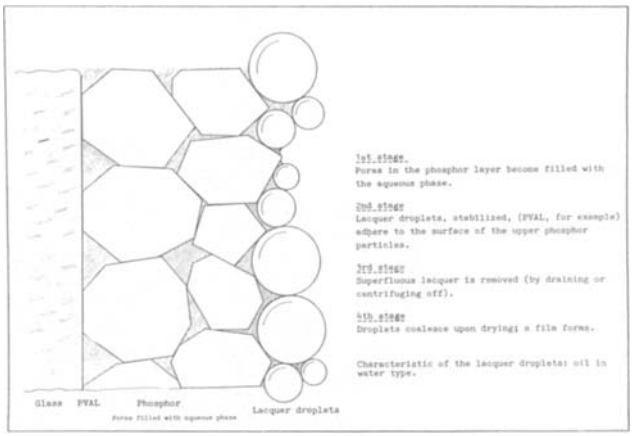

Fig. 6. Creating the lacquer film

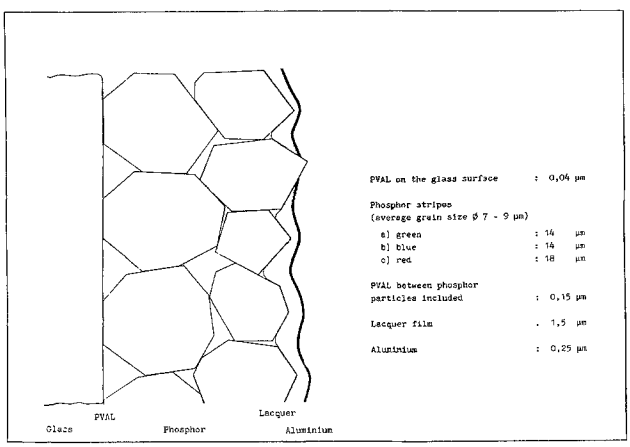

Fig. 7. Structure of the layers on the luminescent screen before bakeout.

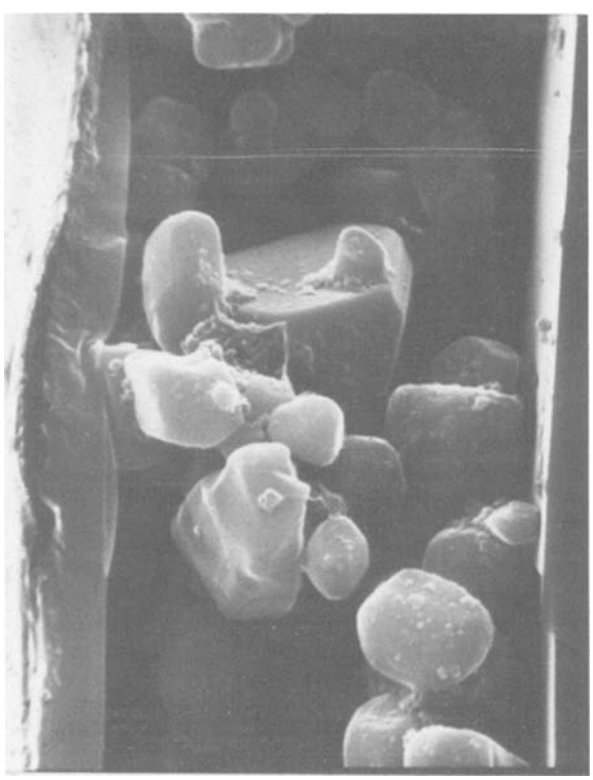

Fig. 8. Layer structure of the phosphor before bakeout. EM photo magnification 1,600× (magnification of the photo 45,000×).

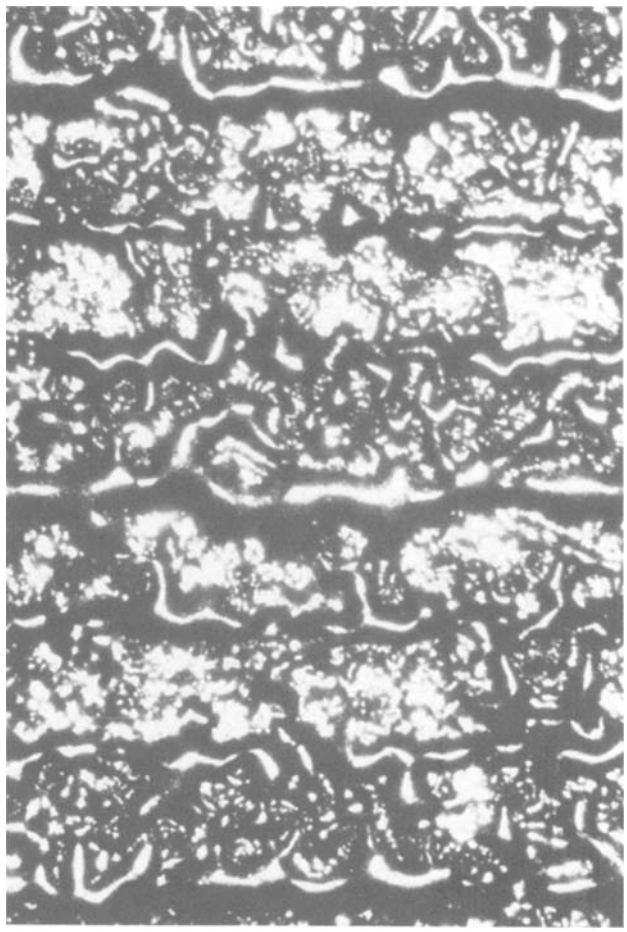

Fig. 9. Aluminum layer in reflected light (with lacquer film). Microphoto, magnified 100× (magnification on the photo 400×).

its life, the organic matter has to be removed again by baking out. During this bakeout, the polymethacrylate/polyacrylate film depolymerizes almost completely. Depolymerization takes the form of a chain reaction; after the initial reaction, the monomers are split off from the end of the chain like a zipper (9) (Fig. 10).

The PVAL is broken down during the bakeout. According to Kaesche-Krischer and Heinrich (10), there is merely dehydration in the first phase up to 260°C. The loss of weight during this initial stage is approximately 32%. At higher temperatures in the second phase, a mixture of various hydrocarbons is created. Above 390°C, the carbon structure collapses (Fig. 11).

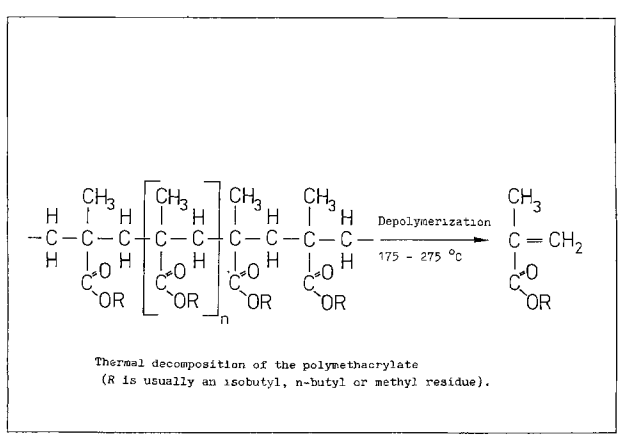

Fig. 10. Depolymerization reaction of the lacquer film in the course of baking out the luminescent screen.

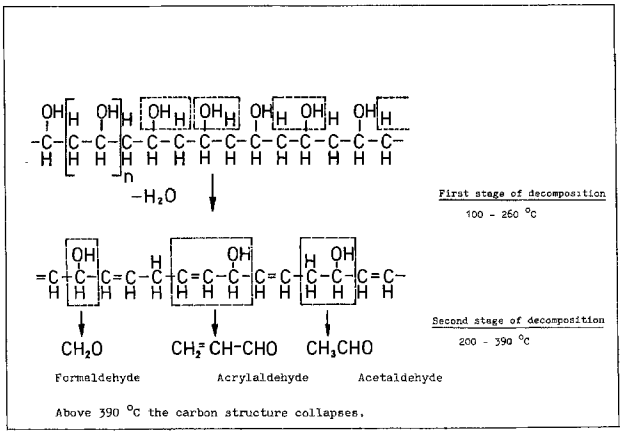

Fig. 11. Decomposition reaction of the PVAL layers in the course of baking out the luminescent screen.

Depolymerization of the lacquer film commences at temperatures above approximately 175°C. Simultaneously, the first phase of the decomposition of the PVAL starts. Above 260°-280°C, after the lacquer film has been decomposed, the subsequent phases of decomposition of the PVAL take place. The monomers and other products of decomposition diffuse through the aluminum backing. These relatively slow processes avoid damaging the phosphor or blistering the aluminum backing by preventing rapid formation of gaseous products.

In addition, decomposition takes place from the coating side inwards; this means that the PVAL layers on the surface of the glass are broken down last. The presence of any PVAL after baking out could not be proved with the iodine/boric acid (3) reaction.

For direct proof of the change in the PVAL layers and the lacquer film, the thickness of the coatings was measured before and after bakeout. The measurements, carried out on the green phosphor stripe without lacquer by means of a light section microscope, showed that the phosphor layer had decreased in thickness by roughly 10%, *i.e.*, approximately 1.5 μm (Fig. 12).

This decrease is markedly greater than all the PVAL layers before bakeout on the surfaces of the phosphor and glass at the contact points. Obviously, the phosphor layer must have become more compact. This reduction in the distance between surfaces leads us to conclude that ions on the surface of the solids in contact have changed place due to the heat-treatment, resulting in sintering. At the same time, ion bonds have occurred. The reduced spacings also favor the dispersion forces (Fig. 13).

This has been confirmed also by measurement of grain-size distribution (green phosphor): before bakeout, average 7.08 μm

	n	$\bar{x}$ µm	s µm
1.) before baking out	10	16,0	1,0
2.) after baking out	10	14,5	1,6

Difference in the two series of measurements

Δ = 1,5 µm

The measurements were carried out on the green phosphor stripe without a lacquer film, using a light section microscope.

Fig. 12. Layer thickness measurements

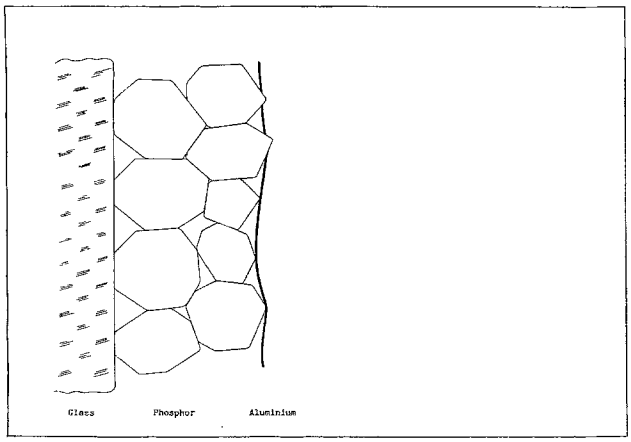

Fig. 13. Structure of the layers on the luminescent screen after bakeout.

<5 μm 17%

<10 μm 14.8%

and after bakeout, average 7.7 μm

<5 μm 12%

<10 μm 21%

Adhesion Measurements

What influence has the baking-out procedure on the adhesion of the phosphor particles to each other and to the surface of the glass? To establish this, adhesion tests were carried out on screens that had been through the various stages of the manufacturing process. The method used was to direct a jet of water of a certain size against various positions on the screen for a certain time. The pressure of the jet of water was increased until a hole became clearly visible. The pressure of the jet, measured by the differential pressure method with a mercury manometer, is the indicator of the adhesive strength. This test, which was done several times on lacquered and unlacquered phosphor screens before and after bake out, indicated no decrease in the adhesive strength of the phosphor layer to the glass after bakeout (Fig. 14). Even after three bakeouts, there was no change.

No difference was found in the adhesion of the phosphor particles to one another nor to the glass either. This confirms the supposition that powerful adhesion forces have been created by the bakeout. When watching the formation of the hole by the water jet, the hole in the screen is seen to occur and is immediately visible on the glass surface.

Composition of layer	Not baked-out	Baked-out once	Baked-out three times
Phosphor sedimented in H_2O	< 1	> 67	-
Phosphor suspension (+ PVAL and ADC) not exposed	1,5	> 67	-
Phosphor suspension (+ PVAL and ADC) after exposure to ultraviolet light	> 67	> 67	> 67

Fig. 14. Adhesion measurements on phosphor coatings (green); adhesive strength stated in kPa.

The Aluminum Layer after Baking

The attaching mechanism of the phosphor layers to the aluminum is also changed by baking-out. The foundation layer of lacquer, previously between phosphor and aluminum, has been completely removed, leaving empty spaces in between. Figure 15 shows the aluminum lacquer in transmitted light. One can see several holes in the aluminum layer.

The aluminum skin is now only attached to those points where it is lying on the phosphor crystals or where holes have been made in the former lacquer coating by sharp points in the phosphor layer during the drying process. It has been proved by several experiments that the adhesion of the aluminum increases with the number of holes. The adhesion of the aluminum layer is affected by dispersion forces in those places where the aluminum is in close contact with the phosphor or by mechanical forces (clamping phenomena). Figure 16 shows an electron microscope photo of a hole where the aluminum is attached.

Conclusion

From the experiments and conceptions on the adhesion of phosphor layers in color picture tubes before and after bakeout, the following can be concluded for the changes in adhesion forces:

1. In the course of luminescent screen production, PVAL and the polymethacrylate/polyacrylate film form high molecular intermediate layers. The PVAL layers adhere to the surface of the solids, partly by covalent bonds with the glass and partly by H-bridges of the PVAL molecules with the phosphor and lacquer. The aluminum baking, evaporated onto the lacquer, adheres by dispersion forces.

2. Exposure of the flow-coated phosphor screen to ultraviolet light irreversibly changes the PVAL in the PVAL/ADC intermediate layer itself. It loses the ability to swell up. After the photoreaction the oxidized compounds of the PVAL molecules become complex bonds, with Cr^{3+} as the complex forming ion.

3. During bakeout, all the intermediate layers of the phosphor screen are removed. The phosphor layer becomes more compact. Adhesion is affected by directly influencing the surfaces with respect to each other by means of sintering (ion bonding) by dispersion forces and by mechanical forces.

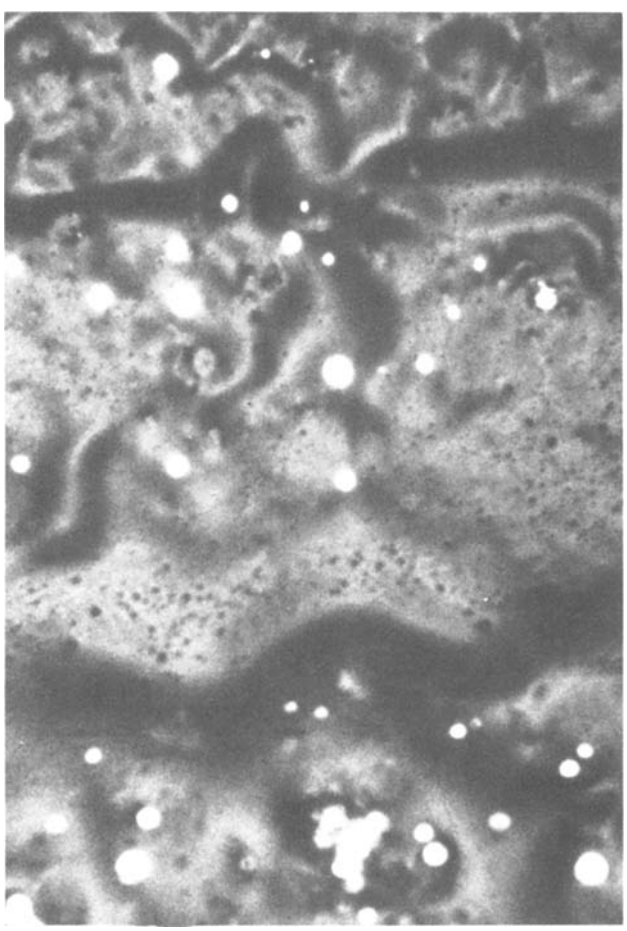

Fig. 15. Aluminum layer in transmitted light. Magnified 100× (magnification on the photo 400×).

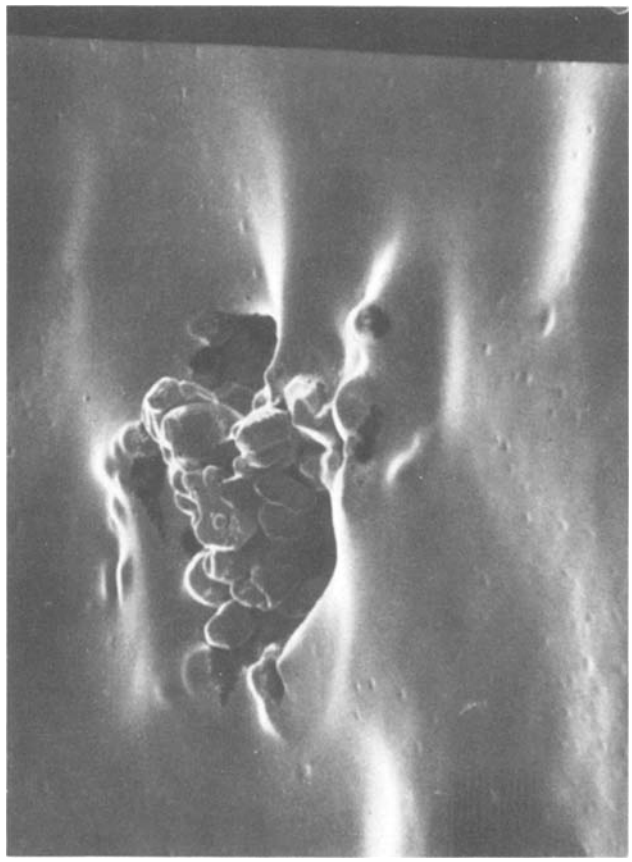

Fig. 16. Electron microscope photo of a point of attachment for the aluminum backing. Magnified 5,600× (magnification on the photo 15,000×).

Manuscript submitted Feb. 1, 1982; revised manuscript received *ca.* Dec. 1, 1982. This was Paper 218 presented at the St. Louis, MO, Meeting of the Society, May 11-16, 1980.

Any discussion of this paper will appear in a Discussion Section to be published in the June 1984 JOURNAL. All discussions for the June 1984 Discussion Section should be submitted by Feb. 1, 1984.

Valvo Bildrohrenfabrik der Philips GmbH assisted in meeting the publication costs of this article.

REFERENCES

1. E. Scharrer, *Angew. Chem.*, **75,** 1108 (1963); *Valvo Berichte,* **10,** 101 (1964).
2. F. A. Dünewald, Dissertation, RWTH Aachen, Aachen, Germany (1967).
3. J. Horacek, *Z. Anal. Chem.*, **199,** 220 (1964).
4. E. Jenkel and B. Rumbach, *Z. Elektrochem.*, **55,** (1951).
5. F. J. Fleer, L. K. Koopal, and J. Lyklema, *Kolloid Z. and Z. Polymere,* **250** (1972).
6. B. Duncalf and A. S. Dunn, *J. Appl. Polym. Sci.*, **8,** 1763 (1964); K. Schläpfer, Dissertation ETH (1965).
7. L. Grimm, K.-J. Hilke, E. Scharrer, and U. Schlenker, *Valvo Ber.*, **18,** 77 (1974); to be published in *This Journal;* E. Scharrer, L. Grimm, and K.-J. Hilke, *Chemie in Unserer Zeit,* **9,** 163

(1975).
8. E. Scharrer, L. Grimm, K.-J. Hilke, and U. Schlenker, *Valvo Ber.*, **19**, 41 (1974).
9. H. Rauch-Puntigam and T. Völker, "Acryl- und Methacrylverbindungen," Springer-Verlag, Berlin (1967).
10. B. Kaesche-Krischer and H.-J. Heinrich, *Chem. Ing. Techn.*, **32**, Parts I and II (1960).

The Mechanism of the Cross Linking of Poly(Vinyl Alcohol) by Ammonium Dichromate with U.V.-Light

L. Grimm, K.-J. Hilke, and E. Scharrer

Valvo Bildröhrenfabrik der Philips GmbH, 5100 Aachen-Rothe Erde, Germany

ABSTRACT

The phosphor raster of color TV screens is produced by the exposure of photosensitive coats to ultraviolet light. On the basis of existing papers and our own experiments, a model is presented showing the mechanism of the photosensitive reaction between poly(vinyl alcohol), ammonium dichromate, and water. A complex redox reaction takes place between the three components, leading to chromium (III) ions and poly(vinyl alcohol) cleavage products with terminal carboxyl groups. There is interaction to chelate complexes, thus resulting in a three-dimensional poly(vinyl alcohol) network insoluble in water.

During the production of color TV screens, a phosphor raster is created by exposing photosensitive coatings to ultraviolet light. The photosensitive layer consists of phosphor, poly(vinyl alcohol) (PVAL), ammonium dichromate (ADC), and water. A high pressure mercury-vapor lamp is used as the source of ultraviolet light. The actual photosensitive system comprises ammonium dichromate, poly(vinyl alcohol), and water, so the phosphor need not be taken into account when further considering the photoreaction.

Poly(vinyl alcohol) is a thread-like polymer with a molecular weight of approximately 100,000. This corresponds to approximately 2500 monomer molecules. Poly(vinyl alcohol) is soluble in water. Figure 1 illustrates a section with two building blocks. The OH groups are arranged in a 1,3 position. They are attached to a secondary carbon atom and correspond in their characteristics to the hydroxyl groups of secondary alcohols.

The second part of Fig. 1 shows the smallest analogous polyol, 2,4-pentanediol. This compound was taken as a model substance for the experiments on the oxidation of PVAL by chromate described below.

In the presence of water, ammonium dichromate reaches an equilibrium with ammonium hydrogen chromate

$$[2(NH_4)^+] + Cr_2^{VI}O_7^{--} + H_2O \rightleftharpoons 2HCr^{VI}O_4^- + [2(NH_4)^+]$$

Both types of ions act as oxidants. Their maximum light absorption level is around 360 nm. In both compounds, the chromium is hexavalent. Figure 2 reproduces the absorption spectrum of an ammonium dichromate solution in connection with the emission spectrum of a high pressure mercury-vapor lamp. The reciprocal effect between ammonium dichromate and ultraviolet light is possible, because the absorption maximum of the ammonium dichromate and a strong emission line of the mercury-vapor lamp both lie around 360 nm.

That poly(vinyl alcohol) is oxidized and chromium(VI) is reduced to chromium(III) during the photoreaction has been known for a considerable time.

Schläpfer (1) formulated, for example, the oxidation of a hydroxyl group of the PVAL to a keto group as the reaction of a secondary alcohol with ammonium dichromate

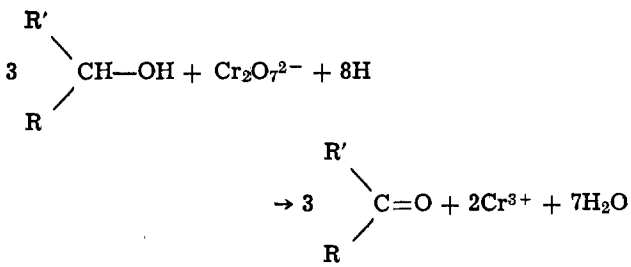

Schläpfer (1). Duncalf and Dunn (2, 3), van Nice and Farlee (4), all assume that complexing occurs between the chromium(III) thus formed and the PVAL, joining the PVAL chains together to create a three-dimensional network. This makes the PVAL insoluble in water. There are varying views on the nature of the complex formation.

Our own research (5, 6) indicates that the oxidation of PVAL with ADC continues until the molecular chains are split. Subsequently, true chelate complexes form with chromium(III). Two facts would seem to support this result: (*i*) The loss of viscosity in a

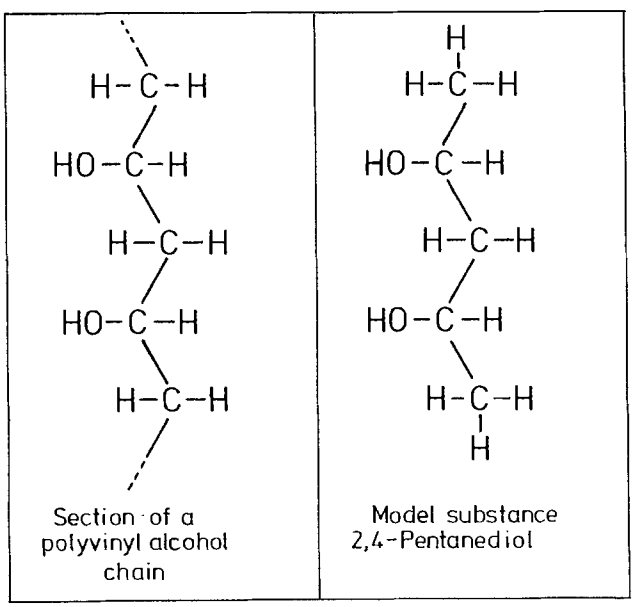

Fig. 1. Poly(vinyl alcohol) (PVAL)

Key words: dark reaction, chain cleavage, model substance 2,4-pentanediol.

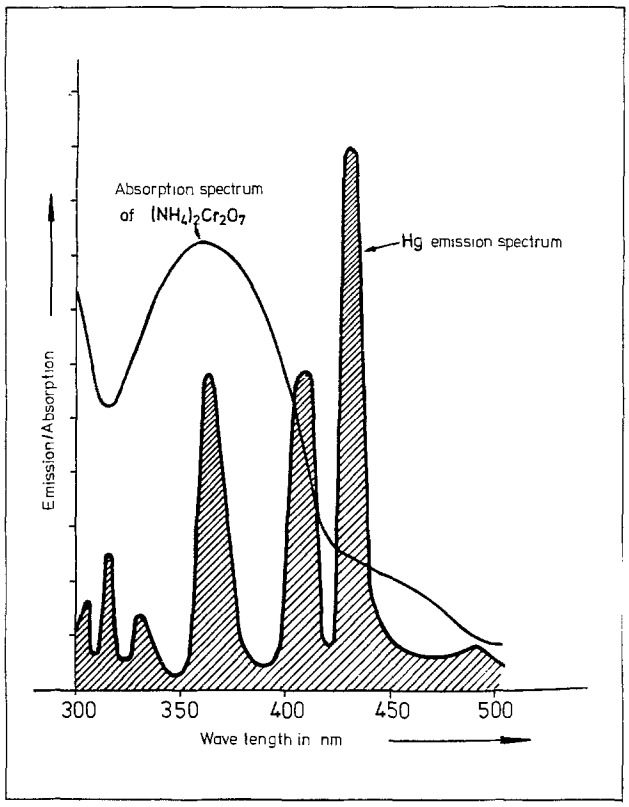

Fig. 2. Emission spectrum of a high pressure mercury vapor discharge lamp and absorption spectrum of ADC.

phosphor suspension and (*ii*) experiments with 2,4-pentanediol as a model substance for PVAL

Figure 3 shows how the viscosity in a photosensitive phosphor suspension behaves as a function of time. The readings were taken on freshly made-up phosphor suspensions to the exclusion of ultraviolet light. A redox reaction takes place in these suspensions which is known as the "dark reaction." The proof that a redox reaction occurs is that the chromium(III) contained in the suspension increases at the same time. After 24 hr, roughly 4% of the original chromium(VI) is present in the form of chromium(III) due to the dark reaction (Fig. 4).

In addition to this, the *p*H-value rises during this period from 5.3 to 5.8, since protons are consumed during the chromate oxidation. Our experiments indicated that the dark reaction ceased after several days at a chromium(III) content of 6-7% of the original chromium(VI). The *p*H value rose from 0.5 to 0.7 *p*H units. Presumably, the rise in the *p*H-value limits the dark reaction.

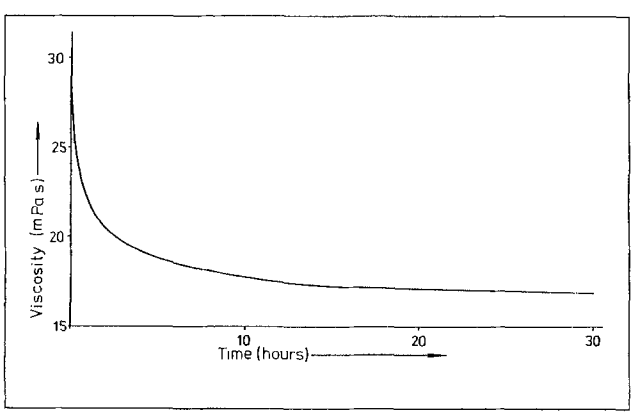

Fig. 3: Viscosity behaviour of a phosphor suspension

Fig. 3. Viscosity behavior of a phosphor suspension

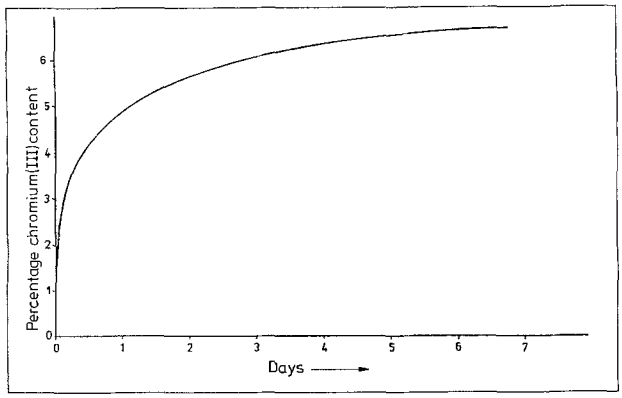

Fig. 4. Increase of chromium (III) in phosphor suspensions dependent on time (dark reaction).

The surprising fact that a redox reaction between PVAL and ADC can take place even without the effect of light led to a thorough investigation of the dark reaction. We discovered that in a dilute aqueous solution of PVAL and ADC, corresponding in concentration to a phosphor suspension, no measurable formation of chromium(III) ions and no loss of viscosity took place within the period of one week. If, however, a sulfidic phosphor or dissolved sulfide ions are added, the dark reaction described above can be observed. It is not possible to induce a dark reaction with oxidic phosphors or insoluble oxides such as SiO_2, Al_2O_3, or TiO_2. It may, therefore, be assumed that in the case of the dark reaction, the redox reaction between PVAL and ADC is induced by a reaction between sulfide ions and ADC.

It is true the photoreaction is initiated in a different manner from the dark reaction, but it may be assumed that during the course of the dark reaction, the same reaction sequence with respect to the oxidation of the poly(vinyl alcohol) occurs as in the layer. There will, however, be a considerably slower reaction rate. This would appear to be confirmed by the fact that, similarly to the dark reaction, the formation of chromium(III) ions is limited in the photoreaction as well. A maximum of about 25% of the chromate present can be reduced to chromium(III), as our experiments have shown. The view that the dark reaction has an analogous reaction sequence is supported by the fact that the flow-coated layers become insoluble by a sufficiently long dark reaction.

According to Staudinger's theory (7), the loss in viscosity observed means a lowering of the mean chain length, *i.e.*, PVAL chains must be getting cleaved. A reduction in viscosity due to hydrolysis can be discounted. Neither the acid reaction of the dichromate ions, nor the presence of solid surfaces alone influences the viscosity of the PVAL solution, as our experiments have indicated.

The object of our work is to investigate in greater depth the sequence of PVAL oxidation by ADC. Since Duncalf and Dunn's (2) experiments have shown that it is difficult to prove the existence of intermediate products during PVAL oxidation, we have used—as Schläpfer did—2,4-pentanediol as a model substance for some experiments. While Schläpfer (1) used a surplus of ADC, we have used an ADC/2,4-pentanediol ratio corresponding to the quantities of ADC and PVAL in phosphor suspensions. During the course of our experiments, we made the following observations: 2,4-pentanedione (acetylacetone) forms a very stable chelate complex, chromium acetylacetonate, with chromium(III) (8). If 2,4-pentanediol, our model substance for PVAL, were to be oxidized with ADC to a diketone, chromium acetylacetonate would also be bound to form. However, we found upon treating 2,4-pentanediol with ADC not chromium acetylacetonate or 2,4-pen-

tanedione but 3-penten-2-one (9). This means that dehydration takes place after the oxidation of the first hydroxyl group to a ketone group. The existence of these reaction products was proved by gas chromatography and infrared spectroscopy with the aid of synthesized comparative substances (Fig. 5).

We must, therefore, exclude the possibility of the PVAL being oxidized to a diketone grouping and thus the formation of a similar complex with chromium(III) to that forming with acetylacetone.

Unsaturated ketones are, nevertheless, very liable to oxidation and easily cleaved. These findings have led us to put to discussion the following model for the mechanism of the photoreaction between PVAL and ADC. For the start of the photoreaction, we have taken over the mechanism of the oxidation of a secondary alcohol with ADC, according to Weber and Asperger (10), designed on the basis of kinetic investigations into the photochemical oxidation of glycerine with dichromate. The first photochemical reaction, accordingly, consists of an electron in the hydrated dichromate ion being raised to a higher level by the adsorption of light. This makes the ion unstable and it decays, forming chromium trioxide, an unstable monomeric intermediate (first reaction). As is well known, chromium trioxide is a strong Lewis acid and is able to form an ester with an OH-group of the poly(vinyl alcohol) (second reaction)

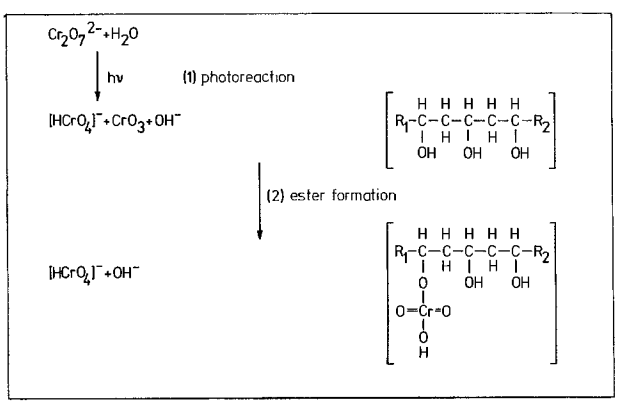

Chromium esters, as intermediate stages during the oxidation of alcohols, were detected by Westheimer (11, 12, 13), Kläning (14, 15), and Carrington (16). It may, therefore, be safely assumed that the chromate oxidation of a secondary alcohol takes place via the formation of a chromate alcohol ester (17). These esters are not very stable and are also sensitive to light, as Kläning (14, 15) has shown. They decompose easily upon exposure to ultraviolet light, creating a keto group and a compound of tetravalent chromium in the process (third reaction)

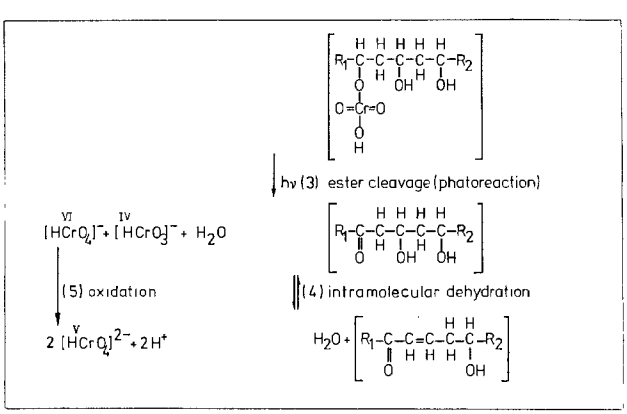

In the literature, only the third reaction (ester cleavage) is considered to be a photosensitive reaction. We are of the opinion that Weber and Asperger's mechanism (first photoreaction) can also be integrated in the photoreaction scheme as favoring the formation of chromium esters. It is generally assumed (17) that the first step in the redox reaction between chromate and alcohol is a two-electron reaction, as was formulated here. Nice and Farlee (4) have another interpretation. They conclude from EPR measurements, in which chromium(V) occurred as an intermediate stage, that the PVAL-Cr(VI) ester becomes a PVAL-Cr(V) ester via a charge transfer process by absorbing radiation during exposure. That chromium(V) can also be present as a result of another subsequent reaction will be shown later. The partly oxidized poly(vinyl alcohol), occurring as a result of the third reaction, does not at first oxidize further. Instead, intramolecular dehydration sets in, as we have shown by our model experiments. The formation of an α,β-unsaturated ketone group (fourth reaction) takes place. The low water content in the coating favors this reaction. Duncalf and Dunn (2) also discovered unsaturated ketone groups in partly oxidized PVAL films. The fourth reaction is an equilibrium reaction, similar to the equilibrium described by Pressman *et al.* (18), between mesityl oxide and diacetone alcohol. Resultant reactions will displace this equilibrium in the direction of a dehydration.

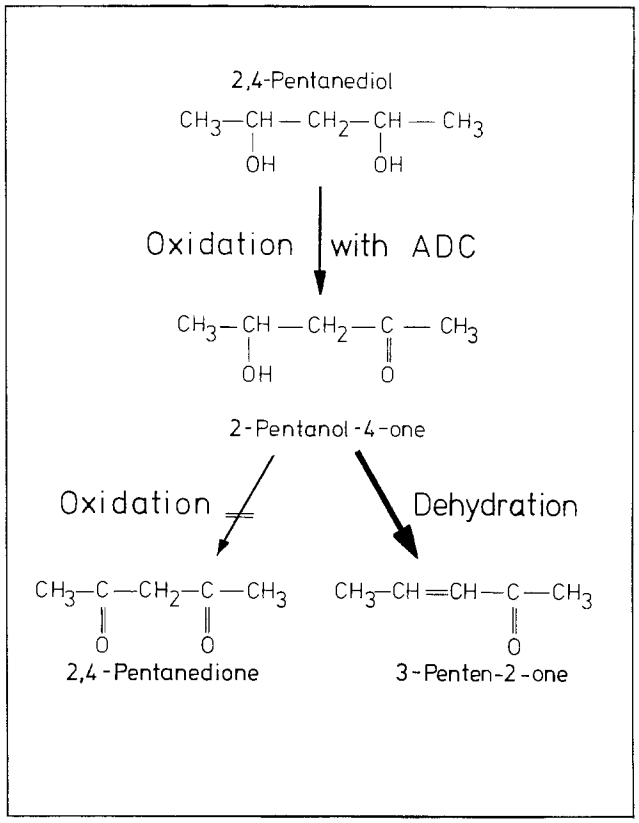

Fig. 5. Oxidation of 2,4-pentanediol

Presence of chromium(V) as an intermediate stage in the oxidation of alcohol has been proved by several authors (3, 11, 19) and so can be reckoned to be certain. It may also be assumed that this chromium(V) oxidizes alcohol or intermediate products of the alcohol oxidation in a two-electron reaction and becomes chromium(III) in the process. However, there are various views on how chromium(V) is formed.

On the one hand, there is the viewpoint of Westheimer *et al.* (12); according to this, Cr(IV) is oxidized by Cr(VI) to Cr(V)

$$\mathrm{Cr(IV)} + \mathrm{Cr(VI)} \rightarrow 2\,\mathrm{Cr(V)}$$

This mechanism is supported by the experiments of Haight *et al.* (20) and also by Bontchev *et al.* (21). But,

on the other hand, there is the opinion held by Rocek *et al.* (22, 23) that the Cr(IV) reacts with more alcohol, forming a radical and Cr(III). The radical plus Cr(VI) then yields Cr(V) and becomes a ketone

$$R_2CHOH + Cr(IV) \rightarrow R_2\dot{C}OH + Cr(III)$$

$$R_2\dot{C}OH + Cr(VI) \rightarrow R_2C{=}O + Cr(V)$$

Experiments by Rocek *et al.* (22) and Wiberg *et al.* (19) tend to support the radical mechanism. Both authors worked under reaction conditions which in some respects were considerably different to those existing in the photosensitive phosphor suspension. As the reaction conditions in the case of Bontchev *et al.* resemble those in PVAL oxidation most, we decided to use the Westheimer mechanism and have formulated the fifth reaction accordingly: the Cr(IV) is oxidized to Cr(V) by Cr(VI), which, being a very strong oxidant, reacts preferentially in the course of the process.

Compounds with double bonds, which are also polarized by the proximity of keto groups, are liable to oxidize (24, 25, 26). We assume that during this oxidation, an intermediate is first formed by addition of chromium acid to the double bond (27). We have formulated this intermediate as an ester of the pentavalent chromate (sixth reaction). Such cyclic esters are known to formulate when double bonds are oxidized in the presence of osmium tetroxide (28). The cyclic chromate ester is hydrolized in this reaction environment and a 1,2-glycol forms (seventh reaction)

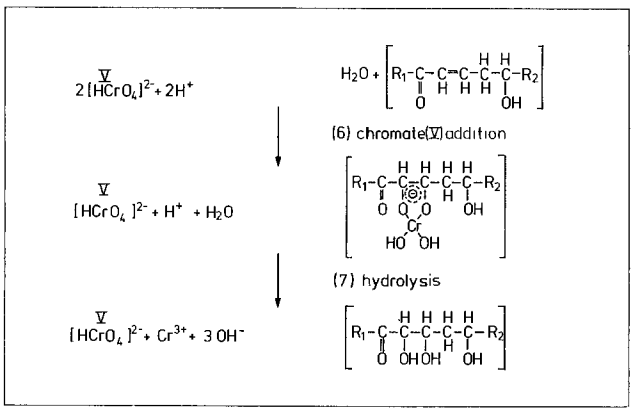

Under such circumstances, glycols are not stable. They get cleaved by surplus dichromate and continue oxidizing to two carbonic acid groups. There is no reference in the literature to an obvious mechanism for the oxidative cleavage of glycol. We have, therefore, limited ourselves to giving a total formula for this stage of the reaction. In the case of the PVAL-ADC photochemical system, this reaction leads to a cleavage of the chain, the chain ends having the structure of α-ketonic and β-hydroxy acid (eighth reaction)

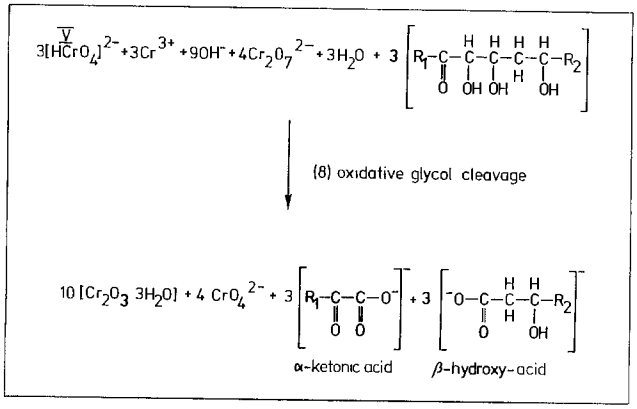

The poly(vinyl alcohol)/ammonium dichromate reaction mechanism, already discussed in detail, is now shown schematically in Fig. 6.

Differing mechanisms are put forward to explain the cross-linking of the poly(vinyl alcohol) by the chromium(III) ions which have formed. Duncalf and Dunn (2) and van Nice and Farlee (4) assume that cross-linking occurs by formation of a hexacoordination around the trivalent chromium with the help of poly(vinyl alcohol) hydroxyl groups.

On the basis of our experiments, we arrive at a stoichiometrical complexing formulation. This happens in the following manner: the poly(vinyl alcohol) cleavage products with terminal carboxyl groups created during the redox reaction make octahedral chelate complexes with the chromium(III) ions formed. Because of their configuration, the α- or β-fixed polar groups can develop coordinating linkages. In this way a maximum of three chain ends can be joined up to each other

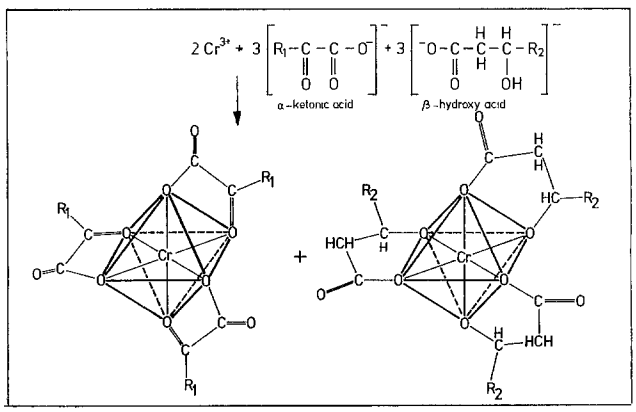

Similar complexes can be formed with one or two chelate groups. The remaining coordination points on the chromium can be saturated by polar groups of other poly(vinyl alcohol) chains. This would also lead to a three-dimensional cross-linkage and thus considerably reduces the solubility of PVAL in water.

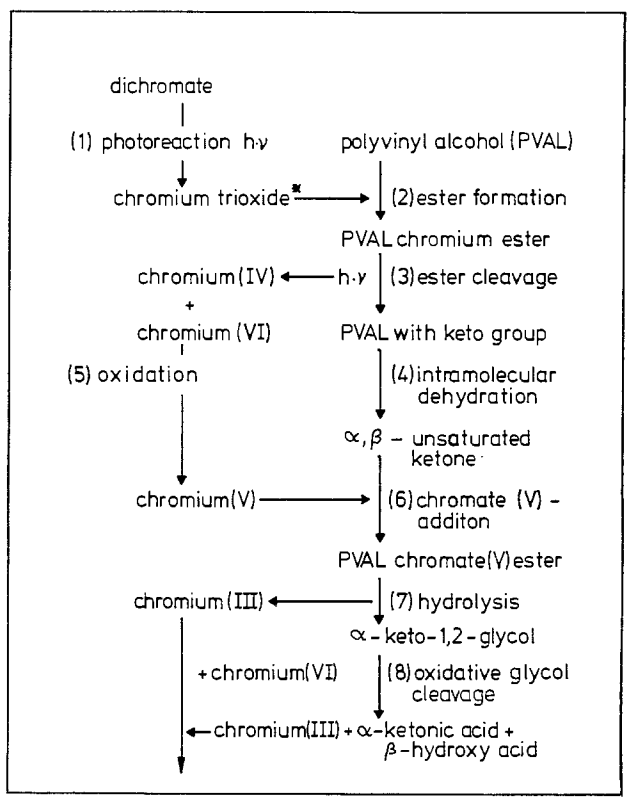

Fig. 6. Mechanism of the PVAL-ADC reaction

This combination of both model concepts is presumably closest to the situation in the flow coat layer.

Upon considering the summation equation of the photoreaction, it is clear that water will be consumed

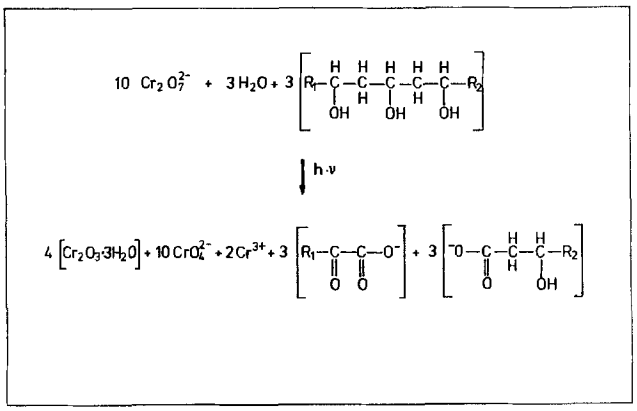

From experience, we also know that too little moisture in the phosphor layer inhibits the reaction. On the other hand, superfluous water in the layer impedes three-dimensional cross-linkage. The necessary trivalent chromium created during the photoreaction can then form stable hexaquo complexes with water in a competing reaction. These hexaquo complexes no longer contribute to cross-linking. This is why a certain limited moisture content must be maintained in the phosphor layer during exposure to obtain a faultless phosphor raster. This is ensured by holding the climatic conditions in the flow coat room within very tight limits.

Manuscript submitted Feb. 1, 1982; revised manuscript received *ca.* Dec. 1, 1982. This was Paper 223 presented at the St. Louis, MO, Meeting of the Society, May 11-16, 1980.

Any discussion of this paper will appear in a Discussion Section to be published in the June 1984 JOURNAL. All discussions for the June 1984 Discussion Section should be submitted by Feb. 1, 1984.

Valvo Bildrohrenfabrik der Philips GmbH assisted in meeting the publication costs of this article.

REFERENCES

1. K. Schläpfer, *Schweiz. Archiv. Angew. Wiss. Techn.*, **31**, 154 (1965).
2. B. Duncalf and A. S. Dunn, *J. Appl. Polym. Sci.*, 1763 (1964).
3. B. Duncalf and A. S. Dunn, in "Polyvinyl Alcohol," C. A. Finch, Editor, Chap. 18, p. 461, Wiley and Sons, London (1973).
4. H. L. van Nice and R. Farlee, *Polym. Eng. Sci.*, **17**, 359 (1977).
5. E. Scharrer, L. Grimm, K.-J. Hilke, and U. Schlenker, *Valvo Ber.*, **18**, 77 (1974); **19**, 41 (1974).
6. E. Scharrer, L. Grimm, and K.-J. Hilke, *Chemie in Unserer Zeit*, **9**, 163 (1975).
7. H. Staudinger, "Organische Kolloidchemie," 5. Auflage, Viewag-Verlag, Braunschweig (1950).
8. J. F. Steinbach and J. H. Burns, *J. Am. Chem. Soc.*, **80**, 1839 (1958).
9. L. Grimm, K.-J. Hilke, and H. Mayatepek, Internal paper, Valvo Bildröhrenfabrik, Aachen (1970).
10. K. Weber and S. Asperger, *J. Chem. Soc.*, 2119 (1948).
11. F. H. Westheimer, *Chem. Rev.*, **45**, 419 (1949).
12. W. Watanabe and F. H. Westheimer, *J. Chem. Phys.*, **17**, 61 (1949).
13. F. Holloway, M. Cohen, and F. H. Westheimer, *J. Am. Chem. Soc.*, **73**, 306 (1951).
14. U. Kläning, *Acta Chem. Scand.*, **12**, 807 (1958).
15. U. K. Kläning and M. C. R. Symons, *J. Chem. Soc.*, **1960**, 977.
16. A. Carrington and M. C. R. Symons, *Chem. Rev.*, **63**, 443 (1963).
17. K. B. Wiberg, in "Oxidation in Organic Chemistry," pp. 159-170, Academic Press, New York (1965).
18. D. Pressman, L. Breuer, and H. J. Lucas, *J. Am. Chem. Soc.*, **64**, 1112 (1942).
19. K. B. Wiberg and H. Schäfer, *ibid.*, **91**, 927, 933 (1969).
20. G. P. Haight, T. J. Huang, and B. Z. Shakhashiri, *J. Inorg. Nucl. Chem.*, **33**, 2169 (1971).
21. P. R. Bontchev, A. Malinovski, M. Mitewa, and K. Kabassonov, *Inorg. Chim. Acta*, **6**, 499 (1972).
22. J. Rocek and E. A. Radkowsky, *J. Am. Chem. Soc.*, **90**, 2986 (1968).
23. M. Rahman and J. Rocek, *ibid.*, **93**, 5462 (1971).
24. W. J. Hickinbottom, D. Peters, and D. G. W. Wood, *J. Chem. Soc.*, 1360 (1955).
25. W. J. Hickinbottom and G. E. M. Moussa, *ibid.*, 4195 (1957).
26. G. E. Moussa, *J. Appl. Chem.*, **12**, 385 (1962).
27. H. H. Zeiss and F. R. Zwanzig, *Chem. and Ind.*, 545 (1956).
28. E. S. Gould, "Mechanismus und Struktur in der organischen Chemie," 2nd ed., pp. 646-647, Verlag Chemie, Weinheim (1971).

JOURNAL OF THE ELECTROCHEMICAL SOCIETY

ACCELERATED

—BRIEF COMMUNICATIONS—

AUGUST 1983

Reduction of Carbon Dioxide to Methanol on n- and p-GaAs and p-InP. Effect of Crystal Face, Electrolyte and Current Density

D. Canfield and K. W. Frese, Jr.*

Materials Research Laboratory, SRI International, Menlo Park, California 94025

As part of a program to study the conversion of inorganic substances into fuels, we have been investigating the reduction of CO_2 to CH_3OH on semiconductor electrodes. A good example study of CO_2 reduction on metal electrodes is reference (1). In this communication we report the conversion of CO_2 into CH_3OH at n and p-GaAs, and p-InP electrodes and give Faradaic yields for methanol and formaldehyde and methane.

ELECTROLYSIS

The electrolysis of CO_2 saturated electrolytes was carried out in a closed system consisting of a 1.1 ℓ CO_2 reservior, a teflon circulation pump, and an electrolysis cell. The anode and cathode compartments were separated by a Na_2SO_4/agar bridge. Electrolytes, 0.2 M, (25 ml) were prepared from either reagent grade Na_2SO_4 and distilled-deionized water, electrolyte A; or 99.999% Na_2SO_4 and 1.6 x 10^7 ohm cm conductivity water (milligard filters), electrolyte B. The experiments were performed galvanostatically in the dark for n-type and under illumination (tungsten-halogen lamp) for p-type. Typically 10-20 coulombs of charge were passed. The initial pH of the cathode compartment was 4.0; due to removal of H^+ in the reaction, final pH values were 5-6. The electrodes were chemomechanically etched first with 1% Br_2/CH_3OH (V/V) followed by 1% sodium hypochlorite in 0.1 M disodium ethylenediammine tetracetic acid at pH = 9-10.

PRODUCT ANALYSIS

Formaldehyde was determined by the chromotropic acid colorimetric method. Plots of absorbance versus concentration were linear from 10^{-4} to 10^{-6} M.

Methanol was detected by flame ionization gas chromatography (FID) using a column of Porapak N. To obtain good separation from H_2O and reproducibility in the results, we had to analyze the CH_3OH/H_2O vapor in equilibrium with the CH_3OH/Na_2SO_4 electrolyte. Peak area versus CH_3OH concentration in the liquid was linear from 10^{-4} to 5 x 10^{-2} M. Methane was also analyzed by FID using Porapak R and Q. We found varying amounts up to 10^{-7} M in the CO_2 reactant gas. We could detect CH_4 at $\lesssim 10^{-8}$ M in a calibration of CH_4/N_2 mixtures.

RESULTS AND DISCUSSION

Tables I summarizes our typical results on Faradaic efficiency for methanol production for CO_2 saturated Na_2SO_4 electrolytes using n-GaAs electrodes. Note that two electrolytes, A and B, as well as crystal face and current density are compared. The efficiency-current density data are presented in corresponding pairs in a certain current density range. High faradaic efficiences were obtained using the (111) As face in reagent grade Na_2SO_4, (A). As evident from Table I, as the current density increased the yield of methanol decreased. When the electrolysis of CO_2 was performed in high purity electrolyte (B), no methanol could be found at low current density. The importance of electrolyte

*Electrochemical Society Active Member

Key words: CO_2 reduction, methanol, GaAs, InP electrodes.

purity has been stressed in the past. Auger electron spectroscopy experiments are in progress to obtain information about the GaAs surface after electrolysis in both A and B electrolytes.

Available efficiency data obtained with the (111)Ga face show that methanol is produced in either electrolyte. In electrolyte A, the efficiencies are close to those of the (111)As face at comparable current density. In electrolyte B, the results indicate much better yields even at the high current density (340 $\mu A/cm^2$). The methanol yields with the (100) and (110) faces are evident in the remainder of Table I. Generally, these faces gave low yields of methanol.

Table II shows comparable data obtained using p-GaAs and p-InP electrodes. The pattern with respect to current density is similar to that observed with n-type. However n-type As face might give higher yields than p-type at the same current density.

The effect of photo current density is clear in the InP results. In addition this material works well in both electrolytes A and B.

In all cases presented here, no CH_4 due to electrolysis was detected. Faradaic efficiencies for formaldehyde were always $\lesssim 0.001$.

We will report more detailed results of CO_2 reduction in the near future.

Acknowledgement -- The authors thank the Basic Research Division of the Gas Research Institute for support of this work.

REFERENCES

1) P. G. Russell, N. Kovac, S. Srinivasan, and M. Steinberg. J. Electrochem. Soc. 124, 1329 (1977).

Manuscript submitted May 6, 1983.

SRI assisted in meeting publication costs of this article.

Table I
FARADAIC EFFICIENCY FOR METHANOL USING n-GaAs ELECTRODES

Crystal Face	Current[a] $\mu A/cm^2$	Electrolyte[b]	Efficiency
(111)As	160-200	A	1.0-1.0
	160-240	A	0.89-0.85
	360-400	A	0.28-0.24
	100-130	B	0.0[c]
(111)Ga	290-390	A	0.27-0.14
	340	B	0.30-0.80
(110)	130	A	0.14
	150-240	B	0.04-0.04
(100)	145-160	A	0.01-0.0

a) Typical electrode potentials were -1.2 to -1.4 V vs SCE.
b) See text for explanation
c) 3 trials

Table II
FARADAIC EFFICIENCY FOR METHANOL USING p-GaAs AND p-InP ELECTRODES

Crystal Face	Photo Current[a] $\mu A/cm^2$	Electrolyte	Efficiency
(111)As	80-100	A	0.52-0.57
	165	A	0.27
	100	B	0.07
(111)Ga	120	A	0.27
	415	A	0.09
	240	B	0.11
	850	B	0.14
(111)P	60-66	A	0.80-0.69
	100	A	0.44
	60	B	0.80

[a]Electrode potentials -1.2 to -1.4 V vs SCE.

Surface Enrichment of Nitrogen during Passivation of a Highly Resistant Stainless Steel

Y. C. Lu[1,3], R. Bandy, C. R. Clayton*,[1], and R. C. Newman*

Brookhaven National Laboratory, Upton, New York 11973

A stainless steel with 0.44 wt.% N and 6.1 wt.% Mo has been shown to have exceptional resistance to localized corrosion (1). This resistance is superior to that of commercial alloys based on Fe-Cr-Ni-Mo, and at least equal to that of more expensive Ni-Mo-Cr alloys. The alloy also represents a significant improvement on laboratory materials with somewhat lower N or Mo concentrations (1-3). We have analyzed the surface of the alloy after passivation, and have obtained evidence for a surface enrichment of N. The role of Mo remains obscure.

The composition of the high-nitrogen alloy, designated #30, is given in Table 1. It was used in the solution annealed condition, where it has an austenitic structure and most of the nitrogen is in solid solution (1). For comparison, the commercial low-nitrogen alloy AL 6X was also analyzed. A 10 x 7 x 1 mm coupon of each alloy was polished with diamond paste to a 0.25 μm finish, cleaned with acetone and immersed in Ar-deaerated 0.5M H_2SO_4 at 22°C. After passivating at +500 mV (SCE) for 24 hours, the specimen was rinsed with deaerated, distilled water and transferred to a Vacuum Generators ESCA 3 (Mark 2) electron spectrometer. All these operations were performed in an argon atmosphere, using a glove box and a transfer device.

Auger electron and X-ray photoelectron analyses were carried out using a hemispherical electrostatic analyzer. The Auger electrons were excited by an electron beam with a diameter of 5 μm and a beam current of 1.8 μA. The Auger electron spectra were recorded in the differential mode using a modulation voltage of 3 V peak-to-peak. The X-ray source was Al Kα radiation. The photoelectron spectra were processed and displayed by a VGS 1000 Datasystem. The pressure during analysis was about 10^{-9} torr. Depth profiling was performed using a beam of Xe ions incident at 60° to the specimen surface, with a current of 2 μA and an accelerating voltage of 2 kV. The pressure of Xe was 10^{-6} torr. Under identical conditions, the etching rate of type 304 stainless steel is about 0.01 nm/s (4).

Figure 1 shows Auger electron spectra at three stages in the analysis of the #30 alloy. The second spectrum was recorded at the position of maximum nitrogen concentration. Figures 2 and 3 are depth profiles of the passivated #30 and AL 6X alloy surfaces. No nitrogen was detected on the AL 6X alloy. The main features of the #30 alloy surface are summarized as follows:

1. The outer region of the film contains no detectable Mo, and is essentially a Cr-Fe-Ni oxide (or hydroxide).
2. The maximum N signal occurs at a point where the O signal has fallen substantially below its level in the outermost part of the film.
3. The apparent maximum N concentration is about 7 times its bulk level, assuming constant sensitivity and no preferential sputtering.
4. If the etching rate is comparable with that of type 304 stainless steel (4), the O-rich part of the film is about 1 nm thick, compared with ∿2 nm for AL 6X (Figure 3). Most of the excess N is localized within a layer 3 nm thick.
5. No enrichment of Mo is detected.

Examination of the nitrogen signal distribution reveals some evidence for a specific localization of nitrogen on the metal side of the metal-oxide interface. The descending

*Electrochemical Society Active Member.
[1]Department of Materials Science, SUNY, Stony Brook, NY

[3]Visiting scholar on leave from Guangzhou Res. Inst. of Elec. Appliances, Guangzhou, China

Key words: alloy, corrosion, passivity.

part, between 180 and 600 s etching, is roughly parallel to the oxygen distribution. Oxygen is not really distributed in this fashion - the effect is caused by surface roughness and/or ion beam damage. There must, therefore, be a sharp fall in nitrogen concentration between 200 and 300 s etching (that is, within about 1 nm). Similarly, the rising part of the nitrogen distribution (0-90 s etching) is distorted by sub-surface emission. The mean free path of the 379 eV nitrogen Auger electrons is about 1 nm (5). The oxide film may therefore contain little or no nitrogen. Given the estimated etching rate of 0.01 nm/s, we conclude that at least 75% of the excess nitrogen is localized within 1 nm of the metal-oxide interface, and is in (or on) the metal rather than incorporated into an oxide. We are therefore seeing a segregation or adsorption of nitrogen near the metal-film interface, resulting from selective removal of metal atoms.

X-ray photoelectron spectroscopy (XPS) showed that the N(1s) binding energy was 396.9±0.1 eV at all stages of ion etching, including the end of the profile where the N was in solid solution in the alloy. Species such as NH_4^+ and NO_2^- are therefore ruled out (6). There is evidently no specific association of N and Mo; a subtle explanation is therefore required for the reported synergism between these two elements in passivity (1). More detailed XPS surface analyses will be described in a longer paper (7); they show, *inter alia*, that the composition of the #30 alloy surfaces is similar whether H_2SO_4 or HCl is used as the passivating medium at +500 mV (SCE). Since a low nitrogen alloy pits in HCl solution under the same conditions, we will conclude that the interfacial nitrogen enrichment is responsible for the resistance of the #30 alloy to localized corrosion.

Conclusions

1. Nitrogen, probably in an uncharged form, is enriched on the metal side of the metal-film interface after passivation of the #30 alloy.
2. Molybdenum is probably present in the oxide film, but is depleted compared with the bulk alloy and shows no obvious association with nitrogen.
3. The improvement of passivity by alloying with nitrogen probably results from segregation of nitrogen to the metal surface during preferential dissolution of metal atoms, rather than from its incorporation into an oxide film.

Acknowledgements

This work developed from a program at Brookhaven National Laboratory funded by the U.S. Department of Energy (Contract No. DE-AC02-76CH00016). The contributions of R. Bandy and R. C. Newman were funded by the Divisions of Geothermal Energy and Basic Energy Sciences, respectively. Discussions with D. van Rooyen are acknowledged. The VGS Electron Spectrometer and VGS 1000 Datasystem were acquired from equipment awards DMR7718319 and DMR811732 from the National Science Foundation, Washington, DC, to SUNY, Stony Brook, NY

Table I. Composition of Alloys

wt.%	Cr	Ni	Mo	N	C	S	P
#30	24.3	19.9	6.06	0.44	0.018		
AL 6X	20.5	24.65	6.19	0.04	0.2	.002	.03

References

1. R. Bandy and D. van Rooyen, Paper No. 71, Corrosion/82, Houston, 1982; Corrosion (in press).
2. J. E. Truman, M. J. Coleman and K. R. Pirt, Br. Corros. J., 12, 236 (1977).
3. Avesta 254 SMO (Preliminary Data Sheet) Information Bulletin no. 7719, Avesta Jernverks AB, Sweden.
4. C. R. Clayton, Y. F. Wang and G. K. Hubler, proceedings of 5th International Symposium on Passivity, Bombannes, France, 1983 (submitted).
5. M. P. Seah and W. A. Dench, Surf. Interface Anal, 1, 2 (1979).
6. C. D. Wagner, "Handbook of X-ray Photoelectron Spectroscopy", p. 40. Perkin-Elmer Corporation, Eden Prairie, Minn. (1979).
7. Y. C. Lu, R. Bandy, C. R. Clayton and R. C. Newman, J. Electrochem. Soc. (in preparation).

Manuscript submitted April 11, 1983.

Brookhaven National Laboratory assisted in meeting publication costs of this article.

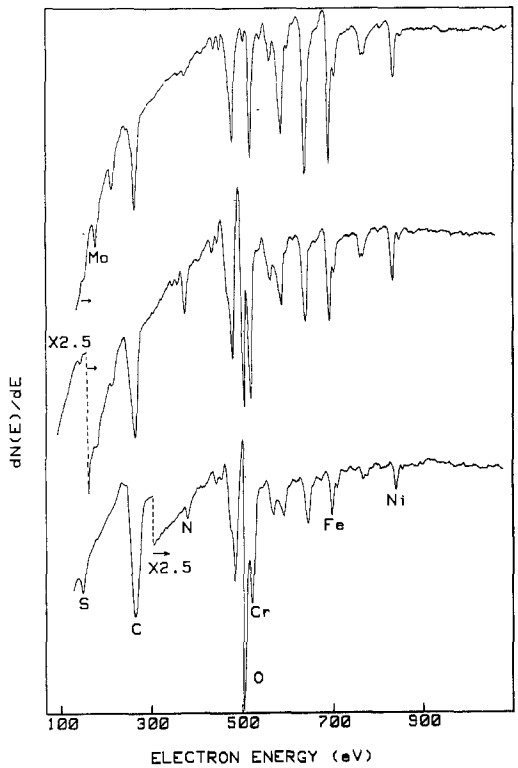

Fig. 1 Auger electron spectra of the passivated surface of high-nitrogen alloy #30 (0.5M H_2SO_4, +500 mV (SCE), 24 h). Times of Xe^+ etching and peaks used for quantification are indicated.

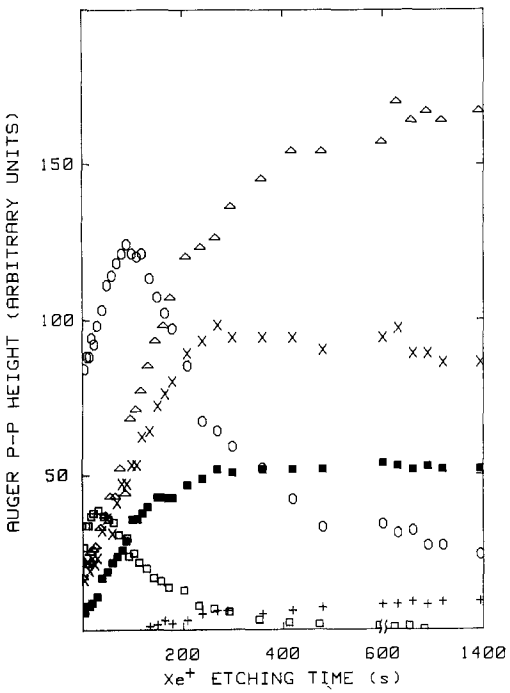

Fig. 3 Auger depth profile of passivated surface of alloy AL 6X (0.5M H_2SO_4, +500 mV (SCE), 24 h). Carbon is omitted.

△... Fe (703 eV),x2 +... Mo (186 eV)
X... Ni (848 eV),x2 ○... O (503 eV)
■... Cr (529 eV) □... S (151 eV)

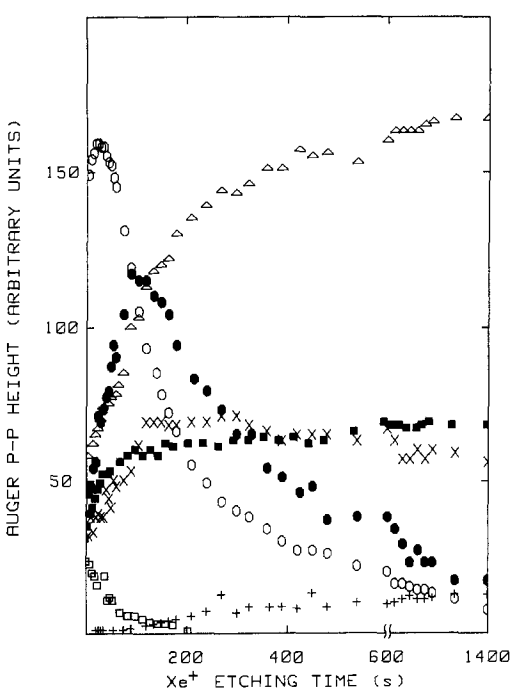

Fig. 2 Auger depth profile of passivated surface of high-nitrogen alloy #30 (0.5M H_2SO_4, +500 mV (SCE), 24 h). Carbon is omitted for clarity - see Fig. 1 for typical contamination levels.

△... Fe (703 eV),x2 ○... O (503 eV)
X... Ni (848 eV),x2 ●... N (379 eV),x5
■... Cr (529 eV) □... S (151 eV)
+... Mo (186 eV)

Reactive Ion Etching of Copper Films

G. C. Schwartz* and P. M. Schaible

IBM, East Fishkill Facility, Hopewell Junction, New York 12533

We have demonstrated that it is feasible to reactively ion etch (RIE) copper films. The etch rate is about an order of magnitude higher than the sputter etch rate. There is no undercut of an inert mask and the patterns formed have vertical sidewalls.

The vapor pressure of copper chloride is substantially lower, than that of aluminum chloride. Nevertheless, Al/4-6% Cu films can be etched, residue free, in CCl_4 containing plasmas, when a heated cathode is used in the reactor (1). Therefore, we expected that RIE of copper films would require elevated cathode temperature.

In reactive ion etching, both chemical reactivity and sputtering contribute to the overall reaction rate (2). Because of the low vapor pressure of copper chloride, we predicted that high ion bombardment energies (high input power densities) would be essential for additional substrate heating and for sputter etching partially reacted surface layers or reaction products of marginal volatility.

RIE of AlCu films was reproducible in CCl_4 but not in Cl_2 plasmas. The superior results obtained in CCl_4 were related to its ability to remove the protective native oxide on aluminum and to getter oxygen and water vapor, thereby preventing re-oxidation. Since the oxide formed on copper is not protective and can be removed readily, we assumed that Cl_2 plasmas would be suitable for RIE of copper. However, a black "smut" was formed on the surface of the copper film and little or no etching occurred. We postulate that, in the presence of oxygen from the SiO_2 cathode plate and water vapor from outgassing of the chamber, copper oxychloride is formed and inhibits etching. Therefore, the gettering action of CCl_4 is required for etching copper as well as for etching aluminum.

The reactor used in these experiments has been described previously (1). The etch rate of copper increases with increasing input power density, cathode temperature, and reactant partial pressure. We did not investigate the effect on etch rate of total pressure, reactant flow rate, or loading. We did not observe corrosion on the etched samples in the laboratory, but have not subjected them to accelerated testing in a hostile environment. However, the reaction of copper with Cl^- is probably self-limiting as opposed to the catalytic effect of Cl^- on corrosion of aluminum (aluminum/copper).

Process optimization is incomplete, but etch rates of about 5000Å/min. were obtained using the following RIE paramenters: rf power density (13.56 MHz), 1.3W/cm^2; gas composition, 5mTorr Ar/5mTorr CCl_4; CCl_4 flow rate, 2.5 sccm; cathode temperature, 225°C.

Thin films of copper (10,000Å) were etched in CCl_4/Ar plasmas using plasma-hardened photoresist as a mask. The resist etched at about half the rate of copper. However, the mask could not be stripped in solvents, e.g., J-100. Ashing, in the presence of chlorinated residues, resulted in the formation of thick layers of copper oxychloride. Therefore an inor-

---

*Electrochemical Society Active Member

Key words: reactive ion etch (RIE), chlorinated plasma, CCl_4 plasma, copper film

ganic mask was required.

MgO is an excellent mask, but does not adhere to copper. We have found that a thin (2000A) film of molybdenum is an effective barrier against copper diffusion and that MgO adheres well to it. CCl_4 plasmas etch molydenum readily. The masking procedure for reactive ion etching of copper requires, therefore, the deposition of a thin film of molybdenum on the copper surface, formation of a simple lift-off stencil on the molybdenum film, evaporation of MgO, and lift-off of the superfluous MgO. After RIE of copper, the MgO is dissolved in a warm aqueous solution of oxalic acid and the molybdenum dissolved in an alkaline solution of potassium ferricyanide at room temperature with no attack on the underlying copper.

Figure 1 shows the result of etching, with an MgO mask, a composite film on a thermally oxidized silicon substrate: 2000A Ti (adhesion layer)/ 30,000A Cu/ 2000A Mo. The narrowest space is about 2 μm. There is no undercut of the mask, although there is occasional lateral attack of the vertical sidewall.

In reactive ion etching of copper, the narrower spaces clear more slowly than the wider ones, whereas in RIE of aluminum and aluminum/copper, the narrower spaces clear more rapidly. This is illustrated for RIE of copper in Fig. 2; a hardened resist mask was used. This geometric effect is also illustrated in Figs. 3a and b; the patterns are positive and negative images of the same dimensions. Isolated lines etched to a clear background although, in the same time, isolated spaces did not clear. Since the application of RIE of copper is directed toward defining relatively widely spaced conductor patterns, this effect does not appear to be a significant drawback.

Because of the large sputtering component of the etch process, etch rate ratios are, in general, not large. However, the erosion rate of the MgO mask is very low so that suitable masking is possible. Since the application is the formation of copper conductors on ceramic substrates, the loss of substrate due to sputtering is acceptable. Figure 4 shows the result of RIE in CCl_4/Ar of a Cr/Cu/Cr layer, 5 μm thick, deposited on a ceramic substrate.

ACKNOWLEDGEMENT

The assistance of J. P. Anderson and V. Platter is gratefully acknowledged.

REFERENCES

1. P. M. Schaible, W. C. Metzger, and J. P. Anderson, J. Vac. Sci. Technol., 15, 334, (1978)

2. J. L. Mauer, J. S. Logan, L. B. Zielinski, and G. C. Schwartz, J. Vac. Sci. Technol., 15, 1734, (1978)

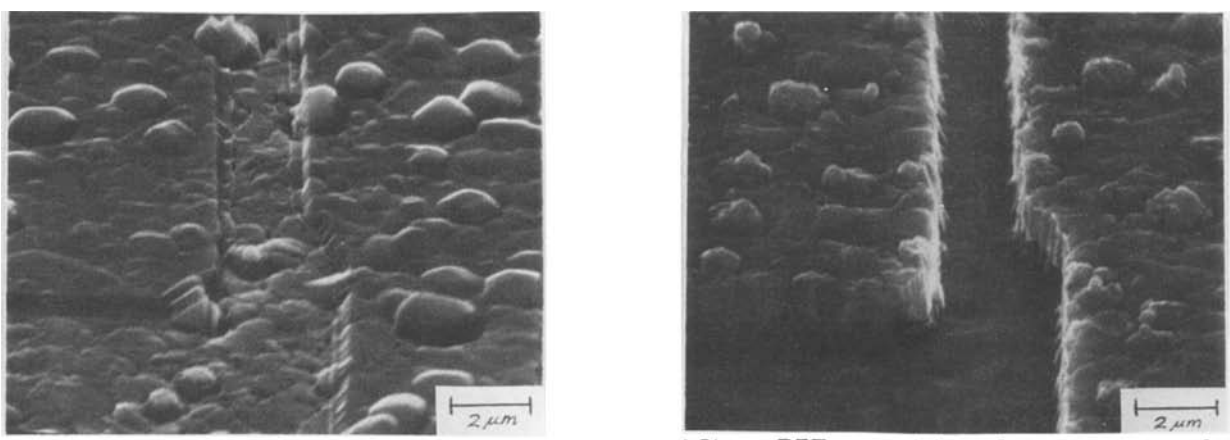

Before RIE

After RIE, masking layer removed

Fig. 1 MgO masked sputtered copper/titanium/thermal SiO_2

Manuscript submitted April 21, 1983; revised manuscript received May 9, 1983.

IBM assisted in meeting publication costs of this article.

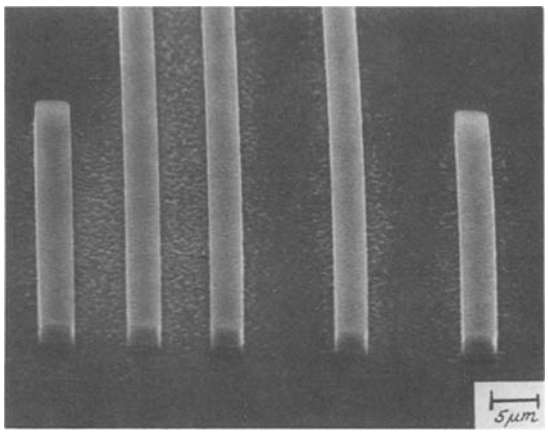

Fig. 2 Hardened photoresist/copper/titanium/thermal SiO_2

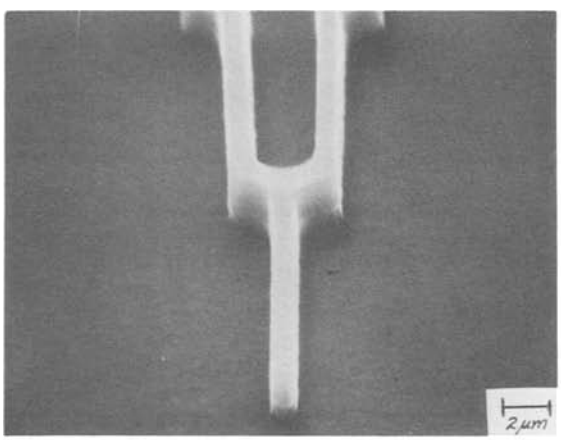

(a)

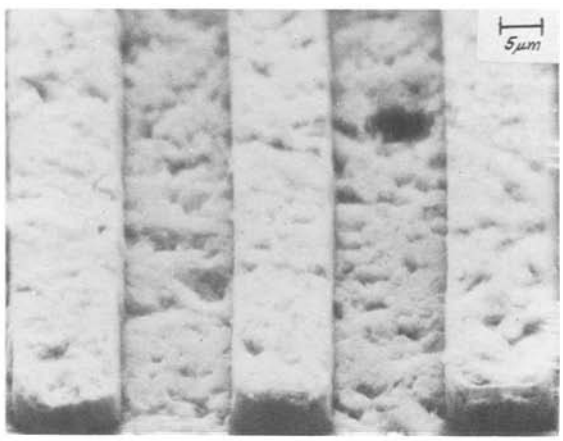

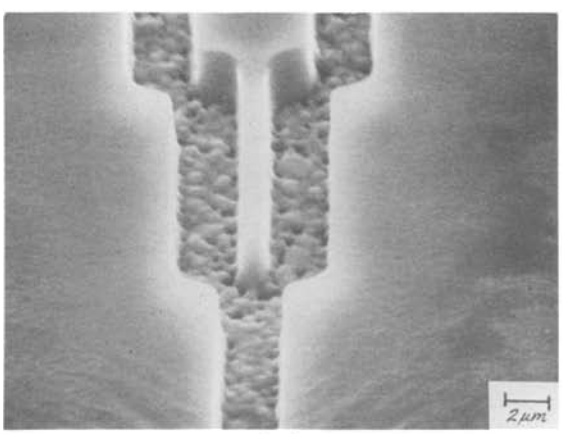

(b)

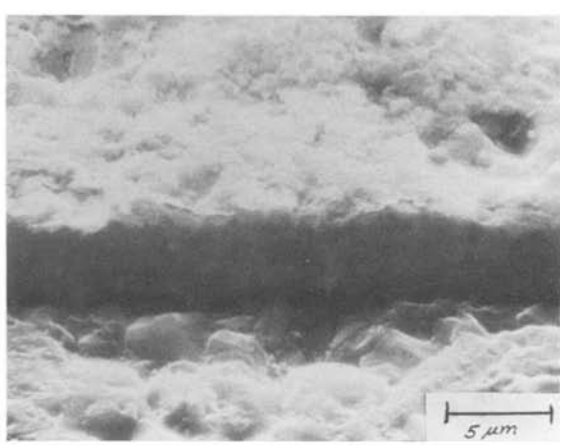

Tin Doping of Gallium Arsenide by Metal Organic Chemical Vapor Deposition (MOCVD)

J. D. Parsons* and F. G. Krajenbrink

Hughes Research Laboratories, Malibu, California 90265

We report here the results of a study to determine the feasibility of growing Sn doped GaAs by MOCVD. Tin is a very desirable n-type dopant for MOCVD grown III-V compounds because of its low vapor pressure and low compensation. The most commonly used n-type dopants for MOCVD grown III-V compounds are S,Se and Te. These elements are effective, low compensation dopants; however, they have very high vapor pressures (Figure 1) which result in the so called 'memory effect'. As a result, it is not possible to grow epilayers with abrupt high-low doping profiles. Silicon, like Sn, has a low vapor pressure but exhibits a considerable amphoteric nature in III-V compounds and alloys.

We have completed a series of experiments in which we determined that: (a) tetramethyltin (TMT) can be used as a Sn source for n-type doping of MOCVD grown GaAs; (b) Sn incorporation can be controlled over a broad range of carrier concentrations, and (c) no surface pile-up of Sn occurs in III-V epilayers grown by atmospheric pressure MOCVD.

The TMT used for this study was supplied by Thiokol/Ventron Division. High carrier concentrations ($>10^{18}cm^{-3}$) were achieved by passing carrier gas through liquid TMT maintained at approximately -50°C. Carrier concentrations between $\sim10^{17}cm^{-3}$ and $10^{18}cm^{-3}$ were obtained by using the TMT bubbler as an effusion cell and passing the H_2 carrier gas by the bubbler outlet tube.

Excellent room temperature mobilities were obtained (Figure 2) in Sn doped GaAs epilayers with carrier concentrations ranging from $9 \times 10^{16}cm^{-3}$ to $8 \times 10^{18}cm^{-3}$. Compensation ratios in the Sn doped GaAs epilayers decreased from about 2 at $8 \times 10^{18}cm^{-3}$ to about 1 at $3 \times 10^{17}cm^{-3}$. This may be due to a decrease of carbon incorporation from the TMT source.

Our experiments show that the problems of Sn doping experienced by LPE and MBE are easily overcome with atmospheric pressure MOCVD. High carrier concentrations are difficult to achieve with Sn in GaAs by LPE (1); however, high carrier concentrations are readily achieved by MOCVD with Sn, as discussed above. All surface morphologies were excellent and no surface pile-up of Sn [often observed in MBE(2)] was detected by SIMS or microscopic examination.

In conclusion, epitaxial films of Sn doped GaAs, having excellent morphologies and Hall mobilities, have been grown by MOCVD. We are in the process of modifying our MOCVD system so that we may grown Sn doped GaAs epilayers with carrier concentrations ranging from $\sim5 \times 10^{15}cm^{-3}$ to $\sim10^{19}cm^{-3}$. Growth parameters will be empirically determined so that GaAs films with carrier concentrations in the above mentioned range can be grown in a predictable and reproducible manner.

---

*Electrochemical Society Active Member

Key words: semiconductors, epitaxy, growth

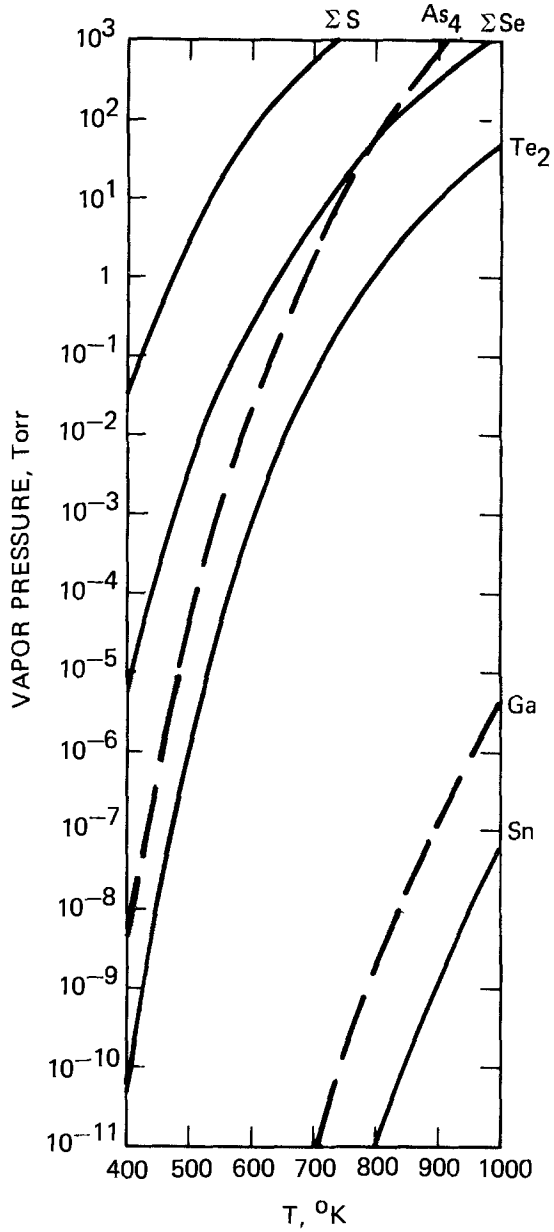

Figure 1. Vapor pressures of Sn and n-type GaAs dopants commonly used by MOCVD.

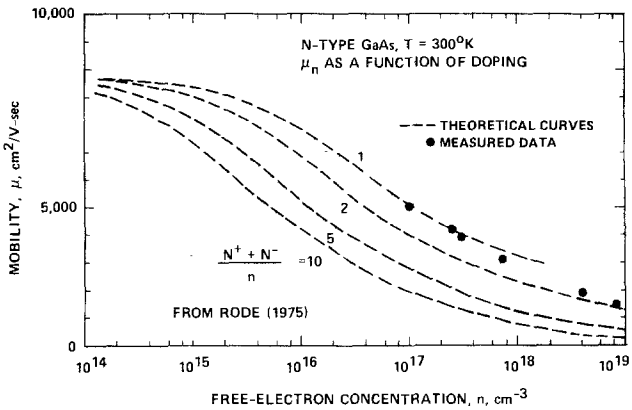

Figure 2. Hall mobility as a function of carrier concentration for Sn doped GaAs grown by MOCVD. (---) theory, (●) measured data.

REFERENCES

1. C.S. Wang and P.D. Greene, Proc. Inst. Symp. On Gallium Arsenide, 2nd. Inst. Phys., Phys. Soc. Conf., Ser. No. 7 p. 18 (1968).

2. J.J. Harris, B.A. Joyce, J.P. Gowers and J.H. Neave, Appl. Phys. A, 28, 63 (1982).

Manuscript submitted March 14, 1983; revised manuscript received May 13, 1983.

Hughes Research Laboratories assisted in meeting publication costs of this article.

Use of Diethylberyllium for Metal Organic Chemical Vapor Deposition of Beryllium-Doped Gallium Arsenide

J. D. Parsons* and F. G. Krajenbrink

Hughes Research Laboratories, Malibu, California 92065

A new dopant source [diethylberyllium (DEB)] has been successfully employed to grow Be-doped GaAs epilayers with excellent surface morphology and transport properties. This is the first time that DEB has been used as a Be source for p-type doping of MOCVD-grown GaAs epilayers. Room temperature electrical properties and Hall mobilities of Be doped GaAs epilayers, grown to date, are presented in Table I.

Beryllium has a much lower vapor pressure than Cd, Zn and Mg (Figure 1). As a consequence, the memory effects observed in MOCVD reactors can be substantially reduced. This will significantly increase the range of device structures that can be grown in a single reactor, and reduce compensation effects at p-n junctions.

Studies to determine the feasibility of using DEB as a Be source for p-type doping of GaAs by MOCVD have been completed. We have determined that DEB has several important advantages over other potential Be sources. First, it is a liquid below room temperature (1); thus, carrier gas saturation can be easily controlled. Second, the vapor pressure of DEB is high enough to permit the bubbler temperatures to be kept below room temperature (2) so that condensation on inlet tube walls can be easily avoided. Third, no reactions which can adversely affect doping efficiency occur in the gas phase or at the gas/epilayer interface. The only difficulty experienced with DEB is Si contamination which is probably caused by $(CH_3)_4Si$ in the DEB bubbler. This has caused a degredation in the transport properties of p-type epilayers with concentrations in the low 10^{18} cm^{-3} range due to compensation effects. We plan to distill our DEB source so that it can be used to grow epilayers with carrier concentrations below $10^{18}cm^{-3}$. Carrier concentrations ranging from $\sim 10^{15}cm^{-3}$ to $\sim 10^{20}cm^{-3}$ may be obtainable with DEB when high purity sources become available.

We are deeply grateful to the Ventron Corporation, Alfa division, for their special efforts to provide us with an experimental sample of DEB. A very special thanks is extended to Mr. Andreas Melas of the Ventron Corporation whose efforts made it possible for us to obtain the DEB used for this investigation.

Table I. Room Temperature Hall Data for Be Doped GaAs Epilayers Grown by MOCVD.

SAMPLE	μ_H ($cm^2/V \cdot s$)	ρ (Ω-cm)	p (cm^{-3})
1	45	8.7×10^{-4}	1.6×10^{20}
2	64	1.4×10^{-3}	7.0×10^{19}
3	72	2.8×10^{-3}	3.1×10^{19}
4	72	3.5×10^{-3}	2.5×10^{19}
5	82	5.0×10^{-3}	1.5×10^{19}
6	76	2.6×10^{-2}	3.2×10^{18}

*Electrochemical Society Active Member

Key words: semiconductors, doping, epitaxy.

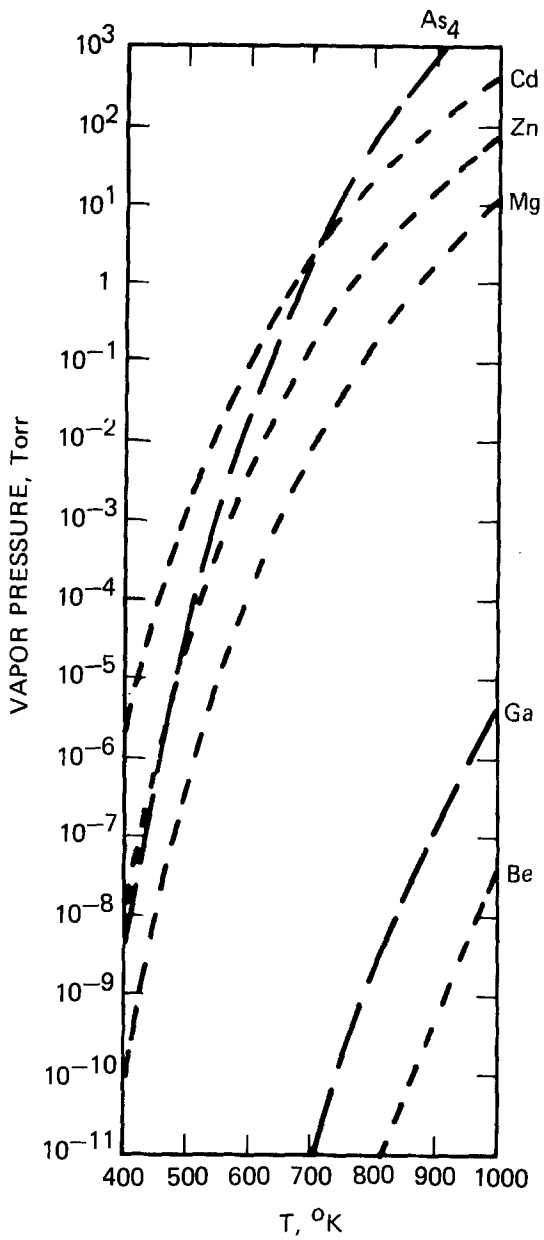

Figure 1. Vapor Pressures of GaAs p-type Dopants Used by MOCVD.

Manuscript submitted March 14, 1983; revised manuscript received May 13, 1983.

Hughes Research Laboratories assisted in meeting publication costs of this article.

REFERENCES

1. Handbook of Organometallic Compounds, Eds. N. Hagihara, M. Kumada and R. Okawara, W.A. Benjamin Inc., (1968).

2. CRC handbook of Chem. and Phys., 58th Ed., (1977-78).

A One-Volt p-InP/n-CdSe Regenerative Photoelectrochemical Cell

P. G. P. Ang* and A. F. Sammells*

Eltron Research Inc., Naperville, Illinois 60540

Photoelectrochemical (PEC) cells have the potential utility of being used for either the direct conversion of solar energy to electricity as in regenerative devices or to generate stored redox species which can later be electrochemically discharged in a suitable cell. This latter approach has been particularly intriguing to us over the last few years. However, although several photoelectrochemical storage cells have been discussed by ourselves and others (1-5), it has become increasingly desirable to have a high-voltage (≃1 V) PEC cell, so that the storage cell with which it is associated has some hope of being competitive with presently available commercial batteries.

One approach whereby liquid-junction photoelectrochemical cells might be used as an electrical energy storage device is to identify regenerative systems possessing sufficient photopotential for the direct charge of an ex situ electrochemical storage cell, where a bipolar electrode configuration between the PEC and the electrochemical cell might be feasible. The use of this type of cell configuration, shown schematically in Figure 1, could lead to a considerable simplification in the interfacing between PEC solar cells and the ex situ electrochemical storage device. Such an approach would have merit if the ex situ stored redox couple has a sufficiently high voltage (i.e. >0.5 V) so that in spite of the inevitable overpotential losses, electrochemical energy efficiencies of ≃75% might be achievable for the discharge reaction at practical current densities. An incidental benefit might be in achieving some degree of thermal management within the cell due to the circulation of the storage redox electrolytes.

The incentive to identify such a regenerative cell came from our earlier work with photoelectrochemical storage cells, one of the most recently discussed (5) having the over-all configuration p-InP/S_n^{2-},S^{2-}/I^-,I_2/n-WSe_2. With this later cell the photopotential generated was typically between 1.1 and 1.2 V. This was sufficient to charge the one-volt sulfide/iodine redox couple at current densities in the 1 to 5 mA/cm^2. Two major issues, however, presently limit further progress on this cell. The first is the absence of suitably efficient polycrystalline n-WSe_2 photoanodes. While some progress has recently been reported (6) on fabricating such materials, the efficiencies are still too low to warrant use in a PEC storage cell. This is a result of nonproductive recombination of the photogenerated carriers which occur at the edge steps of this layer compound leading to a low over-all efficiency for the desired photoelectrochemical reaction. The second is the reduction in effective light transmittance through the electrolyte to the photoanode during photo-oxidation of the iodide/iodine couple upon cell photo-charge. Here the realizable power conversion efficiency was observed to progressively decrease during the photocharging process.

We wish to report here on a two-photoelectrode regenerative PEC cell which has shown a combined photovoltage in excess of one volt. The cell consists of n-CdSe as the photoanode and p-InP as the photocathode in an aqueous sulfide/polysulfide electrolyte. All work reported here is with single-crystal materials.

n-CdSe single crystal was obtained from Cleveland Crystal Inc. Ohmic contact was made by the use of a gallium-indium eutectic followed by contacting a titanium wire via silver epoxy. After appropriate insulation of the semiconductor current collector, the photoanode was initially etched in concentrated HCl for 30 seconds, followed by rinsing with distilled water. The unoptimum performance characteristics of this photoanode under 100 mW/cm^2 ELH illumination were: V_{oc} = -700 mV; I_{sc} = 21 mA/cm^2; FF = 0.4; and η = 5.6%. The p-InP single-crystal photocathode used in this work was obtained from Crysta Comm. Inc. (Zn-doped, carrier density 10^{16}/cm^3, the <111> surface used). Ohmic contact to this material was performed by first sputtering gold, followed by zinc electro-

*Electrochemical Society Active Member

Key Words: cadmium chalcogenides, indium phosphide, photoelectrochemical regenerative cell.

deposition and a final sputtered gold layer. The whole electrode assembly was then annealed at 450°C for one minute. Current collection was achieved by the use of nickel wire contacted with silver epoxy. Insulation of the current collector was performed as before using a non-conducting epoxy. Previous work reported by us has shown that the photoelectrochemical performance of p-InP for photoreduction of aqueous sulfide/polysulfide solutions was enhanced by the incorporation of cobalt sulfide onto the p-InP surface (7). For work reported here, the photocathode was initially etched in 12M HCl for two minutes. This was immediately followed by immersion in a sulfide/polysulfide electrolyte of nominal initial composition 2M Na_2S + 1M S + 1M NaOH. Upon removal of the wetted crystal surface from this solution, a drop of 0.2M $CoCl_2$ was added to its surface. This resulted in the immediate formation of a black precipitate of cobalt sulfide. After this, the crystal surface was rinsed thoroughly with distilled water to remove excess cobalt sulfide. The performance of p-InP in sulfide/polysulfide electrolyte treated in this manner under 75 mW/cm^2 ELH illumination has previously been discussed by us (7) where the following characteristics were observed: V_{oc} = 500 mV; I_{sc} = 17 mA/cm^2; FF = 0.57; η = 6.4%. The single crystal p-InP used in conjunction with n-CdSe in this work under 100 mW/cm^2 ELH illumination gave the performance characteristics: V_{oc} = 500 mV; I_{sc} = 31 mA/cm^2; FF = 0.30; η = 4.7%.

Upon simultaneous illumination of both a n-CdSe photoanode and a p-InP photocathode in a common electrolyte (2M Na_2S + 1M S + 1M NaOH) under 100 mW/cm^2 ELH light, the photoelectrochemical performance curve shown in Figure 2 was obtained. With this unoptimized regenerative cell, its performance can be summarized as V_{oc} = 1.15 V; I_{sc} = 24 mA/cm^2; FF = 0.40; and η = 5.5%. Each photoelectrode had an area of 0.1 cm^2. Current density was probably limited by the photoanode.

Although these preliminary results have not been performed under optimum conditions, the photopotentials generated appear sufficient for the external charge of a number of redox battery couples, including the sulfide/iodine system previously discussed (5).

If this one-volt regenerative system is to have merit of being developed into a useful device, the use of polycrystalline photoelectrodes must be, of course, pursued. For n-CdSe a number of interesting techniques are presently available, including aqueous slurry coating (8,9), electrophoretic deposition (10), thin-film vacuum evaporation (11), spray pyrolysis (12), and electrochemical deposition (13). Clarification of photocorrosion processes in semiconductor materials are being obtained (14) with a variety of interesting approaches identified for arresting such corrosion (15-21). All of this gives encouragement and promise that n-CdSe will eventually be fabricable into an efficient, stable, and cost-effective polycrystalline photoanode for application in this regenerative cell. For this regenerative cell, the direct individual illumination of both the n-CdSe and p-InP will probably be necessary. Substitution of n-CdS for the n-CdSe may allow the direct in-series illumination of this two-photoelectrode cell because of the transparent properties of this former material. This approach is presently being pursued.

Less work has been performed on the preparation of polycrystalline p-InP; however, encouraging progress is being made for solid state cells using chemical vapor deposition techniques (22-24).

We are presently evaluating several approaches for the use of polycrystalline photoelectrodes in this two-photoelectrode regenerative cell. This will be discussed in later communications by us.

REFERENCES

1. G. Hodes, J. Manassen, and D. Cahen, Nature, 261, 403 (1976).
2. P. G. P. Ang and A. F. Sammells, Faraday Div. of the Chem. Soc., Gen. Disc. No. 70, Photoelectrochemistry, St. Catherine's Coll., Oxford (1980).
3. J. Manassen, G. Hodes, and D. Cahen, This Journal, 124, 532 (1977).
4. P. G. P. Ang and A. F. Sammells, This Journal, 129, 233 (1982).
5. P. G. P. Ang, C. J. Liu, A. A. Rossignuolo, A. J. Tiller, and A. F. Sammells in "Measurement Techniques for Photoelectrochemical Solar Cells," W. L. Wallace, A. J. Nozik, S. K. Deb, and R. H. Wilson, Eds., Proc. Electrochem. Soc. Symp., Vol. 82-3, p. 697 (1982).
6. D. S. Ginley, R. M. Biefeld, B. A. Parkinson, and K. Keung-Kam, This Journal, 129, 145 (1982).
7. C. J. Liu, P. G. P. Ang, and A. F. Sammells, This Journal, 129, 1387 (1981).
8. G. Hodes, Nature (London), 285, 29 (1980).
9. X. Xiao and H. T. Tien, This Journal, 130, 55 (1983).
10. Y. Ueno, H. Minoura, T. Nishikawa, and M. Tsuiki, This Journal, 130, 43 (1983).
11. M. A. Russak and J. Reichman, This Journal, 129, 542 (1982).

12. P. G. Ang, C. J. Liu, and A. F. Sammells, Final SERI Report on contract No. XG-0-9175-1, February 1983.
13. M. Tomkiewicz, I. Ling, and W. S. Parsons, This Journal, 129, 2016 (1982).
14. K. W. Frese Jr., This Journal, 130, 28 (1983).
15. M. S. Wrighton, R. G. Austin, A. B. Bocarsly, J. M. Bolts, O. Haas, K. O. Legg, L. Nadjo, and M. C. Palaggoto, J. Am. Chem. Soc., 100, 1602 (1978).
16. R. Noufi, D. Tench, and L. F. Warren, This Journal, 127, 2310 (1980).
17. R. Noufi, A. J. Frank, and A. J. Nozik, J. Am. Chem. Soc., 103, 1849 (1981).
18. F.-R. F. Fan, B. L. Wheeler, A. J. Bard, and R. Noufi, This Journal, 128, 2042 (1981).
19. T. Skotheim, I. Lundstrom, and J. Prajza, This Journal, 128, 1625 (1982).
20. R. Noufi, D. Tench, and L. F. Warren, This Journal, 128, 2596 (1982).
21. R. Noufi, A. J. Nozik, J. White, and L. F. Warren, This Journal, 129, 2261 (1982).
22. M. Inuishi and B. W. Wessels, Thin Solid Films, 88, 195 (1982).
23. M. Inuishi and B. W. Wessels, This Journal, 127, 2747 (1980).
24. T. L. Chu, S. S. Chu, C. L. Lin, Y. C. Tzeng, L. L. Kazmerski, and P. J. Ireland, This Journal, 128, 855 (1981).

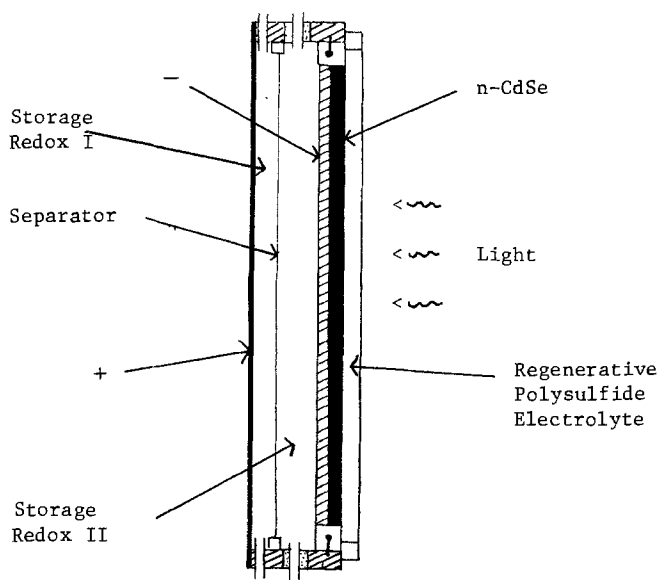

Figure 1. SCHEMATIC p-InP/n-CdSe REGENERATIVE PHOTOELECTROCHEMICAL CELL WITH REDOX STORAGE CAPACITY -- p-InP IN SAME PLANE AS n-CdSe, BUT ITS CURRENT COLLECTION IS TO POSITIVE OF STORAGE CELL.

Manuscript submitted March 29, 1983; revised manuscript received June 1, 1983.

Eltron Research, Inc. assisted in meeting publication costs of this article.

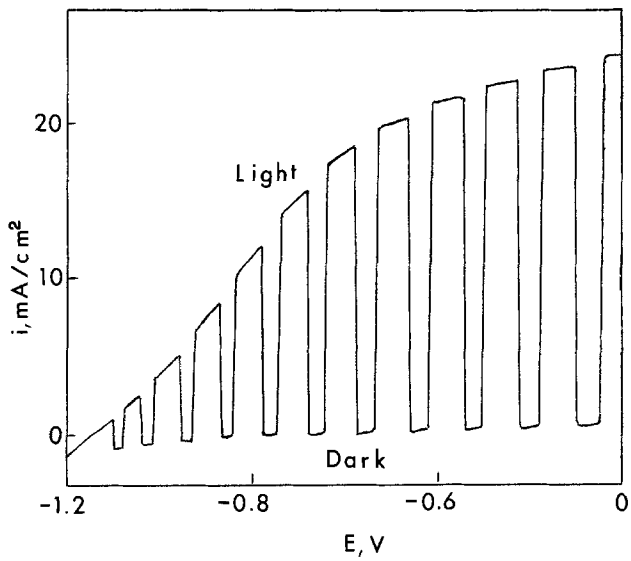

Figure 2. CURRENT-VOLTAGE CHARACTERISTICS OF A TWO-PHOTOELECTRODE PHOTOELECTROCHEMICAL CELL (n-CdSe vs. p-InP Single Crystals in 2M Na_2S + 1M S + 2M NaOH) UNDER ELH ILLUMINATION (100mW/cm^2). (V_{oc} = 1.15V; i_{sc} = 24mA/cm^2; FF = 0.40; n = 5.5%)

Ion Insertion at a Vanadium Pentoxide Cathode

P. G. Dickens and S. J. Hibble

Inorganic Chemistry Laboratory, South Parks Road, Oxford, England

R. H. Jarman

Exxon Research and Engineering Company, Linden, New Jersey 07036

The discharge of a vanadium pentoxide cathode using an aqueous ammonium salt solution (4M) as electrolyte leads to the characteristic shape of potential vs. charge passed shown in Figure 1. Our results agree with those of Shukler and Kuz'min (1) for comparable current densities. The final reduction products on examination prove not to be those suggested by these authors (V_2O_4 or V_2O_3), however, but in fact involve the incorporation of ammonium into a new solid cathodic phase. This result may be of general interest in relation to the use of ammonium salts as supporting electrolytes in the presence of other metal oxide cathodes.

The plateau in Fig. 1 is characteristic of the co-existence of two solid phases; Shukler and Kuz'min identify these as V_2O_5 and V_2O_4 and the corresponding redox reaction as,

$$V_2O_5 + 2H^+ + 2e^- = V_2O_4 + H_2O \qquad [1]$$

This is unsatisfactory, however, since the end of the plateau region in Fig. 1 corresponds to 0.6 e^- passed per V_2O_5 and not $2e^-$ as implied by [1]. Moreover, the X-ray powder pattern of the product reveals no lines characteristic of V_2O_4. The X-ray powder pattern is identical with that of a compound "$V_3O_5(OH)_4$" reported by Glemser (2) as the product of a chemical reduction of V_2O_5 by Zn in NH_4Cl solution (Table I).

Keywords: Solid, cathode, phases, reduction.

Table I. X-Ray Powder Data for $(NH_4)_{1+x}V_3O_8$, d_{obs}/Å

Cathodic Product $(NH_4)_{1.92}V_3O_8$		$V_3O_5(OH)_4$	h	k	l
M 5.587	S 5.549	VS 5.54	0	0	1
	VW 4.432	WM 4.46	0	2	0
M 3.982	S 3.970	VS 3.97	1	2	0
VVW 3.481	W 3.471	S 3.46	0	2	1
M 3.236	S 3.233	VS 3.23	1	2	1
W 2.814	M 2.811		1	3	0
	W 2.784		0	0	2
	VVW 2.737	S 2.74	2	2	1
UW 2.510	M 2.511	MS 2.50	1	3	1
	VW 2.466		2	3	0
	VW 2.280		1	2	2
	VW 2.257	W 2.25	2	3	1
	VVW 2.156	W 2.15	1	4	0
	VVW 2.095	W 2.09	3	3	0
VVW 1.989	W 1.991		2	4	0
VVW 1.977	W 1.982	MS 1.98	1	3	2

a = 8.897(3)Å*	a = 8.905(3)Å**
c = 5.561(4)Å*	c = 5.572(2)Å**

We have shown by repeating the synthesis of this compound following Glemser's prescription, that the black product formed, and the product of electrochemical reduction using 2M $(NH_4)_2SO_4$ as electrolyte, are the same. Careful chemical analysis of a series of synthetic products shows that their mean composition is $(NH_4)_{1+x}V_3O_8$ $(0.8 < x < 1)$, and not $V_3O_5(OH)_4$ as reported by Glemser. The IR spectrum of the synthetic material shows a peak at 1400 cm^{-1} characteristic of NH_4^+. The relevant analytical data are given in Table II.

*Cathodic product.
**$(NH_4)_{1.92}V_3O_8$

Table II. Analytical Data for Synthetic $(NH_4)_{1+x}V_3O_8$

Sample	%N	%H	$\%NH_3$*	MW	Mean Oxidn State of V	Formula
1	8.44	2.48	-	318.0	4.68	$(NH_4)_{1.92}V_3O_{8.0}$
2	8.30	2.38	-	316.2	4.78	$(NH_4)_{1.86}V_3O_{8.10}$
3	8.45	2.35	10.25	314.7	4.74	$(NH_4)_{1.86}V_3O_{8.01}$

*Kjeldahl method

The mean oxidation state of vanadium in the synthetic materials is ∿4.7 which agrees with the degree of cathodic reduction shown in Fig. 1.

$(NH_4)_{1+x}V_3O_8$ is isostructural with $K_2V_3O_8$ and $Rb_2V_3O_8$ as the lattice parameters indicate:

$(NH_4)_{1.92}V_3O_8$	$K_2V_3O_8$(3)	$Rb_2V_3O_8$(3)
a = 8.905Å	a = 8.897Å	a = 8.891Å
c = 5.571Å	c = 5.246Å	c = 5.542Å

We conclude that the cathodic reduction of V_2O_5 in the presence of NH_4^+ leads to the formation of an ammonium insertion compound as the final product according to the approximate overall reaction:

$$3/2\ V_2O_5 + 2NH_4^+ + 1/2\ H_2O + e^- = (NH_4)_2V_3O_8 + H^+$$

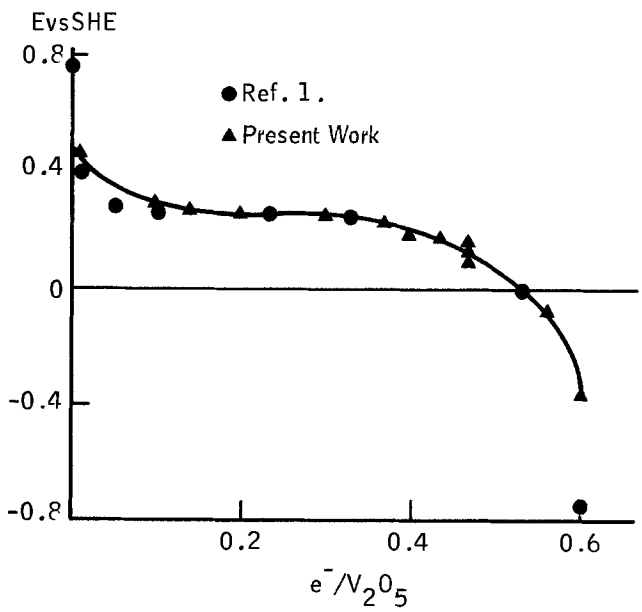

FIGURE 1

Discharge curve of V_2O_5 electrode (Electrolyte, $2M(NH_4)_2SO_4$(aq))

REFERENCES

1. Y. S. Shukler and L. L. Kuz'min, Shurnal Prikladnoi Khimii, 39, 1327 (1966).
2. O. Glemser and E. Schwarzmann, Z. Anorg. Allg. Chem., 278, 249 (1955).
3. a) M. Pouchard, Doctoral Thesis, Bourdeaux University, 1967.
   b) M. Pouchard, J. Galy, L. Rabardol, and P. Hagenmuller, C. R. Acad. Sci. Paris, 264, 1943 (1967).
   C) J. Galy and A. Carpy, Acta Cryst., B31, 1794 (1975).

Manuscript submitted March 11, 1983.

Exxon Research and Engineering Company assisted in meeting publication costs of this article.

Thickness of Electrolyte Layers on Emersed Pt Electrodes

F. T. Wagner* and P. N. Ross, Jr.*

Lawrence Berkeley Laboratory, Materials and Molecular Research Division, Berkeley, California 94720

Ex situ analytical methods show promise for elucidating the elementary steps in electrocatalysis and for determining electrode structure at the atomic scale (1). However, the details of the electrode emersion process must be understood if definitive results are to be obtained. The works of Hansen, Kolb, et al. (2,3,4) indicate that, at least in some cases, electrodes can be emersed with the double layer intact. Of equal importance to the application of ex situ techniques is the question of how much bulk electrolyte adheres to the electrode upon emersion. Gordon (5), using a total attenuated reflectance method, has measured an electrolyte thickness of 38Å on a Ag electrode emersed from 0.1 M NaF into water vapor-saturated Ar, with smaller, potential-dependent thicknesses measured after emersion into unsaturated argon. The extent to which such behavior is typical of electrode-electrolyte systems in general remains to be determined. The present work was carried out using a cell designed to allow the clean transfer of the electrode to an ultra-high vacuum surface analytical chamber. The order of magnitude of the thickness of electrolyte remaining on the surface after emersion was determined by quantitative Auger electron spectroscopy (AES) applied to the non-volatile sodium residue from a HF-NaF aqueous electrolyte.

The electrochemical cell is shown in Fig. 1. After preparation in UHV the single-crystal Pt(100) electrode was moved to a transfer chamber which was then backfilled with purified research grade Ar. The cell, consisting of a Pt ring counterelectrode and an α-PdH reference disk, was loaded with about 100 μℓ of electrolyte through a PTFE capillary connected to an external PTFE reservoir. Contact of the crystal with the electrolyte (under potentiostatic control) left a ca. 0.5 mm electrolyte- filled gap between the working electrode and the counter-reference assembly. Hydrophilic contact angles were always observed on Pt electrodes. The transfer chamber was then pressurized, and the electrolyte drained across the crystal surface in about 5s and out the PTFE capillary. The surface appeared free from water except about a 0.1 mm^2 droplet which was trapped between the crystal and the drain capillary. The scanning capabilities of the Auger system allowed this spot to be analyzed separately. After emersion, the Pt crystal was withdrawn from the cell, the transfer chamber was pumped down, and the crystal was returned to the main UHV chamber for surface analysis.

Figures 2a and b show Auger spectra for Pt(100) emersed from 0.3 M HF and 0.3 M HF + 5×10^{-3} M NaOH, respectively. Emersion from the latter electrolyte yielded a Na 990 eV/Pt 1722 eV ratio of 0.2. The amount of sodium remaining as Na_2O or NaOH on the surface after evaporation of the electrolyte film can be estimated using standard reference spectra of Pt and $Na_{0.7}\ WO_3$ (6):

$$Na^+/cm^2 = \frac{Na^{meas.}_{990}\ @\ 5\ kV}{Pt^{meas.}_{1722}\ @\ 5\ kV} \times \frac{I^{3\ kV}_{990}/I^{5\ kV}_{990}}{I^{3\ kV}_{1722}/I^{5\ kV}_{1722}}$$

$$\times \frac{Pt_{1722},\ Pt\ std.}{Na_{990},Na\ std.} \times \frac{Na_{990}\ bulk\ std.}{Na_{990}\ monolayer\ std.}$$

$$\times\ Na^+/cm^2\ Na_{0.7}\ WO_3$$

$$= 1 \times 10^{14}\ Na^+/cm^2$$

The first factor to the right of the equals sign is the experimental Auger peak ratio (0.2) which was taken with a primary beam energy of 5 kV to maximize the signal-to-noise ratio. The second factor (2.3) corrects the data to the 3 kV beam energy used in the standard spectra in Ref. (6). The third factor gives the ratio of peak intensities for bulk Pt and for sodium in

Keywords: emersed electrode, platinum, Auger electron spectroscopy, sodium ion

* Electrochemical Society Active Members

bulk $Na_{0.7}$ WO_3 (6). The fourth factor is a calculation of the ratio of the 990 eV Auger emission intensity from bulk $Na_{0.7}$ WO_3 to that for a single surface layer of $Na_{0.7}$ WO_3 derived from Lambert's law of exponential attenuation (7),

$$\frac{Na_{990},\ \text{bulk}}{Na_{990},\ \text{one layer}} = [1-\exp(-d/\lambda\cos 42°)]^{-1}$$

where d is the distance between Na-containing (100) planes (approximately 3.85 Å for the sodium tungsten bronze lattice, Ref. 8), λ is the Auger electron mean free path (11 Å for 1 kV electrons in WO_3 as calculated by Powell Ref. 9),and 42° is the acceptance angle of the cylindrical mirror electron energy analyzer. Attenuation of the Pt signal was ignored in this calculation because only small fractions of a monolayer of sodium were observed in these experiments. The Na^+ surface density of (100) $Na_{0.7}$ WO_3 (4.7×10^{14} Na^+/cm^2) is derived from the structure in Ref. 8. The experimental Auger spectra yield a sodium ion density of 1.1×10^{14} Na^+/cm^2 (1.8×10^{-10} g ions/cm^2) on the Pt(100)-1 x 1 surface (1.30×10^{15} Pt/cm^2), or a Na/Pt surface atomic ratio of 0.08. The accuracy of the calculation suffers from uncertainties in λ, matrix effect differences between the Na_2O or NaOH experimental deposit and the $Na_{0.7}$ WO_3 reference material, and the backscattering effect of a high atomic weight substrate on the low atomic weight overlayer. The last effect would tend to make the calculated Na coverage high (by a factor of up to ~2), but is partially compensated for by the W in the reference material. More accurate calibration will require Auger studies of single Na monolayers evaporated onto Pt(100) and subsequently oxidized, but the present calculation yields at least the proper order of magnitude for the amount of Na on the surface.

Similar sodium signals were seen on electrodes emersed at 0.8 V, 1.2 V, and 1.9 V RHE. Emersion at 0.08 V led to Na signals ca. 2- fold smaller. If the detected sodium were due to ions electrostatically bound to the surface one would expect a significantly higher Na signal for emersion at 0.08 V (below the point of zero charge) than for the other measurements. The sodium coverage above the point of zero charge is 10^2- fold larger than the 1.2×10^{-12} g ions/cm^2 specific Na^+ adsorption on Pt between 0.3 and 0.8 V RHE in 10^{-3} N NaF + 10^{-3} H_2SO_4 reported by Balashova and Kazarinov (10). The sodium measured here is thus the nonvolatile residue left behind by the evaporation of the electrolyte film remaining on the surface after emersion. The thickness of this electrolyte film, t, before evacuation can be determined from the measured Na^+ surface concentration as follows:

$$t = 1.1 \times 10^{14}\ Na^+/cm^2 \times \frac{1000\ cm^3}{5 \times 10^{-3}\ \text{moles}\ Na^+} \times \frac{1\ \text{mole}\ Na^+}{6.02 \times 10^{23}\ Na^+} \times \frac{10^8\ Å}{1\ cm} = 4 \times 10^3\ Å$$

No fluorine Auger signals were observed on properly emersed electrodes - fluoride evaporates from the acidic electrolyte as HF, leaving a residue of NaOH (or Na_2O). Higher levels of sodium and sometimes fluorine were observed in the capillary separation spot or when improper draining left visible droplets in the interelectrode gap. Attempts to emerse the crystal by dropping the counter-reference assembly vertically away from it left larger electrolyte drops on the surface. Residue from these drops interfered with surface analysis even when the electrolyte was nominally residue-free HF.

Auger analysis was also performed for sodium residues on Cu(111) and polycrystalline Ni electrodes. Emersion of Cu(111) at -0.12 V RHE from a NaF - NaOH solution 5×10^{-3} M in Na^+ led to a calculated film thickness of 2×10^4 Å. Polycrystalline Ni emersed at 1.5 V RHE from bicarbonate-carbonate buffers 2×10^{-3} and 2×10^{-2} M in Na^+ gave film thicknesses of 2×10^4 Å and 1×10^4 Å, respectively. The potential dependence of the emersion layer thicknesses on Cu and Ni have yet to be studied. The 10^3-10^4 Å electrolyte thicknesses measured here, while much greater than those measured by Gordon on Ag (5), are still sufficiently small to allow the application of UHV techniques to electrode surfaces emersed from electrolytes with non-volatile solutes up to at least 10^{-2} M in concentration (<0.2 monolayer of residue) as confirmed by LEED patterns of Cu(111) emersed from bicarbonate buffer. Since specifically adsorbed ions can drastically alter the electrochemical properties of a surface at bulk concentrations as low as 10^{-5} M (11), it appears that specific adsorption at electrodes can also be studied using ex situ UHV techniques. The 10^3-10^4 Å emersed film thickness is of the same order of magnitude as the thicknesses reported by Muller (12) for vertical films on Ni at a point 1 cm above the 3.4 M KOH bulk electrolyte surface. The agreement may be fortuitous, as the electrode surface here is horizontal and the film drawn by differential pressure rather than by gravity. The disagreement with the 40 Å thicknesses reported by Gordon (5) for a system apparently closer to ours in geometry and electrolyte is not easily explained. It suggests the necessity of independent measurements for each electrode-electrolyte pair and every emersion geometry.

Acknowledgment

This work was supported by the Assistant Secretary for Conservation and Renewable Energy, Office of Advanced Conservation Technology, Division of Electrochemical Systems Resources of the U.S. Department of Energy under Contract No. DE-AC03-76SF00098.

REFERENCES

1. F. T. Wagner and P. N. Ross, Jr., J. Electroanal. Chem., in press.
2. W. N. Hansen, C. L. Wand and T. W. Humphreys, J. Electroanal. Chem., 90, 137 (1978); 93, 87 (1978).
3. D. M. Kolb and W. N Hansen, Surface Sci., 79, 205 (1979).
4. W. N. Hansen, D. M. Kolb, D. L. Rath, and R. Wille, J. Electroanal. Chem., 110, 369 (1980).
5. J. G. Gordon, II, "Extended Abstracts," 82-1, p. 1055, ECS Montreal meeting (1982).
6. L. E. Davis, et al., "Handbook of Auger Electron Spectroscopy," 2nd ed., Physical Electronics, Eden Prairie, MN, 1976.
7. F. T. Wagner, Ph.D. Thesis, University of California, Berkeley, 1981.
8. P. J. Wiseman and P. G. Dickens, J. Solid State Chem., 17, 91 (1976).
9. C. J..Powell, Surface Sci., 44, 29 (1974).
10. N. A. Balashova and V. E. Kazarinov, Elektrokhimiya, 1, 512 (1965).
11. J. C. Huang, W. E. O'Grady and E. Yeager, J. Electrochem. Soc., 124, 1732 (1977) and J. C. Huang, Ph.D. thesis, Case Western Reserve University, 1976.
12. R. H. Muller, J. Electrochem. Soc., 113, 943 (1966).

Figure Captions

Fig. 1. Electrochemical cell showing a.) single crystal Pt working electrode goldbrazed to Ta cylinder, b.) Pt ring counter electrode (cut off flush with top of PTFE plate), c.) Pd-H reference electrode, and d.) PTFE capillary for introduction and removal of electrolyte.

Fig. 2. Auger spectra for Pt(100) electrodes emersed from a.) 0.3 M HF at 1.8 V RHE and b.) 0.3 m HF + 5×10^{-3} M NaOH at 1.9 V RHE. c.) is b.) scaled to give same Pt signal as a.). E_p = 5 kV, V_M = 10V p-p.

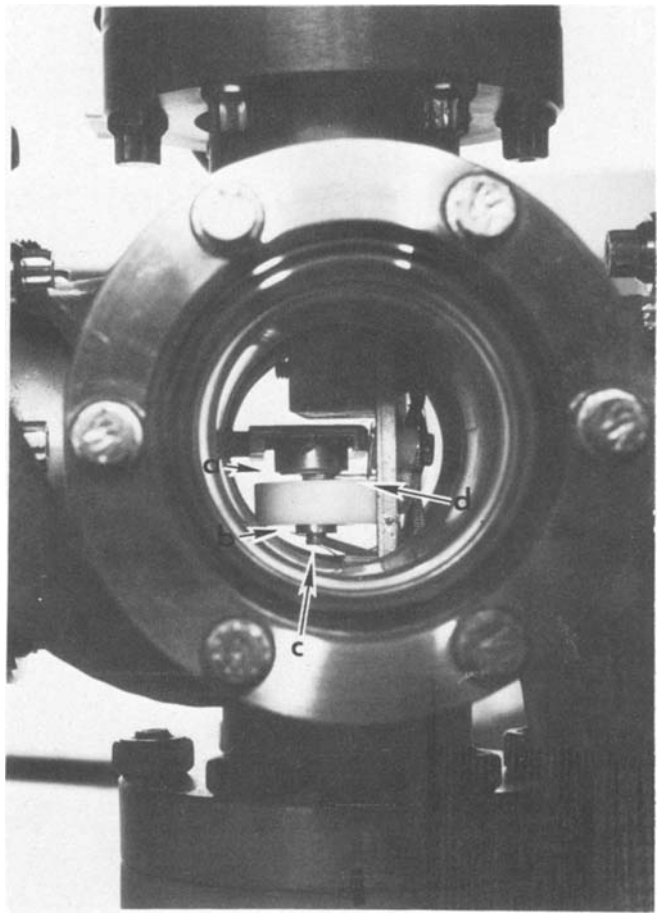

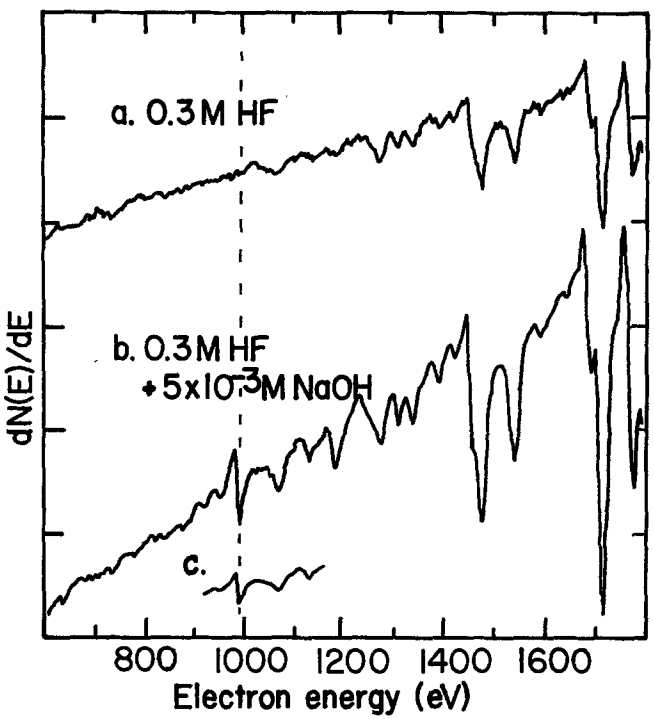

Manuscript submitted Feb. 17, 1983; revised manuscript received April 28, 1983.

Lawrence Berkeley Laboratory assisted in meeting publication costs of this article.

Chloride Ion Penetration of Passive Films on Iron

O. J. Murphy,* J. O'M. Bockris,* and T. E. Pou

Department of Chemistry, Texas A&M University, College Station, Texas 77843

L. L. Tongson and M. D. Monkowski

Materials Research Laboratory, Pennsylvania State University, University Park, Pennsylvania 16802

Models of the passive layer on iron are of two kinds--hydrated amorphous (1) or anhydrous polycrystalline (2).

While the assumption of initial adsorption of chloride ions on passive film surfaces is common to almost all approaches of chloride breakdown mechanisms (3), the further action of these ions is unclear. Two possibilities can be entertained (4-6).

1. The chloride ions locally remove some metal cations from *defects* on the surface, which initiates local pitting in the passive film (4). Once this removal has commenced, the local anodic field will begin to increase as the distance between the bottom of the pit and the metal surface decreases, in a manner which facilitates enhanced anodic dissolution until a visible pit is formed. The formation of a sufficient number of pits leads to the breakdown of the film.†

2. Chloride ions penetrate through the passive film without forming visible pits (5,6). Several mechanisms for this have been suggested (5-7), including passage through a channel already present in the film (8). When the chloride ions reach the iron/iron oxide interface, they aid the removal of ferrous ions from the metal lattice {cf., a similar event in active dissolution (9)}, and the resulting complexes diffuse upward through channels to the outer metal oxide/solution interface.

The air-formed oxide on iron electrodes (99.99% purity, Alfa Ventron Corp., Danvers, Mass.) was removed (10), and the electrode potential was then stepped from the resting value to +0.30 V (NHE) in a freshly added (10) borate buffer solution (pH = 8.4) and held at this value for 45 minutes in each case. The solution was then replaced with a 0.5 M sodium chloride-containing borate buffer solution, and the passivated specimens exposed to this solution at +0.30 V (NHE) for the times shown in Table I.

TABLE I

Passivated Sample Number	Time of Exposure to Cl^- in Seconds
1	40
2	80
3	163
4	205
5	420

After washing with triply distilled water, samples were removed from the cell in a glove box and transferred in argon atmosphere-containing glass vials to a SIMS-SIPS instrument, where SIMS analysis was carried out. Sputtering was performed with Ar at a sputtering rate of approximately 0.3 Å sec^{-1}.

The current density versus time curve for a passivated iron electrode in 0.5 M buffered chloride solution is shown in Figure 1. Also marked on this diagram are the times of withdrawal from the solution of the various passivated specimens. It can be seen that breakdown of passive iron begins, under the conditions used, after ca. 160 seconds (electrode 3). After this time, the current begins to increase sharply. Electrode 5 showed signs of a rust-colored film.

The SIMS data presented in Figure 2 for the passivated iron specimens illustrated in Figure 1 reveal surprising features: (i) for increasing exposure times (40, 80 and 163 seconds) up to breakdown time, increasing amounts of chloride ions penetrate the passive films, reaching a maximum around breakdown; (ii) for

---

* Electrochemical Society Active Members.

† A difficulty of this model involves the probable filling of pits with gelatinous iron hydroxide arising from dissolution of the metal at high local current densities.

Key words: passive films, iron, chloride ions, penetration of, SIMS.

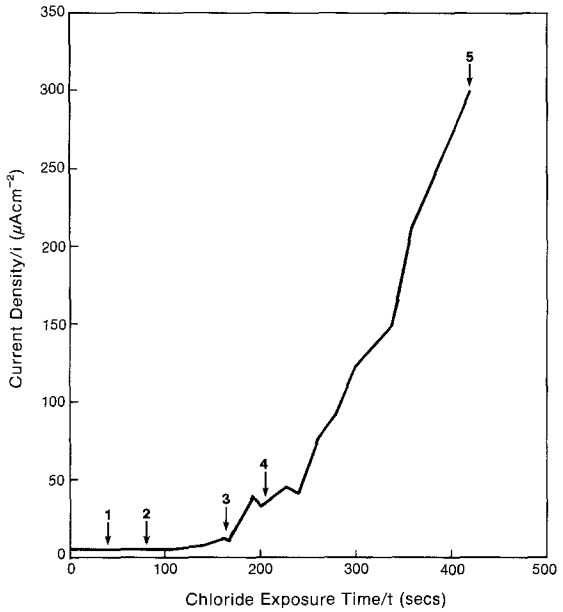

FIGURE 1. Variation of current density with time for a passivated iron electrode {0.30 V (NHE) for 45 minutes in borate buffer, pH = 8.4} in a 0.5 M chloride-containing borate buffer solution held at 0.30 V (NHE).

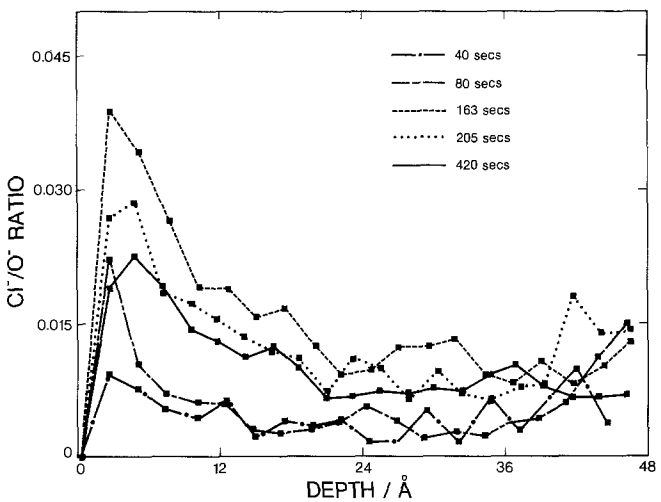

FIGURE 2. Variation of $Cl^-:O^-$ ratios, obtained from SIMS negative ion spectra, with depth into passive films which were previously held at 0.30 V (NHE) in 0.5 M chloride-containing borate buffer solutions for various times: —•— 40 secs; — — — 80 secs; — — — 163 secs; ••• 205 secs; —— 420 secs.

exposure times longer than breakdown, however (205 and 420 seconds), a *decrease* in the chloride content of the passive films† is apparent, the Cl^- concentration within the film becoming lower for the larger exposure time (electrode 5). Chloride ions penetrate passive films right up to the metal/film interface.

In the hydration model of passivity (1), film breakdown would arise through removal of the water. The present results establish chloride penetration (unambiguously for the first time) into the passive film on iron, and it may be thought probable that the coordinating ligand, Cl^- ion, would displace bound water, as both ligands give rise to similar crystal field splittings on forming transition metal octahedral complexes (11), and chloride ion is a stronger Lewis base compared to either water or hydroxyl ions (12). Chloride itself coordinates with Fe^{3+} ions, thus, removing what, in this model, is the essential species $\{Fe^{3+}\text{-}OH_2\}$ in the passive layer.

The necessity of water within passive films for chloride ion penetration of the latter has been stressed in the case of the breakdown of passivated titanium alloys (12). Displacement of water by the stronger Lewis base, chloride ion, and resulting modification of the film structure leading to penetration by chloride ions was assumed (12) to occur.

The anhydrous model appears to be less consistent with the facts reported here in Figure 2. (i) O^{2-} would be much less easy to displace by Cl^- when coordinated with Fe^{3+} than would be H_2O (13). (ii) At potentials positive to +0.30 V (NHE), breakdown with this model would imply migration of O^{2-} against the electric field gradient. (iii) Considering the time to breakdown, a diffusion coefficient for chloride ions within the passive film of at least 10^{-15} cm^2 sec^{-1} must be expected. Although literature data is not available for this process, an extrapolated diffusion coefficient for the related phenomena of water diffusion through *crystalline* silica (14) yielded the much lower value of 6×10^{-19} cm^2 sec^{-1}. Amorphous structures (as with the model of the hydrated passive film) tend to give rise to faster diffusion (15).

In respect to the surprising decrease of chloride ions with time in passive films (cf., Fig. 2), some dissolution of the passive film itself takes place, as is evidenced by the

†These changes occur throughout the films, but are more marked in the first 12-15 Å.

rotating ring-disc work of Heusler and Fischer (16), which showed Fe^{3+} species arising after exposure of passivated iron discs to chloride solution. This process would account for the observations of Figure 2.

This communication serves to resolve the inconsistencies between those workers who found chloride ions in depassivated films (5) and those who did not (17). It is evidently a matter of time after depassivation at which the observations are made.

ACKNOWLEDGEMENTS

The authors are grateful for the support of this work by the Department of the Interior (DOI) under grant #14-34-0001-9446 and to Dr. W. McCoy for discussion.

The authors are also grateful to Mrs. Lynn McCartney-Murphy for her editing and typing of this manuscript.

REFERENCES

1. W. E. O'Grady, *This Journal*, 127, 555 (1980).
2. K. Kuroda, B. D. Cahan, G. Nazri, E. Yeager and T. E. Mitchell, *This Journal*, 129, 2163 (1982).
3. J. Kruger, in: "Passivity and Its Breakdown on Iron and Iron-Base Alloys," eds., R. W. Staehle and H. Okada, p. 91, NACE, Houston (1976).
4. T. P. Hoar and W. R. Jacob, *Nature*, 216, 1299 (1967).
5. C. L. McBee and J. Kruger, in: "Localized Corrosion," eds., R. W. Staehle, B. F. Brown and J. Kruger, p. 252, NACE, Houston (1974).
6. M. J. Pryor, in: "Localized Corrosion," eds., R. W. Staehle, B. F. Brown and J. Kruger, p. 2, NACE, Houston (1974).
7. T. P. Hoar, D. C. Mears and G. P. Rothwell, *Corr. Sci.*, 5, 279 (1965).
8. J. A. Richardson and G. C. Wood, *This Journal*, 120, 193 (1973).
9. J. O'M. Bockris, D. Drazic and A. Despic, *Electrochim. Acta*, 4, 325 (1961).
10. D. L. Cocke, P. Nilsson, O. J. Murphy and J. O'M. Bockris, *Surf. Interface Anal.*, 4, 94 (1982).
11. J. E. Huheey, "Inorganic Chemistry Principles of Structure and Reactivity," p. 363, Harper & Row, New York (1978).
12. P. Fugassi and E. G. Haney, in: "Titanium Science and Technology," eds., R. I. Jaffee and H. M. Burte, p. 2611, Plenum Press, New York (1973).
13. K. J. Vetter and H. H. Strehblow, in: "Localized Corrosion," eds., R. W. Staehle, B. F. Brown and J. Kruger, p. 240, NACE, Houston (1974).
14. K. Nassau, *Mat. Res. Bull.*, 13, 67 (1978).
15. J. P. Randin and R. Viennet, *This Journal*, 129, 2349 (1982).
16. K. E. Heusler and L. Fischer, *Werkst. Korros.*, 27, 551 (1976); 27, 697 (1976); 27, 788 (1976).
17. M. Janik-Czachor, *Zashch. Met.*, 16, 256 (1980).

Manuscript submitted Jan. 7, 1983; revised manuscript received June 21, 1983.

Texas A&M assisted in meeting publication costs of this article.

Direct Hydrogen Profile Determination in TiO_2 after Electrochemical Treatment

P. Clechet,* C. Martelet, and R. Olier

Ecole Centrale de Lyon, Ecully, France

J. P. Thomas and M. Fallavier

Institut de Physique Nucléaire, Villeurbanne, France

Electrochemical treatments of titanium dioxide are well known as leading to important changes in physical (color, IR absorption), electrical (capacitance, conductivity) and photoelectrochemical properties either for single crystal material (1-4) or rf reactively sputtered (5) or thermally grown thin layers (6,7). Here we report similar observations on highly doped ($\sim 10^{19}$ cm^{-3}) 200 nm thick layers obtained by anodic oxidation of bulk electropolished titanium, at 80 V in 1 M sulfuric acid (8).

A treatment at - 2 V/SCE in 1 M NaOH solution gives an enhancement of the photoelectrochemical effect as illustrated in figure 1. Such a treatment, continued for three hours seems not affect layer thickness, reflexion spectra of the sample being almost unchanged. Although such observations, first made by Asatiani (6) have generally been explained by the incorporation of hydrogen species into the material, to date no experimental evidence of this phenomenon has been reported.

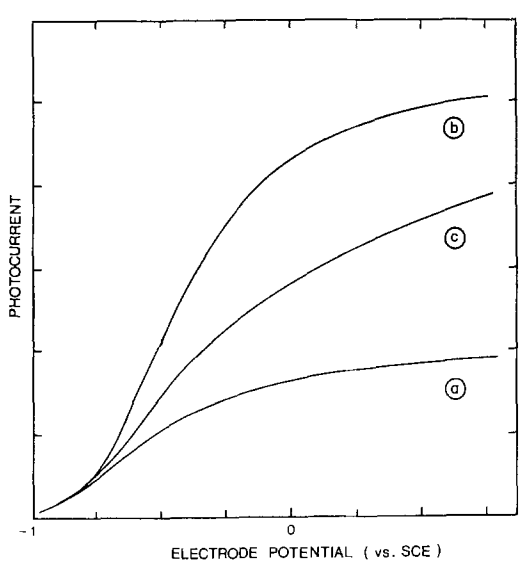

FIGURE 1 - Photocurrent (arbitrary units) vs electrode potential (see text)
a) as anodized
b) after cathodic treatment
c) after subsequent anodic treatment.

A direct proof of such a phenomenon is given here using nuclear microanalysis and more specifically the ^{15}N induced resonant nuclear reaction on hydrogen (9). Briefly summarized the principle of such non destructive depth profiling technique is based on the detection of the characteristic 4.43 MeV X-Ray emission occuring at a depth within the sample corresponding to the energy loss between the ^{15}N incident ion energy and the resonance energy of the reaction ($\sim$ 6.4 MeV) Varying the incident energy above the resonance energy leads to probe the hydrogen distribution with a depth resolution related to the resonance energy width ($\sim$ 7 keV) which corresponds to about 30 Å at the titanium oxide surface.

Figure 2 shows the essential features of our study. From the curve (a) it appears that the anodic layer is quite hydrogen free while a three hour cathodic ageing at - 2 V/SCE in 1 M NaOH solution ($V_{fb} \simeq$ - 1 V/SCE leads to a large hydrogen incorporation. As already observed in other hydrogenated materials (10) this hydrogen distribution is evolving under beam impact from an initial distribution (extrapolated at zero fluence) to a stable one (respectively curve b and c). This loosely bonded hydrogen is mainly confined in the anodic layer and can be related to the labile species mentioned by Ginley (3) from electron stimulated desorption and by Harris (2) and Weber (5) using voltamperometry and capacitance measurements.

After a subsequent anodic treatment — fourteen hours at + 2 V/SCE in 1 M NaOH solution — of these cathodically loaded layers we observed a decrease in the hydrogen content. Within the exception of the near surface region ($\sim$ 50 nm) where hydrogen is still

* Electrochemical Society Active Member

Keywords : TiO_2 films, photoanode, nuclear analysis

highly mobile under beam impact the depth distribution does not evolve significantly (curves d and e). The shape of the stable species distribution remains unchanged but the total amount is significantly smaller than for the cathodically loaded layer (curves c and e). Furthermore the characteristic shape of the distribution is conserved after 450°C annealing under vacuum and has been observed for all the tested samples.

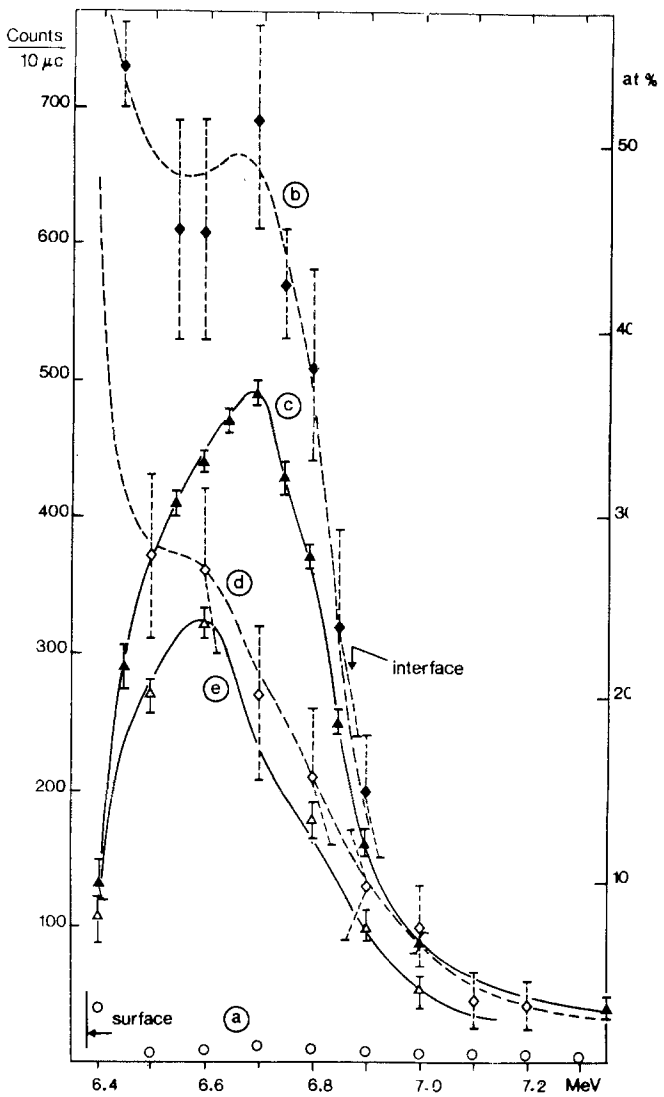

FIGURE 2 - Hydrogen depth distribution (see text)
a) as anodized
b) after cathodic treatment (initial depth distribution)
c) after cathodic treatment (stable species)
d) after subsequent anodic treatment (initial depth distribution)
e) after subsequent anodic treatment (stable species).

Thus, such a depth distribution would be characteristic of bonded species. Moreover the same kind of profile has been found for other anodization voltages (i.e. other oxide thicknesses).

In accordance with Schumacher's observations the anodic or annealing removal of hydrogen is accompanied by a decrease of the photocurrent (curve b figure 1). We did not succeed by any treatment in completly removing the incorporated hydrogen and correspondingly values of the photocurrent never come back to the starting value of the hydrogen free layer.

Thus, nuclear analysis brings out the direct evidence of the existence of at least two forms of incorporated hydrogen within TiO_2 layers as is often proposed in the literature. Incorporation mechanism seems to be intricate and hydrogen profile in our samples cannot be explained by a simple diffusion law. Probably some hydrogen species are trapped on defects resulting from crystallization during film growth (11).

REFERENCES

1. L.A. HARRIS, M.E. GERSTNER, R.H. WILSON
This Journal 126, 850 (1979).

2. L.A. HARRIS, R. SCHUMACHER
This Journal 127, 1186 (1980).

3. D.S. GINLEY, M.L. KNOTEK
This Journal 126, 2163 (1979)

4. R. SCHUMACHER
Ber. Bunsenges. Phys. Chem. 84, 125 (1980)

5. M.F. WEBER, L.C. SCHUMACHER, M.J. DIGNAM
This Journal 129, 2022 (1982).

6. A.L. ASATIANI, T.V. DZHAVRISHVILI, Z.A. ROTENBERG
Sov. Electrochem. 13, 264 (1977).

7. J.P. FRAYRET, A. CAPRANI, R. POINTEAU
Proc. 33th ISE Meeting Lyon 1982 p. 833.

8. R. OLIER, P. CLECHET, C. MARTELET, J.R. MARTIN, A. CACHARD
J. Less Common Metals 69, 73 (1980).

9. J.P. THOMAS, C. PIJOLAT, M. FALLAVIER
Rev. Phys. Appl. 13, 433 (1978).

10. J.P. THOMAS, M. FALLAVIER, J. TOUSSET,
Nucl. Instr. Meth. 187, 573 (1981).

11. C.K. DYER, J.S.L. LEACH
This Journal 125, 1032 (1978).

Manuscript submitted May 5, 1983.

Ecole Centrale de Lyon assisted in meeting publication costs of this article.

JOURNAL OF THE ELECTROCHEMICAL SOCIETY

ELECTROCHEMICAL SCIENCE AND TECHNOLOGY

SEPTEMBER 1983

The Effect of Alloying with Sb and Ca/Sn on the Electrochemical Properties of Solid Lead

J. A. Bialacki and N. A. Hampson

Chemistry Department, University of Technology, Loughborough, Leicestershire, LE11 3TU, England

K. Peters*

Chloride Technical Limited, Swinton, Manchester, M27 2HB, England

ABSTRACT

The electrochemistry of various solid Pb alloys in two different H_2SO_4 concentrations (5.0 and 5.5M) has been studied using linear sweep voltammetry (LSV). It was found that the Ca-Sn-Pb alloys were more susceptible to corrosion than pure lead or various antimonial lead alloys in 5.0 and 5.5M H_2SO_4.

Various metals, and even their oxides and sulfates (1), have been added to the material of the support grids of lead-acid batteries in order to impart many desirable properties such as longer service life, improved castability, etc. Antimony in automotive positive grids extends the life of the battery by producing further resistance to deep cycling and extensive overcharge. This is probably due to the corrosion layer, formed by the Pb/Sb alloy, adhering well to the active material and not causing an intergranular attack on the crystallites in the grid alloy. The only technical disadvantage of the addition of Sb is that the hydrogen overvoltage of the cell is lowered because the additive deposits itself on the negative plate resulting in a decrease in the potential of hydrogen evolution at that electrode. It has also been discovered that at low antimony concentrations, the retention characteristics of the positive paste on the support grids are usually observed to be poor.

Other materials have been used instead of antimony, such as calcium, tin, aluminum, magnesium, titanium, and bismuth (2). The first three metals mentioned have been used successfully in alloys in various countries because they seem to suppress markedly the hydrogen evolution reaction; however, removing antimony from the positive grids results in rather inferior cycle lives.

This paper records the LSV measurements carried out and compares the data obtained on pure lead and various lead alloys in two different H_2SO_4 concentrations, *i.e.*, 5.0 and 5.5M (the range of maximum operative concentration). However, it should be noted that in industry, battery discharge techniques are carried out at rates equivalent to extremely slow sweeps whereas here a faster cycle range is employed.

Experimental

The working electrodes were prepared from pure and alloy lead rods (CTL-metals, diameter = 0.3 cm) shrouded in Teflon which could be rotated at a known constant speed. The linear sweep experiments were performed using the computer-controlled potentiostat recently referenced (3).

All potential measurements were made at 23°C with an Hg/Hg_2SO_4 reference electrode which was in the same H_2SO_4 electrolyte solution as the working electrode.

The alloys used contained

Code	Analysis, weight percent Sb	Ca	Sn	Pb
A	—	—	—	99.999
B	0.58	—	—	Remainder
C	1.88	—	—	Remainder
D	4.18	—	—	Remainder
E	—	0.086	0.34	Remainder
F	—	0.076	0.75	Remainder

The experiments consisted of cycling to a constant response between 500-1500 mV at a series of sweep rates (10-100 $mVsec^{-1}$) in both H_2SO_4 concentrations. The time needed for constancy was approximately 1.5 hr.

Results and Discussion

Figure 1 shows stabilized current response curves for pure lead and varying degrees of antimonial lead in 5.0M H_2SO_4. As can be seen, pure lead undergoes greater anodic attack than the other antimonial alloys showing that the presence of antimony or other impurities exert a protective effect. Alloy D is corroded the least, and the PbO_2 peak corresponding to it occurs at a lower potential. Alloys B and C have very similar maximum peak current values (i_p) which are highlighted in Table I, although in the case of the former,

Table I. A comparison of i_p, E_p, and anodic charge values for pure Pb(A) and the alloys (B-F) at $\nu = 100$ mV sec^{-1} in 5.0M H_2SO_4

Alloys	i_p/mA-cm^{-2}	E_p/V	Charge, Q/mCcm^{-3}
A	2.394	1.213	3.333
B	0.901	1.248	2.554
C	0.930	1.191	2.828
D	0.730	1.177	2.190
E	3.296	1.260	7.087
F	2.592	1.200	5.412

* Electrochemical Society Active Member.

Key words: batteries, lead, alloys, antimony, calcium.

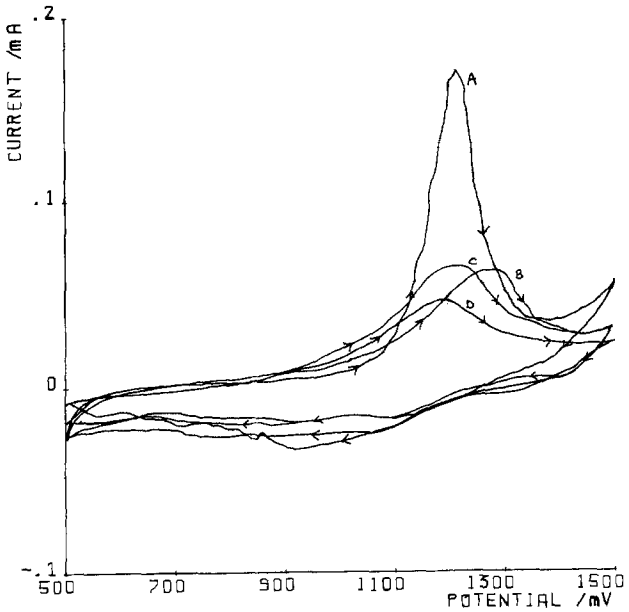

Fig. 1. 5.0M H_2SO_4 electrolyte. Digitally drawn voltammograms of A, pure Pb; B, Pb-Sb (0.58%); C, Pb-Sb (1.88%); D, Pb-Sb (4.18%). (500-1500 mV, $\nu = 100$ mV sec^{-1}) after cycling for 1.5 hr.

the peak potential (E_p) appears at a higher value than for pure lead. The peaks appear broad, comparable to those obtained by Kelly *et al.* (4), indicating that the PbO_2 formed on the electrodes is quite porous and thus the reaction can be driven deeper into the porous layer as the potential is increased.

Figure 2 displays the potential curves for the same alloys used for Fig. 1 but in 5.5M H_2SO_4. This reveals that although pure lead undergoes more anodic attack than the other alloys, the effect is not so prominent and again the placing of the antimonial alloy peaks is similar to those in Fig. 1. However, as described recently (3), the amount of charge contained in the positive-going sweep (sweep rate, $\nu = 100$ mVsec^{-1}) for all the alloys (A-F) decreases dramatically in 5.5M H_2SO_4 when compared with the charge values in 5.0M H_2SO_4. (See Tables I and II).

Figure 3 exhibits the LSV curves for pure lead and ternary alloys (Ca-Sn-Pb) in 5.0M H_2SO_4; Fig. 4

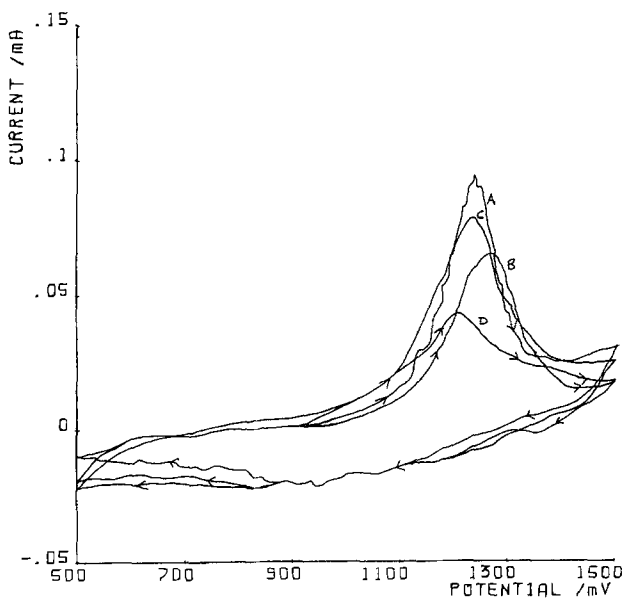

Fig. 2. The same conditions as in Fig. 1, but LSV's carried out in 5.5M H_2SO_4.

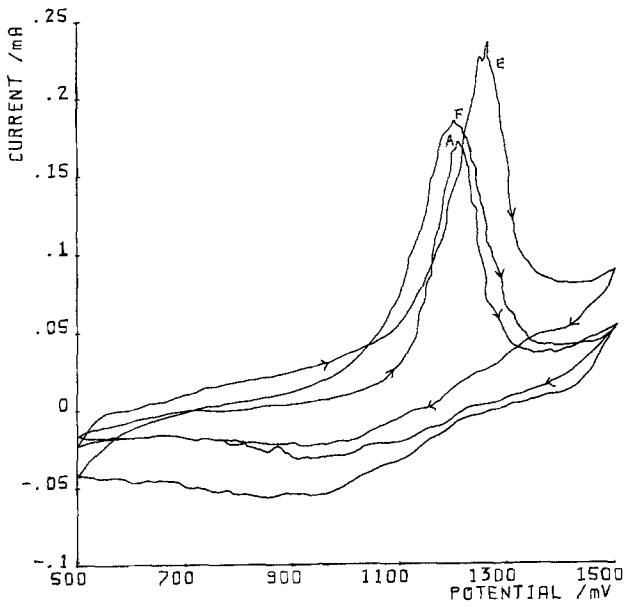

Fig. 3. 5.0M H_2SO_4 electrolyte. Digitally drawn voltammograms of A, pure Pb; E, Pb-Ca (0.086%)-Sn (0.34%); F, Pb-Ca (0.076%)-Sn (0.75%). (500-1500 mV, $\nu = 100$ mV sec^{-1}) after cycling for 1.5 hr.

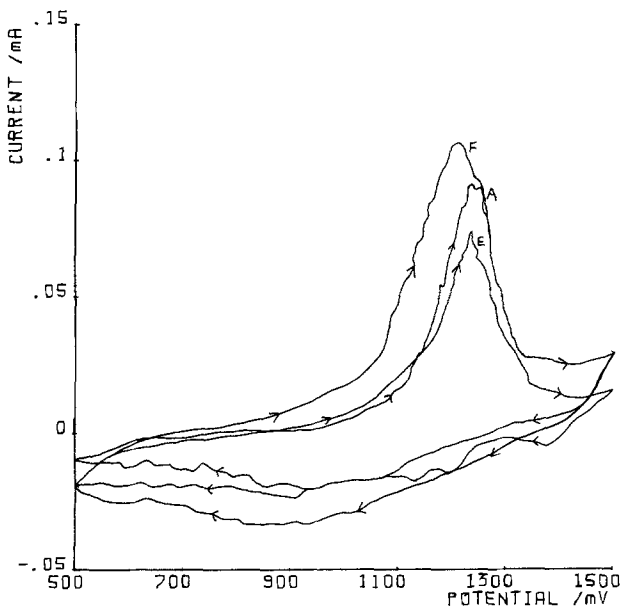

Fig. 4. The same conditions as in Fig. 3, but LSV's carried out in 5.5M H_2SO_4.

corresponds to the same metals employed in 5.5M sulfuric acid.

In Fig. 3, the ternary alloys undergo more corrosive attack than pure Pb, especially alloy E. This highlights the point mentioned earlier that the reduction of Sb, or even lack of it in the positive grids results in rather poor cycle life. Hence, adding Ca/Sn to pure Pb produces a PbO_2 deposit which is more analogous to that of a freshly plated more reactive elec-

Table II. Repeat of Table I, but in 5.5M H_2SO_4

Alloys	i_p/mA-cm^{-2}	E_p/V	Charge, Q/mC-cm^{-2}
A	1.324	1.248	2.238
B	0.963	1.251	1.711
C	1.155	1.209	2.279
D	0.675	1.202	1.608
E	1.037	1.230	1.889
F	1.577	1.209	3.430

trode as described by Fleischmann [whose research used lead freshly electroplated onto massive lead (5)] than to the deposit produced on flat lead and Pb/Sb electrodes.

Figure 4 shows that alloy E has a lower i_p value than pure lead and alloy F, thus varying the acid concentration has a marked effect on the formation of the PbO_2 deposit on these Ca-Sn-Pb alloys.

The relationship between peak potential (E_p) in the oxidation of $PbSO_4$ to PbO_2 and sweep rate (ν) in the form of E_p *vs.* $\log_{10}$ (sweep rate) is displayed in Fig. 5 for the 5.0M H_2SO_4 case. The equation for this relationship was developed by Canagaratna *et al.* (6) for the production of a single layer on an electrode. As can be seen from the straight line plots in Fig. 5, for alloys D and F, the formation of PbO_2 occurs at a much less positive potential than on the pure metal. In 5.5M sulfuric acid when E_p is plotted against $\log_{10}$ (sweep rate), all the alloys (B-F) form PbO_2 at a much less positive potential than pure Pb.

Figure 6 exhibits the i_p-(sweep speed, ν)$^{1/2}$ relationship in 5.0M H_2SO_4, and straight lines were obtained with the pure lead and the alloys in the range ν = 10-100 mVsec^{-1}. The linearity of the plots indicate that the process for each alloy and pure Pb is a simple first order charge transfer reaction. The i_p *vs.* $\nu^{1/2}$ relationship still remained intact for most of the alloys in 5.5M sulfuric acid.

Tables I and II show that the i_p values corresponding to the sweep rate, ν = 100 mVsec^{-1} were higher in 5.0M H_2SO_4 for pure Pb and alloys D, E, and F. Alloys B and C had higher i_p values in 5.5M H_2SO_4. However, in 5.0M H_2SO_4 more charge was obtained with the ternary alloys.

In 5.0M sulfuric acid, using pure Pb (99.999%, Koch-Light) instead of precast lead (contains many minute impurities and is thus <99.999% pure) which Kelly *et al.* (4) used, it would seem that more charge is obtained than with the antimonial alloys. This may be due to the fact that the PbO_2 deposited on the pure Pb metal is more porous than the antimony/lead binary alloys and does not produce a passivating layer which is tight and mechanically sound (4). Even at slower sweep rates, the pure metal still produced more charge in the LSV curves, although it was expected that the antimonial alloys would undergo more anodic attack since it has been observed that some stationary batteries containing Pb-Sb components exhibit a large amount

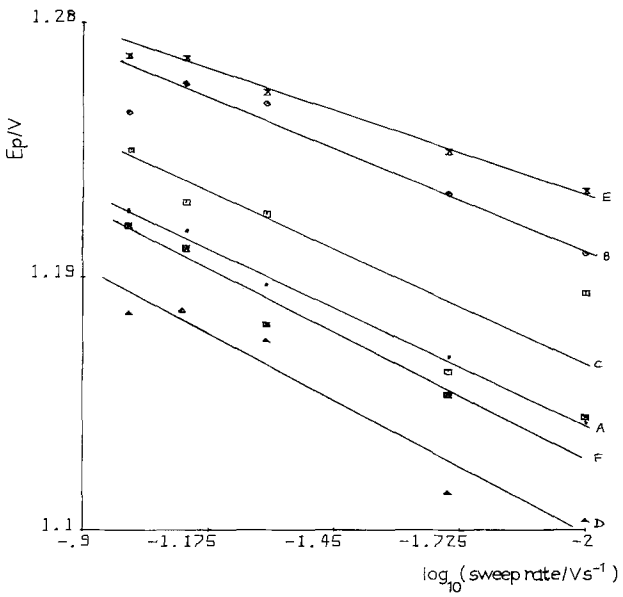

Fig. 5. Plot of E_p *vs.* $\log_{10}\nu$ for: ● = A, pure Pb; ◈ = B, Pb-Sb (0.58%); ⊡ = C, Pb-Sb (1.88%); △ = D, Pb-Sb (4.18%); × = E, Pb-Ca (0.086%)-Sn (0.34%); ⊠ = F, Pb-Ca (0.076%)-Sn (0.75%); in the range 10-100 mV sec^{-1}.

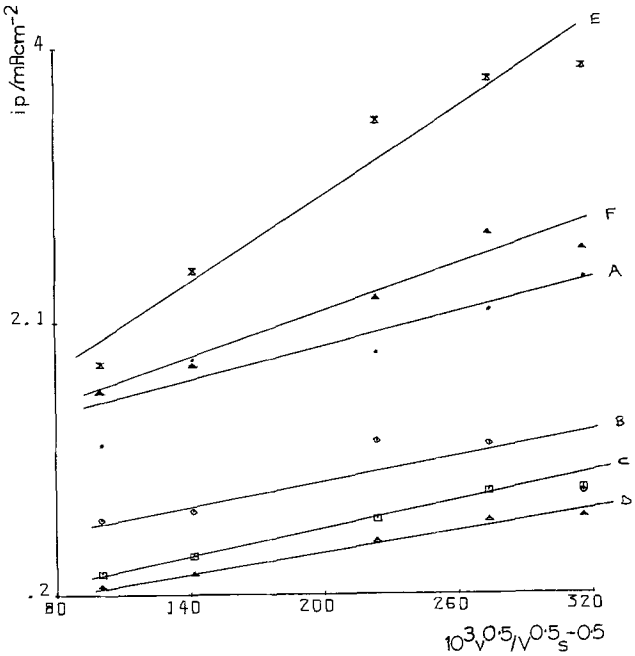

Fig. 6. Plot of i_p *vs.* $\nu^{1/2}$ for: ● = A, pure Pb; ◈ = B, Pb-Sb (0.58%); ⊡ = C, Pb-Sb (1.88%); △ = D, Pb-Sb (4.18%); × = E, Pb-Ca (0.086%)-Sn (0.34%); ▲ = F, Pb-Ca (0.076%)-Sn (0.75%); in the range 10-100 mV sec^{-1}.

of corrosion. In the authors' experiments in 5.5M sulfuric acid, however, only 1.88% antimonial lead displayed higher charge content in the linear sweep voltammogram than the pure metal.

In these experiments, the pure lead undergoes more anodic attack than the Pb-Sb alloys. This is probably due to the lack of impurities because, as mentioned recently (3), additives such as Ag, Cu, Ti, and Bi in lead metal can exert a protecting effect and considerably reduce corrosion. Also, as reasoned earlier, the pure Pb may produce a PbO_2 layer which is more porous than with the antimonial alloys, thus resulting in a greater degree of corrosion evidenced by voltammograms containing more charge for the pure lead. These results may be considered at variance with those of an earlier investigation (4); however, the number of sweeps taken to obtain steady states for each alloy and the sweep speed range were comparable with those reported by Kelly *et al.* (4). However, the potential limits were different; in this case, they were 500-1500 mV, whereas Kelly (4) used the limits of 400-1520 mV.

Conclusions

1. In 5.0M H_2SO_4, the Ca-Sn-Pb alloys are more susceptible to anodic attack than either pure lead or (0.58-4.18%) antimonial lead.

2. There was more charge in the voltammogram corresponding to pure lead in 5.0M H_2SO_4 than with the Pb-Sb alloys.

3. In 5.5M H_2SO_4, more charge was obtained with electrode C than with pure lead and the other two Pb-Sb electrodes.

4. In 5.0M and 5.5M H_2SO_4, the i_p values corresponding to pure lead were higher than those obtained with the lead/antimony binary alloys.

Acknowledgment

The authors are grateful to Chloride Technical Limited for financial assistance.

Manuscript submitted July 26, 1982; revised manuscript received April 22, 1983.

Chloride Technical Limited assisted in meeting the publication costs of this article.

REFERENCES
1. S. Hattori, M. Yamaura, M. Kono, M. Yamone, H. Nakashima, and J. Yamashita, Semiannual Report of the ILZRO Project LE-197 (1974).
2. N. A. Hampson, S. Kelly, and K. Peters, *This Journal*, **127**, 1456 (1980).
3. J. A. Bialacki, N. A. Hampson, and K. Peters, *J. Appl. Electrochem.*, **12**, 627 (1982).
4. N. A. Hampson, S. Kelly, and K. Peters, *ibid.*, **10**, 91 (1980).
5. M. Fleischmann and H. R. Thirsk, *Trans. Faraday Soc.*, **51**, 71 (1955).
6. S. G. Canagaratna, P. Casson, N. A. Hampson, and K. Peters, *J. Electroanalyt. Chem.*, **79**, 273 (1977).

The Electrochemical Cycling of Pasted Sb and Ca/Sn Lead Electrodes (Positives)

J. A. Bialacki and N. A. Hampson

Chemistry Department, University of Technology, Loughborough, Leicestershire, LE11 3TU, England

K. Peters*

Chloride Technical Limited, Swinton, Manchester, M27 2HB, England

ABSTRACT

Linear sweep voltammetry (LSV) has been employed to study the electrochemical behavior of various pasted lead electrodes (positives) in two different H_2SO_4 concentrations (5.0 and 5.5M). The early cycle histories of the porous Sb-based electrodes displayed that they discharged more deeply in 5.0M H_2SO_4 when sweeping back and forth between the PbO_2 and $PbSO_4$ regions. The case was different for the porous Ca/Sn lead electrodes which gave larger reduction peak current values (i_p) in 5.5M sulfuric acid.

The capability of a lead-acid battery to accept charge and then redischarge (1) depends on factors such as construction, condition, age, charging conditions, and the temperature of the cell. If the battery is charged too fast and not effectively controlled, gassing occurs together with high temperatures and sizeable particles from the positive plates can be torn away resulting in PbO_2 sludge which would prematurely reduce the capacity of the cell. Some of the sludge is carried over to the negative plates as a positive-charged colloid via electrophoresis or convection. At these plates, the colloid is reduced to Pb which in turn can lead to short-circuiting. Also, sulfate conversion can be affected making charging more difficult and the expanders will be rendered inoperative. However, if charging is stopped before gas evolution the active material does not become fully charged, and this results in the cell having a low overall capacity.

Antimony is employed as the grid alloying additive for the lead-acid positive plate in automotive batteries, as described by Kelly *et al.* (2, 3). However, a technical disadvantage of the metal's presence in the cell is that antimony released from the positive electrode deposits itself on the negative plate resulting in a reduction of the hydrogen overvoltage at that electrode.

The use of calcium (<0.09 weight percent [w/o]) (4-6) and tin as alloying agents in lead-acid cells was especially developed for float service; they increase the tensile strength of lead without introducing harmful side reactions into the cells. During float periods, the small overvoltage applied to the cell results in a current which is just sufficient to prevent internal self-discharge processes. At the same time, this low current keeps the loss of water by electrolysis to a minimum. With antimonial grid, because the hydrogen overvoltage is depressed by the presence of antimony on the negative electrode, the float current increases during service. However, removal of antimony from the positive grids gives rise to very poor cycle lives (2).

The LSV experiments were carried out on all the pasted lead alloy electrodes in 5.0 and 5.5M sulfuric acid; the reason for the latter value was discussed recently (7). Also, the base lead alloys used here are the same as those previously employed (7).

* Electrochemical Society Active Member.
Key words: batteries, lead, antimony, calcium.

Experimental

The computer-controlled experimental set up was recently described (7, 8). The porous electrodes were prepared by arranging a solid support (various lead-based alloys) to lie beneath the level of a Teflon shrouding. By forcing the positive paste into the cavity, a porous layer was produced (3 mm diam; 0.76 mm deep) which terminated the lead electrode. The density of the high capacity positive paste (15% red lead) used here was 4.2 gcm^{-3}, and the charging of the electrodes was performed in 0.3M H_2SO_4 as reported by Kelly *et al.* (3).

For each concentration of sulfuric acid, an Hg/Hg_2SO_4 reference electrode was used, and all the experiments were carried out at 23° ± 1°C.

The base lead alloys used in the LSV experiments were

Code	Analysis, w/o Sb	Ca	Sn	Pb
B	0.58	—	—	Remainder
C	1.88	—	—	Remainder
D	4.18	—	—	Remainder
E	—	0.086	0.34	Remainder
F	—	0.076	0.75	Remainder

Results and Discussion

The linear sweep experiments were carried out between the limits of 1240 mV (PbO_2) and 700 mV ($PbSO_4$), the sweep-speed being always 10 $mVsec^{-1}$.

Figures 1-5 correspond to a series of voltammograms for the early cycle histories of each pasted Pb-alloy electrode, that is, B-F, all in 5.0M H_2SO_4. Figures 6-10 correspond to the same electrodes, but the potentiodynamic cycling experiments were performed in 5.5M sulfuric acid.

As can be seen from the ten figures, there is a decrease in peak current values (i_p) with cycling (PbO_2 → $PbSO_4$ reduction peak). The major difference is between the i_p values for the first and second cycles for all the electrodes as highlighted by Tables I and II.

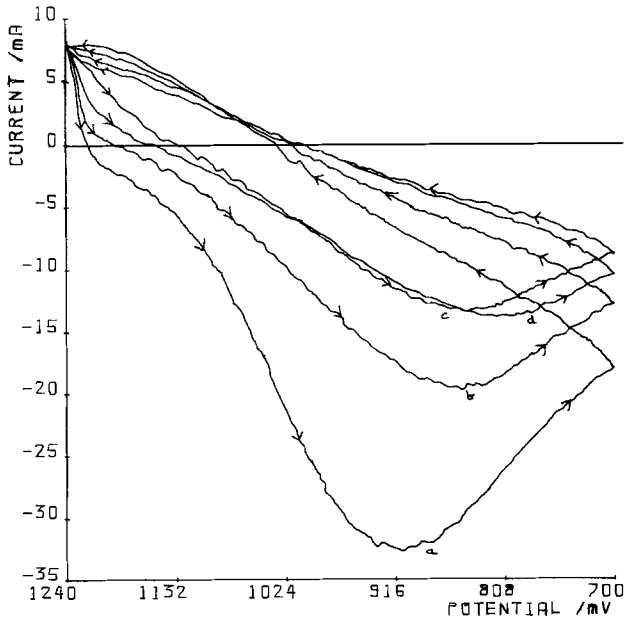

Fig. 1. Digitally drawn voltammograms for B, pasted Pb-Sb (0.58%) positive in 5.0M H_2SO_4. (1240-700 mV, $\nu = 10$ mV sec^{-1}, nominal surface area = 0.07 cm^2). a, first cycle; b, second cycle; c, third cycle, d, fourth cycle.

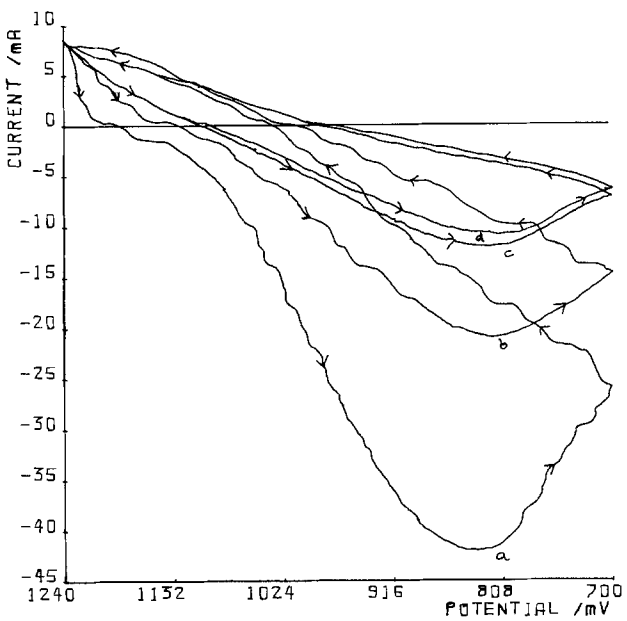

Fig. 2. As in Fig. 1, but for C; pasted Pb-Sb (1.88%) positive

The large initial reduction current is due to a passivated form of $PbSO_4$ being produced which resists oxidation to PbO_2 during the anodic sweep (3). If the higher potential limit is raised above 1240 mV, oxygen bubbles are formed in the electrode matrix which would interfere with the charging/discharging operation.

The electrodes had to be reoxidized galvanostatically (25 $mAcm^{-2}$ in 0.3M H_2SO_4) in an upward-facing position after a series of cycles. This is because the layer of passivated lead sulfate crystals formed on the Pb electrodes is such that in order to reproduce lead dioxide a large overpotential is needed.

Table I shows that in 5.0M H_2SO_4, the pasted alloy-D electrode has a larger initial i_p value than that of the other porous Pb-Sb electrodes. Also, the pasted alloy positive attains a constant response after approximately 15 cycles, the i_p and position of i_p (E_p) values

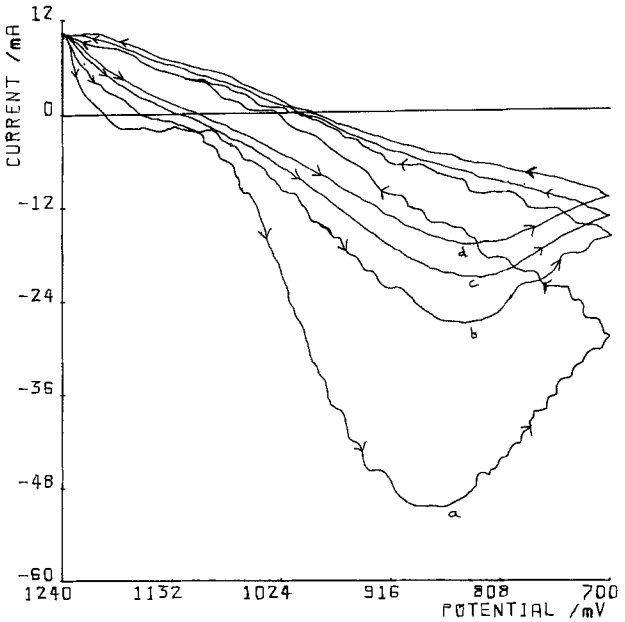

Fig. 3. As in Fig. 1, but for D; pasted Pb-Sb (4.18%) positive

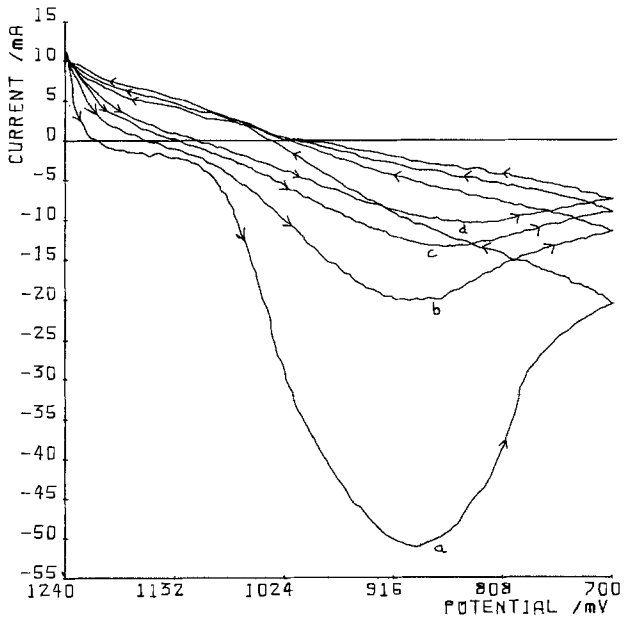

Fig. 4. As in Fig. 1, but for E; pasted Pb-Ca (0.086%)-Sn (0.34%) positive.

remaining constant. Pasted alloys B and C reach constant responses after 11 and 14 cycles, respectively. However, the pasted alloy-E electrode discharges more

Table I. A comparison of i_p with linear sweep cycling of the porous Pb-alloy electrodes (1240-700 mV, 10 mV sec^{-1}) in 5.0M H_2SO_4

Alloys	Cycle number	Reduction peak current, i_p/mA	Position of ip, E_p/mV
B	1	32.79	912
	2	20.00	851
	3	13.53	844
C	1	42.00	842
	2	20.00	824
	3	15.40	821
D	1	50.00	873
	2	26.00	840
	3	21.00	833
E	1	50.80	894
	2	20.60	891
	3	13.80	866
F	1	45.13	882
	2	20.55	862
	3	13.90	848

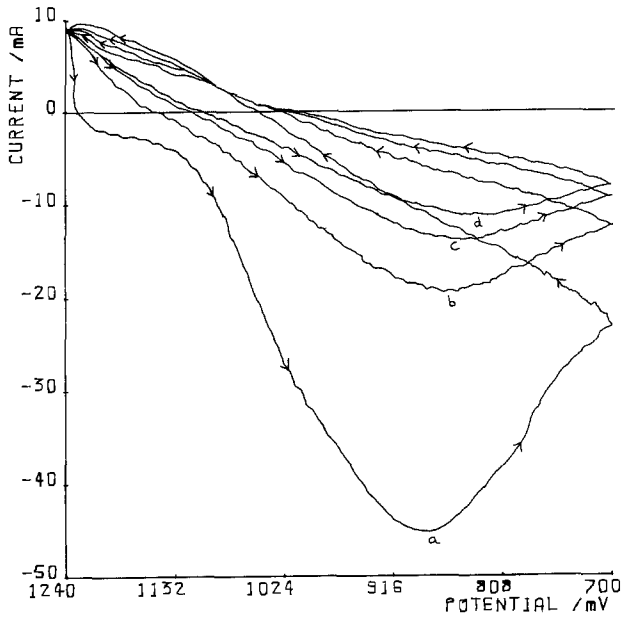

Fig. 5. As in Fig. 1, but for F; pasted Pb-Ca (0.076%)-Sn (0.75%) positive.

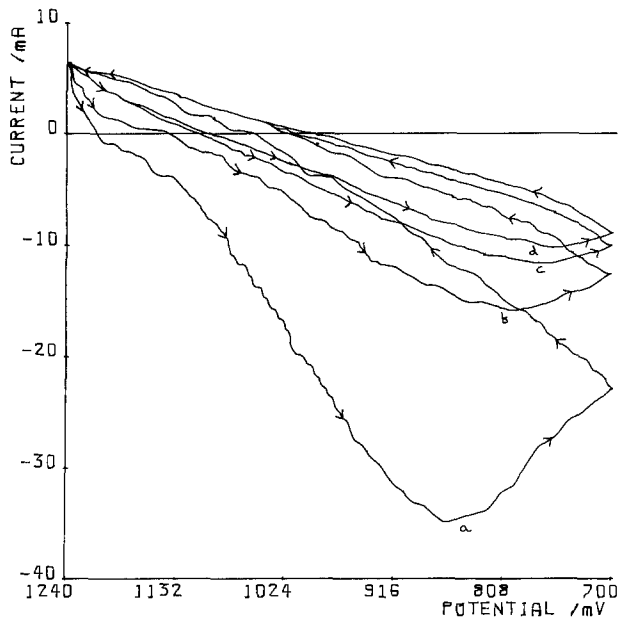

Fig. 6. Digitally drawn voltammograms for B in 5.5M H_2SO_4. (1240-700 mV, ν = 10 mV sec^{-1}, nominal surface area = 0.07 cm^2). a, first cycle; b, second cycle; c, third cycle; d, fourth cycle.

deeply on the first cycle than the porous antimonial lead electrodes as highlighted by Table I. This may be attributed to the fact that a more reactive PbO_2 deposit is produced on Ca-Sn-Pb alloys (7) than the deposit formed on pure lead and most Pb-Sb alloys. Hence, the porosity of the pasted Ca-Sn-Pb electrode matrix when charged may have been further increased. Porous alloy-E positive has a higher initial i_p value than the porous alloy-F electrode, and they both obtain a constant response after 11 cycles no matter what subsequent cycling experiments are carried out. (This applies to the previous pasted Pb-Sb positives.) It would seem, as described by Kelly *et al.* (3), that the $PbSO_4$ produced reaches an equilibrium form with some of the "unpassivated" lead sulfate present in the porous matrix which can be oxidized (to PbO_2) and reduced (back to $PbSO_4$) by sweeping potentiodynamically.

Table II shows that in 5.5M sulfuric acid the pasted alloy-D positive has a greater initial i_p value than that of the other two porous Pb-Sb electrodes but is in turn lower than the initial i_p value of the positive-F electrode. A strange feature of the higher concentration of H_2SO_4 (*i.e.*, 5.5M) is that the pasted alloy-C electrode undergoes partial ohmic control after 10 cycles. With

Table II. Repeat of Table I, but in 5.5M H_2SO_4

Alloys	Cycle number	Reduction peak current, i_p/mA	Position of ip, E_p/mV
B	1	35.00	858
	2	16.00	786
	3	11.60	776
C	1	38.00	850
	2	18.40	813
	3	13.40	808
D	1	55.00	866
	2	24.00	848
	3	17.40	826
E	1	51.17	869
	2	23.00	858
	3	15.00	835
F	1	58.00	950
	2	21.40	861
	3	16.00	840

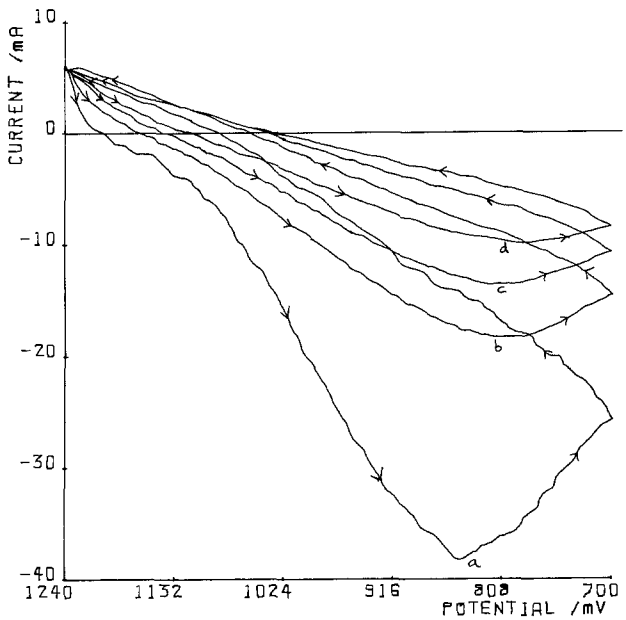

Fig. 7. As in Fig. 6, but for C

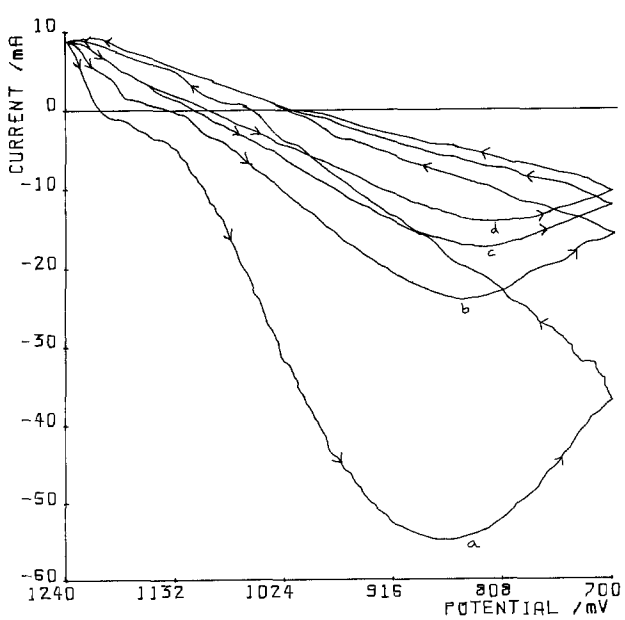

Fig. 8. As in Fig. 6, but for D

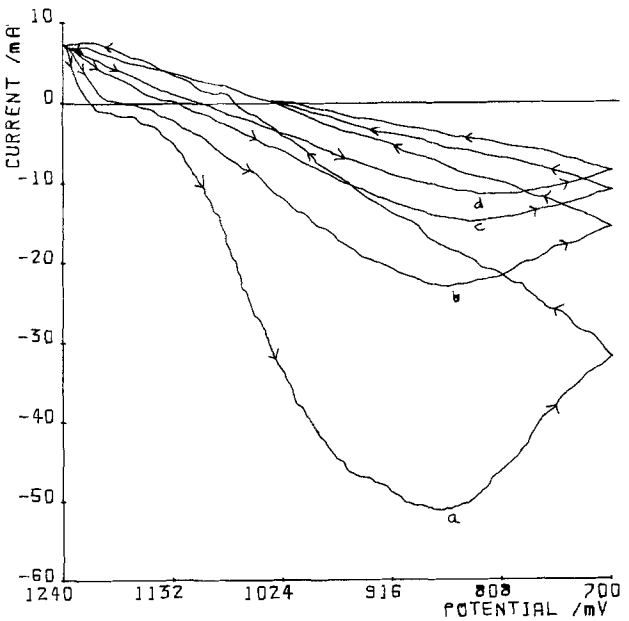

Fig 9. As in Fig 6, but for E

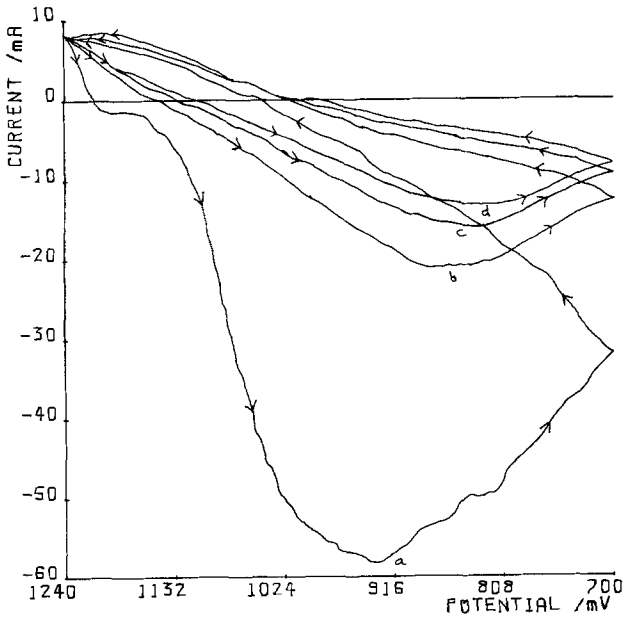

Fig. 10. As in Fig. 6, but for F

the other porous electrodes, their voltammograms reach constancy after a larger number of cycles than the corresponding electrodes in 5.0M H_2SO_4. The pasted Ca-Sn-Pb electrodes discharge more initially in 5.5M H_2SO_4 than in 5.0M sulfuric acid, whereas the situation is completely the opposite with the pasted Pb-Sb positives. It would seem that varying the acid concentration has a marked effect on the PbO_2 porous matrix on the base Ca-Sn-Pb metals.

Comparing the reported data (7) on flat unpasted electrodes to those exhibited here, one notices a few major differences. With the flat unpasted electrode, the PbO_2 peak is dominant (7) and the data obtained correspond to the production of a single layer on an electrode with no thickening of the deposit occurring. With the porous electrode, the prominent PbO_2 formation peak is absent because the lead dioxide produced grows in layers (9), and thus a broad band is observed made up of many different oxidation peaks overlapping with each other. Another significant difference between the two electrodes is that with the porous one, larger current and hence charge values are obtained.

A look at the voltammograms of the flat and pasted electrodes shows that the reduction peaks ($PbO_2 \rightarrow PbSO_4$) are clearly different. With the flat electrode, the reduction "peak" is hardly visible; for the pasted electrode, a long "reduction tail" (3) is displayed which is indicative of newly produced porous PbO_2, where the discharge is being driven deep into the porous matrix.

The i_p, and hence charge values obtained for the pasted Pb-Sb electrodes, are higher than those reported by Kelly *et al.* (3). This is due to the fact that the paste used here was such that it could sustain more charge than the standard automotive paste employed by them (3).

Conclusions

1. The Ca-Sn-Pb electrodes initially discharge more deeply than the Pb-Sb electrodes in 5.0 and 5.5M H_2SO_4 although electrode D (containing 4.18% Sb) performs very similarly to electrodes E and F.
2. After the first cycle the reduction peak current values (i_p) for the porous Pb-Sb electrodes were higher in 5.0M H_2SO_4 than in 5.5M H_2SO_4.
3. The porous Ca-Sn-Pb electrodes had higher reduction peak current values (i_p) in 5.5M H_2SO_4 than in 5.0M H_2SO_4.

Acknowledgment

The authors thank Chloride Technical Limited for financial support and for permission to publish.

Manuscript submitted July 26, 1982; revised manuscript received March 14, 1983.

Chloride Technical Limited assisted in meeting the publication costs of this article.

REFERENCES

1. H. Bode, "Lead-Acid Batteries," John Wiley, New York (1977).
2. N. A. Hampson, S. Kelly, and K. Peters, *J. Appl. Electrochem.*, **10**, 91 (1980).
3. N. A. Hampson, S. Kelly, and K. Peters, *ibid.*, **11**, 595 (1981).
4. H. E. Haring and U. B. Thomas, *Trans. Electrochem. Soc.*, **68**, 293 (1935).
5. E. E. Schumacher and G. S. Phipps, *ibid.*, **68**, 309 (1935).
6. U. B. Thomas, F. T. Forster, and H. E. Haring, *ibid.*, **92**, 313 (1947).
7. J. A. Bialacki, N. A. Hampson, and K. Peters, *This Journal*, **130**, 1797 (1983).
8. J. A. Bialacki, N. A. Hampson, and K. Peters, *J. Appl. Electrochem.*, **12**, 627 (1982).
9. P. Casson, Ph.D. Thesis, Loughborough University (1978).

Corrosion Behavior of SiC/Al Metal Matrix Composites

P. P. Trzaskoma* and E. McCafferty*

Naval Research Laboratory, Washington, DC 20375

C. R. Crowe

Naval Surface Weapons Center, Silver Spring, Maryland 20910

ABSTRACT

The effect of the SiC phase on the corrosion behavior of SiC/Al metal matrix composites has been studied in 0.1 and 0.6N NaCl, both in the presence and absence of dissolved oxygen. Anodic polarization behavior has been determined, and pitting potentials have been measured for three composite systems: SiC/Al 2024, SiC/Al 6061, and SiC/Al 5456. General corrosion behavior and the effects of anodizing on the corrosion resistance of the composites have been studied by a-c impedance techniques. The results show that pitting susceptibility is about the same for the composites and their corresponding alloys, except for Al 2024. In this system, the composite is less resistant to pit initiation than the corresponding wrought aluminum alloy. General corrosion is more significantly affected by the presence of oxygen than by the SiC phase. In the absence of oxygen, corrosion resistance is improved for both the alloys and composites. In addition, the corrosion resistance of the composites can be improved by anodizing.

Recent advances in the fabrication and characterization of SiC/Al composites have resulted in a new generation of engineering materials that are under consideration for a variety of structural, defense, and aerospace applications. These materials consist of an aluminum alloy matrix into which SiC (*i.e.*, flakes, whiskers, or fibers) is incorporated, using various metallurgical techniques, to enhance the physical and mechanical properties of the matrix material. The amount of SiC typically varies between 10 and 50 volume percent (v/o). Composite materials have particular appeal because, within limits, they can be designed and fabricated to fit the mechanical requirements of a given application (1).

Addition of a second phase to a metal alloy, however, could significantly change corrosion behavior. Structural flaws (*i.e.*, crevices, pores) and/or galvanic coupling within the material could result in increased localized corrosion of the matrix. In addition, surface variations could affect the integrity of the protective air-formed film and promote increased localized or general attack.

Several investigators have reported modest to significant increases in the corrosion rates of composites as compared to the matrix for a variety of systems (*i.e.*, boron/aluminum, boron/copper, boron/nickel, graphite/Al 6061, and depleted uranium-0.75% titanium/tungsten) in chloride environments (2-4). Dull *et al.* have studied the corrosion behavior of graphite/Al 6061 in 3.5% NaCl (3). For this composite, an increased corrosion rate was found to be a result of crevice corrosion promoted by galvanic coupling between the matrix and graphite fibers. Boron/aluminum composites have been studied in NaCl solutions by Sedriks *et al.* (5) and Pohlman (6). In the former work, boron fibers were tungsten-coated and diffusion-bonded to aluminum alloy foils; in the latter, uncoated boron filaments were hot pressed in the alloy matrices. In both studies, preferential localized corrosion was observed at the matrix-filament interfaces. Sedriks attributed this behavior to an increase in anodic sites as a result of compositional changes and/or fissures at the filament matrix boundary. Pohlman showed that increased localized attack was a result of galvanic coupling between the matrix and an aluminum boride intermetallic compound which formed during fabrication and heat-treatment of the composite.

The purpose of this investigation is to study the effects of the SiC phase on the corrosion behavior of SiC/Al composites for three alloy systems: Al 2024, Al 5456, and Al 6061. Pitting potentials were measured to compare the pitting susceptibility of the composites with that of their base alloys. General corrosion resistance and the effect of anodizing were studied through a-c impedance techniques.

* Electrochemical Society Active Member.

Key words: impedance, polarization, composites, corrosion, pitting.

Experimental

The aluminum alloy samples were wrought extruded rods of nominal composition given in Table I. Composite samples of the corresponding alloys were extruded rods prepared by powder metallurgy techniques. The composites contained 20 v/o SiC whiskers with diameters of 0.5-1 μm and lengths up to 50 μm. More detail on sample preparation is given elsewhere (1), but in brief, the SiC whiskers were blended with commercially available alloy powders of −325 mesh and were then cold compacted, hot pressed, and cold extruded. Both the composites and wrought alloys were given a T-6 heat-treatment.

Figure 1 shows SEM photomicrographs of a cross-sectional area of a typical composite sample. The light areas are the SiC particles; dark areas are the metal matrix. The top micrograph shows that the SiC particles are distributed unevenly throughout the matrix resulting in a concentration of particles in some areas and an absence of particles in other areas. The bottom micrograph at a higher magnification shows the irregular shape and random orientation of the SiC particles.

Anodized samples were prepared by a sulfuric acid anodizing process. Both Type II (porous, conventional) and Type III (porous, hardcoat) coatings were tested. Prior to anodizing, surfaces were polished to 600 grit and cleaned thoroughly. Type II anodizations were carried out at 23°C and 27 mA/cm^2 ($\approx$ 18V) for 30 min in 16 weight percent (w/o) H_2SO_4. Type III anodizations were prepared in the same solution at −1°C by raising the anodizing voltage 1V (*vs.* a counterelectrode) every 10 min up to 30V. Following anodization, the specimens were sealed in boiling water for 30 min (7).

For the polarization measurements, samples were mounted in epoxy, abraded through 600 grit paper,

Table I. Nominal composition of the aluminum alloys* (w/o)

	Cu	Mn	Mg	Cr	Si
2024	4.4	0.6	1.5		
5456		0.8	5.1	0.12	
6061	0.27		1.0	0.2	0.6

* "Metals Handbook," 8th ed., Vol. 7, p. 241, American Society for Metals, Metals Park, Ohio (1972).

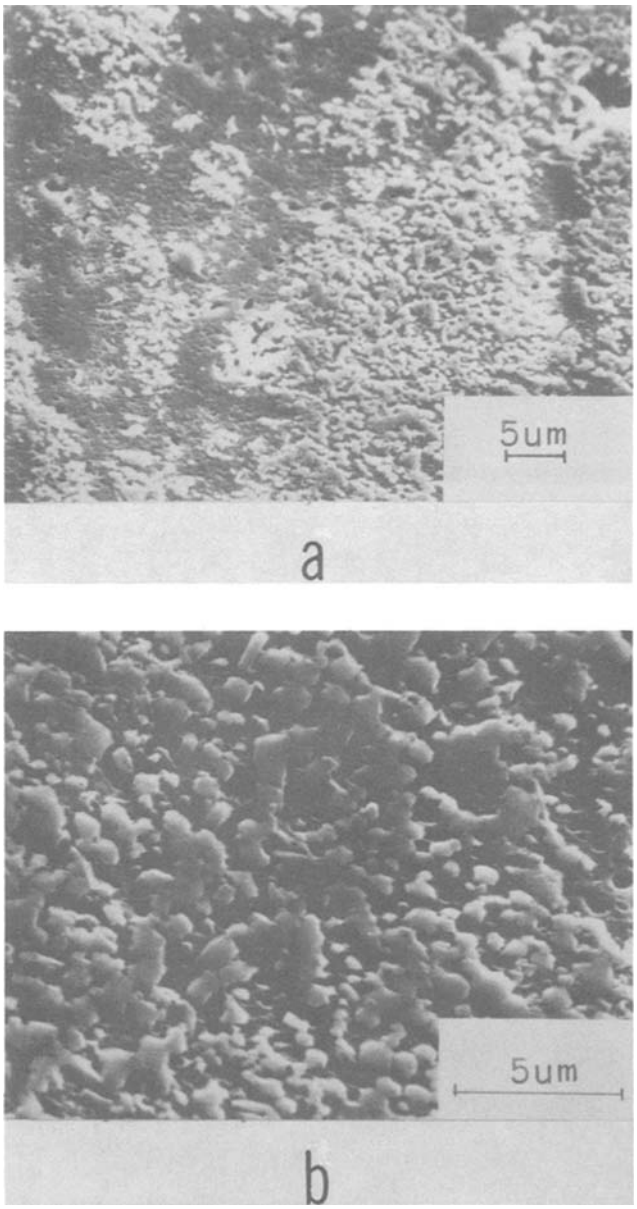

Fig. 1. Scanning electron micrograph of SiC/Al 6061 after polishing with diamond paste and etching for 40 sec in Keller's reagent. The top figure shows the uneven distribution of SiC particles and the bottom figure shows their irregular shape and random orientation.

rinsed with water, air dried, and stored in a dessicator until used. The exposed area of the samples was about 1 cm^2, and the edges at the epoxy mold were masked with lacquer to prevent crevice corrosion.

Solutions were prepared with Fisher certified reagent dissolved in distilled water (10^{-6} Ω^{-1} cm^{-1} conductivity). Solutions were deaerated by bubbling with argon for at least 12 hr prior to immersion and during the polarization run. For runs in solutions containing oxygen, the solutions were quiescent and open to the air.

Measurement of Pitting Potentials

Pitting potentials were determined by the anodic potentiostatic polarization method. Samples were immersed in solution for approximately 2 hr until a steady open-circuit potential (E_{corr}) was recorded; at this time, the potential was increased in 10 mV intervals and the steady current recorded (usually after 10 min). The potential at which the current continuously increased was interpreted to be the pitting potential (E_{pit}). In most cases, visible pits and gas evolution were observed at this time. At the pitting potential and at potentials anodic to the pitting potential, the rising currents were recorded at 1 and 10 min intervals. After 10 min a new potential was set, the currents recorded as described, and so on until the end of the run.

SEM Studies

In order to examine the effect of SiC on pit morphology, SEM studies were performed on one alloy system (Al 6061) after pitting in deaerated 0.1*N* NaCl. For these studies, epoxy-mounted samples were polished with diamond paste (0-1 μm), immersed in solution, allowed to reach a steady potential, and then polarized at a potential about 50 mV positive (−0.610V) to E_{pit} for 30 min. About half of the total surface area (0.5 cm^2) was masked with lacquer before the run in order to compare exposed and nonexposed areas simultaneously in the SEM.

Impedance Measurements

Impedance measurements were made at 25°C in a three-electrode cell containing aqueous 0.6*N* NaCl solution. A PAR Model 173 potentiostat and a Solartron Model EMR 1172 frequency response analyzer were connected to the cell. Potential control of the working electrode was maintained using the potentiostat and a saturated calomel reference electrode. The reference electrode was immersed in the cell by means of a Luggin probe which was isolated by a PAR Model 178 isolation amplifier. The cell current was measured using a PAR Model 376 current to voltage converter. Data were collected and reduced using an HP9835 minicomputer, and results were automatically plotted on the plotter.

The measurement system was calibrated by replacing the electrochemical cell by an electrical analog with known values for the components. No phase shifts or measurement errors greater than 4% were measured over the entire frequency range investigated. At 10 kHz, repetitive measurements on an anodized aluminum sample showed a standard deviation of 0.8° in phase angle and 3.0 Ω-cm^2 in impedance over 20 measurements. Impedance measurements were started 1 hr after immersion. First the open-circuit electrode potential, E_{corr}, of the sample was measured relative to the SCE, and potential control was established at this value. Impedance measurements were then performed by connecting the generator stage of the frequency response analyzer to the input control of the potentiostat. This superimposed a 10 mV a-c excitation signal with a programmable frequency range of 10^4-10^{-4} Hz on the control potential. Both sinusoidal (+10 mV rms) and triangular (±10 mV peak-to-peak) wave forms were used.

Results and Discussion

Polarization behavior and pitting potentials.—The anodic polarization curves for alloys Al 2024 and Al 6061 and their respective composites in deaerated 0.1*N* NaCl are shown in Fig. 2 and 3. Figures 4 and 5 show the corresponding curves in quiescent solutions open to air. Points including arrows indicate the current rise (at a given potential, in a 10 min interval) during active pitting. All other points on the curves are steady current readings. These curves show that the polarization behavior of the composites and alloys is similar. In deaerated solution, a constant current region (200-700 mV) is observed between the corrosion potential and pitting potential, whereas in the presence of oxygen, the corrosion potential is shifted to within 20 mV of the pitting potential.

Table II is a summary of the pitting potentials (E_{pit}) and corrosion potentials (E_{corr}) in 0.1*N* NaCl. It can be seen that the pitting potentials are independent of the presence of dissolved oxygen in solution for all the alloys and composites studied. In comparing a given alloy with its SiC composite, the pitting potentials are

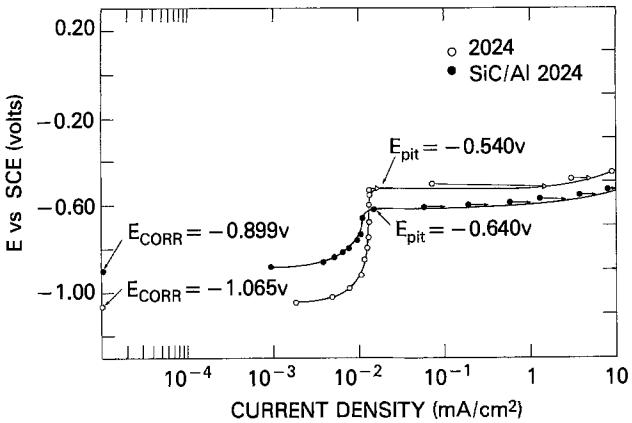

Fig. 2. Potentiostatic polarization curves for Al 2024 and SiC/Al 2024 in deaerated 0.1*N* NaCl. (Arrows show the increase in current density with time, in the initial 10 min interval at a given potential, after the onset of pitting.)

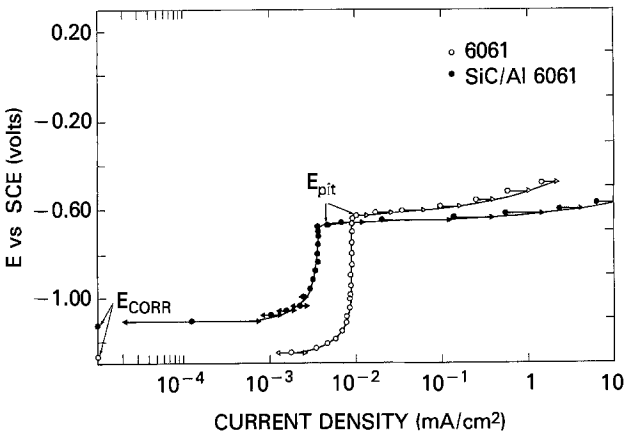

Fig. 3. Potentiostatic polarization curves for Al 6061 and SiC/Al 6061 in deaerated 0.1*N* NaCl. (Arrows show the increase in current density with time, in the initial 10 min interval at a given potential, after the onset of pitting.)

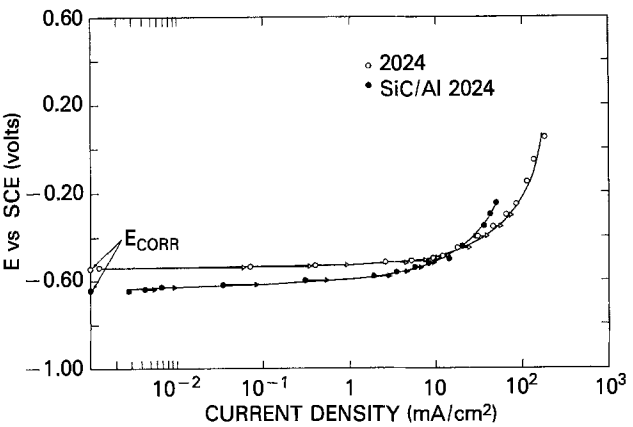

Fig. 4. Potentiostatic polarization curves for Al 2024 and SiC/Al 2024 in quiescent 0.1*N* NaCl open to the air. (Arrows show the increase in current density with time, in the initial 10 min interval at a given potential, after the onset of pitting.)

the same for the alloy and composite except for the Al 2024 system. In this system, E_{pit} of the composite is 100 mV more negative than that of the alloy.

This lower value of E_{pit} for the 2024 composite cannot be attributed to possible differences in matrix structure between the wrought alloy and the powder metallurgy alloy. To investigate this possibility, an Al 2024 sample was fabricated from powders in the same way as the composites (except that SiC was excluded). The

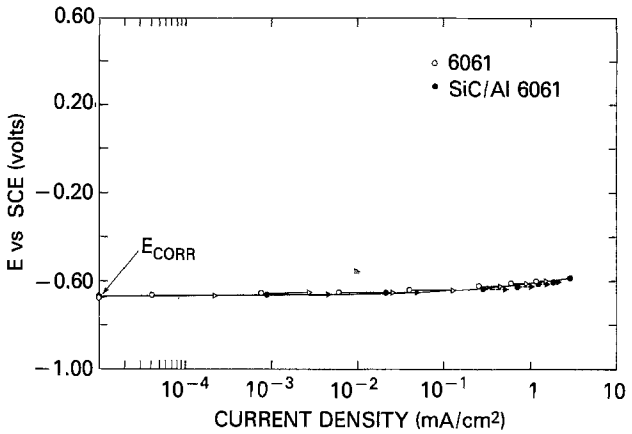

Fig. 5. Potentiostatic polarization curves for Al 6061 and SiC/Al 6061 in quiescent 0.1*N* NaCl open to the air. (Arrows show the increase in current density with time, in the initial 10 min interval at a given potential, after the onset of pitting.)

measured pitting potential of this powder product was the same (−0.540V) as the wrought alloy. Therefore, possible differences in matrix structure or composition as a result of fabrication do not contribute to the lower value of E_{pit} for Al 2024 when SiC is present.

Thus, the SiC phase does not affect the susceptibility to pit initiation of the composites tested, except for Al 2024. In this system, the composite is somewhat more susceptible to pit initiation than the matrix alloy. Additionally while alloy Al 2024 is the least susceptible to pit initiation in chloride solution, the pitting susceptibility of the other alloys and composites is about the same.

Table II also shows the effect of solution deaeration and of SiC additions on the open-circuit corrosion potentials. In the deaerated solutions, E_{corr}, for all samples, is several hundred millivolts negative to the values found for solutions containing oxygen. This effect has been observed previously for aluminum alloys in chloride media (8). The effect of SiC on the corrosion potential is not as clear, however. The addition of SiC tc the alloy can result in E_{corr} being more positive, more negative, or unchanged, depending on the alloy system and on deaeration conditions.

Pit Morphology

Figure 6 shows SEM photomicrographs of Al 6061 and the corresponding SiC composite after pitting in deaerated 0.1*N* NaCl at −0.610V for 30 min. It can be seen that pits on the composite differ in size and structure from those on the base alloy. Small rounded shallow pits develop on the composite whereas larger irregularly shaped deeper pits are observed on the alloy. In addition, pits develop on the composite both in regions of high and low density of SiC.

Figure 7 shows the details of two typical pits found on the composite. In Fig. 7a, a pit is shown developing in a region of low density of SiC. Figure 7b shows a pit developing around a cluster of SiC particles. Here, the growth of the pit appears to have been interrupted by the presence of the SiC particles.

Table II. Open-circuit potentials (E_{corr}) and pitting potentials (E_{pit}) (vs. SCE) in 0.1*N* NaCl solutions

	Open to the air		Deaerated	
	E_{corr}	E_{pit}	E_{corr}	E_{pit}
2024	−0.546	−0.540	−1.065	−0.540
SiC/Al 2024	−0.652	−0.640	−0.899	−0.640
5456	−0.704	−0.690	−1.091	−0.680
SiC/Al 5456	−0.705	−0.695	−1.097	−0.690
6061	−0.683	−0.673	−1.272	−0.640
SiC/Al 6061	−0.669	−0.660	−1.108	−0.665

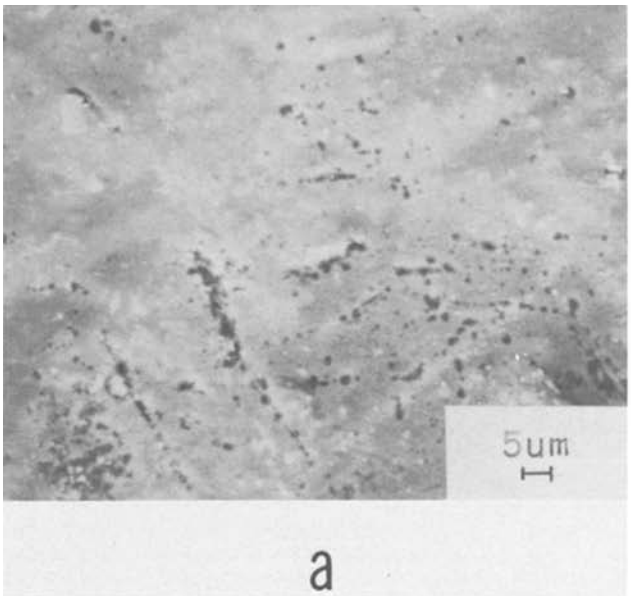

Fig. 6. Pits on (a) SiC/Al 6061 and (b) Al 6061 after polarization in deaerated 0.1*N* NaCl at −0.610V for 30 min.

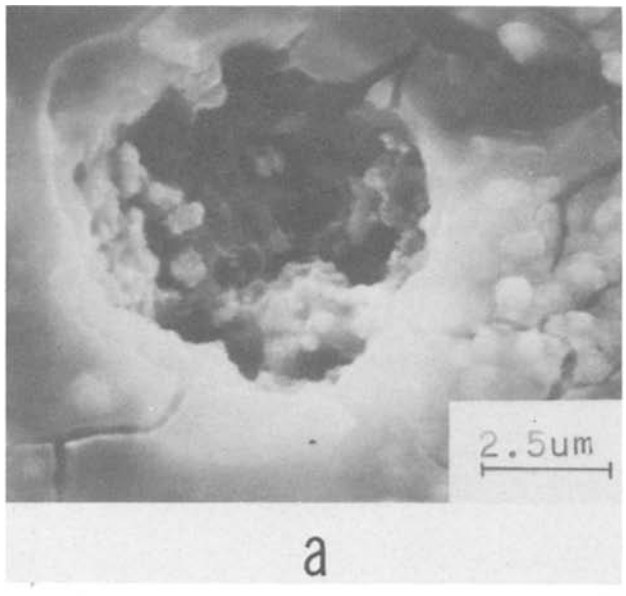

Fig. 7. Typical pits observed on SiC/Al 6061 after polarization in deaerated 0.1*N* NaCl at −0.610V for 30 min.

Thus, although pit initiation for this system is unaffected by the SiC particles, their presence affects the morphology and growth of pits.

A-C Impedance Measurements

Impedance spectra for alloys Al 2024, Al 5456, and Al 6061 and their respective SiC composites in 0.6*N* NaCl quiescent solutions open to the air are shown in Fig. 8-10. The curves are made up of three distinct regions. At high frequency (>10 Hz), the electrode behavior is controlled by the double layer capacitance. Slopes of −1 on the curves indicate purely capacitive behavior, whereas slopes less negative than −1 indicate the possibility of some diffusion effect at the electrode. In all cases except for the wrought Al 2024 and the SiC/Al 6061 specimens, the slopes are nearly −1, and the samples exhibit double layer capacitances ranging from 6 to 16 μf/cm^2. The wrought Al 2024 shows only a limited capacitance, and the capacitance of the SiC/Al 6061 material is affected by diffusion. At intermediate frequencies (10^{-2} to 1 Hz), the curves either plateau or go through a maximum.

The value of the maximum is expected to be directly related to the polarization resistance of the material and therefore to the instantaneous corrosion rate in the Stern-Geary relationship (9)

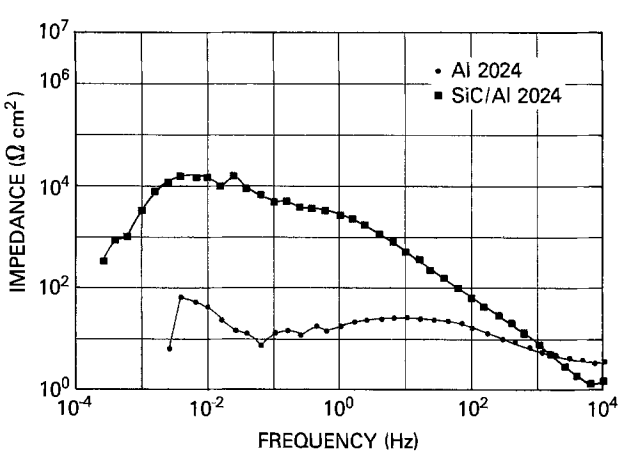

Fig. 8. Impedance spectra for Al 2024 and SiC/Al 2024 in quiescent 0.6*N* NaCl open to the air.

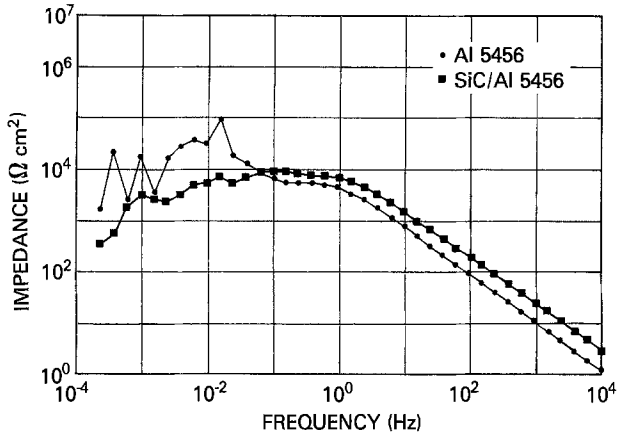

Fig. 9. Impedance spectra for Al 5456 and SiC/Al 5456 in quiescent 0.6*N* NaCl open to the air.

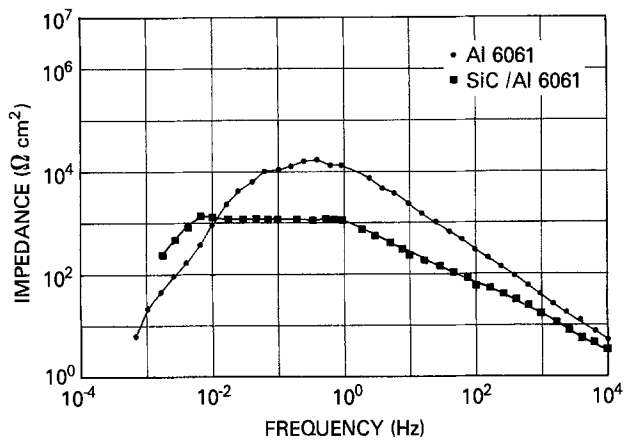

Fig. 10. Impedance spectra for Al 6061 and SiC/Al 6061 in quiescent 0.6*N* NaCl open to the air.

$$\frac{1}{Z} = \frac{1}{R_P} = 2.303\, I_{corr} \frac{(b_a + b_c)}{(b_a b_c)}$$

where Z is the faradaic impedance from the impedance plot, R_P is the polarization resistance, I_{corr} is the corrosion current, and b_a and b_c are the anodic and cathodic Tafel constants, respectively. Thus, the corrosion resistance varies directly with the values of impedance in the plateau region. In the Al 5456 and Al 6061 systems, the composites exhibit slightly less corrosion resistance than the wrought material. In the Al 2024 system, this trend is reversed. At very low frequencies (10^{-2} Hz), the impedance decreases with decreasing frequency. This apparent inductive behavior has been observed in other corroding systems (10, 11). While this effect is not well understood, it has been attributed to double layer capacitances with distributed time constants (10). In the present case, it is believed that this apparent inductance results from current spikes occurring because of breakdown and repassivation of the Al_2O_3 layer on the material. In the oxygen containing solutions, pitting was observed to occur during the course of the low frequency measurements. The low frequency measurements require several hours to make and therefore are presumed to overlap the incubation time for the onset of pitting. The resulting current spikes are integrated into the current measurement, and therefore the calculated $Z = \Delta E/\Delta I$ has a decreased value. The lower the frequency and the longer the measurement time, the more current bursts are integrated into the current measurement, and therefore the impedance is expected to decrease with decreasing frequency.

Figure 11 shows the impedance curves for the composites in deaerated solutions. The impedance behavior of all composites was essentially the same in deaerated solutions. Plateau values were at least an order of magnitude greater than those observed in quiescent solutions, and inductive behavior was significantly less. These characteristics indicate, first, that oxygen content in the solution is the primary factor in determining the corrosion characteristics of the composite, and second, that film breakdown (in the absence of oxygen) is of shorter duration and/or less frequent in the passive film breakdown-repair cycle. In cases where pitting is suppressed, decreases in low frequency impedance are expected to be reduced but not eliminated. This is because passive film breakdown and repassivation events still occur but with reduced integrated current bursts. This interpretation is supported by the fact that where pitting is suppressed (specimens at E_{corr} in deaerated solutions), less inductive behavior is observed in the impedance measurements. Compare Fig. 11 with Fig. 8-10.

Figure 12 shows impedance spectra for anodized SiC/Al 6061 in quiescent 0.6*N* NaCl open to the air. Comparison of these curves with Fig. 10 shows that the Type III coating increases the plateau impedance value and decreases the apparent inductance. Type II anodization, on the other hand, lowers the impedance curves over the entire frequency range and is actually detrimental to corrosion resistance. This indicates that the alumina film formed during Type II anodization contains weak spots which become preferred sites for pitting.

Summary

1. Pitting potentials are independent of the presence of oxygen in 0.1*N* NaCl for all alloys and composites studied.

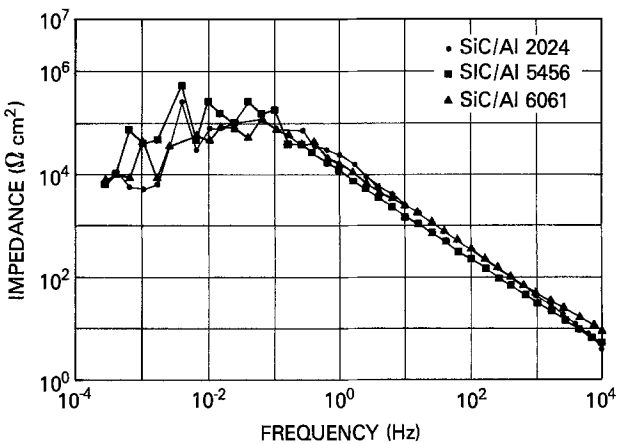

Fig. 11. Impedance spectra for SiC/Al 2024, SiC/Al 5456, and SiC/Al 6061 in deaerated 0.6*N* NaCl.

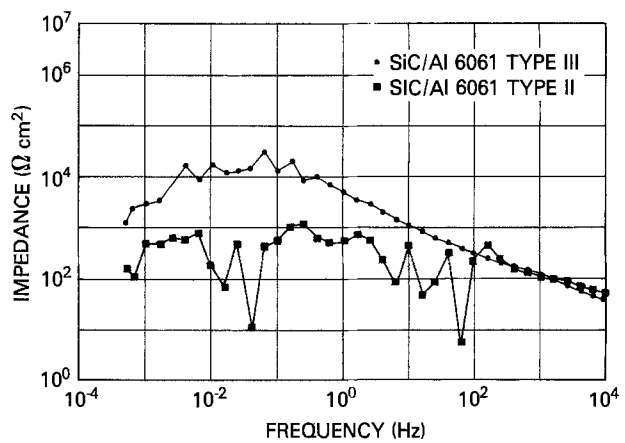

Fig. 12. Impedance spectra for Types II and III anodized SiC/Al 6061 in 0.6*N* quiescent NaCl open to the air.

2. For all specimens in the absence of oxygen, E_{corr} is several hundred millivolts active to E_{corr} in solutions containing dissolved oxygen. While pitting initiates in the freely corroding state in the presence of oxygen, this is not the case in deaerated solutions.

3. The susceptibility to pit initiation is unaffected by the presence of SiC whiskers for all alloys except Al 2024. For this system, the composite exhibits less resistance to pit initiation than the base alloy. Of the specimens tested, Al 2024 is least susceptible to pit initiation in chloride solutions.

4. Pit morphology is affected by the presence of SiC for Al 6061. In this system, large irregularly shaped pits form on the alloy whereas much smaller rounded shallow pits form on the SiC composite.

5. General corrosion is most significantly affected by the presence of oxygen rather than by the alloy type or SiC phase. The corrosion rate for all specimens is significantly lower in deaerated solutions.

6. Type III anodization significantly improves the corrosion resistance of the composites. Corrosion control of these composites should be approached from the standpoint of improvement of the oxide film.

Acknowledgment

The authors wish to acknowledge Dr. S. G. Fishman of the Naval Surface Weapons Center for his guidance and financial support of this work.

Manuscript submitted Nov. 1, 1982; revised manuscript received May 9, 1983.

Naval Research Laboratory assisted in meeting the publication costs of this article.

REFERENCES

1. A. P. Divecha, S. G. Fishman, and S. D. Karmarkar, *J. Metals*, **33**, (9) 12 (1981).
2. M. C. Porter and E. G. Wolff, in "Advances in Structural Composites," Paper No. AC-14, Society of Aerospace Materials Process Engineering, 12th National Symposium Exhibition, Western Period. Co., North Hollywood, CA (1967).
3. D. L. Dull, W. C. Harrington, Jr., and M. F. Amateau, in "Proceedings of the 1974 Triservice Corrosion of Military Equipment Conference," Vol. 1, F. H. Meyer, Editor, p. 399, Air Force Materials Laboratory Report AMFL-TR-75-42, Dayton, OH (1975).
4. P. P. Trzaskoma, *This Journal*, **129**, 1398 (1982).
5. A. J. Sedriks, J. A. S. Green, and D. L. Novak, *Metal. Trans.*, **2**, 871 (1971).
6. S. L. Pohlman, *Corrosion*, **34**, 156 (1978).
7. "Metal Finishing Guidebook and Directory," Vol. 76, p. 534, (Issued as a supplement to *Metal Finishing*), Metals and Plastics Publication, Inc., Hackensack, NJ (1978).
8. S. C. Dexter, *Corrosion*, **36**, 423 (1980).
9. I. Epelboin, C. Gabrielli, M. Keddam, and H. Takenouti, in "Electrochemical Corrosion Testing," ASTM STP 727, F. Mansfield and U. Bertocci, Editors, p. 150, American Society for Testing and Materials, Philadelphia, PA (1981).
10. I. Epelboin and M. Keddam, *This Journal*, **117**, 1052 (1970).
11. S. Haruyama and T. Tsuru, in "Electrochemical Corrosion Testing," ASTM STP 727, F. Mansfield and U. Bertocci, Editors, p. 167, American Society for Testing and Materials, Philadelphia, PA (1981).

Optical Anisotropy and Electrostriction in the Anodic Oxide of Tantalum

J. L. Ord* and W. P. Wang*

Department of Physics, University of Waterloo, Waterloo, Ontario, Canada N2L 3G1

ABSTRACT

The anodic oxidation of tantalum in sulfuric acid electrolyte is studied using potential stepping transients to study the optical anisotropy of the oxide film under anodizing conditions and the strain induced in the film by changes in the field. The optical measurements are made with a self-nulling ellipsometer, and galvanostatic transients are used to study the changes in low frequency dielectric constant associated with the field-induced refractive index and film thickness changes. Two different analysis techniques are used to determine values for beta, the degree of anisotropy (the ratio between refractive index changes parallel and transverse to the field). The beta values obtained using the two techniques, 1.95 and 2.04, are not greatly different, but we regard the 2.04 value as more accurate because the technique used to obtain it is relatively insensitive to common systematic errors. The film thickness increases and the refractive indexes parallel and transverse to the field decrease when the field is applied. Both thickness and index exhibit dependences on field which curve away from the field axis, but the curves are not the parabolas predicted by the theory of electrostriction. The low frequency dielectric constant also decreases when the field is applied, but the charge-discharge cycles exhibit considerable hysteresis, and the dependence on field is not as clearly defined as it is at optical frequencies. The results of the study of tantalum oxide are compared with results of studies of the oxides of niobium, tungsten, and molybdenum carried out under similar experimental conditions. The electrostrictive behavior of these oxides and the absence of electrostriction in the anodic oxides of bismuth and zirconium pose a number of questions which theory cannot answer at present.

This is the last in a series of three papers reporting the results of studies of optical anisotropy and electrostriction in valve-metal oxides. The previous papers reported the results of similar studies on the anodic oxides of molybdenum (1) and niobium (2). Interest in electrostrictive effects was initially sparked by the observation that, contrary to "condenser pressure" predictions, the film thickness increases when a field is applied to the oxide. The changes in film thickness were found to be much larger than had been expected, but the resulting changes in the density of the oxide appeared to be of the magnitude required by the Clausius-Mossotti relation to account for the associated changes in both the refractive index and the low frequency dielectric constant. We reached these conclusions in the paper in which we originally reported electrostrictive effects in valve-metal oxides (3), and subsequent work appeared to support our conclusions. When we investigated the theory of electrostriction to see how the film thickness could increase when the field is applied, we found that the theory had more trouble with the decrease in dielectric constant than with the increase in film thickness (4). In the theory, energy conservation requires the dielec-

* Electrochemical Society Active Member.
Key words: capacitance, dielectrics, ellipsometry.

tric constant to increase when the field is applied if its variation is due to the change in the density of the oxide. This clash between theory and experiment motivated the experiments reported in this and the two previous papers.

Apart from our original study which did not attempt an anisotropic optical analysis (3), there has been only one study of electrostriction in tantalum oxide (5). Optical measurements are difficult in the tantalum system because the electrostrictive effects are smaller than in the other valve-metal systems which have been studied, but the tantalum system is very important because of the vast amount of work which has been done on its oxidation kinetics. Of particular relevance to the present study is the recent work (6, 7) on quantitative analysis of the relaxation processes associated with overshoot phenomena and their possible relation to the dielectric relaxation processes involved in electrostriction. Our specific objectives in this paper are to analyze the field-induced strain and optical anisotropy in tantalum oxide using the techniques developed in our niobium study (2) and to use galvanostatic transients (8) to study the associated changes in the low frequency dielectric constant. We include with our findings a summary of the recent work on electrostriction in valve-metal oxides.

Experimental

The equipment used and the procedures followed in this work are similar to those used in the niobium study (2). The ellipsometer is a modified version (9) of the self-nulling instrument which has been used in this laboratory for many years (10). Quadrature Faraday modulation is decoded by a two-phase lock-in amplifier and the d-c error signals are fed back to the stepping motor drives through voltage-to-frequency converters. The sine-cosine quadrature drives have a nominal resolution of 1/1600th of a degree, and under typical operating conditions, the instrument has a response time of a few tenths of a second and a resolution of a few thousandths of a degree. A helium-neon laser is the light source, and all refractive indexes quoted in this paper are for a wavelength of 6328Å. The hollow equilateral glass prism used as a cell requires an angle of incidence of 60°. The cell has standard taper joints through which the electrode holder, a platinum counterelectrode, a mercury-mercurous sulfate reference electrode, and a gas dispersion tube are inserted. The cell was filled with 0.1M sulfuric acid electrolyte, and all experiments were performed at 22°C.

The circuitry used with the cell is operated by the HP 2114B process control computer which logs the optical data and operates the on-line displays (two storage oscilloscopes and an X-Y plotter). The current source consists of a digital-to-analog converter connected to a high voltage operational amplifier, and a second amplifier follows the potential of the reference electrode relative to the working electrode which is held at virtual ground. A programmable amplifier interfaces the follower to a 16-bit analog-to-digital converter with a 25 μsec conversion time.

The cylindrical working electrode, prepared from a single crystal of tantalum, exposes a vertical surface 1.11 cm^2 in area to the electrolyte when it is clamped between Teflon washers in a glass electrode holder. The optical measurements are made on a flat ground on one side of the cylinder. The surface was prepared for optical measurements by electropolishing in an electrolyte consisting of two parts hydrofluoric, two parts nitric, and five parts sulfuric acid. Between experiments, the electrode was stored with a thick oxide film on its surface, and hydrofluoric acid saturated with ammonium fluoride was used to remove oxide films from the surface of the electrode.

Results and Discussion

The results of the experiment used to study the optical anisotropy induced in tantalum oxide by the anodizing field are shown in Fig. 1. The plot of potential *vs.* time for the experiment is shown in the lower portion of the figure, and the corresponding locus traced out by the null settings of the polarizer and analyzer of the ellipsometer is shown in the upper portion. The potential scale uses as its zero the potential at which the optical analysis indicates that the thickness of the oxide film extrapolates to zero. The 225 μA/cm^2 current is switched on at point A, and anodization continues to point K interrupted by transients at points B through H. The transients used in the optical analysis are those applied at points B, C, F, and H in the regions where the polarizer null setting passes through its maximum and minimum values. The overpotential is stepped to zero (actually far enough above zero to avoid faradaic processes) in eight equal steps of 3 sec duration; then it is stepped up and down five steps before being stepped back eight steps to its initial value. The 3 sec time constant is chosen to suit the response times of the ellipsometer and the program which varies the current to produce the potential steps. Over the lower three-quarters of the potential range, the oxidation current is not significant and the optical readings at the 3 sec point on a step are virtually identical with the readings at the 2 sec point. The stepped "W" transients applied at points E and G in Fig. 1 are not used in the optical analysis. At point D, the oxidation current is lowered by a factor of 16 and a fast galvanostatic "W" transient is applied in order to study the field dependence of the low frequency dielectric constant.

In the tantalum system, the effect of anisotropy on the optical data is not clearly resolvable on the scales used in Fig. 1, and only the first-cycle data are actually shown in the figure. Uniaxial negative anisotropy causes the second cycle to be displaced to slightly higher polarizer null settings, and the most direct approach to analyzing the anisotropy uses the interloop spacing and the zero-field offset in the maximum and minimum polarizer regions to determine the degree of anisotropy. We show the data recorded in these regions along with theoretical curves determined

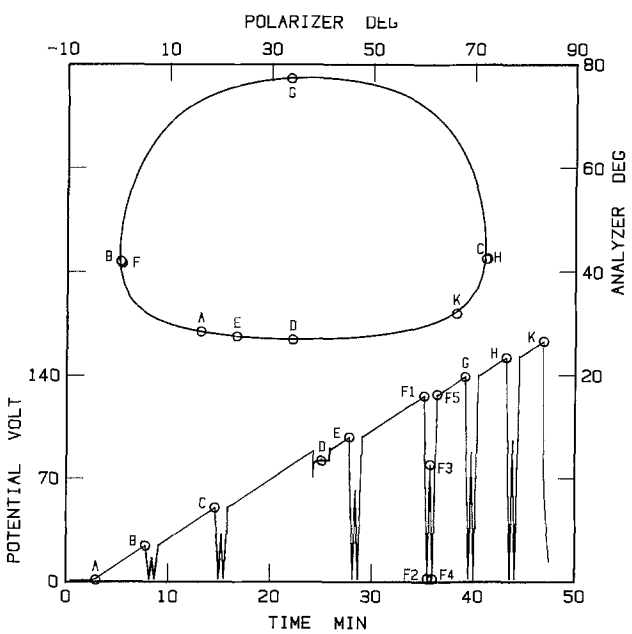

Fig. 1. Anodic oxidation of tantalum at 225 μA/cm^2 in 0.1M sulfuric acid electrolyte with stepped potential transients for studying electrostriction applied at B, C, E, F, G, and H. At point D, the current was reduced by a factor of 16, and a fast galvanostatic transient was applied to study dielectric constant variation.

by this approach on greatly expanded scales in Fig. 2. The transients shown are those recorded at points B, C, F, and H in Fig. 1, and the 1 through 5 numbering scheme is that shown on transient F in Fig. 1. The data plotted are the points recorded at the end of the 3 sec intervals on the first downward stepping segment of the transient. The data from the remaining segments exhibit some hysteresis on a field plot but superimpose on a polarizer-analyzer plot and are omitted from the figure for clarity.

The interloop spacing in Fig. 2 is about the same in the high and low polarizer regions, but the field-switching data behave differently in the two regions, shifting toward a zero-field point to the left of the anodization curves at low P, and between them at high P. If the optical anisotropy were to relax completely at zero-field, then points B2-F2 and C2-H2 would fall on curves parallel to the anodization curves. Their failure to do so, apparent in Fig. 2, is taken as evidence for residual anisotropy at zero-field under our stepping conditions. If the degree of zero-field anisotropy is assumed to be independent of film thickness, an extrapolation scheme can be devised to locate an isotropic curve which is consistent with the data, and this curve, for a film with index 2.1944, is shown in the figure. The problem is then to find a value for the degree of anisotropy, beta, defined as the ratio of index change in the field direction to index change transverse to the field, which enables the anodization curves in Fig. 2 to be fitted with common values of Nz, the index in the field direction, and Nx, the index transverse to the field. The theoretical curves in the figure are plotted for a beta value of 1.95 and index values Nz = 2.17705, Nx = 2.1855.

The analysis procedure described above relies heavily on interloop spacings: the B2-F2 and C2-H2 spacings to locate the isotropic curve and the B1-F1 and C1-H1 spacings along with their offsets from the isotropic curve to determine the degree of anisotropy. Consequently, the results of the analysis will be quite sensitive to any factor (such as a change in the surface roughness) which can cause the optical readings to "drift" slightly with progressive film growth. In a previous paper (2), we developed an analysis technique which relies primarily on the field dependent shifts B1-B2, C1-C2, F1-F2, and H1-H2 to determine the degree of optical anisotropy. As with the analysis described above, the procedure begins by locating an isotropic reference curve, but the analysis is not sensitive to how the curve is located. Then for a series of values of beta, index and fractional film thickness changes are calculated for each of the four transients. The best value for the beta is then taken to be the one which gives the most consistent index and fractional thickness changes for all four transients.

Figure 3 shows the fractional thickness changes calculated from the data in Fig. 2 using this procedure. The lower 5/8ths of each transient is fitted using least squares to determine the fractional thickness change as the field is reduced from 3.8×10^6 V/cm to zero, and this is the quantity which is plotted *vs.* beta in Fig. 3 for each transient. Note that it is transient H at the right of the second optical loop which is most sensitive to the value of beta. The standard deviation from the four-transient average fractional thickness change is plotted *vs.* beta in Fig. 4 along with the corresponding deviation in the refractive index transverse to the field. The curves in Fig. 4 have their minima at slightly different beta values, but neither curve is significantly above its minimum at beta equals 2.04, the average of the values at the two minima. Note that this value gives a significantly better fit to the field switching data than does the 1.95 value determined above. We regard 2.04 as a more accurate value for beta than 1.95

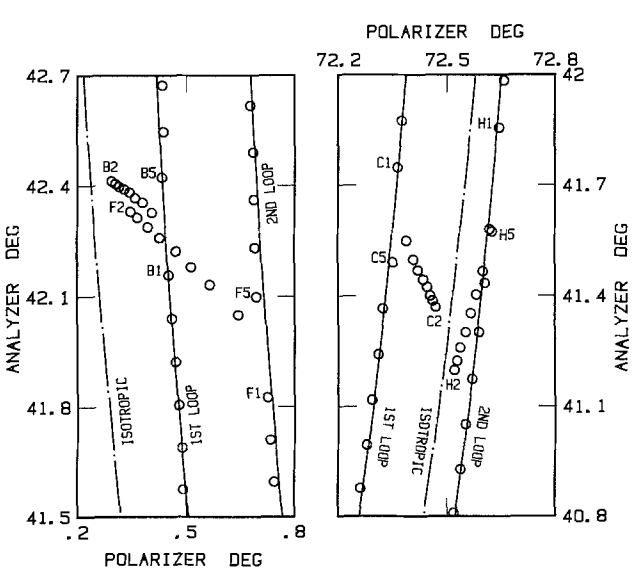

Fig. 2. Optical data in the region of transients B, C, F, and H in Fig. 1 along with theoretical curves for an isotropic film of index 2.1944 and an anisotropic film with transverse index 2.1855 and index 2.17705 in the field direction. The numerical labeling follows the scheme shown on transient F in Fig. 1.

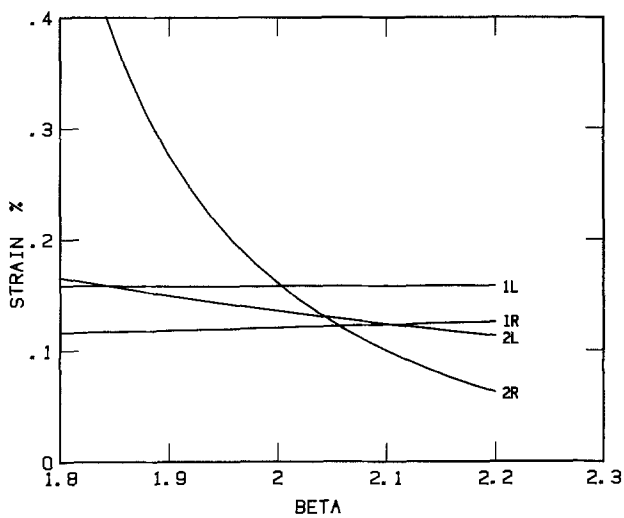

Fig. 3. Calculated strain values for the four transients in Fig. 2 for a range of assumed values of beta, the degree of anisotropy. The strain values plotted are for a field change from 3.8×10^6 V/cm to zero.

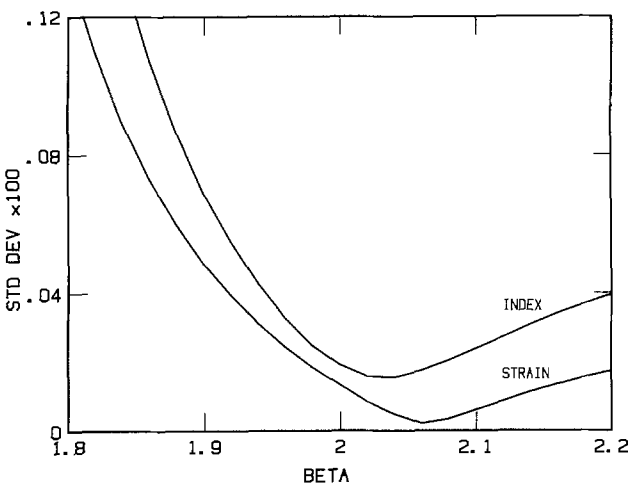

Fig. 4. Standard deviation as a function of beta for the strain values in Fig. 3 and the corresponding standard deviation in transverse index values.

because it is deduced from field switching transients which replicate under conditions where interloop spacings and zero-field offsets vary considerably. The value originally reported for the degree of anisotropy in tantalum oxide is 1.6 (5), a value which is outside of our plotting range in Fig. 3 and 4.

Once we have determined the degree of anisotropy, we can determine how the refractive index of the film and the strain in it depend on the applied field without further difficulty. Transient F is the most suitable one to use for this purpose because the low P region gives the best separation between thickness and index effects and because field-induced thickness changes are proportionately greater at the greater film thicknesses of the second optical cycle. Figure 5 shows how the strain and transverse index depend on the field for transient F. The strain values at the anodizing field, points F1 and F5 in Fig. 2, require extrapolation and correction for film growth and are not shown in the figure although corresponding index values are. Between zero-field and the anodizing field, the film thickness increases by about one-quarter of a percent, and the transverse index decreases by about the same amount. Normal incidence optical measurements depend on the product of transverse index and thickness and hence can detect only second-order differences between the thickness and index changes. Although both strain and index curve away from the field axis, neither dependence is the parabolic one predicted by the theory. The curves exhibit some hysteresis, but the various segments differ little in shape. When we come to compare tantalum with other materials, we will use a curve fitted to the Nz variation over segment F1-F2 rather than the Nx curves in Fig. 5, but the two curves differ only by a scale factor of 2.04.

The changes in the low frequency dielectric constant which accompany the field-induced changes in film thickness and refractive index are studied using a galvanostatic transient with a similar "W"-shape to the transient used for the optical measurements, but with a much shorter time constant. One such transient, applied at a relatively high anodizing voltage, is shown in Fig. 6. The anodizing current density, initially 90 μA/cm^2, was reduced by a factor of 32, and the system was allowed to return to a steady state before the cycling current, also 90 μA/cm^2, was applied. The factor of 32 was used to reduce any uncertainty introduced into the

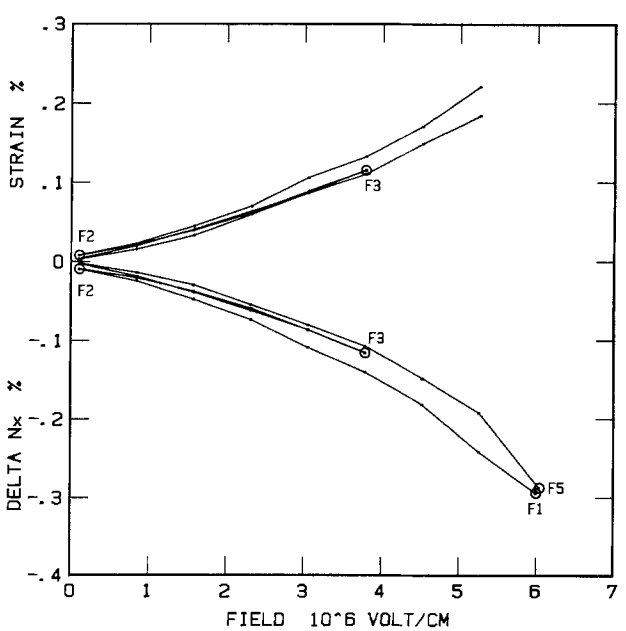

Fig. 5. Strain and change in transverse refractive index as a function of field for transient F in Fig. 1 calculated using the optimum beta of 2.04 from Fig. 4.

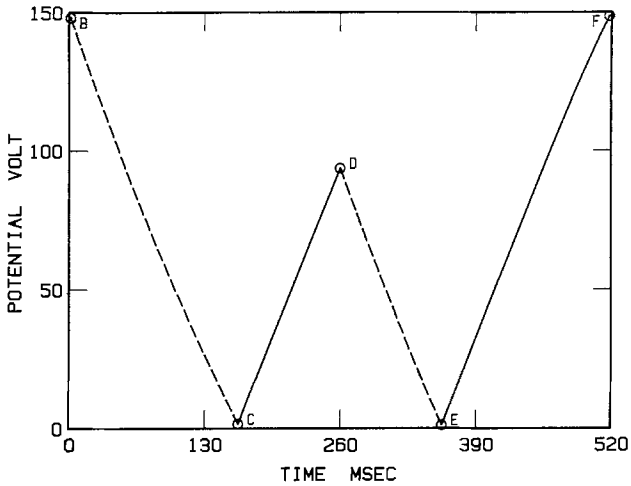

Fig. 6. Galvanostatic "W"-transient with alternating cathodic (broken curve) and anodic (solid curve) segments. The charge-discharge current density, 90 μA/cm^2, is 32 times the initial steady-state current density.

charge calculations by the functional form used to correct for ionic current flow. We have given a detailed description of the procedure used to acquire the data elsewhere (8) and have since applied the technique in studies on molybdenum (1) and niobium (2).

The charging curve derived from the "W"-transient in Fig. 6 is shown in Fig. 7. Corresponding segments bear the same labels in the two figures. The discharge segments curve away from the charge axis in Fig. 7, but the charging segments have opposite curvature and the system exhibits significant hysteresis. This type of charging experiment was initially devised to look for upward curvature in charging curves, and the first system studied, tungsten (8), exhibited upward curvature on both charge and discharge segments even though the hysteresis was significant. The tantalum system, however, does not exhibit as much curvature, and the hysteresis appears to dominate the charge segments, causing them to curve toward the charge axis. Relaxation effects and hysteresis make it difficult to determine how the dielectric constant depends on the applied field without studying the kinetics of the processes involved, but we can see how the magnitude of the effect varies from system to system by comparing results obtained by analyzing only the initial discharge segments. (The technique was designed to average over the charge-discharge cycle in the middle

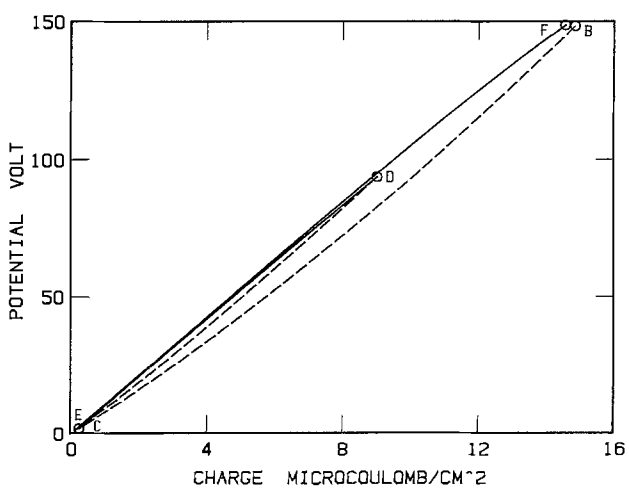

Fig. 7. Charging curve deduced from the "W"-transient in Fig. 6, broken curves indicating cathodic segments, solid curves anodic segments.

of the "W", but we do not wish to defend such an averaging process at this time.)

Dielectric constant values for tantalum oxide determined from the initial discharge cycle in Fig. 7 are plotted *vs.* field in Fig. 8 along with corresponding results for the anodic oxides of tungsten, molybdenum, and niobium. Although the field spanned by the transient is greater for tantalum oxide than for the other oxides, the change in dielectric constant is smaller. Among materials with similar elastic properties, the classical theory of electrostriction predicts larger electrostrictive effects in materials with higher dielectric constants. The data in Fig. 8 are consistent with this prediction under the assumption that the tantalum-niobium and molybdenum-tungsten pairs of oxides have similar elastic properties, and the molybdenum-tungsten pair is more strongly electrostrictive than the tantalum-niobium pair.

A refractive index plot for the four oxides is given in Fig. 9. The field scale is the same as in Fig. 8, and the index plotted is the index in the field direction. Again, tantalum oxide exhibits the smallest electrostrictive effect, and the other oxides exhibit effects consistent with their low frequency dielectric constant variation. Note that it is the d-c field, not the optical field, which produces the electrostriction, and hence it is the low frequency dielectric constant, not the refractive index, whose magnitude influences the size of electrostrictive effects.

Some electrostrictive information is available for three additional anodic oxides. Clayton and DeSmet (11) studied the optical anisotropy of vanadium oxide under anodizing conditions, and their published data is used to estimate the size of electrostrictive effects in vanadium oxide. We estimate a value of 1.8 for beta, and find that the index in the field direction increases from 2.328 at a field of 2.7×10^6 V/cm to 2.351 at zero-field. Vanadium oxide has a higher refractive index than molybdenum oxide, but the two oxides have virtually the same residual anisotropy, anodizing field, and electrostrictive behavior. There is nothing surprising in this result, but it does broaden the range of anodic oxides exhibiting electrostrictive effects.

What is surprising is the finding by Hopper, Wright, and DeSmet (12) that zirconium oxide shows no electrostrictive effects and our finding of the same result for bismuth oxide. Bismuth and zirconium both have characteristics which distinguish them from other valve metals, but electrostriction is thought to be a universal second-order effect exhibited by all dielectric materials at high electric fields. Bismuth is itself an optically anisotropic material, and although this complicates the analysis of ellipsometric data, it is not the reason that no ellipsometric studies of the anodic oxidation of bismuth have been published. The problem with bismuth is the electrochemical anisotropy of the surface and the changes in surface topography which accompany polishing and oxidation processes. These changes strongly affect optical measurements, and it is not surprising that even some straight electrochemical studies have resorted to using mechanical polishing as a final surface treatment (13, 14).

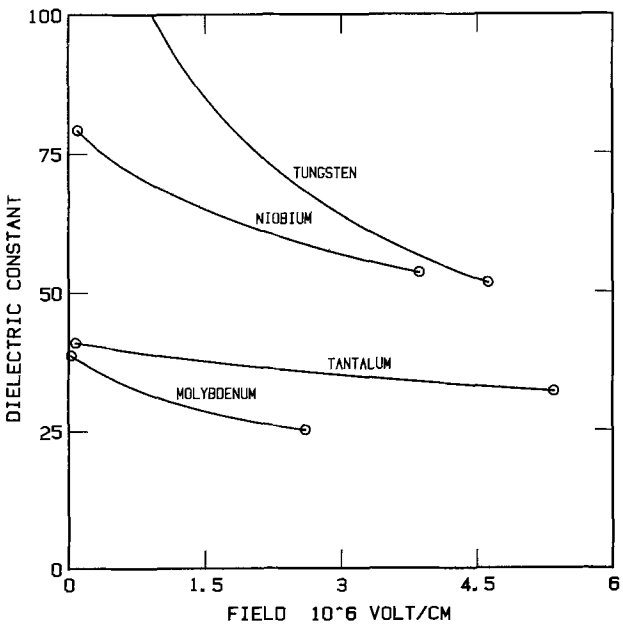

Fig. 8. Dependence of the dielectric constant of tantalum oxide on field (for segment BC of the charging curve in Fig. 7) along with corresponding curves for other valve metals.

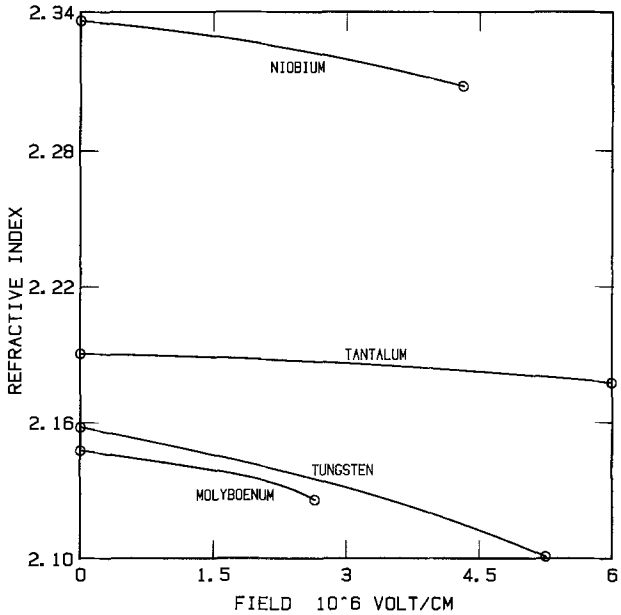

Fig. 9. Refractive index in the field direction *vs.* field for the anodic oxides of tantalum, niobium, tungsten, and molybdenum.

This then completes our re-examination of the experimental evidence of electrostriction in valve-metal oxides; Fig. 8 and Fig. 9, along with the values quoted for vanadium and the negative findings on zirconium and bismuth, summarize the current experimental status. At present, the theory of electrostriction says more about what the results do not mean than it says about what they mean, and more theoretical work will be required before we can begin to understand the significance of our experimental findings.

Acknowledgment

This work received partial support from the Natural Sciences and Engineering Research Council Canada under Grant No. A-1151.

Manuscript submitted Jan. 20, 1983; revised manuscript received May 2, 1983.

REFERENCES

1. D. J. DeSmet and J. L. Ord, *This Journal*, **130,** 280 (1983).
2. C. G. Matthews, J. L. Ord, and W. P. Wang, *ibid.*, **130,** 285 (1983).
3. J. L. Ord, M. A. Hopper, and W. P. Wang, *ibid.*, **119,** 439 (1972).
4. J. L. Ord, *ibid.*, **127,** 2682 (1980).
5. W. D. Cornish and L. Young, *Proc. R. Soc. London, Ser. A*, **335,** 39 (1973).
6. D. F. Taylor and M. J. Dignam, *This Journal*, **120,** 1299 (1973).
7. L. Young and D. J. Smith, *ibid.*, **126,** 765 (1979).
8. J. L. Ord, *ibid.*, **129,** 2038 (1982).
9. J. L. Ord, *SPIE Proc.*, **112,** 58 (1977).
10. J. L. Ord, *Surface Sci.*, **16,** 155 (1969).

11. J. C. Clayton and D. J. DeSmet, *This Journal*, **123**, 1886 (1976).
12. M. A. Hopper, J. A. Wright, and D. J. DeSmet, *ibid.*, **124**, 44 (1977).
13. I. A. Ammar and M. W. Khalil, *Electrochim. Acta*, **16**, 1379 (1971).
14. B. Lovrecek and M. Metikos-Hukovic, *J. Electroanal. Chem.*, **106**, 127 (1980).

Deposition of Metals at a Flow-Through Reticulated Vitreous Carbon Electrode Coupled with On-Line Monitoring of the Effluent

J. Wang* and H. D. Dewald

Department of Chemistry, New Mexico State University, Las Cruces, New Mexico 88003

ABSTRACT

Flow electrolysis at reticulated vitreous carbon (RVC) electrodes was employed for decontaminating heavy metal solutions. Continuous clean up of Cu(II), Ag(I), and Pb(II) solutions (starting concentration, $\sim 10^{-6}$M) was carried out under controlled potential conditions. The decrease in metal ion concentration was monitored by intermittent stripping voltammograms recorded at a downstream flow detector. Electron microscope photographs showed the nature of the electrodeposited metal films. Due to high clean-up efficiency, durability under prolonged flow-through conditions, economy, and simplicity, RVC competes with prevalent metallic and carbonaceous porous materials.

Flow-through porous electrodes are attractive for industrial and environmental applications since they provide intimate contact between the flowing stream and the electrode surface. The idea of using flow-porous electrodes for removal or recovery of metal ions from waste process streams has been investigated since 1972 (1), and has been further developed both in the laboratory and on a pilot plant scale. Various materials, in different forms, have been employed as porous electrodes to obtain the high electrolytic yields. Of the porous matrices employed for these purposes, those made of carbon are becoming popular as compared to metallic matrices. Different forms of flow-through porous carbon electrodes have been reported in connection with removal of metal ions from aqueous media. These include columns packed with finely divided graphite chips (1) or granules (2), glassy carbon grains (3), crushed graphite (4), and screens made of graphite (5) or carbon (6).

The authors report here on the application of RVC as an electrode material for removal and recovery of metal ions from flowing streams. RVC is a relatively new honeycomb carbonaceous material which appears to be well-suited as a versatile electrode material (7). It combines the electrochemical properties of glassy carbon with many structural and hydrodynamic advantages (8, 9). RVC has been employed recently in a variety of electroanalytical applications, mainly as an effective detector in flowing streams (8, 10, 11). In spite of its unique properties, RVC has not been exploited yet for removal of metal ions from flowing streams. (Stripping voltammetry of trace metals at mercury coated RVC has been reported (12).) Some properties of RVC make it especially suitable for extraction of metals from effluents: high surface area results with electrolysis yields up to 100%; due to its high void volume and large pore dimensions, sufficient porosity and low resistance to flow is retained even after deposition of thick metal films; self-supporting rigid matrix that is advantageous compared to a bed of loose particles; and finally, electrodes are very inexpensive and easily fabricated.

In the present work, the clean-up efficiency of the effluent solution was monitored continuously at a downstream flow cell, operated in the sensitive differential pulse stripping mode. Anodic stripping voltammetry (ASV) has been adapted recently to analysis of flowing streams, in particular, for the monitoring of heavy metals in natural waters (13, 14). A dual cell assembly, similar to the one employed in this study, was used recently to minimize various problems associated with ASV measurements; mercury coated RVC cylinder was employed (15). The characteristics of the dual cell assembly for the electrolytic clean-up of metal ions solutions at an upstream RVC cell, accompanied by a simultaneous ASV monitoring of the effluent at a wall-jet detector, are explored in this study.

* Electrochemical Society Active Member.
Key words: RVC, electrolysis, metals, stripping voltammetry.

Experimental Section

Apparatus.—The dual-flow cell design is shown in Fig. 1. The cylindrical body of the upper cell was made of Plexiglas (3.18 cm diam, 7.30 cm length). A solution flow channel (0.55 cm diam) was drilled through the Plexiglas body. The working electrode was composed of a reticulated vitreous carbon cylinder (RVC type: 2 × 3 S; 100 ppi; 1.3 cm length, 0.55 cm diam; purchased from Fluorocarbon Company (the production rights were transferred recently to ERG Incorporated, Oakland, California)). The RVC cylinder was positioned at the lower end of the solution channel by a snug fit. Electrical contact to the RVC was made by pressure to one end of a short glassy carbon rod (0.25 cm diam) sealed with nonconducting epoxy through a hole in the cell wall. The Ag/AgCl (3M NaCl) reference and the platinum wire (0.33 mm diam) auxiliary electrodes were introduced to the flow channel of the upper cell through two holes in its wall.

The lower wall jet detector was described in detail previously (16). The working electrode was a glassy carbon disk (0.25 cm diam) onto which a solution stream was directed from an inlet nozzle (0.34 mm diam). The distance between the nozzle tip and surface of the electrode was 0.25 mm. The glassy carbon disk was polished by a 1 μm alumina slurry, until a mirror-like surface was obtained, and washed with nitric acid and deionized water. All potentials were determined with respect to an Ag/AgCl (3M NaCl) reference electrode. The cell was connected to the RVC electrode cell via a 1.5 cm long Teflon tubing.

The sample and mercury(II) solutions were stored in 250 ml and 400 ml Nalgene beakers, respectively, fitted with covers. Solution flow was maintained with an FMI Lab pump (Model RP-SY, Fluid Metering, Incorporated, Oyster Bay, New York) located between the solution reservoirs and the RVC electrode cell. The reservoirs were connected, through Teflon tubing (1.0 mm inside diameter, 2.0 mm outside diameter), to a three-way Teflon stopcock and connected to

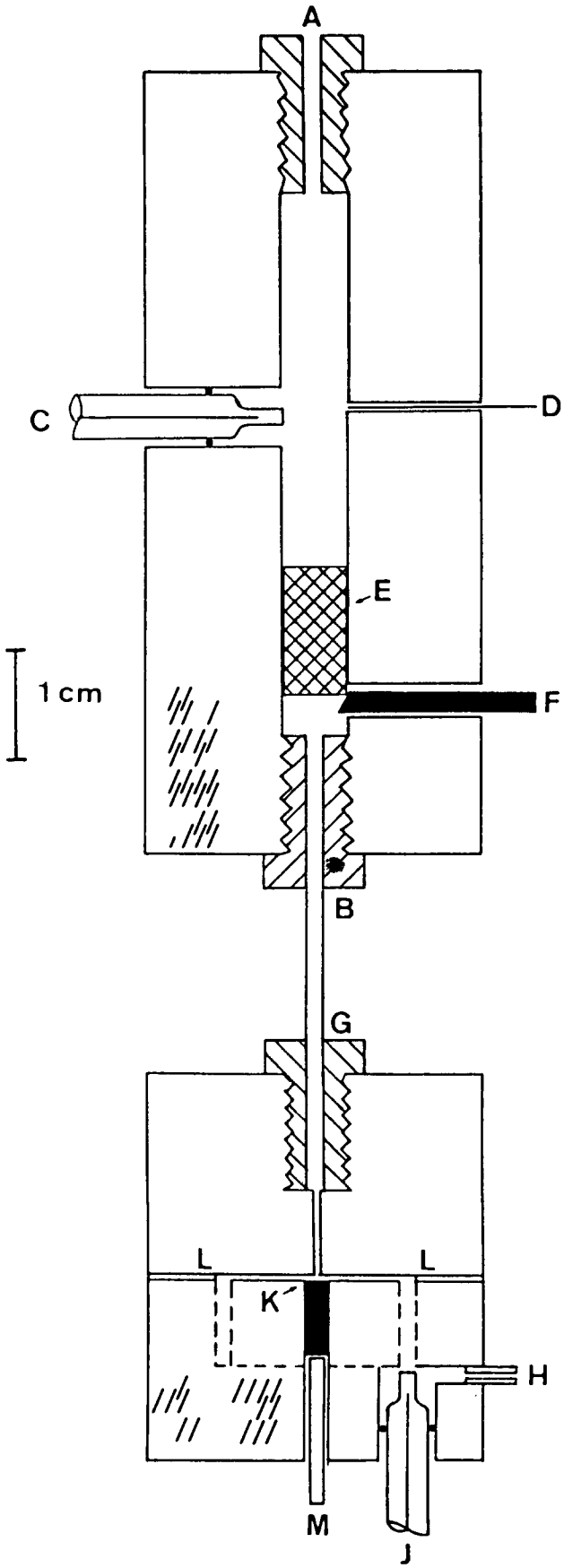

Fig. 1. Dual flow cell assembly: (A, G) solution inlets, (B, H) solution outlets, (C, J) reference electrodes, (D) auxiliary electrode, (E) RVC cylinder, (F) lead to RVC, (K) glassy carbon disk, (L) Teflon spacers, (M) lead to glassy carbon disk.

the pump. Other connecting tubing was Teflon (0.5 mm ID, 1.5 mm OD). All tubing was sealed inside Tygon tubing to reduce oxygen interference. The RVC electrode cell was connected to a Princeton Applied Research Model 364 polarographic analyzer. Stripping voltammograms at the voltammetric detector were recorded with a Sargent-Welch Model 4001 polarograph.

Reagents.—Stock solutions of 10^{-3}M Ag(I), Cu(II), Hg(II), and Pb(II) were prepared by dissolving the metal or its nitrate salt in nitric acid and diluting as required with deionized water. The solutions were stored in polyethylene containers. The Ag(I) solution container was wrapped in aluminum foil. Portions of these solutions were diluted as required for clean-up experiments. A 5×10^{-5}M Hg(II) solution was used for mercury film plating as required. Sample solutions were prepared in 0.1M potassium nitrate supporting electrolyte.

Procedure.—A preplated mercury film was used for the downstream ASV detection of the metals (except for silver which cannot be determined at mercury due to its anodic peak potential). A 5×10^{-5}M $Hg(NO_3)_2$-0.1M KNO_3 solution was purged with N_2 for 20 min. The glassy carbon wall-jet working electrode was filmed by holding its potential at −0.7V and passing the mercury(II) solution through the cell at 0.3 ml/min for 20 min. After this period, the mercury film electrode was held at +0.05V (+0.5V was used for the bare glassy carbon employed in the silver experiments). Following this conditioning, the stopcock was turned to allow flow of the deaerated sample through the dual cell assembly. Removal of the metals began by applying the appropriate potential at the RVC electrode; at the same time the ASV plating potential was applied at the downstream wall-jet electrode. Following the ASV plating period (usually 2 min) the solution flow was stopped; after a 15 sec rest period, a differential pulse potential ramp was initiated and the voltammogram was recorded simultaneously. The scan terminated at +0.05 (+0.5V when Ag was measured). Solution flow was renewed for 90 sec to allow cleaning of the mercury film, readying the system for the next determination. The metals deposited on the RVC electrode and the mercury film were removed at the end of a series of experiments by holding the electrodes at +0.5V for 20 min.

SEM procedure.—Electrodes prepared for scanning electron microscope (SEM) photographs were stored in covered test tubes and handled with gloves. Metal deposition was performed from 5×10^{-5}M metal ion-0.1M KNO_3 solutions for 20 min under continual solution flow of 0.35 ml/min. Samples were prepared for topographical investigation by evaporative coating with gold and were examined with a Phillips 501B-SEM at 320 magnification and 5-9 kV accelerating voltage.

Results and Discussion

Blaedel and Wang (8) studied the mass transport characteristics at flow-through RVC electrodes using $K_3Fe(CN)_6$ solutions. Good agreement was found between the experimental results and the theory of the porous electrode reactor (17). Accordingly, the degree of conversion (R) is a function of the electrolyte flow rate and the electrode length; using a 1 cm long RVC cylinder and low flow rates (<1 ml/min), R approaches 1.0. Based upon these data, similar conditions have been employed in this study. For various practical purposes, a longer electrode would allow the use of high flow rates while maintaining a high degree of conversion.

Figure 2 demonstrates the high degree of clean-up efficiency obtained with the RVC electrode. It shows stripping voltammograms for a Cu(II) solution recorded at the downstream flow detector. Voltammograms a and b are the response for the blank (0.1M KNO_3) solution and following an addition of 10^{-6}M Cu(II), respectively, while the deposition potential is not applied at the upstream RVC electrode. A defined

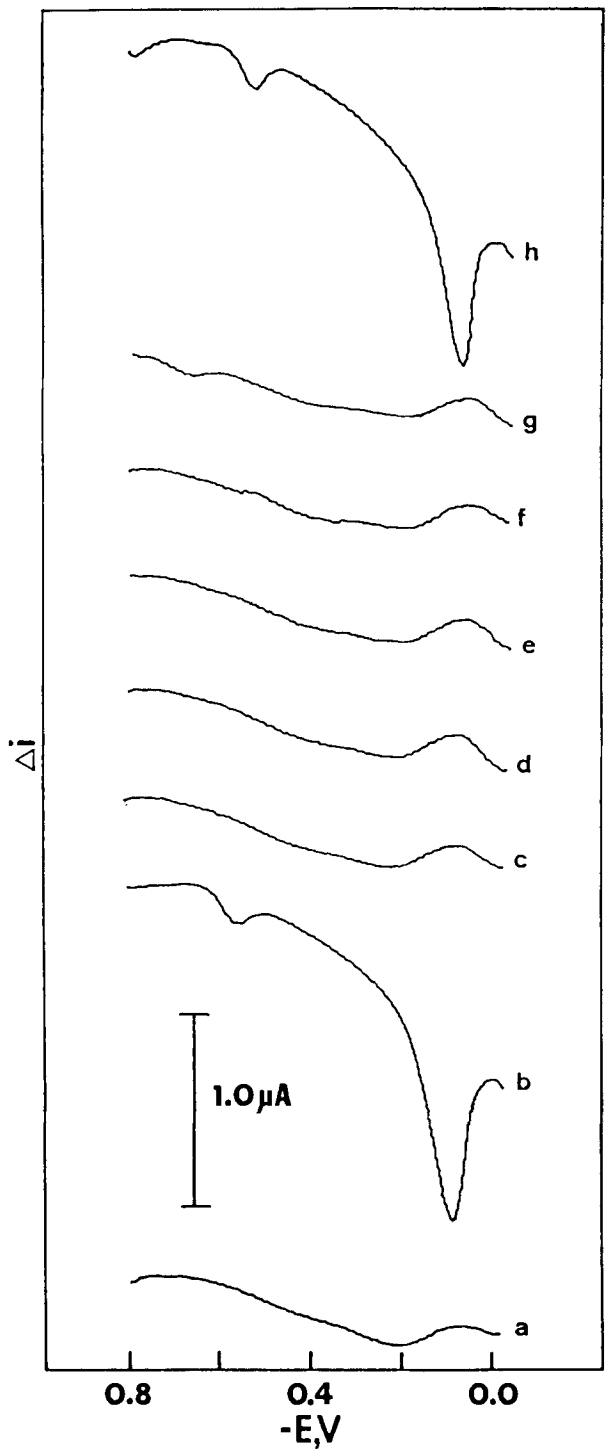

Fig. 2. Characteristic stripping voltammograms recorded at the downstream detector for the 0.1M KNO_3 blank (a) and a 10^{-6}M Cu(II) (b-h) solutions. RVC potential, +0.05V (a, b, h), −0.5V (c-g). Flow rate, 0.2 ml/min. ASV conditions: deposition at −0.8V for 2 min; differential pulse ramp, 50 mV amplitude, 0.5 V/min scan rate, 0.5 sec repetition time.

copper peak is observed at +0.1V (the small peak at +0.55V is due to impurity of lead). Once the Cu(II) is deposited at the RVC electrode, the voltammograms recorded downstream (curves c-g) are very similar to that of the blank solution (curve a), *i.e.*, effective clean-up of Cu(II). The detection cycle at the downstream cell consists of 2 min deposition period, 2 min stripping step, and 90 sec cleaning period, *i.e.*, a complete cycle takes 6 min (or a rate of ten measurements per hour). Curves c-g were recorded over an uninterrupted 30 min period through which the RVC potential was −0.5V. The absence of a copper stripping peak in these curves indicates that the RVC maintains its clean-up characteristics under continuous operation conditions. Following this operation, the potential of the RVC was switched to +0.05V at which copper is not deposited; the corresponding "downstream" voltammogram (curve h) shows copper and lead peaks identical to those recorded at the beginning of the experiment (curve b). This demonstrates the suitability of the flow ASV detection for this purpose. For a starting metal concentration of 10^{-6}M, 99% clean-up efficiency corresponds to a final concentration of 10^{-8}M, which can be detected electroanalytically only by ASV. The high sensitivity of the present detector is the result of combining the effective mass transport of the wall-jet detector with the sensitive differential pulse stripping mode. More rapid detection methods, such as square wave polarography (18), can be utilized in purification of 10^{-4}M solutions, where the final concentration (99% efficiency) is 10^{-6}M.

Figure 3 shows the dependence of the clean-up efficiency on the potential applied at the RVC electrode. The clean-up efficiency was calculated from the ratio of the ASV peak current at a given RVC potential, to that obtained while the RVC was held at +0.05V (no deposition). Satisfactory clean-up efficiency (exceeding 90%) is obtained at potentials more negative than −0.5V. Dependence with similar shape was reported for Cu(II) deposition at graphite cloth electrodes (19). The experiment also included applied potentials of −0.9V and −1.2V, at which complete clean-up was maintained (not shown).

Figure 4 shows ASV monitoring of silver ion in the effluent solution. Curves a and b represent the response of the blank solution and the 10^{-6}M Ag(I) solution, respectively, obtained while holding the RVC electrode at +0.5V. A defined silver peak is observed at +0.37V. Curves c-e were obtained while the silver was electrodeposited at the upstream RVC electrode (E_{RVC} = −0.5V); the response is similar to that of the blank

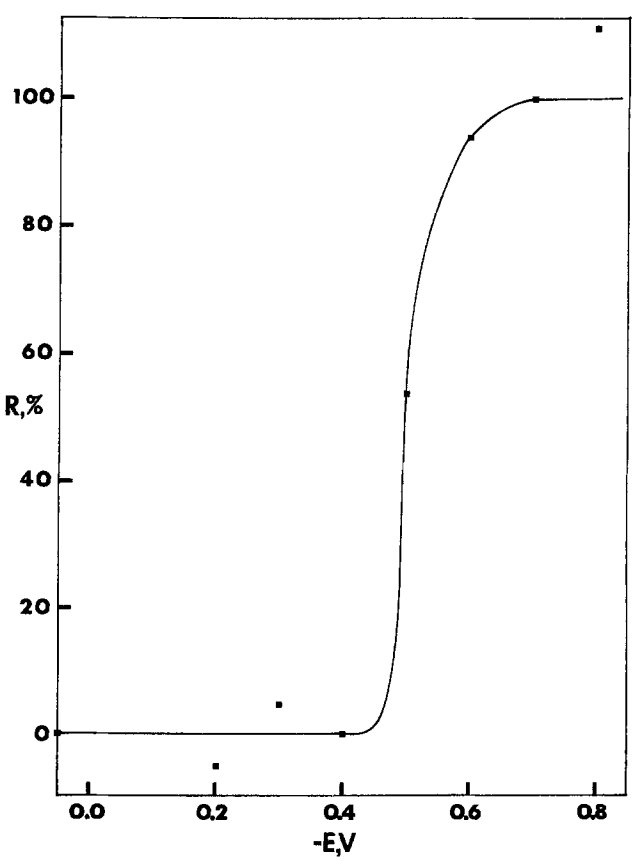

Fig. 3. Dependence of clean-up efficiency on imposed potential. 2.5 × 10^{-6}M Cu(II); 0.1M KNO_3; flow rate, 0.19 ml/min^{-1}. ASV detection conditions, as in Fig. 2.

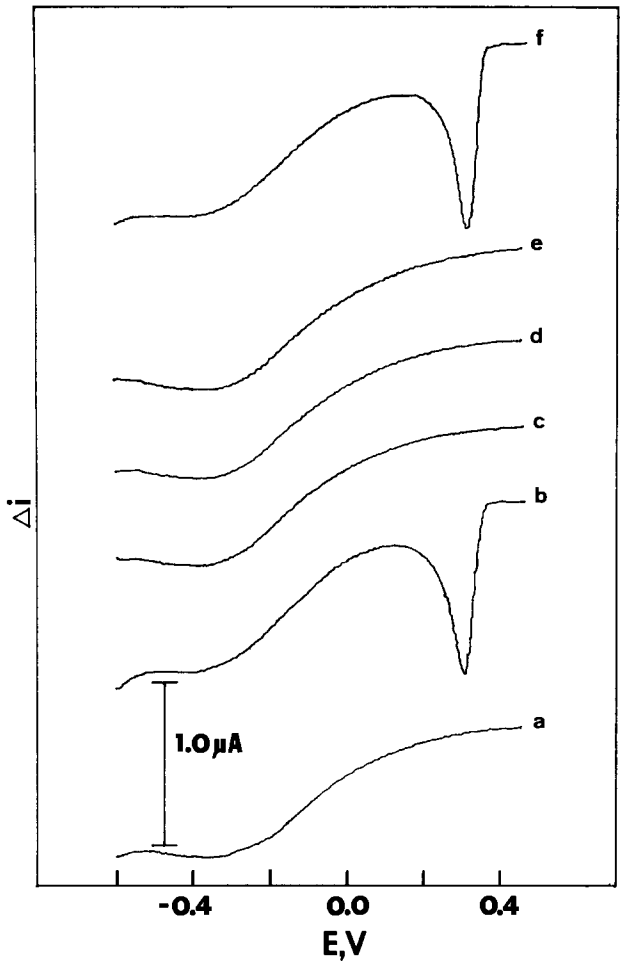

Fig. 4. Characteristic stripping voltammograms recorded at the downstream detector for the blank (a) and 10^{-6}M Ag(I) (b-f) solutions. RVC potential, +0.5V (a, b, f), −0.5V (c-e). Flow rate, 0.24 ml/min. ASV conditions: deposition at −0.6V for 5 min; differential pulse ramp, as in Fig. 2.

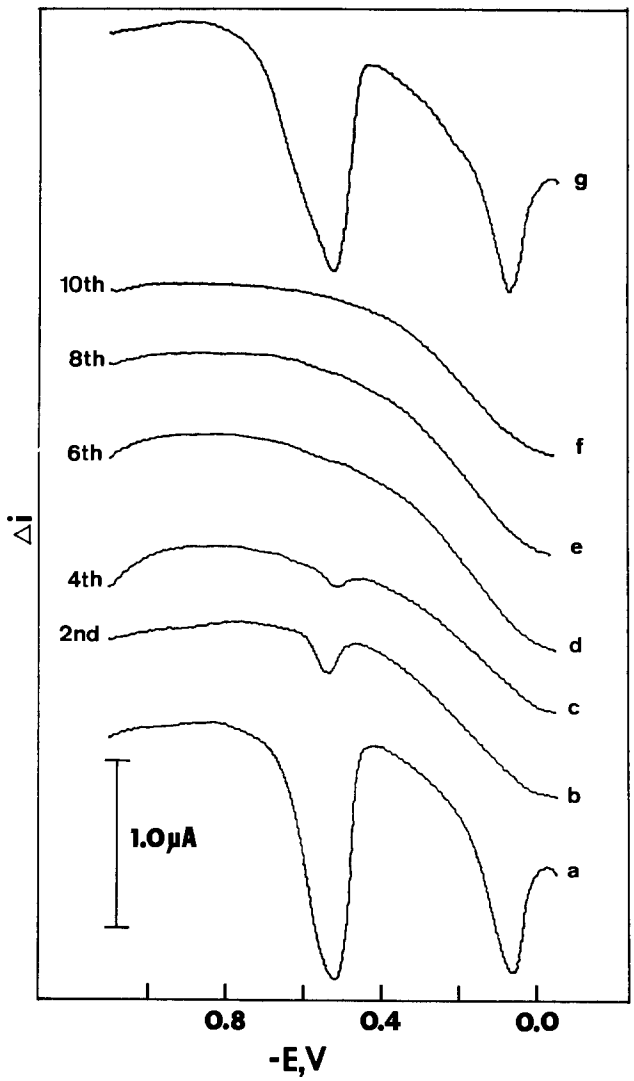

Fig. 5. Characteristic stripping voltammograms recorded at the downstream detector for a solution of 1×10^{-6}M Cu(II) and Pb(II) in 0.1M KNO_3. RVC potential, +0.05V (a, g), −1.1V (b-f). Flow rate, 0.22 ml/min. ASV conditions: deposition at −1.1V for 2 min; differential pulse ramp, as in Fig. 2.

solution (curve a). Following this series, the potential of the RVC was switched back to +0.5V, and a voltammogram, similar to that recorded earlier under similar conditions was obtained (compare curves b and f). Because of its anodic peak potential, silver was monitored at a bare glassy carbon disk, rather than at the mercury electrode; this simplifies the procedure employed, since detector conditioning (mercury plating) is not required. The determination of silver in flowing streams by ASV has not been reported yet.

Figure 5 shows ASV monitoring for a mixture of copper and lead ions, starting concentration 10^{-6}M in each ion. Curve a was obtained without removal of the metals at the RVC electrode. The capability of ASV for measuring mixtures of ions, shown in this curve, is an advantage of the method (in addition to the advantages of high sensitivity and on-line monitoring). Curves b-f are part of a series of ten successive measurements, over 60 min of continuous operation through which the RVC electrode was held at −1.1V. At this potential, both copper and lead coplated at the RVC electrode, as indicated from the ASV response of the effluent. Throughout this period, complete clean-up of copper, similar to that of Fig. 2, is observed. The first two curves (b, c) show incomplete clean-up of lead (~85%, 95% efficiency, respectively), following which complete removal is maintained over the rest of the series. Similar phenomenon was observed in experiments in which only lead was plated (not shown) and is attributed to simultaneous evolution of hydrogen bubbles that occurs at the potential employed. Following the 1 hr period of curves b-f, the potential of the RVC electrode was switched back to +0.05V, at which no deposition occurs; the resulting voltammogram (curve g) is similar to that recorded at the beginning of the experiment, under similar conditions.

Figures 6, 7, and 8 show SEM photographs of the bare RVC electrode, and after deposition of copper and silver, respectively. For both metals, the deposit formed is discontinuous, with certain regions of the RVC left bare. Similar photographs were obtained following depositions of lead and mercury under similar conditions (not shown). Such discontinuities in the electrode surface coverage have been reported for nonporous glassy carbon, and attributed to the presence of surface active sites (20). The nature of the deposit may depend on the deposition potential, that affects the number of active sites (21). The SEM photographs show no appreciable clogging of the RVC. Although 20 min depositions were employed, these data indicate that the RVC retains sufficient porosity even after deposition of thicker metal films. In some experiments, continuous clean-up operation was performed over more than 6 hr, yielding satisfactory efficiency throughout.

In conclusion, the above results confirm the feasibility of exploiting RVC as a working electrode in flow systems concerned with the removal and recovery of dissolved metallic contaminants. The material competes with prevalent metallic and carbonaceous materials utilized for electrodeposition purposes. Electrodes are easily fabricated and are inexpensive enough

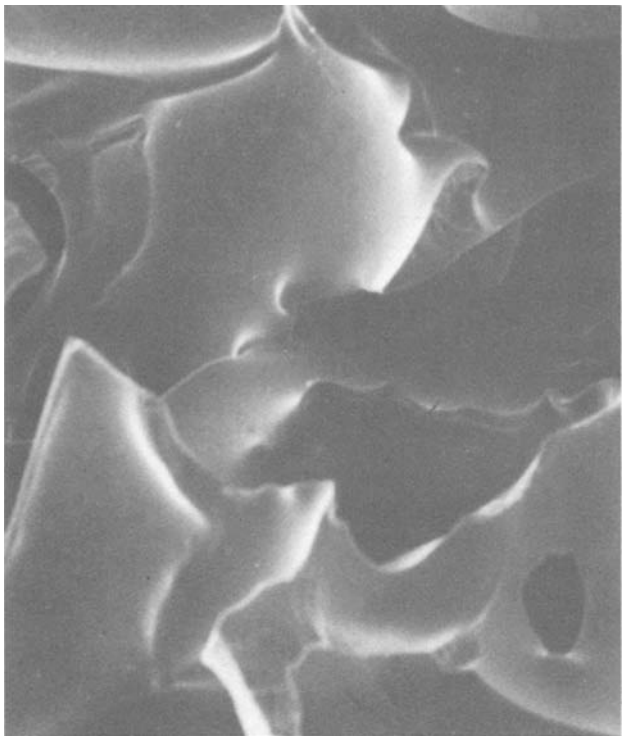

Fig. 6. SEM photograph of RVC. Magnification 320×

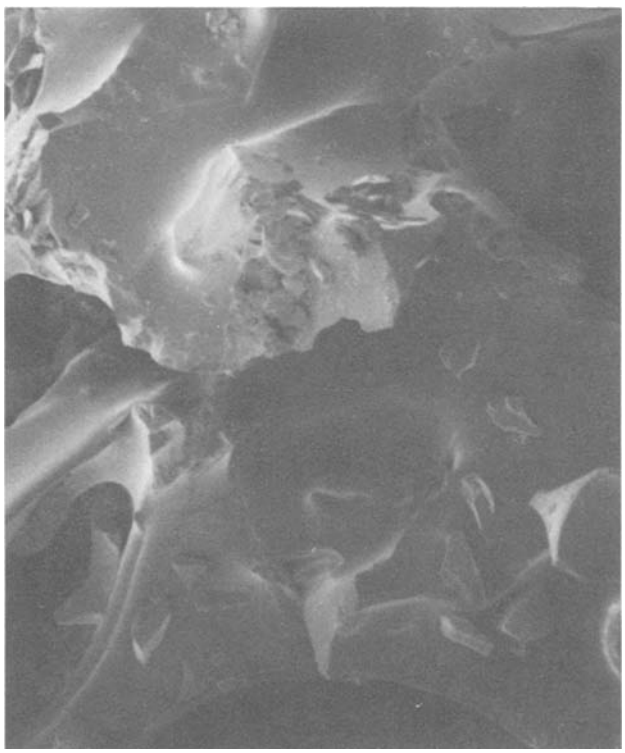

Fig. 7. SEM photograph of RVC after deposition of copper at −0.7V. Magnification 320×. 5 × 10^{-5}M Cu(II) in 0.1M KNO_3. Deposition period, 20 min; flow rate, 0.35 ml/min.

to be disposable. A scale-up of this removal process, employing longer RVC electrodes, would allow the use of higher flow rates, while maintaining the high clean-up efficiency. The downstream ASV cell allows real-time monitoring of the effluent and simultaneous determination of mixtures.

Acknowledgments

This work was supported by a grant from the U.S. Department of the Interior through the New Mexico Water Resources Research Institute.

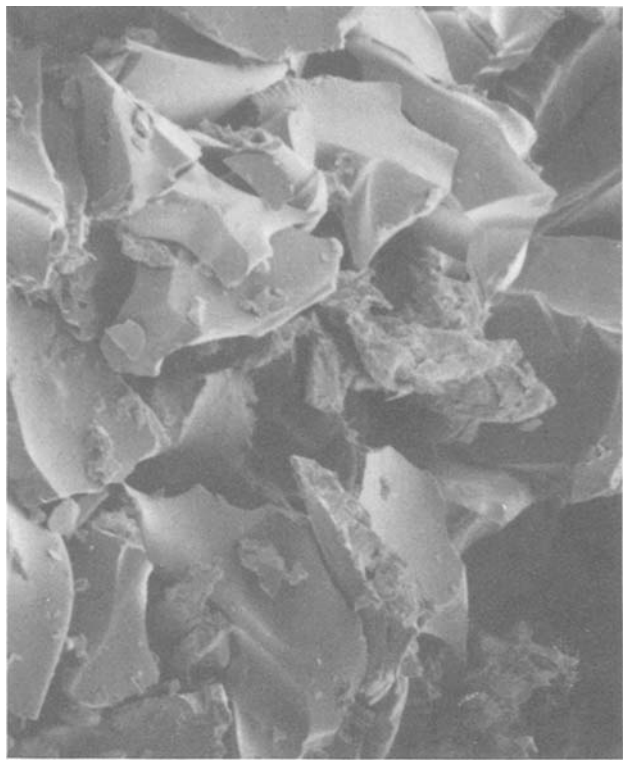

Fig. 8. SEM photograph of RVC after deposition of silver at −0.6V. Magnification 320×. 5 × 10^{-5}M Ag(I) in 0.1M KNO_3. Deposition period, 20 min; flow rate, 0.35 ml/min.

The authors acknowledge H. P. Adams (EML, NMSU) for taking the SEM photographs.

Manuscript submitted Dec. 27, 1982; revised manuscript received April 15, 1983.

REFERENCES

1. D. N. Bennion and J. Newman, *J. Appl. Electrochem.*, **2**, 113 (1972).
2. A. K. P. Chu, M. Fleischmann, and G. J. Hills, *ibid.*, **4**, 323 (1974).
3. T. Fujinaga and S. Kihara, *Crit. Rev. Anal. Chem.*, **6**, 223 (1977).
4. W. J. Blaedel and J. H. Strohl, *Anal. Chem.*, **36**, 1245 (1964).
5. D. Yaniv and M. Ariel, *J. Electroanal. Chem. Interfacial Electrochem.*, **79**, 159 (1977).
6. E. Suzkover, D.Sc. Thesis, Technion—I.I.T., Haifa (1977).
7. J. Wang, *Electrochim. Acta*, **26**, 1721 (1981).
8. W. J. Blaedel and J. Wang, *Anal. Chem.*, **51**, 799 (1979).
9. W. R. Heineman and P. T. Kissinger, *ibid.*, **52**, 138R (1980).
10. A. N. Strohl and D. J. Curran, *ibid.*, **51**, 1045 (1979).
11. J. Wang and H. D. Dewald, *Talanta*, **29**, 453 (1982).
12. W. J. Blaedel and J. Wang, *Anal. Chem.*, **51**, 1724 (1979).
13. S. H. Lieberman and A. Zirino, *ibid.*, **46**, 20 (1974).
14. J. Wang and M. Ariel, *Anal. Chim. Acta*, **99**, 89 (1978).
15. J. Wang and H. D. Dewald, *Anal. Chem.*, **55**, 933 (1983).
16. J. Wang and H. D. Dewald, *Anal. Chim. Acta*, **136**, 77 (1982).
17. R. E. Sioda, *Electrochim. Acta*, **15**, 783 (1970).
18. J. Wang, E. Ouziel, Ch. Yarnitzky, and M. Ariel, *Anal. Chim. Acta*, **102**, 99 (1978).
19. D. Yaniv and M. Ariel, *J. Electroanal. Chem.*, **129**, 301 (1981).
20. W. E. Van Der Linden and J. W. Dieker, *Anal. Chim. Acta*, **119**, 1 (1980).
21. M. Stulikova, *J. Electroanal. Chem.*, **48**, 33 (1973).

A Highly Stable Nonaqueous Suspension for the Electrophoretic Deposition of Powdered Substances

J. Mizuguchi

Sony Corporation, Research Center, Yokohama, Japan

K. Sumi

Motomiya Denshi Corporation, Fukushima, Japan

T. Muchi

Sony Corporation, Development Center, Tokyo, Japan

ABSTRACT

A higly stable nonaqueous suspension for the electrophoretic coating of alumina powders on double helical filaments has been developed. This suspension enables uniform coating in less than a second at a voltage of 300-600V with an average current density of about 1 mA/cm^2. The suspension is composed of dispersing powders, acetone, nitrocellulose, and a small amount of strong base and strong acid. A variety of powders can be anodically deposited uniformly using the same composition. Successful results are obtained for Al_2O_3, (Ba,Sr,Ca)CO_3, MgO, ZnO, TiO_2, SiO_2, SiO, In_2O_3, LaB_6, WC, and CdS powders; for phosphors such as ZnS:Cu,Al, ZnS:Ag, ZnS:Au,Ag,Al, Y_2O_2S:Eu, Y_2O_3:Eu, Y_2O_2S:Tb, and CaS:Ce; and for metallic powders such as W, Mo, Ni, Al, Zn, and Ru.

A number of investigations have been carried out on the electrophoretic deposition of powders in aqueous solutions (1-5), but there have been relatively few investigations in nonaqueous media (6-9). One of the appealing features of this technique is the uniformity of the deposit and the elimination of the waste encountered in the dipping or spraying operations. This method has been applied in the fabrication of oxide-coated cathodes and in the coating of tungsten spirals with an insulating layer of Al_2O_3 (1, 2, 6-9), and in the formation of uniform and even phosphor screens for high resolution oscilloscope (3-5).

Electrophoretic deposition from aqueous solutions or nonaqueous media containing some percentage of water is generally achieved by using magnesium and aluminum nitrates as electrolytes in the presence of an appropriate amount of organic solvent such as alcohol or acetone which minimizes the electrolysis of the liquid and attendant gassing at the electrodes (1-5). Lanthanum and/or calcium nitrates are sometimes used instead of magnesium and aluminum nitrates for phosphor coating because these nitrates have less effect on the luminescent properties of phosphors (3, 4). Metallic ions adsorbed on the powders are the charge determining ions, so the suspended powders are deposited at the cathode. Although this type of suspension is widely used, it has some disadvantages because of the electrolysis of water which inevitably occurs in aqueous or water containing nonaqueous solutions. The formation of hydrogen at the cathode prevents the deposition of a uniform adhering layer, yielding coarse layers with pin holes caused by gas evolution. Hydrogen also causes transparent oxide electrodes such as In_2O_3 and SnO_2:Sb to brown on the glass substrate, a serious drawback in using this method to apply a phosphor coating to the face plate. Because of the electrolysis of water which occurs in parallel with the powder deposition, current efficiency is low and it takes considerable time to obtain a powdered layer of significant thickness.

These difficulties are, however, entirely eliminated by using nonaqueous organic dispersion media. In nonaqueous media, even at very high voltages, current efficiency is high because there is no gas development at the electrodes caused by water decomposition. Hamaker *et al.* (6, 7) first proposed a system in which the suspension is prepared by grinding the alumina in an organic medium, such as alcohol or acetone, with the dispersion fluid in a ball mill.

Yabumoto (8) has suggested a different approach which requires no grinding and which includes nitrocellulose dissolved in alcohol and ether (collodion). Deposition time was about 20-30 sec to obtain an appropriate thickness. Tomita (9) investigated a similar type of suspension composed of methyl isobutyl ketone, nitrocellulose, and alumina powders. He examined the influence of water content in the suspension as well as that of the cosolvents for nitrocellulose on the electrodeposition characteristics of various pretreated alumina powders. Deposition time was around 10 sec with an applied voltage of 500V. However, the detail of the suspension, for example, its stability and reproducibility are not presented and the origin of the potential determining species remains obscure.

The authors investigated the suspension containing nitrocellulose in some detail and found that the required deposition time was about 1 sec and that the surface of the closely packed deposited film was very smooth. Unfortunately, the authors also found that this type of suspension was unstable (*i.e.*, it had a short pot life) and that its reproducibility was poor. An attempt was made to solve these problems by clarifying the mechanism of the deposition process. The authors began by identifying the charge determining species of the dispersed particles and considered the potential distribution in the plating cell ideal for electrophoretic deposition. The potential distribution must be as shown in Fig. 1 in order to supply voltages at the electrode interfaces just sufficient for deposition while retaining the maximum potential gradient in the bulk necessary for mass transfer. Such a potential distribution can be realized by adding an appropriate amount of electrolyte to the solution to control its resistance. If the amount of electrolyte is insufficient, no deposition voltages are applied at the electrode interfaces and thus no deposition will occur. but if too much electrolyte is added. the potential gradient is flat in the bulk and there will be no electrophoresis.

The authors report here a highly stable nonaqueous suspension which enables a uniform and very dense coating using almost any kind of powder in less than a second at a voltage of 300-600V with an average current density of about 1 mA/cm^2. A distinguishing

Key words: electrophoretic depositiion, insulator, phosphor.

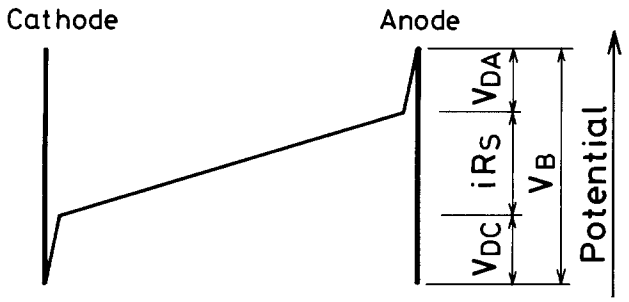

Fig. 1. The potential gradient ideal for electrophoretic deposition, where the anodic and cathodic deposition voltages are denoted by V_{DA} and V_{DC}, respectively, and that bath voltage, the resistance of the solution, and the flowing current by V_B, R_S, and i, respectively.

feature of the method used is the use of a very small amount of strong base and strong acid in the presence of acetone which contains nitrocellulose. The base gives the necessary conductivity to the suspension and the acid imparts a negative charge to the suspended particles.

Experimental

Chemicals.—Acetone of "electronic grade" and tetramethyl ammonium hydroxide (10 weight percent [w/o] methyl alcohol solution, hereafter abbreviated to TMAH) and sulfuric acid of guaranteed grade were obtained from Kanto Chemical Company, Incorporated. Nitrocellulose of RS-60, $[C_6H_7O_2(ONO_2)_2(OH)]_{n=720}$, was obtained from Daicel Limited. It was dried in a water bath at 80°C for 3 hr, after which the nitrocellulose was dissolved in acetone and kept as a stock solution. α-Al_2O_3 (38-900, 5 μm in average diameter) was obtained from Norton Company Limited, U.S.A. Since alumina usually contains a variety of electrolytes which might lead to instability and irreproducibility of the suspension, the powders were washed before use with deionized water using the decantation technique or using a glass filter until the conductivity of the supernatant solution reached nearly the conductivity of the initial deionized water. After washing, the powders were dried at 160°C for 3 hr to completely remove the water. The same treatment was also applied to the other powders.

Plating cell and plating conditions.—Electrophoretic deposition was carried out in a cylindrical cell of about 250 ml whose diameter was about 60 mm, with a d-c power supply of 0-630V/0.5A (Metronix Company Limited, Model 419-630). The applied voltages were between 300 and 600V. The deposition time was 1 sec or less for a coating of about 150 μm. Since the sulfate ions are adsorbed onto the surface of the particles, as will be described later, the particles are negatively charged and deposited at the anode. The electrodes coated were a tungsten filament containing 3% Re for the Al_2O_3 coating and a glass substrate of 40 × 50 mm^2 coated with transparent electrodes such as In_2O_3 or SnO_2:Sb for the coating of phosphor materials. For other powders, an aluminum plate was employed. As a counterelectrode, an aluminum cylinder was used for the alumina coating while a parallel plate of aluminum was employed for other powders.

Preparation of the suspension.—First, 100g of the desired powder was suspended in 500 ml of a 5 mM of nitrocellulose in acetone (monomeric concentration). To this suspension, 60 μl of 10 w/o TMAH was added. Then, approximately 250 ml of this suspension was placed into the electrolytic cell, and 5 μl of concentrated sulfuric acid was added. Hereafter the above composition will be called the "standard composition."

Conductivity and pH measurements.—Conductivity and pH measurements of the supernatant solution of the suspension were made at room temperature with a Model CM-20A conductivity meter and a Model HM-5A pH meter, both from TOA Electronics Limited. The conductivity was measured 1 min after the electrodes were immersed in the solution, while the pH values were measured after 5 min.

Moving boundary method.—The authors used a Burton tube 10 mm in diameter and a pair of platinum disk electrodes 8 mm in diameter. The distance between the electrodes was 20 cm, and the 1000V was applied between the electrodes (50 V/cm). The sharp boundary was initially made by pouring the white suspension ("standard composition") whose color was caused by alumina, followed by the pouring of the supernatant of the suspension which had been made in advance by centrifuging.

Determination of the nitrocellulose concentration in the suspension.—A given amount of nitrocellulose was dissolved in 500 ml of acetone in which 100g of alumina had been suspended. The suspension was then centrifuged and the supernatant was analyzed by polarographic method (10, 11). Correction was made for nitrocellulose adsorbed on the vessel.

Results and Discussion

Characteristics of the electrophoretic deposition.—When the alumina suspension was prepared according to the standard composition, the following characteristics were observed. Figures 2a and 2b show the relation of the transient current *vs.* deposition time and the amount of deposit per unit area *vs.* deposition time, respectively. The applied voltage was fixed at 500V in both cases, and the electrode to be coated was an aluminium wire 0.5 mm in diameter. The distance between the electrodes was about 15 mm. One can see

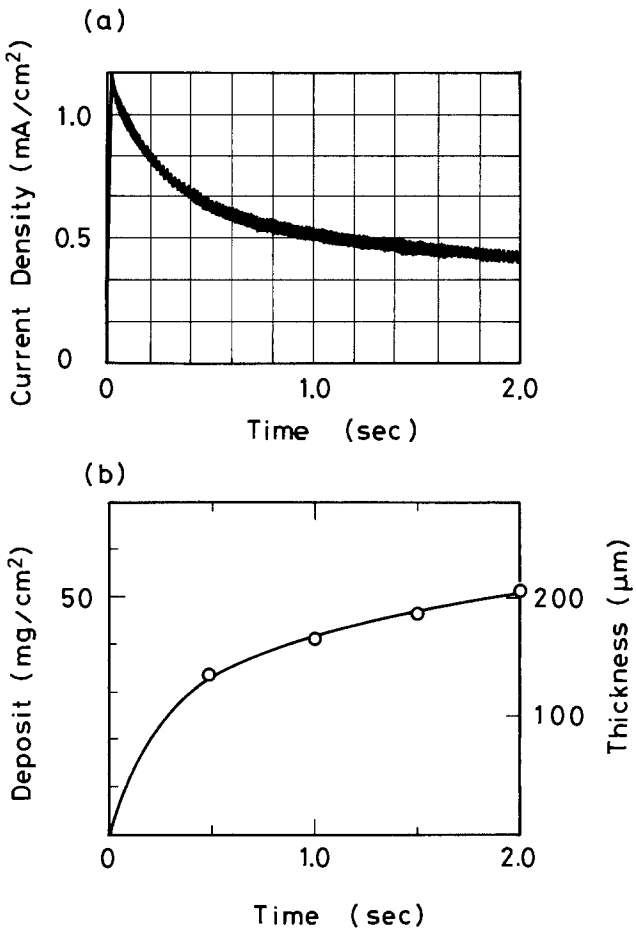

Fig. 2. (a) Transient current *vs.* deposition time, and (b) the amount of the deposit *vs.* deposition time. The applied voltage was 500V in both cases.

that the current decreases rapidly as the amount of deposit increases. The decrease in current is caused by the deposition of the highly resistive alumina powder. What is surprising is the extremely high deposition rate. As can be seen from Fig. 2a, the maximum current density is only 1 mA/cm^2. In a single second, the outer and inner side of the filament is covered with a uniform layer of closely packed Al_2O_3 particles.

The decrease in current described above was also observed in the case of metallic powders, but the decrease was much slower. This decrease can also be attributed to the deposition of metallic powders whose surface is covered with an insulating polymer of nitrocellulose. (see section on adsorption of nitrocellulose)

Figure 3 shows the amount of the deposit per unit area against deposition time as a function of applied voltage. The amount of deposit increases with deposition time, and there is a tendency for the deposit to saturate at voltages of between 300 and 600V. Throwing power of the deposition increases with voltage so that at voltages above 300V, the throwing power is sufficient to coat the double helical filaments with alumina.

Powders other than alumina can also be deposited uniformly and with good adherence with the same bath composition under the same experimental conditions. An example is shown in Fig. 4 where a white emitting mixed phosphor of ZnS:Au, Ag, Al, and Y_2O_2S:Eu (P4A, Kasei Optronix) was deposited on a glass substrate coated with In_2O_3. It can be seen how the surface of the closely packed phosphor layer has been deposited very evenly. This even deposition allows application to phosphor screens where high resolution and low noise, characteristics which depend on the flatness of the surface of the phosphor screen, are required. Since the deposition rate is high, powders with a different specific gravity can be simultaneously deposited in order to obtain a layer which possesses the same composition as the suspension. Another feature of this method is that one can use the face plate with transparent oxide electrodes such as In_2O_3 and SnO_2:Sb for phosphor screen. These transparent oxide films were not subject to coloration due to electrolytic attack of hydrogen during electrodeposition because the powders were deposited at the anode where if any oxygen were evolved, it could not result in the browning of the transparent electrodes.

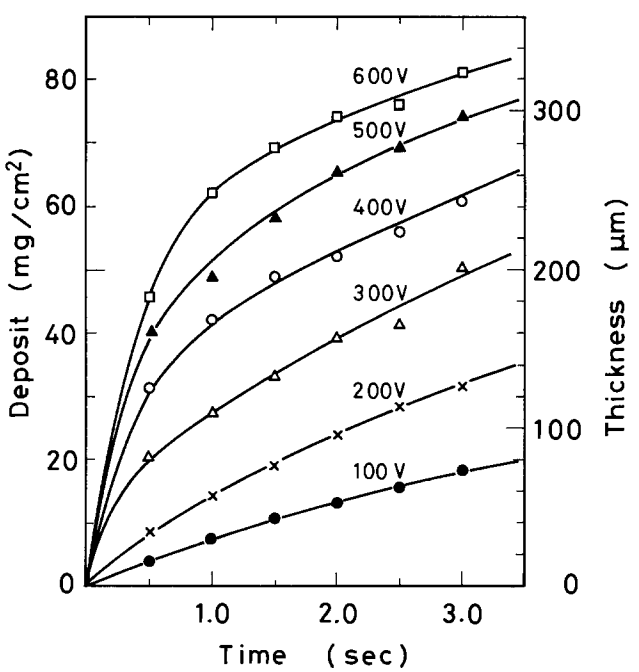

Fig. 3. Deposit *vs.* deposition time as a function of applied voltage.

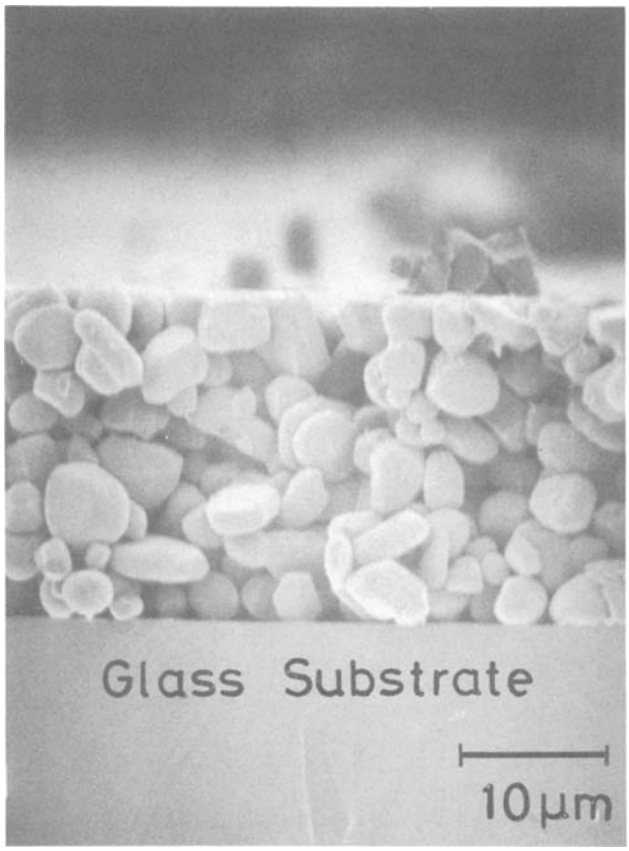

Fig. 4. Microphotograph of the phosphor deposited on an In_2O_3/glass substrate. Pieces of phosphor particles on the top of the layer fell there when the glass covered with the phosphor was cleaved in order to prepare the SEM sample.

Microelectrophoretic deposition of a stripe was also possible, as is shown in Fig. 5, where deposition was performed on a transparent raster-type cell of In_2O_3 (10 × 10 mm^2). The electrode was made in the form of two interpenetrating combs by using a photoetching technique. One group of stripes was first deposited with blue phosphors, then the other group of stripes was coated with green phosphor. Deposition was carried out at a low voltage of 30V for 0.1 sec. The 50 μm wide stripe was successfully coated with phosphors whose average diameter was 4 μm. Finer patterns are clearly possible if finer phosphor particles are used. With microelectrophoretic deposition, a very low voltage of 30V or even less is sufficient because the electric field can be concentrated on a very fine stripe.

Addition of TMAH.—As noted previously, a certain amount of electrolyte must be added to the suspension to lower its resistance. The authors examined TMAH and sulfuric acid added separately to the suspension in the presence and in the absence of alumina and nitrocellulose while monitoring the change in conductivity. The experiment was performed with the standard composition of the suspension while varying the concentration of alumina from 20 to 140g per 500 ml of acetone.

As shown in Fig. 6, no significant increase in conductivity was observed in the suspension of acetone and alumina and in the solution of acetone and nitrocellulose when compared with the conductivity of pure acetone (about 0.2 μS/cm). The addition of TMAH increases the conductivity to some extent, especially in the region of the low concentration of alumina. What is remarkable is that the conductivity increases drastically when TMAH and nitrocellulose are present together. This mechanism may be explained as follows: no considerable increase in conductivity suggests that

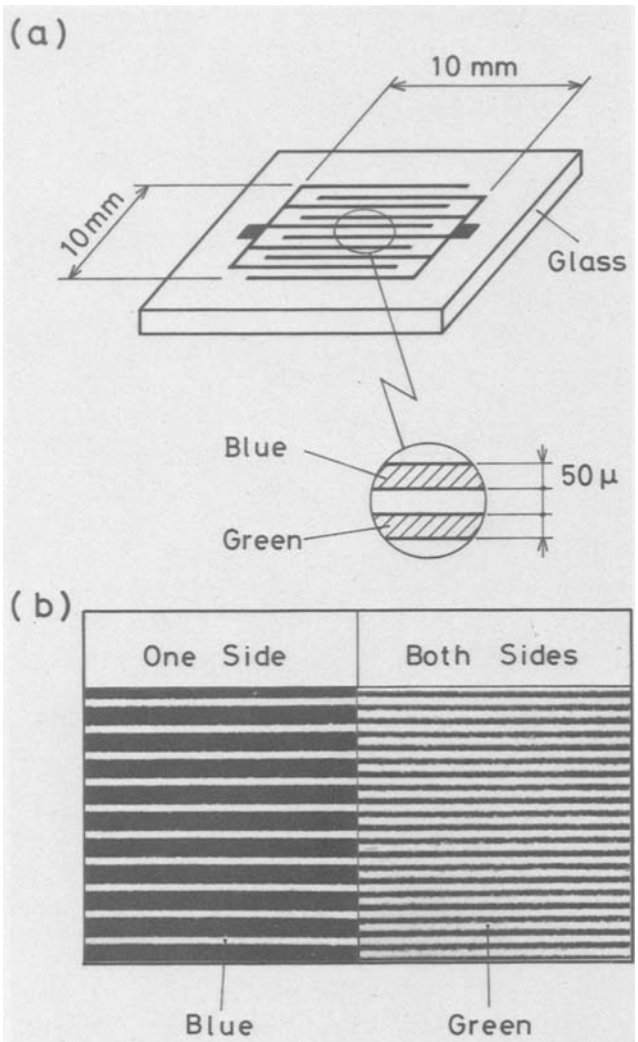

Fig. 5. Fine phosphor stripes prepared by electrophoretic deposition. (a) Transparent electrode (In_2O_3) is photoetched to form a raster cell. (b) One side is covered with blue phosphor, then the other side is coated with green phosphor.

both hydroxide anions and quaternary cations of TMAH are adsorbed on the alumina as is shown by the fact that the conductivity decreases as the alumina concentration increases. When nitrocellulose is added, the nitrocellulose causes these ions to be desorbed from the adsorption sites of the alumina to the suspension, and the nitrocellulose is, in return, adsorbed on these sites—replacement of the adsorbate on the adsorption sites. The increase in conductivity can thus be explained in terms of the ions extruded from the alumina surface. The conductivity of the suspension of around 10-15 μS/cm was found to be the optimum for the electrophoretic deposition.

When sulfuric acid is added instead of TMAH, no significant increase in conductivity is observed regardless of the presence or absence of nitrocellulose. (Almost the same conductivity curve in the presence of acetone and nitrocellulose in Fig. 6). The reason for this is related to the charge determining ions of alumina described in the following discussion.

Influence of sulfuric acid on the electrophoretic deposition.—The suspension without sulfuric acid exhibited no significant deposition; however, when just a trace of sulfuric acid was dropped into the suspension, considerable deposit occurred. Sulfate ions here control the surface charge of the particles. The optimum concentration of sulfuric acid was determined by adding the acid drop by drop, if necessary diluted with acetone, until the film of the optimum adherence and smoothness was obtained. The suspension kept then its optimum state for 8 hr or more unless over 50% of the suspended alumina was taken out of the bath by electrophoretic deposition.

Figures 7a and 7b show the conductivity, pH values, and the amount of deposit per second per unit area when a weighed amount of sulfuric acid was added to the suspension of the standard composition. The applied voltage was 500V. The initial conductivity of approxi-

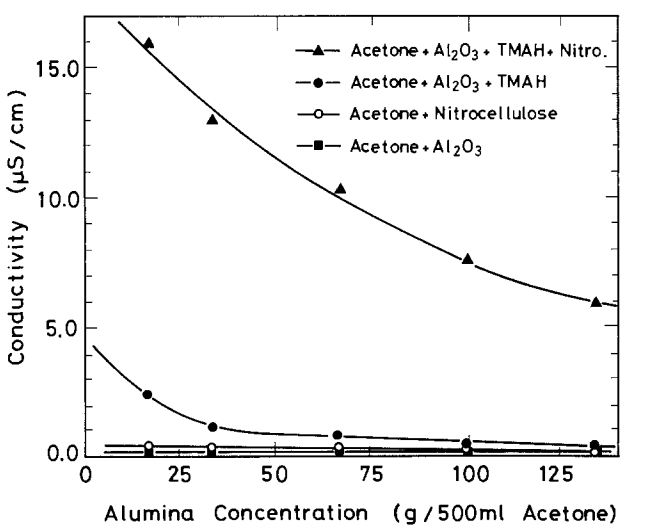

Fig. 6. Conductivity of the various suspensions as a function of the concentration of alumina.

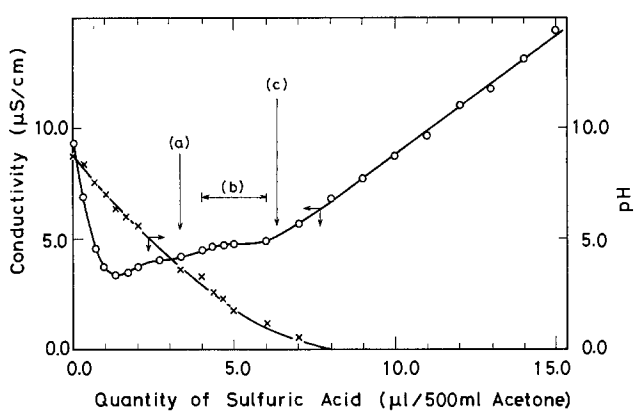

Fig. 7a. Conductivity and pH vs. quantity of sulfuric acid. (a) Point where significant amount of deposit can be observed. (b) Region in which electrophoretic deposition can be optimally achieved. (c) Point where the throwing power begins to be reduced, while the amount of deposit continues to increase.

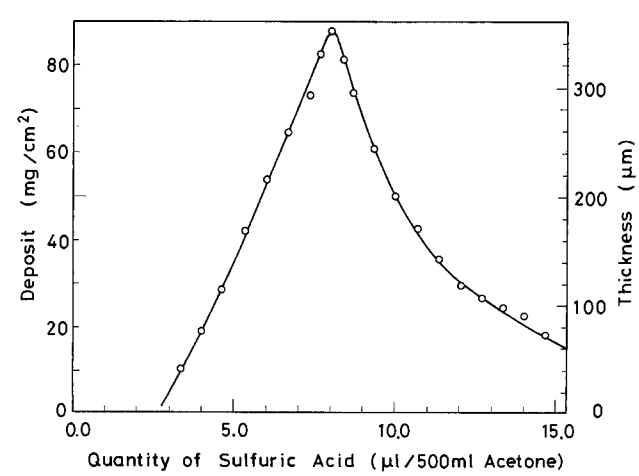

Fig. 7b. Deposit and thickness vs. quantity of sulfuric acid

mately 10 μS/cm is due to TMAH. The initial decrease in conductivity in Fig. 7a is caused by the neutralization reaction of hydroxide ions from TMAH with protons from sulfuric acid, $H^+ + OH^- \rightleftharpoons H_2O$. Conductivity then gradually increases until 4 μl of sulfuric acid, after which it hardly increases until 6 μl of sulfuric acid is added. The deposition of alumina begins abruptly at the point of 3 μl of sulfuric acid and increases linearly up to 8 μl as shown in Fig. 7b. The fact that the amount of deposit increases while no considerable increase in conductivity suggests that the sulfate ions may be adsorbed on the particles. The slow increase in conductivity mentioned above is considered to be caused by reaction of sulfuric acid with adsorbed TMAH releasing quaternary cations of TMAH into the solution while sulfate is being adsorbed. The usual abrupt break corresponding to the beaks in the conductivity was not observed in the pH curve in Fig. 7a. This state of affairs can be attributed to the fact that the dissociation constant of water, which is $[H^+][OH^-] = 10^{-14}$ in aqueous solutions, is expected to be quite different in nonaqueous solutions and that the pH value measured in nonaqueous media does not correspond to the one measured in aqueous solutions.

Successive addition of acid causes an increase in conductivity as shown in Fig. 7a, while the amount of deposit still increases and shows the deposition maximum at 8 μl of sulfuric acid and then decreases, as can be seen in Fig. 7b. The decrease in the amount of deposit can be explained as follows: when all the adsorption sites on the alumina surface are occupied with sulfate ions, all sulfate ions added subsequently remain in the suspension and cause the increase in conductivity. The mass transfer of negatively charged alumina decreases due to the reduced potential gradient in the bulk and, at the same time, two different ionic species, negatively charged alumina and sulfate ions, compete at the anode which result in the decrease in deposition efficiency of alumina.

The optimum throwing power which enables one to coat the outer and inner side of the filament was observed in the region b in Fig. 7a, while the deposition maximum occurs with a larger quantity of sulfuric acid as shown in Fig. 7b. This fact indicates that an optimum quantity of surface charge is necessary for the electrophoretic deposition with high throwing power.

Figure 8 shows the charged species before and after the addition of sulfuric acid. Under the optimum composition, no competing anions with negatively charged alumina exist at the anode, so a high current efficiency is assured.

Confirmation of the adsorption of sulfate ions.—In order to confirm directly the adsorption of sulfate ions, the moving boundary method (12) was employed. Figure 9 shows the moving distance toward the anode after 15 min application of the voltage plotted against the quantity of sulfuric acid. In this figure is also shown the amount of the deposit per unit area as obtained from a separate experiment. A minus value of the moving distance indicates a sedimentation of the boundary caused by particles with not enough charge moving toward the anode. One can see that the moving distance increases with the addition of sulfuric acid to a certain point, after which the distance decreased. The same tendency was observed in the amount of deposit. These observations confirm that the charge determining species are sulfate ions.

Adsorption of nitrocellulose.—Nitrocellulose is adsorbed on the alumina surface and causes an increase in the dispersion power of the particles. A minute change in adsorption affects the process of electrophoretic deposition. When the concentration of nitrocellulose in the suspension is small, the deposit is so poorly adherent that it cannot be removed intact from the bath. An increase in the concentration of nitrocellulose improves adherence, but the throwing power of the suspension decreases when the amount of nitrocellulose exceeds a certain point. Because of this, it is important to determine the quantity of nitrocellulose being adsorbed on the surface. The amount of nitrocellulose adsorbed on the surface was determined using a polarographic technique which monitors the reduction wave of $-NO_2$ to $-NHOH$ (10, 11). This analytical method is accurate within 0.1%.

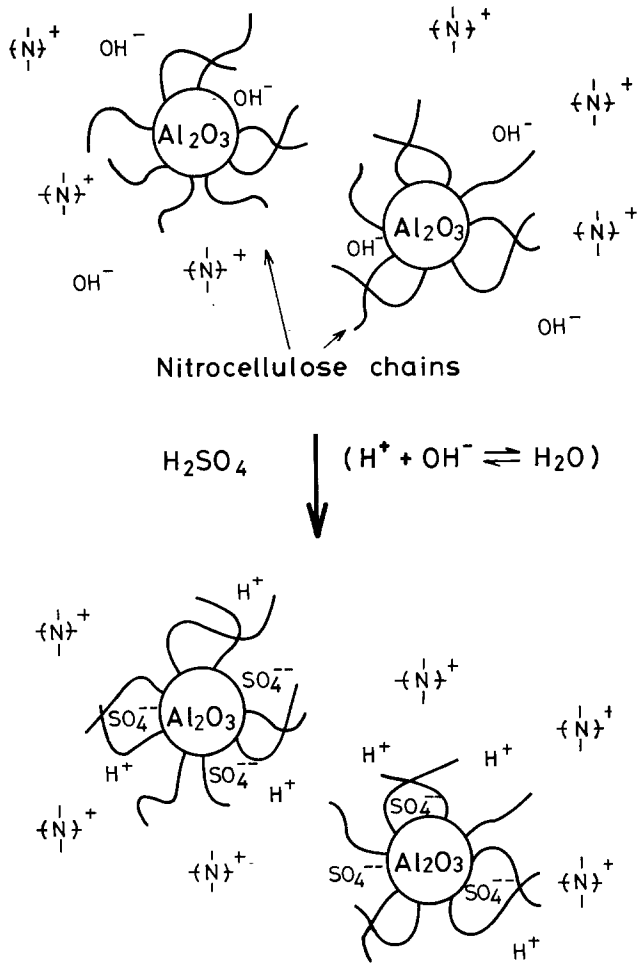

Fig. 8. Charged species before and after the addition of sulfuric acid.

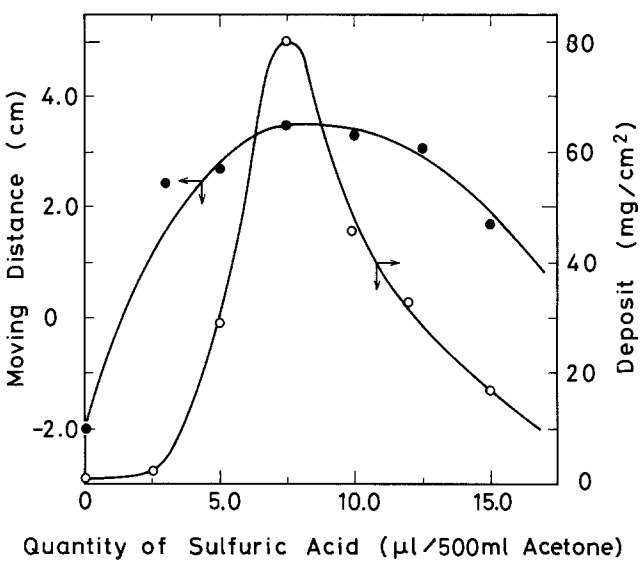

Fig. 9. Moving distance and amount of deposit vs. quantity of sulfuric acid.

Figure 10 shows the relation between the nitrocellulose quantity dissolved in the suspension and the quantity adsorbed by the alumina. At a concentration of 1.25g of nitrocellulose per 500 ml of acetone (about 5 mM), about 40% of the dissolved nitrocellulose was adsorbed on the alumina surface. If we take a nitrocellulose density of 1.6 and assume the average diameter of the alumina particles to be 5 μm, a simple calculation shows that the adsorbed layer of nitrocellulose is about 100A. This thickness is acceptable if, as has been suggested by Crowl (13), the stabilization of dispersion of small particles of Al_2O_3 by an adsorbed layer mechanism requires an adsorbed layer of at least 50A thick.

Deposition mechanism at the anode.—As the Verwey-Overbeek theory (14) predicts, the particles are brought up to the electrode under the influence of an electric field which exerts sufficient force to overcome the mutual repulsion, thus allowing the particles to come close enough for the London-van der Waals force of attraction to predominate. Alumina particles migrate to the anode by electrophoresis, so the concentration of the particles is high around the electrode in comparison with the concentration in the bulk. The moment the sulfate ions on the surface of the particles discharge at the anode, the particles lose their surface charges and come closer to each other so that the nitrocellulose chains on the alumina surface may form the necessary bridges to cause them to deposit at the anode (see Fig. 11). The adhesion force due to nitrocellulose polymer is much greater than when it depends only on the London-van der Waals attractive force.

Brown (15) has a similar explanation of the electrolytic reaction found in an aqueous suspension containing aluminum chloride as an electrolyte. In Brown's system, it is known that a polymeric hydroxide is initially formed at the cathode from the aluminum chloride and the resulting chains are adsorbed onto the particles, as they are brought up to the cathode, to hold them together. Another similar mechanism is found in the fact that the addition of a prolamine such as zein to the suspension of metallic and nonmetallic powders results in improved adhesion of the deposit in the absence of any electrolytes (16, 17). The zein will be adsorbed strongly onto the particles and form the necessary bridges.

Role of the chemicals.—Acetone acts as a solvent for nitrocellulose. Any ketonic solvent can replace the acetone. Nitrocellulose plays the following three important roles in the suspension. The first role is that of a dispersant. In general, there are two methods of preventing particles from being coagulated. One method is to impart a charge to the particles so that the electric repulsive force of the particles prevents the particles from approaching each other, thus resulting in a good dispersive effect. The other method is to use polymers which can be adsorbed on the surface of the particles. The polymer chains, one end of which is adsorbed onto the particle while the other end of which is free in the solvent, prevent the particles from converging by steric hindrance. Nitrocellulose in the present system works as a dispersant in the latter mechanism. A negative surface charge caused by sulfate ions might also be expected to increase the dispersive effect according to the former mechanism. The second role is that of a binder. Adhering strength depends on how active the surface is (the wetting effect) and how strong the chemical binding force is between particles. Nitrocellulose is an effective surface active agent and works as a binder. Nitrocellulose in its third role causes the ions of TMAH to be desorbed from the alumina surface to the suspension so that the conductivity of the suspension increases remarkably.

TMAH is an electrolyte which increases the conductivity of the suspension. TMAH is not the only electrolyte which can aid electrophoretic deposition. Any alkaline strong electrolyte, such as sodium hydroxide, potassium hydroxide, tetra-alkyl ammonium salts of $(N(C_nH_{2n+1})_4X, X = Cl, Br, I, OH)$ is effective in the present system. However, there is a definite advantage in using tetra-alkyl hydroxides, since they are composed of only noncontaminating atoms for the insulating and luminescent properties of the powders. Furthermore, these reagents are popular supporting electrolytes in the field of polarography and available in high purity. Alkali metals such as sodium and potas-

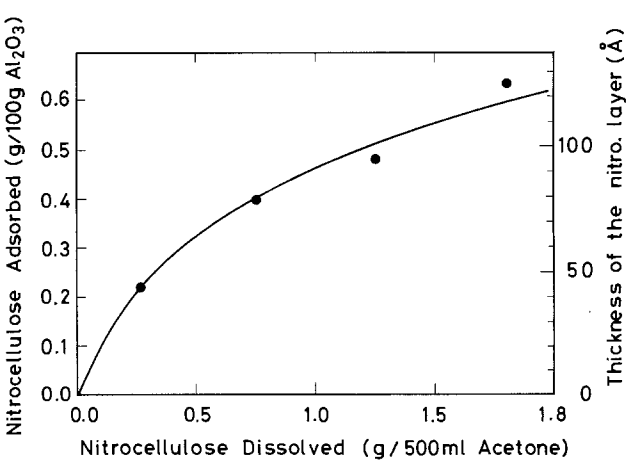

Fig. 10. Adsorption of nitrocellulose on the surface of the alumina powder. Concentration of nitrocellulose is plotted against the prepared concentration of nitrocellulose.

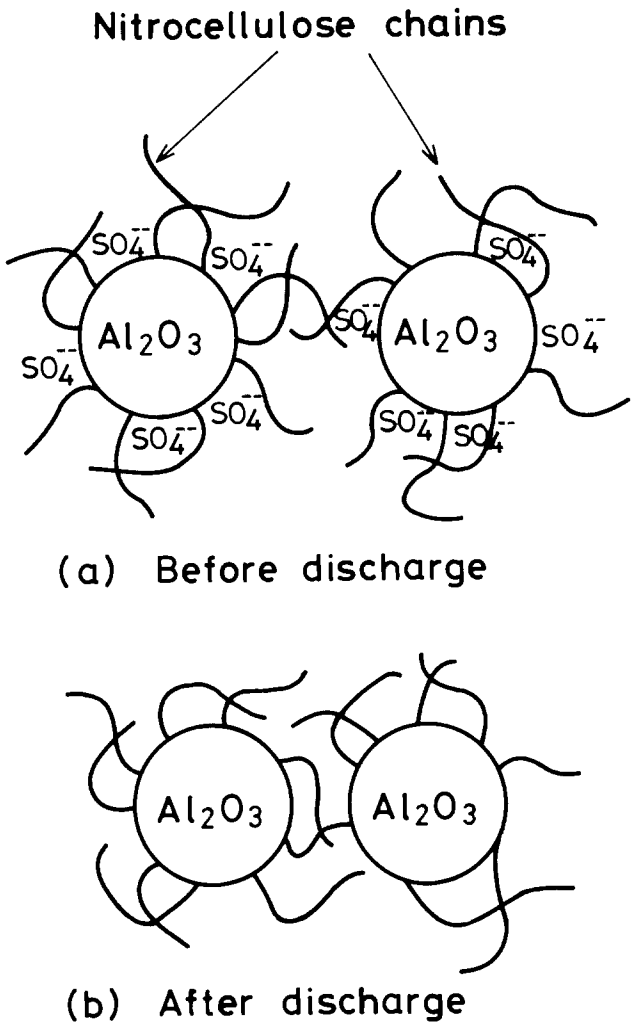

Fig. 11. Particles before and after discharging their charges at the electrode.

sium sometimes work as a flux, assisting the crystal growth of the powder, or sometimes cause leakage of the current. Chlorine is also known to cause coloration of phosphors under electron beam radiation.

Sulfuric acid imparts a negative charge to the particles. The authors extensively investigated acids which could replace sulfuric acid, but the only possible alternative proved to be phosphoric acid.

Further application of powder deposition.—Since nitrocellulose covers the powder's surface, on which sulfate anions are preferentially adsorbed, in principle any powders can be electrophoretically deposited under the same conditions if nitrocellulose can be effectively adsorbed on the surface of the particles and if the powder is not soluble in the solvent. Successful results are obtained for (Ba, Sr, Ca)CO_3, MgO, ZnO, TiO_2, SiO_2, SiO, In_2O_3, LaB_6, WC, and CdS for phosphors such as ZnS:Cu,Al, ZnS:Ag, ZnS:Au,Ag,Al, Y_2O_3:Eu, Y_2O_2S:Eu, Y_2O_2S:Tb, CaS:Ce, and for metallic powders such as W, Mo, Ni, Al, Zn, and Ru.

Acknowledgments

The authors would like to express sincere thanks to J. Seto, K. Ueno, and S. Soyama for suggestions and discussions throughout the course of the investigation. Thanks are also due to G. P. Satô of Sophia University for valuable discussions.

Manuscript submitted Dec. 7, 1982; revised manuscript received May 7, 1983.

Sony Corporation, Research Center, assisted in meeting the publication costs of this article.

REFERENCES

1. F. Rosebury, "Handbook of Electron Tube and Vacuum Techniques," Addison-Wesley Publishing Company, Inc., p. 85 (1965).
2. Y. Tomita, *Hitachi Hyôron*, **49**, 40 (1967).
3. R. G. Liversey and E. Lyford, *J. Phys. E.*, Ser. 2, **1**, 948 (1968).
4. P. F. Grosso, R. E. Rutherford, Jr., and D. E. Sargent, *This Journal*, **117**, 1456 (1970).
5. E. I. Szabo and S. L. Gertsman, *ibid.*, **118**, 2059 (1971).
6. J. H. De Boer, H. C. Hamaker, and E. J. W. Verwey, *Rec. Trav. Chim.*, **58**, 662 (1939).
7. H. C. Hamaker, *Trans. Faraday Soc.*, **36**, 279 (1940).
8. C. Yabumoto, Jpn. Patent 173952 (1946).
9. Y. Tomita, *Hitachi Hyôron*, **50**, 39 (1968).
10. J. Mizuguchi and K. Ueno, *Rev. Polarog.*, **18**, 51 (1972).
11. J. Mizuguchi, *This Journal*, **129**, 1520 (1982).
12. S. Glasstone, "An Introduction to Electrochemistry," D. Van Nostrand Company, Inc., p. 536 (1942).
13. V. T. Crowl, *J. Oil. Col. Chem. Assoc.*, **50**, 1023 (1967).
14. E. J. W. Verwey and J. T. G. Overbeek, "Theory of the Stability of Lyophobic Colloids," Elsevier Publishing Company, Amsterdam-New York (1948).
15. D. J. Brown and W. Salt, *J. Appl. Chem.*, **15**, 40 (1965).
16. P. Gutierrez, J. R. Mosley, and T. C. Wallace, *This Journal*, **109**, 923 (1962).
17. Vitro Corp. of America, U.S. Pat. 2,982,707.

Study of a Decomposing Hydride Phase at Nickel Cathodes by Measurement of Open-Circuit Potential Decay

B. E. Conway,* H. Angerstein-Kozlowska, and M. A. Sattar

Chemistry Department, University of Ottawa, Ottawa, Ontario, K1N 9B4 Canada

B. V. Tilak*

Occidental Chemical Corporation, Hooker Research Center, Grand Island, New York 14072

ABSTRACT

At Ni or Raney Ni Al-type electrodes subjected to cathodic polarization with H_2 evolution in alkaline solutions, characteristic time dependent currents are observed when measurements are made in the direction of increasing or decreasing potentials. Also, after polarization to high cathodic overvoltage, appreciable quantities of H_2 continue to be evolved after interruption of the current or an anodic current is observed at low cathodic overpotentials as the potential is reduced, that is at potentials still negative to the H_2 reversible potential. These observations suggest that a three-dimensional hydride is formed which undergoes decomposition at low overpotentials. The kinetics of decomposition of such a surface or thin layer metal hydride were evaluated by means of open-circuit potential decay measurements. A mixed "corrosion"-type mechanism is considered with anodic hydride decomposition

$$MH + OH^- = M + H_2O + e \quad [1]$$

coupled concurrently with cathodic H_2 evolution through the steps

$$M + H_2O + e = MH_{ads} + OH^- \quad [2a]$$

and

$$MH_{ads} + H_2O + e = M + H_2 + OH^- \quad [2b]$$

Evidence shows that the anodic process [1] is not Al dissolution. Kinetic treatment of the potential decay on open circuit is given in terms of the above mechanism involving adsorbed H and decomposition of a bulk hydride. Certain conditions are shown to correspond with the observed experimental behavior. Similar behavior with respect to potential decay and H_2 evolution is found with electroplated Ni-Mo-Cd-coated cathode preparations.

A striking feature of cathodic H_2 evolution behavior on Raney-type leached Ni-Al alloys or on electrolytically prepared Ni-Mo-Cd electrodes is that the decadic Tafel slopes are changed dramatically from *ca.* 100 mV on bulk Ni to *ca.* 20 ~ 30 mV on the composite surfaces. Correspondingly, unusually low potential decay slopes, dE/d log t, are observed which indicate that discharge of some capacitance as well as that of the double-layer is involved.

* Electrochemical Society Active Member.

Key words: hydrogen cathodes, hydrides, open-circuit potential, nickel cathodes.

During the evaluation of the cathodic polarization behavior of some Raney Ni-Al and Ni-Mo-Cd electrodes, an interesing time dependence of hydrogen overpotential (η) was observed in the directions of increasing or decreasing current density, i. Also, appreciable quantities of H_2 continue to be evolved after interruption of the current and an anodic current is observed at low but still cathodic H_2 overpotentials as the potential is reduced in a stepwise manner in a potentiostatic experiment. These observations suggest that some species forming a two- or three-dimensional phase are formed which undergo decomposition, leading to evolution of H_2 on open circuit or to the anodic current observed at low cathodic η. It will be shown that it is likely that a nickel hydride species is formed.

It may be significant that H_2 overpotentials are lowest at those metals, *e.g.*, Pt, Ir, Rh, on which a two-dimensional surface hydride (strongly chemisorbed H at full site coverage) exists already at or before the reversible hydrogen potential. Thus, H_2 evolution occurs on an already completed chemisorbed H film. On the other hand, previous work on Ni electrodes indicates (1, 2, 3) that at that metal, full coverage by atomic H is not attained at the reversible hydrogen potential, but a three-dimensional hydride can develop on cathodic polarization (4, 5) and gives rise to a surface having good electrocatalytic properties for H_2 evolution similar to those associated with the two-dimensional hydride surfaces at Pt, Rh, etc. (6).

It appears that in generating a highly active surface of Ni from Raney-Ni alloys by leaching, or by electrodeposition of Ni-Mo alloys with cathodic co-evolution of H_2 and hence codeposition of H, some kind of hydride phase is formed having desirable electrocatalytic properties, in particular low Tafel slopes that are as important as high exchange current densities for minimizing overpotential. Thus, it is not necessarily generation of large real/apparent area that is the only or even the key factor in leading to high performance of such H_2 cathode materials; however, the importance of distinguishing the real area factor from other intrinsic surface chemical and reaction mechanism factors in evaluating electrocatalyst materials must be stressed (7, 8). These considerations are material to the development of electrolytically prepared alloy cathodes containing Mo [cf. Ref. (9)] or Ti where the role of the alloy element in Ni may be to facilitate formation of a hydride phase.

In this paper, investigations of the hydride question are made by means of studies of time variation of cathodic H_2 overpotential on some Raney Ni-Al and Ni-Mo-Cd electrode preparations in relation to open-circuit decay of potential and the observation of simultaneously evolved H_2 on open circuit following previous cathodic polarization.

Experimental

Electrodes.—Nickel rods with Ni/Al plasma-sprayed coatings on the surface were used in part of the work. Only the surface of the bottom of the rod was exposed to the solution so that its working area was well defined. The sides, after being smoothed by grinding, were covered by shrinkable Teflon. The latter operation was necessary to prevent the electrolyte creeping up the pores in the walls of the electrode, thus leading to a change of reactive surface area. The electrodes were activated in concentrated boiling NaOH for 24 hr during which period visible H_2 evolution had ceased.

Electrolytically deposited or thermally prepared (9) Ni-Mo alloy materials are also active for cathodic H_2 evolution and have performance characteristics similar to those of Raney-Ni preparations. Such electrodes were prepared by electrocodeposition of Ni, Mo, and Cd (9) onto chemically polished Ni electrodes from a plating solution having the following composition in molar concentrations of its constituents: Na_2MoO_4, 0.033M; $NiCl_2$, 0.073M; $Na_4P_2O_7 \cdot 10H_2O$, 0.145M; $NaHCO_3$, 0.892M; NaCl, 1.28M; $N_2H_4 \cdot H_2SO_4$, 0.025M; $Cd(NO_3)_2$, 3.9×10^{-4}M; and KSCN, 2×10^{-4}M. Compositions of the coated Ni electrodes were determined by x-ray emission analysis. The electrodes used were thoroughly washed free of the plating solution and then leached for several hours at 95°C in strong aqueous NaOH.

Solutions.—The electrolyte solution was aqueous 10M NaOH pre-electrolyzed for many hours in a small scale Nafion membrane Cl_2 electrolysis cell as used by Hooker Chemical Company, Niagara Falls, New York. This electrolyte was shown, in parallel cyclic voltammetry experiments at Pt, to be remarkably pure by the standards previously published for high purity electrochemical surface work (10).

Polarization curves.—Fresh electrodes, prepared by the leaching procedure, were polarized cathodically at -0.250V E_H for up to 2 hr in order to obtain the most reproducible results. The ascending and descending polarization curves were made by registering the initial and the reasonably steady currents for potentials changed in intervals of 10 mV.

Cathodic and anodic potential steps.—In order to study the anodic decomposition of the supposed nickel hydride, potential steps from a cathodic polarization into the anodic potential region (but still negative to the H_2 reversible potential for that solution) for the hydride oxidation reaction were made potentiostatically.

In another type of experiment, a small ascending or descending potential step of about 10 mV was imposed on the electrode in the potential range of the potential time effects and the change of current with time was recorded.

Open-circuit decay of potential.—In order to ensure that the initial state of electrodes used was the same in each experiment, all electrodes were first prepolarized to give reproducible behavior (see section on polarization curves) and then allowed to reach a steady potential on open circuit. The electrode was then polarized cathodically in successive measurements to constant potentials of -0.100, -0.200, and -0.250V, E_H for 5 min before the current was interrupted and the variation of the potential of the electrode was recorded in time.

Results and Discussion

Introduction.—An indication of unusual behavior of the Raney Ni and Ni-Mo-Cd H_2 cathodes was given by three phenomena observed during cathodic polarization and open-circuit decay experiments.

1. During cathodic H_2 evolution at the Raney Ni-Al or Ni-Mo-Cd electrodes, the current density, i, is not steady at a constant potential (Fig. 1); it decreases with time when a given η is approached from lower η while it increases with time when the η change is in the opposite direction. The relatively most significant changes of i with time occur at low η, 0.04 ~ 0.08V. This time dependence of η is a characteristic feature of cathodic polarization of Ni-based cathodes evolving H_2, and its understanding is basic to the improvement of Ni cathode performance. The time dependence of potential, at low overpotentials, is observed not only at the Raney Ni-Al electrodes but also at electrodeposited Ni-Mo-Cd coatings at Fe or at Ni-electrodeposited on Fe, as well as at the bulk Ni-Mo alloys, as may be seen from Fig. 1b. This figure also shows a comparison of the Tafel lines for these electrode preparations from which it is seen how the Tafel slope for H_2 evolution is quite dependent on the electrode composition or preparation.

2. Upon interruption of a cathodic current at $\eta >$ 0.10V, continuing evolution of H_2 gas is observed which is quite vigorous for 5 ~ 6 min and slower for a further several minutes. During this time, the potential drifts slowly from *ca.* -0.075 to -0.010V but does not

drop to 0.0V E_H. This suggests that a process different from the reversible H_2/H_2O reaction, with E_{rev} changing with time, occurs at the electrode in parallel with H_2 evolution.

When η is lowered to −0.040V or less, a rapidly diminishing anodic current is first observed at nominally cathodic overvoltages (*i.e.*, w.r.t. the H_2 reversible potential for the same solution) indicating that, besides H_2 evolution, another process occurs on the electrode having an E_{rev} more negative than that for H_2 evolution. The observed behavior also indicates that this E_{rev} changes with time during polarization.

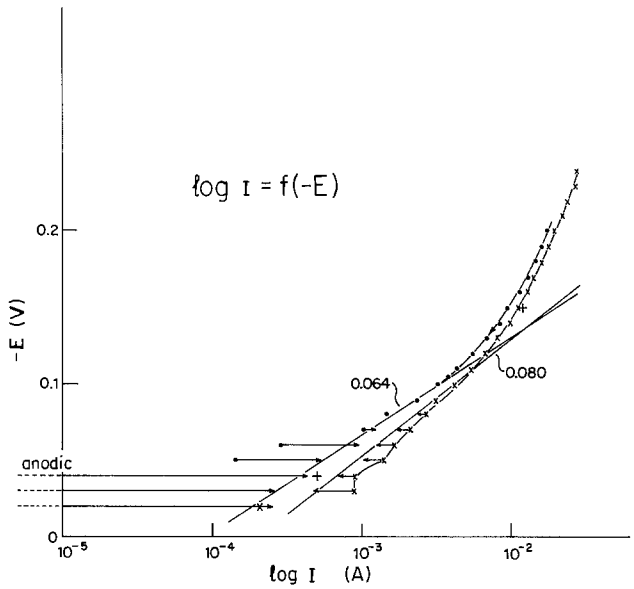

Fig. 1a. Polarization curves for hydrogen evolution on Ni-Al electrodes in MX cell solutions (5M aqueous NaCl solutions at 298 K). x—ascending curve; ●—descending curve; +—steady-state values in potential steps. Arrows show directions of potential change with time.

3. When cathodic current is interrupted, a rapid fall of potential (due to iR drop) is first observed followed by a remarkably slow further decay of potential (Fig. 2a), unlike that normally observed when discharge of the double-layer capacitance is involved. This suggests participation of a large pseudocapacitance (11). Only in potential decay traces taken from higher η, where the pseudocapacitance seems to have become almost completely charged, corresponding to a saturation condition, does the potential decay trace assume a more normal curved (Fig. 2b) form which, however, soon goes into a region of very slow further fall of potential as in Fig 2a.

In the following, we examine the time dependent changes of current following changes of potential and the potential decay behavior and make some quantitative interpretations. Changes of state of a hydride phase will form the basis of this approach.

Current response to stepwise changes of potential.— When the electrode potential is stepped from higher to lower cathodic polarization for H_2 evolution, *e.g.*, from −0.150 to −0.040V, the cathodic current, $i_{c,0.15}$, changes not as expected to a lower cathodic value at the lower potential but first to an anodic current, $i_{a,0.04}$. The latter diminishes at first rapidly then more slowly, reaching zero after about 20 sec. Similar effects, but in the opposite direction, occur if the overpotential is raised in a stepwise manner in the range −0.010 to −0.150V. After further time, following the transient anodic current at 0.040V, the current becomes cathodic and eventually attains a steady-state value, $i_{c,0.04}$, after about 60 sec. Such an i-t transient is shown in Fig. 3.

The occurrence of an anodic current at cathodic polarization with respect to the H_2 evolution process indicates that, in fact, the potential step was made to a potential region below the reversible potential for the formation of some species, other than H_2, present on the surface or in the electrode and an adjustment of concentration of this species is taking place during the i-t transient.

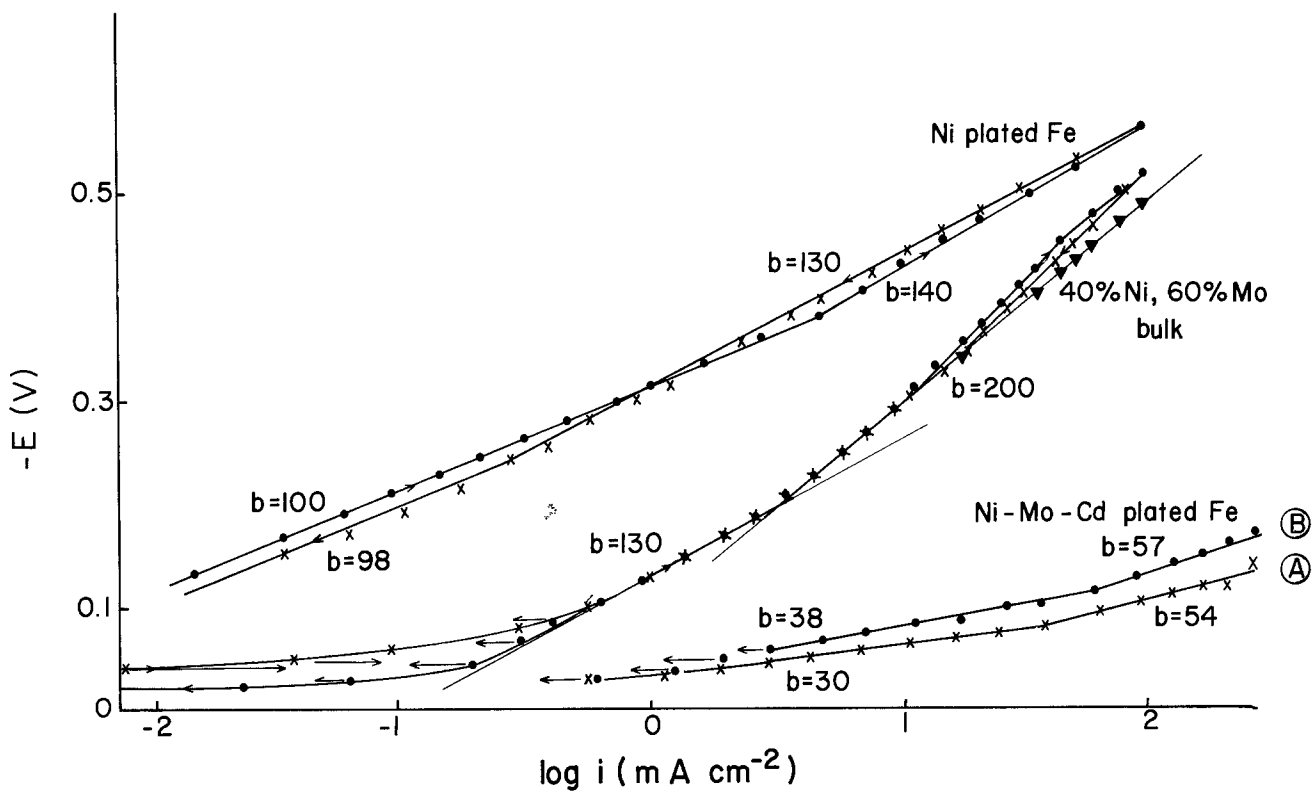

Fig. 1b. Comparison of polarization curves for H_2 evolution on Ni-plated Fe, bulk Ni-Mo alloy as indicated, and Ni-Mo-Cd electroplated coating on Fe. 5.0M NaCl at 368 K. Note marked differences of Tafel slopes.

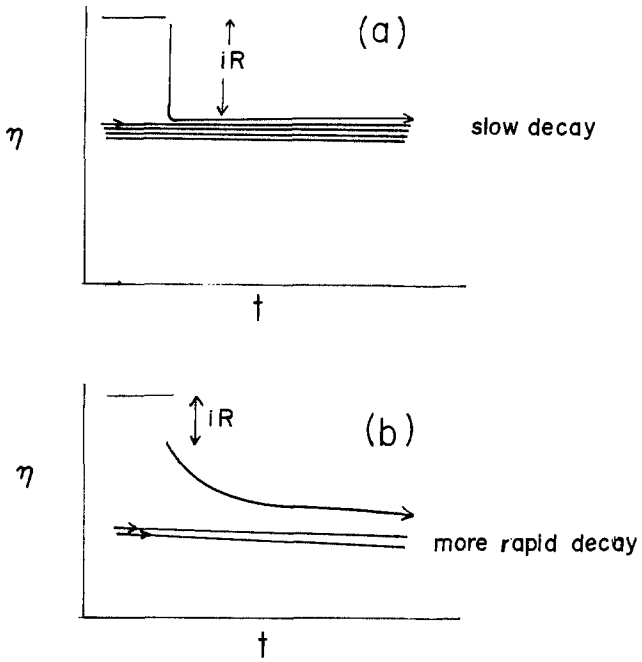

Fig. 2. Potential drop on open circuit for an electrode with large pseudocapacitance. (a)—Oscilloscope record of the fall of potential after current interruption at a Raney Ni electrode. (b)—As in (a) but from a higher cathodic potential.

The observed changes of current in response to a potential step take place over a time scale of seconds or minutes. Such a rate of change of current excludes adjustment of coverage θ_H of adsorbed H, which is normally completed in milliseconds, or of double-layer charge, which takes place on an even shorter time scale.

An accurate measurement of the $i = f(t)$ curve is difficult because of the high degree of reversibility of the reaction which occurs, *i.e.*, it is associated with a large exchange current density, i_o. Thus, the potentials involved are nearly the same as the reversible potential of the process. Even a potential shift of 1 mV changes the current by 30-50%, and 1 mV is just the practical limit of stability of most potentiostats. Nevertheless, it was established from the experimental results that more than one type of current-time dependence can be distinguished. Thus, the shape of the total current i_t *vs.* time t curve, shown in Fig. 3, indicates that at least two rate determining processes are operating. At shorter times, i_t changes linearly with log t (Fig. 4) while, at longer times in certain experiments, i_t as $f(t)$ has a region in which i_t is proportional to $t^{1/2}$ (Fig. 5) indicating the role of diffusion control. At even longer times, as i_t approaches the steady-state value at this potential, the changes in i_t are small so that it is difficult to evaluate precisely the form of the dependence of i_t on t.

The dependence of current on $t^{1/2}$ over some of the t range indicates that the reacting species are not only present on the surface of the electrode but also in the bulk of the electrode. This is what would be expected if a bulk metal hydride was involved as the reacting species as is the case with a Pd electrode (12, 13).

Response to small potential steps ($\Delta E = E_2 - E_1$).— In order to investigate the first process, small potential steps ΔE from a potential E_1-E_2 of 10 mV were imposed on the electrode in the potential range from −0.090 to −0.027V, and the resulting change of current with time was recorded on an oscilloscope. Such an oscillogram for a step ΔE of ~10 mV from $E_1 = -0.0980 \sim -0.0982$ to $E_2 = -0.0877 \sim -0.0876$V is shown in Fig. 6, trace a. At the moment the potential is changed from E_1 to E_2, the cathodic current drops from the steady-state value i_{E_1} to below the steady-state current for E_2 but then slowly recovers by increasing to the steady-state value i_{E_2} for potential E_2. The increase of the current is logarithmic in time (Fig. 7a) on the time scale of the oscillogram, followed by a

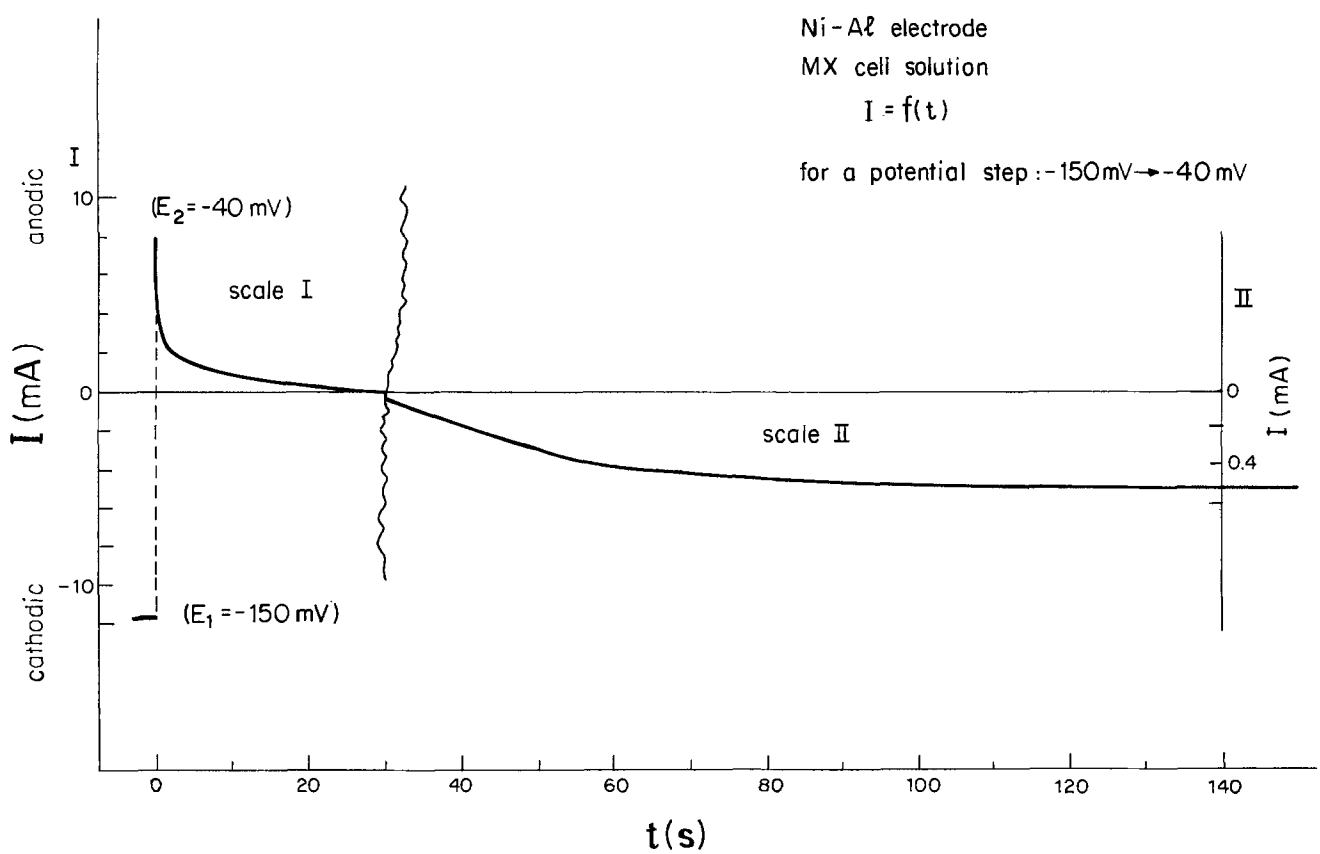

Fig. 3. Change of current i_t with time following a potential step from −0.150 to −0.040V

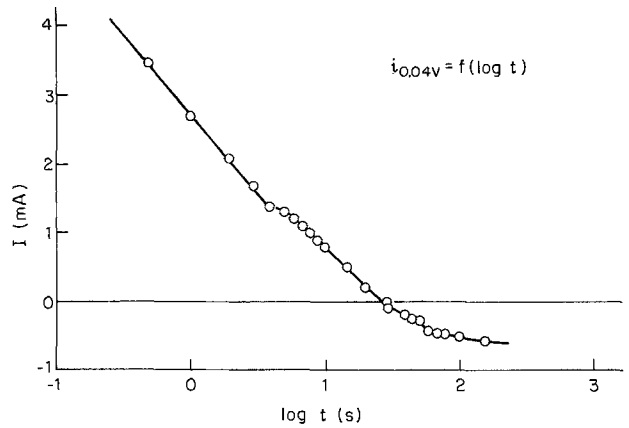

Fig. 4. Change of current i_t with log t following a potential step from —0.150 to —0.040V.

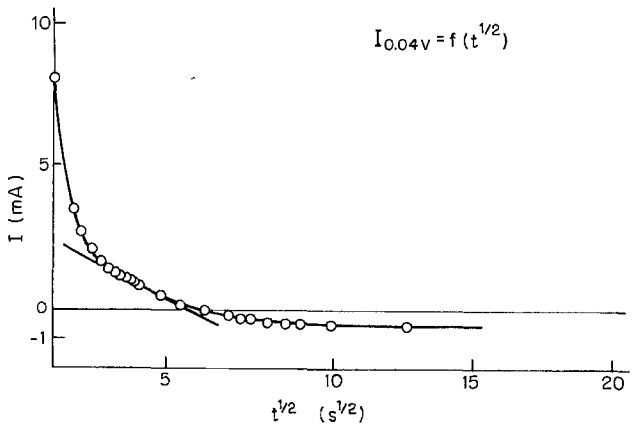

Fig. 5. Change of current i_t with $\sqrt{t}$ following a potential step from —0.150 to —0.040V.

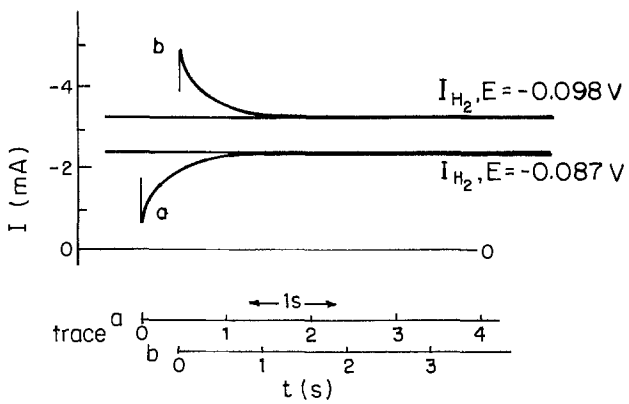

Fig. 6. The oscilloscope traces of current as a function of time for potential step

(a) —0.0980 → —0.0877V

(b) —0.0876 → —0.0981V

much slower increase as was shown in Fig. 4. This slow adjustment of the current takes a longer time when the potential step is made at lower potentials (Fig. 8).

In the case of trace b, Fig. 6, the potential step was made in the opposite direction to that in trace a, *i.e.*, from a lower E_1 value of —0.0876V to a more negative value of $E_2 \simeq$ —0.0980V. The current increased momentarily after the step was made but then decreased again logarithmically in time, (Fig. 7b).

The magnitude of the first sharp increase or decrease of the current depends on the time of polarization as can be seen in Fig. 8 which shows the current changes which arise in response to potential steps applied to the electrode after (*i*) a steady state was reached or

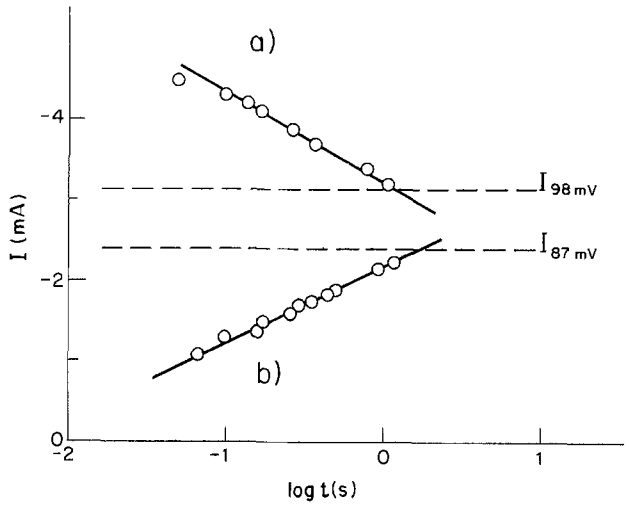

Fig. 7. Currents as a function of log t after potential steps as in Fig. 6.

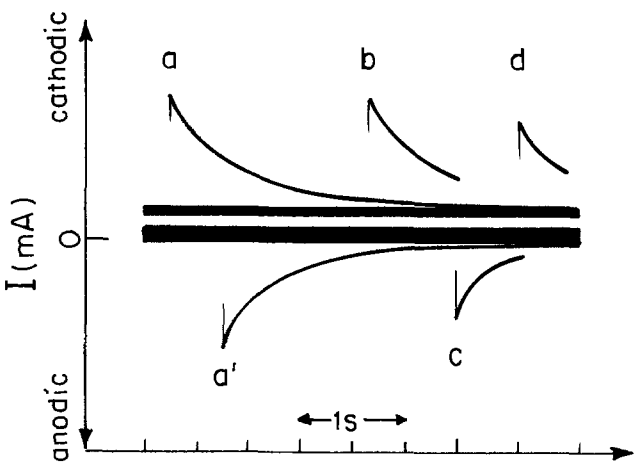

Fig. 8. Oscilloscope traces of current as a function of time for potential steps from $E_1 \simeq$ —0.038V to $E_2 \simeq$ —0.028V. (a)—step after a steady state is reached at E_1; (a^1)—step after a steady state is reached at E_2; (b)—step after 6 s at E_1; (c)—step after 1.7 s at E_2 (after trace b); (d)—step after 1.2 s at E_1 (after trace c).

(*ii*) after various short periods of time at the potential of the beginning of the step.

Significance of time dependent currents.—It will be necessary to treat several possibilities that arise for the mechanism of time dependence of currents and the observed open-circuit evolution of H_2. The hydride model referred to earlier will be considered. In order to provide some indication whether the experimental behavior observed can be explained in terms of such a model, we investigate mathematically the consequences of various mechanistic possibilities and compare them with experiment.

Two types of behavior will be considered: (*i*) the time dependent currents that result (Fig. 6a, 6b) when an "ascending" or "descending" potential step is applied to a porous catalytic Ni electrode acting as a cathode for H_2 evolution, and (*ii*) the open-circuit evolution of H_2 and the associated decay of potential with time.

Responses of current to a potential step.—The results of the potential step method are treated in terms of the possible formation of a nickel hydride[1] phase

[1] The nickel hydride is written here as Ni_2H rather than NiH_x for reasons of convenience in order to relate all equations to a one-electron process and not to one involving a fraction of an electron.

$$x\text{Ni} + \text{H}_2\text{O} + e \rightarrow \text{Ni}_x\text{H} + \text{OH}^- \quad [1]$$
$$i - X_\text{H} \qquad X_\text{H}$$

in parallel with hydrogen evolution

$$\text{H}_3\text{O}^+ + e \rightarrow \text{H}_2\text{O} + \tfrac{1}{2}\,\text{H}_2 \quad [2]$$

on nickel atom sites on the surface of the electrode. In Eq. [1], X_H represents the site fraction of H in the metal lattice and x the stoichiometry (see footnote) of the nickel hydride phase.

The response to a change of potential is associated with the anticipated property that X_H in the hydride is dependent on potential according to some three-dimensional "Langmuir type" sorption equation of the form [cf. that for two-dimensional electrochemical adsorption (14, 15)]

$$X_\text{H}/1 - X_\text{H} = K \exp\left[-\mathbf{F}V_\text{H}/RT\right] \cdot C_{\text{H}^+} \quad [3]$$

so that X_H increases as V_H becomes more negative. A similar relation applies to three-dimensional Li^+ sorption in TiS_2 (16). It is important to note that Eq. [3] corresponds to a continuous variation of reversible potential V_H for the hydride phase with increasing or decreasing X_H, as with an ionic redox electrode where the reversible potential depends logarithmically on the ratio of activities of [ox] and [red] species. Hence, a readjustment of X_H occurs in response to a change of V_H, or vice versa, but any change of X_H requires faradaic charge transfer, anodic or cathodic in direction, depending on the direction of change of V_H.

The total current i_t will be the sum of the hydrogen evolution current i_{H_2} and a hydride formation current $i_{\text{Ni}_x\text{H}}$

$$i_t = i_{\text{H}_2} + i_{\text{Ni}_x\text{H}} \quad [4]$$

In the steady-state condition at potential E_1, before a potential step is applied, the hydride lattice fraction X_{H,E_1} will be constant and the current for the hydride formation, $i_{\text{Ni}_x\text{H}} = 0$. The total current will therefore be only the current due to H_2 evolution, $i_t = i_{\text{H}_2}$. After the potential of the electrode is stepped downwards from E_1 to E_2, the nickel hydride H lattice fraction, X_H, has to become adjusted from X_{H,E_1} to X_{H,E_2}, the value at the new potential E_2. The corresponding current for the decomposition of the hydride ($E_2 < E_1$) is then an anodic one given by

$$Q_{\text{Ni}_x\text{H}}\left(\frac{dX_\text{H}}{dt}\right) = i_{\text{Ni}_x\text{H}} = \vec{i} - \overleftarrow{i}$$
$$= Q_{\text{Ni}_x\text{H}}\left[k_1(1 - X_\text{H})c_{\text{H}_2\text{O}}\right] \exp\left[-(1-\beta)\mathbf{F}V/RT\right]$$
$$- k_{-1}X_\text{H}c_{\text{OH}^-} \exp\left[\beta V\mathbf{F}/RT\right] \quad [5]$$

The adjustment of surface coverage θ_H by H_{ads} involved in reaction [2] from a value θ_{H,E_1}-θ_{H,E_2} occurs in a shorter time than the time scale of the measurements analyzed here; therefore the current due to this adjustment does not have to be considered. Also the double-layer charging occurs over a much shorter time than that measured here.

The nickel hydride current, $i_{\text{Ni}_x\text{H}}$, diminishes with time, reaching zero in the eventual steady-state condition at the potential E_2. The time dependence of $i_{\text{Ni}_x\text{H}}$ can be found as follows

Equation [5] can be rewritten with

$$k_1c_{\text{H}_2\text{O}} \exp\left[-(1-\beta)\mathbf{F}V/RT\right] \equiv \mathbf{A}$$
$$\text{and } k_{-1}c_{\text{OH}^-} \exp\left[\beta\mathbf{F}V/RT\right] \equiv B \quad [6]$$

as

$$\frac{dX_\text{H}}{dt} = A(1 - X_\text{H}) - BX_\text{H} \quad [7]$$

Rearranging Eq. [7] and integrating gives

$$\frac{1}{A+B}\ln\left[A - (A+B)X_\text{H}\right] = -t - C \quad [8]$$

At $t = 0$, $X_\text{H} = X_{\text{H},E_1}$, the H lattice fraction at potential E_1 and C, the integration constant, is

$$-C = \frac{1}{A+B}\ln\left[A - (A+B)X_{\text{H},E_1}\right] \quad [9]$$

From Eq. [8] and [9], the lattice fraction X_H as a function of time is

$$X_\text{H} = -e^{-(A+B)t} \cdot \frac{(A+B)X_{\text{H},E_1}}{A+B} + \frac{A}{A+B} \quad [10]$$

The change of X_H with time is

$$dX_\text{H} = -\left[A - (A+B)X_{\text{H},E_1}\right] \exp -(A+B)t \cdot dt \quad [11]$$

and the current for hydride oxidation

$$-i_{\text{Ni}_x\text{H}} = \mathbf{F}\frac{dX_\text{H}}{dt} \quad [12]$$

is

$$i_{\text{Ni}_x\text{H}} = \mathbf{F}\left[A - (A+B)X_{\text{H},E_1}\right] \exp -(A+B)t \quad [13]$$

or

$$\ln|i_{\text{Ni}_x\text{H}}| = \ln\left|\mathbf{F}\left[A - (A+B)X_{\text{H},E_1}\right]\right| - (A+B)t \quad [14]$$

The log of the hydride formation or oxidation current, as can be seen from Eq. [13], is hence a linear function of time.

To check if the potential transients correspond to a reaction mechanism leading to Eq. [13], the total current i_t minus the steady-state current at E_2 was plotted as a function of time. An example of such a plot is shown in Fig. 9. The rather good straight lines obtained confirm the possibility that reaction [1] is the operating process, *i.e.*, a nickel hydride is formed and determines the H_2 evolution characteristics of the electrode.

Continuing H_2 evolution at Ni electrodes on open-circuit after cathodic polarization and the time variation of overvoltage.—Origin of the observed effects.— An important phenomenon associated with the cathodic evolution of H_2 at Ni is the observation of continuing H_2 gas evolution on open circuit at Ni cathodes, especially at the porous-leached Raney Ni-Al electrodes after cathodic polarization. The behavior is observed to be related to the time dependence of cathodic overvoltage, η_i at Ni at various current densities, i, and to the decay of potential on open circuit after interruption of cathodic polarization.

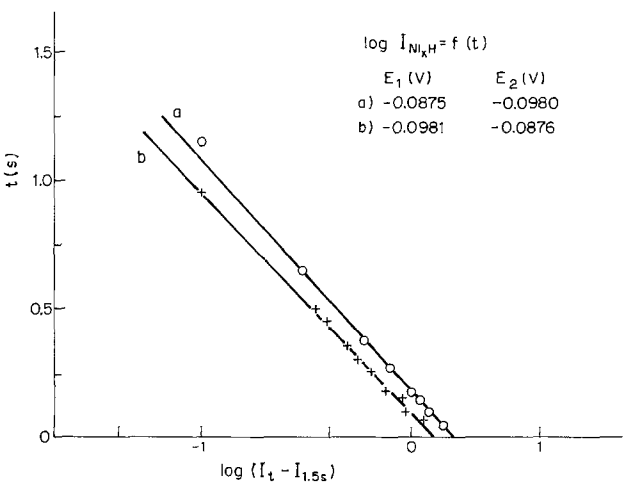

Fig. 9. Log of oxidation (a) and formation (b) currents for nickel hydride after a potential step as a function of time.

(a) −0.0980 → −0.0877V

(b) −0.876 → −0.0981V

When η is lowered to -0.04V or less, the rapidly diminishing anodic current, referred to in the section on current response to stepwise changes of potential, is first observed at nominally cathodic overvoltages (*i.e.*, w.r.t. the H_2 reversible potential for the same solution) indicating that the E_{rev} for the electrode process changes during polarization. Upon interruption of the current, H_2 evolution was observed to continue for 5 min, and the potential of the electrode, instead of dropping to 0.0V E_H, drifted slowly over *ca.* 20 min from *ca.* -0.075 to -0.010V. The decay of this potential is logarithmic with time t, a feature of the behavior that will be treated in more detail below.

The observed change of apparent reversible potential for H_2 at the Raney Ni or alloy electrodes could arise on account of the following possibilities: (*i*) increased H_2 pressure in pores of the electrode during electrolysis, (*ii*) formation, during cathodic polarization, of a species such as hydride Ni_xH on the electrode having a reversible potential more negative than that of the hydrogen electrode, or (*iii*) adsorption or deposition of impurities. The latter is not a realistic possibility since it could not lead to macroscopic H_2 gas evolution on open circuit. Also, the processes involved would be diffusion controlled which they are not; *cf.* the log t behavior.

Possibility (*i*) is eliminated if the pressure of H_2 in pores required to account for the slow fall of the observed quasireversible potentials from -0.075 to *ca.* -0.005V is calculated from the Nernst equation: 259 atm at -0.075V E_H. From the nature of the electrode materials, it is unlikely that the observed shift of 0.07V could be accounted for in the above way as a change of reversible H_2 potential with pressure.

Corrosion of residual Al in the Raney electrodes could also give rise to time dependent changes of current with changing potential or to the open circuit evolution of H_2. This seems unlikely for the following reasons: α, the characteristic behavior in Fig. 6, is repeatable indefinitely, with positive or negative-going changes of potential; it could not arise in the cathodic direction since redeposition of any dissolved Al is not possible. β, the materials which show these effects, had previously been leached vigorously in KOH at 95°C. γ, the effects, depend on the potentials and times of previous cathodic polarization, *i.e.*, the extents to which a hydride phase could have been formed.

Possibility (*ii*), the formation and decomposition of a nickel hydride, Ni_xH, is therefore indicated. This hydride, as mentioned earlier, would be formed either as a surface or bulk phase by process [1] in parallel with cathodic H_2 evolution (process [2]) and decomposed by the reverse of this process on anodic polarization. Decomposition of Ni_xH can, however, also proceed on open circuit as treated in the following section.

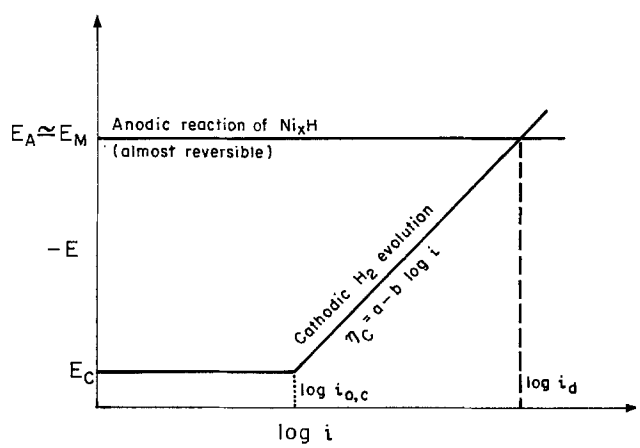

Fig. 10. Evans diagram for decomposition of the hydride through an electrochemical mixed process.

The decay of potential on open circuit at Ni-based cathodes.—Experimental potential vs. log [time] plots.—Typical changes of potential with time on open circuit after polarization for 5 min at each of three potentials, as indicated, are shown in Fig. 11; lines in series a are for the Raney Ni electrodes while those in series b are for bulk Ni-Mo alloy (80-20). The changes in potential are linear in log t with the slopes indicated on the figure. Unlike the situation for potential decay at Hg or for anodically polarized electrodes of Ni evolving O_2, the slopes depend on the initial polarization potential. This is probably connected with the state of hydridization of the electrodes as referred to in other ways elsewhere in this paper. As $t \to \infty$, the potentials asymptotically approach the rest potential of *ca.* -0.01V, as expected. The behavior is excellently reproducible, as exemplified in Fig. 12 for the Raney Ni electrode, with respect to 2 runs.

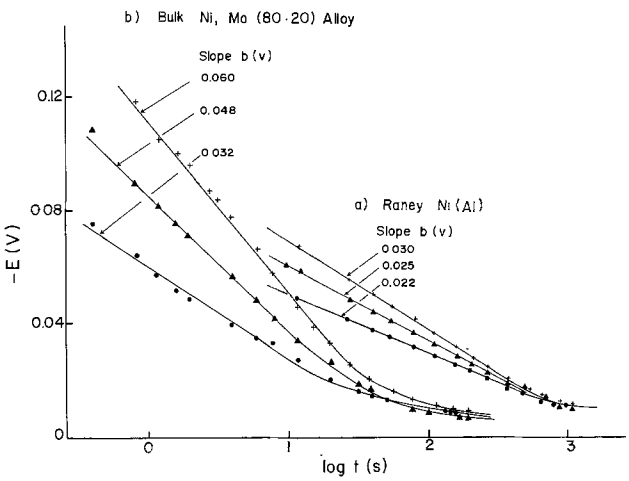

Fig. 11. Decay of open-circuit potential with log [time, sec] at Raney Ni (Al) and bulk Ni (80%)-Mo (20%) alloy electrodes after cathodic polarizations for 5 min at the potentials as indicated

a) ○ -0.10V; -0.20V; + -0.25V E_H for Raney Ni (Al) electrode.

b) x -0.30 or -0.45V; ▲ -0.25V; ○ -0.18V E_H for 80:20 Ni-Mo alloy electrode.

Each at 368 K in 5.0M aqueous NaCl.

The nature of self-discharge processes involving H_2 evolution.—When a hydride phase, *e.g.*, Ni_xH, is present which can establish a range of quasireversible potentials more negative than the H_2/H_2O, OH^- reversible potential, depending on x, self-discharge can

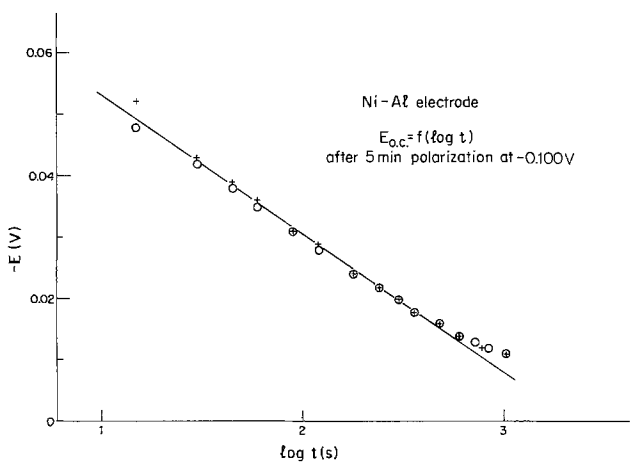

Fig. 12. Reproducibility of open-circuit potential decay after polarization for 5 min at -0.100V for the Raney Ni (Al) electrode of Fig. 11.

take place on open circuit by means of an anodic and cathodic process coupled as parallel reactions, *viz.*, through the formal scheme

$$Ni_xH + OH^- \rightleftharpoons xNi + H_2O + e \text{ (anodic)} \quad [-1]$$

$$e + H_2O \rightarrow OH^- + \tfrac{1}{2} H_2 \text{ (cathodic)} \quad [2']$$

The H_2 evolution in [2'] proceeds by one of the usual two-step reactions involving adsorbed H as the intermediate either on Ni or Ni_xH sites. The above anodic and cathodic processes are coupled as in a corrosion-type process with the net reaction of Ni_xH decomposition taking place at some mixed potential, E_M.

The above type of self-discharge is to be contrasted with that involved in desorption of adsorbed H in the H_2 evolution reaction itself on various other metals where processes (for alkaline pH's) such as $H_2O + e + M \rightarrow MH_{ads} + OH^-$ followed by $MH_{ads} + H_2O + e \rightarrow H_2 + OH^- + M$ must take place, as treated in previous papers (17, 18). The latter two processes will, however, be involved in the cathodic partial reaction, step [2'], of H_2 evolution.

The mixed potential E_M of the local cell in which processes [-1] and [2'] are occurring in a coupled manner, will be determined by the potential of the more reversible of the two coupled processes, as shown schematically in the Hoar-Evans diagram, Fig. 10. In this figure, the anodic process is drawn as almost reversible (potential E_A) while the cathodic process with reversible potential E_C and exchange current density $i_{o,c}$ is polarized with a Tafel slope b. As usual, the "mixed potential" is determined by the potential of the more reversible process, *i.e.*, E_A, so that $E_A \simeq E_M$ and the decomposition current i_d is determined at all potentials by the kinetics of the process of cathodic evolution of H_2 on the hydrided surface. The situation is analogous to that treated by Conway and Bourgault (19, 20) for decomposition of the surface oxide at nickel oxide battery cathodes where O_2, rather than H_2, is evolved on open circuit. They showed that the kinetics of the rate controlling coupled process in the open-circuit reaction could be evaluated from an analysis of the open-circuit decay of potential with log [time]. This approach can be adapted to the reactions occurring here at nickel cathodes evolving H_2. The experimental decay behavior for two types of electrodes is shown in Fig. 11 and 12 and will be discussed in relation to mechanisms in the section comparison with experiment.

Kinetics of the potential decay, and capacitance.—When, in a system with two parallel reactions, as in Fig. 6, a polarizing current is interrupted, the potential V of the electrode will fall with time on open circuit on account of continuing passage of current across the double layer causing discharge of the double-layer capacitance, C, and the additional (pseudo-) capacitance, C_ϕ (3), arising on account of the potential dependence of the lattice fraction X_H of sorbed species (H), Eq. [3]. Thus, the open-circuit process involves "discharge" of this C_ϕ (decomposition of the sorbed species) in parallel with that of C (cf. Ref. 13, 15)

$$i_t = (C_\phi + C)\, dV/dt \quad [15]$$

or

$$i_t \doteq C_\phi\, dV/dt \quad [16]$$

since normally $C_\phi >> C$ except as $X_H \rightarrow 0$ or $X_H \rightarrow 1$ (3).

It should be mentioned that any species which can be formed or decomposed at potentials negative to the H_2 reversible potential for the solution involved and whose reversible potential V_{rev} depends on a two- or three-dimensional lattice occupancy fraction (by H) in the way mentioned earlier can provide the pseudocapacitance the discharge of which will allow evolution of H_2 on open circuit, as observed.

The formation of $Ni(OH)_2$, rather than anodic decomposition of hydride (process [-1], is unlikely as it could occur, according to the Pourbaix diagram, only at potentials more positive than the H_2 reversible potential. This is confirmed by potentiodynamic *i vs. V* profiles for a Ni electrode in alkaline solution (Fig. 13) which show that a surface oxide is formed only irreversibly at Ni at potentials positive to the H_2 reversible potential.

In the system investigated, no species other than nickel hydride is therefore likely to be formed and to behave in the way observed.

The anodic reaction in the corrosion-type mechanism (processes [-1] and [2']).—The values of the open-circuit potential indicate that the decomposition of hydride can be considered as occurring almost reversibly without any limitation by activation or by diffusion. Therefore, the rate of the mixed hydride decomposition process is determined, as indicated in Fig. 10, by the H_2 evolution reaction kinetics (process [2']; see Eq. [21a], [-21a], and [21b] below).

The reversible potential for reaction [1], almost equal to the mixed potential, E_M, will depend on the lattice site fraction, X_H (cf. Eq. [3])

$$E_{rev} = E^\circ + \frac{RT}{\mathbf{F}} \ln \frac{(1 - X_H)\, c_{H_2O}}{X_H c_{OH^-}} \quad [17]$$

The extent of open-circuit evolution of H_2 on the porous Ni electrodes will be determined by the amount of the NiH_x hydride species in the electrode material, so that a capacitance analogous to the adsorption pseudocapacitance C_ϕ (15) should be written in terms of X_H (Eq. [3] and [20]) as

$$C_{Ni_xH} = Q_{Ni_xH} \frac{n\mathbf{F}}{RT} (X_H)(1 - X_H) \quad [18]$$

Then the kinetic equation for self-discharge of C_{Ni_xH} involves X_H and the rate of the step [21b] (see below), with θ_H the coverage of H on the hydride at the surface.

The course of decay of potential on open circuit in relation to a decrease of X_H and coupled evolution of H_2 can be conveniently illustrated by reference to a working diagram (Fig. 14).

Thus, in region I (Fig. 14), the potential drop on open circuit, *e.g.*, from E_2 to E_1, is associated with change of X_H down the X_H *vs.* E line from $X_{H,1}$ to $X_{H,2}$, with evolution of H_2 on open circuit. The H_2 current is coupled with the state of the hydride measured by the X_H and the corresponding E values.

In region II (Fig. 14), where the hydride has reached a state of saturation ($X_H \rightarrow 1$) and the cathodic potential E_2 is greater than the potential for $X_H = 1$,[2] open-

[2] Strictly, as $X_H \rightarrow 1$, the potential tends to infinity (−) according to Eq. [3]. Here a practical limit of X_H = *ca.* 0.95 can be considered.

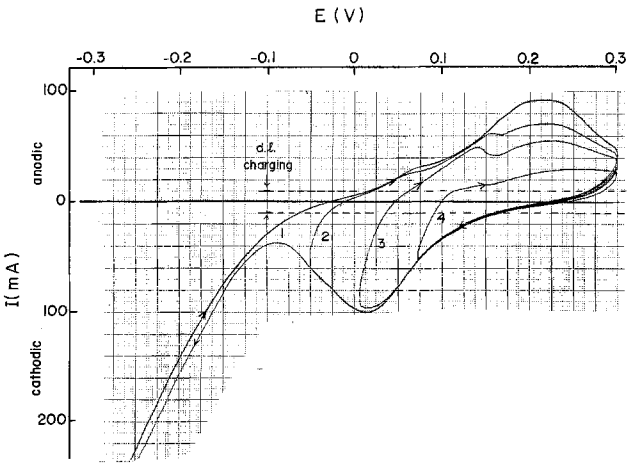

Fig. 13. Potentiodynamic *i vs. V* profile for Raney Ni electrode, previously leached in NaOH, $s = 25$ mV s^{-1}, $T = 298$ K.

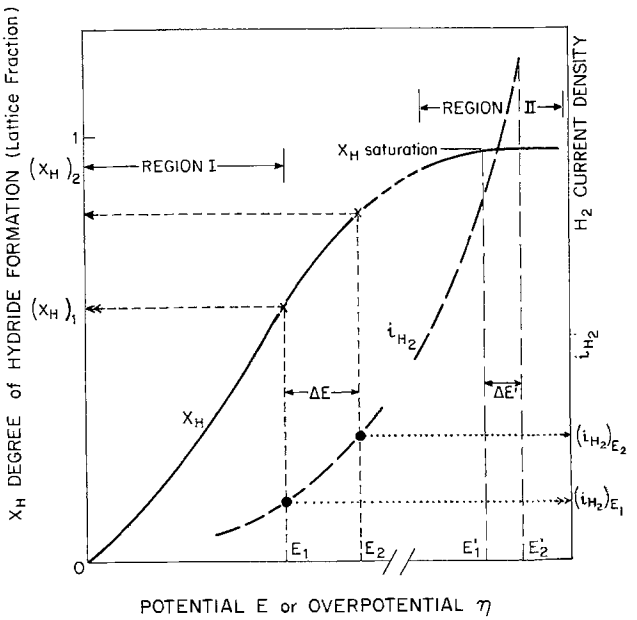

Fig. 14. Working diagram illustrating open-circuit discharge of hydride pseudocapacitance in terms of change of lattice fraction X_H of H with potential according to the corresponding sorption isotherm for H in relation to currents for H_2 evolution as a function of potential.

circuit changes of potential are initially determined mainly by the double-layer capacity (as in Fig. 2b) until $E < E'_1$, when continuing fall of potential follows the X_H curve with a much larger capacitance (hence slower decay of potential). Then the potential decay follows the representation shown in region I, according to the curve of X_H *vs.* E in a descending direction.

In terms of the proposed equilibrium state of Ni_xH, its formation and removal rates, $i_1 = i_{-1}$, give for alkaline pH's

$$k_1 c_{H_2O}(1 - X_H) \exp[-(1-\beta)VF/RT] = k_{-1} c_{OH^-} X_H \exp[\beta VF/RT] \quad [19]$$

(β is assumed the same for cathodic and anodic directions of (1), *i.e.*, $\beta = 0.5$.) Hence

$$X_H = \frac{K_1 c_{H_2O}(c_{OH^-})^{-1} \exp[-VF/RT]}{1 + K_1 c_{H_2O}(c_{OH^-})^{-1} \exp[-VF/RT]} \quad [20]$$

where $K_1 = k_1/k_{-1}$. This type of relation is the isotherm for "intercalation" of H, *e.g.*, similar to that known for Li^+ into TiS_2 (16). This analogy is useful to make.

The cathodic process.—In the case of the Ni cathode, the initial open-circuit potential is *ca.* −0.075V, indicating that the decomposition of the hydride is not the limiting step, so that the rate controlling process should be one of the steps in the H_2 evolution reaction (Eq. [21a,b] below) proceeding according to the Volmer-Heyrovsky pathway as indicated in previous published literature

$$Ni + H_2O + e \rightleftharpoons NiH_{ads} + OH^- \quad (pH > 7) \quad [21a, -21a]$$

$1 - \theta_H$ (V) θ_H c_{OH^-}

coupled with

$$NiH_{ads} + H_2O + e \rightarrow Ni + OH^- + H_2\uparrow \quad [21b]$$

θ_H (V)

leading to H_2 evolution.

Here it must be stressed that there is a basic difference between adsorbed H (NiH_{ads} at coverage θ_H) in steps [21a] and [21b] and Ni_xH in processes [1] and [-1]. Ni_xH is a phase compound existing at and near the surface while H_{ads} is a chemisorbed intermediate in the H_2 evolution reaction. Probably H_{ads} is adsorbed on the surface of the interphasial (> monolayer) Ni-hydride, Ni_xH; this is analogous to the situation proposed for H_2 evolution at Pt where the kinetically involved H is weakly adsorbed on a monolayer surface compound of PtH with H in 4 ~ 5 multiple states of chemisorption, strongly bound.

The state of H as Ni_xH should probably be treated in terms of a lattice site fraction X_H (cf. Eq. [20]) in the Ni lattice in an interphasial region (order of 1 ~ 5 nm near the surface?). However, the state of chemisorbed H must be treated differently but in the usual way in terms of the two-dimensional surface site fraction, θ_H, that is for H adsorbed at the surface of the Ni and Ni_xH phases. Experimentally, it is not possible to distinguish the adsorbed H from the hydride H by the electrochemical procedures used in the present work but this does not affect the general interpretation of the results reported here.

At Ni, previous work (2, 18) indicates that cathodic H_2 evolution occurs at current densities determined by the rate constant of step [24], and with a coverage θ'_H of H which is rather low (3) ($\theta_H <$ *ca.* 0.1). Then reaction [23a] will be at quasiequilibrium, and the coverage of H on electrode surface sites (θ_H) can be written for this process in the usual way as follows

$$\theta_H = \frac{K_{21a} c_{H_2O}(c_{OH^-})^{-1} \exp[-VF/RT]}{1 + K_{21a} c_{H_2O}(c_{OH^-})^{-1} \exp[-VF/RT]} \quad [22]$$

In order to pursue the consequences of the hydride decomposition model, it is necessary to assume that the change of lattice fraction, X_H, in nickel hydride is not substantially affecting the overvoltage of hydrogen, *i.e.*, the changes of electrode mixed potential E_M due to the change of the reversible potential of reaction [1], E_1, are much greater than the change of hydrogen overvoltage. This, of course, can only be a first approximation but will apply so long as no great fraction of the hydride is consumed.

The overall rate of H_2 evolution according to this model, with step [21b] rate controlling, is given by

$$i = 2F k_{21b} c_{H_2O} \theta_H \exp[-(1-\beta)VF/RT] \quad [23]$$

Then, substituting for θ_H in terms of its potential dependence given by Eq. [22]

$$i = \frac{2F K_{21a} k_{21b} c^2_{H_2O}(c_{OH^-})^{-1} \exp[-(2-\beta)VF/RT]}{1 + K_{21a} c_{H_2O}(c_{OH^-})^{-1} \exp[-VF/RT]} \quad [24]$$

This will be the current which will discharge the capacitance, associated with hydride, as given by Eq. [16], until the reversible potential of H_2/H_2O is attained so that there would then be no further tendency for self-discharge to occur.

Time dependence of open-circuit potential.—The expression which represents the time course of electrode potential during self-discharge with evolution of H_2 is required. This is given by solving the differential Eq. [16], but using the capacitance associated with bulk Ni_xH as expressed by Eq. [18]-[20] giving X_H.

Then, from Eq. [20] to [24], and noting the reactions [1], [-1]

$$\frac{2Q_{Ni_xH}F}{RT}\left[\frac{K_1 c_{H_2O}(c_{OH^-})^{-1}\exp(-VF/RT)}{1 + K_1 c_{H_2O}(c_{OH^-})^{-1}\exp(-VF/RT)} - \left(\frac{K_1 c_{H_2O}(c_{OH^-})^{-1}\exp(-VF/RT)}{1 + K_1 c_{H_2O}(c_{OH^-})^{-1}\exp(-VF/RT)}\right)^2\right]\frac{dV}{dt} = \frac{2F k_{21b} K_{21a} c^2_{H_2O}(c_{OH^-})^{-1}\exp-(2-\beta)VF/RT}{1 + K_{21a} c_{H_2O}(c_{OH^-})^{-1}\exp(-VF/RT)} \quad [25]$$

This equation involves the quantity of charge Q_{Ni_xH}

associated with the amount of Ni_xH, but a rate of discharge controlled by the surface reactions involving adsorbed H (steps [21a] and [21b]).

Eq. [25] simplifies to

$$Q_{Ni_xH} \cdot \frac{F}{RT} \frac{[1 + K_{21a}c_{H_2O}(c_{OH^-})^{-1}\exp(-VF/RT)] \cdot \exp(2-\beta)VF/RT \cdot K_1 \exp\left(\frac{-VF}{RT}\right)}{k_{21b}K_{21a}c_{H_2O}[1 + K_1c_{H_2O}(c_{OH^-})^{-1}\exp(-VF/RT)]^2} dV = dt \quad [26]$$

In order to evaluate the time course of potential on open circuit (potential decay), this equation has to be integrated. This can be done for four limiting cases, several of which correspond to realistic conditions.

Case a: Coverage θ_H and extent of sorption X_H are high, *i.e.*, K_1 and K_{21a} are large. Then

$$K_1c_{H_2O}(c_{OH^-})^{-1}\exp(-VF/RT) >> 1$$

and

$$K_{21a}c_{H_2O}(c_{OH^-})^{-1}\exp(-VF/RT) >> 1$$

Integration then gives the potential decay relation

$$V(t) = \frac{2RT}{3F}\ln[t + A\exp(3FV_{in}/2RT)] - \frac{2RT}{3F}\ln A \quad [27]$$

where V_{in} is the initial potential (at $t = 0$) and A is given by

$$A = \frac{2Q_{Ni_xH}}{3F} \cdot \frac{c_{OH^-}}{k_{21b}K_1c^2_{H_2O}} \quad [28]$$

The main conclusion of interest here is the slope of the potential decay relation at appreciable times, *viz.* $2RT/3F$ or 0.040V in log t at 298 K which can be compared with experiment. The behavior for other cases follows analogously.

Case b: X_H is high, θ_H low, *i.e.*, K_1 is large, K_{21a} small. Proceeding as in case a, gives a potential decay law

$$V(t) = \frac{2RT}{5F}\ln[t + A'\exp(5FV_{in}/2RT)] - \frac{2RT}{5F}\ln A' \quad [29]$$

The slope of the relation in ln t is thus $2RT/5F$ or 0.024V in log t.

Case c: low X_H and low θ_H, *i.e.*, both K_1 and K_{21a} small. These conditions give a potential decay law

$$V(t) = \frac{2RT}{F}\ln[t + A'\exp(FV_{in}/RT)] - \frac{2RT}{F}\ln A'' \quad [30]$$

This gives a slope of the potential decay in ln t of $2RT/F$ or 0.120V in log t.

Case d: low X_H but high θ_H. This case is physically unrealistic. Processing of the equations leads to a relation in which formation of hydride would occur in time, *i.e.*, V would increase. By *reductio ad absurdum*, this result indicates that the conditions for case d cannot arise in reality. The results for these cases are summarized in Table I.

Similar calculations made for the first step in hydrogen evolution, the Volmer discharge reaction (Eq. [21a]), as the rate determining step show that, after sufficiently long times, the open-circuit potential will decay logarithmically in time with a slope of 0.040V for large X_H. For small X_H, however, the decay slope expected is 0.120V, indicating that it is not decomposition of the hydride that would occur but an increase in X_H which is an unrealistic situation.

The assumption made in an earlier paragraph that hydrogen overvoltage does not depend on the lattice fraction of hydride is, of course, a speculative approximation. As was mentioned in the introduction, however, there are indications that hydrogen overvoltage is lower on a hydride than on a bare metal surface so that, practically, H_2 should be evolved mainly on the hydride. Based on this model, the slopes of the time dependence of the open-circuit potential decay were calculated in a similar way to that used above but taking into account the expectation that the surface area at which the hydrogen evolution takes place should be proportional to X_H. Then reactions [21a, b] have to be written in the following manner

$$Ni_xH + H_2O + e \leftrightarrows (Ni_xH)\,H_{ads} + OH^- \quad [21a']$$

$$(Ni_xH)\,H_{ads} + H_2O + e \rightarrow Ni_xH + OH^- + H_2\uparrow \quad [21b']$$

As was done earlier in this paper, the value of the lattice pseudocapacitance, C_{Ni_xH}, of nickel hydride (Eq. [18]) and the current for hydrogen evolution, I, are introduced in Eq. [16]. Previously, the area of the electrode was taken as constant; therefore the current density i could be used. Now the reaction area is proportional to the lattice fraction of hydride so that current is $I = aX_Hi$, where a is a proportionality factor with the dimensions of cm².

Equation [16] with Eq. [18] gives

$$Q_{Ni_xH}\frac{F}{RT}X_H(1 - X_H) \cdot dV = aX_Hi \cdot dt \quad [31]$$

and, after rearrangement

$$\frac{Q_{Ni_xH}}{RT} \cdot \frac{[1 + K_{21a}c_{H_2O}(c_{OH^-})^{-1}\exp(-FV/RT)]}{[1 + K_1c_{H_2O}(c_{OH^-})^{-1}\exp(-FV/RT)]} \cdot \frac{c_{OH^-}\exp[(2-\beta)FV/RT]}{ac^2_{H_2O}k_{21b}K_{21a}} dV = dt \quad [32]$$

Table I. Mechanisms and potential decay slopes, dV/d log t, for the H_2 evolution process on Ni metal sites at Ni in the presence of hydride Ni_xH

Mechanism	Case	Condition	$\frac{dV}{d\log t}$	A
Mixed process	a	K_1, K_{21a} large	0.040	$\frac{2Q}{3F} \cdot \frac{c_{OH^-}}{k_{21b}K_1c^2_{H_2O}}$
Anodic reaction: (1), fast $Ni_xH + OH^- \rightarrow xNi + H_2O + e$				
Cathodic reaction: (21) with (21b) r.d.s. a) $Ni + H_2O + e \rightleftarrows NiH_{ad} + OH^-$ b) $NiH_{ad} + H_2O + e \rightarrow Ni + OH^- + H_2\uparrow$	b	K_1 large K_{21a} small	0.024	$\frac{2Q}{5F} \cdot \frac{c^2_{OH^-}}{k_{21b}K_{21a}K_1c^3_{H_2O}}$
	c	K_1 and K_{21a} small	0.120	$\frac{2Q}{F} \cdot \frac{K_1}{k_{21b}K_{21a}c_{H_2O}}$
	d	K_1 small K_{21a} large	Physically unrealistic	
Cathodic reaction with (21a) r.d.s	a	K_1 large	0.040	
	b	K_1 small	−0.120V, physically unrealistic	

which is to be compared with Eq. [26]. Again, four limiting cases can be distinguished.

Case a: K_1 and K_{21a} are large—Eq. [32] simplifies to

$$\frac{Q_{Ni_xH}}{RT} \cdot \frac{c_{OH^-} \exp[(2-\beta)\mathbf{F}V/RT]}{aK_1c^2_{H_2O}k_{21b}} dV = dt \quad [33]$$

which is identical with the equation derived before, *i.e.*, the slope $dV/d \log t$ is 0.040V as derived earlier.

Case b—K_1 is large, and K_{21a} is small. Again, Eq. [32] simplifies to an equation identical with the one derived before

$$\frac{Q_{Ni_xH}}{RT} \cdot \frac{c^2_{OH^-} \exp[(3-\beta)\mathbf{F}V/RT]}{aK_1K_{21a}k_{21b}c^3_{H_2O}} dV = dt \quad [34]$$

giving the same value for $dV/d \log t = 0.024$V.

Case c—K_1 and K_{21a} are small. Equation [32] gives then

$$\frac{Q_{Ni_xH}}{RT} \cdot \frac{c_{OH^-} \exp[(2-\beta)\mathbf{F}V/RT}{ak_{21b}K_{21a}c^2_{H_2O}} dV = dt \quad [35]$$

which is different from the result derived before for this case but it has the same general form as Eq. [33]. $dV/d \log t$ is therefore 0.040V.

Case d—K_1 is small, and K_{21a} is large. Because of the model used here, this case must be different from the corresponding previous one. Equation [32] simplifies to

$$\frac{Q_{Ni_xH}}{RT} \cdot \frac{\exp[(1-\beta)\mathbf{F}V/RT]}{c_{H_2O}ak_{21b}} dV = dt \quad [36]$$

which, after integration and rearrangement, gives

$$V = \frac{2RT}{\mathbf{F}} \ln[t + A \exp(\mathbf{F}V_{in}/2RT)] - 2RT/\mathbf{F} \ln A \quad [37]$$

with

$$A \equiv \frac{2Q_{Ni_xH}}{\mathbf{F}} \cdot \frac{1}{k_{21b}c_{H_2O}} \quad [38]$$

For sufficiently long times

$$V = 0.120 \log t - 0.120 \log A \quad [39]$$

so that $dV/d \log t = 0.120$V. The results of this treatment are summarized in Table II.

Comparison with experiment.—The slopes of the experimental decay plots are unusually low, in the range 0.022 ~ 0.030V (Fig. 11, 12). This indicates that case (b) applies.

Physically, the treatment given in this paper involves the difficult concept that sorbed H as Ni_xH behaves like a surface film capacitance. However, as we have mentioned, analogous systems are known in three dimensions (16), and have been proposed for H in Ni (11). The observed release of a macroscopic volume of H_2 on open circuit during some minutes and the observed anodic current on cathodic polarization after application of a potential step provide the physical support for the view that a nickel hydride is involved but the kinetics of the mixed process are determined by the H_2 evolution reaction.

Relevance to nickel cathode performance.—The performance (overpotential *vs.* ln *i* relation for H_2 evolution) of nickel-based cathodes of the kind we have investigated is much superior to that of bulk nickel metal cathodes, *e.g.*, Tafel slopes are lower. We believe that the presence of a hydride phase, as indicated by the present work on potential decay, could be the important, if not essential, condition for low overpotential behavior in nickel cathode performance and for relatively small depreciation of performance with time over extended periods. In the case of the electrolytically deposited Ni-Mo electrodes, the codeposition of H and the coevolution of H_2 [cf. Ref. (22)] may be important.

Table II. Mechanisms and potential decay slopes, $dV/d \log t$, for the H_2 evolution process on Ni hydride sites at the Ni electrode surface

Mechanism	Case	Condition	$dV/d \log t$
Mixed process	a	K_1, K_{21a}' large	0.040
Anodic reaction:			
(1) fast $Ni_xH + OH^- \rightarrow xNi + H_2O + e$	b	K_1 large K_{21a}, small	0.024
Cathodic reaction:			
(21a', b') with (21b') r.d.s.	c	K_1, K_{21a}, small	0.040
a) $Ni_xH + H_2O + e \rightarrow (Ni_xH)H_{ad} + OH^-$	d	K_1 small	0.120
b) $(Ni_xH)H_{ad} + H_2O + e \rightarrow Ni_xH + OH^- + H_2\uparrow$		K_{21a}, large	

Note on Table II: The potential decay slopes for the conditions here do not follow the expectations for regular consecutive reaction steps as treated in Ref. (17) and (18) because the surface site availability is assumed to be proportional to X_H (Eq. [20]) which introduces a potential dependent quantity in addition to that arising from θ_H (Eq. [22]).

Acknowledgment

Grateful acknowledgment is made to Hooker Chemicals and Plastics Corporation for support of this work at University of Ottawa. Thanks are due to Dr. D. Pouli and Dr. J. Stachurski for useful practical discussions. Data on the potential decay behavior at bulk Ni-Mo alloy electrodes were obtained by Dr. M. A. Sattar in this Laboratory and will be reported in more detail elsewhere.

Manuscript submitted Dec. 29, 1982; revised manuscript received April 5, 1983. This was Paper 514 presented at the Minneapolis, Minnesota, Meeting of the Society, May 10-15, 1981.

The University of Ottawa assisted in meeting the publication costs of this article.

REFERENCES

1. L. Angely, G. Bronoel, and G. Peslerbe, *J. Electroanal. Chem.*, **96**, 183, 191, 203 (1979).
2. J. O'M. Bockris and E. C. Potter, *J. Chem. Phys.*, **20**, 614 (1952).
3. M. A. V. Devanathan and B. Selvaratnam, *Trans. Faraday Soc.*, **56**, 1820 (1960).
4. B. Baranowski, *Bull. Acad. Pol. Sci., Ser. Sci. Chim.*, **7**, 897 (1959).
5. A. Janko, *ibid.*, **8**, 131 (1960).
6. F. G. Will and C. A. Knorr, *Zeit. Electrochem.*, **64**, 258 (1960).
7. M. Vuković, H. Angerstein-Kozlowska, and B. E. Conway, *J. Appl. Electrochem.*, In press.
8. "Electrocatalysis," M. Breiter, Editor, The Electrochemical Society Softbound Proceedings Series, Princeton, NJ (1974).
9. J. Stachurski, D. Pouli, G. Pokrzyk, and J. Ripas, U.S. Pat. 4,354,915 (1982); S. Anderson, D. E. Brown, S. M. Hall, M. N. Mahmood, M. C. M. Man, A. K. Turner, and D. Wood, Abstract 507a, p. 1254, The Electrochemical Society Extended Abstracts, Vol. 81-1, Minneapolis, MN, May 10-15, 1981.
10. B. E. Conway, H. Angerstein-Kozlowska, W. B. A. Sharp, and E. Criddle, *Anal. Chem.*, **45**, 1331 (1973).
11. H. H. Ewe, *Electrochim. Acta*, **17**, 2267 (1972).
12. M. Enyo and T. Maoka, *J. Electroanal. Chem.*, **108**, 227 (1980).
13. M. W. Breiter, *ibid.*, **81**, 275 (1977).
14. A. Eucken and B. Weblus, *Zeit. Elektrochem.*, **55**, 114 (1951).
15. B. E. Conway and E. Gileadi, *Trans. Faraday Soc.*, **58**, 2493 (1962).

16. A. H. Thompson, *This Journal*, **126**, 608 (1979).
17. B. V. Tilak and B. E. Conway, *Electrochim. Acta*, **21**, 745 (1976).
18. B. V. Tilak, C. G. Rader, and B. E. Conway, *Electrochim. Acta*, **22**, 1117 (1977).
19. P. D. Lukovstev, J. Lewina, and A. N. Frumkin, *Acta Physicochim. U.R.S.S.*, **11**, 21 (1939).
20. B. E. Conway and P. L. Bourgault, *Can. J. Chem.*, **37**, 292 (1959).
21. B. E. Conway and P. L. Bourgault, *Trans. Faraday Soc.*, **58**, 593 (1962).
22. R. Dorsch, *J. Electroanal. Chem.*, **21**, 495 (1969).

Hydrogen Overvoltage on Tin Self-Cleaning Rotating Electrode (SRE) in Absence and Presence of Surface Active Ions

C. I. Noninski, I. P. Ivanov,[1] and M. Vassileva-Dimova[1]

Higher Institute of Chemical Technology, Sofia, Bulgaria

ABSTRACT

An investigation of hydrogen overvoltage on tin self-cleaning rotating electrode (SRE) in sulfuric acid solution in the presence and absence of some halogen ions was carried out. It was established that the rate of the mechanical renewal exerts significant influence on the hydrogen evolution overvoltage decreasing it about 0.120V. It was found that the halogen ion adsorption practically does not change the magnitude of the overvoltage decrease which remains of the same order as it is in pure sulfuric acid. It was shown that the effective energy of activation of the hydrogen evolution process upon a continuously renewed surface decreases about two times in comparison with an unchanged surface.

Tomashov *et al.* (1, 2) were the first to carry out measurements of hydrogen evolution on continuously mechanically renewed electrode surfaces of metals with various hydrogen overvoltage. These authors found out that the electrode surface renewal decreases the hydrogen overvoltage only in the case of metals characterized by low hydrogen overvoltage (Fe, Ni, and Pd), but does not influence the overvoltage in the case of the metals of high hydrogen overvoltage used in the study (Sn and Pb), which probably is due to screening of the electrode surface by the rotating corundum disk used. The preliminary investigations carried out by Noninski (3) with the help of his SRE (4) whose working electrode surface is nearly free (nonscreened) during the renewal, show that the mechanical renewal exerts a significant influence on the value of hydrogen evolution overvoltage on Sn and Zn electrodes by decreasing the overvoltage about 100 mV. If it is proceeded by the common concepts used by Tomashov *et al.* (1, 2), these results evidently contradict the dominating theory of charge transfer. It was necessary that the mentioned preliminary investigations done by Noninski (3) be continued while strictly keeping the contemporary requirements when measuring the hydrogen evolution overvoltage. Such a study was done by the authors using SRE of metals with different values of hydrogen overvoltage (5) and on Cd SRE (5-7) in H_2SO_4 solutions.

In this paper, the influence of the rate of the continuous mechanical renewal of the cathode surface on the hydrogen evolution overvoltage and on the energy of activation of the process on Sn SRE in sulfuric acid solution is studied. The influence of some halogen ions on the hydrogen overvoltage value on nonrenewed and on the continuously mechanically renewed surface of the electrode is studied as well.

Experimental

When constructing the apparatus, schematically shown in Fig. 1, measures were taken to keep the highest solution purity and to avoid (to the highest possible extent) the penetration of atmospheric oxygen and oxygen from the anodic compartment of the cell into the cathodic compartment. All the connections were made through glass weldings, and the sleeves and taps were made tight by specially manufactured detents filled with mercury K. The SRE, F, with which the experiments were carried out was situated in the central part of the electrolytic cell, A, whose hermeticity was ensured also through a mercury detent, D. In the compartment B, the counter-

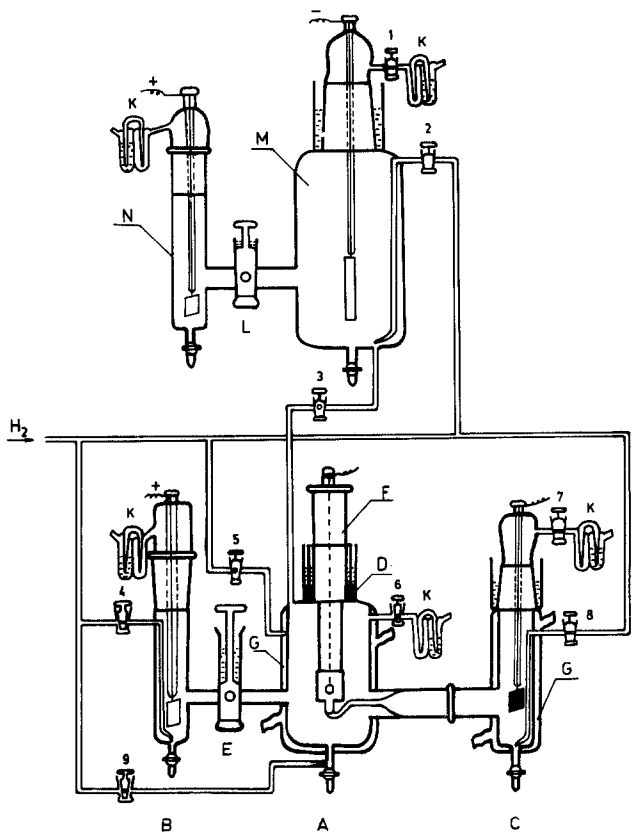

Fig. 1. Scheme of the apparatus for measuring hydrogen overvoltage: A—working electrode compartment; B—counterelectrode compartment; C—reference electrode compartment; M—pre-electrolysis cell; N—anode; F—SRE; D—mercury detent; K—hydraulic detents; G—water jacket; E, L, 1-9—taps.

[1] Present address: Department of Chemistry, Medical Academy, 1431 Sofia, Bulgaria.

Key words: self-cleaning rotating electrode, continuously mechanical renewal, decreasing of hydrogen overvoltage, energy of activation.

electrode was situated, and in compartment C, the normal hydrogen electrode used as a reference was situated. In order to avoid the ohmic potential drop between the cathode and the Luggin capillary end, the latter was situated in the near vicinity of the renewing surface at a distance of about 0.1-0.2 mm. The cathode compartment and that of the hydrogen electrode were supplied with water jackets, G, which maintained the desired temperature and was measured by an ultrathermostat with accuracy ±0.1°C.

The solutions were prepared with H_2SO_4 (pure specimen [p.a.]) and fresh bi-distilled water. The salts, KI and KBr (p.a.), used were additionally purified through double recrystallization in bi-distilled water. Final purification of the solutions was reached through pre-electrolysis on an auxiliary tin electrode in cell M at $2 \cdot 10^{-1}$ A-cm^{-2} current density for 20 hr. In order to avoid the influence of side depolarizers, all the experiments as well as the preliminary electrolysis of the solutions were carried out in hydrogen atmosphere at closed E and L taps separating the anode from the cathode compartment. After placing the SRE, F, in the electrolytic cell and blowing hydrogen through the latter for several hours, tap 3 was opened to let the pre-electrolyzed solution passing into the central part A of the cell where it was distributed in the anode B and the reference electrode C compartments. Throughout the whole course of taking the polarization curves, a continuous blowing of hydrogen through all three compartments of the cell was ensured. This hydrogen was obtained through electrolysis of 20% KOH (Fig. 2). The pressure necessary for blowing the hydrogen obtained in the electrolyzers, 2 and 3, in Fig. 2 was ensured through an additional water column (tube 1). Special attention was paid to the purification of the hydrogen from traces of oxygen. For this purpose, after the hydrogen was passed through washing bottles containing alkali solution of pyrogalol (5), sulfuric acid solution (6), and bi-distilled water (7), it was passed consecutively through a furnace with copper wadding and through furnaces with palladized asbestos (9, 10) at 350°-380°C. For catching the last traces of oxygen the hydrogen was passed through a furnace with palladized asbestos (11) at 600°C. After that the hydrogen was passed through washing bottles containing $Pb(CH_3COO)_2$ solution (12), H_2SO_4 solution (13), and working solution (14).

For ensuring rotating motion of the SRE a d-c electromotor motor generator type was used. The rotation rate of the SRE was judged by the voltage of the generator winding. All the parts of the SRE whose construction is shown in Fig. 3 (4) were made of Teflon. The working electrode surface was renewed using a cleaner specially constructed for the aim 5 which was attached immovably at the bottom cap 6 of the SRE. The appliance for renewal (the cleaner)

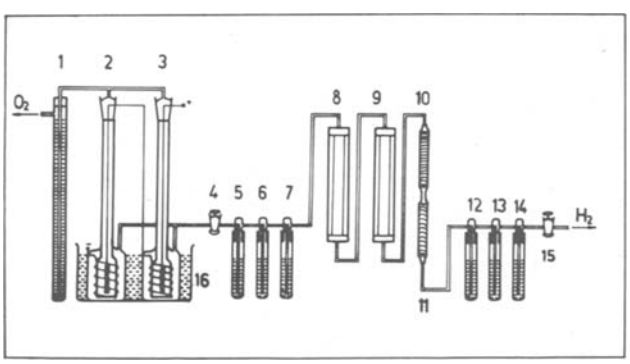

Fig. 2. Scheme of the system for the production and purification of hydrogen: 1—water column; 2, 3—electrolyzers; 5, 6, 7, 12, 13. 14—washing bottles; 16—bath with flowing water; 8—furnace with copper wadding; 9, 10, 11—furnaces with asbestos + Pd.

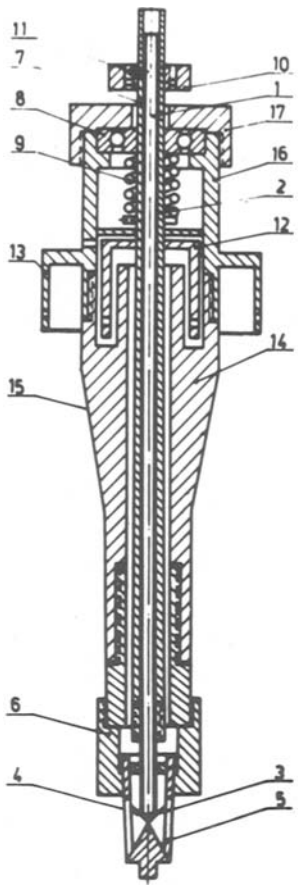

Fig. 3. Construction of the SRE: 1—metal wire; 2—insulating layer; 3—working electrode surface; 4—edges of the sharpener; 5—sharpener; 6—screwing up lid; 7—tube; 8—ball bearing; 9—spring (or heavy washers); 10—connector; 11—small screw to connect the electrode 1 with the connector; 12, 13—water or mercury detents; 14—body of the SRE; 15—sleeve; 16—bearing case; 17—lid.

is made of corundum. The cleaner consists of four cutters whose edges ensure continuous renewal of the whole working surface of the electrode. It is very essential that the edges of the appliance for renewal touch a very small part of the electrode surface and that the remaining part from the electrode solution interface, where the electrode process in fact takes place, is entirely free and nonscreened. An electrode made of spectrally pure Sn with a cone working surface of 0.1 cm^2 was used as a working electrode. The measurements were carried out in potentiostatic regime *vs.* normal hydrogen electrode at 24° ± 0.1°C. Besides that, investigations were carried out at various temperatures.

Results and Discussion

The experimental results obtained by the authors are represented in Fig. 4-8 and in Table I.

In Fig. 4, the influence of the rate of continuous mechanical renewal of the electrode surface on the hydrogen evolution overvoltage on Sn SRE in 2*N* H_2SO_4 is shown. As it is seen from the figure, the rate of mechanical renewal exerts significant influence on the hydrogen evolution overvoltage as the latter decreases, reaching about 0.120V at rate of electrode rotation $n = 50$ sec^{-1} and current density $i = 1 \cdot 10^{-3}$ A-cm^{-2} (curve 5). At very high rates of renewal ($n >$ 50 sec^{-1}), the decrease in the overvoltage remains practically the same as at lower rates of renewal. From Fig. 4, it is also seen that in the polarization curves η-log i taken both on nonrenewed and on a continuously mechanically renewed surface, a sharp drop of the overvoltage reaching 0.25-0.30V is observed at

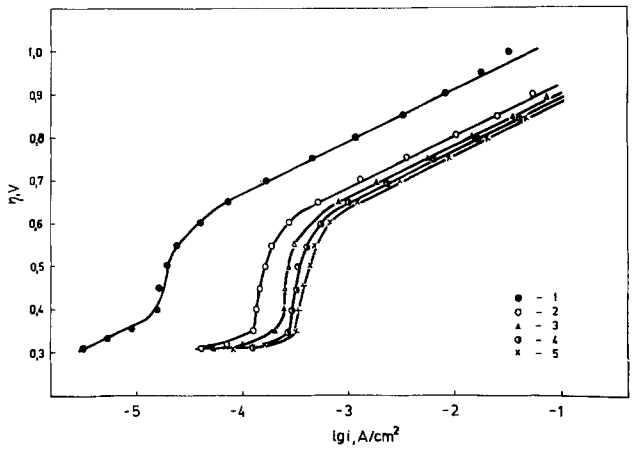

Fig. 4. Dependence of the hydrogen evolution overvoltage on the logarithm of current density on Sn SRE in 2N H_2SO_4 at various rates of mechanical renewal of the electrode surface: 1—on nonrenewed surface, $n = 0$ sec^{-1}; 2—on renewed surface, $n = 9.7$ sec^{-1}; 3—$n = 29$ sec^{-1}; 4—$n = 70$ sec^{-1}; 5—$n = 50$ sec^{-1}, at 24°C.

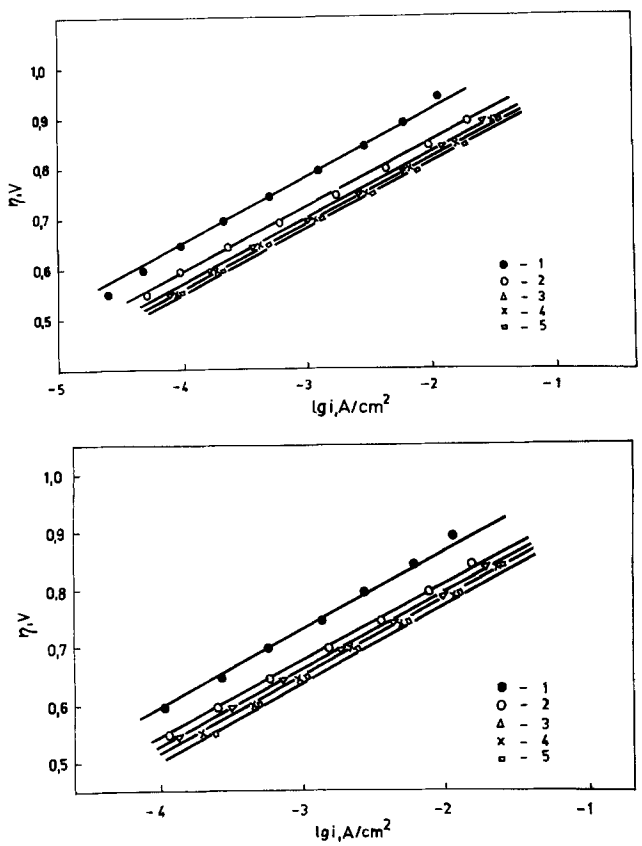

Fig. 5. Dependence of η-log i on Sn SRE obtained in 1N H_2SO_4 + 0.01N KBr(a) and in 1N H_2SO_4 + 0.1N KBr(b): 1—nonrenewed surface; 2—$n = 9.7$ sec^{-1}; 3—$n = 29$ sec^{-1}; 4—$n = 50$ sec^{-1}; 5—$n = 70$ sec^{-1}, at 24°C.

overvoltage of about 0.6V. On a nonrenewed electrode surface, two linear Tafel regions are formed in the η-log i polarization curve having different constant a values and approximately equal constant b values. On a continuously mechanically renewed electrode surface, the second linear region is not observed.

The sharp drop of hydrogen overvoltage is due to passing through the zero charge potential of the metal which for Sn is about −0.4V (8). Such a drop of overvoltage when passing from a negatively charged metal surface to a positively charged surface, as it is known, was observed long ago by other authors. The constant a values found out by the authors (on a negatively

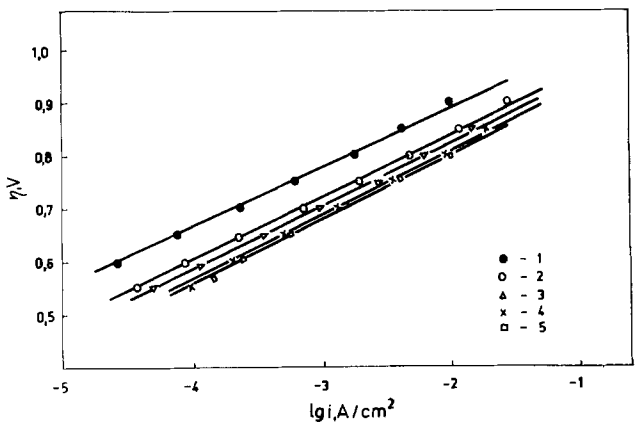

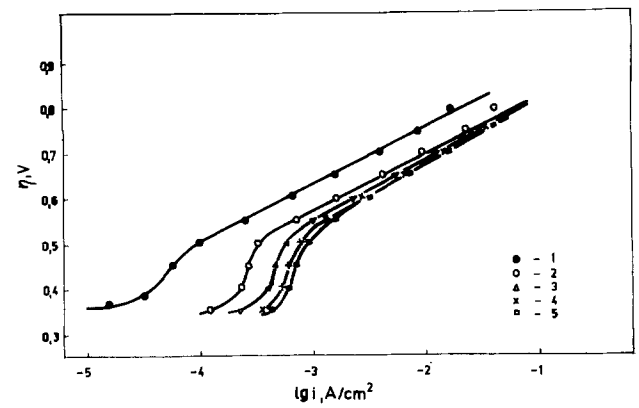

Fig. 6. Polarization curves obtained on Sn SRE in 1N H_2SO_4 + 0.01N KI(a, top) and in 1N H_2SO_4 + 0.1N KI(b, bottom). The indications are the same as in Fig. 5, at 24°C.

charged nonrenewed electrode surface, $a = 1.16$V, while on a positively charged nonrenewed electrode surface, $a = 0.88$V) are near to those of Kilimnik and Rotinjan (9).

Experiments in H_2SO_4 solutions containing the halogen ions I^- and Br^- were carried out to examine the way the surface active ions influence the hydrogen evolution overvoltage. In Fig. 5a and 5b, are shown the polarization curves η-log i obtained in 1N H_2SO_4 in the presence of 0.01N KBr (Fig. 5a) and 0.1N KBr (Fig. 5b) while in Fig. 6a and 6b the same curves are given in presence of 0.01N KI (Fig. 6a) and 0.1 KI (Fig. 6b). From Fig. 5 and 6 it is seen that in sulfuric acid solution containing the surface active ions Br^- and I^-, the continuous mechanical renewal of the Sn electrode exhibits approximately the same influence on the hydrogen evolution overvoltage as in pure H_2SO_4 solution. The overvoltage decrease due to mechanical renewal is practically the same as in pure H_2SO_4 solution which is better seen from Table I in which data obtained on the basis of the curves in Fig. 5 and 6 at

Table I. Hydrogen overvoltage (V) on tin Sn SRE in 1N H_2SO_4 and in H_2SO_4 solution containing surface active ions Br^- and I^- at various rates of renewal of the electrode surface and at $i = 1 \cdot 10^{-3}$ A-cm^{-2}

Composition of the electrolyte	Nonrenewed surface	Continuously mechanically renewed surface			
	$n = 0$ sec^{-1}	$n = 9.7$ sec^{-1}	$n = 29$ sec^{-1}	$n = 50$ sec^{-1}	$n = 70$ sec^{-1}
1N H_2SO_4	0.810	0.735	0.720	0.700	0.690
1N H_2SO_4 + 0.01N KBr	0.785	0.720	0.700	0.685	0.685
1N H_2SO_4 + 0.1N KBr	0.775	0.715	0.700	0.690	0.680
1N H_2SO_4 + 0.01N KI	0.735	0.675	0.610	0.605	0.600
1N H_2SO_4 + 0.1N KI	0.625	0.570	0.550	0.545	0.540

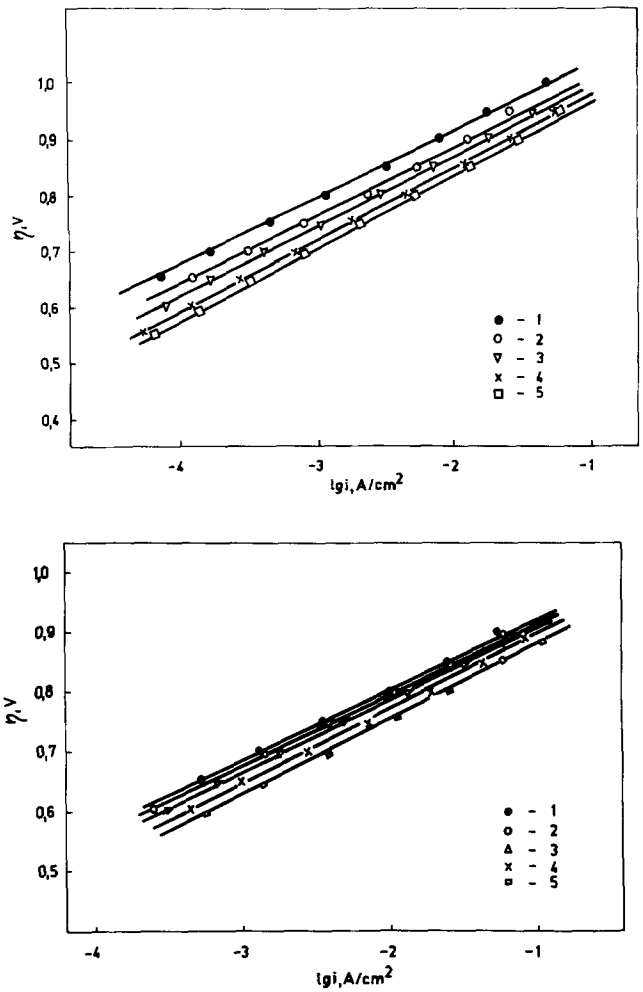

Fig. 7. Dependence of hydrogen evolution overvoltage on the logarithm of current density in 2N H_2SO_4 on nonrenewed (a, top) and continuously mechanically renewed (b, bottom) cathode surfaces of the Sn electrode, $n = 9.7$ sec^{-1}: 1—24°; 2—34°; 3—41°; 4—50°; and 5—60°C.

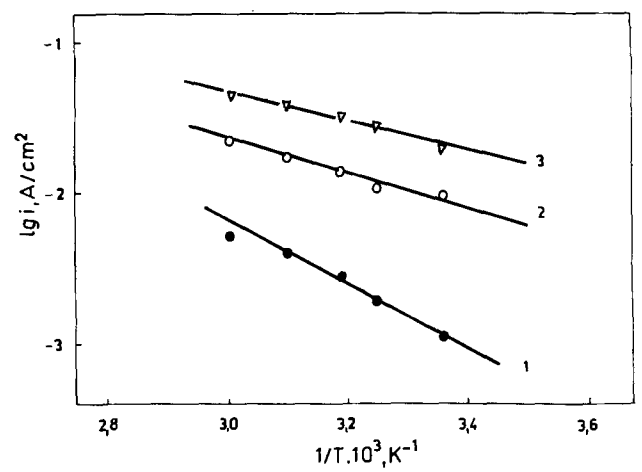

Fig. 8. Dependence of the logarithm of current density on the reciprocal value of the temperature at $\eta = 0.8$V and at various rates of electrode rotation: 1—nonrenewed electrode surface; 2—at $n = 9.7$ sec^{-1}; 3—$n = 30$ sec^{-1}.

$i = 1 \cdot 10^{-3}$ A-cm^{-2} are shown. From Table I, it is seen that the hydrogen evolution overvoltage observed in H_2SO_4 solution after the addition of the surface active ions Br^- and I^- is decreased both on nonrenewed and on continuously mechanically renewed cathode surfaces of the Sn electrode. In the same concentration, the influence of KI is expressed more strongly than the same of KBr which corresponds to the increase of the surface activity of the ions F^-, Cl^-, Br^-, and I^-. From the table, it is also seen that the influence of ions on the hydrogen overvoltage is more expressed for higher concentrations. The investigations carried out by the authors as it was mentioned show that halogen ion adsorption practically does not change the magnitude of the overvoltage decrease which remains of the same order as it is in pure H_2SO_4. From the above investigations, a conclusion can be drawn that the adsorption of the studied surface active ions, I^- and Br^-, takes place at a rate higher than the rate of renewal of the electrode surface. This fact can be judged by the total shift of the η-log i polarization curves compared to the same but taken in absence of the surface active ions.

In order to establish how the rate of mechanical renewal influences the effective activation energy of hydrogen evolution on a tin electrode, the temperature dependence of the rate of electrolytic evolution of hydrogen in sulfuric acid solution was studied. It is necessary to note that in the literature there are no data for the activation energy not only for a mechanically renewed tin electrode surface but also for a nonrenewed surface. In Fig. 7a and 7b, the dependence of the overvoltage on the logarithm of current density is shown, respectively, for nonrenewed and for continuously mechanically renewed cathode surface at temperatures of 24°, 34°, 41°, 50°, and 60°C. From curves in Fig. 7a and 7b, it is seen that the temperature has a much weaker influence on the hydrogen overvoltage of a mechanically renewed electrode surface.

In Fig. 8 the dependence of the logarithm of the current density on the reciprocal value of the temperature is shown at overvoltage $\eta = 0.8$V for a nonrenewed surface (curve 1) and for a continuously renewed electrode surface at a rate of electrode rotation $n = 9.7$ sec^{-1} (curve 2) and at $n = 30$ sec^{-1} (curve 3). From Fig. 8, it is shown that the effective activation energy of hydrogen evolution on a nonrenewed surface has a value $E_a = 42$ kJ-mol^{-1}, while on a continuously mechanically renewed surface at a rate of electrode rotation $n = 9.7$ sec^{-1} and $n = 30$ sec^{-1}, the activation energy has values $E_a = 23$ kJ-mol^{-1} and $E_a = 20$ kJ-mol^{-1}, respectively. From the obtained data it is seen that the mechanical renewal of the electrode surface influences the effective activation energy of hydrogen evolution by decreasing it about two times.

In general, the results in this paper are a new confirmation of the influence, observed by Noninski (3), of the cathode surface renewal both on the activation energy and on the hydrogen evolution overvoltage on metals with high hydrogen overvoltage and in the absence and presence of surface active ions. The experimental results obtained by the authors with the help of SRE when studying the influence of the continuous mechanical renewal on the overvoltage and the activation energy of hydrogen evolution can hardly be explained by the widely accepted theories for this process: theory of recombination and the theory of charge transfer. The authors agree with Tomashov *et al.* (1, 2) that if it is proceeded from the theory of delayed recombination only the decrease of the hydrogen overvoltage of metals with low one can be explained where measurable adsorption of atomic hydrogen can be observed. As for the metals with high hydrogen overvoltage at which there is practically no such adsorption, Tomashov *et al.* (1, 2), accepting that here the theory of charge transfer is valid, rightfully consider that on these metals the continuous mechanical renewal should not influence the hydrogen evolution overvoltage. The authors observed that a decrease of hydrogen overvoltage on metals characterized by high hydrogen overvoltage where there is practically no adsorption of atomic hydrogen leads them to be-

lieve that also for metals with low hydrogen overvoltage, the decrease of the latter is not connected with the adsorption of atomic hydrogen but with some other reason.

According to some of the main theses developed in Ref. (10), it can be accepted that the electrode potential influences the electrode process rate mainly by changing the total number of collisions of the ions on the electrode surface through respective change of the rate of the translational movement and the concentration of the neutralizing ions. At that the electrode potential influences the electrode process rate not by increasing the rate of the translational movement of the ions that much but by increasing their concentration at the electrode surface. According to the concepts in Ref. (10), at the stationary process the main reason for the electrode overvoltage is the increased concentration of the ions at the electrode surface. It is important to note that the above-mentioned increase of the ion concentration is connected with the increase of the intensity of the electrostatic field. As a result of the mechanical renewal of the electrode surface, an efficient stirring of the solution is obtained because the immovable liquid layer lying next to the electrode surface is stirred. This energetic stirring leads to leveling the ion concentration at the electrode surface with their concentration in the bulk of the solution. As a result of this, the energy is hindered along the path of the neutralizing ion in such a way that the hydrogen overvoltage and the activation energy are decreased.

As it is known, the continuous mechanical renewal changes the electron work function, and therefore the contact potential difference between the cathode metal and platinum will also be changed.[2]

According to the equation

$$\eta = a_{Pt} + U_{PtMe} + b \log i \qquad [1]$$

(a_{Pt} and b-Tafel constants)

[2] More exactly, according to Ref. (11) there should be considered the difference between the zero charge potentials of the platinium and the cathode metal.

established on the basis of significant experimental data (11), it is natural to expect a change of the overvoltage as a result of mechanical renewal because it includes the contact potential difference U_{PtMe}. From Eq. [1], it is also seen that if the same metal which is used for a cathode is taken as a reference electrode then it is to be expected that the measured overvoltage on all metals will be the same as that on platinum. The hydrogen overvoltage, however, includes in itself the contact potential difference U_{PtMe} and namely because of this it will depend on the nature of the cathode metal.

According to the shortly explained concepts (10, 11) it seems most probable that the continuous mechanical renewal influences the hydrogen overvoltage both by leveling the ion concentration at the electrode surface with that in the bulk of the solution and by changing the contact potential difference U_{PtMe}.

Manuscript submitted March 18, 1982; revised manuscript received *ca.* May 24, 1983.

REFERENCES

1. N. D. Tomashov, N. M. Strukov, and L. P. Vershinina, *Dokl. AN USSR*, **171**, 1134 (1965); *Elektrokhimiya*, **5**, 26 (1969).
2. N. D. Tomashov and L. P. Vershinina, *Electrochim. Acta*, **15**, 502 (1970).
3. C. I. Noninski, *Khim. Ind. (Sofia)*, **44**, 121 (1972).
4. C. I. Noninski, Invention No. 23842 G-01, No. 27/28, Bulgaria (1976).
5. I. P. Ivanov, Thesis, Sofia, Bulgaria (1976).
6. C. I. Noninski and I. P. Ivanov, *Khim. Ind. (Sofia)*, **47**, 70, 304 (1975).
7. C. I. Noninski, *Bull. Soc. Chim. Fr.*, **9-10**, 1283 (1976).
8. V. L. Heifetz, B. S. Krasikov, and A. L. Rotinjan, *Elektrokhimiya*, **6**, 916 (1970).
9. A. B. Kilimnik and A. L. Rotinjan, *Elektrokhimiya*, **5**, 1234 (1969); *Zh. Prikl. Khim.*, **44**, 673 (1971).
10. C. I. Noninski, Ann. *Inst. Chim. Technol. Sofia*, **4**, 145 (1957).
11. C. I. Noninski, *Proc. Bulgar. Acad. Sci.*, **6**, 407 (1956).

Maskless Laser Patterning for Gold Plating of Microelectronic Materials

R. J. von Gutfeld,* M. H. Gelchinski, and L. T. Romankiw*

IBM Thomas J. Watson Research Center, Yorktown Heights, New York 10598

ABSTRACT

The authors have developed a method for producing small area patterns using any one of several organic coatings, including photoresist in conjunction with a Q-switched Nd-YAG laser. The laser removes the coating locally leaving a clean metal surface which can then be plated by conventional means. The authors have laser patterned coated substrates of copper, nickel, nickel-plated Be-Cu, and gold plated the patterned 1/2-1 mm diam regions. These areas are typical of those required on microelectronic connector parts and serve to demonstrate the potential of this simple technique for conserving precious metals. Laser and coating parameters are described together with details of the patterning method.

The increasing cost and scarcity of precious metals for microelectronic applications have created a strong need for conserving these resources. This can be accomplished by either finding cheaper substitute metals or alloys at a cost of decreasing the performance or using the same precious metals more efficiently. The most recent approach in the plating industry is to seek methods for increasing the efficient use of precious metals by patterning the part so that only the essential areas are plated. Several masking schemes for local plating of electronic parts have been devised including moveable masks that are brought into contact with the part during plating and subsequently released when plating is completed (1). Such contact masks are usually made of vinyl and have to be especially fabricated for each specific application. More complicated contact masks have been designed for use with reel-to-reel jet plating machines. Here, the mask continuously rotates to make and break contact in synchronism with the part as it moves through the plating cycle. The use of photoresist in conjunc-

* Electrochemical Society Active Member.

tion with preformed masks can also be used but is a costly time consuming multistep process, not well suited for most electronic connector parts, particularly in reel-to-reel plating machines. Further, the standard photoresist technique is fairly inflexible since new masks must be fabricated with every change in plating pattern.

The authors report a simple inexpensive method for forming patterns for localized plating without the use of a preformed mask. The scheme uses a focused laser beam to remove locally a thin masking material which has been preapplied over the entire part. This results in a clean metallic region for plating while maintaining electrical insulation over the remainder of the part. The technique is particularly applicable for reel-to-reel plating machines in conjunction with a high repetition rate laser to form the required maskless pattern on an array of moving parts. The authors have termed this patterning process "laser ablation technique."

Experimental Procedures and Results

Maskless plating patterning using the laser ablation technique requires the following steps: (*i*) immersion of the part to be locally plated in any one of a number of liquid dielectric materials to obtain a thin coating which upon solidification is electrically insulating with good adhesion to the substrate and insoluble in water. This coating can also be applied by controlled spraying of the dielectric liquid onto the part. (*ii*) Absorption of one or more laser pulses by the coated part to remove completely the desired area of dielectric. The size of the area uncovered or patterned is controlled by the laser spot diameter, power density, wavelength, and pulse width. (*iii*) Plating of the part by conventional, jet, or laser plating techniques (2-4) after cleaning to remove solid remnants of the ablation followed by (*iv*) rinsing in the appropriate solvent to dissolve the remaining dielectric coating material not previously removed by the laser patterning step.

A number of organic dielectric masking materials were used in the first studies including glycol phthalate, paraffin, and AZ® photoresist (Shipley Company), all applied to pure nickel or nickel-plated beryllium-copper stock, ~8 mil thick. Nickel-plated beryllium-copper is typically used in the electronic connector industry so that most of our later experiments concentrated on the use of this material in conjunction with gold and gold alloy electroplating. Initial experiments with glycol phthalate as a dielectric coating were made by dipping the samples in a solution of glycol phthalate dissolved in acetone followed by air drying. Laser ablation occurred with the samples immersed in a gold plating solution using millisecond pulses from a mechanically modulated multiline 8 w cm argon laser. Although resulting gold-plated sections were found to be adherent and of reasonable quality, two problems were observed: (*i*) nonuniform removal of the dielectric coating due to some melting and charring of the coating. This resulted in some local spots of charred residue and uneven plating patterns, especially around the outer periphery, and (*ii*) contamination of the plating solution from accumulation of ablated dielectric material The detailed effects of this organic contamination on the quality of plating were not determined or investigated but are known to be detrimental to the plating solution performance with long term usage (5). In order to eliminate the possible contamination of the plating bath, the experimental procedure was altered to produce patterning in air. Also, a Nd-YAG laser that could be Q-switched to produce pulses as short as 20 nsec at 1.06 μm wavelength was used. Pulse widths of 100 μsec, 1 msec, 2 msec, and 5 msec were also available as non-Q-switched pulsed modes. The advantages of this laser for laser ablation are the short pulses and weak absorption by the organic coatings at 1.06 μm.

It was found that a single 5 msec pulse burned the glycol dielectric coating applied to a nickel-coated Be-Cu substrate. Consequently, a rough poorly adhering nodular deposit was obtained, presumably due to the remnant residue layer. This type of deposit is shown in the scanning electron microscope micrographs of Fig. 1. In addition to the poor surface cleaning resulting from this relatively long pulse, heat dissipation caused a weakening of the adhesion of the glycol phthalate at the periphery of the ablated spot and led to the underplating evident in Fig. 1a. Short Q-switched pulses, on the other hand, resulted in uniform cleanly ablated patterns as well as a smooth surface for subsequent plating. Plating obtained on such surfaces resulted in uniform and bright deposits as shown in Fig. 2. In addition, the damage to the substrate adhesion of the glycol phthalate at the periphery took place over a much smaller circumferential area.

Although experiments with glycol phthalate showed feasibility, it was of interest to explore other coating materials. In the first experiments with AZ® photo-

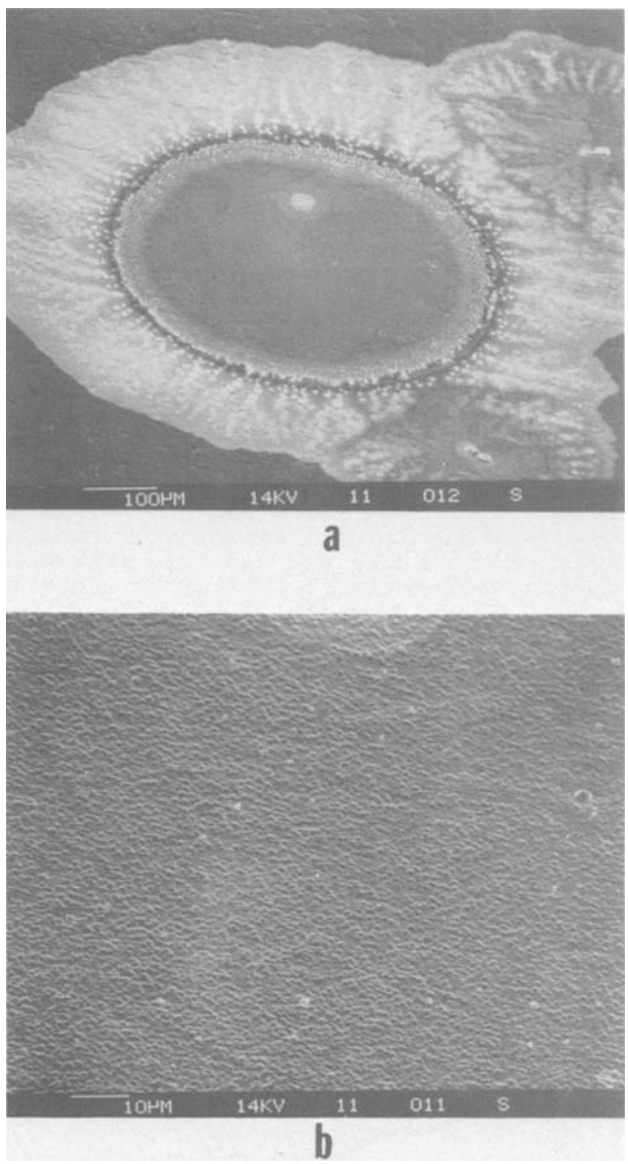

Fig. 1. (a) SEM micrograph of gold plating on nickel-plated Be-Cu using glycol phthalate dielectric oblated with one 5 msec Nd-YAG laser pulse. Note the underplating along the circular periphery caused by overheating during ablation. (b) Gold surface morphology near the center.

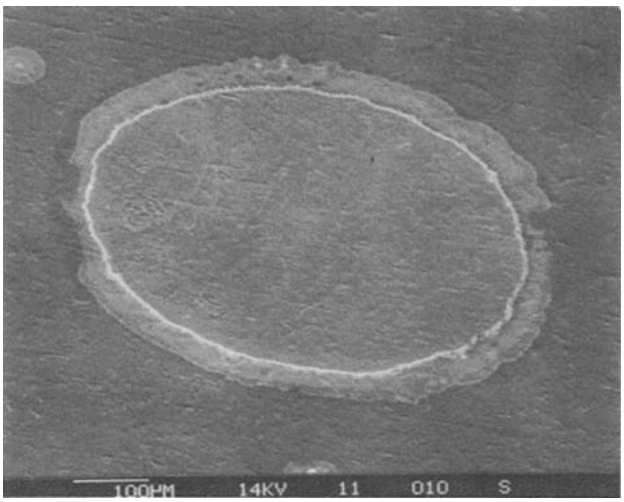

Fig. 2. Same as Fig. 1 but using the 20 nsec Q-switched Nd-YAG pulse to form the ablation. Note the improvement in the decreased underplating.

resist, standard spinning (2000 rpm) and baking at 80°C for 20 min of the photoresist coatings on the part were utilized. Ablation was carried out with 5 msec pulses which caused carbonization of the photoresist and did not provide a clean ablated surface for plating. Q-switched pulses, on the other hand, resulted in a uniform ablation pattern. In addition, the rather cumbersome techniques of spinning and baking the photoresist were found to be unnecessary for successful laser ablation. Experimentation showed that coatings could be reliably produced by dipping the part in a dilute resist solution followed by air drying. The laser power required for ablating was found to be independent of the coating thickness when 20 nsec Q-switched pulses were used. Typical laser energy per pulse was 5 mJ producing ablated spots on the order of 1 mm in diameter. The relative independence of laser energy with coating thickness and the very weak absorption in photoresist at 1.06 μm as shown in Fig. 3 implies that laser absorption occurs in the metal substrate giving rise to heating at the photoresist-metal interface. Peak temperature increases at the interface resulting from the 5 mJ Q-switched pulses are estimated for a perfectly smooth surface to be on the order of ~500°C based on a one-dimensional thermal diffusion calculation using the thermal parameters of the substrate and a reflectivity of ~70% (6). At these laser power levels, however, the rough surface peaks, typical of sulfamate nickel plating, are melted (on the order of 1-2 μm) creating a smoother surface texture. This smoothing effect is shown in Fig. 4, where two sulfamate nickel-coated surfaces are compared, one laser treated, the other untreated.

The weak dependence of laser power (for successful ablation) as a function of photoresist thickness leads the authors to conclude that material removal is due to differential expansion as well as possible thermal shock from locally intense thermoelastic expansions. This results in local fracture of the photoresist layer and a clean metal area without organic residue in the immediate region of laser absorption. This model is consistent with the two to three times higher thermal expansion coefficient of resist compared to nickel and copper. Film or coating fragments have been observed in close proximity to the ablated regions indicative of shattering rather than vaporization or melting of the dielectric.

After the ablation steps with from one to three Q-switched laser pulses, the following procedure was carried out to obtain the final gold-patterned product. First, the samples were subjected to a stream of air to remove the shattered film fragments. This was fol-

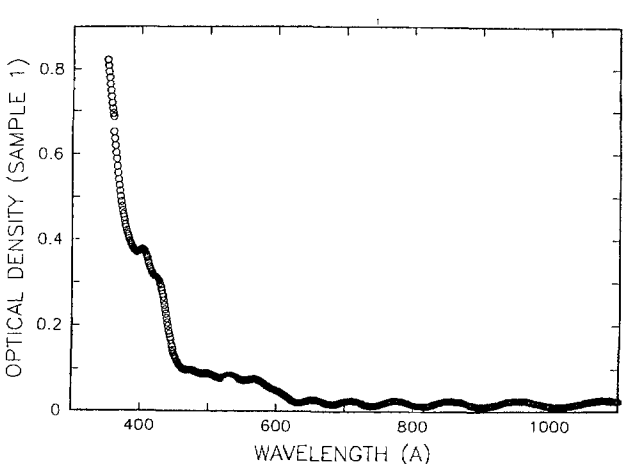

Fig. 3. Optical absorption as a function of wavelength resulting from an air-dried AZ® photoresist material on glass. Note the very low absorption at the Nd-YAG (1.06 μm) wavelength.

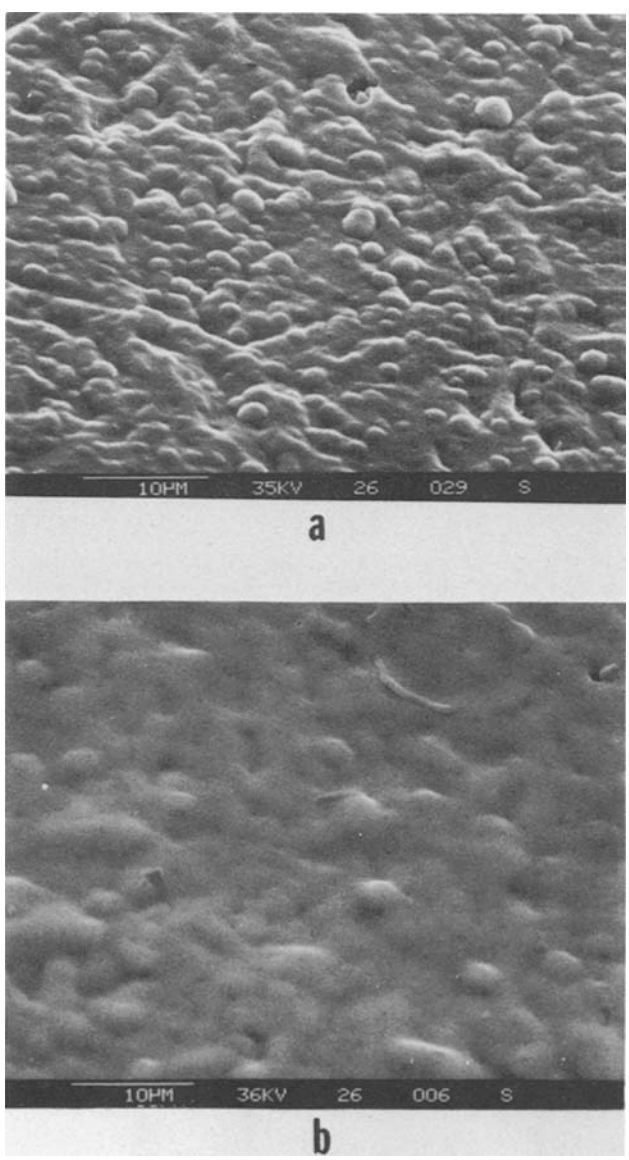

Fig. 4. Smoothing of rough sulfamate nickel-coated Be-Cu surface as produced by laser absorption: (a) substrate surface after removal of photoresist with acetone; (b) after removal of photoresist with one Q-switched laser pulse. Here isolated fragments of photoresist "flakes" are also visible.

lowed by immersion in a 1:1 HCl solution for 1 min followed by a quick water rinse. The samples were subsequently immersed in Autronex N (Selrex Corporation) solution and electroplated in a conventional two-electrode cell at constant potential for 35 min. This was followed by a water, acetone, and alcohol rinse. The acetone removed the remaining photoresist not previously removed by the laser ablation step. Micrographs of a plated region are shown in Fig. 5a, b while a photograph of the patterned array of nickel-gold spots is shown in Fig. 6. These areas were fabricated to serve as gold contacts and were tested for adhesion, electrical conductivity, and porosity. Tests showed them to be entirely similar in these properties to the gold contact dots produced conventionally on similar substrates. It was observed that the surface quality of the gold improved with the slightly higher intensity laser ablation pulses which smoothed out the substrate surface. The slight substrate melting, as previously described, is believed to provide a better surface for the electroplated gold layer which leads to a decrease in the porosity of the gold deposition (7).

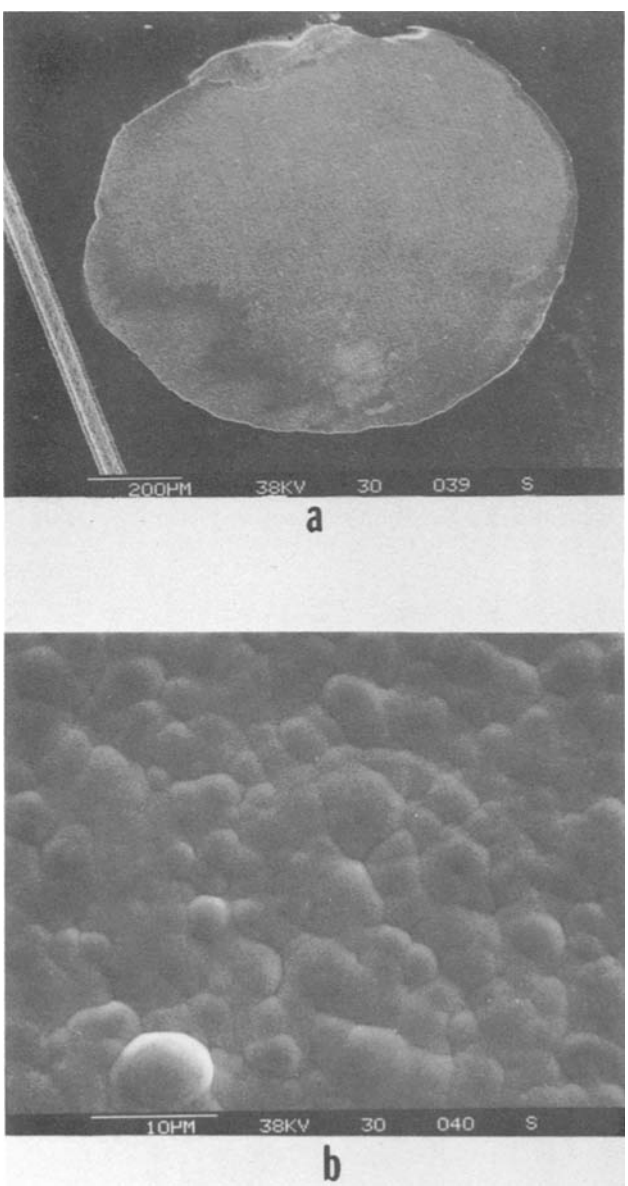

Fig. 5. (a) SEM micrograph of selectively plated gold (Antronex N) using conventional d-c plating for 35 min on a sulfamate nickel-plated Be-Cu sample. Here AZ® photoresist was ablated to achieve the pattern. Gold thickness is ~6 μm. (b) SEM of gold region of (a) showing surface morphology.

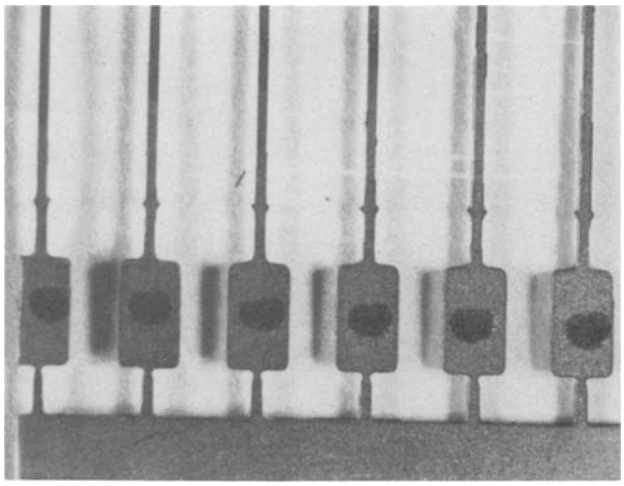

Fig. 6. An array of parts (sulfamate nickel-plated Be-Cu) showing a single gold-plated spot on each part to obtain selective plating via the ablation technique.

Figure 7 is a photograph of a metallurgical section of ~1.5 μm thick nickel-gold sample, a thickness suitable for typical contact applications. Electrical contact measurements of this pore-free sample compared favorably with a gold-on-gold sample used as a reference standard for contact resistivity.

In the experiments, the authors studied the plating quality on ablated regions as a function of laser power density, pulse width, and number of pulses/site. For ~1 mm diam ablation areas with AZ® photoresist, best results occurred with the sample ablated in air using Nd-YAG 20 nsec Q-switched pulses, one to three pulses/site, ~5 ± 2 mJ/pulse. Repetition rates were ~40/min preventing any average heating of the substrate between successive pulses. It was also found that photoresist gave the most reproducible ablation and plating quality compared to the other dielectrics used, *i.e.*, glycol phthalate and paraffin. Furthermore, it was realized that glycol phthalate may be hydrolyzed in acid solutions. Hydrolysis could result in plating solution contamination as well as a dissolution of the dielectric mask. Problems arising from patterning with values of laser parameters outside of the above-mentioned parameters, *i.e.*, the "process window" were (*i*) charring, burning, or melting of the dielectric layer which resulted in poor adhesion and led to underplating (plating underneath coating regions not ablated), (*ii*) damage to the substrate, and (*iii*) incomplete removal of the dielectric causing irregular or nodular gold plating and inadequate adhesion. The incomplete removal may consist of a very thin layer, probably less than 100Å in thickness in the form of an organic or carbon residue which prevents high electrical conduction to the substrate and causes poor plating adhesion. However, operating within the process window

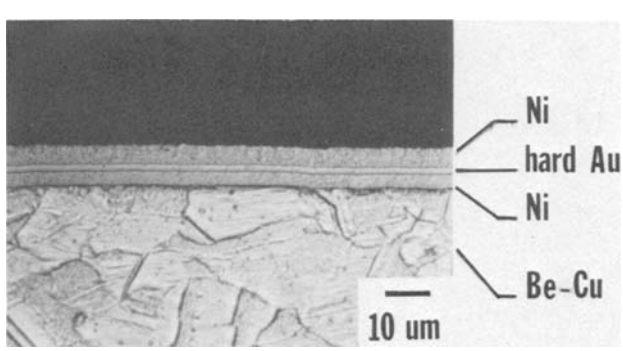

Fig. 7. Metallurgical cross section of nickel-gold contact plated after laser ablation of photoresist. The substrate is sulfamate nickel-plated Be-Cu. (See text.)

eliminates all of the above difficulties and results in a clean surface and excellent plating with good adhesion.

Summary and Conclusions

Experiments with a number of dielectric coating materials on metal substrates have been undertaken to attempt maskless laser patterning for subsequent electroplating of the patterned area. The patterning by way of laser ablation has been undertaken both with the sample in air and submerged either in water or a gold plating solution. Glycol phthalate, paraffin wax, and AZ® photoresist were used as dielectric coatings, all with some success. Optimum patterning on Be-Cu substrates results from the use of AZ® photoresist in conjunction with a Q-switched Nd-YAG laser. This optimum was measured in terms of the quality of the resulting gold plating, its adhesion, uniformity, microscopic structure, and electrical conductivity. The laser parameters were found to be optimal for these cases where the laser wavelength is not absorbed by the coating material but by the substrate at the dielectric coating-substrate interface. This method of maskless patterning should find interesting applications in a number of areas requiring selective plating or etching patterns.

Acknowledgments

The authors are grateful to Dr. P. Perry for conducting absorption and reflection measurements of the AZ® photoresist and for the invaluable technical assistance from D. Vigliotti, A. Pfeiffer, and E. Dibble.

Manuscript submitted Dec. 3, 1982; revised manuscript received *ca.* May 11, 1983.

IBM assisted in meeting the publication costs of this article.

REFERENCES

1. F. H. Reid and W. Goldie, "Gold Plating Technology," p. 203, Electrochemical Publ. Limited (1974).
2. R. J. von Gutfeld, E. E. Tynan, R. L. Melcher, and S. E. Blum, *Appl. Phys. Lett.*, **35**, 651 (1979).
3. R. J. von Gutfeld, R. E. Acosta, and L. T. Romankiw, *IBM J. Res Dev.*, **26**, 136 (1982).
4. M. H. Gelchinski, L. T. Romankiw, and R. J. von Gutfeld, Abstract 131, p. 206, The Electrochemical Society Extended Abstracts, Vol. 82-2, Detroit, MI, Oct. 17-21, 1982.
5. F. H. Reid and W. Goldie, "Gold Plating Technology," p. 143, Electrochemical Publ. Limited (1974).
6. H. S. Carslaw and J. C. Jaeger, "Conduction of Heat in Solids," 2nd ed., Chap. II, Oxford University Press (1959).
7. S. M. Garte, *Plating*, **53**, 1335 (1966).

The Effect of Pressure on the Product Distribution in Kolbe Electrolysis

J. E. Sanderson,[1] P. F. Levy, L. K. Cheng, and G. W. Barnard[2]

Dynatech Research and Development Company, Chemical Engineering Group, Cambridge, Massachusetts 02139

ABSTRACT

Experiments have been run which demonstrate that electrochemical oxidation of n-alkanoic acids (in the range of C_4-C_6) in aqueous solution at a smooth platinum anode gives higher yields of alkane dimer product when run at elevated pressures than an equivalent experiment at atmospheric pressure. This phenomenon has been observed over a wide range of reaction conditions. A plausible explanation for this result is that under high pressure conditions, olefin accumulates at the anode surface which helps to prevent the water, required to stabilize intermediates in the formation of competitive products, from reaching the electrode surface.

The electrochemical oxidation of aliphatic carboxylic acids is among the oldest of organic reactions. Kolbe described the decarboxylation and dimerization of organic acids to produce alkanes (1). Hofer and Moest described the decarboxylation of organic acids to produce alcohols (2). In addition, a variety of other products have been observed under both sets of reaction conditions particularly when acids other than acetic are electrolyzed including olefins, esters, nondimerized alkanes, and cyclopropane derivatives (3, 4).

The stoichiometry for the Kolbe and Hofer-Moest reactions are, respectively

$$RCOOH + R'COOH \rightarrow R{-}R' + 2CO_2 + H_2 \quad [1]$$

$$RCOOH + H_2O \rightarrow R^*OH + CO_2 + H_2 \quad [2]$$

where R* refers to R and isomers of R collectively.

The former (Kolbe) reaction (Eq. [1]) is predominant at smooth platinum anodes with acetic acid and the longer chain fatty acids (C_6 and up) (5). The second (Hofer-Moest) reaction (Eq. [2]) is observed to predominate at carbon anodes (6). In both cases, under most conditions the main side product is olefin

$$RCOOH \rightarrow R'HC = CHR'' + CO_2 + H_2 \quad [3]$$

where R′ and R″ are either hydrogen or organic radicals. With most other electrode materials and at low current densities, the primary side product (in aqueous solution to which this discussion is limited) is oxygen.

Speculation as to the mechanism of the Kolbe and Hofer-Moest reactions has been going on almost since the reactions were discovered. The evolution of the current view of the mechanism of these reactions is documented in reviews such as those by Utley (4), Weedon (5), or Eberson (6). Figure 1 presents a dia-

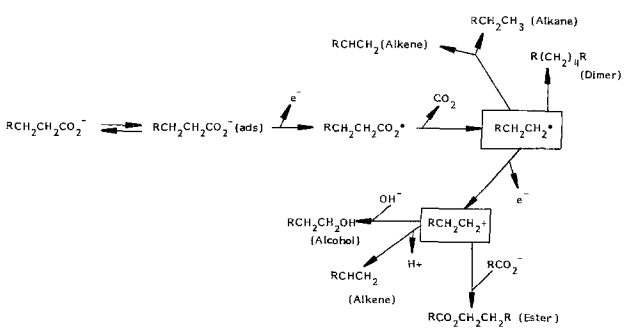

Fig. 1. Anodic oxidation of carboxylates reaction mechanism

[1] Present address: Moleculon Research, Cambridge, Massachusetts.
[2] Present address: Earthscan, London, England.

gram similar to the one constructed by Utley (4) indicating the mechanism of the Kolbe and Hofer-Moest reactions. Table I shows typical product distributions. No method has been reported which is capable of increasing the yield of alkane dimer above the levels usually obtained for a given organic acid (6). This paper suggests a technique for increasing the yield of alkane dimer and presents an explanation for this effect.

Experimental

The electrolysis reactions under investigation take place in a flow-through electrolytic cell manufactured by ECO, Incorporated, Cambridge, Massachusetts. A schematic diagram of the cell is shown in Fig. 2. The cell has been modified and reinforced to allow it to be operated at pressures up to 1.5 MPa. The electrodes are separated by cardboard gaskets giving an electrode spacing of approximately 0.15 mm. The exposed internal surface area of the electrodes is 36 cm^2. The inlet and outlet ports are both located on the cathode side of the cell.

The cell is integrated into a circulating system shown in Fig. 3 which is capable of measuring and regulating liquid temperature and liquid flow rate as well as current, potential difference, gas flow rate, and pressure. A BIF® diaphragm pump draws the aqueous acid solution from a 1 liter holding vessel and circulates it through the electrolytic cell. The liquid and generated gas return to the holding vessel, and the gaseous products exit through a back pressure regulator.

The system pressure is measured by a pressure gauge connected to the holding vessel and maintained by adjustment of the back pressure regulator. The electrolytic cell is connected to a Sorenson SRL10-100 d-c power supply, capable of delivering up to 100A at between 0 and 10V. The current is monitored by a Sargent-Welsh ammeter connected in series between the anode and positive terminal of the power supply.

Experiments have been run up to 1.5 MPa and up to 150°C. For experiments over 100°C, a condenser was added to the system to minimize water loss in the gas stream. In all experiments, water vapor is removed from the exit gas stream by using a "U" tube filled with indicating Drierite®. Once a satisfactory balance between decarboxylated products and carbon dioxide production was demonstrated, another "U" tube containing indicating Ascarite® was added to the system to remove CO_2 from the exit gas to simplify the analysis of the gas composition. Gas production was measured either by water displacement or by a wet test meter. The *p*H of the liquid in the holding vessel is checked at the start and end of each experiment.

All reagents were reagent grade materials obtained from major supply houses and were used without purification. In many experiments, sodium sulfate

Table I. Kolbe electrolysis of aliphatic monobasic carboxylates

Acid	Structure	Percentage yield		
		Paraffin	Olefin	Ester
Ethanoic	CH_3COOH	85	2	2
Propanoic	C_2H_5COOH	8	66	5
n-Butanoic	C_3H_7COOH	14.5	53	10
2-Methyl-propanoic	$(CH_3)_2CHCOOH$	trace	62	10
n-Pentanoic	C_4H_9COOH	50	18	4
3-Methyl-butanoic	$(CH_3)_2CHCH_2COOH$	43	42	5
Methyl ethyl ethanoic	$(CH_3)(C_2H_5)CHCOOH$	10	42	10
Trimethyl ethanoic	$(CH_3)_3C\,COOH$	13	52	0
n-Hexanoic	$C_5H_{11}COOH$	75	7	1.5

From Allen, p. 103 (7).

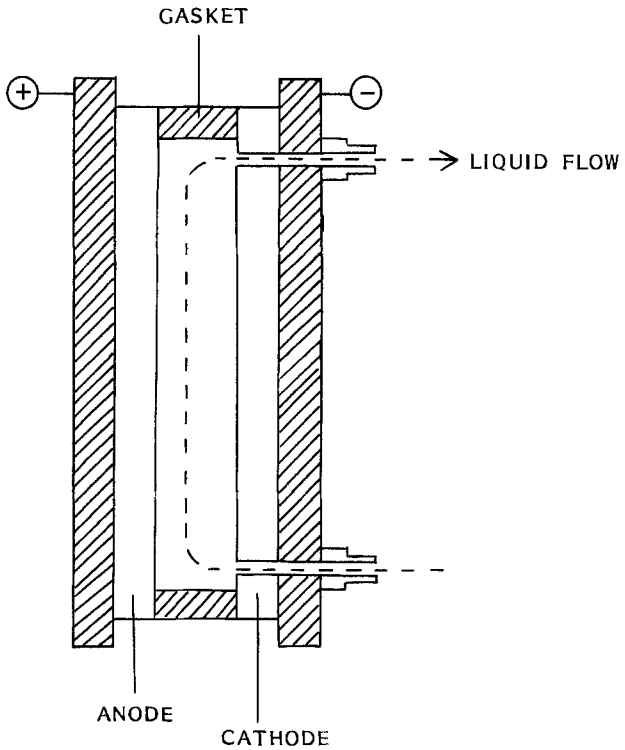

Fig. 2. Schematic diagram of electroprep[1M] electrolysis cell

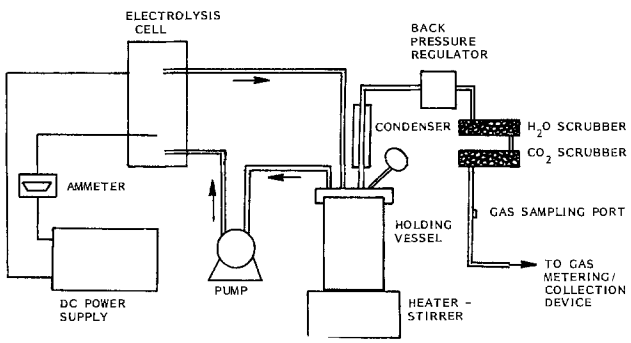

Fig. 3. Diagram of integrated electrolysis system

was used as a supporting electrolyte to reduce the electrical resistance of the electrolyte solution.

Gaseous products (olefins, etc.) are separated and quantified using a Gow-Mac 750 gas chromatograph equipped with a flame ionization detector. These products are separated on a ⅛ in. × 20 ft stainless steel column packed with n-octane on Durapak using nitrogen carrier gas at 48°C. The water immiscible products are analyzed on a programmable Perkin-Elmer F30 gas chromatograph equipped with a flame ionization detector. Glass columns ¼ in. diam × 6 ft packed with Chromasorb 101 (no liquid phase) are used with nitrogen carrier gas to separate these products at 130°-230°C. Water soluble components are quantified using the same instrument by injection of the acidified aqueous solution using the same temperature program.

Results

Numerous experiments have been run under a wide variety of conditions of electrolyte concentration, temperature, *p*H, current density, etc., in which the product distribution at elevated pressures has been compared with the product distribution under the same conditions, but at atmospheric pressure. Table II presents the results of one such experiment using 2M n-butanoic acid at *p*H 5.2 and an anodic current density of 0.28 A/cm^2. Although in this case, ester appeared to be the primary beneficiary of increased pressure, some hexane was identified in the product mix. These

Table II. Effect of pressure on the product yields from the electrolysis of butanoic acid on platinum in aqueous solution

Pressure product	100 kPa, Run 82 % yield	1.1 MPa, Run 81 % yield
Hexane	0	2.7
Propyl butanoates	53.0	67.0
Isopropanol	3.1	2.3
n-propanol	1.0	0.9
Propene	42.0	27.0
pH range	5.0-5.2	5.0-5.3
Concentration	2.0M	2.0M

data are included because they represent the only relevant n-butanoic acid data to date. Also, they clearly show the reduction in olefin yield as a result of pressure.

Table III presents typical results for the electrochemical oxidation of n-pentanoic acid. Each result represents the average of two experiments using 2M n-pentanoic acid at pH 7.5 and an anodic current density of 0.28 A/cm^2. In these experiments, the amount of olefin formed was reduced by half and the n-octane yield was increased significantly. Similarly, in the case of n-hexanoic acid, Table IV presents the product distribution for experiments using 1M n-hexanoic acid at pH 8.0, also at 0.28 A/cm^2. Although the alkane dimer yield is quite high even at atmospheric pressure, it increases further at elevated pressure at the expense of olefin formation. Table V shows the alkane dimer yield for four sets of paired reactions under a variety of conditions using n-pentanoic and n-hexanoic acids, plus run 75 which is included even though no run under exactly the same conditions, except for pressure, was performed because it represents the highest alkane dimer yield obtained to date with n-pentanoic acid in the 1 MPa pressure range.

Discussion and Conclusions

It is clear that electrolytic oxidation of organic aliphatic acids in aqueous solution at elevated pressures produces smaller amounts of olefin sideproducts than does an equivalent experiment run at lower pressure and that the primary beneficiary is alkane dimer. There are two apparent explanations for this result.

Table III. Effect of pressure on the product yields* from the electrolysis of n-pentanoic acid on platinum in aqueous solution

Pressure product	100 kPa, % yield	1.1 MPa, % yield
n-octane	42.9	63.3
sec-butyl pentanoate	2.7	3.4
n-butyl pentanoate	0.9	0
sec-butanol	4.1	1.7
n-butanol	1.4	1.3
other aqueous	10.5	2.1
1-butene	15.5	8.9
trans-2-butene	5.5	2.1
cis-2-butene	4.1	1.7
n-butane	2.3	0.8
other gaseous	10.0	4.2
uncollected	0	10.5
pH range	7.4-9.2	7.4-8.2

* Mol percent of acid consumed to produce the specified products.

Table IV. Effect of pressure on the product yields from the electrolysis of n-hexanoic acid on platinum

Pressure product	100 kPa, % yields*	1.2 MPa, % yield
Decane	76.0	88.0
Pentyl hexanoates	0	0
2-Pentanol	3.3	1.0
1-Pentanol	0	0
Pentenes	20.0	11.0
pH range	7.4-8.9	7.4-8.0

* Average of two runs.

Table V. Effect of pressure on linear alkane yield

Run number	Acid	pH range	Pressure	Concentration	% Alkane*
71	n-Pentanoic	7.5-8.6	1.1 MPa	0.7M	67
72	n-Pentanoic	7.5-9.1	100 kPa	2.0M	51
73	n-Pentanoic	7.4-9.2	100 kPa	2.0M	45
74	n-Pentanoic	7.4-8.2	1.1 MPa	2.0M	59
75	n-Pentanoic	7.0-7.5	1.1 MPa	2.0M	71
76	n-Hexanoic	7.7-8.3	1.1 MPa	1.0M	80
77	n-Hexanoic	7.4-8.8	100 kPa	1.0M	68
78	n-Hexanoic	7.4-8.0	1.1 MPa	1.0M	88
79	n-Hexanoic	7.4-8.9	100 kPa	1.0M	76

* Mol percent of acid consumed to form alkane dimer product.

The first explanation is that the formation of olefin from 1-electron oxidation product is a reversible reaction. The pressure increases the activity of olefin in the system, which increases the rate of the reverse reaction. However, there are no data to support this hypothesis. In particular, in the electrolysis of pentanoic and longer acids, a substantial amount of the olefin product is 2-olefin. By any conceivable reverse reaction from a 2-olefin to alkane dimer, the alkane dimer would be nonlinear. Nobody has reported the identification of nonlinear alkane dimer in this type of reaction. Furthermore, in the current work, considerable effort has been expended to identify isoalkane dimer in the product mix without success. Typically, in an experiment run at 1+ MPa, the yield of alkane exceeds the atmospheric yield by 20-50% of the atmospheric yield. Also, typically, the 2-olefin comprises about 50% of the total olefin produced. If one assumes that the increase in alkane yield is a result of back reaction and that the 1-olefin and 2-olefin are equally reactive, then one would expect at least 10% of the alkane product to be isomeric. It is unlikely that this amount of isomeric alkane could have escaped detection.

Another approach to attempt to demonstrate the reversibility of the radical-to-olefin reaction was to perform an electrolysis of n-pentanoic acid in a vessel pressurized with propene. A reaction of this type would be expected to produce normal and isomeric heptanes, decanes, and undecanes along with the usual n-octane product if the aforementioned hypothesis were true. This approach had been previously successful in demonstrating that under electrolysis reaction conditions at a carbon anode that olefin could be converted to alcohol. Figure 4 shows a gas chromatogram of the aqueous product fraction of an electrolysis of n-pentanoic acid in a vessel prepressurized with propene. The presence of n-propanol and i-propanol along with the usual butanol products are apparent. These peaks do not appear when propene is not added. However, in the experiment to demonstrate formation of heptanes, decanes, and undecanes, none were identified.

Some researchers have reported the trapping of methyl radicals produced by electrolysis of acetate by added olefins in which two methyl groups are added to the olefin (4), but this reaction may be peculiar to methyl radicals.

Another hypothesis which has proven more resilient to scrutiny is that the yield of linear alkane is increased as a result of an increase in the partial pressure of olefin in the electrolysis cell because the pressure increases the amount of olefin at the electrode surface. This olefin, along with 1-electron oxidation intermediates (alkyl radicals perhaps) form a lipophilic layer at the electrode surface which serves to keep water (or other polar solvents) away from the electrode surface. It is not difficult to imagine that since carbonium ion products are often observed to form at lower potentials than radical products that, in the presence of water or other polar material which will serve to stabilize the transition state as well as

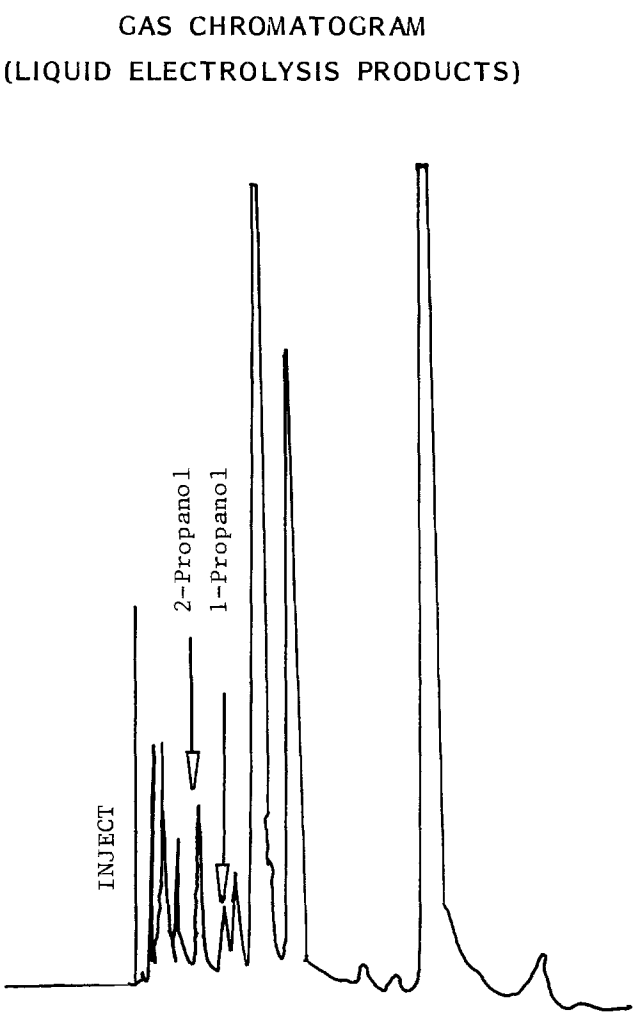

Fig. 4. Gas chromatograms of liquid products from oxidation of pentanoic acid on carbon anode with propene in headspace.

the carbonium ion intermediate, 2-electron oxidation products will be favored. Table VI lists the vapor pressures of various olefins calculated from the data given using the Clausius-Clapeyron relationship. These data indicate that all of the olefins of interest, with the possible exception of propene, are liquids under the high pressure electrolysis conditions employed. It is interesting to note that alkane dimer only becomes the major product at room temperature and atmospheric pressure in aqueous solution when the acid used is n-hexanoic or longer. The olefin sideproducts from these acids are liquids at room temperature.

The notion that alkane dimer is favored by high current densities because the alkane dimer is the product of a second order radical coupling reaction has been prevalent in the literature for some time. An alternative explanation is based on the fact that in the absence of competitive reactions, the radical concentration on the electrode surface will simply build up until the rate of dimerization equals the rate of generation. It may be that the formation of lipophilic products, alkane dimer and olefin, augment the formation of alkane dimer in the sense that their presence impedes the flow of water to the electrode surface necessary to stabilize carbonium ion formation required for the production of sideproducts. Muck and Wilson (8) have proposed an explanation of increased dimer yield with long chain carboxylates due to stacking or layering of the organic acids caused by hydrophobic attraction between the alkyl chains. This stacking occurs perpendicular to the electrode surface and tends to trap CO_2 between the anode and the alkyl radicals formed after decarboxylation. The separation of alkyl radicals from the electrode surface will tend to decrease the efficiency of the second electron transfer to form the carbonium ion and favor dimer formation. Our data do not contradict this explanation. The exclusion of water from the electrode surface by lipophilic products, however, also helps to explain the difference observed in dimer yields for the shorter chain (C_4-C_6) carboxylates at elevated pressure.

Table VI. Vapor pressure of olefins 35°C

Olefin	BP_{760}	ΔH_V cal/g*	ΔH_V cal/mol	Vapor pressure, 35°C
Propene	−47.7°C	104.6 (47.7°C)	4393	1.4 MPa
1-Butene	− 6.3°C	86.8 25°C	4861	0.34
cis-2-Butene	+ 3.7°C	86.8 25°C	4861	0.25
trans-2-Butene	0.88°C	91.8 25°C	5141	0.28
1-Pentene	30°C	85 est	5950	0.12
2-Pentene	37.1°C	85 est	5950	0.9

* From Lange, "N.A. Handbook of Chemistry," 9th ed., Handbook Publishers, Sandusky, Ohio (1956).

The explanation is further supported by a series of experiments in which butanoic acid and mixtures of butanoic and hexanoic acids were the reacting species. These experiments were performed at room temperature, atmospheric pressure, and 0.28 A/cm² current on platinum anodes. The aqueous electrolysis solutions contained 1.4M butanoic acid or 0.7M butanoic plus 0.7M hexanoic acids. Solutions were neutralized with sodium hydroxide to pH 7. The results (summarized in Table VII) show a marked increase in the formation of 1-electron product from butanoic acid in the presence of hexanoic acid. Both experiments where butanoic-hexanoic mixtures were used produced more alkane dimer from butanoic (hexane and octane) and less olefin than the experiment using butanoic alone. The ratio of butanoic to hexanoic acid reacted was 1:3 when equimolar concentrations were used and 1:2 when twice as much butanoic as hexanoic was used. This may result from the more favorable partitioning of hexanoic acid from the bulk aqueous solution into the lipophilic layer surrounding the anode.

The shift of butanoic acid products to 1-electron products in the presence of hexanoic acid may be explained by a similar mechanism as the shift caused by increasing the reactor pressure—providing a more substantial lipophilic layer. Thus, the product distribution (1-electron *vs.* 2-electron oxidations) is controlled by the integrity of the lipophilic layer and its effectiveness in excluding water from the anode.

The significance of the ability to increase dimer yields at elevated pressures can best be appreciated by quoting Eberson (6) in a review article on the electrochemical behavior of carboxylic acids:

"Since the possibility of two competing pathways in the Kolbe reaction exists, the immediate prob-

Table VII. Product distribution from electrolytic oxidation butanoic hexanoic acid mixtures*

Product	% Yield from butanoic alone	% Yield from 0.7M butanoic + 0.7M hexanoic		% Yield from 1.4M butanoic + 0.7M hexanoic	
	Butanoic	Butanoic	Hexanoic	Butanoic	Hexanoic
Propane	2.0	4.7	—	2.5	—
Propene	31.1	15.6	—	10.7	—
n-Hexane	17.0	21.9	—	31.5	—
n-Octane	—	31.3	9.5	45.3	26.9
Propanols	45.7	15.6	—	2.9	—
Esters	4.0	11.0	3.3	7.0	4.4
Decane	—	—	66.4	—	49.8
Pentanols	—	—	4.7	—	0.3
Pentane	—	—	3.3	—	4.9
Pentenes	—	—	12.8	—	13.7

* Percent yields are based on mols acid reacted to form products recovered. One mol of each acid is reacted to form each mol of n-octane.

lem to answer is whether one can influence the direction of a given process by proper manipulation of experimental variables so that either the radical or carbonium ion mechanism is favored. As we shall see, unidirectional selectivity can easily be achieved, in that one can always find conditions to favor the cationic mechanism; on the other hand, in many cases, because of structural features in the substrate, it may not be possible to realize the radical pathway even under the most favorable experimental conditions.

In short, to date, Kolbe electrolysis has not been used commercially for the conversion of mixed and/or dilute organic acids to hydrocarbons because no technique was available whereby the yield of alkane dimer could be increased above those which have been observed for years, as given in Table I. By running electrolyses at elevated pressures, these values have been substantially exceeded in the current work.

Acknowledgment

This work was carried out through the sponsorship of the Department of Energy, Division of Advanced Energy Projects, Office of Basic Energy Sciences under Contract No. DE-AC02-81ER10914-1 and the direction of Dr. Ryszard Gajewski.

Work performed at Dynatech Research and Development Company, Cambridge, Massachusetts 02139.

Manuscript submitted Jan. 31, 1983; revised manuscript received April 25, 1983.

Dynatech Research and Development Company assisted in meeting the publication costs of this article.

REFERENCES

1. H. Kolbe, *Ann. Chem.*, **69**, 257 (1849).
2. H. Hofer and M. Moest, *Ann. Chem.*, **323**, 284 (1902).
3. W. J. Koehl, Jr., *J. Am. Chem. Soc.*, **86**, 4686 (1964).
4. J. H. P. Utley, in "Techniques of Chemistry," Vol. 5, N. L. Weinberg, Editor, p. 793, Wiley, New York (1974).
5. B. C. L. Weedon, *Quart. Rev. (London)*, **6**, 380 (1952).
6. L. Eberson, in "Organic Electrochemistry," M. Baizer, Editor, p. 469, Marcel Dekker, New York (1973).
7. M. J. Allen, "Organic Electrode Processes," Reinhold, New York (1958).
8. D. L. Muck and E. R. Wilson, *This Journal*, **117**, 1358 (1970).

Polarographic and Potentiostatic Reduction of Carbodiimides in Nonaqueous Solvents

R. C. Duty and M. Garrosian

Chemistry Department, Illinois State University, Normal, Illinois 61761

ABSTRACT

The polarographic reduction of unsubstituted and substituted phenyl carbodiimides in dimethylformamide and acetonitrile reduced in one wave ($E_{\frac{1}{2}}$ = 1.48-1.87 at 25°C *vs.* Ag/AgBr reference electrode). A plot of E_{dme} *vs.* $(i/i_d\text{-}i)$ revealed a one-electron reduction for the rate controlling step. A postulated mechanism for this reduction was a carbene intermediate. A large scale reduction in dimethylformamide produced diphenylurea which was formed by the carbene abstracting oxygen from the solvent. In acetonitrile as the solvent, the abstraction of hydrogen was not possible, and the carbene was reduced to *N,N*-diphenylmethanediamine. A Hammett substituent plot produced a reaction constant (ρ) of +0.489 which was in agreement with the suggested mechanism.

Carbodiimides have not been previously studied polarographically, but cumulated double bonds have been reduced by Peover *et al.* (1). Peover polarographically reduced tetraphenylallene and found that allene structures were reduced by one electron to a radical anion which was rapidly protonated and reduced by a second electron to the allyl carbanion. Brominated allenes have been reduced by Simonet *et al.* (2), but in their study, the bromo group was reduced in two one-electron steps to the allene carbanion which is a resonance structure of a three-propyne anion.

Carbenes have been generated electrolytically, and Wawzonek *et al.* (3) were the first to report such an intermediate dichlorocarbene generated from the electrolytic reduction of carbon tetrachloride. A second reported carbene intermediate was generated electrolytically from 9,9-dichlorofluorene where difluorenylidene was the dimerized product of the carbene, fluorenylidene (4).

This investigation was begun to ascertain if carbenes could be generated from the carbodiimide functional group (Ph—N=C=N—Ph). With cumulated double bonds, flanked on either side with strong electronegative nitrogen atoms, a two-electron reduction would result in a carbene intermediate (PhNH—C̈—NH—Ph). Isolated products, Hammett reaction constant, and the number of electrons involved in the reduction steps were used to prove the existence of the carbene intermediate.

Experimental

Apparatus.—A Heath Model EUW-401 polarograph with a Heath Model EUW-19-2 operational amplifier was used to record the polarograms on a Heath recorder EUW-20A. The potentiostat used in the large scale reductions was a Beckman Electroscan 30 with a reference voltage span of ±5.0V with ±10 mV accuracy. Infrared spectra were recorded on a Beckman IR-8 spectrophotometer and NMR spectra were recorded on a Hitachi Perkin-Elmer R-20 high resolution NMR spectrophotometer. The mass spectrometer was a Finnigan Model 3000.

Reagents.—Fisher reagent grade *N,N*-dimethylformamide was purified as previously described (4). The supporting electrolyte was Eastman reagent grade tetra-n-butylammonium bromide (0.175M) and was recrystallized several times from anhydrous ethyl acetate until polarographically pure.

Acetonitrile (Mallinckrodt Nanograde) was refluxed with sodium hydride (approximately 1 g/liter) and distilled, under nitrogen, through a 30 cm fractionating column filled with glass helices. The first and last 10% fractions were discarded, and the distilled acetonitrile was stored under nitrogen.

Carbodiimides.—Seven aromatic carbodiimides (p-H, p-CH_3, p-CH_3O, p-Br, p-Cl, m-CH_3, and o-F) were prepared for this study by the method of Campbell (5).

Diphenylcarbodiimide, bp 130°-131°C at 0.5 Torr, 90% yield. Bis-(p-chlorophenyl)-carbodiimide, mp 56°-57°C (lit. mp 56°-57°C) (5). 4,4'-Ditolylcarbodiimide, mp 54°-55°C (lit. mp 56.5°-57.5°C) (5), 72% yield. 3,3'-Ditolylcarbodiimide, 145°-146°C at 0.375 Torr, 94% yield. Bis-(o-fluorophenyl)-carbodiimide, 147° at 0.05 Torr, 96% yield. Bis-(p-methoxy-phenylcarbodiimide) mp 51°-52°C (lit. mp 52°-53°C) (6), 98% yield. Bis-(p-bromophenyl)-carbodiimide, mp 64°-65°C, 89% yield. o-Fluoro and p-bromo had not been prepared previously and these were confirmed by their characteristically strong infrared stretching frequency for carbodiimides between 2000 and 2140 cm^{-1}.

The catalyst, 3-methyl-1-phenyl-3-phosphalene-1-oxide, for the carbodiimide synthesis was prepared from dichlorophenyl phosphine and isoprene in 40% yield, bp 160°-162°C at 0.40-0.45 Torr (6).

Procedure.—A current-voltage curve was recorded for a solution concentration of the order of 1×10^{-3}M in carbodiimide and 0.175M for supporting electrolyte. The capillary had a drop time of 3.45 sec (6.92 mg/drop) at 60 cm of mercury with an $m^{2/3}t^{1/6}$ value of 4.46.

The large scale reduction cell (4) had approximately 25 ml compartments of catholyte and anolyte. The catholyte was charged with 1g of carbodiimide and 20 ml of 0.175M supporting electrolyte. The anolyte contained only the 0.175M supporting electrolyte. The cathode was a 7 cm^2 pool of mercury which was stirred magnetically, and both anolyte and catholyte were degassed with purified nitrogen before and during the reduction. The reductions were conducted in a 0°C constant temperature bath, and the reduction potential was −1.95V *vs.* an Ag/AgBr reference electrode. The reduction time was 10 hr, and the current had dropped to 9 mA. During the course of the reduction, the clear catholyte turned dark green and the anolyte dark red.

The catholyte was rotary evaporated to a dark viscous liquid (2.82g) which was extracted with ether. The ether extract yielded 0.19g of a yellow-white material which melted above 400°. This ether extract contained less than 1% diphenylcarbodiimide as compared by infrared with a known 1% solution. The ether insoluble residue was washed with distilled water and produced 0.710g of crude diphenylurea mp 234°-239°C. Recrystallization from 95% ethanol yielded 0.312g (28.5% yield) of pure diphenylurea, 236°-237°C; ir (KBr) 3280, 1601 cm^{-1} (lit. mp 234°-236°C) (7).

The reduction of diphenylcarbodiimide in acetonitrile was accomplished in the exact manner as in dimethylformamide except that the reduction was done at a potential of −1.90V *vs.* Ag/AgBr electrode and was run for a total time of 22 hr. The initial current was 140 mA which fell to 0.2 mA at the end of the reduction. The catholyte was dark green at the end of the reduction and had no evidence of any diphenylcarbodiimide peak between 2100 and 2200 cm^{-1} in the infrared.

The catholyte was rotary evaporated to dryness (2.62g) and washed with 40 ml of ether. Evaporation of the ether produced a yellow-white residue which was recrystallized once from 95% ethanol and twice from n-hexane to yield 0.043g of 4,4'-diaminodiphenylmethane, 4.3% yield, mp 96°-98°C, lit. mp 93°C (8), IR (KBr) 3390, 3260, 3060, and 1490 cm^{-1} mass spectrum (70 eV) m/e (vol. intensity) 198 (9), 197 (18), 196 (63), 106 (100), 105 (63). Molecular weight range 100-210.

Results and Discussion

A potentiostat (Beckman Electroscan 30) was used in conjunction with the Heath polarograph (Model EUW 401) to establish a possible mechanism for the reduction of aromatic carbodiimides. The reduction of

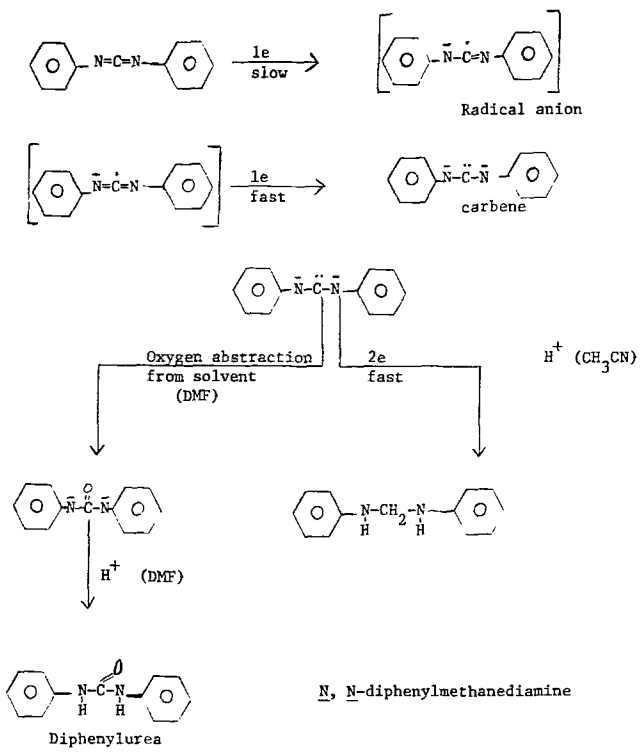

Fig. 1. Proposed mechanism for the reduction of diphenylcarbodiimide.

diphenylcarbodiimide may proceed via a one-electron rate controlling step to a radical anion which rapidly reduces to a carbene via a second fast electron addition. A proposed mechanism for this reduction is given in Fig. 1.

Seven different carbodiimides were prepared for this study and reduced polarographically. The polarographic results for these carbodiimides are given in Table I where their half-wave potentials and diffusion current constants are given. The half-wave potentials were plotted against the Hammett substituent constants, and this graph is shown in Fig. 3. The slope of this plot, the reaction constant (ρ), was +0.489. The fact that a positive slope exists indicates there is a mechanistic relationship between the half-wave potential and the substituent groups. It was shown (10, 11) for positive reaction constants for polarographic reductions that the reactant in the rate controlling step is stabilized by electron contributing groups. If one assumes two one-electron steps in the reduction of carbodiimides (see Fig. 1), the first step would have to be the rate determining step to be in accord with the Hammett plot of Fig. 2.

To ascertain the number of electrons involved in the rate controlling step, the polarograms were analyzed according to the procedure of Meites (12). In this method a plot of E_{dme} *vs.* $\log \frac{i}{i_d - i}$ was constructed for diphenylcarbodiimide as shown in Fig. 3. The values of D_{dme} and i were taken at each equal incre-

Table I. Polarographic half-wave potentials and diffusion current constants for aromatic diphenylcarbodiimides

Compound	Half-wave potential ($E_{1/2}$)	Diffusion current constant (I_d)
ϕ—N=C=N—ϕ	1.64	2.02
p—CH_3—ϕ—N=C—N—ϕ—CH_3—p	1.78	1.34
m—CH_3—ϕ—N=C=N—ϕ—CH_3—m	1.77	1.15
p—CH_3—O—ϕ—N=C=N—ϕ—OCH_3—p	1.87	1.30
o—F—ϕ—N=C=N—ϕ—F—o	1.62	0.937
p—Br—ϕ—N=C=N—ϕ—Br—p	1.54	0.804
p—Cl—ϕ—N=C=N—ϕ—Cl—p	1.48	1.00

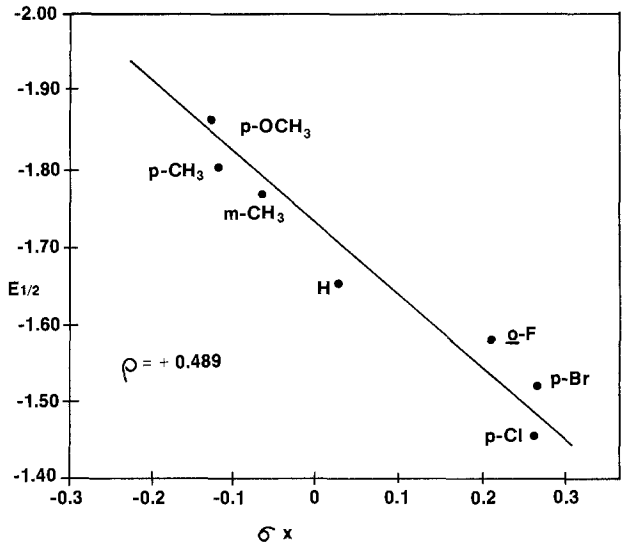

Fig. 2. Graph of $E_{1/2}$ values vs. sigma values of substituent groups of carbodiimides.

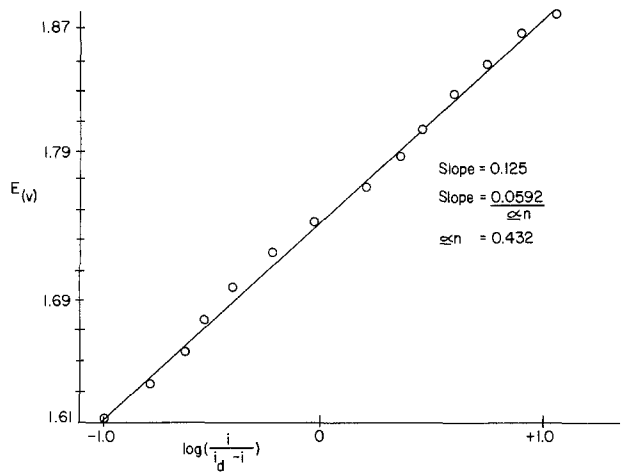

Fig. 3. Graph of $E_{1/2}$ values vs. log $(i/i_d - i)$ of diphenylcarbodiimide at 60 cm mercury height.

ment of 20 mV where the scan rate was stopped and the current read. This operation was done through the rising portion of the polarogram. The slope of this plot is equal to $-0.054/\alpha n$ where α is the transfer coefficient and n is the number of electrons in the rate controlling step. The value of αn has been shown to fall in the range of 0.4 to 0.6 for a one-electron reduction of a rate controlling step (13, 14). Consequently, since the αn from Fig. 3 was 0.432 for diphenylcarbodiimide, this is consistent with a mechanism which postulates the addition of one electron in the rate controlling step. Therefore, the Hammett plot plus the one-electron addition in the rate controlling step support the mechanism postulated in Fig. 1.

To ascertain whether the polarographic currents were kinetic currents, adsorption currents, or diffusion controlled currents, four carbodiimides (diphenyl, 4,4'-ditolyl, bis-(p-methoxylphenyl, and bis(p-chlorophenyl) each were run at 40, 50, 60, and 70 cm heights. The diffusion currents were plotted *vs.* the square root of height and every plot gave a linear positive slope which indicated a diffusion controlled current was produced.

To help substantiate the mechanism given in Fig. 1, the diphenylcarbodiimide was reduced potentiostatically and the products of the reduction were analyzed. In the solvent, dimethylformamide, two products could be expected to form: *N,N*-diphenylmethanediamine ($PhNHCH_2NHPh$) and/or diphenylurea ($PhNHCONHPh$). The latter product is produced from an oxygen abstraction reaction of the carbene with the solvent. Carbenes and atomic carbon are known to abstract oxygen, and Skell (15) has reported that oxygen is abstracted from acetone by atomic carbon to form carbon monoxide. In this laboratory, the carbene from 9-anthrone was shown to abstract oxygen from phosphorus oxychloride and, also, triethylphosphate as illustrated (16)

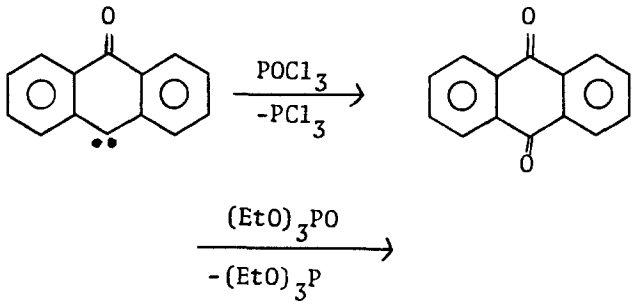

In each of these cases, the bond energies favor the formation of anthraquinone. Bond dissociation energies (17) for $POCl_3$ and $(EtO)_3PO$ are 127.5 and 150.7 kcal/mol, respectively, for the phosphorus-oxygen bond, and the bond energy for a carbon-oxygen double bond is 185.6 kcal/mol (18).

If the reaction between the carbene and dimethylformamide is to occur, the bond energy for the carbon-oxygen double bond should be stronger for diphenylurea than for dimethylformamide. Unfortunately, these bond energies are not available, but one would expect the resonance contribution from two nitrogens in the urea molecule to add additional bond strength to the carbon-oxygen double bond as compared to one nitrogen for dimethylformamide.

When 1g of diphenylcarbodiimide was reduced at a stirred mercury pool cathode in dimethylformamide, no *N,N*-diphenylmethanediamine was produced, but a 28.5% yield of diphenylurea was found. Every effort was made to ensure that the dimethylformamide was anhydrous; to maintain these anhydrous conditions, dry nitrogen was bubbled through the cell throughout the entire potentiostatic reduction period. Consequently, since diphenylurea was formed, the oxygen must have come from the oxygenated solvent, dimethylformamide.

To further prove the abstraction of oxygen reaction, the potentiostatic reduction was run in an aprotic non-oxygenated anhydrous solvent, acetonitrile. When these reduction products were analyzed, as discussed in the experimental section, no diphenylurea was formed. However, from the ether extract, after two recrystallizations, a 4.3% yield of 4,4'-diaminodiphenylmethane was recovered. Wagner (8) had earlier shown that *N,N*-diphenylmethanediamine would easily rearrange to *N*-(4-aminophenylmethyl)-aniline and finally to the 4,4'-diaminodiphenylmethane.

Manuscript submitted Nov. 16, 1982; revised manuscript received May 26, 1983.

REFERENCES

1. R. Dietz, M. E. Peover, and R. Wilson, *J. Am. Chem. Soc.*, **68**, 75 (1968).
2. J. Simonet, H. Doupeux, and D. Bretelle, *C.R. Acad. Sci. Paris*, **270**, 59 (1970).
3. S. Wawzonek and R. C. Duty, *This Journal*, **108**, 1135 (1961).
4. R. C. Duty, G. Biolchini, and W. Matthews, *Anal. Chem.*, **46**, 167 (1974).
5. T. W. Campbell and J. J. Monagle, *J. Am. Chem. Soc.*, **87**, 3673 (1962).
6. W. B. McCormack, U.S. Pat. 2,633,737 (1953); *C.A.*, **49**, 7601a (1955).
7. H. Hentschel, *J. Prakt. Chem.*, **27**, 449 (1883).
8. E. C. Wagner, *J. Chem. Soc.*, **56**, 1934 (1946).
9. J. W. Sease, F. G. Burton, and S. L. Nickol, *J. Am. Chem. Soc.*, **90**, 2595 (1968).
10. J. Seare and P. Chang, *ibid.*, **86**, 3154 (1964).

11. A. Streitwieser, Jr., and C. Perrin, *ibid.*, **86**, 4938 (1964).
12. L. Meites, "Polarographic Techniques," 2nd ed., p. 1, Interscience Publishers, New York (1965).
13. R. Annion, R. E. Erickson, J. Michalovic, and B. McKay, *J. Am. Chem. Soc.*, **88**, 4424 (1966).
14. R. E. Erickson, R. Annino, M. D. Scanlon, and G. Zany, *ibid.*, **91**, 1767 (1969).
15. P. S. Skell, J. H. Plonka, and R. R. Engel, *ibid.*, **86**, 4938 (1964).
16. R. E. Hallstein, Master's Thesis, Illinois State University (1969).
17. C. T. Mortimer, "Reaction Heats and Bond Strengths," p. 189, Addison-Wesley Publishing Co., Inc., New York (1962).
18. K. S. Pitzer, *J. Am. Chem. Soc.*, **90**, 2140 (1948).

Oxygen Electrocatalysis on Some Oxide Pyrochlores

H. S. Horowitz, J. M. Longo, and H. H. Horowitz*

Exxon Research and Engineering Company, Corporate Research Laboratories, Linden, New Jersey 07036

ABSTRACT

Pyrochlore structure oxides described by the formula $A_2[B_{2-x}A_x]_{7-y}$, where A = Pb or Bi, B = Ru or Ir, $0 \leq x \leq 1$ and $0 \leq y \leq 0.5$, have been evaluated for oxygen electrocatalysis. In alkaline electrolyte between room temperature and 110°C, these materials display significantly lower polarizations than any other catalyst for O_2 evolution and are among the best for O_2 reduction. Rotating ring disk experiments have not detected soluble H_2O_2 as an intermediate during O_2 reduction. It has been established that reasonable activity maintenance is achievable over relatively long periods (500-1800 hr).

One particularly troubling aspect of modern oxygen electrochemistry technology is the lack of reversible bidirectional electrocatalysts, *i.e.*, there are few known materials that can reversibly, or nearly reversibly, catalyze both the electroreduction and electroevolution of oxygen. Metal oxides and mixed metal oxides have shown promise as oxygen electrocatalysts (1, 2), but are often limited by low electric conductivity or low specific surface area.

One family of oxides that does function bidirectionally and reduces activation overvoltages for both O_2 reduction and evolution has been discovered (3, 4). These catalysts, which have the pyrochlore structure, may be described by the formula $A_2[B_{2-x}A_x]O_{7-y}$ where: A = Pb or Bi; B = Ru or Ir; $0 \leq x \leq 1$ and $0 \leq y \leq 0.5$. In alkaline electrolyte between room temperature and 110°C, these materials display significantly lower polarizations than any other catalyst for O_2 evolution and are among the best for O_2 reduction. This paper describes the behavior of these catalysts during oxygen reduction and evolution. Data on the ability of these catalysts to promote the oxidation of organics including alcohols, ketones, and olefins (5) have already been presented. The data presented here deal primarily with the $Pb_2[Ru_{2-x}Pb_x^{4+}]O_{6.5}$ series, with which the great majority of our experimental data has been collected.

Experimental

The synthesis and characterization of the pyrochlore oxide catalysts used in this study have been reported in Ref. (3). The alkaline solution synthesis technique which has previously been reported (6), eliminated the need for any reaction at elevated temperature and thus provided pyrochlore oxide catalysts with high surface area (50-200 m^2/g, by the BET method). Because the solution-synthesized catalysts demonstrated superior catalytic activity, and because this synthesis route represents the simplest and most reproducible method of preparing pyrochlore electrocatalyts over a wide compositional range, most of the electrocatalytic results presented here were obtained on materials synthesized by this solution route.

Teflon-bonded porous electrodes (5 cm^2 in area) were fabricated according to the following procedure: weighed amounts of catalyst and Teflon (du Pont No. 42 suspension) were gently mixed with a few drops of water to coagulate the Teflon. The electrodes were always 20 weight percent (w/o) Teflon. The catalyst loading usually employed was approximately 60 mg/cm^2. The gummy product was then spread on a gold-expanded metal screen and pressed dry between filter paper. The electrode was then cold-pressed for 0.5 min at 2000 psi, allowed to air dry for a minimum of 30-45 min, and then hot pressed at 325°C, 500 psi for 30 min. The hot pressing was usually done in an inert atmosphere since the presence of oxygen often led to combustion of the organic constituents in the electrode. After cooling, the electrode was weighed to determine its loading and then placed in the electrochemical cell for testing.

The cell, schematically illustrated in Fig. 1, consisted of a thermostated liquid phase compartment and a gas phase compartment. The liquid compartment contained the electrolyte, counterelectrode, saturated calomel reference electrode (in communication with the test electrode via a Luggin capillary), and magnetic stirrer. The gas phase compartment contained a gas inlet and outlet and a stopcock to drain off any condensate. The test electrode, situated between the two compartments, was held in place between two Teflon washers with an annular gold current collector pressing against it. In a few cases specifically mentioned in the text, the working electrode was submerged in the electrolyte and no gas phase compartment was used.

The cell was connected to a Princeton Applied Research Model 173 potentiostat equipped with a programmer and logarithmic current convertor. Outputs of potential *vs.* log current density (based on geometric surface area) were directly recorded. The electrochemical potential was experimentally measured

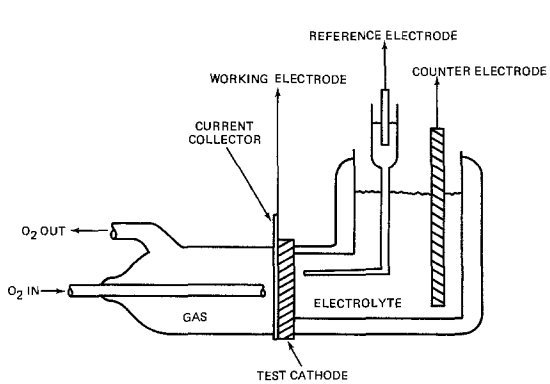

Fig. 1. Interface maintaining electrode cell

* Electrochemical Society Active Member.
Key words: inorganic, electrode, overvoltage, stoichiometry.

against a saturated calomel reference electrode (SCE). This potential was later referenced to the reversible hydrogen electrode (RHE) by experimentally measuring, in the same electrolyte, the potential of an SCE against a freshly platinized platinum coil contained in a tube through which hydrogen was bubbled. The referencing of each SCE *vs.* RHE was carried out at least once per week to ensure that the reference electrodes were not changing with time. All polarization curves presented in this paper are experimentally obtained and are not *IR* corrected. The electrode resistances, as measured by the application of voltage steps, were of the order of 0.5 Ω-cm².

Performance curves were generally obtained at a programmed polarization rate of 0.2 mV/sec The only exceptions were those steady-state performance curves referred to in the text. Life tests were usually designed to run continuously at constant current density while the electrode potential was monitored. During life tests, titrations of the electrolyte were made at least every few days, and water or fresh alkali added, if necessary, to maintain the appropriate pH.

X-ray diffraction was routinely performed on the electrodes after testing to detect any major phase changes. Significant changes in the lattice parameter could also be detected in this manner. Catalyst stability was also monitored by analyzing the electrolytes for the presence of metal cations (Pb, Bi, Ru). These analyses were performed by differential pulse polarography on a dropping mercury electrode.

Diagnosis of the causes of electrode failure was aided by chronoamperometric measurements which were made following the application of a voltage step to the electrode. These current *vs.* time plots (fraction of a second time scale) were recorded on a Tektronix Model 5103N data storage oscilloscope. The electrode was kept under nitrogen for this experiment. These measurements were usually made on an electrode at various stages during the course of a life testing experiment.

The stability of lead ruthenate as a function of its composition, surface area, and method of preparation were also monitored in separate immersion tests. Catalyst powders, Teflon-bonded onto gold screens, as above, were suspended in stirred 3*N* KOH at room temperature and potentiostated at 1.25V *vs.* SCE. The counterelectrode was maintained in a separate chamber separated by a porous glass frit to minimize metal deposition. Each day samples were analyzed for lead and ruthenium by differential pulse polarography using a Princeton Applied Research Electrochemistry System Model 170. When the concentrations reached a constant value, the electrolyte was changed and the test continued.

Tests for the formation of hydrogen peroxide as an intermediate in the reduction of oxygen on lead ruthenate were carried out on a rotating ring disk electrode. Both the ring and the disk were made of gold, but the disk was depressed about 1 mm below the surface and the space thus formed was packed with powdered lead ruthenate bonded by 20% Teflon. Tests were run at room temperature in 0.1*N* NaOH at 1000, 2000, and 3000 RPM. The ring was kept at +150 mV *vs.* the saturated calomel reference electrode to oxidize any H_2O_2 to O_2. The disk was held at varying potentials from 0 to −510 mV/SCE at 30 mV intervals and the disk and ring were monitored for current.

Results

Oxygen reduction.—Figure 2 compares steady-state polarization curves for the electroreduction of O_2 on a typical pyrochlore catalyst, $Pb_2[Ru_{1.42}Pb_{0.58}^{4+}]O_{6.5}$, and 15 w/o platinum on carbon. The latter was considered representative of conventional supported noble metal electrocatalysts. The activities of both catalysts

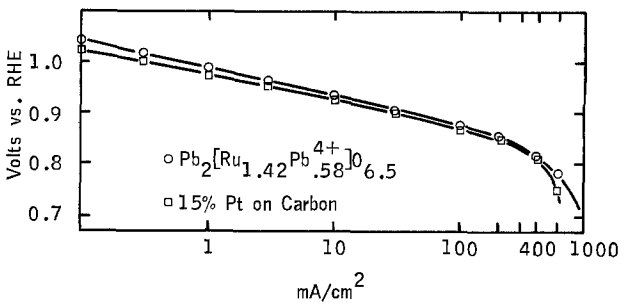

Fig. 2. Steady-state polarization curves for O_2 reduction in 3M KOH, 75°C on $Pb_2[Ru_{1.42}Pb_{0.58}^{4+}]O_{6.5}$, and 15 w/o Pt on carbon. Catalyst loadings are 60 and 50 mg/cm², respectively.

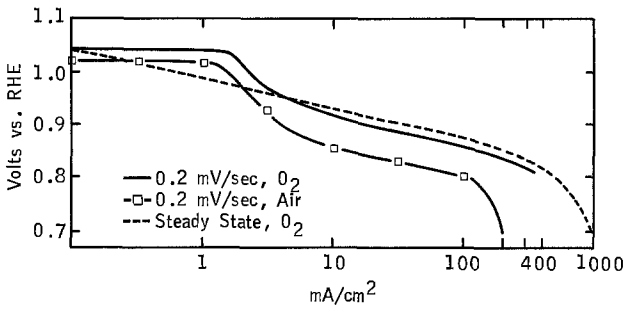

Fig. 3. O_2 reduction in 3M KOH, 75°C on $Pb_2[Ru_{1.42}Pb_{0.58}^{4+}]O_{6.5}$ using O_2 (dynamic and steady-state polarization) and air (dynamic polarization only) as feed gases. Catalyst loading is 60 mg/cm².

are quite comparable.[1] Figure 3 presents oxygen reduction curves for the same pyrochlore catalyst run under steady-state as well as dynamic scan conditions (0.2 mV/sec). The constant polarization at low current densities observed for the pyrochlore run under dynamic scan conditions is a consequence of pseudocapacitance charging currents. (Lead ruthenate with surface areas of 60-80 m²/g has a pseudocapacitance of more than 100 farads/g; thus, voltammograms under N_2 at 0.2 mV/sec showed capacitance currents of 3-8 mA/cm².) However, it is apparent that in the current density range of practical interest (*i.e.*, ten to several hundred mA/cm²) there is little difference between the curves. Thus, the dynamic scan conditions are adequate for providing data that realistically characterize the inherent catalytic activity of these materials at significant current densities. Also included in Fig. 3 for comparison is a polarization curve obtained using air as the feed gas.

Figure 4 illustrates the O_2 electroreduction activity of a number of lead ruthenate pyrochlores, $Pb_2[Ru_{2-x}Pb_x^{4+}]O_{6.5}$, where $0 \leq x \leq 1.0$. These data along with that of Table I demonstrate that catalysts of roughly equivalent activity can be synthesized over the entire compositional range. In the two examples where the activity is noticeably lower ($x = 0.04$ and $x = 0.98$), the synthesis conditions were such that the surface areas of the catalysts were quite low (<15 m²/g). Thus, the qualitative conclusion drawn from these activity curves is that the catalyst activity does not appear to be significantly dependent upon composition; surface area does appear to be the predominant factor.

In order to determine whether the electrocatalytic activity of the lead ruthenate pyrochlores was significantly different from RuO_2 and whether the activity

[1] Subsequent work performed in this laboratory by J. S. Batzold and R. B. McCormick, with regard to the comparative oxygen reduction performance of lead ruthenate pyrochlores and carbon-supported platinum, has emphasized the optimization of low loaded electrode structures for both catalysts. This more quantitative study concluded that the specific activity of lead ruthenate (in terms of milliamperes per milligram of noble metal content) is approximately equal, within a factor of two (10-15 mV), to platinum.

Table I. O_2 reduction activity on $Pb_2[Ru_{2-x}Pb_x^{4+}]O_{6.5}$ as a function of composition (test conditions: 3M KOH, 75°C)

Composition (X)	Potential at 100 mA/cm² (mV vs. RHE)	Surface area (m²/g)
0.04	830	5
0.11	880	28
0.18	860	24
0.30	888	89
0.33	895	85
0.41	890	109
0.50	700	83
0.58	926	67
0.65	910	82
0.68	900	63
0.71	905	63
0.82	902	60
0.89	899	57
0.94	881	81
0.98	840	13

of the pyrochlores could possibly be attributed to impurity phases of ruthenium oxide, several comparative tests were performed. Figure 5 compares the oxygen reduction activity of $Pb_2[Ru_{1.42}Pb_{0.58}^{4+}]O_{6.5}$ (67 m²/g) with amorphous hydrated ruthenium oxide (21 m²/g), crystalline RuO_2 synthesized by heat-treating the hydrated ruthenium oxide at 600°C for 48 hr (4 m²/g), and amorphous hydrated ruthenium oxide prepared by precipitation in alkali of a ruthenium nitrate solution (145 m²/g). The results show that each form of ruthenium oxide tested demonstrated activity that was inferior to the lead ruthenate. The amorphous ruthenium oxides imparted a deep amber color (due to the ruthenate ion) to the electrolyte, thereby indicating severe stability problems.

The effect of both temperature and $[OH^-]$ on O_2 reduction activity is shown in Fig. 6. The almost temperature independent behavior most likely resulted

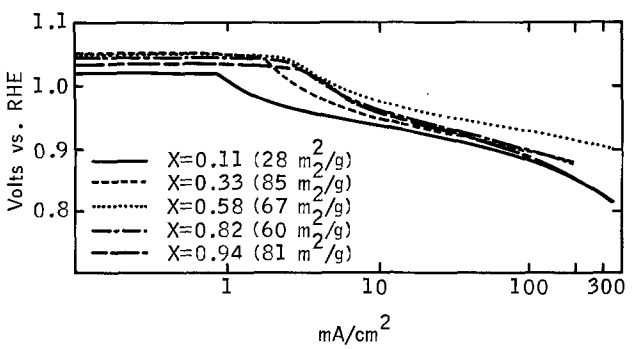

Fig. 4. O_2 reduction in 3M KOH, 75°C on $Pb_2[Ru_{2-x}Pb_{0.58}^{4+}]O_{6.5}$ as a function of X. Catalyst loading is 60 mg/cm².

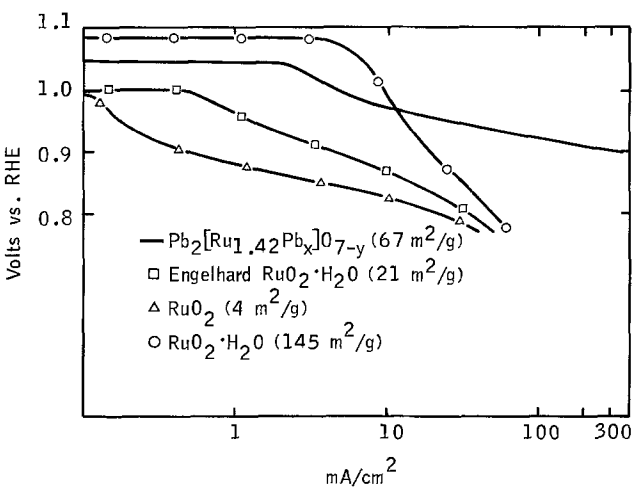

Fig. 5. O_2 reduction in 3M KOH, 75°C on $Pb_2[Ru_{1.42}Pb_{0.58}^{4+}]O_{6.5}$ and several ruthenium oxides. Catalyst loading is 60 mg/cm² in all cases.

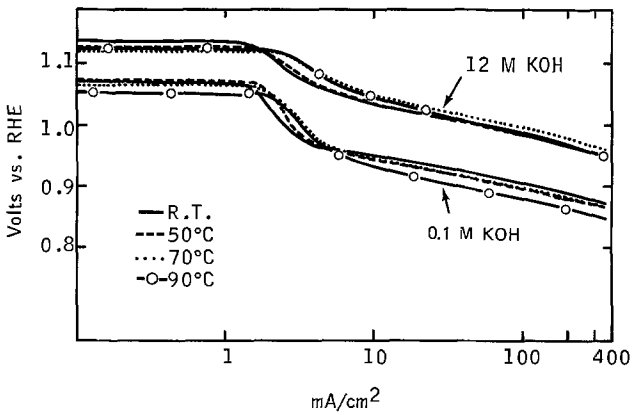

Fig. 6. O_2 reduction in 3M KOH, 75°C on $Pb_2[Ru_{1.41}Pb_{0.59}^{4+}]O_{6.5}$ (67 m²/g) as a function of electrolyte temperature and $[OH^-]$. Catalyst loading is 60 mg/cm².

from the compensating effects of an Arrhenius type behavior *vs.* a decrease in either the hydrophobicity of the electrode or the oxygen solubility of the electrolyte with increasing temperature. The effect of $[OH^-]$ is quite pronounced, with a change from 0.1 to 12M KOH resulting in an increase of O_2 reduction potential of approximately 100 mV relative to the reversible hydrogen potentials in each electrolyte.

In Fig. 7 are shown polarization curves for the reduction of oxygen on a number of bismuth ruthenates, $Bi_2[Ru_{2-x}Bi_x]O_{7-y}$. As was the case with the lead ruthenates, activity does not appear to be significantly dependent upon composition. The level of oxygen reduction activity is seen to be comparable to that obtained with the lead ruthenates.

Oxygen evolution.—Figure 8 shows polarization curves for oxygen evolution on a number of pyrochlores, $Pb_2[Ru_{2-x}Pb_x^{4+}]O_{6.5}$, where $0 < x < 1$. It can be seen from these curves and Table II that catalysts of roughly equivalent activity can be synthesized over very nearly the entire compositional range; surface area again appears to be the predominant factor affecting activity. Note again the predominating effect of pseudocapacitance at low current densities.

The data in Fig. 8 illustrate the fact that $Pb_2[Ru_{2-x}Pb_x^{4+}]O_{6.5}$ pyrochlores are even more effective catalysts for oxygen evolution than they are for oxygen reduction. A typical good $Pb_2[Ru_{2-x}Pb_x^{4+}]O_{6.5}$ catalyst evolves oxygen at 100 mA/cm² at a polarization of approximately 120 mV from the theoretical potential (1.18V *vs.* RHE, 3M KOH, 75°C) as compared to a polarization of approximately 260 mV from

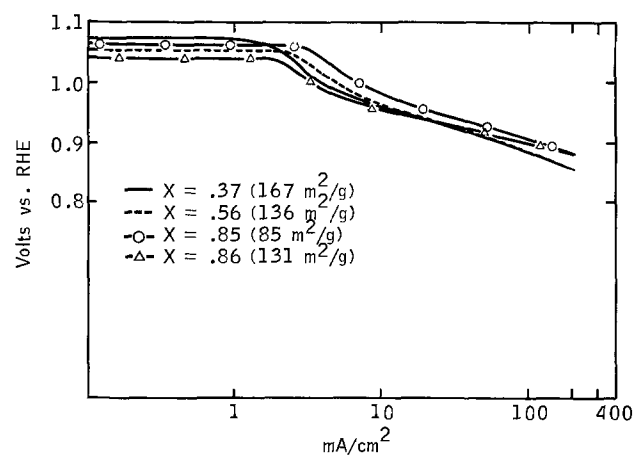

Fig. 7. O_2 reduction in 3M KOH, 75°C on several $Bi_2[Ru_{2-x}Bi_x]O_{7-y}$ catalysts. Catalyst loading is 60 mg/cm².

Table II. O_2 evolution activity on $Pb_2[Ru_{2-x}Pb_x^{4+}]O_{6.5}$ as a function of composition (test conditions: 3M KOH, 75°C)

Composition (X)	Potential at 100 mA/cm² (mV vs. RHE)	Surface area (m²/g)
0.10	1355	12
0.14	1335	33
0.25	1328	28
0.30	1319	39
0.33	1302	85
0.41	1310	109
0.54	1349	74
0.58	1318	67
0.64	1335	85
0.68	1312	63
0.70	1339	30
0.87	1385	15
0.89	1370	92
0.98	1423	14

theory for oxygen reduction at the same current density. This extraordinarily low anodic polarization is further demonstrated by the oxygen evolution activity comparisons, shown in Fig. 9, between $Pb_2[Ru_{1.67}Pb_{0.33}^{4+}]O_{6.5}$ and some competitor electrocatalysts. Data for Pt black, RuO_2, 1% Mg-doped $NiCo_2O_4$ supported on Ni sheet, and Ni sheet are included along with the pyrochlore. It should be noted that RuO_2, while included in the comparison, is found not to be stable in alkali under anodic polarization.

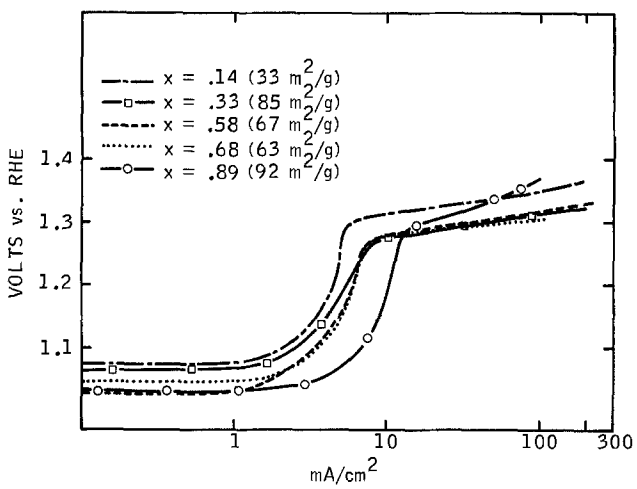

Fig. 8. O_2 evolution in 3M KOH, 75°C $Pb_2[Ru_{2-x}Pb_x^{4+}]O_{6.5}$ as a function of x. Catalyst loading is 60 mg/cm².

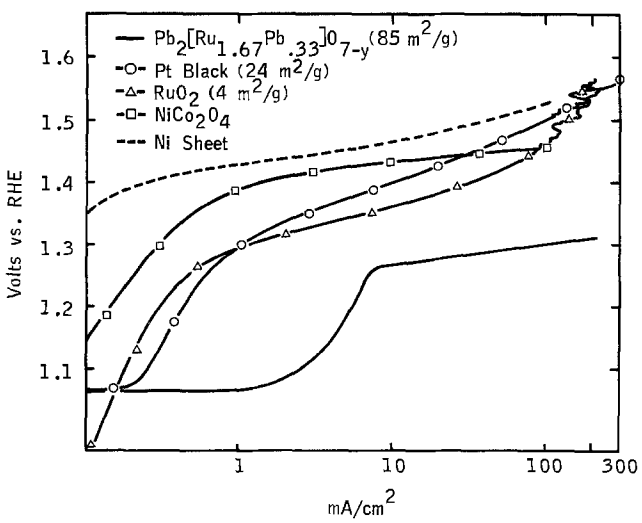

Fig. 9. O_2 evolution in 3M KOH. 75°C on various catalysts. Catalyst loadings were: 60 mg/cm² for the pyrochlore; 33 mg/cm² for the Pt black; and 62 mg/cm² for the RuO_2. The catalyst loading for $NiCoO_4$ spinel was not recorded.

The performance of Ni could probably have been substantially improved by using a higher surface area form of the metal, but there are no reports in the literature of achieving oxygen evolution activities with nickel that are any better than can be obtained with $NiCo_2O_4$.

As illustrated by Fig. 10, polarization of the oxygen evolution reaction decreases with increasing temperature, in contrast to the oxygen reduction reaction. It is a reasonable assumption that the oxygen solubility is not a factor in the evolution reaction. In addition, the loss of electrode structure effectiveness with increasing temperature, invoked for oxygen reduction, is of diminished importance here since maintenance of a delicate three-phase interface (catalyst-gas-electrolyte) is not critical for oxygen evolution. Figure 11, when compared with Fig. 10, shows that a decrease in the OH^- concentration of the electrolyte leads to a decrease in activity.

Electrode life testing/activity maintenance.—Figure 12 shows the results of several galvanostatically controlled life tests of oxygen reduction activity. In Fig. 12a, the catalyst $Pb_2[Ru_{1.83}Pb_{0.17}^{4+}]O_{6.5}$ was tested at 50 mA/cm². The low surface area (8 m²/g) resulted in a relatively low potential. The catalyst contained a trace impurity of RuO_2; however, as was previously demonstrated, this trace impurity cannot contribute significant electrocatalytic activity to the lead ruthenate pyrochlore. The test, which was voluntarily terminated after 1176 hr, was interrupted at 745 hr as well as at 1176 hr, and at each interruption the electrode was removed from the cell, x-rayed, and then reinstalled. No change in the x-ray pattern could be

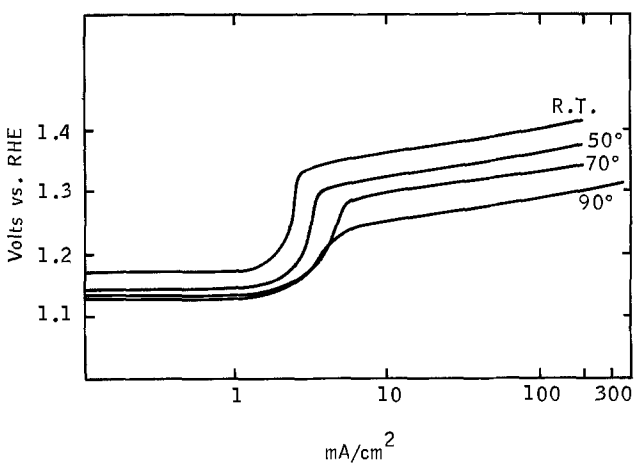

Fig. 10. O_2 evolution in 3M KOH on $Pb_2[Ru_{1.41}Pb_{0.59}^{4+}]O_{6.5}$ (63 m²/g) as a function of electrolyte temperature.

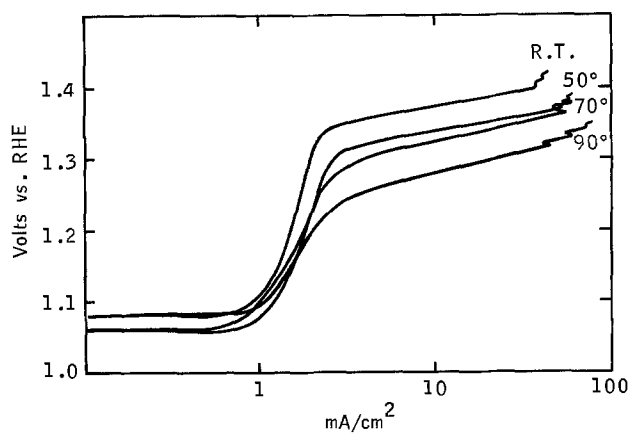

Fig. 11. O_2 evolution in 0.1M KOH on $Pb_2[Ru_{1.66}Pb_{0.34}^{4+}]O_{6.5}$ (74 m²/g) as a function of electrolyte temperature.

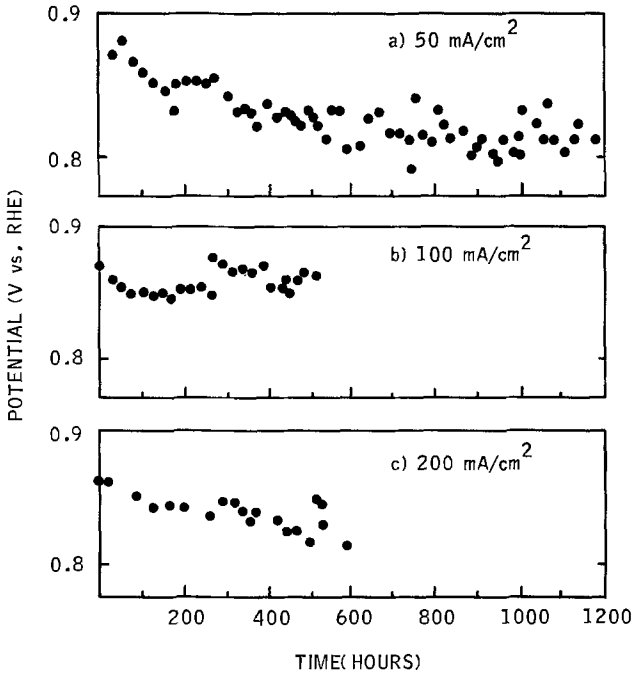

Fig. 12. O_2 reduction life tests in 3M KOH, 75°C on (a) $Pb_2[Ru_{1.83}Pb_{0.17}^{4+}]O_{6.5}$ (8 m^2/g), (b) $Pb_2[Ru_{1.79}Pb_{0.21}^{4+}]O_{6.5}$ (86 m^2/g), and (c) $Pb_2[Ru_{1.44}Pb_{0.56}^{4+}]O_{6.5}$ (76 m^2/g). Catalyst loading was 60 mg/cm^2 in each case.

detected. It can be seen that most of the activity loss was suffered in the first 300 hr.

The results of a life test run on $Pb[Ru_{1.79}Pb_{0.21}^{4+}]O_{6.5}$ (86 m^2/g) at 100 mA/cm^2 is shown in Fig. 12b. There was little voltage decay during the course of the test. The test was voluntarily terminated at 500 hr; at this time the electrode was "weeping" badly (*i.e.*, electrolyte had passed through to the gas side). Figures 13a and 13b show pre-test and post-test polarization curves for oxygen reduction and oxygen evolution, respectively. The decay in oxygen reduction is probably due primarily to the flooded condition of the electrode. This conclusion is supported by the fact that the oxygen evolution activity, which is not dependent upon the maintenance of the three-phase interface, was not affected. The x-ray diffraction pattern of the electrode showed no changes relative to the original catalyst.

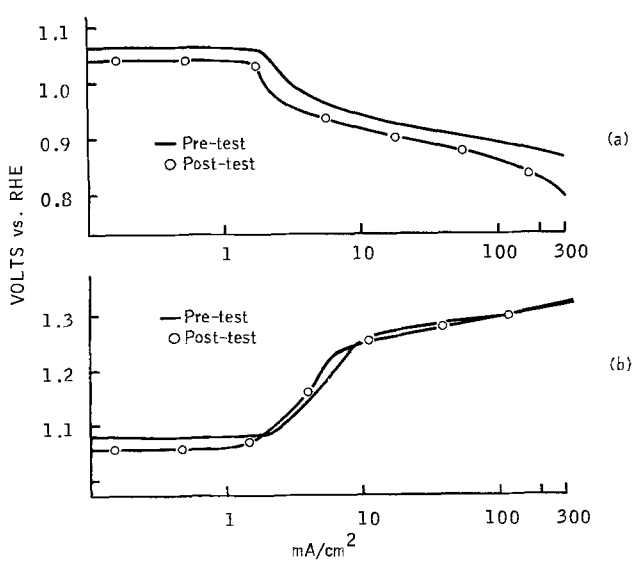

Fig. 13. Pre-test and post-test polarization for (a) O_2 reduction and (b) O_2 evolution in 3M KOH, 75°C for the life tested $Pb_2[Ru_{1.79}Pb_{0.21}^{4+}]O_{6.5}$. (See Fig. 12b.)

An O_2 reduction life test at an even higher current density, 200 mA/cm^2, was run on the catalyst $Pb_2[Ru_{1.44}Pb_{0.56}^{4+}]O_{6.5}$ (76 m^2/g). A steady decline amounting to 43 mV over the 587 hr of the test is observed in Fig. 12c. X-ray diffraction of the tested electrode showed a contraction of the lattice parameter indicating that the extent of lead substitution on the "B" site, x, had decreased (3) yielding the composition $Pb_2[Ru_{1.65}Pb_{0.35}^{4+}]O_{6.5}$.

A chronoamperometric measurement, made on the electrode after completion of the life test, is displayed in Fig. 14 along with the corresponding current decay curve obtained on the electrode before the test. In the pre-test measurement, the initially high currents decay quite rapidly with time. In contrast, the post-test measurement displays a rapid decay of the initial current with time followed by a very slow decay of smaller currents for a longer time. It is speculated that the pretest current decay behavior is characteristic of an electrode where the catalyst is in good contact with the current collector grid, whereas the post-test data is characteristic of separation of the catalyst layer from the grid. The low resistance and capacitance associated with the first decay process of the post-test measurement would correspond to the grid wires and any catalyst still in good contact with them. The second, slower decay process is attributed to the bulk of the porous high surface area catalyst which is separated from the grid by a high electronic resistance.

Figures 15 and 16 show the results of cycling mode life tests. In both experiments, the electrode was operated at 25 mA/cm^2 in O_2 reduction for 8 hr periods followed by 12.5 mA/cm^2 O_2 evolution periods of 16 hr duration. Figure 15 shows the results for $Pb_2[Ru_{1.61}Pb_{0.39}^{4+}]O_{6.5}$ (67 m^2/g) which suffered a steady activity decay. At the 293 hr mark, the elec-

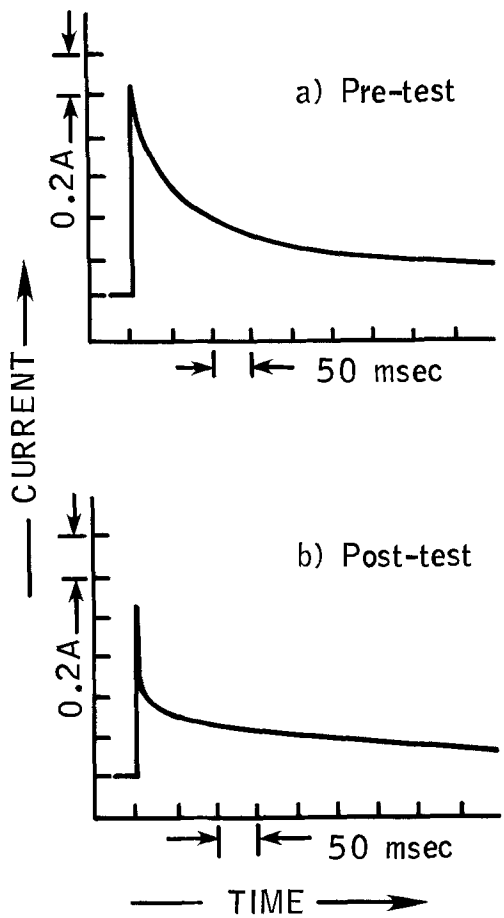

Fig. 14. Pre-test and post-test chronoamperometric measurements on the life tested $Pb_2[Ru_{1.44}Pb_{0.56}^{4+}]O_{6.5}$. (Fig. 12c). $\Delta mV = 30$.

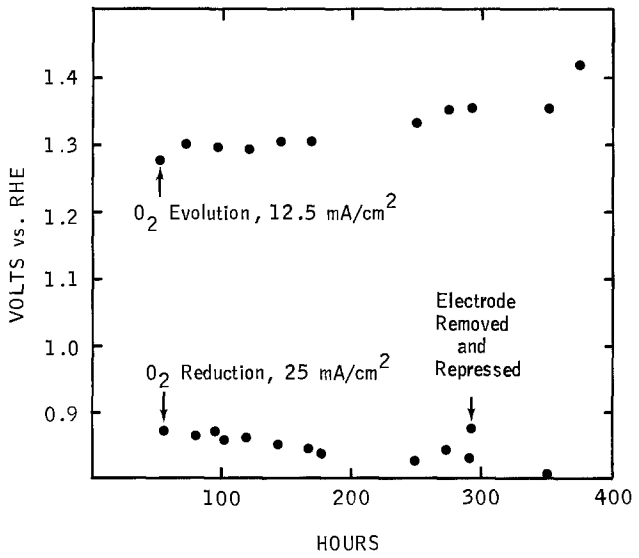

Fig. 15. O_2 reduction/evolution cycling mode life test in 3M KOH, 75°C on $Pb_2[Ru_{1.61}Pb_{0.39}^{4+}]O_{6.5}$ (67 m^2/g). Catalyst loading is 60 mg/cm^2.

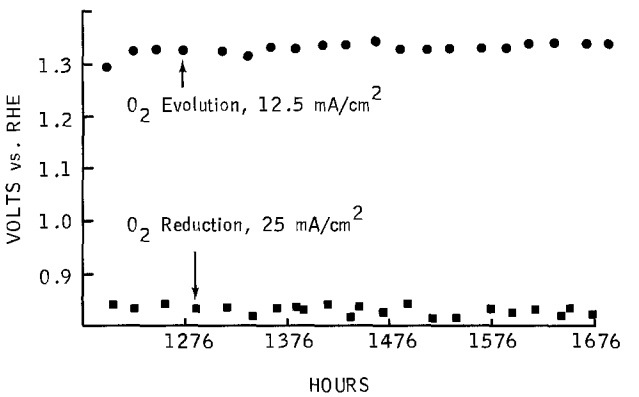

Fig. 16. O_2 reduction/evolution cycling mode life test in 3M KOH, 75°C on $Pb_2[Ru_{1.83}Pb_{0.17}^{4+}]O_{6.5}$ (8 m^2/g). Catalyst loading is 60 mg/cm^2.

trode was "weeping" badly. In addition, a chronoamperometric curve obtained at this stage displayed the characteristic change in shape suggestive of catalyst separation from the current collector (Fig. 17). The electrode was removed from the cell, cold-pressed, and then reinstalled in the cell. The electrode still "weeped" quite badly, but the capacitance curve had regained the shape characteristic of a freshly fabricated electrode (see Fig. 17), and the measured electrode resistance and capacitance had recovered to values not very much different than the pre-life test values. The improvement in activity that was achieved with repressing is evident in the series of oxygen reduction polarization curves shown in Fig. 18. This clearly supports the authors' belief that the observed activity maintenance difficulties are related to electrode structure problems. It should be noted that the activity improvement achieved by repressing was temporary; when the life test was continued, structure deterioration as evidenced by "weeping," was again noted. The resultant decline in activity is seen in Fig. 15.

X-ray diffraction of the electrode after termination of the life test showed a contraction of the lattice parameter indicating that the composition of the catalyst had changed to approximately $Pb_2[Ru_{1.75}Pb_{0.25}^{4+}]O_{6.5}$. This occurred via dissolution into the electrolyte. Some metal deposition occurred on the counterelectrode when it was polarized cathodically and this disappeared when it was cycled anodically. Analyses of

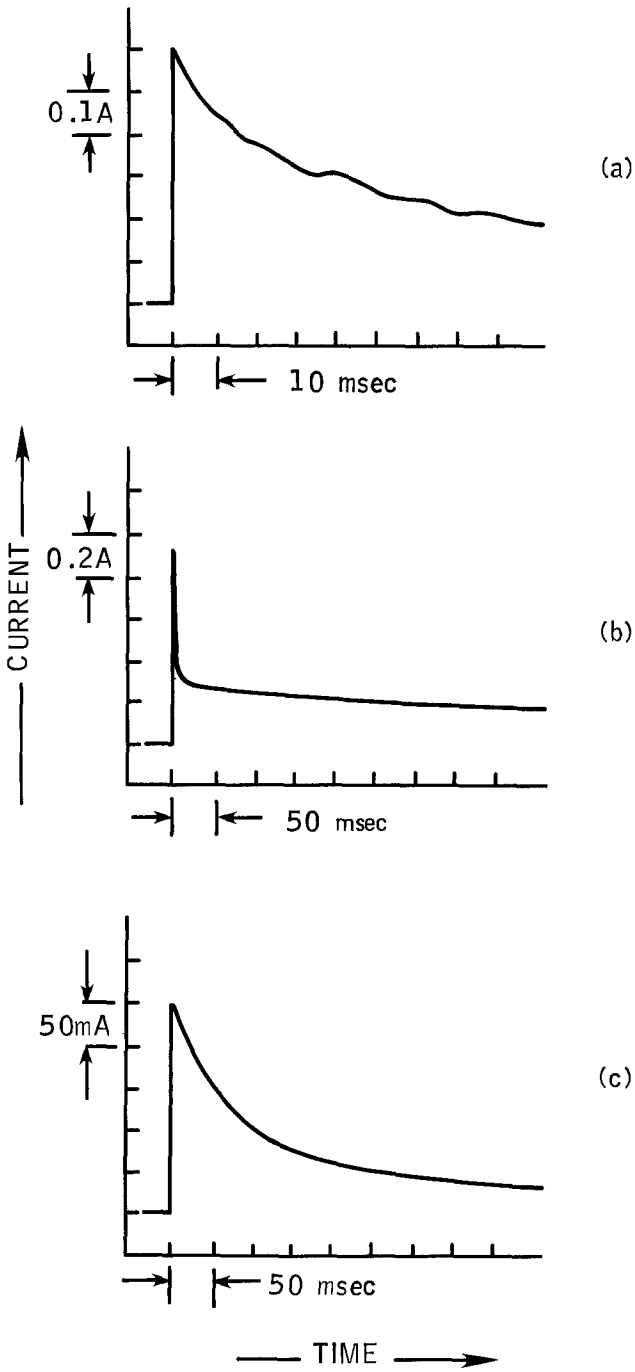

Fig. 17. Chronoamperometric meosurements made on life tested $Pb_2[Ru_{1.61}Pb_{0.39}^{4+}]O_{6.5}$ (see Fig. 14) in (a) pre-test condition, (b) post-test condition, and (c) post-test condition plus repressing. $\Delta mV = 10$.

the electrolyte taken when the counterelectrode was clean showed 4×10^{-4}M Pb and 9×10^{-6}M Ru. While it is apparent that the catalyst did undergo some chemical changes during this test, no gross chemical instability was observed, and it appears that the activity decline was primarily associated with electrode structure problems.

The second cycling test shown in Fig. 16 was run on the same electrode that had previously been tested for 1176 hr in O_2 reduction (Fig. 12a). The cycling was continued for 524 hr at which time the electrode was again removed and x-rayed. No crystallographic changes could be detected. As can be seen from the figure, no additional activity loss was observed during this period of cycling.

In Fig. 19 are shown the results of several O_2 evolution life tests. The catalyst in Fig. 19a was $Pb_2[Ru_{1.49}Pb_{0.51}^{4+}]O_{6.5}$ impregnated into a porous

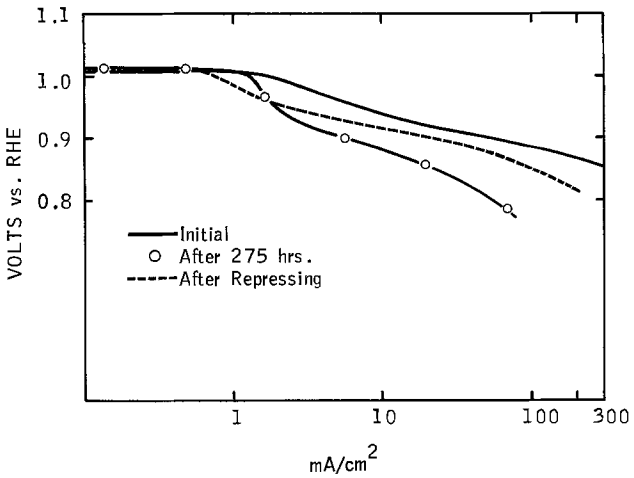

Fig. 18. O_2 reduction performance in 3M KOH, 75°C on $Pb_2[Ru_{1.61}Pb_{0.39}^{4+}]O_{6.5}$ at various stages of life testing (see Fig. 15).

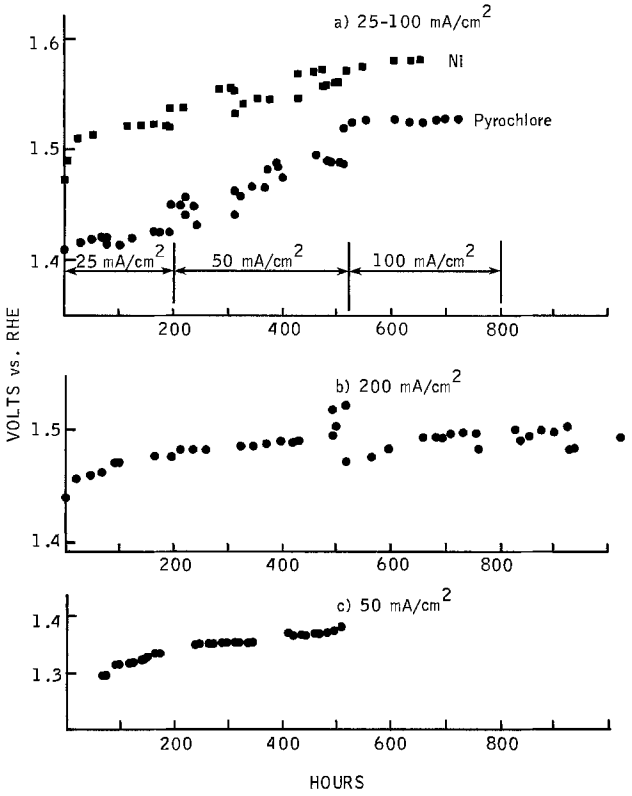

Fig. 19. O_2 evolution life tests in 3M KOH, 75°C on (a) $Pb_2[Ru_{1.49}Pb_{0.51}^{4+}]O_{6.5}$ and porous nickel, (b) $Pb_2[Ru_{1.49}Pb_{0.51}^{4+}]O_{6.5}$, and (c) $Pb_2[Ru_{1.85}Pb_{0.15}^{4+}]O_{6.5}$.

nickel substrate at a loading of 6 mg/cm². The immersed electrode was maintained in continuous O_2 evolution starting at 25 mA/cm² and subsequently at 50 and 100 mA/cm². There appeared to be an increase in polarization for about the first 500 hr of the test, but during the last 200 hr, the polarization remained constant. The test was terminated at 722 hr. Electrolyte analyses revealed no detectable concentrations of ruthenium, and lead concentrations of $\sim 2.3 \times 10^{-5}$M. X-ray diffraction of the electrode showed no changes in the catalyst. Simultaneous with this experiment, a comparative life test was run on the porous nickel support. These data are also included in Fig. 19a, and it can be seen that the activity of the support material is significantly lower than the lead ruthenate. The relatively low activity of the lead ruthenate (compared to polarization curves shown earlier) is thought to be due to the low (1.2 mg Ru/cm²) catalyst loading and nonoptimized support technique.

A supported lead ruthenate electrode ($Pb_2[Ru_{1.49}Pb_{0.51}^{4+}]O_{6.5}$), identical to the one used in Fig. 19a was again life tested in oxygen evolution, but this time at a constant current density of 200 mA/cm². The test was run for 1019 hr, and the activity maintenance, as shown by Fig. 19b was quite good. X-ray diffraction indicated the catalyst had not undergone any change, and the electrolyte analysis results were essentially the same as those obtained on the previous experiment run with this type of electrode.

An improvement in oxygen evolution activity can be achieved by using a higher loading (62 mg/cm²), Teflon-bonded, interface maintaining electrode; but activity maintenance problems become more severe with this type of electrode. Figure 19c shows the results of an oxygen evolution life test run at 50 mA/cm². The polarization was relatively low, but there was a definite increase in polarization with time. By the time the test was terminated at 504 hr, the electrode had started to physically disintegrate with portions of the current collector becoming visible where parts of the catalyst layer had become separated. The chronoamperometric curve obtained at the end of the life test showed the characteristic shape suggestive of catalyst layer separation from the current collector. The results of this experiment highlight the need for a much more rugged electrode structure in applications involving O_2 evolution. X-ray diffraction could not detect any changes in the catalyst, but polarographic analysis of the electrolyte revealed Pb present at 3×10^{-4}M and Ru present at 4×10^{-5}M (in an electrolyte volume of 250 ml).

In order to determine the activity maintenance characteristics of bismuth ruthenate pyrochlores, the catalyst $Bi_2[Ru_{1.63}Bi_{0.37}]O_{7-y}$ (167 m²/g) was life tested. The electrode was first operated in oxygen reduction at 50 mA/cm² for 240 hr and then switched to a cycling mode (8 hr of O_2 reduction at 25 mA/cm² and 16 hr of O_2 evolution at 12.5 mA/cm²). The test was voluntarily terminated at 1174 hr of operation due to bad leaks in the electrode. As can be seen in Fig. 20, there was little or no activity decay. Electrolyte analyses conducted during the test detected Bi at levels of $\sim 6 \times 10^{-5}$M and Ru at $\sim 4 \times 10^{-5}$M. X-ray diffraction of the tested electrode did not reveal any catalyst changes.

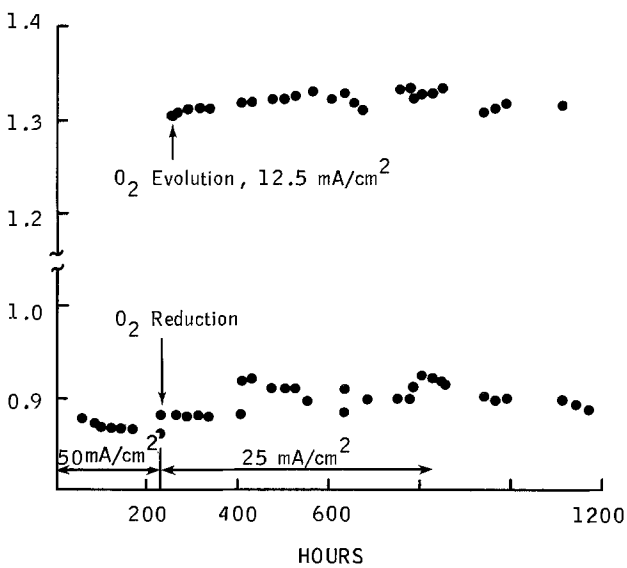

Fig. 20. O_2 reduction/evolution cycling mode life test in 3M KOH, 75°C on $Bi_2[Ru_{1.63}Bi_{0.37}]O_{7-y}$ (167 m²/g). Catalyst loading is 60 mg/cm².

Electrolyte immersion tests at the potential of incipient oxygen evolution, as described in the experimental section, were also used to measure catalyst stability, particularly with respect to the effects of compositional variations. In a typical experiment, plumbate and ruthenate ions would be detected in the electrolyte, and their concentrations in solution would rise within a few days to a virtually constant value in the range of 10^{-4}-10^{-6}M of lead ions (20-0.2 ppm). The ruthenium concentration was almost always slightly lower, 1/2-2/3 that of the lead. Most of this level was reached during the first day.

When the electrolyte was changed, the concentration of ions would again rise to a nearly steady value, lower than before. This would continue for several electrolyte changes until this final concentration decreased quite slowly from run to run. These ultimate steady-state concentrations were in the range of 10^{-5} to less than 10^{-6}M in lead (2-0.2 ppm) depending on the catalyst composition. The tendency was for the final concentrations of dissolved lead and ruthenium to decrease with decreasing surface area and with decreasing x (where x is given by the formula, $Pb_2[Ru_{2-x}Pb_x]O_{6.5}$). The best sample tested showed a final lead concentration of 7×10^{-7}M (0.15 ppm). This sample had a composition $x = 0.18$ and a surface area of 24 m^2/g. It was prepared by ceramic techniques at 600°C.

As the concentration of alkali or the temperature was increased, the concentrations of lead or ruthenium cations in the electrolyte rose. However, it was still possible to find 1.1×10^{-6}M Pb^{2+} at 40°C in 2M KOH with $Pb_2[Ru_2]O_{6.5}$ having a surface area of 2.4 m/g. At lower voltages in the realm of oxygen consumption, compositions where $x = 0$ gave $[Pb^{2+}] < 10^{-6}$M, even in 20% NaOH at 80°C with a catalyst of 33 m^2/g surface area.

The intermediacy of hydrogen peroxide.—Using the compacted lead ruthenate disk and gold ring rotating electrode assembly described in the experimental section, an attempt was made to detect hydrogen peroxide during oxygen reduction in 0.1M NaOH. The low concentration of alkali was used to maximize oxygen solubility to make detection of even small amounts of H_2O_2 easy; yet none was observed at potentials of 0 to −510 mV *vs.* SCE, a range where oxygen reduction current on the disk was very evident.

Control runs made with H_2O_2 added to the electrolyte showed that H_2O_2 yields of 1% of the oxygen consumed could be detected in this apparatus. The ring collection efficiency, as measured with ferricyanide solutions, was just under 30%. Thus it can be said that up to 3000 rpm less than 1% of H_2O_2 was produced as an intermediate in the reduction of oxygen.

The addition of hydrogen peroxide to an open-circuited lead ruthenate electrode at 50°C in 1.5M KOH caused the formation of O_2 bubbles and a small but definite reduction in potential to just about 1.0V *vs.* the reversible hydrogen potential. This suggests that lead ruthenate catalyzes the anodic oxidation of peroxide to oxygen thereby reducing the mixed potential.

Summary and Discussion of Results

The data presented in this paper have established that a new class of mixed metal oxides that substantially reduce the activation energy overvoltages associated with oxygen electrocatalysis have been discovered. Specifically, it is found that these catalysts, in aqueous alkaline media near ambient temperature, are superior to any other oxygen evolution catalyst and are equal in performance to the best known oxygen reduction catalysts. As bidirectional oxygen electrocatalysts, they appear to be unmatched.

It has been established that reasonable activity maintenance is achievable over relatively long testing periods (500-1800 hr). The principal difficulties associated with activity maintenance appear to be related to electrode structure. These difficulties may be due, in part, to the fact that the Teflon concentration used in test electrodes was optimized for initial performance rather than for activity maintenance. While no indications of gross chemical/electrochemical instability were noted, evidence of finite catalyst solubility was established. Interestingly, this observed corrosion appeared to have no significant effect on catalytic activity.

There are several physical and chemical characteristics of the oxide pyrochlores under discussion which may contribute to their high electrocatalytic activity. The previously described alkaline solution synthesis technique (6) has provided these materials with surface areas typically ranging from 50 to 200 m^2/g. Thus one of the basic requirements for an effective electrocatalyst has been satisfied: the electrocatalytic activity is not limited by the unavailability of catalytically active surface sites, as is so often the case with metal and mixed metal oxides.

Since all the catalysts investigated in this study display metallic or near metallic conductivity, the additional basic requirement of minimizing ohmic losses within the catalyst and between the catalyst and current collector has also been satisfied.

While high surface area and metallic conductivity are beneficial to electrocatalysis, they do not alone explain the high catalytic activity. Our speculations in this matter center around two themes: the variable oxygen stoichiometry of the pyrochlore lattice, and the multiple valence states of the cations, particularly the ruthenium.

Noble metal pyrochlores were originally considered by the authors as prime electrocatalyst candidates because of their ability to accommodate oxygen vacancies in up to one seventh of the anion sites. Changes in the average valence of the ruthenium can be expected to accommodate any such stoichiometry changes in $Pb_2[Ru_{2-x}Pb_x]O_{6.5}$. The existence of higher and lower valent oxides (either surface or bulk) in the potential range of interest appears to be a characteristic of many oxygen electrocatalysts such as Pt, Ag, Ni (for oxygen evolution), Au, etc. The reasons for this have never been explained exactly, although the ability of the surface to interact with or adsorb the potential intermediate peroxide or hydroperoxide ion on its surface is often invoked.

In the case of lead ruthenate, the oxygen nonstoichiometry concept can be developed further by combining it with the known reactions of the variable valence ruthenium. It is known that these same catalysts can cleave carbon-carbon double bonds (5) in a manner analogous to that of osmium and ruthenium tetroxide (7). It is known (8) that OsO_4 (and presumably RuO_4) cleave olefins via complexes with the structure

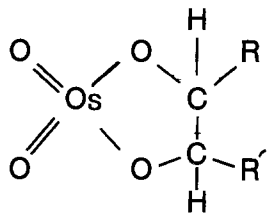

The fact that these catalysts can carry out the very same cleavage suggests that they can form moieties similar to the tetroxide on their surfaces. By analogy, it is possible that the ruthenium atoms at the surface of the crystal lattice can react with oxygen molecules so as to form these same surface complexes

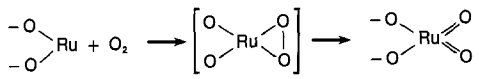

These can be reduced stepwise to regenerate the starting structure

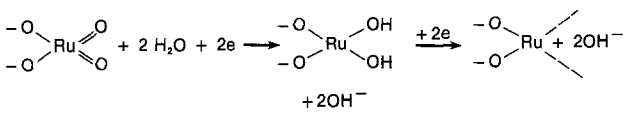

This or a similar set of reaction steps would avoid the formation of hydrogen peroxide consistent with the results of the rotating disk electrode experiment.

Acknowledgments

The authors would like to thank B. Bowling, H. Brady, and J. Lewandowski for assistance in the synthesis and materials characterization of the catalysts used in this study; J. Haberman, K. Strohmaier, and L. Yacullo for the electrochemical measurements; and J. Batzold and R. McCormick for making their data available as well as for helpful discussions.

Manuscript submitted March 22, 1982; revised manuscript received *ca.* May 3, 1983. This was Paper 528 presented at the Minneapolis, Minnesota, Meeting of the Society, May 10-15, 1981.

Exxon Research and Engineering Company assisted in meeting the publication costs of this article.

REFERENCES

1. A. C. C. Tseung and H. L. Bevan, *Electroanal. Chem. Interfacial Electrochem.*, **45**, 429 (1973).
2. H. L. Bevan and A. C. C. Tseung, *Electrochim. Acta*, **19**, 201 (1974).
3. H. S. Horowitz, J. M. Longo, and J. T. Lewandowski, *Mater. Res. Bull.*, **16**, 489 (1981).
4. H. S. Horowitz, J. M. Longo, and J. I. Haberman, U.S. Pat. 4,146,458 (1979).
5. H. H. Horowitz, H. S. Horowitz, and J. M. Longo, in "Electrocatalysis," W. E. O'Grady, P. N. Ross, Jr., and F. G. Will, Editors, p. 285, The Electrochemical Society Softbound Proceedings Series, Pennington, NJ (1981).
6. H. S. Horowitz, J. M. Longo, and J. T. Lewandowski, U.S. Pat. 4,129,525 (1978).
7. C. Djerasssi and R. R. Engle, *J. Am. Chem. Soc.*, **75**, 3838 (1953).
8. R. Criegee, *Ann.*, **522**, 75 (1936).

Computer-Controlled Apparatus for Interfacial Tension Measurements

M. Carlà, G. Aloisi, G. Papeschi, and S. Bordi*

Università di Firenze, Istituto di Chimica Fisica, I 50121 Firenze, Italy

ABSTRACT

A fully computer-controlled apparatus for interfacial tension measurements at the mercury/solution interface is described. The apparatus is based on the drop time method, whose reproducibility and accuracy have been improved by a new calibration technique and the use of a glass polyethylene dropping electrode.

This paper describes a fully automated apparatus, based on the drop time method, that has been implemented for interfacial tension measurements. The need for automation comes mainly from the amount of data that must be collected and elaborated to carry out adsorption studies on families of organic compounds (up to 5,000-10,000 data for each family). The drop time technique has been chosen for its ease of automation, unlike the capillary electrometer and the sessile drop methods that are very difficult to be automated (1). Moreover the drop time measurements are affected by a random scatter of each point fairly smaller than the one obtainable with the other techniques. This is particularly important in this kind of measurement because the mathematical elaboration involves several differentiations of the experimental data. The drop time method has been frequently regarded as scarcely accurate so that alternative methods, such as the maximum bubble pressure and the capillary electrometer methods, have been preferred (2). This attitude is mainly due to the fact that the proportionality relation between interfacial tension and drop time (namely Tate's formula) is only approximate. Several side effects, difficult to be compensated or computed exactly (3, 4, 5), are responsible for deviations from Tate's formula and for some of them [*e.g.* Harkin's effect (6)], there is not even a full agreement about their actual relevance. This difficulty has been overcome by calibrating the apparatus on a whole reference electrocapillary curve, rather than on a single electrocapillary maximum, so as to obtain empirical correction terms to Tate's formula. Another drawback of the drop time method consists in the difficulty of preparing satisfactory and durable dropping electrodes since the precision of the drop time measurements depends dramatically on the precision of the drop growth and detachment which, in turn, depends on the sharpness of the electrode orifice. These requirements have been usually satisfied with glass capillaries drawn on a gas flame and internally siliconized, but this technique of preparation requires a high degree of skill and many trials. Moreover, these capillaries cannot be employed with certain electrolytes which have the very useful property of being not specifically adsorbed [say, NaOH, HF, dilute NaF (7, 8)]. This difficulty has been overcome by devising a quite reproducible procedure for constructing combined glass-polyethylene dropping electrodes with the required mechanical and chemical properties (9).

* Electrochemical Society Active Member.

Key words: drop time, interfacial tension, computer control.

System Description

The whole system is shown in Fig. 1. It consists of three sections: the digital control section, the measuring cell, and the auxiliary devices (emptying and filling system).

Digital section.—The computer is a 960A Texas Instruments with 16-bit word and 32-K words of main memory. The peripheral configuration for electrocapillary measurements includes console, printer, tape puncher, and X-Y display. Interfacing with the other sections is accomplished through (*i*) a digital-to-analog converter (DAC) to set up the polarization potential

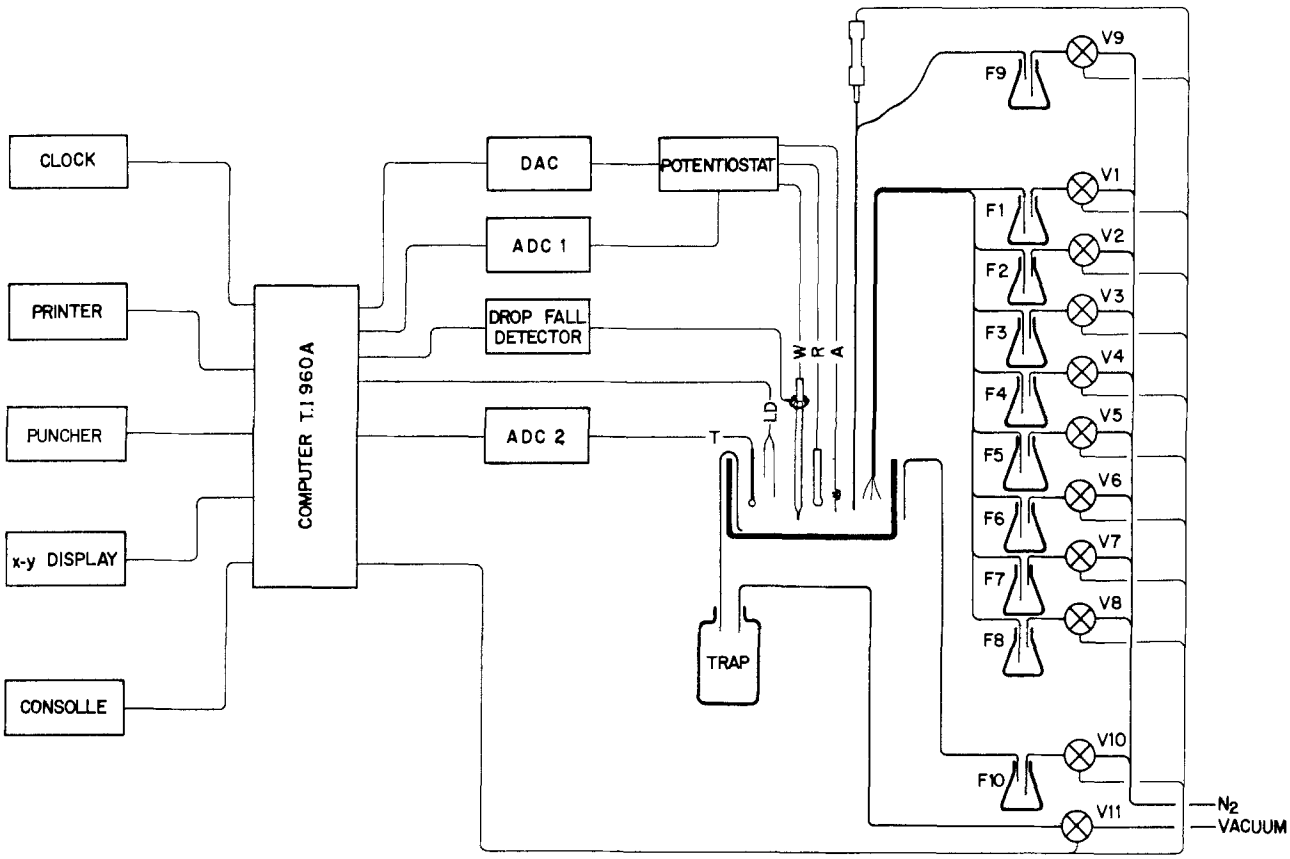

Fig. 1. Block diagram of the system. (W—dropping electrode; R—reference electrode; A—auxiliary electrode; T—thermometric probe; LD—solution level detectors; F1-F8—work solution flasks; F9-F10—humidification flasks; V1-V11—electropneumatic valves.)

across the metal-solution interface (12 bits, 1 mV resolution, 250 μV accuracy); (*ii*) an analog-to-digital converter (ADC1) (12 bits) to sample the current flowing across the dropping electrode; (*iii*) an analog-to-digital converter (ADC2) (12 bits) to monitor the cell temperature; (*iv*) an interrupt line from the drop fall detector [described in detail in Ref. (10)] to measure the drop time (resolution: 1 msec); (*v*) two level detector lines (LD) to sense when the solution in the measuring cell reaches any of two pre-established levels during the filling operation; (*vi*) a valve control bus to control the electropneumatic valves (V1-V11) which drive the emptying, washing, filling, and deaerating operations on the cell.

The operating system is memory resident and supports a compiled Basic with multitask and time sharing capabilities, implemented in this laboratory (11). A full run can be programmed for any number of electrocapillary curves, by pre-establishing for each curve the potential range and steps and by selecting the proper washing and deaerating cycle as well as the flask (F1-F8) from which the working solution must be drawn. During the run, the presence of the operator is required only to change the solution flasks (the system can accommodate up to eight flasks at a time). Apart from this intervention, measurements proceed unattended, preferably by night, when possible sources of vibration are reduced to a minimum.

During the measurements, for each point of a curve, the system records on the printer the time, the drop time averaged over three consecutive drops, the cell temperature, and the current flowing across the interface. At the end of each curve, the drop times are punched on paper tape for further elaboration.

Measuring cell.—A schematic picture of the cell assembly is shown in Fig. 2. A copper cage (1), contained in a Dewar vessel (2), is suspended to a bar, fixed into a main wall of the laboratory. The measuring cell (4) is made of Pyrex glass with a Teflon plug which holds all the electrodes. Both this cell and the capillary that regulates the mercury flow (5) are contained in the cage and are thermostated by a Peltier cell (6) at 25° ± 0.1°C. Besides the dropping electrode, the cell contains: (*i*) a saturated calomel electrode (8), made in this laboratory and employing a low leakage junction; (*ii*) a platinum counterelectrode (9); (*iii*) a thermometric probe (10); (*iv*) two platinum pins to "sense" the solution level (11) (*v*) eight polyethylene tubes (12) (for the filling operations) which are connected to the eight flasks F1-F8 of Fig. 1; (*vi*) a tube (13) which draws the solution and the mercury from the bottom of the cell; (*vii*) a deaeration tube (14) which can be moved up and down by actuator (19) and that delivers nitrogen to the cell either through or over the solution. Nitrogen can also be blown outside the cell, through tube (18) to remove oxygen from the Dewar vessel. The whole cell assembly, the eight flasks for filling the cell, and the flasks for humidifying nitrogen (F9 and F10 in Fig. 1) are installed in a cabinet thermostated at 25° ± 0.5°C.

Emptying and filling system.—Working solutions are lifted into the cell by transmitting a nitrogen pressure to the filling flasks through the electropneumatic valves (V1-V8 in Fig. 1) operated by the computer. The filling operation is controlled through the two level detectors (LD): a lower level for the working solution and a higher level for the washing operation. Usually, two washing operations are performed before filling the cell for the measurements; on the whole, this procedure requires about 70 cm^3 of solution. The emptying system consists of a vacuum pump, a valve (V11 in Fig. 2), and a trap balloon.

Calibration and Results

In drop time measurements, where only the applied potential and the solution composition are varied under otherwise identical experimental conditions, the drop time t is commonly considered to depend

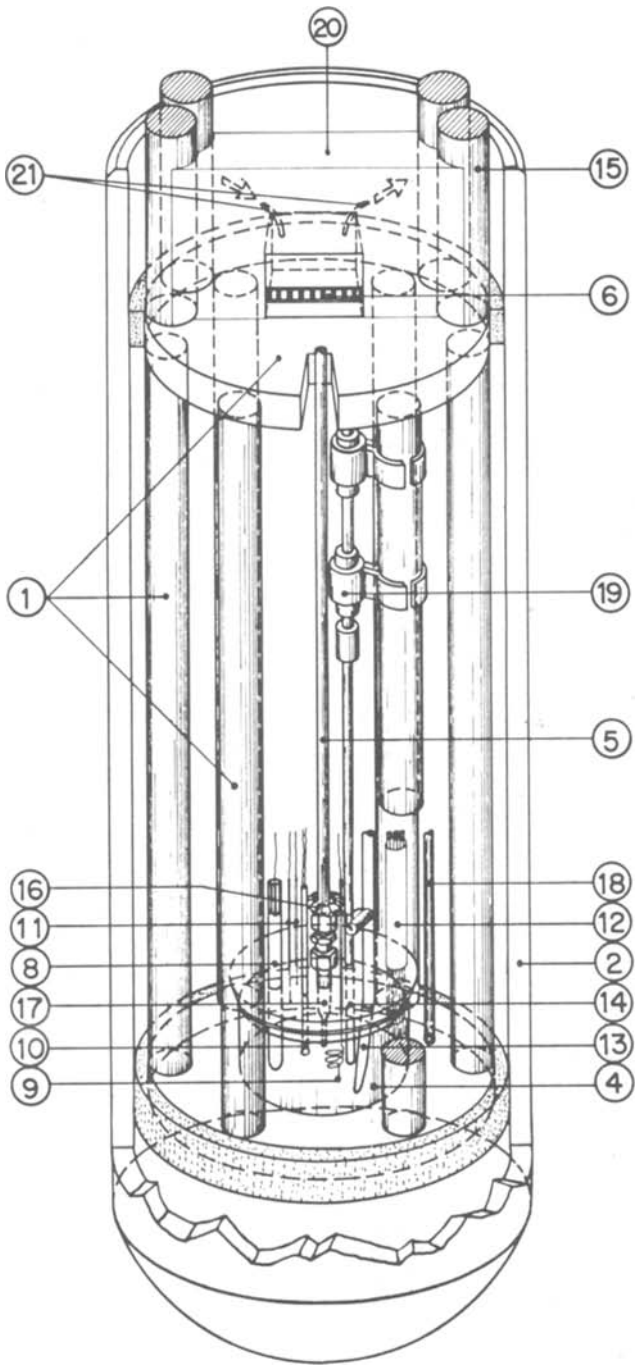

Fig. 2. Cell assembly. (1—copper cage; 2—Dewar vessel; 4—measuring cell; 5—glass capillary; 6—Peltier cell; 8—reference electrode; 9—auxiliary electrode; 10—thermometric probe; 11—solution level detectors; 12—filling tubes; 13—emptying tube; 14—deaeration tube; 15—suspension bars; 16—signal pick-up of the drop fall detector; 17—dropping polyethylene tip; 18—deaeration tube; 19—actuator; 20—thermal insulator; 21—Peltier cell cooling circuit.)

explicitly only upon the interfacial tension γ and upon the solution density d. According to Corbusier and Gierst (4) and to Barradas and Kimmerle (5), the functional dependence of t upon γ and d has the general form

$$\frac{\gamma}{\gamma_r} = \frac{D-d}{D-d_r} f\left(\frac{t}{t_r}\right)$$

where γ_r and t_r are the γ and t values of the electrocapillary maximum of the reference solution, d_r is the density of this solution, and D is the density of mercury. No agreement exists on the exact form of $f(t/t_r)$, but that it is close to linear. Upon expanding this function in a power series and fitting the directly obtained experimental data to those of the reference solution by the least squares method, it was found that only the powers up to the second need to be retained. The equation employed for the calibration has, therefore, the form

$$\frac{\gamma}{\gamma_r} = \frac{D-d}{D-d_r}\left[1 + A\cdot\frac{t-t_r}{t_r} + B\cdot\left(\frac{t-t_r}{t_r}\right)^2\right]$$

Figure 3 shows the reference electrocapillary curve for 0.1M KCl, as obtained by Vos and Los (12) with the sessile drop method, together with the one obtained with the drop time method by the above calibration procedure ($A = 0.933$, $B = -0.065$).

After the above calibration, electrocapillary curves were measured in several solutions for which γ values, as obtained by the capillary electrometer or the maximum bubble pressure methods, are available in the literature. Results obtained in 0.1M $HClO_4$ (13), 1M KCl (5), and 0.1M Na_2SO_4 (14) solutions are shown in Fig. 4, 5, and 6. Agreement is very good for the first two solutions (maximum deviation—0.5 dynes cm^{-1}), while it is slightly less satisfactory for the third solution (maximum deviation—1 dyne cm^{-1}).

These discrepancies are quite consistent with the data accuracy that may be expected on the basis of the accuracy of the several calibration standards that

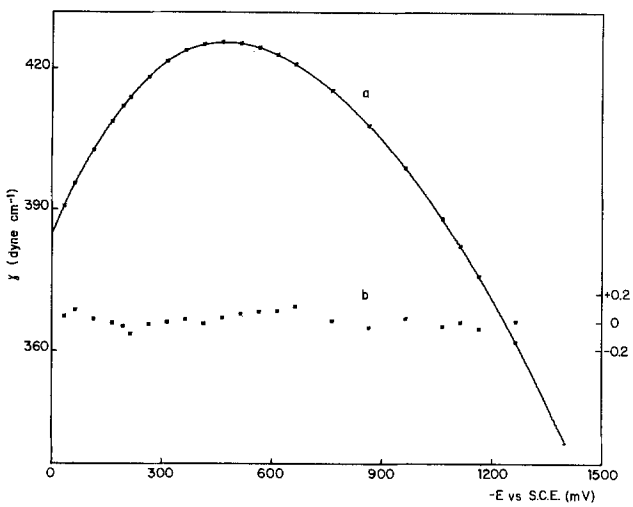

Fig. 3. Electrocapillary curve of 0.1M KCl. a. Solid line—authors' data; squares—data from Vos and Los (12). b. Differences between the two sets of data.

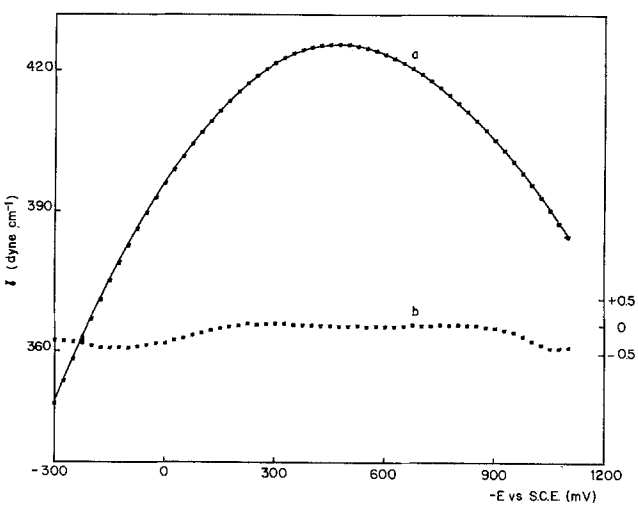

Fig. 4. Electrocopillary curve of 0.1M $HClO_4$. a. Solid line—authors' data; squares—data from Baikerikar *et al.* (13). b. Differences between the two sets of data.

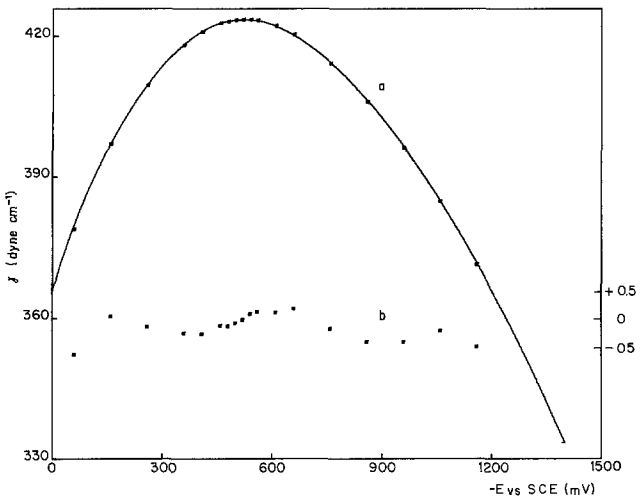

Fig. 5. Electrocapillary curve of 1M KCl. a. Solid line—authors' data; squares—data from Barradas *et al.* (5). b. Differences between the two sets of data.

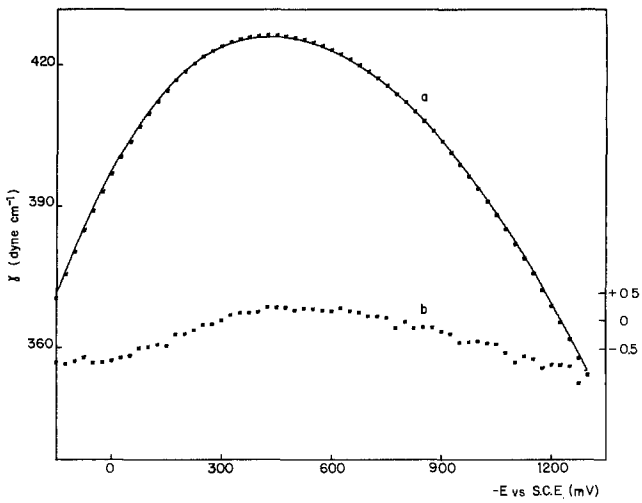

Fig. 6. Electrocapillary curve of 0.1M Na_2SO_4. a. Solid line—authors' data; squares—data from Nakadomari *et al.* (14). b. Differences between the two sets of data.

have been used. Internal accuracy (reproducibility) of the apparatus is really much better, but this is little help in obtaining more accurate data as long as a more accurate absolute calibration standard is not available. This reproducibility has been tested in several runs for different substances and a data scatter better than 0.2 dyne cm^{-1} has been observed as the worst case value even for organic compounds. For simple inorganic systems, the data reproducibility reaches 0.03 dyne cm^{-1}. This value is close to the one reported by Mohilner (15) and obtained with the maximum bubble pressure technique. This error is small if compared with the error of the best available standards (0.3 dyne cm^{-1}).

Manuscript submitted Dec. 12, 1982; revised manuscript received *ca.* April 8, 1983.

Università di Firenze, Istituto di Chimica Fisica assisted in meeting the publication costs of this article.

REFERENCES

1. H. H. Girault, D. J. Schiffrin, and B. D. V. Smith, *J. Electroanal. Chem.*, **137**, 207 (1982).
2. J. Lawrence and D. M. Mohilner, *This Journal*, **118**, 1596 (1971).
3. G. S. Smith, *Trans. Faraday Soc.*, **47**, 63 (1951).
4. P. Corbusier and L. Gierst, *Anal. Chimica Acta*, **15**, 254 (1956).
5. R. G. Barradas and F. K. Kimmerle, *Can. J. Chem.*, **45**, 109 (1967).
6. W. Harkins, *Int. Crit. Tables*, New York, **4**, 435 (1928).
7. R. Payne, *J. Electroanal. Chem.*, **41**, 277 (1973).
8. L. Novotny, J. Kuta, and I. Smoler, *ibid.*, **88**, 161 (1978).
9. M. Carlà and G. Aloisi, *This Journal*, **130**, 637 (1983).
10. M. Carlà, G. Aloisi, G. Papeschi, and S. Bordi, *ibid.*, **130**, 1327 (1983).
11. M. Carlà, *Automazione e Strumentazione*, **3**, 82 (1982).
12. H. Vos and J. M. Los, *J. Coll. Interf. Sci.*, **74**, 360 (1980).
13. K. J. Baikerikar, J. Buckfelder, and R. S. Hansen, *J. Electroanal. Chem.*, **108**, 17 (1980).
14. H. Nakadomari, D. M. Mohilner, and P. R. Mohilner, *J. Phys. Chem.*, **80**, 1761 (1976).
15. D. M. Mohilner and T. Kakiuchi, *This Journal*, **128**, 350 (1981).

The Electrolytic Maintenance of Homogeneous Catalytic Activity

J. B. Davison,[1] P. J. Peerce-Landers,*[2] and R. J. Jasinski*

Occidental Research Corporation, Irvine, California 92714.

ABSTRACT

The lifetimes of homogeneous nickel and palladium catalysts used in the cyanation of aryl chlorides were increased several fold by the application of a reducing potential. Catalytically inactive metal species formed in deleterious side reactions with cyanide were electrochemically intercepted and restored to a catalytically active state. The low number of electrons consumed per mol of product, 0.02-0.04 for nickel and 0.06-0.25 for palladium, suggests that the charge consumed was only used to maintain catalyst activity. The low power consumption makes electrolytic maintenance a commercially attractive method for prolonging catalyst lifetimes.

The short lifetimes of many homogeneous transition metal catalysts preclude their use in commercial processes. Catalyst deactivation frequently results from redox reactions between the catalyst and impurities, reactants, and/or products. It occurred to the authors that the lifetimes of such redox deactivated catalysts might be prolonged by electrochemical means. This requires that the deactivated metal complexes be electroactive and convertible to some species within the catalytic cycle. To be an efficient process, only the deactivated complex should be electroactive at the potentials employed.

* Electrochemical Society Active Member.
[1] Present address: J. C. Schumacher Company, Oceanside, California 92054.
[2] Present address: Betz Laboratory, The Woodlands, Texas 77380.
Key words: nickel triphenylphosphine, palladium triphenylphosphine, electrocatalysis, aryl chlorides, catalysis.

A system meeting these requirements is the tetrakis-(triphenylphosphine) nickel (0) (NiL_4, L = PPh_3) catalyzed cyanation of aryl chlorides in ethanol (1)

$$ArCl + CN^- \xrightarrow[EtOH,\ 55°C]{NiL_4} ArCN + Cl^-$$

The reaction proceeds under rather mild conditions. However, the number of catalyst turnovers obtained is low, generally < 50. Cassar has reported that the nickel catalyst is readily poisoned by excess cyanide (1). The authors have found that the formation of tetracyanonickelate, $Ni(CN)_4^{-2}$, accompanies cessation of catalytic activity (2).

Electroreduction of $Ni(CN)_4^{-2}$ in ethanol did not result in the formation of NiL_4 even in the presence of large excesses of triphenylphosphine (mol ratios of L:Ni > 25). Only nickel metal was obtained. Similar results were obtained when electrochemical regeneration of NiL_4 was attempted in spent reaction mixtures. Moreover, NiL_4 could not be electrogenerated from Ni(II) in the presence of four equivalents of cyanide. However, Ni(II) was reducible to NiL_4 in the presence of one or two equivalents of cyanide. Therefore, it was reasoned that the continuous application of a reducing potential might prolong catalyst activity by electrochemically restoring intermediate inactive nickel species to the catalytic cycle.

Neither the aryl chlorides used, the product nitriles, nor the intermediate aryl nickel complexes were reducible at the potentials required to form NiL_4. Tetrakis (triphenylphosphine) palladium (0) (PdL_4, L = PPh_3) was also tested since it too was found to catalyze the cyanation of aryl chlorides and was readily poisoned by excess cyanide.

Experimental

All chemicals were reagent grade and used as received unless otherwise specified. NiL_4 was prepared by the literature method (3); PdL_4 was obtained from Strem. All chloroarenes, tetraethylammonium cyanide (TEACN, Lachat), and tetraethylammonium chloride (TEAC, Eastman) were commercial materials. Absolute ethanol and DMF were stored over molecular sieves and thoroughly degassed prior to use. The HMS carbon fibers used as electrodes were obtained from Hercules.

All electrochemical experiments were conducted using a Princeton Applied Research (PAR) Model 173 Potentiostat/Galvanostat in conjunction with a PAR Model 175 Universal Programmer and a PAR Model 179 Digital Coulometer. The electrochemical cell was a conventional three-compartment cell which isolated the working and auxiliary electrodes with provision for degassing the solution in the working electrode compartment and maintenance of an inert atmosphere. The top of the working electrode compartment was fitted to a reflux condenser which was connected to a mineral oil bubbler. In addition, there was a septum port on the working electrode compartment top through which TEACN solution was introduced and GC samples were withdrawn. The auxiliary and working electrodes consisted of several 2 in. diam loops of HMS carbon fibers to which electrical contact was made using an alligator clip connected to a copper lead wire.

Nickel potentials were measured and are reported relative to an Ag/Ag^+ (0.1M $AgBF_4$/EtOH) reference electrode. The potential of this reference electrode was 0.510 ± 0.01V *vs.* SCE. Palladium potentials were measured and are reported relative to an Ag/AgI (0.1M I^-/DMF) reference electrode. The potential of this reference electrode was −0.5V *vs.* SCE. Contact of the reference electrodes with the solution in the working electrode compartment was made via a salt bridge filled with either 0.1M TBAP/EtOH (nickel) or 0.1M TBAP/DMF (palladium). A 0.1M solution of TEAC was used as the supporting electrolyte.

Gas chromatographic analyses of the reaction mixtures were performed on a Hewlett-Packard 5840 gas chromatograph equipped with a 12m 0V-101 capillary column. Infrared spectra were recorded on a Beckman 4260 spectrometer.

General procedure for electrolytic reactions.—In the dry box, the working compartment was loaded with 0.25 mmol NiL_4 or 0.125 mmol PdL_4 catalyst, a threefold excess of L (based on Ni or Pd), 10 mmols naphthalene (internal GC standard), 100 mmols aryl chloride, 40 ml of 0.1m TEAC in ethanol (Ni) or DMF (Pd), and a magnetic stirring bar. The other two compartments were filled with the TEAC supporting electrolyte solution. The cell was stoppered, removed from the dry box, fitted with a reflux condenser connected to a mineral oil bubbler to monitor a very slow argon purge, and placed in an oil bath at 55°C (Ni) or 130°C (Pd).

General procedure for control reactions.—The control reactions were set up as above but in a two-neck round bottom flask fitted with a reflux condenser and rubber septum. The control reactions were not electrolyzed but did contain 40 ml of the supporting electrolyte solution.

Both the control and electrolysis reaction mixtures were permitted to stir for 30 min at temperature. During this time, the solids dissolved. The solutions were a homogeneous yellow orange when controlled addition of the TEACN solution was begun. For the nickel reactions, an ethanolic solution of 3M TEACN was used. For the palladium reactions, a 0.42M TEACN solution in DMF was employed. The rate of addition was maintained by a syringe pump at 3.6 mmols TEACN per hour for the nickel reactions. See Table II for the cyanide addition rates in the palladium reactions. GC samples from both the control and electrolysis reaction mixtures were withdrawn hourly by syringe and analyzed.

Results and Discussion

To determine whether the lifetimes of the nickel and palladium catalysts could be electrolytically prolonged, the aryl chloride cyanation reactions were run in the presence of a reducing potential. A potential sufficient to reduce M(II) to M(0) was applied to the working electrode: −1.2 to −1.6V for Ni; −0.3 to −0.8V for Pd. The reactions were also run at a constant current of 5 mA. Each electrochemical experiment was run concurrently with a nonelectrolytic control.

Prolonging the catalytic activity of NiL_4.—The results of the cyanation reactions catalyzed by NiL_4 are shown in Table I. With the exception of *para*-dichlorobenzene, at least a two-fold enhancement in catalyst lifetime was observed in all the electrolytic reactions. No attempt was made to optimize conditions. In some cases, reactions were arbitrarily terminated before catalytic activity had been lost. The results show that the observed effect is general for aryl chlorides bearing electron withdrawing or electron donating groups in the *meta* and *para* positions. The number of electrons consumed per mol of product was quite low: 0.02-0.04. This suggests that the charge consumed was only used to maintain catalyst activity.

The data from the electrolytic and the homogeneous control experiments for reaction 1 in Table I are graphically compared in Fig. 1. The rate of the product formation in both cases was governed by the TEACN addition rate. After about 4 hr, the catalyst in the control reaction was inactive. However, in the presence of a reducing potential, catalyst activity was maintained for over 12 hr.

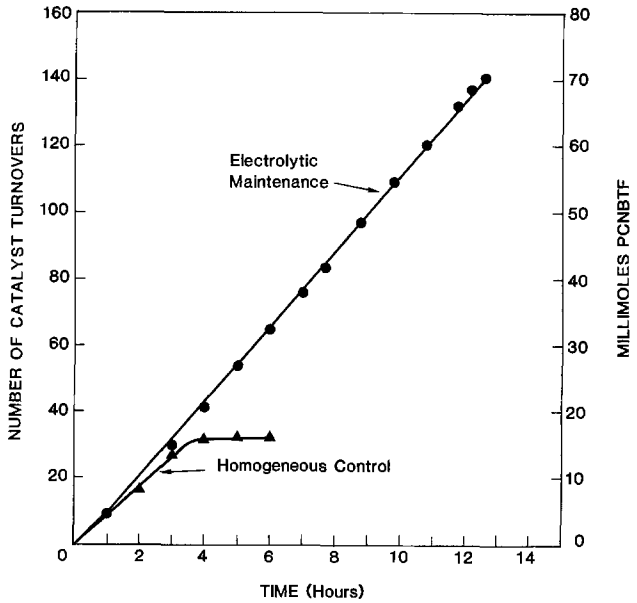

Fig. 1. Comparison of nickel catalyst performance in the presence and absence of an applied reducing potential. The reaction is the conversion of parachlorobenzotrifluoride (PCBTF) to paracyanobenzotrifluoride (PCNBTF). (Cf. reaction 1 in Table II.)

Figure 2 shows the infrared spectra of samples withdrawn from both reactions at various times. At $t = 0$, before CN^- addition was begun, both spectra were identical. At $t = 3$ hr, the spectra were still indistinguishable. Both exhibited an absorbance at 2230 cm^{-1} attributable to the C≡N stretch of the product, *para*-cyanobenzotrifluoride. After 4 hr, the spectra of the two reaction mixtures differed. The spectrum of the electrolytic reaction showed only a more intense product peak. However, little change was observed in the intensity of the product band in the spectrum of the control reaction. In addition, a new band was observed at 2124 cm^{-1} due to the C≡N stretch of $Ni(CN)_4^{-2}$. The appearance of $Ni(CN)_4^{-2}$ after 3 hr correlated with the loss of catalytic activity (cf. Fig. 1). After 5 hr, the spectrum of the control reaction exhibited an additional band at 2078 cm^{-1} due to unreacted TEACN. Only the product band was observed between 5 and 13 hr (not shown) in the spectrum of the electrolytic reaction mixture. These spectroscopic data indicate that catalytically inactive nickel species were electrochemically intercepted and the rate of formation of $Ni(CN)_4^{-2}$ minimized.

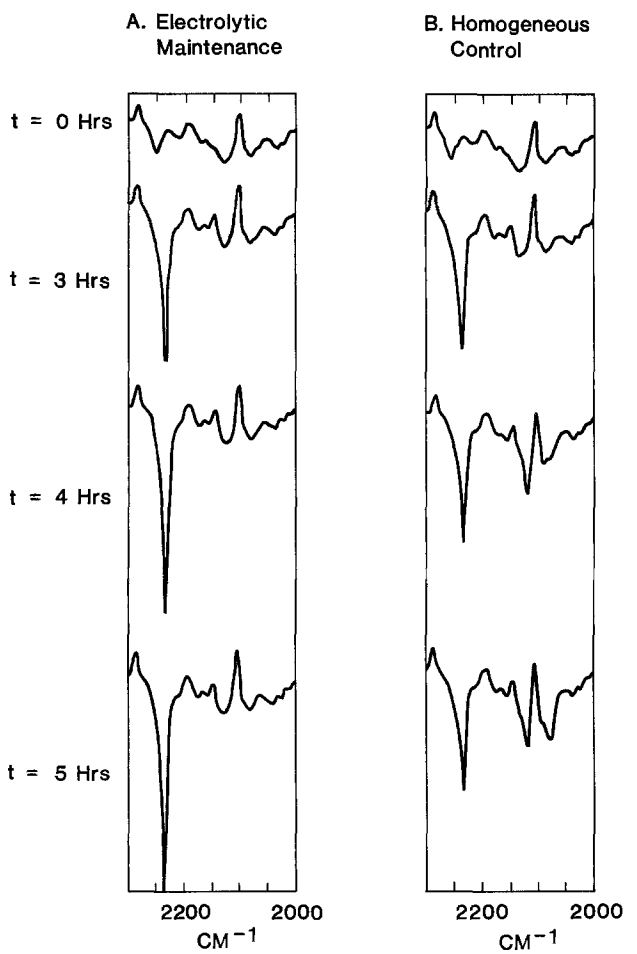

Fig. 2. Infrared spectra in the 2000-2300 cm^{-1} region of aliquots taken from the two reactions depicted in Fig. 1. Times refer to the time elapsed since the addition of cyanide was begun.

Eventually, catalytic activity was lost in most of the electrolytic reactions. The presence of $Ni(CN)_4^{-2}$ in the spent reaction mixtures was detected by infrared. [Loss of catalytic activity was generally accompanied by a change in solution color from amber to pale yellow (2).] The cause of catalyst deactivation in these cases was not investigated in detail. It may have resulted from passivation of the working electrode. An insoluble coating was observed on the working electrode during reaction 8. It is also possible that not all of the inactive nickel species formed are reducible to catalytically active species. As those inactive species accumulate, the concentration of free cyanide will increase (since the rate of addition of cyanide is constant) and irreversible catalyst poisoning will result.

Prolonging the catalytic activity of PdL_4.—Electrolytic maintenance of catalyst activity was also demonstrated for the PdL_4 catalyzed cyanation of aryl chlorides

$$ArCl + CN^- \xrightarrow[DMF,\ 130°C]{PdL_4} ArCN + Cl^-$$

A higher temperature, 130°C, and a higher boiling solvent, DMF, were required because palladium did not insert into the aryl carbon-chlorine bond at lower temperatures. To the authors' knowledge, there is no literature precedent for this reaction.

Comparison of electrolytic and homogeneous control experiments for five aryl chlorides is given in Table II. With the exception of orthochlorobenzotrifluoride, the electrolytic experiments outperformed the controls. The effect of TEACN addition rate on catalyst turnover number was studied in reactions 9, 10, and 11. In these reactions, the electrochemical experiment was run at a constant current of 5 mA.

In the control reaction, as the rate of addition of CN^- was increased, the number of turnovers observed decreased. This result demonstrates the sensitivity of the palladium catalyst to excess cyanide. A band at 2124 cm^{-1} was observed in the infrared spectra of spent reaction mixtures suggesting the presence of $Pd(CN)_4^{-2}$. In contrast to the control experiments, in the presence of a reducing potential, the palladium catalyst performed just as well or better at higher CN^- addition rates. The number of electrons consumed per mol of product decreased with increasing CN^- addition rate. This suggests that part of the current was expended in side reactions at the slower CN^- addition rates.

There were some differences in activity between the palladium and nickel systems. For example, no reaction was obtained with parachlorotoluene using PdL_4. However, this aryl chloride was very reactive in the nickel system. Conversely, chlorobenzene underwent cyanation with the palladium catalyst, but not with nickel. Therefore, PdL_4 and NiL_4 are complementary aryl chloride cyanation catalysts.

Table I. Comparison of homogeneous catalysis and electrolytic catalyst regeneration for the cyanation of aryl chlorides. $Ni(PPh_3)_4$ catalyst

Reaction No.	ArCl	Product	Number of catalyst turnovers		Electrons consumed/ mol of product
			Homogeneous	Electrolytic	
1	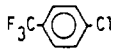	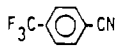	32	142	0.04
2	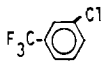	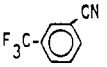	55	124	0.03
3	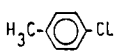	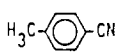	25	160	0.03
4	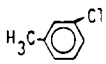	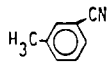	54	230[a]	0.02
5	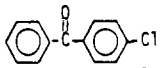	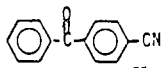	84	200[a]	0.04
6			46	185	0.04
7	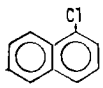	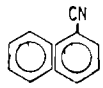	16	200[a]	0.04
8	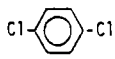	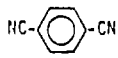	46	81[b]	0.03

a. Reaction arbitrarily terminated; catalyst was still active.
b. Insoluble coating formed on working electrode and probably prevented further electrolytic regeneration.

Table II. Comparison of homogeneous catalysis and electrolytic catalyst regeneration for the cyanation of aryl chlorides. $Pd(PPh_3)_4$ catalyst

Reaction No.	ArCl	Product	CN^- Addition rate mmols/hr	Number of catalyst turnovers		Electrons consumed/ mol of product
				Homogeneous	Electrolytic	
9	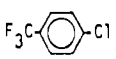	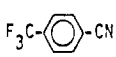	1.4	58	113	0.24
10	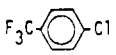	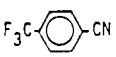	2.1	38	116	0.11
11	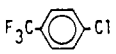	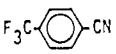	3.5	8	162	0.06
12	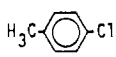	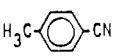	2.1	0	Ca · 2	0.10
13	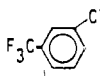	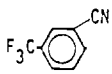	1.4	18	130	0.14
14		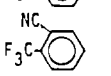	1.0	Trace	Trace	—
15			1.0	Trace	96	0.25

Conclusions

Metal complexes that exit a catalytic cycle due to redox side reactions may be electrochemically returned to the cycle *in situ*. In this way, the lifetimes of homogeneous nickel and palladium catalysts were prolonged severalfold. Ideally, only the catalytically inactive metal species are electroactive at the potentials employed. Under these conditions, the power consumption is only a fraction of the stoichiometric requirement. Electrolytic maintenance of catalyst activity may permit the exploitation of catalysts previously considered too inefficient and shortlived for commercial use.

Manuscript submitted Jan. 24, 1983; revised manuscript received May 26, 1983.

Occidental Research Corporation assisted in meeting the publication costs of this article.

REFERENCES

1. L. Cassar, *J. Organomet. Chem.*, **54**, C57 (1973); L. Cassar, S. Ferra, and M. Foa', *Advan. Chem. Ser.*, **132**, 252 (1974).
2. J. B. Davison and P. J. Peerce-Landers, Manuscript in preparation.
3. R. A. Schunn, *Inorg. Syn.*, **13**, 124 (1971).

Semiconductor Electrodes

LI. Efficient Electroluminescence at ZnS Electrode in Aqueous Electrolytes

F.-R. F. Fan,* P. Leempoel, and A. J. Bard*

Department of Chemistry, The University of Texas at Austin, Austin, Texas 78712

ABSTRACT

Electroluminescence (EL) on ZnS was studied in aqueous solutions containing various redox species. For species able to generate strongly oxidizing intermediates, such as peroxydisulfate or hydrogen peroxide, bright blue luminescence was observed during cathodic polarization at potentials near to or negative of flatband potential (V_{FB}) of ZnS. For solutions containing supporting electrolyte alone at various pH's, no emission was detectable even at potentials 7V negative of V_{FB}. This suggests that minority carrier (hole) injection is responsible for the initiation of EL. The peak energy of the EL spectrum was much smaller (by 1 eV) than the bandgap of ZnS, suggesting that the radiative recombination is through intermediate luminescent centers. Under steady-state conditions, the EL intensity was proportional to the square of the current, suggesting that EL intensity is dominated by the recombination of electron hole pairs at luminescent centers. In the early part of a potential pulse (especially the first pulse), the growth behavior of EL intensity was strongly affected by the electron trapping of the empty upper luminescent states. The location of the EL spectra depended on the current density and EL intensity; with increasing EL intensity, a significant blue shift of the emission peak was observed. These results suggest that the overall radiative recombination rate might be limited by electron transfer (through a tunneling mechanism) from the occupied upper luminescent states to the empty lower luminescent states. An EL efficiency of 0.2% can be achieved by operating at a current density of 25 mA/cm^2.

The study of interfacial charge transfer processes at semiconductor electrodes is under active investigation (1-5). Luminescence techniques have been employed successfully as probes to study surface recombination and excited state processes (6-9). Recently Ellis *et al.* (6) have carried out extensive studies on the electroluminescence and photoluminescence of cadmium chalcogenides, for example CdS and CdSe, and, by comparison with photogenerated charge transfer obtained information about the reaction processes at these electrodes. The efficiency of the room temperature emission of these materials in the visible spectral region is quite low, as is that of most other semiconductors (*e.g.* quantum yields $< 10^{-3}$).

Wide bandgap II-VI compounds are potentially useful electrode materials for visible electroluminescence in solution; the zinc chalcogenides are especially good candidates for such applications. Indeed, low voltage solid-state devices which produce electroluminescence have been described; however, it is difficult to produce a good p-n junction necessary for efficient charge injection due to self-compensation by native defects. Less complex Schottky junctions have been attempted with some degree of success (10-12). There have been few reports of solution studies of electroluminescence of ZnS (13, 14). In an early letter (14), emission was reported for a ZnS electrode immersed in fuming sulfuric aicd; this was attributed to the formation of an inversion layer at ZnS surface. More recently a brief report by Tyagai *et al.* (13) described the blue emission of a ZnS cathode in H_2O_2, which was attributed to hole injection from the reduction intermediate, ·OH, into the valence band of ZnS. However, details of the process, the mechanism of emission, and the dependence of the spectral distribution on a variety of electrochemical parameters were not explored. The authors thought it of interest to examine the electroluminescence of ZnS as a probe of the energetics at the ZnS/electrolyte interface and for possible application to display devices.

In this paper, the authors examine the electrochemical and electroluminescent properties of single-crystal n-type ZnS electrodes with various redox couples. They demonstrate that the electroluminescence (EL) is initiated by hole injection from solution redox couples and under steady-state conditions, the EL intensity is dominated by the recombination of electron hole pairs at luminescent centers. Neither electron transfer to the upper states nor hole transfer to the lower state controls the rate of emission in the condition studied. The effect of trapping on the growth of EL and the factors affecting the intensity and spectral distribution of the EL are discussed. The EL efficiency at room temperature is among one of the highest in the photoelectrochemical-type luminescent cells or low voltage solid-state electroluminescence devices (22). An EL efficiency of 0.2% can be achieved by operating at a current density of 25 mA/cm^2.

Experimental Section

Materials.—Al-doped ZnS single crystals were generously donated by J. O. McCaldin or were grown by iodine chemical vapor transport (15). These crystals usually had high resistivities ($> 10^{10}$ Ω-cm). The crystals were heated in a molten 90% Zn-10% Al mixture at 900 C for 10-24 hr. This treatment reduced the resistivity of some crystals to 20-10^4 Ω-cm. The crystals with low resistivity were used in the EL experiments. They were cut into slices along the (111) plane and were subsequently polished by carborundum (1 μm grit size) and alumina (0.5 μm particle size). Ohmic contact was made according to the method given by Kaufman and Dowber (16). The crystals were mounted as electrodes as described previously (17). Before a series of experiments, the electrode was etched in a potassium dichromate-H_2SO_4 cleaning solution at 70°C for 5 min. Reagent grade chemicals were used without further purification. All solutions were prepared from triply distilled water and were deoxygenated, if not otherwise mentioned, for at least 30 min with purified nitrogen before each experiment. These experiments were carried out with the solution under a nitrogen atmosphere.

Electrochemical measurements.—All electrochemical measurements were performed with the same electrochemical cells, apparatus, and procedures as reported previously (17). The impedance measurements were carried out with an aqueous solution containing 1.0M $NaClO_4$. The pH of the solution was adjusted with $HClO_4$ or concentrated NaOH (10M). The apparatus and procedures for impedance measurements were based on those reported previously (18).

* Electrochemical Society Active Member.

Key words: electroluminescence, luminescence, display, semiconductor.

Two a-c frequencies (100 and 300 Hz) were employed and no significant dispersion was found.

Electroluminescence measurements.—The EL spectra were mainly obtained with a PAR Model 1215 OMA2 optical multichannel analyzer including a silicon intensifier target vidicon detector with a vacuum u.v. scintillator to enhance the u.v. response. This detection system has an essentially flat response in the wavelength range of the ZnS EL spectrum, 350-550 nm. To obtain the EL spectra, the electrode was pulsed between 0.0V *vs.* SCE and a given negative potential. The EL signal was detected by synchronizing the OMA detection system with the potential pulses applied to the electrode. Another detection system was constructed based on an Oriel monochromator equipped with gratings blazed at 500 or 1000 nm. The monochromator was interfaced to a highly red-sensitive photomultipler tube (PMT) (Hamamatsu R928). Signals from the PMT were amplified by a lock-in amplifier and displayed on a Houston Model 2000 X-Y recorder. In the transient experiments, the EL signal was detected by a PMT with attached neutral density filters and a 460 nm bandpass filter. Signals from the PMT were amplified by a current-to-voltage converter and displayed together with the chronoamperometric curves on a Nicolet Model 1090A digital oscilloscope and then recorded on a Houston Model 2000 X-Y recorder.

The integrated EL efficiency, $\bar{\phi}_{EL}$, was determined by an integrating sphere photometric detection system as described by Itaya and Bard (19) and by Bezman and Faulkner (20).

The total photometric apparatus consisted of an integrating sphere and an EG&G radiometer attached to the viewing port of the sphere. The sensitivity, S, of the integrating sphere was calibrated with an He-Ne laser or by a light beam (10 nm bandwidth) obtained from a 450W Xe-lamp and an interference bandpass filter at 460 nm. The calibration factor, C, of the EG&G radiometer was obtained by a standard actinometric procedure with a 0.1M ferrioxalate actinometer. The sample cell for EL experiments was inserted into the sphere and was held in position by a standard taper joint attached to the sphere. The electrode was pulsed and the total charge passed was measured with a digital coulometer. The total photon energy emitted was measured by the integrating sphere photometric apparatus. The integrated number of photons can be calculated based on Eq. [1] given in Ref. (19) or approximately

$$\text{the total number of photons (einsteins)} \cong S \times C \times \text{total photon energy (joules) measured}/\mathbf{F} \times \text{photon energy } \lambda_{max} \quad [1]$$

in which $\mathbf{F}$ is Faraday's constant and λ_{max} is the wavelength at the peak of EL spectrum. In this equation, the average energy per photon is taken as the photon energy at λ_{max}. This is only an approximation since the EL spectra are not narrow enough to be treated as line spectra. However, they are quite symmetric and the half-width is narrow as compared with the photon energy at λ_{max}.

Results

Electrochemical behavior.—Flatband potential (V_{FB}).—Studies of the capacitance of n-ZnS electrodes were conducted in deaerated aqueous solutions containing 1M $NaClO_4$ at different *p*H's. As shown in Fig. 1, a Schottky depletion layer was formed at the surface of ZnS, as indicated by the linear dependence of the reciprocal of the square of the capacitance on the potential (Mott-Schottky plot). V_{FB} of this ZnS electrode was −1.61V *vs.* SCE at *p*H 1.95 and shifted about 55 mV negatively per *p*H unit increment. The uncompensated ionized charge density, found from the slope of the Mott-Schottky plots and the dielectric constant ($\epsilon = 8.3$) (21) was 9.1×10^{17} cm^{-3}.

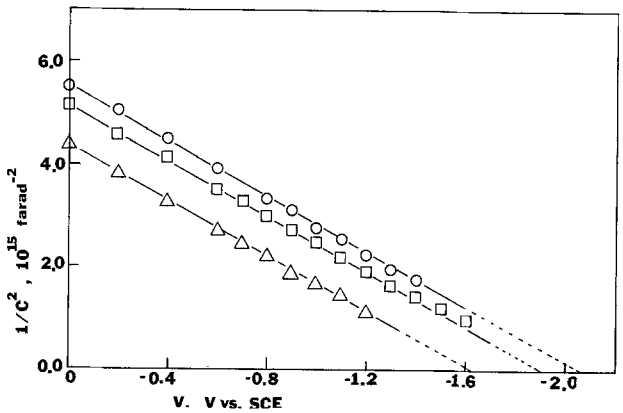

Fig. 1. Mott-Schottky plots of ZnS electrodes in 1M $NaClO_4$ at different *p*H. A-C frequencies, 100 and 300 Hz. △, *p*H 1.95; □, *p*H 7; ○, *p*H 10.

Voltammetric behavior.—Cyclic voltammetric studies on n-ZnS were conducted in deaerated 1M NaCl solution at different *p*H's. As shown in Fig. 2, in the absence of peroxydisulfate at *p*H 11.4, no appreciable cathodic current was observed at potentials positive of −2.0V *vs.* SCE (curve a). The introduction of 20 mM $K_2S_2O_8$ into the solution caused an increase in the cathodic current for potentials negative of −1.8V *vs.* SCE (curve b). This enhanced cathodic current is apparently due to the reduction of $S_2O_8^{2-}$ at the ZnS electrode. When the *p*H of the solution used in b was decreased to 2.2, a diffusion-controlled reduction wave with a peak current, i_p, proportional to

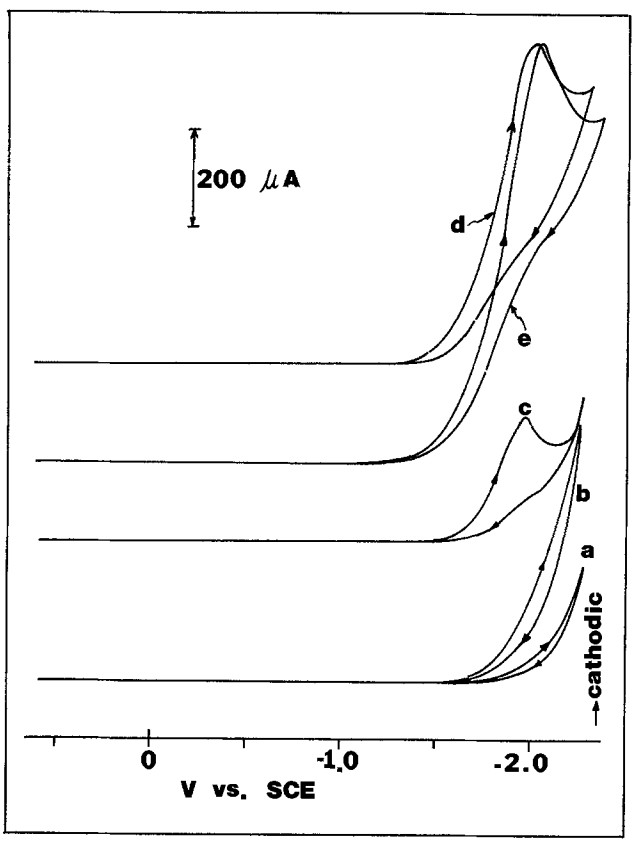

Fig. 2. Cyclic voltammograms on ZnS electrodes. Scan rate; 100 mV/sec in (a) 1.0M $NaClO_4$, *p*H 11.4; (b) 1.0M $NaClO_4$, 20 mM $K_2S_2O_8$, *p*H 11.4; (c) 1.0M $NaClO_4$, *p*H 2.3; (d) 1.0M $NaClO_4$, 20 mM $K_2S_2O_8$ at *p*H 2.2; (e) 1.0M $NaClO_4$, 20 mM $K_2S_2O_8$ at *p*H 2.0. Solution *p*H was adjusted with concentrated NaOH (10M) and $HClO_4$.

the square root of scan rate and a peak potential, E_p, at about −1.85V *vs.* SCE appeared (curve d). This wave can mainly be attributed to proton reduction, because the peak height increases with the proton concentration (cf. curve e with curve d) and the peak position was essentially the same as that corresponding to proton reduction in a solution not containing $S_2O_8^{2-}$ (see curve c). However the different i_p-values in curves d and c suggest partial contribution by the reduction of peroxydisulfate species. The reduction of $S_2O_8^{2-}$ does not appear to be strongly *p*H dependent over the *p*H range studied. Note that the peak position for $S_2O_8^{2-}$ reduction of graphite electrodes is essentially *p*H independent (see Fig. 3).

Interfacial energy scheme.—The interfacial energy scheme at the (ZnS/electrolyte) interface at pH 1 is summarized in Fig. 4. The location of the bandedges of ZnS with respect to SCE were calculated based on the procedures reported previously (18) and on the following quantities: the resistivity of the sample, $\rho \cong 20$ Ω-cm; the effective mass of electron, $m_e^* = 0.34\ m_o$ (21) (m_o is the mass of free electron); the electron mobility, $\mu_e = 160$ cm²/Vsec (22); the bandgap, $E_g = 3.66$ eV (21, 22) and the flatband potential at *p*H 1, $V_{FB} = -1.54$V *vs.* SCE. The conduction bandedge, E_c, was found to be −1.74V *vs.* SCE. This put the valence bandedge, E_v, at a potential of 1.92V *vs.* SCE. The normal potentials of the ($OH^- \cdot OH$) and (SO_4^{2-}/SO_4^{-}) couples have been estimated to be 2.7 and 3.2V *vs.* SCE, respectively (23).

Electroluminescence (EL).—Studies of EL from n-ZnS electrodes were conducted in deaerated aqueous solutions containing various redox couples given in Fig. 4 or in oxygen-saturated solution containing no redox couples other than supporting electrolyte, 1M $NaClO_4$. In the presence of peroxydisulfate or hydrogen peroxide, a bright blue emission was observed starting at potentials negative of V_{FB} that was readily observable under daylight conditions (Fig. 5). No detectable EL was observed in solution containing only supporting electrolyte even at an applied potential of −10V *vs.* SCE. In Ce(IV) solution, the blue emission was found at potentials far negative of V_{FB}, such as −5V *vs.* SCE. EL with peroxydisulfate was studied most extensively, and details of the results in solutions containing 0.2-1M $S_2O_8^{2-}$ at different *p*H's are given below.

Steady-state current and EL-potential properties.—As shown in Fig. 6a, the current, *i*, increases exponentially with potential, and some cathodic current flows when the potential is positive of V_{FB}. This exponential dependence is consistent with the capacitance measurements which indicate the formation of a Schottky depletion layer at the surface of ZnS. When the potential is well negative of V_{FB}, the i-ΔV (where $\Delta V = V - V_{FB}$) characteristic obeys a power law relationship over a wide range of applied potential of the form $i \propto \Delta V^n$ with n equal to 2. This suggests that the current in this potential range is dominated by double injection (24). A current doubling effect is expected with this system based on the interfacial energy scheme shown in Fig. 4.

Different from the i-ΔV behavior, significant EL intensity is only detected at potentials near to or negative of V_{FB} (see Fig. 6b), where double injection

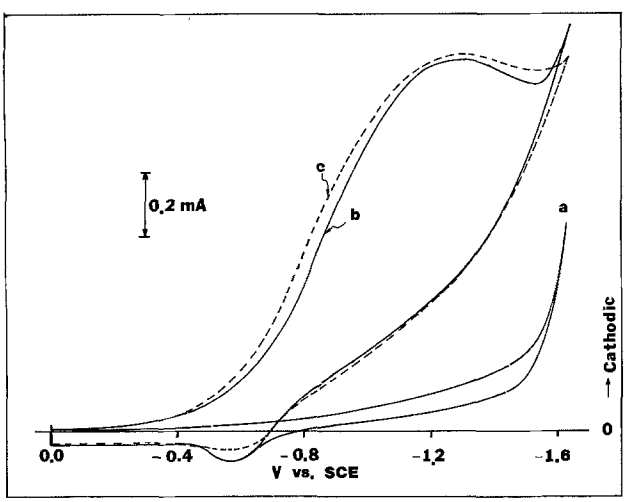

Fig. 3. Cyclic voltammograms on graphite electrode. Scan rate, 100 mV/sec in (a) 1.0M $NaClO_4$, *p*H 11.4; (b) 1.0M $NaClO_4$, 20 mM $K_2S_2O_8$, *p*H 11.4; (c) 1.0M $NaClO_4$, 20 mM $K_2S_2O_8$, *p*H 2.2.

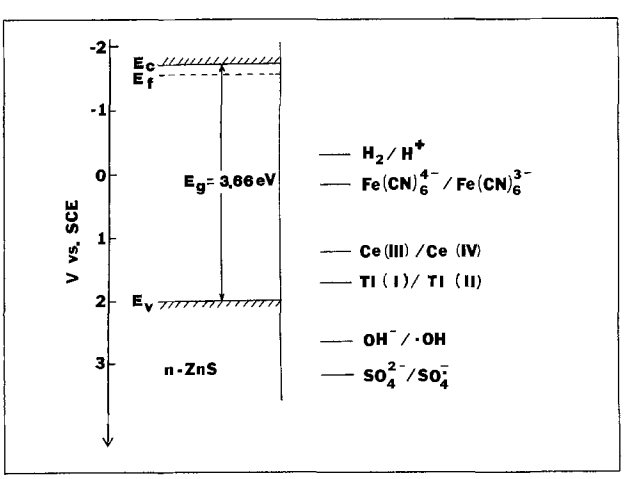

Fig. 4. Energy scheme at ZnS/electrolyte interface

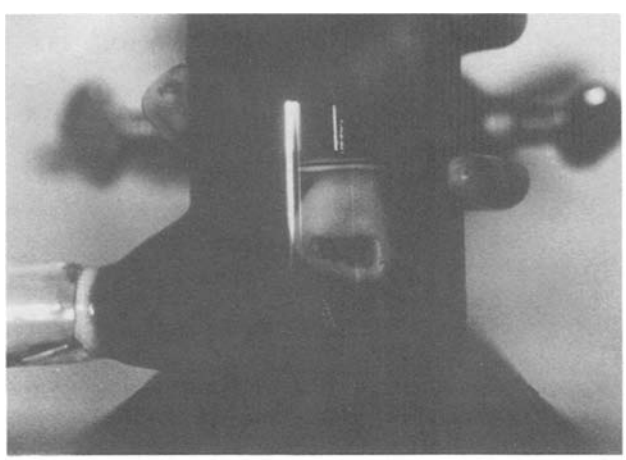

A

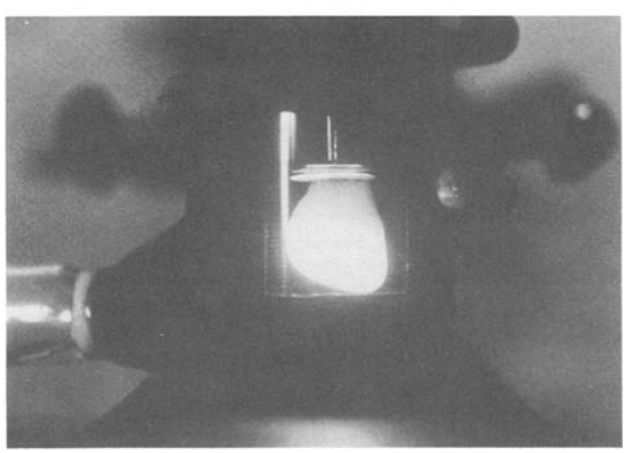

B

Fig. 5. Photo of EL at ZnS electrode

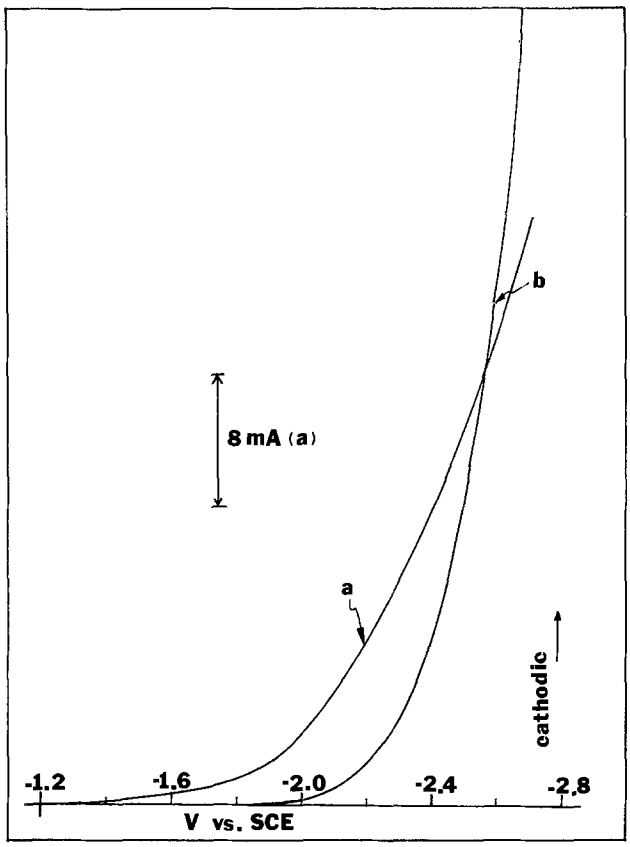

Fig. 6. Current-(curve a) and EL intensity-(curve b) *vs.* potential at ZnS electrodes in 1.0M $NaClO_4$ and 0.2M $(NH_4)_2S_2O_8$ at pH 8.4. Scan rate, 20 mV/sec.

takes place. Moreover, the EL intensity rises more steeply, as compared with the current, with increasing negative potential. As shown in Fig. 7, the EL intensity, I, varies according to a relationship of the form $I \propto i^n$, with n equal to 2 over the current range studied.

Spectral distribution.—EL spectra were obtained by repetitively pulsing the electrode between 0.0V and a potential negative of V_{FB}. The bright blue emission could be seen easily with the naked eye even under ordinary room light conditions. The EL spectra were obtained by synchronizing the OMA detection system with the potential pulses applied to the electrode.

Since the intensity and the spectral distribution of the EL vary with time during the first several potential pulses and reach a steady-state condition only after some period of cycling, the EL spectra shown were recorded under steady-state potential pulsing conditions, if not otherwise mentioned. The EL growth behavior is described in the following sections.

The EL spectra, shown in Fig. 8, are characterized by a single broad band with maximum EL intensity at about 460 nm. The exact peak position, λ_{max}, of the EL spectrum depends on several parameters which will be discussed in the following sections. Because the sensitivity of the OMA detection system was low at wavelengths beyond 700 nm, a highly red-sensitive photomultiplier tube (Hamamatsu R928) was used to check the EL spectrum in this region. No other bands were observed out to 1000 nm.

Effects of potential on EL intensity and spectral distribution.—As shown in Fig. 8, significant changes in the intensity and shifts in spectral distribution of the EL were found with small changes of the negative potential limit. More negative step potentials increased the EL intensity and produced a blue shift in the EL spectrum (by about 35 nm in λ_{max} with a potential change of −1.95 to −2.25V *vs.* SCE). The EL spectrum also was broadened with decreasing negative limits (half-width of 92 nm at −1.95V *vs.* 84 nm at −2.25V *vs.* SCE). Note that the EL spectrum with the higher emission intensity had a sharper high energy edge than that with low emission intensity. This is shown more clearly in Fig. 9 by normalizing curve e in Fig. 7 to the same peak height as curve a and then translating this normalized curve by 35 nm to shorter wavelengths to match the peak positions of the two curves.

Development of electroluminescence and current during sequential potential pulses.—The growth and decay of the EL intensity and current during a sequence of potential pulses between 0 and −2.75V *vs.* SCE is shown in Fig. 10. In the first pulse, the current (the lower curve) reaches a peak value within 5 μsec, which is very close to the rise time of the potential step generated from the potentiostat. After reaching

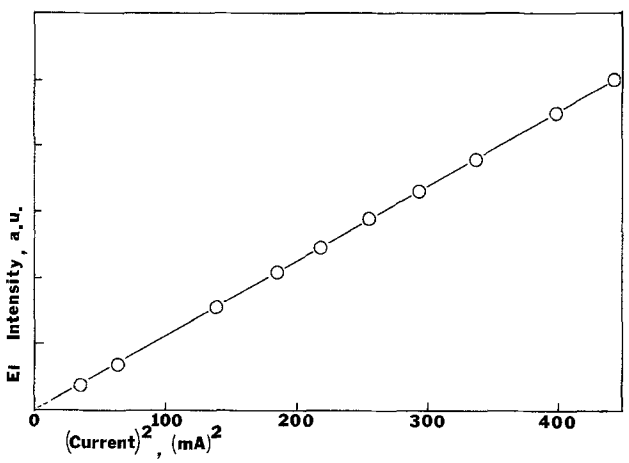

Fig. 7. EL intensity *vs.* current for ZnS electrodes in 1.0M $NaClO_4$ and 0.2M $(NH_4)_2S_2O_8$ at pH 8.4.

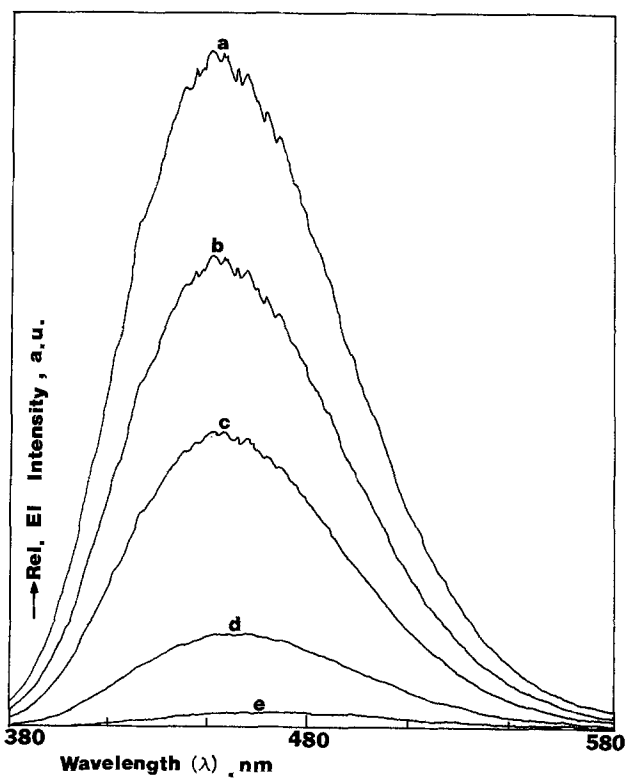

Fig. 8. Steady-state EL spectra at different step potentials on ZnS electrodes in 1.0M $NaClO_4$ and 0.2M $(NH_4)_2S_2O_8$ at pH 8.9. The positive limit potential was 0V *vs.* SCE. Negative limit potentials: (a) −2.25V, (b) −2.20V; (c) −2.15V; (d) −2.10V; (e) −2.05V *vs.* SCE.

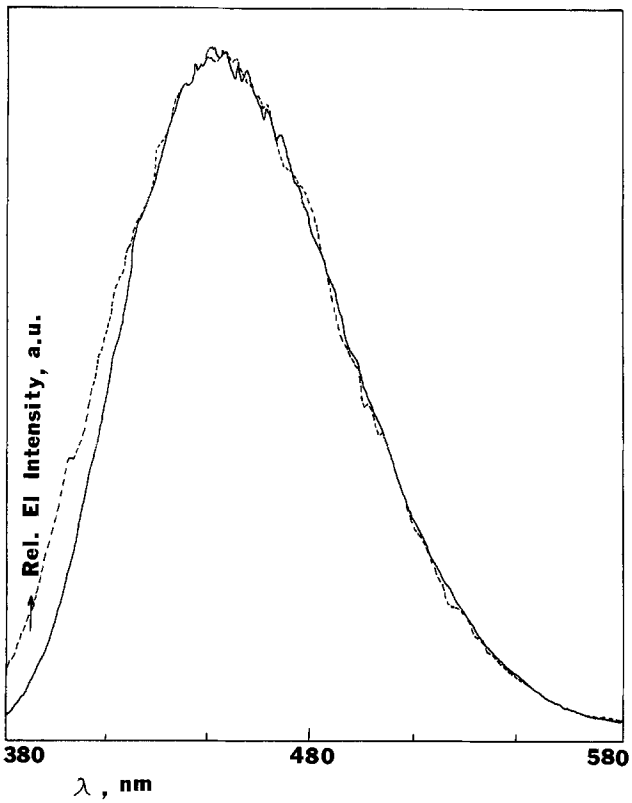

Fig. 9. EL spectra from curves a and e in Fig. 8 normalized curve e to the same peak height as curve a and then this normalized curve translated 35 nm to shorter wavelengths to match the peak positions of these two curves.

the maximum, the current decays exponentially to a steady-state value. In the subsequent pulses, this current overshoot disappears gradually and the current more rapidly (~20 μsec) attains the steady-state value. In the reverse (positive) potential step, the current decays to zero within 20 μsec and occasionally shows an oscillation. The increase of EL intensity was slower than the corresponding rate of current increase and no significant decay occurred during the cathodic step, if the pulse width was short (≤5 msec) (Fig. 10). The EL intensity increased with sequential potential pulses and reached a steady-state value after about 10 pulses, if the cathodic step potential was negative of −2.5V *vs.* SCE. The decay time of EL (≤20 μsec) was much shorter than its rise time. The rise time depended on the history of pulsing and the step potential. Extensive potential pulsing and/or a large amplitude potential step decreased the rise time of EL. A rise time of 200 μsec can be achieved after extensive pulsing of the ZnS electrode between 0 and −3.5V *vs.* SCE. There was always a dead zone at the beginning of the first potential pulse of a sequence where significant current was observed without generation of a significant amount of EL.

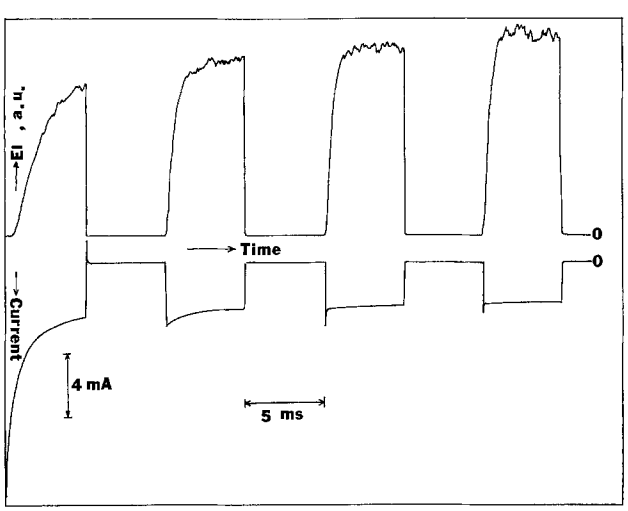

Fig. 10. Bottom: Current time characteristics of ZnS electrodes in 1M $NaClO_4$ and 0.2M $(NH_4)_2S_2O_8$ at pH 8.4. The potential was pulsed between 0 and −2.75V *vs.* SCE at a frequency of 100 Hz. Top: corresponding EL intensity-time characteristics.

Accompanying the growth of the EL intensity during a sequence of pulses, a blue shift of the EL spectrum was observed. As shown in Fig. 11, the integrated EL intensity during a single pulse increased with pulse number. This is consistent with the result shown in Fig. 10. The integrated EL intensity in the 26th pulse was about 100 times higher than that of the first pulse. Moreover, a pronounced blue shift of about 20 nm in λ_{max} was observed on the EL spectrum of the 26th pulse compared to that of the first.

Effects of pH on EL intensity and spectral distribution.—Studies of pH effects on the EL were conducted in deaerated solutions containing 0.2M $(NH_4)_2S_2O_8$ and 1M $NaClO_4$. The pH of the solution was adjusted with 10M NaOH and $HClO_4$. The peak intensity of the EL was a function of pH (Fig. 12). When the potential of the ZnS electrode was pulsed between 0 and −3V *vs.* SCE with a 5 msec pulse width, the EL intensity reached a maximum value at pH 7-9 and decreased gradually at lower pH and more steeply at higher pH. An increase in pH from 8.0 to 10.1 caused a large decrease in the EL intensity and a red shift of 35 nm in the EL spectrum. Similarly, a decrease of pH from 8.0 to 1.2 decreased the EL intensity and caused a red shift (~18 nm) of the EL spectrum (Fig. 13).

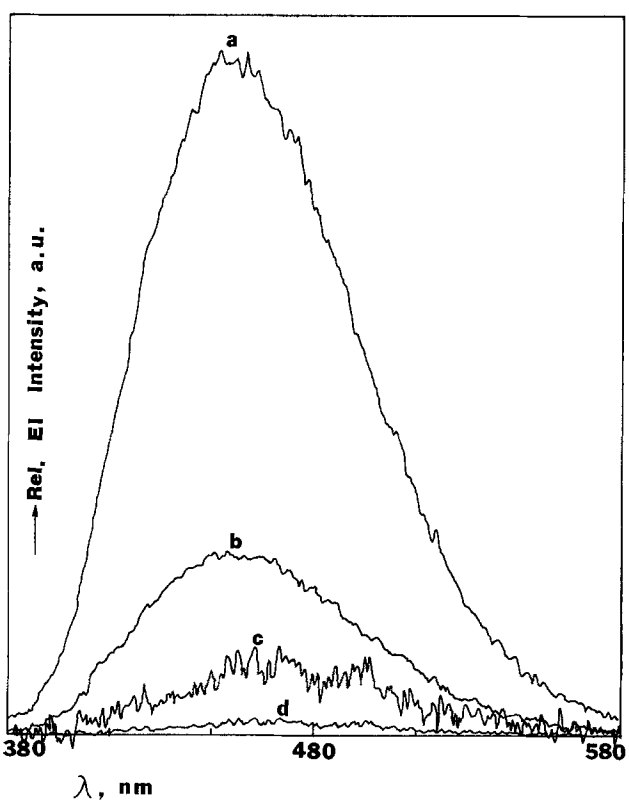

Fig. 11. Development of EL spectra for different potential pulses on ZnS electrodes in 1.0M $NaClO_4$ and 0.2M $(NH_4)_2S_2O_8$ at pH 8.9. Curve a—26th pulse; curve b—11th pulse; curve d—first pulse; curve c—five times expansion of the EL scale in curve d. Potential of the electrode was pulsed between 0 and −2.25V *vs.* SCE at a frequency of 100 Hz.

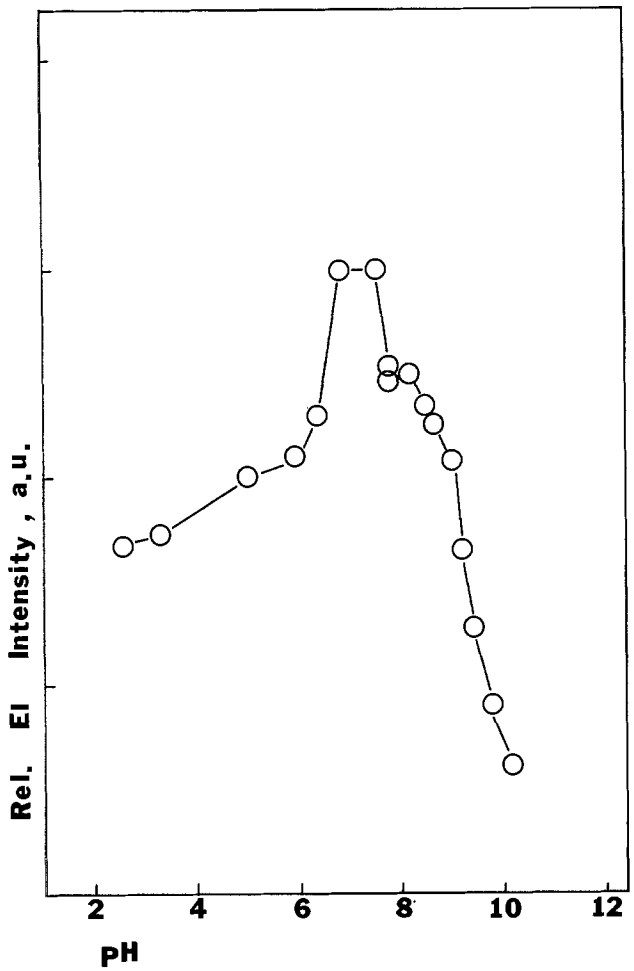

Fig. 12. EL peak intensity *vs.* pH characteristics of ZnS electrodes in 1M $NaClO_4$ and 0.2M $(NH_4)_2S_2O_8$. The electrode was pulsed between 0 and −3V *vs.* SCE at a frequency of 100 Hz.

Electroluminescence in the first potential pulse.—The growth of EL during the first pulse was usually very different from that observed under steady-state pulse conditions. The effect of the negative potential limit is shown in Fig. 14. At smaller negative potentials (*e.g.*, positive of −2V *vs.* SCE), the EL intensity was very low and increased linearly with time (see curve 14a). As the limit was made more negative, the EL intensity increased linearly with time at the very beginning and exponentially approached a saturation value at longer times (see curve 14c), indicating a faster growing-in of EL as compared with that at less negative potentials. A faster rate in EL growth could also be achieved at less negative potentials, if the electrode was prebiased to a potential where no EL was generated but a significant current was observed (for example, a prebias at any potential between −1.4 and −1.8V *vs.* SCE at pH 8.4).

The effect of prebias on the growth behavior of EL at −2.25V *vs.* SCE is shown in Fig. 15. Without prebias, the EL intensity was low and grew very slowly (see curve b). The corresponding chronoamperometric curve (curve d) showed a significant current overshoot and sharp decay to a steady-state value. Prebias of the electrode for 30 sec at −1.72V *vs.* SCE, where no EL but a significant transient current was detected, not only enhanced the EL intensity but also accelerated the growth of EL (see curve a). The current overshoot in curve d disappeared and the current reaches the steady-state value within a few tens of μsec (see curve c).

Efficiency and stability of ZnS electrode.—The EL efficiency was determined in a pulse experiment with

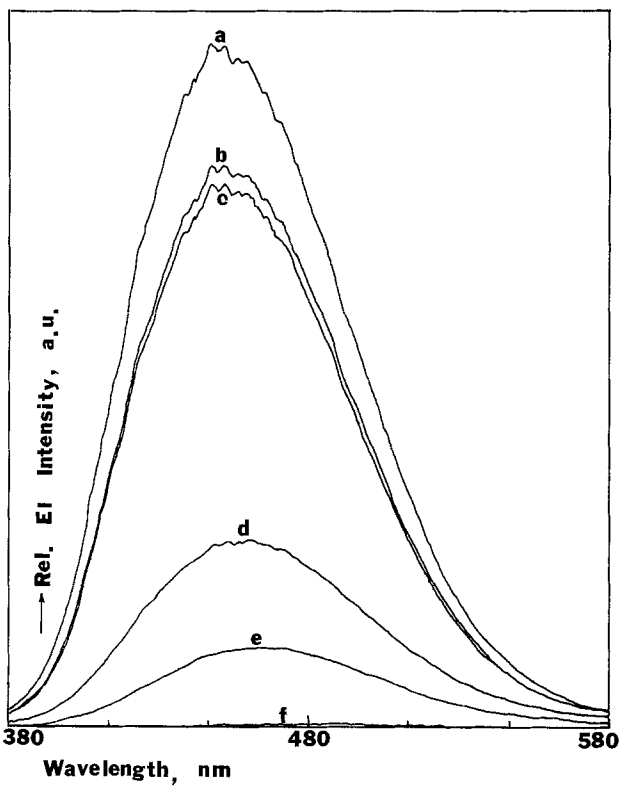

Fig. 13. EL spectra at different pH on ZnS electrodes in 1M $NaClO_4$ and 0.2M $(NH_4)_2S_2O_8$. The electrode was pulsed between 0 and −2.25V *vs.* SCE at a frequency of 100 Hz. Curve a—pH 8.0; b—pH 7.4; c—pH 5.0; d—pH 2.7; e—pH 1.2; f—pH 10.1.

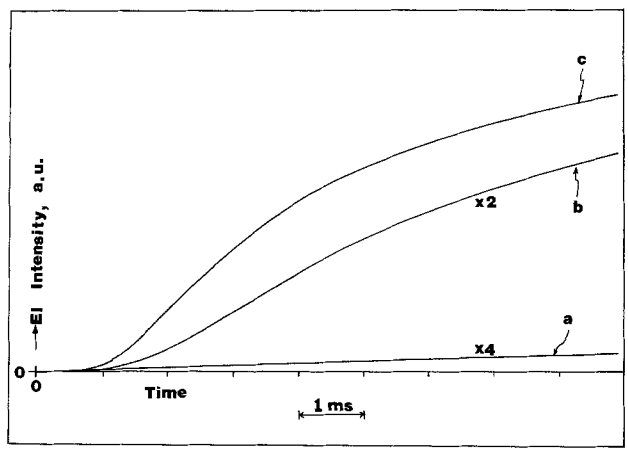

Fig. 14. Growth behavior of EL of ZnS electrodes during the first pulse. Solution contained 1.0M $NaClO_4$ and 0.2M $(NH_4)_2S_2O_8$ at pH 4.0. The cathodic step potential: −2.0V *vs.* SCE (curve a); −3.0V (curve b); −3.5V (curve c).

a step potential to −2.5V *vs.* SCE where a steady-state current density of 25 mA/cm² was obtained. An integrated EL efficiency, ϕ_{EL}, was calculated based on Eq. [2]

$$\bar{\phi}_{EL} = \frac{\text{total light emitted} \times \mathbf{F}}{\text{total charge passed through the electrode}} \quad [2]$$

in which **F** is Faraday's constant, the light emitted was in einsteins, and the charge in coulombs. The total light energy, in joules, was converted to einsteins at 460 nm. The broad (FWHM of ~80 nm) but quite symmetric feature of the EL spectrum makes this only an approximation. The EL efficiency at a current density of 25 mA/cm² ranged from 0.2 to 0.35%, depending on the particular electrode. Since the EL intensity depends in a nonlinear way on the current density, as illustrated in Fig. 7, so does ϕ_{EL}. To in-

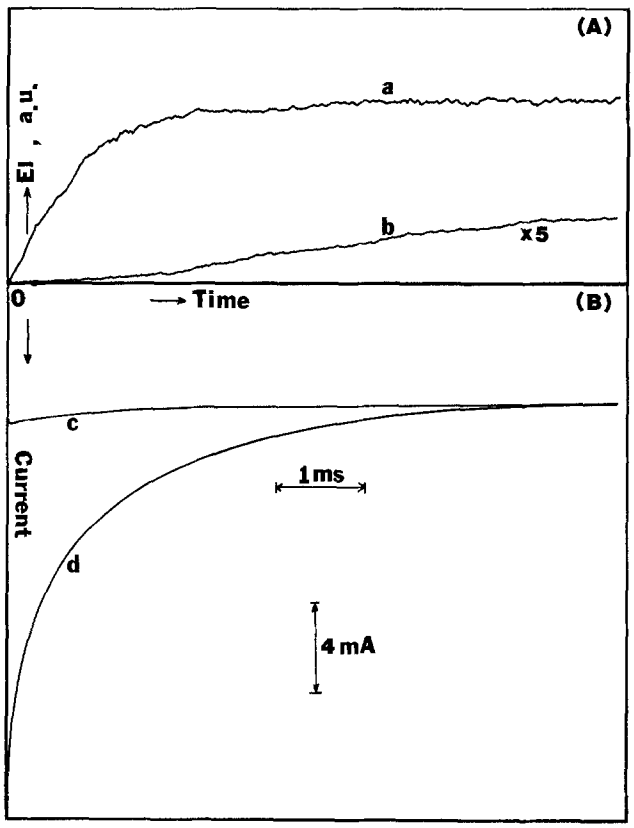

Fig. 15. Effect of prebias on the growth of EL and current for the first potential pulse. Solution and electrode, same as in Fig. 14. Curves a (EL) and c (current)—electrode was prebiased at −1.75V vs. SCE for 30 sec before step to −2.25V; curves b (EL) and d (current)—without prebias.

vestigate the stability of the ZnS electrodes in aqueous solution containing peroxydisulfate, the authors performed a long-term pulse experiment. The electrode was immersed in a solution containing 0.2M $(NH_4)_2S_2O_8$ and 1M $(NH_4)_2HPO_4$ (pH ~ 8) and was pulsed between 0 and −2.5V *vs.* SCE with a pulse width of 5 msec. The EL intensity was monitored occasionally with a radiometer. Since peroxydisulfate is reduced irreversibly on the ZnS electrode and is not regenerated at the counterelectrode, an additional amount of peroxydisulfate was introduced daily into the solution. The pH of the solution was kept at ~8. The EL intensity showed some short-term fluctuation but the electrode glowed continuously for at least 11 days, after which time the experiment was terminated. The surface of the electrode after this test was darker colored than originally but the weight loss was <1%. At present, the authors are uncertain as to the origin of the apparent change of the electrode surface color. The darkening of the electrode surface did not decrease the EL intensity, and the surface film was difficult to remove by etching with dichromate cleaning solution.

Discussion

Interfacial energetics and mechanism of electroluminescence.—The fact that significant EL intensity near V_{FB} occurs only in solutions containing redox couples, such as H_2O_2 and $S_2O_8^{2-}$, whose reduction produces intermediates that are sufficiently oxidizing to inject holes into the valence band of n-ZnS (see Fig. 4), supports the minority carrier injection mechanism of electroluminescence (6-8, 13). The lack of EL in supporting electrolyte alone and the observation of little EL in solutions containing weakly oxidizing species, such as $Fe(CN)_6^{3-}$, even at a potential far negative of V_{FB} (for example −8.0V *vs.* SCE), rules out the possibility that the energetic holes required for EL are generated by high electric field processes inside the semiconductor, *e.g.*, field-assisted electron tunneling from valence band to conduction band. In solutions containing redox couples with potentials located within the bandgap but close to the valence bandedge of n-ZnS, such as Ce(IV)/Ce(III) and Tl(II)/Tl(I), significant EL was observed only when the n-ZnS electrode was biased at a potential at least 1V negative of V_{FB}. The requirement of this overpotential is understandable simply based on the energetics for interfacial hole transfer. Both Ce(IV) and Tl(II) are energetically insufficient to inject holes into the valence band of n-ZnS. However, efficient hole injection can occur, if a significant net change in the potential drop across the double layer is allowed or a strong negative bias is applied to the electrode so that electron tunneling from the valence band to the solution species can take place. This seems the case for Ce(IV) and Tl(II).

The mechanism proposed for the electroluminescence in $S_2O_8^{2-}$ or H_2O_2 is shown in Scheme I. This scheme has long been applied to explain the edge emission from GaP, CdSe, etc.

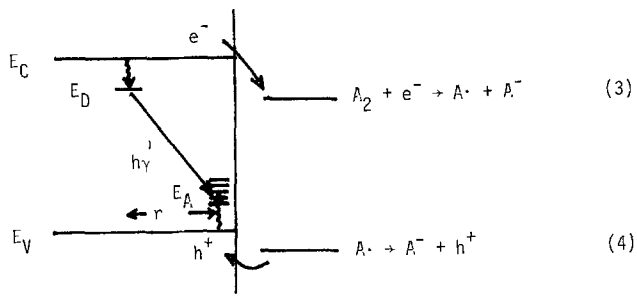

Scheme I

The first stage (Eq. [3]) involves the reduction of $S_2O_8^{2-}$ or H_2O_2 by conduction band electrons of the n-ZnS electrode. This produces $SO_4^{\cdot-}$ or · OH; these are sufficiently oxidizing to capture electrons from the valence band in the second stage (Eq. [4]). The radiative recombination of these injected holes with conduction band electrons does not produce edge emission (corresponding to E_g) in the present experiment. The peak energy (2.74 eV) of the EL spectrum is substantially smaller than the bandgap (3.66 eV) of ZnS. This subbandgap emission can only be explained based on radiative recombination through intermediate levels, such as the donor impurity level E_D and/or acceptor impurity level E_A.

The interfacial energetics can also be changed by varying the pH of the solution. Capacitance measurements clearly show the strong pH dependence of V_{FB} of n-ZnS electrodes. Increasing the pH, shifts V_{FB} towards more negative values. This favors hole injection (Eq. [4] in Scheme I) but makes electron transfer from the conduction band of n-ZnS to solution species (the first step or Eq. [3] in Scheme I) less favorable. Thus at a given potential, the current density and the corresponding EL intensity decrease with an increase in pH. This is consistent with the results shown in Fig. 12 when the pH is beyond 8. The decrease of EL intensity with a decrease in pH at pH < 7 does not fit this argument. The decrease of EL intensity in this pH range might be caused by at least two factors. The first involves the competition between the reduction of proton and $S_2O_8^{2-}$ on the ZnS electrode. This is illustrated in Fig. 2. Proton reduction which produces no EL, would decrease the contribution of the reduction of $S_2O_8^{2-}$ to the total current density and thus reduces the EL intensity. The second factor pertains to the instability of ZnS in acidic solution. Significant weight loss (~5%) was observed after a ZnS crystal was immersed in an air-saturated solution containing 1M $(NH_4)_2S_2O_8$ at pH 1 for 2 months.

Spectral distribution and intensity of electroluminescence.—That EL spectra are more asymmetric at high emission intensity than at low intensity as shown in Fig. 9 might be partially due to the effect of self-absorption. If holes can be transferred from some distance into the ZnS, the photons emitted there (especially those with shorter wavelength) could be recaptured to promote photo-induced electron transfer from traps. Experiments showing a photo-enhanced cathodic current and photoquenching of EL, which will be discussed in a separate paper, support this argument. The sharper rise in intensity in the high energy edge is expected from reabsorption of the luminescence by the transition between the band tail (caused by heavily doping) and filled intermediate levels. These results suggest that EL from ZnS is produced in a region extending from the semiconductor/solution interface into a certain depth of the semiconductor. However, due to the much lower (~16 times) hole mobility compared with the electron mobility, the emission zone could be quite thin.

One of the interesting features of the EL spectrum on the ZnS electrode is the blue shift of λ_{max} with increasing excitation rate (current density) and thus EL intensity. Several experiments have been conducted to illustrate this phenomenon. These include (*i*) the effect of cathodic step potential (see Fig. 8), (*ii*) the time dependence of EL spectrum (see Fig. 11), and (*iii*) the pH effect (see Fig. 13). Such peak shifts might be attributed to a kinetic effect involving the rate of filling of holes in a band of acceptor levels involved in the radiative process. Thus, at low currents only, the upper acceptor levels would be populated, resulting in lower energy transition, while at high currents, lower acceptor levels would be involved and a higher energy transition would be observed. If this mechanism applies, one would expect the low energy edge of the EL spectrum to reproduce approximately the shape of the acceptor band at the low energy tail. This seems consistent with the experiment, if the impurity band has an exponential distribution of states at the low energy edge. However, the high energy edge of the EL spectrum should be a rather abrupt cutoff before the impurity band is completely filled. The experiment does not show this behavior especially at low current densities (low EL intensities).

One of the accepted models to explain this phenomenon and most of our results on luminescence (including photoluminescence and photoquenching of EL which are not reported here) at ZnS involves tunneling between spatially separated upper (or donor) and lower (or acceptor) states (see Scheme 1). This concept was proposed about two decades ago by Williams and co-workers (25) to explain luminescence from Cu-doped and Cu In-doped ZnS. Similar recombination processes by electron tunneling have been identified for donor acceptor pairs in many semiconductors (26-28) and in alkali halides (29).

The energy of the emitted light due to the transition from the donor level to the acceptor level in a donor acceptor pair separated by a distance, r, is given by Eq. [5] (21), if the phonon coupling is neglected

$$E(r) = E_g - (E_A + E_D) + e^2/\epsilon_0 r \qquad [5]$$

in which E_g is the bandgap, E_A and E_D are the depth of the donor and acceptor, respectively, e is the elementary charge, and ϵ_0 is the static dielectric constant. The electron tunneling probability between two states can be written (30, 31)

$$W(r) = W_0 \exp(-2r/a) \qquad [6]$$

where a is the effective radius for overlap of the donor wave functions with the acceptor wave functions and W_0 is a parameter independent of r.

Based on the tunneling model, the rate determining step for the overall radiative recombination process is the electron transfer (through a tunneling mechanism) between the occupied upper states and the empty lower states. With progressive excitation by a potential pulse of large amplitude, electrons are accumulated in the upper luminescent levels and holes in the lower levels. This increases the density of excited luminescent states and thus statistically shortens the average interimpurity distance. A blue shift of the emission peak (Eq. [5]) with increasing transition probability (Eq. [6]) should be observed. However, since the number of possible pairings decreases as r decreases (25c, 26c), the emission intensity must go through a maximum as the separation r is varied. Qualitatively, this model explains the relation between the spectral distribution and the EL intensity quite satisfactorily.

Electroluminescence intensity-current relationship.—The intensity (I)-current (i) relationship of the form $I \propto i^2$ suggests that the radiative recombination of electron hole pairs at the luminescent centers is the rate determining step of the EL under steady-state conditions. Neither electron transfer to the upper states nor hole transfer to the lower state controls the rate of emission. This is consistent with the tunneling model discussed above.

At steady state, the electron density of the upper occupied state, n_u, is proportional to exp $[e(\text{QFLE})/kT]$ and the density of free electrons, n. The QFLE term represents the quasi-Fermi level of electrons, k is the Boltzmann constant, and T is the absolute temperature. Assuming that the diffusive component of the current is negligibly small as compared to the migration term, the current density is thus proportional to N. Hence

$$n_u \propto i \qquad [7]$$

The hole density of the lower empty state, p_l, is proportional to exp $[e(\text{QFLH})/kT)]$ and the density of free holes, p. The QFLH term is the quasi-Fermi level of holes. p is proportional to the rate of hole injection which contributes one-half of the total current. The splitting of QFLH and QFLE from the equilibrium Fermi level arises because electrons accumulate in the donor levels and holes accumulate in the lower acceptor states. Thus

$$p \propto i \qquad [8]$$

Since the emission rate is proportional to the product of n_u and p_l, if the radiative recombination process is the rate determining step, a square law for the intensity-current relationship is predicted.

Effect of trapping on the growth of electroluminescence.—Several experimental results demonstrate the existence of electron trapping, which strongly affects the EL on ZnS: (*i*) there is a potential region where no EL intensity is detected but significant current is observed (see Fig. 6); (*ii*) the current overshoots in the first potential pulse; prebiasing the electrode or pulsing the electrode continuously eliminates this current overshoot (see Fig. 10 and 15)—this suggests that the current overshoot at the beginning of the first potential pulse is not controlled by solution double layer; (*iii*) at a low negative step potential, the EL intensity is very low and increases linearly with time (see Fig. 14). Progressively pulsing the electrode accelerates the growing-in of EL and increases also the EL intensity (see Fig. 10). The increase of cathodic limit potential has the same effect on the growth of EL (see Fig. 14).

A simple rate equation is adequate to illustrate qualitatively these points (see Scheme II). If the upper (donor) states are sufficiently deep that the detrapping of electrons to the conduction band can be neglected, the rate of electron filling of the initially

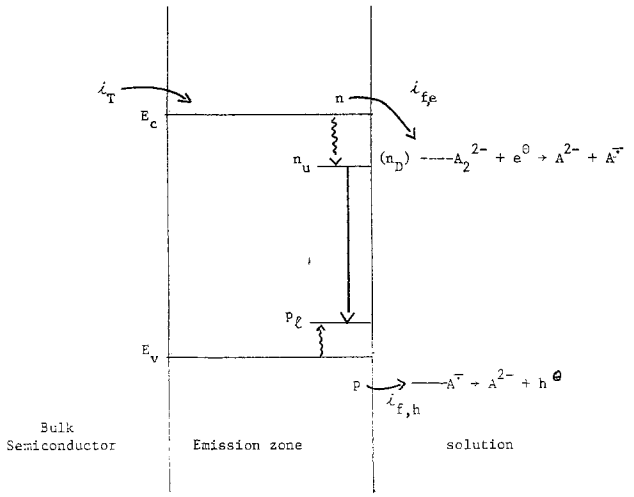

Scheme II

empty upper (donor) states is given by

$$\frac{dn_u}{dt} = A_1 n(n_D - n_u) - A_2 n_u p_l - A_3 n_u p_l \qquad [9]$$

in which n_u is the density of occupied upper (donor) states, n the density of electrons in the conduction band, n_D the total number of upper states (empty and occupied) per unit volume, p_l the density of empty lower (acceptor) states, and A_1 and A_2 are constants describing the rate of generation of n_u, the radiative recombination rate and the nonradiative recombination through n_u and p_l, respectively.

The authors assume that before most of the upper states are filled, electron trapping by these states is the predominant process for the consumption of electrons injected from the bulk of semiconductor into the emission zone. Thus, in the early part of the pulse, n, p, and p_l are small and only slowly varying variables, *i.e.*

$$\frac{dn}{dt} \sim 0 \qquad [10a]$$

$$\frac{dp}{dt} \sim 0 \qquad [10b]$$

$$\frac{dp_l}{dt} \sim 0 \qquad [10c]$$

By integration of Eq. [9] with $n_u = 0$ at $t = 0$ and the assumptions in Eq. [10a], [10b], and [10c]

$$n_u = n_u^{\infty} [1 - \exp(-t/\tau)] \qquad [11]$$

in which

$$n_u^{\infty} = A_1 n n_D / (S_1 n + A_2 p_l + A_3 p_l) \qquad [12]$$

and

$$\tau = 1/(A_1 n + A_2 p_l + A_3 p_l) \qquad [13]$$

The EL intensity is given by

$$I = A_2 n_u p_l = A_2 p_l n_u^{\infty} [1 - \exp(-t/\tau)] \qquad [14]$$

This exponential growth of EL was observed at high step potentials and in the time domain away from the beginning of a potential step (Fig. 14).

When $t/\tau \rightarrow 0$, Eq. [14] reduces to

$$I = A_2 p_l n_u^{\infty} t/\tau \qquad [15]$$

This linear growth behavior of EL is observed at the beginning of any potential step or throughout the whole width of potential pulse, when its amplitude is small (see curve a of Fig. 14).

The conservation of charges gives

$$\frac{dn_u}{dt} + \frac{dn}{dt} - \frac{d}{dt} - \frac{dp_l}{dt} = i_d \qquad [16]$$

with

$$i_d = i_T - (i_{f,e} + i_{f,h}) \qquad [17]$$

i_d in these equations should represent the current overshoot in the chronoamperograms in the first potential pulses. Combination of Eq. [10a], [10b], [10c], [12], and [16] yields

$$i_d = (n_u^{\infty}/\tau) \exp(-t/\tau) \qquad [18]$$

This current transient is clearly shown in the first potential pulse in Fig. 10. The time constant for the increase of EL is very similar to that for the current decay, as expected from Eq. [14] and [18]

The actual mechanism is certainly more complicated than that given above and involves radiationless recombinations between n and p, probably via trapping levels. These radiationless processes are what contribute to the modest efficiency of the observed EL. Additional surface quenching processes by solution species also occur. Such processes are currently under investigation.

Conclusions

Bright blue EL results from the electrochemical reduction of peroxydisulfate at an n-ZnS electrode. This luminescence arises from recombination of an electron with a hole injected by an intermediate $(SO_4^{-\cdot})$ in the reduction.

Acknowledgment

The support of this research by the Solar Energy Research Institute and the Office of Naval Research is greatly appreciated. The authors are indebted to Professor J. D. McCaldin of Cal Tech for supplying several ZnS crystals. P. Leempoel was partially supported by a Fulbright grant.

Manuscript submitted Dec. 20, 1982; revised manuscript received March 30, 1983.

REFERENCES

1. A. Heller, *Acc. Chem. Res.*, **14**, 154 (1981).
2. A. J. Bard, *Science*, **207**, 139 (1980).
3. M. S. Wrighton, *Acc. Chem. Res.*, **12**, 303 (1979).
4. A. J. Nozik, *Annu. Rev. Phys. Chem.*, **29**, 189 (1978).
5. H. J. Gerischer, *J. Electroanal. Chem. Interfacial Electrochem.*, **58**, 263 (1975).
6. H. H. Strickert, J.-R. Tong, and A. B. Ellis, *J. Am. Chem. Soc.*, **104**, 581 (1982); B. R. Karas, H. H. Strickert, R. Schreiner, and A. B. Ellis, *ibid.*, **103**, 1648 (1981); B. R. Karas and A. B. Ellis, *ibid.*, **102**, 968 (1980); B. R. Karas and A. B. Ellis, *ibid.*, **101**, 236 (1979); H. H. Strickert, J.-R. Tong, and A. B. Ellis, *ibid.*, **104**, 581 (1982).
7. B. Pettinger, H.-R. Schoppel, and H. Gerischer, *Ber. Bunsenges. Phys. Chem.*, **80**, 849 (1976).
8. K. H. Beckmann and R. Memming, *This Journal*, **116**, 368 (1969).
9. J. D. Luttmer and A. J. Bard, *ibid.*, **126**, 414 (1979); *ibid.*, **125**, 1424 (1978); R. N. Noufi, P. A. Kohl, S. N. Frank, and A. J. Bard, *ibid.*, **125**, 246 (1978).
10. M. Aven and J. Z. Devine, *J. Luminesc.*, **7**, 195 (1973).
11. M. E. Ozsan and J. Woods, *Appl. Phys. Lett.*, **25**, 489 (1975).
12. H. Katayama, S. Oda, and H. Kukimoto, *Appl. Phys. Lett.*, 27, 697 (1975).
13. V. A. Tyagai, M. K. Sheinkman, E. L. Shtrum, G. Ya. Kelbasov, and N. K. Moiseava, *Sov,. Phys. Semicond.*, **14**, 112 (1980).
14. L. J. Van Ruyven and F. E. Williams, *Phys. Rev. Lett.*, **16**, 889 (1966).
15. R. Nitsche, *J. Phys. Chem. Solids*, **17**, 163 (1960).
16. R. G. Kaufman and P. Dowbor, *J. Appl. Phys.*, **45**, 4487 (1974).
17. F.-R. Fan, H. S. White, B. L. Wheeler, and A. J. Bard, *J. Am. Chem. Soc.*, **102**, 5412 (1980).
18. F.-R. Fan and A. J. Bard, *This Journal*, **128**, 945 (1981).
19. K. Itaya and A. J. Bard, *J. Phys. Chem.*, **85**, 1358 (1981).
20. R. Bezman and L. R. Faulkner, *Anal. Chem.*, **43**, 1749 (1971).
21. J. I. Pankove, "Optical Processes in Semiconduc-

tors," p. 412, Prentice-Hall, Englewood Cliffs, NJ (1971).
22. Y. S. Park and B. K. Shin, "Topics in Applied Physics," Vol. 17, J. I. Pankove, Editor, p. 136, Springer-Verlag, Berlin (1977).
23. R. J. Memming, *This Journal*, **116**, 785 (1969).
24. M. A. Lampert and A. Rose, *Phys. Rev.*, **121**, 26 (1961).
25. J. S. Prener and F. E. Williams, *This Journal*, **103**, 342 (1956) E. F. Apple and F. E. Williams, *ibid.*, **106**, 224 (1960); F. E. Williams, *J. Phys. Chem. Solids*, **12**, 265 (1960).
26. J. J. Hopfield, D. G. Thomas, and M. Gershenzon, *Phys. Rev. Lett.*, **10**, 162 (1963); D. G. Thomas, M. Gershenzon, and F. A. Trumbore, *Phys. Rev.*, **133**, 269 (1964); D. G. Thomas, J. J. Hopfield, and W. M. Augustyniak, *Phys. Rev.*, **A140**, 202 (1965).
27. D. Redfield, J. P. Wittke, and J. L. Pankove, *Phys. Rev.*, **B2**, 1830 (1970).
28. R. A. Street, *Adv. Phys.*, **30**, 593 (1981).
29. C. J. Delbecq, Y. Toyozawa, and P. H. Yuster, *Phys. Rev.*, **B9**, 449 (1974).
30. A. Miller and E. Abrahams, *E. Phys. Rev.*, **120**, 745 (1960).
31. F. Mott, *Phil. Mag.*, **19**, 835 (1969).

Technical Note

Electrochemical Reduction of Calcium Chromate

F. M. Delnick*

Sandia National Laboratories, Exploratory Batteries Division 2523, Albuquerque, New Mexico 87185

D. K. McCarthy

Sandia National Laboratories, Battery Development Division 2522, Albuquerque, New Mexico 87185

A saturated solution of $CaCrO_4$ in LiCl-KCl eutectic is used as the cathode in $Ca/CaCrO_4/Fe$ thermally activated batteries. Upon activation to the molten state, CrO_4^{-2} is reduced at the Fe cathode current collector and Ca is oxidized via a Ca-Li alloy intermediate at the anode (1-4). Since the CrO_4^{-2} solution is in intimate contact with the anode, the CrO_4^{-2} is also reduced at the anode in a side reaction parallel to Ca oxidation. These CrO_4^{-2} reductions at both the cathode and anode produce insoluble product layers which partially control the discharge behavior of the $Ca/CaCrO_4/Fe$ thermal battery (4, 5).

The insoluble chromate reduction product at the anode has been identified by Nissen (4) as primarily Ca_2CrO_4Cl. In partially discharged batteries, Hlava and Headley (6) have identified both $Ca_5(CrO_4)_3Cl$ and Ca_2CrO_4Cl.

Laitinen and co-workers (7-14) have studied extensively the electrochemical reduction of dilute solutions of CrO_4^{-2} in LiCl-KCl eutectic and have observed neither of the above two Cr(V) compounds.

By controlled potential coulometry, Ferguson (15) and Bhatia (16) observed that three Faradays of charge were required to reduce one mol of CrO_4^{-2} in a single reduction wave. Using chronopotentiometry in the presence and absence of O^{-2}, Laitinen and Bankert (7) concluded that this three-electron single-step reduction resulted in the formation of the intermediate CrO_4^{-5} which subsequently decomposed to CrO_3^{-3} and O^{-2}. Propp and Laitinen (8) examined the reduction of K_2CrO_4 in the presence of Mg^{+2}. A nonstoichiometric Cr(III) compound was obtained: $Li_xMg_yCrO_4$, $(x + 2y = 5)$. Hanck and Laitinen (10) obtained $LiZn_2CrO_4$ in the presence of Zn^{+2} and either Co_2CrO_4 or $LiCo_2CrO_4$ (depending on specific conditions) in the presence of Co^{+2}. Nezu and Laitinen (11), however, were not able to identify the reduction product of CrO_4^{-2} in the presence of Ca^{+2}. Uchida and Laitinen (12) concluded that Ca^{+2} has no effect on the reduction of CrO_4^{-2}, and that water associated with hygroscopic $CaCl_2$ does influence the reduction mechanism and accounts for the irreproducible results of Nezu and Laitinen (11).

By evaluation of the diffusion coefficients and shifts in chronopotentiometric quarter-wave potentials of the CrO_4^{-2} reduction reaction in the presence of divalent metal cations M(II) = Zn^{+2}, Mg^{+2}, and Ni^{+2}, Hanck and Laitinen (10) concluded that CrO_4^{-2} reduction does not proceed in a single-step three-electron reduction reaction to an oxy-anion such as CrO_4^{-5} [Laitinen and Bankert (7)] but that it must proceed via an intermediate oxidation state of chromium.

The discovery of Niki and Laitinen (13) that chemically synthesized Li_3CrO_4 is stable in LiCl-KCl eutectic has led Niki, Uchida, and Laitinen (14) to propose that the Cr(V) compound Li_3CrO_4 is a possible intermediate in the electrochemical reduction of CrO_4^{-2} in LiCl-KCl according to the equation

$$CrO_4^{-2} + 3Li^+ + e^- \rightleftarrows Li_3CrO_4 \text{ (solid)} \quad [1]$$

These authors, however, did not report the synthesis of Li_3CrO_4 by the electrochemical reduction of CrO_4^{-2}. The subsequent disproportionation according to Eq. [2] or further reduction according to Eq. [3] of Li_3CrO_4 leads to $LiCrO_2$, the final product in the overall reduction of CrO_4^{-2} in LiCl-KCl eutectic (13, 14)

$$3Li_3CrO_4 \rightleftarrows 2Li_2CrO_4 + LiCrO_2 + 2Li_2O \quad [2]$$

$$Li_3CrO_4 + 2e^- \rightleftarrows LiCrO_2 \text{ (solid)} + 2\,O^{-2} + 2Li^+ \quad [3]$$

In this report, Li_3CrO_4 has been electrochemically synthesized by reducing CrO_4^{-2} in LiCl-KCl eutectic, thus confirming the hypothesis of Niki, Uchida, and Laitinen (14). The authors have also synthesized $Ca_5(CrO_4)_3Cl$ and Ca_2CrO_4Cl by electrochemical reduction of CrO_4^{-2} in the presence of Ca^{+2}. Li_3CrO_4, Ca_2CrO_4Cl, and $Ca_5(CrO_4)_3Cl$ have each been further

* Electrochemical Society Active Member.
Key words: battery cathode, electrosynthesis, molten salt, high temperature.

reduced to $LiCrO_2$, the final product in the overall reduction of CrO_4^{-2}.

Experimental

Polarographic grade LiCl-KCl eutectic was supplied by Anderson Physics Laboratories, Incorporated and was used without further purification. $CaCl_2$-NaCl-KCl ternary eutectic was prepared in our laboratory from reagent grade chemicals and was also used without further purification. Potentiostatic reductions were conducted on gold flags (99.5% purity) or spectroscopic grade graphite electrodes. Solid products were rinsed lightly with water to remove the halide electrolyte. The major constituents were then identified by x-ray powder diffraction. When Cr(V) compounds constituted the major reduction products, their identification was not impeded by hydrolysis reactions. These hydrolysis reactions did, however, prohibit the identification of Cr(V) minor constituents. Cyclic voltammograms were measured on gold disk electrodes fabricated by fusing gold wire onto alumina tubes. The end of the gold-filled tube was cut flat and polished to expose a gold electrode of circular cross section (area = 0.03 cm^2). All experiments were performed in a quartz cell under an argon atmosphere (AR = 99.9995% purity). All potentials are reported *vs.* the Ag/Ag^+ (0.1m) reference electrode (17), and all concentrations are expressed in molality, m.

Results and Discussion

The cyclic voltammograms of 0.11m solutions of K_2CrO_4 and $CaCrO_4$ are shown in Fig 1. In the absence of Ca^{+2}, a two-step CrO_4^{-2} reduction sequence is observed. The first step at $E = -0.1V$ corresponds to Li_3CrO_4 formation according to Eq. [1]. The current peak at $E = -0.45V$ represents the subsequent reduction of Li_3CrO_4 to $LiCrO_2$ according to Eq. [3] (13, 14). Potentiostatic reduction of concentrated (>0.1m) solutions of K_2CrO_4 in LiCl-KCl eutectic on a gold flag at $E = -0.2V$ yields a dark crystalline solid identified as Li_3CrO_4[1] by x-ray diffraction. In the presence of Ca^{+2} ions, a three-step reduction sequence is observed. By analogy, the first and third steps (at $E = -0.1$ and $-0.47V$) represent Li_3CrO_4 and $LiCrO_2$ formation, respectively. The second reduction wave at $E = -0.22V$ represents the formation of $Ca_5(CrO_4)_3Cl$. Successive cyclic scans on the reduction product substrate (Fig. 2) show the complete domination of the $Ca_5(CrO_4)_3Cl$ reaction. After the second scan, the Li_3CrO_4 reduction reaction cannot be resolved, and the $LiCrO_2$ current peak is reduced. Potentiostatic reduction of concentrated (>0.1m) solutions of $CaCrO_4$ in LiCl-KCl eutectic at $E = -0.3V$ yields $Ca_5(CrO_4)_3Cl$.[2] When this product is removed from the $CaCrO_4$ solution, washed, vacuum dried, and then placed into an LiCl-KCl electrolyte containing no $CaCrO_4$, further solid-state reduction occurs but at a much slower rate. The product of this solid-state reaction is $LiCrO_2$.[3]

In LiCl-KCl eutectic, the Cr(V) compound $Ca_5(CrO_4)_3Cl$ is the initial major product of the reduction of concentrated solutions of $CaCrO_4$ over the potential range of $E = -0.05V$ to $E = -0.4V$ and temperature range T = 400°-600°C. As concentrated solutions of $CaCrO_4$ are reduced to completion at potentials more negative than $E = -0.2V$, however, a distribution of reduction products consisting of $Ca_5(CrO_4)_3Cl$ and $LiCrO_2$ is obtained. The final reduction product is $LiCrO_2$.

In $CaCl_2$-NaCl-KCl ternary eutectic, the potentiostatic reduction of concentrated solutions of CrO_4^{-2} yields Ca_2CrO_4Cl[4] exclusively. This Cr(V) compound undergoes no further reduction in the ternary eutectic. Similarly, when $Ca_5(CrO_4)_3Cl$ is introduced into this Li^+ free electrolyte it undergoes no further reduction.

[1] Joint Committee Powder Diffraction Standards, Sets 1-31, Powder Diffraction File (PDF) 27-1229 (1982).
[2] *Ibid.*, Sets 1-31, PDF 12-246 (1982).
[3] *Ibid.*, Sets 1-31, PDF 25-476 (1982).
[4] *Ibid.*, Sets 1-31, PDF 19-217 (1982).

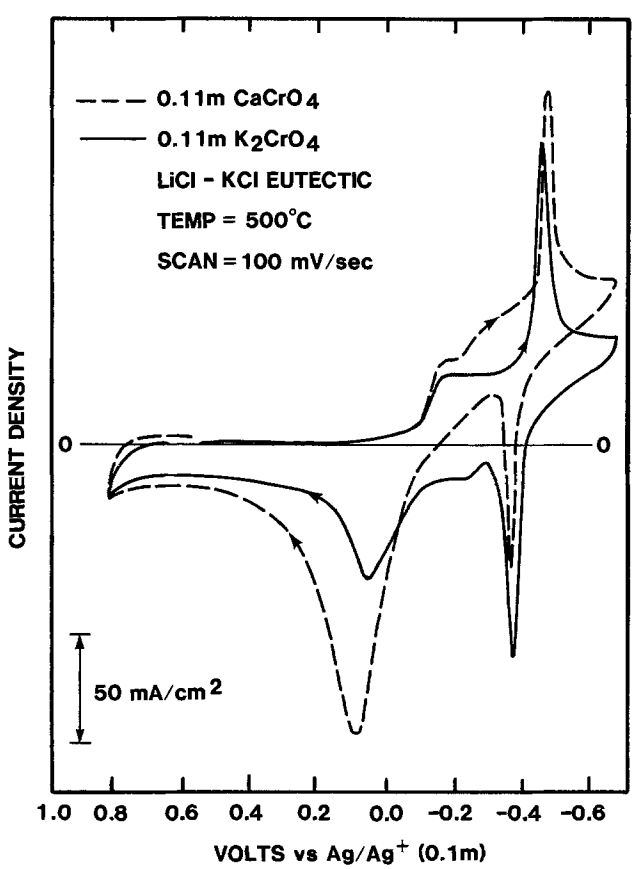

Fig. 1. Cyclic voltammogram of $CaCrO_4$ and K_2CrO_4 solutions on a gold disk electrode.

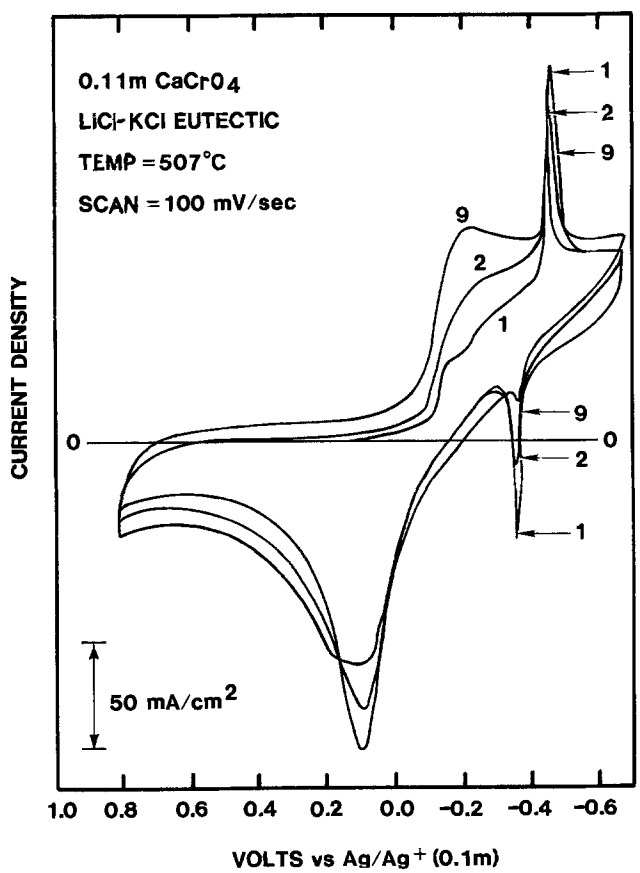

Fig. 2. Successive cyclic voltammograms of a $CaCrO_4$ solution on a gold disk electrode. The 1st, 2nd, and 9th cycles are shown.

On the other hand, when Ca_2CrO_4Cl is introduced into LiCl-KCl eutectic, it can be completely reduced to $LiCrO_2$.

Cyclic voltammograms of dilute solutions (<0.04m) of $CaCrO_4$ in LiCl-KCl eutectic yield a single-step irreversible charge transfer reaction. Potentiostatic reduction at $E = -0.4V$ requires 3.03 Faradays of charge per mol of CrO_4^{-2}. The product of this reduction is identified by x-ray diffraction as $LiCrO_2$ exclusively. In dilute solutions, Ca^{+2} is not incorporated into the CrO_4^{-2} reduction products and apparently exerts no influence on the overall reduction reaction. This agreement with Uchida and Laitinen (12) suggests that the CrO_4^{-2} reduction product is not only strongly dependent on the cations present (8, 10) but also dependent upon cation and CrO_4^{-2} concentrations. Laitinen, *et al.* (7-10, 12) confined their work to concentration ranges approximately one order of magnitude lower than those used in this report and, therefore, never observed direct evidence of a Cr(V) intermediate in the chromate reduction reaction [indirect evidence attributed to a Cr(IV) intermediate was obtained by Hanck and Laitinen (10)]. The reduction products containing Cr(V) are favored at the higher concentrations of Ca^{+2}. The availability of Li^+ (not considered by Laitinen and co-workers) also exerts an influence on the reduction mechanism.

Conclusions

The electrochemical reduction of CrO_4^{2-} proceeds through a Cr(V) intermediate, CrO_4^{-3}. The reaction of this intermediate with the available cations and the concentrations of these cations determine the overall reaction mechanism and the ultimate reduction product. In LiCl-KCl eutectic, $CaCrO_4$ ($\gtrsim$ 0.1m) is reduced to the stable intermediate $Ca_5(CrO_4)_3Cl$. In $CaCl_2$-KCl-NaCl ternary eutectic $CaCrO_4$ ($\gtrsim$ 0.1m) is reduced to the stable intermediate Ca_2CrO_4Cl. In the presence of Li^+, each of these Cr(V) compounds is further reduced to $LiCrO_2$. No subsequent reduction of $Ca_5(CrO_4)_3Cl$ or Ca_2CrO_4Cl occurs in $CaCl_2$-KCl-NaCl ternary eutectic.

Acknowledgment

This work was performed at Sandia National Laboratories supported by the U.S. Department of Energy under contract number DE-AC04-76DP00789.

Manuscript submitted Jan. 13, 1983; revised manuscript received May 10, 1983.

Sandia National Laboratories assisted in meeting the publication costs of this article.

REFERENCES

1. D. M. Bush, Sandia National Laboratories Report SAND74-0007, p. 10 (1964).
2. R. P. Clark and K. R. Grothaus, Sandia National Laboratories Report SC-RR-710037, p. 1 (1971).
3. D. A. Nissen, Sandia National Laboratories Report SC-RR-72018, p. 15 (1972).
4. D. A. Nissen, *This Journal*, **126**, 176 (1979).
5. R. A. Guidotti and F. M. Delnick, Paper 78 presented at The Electrochemical Society Meeting, Denver, CO, Oct. 11-16, 1981.
6. P. F. Hlava and T. J. Headley, Sandia National Laboratories SAND77-1317 (1977).
7. H. A. Laitinen and R. D. Bankert, *Anal. Chem.*, **39**, 1790 (1967).
8. J. H. Propp and H. A. Laitinen, *ibid.*, **41**, 644 (1969).
9. B. Popov and H. A. Laitinen, *This Journal*, **117**, 482 (1970).
10. K. W. Hanck and H. A. Laitinen, *ibid.*, **118**, 1123 (1971).
11. H. Nezu and H. A. Laitinen, Unpublished results. See Ref. (6) in I. Uchida and H. A. Laitinen, *This Journal*, **123**, 829 (1976).
12. I. Uchida and H. A. Laitinen, *ibid.*, **123**, 829 (1976).
13. K. Niki and H. A. Laitinen, *J. Inorg. Nucl. Chem.*, **37**, 91 (1975).
14. K. Niki, I. Uchida, and H. A. Laitinen, *This Journal*, **123**, 20 (1976).
15. W. S. Ferguson, 15th monthly report, Contract No. DAI-49-186-502-ORD (P)-187, University of Illinois (1955).
16. B. B. Bhatia, Ph.D. Thesis, University of Illinois (1959).
17. S. Levy and F. Reinhardt, *This Journal*, **122**, 200 (1975).

JOURNAL OF THE ELECTROCHEMICAL SOCIETY

SOLID-STATE SCIENCE AND TECHNOLOGY

SEPTEMBER 1983

Leakage and Breakdown in Thin Oxide Capacitors—Correlation with Decorated Stacking Faults

P. S. D. Lin, R. B. Marcus, and T. T. Sheng

Bell Laboratories, Murray Hill, New Jersey 07974

ABSTRACT

Thin oxide MOS capacitors which exhibited high leakage and lowered breakdown strength were studied by a number of methods in order to identify the mechanism responsible for the degradation. Electron beam-induced current (EBIC) studies, Secco etching, transmission electron microscope imaging, and energy dispersive x-ray spectroscopy were all applied to this problem. The results indicated that the defects responsible for the poor dielectric properties are impurity (Cu,Ni,Fe,Zn,Sn)-decorated stacking faults about 1μ in length, located in silicon near the silicon-silicon dioxide interface. This study establishes that decorated stacking faults degrade the quality of MOS capacitors by increasing capacitor leakage and decreasing breakdown strength.

High quality thin silicon dioxide film is of basic importance to integrated circuit MOS technology. As lateral dimensions of device elements become smaller, gate oxide thickness is also reduced in order to lower the operating voltage and thereby the power consumption. Gate oxides 25 nm thick are now commonly used in VLSI devices and the thickness is expected to be further reduced in the future.

An additional advantage of thin oxide is its high intrinsic breakdown strength. Both experimental and theoretical studies (1, 2) indicate that the field strength at breakdown improves as the thickness decreases: from about 9 MV/cm at 50 nm to 15 MV/cm at 10 nm; and for very thin silicon dioxide films, the intrinsic breakdown field strength is about 30 MV/cm. On the other hand, such ideal strengths are not usually attained. The breakdown strength of the oxide film in practice is ultimately limited by extrinsic factors. In this regard, the influence of mobile ions, sodium ion clustering (3), or pinholes (4), etc. on oxide breakdown strength has attracted much attention.

This paper reports on the results of a study of the cause of leakage and low voltage breakdown in a group of capacitors made with 22 nm oxides. This study involved the identification of extrinsic defects which were responsible for poor capacitor performance. The identification was made with a number of tools and methods including EBIC microscopy with the scanning electron microscope (SEM), and transmission electron microscopy (TEM).

The EBIC observations and the correlation between the breakdown sites and EBIC spot sites are described in a later section. Leakage current and breakdown field strength measurements are presented and correlated with the number density of EBIC spots in the section on breakdown and leakage measurements. Experiments aimed at identifying the defects responsible for leakage and breakdown are reported in the section on defect characterization. Techniques applied to this identification include EBIC imaging of Schottky diodes fabricated from MOS capacitors, preferential chemical etching of oxidized silicon wafers, and characterization by TEM and energy dispersive x-ray emission spectroscopy (EDXES).

Key words: silicon, stacking faults, EBIC, impurity, oxide leakage.

Experimental

Specimen characteristics.—The specimens studied were capacitors formed on field and gate oxides on three 3 in. diam (100) p-type, 6-8 Ω-cm, 0.51 mm thick silicon wafers. All wafers were degreased and cleaned prior to oxidation. Field oxides were formed by growing 100 nm dry oxide at 1000°C for 100 min in O_2/HCl, followed by 250 nm of steam/N_2 oxide at 950°C. Thin gate oxides were grown in O_2/HCl at 1000°C for 16 min. Square-shaped capacitors 0.5 mm a side were formed using field plates described in Table I.

EBIC imaging of capacitor defects and breakdown sites.—Figure 1 shows the experimental setup for EBIC mode of imaging of MOS capacitors. It consisted of an SEM (Cambridge Steroscan S4) operated from 1.0 to 30 kV and the preamplifier, a battery-powered 30V d-c bias supply, a Tektronix 569 curve tracer, and a micromanipulator with an etched tungsten probe. The current was taken directly from the back contact of the silicon wafer to the low noise preamplifier mounted to one port of the specimen chamber. The values of the feedback resistors were chosen to be 1/(current sensitivity) to provide unit voltage gain. The frame scan rates used were 20 and 60 sec for current ranges of 10 and 1 nA, respectively.

Conventional EBIC imaging of capacitors with relatively thick oxide proceeds by biasing the capacitor

Table I. Specimens studied

Specimen	Field plate doping	Gate oxide thickness	Field plate material/thickness (nm)
1	PBr_3, 950°C	22	Poly/350
2	As^+ implant, 900°C anneal	225	Poly/350
3	As^+ implant, 900°C anneal	22	Poly/150 nm over metal silicide/80 nm

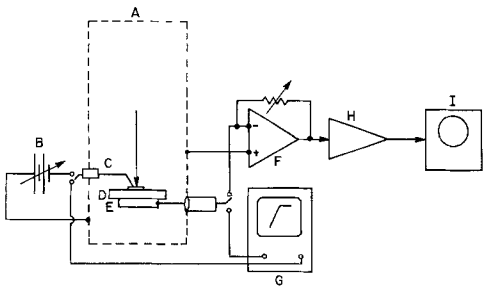

A= SCANNING ELECTRON MICROSCOPE
B= BATTERY OPERATED BIAS SUPPLY, 0 TO ±30V
C= MICROMANIPULATOR AND W PROBE
D= SPECIMEN (3" WAFER)
E= SPECIMEN STAGE
F= CURRENT PREAMPLIFIER
G= CURVE TRACER (TEKTRONIX 576)
H= VOLTAGE AMPLIFIER
I= CRT DISPLAY

Fig. 1. Diagram of the experimental arrangement for electron beam-induced current mode imaging and breakdown strength measurement of MOS capacitors.

into depletion so that the depletion region in silicon can be used to separate the beam-induced carriers. This technique was used as well as one in which the capacitors were biased into deep accumulation. In the latter case, a high field exists across the oxide, and regions of enhanced tunneling of charges showed up as bright spots in EBIC images.

Figure 2 shows EBIC images of capacitors with (a) thin gate oxide and (b) thick field oxide. These micrographs were taken while the capacitors were biased in depletion, and they show distinct white/black spots which were found to correlate with leakage and locations of breakdown (see below). Figures 3a-3d show a set of micrographs taken on another capacitor. In the secondary electron image (a), the capacitor appears normal. In the low field EBIC image (b), a number of EBIC spots similar to those in Fig. 2 were present. When the bias was increased to above 6 MV/cm, a number of bright spots appeared both at the low field EBIC spot sites and at some extra places. The extra spots appeared to have lower brightness in comparison with the low field EBIC spots. After stressing the capacitor to breakdown, one of the sites which was imaged before breakdown was found to coincide with the breakdown site (arrow, site D).

The coincidence of EBIC spots with breakdown sites was observed in many cases. Figure 4 gives two more examples in which breakdown sites coincided with the EBIC spots for two capacitors with widely different numbers of EBIC spots (9 *vs.* 220).

Breakdown and leakage measurements.—Before specimens 1 and 2 were examined in the SEM, the voltage required to give a leakage current of 10 μA was measured for each capacitor. The distributions were found to be bimodal on both specimens, with the populations (about) equally distributed on each specimen. Wafer maps showed that the capacitors in the lower voltage range were grouped together (spatially) on each specimen, and were the only capacitors which had the EBIC spots described in the previous section.

The leakage and breakdown characteristics of capacitors on specimens 1 and 2 were measured using an HP-4061A automated current voltage measurement system. The voltage was applied in 0.25V steps with 3 sec settling time until irreversible breakdown, and the I-V values were recorded. Figure 5 shows typical I-V curves thus recorded for two capacitors with (curve S8) and without (curve E2) EBIC spots; it shows that both the leakage current at a fixed voltage and the breakdown voltage were affected by the total number of EBIC spots per capacitor. Figures 6a and 6b show that the leakage current increased by two to three orders of magnitude as the EBIC spot

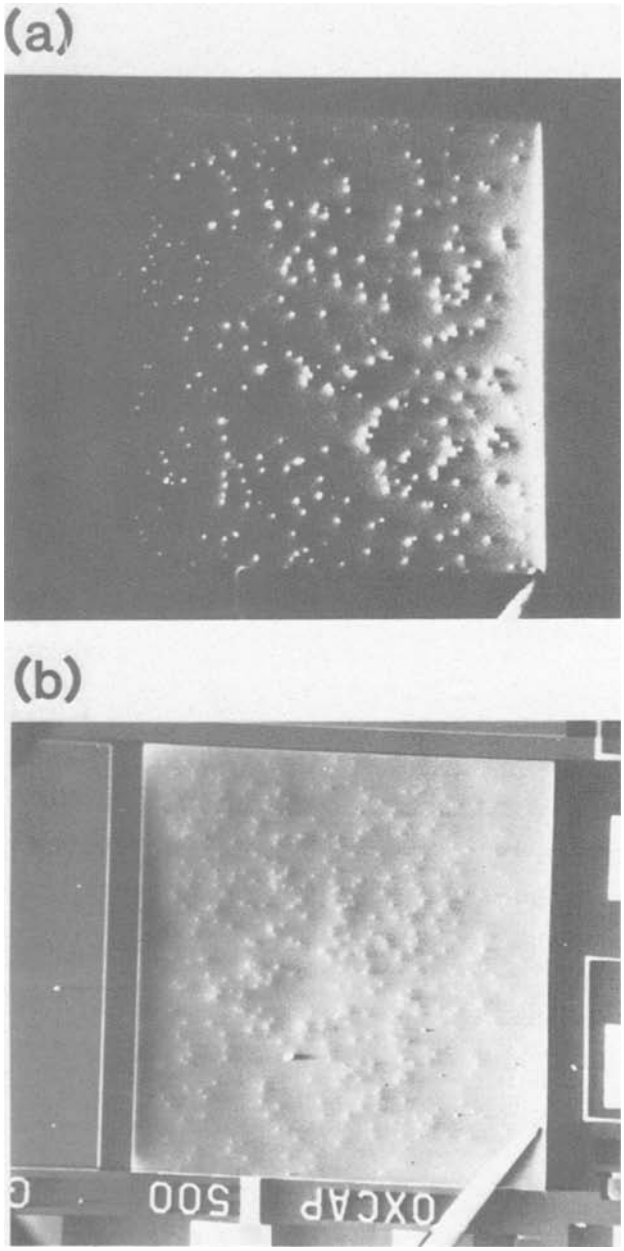

Fig. 2. Typical EBIC images of capacitors with thin (22 nm) gate oxide (a), specimen 1 and thick (350 nm) field oxide (b), specimen 2. Each side of the capacitors is 0.5 mm in length.

density (total number of spots/capacitor area) varied over the range 0-10^5/cm^2. Figures 7a and 7b show that the breakdown voltage decreased by about a factor of two for the same set of capacitors. These data indicate that defects responsible for EBIC spots also contribute to excessive leakage current and initiate oxide breakdown events.

Defect characterization.—A number of analysis techniques were used to characterize and identify the defects which produced the EBIC spots and leakage and reduced breakdown voltage.

EBIC studies.—It is known that the Schottky metal semiconductor barrier can be used to image defects in semiconductors in the EBIC mode. This technique is ideally suited to determining whether the defects reside in the silicon substrate or in the oxide or the field plate.

A number of capacitors of specimen 1 were prepared into Shottky diodes by first removing the polysilicon field plate in CF_4 plasma and the gate oxide in buffered HF, and then depositing a thin (20-50

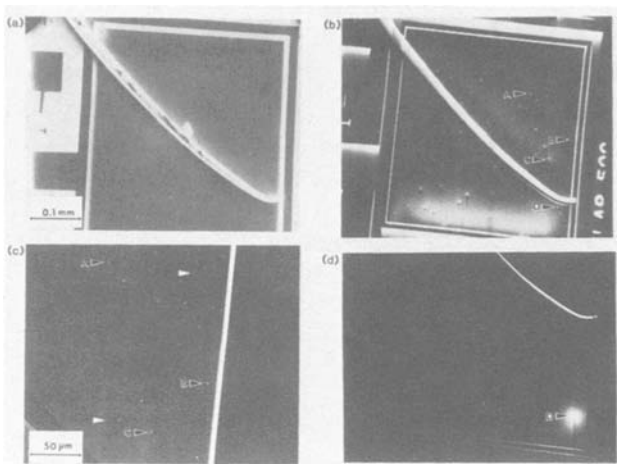

Fig. 3. Secondary electron image (a); EBIC image at E = 0.5 MV/cm (b); high field (6.5 MV/cm) EBIC image at a higher magnification (c). The corresponding sites in (b) and (c) are labeled as A, B and C. (d) shows a breakdown site D coincident with site D in (b). Two white arrows in (c) point to extra bright spots which have no correspondence in (b). Specimen 1.

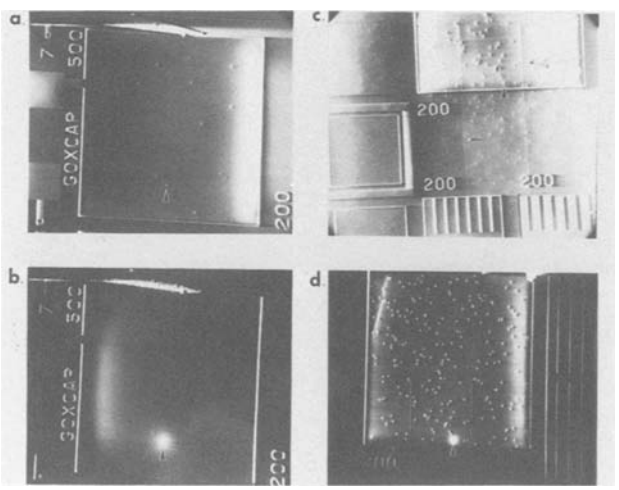

Fig. 4. Micrographs showing the coincidence of EBIC spots with breakdown sites, independent of defect density of the capacitors. Arrows point to EBIC spots in (a) and (c), and to corresponding breakdown sites in (b) and (d). Specimen 1.

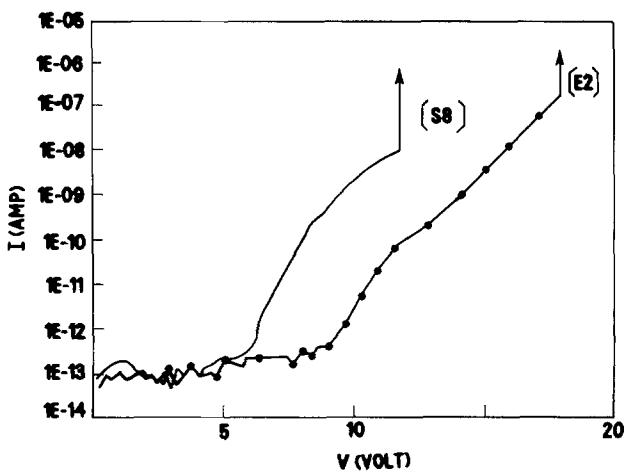

Fig. 5. I-V characteristics of capacitors with 485 EBIC spots (curve S8) and no spots (curve E2). Specimen 1.

nm) layer of aluminum to serve as a Schottky barrier field plate. Schottky diodes thus fabricated were then examined in the EBIC mode. Figures 8a and 8b show

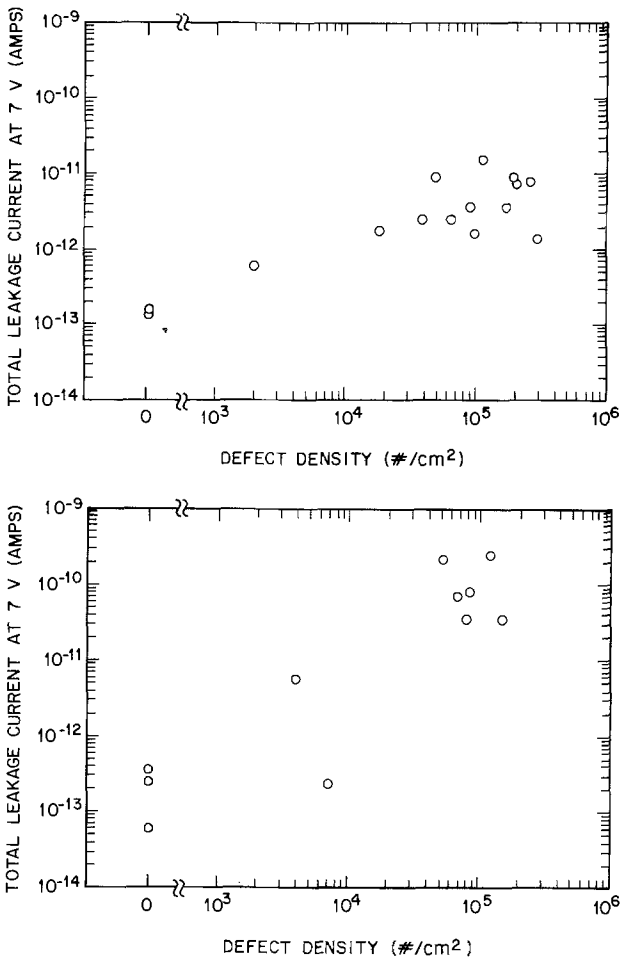

Fig. 6. Leakage current at 7V (accumulation) as a function of EBIC corresponding density for specimens 1 (a, top) and 2 (b, bottom).

that there is an exact one-to-one correspondence between the defects imaged in an MOS capacitor and in the Schottky diode fabricated from it. At a higher magnification (Fig. 8c), two Schottky EBIC defects appear rectangular in shape and oriented perpendicular to each other; one is parallel to the wafer flat, which suggests that the defects may be stacking faults in the substrate.

EBIC imaging and Secco etching.—Part of sample 3 was first studied in the EBIC mode and then treated with buffered HF to remove the polysilicon/metal silicide field plate and the oxide. The sample was then Secco (5)-etched for 30 sec, and reexamined in the SEM. Figures 9a and 9b show that the EBIC spots coincide with defects revealed by Secco etch. Some etch pits are seen at higher magnification in the SEM micrograph of Fig. 9c. The 1 μm long etch pits are oriented parallel and perpendicular to the wafer flat and have similar dimensions to the Schottky diode defects in Fig. 8c.

Transmission electron microscopy and x-ray emission spectroscopy.—In order to locate specific EBIC spot sites in the TEM it is necessary to first generate fiducial marks convenient to spot sites and use these marks to again locate the defect area in the TEM after TEM sample preparation. The method chosen was to "write" orthogonal lines of polymerized hydrocarbon with the SEM electron beam, and use these lines as a set of fiducial marks. Two such lines written orthogonally on a capacitor plus the capacitor edges served to locate the EBIC sites in the TEM sample (Fig. 10).

Samples were studied by TEM at 120 and 200 keV; EDXES detection was used for specimen composition analysis.

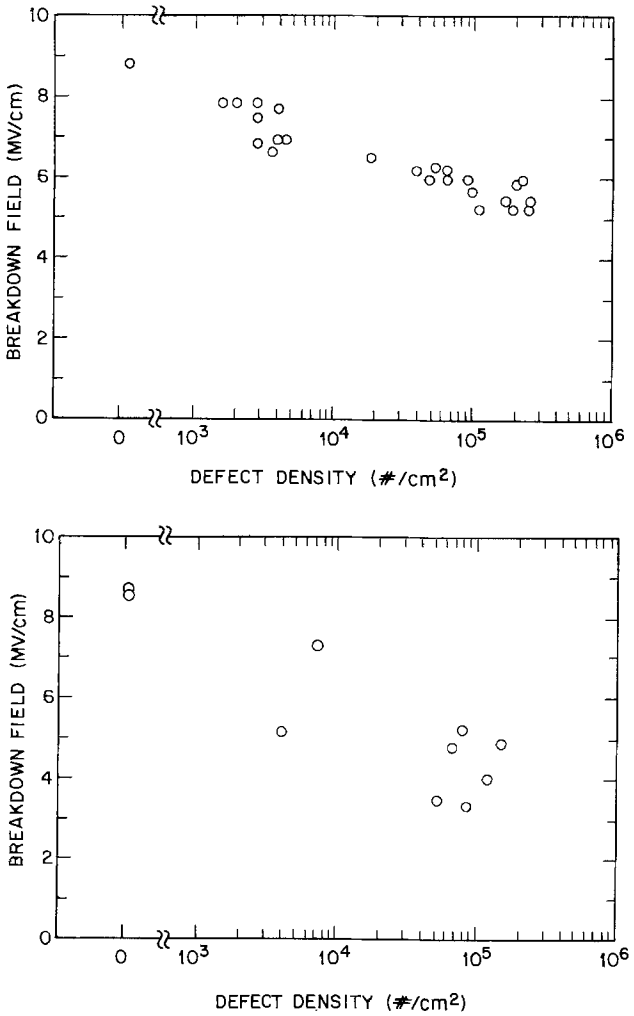

Fig. 7. Breakdown field as a function of EBIC spot density for specimens 1 (a, top) and 2 (b, bottom).

Figures 11 and 12 show TEM micrographs of three defects at high magnification. Each defect consists of a stacking fault with precipitates. The stacking faults dimensions are approximately 1 × 0.2 μm, close to those of Secco-etched pits and the EBIC defects revealed in the Schottky diode. Precipitates clustered at the defect are clearly visible (arrows, Fig. 11, 12). The precipitates were sensitive to electron irradiation and disappeared after 5 min exposure to a 1 × 10^{-11}A, 120 keV beam (compare Fig. 11a, b). EDXES analysis was carried out by focusing a reduced diameter beam on the precipitates. Figure 13a shows the same stacking fault as in Fig. 11b, together with two circular contamination marks which indicate the size of the sampled area and were made while analyzing the silicon background. The EDXES spectra shown in Fig. 13b and 13c and other analyses on three defect sites showed the presence of copper, tin, zinc, iron and nickel in precipitate regions. Further TEM characterization of the defects is in progress.

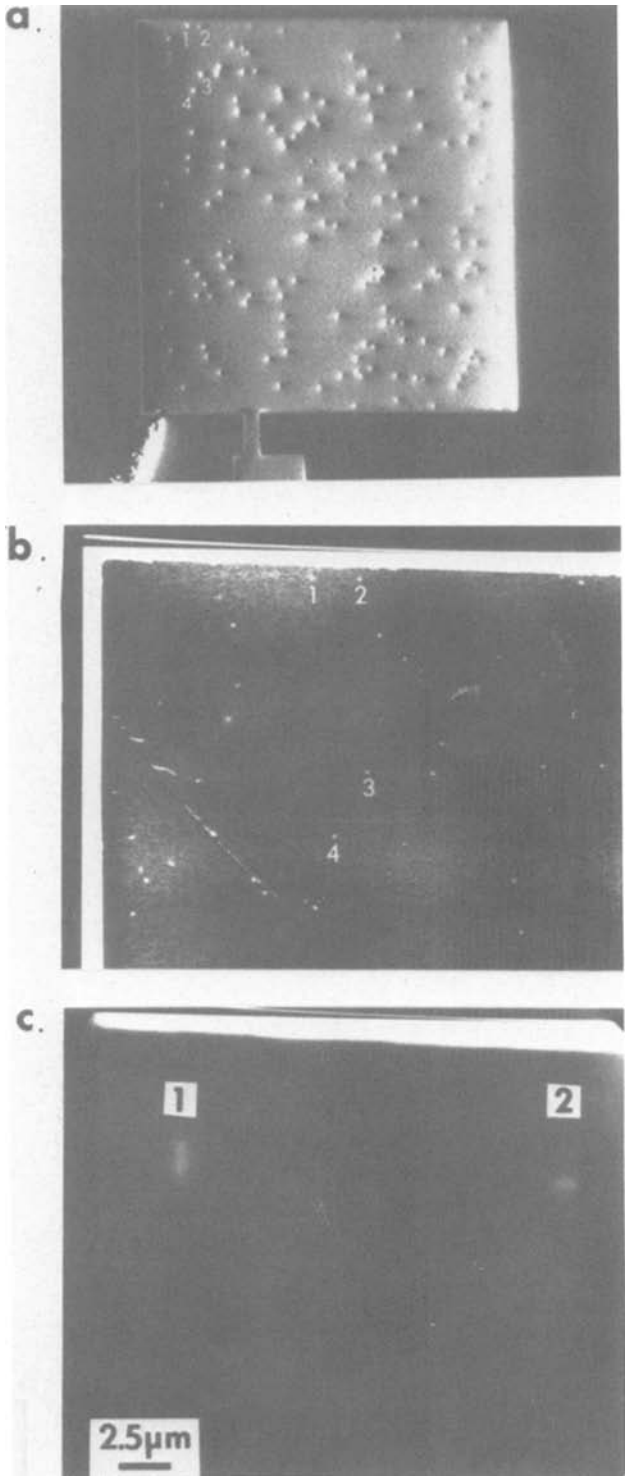

Fig. 8. Defects found by EBIC study in a capacitor (a) and in the Schottky diode prepared from it (b). Labels 1-4 mark corresponding sites. A higher magnification image of defects 1 and 2 (c) shows that they are oriented perpendicular to each other. Specimen 1.

Discussion

Morphology and origin of defects.—The defects revealed by EBIC, Secco etch, and TEM analysis are identified as decorated stacking faults. The uniform length of the defects and their mutually perpendicular orientation suggest that they were formed in the surface layer of silicon during oxidation; and in fact similar defects have been identified by EBIC, TEM, and optical microscope study of oxidized, Secco-etched silicon wafers (6, 7). Secco etch studies of a 2°-lapped piece from sample 3 showed the absence of pits under the surface, confirming that the defects are not bulk stacking faults. Most of the Secco-etched pits seen in Fig. 9c are not symmetrically shaped and are similar to those shown in Fig. 4b-4d of Ref. (6); these shapes had been attributed to oxidation-induced stacking faults with impurity decoration.

The size of stacking faults depends on oxidation conditions. At temperatures lower than 1150°C, stacking faults grow with increasing oxidation time, and at higher temperatures, they shrink after an initial growth period and eventually disappear. The processing step which is considered most likely to be responsible for stacking fault formation is the 950°C

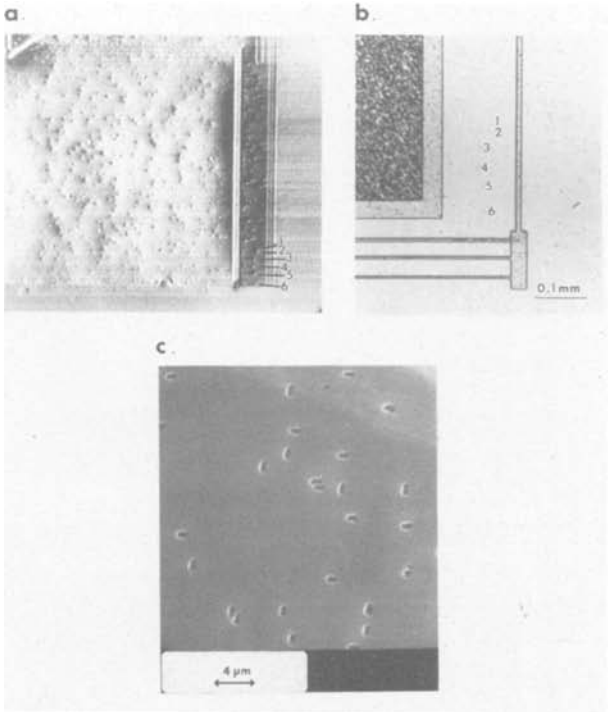

Fig. 9. Coincidence of EBIC spots in (a) with Secco-etched pits in (b); No. 1-6 mark corresponding sites. (c) is a secondary electron image showing etch pits on the sample. Specimen 3.

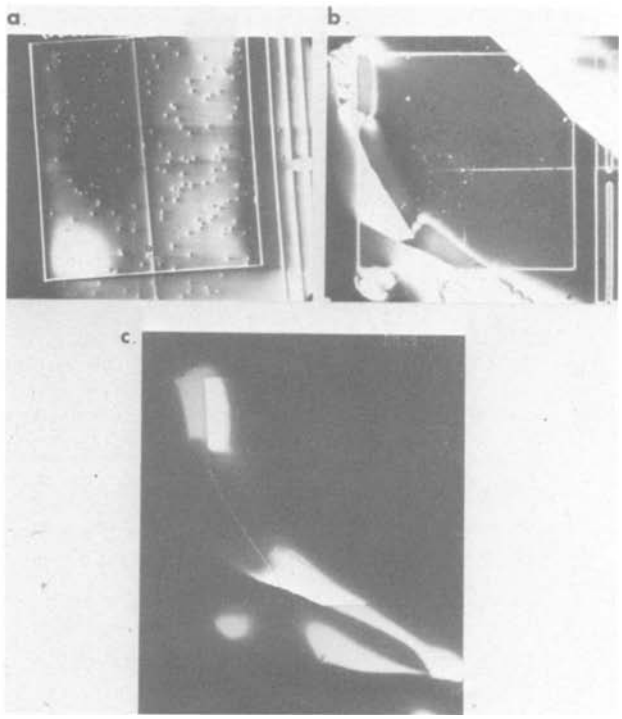

Fig. 10. EBIC image of a capacitor before thinning for TEM study (a), and optical micrograph (b), and electron micrograph (c) of the same capacitor after thinning. The two lines dividing the capacitor into quadrants are polymerized hydrocarbon written by the SEM electron beam, and serve as fiducial marks in locating the defects in TEM. EBIC spot sites a-g (a) were relocated by TEM after sample thinning. Specimen 1.

wet field oxidation step. Reference (8) gives a general relation for the stacking fault length growth rate dl/dt in (100) silicon in dry or steam O_2 ambient

$$\frac{dl}{dt} = k_1 \left(\frac{dx}{dt} \right)^{0.4} - k_2 \qquad [1]$$

where

$$k_1 = 1.58 \times 10^{10} \exp\,(-2.4\,\text{eV}/kT)\,(\mu/\text{hr})^{0.6}$$
$$k_2 = 6.45 \times 10^{17} \exp\,(-4.8\,\text{eV}/kT)\,(\mu/\text{hr}) \qquad [2]$$
$$\frac{dx}{dt} = \text{rate of growth of oxide thickness } x$$

Applying this equation to calculate the stacking fault growth length, a total length of 1.44μ at the rate of 1.02 μ/hr is calculated. This length is indeed close to the length of EBIC defects and Secco etch pits observed (1-1.5μ).

Coincidence of breakdown sites with defects.—The coincidence of breakdown sites with oxidation-induced stacking fault sites is a new and important observation. Although many SiO_2 breakdown mechanisms have been suggested, to the authors' knowledge no direct observation or correlation with substrate crystallographic defect sites has previously been made. Among various proposed breakdown mechanisms, the one advanced in Ref. (1) is of particular interest. In this model, electrons are injected from the cathode into the oxide by Fowler-Nordheim tunneling and accelerated by the oxide field. The model can be applied to the present experiment, if it is assumed that precipitates at the faults cause enhanced electron tunneling from the cathode. In fact, local increase of current at defect sites under high field strengths (above 6 MV/cm) at which the induced current follows Fowler-Nordheim behavior has been confirmed in another study (9).

Although the role of decoration is not certain, it should be pointed out that the amount of impurity present at a crystallographic defect has been found to correlate both with the extent of electrical activity at an EBIC recombination center (10, 11) and with p-n junction leakage (6). By inference, it might be

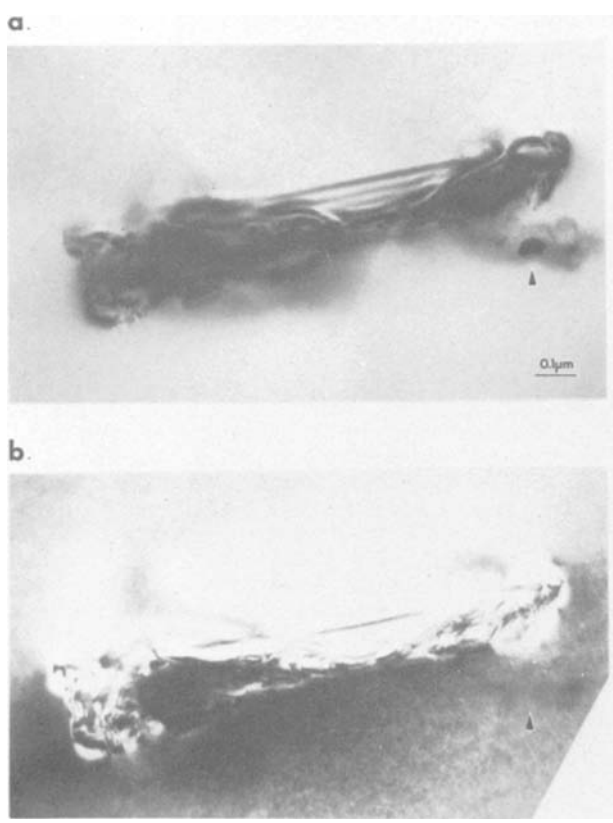

Fig. 11. TEM micrographs of a stacking fault with impurity precipitates (arrow) which disappeared after beam irradiation (1). Specimen 1.

suspected that in the present case the gate oxide leakage and breakdown might also depend on the

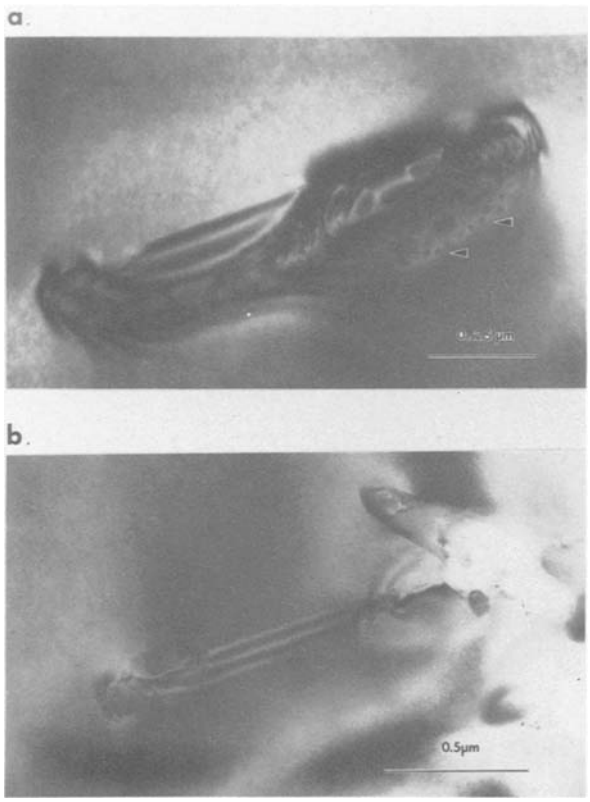

Fig. 12. Two other decorated stacking faults imaged by TEM. Notice the precipitates (arrow) in (a). Specimen 1.

type and amount of impurity precipitates present at the stacking fault. Further study on this question is underway.

Conclusion

The authors' observations indicate that impurity-decorated oxidation-induced stacking faults located in silicon near the silicon-silicon dioxide interface degrade the quality of MOS capacitors. This is the first time that a correlation has been established between such defects and leakage and breakdown in thin oxide capacitors.

Acknowledgments

The authors thank R. Kushner and N. Lifshitz for bringing our attention to the study and for supplying samples. They are also grateful to G. S. N. Chu for the 2° angle-lapped sample, P. Burns for preparing the Schottky electrode, and M. Read for Secco etching.

Bell Laboratories assisted in meeting the publication costs of this article.

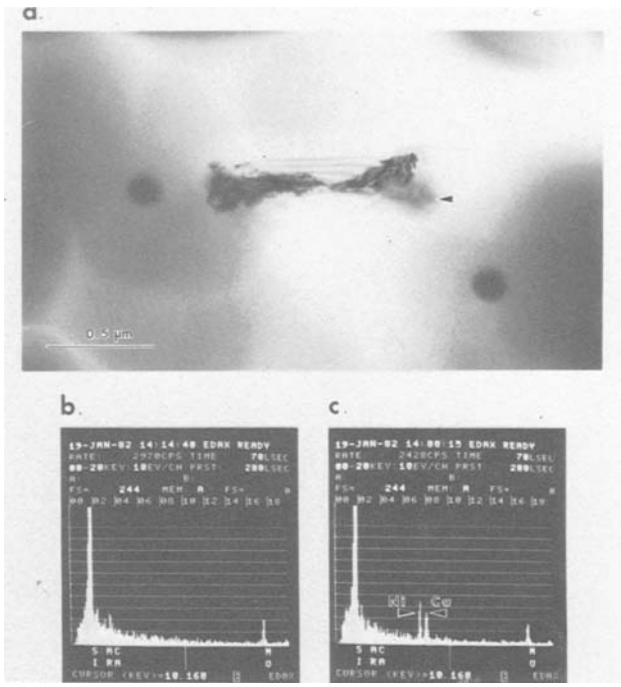

Fig. 13. A TEM image of the decorated stacking fault as in Fig. 11b (a), EDXES spectra from the silicon matrix (b), and precipitate region (c); the probe diameter for EDXES study is approximately the diameter of the contamination disks. Arrow indicates area sampled for EDXES analysis of the precipitate. The extra peaks in (c) correspond to Cu and Ni. The Mo peak in both (b) and (c) is due to the sample retaining ring. Specimen 1.

REFERENCES

1. T. H. DiStefano and M. Shatzkes, *J. Vac. Sci. Technol.*, **12**, 37 (1975).
2. C. M. Osburn and D. W. Ormond, *This Journal*, **119**, 597 (1972).
3. T. H. DiStefano, *J. Appl. Phys.*, **44**, 527 (1972).
4. R. A. Williams and M. M. Beguwala, *Solid State Technol.*, **24**, 65 (1981).
5. F. Secco D'Aragora, *This Journal*, **119**, 94 (1932).
6. J. M. Dishman, S. E. Haszko, R. B. Marcus, S. P. Murarka, and T. T. Sheng, *J. Appl. Phys.*, **50**, 2689 (1978).
7. W. T. Stacy, D. F. Allison, and T. C. Wu, *This Journal*, **129**, 1128 (1982).
8. A. Miin-Ron Lin, R. W. Dutton, D. A. Antmiadir, and W. A. Tiller, *ibid.*, **128**, 1121 (1981).
9. P. S. D. Lin and H. J. Leamy, *Appl. Phys. Lett.*, **42**, 717 (1982).
10. R. B. Marcus, M. Robinson, T. T. Sheng, S. E. Haszko, and S. P. Murarka, *This Journal*, **124**, 425 (1977).
11. E. Blumtritt, R. Gleichman, J. Heydenreich, and H. Johansen, *Phys. Status Solidi A*, **55**, 611 (1979).

Effect of CaO and MgO on Crystallization in Lead Borosilicate Glasses

S. Sachdev and R. C. Buchanan*

Department of Ceramic Engineering, University of Illinois at Urbana-Champaign, Urbana, Illinois 61801

ABSTRACT

The effects of crystallization of CaO and MgO additions to high lead borosilicate glasses were investigated. Both oxides were found to promote crystallization when added in amounts > 10 mol percent (m/o), with CaO being the more effective additive. Crystal phases $4PbO \cdot 3CaO \cdot SiO_2$ and $8PbO \cdot MgO \cdot 6SiO_2$ were identified in the crystallized CaO and MgO containing glasses, respectively. Morphology of the crystals was hexagonal.

Glasses in the ternary system $PbO \cdot B_2O_3 \cdot SiO_2$ find extensive use as dielectric insulation and for many low melting solder glass compositions (1, 2). Stable glasses have been found to exist in this system for compositions with PbO content between 30 and 70 m/o and SiO_2 content below 30 m/o (3-5). Crystallized glasses in this system are of interest because they introduce desirable properties of hardness, mechanical strength, thermal stability, and higher deformation temperatures compared to the vitreous glasses.

Generally, the usefulness of a particular modifying oxide in promoting crystallization of the glass during heat-treatment depends upon the charge/size ratio or field strength of the cation (6). Small cations of high field strengths will tend to be surrounded by a more ordered arrangement of oxygen ions compared to larger cations of equivalent charge. The transition to the more ordered structure with small cations is readily accomplished (6) for simple component systems. Of the alkaline earth modifier oxides, MgO would be the most effective in inducing crystallization since the field strength of the Mg^{2+} cation is higher than those for Ca^{2+}, Sr^{2+}, or Ba^{2+} ions. Higher concentrations of these cations would, therefore, be needed for equivalent crystallization.

Embabi *et al.* (7) studied the crystallization behavior of a $PbO \cdot SiO_2$ glass, modified with B_2O_3, Al_2O_3, R_2O (R=Na, K, Li) and RO (R=Ca, Mg, Zn) oxides, by observing the changes in the electrical resistivities of the modified glass as a function of temperature. These experiments showed the devitrification tendency to be suppressed by the R_2O and R_2O_3 oxides as well as by MgO and ZnO, but not by CaO. The apparent anomaly in the crystallization tendency of MgO is of significance since CaO and/or MgO are frequently incorporated in low melting lead borosilicate glass compositions for viscosity and expansion control. In contrast, studies in other glass systems of the type $SiO_2 \cdot G_2O_3 \cdot Al_2O_3 \cdot RO \cdot R_2O$, where the RO oxides were CaO, MgO, and BaO, showed a lowering of viscosity and expected devitrification tendency in the order MgO > CaO > BaO (8).

This study was intended to further investigate the effects of RO (R = Ca, Mg) oxides on the crystallization tendency of lead borosilicate glasses, in view of their common usage in these low melting glass compositions.

Experimental

The base glass used was 43 m/o PbO, 30 m/o B_2O_3, and 27 m/o SiO_2. This composition is close to a small immiscibility region in the $PbO \cdot B_2O_3 \cdot SiO_2$ ternary diagram given by Pavlushkin and Zhuravlev (5). Substitution of modifier oxides CaO and MgO was made at the expense of B_2O_3, since this would have the effect of increasing the crystallization tendency. Crystallization observations were made visually, as well as by scanning (SEM) and transmission (TEM) electron microscopy, optical microscopy, and x-ray diffraction (XRD) analysis. Phase identification and composition were determined using electron microprobe and XRD analysis techniques.

Table I gives the base glass composition as well as the CaO and MgO substitutions made. Reagent grade chemicals were used for all batch constituents. The batches were melted in platinum crucibles in a globar furnace at temperatures between 1125° and 1225°C for approximately 1 hr in a slightly reducing air ambient. The glasses, after homogenization, were fritted by quenching in water or were cast in graphite molds and furnace cooled.

Differential thermal analysis (DTA) traces were made of the vitreous frits (ground to ~70 μm) to determine the glass transition (T_g) and the crystallization temperatures (T_{x1}). The DTA experiments were carried out up to ~800°C, using a du Pont 1090 thermal analyzer system with Pt crucibles and Al_2O_3 standards. DTA traces of glasses (1, 6, 7) in Table I are shown in Fig. 1 as curves a, b, c, respectively. The glass transition temperature, T_g, is seen to be in the range 390°-420°C. A nucleation peak for the Ca containing glass (b) is indicated to be 445°C, from which the nucleation region was estimated to be between 430° and 460°C. The DTA traces also showed a crystallization peak in the region of 560°C for the Ca glass. Investigation of the crystal growth phase was, however, carried out both above and below this temperature in the range of 550°-600°C.

An investigation into the growth of the main x-ray intensity peak ($2\theta = 32.2°$) for the crystal phase in the 12.4 m/o CaO containing sample, as a function of soak time at 580°C, showed that almost 90% crystallization had occurred after 4 hr. This data is given in Fig. 2. The increase in the relative integrated intensity with soak time up to 24 hr would primarily indicate growth in crystallite size with time.

Accordingly, the thermal cycle used to induce crystallization in the glass samples was as follows: the ground (~70 μm) glass powders were (*i*) placed in small platinum dishes; (*ii*) heated at 10°C/min to 450°C; (*iii*) held at 450°C for 20 min to aid nucleation; (*iv*) heated to 580°C and held for 4 hr to achieve crystallization; then (*v*) furnace cooled. Samples cooled in

Table I. Lead borosilicate glass compositions

Oxides	Compositions (m/o) 1*	2	3	4	5	6	7
PbO	43.0	43.0	43.0	43.0	43.0	43.0	43.0
B_2O_3	30.0	25.0	20.0	25.0	17.6	17.6	—
SiO_2	27.0	27.0	27.0	27.0	27.0	27.0	—
CaO	—	5.0	10.0	—	—	12.4	—
MgO	—	—	—	5.0	10.0	—	12.4

* Base composition.

* Electrochemical Society Active Member.

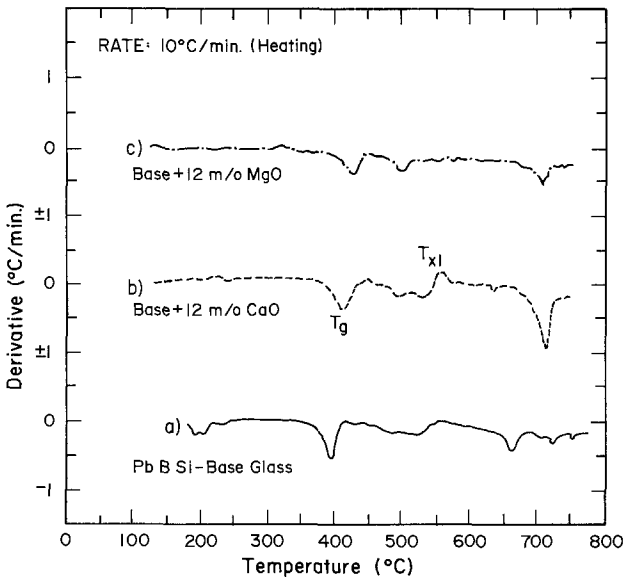

Fig. 1. DTA heating traces for base, Ca and Mg glasses (1, 6, 7) in Table I.

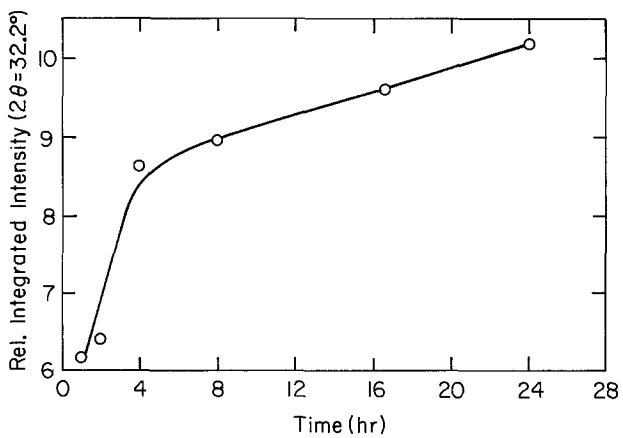

Fig. 2. Relative integrated x-ray intensity peak ($2\theta = 32.2°$) as a function of soak time at 580°C.

graphite molds were also held at 580°C both on cooling and on reheating from room temperature. This was to observe any crystallization in the bulk samples.

The crystal phases developed were observed visually and with the aid of SEM, TEM, and optical microscopy. Identification of the unknown phases was made using an x-ray Phillips Norelco diffractometer with monochrometer and a Debye-Scherrer powder camera. Nickel-filtered copper $K\alpha$ radiation was used with an accelerating voltage of 25 kV and a filament current of 10 mA. The powder camera specimens were prepared using standard powder camera techniques. Exposure time was 12 hr. Diffractometer scans were made at the rate of 2° 2θ/min from 15° to 75° 2θ. Scans of 0.5° 2θ/min were used for accurate identification of particular angles.

Electron microprobe (beam size ~1 μm) analysis was carried out, using ARL-FMX electron microprobe, to determine the chemical composition of the phases. The samples used were polished to one-quarter micron surface finish with diamond paste. The analysis was made using samples of diopside ($CaMgSi_2O_6$), jadeite ($NaAlSi_2O_6$), and galena (PbS) as standards.

Results and Discussion

The DTA traces in Fig. 1 show glass transition temperatures (T_g), indicated by endothermic peaks at ~395°, 410°, and 420°C for the base, Ca and Mg glasses, respectively. The relative increase in T_g over the base glass is in line with the higher field strength for the Mg^{2+} ion compared to Ca^{2+}. As indicated also for the Ca containing glass, the exothermic peaks at ~445° and 560°C can be attributed respectively to apparent nucleation and to crystallization in the glass. Both events, as expected, were absent in the base glass. The Mg glass showed no detectable nucleation at 445°C and only slightly crystallization at 560°C, indicating a lower crystallization tendency for the glass.

Endothermic reactions in the region 470°-530°C likely represent coalescence and flow of the glass particles, since smooth transparent films were generally obtained after heat-treatment at 580°C. Endothermic peaks at ~705° and 715°C in the Mg and Ca containing glasses can be attributed to melting of the respective crystalline phases. The magnitude of the peaks again relate to the degree of crystallinity in the two glasses since the sample volumes were the same. All three glasses showed a melt endotherm at ~670°C. On cooling from 800°C, the DTA traces for the glasses were uneventful, except for glass transitions, T_g, which occurred at slightly lower temperatures than on heating.

The results of heating the different powdered glass samples through the prescribed crystallization cycle may be summarized as follows.

The base glass showed slight cloudiness when observed visually. However, examination of the unmilled frit by TEM showed no evidence of either immiscibility or crystallinity. The cloudiness was therefore attributed to the presence of small bubbles. With CaO or MgO in amounts of approximately 5 m/o, the glasses were visually clear and no trace of crystallinity was detected, either optically or with the SEM.

Glasses containing >10 m/o CaO or MgO showed a significant degree of crystallization when processed through the crystallization cycle. The effect was more pronounced with CaO than with MgO in line with the DTA results and as illustrated in Fig. 3a and 3b, which show SEM photomicrographs of the surface of the 12.4 m/o CaO and MgO crystallized samples, respectively. The hexagonal morphology of the crystallites is clearly evident. The larger size crystals obtained with the MgO samples would indicate that fewer nuclei were formed; hence, the glasses could be considered more stable. With the >10 m/o CaO or MgO glasses, which were cooled in graphite molds and kept at 580°C for 4 hr, no crystallinity was detected. Crystallinity was developed, however, when the bulk samples were cooled to room temperature and heated through the crystal-

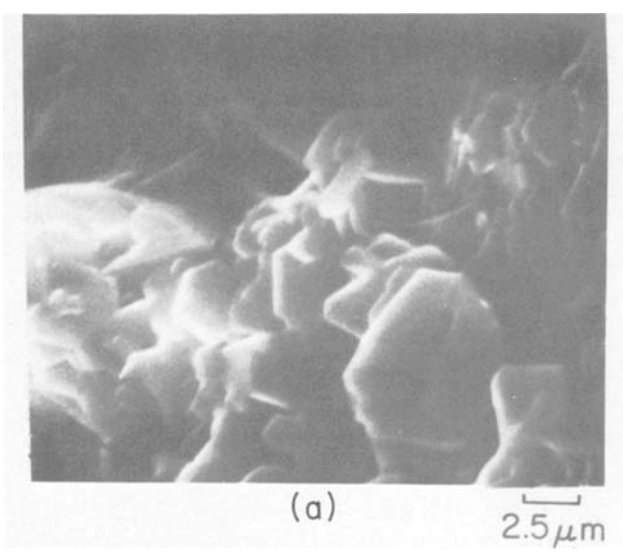

Fig. 3a. SEM photomicrograph of fracture surface of 12.4 m/o CaO-crystallized sample showing hexagonal crystals.

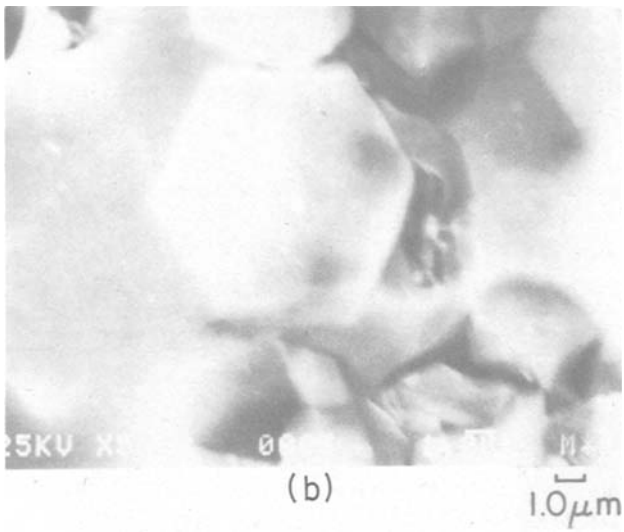

Fig. 3b. SEM photomicrograph of fracture surface of 12.4 m/o MgO-crystallized sample showing hexagonal crystals.

lization cycle, but to a lesser degree. This would be expected from the lack of surface nuclei and the DTA observations.

Table II gives the prominent x-ray lines obtained for the 12.4 m/o CaO-crystallized glass sample. The measured interplanar "d" spacings are seen to correspond to those given for a lead calcium silicate phase (tentatively identified as $Ca_2Pb_3Si_3O_{11}$) by Ito (9). The melting point of the crystal phase in the 12.4 m/o CaO sample was determined by DTA to be ~715°C.

Despite the apparent close x-ray similarity between Ito's data (9) and the data given in Table II, electron microprobe analysis of the phase crystallized from the calcium containing glasses indicated a composition close to $4PbO \cdot CaO \cdot 3SiO_2$. To further examine this composition, without influence from other oxides, a glass sample was prepared as described, using only PbO, CaO, and SiO_2 in the molar ratios (4:1:3), and was crystallized using the same thermal cycle as for the other glasses. X-ray diffraction analysis showed the 4:1:3 (lead calcium silicate) compound to be highly crystalline. The normaliized x-ray intensity patterns are compared in Fig. 4, which shows the $4PbO \cdot CaO \cdot 3SiO_2$ compound to be identical to the crystalline phase in the Ca glass, except for intensity differences.

Table III shows the measured interplanar spacings for the 12.4 m/o MgO-crystallized samples. The d spacings are again compared to those of magnesium barysilite ($Pb_8Mg(Si_2O_7)_3$), which shows good correspondence.

Table II. Interplanar "d" spacings from CaO-crystallized glass compared with calcium lead silicate phase

CaO-crystallized glass (measured)		Calcium lead silicate phase (ASTM Card 20-220)	
d(A)	Intensity	d(A)	Intensity
4.869	S	4.94	VS
4.446	S	4.44	S
4.245	S	4.27	M
3.536	S	3.55	VS
3.390	S	3.39	M
3.232	S	3.23	M
3.069	VS	3.08	VS
—	—	2.976	VW
2.853	VS	2.850	VS
2.850	VS	2.801	S
2.718	S	2.730	S
2.347	M	2.339	W
2.131	W	2.136	W
1.996	M	1.999	M
1.944	M	1.943	W
1.809	M	1.808	M
1.729	W	1.721	W
1.688	VW	1.700	VW
1.514	VW	1.516	VW
1.468	W	1.468	VW
1.414	W	1.414	VW

Table III. Interplanar "d" spacings from MgO-crystallized glass compared with Mg-barysilite ($Pb_8Mg(Si_2O_7)_3$)

MgO-crystallized glass (measured)		Mg-barysilite (JCPDS)	
d(A)	Intensity	d(A)	Intensity
4.86	VW	4.91	VW
4.56	M	4.57	M
4.23	W	4.18	W
3.52	M	3.50	M
3.23	W	3.20	VS
2.98	M	2.96	VS
3.87	W	2.82	M
2.72	M	2.77	S
2.72	S	2.68	VS
2.58	W	2.60	W
2.34	W	2.35	W
2.28	W	2.30	M
2.15	VS	2.26	W
2.09	VS	2.10	W
2.04	S	2.00	W
1.98	M	1.95	W
1.94	S	1.94	M
1.89	W	1.88	VW
1.83	W	1.84	M
1.72	M	1.70	M
1.58	VW	1.59	W

Electron microprobe analysis was carried out on large single crystal grains in the polished surface of the Ca-crystallized glass sample. The microprobe results showed nearly identical composition for the 4:1:3 lead calcium silicate and the 12.4 m/o CaO-crystallized samples. Typical analysis for the samples is given in Table IV. The K ratio values shown in Table IV indicate the characteristic x-ray intensity for an element within the sample compared to the standard sample, corrected for background. The data show the existence of identical phases with a chemical formula approximating $4PbO \cdot CaO \cdot 3SiO_2$. It was concluded, therefore, that this was the most likely formula for the phase identified by Ito (9). Figure 5 shows an SEM photomicrograph of the surface of the (4:1:3) crystallized lead calcium silicate sample. The crystallites appear to be of rhombohedral morphology although, as indicated, they were chemically identical with the 12.4 m/o CaO-crystallized samples shown in Fig. 3. The different morphology no doubt reflected the different growth conditions. Table V shows the electron microprobe results for the 12.4 m/o MgO-crystallized sample. The microprobe confirmed the chemical formula

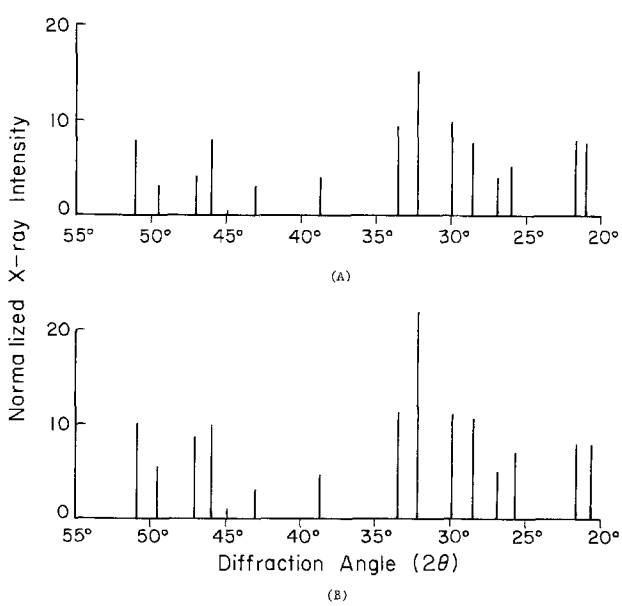

Fig. 4. Comparison of x-ray peak positions (normalized) as a function of diffraction angle 2θ for crystallized 12.4 m/o CaO (A) and $4PbO \cdot CaO \cdot 3SiO_2$ samples (B).

Table IV. Electron microprobe analysis on crystals in 12.4 m/o CaO-crystallized samples compared with $4PbO \cdot CaO \cdot 3SiO_2$ phase

Element	K-ratio	w/o (meas)	w/o (calc)	a/o (meas)	a/o (calc)	Molar (meas)		Ratios (calc)
Pb (M_α)	0.7752	73.56	73.41	21.48	21.05	3.90	PbO	4.0
Ca (K_α)	0.1812	3.64	3.55	5.50	5.26	1.0	CaO	1.0
Si (K_α)	0.3367	8.12	7.46	17.51	15.79	3.18	SiO_2	3.0
O*	—	14.68	15.59	55.51	57.89		—	—

* By difference.

Table V. Electron beam microprobe analysis on 12.4 m/o crystallized samples compared with $8PbO \cdot MgO \cdot 6SiO_2$ phase

Element	K-ratio	w/o (meas)	w/o (calc)	a/o (meas)	a/o (calc)	Molar (meas)		Ratios (calc)
Pb (M_α)	0.7182	80.13	75.8	27.45	22.20	8.07	PbO	8.0
Mg (K_α)	0.0140	1.16	1.11	3.40	2.78	1.0	MgO	1.0
Si (K_α)	0.1386	7.26	7.71	18.35	16.67	5.34	SiO_2	6.0
O*	—	11.45	15.37	50.80	58.33		—	—

* By difference.

of the crystals to be $Pb_8Mg(Si_2O_7)_3$. The electron microprobe traces are compared in Fig. 6 for the crystallized Ca and Mg glass samples.

In summary, CaO was observed to promote a greater degree of crystallization than MgO in the lead borosilicate glasses studied. This may simply reflect the lower viscosity of the CaO glass (10) compared to the MgO glasses at the nucleation and crystal growth temperatures, which would have the effect of increasing nuclei formation and mass transport during crystallization. Work by Kim (11) has shown that molar additions of MgO to a lead borosilicate glass of like composition resulted in a higher density (and lower molar volume) than equivalent CaO addition. This resulted also in higher softening point, glass transition temperature, activation energy for electrical conduction, and electrical resistivity but lower thermal expansion coefficient for the MgO glasses. These data would indicate that the higher field strength of the Mg^{2+} ($Mg^{2+} \sim 4.7$; $Ca^{2+} \sim 2.4$) ions exert a greater stabilizing influence on the relatively low SiO_2 content lead borosilicate glasses. This in turn would result in the lower crystallization tendency observed.

Conclusions

The conclusions reached from this study were as follows:

1. CaO and MgO induce crystallization in high lead borosilicate glasses, when present in concentrations greater than 10 m/o.

2. CaO was found to promote crystallization to a greater degree than MgO.

3. The compound $4PbO \cdot CaO \cdot 2SiO_2$ was identified as the crystalline phase in the Ca containing glasses.

4. A crystal phase $Pb_8Mg(Si_2O_7)_3$ was identified in the MgO-crystallized glasses.

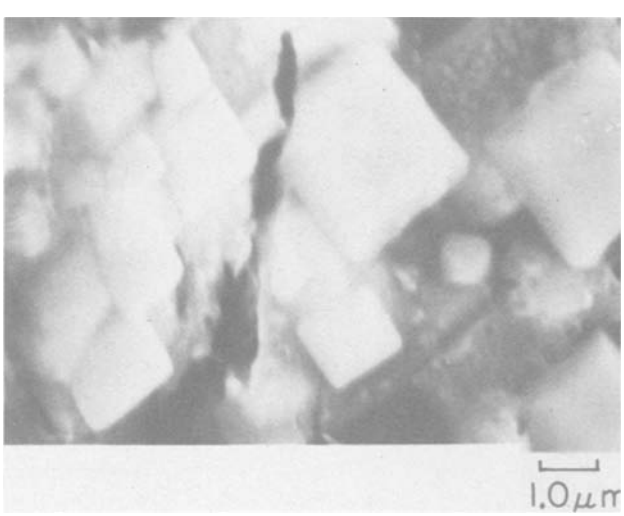

Fig. 5. SEM photomicrograph of fracture surface of synthetic crystallized sample containing (4:1:3) PbO, CaO, and SiO_2 showing rhombohedral crystals.

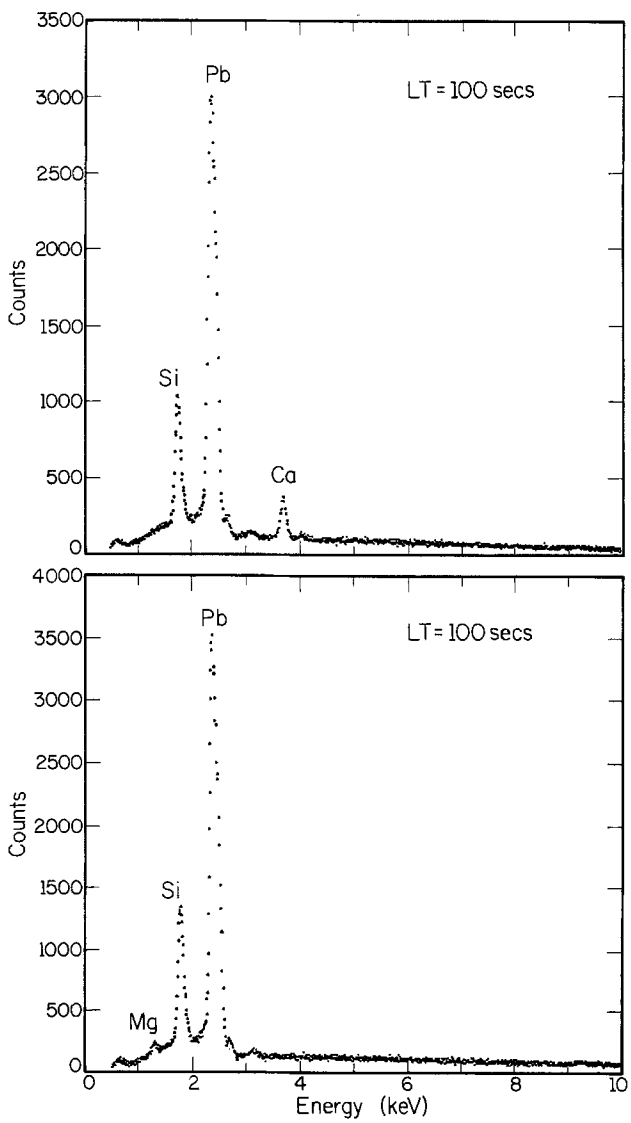

Fig. 6. Comparison of electron microprobe data for 12.4 m/o CaO- and MgO-crystallized glass samples.

Acknowledgments

This work was supported by the Computer Based Education Research Laboratory and in part by the National Science Foundation under MRL grant DMR-80-20250.

Manuscript submitted Sept. 21, 1982; revised manuscript received May 18, 1983.

REFERENCES

1. J. Gallup and A. G. F. Durwall, *Am. Ceram. Soc. Bull.*, **36**, 47 (1957).
2. R. C. Buchanan and M. A. Zuegel, *J. Am. Ceram. Soc.*, **57**, 28 (1968).
3. R. F. Geller and E. N. Bunting, *J. Res. Nat. Bur. Stand.*, **23**, 275 (1939).
4. D. W. Johnson and F. A. Hummel, *J. Am. Ceram. Soc.*, **51**, 196 (1968).
5. N. M. Pavlushkin and A. K. Zhuravlev, *Izv. Akad. Nauk, SSSR, Neorg. Mater.*, **5**, 572 (1969).
6. P. W. McMillan, "Glass Ceramics," 2nd Printing, Academic Press, London (1969).
7. H. K. Embabi, M. N. Alaya, and A. E. Mahoyoub, *Trans. J. Br. Ceram. Soc.*, **73**, 20 (1974).
8. J. D. Schnapp, A. Petzold, H. Busch, and H. Eifer, *Silikatech*, **26**, 219 (1975).
9. J. Ito, *The Am. Mineralogist*, **53**, Jan.-Feb. (1968).
10. S. English, *J. Soc. Glass Tech.*, **8**, 205 (1924).
11. S. B. Kim, M.S. Thesis, University of Illinois (1977).

A Theoretical Study of the Low-Temperature Chemical Vapor Deposition of SiO_2 Films

C. Cobianu and C. Pavelescu

Microelectronica, R-72996, Bucharest, Romania

ABSTRACT

The silicon dioxide deposition on silicon substrates in the SiH_4-O_2-N_2 system was investigated in the temperature range from 80° to 400°C on a nozzle-type reactor at atmospheric pressure. An exponential temperature dependence (of Arrhenius type) with a break at 250°C has been observed for the O_2/SiH_4 ratio corresponding to the maximum deposition rate and also for the O_2/SiH_4 ratio corresponding to near-zero deposition rate in the retardation region. Within the bimolecular surface reaction theory (Langmuir-Hinshelwood mechanism), these results are explained, and the break is interpreted as a change in the adsorption mechanism of the reactant gases with temperature. The apparent activation energy of the surface reaction (5.2-6.5 kcal/mol) in the temperature range from 80° to 400°C has been derived from the Arrhenius plot of the maximum deposition rate, in agreement with the above theory. An empirical reaction rate equation has been proposed which, in addition, explains the linear dependence of the maximum deposition rate on silane flow rate at constant O_2/SiH_4 ratio.

The study of the low-temperature silane oxidation has been made in two directions: homogeneous and heterogeneous reactions.

The homogeneous reaction between oxygen and silane was studied by Emeleus and Stewart (1), who found the lower and upper limits of the explosion in the temperature range from 15° to 200°C. They concluded that the gas-phase oxidation of the silane is a branching chain reaction. Strater (2) studied the formation of silicon dioxide in the gas-phase or on the reactor walls for SiH_4-O_2-N_2 mixtures. He observed that the temperature of reaction initiation increased with O_2/SiH_4 increase. For temperatures ranging from 240° to 450°C the reaction is

$$SiH_4 + O_2 = SiO_2 + 2H_2 \quad [1]$$

Shintani *et al.* (3) determined the variation of the number and dimension of SiO_2 submicron particulates dispersed in a CVD reactor as a function of CVD conditions.

The heterogeneous reaction between silane and oxygen for SiO_2 and PSG film deposition at temperatures ranging from 250° to 500°C was extensively studied (4-11). Baliga and Ghandhi (7) suggest that the deposition reaction obeys the theory of heterogeneous reaction at a solid surface.

This paper presents our experimental results of SiO_2 deposition kinetics in the temperature range from 80° to 400°C on a nozzle-type reactor. In addition, we interpret our data as well as those of other workers using the bimolecular surface reaction theory (12). In this way the variation of the deposition rate with the processing variables can be explained, and thus a step in the explanation of the complex mechanism of the reaction can be made.

Key words: silane, oxygen, adsorption.

Experimental

A continuous nozzle-type reactor employing separate, nitrogen-diluted oxygen and silane streams that are directed toward the substrate by laminar flow nozzles [Fig. 2D from Ref. (13)] was used for the SiO_2 film deposition. The temperature profile on the susceptor surface was measured with a Technoterm 9500 digital thermometer, and we found a ±5% variation around the set point value across the susceptor surface. Five percent silane in argon and oxygen, both diluted in nitrogen were used for film deposition. A total flow rate of 8.2 liters/min was maintained constant in all experiments except for the case when the effect of the carrier gas flow was studied.

The layers were deposited on polished silicon wafers cleaned before deposition by degreasing in boiling trichloroethylene, alcohol and then etched in 5% HF. The wafers were heated on the susceptor for 5 min before deposition in order to attain equilibrium temperature.

The oxide thickness was measured by profilometer method with a stylus type profilometer, and was verified with an ellipsometer for thicknesses less than 500Å.

Results

Our experimental results of the low-temperature chemical vapor deposition (LTCVD) of SiO_2 films obtained on a nozzle-type reactor agree from a qualitatively point of view with the data published for horizontal (11) and vertical (9) reactors.

However, our experimental work performed with high silane concentration has allowed the SiO_2 film formation at temperatures as low as 80°C.

The effective results obtained on the nozzle-type reactor, which also support the application of bimolecular surface reaction theory to the kinetic study of the low temperature SiO_2 deposition, are presented below.

Thus, the variation of growth rate at 350°C with O_2/SiH_4 ratio on the abscissa and silane flow rate as a parameter is shown in Fig. 1. At a given silane flow rate, we obtained an increase-maximum-decrease dependence of deposition rate on O_2/SiH_4 ratio. Moreover, for different silane flow rates (30, 45, 60 cm³/min), the maximum deposition rate appeared at the same O_2/SiH_4 ratio. In addition, in the region where the deposition rate decreased with respect to the O_2/SiH_4 ratio (retardation region), the deposition rate tended to become independent of the silane flow rate and the inhibition of the reaction seemed to appear at about the same O_2/SiH_4 ratio when silane flow rate was varied. A similar behavior was obtained at 250°, 300°, and 400°C for different silane flow rates.

In order to gather more information about this heterogeneous deposition process we studied the SiO_2 film formation in the temperature range from 80° to 400°C at a silane flow rate of 45 cm³/min (Fig. 2). At all temperatures investigated, the O_2/SiH_4 ratio corresponding to the maximum deposition rate and that corresponding to the inhibition of the reaction in the retardation region increased with temperature increase. The maximum deposition rate increases with temperature increase, but at 400°C the increase seemed to be reduced with respect to that obtained at 350°C.

The effect of the silane flow rate on the SiO_2 deposition rate at 400°C, with SiH_4/O_2 ratio on the abscissa and oxygen flow rate as a parameter, was also represented by an increase-maximum-decrease variation (Fig. 3). The maximum deposition rate for an oxygen flow rate of 400 cm³/min was twice the value for an oxygen flow rate of 200 cm³/min but the maxima appeared at the same SiH_4/O_2 ratio. The same behavior was observed by representing Goldsmith and Kern's data (4) in a similar manner.

The deposition rate variation at 400°C with the total gas flow rate on the abscissa at a given O_2/SiH_4 ratio

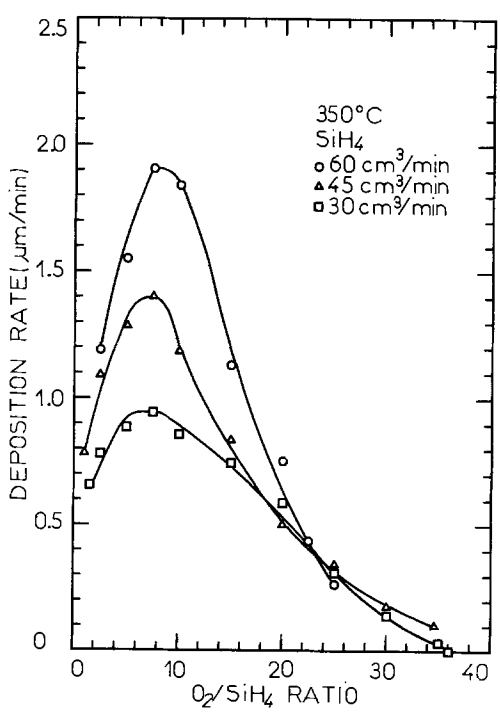

Fig. 1. Film deposition rate vs. oxygen/silane ratio, at 350°C with silane as a parameter.

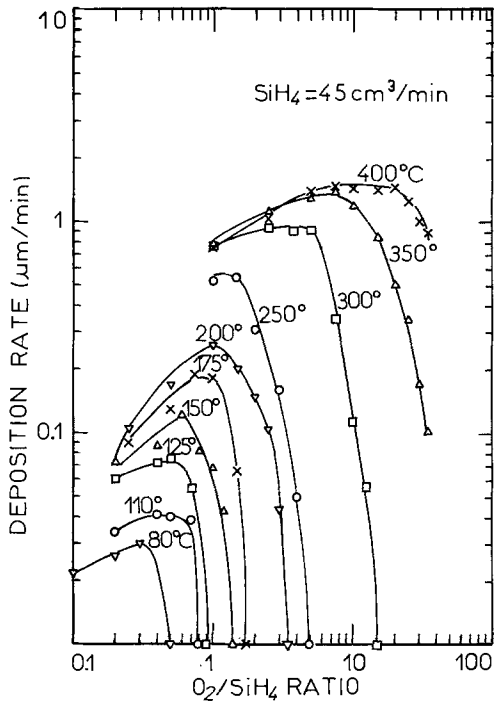

Fig. 2. Film deposition rate vs. oxygen/silane ratio, at temperatures from 80° to 400°C with silane flow rate of 45 cm³/min.

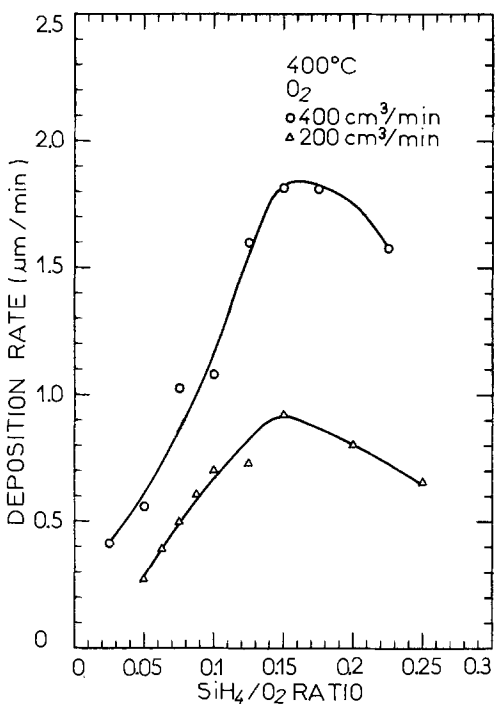

Fig. 3. Film deposition rate vs. silane/oxygen ratio, at 400°C with oxygen flow rate as a parameter.

(silane flow rate is kept constant) is presented in Fig. 4. We observed an increase-maximum-decrease variation as predicted by Kern (9, 10).

Discussion

The temperature dependence of the experimental data.—The increase of the O_2/SiH_4 ratio corresponding to the maximum deposition rate with temperature increase (Fig. 2) suggested an exponential temperature relationship for this dependence. In Fig. 5 (curve 1) the logarithm of the O_2/SiH_4 ratio for the maximum deposition rate is plotted against the reciprocal absolute temperature for our data (silane flow rate of 45 cm³/min) over the 80°-350°C range, as well as those

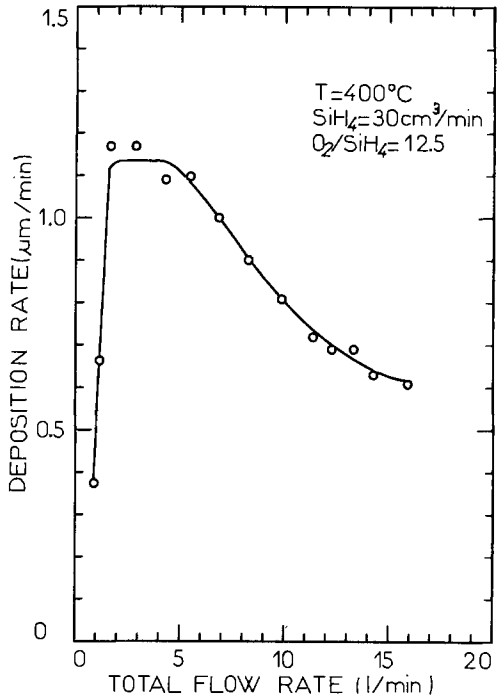

Fig. 4. Film deposition rate vs. total gas flow rate at 400°C

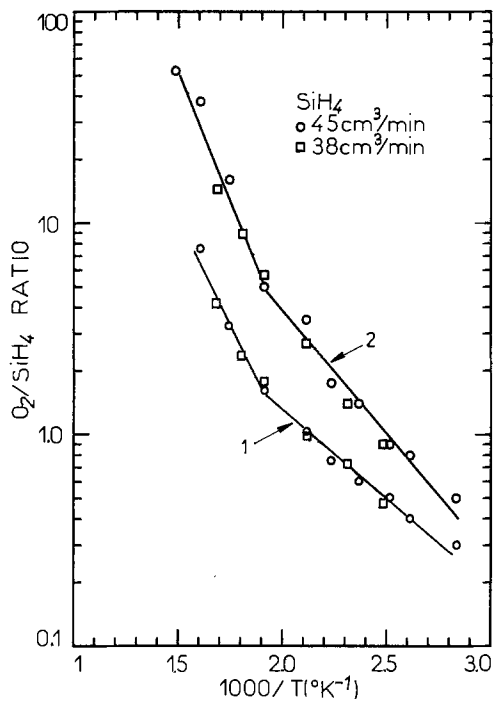

Fig. 5. Oxygen/silane ratio corresponding to *(i)* maximum deposition rate (curve 1), and *(ii)* near-zero deposition rate (curve 2) vs. temperature (80°-350°C): ○, our data; □, Taft's data (11).

of Taft (silane flow rate of 38 cm³/min) (11) in the 130°-320°C range. For both sets of data, we obtained two straight lines that broke at 250°C. As the experimental points reported in (11) and in this paper were too close to one another, we have drawn a single curve through them using the least squares method (applied throughout this work where it was the case). The activation energies (E_1) associated with this temperature variation are presented in Table I. The same temperature dependence was observed for the O_2/SiH_4 ratio corresponding to the near-zero deposition rate in the retardation region, as shown in Fig. 5 (curve 2). The activation energies derived from the slopes of these straight lines (noted by E_2) are listed in Table I.

The temperature dependence of the maximum deposition rate at a given silane flow rate (Fig. 2) fitted an Arrhenius law as shown in Fig. 6. For our data as well as for those of Taft (11) the slopes of the straight lines corresponding to different silane flow rates were close to one another. The values of the corresponding activation energies (noted by E_3) are also listed in Table I. The processes including these energetic barriers (E_1, E_2, E_3) are identified according to the bimolecular surface reaction theory.

Theory and model.—The deposition rate of the LTCVD SiO_2 films which presents a maximum when the partial pressure of oxygen is varied and the partial pressure of silane is kept constant (Fig. 1, 2) and another maximum when silane is varied and oxygen is kept constant (Fig. 3) have led us to interpret the experimental data on the basis of the theory of bimolecular surface reactions (12), Langmuir-Hinshelwood mechanism (see Appendix). Moreover, our experimental results on the efficiency of the silane oxidation reaction in the deposition of SiO_2 films, which have shown an increase-maximum-decrease dependence on O_2/SiH_4 ratio were consistent with this theory (14).

In our case, the reaction surface is the outer surface of the growing SiO_2 while the adsorbed gases are oxygen and silane whose partial pressures are p_{O_2} and p_{SiH_4} (calculated by dividing the flow rate of the gas by the total flow rate). At this stage we neglect the possible adsorption of the nitrogen and/or argon or reaction products. According to Eq. [A-11] of the Appendix, for both sufficiently strongly adsorbed gases, the O_2/SiO_4 ratio corresponding to the maximum deposition rate is given by

$$p_{O_2}/p_{SiH_4} = K_{01} \exp(-E_1/RT) \quad [2]$$

where K_{01} is defined by Eq. [A-12] and depends on the nature of the adsorbed molecules, while E_1 according to Eq. [A-13] is

$$E_1 = E_{O_2} - E_{SiH_4} \quad [3]$$

where E_{O_2} and E_{SiH_4} are the energies liberated at 0 K per oxygen and silane molecule adsorbed. According to

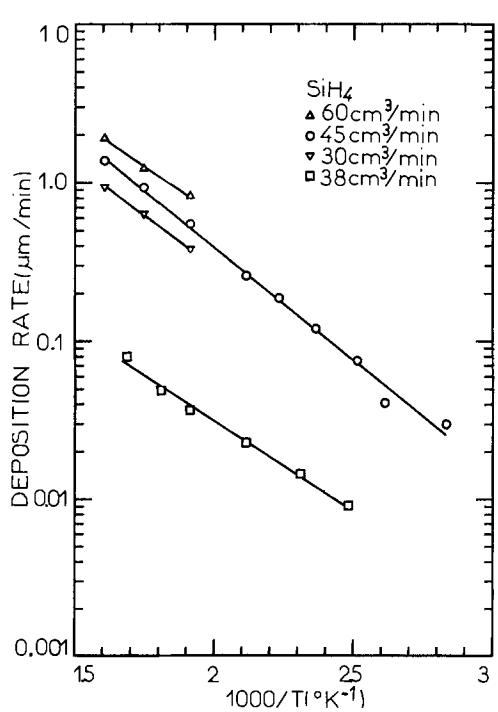

Fig. 6. Arrhenius plot of maximum deposition rate at temperatures ranging from 80° to 350°C: △, ○, ▽, our data; □, Taft's data (11).

Table I. The activation energies of the silicon dioxide deposition process on silicon substrates

Experimental data	Temperature range (°C)	Reactor	Activation energies (Kcal/mole)			
			Adsorption of reactant gases corresponding to		Surface reaction	
			Maximum deposition rate (E_1)	Near-zero deposition rate (E_2)	Apparent (E_3)	True (E_r)
Present work	80-250	Nozzle-type	3.60	5.16	6.52	4.72
	250-400		9.97	11.23		1.53
Ref. [11]	130-250	Horizontal	4.46	6.49	5.20	2.97
	250-320		7.55	8.16		1.42

this theory, the activation energies (E_1) derived from Fig. 5 can be called apparent activation energies of the adsorption of the two reactant gases corresponding to the maximum deposition rate. Their values (3.6-9.9 kcal/mol) lead us to the conclusion that the two gases are probably chemisorbed on the SiO_2 surface, rather than physically adsorbed (where the heats evolved are in the range of few hundred cal/mol). The break in the activation energy, E_1, at 250°C, (Fig. 5) may indicate a change in the adsorption mechanism for silane and/or oxygen with temperature.

The experimental activation energy, E_2, derived from the exponential temperature dependence of the O_2/SiH_4 ratio corresponding to a near-zero deposition rate can be interpreted according to Eq. [A-29]-[A-31] as follows:

$$p_{O_2}/p_{SiH_4} = K_{02} \exp(-E_2/RT) \qquad [4]$$

where K_{02} is a constant defined by Eq. [A-30]. According to Eq. [A-31], E_2 can be called the apparent activation energy of the adsorption of the two reactant gases corresponding to the near-zero deposition rate and is given by

$$E_2 = E_r + E_{O_2} - E_{SiH_4} \qquad [5]$$

In Eq. [5], E_r is the activation energy of the reaction, while E_{SiH_4} and E_{O_2} are the energies liberated at 0 K for an adsorbed molecule of SiH_4 or O_2 corresponding to the surface fractions θ_{O_2} and θ_{SiH_4} covered by the two gases at near-zero deposition rate. In fact, the activation energy E_2 may be qualitatively inferred by considering that the inhibition of the reaction correlates with a certain $0_{O_2}/0_{SiH_4}$ ratio, giving an equation similar to Eq. [2]. The values of the experimental activation energy of the adsorption corresponding to a near-zero deposition rate are higher than those of the adsorption corresponding to the maximum deposition rate.

According to the Langmuir-Hinshelwood mechanism, the maximum deposition rate for sufficiently strongly adsorbed oxygen and silane (Eq. [A-8]) is given by

$$v_M = k_r/4 = k_{03} \exp(-E_3/RT) \qquad [6]$$

where k_r is the rate constant of the reaction (which obeys the Arrhenius law), $k_{03} = k_{0r}/4$ and $E_3 = E_r$ (Eq. [A-4]). Therefore, the quantity E_3 derived from the slope of straight line shown in Fig. 6 is the apparent activation energy of the limiting reaction between the molecules adsorbed on the surface.

However, Eq. [6] cannot explain the linear dependence of the maximum deposition rate on the silane flow rate (at constant O_2/SiH_4 ratio, at a given temperature) as shown in Fig. 7. In fact, the increase of the maximum deposition rate by a factor, when the silane introduced is multiplied by the same factor, correlated with the oxygen increase by the same factor (to keep the O_2/SiH_4 ratio constant) is equivalent with a linear dependence of the maximum deposition rate with respect to the square root of the product of silane and oxygen partial pressures. On the other hand, the reaction rate equation for competitively and sufficiently strong adsorption of silane and oxygen, depending only on the ratio of the partial pressures of the two gases (Eq. [A-14]) cannot predict this linear increase with the silane at constant O_2/SiH_4 ratio. On this basis, in order to describe more completely the experimental results, we suggest an empirical reaction rate equation of the Langmuir-Hinshelwood type which is multiplied by the square root of the product of the silane and oxygen partial pressures

$$v = k_r K_{O_2} K_{SiH_4} p_{O_2} p_{SiH_4} / (1 + K_{O_2} p_{O_2} + K_{SiH_4} p_{SiH_4})^2 \qquad [7]$$

This empirical reaction rate equation also predicts an increase-maximum-decrease behavior of the deposition rate with respect to both silane and oxygen partial pressures when one is varied and the other is kept constant. The coordinates of the maximum deposition rate are given by Eq. [A-16] and [A-17]. In addition, Eq. [A-18] and [A-20] show the same exponential temperature dependence for the O_2/SiH_4 ratio corresponding to the maximum deposition rate as that provided by Eq. [3]. The linear dependence of the maximum deposition rate on the square root of the product of silane and oxygen (Eq. [A-25]) or on the silane partial pressure (Eq. [A-21]) is obtained as follows

$$v_M = k_{0M} p_{SiH_4} \exp(-E_a/RT) \qquad [8]$$

where k_{0M} is a constant given by Eq. [A-22] and E_a is an apparent activation energy

$$E_a = E_r + (E_{O_2} - E_{SiH_4})/2 \qquad [9]$$

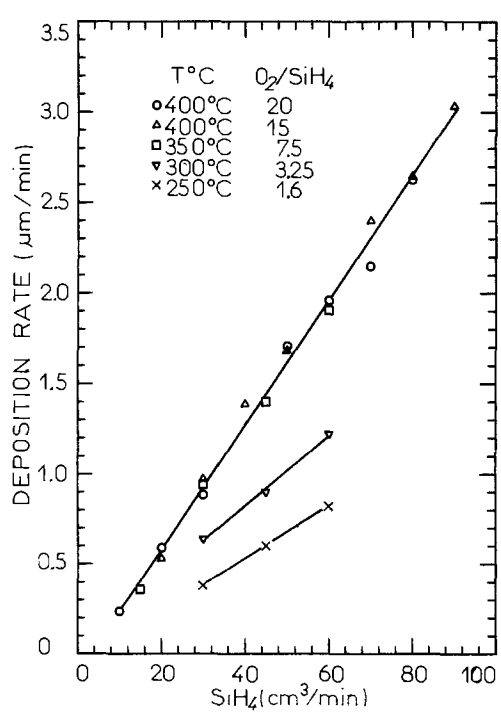

Fig. 7. Film deposition rate vs. silane flow rate at temperatures from 250° to 400°C with oxygen/silane ratio as a parameter.

In this equation E_r is the true activation energy of the reaction while E_{O_2} and E_{SiH_4} were defined in Eq. [3]. If we consider in this case that $E_a = E_3$ and $E_{O_2} - E_{SiH_4} = E_1$, where E_3 and E_1 are known from Table I, then we can calculate the values of E_r according to Eq. [9]. The break in the true activation energy of the reaction at 250°C is due to the two regimes in the activation energy of adsorption of the two gases at the maximum deposition rate. This result is in agreement with the fact that the surface reaction mechanism is determined by the heat evolved in the adsorption process. On this basis, the change in the adsorption mechanism of the reactant gases (at about 250°C) is also made responsible for the break observed in the exponential temperature dependence of the reciprocal of the absorption coefficient corresponding to 880 cm^{-1} (15). Thus, this empirical reaction rate equation can predict the determination of the reaction process by the adsorption of the reactant gases in the complex mechanism of SiO_2 deposition reaction.

Specific to this empirical equation is the retardation of the reaction rate by the square root of the partial pressure of the reactant gas more strongly adsorbed on the surface. In this case, the exponential temperature dependence of the O_2/SiH_4 ratio corresponding to near-zero deposition rate could be explained on the basis of a certain $\theta_{O_2}/\theta_{SiH_4}$ ratio at the inhibition of the reaction.

The inhibition of the SiO_2 film deposition reaction by the carrier gas.—The experimental results (4, 9-10) have shown that with the increase of the nitrogen flow rate over a given value (the other CVD conditions kept constant) the deposition rate begins to decrease (Fig. 4). The theory of the inhibition of the bimolecular surface reactions by a third gas (poison) can explain these results. Thus, at higher partial pressures of nitrogen the surface fractions covered by the reactant gases begin to decrease due to the third gas adsorbed on the same surface. Therefore, the reaction rate (Eq. [A-32]) is decreased because of the lower probability of the two reactant gases to be adsorbed on neighboring sites of the surface.

Conclusions

The bimolecular surface reactions theory (Langmuir-Hinshelwood mechanism) was applied to explain the kinetics of the low temperature (80°-400°C) SiO_2 film deposition. The experimental dependence of the deposition rate with respect to silane, oxygen and nitrogen flow rates are explained within this theory. The exponential temperature dependences (of Arrhenius-type) experimentally obtained, for (*i*) the O_2/SiH_4 ratio corresponding to the maximum deposition rate, (*ii*) the O_2/SiH_4 ratio corresponding to near-zero deposition rate, and (*iii*) the maximum deposition rate are explained by means of this theory. The corresponding activated processes which have been identified according to the Langmuir-Hinshelwood mechanism are the adsorption of the reactant gases corresponding to the maximum deposition rate (E_1), the adsorption of the reactant gases corresponding to the near-zero deposition rate, in the retardation region (E_2) and the surface reaction (E_3), respectively. The break observed in the activation energies E_1 and E_2 at 250°C was interpreted as a change in the adsorption process of the reactant gases.

In addition, we have proposed an empirical reaction rate equation which explains the linear dependence of the maximum deposition rate with respect to the silane flow rate at constant O_2/SiH_4 ratio. According to this empirical equation, a compensation effect between the adsorption and reaction processes has been found to explain the same value of the apparent activation energy of reaction when the temperature was varied from 80° to 400°C.

Manuscript submitted Jan. 27, 1983; revised manuscript received April 22, 1983. This was Paper 208 presented at the Montreal, Quebec, Canada, Meeting of the Society, May 9-14, 1982.

APPENDIX

Adsorption of two gases on the same surface.—In the case of the competitive adsorption of two gases A and B without dissociation on a perfectly smooth surface, with no interaction between the adsorbed molecules the fractions of the surface covered by the two adsorbed gases, θ_A and θ_B are (12)

$$\theta_A = K_A p_A/(1 + K_A p_A + K_B p_B) \quad [A\text{-}1]$$

and

$$\theta_B = K_B p_B/(1 + K_A p_A + K_B p_B) \quad [A\text{-}2]$$

where p_A and p_B are the partial pressures of the reactant gases while K_A and K_B are the equilibrium constants for the adsorption of the two gases.

Langmuir-Hinshelwood mechanism for bimolecular surface reactions.—According to the Langmuir-Hinshelwood hypothesis, the adsorption equilibrium is undisturbed by the occurrence of the reaction between the two gases A and B and the reaction rate is proportional to the product of the surface fractions covered by A and B, θ_A and θ_B, respectively (12)

$$v = k_r \theta_A \theta_B = k_r K_A K_B p_A p_B/(1 + K_A p_A + K_B p_B)^2 \quad [A\text{-}3]$$

where the rate constant k_r obeys the Arrhenius law

$$k_r = k_{0r} \exp(-E_r/RT) \quad [A\text{-}4]$$

If the partial pressure p_A is kept constant and p_B is varied, the reaction rate has an increase-maximum-decrease variation. There is a similar variation with respect to p_B if p_A is kept constant. With p_B kept constant and p_A as a variable, the maximum reaction rate is obtained for

$$p_A = (1 + K_B p_B)/K_A \quad [A\text{-}5]$$

For this value of p_A, the maximum reaction rate is

$$v_M = k_r K_B p_B/[4(1 + K_B p_B)] \quad [A\text{-}6]$$

If we consider now a sufficiently strong adsorption of the gas B ($K_B p_B >> 1$), Eq. [A-5] and [A-6] become

$$p_A/p_B = K_B/K_A \quad [A\text{-}7]$$

and

$$v_M = k_r/4 = k_{03} \exp(-E_3/RT) \quad [A\text{-}8]$$

where $k_{03} = k_{0r}/4$ and $E_3 = E_r$ is the activation energy defined by Eq. [A-4]. If we take into account Eq. [A-7], we obtain $p_A K_A = p_B K_B >> 1$, and the conclusion is that at the maximum reaction rate, a sufficiently strong adsorption of one gas implies the strong adsorption of both of them.

The statistical treatment of the ideal adsorption of two gases on the same surface gives the next expressions for K_A and K_B (16)

$$K_A = K_{0A}(T) \exp(E_A/RT) \quad [A\text{-}9]$$

and

$$K_B = K_{0B}(T) \exp(E_B/RT) \quad [A\text{-}10]$$

where E_A and E_B are the energies liberated at 0 K per adsorbed molecule A and B, respectively, and $K_{0A}(T)$, $K_{0B}(T)$ are quantities whose temperature variations are small compared with the rapid variation of the exponential terms. With K_A and K_B given by Eq. [A-9] and [A-10], Eq. [A-7] that gives the abscissa of the maximum reaction rate becomes

$$p_A/p_B = K_{01} \exp(-E_1/RT) \quad [A\text{-}11]$$

where K_{01} and E_1 are given by

$$K_{01} = K_{0B}(T)/K_{0A}(T) \quad [A\text{-}12]$$

and

$$E_1 = E_A - E_B \quad [A\text{-}13]$$

In the same manner, one can obtain the values for the maximum reaction rate and the corresponding p_B/p_A ratio when p_A is kept constant and p_B is varied.

In the hypothesis of both gases competitively and sufficiently strongly adsorbed so that $K_A p_A + K_B p_B >>$

1, the reaction rate equation depends on the ratio of the partial pressures of the two gases

$$v = k_r K_A K_B p_A p_B/(K_A p_A + K_B p_B)^2 = k_r a r/(ar + 1)^2 \quad [A\text{-}14]$$

where $a = K_A/K_B$ and $r = p_A/p_B$. The maximum reaction rate and the corresponding abscissa are the same as those given by Eq. [A-7] and [A-8].

Empirical reaction rate equation.—In order to improve the fit of the theory to experiment we propose the equation

$$v = k_r K_A K_B p_A^{3/2} p_B^{3/2}/(1 + K_A p_B + K_B p_B)^2 \quad [A\text{-}15]$$

for the reaction rate. With p_B kept constant and p_A varied, the abscissa of the maximum reaction rate is

$$p_A = 3(1 + K_B p_B)/K_A \quad [A\text{-}16]$$

and the maximum reaction rate becomes

$$v_M = 3^{3/2} k_r K_B p_B^{3/2}/[16 K_A^{1/2} (1 + K_B p_B)^{1/2}] \quad [A\text{-}17]$$

In the case of sufficiently strong adsorption of the gas B ($K_B p_B >> 1$), Eq. [A-15] and [A-16] become

$$p_A = 3K_B p_B/K_A \quad [A\text{-}18]$$

and

$$v_M = (3^{3/2}/16)\, k_r\, (K_B/K_A)^{1/2}\, p_B \quad [A\text{-}19]$$

If we take into account Eq. [A-9] and [A-10], then Eq. [A-18] and [A-19] become

$$p_A/p_B = 3K_{01} \exp(-E_1/RT) \quad [A\text{-}20]$$

where K_{01} and E_1 are defined in Eq. [A-12]-[A-13], and

$$v_M = k_{0M} \exp(-E_a/RT) p_B \quad [A\text{-}21]$$

in which the constant k_{0M} and the apparent activation energy E_a are given by the following equations

$$k_{0M} = (3^{3/2}/16)\, K_{01}^{1/2}\, k_{or} \quad [A\text{-}22]$$

and

$$E_a = E_r + (E_A - E_B)/2 \quad [A\text{-}23]$$

where k_{or}, E_A, and E_B are previously defined, and E_r is the true activation energy of the reaction. From Eq. [A-18], by multiplying with p_B in each part of the equality, we obtain

$$p_B = (1/3^{1/2})\, (K_A/K_B)^{1/2}\, (p_A/p_B)^{1/2} \quad [A\text{-}24]$$

and therefore, Eq. [A-19] becomes

$$v_M = (3/16)\, k_r\, (p_A p_B)^{1/2} \quad [A\text{-}25]$$

Similar results can be obtained with p_B as a variable and p_A kept constant.

Inhibition of the bimolecular surface reaction by the reactant gases.—The falling off of the reaction rate (Eq. [A-3]) is obtained when the partial pressure of the gas that is varied, p_A, begins to fulfil the condition

$$K_A p_A >> 1 + K_B p_B \quad [A\text{-}26]$$

In this case, the reaction rate equation becomes

$$v = k_r (K_B/K_A)\, (p_B/p_A) \quad [A\text{-}27]$$

If we denote by v_o a reaction rate close to the experimental zero deposition rate, and we consider this amount as a threshold value for the total inhibition of the reaction independent of temperature, then the corresponding ratio of the reactant gases becomes

$$p_A/p_B = (k_r K_B)/(K_A v_o) \quad [A\text{-}28]$$

From Eq. [A-28], the temperature dependence of p_A/p_B that gives near-zero deposition rate is

$$p_A/p_B = K_{02} \exp(-E_2/RT) \quad [A\text{-}29]$$

where K_{02} and E_2 are

$$K_{02} = k_{or} K_{01} \quad [A\text{-}30]$$

and

$$E_2 = E_r + E_A - E_B \quad [A\text{-}31]$$

In the above equation E_2 is the apparent activation energy of the adsorption corresponding to the near-zero deposition rate and E_r is the true activation energy of the reaction defined in Eq. [A-4]. E_A and E_B correspond now to the surface fractions covered by the two gases at the inhibition of the reaction.

Inhibition of the bimolecular surface reaction by the diluent gas.—In addition to the Langmuir-Hinshelwood mechanism presented, if the effect of a third gas of partial pressure p_i that is adsorbed on the same surface is considered, the reaction rate becomes

$$v = k_r K_A K_B p_A p_B/(1 + K_A p_A + K_B p_B + K_i p_i)^2 \quad [A\text{-}32]$$

where K_i is the equilibrium constant of the third gas. A similar expression could be adopted for our empirical reaction rate equation in the case of higher partial pressures of nitrogen.

REFERENCES

1. H. J. Emeléus and K. Stewart, *J. Chem. Soc. (London)*, Part I, 1182 (1935), Part II, 677 (1936).
2. K. Strater, *RCA Rev.*, **29**, 618 (1968).
3. A. Shintani, K. Suda, M. Suzuki, M. Maki, and K. Takami, *This Journal*, **124**, 1771 (1977).
4. N. Goldsmith and W. Kern, *RCA Rev.*, **28**, 153 (1967).
5. W. Kern and A. W. Fisher, *ibid.*, **31**, 715 (1970).
6. W. Kern and R. C. Heim, *This Journal*, **117**, 562 (1970).
7. B. J. Baliga and S. K. Ghandhi, *J. Appl. Phys.*, **44**, 990 (1973).
8. M. Shibata and K. Sugawara, *This Journal*, **122**, 155 (1975).
9. W. Kern, G. L. Schnable, and A. W. Fisher, *RCA Rev.*, **37**, 3 (1976).
10. W. Kern and R. S. Rosler, *J. Vac. Sci. Technol.*, **14**, 1082 (1977).
11. E. A. Taft, *This Journal*, 126, 1728 (1979).
12. K. J. Laidler, in "Catalysis," Vol. I, P. H. Emmett, Editor, p. 151, Reinhold Publishing Co., New York (1954).
13. W. Kern, *Solid State Technol.*, **18**, 25 (1975).
14. C. Cobianu and C. Pavelescu, *Thin Solid Films*, **102**, 361 (1983).
15. C. Pavelescu, C. Cobianu, and A. Vancu, *This Journal*, **129**, 328C (1982).
16. K. J. Laidler, in Catalysis," Vol. I, P. H. Emmett, Editor, p. 98, Reinhold Publishing Co., New York (1954).

Oxide Isolation for Double-Polysilicon VLSI Devices

R. M. Levin*,[1] and T. T. Sheng

Bell Laboratories, Murray Hill, New Jersey 07974

ABSTRACT

A novel method for the formation of an isolation layer between the polysilicon layers in double-polysilicon VLSI devices is described. The intermediate oxide is realized by means of CVD oxide or a combination of polyoxide on top of the first polysilicon layer and CVD oxide on its walls. The isolation can be applied also to structures having a first conductor level which is difficult to oxidize. Test capacitors indicate that very low freak population, low leakage currents, and breakdown voltages higher than 50V between the polysilicon layers can be achieved by the use of the method. The results are compared to double-polysilicon structures having thermally grown sidewall oxide.

Double-polysilicon gate MOS structures are extensively utilized in MOS and CCD memories (1-3). In conventional processes, the isolation between the sidewall of the first polysilicon layer and the overlapping polysilicon layer is realized by an intermediate oxide which is thermally grown from the first polysilicon level, simultaneously with the second gate oxide (1, 4-6). In comparison to oxides grown on single-crystal silicon, oxides grown on polysilicon have lower breakdown fields and are more conductive for a given average field (4, 7-9). Therefore, it is very important to have a thick intermediate oxide. With a thicker intermediate oxide, the parasitic capacitance between the two polysilicon levels is also reduced, and the performance of most circuits is improved. It has been demonstrated recently that when oxidation is carried out in the temperature range of 700°-900°C, heavily doped polysilicon is oxidized two to four times faster than single-crystal silicon (10-12). This effect has been used to grow intermediate oxides which are significantly thicker than the second gate oxide and therefore have high breakdown voltages and low leakage currents (5, 6).

The strong dependency between the thickness of the second gate oxide and that of the intermediate oxide is the major disadvantage of the conventional isolation methods. The continuous reduction in device dimensions forces a reduction in the gate oxide thickness and, as a result, a thinning of the intermediate oxide. The methods which are strongly dependent on the oxidation properties of polysilicon face even more severe problems in VLSI technology. As a result of the reduction in device dimensions, the line width and the thickness of the polysilicon runners are also reduced, and their resistance is increased. To overcome the increased resistance of the interconnects, composite structures consisting of a refractory metal or a refractory metal silicide on top of polysilicon have been considered (13, 14). Some of the metals proposed for this structure cannot be oxidized easily; others may be oxidized more slowly than doped polysilicon and will yield a very thin intermediate oxide as isolation between the conductor levels.

In this paper, the authors present and characterize a novel method for applying an isolation oxide between two polysilicon levels. The process is outlined in Fig. 1. After the deposition of the first polysilicon gate layer, a thick oxide layer is grown (or deposited) on top, and the first gate level is defined using etching techniques which yield vertical oxide/polysilicon walls (Fig. 1a). After resist removal, a desired thickness of oxide is deposited (Fig. 1b) and etched anisotropically together with the underlaying first gate oxide to expose the silicon surface at the second gate regions, leaving an oxide layer on the polysilicon sidewalls (Fig. 1c). The second gate oxide is now thermally grown, and the second polysilicon gate is applied (Fig. 1d). Glass deposition followed by an anisotropic etching has been used recently to achieve sidewall spacers in the fabrication of novel MOFET structures (15-17).

Because the intermediate oxide is applied separately from the oxidation of the second gate, its thickness is independent of the second gate oxide thickness. Also, the intermediate oxide can be applied over gates made of a variety of materials. Structures with very thin second gate oxide but high breakdown voltage, low poly I-poly II leakage currents, and low parasitic capacitance between the two gate levels can be fabricated by the use of this method.

Requirements for the CVD Isolation Process

The requirements for good CVD isolation process with uniform sidewall oxide thickness can be summarized as follows:

(*i*) Vertical walls at the SiO_2/poly I gate edge—This requirement is met by many of the recent dry etching processes because it is imperative for the VLSI technology (18). If the walls are not vertical, part of the oxide deposited on the walls is etched off during the etching of the CVD/first gate oxides, its thickness is reduced, and its electric isolation properties are degraded.

(*ii*) Anisotropic SiO_2 etching—The etching of the CVD/first gate oxides should be anisotropic to avoid any etching and thinning of the sidewall oxide.

(*iii*) Good thickness uniformity of the deposited glass—It has been reported that excellent thickness uniformity can be obtained in the deposition of undoped SiO_2 glass films (19, 20).

(*iv*) Uniform step coverage of the deposited glass—If the step coverage of the glass is not uniform, reentrant angles may appear at the base of the steps. This means that the oxide thickness is not uniform along the step. Also, after anisotropic etching of the second polysilicon layer, residual polysilicon within the re-entrant angles may short between adjacent second gates. Glass deposition processes with the capability of very good step coverage have been recently demonstrated (21-23).

Fulfillment of these four requirements is important to assure good control on the sidewall oxide thickness. However, even if they are not completely fulfilled, the desired final sidewall oxide thickness (and electrical isolation properties) can be achieved after characterization of the complete process by depositing glass films which are thicker than the final required oxide thickness.

Experimental

Sample preparation.—Double-polysilicon capacitor structures were fabricated on 3 in. p-type silicon wafers, <100> oriented, 6-30 Ω-cm. The processing sequence is outlined in Table I.

An 8000Å thick polysilicon film was deposited (LPCVD, SiH_4, 630°C) onto 4000Å thermally grown

* Electrochemical Society Active Member.
[1] Present address: National Semiconductor, Santa Clara, California 95051.

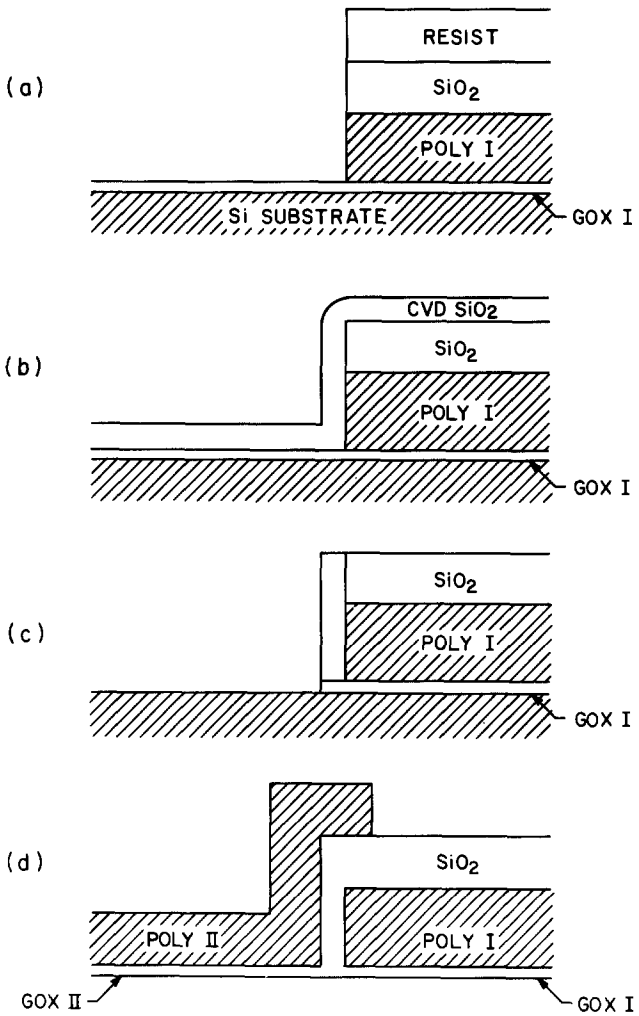

Fig. 1. Process sequence for the CVD isolation method

silicon dioxide. After phosphorus doping of the polysilicon from a PBr_3 source at 950°C for 60 min, the P-glass film grown on top of the polysilicon during the doping was dip etched in diluted HF solution (50 parts H_2O:1 part by volume of 49% HF acid) and 4000Å oxide was grown in steam at 950°C on top of the polysilicon layer. The first polysilicon level was patterned using a trilevel resist structure (24) and optical photolithography. The top oxide and the polysilicon were reactive ion etched (RIE) anisotropically in CHF_3/NH_3 and Cl_2, respectively. The resist was stripped, and various thicknesses of undoped SiO_2 glass were deposited at 630°C by decomposing tetraethyl orthosilicate (TEOS) at reduced pressure (20, 25). The CVD oxide thickness was measured on flat silicon monitors. The CVD oxide and 250Å of the thermally grown SiO_2 were RIE anisotropically in CHF_3/NH_3. The additional etching of thermally grown oxide simulates the etching of 250Å thick first gate oxide which is a typical gate oxide thickness in submicron channel devices (26). The samples were then oxidized in dry T_2/HCl ambient at 1000°C for 16 min to simulate the growth of 250Å second gate oxide. The second polysilicon layer was deposited, phosphorus doped, patterned and RIE. Finally, the exposed oxide was etched from top of the first polysilicon level to permit contact to this level. (It should be mentioned that an HF dip can be used prior to the deposition of the second polysilicon layer without having the previously reported (27) fast etching of the CVD oxide at the step.)

A TEM cross section through a complete sample is shown in Fig. 2. The structure is similar to that shown in Fig. 1d, with the thickness of GOX I and GOX II approximately equal to 4000Å. Thick oxide was used underneath the polysilicon layers rather than thin gate oxides to assure that shorts and leakage currents between the polysilicon levels do not occur through the substrate. The structure consists of two capacitors between the two polysilicon levels which are connected in parallel: an overlapping capacitor and a sidewall capacitor. The former capacitor has a thick (4000Å) dielectric oxide (on top of poly I). The later capacitor has a sidewall dielectric oxide which is varied over the range 200-930Å. Only the thin oxide region (sidewall) may be sensitive to electrical breakdown and leakage currents at low voltages. The length of the sidewall capacitor is 2.0 cm and its width (the height of poly I) is 0.6μ, yielding a capacitor area of 1.2×10^{-4} cm^2. The area of the overlapping capacitor is 8.0×10^{-4} cm^2.

For comparison, similar double-polysilicon structures with thermally grown intermediate sidewall oxides were prepared. The process sequence is identical to that outlined above, except for the oxide deposition and etching (steps 8 and 9 in Table I) which were skipped.

Electrical measurements.—The electrical breakdown properties of the double-polysilicon structures were measured by an automated system on more than 130 capacitors for each of the oxide sidewall thicknesses (at least two wafers for each thickness). Every capacitor was stressed in incremental steps to high voltages for 50-100 msec. After every step, the voltage was lowered to 2V and the current passed through the capacitor was measured. Breakdown voltage was defined as the highest voltage applied to the capacitor before current of 2 μA was measured at 2V (28). No capacitors were found to pass this current without having previously suffered a destructive breakdown.

Poly I-poly II leakage current characteristics were measured using a logarithmic picoammeter and a ramped voltage source.

Experimental Results and Discussion

TEM study.—TEM cross sections through the first gate edge are presented in Fig. 3 and 4. The sidewall oxide in Fig. 3 was formed during the oxidation step, which simulated the growth of 250Å second gate oxide on <100> single-crystal silicon. The sidewall oxide thickness varies between 200-400Å. Thinning of the oxide is evident at the top and the base corners of poly I. The surface of the poly I sidewall is very

Table I. Process sequence for CVD intermediate oxide method

1. Grow oxide (Steam, 950°C, 4000Å).
2. Deposit polysilicon (8000Å).
3. Phosphorus doping (PBr_3, 950°C, 60 min).
4. Grow oxide (Steam, 950°C, 4000Å).
5. Poly I lithography (Trilevel resist structure).
6. RIE SiO_2 (CHF_3/NH_3).
7. RIE polysilicon (Cl_2).
8. Deposit SiO_2 glass (TEOS, 630°C).
9. RIE CVD SiO_2 + 250Å thermally grown SiO_2.
10. Grow oxide (dry O_2/HCl, 1000°C, 16 min).
11. Deposit polysilicon (3000Å).
12. Phosphorus doping (PBr_3, 950°C, 30 min).
13. Poly II lithography.
14. RIE polysilicon (Cl_2).
15. RIE SiO_2 (CHF_3/NH_3).

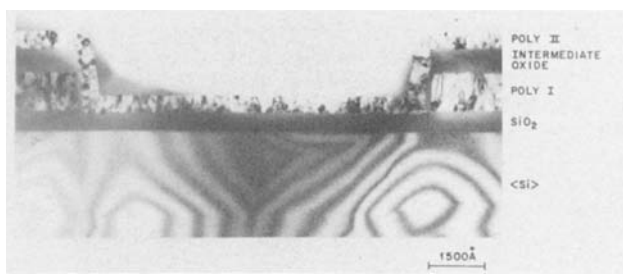

Fig. 2. A TEM cross section through a complete double-polysilicon structure.

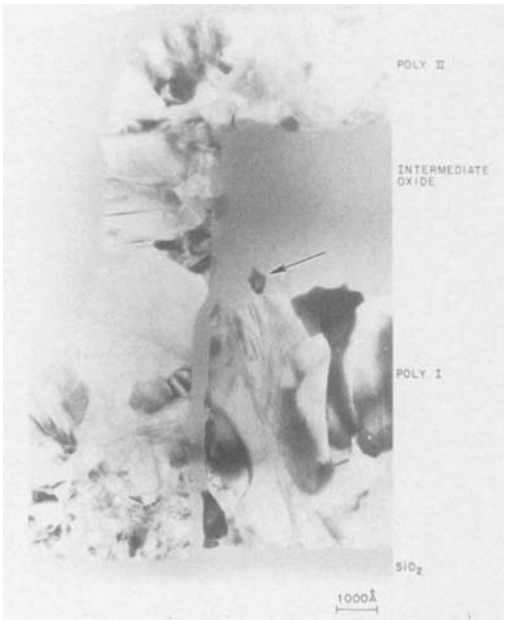

Fig. 3. A TEM cross section through the edge of the first gate. The sidewall oxide was thermally grown.

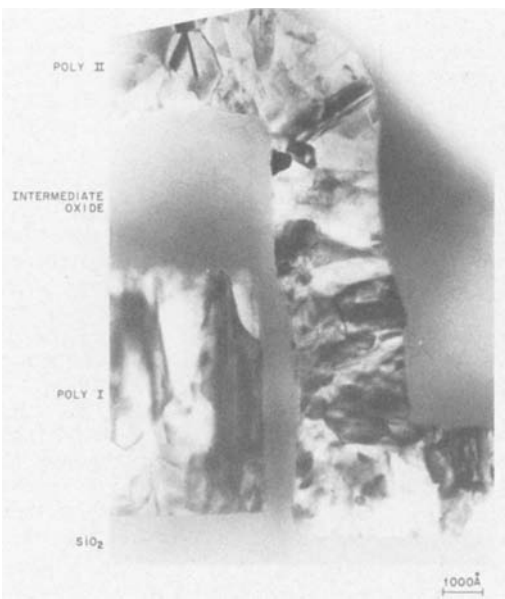

Fig. 4. A TEM cross section through the edge of the first gate. The sidewall oxide is CVD oxide, with additional oxidation in dry O_2/HCl ambient at 1000°C for 16 min.

rough with sharp protuberances. On the other hand, the sidewall oxide in Fig. 4, which is a deposited glass film, is fairly uniform (650-850Å), and the poly I sidewall is smooth.

Oxide thinning is known to occur at sharp corners of single-crystal silicon (29) or phosphorus-doped polysilicon (3, 6), as well as the occurrence of increased roughness of the polysilicon surface after its oxidation (9, 30-32). Protuberances and bumps on the polysilicon surface are expected to lower the breakdown field and increase the leakage current passing through the capacitor by enhancing the local electric field (33). Local electric field enhancement may be emphasized when a thick oxide film is thermally grown from a polysilicon layer, as is done in the conventional double-polysilicon processes, because some of the protuberances may extend very deep into the oxide causing a significant local oxide thinning (31). This is demonstrated in Fig. 3 which shows a large polysilicon projection into the thick polyoxide (shown by the arrow).

Breakdown voltage.—Electrical breakdown results are presented in Fig. 5 on a log-normal scale. For the thermally grown sidewall oxide, the median breakdown voltage is 12V. Five percent of the capacitors fail at voltages lower than 5V, which is a typical circuit operation voltage. Three percent of the capacitors fail to pass even the first test at 2V. The CVD sidewall capacitors (with the additional oxidation under GOX II conditions) do not exhibit early breakdown behavior even for a nominal oxide thickness of 390Å. The median breakdown voltages are 13, 32, and 60V for nominal CVD oxide thicknesses of 390, 620, and 930Å, respectively. The corresponding median breakdown fields are 3.3, 5.2, and 6.5 MV/cm. It should be mentioned however that the oxide thicknesses which are used to calculate the fields are the nominal thicknesses and may not be the actual thicknesses. Breakdown measurements (34) which have been conducted recently on flat capacitors indicate that the breakdown field of CVD oxide after densification at 1000°C in argon for 30 min is higher than 5 MV/cm in the range of thicknesses used in the present work.

On isolated areas on a few wafers, the breakdown voltages were significantly lower than those measured on most of the capacitors having similar sidewall oxide thicknesses. This manifests itself by the weak tail in the breakdown distribution of the samples having sidewall oxide 930Å thick (Fig. 5). This phenomenon is attributed to nonuniformities in the sidewall oxide thickness across the wafers and may be caused by any of the four reasons given in the second section of this paper. Actually, it has been found that the slope of the poly I edge in these areas is 75°-80°, compared to 88°-90° elsewhere on the wafers.

The results presented in Fig. 5 were obtained with the first polysilicon level biased positively with respect to the second polysilicon level. Measurements conducted with opposite polarity did not yield significantly different results.

Leakage current.—Results of leakage current through a CVD sidewall oxide (nominal thickness 830Å) and through a thermally grown sidewall oxide are shown in Fig. 6. The constant currents at low voltages are displacement currents due to capacitor charging. The advantage of the CVD isolation method over the thermal oxidation method is clear, since the leakage current through this capacitor is much lower. The lower current measured in the second sweep is due to charge trapping in the oxides (35, 36). Subse-

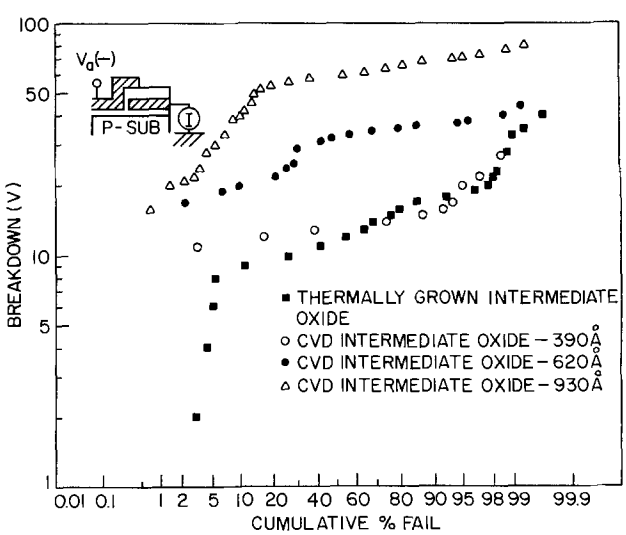

Fig. 5. Electrical breakdown distribution for double-polysilicon capacitor structures.

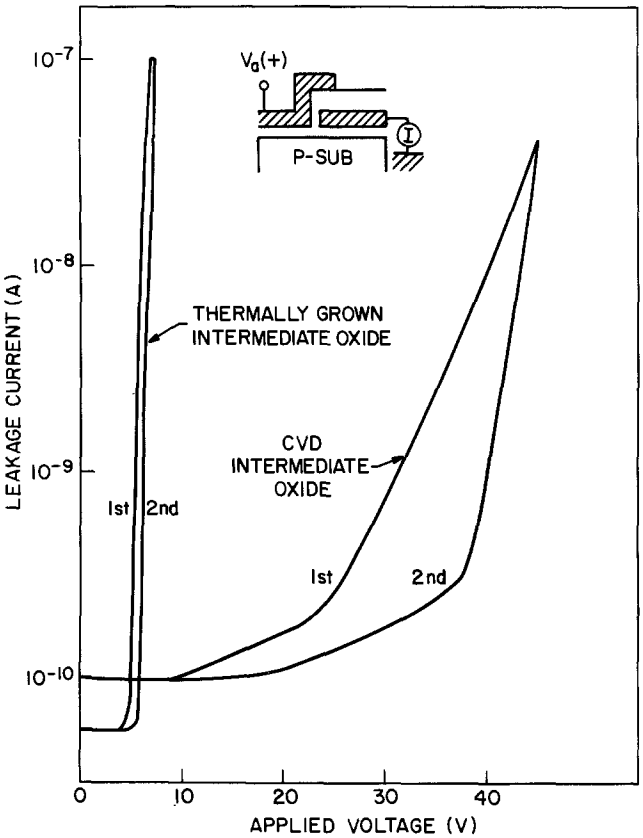

Fig. 6. Leakage currents through a thermally grown sidewall oxide and an 830Å thick CVD sidewall oxide (the oxide deposition is followed by an oxidation in dry O_2/HCl ambient at 1000°C for 16 min).

quent sweeps result in only very small changes in the leakage current.

Conclusions

A novel method for the formation of an isolation layer between two polysilicon layers by means of oxide deposition has been described. Measurements conducted on test capacitors indicate that double-polysilicon structures with zero freak population, high breakdown voltages, and low leakage currents can be obtained by the use of the proposed method. In contrast, double-polysilicon structures with sidewall isolation oxide which is grown simultaneously with the second gate oxide (250Å in this study) exhibit freak population, low breakdown voltages ,and high leakage currents.

The main advantage of the CVD isolation method is the interdependency between the intermediate oxide thickness and the second gate oxide thickness. As a result, an intermediate oxide as thick as necessary can be formed to achieve any desired electrical isolation strength. In the course of this work, structures with sidewall oxides of 200-3000Å thick were fabricated. The isolation can be realized even when the first gate material cannot be oxidized.

The requirements for the CVD isolation method, vertical SiO_2 and polysilicon walls, anisotropic SiO_2 etching and good thickness uniformity and step coverage of the deposited glass are not special for this method because they are imperative for VLSI technology.

Acknowledgments

The authors wish to thank P. Heimann, E. Kinsbron, W. T. Lynch, R. B. Marcus, T.E. Smith, and M. Sternheim for valuable discussions, and E. I. Povilonis and the MOS Fabrication Group for assistance in the sample preparation.

Manuscript submitted Dec. 2, 1982; revised manuscript received May 31, 1983.

The National Semiconductor Corporation assisted in meeting publication costs of this article.

REFERENCES

1. C. H. Sequin, D. A. Sealer, W. J. Bertram, Jr., R. R. Buckley, F. J. Morris, T. A. Shankoff, and M. F. Tompsett, in "International Solid State Circuits Conference, Digest of Technical Papers," p. 24 (1974).
2. C. N. Ahlquist, J. R. Breivgel, J. T. Koo, L. McCollum, W. G. Oldham, and A. L. Renningern, *ibid.*, p. 128 (1976).
3. S. Matsue, H. Yamamoto, K. Kobagashi, T. Wada, M. Maeda, T. Okuda, and Y. Inagaki, *ibid.*, p. 232 (1980).
4. A. K. Sinha, T. T. Sheng, T. A. Shankoff, W. S. Lindenberger, E. N. Fuls, and C. C. Chang, in "Reliability Physics Symposium Technical Digest,"**17**, 35 (1979).
5. J. J. Barnes, J. M. DeBlasi, and B. E. Deal, *This Journal*, **126**, 1779 (1979).
6. H. Sunami, M. Koyanagi, and N. Hashimoto, *ibid.*, **127**, 2499 (1980).
7. D. J. DiMaria and D. R. Kerr, *Appl. Phys. Lett.*, **27**, 505 (1975).
8. S. A. Abbas and C. A. Barile, in "Reliability Physics Symposium Technical Digest," **13**, 1 (1975).
9. R. M. Anderson and D. R. Kerr, *J. Appl. Phys.*, **48**, 4834 (1977).
10. B. E. Deal and M. Sklar, *This Journal*, **112**, 430 (1965).
11. C. P. Ho, J. D. Plummer, J. D. Meindl, and B. E. Deal, *ibid.*, **125**, 665 (1978).
12. H. Sunami, *ibid.*, **125**, 892 (1978).
13. T. Mochizuki, K. Shibata, T. Inoue, and K. Ohuchi, *Jpn. J. Appl. Phys. Suppl.*, **17**, 37 (1977).
14. S. P. Murarka, D. B. Fraser, A. K. Sinha, and H. J. Levinstein, *IEEE Trans. Electron Devices*, **ed-27**, 1409 (1980).
15. C. J. Koeneke, S. M. Sze, R. M. Levin, and E. Kinsbron, *IEEE IEDM Tech. Digest*, 367 (1981).
16. T. Shibata, K. Hieda, M. Sato, M. Konaka, R. L. M. Dang, and H. Iizuka, *ibid.*, 647.
17. S. Ogura, P. J. Tsang, W. W. Walker, D. L. Critchlow, and J. P. Shepard, *ibid.*, 651.
18. D. N. K. Wang, D. Maydan, and H. J. Levinstein, *Solid State Technol.*, **23**, 122, Aug. (1980).
19. R. S. Rosler, *Solid State Technol.*, **20**, 63 (1977). (1977).
20. A. C. Adams and C. D. Capio, *This Journal*, **126**, 1042 (1979).
21. L. W. Winkle and C. W. Nelson, *Solid State Technol.*, **24**, 123 (1981).
22. J. W. Peters, *IEEE IEDM Tech. Digest*, 240 (1981).
23. R. M. Levin and K. Evans-Lutterodt, *Mater. Lett.*, **1**, 29 (1982); *J. Vac. Sci. Technol.*, **B1**, 54 (1983).
24. J. M. Moran and D. Maydan, *Bell System Tech. J.*, **58**, 1027 (1979).
25. R. M. Levin and A. C. Adams, *This Journal*, **129**, 1588 (1982).
26. W. Fichtner, E. N. Fuls, F. L. Johnston, T. T. Sheng, and R. K. Watts, *IEEE IEDM Tech. Digest*, 24 (1980).
27. A. Hiraiwa, K. Mukai, S. Harada, T. Yoshima, and S. Itoh, *Jpn. J. Appl. Phys.*, **18**, 191 (1979).
28. W. S. Lindenberger and P. A. Heimann, Private communication.
29. R. B. Marcus and T. T. Sheng, *This Journal*, **127**, 705 (1980).
30. E. A. Irene, E. Tierney, and D. W. Dong, *ibid.*, **127**, 705 (1980).
31. R. B. Marcus, T. T. Sheng, and P. Lin, *ibid.*, **129**, 1282 (1982).
32. M. Sternheim, E. Kinsbron, J. Alspector, and P. A. Heimann, Private communication.
33. B. K. Ridley, *J. Appl. Phys.*, **46**, 998 (1975).
34. R. M. Levin, Unpublished results.
35. C. Hu, Y. Shum, T. Klein, and E. Lucero, *Appl. Phys. Lett.*, **35**, 189 (1979).
36. H. Lee and C. Feng, *Appl. Phys. Lett.*, **37**, 1080 (1980).

The Effects of Arsenic Doping in Reactive Ion Etching of Silicon in Chlorinated Plasmas

G. C. Schwartz* and P. M. Schaible

IBM General Technology Division, East Fishkill Facility, Hopewell Junction, New York 12533

ABSTRACT

The results of a study of the influence of arsenic doping of silicon and Cl_2 and CCl_4 reactant concentrations on etch rate and etch profile are described. From approximately 10^{16} to 10^{20} As/cm^3, the etch is anisotropic and the etch rate does not increase in either Cl_2 or CCl_4 plasmas. At concentrations above 10^{20} As/cm^3, mask undercutting occurs and the etch rate rapidly increases (approximately 300% for 1.5×10^{21} As/cm^3), although the functional form of the relationship between etch rate and As concentration depends on the reactant, reactant supply, and silicon load. Temperature effects are also described.

Among the dry etching processes required for fabrication of VLSI semiconductor devices is an anisotropic etch to form deep trenches in single-crystal silicon. Silicon can be reactively ion etched in CCl_4 and Cl_2 plasmas without undercut of a permanent mask. However, when the silicon is heavily doped with arsenic for buried subcollectors, undercut occurs during trench etching (1, 2). It was also observed that the undercut occurred more readily in Cl_2 than in CCl_4.

In this paper, the authors present the results of a study of the influence of arsenic doping and Cl_2 and CCl_4 reactant concentrations on both etch rate and etch profile. It has been found that both plasmas exhibit a combination of spontaneous and ion-assisted reactions as the arsenic concentration exceeds 10^{20}/cm^3.

Experimental Procedures

The apparatus and the operating procedures have been described previously (1, 3). The depths of the etched slots were measured with a Taylor-Hobson Talystep after removing the patterned Al_2O_3 mask. When there is undercutting of the mask, a pile-up of scattered material beneath the edges of a proximity mask (*e.g.*, a silicon chip placed on the wafer) can make it difficult to interpret the Talystep traces. Therefore, a mask of Al_2O_3 evaporated through a lift-off stencil was used. Etch rates were calculated from the ratio of etched depth (after mask removal) to total etch time; this assumes a constant etch rate.

High concentrations of arsenic in single-crystal silicon, relatively constant for a depth of at least 1 μm, were obtained by capsule diffusion at 1050°C followed, when required, by a drive-in at the same temperature. The protective oxide was removed in buffered HF before further processing. The concentration and the concentration profile of arsenic in the silicon were measured by 2 MeV $^4He^+$ nuclear backscattering spectrometry (NBS). A typical spectrum is shown in Fig. 1a. The arsenic concentration profiles are not known beyond a depth of 1 μm because this is the depth limit of the method. The highest concentration of arsenic obtainable was 1.6×10^{21} As/cm^3, *i.e.*, approximately 3 atomic percent (a/o). Figure 1b is a plot of the sheet resistance of some of the silicon samples (used in these experiments) as a function of arsenic concentration. Samples containing different concentrations of arsenic were etched in a single run to eliminate the effects of run-to-run variations. The reference sample was a P-type silicon wafer, chosen because it was readily available. It had been shown previously (4) that when the wafers were not bonded to the cathode, an N-type (0.1 Ωcm) wafer etched 8% faster than a P-type (2 Ωcm) wafer (in 20% CCl_4) whereas bonded wafers etched at the same rate. The difference in etch rates of the unbonded wafers was attributed to the fact that the N-type wafer was cooler.

Etch times were relatively short (usually 5 min) to try to ensure, whenever possible, that only the uniformly doped region was etched. The influence of

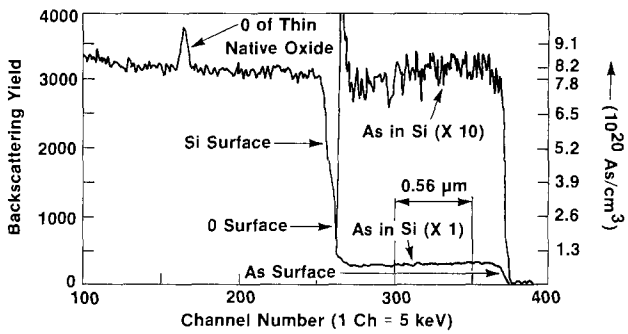

Fig. 1a. Energy spectrum for 2 McV ^4He ions backscattered from silicon doped with 8×10^{20} As/cm^3. The ordinate is the backscattering yield counts and it is proportional to concentration. The abscissa is the energy of the backscattered ^4He ions given in terms of channel number (1 channel = 5 keV); it is proportional to depth of arsenic in the silicon sample.

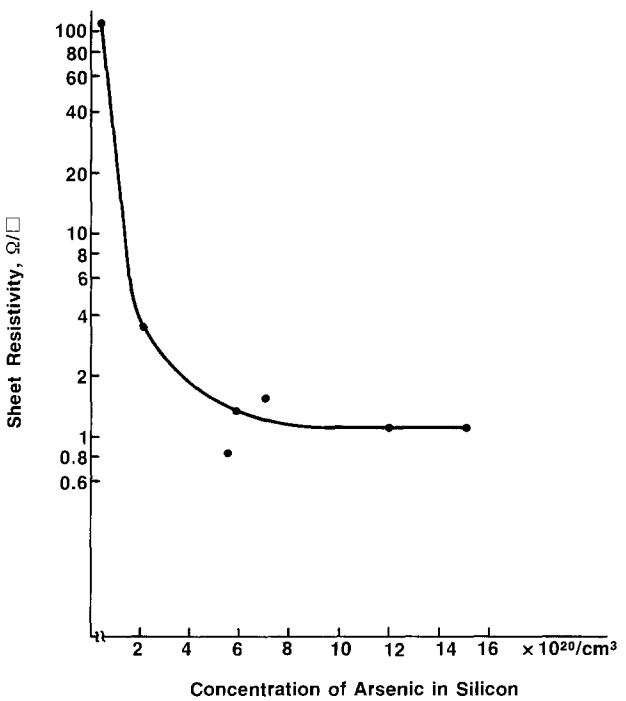

Fig. 1b. Sheet resistivity of silicon (Ω/□) as a function of arsenic concentration.

*Electrochemical Society Active Member.

Key words: reactive ion etching (RIE), chlorinated plasmas, arsenic-doped silicon, etch profiles.

temperature was examined by comparing, in the same run, samples resting on the water-cooled cathode (*i.e.*, unbonded) and samples thermally bonded to it with a heat conducting silicone grease, Dow Corning No. 340. The authors have shown (4) that bonding a wafer to the cathode changes its temperature, not its electrical coupling. In all the experiments reported here, the input power density was 0.8 W/cm^2 and the system pressure, before ignition of the flow, was 10 mTorr. The flow rate Q of the reactant gas was adjusted, at constant throttle setting, to produce the required pressure in the chamber. Pressures of 2, 5, and 10 mTorr CCl_4 and 0.5, 2, 5, and 10 mTorr Cl_2 were used in these experiments; argon was added, where necessary, to bring the total pressure to 10 mTorr. When the initial reactant pressure was, *e.g.*, 2 mTorr, the reactant concentration was called 20%; any differential pumping was ignored. Since the only diluent used was argon, it is understood that 20% Cl_2 means 20% Cl_2 in Ar. The pump speed for CCl_4 was 24.0 liter/sec (*i.e.*, $Q(CCl_4)$ was 3.75 sccm at 2 mTorr CCl_4); for Cl_2 it was 68.4 liter/sec.

The wafer load was the equivalent of one 57 mm wafer masked with a pattern that exposed 60% of the silicon surface, except for experiments in which the effect of loading with silicon wafers was investigated.

At an input power of 0.8 W/cm^2 and a pressure of 10 mTorr, the peak-to-peak rf voltage V_{pp} was approximately 2000V in argon, 1850V in Cl_2, 1900V in CCl_4 at $Q(CCl_4) = 2.0$ sccm, and 1500V in CCl_4 at $Q(CCl_4) = 30$ sccm. When $Q(CCl_4) < 8$ sccm, the pressure in the reactor decreased when the glow was ignited; at $Q(CCl_4) > 8$ sccm it increased. The decrease in pressure probably contributes to the observed increase in V_{pp} at low values of the flow rate. Also, the species in the plasma probably change in concentration and in nature (oligimers or fragments) as the flow rate is changed. The bias became more negative when part of the SiO_2 surface was covered by silicon wafers.

Fractured sections were examined in a scanning electron microscope (ISI Super Mini-SEM) to obtain the etch profiles.

Experimental Results

Etch rates.—Etch rates at constant throttle and constant load.—Figures 2a, b, c, and d show the influence of arsenic concentration on the etch rates of single-crystal silicon in both Cl_2 and CCl_4 plasmas. In most cases, etch rates are given for both unbonded and bonded wafers.

The etch rate of unbonded silicon wafers doped with 10^{20} As/cm^3 was, at most, approximately 10% greater than that of a P-type silicon wafer (2 Ωcm). There was no significant difference in etch rates when the wafers were bonded. As the arsenic concentration was increased from 10^{20} to 1.5×10^{21}/cm^3 (*i*) in 5, 20, and 50% Cl_2 and in 20% CCl_4, the slope of the curve, etch rate *vs.* concentration of arsenic, increased with increasing concentration and (*ii*) in 50 and 100% CCl_4 and 100% Cl_2, the etch rate increased linearly with increasing concentration of arsenic.

There was a tendency for the cooler wafers to etch faster when the concentration of arsenic was lower, with the trend reversed at the higher doping levels. In both plasmas, the higher the concentration of reactant, the greater the influence of temperatures on the etch rates of doped silicon.

In 100% Cl_2 and CCl_4, in which the largest increases in etch rate occurred, the rates were tripled (approximately) for the unbonded wafers as the arsenic concentration was increased from 1×10^{20} (0.2 a/o) to 1.5×10^{21}/cm^3 (3 a/o). The enhancement of etch rate with increasing dopant concentration was significantly smaller for the bonded (cooler) wafers.

Influence of the flow rate of CCl_4.—In one series of experiments, at 10 mTorr CCl_4, the throttle was adjusted to reduce the flow rate from 19 to 6 sccm. Figure 3 compares the etch rates obtained at these two flow rates: A and A′ for 19 sccm (from Fig. 2d), and B and B′ for 6 sccm.

At the lower flow rate, there is a gradual increase in the etch rates at the lower concentrations of arsenic with a more rapid increase in etch rates at higher concentrations. At the higher flow rate, however, the etch rates increase linearly with increasing concentration of arsenic. The increase in etch rate due to the increase in flow rate is significantly greater for heavily doped than for lightly doped wafers, particularly in the case of the unbonded (hotter) wafers.

Influence of wafer load.—The authors had shown that in RIE of lightly doped silicon there was a loading effect in both Cl_2 and CCl_4 plasmas (5); the decrease in etch rate with increasing load is most rapid at small loads (less than 10% of the SiO_2 cathode plate covered by silicon). Therefore, the loading effect for P-type silicon was compared with that for silicon heavily doped with arsenic.

When six unmasked 57 mm P-type silicon wafers were added to the standard load for RIE in 20% Cl_2, the etch rates of both P-type silicon and silicon doped with 1.5×10^{21} As/cm^3 decreased in about the same proportion, *i.e.*, approximately 40%. (Compare points labeled AL and A′L with curves A and A′ in Fig. 2b.) Several runs were made in 100% CCl_4, $Q(CCl_4) = 6$ sccm, in which 1/16 of a wafer was used instead of the standard load of one wafer. The increase in etch rate of the heavily doped wafers was significantly greater than that of the P-type substrate. The increase was approximately 25% for P-type, approximately 90% for 6×10^{20} As/cm^3, and approximately 220% for 1.2×10^{21} As/cm^3. (Compare points labeled BL with curve B in Fig. 3.)

Etch profiles.—Scanning electron micrographs of fractured sections of typical wafers whose etch rates are given in Fig. 2 and 3 are shown in Fig. 4-10.

Unbonded wafers, Cl_2 plasmas.—The undercut profiles had a smooth taper with a positive slope (Fig. 4-7). In 20% Cl_2, there appears to be no undercut on the sample doped with 1×10^{20} As/cm^3 (Fig. 5a). However, if the sample is then etched for 30 min, instead of the usual 5 (chosen to limit etching to the uniformly doped region), undercut does occur (Fig. 5e), but only in the doped region. The extent of undercut is comparable to that observed in the N^+ region (10^{20} As/cm^3) after RIE through an $N/N^+/P$ layered structure to form a deep slot (etch time approximately 30 min) (1).

Unbonded wafers, CCl_4 plasmas.—There was no undercut of the mask when wafers heavily doped with 1.5×10^{21} As/cm^3 wafers were etched in 20% CCl_4, nor was there undercut of the N^+ layer when the $N/N^+/P$ structure (mentioned above) was etched for 30 min (1). Undercut occurred in 50% CCl_4; the slope was positive, except on the sample doped with 1.5×10^{21} As/cm^3 (Fig. 8e). In 100% CCl_4, undercut depended on the flow rate of CCl_4; at high flow (Fig. 9) the slope was positive (the highest doping level was 1.2×10^{21} As/cm^3); at low flow, (Fig. 10) the slope changed from positive to negative at a doping level between 2 and 4×10^{20} As/cm^3.

Extent of undercut on unbonded wafers.—To estimate the extent of undercut, the lateral and vertical etch distances were measured on the micrographs of Fig. 4-10. There is a wide scatter in the results, probably due to the sensitivity of the measurements to the angle of fracture, angle of view, and acuity of focus.

Figure 11a is a plot of the extent of undercut (lateral etch distance/vertical etch distance) on wafers etched for 5 min in Cl_2 plasmas, as a function of dopant concentration. In 5 and 20% Cl_2, undercut increases with increasing arsenic concentration. In 50 and 100% Cl_2, undercut is independent of arsenic concentration

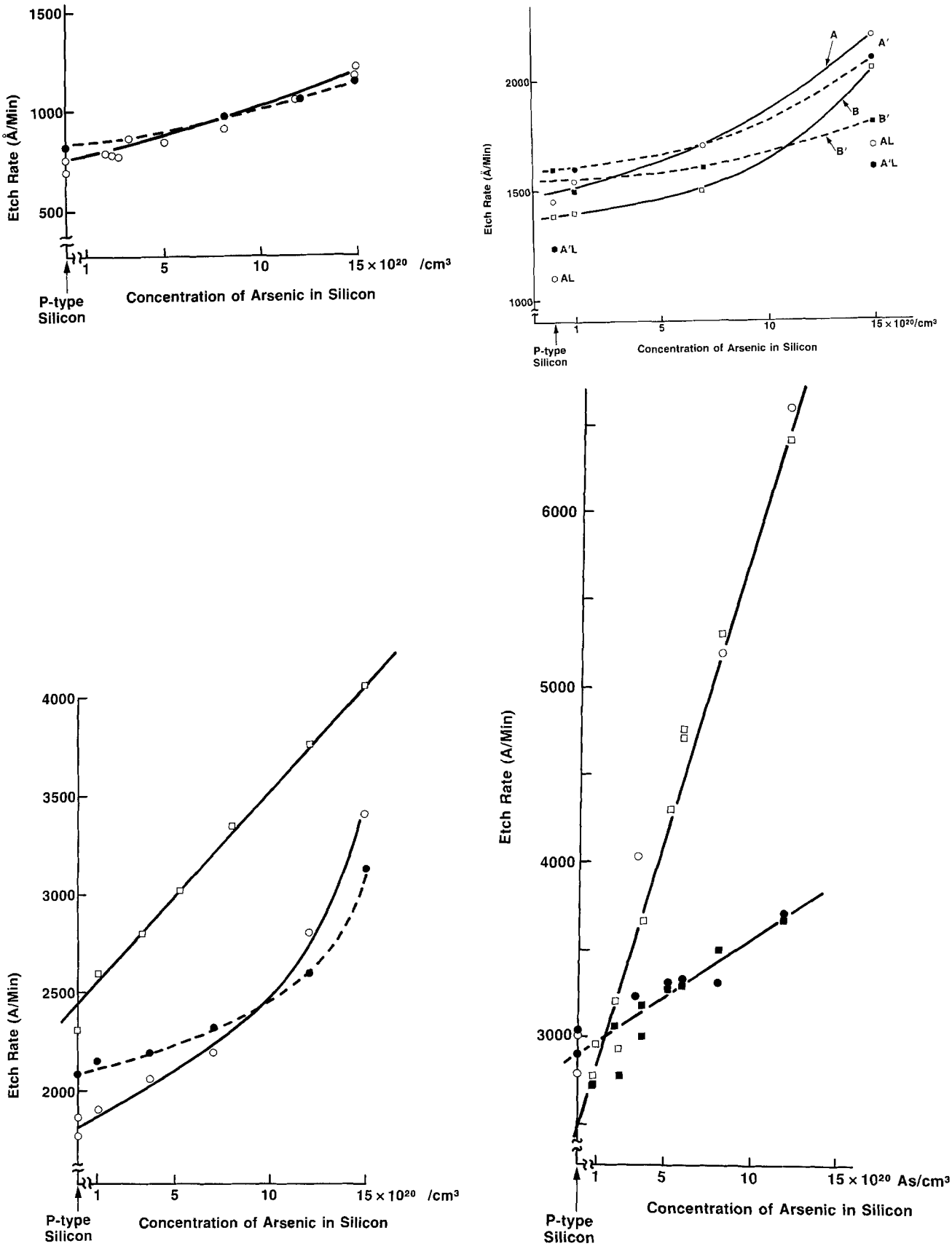

Fig. 2. The reactive ion etch rate of the arsenic-doped silicon as a function of arsenic concentration. Input power density, 0.8 W/cm²; total pressure, 10 mTorr. Data are given for wafers resting on the cooled cathode (open symbols) and (in most cases) for wafers thermally bonded to it (closed symbols). Etch rates in Cl_2 (○); in CCl_4 (□). a (upper left), In 5% Cl_2; b (upper right), in 20% Cl_2 and CCl_4; in Cl_2 with load of six Si wafers (○); c (lower left), in 50% Cl_2 and CCl_4; d (lower right), in 100% Cl_2 and CCl_4.

at concentrations $> 3 \times 10^{20}/cm^3$. From 5 to 50% Cl_2, undercut increases with increasing concentration of Cl_2. Undercut is similar in 50 and 100% Cl_2. The maximum ratio of lateral to vertical etch depth is about 0.7. In isotropic etching the ratio is one.

Figure 11b is a plot of undercut *vs.* arsenic concentration for wafers etched in CCl_4 plasmas. As stated above, no undercut was observed in 20% CCl_4 plasmas. In 50 and 100% CCl_4, undercut is independent of arsenic concentration at concentrations greater than ap-

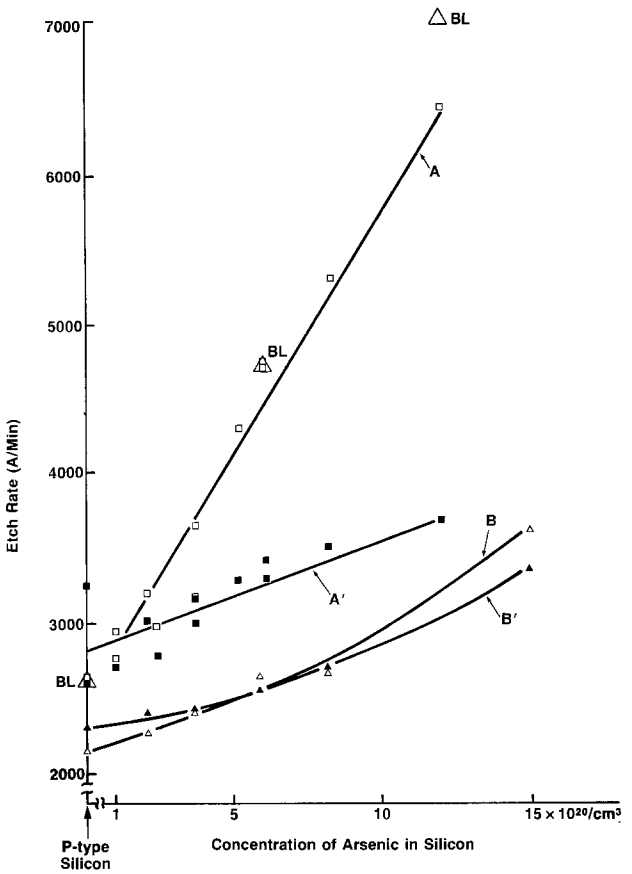

Fig. 3. Influence of flow rate and loading on etch rate in 100% CCl_4. Standard load: 19 sccm (□); 6 sccm (△). One sixteenth standard load, 19 sccm (△). Open symbols, unbonded samples; closed symbols, bonded samples.

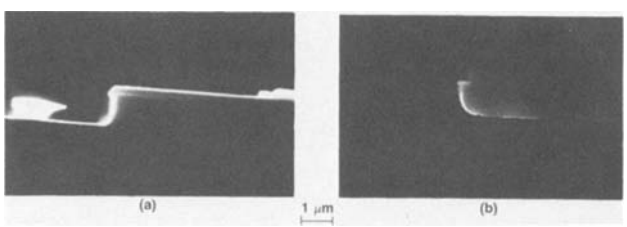

Fig. 4. Scanning electron micrographs of fractured sections of unbonded silicon wafers doped with several concentrations of arsenic reactively ion etched in a 5% Cl_2 plasma. Input power density, 0.8 W/cm^2; total pressure, 10 mTorr; run time, 10 min. a, 3.3 × 10^{20} As/cm^3; b, 1.5 × 10^{21} As/cm^3.

proximately 4 × 10^{20}/cm^3. In 100% CCl_4, when the flow rate was reduced from 19 to 6 sccm, the extent of undercut was reduced by about 25%. The maximum ratio of lateral to vertical depth is about 0.4.

The effect of loading with silicon wafers was the reduction, by the same fraction, of both vertical and horizontal etch rates. This is illustrated in Fig. 12.

Bonded wafers.—Heat sinking the heavily doped wafers to the water-cooled cathode inhibits undercutting. There was no mask undercut on bonded wafers etched in 20 and 50% Cl_2. Undercut occurred in 100% Cl_2 but the profiles were unusual; a typical profile is shown in Fig. 13. The edge is vertical at the topmost third of the slot; at greater depth, the typical undercut profile is seen. The ratio of lateral to total vertical depth is about 0.3.

There was no undercut on bonded wafers etched in CCl_4 plasmas.

Enhanced etching adjacent to etched walls.—Enhanced etching adjacent to the etched walls (also called

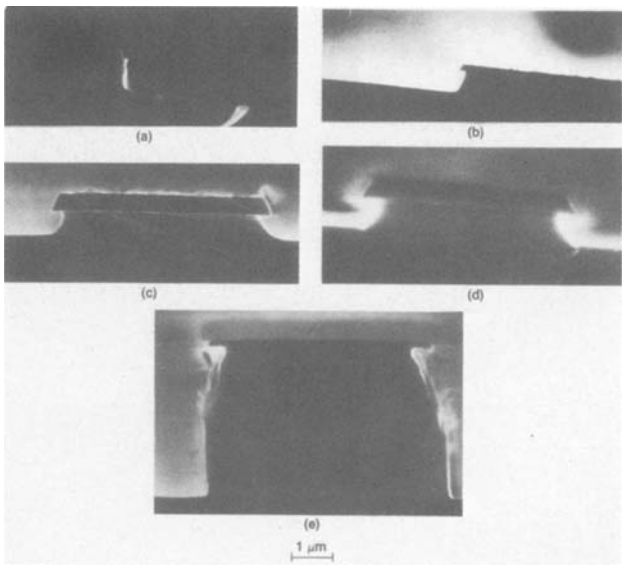

Fig. 5. Scanning electron micrographs of fractured sections of unbonded silicon wafers doped with several concentrations of arsenic reactively ion etched in a 20% Cl_2 plasma. Input power density, 0.8 W/cm^2; total pressure, 10 mTorr; run time, 5 min (except e). a, 1 × 10^{20} As/cm^3; b, 3.3 × 10^{20} As/cm^3; c, 7 × 10^{20} As/cm^3; d, 1.2 × 10^{21} As/cm^3; e, 1 × 10^{20} As/cm^3 (30 min).

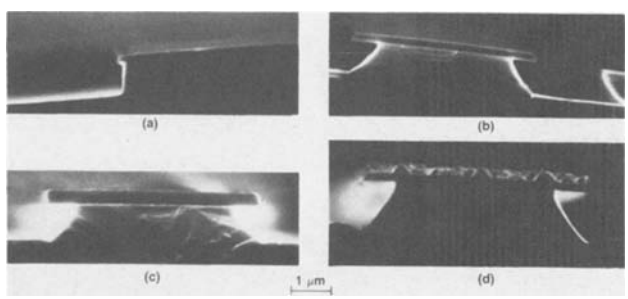

Fig. 6. Scanning electron micrographs of fractured sections of unbonded silicon wafers doped with several concentrations of arsenic reactively ion etched in a 50% Cl_2 plasma. Input power density, 0.8 W/cm^2; total pressure, 10 mTorr; run time, 5 min. a, 1 × 10^{20} As/cm^3; b, 3.7 × 10^{20} As/cm^3; c, 7.0 × 10^{20} As/cm^3; d, 1.5 × 10^{21} As/cm^3.

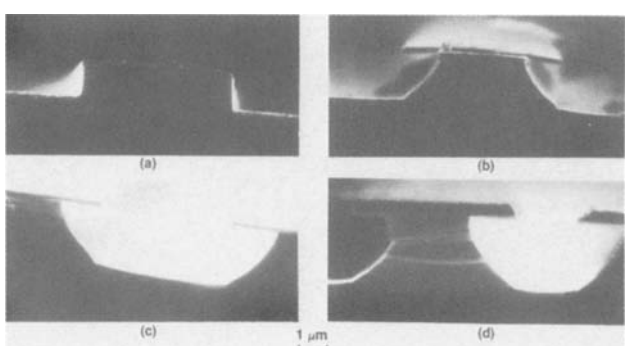

Fig. 7. Scanning electron micrographs of fractured sections of unbonded silicon wafers doped with several concentrations of arsenic reactively ion etched in 100% Cl_2 plasma. Input power density, 0.8 W/cm^2; total pressure, 10 mTorr; run time, 5 min. a, P-type silicon; b, 3.3 × 10^{20} As/cm^3; c, 8.2 × 10^{20} As/cm^3; d, 1.2 × 10^{21} As/cm^3.

trenching or grooving) was not seen after RIE in 5% Cl_2; it was seen only on the most heavily doped (1.5 × 10^{21} As/cm^3) sample in 20% Cl_2. In 50% Cl_2, there was no trenching on samples doped with less than approximately 3× 10^{20} As/cm^3; at greater con-

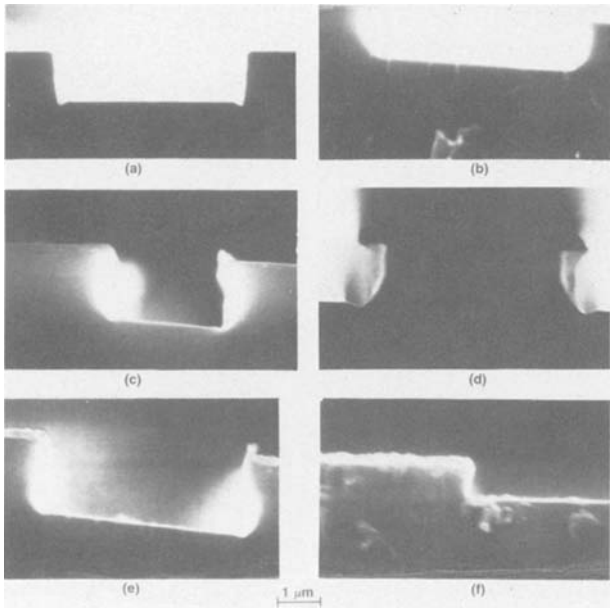

Fig. 8. Scanning electron micrographs of sections of unbonded silicon wafers doped with several concentrations of arsenic reactively ion etched in a 50% CCl_4 plasma. Input power density, 0.8 W/cm^2; total pressure, 10 mTorr; run time, 5 min (except f). a, 1 × 10^{20} As/cm^3; b, 3.3 × 10^{20} As/cm^3; c, 8.2 × 10^{20} As/cm^3; d, 1.2 × 10^{21} As/cm^3; e, 1.5 × 10^{21} As/cm^3; f, 1.5 × 10^{21} As/cm^3 (3 min).

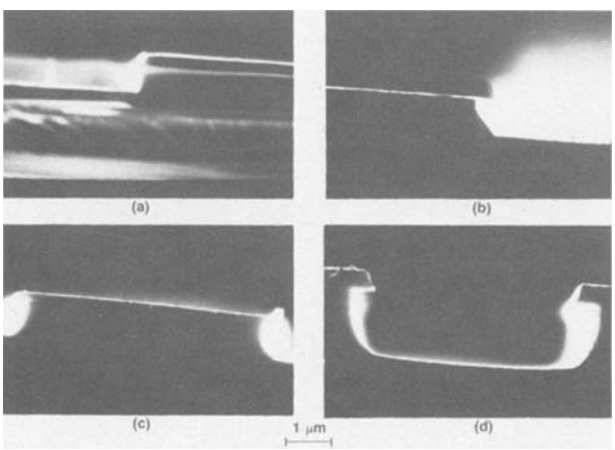

Fig. 9. Scanning electron micrographs of sections of unbonded silicon wafers doped with several concentrations of arsenic reactively ion etched in a 100% CCl_4 plasma. Input power density, 0.8 W/cm^2; total pressure, 10 mTorr; flow rate of CCl_4, 19 sscm; run time, 3 min. a, 1 × 10^{20} As/cm^3; b, 2.4 × 10^{20} As/cm^3; c, 3.7 × 10^{20} As/cm^3; d, 1.2 × 10^{21} As/cm^3.

centrations of As, the depth of the trench increased with doping level.

In 100% Cl_2, however, trenching was barely perceptible; its extent appeared to be the same on all the As-doped wafers. In 50% CCl_4, grooving was sporadic; in 100% CCl_4 (at both flow rates) it was evident only on the more lightly doped wafers.

Bonding the heavily doped wafers to the cathode eliminated trenching, except for the most heavily doped sample etched in 100% Cl_2.

Increasing the silicon load reduced the trench depth in Cl_2 but increased the depth in CCl_4 RIE of heavily doped wafers.

Boron doping.—The authors looked briefly at the effect of high concentration of P-type impurities. A wafer heavily doped with boron (1.3 × 10^{21} B/cm^3 at the surface decreasing to 6 × 10^{20} B/cm^3 at a depth of 1 μm) etched at the same rate as P-type silicon wafer

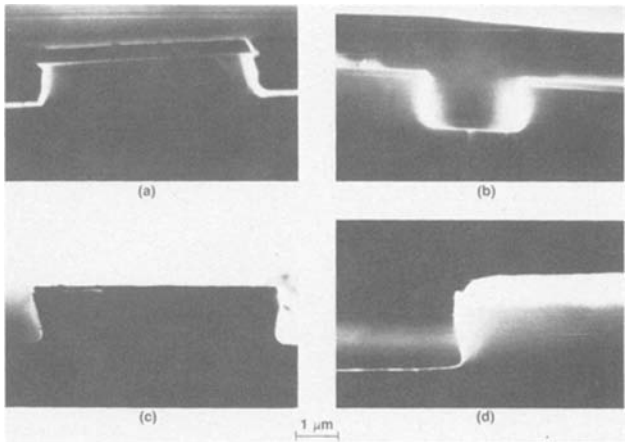

Fig. 10. Scanning electron micrographs of fractured sections of unbonded silicon wafers doped with several concentrations of arsenic reactively ion etched in a 100% CCl_4 plasma. Input power density, 0.8 W/cm^2; total pressure, 10 mTorr; flow rate of CCl_4, 6 sccm; run time, 3 min. a, 2.1 × 10^{20} As/cm^3; b, 5.9 × 10^{20} As/cm^3; c, 8.2 × 10^{20} As/cm^3; d, 1.5 × 10^{21} As/cm^3.

containing < 10^{16} B/cm^3 in both 20 and 50% Cl_2, and the mask was not undercut. However, in 50% Cl_2, there was a very small trench adjacent to the etched walls.

Discussion

As the concentration of arsenic in single-crystal silicon was increased from approximately 10^{16} to 10^{20}/cm^3, the reactive ion etch rate did not increase in either Cl_2 or CCl_4 plasmas at 10 mTorr. When the concentration was increased beyond 10^{20} As/cm^3, the etch rate increased with increasing dopant concentration. The functional form of the relationship between etch rate and concentration of arsenic in silicon depended on the reactant and the reactant supply. In 5-50% Cl_2, in 20% CCl_4, and in 100% CCl_4 at low flow rate, there was a gradual increase in etch rate at the lower concentrations and a more rapid increase at the higher concentrations. In 50 and 100% CCl_4 and in 100% Cl_2, the etch rate increased linearly with increasing dopant concentration.

Similar results have been reported by Koike *et al.* (6). They measured the etch rate of phosphorous-doped polysilicon. The relative etch rate (doped/undoped polysilicon) increased very slowly with decreasing resistance reaching a value of approximately 1.1 at 250 Ω/□; it increased gradually to approximately 1.35 as the resistance decreased to 75 Ω/□; and finally it increased very rapidly to approximately 3 at 25 Ω/□.[1] They also reported that the relative etch rate approached unity as the d-c bias was increased.

The authors attribute the increase in etch rates of very heavily doped silicon to the increasing importance of the chemical component of the etching reaction as compared with the ion-assisted component. Some of the evidence which supports this view follows. As shown in Fig. 2, the more heavily doped the silicon, the greater was the increase in etch rate in response to an increase in the reactant concentration (which decreased the rf peak-to-peak voltage and therefore the cathode bias) and to an increase in temperature. This point about reactant supply can be demonstrated in a somewhat different way by replotting some of the data of Fig. 2 as has been done in Fig. 14. Figure 14 shows that although the etch rates of both lightly and very heavily doped single crystal silicon increase monotonically with increasing reactant concentration, the rate of increase is significantly greater for the heavily doped silicon.

[1] Since the thickness of the polysilicon was not given by Koike *et al.*, dopant concentrations could not be calculated. The authors can make an estimate: at about 75 Ω/□, [P] is about 5 × 10^{18} for a polysilicon thickness of 2 μm and 2 × 10^{19}/cm^3 for a polysilicon thickness of 0.5 μm.

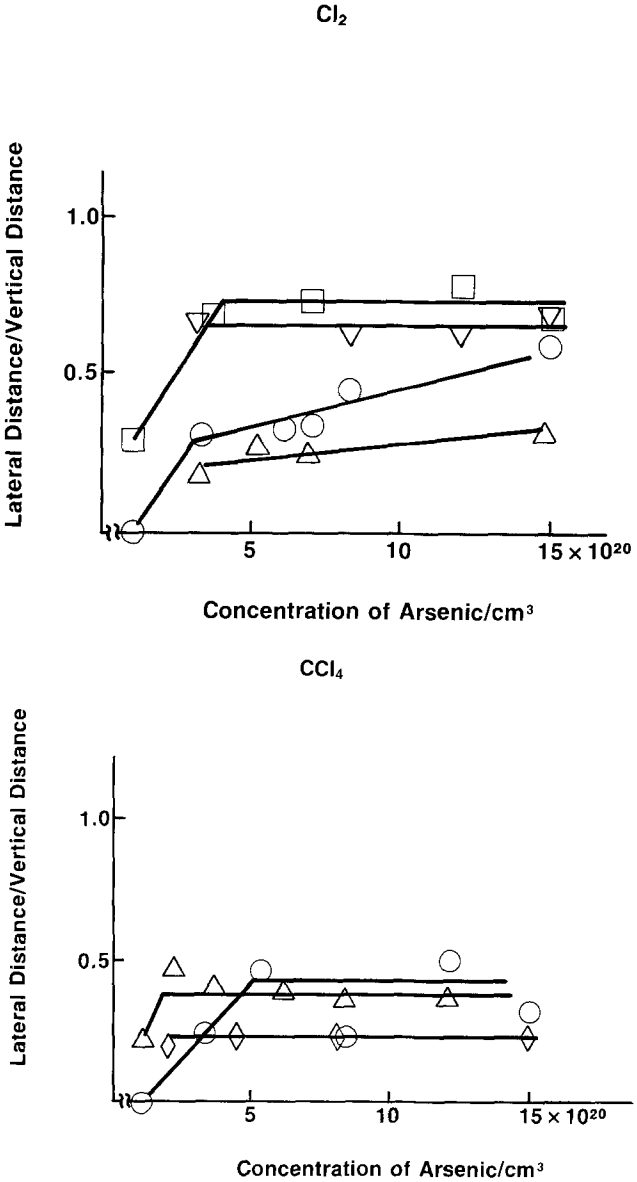

Fig. 11. Extent of undercut in reactive ion etching unbonded wafers in chlorinated plasmas as a function of arsenic concentration at 0.8 W/cm² input power density, 10 mTorr total pressure. Undercut is expressed by:

$$\frac{\text{lateral distance}}{\text{vertical distance}}$$

The distances are estimated from scanning electron micrographs of fractured sections. a, In 5 (△), 20 (○), 50 (□), and 100% (▽) Cl_2; b, in 50 (○) and 100% CCl_4, flow rate = 10 sscm (△), flow rate = 6 sscm (◇).

Also, the decrease in etch rate which resulted when (at 10 mTorr CCl_4) the flow rate was reduced (and the rf peak-to-peak voltage thereby increased) was greater for the more heavily doped wafers. Finally, the loading effect in 100% CCl_4 was almost ten times larger for a wafer doped with 1.2×10^{21} As/cm³ than for a very lightly doped wafer.

Undercut during RIE can occur only as the result of a chemical reaction in which a volatile product is formed directly (*i.e.*, without the assistance of ion bombardment). It is speculated that high concentrations of arsenic in silicon promote such a reaction since undercut does not occur during RIE of lightly doped silicon using the same conditions of chlorinated species supply and ion bombardment. The volume of material removed from beneath the mask was too large to be accounted for by a reaction only of arsenic.

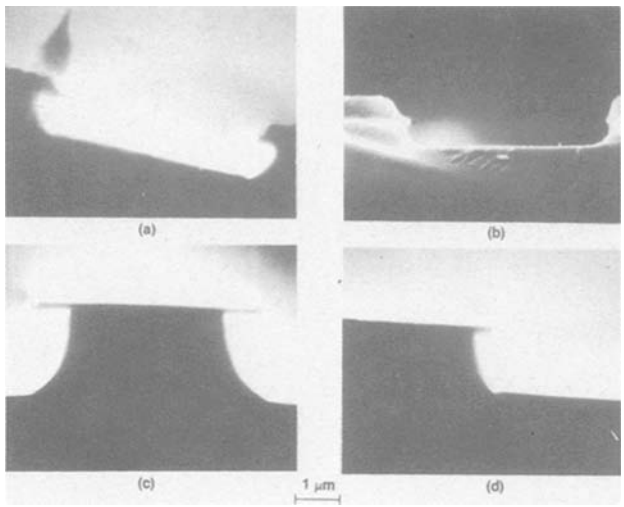

Fig. 12. Scanning electron micrographs of fractured sections to show effect of silicon loading on profile of arsenic-doped silicon reactively ion etched in chorinated plasmas. The input power density is 0.8 W/cm²; total pressure, 10 mTorr; and run time, 5 min. a, 20% Cl_2 in Ar, 1.5×10^{21} As/cm³, 1/16 of a masked 57 mm wafer; b, as in a, with six additional unmasked 57 mm silicon wafers; c, 100% CCl_4, 6.1×10^{20} As/cm³, 1/16 of a masked 57 mm wafer; d, As in c, with one additional unmasked 57 mm silicon wafer.

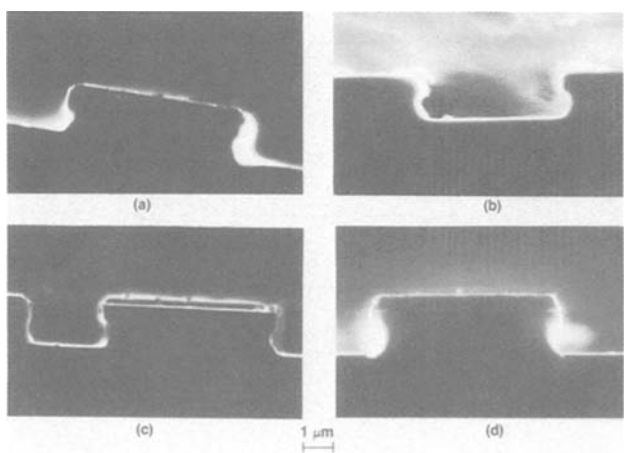

Fig. 13. Scanning electron micrographs of fractured sections of bonded silicon wafers doped with several concentrations of arsenic reactively ion etched in a 100% Cl_2 plasma. Input power density, 0.8 W/cm²; total pressure, 10 mTorr; run time, 5 min. a, 3.3×10^{20} As/cm³; b, 5.2×10^{20} As/cm³; c, 8.2×10^{20} As/cm³; d, 1.2×10^{21} As/cm³.

As it has been noted, undercut occurs when the concentration of dopant exceeds about 10^{20} As/cm³; the exact doping level at which it is first seen depends on the nature of the reactant, its concentration in the feed gas, the substrate temperature, and the run time. It required a higher concentration of CCl_4 than Cl_2 in the feed gas to produce an undercut. The maximum undercut was almost twice as great in Cl_2 as in CCl_4. Cooling the substrates to 25°C completely eliminated undercutting in CCl_4 plasmas and in 50% Cl_2. The difference between the plasmas may be due to the fact that in CCl_4 sidewall passivation (7) (by recombination or oligerimization) may provide additional protection against undercut. Since undercut is due to a purely chemical reaction, it is not unexpected that reducing the temperature inhibits it.

The authors attributed the higher etch rates observed for very heavily doped wafers, particularly at high reactant concentrations, to the increasing importance of the chemical component of RIE. However, since the

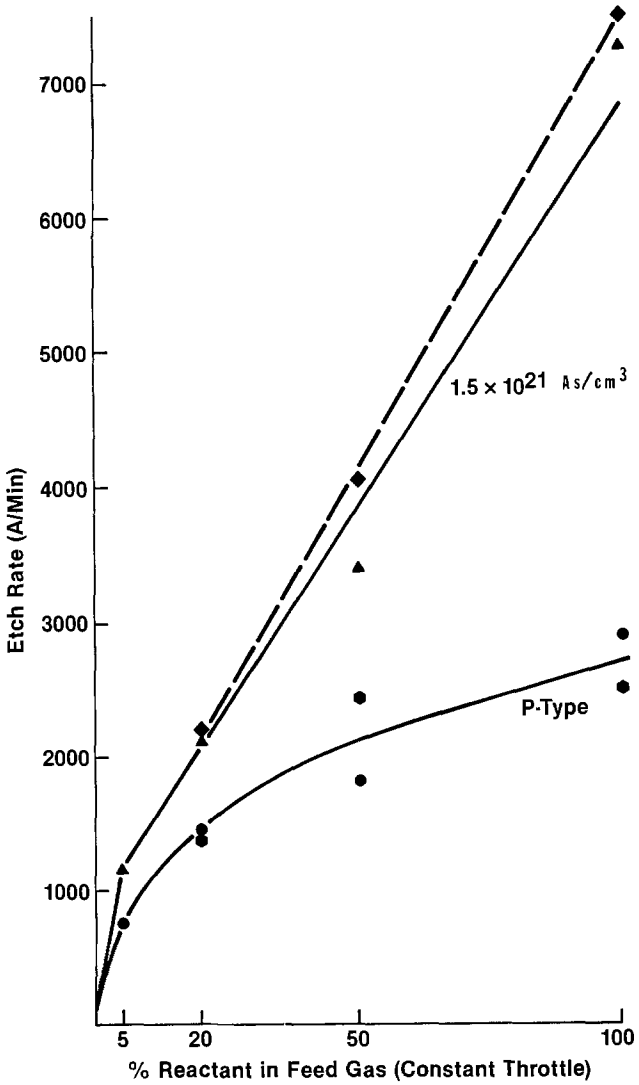

Fig. 14. The reactive ion etch rate of silicon as a function of reactant concentration (at constant throttle setting) for a P-type sample (○ Cl_2, ○ CCl_4) and a wafer doped with 1.5 × 10^{21} As/cm^3 (△ Cl_2, ◇ CCl_4).

undercut reaches a limiting value, less than one, it appears that the purely chemical reaction has a limited effect on the etch rate in the absence of the synergistic interaction of chemistry and ion bombardment.

How does a relatively small amount of arsenic in silicon, *i.e.*, 0.2-3 a/o, result in an acceleration of the etch rate and undercut of the mask? Boron doping does not have the same effect. Mogab and Levinstein (7) attributed the enhancement of the etch rate of phosphorus-doped (5 × 10^{-4} Ωcm) polycrystalline silicon (in C_2F_6/Cl_2 mixtures in a high pressure/high flow reactor) and the difference between boron and phosphorus doping, to the presence in P-doped polysilicon, to a high concentration of free electrons which increase the rate of chemisorption of Cl atoms. Certainly, the fact that there is no acceleration in etch rate when silicon is heavily doped with boron makes the role of electrons plausible. However, if high concentrations of electrons, per se, are responsible for the increase in the rate of the etching reaction, it is reasonable to expect some correlation between the change in electron concentration and the change in etch rate as the doping level is increased.

The concentration of electrons in n-type silicon increases monotonically with increasing dopant concentration in the range 10^{16}-10^{20}/cm^3, although the rate of increase decreases markedly at the higher (*i.e.*, > 3 × 10^{20}/cm^3) dopant concentrations (8, 9). However, the etch rates of n-type silicon do not parallel this trend. This is seen clearly in Fig. 15 in which the quantity $(\Omega/\square)^{-1}$ (which is an approximate measure of electron concentration) and the etch rates of unbonded wafers in 50% CCl_4 and Cl_2 are plotted as a function of arsenic concentration, as well as in the results of Koike on phosphorus-doped polysilicon. From Koike's results, one might conclude that significant etch rate acceleration occurs when phosphorus-doped silicon becomes degenerate. In arsenic-doped single-crystal silicon, the fact that the carrier concentration increases more slowly than the atomic concentration (above about 10^{20}/cm^3) has been attributed to cluster formation (8). There appears to be a correlation between the onset of clustering and the onset of etch rate acceleration and undercut in RIE of the doped single-crystal silicon in CCl_4 and Cl_2. It is not known whether this is a coincidence or whether this suggests a mechanism. Although the structure of the cluster has not been determined, a configuration, As-V^{--}-As, has been proposed (10). The stabilized doubly charged negative vacancy may play a role in enhancing the chemical component of the etching reaction.

To distinguish between the importance of arsenic in clusters and the importance of free carriers (electrons) in etch rate acceleration and lateral etching in RIE of heavily doped (> 10^{20} As/cm^3), the following experiment (which the authors were unable to do) should be instructive. By the use of laser annealing, silicon can be doped by ion implantation with electrically active arsenic above its solubility limit. Therefore, one could compare etch rates and extent of undercut of laser-annealed silicon and laser-annealed silicon which was subsequently thermally annealed to form clusters.

In physical sputtering, trenching has been attributed to the dependence of sputtering yield on the angle of incidence of the bombarding ions, forward sputtering, and enhancement of the ion flux at mask edges. Previously (1), the authors had related trenching during RIE of lightly doped silicon in chlorinated plasmas to the sputtering component of RIE; they reported a correspondence between the extent of grooving and the RIE parameters such as input rf power and frequency, system pressure, ion mass, and loading. While sputtering effects undoubtedly are operative, they cannot explain all the observations reported in this paper.

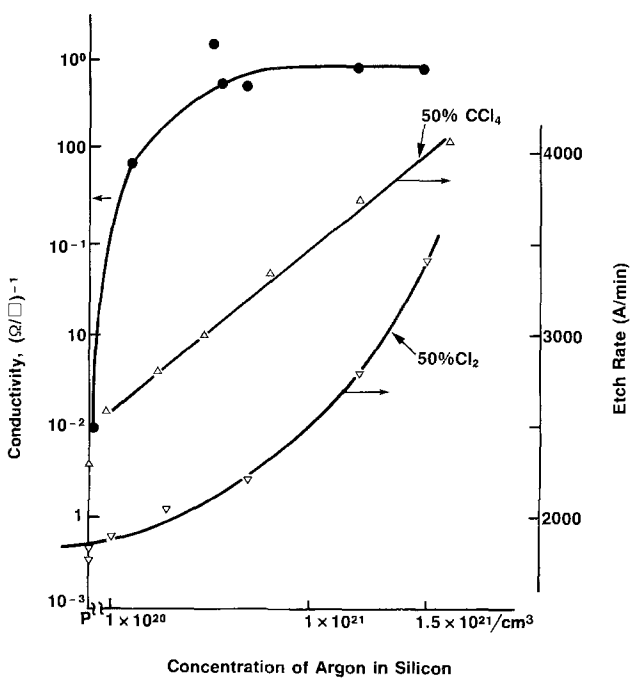

Fig. 15. The reactive ion etch rate, in 50% Cl_2 and CCl_4, and the conductivity $(\Omega/\square)^{-1}$ of silicon as a function of arsenic concentration.

Chemical effects also contribute to trench formation. For example, in 20 and 50% Cl_2 plasmas, trenches of different depths were formed on wafers etched at the same time. There was a correlation between the trench depth and the concentrations of both reactant and dopant. Despite the lower cathode bias in 50% Cl_2, compared with 20% Cl_2 the trenches were deeper after RIE in 50% Cl_2. In 100% Cl_2, however, the lower cathode bias seems to be the dominant factor; trenches were shallow and the same for all the arsenic-doped wafers despite the higher reactant supply. The authors cannot explain the results obtained in the CCl_4 plasmas; the extent of trenching followed no consistent pattern with respect to cathode bias, reactant supply, or dopant concentration.

Conclusions

Doping of silicon with arsenic increases the chemical component of etching relative to the ion-assisted component when reactive ion etching silicon in chlorinated plasmas. As the chemical component becomes more important, the dependence of etch rate on temperature becomes more pronounced and etch profiles become more isotropic. The exact dependencies of etch rate and etch profile on temperature, reactant concentration, reactant flow, and wafer load are different for CCl_4 and Cl_2 plasmas, but both plasmas exhibit a combination of free radical and ion-assisted reactions as the arsenic concentration exceeds $10^{20}/cm^3$.

The mechanism by which arsenic enhances the reaction rate of silicon is in question. The etch rate does not correlate with free electron density which could enhance Cl adsorption. Clustering, which is operative in the As-Si system above about $10^{20}/cm^3$ As, coincides with the onset of etch rate acceleration, but the role that a cluster would play in etching needs further investigation.

Acknowledgments

The authors thank J. P. Anderson, V. Platter, and R. Carruthers for their technical assistance. They thank E. Mayen for preparing the arsenic-doped samples. They are indebted to W. K. Chu and R. Lever for nuclear backscattering analyses and to R. Kastl for SIMS profiles. They also thank J. S. Logan, R. Lever, and W. K. Chu for many valuable discussions during the course of this investigation.

Manuscript submitted Dec. 8, 1982; revised manuscript received April 5, 1983.

IBM assisted in meeting publication costs of this article.

REFERENCES

1. G. C. Schwartz and P. M. Schaible, *J. Vac. Sci. Technol.*, **16**, 410 (1979).
2. H. B. Pogge, J. A. Bondur, and P. J. Burkhardt, *This Journal*, **125**, 470C (1978).
3. P. M. Schaible, W. C. Metzger, and J. P. Anderson, *J. Vac. Sci. Technol.*, **15**, 334 (1978).
4. G. C. Schwartz and P. M. Schaible, in "Plasma Processing," R. G. Frieser and C. J. Mogab, Editors, p. 133, The Electrochemical Society Softbound Proceedings Series, Pennington, NJ (1981).
5. G. C. Schwartz and P. M. Schaible, Abstract 612, p. 1535, The Electrochemical Society Extended Abstracts, Vol. 79-1, Boston, MA, May 6-11, 1979.
6. A. Koike, K. Imai, S. Hosoda, A. Tomozawa, and T. Agatsuma, Abstract 213, p. 343, The Electrochemical Society Extended Abstracts, Vol. 82-1, Montreal, Que., Canada, May 9-14, 1982.
7. C. J. Mogab and H. J. Levenstein, *J. Vac. Sci. Technol.*, **17**, 721 (1980).
8. R. O. Schwenker, E. S. Pan, and R. F. Lever, *J. Appl. Phys.*, **42**, 3195 (1971); M. Y. Tsai, F. F. Morehead, J. E. E. Baglin, and A. E. Michel, *ibid.*, **51**, 3230 (1980).
9. S. Solmi, M. Severi, R. Angelucci, L. Baldi, and R. Bilenchi, *This Journal*, **129**, 1811 (1982).
10. W. K. Chu and B. J. Masters, in "American Institute of Physics Conference Proceedings," p. 305, Boston, MA (1978).

Properties of Hot-Pressed Zirconium Pyrovanadate Ceramics

R. C. Buchanan* and G. W. Wolter

Department of Ceramic Engineering, University of Illinois at Urbana-Champaign, Urbana, Illinois 61801

ABSTRACT

Zirconium pyrovanadate powders prepared from solution precipitation and by solid-state reaction were hot pressed below 800°C. Unit cell parameter and thermal expansion were found to have a negative slope above 150°C, attributed to flexing of the bond angles in the ZrV_2O_7 structure. Thermal expansion coefficient determined was 72×10^{-7}/°C. Electrical conductivities measured were in the range $10^{-5} - 10^{-6}$ $(\Omega\text{-cm})^{-1}$ at 25°C with activation energy of 0.2 eV. Conduction was determined to be n-type and was attributed to the presence of V^{4+} ions in the hot-pressed ZrV_2O_7. Infrared transmission was significant in the range 2.5 −10 μm with a maximum (85%) at 7.5 μm.

Although zirconium pyrovanadate, ZrV_2O_7, was first reported in 1942 by Peyronel (1), very little has been reported concerning its properties. This is due to the difficulty of forming high purity ZrV_2O_7 since the reactions involved in the formation are extremely slow. Also, there is difficulty in obtaining dense compacts of the material, owing to its tendency to decompose in the temperature range where normal solid-state sintering would occur.

The system V_2O_5-ZrO_2 was studied by Burdese and Borlera (2) and by Cirilli, Burdese, and Brisi (3). Only one compound, ZrV_2O_7, was found to exist in the system. It melts incongruently at 747°C to ZrO_2 plus a liquid of composition 64% V_2O_5-36% ZrO_2 which melts at about 670°C. No areas of solid solubility were reported.

Zirconium pyrovanadate has been prepared by two methods: a solution method reported by Peyronel (1) and by the direct reaction of ZrO_2 and V_2O_5 (2-5). The method reported by Peyronel involved the reaction of NH_4VO_3 and $ZrO(NO_3)_2$ in aqueous solution in the presence of H_2O_2. In the *p*H range from 2.1 to 6.9, a zirconyl vanadate, $3ZrO_2 \cdot 2V_2O_5 \cdot 9H_2O$, was formed. The zirconyl vanadate was yellow in color, amorphous, and insoluble in water. If the *p*H of the solution was below 3.0, HVO_3 was also formed and was absorbed on the surface of the $3ZrO_2 \cdot 2V_2O_5 \cdot 9H_2O$. After heating to 260°-270°C, these adsorption products decomposed to form ZrV_2O_7.

* Electrochemical Society Active Member.
Key words: inorganic, infrared, synthesis, conductance.

Formation of ZrV_2O_7 by direct reaction of ZrO_2 and V_2O_5 has been reported by Burdese and Borlera (2), Craig and Hummel (4), and Pedregosa *et al.* (5). Incomplete formation of the ZrV_2O_7 was reported after reacting a stoichiometric mixture of ZrO_2 and V_2O_5 for 1000 hr at temperatures of 650°-700°C. The reaction was described as "extraordinarily slow".

Reactions in the system ZrO_2-V_2O_5 were studied by Tsujii *et al.* (6). High temperature x-ray diffraction (XRD), differential thermal analysis (DTA), and infrared spectroscopy were used to examine the reactions. The decomposition of ZrV_2O_7 to ZrO_2 plus liquid was reported to occur at temperatures above 800°C.

The crystal structure of ZrV_2O_7 has been determined to be cubic with a reported lattice constant of 8.74A [Peyronel (1)], 8.742A [Burdese and Borlera (2)], 8.777A [Craig and Hummel (4)], and 8.787A [Pedregosa *et al.* (5)]. This results in a theoretical density of 2.93 g/cm^3.

The space group of ZrV_2O_7 was determined to be Pa3 by Pedregosa *et al.* (5), using x-ray powder diffraction methods. The Pa3 space group is typical of many MeX_2O_7 compounds, such as the ZrP_2O_7 structure. The ZrP_2O_7 structure consists of an NaCl-like distribution of Zr^{4+} and $P_2O_7^{4-}$ ions (7). Each Zr^{4+} ion is surrounded by six O^{2-} ions. Levi and Peyronel (8) report that the $P_2O_7^{4-}$ groups in the ZrP_2O_7 lattice are centrosymmetric and occupy the special positions in the Pa3 lattice.

The thermal expansion behavior for ZrV_2O_7 was investigated by Craig and Hummel (4). Two rapid reversible inversions were reported at about 80° and 100°C. Above 150°C, the expansion was found to be negative, with an expansion coefficient of -68×10^{-7}/°C between 200° and 600°C. Hot stage XRD was used to determine the effect of temperature on the unit cell dimensions. The variation in a_o with temperature was found to be similar to the bulk thermal expansion. The two low temperature inversions reported by Craig and Hummel (4) were apparently transitions from a low temperature cubic structure to a high temperature structure which is also cubic. The large area of negative expansion probably resulted from the open structure of the ZrV_2O_7 which allows changes in coordination or bond angles without drastic changes in the structure. Similar behavior was noted by Harrison, McKinstry, and Hummel (9) for ZrP_2O_7 and other MeX_2O_7 compounds.

The pronounced negative expansion and unit cell characteristics suggested interesting anomalies in the electrical properties, analogous to the ZrP_2O_7 (7).

The goals of this study, therefore, were to investigate hot pressing as a technique for producing dense samples of ZrV_2O_7, and to characterize the samples produced, with respect to microstructure, optical, and electrical properties.

Experimental

Zirconium pyrovanadate powders used in this study were prepared both from solution precipitation and by solid-state reaction. For the solution preparation, reagent grade NH_4VO_3 and $ZrO(NO_3)_2$ powders were used as precursors. A typical batch consisted of 13.96g NH_4VO_3 and 15.94g $ZrO(NO_3)_2$. The constituents were dissolved separately in 500 ml of deionized water; however, the NH_4VO_3 solution required heating to near boiling to achieve complete dissolution. The $ZrO(NO_3)_2$ solution plus 70-80 ml of H_2O_2 was then added to the NH_4VO_3 solution, while stirring. After the reaction subsided, the pH was adjusted to 2.5-2.8 by adding nitric acid. The resultant precipitate on cooling was separated from the supernate by vacuum filtration. Calcination of the precipitate above 350°C for 8 hr produced ZrV_2O_7. Any unreacted V_2O_5 present (determined from DTA and XRD) could be substantially removed by milling of the powders in deionized water.

To obtain the solid-state-reacted powders, ZrO_2 and V_2O_5 powders were combined in equimolar ratios to obtain a 100g batch. The mixed powders were placed in a platinum crucible and reacted in air at 650°C for 72 hr, 700°C for 48 hr, and 720°C for 50-250 hr. Approximately every 25 hr, the reaction products were crushed with a mortar and pestle and examined by XRD and DTA. The final powder, which was determined to be ZrV_2O_7, was obtained after calcination at 720°C for 240 hr. Figure 1 shows the reaction sequence from initial powder to ZrV_2O_7 product. The ZrV_2O_7 powder was then milled for 6 hr in polyethylene jars with zirconia balls to reduce the particle size.

Hot pressing was used to densify the ZrV_2O_7 samples. Hot pressing was employed since normal solid-state sintering would not produce dense compacts due to the low decomposition temperature for ZrV_2O_7, which is shown in Fig. 2 to be 840°C. The decomposition effectively limited hot pressing temperatures to below 800°C.

The hot pressing apparatus used consisted of a press with furnace, water-cooled platens, temperature controller, and dial gauge to measure platen movement. Several die materials were investigated including

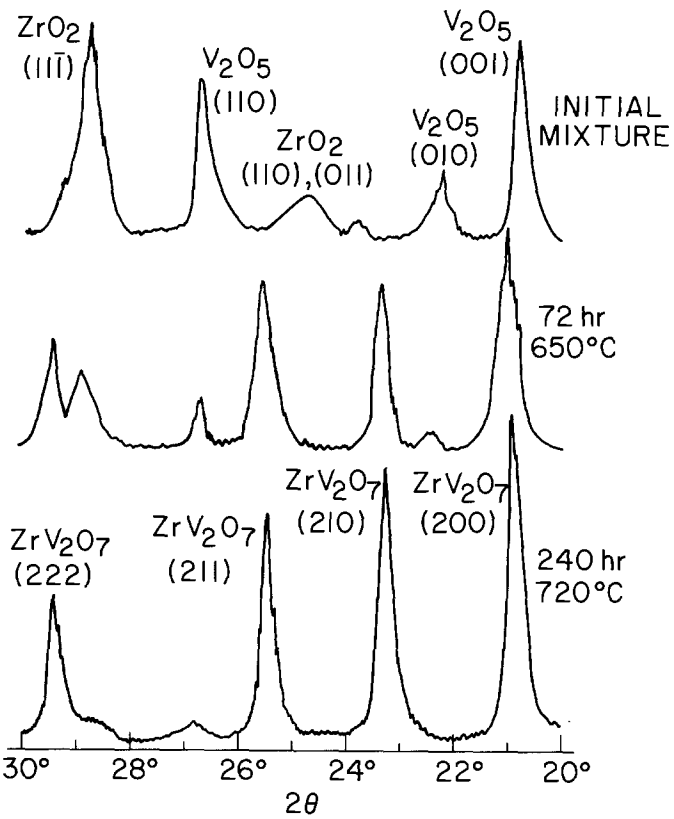

Fig. 1. X-ray diffraction patterns showing progressive formation of ZrV_2O_7 from powder reactants ZrO_2 and V_2O_5 taken at various calcination times and temperatures.

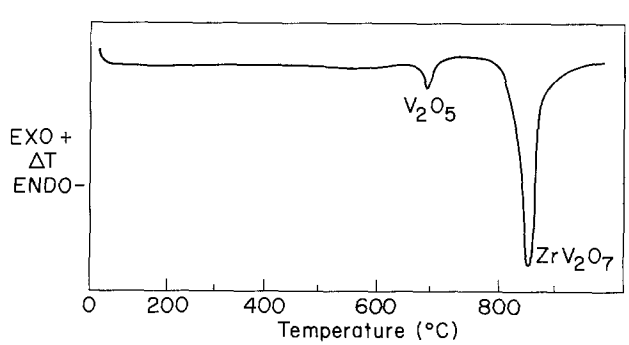

Fig. 2. Typical DTA curve for solid state reacted ZrV_2O_7 powder

graphite, stainless steel, boron nitride and alumina. Alumina was finally chosen as the die material. Graphite dies proved unsatisfactory since they reduced the ZrV_2O_7 sample. Stainless steel and boron nitride dies deformed under load at pressing temperatures, rendering sample ejection impossible without destroying the die. Boron nitride also appeared to reduce the sample, although not as drastically as graphite. Alumina was found to possess sufficient hot strength to serve as a die material. However, a eutectic reported between V_2O_5 and Al_2O_3 at 658°C (10) suggested the possibility of a reaction between the ZrV_2O_7 and the die. This reaction was eliminated by encasing the sample in platinum foil. The punches were made of 12.5 mm diam McDanel[1] 998 alumina, and the die was a 13 mm ID McDanel ALGT 3106 alumina tube with a jacket of castable refractory. The dense alumina tube provided thermal mass to reduce temperature fluctuation of the die. The furnace used was a wire-wound kanthal tube furnace. Pressures up to 80 MPa were typically used at die temperatures just below 820°C.

For hot pressing, the ZrV_2O_7 powder was prepressed at 35 MPa in a 12.7 mm steel die with a hand hydraulic press to provide mechanical strength for sample handling. The prepressed sample was placed in the hot press (alumina) die assembly and was heated from room temperature to 700°C in 1 hr. The heating rate was then reduced, and at ~20°-30°C below the desired pressing temperature (750° ± 10°C), pressure (80 MPa) was applied to the sample. The pressing time (60-90 min), temperature and platen position were recorded. The actual sample temperature was about 50°C lower than the measured die temperature. After the sample was hot pressed for the desired time at temperature, the pressure was released, the bottom punch support removed, and the press was used to eject the sample through the lower end of the die. The sample was allowed to cool slowly, resting on the bottom punch in the lower part of the furnace.

Low temperature reactions in the ZrV_2O_7 powders were investigated using a pressure DSC cell with a du Pont 900 thermal analyzer. DTA and TGA analyses were also made on the powders. Powder samples as well as crushed hot-pressed ZrV_2O_7 samples were analyzed by XRD. A Phillips Norelco diffractometer with monochrometer and Debye-Scherrer powder camera were used in the analysis with nickel filtered copper K_α radiation. Lattice parameter variations with temperature were investigated using a hot stage and pulse height analyzer (PHA) with the diffractometer.

The infrared absorption spectra was investigated using a Beckman 12 spectrophotometer and a Cary 14 spectrophotometer. Samples consisted of 1 mg of ZrV_2O_7 in 200 mg of KBr pressed into a pellet. Absorption spectra from 2.5 to 35 μm were obtained with the Beckman unit, and spectra from 0.6 to 2.6 μm were measured with the Cary 14 unit.

Electron paramagnetic resonance (EPR) was used to determine the presence of V^{4+} ions in calcined ZrV_2O_7 powder and crushed hot-pressed samples. Since the EPR signal is dependent on the number of unpaired electrons in the material being examined and none of the ions in the ZrV_2O_7 normally has unpaired electrons, an EPR signal should result only when V^{4+} ions (unpaired d^1 electrons) are present. Samples for EPR consisted of 70 μm sized powders which were placed in fused quartz tubes 4 mm diam and 8 cm long. A Varian EPR unit was used for measurements. All measurements were made at room temperature. Microwave frequencies of 9.1-9.3 GHz and a scan range from 2200-4200 gauss was covered.

The microstructure of fractured and polished sections for hot-pressed ZrV_2O_7 were examined using JEOL JSM U3 scanning electron microscope. Energy dispersive x-ray analysis (EDAX) was used to determine elemental distribution in the samples. The thermal expansion of ZrV_2O_7 was determined using a modified du Pont 940 thermochemical analyzer (TMA). The sample size used was 6 mm and the heating rate was 10°C/min. Expansion was measured from 22° to 500°C. The instrument was standardized using Al, Fe, and quartz standards.

Samples for electrical measurements were lapped plane parallel and electroded with a platinum paste which was fired on at 600°C for 10 min. D-C conductivity was measured as a function of temperature over the range 22°-500°C using an electrometer. A-C electrical properties were measured using a Hewlett-Packard 4815A impedance bridge. Measurements were made at a frequency of 1 MHz. The sample impedance (Z) and phase angle (θ) were measured at temperatures from 22° to 500°C.

The type of charge carrier present in ZrV_2O_7 was determined from the thermoelectric or Seebeck effect. A temperature gradient placed across the material caused the majority carriers from the higher temperature region to diffuse toward the colder regions. This resulted in a voltage being developed across the sample, which was detected with a galvanometer, the direction of this voltage indicating the carrier type.

Results and Discussion

The ZrV_2O_7 powders prepared from aqueous solution and by solid-state reaction showed essentially similar properties. With the aqueous solution method of preparation, pH control in the range 2.2-3.0 was necessary, but otherwise the ZrV_2O_7 compound was readily obtained.

The solid-state reaction of ZrO_2 and V_2O_5 to form ZrV_2O_7 was confirmed to be very slow. This can be seen from the XRD patterns shown in Fig. 1. After 72 hr of calcining at 650°C, the reaction was incomplete. X-ray diffraction peaks indicated that significant amounts of ZrO_2 and V_2O_5 were still present. After 240 hr at 720°C, a trace of the V_2O_5 (110) peak was still evident. Powders were calcined until no trace of the initial oxides could be detected from the diffraction patterns. This material was determined to contain less than 0.5 weight percent (w/o) unreacted oxides from DTA studies.

The crystal structure for ZrV_2O_7 was found by XRD analysis to be primitive cubic, with a lattice constant of 8.778A corresponding to a theoretical density of 2.997 g/cm^3. The variation of the lattice constant with temperature was similar to that obtained by Craig and Hummel (4). The lattice size increased up to 150°C, with a sudden change in a_o at 80°C. Above 150°C, the lattice constant decreased linearly. Except for the shift in d spacings due to the variation of a_o, the XRD patterns were identical at all temperatures. No extinction or change in intensity of any peak was noted.

A DTA heating trace for the ZrV_2O_7 sample prepared by solid-state reaction is given in Fig. 2. Only the melting endotherms for the V_2O_5 (670°C) and ZrV_2O_7 (840°C) were observed, in contrast to the precipitated powders where several lower temperature events were noted. DSC studies of the ZrV_2O_7 also showed reversible endothermic reaction peaks at 78° and 107°C. These endotherms correspond to DTA endotherms reported by Craig and Hummel (4) and were only observed in samples calcined above 650°C. These reactions appear to be transitions from a low temperature cubic phase to high temperature cubic ZrV_2O_7, similar to the transition observed in ZrP_2O_7 by Harrison *et al.* (9). This transition in ZrP_2O_7 was determined by Lazerev and Tenisheva (10) to be a result of bond angle changes within the $P_2O_7^{4-}$ group, changing from a "bent" structure to a statistically centrosymmetric structure. This structural rearrange-

[1] McDanel Corporation, Beaver Falls, Pennsylvania.

ment between the low and high temperature cubic phases appears to be subtle since XRD studies showed no intensity change in any peak as the temperature was varied.

Samples hot pressed under the conditions of 70-80 MPa at 740°-760°C for 60-90 min gave densities in the range 2.84-2.86 g/cm^3 (>95% theoretical). The samples were brown in color, with the center portion occasionally being darker than the edges, due possibly to variation of oxygen partial pressure over the sample during hot pressing. Rupture strengths for the dense samples were estimated to be in the range 70-130 MPa. Samples which were hot pressed above 770°C appeared to consist of two phases. These samples showed lower strength and higher porosity and were not used for property measurements.

Figures 3a and 3c show, respectively, SEM photomicrographs of the solid-state-reacted (calcined) and solution-precipitated powders. The corresponding fracture sections for the hot-pressed samples are shown in Fig. 3b and 3d. Comparison of the two starting powders showed the particles of the calcined material to be larger (2.0 *vs.* 0.6 μm average particle size) and more spherical, compared to the more acicular-shaped precipitated particles (Fig. 3c).

Figures 3b and 3d show significant grain growth occurring in the hot-pressed samples. However, the relative size and shape differences remain (~7.0 *vs.* 2.0 μm), as can be seen from Fig. 3d which show sharply angular grains (and high density) for the hot-pressed precipitated powder. Figure 3b and 3d show little evidence of plastic flow in the hot-pressed samples. Considering the relatively low hot pressing temperature and time (750°C/1 hr), the most likely mechanism for the marked densification and grain growth observed for the ZrV_2O_7 samples is liquid phase-assisted sintering. The liquid would be provided by the residual V_2O_5 content (~0.5 w/o) in the prepared powders. However, no second phase was detected in any of the hot-pressed samples examined. Vanadium EDAX scans of polished sections showed no anomalously high concentrations nor any evidence of a vanadium rich phase in the grain boundaries, except possibly at some triple point regions. This would be expected from the low free V content and is consistent also with a liquid phase-assisted mechanism.

The infrared absorption spectrum for ZrV_2O_7 was measured from 0.7 to 40 μm. The spectrum from 2.5 to 40 μm is shown in Fig. 4. Absorption bands were observed at 25.6, 14.3, and 11.8 μm, in agreement with the results of Hubin and Tarte (12). The peak at 25.6 μm was attributed to the antisymmetic deformation of the VO_3 group. The other two peaks were attributed to valence vibrations of the VO_3 group, one symmetric and the other (11.8 μm) antisymmetric.

Significant infrared transmission is seen to occur throughout the range 2.5 to 10 μm with 85% transmission at the 7.5 μm peak position. The small absorption peak at 6.13 μm (0.202 eV) corresponded closely to the measured activation energy for electrical conduction in the ZrV_2O_7 samples. This very likely represents, therefore, the absorption or activation energy for electron hopping between V^{4+} and V^{5+} ions. For the near infrared region, the infrared spectra showed a gradual decrease in transmission from 2.5 to 0.6 μm, except for an absorption band at 2.19 μm which was not previously reported, since studies did not include these wavelengths.

The thermal expansion curve determined for the hot-pressed ZrV_2O_7 is shown in Fig. 5. The curve is similar to that obtained by Craig and Hummel (4) and to the measured x-ray expansion data. The material expanded linearly up to 70°C at which point there was a sudden expansion. Expansion continued up to 120°C. Above 150°C, there was negative linear expansion up to at least 400°C. Above 400°C, the TMA data were not reproducible due to equipment limitations. Also, the error in XRD measurements increased due to broadening of the diffraction peaks. However, the negative expansion appeared to continue above 400°C as reported by Craig and Hummel

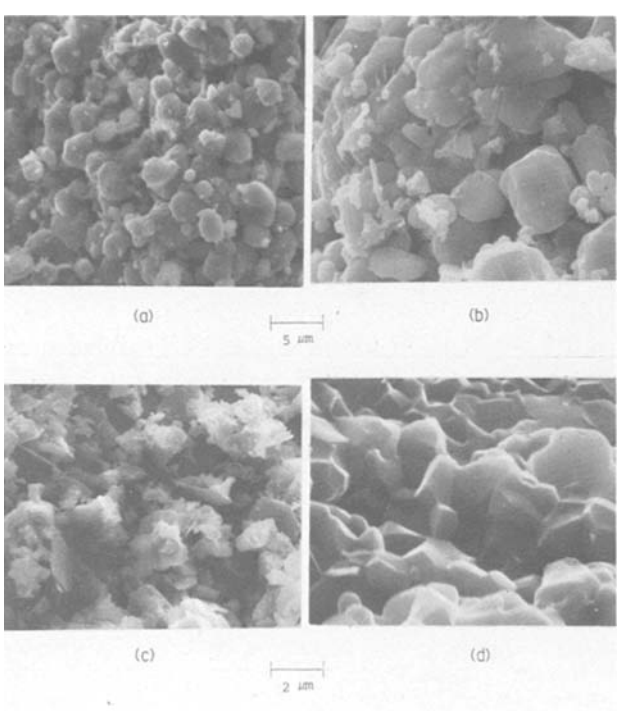

Fig. 3. SEM photomicrographs of ZrV_2O_7 samples: a) solid-state-reacted powder with b) hot-pressed fracture section and c) precipitated powder with d) hot-pressed fracture section.

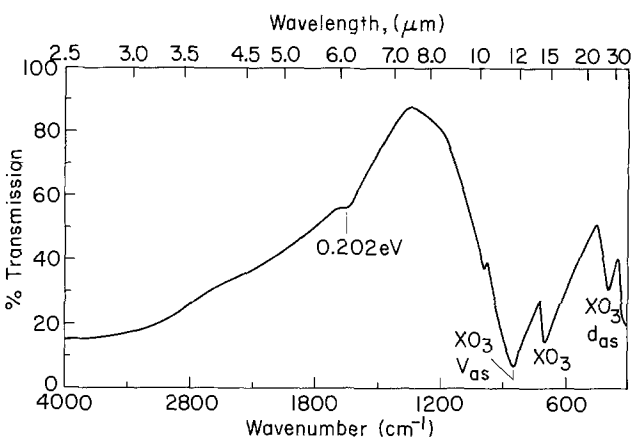

Fig. 4. Infrared absorption spectrum for ZrV_2O_7 sample (30-2.5 μm).

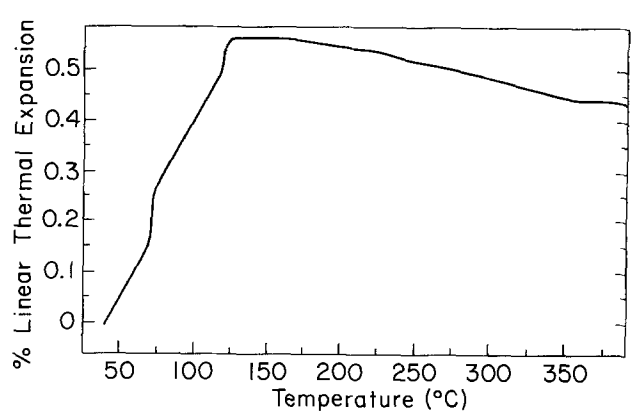

Fig. 5. Thermal expansion of ZrV_2O_7 sample (behavior was similar for both solid-state-reacted and precipitated ZrV_2O_7).

(4). The high temperature expansion was determined to be -72×10^{-7}/°C. This negative expansion appears to be due to a rearrangement in the ZrV_2O_7 structure, likely a change in the angle of the V-O-V bonds in the $V_2O_7^{4-}$ group. This type of bond angle change has been reported for similar compounds (11).

Typical electrical conductivity values obtained for ZrV_2O_7 ranged from 10^{-5}-10^{-6} $(\Omega\text{-cm})^{-1}$ at 25°C, depending on sample preparation. Arrhenius plots of the data are shown in Fig. 6. These plots show linear behavior throughout the temperature range with a small deviation from linearity at about 80°C. This temperature corresponded to the transition noted from DSC and thermal expansion data.

The activation energy for conduction, E_a, was determined to be 0.20 ± 0.01 eV in line with the infrared absorption band seen at 0.202 eV. This activation energy was identical to that obtained by Allersma *et al.* (13) for V_2O_5 which had a conductivity three orders of magnitude higher than ZrV_2O_7. The activation energy for V_2O_5 was attributed to the mobility for electron hopping from V^{4+} to V^{5+} ions (13-15). Since EPR measurements indicated that V^{4+} was present in the hot-pressed ZrV_2O_7 samples (Fig. 7), a similar conduction mechanism can be proposed. The lower conductivity for the ZrV_2O_7 samples as compared to that of V_2O_5 may be attributed to the lower concentration of V^{4+} ions. The carrier concentration was not determined, but Seebeck effect measurements showed ZrV_2O_7 to be an n-type conductor which also agrees with the proposed conduction mechanism.

The activation energy was similar for hot-pressed samples prepared from both solid-state-reacted and precipitated powders. Conductivity values, however, were an order of magnitude higher for the solid-state-reacted powders. This agreed with the higher V^{4+} content indicated from the EPR measurements (Fig. 7). The conductivity of the solid-state reacted powders could, however, be decreased to that of the precipitated ZrV_2O_7 by annealing in air at 700°C, which treatment would have the effect of decreasing the V^{4+} content.

A-C impedance and phase angle data for the ZrV_2O_7 are shown in Fig. 8. An impedance bridge was used for measurements since the material was too lossy for measurements with a capacitance bridge. The results are as expected for a lossy dielectric. Measured impedance values were low ($Z \sim 1000\Omega$) which indicated a high concentration of charge carriers. The impedance decreased rapidly with temperature, accompanied by a phase angle change from near −90° (a pure capacitor) at low temperature to near 0°C (a pure resistor) at high temperature. These changes reflect an increase in carrier mobility with temperature. It was also noted that the impedance for the samples formed from the precipitated powders was higher than that for solid-state-reacted powders indicating lower carrier concentration, in agreement with the d-c conductivity data.

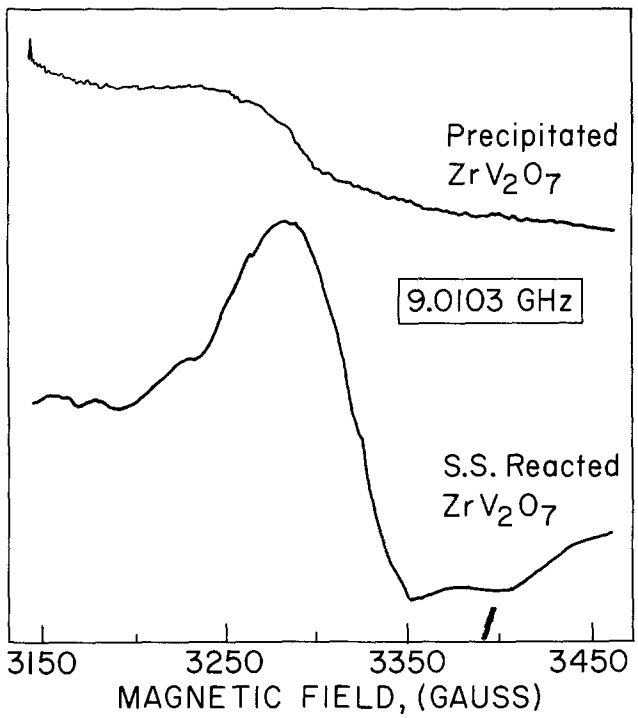

Fig. 7. Typical EPR spectrum for precipitated and solid-state-reacted ZrV_2O_7 samples showing V^{4+} peak in the reacted sample.

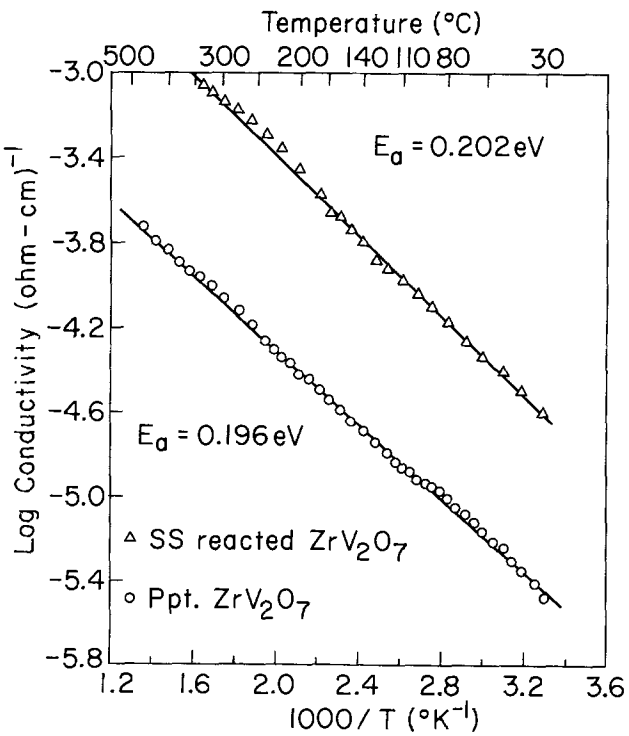

Fig. 6. D-C conductivity as a function of inverse absolute temperature for ZrV_2O_7.

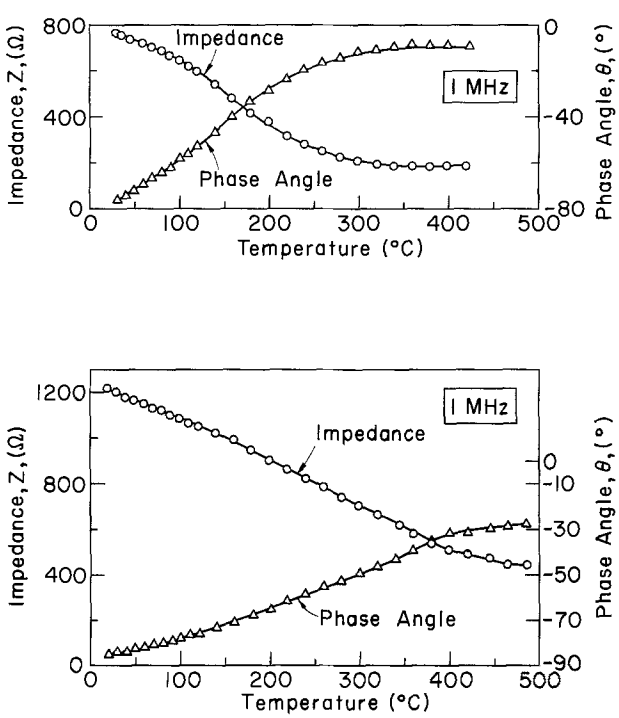

Fig. 8. A-C dielectric properties of hot pressed ZrV_2O_7 samples: a) solid-state-reacted ZrV_2O_7, and b) precipitated ZrV_2O_7.

Summary

1. Zirconium pyrovanadate was prepared by solid-state reaction of ZrO_2 and V_2O_5 and by solution reaction of NH_4VO_3 and $ZrO(NO_3)_2$.

2. Hot pressing was used to densify ZrV_2O_7 to greater than 95% of theoretical density. The resulting samples were determined to be single-phase.

3. Normal thermal expansion was observed to 120°C with two areas of rapid expansion noted at 78° and 110°C corresponding to reversible endothermic reactions. These reactions were attributed to slight angular rearrangements within the ZrV_2O_7 crystal lattice.

4. A large area of negative thermal expansion was observed above 150°C. The expansion coefficient determined was -72×10^{-7}/°C.

5. Electrical conduction was found to be due to V^{4+} defects in the material which allowed electron hopping between V^{4+} and V^{5+} cations. The activation energy for conduction was 0.2 eV with conductivity values in the range of 10^{-5}-10^{-6} $(\Omega\text{-cm})^{-1}$ at room temperature. Conduction was determined to be n-type.

6. A-C impedance measurements indicated high carrier concentration and mobility for the hot-pressed ZrV_2O_7.

Acknowledgments

This work was supported by the Office of Naval Research under contract N-00014-C-78-0279 and in part by the National Science Foundation under MRL grant DMR-80-20250.

Manuscript submitted Sept. 21, 1982; revised manuscript received May 16, 1983.

REFERENCES

1. G. Peyronel, *Gazz. Chim. Ital.*, **72**, 77 (1942).
2. A. Burdese and M. L. Borlera, *Anal. Chim. (Rome)*, **50**, 1570 (1960).
3. V. Cirilli, A. Burdese, and C. Brisi, *Atti. Acad. Sci. Torino*, **95**, 14 (1961).
4. D. F. Craig and F. A. Hummel, *J. Am. Ceram. Soc.*, **55**, 532 (1972).
5. J. C. Pedregosa, E. J. Baran, and P. J. Aymonino, *Anales. Asoc. Quim. Argentia*, **60**, 397 (1972).
6. Y. Tsujii, E. Miura, M. Hashiba, Y. Nurishi, and T. Hibino, *Gifu Diagaku Kogakubu Kenkyu Hokoku*, **28**, 89 (1978).
7. R. Sacks, Y. Avigal, and E. Banks, *This Journal*, **129**, 726 (1982).
8. G. R. Levi and G. Peyronel, *Z. Krist.*, **92**, 190 (1935).
9. D. E. Harrison, H. A. McKinstry, and F. A. Hummel, *J. Am. Ceram. Soc.*, **37**, 277 (1954).
10. D. Barham, *Trans. Br. Ceram. Soc.*, **64**, 371 (1965).
11. A. N. Lazarev and Tenisheva, "Structural Transformations in Glasses at High Temperatures," N. A. Popov and E. A. Porai-Koshits, Editors, pp. 202-222, Consultants Bureau, New York (1965).
12. R. Hubin and P. Tarte, *Spectrochim. Acta*, **23**, 1815 (1967).
13. T. Allersma, R. Hakim, T. N. Kennedy, and J. D. Mackenzie, "Structure and Physical Properties of Solid and Liquid Vanadium Pentoxide," Technical Report No. 2, Contract No. Nonr-591(21), Rensselear Polytechnic Institute (1966).
14. J. Boros, *Z. Phys.*, 721 (1979).
15. A. I. Ivon and I. M. Cherneńko, *Soviet Physc. J.*, **21**, 111 (1978).

Autodoping Phenomena in Epitaxial Silicon

G. K. Ackermann*

Technische Fachhochschule Berlin, Germany

E. Ebert

IBM Research and Development Laboratory, Böblingen, Germany

ABSTRACT

Autodoping experiments were performed using a radiation-heated Applied Materials Corporation (AMC) 7600 epitaxial reactor, (100) n-doped silicon wafers, arsenic-doped buried layers (subcollector) of total implanted or diffused dose of $7 \times 10^{15} - 3 \times 10^{16}$ cm^{-2}, and buried layer areas between 10 and 100% wafer area. Intentionally undoped epitaxial layers of 1.4 μm thickness were grown. The lateral autodoping was found to be very uniform with no distinct flow pattern-induced spatial distribution. Autodoping follows a square root law with respect to buried layer area. Autodoping shows a linear relationship with respect to buried layer doping. An analysis of the buried layer doping profile identifies the out-diffusion source with electrically inactive arsenic, about 50% of total implanted or diffused dopant. Less than 1% of the out-diffusing arsenic is incorporated into the wafer surface and growing epitaxial layer.

The out-diffusion of dopants out of highly doped wafer areas during the epitaxial process and the incorporation into the wafer surface during prebake and into the growing epitaxial layer during deposition is called autodoping. Various papers have appeared to describe this undesired epitaxial doping and the dependence on process parameters like prebake time, prebake temperature, hydrogen velocity and pressure within the epitaxial reactor, and growth rate. A review of many important results and an extended bibliography is given in the report by Srinivasan (1). Most authors use rf-heated epitaxial reactors with defined horizontal H_2 gas flow which results in a distinct flow pattern within the autodoping distribution, the so-called lateral autodoping. Only the work published by Lewe (2) is performed using an AMC 7000 radiation-heated system.

The aim of this work is to investigate the influence of the very complex flow characteristic of the radiation-heated AMC 7600 epitaxial reactor on lateral autodoping.

A main point of interest is an analysis of the buried layer doping profile before and after out-diffusion in order to locate the out-diffusion source within the buried layer. In addition, the relationship between autodoping and buried layer doping level as well as buried layer area will be examined. Skelly and Adams (4) found a linear relationship between the autodoping level and the buried layer doping level in the range of 4×10^{18}-4×10^{19} cm^{-3}. Srinivasan (5)

* Electrochemical Society Active Member.
Key words: epitaxy, impurity, mass transport.

published a square root dependence of autodoping on buried layer area.

Experimental

Autodoping experiments were performed using n⁻ silicon wafers with (100) orientation and 82 mm diam. Arsenic-buried layers were diffused (capsule diffusion, 1105°C, 135 min) or implanted (Extrion, 50 kV), doses varying between 7×10^{15} and 2.9×10^{16} cm^{-2}. Buried layer areas varied between 10 and 100% of total wafer area. Intentionally undoped epitaxial layers of 1.4 μm thickness were grown under normal pressure with H_2 carrier gas. Throughput was 300 liter/min. Besides the vertical gas stream of the down flow system, which carries one half of the total throughput, there are two jet inlets perpendicular to the axis of rotation, which carry the other half, and 0.06 mol percent (m/o) $SiCl_4$ for the epitaxial deposition. The linear velocity of the gas volume calculated from throughput and reactor geometry is about 2-3 cm/sec. The velocity is small compared with the thermal velocity of the gas molecules. The prebake and deposition temperature was 1150°C, realized by 70 halogen lamps powered as proposed by AMC.

Table I contains the essential process parameters of the lots processed. Two groups of wafers were processed. Group 1 consisted of four dots (No. 516-519) with an almost constant buried layer doping dose of 2×10^{16} cm^{-2}, and subcollector areas varying between 10 and 70%. Group 2 consisted of five lots with 100% buried layer area and varying buried layer (subcollector) doping dose. Lots 513 and 514 have an epitaxial doping of about 2×10^{16} cm^{-3}. These lots were mainly used for buried layer doping profile analysis. Lot 521 of group 2 can be counted also to group 1 to complete the lots with varying buried layer area.

After the epitaxial process, about 150 nm SiO_2 were grown and aluminum dots evaporated, defining MOS capacitors. Some measurements discussed below were performed without aluminum dots using a mercury probe built by Hagmann and Voelmle (8). In order to determine the doping profile of the epitaxy, in most cases the pulsed capacitance voltage (PCV) method was applied (6). The PVC apparatus used during this work was built by the German Manufacturing Technology Center of IBM (7). The IBM 5100 desk computer attached to the measuring unit delivered the doping profile data and a graph of the profile. Because of the limits given by the breakdown voltage of the oxide and the dielectric breakdown of silicon, the above-mentioned thin epitaxial layer of 1.4 μm thickness was grown in order to get close to the epitaxy-substrate interface.

To determine the buried layer doping profile, the two-point spreading resistance probe (SR) and secondary ion mass spectroscopy (SIMS) were used. It is impossible to determine the epitaxial doping profile by SR or SIMS in the range below 10^{16} cm^{-3} of epitaxial doping. In the case of SR, it is known that a low doped layer (epitaxy) on top of a high doped layer (subcollector) is difficult to measure due to artifacts created by the correction algorithm (9). New algorithms are published to ease or accelerate the computation (10, 11); however, the basic just-mentioned disadvantage restricts the application of SR. In the case of SIMS, the low sensitivity is the limiting factor, 10^{17} cm^{-3} for the apparatus used in the Böblingen laboratory (12). This value is well above the epitaxial doping or autodoping level of about 10^{16} cm^{-3}.

Table I. Hardware of autodoping experiments

Lot No.	Buried layer area percentage of total area	Buried layer doping dose cm^{-3}	Remarks
513	100	7×10^{15}	Epiprocess with doping 2×10^{16} cm^{-3}
514	100	2.2×10^{16}	
516	50	1.9×10^{16}	Diffused
517	30	2.1×10^{16}	Implanted
518	70	2.1×10^{16}	Implanted
519	10	2.1×10^{16}	Implanted
520	100	1.4×10^{16}	Implanted
521	100	1.9×10^{16}	Implanted
522	100	2.5×10^{16}	Implanted
523	100	2.9×10^{16}	Diffused
524	100	7×10^{15}	Implanted

In order to characterize the epitaxial doping level due to autodoping, many authors [*e.g.*, (1)] take the autodoping peak concentration value close to the epitaxy-substrate interface. Due to the breakdown restrictions mentioned above, this peak value could not be measured by PCV. Skelly and Adams (4) characterized the autodoping by taking the epitaxial doping level derived from CV measurements. Measurements on many wafers showed that in this case the doping within the epitaxy is a sensitive indicator for the amount of autodoping.

Results

Lateral autodoping.—Using a horizontal rf-heated reactor, Srinivasan (1) found that the peak value of autodoping measured as a function of the distance from the buried layer edge decreases. The slope is very steep for the upstream direction and moderates in the downstream direction. After the theory given in Srinivasan's paper, this is to be expected.

The experimental results found in this study are quite different. Figure 1 contains five PCV profiles taken almost at the buried layer edge (profile 7) up to a distance of 40 mm from the edge. The profiles were taken following the arrow in the wafer sketch given in the upper right corner of Fig. 2. The profiles of Fig. 1 indicate a slight increase of epitaxial doping with increasing distance from the buried layer edge. In order to get one number to characterize the autodoping, one could take the doping concentration N_x at a fixed penetration depth x within the epitaxy. The doping concentration at $x = 0.4$ μm, $N_{0.4}$, was taken to characterize the autodoping. Of course, a number $N_{0.3}$ or $N_{0.5}$ would do the same. Measurements

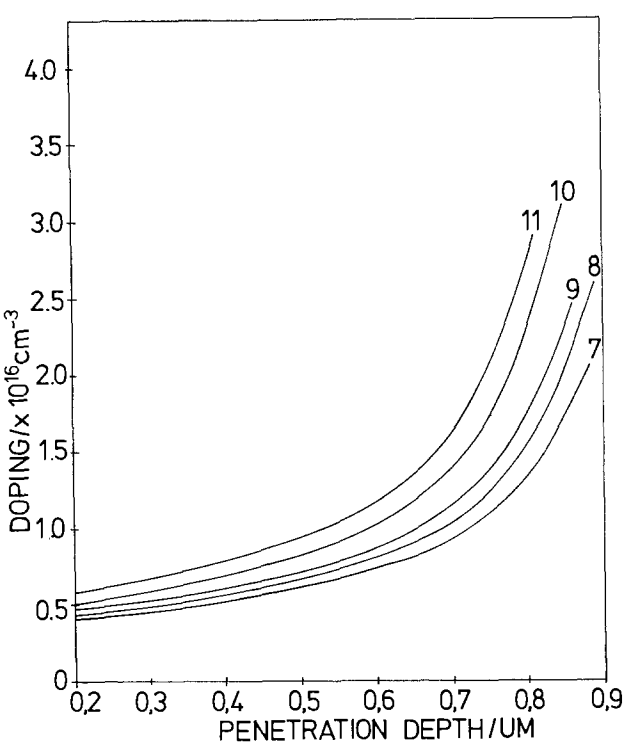

Fig. 1. Five PCV profiles taken close to the buried layer edge (profile 7) up to 40 mm apart (profile 11).

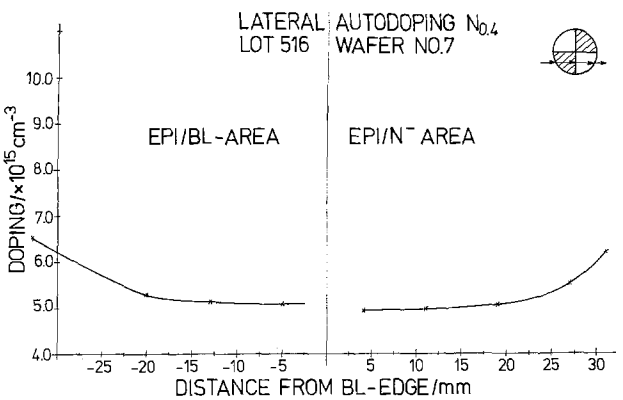

Fig. 2. Lateral autodoping $N_{0.4}$ of a 50% buried layer wafer, abscissa displays the distance from buried layer-(BL) edge. The measurements follow from left to right the line indicated in the schematic in the upper right corner of figure.

of many wafers show that indeed $N_{0.4}$ does not vary as long as the process is constant. In addition, this number is more sensitive to process variations and/or autodoping variations as an integrated value like sheet resistance. $N_{0.4}$ should represent the doping at a given distance from the autodoping peak concentration. However, because $x = 0.4$ μm is measured from the epitaxy surface, fluctuations in epi thickness will influence the distance from the autodoping peak, which should be constant 1.0 μm. Thickness fluctuations will result in apparent $N_{0.4}$ fluctuations. Such epitaxial thickness fluctuations have been observed and the data corrected, if possible. Figure 2 gives the autodoping $N_{0.4}$ with respect to position on the wafer surface. The distribution of subcollector and buried layer free area is given in the upper right of Fig. 2. The main result is that autodoping is almost flat over the whole wafer regardless of a buried layer underneath the epitaxy and independent of distribution of buried layer area. A distinct increase is found near the wafer edge (rim). Similar results are reported by Langer and Goldstein (13) and Skelly and Adams (4). The flat autodoping $N_{0.4}$ over the wafer area must be due to the above-mentioned very complex flow characteristic. A distinct flow pattern-induced autodoping distribution was always found in epitaxial systems with smooth vertical or horizontal gas flow.

The increase of autodoping near the wafer rim relates other authors (13, 4) to autodoping from the back of the wafer. In this case, such a source is very unlikely because the wafer back is oxidized prior to the buried layer diffusion process. Nevertheless, some out-diffusion out of the rim of the wafer itself cannot be ruled out. If the susceptor is an important autodoping source too, then the rim of the wafer should be more affected than the center. The analysis of the autodoping profiles given later shows that some contribution of the susceptor is very likely.

Autodoping and buried layer doping.—Table I gives the five lots processed with varying subcollector doping. Some were processed by diffusion (capsule, 1105°C, 135 min) and some by ion implantation (Extrion/Varian, 50 keV, redistribution: 1100°C, 75 min). The subcollector reoxidation process is identical for both diffusion processes; 970°C, 95 min.

Figure 3 contains five doping profiles for wafers of lot 524 (lowest curve), 520, 521, 522, 523 (upper most curve). These PCV profiles show that the epitaxial doping due to autodoping increases with increasing buried layer doping. Again. $N_{0.4}$ is taken and this value investigated as a function of buried layer doping, which was determined by x-ray fluorescence. From Fig. 4, the linear relationship between $N_{0.4}$ and buried layer doping is quite obvious. There may be

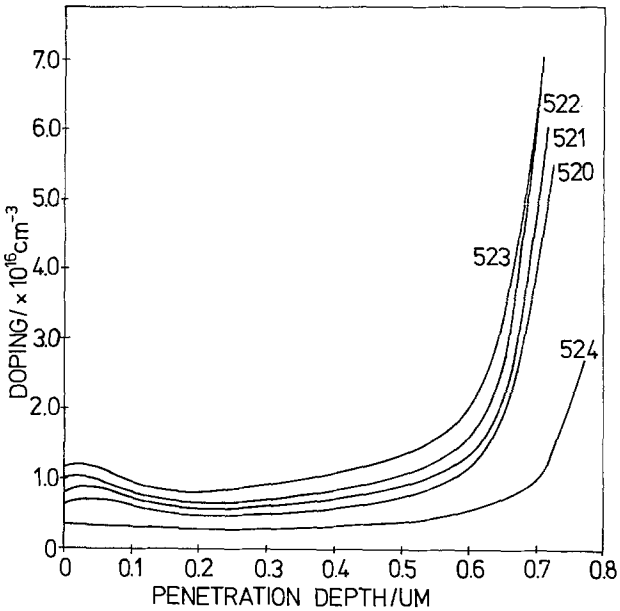

Fig. 3. PCV profiles of lots with different buried layer doping ranging from 7 $\times$ 10^{15} (lot 524) up to 2.9 $\times$ 10^{16} cm^{-2} doping dose (lot 523); see aso Table I.

a slight leveling off for substrate doping dose higher than 2 $\times$ 10^{16} cm^{-2}. The few data do not allow a more exact determination of the mean curve in this area. Skelly and Adams (4) found a similar relation for subcollector doping up to 4 $\times$ 10^{19} cm^{-3}. The data given here correspond to subcollector doping levels up to 3 $\times$ 10^{20} cm^{-3} (roughly 1 μm penetration depth was processed). The data of Skelly and Adams cannot be compared directly with the data given in Fig. 4, because total subcollector doping and electrically active doping differ quite a lot as will be shown below. The increase of epitaxial doping close to the epitaxial surface (Fig. 3, $\leq$ 0.1 μm) is an artifact and will not be discussed.

Electrically active dose.—In order to examine the out-diffusion process and the autodoping mechanism in more detail, the electrically active buried layer doping dose was compared with the total buried layer doping dose before the epitaxy process. Figure 5 contains these data. The points given in Fig. 5 compare the electrically active dose (ordinate left-hand reading) determined by sheet resistance and penetration depth (bevel and stain) measurements as well as

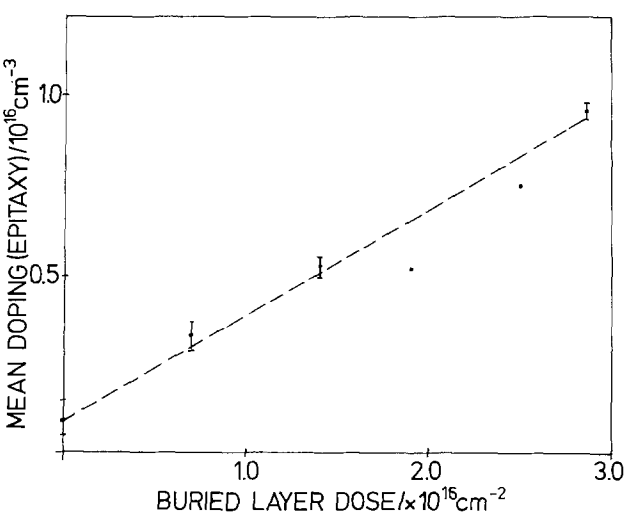

Fig. 4. Mean epitaxial autodoping level $N_{0.4}$ as a function of total built-in buried layer dose, measured by x-ray fluorescence technique.

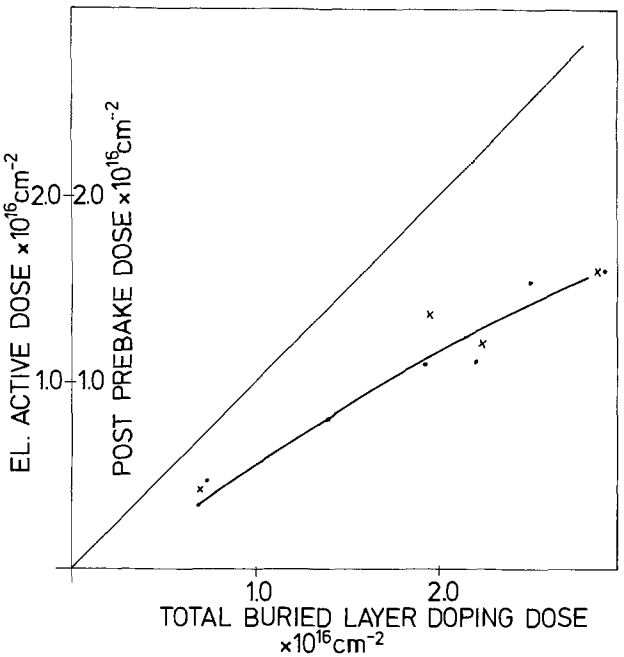

Fig. 5. Buried layer electrical active dose as a function of total built-in doping dose postburied layer diffusion process (points), and total built-in dose post prebake cycle of epitaxial process (crosses) as a function of total built-in dose.

SR data with the total buried layer doping dose from x-ray fluorescence analysis (abscissa). If all the arsenic would be electrically active, a straight line with slope 1 would be expected. This line is given in Fig. 5, too. The actual curve differs quite a lot from this line. Roughly 50% of the diffused or implanted arsenic is electrically active. There is no difference between implanted or diffused arsenic as far as this percentage is considered.

If one compares the total buried layer doping dose before and after a 10 min prebake (ordinate right-hand reading), a reduction of about 50% is found. This is indicated by the crosses in Fig. 5. They define almost the same curve as the points. It follows that the electrically active arsenic stayed in the substrate and the inactive arsenic diffused out during prebake. Obviously, a 10 min prebake is sufficient for out-diffusion of all electrically inactive arsenic. This was confirmed by two additional 10 min heating cycles which did not change the buried layer doping measured after the first prebake.

Srinivasan (14) reported a decrease of lateral autodoping with increasing prebake time. The author's results would indicate that this is due to the fact that the autodoping source ceases and the autodoped surface areas are bleached out.

Buried layer doping profile analysis.—In order to get direct information about the decrease of arsenic within the buried layer during processing, the buried layer profile was measured by SR and by SIMS before prebake and after the epitaxial process including prebake and growth of a 1.4 μm slightly doped epitaxial layer. The SR data give the electrically active arsenic; the SIMS profile shows the total amount of arsenic within the buried layer. Figure 6 gives the data accumulated for lot 514 (see Table I). The total buried layer doping dose measured by x-ray fluorescence technique was 2.2×10^{16} cm^{-2}; the electrically active dose (sheet resistance and penetration depth) was 1.1×10^{16} cm^{-2}.

First, the profiles postdiffusion process (Fig. 6: SC-Reox) will be compared. The SIMS profile containing all arsenic diffused in shows the well-known surface pile-up because of the high segregation coefficient (Si/SiO_2) of ten for arsenic. The semilog plot

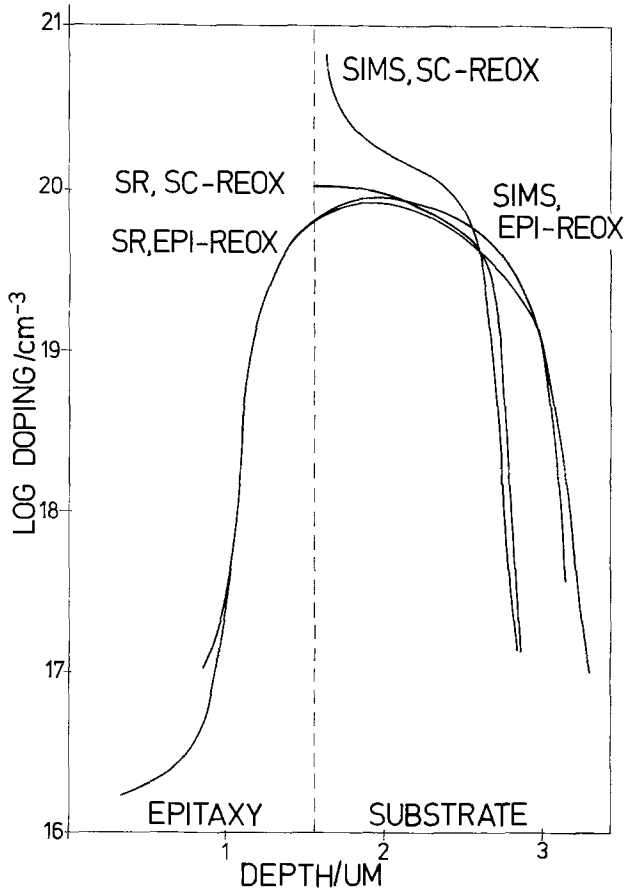

Fig. 6. Spreading resistance two-point probe and SIMS buried layer doping profiles postdiffusion process (BL-Reox) and post epitaxial process (Epi-Reox) indicating the difference between electrical active and total built-in dose post BL-Reox (lot 514).

shows a huge difference between total (SIMS) and electrically active (elac) (SR) arsenic. Figure 7 gives the differential curve $N(x)$ *vs.* penetration depth

$$N(x) = N(x)_{tot} - N(x)_{elac} \qquad [1]$$

whereas $N(x)_{tot}$ is the total amount of dopant at depth x and $N(x)_{elac}$ is the electrically active dopant. Integration of the curve given in Fig. 7 yields a dose difference ΔD

$$\Delta D = 1 \times 10^{16} \text{ cm}^{-2}$$

in accordance with the x-ray fluorescence and sheet resistance data given above.

The profiles of the buried layer after the epitaxy process (Fig. 6: Epi-Reox) do not differ at all within the measurement accuracy. The profiles show the same increased penetration depth due to the additional heat cycle, but there is no difference between electrically active and total amount of buried layer doping.

Discussion

The results presented in the last sections were not given to repeat measurements made by other authors in detail. Therefore, the layout of the system was not changed with respect to gas flow properties, prebake time, or prebake temperature. The aim was to check an existing system with respect to lateral autodoping and dependence of autodoping on buried layer doping (arsenic) and buried layer area (Fig. 8).

Lateral autodoping.—The smooth lateral autodoping found is very promising considering a commercial epitaxial system used in the process of developing integrated circuits. There is no distinct direction of gas flow with respect to buried layer edge. The complex flow pattern of the AMC 7600 epitaxial re-

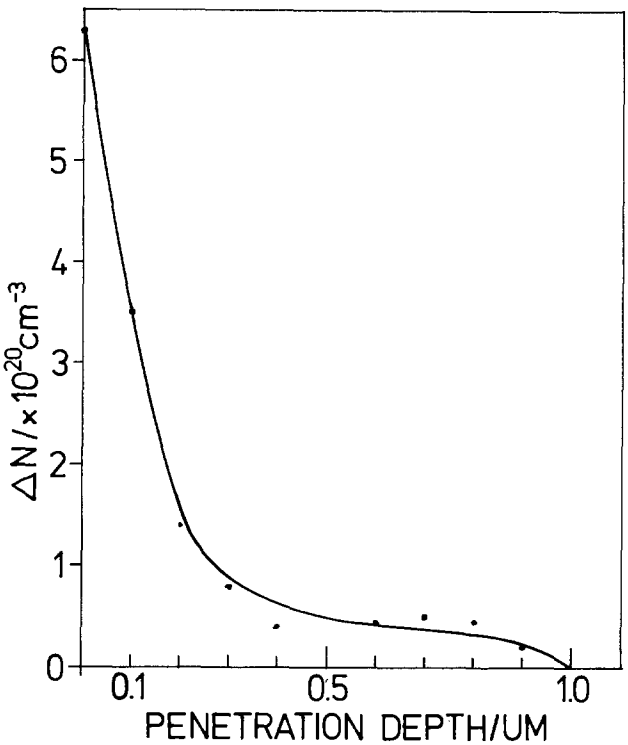

Fig. 7. Differential curve derived from SR, BL-Reox and SIMS, BL-Reox curves of Fig. 6. ΔN is the difference in doping dose calculated by integration. The penetration depth is measured from the epitaxial-substrate interface.

actor prevents any spatial dependence of autodoping. This is an advantage with a view to application.

Square root law.—The square root law of autodoping with respect to buried layer area detected by Srinivasan (5) was verified. The measurements accumulated during this work fit well with Srinivasan data. The theory given by Srinivasan (5) shows that for point grids with small grid sizes 10 μm, the square root dependence of autodoping on buried layer area indeed holds. Here, autodoping sources were investigated up to 100% wafer area, no small point grids but large sources only. Instead of a point grid, which may explain the integrated circuit wafer, an area is assumed large in diameter compared with the boundary layer thickness (15, 16)), which can be calculated from basic theory (17) to be about 1 cm. A sketch is given in Fig. 9. The buried layer penetration depth is not on the same scale. Of the out-diffusing arsenic, only particles remaining in the boundary layer will contribute to the autodoping. Therefore, responsible for the autodoping is the area formed by the boundary layer height and the circumference of the buried layer, which in a first approximation is proportional to the square root of the buried layer area. After this assumption, the square root law is a consequence of the boundary layer.

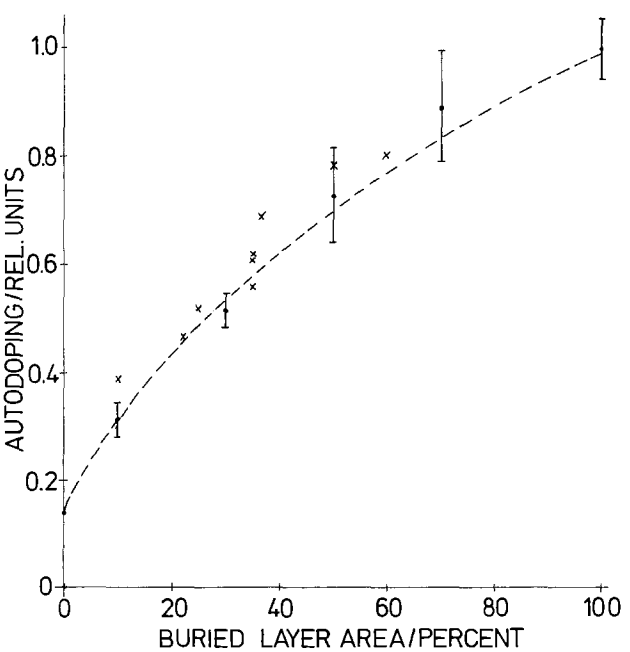

Fig. 8. Autodoping level within epitaxial layer in relative units vs. percentage of buried layer area. Figure contains measurements of Srinivasan (5) (crosses) and data of this paper (bars).

Autodoping source.—The main problem was to detect and analyze the autodoping source within the arsenic-buried layer. From the data given (Fig. 6), it is quite clear that with postburied layer diffusion and redistribution almost half of the arsenic is electrically inactive. Only the inactive arsenic diffuses out during the prebake process. Obviously for the AMC 7600 reactor, a 10 min prebake at a temperature of 1150°C is sufficient for the out-diffusion of all inactive arsenic. A second and third prebake do not change the amount of arsenic within the buried layer as shown. The additional prebake cycles show that the electrically active arsenic incorporated within the silicon lattice does not diffuse out and cannot be turned into electrically inactive arsenic at a temperature of 1150°C.

Surprisingly, even for the lowest doping dose of 7×10^{15} cm^{-2} about 50% of the arsenic is electrically inactive. One would have expected, that for very low doping doses the amount of electrically inactive arsenic is small compared with high doping doses. Figure 5 shows some indication of a saturation effect for doping doses of about 3×10^{16} cm^{-2}. But the effect is not very pronounced.

Autodoping profile.—From the results accumulated, it is very difficult to derive a conclusive model or to test one of the existing autodoping models. This is due to the fact that the PCV data do not deliver the autodoping maximum. Generally, it is difficult to measure a profile with an in depth increasing impurity concentration by PCV. The capacitance changes with increasing voltage step are too small within the steep part of the profile. Spreading resistance measurements would not show this problem, but it is always difficult to get the correct low concentration amount (epitaxy) on top of a high concentration (buried layer) by SR due to correction program artifacts (9). In this work, the correct amount of doping within the epitaxy was the interesting number. There-

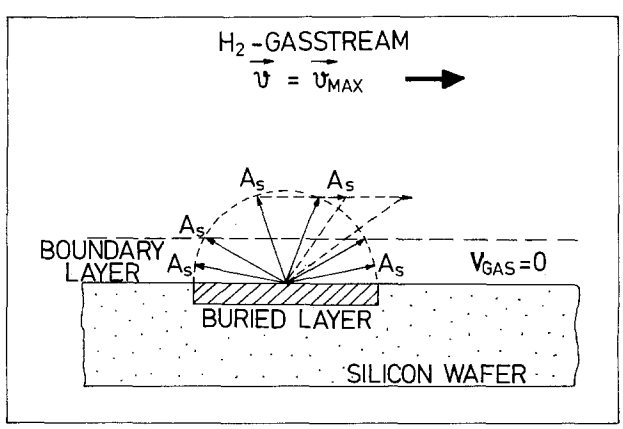

Fig. 9. Schematic drawing of boundary layer; arrows indicate some directions of out-diffusing arsenic out of the buried layer.

fore, the authors took the PCV technique instead of SR. In order to get very close to the autodoping maximum, the very thin epitaxy (1.4 μm) was processed.

The results published by Lewe (2) for another radiation-heated epitaxial reactor (AMC 7000) show that the absorption layer model published by Tabe and Nakamura (18) is a good tool to describe autodoping profiles. Of course, because of lack of data, this model cannot be proven. The exponential law of autodoping concentration $C(z)$ as a function of penetration depth z, measured from the epitaxy-substrate interface is indicated in the steep part of Fig. 10

$$C(z) \propto e^{-\frac{k_2}{k_2'}z} \quad [3]$$

k_2, k_2' are equilibrium constants (2, 18) for the incorporation of out-diffused arsenic into the growing epitaxial layer (k_2) and for the out-diffusion of incorporated arsenic (k_2'). Tabe and Nakamura consider also the influence of the susceptor to the autodoping amount. The normally clean susceptor ($\lesssim 5 \times 10^{13}$ cm^{-3}) will absorb some of the out-diffused arsenic. This will then be incorporated in the growing epitaxial layer. That this process may be important for the first half micrometer within the epitaxy can be seen in Fig. 10. The impurity concentration within this part of epitaxy cannot be explained by the exponential law given above. It could be the result of a constant contribution of some doping source, possibly the susceptor.

Assuming that the interface is at 1.4 μm in accordance with epi thickness measurements, one can get an estimate of the total amount of arsenic built in due to autodoping and compare this number with the total out-diffused arsenic doping dose. In Fig. 10, the profile for lot 516 is given. The out-diffused arsenic was 1×10^{16} cm^{-2} (Fig. 5, Table I). Integrating the exponential law and taking the same amount of arsenic on both sides of the interface results in 3×10^{13} cm^{-2}. In spite of the low accuracy of this number, it is quite clear that only a small part of less than 1% of the out-diffused arsenic is built into the growing epitaxial layer. A similar value was found by Skelly and Adams (4).

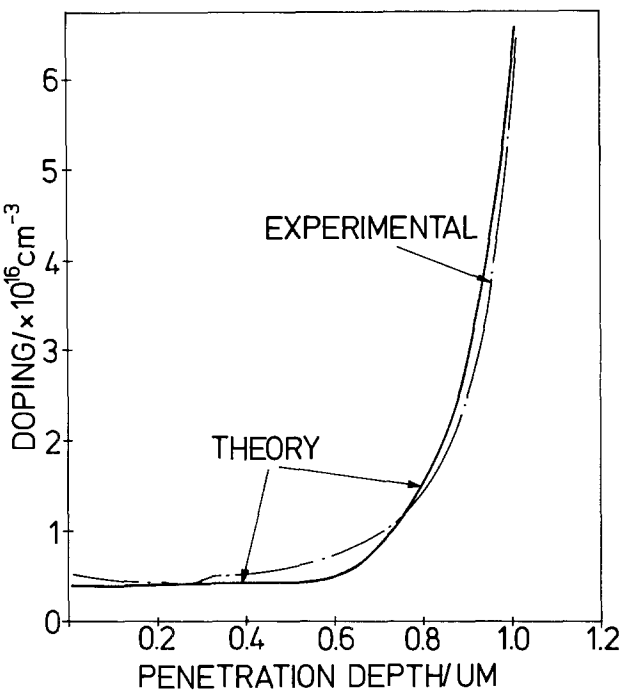

Fig. 10. PCV profile of a wafer of lot 516; given is the theoretical curve following the absorption layer model by Tabe and Nakamura (18).

Conclusion

It has been shown that the source of autodoping is electrically inactive arsenic, about 50% of the total dose diffused during the buried layer process. This inactive arsenic out-diffuses during prebake of the epitaxial process. The square root dependence of autodoping on buried layer area was verified.

The autodoping profiles measured by PCV are consistent with the absorption layer model published by Tabe and Nakamura (18).

Acknowledgments

One of the authors (G.K.A.) acknowledges the financial support of IBM Germany during the sabbatical half-year spent in the laboratory. The steady support of Dr. P. Schweitzer and Dr. G. Hübner from UV Wissenschaft as well as the interest and help of Prof. Dr. O. G. Folberth and Dr. A. Heinemann of the hardware house of the Böblingen laboratory are very gratefully acknowledged.

Both authors appreciate the intensive and patient help of the line staff during processing and measuring and of Mrs. V. Schott for typing the manuscript.

Manuscript submitted April 22, 1982; revised manuscript received *ca.* May 7, 1983. This was a Recent News Paper presented at the Denver, Colorado, Meeting of the Society, Oct. 11-16, 1981.

IBM Research and Development Laboratory, Germany, assisted in meeting publication costs of this article.

REFERENCES

1. G. R. Srinivasan, *This Journal*, **127**, 1334 (1980).
2. V. Lewe, *Proc. ESSDERC*, **4H**, 182 (1980).
3. Applied Materials Corporation 7600 Instruction Manual.
4. G. Skelly and H. C. Adams, *This Journal*, **120**, 116 (1973).
5. G. R. Srinivasan, *ibid.*, **127**, 2305 (1980).
6. W. v. Gelder and E. H. Nicollian, *ibid.*, **118**, 138 (1971).
7. Instructions for use of the PCV/Tester, G. E. Schmid, GMTC Sindelfingen.
8. D. Hagmann and K. H. Voelme, To be published.
9. C. W. Magee, Abstract 366, p. 880, The Electrochemical Society Extended Abstracts, Vol. 81-2, Denver, CO, Oct. 11-16, 1981.
10. Y. Lida, H. Abe, and M. Kondo, *This Journal*, **124**, 1118 (1977).
11. D. C. D'Avanzo, R. D. Rung, A. Gat, and R. W. Dutton, *ibid.*, **125**, 1171 (1978).
12. E. E. Biedermann and W. Garben, Private communication.
13. P. H. Langer and J. I. Goldstein, *This Journal*, **124**, 591 (1977).
14. G. R. Srinivasan, *ibid.*, **125**, 146 (1978).
15. M. Ogirima, H. Saida, and M. Maki, *ibid.*, **125**, 1879 (1978).
16. R. L. Bratter, R. L. Mehado, and A. K. Gaind, IBM T.R. 22.1599 (1973).
17. A. S. Grove, "Phys. and Techn. of Sem. Dev.", Wiley and Sons, New York (1967).
18. M. Tabe and H. Nakamura, *This Journal*, **126**, 822 (1979).

Correlation of Lifetime with Recombination Centers in Electron-Irradiated P-Type Silicon

B. J. Baliga* and A. O. Evwaraye

General Electric Company, Corporate Research and Development Center, Schenectady, New York 12345

ABSTRACT

Four majority carrier trap levels have been observed in p-type (boron-doped) silicon after 1.5 MeV electron irradiation. By correlation of the annealing rate of the minority carrier recombination lifetime with the concentration of these levels, it has been found that the divacancy-induced level at (E_V + 0.23 eV) controls the lifetime. Since this level begins to anneal out only at temperatures above 300°C, it can be concluded that electron irradiation of p-base silicon devices can be used to control their switching speed.

With the development of transient capacitance techniques, the study of defects in silicon has been rapidly advancing in recent years. Among these measurement techniques, deep level transient spectroscopy (DLTS) has been found to be the most convenient to measure the energy level and capture the cross section of the defect levels (1). The study of defect levels induced by electron irradiation has been performed using this technique to understand the nature of defect levels and to correlate the defect level position with defect structure identified using EPR (2-4).

From a device point of view, the study of electron irradiation-induced damage is important because it can be used to evaluate device degradation in harsh environments where a high flux of energetic electrons may be present. In addition, electron irradiation of power devices has been deliberately performed as a method for controlling lifetime in order to adjust the switching speed (5). In these cases, it would be useful to be able to determine which of the many electron irradiation-induced defects is responsible for determining the recombination lifetime. This has been performed in a previous study for n-type silicon (6). This paper reports a corresponding study performed to correlate defect levels produced in p-type (boron-doped) silicon by electron irradiation.

Experimental Technique

To study electron irradiation-induced defects in p-type silicon, ($n^+ p p^+$) junction diodes were fabricated by using 5 Ω-cm boron-doped Czochralski starting material. The heavily doped P^+ contact layer was first formed by boron diffusion using boron nitride as a source. The n^+ diffusion was then performed using $POCl_3$ as a source. These diodes were mounted on TO-5 packages for the measurements. The defect levels were measured by using DLTS with temperature sweeps from 77 K to room temperature. The minority carrier recombination lifetime was measured by using the reverse recovery technique (7).

The electron irradiation was performed at room temperature using a 1.5 MeV electron beam at flux of up to 2.5 × 10^{14} electrons per cm^2. The devices were mounted on a cooling block with forced air cooling to minimize the temperature rise during radiation. Measurements of the DLTS spectrum and the lifetime were then conducted immediately after radiation as well as after annealing.

Defect Levels

Immediately following the electron irradiation, four majority carrier defects levels were observed. These levels are shown in Fig. 1[2] and identified as M1-M4. It was found that the level M3 annealed upon storage of the diodes at room temperature. The annealing out of the level M3 was found to be accompanied by a growth in the concentration of level M4. A DLTS spectrum of a diode after room temperature annealing for 1 week is shown in Fig. 2. Note the absence of the M3 peak. Due to this observed annealing at room temperature, further measurements were conducted only after stabilizing the diodes at room temperature. The results of measurements of the DLTS peak heights and the lifetime were then conducted as a function of the radiation dose. It was found that the concentration of the levels increased with increasing radiation dose as illustrated in Fig. 3. In this figure, the variation in the lifetime with radiation dose is also shown. Throughout this paper, the reciprocal of the lifetime has been used for purposes of comparison with the DLTS peak heights because the lifetime is inversely proportional to the concentration of the recombination level. It can be seen that the variation in the lifetime correlates with the concentration of both levels M2 and M4.[2] To determine which of these levels is responsible for controling the lifetime, it was therefore necessary to perform studies of the behavior of these levels and the lifetime as a function of anneaing.

* Electrochemical Society Active Member.

[1] The rate windows used to obtain the DLTS spectra shown in the figures range from 1 to 10 msec.

[2] Note that the M1 level is too shallow to influence minority carrier lifetime and its annealing behavior is therefore not discussed in this paper.

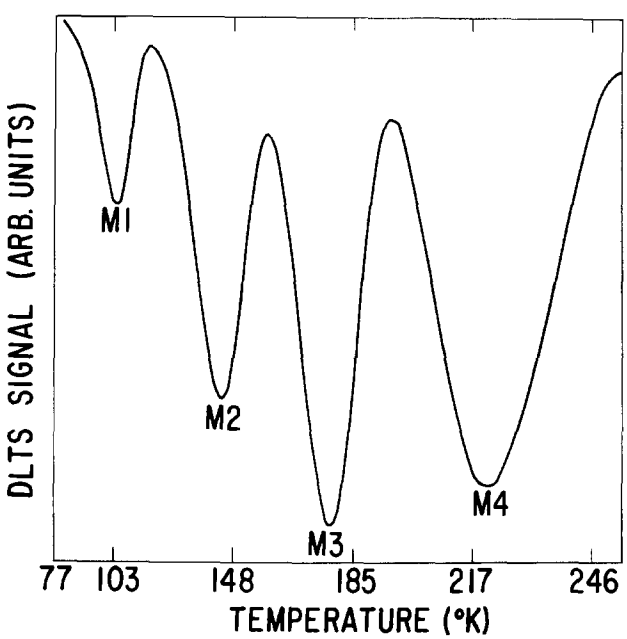

Fig. 1. Deep levels observed in p-type (boron-doped), 5 Ω-cm, silicon immediately after 1.5 MeV electron irradiation at room temperature.

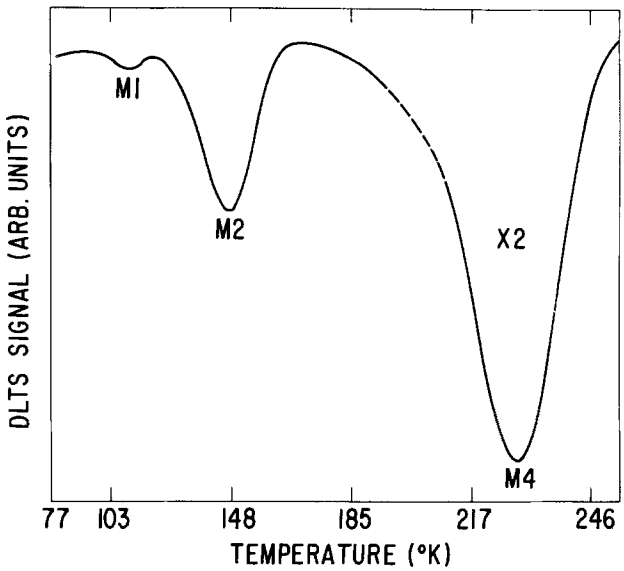

Fig. 2. Deep levels observed in p-type (boron-doped) 5 Ω-cm silicon after 1.5 MeV electron irradiation and room temperature annealing.

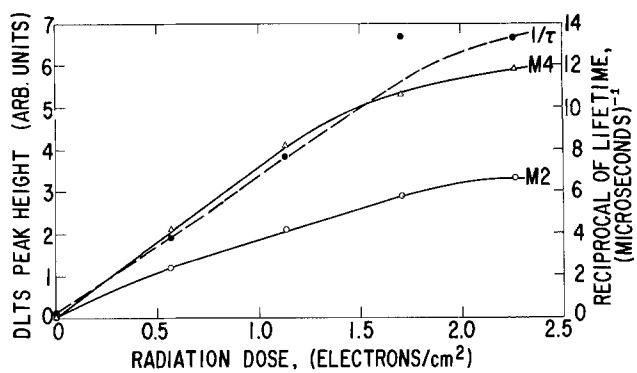

Fig. 3. Increase in concentration of defect levels M2 and M4 as a function of radiation dose. The corresponding reduction in the minority carrier recombination lifetime (τ) is also shown. (The radiation dose is in units of 10^{14} electrons per cm^2.)

Annealing Experiments

In order to correlate the defect level position with the lifetime, isothermal annealing of the diodes was performed at temperatures ranging from 200° to 500°C. During this annealing, the defect level concentration was periodically measured by using DLTS and the lifetime measured by the reverse recovery technique. It was found that below 400°C, the defect levels M2 and M4 exhibited distinctly different annealing behavior. The level M4 was found to either increase in concentration or remain relatively stable. In contrast, the level M2 was found to anneal out at between 300° and 400°C. This allowed correlation of the behavior of the lifetime to the defect level reponsible for determining the recombination of minority carriers. Figures 4 and 5 show typical results observed in this study for the variation of the lifetime and the defect level (M2 and M4) concentration at 350° and 400°C, respectively. It can be seen that in both cases the lifetime variation exhibits a very good correlation with the annealing behavior of the level M2. From these data, it can be concluded that the recombination lifetime is being controlled by defect level M2 and not by defect level M4. This is an unexpected observation because levels located closer to midgap are usually found to be the dominant recombination centers.

Discussion and Conclusions

In this study, four majority carrier levels were observed after electron irradiation of p-type silicon.

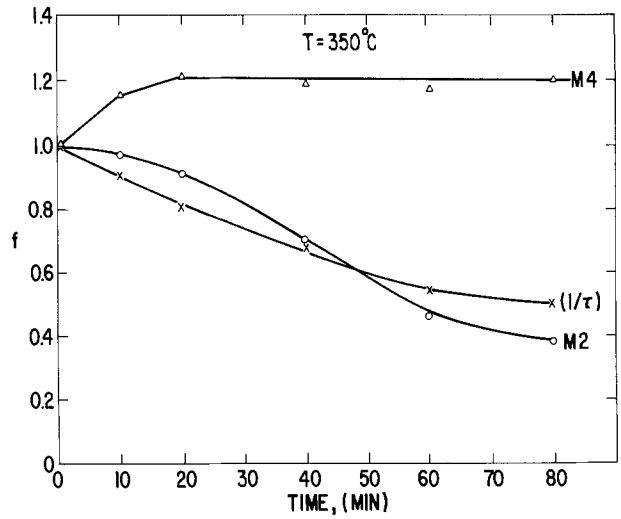

Fig. 4. Annealing behavior of defect levels M2 and M4 and the lifetime for isothermal annealing at 350°C. Note that fractional changes are being compared here for purposes of correlation.

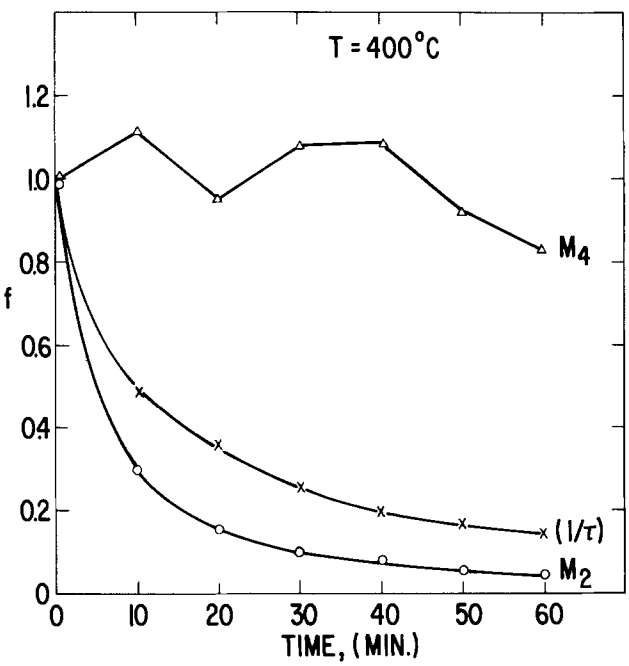

Fig. 5. Annealing behavior of defect levels M2 and M4 and the lifetime for isothermal annealing at 400°C. Note that fractional changes are being compared here for purposes of correlation.

Table I gives a list of deep levels reported in earlier studies corresponding to the levels M1-M4 observed in this study. The annealing out of level M3 observed in this study at room temperature with the corresponding increase in the concentration of level M4 has also been observed in the earlier studies (2, 3). The observed annealing out of the M2 level at lower tem-

Table I. Defects in electron-irradiated p-type silicon

This study	Walker/Sah	Kimerling	Mooney *et al.*
M1 (E_V + 0.18 ± 0.05 eV)	E_V + 0.18 eV	E_V + 0.09 eV	E_V + 0.18 eV
M2 (E_V + 0.23 ± 0.05 eV)	E_V + 0.24 eV	E_V + 0.21 eV	E_V + 0.23 eV
M3 (E_V + 0.29 ± 0.05 eV)	E_V + 0.29 eV	E_V + 0.27 eV	—
M4 (E_V + 0.36 ± 0.05 eV)	E_V + 0.35 eV	E_V + 0.33 eV	E_V + 0.38 eV

peratures than the M4 level in this study is also in agreement with the results reported in all the earlier studies (2-4). Based upon these comparisons, the levels M1-M4 can be related to the defect levels reported in the earlier studies as shown in Table I. Mooney *et al.* (4) have argued that the level M4 at (E_V + 0.38 eV) is a vacancy carbon oxygen complex called the K-center while the level M2 at (E_V + 0.23 eV) is due to the divacancy defect center. Based upon the correlation of the annealing behavior of the minority carrier lifetime with the concentration of level M2 observed in this study, it can be concluded that the lifetime in electron-irradiated, p-type (boron-doped) silicon is controlled by the divacancy defect center. It is worth noting here that the divacancy center was also observed to control the lifetime in lightly doped n-type silicon (6). In addition to these conclusions, the results of this study also indicate that the defect controlling the lifetime in p-type silicon does not anneal out until temperatures over 300°C are reached. Since power devices are generally operated at well below junction temperatures of 200°C, these results indicate that electron irradiation can be used to control lifetime in p-base devices without encountering changes in device characteristics during operation.

Manuscript submitted Nov. 22, 1982; revised manuscript received *ca.* May 9, 1983. This was Paper 65 presented at the Philadelphia, PA, Meeting of the Society, May 8-13, 1977.

General Electric Company assisted in meeting the publication costs of this article.

REFERENCES

1. D. V. Lang, *J. Appl. Phys.*, **45**, 3023 (1974).
2. J. W. Walker and C. T. Sah, *Phys. Rev. B*, **7**, 4587 (1973).
3. L. C. Kimmerling, *IEEE Trans. Nucl. Sci.*, **ns-23**, 1497 (1976).
4. P. M. Mooney, L. J. Cheng, M. Suli, J. D. Gerson, and J. W. Corbett, *Phys. Rev. B*, **15**, 3836 (1977).
5. B. J. Baliga and E. Sun, *IEEE Trans. Electron Devices*, **ed-24**, 685 (1977).
6. A. O. Evwaraye and B. J. Baliga, *This Journal*, **124**, 913 (1977).
7. D. C. Lewis, *Solid-State Electron.*, **18**, 87 (1975).

On the Formation of Planar-Etched Facets in GaInAsP/InP Double Heterostructures

L. A. Coldren, K. Furuya,[1] and B. I. Miller

Bell Laboratories, Holmdel, New Jersey 07733

ABSTRACT

Techniques to predict and control the etched wall profile at a mask edge are developed. An understanding of the etch rate *vs.* substrate orientation angle is used to predict and experimentally realize desired etched wall profiles on (001) GaInAsP/InP double heterostructure (DH) wafers. The identification and utilization of crystallographic stop etch planes is key to ensuring planar and reproducible etched facets. Fabrication procedures employing wet and dry etching techniques are outlined for either isolated step-etched vertical wall profiles or narrow groves.

The promise of integrated optics and/or electronics in the GaInAsP/InP material system (1) depends upon a detailed knowledge of the etching properties of the various epi layers both individually and in combination. A number of papers have contributed to this knowledge over the years (2-8). Perhaps the most important aspect of etching in the present context is the resulting wall profile, slope, and undercut at the edge of some mask, since masked etching is usually the primary means of defining the necessary surface topology. Alternative techniques of selective epi growth (9) or etching with a beam of limited extent (10-12) are still in exploratory stages.

Recently, there have been several important papers that addressed the topic of etching in GaInAsP/InP (13-16), but still lacking are detailed procedures for obtaining a desired wall profile (such as vertical) or an understanding of how to proceed to develop such procedures for a new problem. Earlier work in GaAlAs/GaAs went some distance in addressing these questions (17-20) but much of the information is limited to that system. In this paper we attempt to supply some of the missing information for the GaInAsP/InP system. In particular, we begin by considering the factors that affect wall profiles at mask edges. Starting with InP alone, it is shown that a knowledge of the relative etch rates of the various planes containing the mask edge line (together with some information about mask adhesion) allows the prediction of the etched wall evolution given some starting surface plane. Armed with this information, we then proceed to focus on the important and most critical practical problem of creating smooth, planar, and vertical-etched facets in GaInAsP/InP DH configurations for laser mirrors (15, 16, 21-23). In this multilayer situation, it is found to be advantageous to use multiple etching steps to control the wall profile (21, 23). Also, in order to etch narrow grooves with vertical walls, procedures to avoid undercutting have been developed (23, 24). These procedures are given in detail.

Although the focus is on the important example of laser mirrors, it is emphasized that the general basis of the approach can be used to obtain any number of preferred results, provided only that material-etchant combinations giving the necessary etch rate *vs.* surface orientation angle characteristics are found. Prediction of this characteristic from the materials involved and the crystal structure would provide procedures based truly on fundamentals. Although we certainly do not go that far, the connection between crystal structure and the etch rate curves in these III-V compounds is discussed.

Wall Profiles at Mask Edges—InP

Conventional wet chemical etching (WCE).—With the possible exception of the etching depth, the quality and nature of the wall profile is the most important result of chemical etching on a masked substrate. (Here "wall profile" is used to generally refer to all aspects of the resulting wall unless other qualities, *e.g.*, smoothness, mask undercut, slope, etc., are specifically stated.) The wall profile becomes especially crucial in devices that directly use the etched wall as an integral

[1] Present address: Tokyo Institute of Technology, Tokyo, Japan.

Key words: lasers, reactive ion etching, crystallographic etching, integrated optics.

component (*e.g.*, mirrors in etched facet lasers or waveguide sidewalls in BH and buried crescent [BC] lasers). Generally, one desires a predictable and reproducible result. In this section, the groundwork is laid for understanding and predicting wall profiles given the masking and substrate materials, their orientation, and the chemical etchant. We will first concentrate on InP.

Figure 1 illustrates a number of wall profiles that can be obtained using Si_3N_4 masks on either (100) or (110) wafers. At least to a degree, the differences that occur among the various combinations are related to the anisotropy introduced by the relative orientation of the polar {111} planes. The more chemically inert {111}A In planes [(111), ($1\bar{1}1$), ($\bar{1}1\bar{1}$)] form approximate "stop etch" planes for all known wet etches. This fact is clearly reflected by the results in Fig. 1. Put another way, the factors that cause the {111}A surfaces to differ chemically from the more active {111}B P surfaces (*e.g.*, number of unbonded valence electrons (2), etc.) probably exist to some degree on other nearby or related surfaces. Our initial task here is to understand the effects of these differences in etch rate on the resulting wall profiles at mask edges.

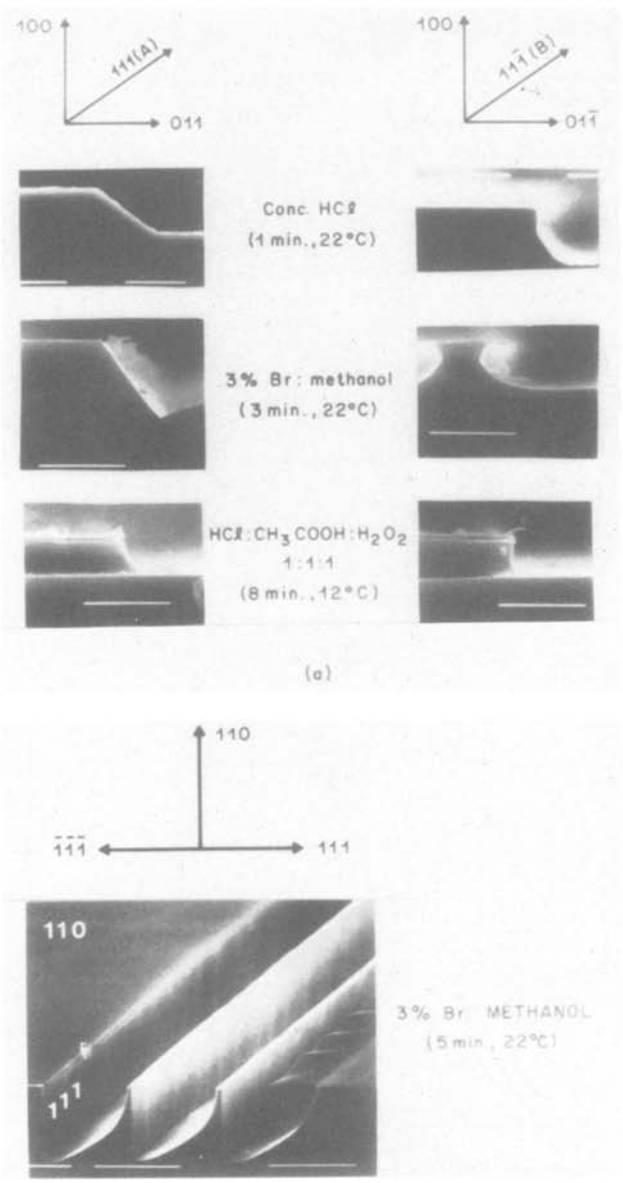

Fig. 1. (a) SEM cross sections of etched wall profiles at Si_3N_4 mask edges for (100) InP with three different etches. (b) SEM perspective view of Br:methanol etching on (110) InP with a three slot Si_3N_4 mask. Markers ≡ 10 μm.

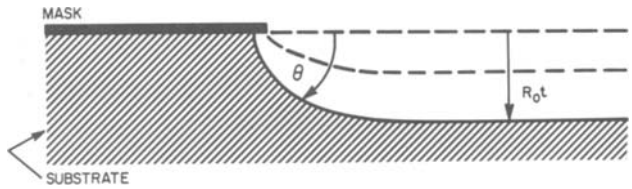

Fig. 2. Schematic representation of the results of chemical etching near a mask edge for time t. Dashed lines represent the original surface and an intermediate depth profile.

Figure 2 schematically traces the progress of etching at the edge of a mask. The important observation one can make from this general illustration is that there must be a rotation of the surface normal near the edge of a mask as the etching proceeds. This sloping of the surface is necessary to connect the unetched and etched regions. Thus, the variation of etch rate, R, with surface rotation angle about the mask edge, θ, is important in determining the eventual wall profile for the materials, orientations, and etchants involved. In fact, for a number of special case R *vs.* θ characteristics, the wall profile can be predicted by inspection.

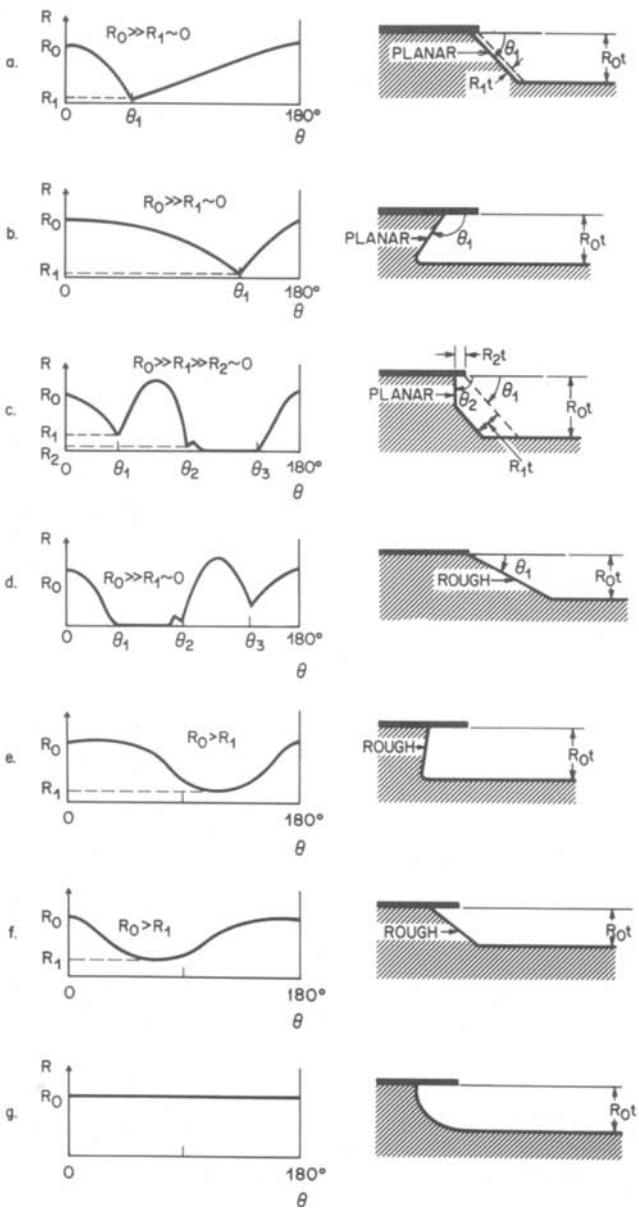

Fig. 3. Hypothetical etch rate R vs. substrate orientation angle θ (left) and predicted wall profile cross section at a mask edge (right).

Figure 3 gives several hypothetical examples of special R *vs.* θ characteristics with resulting wall profiles. Here, because of the inequalities ($R_0 >> R_1$, etc.) and the effective stop etch planes ($R_2 \approx 0$, etc.), the resulting wall slopes can be easily predicted quantitatively. However, we must presume that etching conditions near the mask edge approximate those under which the R *vs.* θ curve was obtained. That is, the rate controlling etching mechanism must not be varied. Also, one can predict that very smooth surfaces should result if a sharp local minimum in etch rate occurs at that orientation angle. (See Fig. 3a—θ_1, 3b—θ_1, 3c—θ_1 and θ_2.) These planes tend to be very smooth simply because any ± surface irregularity will be subjected to a much higher etch rate and quickly disappear. We have termed these "crystallographic planes," since a particular crystal plane usually coincides. Note that stop etch orientation angles are not always "crystallographic," under our definition, since $R \sim 0$ at some angle is not always associated with a large etch rate for both $\pm \Delta\theta$ deviations from this angle. (See Fig. 3c—θ_3, 3d—θ_1, 3e—θ_1, 3f—θ_1.) Thus, these surfaces have been labeled, as well as any other that do not fall under the crystallographic etching definition as "rough."

In Fig. 3a-f, we have actually only illustrated three material combinations similar to the actual results with (100) InP using Br:methanol in (a) and (b), HCl in (c) and (d), and HCl + HNO_3 in (e) and (f) for mask edges lying in the (011) and (01$\bar{1}$) planes, respectively. Because of symmetry, the R *vs.* θ characteristics are mirror image pairs in this case, and inverting the crystal to its rear surface (starting from $\theta = 180°$) is equivalent to using the orthogonal (rotated by 90° on the surface) mask orientation. Figure 3g is obviously an isotropic example not characteristic of any of the III-V's.

The prediction of mask undercutting is a bit more complicated, even in the special cases illustrated in Fig. 3. First, we must know or assume something about the etching properties of the mask-substrate interface. Then, we must somehow calculate how much undercutting occurs before a stable stop etch or slow etch orientation is established (25). From this point, they again can use the rate multiplied by the time for the stable wall orientation angle, provided as always that the R *vs.* θ characteristic is still valid for the changing geometry.

The schematic wall profiles in Fig. 3 also illustrate undercutting. In most cases, the first assumption is that no increase or decrease in etch rate occurs due to the mask-substrate interface. Secondly, it is noted that for cases with stop etch planes where $0 < \theta_1 \leq 90°$ there should be very little undercutting before this stable plane is established. This assumption follows from the first since the wall would tend initially to proceed beneath the mask only with a perpendicular intersection angle. (See Fig. 3g—isotropic case.) But with a stop etch plane at $\theta \leq 90°$, essentially no undercutting will initially occur, since the plane is reached at the mask edge almost instantaneously. Thus, in these cases, the undercut is $R_1 t/\sin\theta_1$ unless another stop etch plane with a still lower etch rate is encountered for $\theta \leq 90°$ as in Fig. 3c. Then $R_2 t/\sin\theta_2$ determines the undercut. In practice, the above analysis gives good predictions.

If the stop etch plane occurs for $\theta_1 > 90°$, (*e.g.*, Fig. 3b) it may never be established under the assumptions that there is no reduction in etch rate at the mask interface or with increasing undercut. In practice, using Br:methanol on InP, a significant dependence on the choice of masking material has been observed. In some cases, the stop etch plane is quickly established; in other cases it never is reached (25). Thus, the amount of undercutting is generally dominated by process dependent factors, such as mask-to-substrate strain, and not the side etching of the stop etch plane in the $\theta_1 >$ 90° cases. One must, therefore, characterize his own process in order to predict undercutting in these cases. Also, diffusion of reactants or products to or away from the region immediately under the mask can be important for large undercuts.

In cases where there are no stop etch orientations [$R(\theta) \approx 0$] or crystallographic planes [$R(\theta) << R(\theta \pm \Delta\theta)$], the wall profile cannot be quantitatively predicted as easily. (See Fig. 3e, f.) However, qualitatively the same thing happens if there are even weak minima in R *vs.* θ. That is, the final wall profile will tend to be characterized by slopes given by $\theta \approx \theta_{min.}$, and undercutting will tend to proceed at $R(\theta_{min.})t/\sin\theta_{min.}$ if $\theta \leq 90°$. Again, assumptions concerning the mask-substrate interface and R *vs.* θ for the etching geometry must be made. For $\theta_{min.} > 90°$, the undercutting situation is much less predictable as mentioned above since etching near the mask-substrate interface predominates.

Figure 4 gives the actual measured plots of R *vs.* θ for the cases shown schematically in Fig. 3a-f, as well as one other. The data was obtained with planar-masked samples that had been polished to a number of different surface orientations as shown. The same substrate material was used for all etchants. From these data, we can determine the values R_1, R_2, θ_1, θ_2, etc. for a particular case shown in Fig. 3 to obtain a quantitative prediction of wall profile. For example, with HCl (Fig. 3c) they obtain: $R_0 = 8$ μ/min, $\theta_1 = 55°$, $R_1 = 1.2$ μm/min; $\theta_2 = 90°$, $R_2 = 0.4$ μm/min, and $\theta_3 = 140°$.

One should be cautioned, however, that quantitative predictions from these data are restricted by several factors: (*i*) the etch rate is generally nonlinear with time. The rate is usually significantly higher during the first few seconds of etching (2) so Fig. 4 is only quantitatively valid near the etching time used. The qualitative form, however, does appear to hold for a wide variety of etching times. (*ii*) Geometry may change the etch rate, especially in reactions that are partially limited by diffusion of reactants or products to or away from the region. Deep grooves and walls with large undercutting are examples of limiting geometries. It is also noted from Fig. 4 that θ_1 and θ_2 are crystallographic minima but that θ_3 is only a stop etch angle. Of course, θ_3 is not a factor since $R_2 \approx 0$, unless etching

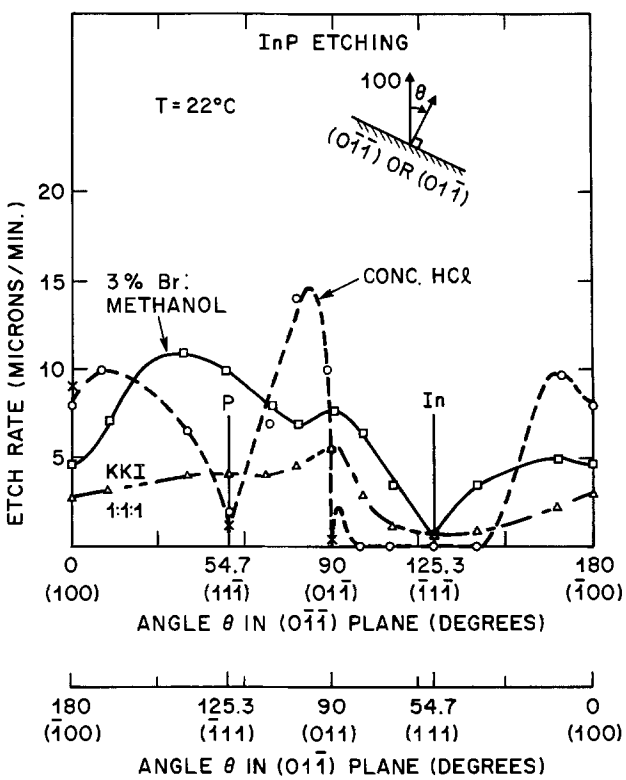

Fig. 4. Measured etch rate *vs.* InP substrate orientation angle from the (100) for rotation about either the [0$\bar{1}$1] or [01$\bar{1}$] axes.

proceeds from the $\theta = 180°$ side. Equivalently for θ_3, the lower abcissa with $\theta_1 \approx 40°$ analogous to Fig. 3d is used.

The small bump or maximum for HCl in Fig. 4 for $\theta \sim 95°$ is believed to exist, but it has only been observed qualitatively. Its amplitude and width have not been measured accurately. The best evidence for its existence is the very smooth appearance of a resulting etched $(01\bar{1})$ facet, indicating crystallographic behavior as shown in the experiments below. It is entirely possible that there is no bump in the plane but that the {011} is a sharp minimum in some other orthogonal plane.

Figure 5 shows some experimental results of wall profile and surface texture for HCl etching analogous to the schematics in Fig. 3c, d. Part (a) considers the mask edge in the $(01\bar{1})$ plane (Fig. 3c or upper abcissa in Fig. 4). In this case, the authors observe the two predicted crystallographic facets labeled $(11\bar{1})$ and $(01\bar{1})$ for $\theta_1 = 55°$ and $\theta_2 = 90°$, respectively. Here the etching time was 90 sec, so $R_0 t = 12$ μm, $R_1 t = 1.8$ μm, and $R_2 t = 0.6$ μm from Fig. 4. The measured values from Fig. 5 of 11, 2.4, and 0.5 μm, respectively, for the depth, slope erosion, and mask undercut are in good agreement with the prediction. Also, the extreme smoothness of these facets shown by the perspective views is characteristic of the predicted crystallographic etching.

The triangular mesas, which depart from planarity in Fig. 5a, are the result of mask roughness. Of practical significance is the fact that the wall eventually becomes smooth even if the mask is rough, provided only its average edge line falls in the $(01\bar{1})$ plane. These characteristic features are useful in distinguishing $(01\bar{1})$ *vs.* (011) under the convention adopted. That is, triangular mesas that point away from the designated (100) surface signify a $(01\bar{1})$ edge surface, and mesas that point toward the (100) signify a (011) facet (26).

The above-mentioned mesas are believed to account for the occasional apparent deviation of the resulting etch profile from 90°. Deviation from the vertical of ~2°-5° (*i.e.*, $\theta_2 = 92°$-$95°$) have been observed by others (14, 15) and ourselves. Arrays of very small mesas can explain this phenomena. However, it can also be argued that θ_2 is not 90° but must be slightly greater than 90° to break the chemical degeneracy between (011) and $(01\bar{1})$. When $\theta_2 > 90°$, the surface has more In atoms than P and vice versa. Perhaps the surface must be slightly In rich to inhibit HCl etching, for it is well established that the In rich surfaces are more inert than the P rich ones. Regardless of the explanation, this slight tilt does exist, but fortunately its effect on laser mirror reflectivity is small (15).

Figure 5b gives the results of HCl etching with the mask edge in the (011) plane. In this case, we again observe a well defined stop etch angle ($\theta_1 \approx 40°$) as predicted from Fig. 4 (lower abcissa), but the etching is clearly not crystallographic in our definition, since the surface is textured and rough. The roughness appears to follow the mask edge roughness. With smoother mask edges the wall could be improved, but the point here is that the etching does not naturally provide a smooth surface despite edge roughness as in Fig. 5a. The undercutting is too small to measure with such a rough surface.

Figure 6 gives similar results for etching with 3% Br:methanol. For both mask orientations, the {111}A plane defines the crystallographic stop etch orientation angle analogous to the schematics in Fig. 3a, b. The surface smoothness is good in both cases. The etching depth corresponds to the rate $R_0 = 4$ μm/min obtained again from the plot in Fig. 4. The undercutting for the mask edge in the (011) plane, as mentioned above is predictable, and it agrees with the value $R_1 = 0.4$ μm/min from Fig. 4. For the orthogonal orientation (Fig. 6a), the undercutting is very nonlinear with etching time as also suggested in the Fig. 3 discussion. (Note that this is a wall angle effect, not the initial transient in etch rate referred to in the Fig. 4 discussion.) During the first 10 or 20 sec with this 3% concentration and an Si_3N_4 mask, the wall is approximately perpendicular to the mask, and the side etching is approximated by $R(\theta \sim 90°) \approx 7$ μm/min. Then after the stop etch plane is established, $R(\theta \sim 125°) \approx 0.4$ μm/min, the side etching is relatively insignificant.

As mentioned earlier, this situation can vary dramatically, dependent mainly upon the degree of etch rate enhancement or suppression at the mask-substrate interface (25). Only slight changes in etch rate are necessary to change the wall slope, which is the dominate factor in determining undercutting in this case. For other masks, such as some photoresists and some forms of SiO_2, the undersloping {111}A stop etch

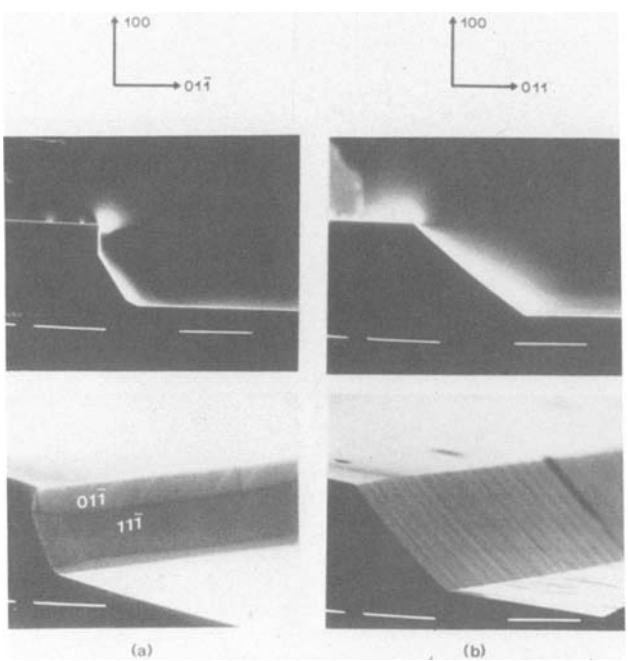

Fig. 5. SEM cross sections (top) and perspectives (bottom) of steps on (100) InP etched with HCl for 90 sec using mask edges lying in either the (a) $(01\bar{1})$ or (b) (011) planes. Mask is plasma deposited Si_3N_4. Markers ≡ 10 μm.

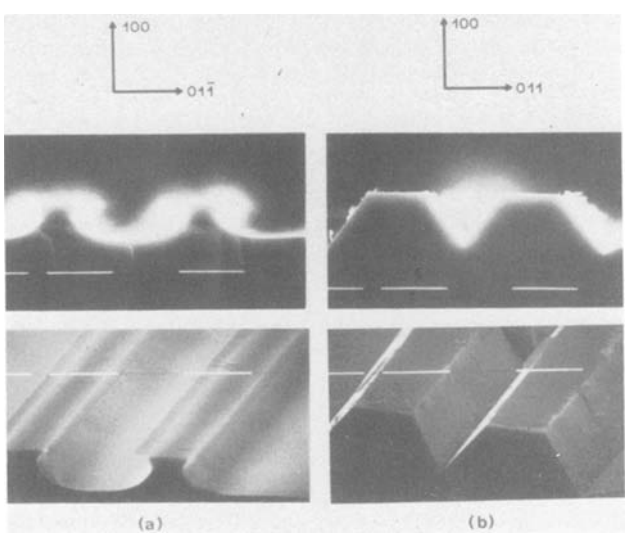

Fig. 6. SEM cross sections (top) and perspectives (bottom) of ridges on InP etched with 3% Br in methanol for 120 sec using two Si_3N_4 mask stripes 10 μm wide spaced by 10 μm in the orientations indicated.

plane is never obtained for this orientation, and the side etching continues at some intermediate rate. These relatively subtle interface changes have little effect on undercutting for the first orientation [Fig. 6b—mask edge in (011) plane] or any other case in which the stop etch orientation angle $\theta \leq 90°$ as stated above.

The enhancement or suppression of etch rate at the mask-substrate interface is not always subtle. Metal masks on InP offer some examples. Figure 7 gives example SEM's of HCl etching with Ti masks. For both mask orientations the interface undercutting is dramatic. This example used an RIE first step, but the same "wild" undercutting has been observed in other cases as well. Similar results have been observed with photoresist-over-Au masks and Br:methanol etching. These results suggest some sort of electrochemical cell action or the formation of an easily etched interface compound. The former is believed to be more likely in these cases.

Reactive ion etching (RIE).—A number of dry etching procedures, including the low pressure reactive ion etching (RIE), have been studied for use on InP and GaInAsP/InP device structures. Since these studies are well documented in the literature (24, 27, 28), the results will not be discussed in any great detail here. However, a review of the salient characteristics of certain processes that have been used to overcome the limitations of WCE is needed. Although some of the same results can be obtained with the generally higher pressure plasma etching processes (29-31), we will concentrate on the highly directional etching properties of RIE. We will also only discuss Cl_2:O_2:Ar gas mixtures although other possibilities exist (27).

The first, and perhaps most significant, property of RIE in this context is the lack of any significant etching dependence on crystal orientation. That is, wall profiles are generally not dependent on crystal orientation, but they are dependent on the etching conditions and parameters of RIE. This is in distinct contrast to the higher pressure plasma etching results using Cl_2 on GaAs (31) where much lower ion energies have allowed the observation of crystal orientation effects. The second significant feature of RIE is that mask undercutting is practically nonexistent. Etching occurs only where the collimated ions strike the surface. Figure 8 gives examples of InP etching with a Cl_2 + O_2 mixture for two different etching conditions. The change in wall profile and roughness with changing conditions is apparent. No orientation effect was observed, and in all cases no undercutting of the mask is evident. It should be noted, however, that mask erosion is a more significant problem with RIE as compared to WCE because of the poorer mask *vs.* substrate etching selectivity. Metal masks are usually required to withstand the sputter etching effect of the incident ions. Nevertheless, mask erosion is not the cause of the wall slopes generally observed for normally incident ion beams. The sloping effect is generally attributed to nonvolatilized etch products that "mask" the wall (28).

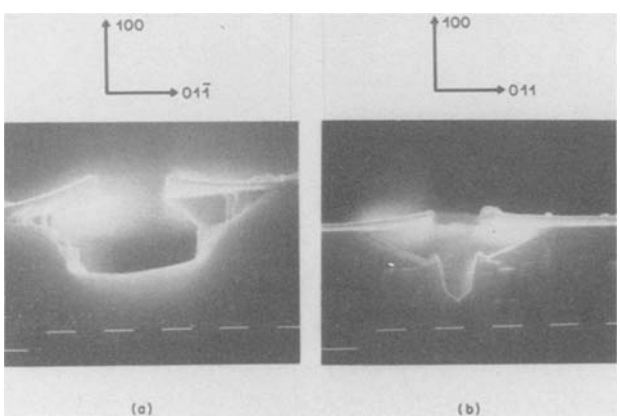

Fig. 7. SEM cross sections of InP etched with HCl for 10 sec following RIE with a Ti mask. Markers ≡ 1 μm.

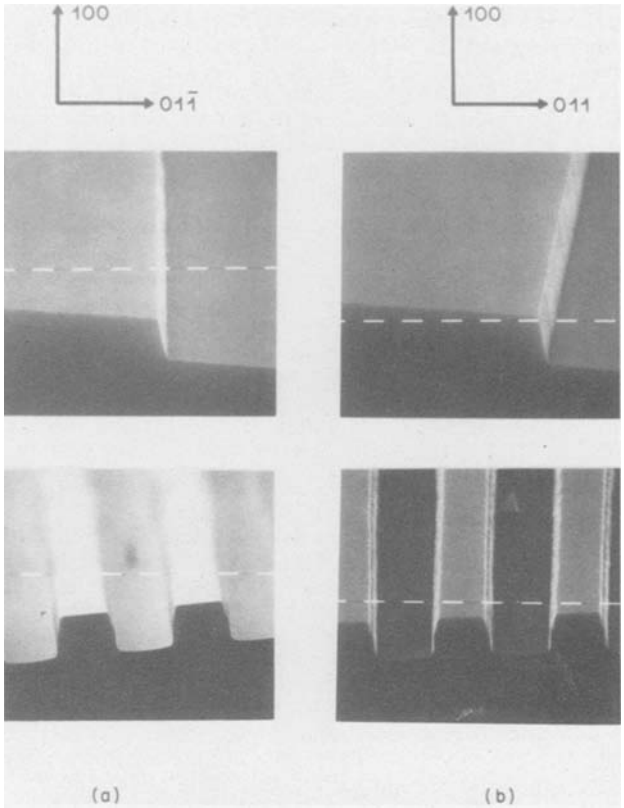

Fig. 8. SEM perspective of InP etched by RIE. Etching conditions: top—80% Cl_2 + 20% O_2 gas mixture at 2 mTorr pressure; 0.33 W/cm^2 applied rf power; substrate temperature 250°C; etching time was 20 min. Bottom—80% Cl_2 + 20% O_2; 4 mTorr; 0.33 W/cm^2; 30°C, 20 min. Markers ≡ 1 μm.

The top part of Fig. 9 illustrates RIE groove etching for Ti/Si_3N_4 masks with edges in either the (011)

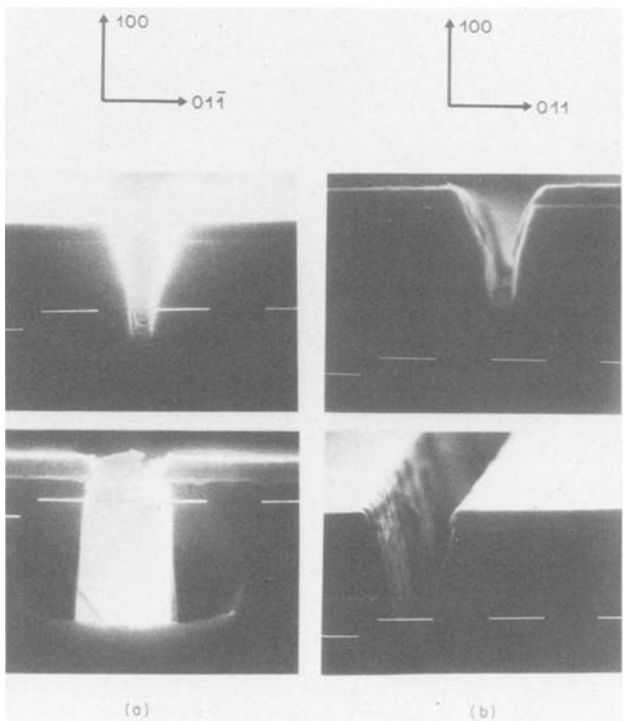

Fig. 9. SEM cross sections showing at the top, RIE grooves (80% Cl_2 + 20% O_2, 2 mTorr, 0.33 W/cm^2, 25°C, 20 min) formed with a Ti over Si_3N_4 mask, and at the bottom, the results of subsequent etching in HCl for 10 sec.

or $(01\bar{1})$ planes. No difference can be observed. Also, the capability of RIE to etch narrow grooves is noted. The bottom part gives the result of post etching in HCl for 10 sec. The distinction observed earlier is clearly evident. The near zero etch rate for $40° < \theta < 85°$ with the mask edge in the (011) plane (Fig. 9b) results in no HCl effect on the rough RIE surface. Even the small (~1000Å) striations are unaffected on the RIE wall which here has a $\theta \sim 75°$ slope. For the $(01\bar{1})$ case, the walls etch quickly to a smooth and near vertical state as shown previously. The Ti/Si_3N_4 mask used in Fig. 9 allows prolonged RIE (several hours), plus the capability to immediately WCE/HCl without the wild undercutting effects shown in Fig. 7. This capability is important in narrow-grooved device structures (23).

Combined RIE-WCE grooves, (011) facets.—Figure 9, discussed above, suggests combining an RIE step with a subsequent WCE step to obtain narrow, high aspect ratio grooves in InP. Later, it will also be seen that this combination is particularly useful with GaInAsP/InP heterostructures. For InP alone, the principal advantage of preceding HCl-WCE by RIE is to lessen the undercutting. Since the side etching rate with HCl for $(01\bar{1})$ walls is about one-tenth the vertical rate ($R_2/R_0 \sim 0.05$ from Fig. 4), a groove will widen by about 10% of the etched depth (two times undercut), if only HCl is used. The formation of the {111}B facets at the groove bottom require even longer etching if the height of the $(01\bar{1})$ wall is of primary interest. That is, the useful depth is reduced by the "V" formed at the bottom by an amount $w_g/2 \tan 55° = 0.71\ w_g$, where w_g is the groove width. However, if RIE is first used to the desired depth, only a few seconds in HCl will planarize the wall to the $(01\bar{1})$ as in Fig. 9a. This planarization is particularly rapid, since the wall slope left by RIE is typically $\theta_R \sim 75°$, and from Fig. 4 a maximum in etch rate is observed near this orientation ($R_{75} \sim 12$ μm/min). Also, no low etch rate orientation now separates the starting from the final ($\theta \sim 90°$) wall angles. Thus, in a typical HCl dip time of 5 sec, a mask undercutting of $R_2 t \sim 350$Å is obtained from Fig. 4. For such small amounts of etching it is sometimes desirable to dilute the HCl slightly with water. A 1:1 dilution slows the etch rate by about an order of magnitude, but the qualitative features of Fig. 4 remain.

Another important possibility with combined RIE and WCE steps is the formation of (011) vertical facets on (100) InP (32). To the author's knowledge, no WCE will provide a wall angle $\theta > 55°$ when the masking edge is in the (011) plane. The reason, of course, is the coincidence of the {111}A stop etch plane which is effective for all known WCE etchants. With RIE this is not the case.

Figure 10a shows that RIE can provide $\theta > 90°$ if the ion beam is angled relative to the substrate normal (23, 33). From Fig. 4, using the lower abcissa, it is observed that with $\theta > 90°$ the wall surface has moved out of the zero etching range $40° < \theta < 90°$ and into a range where HCl will quickly planarize the wall back to the (011). Figure 10b illustrates the experimental result of briefly post etching the angled RIE sample of Fig. 10a in HCl. The vertical (011) facet is clearly designated by the upward pointing triangular mesas. The mask for this WCE step is actually at the bottom of the RIE wall where θ becomes <90°, and the etch rate falls to zero. Below this depth of RIE, the wall takes on the characteristic wall angle, $\theta \sim 40°$, and rough texture observed previously in Fig. 5b. The situation after RIE in Fig. 10 is entirely analogous to that in Fig. 9. The RIE has provided a wall surface oriented between the {111}B and the vertical. The high HCl etch rate in this region angles the wall slope to the crystallographic stop etch orientation near the vertical. The primary difference is the location of the effective mask.

Figure 10c shows an alternative method to obtain a (011) facet, and this time all steps are WCE. The trick

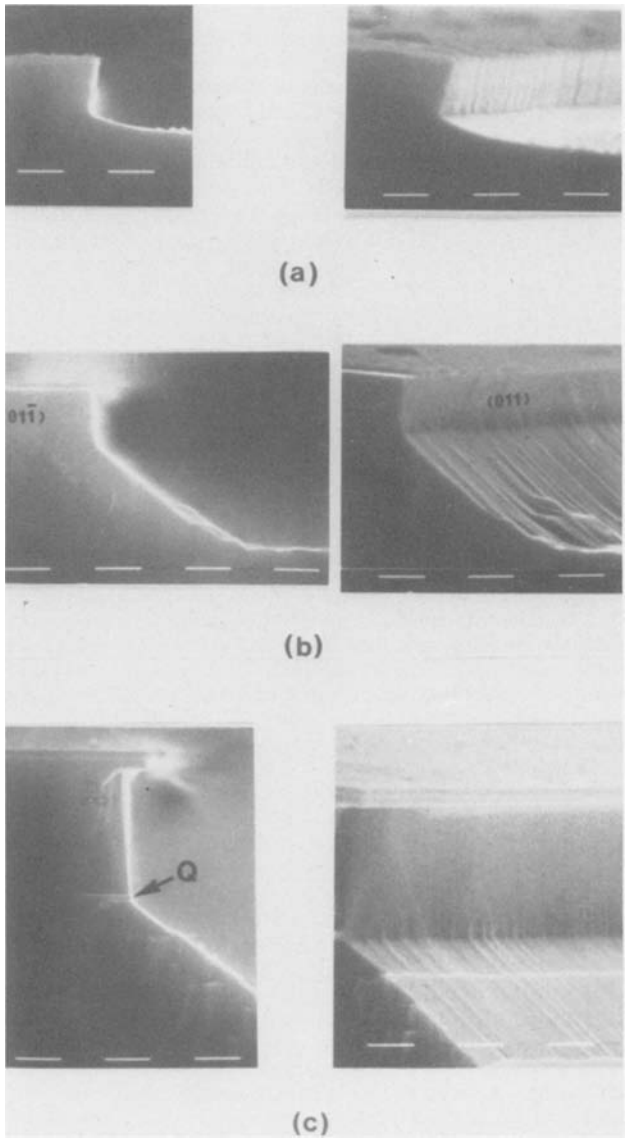

Fig. 10. SEM cross sections and perspectives of (011) facets after (a) 40°-angled RIE (60% Cl_2 + 30% O_2 + 10% Ar, 2 mTorr, 0.33 W/cm², 25°C, 150 min), and (b) additional etching of in HCl for 10 sec. Mask for (a) and (b) is Ti/Si_3N_4. (c) Results of all WCE procedure incorporating (1) etching in HCl for 30 sec, (2) etching in a 6:4:35 by wt $K_3Fe(CN)_6$:KOH:H_2O solution for 60 sec, and (3) etching in HCl for 20 sec. Mask for (c) is Si_3N_4; all markers ≡ 1 μm.

is to provide a different composition buried epi layer that can be selectively etched to provide the necessary undercut masking line. Here a three-step procedure is employed to (*i*) cut through the InP to a GaInAsP layer, (*ii*) selectively etch away the buried GaInAsP layer to beneath the top mask, and (*iii*) then etch in HCl to planarize the wall above the GaInAsP mask, etching from the bottom-up.

GaInAsP/InP Heterostructure Wall Profiles

One-step etching.—Most commonly, multilayer structures in this material system are etched with a single etchant at any given masking level. If all layers are to be cut at some mask edge, it is desirable to choose an etchant that etches both the quaternary and InP layers at about the same rate so that no protrusions or recession of any single layer occurs. A number of studies have proposed etching mixtures to satisfy this criteria (13-15) and thereby yield a uniform wall profile across a multilayer heterostructure. For etched mirror facets in lasers, this wall should be "vertical" or perpendicular to the surface. Of all the etchants that have been

proposed, however, none use a crystallographic stop etch plane to provide a reproducible and planar facet as illustrated with HCl above for InP alone. The one mixture that does reproducibly give a planar wall across all layers, Br:methanol, provides a {111}A crystallographic plane, which is not compatible with simple two-mirror lasers on (100) substrates. There has been some work with Br:methanol and mask edges in the $(01\bar{1})$ plane, in which the etching did not limit at the $\theta = 125°$ {111}A plane (15). In these cases, the mask-substrate combination apparently inhibited the formation of the undersloping wall by favoring continuing undercutting. But here again, the reproducibility and planarity advantages of a stop etch plane are not being utilized, and the wall profile is rounded as in other such cases (13-20).

To our knowledge, no single etchant which limits at the $(01\bar{1})$ plane in both the quaternary and InP has been identified. Without this stop etch action, we can only hope to approximate a vertical wall, *e.g.*, $(01\bar{1})$, and the etch rates of the quaternary and InP must be exactly equal to avoid any step at a buried interface. Figure 11 illustrates the optimization of an HCl + xHNO$_3$ mixture to eliminate this step by adjusting x. This interesting mixture is a combination of an etchant that etches InP but not GaInAsP-HCl and one that etches GaInAsP but not InP-HNO$_3$. Although it retains some of the anisotropic characteristics of HCl so that $(01\bar{1})$ walls are approximated, the addition of HNO$_3$ removes the crystallographic stop etching quality. The undercutting rate is ~2 μm/min or about one-fourth the vertical rate. In other words, the R *vs.* θ characteristic shows only a weak minimum at $\theta = 90°$, unlike pure HCl. In our experience, the resulting wall profile for the optimized mixture ($x = 2$ in this case) is about as good as can be done with a single etching step.

RIE again provides an alternative way of obtaining a desired wall slope in GaInAsP/InP heterostructures. Because of the collimation of the ion beam and since etching only occurs where the ions strike, there is no tendency for a step to form at a buried layer in this case, even if a different etch rate exists. Thus, the wall profiles are similar to those shown earlier in Fig. 8 for InP alone. In most cases, it is impossible to discern the location of a buried quaternary layer in InP. The chief qualitative difference between the WCE result of Fig. 11 and RIE with a properly angled ion beam is the lack of mask undercutting in the latter dry etching case. Wall striations and slope are qualitatively of the same order. Also, RIE can provide the same wall regardless of orientation. Laser thresholds using either one-step WCE or RIE are increased by ~0-50% over cleaved control samples.

Two-step etching.—In order to improve the quality and reproducibility of wall profiles resulting from a first etching step, we have proposed a second crystallographic stop etching step to smooth and planarize the wall. For $(01\bar{1})$ walls, HCl is the only etchant found that provides a definite crystallographic stop etching in InP. Of course, the major difficulty in the heterostructure is that HCl will not etch GaInAsP at all. Thus, the first step must leave the wall very nearly planar at the $(01\bar{1})$ so that a brief HCl etching (5-20 sec) will not create a large protrusion of the quaternary layers of interest. Figure 12 illustrates the results that can be obtained with a WCE first step. The wall illustrated deviates less than ~500Å from planarity.

If angled RIE is used for the first step, (011) facets as well as $(01\bar{1})$ can be obtained. For $(01\bar{1})$ facets, the results are similar to Fig. 12 but with reduced undercut. The technique for (011) facets is the same as used for Fig. 10. That is, the RIE is angled to provide a very slightly undersloping wall, exposing to the HCl a wall surface that can be etched back to the (011) with the bottom of the wall acting as a mask. The results, shown in Fig. 13, also include a supplementary material selective etching of the quaternary (Q) layer and another brief HCl etching to reduce the quaternary protrusion. Such supplementary steps have also been found to improve the yield of $(01\bar{1})$ facets as in Fig. 12. The next section will review these and other multistep etching procedures.

Multistep and sequential layer etching facets and grooves.—By multistep etching, we refer to an extension of the two-step procedures discussed above. That is, they have found that it is possible to improve the yield and have more predictable wall profile results if additional "fine tuning" steps are included. Also, certain of the steps can be reiterated to converge on the desired smooth and planar walls.

Table I outlines a general multistep procedure for obtaining mirror quality $(01\bar{1})$ walls in DH laser wafers. Here, the first step is assumed to cut through all important layers of the device structure. Subse-

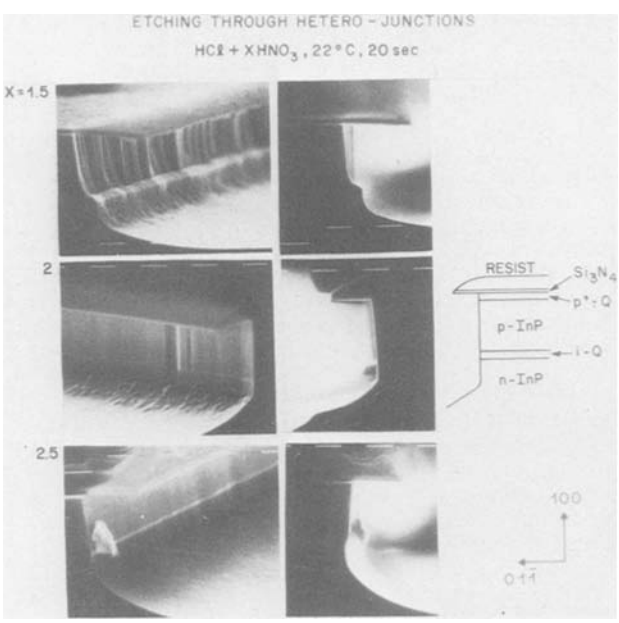

Fig. 11. SEM perspectives and cross sections of GaInAsP/InP DH etching in HCl + xHNO$_3$ for $x = 1.5$, 2.0, and 2.5. Mask is negative resist on Si$_3$N$_4$; markers ≡ 1 μm.

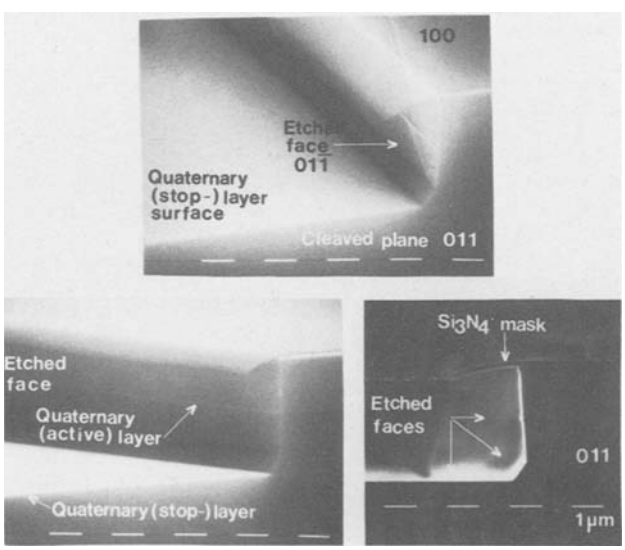

Fig. 12. SEM perspectives and cross sections of two-step WCE DH wall profiles after etching in (1) 1:1.5-HCl:HNO$_3$ as in Fig. 11 and (2) pure HCl for 10 sec.

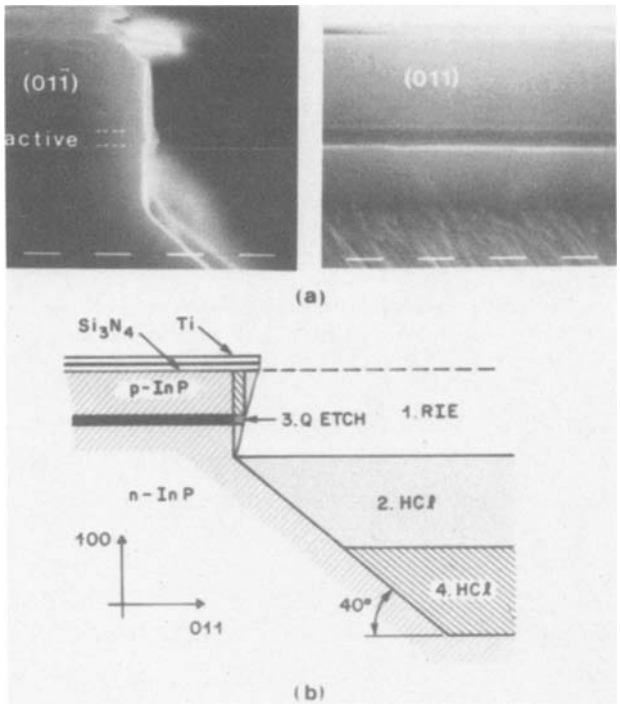

Fig. 13. (a) SEM cross section and perspective of a (011) facet on a DH wafer. (b) Schematic illustration of steps employed. Marker ≡ 1 μm.

quent etching is applied to improve the result, primarily by side etching. The simple two-step procedure discussed above is a special case in which no optional steps are employed. As noted, angled RIE can also be used to form (011) facets. All etchants in step 1 will etch all layers of the DH. Step 2 uses a selective Q-etch to recess the active Q layer by ~1000Å, or the assumed striation deviation from the (01$\bar{1}$) plane left by step 1. Step 3 planarizes the wall with the crystallographic HCl etchant. Step 4 includes additional side etching steps of ever decreasing duration (or extent) always ending with the important HCl crystallographic etching. Figure 14 gives an etched DH facet example in which some optional steps were employed. The mirror quality was uniformly good over most of the wafer. Note that the optional step 2 may be skipped initially and then included in step 4. It is important to realize in considering this multitude of possibilities that the primary etching is done in steps 1 and 3. The remaining steps are only for fine tuning that which should already be a good result.

Table II outlines a different kind of approach, in which individual layers of a DH are removed sequentially from the top. This approach is particularly useful for narrow groove etching since RIE can be used for cutting all Q layers without any mask undercutting, and then that Q-layer becomes the mask for crystallographic etching of the underlying InP layer with little associated undercutting. Of course, the narrowest grooves are still obtained by etching deeply with RIE

Table I. Multistep etching, (01$\bar{1}$) facets

Step	Etchant	Comment
1.	$HCl:HNO_3$ $HCl:CH_3COOH:H_2O_2$ $Br:CH_3OH$ $\angle$ RIE ~ 40°	Cut all layers approx. vertical [RIE → (011) also]
2. [optional]	$K_3Fe(CN)_6:KOH:H_2O$ $H_2SO_4:H_2O_2:H_2O$ HNO_3	Selective Q-etch to recess Q—layers (~1000Å)
3.	HCl	Planarize at (01$\bar{1}$)
4. [optional]	As above	Repeat 1-3, 1 and 3, or 2 and 3 to improve facet

Table II. Sequential layer etching, (01$\bar{1}$) facets and grooves

Step	Etchant	Comment
1.	a. $K_3Fe(CN)_6:KOH:H_2O$ $H_2SO_4:H_2O_2:H_2O$ HNO_3	Cut through Q—cap; a. selective b. nonselective [RIE → no undercut]
	b. $HCl:HNO_3$ $Br:CH_3OH$ $\perp$ RIE	
2.	HCl	Cut to Q-active with little undercut
3.	a. $K_3Fe(CN)_6:KOH:H_2O$ $H_2SO_4:H_2O_2:H_2O$ HNO_3	Cut through Q—active a undercutting a problem b. relative undercutting [RIE → no undercut]
	b. $HCl:HNO_3$ $\angle$ RIE ± 5°	
4. [optional]	$K_3Fe(CN)_6:KOH:H_2O$ $H_2SO_4:H_2O_2:H_2O$ HNO_3	Recess protruding Q—layers after step 3b.
5.	HCl	Etch below Q-layer and planarize at (01$\bar{1}$)
6. [optional]	As above	Repeat 3-5 or 3 and 5 to improve facet

to avoid the necessity of prolonged WCE for the desired depth.

As shown in Table II, the first step is used to cut through the cap or contact Q-layer shown schematically in Fig. 11 above. Etchant group (a) is material selective so that stop etching will occur at the InP cladding layer for depth control. Undercutting or side etching does not self-limit in these cases. The second step uses HCl to cut vertically to the active Q-layer. With the group b etchants in step 3 (RIE or HCl + HNO_3), the active layer can be cut with no undercutting relative to the adjacent InP. (The HCl + HNO_3 mixture etches both at the same rate, undercutting both together.) However, with the material selective etchants of 3a the Q-layer always is undercut slightly relative to the upper InP cladding layer. It then is generally very difficult to avoid an undercutting step at the active layer after subsequent HCl etching. Figure 15a illustrates an example of the resulting wall profiles in a groove. Only by very careful timing of the etching can the lower edge of the Q-layer be kept roughly in line with the masking InP cladding layer to avoid this phenomenon. See Fig. 15b.

Slightly angled RIE, on the other hand, can be used to cut the active layer with no undercutting or stepping problems. Thus, it becomes the preferred etchant in

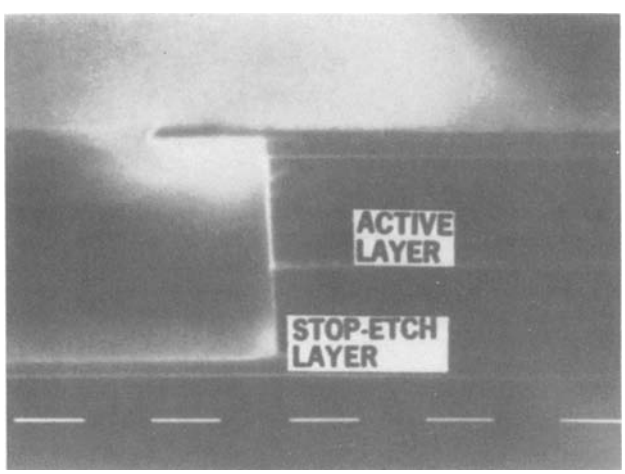

Fig. 14. SEM cross section of an (011) DH facet using multistep etching on a wafer with a buried Q stop etch layer. Step 1 used $HCl:HNO_3$-1:3 for 15 sec. Step 2 used $K_3Fe(CN)_6:KOH:H_2O$-6:4:70 for 7 sec. Step 3 used HCl for 10 sec. Markers ≡ 1 μm.

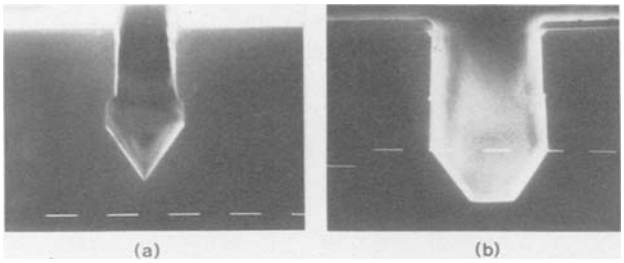

Fig. 15. SEM cross sections of etched grooves in DH using sequential layer etching. Step 1—RIE; step 3—$K_3Fe(CN)_6$:KOH:H_2O; step 4 and 6—not used. Part (a) results of over etching in step 3; (b) proper etch times.

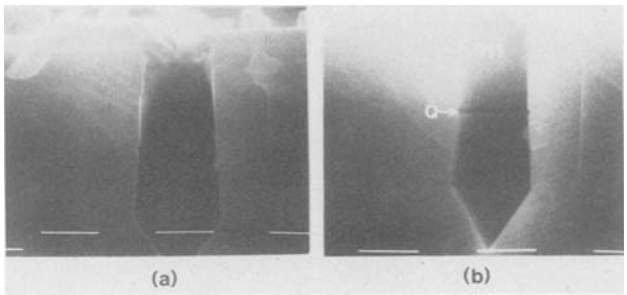

Fig. 16. SEM cross section (a) and perspection (b) of DH groove using a different etchant sequence. Step 1—RIE; step 3—∠ RIE at 5°; step 4—$K_3Fe(CN)_6$:KOH:H_2O; no step 6. Markers ≡ 1 μm.

step 3 for narrow grooves. The optional step 4 is useful to recess the active Q-layer slightly following the use of the group 3b etchants analogous to step 2 in Table I. Step 5 extends the $(01\bar{1})$ facet to below the active Q-layer, using it as its mask. Figure 16 shows the result using the RIE based procedure (RIE in steps 1 and 3).

Summary and Conclusions

In this work, an understanding of the etch rate *vs.* substrate orientation angle has been used to predict and experimentally realize desired etched wall profiles on GaInAsP/InP DH wafers. Crystallographic stop etch planes were employed to ensure the quality and reproducibility of the results. Etched mirror fabrication procedures combining WCE and RIE techniques were outlined in some detail in Tables I and II.

The results indicate that high quality laser mirror facets can be obtained with all WCE using a basic two-step etching procedure, starting with an HCl:HNO_3 mixture and finishing with an HCl planarizing step. Optional refinement, as shown in Table I, may be desirable. For narrow grooves to be used as partially transmissive mirrors, a sequence of RIE and HCl WCE steps as outlined in Table II gives the best results on (001) GaInAsP/InP DH laser wafers.

Despite the success we have demonstrated, a simpler one-step procedure would still be desirable. However, in this case it is believed that an etchant which stop etchs at the same vertical plane for both the InP and Q layers must be found. Identical etch rates in the two materials are not enough.

For applications where other types of wall profiles are desired, the etch rate *vs.* angle characteristics of various possible etches again can provide the starting point. For reproducibility and planarity, stop etch planes should be identified and utilized.

Acknowledgment

Manuscript submitted Nov. 8, 1982; revised manuscript received March 30, 1983.

Bell Laboratories assisted in meeting publication costs of this article.

REFERENCES

1. J. J. Hsieh, *Appl. Phys. Lett.*, **28,** 283 (1976).
2. B. Tuck and A. J. Baker, *J. Mater. Sci.*, **8,** 1559 (1973).
3. H. C. Gatos and M. C. Lavine, *This Journal*, **107,** 427 (1960).
4. J. W. Faust, Jr., in "Compound Semiconductors Vol. 1: Preparation of III-V Compounds," p. 445 Reinhold, New York (1963).
5. R. Becker, *Solid-State Electron.*, **16,** 1241 (1973).
6. T. Kotami, S. Komiya, S. Nakai, and Y. Yamaoka, *This Journal*, **127,** 2273 (1980).
7. S. B. Phatuk and G. Kelner, *ibid.*, **126,** 287 (1979).
8. S. Adachi and H. Kawagushi, *ibid.*, **128,** 1342 (1981).
9. F. A. Blum, K. L. Lawley, F. H. Doerbeck, and W. C. Holton, *Appl. Phys. Lett.*, **25,** 620 (1974).
10. R. L. Seliger, J. W. Ward, V. Wang, and R. L. Kubena, *ibid.*, **34,** 310 (1979).
11. D. J. Ehrlich, R. M. Osgood, Jr., and T. F. Deutsch, *ibid.*, **36,** 698 (1980).
12. J. W. Coburn and H. F. Winters, *J. Appl. Phys.*, **50,** 3189 (1979).
13. T. Kambayashi, C. Kitahara, and K. Iga, *Jpn. J. Appl. Phys.*, **19,** 79 (1980).
14. S. Adachi, Y. Noguchi, and H. Kawaguchi, *This Journal*, **129,** 1053 (1982).
15. P. D. Wright, R. J. Nelson, and R. B. Wilson, *IEEE J. Quantum Electron.*, **qe-18,** 249 (1982).
16. K. Iga and B. I. Miller, *ibid.*, **qe-18,** 22 (1982).
17. R. A. Logan and F. K. Reinhart, *J. Appl. Phys.*, **44,** 4172 (1973).
18. R. P. Tijburg and T. van Dongen, *This Journal*, **123,** 687 (1976).
19. C. E. Hurwitz, J. A. Rossi, J. J. Hsieh, and C. M. Wolfe, *Appl. Phys. Lett.*, **27,** 241 (1975).
20. J. L. Merz and R. A. Logan, *J. Appl. Phys.*, **47,** 3503 (1976).
21. K. Furuya, L. A. Coldren, B. I. Miller, and J. A. Rentschler, *Electron. Lett.*, **17,** 582 (1981).
22. S. Adachi, H. Kowaguchi, K. Takahei, and Y. Noguchi, *J. Appl. Phys.*, **52,** 5843 (1981).
23. L. A. Coldren, K. Furuya, B. I. Miller, and J. A. Rentschler, *IEEE J. Quantum Electron.*, **qe-18,** 1679 (1982).
24. L. A. Coldren, K. Iga, B. I. Miller, and J. A. Rentschler, *Appl. Phys. Lett.*, **37,** 681 (1980).
25. R. B. Wilson, P. D. Wright, P. A. Barnes, and R. J. Nelson, Unpublished.
26. L. W. Stulz and L. A. Coldren, Unpublished.
27. R. E. Howard, E. L. Hu, and L. A. Coldren, Proc. Top. Meet. Integ. and Guided Wave Opts., WA-2, Incline Village, NV, Optical Soc. of Am. (1980).
28. L. A. Coldren and J. A. Rentschler, *J. Vac. Sci. Technol.*, **19,** 225 (1981).
29. R. H. Burton and G. Smolinsky, *This Journal*, **129,** 1599 (1982).
30. R. A. Baker, T. M. Mayer, and R. H. Burton, *Appl. Phys. Lett.*, **40,** 583 (1982).
31. D. E. Ibbotson, D. L. Flamm, V. M. Donnelly, and B. S. Duncan, *J. Vac. Sci. Technol.*, **20,** 489 (1982).
32. L. A. Coldren, K. Furuya, B. I. Miller, and J. A. Rentschler, *Electron. Lett.*, **18,** 235 (1982).
33. M. A. Bösch, L. A. Coldren, and E. Good, *Appl. Phys. Lett.*, **38,** 264 (1981).

Liquid Phase Epitaxial Growth Conditions of Lattice-Matched $Al_{0.48}In_{0.52}As$ and $Al_xGa_yIn_{1-x-y}As$ Layers Without Surface Defects

K. Nakajima, T. Tanahashi, S. Komiya, and K. Akita

Semiconductor Materials Laboratory, Atsugi Laboratories, Fujitsu Laboratories Limited, Ono, Atsugi, 243-01 Japan

ABSTRACT

The liquid phase epitaxial (LPE) growth conditions for lattice-matched $Al_{0.48}In_{0.52}As$ and $Al_xGa_yIn_{1-x-y}As$ layers with various compositions and energy gaps were determined by using the x-ray diffraction and photoluminescence measureements. The epitaxial layers were grown on InP (111)A and (100) substrates. By using these LPE growth conditions, the lattice-matched epitaxial layers can be grown in the energy gap range from 0.8 to 1.44 eV. The Hall measurements of unintentionally doped $Al_{0.48}In_{0.52}As$ layers which were grown without using special baking methods were performed at room temperature. The carrier concentration was 4.7×10^{15} and 5.9×10^{15} cm^{-3}, and the Hall mobility was 4549 and 4466 $cm^2/Vsec$. The compositional grading in $Al_xGa_yIn_{1-x-y}As$ layers was studied by the $CuK\alpha_1$ rocking curves. It was found that the epitaxial layers with mirror surface were more easily obtained on (111)A InP than on (100) InP. The composition dependence of the growth rate of $Al_xGa_yIn_{1-x-y}As$ was studied. The possibility of obtaining heterostructures such as $Al_xGa_yIn_{1-x-y}As/Al_{0.48}In_{0.52}$ As and $In_{0.53}Ga_{0.47}As/Al_{0.48}In_{0.52}As$ was also studied.

$Al_xGa_yIn_{1-x-y}As$ can be lattice matched to InP and can be used to obtain optical devices designed for the wavelength range from 0.86 to 1.68 μm. $Al_{0.48}In_{0.52}As$ is one of the terminal compounds of the lattice-matched $Al_xGa_yIn_{1-x-y}As/InP$ system and has a larger energy gap than InP (1). Therefore, it is especially interesting that this alloy system has a possibility of achieving laser emission in the 1.0-1.2 μm range in which effective carrier confinement effects cannot be expected in $InP/In_{1-x}Ga_xAs_{1-y}P_y/InP$ double heterostructure lasers. $Al_{0.48}In_{0.52}As$ can also be used as thin intermediary layers to increase Schottky barrier heights for $In_{0.53}Ga_{0.47}As$ field effect transistors because $Al_{0.48}In_{0.52}As$ has a higher Schottky barrier height than InP (2). $Al_{0.48}In_{0.52}As$ and $Al_xGa_yIn_{1-x-y}As$ can also be expected as materials for detectors because of their wide wavelength range.

It has been generally believed that the liquid phase epitaxial (LPE) growth of $Al_{0.48}In_{0.52}As$ and $Al_xGa_yIn_{1-x-y}As$ is difficult due to the very large distribution coefficient of Al (3). Therefore, molecular beam epitaxy (MBE) has been used for the growth of these materials (2, 4-9). However, undoped $Al_{0.48}In_{0.52}As$ epitaxial layers grown by MBE were found to be semi-insulating due to the presence of high density of deep level traps (2, 4). In order to obtain high purity $Al_{0.48}In_{0.52}As$ and $Al_xGa_yIn_{1-x-y}As$, it is necessary to grow them by the LPE method. Recently, we found for the first time that lattice-matched $Al_{0.48}In_{0.52}As$ (10) and $Al_xGa_yIn_{1-x-y}As$ (11) epitaxial layers could be grown on InP by LPE. Relatively high growth temperatures such as 700° and 800°C were used to grow epitaxial layers of these materials in order to avoid the violent depletion of Al in the growth solutions. In these previous works, however, sufficient information required for the growth of lattice-matched $Al_xGa_yIn_{1-x-y}As$ layers with various compositions was not supplied.

In this work, the LPE growth conditions for lattice-matched $Al_{0.48}In_{0.52}As$ and $Al_xGa_yIn_{1-x-y}As$ with various compositions were obtained. The epitaxial layers were grown on InP (111)A and (100) substrates, and the growth conditions to obtain epitaxial layers without surface defects were found by studying the substrate orientation dependence of the surface morphology. A possibility of growing heterostructure wafers such as $Al_xGa_yIn_{1-x-y}As/Al_{0.48}In_{0.52}As$ and $In_{0.53}Ga_{0.47}As/Al_{0.48}In_{0.52}As$ was also studied for device applications. In order to know whether thick $Al_xGa_yIn_{1-x-y}As$ epitaxial layers can be grown or not, the composition dependence of the growth rate of $Al_xGa_yIn_{1-x-y}As$ was investigated. The compositional grading in $Al_xGa_yIn_{1-x-y}As$ layers was studied by the half-width of the $CuK\alpha_1$ rocking curves. The energy gaps of lattice-matched $Al_{0.48}In_{0.52}As$ and $Al_xGa_yIn_{1-x-y}As$ were experimentally determined by photoluminescence measurements. The Hall measurements of unintentionally doped $Al_{0.48}In_{0.52}As$ layers were performed at room temperature, and the carrier concentration and Hall mobility were derived from the measurements.

Key words: AlGaInAs, LPE growth, matching, thin film.

Experimental Procedure and Results

LPE growth conditions for lattice-matching.—$Al_xIn_{1-x}As$ and $Al_xGa_yIn_{1-x-y}As$ epitaxial layers were grown onto InP (111)A and (100) substrates by the LPE method. The solution compositions for the growth were determined on the basis of the previously calculated phase diagrams (10, 11). These values are listed in Tables I and II. The experimental apparatus consisted of a horizontal furnace system and a conventional sliding graphite boat as reported previously (12). Pd-purified H_2 flowed through the fused silica tube set in the furnace. Materials used were semiconductor grade Al, In, GaAs and InAs. AlIn mother alloy which contained 0.1 atomic percent (a/o) Al was used as the Al source because it was very difficult to dissolve Al into In melts directly at the growth temperatures, by reason of the miscibility gap in the liquid state of the Al and In binary system (13).

At the start of the growth run, the furnace was heated rapidly to 30°-40°C above the starting growth temperature, and the growth solution was held there for about 30 min. It was then cooled with a constant cooling rate of 0.5°C/min. Prior to growth, the thermal damage of the surface of the InP substrates was removed using an undersaturated In + P solution.

For the growth of $Al_xIn_{1-x}As$, 685°, 770° and 790°C were used as the starting growth temperatures. The exact amount of supercooling is not clear because of the lack of an experimental phase diagram, but it is sure that the epitaxial layers were grown from supercooled solutions (10). When the growth temperature interval was 9°C, the thickness of epitaxial layers grown on InP (111)A substrates was 0.1 and 0.5 μm for the starting growth temperatures of 685° and 790°C, respectively.

Lattice constants of these layers were measured by a double crystal x-ray diffraction technique with a symmetric parallel arrangement [+(333), −(333)].

Table I. Starting growth temperatures, solution compositions, substrate orientations, lattice constants a (Å), and energy gaps E_g (eV) at 300 K for $Al_xIn_{1-x}As$ grown on InP substrates

Starting growth temperature, (°C)	Solution compositions X_{Al}^l	X_{As}^l	X_{In}^l	Face	a (A)	E_g (eV)
685	0.00026	0.077	0.92274	(111)A	5.886	—
	0.00027	0.076	0.92373		5.881	—
	0.00030	0.070	0.9297		5.864	—
770	0.00067	0.1399	0.85943	(111)A	5.8825	1.425
	0.00068	0.139	0.86032		5.885	1.431
	0.00070	0.138	0.8613		5.880-5.882	1.437
	0.00073	0.134	0.86527		5.870	1.443
790	0.00075	0.162	0.8372	(111)A	5.914	—
	0.00080	0.157	0.8422		5.885	—
	0.00085	0.152	0.8471		5.870-5.872	1.44
	0.00090	0.147	0.8521		5.861	—

Table II. Starting growth temperatures, solution compositions, substrate orientations, lattice constants a (Å), and energy gaps E_g (eV) at 300 K for $Al_xGa_yIn_{1-x-y}As$ grown on InP substrates

Starting growth temperature, (°C)	Solution compositions X_{Al}^l	X_{Ga}^l	X_{In}^l	X_{As}^l	Face	a (A)	E_g (eV)
685	0.00012	0.025	0.07795	0.89693	(111)A	5.866-5.870	0.8305
	0.00012	0.030	0.07514	0.89474		5.858	0.7858
	0.00015	0.015	0.0776	0.90725		5.879	1.033
	0.00015	0.020	0.0750	0.90485		5.865	0.960
790	0.0003	0.020	0.8097	0.170	(111)A	5.931	—
	0.0003	0.025	0.8077	0.167		5.919	—
	0.0003	0.038	0.8047	0.157		5.862-5.867	0.808
	0.0003	0.040	0.8037	0.156		5.863	0.793
	0.0004	0.020	0.8206	0.159		5.884-5.878	1.057
	0.0004	0.025	0.8196	0.155		5.873	1.010
	0.0004	0.030	0.8186	0.151		5.865-5.859	0.887
	0.0005	0.010	0.8345	0.155		5.877-5.884	1.240
	0.0005	0.014	0.8345	0.151		5.873	1.028
	0.0005	0.016	0.8335	0.150		5.866	1.040
	0.0006	0.003	0.8489	0.1475		5.868	1.352
	0.0006	0.005	0.8484	0.146		5.862	1.259
	0.0006	0.008	0.8474	0.144		5.857	1.252
	0.0005	0.007	0.8355	0.157	(100)	5.878	1.288
	0.0005	0.010	0.8345	0.155		5.873	1.269
	0.0005	0.015	0.8335	0.151		5.850	1.277

The precise diffraction angle of the layers was determined from the (333) $CuK\alpha_1$ reflection by using the substrate reflection as an internal standard. The measured results are listed in Table I. Figure 1 shows the lattice constant of $Al_xIn_{1-x}As$ epitaxial layers grown on InP (111)A substrates starting from 685°, 770°, and 790°C as a function of X_{Al}^l, where X_i^l represents the atomic fraction of the element i in the solution. The broken line represents the lattice constant of InP. Figure 1 also shows the previously determined lattice constant of $Al_xIn_{1-x}As$ layers grown on InP (100) substrates (10). The starting growth temperature was between 790° and 770°C (10). When $Al_xIn_{1-x}As$ layers were grown from solutions with the same composition, the lattice constant of a layer grown on the (111)A face is larger than that of a layer grown on the (100) face. The solution compositions for the growth of lattice-matched $Al_{0.48}In_{0.52}As$ on InP can be determined from Fig. 1

For the growth of $Al_xGa_yIn_{1-x-y}As$, 685° and 790°C were used as the starting growth temperatures. The quaternary epitaxial layers were grown on InP (111)A and (100) substrates. Lattice constants of these layers were also determined from the (400) and (333) $CuK\alpha_1$ reflections by using the double crystal x-ray diffraction technique. The precise diffraction angle of the layers was determined by using the substrate reflection as an internal standard. The results are listed in Table II. Figure 2 shows the lattice constant of $Al_xGa_yIn_{1-x-y}As$ layers grown on InP (111)A and

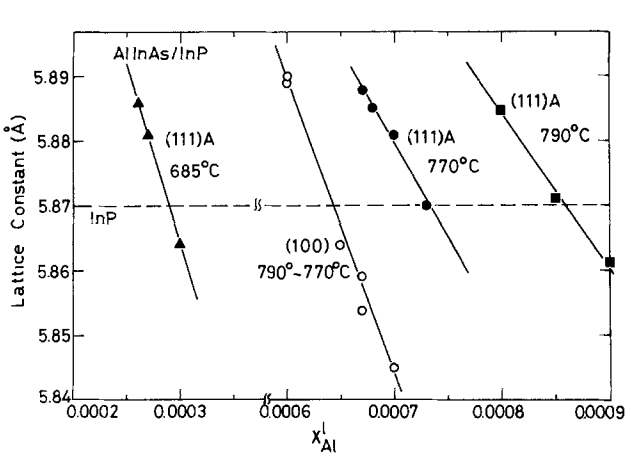

Fig. 1. Lattice constants of $Al_xIn_{1-x}As$ layers grown on (111)A and (100) InP substrates. The starting growth temperatures are 685°, 770°, and 790°C for the (111)A face, and between 790°-770°C for the (100) face.

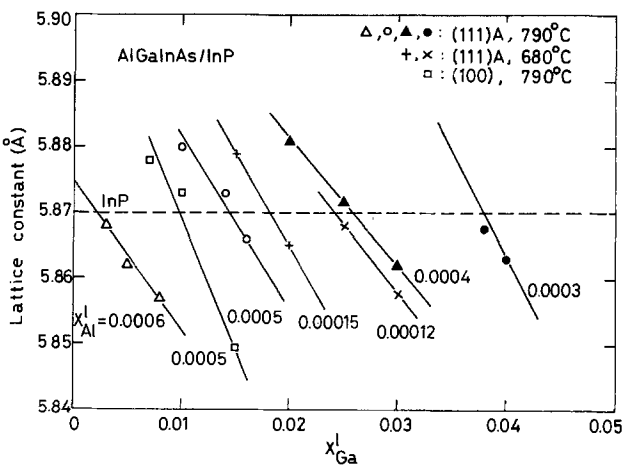

Fig. 2. Lattice constants of $Al_xGa_yIn_{1-x-y}As$ layers grown on (111)A and (100) InP substrates. The starting growth temperatures are 685° and 790°C for the (111)A face and 790°C for the (100) face.

(100) substrates starting 685° and 790°C. The growth solutions containing $X_{Al}^{l} = 0.00012$ and 0.00015 at 685°C ,and $X_{Al}^{l} = 0.0003$, 0.0004, 0.0005, and 0.0006 at 790°C were used for the (111)A face. The growth solution with $X_{Al}^{l} = 0.0005$ were used for the (100) face. When $Al_xGa_yIn_{1-x-y}As$ layers were grown from solutions with the same composition, the lattice constant of a layer grown on the (111)A face is also larger than that of a layer grown on the (100) face. The solution compositions for the growth of lattice-matched $Al_xGa_yIn_{1-x-y}As$ on InP can be found from Fig. 2.

Figure 3 shows solution compositions, X_{Ga}^{l}, X_{As}^{l}, and X_{Al}^{l}, required for the LPE growth of lattice-matched $Al_{0.48}In_{0.52}As$ and $Al_xGa_yIn_{1-x-y}As$ layers with various compositions. These data were derived from Fig. 1 and 2 and the calculated liquidus isotherms (10, 11). The starting growth temperatures of 685° and 790°C were used. As shown in Fig. 3, X_{Ga}^{l} and X_{As}^{l} decrease as X_{Al}^{l} increases. When growth solutions have the same X_{Al}^{l}, X_{Ga}^{l} is smaller for the (100) face than for the (111)A face. The data for $X_{Ga}^{l} = 0.0$ gives the solution compositions for the growth of lattice-matched $Al_{0.48}In_{0.52}As$ on InP.

Rocking curves of $Al_xGa_yIn_{1-x-y}As$ layers.—Figures 4 and 5 show the $CuK\alpha_1$ rocking curves for the (333) reflection of $Al_xGa_yIn_{1-x-y}As$ LPE layers grown on InP (111)A substrates. These layers were grown starting from 790°C at a constant cooling rate of 0.5°C/min. The quaternary layer shown in Fig. 4 has the thickness of 0.8 μm, the wavelength of 0.99 μm, and the lattice misfit of -2.22×10^{-3}. The half-width of the diffraction peak is about 51 sec, and it is a little larger than that of InP (about 34 sec). This means that the compositional grading in the 0.8 μm thick $Al_xGa_yIn_{1-x-y}As$ LPE layer is small. The quaternary layer shown in Fig. 5 has the thickness of 3.7 μm, the wavelength of 1.53 μm, and the lattice misfit of -4.8×10^{-4} to -1.34×10^{-3}. The half-width of the diffraction peak is about 100 sec, and it is larger than that of InP (about 36 sec). This indicates that the 3.7 μm thick $Al_xGa_yIn_{1-x-y}As$ layer has a compositional grading, and the lattice constant of the layer is estimated between 5.867 and 5.862Å. The half-width of the 3.7 μm thick $Al_xGa_yIn_{1-x-y}As$ LPE layer is comparable to that of the 4.3 μm thick $In_{1-x}Ga_xAs_{1-y}P_y$ LPE layer which was grown starting from 650°C at a constant cooling rate of 0.5°C/min (14). Therefore, the degree of the compositional grading of $Al_xGa_yIn_{1-x-y}As$ is almost comparable with that of $In_{1-x}Ga_xAs_{1-y}P_y$.

Energy gaps of lattice-matched alloys.—The energy gap of undoped $Al_xIn_{1-x}As$ and $Al_xGa_yIn_{1-x-y}As$ layers was determined by photoluminescence (PL) measurements at 300 and 77 K. A CW 200-mW Ar ion laser at 5145Å was used as the optical pumping source.

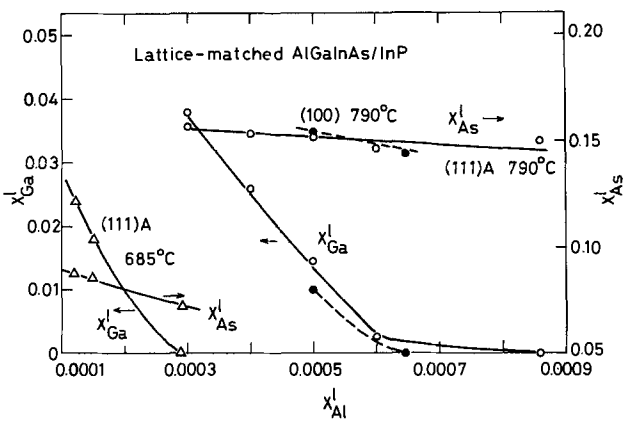

Fig. 3. Solution compositions, X_{Ga}^{l}, X_{As}^{l}, and X_{Al}^{l}, required for the LPE growth of lattice-matched $Al_{0.48}In_{0.52}As$ and $Al_xGa_yIn_{1-x-y}As$ layers with various compositions.

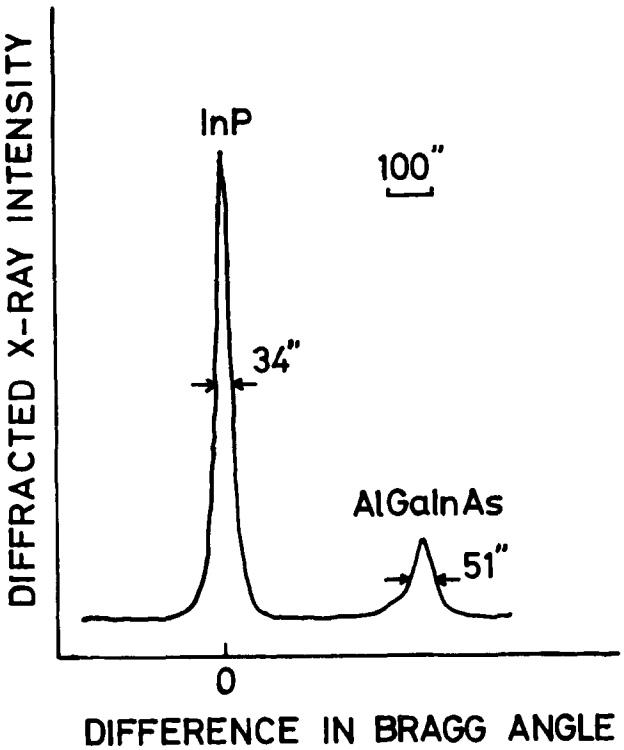

Fig. 4. $CuK\alpha_1$ rocking curve for the (333) reflection of a 0.8 μm thick $Al_xGa_yIn_{1-x-y}As$ layer grown on (111)A InP.

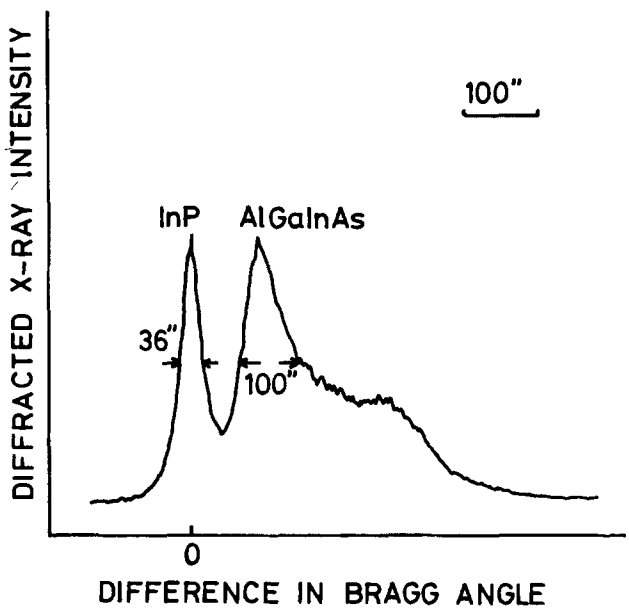

Fig. 5. $CuK\alpha_1$ rocking curve for the (333) reflection of a 3.7 μm thick $Al_xGa_yIn_{1-x-y}As$ layer grown on (111)A InP.

The laser light was chopped at a frequency of 200 Hz and focused on the sample to a spot about 0.5 mm in diameter. For the PL measurements of longer wavelengths than 0.9 μm, a JASCO CT-50 monochromator with a PbS detector cooled at 77 K and a PAR HR-8 lock-in amplifier were used. For the PL measurements of shorter wavelengths than 0.9 μm, a NARUMI RM-21 monochromator with an Si photodiode (HTV S1336) at room temperature and an NF LI-573 lock-in amplifier were used. The measured results are listed in Tables I and II.

A typical PL spectrum of an $Al_xGa_yIn_{1-x-y}As$ layer is shown in Fig. 6. The spectrum was measured at 300 K. The peak wavelength is 1.028 μm. The thickness and lattice constant of the quaternary layer are 0.5 μm and 5.873Å, respectively. This layer was grown on

(111)A InP starting from 790°C at a constant cooling rate of 0.5°C/min. The half-width of the PL spectrum shown in Fig. 6 is 57 meV, and this value is comparable to the half-width of the PL spectra of $In_{1-x}Ga_xAs_{1-y}P_y$ layers whose thickness was 1 μm (15). This means that the composition variation in this $Al_xGa_yIn_{1-x-y}As$ epitaxial layer is not large. This is consistent with the results of the rocking curves.

Figure 7 shows the energy gap of $Al_xIn_{1-x}As$ as a function of X_{Al}^1. The energy gap of $Al_xIn_{1-x}As$ epitaxial layers grown on InP (111)A and (100) substrates was measured at 300 and 77 K. The starting growth temperature was 770°C for the (111)A face, and it was between 790° and 770°C for the (100) face (10). The energy gap of lattice-matched $Al_{0.48}In_{0.52}As$ was measured to be 1.44 eV. This value is slightly larger than our previously reported value of 1.42 eV (10), and it is comparable to Lorentz and Onton's value of 1.45 eV (1). The energy gap increases gradually with X_{Al}^1 for both faces. The energy shift between the energy gaps at 300 and 77 K was found to be 0.06 eV.

Figure 8 shows the energy gap of lattice-matched (111)A oriented $Al_xGa_yIn_{1-x-y}As$ epitaxial layers as a function of X_{Al}^1 at 685° and 790°C. The energy gap was measured at 300 K. The energy gap varies abruptly with increasing X_{Al}^1 in the range of the wider energy gap than 0.8 eV. The terminal value at $X_{Al}^1 = 0.0$ corresponds to the value of $In_{0.53}Ga_{0.47}As$, and the terminal values at $X_{Al}^1 = 0.00025$ and 0.00086 correspond to that of $Al_{0.48}In_{0.52}As$ for the two different growth temperatures. From the information presented in Fig. 3 and 8, the LPE growth conditions for lattice-matched $Al_xGa_yIn_{1-x-y}As$ layers with desired energy gaps can be easily determined.

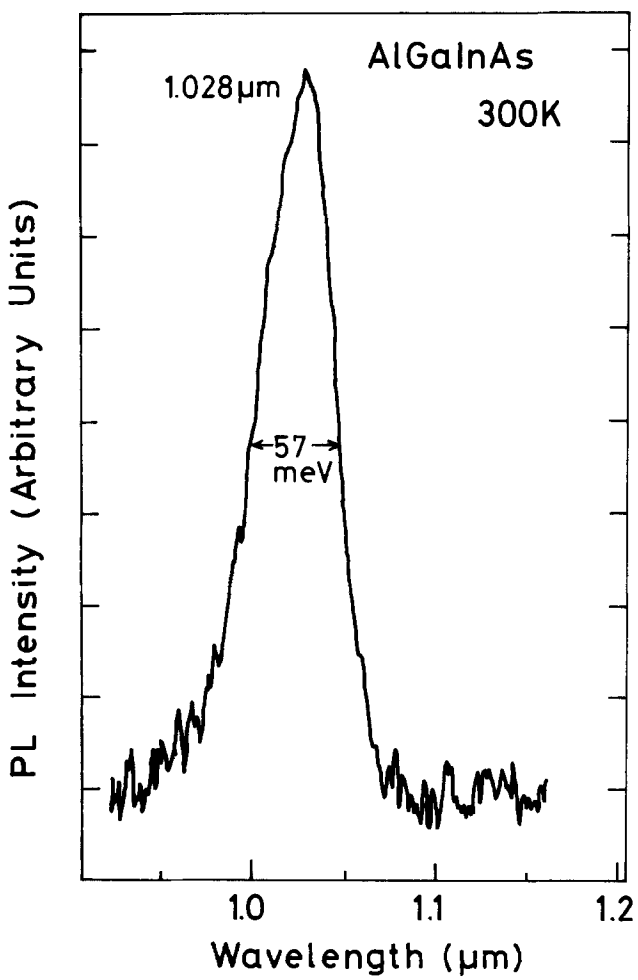

Fig. 6. Typical PL spectrum of an $Al_xGa_yIn_{1-x-y}As$ layer

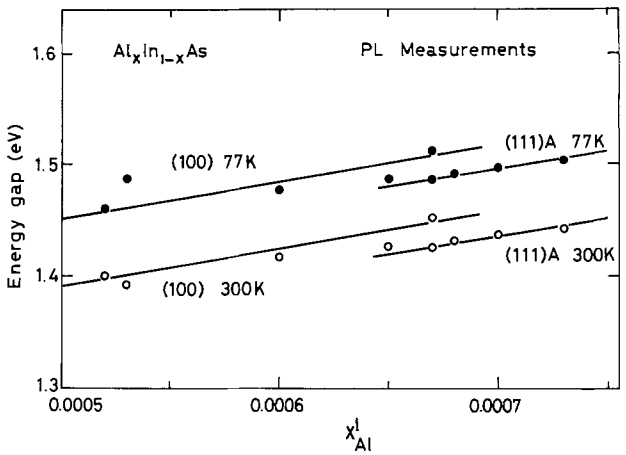

Fig. 7. Energy gap of $Al_xIn_{1-x}As$ grown on InP (111)A and (100) substrates as a function of X_{Al}^1.

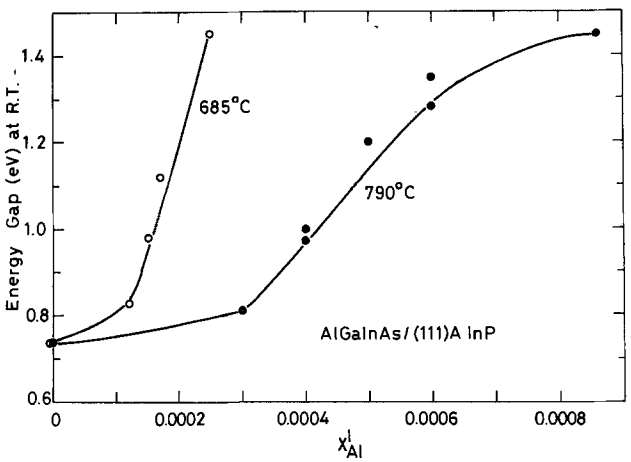

Fig. 8. Energy gap of lattice-matched (111)A-oriented $Al_xGa_yIn_{1-x-y}As$ layers as a function of X_{Al}^1 at 685° and 790°C.

Hall measurements of unintentionally doped $Al_{0.48}In_{0.52}As$ layers.—The Hall measurements of unintentionally doped $Al_{0.48}In_{0.52}As$ layers were performed at room temperature, and the carrier concentration, n, and Hall mobility, μ, were derived from the measurements. The method of the Hall measurements was the same as in the previous work (16). Two samples of 0.5 μm thick $Al_{0.48}In_{0.52}As$ layers grown on Fe-doped semi-insulating (10^6 Ω-cm) (111)A InP were used for the Hall measurements. In this growth, any baking methods of growth solutions described previously (17) have not been employed to obtain high purity LPE $Al_{0.48}In_{0.52}As$ layers. The results of the Hall measurements were $\mu = 4549$ cm²/Vsec at $n = 4.7 \times 10^{15}$ cm^{-3}, and $\mu = 4466$ cm²/Vsec at $n = 5.9 \times 10^{15}$ cm^{-3}. These Hall mobilities are the highest of those reported until now, and these carrier concentrations are the lowest of those reported until now. The room temperature Hall mobility of $Al_{0.48}In_{0.52}As$ layers grown by MBE was reported by Cheng *et al.* (6). According to their data, the Hall mobility was lower than 800 cm²/Vsec at $n = 1 \times 10^{17}$ cm^{-3}. The Hall mobility and carrier concentration of undoped $Al_{0.48}In_{0.52}As$ has not been reported. However, the Hall mobilities of $Al_{0.48}In_{0.52}As$ grown by LPE are obviously higher than those of $Al_{0.48}In_{0.52}As$ grown by MBE. High purity $Al_{0.48}In_{0.52}As$ layers with carrier concentrations of 5×10^{15} cm^{-3} can be easily obtained by LPE without special purification methods such as the baking technique (17).

Substrate orientation dependence of surface morphology.—The surface morphology of $Al_{0.48}In_{0.52}As$

and $Al_xGa_yIn_{1-x-y}As$ depends strongly on the orientation of the substrates. For the starting growth temperature of 685°C, the typical surface morphologies of $Al_xIn_{1-x}As$ grown on InP (100) and (111)A substrates are shown in Fig. 9a and b, respectively. As shown in Fig. 9a, only small growth islands appear on the surface of the (100) substrate, and it is very difficult to grow an $Al_xIn_{1-x}As$ epitaxial layer all over the (100) surface. However, it is easy to grow an $Al_xIn_{1-x}As$ epitaxial layer on the (111)A substrate as shown in Fig. 9b. For the high starting growth temperature of 790°C, an $Al_xIn_{1-x}As$ epitaxial layer can be grown all over the surface of the (100) InP substrate as shown in Fig. 10a. However, many surface defects often appear on the (100) surface. In order to obtain $Al_xIn_{1-x}As$ epitaxial layers without surface defects, the epitaxial layers must be grown on the (111)A substrates. Figure 10b shows the typical surface of an $Al_xIn_{1-x}As$ layer grown on (111)A InP starting from 790°C. The (111)A surface is very smooth, and such surface defects as shown in Fig. 10a are not observed at all. For the growth of $Al_xGa_yIn_{1-x-y}As$, epitaxial layers with smooth surface can also be easily grown on the (111)A substrates.

The reason why the surface defects easily appear on the (100) surface of $Al_xIn_{1-x}As$ layers is related to dissolution of the InP (100) substrates. When $Al_xIn_{1-x}As$ layers were completely removed by using a selective etchant of $HF:HNO_3 = 1:1$, many small holes were observed on the surface of the InP (100) substrates. However, such holes were not observed on the surface of the InP (111)A substrates. As reported previously (18), the (111)A face is more stable to dissolution than the (100) face. Therefore, the surface defects due to dissolution of the substrates appear more easily on the (100) face than on the (111)A face.

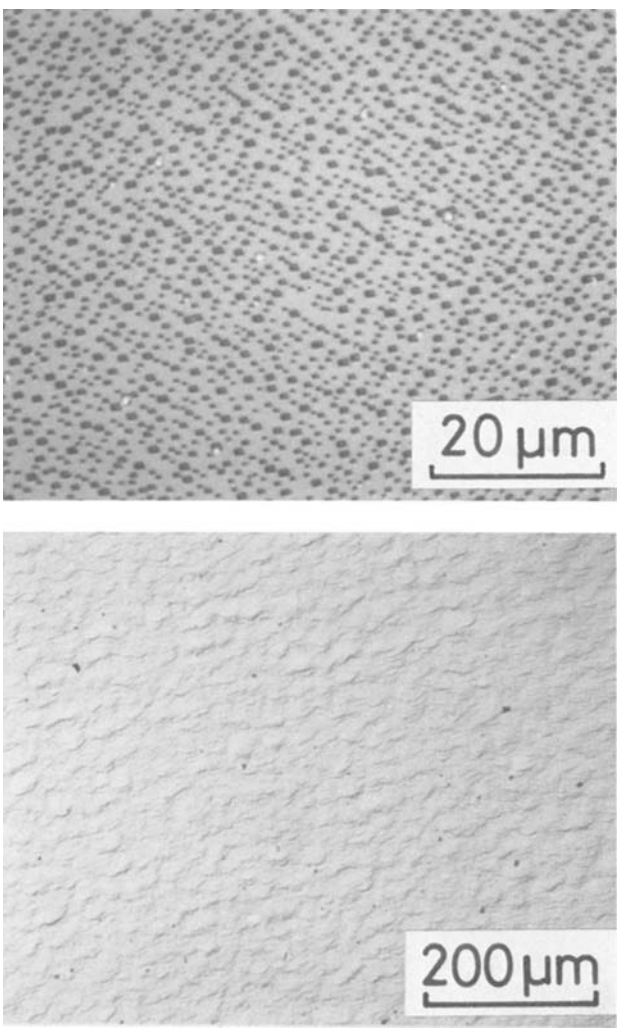

Fig. 9. (a) Typical surface of $Al_xIn_{1-x}As$ grown on (100) InP starting from 685°C. (b) Typical surface of $Al_xIn_{1-x}As$ grown on (111)A InP starting from 685°C.

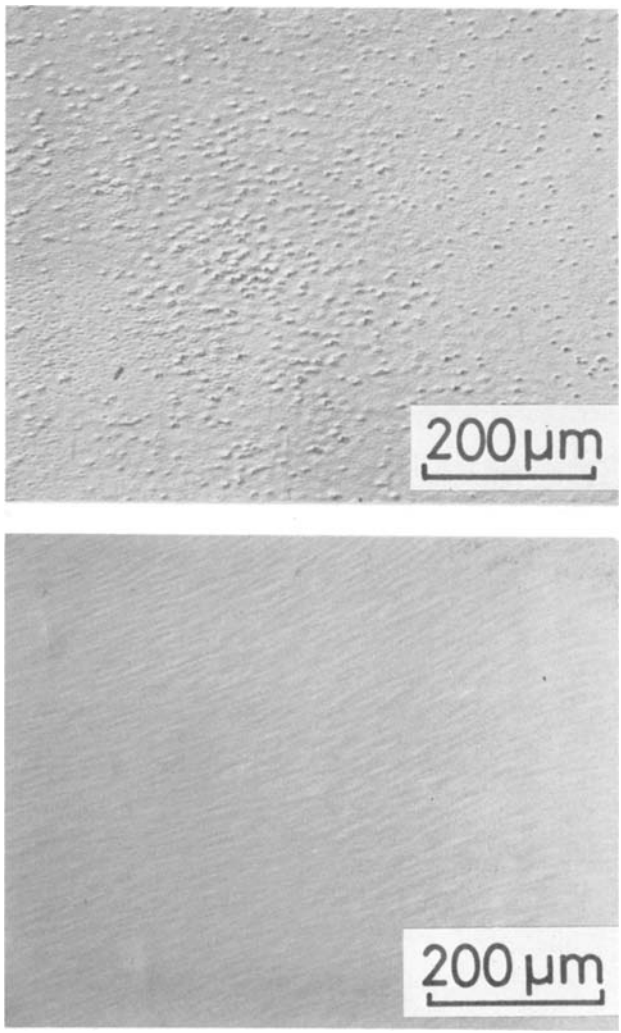

Fig. 10. (a) Typical surface of $Al_xIn_{1-x}As$ grown on (100) InP starting from 790°C. (b) Typical surface of $Al_xIn_{1-x}As$ grown on (111)A InP starting from 790°C.

Growth rate of $Al_{0.48}In_{0.52}As$ and $Al_xGa_yIn_{1-x-y}As$. —Figure 11 shows the layer thickness of lattice-matched $Al_{0.48}In_{0.52}As$ and $Al_xGa_yIn_{1-x-y}As$ as a function of $X_{Al}{}^1$. These layers were grown on InP (111)A substrates by the ramp cooling method. A constant cooling rate of 0.5°C/min was used. The starting growth temperatures were 685° and 790°C, and the cooled temperature interval was 9°C. As shown in Fig. 11, the layer thickness of $Al_xGa_yIn_{1-x-y}As$ increases as $X_{Al}{}^1$ decreases. This means that the layer thickness of $Al_xGa_yIn_{1-x-y}As$ increases as x (Al content in the alloy) decreases. The growth rate of $Al_{0.48}In_{0.52}As$ ternary layers is the smallest of the Al-Ga-In-As system. The growth rate of Al_xGa_y-$In_{1-x-y}As$ increases rapidly when $X_{Al}{}^1$ becomes smaller than 0.0005.

Figure 12 shows the layer thickness of $Al_xIn_{1-x}As$ grown for 1 min as a function of the starting growth temperature. The growth was performed on (111)A InP by the ramp cooling method. A constant cooling rate of 0.5°C/min was used. As shown in Fig. 12, the layer thickness per 1 min was only 60Å at 685°C and 240Å at 790°C. Therefore, very thin layers can be

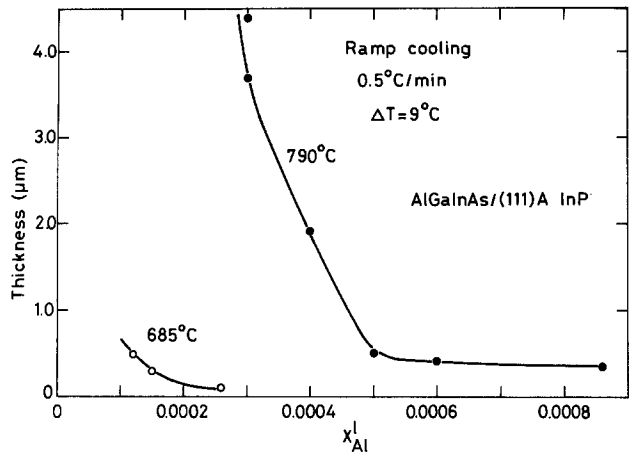

Fig. 11. Layer thickness of lattice-matched $Al_{0.48}In_{0.52}As$ and $Al_xGa_yIn_{1-x-y}As$ grown on (111)A InP starting from 685° and 790°C.

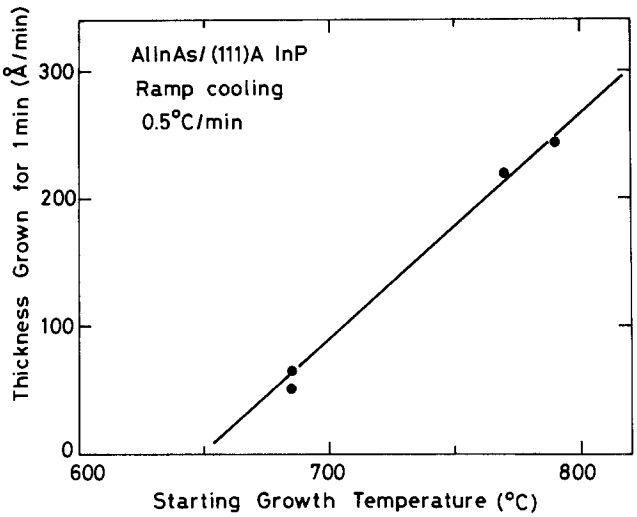

Fig. 12. Layer thickness of $Al_xIn_{1-x}As$ grown for 1 min as a function of the starting growth temperature.

grown under good control by using the ordinary LPE growth apparatus with a sliding graphite boat. It is expected that a 40Å thick layer can be grown at 790°C for the growth time of 10 sec.

Growth of heterostructures.—In order to fabricate devices using $Al_{0.48}In_{0.52}As$ or $Al_xGa_yIn_{1-x-y}As$, it is necessary to obtain heterostructures. $Al_xGa_yIn_{1-x-y}As$ can be grown on $Al_{0.48}In_{0.52}As$ without dissolution. $Al_{0.48}In_{0.52}As$ can also be grown on $Al_xGa_yIn_{1-x-y}As$, but the dissolution of $Al_{0.48}In_{0.52}As$ into the Al-Ga-In-As growth solution becomes more severe as the Al content in the quaternary alloy decreases. Figure 13 shows the $Al_xGa_yIn_{1-x-y}As/Al_{0.48}In_{0.52}As/Al_xGa_yIn_{1-x-y}As$ heterostructure grown on (111)A InP. The starting growth temperature was 790°C. The wavelength of the $Al_xGa_yIn_{1-x-y}As$ layers was 1.0 μm at 300 K. $In_{0.53}Ga_{0.47}As$ can be grown on $Al_{0.48}In_{0.52}As$ as shown in Fig. 14. These layers were grown on (111)A InP. $In_{0.53}Ga_{0.47}As$ was grown on $Al_{0.48}In_{0.52}As$ at 650°C by the ramp cooling method. $In_{1-x}Ga_xAs_{1-y}P_y$ can also be grown on $Al_{0.48}In_{0.52}As$, but the growth of $Al_{0.48}In_{0.52}As$ on $In_{0.53}Ga_{0.47}As$ was more difficult.

Figure 15 shows a multilayer structure consisting of $Al_{0.48}In_{0.52}As$ and $Al_xGa_yIn_{1-x-y}As$ grown on (111)A InP. The thickness of the $Al_{0.48}In_{0.52}As$ and $Al_xGa_yIn_{1-x-y}As$ layers were about 0.05 and 0.1 μm, respectively. The growth was started from 781°C at a constant cooling rate of 0.5°C/min, and the growth time of each layer was 1 min. Since a sightly super-

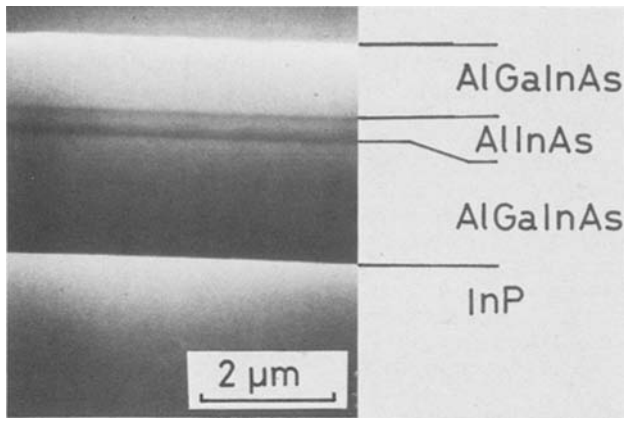

Fig. 13. $Al_xGa_yIn_{1-x-y}As/Al_{0.48}In_{0.52}As/Al_xGa_yIn_{1-x-y}As/$ (111)A InP heterostructure.

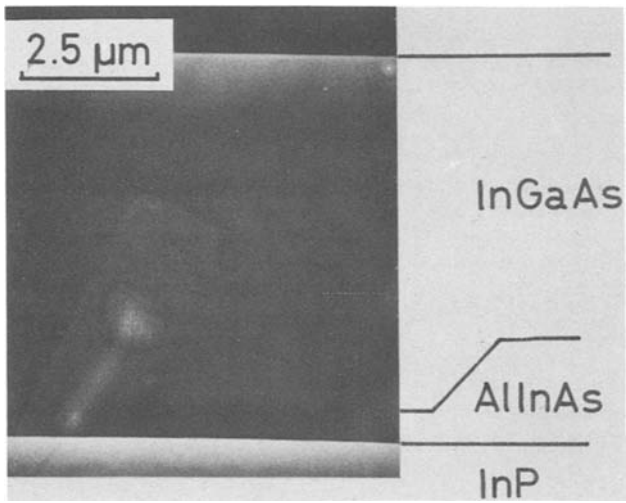

Fig. 14. $In_{0.53}Ga_{0.47}As/Al_{0.48}In_{0.52}As/(111)A$ InP heterostructure.

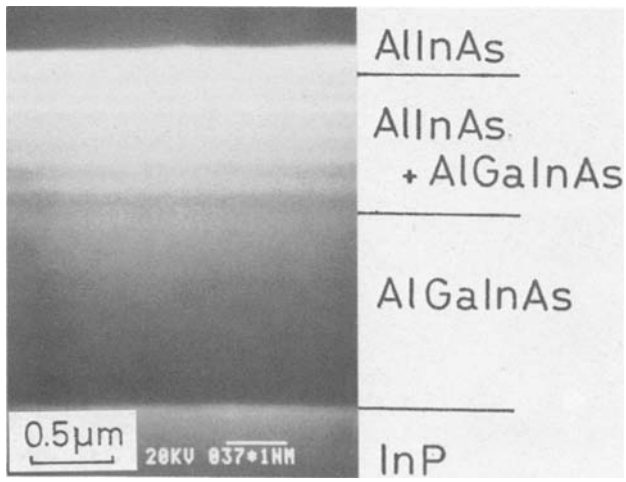

Fig. 15. Multilayer structure consisted of $Al_{0.48}In_{0.52}As$ and $Al_xGa_yIn_{1-x-y}As$ grown on (111)A InP.

cooled (2°-3°C) solution was used for the growth of $Al_{0.48}In_{0.52}As$ layers, the growth rate was higher than that shown in Fig. 12. The wavelength of the $Al_xGa_yIn_{1-x-y}As$ layers was 0.98 μm at 300 K. Figure 16 shows the O_2^+/SIMS depth profile of ^{71}Ga from the surface of this sample. As shown in Fig. 16, this sample has 11 layers. The abruptness of the hetero-interfaces cannot be accurately known from Fig. 16 because of the limit of resolution of SIMS depth pro-

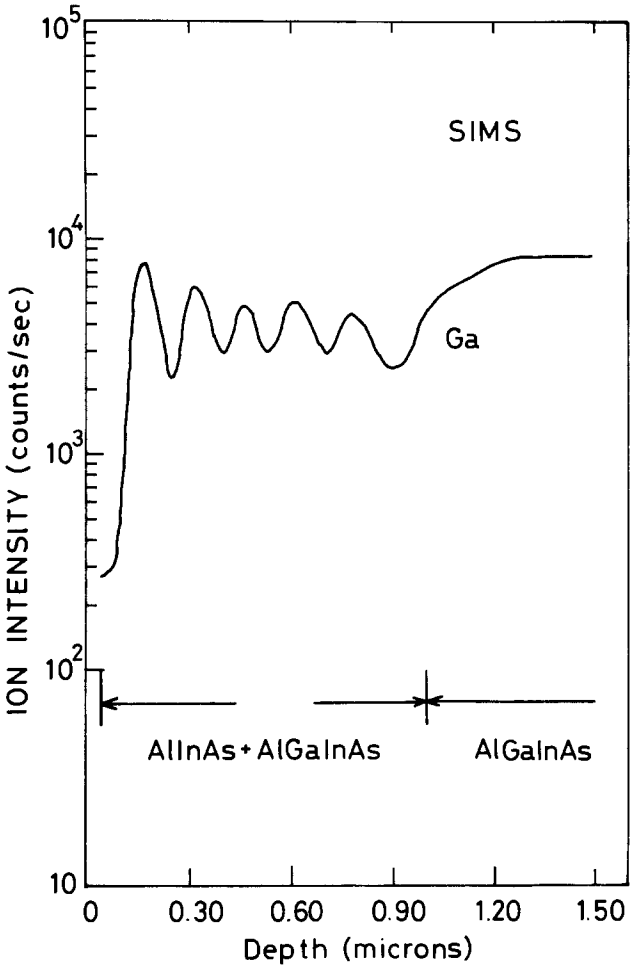

Fig. 16. O_2^+/SIMS depth profiling measurements of ^{71}Ga in the multilayer structure wafer consisted of $Al_{0.48}In_{0.52}As$ and $Al_xGa_yIn_{1-x-y}As$.

filing measurements. A thinner multilayer structure can be grown by using a shorter growth time.

Discussion

It is generally considered that the LPE growth of $Al_{0.48}In_{0.52}As$ and $Al_xGa_yIn_{1-x-y}As$ is difficult due to the very large distribution coefficient of Al. However, it is found that the LPE growth becomes possible by using the high growth temperatures and by protecting properly InP substrates from thermal damage. Especially, very smooth surfaces without defects can be obtained for the (111)A face. It was reported that the (111)A face can be used for optical devices such as avalanche photodiodes (19). Therefore, it is expected that the (111)A-oriented $Al_{0.48}In_{0.52}As$ and $Al_xGa_yIn_{1-x-y}As$ can be used for optical devices and field effect transistors. For the growth of (100)-oriented $Al_{0.48}In_{0.52}As$ and $Al_xGa_yIn_{1-x-y}As$ with smooth surfaces, it will be necessary to use large amounts of supersaturation. These materials are unsuitable for the growth of thick layers because of the very small growth rate, but they are suitable for the controllable growth of thin layers. Moreover, various kinds of heterostructures can be obtained. Therefore, $Al_{0.48}In_{0.52}As$ and $Al_xGa_yIn_{1-x-y}As$ can be applied to various devices.

Summary

The LPE growth conditions for lattice-matched $Al_{0.48}In_{0.52}As$ and $Al_xGa_yIn_{1-x-y}As$ layers with various compositions were determined at 685° and 790°C. By using these growth conditions, the lattice-matched epitaxial layers can be grown in the energy gap range from 0.8 to 1.44 eV. The results of the room temperature Hall measurements of unintentionally doped $Al_{0.48}In_{0.52}As$ showed $\mu = 4549$ cm²/Vsec at $n = 4.7 \times 10^{15}$ cm^{-3}, and $\mu = 4466$ cm²/Vsec at $n = 5.9 \times 10^{15}$ cm^{-3}. High purity $Al_{0.48}In_{0.52}As$ layers with carrier concentrations of 5×10^{15} cm^{-3} can be easily obtained by LPE without special purification methods. Epitaxial layers without surface defects were more easily obtained on (111)A InP than on (100) InP. The growth rate of $Al_xGa_yIn_{1-x-y}As$ increases as the Al content in the alloy decreases, and the growth rate of $Al_{0.48}In_{0.52}As$ was the smallest of the Al-Ga-In-As system. The layer thickness of $Al_xIn_{1-x}As$ grown for 1 min was only 240Å when the starting growth temperature was 790°C, so very thin layers can be controllably grown by the ordinary LPE growth method. The compositional grading in thin $Al_xGa_yIn_{1-x-y}As$ layers with the thickness of 0.8 μm is small. The heterostructures of $Al_xGa_yIn_{1-x-y}As/Al_{0.48}In_{0.52}As/Al_xGa_yIn_{1-x-y}As/InP$, $In_{0.53}Ga_{0.47}As/Al_{0.48}In_{0.52}As/InP$, and $In_{1-x}Ga_xAs_{1-y}P_y/Al_{0.48}In_{0.52}As/InP$ can be obtained by LPE.

Acknowledgments

The authors wish to acknowledge the photoluminescence measurements of A. Yamaguchi. Useful discussions were held with I. Umebu, S. Yamakoshi, and T. Kaneda.

Manuscript submitted Dec. 22, 1982; revised manuscript received March 24, 1983.

Fujitsu Laboratories Limited assisted in meeting publication costs of this article.

REFERENCES

1. M. R. Lorentz and A. Onton, in "Proceedings of the 10th International Conference on the Physics of Semiconductors," p. 444, U.S. Atomic Energy Commission, Washington, DC (1970).
2. H. Ohno, C. E. C. Wood, L. Rathbun, D. V. Morgan, G. W. Wicks, and L. F. Eastman, *J. Appl. Phys.*, **52**, 4033 (1981).
3. E. H. Perea, C. G. Fonstad, and M. Quillec, *ibid.*, **49**, 4577 (1978).
4. H. Ohno, J. Barnard, C. E. C. Wood, and L. F. Eastman, *IEEE Trans. Electron Devices Lett.*, **edl-1**, 154 (1980).
5. W. T. Tsang, *J. Appl. Phys.*, **52**, 3861 (1981).
6. K. Y. Cheng, A. Y. Cho, and W. R. Wagner, *ibid.*, **52**, 6328 (1981).
7. K. Y. Cheng, A. Y. Cho, and W. R. Wagner, *Appl. Phys. Lett.*, **39**, 607 (1981).
8. K. Y. Cheng, A. Y. Cho, T. J. Drummond, and H. Morkoc, *ibid.*, **40**, 147 (1982).
9. K. Y. Cheng and A. Y. Cho, *J. Appl. Phys.*, **53**, 4411 (1982).
10. K. Nakajima, T. Tanahashi, and K. Akita, *Appl. Phys. Lett.*, **41**, 194 (1982).
11. K. Nakajima and K. Akita, *J. Cryst. Growth*, **54**, 232 (1981).
12. K. Nakajima, T. Kusunoki, K. Akita, and T. Kotani, *This Journal*, **125**, 123 (1978).
13. M. Hansen, in "Constitution of Binary Alloys," 2nd ed., R. F. Mehl and M. B. Bever, Editors, p. 100, McGraw-Hill, New York (1958).
14. K. Nakajima, S. Komiya, K. Akita, T. Yamaoka, and O. Ryuzan, *This Journal*, **127**, 1568 (1980).
15. K. Nakajima, A. Yamaguchi, K. Akita, and T. Kotani, *J. Appl. Phys.*, **49**, 5944 (1978).
16. K. Akita, A. Yamaguchi, K. Nakajima, and T. Takanohashi, *Electron. Lett.*, **17**, 921 (1981).
17. K. Nakajima, S. Yamazaki, T. Takanohashi, and K. Akita, *J. Cryst. Growth*, **59**, 572 (1982).
18. K. Nakajima, S. Yamazaki, and K. Akita, *Jpn. J. Appl. Phys.*, **21**, L237 (1982).
19. T. Shirai, S. Yamazaki, K. Yasuda, T. Mikawa, K. Nakajima, and T. Kaneda, *Electron Lett.*, **18**, 575 (1982).

On the Preferential Etching of GaAs by H_2SO_4-H_2O_2-H_2O

D. N. MacFadyen[1]

Department of Electronic and Electrical Engineering, Glasgow University, Glasgow, Scotland

ABSTRACT

The preferential etching of gallium arsenide in H_2SO_4-H_2O_2-H_2O has been studied. A mechanism for the etching process is discussed drawing on observation by optical and scanning electron microscopy, published results on U H V surface analysis, and surface state models. The etch rates of the revealed planes are related to surface step densities, and the exposure of "equilibrium" step density surfaces is related to the surface migration lengths of probable reactant species.

The wet chemical etching of GaAs has found considerable application in device fabrication. The H_2SO_4:H_2O_2:H_2O etchant has been used to define stripe lasers (1), waveguides (2), and gratings (3), and also for etching laser mirrors (4). However, etchants have largely been selected on an empirical basis, and, although recent papers have characterized the kinetics of the etch reaction, little attention has been paid to the reaction mechanism itself.

The early work of Gatos and Levine (5) showed that the preferential etching of the surfaces of III-V semiconductor crystals could be related to the surface density of group V atoms. Tarui *et al.* (6) reported a variety of pit profiles etched in GaAs through silica masks of differing orientations using a dilute (5%) bromine-methanol etch. The revealed planes were identified as A {111}. They also measured etch depth as a function of time for the nonpolar {110} and {100} planes, showing that the etch rates for the various planes proceeded in the order {110} $\geqq$ B {111} $\geqq$ {100} $\geqq$ A {111}. Koszi and Rode (7), again etching GaAs in the bromine-methanol system, found that at etch concentrations greater than 1% bromine, the revealed plane was of the {322} type, lying at an angle of 10° to the nearest A {111} plane.

The etchant system used in this work, H_2SO_4:H_2O_2:H_2O, was reported in the context of etching beneath a mask of Iida and Ito (8) who used a variety of etch solutions to produce a ternary etch rate diagram for the system (with respect to etching in the {100} direction). The measured angles of the revealed planes for a variety of mask orientations on various surfaces were shown, and results were found to vary considerably from those expected purely from exposure of A {111} planes. A variety of other "Ga" planes, namely the A {223}, {335}, {112}, {113}, {115}, and {117}, were considered as slow etch planes all of which lie on the great circles connecting the A {111} planes in stereographic projection. The fact that measured angles did not coincide exactly with these planes was attributed to poor mask alignment.

The final shelf life of the H_2SO_4:H_2O_2:H_2O etch can limit the reproducibility of results. Mori and Watanabe (9) showed that the replacement of sulfuric by phosphoric acid provides greater stability. They suggested a kinetic model for the etching system based on the assumption of five stages in the reaction process: (*i*) adsorption of m molecules of H_2O_2 onto an active center; (*ii*) formation of oxidized products; (*iii*) adsorption of n molecules of H_3PO_4 on oxidized product; (*iv*) dissolution of oxidized products; and (*v*) desorption of dissolved complex into solution.

The factors m and n were determined experimentally to be 1 and 2, respectively, giving the reaction orders for stages (*i*) and (*iii*) of the process. The experimental results presented below are in agreement with these measurements. However, the main emphasis of the experimental work was the accurate determination of the orientation and surface structure of the exposed planes. The discussion which follows relates the experimental results to the mechanism of stages (*i*) and (*iv*) above.

Experimental Procedure

The GaAs specimens were prepared by chemical polishing in Br/CH_3OH with subsequent cleaning in methanol, acetone, and isopropyl alcohol. Positive photoresist AZ 1350J was used to produce a series of masking stripes on the specimens. To use the photoresist as a mask for subsequent etching, it was necessary to bake it for 15 min at 130°C. Alternatively, aluminum masks could be produced by evaporation and lift-off.

The etchant was prepared from Aristar grade hydrogen peroxide and sulfuric acid with distilled water and used within hours of preparation in an attempt to avoid ambiguities introduced by possible decomposition of the peroxide. The etchant compositions referred to subsequently are volume percentages of 30% H_2O_2 (by volume), concentrated H_2SO_4, and distilled water.

Etching was carried out at a range of temperatures from −10° to +30°C in a circulating thermostatic bath containing a methanol/water mixture. Temperature was controlled to ±0.5°C, and etchant was stored in the bath prior to use to ensure it was at the correct temperature.

Subsequent to etching, the specimens were cleaved normal to the mask strips and mounted for observation in the optical and scanning electron microscopes. Measurements of etch pit dimensions were made from photographs taken in an optical microscope by comparison with a similarly photographed calibration graticule. Etch rates of smaller specimens were made in the scanning electron microscope using photographs with electronically superimposed marker bars. The marker bars and camera distortions were calibrated by photographing a scribed diffraction grating.

The type of pit profiles produced by the etchant are shown in Fig. 1. Measurements were made of the etch rate in the {001} direction, the mask undercutting rate, and the angles α and β which identified the plane exposed at the pit side wall and the relative etch rates of the {001} and B {111} surfaces exposed. By cleaving specimens with aluminum masks (semitransparent to the electron beam) or photoresist masks (semi-

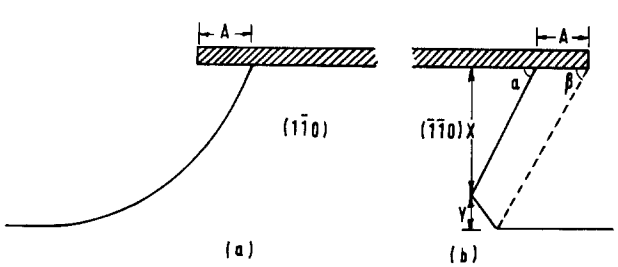

Fig. 1. Diagrams illustrating the pit profiles observed when preferentially etching masked (001)-oriented GaAs.

[1] Present address: Barr and Stroud Limited, Anniesland, Glasgow, Scotland.

transparent to light), the etch rate of the {110} surface could also be measured.

In the subsequent discussion, the etching characteristics of the various parameters measured are related to the structure of atomically clean surfaces of similar orientation.

Results and Discussion

Gatos and Levine (5) identified the differing etch rates of the A {111} and B {111} planes of the GaAs crystal, the A (Ga) planes etching at a much slower rate than the B (As) planes.

The difference was explained on the basis that the removal of the triply bonded surface atoms was rate controlling as the underlying (singly bonded) atoms of the other element could be expected to be highly unstable. This is an oversimplified one-dimensional model.

Figure 2 shows a zinc blend lattice structure with {111}-type top surfaces, the lines joining the lattice points indicating the direction of the interatomic bonds.

Figure 3 represents a plan view of the {111} plane, the atom circles joined by bold lines representing the surface layer and those joined by dashed lines the underlying layer. The double circles represent atoms directly below atoms on the surface. The surface layer of atoms is buckled as shown in Fig. 2.

If the atom marked "X" is removed from the "stable" surface (all atoms triply bonded to the substrate), then, rather than leaving a singly bonded atom (as assumed by Gatos), the surface indentation produced will have three side walls of triply bonded atoms of the alternate (white) atom (1). When these atoms are removed, they reveal double-bonded (black) atoms which on reaction will again reveal triply bonded (white) atoms (2).

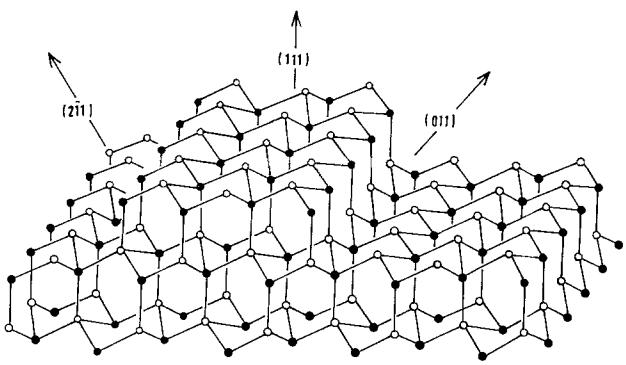

Fig. 2. Diagram of the zinc blend (111) surface

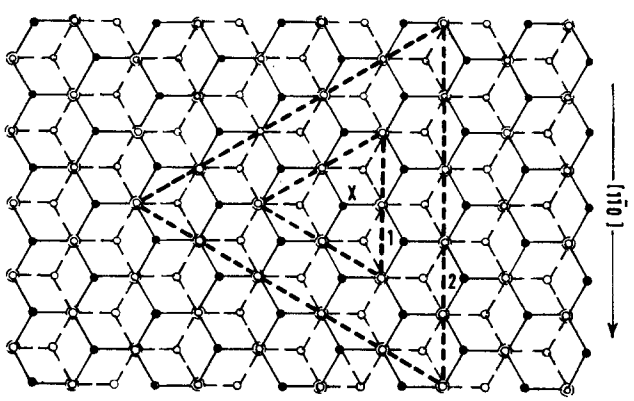

Fig. 3. Plan view of the (111) surface of the zinc blend lattice. Solid lines represent bonds between surface atoms. Fine dashed lines represent bonds between atoms in the second layer. Double circles indicate interplanar bonds to an underlying (black) atom. Bold dashed lines indicate progress of surface etching steps.

Assuming that the reactivity of a surface atom is dependent on the number of bonds binding it to the substrate (*i.e.*, the order of stability of surface states is 3A, 3B, 2A, 2B, 1A, 1B where the numbers represent the number of bonds in the substrate direction and the A and B represents Ga and As atoms, respectively), a laminar model for the etching process emerges.

If triply bonded A and B atoms are regarded as considerably more stable than the other four possible states, and similarly a 3A atom is much more stable than a 3B atom, then despite the low reactivity of an A {111} surface, once one atom has been removed the entire surface layer can be removed by the lateral etching of steps comprising triply bonded B atoms followed by doubly bonded A atoms.

A further extension of this argument is revealed by again referring to the lattice model of Fig. 2. Once an edge of 3B atoms has been established as illustrated, then the removal of one atom from such an edge will produce a pair of "jogs" (by analogy with edge dislocations) whose edges are comprised of 2A and 2B atoms and which could be expected to propagate rapidly in a direction perpendicular to the initial surface step encountering no triply bonded atoms to impede progress. Which of the three types of site for atom removal dominates the etch mechanism is also effected by the fact that the sites are two-, one-, and zero-dimensional with respect to the planar surface, a step, and a jog.

The simple model of a two-dimensional square lattice was used to simulate the etching of steps of 3B atoms on an A {111} surface when the relative atom removal rates of the 3B atoms and 2A atom sites are assumed to be rate controlling.

Results taken from a range of reaction probability ratios of 1:1 to 128:1 (step:surface) show the following simple relationship between reaction probability and reaction occurrence at the two types of site

$$(\text{reaction rate ratio}) = (\text{reaction probability ratio})^{1/2} \quad [1]$$

and similarly

$$(\text{reaction rate}) = \frac{1}{(\text{reaction rate ratio})} \quad [2]$$

The state of the array during etching shows a decrease in edge site density (number of step sites/number of surface sites) from 0.5 for a 2:1 reaction probability ratio (counting step and surface double sites as step sites) to less than 0.1 for a reaction probability ratio of 128:1.

When etching a B {111} surface, the reactant is presented with a highly reactive surface on which less reactive steps with A-type construction are exposed when surface atoms are removed. For the case where step sites are less reactive than surface sites for the same range of reaction probability ratios, reaction rate decreases asymptotically to the surface site reaction rate.

If it is assumed that the results of this simple example can be used as a basis for understanding the etching of a three-dimensional system, the following conclusions may be drawn from the exercise: (*i*) when a highly stable surface etches to reveal reactive steps which can propagate laterally, the removal of atoms at such steps is the dominant etch mechanism, but the etch rate itself is determined by the reactivity of the surface atoms because that reactivity determines the step site density; and (*ii*) the presence of stable steps on a reactive surface has little influence on either the surface topography or reaction rate, the step density being similar to that found when reaction rates are identical.

The dependance of etch rate on surface step density is verified by the experimental results in Fig. 4,

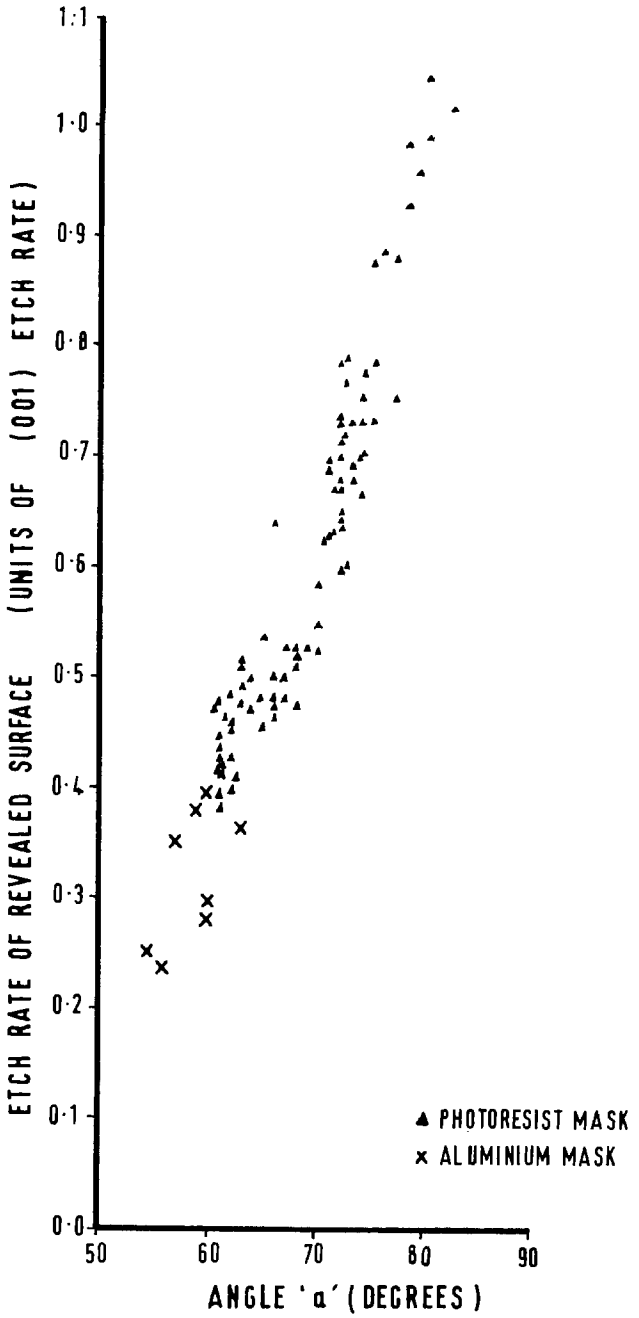

Fig. 4. 'A' plane etch rate as a function of angle to the (001) surface with results normalized to the etch rate in the [001] direction.

showing the etch rates of the large range of A-type planes revealed due to variations in the undercutting rate produced by variation in mask adhesion quality. The etch rate of the B {111} surface was unaffected by mask adhesion, and therefore a larger area of B {111} surface was revealed in cases of poor adhesion and high angled side planes. Etch rates of the revealed planes are expressed as a fraction of the etch rate of the adjacent (001) surface with results taken over a range of temperatures from −9° to +25°C. The etch rate increase is approximately linear with angle and is nonzero at 54.7°, the angle of the A {111} plane. Figure 5 shows the atomic arrangement in two atomic layers of a $(\bar{1}\bar{1}0)$ section through a GaAs crystal (normal to the mask direction).

The three sections of the A $(1\bar{1}\bar{1})$, A $(2\bar{2}\bar{1})$, and $(\bar{1}\bar{1}0)$ planes show how each surface can be constructed with a minimum number of dangling bonds, and hence a minimum surface-free energy, by a series of monatomic steps of B {111} plane (As atoms) with

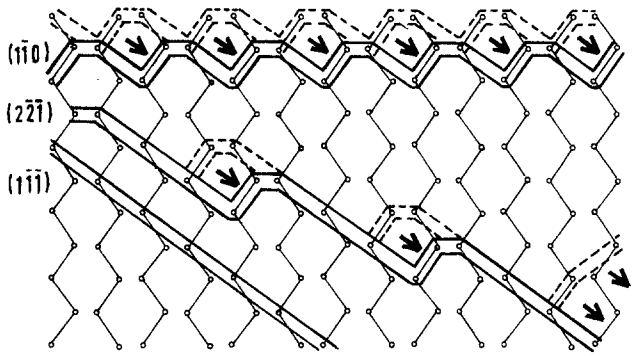

Fig. 5. A (110) section of the zinc blend lattice showing minimum dangling bond construction of three planes with a [110] zone axis. Bold atoms = top layer; fine atoms = second layer.

surface densities of 0, 0.25, and 0.5, respectively. Dangling bond As atom densities for the whole range of surfaces from the A {111} to the B {111} are shown in Fig. 6 with results normalized to the density of dangling bonds on the B {111} surface. For the range of planes between A {111} and {110} (54.7°, −90°), dangling bond density is equal to step density.

Step density increases linearly with angle in the range of experimental results, and this corresponds to the linear increase in the etch rate with step density shown in Fig. 4. The gradients of the two graphs are similar, but the experimental results show a finite etch rate for the A {111} surface corresponding to a "random" surface step density of 0.1 and giving no contribution to the macroscopic planar angle. However, the two components cannot be simply added together. A significant factor is the surface lifetime of the steps. Reference to Fig. 3 shows that in the three-dimensional case, the step density contribution from individual sites is not constant but will increase with time. The eventual limit is determined by the point at which the triangular steps defect from neighboring reaction sites, overlap and annihilate each

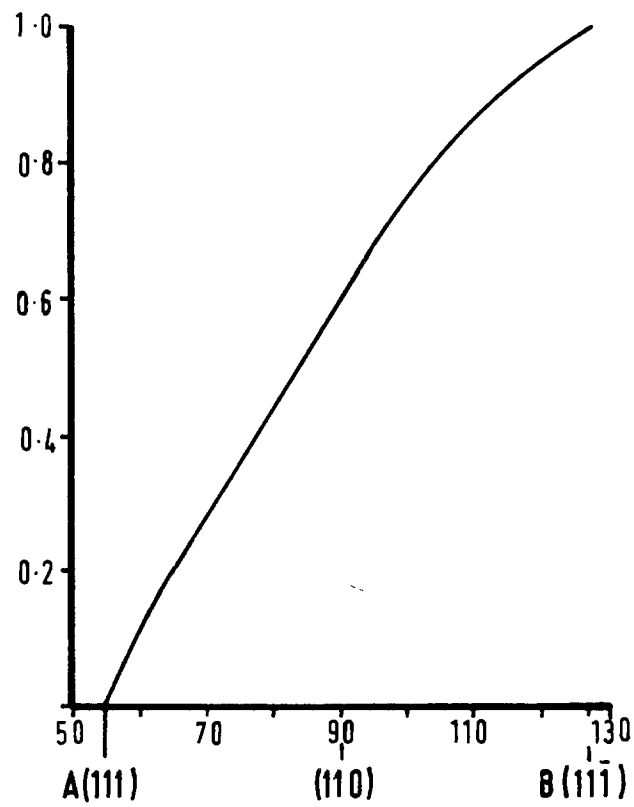

Fig. 6. Normalized dangling bond density as a function of angle to the (001) plane.

other. When there is a constant additional source of steps which sweep across the specimen with a regular frequency (as provided by a surface mask), the A {111} surface reactivity contribution to the etch rate will be reduced because the average number of step sites created per "surface" reaction will be reduced as a function of density of steps on the surface.

A second restraint on the extent to which step density determines the etching rate of an exposed surface follows.

Each step envisaged on the vicinal A surface exposed during etching would lie in the direction of the mask edge, and the surface generated by rows of equally spaced parallel steps on an A {111} surface. Each step has a surface consisting of Ga atoms triply bonded to the substrate in a manner completely analogous to the bonding on a B {111} surface. It might, therefore, be assumed that the etch rate of the steps on the A-type vicinal surface would be equal to that of the B {111} surface. The situation is illustrated by referring to Fig. 5. Etching perpendicular to the macroscopic surface is due to steps moving in the $[11\bar{1}]$ direction. As the angle of the plane increases, the step density increases, and if their velocity is constant (giving the observed experimental relationship between etch rates), then the number of steps passing a fixed point on the plane will also increase. An increased flux of steps arriving at the B surface would account for its faster growth rate in the presence of higher angle side planes as observed experimentally. However, if the etch rate is determined by the dangling bond density on the surface, the B {111} surface would etch at the same rate as the steps on the A plane surface and it would not grow. Therefore, there must be a limiting factor on etch rate other than dangling bond density.

A second example of additional etch rate limiting factors is given in the cases where the mask is completely undercut. If side wall etch rate is determined by the progress of surface steps away from the substrate/mask interface, then undercutting is determined by the "release" rate of steps from the interface. On this basis, a very fast undercutting rate could be expected to reveal a {110} surface or (ultimately) a B {111} surface. Figure 7 shows that this does not happen. An increase in the undercutting rate of the mask has caused the formation of a new {001} surface, but the A-type side wall of the rib has maintained the same angle as that in the region of the rib where the mask is still intact. In previous examples, the angle of the exposed A-type side wall could be related to mask adhesion quality, but here there is no mask adhesion and yet the side wall has remained.

Figure 7b shows a $(\bar{1}\bar{1}0)$ section through a specimen and illustrates the development of a vicinal A surface at the intersection of the (110) side of the specimen and the (001) top surface. The adjacent masked rib structure has etched to reveal lower angle side walls with lower step density determined by mask adhesion.

In order to understand the observation of "equilibrium" step density surfaces where the vicinal angle adopted is determined by the reaction conditions instead of masking of the surface, a discussion of the reaction mechanism is required.

The surface of GaAs oxidizes to a thickness of a few angstroms when exposed to the atmosphere (10). It is assumed that the chemical etching reaction can be related to the surface structure of an atomically clean surface for which it is possible to draw on the numerous published RHEED and LEED results available from experiments conducted in UHV.

Although surface steps have been discussed above in the context of a laminar etching mechanism, it has long been recognized that their presence on vicinal surfaces in regular arrays is also a mechanism of free energy minimization (11, 12).

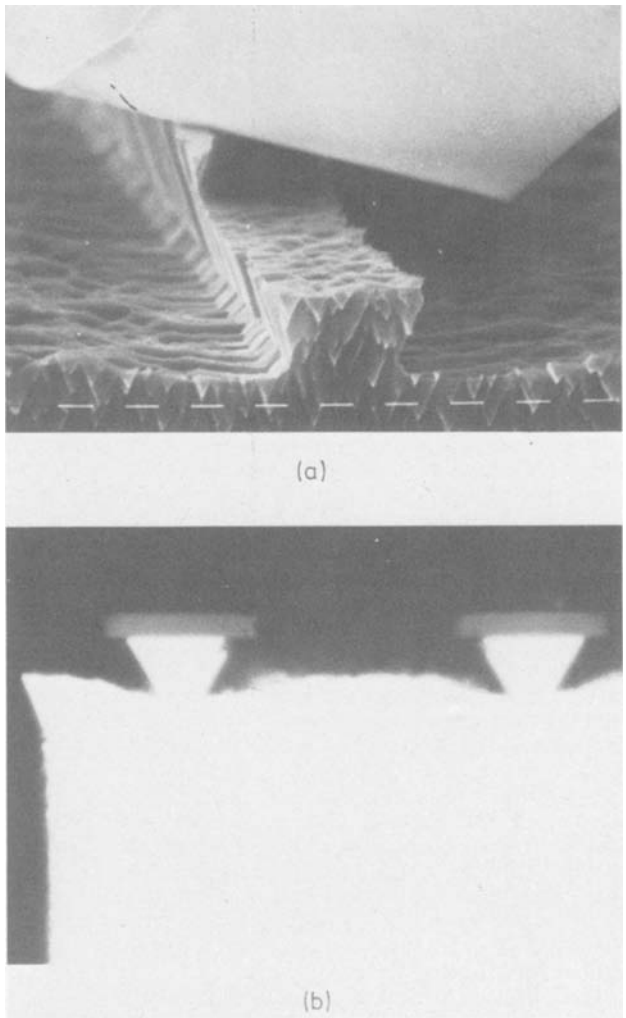

Fig. 7. Examples of the exposure of "equilibrium" step density surfaces. (a) Electron micrographs (1 μm markers). (b) Optical micrographs ($\times$ 3000).

The surface state model of Gregory and Spicer (13) for the GaAs {110} surface has two surface state bands, an As-associated band lying at the top of the valence band and hence filled, and an empty Ga-associated band just below the conduction band. This is the equivalent of the simple Gatos atomic model with the As surface atom maintaining five electrons (one dangling bond) and the Ga atom three electrons (no dangling bond) in accordance with their atomic valence numbers. The theoretical analysis of Mele and Joannopoulos (14) predicts these surface states and also explains the different results observed on defect-covered surfaces. They suggest that when defects occur on the cleaved surface, the crystal is trying to cleave on two adjacent (110) planes.

Although these additional {110} planes will not themselves alter the surface states present, the interaction of the two planes must involve the presence of double dangling bonds. Analysis of a {110} surface with every second surface bond broken produces new surface states which would be associated, for instance, with jogs in surface steps. Interaction between the two dangling bonds on each atom results in split energy levels giving a filled As-like sp-derived state below the valence maximum and an empty As-derived transverse p-state in the upper half of the bandgap. The Ga atom gains a filled sp-type state in the lower bandgap and an empty transverse p-state in the upper half of the bandgap.

This analysis shows that a surface Ga atom with only two bonds to the substrate will have a dangling

bond associated with it, and a doubly bonded As atom will still only have a single dangling bond. Therefore, the chemical reactivity of doubly bonded Ga and As atoms may be expected to be similar to that of a triply bonded As atom.

Studies of surface states can provide useful information about the reactivity of atoms in the various possible surface configurations, but the mechanism of surface adsorption is also of prime importance in the discussion of chemical reaction. Gojstein (15) showed that differences in heat of adsorption between sites of less than 10% could give orders of magnitude difference in absorption probability.

Goddard *et al.* (16) presented a theoretical evaluation of adsorption to GaAs {110} surfaces using the chemical approach of modeling a small complex of atoms—a gallium or arsenic atom with three (substrate-oriented) bonds terminated with hydrogen atoms. The surface states predicted were in agreement with Mele and Joannopoulos, and it was shown that the chemisorption of atomic oxygen occurs between an empty p-orbital and the As dangling bond; molecular oxygen is only weakly physisorbed and atomic oxygen is only weakly adsorbed to Ga sites.

An important aspect of this work is the accuracy of a few atom models in predicting surface behavior, suggesting that local structure rather than the orientation of the surface dominates surface reactivity. In this light, the {110} surfaces may be regarded as a corrugated surface of alternate A- and B-type {111} monatomic steps.

Hydrogen peroxide has the electronic structure shown schematically in Fig. 8, having two hydrogen atoms in separate planes with a common axis through the two oxygen atoms (18). Comparison of this structure with that of the oxygen molecule shows that there are none of the empty orbitals which provide the basis for the chemisorption of the oxygen molecule at As dangling bonds.

The reaction ultimately required of the H_2O_2 is

$$*H_2O_2 \rightarrow H_2O + *O \quad [3]$$

where the * refers to an adsorption site such that adsorbed atomic oxygen becomes available for oxidation of the surface. The addition of oxygen to both organic and inorganic compounds which possess unshared electrons frequently occurs, but there are no obvious sites on the GaAs surface to provide unshared electrons, and alternative reactions must be sought.

Discussing the catalytic decomposition of hydrogen peroxide at the surfaces of silver and gold, Goszner and Bischof (17) showed a strong correlation between oxygen affinity and surface activity.

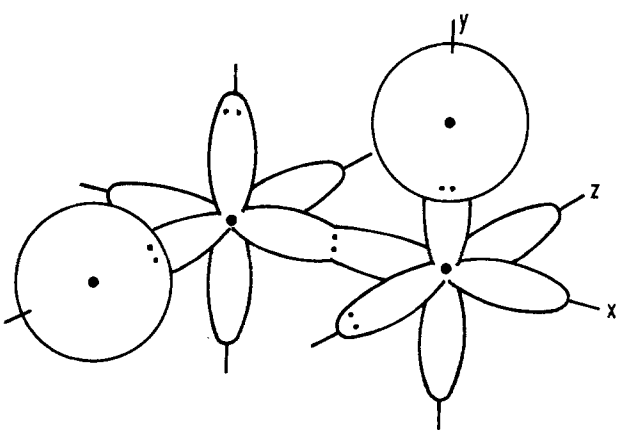

Fig. 8. A representation of the electronic structure of the hydrogen peroxide molecule. The oxygen 1s and 2s orbitals are full and not illustrated.

A possible initial reaction step for both gold and silver surfaces was given as

$$H_2O_2 + e + * \rightarrow *OH + OH^- \quad [4]$$

$$OH^- + * \rightarrow *OH^- \quad [5]$$

Splitting the H_2O_2 molecule down the center in this manner leaves one OH molecule with an empty p-orbital (suitable for bonding to an As atom) and one with both p-orbitals full which could be envisaged as bonding to the empty d-orbital of an adjacent surface Ga atom, although such a bond would be weak. Further reaction requires additional peroxide to form an OOH^- ion which will subsequently release an oxygen atom

$$*OH^- + H_2O_2 \rightarrow *OOH^- + H_2O \quad [6]$$

$$*OOH^- \rightarrow *O + OH^- \quad [7]$$

Such an oxygen atom would be adsorbed on a Ga triply bonded site as this is most suited to the OOH^- ion with its hydrogen-free oxygen atom having two filled p-orbitals. However, as atomic oxygen is only weakly adsorbed to Ga (16), it is likely to migrate to an As site (or other suitable reaction site) by a surface diffusion mechanism. If the weakly adsorbed reactant is assumed to have a finite surface lifetime, then for the range of surfaces where the distance between reaction sites is greater than the surface path length of the reactant, the probability of reaction at a particular site will be constant. However, when the surface site separation is less than the surface path length of the reactant, there will be an excess of reaction sites and the probability of reaction at a particular site will drop.

The vicinal surface whose site separation is equal to the reactant migration length, and all those with higher site densities, will have equal bulk etch rates because the increase in site density will not increase the probability of reaction.

In terms of the observed effects, the range of vicinal A surfaces with low step densities would have reaction rates determined by the step density while reaction rates of surfaces such as the basal B {111} plane and the {110} surface will be limited by the arrival rate of reactant. At a mask/substrate interface, if the separation of surface steps released from the interface is greater than the surface path length of the reactant, then the steps produced by the process of undercutting will be evenly distributed down the side wall of the etch pit. However, if undercutting occurs faster than the critical rate, the velocity of the surface steps will decrease, increasing their density. Under these circumstances, the defects introduced at the mask/substrate interface will not be accommodated into the vicinal A surface, and the mask adhesion will "fail," the excessive undercutting revealing an {001} surface. If a vicinal A surface has been formed before failure of the mask, then at the interface between it and the new {001} surface there will be a large source of surface steps, but the limited surface density of reactant on the vicinal A surface will limit the movement of steps from this large source onto the side wall. This mechanism determines the equilibrium step density described above.

A maximum etch rate, independent of reaction site density, whereby reaction rates of individual sites on high site density surfaces are inversely proportional to site density, also explains the observed faceting of the {001} and etched {110} surfaces.

The specimen illustrated in Fig. 9a shows a corner intersection of the (001), $(1\bar{1}0)$, and $(\bar{1}\bar{1}0)$ surfaces. The (001) surface was prepared by chemical/mechanical polishing and exhibits the typical elongated pyramidal structure, detail of which is shown in Fig. 9b. The two {110} surfaces were cleaved immediately

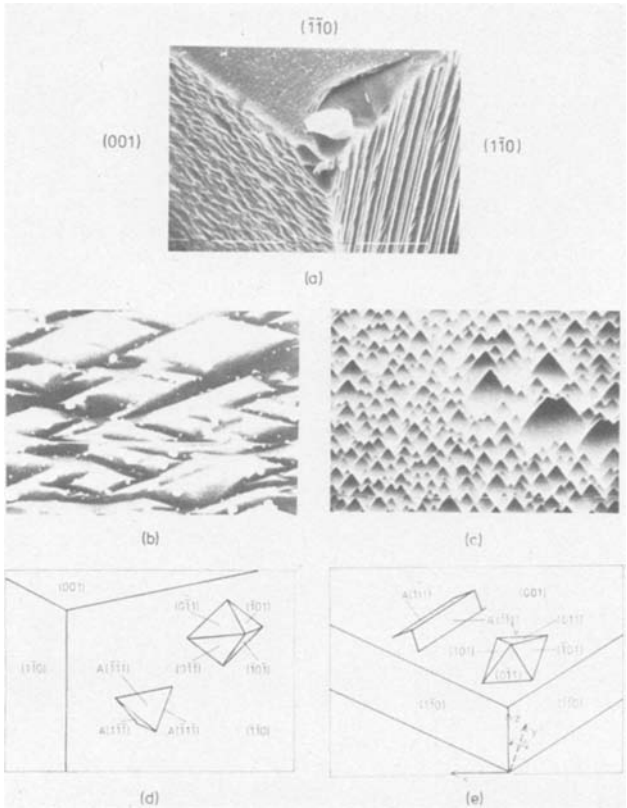

Fig. 9. Electron micrographs of preferentially etched GaAs surfaces. Markers in (a) = 10 μm; markers in (b) and (c) = 1 μm.

prior to etching. The (1̄10) (top) surfaces are etched flat from an initially good cleave. In contrast, the cleaved surface of the (1̄10) plane was interrupted by an array of cleavage defects lying in a [111] direction, and these have acted as nucleation sites for the exposure of the observed defects.

Figure 9c illustrates a third {110} surface topography observed after etching. Diagrams d and e show the derivation of the constituent planes of these structures. Figure 9e shows the orientation of the four {110}-type surfaces and two A {111} surfaces which intersect the (001) surface. The pyramids revealed by etching the (001) surface are elongated in the [1̄10] direction and are therefore comprised of planes lying between the {110} and A {111} planes with a common zone axis.

Figure 9d illustrates that A (111)/(110) vicinal planes lead to the formation of the structures in the micrographs a and c. The tendency to form surfaces with an equilibrium step density is explained by random variation occurring in site density during etching.

Having identified a reaction model based on the exposure of surfaces with an equilibrium density of reactive surface steps, variation of the equilibrium step density with etch composition and temperature are discussed. Figure 10 shows the dependence of various etch parameters with the amount of peroxide in the etch. There is a first-order relationship between the peroxide concentration and both mask undercutting rate and {001} etch rate. The size of the exposed B {111} surface is constant, so its size relative to the exposed A-type size wall decreases with peroxide concentration. Figure 11 shows the results of measurement of the etch angle of the apex between the B (111) and (100) surfaces, interpreted as a measure of the relative etch rates of the two planes. There is a variation of 20% in the relative etch rates for the range of peroxide concentration examined.

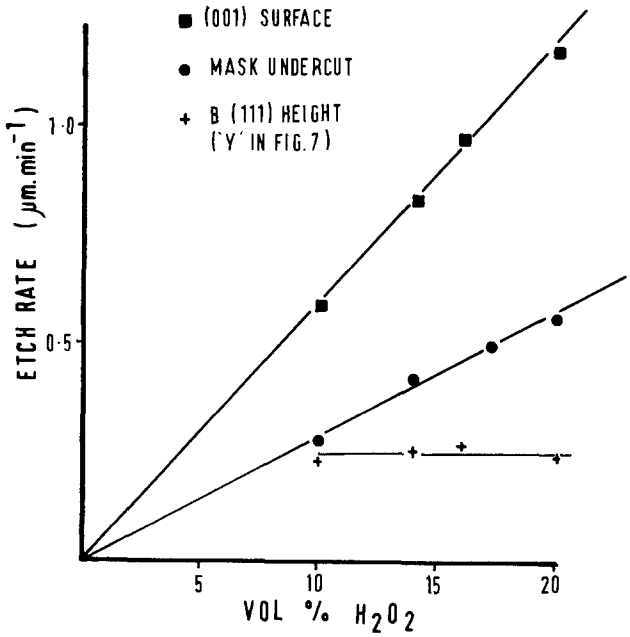

Fig. 10. Variation in etching parameters with etch composition. Etch temp. = 21°C; etch time = 4 min.

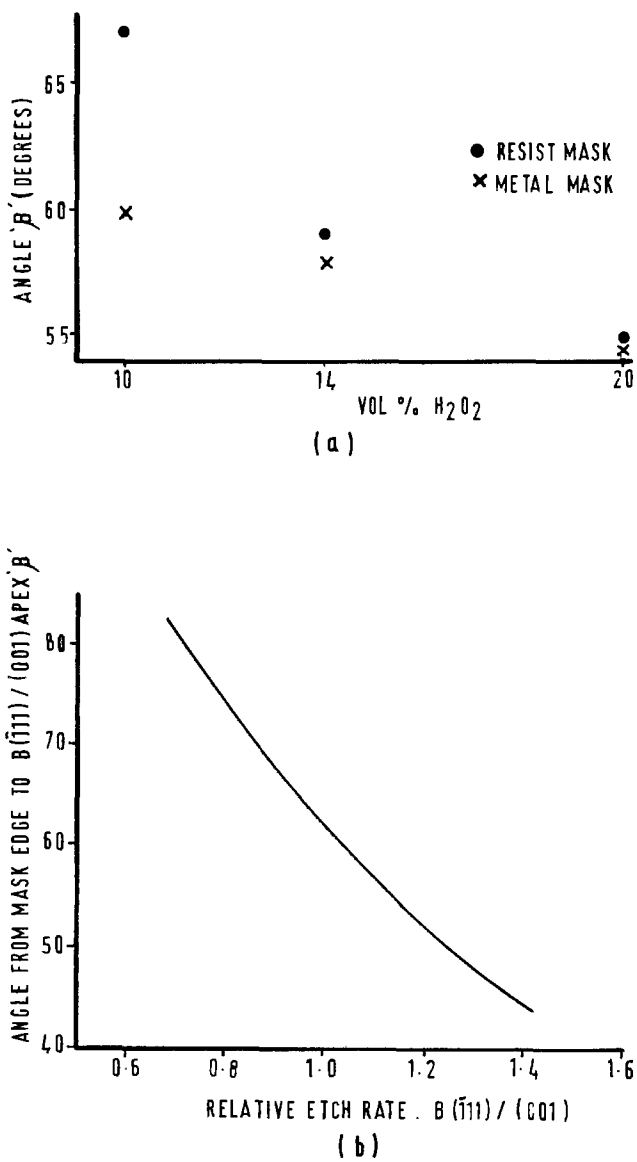

Fig. 11. Graphs showing the dependence of B {111}/(001) etch rate ratio on peroxide concentration.

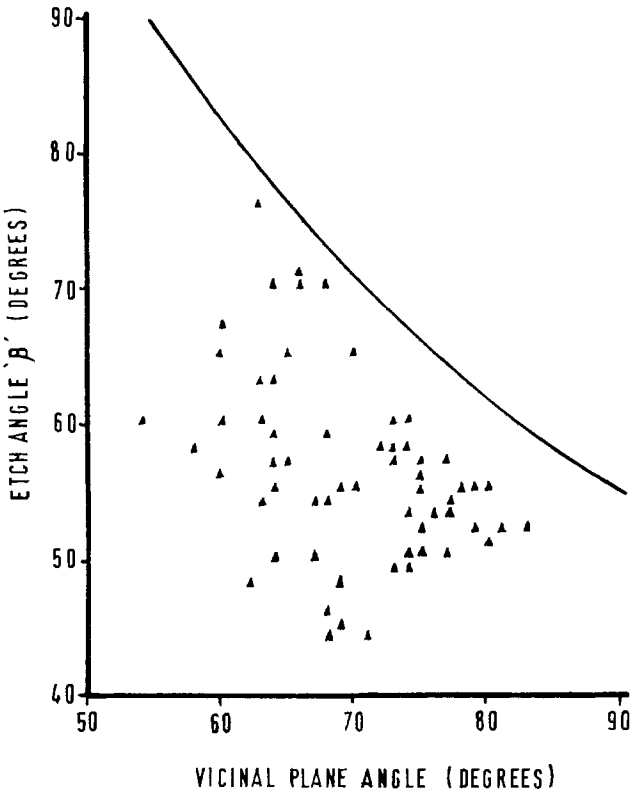

Fig. 12. Comparison between (a) the theoretical relationship between the etch angle of B ($\bar{1}11$)/(001) apex and the angle to the (001) surface of the "equilibrium" vicinal surface lying between the A (111) and (110) surfaces and (b) experimental points indicating the etch angle of the B ($\bar{1}11$)/(001) apex associated etch pit side wall angle.

A second series of experiments in which the acid concentration in the etch was varied showed that for masks orientated in the [110] direction the rate of mask undercutting, shown in Fig. 10 to be proportional to peroxide concentration, was also independent of acid concentration (see Fig. 13). In the theoretical discussion, the undercutting rate was related to the release rate of steps from the interface between the mask and the etch pit side wall. This has now been directly related to peroxide concentration which therefore controls step movement.

The number of reaction sites on the surface steps which are oxidized will depend on the probability of removal of oxidized reaction product, and therefore for the same vicinal plane, the density of reaction sites will depend on acid concentration, and the "equilibrium" reaction site separation cannot be directly measured from the macroscopic planar angle.

The etch rate of the (001) surface, shown to be proportional to peroxide concentration, maintains this relationship because the surface will always facet to reveal surfaces with equilibrium step density, the macroscopic angle of which will vary with acid:peroxide ratio but whose reaction site separation, and therefore reactivity, will be determined by the surface lifetime of the peroxide-derived reactant. The pyramidal facets observed on the (001) surface have mirror symmetry in the (110) plane (the plane of the sections used in experimental measurements). The graph in Fig. 12 shows the relationship between the angle to the (001) direction of the components of the etch vectors of the faceted surface in the (110) plane and the angle of the vicinal surfaces to the (001) surface. The experimental points plotted on the graph relate the measured angles of the revealed side planes and the angle to the apex between the (001) and B {111} surfaces. The majority of the points lie well below the theoretical curve as would be expected if mask

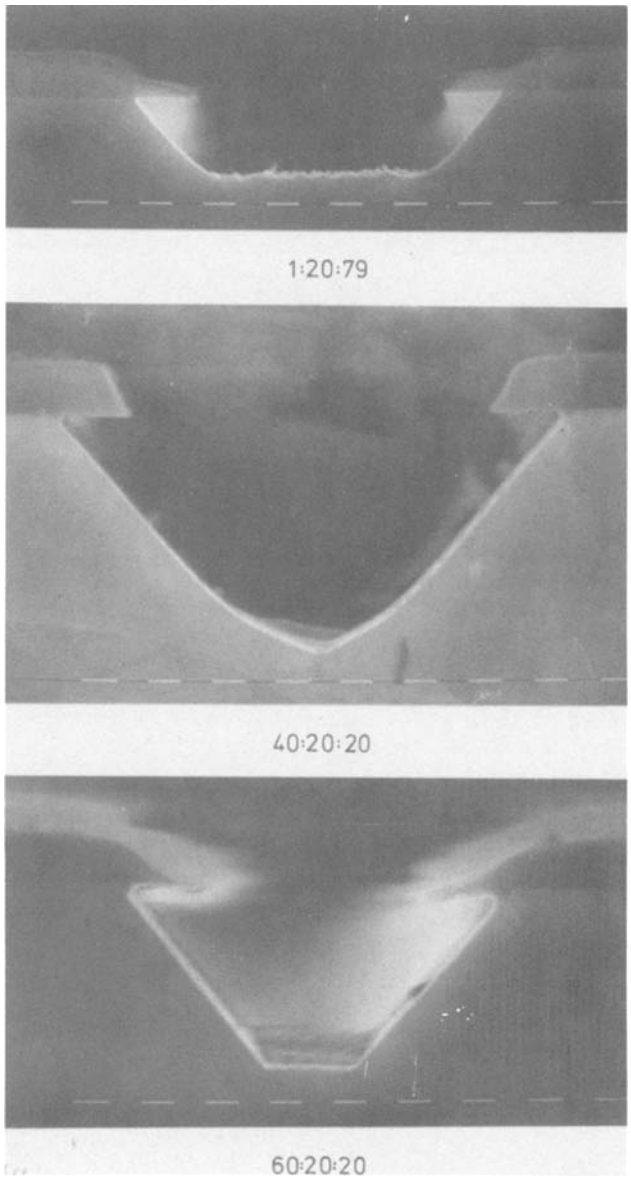

Fig. 13. ($1\bar{1}0$) sections of channels etched between ($1\bar{1}0$)-oriented masks on the (001) surface with various H_2SO_4:H_2O_2:H_2O etch compositions. (1 μm markers.)

adhesion is producing a side wall angle with less than the equilibrium step density. Those results which lie close to the theoretical curve correspond to cases where the mask had failed and indicate that the growth of the (001) surface under the mask is in the direction of the etch vectors of surface facets with "equilibrium" step density.

Figure 14 shows an Arrhenius plot for various measured parameters over the temperature range 30°-10°C using a 2:14:84 etching solution. The temperature dependence of etch rate in the (001) direction and of undercutting of the mask are the same with an activation energy of 5 kcal · mol^{-1}, comparing well with the value of 6-8 kcal · mol^{-1} (depending on composition) quoted by Iida (8) However, the parameters marked X and Y in Fig. 1, the distance from the mask to the apex between the A and B planes, and the height (in the (001) direction) of the B {111} plane have a different dependence. The general trend indicated is a reduction in the exposed area of B {111} plane as the temperature is reduced.

The surface oxide removing stage has the higher activation energy as it becomes less effective at lower temperatures. Therefore, as temperature is reduced there will be an increase in step density on the equi-

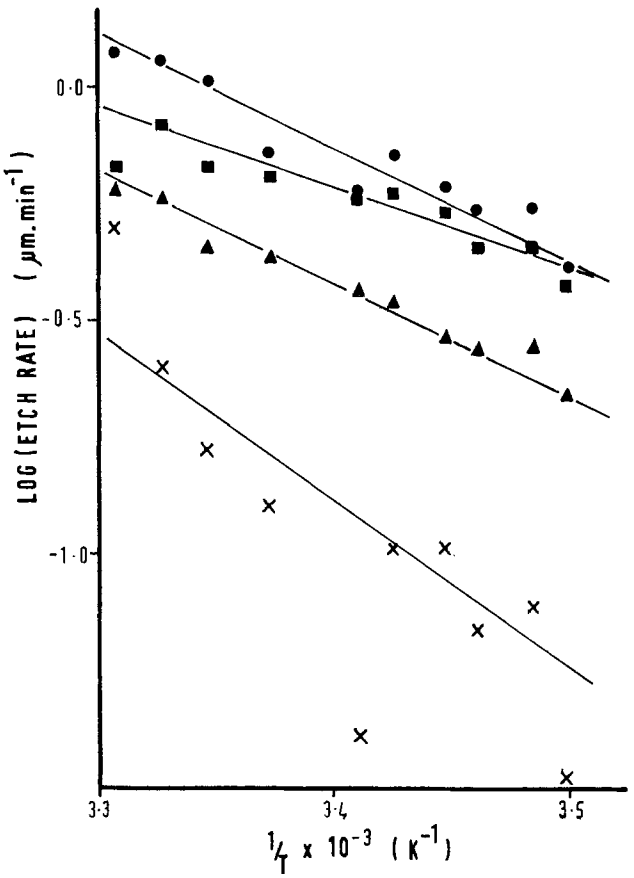

Fig. 14. Arrhenius plots of log (etch rate) for various parameters against reciprocal temperature; ● = (001) etch rate, ▲ = mask undercutting rate, ■ = parameter X growth rate, and × = parameter Y growth rate.

librium surface confirmed by the results of Fig. 14 showing the variation in angle β with temperature and partly accounting for the decrease in area of exposed B {111} surface. The angle of the revealed side wall showed no significant change with temperature.

Summary

A mechanism for preferential chemical etching of GaAs in H_2SO_4:H_2O_2:H_2O has been proposed based on the known characteristics of the etchant and the GaAs surface. All the topographies observed experimentally are explained by this mechanism as are the results of other workers in the field.

Model building of GaAs crystal surfaces showed that the preferred etch planes observed could be constructed by adding regular arrays of surface steps to the fundamental A {111} surfaces. Investigation of the relative etch rates of the observed surfaces with respect to surface step density showed that there was a limit to the etch rate increase caused by increasing the step density suggesting a surface migration limited reaction rate. Studies of the characteristics of various etch compositions lead to the conclusion that there was also an equilibrium surface density of oxidized steps which influenced the macroscopic angle of the equilibrium surface.

Acknowledgments

This work was funded by the SRC. The author thanks Professor Lamb for the provision of facilities and C. Stanley for supervision of the project.

Manuscript submitted March 15, 1982; revised manuscript received March 29, 1983.

REFERENCES

1. R. P. Tijburg and T. van Dongen, *This Journal*, **123**, 687 (1976).
2. R. A. Logan and F. K. Reinhart, *J. Appl. Phys.*, **44**, 4172 (1973).
3. W. T. Tsang and S. Wang, *Appl. Phys. Lett.*, **28**, 44 (1976).
4. J. L. Mertz, R. A. Logan, and A. M. Sergent, *IEEE J. Quant. Electron.*, **qe-15**, 72 (1979).
5. H. C. Gatos and M. C. Levine, *This Journal*, **107**, 427 (1960).
6. Y. Tarui, Y. Komiya, and Y. Harada, *ibid.*, **118**, 118 (1971).
7. L. A. Koszi and D. L. Rode, *ibid.*, **122**, 1676 (1975).
8. S. Iida and K. Ito, *ibid.*, **118**, 768 (1971).
9. Y. Mori and N. Watanabe, *ibid.*, **125**, 1511 (1978).
10. F. Lukes, *Surf. Sci.*, **30**, 91 (1972).
11. C. Herring, *Phys. Rev.*, **82**, 87 (1951).
12. F. Hottier and J. B. Theeten, *Surf. Sci.*, **65**, 563 (1977).
13. P. E. Gregory and W. E. Spicer, *Appl. Phys. Lett.*, **25**, 511 (1974).
14. E. J. Mele and J. D. Joannopoulos, *Phys. Rev.*, **19**, 2928 (1979).
15. N. A. Gojstein, *Acta Met.*, **11**, 957 (1963).
16. W. A. Goddard, J. J. Barton, A. Redondo, and T. C. McGill, *J. Vac. Sci. Technol.*, **15**, 1274 (1978).
17. K. Goszner and H. Bischof, *J. Catal.*, **32**, 175 (1974).
18. W. C. Shumm, C. N. Satterfield, and R. L. Wentworth, "Hydrogen Peroxide," Reinhold Publication Corp., New York (1955).

Effects of Back-Side Oxidation of Si Substrates on Sb Diffusion at Front Side

S. Mizuo and H. Higuchi*

Hitachi Limited, Central Research Laboratory, Kokubunji, Tokyo 185, Japan

ABSTRACT

The effect of back-side oxidation of Si wafers on the diffusion of Sb in the front of wafers is investigated with back-side selective oxidation (BSO) at 1100°C in dry O_2 ambients. It is found that the diffusion of Sb in the front of the wafers is retarded by BSO only for FZ Si substrates under directly formed Si_3N_4 films, and that Sb diffusion in CZ Si substrates and under double-layered SiO_2-Si_3N_4 films in both FZ and CZ substrates is not affected by BSO. The effective range over which BSO affects Sb diffusion is found to increase with oxidation time. The range and extent of oxidation retarded diffusion (ORD) for Sb are shown to agree with those of oxidation enhanced diffusion (OED) for B and P. These results are explained with a proposed model: *(i)* there is a thermal equilibrium between vacancies and interstitials, and *(ii)* the Si-SiO_2 interface provides sinks and generation centers for point defects in Si, though the Si-Si_3N_4 interface does not react with point defects.

It is well known that diffusion of Group III and and V elements in Si is affected by thermal oxidation. Diffusion of B, P, and As has been found to be enhanced by thermal oxidation (1-3). This phenomenon has been discussed in relation to the mechanism of impurity diffusion and point defect structure in Si using several different models.

The authors have found ORD of Sb in Si and proposed that there is a local equilibrium between interstitials and vacancies (4). Moreover, they have found that the range of B- and P-diffusion enhancement effect by thermal oxidation increases with oxidation time (5-6). If local equilibrium between interstitials and vacancies exists, the Sb ORD range due to oxidation should be equal to the OED range for B and P and should expand with oxidation time.

In this paper, the ORD range for Sb is investigated by BSO to clarify the existence of local equilibrium.

Point Defect and Impurity Diffusion Model

Formerly, impurity diffusion in Si was explained using a vacancy model (7). However, this model cannot explain the coexistence of OED for both B and P in Si, and extrinsic stacking fault growth during thermal oxidation (8).

Gosele *et al.* claimed that B and P diffuse in Si only through interstitials in both inert and oxidizing ambients (9). They explained the OED for B and P in Si in terms of the increase in concentration of interstitials at the oxidizing Si-SiO_2 interface.

Hu and Antoniadis *et al.* have proposed a dual diffusion mechanism model. According to their model, an impurity atom diffuses in Si via both interstitials and vacancies (10, 11).

Taniguchi *et al.* assumed from experimental results that B and P diffuse in Si via vacancies that have developed from treatment with inert ambients and that they diffuse via both vacancies and interstitials with the use of oxidizing ambients. However, these two models encountered problems with the finding of ORD of Sb in Si (12).

The authors have found that the ratio of impurity diffusion coefficient under oxidizing and nonoxidizing condition (D_O/D_N) for B and P is inversely proportional to D_O/D_N for Sb (4). Moreover, they have found that B, P, Al, and Ga have similar D_O/D_N values (13, 14). This strongly suggests that the four elements diffuse in Si by only one mechanism. It would be incredible for all these elements to have similar fractions of interstitial diffusion, f_I, with values other than unity in spite of the differences in ionic radii and in periodic table grouping. Consequently, the authors have concluded that they diffuse only by interstitials.

Recently, Antoniadis *et al.* investigated the effects of oxidation and obtained fractions of f_I (15). Their values are 0.30 for B and 0.38 for P at 1000°C. However, Tan *et al.* showed that f_I must be greater than 0.5 for enhanced diffusion in the case of interstitial supersaturation at equilibrium between interstitials and vacancies (16). Therefore, the f_I values of Antoniadis *et al.* must be analyzed in more detail. Thus, even if diffusion of B and P do not proceed entirely by interstitials, they can be regarded as playing the dominant role in such diffusion. Antimony can be regarded to diffuse by vacancies. The f_I value of Antoniadis *et al.* for Sb, which is 0.03, indicates the dominant role of vacancies in Sb diffusion (15). The above models were proposed to explain experimental results assuming the changes in concentration of interstitials and vacancies. More experimental data is necessary to show the validity of this model. The experimental data of this subject could be summarized as follows.

Taniguchi *et al.* found that the OED range from the oxidizing Si-SiO_2 interface is 25 μm and is independent of oxidation time (12). They proposed that vacancies only develop in Si with heat-treatment using inert ambients and that interstitials are generated only at the oxidizing Si-SiO_2 interface.

The authors found ORD of Sb in Si under the same condition in which B and P exhibit OED (4). This result indicates that the increase in point defect concentration causing B and P diffusion and the decrease in concentration of defects causing Sb diffusion, occur at the same time. Consequently, they proposed the equilibrium between interstitials and vacancies to be

$$I + V \leftrightharpoons \text{Null} \qquad [1]$$

where I, V, and Null denote interstitials, vacancies, and perfect crystal, respectively. Hence, the following relation holds regardless of ambient or location in Si

$$C_I \times C_V = \text{constant} \qquad [2]$$

where C_I and C_V denote the concentration of interstitials and vacancies.

Recently, Tan *et al.* found OED of Sb in (111) Si under the condition in which B and P exhibit ORD (17). This shows that undersaturation of interstitials and supersaturation of vacancies actually occur at the same time and strengthens the model that interstitials and vacancies in Si effect thermal equilibrium.

On the other hand, Antoniadis *et al.* found that ORD of Sb in Si occurs about an hour after the beginning of oxidation at 1100°C (15). Their results show that the equilibrium reaction of Eq. [1] takes several hours.

* Electrochemical Society Active Member.
Key words: silicon, Sb diffusion, oxidation, anomalous diffusion.

Gosele *et al.* proposed that the above delay is caused by an entropy barrier (18). They showed that some time duration is necessary to achieve thermal equilibrium.

In this experiment, the ORD range of Sb is investigated in detail to clarify the validity of the model that local equilibrium between interstitials and vacancies holds.

Experimental

The sample preparation procedure for this experiment is shown in Fig. 1. The substrates used were p-type FZ- or CZ-grown (100)-oriented wafers with electrical resistivities of 20-30 Ω-cm. The wafers were 400 μm thick. Antimony predeposition diffusion was carried out at 1175°C in an N_2 ambient for 30 min with Sb_2O_3 as the diffusion source (19). The sheet resistivity of the Sb-diffused layers was 40 Ω/□ and the junction depth was 0.8 μm. The samples were oxidized at 1000°C in dry O_2 for 60 min to grow 50 nm thick SiO_2 films.

Silicon nitride films 75 nm thick were grown on the back surface of the wafers at 800°C with SiH_4 and NH_3 as sources. These Si_3N_4 films at the back were selectively removed by photoetching. The etching mask pattern is shown in Fig. 2.

Striped patterns with frames were used to preserve the stiffness of the samples after Si etching. The SiO_2 films on the surface of the samples were removed by chemical etching with a buffered HF etchant. The 75 nm thick Si_3N_4 films were deposited by chemical vapor deposition on the front surface of the samples. Then, the uncovered areas on the back of the wafers were etched to reduce their thickness. A 40 weight percent (w/o) KOH aqueous solution was used at 80°C for this Si etching. The depth of the Si etching ranged from 100 to 300 μm.

A microphotograph of a cross section of the samples after Si etching is shown in Fig. 3, and a schematic cross section of the sample is shown in Fig. 4a. Impurity diffused layers directly covered with Si_3N_4 films were formed on the front of the samples (top of Fig. 4a). There are two areas on the back of the samples (bottom of Fig. 4a); one is the area covered with double-layered SiO_2-Si_3N_4 films (the BN area), and the other is the bare Si-etched area (the BO area).

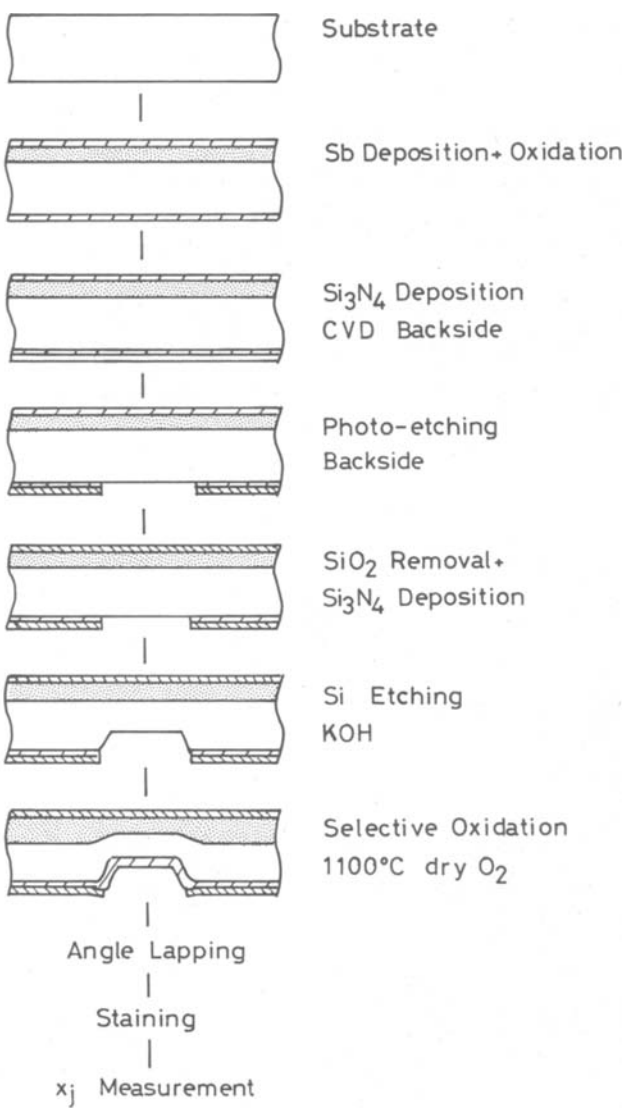

Fig. 1. Sample preparation procedure

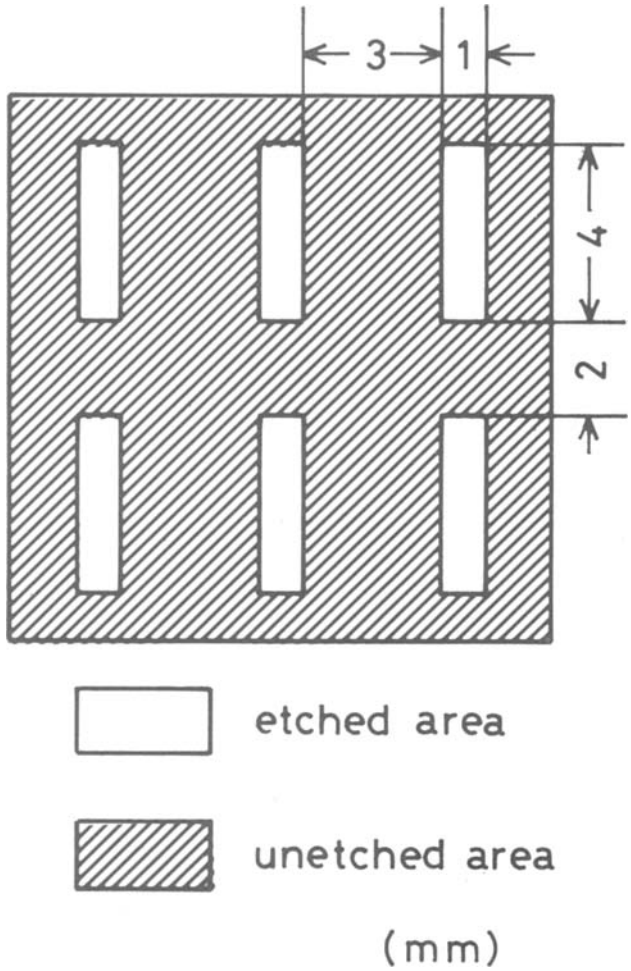

Fig. 2. Photoetching mask pattern

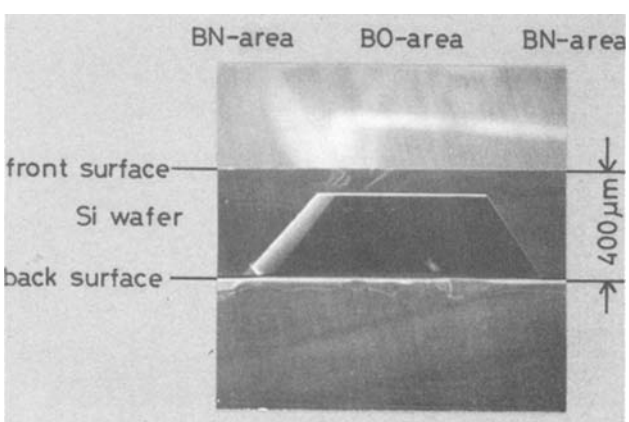

Fig. 3. Cross-sectional view of the samples (SEM microphotograph)

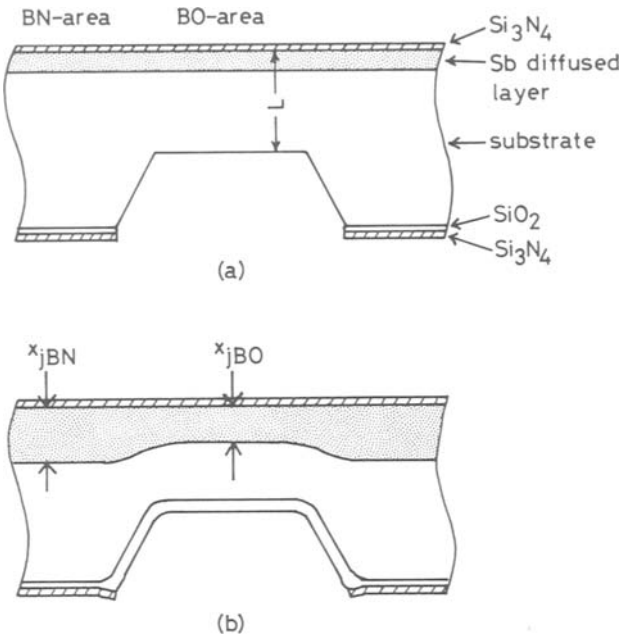

Fig. 4. Schematic cross section of the samples: (a) before BSO, (b) after BSO.

The back-sides of the samples were oxidized at 1100°C in dry O_2. The oxidation times ranged from 500 to 4000 min. A schematic cross section of the samples after oxidation is shown in Fig. 4b. Then, the samples were angle-lapped with Al_2O_3 powder, and the pn junction was revealed by staining (20). The junction depths in both the BN and BO areas (x_{jBN} and x_{jBO} in Fig. 4b) were measured using a microscope and scale.

Experimental Results

The results of 500 min BSO at 1100°C in dry O_2 are shown in Fig. 5. The horizontal axis is the distance L between the oxidized Si-SiO_2 interface and the front surface (L = wafer thickness minus Si etching depth). The vertical axis is the ratio of x_j in the BO area to that in the BN area. This can also be represented as the time average of the square root of the ratio of the impurity diffusion coefficient in the BO and BN areas. That is

$$\frac{x_{jBO}}{x_{jBN}} = \sqrt{\frac{D_{BO}}{D_{BN}}} \quad [3]$$

where, D_{BO} and D_{BN} denote the time average of the impurity diffusion coefficient in the BO and BN areas. Deviation of x_{jBO}/x_{jBN} from unity signifies enhancement or retardation of diffusion by BSO in the BO area. It can be seen that x_{jBO}/x_{jBN} in the FZ Si substrates masked with Si_3N_4 films (white circles) is smaller than unity, indicating diffusion retardation by BSO. The deviation of x_{jBO}/x_{jBN} from unity is larger for a smaller L. This indicates that the effect of BSO on Sb diffusion is reduced with an increase in distance from the oxidizing Si-SiO_2 interface. The range for Sb of ORD (the value of L at which x_{jBO}/x_{jBN} becomes unity) is about 300 μm.

x_{jBO}/x_{jBN} in CZ substrates under Si_3N_4 films (white cube) does not significantly deviate from unity, indicating that the range of ORD effect for BSO is very small in comparison to that in FZ substrates. This x_{jBO}/x_{jBN} under double-layered SiO_2-Si_3N_4 films for both FZ and CZ substrates (black circle and cube) is unaffected by BSO. These results are similar to those for B and P diffusion (6).

The results for 1000 min BSO are shown in Fig. 6. Characteristics for 500 min oxidation are not changed. However, the deviation of x_{jBO}/x_{jBN} from unity is larger and the range of effect of BSO is also larger. The results for both 2000 and 4000 min oxidation are shown in Fig. 7 and 8. The increase in ORD range seems to begin to saturate.

The shape of the pn junction at the boundary between the BO and BN areas is shown in Fig. 9. The slope of the pn junction at the pattern edge is gradual. This is similar to the case for B and P diffusion (6) and suggests that the effect of oxidation spreads not only vertically but also horizontally. The results also suggest that lattice strain caused by selective oxidation does not affect Sb diffusion.

The results of this experiment and those of B and P experiments (6) are summarized in Fig. 10. It can be seen from that figure that the range of OED for B and P and the ORD range for Sb are similar. Moreover, the deviation of x_{jBO}/x_{jBN} from unity for B and P is similar to that for Sb. This suggests the existence of local equilibrium between interstitials and vacancies.

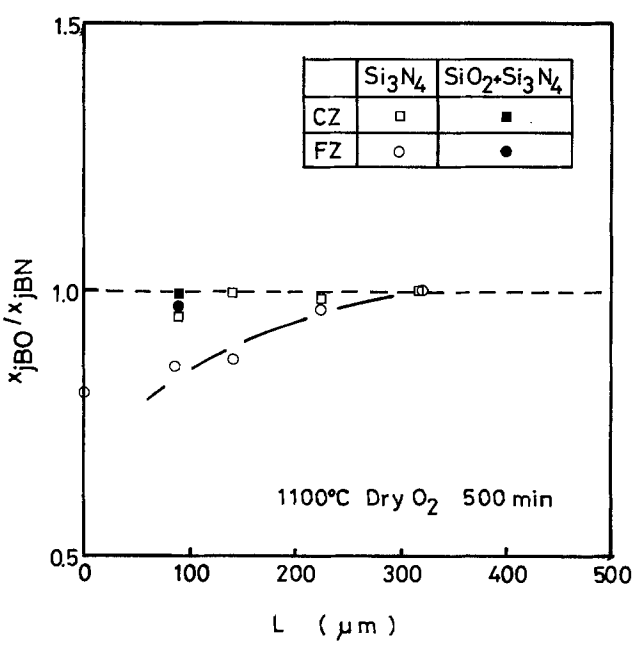

Fig. 5. x_{jBO}/x_{jBN} vs. L: 1100°C, dry O_2, 500 min

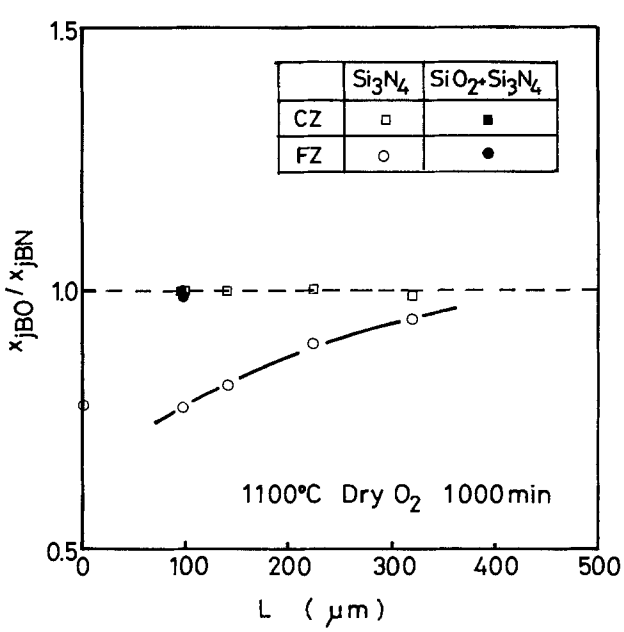

Fig. 6. x_{jBO}/x_{jBN} vs. L: 1100°C, dry O_2, 1000 min

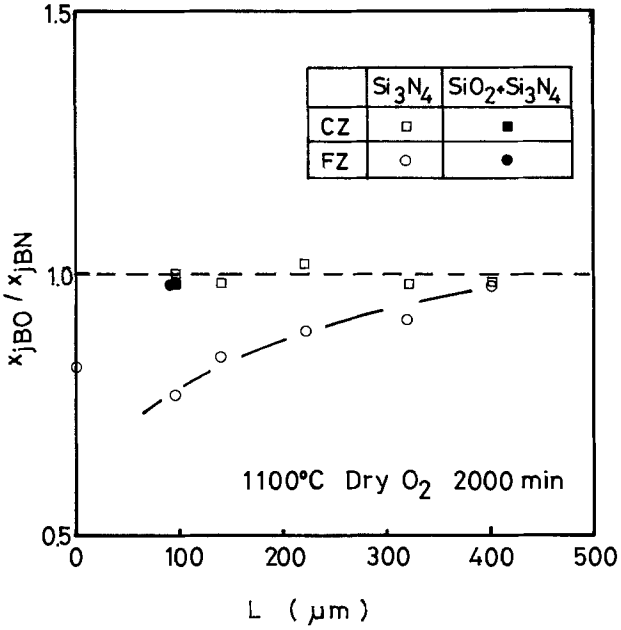

Fig. 7. x_{jBO}/x_{jBN} vs. L: 1100°C, dry O_2, 2000 min

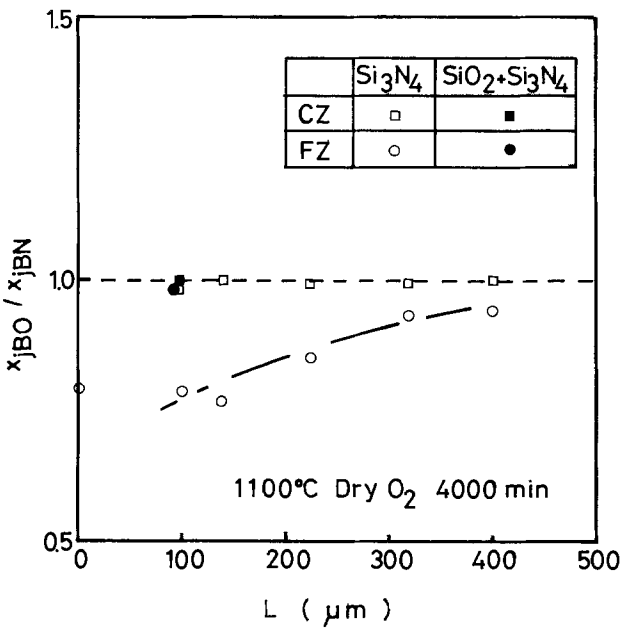

Fig. 8. x_{jBO}/x_{jBN} vs. L: 1100°C, dry O_2, 4000 min

Discussion

The results of this experiment can be summarized thusly:

1. The ORD range of Sb due to BSO increases with oxidation time.
2. The ORD range of Sb due to BSO agrees with that of OED for B and P.
3. The extent of ORD for Sb is similar to that of OED for B and P.
4. Sb diffusion at the front of FZ Si substrates that are directly covered with Si_3N_4 films is retarded by BSO.
5. Sb diffusion at the front of FZ Si substrates masked with double-layered SiO_2-Si_3N_4 films is not affected by BSO.
6. Sb diffusion at the front of CZ Si is not affected by BSO under either Si_3N_4 or SiO_2-Si_3N_4 films.

The above results can be considered in relation to the point defect structure in Si, and the defect model can be deduced.

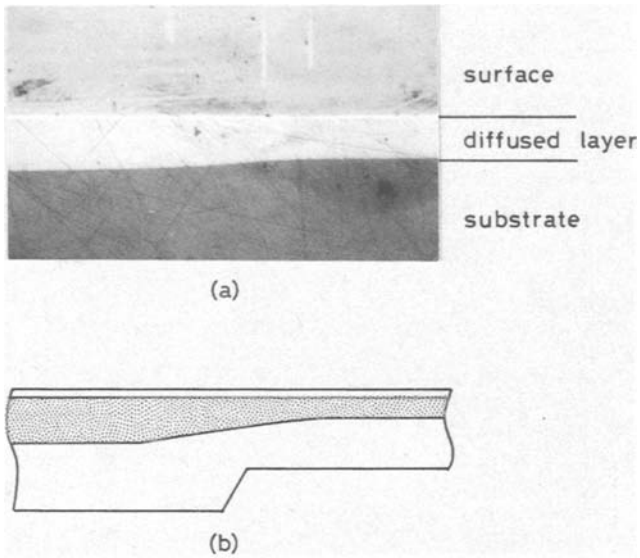

Fig. 9. Junction shape at the boundary between the BO and BN areas: 1100°C, dry O_2, 2000 min.

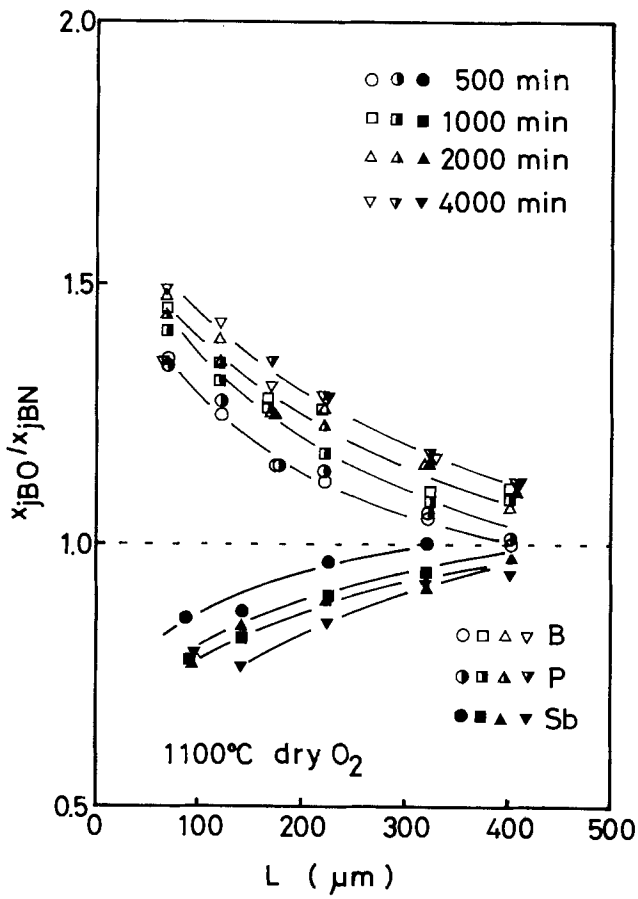

Fig. 10. x_{jBO}/x_{jBN} vs. L for B, P, and Sb: 1100°C dry O_2

Point defect structure and impurity diffusion.—Result 1 shows that the distribution of point defects contributing to Sb diffusion increases with BSO duration. This suggests that distribution of point defects is determined by their diffusion.

As is mentioned in the section on point defect and impurity diffusion model, B and P can be regarded as diffusing, at least mainly, by interstitials. Therefore, the OED range from the oxidizing Si-SiO_2 interface represents the distribution of supersaturated interstitials. Similarly, the ORD range of Sb can be considered to correspond to the distribution of under-

saturated vacancies. Hence, Result 2 shows that the increase in supersaturated interstitial distribution agrees with that of undersaturated vacancy distribution. This supports the model that interstitials and vacancies effect thermal equilibrium.

Result 3 supports the proposal that the fraction of f_I is unity for B and P and that f_I is zero for Sb.

Antoniadis *et al.* found that ORD of Sb in Si occur about an hour after the beginning of oxidation at 1100°C (15). However, this does not negate the presence of thermal equilibrium between interstitials and vacancies. If the time delay in Sb ORD proposed by Antoniadis *et al.* exists, the range of OED for B and P and that of ORD for Sb may differ. However, the results in Fig. 10 show no significant difference in these ranges. This may be due to the long BSO time in this experiment. A BSO experiment with smaller L and shorter BSO time will clarify the effect of time delay.

Effect of surface films on impurity diffusion.—In this experiment, retarded diffusion by back-side oxidation is found only under directly formed Si_3N_4 films. This is similar to the case of B- and P-enhanced diffusion by back-side oxidation (6). The authors have found anomalous-enhanced diffusion of B and P in CZ Si under directly formed Si_3N_4 films (21, 22) and have proposed that (*i*) the Si-SiO_2 interface reacts with point defects in Si and preserves their concentration and (*ii*) the Si-Si_3N_4 interface does not react with point defects in Si.

The effect of surface films in this experiment can be explained by the above model. Excess Si atoms introduced into Si crystals while oxidizing the back surface diffuse toward the front surface. In the case of directly formed Si_3N_4 film at the front surface, excess Si atoms reaching the front surface decrease the vacancy concentration near the front surface. Consequently, Sb diffusion is retarded. On the other hand, in the case of double-layered SiO_2-Si_3N_4 films, excess Si atoms reaching the front surface react with the Si-SiO_2 interface and vanish. Therefore, no decrease in vacancy concentration or Sb-retarded diffusion occurs.

Hu found that the shrinkage of oxidation-induced stacking faults (OSF's) is interrupted by directly formed Si_3N_4 films (23). Recently, the authors found that OSF's under directly formed Si_3N_4 films grow due to BSO but that those under double-layered SiO_2-Si_3N_4 films shrink (24). These OSF behaviors strengthen the difference in interface characteristics.

Effect of substrate crystal growing method.—The results of this experiment show that Sb-retarded diffusion does not occur in CZ Si crystals even under directly formed Si_3N_4 films. Two effects cause this phenomenon. One is that oxygen precipitate formation with subsequent supersaturation of interstitials and undersaturation of vacancies occurs in CZ Si during BSO. The changes in point defect concentration affect impurity diffusion under directly formed Si_3N_4 films: B and P diffusion is enhanced and Sb diffusion is retarded (21, 22, 25). This effect occurs not only in the BO area but also in the BN area (21, 22). Consequently, the difference in diffusion caused by BSO between the two areas is canceled.

The other effect is that oxygen precipitates formed in CZ Si crystals make extrinsic stacking faults and they act as sinks for excess Si atoms. The excess Si atoms diffusing from the oxidizing back surface toward the front surface in the BO area are captured by stacking faults in the crystal bulk and cannot reach the front surface. Hence, Sb-retarded diffusion does not occur in CZ crystals. On the other hand, the concentration of oxygen in FZ Si is very low and precipitate formation does not occur. Therefore, excess Si atoms diffusing from the oxidizing back surface can reach the front surface.

The fact that the OED range obtained by Taniguchi *et al.* in CZ Si is small compared to that in FZ Si supports the above explanation (5, 6, 12).

Remaining questions.—The results of this paper strongly suggest the existence of local equilibrium between interstitials and vacancies. However, several questions remain. One is the ratio of the concentration of interstitials to the concentration of vacancies, which is not clear at this point. Another question is which point defect is the major diffusant in Si crystals. Further investigation is necessary to clarify both these questions. The latter question may be solved by experiments with the effect of oxidation on self-diffusion of Si. That is, if interstitials are the major diffusant, self-diffusion of Si would be enhanced by thermal oxidation. On the other hand, if Si atoms move in Si by vacancies, self-diffusion of Si would be retarded by oxidation.

Conclusion

The range of ORD from the oxidizing Si-SiO_2 interface has been investigated for Sb diffusion in Si by BSO. The experimental results can be summarized as follows:

1. Sb diffusion at the front of FZ Si substrates directly covered with Si_3N_4 films is retarded by BSO.
2. Sb diffusion at the front of FZ Si substrates masked with double-layered SiO_2-Si_3N_4 films is not affected by BSO.
3. Sb diffusion at the front of CZ Si is not affected by BSO under either Si_3N_4 or SiO_2-Si_3N_4 films.
4. The range of ORD due to BSO increases with oxidation time.
5. The ORD ranges of Sb with BSO are almost equal to the OED ranges of B and P with BSO.

These results confirm that the ORD of Sb is the inverse effect of OED of B and P. This phenomenon is explained most consistently by a model with local equilibrium between interstitials and vacancies.

Acknowledgment

The authors wish to thank S. Nakamura for his help with Sb diffusion.

Manuscript submitted July 30, 1982; revised manuscript received *ca.* Feb. 15, 1983.

Hitachi Limited assisted in meeting publication costs of this article.

REFERENCES

1. W. G. Allen and K. V. Anand, *Solid-State Electron.*, **14,** 397 (1971).
2. G. Masetti, S. Solmi, and G. Soncini, *Philos. Mag.*, **33,** 613 (1976).
3. Y. Ishikawa, Y. Sakina, H. Tanaka, S. Matsumoto, and T. Niimi, *This Journal*, **129,** 644 (1982).
4. S. Mizuo and H. Higuchi, *Jpn. J. Appl. Phys.*, **20,** 739 (1981).
5. S. Mizuo and H. Higuchi, *ibid.*, **21,** 272 (1982).
6. S. Mizuo and H. Higuchi, *This Journal*, **129,** 2292 (1982).
7. S. M. Hu, "Atomic Diffusion in Semiconductor," D. Shaw, Editor, p. 217, Plenum Press, London (1973).
8. U. Gösele, F. Morehead, H. Foll, W. Frank, and H. Strunk, "Semiconductor Silicon 1981," H. R. Huff, P. J. Kriegler, and Y. Takeishi, Editors, p. 766, The Electrochemical Society, Pennington, NJ (1981).
9. U. Gosele and H. Strunk, *Appl. Phys.*, **20,** 265 (1979).
10. S. M. Hu, *J. Appl. Phys.*, **45,** 1567 (1974).
11. D. A. Antoniadis, A. G. Gonzalez, and R. W. Dutton, *This Journal*, **125,** 813 (1978).
12. K. Taniguchi, K. Kurosawa, and M. Kashiwagi, *ibid.*, **127,** 2243 (1980).
13. S. Mizuo and H. Higuchi, *Jpn. J. Appl. Phys.*, **21,** 56 (1982).
14. S. Mizuo and H. Higuchi, *Denki Kagaku*, **50,** 338 (1982).
15. D. A. Antoniadis and I. Moskowitz, *J. Appl. Phys.*,

53, 6788 (1982).
16. T. Y. Tan and U. Gösele, *Appl. Phys. Lett.*, **40**, 616 (1982).
17. T. Y. Tan and B. J. Ginsberg, *ibid.*, (1983).
18. U Gösele, W. Frank, and A. Seeger, *Solid State Commun.*, **45**, 5 (1983).
19. M. Nanba, *This Journal*, **128**, 420 (1981).
20. W. R. Runyan, "Semiconductor Measurements and Instrumentation," p. 207, McGraw-Hill, New York (1975).
21. S. Mizuo and H. Higuchi, *Jpn. J. Appl. Phys.*, **20**, 791 (1981).
22. S. Mizuo and H. Higuchi, *ibid.*, **21**, 281 (1982).
23. S. M. Hu, *J. Appl. Phys.*, **51**, 3666 (1980).
24. S. Mizuo and H. Higuchi, *Jpn. J. Appl. Phys.*, **21**, 1547 (1982).
25. S. Mizuo and H. Higuchi, *Denki Kagaku*, **51**, 403 (1983).

Effects of Exposure Atmosphere and Ejected Electrons on PGMA Negative Resist Cross-Linking in X-Ray Lithography

K. Okada, K. Suzuki, and J. Matsui

NEC Corporation, Microelectronics Research Laboratories, 4-1-1, Miyazaki, Miyamae-ku, Kawasaki 213, Japan

ABSTRACT

The exposure atmosphere effect for poly (glycidyl methacrylate) (PGMA) in x-ray lithography using an Al x-ray source has been studied with special reference to the interaction with electrons ejected from the gold film on the x-ray mask. The exposures were performed in a pressure-controlled exposure chamber, using a 1.7 kW stationary Al source and a gap-controlled mask and wafer assembly. PGMA cross-linking distinctly increases, as the atmosphere pressure is increased from 6.7 to 2670 Pa, when using the x-ray masks with thin gold films. As the mask-to-wafer gap is increased from 6 μm to 1 mm, PGMA cross-linking markedly decreases when using these masks. An interpretation of the mechanism for the observed effects is also presented. Furthermore, protective films, such as Mylar, polyimide, and silicon nitride, have been examined to suppress electrons ejected from the gold film.

X-ray lithography is a promising technology for replicating very high resolution patterns. However, for replication of submicron-size features, problems such as the effects of photoelectrons and Auger electrons from the x-ray mask (1, 2) and exposure atmosphere effect (3, 4) should be elaborately investigated. Maldonado *et al.* (1) have studied the effects caused by the continuous radiation when using Rh and Pd x-ray sources. It has been reported that the photoelectrons and Auger electrons ejected from the x-ray mask, and also from the resist substrate, decrease the resolution and contrast of the exposed pattern. Moran *et al.* (3) have shown the exposure atmosphere effect in the mixture of 92.5 weight percent (w/o) poly (2,3-dichloro-1-propyl acrylate) and 7.5 w/o COP (DCOPA). According to Ref. (3), the 1 μm resolution for DCOPA negative resist cannot be accomplished without a carefully controlled atmosphere of nitrogen and oxygen when using a Pd x-ray source. Saitoh *et al.* (2) have reported the effects of photoelectrons and Auger electrons ejected from the x-ray mask on the contrast and resolution in resist pattern replication when using an Mo x-ray source.

To date, studies concerning the above problems have been made using the x-ray sources in the shorter wavelength range from 0.4 to 0.6 nm. A previous work (4) pointed out the exposure atmosphere dependence of PGMA negative resist cross-linking when using an Al x-ray source. In the present work, the exposure atmosphere effect on PGMA cross-linking was examined in connection with the effects of the electrons ejected from the gold film fabricated on the x-ray mask. The exposure-atmosphere pressure dependence, the mask-to-wafer gap dependence, and the effect of using protective films are described.

Experimental

The schematic of the x-ray exposure system used is illustrated in Fig. 1. The source contains a water-cooled 1.7 kW stationary Al target which is columnar in shape and has ten exchangeable foci formed on the side of the column. Focus exchange can easily be obtained by revolving the target at small angle increments in the mounting to the x-ray tube. The exposure chamber is separated from the source chamber by a 25 μm thick Be window. The pressure in the exposure chamber is varied in the range from 1 to 10^4 Pa by controlling a rotary pump evacuation with a vacuum valve. A mask and wafer assembly in the exposure chamber is set 22 cm from the target. The mask-to-wafer gap is varied in the range from a few μm to 10^3 μm using Mylar or stainless steel spacers. The incident x-ray flux density Φ is given by

$$\Phi = \eta \cdot P \cdot Tw \cdot Td \cdot Tm \cdot \frac{1}{l^2} \qquad [1]$$

where η is the radiated characteristic x-ray power per watt per steradian (5), P the input power, Tw the transmission factor for the window, Td the transmission factor for the target-to-mask atmosphere, Tm the

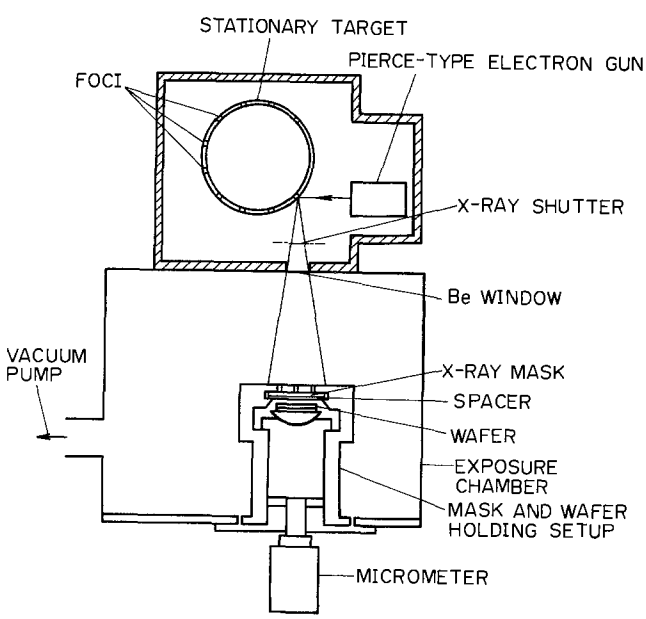

Fig. 1. X-ray exposure system schematic

Key words: pressure, polymers, absorption, integrated circuits.

transmission factor for the mask, and l the target-to-mask distance. Exposure time is decided upon based on the equation $T = D/\Phi$, where D is the required radiation dose per unit area.

The x-ray mask substrates were silicon nitride membranes made by plasma-CVD method (6). Thin gold films were deposited on the substrate by rf-sputtering, and several protective layers were overlaid on the gold film. The exposure aspect for x-ray mask, spacer and resist-coated Si wafer is illustrated in Fig. 2. The spacer and the Si ribs of the x-ray mask were utilized as x-ray absorbers.

The PGMA was obtained from Tokyo Ohka Kogyo Company, Limited. Its weight average molecular weight and polydispersity were 89,000 and 1.47, respectively. The resist films were prebaked at 80°C in nitrogen gas for 10 min. The average resist thickness was 0.74 μm. Exposed samples were developed by immersing them in a 7:1 mixture of methyl ethyl ketone and ethanol at 23°C for 2 min. They were then rinsed in methyl isobutyl ketone at 23°C for 1 min. The resist thickness was measured with a Talystep.

Results and Discussion

The PGMA sensitivity curve by Al Kα x-ray irradiation was obtained under 6.7 Pa pressure in the exposure chamber. The dose required to leave 60% resist thickness under no x-ray mask condition was 30 mJ/cm². For all exposures, the dose to PGMA resist and the electron accelerating voltage to Al target were maintained at 30 mJ/cm² and 17 kV, respectively. Air was used as a gas medium in the exposure chamber. Therefore, for all exposures performed here, the exposure time was adjusted to provide the Al Kα dose of 30 mJ/cm² to PGMA resist, since gas absorption increases with an increase in air pressure.

Figure 3 shows the pressure dependence of the remaining PGMA film thickness. Under no x-ray mask condition, the remaining PGMA film thickness gradually decreased as the pressure in the space separating mask and resist-coated wafer was increased from 6.7 to 2670 Pa. As is generally known (3), this is attributed to PGMA cross-linking retardation by oxygen molecules. On the contrary, when an x-ray mask with a 17 nm thick gold film on the silicon nitride membrane was employed, the remaining PGMA film thickness distinctly increased with an increase in pressure. Here, the mask-to-wafer gap was kept at 20 μm. Furthermore, the pressure dependence was examined in the case of the x-ray masks with 42 and 90 nm thick gold films. The results obtained were nearly the same as in the case of the x-ray mask with 17 nm thick gold film.

A study was undertaken to examine the above-mentioned novel pressure dependence. The effect of the mask-to-wafer gap on the remaining PGMA film thickness is shown in Fig. 4. Here, the pressure used, which was the highest value attainable in the system, was kept at 2670 Pa. As the mask-to-wafer gap was increased from 6 μm to 1 mm, the remaining PGMA film thickness markedly decreased and approached the value under no x-ray mask condition. Gold film thickness dependence was not recognized.

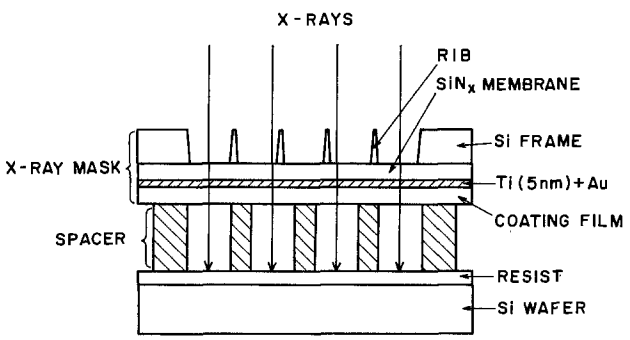

Fig. 2. Cross-sectional representation of x-ray mask, spacer, and resist-coated Si wafer under exposure condition.

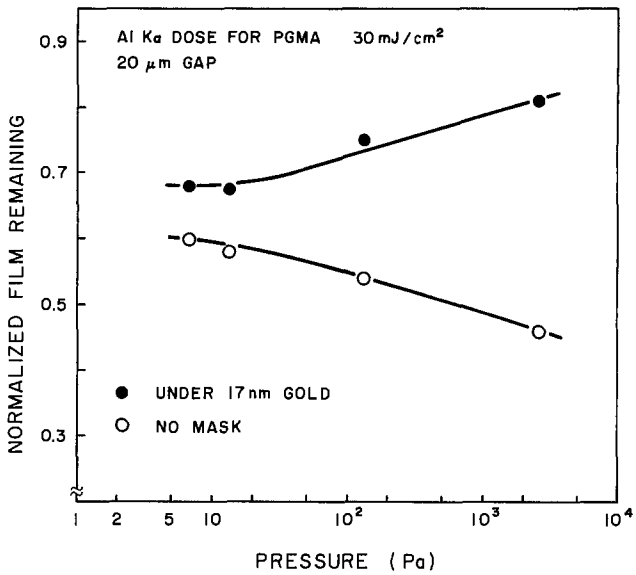

Fig. 3. Exposure-atmosphere pressure dependence of the remaining PGMA film thickness.

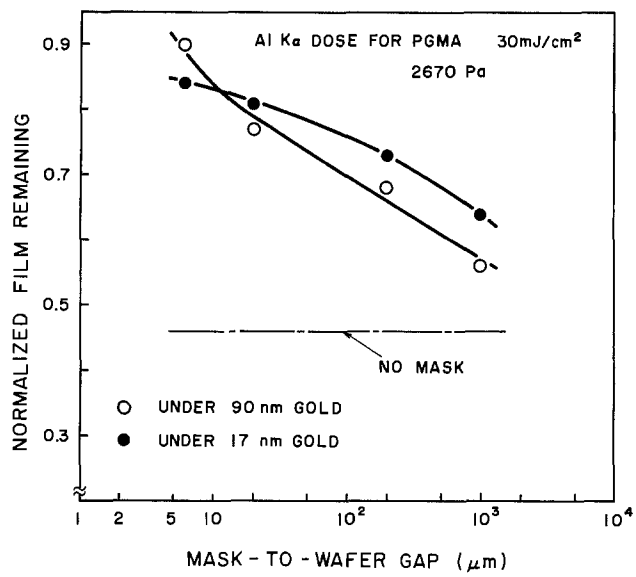

Fig. 4. Mask-to-wafer gap dependence of the remaining PGMA film thickness. Pressure was maintained at 2670 Pa.

The authors postulate a mechanism that can account for the observed effects. In the energy region below 10 keV, the range-energy relation $R = 900\ \rho^{-0.8}E^{1.3}$ was found with R in Å, ρ in g cm^{-3}, and E in keV (7). Thereby, R in the gas medium (air) is estimated to be more than ~0.36 mm in the pressure range used here, assuming that $E = \sim 1$ keV. Therefore, the majority of electrons ejected from the gold film appear to reach the PGMA film, since the mask-to-wafer gap is 20 μm: (*i*) Photoelectrons and Auger electrons are ejected into the mask-to-wafer space by the absorption of x-rays in the gold film on the x-ray mask. (*ii*) With the ionization of the constituents of air by these electrons, a large number of secondary electrons are produced in the space. (*iii*) PGMA cross-linking is promoted to a greater extent by the total electrons comprising both electrons ejected from the gold film and those produced by secondary ionization.

For the results indicated in Fig. 3, it should be noted that the amount of photoelectrons and Auger electrons in each point, ejected from the gold film, is theoretically constant even in the case of pressure variations. Therefore, the mechanism for surplus secondary elec-

tron production through the ionization of air appears most relevant. The stopping power (8), which indicates the standard ionization quantity, is approximated by

$$-\frac{dE}{dx} \propto N \cdot Z \qquad [2]$$

where N is the number of atoms per unit volume, Z atomic number, E incident energy, and x electron trajectory. Equation [2] represents that the stopping power is proportional to the density of air. An increase in the pressure in the mask-to-wafer space leads to an increase in the density of air. Consequently, it is interpreted that surplus secondary electrons are produced with an increase in pressure. The mask-to-wafer gap dependence of the remaining PGMA film thickness (Fig. 4) also appears to support the above mechanism. Namely, it is appropriate to consider that the energy absorption of electrons ejected from the gold film in the air in the mask-to-wafer space, as a general tendency, decreases with an increase in the gap (9). Finally, the observed effects seem to be temporarily interpreted by the above mechanism.

In order to suppress the photoelectrons and Auger electrons generated from the gold film on the x-ray mask, a few protective films covering the gold film were tested. Figure 5 shows the pressure dependence of the remaining PGMA film thickness when using Mylar films as a protective layer. The mask-to-wafer gap was kept at 20 μm, and a 4 μm thick Mylar film was put on the x-ray mask. As shown in this figure, the data for both a 4 μm thick Mylar film mask alone and the 17 nm thick gold film mask covered with a 4 μm thick Mylar film almost agree with those under direct x-ray exposure. The results indicate that electrons ejected from the gold film on the x-ray mask can be effectively eliminated by the Mylar film and that almost no electrons are ejected from the Mylar film itself. Results for polyimide films used as a protective layer are shown in Fig. 6. The polyamic acid was spin-coated on the x-ray masks and next converted to polyimide by curing the film at 150°C for 30 min and then at 300°C for 1 hr. As the pressure was increased from 6.7 to 2670 Pa, the remaining PGMA film thickness was much more retarded under a 1.4 μm thick polyimide film mask than under direct x-ray exposure. In addition, when using the 20 nm thick gold film mask coated by a 1.4 μm thick polyimide film, the remaining PGMA film thickness was much more retarded with an increase in pressure than when using a 1.4 μm

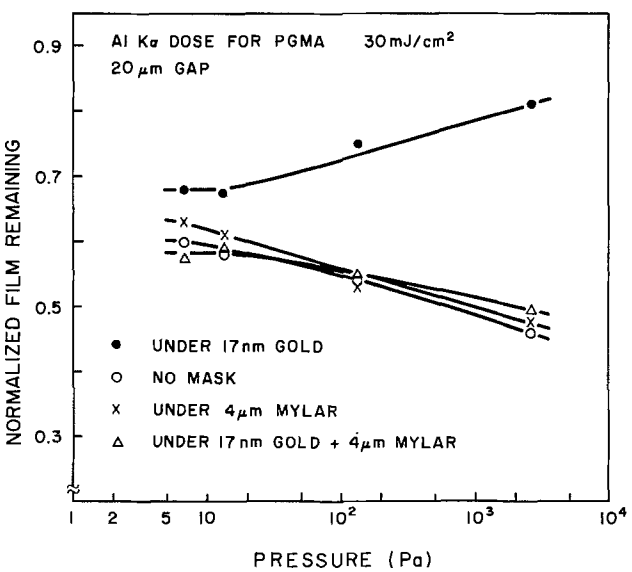

Fig. 5. Effect of Mylar films utilized as a protective layer. The pressure dependence of the remaining PGMA film thickness is demonstrated.

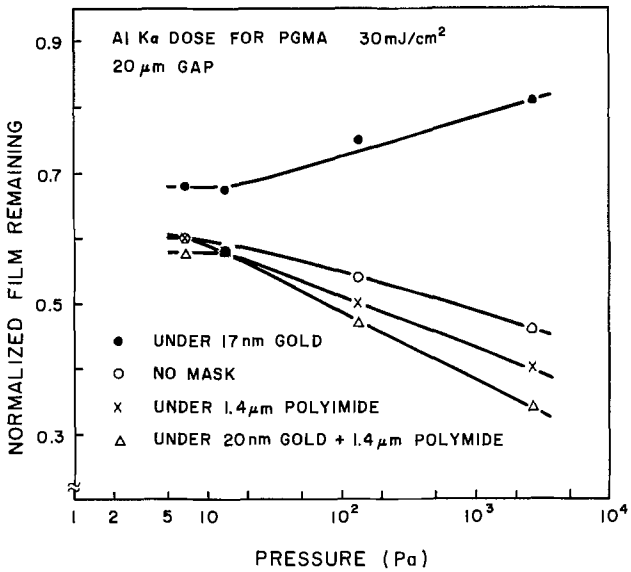

Fig. 6. Effect of poyimide films utilized as a protective layer

thick polyimide film mask. In the previous work (4), we indicated similar tendencies in experiments employing polyimide film masks. Comparisons, however, were made first in this study between polyimide film masks and direct x-ray exposure. Silicon nitride films, produced by plasma CVD method, were tried as an example of inorganic protective layer. As indicated in Fig. 7, the data for a 1.2 μm thick silicon nitride film mask alone and the 20 nm thick gold film mask covered with a 0.9 μm silicon nitride film agree fairly well with those under direct x-ray exposure. With a silicon nitride film of a suitable thickness, it appears that photoelectrons and Auger electrons generated from the x-ray mask are effectively stopped.

Conclusions

Results on the exposure obtained with an Al x-ray source are summarized as follows:

1. PGMA cross-linking distinctly increases, as the exposure atmosphere pressure is increased from 6.7 to 2670 Pa, when using the x-ray masks with thin gold films.
2. As the mask-to-wafer gap is increased from 6 μm to 1 mm, PGMA cross-linking markedly decreases and approaches the value pertaining under direct x-ray exposure when using these masks.

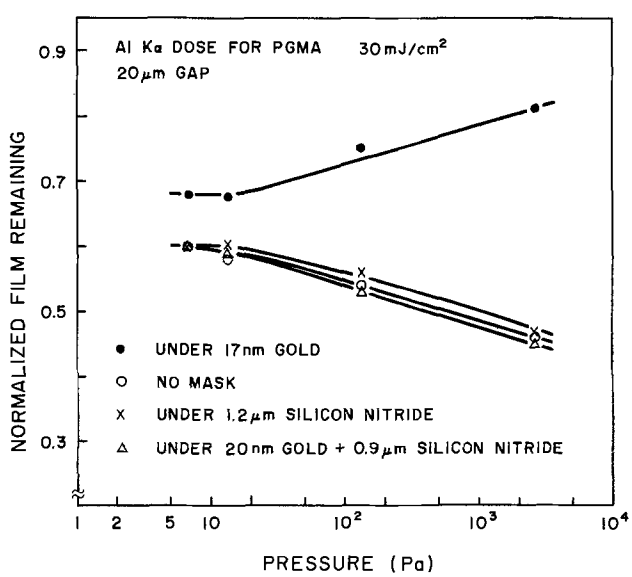

Fig. 7. Effect of silicon nitride films utilized as a protective layer.

3. These observations are temporarily interpreted in terms of PGMA cross-linking variation basically dependent on the ionization quantity of air caused by electrons ejected from the gold film fabricated on the x-ray mask.

4. In order to suppress electrons ejected from this gold film, a few protective films have been examined. It appears that silicon nitride and Mylar films satisfy the demand.

Acknowledgment

The authors wish to thank Drs. S. Asanabe, K. Ayaki, D. Shinoda, and Y. Okuto for their continuous encouragement.

Manuscript submitted Dec. 27, 1982; revised manuscript received April 21, 1983.

NEC Corporation assisted in meeting publication costs of this article.

REFERENCES

1. J. R. Maldonado, G. A. Coquin, D. Maydan, and S. Somekh, *J. Vac. Sci. Technol.*, **12**, 1329 (1975).
2. Y. Saitoh, H. Yoshihara, and I. Watanabe, *Jpn. J. Appl. Phys.*, **21**, L52 (1982).
3. J. M. Moran and G. N. Taylor, *J. Vac. Sci. Technol.*, **16**, 2020 (1979).
4. K. Okada, *Jpn. J. Appl. Phys.*, **20**, L22 (1981).
5. D. Maydan, G. A. Coquin, J. R. Maldonado, S. Somekh, D. Y. Lou, and G. N. Taylor, *IEEE Trans. Electron Devices*, **ed-22**, 429 (1975).
6. K. Suzuki and J. Matsui, *J. Vac. Sci. Technol.*, **20**, 191 (1982).
7. H. J. Fitting, *Phys. Status Solidi A*, **26**, 525 (1974).
8. See, for example, H. A. Bethe, "Handbuch der Physik," Vol. 34, S. Flugge, Editor, p. 62, Springer-Verlag, Berlin (1958).
9. See, for example, L. V. Spencer and U. Fano, *ibid.*, p. 121.

Modeling and Analysis of Low Pressure CVD Reactors

K. F. Jensen and D. B. Graves

Department of Chemical Engineering and Materials Science, University of Minnesota, Minneapolis, Minnesota 55455

ABSTRACT

A detailed mathematical model for the hot wall multiple-disk-in-tube LPCVD reactor is developed by using reaction engineering concepts. This model includes the convective and diffusive mass transport in the annular flow region formed by the reactor wall and the edges of the wafers as well as the surface reactions on the reactor wall. In addition, the model describes the coupling of diffusion between and reaction on the wafers. Variations in gas velocities and diffusion fluxes due to net changes in the number of mols in the deposition are also taken into account as are nonisothermal operating conditions. The combined reactor equations are solved by orthogonal collocation. The deposition of polycrystalline Si from SiH_4 is considered as a specific example, and the model is employed in estimation of kinetic rate constants from published reactor measurements. The effects on the growth rates and film thickness uniformity (within each wafer and from wafer to wafer) of variations in flow rates, reactor temperature profiles, and SiH_4 concentration in the feed stream are analyzed. The model predictions show good quantitative agreement with published experimental data from different sources. Finally, recycle of reactor effluent is considered a typical commercial operating conditions, and it is demonstrated that this modification produces higher growth rates and better film uniformity than can be achieved in conventional LPCVD processing.

Chemical vapor deposition (CVD) is a key process in the semiconductor industry for growing thin solid films, in particular polycrystalline Si, Si_3N_4, and SiO_2 films. These materials are grown predominantly in tubular, hot wall, low pressure chemical vapor deposition (LPCVD) reactors which have replaced the earlier cold wall atmospheric pressure reactors. This change has come about because LPCVD reactors allow a larger number of wafers to be processed with better uniformity of film thickness and composition within and among the wafers. Table I gives a summary of LPCVD process conditions for polycrystalline Si, Si_3N_4, and SiO_2. The very large packing densities of wafers that can be realized in LPCVD reactors are possible because at the low process pressures (0.5-1 Torr), the diffusion coefficients are three orders of magnitude larger than at atmospheric pressure so that the chemical reactions at the surface of the wafers are rate controlling rather than mass transfer processes. Moreover, in spite of the low pressures, rates of deposition in LPCVD are only five to ten times less than those obtained in atmospheric CVD since the reactants are used with little or no diluent in LPCVD whereas they are strongly diluted in conventional CVD (1). The wall deposits, which are avoided in cold wall reactors, could create particulate problems in LPCVD processes. However, these potential problems may be avoided by keeping the cumulative wall deposit thin by periodic reactor cleaning.

Key words: LPCVD, polycrystalline Si, modeling, reactors.

The development of CVD reactors and the selection of operating regimes have hitherto mainly been based on empirical design rules. This limits the operation of existing reactors to certain fixed conditions and severely hampers the development of novel deposition processes. Furthermore, the decrease of feature sizes in large scale integrated circuits necessitates the growth of films of highly uniform thickness and composition. This must, of course, be achieved by efficient, economical use of resources. Thus, reaction engineering analysis and design should be a key element in the development and operation of CVD reactors.

CVD in cold wall reactors at atmospheric pressure has been analyzed for two major reactor geometries. Eversteijn *et al.* (2), Rundle (3), and Takahashi *et al.* (4) used various simplifying asumptions to consider the deposition of Si in a horizontal reactor with a flat plate susceptor. Fujii *et al.* (5), Dittman (6), and Manke and Donaghey (7) modeled to various degrees of accuracy the epitaxial growth of Si in a "barrel"

Table I. Typical deposition conditions in LPCVD reactors (1), (21)

Film	Reactant gases	Temperature, °C	Pressure, Torr	Total gas flow, sccm	Dep. rate, Å/min
Poly-Si	SiH_4	620	0.3	70-100	100-120
	SiH_4/N_2	640	0.5	500-1000	140-160
Si_3N_4	SiH_4/NH_3	800	0.3	100-200	40-60
SiO_2	SiH_2Cl_2/N_2O	800-900	0.6	200-300	80-120

reactor. None of the investigators took into account that the barrel-formed susceptor may rotate during reactor operation. There have been few and mostly descriptive modeling efforts for LPCVD reactors. Gieske *et al.* (8) and Hitchman *et al.* (9) have presented experimental data and discussed flow fields, mass transfer effects, and possible kinetics but have not formulated a detailed model. Recently, in fact after we had completed this work, Kuiper *et al.* (10) published a model for the LPCVD growth of polycrystalline Si. This simple model omits effects of diffusion in the space between wafers and the significant volume expansion associated with SiH_4 reacting to Si and $2H_2$. Furthermore, the model in its present form is restricted to isothermal conditions and therefore cannot predict reactor temperature profiles that will yield uniform growth rates throughout the reactor. The authors make no attempt to compare the model predictions with experimental observations.

In this paper, we develop a detailed mathematical model for the commercial, multiple-disk-in-tube LPCVD reactor illustrated in Fig. 1. This model includes the physicochemical processes in the annular flow region formed by the tube wall and the edges of the wafers as well as those occurring in the spaces between the wafers. The changes in gas velocity and diffusion fluxes, due to a net production/reduction of mols in the gas phase during the reactions, are taken into account as is the deposition of material on the reactor wall and wafer carrier. A general nonisothermal furnace profile is considered such that variations in growth rates from wafer to wafer may be minimized. We shall demonstrate that the mathematical model correctly predicts experimental observations and gives a quantitative comparison with published experimental data from separate reactor studies. In addition, we shall use the reactor analysis to compare growth rates and thickness uniformities across individual wafers as well as from wafer to wafer for different operating conditions. In particular, the effects of flow rates, diluent (N_2), temperature profiles, and recycle of reactor effluent are elucidated.

Model Development

The modeling approach that we present is not restricted to any specific deposition kinetics. However, in order to compare model predictions and experiments, we focus on the low pressure CVD of polycrystalline Si from SiH_4 which is a major LPCVD process for which experimental data have been published. We consider the usual commercial LPCVD reactor illustrated in Fig. 1. The wafers are placed perpendicular to main direction of flow and concentrically inside a quartz tube. The flow in the annular region formed by the reactor tube and the wafer edges, *i.e.*, $R_w \leq r \leq R_t$, is laminar. Because of the low pressures, diffusion is the dominant mode of transport in the spaces between the wafers, and the mixing caused by the flow past the wafer edges is negligible. The reactor temperature is controlled by a three-zone heater, and the heats of reaction associated with the deposition are small because of the slow growth rates. Moreover, at the low pressures and high temperatures encountered in LPCVD, heat transfer occurs mainly by radiation. Therefore, we may assume that the temperature profile is determined solely by the furnace settings.

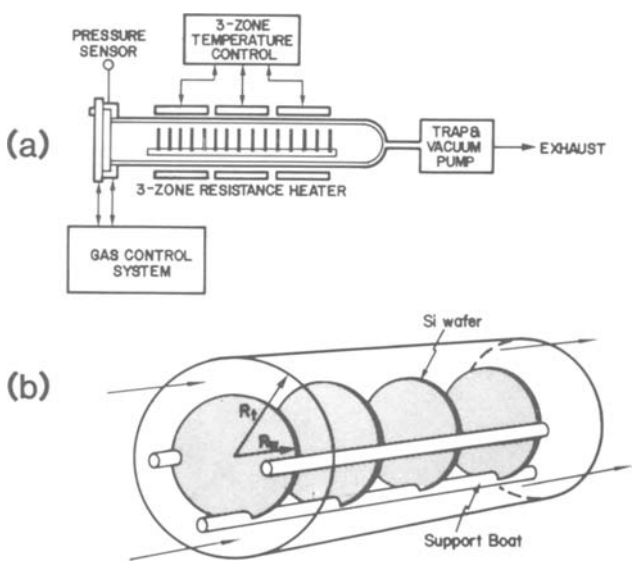

Fig. 1. Schematic of LPCVD reactor: (a) overall system, (b) details of wafer positioning.

Even though there have been a number of experimental studies of Si deposition from SiH_4, the kinetic mechanism is not understood (11). It is possible that SiH_4 decomposes in the gas phase (12, 13) according to the reaction

$$SiH_4 \rightleftarrows SiH_2 + H_2 \quad [1]$$

The formed SiH_2 then adsorbs on the Si surface

$$SiH_2 + * \rightleftarrows SiH_2* \quad [2]$$

where it diffuses to a reaction site and decomposes to Si releasing H_2

$$SiH_2* \rightarrow Si(s) + H_2(g) + * \quad [3]$$

Since there are no rate data available for the individual reaction steps, we assume, as did Claassen *et al.* (14), that the surface reaction is rate controlling and follows the rate expression

$$\mathcal{R} = \frac{kP_{SiH_4}}{1 + K_1P_{H_2} + K_2P_{SiH_4}} \text{ [mol Si/m}^2\text{ sec]} \quad [4]$$

This particular form may be justified by the mechanism (Eq. [1]-[3]) and reflects the experimental observations: (*i*) the rate is inhibited by H_2, (*ii*) the rate is first order in SiH_4 at low SiH_4 partial pressures ($\lesssim$10 m Torr), and (*iii*) the rate approaches zero order in SiH_4 at high partial pressures ($\sim$1 Torr) (14). In addition, we may neglect the homogeneous reactions (Eq. [1]) in the ensuing model development and the lumped rate expression (Eq. [4]) used. Considering the lack of detailed kinetic data, the inclusion of the kinetic scheme (Eq. [1]-[3]) in the model would only obscure the reactor analysis.

With the above assumptions and remarks, we are able to construct mathematical models for the stationary operation of the LPCVD reactor shown in Fig. 1. The concentration of the reactant SiH_4 between the wafers is governed by the continuity equation

$$\nabla \cdot N_1 = 0 \quad [5]$$

where N_1 is the molar flux of SiH_4 and

$$N_1 = -\frac{P}{RT} D_{1m} \nabla x_1 + x_1 \sum_{i=1}^{3} N_i \quad [6]$$

Here D_{1m} is an effective binary diffusivity and x represents the mol fraction of SiH_4. The boundary conditions are

$$x_1(r = R_w) = x_{1b} \qquad \left.\frac{\partial x_1}{\partial r}\right|_0 = 0 \qquad z_l < z < z_l + \Delta \quad [6a]$$

$$-N_{1z}|_{\text{wafer } l} = \mathcal{R} \qquad N_{1z}|_{\text{wafer } l+1} = \mathcal{R} \qquad 0 < r < R_w \quad [6b]$$

where expression [6b] states that the molar flux to the wafer surfaces equals the rate of deposition of Si per unit area. Since the wafer spacing Δ is small compared to the radius of the wafer R_w, *i.e.*, $\Delta/R_w < 0.1$, and the reactant concentration varies smoothly over the length of the reactor, we may neglect the variation in the

z-direction within each cell formed by the wafers and use an average SiH_4 concentration. By the averaging process, the boundary conditions (expression [6b]) are incorporated into the continuity balance which now takes the form

$$-\frac{\Delta}{2r}\frac{d}{dr}(rN_1) = \mathcal{R} \qquad [7]$$

By using Eq. [6], that $2N_1 = -N_2$ according to the stoichiometry, and that the flux of inerts $N_3 \doteq 0$, the balance takes the form

$$\frac{\Delta}{2r}\frac{P}{RT}D_{1m}\frac{d}{dr}\left(\frac{r}{1+x_1}\frac{dx_1}{dr}\right) = \mathcal{R} \qquad [8]$$

with boundary conditions

$$x_1(r = R_w) = x_{1b} \quad \text{and} \quad \left.\frac{dx_1}{dr}\right|_0 = 0 \qquad [9a, b]$$

The continuity balance over SiH_4 in the annular flow region has the form

$$\nabla \cdot cD\nabla x_1 - \nabla \cdot (cx_1 v) = 0 \qquad [10]$$

D is a dispersion coefficient and $D \doteq D_{1m}$ since at low pressures and small Re the mixing occurs mainly by molecular diffusion. The boundary conditions are

$$-D\left.\frac{\partial x_1}{\partial z}\right|_0 = v_0[x_{10} - x_1] \qquad [11a]$$

$$R_w < r < R_t$$

$$\left.\frac{\partial x_1}{\partial z}\right|_L = 0 \qquad [11b]$$

and

$$-\frac{P}{RT}D\left.\frac{\partial x_1}{\partial r}\right|_{R_t} = \mathcal{R}(R_t) \qquad [11c]$$

$$0 < z < L$$

$$\frac{P}{RT}D\left.\frac{\partial x_1}{\partial r}\right|_{R_w} = \left[\frac{R_w}{\Delta}\eta + \alpha\left(\frac{R_t}{R_w}\right)\right]\mathcal{R}(R_w) \qquad [11d]$$

Equations [11a] and [11b] are the same as Danckwerts' boundary conditions for fixed bed reactor models. With these boundary conditions, the dispersion model becomes identical to the continuously stirred tank reactor (CSTR) in the limit of very large dispersion coefficients, and it approaches the plug flow reactor (PFR) in the limit of very small dispersion coefficients where convection dominates. The boundary condition (Eq. [11c]) represents the deposition on the hot reactor wall. The first term on the right-hand side of condition (Eq. [11d]) gives the flux of SiH_4 between the wafers due to the deposition of Si. The quantity η is analogous to the effectiveness factor in heterogeneous catalysis (16) and is defined as the ratio of the total rate of reaction on each pair of wafers to that which we would obtain if the concentration were equal to the bulk concentration everywhere in the cell formed by the two wafers, *i.e.*

$$\eta = \frac{2\int_0^{R_w} r\mathcal{R}(x_1(r))\,dr}{R_w^2\mathcal{R}(x_1(R_w))} \qquad [12]$$

Thus, if the surface reaction is the rate controlling step, $\eta \doteq 1$; whereas if the diffusion between the wafer controls is the rate controlling step, $\eta < 1$. In the limit of strong diffusion resistance, the deposition is confined to a narrow outer band of the wafers and a strongly nonuniform film results. The second term on the right-hand side of Eq. [11d] refers to the deposition on the wafer carrier. α is the area of the carrier relative to reactor tube area.

The pressure drop over the LPCVD reactor is very small (9) so that the total pressure, P, may be considered constant. Therefore, the increase in the number of mols by the deposition reaction $SiH_4 \rightarrow Si + 2H_2$ means an increase in the volumetric flow. To effectively treat this effect, we express the concentration of species in terms of the overall conversion (x) and the fractional change in volume between no conversion and complete conversion (ϵ) (see Ref. (20) for details). The stoichiometry implies that $\epsilon = x_{10}$. The mol fractions of SiH_4 and H_2 are then given by

$$x_1 = \frac{(1-x)x_{10}}{1+\epsilon x} \qquad x_2 = \frac{x_{20} + 2xx_{10}}{1+\epsilon x} \qquad [13]$$

The gas flow is parallel to the axis of the reactor (the z-direction) and

$$v = v_0(1+\epsilon x)T/T_0 \qquad [14]$$

where v_0 is the entrance velocity.

At the low pressures employed in LPCVD, diffusion coefficients are approximately 1000 times larger than those at atmospheric conditions and consequently, the radial mixing is rapid in the annular flow region. Furthermore, the time scale associated with deposition is larger than that for diffusion, *i.e.*, the generalized Damköhler number, $\mathcal{R} \cdot (R_t - R_w)/C_0D_{1m}$ is small. Therefore, we assume perfect radial mixing and average over the continuity balance by using

$$\langle\cdot\rangle = \frac{\int_0^{2\pi}\int_{R_w}^{R_t} r \cdot dr d\theta}{\int_0^{2\pi}\int_{R_w}^{R_t} r dr d\theta} \qquad [15]$$

This averaging eliminates the r-component and includes the boundary conditions Eq. [11c] and [11d] in the one-dimensional continuity balance. Then by making use of the expressions [13] for the mol fractions, the axial velocity (expression [14]), and the temperature dependence of the diffusivity $D/D_0 = (T/T_0)^{1.65}$, we derive the following balance in terms of the conversion, x

$$D_0\frac{d}{dz}\left(\psi\frac{dx}{dz}\right) + v_0\frac{dx}{dz} - \frac{2\mathcal{R}}{(R_t^2 - R_w^2)C_{10}}\left[R_t(1+\alpha) + \frac{R_w^2}{\Delta}\eta\right] = 0 \qquad [16]$$

where

$$\psi = -\frac{(1+\epsilon)}{(1+\epsilon x)^2}\left(\frac{T}{T_0}\right)^{0.65} \qquad [17]$$

The boundary conditions take the form

$$D_0\left.\frac{dx}{dz}\right|_0 = v_0(1+x\epsilon)x \qquad \left.\frac{dx}{dz}\right|_L = 0 \qquad [18]$$

To set forth the fundamental parameter combinations associated with the deposition process, we make the modeling equations dimensionless by defining

$$\mathrm{Da}_1 = \frac{2LR_t(1+\alpha)}{v_0(R_t^2 - R_w^2)c_{10}}\mathcal{R}(x=0)$$

$$\mathrm{Da}_2 = \frac{2L\,R_w^2/\Delta}{v_0(R_t^2 - R_w^2)c_{10}}\mathcal{R}(x=0)$$

$$g(x) = \frac{\mathcal{R}(x)}{\mathcal{R}(x=0)} \qquad \mathrm{Pe} = \frac{v_0L}{D_0}$$

$$\zeta = \frac{z}{L} \qquad \xi = \frac{r}{R_w} \qquad \Phi^2 = \frac{2R_w^2\mathcal{R}(x=0)}{\Delta c_{10}D_{1m0}(T/T_0)^{0.65}} \qquad [19]$$

The reactor Eq. [16] then takes the form

$$\frac{d}{d\zeta}\left(\psi\frac{dx}{d\zeta}\right) + \mathrm{Pe}\frac{dx}{d\zeta} - \mathrm{Pe}(\mathrm{Da}_1 + \eta\mathrm{Da}_2)g(x) = 0 \quad [20]$$

with boundary conditions

$$\left.\frac{dx}{d\zeta}\right|_0 = \mathrm{Pe}(1 + x(0)\epsilon)x(0) \quad \text{and} \quad \left.\frac{dx}{d\zeta}\right|_1 = 0 \quad [21a, b]$$

and

$$\eta = 2\int_0^1 \xi \frac{g(x(\xi))}{g(x_b)}d\xi \quad [22]$$

The reaction-diffusion problem governing the wafers becomes

$$\frac{1}{\xi}\frac{d}{d\xi}\left(\frac{\xi}{1+\epsilon x}\frac{dx}{d\xi}\right) + \Phi^2 g(x(\xi)) = 0 \quad [23]$$

with boundary conditions

$$x(\xi = 1) = x_b(\zeta) \quad \text{and} \quad \left.\frac{dx}{d\xi}\right|_0 = 0 \quad [24a, b]$$

The parameters each have specific physical significances. The Damköhler numbers Da_1 and Da_2 represent the ratios of reactor space time to the characteristic time for deposition on the reactor wall and on the wafers, respectively. The axial Peclet number (Pe) represents the ratio of the time constant for convective transport to that for diffusive transport. The parameter, Φ, is equivalent to the Thiele modulus (ϕ) used extensively in analysis of heterogeneous reactions. It denotes the ratio of the characteristic time for diffusion in between the wafers to the characteristic time for deposition of Si on the wafer surfaces. Thus, if Φ is large, the deposition is hindered by diffusion and a nonuniform film results. This effect is completely analogous to that of a large Φ for a porous catalyst. In fact, the modeling Eq. [20]-[24] are similar to those for a catalytic fixed bed reactor.

Numerical Solution of the Modeling Equations

The modeling equations form two nonlinear boundary value problems which must be solved by some suitable numerical technique. Here we use the orthogonal collocation method which has been applied successfully to many chemical reaction engineering problems, especially fixed bed reactors [(17), (18) and references therein]. In this method, the first and second spatial derivatives are approximated by a weighted sum of values of the dependent variable at the collocation points

$$\left.\frac{dx}{d\zeta}\right|_{\zeta_i} = \sum_{j=0}^{N+1} A_{ij}x_j \qquad i = 0, 1, \ldots, N+1 \quad [25]$$

$$\left.\frac{d^2x}{d\zeta^2}\right|_{\zeta_i} = \sum_{j=0}^{N+1} B_{ij}x_j \qquad i = 0, 1, \ldots, N+1 \quad [26]$$

The weight matrices depend on the trial functions which in our case are the first N Jacobi polynomials $P_i^{(\alpha,\beta)}(\zeta)$ with weight function $\zeta^\alpha(1-\zeta)^\beta$ (17, ct. 3). Since there is no special symmetry in the tubular reactor problem Eq. [20], we use $(\alpha, \beta) = (0, 0)$ for that equation. However, for the wafer problem (Eq. [23]), advantage is taken of the radial symmetry and the Dirchlet condition (Eq. [24a]) by using $(\alpha, \beta) = (1, 0)$. The collocation points are in each case the zeros of the orthogonal polynomium, $P_N^{(\alpha,\beta)}(\zeta)$. By discretizing the reactor Eq. [20], [21], we obtain the following set of nonlinear algebraic equations for the interior

$$\psi_i \sum_{j=0}^{N+1} B_{ij}x_j + \left[\mathrm{Pe} + \sum_{j=0}^{N+1} A_{ij}\psi_j\right]\sum_{j=0}^{N+1} A_{ij}x_j - \mathrm{Pe}(\mathrm{Da}_1 + \eta(x)\mathrm{Da}_2)g(x_i) = 0 \qquad i = 1, \ldots, N \quad [27]$$

and for the boundary

$$\sum_{j=0}^{N+1} A_{0j}x_j - \mathrm{Pe}(1 + x_0\epsilon)\,x_0 = 0 \quad [28]$$

$$\sum_{j=0}^{N+1} A_{N+1,j}x_j = 0 \quad [29]$$

In order to solve this system of equations, we need to evaluate $\eta(x_i)$ from the solution to the wafer problem, (Eq. [23]). Since the variations in film thickness across the individual wafers is small (<5%) in most LPCVD reactors, we expect Φ to be small. In that case, it is possible to obtain an accurate solution to the wafer problem by using just one interior collocation point. This technique has been demonstrated to give accurate results for the analogous catalyst particle problem even for moderately large values of Φ (19). Then by using the one-point collocation technique (19), the wafer problem is approximated as

$$\epsilon\Phi^2 g(x(\xi_1)) = 6\ln\left[\frac{1+\epsilon x(\xi_1)}{1+\epsilon x(1)}\right] \quad [30]$$

This equation can be solved for given ϕ^2, ϵ, and $x(1)$ to yield $x(\xi_1)$. One can then evaluate η_i by Radau quadrature (17, 19) as

$$\eta_i = \frac{2}{g(x(1))}\left[\tfrac{3}{8}\cdot g(x(\xi_1)) + \tfrac{1}{8}g(x(1))\right] = \frac{1}{4}\left[1 + 3\frac{g(x(\xi_1))}{g(x(1))}\right] \quad [31]$$

By combining these equations with the $N + 2$ nonlinear algebraic equations for the reactor tube (Eq. [27]-[29]), we can find the solution to the entire LPCVD problem by Newton-Raphson iteration. This, in turn, enables us to predict growth rates and variations in film thickness within and among wafers. The growth rate on the wall is determined by

$$G_t = \overline{V}_{si}\Re(x = 0)g(x) \quad [32]$$

while the average growth rate on each wafer is

$$\overline{G}_w = \overline{V}_{si}\Re(x = 0)g(x)\eta \quad [33]$$

The average growth rate on all wafers in the reactor is computed by quadratures

$$\overline{G} = \overline{V}_{si}\Re(x = 0)\int_0^1 g(x)\eta d\zeta \doteq \overline{V}_{si}\Re(x = 0)\sum_{i=1}^{N} w_i g(x_i)\eta_i \quad [34]$$

where the w_i's are Gauss quadrature weights corresponding to the N interior collocation points. The variation in growth rates and thus film thickness is determined as

$$\sigma^2 = \int_0^1\left[\frac{\overline{G} - \overline{G}_w(\zeta)}{\overline{G}}\right]^2 d\zeta = \frac{\int_0^1 [g(x)\eta]^2 d\zeta}{\left[\int_0^1 g(x)\eta d\zeta\right]^2} - 1 \quad [35a]$$

for the reactor

$$\sigma_w^2 = 2\int_0^1 \xi\left[\frac{G_w - \overline{G}_w}{\overline{G}_w}\right]^2 d\xi = \frac{2}{\eta^2}\int_0^1 \xi\left[\frac{g(x(\xi))}{g(x(1))}\right]^2 d\xi - 1 \quad [35b]$$

within each wafer

These integrals can also be evaluated by quadrature. With the developed mathematical model, we are now able to analyze experimental observations and to draw comparisons between growth rates and possible levels of uniformity at different operating conditions.

Evaluation of Kinetic Parameters

Since detailed rate data for the pyrolysis of SiH_4 are scarce and often contradictory (11), we chose to evaluate the parameters k, K_1, and K_2 in expression [4] from experimental data for the deposition of polycrystalline Si in an LPCVD reactor obtained by Claassen *et al.* (14). The reactor was loaded with 50 76.2 mm diam wafers spaced 10 mm apart and it was kept isothermal. Very low concentrations of SiH_4 ($x_{10} = 0.0047$) were used in mixtures of H_2 and N_2. The relative amount of the carrier gases, H_2 and N_2, was varied to demonstrate the inhibition of Si deposition by H_2. Figure 2 shows the experimental data from Claassen *et al.* (14) and the theoretical predicted growth rates as a function of the dimensionless axial reactor position, ζ.

The model predicts quite well the decrease in growth rates along the reactor length due to depletion of SiH_4 as well as the inhibiting effect of increased H_2 concentration.

The rate constants determined from this comparison with experimental data are

$$k = 1.25\ 10^9 \exp(-18{,}500/T)\ \text{mol/m}^2\text{/atm/sec}$$

$$K_1 = 1.75\ 10^3\ \text{atm}^{-1}$$

$$K_2 = 4.00\ 10^4\ \text{atm}^{-1}$$

The activation energy for k is not determined but instead extracted from Bryant's survey of the temperature dependence of Si deposition (11). The "adsorption parameters," K_1, K_2, are considered temperature independent in the range of temperatures of interest in LPCVD of polycrystalline Si, 600°-650°C, because of insufficient data. The rate constants were not determined by any statistical technique although the modeling equations could form the basis for nonlinear least squares parameter estimation. However, that falls outside the scope of the present work.

In order to test the ability of our mathematical model to predict growth rates at different conditions than those used in the evaluation of the kinetic parameters, we consider the effect of varying the deposition area by removing wafers. Figure 3 shows measured growth rates by Claassen *et al.* (14) and predicted growth rates for the cases of 5 and 50 wafers in a 0.5m reaction zone. The model matches the trend of the experimental observations and demonstrates that, as expected, the growth decreases more rapidly in the case of the larger deposition area (50 wafers) because of the faster depletion of the reactant, SiH_4. The assumption of a small wafer spacing relative to the wafer radius (*i.e.*, $\Delta/R_t << 1$), which was used to eliminate the z-dependence in the wafer problem (Eq. [5], [6]), clearly does not hold for the five-wafer case. This may explain the slightly larger differences between model predictions and experimental observations for the five-wafer run than those for the 50-wafer run.

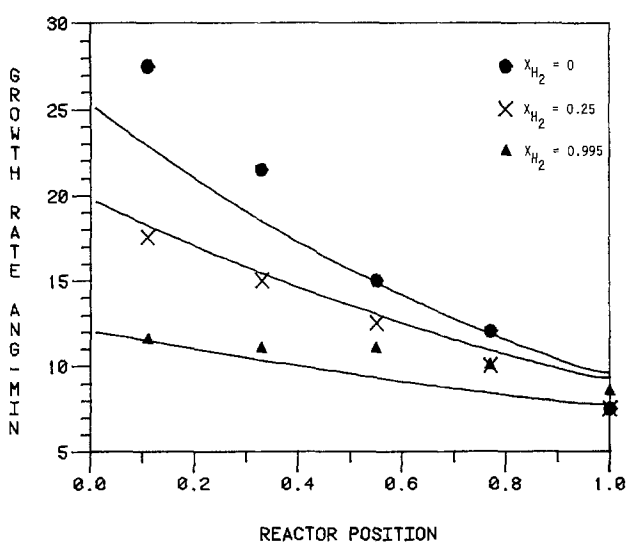

Fig. 2. Model predictions (solid line) vs. experimental data (14) of growth rate profiles as a function of inlet H_2 concentration. Reactor conditions: $P = 0.53$ Torr, $T = 625$°C, flow = 1000 sccm, $X_{SiH_4} = 0.0047$.

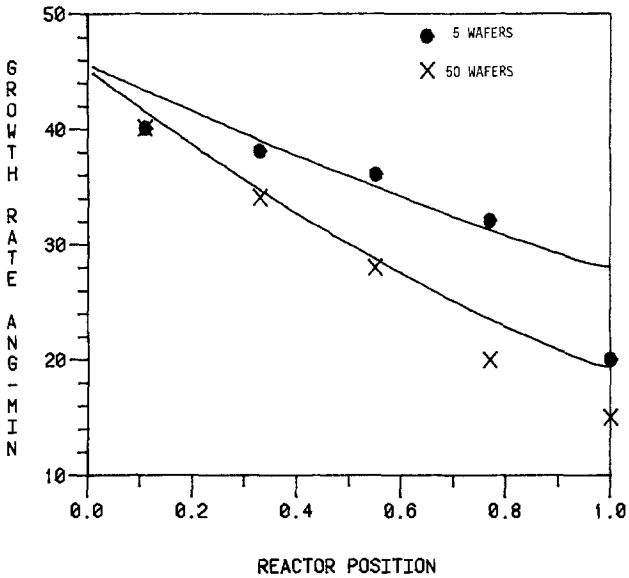

Fig. 3. Model predictions (solid line) vs. experimental data (14) of growth rate profiles as a function of number of wafers in the reactor. Reactor conditions: $P = 0.53$ Torr, $T = 625$°C, flow = 1000 sccm, $X_{SiH_4} = 0.0047$.

Comparison of Model Predictions and Commercial Process Data

In order to further test the mathematical model, we consider deposition data obtained by Rosler (1) with a different LPCVD reactor system, and at SiH_4 concentrations two orders of magnitude larger than those used in the above evaluatins of the kinetic constants. The same size wafer (76.2 mm diam) was used in the experimental study. The reactor contained 110 wafers spaced at 4.7 mm as well as five dummy wafers at each end of the wafer zone. The possible growth rates and film thickness uniformities for two typical conditions for commercial LPCVD reactors, pure SiH_4 feed and SiH_4 diluted with N_2, were compared, and the effects of flow rates, reactor temperature profile, and dilution were demonstrated experimentally.

Figure 4 illustrates the measured growth rates (1) and the predicted rates as functions of the wafer position in the reactor for a ±15% change in SiH_4 feed rates around the base case of 47 sccm pure SiH_4 feed. The reactor temperature is varied from 607° to 654°C along the length of the reactor by using the 3-zone furnace to produce a nearly uniform thickness of the polycrystalline Si layer in the base case. The model predictions accurately predict the trends in the experimental data. When the feed rate of SiH_4 is stepped up 15%, the growth rates, as reflected by the Si-thickness, increase along the length of the reactor since there is excess reactant available relative to the base case. A flat thickness profile could clearly be achieved by lowering the temperature gradient along

the length of the reactor. Similarly, if the flow rate of SiH_4 is dropped, the rates of deposition of Si tail off. Again a flat thickness profile could be reestablished by readjusting the temperature profile, this time by increasing the temperature gradient.

The slight wavelike appearance of the model predictions comes about because the deposition rate depends exponentially on the reactor temperature which varies piecewise linearly along the reactor. In order to obtain a quantitative agreement between model and experiments, we have used a slightly smaller temperature variation, 607°-650°C, rather than 607°-654°C, and a shorter deposition time, 30 min rather than 45 min. Nevertheless, the accurate prediction of the trends and the good quantitative agreement between model predictions and experiments obtained with those minor changes demonstrates the usefulness of our modeling approach, in particular when considering that the kinetic rate constants are based on deposition at very low SiH_4 concentrations and on different substrates than in the present case.

Because of the high sensitivity to SiH_4 flow rate variations and the large temperature gradients required to produce a flat growth profile in LPCVD processing with pure SiH_4, dilution with N_2 is often employed. This process modification reduces the sensitivity to flow variations and to temperature gradients as seen by comparing Fig. 4 and 5. The latter figure shows experimental data for dilute processing (23% SiH_4 in N_2), obtained by Rosler (1), and model simulations. Again the model predicts the trends quite well, but lower temperatures were used in the model simulations in order to compensate for our imperfect knowledge of the rate constants.

The growth rates obtained by using pure SiH_4 are less than those obtained in dilute processing, approximately 125 Å/min *vs.* 200 Å/min. However, this difference is caused by the larger SiH_4 flow rate used in dilute processing. For the same feed rates of SiH_4, the growth rate is larger for pure SiH_4 feed than for dilute feed. Nevertheless, the dilute processing offers the advantages of a small sensitivity to flow disturbances and a small temperature gradient along the reactor. The latter effect is especially advantageous since it produces more uniform grain sizes and consequently more uniform electronic properties than

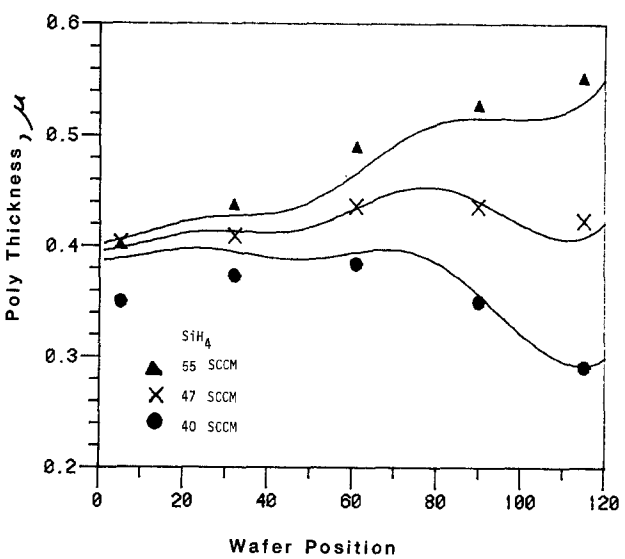

Fig. 4. Model predictions (solid line) *vs.* experimental data (1) of film thickness profiles as a function of (pure) SiH_4 flow rate. Reactor conditions $P = 0.6$ Torr, wafer spacing = 0.00476m, reactor length = 0.625m (assumed); experimental temperature profile and deposition time: 607°, 629°, 654°C; $t = 45$ min; model temperature profile and deposition time: 607°, 614°, 650°C; $t = 30$ min.

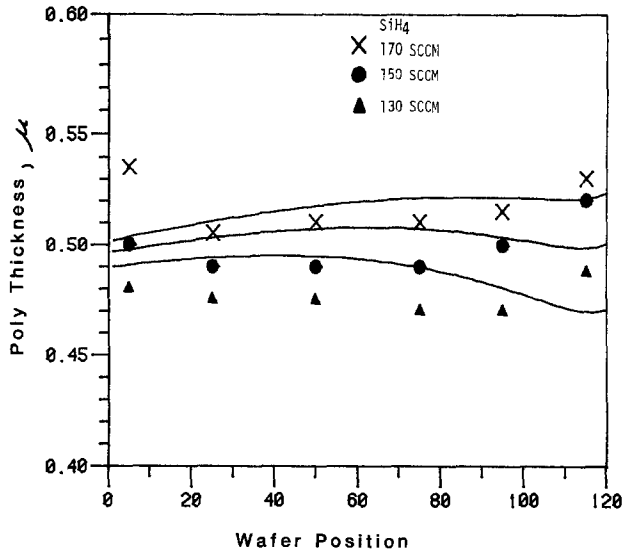

Fig. 5. Model predictions (solid line) *vs.* experimental data (1) of film thickness as a function of (dilute) SiH_4 flow rate. Reactor conditions same as in Fig. 4 except: $P = 0.7$ Torr, N_2 flow = 500 sccm; experimental temperature profile and deposition time: 643°, 643°, 647°C; 25 min; model temperature profile and deposition conditions: 625°, 629°, 633°C; 25 min.

can be achieved in a process with pure SiH_4 feed where larger temperature gradients are needed to give uniform film thickness. The disadvantages of the dilute processing are the high flow rates and the associated pumping speeds. Furthermore, there is an increased cost of SiH_4 since less SiH_4 is converted over the reactor.

An LPCVD Reactor with Recycle

The ultimate goal in LPCVD deposition of polycrystalline Si is to grow Si films with constant thickness and material properties. Because of the distributed nature of the LPCVD reactor, it has been necessary to either vary the wafer temperature along the length of the reactor or to use dilute processing in order to at least approach this goal. Neither of the two approaches is ideal as demonstrated in the above discussion. A continuously stirred tank reactor would give uniform films, but there are difficulties such as particulate and wafer loading problems associated with the design and operation of a CSTR reactor. On the other hand, these problems are avoided in the tubular LPCVD reactor. By recycling a fraction of the reactor effluent to the reactor inlet as illustrated in Fig. 6, one can combine the benefits of the CSTR and the conventional LPCVD reactor. If we define the recycle ratio, λ as

$$\lambda = \frac{\text{reactor effluent returned to the reactor inlet}}{\text{total reactor effluent}} = \frac{F_r}{F_{exit}}$$

then the recycle reactor will behave as CSTR in the limit $\lambda \to 1$ and obviously as a conventional LPCVD reactor in the limit $\lambda \to 0$ [see Ref (20)]. Thus, the

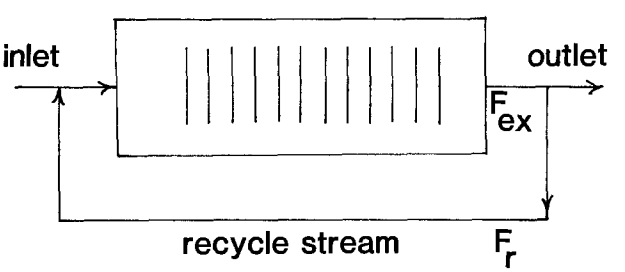

Fig. 6. LPCVD reactor schematic with recycle. Recycle ratio $\equiv F_r/F_{exit}$.

recycling provides a means for obtaining various degrees of mixing with the LPCVD reactor.

If we assume that the recycle stream is quenched to avoid reactions in the recycle line and then mixed with the inlet stream at the same temperature, a total mol balance over the mixing point yields

$$F_o + F_r = F_o' \quad [36]$$

where F_o, F_r, F_o' are the molar flow into the system, in the recycle loop, and into the reactor, respectively. By using $F_r = \lambda F_o'[1 + \epsilon(x_e - x_i)]$ we find the flow into the reactor is

$$F_o' = \frac{F_o}{1 - \lambda[1 + \epsilon(x_e - x_i)]} \quad [37]$$

where x_i is the conversion of SiH_4 in the combined feed to the reactor and x_e represents the exit conversion. A balance over SiH_4 gives

$$F_o X_{10} + F_r X_{1e} = F_o' X_{1i} \quad [38]$$

which by using Eq. [13] can be written in terms of the inlet and exit conversions, x_i and x_e, as

$$\frac{F_o}{F_o'} = -\frac{\lambda(1 - x_e)[1 + \epsilon(x_e - x_i)]}{1 + \epsilon x_e} + \frac{(1 - x_i)}{1 + \epsilon x_i} \quad [39]$$

In addition, the inlet boundary condition (Eq. [21a]) has to be reformulated and now takes the form

$$\left.\frac{dx}{d\zeta}\right|_0 = \mathrm{Pe}(x - x_i)\frac{(1 + \epsilon x)}{(1 + \epsilon x_i)} \quad [40]$$

By combining Eq. [37], [39], and [40] with the reactor modeling Eq. [20]-[24], and by employing the same numerical procedure as described above, the conversion and growth rate profiles for the recycle reactor are determined. The Damköhler and Peclet numbers have to be calculated in the numerical solution since they depend on the flows into the reactor.

In the following section, we compare the performance of the LPCVD reactor with pure SiH_4 feed, dilute feed, and recycle for the conditions reported by Rosler (1). These conditions correspond to those used commercially. The performance of the reactor is evaluated in terms of (*i*) the necessary temperature increase over the reactor to achieve a flat growth profile, ΔT; (*ii*) the average growth rate, $\overline{G}$; (*iii*) the effective use of SiH_4, E, *i.e.*, SiH_4 used to deposit Si on the wafers contrary to SiH_4 wasted on the walls and carried out of the reactor system; and (*iv*) the standard deviation in growth rates across the reactor, σ, calculated with Eq. [34]. In order to have an equitable comparison of the reactor operations, they are considered for constant temperature difference (ΔT), total flow through the reactor, and SiH_4 flow into the reactor system. The latter conditions imply that the pumping and reactant costs are maintained constant.

Table II summarizes the performance measures, $\overline{G}$, E, and σ for different values of λ. For the case of pure SiH_4 feed (no recycle), a temperature increase of 25°C is needed to make the growth rates somewhat uniform over the reactor. As the recycle increases, the needed ΔT decreases, and at 90% recycle only 4°C are necessary to produce a very uniform film thickness from wafer to wafer. At the same time, $\overline{G}$ and E have gone up. It is noted that E will always be less than 100% since wall deposits cannot be avoided. On the other hand, for the dilute processing conditions, the average growth rate and consequently the effective use of SiH_4 fall off with increasing N_2 content in the feed. Moreover, the standard deviation rises with X_{N_2}, except at large dilutions where the growth rate is so diminished that the standard deviation also is reduced. This comparison of LPCVD operating alternatives clearly demonstrates the advantages of including the recycle stream. It also shows that dilute processing is an attractive alternative only if additional SiH_4 is added to improve growth rates as was done in the cases discussed in the previous section.

Table II. Comparison of model predictions between one-pass reactor operation and reactor with recycle. Reactor conditions: P = 0.6 Torr, reactor length = 0.65m, reactor diameter = 0.12m, 100 wafers, wafer diameter = 0.0762m, wafer spacing = 0.0047m, make-up SiH_4 flow rate = 47 sccm

	Recycle				Dilute			
λ	ΔT °C	$\overline{G}$ A/min	E %	σ %	x_{N_2}	$\overline{G}$ A/min	E %	σ %
0	25	132	63	2.1	0.0000	—	—	—
0.25	21	141	68	1.7	0.3865	129	62	11.6
0.50	15.5	152	73	1.1	0.6775	125	60	22.1
0.75	9.5	163	78	0.5	0.8700	117	56	27.3
0.90	4.0	170	81	0.6	0.9536	96	46	22.2

Conclusion

In this paper, we have developed a detailed mathematical model for the LPCVD reactor by using reaction engineering concepts. This model encompasses the convection and diffusion processes in the annular region between the reactor wall and the edges of the wafers as well as the surface reactions on the reactor walls. In addition, the model describes explicitly the interaction between diffusion and between surface reaction on the wafers. The variations in gas velocities and diffusion fluxes due to net changes in the number of mols in the gas phase in the deposition reactions are taken into account. These are significant in CVD reactions but have been neglected in most previous modeling studies. The combined reactor equations have the same form as the ones for a catalytic-fixed bed reactor, and consequently the concepts developed for fixed bed reactors also apply to LPCVD reactors.

The modeling equations were solved by orthogonal collocation which is a powerful numerical technique and particularly useful for reactor problems (17). By using experimental data obtained by Claassen *et al.* (14), it was demonstrated that the model could be used to estimate kinetic parameters. The model could, in turn, predict experimental observations obtained at different reaction conditions than those used in the parameter estimation. In this way, the observations made by Rosler (1) for commercial LPCVD reactor conditions were analyzed for effects of flow rate changes and temperature gradients on the growth rates of polycrystalline Si. In addition, we considered recycling a fraction of the reactor effluent back to the reactor inlet. This modification allows us to manipulate the degree of backmixing in the reactor and produce large growth rates with high degrees of uniformities within wafers as well as from wafer to wafer. Furthermore, only a small temperature rise (<5°C) over the reactor is then necessary to ensure uniform growth rates. The H_2 content in the recycle reactor is not substantially different from that in standard LPCVD reactors. Thus, the recycle reactor is not expected to alter the film composition. For the same pumping speed and reactant feed, the recycle reactor out performs the conventional LPCVD reactor even when compared to so-called dilute processing. This indicates that future reactor design should emulate the CSTR while minimizing particulate problems and providing for easy wafer loading.

In all the cases considered in this paper, the film thickness varied <1% within each wafer. Thus, the surface reaction controlled the deposition on the wafers which was reflected in small values of Φ. Increases in the pressure which decreases the diffusivity for closer wafer spacing would increase the diffusion resistance. This would cause the deposited film to become thinner towards the center of the wafer. At the low pressures encountered in LPCVD, Knudsen diffusion becomes the dominant mode of mass transport

with small wafer spacings (~2 mm). For faster surface reactions than considered in this paper, the diffusion of reactants between wafers could be rate controlling with standard 3/16 in. spacings. This appears to be the case in some SiO_2 and Si_3N_4 deposition schemes (1).

The quantitative agreements with experimental data and the good predictions derived from this modeling approach demonstrate the power in analyzing deposition processes. The approach is not restricted to any particular deposition reaction. The growth of polycrystalline Si and SiH_4 was considered as an example because of the importance of LPCVD-grown Si. The analysis can easily be extended to the deposition of materials such as SiO_2 and Si_3N_4 as well as doping of films, provided the reaction kinetics are known. Unfortunately, kinetic rate expressions are scarce for most deposition reactions. The modeling approach used here offers the ability to estimate overall parameters as we have shown for SiH_4. However, the entire deposition mechanism composed of homogeneous and heterogeneous reactions can only be discovered by experiments involving carefully controlled flow fields and surfaces. This is currently under investigation.

Acknowledgment

The authors are grateful to the Graduate School of the University of Minnesota for support for this work.

Manuscript submitted Nov. 25, 1982; revised manuscript received May 11, 1983.

LIST OF SYMBOLS

$\underline{\underline{A}}$	matrix of differentiation weights, see Eq. [25]
$\underline{\underline{B}}$	matrix of differentiation weights, see Eq. [26]
c_o	total inlet concentration
D	dispersion coefficient $\doteq D_{1m}$
D_{im}	diffusivity of component i in the gas mixture
Da_1, Da_2	Damköhler numbers, see Eq. [19]
E	effective use of SiH_4
F_o, F_r, F_o'	molar flow into reactor system, in recycle loop, into reactor
$g(x)$	dimensionless rate, see Eq. [19]
$\overline{G}$	growth rate averaged over length of reactor, see Eq. [34]
G_t	growth rate on reactor wall, see Eq. [32]
$\overline{G}_w$	growth rate averaged over wafer, see Eq. [33]
k, K_1, K_2	rate constants, see Eq. [4]
N_i	molar flux of component i
P	pressure
Pe	Peclet number, see Eq. [19]
r	radial coordinate
R	gas constant
$\mathcal{R}$	reaction rate, see Eq. [4]
R_w	radius of wafer
R_t	radius of reactor tube
T	temperature
v	linear velocity in annulus
w	Gaussian quadrature weights
x_i	mol fraction component i
z	axial coordinate
α	area of wafer carrier relative to reactor tube area
Δ	wafer spacing
ϵ	volume expansion coefficient, cf. Eq. [13], [14]
ζ	dimensionless axial coordinate, see Eq. [19]
η	effectiveness factor, see Eq. [12]
λ	recycle ratio
ξ	dimensionless radial coordinate, see Eq. [19]
σ^2	variation in film thickness along reactor, see Eq. [34]
σ_w^2	variation in film thickness across wafer, see Eq. [35]
Φ	Thiele modulus, see Eq. [19]
χ	conversion
χ_i, χ_e	inlet and exit conversion
ψ	see Eq. [17]

Subscripts

b	bulk conditions
1	SiH_4
2	H_2

REFERENCES

1. R. S. Rosler, *Solid State Technol.*, **20**, 63 (1977).
2. F. C. Eversteijn, P. J. W. Severin, C. H. J. van den Brekel, and H. L. Peek, *This Journal*, **117**, 925 (1970).
3. P. C. Rundle, *J. Cryst. Growth*, **11**, 6 (1971).
4. R. Takahashi, Y. Koga, and K. Sugawara, *This Journal*, **119**, 1406 (1972).
5. E. Fujii, H. Nakamura, K. Hariuna, and Y. Koga, *ibid.*, **119**, 1106 (1972).
6. F. W. Dittman, *Adv. Chem. Ser.*, **133**, 463 (1974).
7. C. W. Manke and L. F. Donaghey, *This Journal*, **124**, 561 (1977).
8. R. J. Gieske, J. J. McMullen, and L. F. Donaghey, in "Chemical Vapor Deposition," L. F. Donaghey, P. Rai-Choudhury, and R. N. Tauber, Editors, p. 151, The Electrochemical Society Softbound Proceedings Series, Princeton, NJ (1977).
9. M. L. Hitchman, J. Kane, and A. E. Widmer, *Thin Solid Films*, **59**, 231 (1979).
10. A. E. T. Kuiper, C. J. H. van den Brekel, J. de Groot, and G. W. Veltkamp, *This Journal*, **129**, 2288 (1982).
11. W. A. Bryant, *Thin Solid Films*, **60**, 19 (1979).
12. C. G. Newman, H. E. O'Neal, M. A. Ring, F. Leska, and N. Shiply, *Int. J. Chem. Kinet.*, **11**, 1167 (1979).
13. C. H. J. van den Brekel and L. J. M. Bollen, *J. Cryst. Growth*, **54**, 310 (1981).
14. W. A. P. Claassen, J. Bloem, W. G. J. N. Valkenburg, and C. H. J. van den Brekel, *J. Cryst. Growth*, **57**, 259 (1982).
15. A. Varma and R. Aris, "Chemical Reactor Theory—A Review," L. Lapidus and N. R. Amundson, Editors, Prentice Hall, Englewood Cliffs, NJ (1977).
16. R. Aris, "The Mathematical Theory of Reaction and Diffusion in Permeable Catalysts," Clarendon Press, Oxford (1975).
17. J. Villadsen and M. L. Michelsen, "Solution of Differential Equation Models by Polynomial Approximation," Prentice Hall, Englewood Cliffs, NJ (1978).
18. K. F. Jensen and W. H. Ray, *Chem. Eng. Sci.*, **37**, 199 (1982).
19. W. E. Stewart and J. Villadsen, *AIChE J.*, **15**, 28 (1968).
20. O. Levenspiel, "Chemical Reaction Engineering," 2 ed., Wiley, New York (1972).
21. Y. Yasuda, *Thin Solid Films*, **90**, 259 (1982).

Technical Notes

Substrate Biasing for Plasma Etching

T. D. Mantei

Department of Electrical and Computer Engineering, University of Cincinnati, Cincinnati, Ohio 45221

Most plasma etching processes require negative substrate biasing to ensure directional ion bombardment. The electrodes of an rf-driven plasma etch reactor, for example, acquire a negative self-bias voltage due to partial rectification of the applied rf electric field by the plasma sheath surrounding the platens (1-3). In many cases, however, it may be desirable to apply an additional separately controllable substrate bias or to establish a substrate bias in a quiescent plasma in which self-bias is negligible. This note shows that the negative d-c substrate bias resulting from the application of an external alternating voltage to a substrate can be accurately predicted by a simple calculation. The result is confirmed by bias measurements in a quiescent plasma.

Figure 1a shows a substrate immersed in plasma and driven by an externally applied alternating voltage $V_{rf} \cos \omega t$. The capacitor prevents the extraction of net current from the plasma. The Langmuir current-voltage characteristic (4) in Fig. 1b shows that the thermal currents of the electrons and the heavier less mobile ions are unequal. With no applied rf signal, the substrate potential will therefore settle at a negative value (V_F), the floating potential (4), relative to the ambient plasma potential (V_p). At the floating potential, the random electron and ion thermal currents falling to the substrate surface just cancel. When the alternating voltage ($V_{rf} \cos \omega t$) is applied, a more negative steady bias voltage ($V_{d.c.}$) is established (Fig. 1) at which the time-average electron and ion current components again cancel; that is

$$<I_e + I_i> = 0 \qquad [1]$$

where the brackets denote time-averaging. For a Maxwell-Boltzmann electron energy distribution, Eq. [1] becomes

$$nqA\left(\frac{KT_e}{2\pi m_e}\right)^{1/2} \cdot \left\{ \exp\left(q\frac{V_{d.c.}}{KT_e}\right) \cdot \frac{1}{2\pi}\int_0^{2\pi} \exp\left(q\frac{V_{rf}\cos\omega t}{KT_e}\right) d\omega t - \left(\frac{\pi m_e}{2m_i}\right)\right\} = 0 \qquad [2]$$

where n is the electron density, q the electronic charge, A the substrate area, T_e the electron temperature, K is Boltzmann's constant, m_i and m_e are the ion and electron masses, and $V_{d.c.}$ is the resulting negative d-c substrate bias voltage relative to V_p. The integral can be recognized as a form of I_0, the zero-order Bessel function of the second kind (5). Equation [2] thus gives the compact relation

$$V_{d.c.} = -V_F - V_e \ln (I \cdot [V_{rf}/V_e]) \qquad [3]$$

where

$$V_F = V_e \ln (2m_i/\pi m_e)^{1/2}$$

is the floating potential and V_e [$= KT_e/g$] is the electron temperature expressed in volts. A similar result has been reported for an undriven Langmuir probe in an electrically noisy plasma (6).

In the limit $V_{rf} \to 0$, $V_{d.c.}$ reduces to $-V_F$. When $V_{rf} > 10\ V_e$, then

$$\ln I \cdot (V_{rf}/V_e) \approx V_{rf}/V_e - \ln (2\pi V_{rf}/V_e)^{1/2}$$

and

$$V_{d.c.} \approx -V_F - V_{rf} + V_e \ln (2\pi V_{rf}/V_e)^{1/2}$$

Thus for large V_{rf} [$> 10\ V_e$], the negative substrate bias ($V_{d.c.}$) equals the floating potential plus the peak applied rf voltage minus a positive correction term.

Figure 2 shows measured values of $V_{d.c.}$ plotted *vs.* V_{rf}, obtained in a quiescent plasma discharge currently

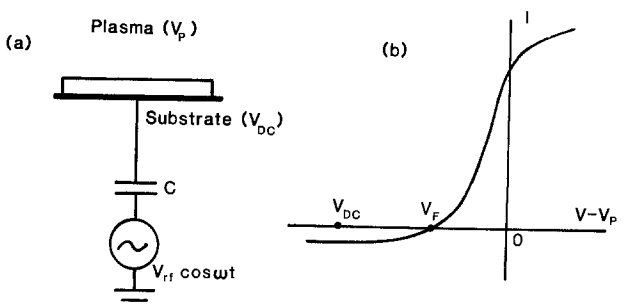

Fig. 1. a. Simplified sketch of biased substrate immersed in plasma. b. Sketch of Langmuir current-voltage relation showing the floating potential (V_F) and final steady substrate bias voltage ($V_{d.c.}$).

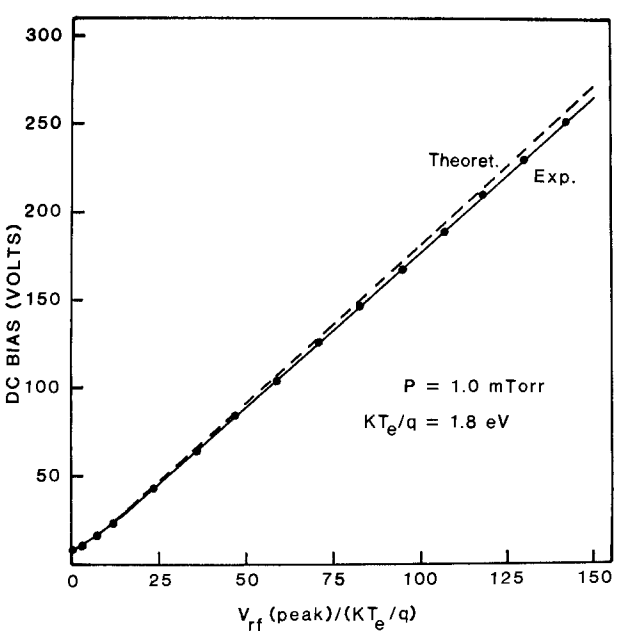

Fig. 2. Steady d-c electrode bias as a function of peak applied rf voltage in argon 1.0 mTorr. Dashed line is Eq. [3] with T_e = 1.8 eV and V_F = −7.9V.

Key words: semiconductor, plasma, etching.

being developed for plasma etching (7). For this comparison, a small cylindrical platinum probe was driven by an audio oscillator supplying an alternating voltage ($V_{rf} \cos \omega t$) relative to the grounded chamber wall in an argon plasma with $P = 1.0$ mTorr, $n = 6.3 \times 10^{10}$ cm^{-3}, $V_e = 1.8$ eV, and $\omega/2\pi = 4$ kHz. The solid line and circles represent the experimental points while the dashed line represents Eq. [3] using the measured value $V_F = -7.9$V. The measured points lie within 3% of the calculated values of $V_{d.c.}$. Better agreement can in fact be obtained by using a more detailed treatment of ion collection (8), but the additional complexity does not seem justified for most applications.

Similar measurements have been carried out using fluorinated etch gases in the same quiescent plasma etch reactor with qualitatively identical results. An inert gas was used for the comparison presented above simply to avoid the ambiguity introduced by the presence of negative ions.

Acknowledgment

The author thanks T. Wicker for his able assistance with the experiment.

Manuscript submitted Feb. 25, 1983; revised manuscript received May 5, 1983.

REFERENCES

1. J. L. Vossen, *This Journal*, **126**, 319 (1979).
2. B. N. Chapman, "Glow Discharge Processes," p. **143**, Wiley-Interscience, New York (1980).
3. H. S. Butler and G. S. Kino, *Phys. Fluids*, **6**, 1346 (1963).
4. J. D. Cobine, "Gaseous Conductors," pp. **139**, Dover, New York (1958).
5. G. N. Watson, "A Treatise on the Theory of Bessel Functions," p. 79, Macmillan, New York (1944).
6. A. Garscadden and K. G. Emeleus, *Proc. Phys. Soc.*, **79**, 535 (1962).
7. *Appl. Phys. Lett.*, To be published.
8. J. G. Laframboise, Rep. No. 100, Inst. Aerospace Studies, Univ. of Toronto (1966).

Chlorine Redistribution in HCl Oxides Due to High Temperature Annealing

B. C. Beard

Center for Surface and Coatings Research, Lehigh University, Bethlehem, Pennsylvania 18015

S. Titcomb and S. R. Butler*

Sherman Fairchild Laboratory, Lehigh University, Bethlehem, Pennsylvania 18015

The incorporation of chlorine in the growing SiO_2 film during O_2/HCl oxidation of silicon has been studied by a number of workers (1, 2). It has been well established that under certain oxidation conditions a Cl-rich phase develops at the interface of the SiO_2 film and the Si substrate (3, 4). In this report, the redistribution of the Cl from the SiO_2/Si interface region in response to high temperature annealing is discussed.

Rutherford backscattering (RBS) studies of the Cl redistribution have recently been presented by Butler *et al.* (4). In a parallel study, secondary ion mass spectrometry (SIMS) analysis was performed on a number of Cl containing specimens. The superior depth resolution of SIMS (<18 nm) over RBS (35 nm) allowed for more detailed depth profiles of Cl.

Materials

The SiO_2 films were grown in a O_2 ambient containing 4% HCl for 30 min at 1200°C. For this oxidation condition, it has been shown that a Cl-rich phase forms at the Si/SiO_2 interface (5). The resulting oxide thickness was 165 nm. The samples were then annealed for up to 16 hr at 1200°C in N_2 containing 4 ppm H_2O.

Experimental Conditions

The SIMS experiments were performed at an ion flux of 4.0×10^{14} ion/sec cm^2, at an energy of 8 keV, corresponding to an SiO_2 sputter rate of 0.046 ± 0.003 nm/sec. The ion beam was composed of Ar^+ ions unfocused from the duoplasmitron source. The ion beam was refined through a Ta aperture such that only a small uniform portion of the beam struck the specimen.

* Electrochemical Society Member.

Key words: silicon dioxide, Cl incorporation, SIMS, RBS.

Results

Figure 1 illustrates a collection of SIMS profiles of a sample before and after a 12 hr 1200°C anneal. The initial Cl-rich phase thickness is ≤18.5 nm, which upon annealing migrated away from the interface to a resulting thickness of ≈69 nm. Based on the integrated areas, the annealed specimen can be seen to have less Cl. Figure 2 more clearly shows the SIMS Cl concentration *vs.* depth profile after the anneal. The bulk of the Cl has moved into the SiO_2 away from the interface. The shoulder on the Si side of the

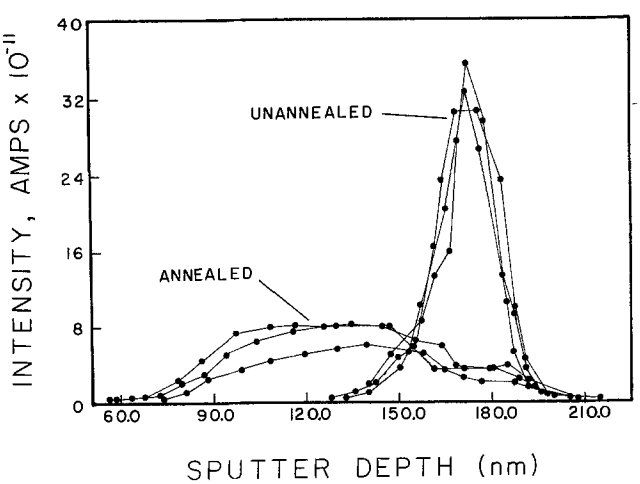

Fig. 1. The SIMS chlorine depth profiles for an unannealed specimen and for a specimen annealed in N_2 (4 ppm H_2O) at 1200°C for 12 hr. Several runs were made on each sample as a reproducibility test. The width of the unannealed peak indicates a Cl phase thickness of ≤ 18.5 nm.

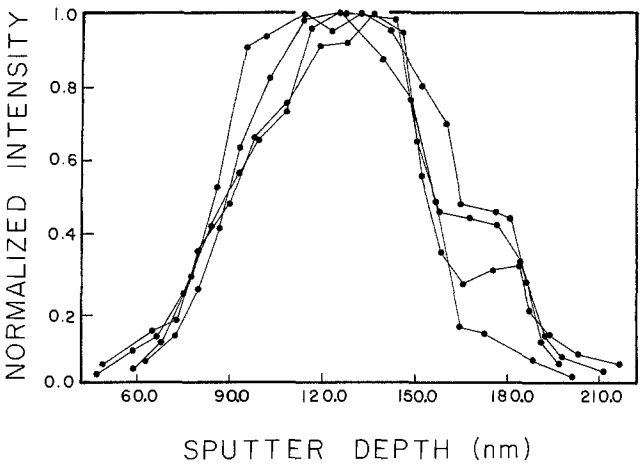

Fig. 2. SIMS Cl depth distribution profiles of an annealed specimen. The majority of the Cl is found in the SiO_2, extending from the original pre-anneal interfacial (165 nm) region well into the bulk of the oxide layer.

distribution in each run may indicate nonuniform sputtering in the interface region. Contributions to the Cl signal from the sputter crater edge or redeposition of Cl during sputtering could also account for the observed shoulder.

RBS analysis also suggested a thickening of the Cl-rich particles. Figure 3 illustrates the movement of the Cl phase outward into the SiO_2 for annealing times of 4 and 16 hr. Note that at 4 hr the Cl distribution has reached nearly maximum width (see Fig. 4) and that the concentration is significantly reduced. (The maximum distribution width at anneal time >4 hr can be assigned as ≈69 nm from the SIMS results.) At 16 hr, the Cl concentration is considerably less with little further increase in the width.

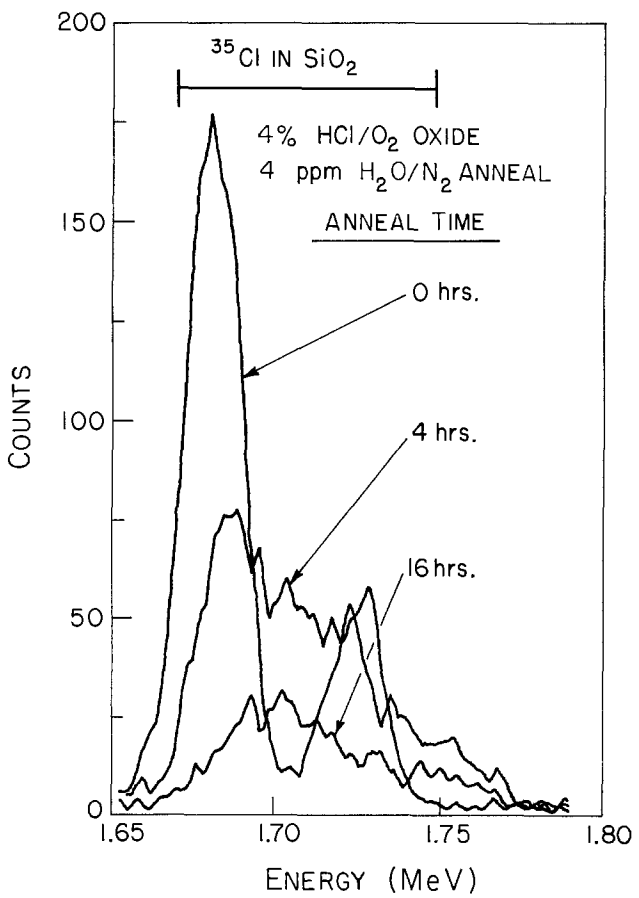

Fig. 3. RBS spectra (chlorine region) of unannealed and annealed (4, 16 hr) specimens.

Discussion

It was suggested in Ref. (4) that the apparent spreading of the Cl distribution outward from the interface region was due to a coarsening of the larger third-phase particles. That is, the smaller particles redissolve and the larger ones grow due to lateral diffusion of Cl. In a somewhat slower process, the Cl is removed from the surfaces of the large particles and diffuses out through the oxide. The low solubility of Cl in SiO_2 limits the out-diffusion process, Fig. 5.

Both the RBS and SIMS data support the out-diffusion of Cl away from the interface. Both techniques also indicate a simultaneous loss of Cl as a function of annealing time. The distribution of the Cl, how-

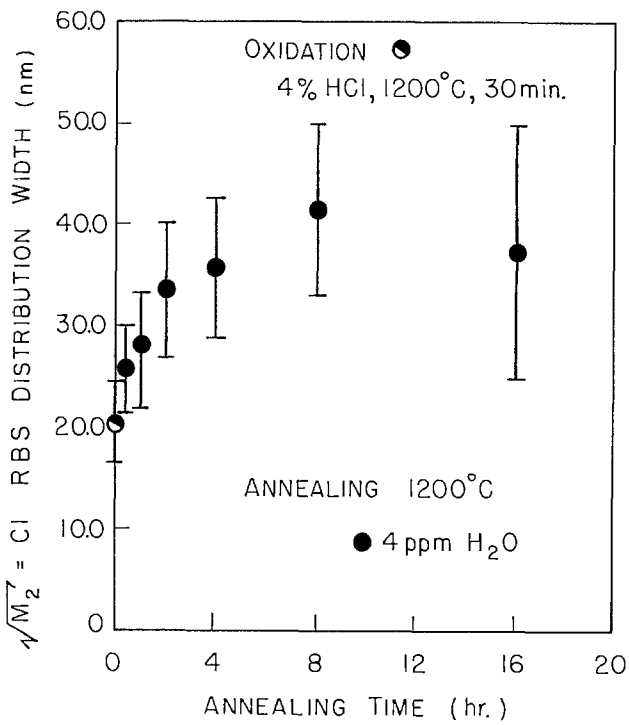

Fig. 4. Effective Cl distribution width based on moment analysis of RBS spectra of specimen annealed up to 16 hr.

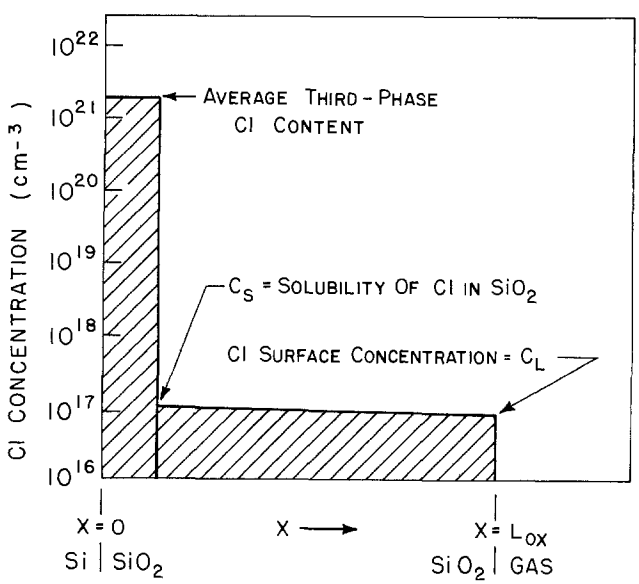

Fig. 5. Schematic model of Cl distribution during annealing. The low solubility of Cl in SiO_2 (~10^{17} Cl/cm^3) limits out-diffusion thus allowing third-phase particles to coarsen.

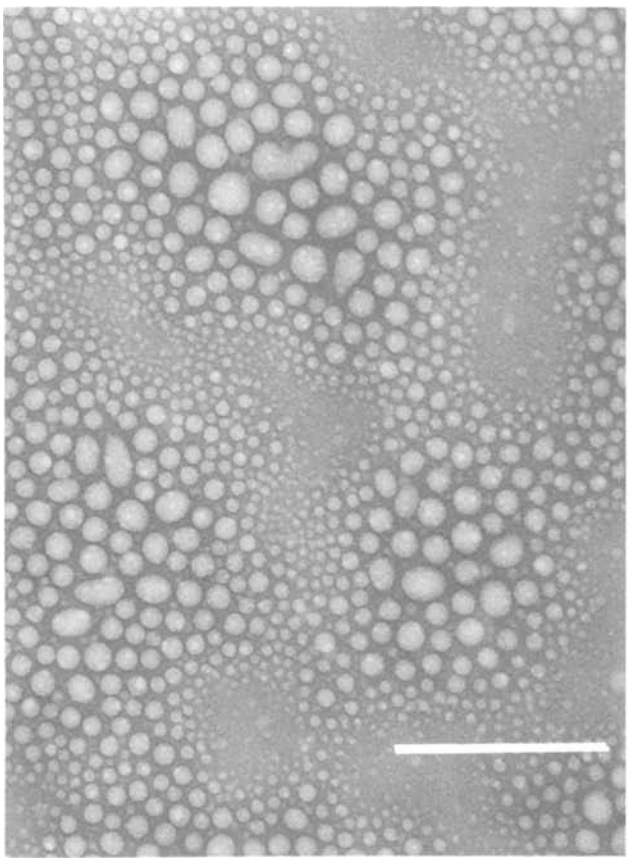

Fig. 6. TEM micrograph of a 6% HCl, 1200°C, 30 min unannealed oxide (0.5μ marker).

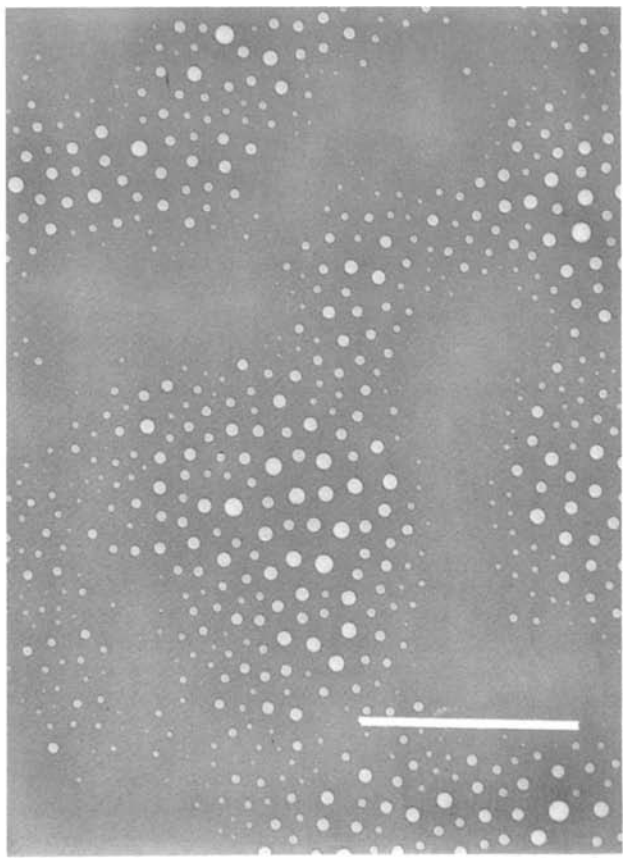

Fig. 7. TEM micrograph of a 6% HCl, 1200°C, 30 min oxide, which has been annealed 1 hr in N_2 at 1200°C (0.5μ marker).

ever, does not continually broaden with time; it appears to actually recede toward the interface. This observation suggests a rapid coarsening of the Cl-rich phase superimposed on a steady low level loss of Cl. Recent transmission electron microscopy (TEM) studies (5) tend to indicate the coarsening of small third-phase particles as a result of annealing, Fig. 6 and Fig. 7. The TEM results may add further support to the SIMS and RBS data which suggest a simultaneous coarsening/out-diffusion of the Cl-rich phase during high temperature annealing.

REFERENCES

1. J. Monkowski, R. E. Tressler, and J. Stach, *This Journal*, **125**, 1867 (1978).
2. A. Rohatgi, S. R. Butler, and F. J. Feigl, *ibid.*, **126**, 143 (1979).
3. B. E. Deal, A. Hurrle, and M. J. Schulz, *ibid.*, **125**, 2024 (1978).
4. S. R. Butler *et al.*, in "Materials Science Research," Vol. 14, J. Pask and A. Evans, Editors, pp. 367-377, Plenum, New York (1981).
5. H.-L. Tsai, Ph.D. Thesis, Lehigh University, Bethlehem, PA (1982).

JOURNAL OF THE ELECTROCHEMICAL SOCIETY

ACCELERATED

BRIEF COMMUNICATIONS

SEPTEMBER 1983

Copolymers of Trimethylsilylstyrene with Chloromethylstyrene for a Bi-Layer Resist System

M. Suzuki, K. Saigo, H. Gokan, and Y. Ohnishi

Fundamental Research Laboratories and Microelectronics Research Laboratories, NEC Corporation, Kawasaki-City Kanagawa Prefecture 213 Japan

Copolymers of trimethylsilylstyrene (SiSt) with chloromethylstyrene (CMS) have been developed as the top imaging layer resist in a bi-layer resist system, since these organosilicon polymers were expected to be quite resistive to O_2-RIE (1). This paper describes the organosilicon polymers etching characteristics, E.B. and deep UV exposure characteristics for the homo- and the co-polymers of trimethylsilylstyrene. It also reports the copolymer application to a bi-layer resist system.

Multi-layer resist systems were developed(2-7) to obtain fine high aspect ratio patterns, even on the steps of the substrate. Among them, the bi-layer resist system, using O_2-RIE, is the most attractive from the process standpoint. In this resist system, polymers with high dry etch resistance (such as AZ-1350J photoresist) are used as the bottom planarizing layer, and the resist material with high resistance to O_2-RIE is used as the top imaging layer. Gokan et al. examined the metal-free organic polymer resistance to the oxygen ion-beam etching extensively and showed the etch rate was inversely proportional to the effective carbon content in the polymer(8). Carbon itself is the most resistive material among all the metal-free organic polymers. However, the etch rate ratio between carbon and AZ-1350J photoresist is only 1 to 3. No metal-free organic polymer can be expected to be suitable for the top layer in a bi-layer resist system. On the other hand, metals and silicon are reported to be highly resistive to oxygen ion-beam etching (9). Therefore, polymers containing metal or Si atoms are promising candidates for the top imaging layer in a bi-layer resist system (10). Especially, polymers containing Si atoms are favorable, because the contamination problem appearing in making integrated circuits is avoided. Thus, Si atoms were introduced in the organic polymer resists whose sensitivity and resolution were proved to be excellent.

Key Words: electron beam, deep UV light, negative resist, multi-layer resist

Organosilicon polymers were synthesized from the corresponding monomers, where trimethylsilylstyrene was derived from chlorostyrene. The polymers investigated are listed in Table I. The copolymer compositions were determined by elemental analysis.

The organosilicon polymers etching characteristics under O_2-RIE condition are shown in Fig. 1. AZ-1350J photoresist etching characteristics are also shown. AZ-1350J photoresist was hard baked at 250°C for 1hr. The film thickness was measured with a Taylor Hobson "Taly Step" instrument. The RIE system is a parallel plate reactor, operated at 1.1 Pa pressure and a power density of 0.096 W/cm^2, and a 4sccm O_2 flow rate.

Organosilicon polymers show an interesting etching characteristic. After some reduction in film thickness, organosilicon polymers etch rates become a few Å/min, i.e., etching in these polymers practically stops. The thickness reductions in organosilicon polymers until the practical stop of etching, and the number of Si atoms contained in these etched layers are summarized in Table II. In the calculation the polymer densities were assumed as being 1.2 (11). From Table II, it is found that organosilicon polymer etching practically stops when a polymer layer containing 1-3x10^{16} atoms/cm^2 is etched. Si atoms would be accumulated on the surface in the form of SiO_2 or SiO as a protecting layer. This was confirmed by Auger spectroscopy and is discussed later. On the other hand, AZ-1350J photoresist was etched continuously at a rate of 800 Å/min. From Fig. 1 and Table II, it was concluded that very thin (220-2200 Å) organosilicon polymer layers can be used as an etch mask for pattern transfer to the underlying planarizing polymer in O_2-RIE.

The PSiSt surface after O_2-RIE was investigated by Auger spectroscopy. The result shows Si atoms are accumulated in the form of silicon oxide (SiO_2 or SiO), instead of pure Si. Depth profiles for Si, O, and C were measured by monitoring Auger signal

intensities while removing surface layers by Ar ion milling. The surface layers milling rate was assumed to be the same as that for SiO_2. In the profile measurement, only the total Si amount was measured,since it was difficult to assign signals for Si to silicon oxide or pure Si exactly. Up to the depth of 200Å, the oxygen amount decreased and the carbon amount increased gradually with increasing depth, while the silicon amount was constant. This shows that the PSiSt surface gradually changed into silicon oxide during the O_2-RIE.

The PSiSt homopolymer and copolymers of SiSt with CMS are selected, considering O_2-RIE resistance. Their sensitivities and resolutions have been evaluated. Both polymers were fractionated to obtain polymers with narrow molecular weight distribution. The fractionated polymers are listed in Table III. These polymers were spun on silicon wafers from xylene solutions. Prebaking was carried out at 100°C for 30 min in a nitrogen atmosphere. Electron beam (20 KeV) exposure was carried out with JEOL JBX-5A electron beam exposure system. Canon PLA-521F contact printer (equipped with cold mirror CM 290) was used to expose deep UV light. After the exposure, the wafers were soaked in a suitable developer for 1 min, and then rinsed in isopropyl alcohol (IPA) for 1 min. For PSiSt, 35:65 tetrahydrofuran (THF) and ethanol (EtOH) solution was chosen and for $P(SiSt_{90}\text{-}CMS_{10})$, 45:55 THF and EtOH solution was chosen as a developer to minimize swelling. Half micron lines and spacings are easily resolved in 0.2 μm thick resist layers. The gel doses (D_g^i) for E.B. exposure are summarized in Table III. The PSiSt sensitivity is 1.5 times as high as that of polystyrene. However, this sensitivity is not sufficient for practical device fabrication. Copolymerization with CMS is very effective to improve the sensitivity. The sensitivity is enhanced ten times as high as that of PSiSt by copolymerizing with 10 mol% CMS. The copolymer of SiSt with CMS is also sensitive to deep UV light. For $P(SiSt_{90}\text{-}CMS_{10})$ F1, total crosslinking occurs at 60 mJ/cm^2 deep UV exposure.

Fine pattern fabrication was carried out using $P(SiSt_{90}\text{-}CMS_{10})$ F1 as the top imaging layer in a bi-layer resist system. A 1.6 μm thick layer of AZ-1350J photoresist was used as the bottom planarizing layer. After E.B. (4.5μC/cm^2) or deep UV (60 mJ/cm^2) exposure and development, the fine patterns in 0.2μm thick $P(SiSt_{90}\text{-}CMS_{10})$ layer were transferred into the thick AZ-1350J photoresist layer by O_2-RIE. The resultant steep profile pattern is shown in Fig.2.

Organosilicon polymers have been found to be attractive materials as the top imaging layer in a bi-layer resist system, since they are very resistive to O_2-RIE. The minimum Si content to form a sufficient protecting layer under O_2-RIE condition has been clarified. From the above consideration, $P(SiSt_{90}\text{-}CMS_{10})$ has been developed as a highly sensitive resist material, keeping high dry etch resistance and high resolution. It is a novel resist material suitable for a bi-layer resist system.

ACKNOWLEDGEMENTS

The authors are grateful to D. Shinoda and S. Fujiwara for their encouragement. They also thank K. Tanigaki, A. Morimoto and N. Endo for their helpful discussions, and Y. Kamejima and T. Jitsukawa for their Anger spectra measurements.

REFERENCES

1) M. Suzuki and K. Saigo, Proc. of 23rd Symposium on Semicon. and Integ. Circuits Technol. P. 18 Dec. 1982 Tokyo.
2) J. M. Moran and D. Maydan, J. Vac. Sci. Technol., 16, 1620 (1979).
3) B. J. Lin, IEDM82-391.
4) K. L. Tai, R. G. Vadimsky and E. Ong, Proc. of 1982 Symposium on VLSI Technology, P.90 (1982) Oiso.
5) K. L. Tai, W. R. Sinclair, R. G. Vadimsky, J. M. Moran and M. J. Rand, J. Vac. Sci. Technol., 16, 1977 (1979)
6) M. Hatzakis, J. Paraszczak and J. Shaw, Proc. Microcircuit Eng. (Lausanne), P.396, Sept. 1981.
7) J. M. Shaw, M. Hatzakis, J. Paraszczak, J. Liutkus and E. Babich, Proc. Sixth International Technical Conference on Photopolymers, P.285, Nov. 1982 Ellenville.
8) H. Gokan, S. Esho and Y. Ohnishi, This Journal, 130, 143(1983).
9) P. D. DeGraff and D. C. Flanders, J.Vac. Sci. Technol., 16, 1906 (1979).
10) S. A. MacDonald , A. S. Steinmann, H. Ito, W. Lee, H. Hiraoka, C. G. Wilson, M.Hatzakis, J. Shaw and J. Paraszczak, Title announced in Program of 1983 Int. Symp. on EIPB, May 31-June 3, 1983 Los Angeles.
11) "Polymer Handbook", 2nd ed., J. Brandrup and E. H. Immergut, Editors, P. v- 55, John Wiley & Sons, Inc. New York (1975).

Table I. List of organosilicon polymers

	Name
PSiMA	Polytrimethoxysilylpropyl methacrylate
P(SiMAm-GMAn)	Poly(trimethoxysilylpropyl methacrylate-co-glycidylmethacrylate)
PSiSt	Polytrimethylsilylstyrene
P(SiStm-CMSn)	Poly(trimethylsilylstyrene-co-chloromethylstyrene)
P(SiStm-GMAn)	Poly(trimethylsilylstyrene-co-glycidylmethacrylate)

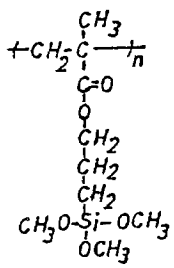

PSiMA

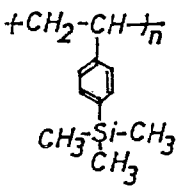

PSiSt

Table II. Number of Si atoms in the layer etched by O_2-RIE

Polymer	Thickness Reduction (A)	Si ($\times 10^{16}$ atoms/cm^2)
PSiSt	220	0.9
P($SiSt_{80}$-CMS_{20})	290	1.2
P($SiSt_{40}$-GMA_{60})	1700	3.0
PSiMA	510	1.5
P($SiMA_{20}$-GMA_{80})	2200	2.0
P($SiMA_{50}$-GMA_{50})	620	1.2

Table III. Organosilicon polymers molecular weights and gel doses

Polymer	Mw ($\times 10^4$)	Mn ($\times 10^4$)	Mw/Mn	D_g^1 ($\mu C/cm^2$)
PSiSt F1	19.8	15.1	1.3	15
PSiSt F2	12.6	9.9	1.3	30
P($SiSt_{90}$-CMS_{10}) F1	28.6	22.2	1.3	1.1
P($SiSt_{90}$-CMS_{10}) F2	15.0	11.1	1.4	2.1
P($SiSt_{80}$-CMS_{20})*	5.5	2.5	2.2	3.8

*This polymer was not fractionated.

Manuscript submitted May 26, 1983.

NEC Corporation assisted in meeting publication costs of this article.

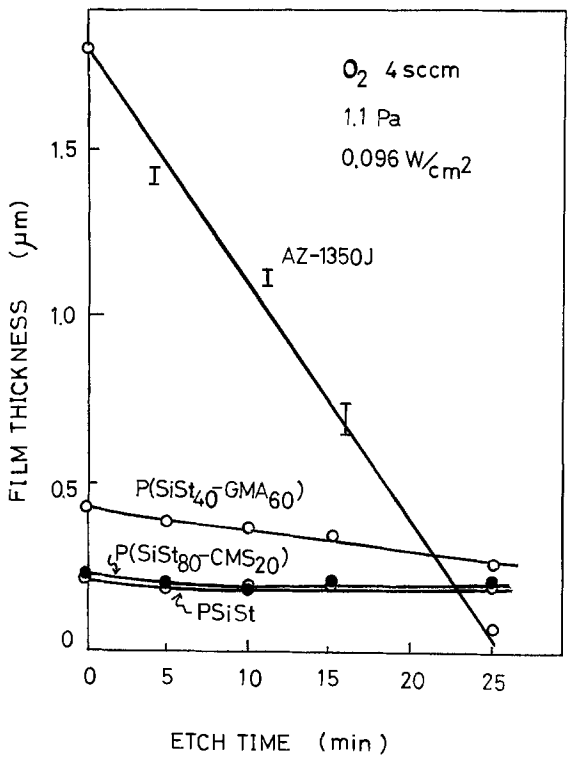

Fig. 1 Organosilicon polymers etching characteristics under O_2-RIE condition
Etching condition: 1.1Pa, 4sccm, 0.096W/cm^2

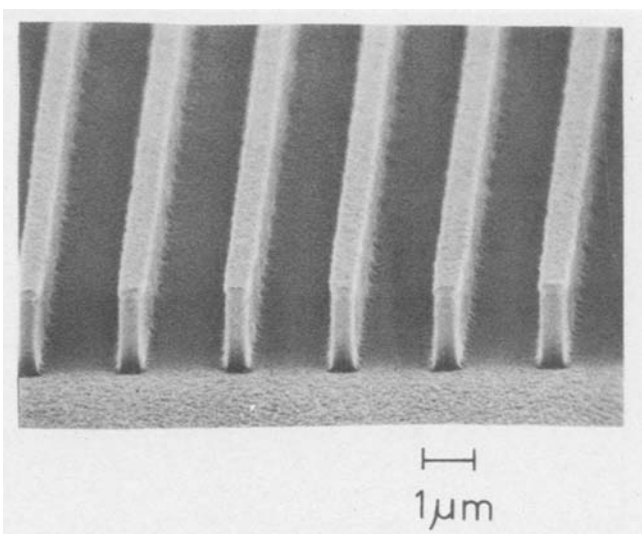

Fig.2 Resultant high aspect ratio pattern obtained using 0.2μm thick P($SiSt_{90}$-CMS_{10}) F1 as the top imaging layer on the 1.6 μm thick AZ-1350J film. (4.5μC/cm^2)

Polymer-Coated Electrodes in Ambient Temperature Molten Salts

P. G. Pickup and R. A. Osteryoung

Department of Chemistry, State University of New York at Buffalo, Buffalo, New York 14214

We were interested in investigating redox polymer films on solid electrodes (1) in a molten salt. We have therefore investigated the electrochemistry of poly-$[Ru(2,2'\text{-bipyridine})_2(4\text{-vinylpyridine})_2]^{2+}$ (2), polyvinylferrocene (PVF) (3,4) and thionine polymer (5) coated glassy carbon electrodes in various compositions of the ambient temperature molten salt system aluminum chloride:n-butylpyridinium chloride (BuPyCl) (6) at 40°C. Electrodes were coated with polymer as described in references 2, 4, and 5 respectively. Surface coverages were measured by cyclic voltammetry in 0.1 M Et_4NClO_4/CH_3CN for the ruthenium and PVF polymers and in 0.05 M aqueous H_2SO_4 for the thionine polymer.

We have used the 0.95:1 (basic), 1:1 (neutral) and 1.2:1 (acidic) $AlCl_3$:BuPyCl mole ratio melts in which the dominant equilibrium is (7):

$$2AlCl_4^- \rightleftarrows Al_2Cl_7^- + Cl^- \quad K < 4 \times 10^{-13}$$

The "neutral" melt can be described as $BuPy^+$ $AlCl_4^-$. The basic melt may be considered to consist of $BuPy^+$, Cl^- and $AlCl_4^-$ ions and the acidic of $BuPy^+$, $Al_2Cl_7^-$ and $AlCl_4^-$, the content depending on the stoichiometric ratio of $AlCl_3$ to BuPyCl. Potentials are quoted relative to Al in a 2:1 melt, which is ca. +140 mV relative to SCE in CH_3CN (8).

The cyclic voltammetry of a C/poly-$[Ru(bpy)_2(vpy)_2]^{2+}$ electrode in an acidic melt (Figure 1) was almost featureless on the first scan. Additionally, no electrochemistry of dissolved ferricenium ($E^{o'}$ = 0.24 V) was observed. On subsequent scans a well defined, reversible wave developed at E^o = +1.26 V and after this wave had reached ca. 80% of its final size a small membrane diffusion type wave (9) for ferricenium reduction developed at ca. + 0.3 V. The voltammogram of Figure 1 reached steady state after about 40 scans and the final charge

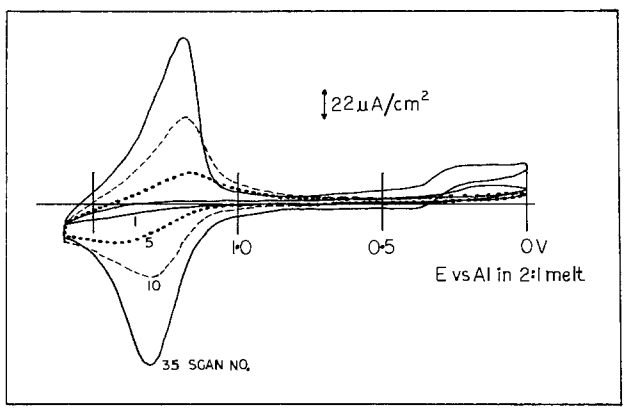

Figure 1. Cyclic voltammograms at 40°C of a C/poly-$[Ru(bpy)_2(vpy)_2]^{2+}$ electrode (surface coverage = 2.0×10^{-9} mol/cm^2) in 1.2:1 $AlCl_3$:BuPyCl melt containing ferricenium (ca. 1 mM). Scan speed = 100 mV/s.

under the wave at +1.26 V corresponded to 100% of the polymer originally present. Thicker films require a longer break-in period.

We interpret the above behavior as indicating slow permeation of melt and ferricenium ions into the polymer film. This permeation is facilitated by repeated oxidation and reduction of the polymer since it does not occur when the polymer is maintained in its reduced state and it is very slow when the polymer is exhaustively oxidized. Presumably the counter-ion and polymer backbone movements associated with oxidation and reduction of the polymer (4,10) allow melt to diffuse into the polymer. This interpretation is supported by the gradual appearance of chloride (from $AlCl_4^-$ or $Al_2Cl_7^-$) oxidation and Al deposition at the limiting potentials of the acidic melt if the potential is scanned through the normal electrochemical window of the melt (6) during break-in. Once an electrode has been broken in it remains electroactive for extended periods (days) in the melt. This type of break-in behavior has been observed by other workers, using different polymers and more conventional solvents (water (4) and acetonitrile (10)).

* Electrochemical Society Active Member
Key Words: Fused salts, electrode, voltammetry

Once a ruthenium polymer film has been broken in it exhibits well defined electrochemistry in both neutral and acidic melts (the basic melt is more easily oxidized than the polymer). For films of 3×10^{-9} mol/cm^2 or less, reversible electrochemistry is observed at scan speeds as high as 500 mV/s. Peak separations are constant and peak currents vary linearly with scan speed, characteristic of a surface bound redox couple. Thicker films show evidence of slow charge transport at scan speeds above 100 mV/s, with increasing peak separation and decreasing charge as the scan speed is increased. The formal potential of the polymer in the melt is about 100 mV greater than expected in comparison to ferrocene/ferricenium, the respective redox potentials of these couples being 1.22 V and 0.38 V vs SCE in acetonitrile.

To obtain a well defined voltammogram of a drop coated C/polyvinylferrocene electrode required that it first be cycled through the PVF redox wave in neutral or basic melt (the polymer dissolves in acidic melt) and then in acetonitrile/Et_4NClO_4. After washing with acetone to remove Et_4NClO_4 from the polymer and drying in the vacuum port of the dry-box the electrode shows well defined electrochemistry in the melt after a break-in period similar to that observed for the ruthenium polymer. Generally, the final voltammogram (Figure 2) shows stable, reversible electrochemistry at E^0 ~0.25 V. However, the quantity of polymer as deduced from the charge is always significantly less than was originally deposited onto the electrode, usually corresponding to 5-20 monolayers of monomer units.

Thionine polymer also exhibits a break-in period in the melt. Final voltammograms (Figure 3) show quasi-reversible electrochemistry at $E^{0'}$ ~0.25 V with the peak separation increasing with scan speed. However, the voltammograms in the melt compare well with those obtained in aqueous sulphuric acid (5).

The results presented here indicate that three very different redox polymer coated electrodes function well in these anhydrous, highly conducting ambient temperature ionic liquids and we feel there is great potential for the use of such electrodes in such media. Other ambient temperature ionic liquids, such as the dialkylimidazolium chloroaluminates (11) would also appear to be useful for studies of polymeric electrodes. The use of such liquids for studies of electronically conducting polymers such as polyacetylenes, polypyrroles and others also appears to have considerable scientific and perhaps technological significance. Smyrl and co-workers

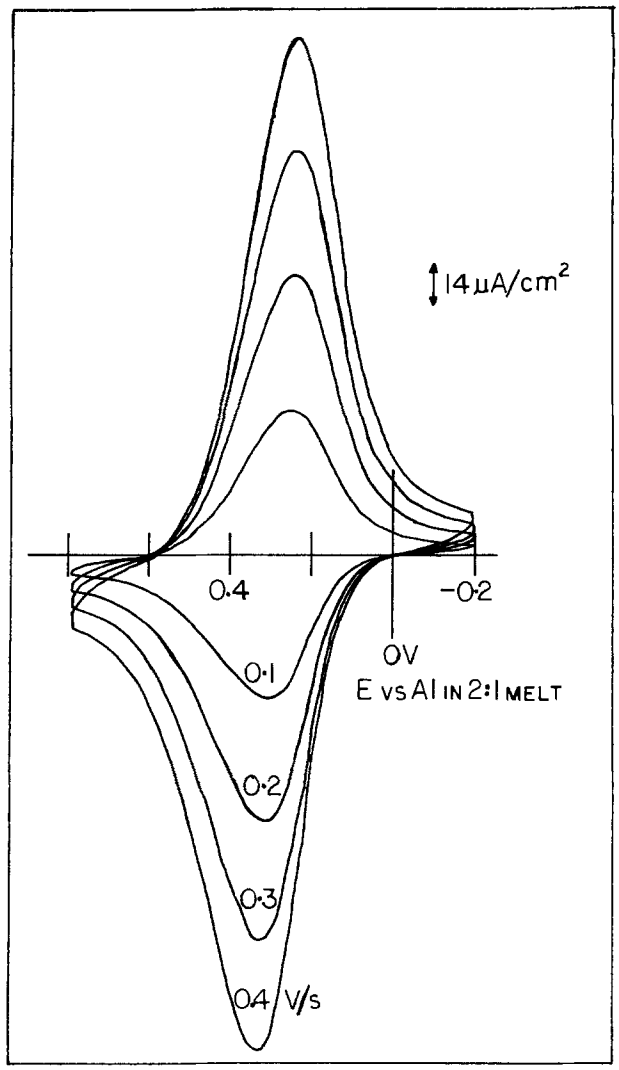

Figure 2. Cyclic voltammograms at 40°C of a C/polyvinylferrocene electrode (final surface coverage = 1.3×10^{-9} mol/cm^2) in 0.95:1 $AlCl_3$: BuPyCl melt.

recently reported on impedance studies at polyacetylene coated electrodes in a 2:1 $AlCl_3$:BuPyCl melt (12); in this melt composition only the oxidation of the polyacetylene could be observed since the melt "window" is ~2 V. However, use of a "neutral" system, either the butylpyridinium chloride or dialkylimidazolium chloride - aluminum chloride ionic liquid, might render such conducting polymers susceptible to both oxidation and reduction, since solvent limits of ca. 3.5 and 4.5 V, respectively, are observed (13). There are possible applications of polymer coated electrodes in these molten salt systems in the fields of electrocatalysis, fuel cells, photoelectrochemistry and batteries. Additional studies in this area are in progress in our laboratory.

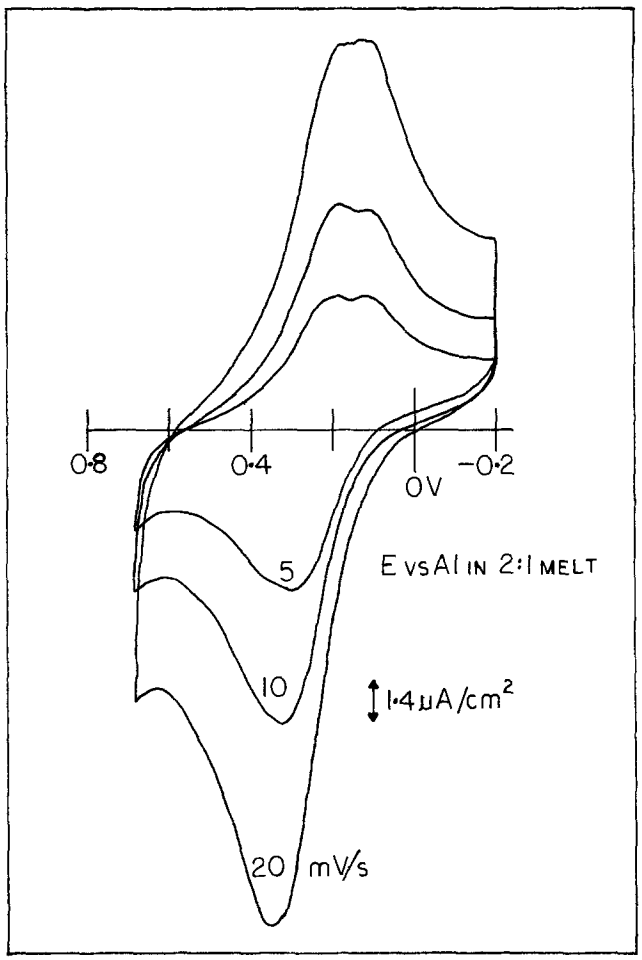

Figure 3. Cyclic voltammograms at 40°C of a C/thionine polymer electrode (surface coverage = 1.9×10^{-9} mol/cm^2) in 0.95:1 $AlCl_3$:BuPyCl melt.

ACKNOWLEDGMENT

We would like to thank Prof. Royce Murray for supplying material from which the polymeric electrodes were prepared.

This work was supported in part by the Air Force Office of Scientific Research and the Office of Naval Research.

Manuscript submitted June 1, 1983.

REFERENCES

1. R. W. Murray, "Chemically Modified Electrodes", Chapter 3 in Electroanalytical Chemistry, Vol. 13, A. J. Bard, Ed., M. Dekker, New York, (in press) (1982).
2. P. Denisevich, H. D. Abruna, C.R. Leidner, T. J. Meyer and R. W. Murray, Inorg. Chem. 21, 2153 (1982).
3. A. Merz and A. J. Bard, J. Am. Chem. Soc. 100, 3222 (1978).
4. P. Daum and R. W. Murray, J. Phys. Chem. 85, 389, (1981).
5. W. J. Albery, A. W. Foulds, K. J. Hall and A. R. Hillman, This Journal, 127, 654 (1980).
6. J. Robinson and R. A. Osteryoung, J. Am. Chem. Soc. 101, 323 (1979).
7. R. J. Gale and R. A. Osteryoung, Inorg. Chem. 18, 1603, (1979).
8. J. Robinson and R. A. Osteryoung, J. Am. Chem. Soc. 102, 4415, (1980).
9. T. Ikeda, R. Schmehl, P. Denisevich, K. Willman and R. W. Murray, J. Am. Chem. Soc. 104, 2683 (1982).
10. F. B. Kaufman, A. H. Schroeder, E. M. Engler, S. R. Kramer and J. Q. Chambers, J. Am. Chem. Soc. 102, 483, (1980).
11. J. S. Wilkes, J. A. Levisky, R. A. Wilson and C. L. Hussey, Inorg. Chem. 21, 1263 (1982).
12. W. H. Smyrl, S. R. Kurtz, C. D. Jaeger, J. M. Zeigler and D. S. Ginley, paper presented to the Electrochemical Society Spring Meeting, San Francisco, CA, May, 1983.
13. M. Lipsztajn and R. A. Osteryoung, This Journal, to be published. Recent News Paper, 4th International Symposium on Molten Salts, The Electrochemical Society, Spring Meeting, San Francisco, CA, May, 1983.

Increased Electrochemical Window in Ambient Temperature Neutral Ionic Liquids

M. Lipsztajn and R. A. Osteryoung*

Department of Chemistry, State University of New York, Buffalo, New York 14214

In the past several years, low temperature molten salt systems composed of aluminum chloride and alkylpyridinium salts have been found (1-3) to be useful solvents for electrochemical and spectroscopic studies of both organic and inorganic species. Recently Wilkes et al (4) have developed a group of dialkyl-imidazolium chloroaluminate melts having a wider cathodic limit than the alkylpyridinium chloroaluminates.

Both cathodic and anodic limits of these solvents depend on the mole ratio of components taken for the preparation of the molten salt. For so-called basic melts ($MC = \frac{n_{AlCl_3}}{n_{RCl}} < 1$) the anodic limit corresponds to the electrooxidation of chloride ions and is identical (5) for both N-n-butylpyridinium chloride (BuPyCl)-$AlCl_3$ and 1-methyl-3-ethylimidazolium chloride (ImCl)-$AlCl_3$ melts. The cathodic limit for basic melts corresponds to the electroreduction of the organic cation ($BuPy^+$ or Im^+).

For acidic melts ($MC > 1$) the anodic and cathodic limits are identical (5) for both RCl-$AlCl_3$ melts ($R = BuPy^+$ or Im^+) and correspond to, respectively, tetrachloroaluminate ($AlCl_4^-$) oxidation, to yield chlorine, and heptachloroaluminate ($Al_2Cl_7^-$) reduction, to yield Al.

The electrochemical windows for these melts measured at a tungsten electrode are shown in Figure 1.

The purpose of this communication is to present the great advantage of use of a neutral melt (MC = 1.00); preparation of this melt consists of weighing appropriate amounts of $AlCl_3$ and RCl, and mixing. This roughly neutral melt is subsequently adjusted by addition of small amounts of either $AlCl_3$ or RCl to obtain the proper electrochemical window. As shown in Figure 1 the limits established for neutral melts correspond to anodic oxidation of $AlCl_4^-$ and cathodic reduction of R^+, giving a very wide electrochemical window (~3.6 V for 1:1 $AlCl_3$-BuPyCl and ~4.4 V for 1:1 $AlCl_3$-ImCl melts respectively). This extension of the electrochemical window enables us to investigate several redox systems inaccessible for study in melts prepared by use of an excess of basic (RCl) or acidic ($AlCl_3$) components. Some of these systems are of fundamental importance in understanding the chemistry of these melts.

As an example, the electrochemistry obtained at a tungsten electrode in a 30 mmol solution of BuPyCl in neutral $AlCl_3$-ImCl melt is presented in Figure 2. The quasi-reversible oxidation of Cl^- is observed (4) as a discrete anodic voltammetric wave, while cathodically the reduction of $BuPy^+$ occurs. More detailed studies of Cl^- oxidation and $BuPy^+$ reduction will be presented in subsequent publications; however it is worth mentioning that this first process is convective diffusion controlled at a rotating disc electrode and that the Cl^- oxidation wave can be very useful in studies of many chemical reactions, particularly those involving chloride complexation with a metal ion.

In a melt symmetric to that discussed above (i.e. a neutral melt with a small excess of $AlCl_3$ added (6)) the convective - diffusion controlled reduction of $Al_2Cl_7^-$ at a rotating disc electrode is observed and this wave can be also very useful.

The very wide electrochemical window of neutral $AlCl_3$-RCl melts appears very promising from the point of view of use as a solvent for new high energy density batteries. Applicability of this system to studies involving redox and conducting polymeric electrodes is in progress (7).

*Electrochemical Society Active Member

Key Words: Fused salts, depolarization, discharge, voltammetry

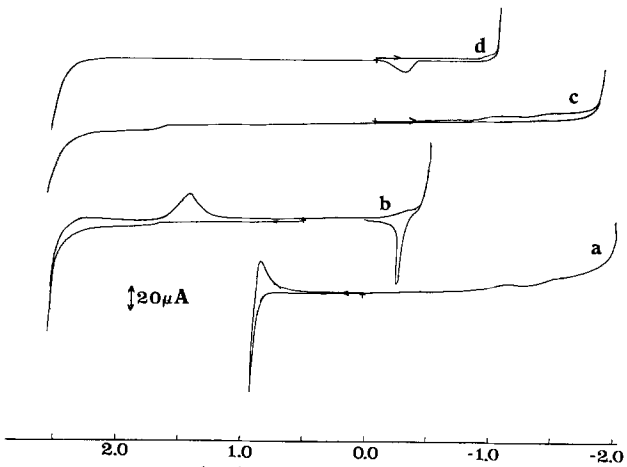

1. Cyclic voltammetric curves recorded on tungsten electrode (area 0.0784 cm^2) in (a) basic $AlCl_3$-ImCl melt (MC = 0.67) (b) acidic $AlCl_3$-ImCl melt (MC = 1.2) (c) neutral $AlCl_3$-ImCl melt (MC = 1.00) (d) neutral $AlCl_3$-BuPyCl melt (MC = 1.00) Sweep rate = 0.05 V s^{-1}, temperature = 30°C.

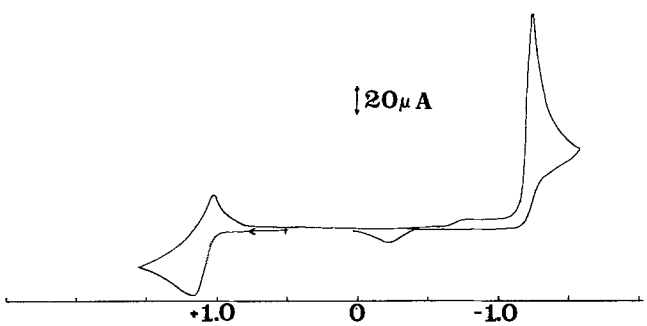

2. Cyclic voltammetric curve recorded on tungsten electrode (area 0.0784 cm^2) at 30°C in 30 mmol solution of N-n-butylpyridinium chloride in neutral $AlCl_3$-ImCl melt (MC = .994), sweep rate 0.05 V s^{-1}.

ACKNOWLEDGMENT

This work was supported in part by the Air Force Office of Scientific Research and the Office of Naval Research.

This paper was presented in part at the 4th International Symposium on Molten Salts, the Electrochemical Society Meeting, San Francisco, May 1983.

Manuscript submitted June 6, 1983.

REFERENCES

1. H. L. Chum, V. R. Koch, L. L. Miller and R. A. Osteryoung, J. Amer. Chem. Soc., 97, 3264 (1975).
2. J. Robinson and R. A. Osteryoung, ibid, 101, 323 (1979).
3. R. J. Gale and R. A. Osteryoung, Inorg. Chem., 18, 1603 (1979).
4. J. S. Wilkes, J. A. Levisky, R. A. Wilson and C. L. Hussey, ibid., 21, 1263 (1982).
5. Z. Karpinski and R. A. Osteryoung, in preparation.
6. J. Robinson and R. A. Osteryoung, This Journal, 127, 122 (1980).
7. P. G. Pickup and R. A. Osteryoung, This Journal, submitted for publication.

Phenomenological Model for Silicon Oxidation in Dry Oxygen in the Presence of HCl

A. I. Ellis,* K. M. Gardiner, and T. E. Cyr

Solid State Electronics Division, Honeywell Incorporated, Plymouth, Minnesota 55441

INTRODUCTION

Thermal oxidation of silicon to form a thin SiO_2 layer is one of the most important processes in VLSI and VHSIC technology. Presently, some commercially available, high performance MOS memory circuits use gate oxides as thin as 400 Å. There is a wide body of experimental evidence which indicates that such thin layers of SiO_2 are substantially different from thicker layers. These differences include growth kinetics, optical properties, breakdown characteristics, and physical structure. In spite of the pioneering studies of Deal and Grove [1] and several other authors [2-4], the growth of the first several hundred angstroms of oxide has not yet been quantitatively explained. In this paper we propose a conceptually simple modification of the Deal -Grove model based on the assumption that the oxygen atoms impacting the oxide surface have a definite probability of penetrating to a certain depth. Expressions useful for data analysis and simulation (SUPREM II and III) are given.

DRY OXIDATION MODEL

Blanc [3] proposed a simple model which explains well the anomalously high oxidation rate of thin oxide. This model assumes that although oxygen diffuses molecularly during the dry oxidation, the actual oxidant is atomic oxygen; this leads to a conceptually simple modification of the Deal-Grove model. Blanc's model was tested in both the thin and thick oxide regions and was found inadequate for the simulation of both oxide regimes. Therefore, here we suggest a semiempirical modification of the Deal-Grove formula. It was assumed after Deal and Grove, that the oxidation mechanism arises from the diffusion transport of oxidant through the growing amorphous SiO_2 layer followed by the reaction of Si with oxidant at the advancing interface. The equation of Deal and Grove which describes the change of oxide thickness, Z_{ox}, with the oxidation time, t, has the following form:

$$\frac{dZ_{ox}}{dt} = \frac{K_1 K_p}{2K_1 Z_{ox} + K_p} \qquad (1)$$

Here K_1 and K_p are the linear and parabolic growth rates respectively. They are related to the linear and parabolic rate constants A and B by $A = K_p/K_1$ and $B = K_p$. We suggest that for thin oxides the linear growth rate K_1 should be replaced by K_n, where

$$K_n = K_1 (1 + Z_f \exp(-Z_{ox}/Z_1)) \qquad (2)$$

The new model parameters are: Z_f the growth acceleration factor, and Z_1 the effective penetration depth. Their temperature dependences (for dry O_2) as determined by comparison to experimental data are:

$$Z_f = 39.965 - .08145 + 4.2552 \times 10^{-5} T^2 \qquad (3)$$

$$Z_1 = 1/(692 - 1.3641T + 6.876 \times 10^{-4} T^2) \text{ (microns)} \qquad (4)$$

where T is in °C.

Integrating equation (1) one obtains the well known dependence (Grove's equation):

$$t = \frac{Z_{ox}^2}{K_p} + \frac{Z_{ox}}{K_1} \qquad (5)$$

This equation will take the following form if K_n is substituted for K_1 in Eq (1):

---

* Electrochemical Society Active Member.

Key words: oxidation, growth, kinetics.

$$t = \frac{Z_{ox}^2}{K_p} + \frac{Z_{ox}}{K_1} + \frac{Z_1}{K_1} \ln \left[\frac{1 + Z_f e^{-Z_{ox}/Z_1}}{1 + Z_f} \right] \quad (6)$$

Equation (6) differs from equation (5) by an additional term which causes faster growth for thin oxides but is negligible for oxides 3 to 4 times thicker than Z_1.

The SUPREM II-05 program models the oxide growth by employing approximate empirical correction factors to the usual linear parabolic growth law. The model proposed here improves the predictive capabilities of SUPREM. In Fig.1 we compare the oxide growth rate dZ_{ox}/dt calculated from the Deal and Grove model with that predicted by the new model. Also shown is the growth rate which was used in the SUPREM II-05 program. Note the sharp discontinuity in the SUPREM II-05 curve. This is due to the attempt to fit the experimental data with a constant acceleration factor.

The analysis of the data [1,2,4,5] at 700, 780, 893, 980 and 1100°C further confirm the validity of the proposed model. Figure 2 shows the comparison of the theory with experimental data for oxidation in dry O_2 at 893°C. The dashed curve is the result of the SUPREM II-05 calculations and the solid curve shows that the new model provides a smooth transition from the accelerated to the linear growth regions while maintaining a good fit to experimental data for thick oxides. Such a good fit, over the entire oxide thickness range was not possible with Deal and Grove model.

OXIDATION IN HCL/O_2 MIXTURES

One of the most significant developments in the passivation of thermally grown silicon-dioxide films over the past several years has been the addition of a chlorine species during silicon oxidation. This so-called HCl oxidation has many benefits [6]. It reduces the instabilities due to the presence of mobile ions in the oxide and increases the lifetime of the minority carriers in the underlying silicon. It also reduces the number of oxide defects and therefore improves the dielectric breakdown characteristics of the oxide. The interface state density is reduced and a reduction in surface charge density in the oxide is observed. Also, the HCl oxidation reduces the stacking fault density in the underlying silicon. Not all of the effects of chlorine, however,are advantageous; the chlorine, is responsible for anisotropic etching of the underlying silicon and the separation of the oxide from the silicon. Because of the practical interest in the HCl oxidation a good understanding of the oxidation process is of considerable importance. Most of the work reported in the literature to date has concentrated on expanding the experimental data to gain better insight into the reaction kinetics of this system [6-9]. Monkowski and his coworkers [10] proposed a model which explains the development of chlorinated oxides. It accounts for the development of two additional chlorine-rich phases at the oxide-silicon interface during HCl oxidation by analogy to the corrosion of metals by two oxidants. It does not provide, however, quantitative information on the mechanism of the oxidation, and as such is not useful for process modeling and simulation.

In our present work we suggest a simple expansion of the kinetic model proposed in the previous chapter to include chlorine oxidation. In the light of the research work of Hess and Deal [6] the parabolic rate constant (B) gradually increases with increasing HCl concentration; there is no variation of B with silicon orientation. On the other hand, the linear rate constant B/A involves the reaction rate constants at the SiO_2 surface and at the silicon surface and exhibits a strong orientation dependence which decreases with increasing temperature. It shows an initial increases due to the addition of 1% HCl to the dry oxygen atmosphere, but further HCl additions have only a small effect on B/A. Hess and Deal explain this last behavior of B/A as related to enhanced Si-Si bond breaking due to etching by a chlorine species. Because Arrhenius plots of the rate constants for the O_2/HCl oxidations were not linear they concluded that more than one process is occurring during silicon oxidation in these mixtures.

Based on the reported observations we included chlorine oxidation effects in the equation of Deal and Grove (Eq. 1-4) by modifying the linear and parabolic growth rates in a fashion which would allow us to extract expressions useful for data analysis and simulation. We have assumed that the presence of chlorine in the oxidizing gas affects both the growth acceleration factor, Z_f, and the effective penetration depth, Z_1. The parabolic growth rate, K_p is also modified. We introduce three new model parameters which are defined through the following relationships

$$Z_f^{Cl} = Z_f * A_f \quad (7)$$

$$Z_1^{Cl} = Z_1 * A_1 \quad (8)$$

$$K_p^{Cl} = K_p * A_p \quad (9)$$

The new coefficients: A_f, A_1 and A_p are functions of the HCl concentration, and temperature.

To define the A parameters we used a curve fitting procedure. The only data of sufficient precision, at sufficiently close intervals of temperature and extending from low to high percentages of HCl appear to be those of Deal, Lie and Razouk.[11] We have supplemented their data by including a set of unpublished oxidation data[12] taken for <100> silicon at 975°C for 4% HCl in dry O_2. All the wafers were p-type with a nominal resistivity of 9 - 13 Ω-cm. This low resistivity value has no influence on the oxidation process [13]. The oxide thicknesses were measured using AME-500 ellipsometer at an angle of incidence of 70° and a wavelength of 0.5461 μm.

Table 1. The chlorine oxidation model coefficients A_f, A_1 and A_p (Eq. 7-9) from a fit of the calculated oxide thicknesses to the data (Ref. 11.)

TEMP / % HCl	A_f			A_1			A_p		
	900°C	1000°C	1100°C	900°C	1000°C	1100°C	900°C	1000°C	1100°C
1%	2.22	1.59	2.14	1.48	1.31	0.56	1.12	1.59	1.35
5%	2.80	2.09	2.97	1.29	1.05	0.38	1.45	2.03	1.61
10%	3.16	2.53	3.20	0.95	0.69	0.30	1.98	2.70	2.03

A standard least squares optimization method was used in SUPREM II-05 to obtain the parameters shown in Table 1. All three coefficients exhibit a nonlinear behavior as a function of temperature and percentage of chlorine. These results were then utilized in defining the functional dependence of the A coefficients on the temperature and percentage of chlorine. This relationship was assumed to have the form of an equation

$$F(P, T) = a + bP + cT + dT^2 + ePT + fP^2 \quad (10)$$

where P is the percentage of HCl and T represents the oxidation temperature in °C.

The parameters a, b, c, d, e, and f are strictly numerical coefficients and cannot be directly correlated with physical parameters of the oxidation system.

Equation (10) was solved numerically for each of the A coefficients using least squares, and the following parametric equations were obtained

$$A_f = 69.79 + 0.150P - 0.13682T + 6.838 \times 10^{-5}T^2 + 5.18 \times 10^{-5}PT - 8.54 \times 10^{-3}P^2 \quad (11)$$

$$A_1 = -12.20 - 0.198P + 3.221 \times 10^{-2}T - 1.871 \times 10^{-5}T^2 + 1.636 \times 10^{-4}PT - 1.92 \times 10^{-3}P^2 \quad (12)$$

$$A_p = -51.12 + 0.182P + 0.10414T - 5.143 \times 10^{-5}T^2 - 1.059 \times 10^{-4}PT + 2.55 \times 10^{-3}P^2 \quad (13)$$

where T is in °C.
Equations (3-5), (7-9), (11-13) were directly implemented into the SUPREM II program (Subroutine OXDEP) to account for the effect of chlorine in the dry O_2 oxidizing gas.

To verify our phenomenological model we have calculated the oxide thickness as a function of the oxidation time for dry O_2 oxidation of <100> silicon at 975°C and with 4% HCl. The calculation is compared with the measured values [12] in Figure 3. It is seen that our oxidation model agrees closely with the experimental data in both the linear and parabolic regimes. The dashed curve represents the calculations done assuming that there is no oxide present on the silicon surface at time t = 0. Usually however there is initially a thin layer of oxide present and this can easily be included in the calculations by using the DEPOSITION step in the SUPREM Input Data File before the OXIDATION steps are simulated. The full curve represents results of calculations for initial oxide thickness of 25 Å with a 9 minute push-in simulated prior to the high temperature oxidation. Incorporation of these two processing steps brings the theory into much closer agreement with the experimental data, especially in the thin oxide regime. The growth of the initial 25 Å

of oxide can be easily associated with the standard R.C.A. cold clean process through which wafers went before high temperature oxidation.

CONCLUSION

The phenomenological model presented here should be useful for most (chlorine) oxidations of practical interest, within the range of conditions for which data is currently available. Better understanding of the mechanisms involved will be necessary, however, for complete predictive capability particularly outside the available data range.

ACKNOWLEDGMENT

The authors are indebted to J. S. T. Huang for comments and helpful suggestions. Special thanks are due to D. Suhl, S. Peck and G. Kirchner for supplying us with their experimental data and for helpful discussions.

REFERENCES

1. B.E. Deal and A.S. Grove, J. Appl. Phys., 36, 3770 (1965)
2. E.A. Irene and Y.J. Van der Meulen, J. Electrochem. Soc, 23, 1380 (1976)
3. J. Blanc, Appl. Phys. Lett. 33, 424 (1978)
4. E.A. Irene J. Electrochem. Soc. 125, 1708 (1978)
5. G. Wright, Private Communication
6. D.W. Hess and B.E. Deal, J. Electrochem. Soc. 124, 735 (1977)
7. B.E. Deal, J. Electrochem. Soc. 125, 576 (1978)
8. C. Hashimoto, S. Muramoto, N. Shiono, and O. Nakajima, J. Electrochem. Soc. 127, 129 (1980)
9. R.W. Dutton et. al. "Oxidation and Epitaxy", Tech. Report No. 5021-1, Stanford University, Stanford, California (1977)
10. J.R. Monkowski, J. Stach, and R.E. Tressler "A Model of Silicon Oxidation in Chlorine-Containing Ambients: Competition between two oxidants", IEEE Proc. Electron. Components Conf.,San Francisco, Calif., 61 (1980)
11. B.E. Deal, L.N. Lie and R.R. Razouk "Characterization of Silicon Oxidation in High Pressure Dry O_2", Technology Modeling Seminar, Stanford University, Stanford, California (1981)
12. G. Kirchner, S. Peck and D. Suhl, Private Communication
13. E.A. Irene, J. Electrochem. Soc., 121, 1631 (1974)

Manuscript submitted June 1, 1982; revised manuscript received Sept. 10, 1982.

Honeywell Incorporated assisted in meeting publication costs of this article.

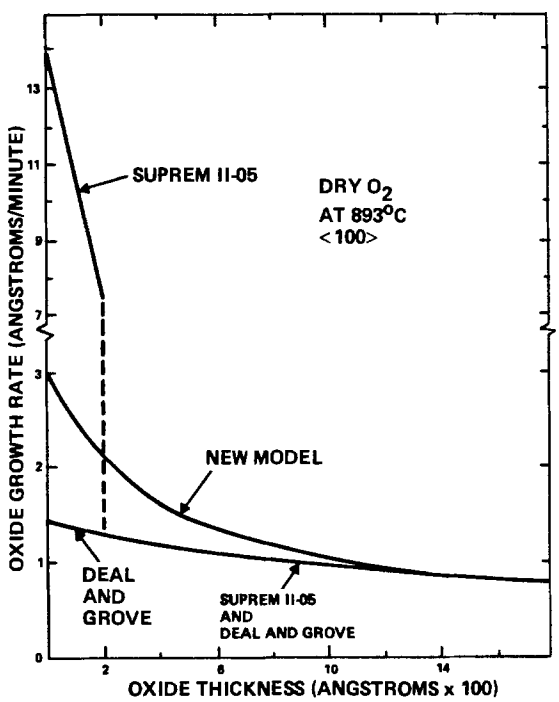

Fig. 1. Comparison of the predicted oxide growth rate for the new dry oxidation model with that of Deal and Grove and that used in SUPREM II-05.

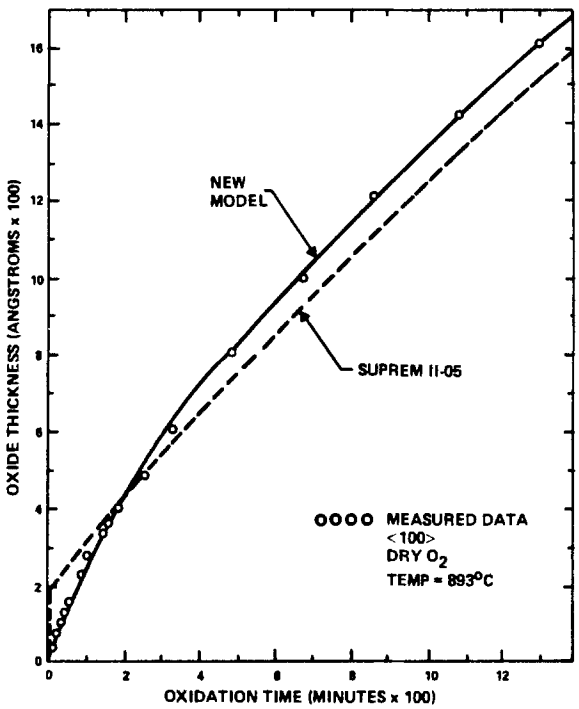

Fig. 2. Comparison of the theory with experimental data[1,2,4,5] for <100> silicon oxidation in dry O_2 at 893°C.

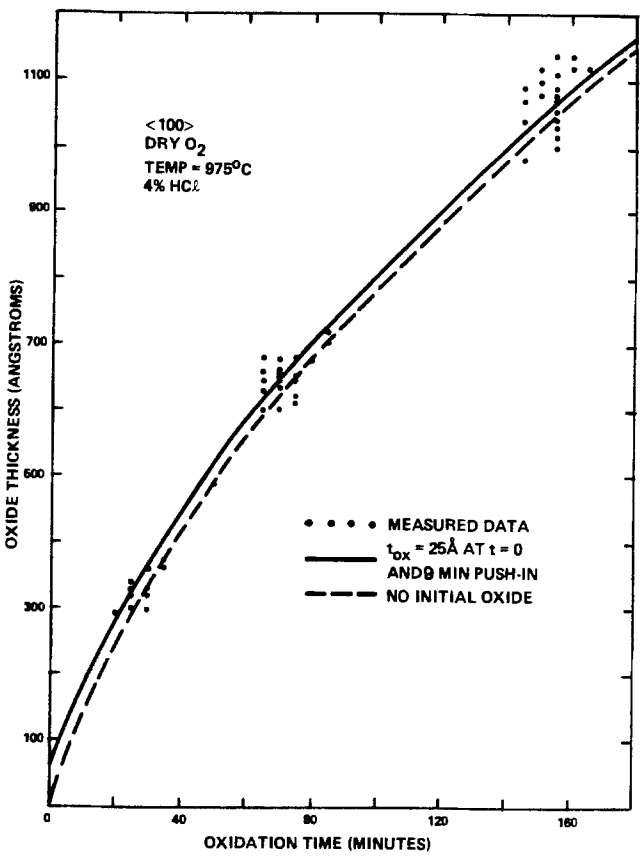

Fig. 3. Comparison of the theory with experimental data[12] for <100> silicon oxidation in dry O_2 with 4% HCl at 975°C. The dashed curve was calculated assuming that t_{ox} = 0 at t=0. The full curve represents results of calculations for initial oxide thickness of 25 Å with a 9 minute push-in simulated before the high temperature oxidation.

JOURNAL OF THE ELECTROCHEMICAL SOCIETY

REVIEWS AND NEWS

SEPTEMBER 1983

Report of the Electrolytic Industries for the Year 1982[1]

M. Y. C. Woo*

Engelhard Corporation, Engelhard Industries Division, Iselin, New Jersey 08830

R. D. Varjian*

Dow Chemical Company, Louisiana Applied Science and Technology Laboratory, Plaquemine, Louisina 70765

Chlorine-Caustic Soda

Production and capacity.—United States.—The U.S. industry produced 9.17 million tons of chlorine in 1982, down 15% from 1981, the lowest level since 1975. In December 1982, capacity stood at 39,995 tons/day, compared to 40,629 a year earlier. The industry operating rate dipped to 57.8%, just a shade above the August low of 57% (1).

United States chlorine production capacity is given in Table I (2).

Ten percent of chlorine is manufactured in small plants of less than 275 tons capacity per day. These small plants are vulnerable to shutdown considering the depressed state of the industry (3).

One plant expansion was announced. Vulcan plans to expand its Geismar, Louisiana, capacity by 12% in the fall of 1983. Capacity at that time will reach 675 tons/day chlorine and 720 tons/day of caustic. Project cost is estimated at $12.5 million (4, 5, 6).

PPG has announced a modernization program for its operation at Natrium, West Virginia. New technology will reduce energy demands by 10% (7).

Linden Chemicals and Plastics purchased International Minerals and Plastics chlorine-caustic soda plant in Orrington, Maine, as well as chlorine-caustic plants at Ashtabula, Ohio, and Niagara Falls, New York (8, 9).

A number of plant closures or cutbacks took place in 1982.

Occidental Chemical closed its Montague, Michigan, facility indefinitely in reaction to depressed operating conditions throughout the industry (10). The plant capacity is 74,000 metric tons of chlorine per year, or about 7% of Oxy's total (11).

Linden Chemicals and Plastics plant in Linden, New Jersey, is on stand-by (10).

Pennwalt closed its 330 ton/day Calvert City, Kentucky, plant in the spring (12, 13).

Dow has mothballed its Midland, Michigan, plant, holding it on stand-by for 6 to 18 months. The plant had an estimated 282,000 metric ton/year capacity, or about 6% of Dow USA's 4.47 million metric ton capacity (14).

Olin temporarily closed its mercury cell plant at McIntosh, Alabama, because of poor market conditions. Plant capacity is 350 tons/day of chlorine (15).

PPG closed two production units at Lake Charles, Louisiana, described as outmoded diaphragm cells already scheduled for modernization. Capacity will be restored in 1983 when the old units are replaced by low energy bipolar electrolyzers (16).

Occidental Chemical cut output by 50% at its Taft, Louisiana, plant. Name plate capacity is 503,000 tons/year caustic soda (17).

Utilities on the Gulf Coast face vast capital expenditures converting from gas to coal. Other regions where nuclear and coal-fired generators are in place might be more attractive. Plants might be replaced with new facilities in the Northwest and western Canada where cheap hydropower exists (18).

Canada.—Canadian chlorine production capacity is given in Table II (2).

Japan.—1981 production of soda chemicals in Japan was 5.5 million tons, down 5.3% from 1980. 1981 was the second consecutive year of negative growth in the industry (19).

65.1% of Japanese plants have switched from mercury cells to diaphragm cells. Diaphragm plants account for 2.5 million tons/year and mercury plants

Table I. U.S. chlorine production capacity 1982—thousands of metric tons per year (2)

Convent Chemical	377
Diamond Shamrock	1,147
Dow Chemical USA	3,811
DuPont	602
Georgia-Pacific	429
Linden Chemicals and Plastics	407
Occidental Chemical	1,049
Olin	878
Pennwalt	362
PPG	1,348
Vulcan	438
Others	1,789
	12,637

Table II. Canadian chlorine production capacity, 1982—thousands of metric tons per year

American Can of Canada	10.6
Canadian Occidental	176.0
Canso Chemicals	24.0
CIL	320.0
Dow Chemical Canada	725.0
FMC of Canada	49.0
Great Lakes Forest Products	15.0
PPG (Stanchem)	105.0
Prince Albert Pulp	30.0
Reed Paper	20.0
St. Anne Chemical	10.0
Total	1,484.6

* Electrochemical Society Active Member.

[1] This report is sponsored by the Industrial Electrolytic Division of The Electrochemical Society. It represents a summary of the published information on production, plant capacities, consumption, markets and trends, prices, raw materials, new developments, and health and environmental aspects in the electrolytic and related industries.

The material presented herein has been obtained from many sources, as noted in the list of references, and does not necessarily represent the opinions of the authors.

The Industrial Electrolytic Division is grateful for the support received from the Vittorio de Nora-Diamond Shamrock Fund which assisted with the publication costs of this report.

produce 1.3 million tons/year of NaOH. Total capacity is 3.8 million tons. The change to diaphragm cell plants should be complete by the end of fiscal 1984 (20).

Asahi Glass has changed its diaphragm cell plant in Kitakyushu to a membrane plant. Diamond Shamrock DS cells were converted from asbestos diaphragms to Asahi Glass membranes. Caustic capacity was doubled from 750 ton/month to 1500 tons/month. Cost was 400 million yen (23).

Asahi Chemical has started its 40,000 ton/year membrane cell plant at Nobeoka. Now, the company can produce all its capacity via the membrane cell process (22, 23).

The Japan Soda Industry has started negotiations with Mexico's Exporta dosa de Sal, held 49% by Mitsubishi, in order to cut the supply of salt by 30% from 1983 levels. Sluggish demand for caustic soda is causing reduced salt consumption (24).

Europe.—Billerud-Uddeholm has purchased ICI FM21 membrane cells for 45,000 metric ton/year plant expansion in Skoghall, Sweden. Startup is slated for December 1983 (25).

Akzo Zout is building the first world scale membrane plant near Rotterdam, The Netherlands. The plant uses Asahi Chemical technology and is rated at 280,000 metric tons/year (26).

Markets and prices.—Chlorine.—Chlor-alkali producers were hit hard during 1982 by demand cutbacks. Industry operating rates remained near 60% all year. Producers tried to maintain margins by raising caustic prices. However, caustic demand went soft and prices fell $50-$60 per ton. Near the end of the year, a $10 price increase for chlorine was obtained (27).

In midyear, producers were waiting for an improvement in the entire economy to help strengthen chlorine markets. Inventories remained low in anticipation of an economic turnaround (10).

The U.S. International Trade Commission ruled that the domestic industry was not being hurt by chlorine imports from Canada. Diamond Shamrock, Olin, and Pennwalt complained that material from CIL, Incorporated was being sold at less than fair value (28).

Most forecasters foresee lower than historic growth for chlorine in the future.

Chlorine's real price has not changed since 1977. Annual growth rates are expected to be in the 2-3% range, down from the 5-7% growth rate experienced prior to 1979. Little or no chlorine plant capacity will be added over the next 5 years (3).

World consumption of chlorine will grow 9.2% per year through 1990 according to a C.H. Kline study. Chlor-alkalis are a growth industry in the developing countries of Asia, Africa, and Latin America where consumption grew at 11.6%/year between 1975 and 1980. During the same period in industrialized countries, the growth rate was 2.8%/year. The only promise for better than average growth is in caustic-enhanced oil recovery (29).

The chlor-alkali industry will grow at just 3.6%/year through 1995 compared to the historic level of 4.4% according to Predicasts (30).

Caustic soda.—Caustic soda markets finally reached a ceiling after a decade of growth. Prices have fallen. Caustic has gone off allocation. 2-5% of caustic consumers could shift to soda ash. Enhanced oil recovery and pollution control could help future caustic markets (3).

U.S. caustic soda exports in 1981 were 1.33 million tons valued at $271 million. This was a 5.9% drop in tonnage but a 33% increase in value over 1980 (31).

Japanese caustic soda production dropped to an estimated 2.77 million tons in 1982, the lowest level since 1970 (32).

Technological developments.—Membrane cell developments are continuing. Asahi Chemical, Asahi Glass, DuPont, and Tokuyama Soda are jockeying for positions in the world wide membrane cell market. ICI estimates that non-Communist chlor-alkali producers will add 22 billion lb/year of capacity by 1990. If all were membrane cells, they would require 3.3-4.4 million square feet of membrane (33).

PPG has offered its new bipolar membrane cell for license. Olin has started up its first commercial cell using the DuPont Nafion membrane and is designing new cells to operate at 5,000 to 10,000 amp/sq meter, three times higher than currently available commercial cells. Dow and Oronzio de Nora Impianti Elettrochimici (Italy) are studying solid polymer electrolytes where the membrane is bonded to the electrode (34). Dow has developed a new ion exchange membrane (35).

Asahi Glass and Solvay have agreed to mutual membrane cell development program (36). The agreement is the sixth of its kind for Asahi Glass (37).

PPG and Asahi Glass have a production prototype unit designated the "Bizec" electrolyzer operating at Lake Charles, Louisiana. The commercial scale unit produces 25 tons/day of chlorine (38).

Georgia-Pacific has started an operational pilot plant at Phoenix, Arizona, using Diamond Shamrock technology and DuPont's Nafion 901 membrane (39).

Asahi Chemical started up an ion exchange membrane manufacturing plant. Monomer synthesis and polymerization facilities are located in Nobeoka, Japan. The membranes are made in Kawasaki. Present plant capacity can provide membranes for 1.2 million metric tons/year of chlorine and could be expanded (40). Asahi Chemical has decided to sell the membrane separately as well as selling entire electrolysis facilities (41).

Asahi Chemical was awarded patents for its chlor-alkali production know-how featuring use of an ion-exchange membrane (42, 43).

Electrochemical Technologies is a joint venture between Diamond Shamrock and Chemnor (Geneva). The new company will conduct research, manufacturing, and distribution functions previously handled by the two parent companies (43).

Membrane cell plants in operation or construction in the U.S., Canada, Japan, and western Europe are given in Table III (2).

Environmental and toxicological developments.—Caustic soda will be added to dioxin-contaminated soil

Table III. Membrane cell plant capacity, 1982—thousands of metric tons per year of chlorine (2) (technology developer listed at right)

United States		
Fort Howard Paper, Muskogee, OK	5	Hooker
Georgia-Pacific, Phoenix, AZ	2	Diamond Shamrock
Vulcan, Wichita, KS	68	Diamond Shamrock (1983 startup)
Canada		
American Can of Canada	10.6	Ionics
Great Lakes Forest Prod., Dryden, Ont.	15	Hooker
Prince Albert Pulp, Saskatoon, Sas.	30	Asahi Chemical
St. Anne Chemical, Nackawic, N.B.	10	ICI
Japan		
Asahi Chemical, Nobeoka	120	Asahi Chemical
Denki Kagasu Kogyo, Ohmi	52.6	Asahi Chemical
Asahi Glass, Kansai	10	Asahi Glass
Nihon Carbide, Uozu	10	Asahi Glass
Showa Chlorine, Okinawa	2.2	Diamond Shamrock
Tokuyama Soda, Tokuyama	10	Tokuyama
Western Europe		
Finnish Chemicals, Joutseno, Fld.	56	ICI, 1984 startup
Bayer, West Germany	0.7	ICI
Akzo Zout Chemic, Rotterdam The Netherlands	250.0	Asahi Chemical (1983 startup)
Elkem, Svelgen, Norway	8	Ionics
Tofte Cellulosis, Hurum, Norway	14.5	Hooker/Uhde
Billerud Uddeholm, Skoghall, Swe.	40	ICI and Diamond Shamrock

in an EPA test to determine if the technique might help clean up ground contamination in Missouri. It is hoped that the strong base will strip chlorine from the hazardous materials and reduce their toxicity (44).

EPA has set a limit of 100 ppb for trihalomethanes in drinking water. However, if conventional technology cannot reduce trihalomethanes to this level, then the EPA can grant a variance (45).

Other Alkaline and Chlorine Compounds

Caustic potash.—Caustic potash prices held firm in a relatively stable market, although weak fertilizer demand tipped the market balance this year. Linden Chemicals and Plastics and Diamond Shamrock posted prices of $12/hundredweight. Monsanto's list price is $13.00 (46, 47).

Linden Chemicals and Plastics acquired International Minerals and Chemical's (IMC's) caustic potash plant in Ashtabula, Ohio, plus IMC's share of chlorine-caustic potash production from a joint venture with Occidental Chemical in Niagara Falls, New York (48).

Pennwalt closed its 40,000 ton/year caustic potash operation in Calvert, City, Kentucky. This was Pennwalt's only KOH plant. Pennwalt will remain in the market as a reseller (49).

Soda ash.—Soda ash output for the first 10 months of 1982 was 6.6 million tons, down 6% from the 1981 period (50). Total production for the year was expected to be 8.3 million tons, about equal to 1981's output (51).

Tenneco Minerals started up a mining and milling facility near Green River, Wyoming, in June. The company expects to produce two million tons/year of soda ash at the site by 1984 (52).

Church and Dwight and Allied Corporation have formed a partnership to mine and process trona deposits in Wyoming. Both companies have production facilities near Green River, Wyoming, and trona leases in the southwestern part of the state (53).

Texas Gulf has canceled plans to double production at its trona mine and soda ash processing plant near Rock Springs, Wyoming, because of the poor economy and industry overcapacity. The expansion had been scheduled to go on-line in January, 1984 (54, 55).

Solution mining could significantly lower costs *vs.* mechanical mining or synthetic routes. FMC, Allied, Vulcan, and a partnership of Cleveland-Cliffs Iron and Industrial Resources of Chicago are among those companies attempting to develop the new process (51, 56, 57, 58, 59).

Allied remained the only synthetic soda ash producer in the U.S. in 1982 (60).

Market softness characterized by overcapacity and high inventories caused Green River, Wyoming, producers to cut prices throughout the year. Bulk soda ash prices began the year at $92/ton and fell steadily to $84 by year's end. In October, Kerr-McGee slashed its California prices by $2.00/ton to $107.25 for dense flake soda ash (61, 62, 63, 64).

The end uses for soda ash are shown in Table IV (51).

Five major Wyoming soda ash producers (Allied, FMC, Stauffer Chemical, Texas Gulf, and Tenneco) attempted to form an export association under the auspices of the Webb-Pomerone Act in order to penetrate Japanese markets. However, California-based Kerr-McGee refused to join the cartel. Later in the year, Allied and FMC also pulled out, citing internal difficulties and an inability to attract all U.S. producers to join the group. The remaining three companies continue in the export cartel (65, 66, 67).

The European Commission imposed a provisional antidumping duty on most imports of heavy soda ash from the U.S. Great Britain's ICI initiated the complaint (68, 69).

The British soda ash industry was in poor shape. Output was below 74% of the rated capacity of 1.5 million metric tons/year. ICI's list price for soda ash was $175/metric ton (70).

Analyst Roger E. Shamel and soda ash producer FMC believe that the industry will shift from caustic soda to soda ash as chlorine demand slackens and the caustic market tightens. The imbalance in the chlor-alkali industry provides new markets for soda ash (71, 72).

Sodium chlorate.—Annual U.S. capacity for sodium chlorate is given in Table V (73).

Pennwalt doubled its capacity at its Tacoma, Washington, plant with an expansion completed early in the year (74).

Kerr-McGee has contracted with Huron Chemicals to supply technology, engineering, and equipment for an expansion at its Hamilton, Mississippi, plant. The project will raise capacity to 52,000 tons/year. Start-up is scheduled for the third quarter of 1983. Project cost: $5 million (75, 76, 77).

Erco decided to defer a plan to double its 25,000 ton/year plant at Monroe, Louisiana. Erco has also delayed construction of a new plant in Raleigh-Durham, North Carolina (78).

Canadian capacity is over 325,000 tons/year. Canadian plants ship 65-75,000 tons/year of sodium chlorate to U.S. customers. More Canadian capacity is scheduled. Erco increased the size of its Thunder Bay, Ontario plant from 36,000 to 51,000 tons/year. Canadian Occidental Petroleum started a 7,600 ton/year plant at Nanaimo, British Columbia, in October. BCM Technology has a 20,000 ton/year plant under construction in Amhertsburg, Ontario. PPG Industries Canada will complete expansion of its Stanchem operation at Beaucharnois, Quebec, in the third quarter of 1983, increasing capacity to 80,000 tons/year. Earlier in the year, PPG increased its Stanchem plant by 38,000 to 73,000 tons/year. Que Nord will increase the size of its plant at Magog, Quebec, from 32,000 to 65,000 tons/year. The expansion will cost approximately $21 million (Canadian) (78-87).

Total U.S. demand in 1982 was approximately 375,000 tons. 1986 demand is expected to be 456,000 tons (73).

Published prices for sodium chlorate varied from $420 to $440/ton throughout the year. However, discounts were available for as low as $375.00, especially at year's end as pulp and paper markets softened and excess capacity came on-stream in Canada (73, 78, 88-94).

Table IV. U.S. soda ash end-use—millions of tons per year

Glass	3.91
Chemicals	1.32
Detergents	0.52
Pulp	0.25
Water Treatment	0.25
Other	0.95
Exports	1.10
Total	8.30

Table V. U.S. sodium chlorate capacity (73)
(thousands of short tons/year)

Brunswick Chemical, Brunswick, GA	25
Erco, Monroe, LA	25
Georgia Pacific, Plaquemine, LA	27
Huron Chemicals, Riegelwood, NC	15
Kerr-McGee, Hamilton, MS	38
Kerr-McGee, Henderson, NV	30
Occidental Chemical, Columbus, MS	66
Occidental Chemical, Taft, LA	60
Olin, McIntosh, AL	22
Pacific Engineering, Henderson, NV	6
Pennwalt, Calvert City, KY	50
Pennwalt, Portland, OR	24
Pennwalt, Tacoma, WA	20
Total	408

The primary use for sodium chlorate is paper bleaching, accounting for 82% of the U.S. market. Other uses: other chlorates—7%; uranium—5%; agricultural—4%; miscellaneous—2% (73).

Sodium chlorate's future is largely dependent on the pulp and paper industry. Demand for sodium chlorate is expected to grow at 5-6% annually over the next 5 years. Industry estimates of the market balance point range from the mid-80's to almost 1990 (73, 78).

Metals

"When the new materials which are the lifeblood of modern industry are concentrated in only a few regions of the world, and when basic industries of a nation become significantly dependent on supplies of those raw materials from foreign sources, these become strategically important to the economies of those countries", said B. O. Szuprowicz, author of "How to Avoid Strategic Materials Shortages (95).

Realization of this potentially dangerous dependence on foreign sources is prompting the White House to rebuild the U.S. strategic stockpiles, intensify domestic mining, and open offshore waters for exploration of vital minerals (96). President Reagan submitted the Administration's National Materials and Minerals Program Plan and Report to Congress in 1982. The report addressed four areas of concern: land availability, minerals and materials data collection and analyses, research and development, and strategic and critical materials stockpile policy (97). Before the Reagan Administration's mineral policy can be effective, the General Accounting Office (GAO) recommends that (*i*) the terms "critical" and "strategic" should be defined, (*ii*) method of measuring the scope of the problem should be developed, and (*iii*) impact of short-term action on long-term mineral goals should be assessed (98).

The issue of whether the current stockpile of minerals and metals is a balance stockpile was raised recently. "We have the wrong kind of stockpile, and we are preparing for the wrong kind of emergency", says R. G. Adams, Mineral Economist at Chase Econometrics (99). His rationale was that the stockpile was established in the mid-1950's and therefore does not reflect today's arms technology. One of the examples cited was that the roughly 14 million tons of bauxite, the ore from which some aluminum is made, is largely irrelevant because the U.S. has almost stopped using bauxite and switched to alumina (99).

One way to build stockpile and acquire minerals is via bartering. "When you look at huge surpluses of agricultural goods the government holds, it seems logical to trade for fuels, bauxite, cobalt, and other minerals from nations", said B. Fisher, of Agri-Energy Roundtable Incorporated. One of the problems in bartering, however, may be the possibility of violating GATT (General Agreement on Tariffs and Trade) if the dairy products were involved in foreign trade or barter (100).

Table VI provides a comprehensive illustration of U.S. reliance of selected minerals and metals on foreign sources (95).

Table VI. U.S. net import reliance of selected minerals and metals as a percent of consumption (95)

Minerals and Metals	Major Foreign Sources
Columbium (100%)	Brazil, Canada, Thailand
Mica (sheet) (100%)	India, Brazil, Madagascar
Strontium (100%)	Mexico, Germany, Canada
Graphite (100%)	Mexico, Korea, U.S.S.R., Madagascar
Manganese (98%)	South Africa, Gabon, Brazil, France
Bauxite and Alumina (94%)	Jamaica, Australia, Guinea, Surinam
Cobalt (93%)	Zaire, Belgium-Luxembourg, Zambia, Finland
Chromium (91%)	South Africa, U.S.S.R., Philippines
Tantalum (90%)	Turkey, Thailand, Canada, Malaysia, Brazil
Platinum—Group Metals (88%)	South Africa, U.S.S.R., England
Fluorspar (87%)	Mexico, South Africa, Spain
Tin (79%)	Malaysia, Thailand, Bolivia, Indonesia
Asbestos (78%)	Canada, South Africa
Nickel (73%)	Canada, Norway, Botswana, New Caledonia
Potassium (65%)	Canada, Israel
Zinc (60%)	Canada, Mexico, Spain, Germany
Cadmium (55%)	Canada, Australia, Mexico, Belgium-Luxembourg
Tungsten (53%)	Canada, Bolivia, China, Thailand
Selenium (52%)	Canada, Japan, Yugoslavia
Antimony (48%)	South Africa, Bolivia, China, Mexico
Barium (41%)	Peru, Ireland, Mexico, Morocco
Gypsum (38%)	Canada, Mexico, Spain, Dominican Republic
Titanium (ilmenite) (35%)	Australia, Canada, South Africa
Mercury (28%)	Spain, Algeria, Italy, Japan
Iron Ore (25%)	Canada, Venezuela, Brazil, Liberia
Iron and Steel Scrap (37%)	Net Exports
Gold (18%)	Canada, U.S.S.R., Switzerland
Vanadium (17%)	South Africa, Chile, Canada
Iron and Steel Products (15%)	Japan, Europe, Canada
Copper (14%)	Chile, Canada, Zambia, Peru
Sulfur (12%)	Canada, Mexico
Silver (7%)	Canada, Mexico, Peru, England

Aluminum.—U.S. aluminum producers ended 1982 with smelters operating at 58% of annual rated capacity of 5.54 million tons. Canadian plants are running at 85.7% of their 1.36 million ton capacity. The industry eliminated 668,735 tons of primary production in 1982. Inventories exceeded 6 months supply, well above the normal 3-4 month inventory (101, 102).

The price for primary aluminum ingot began the year at 51.5 cents/lb, nearly one-third below its 76 cent list price. The midyear price fell as low as 43.3 cents, then gained some ground to close the year at 46.5 cents. Production costs are about 70 cents/pound (103-106). Despite the gloomy profit picture, a number of companies are planning new capacity.

Canadian Reynolds Metals will proceed as planned to expand its Baie Comeau, Quebec, smelter from 175,000 tons/year to 300,000 tons/year now that the Quebec government has agreed to halve its electricity rates for 5 years (107, 108).

Alcan has chosen Vandenhoof, British Columbia, as the site for its $750 million (Canadian) smelter. Pechiney Ugine Kuhlman will build a new smelter at Becancour, Quebec. Alumax has plans for a new smelter in Umatilla, Oregon (109-112).

Arco Metals is studying the feasibility of building a $1 billion (Canadian) aluminum smelter in Newfoundland Province. Capacity 200,000 tons/year, expandable to 300,000 (113). A large number of plants experienced shutdowns during 1982.

Reynolds Metals may close its Arkadelphia, Arkansas, primary aluminum reduction plant unless federal officials reverse a 1980 Southwestern Power Authority ruling not to renew a 30 year contract to provide inexpensive hydroelectric power to the plant (114).

Reynolds Metals has shut down two more potlines at Troutdale, Oregon, idling 50,000 tons/year of capacity. One potline remains operational at 30,000 tons/year (115). Reynolds closed the last of seven potlines, idling the entire 202,000 ton capacity of its Histerhill, Alabama, plant (116). Reynolds temporarily shut down 56,000 tons of capacity at its Longview, Washington, plant (117, 188).

Alcoa permanently closed its 145,000 metric ton/year smelter at Port Comfort, Texas. The smelter had been idle for 18 months (119). Alcoa shut the second of eight potlines at its Rockdale, Texas, smelter eliminating 37,400 tons of capacity (120).

Kaiser closed a fourth potline at its Mead, Washington, smelter, cutting the capacity to half its rated output of 220,000 tons/year (121). Kaiser will not restart its Ravenwood, West Virginia, smelter because management and the United Steelworkers could not agree on a number of local issues (122). Kaiser closed an-

other potline in Chalmette, Louisiana, reducing capacity to 137,000 tons/year from 260,000 rated capacity. Currently, Kaiser has only two potlines in operation at Chalmette (122, 105).

Martin Marietta closed 18,000 tons of primary aluminum capacity at The Dalles, Oregon. The smelter had been operating at 100% of its 90,000 ton capacity (124, 125).

Alumax has shut 22,000 tons/year of primary aluminum smelting capacity at the Eastalco smelter in Frederick, Maryland. Partner Howmet Aluminum cut 15,000 tons of its capacity previously (126).

Noranda Aluminum has shut 25% of its 140,000 ton/year capacity at New Madrid, Missouri (127).

Alcan Aluminum cut production at its Arvida, Quebec, smelter by 10% of its total 476,000 ton annual capacity (128).

Consolidated Aluminum has shut down 75% of its last remaining potline at New Johnsonville, Tennessee. Current operating capacity is 9,125 tons annually. Full plant capacity is 146,000 tons (129).

Revere Copper and Brass filed for Chapter 11 bankruptcy on October 27th (130).

Power cost increases in the Northwest by the Bonneville Power Administration are causing aluminum producers in the area to reconsider spending plans. October 1 rates were 26 mils/kwh compared to 22 mils/kwh BPA had forecast earlier. The 1979 average was 3 mils/kW-hr. Kaiser is reconsidering plans to invest $600 million at its Tacoma and Mead, Washington, plants. Alcoa has delayed major improvements on its Vancouver, Washington, smelter. Alumax Pacific may be reconsidering its plan to build a new smelter in Umatilla, Oregon. Producers may build new plants in Brazil and Australia where energy costs are 30-50% lower than in the U.S. (131, 132).

The aluminum industry was able to reduce the amount of energy needed to make a pound of aluminum by 15.4% through the first half of 1981 compared to base year 1972 (133).

The average 1983 car built in the U.S. will contain 135 lb of aluminum, about two pounds more than the average 1982 car. 1985 cars may contain 145-200 lb of aluminum (134, 135).

EPRI is planning a 3 year $600,000 program to scale-up a process for extracting aluminum from fly ash (136).

Anthony Bird Associates projects an industry recovery which began in the last quarter of 1982 and extends to mid-1984. Aluminum production will increase >7.5% in 1983. Chemical Bank forecasts an average annual 4-5% growth in demand for the next 20 years. SRI International predicts a more modest 3.8% growth for the next 10 years. Prices will rise to an average $1,887/metric ton between 1981 and 1985, compared to an average $1,224 between 1976 and 1980. Producers hope the current surplus will diminish once the general economy recovers (137-140).

Beryllium.—Domestic beryllium mineral production in 1982 was about at the same level as that of 1981. Beryllium consumption was as follows: as metal in nuclear reactors and aerospace application, 38%; as an alloy and oxide in electrical equipment, 36%; as an alloy and oxide in electronic components, 17%; and as compounds and metal in other, 9%. Beryllium metal domestically was at $194/lb (141).

The stockpile status as of November 30, 1982, is as follows (in s-tons) (141):

	Goal	Total Inventory
Beryl ore (11% BeO)	720	720
Beryllium-copper master alloy	316	295
Beryllium metal	400	229

Beryllium ore imports for the U.S. were mainly from Brazil, China, India, and Argentina (141). Alloy 25, a copper base containing 2% beryllium, ended 1982 at $7.10/lb. Price of vacuum-cast lump and chipped beryllium increased to $173/lb, and beryllium oxide powder was quoted at $49.60/lb (148).

Increase in beryllium product sales revenues in 1982 was mainly attributed to greater demand from defense-related industries, according to a Brush Wellman spokesman (142). Average selling price of beryllium products was increased by about 8% as of September 1982 (143, 144).

Brush Wellman Incorporated, the only company currently operating a beryllium extraction facility in the western world, announced plans for a $2.5 million modification of its Delta, Utah, plant. The modification will allow the company to process lower grade beryl ore and related minerals. Expected completion date: mid-1983 (145, 146).

During 1982, Brush Wellman received a long-term $3.5 million research contract from U.S. DOE regarding beryllium metal processing. The company also acquired Technical Materials Incorporated, a producer of inlaid metals (148).

New uses of beryllium and beryllium products include magnets for electronic industry containing copper, alumina and beryllium (146) and a beryllium-copper alloy (Mitsubishi MX96) used for connectors, micrometers, slide switches, and others (147).

Chromium.—Chromite consumption through September 1982 decreased 37% compared to the same period in 1981. Consumption of chromium alloys decreased 39% between the two years, owing primarily to the continued decline of stainless steel production (149).

Joslyn Stainless Steels has adopted an experimental technique developed by the Bureau of Mines for in-plant recycling of stainless steel furnace dusts, mill scale, and grinding swarfts. These waste materials can be pelletized and returned to an electric arc furnace so that chromium, nickel, molybdenum, and other valuable constituents can be recovered. The process solves problems of storage and disposal and could improve furnace economics (150).

DuPont has doubled the capacity of its chromium dioxide plant at Newport, Delaware. The company forecasts requirements for the product will grow more than 20%/year through 1990 (151).

American Chrome and Chemicals has started up a new chromium oxide plant in Corpus Christi, Texas (152-154).

Ciba-Geigy has begun a project to expand and modernize its chromate pigment plant at Glens Falls, New York (155).

The Reagan Administration has decided to up-grade chrome ores held in the national defense stockpile in order to help the domestic industry (156).

Noranda Exploration has agreed to spend $750,000 in fees and exploration costs to investigate chromite reserves along the California-Oregon border owned by Baretta Mining (157).

Copper.—In recent years, the copper industry has managed to weather the cyclical storms through a variety of asset management techniques. In 1982, demand for copper had all but disappeared and the first 6 months was a financial disaster for copper producers. With the exception of Newmont Mining Corporation, New York, major copper producers such as Phelps Dodge Corporation, Kennecott of SOHIO, and Asarco posted 9 month losses of $60 million, $119 million, and $35 million, respectively (158).

Copper prices had fallen so low that few, if any, U.S. copper mining companies could recover production costs. And according to G. B. Munroe, Chairman of Phelps Dodge Corporation, major factors in the rise of production costs are escalation energy cost, cost for pollution control, and wages (159).

The year opened with COMEX at 74-1/4 cents/lb and the U.S. producer price (USPP) at 79-1/2 cents/lb. By midyear, COMEX had fallen to 54.2 cents/lb and USPP to 66 cents/lb. A late December rally pushed COMEX over 70 cents/lb. 1982 average prices were 65.8 cents/lb for COMEX and 72.8 cents/lb for USPP (175).

In order to combat losses, copper output was slashed. Producers continued to process metal from leaching and work from inventories to meet customer demand. Cutbacks in buyers commitments resulted in refined copper inventories (by April) as high as three times that of the same period in 1981. Chief culprit in this bleak scenario was demand which was uninspired in 1982 as the auto and housing industry continued to be depressed, and as customers, wary of building inventories, were keeping their stocks lean and their orders based on immediate need (160).

Production/consumption.—Compared to 1982, free world mine production fell by about 385,000 s-tons. There were massive cutbacks in the U.S. and Canada. Offsetting these reductions were 198,000 s-tons increases in Chile and Peru. Refined copper production was down 480,700 s-tons (175). Tables VII and VIII provide a statistical summary.

Copper consumption in the U.S. fell by over 330,000 s-tons (14.7%) and in Canada by 95,700 s-tons (36%) in 1982. Total free world demand was off 343,200 s-tons. Countries showing increases were Japan, England, France, and Belgium. Table IX provides a summary of the free world consumption of refined copper (175).

U.S. activities.—Production cutbacks and work force layoff were the first strategies employed to counter the recession's impact. First major shutdown was by Duval's Mines and Mills for 3 months at the beginning of 1982. Asarco closed its Silver Bell Mine and Inspiration Consolidated Corporation, Phoenix, closed its Christmas mine (158).

Of comparable significance was the indefinite closing of the Ray Mines and Chino Mines, divisions of Kennecott Minerals Company, Salt Lake City, in March of 1982 (160). Three weeks later, Phelps Dodge closed all its production facilities with the exception of its Hidalgo, New Mexico, smelter (158). Newmont Mining Corporation's Magna Copper Company subsidiary closed its 84 million lb/yr. copper mine at Superior, Arizona, for an indefinite period. The copper mine and smelter at San Manuel continued to operate (161).

Despite the slump in copper markets, Kennecott Minerals and Mitsubishi Corporation were proceeding with the final stage of the expansion program at their jointly owned Chino Mine and Mill in Hurley, New Mexico, which is expected to reach full operation by 1985 (162).

Construction of White Pine Copper Division's electrolytic copper refinery in Michigan was 90% complete. Production capacity at White Pine Mine stood at approximately 25,000 tons of copper ore per day. The superior high temperature copper contains on the order of 20 oz of silver per ton (163).

Environmental.—The U.S. Court of Appeals ruled in August that unless the mining company can demonstrate that conforming with the environmental regulation (the Clean Air Act) would be so economically disruptive as to necessitate a shutdown of the plant, exemptions to the Clean Air Act could be granted. Asarco Incorporated, Kennecott Corporation, and the now defunct Bunker Hill Company were the principal petitioners for the regulatory relief. Their suit was joined by Phelps Dodge Corporation, Molycorp Incorporated, and Magna Copper Company (164).

To comply with EPA emission standards, Phelps Dodge expected to spend $50 million for its Ajo smelter and $150 million for its Morenci mines. Phelps Dodge is currently seeking an 18 month extension on the deadline dates for the two plants (158).

Legislation to extend for 5 years, to 1993, the period through which nonferrous smelter orders (NSO's) may be obtained had been introduced in Congress and approved by Committees in the House and Senate. [The NSO basically allowed a smelter to operate temporarily in the absence of stringent and expensive pollution controls. The first Clean Air Act 5 year permit period began in 1977 and the second in January 1983] (158).

Activities outside U.S.—For a variety of social, political, and financial reasons, monolithic blocks of nations which depend to varying degrees on copper for their hard currency earnings did not decrease their production despite depressed prices. According to S. Hobson, Director of Minerals Research Services Limited, London, the production cutbacks took place in North America mainly due to high cost operations, low grade ores, environmental pollution control costs, and the appreciation of the U.S. dollars. Countries such as Chile depreciated their currency and thus cushioned or even eliminated the impact of falling copper prices in terms of their domestic currencies (158).

During 1982, many expansion projects were undertaken in copper exporter countries. These include East

Table VII. Free world mine productions of copper (175)
(000 s-tons)

	1981	1982
U.S.	1,692	1,254
Chile	1,189	1,353
Canada	790	688
Zambia	646	622
Zaire	556	517
Peru	361	396
Philippines	333	314
Australia	249	253
South Africa	232	220
New Guinea	182	187
Yugoslavia	122	132
Mexico	253	253
Other	548	578
Total	7,153	6,767

Table VIII. Free world refined copper production (175)
(000 s-tons)

	1981	1982
U.S.	2,182	1,804
Japan	1,155	1,177
Chile	854	974
Zambia	620	622
Belgium	472	424
Canada	525	330
West Germany	426	435
Australia	211	204
Yugoslavia	146	138
Spain	167	176
England	150	149
Other	1,174	1,227
Total	8,082	7,660

Table IX. Free world consumption of refined copper (175)
(000 s-tons)

	1981	1982
U.S.	2,236	1,881
Japan	1,379	1,441
West Germany	818	803
England	366	407
France	473	479
Italy	403	391
Belgium	286	319
Canada	266	171
Other	1,755	1,733
Total	7,982	7,265

Malaysian, 50,000 tpy copper smelter (165); $265 million expansion of Peru Cobriza Copper Mine (166); Peru Garga new solvent extraction electrowinning plant (167); Sumitomo Metal boost of capacity from 36,000 to 155,000 tpy of copper (168); and others in East Germany (169), Mexico (170), Philippines (171), Turkey (172), and China (173).

Outlook.—According to J. Van Dan, Societe Generale des Minerals of Belgium, developing countries will be increasing their share of refined copper production, and this trend is likely to continue for the next few years. Mine production in the developed economies such as U.S. and Canada will show a dramatic decline. "Wider and more violent fluctuations" in copper prices than in the past are likely to be characteristic of the future, Van Dan claimed (174).

U.S. copper consumption should experience some growth in 1983. An increase in housing and auto should offset reduced capital spending and loss of the copper penny market. Outside the U.S., Japan is projecting a decline in copper consumption; major developing countries are in deep trouble with foreign debt and are not expected to show improvement over 1982. Overall, consumption for the free world is not likely to be better than 1982 (175).

Lithium.—Lithium metal prices advanced slightly during 1982. The early year price was $20.65/lb. Foote Mineral raised its price to $23.35 in April. Lithcoa waited until October to increase its price to $21.70 (176, 177). Foote Mineral and Lithcoa increased prices on technical grade lithium carbonate by 4.8% to $1.48/lb in October (178-181).

Due to sluggish demand, Foote Mineral has shut its 18 million lb/year lithium carbonate plant at Kings Mountain, North Carolina, for a 4-7 month period. In the interim, a second Foote plant at Silver Peak, Nevada, will operate at maximum capacity (182, 183).

Duracell International, Ray-O-Vac, and Union Carbide installed lithium battery manufacturing facilities in Valdese, North Carolina, Appleton, Wisconsin, and Bennington, Vermont, respectively. SRI International estimated the world lithium battery market at $45 million and growing four times as fast as the 8%/year rate for all disposable batteries (184).

The U.S. lithium industry has sufficient capacity in place to supply estimated growth requirements for at least 10 years. The proven reserve position in the U.S. appears adequate for the next 50 years. World-wide resources are adequate to cover any conceivable growth for centuries (185).

Magnesium.—Western World magnesium production fell by over 30% in the first quarter of 1982 compared with same period a year ago (186). U.S. production and shipment of primary magnesium showed little improvement over the first quarter of 1982, according to the Bureau of Mines (187). By the third and fourth quarters, the primary magnesium metal industry was operating at approximately 50% of capacity (188). For the full year, total magnesium output was less than 192,000 s-tons—the first time since 1975 (196).

The published list price for primary magnesium metal in the U.S. in 1982 remained at $1.34/lb (f.o.b. producer's plant) between June 1981 and December 1982 (196).

Sagging auto sales and lower profit made Detroit less willing to pay the incurred expenses by replacing aluminum ($0.40/lb) with magnesium ($1.20/lb). In the late 1970's, Ford predicted that its use of magnesium in the average passenger car would increase by 1985 to 5 lb/car from less than 1 lb/car. The latest projection was that the amount of magnesium would rise to only 1 lb/car by 1985 (189).

Expanding usages of magnesium may come from the galvanizing and high strength magnesium alloys. Centre de Recherches Metallingiques of Liege recently announced the possible improvement in properties of conventional galvanized sheet by the addition of small amounts of magnesium and other metals. The magnesium containing zinc coating offers promising short-term solution from the point of view of corrosion resistance, etc. (190). Pesses Company announced a new nickel-magnesium-developed alloy containing 20% magnesium (thus reducing the amount of alloy being used by one third) which will reduce overall alloy product cost (191). Amax and Dow Chemical are actively developing magnesium alloys having no heavy metal contamination to correct the corrosion problem (189).

Many other concurrent developments in magnesium die casting seem likely to push the superlight metal's use upward sharply in the next few years. A new push by the two major magnesium suppliers, Amax and Dow, to replace the less rigid plastic components with magnesium was underway. Diecasters and metal firms are also zeroing in on the fast growing electronic data processing areas. A plus in the electronics markets is that the high purity alloy resists "microflaking" which can cause failures in computer printers and other peripherals (192).

In the magnesium technology production area, Air Products and Chemicals Incorporated recently announced the development of a process which will eliminate obnoxious fumes and corrosion problems prevalent under the conventional salt flux method. The new system blends carbon dioxide with 2-3% of sulfur hexafluoride to protect magnesium at various stages of operation (193).

Norsk Hydro, the world's second largest producer of magnesium, announced the undertaking of a $50 million modernization project that will allow it to increase capacity (50,000 mt/yr) by 20%. The modernization which includes the replacement of existing electrolytic cells with considerably larger ones was to begin in the fall of 1982 at its Porsgunn facility (194). Modernization of facilities would mean that magnesium production will be temporarily scaled down during the autumn and that a weak result for the year is expected (195).

Magnesium market outlook is expected to show a gradual improvement in 1983. Steel desulfurization and magnesium diecasting markets are expected to show some strengths. The annual growth rate for the total magnesium market is projected to be 3.6% (196).

Manganese.—Manganese metal imports totaled 4,878 tons through October 1982, nearly all from the Republic of South Africa. This was down from 6,551 tons from the same period in 1981 (197, 198). Manganese metal prices settled at 70 cents/lb in June as Elkem Metals and Foote Mineral matched Kerr-McGee's price (199).

Three actions by the Reagan Administration affected the manganese industry. The administration has decided to allow offshore exploration and mining for strategic minerals. A manganese lease off the Georgia-Florida coast was expected to be the first to issue. The administration refused to sign the international Law of the Sea Treaty in 1982 which has been signed by 118 nations. Thus, U.S. companies might be unable to mine manganese nodules in the Pacific Ocean. The main stumbling block was a provision calling for worldwide sharing of mineral revenues. Most companies supported the President's position. The administration endorsed the processing of manganese ore to be held in the national defense stockpile in order to help the domestic industry. However, import quotas or duties were not implemented (200-204).

Brazil is studying proposals from Brazilian and Japanese companies for exploiting a 60 million metric ton manganese ore deposit in the Carajas mountain range (205).

The manganese outlook appears good. Manganese consumption in the U.S., Europe, and Japan is expected to increase by 27% from 1981 levels by the end of the decade according to the president of Cia. Minera Autlan SA de CV of Mexico (206).

Nickel.—1982 was a poor year for the nickel industry. Strikes and weak demand caused Inco and Falconbridge to close mines and refineries for extended periods. Inco idled facilities at Copper Cliffs, Sudbury, and Port Colborne, Ontario, and at Thompson, Manitoba. Falconbridge shut its Sudbury complex temporarily. Shutdowns for portions of 1983 have already been planned. Overall, the industry was operating at approximately 60% of capacity, compared to a 1981 average of 70-73% operating rate. U.S. consumption decreased about 31% compared to 1981. Merchant nickel prices were $2.60-2.75/pound early in the year but fell steadily to as low as $1.55 by year's end (207-217).

Preliminary development of a nickel-cobalt mine continued at Gasquet Mountain, California. California Nickel seeks to open a mine and processing plant there by 1985. Capital costs of the mine should be $300 million. California Nickel and Cook International have agreed to develop a strategic metals reserve at the site (218-221).

Hanna Mining Company closed one of its two operating lines at its refinery in Riddle, Oregon (222).

Completion of Inco's new open pit mine at Thompson, Manitoba, will be delayed until early 1986. 1984 was the previously announced completion data (223, 224).

Gould, Incorporated sold the nickel-cadmium-sealed cell portion of its portable battery division to Saft America, Incorporated. The sale involved Gould's business and manufacturing facilities in Tijuana, Mexico, and St. Paul, Minnesota (225).

Industry forecasts varied. Inco expects annual nickel growth rates of 2%, while London stockbrokers, Shepherd and Chase, predicted a 3.3% annual growth rate through 1984. Both predictions are down significantly from the 6% growth rates experienced prior to 1974 (226, 227).

An industry-sponsored study to determine the effects of nickel exposure on workers was announced (228).

Sodium.—About 80% of total production of metallic sodium is used to manufacture tetraethyl lead and tetramethyl lead antiknock additives for gasoline. However, it is expected that this end use of metallic sodium will continue to decline. The sodium used in the production of metallic titanium constituted about 11%. Other uses of sodium are in the manufacturing of herbicides, pesticides, perfumes, dyes, pharmaceuticals, sodium hydroxide, and sodium borohydride. New potential uses of metallic sodium include application as an electrode in sodium sulfur batteries, as a heat transfer medium in nuclear reactors, and recently as a sodium heat engine which has no moving parts and uses a small quantity of liquid sodium as its working fluid (229, 230).

Metallic sodium capacity in the U.S. in 1982 was 128,700 s-tons, down from 1981 capacity of 138,600 s-tons. Price of metallic sodium averaged 60 cents/lb (or 132.3 cents/kg) in 1982 (231). Production and inventory of metallic sodium are shown in Table X.

Titanium.—In spite of the projection by J. Daniell, President of RMI Company, in late 1981 that prospects are bright for the titanium market in 1982 and beyond (233), overcapacity and excessive inventories coupled with weak economic condition in 1982 had brought an end to a 3 year period of growth and prosperity for the titanium industry (234). Other major factors responsible for the recession in the titanium industry are

Table X. 1982 U.S. production and inventory of metallic sodium (S-tons) (232)

Month	Production	Inventory
Jan	8,979	N.A.
Feb	8,848	2,038
Mar	9,468	N.A.
Apr	9,446	N.A.
May	9,202	3,863
June	8,824	3,748
July	8,961	4,199
Aug	8,123	4,813
Sept	8,121	4,503
Oct	7,882	5,124
Nov	7,389	4,281
Dec	7,780	5,531
Total	103,023	

a reversal of customer inventory policies from accumulation to liquidation, a decline in commercial aircraft building, a growing weakness in electric power plant production (particularly nuclear), and a depressed chemical capital spending (235).

Sponge and ingot producer cutbacks began in the second quarter of 1982. In the fourth quarter, the industry operated at an estimated 35% of capacity, with some U.S. and foreign producers totally suspending operations in November and December (249).

Prices for titanium also declined in 1982, reflecting market conditions. At the beginning of 1982, published prices were $7.65/lb for domestic sponge and $8.85/lb for Japanese sponge. In April, RMI announced a reduction to $5.55/lb. By year's end, primary grade of sponge could be purchased for as low as $5.00/lb. Reflecting lower sponge costs and a substantial inventory accumulation, mill product prices by year's end discounted for 10-20% below 1981 prices (249).

Table XI provides a summary of U.S. production and consumption data for titanium in 1982 (249).

The growing concern about imports from Japan had prompted a cost reduction program to be implemented in U.S. by titanium producers (236). "New record levels of imported Japanese sponge have been set in each of the last four years," according to J. Daniell of RMI (237). The International Trade Administration Department of Commerce conducted an administrative review of antidumping funding on titanium sponge from U.S.S.R. recently (238).

Expansion activities in the U.S. titanium industry include start-up of International Titanium plant in Moses Lake, Washington, (5.5 million lb/year); planned start-up of Albany Titanium, an Oregon plant of high purity sponge (420,000 lb); expansion of Titanium Metals, Henderson, Nevada, 28 million lb/yr capacity to 32 million lb/yr; RMI announced 20% expansion of its Niles, Ohio, 19 million lb/yr ingot facility; and 50% increase in sponge announced by Oregon Metallurgical, Albany, Oregon (241).

Activities overseas in 1982 include the completion of IMI Titanium, Kynoch Limited, Witton, Birmingham, second stage expansion to 7.5 million lb (242); major cutback in production was announced by Osaka Titanium Company and Toho Titanium Company for the third quarter of 1982 (243).

Table XI. U.S. production and consumption of titanium (249) (000 pounds)

	1981	1982
Sponge		
Imports	12,980	3,300
Consumption	63,198	32,700
Scrap consumption	29,590	14,700
Ingot		
Production	91,846	46,600
Consumption	87,050	46,700
Mill products		
Shipments	50,984	35,000
Exports	12,098	6,500
Imports	2,720	2,400

A joint venture plan between Westinghouse Electric Corporation and Mitsubishi International Corporation was announced for the production of titanium ingot (10 million lb/year) at Westinghouse's Ogden, Utah, zirconium and hafnium plant (244). A licensing agreement for the manufacture of titanium alloys in Japan was concluded in late 1982 between IMI and Sumitomo (parent company of Osaka Titanium Company) (245).

The D-H Titanium Company was dissolved in December 1982 by its two partners, the Dow Chemical Company and Howmet Turbine Components Corporation. Market problems rather than failure of technology was the major reason for ending the venture according to spokesmen. The 3 year joint venture was aimed at developing a new technology adapting an electrolytic process for producing a crystal-like titanium product (246). Also in the new technology front, Ishizuka Research Institute in Tokyo is developing an electrolytic chlorinator for the manufacturing of titanium sponge at higher efficiency (247).

Environmental problems developed at International Titanium Incorporated, Moses Lake, Washington, resulted in titanium tetrachloride and chlorine spills. Production was halted during the summer. Staff inexperience and overextended staff were cited as the main reasons (248).

Outlook:—Recovery of the titanium market is not likely before 1984, according to executives from titanium industries around the world while attending the Japan Titanium Society's International Symposium (239). In the U.S., the commercial aerocraft production is not expected to significantly improve until the mid or late 1980's. The titanium industry will have to seek newer and probably much smaller and mundane markets in the future (240). R. L. Kane of Titanium Industries is projecting the nonaerospace free world demand for 1983 will be 21 million lb including areas such as power plant condensers, chemical plant processing equipment, and electrodes for chemical, pulp and paper, desalination, metal treatment, metal refining, and marine and pollution control (239).

Timet forecasted an expected decline in titanium mill product shipments in 1983 to 35 million lb with a resurgence in 1984 to 50 million lb. Other outlooks for the 1983 market are more optimistic. However, the consensus was that it was unlikely that U.S. mill product shipment would again attain 1980-1981 levels until 1985 or later (249).

Zinc.—The worldwide economic recession adversely affected U.S. production and consumption of zinc in 1982. Mine production was down due to mine closings; however, the lack of strikes and the opening of two new mines minimized the production loss relative to 1981. The depressed market and low prices resulted in lower refined metal production. Capacity utilization at primary smelters was about 50% in November (251).

1982 worldwide slab zinc production decreased by 427,000 s-tons from 1981 total of 5.017 million s-tons. Production increased slightly in the western hemisphere and dropped slightly in Western Europe. Production in the remainder of the free market countries also remained at virtually the same levels in 1982. Both U.S. and Canada slab zinc production decreased by about 26% from 1981 levels (see Table XII) (252).

U.S. demand of slab zinc was 810,000 s-tons in 1982 *vs.* 920,000 s-tons in 1981. Major zinc markets such as galvanizing and diecasting continued to be depressed due to poor climate in auto and steel industries (Tables XIII, XIV). After starting the year at 44 cents/lb for high grade zinc, slab zinc prices bottomed out at 35 cents by mid-year. By year's end, prices (252, 253, 255) closed in a split market of 36-40 cents/lb. In order to offset low zinc prices and soft demand, many U.S. zinc producers had to resort to measures such as production cutbacks, permanent plant closings, and union wage-benefit concessions (252). SRI economist reported that only 47% of the zinc producers were able to break even at 40 cents/lb (254).

Table XII. 1982 world zinc production and consumption (252)
(000 s-tons)

	Production				Consumption	
	Mine		Slab		Slab	
	1981	1982	1981	1982	1981	1982
U.S.	377	366	432	317	917	809
Canada	1,206	1,197	681	501	145	116
Other Western Hemisphere	976	1,042	409	435	341	286
Western Europe	1,074	1,052	2,031	1,891	1,772	1,552
Africa	292	290	223	234	176	184
Asia	443	445	910	890	1,227	1,253
Oceanic	534	695	331	323	128	106
Total	4,902	5,097	5,017	4,591	4,706	4,306

Table XIII. U.S. consumption of slab zinc (252)
(000 s-tons)

	1981	1982
Diecasting	268	210
Galvanizing	453	397
Brass	125	101
Rolled zinc	26	50
Zinc oxide	21	23
Other uses	27	29
Total	920	810

Table XIV. U.S. zinc supply and demand (252)
(000 s-tons)

	1981	1982
Supply		
Ore production (recoverable)	344	330
Ore imports (zinc content)	130	51
Total zinc in ore	474	381
Metal production	433	298
Metal imports (for consumption)	664	450
Inventory increase (decrease)	(177)	62
Total metal supply	920	810
Metal Demand		
Consumption	920	810
Exports	0	0
Total demand	920	810

U.S. activities/cutbacks/expansions.—In January of 1982, efforts by private investors to purchase the Bunker Hill mining, smelting, and refining complex in Kellogg, Idaho, collapsed, and the facility was closed. Later in the year, Gulf Resources and Chemical Corporation (parent company) announced the intent to sell portions of the shuttered Bunker Hill lead and zinc operation. A salvage company had expressed interest in purchasing the company's lead smelter and zinc plant. The interested party was not identified (252, 256).

Asarco Incorporated in early 1982 reduced its Corpus Christi, Texas, electrolytic zinc refinery to 50% of capacity due to poor availability of feed materials (257). In October, Asarco suspended indefinitely the Corpus Christi operations. Depressed market and metal prices were cited as the main reasons (258).

Cutbacks during 1982 include the output reduction from the electrolytic zinc refinery of Jersey Minere Zinc Company, Clarkesville, Tennessee. This 50% cutback resulted in an annual produced tonnage of 45,000

s-tons (259). National Zinc Company suspended zinc smelting operation at its Bartlesville, Oklahoma, plant beginning July 3, 1982, due to excessive inventories and low demand. The plant, which has a capacity of 56,000 s-tons/year of slab zinc, had been operating at 95% of capacity for the first half of the year (260).

In December, Gulf & Western announced plans to close indefinitely its zinc mine at Beaver Creek, Tennessee, and the mill at nearby Jefferson City that processed Beaver Creek ore. The mine and mill had been producing about 2,500 s-tons/month of zinc concentrate (252).

St. Joe Resources Company started up three new electrolytic zinc furnaces at its Monaca, Pennsylvania Zinc Smelter in late 1982. The furnaces increased capacity from 75,000 to 85,000 tons at a cost of 3 million (262).

Opportunities.—The new zinc coin, containing 97.6% zinc and 2.4% copper and weighing about 19% less than the old copper coin, had the first volume production in 1982. This new copper-plated zinc penny would account for about 25,000 s-tons of zinc/year (252).

Galfan, a new zinc galvanizing alloy developed by the International Lead Zinc Research Organization Incorporated, awarded a license to Yodugawa Steel Works Limited, Osaka, Japan. Yodugawa, a producer with an annual capacity of 600,000 s-tons of rolled steel, was the ninth company to secure such license (261).

Environmental.—The diecasting and zinc industries were bracing for potentially tighter regulation from the EPA which may include zinc on a new list of hazardous metals in foundries. EPA was expected to issue foundry effluent regulations during the fourth quarter of 1982 (263).

The EPA announced that it had reviewed the standards of performance for primary zinc smelters and proposed not to revise the standards. These standards, established in 1971, were scheduled to be revised every 4 years (264).

Major activities outside the U.S.—The Polaris lead-zinc mine, called the northern-most operation of its kind and located 90 miles from the magnetic North Pole and 900 miles from the true North Pole, made the first shipments of concentrates to Europe in the third quarter of 1982. The Polaris mine has an estimated 25 million tons of reserves and is designed to produce 206,000 tons of zinc concentrates. Polaris mine's parent company is Cominco Limited (265, 266).

Noranda Mines of Canada announced delay in the construction of its $360 million zinc refinery at Bellevue, New Brunswick. The plant is to have a capacity of 110,000 s-tons of zinc/year (267).

Capacity at the Kidd Creek Mines Limited (Canada) electrolytic zinc plant in Ontario was expected to be raised to 11,000 tons/month in 1982. The plant which recently produced its one-millionth ton of zinc is fed zinc concentrates from Kidd Creek Timmons Mine (268).

Other foreign expansion projects were (*i*) the dedication of a $175 million electrolytic zinc refinery at San Luis Potosi by Industrial Mineral Mexico SA. (annual capacity is 125,000 tons of refined zinc) (269); (*ii*) Thai zinc project with an annual capacity of 66,000 s-tons of zinc will direct its product to the South East Asian market. Total investment was $140 million (270).

Foreign cutbacks and shutdowns include the following: (*i*) the 99,000 s-tons zinc plant at Andaluza de Piritas SA in Spain was shutdown due to severe drought (271); (*ii*) production cutback was required at Preussag Metall, a major West German zinc producer, as a result of the conversion of the Harz facility from a primary to a secondary zinc smelter (272); and (*iii*) major zinc smelting companies in Japan such as Mitsui Mining and Smelting and Toho Zinc Company brought operating rates down to around 60% of capacity between June and August of 1982 due to low demand and reduction in available "discount" electrical rates (273).

Outlook.—Despite continued mixed signals in the monthly economic data there appears to be a solid foundation for recovery forming in 1983. Zinc demand should rise and should benefit directly from even a modest recovery in auto production, plus the increased activity in construction and appliances (252).

R. H. Lesemann of Commodities Research Unit Limited predicted zinc consumption will fall to about 1-1.5% in the current decade, reflecting slower economic growth and substitution. Regarding supply, new mine capacity coming on-stream over the next 5 years could be substantial. Prices should be strong in the 1983-1984 period (274).

The Electrical Industry (275)

Despite the severe economic recession and despite the drop in both peak demand and energy sales that utilities experienced during 1982, statistical surveys showed that the utilities maintained a strong construction program. Taking into account adjustments made for a small sample of rural electric cooperatives and public power bodies, capital expenditures for 1982 showed a positive increase.

Total revenues of investor-owned electric utilities hit a record high of $102.3 billion in 1982 compared to $94.3 billion received in 1981. Three hundred and eight electric rate increases were granted in 1982 which amount to a total increase of $7.57 billion, and 180 cases are pending (or $7.69 billion), representing a decrease in rate increases from 1981.

Power generation in the U.S. (275).—Capital expenditures by the electric utility industry in 1982 were $40.2 billion. Generation expenditures continued to account for about 75% of the total utility spending—about $30 billion (see Table XV). The majority of the facilities that were canceled in 1982 were the capital-intensive nuclear plants which have long lead times. For example, 18 nuclear plants with a rated capacity of 22,019 MW were canceled, and another 28 units with a capacity of 31,004 MW were deferred. As for fossil units, 12 units with a rated capacity of 8,006 MW were canceled, and 16 units with a rating of 9,554 MW were deferred.

During 1982, the power industry's capability rose to 649,532 MW (see Tables XVI, XVII). Use of coal as fuel decreased slightly in 1982; oil consumption dropped for the third year in a row; and natural gas use went down 3.2 trillion ft^3 (see Table XVIII). Table XIX indicated energy generated by fuel type continues its "unsteady" trend towards predomination of coal-fired generation.

Total electricity sales fell 1.3% in 1982 to 2.12 trillion kW-hr. 1982 fall-off was triggered by a drop of more than 6% in industrial (large light and power) sales. By comparison, both the residential and small light and power customer classes showed continued growth (Tables XX, XXI, XXII). The Edison Electric Institute is projecting a growth in kW-hr of about 2%. An estimate of 3%/year for the long-term growth of energy is not unreasonable.

Energy sources outlook in the U.S.—According to the Department of Energy's mid-year short-term energy outlook report, although the long-term outlook for nuclear generation is uncertain, nuclear power was the fastest growing energy source in the U.S. By the end of 1982, nuclear energy generation would have accounted for 13.4% of capacity, up from 11.9% in 1981. Coal-fired generation also demonstrated an increase in 1982; oil and gas showed decline (276).

Table XV. Total electric power system* capital expenditures (millions of dollars) (275)

	Generation		Transmission		Distribution		Miscellaneous		Totals	
	Total industry	Investor owned	Total industry	Investor owned	Total industry	Investor owned	Total industry	Investor owned	Total industry	Investor owned
1979	24,875	16,939	3,384	2,221	5,329	4,098	1,666	1,187	35,254	24,445
1980	25,688	17,875	3,280	2,279	5,307	4,365	1,650	1,297	35,925	25,816
1981	25,823	19,217	3,168	2,326	4,950	4,169	1,882	1,543	35,823	27,254
1982	29,836	22,787	3,497	2,595	5,228	4,432	1,654	1,347	40,216	31,161
1983**	28,189	21,649	4,182	3,184	5,496	4,582	1,988	1,659	39,855	31,075

* 50 states; ** Prospective.

Table XVI. Electric power industry capability 1983 and beyond, MW (275)

Fuel type	Total capability (Dec. 31, 1982)		Capability additions (1983 and beyond)		Present capability plus additions	
	MW	%	MW	%	MW	%
Hydro*	78,016	12.0	8,704	7.3	86,720	11.3
Fossil fuel	451,443	69.5	55,023	46.1	506,466	65.9
Nuclear	63,142	9.7	55,482	46.4	118,624	15.4
Internal combustion	5,139	0.8	—	—	5,139	0.7
Combustion turbine	51,792	8.0	200	0.2	51,992	6.7
Total industry	649,532	100.0	119,409	100.0	768,941	100.0

* Includes pumped storage. Source: Energy Information Administration/DOE plus Electrical World's Jan 1983 Capacity Additions Report.

Table XVII. Installed generating capacity by type of ownership* (Dec. 31, 1982)—in MW (275)

	Investor owned	Municipals, state, and power district systems	Cooperatives	Federal agencies	Total
1979	464,040	62,072	13,843	58,343	598,298
1980	476,979	62,064	15,425	59,078	613,546
1981	490,767	64,653	18,406	60,982	634,808
1982	498,643	66,882	21,463	62,544	649,532

* Data includes Alaska and Hawaii. Source: EIA/DOE.

"For the first time since World War II, the electric utility industry, our biggest customer, is registering no growth in the generating of electricity," observed National Coal Association President C. Bagge. With zero growth in the demand for electricity, industrial output at its lowest point since 1977, stagnation in the steel industry, and lagging economics overseas, U.S. coal consumption plus exports were off by 13 million tons in 1982 (*vs.* 1981). However according to the U.S. Energy Information Administration, growth rates in coal use by utilities are expected to average 3.9% over the next 10 years (277).

According to D. Steffes of Planning and Forecasting Consultants, Houston, Texas, "Actual U.S. energy consumption for the decade of the 1980's will be less than the peak year in 1979. . . . With U.S. energy consumption declining and production increasing, the need for imported energy (oil) will decrease significantly. . . . The U.S. cost of oil imports will decline drastically because of the double effect of lower volumes and lower prices." (278).

As for natural gas, according to Merrill Lynch Pierce Fenner and Smith's outlook, the average well head price of gas will jump an estimated 33% in 1982 and as the decontrol schedule continues, the average price will be no greater than $4.25/mcf at the beginning of 1985 (279).

The Institute of Gas Technology estimated current recoverable energy reserves in the U.S. are natural gas, 207 trillion ft^3; natural gas liquids, 7.1 billion bbl; conventional crude oil, 31.6 billion bbl; and coal, 282 billion tons (280).

Energy from fossil fuels.—Synfuels.—Falling oil prices are forcing energy producers to postpone and cancel major investment projects costing billions of dollars. A number of major corporations said they were now working on the assumption that the average contract price of crude oil may not rise at all in real

Table XVIII. Consumption—type of fuel (275)

	Coal—millions of tons	Oil—millions of bbl	Gas—millions of cu ft
1972	351.2	496.6	3,976.9
1973	388.7	562.5	3,660.2
1974	391.2	539.1	3,443.4
1975	405.9	506.6	3,157.7
1976	448.3	556.5	3,080.9
1977	477.0	624.2	3,191.2
1978	481.6	635.8	3,188.4
1979	527.1	523.3	3,490.4
1980	569.5	420.2	3,681.6
1981r	596.8	351.1	3,640.2
1982	594.1	249.7	3,226.6

r = revised.
Source: EIA/DOE. Data includes Alaska and Hawaii.

Table XIX. Energy generated—type of fuel (275)

	Energy generated—billions of kW-hr				
	Nuclear	Coal	Oil	Gas	Total*
1978	276.4	976.6	364.2	305.4	1,922.6
1979	255.2	1,075.0	303.0	329.5	1,967.0
1980	251.1	1,162.0	245.6	346.2	2,010.4
1981	272.7	1,203.2	206.1	345.8	2,034.1
1982	282.8	1,192.5	146.4	305.3	1,932.5

* Includes production from geothermal sources, wood, and waste.
r = revised.
Source: EIA/DOE. Data includes Alaska and Hawaii.

Table XX. Electric customers and revenue

	Electric customers (thousands)* (275)					Electric revenue (millions of dollars)* (275)				
	Residential	Small light & power	Large light & power	Other classifications	Total**	Residential	Small light & power	Large light & power	Other classifications	Total**
1979	79,602r	9,387r	478r	287	89,772r	30,799	22,264	23,825	2,752	70,640
1980	82,153r	9,699r	485	317r	92,653r	37,581	27,370	27,317	3,195	95,462
1981	83,459	9,903	487	311	94,160	43,350	32,331	32,720	3,705	111,584
1982***	85,000	10,118	505	316	95,939	47,810	35,804	34,720	4,049	122,384

r — revised; * — includes Alaska and Hawaii; ** — May not add due to rounding; *** — Estimated by Electrical World.
Source: Edison Electric Institute.

terms during the 1980's. This was affecting their evaluation of schemes such as synthetic fuel plants which could be viable only if the cost of conventional energy sources increased (281).

The U.S. Synthetic Fuels Corporation (SFC) has shown itself, as a direct consequence of Reagan policy, to be unwilling to back the kinds of mammoth projects that companies originally proposed (282). The SFC will be more selective in the types of synfuels project proposals it solicits for review for federal financial support. At its August board meeting, the SFC adopted a solicitation document restricting projects to those based on coals, oil shale, and tar sands (283).

Throughout the year, the SFC had been under tremendous pressure, particularly from the House and Senate (284, 285, 286). "We are not going to give money to any white elephants," said E. E. Noble, the newly appointed chairman of the $20 billion synfuels program. Still, there were concerns among both industry and SFC officials that none of the plants may be built without improved projections of costs for constructing and operating the units. Cost overruns have long been a nightmare for the fledgling synfuels industry (287).

Table XXIII highlights the status of the key synfuels projects in the U.S. (288).

Coal gasification.—The DOE fossil energy budget (December 17, 1982) proposal indicated that the Administration proposed to spend approximately $11.2 million on gasification projects. The House and Senate proposed budgets were $50 and $31.25 million, respectively. The bulk of the funding is expected to be allocated to surface coal gasification projects (289). In spite of a plea to include underground coal gasification in the DOE's budget of promising energy technologies from the American Institute of Chemical Engineering citing that the estimated coal reserves recoverable by underground gasification are five times those recoverable through conventional mining, less than $6 million will be awarded (290).

Construction of the Great Plains, North Dakota, coal gasification project, the nation's first commercial scale synthetic fuels plant of its kind, is proceeding on schedule and should be completed within budget, according to project sponsors (291). The Great Plains project was financed by American Natural Resources (25%), Transco (20%), Tenneco (30%), MidCon (15%), and a new partner, Los Angeles-based Pacific Lighting Corporation (10%) (292).

Blaming in part the global oil glut that has weakened demand for synthetic fuels, the Panhandle Eastern Corporation has scrapped a multimillion dollar coal gasification project in Wyoming. The proposed plant would have been the second largest coal gasification plant in the U.S. capable of producing 26 billion ft^3 of natural gas and 193 million gallons of gasoline annually (293).

The 30 ton/day experimental gasifier built in Salt Lake City, Utah, under the sponsorship of DOE, was completed in late 1982 and is undergoing tests. The "entrained bed" gasifier operates on the principle that coal particles are swept and "entrained" in a stream of oxygen, steam, and the product gases. Unlike the Texaco gasifier, which employs a slurry feeding system, coal is fed to the Salt Lake City unit in dry form. And unlike the K-T (Kopparsi-Totzek gasifier) system, the Salt Lake City unit is pressurized. Only the Shell-Koppers gasifier being developed in Europe by Royal Dutch Shell is both pressurized and fitted with dry coal feeding system. Evaluation of the Salt Lake Unit should be completed in March 1983 (294).

Oil shale.—The Colony Oil Shale Project came to an abrupt halt at the end of April 1982. Most surprising was the announcement by Exxon Corporation that it is closing down the Colony Oil Shale Project in Western Colorado. The reasons cited were high interest rates on capital investment, current low price of crude oil, and the low priority accorded by the Reagan Administration to synthetic fuels development (295). The other government-assisted oil shale project in Colorado operated by Union Oil is more than halfway completed with its first 10,000 bbl/day unit operating (295). The SFC asserted that the Exxon withdrawal only served to emphasize the importance of a govern-

Table XXI. Average annual use and bill* (275)

	Residential		
	Average use kW-hr	Average bill kW-hr	Annual
1972	7,691	2.29¢	$176.39
1973	8,079	2.38¢	$192.35
1974	7,907	2.83¢	$223.73
1975	8,176	3.21¢	$262.26
1976	8,360	3.45¢	$288.39
1977	8,693	3.78¢	$328.99
1978	8,849	4.03¢	$356.74
1979	8,843	4.43¢	$391.30
1980	9,025	5.12¢	$461.81
1981	8,863	5.89¢	$522.24
1982**	8,823	6.42¢	$566.20

r = revised.
* Includes Alaska and Hawaii.
** Estimated by Electrical World.
Source: Edison Electric Institute.

Table XXII. Average annual use and bill* (275)

	Large light and power		
	Average use kW-hr	Average bill kW-hr	Annual
1972	1,761,816	1.09¢	$19,204
1973	1,754,641	1.17¢	$20,529
1974	1,649,133	1.55¢	$25,562
1975	1,578,958	1.92¢	$30,330
1976	1,710,023	2.07¢	$35,370
1977	1,722,567	2.33¢	$40,105
1978	1,702,939	2.59¢	$44,156
1979	1,716,294	2.91¢	$50,012
1980	1,650,037	3.44¢	$56,792
1981	1,628,978	4.03¢	$65,572
1982**	1,514,826	4.66¢	$70,141

r = revised.
* Includes Alaska and Hawaii.
** Estimated by Electrical World.
Source: Edison Electric Institute.

Table XXIII. Status of major federal synfuels program (July 14, 1982) (288)

Project and location	Principals	Capacity	Status
Incentives issued —			
○ Coal gasification Mercer County, ND	Great Plains Gasification Associates	125 million cu ft/day	$2.4 billion loan guarantee; completion date: 1984
○ Oil shale (Colony Project) Parachute, CO	Tosco/Exxon (40%/60%)	50,000 bbl/day	Project shelved. $1.1 billion loan guarantee to Tosco rescinded.
○ Oil shale Garfield County, CO	Union Oil	9,000 bbl/day	About $400 million in price supports and guaranteed prices issued for a $520 million project; completion date: 1983.
Incentives under negotiation			
○ Coal liquefaction Breckinridge County, KY	Ashland Synthetic Fuels; Bechtel Petroleum	25,000 bbl/day	Loan guarantees sought for $2.7 billion project; completion date: 1988.
○ Coal liquefaction Hampshire Energy Gillette, WY	Kaneb Services; Koppers; Northwestern Mutual Life Insurance Co.; SOHIO	19,000 bbl/day	Loan guarantees and price supports sought for $2 billion project; completion date: 1986. Process: indirect liquefaction.
○ Coal gasification Shelby County, TN	Memphis Light, Gas and Water	50 million cu ft/day	Loan guarantee, price subvention and interest rate differential sought for $800 million medium BTU project; decision on negotiation delayed; completion date: 1985.

ment program to offer aid to the fledgling synfuel industry (296).

Other than the large oil shale projects centered in the western states, oil shale in the eastern half of the nation is beginning to attract the attention of developers in Indiana, Ohio, and Kentucky. The attractiveness of eastern oil shale includes (*i*) equivalent amounts of oil recovered (25 gal/ton of oil shale); (*ii*) recoverable energy in the form of light gases and liquid hydrocarbon; (*iii*) strip mining possibility; (*iv*) proximity to water sources, and (*v*) closer markets (297).

Using the Hytort process developed by IGT, IGT claimed that eastern shale may contain as much as 423 billion bbl of oil. Table XXIV illustrates the distribution of this potential (297).

Activities outside the U.S. include the Morocco ONAREP oil shale project. ONAREP has obtained a $20 million loan from the World Bank to help to produce shale oil. Morocco's estimated 20 billion tons of shale are available for oil recovery. Occidental Petroleum and Royal Dutch/Shell expressed interest in the development of this shale deposit (298). The Science Application Incorporated, Golden, Colorado, T^3 process will be used for this development (299).

The Lurgi-Ruhrgas (LR) process developed in West Germany claimed that considerable experience was gained in testing shales from many parts of the world. Tests with Colorado shales suggested 100% recovery of the oil and an overall thermal efficiency of 92.7%. Water consumption is minimal (299).

Coal liquefaction.—Two coal liquefaction projects were selected by the SFC in 1982 as the most promising. The two chosen, for which contracts could be awarded as early as August 1982 and no later than November 1982, are a $2.7 billion coal liquefaction plant to be built in Kentucky's Breckinridge County by Ashland Oil and Bechtel and a $2 billion coal liquefaction plant, planned to be built in Wyoming by a consortium headed by Kaneb Services and Koppers (300).

Table XXIV. Oil recovered by the Hytort process (297)

State	Area suitable for surface mining (sq mi)	Recoverable oil (billion bbl)
Ohio	980	140
Kentucky	2,650	190
Tennessee	1,540	44
Indiana	600	40
Michigan	160	5
Alabama	300	4
Total	6,230	423*

* These resources could, alternatively, yield as much as 2,200 trillion cubic feet of synthetic natural gas, depending on the processing used. Source: Phillips Petroleum.

The Breckinridge plant is expected to produce 25,000 bbl/day via the H-coal direct coal liquefaction process (developed by Dynalectron) (300, 301). Ashland and Hydrocarbon (a subsidiary of Dynalectron) are seeking other sponsors for Phase IV of the H-coal project to further demonstrate the maturity and flexibility of H-coal technology by processing a variety of coals around the world, testing new catalysts and operating conditions, and collecting additional scale-up and engineering data (302).

The Wyoming Hampshire Venture (Gillette, Wyoming) is expected to turn out 22,000 bbl/day of gasoline from methanol via the indirect coal liquefaction Mobil MTG process (300, 301). However, on October 19, 1982, SOHIO, one of the five backers of the project, decided to withdraw based on an economic decision. It is thought that SOHIO represented at least $300 million of equity to Hampshire project (303). Attempts to find a replacement for SOHIO were unsuccessful and late in the year the Hampshire Energy consortium indefinitely suspended its plan to build the 21,000 bbl/day coal-to-gasoline plant near Gillette, Wyoming. Despite, the decision to shelve the project, the Hampshire group continues to press for federal and state permits it would need to begin construction (304, 305).

The Exxon donor solvent coal liquefaction process developed by Exxon has been undergoing a 2 year large-scale pilot plant testing at Baytown, Texas. Since its start up in 1980, the pilot plant accumulated over 10,600 hr of operation and processed more than 80,000 tons of coal. The EDS development program was shared by cosponsors Exxon, DOE, EPRI, Phillips Coal, ARCO's Anaconda Minerals, West Germany Ruhrkohle, ENI of Italy, and a Japanese consortium. Commercial scale application is still some years off (301, 306).

Energy from nuclear sources.—In spite of the fact that nuclear energy is the fastest growing U.S. electric power source (307), the nuclear industry must rebuild its credibility to get public acceptance, says NRC Chairman, N. Palladino. A recent study by Battelle Human Research Center also indicated that the American people express "cautious optimism" in the belief that technology can deal with nuclear plant safety and waste management problems (308).

Energy Information Administration estimated that nuclear power in 1982 would generate 313 billion kW-hr of electricity, or 15% more than 1981's total. Nuclear power accounted for approximately 13% of the total electricity output in the U.S. during 1982 (307). Electricity from coal and natural gas supplied over 50% and 15%, respectively, of the U.S. electricity demand (309).

Less-than-enthusiastic public acceptance, cost overruns, delays and deferrals, and no firm solution to the

problem of waste disposal had resulted in slipping of construction schedules and eventual cancellation of numerous projects. Table XXV provides an up-to-date overview of nuclear capacity in the U.S. (309).

The adverse impact of Three Mile Island on the nuclear industry cannot be downplayed. The recent inspection result from TMI-2 reactor showing no fuel melting was good news (310). Unfortunately, the cancellation list for nuclear power plants continued to grow. TVA scrapped further construction of four partially completed nuclear power plants in August 1982 due to dwindling electricity demand. Houston Lighting Power Company also dropped the Allens Creek Nuclear Power plant at Austin, Texas, citing continuing delays in obtaining a construction plant. Since 1975, 89 reactor years have been lost to delays in nuclear power plants (309).

Many an argument has been triggered on the subject of which fuel generates the least expensive electricity. Basically, capital costs are much higher for nuclear plants than coal-fired plants. But, compared to coal, nuclear fuel costs are extremely small. According to a DOE Energy Information Administration (EIA) study, new nuclear plants will produce power one-half to one-third the cost of operating existing oil and gas-fired plants (311). In a 1982 study by W. W. Brandfon of Sargent and Lundy, nuclear has a 4.7% edge over high sulfur coal and a 13% edge over low sulfur coal. EIA, however, maintained nuclear-generated electricity would cost approximately the same as coal-generated electricity in the future (309).

Unlike the Carter Administration, the Reagan Administration enthusiastically endorsed nuclear power and breeder technology coupled with reprocessing of spent fuel. According to Welske of AIF, "Nuclear power is, after all, not only an economic animal, but a political emotional animal as well" (309). "Clinch River breeder reactor is the epitome of that politicization," said G. Chipman of DOE. Project cost for the breeder was estimated to be $8-12 billion, a major jump from an earlier projection of $3.7 billion (312).

Fuel cells and batteries.—Fuel cells.—As of December 17, 1982, the DOE fossil energy budget for fuel cells development includes the following features: Reagan request, $95 million; House appropriation, $31.5 million (proposed); and Senate appropriation, $28.8 million (proposed) (313). The final budget figure for fuel cell will likely be somewhere between $20-$30 million.

Following the announcement earlier in 1982 that DOE and NASA would fund field testing of commercial-scale fuel cells, the two agencies have now unveiled a 4 year $37 million program to develop alternative fuel cell technology. Westinghouse Electric Corporation, Pittsburgh, Pennsylvania will develop a phosphoric acid fuel cell system based on air-cooled designs (314, 315).

A $40.8 million project being shared by DOE and the Gas Research Institute (GRI) to install 45 fuel cell power plants, each capable of generating 40 kW of electricity in commercial and residential sites across the U.S. will start in mid-1983. NASA will be the contracting agent. United Technologies will provide the fuel cell system (316). The first of 48 units that will be field tested is now humming away quietly behind a laundromat in Portland, Oregon. The succeeding fuel cell began running in October at the Southern New England Telephone Company in Vernon, Connecticut (317).

On a slightly negative note, the 4.8 MW demonstration (United Technology) phosphoric acid fuel cell plant at Con Edison, New York, was further delayed until mid or late Fall of 1982 because of design problem in the reformer-tube unit. The plant was slated to go into operation in June of 1982 (318).

Overseas activities in phosphoric acid fuel cell development are particular strong in Japan. Toshiba Corporation, Fuji Electric Company, and Mitsubishi Electric Corporation all are trying to develop cell technology (319). Mitsubishi Electric Corporation has started joint development of a molten carbonate fuel cell with Energy Research Corporation of Connecticut (320).

Batteries.—The $18.8 million federal research and development funding for 1982 according to General Accounting Office (GAO) was aimed at developing near-term electric vehicle battery technology and producing improved vehicle prototypes. But to date, only General Motors has signaled its intention to market electric vehicles in the near future. A study prepared recently by GAO recommended that the government end its research and development effort, with the exception of a program to develop more efficient advanced electric vehicle batteries such as aluminum-air, lithium-metal sulfide, and sodium sulfide units. For both fiscal 1981 and 1982, DOE provided more than $10 million for specific advanced battery research (321).

In a move toward the advancement of research into the development of the electric automobile, Johnson Controls Incorporated, Milwaukee, Wisconsin, and Exxon Research and Engineering Company, Linden, New Jersey, have agreed to jointly pursue the development of the zinc-bromine battery. The zinc-bromine battery is aimed at providing additional power needed for full "on board" capacity and for load leveling application (322).

In early April, the Strategic Systems Division of GTE Products Corporation, Stamford, Connecticut, received a $5.9 million contract from the Air Force to supply 10,000 A-hr lithium thionyl chloride batteries for the Minuteman ICBM program. In anticipation of the brisk business with the Military, GTE recently opened a $15 million lithium battery production plant at Henderson, Nevada. The other lithium battery developers are Power Conversion Incorporated, Elmwood Park, New Jersey (lithium-sulfur dioxide battery) and Gould, Rolling Meadows, Illinois (lithium-iron sulfide battery) (323).

Fusion and magnetohydrodynamics.—Fusion.—The Tokamak fusion test reactor (based on the principle of "magnetic confinement") at Princeton University Plasma Physics Laboratory was successfully tested December 24, 1982. The test plasma was hydrogen, not fuel (deuterium and tritium). Temperatures attained were only 100,000°C, and the plasma lasted 50 msec. Investigators are expected to reach scientific break-even conditions, *i.e.*, generation of enough heat from fusion reactions to maintain the plasma without ex-

Table XXV. Nuclear power capacity (309)

Number of reactors	Water reactor	Pressurized water reactor	Other	Total	Capacity (MW)
Operating or licensed	25	48	3	76	58,495
In full power	24	45	3	72	55,061
In power ascension	0	2	0	2	2,328
Shut down indefinitely	1	1	0	2	1,106
Construction permit granted	26	49	0	75	83,288
Construction at 20% or more	21	38	0	59	64,870
Construction at less than 20%	5	9	0	14	15,858
No construction	0	2	0	2	2,560
Construction permit pending	5	5	1	11	12,714
Order placed for new plant	0	3	0	3	3,510
Total	56	105	4	165	158,007

ternal heating, by 1985. Target of the Princeton group is to achieve by 1990 the overall goal of engineering break-even, *i.e.*, production of energy equal to that needed to run the entire facility (324).

Based on the principle of "inertial confinement", the group at University of Rochester, Laboratory for Laser Energetics, is attempting to produce energy via laser fusion techniques. Basically, a number of synchronized laser beams are directed at a tiny pellet of deuterium and tritium. Tremendous energy is generated as the escalating temperature of the fuel caused atomic fusion. The energy liberated in the forms of neutrons is "inertially confined" and can be captured for generating electricity (325).

These two man-made approaches to fusion, magnetic and inertial, can potentially solve the world energy problem for millennia at a tolerable fraction of the environmental damage now caused by existing sources. Table XXVI provides an estimate of future sources of energy (326).

MHD.—Coal-fired power plants that emit practically no SO_x, NO_x, or particulates may be possible by using combined magnetohydrodynamics (MHD)/steam generators, according to University of Tennessee's Space Institute. Essentially, MHD generation uses a superheated electrically conductive gas (at 4900°F) which is produced by burning (coal) gas that is preheated to 2,960°F and passing the resultant ionized gas (potassium ions from potassium carbonate seed) through a strong magnetic field to generate electricity. The hot gas leaving the MHD generator is at a temperature of about 3,500°F so it can be used to create steam in a conventional steam generator (327).

A $2.6 million contract for the first phase of the MHD Advanced Power Train (APT) program was awarded to Westinghouse Electric Corporation by NASA. The power train includes the power producing components of the MHD topping cycle. Funding for the contract was scheduled for completion in late 1982 (328).

EPRI, along with DOE, Mountain States Energy, and Montana Power dedicated a $1.5 million inverter for a $40 million MHD test center at Butte, Montana. With MHD, d-c current is generated by the flow of plasma. Electron flows are tapped by electrodes and fed into the inverter. The hot gases are also used to produce steam (329).

A new concept of MHD was expected to be tested at the pilot scale plant at Ben Gurion University in Beersheba, Israel. The methods entail heating a liquid metal which is driven through a high intensity magnetic field to produce an electric current (330).

Geothermal.—The U.S. Geological Survey estimated the quantity of energy recoverable from low temperature and high temperature geothermal sources are 200-300 quadrillion BTU and 85-140 quadrillion BTU, respectively. Just how far geothermal power can go depends strongly on the development of a technology called binary generation—a technology used for extracting energy from low temperature geothermal sources. This binary generation technology requires a large quantity of isobutane-pentane mixture as heat transferring fluid in addition to muds and heat tolerant additive materials for drilling. According to R. Wolke, Manager of Magsobar's Geothermal Division, drilling a 7000 ft well—not unusually deep—would take approximately $50,000 of additives and muds (331).

The number of geothermal wells sunk each year has doubled over the past 8 years to 80 wells. The quantity of installed geothermal power capacity is, however, still small—920 MW (roughly equivalent to a fair-sized nuclear plant). Potential geothermal power capacity in the U.S. according to NSF is 200,000-700,000 MW (331).

The slashing of federal funding from $53 million in fiscal 1982 to $10 million in fiscal 1983 casts a shadow of uncertainty for the future expansion of geothermal energy. Only the attractive economics of geothermal energy could prove a powerful incentive for private development (331). The recent decision by Southern California Edison Company not to undertake the 47 MW plant at Heber, which was to have been the first commercial geothermal facility in the Imperial Valley, was certainly not encouraging (332).

The largest geothermal prospect is in the Imperial Valley of California. Other areas include Hawaii Island, Utah, Nevada, Oregon, and New Mexico (331).

Hydroelectric/wind.—In an era of spiraling fuel prices and widespread concern for air quality, hydro and wind generation represents a stabilizing force for holding down energy costs. In the U.S., almost all primary (high head) hydro resources have already been developed and are being used. Secondary (low head) resources are just beginning to be tapped (333).

Although the DOE's Office of Conservation and Renewable Energy has published final rules for loans for wind-energy systems and small hydroprojects, it only informs the public how to go about obtaining loans. The Congress, however, has thus far not appropriated any funds for the loan program (334).

Feasibility studies were conducted by Tennessee Valley Authority (TVA) on 25 sites for the benefits of possible hydropower developers. Thus far, eight have been evaluated. The results are highlighted in Table XXVII (335).

The Interior Department's Bureau of Reclamation has dedicated two new wind generators near Medicine Bow, Wyoming, with a total capacity of 6.5 MW. Technologies are provided by Hamilton Standard Division of United Technology and Boeing (337).

Solar photovoltaic.—Despite a lot of hard work, the prohibitive cost of converting sunlight directly into electricity has held back the solar/photovoltaic industry for the past decade. While federal cuts are likely to reduce both the number of companies working on solar cells and other technological approaches, many believe that the industry is mature enough and has

Table XXVI. Estimated future sources of energy (326)
("Q" or 10^{18} BTU 10^{21} joules)

	Near terms or known	Total future U.S. supply
Gas and oil	0.6	2.8
Shale oil	0.9	9.6
Coal	5.2	34.0
Nuclear fusion	1.3	70.0 (breeder)
Solar	renewable	renewable
Geothermal, wind; bioconversion	limited	limited
Fusion	250 (lithium)	16,000,000,000 (deuterium)

Note: U.S. energy use rate = approximately 0.1 Q/yr.

Table XXVII. Results of feasibility studies for eight dams (335)

Site	County	Installed capacity (kW)	Average annual energy (MW-hr)	Cost* ($/kW)
Old Columbia	Maury, TN	730	3,200	3,030
Shelbyville	Bedford, TN	230	1,300	3,900
McMinnville	Warren, TN	225	1,400	4,000
Burgess Falls	Putnam, TN	370	1,300	2,570
Sparta	White, TN	300	1,400	2,100
Shoal Creek 1	Lawrence, TN	300	1,100	3,900
DeSoto State Park	DeKalb, AL	700	2,000	2,200
Eve Mills	Monroe, TN	33	100	3,300

* Total cost based on 1981 dollars; estimates do not include primary reclosure and transformer costs.

good enough technology to prosper without federal support (338).

Most recently, Southern California Edison Company has filed for a landuse permit as a first step in what may prove to be one of the most exciting 20th Century ventures—a solar tower installation with an average net output around 100 MW. Estimated cost is $43 million (plus interest); it should take 3.5 years to complete. Location is to be in the high desert region near Victorville, California. The solar heat would come from some 15,400 heliostats (modular mirror). The receiver fluid (potassium or sodium nitrate) would, by heat exchange, convert into steam to drive a generator (339).

Activities in the development of improved solar cells for photovoltaic application are especially high in 1982. Various technologies (Table XXVIII) are competing in the race toward the $1-$2/peak watt cost of photovoltaic cells that is required to justify higher production capacity. And all photovoltaic companies are working on ways to boost cell efficiency, from the current level of about 12-15%, while cutting present cell cost of about $10/peak watt (340).

Mobil Oil Corporation recently has purchased for cash the 20% equity that Tyco Laboratories Incorporated held in Mobil Tyco Solar Corporation, a joint venture since 1974 to develop photovoltaic solar technology. Mobil will continue to develop and manufacture solar cells at the Waltham and Billerica, Massachusetts, plants (341).

Energy Conversion Devices (Troy, Michigan) announced that its joint solar cell venture with Standard Oil of Ohio (SOHIO) is moving headlong toward commercialization. The joint venture (since mid-1981) is aimed at the development of amorphous silicon solar cells. SOHIO has invested approximately $15 million (of the $80 million envisioned) to date. SOHIO also will be getting a share of the ECD-Sharp Corporation, Japan, joint venture (342).

Table XXVIII. Various photovoltaic technologies (340)

Company	Process	Status
Ametek (Paoli, PA)	Electroplates cadmium telluride on a metallic substrate	R&D
Arco Solar (Chatsworth, PA) subs. of Atlantic Richfield)	Pulls silicon crystal from crucible and slices into wafers	Commercial
Chevron Research (Richmond, CA) subs. of Socal	Deposits cadmium sulfide/copper on a glass substrate	Commercial
Chronar (Princeton, NJ)	Deposits silane vapor on a substrate	Near commercialization
Crystal Systems (Salem, MA)	Forms silicon ingot within crucible and slices into wafers	Commercial
General Electric (Philadelphia, PA)	Decomposes silane plasma on a thin film	R&D
Mobile Solar (Waltham, MA) subs. of Mobil Oil	Uses a die to shape a silicon ribbon	Commercial
Photon Power (El Paso, TX) subs. of Libby Owens Ford, Total (France)	Similar to Chevron Research	R&D
Photowatt Internat'l. (Phoenix, AZ) subs. of Elf Aquitaine (France) and others	Similar to Arco Solar	Commercial
RCA (Princeton, NJ)	Similar to GE	R&D
Solarex (Rockville, MD) partially owned by Standard Oil (IN)	Forms rectangular silicon	Commercial
SES (Newark, DE) subs. of Shell	Similar to Chevron Research	R&D
Solar Power (Woburn, MA) subs. of Exxon	Similar to Arco Solar	Commercial
Solavolt (Phoenix, AZ) subs. of Motorola/ Shell	Similar to Arco Solar	Commercial
Telic (Santa Monica, CA) subs. of Dart & Kraft	Deposits copper indium diselinide on a substrate	R&D
Westinghouse (Pittsburgh, PA)	Grows silicon crystals in strips using a dendritic seed	R&D

Other commercial activities include the recent dedication of a 225 kW solar cell power plant at Phoenix Sky Harbor International Airport. This photovoltaic plant is a joint effort of DOE and three other Arizona participants (343). Also included is the Sacremento Municipal Utility District (SMUD) 100 MW photovoltaic project sponsored by DOE, California Energy Commission, and SMUD for the initial $12 million first phase. And ARCO's 1 MW photovoltaic plant near Barstow, California, was tested for the first time under cloudy skies and high winds producing 40 kW (344).

In the Research and Development front, ARCO's P. Wildes indicated that richly colored compounds may soon bring solar energy closer to economic viability. Chemists have used fluorescent dyes with cheap plastic to produce an inexpensive luminescent solar concentrator (LSC) that makes silicon photovoltaic cells more economic to use. These dyes impart additional stability to photovoltaic cells which are under constant bombardment of light (345).

Researchers at Lawrence Berkeley Laboratory (team headed by Professor G. Somorjai) claimed the discovery of doped iron oxide materials capable of splitting water with solar radiation. Somorjai claimed that the doped iron oxide materials will allow one to make use of the visible part of the spectrum, rather than only the ultraviolet (346).

The Texas A and M Hydrogen Research Center also claimed the breakthrough in the development of a process which relies on photovoltaic cells made from single-crystal silicon laced with an inexpensive metal. The Texas A and M group is headed by Professor J. O'M. Bockris and funded by five companies: Atlantic Richfield, Standard Oil of Ohio, Diamond Shamrock, Koppers, and one unidentified company (347).

REFERENCES

1. *Chemical Week*, Feb. 9, 1983.
2. SRI International Report 61-C, Chlorine, 1982.
3. *Chemical and Engineering News*, March 1, 1982.
4. *Chemical and Engineering News*, June 14, 1982.
5. *Chemical Week*, Feb. 17, 1982.
6. *Chemical Marketing Reporter*, Feb. 15, 1982.
7. *Journal of Commerce*, Oct. 29, 1982.
8. *Paper Trade Journal*, April 15, 1982.
9. *Chemical Week*, Feb. 24, 1982.
10. *Chemical Marketing Reporter*, July 5, 1982.
11. *Chemical and Engineering News*, March 15, 1982.
12. *American Metal Market*, Feb. 3, 1982.
13. *Chemical Week*, Jan. 27, 1982.
14. *Chemical and Engineering News*, June 14, 1982.
15. *Chemical Marketing Reporter*, Dec. 6, 1982.
16. *Chemical and Engineering News*, June 18, 1982.
17. *Chemical Week*, Dec. 1, 1982.
18. *Chemical Marketing Reporter*, Jan. 4, 1982.
19. *Japan Chemical Week*, June 24, 1982.
20. *Chemical Economics and Engineering Review*, Sept. 1982.
21. *Chemical Economics and Engineering Review*, Nov. 1982.
22. *Chemical Weekly*, Aug. 31, 1982.
23. *Japan Chemical Week*, April 29, 1982.
24. *Japan Economic Journal*, Sept. 28, 1982.
25. *Paper Trade Journal*, April 30, 1982.
26. *Chemical Marketing Reporter*, March 22, 1982.
27. *Chemical Marketing Reporter*, Jan. 3, 1983.
28. *Chemical Marketing Reporter*, May 17, 1982.
29. *Chemical Marketing Reporter*, July 12, 1982.
30. *Chemical Marketing Reporter*, Aug. 9, 1982.
31. *Journal of Commerce*, Feb. 22, 1982.
32. *Japan Economic Journal*, Jan. 18, 1982.
33. *Chemical and Engineering News*, March 15, 1982.
34. *Chemical Week*, Aug. 25, 1982.
35. *Chemical Week*, Nov. 17, 1982.

36. *Chemical Economics and Engineering Review*, May 1982.
37. *Japan Chemical Week*, May 6, 1982.
38. *Chemical Marketing Reporter*, July 26, 1982.
39. *Chemical and Engineering News*, June 14, 1982.
40. *Chemical Marketing Reporter*, Jan. 25, 1982.
41. *Japan Chemical Week*, Sept. 9, 1982.
42. *Japan Economic Journal*, July 27, 1982.
43. *Wall Street Journal*, April 28, 1982.
44. *Chemical Marketing Reporter*, Dec. 6, 1982.
45. *Chemical and Engineering News*, March 15, 1982.
46. *Journal of Commerce*, Dec. 8, 1982.
47. *Chemical Marketing Reporter*, Nov. 29, 1982.
48. *Paper Trade Journal*, April 15, 1982.
49. *Chemical Marketing Reporter*, Feb. 8, 1982.
50. *Chemical Week*, Jan. 5, 1983.
51. *Chemical and Engineering News*, March 1, 1982.
52. *Chemical Marketing Reporter*, June 7, 1982.
53. *Chemical Week*, Jan. 13, 1982.
54. *Chemical Engineering*, Dec. 13, 1982.
55. *Chemical Week*, Sept. 1, 1982.
56. *Journal of Commerce*, Sept. 7, 1982.
57. *Chemical Marketing Reporter*, Sept. 6, 1982.
58. *Chemical Week*, Aug. 4, 1982.
59. *Chemical Week*, Feb. 16, 1982.
60. *Chemical Marketing Reporter*, July 12, 1982.
61. *Chemical Marketing Reporter*, Oct. 4, 1982.
62. *Chemical Marketing Reporter*, Oct. 11, 1982.
63. *Chemical Marketing Reporter*, Dec. 6, 1982.
64. *Chemical Marketing Reporter*, Jan. 3, 1982.
65. *Chemical Marketing Reporter*, April 26, 1982.
66. *Chemical Marketing Reporter*, Aug. 16, 1982.
67. *Chemical Marketing Reporter*, Sept. 6, 1982.
68. *Chemical Marketing Reporter*, Nov. 22, 1982.
69. *European Chemical News*, Nov. 22, 1982.
70. *Chemical Marketing Reporter*, July 5, 1982.
71. *Chemical Marketing Reporter*, May 17, 1982.
72. *Chemical and Engineering News*, May 31, 1982.
73. *Chemical Marketing Reporter*, Feb. 15, 1982.
74. *Chemical Marketing Reporter*, Feb. 22, 1982.
75. *Chemical Engineering*, Aug. 8, 1982.
76. *Chemical Week*, June 23, 1982.
77. *Chemical Marketing Reporter*, June 14, 1982.
78. *Chemical Marketing Reporter*, Feb. 8, 1982.
79. *European Chemical News*, Oct. 18, 1982.
80. *Chemical Engineering News*, Feb. 22, 1982.
81. *Industrial Mineral (London)*, Sept. 1982.
82. *European Chemical News*, July 5, 1982.
83. *European Chemical News*, Oct. 18, 1982.
84. *Chemical Marketing Reporter*, Oct. 11, 1982.
85. *New York Times*, Feb. 4, 1982.
86. *Chemical Week*, Feb. 10, 1982.
87. *Chemical Marketing Reporter*, July 26, 1982.
88. *Chemical Marketing Reporter*, Jan. 3, 1983.
89. *Journal of Commerce*, June 18, 1982.
90. *Chemical Marketing Reporter*, June 21, 1982.
91. *Chemical Marketing Reporter*, June 14, 1982.
92. *Chemical Marketing Reporter*, March 29, 1982.
93. *Chemical Marketing Reporter*, March 22, 1982.
94. *Chemical Marketing Reporter*, March 15, 1982.
95. *American Metal Market, Strategic Metals Suppl.*, Feb. 18, 1982.
96. *U.S. News & World Report*, Feb. 8, 1982.
97. *Journal of Metals*, pp. 45-47, Nov. 1982.
98. *American Metal Market*, p. 5, June 10, 1982.
99. *Business Week*, Feb. 8, 1982.
100. *American Metal Market*, p. 5, Sept. 11, 1982.
101. *American Metal Market*, Jan. 20, 1983.
102. *Chemical Marketing Reporter*, Jan. 3, 1983.
103. *Business Week*, Jan. 25, 1982.
104. *Business Week*, July 12, 1982.
105. *Business Week*, Dec. 6, 1982.
106. *Chemical Week*, Sept. 15, 1982.
107. *Wall Street Journal*, Nov. 11, 1982.
108. *Chemical Marketing Reporter*, Nov. 15, 1982.
109. *Metal Bulletin (London)*, May 7, 1982.
110. *American Metal Market*, April 29, 1982.
111. *Financial Times (Frankfurt)*, April 27, 1982.
112. *American Metal Market*, April 20, 1982.
113. *American Metal Market*, Dec. 14, 1982.
114. *American Metal Market*, July 26, 1982.
115. *American Metal Market*, July 26, 1982.
116. *Wall Street Journal*, Feb. 26, 1982.
117. *Journal of Commerce*, May 10, 1982.
118. *Chemical Marketing Reporter*, May 10, 1982.
119. *Chemical and Engineering News*, May 31, 1982.
120. *American Metal Market*, Jan. 7, 1982.
121. *New York Times*, May 7, 1982.
122. *American Metal Market*, Nov. 3, 1982.
123. *Chemical Marketing Reporter*, Jan. 18, 1982.
124. *American Metal Market*, May 5, 1982.
125. *American Metal Market*, April 17, 1982.
126. *American Metal Market*, June 25, 1982.
127. *American Metal Market*, June 11, 1982.
128. *Wall Street Journal*, Feb. 23, 1982.
129. *American Metal Market*, Aug. 6, 1982.
130. *American Metal Market*, Oct. 28, 1982.
131. *Chemical Engineering*, Oct. 18, 1982.
132. *Wall Street Journal*, March 25, 1982.
133. *American Metal Market*, Feb. 2, 1982.
134. *American Metal Market*, Dec. 22, 1982.
135. *Materials Engineering*, Oct. 1982.
136. *Light Metal Age*, April 1982.
137. *American Metal Market*, Nov. 2, 1982.
138. *Metal Bulletin (London)*, Aug. 27, 1982.
139. *American Metal Market*, Aug. 17, 1982.
140. *Chemical Marketing Reporter*, May 24, 1982.
141. Mineral Commodity Summaries 1983, U.S. Bureau of Mines.
142. *American Metal Market*, p. 7, Oct. 22, 1982.
143. *American Metal Market*, p. 6, Aug. 19, 1982.
144. *American Metal Market*, p. 10, Aug. 31, 1982.
145. *Industrial Minerals (London)*, p. 15, March 1982.
146. *Japan Chemical Week*, p. 1, July 8, 1982.
147. *New York Times*, p. 36, Sept. 9, 1982.
148. *Engineering and Mining Journal*, p. 124, March 1983.
149. U.S. Bureau of Mines Mineral Industry Survey—Chromium, Dec. 8, 1982.
150. *American Metal Market*, Dec. 15, 1982.
151. *Chemical Marketing Report*, Oct. 25, 1982.
152. *American Metal Market*, June 16, 1982.
153. *Chemical Week*, June 9, 1982.
154. *Chemical Marketing Reporter*, May 31, 1982.
155. *American Paint Coating Journal*, Jan. 25, 1982.
156. *American Metal Market*, Dec. 7, 1982.
157. *American Metal Market*, March 23. 1982.
158. *American Metal Market Suppl.*, Nov. 22, 1982.
159. *Chemical Marketing Reporter*, p. 28, Jan. 25, 1982.
160. *Chemical Marketing Reporter*, p. 16, June 17, 1982.
161. *Chemical Marketing Reporter*, p. 17, Aug. 16, 1982.
162. *Metal Bulletin*, p. 11, Oct. 1, 1982.
163. *World Mining*, p. 168, Oct. 1982.
164. *Chemical Marketing Reporter*, pp. 3, 19, Aug. 9, 1982.
165. *Metal Bulletin*, p. 11, Jan. 19, 1982.
166. *American Metal Market*, p. 5, June 9, 1982.
167. *World Mining*, p. 94, June 1982.
168. *Metal Bulletin (London)*, p. 7, July 30, 1982.
169. *Metal Bulletin (London)*, p. 9, Aug. 10, 1982.
170. *Wall Street Journal*, p. 27, Aug. 9, 1982.
171. *World Mining*, pp. 106-107, Sept. 1982.
172. *Metal Bulletin (London)*, p. 11, Nov. 19, 1982.
173. *American Metal Market*, p. 6, Nov. 24, 1982.
174. *American Metal Market*, p. 6, Oct. 16, 1982.
175. *Engineering and Mining Journal*, pp. 52-54, March 1983.
176. *American Metal Market*, March 31, 1982.
177. *American Metal Market*, Oct. 4, 1982.
178. *Industrial Minerals (London)*, Dec. 1982.
179. *Chemical Marketing Reporter*, Sept. 20, 1982.
180. *American Metal Market*, Sept. 9, 1982.
181. *Chemical Marketing Reporter*, Sept. 6, 1982.
182. *American Metal Market*, Aug. 3, 1982.
183. *Chemical Marketing Reporter*, Aug. 2, 1982.
184. *Chemical Week*, May 12, 1982.
185. *Light Metal Age*, June 1982.
186. *Metal Bulletin (London)*, p. 11, Aug. 27, 1982.
187. Mineral Industry Survey, p. 1, Aug. 31, 1982.
188. Mineral Industry Survey, p. 1, Dec. 3, 1982.
189. *Chemical Week*, pp. 12-13, June 23, 1982.
190. *European Chemical News*, p. 6, March 22, 1982.
191. *American Metal Market*, p. 25, July 19, 1982.
192. *Americal Metal Market*, pp. 20-21, Nov. 29, 1982.
193. *American Metal Market*, p. 20, Nov. 15, 1982.
194. *American Metal Market*, p. 5, Feb. 24, 1982.
195. *Metal Bulletin (London)*, p. 11, Aug. 27, 1982.
196. *Engineering and Mining Journal*, pp. 59-60, March 1983.
197. U.S. Bureau of Mines Mineral Industry Survey—Manganese, Dec. 19, 1982.
198. U.S. Bureau of Mines Mineral Industry Survey—

Manganese, Jan. 6, 1982.
199. *American Metal Market*, June 18, 1982.
200. *Wall Street Journal*, Jan. 20, 1982.
201. *Fortune*, Aug. 23, 1982.
202. *Chemical Week*, April 28, 1982.
203. *Journal of Commerce*, Dec. 22, 1982.
204. *American Metal Market*, Dec. 7, 1982.
205. *Chemical Week*, Feb. 10, 1982.
206. *American Metal Market*, May 27, 1982.
207. *Canadian Chemical Processing*, Nov. 30, 1982.
208. *New York Times*, Oct. 8, 1982.
209. *Journal of Commerce*, Nov. 29, 1982.
210. *Chemical Marketing Reporter*, Jan. 3, 1983.
211. *American Metal Market*, Nov. 3, 1982.
212. *American Metal Market*, Nov. 30, 1982.
213. *American Metal Market*, Dec. 16, 1982.
214. *American Metal Market*, Jan. 15, 1982.
215. Mineral Industry Survey—Nickel, Dec. 30, 1982.
216. *American Metal Market*, Jan. 22, 1982.
217. *American Metal Market*, Dec. 12, 1982.
218. *American Metal Market*, Aug. 24, 1982.
219. *Chemical Engineering*, March 22, 1982.
220. *Financial Times (Frankfurt)*, June 3, 1982.
221. *Wall Street Journal*, Sept. 21, 1982.
222. *New York Times*, March 22, 1982.
223. *World Mining*, Sept. 1982.
224. *World Mining*, Jan. 1982.
225. *American Metal Market*, April 6, 1982.
226. *American Metal Market*, Oct. 12, 1982.
227. *American Metal Market*, March 31, 1982.
228. *Chemical and Engineering News*, May 17, 1982.
229. Mineral Commodity Summaries—Soda Ash, Sodium Sulfate and Sodium. U.S. Dept. of the Interior.
230. "Science News," Vol. 121, Ivars Peterson reports from Washington.
231. SRI Chemical Economics Handbook, CEH Manual of Current Indicators—supplemental data, Dec. 1982.
232. Current Industrial Report, M28A, Inorganic Chemicals, 1982. (Informatiion obtained from D. Kostick, Bureau of Mines).
233. *Journal of Commerce*, p. 9A, Dec. 29, 1981.
234. *American Metal Market*, pp. 1, 12, Feb. 18, 1982.
235. *American Metal Market*, p. 3, Nov. 24, 1982.
236. *Chemical Week*, p. 43, June 30, 1982.
237. *American Metal Market*, p. 28, June 4, 1982.
238. *Federal Register*, pp.. 51176-51177, Nov. 12, 1982.
239. *American Metal Market*, p. 7, Nov. 17, 1982.
240. *Metal Bulletin (London)*, p. 15, Nov. 19, 1982.
241. *Chemical Week*, p. 27, March 31, 1982.
242. *American Metal Market*, p. 6, Dec. 16, 1982.
243. *Japan Economics Journal*, p. 5, Aug. 31, 1982.
244. *American Metal Market*, p. 15, Aug. 13, 1982.
245. *American Metal Market*, p. 16, Nov. 19, 1982.
246. *American Metal Market*, p. 14, Dec. 30, 1982.
247. *American Metal Market*, p. 9, July 20, 1982.
248. *American Metal Market*, p. 9, Oct. 13, 1982.
249. *Engineering and Mining Journal*, pp. 86-90, March 1983.
250. *The Energy Daily*, pp. 1-4, Oct. 12, 1982.
251. Mineral Commodity Summaries 1983, Bureau of Mines, pp. 174-175.
252. *Engineering and Mining Journal*, pp. 56-57, March 1983.
253. *American Metal Market*, p. 1, Nov. 9, 1982.
254. *American Metal Market*, p. 13, Sept. 21, 1982.
255. *American Metal Market*, pp. 1, 16, Dec. 10, 1982.
256. *American Metal Market*, p. 6, Sept. 3, 1982.
257. *New York Times (New York ed.)*, p. 30, Jan. 25, 1982.
258. *American Metal Market*, pp. 1, 20, Oct. 19, 1982.
259. *American Metal Market*, p. 2, April 30, 1982.
260. *American Metal Market*, p. 31, June 28, 1982.
261. *American Metal Market*, p. 5, April 7, 1982.
262. *Chemical Marketing Reporter*, p. 5, Nov. 8, 1982.
263. *American Metal Market*, p. 1, Sept. 24, 1982.
264. *Federal Register*, pp. 44587-44589, Oct. 8, 1982.
265. *American Metal Market*, p. 5, Sept. 30, 1982.
266. *New York Times (New York ed.)*, pp. 25, 28, March 22, 1982.
267. *Metal Bulletin (London)*, p. 11, April 23, 1982.
268. *World Mineral*, p. 51, July 1982.
269. *American Metal Market*, p. 2, Oct. 1982.
270. *World Mineral*, p. 167, Oct. 1982.
271. *American Metal Market*, p. 7, Dec. 18, 1981.
272. *American Metal Market*, p. 7, Jan. 27, 1982.
273. *Japan Economic Journal*, p. 6, July 20, 1982.
274. *American Metal Market*, p. 5, Feb. 24, 1982.
275. *Electrical World*, pp. 61-81, March 1983.
276. *The Energy Daily*, p. 3, May 14, 1982.
277. *Electrical World*, p. 83, Nov. 1982.
278. *Electrical World*, p. 81, Dec. 1982.
279. *Electrical World*, p. 111, March 1982.
280. *Chemical Week*, p. 35, Dec. 8, 1982.
281. *Financial Times (Frankfurt)*, pp. 1, 16, Feb. 22, 1982.
282. *Chemical Marketing Reporter*, pp. 29-31, 33-34, Oct. 18, 1982.
283. *Oil and Gas Journal*, p. 48, Aug. 30, 1982.
284. *Chemical and Engineering News*, p. 5, April 5, 1982.
285. *Chemical and Engineering News*, p. 21, April 19, 1982.
286. *The Energy Daily*, pp. 1, 4, May 6, 1982.
287. *Chemical Week*, pp. 14-15, April 7, 1982.
288. *Chemical Week*, p. 32, July 14, 1982.
289. *The Energy Daily*, p. 2, Dec. 17, 1982.
290. *Chemical and Engineering News*, p. 21, March 15, 1982.
291. *Chemical Marketing Reporter*, Aug. 23, 1982.
292. *The Energy Daily*, pp. 1, 4, May 14, 1982.
293. *The Wall Street Journal*, March 25, 1982.
294. *The Energy Daily*, p. 2, Jan. 5, 1983.
295. *Chemical and Engineering News*, p. 10, May 10, 1982.
296. *Electrical World*, p. 4, June 1982.
297. *Chemical Week*, pp. 30, 33, April 7, 1983.
298. *Chemical Week*, p. 23, April 28, 1983.
299. *Chemical and Engineering News*, p. 60, April 12, 1982.
300. *Chemical Week*, p. 18, June 30, 1982.
301. *European Chemical News*, p. 11, Aug. 30, 1982.
302. *Synfuels*, Feb. 26, 1982.
303. *The Energy Daily*, pp. 1, 4, Oct. 21, 1982.
304. *Chemical Week*, p. 13, Dec. 15, 1982.
305. *American Metal Market*, p. 14, Dec. 15, 1982.
306. *Chemical Marketing Reporter*, p. 49, Aug. 23, 1982.
307. *The Energy Daily*, p. 3, May 14, 1982.
308. *Electrical World*, p. 11, Jan. 1982.
309. *Chemical and Engineering News*, p. 11, Sept. 20, 1982.
310. *Electrical World*, p. 11, Aug. 1982.
311. *The Energy Daily*, p. 4, Sept. 9, 1982.
312. *The Energy Daily*, p. 3, Sept. 15, 1982.
313. *The Energy Daily*, p. 2, Dec. 17, 1982.
314. *Chemical Engineering*, p. 18, July 12, 1982.
315. *Electrical World*, p. 80, Aug. 1982.
316. *Industrial Research and Development*, p. 80, May 1982.
317. *The Energy Daily*, p. 4, May 6, 1982.
318. *Electrical World*, p. 13, May 1982.
319. *Japan Economics Journal*, p. 8, Dec. 21, 1982.
320. *Japan Chemical Week*, p. 3, April 29, 1982.
321. *American Metal Market/Metal Working News*, April 26, 1982.
322. *American Metal Market*, p. 1, Dec. 7, 1982.
323. *American Metal Market*, p. 29, June 14, 1982.
324. *Chemical and Engineering News*, Jan. 10, 1983.
325. *Popular Mechanics*, p. 86, Sept. 1982.
326. *Mechanical Engineering*, p. 23, July 1982.
327. *Electrical World*, p. 96, Feb. 1982.
328. *Chemical Engineering*, p. 33, Sept. 20, 1982.
329. *Electrical World*, p. 9, Dec. 1982.
330. *Chemical Week*, p. 27, Nov. 3, 1982.
331. *Chemical Week*, pp. 29-30, June 30, 1982.
332. *The Energy Daily*, pp. 1, 4, Nov. 19, 1982.
333. *Electrical World*, pp. 77-79, Aug. 1982.
334. *Electrical World*, pp. 9-10, Oct. 1982.
335. *Electrical World*, pp. 28-30, June 1982.
336. *Electrical World*, pp. 24-25, Feb. 1982.
337. *Electrical World*, p. 11, Oct. 1982.
338. *Business Week*, pp. 32D, 32F, July 5, 1982.
339. *Electrical World*, p. 24, Dec. 1982.
340. *Chemical Week*, pp. 28-29, Nov. 3, 1982.
341. *Journal of Commerce*, p. 11A, Sept. 13, 1982.
342. *The Energy Daily*, p. 1, Dec. 15, 1982.
343. *Electrical World*, p. 13, July 1982.
344. *Electrical World*, p. 9, Dec. 1982.
345. *Chemical Week*, p. 66, Aug. 25, 1982.
346. *The Energy Daily*, pp. 1, 4, Sept. 24, 1982.

JOURNAL OF THE ELECTROCHEMICAL SOCIETY

ELECTROCHEMICAL SCIENCE
— AND TECHNOLOGY —

OCTOBER
1983

EST

Thermal Energy Generation of LiAl/FeS Cells

D. M. Chen and H. F. Gibbard*

Gould Incorporated, Gould Research Center, Rolling Meadows, Illinois 60008

ABSTRACT

Two independent methods were employed to determine the rate of thermal energy generation in 200 A-hr lithium-aluminum/iron sulfide cells. The first is an indirect method using thermodynamic calculations based on precise measurements of the cell potential as a function of temperature and state of charge, combined with measurements of the overpotential during discharge. The second is the direct measurement of the cell heat generation using a new high temperature battery calorimeter. The results obtained by these two methods are in excellent agreement. The rate of heat generation is 40-50W per cell during the last 30% of discharge at 100A. Under certain conditions the cell reaction, initially exothermic, becomes endothermic and then exothermic again during discharge. This unusual behavior is caused by the formation of intermediate J-phase ($LiK_6Fe_{24}S_{26}Cl$) and X-phase (Li_2FeS_2) compounds during the course of discharge.

High temperature lithium-aluminum/iron sulfide batteries are under development for vehicle propulsion, off-peak energy storage, and satellite power applications. Thermal management is an important aspect of design of these batteries because of their high specific energy of more than 100 W-hr/kg and operating temperature of 400°-500°C. From the viewpoint of thermal management, the most important property of a battery is the variation of temperature with position and time, which is caused primarily by the generation of thermal energy within the cells.

The objective of the present work was to determine the rate of thermal energy generation in LiAl/FeS cells as a function of current and depth of discharge. The ultimate goal of this research is to establish a thermal model to predict the temperature at all points within a battery, given the current and terminal voltage of each cell and known initial and boundary conditions. Values of the rate of thermal energy generation are essential to this thermal modeling.

Two independent methods were used to find the rate of thermal energy generation $\dot{q}$. The first, indirect, method was to measure the cell potential E as a function of temperature, and the total overpotential η, and to compute $\dot{q}$ using the thermodynamic equation (1)

$$\dot{q} = I[-T(\partial E/\partial T)_{P,\xi} + \eta] \qquad [1]$$

where I is current, taken as positive for discharge; P is pressure; and ξ represents the progress of the cell reaction. Several studies of the temperature coefficient of the cell potential have been published (2-4). However, none of these covers the desired range of temperature and state of charge with sufficient precision for our purpose.

The use of Eq. [1] for calculating the rate of thermal energy generation is valid only if the cell is thermodynamically reversible, as defined by Gibbs (5). This has not been shown previously for LiAl/FeS cells. Thus, we have also directly measured the heat flow from isothermal cycling cells, using a high temperature calorimeter (6) specially designed for this purpose. Equation [1] is strictly applicable only for isothermal operation. This condition is closely met for all of the calorimetric results reported here. Thermal modeling and experimental measurements of internal cell temperature have shown maximum internal temperature differences of less than 1°C for cells operated at the currents used in our calorimetric work, *i.e.*, 40A or less.

Experimental

200 A-hr lithium-aluminum/iron sulfide cells.—The cells used in the present study were five-plate, prismatic cells. They contained three lithium-aluminum alloy negative electrodes, two iron sulfide positive electrodes, boron nitride nonwoven separators, and molten LiCl-KCl-LiF (62.7, 28.2, 9.1 mol percent, respectively; melting point, 397°C) electrolyte. Figure 1 shows details of the cell construction. The cells weighed approximately 2.5 kg and had exterior dimensions of 21 × 13.3 × 3.2 cm; their theoretical capacity based on FeS content was 200 A-hr. The amounts of the electrode materials and electrolyte in the cells are given in Table I.

Apparatus.—A cylindrical constant-temperature furnace was built to house the LiAl/FeS cell under test. The furnace core was a 304 stainless steel can (height, 46 cm; diameter, 20 cm) surrounded by

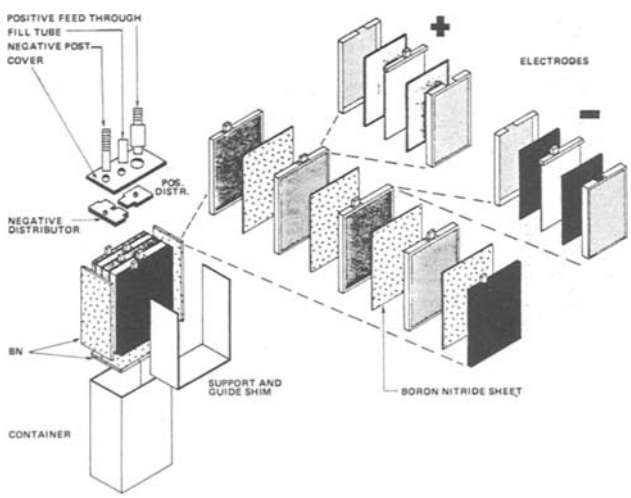

Fig. 1. Five-plate cell construction.

* Electrochemical Society Active Member.
Key words: cell, emf, electrolyte, thermodynamics.

Table I. Masses of components of a 200 A-hr LiAl/FeS cell

Component	Weight, g
Positive electrode	
FeS	185.35
Li_2S	96.74
Fe	129.94
Mo	15.46
C	6.88
LiCl/KCl (eutectic)	134.03
Total positive material	568.40
Negative electrode	
LiAl (18 w/o Li)	237.20
Al	124.80
LiCl/KCl (eutectic)	40.86
Total negative material	402.86
Electrolyte	
LiCl/KCl/LiF (62.7, 28.2, 9.1 mol percent)	536.90

three electrical mica band heaters (Tempco Electric Heater Corporation, Schiller Park, Illinois). This inner container was centered in a cylindrical vessel (height, 112 cm; diameter, 56 cm) filled with thermal insulation material (Fiberfrax Blankets and Fiberfrax Hot Boards, products of Carborundum Company, Niagara Falls, New York). In steady-state operation, this furnace without cell connections, lost to the surroundings the following heats: 195, 182, and 160W at temperatures of 490°, 470°, and 440°C, respectively.

Figure 2 shows schematically the apparatus for the measurement of cell potential. An LiAl/FeS cell was clamped by two constraint plates to eliminate possible shape change of the electrodes and was placed into the furnace. Power cables connected the cell terminals to the battery charge-discharge cycler (Model CDC-50-10, Propel Incorporated, South Plainfield, New Jersey). Two smaller gauge wires were also connected to the cell terminals for potential measurements. Argon gas was passed at a low rate into the furnace to protect the cell terminals from oxidation. The supply of constant power to the heaters through a variable transformer gave a highly stable steady-state temperature, and this method of temperature control was used during measurements of cell potential.

The cell temperature was measured using a calibrated type K thermocouple located at the center of the surface of one of the constraint plates. The cell potential was measured using a Guildline seven-and-one-half-digit multimeter. The precision of the measurements of temperature and cell potential was 0.1°C and 0.01 mV. The criterion of equilibrium was taken as constancy of the cell potential to within 0.01 mV for 1 hr. The time required for attainment of equilibrium after a change of temperature or state of charge was typically 14-18 hr but occasionally reached several days. Changes in state of charge were always carried out at 475°C by 50A constant current charge or discharge. The cell was assumed to be fully charged when its terminal voltage reached 1.55V during charge and completely discharged on reaching 1.00V during discharge. The relatively high current used to change the state of charge has little effect on cell capacity: for discharge at 50A the capacity was 188 A-hr; for 20A discharge it was 194 A-hr; and the theoretical capacity based on the sulfur content of the positive electrode was 200 A-hr. This relatively high current may, however, introduce some uncertainty as to the phases present in the FeS electrode, since no analysis of the electrode was performed. At each depth of discharge, the cell potential was measured from higher temperature to lower temperature and back again.

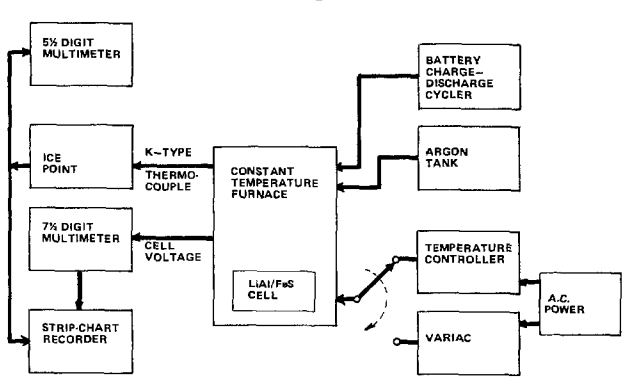

Fig. 2. Block diagram of apparatus used for cell potential measurement.

A high temperature battery calorimeter (Hart Scientific, Provo, Utah) was designed and constructed for measurement of the rate of thermal energy generation of LiAl/FeS cells. The calorimeter was designed with a temperature range of 400°-500°C, a sensitivity of 1 mW, and an upper limit of heat flow of 50W. The details of its construction and principles of operation are presented in Ref. (6).

During early testing of the calorimeter, it was noted that some of the nickel-foil heaters and their power leads oxidized and failed in 15 days of operation. Accordingly, the temperature range of the calorimeter was limited to 410°-435°C. Within these limits the calorimeter functioned as designed. Design changes to remedy its flaws are also presented in Ref. (6).

Results and Discussion

Table II gives the values of the cell potential at various temperatures and depths of discharge. The reproducibility of these results was excellent. For example, at 23% depth of discharge (see Table II), the cell potential was 1.33705V at 476.8°C; after five days at lower temperatures, the cell potential was measured again as 1.33702V at 476.4°C.

The measured cell potentials are plotted in Fig. 3. As can be seen, the temperature derivative of the cell

Table II. Emf of LiAl/FeS cell

Depth of discharge (%)	Temperature (°C)	Emf (V)
0	479.1	1.40476
	464.6	1.40743
	447.2	1.41106
	433.3	1.41398
	417.9	1.41766
12	494.0	1.34681
	471.6	1.34261
	462.4	1.34083
	447.7	1.33796
	416.4	1.33096
	422.8	1.33232
23	476.8	1.33705
	459.9	1.33483
	445.2	1.32276
	415.3	1.33254
	417.5	1.33254
	422.3	1.33190
	428.5	1.33106
	448.3	1.33294
	480.1	1.33773
	488.0	1.33916
	476.4	1.33702
37	474.1	1.33362
	444.0	1.32895
	412.7	1.33267
	418.6	1.33181
	425.4	1.33073
	439.2	1.32872
	483.2	1.33477
	476.0	1.33375
51	485.2	1.32180
	465.6	1.32456
	414.0	1.33284
	430.0	1.33000
	446.3	1.32748
	477.6	1.32270
77	475.3	1.32273
	493.0	1.32011
	439.6	1.32840
	407.5	1.33356
	478.0	1.32204
100	483.2	1.32023
	455.7	1.32649
	428.0	1.33143
	417.0	1.33357
	470.7	1.32292
	474.0	1.32204

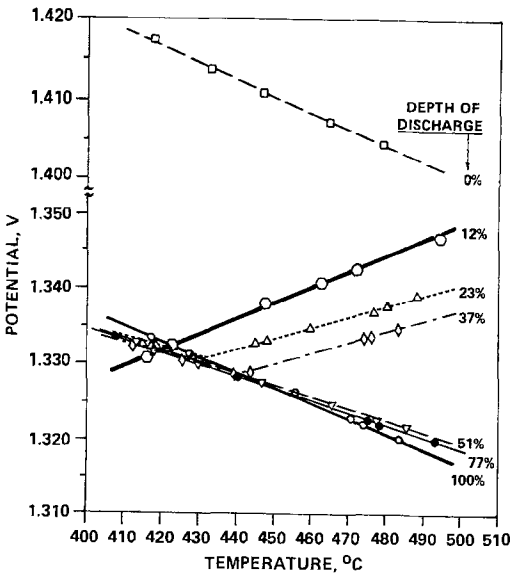

Fig. 3. Cell potential of an LiAl/FeS cell as a function of temperature and depth of discharge.

potential varies strongly with temperature and depth of discharge. For fully charged or discharged cells the temperature coefficient of the emf is negative. However, for partially discharged (23-37% depth of discharge) cells, two linear portions are noted; over the lower portion of the temperature range the temperature coefficient is negative, and at higher temperatures it is positive. The cause of this unusual behavior is believed to be transitions between J-phase ($LiK_6Fe_{24}S_{26}Cl$) and X-phase (Li_2FeS_2) materials identified by workers at Argonne National Laboratories (7, 8). For cells discharged 50% or more, only negative slopes were found over the temperature range of 400°-500°C.

Values of the temperature derivatives at 475° and 420°C, obtained by linear least squares analysis are given in Table III, along with 95% confidence intervals. Figure 4 shows the same results in graphical form.

In addition to the cell potential and its temperature derivative, values of the terminal voltage as a function of current and depth of discharge are required to compute the rate of thermal energy generation. Figure 5 shows the cell voltage during constant-current discharges of 40-100A to a cutoff voltage of 1.00V at 475°C. From these measurements and the cell potentials taken from Fig. 3, the overpotential was calculated, and the rate of thermal energy generation was computed using Eq. [1]. The results are presented in Fig. 6.

The rates of thermal energy generation shown in Fig. 6 are relatively small, even negative (*i.e.*, endothermic), during the first 50% of discharge at 475°C. The reason for this is the positive value of $\partial E/\partial T$ (see Fig. 4), which offsets the polarization heat $I\eta$. Toward the end of discharge, two phenomena contribute to a substantial rise in $\dot{q}$. The thermodynamic contribution

Table III. The emf temperature coefficients of LiAl/FeS cells at various depths of discharge and operating temperatures

Depth of discharge	Temperature coefficient (mV/K)		95% Confidence interval (± mV/K)	
(%)	475°C	420°C	475°C	420°C
0	−0.210	−0.120	0.023	0.023
12	+0.206	+0.206	0.019	0.019
23	+0.147	−0.126	0.020	0.032
37	+0.150	−0.149	0.016	0.008
51	−0.155	−0.155	0.013	0.013
77	−0.159	−0.159	0.012	0.012
100	−0.202	−0.202	0.007	0.007

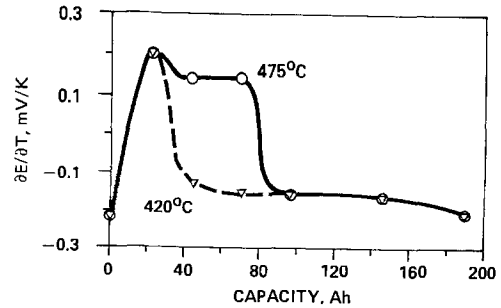

Fig. 4. Temperature derivative of cell potential of a 200 A-hr LiAl/FeS cell.

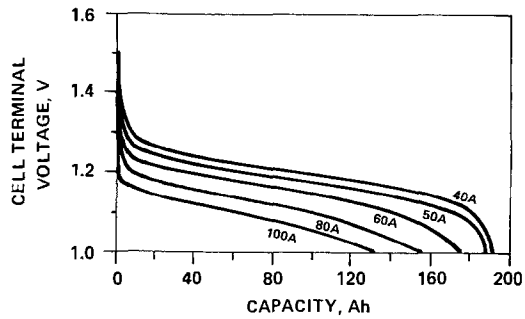

Fig. 5. Discharge curves at various currents at 475°C

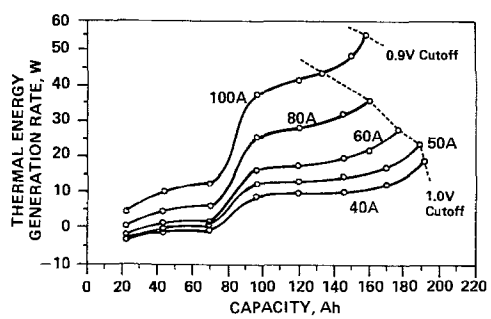

Fig. 6. Thermal energy generation rate of an LiAl/FeS cell during discharge at 475°C.

to $\dot{q}$ changes sign and becomes exothermic, and the cell overvoltage increases rapidly (see Fig. 5). As a result, the rate of thermal energy generation reaches 40 W/cell for a 100A discharge, or 4 kW for a 100-cell battery, such as might be used to power an electric vehicle, for example.

The rates of thermal energy generation measured calorimetrically and computed from Eq. [1] are compared for a 40A discharge at 430°C in Fig. 7. The agreement between the calorimetric (squares, full curve) and the predicted (circles, dotted curve) values of heat flow is seen to be excellent. The polarization heat is also shown; over most of the discharge

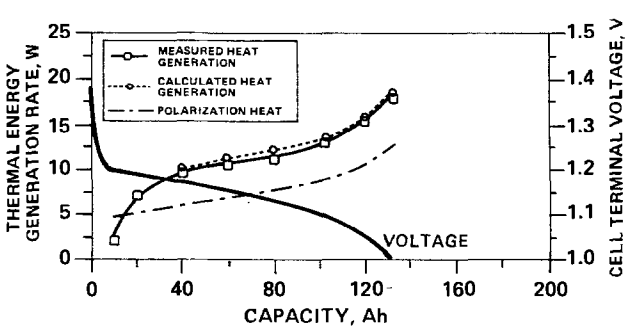

Fig. 7. Thermal energy generation rate and cell terminal voltage of an LiAl/FeS cell at 40A discharge at 430°C.

it lies below and nearly parallel to the curve for the total heat.

Discharge of the cell at a lower rate shows more of the details of the changes in cell thermodynamics. Figure 8 shows the heat flow during a 10A discharge at 435°C. The transition from exothermic to endothermic and back again, which is predicted thermodynamically, is clearly shown by the calorimetric measurements. The agreement between the two methods is not good during the first quarter of the discharge; the calorimetric values are believed more reliable owing to the rapid change of the absolute value of the cell potential with state of charge, which decreased the accuracy of determinations of $\partial E/\partial T$ for high states of charge.

Figures 9 and 10 show the heat flows measured at the lower temperature of 410°C during a 10A discharge. Two points are particularly significant. First, the endothermic effect during discharge was not observed at

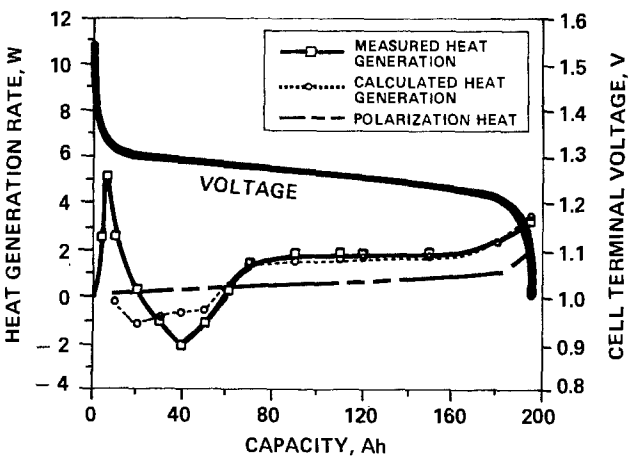

Fig. 8. Thermal energy generation rate and cell terminal voltage of an LiAl/FeS cell during 10A discharge at 435°C.

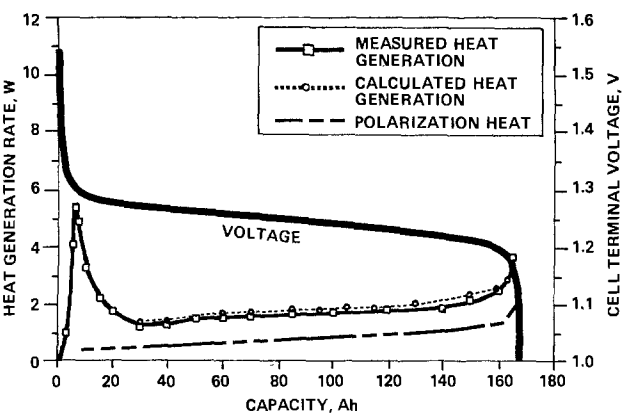

Fig. 9. Thermal energy generation rate and cell terminal voltage of an LiAl/FeS cell during 10A discharge at 410°C.

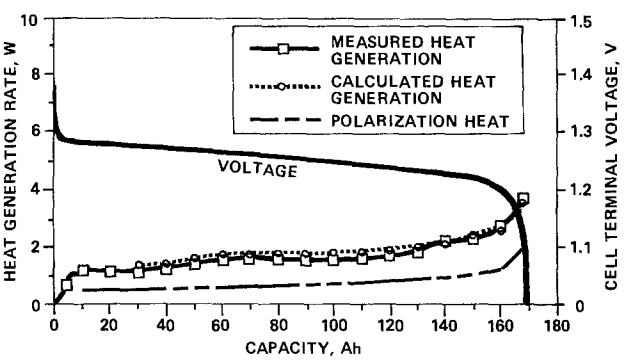

Fig. 10. Thermal energy generation rate and cell terminal voltage of an LiAl/FeS cell during 10A discharge at 410°C.

410°C, in contrast to the case at 435°C (Fig. 8). This result, which is consistent with the emf measurements, indicates that the phase transition of J to X did not occur during discharge at 410°C. Second, at the beginning of discharge, two different heat generation rates were observed (Fig. 9 and 10) because the initial state of the cell was slightly different in each case. For the results in Fig. 9 the cell discharge was begun when the open-circuit voltage was 1.540V. For the results shown in Fig. 10 the cell was allowed to stand at open circuit for several days after a charge to 1.550V; at the beginning of discharge its open-circuit voltage was 1.375V. The exothermic peak during the first 10% of discharge as shown in Fig. 8 and 9 is believed to be associated with the phase transformation of FeS to J (8). Moreover, the absence of this exothermic peak in Fig. 10 indicates that the FeS-to-J transition in a cell charged to 1.55V may take place gradually during open-circuit stand. The cell reaction in the case illustrated by Fig. 10 is believed to be due primarily to the reaction of J to Li_2S.

Figure 11 shows the terminal voltages of an old cell which was overcharged deliberately to 1.98V and subsequently to 1.94V at 420°C at 40A and was then placed on open circuit. The cell voltage dropped during open-circuit stand, underwent a point of inflection in the vicinity of 1.50V, and then leveled off at 1.35V. The transition of FeS to J is thought to be responsible for the inflection.

The entropic contribution to thermal energy generation can be expressed as

$$\dot{q}_S = -IT(\partial E/\partial T)_{P,\xi} = \dot{q} - I\eta \qquad [2]$$

At a particular temperature and state of charge, the temperature derivative is constant. The relationship between $\dot{q}_S$ and I is thus expected to be linear. Figure 12 shows $\dot{q}_S$ for various charge/discharge currents at 50% capacity and a temperature of 420°C. The circles represent the entropic heat, which was obtained by subtracting the polarization heat from the total measured calorimetric heat flow. The solid lines in Fig. 12 indicate the values of $\dot{q}_S$ calculated from the value of $\partial E/\partial T$ derived from emf measurements, −0.155 mV/K. The agreement is excellent for both charge and discharge.

The calorimetric measurements and indirect thermodynamic calculations of thermal energy generation yielded substantially identical results for the types of cells studied in this work. However, battery calorimetry has several advantages over the measurements of cell potentials at open circuit and during current flow.

1. The calorimetric measurement of heat flow is direct and absolute; it requires no assumptions as to the thermodynamic reversibility of the cell.

2. Calorimetry gives precise values for heat flow and does not require differentiation of the results with

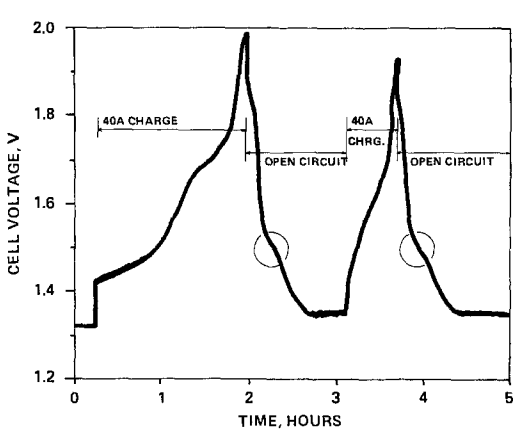

Fig. 11. Cell voltage during overcharge and open circuit

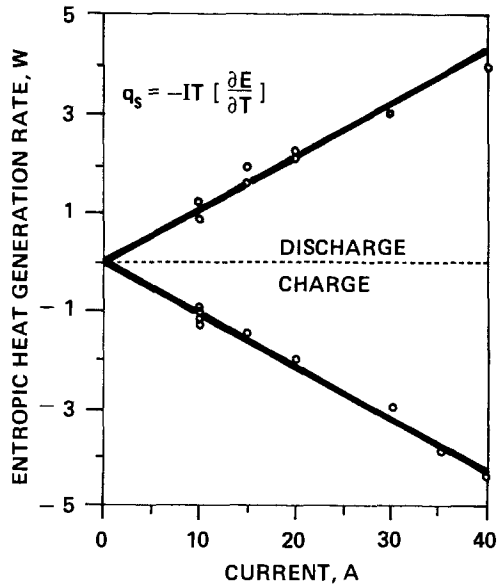

Fig. 12. Entropic heat generation rate as a function of charge/discharge current at 50% capacity at 420°C.

respect to temperature, as does the measurement of emf.

3. Calorimetric measurements are rapid. For the LiAl/FeS cells studied in this work the amount of information collected by calorimetry in one day required more than two weeks to obtain in measurements of cell potentials.

4. The rapidity of calorimetric measurements permits the study of cells in which the state of charge is changing because of a finite rate of self-discharge.

In summary, the precision, speed, and absolute nature of the results of battery calorimetry tend to offset the cost of the instrument, which is higher than that required for precise emf measurements.

Conclusions

The rate of thermal energy generation has been determined for the high temperature lithium-aluminum/iron sulfide cell with boron nitride separator and molten LiCl-KCl-LiF electrolyte by two independent methods. The cell thermal energy generation calculated from a thermodynamic equation is in good agreement with the heat flow measured with an isothermal conduction calorimeter. The results of cell heat generation are valuable for thermal modeling and the temperature control of batteries containing large numbers of cells.

The temperature derivative of the cell potential of the LiAl/FeS cell is a complicated function of temperature and state of charge. The cell reaction for fully charged and fully discharged cells is exothermic; above 430°C, a part of the discharge process is endothermic.

In the calorimetric measurements, cell reactions attributed to the conversions of FeS to J-phase and J- to X-phase during discharge were observed and discussed in this paper. The entropic heat generation of a cell was obtained by subtracting the polarization heat from the total cell heat generation measured by a calorimeter. Although the calculated entropic heat at 50% of capacity is consistent with thermodynamic reversibility, the cell reaction at higher states of charge showed evidence of irreversibility.

Acknowledgments

This work was supported by the U.S. Department of Energy under Contract W-7405-ENG-48 with Lawrence Berkeley Laboratory through subcontract number 4505810. The cooperation of Gould's lithium/iron sulfide group in cell preparation is gratefully acknowledged. One of the authors (D.M.C.) would like to thank J. Phillips and C. C. Chen for many valuable discussions.

Manuscript submitted Jan. 17, 1983; revised manuscript received April 28, 1983.

Gould Incorporated assisted in meeting the publication costs of this article.

REFERENCES

1. H. F. Gibbard, "Thermal Properties of Battery Systems," *This Journal*, **125**, 353 (1978).
2. M. M. Farahat, A. A. Chilenskas, and D. L. Barney, Abstract 86, p. 234, The Electrochemical Society Extended Abstracts, Vol. 80-2, Hollywood, FL, Oct. 5-10, 1980; Argonne National Laboratory Report, ANL-80-49, pp. 58-60 (1980).
3. M. Gauthier, F. Morin, and R. Bellemar, IREQ Report Number 1805C (April 1978).
4. C. Sy, Z. Tomczuk, and M. F. Roche, Argonne National Laboratory Report ANL-77-17, p. 47 (1977).
5. J. W. Gibbs, "Collected Works," Vol. I, pp. 331-349, 406-412, Yale University Press, New Haven (1957).
6. L. D. Hansen, R. M. Hart, D. M. Chen, and H. F. Gibbard, *Rev. Sci. Instrum.*, **53**, 45 (1982).
7. Z. Tomczuk and M. F. Roche, Argonne National Laboratory Report, ANL-79-94, p. 142 (1980).
8. Z. Tomczuk, S. K. Preto, and M. F. Roche, *This Journal*, **128**, 760 (1981).

The Effect of Additives on Current Distribution in Pasted Zinc Electrodes

J. McBreen* and E. Gannon

Brookhaven National Laboratory, Department of Energy and Environment, Upton, New York 11973

ABSTRACT

The effect of additives on current distribution during formation of a pasted zinc electrode was investigated in a two-electrode zinc-nickel oxide cell with a sectioned nickel oxide electrode. The zinc electrodes consisted of zinc oxide, a PTFE binder, and small weight percentage additions of the oxides of high hydrogen overvoltage metals. The square nickel oxide electrode was divided into sixteen square sections, consisting of four center and twelve edge sections. It was assumed that the current to each section was an exact measure of the current to that section of the zinc electrode that was in register with the section. In the case of zinc electrodes with no additive, the average current density at the edge sections was about twice that found at the center sections. Additions of Bi_2O_3, Ga_2O_3, CdO, and HgO had little effect on the current distribution. Additions of Tl_2O_3 and $In(OH)_3$ resulted in very even current distribution over the electrode area. Anomalous effects were found with PbO additions because of leaching of the additive into the electrolyte at the electrode edges.

The principal mode of failure in zinc-silver oxide and zinc-nickel oxide cells with pasted zinc electrodes is shape change. This is a redistribution of the zinc active material that occurs on cycling. When shape change occurs zinc is eroded from the electrode edges and the zinc agglomerates toward the electrode center. Proposed mechanisms for shape change either attribute it to nonuniform current distribution (1) or to separator related electro-osmotic effects which are coupled with electrode reactions to cause nonuniform mass transport (2, 3). Since shape change occurs in cells with microporous separators, which presumably do not give electro-osmotic effects, and is accelerated by membranes which display electro-osmosis, both mechanisms may be operative. Electro-osmosis cannot explain the dramatic effects of substitution of other additives for HgO (4-6), or the incorporation of $Fe(OH)_2$ at the electrode edges (7, 8).

In previous work on the addition of oxides of high hydrogen overvoltage metals to zinc electrodes, it was found that many of these additives were reduced to metal prior to zinc deposition (9). It was also found that some metal oxide additives greatly affect the electrode polarizability and the zinc morphology. It was speculated that the beneficial effects of additives might be due to an improvement in current distribution. The present study was an investigation of current distribution during formation of zinc electrodes with various additives.

Experimental

Cell.—The current distribution cell was very similar in many respects to that described previously (1). The test cell consisted of a standard pasted zinc electrode, a separator system, and a sectioned nickel oxide counterelectrode. A cross section drawing of the cell is shown in Fig. 1. Current distribution was determined by monitoring the current to the various sections of the nickel oxide electrode.

Zinc electrode.—The zinc electrodes consisted of a ZnO/PTFE (polytetrafluoroethylene) mix with the various additives on an expanded silver current collector (Exmet Corporation, 5 Ag12.5-2/0). The method of preparation of the ZnO/PTFE mix (98% ZnO + 2% PTFE) is described elsewhere (9). The ZnO/PTFE mix and the additives were blended in a Waring blender in 120 ml of isopropanol. The suspension was poured over the current collector onto a vacuum table and the liquid drawn off. After that, the electrodes were pressed wet, dried in an oven at 50°C, and given a final dry pressing to the final dimensions (10.52 × 10.52 × 0.073 cm). The vacuum table technique has been described in detail elsewhere (10). Each electrode contained 16.3g of ZnO. Electrodes of the following compositions were evaluated: 98% ZnO + 2% PTFE (control), 89% ZnO + 9.2% Bi_2O_3 + 1.8% PTFE, 96% ZnO + 2% Ga_2O_3 + 2% PTFE, 96% ZnO + 2% CdO + 2% PTFE, 96% ZnO + 2% HgO + 2% PTFE, 96% ZnO + 2% PbO + 2% PTFE, 96% ZnO + 2% Tl_2O_3 + 2% PTFE, 96% ZnO + 2% $In(OH)_3$ + 2% PTFE, 91% ZnO + 2% PbO + 5% Zn + 2% PTFE, 93% ZnO + 5% Zn + 2% PTFE, and 91% ZnO + 5% Zn + 2% HgO + 2% PTFE.

Nickel oxide electrode.—The nickel oxide electrode was prepared by sectioning a nickel plaque into 16 sections (2.54 × 2.54 × 0.13 cm). The sections were then welded on to an array of machined nickel current collectors that were countersunk in an acrylic block (Fig. 1). The spaces between each section and the edges were masked with epoxy. The finished electrode is shown in Fig. 2. The space between each section was 0.12 cm. Except for the coined indentations at the

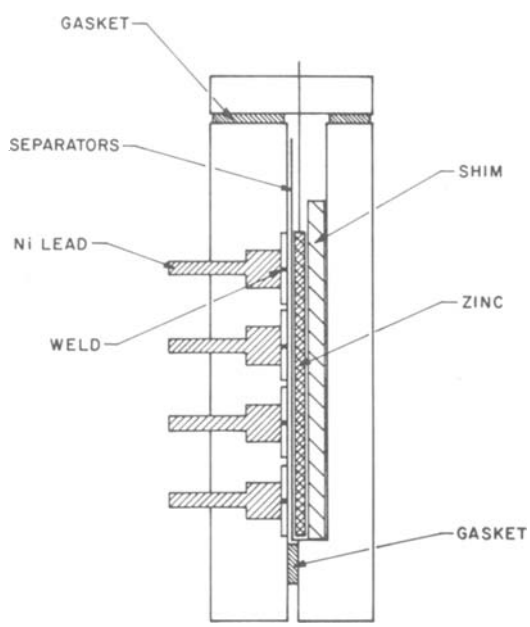

Fig. 1. Schematic of current distribution cell

* Electrochemical Society Active Member.
Key words: battery, cell, electrodeposition.

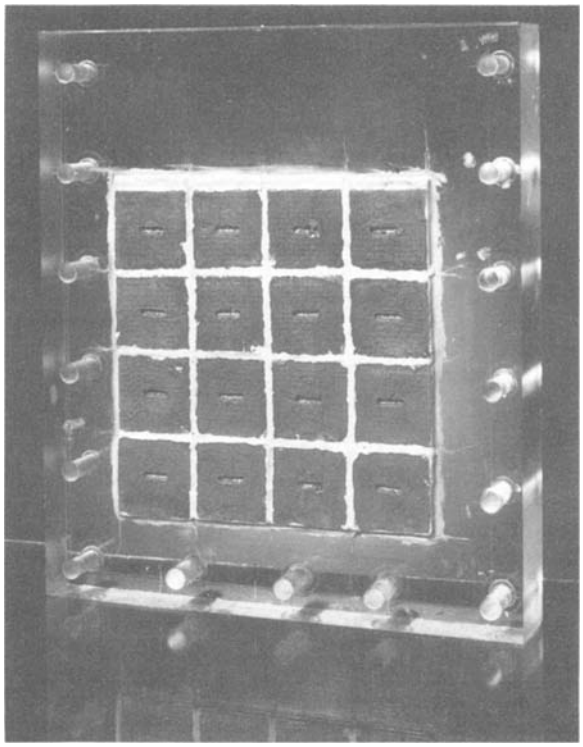

Fig. 2. The sectioned nickel oxide electrode for current distribution measurements.

center welds on each section, the electrode was perfectly flat. The sectioned nickel electrode was impregnated with $Ni(OH)_2$ + 8% $Co(OH)_2$ to a theoretical capacity of 2.87 A-hr using the standard impregnation method (11). The electrode was then given three formation cycles in a 6M KOH + 0.5M LiOH electrolyte.

Cell assembly.—The cell was assembled as follows. A sheet of nonwoven polypropylene (11.0 × 11.0 × 0.013 cm, Pellon Corporation, 2504K4) was placed over the sectioned nickel oxide electrode. The zinc electrode was wrapped in two turns of a microporous separator (Celanese Corporation, Celgard 3501) and then centered over the nonwoven separator, in register with the sectioned nickel oxide electrode. The zinc electrode was placed in such a way that the expanded metal current collector was on the side of the zinc electrode remote from the nickel oxide electrode. The rest of the cell was assembled, as shown in Fig. 1, and bolted together. Provisions were made to ensure an even distribution of thickness in the cell cavity (±0.005 mm). The cell was then wetted down with 20 ml of electrolyte (8.4M KOH + 0.5M LiOH + 0.74M ZnO) and soaked for at least 16 hr prior to the start of the experiment. The cells were operated in the flooded mode with electrolyte extending 2 cm above the top of the zinc electrode.

Experimental procedure.—The cell was first vacuum treated to remove gas bubbles and then connected to the electrical circuitry for measuring the current distribution. This is described in detail elsewhere (1). The cell was charged at 200 mA (1.82 mA/cm²) for 18 hr. The current to the various sections was continuously monitored. After each test the cells were taken apart and the zinc electrodes were visually examined. The nickel oxide electrode was discharged against a nickel sheet electrode, washed three times in hot (60°C) KOH to remove soluble additives, rinsed with distilled water, and allowed to dry overnight at 25°C, prior to the next run.

Results and Discussion

Metal oxide additives and the initial stages of electrode formation.—Depending on the additive, it took up to 20 min for the zinc electrode to reach the zinc deposition potential, during formation. This was true for additions of Tl_2O_3, CdO, HgO, and Bi_2O_3. This was similar to what was observed before (9) and was due to the reduction of the additive oxide to the metal. During this time there were rapid fluctuations in the current distribution. Initially edge sections had a higher current than center sections. However, the current at the edges decreased rapidly as the oxide was consumed and the current to the center sections increased. On reaching the zinc deposition potential, the current distribution reverted to a condition where edge sections had a higher current than center sections. The current distribution became somewhat more even after the first hour of charge and thereafter remained relatively constant. The distribution shown in Fig. 3 is representative of that found for the last 17 hr of charge. In the case of electrodes with no additive and electrodes with additions of Ga_2O_3 and $In(OH)_3$ the zinc deposition potential was reached within seconds. The current to the edge seconds was higher than that to the center sections. The current distribution became more even after about 1 hr and once again the current distribution at the end of charge (Fig. 3) is representative of the current distribution for the last 17 hr of charge. Some of these experiments were repeated several times and the reproducibility was good. The experiments with no additives and with

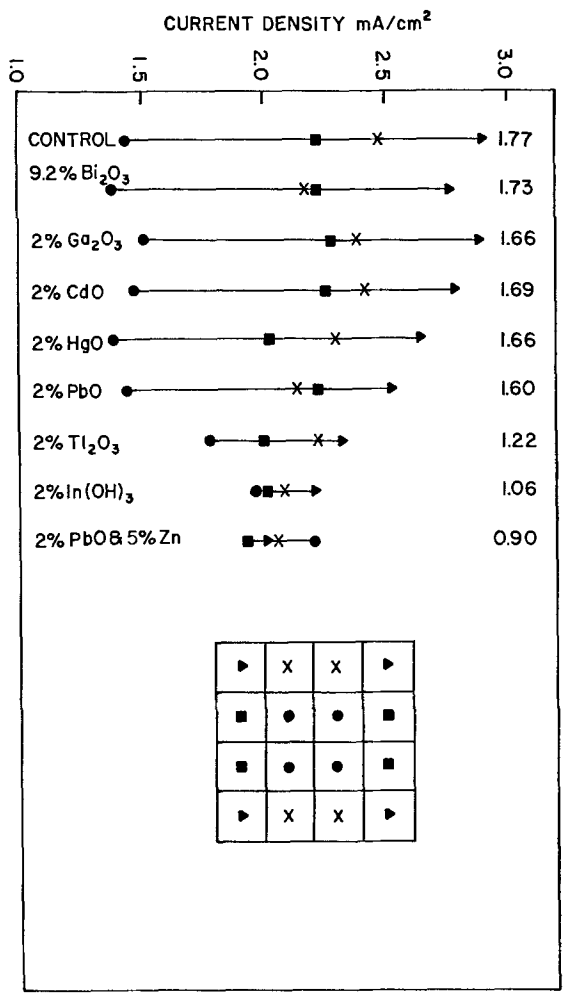

Fig. 3. Current distribution at the end of an 18 hr charge (1.82 mA/cm²) for zinc electrodes with various additives. The currents to the 16 sections are presented as four averages of four sections each. The symbols for the section averages (*e.g.*, ▲ = corner sections and ● = center sections) are indicated in the inset. The numbers to the right of each line are the ratios of the average edge section current density to the average center section current density.

Ga_2O_3 were repeated several times over the course of these experiments to ensure that changes in current distribution from experiment to experiment were not due to some artifact due to aging of the nickel oxide electrode.

The special case of PbO additions.—In the case of the cells with PbO additions, there were rapid fluctuations in the current distribution during the first 10 min of charge. However, the current to the center sections was higher than that to the edge sections. On reaching the zinc deposition potential the current distribution was very uneven with the current density at the electrode edges being as much as eight times higher than that found at the center sections. The current distribution became more even after about 5 hr. The results in Fig. 3 are representative of the current distribution obtained in the last 12 hr of charge. However, the current to the top four sections of the electrode remained abnormally high. The average current to the top four sections was about twice that to the bottom four sections of the electrode. This experiment was repeated several times with similar results. It was observed after the overnight soak that the top edge sections of the zinc electrode (~2 cm wide) were white while the center part of the electrode had the yellowish tinge of PbO. Thus it became evident that the PbO was being leached from the electrode into the electrolyte at electrode edges. The anomalies in the current distribution are attributed to the fact that there was much less additive at the electrode edges. In one test it was found, if the cell was charged for 1 hr and allowed to stand overnight, that on resumption of the charge the current distribution was much more even. This was due to the displacement of soluble lead from the excess electrolyte onto the electrode edge according to

$$HPbO_2^- + OH^- + H_2O + Zn \rightarrow Pb + Zn(OH)_4^=$$

It was then decided to try an electrode formulation consisting of 91% ZnO + 2% PbO + 2% PTFE + 5% Zn (−325 mesh) where the soluble lead would be displaced from the electrolyte by metallic zinc.

Electrode with PbO and Zn additions.—In the case of electrodes with PbO and Zn additions, the zinc deposition potential was immediately established on turning on the charging current. The current distribution was very even throughout charge. A blank run with a 5% Zn addition and one with a 5% Zn + 2% HgO addition gave respective results that were similar to those found for the control and the cell with a 2% HgO addition. The Zn powder displaces the PbO by cementation. The resultant gray Pb could be seen as the electrode was wetted in from the edges, on addition of electrolyte. This result strongly indicates once again that the effect of these additives is related to some substrate effect and is not a codeposition effect (9, 12).

Metal oxide additives and current distribution.—Additives such as Tl_2O_3, PbO, and $In(OH)_2$, which were shown to increase the electrode polarizability (9), result in more even current distribution during electrode formation. However, additives that reduce the polarizability of the electrode do not result in any significant disparity in the measured current distribution over that found for electrodes with no additives. There are at least two possible reasons for this. One, is that the edge sections are large (2.54 × 2.54 cm) and the current is an average over this and does not reflect the true current density at the edge. The other is that the condition here is a current distribution case, wherein both the interelectrode spacing and the polarizability are small. For such a case, it has been shown that even for vanishing polarization the high current density point is very close to the electrode edge (13). Thus there is a limit to the unevenness in current distribution to be expected.

There was qualitative evidence that additives also affect the current distribution within the pores of the zinc electrode. In cells with Ga_2O_3 additives all of the zinc deposit appeared to be in abuttal with the separator. The area around the expanded metal current collector was still white zinc oxide. However, in cells with $In(OH)_3$ and PbO additives most of the zinc deposit was in the vicinity of the current collector. The front of the electrode in abuttal with the separator was largely white zinc oxide. In previous work (9) it was found that additions of Ga_2O_3 yielded electrodes with minimum polarizability and additions of PbO and $In(OH)_3$ gave electrodes with maximum polarizability. The observed distribution of zinc is consistent with this.

Conclusions

1. It has been shown that metal oxide additives can affect the current distribution during formation of pasted zinc battery electrodes.
2. Additives such as Tl_2O_3 and $In(OH)_3$ that increase electrode polarizability improve the current distribution.
3. Leaching effects of soluble additives such as PbO at electrode edges can lead to very uneven current distribution during electrode formation.
4. Results in electrodes with a combination of a PbO/Zn powder additive indicate that the beneficial effect of lead additives is related to a substrate effect and not to a codeposition effect.

Manuscript submitted March 17, 1983; revised manuscript received May 25, 1983.

Brookhaven National Laboratory assisted in meeting the publications costs of this article.

REFERENCES

1. J. McBreen, *This Journal*, **119**, 1620 (1972).
2. K. W. Choi, D. N. Bennion, and J. Newman, *ibid.*, **123**, 1616 (1976).
3. K. W. Choi, D. Hamby, D. N. Bennion, and J. Newman, *ibid.*, **123**, 1628 (1976).
4. A. Himy and O. C. Wagner, U.S. Pat. 4,084,047.
5. O. C. Wagner, A. Almerine, and R. Smith, Proceedings 29th Power Sources Conference, Atlantic City, NJ, June 9-12, 1980. The Electrochemical Society Inc., p. 237 (1981).
6. S-P. Poa, G-M. C. Chiang, and T-C. Lin, *Science Development Monthly (Taiwan)*, **6**, 1013 (1978).
7. J. McBreen, U.S. Pat. 3,876,470.
8. S-P. Poa and C. H. Wu, *J. Appl. Electrochem.*, **8**, 427 (1978).
9. J. McBreen and E. Gannon, *Electrochim. Acta*, **26**, 1439 (1981).
10. J. McBreen, U.S. Pat. 4,000,005.
11. A. Fleischer, *J. (and Trans.) Electrochem Soc.*, **94**, 289 (1948).
12. J. McBreen, M. G. Chu, and G. Adzic, *This Journal*, **128**, 2287 (1981).
13. C. Wagner, *ibid.*, **98**, 116 (1951).

Chloride Accumulation on Indoor Zinc and Aluminum Surfaces

G. B. Munier, L. A. Psota-Kelty, and J. D. Sinclair*

Bell Laboratories, Holmdel, New Jersey 07733

ABSTRACT

The long-term accumulation of chloride and other ions on indoor zinc and aluminum surfaces in 15 U.S. cities has been measured. For most ionic contaminants, the accumulation on zinc and aluminum surfaces is similar, suggesting that particulate deposition is the most likely mode of accumulation. Chloride accumulation on aluminum occurs by particulate deposition, but on zinc surfaces, attack by reactive chlorine containing gases also contributes to accumulation. In New York City and Philadelphia, chloride accumulation is very rapid on all zinc surfaces but not on aluminum surfaces. Volatilization of chloride, probably as HCl or NH_4Cl, seems to contribute to the low chloride concentrations observed on aluminum surfaces in these cities. In Wichita and Houston, deposition of coarse chloride containing particulates produces rapid accumulation of chloride on horizontal zinc and aluminum surfaces while chloride accumulation on vertical surfaces is slow.

As part of a broad study to determine the amounts and effects of major inorganic pollutants in indoor environments (1, 2), the long-term accumulation of chloride on indoor zinc and aluminum surfaces at telephone company switching centers in 15 U.S. cities has been measured (3). In the previous reports (1, 2) on this study, the accumulation of chloride, nitrate, sulfate, sodium, ammonium, potassium, calcium, and magnesium at seven cities was documented. The highly complex nature of the accumulation process and the many indoor, outdoor, and human factors that bear on the accumulation process were discussed, including aerosol size distribution, air flow patterns, temperature and humidity gradients, air filtration systems, air leakage pathways, and concentrations of ammonia, acidic aerosols, and other substances that could interact with surface species to produce volatile products. The sulfate accumulation on zinc and aluminum surfaces was shown to correlate well with sulfate concentrations in the local troposphere but not with SO_2 concentrations, indicating that the primary accumulation process for sulfate is particulate deposition rather than a corrosion reaction with SO_2. Hermance *et al.* (4) have demonstrated that airborne nitrates in the Los Angeles area correlate with nitrate concentrations on surfaces and with the incidence of electrolytic stress corrosion cracking of nickel brass.

For the initial seven cities, the behavior of chloride was highly irregular. In New York City and Council Bluffs (Iowa), chloride accumulation on zinc was rapid, but on aluminum the chloride accumulation was low. In Houston and Cleveland, accumulation on zinc was similar to that on aluminum. It was suggested in the previous reports that preferential volatilization of chloride species from aluminum surfaces might contribute to the lower amounts of chloride at some locations by a process similar to the sulfuric acid aerosol-induced depletion of chloride from sea salt aerosol that has been documented by Hitchcock *et al.* (5). For the sea salt aerosol, the volatile chloride was HCl. In a paper on aerosol chemistry, Weschler and Graedel (6) have discussed evidence that species with saturation vapor pressures $>10^{-7}$ Torr will exist in the vapor phase at remote locations where there are few, if any, local sources, while species with saturation vapor pressures in the 10^{-7}-10^{-8} Torr range will be partitioned between the gas phase and a condensed phase within aerosols. For some indoor surfaces containing chloride, interaction with ammonia or acid ammonium sulfate aerosol could produce NH_4Cl, which has a saturation vapor pressure of 2.4×10^{-5} Torr. Thus, depending on the gas phase concentrations of HCl and NH_3, either HCl or NH_4Cl could volatilize and thereby remove chloride from indoor surfaces.

In this report all the completed field data on chloride and sulfate accumulation are given, as are additional laboratory studies that were intended to further elucidate the cause of the difference in accumulation of chloride on zinc and aluminum.

* Electrochemical Society Active Member.
Key words: corrosion, chloride, aluminum, zinc.

Experimental

The zinc and aluminum surfaces examined in this study were structural surfaces associated with telephone company switching equipment frames. The zinc surfaces were electroplated steel sheets while the aluminum surfaces were 2000 series low copper alloys. These surfaces were not cleaned or disturbed during the accumulation period, which was determined by subtracting the year of manufacture stamped on equipment surfaces from the year in which the equipment was sampled. The sampling was accomplished between October 1978 and October 1982, and most of the equipment was 8-15 yr old. The air exchange rate at these locations was typically in the range of 0.10-0.25 per min. The direction of air flow relative to equipment orientation was variable. The air processing fans were run continuously (except for power outages or servicing). The air filtration systems were equipped to remove most of the large particles (>5 μm aerodynamic diam) from the air intake stream but only about 10% of the fine particles (<2 μm).

Except as noted in previous reports (1, 2), surface extractions were accomplished with moistened pieces (square sections 1.27 cm on a side) of pre-cut Whatman 542 filter paper. The papers were cleaned before placement on a surface by washing them three times with boiling distilled water, and this was followed by oven drying. The volume of water in each paper was determined to be approximately 0.03 ml. The papers were placed on flat surfaces in either a horizontal or a vertical plane and were removed from the surfaces after drying. The sampling interval for each paper was approximately 30 min but was somewhat dependent on the ambient relative humidity. The procedure was carried out three times on each sampled area to insure complete removal of water-soluble contaminants (7). Between 50 and 120 samples were collected from each location. The samples were stored and transported to the laboratory in disposable polystyrene test tubes. In the laboratory, the paper samples were extracted with 10 ml of water, and the extracts were then split for separate cation and anion analysis. All samples were analyzed by ion chromatography. Standard ion exchange pre-columns, separator columns, and suppressor columns were used for the ion analyses. Appropriate blank corrections for the sampling and analytical procedure were made when converting the solution concentrations to surface concentrations. The details and validation of the sampling and analytical procedures are described elsewhere (7).

An adjustment in the total surface concentration of each ion was made to take into account any accumulation that occurred prior to uncrating the equipment at its permanent location. These initial concentrations were estimated by sampling new equipment shortly after uncrating at one location in New York City and

one in New Jersey. A total of 60 samples each on zinc and aluminum surfaces were taken at both locations. The average concentrations of chloride on zinc and aluminum surfaces were 0.04 and 0.24 $\mu g/cm^2$, respectively, while those of sulfate were 0.13 and 0.21 $\mu g/cm^2$.

For surface acidity measurements, at least 60 single paper extracts from a location were jointly extracted in the minimum volume of water necessary to permit measuring the solution pH (on the order of 20 ml). The relative acidities of the surfaces were calculated on an aliquot basis using a water volume of 0.03 ml/paper.

Results and Discussion

Accumulation data.—The accumulation data can be presented either as total surface concentration or as an average annual accumulation based on surface age. Neither method is entirely satisfactory for the purpose of comparing locations or comparing zinc and aluminum surfaces. Clearly, total surface concentrations should not be used to compare surfaces that range from 8 to 15 yr in age. Both total concentration and average annual accumulation are deficient in representing cases in which a species may accumulate to a nearly limiting concentration in the early stages of exposure While it would have been desirable to measure accumulation on a periodic basis and thereby obtain kinetic information, such a study on realistic field surfaces is not practical. In the authors' opinion, the accumulation of chloride and sulfate ions measured in this and the previous work has, except for chloride on aluminum surfaces at some locations, probably occurred at a roughly linear rate. However, presentation of the data as an average annual accumulation in $\mu g/cm^2$ does not imply linearity. Surface passivation could lead to a cessation of accumulation in the case of attack by a corrosive gas. A chemical or physical loss process could also compete equally with accumulation after some exposure interval, halting further apparent accumulation. Both of these possibilities will be considered with regard to the accumulation of chloride on aluminum.

The specific characteristics of the accumulation rate over the exposure period and the units of measure selected for presenting the data will not influence the conclusions of this study. Over short time intervals (hours to weeks), the accumulation rates of particles and gases are likely to vary significantly with outdoor meteorological conditions, indoor RH, loading of the air filters, changes in ambient concentrations, alteration of surface characteristics with time, and numerous other factors. These factors will probably not result in substantial variation in the annual accumulations from year to year.

The average annual accumulations of sulfate on zinc and aluminum surfaces for the cities studied to date are shown in Fig. 1. The data are somewhat scattered, as expected for the highly nonuniform contamination levels typical of field surfaces, but demonstrate a roughly 1:1 correspondence between the accumulation of sulfate on zinc and that on aluminum surfaces. For the limited data presented previously (1, 2) on nitrate, sodium, potassium, calcium, and magnesium, the same type of correspondence was generally evident, though in the case of calcium and magnesium there was a modest preference for zinc surfaces at a few locations.

For the chloride data, as shown in Fig. 2, the accumulation on zinc is roughly similar to that on aluminum in Houston, Wichita, and Orlando. In New York, Philadelphia, Northern New Jersey (Newark and Jersey City), and Council Bluffs, the accumulation on zinc is roughly six to ten times larger than that on aluminum.

These indoor average annual accumulations for chloride and sulfate are about one order of magnitude lower than typical outdoor accumulation rates (8). Indoor and outdoor concentrations of fine particles (<2 μm aerodynamic diam) are usually in the same range, while concentrations of large particles (>2 μm) are usually a factor of 5-10 higher outdoors than indoors (9). In view of the much larger air currents typically present outdoors, an order of magnitude difference in the surface accumulation indoors and outdoors appears reasonable.

The accumulation of chloride, as will be explained, seems to result from three major sources: (a) corrosive gases (primarily HCl); (b) large particulates (primarily crustal materials of aerodynamic diameter >2 μm); and (c) accumulation mode aerosols (primarily of anthropogenic origin with aerodynamic diameters of 0.1-2 μm) (10). In general, the chloride containing gases would be expected to attack horizontal and vertical surfaces with equal efficiency but could attack zinc and aluminum at different rates. The large particulates will accumulate efficiently on horizontal surfaces but usually will not collect on vertical surfaces. The aerodynamic characteristics of the accumulation mode aerosols are expected to produce nearly equal accumulation (assuming all other factors including air flow patterns are identical) on horizontal and vertical surfaces (10). In Table I, the average chloride accumulation on zinc and aluminum surfaces is separated into horizontal and vertical planes. For Houston and Wichita, the accumulation is similarly high on zinc and aluminum horizontal surfaces and considerably lower on the vertical surfaces. Deposition of large particulates is clearly the dominant accumulation process. This result may be related to the dry nature of the crustal materials in these areas. In New York City and Philadelphia, very rapid accumulation takes place on horizontal and vertical zinc surfaces but not on aluminum surfaces. The corrosive gas source most plausibly explains the data, though it is perhaps sur-

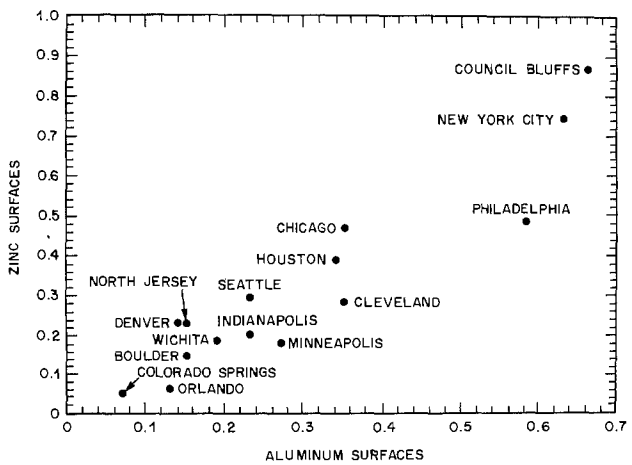

Fig. 1. Average annual sulfate accumulation on zinc and aluminum surfaces ($\mu g/cm^2$).

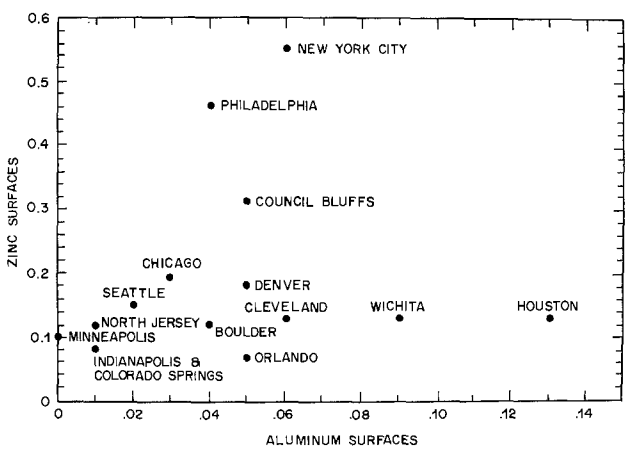

Fig. 2. Average annual chloride accumulation on zinc and aluminum surfaces ($\mu g/cm^2$).

Table I. Chloride average annual accumulation ($\mu g/cm^2$)

City or State		Zinc		Aluminum	
		Horizontal	Vertical	Horizontal	Vertical
Houston	(2)*	0.22	0.03	0.17	0.10
Wichita	(1)	0.23	0.02	0.15	0.03
Council Bluffs	(1)	0.30	0.33	0.03	0.08
Chicago	(2)	0.28	0.09	0.06	0
Seattle	(2)	0.19	0.11	0.04	0
North Jersey	(2)	0.16	0.09	0.01	0
Minneapolis	(2)	0.10	0.09	0	0
Colorado	(3)	0.13	0.13	0.04	0.03
Indianapolis	(2)	0.13	0.03	0.02	0
Cleveland	(2)	0.13	0.13	0.06	0.05
Orlando	(2)	0.09	0.05	0.10	0.01
New York City	(4)	0.49	0.60	0.08	0.05
Philadelphia	(2)	0.56	0.37	0.06	0.01

* Number in parentheses is the number of locations sampled.

prising that the chloride accumulation is a factor of ten greater on zinc than on aluminum. Very little useful data is available on the atmospheric concentrations of corrosive chlorine containing gases in major U.S. cities. Incineration and chemical manufacturing are known to be major sources of HCl that might be expected to produce high concentrations in the Philadelphia and New York City areas. In the majority of cities, combinations of the three chloride sources seem to be responsible for the observed rates.

Accumulation model.—If it is assumed that: (*i*) large particulates accumulate exclusively on horizontal surfaces; (*ii*) small particulates collect at equal rates on horizontal and vertical surfaces; and (*iii*) the accumulation rate on zinc due to corrosive gases at normal ambient concentrations is ten times the rate on aluminum, then

$$Zn_H = G_{Zn} + L + S$$

$$Zn_V = G_{Zn} + S$$

$$Al_H = G_{Al} + L + S$$

$$Al_V = G_{Al} + S$$

where Zn_H, Zn_V, Al_H, and Al_V are the observed rates on zinc and aluminum horizontal and vertical surfaces, G_{Zn} and G_{Al} are the corrosive gas accumulation rates on zinc and aluminum ($G_{Zn} = 10\ G_{Al}$), L is the accumulation rate of large particulates, and S is the accumulation rate of small particulates.

The above system of equations was solved simultaneously using a least squares fit to the observed data. The results are shown in Table II. The negative values in Table II may result, in part, from the approximation $G_{Zn} = 10\ G_{Al}$. All but one of the negative values are for the fine particulate contribution, S. If $G_{Zn}/G_{Al} > 10$, the magnitudes of the negative S values will be reduced. The normal scatter in the data and the limited number of observations also undoubtedly contribute to the negative values. The tabulated values are a quantitative estimate of the qualitative conclusions that have been discussed above.

Explanation of low chloride on aluminum.—Four possible causes for the substantially higher accumulation at some locations of chloride on zinc, under the influence of a corrosive gas, were considered: (*i*) the reaction with aluminum was blocked by the passive oxide film or an unknown environmentally dependent factor; (*ii*) chloride products more readily flake off

Table II. Derived average annual chloride accumulation for the three source categories ($\mu g/cm^2$)

	G_{Zn}	L	S
New York City	0.53	−0.04	0.04
Philadelphia	0.47	0.12	−0.07
Council Bluffs	0.29	0.04	−0.04
Chicago	0.16	0.12	−0.04
Seattle	0.16	0.06	−0.04
North Jersey	0.14	0.04	−0.03
Minneapolis	0.10	0.01	0
Colorado	0.11	0.01	0.02
Indianapolis	0.08	0.06	−0.03
Cleveland	0.09	0.01	0.04
Orlando	0.02	0.06	0.02
Wichita	−0.03	0.16	0.01
Houston	0	0.13	0.07

aluminum surfaces; (*iii*) chloride products were not extractable from aluminum (perhaps due to entrapment in the oxide, the formation of an unknown complex oxychloride, or the existence of an organic film that rendered the surface unwettable); and (*iv*) chloride products on aluminum preferentially volatilize. The oxide film on aluminum is well known to be protective and explanation (*i*) has been assumed to be important. As will be discussed, evidence gathered in this work suggests that explanation (*iv*) is also important at some locations.

Explanation (*ii*) was considered unlikely since the accumulation on vertical surfaces is comparable to that on horizontal surfaces for both zinc and aluminum in the clear-cut cases where a corrosive gas was the major source (New York City and Philadelphia) and in the cases where the corrosive gas and fine particulate sources appear important (Colorado and Cleveland). Gravity effects should produce much lower concentrations on aluminum vertical surfaces if flaking is important. Air currents could influence horizontal and vertical surfaces, though gravity effects would still be expected to yield increased losses from vertical surfaces. Further, gravity and air currents should have roughly the same effect on aluminum surfaces at all locations.

Results pertinent to explanation (*iii*) are shown in Table III. The residues remaining after evaporation of the aqueous extractions of the sampling papers were examined by EDXA. The x-ray intensities are referenced to calcium, which was determined quantitatively in previous work (2) by ion chromatography. Zinc is clearly a significant contributor to the anion-cation balance on zinc surfaces at many locations. The other metal ions observed are present only in trace amounts. On aluminum surfaces, very low contributions to the anion-cation balance were observed for all four metal ions. Thus, very little of the chloride that might have been present on aluminum surfaces in these cities was present as the normally soluble aluminum chloride. If chloride was present, it must have been trapped within the oxide or have formed a considerably less soluble complex salt of unknown composition and structure. EDXA analysis of surfaces removed from normal indoor sites in New York City for subsequent laboratory analysis detected significant amounts of chloride on zinc surfaces but none on aluminum surfaces. While EDXA is not a highly sensitive technique, if chloride in an unextractable form was present on aluminum to the same extent as the extractable chloride on zinc, the chloride should have been detectable by EDXA.

Table III. Relative x-ray intensities of metal ions extracted from surfaces

Metal surface	Ions				
	Calcium	Zinc	Copper	Aluminum	Iron
Zinc	1.0	0.080-0.978	0.017-0.041	0.000-0.073	0.000-0.095
Aluminum	1.0	0.029-0.077	0.020-0.059	0.000-0.008	0.007-0.052

This result demonstrates that chloride is not present, but it does not allow a distinction between passivation effects and volatilization of chloride.

A major fire that occurred at a telephone company switching center in Manhattan in 1975 provided an opportunity to study the volatility of chloride products on aluminum [explanation (*iv*)]. Severe chloride corrosion occurred on both zinc and aluminum surfaces, due to the release of significant amounts of HCl during thermal degradation of wire insulation. These surfaces were sampled by paper extraction during the first 3 months after the fire and then again in 1980. The results are shown in Table IV. The higher chloride concentration on zinc surfaces in 1975 should not be taken as an indication that zinc is more reactive even under the extreme conditions of the fire because: (*i*) normal indoor zinc surfaces of comparable service life in New York City had, on the average, 27 $\mu g/cm^2$ of chloride in 1975 while aluminum surfaces had <2 $\mu g/cm^2$; and (*ii*) the source of the smoke from the fire was closer on the average to the zinc surfaces sampled than to the aluminum surfaces. Five years after the fire, the amount of extractable chloride on aluminum dropped by a factor of five, while that on zinc decreased only slightly. The x-ray spectra in Fig. 3 were taken of heavily corroded aluminum surfaces from the fire location. The spectra show that chloride observed in the pits in 1975 remains present at a high level in 1981. However, in the area adjacent to the pits, appreciable amounts of chloride were detected in 1975 but not in 1981. Presuming that the chloride products did not flake off, it seems very likely from the data in Fig. 3 and Table IV that most of the chloride products from the fire volatilized from the surface between 1975 and 1981 except in the area of the pits. The formation of insoluble complex chlorine containing salts or the trapping of chloride in the surface oxide is not the major cause of the low chloride concentrations that were observed in the extractions of these aluminum surfaces in 1981.

The observations that if indoor HCl concentrations are high enough, aluminum will severely pit and corrode, but when conditions return to normal, that chloride products appear to volatilize, suggest that volatilization may also be significant for normal indoor surfaces.

Volatility of chloride products.—Two cations readily available from sulfate aerosols, hydronium and ammonium, when coupled with chloride yield significantly volatile species. Ammonium is also available from numerous potential indoor sources, including floor and window cleaners, air handling systems, volatile products from construction materials or electronic equipment, and humans. Considering HCl and NH_4Cl, the least volatile is NH_4Cl (as NH_3 and HCl). The Jost cylindrical diffusion model (11) was used to determine if 40 $\mu g/cm^2$ of chloride could be reasonably expected to volatilize in 5 yr from the fire contaminated surfaces, presuming NH_4Cl is the surface specie. In the field environments under study, air convection is clearly important and a diffusion model should substantially underestimate the actual volatilization rate. The model gives $V/t = DqC/l$, where V is the quantity of vapor leaving the top of an assumed evaporation cylinder in time t, D is the diffusivity of the vapor in air, q is the cross-sectional area, C is the equilibrium concentration of the vapor immediately above the solid, and l is the height of the cylinder above which the pressure of the vapor is assumed to be effectively zero. The model substantially oversimplifies the field situation but is adequate for a crude estimation. A reasonable value for l was determined by gravimetrically monitoring the loss of a sample of ammonium carbonate, which is quite volatile ($C = 1$ Torr). The circular sample pan area was 0.28 cm^2. For $l = 1$ cm, V/t (observed) was 1.2 mg/hr while V/t (calculated) was 0.94 mg/hr. Using $l = 1$ cm, and $C = 2.4 \times 10^{-5}$ Torr, V/t (calculated) for NH_4Cl was 1.4×10^{-5} mg/hr, which yields a maximum possible loss of chloride in 5 yr of 1460 $\mu g/cm^2$. The observed chloride loss is a factor of 36 smaller than the calculated maximum loss, indicating that volatilization of NH_4Cl (as NH_3 and HCl), which could be formed by combination of chloride with deposited ammonia, $(NH_4)_2SO_4$, or $(NH_4)HSO_4$, is plausible. Since HCl is more volatile than NH_4Cl, either could reasonably explain the 40 $\mu g/cm^2$ chloride loss.

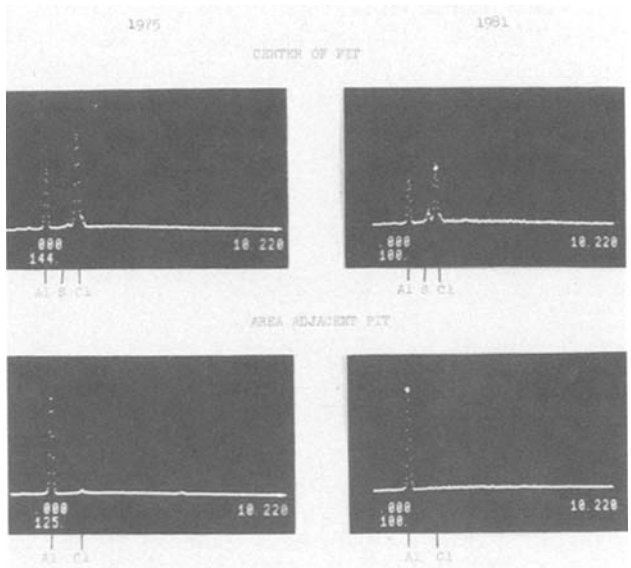

Fig. 3. EDXA analysis of chloride attacked aluminum surfaces from the New York City fire location.

The much greater tendency for apparent volatilization of chloride species from aluminum than from zinc surfaces will require further study to be clearly understood. If aluminum surfaces are more acidic than zinc, volatilization of HCl would more readily occur. From Table V, the average relative surface pH's of aluminum surfaces were found to be lower than for zinc surfaces. Complicating the interpretation, though, is the result that the zinc vertical and aluminum horizontal surfaces have similar acidities, yet the average accumulation rate of chloride on zinc is twice that on aluminum. Either the average surface acidity is not the dominant factor or horizontal and vertical surfaces should not be compared because of the coarse particle influence on the former. These acidities, of course, are from macroscopic measurements. There could well be microscopic areas on aluminum surfaces that are con-

Table IV. Average chloride concentrations of fire-contaminated surfaces from New York City ($\mu g/cm^2$)

Surface	1975	1980
Zinc	114	99
Aluminum	49	10

Table V. Acidity and average annual chloride accumulation for all locations

Surface	pH	Chloride ($\mu g/cm^2$)
Zinc		
Horizontal	5.0	0.26
Vertical	4.6	0.20
Aluminum		
Horizontal	4.7	0.09
Vertical	4.0	0.09

siderably more acidic, due to ongoing pitting or the influence of local atmospheric factors.

The authors have made comparisons of the surface pH and surface chloride concentrations reported here with pH and ammonium concentrations in rainfall as reported by the National Atmospheric Deposition Program (12). No meaningful correlations were found. Unfortunately, insufficient data on gaseous ammonia concentrations and the acidity and ammonium concentrations of aerosols in these cities are available for comparisons. As further atmospheric data become available these comparisons should be made.

Concluding remarks.—The previously reported observation that chloride accumulation on indoor zinc surfaces is considerably greater than on aluminum surfaces at some field locations has been supported by further data from additional cities. The contributions of large particulates, fine particulates, and gaseous substances to the accumulated chloride on these surfaces have been estimated by a simple model for the 15 cities studied to date. The lower chloride concentrations on some aluminum surfaces seems to be best explained by a combination of the passive nature of the oxide film and the volatilization of chloride species. Evidence has been offered that aluminum surfaces are slightly more acidic than zinc surfaces, thereby possibly enhancing HCl evolution, and that NH_4Cl, if it can be formed, is sufficiently volatile to remove large amounts of chloride. The specific nature of the volatilization, if it occurs, remains uncertain.

Acknowledgment

The authors are indebted to C. J. Weschler and G. R. Crane for very helpful discussions during the course of this study.

Manuscript submitted Sept. 10, 1982; revised manuscript received June 14, 1983.

Bell Laboratories assisted in meeting publication costs of this article.

REFERENCES

1. G. B. Munier, L. A. Psota, B. T. Reagor, B. Russiello, and J. D. Sinclair, *This Journal*, **2**, 265 (1980).
2. G. B. Munier, L. A. Psota-Kelty, and J. D. Sinclair, "Atmospheric Corrosion," W. H. Ailor, Editor, p. 275, John Wiley and Sons, Inc., New York (1982).
3. G. B. Munier, L. A. Psota-Kelty, and J. D. Sinclair, Paper 22 presented at The Electrochemical Society Meeting, Montreal, Canada, May 9-14, 1982.
4. H. W. Hermance, C. A. Russell, E. J. Bauer, T. F. Egan, and H. V. Wadlow, *Environ. Sci. Technol.*, **5**, 781 (1971).
5. D. R. Hitchcock, L. L. Spiller, and W. E. Wilson, *Atmos. Environ.*, **14**, 165 (1980).
6. C. J. Weschler and T. E. Graedel, *Rev. Geophys. Space Phys.*, To be published.
7. J. D. Sinclair, *Anal. Chem.*, **54**, 1529 (1982).
8. S. E. Lindberg and G. M. Lovett, p. 46, 4th International Conference on Precipitation Scavenging, Dry Deposition, and Resuspension, Santa Monica, CA, Nov. 28-Dec. 3, 1982.
9. C. J. Weschler, S. P. Kelty, and J. E. Lingousky, Submitted to *J. Air Pollut. Control Assoc.*
10. S. K. Friedlander, "Smoke, Dust and Haze—Fundamentals of Aerosol Behavior," John Wiley and Sons, New York (1977).
11. W. Jost, "Diffusion in Solids, Liquids, Gases," p. 9, Academic Press, Inc., New York (1970).
12. J. H. Gibson, Personal communication, Summary listing for Jan. 1, 1980-Dec. 31, 1980.

Electroplating of Cyclic Multilayered Alloy (CMA) Coatings

U. Cohen,*,[1] F. B. Koch,* and R. Sard*,[2]

Bell Laboratories, Murray Hill, New Jersey 07974

ABSTRACT

A new technique has been developed for producing laminated composites of cyclic multilayered alloy (CMA) electrodeposits. The thickness and composition of the individual layers of the CMA deposits are altered precisely and conveniently by cyclic modulation of the cathodic current or potential during electrodeposition. It is thus possible to modify the structure to obtain laminated composite coatings which may have desirable engineering properties. Wear and corrosion resistances, mechanical hardness and strength, as well as certain magnetic, optic, and electronic properties of the plated composite alloys should be, in principle, straightforward to design and fabricate. The CMA technique was demonstrated by plating a wide variety of Ag-Pd CMA structures. Fine structures, with repeat distances as small as 0.05 μm, were obtained. Both square and triangular waveforms were applied to produce sharp or gradual composition variations, respectively. The resulting deposits were found to correspond closely to the intended structures with respect to thickness and composition, when the individual layers were thicker than about 1000Å. The amplitude of the composition modulation diminished rapidly for layer thicknesses below this limit. For the prospective application of Ag-Pd alloys as a contact finish, CMA structures composed of relatively thin Pd-rich layers alternating with thick Ag-rich layers would offer the high corrosion resistance of Pd combined with the low electrical resistance and low cost of Ag. An initial comparison of the CMA deposits with uniform, d-c plated, Ag-Pd alloys did not show any clear difference in contact properties. However, both types of deposit proved satisfactory in the tests which were made.

Lamellar or banded plating structures obtained with direct current have often been observed in both alloy coatings (1-7) and single metals deposited from additive containing baths (7-11). Such structures are largely due to nonequilibrium or dynamic effects and are usually unintentional. In general, they arise due to periodic fluctuations in the electrocrystallization process accompanied by periodic fluctuations of the cathodic polarization (1, 12). Periodic potential fluctuations were also reported in the deposition of banded Cu alloys (13), Fe-Ni (14), Cd-Zn (15), and Nb-Ge (12).

Vacuum evaporation of composition modulated films was introduced by DuMond and Youtz (16). The technique consisted of evaporating alternate layers of the components onto a common substrate. Utilizing a similar technique, Hilliard *et al.* (17, 18) obtained composition-modulated films with short wavelengths for diffusion studies. They used a rotating pinwheel shutter with radial cutouts to facilitate alternate deposition of the two components, which were simultaneously evaporated from separate crucibles. The tech-

* Electrochemical Society Active Member.
[1] Present address: MPI, Santa Clara, California 95051.
[2] Present address: Oxy Metal Industries, Warren, Michigan 48089.
Key words: alloys, laminated composites, contacts, electrodeposition.

nique was further used to obtain composition-modulated films with enhanced elastic modulus (19), magnetization (20-24), and superconductivity (25). Similarly, molecular beam epitaxy (MBE) was used to obtain fine structures of alternating epitaxial layers of GaAs and $Ga_{1-x}Al_xAs$ (26-28). Electroplated structures of alternating layers were described by Blum (29) as early as 1921. They were obtained by plating alternately from separate electrolytes of the two components. Brenner (1) mentioned (without details) the electrodeposition of Cu-Bi alloy with alternating layers of different compositions from a single electrolyte. They were obtained by automatic switching of the current density between two widely separated values. The deposit was cross sectioned and etched to form a small diffraction grating.

In alloy electrodeposition, the current density generally has pronounced effects upon the deposit composition, structure, and properties (1). Usually, an increase of the current density (or the cathode polarization) causes an increase in the relative amount of the less noble metal in the plated alloy. With such alloys, it is possible to control the composition by changes in the plating current. Regularly modulated structures of a plated alloy, made in this way, offer the promise of new types of materials. The wide versatility of this method is due to the following reasons: (*i*) It should be applicable to most alloy systems that can be electroplated. (*ii*) Potential engineering applications for plated alloy films with tailored layer thicknesses and composition modulations should span a wide spectrum. Material properties which might be enhanced by such structures include mechanical strength, wear resistance, corrosion resistance, superconductivity and magnetic properties. (*iii*) For a given plating system the thickness of each individual layer is determined by the time integrated current (charge), and the current efficiency. Its composition is determined by the current amplitude and other plating conditions. (*iv*) Control of the charge can be achieved with a programmable power supply, completely external to the plating cell. (*v*) The concentration profile within each cycle can also be tailored, up to a point, by changing the plating current waveform, *e.g.*, by changing the amplitude and frequency and by utilizing either triangular or square wave signals to obtain gradual or abrupt variations, respectively.

Limitations of the CMA technique include the limited choice of metal pairs capable of alloy plating and the relatively small magnitude of the composition modulation (usually no more than about 20-30%). With very short spacings (~20Å), limitation on the modulation might involve mass transfer effects and epitaxial and pseudoepitaxial phenomena in the solid, in addition to relaxation times of solutes' redistribution in the diffusion layer in the electrolyte. The plated CMA coatings were characterized by Auger emission spectroscopy (AES) with sputter depth profiling and also by scanning electron microscopy (SEM) on etched cross sections. The latter technique relied on the preferential etching rate of the deposit layers. This rate is sensitive to composition and probably also to the microstructure. It increases with the content of Ag in the alloy.

This paper describes experimental results demonstrating the feasibility of electroplating CMA structures of Ag-Pd alloy coatings from a concentrated chloride bath. This alloy was chosen because it is a potential substitute for hard gold plating on electrical contacts (30). CMA structures of the Ag-Pd alloy coatings may exhibit certain desirable properties in such applications. For example, to minimize cost, reduce electrical resistivity, and increase corrosion-resistance, one could conceivably produce a layered structure composed of relatively thick layers of an alloy rich in Ag, alternating with thin layers rich in Pd. To minimize the formation of tarnish films, the outer surface layer would be Pd-rich. A preliminary comparison is made of contact properties of CMA deposits versus those of uniform Ag-Pd alloys plated with direct current. This comparison is based on several tests relevant to contact finishes (*e.g.*, contact resistance stability and contact wear).

Experimental

Plating Procedure

The Ag-Pd plating bath (with total volume of 1300 ml) consisted of:

LiCl	500g
AgCl	12g
$PdCl_2$	3g
HCl	20 ml
H_2O	1000 ml

It was operated at 85° ± 0.5°C with moderate stirring (about 10 cm/sec flow rate). The experimental plating apparatus and the bath preparation are described in detail elsewhere (30). The electroplating cell consisted of a closed vessel fitted with five ground joint openings for thermometer, stirrer, and three electrodes. The counterelectrode was made of a silver sheet with a surface area of about 15 cm^2. An internal reference electrode was made by immersing a Pd wire (0.050 in. diam) in the plating bath. This electrode had a static potential of about −258 mV *vs.* the Ag/AgCl (sat. KCl) reference electrode and was used to follow the cathode polarization, η, in response to the current modulation. The cathodes, or substrates, consisted of strips masked on their edges and back side so that the exposed area was about 2.5-3.0 cm^2. Some substrates consisted of pure silver, while others were CDA 725 copper alloy (89% Cu-9% Ni-2% Sn) protected with a soft gold undercoating (0.2-0.4 μm thick). For more details of the substrate preparation see Ref. (30).

The applied electric signal was produced and controlled by a combination of a potentiostat/galvanostat (PAR 173) and a signal programmer (PAR 175). The time traces of the current, cell voltage, and cathode potential (*vs.* the Pd wire reference) were monitored by a chart recorder and by an X-Y recorder (HP 7004B).

CMA coatings were prepared with two modes of current modulation; square (or stepped), and triangular (or swept) current waves. CMA structures with palladium-rich last layers and with silver-rich last layers were produced by stopping the plating at the appropriate half-cycle in order to study the effect of having the more corrosion resistant Pd-rich layer at the surface.

Microscopic Analysis

Metallographic cross sections were mechanically polished using alumina powder (0.05μ) and etched for 30 sec in a freshly prepared solution of 5g KCN, 5g $(NH_4)_2S_2O_8$, and 200 ml of deionized water. The mounted cross sections were then coated with ~200Å of gold, by sputtering, to improve their electric conduction for SEM examination.

Auger Analysis

The Auger measurements were made with a scanning Auger microprobe (SAM, PHI Model 650) employing a double pass cylindrical mirror analyzer with a concentric 5 kV gun. Composition-depth profiles were obtained with Ar sputtering. Derivative spectra were taken with 5 kV primary energy, $\sim 10 \times 10^{-7}$A beam current, 3V peak to peak modulation, scan rate 3 eV/sec, time constant 0.03 sec, and sputter rate—either ~250 or 60Å/min at 3 kV in 5×10^{-5} Torr of argon.

The primary information was obtained from the principal MNN lines of Pd and Ag (located at 330

and 351 eV, respectively). The relative sensitivity factor for these lines, S_{Ag}/S_{Pd}, was taken as 1.28 based on the determination by Schwartz (31) for a wrought R156 alloy (60% Pd/40% Ag) and the bulk alloy measurement described below. The composition was then determined from the formula $C_{Ag}/C_{Pd} = (I_{Ag}/I_{Pd})/1.28$ where C_{Ag} and C_{Pd} are in atomic percent (a/o) and I_{Ag} and I_{Pd} are peak to peak intensities of the 351 and 330 eV lines, respectively. The increase in Pd surface concentration (relative to the bulk concentration) produced by sputtering, introduced some error into the determination of the bulk concentrations, as described by Schwartz (31). To estimate this effect, a sample of R156 alloy was sputtered for 40 min. After the surface films were removed in the first minute of sputtering, a constant intensity ratio, $I_{Ag}/I_{Pd} = 0.92$, was obtained This ratio, together with a sensitivity ratio of 1.28, indicated a composition of 42% Ag and 58% Pd, in close agreement with the nominal bulk composition of R156. The Pd enhancement effect from sputtering thus was small in this case. The indicated compositions of the electrodeposited alloys were within about 5 a/o of the values obtained by x-ray analysis in the SEM. The error in the Auger measurement of absolute composition is not a serious problem in the present application where the change in the relative amounts of Ag and Pd as a function of depth is of more interest.

Results

Effect of Current Waveform on Structure

In this section, we compare the intended structures, as determined by the current waveform used, with the results obtained by AES and SEM analysis. The effects of substrate roughness and the displacement reaction of Ag from the substrate or the deposit by Pd are also demonstrated.

Square CMA with modulation ≧1000Å.—Figure 1 depicts the time traces of an applied square current wave, and the corresponding cathode polarization (η *vs.* t). These were obtained during a plating experiment designed to produce a structure of alternating thick (1000Å) Ag-rich layers and thin (100Å) Pd-rich layers. Figure 2 shows SEM photographs of an etched cross section of the resulting deposit. A comparison to the 0.1 μm (1000Å) scale marker indicates that the total cycle thickness is very close to the nominal value of 1100Å. This deposit was plated onto a silver strip substrate which had been chemically etched (in NH_4OH/H_2O_2 1:1), and immersed (with no applied current) for 2 min in the Ag-Pd plating bath prior to the CMA plating. It was also left in this bath (with no applied current) for 1 min following the termination of the CMA plating. Pd-rich layers produced by displacement plating can be seen at the boundary between the Ag substrate and the CMA structure, and also on the outer surface. (The etching procedures make the Pd-rich layers appear white in these SEM photographs.) For more details regarding the displacement reactions, see Ref. (30).

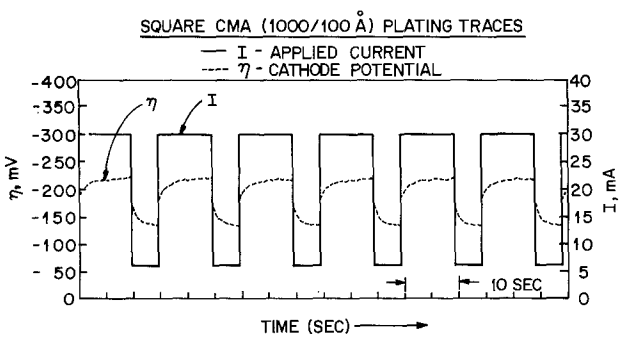

Fig. 1. Time traces of the impressed plating current, *I*, and the cathodic polarization, η (vs. Pd-wire reference electrode), for a square waveform designed to produce alternating 1000Å Ag-rich layers and 100Å Pd-rich layers.

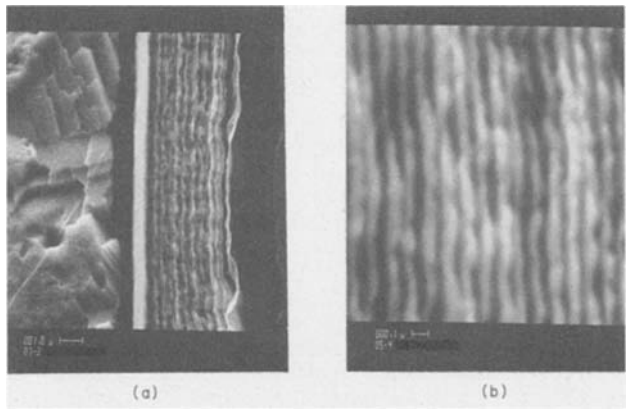

Fig. 2. SEM of an etched cross section of the CMA structure corresponding to Fig. 1. Notice (from left to right) the Ag-substrate, a Pd-enriched displacement layer (white), the 34 cycles of CMA structure, and another Pd-rich displacement layer.

The composition modulation and the Pd surface enhancement of this sample are immediately apparent in the Auger depth profiles shown in Fig. 3. The indicated variation of Pd in the bulk of the sample is between 34 and 37 a/o while corresponding variation in the Ag/Pd ratio is 1.94 to 1.70. The gradual decrease in the amplitude of composition modulation with sputtering time does not represent a real effect in the sample. It results from the gradual loss of depth resolution associated with the analysis technique. This effect is further discussed later. Minor amounts of Cl and S were also detected at about the 1% level. The S was a surface contaminant (presumably a sulfide) which disappears after a sputtering time of less than 1 min. Interestingly, the Cl signal in Fig. 3 shows a moderate peak coinciding with the Pd-rich displacement layer, and very small peaks occur thereafter

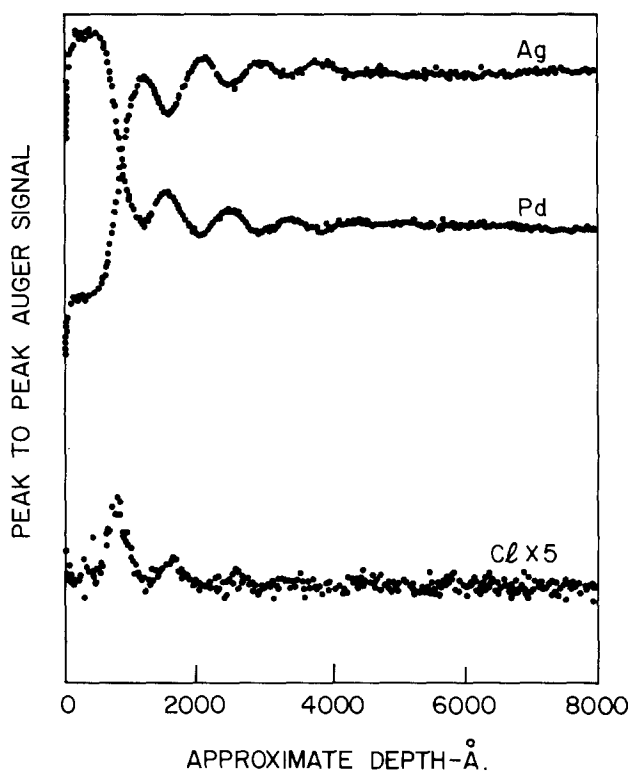

Fig. 3. Auger depth profiles for Ag, Pd, and Cl obtained with the deposit corresponding to Fig. 1 and 2. Notice the Pd-rich outer layer produced by displacement and 3-4 cycles of CMA. Also notice that Cl peaks coincide with Pd peaks.

at depths corresponding to maxima in Pd concentration. When the sputter beam was turned off, the Cl signal increased steadily, indicating this species was migrating to the surface. Presumably, this Cl is incorporated from the plating bath in greater amounts during the intervals of lower current density (*i.e*, Pd-rich layers). The depth profiles in Fig. 3 show quite clearly that the surface layer is enriched in Pd by the displacement reaction. The indicated surface composition is approximately 56% Pd. This surface layer is about 1000Å thick and is variable in thickness from point to point on the sample as can also be seen in Fig. 2.

Results are presented next which illustrate that the Ag-Pd plating tends to smooth small protrusions or irregularities but amplifies large ones. The latter are deleterious since they proceed to develop into nodules, and eventually deteriorate the plating. Figure 5 shows SEM micrographs of an etched cross section of a CMA coating on a very flat and smooth substrate. The Ag substrate was prepared by careful polishing with 0.3 μm alumina. Plating was initiated immediately after immersion, a procedure which avoids the silver displacement reaction with an attendant surface roughening. The applied current waveform and the corresponding time traces of the cathode polarization and cell voltage, obtained during the plating of this sample, are shown in Fig. 4. The designed CMA structure consisted of alternating layers of 1000Å rich in Ag and 200Å rich in Pd. A layer of about 1 μm of soft gold (seen as a white layer) was overplated on this CMA structure in order to facilitate the preparation of the metallographic cross section. Another Ag substrate was roughened by a prolongated etching in NH_4OH/H_2O_2 (1:1) followed by immersion in the plating bath for 2 min with no current applied. Figure 6 shows

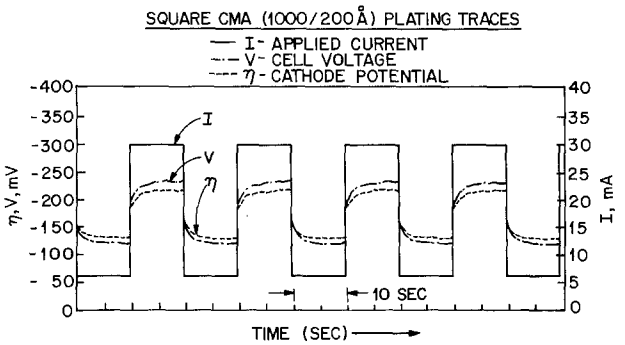

Fig. 4. Time traces of the applied current, the corresponding cathodic polarization, η, and the cell voltage, V, obtained during the plating of a square CMA designed to produce alternating 1000Å Ag-rich layers and 200Å Pd-rich layers.

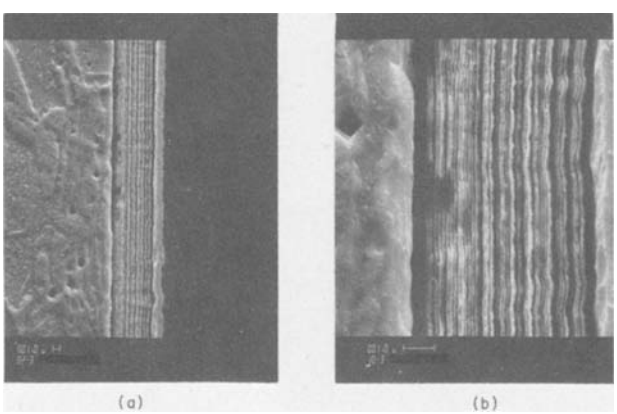

Fig. 5. SEM of an etched cross section of the CMA corresponding to Fig. 4. The outermost layer (white) corresponds to a soft gold (about 1 μm thick) plated over the CMA structure in order to facilitate mechanical polishing of the sample without damage.

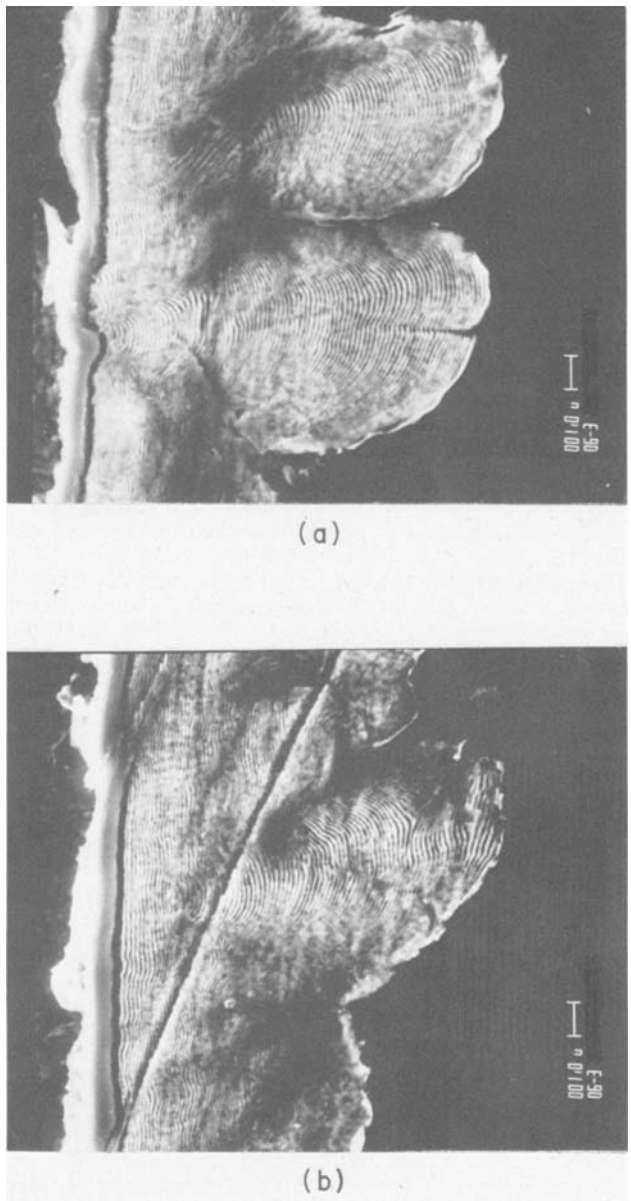

Fig. 6. SEM of an etched cross section demonstrating the effects of substrate roughness (a) and particle inclusions (b) on the stability of the growth interface. CMA structure same as in Fig. 1, 2, and 3.

SEM photographs of the etched cross section of this substrate and the Ag-Pd CMA coating which was plated onto it. The designed CMA structure of this sample was similar to the sample of Fig. 1, 2, and 3 (*i.e.*, alternating layers of 1000Å Ag-rich, and 100Å Pd-rich). Here, however, the substrate roughening produced large protrusions $\geq$0.5 μm which were subsequently amplified in the CMA deposit. A similar effect was also produced by inclusion of solid particles during the plating (cf. Fig. 6b). Small protrusions originating either in the substrate, or within the CMA deposit due to small fluctuations, are seen to be smoothed out as the deposition proceeds.

Square CMA with modulations of 500-1000Å.— Figure 7 shows the time traces of the applied current and the corresponding cathode polarization and cell voltage during the deposition of a CMA structure designed to produce alternating layers of 500Å Ag-rich, and 250Å Pd-rich. SEM photographs of the etched cross section are shown in Fig. 8. Good agreement between the designed and obtained total cycle thickness may be noted. Also evident is the excellent resolution of the microstructure after etching (better than 500Å).

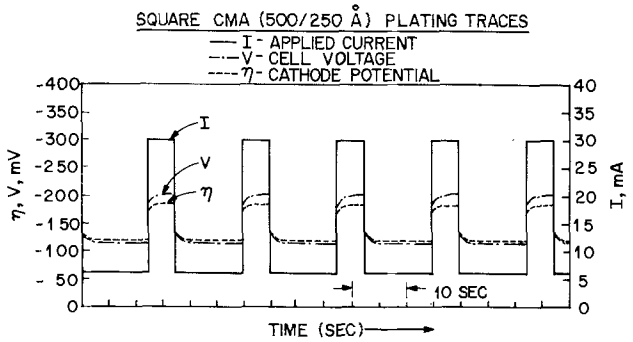

Fig. 7. Time traces obtained during the plating of a square CMA designed to produce alternating 500Å Ag-rich layers and 250Å Pd-rich layers.

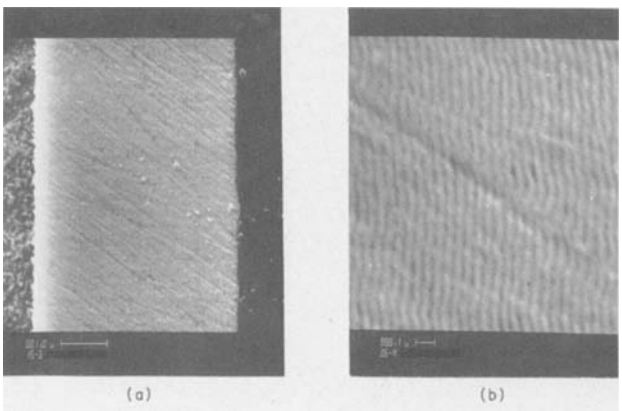

Fig. 8. SEM of an etched cross section corresponding to Fig. 7. Notice the excellent resolution of the etchant. The total deposit thickness is about 6 μm, and there are some 80 cycles, or a total of 160 layers.

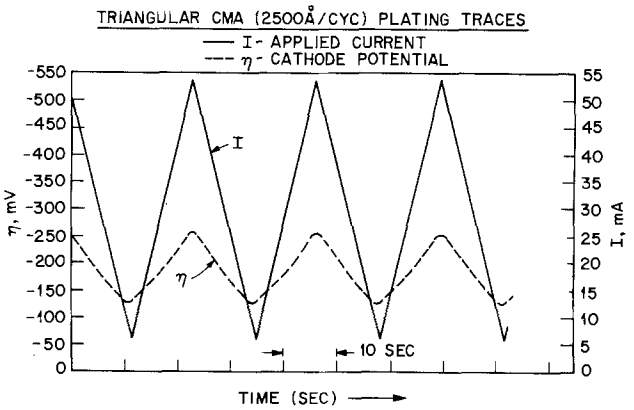

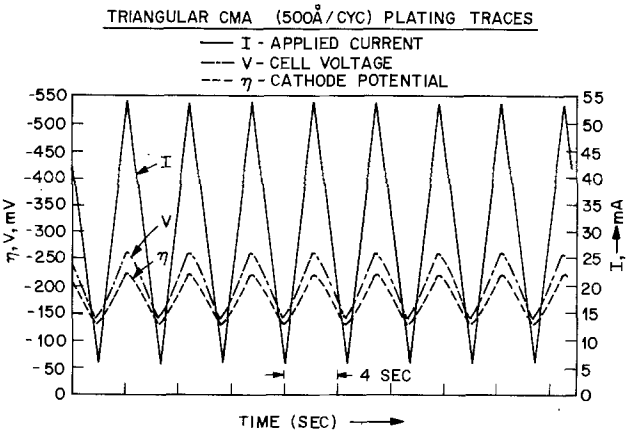

Fig. 9. Time traces obtained during the plating of triangular CMA structures. The current waveforms were designed to produce a structure with cyclic layers 2500Å thick (a) and a structure with cyclic layers 500Å thick (b).

The deep diagonal grooves which run across the coating are probably artifacts caused by minute polishing scratches which were later magnified by the chemical etching procedure. The substrate of this sample consisted of the alloy, CDA 725. It was mechanically polished (with 0.3 μm alumina) and plated with a 0.3 μm thick soft gold undercoating prior to plating of the CMA coating. As discussed elsewhere (30), this procedure avoids vigorous displacement reactions of base metals with the Ag-Pd plating bath. The plating of the CMA structure was started immediately following the immersion of the protected substrate in the Ag-Pd plating bath. Examination of this sample by AES, as well as four other samples with nominal cyclic wavelengths less than 1000Å, failed to show any indication of composition modulation in the sputter profiles. Data scattering was about 2% in the Ag/Pd ratio. Much of the layer delineation seen by SEM for these samples may thus originate from microstructure modulation. The lack of composition resolution by AES depth profiling could also be due to the undulating character of the deposit surface (cf. Fig. 8).

Square CMA with modulation <500Å.—Samples with a designed modulation of less than 500Å show no evidence of modulations by either SEM or AES. Thus, rapid variation of the applied current density does not appear to be reflected in either the deposit microstructure or the composition. This apparent limit on the dynamics of the plating process will be considered in more detail later.

Triangular CMA.—Figures 9a and 9b depict the applied triangular current waveforms, and the time traces η-t and V-t, obtained during the plating of two triangular CMA structures. They were designed to produce structures with cyclic layers of 2500Å and 500Å, respectively. Etched cross sections of similar samples are shown in Fig. 10a and 10b. Whereas it is easy to delineate the CMA structure having cyclic layers of about 2500Å thick (cf. Fig. 10a), a similar delineation is not possible with the deposit designed to produce cyclic layers of 500Å thick (cf. Fig. 10b) nor with several other triangular CMA deposits, designed to have wavelengths shorter than 500Å. The AES depth profiling obtained with a triangular CMA structure having 2500Å wavelength is shown in Fig. 11. In this case, about 3 μm was sputtered away. enough to penetrate through the deposit thickness (nominally 2.75 μm). Approximately 3 or 4 of the 11 layers are resolved and show a triangular variation in the composition. As previously mentioned, the loss of depth resolution, as well as the nonabrupt drop in signal when sputtering had penetrated through the plated alloy, are believed to be artifacts due to sputter-induced microtopographic features. The AES depth profiling was not able to resolve any composition modulation in triangular CMA deposits with designed layer thicknesses of 500Å or shorter, just as with the square CMA structures.

Evaluation of Deposits for Contact Finish Applications

A preliminary evaluation of contact resistance of Ag-Pd CMA and d-c plated alloy coatings was performed. The contact resistance prior to and following exposure to an environment of flowers of sulfur (37) was measured using a four-point probe at 100g force.

One week exposure of both the square CMA and the d-c coatings (50% Ag-50% Pd) to an environment containing flowers of sulfur, 85% relative humidity (RH), and 50°C, had hardly any effect on the contact resistance of either types of deposits. The initial value was about 1.1-1.3 mΩ for all coatings. Figure 12 shows a probability plot of the measured contact resistance values for the wrought R156 alloy, for a uniform (d-c

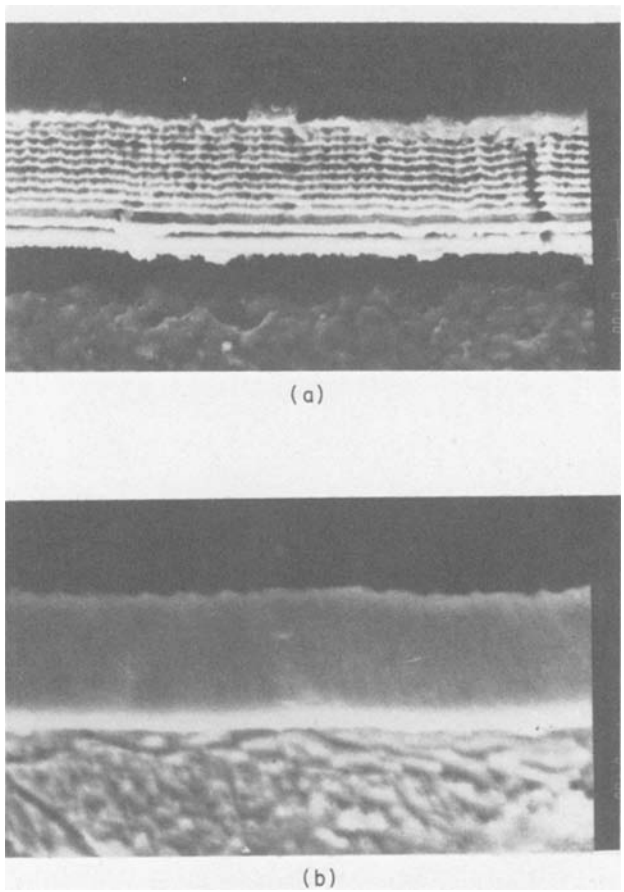

Fig. 10. SEM of etched cross sections of triangular CMA deposits designed to produce a structure with cyclic layers 2500Å thick (a) and a structure with cyclic layers 500Å thick (b). (See text.)

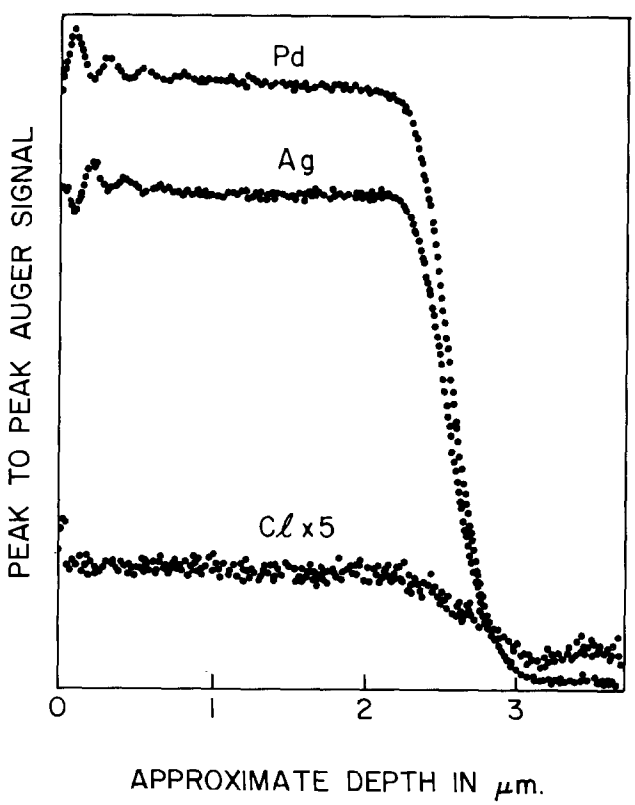

Fig. 11. Auger depth profiles for Ag, Pd, and Cl obtained with samples corresponding to Fig. 9a and 10a. Note the triangular response of the composition to the current.

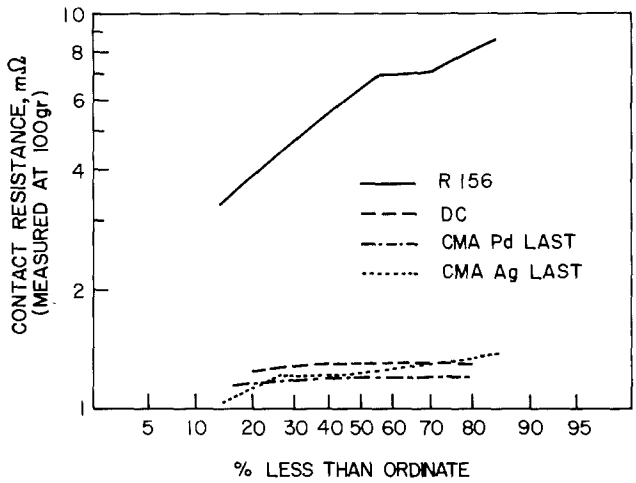

Fig. 12. Contact resistance distribution plot after a flowers of sulfur exposure test. Data were measured with a load of 100 g on a gold probe using the 4 wire method. Samples were exposed to saturated flowers of sulfur for 1 week at 50°C and 85% RH.

plated) deposit, and for two CMA deposits with alternating layers of 1000Å rich in Ag and 200Å rich in Pd. The two CMA deposits differed from each other only in that the plating current was turned off during the plating of an Ag-rich layer (ARL) or during the plating of a Pd-rich layer (PRL). The ARL deposit gave slightly greater scatter than either the PRL or the uniform deposit. However, all three electrodeposits showed substantially less contact resistance increase than did the bulk R156 alloy. This improvement in the contact resistance stability (CRS) of the electrodeposited alloys over the wrought alloy is particularly surprising since the latter contained more Pd than the plated alloys.

The same result was also found in a previous comparison (30) of d-c plated Ag-Pd *vs.* R156 in a flowers of sulfur test. As discussed below, the influence of incorporated Cl and the microstructure will be considered as possible causes for the improved CRS behavior. Wear and friction response of the Ag-Pd CMA coatings was evaluated briefly using the approach described in Ref. (30) and was also found similar to that of d-c Ag-Pd coatings.

CMA and d-c Ag-Pd platings differed in the coating appearance. d-c platings containing less than about 45% Ag had rough surfaces with dark gray matte color. The surface became smoother, and the color lighter, with increased Ag content. Deposits containing more than about 70% Ag exhibited a silver-white color and tended to be powdery. Semi-bright d-c coatings could be obtained only under optimum conditions. CMA deposits, on the other hand, had smoother surfaces and brighter appearance under a wider range of plating conditions. For a given average current density, the brightness increased with the applied wave frequency provided that the high current amplitudes and durations were not excessive (*i.e.*, about 25 mA/cm^2 and 1 min).

Discussion

The analysis of CMA deposits indicates that, within certain limits, the alloy composition and structure do correspond to the applied current waveform. A triangular waveform gives rise to a clearly triangular composition profile (cf. Fig. 11). A square waveform, however, does not appear to cause corresponding sharp composition steps, particularly for short wavelengths. In such cases the composition-depth profiles are rounded, resembling a roughly sinusoidal waveform (cf. Fig. 3). The cathodic polarization also does not change instantaneously with new applied current but approaches a new steady state with a time constant of the order of several seconds. This response time is not

likely to reflect the non-Faradaic effects such as double layer charging, which typically takes place in a millisecond time frame. Rather, this response time probably reflects the ion redistribution in the diffusion layer (concentration polarization) which normally takes place with a time constant of a few seconds (1) such as is observed in Fig. 1. It is thus possible to understand why we observe a clearly defined CMA structure with a cyclic composition only when the wavelength is $\geq$1000Å, corresponding to cycle time >5 sec for the conditions used.

The layers seen in SEM micrographs of CMA deposits where the wavelengths are in the intermediate range (500-1000Å), may reflect a modulation of the microstructure more than of composition (since no modulation is detected by AES profiles of such samples). The general experience in plating both alloys and single metals indicates that microstructure is indeed sensitive to current density variations (1). A study of the microstructure modulations of CMA Ag-Pd deposits by transmission electron microscopy (TEM) of cross sections is planned to confirm this point. A previous study of d-c plated Ag-Pd coatings by TEM and x-ray diffraction (XRD) revealed a homogeneous single phase solid solution with an fcc crystal structure, and very fine grains (100-300Å) (33). Voids of about 20-30Å in size were also noted at the grain boundaries.

It does not seem likely that the loss of AES depth resolution is due to solid-state diffusion. The rates of solid-state interdiffusion of Ag and Pd in the alloy Ag-Pd are extremely low at room temperature. The plating temperature (85°C) is only maintained for short period (about 10 min). Experiments to homogenize adjacent thin layers of Ag and Pd by Tu (34), revealed negligible diffusion after a period of 24 hr at 200°C. Indeed, the diffusion length, computed from the diffusion coefficients of the bulk Ag-Pd alloy, should be only a small fraction of 1Å (during a 24 hr period at 200°C).

Among several possible reasons for the loss of the AES resolution of composition modulations with the depth, we believe that the microtopography of the deposit surface and outer layers is of primary importance. The outer layers of CMA deposits will generally not be perfectly flat. Undulating ripples are clearly seen in Fig. 2, 5, 6, and 8. Before sputtering is begun, the AES analyzing beam excites only the outermost layer surface, regardless of the ripples, so that true surface composition is obtained. However, as depth profiling is set by sputtering, the bottom of the sputtering crater (about 1 mm diameter) advances through the deposit, exposing various depths of a layer, or even more than a single layer, at a time. The topography of the surface will change during the course of the sputtering; it could approach a flat or, more likely, it could develop new microtopography such as the cones often seen on sputtered metals (35). Consequently, the analyzing AES beam (of about 5 μm diameter), focused at the crater's bottom, will generally sample areas at different distances from the original surface at any instant. Such averaging effects add to the rounding of composition profiles of CMA structures obtained with square current waveforms. Esaki and Chang (27) attributed the steady loss of resolution with the sputtering depth to the spatially varying rates on the scale of the area of the focused primary beam.

It is possible to interpret a number of our findings concerning the controlling parameters in the plating process on the basis of a relatively simple model, *i.e.*, that the mass transport of Pd^{+2} ions across the diffusion layer is rate controlling. This is the typical behavior for normal alloy plating where the more noble metal is diffusivity controlled (1). To achieve a maximal effect of modulating the composition, it is necessary to operate under conditions such that modulation of current density produces largest change in the concentration of Pd^{+2} ions at the interface. For the experimental conditions used, increasing the current density modulation, decreasing the total ion concentration of the solution, or decreasing the rate of stirring all should favor larger modulation in the composition of the plated CMA alloy. It is anticipated that CMA Ag-Pd structures with layer thickness $\leq$100Å may be obtained by decreasing the ion concentrations by about an order of magnitude. This, however, may increase erratic fluctuations in composition and morphology of the growth interface.

The smoothness of the deposit is also controlled by the mass transport of the Pd^{+2} ions. We can thus understand that changes in plating parameters which tend to decrease the Pd content in the plated alloy (*e.g.*, increased current density), tend also to destabilize the growth interface of the deposit. In the SEM photographs of etched cross sections (see especially Fig. 6a and 6b), interface protrusions of small dimensions are seen to be gradually smoothed out, whereas protrusions of larger dimensions are seen to be gradually amplified, causing increasing roughness and eventually leading to nodule formation and coating deterioration. Other destabilizing effects due to substrate surface irregularities and particle inclusions during growth can likewise be seen in these figures. The critical size of protrusion which is no longer smoothed is expected to be comparable to the diffusion layer thickness since larger protrusions will penetrate into the diffusion layer, thereby becoming more favored for growth over their surroundings. The faster growth rate on such large protrusions is due to the larger nutrient concentration ahead of the protrusions causing the further amplification of these protrusions. With small protrusions, on the other hand, the diffusion layer can conform to the outlines of the solid surface. The growth of such protrusions is, therefore, not favored over their surroundings. However, the increase of free energy due to the increased interface area of protrusions and the associated surface tension, will tend to smooth out the small protrusions (36, 37).

The SEM photographs of etched cross sections provide insight as to such effects of surface irregularities on rate growth because: (*i*) Each cross-sectional photograph contains a continuous record of the growth interface position and shape. Each contour line (cyclic layer) represents the instantaneous position of the growth interface at a known time (given by the number of lines from the substrate). (*ii*) The growth direction is always normal to the contour lines. (*iii*) The local contour line spacing is proportional to the local rate of growth. *i.e.*, the regions with the largest spacing between lines can be identified as the regions with the fastest growth. In future studies, this information could be more systematically analyzed to provide a new means to study the stability of growth interfaces as well as the macro and microthrowing power of plating baths.

The superior corrosion resistance and contact resistance stability (CRS) of both CMA and d-c plated Ag-Pd alloys (relative to the wrought alloy R-156), as determined in the flowers of sulfur tests, is of practical significance as well as scientific interest. Based on the higher content of Ag in the plated alloy, one would anticipate the opposite behavior. Nevertheless, the plated alloys differ substantially from the wrought alloy in their microstructure and their incorporated trace impurities. As noted previously (30), the grain size of the wrought alloy is of the order of several micrometers, whereas that of the plated alloys is only about 100-300Å. Also, the plated alloy is more homogeneous than its wrought counterpart. The much finer grain size as well as the greater homogeneity of the plated alloy, could reduce the Ag mobility towards the surface, thereby reducing the formation of tarnish films in the sulfiding environment. It is also con-

ceivable that incorporated impurities in the plated alloy may somehow hinder and reduce the mobility of Ag to the surface, thereby improving its tarnish resistance. The presence of incorporated Cl in CMA Ag-Pd coatings, established by AES, may thus contribute to its superior tarnish resistance over that of the wrought alloy.

Summary

With the application of the CMA technique to the plating of Ag-Pd alloys, we have demonstrated the feasibility of preparing new types of laminated composite structures. The technique allows the control of thickness and composition of individual layers within the deposit in a precise and convenient manner. The versatility of the technique has been demonstrated by plating CMA structures by both square and triangular waveforms. The minimum thickness of the individual layers appears to be defined by the response time, of the order of several seconds, required to achieve a new steady state of concentration gradients in the diffusion layer after a change has occurred in the current density. For the conditions of this study, this minimum cycle wavelength was about 500-1000Å. Plating of CMA structures of Ag-Pd alloy with layer thickness below about 100Å is believed to be feasible with lower average current densities and bath concentrations. Detailed studies of etched cross sections of CMA structures provide a new and convenient means to study destabilizing mechanisms of the growth interface and its morphology.

A preliminary comparison between CMA and d-c plated Ag-Pd alloys did not reveal any clear differences in tests relevant to their contact finish properties. Both were found superior to the wrought alloy, R-156, in these tests, although they contained one-third less Pd than the wrought alloy. Indeed the contact finish properties of both types of plated Ag-Pd alloy were found to be generally satisfactory. The only noticeable difference between CMA and d-c plated Ag-Pd alloys was the increasing brightness of CMA deposits with the frequency of the square or triangular waveform.

With the knowledge of the CMA technique gained from the present study, it should be possible to produce other CMA alloys where beneficial effects might be realized from the strongly anisotropic structure. One obvious future application is the preparation of magnetic alloy films for information storage since magnetic properties are sensitive to both film thickness and composition. Other possible areas of application for CMA plating include the preparation of superconducting films, highly protective coatings for use in corrosive environments, and layered structures with optical or improved mechanical properties such as toughness and wear resistance.

Manuscript submitted June 11, 1982; revised manuscript received May 10, 1983. This was Paper 310 presented at the Denver, Colorado, Meeting of the Society, Oct. 11-16, 1981.

Bell Laboratories assisted in meeting publication costs of this article.

APPENDIX A

Design of CMA Structure Parameters

Square Current Wave

The square current wave is characterized by its lower and upper current densities, $i_1 = I_1/A$, and $i_2 = I_2/A$, respectively, and their corresponding periods t_1 and t_2, respectively. Here A is the cathode surface area, and I_1 and I_2 are the applied current steps. The cycle frequency is $f = 1/\tau$, where $\tau = t_1 + t_2$ is the total cycle period. The individual layer thicknesses are calculated from the relationships

$$h_1 = \frac{p_1 I_1 t_1 M_1}{n_1 d_1 A \mathbf{F}} \quad [1]$$

$$h_2 = \frac{p_2 I_2 t_2 M_2}{n_2 d_2 A \mathbf{F}} \quad [2]$$

and

$$\frac{h_1}{h_2} = \frac{p_1 I_1 t_1 M_1 n_2 d_2}{p_2 I_2 t_2 M_2 n_1 d_1} \quad [3]$$

Here p_1 and p_2 are the lower and upper step cathode current efficiencies, respectively, and M_1 and M_2 are the molar weights of the alloy plated at i_1 and i_2, respectively. **F** is the Faraday constant (96,500 coulomb/mol). n_1 and n_2 are the numbers of electrons transferred per formula of the alloys plated at i_1 and i_2, respectively, and d_1 and d_2 are the corresponding densities of these alloys. For small magnitude composition modulation, the average parameters can be considered: $P \simeq P_1 \simeq P_2$; $M \simeq M_1 \simeq M_2$; $n \simeq n_1 \simeq n_2$; and $d \simeq d_1 \simeq d_2$.

For this case

$$h_1 = C\frac{I_1 t_1}{A} \quad [1a]$$

$$h_2 = C\frac{I_2 t_2}{A} \quad [2a]$$

and

$$\frac{h_1}{h_2} = \frac{I_1 t_1}{I_2 t_2} \quad [3a]$$

Here $C = pM/nd\mathbf{F}$ is a constant. For Ag-Pd alloys of about 50% Ag-50% Pd, $C \simeq 1.0 \frac{\text{cm}^2\,\mu\text{m}}{\text{coulomb}}$ when h_1 and h_2 expressed in μm, I_1 and I_2 in amperes, t_1 and t_2 in sec, and A in cm^2.

Triangular Current Wave

Only average parameters are considered here since the current is continuously swept. The lower and upper limit current densities are $i_1 = I_1/A$ and $i_2 = I_2/A$, respectively. The average current density is $i_{avg} = \frac{i_1 + i_2}{2}$, and the sweep rate is

$$\frac{di}{dt} = \frac{2(i_2 - i_1)}{\tau} \quad [4]$$

where τ is the cycle period. The cyclic layer thickness is calculated from

$$h = Ci_{avg}\tau = C\frac{I_{avg}\tau}{A} \quad [5]$$

REFERENCES

1. A. Brenner, "Electrodeposition of Alloys: Principles and Practice," Academic Press, New York (1963).
2. V. Zentner, *Plating*, **52**, 368 (1965).
3. D. W. Endicott and J. R. Knapp, Jr., *ibid.*, **53**, 43 (1960).
4. I. A. Menzies and C. S. Ng, *Trans. Inst. Met. Finish.*, **36**, 48 (1968).
5. J. H. Wiesner and W. B. Distler, *Plating*, **56**, 799 (1969).
6. R. Duva and D. G. Foulke, *ibid.*, **55**, 1056 (1968).
7. E. Raub and K. Muller, "Fundamentals of Metal Deposition," Elsevier, New York (1967).
8. C. A. Snavely, *This Journal*, **97**, 99 (1950).
9. V. A. Lamb, C. E. Johnson, and D. R. Valentine, *ibid.*, **117**, 291C, 341C, 381C (1970).
10. R. Weil and W. N. Jacobus, Jr., *Plating*, **53**, 102 (1966).
11. A. Brenner, V. Zentner, and C. W. Jennings, *ibid.*, **39**, 865, 899, 933 (1952).
12. U. Cohen and W. A. Tiller, To be published.
13. W. R. Meyer and A. Phillips, *Trans. Electrochem. Soc.*, **73**, 377 (1938).
14. K. Aotani, *J. Electrochem. Soc. Jpn.*, **21**, 180 (1953).
15. P. F. Mikhalev, *Compt. Rend. Acad. Sci. URSS*, **24**, 899 (1939).
16. J. DuMond and J. P. Youtz, *J. Appl. Phys.*, **11**, 357 (1940).
17. H. E. Cook and J. E. Hilliard, *ibid.*, **40**, 2191 (1969).
18. E. M. Philofski and J. E. Hilliard, *ibid.*, **40**, 2198 (1969).
19. W. M. C. Yang, T. Tsakalkos, and J. E. Hilliard, *ibid.*, **48**, 876 (1977).

20. B. J. Thaler, J. B. Ketterson, and J. E. Hilliard, *Phys. Rev. Lett.* **41**, 336 (1978).
21. M. B. Brodsky and A. J. Freeman, *ibid.*, **45**, 133 (1980).
22. E. M. Gyorgy, J. F. Dillon, D. B. McWhan, L. W. Rupp, L. R. Testardi, and P. J. Flanders, *ibid.*, **45**, 57 (1980).
23. T. Jarlborg and A. J. Freeman, *ibid.*, **45**, 653 (1980).
24. M. B. Brodsky, *J. Appl. Phys.*, **52**, 1665 (1981).
25. S. T. Ruggiero, T. W. Barbee, and M. R. Beasly, *Phys. Rev. Lett.*, **45**, 1299 (1980).
26. A. Y. Cho, *J. Appl. Phys.*, **41**, 782 (1970).
27. L. Esaki and L. L. Chang, *Thin Solid Films*, **36**, 285 (1976).
28. Z. L. Liau, S. U. Campisano, C. Canali, S. S. Lau, and J. W. Mayer, *This Journal*, **122**, 1696 (1975).
29. W. Blum, *Trans. Am. Electrochem. Soc.*, **40**, 307 (1921).
30. U. Cohen, K. R. Walton, and R. Sard, *This Journal*, To be published.
31. G. P. Schwartz, *Surf. Sci.*, **76**, 113 (1979).
32. A procedure recommended by the B.04 ASTM Committee, designated: "Method of Test for Tarnish Resistance of Electrical Contacts to a Flowers of Sulfur Atmosphere."
33. U. Cohen and S. Nakahara, Unpublished research.
34. K. N. Tu, *J. Appl. Phys.*, **48**, 3400 (1977).
35. G. K. Wehner and D. J. Hajicek, *ibid.*, **42**, 1145 (1971).
36. C. Wagner, *This Journal*, **101**, 225 (1954).
37. A. R. Despic and K. I. Popov, in "Modern Aspects of Electrochemistry," Vol. 7, B. E. Conway and J. O'M. Bockris, Editors, Plenum Press, New York (1972).

Capacitance Characteristics of the Polycrystalline CdS/NaOH and CdS/Cysteine Interfaces

R. Dewitt and A. Kirsch-De Mesmaeker*

Universite Libre de Bruxelles, Faculte des Sciences-CP. 160, Service de Chimie Organique, B-1050 Bruxelles, Belgium

ABSTRACT

Flatband potentials (V_{FB}) of polycrystalline CdS have been determined as a function of pH, in the absence and in the presence of cysteine. From pH 10, the linear dependence of V_{FB} with pH is explained by a hydroxylation of the electrode surface. With cysteine, two V_{FB} negative steps occur at pH's corresponding to the two pK_a's of the reductant, emphasizing the V_{FB} dependence on the degree of ionization of the amino acid.

Several studies (1) have shown that CdS in contact with an aqueous electrolyte solution presents important photoanodic corrosion. Up to now, the most efficient redox electrolytes used to check this are the chalcogenide/polycalcogenide couples (2).

It was interesting to test sulfur containing organic reductants as kinetic inhibitors of CdS photocorrosion (3). According to some choice criteria, cysteine (I) had been chosen as one of these reductants; its behavior at illuminated CdS has been described previously (3). These studies have shown that although cysteine does not behave as an efficient kinetic inhibitor of photocorrosion, the i/V curve characteristics of amorphous CdS are improved under illumination in an aqueous basic solution of cysteine. From x-ray fluorescence and LEEIX measurements (4), it turns out that the photoelectrochemical characteristic improvements can be correlated to hydroxylation of the CdS, strongly enhanced in the presence of cysteine (pH 14).

Nevertheless, a thorough *in situ* study of the CdS-cysteine junction by capacitance measurements could not be carried out because of the nonlinearity of the Mott-Schottky $1/C^2$ *vs.* V plots. This behavior probably stems from the amorphous structure of the studied CdS films, obtained by chemical deposition (5). Consequently, in order to get a deeper insight into the CdS-cysteine interface by capacitance studies, we examined another type of CdS prepared by evaporation and presenting a better crystalline structure. With these samples, we have been able to study more quantitatively the solid-liquid junction, and especially the influence of cysteine and pH on the capacitance characteristics in the dark, which we present in this paper.

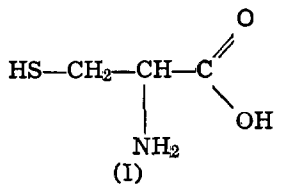

(I)

Experimental

Electrodes.—Polycrystalline n-CdS electrodes prepared by evaporation on brass, were donated by B. Baron (Institute of Energy Conversion, University of Delaware, Newark, Delaware). The microcrystals (hexagonal system) are oriented with the c-axis perpendicular to the support, the thickness of the CdS film is about 25 μm, with an average grain diameter of 1 μm and a resistivity varying between 1 and 3 $\Omega \cdot$ cm from one sample to the other. The donor density ($N_D \simeq 4.5 \pm 0.5\ 10^{18}$ cm^{-3}) was determined by us, from the slope of the Mott-Schottky plot. The N_D value is only indicative because no roughness factor, which can easily reach 2, has been considered. The polycrystalline structure has been checked by SEM (ISI DS 130, no metallization treatment) (Fig. 1) and x-ray diffraction. Figure 1 shows that the surface structure is very different from the nodules of the amorphous CdS (3b) studied before.

Preparation of electrodes.—Each electrode is mounted on a Pyrex support using an insulating glue (Dow Corning RTV 730). Electrical contact is made by a copper wire glued with a conducting silver paint on the back brass surface. Before each measurement, the mounted electrode is etched by HCl 4M (Merck, Titrisol) for 1 min at room temperature in the dark; it is then rinsed five times with tridistilled water and finally the solution is poured into the cell. The measurements are made after a 5 min contact between the solution and the electrode.

* Electrochemical Society Active Member; Research Associate of the National Fund for Scientific Research (Belgium).
Key words: CdS, cysteine, surface modification, flatband potential.

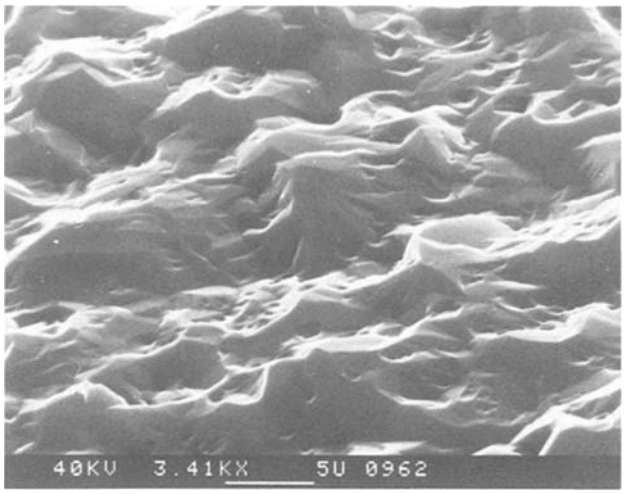

Fig. 1. SEM picture of the CdS film. Beam incidence of 30° with respect to the surface.

Solutions.—All solutions are made with tridistilled water. Traces of ferric ions present in NaOH (P. A. Merck) are removed by coprecipitation with $Mg(OH)_2$ added as $MgSO_4$ to the NaOH stock solution (4M). L-Cysteine ($HSCH_2CH(NH_2)COOH$) (P. A. Aldrich) and $LiNO_3$ (P.A. U.C.B.) are used as such. Na_2SO_4 (P.A. U.C.B.) is recrystallized. The *p*H of each solution is measured with a Philips PR 9403 *p*H meter, equipped with a glass electrode (Philips GA 420, *p*H 0-14). The concentration of cysteine is checked for several experiments by the Ellmann's spectroscopic method (6) (oxidation of cysteine by 3,3′ dithiobis (6 nitrobenzoic) acid giving a free yellow nitro carboxythiolate ion with $\epsilon_{412\,nm} = 13{,}600$). All solutions are deoxygenated by nitrogen bubbling during the solution preparation and before and during the experiments.

Experimental setup.—The impedance measurements are performed by superimposing a sinusoidal signal on a linear potential sweep, applied, via a Tacussel Pit 20-2X Potentiostat, to the CdS working electrode of a one-compartment cell containing also the saturated calomel and counterelectrodes. The resulting cell signal is measured *vs.* the reference signal of the potentiostat, with an Ortec Brookdeal 9503-C Lock-in Amplifier or on a X-t recorder with a signal rectifier.

Results and Discussion

The impedances of the solid-liquid CdS/NaOH and CdS/cysteine junctions are determined in order to point out the cysteine effect on the Schottky barrier. With both junctions, the impedance data fit to a first approximation (within the experimental precision of ± 10%) with a simple equivalent electrical circuit, composed of a resistance R_S in series with a capacitance *C* with a parallel resistance R_P or "shunt resistance," responsible for the faradaic or leak current.

The actual equivalent electrical circuit is probably a little more complicated in the low frequency region where other electrical elements perturbate by less than 15% the behavior of the simple circuit described above. These other elements of the equivalent circuit are probably responsible for the slight frequency dependence of the slopes of the Mott-Schottky lines ($1/C^2$ *vs.* *V*), determined in the low frequency region in the absence or in the presence of cysteine (Fig. 2A and B).

Frequency dispersion in Mott-Schottky plots have been often described (8) and it has been shown recently that such a frequency dependence in a low frequency range vanishes with increasing frequency (9). Nevertheless, as shown by Fig. 2A and B, the extrapolated flatband potential (V_{FB}) remains constant within the experimental error (± 10 mV). The fact that only the slope of the function is frequency dependent allows us to evaluate, without appreciable error, the V_{FB} by extrapolation of the straight line.

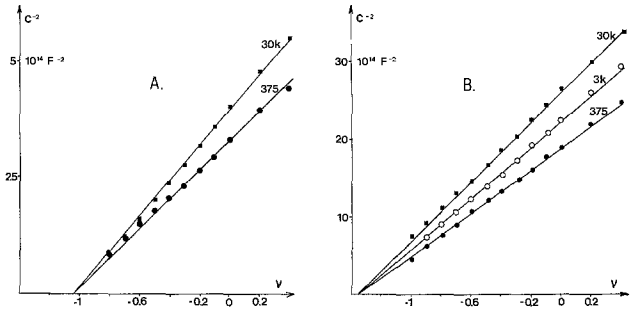

Fig. 2. Mott-Schottky plots for different frequencies. A: CdS/NaOH *p*H 14. B: CdS/cysteine 1M, NaOH *p*H 11.5.

Figure 3 shows the V_{FB} values as a function of *p*H in NaOH alone and with cysteine 1M. All the values are obtained from capacitance measurements made at 375 Hz. We chose this frequency because the $(C\omega)^{-1}$ values are then comprised between 2600Ω ($C \simeq 150$ nF) and 13,000Ω ($C \simeq 30$ nF), which allows to simplify the impedance of the equivalent circuit to the *C* branch only.

For CdS in NaOH alone, as shown in Fig. 3, the V_{FB} remains constant between *p*H 6 and 10, with a value of approximately −0.910V *vs.* SCE. At *p*H 10, the V_{FB} starts increasing linearly with the *p*H, up to *p*H 13.5 with a slope of 30 mV per *p*H unit. The nature of the electrolyte does not seem to have any major influence on V_{FB} ($LiNO_3$ 0.4M or Na_2SO_4 0.2M). It has to be noticed that, in order to obtain reproducible results, an electrode etching with HCl 4M is required before each measurement. Indeed, if two successive measurements are performed, the first one at a higher *p*H and the second one at a lower *p*H, without chemical etching between both experiments, the V_{FB} value at the lower *p*H is quite irreproducible: the values extend from the actual value obtained after etching, to values close to the ones obtained at the higher *p*H. This behavior, always observed without preliminary etching, most probably stems from an irreversible electrode modification by the highly basic aqueous solution.

Figure 3 also shows that in the presence of cysteine 1M, for all the *p*H values, the CdS V_{FB} is shifted cathodically compared to the V_{FB} obtained in NaOH alone. This negative V_{FB} shift is comparable to the one observed with the S^{2-} ions (2b), with however, in the cysteine case, a more complex relation be-

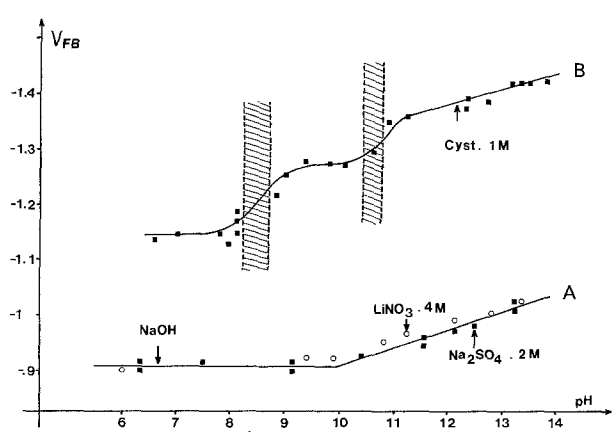

Fig. 3. V_{FB} of nCdS extrapolated from Mott-Schottky plots made at 375 Hz as a function of *p*H. A: NaOH, from *p*H 6 to 13.5; ionic strength is kept constant by adding $LiNO_3$ 0.4M (○) or Na_2SO_4 0.2M (■). B: Cysteine 1M, from *p*H 7 to 14.

tween V_{FB} and the pH. Indeed, as shown in Fig. 3, V_{FB} does not vary linearly with the pH, except for pH higher than 11. Between pH 6 and 11, there are two V_{FB} negative steps as a function of the pH: one around pH 8.5 and the other around pH 10.75. It has not been possible to investigate the pH region lower than 6, because of the cysteine insolubility in acidic medium.

CdS/NaOH junction.—Variation of V_{FB} of CdS in contact with aqueous solutions at different pH has already been investigated by several authors (10); however, the results are somewhat different from one author to the other. Most of the differences could be attributed to different crystallographic faces in contact with the electrolyte which exhibit different V_{FB} dependence with the pH. Recently, this has also been shown in the case of the n-GaAs (10d). Thus we felt that a clarification of the pH effect on our CdS junction was a prerequisite for a study of the effects of cysteine as a function of pH.

In our case, the V_{FB} remains constant from pH 6 to 10 and corresponds to −0.91 V/SCE, in agreement with Watanabe's results; however, from pH 10, contrary to Watanabe's results, the V_{FB} values start shifting negatively by 30 mV/pH up to pH 13.5, similarly to Matsumura's results. This behavior can be explained by taking into account a chemical modification of the CdS induced by the aqueous basic solution under anodic bias. Indeed, it has been shown by x-ray fluorescence and LEEIX measurements (4) that an electrode of amorphous CdS, dipped in an NaOH solution at pH 14, is modified by hydroxyl groups, cadmium oxide, and sulfate-type sulfur. Moreover, under anodic bias with respect to V_{FB}, in the dark and under illumination, the same modification is observed and no sulfur S° from the lattice sulfide oxidation is detected. These experimental observations are in very good agreement with the calculated Pourbaix diagram for CdS (Fig. 4) where the semiconductor between pH 2 and 13.5 corrodes anodically into SO_4^{2-} and Cd^{2+} or different soluble hydroxylated Cd^{2+} or insoluble $Cd(OH)_2$, depending on pH. Such a diagram has already been calculated by Park *et al.* (11) who considered the sulfur S° in the anodic corrosion area. However, the thermodynamic data show that only HSO_4^- and SO_4^{2-} can be considered as the stable thermodynamic sulfur species in the anodic corrosion area of CdS (Fig. 4). Therefore, at $V > -0.5V$ (SCE) where a small oxidation current is observed, the electrode could corrode into SO_4^{2-} and Cd^{2+} ions. The SO_4^{2-} should gradually dissolve into the solution whereas the fate of the Cd^{2+} is critically pH dependent. In neutral or acidic solution, Cd^{2+} is soluble and the electrode merely dissolves without surface chemical modification. On the contrary, in the high pH region (pH 10-13.5), the $Cd(OH)_2$ formed by anodic oxidation would accumulate on the surface and modify the CdS.

Taking into account this chemical modification by corrosion and passivation, the pH effect on the CdS V_{FB} can easily be explained. Indeed, according to the corrosion criteria (*i.e.*, 10^{-6}M for the concentration of soluble species), pH 10 plays a capital role for the CdS/NaOH junction since it represents the boundary between the corrosion ($Cd(OH)^+ + SO_4^{2-}$) and passivation ($Cd(OH)_2 + SO_4^{2-}$) areas. Consequently, for pH < 10, although the electrode is corroding, its superficial chemical composition does not change and is essentially composed of CdS, the V_{FB} of which does not depend on pH. On the contrary, for pH > 10, the electrode surface is passivated by $Cd(OH)_2$, an "active" form of CdO, the V_{FB} of which should be pH dependent as for the oxide semiconductors.

CdS/cysteine junction.—There are two types of cysteine effects on the CdS V_{FB} which are pointed out in Fig. 3. The first one is a negative shift of V_{FB} for

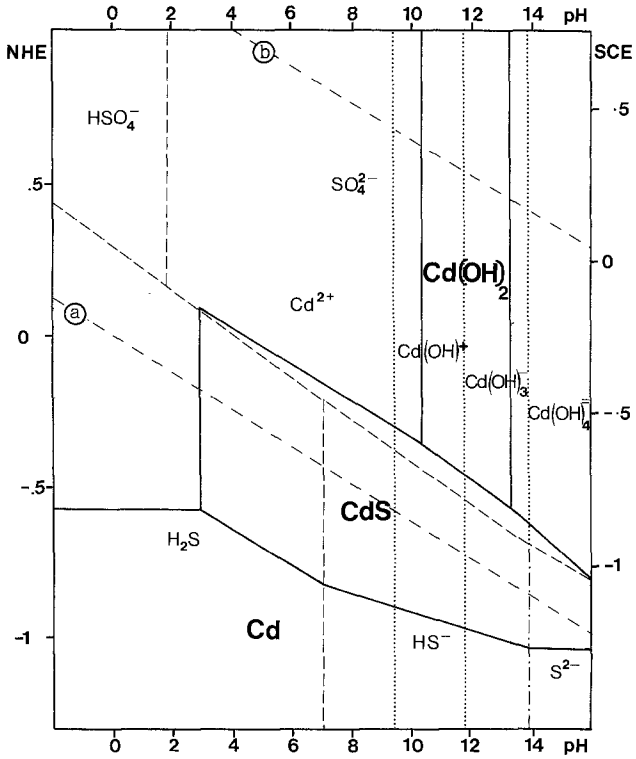

Fig. 4. Pourbaix diagram of CdS. Solid species considered: CdS, Cd, $Cd(OH)_2$, S. Soluble species considered: Cd^{2+}, H_2S, HS^-, HSO_4^-, S^{2-}, SO_4^{2-}, $Cd(OH)^+$, $Cd(OH)_3^-$, $Cd(OH)_4^{2-}$. The thermodynamic data are taken from Ref. (12) and (13). The boundary between two areas involving at least one solid and one soluble species (——) is calculated using the corrosion criterion of 10^{-6}M for the soluble species concentration. (.....) Boundaries between areas involving soluble species of cadmium derivatives; (-----) boundaries between areas involving soluble species of sulfur derivatives. The thermodynamically predominant species are indicated in each area. a and b = redox potentials of water.

all pH values comprised between 7 and 14, compared to the values in NaOH alone. The second is a variation of the amplitude of this shift depending on pH.

Actually, the amino acid (I) has three ionizable acid functions with the following pK_a values (14):

$$R'—COOH \overset{K_a1}{\rightleftharpoons} R'—COO)^{(-)} + H^{(+)} \quad pK_a1 = 1.71$$

$$R'—SH \overset{K_a2}{\rightleftharpoons} R'—S^{(-)} + H^{(+)} \quad pK_a2 = 8.3/8.7$$

$$R'—NH_3^{(+)} \overset{K_a3}{\rightleftharpoons} R'—NH_2 + H^{(+)} \quad pK_a3 = 10.4/10.8$$

These are macroscopic constants. More accurately, the two latter pK_a's can be divided into four microscopic constants:

$$NH_3^{(+)}—R—SH \overset{K_a4}{\rightleftharpoons} NH_3^{(+)}—R—S^{(-)} + H^+ \quad pK_a4 = 8.4/8.7$$

$$NH_3^{(+)}—R—SH \overset{K_a5}{\rightleftharpoons} NH_2—R—SH + H^+ \quad pK_a5 = 8.6/8.9$$

$$NH_3^{(+)}—R—S^{(-)} \overset{K_a6}{\rightleftharpoons} NH_2—R—S^{(-)} + H^+ \quad pK_a6 = 10/10.8$$

$$NH_2—R—SH \overset{K_a7}{\rightleftharpoons} NH_2—R—S^{(-)} + H^+ \quad pK_a7 = 10/10.5$$

where —R— stands for $—CH(COO^{(-)})—CH_2—$.

If we assume that cysteine adsorbs reversibly on the surface when CdS is dipped in a cysteine solution, we can easily interpret our results. For pH lower than pK_a4 and pK_a5 but $> pK_a1$, cysteine is twice ionized, with a negative charge on the carboxylate group and a positive one on the ammonium group, leading to a resulting charge of zero. In this condition, the V_{FB} cathodic shift, between pH 7 and 8, compared to the value in NaOH alone, could be attributed to a potential drop in the OHP, due to the dipole of the adsorbed "neutral" cysteine. Around pH 8.5, the V_{FB} shifts cathodically because of the acid-base reactions 4 and 5 (first shaded area, Fig. 3), leading to an ion with a total negative charge of 1. Around pH 9.5, the right-member products of equilibria 4 and 5 are the preponderant species in solution. Similarly, at pH 10.75, there is a second V_{FB} step with increasing pH, corresponding to the acid-base reactions 6 and 7 (second shaded area, Fig. 3). These equilibria lead to an ion with a total negative charge of 2. The different V_{FB} shifts would thus depend on the different degree of the cysteine ionization. For pH higher than pK_a6 and pK_a7, V_{FB} shifts linearly with pH with a slope of 30 mV per pH unit. This pH dependence indicates probably a superposition of the cysteine effect and of the NaOH one. If we accept that in this high pH region, as discussed before, the electrode surface in contact with the solution, is covered by $Cd(OH)_2$, the sulfur atoms being dissolved as sulfate ions, the persistence of the cysteine effect in the high pH range (11.5-13.5) on the V_{FB} value (compared to the one in NaOH alone), would indicate that cysteine adsorbs on the Cd atoms (hydroxylated or not).

Conclusions

There are two important results which emerge from this work.

The first one concerns the capacitance results obtained with the CdS/NaOH junction. The pH effect on the V_{FB} indicates that the chemical composition of the surface varies with pH. At pH higher than 10, the linear dependence of the V_{FB} with pH and the examination of the Pourbaix diagram lead to the conclusion that the surface gets hydroxylated at least partially. This conclusion has already been suggested before by Matsumura *et al.* (10c) but has never been clearly discussed.

The second result is that, to our knowledge, it is the first time that a V_{FB} shift, depending on the degree of ionization of the reductant in solution, has been clearly pointed out.

Acknowledgments

We are grateful to Dr. B. Baron from the Institute of Energy Conversion at the University of Delaware for donating the polycrystalline CdS samples and to Dr. L. Devos from the University of Brussels (Zoology Department) for taking the SEM photographs. One of us (R.D.) thanks the "Institut pour l'Encouragement de la Recherche Scientifique dans l'Industrie et l'Agriculture" (IRSIA) for a fellowship.

Manuscript submitted Jan. 10, 1983; revised manuscript received May 24, 1983.

REFERENCES

1. (a) H. Gerischer, *J. Electroanal. Chem.*, **82**, 133 (1977); (b) A. J. Bard and M. S. Wrighton, *This Journal*, **124**, 1706 (1977); (c) H. Gerischer and J. Gobrecht, *Ber. Bunsenges. Phys. Chem.*, **82**, 520 (1978).
2. (a) A. B. Ellis, S. W. Kaiser, and M. S. Wrighton, *J. Am. Chem. Soc.*, **98:22**, 6855 (1976); (b) H. Minoura, T. Oki, and M. Tsuiki, *Chem. Lett.*, 1279 (1976); (c) B. Miller and A. Heller, *Nature*, **262**, 680 (1976); (d) A. B. Ellis, S. W. Kaiser, J. M. Bolts, and M. S. Wrighton, *J. Am. Chem. Soc.*, **99:9**, 2839 (1977).
3. (a) A. Kirsch-De Mesmaeker, A. M. Decoster, and J. Nasielski, *Solar Energy Mater.*, **4**, 203 (1981); (b) A. Kirsch-De Mesmaeker, P. Josseaux, J. Nasielski, and C. Defosse, *ibid.*, **6**, 429 (1982).
4. P. Josseaux, Private communication.
5. N. R. Pavaskar, C. A. Menezes, and A. B. B. Sinha, *This Journal* **124**, 743 (1977).
6. G. L. Ellmann, *Arch. Biochem. Biophys.*, **82**, 70 (1959).
7. (a) V. A. Myamlin and Y. V. Pleskov, "Electrochemistry of Semiconductors," Plenum Press, New York (1967); (b) H. Gerischer, "Physical Chemistry," Vol. IX, p. 463, Academic Press, New York (1970).
8. (a) S. Toshima and I. Uchida, *Electrochim. Acta*, **15**, 1717 (1970); (b) D. M. Tench and E. Yeager, *This Journal*, **120**, 164 (1973); (c) M. J. Madou, F. Cardon, and W. P. Gomes, *ibid.*, **124**, 1623 (1977); (d) E. C. Dutoit, R. L. Van Meirhaeghe, F. Cardon, and W. P. Gomes, *Ber. Bunsenges. Phys. Chem.*, **79**, 1206 (1975).
9. M. Tomkiewicz, *This Journal*, **126**, 2220 (1979).
10. (a) T. Watanabe, A. Fujishima, and K. Honda, *Chem. Lett.*, 897 (1974); (b) D. S. Ginley and M. A. Butler, *This Journal*, **125**, 1968 (1978); (c) M. Matsumura, S. Matsudaira, H. Tsubomura, M. Takata, and H. Yanagida, *Ind. Eng. Chem. Prod. Res. Dev.*, **19**, 415 (1980); (d) K. Rajeshwar and T. Mraz, *J. Phys. Chem.*, **87**, 742 (1983).
11. S. Park and M. E. Barber, *J. Electroanal. Chem.*, **99**, 67 (1979).
12. M. Pourbaix, "Atlas d'équilibres électrochimiques à 25°C," Gauthier-Villars, Paris (1963).
13. (a) W. H. Latimer, "Oxidation Potentials," 2nd ed., Prentice Hall (1952); (b) "Handbook of Materials Science," Vol. 1, CRC Press.
14. (a) P. C. Jocelyn, "Biochemistry of the SH Group," Academic Press, New York (1972); (b) M. Friedman, "The Chemistry and Biochemistry of the Sulfhydryl Group in Amino Acids, Peptides and Proteins," Pergamon Press (1973).

BP-Stabilized n-Si and n-GaAs Photoanodes

D. S. Ginley,* R. J. Baughman, and M. A. Butler*

Sandia National Laboratories, Albuquerque, New Mexico 87185

ABSTRACT

Thin boron phosphide overlayers, employed as transparent conductive windows, have been deposited on n-Si and n-GaAs photoanodes. Significantly enhanced stabilities are observed in ferro-ferricyanide electrolytes. Spectral response and I-V data for aging experiments, as well as a discussion of the energy level diagrams for the heterojunctions, are presented.

The use of heterogeneous photocatalysis for solar energy conversion in photoelectrochemical devices has attracted tremendous attention over the last 7 or so years. Whether employed as discrete semiconductor electrodes or in particulate systems, one of the major requirements in any practical system is that of extended stability. This is especially true in view of the increasing tendency to employ small bandgap non-oxide electrode materials.

Because it is very difficult to find intrinsically stable materials and to develop them to device quality, considerable effort has been expended on electrode modification to improve stability and charge transfer properties. Some of the methods employed or suggested include the use of stabilizing redox couples in the electrolyte (1, 2) or chemically bound on the surface (3) and overcoating of unstable semiconductors with stable electronic (4, 5) or ionic conductors (6).

In this paper, the authors demonstrate that the growth of a degenerate layer of n-type boron phosphide (BP) on either n-Si or n-GaAs can impart great stability to these normally quite unstable photoanodes. This paper reports predominantly on the results on Si substrates, with some results being reported for both substrates. Though the application of semiconductor overlayers had been previously proposed (4), the intent there was to collect photocurrents from both layers and augment open-circuit potentials. Prototypes of these devices suffered greatly from bandedge matching problems, and extremely low quantum efficiencies were the result. The intent here was somewhat different. A number of attempts have been made (7, 8) to use thin metal overlayers as protective films, but light transmission and pinhole problems dominated these devices. The authors desire was to use this concept, but to employ a large bandgap stable degenerate semiconductor upon a smaller bandgap unstable semiconductor. For this to be effective, a number of requirements had to be met. There needed to be an effective heterojunction between the two semiconductors; this implied a high density of interfacial states. The bandgap of the overcoating semiconductor had to be significantly larger than that of the small bandgap material so that reasonable conversion efficiencies could be attained. The overcoating material had to be stable in the required electrolyte environment. All of these requirements could be met using BP layers (bandgap 2.0 eV) on n-Si (bandgap 1.1 eV) and n-GaAs (bandgap 1.4 eV).

Experimental

The substrate materials were single-crystal specimens of n-Si and n-GaAs. The silicon samples were Sb-doped to 0.0005-0.20 Ω/cm and cut perpendicular to the <100> axis. The gallium arsenide samples were Si-doped to 6-7 × 10^{17} and were cut perpendicular to the <100> axis. Before growth, all samples were polished with 1/4 μm diamond paste, acid-etched, and rinsed with spectral grade methanol. The Si contacts were Ti/Pt/Au, and the GaAs contacts were Ge-Au/Ni/Au. All contacts were applied by sputtering and were annealed in vacuum and hydrogen, respectively.

Boron phosphide was deposited by chemical vapor deposition (CVD) from mixtures of B_2H_6, PH_3, and H_2 (9).

The gas nutrient materials used in this work were all Matheson gas products. The hydrogen carrier gas, 99.999% pure, was passed through a Matheson hydrogen purifier Model 8363. The diborane, 99.995% pure, was a 1.10% concentration in UHP hydrogen gas. The phosphine, 99.999% pure, was a 4.48% concentration in hydrogen gas. Both the diborane and phosphine were used directly from the gas cylinder.

Matheson gas flow controllers were used to regulate and control all gas flow. The system included mass flow controller Model 8240, mass flow meter Model 8142, and totalizer Model 8122. Each gas system was calibrated for a specific gas mixture. The exhaust gas was passed through a silicone oil gas trap and was then either burned or vented through a hood.

The growth apparatus is shown schematically in Fig. 1. The outer atmosphere chamber, constructed of fused silica, was 31 cm (length) × 5 cm (diam) and supported the desired growth environment. The chamber

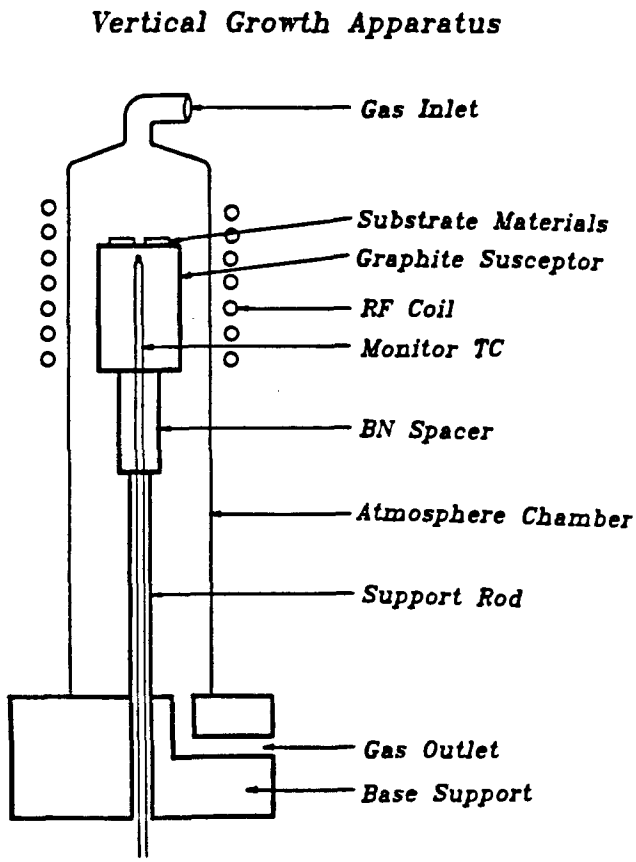

Fig. 1. Schematic of BP vertical growth apparatus

* Electrochemical Society Active Member.

Key words: boron phosphide, corrosion resistant layer, photoelectrochemistry, silicon photoanode, gallium arsenide photoanode.

was friction-fitted into the support base. A gas seal was provided by an "O" ring in the base. This configuration allowed the fused silica growth chamber to disconnect from the base, avoiding rupture in case exhaust tubing became either plugged or restricted during a growth procedure.

All electrochemical measurements were made using a conventional three-electrode electrochemical cell with a saturated calomel reference electrode (SCE), a PAR 173 potentiostat, and a PAR 174 programmer. Illumination was by a 150W Schoeffel medium pressure xenon lamp used with a Schoeffel grating monochrometer where appropriate. Conversion efficiencies were measured using the unfiltered light source attenuated to 80 mW/cm^2.

All electrolytes were prepared from distilled water and analytical purity reagents. The electrolytes employed throughout the bulk of this study were 0.1M potassium ferricyanide and 0.25M potassium ferrocyanide ($pH \cong 7.8$).

All aging experiments were conducted in the above electrolyte in the air. The propensity of the electrolyte to decompose was rectified by periodic electrolyte renewal and by cleaning the cell windows. The BP-coated Si samples were aged at 0.2V *vs.* the ferro-ferricyanide couple (+0.455V [SCE] measured on a Pt metal electrode) to be near the maximum power point of the cell. For the aging experiments, BP-coated GaAs was potentiostated at +0.100V *vs.* SCE and the virgin n-GaAs electrode was potentiostated at +0.260V *vs.* SCE.

Results

Boron phosphide films for this study were grown with P:B atom ratios in the input stream from 1:1 to 24:1. Growth temperature was typically 900°C for both the Si and the GaAs substrates. Total gas flow was held constant at 2500 sccm by correcting with the hydrogen carrier gas flow rate. Normally the layers grown were 2000-5000Å thick, which required growth times from 2 to 4 min for the 1:1 and 24:1 ratios on silicon. BP films are well known to grow epitaxially on silicon (10-12), which was observed in this case. The films, as expected, were grown pinhole-free as viewed in the SEM. The growth on GaAs produced excellent optical quality crystalline films, but grain size and orientation were not determined.

It was determined that sample resistivity (*i.e.*, doping level) was a function of P:B ratio. Figure 2 illustrates a plot of resistivity *vs.* P:B growth ratio for BP on both n- and p-type silicon substrates. It was observed that at P:B ratios below 2:1 the film resistivity, as measured impedance in the PEC, rapidly increased and the films approached an intrinsic value. Even growing at ratios of less than 1:1 would not switch the films from n- to p-type, nor would growing on p-type substrates do so. Above ratios of 2:1, the resistivity rapidly decreased to a low value which was minimum about 12:1. Subsequently, increasing the phosphorous atom percent resulted in a slight increase in conductivity with both the n- and p-substrates. It may be that the additional phosphorous at higher concentrations results in the incorporation of a high density of trap states, reducing majority carrier mobility. To achieve the best results when employing these films as transparent conducting windows, it is desirable to have the conductivity as high as possible but to minimize the number of trap states and defects. This is to assure not only efficient charge transport but to minimize the possibility of decomposition reactions initiating at near surface sites with broken bonds or altered stoichiometry.

The validity of this interpretation seems to be reflected in the dependence of conversion efficiency upon the P:B ratio. Figure 3 illustrates the conversion efficiency *vs.* the P:B ratio for BP on n-Si. This information seems to correlate quite well with that from the previous figure. Where resistance is a minimum, the efficiency is a maximum. As the phosphorous concentration increases past this point, the conversion efficiency decreases. As impedance increases, the efficiency rapidly decreases and reaches zero, where we see the rapid increase in resistivity. The low efficiencies in these cells stem from the nearly linear I-V characteristics between I_{sc} and V_{oc}, producing a very low fill factor. There is also some dark current which gradually decreases with time.

Figure 4 illustrates the I-V curves in ferrocyanide electrolyte for virgin GaAs and BP-coated GaAs electrodes. The overall dark and illuminated I-V curves are quite similar in shape for the virgin and coated electrodes. The leakage current increased somewhat for the coated electrode, although this diminished with time. Fill factors are comparable; the flatband shifted approximately 0.35V to the positive of SCE for the coated electrode.

Aging studies were performed in aqueous ferro-ferricyanide in the air. In retrospect, although the couple was energetically very good, it was particularly inappropriate since it underwent photodecomposition. This required a periodic renewal of the electrolyte and cleaning of the cell windows. The electrode surface was also rinsed in distilled water at these intervals. Much of the erratic nature of the photocurrent with time during aging experiments was a consequence of this electrolyte problem. Figure 5 illustrates a plot of photocurrent *vs.* total interfacial coulombs of a BP-coated Si electrode. The P:B growth ratio of this electrode was 12:1, and the electrode was aged at approximately the maximum power point. Clearly the photocurrent did not decay. In fact, it has a pronounced upward trend indicative of an increasing electrode efficiency. The efficiency increased from roughly 1.97 to 2.75% during the aging experiment, while the dark current dropped somewhat from −1.0 to −0.5 mA at 0.0V (SCE). Open-circuit potentials remained rela-

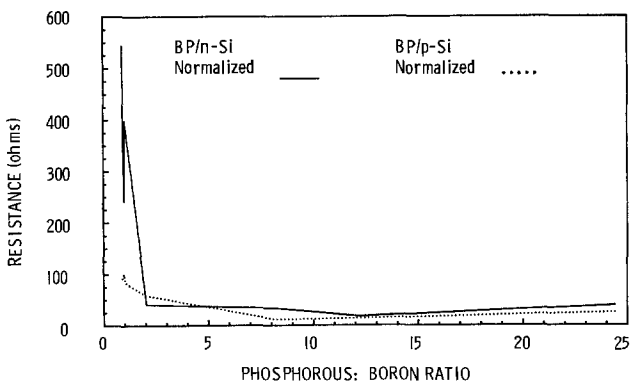

Fig. 2. Plot of sample resistance, as determined by I-V plots in a photoelectrochemical cell *vs.* P:B growth ratio. The solid line is the curve for BP on n-type silicon; the dashed is for BP on p-type silicon.

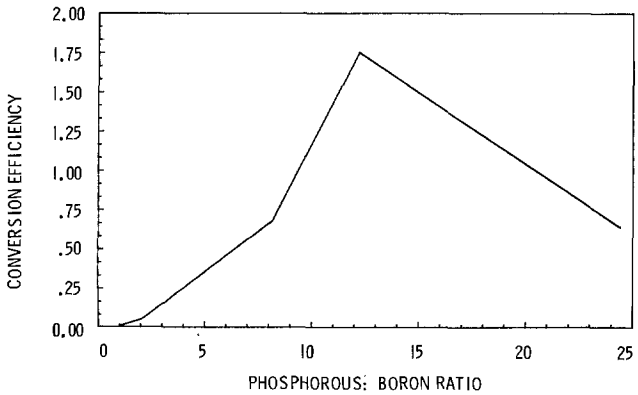

Fig. 3. The plot shows conversion efficiency in percent *vs.* the P:B ratio for a coated p-type silicon substrate in ferro-ferricyanide electrolyte.

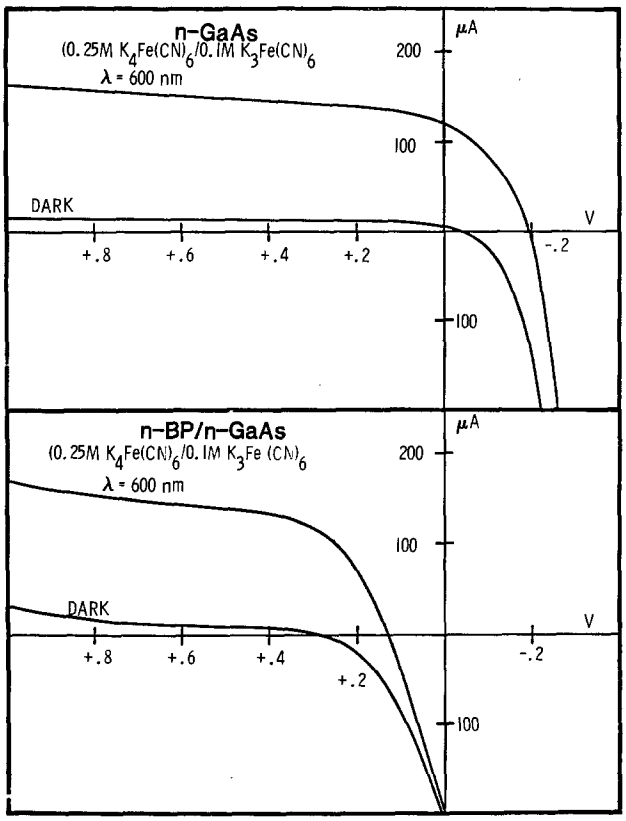

Fig. 4. I-V curves for a virgin n-GaAs photoanode and for a BP-coated n-GaAs photoanode vs. SCE in a ferro-ferricyanide electrolyte.

tively unchanged. The electrode surface showed no change in appearance and showed no pitting or other physical changes under microscopic examination. A virgin n-type silicon electrode was run under comparable conditions in the ferro-ferricyanide electrolyte. Photocurrent decayed to zero after only 0.8C of interfacial current. Figure 6 illustrates the dependence of the spectral response as a function of aging time. The virgin curve looks much as expected with a photocurrent onset near the Si bandedge and a cutoff near the bandedge of the BP. As aging proceeds, there seems to be nonsystematic variations in the longer wavelength portion of the spectrum. These are, however, systematic variations in the short wavelength portion of the spectrum. As aging proceeds, the blue response of the electrode continues to improve.

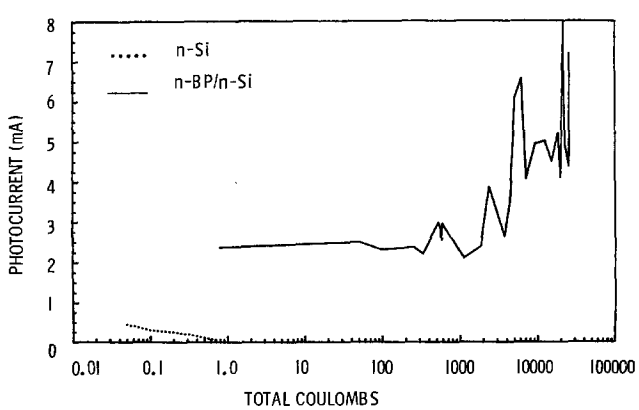

Fig. 5. Plot of extended aging experiment for a virgin n-Si photoanode and a BP-coated n-Si photoanode in a 0.1M $K_3Fe(CN)_6$/0.25M $K_4Fe(CN)_6$ electrolyte. The plot shows photocurrent vs. total interfacial coulombs. The solid line is for the BP-coated electrode; the dashed line is for the uncoated electrode.

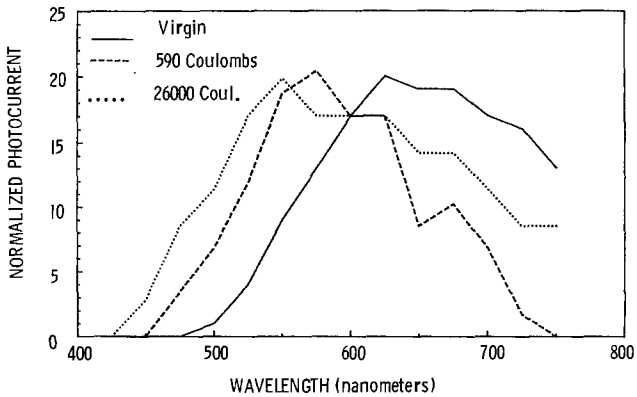

Fig. 6. Spectral response curves as a function of aging for the BP-coated n-silicon electrode shown in Fig. 5. The solid line is before aging; the dashed line is after 590 interfacial coulombs; and the dotted line is after 26,000 interfacial coulombs.

Figure 7 illustrates the aging of a virgin and BP-coated GaAs photoanode in the same ferro-ferricyanide electrolyte. The virgin electrode shows a very rapid decay of photocurrent reaching zero after only 12C. The BP-coated electrode shows an initial rapid decrease of photocurrent followed by a much more gradual decline and by what appears to be a final leveling off. The run was stopped because an orange-green coating began forming on the electrode. Subsequent chemical analysis showed this coating to be composed exclusively of electrolyte decomposition products. When the surface was cleaned, it showed a surface and photoelectrochemical character very similar to that of the preaged electrode.

Discussion and Conclusions

The experiments discussed above illustrate the viability of using a large bandgap semiconductor as a transparent conductive window on smaller bandgap material. In both the n-Si and n-GaAs cases, improved stability was observed while reasonable I-V properties were obtained.

A number of interesting effects were observed relative to the future utility of this method of electrode modification.

Basically, the device inherently resembles a metal overcoated semiconductor electrode. It is, in fact, a solid-state device. This means that the band mismatch between the two semiconductors can play an important role in determining the behavior of the device.

In Fig. 8, the band configurations for BP-overcoated n-Si and n-GaAs are shown. The positions of the bands come from the known bandgaps and the electronegativity model (13). For degenerately doped BP and n-

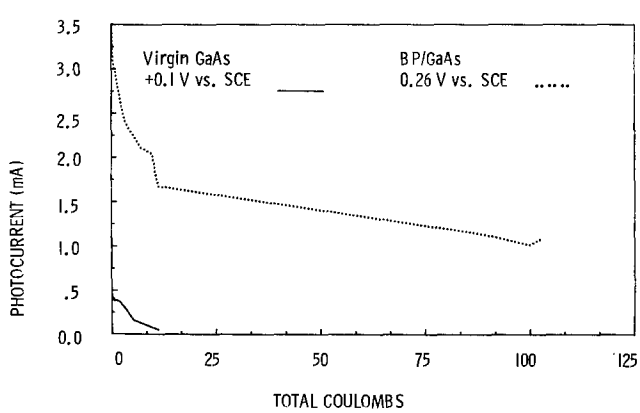

Fig. 7. Plot of extended aging experiment for a virgin n-GaAs photoanode and a BP-coated n-GaAs photoanode in a 0.1M $K_3Fe(CN)_6$/0.25M $K_4Fe(CN)_6$ electrolyte. The plot shows photocurrent vs. total interfacial coulombs. The solid line is for the virgin electrode; the dotted is for the coated electrode.

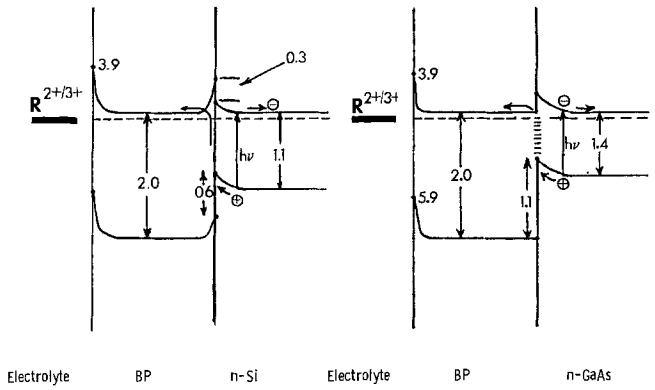

Fig. 8. Expected band structure for BP-coated n-Si and n-GaAs The numbers are band positions and discontinuities in eV.

GaAs, the band positions provide ~0.5V of barrier height at the junction between the two semiconductors. The known position of the ferri-ferrocyanide couple of +0.46V (SCE) suggests that the photocurrent should disappear about 0V (SCE), in reasonable agreement with the data in Fig. 4.

For BP-coated n-Si, the band positions are such that an ohmic contact would be expected between the two, and no photovoltage with the silicon spectral response should be expected. Since both Si and GaAs are quite covalent, Fermi level pinning is expected to occur around 1/3 of the bandgap (14). This is how the band structure is drawn in Fig. 8. Thus, the expected maximum open-circuit voltage is about 0.4V, in reasonable agreement with observations. While Fermi level pinning for GaAs might also be expected, the height of the conduction band discontinuity suggests that pinning would change neither the barrier height nor the maximum open-circuit voltage significantly.

Another important consideration in these systems is the epitaxial growth of protective film on the small gap material. BP grows epitaxially on Si but not on GaAs. It is, however, the GaAs that shows the best junction characteristics, although the Si shows somewhat greater stability. This is to be expected as the higher interface state densities in the GaAs case make it easier for holes to pass through the heterojunction, as shown in Fig. 8. In the Si case, the lack of interface state density impedes the hole transport and provides, in effect, large series resistance for the device. This explains the linear I-V characteristics and poor fill factors that are observed.

The doping of the overcoating semiconductor layer is very important. To achieve the type of device desired—essentially a Schottky barrier device—it is necessary to have sufficient doping for the layer to act essentially as if it were a metal. If doping levels are too low, the device becomes an n/n' heterojunction device of the type envisaged by Wagner and Nozik (4, 5). In this case, minority carrier transport through the heterojunction is impeded by the band discontinuities. If doping levels are too high, a high density of deep trap states can be introduced, resulting in reduced transmission in the desired portion of the spectrum. While a high density of interface states is desirable to achieve efficient Schottky barrier behavior, a high density of deep trap states, as stated above, can be detrimental to electrode performance. These states can originate with lattice imperfections, impurities, and excess dopant (or a compensated situation). These problems seem to effect the BP-coated silicon electrode to some extent. The gradual increase in efficiency *vs.* time for these electrodes may be due to a reduction of deep trap state density.

In general, the device resembles a Schottky barrier solar cell in series with an electrochemical cell. This situation may occur in quite a few surface-modified systems, and especially must be considered when metals are deposited on semiconductor surfaces. BP has demonstrated an exceptional stability in these devices, with 2000Å layers surviving nearly 30,000C with no detectable deterioration. While this type of device may not be eminently practical, it does provide an excellent test bed for investigating new semiconductors for PEC's and does demonstrate the utility of employing semiconductors as stable transparent conductive windows.

Acknowledgment

This work performed at Sandia National Laboratories supported by the U.S. Department of Energy under Contract DE-AC04-76DP00789.

Manuscript submitted April 6, 1983; revised manuscript received *ca.* June 3, 1983.

Sandia National Laboratories assisted in meeting publication costs of this article.

REFERENCES

1. A. B. Bocarsly, D. C. Bookbinder, R. N. Doiney, N. S. Lewis, and M. S. Wrighton, *J. Am. Chem. Soc.*, **102,** 3683 (1980).
2. A. Heller, H. J. Lewerenz, and B. Miller, *ibid.*, **103,** 200 (1980).
3. J. M. Bolts, A. B. Bocarsly, M. C. Palazotto, E. G. Walton, N. S. Lewis, and M. S. Wrighton, *ibid.*, **101,** 1378 (1979).
4. S. Wagner and J. L. Shay, in "Electrode Materials and Processes for Energy Conversion and Storage," J. D. E. McIntyre and S. Srinivasan, Editors, p. 105, The Electrochemical Society Softbound Proceedings Series, Princeton, NJ (1977).
5. R. Noufi, A. J. Frank, and A. J. Nozik, *J. Am. Chem. Soc.*, **103,** 1849 (1981).
6. R. C. Hughes, D. S. Ginley, and A. K. Hays, *Appl. Phys. Lett.*, **40,** 853 (1982).
7. S. Menezes, A. Heller, and B. Miller, *This Journal*, **127,** 1268 (1980).
8. L. A. Harris and J. A. Hugo, *ibid.*, **128,** 1203 (1981).
9. R. J. Baughman and D. S. Ginley, Submitted to *Solid-State Chem.*
10. T. Takenaka, M. Takigawa, and K. Shohno, *Jpn. J. Appl. Phys.*, **15,** 2235 (1976).
11. K. Shohno, H. Ohtake, and J. Bloem, *J. Cryst. Growth*, **45,** 187 (1978).
12. S. Motojima, S. Yokoe, and K. Sugiyama, *ibid.*, **49,** 1, (1980).
13. M. A. Butler and D. S. Ginley, *This Journal*, **125,** 228 (1978).
14. S. M. Sze, "Physics of Semiconductor Devices," Chap. 5, Wiley, New York (1981).

An Analysis of a Back Fed Porous Electrode for the Br_2/Br^- Redox Reaction

John Van Zee* and Ralph E. White**

Department of Chemical Engineering, Texas A&M University, College Station, Texas 77843

ABSTRACT

An experimental analysis of the Br_2/Br^- redox reaction in a porous back fed ruthenium-coated titanium electrode is described. A mathematical model of the steady-state process is presented. Nonlinear regression of the model against the experimental data gives physically meaningful parameter estimates; these parameters and the model provide a design equation for the porous electrode current as a function of specific surface area, bulk Br_2 concentration, average total overpotential, and the Reynolds number. The design equation shows that the back fed electrode could reduce the loss of Br_2 across the separator and the ohmic loss in a Zn/Br_2 battery.

A flow-by back fed porous electrode, as shown in Fig. 1, is a diffusion electrode. The term "flow-by" emphasizes that the reactant flows outside rather than through the electrode. Consequently, fresh reactant must diffuse to a reaction site within the porous electrode. Typically, the reaction occurs on the side closest to the counterelectrode if the catalyst application and the concentration are uniform. Thus, the back fed electrode may be limited by diffusion if it is too thick. This may be the reason it has been ignored by commercial monopolar Zn/Br_2 battery designers (1, 2).

However, this back fed configuration may provide some advantages for a Zn/Br_2 battery or similar electrochemical system. Specifically, the back fed electrode may reduce the ohmic energy loss and the product (*e.g.*, Br_2) loss across the separator. The ohmic energy loss would be decreased because the solution gap between the electrodes would be reduced to approximately half that of the front fed electrode (compare Fig. 1 and 2). This reduction in electrode gap could decrease the cell's specific resistance by more than 25% in Zn/Br_2 batteries if a relatively nonconducting complexing agent (3) is present in the electrolyte. [This decrease in resistance is approximately 25% because the electrolyte between the electrodes contributes only approximately 50% of the ohmic loss in a Zn/Br_2 battery (1, 4).] The same percentage decrease might be observed in gas generating cells. The loss of product across the separator may be reduced because the porous electrode may act as a separator when the reaction occurs preferentially on the back side (fresh solution side) of the porous electrode (Fig. 1). This reduction of the product loss across the separator would probably decrease the self-discharge rate in a Zn/Br_2 battery.

Even though back fed electrodes are limited by diffusion, the limiting current due to diffusion may be adequate for the specific application. This is evident, for example, in the back fed electrode designs of SPE water electrolyzers (5) where the diffusion limiting current is large because the reactant is in abundance. Even if the reactant is present in low concentration, the process may be limited to some current below the diffusion limited current by slow kinetics or by some other feature of the other electrode. For example, in Zn/Br_2 batteries the Br_2 electrode is not required to operate above 50 mA/cm^2 because of zinc dendrite formation at the zinc electrode (1, 2, 4, 6, 7).

Since the design principles for flow-by back fed porous electrodes are not well known, this paper presents an analysis of this electrode design for the bromine/bromide reaction

$$Br_2 + 2e^- \rightarrow 2Br^- \qquad [1]$$

* Electrochemical Society Student Member.
** Electrochemical Society Active Member.
Key words: battery, current density, mass transport, kinetics.

First, a mechanistic model of the steady-state process is developed. Next, an experimental study of the bromine/bromide redox reaction is presented. Then, least squares regression techniques are used to fit the model to experimental data to obtain physically meaningful parameter estimates. Finally, the regression results and the mechanistic model are used to analyze the physical behavior of a flow-by back fed porous Br_2 electrode.

Previous Work

The previous analyses (8-12) of steady-state mass transfer in porous diffusion electrodes pertinent to the back fed model developed below have been reviewed by Newman and Tiedeman (13).[1] In these previous

[1] The approach of these analyses differs from the approach of single-pore models (see Ref. (14), for example) as described by Tilak *et al.* (15) because it uses a pseudo-homogeneous reaction rate and volume average quantities instead of the single-pore concept.

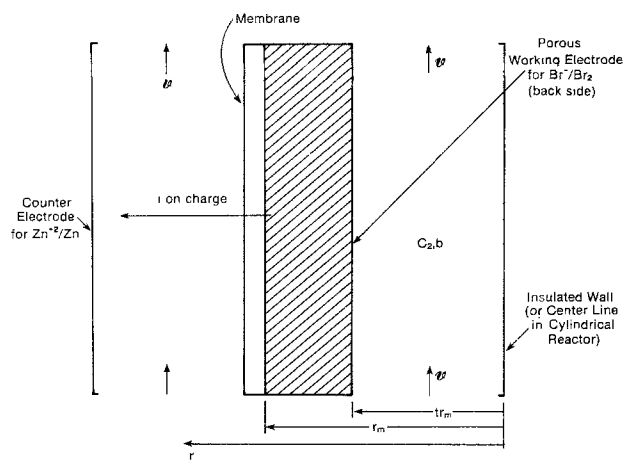

Fig. 1. A schematic of a back fed porous electrode for the bromine/bromide redox reaction in a Zn/Br_2 battery.

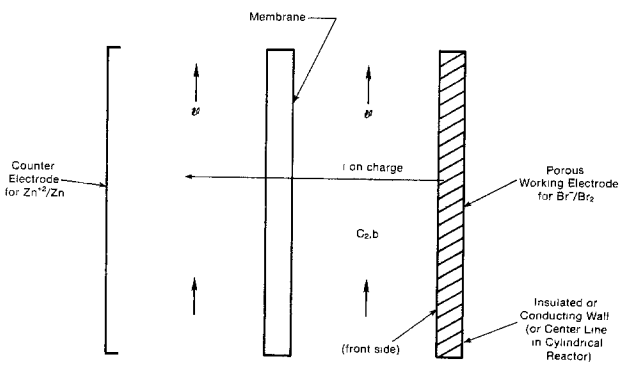

Fig. 2. A schematic of a front fed porous electrode

analyses, the authors have considered redox reactions which have stoichiometric coefficients of +1 and −1 for anodic and cathodic species, respectively, whereas the coefficients used here are +2 and −1 as shown by reaction [1]. These previous models and the model developed here include the assumption of excess supporting electrolyte and, consequently, neglect the effect of ionic migration. The boundary conditions for the concentration in the previous analyses require a known constant concentration of reactant at the edge of the porous region whereas in the model developed below the reactant concentration at the edge of the porous region depends on overpotential, Reynolds number, and the bulk properties of the flowing electrolyte.

The results most closely related to the back fed electrode model presented here are those of Newman and Tiedeman (13) and Austin and Lerner (12) because they neglect the ohmic potential drop in both the matrix and the solution and because they use a complete Butler-Volmer kinetic expression. Newman and Tiedeman (13) give the current/potential relationship in Cartesian coordinates for redox reactions with stoichiometric coefficients of +1 and −1 and a constant concentration at the reservoir-electrode interface. One problem with this fixed concentration boundary condition model is that accurate predictions of the current density from the resulting equations occur only for infinitely large rates of external mass transfer. Austin and Lerner (12) use a stagnant film concept to relax the constant concentration boundary condition and, thereby, include the effect of external mass transport; they show the current potential relationship in Cartesian coordinates in terms of the limiting current. The limiting current density in Ref. (12) could have been but was not given as a function of the external mass transfer coefficient

$$i_L = kc_{i,b}\frac{n\mathbf{F}}{s_i} \qquad [2]$$

This mass transfer coefficient k is included in the back fed model developed below. Austin and Lerner (12) discuss the relative importance of the ohmic drop in the solution phase and they show that its neglection may be a reasonable assumption when the reaction occurs over a very short distance as is the case for the model presented here as discussed below.

Model

The model developed here extends similar developments for steady-state mass transfer in porous electrodes (8-13) by including an external mass transfer coefficient and different stoichiometric coefficients for the reactant and product. That is, redox reactions considered in Ref. (8-13) have stoichiometric coefficients of +1 and −1 for the oxidized and reduced species, respectively, whereas the coefficients used here are +2 and −1 as shown by reaction [1].

The model is presented by first stating the assumptions and then developing the equations. The assumptions used in the development of the model are

a. Steady-state is maintained.

b. The porosity and specific catalytic surface area are uniform and they do not change with time.

c. Dilute solution theory (13) applies.

d. Sufficient supporting electrolyte exists so that ionic migration can be neglected (*i.e.*, no potential drop in the solution).

e. Dispersion and convection are not present in the porous section of the electrode.

f. In the porous region, the only important gradients are those in the direction normal to the fluid flow.

g. The separator at the edge opposite the flowing solution is impermeable to the reacting species.

h. The hydrodynamic profile is known in the nonporous region.

i. The potential drop in the matrix is negligible.

j. The concentration of the anodic reactant, Br^-, is large relative to the concentration of the cathodic reactant, Br_2.

k. The kinetic expression follows a Butler-Volmer type expression where the cathodic reaction order is unity and reaction [1] is assumed to be an elementary step.

l. Isothermal conditions exist.

m. The conversion per pass is small.

These assumptions permit the development of a single analytical expression suitable for design over a large range of overpotentials.

The equations of this model can be developed by considering the cylindrical back fed electrode of Fig. 1. (Cylindrical coordinates are used since the experimental data were obtained with a tubular porous electrode.) Bromine is present at a concentration of $c_{2,b}$ in the stream having an axial velocity v. The redox reaction of interest here occurs in the porous electrode which has an outside radius of r_m and an inside radius of tr_m where t is less than one.

The steady-state material balance for the ith species within the porous electrode can be written as (13)

$$-\nabla \cdot N_i + aj_i = 0 \qquad [3]$$

for reaction [1] with subscript i equal to 1 and 2 for Br^- and Br_2, respectively. The volume average production rate aj_i can be written as (16)

$$aj_i = \frac{-s_i a i_{o,b}}{n\mathbf{F}}\left\{\prod_i\left(\frac{c_i}{c_{i,b}}\right)^{p_i}\exp\left(\frac{\alpha_a\mathbf{F}}{RT}\eta\right) - \prod_i\left(\frac{c_i}{c_{i,b}}\right)^{q_i}\exp\left(\frac{-\alpha_c\mathbf{F}}{RT}\eta\right)\right\} \qquad [4]$$

where

$$i_{o,b} = i_o^{\circ}\prod_i\left(\frac{c_{i,b}}{c_i^{\circ}}\right)^{\gamma_i} \qquad [5]$$

$$p_i = \gamma_i + \frac{\alpha_a s_i}{n} \qquad [6]$$

$$q_i = \gamma_i - \frac{\alpha_c s_i}{n} \qquad [7]$$

and

$$\alpha_a + \alpha_c = n \qquad [8]$$

$$\eta = V - \Phi_2 - \Delta U_b \qquad [9]$$

The reaction orders p_i and q_i in Eq. [4] can be related to the stoichiometry for an elementary step (17): (*i*) for anodic reactants, $p_i = s_i$ and $q_i = 0$ and (*ii*) for cathodic reactants, $q_i = -s_i$ and $p_i = 0$. The concentration dependence on the exchange current density of species i, γ_i, is then related simply to the stoichiometric equation. That is, since reaction [1] is assumed to be an elementary step and if it is assumed that $\alpha_a = \alpha_c = 1.0$, for example, then

$$\gamma_1 = 2 - \frac{(1.0)(2)}{2} = 1.0 \qquad [10]$$

and

$$\gamma_2 = 1 + \frac{(1.0)(-1)}{2} = 0.5 \qquad [11]$$

The total overpotential η in Eq. [4] and [9] is the sum of the surface overpotential and the local overpotential from outside the double layer to the bulk solution. This overpotential includes the effect of a reference electrode which differs from the working electrode by the term ΔU_b where

$$\Delta U_b = U^{\theta} - U_{re}{}^{\theta} - \frac{RT}{n\mathbf{F}}\sum_i s_i \ln\left(\frac{c_{i,b}}{\rho_o}\right) + \frac{RT}{n_{re}\mathbf{F}}\sum_i s_{i,re}\ln\left(\frac{c_{i,re}}{\rho_o}\right) \qquad [12]$$

It is important to note that both $i_{o,b}$ and ΔU_b are based on the same bulk concentration ($c_{2,b}$), and that the potential of the working and reference electrodes must be referenced to the same thermodynamic scale (*e.g.*, H_2 scale).

Neglecting ionic migration according to Assumption d, the specific expression for the flux of Br_2 in the porous electrode is

$$N_2 = -D_e \frac{dc_2}{dr} \quad [13]$$

where

$$D_e = \frac{\epsilon}{\tau} D_2 \quad [14]$$

Substitution of Eq. [4], [13], and [14] into the radial component of the cylindrical form of Eq. [3] yields

$$\frac{d^2c_2}{dr^2} + \frac{1}{r}\frac{dc_2}{dr} - Kc_2 = \frac{-ai_{o,b}}{2FD_e} \exp\left(\frac{\alpha_a F}{RT}\eta\right) \quad [15]$$

where

$$K = \frac{ai_{o,b}}{2FD_e c_{2,b}} \exp\left(\frac{-\alpha_c F}{RT}\eta\right) \quad [16]$$

and the local concentration of Br^- has been assumed to be constant and equal to the bulk concentration of Br^-, according to Assumption j (*i.e.*, $c_1/c_{1,b} = 1.0$).

The following dimensionless variables can be used to simplify Eq. [15]

$$\xi = \frac{r}{r_m}, \quad \theta = \frac{c_2}{c_{2,b}} \quad [17]$$

which when substituted into Eq. [15] yields

$$\frac{d^2\theta}{d\xi^2} + \frac{1}{\xi}\frac{d\theta}{d\xi} - B\theta = -A \quad [18]$$

where

$$B = Kr_m^2 \quad [19]$$

and

$$A = \frac{ai_{o,b}r_m^2}{2FD_e c_{2,b}} \exp\left(\frac{\alpha_a F}{RT}\eta\right) \quad [20]$$

Following Assumptions g, h, and m, the boundary conditions are at

$$r = r_m, \quad \xi = 1 \quad \frac{d\theta}{d\xi} = 0 \quad [21]$$

at

$$r = r_m t, \quad \xi = t \quad \frac{d\theta}{d\xi} = \frac{r_m k}{D_e}(\theta(t) - 1.0) \quad [22]$$

where the gradients are defined to be in the positive direction of ξ. The mass transfer coefficient k in Eq. [22] is an average value over the length of the tubular reactor and is given by (18)

$$k = 1.651 \frac{D_2}{2r_i}\left(N_{Re}N_{Sc}\frac{2r_i}{L}\right)^{1/3} \quad [23]$$

Equation [18] can be solved analytically by assuming a solution of the form

$$\theta(\xi) = \Psi(\xi) + \Gamma \quad [24]$$

where Γ is a constant for a given η and temperature and is given by

$$\Gamma = \exp\left(\frac{2F}{RT}\eta\right) \quad [25]$$

Application of the boundary conditions, Eq. [21] and [22], to the homogeneous part of Eq. [18] gives the solution in terms of modified Bessel functions of the first and second kind (19). The complete solution to Eq. [18] is [see Ref. (20)]

$$\theta(\xi) = G[\theta(t) - 1.0]\left\{\frac{K_1(\sqrt{B})}{I_1(\sqrt{B})} I_o(\sqrt{B}\xi) + K_o(\sqrt{B}\xi)\right\} + \exp\left(\frac{2F}{RT}\eta\right) \quad [26]$$

where the dimensionless surface concentration is

$$\theta(t) = \frac{GK_1(\sqrt{B})I_o(\sqrt{B}t) + GI_1(\sqrt{B})K_o(\sqrt{B}t) - I_1(\sqrt{B})\exp\left(\frac{2F}{RT}\eta\right)}{GK_1(\sqrt{B})I_o(\sqrt{B}t) + GI_1(\sqrt{B})K_o(\sqrt{B}t) - I_1(\sqrt{B})} \quad [27]$$

and

$$G = \frac{r_m k I_1(\sqrt{B})}{D_e\sqrt{B}[K_1(\sqrt{B})I_1(\sqrt{B}t) - I_1(\sqrt{B})K_1(\sqrt{B}t)]} \quad [28]$$

An expression for the current density, consistent with the sign convention that cathodic currents are negative, can be obtained from the dimensional definition of the flux at the inside edge of the porous electrode

$$\frac{i}{2F} = N_2 \Big|_{\xi=t} = kc_{2,b}[\theta(t) - 1.0] \quad [29]$$

In addition, the cross-sectional area at the inside edge of the porous electrode can be used to obtain an expression for the total current

$$I = 4\pi t r_m L F k c_{2,b}[\theta(t) - 1.0] \quad [30]$$

Equation [30] can be used to predict the current being passed by a back fed cylindrical porous electrode as a function of the applied potential and the Reynolds number because it includes the dependence of the concentration distribution on the mass transfer coefficient external to the porous electrode. Also, this equation applies to a front fed configuration where the separator and the counterelectrode are located at some radial position less than tr_m (*i.e.*, close to the center line). Thus, the orientation of the coordinate system would be the same as with the back fed electrode and therefore the boundary conditions of Eq. [21] and [22] would still apply. Conceptually, the boundary condition at $\xi = 1$ would be the same because a backing plate would be considered impermeable. In this front fed configuration, the mass transfer coefficient must be adjusted for flow in an annulus (18). (Analogous equations for Cartesian coordinates are shown in the Appendix).

Equation [30] and the model presented here are limited to small conversions per pass because they include the lumped mass transfer coefficient of Eq. [23] (18). However, a small conversion per pass is a reasonable assumption for flow batteries (*e.g.*, Zn/Br_2, Zn/Cl_2, redox) because large concentration changes occur only after many passes. Thus, the model has utility for flow batteries. Also, the model can be utilized to determine kinetic and mass transfer parameters from a reactor built to satisfy Assumption m; the parameters obtained from this differential reactor (laboratory scale) could then be used to design a more complicated pilot plant scale reactor.

A simple form of Eq. [27] for use in Eq. [30] can be obtained for the case where the pseudo-homogeneous rate constant B is large and the electrode is not too thin; that is, for the cases where

$$\sqrt{B} \geq 88 \quad \text{and} \quad t \leq 0.95 \quad [31]$$

Equation [27] becomes

$$(t) = \frac{kr_m + D_e\sqrt{\bar{B}}\exp\left(\frac{2\mathbf{F}}{RT}\eta\right)}{kr_m + D_e\sqrt{\bar{B}}} \quad [32]$$

or

$$\theta(t) = \frac{1 + P\exp\left(\frac{2\mathbf{F}}{RT}\eta\right)}{1 + P} \quad [33]$$

where

$$P = \sqrt{\frac{D_e a i_{o,b}\exp\left(\frac{-\alpha_c\mathbf{F}}{RT}\eta\right)}{k^2 2\mathbf{F}c_{2,b}}} \quad [34]$$

The dimensionless parameter P in Eq. [34] shows the combined effects of internal, external, and charge transfer resistance on the surface concentration.

Experimental Analysis

The experimental analysis of the flow-by back fed cylindrical porous electrode considered the reduction of bromine to bromide according to Eq. [1] and the oxidation of bromide to bromine according to the reverse reaction of Eq. [1]. The experimental data were obtained by potentiostatic determination of the current for a cylindrical flow-by back fed porous Ti-RuO_2 electrode. The dependent variable was the observed steady-state current and the independent variables were applied potential ($V - \Phi_{re}$) and the electrolyte flow which was equivalent to the Reynolds number (N_{Re}) since ν and r_i were assumed to be constant. The experiments were performed at a constant bulk Br_2 concentration ($c_{2,b}$) at different applied potentials and Reynolds numbers. The order of the experiments (*i.e.*, the order for applying different values of the potential) was randomized to remove the effect of any concentration changes with time. This randomization insured that the experimental errors were independent and therefore the data are consistent with the assumptions of the least squares theory discussed below [see also, *e.g.*, Ref. (21)].

Experimental Apparatus

Reactor system.—A schematic of the reactor system is shown in Fig. 3; the negative electrolyte contacted the zinc terminal (*i.e.*, the counterelectrode in this study) and the positive electrolyte contacted the Br_2/Br^- terminal (*i.e.*, the back fed porous working electrode under investigation here). Fisher flowmeters (No. 448-324) with 0.635 cm outside diameter glass floats were used for volumetric flow measurement. Constant speed magnetic induction centrifugal pumps (Eastern No. MD-15T-G01) were used to circulate the electrolytes; peristaltic (*i.e.*, roller) pumps were not used because of reported problems with the surges in pressure caused by the rollers (22). The recycle streams were a necessary result of the constant speed pumps and they formed the reservoir for each electrolyte. Schedule 40, 1.27 cm PVC pipe was used for the system piping and smaller connections were made with Tygon tubing and hose clamps. Some attack of the tubing by Br_2 was noticed over the life of the experiments (~2 months), but no loss of catalytic activity due to organic poisoning of the Br_2 electrode by any dissolved Tygon was observed.

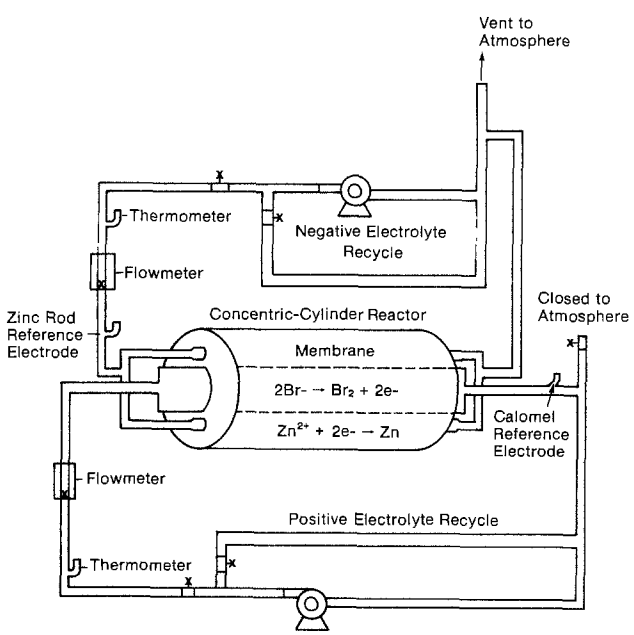

Fig. 3. A schematic of the experimental reactor system shown in the charge mode.

The experimental system was designed as shown in Table I, to be consistent with Assumptions d, i, j, and m used in the development of the theoretical model; the system was also designed in a manner similar to existing Zn/Br_2 batteries (1, 2, 4, 6, 7, 22). The experimental electrolyte was supported wtih excess Na^+ to satisfy Assumption d. Although the specific conductivity κ of the electrolyte was not measured, it was probably about 0.4 Ω^{-1} cm^{-1} (1, 4). Using this κ value, the voltage drop in the solution over the length of a reaction zone on the order of 10^{-2} cm can be calculated by Ohm's law and shown to be on the order of 10 mV (20) at a current density of 50 mA/cm^2 (a small reaction zone is expected for this fast reaction as described below); this voltage drop is consistent with part of Assumption i. The concentration of bromide in Table I is approximately 80 times larger than the limiting reactant, bromine. This concentration ratio is consistent with existing Zn/Br_2 battery design and Assumption j. Table I also shows that the conversion (or production) per pass of bromine is expected to be low for typical currents and Reynolds numbers, as discussed below.

Electrodes.—The zinc terminal (*i.e.*, counterelectrode) consisted of a 2.54 cm OD titanium tube with a wall thickness of 0.125 cm. The negative electrolyte was fed to the inside of the tube through PVC end caps. The end caps fit snugly over the outside of the titanium tube and small leaks were stopped by wrapping Teflon tape around the outside of the tube. The inner electrode hole in the center of the end caps was sealed with an O-ring and the end cap lids. Two equally spaced electrical connections were made between the end caps; no measurable voltage drop existed between the connections or over the length of the counterelectrode. During the anodic or charge mode of the experiment, bromide was oxidized to bromine and zinc was plated at this counterelectrode. Conversely, when cathodic potentials were applied, bromine was reduced to bromide at the porous electrode and zinc was dissolved at the counterelectrode.

Table I. Experimental system design specifications

Negative electrolyte volume	420 ± 10 cm^3
Positive electrolyte volume	580 ± 10 cm^3
Negative electrolyte composition:	
$ZnBr_2$	1.05M
NaBr	2.08M
pH (lowered from 3.8 with HBr)	1-3
Zyonil	100 ppm
Positive electrolyte composition:	
$ZnBr_2$	1.05M
NaBr	2.08M
Br_2	0.0510M
pH	3.8
Negative and positive electrolyte density at 22°C	1.38 g/cm^3
Electrode length	12.7 cm
Counterelectrode plating area	56.2 cm^2
Annulus spacing	0.328 cm
Positive electrode outside diameter ($2r_m$)	0.4572 cm
Positive electrolyte, cathodic reactant conversion per pass for N_{Re} = 100 and 0.25A (assuming 100% faradaic conversion)	8.0%

The flow-by back fed electrode (again, the experimental working electrode) consisted of a titanium tube perforated with 400 holes which were drilled with a No. 57 drill (0.10922 cm diam). The titanium tube wall thickness was 0.0889 cm and the outside diameter of the tube was 0.635 cm. The entire tube was coated with RuO_2 by using a standard dimensionally stable anode (DSA) preparation technique. Table II summarizes the electrode fabrication parameters including the calculated (based on geometry) specific surface area and porosity of the perforated tube electrode.

The catalytic surface area is expected to be much greater than the geometric value shown in Table II because the RuO_2 coating was deposited by thermal decomposition and therefore is highly porous. Reported catalytic surface areas for the DSA coating range up to 1000 times larger than the geometric area due to the roughness of the surface (23, 24). Thus, it is this porous coating that corresponds to the classical concept of a homogeneous porous electrode rather than the drilled holes of the titanium tube. Thus, the ratio of porosity and tortuosity for the porous coating would probably be larger than the geometric value for ϵ/τ shown in Table II.

Also shown in Table II is the length of tube before the porous electrode L_{en}. This entrance length can be considered as the length available for the development of the hydrodynamic profile. The required entrance length is a function of the Reynolds number and it can be estimated (25)

$$L_{en} = 0.036\, N_{Re}(2r_i) \qquad [35]$$

At a Reynolds number of 100, the entrance length from Eq. [35] is 1.64 cm. The actual entrance length in the experiment was greater than this because Tygon tubing with an ID approximately equal to r_i was used between the PVC pipe and the perforated tube electrode.

A saturated calomel electrode (SCE) was used as the reference electrode in the experiment and it was positioned downstream of the working electrode as shown in Fig. 3. The actual location (*i.e.*, upstream or downstream) was unimportant because the conversion per pass was small; hence the reference electrode was bathed in a concentration with an essentially constant ratio of Br_2/Br^- throughout an experimental run. This constant concentration was used to calculate the null potential ΔU_b which can be measured at open circuit. A measured value of $\Delta U_b = 0.757 \pm 0.0005$V was observed for all of the experimental data reported here. A calculated value of $\Delta U_b = 0.772$V is predicted according to Eq. [12] with the concentrations of Table I. This discrepancy of 15 mV between the observed and predicted values of ΔU_b may be attributable to the liquid junction potential between the reference electrode and the positive electrolyte which flowed by the SCE; (according to Ref. (26), liquid junction potentials can be on the order of 20 mV).

Membrane preparation.—The separator used in all experimental runs was a Nafion 315 membrane. The membrane was cut to the required width and then boiled in distilled water for at least 1 hr. The boiling was required to open the pores in the resin of the membrane and distilled water (instead of acid) was used to minimize the diffusion of Br_2 through the Nafion as discussed in Ref. (27). The membrane was allowed to cool to room temperature and then it was wrapped around the outside of the porous electrode. The 0.6 to 0.3 cm seam where the membrane overlapped was glued by using a syringe applicator with an epoxy and hardener (General Electric No. 512 and No. 524). The glue was allowed to dry at room temperature for about 5 days. The electrode/membrane assembly was then tested for leaks with an approximate 30 cm static head of water. The membrane was wrapped tightly around the electrode and hence flow through the electrode (*e.g.*, in one drilled hole and out another) was highly improbable; thus model Assumption e was fulfilled.

Electronics.—Figure 4 shows a schematic of the electrical connections used in the experiment. A Princeton Applied Research potentiostat (PAR 371) was used to control the first independent variable, the applied potential $V - \Phi_{re}$. That is, the potential difference between the porous electrode (*i.e.*, the working electrode) and the SCE were controlled by adjusting the potential applied to the counterelectrode. The applied potential $V - \Phi_{re}$ was not corrected for ohmic drop because the downstream reference electrode was located outside of the potential field which existed between the working electrode and the counterelectrode. Thus, it was assumed that the potential in the solution was the same everywhere in the flow channel and hence $\Phi_{re} = \Phi_2$. Thus, the total overpotential η of Eq. [9] is related to the applied potential $V - \Phi_2 = V - \Phi_{re}$ through the open circuit or null potential ΔU_b (*i.e.*, $\eta = V - \Phi_{re} - \Delta U_b$). Also, the assumption of negligible potential drop within the porous region of the electrode implies that $\Phi_{re} = \Phi_2 = \Phi_{2,o}$. At a given applied potential and

Table II. Experimental back fed porous electrode fabrication parameters. (Values without superscripts were measured.)

Parameter	Value	Units
ϵ/τ	0.172[1]	none
a	112.4[2]	cm^{-1}
L	12.7	cm
r_m	0.3175	cm
r_i	0.2286	cm
t	0.720	none
ν	0.00903[3]	cm^2/sec
L_{en}	12.7	cm
Electrode area at r_i	18.24	cm^2

[1] Assumed $\tau = 1.0$; ϵ was calculated from geometry of the holes in the perforated tube electrode.
[2] Assumed value based on geometric specific surface area of 15.10 cm^{-1} and a roughness factor of 7.443.
[3] Calculated from assumed value of $\mu = 1.25$ g/cm-sec and a measured value of $\rho = 1.384$ g/cm^3.

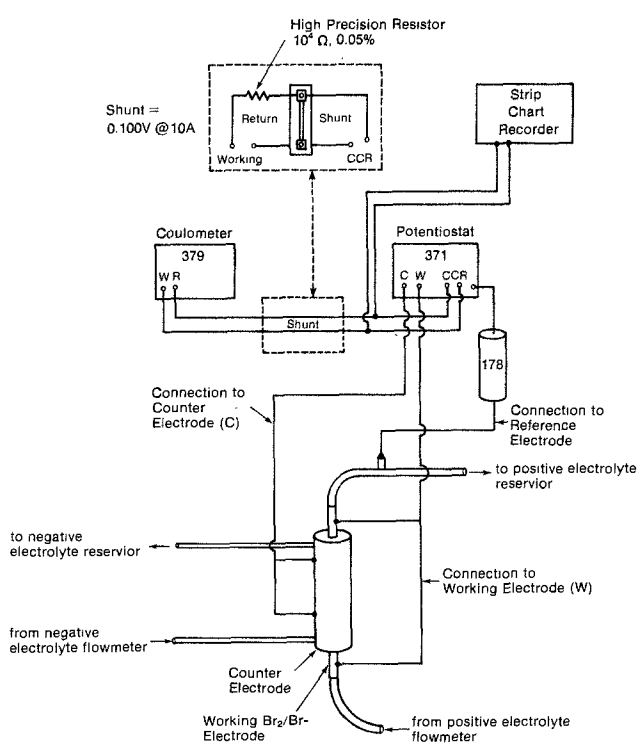

Fig. 4. A schematic of the experimental electronics

Reynolds number, a strip chart recorder (as shown in Fig. 4) was used to verify that steady-state current conditions existed. This current was then read from the analog meter on the PAR 371. The digital coulometer (PAR 379) shown in Fig. 4 was used to record the number of coulombs passed during an experimental run which was then used to calculate the faradaic conversion per pass of the positive electrolyte, as shown in Table I. (The coulometer was connected across a 10,000Ω shunt to reduce the input signal to within the limits of the coulometer.)

Experimental Procedures

Steady-state current measurement.—The procedure for measuring the steady-state current from the back fed electrode began by circulating the electrolyte streams for about an hour until the temperature of each stream was constant followed by an iodometric titration to find the initial Br_2 concentration in the positive electrolyte. Once the bromine concentration was known, the cell was left at open circuit for 30 min and the null potential (*i.e.*, the open-circuit potential between the working electrode and the downstream calomel reference electrode) ΔU_b was recorded every 10 min. Once the null potential was constant, experimental data were obtained; that is, a randomly chosen applied anodic potential difference $V - \Phi_{re}$ was set until a steady-state current was observed on the strip chart recorder. Then, the cell was returned to open circuit and the number of coulombs of charge were recorded. The null potential ΔU_b as measured by the PAR 371 was recorded and the reservoir concentration of the Br_2 above the titrated concentration was calculated by assuming 100% faradaic efficiency. This calculation was used to check the percent conversion.

If the percent conversion was small and if the null voltage was the same after the run as it was for the previous run, the cell was operated according to the above procedure at a randomly chosen cathodic potential difference. If the null potential was different from the value in the prior runs, the cell was charged or discharged at a low rate to adjust the bromine concentration, left at open circuit for 10 min and the null potential checked again. Then, samples were taken to determine the reservoir concentration of Br_2 by titration. If the Br_2 concentration was the same (to within ± 3%) as the previous runs, the cell was operated at a randomly chosen cathodic potential difference according to the above procedure. Then, the above anodic/cathodic sequence was repeated.

Titration of these samples and the measurement of the null potential ΔU_b were used to check the level of the bromine concentration $c_{2,b}$. Thus, the bromine concentration was not controlled during an experimental run but it was measured, and this measurement was used as a basis for including or discarding the results of an experimental data point. However, the titrations involved three 5 ml samples from the reservoir volume which was about 3% of the reservoir volume. Therefore, to minimize additions to the reservoir, samples were taken and titrations were made after four or five experimental runs if the null potential was unchanged. Theoretically, the null potential can be used to predict changes in the bromine concentration to within ± 4% for a 0.5 mV change at the concentrations shown in Table I. Experimentally, an observed change in ΔU_b of 0.5 mV corresponded to a 4% change in the bromine concentration as measured by titration of three samples. Thus, although the bromine concentration was not controlled in the experiment, the experimental error was approximately 4%. To insure that these concentration errors were random, the experimental runs were randomized; hence, any concentration changes with time should not affect the average value of the measured current at a given applied potential and Reynolds number.

Flow control.—The second independent variable, the Reynolds number, was controlled by a needle valve as indicated by a flowmeter. That is, the volumetric flow in the nonporous region of the electrode was adjusted manually so that the Reynolds number remained constant for an experimental data point. The volumetric flow was obtained from a calibration curve which was drawn from manufacturers' data and the experimental kinematic viscosity shown in Table II. The density of the positive electrolyte was measured at 24°C and the viscosity of the electrolyte was obtained from Ref. (1) for this calculation. The approximate error in the experimental Reynolds number was 5%.

Experimental Results

The points in Fig. 5 and 6 show the experimentally determined steady-state current as a function of applied potential and Reynolds number for the perforated tube back fed electrode. The numbers beside each data point correspond to the sequence in which the points were obtained. The data connected by dashed lines indicate the conditions where bubbles were observed in the exit stream. The solid lines in Fig. 5 and 6 are model predictions which are discussed below. The electrode fabrication parameters and electrolyte compositions are shown in Tables I and II. The electrolyte temperature for all data was 28°C. The Br_2 concentration varied by 3% from 0.0510M as shown in the figure but the null potential ΔU_b was essentially constant. The data were reproducible over the 2 month life of the experiment.

The general form of the results in Fig. 5 is similar to the behavior of a rotating disk electrode (RDE) as the rotation speed is increased; that is, the limiting current increases with Reynolds number and thereby shows a region in which external mass transfer controls the rate of reaction. Also, the length of the limiting current plateau decreases as the Reynolds number increases in a manner similar to an RDE system for

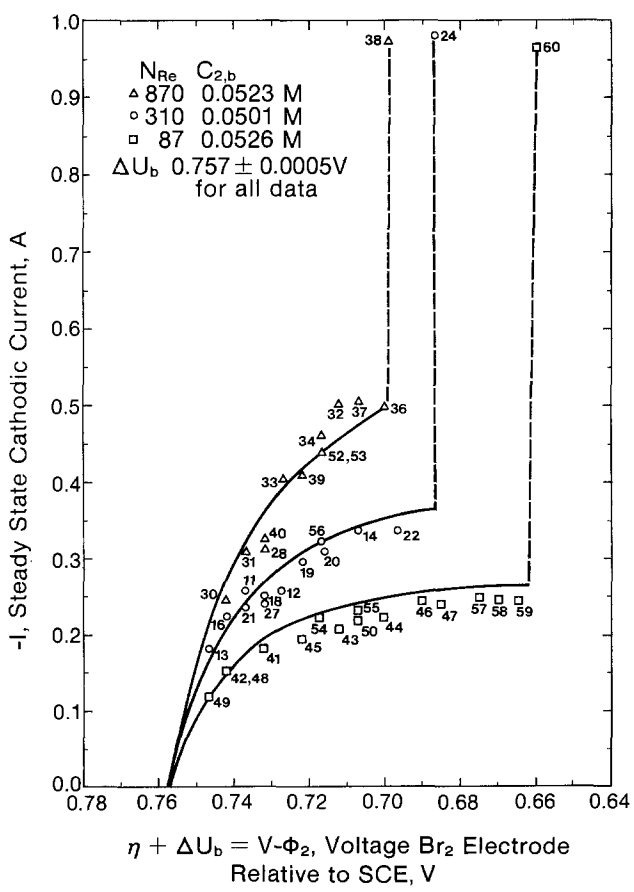

Fig. 5. Experimental cathodic steady-state currents

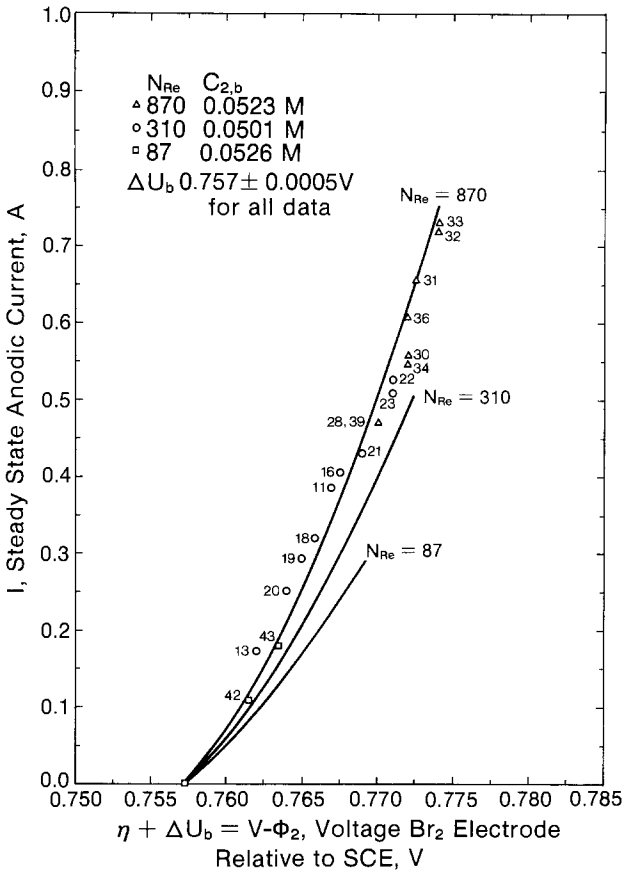

Fig. 6. Experimental anodic steady-state currents

the reduction of Cu^{+2} in acidic electrolyte (28). In Fig. 5, the side reaction characterized by gassing is probably the reduction of hydrogen ion. However, no changes in the pH of the positive electrolyte were noticed, but this could be a result of the small amount of gassing and the large reservoir.

The anodic experimental data in Fig. 6 depend only slightly on the Reynolds number over the range of experimentally applied potentials. This slight dependence is due to the high Br^- concentration in the electrolyte (20).

Least Squares Regression

The model presented above depends on, among other things, the parameters α_c, i_o^o, and D_2. These parameters can be obtained from the literature if available (they are not available for these experimental conditions), determined by independent experiments or determined by applying least squares (LS) regression (21, 29-31) to the model and experimental data. Confidence is gained in the model if the parameter values obtained by LS are physically realistic. If the parameter values are physically realistic, extrapolation beyond the experimental range could be done within the limits of the assumptions. However, even if the parameter values are not physically realistic, LS does provide a set of parameter values suitable for use in the model which could be used for interpolation within the range of the experimental data. It is perhaps this last advantage of LS which is the most important for battery designers. That is, at the LS estimates the model provides the best functional relationship (for the assumed model) between the physical parameters and the experimental data. A better functional relationship may be obtained with a different model but in the absence of another model, the designer should use the LS estimates for interpolation even in preference to literature values.

The LS method consists of minimizing the following nonlinear objective function

$$F(\beta) = \sum_1 \epsilon_1^2 = \sum_1 (I_1 - \hat{I}_1)^2 \qquad [36]$$

where $\hat{I}_1$ = is given by Eq. [30] at the experimental conditions corresponding to the 1th datum. The nonlinearity of Eq. [36] results from the nonlinear model equations, but it does not affect the theory behind LS regression. The computations necessary to minimize this objective function become more complicated with a nonlinear function; however, many computers have subroutine libraries which can perform the necessary calculations [see Ref. (20)]. The nonlinearity does affect the statistical inferences that can be made, and hence, the confidence limits for the parameters are valid only as the number of experimental data points becomes large (29). These confidence limits for the parameters are discussed in Ref. (20) and (32).

Regression Results

Table III presents the results of the application of the LS technique (20). As can be seen in Table III, in the first four cases α_c was set and LS used to determine i_o^o and D_2, and in the last case LS was used to determine α_c, i_o^o, and D_2. The solid lines shown in Fig. 5 and 6 were calculated according to Eq. [30] with the case five parameter values [no noticeable difference in the lines occurs when the case 3 or 4 Table III parameter values are used since the values of Eq. [36] are not significantly different (20)].

Quantitatively, the model predicts all of the experimental data points to within 30% and most of the data to within 10%. The greatest deviations occur at large currents and Reynolds numbers; these deviations could be a result of measurement errors in either the flow rate or bulk Br_2 concentration which are magnified at the large current experimental conditions. This degree of accuracy may be suitable for engineering purposes.

Discussion

Table IV presents a comparison of the LS parameter estimates with literature values. The LS estimate of the diffusion coefficient is the same order of magnitude as the published data which was obtained in a rotating disk experiment (33). The difference in diffusion coefficients may be attributable to the relatively small assumed value of ϵ/τ (0.172). That is, if it is assumed that the value for D_2 given by Osipov *et al.* (33) is correct, then ϵ/τ for the porous electrode

Table III. Least squares estimates

Case[1]	α_c	α_a[2]	$i_o^o \times 10^3$, A/cm²	$D_2 \times 10^5$, cm²/sec	SSE[3]
1	0.50	1.50	190 ± 101	(9.03 ± 2.37)	0.1386
2	0.75	1.25	610 ± 63	(6.99 ± 1.16)	0.1076
3	1.00	1.00	123 ± 41	(5.86 ± 0.73)	0.0965
4	1.50	0.50	58 ± 17	(4.79 ± 0.43)	0.0925
5	1.32 ± 0.52	0.68	79 ± 68	(5.08 ± 1.10)	0.0919

[1] Cases 1-4 are for α_c fixed with i_o^o, and D_2 the LS estimates. Case 5 is for α_c, i_o^o, and D_2 as the LS estimates.
[2] Calculated from Eq. [8] with $n = 2$.
[3] SSE = value of Eq. [36] at LS estimates.

Table IV. Comparison of least squares estimates with literature values for case 5 of Table III

Parameter	Units	Least squares estimate	Literature value/Ref.
D_2	cm²/sec	(5.08 ± 1.10) × 10^{-5}	1.2×10^{-5} (33)
i_o^o	A/cm²	0.079 ± 0.068	0.345 (33)[1]
α_c	none	1.32 ± 0.52	1.2 (32); 1.24-1.57 (35)

[1] i_o^o extrapolated from the reported $i_{o,b}$ values using Eq. [5]-[8] and the LS estimate of $\alpha_c = 1.32$.

studied here would be 0.728. The point is that the product (D_2) (ϵ/τ) (*i.e.*, the effective diffusion coefficient) is the unknown parameter in a porous electrode. The LS estimation procedure gives an estimate of D_2 which when multiplied by the assumed value of ϵ/τ is suitable for design within the range of the data (*i.e.*, for interpolation). The literature value for i_o^o is not directly comparable with the LS estimate in Table IV because the literature value was obtained on a platinum RDE whereas an RuO_2 on Ti electrode was used here. However, the LS estimate for i_o^o is reasonable because platinum should be a better catalyst and therefore result in a larger i_o^o. Another complication in the comparison of i_o^o is that the product of the specific surface area a and the exchange current density appears in the model and the value of a was not measured in this experiment. However, the point is (as with the diffusion coefficient) the LS procedure gives an estimate of i_o^o which can be used in the model with the assumed value of a to interpolate. It should be noted that the LS value of i_o^o gives a relatively large value of $i_{o,b}$ from Eq. [5] which is consistent with the observations of fast Br_2/Br^- kinetics by Zn/Br_2 battery designers (1, 4, 6, 7, 34). The LS estimate of α_c agrees well with the literature values of Ref. (34) and (35). Both i_o^o and α_c have large error bounds due to the small amount of data obtained here for anodic polarizations (see Fig. 6) and for the lack of data on the concentration dependence of γ_i. The model deviations from the experimental anodic data are also a result of the lack of data on the concentration dependence of γ_i.

It is important to note that the model is sensitive to the parameter values throughout the range of the experimental data as demonstrated, for example, by Fig. 7 and 8. Similar predictions can be made for anodic currents (20). It is also important to note that the estimated values of i_o^o and D_2 yield a small ellipse on a contour plot as shown in Fig. 9 with $\alpha_c = 1.0$. Note that the minimum value of the objective appears as a steep narrow ellipse within the vicinity of the LS estimates (case 3, Table III).

With the value of i_o^o obtained by LS and the experimental concentrations, a large value of B results from Eq. [19]. Thus, the model predicts a thin reaction zone as indicated in Fig. 10 by concentration changes only at the edge of the porous region. This implies that only a small fraction of the RuO_2/Ti porous electrode is utilized even at relatively small overpotentials. Figure 10 illustrates an interesting feature of the model presented here. That is, at a given η, $\theta(\xi)$ drops rapidly over a small distance within the porous electrode to a constant value instead of zero as might be expected. The reason for this is the inclusion of the complete Butler-Volmer equation which leads to the Γ term in Eq. [24] (20).

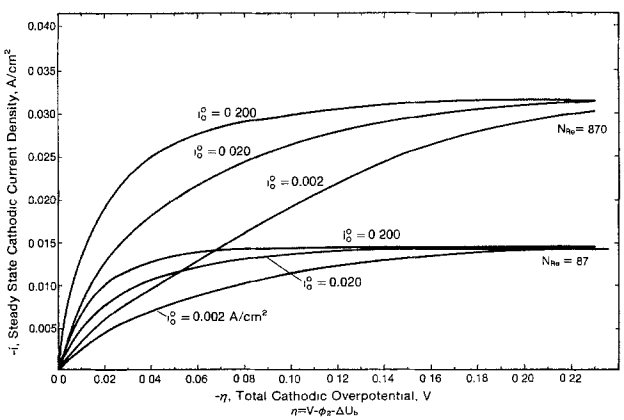

Fig. 7. Model sensitivity to changes in exchange current density for cathodic polarizations at case 5 of Table III values for D_2 and α_c.

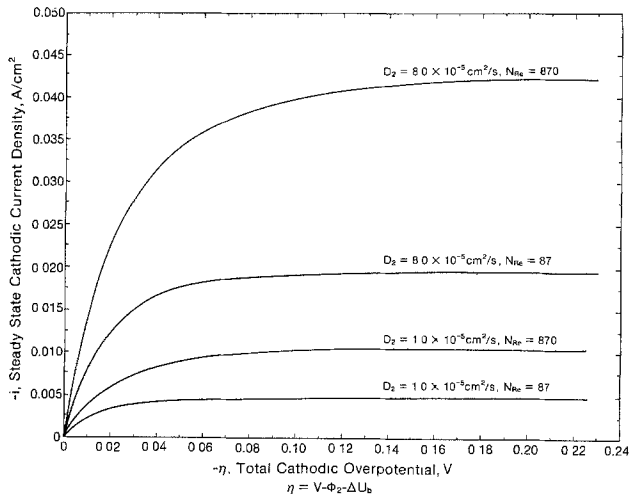

Fig. 8. Model sensitivity to change in the diffusivity for cathodic polarizations at case 5 of Table III values for i_o^o and α_c.

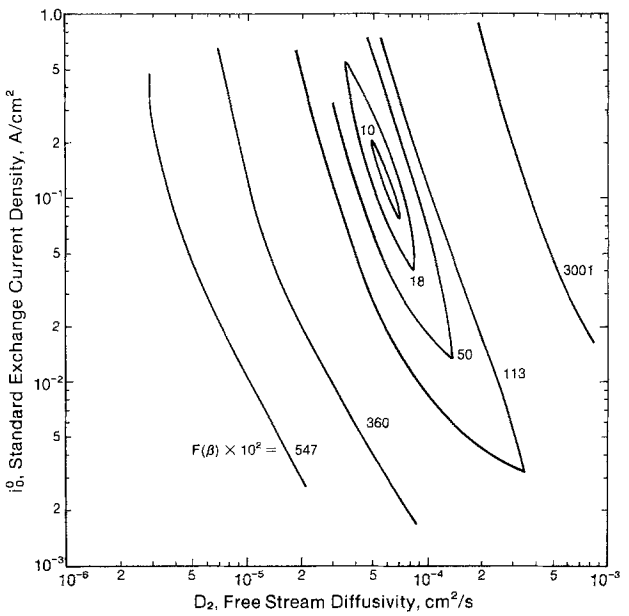

Fig. 9. Contours of the scaled least squares objective function [$F(\beta)$ (as given by Eq. [36]) × 10^2] for $\alpha_c = 1.0$.

Conclusions

This study of a flow-by back fed porous electrode for the reduction of bromine produced a mechanistic model of the steady-state process. The model consists of a single analytical expression (Eq. [30]) suitable for design purposes. The model is applicable over a large range of overpotentials and includes external mass transfer resistance. Also, the model predicts most of the experimental data presented here to within approximately 10%, and the parameter estimates of α_c, i_o^o, and D_2 obtained here compare favorably with literature values.

Analysis of the flow-by back fed porous electrode for the reduction of bromine revealed that its limiting current is similar to a rotating disk; its limiting current density is characterized by a zero concentration at the surface on the side of the fresh reactant. The reaction zone for the fast reaction studied here is less than 5% of the electrode thickness; hence, the concentration profile is horizontal within the porous electrode and the reaction occurs on the back side of the electrode. This small reaction zone thickness indicates that small ohmic energy losses could be achieved by using thin back fed electrodes. The concentration profile shows that the Br_2 concentration at the separator in a Zn/Br_2 battery could be reduced significantly

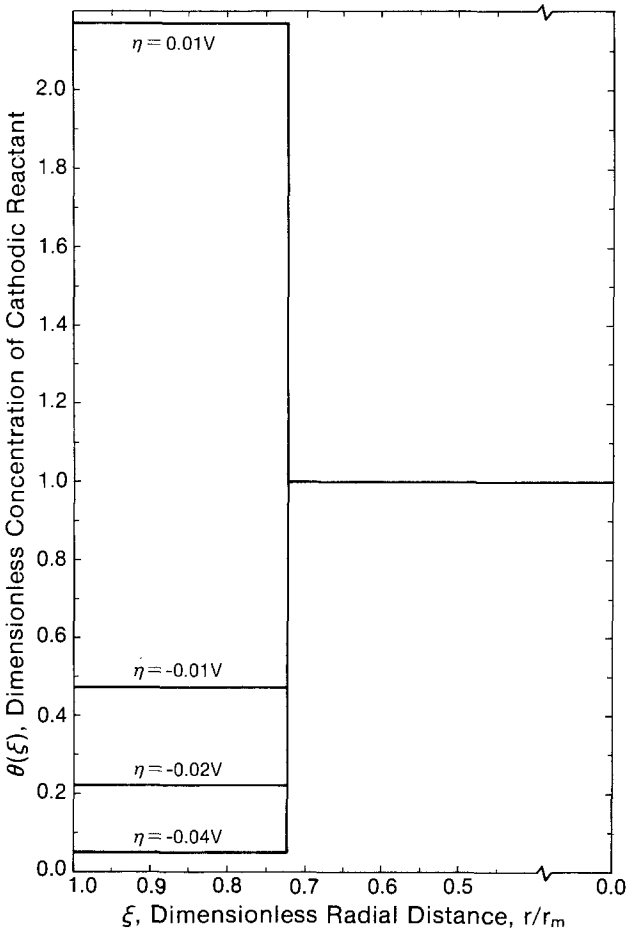

Fig. 10. Concentration profiles in experimental back fed porous electrode for LS parameter estimates of case 5 of Table III.

during discharge which would decrease the loss of Br_2 across the separator. However, on charge, the concentration of Br_2 at the separator would be increased and would cause consequently a greater loss of Br_2.

Acknowledgments

This work was supported by the Center for Energy and Mineral Resources at Texas A&M University. The electrode was coated with catalyst by the Chlor-Alkali Department of the Dow Chemical Company, Texas Division, Freeport, Texas. The experimental Zn/Br_2 reactor was furnished by Gould Incorporated, Rolling Meadows, Illinois. The authors gratefully acknowledge all of this support.

Manuscript submitted Nov. 16, 1982; revised manuscript received *ca.* May 13, 1983.

APPENDIX

The Back Fed Model in Cartesian Coordinates

The governing differential equation for the concentration of a cathodic reactant (*e.g.*, bromine) which corresponds to Eq. [15] in the text is

$$\frac{d^2c_2}{dx^2} - Kc_2 = \frac{-ai_{o,b}}{2FD_e}\exp\left(\frac{\alpha_n F}{RT}\eta\right) \quad [A\text{-}1]$$

where

$$K = \frac{ai_{o,b}}{2FD_e c_{2,b}}\exp\left(\frac{-\alpha_c F}{RT}\eta\right) \quad [A\text{-}2]$$

The following dimensionless variables can be used to simplify Eq. [A-1]

$$\zeta = \frac{x}{x_m}; \quad \theta = \frac{c_2}{c_{2,b}} \quad [A\text{-}3]$$

Then, Eq. [A-1] becomes

$$\frac{d^2\theta}{d\zeta^2} - B\theta = -A \quad [A\text{-}4]$$

where

$$A = \frac{ai_{o,b}x_m^2}{2FD_e c_{2,b}}\exp\left(\frac{\alpha_a F}{RT}\eta\right) \quad [A\text{-}5]$$

and

$$B = K\,x_m^2 \quad [A\text{-}6]$$

The boundary conditions are at

$$x = x_m, \quad \zeta = 1.0, \quad \frac{d\theta}{d\zeta} = 0 \quad [A\text{-}7]$$

at

$$x = 0, \quad \zeta = 0, \quad \frac{d\theta}{d\zeta} = \frac{x_m k}{D_e}(\theta(0) - 1.0) \quad [A\text{-}8]$$

where

$$k = 1.651\frac{D_2}{2r_h}\left(1.5\,N_{Re}\,N_{Sc}\frac{2r_h}{L}\right)^{1/3} \quad [A\text{-}9]$$

and r_h is the hydraulic radius as defined in Ref. (25).

Equation [A-4] can be solved analytically by assuming a solution of the form

$$\theta(\zeta) = \Psi(\zeta) + \Gamma \quad [A\text{-}10]$$

where Γ is a constant at a given η and temperature and is given by

$$\Gamma = \exp\left(\frac{2F}{RT}\eta\right) \quad [A\text{-}11]$$

The general form of $\Psi(\zeta)$ is

$$\Psi(\zeta) = E\sinh(\sqrt{B}\,x) + F\cosh(\sqrt{B}\,x) \quad [A\text{-}12]$$

and application of boundary condition Eq. [A-7] gives

$$F = -E\coth(\sqrt{B}\,x_m) \quad [A\text{-}13]$$

Application of boundary condition Eq. [A-8] gives

$$E = \frac{x_m k}{D_e\sqrt{B}}(\theta(0) - 1.0) \quad [A\text{-}14]$$

Thus, the complete solution for $\theta(\zeta)$ is

$$\theta(\zeta) = E\sinh(\sqrt{B}\,\zeta) - E\coth(\sqrt{B}\,x_m)\cosh(\sqrt{B}\,\zeta) + \exp\left(\frac{2F}{RT}\eta\right) \quad [A\text{-}15]$$

Solving for the unknown surface concentration, $\theta(0)$, in Eq. [A-13] gives

$$\theta(0) = \frac{x_m k\coth(\sqrt{B}\,x_m) + D_e\sqrt{B}\exp\left(\frac{2F}{RT}\eta\right)}{D_e\sqrt{B} + x_m k\coth(\sqrt{B}\,x_m)} \quad [A\text{-}16]$$

Now, consideration of the case where $\sqrt{B} \to 100.0$ gives

$$\theta(0) = \frac{x_m k + D_e\sqrt{B}\exp\left(\frac{2F}{RT}\eta\right)}{x_m k + D_e\sqrt{B}} \quad [A\text{-}17]$$

Finally, an expression for the current density is

$$\frac{i}{2F} = N_2\Big|_{x=0} = kc_{2\,b}(\theta(0) - 1.0) \quad [A\text{-}18]$$

where $\theta(0)$ is defined by Eq. [A-16] or [A-17].

LIST OF SYMBOLS

a	specific catalytic surface area of porous electrode, cm^{-1}
c_1, c_2	concentration of ith species, i = 2 for bromine, mol/cm^3
$c_{i,b}, c_{2,b}$	bulk concentration of ith species, i = 2 for bromine, mol/cm^3
c_i°	standard reference concentration of ith species $= 10^{-3}$ mol/cm^3
$c_{i,re}$	reference electrode concentration of ith species, mol/cm^3

D_e effective diffusion coefficient of bromine, cm²/sec
D_2 free stream diffusion coefficient of bromine, cm²/sec
$\mathbf{F}$ faraday's constant, 96,487 C/mol of electrons
$F(\beta)$ least squares objective function, A²
I total cell current, A
$I_0(\cdot)$ modified Bessel function of the first kind, zero order
$I_1(\cdot)$ modified Bessel function of the first kind, first order
I_l lth experimentally observed current, A
$\hat{I}_l$ model predictions at experimental conditions corresponding to the lth datum, A
i steady-state current density, A/cm²
i_L limiting current density, A/cm²
$i_{o,b}$ exchange current density at bulk concentrations, A/cm²
i_o^* standard exchange current density at 1*M*, A/cm²
j_i average production rate per unit area
K reaction rate function, cm^{-2}
$K_0(\cdot)$ modified Bessel function of the second kind, zero order
$K_1(\cdot)$ modified Bessel function of the second kind, first order
k mass transfer coefficient, cm/sec
L electrode length, cm
L_{en} entrance length, cm (see Eq. [35])
N_i, N_2 flux of ith species, $i = 2$ for bromine, mol/cm²/sec
N_{Re} Reynolds number
N_{Sc} Schmidt number
n number of mols of electrons ($n = 2$ mols of electrons for reaction [1])
p_i, q_i reaction orders for ith species ($p_{Br^-} = 2$, $q_{Br2} = 1$)
R gas constant, 8.313 J/mol/K
r radial coordinate, cm
r_i inside radius of electrode, cm
r_m membrane radius, cm
s_i stoichiometric coefficient of ith species ($s_{Br^-} = 2$, $s_{Br2} = -1$)
T temperature, K
t thickness ratio of porous electrode
U^θ standard open circuit potential of working electrode, V
$U_{re}{}^\theta$ standard reference electrode potential, V
V potential of working electrode, V
v axial velocity behind the back fed electrode, cm/sec

Greek letters

α_a apparent anodic transfer coefficient
α_c apparent cathodic transfer coefficient
β vector of least squares parameters, $= [i_o^* \; D_2 \; \alpha_c]$
γ_i concentration dependence for exchange current density
ϵ porosity of electrode
ϵ_l lth residual of least squares function, A
η total overpotential, V
$\theta(t)$ dimensionless surface concentration
ν kinematic viscosity, cm²/sec
ξ dimensionless radial coordinate
π 3.1416
τ tortuosity of porous electrode
Φ_{re} potential in the solution at the reference electrode, V
Φ_2 potential of the solution in flow channel of porous electrode, V
$\Phi_{2,0}$ potential of the solution just outside the double layer, V

REFERENCES

1. R. A. Putt, "Assessment of Technical and Economic Feasibility of Zinc-Bromine Batteries for Utility Load Leveling", Final Report to Electric Power Research Institute, Palo Alto, CA, EM-1059, Research Project 635-1, May 1979.
2. P. Y. Lu, Workshop on Electrodes for Flowing Solution Batteries, summary by L. Nanis for Electric Power Research Institute, Palo Alto, CA, Special Study Project WS-79-192, Section 2, Feb. 1981.
3. D. J. Eustace, *This Journal*, **127**, 528 (1980).
4. F. G. Will, C. D. Iacovangelo, J. S. Jackowski, and F. W. Secor, "Assessment of the Zinc-Bromine Battery for Utility Load Leveling," Final Report to U.S. Dept. of Energy, Division of Energy Storage Systems, Contract No. 2950, EY-76-C-02-2950, March 1978.
5. B. V. Tilak, P. W. T. Lu, J. E. Colman, and S. Srinivasan, in "Comprehensive Treatise of Electrochemistry," Vol. 2, J. O'M. Bockris, B. E. Conway, E. Yeager, and R. E. White, Editors, p. 63, Plenum Press, New York (1981).
6. R. Bellows, D. Estace, P. Grimes, J. Shropshire, and H. Tslen, in 11th International Power Sources Symposium, p. 301, Brighton, England, Sept. 1978.
7. R. Bellows, H. Einstein, P. Grimes, E. Kanter, and K. Newby, in 15th Intersociety Energy Conversion Engineering Conference, Seattle, WA, p. 1465-1470, Aug. 1980.
8. J. S. Newman and C. W. Tobias, *This Journal*, **109**, 1183 (1962).
9. I. G. Gurevich and V. S. Bagotskii, *Electrochim. Acta*, **9**, 1151 (1964).
10. O. S. Ksenzhek, *Zh. Fiz. Khim.*, **36**, 633 (1962).
11. E. A. Grens and C. W. Tobias, *Electrochim. Acta*, **10**, 761 (1965).
12. L. G. Austin and H. Lerner, *ibid.*, **9**, 1469 (1964).
13. J. Newman and W. Tiedeman, *AIChE J.*, **21**, 25 (1975).
14. J. O'M. Bockris and S. Srinivasan, "Fuel Cells: Their Electrochemistry," p. 234, 254, 256, McGraw Hill, New York (1969).
15. B. V. Tilak, R. S. Yeo, and S. Srinivasan, in "Comprehensive Treatise of Electrochemistry," Vol. 3, J. O'M. Bockris, B. E. Conway, E. Yeager and R. E. White, Editors, p. 70, Plenum Press, New York (1981).
16. J. A. Trainham, Ph.D. Dissertation, University of California, Berkeley, CA (1979).
17. J. Newman, "Electrochemical Systems", p. 174, Prentice-Hall, Inc., Englewood Cliffs, NJ (1973).
18. J. Newman, "Electrochemical Systems," Prentice-Hall, Inc., Englewood Cliffs, NJ (1973).
19. H. S. Mickely, T. K. Sherwood, and C. E. Reed, "Applied Mathematics in Chemical Engineering," 2nd ed., p. 197, McGraw-Hill, New York (1957).
20. J. Van Zee, M. S. Thesis, Texas A&M University, College Station, TX (1982).
21. B. Ostle and R. W. Mensing, "Statistics in Research," 3rd ed., pp. 166-178, Iowa State University Press, Ames, Iowa (1975).
22. R. D. Weaver, "Testing and Evaluation Results of Gould Laboratory Prototype Zinc Bromine Cells," Final Report to Electric Power Research Institute, p. 56, Palo Alto, CA, Dec. (1977).
23. P. C. S. Hayfield and W. R. Jacob, in "Modern Chlor-Alkali Technology," M. O. Coulter, Editor, p. 105, Ellis Horwood Ltd., Chichester, West Sussex, England (1980).
24. D. L. Caldwell and M. J. Hazelrigg, in "Modern Chlor-Alkali Technology," M. O. Coulter, Editor, p. 127, Ellis Horwood, Ltd., Chichester, West Sussex, England (1980).
25. R. B. Bird, W. E. Stewart, and E. N. Lightfoot, "Transport Phenomena," p. 47, John Wiley, New York (1960).
26. J. Newman, "Electrochemical Systems," p. 130, Prentice-Hall, Inc., Englewood Cliffs, NJ (1973).
27. F. Will, *This Journal*, **126**, 36 (1979).
28. R. White and J. Newman, *J. Electroanal. Chem.*, **82**, 176 (1977).
29. W. J. Kennedy, Jr. and J. E. Gentle, "Statistical Computing," p. 426, Marcel Decker, Inc., New York (1980).
30. Y. Bard, "Nonlinear Parameter Estimation," Academic Press, New York (1974).
31. R. J. Freund and P. D. Minton, "Regression Methods," Marcel Decker, Inc., New York (1979).
32. A. R. Gallant, *Am. Stat.*, **29**, 73 (1975).
33. O. R. Osipov, M. A. Novitiskii, Yu. M. Povarov, and P. D. Lukovtsev, *Elektrokhimiya*, **8**, 327 (1972).
34. F. Will, in 11th International Power Sources Symposium, p. 9, Brighton, England, Sept. 1978; Personal communication with F. Will, July 2, 1982.
35. I. Rubinstein, *J. Phys. Chem.*, **85**, 1899 (1981).

Photo-oxidation of Organic Compounds at Doped α-Fe_2O_3 Electrodes

J. H. Kennedy* and D. Dünnwald

Chemistry Department, University of California, Santa Barbara, California 93106

ABSTRACT

Photo-oxidation of organic compounds at doped α-Fe_2O_3 electrodes was investigated in aqueous and nonaqueous solutions. Oxalic and formic acids in 0.5M H_2SO_4 showed distinctly different reactivities. Photo-oxidation of alcohols, *e.g.*, methanol and 2-propanol, was investigated in propylene carbonate and compared to their oxidation in water. The oxidation products (formaldehyde, acetone, and oxygen) were analyzed quantitatively; they accounted for 100% of the current. Competition between methanol and 2-propanol, and between these alcohols and water, is also reported.

Although photoelectrochemistry at iron oxide electrodes has been widely investigated in our laboratory (1-7) and in others (8-17), little work has been carried out on the oxidation of organic compounds (16-17). Stability of α-Fe_2O_3 in acid solution has now been demonstrated (7), so that the photo-oxidation of carboxylic acids and alcohols in acidic aqueous solutions could be undertaken. Also, in the present study, the photo-oxidation of alcohols in anhydrous propylene carbonate has been carried out. Competition between alcohols and water was investigated to help establish their relative reactivities.

Experimental

Electrodes were prepared from high purity α-Fe_2O_3 (99.999%, Alfa Products) by doping with 1 atomic percent (a/o) SiO_2. Pellets were pressed, sintered in air at 1365°C for about 20 hr, and then quenched in air to room temperature. The electrodes were about 1 cm^2 area after sintering and 0.1 cm thick. Electrical connection was made on the back with a sputtered gold film followed by silver epoxy to attach a wire lead. The electrode and the wire lead were then sealed in a glass tube with epoxy resin. The resistances of the electrodes measured at 1 kHz with a conductivity bridge were 60-350Ω.

Experiments with the organic acids were carried out in a two-compartment cell separated by a fritted glass disk. The compartment containing the semiconductor electrode was closed and contained a burette for collection of evolved gases. Experiments with alcohols were carried out in a single-compartment cell.

The light source was a 150W Xe lamp with light focused on the electrode by means of a quartz lens. Photocurrent *vs.* potential plots were taken with PAR Model 174 and X-Y recorders. Potentials were measured *vs.* SCE with all photo-oxidation experiments carried out at +1.2V *vs.* SCE. No attempt was made to adjust for the different junction potentials that were created when nonaqueous media were employed.

All chemicals were reagent grade. Propylene carbonate was distilled *in vacuo* and stored over molecular sieves. Tetra-*n*-butylammonium perchlorate, used as supporting electrolyte at a concentration of 0.1M, was dried *in vacuo* at 120° C before use.

CO_2, CO, and O_2 were analyzed by mass spectrometry. Analysis of formaldehyde was made spectrophotometrically using chromotropic acid. Analysis for acetone was made spectrophotometrically using 2,4-dinitrophenylhydrazine.

Results

Several carboxylic acids were investigated in solutions containing 0.5M H_2SO_4 and 0.1M Na_2SO_4. Citric acid and acetic acid, both at 0.5M concentration, showed no influence on the current-potential curves. Essentially all photocurrent resulted in O_2 production (0.8% CO_2 found with acetic acid). On the other hand, formic acid showed a small change and oxalic acid a large change in the I-V curves, as can be seen in Fig. 1. 0.5M oxalic acid shifted the onset of photocurrent 0.4V cathodically, while formic acid caused little shift. The photocurrents were significantly higher than in sulfuric acid alone.

An attempt was made to understand the large cathodic shift in photocurrent onset in oxalic acid by investigating current transients by on-off switching of the light source. In 0.5M H_2SO_4/0.1M Na_2SO_4, the photocurrent onset was +0.65V *vs.* SCE, but the first cathodic photocurrents were not observed until < +0.25V *vs.* SCE. Between +0.3 and +0.6V *vs.* SCE, anodic transients were observed upon illumination and cathodic transients were observed during dark periods. Both transients increased with anodic potential and had about the same magnitude up to +0.6V, thus resulting in no net steady-state photocurrent. It is probable that the flatband potential is near the lower value of +0.25V *vs.* SCE. When the same transient experiment was carried out with 0.5M oxalic acid in 0.5M H_2SO_4/0.1M Na_2SO_4, the photocurrent onset was at +0.225V *vs.* SCE. No cathodic transients were observed above +0.225V *vs.* SCE, and cathodic photocurrents were observed < +0.10V *vs.* SCE. Thus, the flatband potential appeared to be shifted cathodically only 100-150 mV in oxalic solutions, accounting for only a fraction of the 400 mV cathodic shift in photocurrent onset.

Whereas in H_2SO_4 solutions 100% of the photocurrent resulted in O_2 production, increasing amounts of carboxylic acid led to a decrease in O_2 and an increase in CO_2. Small amounts of CO were also detected. As seen in Fig. 2 and 3, formic and oxalic acids showed clearly different reactivities. 0.5M oxalic acid gave 80% CO_2 production while formic acid was much less

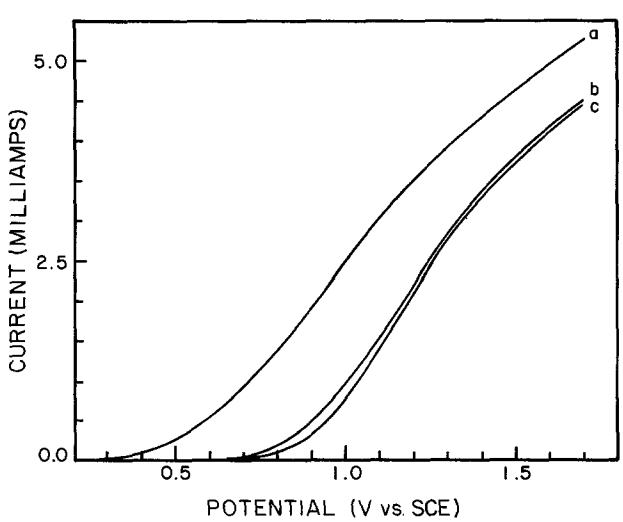

Fig. 1. Photocurrent-potential curves for organic acids in 0.5M H_2SO_4/0.1M Na_2SO_4. (a) 0.5M oxalic acid, (b) 0.5M formic acid, (c) blank.

* Electrochemical Society Active Member.

Key words: α-Fe_2O_3 photoanodes, organic acid photo-oxidation, alcohol photo-oxidation.

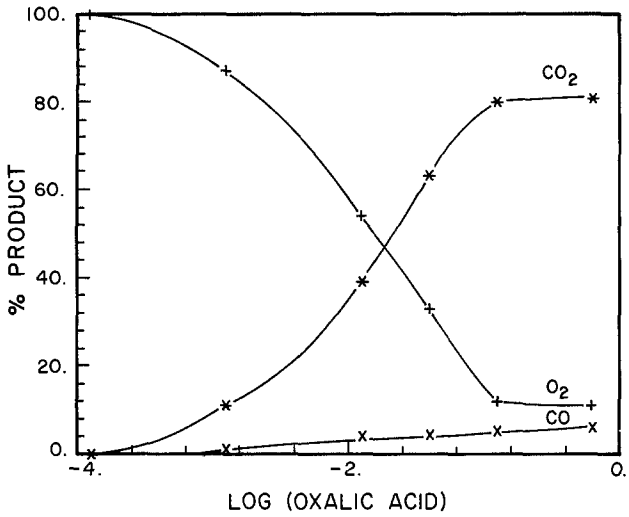

Fig. 2. Photo-oxidation of oxalic acid in 0.5M H_2SO_4/0.1M Na_2SO_4.

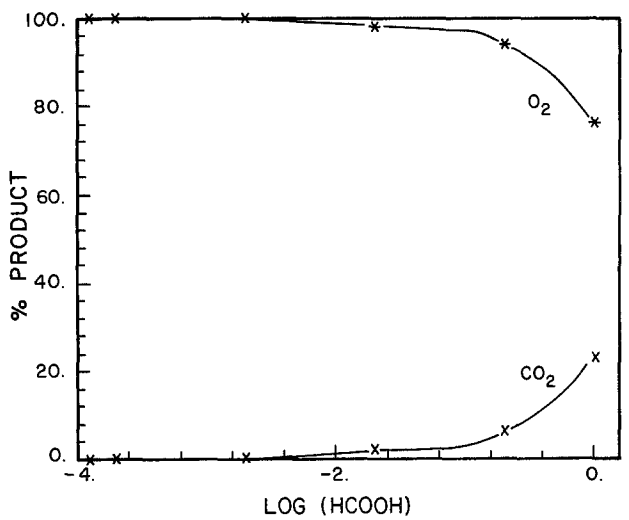

Fig. 3. Photo-oxidation of formic acid in 0.5M H_2SO_4/0.1M Na_2SO_4.

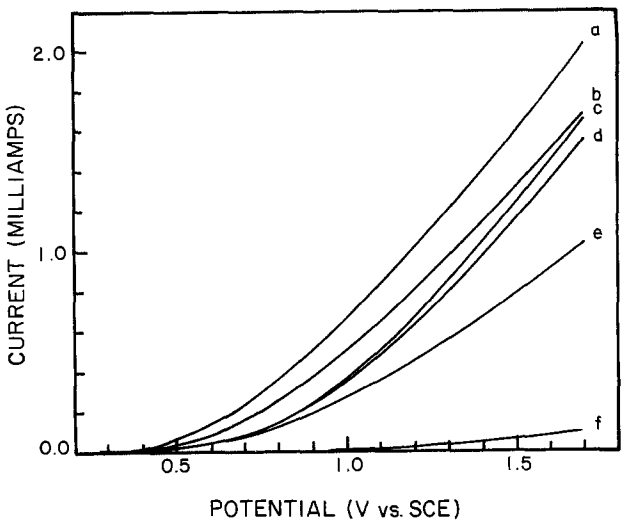

Fig. 4. Photocurrent-potential curves in propylene carbonate containing 0.1M tetra-*n*-butylammonium perchlorate. (a) 2M methanol/2M H_2O, (b) 2M 2-propanol/2M H_2O, (c) 2M methanol, (d) 2M H_2O, (e) 2M 2-propanol, (f) blank.

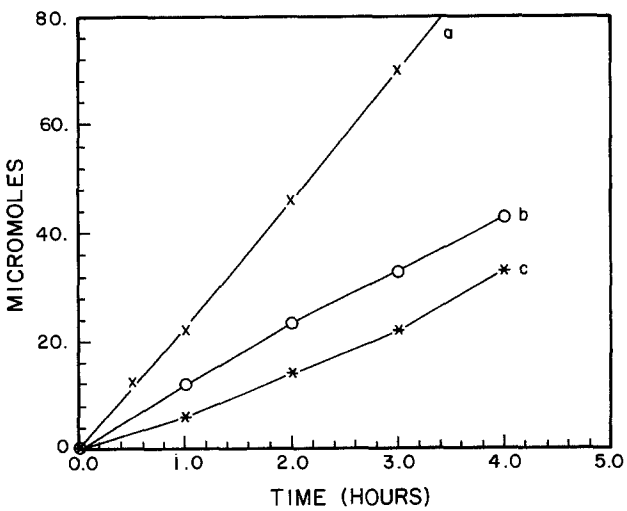

Fig. 5. Photo-oxidation of alcohols. (a) Formaldehyde produced in methanol, (b) formaldehyde produced in 2M methanol in propylene carbonate, (c) acetone produced in 2M 2-propanol in propylene carbonate. All solutions contained 0.1M tetra-*n*-butylammonium perchlorate.

efficient in competing with water for the photogenerated holes.

The photo-oxidation of alcohols was mainly investigated in propylene carbonate (Fig. 4), although the oxidation of pure methanol and aqueous solutions was also carried out. This was possible because the tetra-*n*-butylammonium perchlorate supporting electrolyte was easily soluble in methanol, and a 0.1M solution exhibited a resistance of 350Ω. Pure 2-propanol could not be studied because the electrolyte was only slightly soluble with resistances of about 7 kΩ. The product of photo-oxidation in pure methanol was formaldehyde. It accounted for 100% of the current and increased linearly with time as shown in Fig. 5. However, even in 1:1 methanol:water (0.05M H_2SO_4, 0.1M Na_2SO_4) by volume only 25% of the photocurrent led to formaldehyde. Results from the same experiment with 2-propanol showed that only 2.5% of the photocurrent could be attributed to acetone production.

The following set of experiments was carried out in anhydrous propylene carbonate containing 0.1M tetra-*n*-butylammonium perchlorate, which exhibited resistances of about 400Ω. Except where stated otherwise, the reactant concentration was 2M.

Pure propylene carbonate with 0.1M supporting electrolyte showed only very small photocurrents (Fig. 4). Upon addition of alcohols or water, significant photocurrents were observed and different reactivities for the various reactants could be seen in the I-V curves. Methanol caused the highest increase in anodic photocurrent, followed closely by water, while the effect due to 2-propanol was considerably less. Interestingly, the photocurrent with 1M methanol/1M water mixtures was higher than with 2M methanol or with 2M water, individually.

The photo-oxidation of methanol in propylene carbonate led to formaldehyde as the oxidation product and accounted for 100% of the current. The photocurrent dropped slightly during the experiments, unlike the results observed in pure methanol, thus yielding a nonlinear relationship between illumination time and formaldehyde which was produced (Fig. 5).

The photo-oxidation product of 2-propanol in propylene carbonate was acetone, which also accounted for 100% of the photocurrent. Unlike methanol oxidation, the current increased during the experiments (Fig. 5), leading to smaller differences in photocurrents between the two alcohols than was observed from the initial I-V curves (Fig. 4). However, if the electrode was immersed in the 2-propanol solution for several hours prior to illumination, the photocurrent was stable at the higher value.

Competition between the two alcohols was next studied by photo-oxidation of mixtures containing 2M concentrations of each. Although the analysis for formaldehyde could not be used in the presence of 2-propanol, the amount of acetone could be determined. The amount of formaldehyde was calculated from the coulombs of charge and the yield of acetone. Considerably more methanol was oxidized than 2-propanol, as shown in Fig. 6. Mixtures of methanol and 2-propanol gave less product than additivity would predict. After 4 hr illumination at +1.2V *vs.* SCE, 2M methanol gave 41 μmol of formaldehyde and 2M 2-propanol gave 33 μmol of acetone (Fig. 5). A mixture of 2M methanol/2M 2-propanol gave only 34 μmol of formaldehyde and 16 μmol of acetone under the same conditions (Fig. 6).

Finally, the competition between water and these alcohols was investigated. The presence of 2M H_2O led to a sharp increase in photocurrent (Fig. 4). Surprisingly, the amount of organic product also increased considerably as shown in Fig. 7 and 8. One hundred percent of the additional current resulted in acetone production in 2-propanol/water solution; 80% of the total current resulted in formaldehyde production in methanol/water solutions.

Discussion

In aqueous solutions, it is known that photogenerated holes in α-Fe_2O_3 react rapidly with water or hydroxide ions. Thus, any organic compound that is oxidized in an aqueous medium must compete effectively with water. As can be seen from the results with carboxylic acids, the ability to compete for photogenerated holes varies greatly. Whereas acetic acid is readily oxidized at *n*-TiO_2, this reaction apparently does not proceed at α-Fe_2O_3. Formic acid required high concentrations to show any significant amounts of product, and of the acids studied, only oxalic acid showed high reactivity. Adsorption of the reactants at the α-Fe_2O_3 surface may play a crucial role in determining the reactivity as well as relative rate constants for the competing reactions.

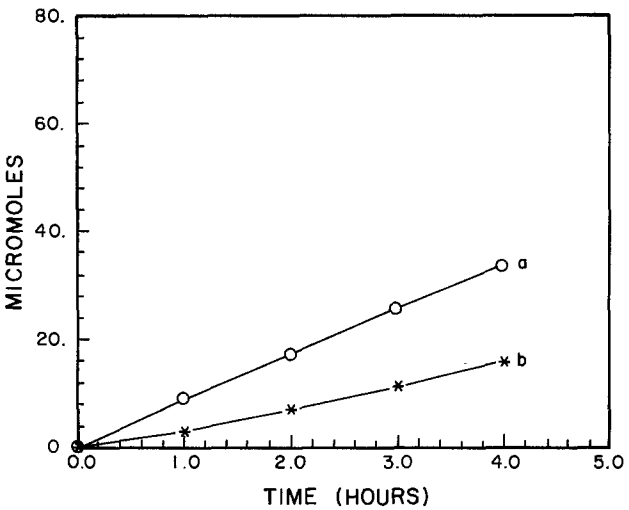

Fig. 6. Competition between 2M methanol and 2M 2-propanol in propylene carbonate. (a) Formaldehyde production, (b) acetone production.

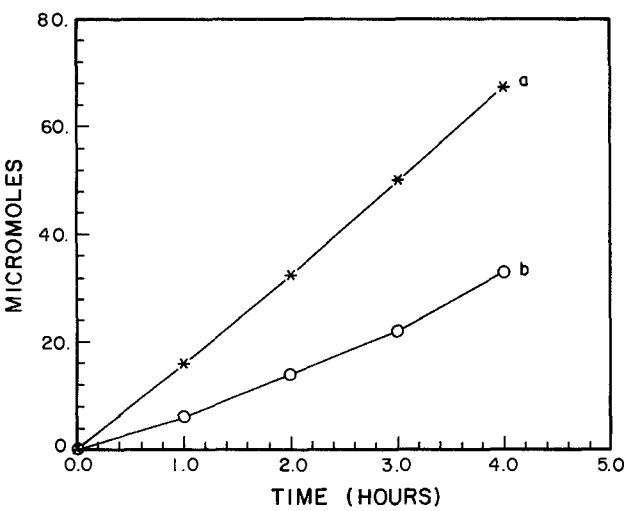

Fig. 7. Effect of water on the photo-oxidation of 2M 2-propanol in propylene carbonate. (a) Acetone production in the presence of 2M H_2O, (b) acetone production in the absence of H_2O.

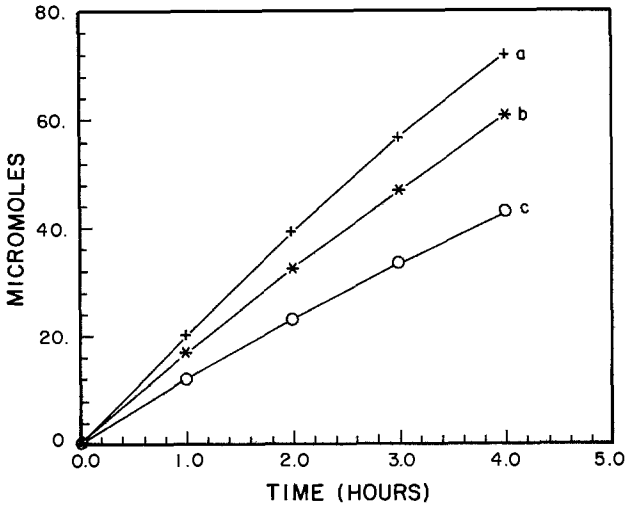

Fig. 8. Effect of water on the photo-oxidation of 2M methanol in propylene carbonate. (a) Calculated amount of formaldehyde if all photocurrent oxidized methanol in the presence of 2M H_2O, (b) amount of formaldehyde produced in the presence of 2M H_2O, (c) amount of formaldehyde produced in the absence of H_2O.

The study of transients showed that the large cathodic shift in photocurrent onset upon addition of oxalic acid was only partially due to a shift in flatband potential. The predominant reason for its high efficiency was the lack of back reaction; *i.e.*, no cathodic transients were observed.

Photo-oxidation of alcohols in aqueous solutions would also require effective competition with water for photogenerated holes. Experiments with 2-propanol in aqueous H_2SO_4 showed almost no organic reaction taking place, but methanol was able to compete reasonably effectively.

However, by working in a nonaqueous solvent, a direct comparison of reactivity could be made. Methanol in propylene carbonate yielded even more photocurrent than water, while 2-propanol was much less reactive. Thermodynamically, each of these substances should be easily oxidized by the photogenerated holes, so the rate of reaction appears to be controlled by the rate of charge transfer compared to surface recombination. It should also be noted that no evidence for current doubling was obtained, which was in contrast to results at TiO_2 electrodes (18) but in agreement with previous reports at iron oxide electrodes (16).

Change in reaction rate with time was also noted for the alcohols. The slight decay in photocurrent observed with methanol solutions may be attributed to a poisoning of the surface by the formaldehyde reaction product. The electrode performance recovered after extensive washing, lending support to this hypothesis. The opposite behavior exhibited by 2-propanol could be accounted for by a slow adsorption process (the slow rate may indicate diffusion into the surface along grain boundaries). This hypothesis is supported by the fact that immersion in 2-propanol solutions for several hours before photo-oxidation produced higher photocurrents.

Direct competition between the two alcohols in propylene carbonate was not additive and, again, may reflect the competition of reactants for active surface sites. The total product formed was not much greater than that from methanol alone, and mixtures of the two alcohols gave less of each product than solutions of the individual alcohols. Methanol was the more effective competitor, with twice as much formaldehyde formed as acetone in a propylene carbonate solution containing 2M methanol and 2M 2-propanol. This is consistent with the photocurrent results shown in Fig. 4. The nonadditivity would be expected if a Langmuir-type adsorption isotherm were involved. With the high concentrations used, it would be expected that most of the active sites would be filled and increases in concentration would result in only small increases in photocurrent as observed. An added complication is the expectation, based on the low photocurrents observed for 2-propanol, that the competition for holes will vary with the species on the surface. Thus, 2-propanol may compete well against methanol for surface sites, but this could lead to more likely surface recombination and lower photocurrents.

The addition of water to propylene carbonate solutions containing alcohol introduced another complication. Two steps in the total oxidation process are observed experimentally. First, the capture of a hole in competition with surface recombination is observed in the form of photocurrent. Second, the final product is observed by chemical analysis. It is quite possible, and indeed the results seem supportive, that one reactant may be effective in capturing a hole to form an active intermediate while another reactant is more effective in its reaction with this intermediate. Thus, the increase in photocurrent observed when water was added to the propylene carbonate solutions containing 2M methanol or 2M 2-propanol indicated the ability of water to capture photogenerated holes. On the other hand, these solutions showed greater production of formaldehyde or acetone when water was added, providing evidence that the alcohols reacted rapidly with the water intermediate, such as the hydroxyl radical. This concept also helps explain the synergistic effect seen in methanol/water mixtures in propylene carbonate in which 1M methanol/1M water gave higher photocurrents than either 2M methanol or 2M water. One reactant, water, was effective in capturing photogenerated holes, while the second reactant was effective in removing the intermediate from the electrode surface to form the final product.

Acknowledgment

This work was supported by the Division of Chemical Sciences, Office of Basic Energy Sciences, U.S. Department of Energy.

Manuscript submitted Jan. 31, 1983; revised manuscript received May 20, 1983.

Chemistry Department, University of California assisted in meeting publication costs of this article.

REFERENCES

1. J. H. Kennedy and K. W. Frese, Jr., *This Journal*, **125**, 709 (1978).
2. J. H. Kennedy and K. W. Frese, Jr., *ibid.*, **125**, 723 (1978).
3. J. H. Kennedy, R. Shinar, and J. D. Ziegler, *ibid.*, **127**, 2307 (1980).
4. J. H. Kennedy, M. Anderman, and R. Shinar, *ibid.*, **128**, 2371 (1981).
5. R. Shinar and J. H. Kennedy, *Sol. Energy Mater.*, **6**, 323 (1982).
6. R. Shinar and J. H. Kennedy, *This Journal*, **130**, 392 (1983).
7. J. H. Kennedy and M. Anderman, *ibid.*, **130**, 848 (1983).
8. K. L. Hardee and A. J. Bard, *ibid.*, **123**, 1024 (1976).
9. K. L. Hardee and A. J. Bard, *ibid.*, **124**, 215 (1977).
10. R. K. Quinn, R. D. Nasby, and R. J. Baughman, *Mater. Res. Bull.*, **11**, 1011 (1976).
11. L. S. R. Yeh and N. Hackerman, *This Journal*, **124**, 833 (1977).
12. H. H. Kung, H. S. Jarrett, A. W. Sleight, and A. Ferretti, *J. Appl. Phys.*, **48**, 2463 (1977).
13. J. S. Curran and W. Gissler, *This Journal*, **126**, 56 (1979).
14. H. Metee, J. W. Otvos, and M. Calvin, *Sol. Energy Mater.*, **4**, 443 (1981).
15. A. F. Sammells and P. G. B. Ang, *This Journal*, **126**, 1831 (1979).
16. S. Miyoshi and A. Kunugi, *Denki Kagaku*, **48**, 476 (1980).
17. R. A. Fredlein and A. J. Bard, *This Journal*, **126**, 1892 (1979).
18. M. Miyake, H. Yoneyawa, and H. Tamura, *Chem. Lett.*, 635 (1976).

The Modulated Flow at a Rotating Disk Electrode

Bernard Tribollet[1] and John Newman*

Department of Chemical Engineering, University of California, Berkeley, California 94720

ABSTRACT

The frequency response analysis for an electrochemical system (current or potential) to a sinusoidal speed modulation at a rotating disk electrode involves, at first, the analysis of the corresponding unsteady laminar flow. This hydrodynamic problem is solved by a numerical integration of the unsteady Navier-Stokes equations, and the four first terms of the instantaneous velocity expansions are given. The study of the unsteady mass transport is the second problem; its solution is a series expansion of $Sc^{-1/3}$, and the two first terms are given. Finally, the expressions of the electrical response of the electrochemical system involves also the element of the electrochemical impedance (the diffusion or convective Warburg impedance, the charge transfer resistance, the electrolyte resistance, and the double-layer capacitance). The results are experimentally confirmed, in potentiostatic and galvanostatic regulations, over a wide frequency range ($10^{-2} < p < 5$) for the reduction of $Fe(CN)_6^{3-}$ to $Fe(CN)_6^{4-}$ in 1M KCl.

The frequency response analysis of an electrochemical system to a sinusoidal speed modulation at a rotating disk electrode is a new experimental method which was originated by Tokuda *et al.* (1) and has been exploited by a few authors (2-4). In these early works, the knowledge of the instantaneous velocity profiles close to the rotating disk was obtained from the work of Sparrow and Gregg (5), which gives a good approximation of this hydrodynamic problem when the modulation frequency is low. The condition of low frequency corresponded to the electrochemical

* Electrochemical Society Active Member.
[1] Present address: Groupe de Recherche No. 4 du CNRS, Physique des Liquides et Electrochimie, Associe à l'Universite Pierre et Marie Curie, 75230 Paris Cedex 05, France.
Key words: hydrodynamic modulation, mass transport, impedance.

measurements of Tokuda *et al.* (1) and Kanzaki and Bruckenstein (6). However, in a recent work of Deslouis *et al.* (4), higher modulation frequencies could be achieved and the limitation of the theoretical analysis appeared.

An important application of this method is the determination of the diffusion coefficient by means of the Schmidt number. In the unsteady state mass transport problems, the Schmidt number occurs as its cube root and, therefore, good accuracy is needed in order to analyze the experimental data.

In this paper, an analysis is made of the unsteady laminar flow about a rotating disk whose angular velocity is perturbed by a sinusoidal modulation of low amplitude. This problem is solved numerically for a large frequency range, and the results are compared to previous works (5, 7).

For a sinusoidal speed modulation, a numerical solution of the response of the electrical quantity (current or potential) specific to the interface is given for a large frequency range. Excellent agreement between theory and experiment is found for a redox reaction below the limiting current in galvanostatic regulation. In potentiostatic regulation, at the limiting current, we show the influence of the kinetics in the high frequency range.

Theoretical Analysis

Hydrodynamic problem.—The steady flow field created by an infinite disk rotating at a constant angular velocity in a fluid with constant physical properties was first studied by von Karman (8).

For a low amplitude modulation, the equation of continuity and the equation of motion can be numerically solved from the steady-state solution. As a necessary prelude to this solution, we briefly review some of the steady-state solution as given by von Karman (8).

Von Karman's suggestion of a separation-of-variables approach to the solution of the time independent Navier-Stokes equation results in a set of three-coupled nonlinear ordinary differential equations for the components of the fluid velocity vector and an equation for the dynamic pressure in the fluid above the disk as follows

$$2F + H' = 0 \quad [1]$$

$$F^2 - G^2 + HF' - F'' = 0 \quad [2]$$

$$2FG + HG' - G'' = 0 \quad [3]$$

$$P' + HH' - H'' = 0 \quad [4]$$

where the prime designates differentiation with respect to $\zeta = z\sqrt{\bar{\Omega}/\nu}$. The variables are defined as

$$\bar{v}_r = r\bar{\Omega}\,F(\zeta) \quad [5]$$

$$\bar{v}_\theta = r\bar{\Omega}\,G(\zeta) \quad [6]$$

$$\bar{v}_z = \sqrt{\nu\bar{\Omega}}\,H(\zeta) \quad [7]$$

$$\bar{P} = \mu\bar{\Omega}\,P(\zeta) \quad [8]$$

where the overbar designates the steady state. The boundary conditions are

$$F(0) = H(0) = 0 \quad [9]$$

$$G(0) = 1 \quad [10]$$

$$F(\infty) = G(\infty) = 0 \quad [11]$$

For the unsteady situation, the instantaneous value Ω of the angular velocity is defined by

$$\Omega = \bar{\Omega} + \Delta\Omega\,\mathrm{Re}\{e^{j\omega t}\} \quad [12]$$

For a low amplitude modulation ($\Delta\Omega << \bar{\Omega}$), to determine the deviations of the flow from the steady state, we write

$$v_r = r\bar{\Omega}\left[F(\zeta) + \frac{\Delta\Omega}{\bar{\Omega}}\mathrm{Re}\{\tilde{f}(\zeta)e^{j\omega t}\}\right] \quad [13]$$

$$v_\theta = r\bar{\Omega}\left[G(\zeta) + \frac{\Delta\Omega}{\bar{\Omega}}\mathrm{Re}\{\tilde{g}(\zeta)e^{j\omega t}\}\right] \quad [14]$$

$$v_z = \sqrt{\nu\bar{\Omega}}\left[H(\zeta) + \frac{\Delta\Omega}{\bar{\Omega}}\mathrm{Re}\{\tilde{h}(\zeta)e^{j\omega t}\}\right] \quad [15]$$

$$P = \mu\bar{\Omega}\left[P(\zeta) + \frac{\Delta\Omega}{\bar{\Omega}}\mathrm{Re}\{\tilde{p}(\zeta)e^{j\omega t}\}\right] \quad [16]$$

where $\tilde{f}$, $\tilde{g}$, $\tilde{h}$, and $\tilde{p}$ are complex functions.

Each component is expressed as the sum of a known function and the real part of a complex function whose amplitude is presumed to be small. The equation of continuity and the unsteady Navier-Stokes equations are linearized, and the quadratic terms proportional to $(\Delta\Omega/\bar{\Omega})^2$ are neglected. The resulting equations may be written

$$\begin{cases} 2\tilde{f} + \tilde{h}' = 0 & [17] \\ j\tilde{f}\mathrm{p} + 2F\tilde{f} - 2G\tilde{g} + H\tilde{f}' + F'\tilde{h} = \tilde{f}'' & [18] \\ j\tilde{g}\mathrm{p} + 2G\tilde{f} + 2F\tilde{g} + \tilde{h}G' + H\tilde{g}' = \tilde{g}'' & [19] \\ j\tilde{h}\mathrm{p} + H'\tilde{h} + H\tilde{h}' + \tilde{p}' = \tilde{h}'' & [20] \end{cases}$$

where $\mathrm{p} = \omega/\bar{\Omega}$ is the dimensionless frequency of modulation. The boundary conditions are

$$\begin{cases} \tilde{f}(0) = \tilde{h}(0) = 0 & [21] \\ \tilde{g}(0) = 1 & [22] \\ \tilde{f}(\infty) = \tilde{g}(\infty) = 0 & [23] \end{cases}$$

After the velocity profiles are determined, the pressure distribution can be calculated directly from the integrated form of Eq. [20]. Each complex function may be written as the sum of a real function (index 1) and an imaginary function (index 2). The set of three coupled Eq. [17], [18], [19] becomes a set of six coupled linear ordinary differential equations

$$\begin{cases} 2f_1 + h_1' = 0 & [24] \\ 2f_2 + h_2' = 0 & [25] \\ -f_2\mathrm{p} + 2Ff_1 - 2Gg_1 + Hf_1' + F'h_1 - f_1'' = 0 & [26] \\ f_1\mathrm{p} + 2Ff_2 - 2Gg_2 + Hf_2' + F'h_2 - f_2'' = 0 & [27] \\ -g_2\mathrm{p} + 2Gf_1 + 2Fg_1 + G'h_1 + Hg_1' - g_1'' = 0 & [28] \\ g_1\mathrm{p} + 2Gf_2 + 2Fg_2 + G'h_2 + Hg_2' - g_2'' = 0 & [29] \end{cases}$$

By using Newman's method of solving this kind of problem (9, 10), we derive, for each dimensionless frequency, the solution of the set of six equations.

Cochran (11) has shown that the system of Eq. [1]-[4] can be satisfied by two sets of series expansions for small and large values of ζ. The series solutions for small values of ζ are very useful for the mass transfer problem close to a rotating disk electrode. Therefore, the derivatives at $\zeta = 0$ (given in Table I) are essential in order to determine the first coefficient of the series expansions. The other coefficients are calculated from the first by using the set of Eq. [24]-[29.] In Table II, we recall the steady-state solution, and we give the values of the four first terms of the series for each function.

As the frequency of modulation tends towards zero, we deduce from Eq. [13] that $rf_1(\zeta)$ tends towards the derivative of $\bar{v}_r$ with respect to $\bar{\Omega}$ and from Eq. [27]

Table I. $\tilde{f}'((0,p)$ and $\tilde{g}'(0,p)$ vs. the dimensionless frequency. In polar coordinates, the amplitude is divided by the amplitude for p = 0.

	$\tilde{f}'(0,p)$				$\tilde{g}'(0,p)$			
	In Cartesian coordinates		In polar coordinates		In Cartesian coordinates		In polar coordinates	
p	$f_1'(0,p)$	$f_2'(0,p)$	$A\{\tilde{f}'(p)\}/A\{f'(0)\}$	$-\theta_f$	$g_1'(0,p)$	$g_2'(0,p)$	$A\{\tilde{g}'(p)\}/A\{g'(0)\}$	$\theta_g - 180°$
0.5	0.7513	−0.1077	0.9917	8.2	−0.9235	−0.1857	1.0196	11.4
1	0.6943	−0.2032	0.9452	16.3	−0.9367	−0.3900	1.0982	22.6
1.5	0.6154	−0.2585	0.8721	22.8	−0.9874	−0.5951	1.2478	31.1
2	0.5429	−0.2802	0.7983	27.3	−1.0656	−0.7780	1.4281	36.1
2.5	0.4845	−0.2842	0.7339	30.4	−1.1551	−0.9354	1.6088	39.0
3	0.4389	−0.2802	0.6804	32.6	−1.2465	−1.0719	1.7794	40.7
3.5	0.4029	−0.2731	0.6360	34.1	−1.3360	−1.1925	1.9383	41.8
4	0.3739	−0.2648	0.5987	35.3	−1.4223	−1.3010	2.0864	42.4
4.5	0.3502	−0.2565	0.5672	36.2	−1.5050	−1.4003	2.2251	42.9
5	0.3303	−0.2484	0.5400	36.9	−1.5842	−1.4922	2.3556	43.3
6	0.2988	−0.2337	0.4956	38.0	−1.7330	−1.6591	2.5968	43.8
7	0.2749	−0.2210	0.4609	38.8	−1.8709	−1.8091	2.8169	44.0
8	0.2559	−0.2100	0.4325	39.4	−1.9996	−1.9465	3.0205	44.2
10	0.2275	−0.1921	0.3890	40.2	−2.2355	−2.1940	3.3903	44.5

Table II. Coefficients of the series expansions for the dimensionless components of the fluid velocity. (The values of $f_1'(0,p)$, $f_2'(0,p)$, $g_1'(0,p)$), and $g_2'(0,p)$ are given in Table I.

	F	G	H	f_1	f_2	g_1	g_2	h_1	h_2
ζ^0	0.0	1.0	0.0	0.0	0.0	1.0	0.0	0.0	0.0
ζ^1	0.51023	−0.61592	0.0	$f_1'(0,p)$	$f_2'(0,p)$	$g_1'(0,p)$	$g_2'(0,p)$	0.0	0.0
ζ^2	−0.5	0.0	−0.51023	−1	0.0	0.0	−p/2	$-f_1'(0,p)$	$-f_2'(0,p)$
ζ^3	0.205307	0.170077	1/3	$\frac{1.23184 - 2g_1' - f_2' \cdot p}{6}$	$\frac{-2g_2' + f_1' \cdot p}{6}$	$\frac{1.02046 + 2f_1' - g_2' \cdot p}{6}$	$\frac{2 \cdot f_2' + g_1' \cdot p}{6}$	2/3	0.0

and [29] that $f_2'(\zeta)$ tends towards zero. Therefore, $\tilde{f}'(0,0) = 3/2\ F'(0) = 0.765345$, and in the same way $\tilde{g}'(0,0) = 3/2\ G'(0) = -0.923883$. These values are used for the calculation of the reduced amplitude of $\tilde{f}'$ and $\tilde{g}'$ in Table I.

The amplitude of $\tilde{g}'(0,p)$ increases with p, and $\tilde{f}'(0,p)$ decreases with p. For mass transfer measurements, that means that the results for an axisymmetric electrode (like a disk or a ring) and a nonaxisymmetric electrode (like a microelectrode off the axis of rotation) may be very different.

Comparison with the results of Sparrow and Gregg (5) and Sharma (7).—Low frequency range.—Sparrow and Gregg (5) solved the unsteady flow problem where the angular rotation speed is a time dependent quantity. Their expressions for the instantaneous components of the fluid velocity were obtained by a series expansion about the value found at a quasi-steady state

$$v_r = r\Omega(F(x) + \beta_1 F_1(x) + \beta_2 F_2(x) + \ldots) \quad [30]$$

$$v_\theta = r\Omega(G(x) + \beta_1 G_1(x) + \beta_2 G_2(x) + \ldots) \quad [31]$$

$$v_z = \sqrt{\Omega\nu}(H(x) + \beta_1 H_1(x) + \beta_2 H_2(x) + \ldots) \quad [32]$$

where $x = z(\Omega/\nu)^{1/2}$ is time dependent, and the expansion parameters depend only on time and are defined by

$$\beta_1 = (d\Omega/dt)/\Omega^2$$

$$\beta_2 = (d^2\Omega/dt^2)/\Omega^3$$

After a numerical integration of the Navier-Stokes equation, Sparrow and Gregg gave the value of the velocity derivatives at x = 0

$$H_0''(0) = -1.0205 \qquad G_0'(0) = -0.61592$$

$$H_1''(0) = 0.40967 \qquad G_1'(0) = -0.36922$$

$$H_2''(0) = -0.046224 \qquad G_2'(0) = 0.021185$$

By using these results for a sinusoidal modulation, we can determine the expressions of $\tilde{f}'(0,p)$ and $\tilde{g}'(0,p)$ following our notation

$$\tilde{f}'(0,p) = (0.765345 - 0.023112p^2) - 0.204835pj \quad [33]$$

$$\tilde{g}'(0,p) = (-0.923883 - 0.021185p^2) - 0.36922pj \quad [34]$$

Sharma (7) solved the set of six equations ([24]-[29]) with an important approximation; he expects f_2, g_2, and h_2 to be small relative to f_1, g_1, and h_1, and he neglects $-pf_2$ and $-pg_2$ in Eq. [26] and [28]. Then he finds with our notation

$$\tilde{f}'(0,p) = 0.765345 - 0.20178pj \quad [35]$$

$$\tilde{g}'(0,p) = -0.923883 - 0.52285pj \quad [36]$$

These are exact only for p = 0, and the accuracy of the asymptotic expressions [33] and [34] from Sparrow and Gregg (5) is always better.

High frequency range.—For the high frequencies, Sharma (7) obtained an asymptotic solution; with our notation the expressions of $\tilde{f}'$ (0,p) and $\tilde{g}'$ (0,p) are

$$\tilde{f}'(0,p) = \frac{1}{\sqrt{2p}} - j\left(\frac{1}{\sqrt{2p}} - \frac{0.313}{p}\right) \quad [37]$$

$$\tilde{g}'(0,p) = -\sqrt{\frac{p}{2}} - j\left(\sqrt{\frac{p}{2}} - \frac{3}{2}\frac{0.510}{p}\right) \quad [38]$$

On Fig. 1 and 2, the asymptotic solution of Sparrow and Gregg (5) (Eq. [33], [34]) is compared with our calculation for the low frequency range, and the asymptotic solution of Sharma (7) (Eq. [37], [38]) is compared for the high frequency range. Expression [34] is an approximate solution for $\tilde{g}'$ up to p = 2, and expression [38] is an approximate solution for p higher than 7. Expression [33] gives a good value of

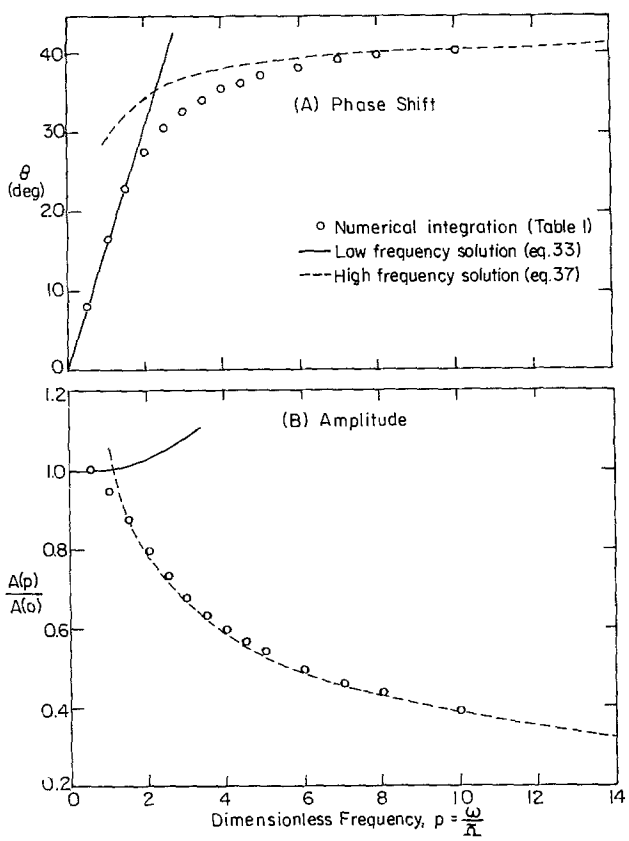

Fig. 1. First coefficient of the series expansion for the unsteady dimensionless component of the radial velocity. Comparison with the results of Sparrow and Gregg (5) and Sharma (7): (A) phase shift of $\tilde{f}'(0,p)$ vs. dimensionless frequency, (B) amplitude of $\tilde{f}'(0,p)$ vs. dimensionless frequency.

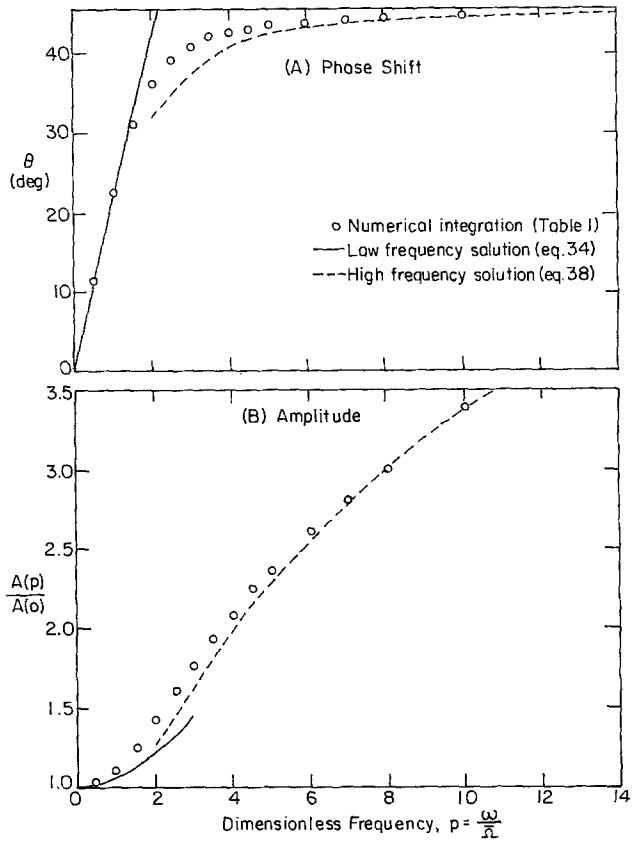

Fig. 2. Second coefficient of the series expansion for the unsteady dimensionless component of the angular velocity. Comparison with the results of Sparrow and Gregg (5) and Sharma (7): (A) phase shift of $\tilde{g}'(0,p)$ vs. dimensionless frequency, (B) amplitude of $\tilde{g}'(0,p)$ vs. dimensionless frequency.

$\tilde{f}'$ only for $p < 1$, and for $p = 1$ the deviation between the expression [33] and our numerical calculation is, for the amplitude, already 6%. The expression [33] may be used with a good accuracy only for $p \leq 0.5$ and the expression [37] for $p \geq 8$.

Mass transport application.—The concentration in the diffusion layer is governed by the unsteady equation of convective diffusion

$$\frac{\partial c}{\partial t} + v_z \frac{\partial c}{\partial z} = D \frac{\partial^2 c}{\partial z^2} \qquad [39]$$

The development of v_z is obtained from Table II and is limited to the two first terms. In order to obtain an analytic solution, Ref. (3) and (4) limited the development to the first term. On the contrary, Tokuda *et al.* (1), for a numerical integration, used the three first terms of the v_z development. By pitting

$$c = \bar{c} + \mathrm{Re}\{\tilde{c}\, e^{j\omega t}\} \qquad [40]$$

and by using the dimensionless variables and parameters

$$a = 0.51023, \quad K = \frac{\omega}{\bar{\Omega}} \left(\frac{9\nu}{a^2 D}\right)^{1/3}, \quad B = \left(\frac{3}{a^4}\right)^{1/3} \qquad [41]$$

and

$$\xi = \frac{z}{\delta} \text{ with } \delta = \left(\frac{3D}{a\nu}\right)^{1/3} \sqrt{\frac{\nu}{\bar{\Omega}}}$$

(δ is a distance characteristic of the thickness of the steady-state diffusion layer; the equivalent Nernst diffusion layer thickness is $\Gamma(4/3)$ times δ) Eq. [39] becomes

$$\frac{d^2\tilde{c}}{d\xi^2} + \left(3\xi^2 - \frac{B\xi^3}{Sc^{1/3}} + \ldots\right)\frac{d\tilde{c}}{d\xi} - jK\tilde{c}$$

$$= -\frac{\Delta\Omega}{\bar{\Omega}}\left(3\frac{\tilde{f}'(0,p)}{a}\xi^2 - \frac{2B\xi^3}{Sc^{1/3}} + \ldots\right)\frac{d\bar{c}}{d\xi} \qquad [42]$$

where

$$\frac{d\bar{c}}{d\xi} = \left.\frac{d\bar{c}}{d\xi}\right|_0 \exp\left(-\xi^3 + \frac{B\xi^4}{4Sc^{1/3}} + \ldots\right) \qquad [43]$$

and where the steady-state derivative at the surface can be expressed as

$$\left.\frac{d\bar{c}}{d\xi}\right|_0 = \frac{c_\infty - \bar{c}_0}{\int_0^\infty \exp\left(-\xi^3 + \frac{B\xi^4}{4Sc^{1/3}} + \ldots\right) d\xi} \qquad [44]$$

Let $\theta(\xi)$ be a solution of the homogeneous equation satisfying the boundary conditions

$$\theta \to 0 \quad \text{as} \quad \xi \to \infty$$

and

$$\theta = 1 \quad \text{at} \quad \xi = 0$$

In terms of the function θ, the solution of Eq. [42] can be obtained by the technique of reduction in order (12) by setting $\tilde{c} = \lambda(\xi)\theta(\xi)$, where λ satisfies

$$\frac{d^2\lambda}{d\xi^2} + \left(3\xi^2 - \frac{B\xi^3}{Sc^{1/3}} + \ldots + \frac{2\theta'}{\theta}\right)\frac{d\lambda}{d\xi}$$

$$= -\frac{\Delta\Omega}{\bar{\Omega}}\left(3\frac{\tilde{f}'(0,p)}{a}\xi^2 - \frac{2B\xi^3}{Sc^{1/3}} + \ldots\right)\frac{1}{\theta}\frac{d\bar{c}}{d\xi} \qquad [45]$$

Integration gives

$$\tilde{c} = K_2\theta + K_1\theta \int_0^{\xi} \frac{\exp\left(-x^3 + \frac{Bx^4}{4Sc^{1/3}} + \dots\right)}{\theta^2(x)}\,dx - \frac{\Delta\Omega}{\bar{\Omega}}\frac{d\bar{c}}{d\xi}\Bigg|_0 \theta \int_0^{\xi} \frac{\exp\left(-x^3 + \frac{Bx^4}{4Sc^{1/3}} + \dots\right)}{\theta^2(x)} \times \int_0^{x} \left(3\frac{\tilde{f}'(0,p)}{a}x_1^2 - \frac{2Bx_1^3}{Sc^{1/3}} + \dots\right)\theta(x_1)\,dx_1 dx \quad [46]$$

where K_1 and K_2 are two integration constants. K_2 can be identified with $\tilde{c}_0$, the value of the amplitude function at $\xi = 0$. K_1 can be obtained from the boundary condition that $\tilde{c}$ approaches zero as ξ approaches infinity, with the result

$$K_1 = \frac{\Delta\Omega}{\bar{\Omega}}\frac{d\bar{c}}{d\xi}\Bigg|_0 W \quad [47]$$

where

$$W = \int_0^{\infty} \left(3\frac{\tilde{f}'(0,p)}{a}\xi^2 - \frac{2B\xi^3}{Sc^{1/3}} + \dots\right)\theta\,d\xi \quad [48]$$

is a dimensionless quantity whose value is worth tabulating.

The general result of this section is a relationship between the concentration and the concentration derivative, both evaluated at the electrode surface. In terms of the dimensional distance z, this can be expressed as

$$\frac{d\tilde{c}}{dz}\Bigg|_{z=0} = \frac{\tilde{c}_0}{\delta}\theta'(0) + \frac{\Delta\Omega}{\bar{\Omega}}\frac{d\bar{c}}{dz}\Bigg|_{z=0} W \quad [49]$$

where $\theta'(0)$ is, for $\xi = 0$, the derivative of $\theta(\xi)$ relative to ξ.

The boundary condition at $z = 0$ determining the value of $\tilde{c}_0$ involves both the mode of regulation and the electrochemical kinetics at the interface. In order to solve the problem, it is not necessary to study, as in Ref. (3, 4), the particular cases of a constant concentration at the interface [improperly called "potentiostatic" in Ref. (3)], or of a constant concentration gradient at the interface [improperly called "galvanostatic" in Ref. (3)]. This general expression [49] is sufficient for studying the electrochemical application in order to obtain an equivalent expression between the observable electrical quantities: the overall potential and the overall current (see Eq. [64]). Determination and tabulation of the quantities $\theta'(0)$ and W thus provide the basis for a rather general treatment subsequently of the interfacial conditions, even though they might have kinetic and double-layer complications not explicitly contemplated here. This point deserves special emphasis.

The numerical calculation of W requires the calculation of the homogeneous solution θ, which is also the solution to the usual convective Warburg impedance problem, where potential or current is modulated instead of rotation speed.

This problem had been studied by a few authors (13-16); in particular Levart and Schuhmann (13) showed how to write θ as a series expansion in $Sc^{-1/3}$

$$\theta(\xi,Sc,K) = \theta_0(\xi,K) + \frac{\theta_1(\xi,K)}{Sc^{1/3}} + \frac{\theta_2(\xi,K)}{Sc^{2/3}} + \dots \quad [50]$$

We solved numerically the corresponding differential equations for θ_0 and θ_1. Since the reciprocal of $\theta'(0)$ is directly related to the convective Warburg impedance, we have tabulated this quantity in terms of the expansion

$$\frac{-1}{\theta'(0)} = Z_0 + \frac{Z_1}{Sc^{1/3}} + \dots \quad [51]$$

When K tends towards zero, $-1/\theta'(0)$ tends towards $\Gamma(4/3)(1 + 0.2980\ Sc^{-1/3})$ which are the two first terms of the expansion of the mass transfer rate for large Schmidt number given by Newman (17) (see Table III).

The expansion for W is more complicated because θ as expanded depends on $pSc^{1/3}$ while $\tilde{f}(0,p)$ in Eq. [48] depends on p without $Sc^{1/3}$. The expansion for W takes the form

$$W = \tilde{f}'(0,p)(t_1 + jt_2) + \frac{1}{Sc^{1/3}}[\tilde{f}'(0,p)(t_3 + jt_4) + t_5 + jt_6 + \dots] \quad [52]$$

where the t's, given in Table IV as functions of $pSc^{1/3}$, are calculated from the following definitions

$$\left.\begin{aligned} t_1 &= \frac{3}{a}\int_0^{\infty} \xi^2 \mathrm{Re}\{\theta_0\}d\xi & t_2 &= \frac{3}{a}\int_0^{\infty} \xi^2 \mathrm{Im}\{\theta_0\}d\xi \\ t_3 &= \frac{3}{a}\int_0^{\infty} \xi^2 \mathrm{Re}\{\theta_1\}d\xi & t_4 &= \frac{3}{a}\int_0^{\infty} \xi^2 \mathrm{Im}\{\theta_1\}d\xi \\ t_5 &= -2B\int_0^{\infty} \xi^3 \mathrm{Re}\{\theta_0\}d\xi & t_6 &= -2B\int_0^{\infty} \xi^3 \mathrm{Im}\{\theta_0\}d\xi \end{aligned}\right\} \quad [53]$$

Table III. Variation of the diffusion or convective Warburg impedance vs. the reduced frequency $pSc^{1/3}$ [$K = 3.258\ pSc^{1/3}$]

$pSc^{1/3}$	$\mathrm{Re}\left\{\frac{Z_0}{\Gamma(4/3)}\right\}$	$\mathrm{Im}\left\{\frac{Z_0}{\Gamma(4/3)}\right\}$	$\mathrm{Re}\left\{\frac{Z_1}{\Gamma(4/3)}\right\}$	$\mathrm{Im}\left\{\frac{Z_1}{\Gamma(4/3)}\right\}$
0	1	0	+0.2980	0
0.1	+0.9883	−0.0956	+0.2789	−0.0898
0.2	+0.9552	−0.1830	+0.2277	−0.1608
0.3	+0.9062	−0.2560	+0.1594	−0.2026
0.5	+0.7866	−0.3519	+0.0301	−0.2045
0.7	+0.6708	−0.3915	−0.0453	−0.1510
1	+0.5367	−0.3935	−0.0740	−0.0700
1.5	+0.4047	−0.3519	−0.0495	−0.0068
2	+0.3343	−0.3101	−0.0247	+0.0074
3	+0.2627	−0.2536	−0.0060	+0.0060
4	+0.1996	−0.1960	−0.0010	+0.0011
5	+0.1816	−0.1789	−0.0007	+0.0007
7	+0.1677	−0.1656	−0.0005	+0.0004
10	+0.1398	−0.1396	−0.0002	+0.0002
15	+0.1140	−0.1129	−0.0001	+0.0001
20	+0.0988	−0.0977	0.0000	0.0000
30	+0.0807	−0.0796	0.0000	0.0000
40	+0.0701	−0.0688	0.0000	0.0000
50	+0.0628	−0.0614	0.0000	0.0000
70	+0.0533	−0.0517	0.0000	0.0000
100	+0.0449	−0.0431	0.0000	0.0000

Table IV. Coefficients of the W expansion vs. the reduced frequency

$pSc^{1/3}$	t_1	t_2	t_3	t_4	t_5	t_6
0	+0.6533	0	+0.7797	0	−0.5963	0
0.1	+0.6511	−0.0396	+0.7726	−0.0829	−0.5934	+0.0407
0.2	+0.6452	−0.0786	+0.7549	−0.1637	−0.5870	+0.0808
0.3	+0.6356	−0.1166	+0.7263	−0.2402	−0.5767	+0.1197
0.5	+0.6060	−0.1874	+0.6408	−0.3738	−0.5452	+0.1918
0.7	+0.5652	−0.2489	+0.5289	−0.4738	−0.5015	+0.2539
1	+0.4904	−0.3201	+0.3405	−0.5537	−0.4215	+0.3241
1.5	+0.3547	−0.3825	+0.0628	−0.5345	−0.2787	+0.3799
2	+0.2338	−0.3910	−0.1107	−0.4179	−0.1540	+0.3782
3	+0.0725	−0.3328	−0.2063	−0.1762	+0.0029	+0.2992
4	−0.0044	−0.2562	−0.1671	−0.0406	+0.0668	+0.2085
5	−0.0364	−0.1931	−0.1105	+0.0154	+0.0838	+0.1391
6	−0.0472	−0.1466	−0.0667	+0.0320	+0.0812	+0.0918
7	−0.0486	−0.1135	−0.0382	+0.0325	+0.0719	+0.0609
10	−0.0386	−0.0600	−0.0055	+0.0169	+0.0435	+0.0195
15	−0.0234	−0.0290	+0.0008	+0.0044	+0.0199	+0.0043
20	−0.0156	−0.0177	+0.0006	+0.0014	+0.0109	+0.0014
30	−0.0086	−0.0092	+0.0002	+0.0003	+0.0047	+0.0003
40	−0.0056	−0.0058	+0.0001	+0.0001	+0.0026	+0.0001
50	−0.0040	−0.0041	0.0000	0.0000	+0.0016	+0.0001
70	−0.0024	−0.0025	0.0000	0.0000	+0.0008	0.0000
100	−0.0014	−0.0014	0.0000	0.0000	+0.0004	0.0000

$\tilde{f}'(0,p)$ is given in Table I for $p \geq 0.5$ and by Eq. [33] for $p < 0.5$.

Table V and Fig. 3 give values of W for three values of Sc (125, 1000, 8000). The value of the first term, without the term in $Sc^{-1/3}$, is also given to illustrate the importance of the Schmidt-number correction. The importance of the correction depends on the frequency as well as the Schmidt number itself. The values on Fig. 3 could be made to fall more nearly on top of each other if plotted against $pSc^{1/3}$ rather than p itself, although this would also make the graph harder to read.

Values of $-W/\theta'(0)$ are given in Table VI and Fig. 4.

Values of $Z_0\tilde{f}'(0,p)\,(t_1 + jt_2)$ are also given to illustrate the importance of the Schmidt-number correction.

Electrochemical application.—The principal result of the preceding section is Eq. [49] relating the oscillating part of the concentration gradient to the oscillating part of the concentration at the surface ($\tilde{c}_0$) and the modulation of the rotation speed ($\Delta\Omega$). Both $\theta'(0)$ and W depend upon the Schmidt number, and a subscript i should be added to all the relevant quantities to denote that different species i can have different values for the diffusion coefficient D_i. We discuss here the application of this equation to the electrochemical impedance, with simplifications directed toward the system and conditions used for the experimental verification of the effect of the term with W, arising from the modulation of the rotation speed.

A single electrode reaction can be written in symbolic form as

$$\sum_i s_i M_i z_i \rightarrow ne^- \qquad [54]$$

For minor species, in the presence of supporting electrolyte and with neglect of double-layer adsorption of these minor species, the concentration gradient is related to the faradaic current density by

$$D_i \frac{\partial c_i}{\partial z}\bigg|_{z=0} = \frac{s_i}{n\mathbf{F}} i_f \qquad [55]$$

and the faradaic current density is governed by a kinetic expression

$$i_f = f(\eta, c_{i0}) \qquad [56]$$

For a simple redox reaction, we have in mind an expression of the form

$$i = i_0 \left[\frac{c_{P0}}{c_{P\infty}} \exp\left(\frac{\alpha_a \mathbf{F}}{RT}\eta\right) - \frac{c_{R0}}{c_{R\infty}} \exp\left(-\frac{\alpha_c \mathbf{F}}{RT}\eta\right) \right] \qquad [57]$$

where η is the total overpotential (sum of concentration overpotential and surface overpotential) and i_0 is the exchange current density at the bulk composition ($c_{P\infty}$ and $c_{R\infty}$). This expression contains the essential features of the concentration overpotential, which may be the only relevant part for an inherently fast reaction. The double-layer capacity is taken to be in parallel across the interface and the diffusion layer in such a manner that the total current density is given by

$$i = i_f + C\frac{d\eta}{dt} \qquad [58]$$

and the electrode potential V measured with respect to a reference electrode placed in the bulk of the solution includes the ohmic potential drop according to

$$V = R_e i + \eta \qquad [59]$$

where R_e is the solution resistance. [Actually, the effect of the nonuniform ohmic potential drop to a disk electrode should be taken into account. but the calculations are then quite complicated (18, 19, 20).]

For impedance calculations, all these expressions can be linearized and the transient parts treated as small departures from the steady-state parts. If a sinusoidal perturbation of very small amplitude is applied to the system, all variables involved will oscillate with the same frequency prescribed by the external perturbation, and each variable can be written as

$$x = \bar{x} + \mathrm{Re}\{\tilde{x}e^{j\omega t}\} \qquad [60]$$

Table V. Variation of W vs. the reduced frequency from Eq. [52]

$pSc^{1/3}$	Sc = 125				Sc = 1000				Sc = 8000			
0	W 0.50179		$\tilde{f}'(0,p)\,(t_1+jt_2)$ 0.50000		W 0.50090		$\tilde{f}'(0,p)\,(t_1+jt_2)$ 0.50000		W 0.50045		$\tilde{f}'(0,p)\,(t_1+jt_2)$ 0.50000	
	A/A(0)	θ	A/A(0)	θ	A/A(0)	θ	A/A(0)	θ	A/A(0)	θ	A/A(0)	θ
0.1	0.9980	4.4	0.9985	3.8	0.9982	3.9	0.9985	3.6	0.9983	3.7	0.9985	3.6
0.2	0.9933	8.8	0.9949	7.6	0.9940	7.8	0.9949	7.3	0.9945	7.4	0.9949	7.1
0.3	0.9857	13.1	0.9892	11.3	0.9873	11.7	0.9891	10.9	0.9885	11.0	0.9891	10.6
0.5	0.9621	21.6	0.9710	18.7	0.9661	19.3	0.9710	18.0	0.9683	18.2	0.9709	17.6
0.7	0.9292	29.9	0.9454	25.9	0.9365	26.7	0.9453	24.8	0.9409	25.2	0.9453	24.3
1	0.8672	41.5	0.8966	36.2	0.8808	37.1	0.8964	34.7	0.8883	35.1	0.8964	33.9
1.5	0.7487	58.8	0.7989	51.8	0.7714	52.6	0.7986	49.4	0.7849	49.8	0.7985	48.3
2	0.6328	73.3	0.6980	65.3	0.6624	65.6	0.6975	62.2	0.6800	62.3	0.6974	60.7
3	0.4465	95.5	0.5224	86.9	0.4810	85.7	0.5216	82.3	0.5018	81.5	0.5214	80.0
4	0.3220	111.35	0.3937	103.3	0.3542	100.0	0.3926	98.0	0.3741	95.2	0.3923	94.1
5	0.2220	124.3	0.2843	117	0.2671	111.4	0.3012	108.4	0.2854	105.3	0.3009	104.5
7	0.1257	139.1	0.1674	134.6	0.1654	124.9	0.1895	123.9	0.1790	118.7	0.1891	118.6
10	0.0651	151.3	0.0872	150.1	0.0922	138.6	0.1032	139.1	0.1030	130.7	0.1094	130.4
15	0.0298	160.7	0.0388	161.5	0.0461	148.8	0.0497	151.7	0.0530	140.4	0.0572	140.4
20	0.0169	165.3	0.0216	166.7	0.0265	157.5	0.0288	158.7	0.0330	146.8	0.0341	147.7
30	0.0076	170.1	0.0095	171.3	0.0121	164.8	0.0131	165.6	0.0163	155.3	0.0168	155.8
40	0.0043	172.2	0.0053	173.5	0.0069	168.2	0.0074	169.3	0.0096	160.5	0.0099	161.3
50	0.0033	174.5	0.0034	174.6	0.0045	170.5	0.0047	171.2	0.0063	164.0	0.0065	164.1
70					0.0024	172.9	0.0025	173.2	0.0033	168.1	0.0034	167.6
100					0.0014	174.7	0.0015	175.0	0.0016	172.0	0.0016	172.1

Table VI. Variation of $-W/\theta'(0)$ vs. the reduced frequency; W is obtained from Eq. [52] and $-1/\theta'(0)$ is obtained from Eq. [51]

	Sc = 125				Sc = 1000				Sc = 8000			
	$-\frac{W}{\theta'(0)}$		$\tilde{Z}_0\tilde{f}'(0,p)(t_1+jt_2)$		$-\frac{W}{\theta'(0)}$		$\tilde{Z}_0\tilde{f}'(0,p)(t_1+jt_2)$		$-\frac{W}{\theta'(0)}$		$\tilde{Z}_0\tilde{f}'(0,p)(t_1+jt_2)$	
$pSc^{1/3}$	A/A(0)	θ	A/A(0)	θ	A/A(0)	θ	A/A(0)	θ	A/A(0)	θ	A/A(0)	θ
0.1	0.9896	10.5	0.9844	9.3	0.9904	9.7	0.9844	9.1	0.9908	9.4	0.9844	9.1
0.2	0.9690	20.8	0.9676	18.4	0.9682	19.2	0.9676	18.1	0.9684	18.7	0.9676	17.9
0.3	0.9163	30.6	0.9315	27.1	0.9234	28.4	0.9314	26.7	0.9275	27.2	0.9891	26.4
0.5	0.8043	48.0	0.8367	42.8	0.8195	44.6	0.8367	42.1	0.8277	42.9	0.8367	41.7
0.7	0.6887	62.5	0.7343	56.2	0.7161	58.1	0.7342	55.1	0.7219	56.0	0.7342	54.6
1	0.5419	79.6	0.5967	72.4	0.5677	74.3	0.5966	70.9	0.5817	71.8	0.5966	70.1
1.5	0.3740	100.7	0.4285	97.2	0.3990	94.0	0.4283	90.4	0.4111	91.3	0.4283	89.3
2	0.2693	116.5	0.3183	108.1	0.2916	108.6	0.3181	105.0	0.3046	105.2	0.3180	103.5
3	0.1530	139.5	0.1907	130.9	0.1701	129.7	0.1904	126.3	0.1803	125.5	0.1904	124.0
4	0.08485	155.9	0.1101	147.8	0.09609	144.5	0.1098	142.5	0.1031	139.7	0.1097	138.6
5	0.05332	168.9	0.07247	161.6	0.06608	156.0	0.07678	153.0	0.07164	149.9	0.07670	149.1
7	0.02792	183.8	0.03946	179.2	0.03783	169.6	0.04467	168.5	0.04155	163.4	0.04457	163.2
10	0.01213	196.3	0.01723	195.0	0.01767	183.6	0.02039	184.0	0.02004	175.7	0.02162	175.3
15	0.00451	205.7	0.00622	206.2	0.00718	193.8	0.00797	196.4	0.0837	185.4	0.00917	185.1
20	0.00221	210.3	0.00300	211.4	0.00357	202.5	0.00400	203.4	0.00452	191.8	0.00474	192.4
30	0.00081	215.1	0.00108	215.9	0.00133	209.8	0.00149	210.2	0.00182	200.3	0.00191	200.4
40	0.00040	217.2	0.00052	218.0	0.00066	213.2	0.00073	213.8	0.00093	205.5	0.00097	205.8
50	0.00027	219.5	0.00030	218.6	0.00038	215.5	0.00041	215.0	0.00055	209.0	0.00057	208.1
70					0.00017	217.9	0.00019	217.3	0.00024	213.1	0.00025	211.7
100					0.00007	219.3	0.00009	218.8	0.00010	216.0	0.00010	215.9

Eq. [56] then becomes

$$\tilde{i}_f = \left(\frac{\partial f}{\partial \eta}\right)_{ci0} \tilde{\eta} + \sum_i \left(\frac{\partial f}{\partial c_{i0}}\right)_{\substack{\eta,cj0 \\ j\neq i}} \tilde{c}_{i0} \qquad [61]$$

The usual charge-transfer resistance R_t can be identified as the reciprocal of $(\partial f/\partial\eta)_{ci0}$, although this may be directly measurable at the prevailing steady-state surface concentration. By substitution of Eq. [49] and [55], we obtain

$$\tilde{\eta} = R_t\tilde{i}_f - \sum_i R_t \left(\frac{\partial f}{\partial c_{i0}}\right)_{\eta,cj0} \left[\frac{\delta_i}{\theta_i'(0)}\frac{s_i}{nFD_i}\tilde{i}_f - \frac{\Delta\Omega}{\bar{\Omega}}\frac{W_i\delta_i}{\theta_i'(0)}\frac{s_i\bar{i}}{nFD_i}\right] = R_t\tilde{i}_f + Z_D\tilde{i}_f + \frac{\Delta\Omega}{\bar{\Omega}}\frac{\bar{i}R_t}{nF}\sum_i \left(\frac{\partial f}{\partial c_{i0}}\right)_{\substack{\eta,cj0 \\ j\neq i}} \frac{W_i\delta_i}{\theta_i'(0)}\frac{s_i}{D_i} \qquad [62]$$

where

$$Z_D = -R_t \sum_i \left(\frac{\partial f}{\partial c_{i0}}\right)_{\substack{\eta,cj0 \\ j\neq 1}} \frac{\delta_i s_i}{nFD_i\theta_i'(0)} \qquad [63]$$

can be termed the diffusion or convective Warburg impedance.

Inclusion of the ohmic potential drop and double-layer capacity according to Eq. [58] and [59] causes Eq. [2] to become

$$\tilde{V} = Z\tilde{i} + \frac{\Delta\Omega}{\bar{\Omega}}\frac{1}{1+j\omega C(R_t+Z_D)}\frac{\bar{i}R_t}{nF} \times \sum_i \left(\frac{\partial f}{\partial c_{i0}}\right)_{\substack{\eta,cj0 \\ j\neq i}} \frac{W_i\delta_i}{\theta_i'(0)}\frac{s_i}{D_i} \qquad [64]$$

where

$$Z = R_e + \frac{R_t + Z_D}{1+j\omega C(R_t+Z_D)} \qquad [65]$$

is the electrochemical impedance $(\tilde{V}/\tilde{i})_{\Delta\Omega=0}$. Under the conditions of the experiments, ω is low enough for ωCR_t and ωCZ_D to be neglected compared to unity.

Furthermore, the formulation based on Eq. [56] obscures the simple relationships which prevail if the kinetics are inherently fast and the overpotential reduces to the concentration overpotential

$$\eta = \eta_c = \frac{RT}{nF}\sum_i s_i \ln\left(\frac{c_{i\infty}}{c_{i0}}\right) \qquad [66]$$

or

$$\tilde{\eta} = \tilde{\eta}_c = -\frac{RT}{nF}\sum_i s_i\frac{\tilde{c}_{i0}}{\bar{c}_{i0}} \qquad [67]$$

Equation [64] would then be replaced by

$$\tilde{V} = Z\tilde{i} + \frac{\Delta\Omega}{\bar{\Omega}}\frac{1}{1+j\omega CZ_D}\frac{\bar{i}RT}{nF}\sum_i \frac{W_i\delta_i}{\theta_i'(0)}\frac{s_i^2}{nFD_i\bar{c}_{i0}} \qquad [68]$$

where

$$Z = R_e + \frac{Z_D}{1+j\omega CZ_D}$$

and

$$Z_D = \frac{RT}{nF}\sum_i \frac{s_i}{\bar{c}_{i0}}\left(-\frac{\delta_i}{\theta_i'(0)}\frac{s_i}{nFD_i}\right) \qquad [69]$$

Galvanostatic mode, $\tilde{i} = 0$: Eq. [64] yields

$$\frac{\tilde{V}}{\Delta\Omega} = \frac{\bar{i}R_t/nF\bar{\Omega}}{1+j\omega C(R_t+Z_D)}\sum_i \left(\frac{\partial f}{\partial c_{i0}}\right)_{\substack{\eta,cj0 \\ j\neq i}} \frac{W_i\delta_i s_i}{\theta_i'(0)D_i} \qquad [70]$$

If the diffusion coefficients are equal for reactants and products, W_i becomes a constant in the sum, and this simplifies to

$$\frac{\tilde{V}}{\Delta\Omega} = \frac{-\bar{i}Z_D/\bar{\Omega}}{1+j\omega C(R_t+Z_D)}W \qquad [71]$$

Equations [68] and [69] yield to Eq. [71] with $R_t = 0$.

For the relatively low values of ω dealt with here, the approximate form would be

$$\frac{\tilde{V}}{\Delta\Omega} = -\frac{\bar{i}}{\bar{\Omega}}Z_D W \qquad [72]$$

If we normalize $(\tilde{V}/\Delta\Omega)$ by dividing by its value for $\omega = 0$, we obtain a function of only two parameters p and $Sc^{1/3}$. For this reason, values of $-W/\theta'(0)$ were given in Table VI and Fig. 4.

In the potentiostatic mode, $\tilde{V} = 0$, and Eq. [64] defines the value of the ratio $\tilde{i}/\Delta\Omega$. Where, again, the diffusion coefficients of reacting species are equal, this yields

$$\frac{\tilde{i}}{\Delta\Omega} = \frac{\bar{i}}{\bar{\Omega}}\frac{1}{1+j\omega C(R_t+Z_D)}\frac{Z_D}{Z}W \qquad [73]$$

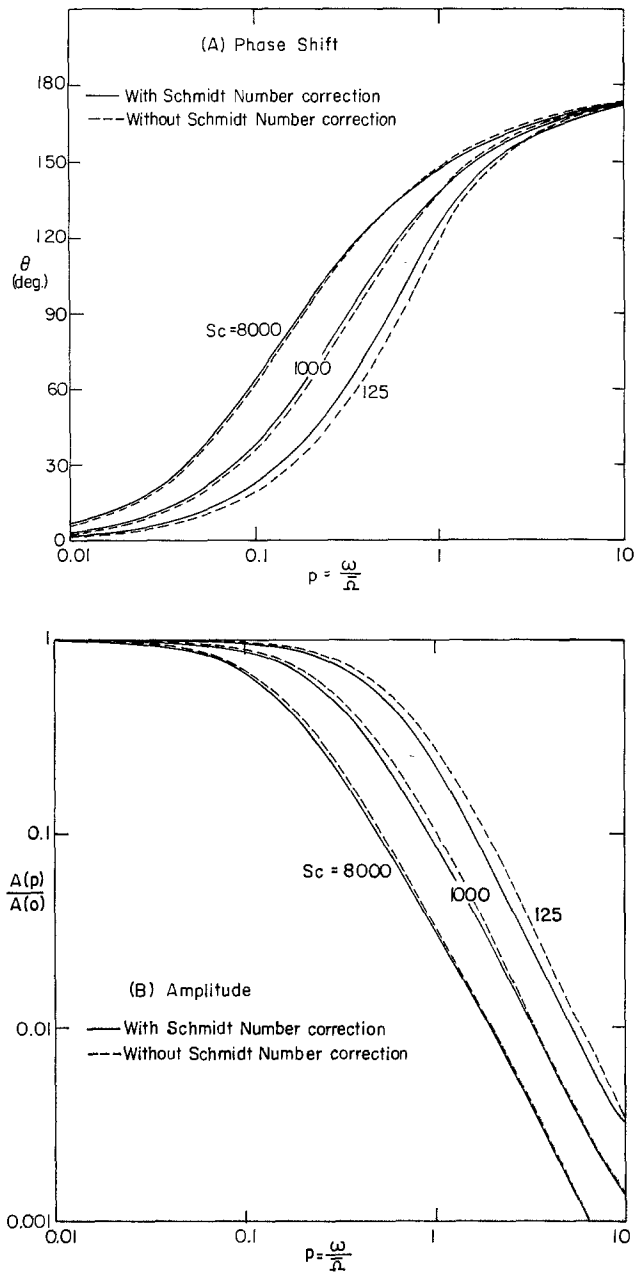

Fig. 3. (A) Phase shift of W vs. dimensionless frequency, (B) normalized amplitude of W vs. dimensionless frequency. In conditions of Eq. [75] or [79], the normalized quantities $(\tilde{i}/\Delta\Omega)$ and W are identical.

In the presence of an excess of supporting electrolyte and for the frequency used in this experiment, the electrolyte resistance (R_e) may be neglected compared to the sum of the charge-transfer resistance (R_t) and the convective-Warburg impedance (Z_D). Then Eq. [73] becomes

$$\frac{\tilde{i}}{\Delta\Omega} = \frac{\bar{i}}{\bar{\Omega}} \frac{Z_D}{R_t + Z_D} W \qquad [74]$$

With the assumption of a small electrolyte resistance Eq. [68] and [69] yield to

$$\frac{\tilde{i}}{\Delta\Omega} = \frac{\bar{i}}{\bar{\Omega}} W \qquad [75]$$

As an aside, we may note from Eq. [64] that if Z denotes the electrochemical impedance $(\tilde{V}/\tilde{i})_{\Delta\Omega=0}$, then it follows that

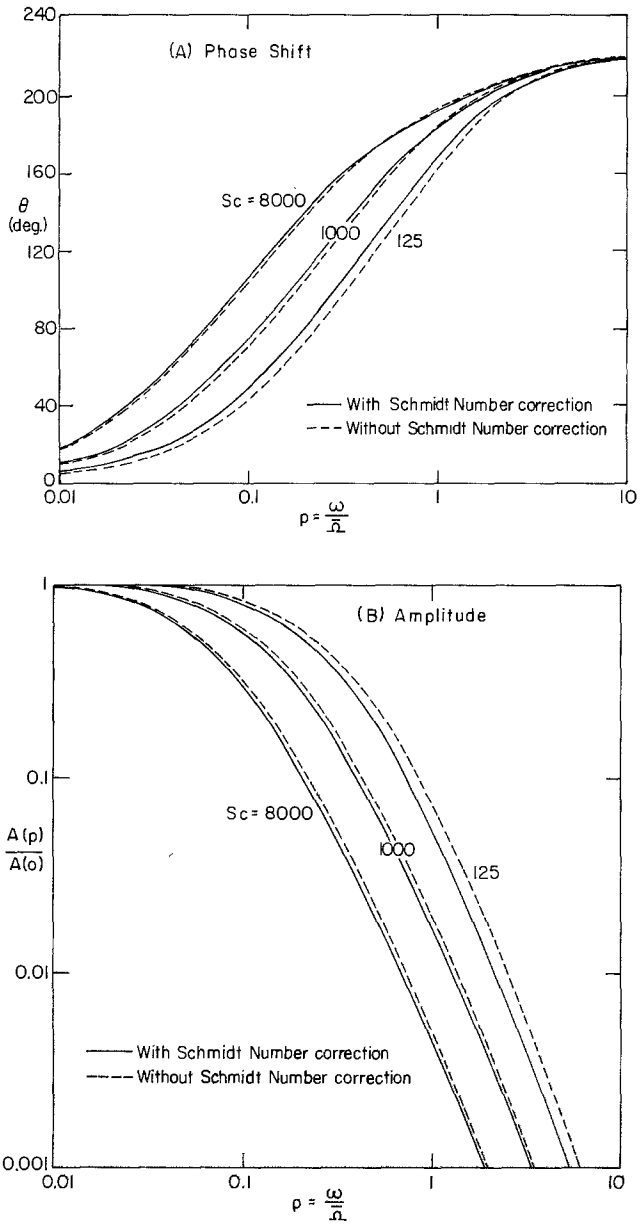

Fig. 4. (A) Phase shift of $-W/\theta'$ (0) vs. dimensionless frequency, (B) normalized amplitude of $-W/\theta'$ (0) vs. dimensionless frequency. In conditions of Eq. [72], the normalized quantities $(\tilde{V}/\Delta\Omega)$ are identical.

$$\left(\frac{\tilde{i}}{\Delta\Omega}\right)_{V=0}^{\sim} = -\left(\frac{\tilde{V}}{\Delta\Omega}\right)_{i=0}^{\sim} \frac{1}{Z} \qquad [76]$$

which is similar to the relation (21)

$$\left(\frac{\partial i}{\partial \Omega}\right)_V = -\left(\frac{\partial V}{\partial \Omega}\right)_i \left(\frac{\partial i}{\partial V}\right)_\Omega \qquad [77]$$

Assuming that we understand the electrochemical impedance Z of the system, the test under hydrodynamic modulation, whether it be potentiostatic or galvanostatic or otherwise, essentially tests for the applicability of the theory developed for W.

We can pick out the value of W for the oxidized or reduced species separately, without the assumption that $D_R = D_P$, by choosing our steady state under conditions where one term or the other in Eq. [57] is negligible. If we are on the cathodic limiting current plateau, we can regard our fixed potential conditions to mean that $c_R = 0$ or that both $\bar{c}_R$ and $\tilde{c}_R$ are zero. The clearest route to the hydrodynamic impedance is then Eq. [45] applied to species R. With Eq. [55], [58],

and [59], we have

$$\frac{\tilde{i}}{\Delta\Omega} = \frac{\bar{i}_{lim}/\bar{\Omega}}{1 + j\omega CR_e} W_R \qquad [78]$$

Again, we can test the theory for W_R. Equation [78] can also be obtained from Eq. [73] by recognizing that Z_D becomes infinite under limiting current conditions. For the values of ω used here, Eq. [78] simplifies further to

$$\frac{\tilde{i}}{\Delta\Omega} = \frac{\bar{i}_{lim}}{\bar{\Omega}} W_R \qquad [79]$$

This relation is similar to Eq. [75] obtained with the assumption that the kinetics are inherently fast and that $R_e << Z_D$.

Experimental

The aim of these experimental measurements is to obtain a comparison with theory on a large frequency range for galvanostatic and potentiostatic regulation. For this reason, we use a well-known electrochemical reaction: the reduction step of a rapid redox system (potassium ferricyanide-ferrocyanide (0.005M) with 1M KCl as supporting electrolyte). The temperature was fixed at 25°C, and the Schmidt number was 1200.

The electrical scheme of the experimental device had been given in Ref. (2) and (4). However, for the present study, a new electrooptical tachometer has been used in order to obtain good regulation of the instantaneous angular velocity even for a low mean velocity (as low as 60 rpm). The measurements are performed thanks to a two-channel transfer function analyzer (DFTA). The remaining parasitic noises are diminished by supplying the potentiostat by Ni-Cd batteries and by using a battery and a large resistance as a galvanostat.

In Fig. 5a and 5b, we give the experimental results obtained at 120 rpm (2 Hz) with a platinum rotating disk electrode (diam = 5 mm) for galvanostatic regulation at $\bar{i} = \frac{1}{2}\, i_{lim}$ ($i_{lim} = 170\ \mu A$). The theoretical curve is obtained from expression [72] with the Schmidt number correction; and for the amplitude, the experimental curve is normalized by the experimental value of $\tilde{V}/\Delta\Omega$ when p tends towards zero. The agreement between the theory and experiment is good for both the phase shift and the amplitude over the whole frequency range.

In Fig. 6a and 6b, we give the experimental results obtained at 120 rpm with the same rotating disk electrode but for potentiostatic regulation at the limiting current ($V = -100$ mV *vs.* saturated calomel reference electrode). The theoretical curve is obtained from expression [79] (with the assumption that $\tilde{c} = 0$ at the interface and $\omega CR_e << 1$).

For $p < 1$, the agreement between theory and experiment is good. For higher frequencies, the deviation increases with p. This deviation may be due to the assumption of $\tilde{c} = 0$ at the interface, which is equivalent to $(R_t + R_e) << Z_D$. Z_D decreases with the frequency, and for p higher than 1, the assumption may not be valid; therefore, it is necessary to use the general expression [73].

From Eq. [57] we have

$$\bar{i} = -\bar{i}_0 \left[\frac{\bar{c}_{R0}}{c_{R\infty}} \exp\left(-\frac{\alpha_c \mathbf{F}}{RT} \bar{\eta} \right) \right] \qquad [80]$$

and

$$R_t = \frac{RT}{\alpha_c \mathbf{F}} \cdot \frac{1}{\bar{i}} \qquad [81]$$

With $\alpha_c = 0.5$, $\bar{i} = 850\ \mu A/cm^2$, $R = 8.314$ J/mol · K, $T = 298$ K, and $\mathbf{F} = 96487$ C/equiv., we obtain 60 $\Omega \cdot cm^2$. And from Eq. [53] with $D_R = 0.765 \cdot 10^{-5}$ cm^2/sec and $\nu = 0.0094$ cm^2/sec, $Z_D(\omega = 0) = \frac{2 \cdot 10^{-4}}{\bar{c}_{R0}}\ \Omega \cdot cm^2$.

The measurements correspond to the beginning of the plateau; then we may assume $\bar{c}_{R0} = 0.01\ c_{R\infty}$ and $Z_D(\omega = 0) = 4\ k\Omega \cdot cm^2$. With these values, R_e is negligible compared to R_t and Z_D, and we may use Eq. [74]. The values of Z_D may be obtained from Table V, and we may calculate the ratio $Z_D/(R_t + Z_D)$. The results are given in Table VII, and the corre-

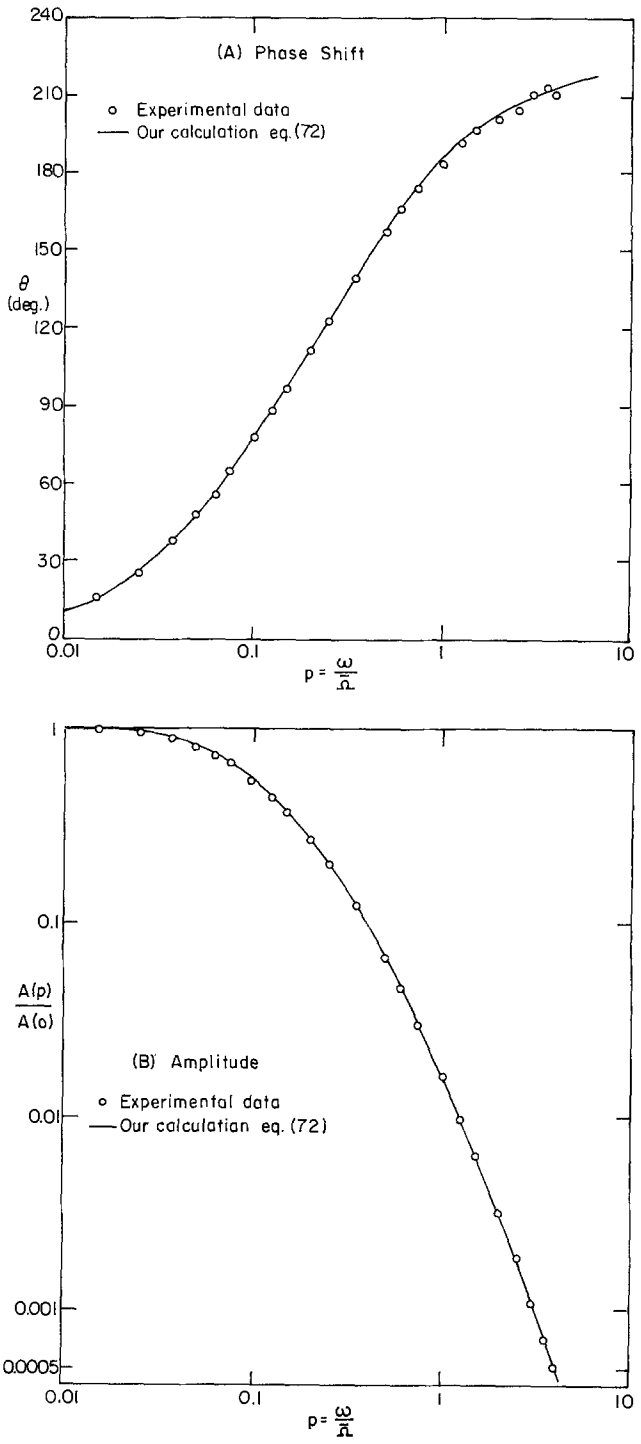

Fig. 5. Comparison between the theoretical curve from Eq. [72] and the experimental data in galvanostatic mode. The data were obtained with the $Fe(CN)_6^{3-}/Fe(CN)_6^{4-}$ system at $i = 1/2\ i_{lim}$. Supporting electrolyte $|KCl| = 1M$, $Sc = 1200$. $\bar{\Omega} = 120$ rpm: (A) phase shift *vs.* dimensionless frequency, (B) normalized amplitude *vs.* dimensionless frequency.

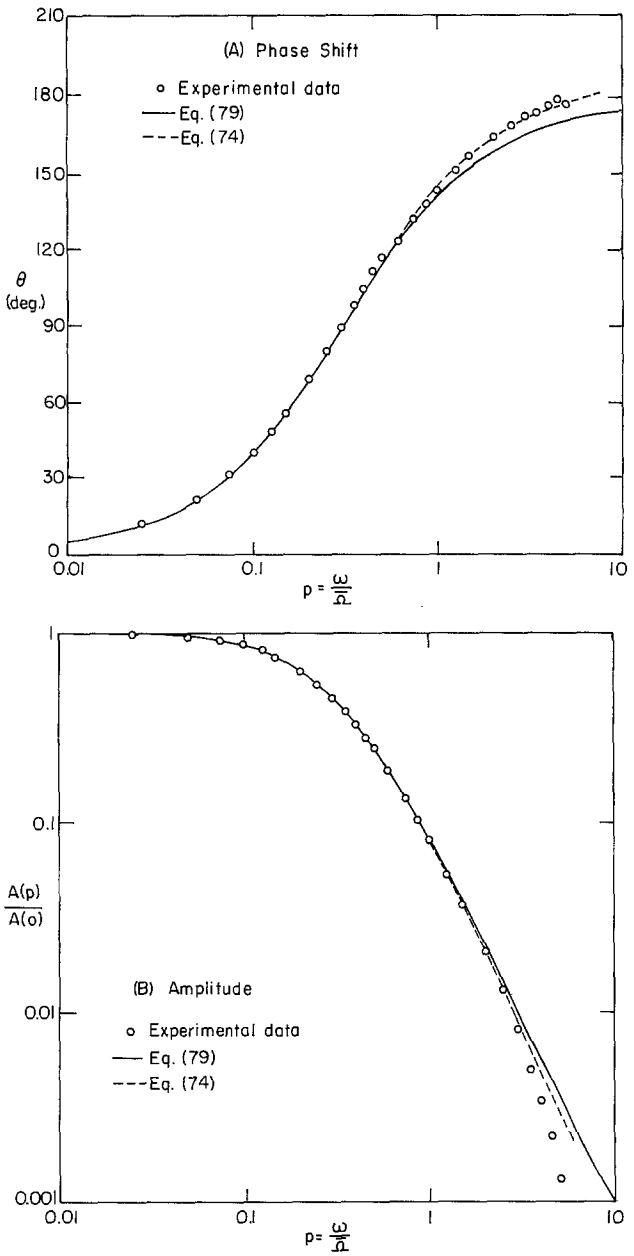

Fig. 6. Comparison between the theoretical curve and the experimental data in potentiostatic mode at the limiting current, the solid lines correspond to Eq. [79] and the dashed lines to Eq. [74]: (A) phase shift vs. dimensionless frequency, (B) normalized amplitude vs. dimensionless frequency.

sponding corrections are given in dashed lines on Fig. 6a and 6b.

With this correction, the agreement between the theory and experiment is good over the whole frequency range for the phase shift and until p = 3 for the amplitude. The deviation for the higher frequencies may be due to the weakness of the signal compared to the residual noise of the electronic device, in particular the potentiostat. This problem is less important in galvanostatic regulation because the galvanostat made with a battery may be considered without noise.

From the comparison of our experimental measurements to the theoretical curve, we have shown on the diffusion plateau the effect of the charge-transfer resistance for higher frequencies. This effect may be more important for intermediate kinetics because R_t is higher and Z_D is smaller. Then below the limiting current, with the assumption $D_R = D_P$ and $\omega C(R_t + Z_D) << 1$, the analysis of the normalized data is easier in galvanostatic regulation (their values depend

Table VII. Variations of $\frac{Z_D}{R_t + Z_D}$

p	1	1.5	2	3	4	5
A	0.95	0.93	0.925	0.91	0.90	0.89
θ	3	3.5	4	5	5.5	6

only on the dimensionless frequency p($p = \omega/\bar{\Omega}$) and the cubic root of the Schmidt number). However in potentiostatic regulation at limiting current, this nonstationary method may give some original information because the electrochemical impedance cannot be used in this low frequency range.

An application of this method is the determination of the diffusion coefficient for the electroactive species. These electrohydrodynamical impedances, in galvanostatic or potentiostatic mode, may be written as a series expansion of $Sc^{-1/3}$; in order to obtain sufficient accuracy, it is necessary to use the two first terms of this series. A best accuracy is obtained if the data analysis is done on a large frequency range. Then, for example, comparison of Fig. 6 with Fig. 3 or of Fig. 5 with Fig. 4 would permit the determination of Sc, with a minor difficulty being associated with the inclusion of the Schmidt number correction. Since we are working with a well-known mass transfer system, it has not been necessary for us to try to infer here the value of the Schmidt number from the experimental results. Tables I-V give results of integration of the unsteady Navier-Stokes equations to cover all frequencies which can be achieved experimentally.

Acknowledgment

This work was supported by the National Science Foundation through an Exchange Visitor Program with Centre National de la Recherche Scientifique No. G050252.

Manuscript submitted July 8, 1982; revised manuscript received Oct. 5, 1982.

LIST OF SYMBOLS

a	constant = 0.51023
B	constant = $(3/a^4)^{1/3}$
c	concentration of the electroactive species, mol/cm³
C	double layer capacity, farad/cm²
D	diffusion coefficient, cm²/sec
f	dimensionless unsteady component of the radial velocity (see Eq. [13])
F	dimensionless steady component of the radial velocity
$\mathbf{F}$	Faraday's constant, 96,487 C/equiv.
g	dimensionless unsteady component of the angular velocity
G	dimensionless steady component of the velocity in θ-direction
h	dimensionless unsteady component of the axial velocity
H	dimensionless steady component of the axial velocity
i	current density, A/cm²
i_o	exchange current density at the bulk composition, A/cm²
i_f	Faradaic current density, A/cm²
i_{lim}	limiting current density, A/cm²
j	$=\sqrt{-1}$
K	dimensionless frequency = 3.2576 p $Sc^{1/3}$
K_1, K_2	integration constants (see Eq. [46])
n	number of electrons involved in electrode reaction
p	dimensionless unsteady component of the dynamic pressure
p	dimensionless frequency = $\omega/\bar{\Omega}$
P	dynamic pressure, dyne/cm²
P	dimensionless steady component of the dynamic pressure
r	radial distance in cylindrical coordinates
R	universal gas constant, 8.3143 J/mol-K
R_e	electrolyte resistance, Ω · cm²
R_t	charge transfer resistance, Ω · cm²

s_i	stoichiometric coefficient of species i in electrode reactions
Sc	Schmidt number
t	time, sec
t_j	parameters of the W expansion ($j = 1$ to 6) (see Table IV)
T	absolute temperature, K
v_r	radial component of the fluid velocity, cm/sec
v_θ	angular component of the fluid velocity, cm/sec
v_z	axial component of the fluid velocity, cm/sec
V	electrode potential measured with respect to a reference electrode placed in the bulk of the solution, V
W	function defined in Eq. [48] (see Table V, Fig. 3)
z	axial distance in cylindrical coordinates, cm
z_i	charge number of species i
Z	electrochemical impedance, $\Omega \cdot cm^2$
Z_D	diffusion or convective Warburg impedance, $\Omega \cdot cm^2$
Z_o, Z_1	coefficients of the series expansion of $-1/\theta'(o)$ in $Sc^{-1/3}$, (see Eq. [45], Table III)
α_a, α_c	transfer coefficients
β_1, β_2	expansion parameters (see Eq. [30]-[32])
$\Gamma(4/3)$	$= 0.89298$, the gamma function of 4/3
δ	distance characteristic of the thickness of diffusion layer, see Eq. [34], cm
ζ	dimensionless axial distance from disk $(=z\sqrt{\Omega/\nu})$
η	total overpotential, V
θ	solution of the unsteady homogeneous equation of convective diffusion
θ	angle in cylindrical coordinates, radian
θ_j	coefficients of the series expansion of θ in $Sc^{-1/3}$, ($j = 0, 1, 2 \ldots$)
μ	viscosity, g/cm-sec
ν	kinematic viscosity, cm^2/sec
ξ	dimensionless axial distance from disk $(=z/\delta)$
ω	modulation frequency, radian/sec
$\Delta\Omega$	amplitude modulation of the rotation speed, radian/sec
Ω	disk rotation speed, radian/sec
χ	dimensionless axial distance from disk $(= z\sqrt{\Omega/\nu})$

Subscripts

o	at electrode surface
∞	in bulk solution
i	relative to species i
P	produced species
R	reacting species

Superscripts

overbar	steady state
~	unsteady component

REFERENCES

1. K. Tokuda, S. Bruckenstein, and B. Miller, *This Journal*, **122**, 1316 (1975).
2. C. Deslouis, I. Epelboin, C. Gabrielli, and B. Tribollet, *J. Electroanal. Chem.*, **82**, 251 (1977).
3. W. J. Albery, A. R. Hillman, and S. Bruckenstein, *ibid.*, **100**, 687 (1979).
4. C. Deslouis, C. Gabrielli, Ph. Sainte-Rose Fanchine, and B. Tribollet, *This Journal*, **129**, 107 (1982).
5. E. M. Sparrow and J. L. Gregg, *J. Aerospace Sci.*, **27**, 252 (1960).
6. Y. Kanzaki and S. Bruckenstein, *This Journal*, **126**, 437 (1979).
7. V. P. Sharma, *Acta Mechanica*, **32**, 19 (1979).
8. Th. Von Karmán and Z. Angew, *Math. Mech.*, **1**, 233 (1921).
9. J. Newman, "Electrochemical Systems," Prentice Hall, Inc., Englewood Cliffs, NJ (1973).
10. J. Newman, *Ind. Eng. Chem.*, **7**, 514 (1968).
11. W. G. Cochran, *Proc. Cambridge Phil. Soc.*, **30**, 365 (1934).
12. F. B. Hildebrand, "Advanced Calculus for Applications," p. 29, Prentice Hall, Inc., Englewood Cliffs, NJ (1948).
13. E. Levart and D. Schuhmann, *J. Electroanal. Chem.*, **28**, 45 (1970).
14. C. Deslouis, Thése de Doctorat d'Etat, Paris, No. A.O. 11014 (1975).
15. D. A. Scherson and J. Newman, *This Journal*, **127**, 110 (1980).
16. R. V. Homsy and J. Newman, *ibid.*, **121**, 521 (1974).
17. J. Newman, *J. Phys. Chem.*, **70**, 1327 (1966).
18. J. Newman, *This Journal*, **113**, 1235 (1966).
19. J. Newman, *ibid.*, **117**, 198 (1970).
20. P. Appel, Ph.D. Dissertation, University of California, Berkeley (1976).
21. C. Deslouis, I. Epelboin, C. Gabrielli, Ph. Sainte-Rose Fanchine, and B. Tribollet, *J. Electroanal. Chem.*, **107**, 193 (1980).

The Kinetic Parameters of the $Fe(CN)_6^{3-/4-}$ Redox System

New Results with the Ring Electrode in Turbulent Pipe Flow

T. Iwasita and W. Schmickler*

Institut für Physikalische Chemie, Universität Düsseldorf, Düsseldorf, Germany

J. Herrmann and U. Vogel

Institut für Physikalische Chemie, Universität Bonn, Bonn, Germany

ABSTRACT

A theoretical analysis of a ring electrode in turbulent pipe flow is given in order to estimate the limits of resolution of a given experimental setup. Special attention is paid to error analysis, which is necessary for the correct evaluation of the data. To demonstrate the potentialities of this method for kinetic studies, the apparent exchange current density of the ferro-ferricyanide system was measured. The values obtained are higher than those reported in the literature.

The study of electrode kinetics has been improved with the development of the methods to measure the reaction rates with increasing accuracy. Stationary and nonstationary methods are employed in a more or less successful way in order to eliminate the diffusional contribution to the electrode process in systems having standard rate constants, k_o, smaller than about 10^{-3} cm/sec. Above this limit the selection of the appropriate technique becomes more and more difficult. With the rotating disk electrode (RDE) rate

* Electrochemical Society Active Member.

Key words: mass transport, kinetics.

constants in the order of 10^{-2} cm/sec have been measured. Some transient techniques have extended this limit by less than one order of magnitude. A rapid analysis of the data for the system $Fe(CN)_6^{3-/4-}$ given in Table I shows that the values of k_o obtained by different methods under the same conditions (electrode metal and supporting electrolyte), vary by a factor greater than two. The differences come probably from the fact that the limit of the methods employed has been exceeded. Factors such as uncompensated *IR* drop or electrode pretreatment can also be reasons for the differences observed, and they contribute to enlarge the errors to a higher extent, thus making the situation even more unfavorable.

Very seldom can one find in the literature a correct limit for the use of an experimental method. The maximum measurable rate constant is normally overestimated on the basis of theoretical calculations without real experimental proof. These idealized limits do not take into account the increasing technical problems one has to confront in a real experiment as the reaction rate becomes larger.

From the transient techniques, the one offering the most attractive possibilities is probably the coulostatic pulse method. Its main advantage is the absence of ohmic drop effects. If the voltage recording system has very fast recovery properties, the η-t curve can be measured at very short times (0.5 μsec after cessation of the pulse), before the diffusional process becomes important (6). Theoretically, rate constants as large as 0.4 cm/sec can be evaluated by means of a simple log η-t relationship, or with cumbersome mathematical treatment 1-5 cm/sec could eventually be measured (6). These limits have still not been experimentally demonstrated.

Recently, a ring electrode in turbulent pipe flow (RTP) has allowed the determination of the rate constant of the redox couple $Fe(bipy)_3^{3+/2+}$, $k_o = 0.9$ cm/sec, with data from stationary current-potential curves (7, 8). In order to achieve high enough stationary flow rates in a 1 cm diam pipe, the experimental arrangements required a relatively large amount of solution (about 5 liters). In our laboratory, the experimental setup was improved in order to reduce the required volume to about 300 ml (9) and to allow a satisfactory reduction of the ohmic resistance. As a test of the new device, the often investigated system $Fe(CN)_6^{3-/4-}$ was measured on platinum and gold electrodes. The results obtained at the ring in turbulent pipe flow are compared with those of RDE experiments and with those of some nonstationary methods. The rotating disk electrode so far has been considered to be sufficient to measure the rate constant of the redox couple $Fe(CN)_6^{3-/4-}$ (3, 10).

The Theoretically Expected Limitations of RTP Measurements

The method of evaluation of the kinetic parameters from the experimental stationary current-potential curve.—In the following discussion we refer to the reaction rate in terms of the standard exchange current density j_{oo} which is defined as follows (11)

$$j_{oo} = nFk_oc^* \qquad [1]$$

where c^* is a standard concentration $= 10^{-3}$ mol/cm^3 and F = the Faraday constant, *ca.* 10^5 As/equivalent. A rate constant $k_o = 1$ cm/sec is equivalent to a standard exchange current density of about 100 A/cm^2. The exchange current density at concentrations c_{ox} and c_{red} is related to the standard rate constant according to

$$j_o = j_{oo}\left[\frac{c_{ox}}{c^*}\right]^{\alpha}\left[\frac{c_{red}}{c^*}\right]^{(1-\alpha)} \qquad [2]$$

with c_{ox}, c_{red} = bulk concentrations in mol/cm^3.

The experimental stationary current-potential curves corrected for ohmic drop result from the contribution of mass and charge transfer. A reaction having an infinite rate of charge transfer (k_o or $j_{oo} \to \infty$) can be described in terms of a reversible current, I_{rev}

$$I_{rev} = \frac{I_{lim}^a\,[1 - \exp(-nF\eta/RT)]}{1 + \frac{I_{lim}^a}{I_{lim}^c}\exp(-nF\eta/RT)} \qquad [3]$$

Equation [3] can be easily obtained for stationary conditions, when the mass transport is proportional to the concentration gradient (I_{lim}^a, I_{lim}^c = anodic and cathodic limiting currents). The reversible current is determined only by the parameters affecting the mass transfer (via I_{lim}^a and I_{lim}^c) and by the overpotential.

For a reaction having a finite rate of charge transfer ($0 < k_o < \infty$) the observed current I, will be smaller than I_{rev} under the same experimental conditions. The evaluation method (8, 12) uses the relationship of both currents introducing a dimensionless parameter u defined as follows

$$u = \frac{2}{3}\frac{I_{rev}}{I_k} \qquad [4]$$

where I_k is the current associated with a reaction controlled by charge transfer alone

$$I_k = I_o \exp(\alpha nF\eta/RT)\,[1 - \exp(-nF\eta/RT)]$$

It can be easily seen that

$$u = \frac{2I_{lim}^a/A}{3j_o\exp(\alpha nF\eta/RT)\left[1 + \frac{I_{lim}^a}{I_{lim}^c}\exp(-nF\eta/RT)\right]} \qquad [5]$$

with A = electrode area. The current ratio I/I_{rev} is related to the parameter u

$$I/I_{rev} = 1 - 2u + 2u^2\ln(1 + 1/u) \qquad [6]$$

Equation [6] contains the experimental current I and the reversible current I_{rev} which can be calculated from the measured limiting currents according to Eq. [3]. Once the value of u is known for several given overpotentials, the exchange current density j_o and the transfer coefficient α can be evaluated from Eq. [5]. A computer fitting procedure can give reliable statistical mean values of the kinetic parameters.

At high overpotentials Eq. [5] can be written

$$-\ln u = -\ln\frac{2}{3}\frac{I_{lim}^a}{Aj_o} + \frac{\alpha nF\eta}{RT}, \quad \text{for} \quad \eta >> \frac{RT}{F}$$

and [7]

$$-\ln u = -\ln\frac{2}{3}\frac{I_{lim}^c}{Aj_o} + \frac{(1-\alpha)nF\eta}{RT}, \quad \text{for} \quad \eta << -\frac{RT}{F}$$

These linear ln u *vs.* η relationships can be used as an alternative for the calculation.

The evaluation procedure described above makes use of the experimental limiting currents. For systems having poorly defined limiting currents it is possible to obtain I_k by extrapolating the current I to infinitely fast mass transport; details are given elsewhere (13).

Simulated current-potential curves for the RTP and RDE methods.—A better understanding of the potentialities of the methods can be achieved by simulating with a computer the expected current-potential curves for different values of j_{oo} at given mass transfer conditions determined by the experimental setup.

The theoretical current-potential curves for the RTP were calculated by means of Eq. [3]-[6] and the following expression for the limiting current (8, 9)

$$I_{\lim}{}^{a} = 0.276AnFD_{red}{}^{2/3}\nu^{1/3}Re^{7/12}L^{-1/3}d^{-2/3}c_{red} \quad [8]$$

where D = diffusion coefficient, ν = kinematic viscosity, Re = Reynolds number, L = electrode length, d = pipe diameter, and A = electrode area.

The computer generated curves are shown in Fig 1. The values of the parameters employed are indicated in the figure.[1]

In the case of the RDE the curves I_{rev} and I *vs.* η were simulated with the help of Eq. [3] and the equation for the kinetic and diffusion-controlled current as follows (3, 15)

$$\frac{1}{I} = \frac{1}{Aj_o \exp(\alpha n\mathbf{F}\eta/RT)[1 - \exp(-n\mathbf{F}\eta/RT)]} + \frac{1 + \dfrac{I_{\lim}{}^{a}}{I_{\lim}{}^{c}}\exp(-n\mathbf{F}\eta/RT)}{I_{\lim}{}^{a}[1 - \exp(-n\mathbf{F}\eta/RT)]} \quad [9]$$

where the limiting current is given by (15)

$$I_{\lim}{}^{a} = 0.620AnFD_{red}{}^{2/3}\nu^{-1/6}c_{red}\omega^{1/2} \quad [10]$$

The respective I_{rev} and I curves are shown in Fig. 2. The selected parameters are also indicated.

In the limit of $j_o \to \infty$, Eq. [9] and [3] are identical. For intermediate kinetics ($0 < j_o < \infty$), a dimensionless parameter u can be defined for the RDE as follows

$$u = \frac{I_{\lim}{}^{a}/A}{j_o \exp(\alpha n\mathbf{F}\eta/RT)\left[1 + \dfrac{I_{\lim}{}^{a}}{I_{\lim}{}^{c}}\exp(-n\mathbf{F}\eta/RT\right]} \quad [11]$$

and the observed current I is given by

$$I/I_{rev} = (1 + u)^{-1} \quad [12]$$

The average flow velocity used to simulate the curves in Fig. 1 (v = 13.77 m/sec, Re number = 30,000) can be easily attained with our experimental arrangement. On the other hand, the rotation speed used to simulate the curves at the RDE (Fig. 2) is almost the practical limit of this technique. Therefore, a comparison of Fig. 1 and 2 clearly shows the superiority of the RTP method. The resolution of the curves for different values of the exchange current density attained with the RTP cannot be reached by the RDE even at a high speed of rotation (10,000 rpm).

[1] The diffusion coefficients and kinematic viscosity correspond to a solution of $Fe(CN)_6^{3-/4-}$ in 0.5M K_2SO_4 at 20°C.

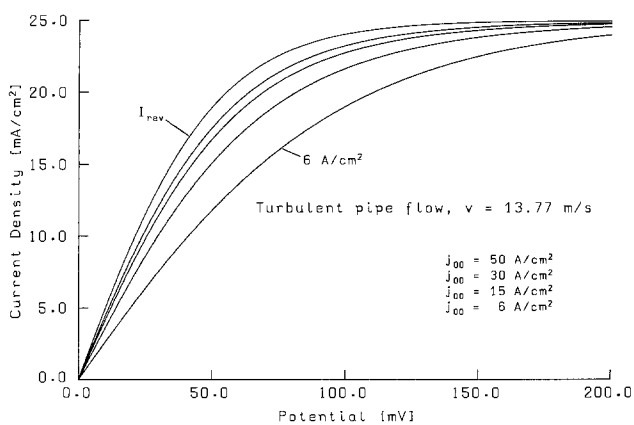

Fig. 1. Computer simulated current-potential curves for the ring electrode in turbulent pipe flow. Electrode length = 0.01 cm; pipe diameter = 0.22 cm, T = 20°C, $c_{ox} = c_{red}$ = 2.5 · 10⁻³M, D_{ox} = 6.22 · 10⁻⁶ cm²/sec, D_{red} = 5.93 · 10⁻⁶ cm²/sec, kinematic viscosity = 1.01 · 10⁻² cm²/sec, α = 0.5. The average flow velocity v corresponds to an Re number of 30,000.

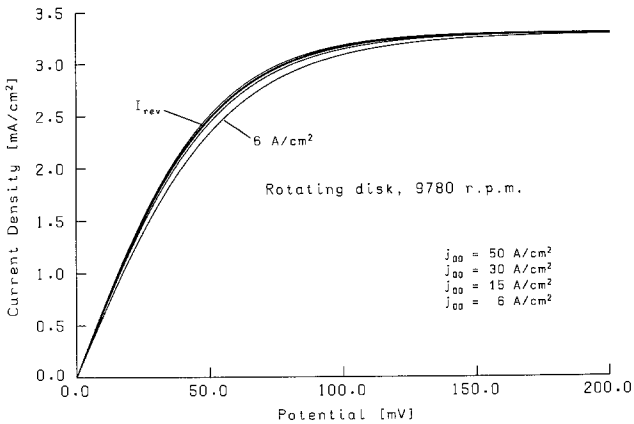

Fig. 2. Computer simulated current-potential curves for the rotating disk electrode. T = 20°C, $c_{ox} = c_{red}$ = 2.5 · 10⁻³M, D_{ox} = 6.22 · 10⁻⁶ cm²/sec, D_{red} = 5.93 · 10⁻⁶ cm²/sec, kinematic viscosity = 1.01 · 10⁻² cm²/sec, α = 0.5.

From the plots of Fig. 2 we can conclude that the maximum value for the standard exchange current density to be measured with the RDE is about 10A cm⁻². This limit can be reached only under optimum experimental conditions. The curves also show that the extrapolated exchange current density is very sensitive to small errors in the current and/or overpotential. This effect is even more pronounced at lower speeds of rotation. Therefore, it is convenient to perform the evaluation of j_o and α from experimental data taken at the highest possible speed of rotation and by means of a fitting procedure through Eq. [9] or [11]. The accurate control of the *IR* drop is also of great importance. Equations [5] and [11] represent important steps in the calculation of the experimental data of the RTP and RDE methods, respectively. The statistical fitting of these relationships gives reliable results that can be conveniently presented in the form of a ln u-η plot. Such curves were simulated for the RTP with selected mass and charge transfer conditions as shown in Fig. 3.

Increasing the convective mass transfer produces a displacement of the curves to higher u values. The linear relationship at high overpotentials predicted by Eq. [7] can also be observed.

Estimation of error in the RTP method.—The errors in the RTP method, as in any experimental technique, can be systematic or random. In the first group we include the instrumental errors, the uncontrolled *IR*

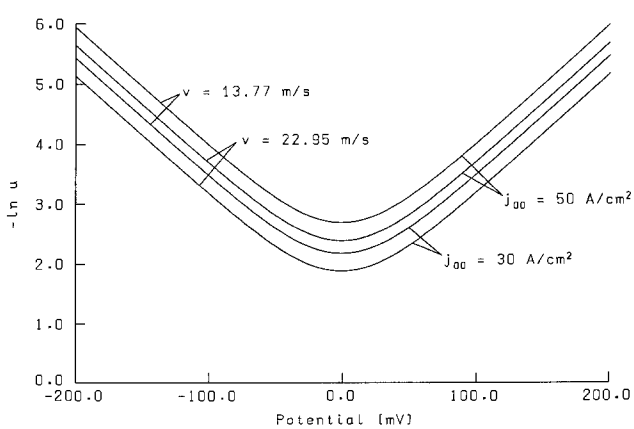

Fig. 3. Computer simulated semilogarithmic plot of the potential dependence of the parameter u for a ring electrode under the same conditions as in Fig. 1.

drop, the errors produced by impurities in the solution, and the failure in the temperature control. In the RTP method in particular, an unsatisfactory mounting of the ring electrode can produce large systematic errors. On the other hand, a test of the state of the ring electrode can be easily done by taking a cyclic voltammogram in 0.5M H_2SO_4 and by checking that the relationship I_{lim}-$Re^{7/12}$ (Eq. [8]) is obeyed. The cyclic voltammogram allows a control of the electrode surface and the I-$Re^{7/12}$ plot proves the fulfillment of the hydrodynamic conditions for the validity of the evaluation procedure.

In the course of one experiment an increase of several degrees in temperature can be observed if the solution is not properly cooled. Therefore, the temperature has to be measured and kept constant, and the temperature control device must be placed very close to the electrode.

The main random error is obviously given by the precision of the instrumental device used to record the current-potential curve. In the case of very fast reactions the ratio I/I_{rev} can be very close to unity giving very low values of the parameter u (see Eq. [6]). Therefore, the propagation of the uncertainty in the I/I_{rev} ratio on the parameter u is of great interest. The current depends on the applied potential. Therefore, the error in the current may come from its own inherent uncertainty and from the random fluctuations of the potential. The reversible current can be determined with high accuracy, especially if there exists a well-defined limiting current region. This is the case for the $Fe(CN)_6^{3-/4-}$ redox system on noble metal electrodes which we have used as a test system. We, therefore, assume that the error ΔI_{rev} is negligible. The propagation of the undetermined error (14) ΔI for the evaluation of the parameter u is given by the relationship

$$\Delta \ln u \simeq \frac{\Delta I}{I_{rev} u} [-2 + 4u \ln (1 + 1/u) - 2/(1 + 1/u)]^{-1} \quad [13]$$

which is obtained from Eq. [6] by differentiation.

Equation [13] shows that the error $\Delta \ln u$ will vary during one experiment due to its complex dependence on u, ΔI, and I_{rev}. For a given error ΔI, Eq. [13] implies smaller $\Delta \ln u$ errors for increasing I_{rev} and u values. At a given overpotential these two parameters can be increased by accelerating the rate of convective mass transport. On the other hand, ΔI can be diminished by improving the sensitivity of the recording system. The random error in the current depends on the particular experimental arrangement used. We have used Eq. [13] to calculate the errors in our experimental u values. They are reported together with our results.

Experimental

Apparatus.—The electrolysis cell used (Fig. 4) consists of a single compartment with a capacity of about 400 cm^3. The counterelectrode and the thermometer are placed directly through standard joints. The solution can be deaerated by bubbling nitrogen or argon through a frit. The temperature is controlled by means of a double spiral inside the cell connected to a cryostat. The hydrodynamic conditions at the working electrode are determined by the pipe which consists of a glass tube of about 18 cm length with an inside diameter of 0.22 cm. It is placed in the cell through a standard joint.

Two metal rings at about 3 cm from the end of the pipe are used as reference and working electrodes (Fig. 5). The pump, a Verder 114-ty-316 Micropump capable of producing a maximal pressure of 5 bar, allows the controlled circulation of the solution with an adjustable velocity. The maximum average velocity is 16 m/sec at 20°C and the maximum Reynolds number is near 35,000.

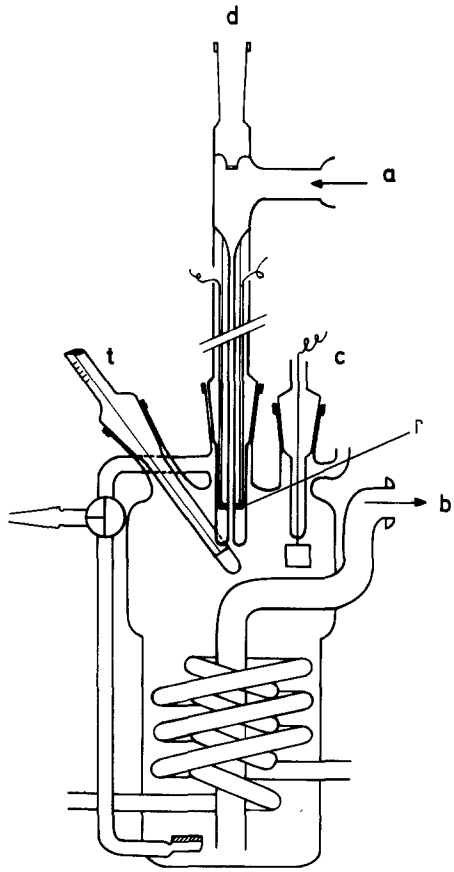

Fig. 4. Electrolysis cell with pipe assembly. The direction of the flow is indicated by the arrows a and b, r = ring electrodes (see details in Fig. 5), c = counterelectrode, d = compartment for an extra reference electrode, t = thermometer.

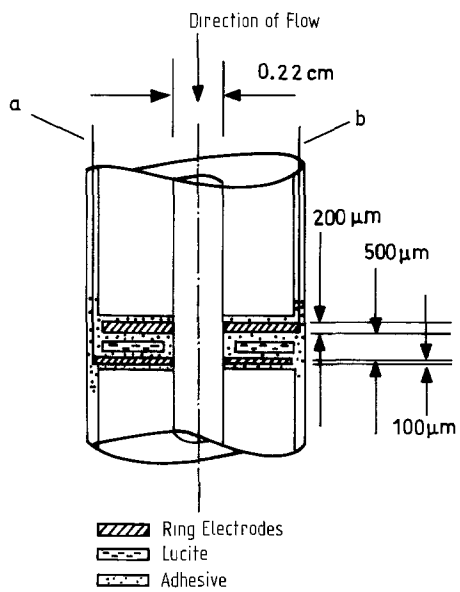

Fig. 5. Diagram showing the double ring electrode assembly. The first ring in the direction of the flow is the reference electrode, the second is the working electrode. a and b are the external contacts.

The potentiostatic current-potential curves were obtained by applying a slow (6 mV/sec) potential sweep through a potentiostat Stonehart BC 1200. The curves were plotted on a X-Y-Recorder Hewlett Packard 7004 B.

The double ring electrode and the control of the ohmic drop.—Pt and Au were employed as metals for the double ring electrode (Fig. 5). Special care was taken in the construction of this unit. Two metal sheets

(0.2 and 0.1 mm thick) separated by a thin Lucite or plastic ring were stuck together between two capillary tubes of 2.2 mm inner diameter. Glycidether-Epikure 113 from Shell was used as adhesive. The metals were then drilled to 1.6 mm diam. By grinding capillary tubes of 2.2 mm inner diameter. Glycidether-sults. After polishing with Al_2O_3 (13 to 1μ mesh) with the help of a Lucite rod and finally with a PTFE coated spindle, a smooth surface is obtained.

The first (0.2 mm thick) ring was used as a reference electrode and the second (0.1 mm thick) as a working electrode. The ohmic resistance between both rings was 2.6Ω in KF and 3.5Ω in K_2SO_4).[2] All overpotentials were corrected for these values. In our case, however, the correction amounts to about 3.5% for the exchange current density.

As an alternative procedure a parallel series of measurements was performed with a calomel reference electrode. This can be of interest if the flow system is constructed with only one ring or if the two rings are to be used as working electrodes as in some kinetic studies (9). In this case the reference electrode was placed in a separate compartment 2 cm before the entrance of the pipe (see Fig. 4). The high ohmic resistance can produce a considerable potential drop between the working and reference electrodes, although our measurements show that the current in this part of the circuit is only about 8-10% of the total current.

A five-electrode arrangement in order to eliminate the ohmic drop in continuous flow systems (16) was used here (Fig. 6). Two extra electrodes, a calomel electrode R_2 and a Pt (or Au) wire W_2 were included in the circuit. R_2 is connected to the input of a second potentiostat P_2. The output is connected to the first reference electrode R_1 and to the counterelectrode C. This arrangement makes the potential drops W_2-R_2 and W_2-R_1 equal so that the return loop current vanishes.

Solutions.—The solutions were prepared with water purified by a double deionization procedure followed by filtration through a Milli-Q unit from Millipore. Potassium ferri- and ferrocyanide were Merck reagent grade. The supporting electrolytes were potassium sulfate Merck reagent grade and potassium fluoride Merck Suprapur.

Pretreatment of the electrodes.—The current-potential curves of the $Fe(CN)_6^{3-/4-}$ redox couple are highly sensitive to small traces of impurities that can be adsorbed at the electrode, producing a partial blocking of the surface. Therefore, special care has to be taken for the cleaning procedure of the pump, the cell, the electrodes, and all materials in contact with the solution. Before taking a curve the electrode was activated by cycling the potential at about 1 V/sec, between the onset of H_2 evolution and shortly before the beginning of O_2 evolution. After a pause of 10 sec at the cathodic end, the curves were recorded at a sweep rate of 6 mV/sec.

A set of current-potential curves at a platinum electrode in K_2SO_4 as supporting electrolyte is shown in Fig. 7. A good test for the experimental arrangement, in particular for the quality of the electrode, is the linear dependence of the limiting current on $Re^{7/12}$, which is shown in Fig. 8.

The roughness factor of the electrodes, measured by the potentiodynamic sweep technique (17-19) was between 2 and 3.5 for Pt and between 2.5 and 6 for Au. Repeated experiments showed that the current per geometric area of the electrode is independent of the roughness factor, so all our results are referred to the geometric area. Apparently it is the geometric area of the ring which determines the rate of mass transport to the electrode and hence the current. Only when the surface roughness is so considerable that it disturbs the flow in the boundary layer, does it affect the experiments (7, 8). The electrode preparation described above assured smooth surfaces and an undisturbed flow of the solution.

[2] Measured via a potentiostatic square wave function and the *IR* drop correction bridge of the Stonehart potentiostat.

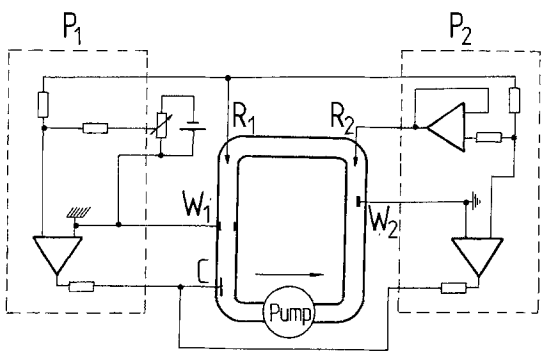

Fig. 6. Diagram of the five-electrode circuit for ohmic drop control. P_1, P_2 = potentiostats, W_1 = working electrode, C = counterelectrode, R_1 = reference electrode, R_1 and R_2 are identical, W_1 and W_2 are of the same metal.

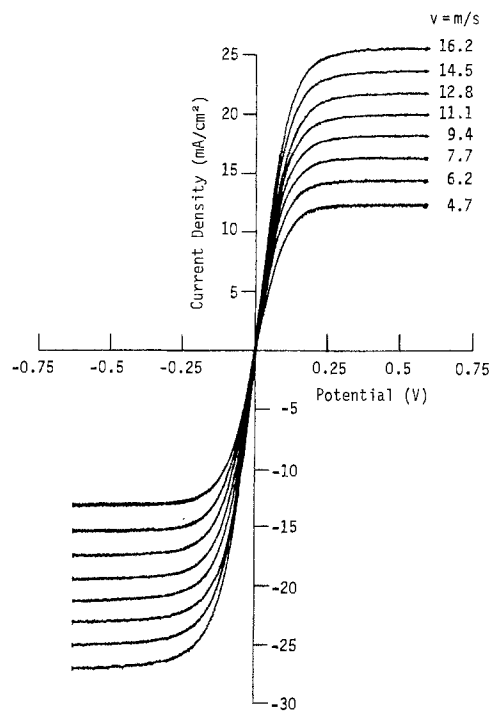

Fig. 7. Experimental current-potential curves for $Fe(CN)_6^{3-/4-}$ redox system at a Pt ring electrode in turbulent pipe flow. The experiments were made with a calomel reference electrode and the five-electrode arrangement shown in Fig. 6. T = 20°C, c_{ox} = 2.5 · 10^{-3}M, c_{red} = 2.5 · 10^{-3}M, 0.5M K_2SO_4.

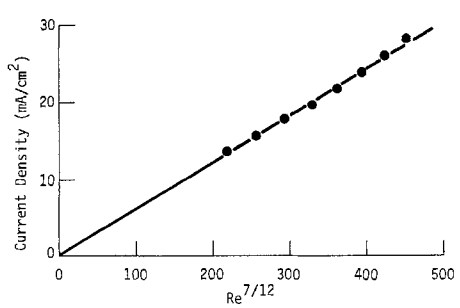

Fig. 8. Plot according to Eq. [8] of the I_{lim}-$Re^{7/12}$ dependence for the anodic branch of the curves shown in Fig. 7.

Table I. Values of the apparent standard rate constant for the system $Fe(CN)_6^{3-/4-}$ obtained by different methods as reported in the literature

Metal	Supporting electrolyte	Concentration* (mol/liter)	Technique	T (°C)	k_o (cm/sec)	Reference
Pt	1M KCl	10^{-2}	Current pulse	25	0.24	(1)
Pt	1M KCl	$\sim 5 \cdot 10^{-4}$	Faradaic impedance	20	0.09	(2)
Pt	0.5M K_2SO_4	10^{-2}	RDE	25	0.067	(3)†
Pt	0.5M K_2SO_4	$\sim 5 \cdot 10^{-4}$	Faradaic impedance	20	0.13	(2)
Au	0.1-10M KF	$5 \cdot 10^{-3}$	Coulostatic pulse	—	0.01 to 0.3	(4)‡
Au	1M KF	$3 \cdot 10^{-2}$-$2 \cdot 10^{-3}$	Potential step	—	0.037	(5)

* Bulk concentration of each component of the redox couple.
† Value calculated from the standard exchange current density, given in the reference, in A cm^{-2}.
‡ The values of k_o are dependent on the concentration of the supporting electrolyte.

Evaluation of the measurements.—The evaluation of the kinetic parameters, j_{oo} and α was performed according to the procedure already described. A computer program was used to calculate the parameter u and to fit the u-η values by a least squares method (20) in Eq. [5]. According to the dependence of the error $\Delta \ln u$ on the u and I_{rev} value (Eq. [13]), smaller statistical weights were given to the values at both extremes (high and low overpotentials) of the curve.

Results and Discussion

A semilogarithmic ln u-η plot of the experimental results for a gold electrode in KF as supporting electrolyte is shown in Fig. 9. The continuous curve corresponds to the fitted values. The error $\Delta \ln u$ was calculated with help of Eq. [13]. The random error ΔI was assumed to be given by the precision of the readings of the current-potential data on the millimeter paper of the X-Y recorder. To a first approximation $\Delta I = \pm \Delta r$ cm · scale factor, with Δr between 0.05 and 0.2. In Table II are included some values of u, I_{rev}, and ΔI used in Eq. [13] to calculate $\Delta \ln u$ for the curve shown in Fig. 9. The errors, represented by vertical traces on the experimental points, are larger at high and low overpotentials. Accordingly, smaller statistical weights were given to these points in the fitting procedure. The standard error for j_{oo} given in Fig. 9 is a measure for the deviation of the experimental values from the fitted curve for a single experiment. The reproducibility of the method can be better described by the standard deviation (14) of a set of different experiments.

In Table III the values of the standard exchange current density and transfer coefficient at Pt and Au electrodes are given for the two supporting electrolytes employed. The standard deviation reported in Table III indicates quite a good reproducibility of the data and a high precision of the method.

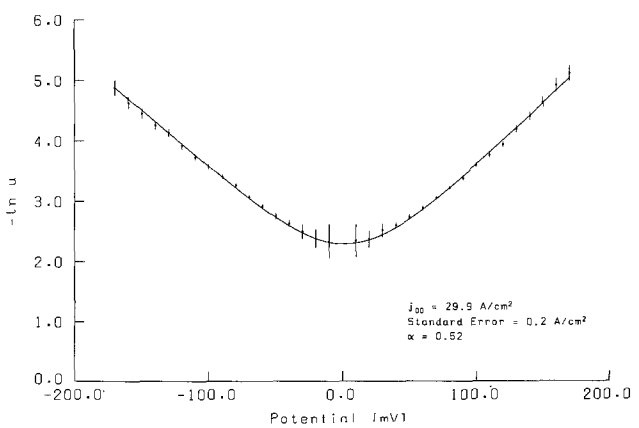

Fig. 9. Experimental ln u-η plots for $Fe(CN)_6^{3-/4-}$ at an Au ring electrode in turbulent pipe flow. $T = 20°C$, $c_{ox} = 2.2 \cdot 10^{-3}$M, $c_{red} = 2.5 \cdot 10^{-3}$M, 1M KF. The continuous line represents the fitted curve. The vertical traces represent the error, according to Eq. [13].

Table II. Parameters I_{rev}, u, and the estimated random error ΔI used in Eq. [10] to calculate the propagated error $\Delta \ln u$

mV	ΔI (μA)	I_{rev} (μA)	u (10^2)	$\Delta \ln u$
−170	± 0.23	134.69	0.759	0.120
−140	± 0.23	133.99	1.412	0.068
−110	± 0.23	131.77	2.412	0.044
−80	± 0.23	124.70	3.834	0.029
−50	± 0.45	103.83	6.390	0.049
−20	± 0.91	53.01	9.237	0.150
+20	± 0.91	56.28	9.352	0.150
+50	± 0.45	117.22	6.497	0.043
+80	± 0.23	144.58	3.997	0.026
+110	± 0.23	154.18	2.335	0.038
+140	± 0.23	157.25	1.221	0.066
+170	± 0.23	158.20	0.605	0.127

Table III. Values of the apparent standard rate constant, apparent standard exchange current density, and transfer coefficient measured with the ring electrode in turbulent pipe flow at 20°C. The standard deviation for a number N of experiments is also given.

Metal	Supporting electrolyte	k_o (cm sec^{-1})	j_{oo} (A cm^{-2})	α	N
Pt	1M KF	0.42	40 ± 6	0.48 ± 0.04	9
Pt	0.5M K_2SO_4	0.35	34 ± 4	0.51 ± 0.03	14
Au	1M KF	0.38	37 ± 4	0.47 ± 0.01	8
Au	0.5M K_2SO_4	0.27	26 ± 2	0.49 ± 0.03	11

In order to compare our results with those of the literature (Table I), we report in Table III the k_o values too. It is evident that with the RTP method we have obtained the highest values for the rate constant of the $Fe(CN)_6^{3-/4-}$ system reported up to the present.

In view of our previous theoretical analysis of the features of this technique in comparison to the RDE, it is obvious that such high reaction rates cannot be measured by the latter method, and the results reported in the literature reflect the enormous effect that small errors can produce when the RDE is used beyond the limits of its possibilities. In the case of the transient techniques for us, the question of the limit of validity remains open, and a revision of the results that have led to a mechanistic interpretation of the ferri-ferrocyanide reaction (4, 5, 21-23) seems to be necessary.

Acknowledgments

The authors are indebted to Professors W. Vielstich and J. W. Schultze for helpful discussions. Financial support by the Deutsche Forschungsgemeinschaft is gratefully acknowledged. This paper is dedicated to Professor W. Vielstich on the occasion of his 60th birthday.

Manuscript submitted Nov. 15, 1982; revised manuscript received May 25, 1983.

Universität Bonn assisted in meeting the publication costs of this article.

LIST OF SYMBOLS

A	electrode area
c^*	standard concentration in 10^{-3} mol/cm^3

c_{ox}, c_{red} bulk concentrations in mol/cm³
D diffusion coefficient
d ring electrode diameter
I experimental current
I_{lim}^a, I_{lim}^c anodic and cathodic limiting currents
I_k current for pure kinetic control
I_{rev} current for pure mass transfer control
j_o exchange current density
j_{oo} apparent standard exchange current density
k_o apparent standard rate constant
L electrode length
Re Reynolds number
u dimensionless parameter relating I to I_{rev}
ν kinematic viscosity
ω angular rotation speed

REFERENCES

1. P. H. Daum and C. G. Enke, *Anal. Chem.*, **41**, 653 (1969).
2. J. E. B. Randles and K. W. Somerton, *Trans. Faraday Soc.*, **48**, 937 (1952).
3. D. Jahn and W. Vielstich, *This Journal*, **109**, 849 (1962); W. Vielstich, Private communication.
4. L. M. Peter, W. Dürr, P. Bindra, and H. Gerischer, *J. Electroanal. Chem.*, **71**, 31 (1976).
5. V. Marecek, Z. Samec, and J. Weber, *ibid.*, **94**, 169 (1978).
6. H. P. van Leeuwen, *Electrochim. Acta*, **23**, 207 (1978).
7. Ch. Bernstein, A. Heindrichs, and W. Vielstich, *J. Electroanal. Chem.*, **87**, 81 (1978).
8. Ch. Bernstein and W. Vielstich, in "Electrode Processes," p. 350, The Electrochemical Society Softbound Proceedings Series, Princeton, NJ (1980).
9. J. Herrmann, Dissertation, Bonn (1983).
10. D. H. Angel and T. Dickinson, *J. Electroanal. Chem.*, **35**, 55 (1972).
11. W. Vielstich and W. Schmickler, "Elektrochemie II," Steinkopff Verlag, Darmstadt (1976).
12. L. N. Klatt and W. J. Blaedel, *Anal. Chem.*, **39**, 1065 (1967).
13. T. Iwasita, W. Schmickler, and J. W. Schultze, in "The Chemistry and Physics of Electrocatalysis," The Electrochemical Society Softbound Proceedings Series, Pennington, NJ (1983).
14. E. Hulzsch, Ausgleichs-Rechnung, Akademische Verlagsgesellschaft, Leipzig (1966).
15. Yu. U. Pleskov and V. Yu. Filinovskii, "The Rotating Disk Electrode," Consultants Bureau, New York (1976).
16. B. A. Coles, N. A. Hampson, A. T. Chadwick, and W. J. Albery, *J. Electroanal. Chem.*, **71**, 125 (1976).
17. R. Woods, in "Electroanalytical Chemistry," Vol. 9, A. J. Bard, Editor, Marcel Decker, New York (1976).
18. D. Dickertmann, J. W. Schultze, and K. J. Vetter, *J. Electroanal. Chem.*, **55**, 429 (1974).
19. A. A. Michri, A. G. Pschenichnikov, and R. Kh. Burshtein, *Elektrokhimiya*, **8**, 364 (1972).
20. D. W. Marquardt, *J. Soc. Industr. Appl. Math.*, **11**, 431 (1963).
21. R. Sohr and L. Müller, *Electrochim. Acta*, **20**, 451 (1975).
22. L. Müller and S. Dietzsch, *J. Electroanal. Chem.*, **121**, 255 (1981).
23. R. R. Dogonadze, J. Ulstrup, and Yu. Kharkats, *ibid.*, **39**, 47 (1972).

Standard Potentials of Li, Na, and K Electrodes and Transfer Free Energies of LiCl, NaCl, and KCl in Selected Ethanol-Water and Methanol-Water Solvents

J. Mazzarese and O. Popovych

Department of Chemistry, Brooklyn College of the City University of New York, Brooklyn, New York 11210

ABSTRACT

Standard potentials of the cell M(Hg)(l)|M^+, Cl^-|AgCl(s); Ag(s) (where M = Li, Na, and K) were determined at 25°C in a number of ethanol-water and methanol-water solvents, and the corresponding standard potentials of the M^+/M electrodes were calculated with the aid of literature data. The Li and Na cells were studied over the entire range of ethanol-water solvents at about 10 weight percent (w/o) intervals of solvent composition, but only in a limited number of methanol-water media. The K cell was studied only in ~ 30, 50, 70, 90, and 100 w/o methanol. For each of the solvent-electrolyte combinations, a function describing the mean ionic activity coefficients of MCl was obtained. Changes in the standard free energy of MCl upon transfer from water to each of the nonaqueous media were calculated from the $E°$'s. Variation of the transfer free energies with solvent composition was interpreted in terms of individual ionic contributions.

The long-term objective of research in this laboratory has been to study ion-solvent interactions in nonaqueous media, with particular emphasis on the determination of the transfer free energies of electrolytes and ions. The transfer free energy, $\Delta G°_t(i)$, and the transfer activity coefficient (medium effect), $_m\gamma_i$, are commonly defined as follows

$$\Delta G°_t(i) \equiv {}_sG°_i - {}_wG°_i = RT \ln {}_m\gamma_i \qquad [1]$$

where ${}_sG°_i$ and ${}_wG°_i$ are the (partial molal) standard free energies of the solute i in the nonaqueous solvent and in water, respectively. Transfer activity coefficients provide a quantitative correlation between equilibrium constants, rate constants, ion activity scales, and emf series in different solvents. The subject of correlating the energic properties of solutes in different solvents, including the methods of evaluating transfer activity coefficients, has been reviewed (1-3).

A common method of determining $\Delta G°_t$ values utilizes the standard potentials, $E°$, of electrodes reversible to the ions of interest. Recalling that for any electrode process, $\Delta G° = -nF\Delta E°$, one can obtain, for example, the sum $[\Delta G°_t(M^+) + \Delta G°_t(Cl^-)]$ from the $E°$'s of cell I in water and given nonaqueous solvent

$$M(Hg)(1)|M^+, Cl^-|AgCl(s); Ag(s) \qquad [I]$$

In the present study, the $E°$'s of cell I were determined in methanol-water and ethanol-water media using dropping amalgam electrodes, where M = Li, Na, and K. These measurements were carried out at intervals of about 10 w/o of each alcohol for those electrolyte-solvent combinations where literature data were either

Key words: electrode potentials, transfer free energies, lithium, sodium, potassium, methanol, ethanol, water.

unavailable or conflicting. The primary objective was to determine the transfer free energies of LiCl, NaCl, and KCl from water to each of the alcohol-water media. Furthermore, from emf measurements of cell I with amalgams of accurately known composition, the standard potentials of the M^+/M electrodes and an expression for the activity coefficients of MCl in each of the solvents were derived.

Analogous work using cell I with K(Hg) electrodes was already reported from this laboratory for the entire range of ethanol-water solvents (4). Here the studies using the K(Hg) electrode were extended to methanol-water mixtures containing about 30, 50, 70, 90, and 100 w/o methanol. Measurements of cell I with Na(Hg) and Li(Hg) electrodes were carried out over the entire range of ethanol-water solvents. In the methanol-water system, the Li(Hg) electrode was studied in water and in 30, 50, 70, 90, and 100 w/o methanol, while the Na(Hg) electrode was investigated only in 70 and 100 w/o methanol. For the methanol-water mixtures omitted from this study, the values of $\Delta G°_t$ of KCl, NaCl, or LiCl were already reported in the literature (5, 6). Values of $\Delta G°_t$ for KCl over the entire methanol-water range were determined previously in this laboratory by two different methods not involving amalgam electrodes (7); they were partially duplicated here because of a history of discrepancies among the literature values.

Experimental

Materials.—Anhydrous methanol was prepared by refluxing 4 liters of Fisher spectroanalyzed or Baker Photrex reagent absolute methanol over 21g of Al powder and 5g of $HgCl_2$ for 24 hr and then distilling through a 22 cm vigreux column, collecting the middle 3 liters. The purified methanol had a density of 0.7865 g/ml at 25°C, in agreement with the literature values of 0.78654 (8) and 0.7866 g/ml (9). The water was deionized with a specific conductance of (2-4) $\times$ 10^{-7} mho cm^{-1}. Methanol-water mixtures were prepared as previously described (10). Also the purification of ethanol, the preparation of ethanol-water mixtures, and that of the alkali-halide solutions were carried out as before (4). LiCl, NaCl, KCl, LiOH, NaOH, and KOH were all Fisher-certified ACS reagent grade and were dried before use.

Electrodes and measurements.—Amalgam electrodes were prepared by electrolysis of the corresponding 1m hydroxides employing a procedure described previously (4). The Li(Hg) contained 0.001-0.003 w/o Li; the Na(Hg), 0.01-0.02 w/o Na; and the K(Hg), 0.02-0.04 w/o K. The Ag-AgCl electrodes were of the thermal electrolytic type prepared by a procedure described by Bates (11). The voltages were measured with an Electro Scientific Instruments Model 330 potentiometer to $\pm$0.1 mV. The apparatus and the measuring procedure were the same as described previously in great detail (4).

Results and Discussion

Standard electrode potentials and activity coefficients.—The potential E_I of cell I at 25°C is given by

$$E_I = E°_I + 0.05916 \log a_{M(Hg)} - 0.05916 \log a_{MCl} \quad [2]$$

where $E°_I = E°_{AgCl} - E°_{M(Hg)}$, referred to $E°_H = 0$ in the given solvent, $a_{M(Hg)}$ is the activity of the alkali metal in the amalgam, and a_{MCl} is the activity of the alkali-metal halide in solution. In order to evaluate $E°_I$ and the activity coefficients of MCl, it is convenient to define the quantity $E°'$

$$E°' = E°_I + 0.05916 \log a_{M(Hg)} \quad [3]$$

and to express the electrolyte activity in terms of its molality, m_{MCl}, the mean molal activity coefficient, $\gamma_\pm$, and the degree of dissociation, α. Upon rearrangement, Eq. [2] becomes

$$E_I + 0.1183 \log (\alpha m_{MCl}) = E°' - 0.1183 \log \gamma_\pm \quad [4a]$$

For purposes of extrapolation, it is now common practice (4, 7, 12) to express $\log \gamma_\pm$ as a polynominal in $I^{1/2}$, where I is the ionic strength. Then, $E°'$ is obtained as the intercept from a plot of the left-hand side of Eq. [4a] *vs.* $I^{1/2}$. In the present study, these plots were straight lines, indicating that the data could be adequately represented by Eq. [4b]

$$E_I + 0.1183 \log (\alpha m_{MCl}) = E°' + 0.1183 AI^{1/2} \quad [4b]$$

Consequently, for each electrolyte-solvent combination, the constant A obtained from the slope of Eq. [4b] can be used to calculate the activity coefficients of MCl in the concentration range employed here by using the relationship $-\log \gamma_\pm = AI^{1/2}$. Values of $E°_I$ were calculated from those of $E°'$ and the literature data on amalgam activities with the aid of Eq. [3]. Complete ionic dissociation could be assumed for all of these solutions, except those of LiCl in 50-100% ethanol and of NaCl in 100% ethanol, which exhibited slight ion pairing. For these systems, the values of α required in Eq. [4b] were calculated from the literature values of the ion pair association constants (13-15). The ranges of the α's involved are indicated in the footnotes of Tables I and II. The calculations were carried out on an IBM 370-145 computer.

A fundamental quantity in electrochemistry is the standard potential of an alkali-metal electrode, $E°_M$. It is the standard potential of the cell

$$Pt; H_2(g) | H^+ || M^+ | M(s) \quad [II]$$

which cannot be determined directly in solvents that react with alkali metals, but is evaluated by combining the $E°$'s of cells I, III, and IV

$$M(Hg)\ (1) | M^+\ (\text{inert solvent}) | M(s) \quad [III]$$

$$Pt; H_2(g) | H^+, Cl^-\ (\text{given solvent}) | AgCl(s); Ag(s) \quad [IV]$$

It is obvious that

$$E°_M = E°_{III} + E°_{IV} - E°_I \quad [5]$$

From the standard potentials $E°_I$ determined in this study, the authors calculated the values of $E°_{Li}$, $E°_{Na}$, and $E°_K$ in each of the solvents with the aid of Eq. [5] by using the relevant literature data for $E°_{III}$ and $E°_{IV}$.

Table I summarizes the results derived from the emf of Li(Hg)—Ag-AgCl cell in solutions of LiCl. Each $E°_I$ was calculated via Eq. [3] from an experimentally determined $E°'$ using literature values (16) for the activity coefficients of Li in its amalgams and $E°_{III} = -0.8480$V, which was determined for the Li cell containing propylene carbonate as the inert solvent (17). Throughout this study, values of $E°_{IV}$ were interpolated for the exact solvent compositions from large-scale graphs of literature data for ethanol-water (18-24) and methanol-water (20, 25-29) solvents.

Table II summarizes the results derived from the emf of the Na(Hg)—Ag-AgCl cells in solutions of NaCl. Since the activities of Na in its amalgams as reported by Bent and Swift (30) are referred to sodium metal (rather than to an infinitely dilute amalgam) as the standard state, the experimentally determined $E°'$ values were converted directly to the tabulated quantity $(E°_{III} - E°_I)$, rather than to $E°_I$.

Table III lists the results derived from the emf of K(Hg)—Ag-AgCl cells in solutions of KCl. The amalgam actvities required to convert $E°'$ to $E°_I$ were interpolated from the data of Armbruster and Crenshaw (31). For the potassium cell, $E°_{III} = -0.9521$V, as reported from this laboratory previously (4), based on the data of Lewis and Keyes (32).

The results in Tables I-III were subjected to a complete error analysis from which the following absolute precisions of the $E°$'s of the alkali-metal electrodes were calculated by the method of propagation of errors. Most of the $E°_M$ values are precise to 0.001V. A pre-

Table I. Results derived from the emf of cell Li(Hg)(I) | Li^+, Cl^- | AgCl(s); Ag(s)*

Solvent	Eq. [4b] A	Eq. [4b] $E^{\circ\prime}$	E°_I	E°_{IV}	Eq. [5] E°_{Li}	Eq. [1] ΔG°_t(LiCl) kcal/mol	Eq. [1] (log $m\gamma_{Li}$ + log $m\gamma_{Cl}$) (molal scale)
Water	0.475	2.2192	2.4126	0.22234	−3.0383	0	0
	0.533	2.2184	2.4139	0.22234	−3.0386	0	0
	0.487	2.2314	2.4135	0.22234	−3.0392	0	0
	0.467	2.2319	2.4135	0.22234	−3.0392	0	0
w/o Ethanol							
10.0	0.968	2.1900	2.3920	0.2146	−3.025	0.493	0.362
20.1	1.060	2.1765	2.3737	0.2074	−3.014	0.915	0.671
30.4	1.066	2.1708	2.3536	0.2001	−3.002	1.379	1.011
40.3	1.107	2.1350	2.3364	0.1934	−2.991	1.775	1.302
49.9	1.010	2.1297	2.3197	0.1848	−2.983	2.160	1.584
60.3	0.927	2.0845	2.2992	0.172	−2.975	2.633	1.930
70.3	1.491	2.0762	2.2680	0.155	−2.961	3.35	2.46
80.4	1.144	2.0454	2.231	0.127	−2.952	4.20	3.08
90.4	1.798	1.9752	2.181	0.088	−2.942	5.35	3.92
100.0	3.338	1.9102	2.087	−0.081	−3.016 [−3.042(33)]	7.53	5.52
w/o Methanol							
30.0	0.585	2.1748	2.3747	0.2031	−3.020	0.892	0.654
50.3	0.652	2.1301	2.3429	0.1904	−3.001	1.625	1.192
69.3	0.678	2.1081	2.3148	0.1684	−2.994	2.273	1.667
90.0	1.486	2.0713	2.2716	0.1135	−3.006	3.269	2.397
100.0	1.522	2.0581	2.2368	−0.0101	−3.095 [−3.653(34), −3.045(35), −3.0845(36)]	4.07	2.985

* All E° values are in volts. E°_{III}(Li) = −0.8480V (17). The concentration range of LiCl was generally 0.02-0.05 or 0.06m. In the ethanol-water system, the α range was 0.88-0.92 in 100% ethanol, 0.90-0.93 in 90.4%, 0.92-0.94 in 80.4%, 0.94-0.95 in 70.3%, 0.94-0.96 in 60.3%, 0.96-0.97 in 49.9%.

Table II. Results derived from the emf of cell Na(Hg)(I) | Na^+, Cl^- | AgCl(s); Ag(s)*

Solvent	Eq. [4b] A	Eq. [4b] $E^{\circ\prime}$	($E^\circ_{III} - E^\circ_I$)	E°_{IV}	Eq. [5] E°_{Na}	Eq. [1] ΔG°_t(NaCl) kcal/mol	Eq. [1] (log $m\gamma_{Na}$ + log $m\gamma_{Cl}$) (molal scale)
w/o Ethanol							
10.0	0.494	1.9927	−2.9157	0.2145	−2.701	0.457	0.335
20.4	0.443	1.9627	−2.8953	0.2072	−2.688	0.927	0.680
30.8	0.535	1.9398	−2.8715	0.1998	−2.672	1.476	1.082
40.6	0.647	1.9202	−2.8491	0.1932	−2.656	1.992	1.460
50.5	0.795	1.8935	−2.8232	0.1842	−2.639	2.589	1.898
60.6	0.833	1.8706	−2.7972	0.171	−2.626	3.189	2.338
69.9	0.939	1.8394	−2.7640	0.157	−2.607	3.954	2.899
80.0	0.946	1.7896	−2.7249	0.128	−2.597	4.856	3.560
90.5	2.14	1.7118	−2.644	0.087	−2.557	6.73	4.93
100.0	2.83	1.6299	−2.562	−0.081	−2.643 [−2.657(33), −2.646(37)]	8.62	6.32
w/o Methanol							
69.8	0.804	1.8678	−2.7953	0.1686	−2.627	3.232	2.370
100.0	1.390	1.7908	−2.7157	−0.0101	−2.726 [−2.7152(34), −2.7132(34), −2.728(38)]	5.068	3.715

* All E° values are in volts. The concentration range of NaCl was generally 0.02-0.05 or 0.06m, except in 100% ethanol where it was 4×10^{-3}—1×10^{-2}m. In ethanol, the α range was 0.97-0.98.

Table III. Results derived from the emf of cell K(Hg)(I) | K^+, Cl^- | AgCl(s); Ag(s)*

Solvent w/o Methanol	m range of KCl	Eq. [4b] A	Eq. [4b] $E^{\circ\prime}$	E°_I	E°_{IV}	Eq. [5] E°_K	Eq. [1] ΔG°_t(KCl) kcal/mol	Eq. [1] (log $m\gamma_K$ + log $m\gamma_{Cl}$) (molal scale)
28.9	0.01-0.06	0.582	1.9761	2.1399	0.2037	−2.888	1.229	0.901
49.7	0.01-0.1	0.547	1.9335	2.0994	0.1908	−2.861	2.163	1.586
70.1	0.02-0.07	0.867	1.8779	2.0490	0.1682	−2.833	3.325	2.438
90.6	0.02-0.05	1.080	1.8413	1.9933	0.1096	−2.836	4.609	3.379
100.0	0.018-0.044	1.271	1.8012	1.966	−0.0101	−2.928 [−2.9116(34), −2.9362(36), −2.933(39)]	5.238	3.840

* All E° values are in volts. E°_{III}(K) = −0.9521V (4).

cision of 0.002V was found for E°_{Li} in 80.4, 90.4, and 100.0% ethanol and in 100.0% methanol, as well as for E°_{Na} in 90.5 and 100.0% ethanol. In another test of the precision and also of the accuracy of our results, the E°_{Li} in water was determined four times using different amalgam concentrations. The four results (shown in Table I) gave an average E°_{Li} = −3.0388 ± 0.0004V. Modern literature values of E°_{Li} in water are −3.0401 (33) and −3.0431V (17). Literature values of the $E^{\circ\prime}$s of the alkali metals in the anhydrous alcohols are included in the tables for comparison with these results.

Transfer free energies.—The changes which the standard free energies of the alkali-metal chlorides experience upon transfer of the electrolytes from water to the alcohol-water mixtures, ΔG°_t, and the corresponding transfer activity coefficients, log $_m\gamma$, are compiled in the last two columns of Tables I-III. The quantity (log $_m\gamma_M$ + log $_m\gamma_{Cl}$) was calculated from the corresponding E°'s of cell I in water, $_wE^\circ_I$, and the nonaqueous solvent, $_sE^\circ_I$, at 25°C using the equation

$$\log {}_m\gamma_M + \log {}_m\gamma_{Cl} = \frac{{}_wE^\circ_I - {}_sE^\circ_I}{0.05916} \qquad [6]$$

ΔG°_t and log $_m\gamma$ are related via Eq. [1].

As pointed out in the introduction, most of the present work in methanol-water media was complementary in nature, *i.e.*, designed to fill the gaps in the existing data on ΔG°_t of alkali-metal halides. Intentional duplication of literature data was carried out only for KCl in the methanol-water system, where serious discrepancies have existed among some of the reported values. In order to compare our results with those from other sources, minor graphical interpolation to integral solvent composition was usually necessary. The existing data on the ΔG°_t of KCl from water to methanol-water solvents are compared in Table IV. While agreement among different laboratories and techniques is good in the middle range of methanol-water composition, it is less than satisfactory at both extremes of the solvent scale. Based on the method of propagation of errors, the precision of the ΔG°_t values should be no worse than 0.01 kcal/mol for most systems and of the order of 0.02 kcal/mol for some media of high alcohol content. The complementary data on ΔG°_t of LiCl and NaCl obtained in methanol-water media fit well on the curves (not shown here) of existing literature data (5, 6) as a function of solvent composition. The values of ΔG°_t for LiCl, NaCl, and KCl in the alcohol-water media experience a monotonous increase with increasing alcohol content in the mixed solvent.

Additional insight into the ion-solvent interactions that determine the variation of ΔG°_t(MCl) as a function of solvent composition can be gained by apportioning the corresponding transfer activity coefficients into their individual ionic contributions. Here, this can be done only for the ethanol-water system, for which transfer activity coefficients of the chloride ion, log $_m\gamma_{Cl}$, have been estimated (40) by the well-known tetraphenylborate assumption. In this assumption, log $_m\gamma$ of the tetraphenylborate anion is set equal to that of the tetraphenylarsonium or the tetraphenylphosphonium cation and the log $_m\gamma$ values for all other ions are calculated on that basis (2, 3). Table V shows the quantities (log $_m\gamma_{Li}$ + log $_m\gamma_{Cl}$) and (log $_m\gamma_{Na}$ + log $_m\gamma_{Cl}$) determined in this study (interpolated to integral solvent composition), the literature values of log $_m\gamma_{Cl}$) determined in this study (interpolated to obtained by difference. The variation of the ionic transfer activity coefficients in ethanol-water media is depicted in Fig. 1. A positive log $_m\gamma$ means that the ion exists in a lower energy state in water (more favorable solvation) than in the nonaqueous medium and vice versa. The behavior of the log $_m\gamma$ of ions as a function of ethanol-water composition depicted in Fig. 1 can be analyzed in terms of a superimposition of two types of major ion-solvent interactions. These are (*i*) the nonspecific long-range interactions and (*ii*) specific chemical interactions in the primary solvation shell. Long-range electrostatic interactions, the magnitude of which has been traditionally estimated from the Born charging equation, make a positive contribution to log $_m\gamma$ of all ions transferred from water to solvents of lower dielectric constant, as can be seen from Eq. [7]

$$\log {}_m\gamma(\text{Born}) = \frac{121.6}{r}\left[\frac{1}{{}_sD} - 0.0128\right] \qquad [7]$$

where r is the ionic radius in angstroms and $_sD$ is the dielectric constant of the nonaqueous solvent. Because this contribution increases as the dielectric constant of the medium decreases, all curves in Fig. 1 would exhibit a continuous rise if Born charging were the major governing energy term. Among the ions represented in Fig. 1, only Na^+ follows very roughly the type of function predicted by the Born equation, since it is an ion which is relatively free of specific solvent interactions in contrast to Li^+ and Cl^- ions for which there is evidence of significant contributions from

Table IV. Standard free energies of transfer for potassium chloride from water to methanol-water solvents, ΔG_t° (kcal/mol, molal scale) in 25°C

w/o Methanol	This study	Ref. (5)	Ref. (6)[1]	Ref. (7)		Ref. (34)
				From solubility[2]	From emf	
10		0.407	0.413	0.250	0.281	
20		0.837	0.844	0.690	0.554	
30	1.277			1.22	1.22	
40		1.723	1.739	1.65	1.65	
50	2.179			2.15	2.15	
60		2.732	2.75	2.74	2.74	
70	3.320			3.26	3.26	
80		3.974	3.97	3.98	3.93	
90	4.574			4.65	4.65	
99		5.160		5.25	5.75	
100	5.238			5.31	5.90	5.056

[1] Calculated in Ref. (5) from data in Ref. (6). [2] Calculated from the solubility of KCl in water and the methanol-water solvents. [3] Calculated from the emf of a cell composed of a K-glass electrode and a calomel electrode.

Table V. Transfer activity coefficients of LiCl, NaCl, and of the individual ions in ethanol-water solvents

w/o Ethanol	(log $_m\gamma_{Li}$ + log $_m\gamma_{Cl}$)	(log $_m\gamma_{Na}$ + log $_m\gamma_{Cl}$)	log $_m\gamma_{Cl}$(40)	log $_m\gamma_{Li}$	log $_m\gamma_{Na}$
10.0	0.362	0.330	0.05	0.31	0.28
20.0	0.668	0.666	0.19	0.48	0.48
30.0	0.999	1.050	0.43	0.57	0.62
40.0	1.294	1.436	0.79	0.50	0.65
50.0	1.587	1.876	1.24	0.35	0.64
60.0	1.920	2.313	1.59	0.33	0.72
70.0	2.44	2.906	1.98	0.46	0.93
80.0	3.06	3.560	2.24	0.82	1.32
90.0	3.89	4.87	2.67	1.22	2.20
100.0	5.52	6.32	3.45	2.07	2.87

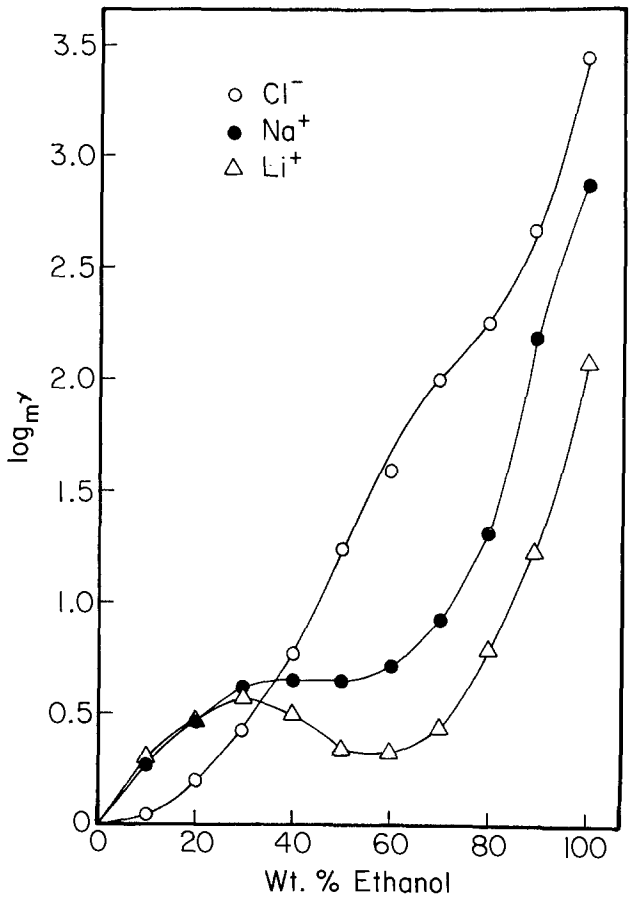

Fig. 1. Transfer activity coefficients of ions in ethanol-water solvents.

short-range ion-solvent interactions. The data for log $_{m}\gamma_{K}$, though available from our previous study (40), were not included in Fig. 1 because they would almost overlap the log $_{m}\gamma_{Na}$ curve. Hydration of the Cl^- ion is known to be reinforced through hydrogen bonding to water molecules. Since the relative H-bonding ability of water is superior to that of ethanol and its mixtures, the transfer of Cl^- from water to these media is energetically disfavored, leading to even more positive values of log $_{m}\gamma_{Cl}$ than would be expected on the grounds of lower dielectric constants alone. More interesting, however, is the behavior of log $_{m}\gamma_{Li}$, which first rises at low ethanol contents, then drops to a minimum in the middle range of solvent composition and finally rises again steeply in the ethanol-rich region. It is noteworthy that the above pattern parallels the behavior of the transfer activity coefficient of the hydrogen ion, log $_{m}\gamma_{H}$, in ethanol-water media, which was already reported from this laboratory (40). The appearance of the minimum in log $_{m}\gamma_{H}$ roughly in the middle range of ethanol-water composition was interpreted (3, 40) in terms of changes in the solvent structure that produce an ethanol-water mixture of maximum basicity. This corresponds to a minimum in log $_{m}\gamma_{H}$, which has the value of −0.86 at 70 w/o ethanol (40). While in the case of the Li^+ ion, the minimum occurs at a positive value of log $_{m}\gamma_{Li}$ (0.33), meaning that water is still the preferred solvator for Li^+ (and that $H^+$is a stronger acid than Li^+), the extent to which log $_{m}\gamma_{Li}$ is lowered relative to "normal" behavior, such as approximated by Na^+, indicates that specific acid-base-type interactions between Li^+ and ethanol-water solvents do make a significant contribution. The Li^+-solvent interaction involved here is of the type usually referred to as lone pair donation from the oxygens of the solvent molecules and it increases with the donor ability (basicity) of the solvent. It is not surprising that this specific interaction is greatest for the smallest cation, Li^+ (r = 0.60Å), which has the highest charge density, and significantly less pronounced for the larger cations, Na^+ (r = 0.95Å) and K^+ (r = 1.33Å) (K^+—not shown here) with log $_{m}\gamma_{Na}$ and log $_{m}\gamma_{K}$ exhibiting plateaus rather than minima in the middle range of ethanol-water composition.

The interesting maximum in the log $_{m}\gamma_{Li}$ at low ethanol content also mirrors its counterpart in log $_{m}\gamma_{H}$ (40). This maximum is believed to occur in a region where water structure has been reinforced by the presence of small amount of ethanol. The transfer of a strongly interacting ion like Li^+ from water to a solvent that is even more structured is enthalpically disfavored (3), leading to a positive contribution to log $_{m}\gamma_{Li}$.

This qualitative interpretation of ionic solvation is obviously far from complete. Significant contributions to transfer free energies can be expected to originate also from ion-dipole, ion-quadrupole, dispersion, and nonelectrostatic interactions, to name just the major components of solvation energy. Unfortunately, present knowledge of the structure of nonaqueous (including mixed) solvents and of the parameters that govern ionic solvation in them is too limited to attempt a more ambitious interpretation.

Acknowledgment

This research was supported in part by Grant 13681 from the PSC-CUNY Research Award Program of the City University of New York.

Manuscript submitted Feb. 28, 1983; revised manuscript received May 19, 1983.

REFERENCES

1. O. Popovych, *Crit. Rev. Anal. Chem.*, **1**, 73 (1970).
2. O. Popovych, in "Treatise on Analytical Chemistry," Part I, Vol. I, 2nd ed., I. M. Kolthoff and P. J. Elving, Editors, Chapter 12, Wiley-Interscience, New York (1978).
3. O. Popovych and R. P. T. Tomkins, "Nonaqueous Solution Chemistry," Chapter 5, John Wiley and Sons, New York (1981).
4. A. J. Dill, L. M. Itzkowitz, and O. Popovych, *J. Phys. Chem.*, **72**, 4580 (1968).
5. D. Feakins and P. J. Voice, *J. Chem. Soc.*, 1390 (1972).
6. G. Akerlof, *J. Am. Chem. Soc.*, **52**, 2353 (1930).
7. L. Malahias and O. Popovych, *J. Chem. Eng. Data*, **27**, 105 (1982).
8. V. A. Griffith, *J. Chem. Soc.*, 860 (1954).
9. R. G. Bates and R. A. Robinson, in "Chemical Properties of Ionic Solutions," B. E. Conway and R. G. Barradas, Editors, Chapter 12, John Wiley and Sons, New York (1966).
10. P. J. LaBrocca, R. Phillips, S. S. Goldberg, and O. Popovych, *J. Chem. Eng. Data*, **24**, 215 (1979).
11. R. G. Bates, "Determination of pH," p. 281, John Wiley and Sons, New York (1964).
12. D. Sen, D. A. Johnson, and R. N. Roy, *J. Phys. Chem.*, **71**, 1523 (1967).
13. A. J. Dill and O. Popovych, *J. Chem. Eng. Data*, **14**, 156 (1969).
14. R. L. Kay, *J. Am. Chem. Soc.*, **82**, 2099 (1960).
15. H. O. Spivey and T. Shedlovsky, *J. Phys. Chem.*, **71**, 2165 (1967).
16. P. Longhi, S. Rondini, S. Ardizzone, and T. Mussini, *Ann. Chim.*, **67**, 177 (1977).
17. S. Rondini, P. Longhi, and T. Mussini, *ibid.*, **67**, 305 (1977).
18. A. Patterson and W. A. Felsing, *J. Am. Chem. Soc.*, **64**, 1478 (1942).
19. H. S. Harned and D. S. Allen, *J. Phys. Chem.*, **58**, 191 (1954).
20. I. T. Oiwa, *ibid.*, **60**, 754 (1956).
21. G. Scatchard, *J. Am. Chem. Soc.*, **48**, 2026 (1926).
22. H. S. Harned and M. E. Fleyscher, *ibid.*, **47**, 82 (1929).
23. K. Schwabe and M. Kunz, *Z. Elektrochem.*, **64**, 1188 (1960).
24. H. Taniguchi and G. J. Janz, *J. Phys. Chem.*, **61**, 688 (1957).

25. H. S. Harned and H. C. Thomas, *J. Am. Chem. Soc.*, **57**, 1666 (1935).
26. R. G. Bates, M. Paabo, and R. A. Robinson, *Anal. Chem.*, **37**, 462 (1965).
27. R. G. Bates and D. Rosenthal, *J. Phys. Chem.*, **67**, 1088 (1963).
28. R. A. Robinson and R. H. Stokes, "Electrolyte Solutions," p. 470, Buttersworth, London (1959).
29. B. E. Conway, "Electrochemical Data," Elsevier, Amsterdam (1952).
30. H. E. Bent and E. Swift, Jr., *J. Am. Chem. Soc.*, **58**, 2216 (1936).
31. M. H. Armbruster and J. L. Crenshaw, *ibid.*, **56**, 2525 (1934).
32. G. N. Lewis and F. G. Keyes, *ibid.*, **34**, 119 (1912).
33. A. McFarlane and H. Harley, *Phil. Mag.*, **13**, 425 (1932).
34. M. Solomon, "Physical Chemistry of Organic Solvent Systems," A. K. Covington and T. Dickinson, Editor, Ch. 2, Part 2, Plenum Press, London (1973).
35. H. Hartley and A. McFarlane, *Phil. Mag.*, **10**, 611 (1935).
36. A. M. Shkodin and L. Ya. Shapovalova, *Izv. Vyssh. Ucheb. Zaved. Khim. Tekhnol.*, **9**, 563 (1966).
37. N. A. Izmaylov and E. F. Ivanova, *Zh. Fiz. Khim.*, **29**, 1614 (1955).
38. P. S. Buckley and H. Hartley, *Phil Mag.*, **8**, 320 (1929).
39. K. Bräuer and H. Strehlow, *Z. Phys. Chem., N.F.*, **17**, 346 (1958).
40. O. Popovych, A. Gibofsky, and D. H. Berne, *Anal. Chem.*, **44**, 811 (1972).

Effect of Carbon on the Reactivity of Lithium with SO_2 and $SOCl_2$ Battery Electrolytes

Stanley D. James,* Patricia H. Smith,* and William P. Kilroy*

Electrochemistry Branch, Naval Surface Weapons Center, Silver Spring, Maryland 20910

ABSTRACT

The normal inertness of lithium to $SOCl_2$ and SO_2 battery electrolytes changes dramatically if the Li has first been ground with carbon black. Spontaneous ignition on mixing then becomes common, especially with $SOCl_2$ electrolyte. We examined the effect of the nature and proportion of carbon in Li-C grinds on their reactivity. We concluded that the carbon's external surface area acting via local electrochemical cells is crucial to its catalytic activity.

Recent investigations in our laboratory indicate that carbon black, which is the cathode substrate for most primary lithium cells, may act as a powerful catalyst for the reaction of lithium with thinoyl chloride or sulfur dioxide. It is known that lithium is relatively inert to the $SOCl_2$ or SO_2 battery electrolytes. This is due to the formation of a protective film which prevents continuing reaction while allowing discharge to proceed via mobile Li ions. However, the presence of carbon results in an increased activation of the reaction between lithium and the battery oxidant (1, 2). This effect may generate potentially hazardous situations with lithium batteries. In an attempt to study the behavior of various carbon blacks, a qualitative and quantitative (calorimetric) investigation of the reactivity of thionyl chloride or sulfur dioxide electrolytes with intimate mixtures of carbon and lithium was undertaken.

Experimental

Qualitative studies were performed in a Dry Room (< 0.5% relative humidity) by measuring the relative reactivity of lithium-carbon mixtures with $SOCl_2$ or SO_2 electrolyte. The mixture reactivity was assessed using the following qualitative scale: (A) no reaction, (B) electrolyte boiled, (C) sparks observed, or (D) spontaneous ignition.

Weighed amounts (7 mg) of lithium (99.9% Foote Mineral) and carbon (outgassed at 120°C for two days) were vigorously ground in a Pyrex ignition tube (Corning No. 9860-10) using the flame-polished end of a Pyrex rod. The uniform black, compacted mass thus produced was broken up with a stainless steel spatula and the process was repeated once or twice more till the mixture appeared homogeneous. The grinding procedure took about 10 min at which time the reactivity was recorded after adding 70 μl of electrolyte. A 1.6M $LiAlCl_4$-$SOCl_2$ electrolyte was prepared by adding Polaroquality $LiAlCl_4$ to $SOCl_2$ (J. T. Baker) that had been refluxed under argon for 20 hr with lithium followed by distillation under argon. The SO_2 electrolyte was 72.8, 18.2, and 8.9 weight percent (w/o) in SO_2, CH_3CN, and $LiAsF_6$, respectively. It was prepared by Honeywell Power Sources Incorporated, Horsham, Pennsylvania and is referred to as "reserve electrolyte."

A quantitative investigation of the carbon-catalyzed Li-$SOCl_2$ electrolyte reaction was accomplished by measuring the heat liberated when Li-C mixtures were added to 1.5M $LiAlCl_4$-$SOCl_2$ electrolyte (obtained from Lithium Corporation of America) in a calorimeter under an inert argon atmosphere. Samples were prepared by grinding carbon (outgassed at 100°C) and lithium (1:1 weight ratio) with a glass mortar and pestle in a helium glove box. The compacted mass which was produced was broken up with a stainless steel spatula and the process repeated for approximately 15 min until the Li-C particles were no larger than 2-3 mm in diameter. Between 30-60 mg of this mixture were accurately weighed into a glass ladle and set inside the head of the calorimeter (Fig. 1). The body of the calorimeter contained 25 ± 1 ml of electrolyte and a Teflon-coated stirring bar. After the calorimeter was assembled, the entire apparatus was insulated with a ½ in. layer of Fiberfrax then wrapped with several layers of Al foil. When the calorimeter had reached thermal equilibrium, the ladle was lowered into the stirred $SOCl_2$-$LiAlCl_4$ solution and the temperature change recorded. Calibration of the system was accomplished at the end of each run by determining the quantity of electrical work ($i \times V \times t$) required to yield a comparable increase in temperature. During this process a d-c current, i, of 2.5A, was passed through the heating coil during a known time interval, t, while the potential, V, across the heating coil was recorded. The heat capacity of the system was found to be constant from run to run.

* Electrochemical Society Active Member.
Key words: battery, carbon, catalysis, cathode.

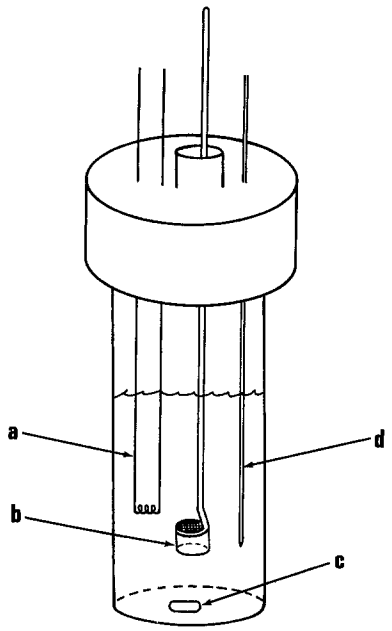

Fig. 1. Schematic diagram of Teflon calorimeter, (a) heater, chromel A; (b) Pyrex sample ladle with stainless steel mesh lid; (c) Teflon-coated stirrer; (d) Chromel-Alumel thermocouple.

Results and Discussion

A recent differential scanning calorimeter (DSC) study revealed that carbon black catalyzes reactions of Li with battery oxidant (1). The mixtures were highly reactive with an unpredictable initiation temperature, indicating that carbon greatly enhances the reactivity of Li with $SOCl_2$ or SO_2 battery electrolytes. The results of the present study reaffirm these observations.

Qualitative study.—Table I summarizes the effect of carbon content on the average reactivity of ground Li-C mixtures with SO_2 reserve electrolyte and $SOCl_2$ electrolyte. Each entry averages the results of 3 to 5 tests. It was observed that traces of carbon are insufficient to activate the lithium-oxidant reaction. Only when the carbon content of Li-C mixes rose above approximately 12 and 40 w/o, respectively, for the $SOCl_2$ and SO_2 electrolytes, was perceptible energy liberated. Of the two electrolytes, the $SOCl_2$ electrolyte was substantially more reactive; spontaneous ignition routinely occurred above about 25 w/o carbon. Spontaneous ignition occasionally occurred with SO_2 electrolyte above 60% carbon but this is not apparent in Table I which depicts only average reactivities. For both electrolytes, decreasing carbon content led to a fall in spontaneous flammability.

Several other variables were qualitatively examined. Investigations on the degree of mixing Li and C revealed that mixtures activated by some grinding or by hammering the Li and C together were substantially more reactive to $SOCl_2$ or SO_2 electrolyte than mixtures of Li and C that were merely "pressed." Pressed mixtures containing 50-91% carbon only warmed the $SOCl_2$ electrolyte (class B). This contrasts with the far greater reactivity of ground mixtures where typical reactivities were found to belong to class D. Ground mixtures were also found to be far more reactive than pressed mixtures to SO_2 reserve electrolyte.

Table I. Reactivity of Li-C ground mixtures with 1.6M $LiAlCl_4$-$SOCl_2$

Li/C ratio	w/o C	SO_2 reactivity	$SOCl_2$ reactivity
0.1	91	Class C	Class D
0.5	67	Class C	Class D
1.0	50	Class B	Class D
1.5	40	Class B	Class D
2.0	33	Class A	Class D
2.5	29	Class A	Class D
3.0	25	—	Class D
4.0	20	—	Class C
5.0	17	—	Class B
7.0	12	—	Class B
8.0	11	—	Class A
9.0	10	—	Class A

Class A; no reaction; class B; electrolyte boiled; class C; sparks observed; class D; spontaneous ignition.

Further studies were performed to determine what effect the SO_2 concentration and the nature of the conducting salt might have on the reactivity of 1:1 (by weight) Li-C mixtures with SO_2. Eight tests conducted on each of LiBr and $LiAsF_6$-sulfur dioxide battery electrolyte, revealed no divergence from a class B reactivity. As the SO_2 concentration in the electrolyte decreased from 14M SO_2, the observed reactivity similarly decreased to the point where very dilute SO_2 solutions were no more reactive than AN or AN-$LiAsF_6$ solutions totally free of SO_2.

We compared the reactivities of ground 1:1 Li-C mixtures with (*i*) various distillate fractions of $SOCl_2$ and (*ii*) 1.6M $LiAlCl_4$-$SOCl_2$ (Polaroquality salt) *vs.* 1.6M $AlCl_3$ in $SOCl_2$ saturated with LiCl. No noticeable difference in reactivity was observed in either case, with the exception that the LiCl-saturated solutions were more reactive (class D) than the $LiAlCl_4$ solutions (class A) with Li-C mixtures containing 12 w/o carbon.

The effect of omitting salt from the electrolyte was studied. Pressed Li-C mixtures (50% carbon) consistently (6 tests out of 6) caused $LiAlCl_4$-$SOCl_2$ to boil (class B), whereas they were totally (4 tests out of 4) unreactive to salt-free $SOCl_2$. Ground mixtures were equally reactive (class D) whether salt was present or absent. As the carbon content of the ground Li-C mixtures decreased, the reactivity to salt-free $SOCl_2$ decreased until at 13% carbon, the mixtures appeared totally inert.

Quantitative study.—The reactivity of 1:1 (by weight) ground mixtures of lithium and carbon with $SOCl_2$ electrolyte was quantitatively measured under an inert helium atmosphere. Table II summarizes the calorimetric data together with various physical and chemical parameters of the carbons investigated. As the particle size decreases or the BET surface area of the carbon blacks increases (Fig. 2), the reactivity of the Li-C mixtures with $SOCl_2$ electrolyte increases. This is not entirely unexpected as an increase of activity with carbon black surface area has been observed in other reactions (3). However, surface area or particle size is critical, as indicated by the apparent nonreactivity of the Sterling FT carbon black (15 m^2/g) which contrasts with the sudden rise in reactivity with a relatively small increase in surface area. Conflicting trends in Table II show that degree of crystallinity is not a controlling factor though it may have secondary importance. The similar unreactivity of Sterling and Superior Graphite 9039 correlates with their similar surface area rather than with their very different crystallinity. On the other hand, the amorphous Monarch 1300 was significantly more reactive than the crystalline Superior Graphite 9042 though their areas were very close. Thus crystallinity seems to confer some degree of inertness. It should be noted that the lithium/carbon black ground mixtures were solid black masses whereas a similar mixture of lithium with the Superior Graphite 9039 yielded a golden metallic material, similar in appearance to LiC_6 and showed no evidence of dispersed carbon particles.

Shawinigan carbon black containing Teflon was ground with lithium and its average reactivity with $SOCl_2$ electrolyte was compared to the average reactivity without Teflon. The presence of Teflon enhanced the exothermicity by approximately 56%. The heats of reaction listed in Table II are much smaller than

Table II. Effect of carbon type on the reactivity of Li-C ground mixtures (50 w/w %) with 1.5M $LiAlCl_4$-$SOCl_2$

Carbon (manufacturer)	Type	Particle size (mμ)	Carbon purity (%)	B.E.T. surface area (m^2/g)	Reactivity (calories/g mixture)	2σ (number of runs)
Sterling FT (Cabot)	Carbon black	180[a]	99.5[a]	15[a]	0	0 ($n = 4$)
Shawinigan (Gulf Oil)	Carbon black	42[b]	99.5[b]	60[b]	3550	616 ($n = 4$)
Elftex 12 (Cabot)	Carbon black	37[c]	99.0[c]	47[d]/43[c]	3984	875 ($n = 3$)
Vulcan 6 (Cabot)	Carbon black	22[a]	99.0[a]	119[a]	4311	166 ($n = 3$)
Monarch 700 (Cabot)	Carbon black	18[c]	98.5[c]	200[c]	5190	714 ($n = 4$)
Monarch 1300 (Cabot)	Carbon black	13[c]	90.5[c]	560[c]	7456	880 ($n = 4$)
9039 (Superior Graphite)	Synthetic graphite	5000[e]	—	16[d]	0	— ($n = 2$)
9042 (Superior Graphite)	Synthetic graphite	<500[e]	—	574[d]	4975	— ($n = 2$)
80% Shawinigan, 20% Teflon (Honeywell)	—	—	—	—	5528	— ($n = 2$)

[a] Cabot pigment brochure.
[b] Data supplied by Gulf Oil Chemical Company.
[c] Cabot Technical report S-36.
[d] Analysis performed by Micromeritics (Norcross, Georgia).
[e] Data supplied by Superior Graphite.

the calculated value for the generally accepted battery reaction ($4Li + 2SOCl_2 = 4LiCl + SO_2 + S$), $\Delta H = -364$ kcal/mol of Li or -26 kcal/g of 1:1 Li-C mixture. Thus the greatest heat listed in Table II, 7.456 kcal/g corresponds to about 29% reaction of the Li.

Mechanism of carbon catalysis.—We explored four possible mechanisms for the catalytic behavior of carbon: (*i*) local electrochemical cell, (*ii*) increased lithium surface area, (*iii*) formation of an active compound during the grind, and (*iv*) surface functional groups on the carbon.

In the first mechanism, each carbon particle in contact with lithium is viewed as a small cathode which is short-circuited to the lithium anode. When an electrolyte solution containing $SOCl_2$ or SO_2 is added, this short-circuited cell discharges at a high rate generating sufficient heat to cause, in the extreme case, ignition. This agrees with data (4) showing that the corrosion of a variety of metals in $LiAlCl_4$-$SOCl_2$ electrolyte is greatly accelerated if the metal is electrically contacted to carbon. By analogy with the behavior of large scale cells, one would expect that eliminating the supporting electrolyte salt from the electrolyte solution would significantly increase the solution resistance, reduce the rate at which the short-circuited cells could discharge, and, thus, reduce the heat that would be generated. This was found to be the case with pressed 1 to 1 Li-C mixtures. In six out of six tests, pressed Li-C caused $LiAlCl_4$-$SOCl_2$ solutions to boil, whereas, the Li-C mixture was totally unreactive in four tests in salt-free $SOCl_2$. In contrast, however, ground 1 to 1 Li-C mixtures were highly reactive toward salt-free $SOCl_2$. We suggest that these results can, nonetheless, be understood in terms of a shorted cell mechanism. Grinding the mixtures creates an extensive Li-C interface effectively lowering the path length for electrolyte conduction in shorted cells to the range of the diffusion layer thickness. Thus in this case, the absence of supporting electrolyte salt is relatively unimportant, as significant currents can be maintained through diffusion of the ions produced by the anode and cathode reactions. With pressed mixtures, on the other hand, the combination of high path length and low conductance in salt-free $SOCl_2$ apparently depresses the shorted cell currents to negligible levels.

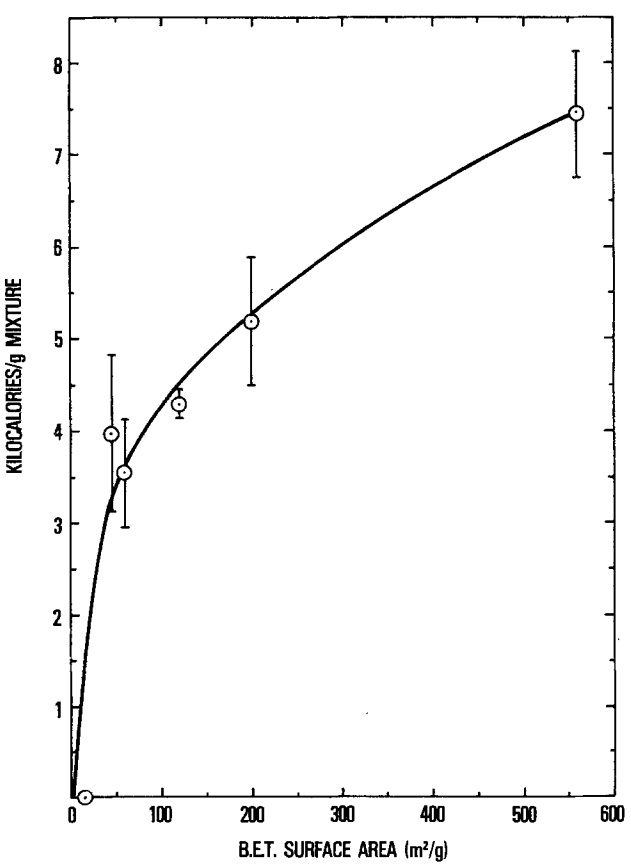

Fig. 2. Reactivity vs. surface area for ground mixtures of Li and C (1:1 by weight) with 1.5M $LiAlCl_4$-$SOCl_2$.

Another explanation of carbon catalysis may be increased Li surface area. In this case finely divided carbon is just a vehicle for producing a very extensive Li-$SOCl_2$ interface. When the carbon becomes coated with Li the reaction interface is raised by many orders of magnitude. Thus when electrolyte is added, in spite of Li passivation, enough heat is generated for ignition to occur. This theory was tested by grinding lithium with powdered Al_2O_3 (surface area, 200 m^2/g). If carbon were simply a vehicle for dispersion of Li. then the alumina should also give rise to increased activation. However, a calorimetric study indicated that a ground mixture of Li and alumina (1:1 weight ratio) was quite inert to $LiAlCl_4$-$SOCl_2$.

A third plausible explanation involves the formation of an active compound when grinding the lithium and carbon together. This active compound would then be responsible for the catalytic effect. X-ray analysis

of ground Li-carbon black mixtures indicated formation of an Li-C compound other than acetylide (5). The 2θ values differed by approximately 1° from a stage 5 lithium-graphite compound. Perhaps this difference is due to the fact that relatively amorphous carbon black was used in place of graphite. We ruled out the participation of other active compounds such as Li_2C_2, Li_3N, Li_2O, Li_2O_2 by testing their reactivity to battery electrolyte, both alone and after grinding with lithium. All were inert. The intercalation compound, LiC_6, was also found to be inert to $SOCl_2$-$LiAlCl_4$. It remains possible however that some unidentified amorphous, Li-C compound, formed during the grinding, played a part in the enhanced reactivity.

Finally we considered the possibility that surface functional groups on the carbon particles are responsible for the catalysis. Carbon black is known to contain superficial H and O which may control its absorptive, catalytic, and electrical behavior (6). Recent studies of Shawinigan carbon black have revealed a substantial ESR signal (7). Energetic surface groups might react with $SOCl_2$ forming labile species (8) which could accelerate its reactivity. To check this hypothesis we heat-treated a sample of Shawinigan black so as to drive off its O and H content. The carbon was fired in an He atmosphere at 950°C for 5 hr. This should remove all of its O and most of its H (9). The carbon was then cooled under He, ground in He with Li (50% mixture) and transported in sealed containers for immediate testing in an Ar glove-bag. Qualitative reactivity testing with five samples of these ground mixtures showed a high, consistent reactivity identical with that of untreated carbon. Thus it is unlikely that superficial O or H are involved in carbon black's catalysis of the Li-$SOCl_2$ reaction.

Conclusions

1. Carbon black promotes reactivity of lithium with Li/SO_2 or Li/$SOCl_2$ battery electrolytes. Lithium-carbon mixtures that are ground together (as may occur in severely warped or sheared batteries) can spontaneously ignite with SO_2 or $SOCl_2$ battery electrolytes. This reactivity occurs both in dry air and also in inert gas atmosphere thus excluding air contamination as a factor in this type of hazard.

2. The order of reactivity of the various battery electrolytes to ground Li-C mixes was $SOCl_2$-$LiAlCl_4$ >> SO_2-AN-$LiAsF_6$ ~ SO_2-AN-LiBr. Decreasing the concentration of SO_2 in the SO_2 battery electrolyte lowers its reactivity.

3. Traces of carbon are insufficient to activate the Li-oxidant reaction. Perceptible energy is liberated only when the C content (in Li-C mixes) exceeds 12 and 40 w/o, respectively, for the $SOCl_2$ and SO_2 electrolytes. Lowering the carbon content of Li-C mixes gives rise to decreasing flammability with battery electrolyte.

4. A variety of carbons was examined. The external surface area of the particles was judged to be the most important factor in the ability of carbon to promote reactivity.

5. No evidence was uncovered for any mechanism of carbon's catalytic activity on the Li-oxidant reactions other than that of shorted electrochemical cells. Grinding of Li with C black generated some Li-C compound but this could neither be identified nor specifically linked with enhanced reactivity.

Acknowledgments

The authors thank the Independent Research Program of the Naval Surface Weapons Center and the Naval Sea Systems Command, Electrochemistry Technology Block Program for financial support of this work.

We also thank Dr. JoAnne Milliken for the x-ray studies, Dr. Victor R. Deitz of the Naval Research Laboratory, Washington, D.C., and Mr. Larry Newman of Cabot Corporation for providing samples of carbon.

Manuscript submitted Dec. 21, 1982; revised manuscript received April 27, 1983.

The Naval Surface Weapons Center assisted in meeting publication costs of this article.

REFERENCES

1. S. Dallek, S. D. James, and W. P. Kilroy, *This Journal*, **128**, 508 (1981).
2. W. P. Kilroy and S. D. James, *ibid.*, **128**, 934 (1981).
3. R. Yoshida, A. Arkawa, K. Kaiko, and O. Ogawa, *Netsv. Sokutei*, **81**, 2 (1981).
4. A. N. Dey, Final Report ERADCOM DELET TR 74-0109-E, July 1978.
5. W. P. Kilroy, S. D. James, and J. Milliken, NSWC TR 81-127, Sept. 1981.
6. R. N. Smith, *Quart. Rev.*, **13**, 287 (1959).
7. R. Ake, D. M. Oglesby, and W. P. Kilroy, Paper 298 presented at The Electrochemical Society Meeting, Detroit, MI, Oct. 17-21, 1982.
8. R. W. Murray, *Accounts of Chem. Res.*, **13**, 135 (1980).
9. W. R. Smith, "Encyclopedia of Chemical Technology," Kirk-Othmer, 2nd ed., Vol. 4, p. 253, Interscience, New York (1964).

Technical Notes

Solution Growth and Electrodeposited $CuInSe_2$ Thin Films

R. N. Bhattacharya*

Department of Structural Chemistry, The Weizmann Institute of Science, 76100 Rehovot, Israel
and
Thin Film Solid State Technology Cell, Department of Physics, I. I. T., Delhi, India

The solution growth deposition of Bi_2Se_3 (1), Bi_2S_3 (2), Sb_2Se_3 (3), α-PbO_2 and Tl_2O_3 (4), and $Cu_{1.8}S$ and TlSe (5) thin films have been reported previously. The growth and photoelectrochemical solar cell based on electrodeposited $CdSe_{1-x}Te_x$ thin films have also been reported (6-8). The deposition of $CuInSe_2$ thin films by solution growth and also by the electroplating method is presented here. The primary interest in such semiconductor films has been directed toward the application for photovoltaic cells.

Present address: Department of Chemistry, The University of Texas at Arlington, Arlington, Texas 76019.

Solution Growth Method

Thin $CuInSe_2$ films with a thickness in the range of 200-300Å are produced by the solution growth method on glass and SnO_2:F coated conducting glass substrates at room temperature. The conducting base SnO_2:F is

Table I. X-ray diffraction and TEM data for CuInSe$_2$ thin films: calculated and experimental values

Calculated				Observed d	
d	2θ (deg)	hkl	Relative intensity	TEM	X-ray
5.2	17.05	101	4	—	—
3.34	26.69	112	100	3.33	3.33
3.22	27.71	103	3	—	—
2.52	35.63	211	4	—	—
2.155	41.92	105,213	2	—	—
2.04	44.42	220,204	70	2.03	2.02
1.743	50.50	116,312	40	1.75	1.79
1.445	64.49	400,008	11	1.44	1.44
1.327	71.04	332,316	16	1.32	1.32

obtained by spray pyrolysis on glass substrates. The film thicknesses are measured using a Taylor Hobson Talystep instrument.

The deposition of CuInSe$_2$ films is based on the slow reaction between a solution of triethanolamine complexed with both In^{3+} and Cu^{1+}, and sodium selenosulfate solution. The sodium selenosulfate solution is prepared by refluxing 5g selenium powder with 12g of sodium sulfite in 200 ml water for about 10 hr. The deposition mixture contains 12.5 ml 0.05M In^{3+} solution, 10 ml 0.05M Cu^{1+} solution, 20 ml 0.3M sodium selenosulfate solution, ~0.03% (volume) triethanolamine, and ~0.04% (volume) ammonia solution.

The films are analyzed by transmission electron diffraction (TEM) and x-ray diffraction methods. Postdeposition treatments are used for the films deposited on glass substrates. This included annealing in argon gas, which results primarily in the recrystallization of the films. The films deposited on SnO_2:F coated glass substrates are polycrystalline with a grain size of about 0.08 μm. The calculated and experimental values of x-ray diffraction and TEM data are given in Table I.

The bandgap is obtained from transmission measurements made using Unicam SP 700 A Spectrophotometer. The transmission T as a function of photon energy $h\nu$ is measured from four different samples deposited on glass substrates with different film thickness d (d_1:800Å; d_2:1000Å; d_3:2000Å; d_4:3000Å). The optical energy gap is found to be 1.08 eV (Fig. 1). The bandgap is determined from the variation of α^2 as a function of energy $h\nu$ (α: absorption coefficient).

Electroplating Method

The electrodeposited CuInSe$_2$ thin films are prepared under potentiostatic conditions on conducting glasses (SnO_2:F coated). For the electroplating, the plating solution is prepared from 0.018M $InCl_3$, 0.018M CuCl, 0.025M selenium dioxide solution, 0.006% (volume) triethanolamine, and 0.007% (volume) ammonia solution. The pH of the deposition mixture is adjusted at ~1 by adding dilute HCl. The deposition is carried out under constant stirring and at room temperature. The voltage is maintained at ~700 mV *vs.* SCE. The plating current is ~15 mA/cm^2.

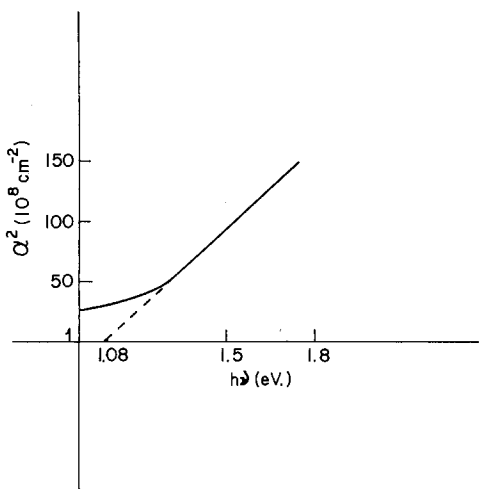

Fig. 1. Variation of α^2 as a function of energy $h\nu$ for solution growth CuInSe$_2$ thin films deposited on glass substrates.

Fig. 2a. X-ray pattern of the as-deposited electroplated CuInSe$_2$ thin films (scale: 4 × 10^2 CPS).

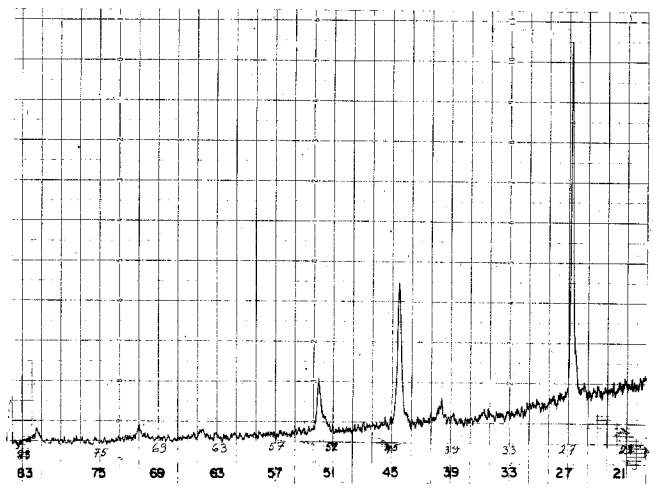

Fig. 2b. X-ray pattern of the electrodeposited and annealed CuInSe$_2$ thin films (scale: 4 × 10^2 CPS).

The x-ray analysis of the films is shown in Fig. 2a and b. Figure 2a represents the as-deposited electroplated films. Figure 2b shows the x-ray diffraction pattern for the single-phase CuInSe$_2$ films when the electroplated films are annealed in argon gas at ~600°C for 1 hr.

Recently the films have also been deposited (both solution growth and electroplated) on titanium substrates. The photoelectrochemical solar cell studies of the CuInSe$_2$ thin films are in progress.

Acknowledgment

The author wishes to express his thanks to Professor K. L. Chopra of Thin Film Solid State Technology Cell, Department of Physics, I.I.T. Delhi, India and also to Dr. David Cahen and Dr. Gary Hodes of The Weizmann Institute of Science, Israel) for their gracious hospitality during the experiments.

Manuscript submitted March 4, 1983; revised manuscript received May 25, 1983.

REFERENCES

1. P. Pramanik, R. N. Bhattacharya, and A. Mondal, *This Journal*, **127**, 1857 (1980).
2. P. Pramanik and R. N. Bhattacharya, *ibid.*, **127**, 2087 (1980).
3. R. N. Bhattacharya and P. Pramanik, *J. Solid State Chem.*, **44**, 425 (1982).
4. R. N. Bhattacharya and P. Pramanik, *Bull. Mater.*

Sci., 2, 287 (1980).
5. R. N. Bhattacharya and P. Pramanik, *ibid.*, 3, 403 (1981).
6. G. Hodes, J. Manassen, S. Neagu, D. Cahen, and Y. Mirovsky, *Thin Solid Films*, 90, 433 (1982).
7. Y. Mirovsky, R. Tenne, G. Hodes, and D. Cahen, *ibid.*, 91, 349 (1982).
8. R. N. Bhattacharya, S. P. S. Arya, D. K. Pandya, and K. L. Chopra, Solar Energy India Symposium, December 1982.

Stability of Conducting Polythiophene and Derivatives

G. Tourillon* and F. Garnier

Laboratoire de Photochimie Solaire, CNRS., 94320 - Thiais, France

Many organic conducting polymers such as polyacetylene, PA (1); polyparaphenylene, PPP (2); polyparaphenylenesulfide, PPS (2); and polypyrrole, PP (3) have been proposed in the literature. These polymers show reversibility of the doping-undoping process, making them of interest in energy storage. One of the key problems, however, is the poor stability of most of these polymers. Polyacetylene, PA, must be prepared and stored under a rigorously O_2 free atmosphere and at a low temperature (4). Polypyrrole, PP, although stable in its conducting state, is also sensitive to O_2 in its semiconducting undoped state (5). As a matter of fact, a progressive redoping by O_2 occurs due to the value of the polymer oxidation potential ($E_{ox} \simeq -0.3$) which lies in the same range as that for the reduction of O_2.

PPP and PPS show a higher oxidation stability mainly in the undoped state ($E_{ox} \simeq +1.6$V), and their sensitivity to O_2 is less pronounced, but information on the doped state is scarce. The authors recently reported the electrochemical generation of thin films of new organic conducting polymers, polythiophene, polyfuran, and derivatives (6) which also appear as interesting candidates for organic electrodes for energy storage or display.

In this paper, the stability characteristics of these new polymers is presented under various experimental conditions (O_2, H_2O, H^+, OH^-, temperature).

Experimental

The polymers have been generated, as previously described (6), either as thin films grafted on a Pt electrode or as thick deposits which are then scratched off, rinsed, and dried. The analyzed polymers were polythiophene, PT; poly-3-methylthiophene, PMeT; poly-3,4 dimethylthiophene, $P(Me)_2T$; and polypyrrole, PP doped with $CF_3SO_3^-$ from $N(Bu)_4$ CF_3SO_3 salt.

They were characterized by infrared, ESR, elemental microanalysis, and d-c conductivity initially, just after their synthesis, and after 8 months storage in air at room temperature.

The stability in electrolytic medium [CH_3CN, $N(Bu)_4$ PF_6] has also been determined after 20 cycles between oxidized and reduced state, using XPS (AEI, Mg kα anticathode 1253.6 eV).

Results and Discussion

The doped PMeT properties (Table I) show that the storage in air affects neither the $CF_3SO_3^-$ doping level nor the conductivity. These results are confirmed by the infrared analysis: this conducting polymer is characterized by a large broad band in the near infrared (4000-1600 cm^{-1}) due to free carriers and by absorption patterns (1600-600 cm^{-1}) associated with the dopant $CF_3SO_3^-$ (Fig. 1). After 8 months storage time in air, a very similar absorption spectrum is obtained which bears out the long term stability.

The undoped PMeT behaves in the same way. After 8 months storage in ambient air, neither oxygen nor H_2O could be detected, in contrast to polypyrrole which has been shown to be very sensitive to oxygen. Furthermore, PMeT can be doped again after 8 months by electrochemical oxidation to the same level as before, about 25-30%.

Table I. Physicochemical and electrical properties of a $SO_3CF_3^-$ doped PMeT just after synthesis and after being kept 8 months in air.

Physicochemical properties	Just after synthesis	Kept 8 months in air
Microanalysis (anion doping level per monomer unit)	25%	24.5%
Conductivity $\sigma(\Omega^{-1}cm^{-1})$	12	10

PT and $P(Me)_2T$ show the same interesting stability characteristics, compared to the experimental precautions which must be taken with other types of organic conducting polymers.

These materials have great thermal stability; 200°-250°C in air and 700°-800°C in inert atmosphere or vacuum. They are stable in concentrated acidic medium but are slowly attacked in basic solution.

The stability under electrochemical treatment was also studied. PP and PMeT were polarized between their oxidized and reduced neutral states during 20 cycles in CH_3CN-$N(Bu)_4PF_6$ medium. Their I-V and XPS characteristics were recorded before and after this polarization (Fig. 2 and 3).

With PP, the oxidation and reduction peaks are not well defined and XPS spectra are greatly modified: the peak due to P is no longer detected, the intensity of the F peak decreases, but the O peak increases. Similar results were recently obtained by Salaneck *et al.* (7) and Street *et al.* (8).

These results show that the dopant PF_6^- is replaced by O_2 during the electrochemical treatment. The authors do not agree with the results of Street *et al.* (8) who proposed that a complex is formed between the oxygen and the nitrogen atom of the cycle: only one nitrogen chemical type was always detected. The same result was also observed with the carbon element. So oxygen must have the same doping property as I_2 or AsF_5.

In contrast, PMeT exhibits good electrochemical stability as shown by the same I-V curve and XPS spectra before and after polarization. Two parameters

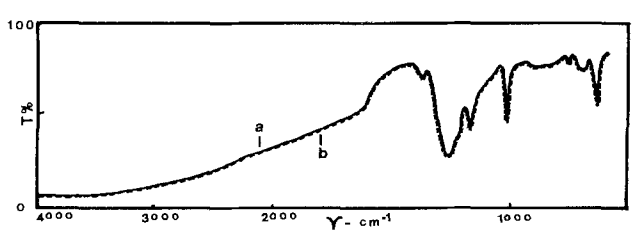

Fig. 1. Infrared spectra of an $SO_3CF_3^-$ doped PMeT a) just after synthesis; b) after 8 months in air.

* Electrochemical Society Active Member.
Key words: organic conducting polymer, thin films, stability.

Sci., 2, 287 (1980).
5. R. N. Bhattacharya and P. Pramanik, *ibid.*, 3, 403 (1981).
6. G. Hodes, J. Manassen, S. Neagu, D. Cahen, and Y. Mirovsky, *Thin Solid Films*, 90, 433 (1982).
7. Y. Mirovsky, R. Tenne, G. Hodes, and D. Cahen, *ibid.*, 91, 349 (1982).
8. R. N. Bhattacharya, S. P. S. Arya, D. K. Pandya, and K. L. Chopra, Solar Energy India Symposium, December 1982.

Stability of Conducting Polythiophene and Derivatives

G. Tourillon* and F. Garnier

Laboratoire de Photochimie Solaire, CNRS., 94320 - Thiais, France

Many organic conducting polymers such as polyacetylene, PA (1); polyparaphenylene, PPP (2); polyparaphenylenesulfide, PPS (2); and polypyrrole, PP (3) have been proposed in the literature. These polymers show reversibility of the doping-undoping process, making them of interest in energy storage. One of the key problems, however, is the poor stability of most of these polymers. Polyacetylene, PA, must be prepared and stored under a rigorously O_2 free atmosphere and at a low temperature (4). Polypyrrole, PP, although stable in its conducting state, is also sensitive to O_2 in its semiconducting undoped state (5). As a matter of fact, a progressive redoping by O_2 occurs due to the value of the polymer oxidation potential ($E_{ox} \simeq -0.3$) which lies in the same range as that for the reduction of O_2.

PPP and PPS show a higher oxidation stability mainly in the undoped state ($E_{ox} \simeq +1.6$V), and their sensitivity to O_2 is less pronounced, but information on the doped state is scarce. The authors recently reported the electrochemical generation of thin films of new organic conducting polymers, polythiophene, polyfuran, and derivatives (6) which also appear as interesting candidates for organic electrodes for energy storage or display.

In this paper, the stability characteristics of these new polymers is presented under various experimental conditions (O_2, H_2O, H^+, OH^-, temperature).

Experimental

The polymers have been generated, as previously described (6), either as thin films grafted on a Pt electrode or as thick deposits which are then scratched off, rinsed, and dried. The analyzed polymers were polythiophene, PT; poly-3-methylthiophene, PMeT; poly-3,4 dimethylthiophene, $P(Me)_2T$; and polypyrrole, PP doped with $CF_3SO_3^-$ from $N(Bu)_4$ CF_3SO_3 salt.

They were characterized by infrared, ESR, elemental microanalysis, and d-c conductivity initially, just after their synthesis, and after 8 months storage in air at room temperature.

The stability in electrolytic medium [CH_3CN, $N(Bu)_4$ PF_6] has also been determined after 20 cycles between oxidized and reduced state, using XPS (AEI, Mg kα anticathode 1253.6 eV).

Results and Discussion

The doped PMeT properties (Table I) show that the storage in air affects neither the $CF_3SO_3^-$ doping level nor the conductivity. These results are confirmed by the infrared analysis: this conducting polymer is characterized by a large broad band in the near infrared (4000-1600 cm^{-1}) due to free carriers and by absorption patterns (1600-600 cm^{-1}) associated with the dopant $CF_3SO_3^-$ (Fig. 1). After 8 months storage time in air, a very similar absorption spectrum is obtained which bears out the long term stability.

The undoped PMeT behaves in the same way. After 8 months storage in ambient air, neither oxygen nor H_2O could be detected, in contrast to polypyrrole which has been shown to be very sensitive to oxygen. Furthermore, PMeT can be doped again after 8 months by electrochemical oxidation to the same level as before, about 25-30%.

Table I. Physicochemical and electrical properties of a $SO_3CF_3^-$ doped PMeT just after synthesis and after being kept 8 months in air.

Physicochemical properties	Just after synthesis	Kept 8 months in air
Microanalysis (anion doping level per monomer unit)	25%	24.5%
Conductivity $\sigma(\Omega^{-1}cm^{-1})$	12	10

PT and $P(Me)_2T$ show the same interesting stability characteristics, compared to the experimental precautions which must be taken with other types of organic conducting polymers.

These materials have great thermal stability; 200°-250°C in air and 700°-800°C in inert atmosphere or vacuum. They are stable in concentrated acidic medium but are slowly attacked in basic solution.

The stability under electrochemical treatment was also studied. PP and PMeT were polarized between their oxidized and reduced neutral states during 20 cycles in CH_3CN-$N(Bu)_4PF_6$ medium. Their I-V and XPS characteristics were recorded before and after this polarization (Fig. 2 and 3).

With PP, the oxidation and reduction peaks are not well defined and XPS spectra are greatly modified: the peak due to P is no longer detected, the intensity of the F peak decreases, but the O peak increases. Similar results were recently obtained by Salaneck *et al.* (7) and Street *et al.* (8).

These results show that the dopant PF_6^- is replaced by O_2 during the electrochemical treatment. The authors do not agree with the results of Street *et al.* (8) who proposed that a complex is formed between the oxygen and the nitrogen atom of the cycle: only one nitrogen chemical type was always detected. The same result was also observed with the carbon element. So oxygen must have the same doping property as I_2 or AsF_5.

In contrast, PMeT exhibits good electrochemical stability as shown by the same I-V curve and XPS spectra before and after polarization. Two parameters

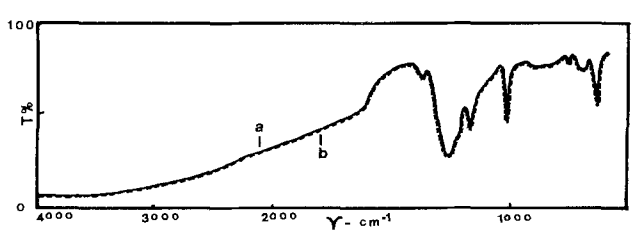

Fig. 1. Infrared spectra of an $SO_3CF_3^-$ doped PMeT a) just after synthesis; b) after 8 months in air.

* Electrochemical Society Active Member.
Key words: organic conducting polymer, thin films, stability.

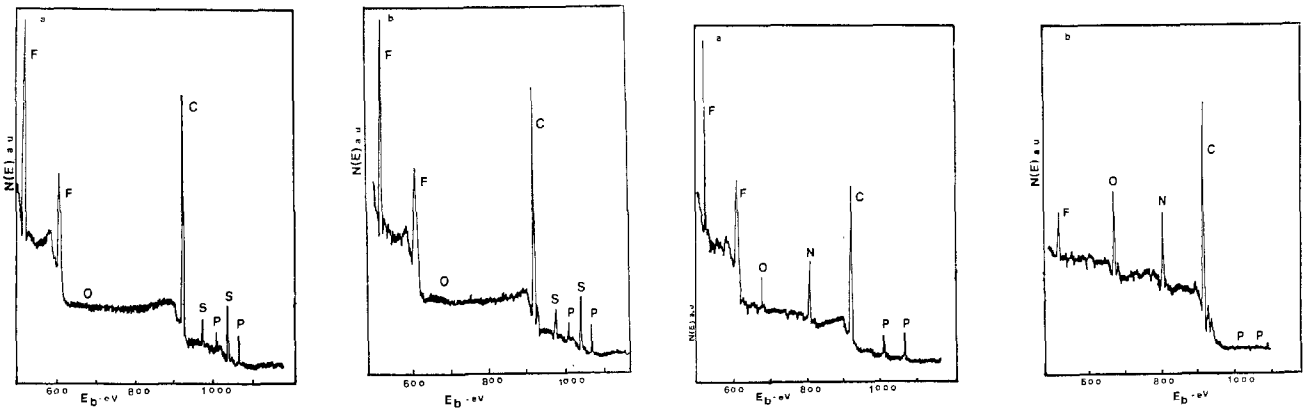

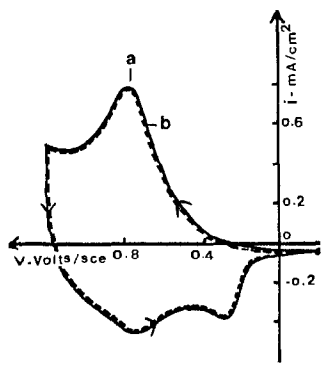

Fig. 2. I-V curves and XPS spectra of thin PMet grafted on Pt sweep rate, 50 mV/sec; electrolytic medium, CH_3CN-$N(Bu)_4PF_6$ 10^{-1} M/liter; XPS spectra, AEI with Mg anticathode; kinetic energy, 1253.6 eV. a) XPS spectrum just after polymerization; b) XPS spectrum after 20 cycles between oxidized and reduced states.

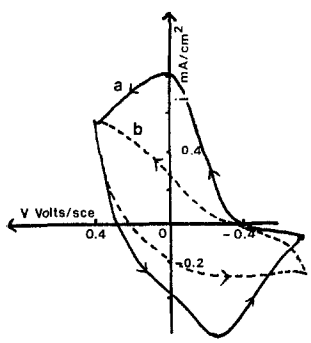

Fig. 3. Same as Fig. 2 but for polypyrrole instead of PMeT

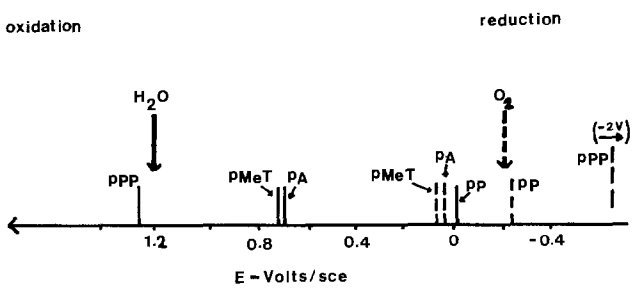

Fig. 4. Oxidation and reduction potentials of several polymers compared with O_2 reduction potential and H_2O oxidation potential. (PP, polypyrrole; PA, polyacetylene; PPP, polyparaphenylene; PMeT, poly-3 methyl thiophene). Solid line, oxidation; dashed line, reduction.

appear to be important for obtaining stable polymers; their oxidation-reduction potentials and their chemical reactivity. In Fig. 4, the authors have reported the oxidation and reduction potential ranges of several polymers together with the O_2 reduction potential and the H_2O oxidation potential. The scheme clearly shows why PP, for example, is not stable in its undoped (reduced) neutral state: it lies close to the O_2 reduction potential and will be slowly oxidized by O_2 to a conducting state which is the electrochemical stable form.

In the same manner, PPP, with a very high oxidation potential (+1.6V), higher than the oxidation potential of water, should be not stable to H_2O in its doped state but should be stable in its neutral form. With this scheme, PMeT and PA should be stable in both states due to the fact that their oxidation-reduction potentials lie between those for O_2 reduction and H_2O values. This is verified in the case of PMeT but not with PA. In this last case with PA, the other important parameter is the chemical reactivity of the material. It is composed of linear chains with an alternation of single and double bonds. Chemical reaction of O_2 with a double bond can easily occur and leads either to oxygen bridging between chains or to a break down of the chains. There is no more π electron delocalization and the electrical properties are greatly affected. In contrast, PMeT is more stable to O_2, as the authors have seen. This stability must be related to the bridging of the polymer double bonds by the sulfur hetero atom.

In conclusion, electrochemically generated PT and derivatives show good stability to O_2 and moisture in both doped and neutral states. Compared to other polymers such as PA or PP, where drastic conditions must be employed to avoid exposure to air and moisture, these new polymers appear to be very attractive.

Their stabilities argue for exploitation of the very promising electrochromic properties that the authors have recently observed (9). It must also be pointed out that these polymers can be obtained either in thin-grafted films or as thick deposits with a very high reproducibility.

Manuscript submitted March 17, 1983; revised manuscript received June 22, 1983.

REFERENCES

1. H. Shirakawa, E. J. Louis, A. G. Mac Diarmid, C. K. Chiang, and A. J. Heeger, *J. Chem. Soc. Chem. Commun.*, 578 (1977).
2. R. H. Baughman, J. L. Bredas, and R. R. Chance, "Polymer Science and Technology," Vol. 15, R. B. Seymour, Editor, p. 137, New York (1982).
3. A. F. Diaz and K. K. Kanazawa, in "Extended Linear Chain Compounds," Vol. 3, G. S. Miller, Editor, p. 417, Plenum Press, New York (1982).
4. H. Naarman, in "Polymeres Electro-Actifs," Font-Romeu, France (1982).
5. A. F. Diaz, J. Crowley, J. Baryon, G. P. Gardini, and J. B. Torrance, *J. Electroanal. Chem.*, **121**, 355 (1981).
6. G. Tourillon and F. Garnier, *ibid.*, **135**, 173 (1982).

7. W. R. Salaneck, R. Erlandsson, J. Prejzci, I. Lundström, C. B. Duke, and W. K. Ford, Organic Polymers, p. 120, American Chemical Society Meeting, Las Vegas, NV (1982).
8. P. Pfluger, M. Krounbi, G. B. Street, and G. Weiser, *J. Phys. Chem.*, In press.
9. F. Garnier, G. Tourillon, M. Gazard, and J. C. Dubois, *J. Electroanal. Chem.*, **198**, 299 (1983).

An Analytical Solution of the Nonsteady Convective Diffusion Equation for Rotating Electrodes

C. Deslouis, C. Gabrielli, and B. Tribollet

Groupe de Recherche No. 4 du CNRS, Physique des Liquides et Electrochimie, associé à l'Université Pierre et Marie Curie, 75230 Paris Cedex 05, France

In electrochemistry, the study of mass transport is often carried out by means of rotating electrodes. The development of nonsteady-state techniques such as electrochemical (1, 2) or electrohydrodynamical (3, 4) impedances leads to derivations in which increasingly more complex forms of the convective diffusion equation are involved.

So far, this equation has only been analytically solved in a few cases. However, an analytical solution can be interesting, especially for performing a fitting procedure on experimental data. Therefore, in this paper an approximate analytical solution of the convective diffusion equation is given in the vicinity of a rotating electrode. This derivation is applicable both to steady-state and nonsteady-state (impedances) conditions, as will be demonstrated by some examples.

The convective diffusion equation is generally written as

$$\frac{\partial c}{\partial t} = D\,\nabla^2 c - \vec{V}\,\overrightarrow{\text{grad}}\,c \qquad [1]$$

where c is the concentration of the diffusing species, D the diffusion coefficient, and $\vec{V}$ the fluid velocity, the normal component of which is proportional to the square of the distance to the electrode. For a sinusoidal modulation of small amplitude, the concentration is

$$c = c_0 + \delta c \exp j\omega t \quad (j = \sqrt{-1})$$

where c_0 is the steady-state concentration, and ω the angular frequency.

By using a concentration $U_0 + \delta U \exp j\omega t$, a normal coordinate η, and a frequency K put into a dimensionless form according to the geometry, the nonsteady part of Eq. [1] can be generally written as

$$\frac{d^2\delta U}{d\eta^2} + a\eta^2\frac{d\delta U}{d\eta} - (b\eta + j\mathrm{K})\,\delta U = f(\eta, j\mathrm{K}) \qquad [2]$$

with boundary condition

$$\delta U \to 0 \quad \text{when} \quad \eta \to \infty$$

By means of the variable change

$$x = (b + a)^{1/3}\eta \qquad [3]$$

$$s = (b + a)^{-2/3}\mathrm{K}j \qquad [4]$$

and the function change

$$\phi(x, s) = \delta U\,(x, s)\exp\left(+\frac{a}{a+b}\frac{x^3}{6}\right) \qquad [5]$$

Eq. [2] leads to

$$\frac{d^2\phi}{dx^2} - \left(x + \frac{a}{a+b}\frac{x^4}{4} + s\right)\phi = g(x, s) \qquad [6]$$

where

$$g(x, s) = (b + a)^{-2/3} f(x, s)\exp\left(\frac{a}{a+b}\frac{x^3}{6}\right)$$

By the above procedure, $0 \leq x \leq 1$, so $x > x^4$, and we must consider the following cases: at mean and high frequencies $|s + x| >> x^4$ and the term $\frac{a}{a+b}\frac{x^4}{4}\phi(x, s)$ can be neglected. At low frequencies, we can substitute for the term $\frac{a}{a+b}\frac{x^4}{4}\phi(x, s)$ the first term of its Taylor expansion in s (*i.e.*, $\frac{a}{a+b}\frac{x^4}{4}\phi(x, 0)$) with

$$\phi(x, 0) = U_0\,(x)\exp\left(\frac{a}{a+b}\frac{x^3}{6}\right)$$

In Eq. [5], indeed, $\delta U(x, 0)$ may be replaced by the stationary solution $U_0(x)$.

Hence, Eq. [6] becomes

$$\frac{d^2\phi}{dx^2} - (x + s)\,\phi = g(x, s) + \frac{a}{a+b}\frac{x^4}{4}U_0(x)\exp\left(\frac{a}{a+b}\frac{x^3}{6}\right) \qquad [7]$$

The homogeneous equation derived from [7] is an Airy's equation whose solution is an Airy function $Ai(x + s)$ of the first kind according to the boundary condition.

The solution of full Eq. [7] may then be put as

$$\phi = Ai\{x + s\} \cdot q(x, s) \qquad [8]$$

and one finds

$$\mathrm{Ai}\{x + s\} \cdot q'' + 2Ai'\{x + s\} \cdot q' = g(x + s) + \frac{a}{a+b}\frac{x^4}{4}U_0(x)\exp\left(\frac{a}{a+b}\frac{x^3}{6}\right) \qquad [9]$$

If

$$q' = Ai^{-2}\{x + s\} \cdot Y(x, s) \qquad [10]$$

then

$$Y'(x, s) = Ai\{x + s\} \cdot g(x, s) + \frac{a}{a+b}\frac{x^4}{4}U_0(x)\exp\left(\frac{a}{a+b}\frac{x^3}{6}\right) \qquad [11]$$

Hence

$$\delta U(x, s) = \exp\left(-\frac{a}{a+b}\frac{x^3}{6}\right)Ai\{x + s\} \left\{\int_0^x (Ai\{\xi + s\})^{-2}\left[\int_0^\xi Ai\{\xi' + s\} \cdot g(\xi', s)\,d\xi' + K_1(s) + \int_0^\xi Ai\{\xi' + s\} \cdot \frac{a}{a+b}\frac{\xi'^4}{4}U_0(\xi')\exp\left(\frac{a}{a+b}\frac{\xi'^3}{6}\right)d\xi' + K_0(s)\right]d\xi + K_2(s)\right\} \qquad [12]$$

$K_2(s)$ is obtained by using the boundary condition at the electrode surface ($x = 0$) which depends on the analyzed problem. The boundary condition at infinity ($x \to \infty$) leads to

$$K_1(s) = -\int_0^\infty Ai\{\xi' + s\}\, g(\xi', s)\, d\xi' \qquad [13]$$

and for low frequencies

$$K_0(s) = -\int_0^\infty Ai\{\xi' + s\}\, \frac{a}{a+b}\, \frac{\xi'^4}{4}\, U_0(\xi') \exp\left(\frac{a}{a+b}\, \frac{\xi'^3}{6}\right) d\xi' \qquad [14]$$

If $Ai\{\xi' + s\}$ is expanded as a Taylor series

$$Ai\{\xi' + s\} = Ai\{\xi'\} + sAi'\{\xi'\} + \ldots + \frac{s^n}{n!} Ai^n\{\xi'\} + \ldots \qquad [15]$$

$K_0(s)$ can be calculated as

$$K_0(s) = I_0 + sI_1 + \ldots + \frac{s^n}{n!} I_n + \ldots \qquad [16]$$

where

$$I_n = -\frac{s^n}{n!} \int_0^\infty Ai^n\{\xi'\}\, \frac{a}{a+b}\, \frac{\xi'}{4}\, U_0(\xi') \exp\frac{a}{a+b}\, \frac{\xi'^3}{6}\, d\xi' \qquad [17]$$

The corrective term $K_0(s)$ can be determined when the stationary solution $U_0(x)$ is known. For mean and high frequencies $K_0(s) = 0$.

Diffusion impedance for a rotating disk electrode—A numerical solution of this problem has been given by Levart and Schuhmann (5). In that case, the relevant values of the parameters in Eq. [2] are, for large value of Sc, $a = 1$, $b = 0$, $f(\eta, j\mathrm{K}) = 0$, and $\eta = (0.51023\ \mathrm{Sc})^{1/3} \sqrt{\Omega/\nu}\, z$. For a single electron transfer process the current may be written as

$$I = n\mathbf{F}Ak\, c_0(0) \exp(\alpha V) \qquad [18]$$

A is the electrode area, $\mathbf{F}$ the Faraday number, k the reaction rate, and α the Tafel slope.

The diffusion impedance Z_D is then defined as

$$Z_D(s) = \frac{1}{\alpha c_0}\, \frac{\delta c}{\delta I}\bigg|_0 = -\frac{1}{n\mathbf{F}DA\alpha c_0} \cdot \frac{\delta c|_0}{\dfrac{\partial(\delta c)}{\partial z}\bigg|_0} \qquad [19]$$

where

$$Z_D(s) = \frac{1}{n\mathbf{F}DA\alpha c_0} \cdot \frac{\delta U|_0}{\dfrac{\partial \delta U}{\partial x}\bigg|_0 \cdot \dfrac{\partial x}{\partial z}} \qquad [20]$$

The exact solution of the stationary problem with the boundary conditions

$$U_0(x) \to 0 \quad \text{when} \quad x = \infty$$

$$U_0(0) = 1 \quad \text{when} \quad x = 0$$

is

$$U_0(x) = 1 - \frac{\displaystyle\int_0^x \exp\left(-\frac{t^3}{3}\right) dt}{\displaystyle\int_0^\infty \exp\left(-\frac{t^3}{3}\right) dt} \qquad [21]$$

After Eq. [12], the nonstationary solution is

$$\delta U(x, s) = \exp\left(-\frac{x^3}{6}\right) Ai\{x + s\} \left\{ \int_0^x (Ai\{\xi + s\})^{-2} \left[\int_0^\xi Ai\{\xi' + s\}\, \frac{\xi'^4}{4}\, U_0(\xi') \exp\left(\frac{\xi'^3}{6}\right) d\xi' + K_0(s) \right] d\xi + K_2(s) \right\} \qquad [22]$$

where

$$K_0(s) = -\int_0^\infty Ai\{\xi' + s\}\, \frac{\xi'^4}{4}\, U_0(\xi') \exp\left(\frac{\xi'^3}{6}\right) d\xi' \qquad [23]$$

$$K_2(s) = \frac{1}{Ai(s)} \quad (U(0, s) = 1) \qquad [24]$$

Hence

$$Z_D(s) = -\frac{1}{n\mathbf{F}DA\alpha c_0\, a^{1/3}}\, \frac{Ai\{s\}}{Ai'\{s\}} \left[\frac{1}{1 + \dfrac{K_0(s)}{Ai'(s)}} \right] \qquad [25]$$

From Ref. (10)

$$Ai'(s) = -0.25882\ (1 + s^3/3) + 0.35502\, s^2/2$$

and from Filinovskii *et al.* (6)

$$\frac{Ai(s)}{Ai'(s)} = -\frac{\sqrt{1.877 + s}}{1 + s} \qquad [26]$$

After computation of I_0, I_1, I_2, I_3, by Eq. [17] one can get for $|s| < 1$ the expression of Z_D

$$Z_D = -\frac{1.2514}{n\mathbf{F}DA\alpha c_0} \cdot \frac{\sqrt{1.877 + s}}{1 + s}\ (0.93844 + 0.07591\, s - 0.07392\, s^2 + 0.06769\, s^3) \qquad [27]$$

When $|s| > 1$, $K_0(s) = 0$ and the Eq. [27] is simplified

$$Z_D = -\frac{1.2514}{n\mathbf{F}DA\alpha c_0}\, \frac{\sqrt{1.877 + s}}{1 + s} \qquad [27a]$$

whence the asymptotic expression of Warburg

$$Z_D \propto -s^{-1/2}$$

For comparison, the values of the real (X_0) and imaginary (Y_0) parts of the diffusion impedance calculated by Levart and Schuhmann (5) are given in Table I along with the values calculated from Eq. [27] and [27a]. Agreement is good over the whole frequency range.

Electrohydrodynamical impedance for a rotating disk electrode.—The electrohydrodynamical impedance is the transfer function between the sine wave modulation of the rotating speed and the response of the electrochemical interface.

The convective diffusion equation is Eq. [2] where $a = 1$, $b = 0$, and $f(\eta, j\mathrm{K}) = \eta^2 \exp(-\eta^3/3)$. The analytical solution is given in Ref. (8).

Diffusion impedance on a hemispherical rotating electrode.—Recently this problem has been analyzed by Chin (9). The author has showed that the adimensional concentration M can be expanded in a spherical coordinate system as a function of the angular coordinate θ

$$M = [M_1(z) + \theta^2 M_3(z) + \ldots]\, e^{j\mathrm{KSc}^{1/3}/\tau} \qquad [28]$$

The notations used are those of Ref. (9), where τ is the adimensional time and $\tau = \Omega t$ (Ω is the angular rotation speed). The convective diffusion equation is then equivalent to the system

Table I. Real and imaginary components of the diffusion impedance on a rotating disk electrode

	Numerical From (5)		Analytical From Eq. [25]	
1.566 K	X_o	$-Y_o$	X_o	$-Y_o$
0.01	1.6109	0.010	1.611	0.010
0.02	1.6107	0.0199	1.611	0.021
0.05	1.6090	0.0498	1.609	0.052
0.07	1.6071	0.0696	1.607	0.073
0.1	1.6033	0.0992	1.600	0.104
0.2	1.5806	0.1944	1.574	0.204
0.5	1.4431	0.4314	1.426	0.445
0.7	1.3205	0.5353	1.302	0.553
1	1.1362	0.6183	1.125	0.663
2	0.7304	0.5999	0.7098	0.5962
5	0.4097	0.3961	0.4082	0.3939
7	0.3419	0.3344	0.3406	0.3332
10	0.2840	0.2797	0.2828	0.2789
20	0.1998	0.1978	0.1987	0.1974
50	0.1263	0.1250	0.1253	0.1250
70	0.1068	0.1058	0.1059	0.1057
100	0.0896	0.0884	0.0886	0.0884
200	0.0635	0.0626	0.0626	0.0626
500	0.0404	0.0396	0.0396	0.0396
1000	0.0287	0.0280	0.028	0.028

From (5) ($Sc \to \infty$).
From Eq. [25] with LF correction.

$$\frac{d^2M_1}{dz^2} + 0.51023\, z^2 Sc \frac{dM_1}{dz} - jKSc^{2/3} M_1 = 0 \quad [29]$$

$$\frac{d^2M_3}{dz^2} + 0.51023\, z^2 Sc \frac{dM_3}{dz} - (1.02046\, zSc + jKSc^{2/3}) M_3 = 0.52762\, z^2 Sc \frac{dM_1}{dz} \quad [30]$$

with the boundary condition in $z = 0$: $dM_1/dz = -1$ and $dM_3/dz = 0$.

These equations have been numerically solved in (9). However, by using the previous derivation an approximate analytical solution can be obtained. Equation [29] is equivalent to Eq. [2] where $a = 0.51023$ Sc, $b = 0$, and $f(\eta, K) = 0$. This problem is similar, as mentioned by Chin, to that of the diffusion impedance on a rotating disk electrode. However, the boundary condition in $z = 0$ ($dM_1/dz = -1$) is different from that given previously.

The solution of Eq. [29] for $K = 0$ is then

$$M_1^\circ(z)\, Sc^{1/3} = 1.611 - Sc^{1/3} \int_0^z \exp\left(-\frac{0.51023\, Sc}{3} \xi^3\right) d\xi \quad [31]$$

and

$$\frac{dM_1^\circ}{dz} = -\exp\left(-\frac{0.51023\, Sc}{3} z^3\right)$$

Equation [30] is equivalent to Eq. [2] where $a = 0.51023$ Sc, $b = 1.02046$ Sc, and $f(z, Kj) = 0.52762\, z^2\, Sc\, dM_1/dz$.

For $K = 0$, an approximate analytical solution of the Eq. [30] is

$$M_3^\circ(z) Sc^{1/3} = 0.20682\, Sc^{1/3} z \exp\left(-\frac{a}{3} z^3\right) + 0.69337\, Ai\{(3a)^{1/3} z\} \exp\left(-\frac{az^3}{6}\right) \quad [32]$$

By the way described in the first part of this paper, an analytical solution of Eq. [30] can then be calculated. In the low frequency range by using a Taylor expansion, we obtain

$$M_{30}Sc^{1/3} = (0.246 - 1.19\, K^2) - j\, 0.53\, K \quad [33]$$

For $|s| > 1$, then for $K > 0.6$ $K_o(s) = 0$ and the analytical expression of $M_{30}Sc^{1/3}$ can be used

Table II. Values of $M_{30}\, Sc^{1/3}$

	Analytical from Eq. [33]		Numerical Ref. (9)	
K	Real part	Imaginary part	Real part	Imaginary part
0.01	0.246	−0.0053	0.24324	−0.00542
0.015	0.2457	−0.00795	0.24309	−0.00760
0.02	0.2455	−0.0106	0.24297	−0.01013
0.03	0.2449	−0.0159	0.24258	−0.01519
0.04	0.2441	−0.0212	0.24207	−0.02021
0.06	0.2417	−0.0318	0.24066	−0.03022
0.08	0.2384	−0.0424	0.23868	−0.04004
0.1	0.2341	−0.053	0.23617	−0.04967
	Analytical from Eq. [35]		Numerical Ref. (9)	
8	0.00206	0.000015	0.00216	0.00011
10	0.00132	0.000007	0.00136	0.00001
20	0.00033	0.0000006	0.00033	~0
30	0.000147	0.0000002	0.00015	~0
40	0.000083	0.0000001	0.00008	~0
60	0.000037	~0	0.00004	~0
80	0.000021	~0	0.00002	~0
100	0.000013	~0	0.000013	~0
150	0.0000059	~0	0.000006	~0

$$M_{30}Sc^{1/3} = -1.294 \int_0^\infty \frac{x^2 Ai\{x + s\}\, Ai'\left\{\frac{x}{3^{1/3}} + 3^{2/3} s\right\} dx}{Ai'\{s\}\, Ai'\{3^{2/3} s\}} \quad [34]$$

For large value of K, an equivalent of $M_{30}Sc^{1/3}$ can be obtained by substituting the Airy's function by their expansions (10).

$$M_{30}Sc^{1/3} = -\frac{0.132}{K^2} - j\frac{0.0223}{K^{7/2}} \quad [35]$$

The agreement is very good with the numerical solution given in (9) for $K \geq 10$ (see Table II).

In conclusion, analytical solutions of the convective diffusion equation have been derived for fluid flows of the same type as the rotating disk system. These solutions corresponding to the general Eq. [12] are complementary to a numerical solution of a problem. They clearly establish the asymptotic behavior and they can be used for a fitting of the parameter to the experimental results. [Sc, for instance, and electrical elements of the equivalent circuit in impedance measurements (2)].

Three applications have been presented in this note; however, this derivation can be applied to the impedance problem for a ring electrode, a cone electrode or a Couette flow. More generally, this type of derivation could be extended to any axisymmetrical problem.

Manuscript submitted April 17, 1981; revised manuscript received June 17, 1982.

Groupe de Recherche No. 4 du CNRS assisted in meeting the publication costs of this article.

REFERENCES

1. C. Deslouis, I. Epelboin, M. Keddam, and J. C. Lestrade, *Electroanal. Chem. Interfacial Electrochem.*, **28**, 57 (1970).
2. C. Deslouis and B. Tribollet, *Electrochim. Acta*, **23**, 935 (1978).
3. K. Tokuda, S. Bruckenstein, and B. Miller, *This Journal*, **122**, 1316 (1975).
4. C. Deslouis, I. Epelboin, C. Gabrielli, and B. Tribollet, *J. Electroanal. Chem.*, **82**, 251 (1977).
5. E. Levart and D. Schumann, *ibid.*, **28**, 45 (1970).
6. V. Y. Filinovskii and V. A. Kir'Yanov, *Dokl. Akad. Nauk. S.S.R.*, **156**, 1412 (1964).
7. W. J. Albery, A. R. Hillman, and S. Bruckenstein, *J. Electroanal. Chem.*, **100**, 687 (1979).
8. C. Deslouis, C. Gabrielli, Ph. Sainte-Rose Fanchine, and B. Tribollet, *This Journal*, **129**, 107 (1982).
9. D-T. Chin, *ibid.*, **127**, 2162 (1980).
10. M. Abramovitz and I. A. Stegun, "Handbook of Mathematical Functions," N.B.S., Washington, DC (1964).

JOURNAL OF THE ELECTROCHEMICAL SOCIETY

SOLID-STATE SCIENCE AND TECHNOLOGY

OCTOBER 1983

Evaluation of Crystalline Quality by Ultraviolet Reflectivity Measurement (UVRM)

T. Itoh* and H. Takai

School of Science and Engineering, Waseda University, Tokyo 160, Japan

ABSTRACT

The damage distribution in ion-implanted silicon and the crystalline quality of epitaxial films are evaluated by detecting the reflectivity change in a sample at 275 nm with reference to the reflectivity at 330 nm, and experimental results are compared with the Rutherford backscattering spectra. The damage distribution induced by P^+ implantation is clearly distinguished from that by Si^+ implantation in both P^+- and Si^+-implanted samples. The recrystallization process of the Si^+-implanted region is identified by UVRM. The distribution profile of crystalline imperfection in a silicon epitaxial film on a porous silicon layer is evaluated by UVRM, and is in good agreement with the depth profile of dechanneled fraction obtained by RBS measurement.

Since ion implantation became an indispensable technique to fabricate silicon devices, many workers have attempted to investigate the damage distribution and the recrystallization process in ion-implanted regions. Successive results can be obtained by Rutherford backscattering (RBS) measurements and transmission electron microscope (TEM) observations, but it is difficult to obtain accurate depth profiles of the damage distributions and the recrystallization in the region of interest.

The optical reflectivity measurement coupled with stripping of surface layers by anodic oxidation is one of the most practical techniques for obtaining the depth profile of crystalline imperfection in silicon (1-3). The crystalline damage induced by the ion implantation causes variations of the optical parameters of silicon. The optical reflectivity of the crystalline silicon show sharp peaks at the wavelengths of 275 nm and 340 nm, which correspond to the threshold energies for the direct interband transition at χ and Γ points, respectively. On the other hand, the reflectivity at 330 nm changes only 1-3% for the state from the single-crystal to amorphous. Evaluation of the crystalline imperfection by UVRM presented in this paper is based on detecting variations of the optical reflectivity in samples.

The authors have developed an apparatus for measuring UV reflectivity, and have investigated the damage distribution profiles in ion-implanted silicon wafers by measuring the relative reflectivity at 275 nm with reference to the reflectivity at 330 nm. In addition, the authors have applied UVRM to evaluate the crystalline quality of silicon epitaxial film grown on a porous silicon layer. Profiles of the crystalline imperfection obtained by UVRM are compared with results obtained by RBS.

Experimental

Figure 1 shows the apparatus developed in order to measure variations of UV reflectivity on a sample surface. The system consists of a monochromatic light source, reflectors, and a detector. The incident light transmits through the half mirror and the polarizer and is reflected on the sample surface. The intensity of reflected light is detected by the photomultiplier. The intensity of incident light is monitored by a solar cell. The system is set in a box filled with dry N_2 gas to reduce the absorption of UV light by oxygen in air. In this optical system, the reflected light intensity I is given by the following relation

$$I = T_{HM} \times T_P^2 \times R_{HM} \times R_S^2 \times R_R \times I_i$$

where T_{HM} and T_P correspond to the transmissivity of the half mirror and the polarizer, and R_{HM}, R_R, and R_S to the reflectivity of the half mirror, the reflector, and the sample surface, respectively. The crystalline imperfection in surface region of a sample is defined as the following equation

$$\text{Imperfection} = \frac{I_c(\lambda_1)/I_c(\lambda_2) - I_s(\lambda_1)/I_s(\lambda_2)}{I_c(\lambda_1)/I_c(\lambda_2) - I_a(\lambda_1)/I_a(\lambda_2)}$$

where $I(\lambda_1)$ and $I(\lambda_2)$ correspond to the reflected light intensities at 275 and 330 nm, respectively, and c and a denote the control samples for the crystalline and amorphous, respectively, and s to the sample under test. Values of the crystalline imperfection given by this method have a correlation to the density of defects and the degree of damage in a sample. Optical

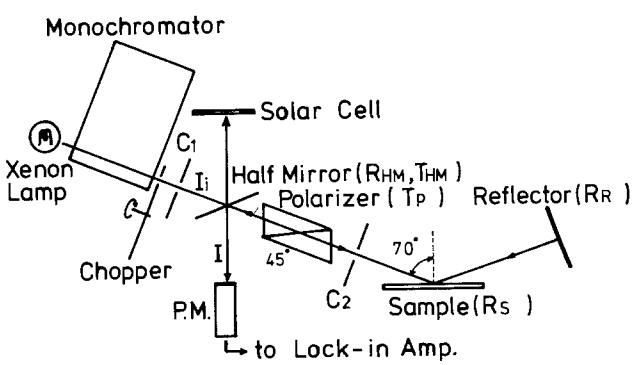

Fig. 1. Schematic diagram of the apparatus for UVRM. C_1, C_2: collimator, P.M.: photomultiplier.

* Electrochemical Society Active Member.

parameters depending on the system are eliminated by calculating the difference of the reflected light intensities between the measured sample and the control samples. The experimental errors due to the surface contaminations can be minimized by calculating the ratio of the reflected light intensities at λ_1 and λ_2. A depth profile of the crystalline imperfection, *i.e.*, crystalline damage and quality in a sample, is obtained by successive reflectivity measurements followed by the anodic oxidization and stripping of surface layer. In the anodic oxidation process, a mixture of N-methylacetamide (NMA) and potassium nitride (KNO_3) is used as the electrolyte in order to form constant oxide thickness in silicon wafers with various impurity concentrations and defect densities. The depth of stripping by each anodic oxidization process was defined as an averaged value calculated from total etched depth and numbers of anodic oxidization.

To investigate distribution profiles of damage induced by ion implantation, P^+ and Si^+ were implanted into (100) oriented silicon wafers at room temperature. Thermal treatments at various temperatures were performed in dry N_2 gas for 10 min. Crystalline quality of silicon epitaxial film was also evaluated by UVRM. A silicon film with a thickness of 200 nm was grown on a porous silicon layer by means of the plasma dissociation of pure silane (4). A porous silicon layer of 2 μm was formed in a p-type silicon wafer with a resistivity of 0.003 Ω-cm by the anodization in 50% HF solution. The anodic current density was controlled at 5 mA/cm^2. Damage distribution profiles and the recrystallization process in ion-implanted regions, and the crystalline quality of epitaxial film were also evaluated by RBS with 400 keV $^3He^+$.

Results and Discussion

Figure 2 shows an aligned and a random RBS spectra from a P^+- and Si^+-implanted sample. Silicon ions of 5×10^{14}/cm^2 were implanted with the energy of 140 keV before P^+ implantation of 5×10^{14}/cm^2 at 100 keV. These spectra show only that the amorphous state is formed by the ion implantations except for the surface region. On the other hand, the depth profile of the crystalline imperfection in the same sample obtained by UVRM indicates, as shown in Fig. 3, that

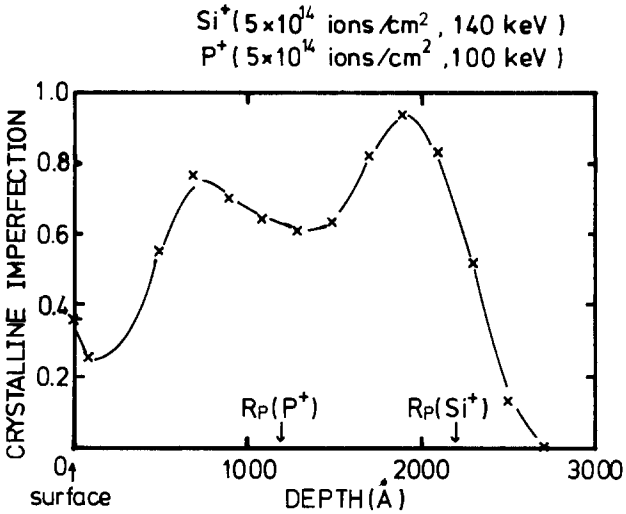

Fig. 3. Depth profile of the crystalline imperfection in P^+- and Si^+-implanted sample.

the amorphous state is not formed in the ion-implanted region. Two peaks of the crystalline imperfection are clearly detected by UVRM at the depth of 80 and 200 nm. These peaks seem to correspond to distributions of damage induced by P^+ and Si^+ implantation, respectively. It is revealed that UVRM has high resolution upon the degree of damage compared with RBS measurement.

Figure 4 shows RBS spectra of Si^+-implanted silicon. Silicon ions of 1×10^{15}/cm^2 were implanted with the energy of 110 keV. The aligned spectra after the ion implantation seem to indicate that the amorphous region is formed in the implanted region except for the surface layer of 40 nm. After the annealing at 500°C, the aligned spectrum of the implanted region shows that the recrystallization proceeds from the surface region in addition to the recrystallization from the substrate. The aligned yield from the implanted region decreases with increasing the annealing temperature, however, the depth profile of residual dam-

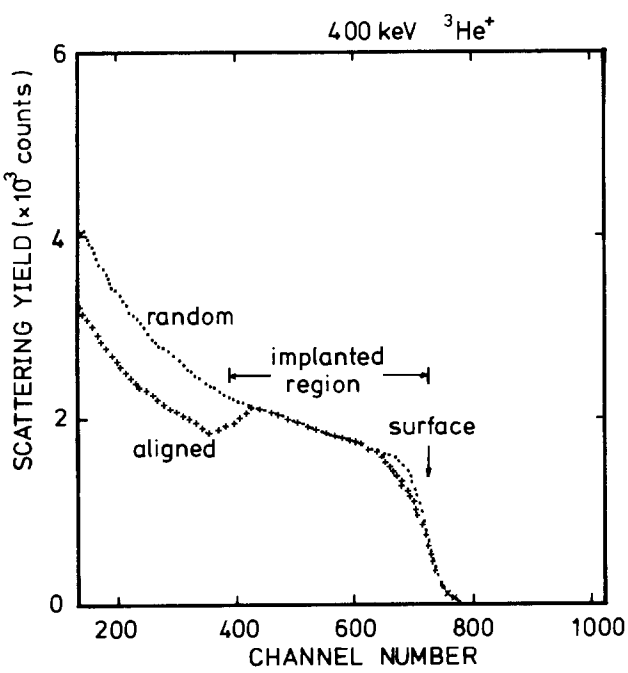

Fig. 2. Backscattering spectra of P^+- and Si^+-implanted silicon. Silicon ions of 5×10^{14}/cm^2 are implanted with the energy of 140 keV before P^+ implantation of 5×10^{14}/cm^2 at 100 keV.

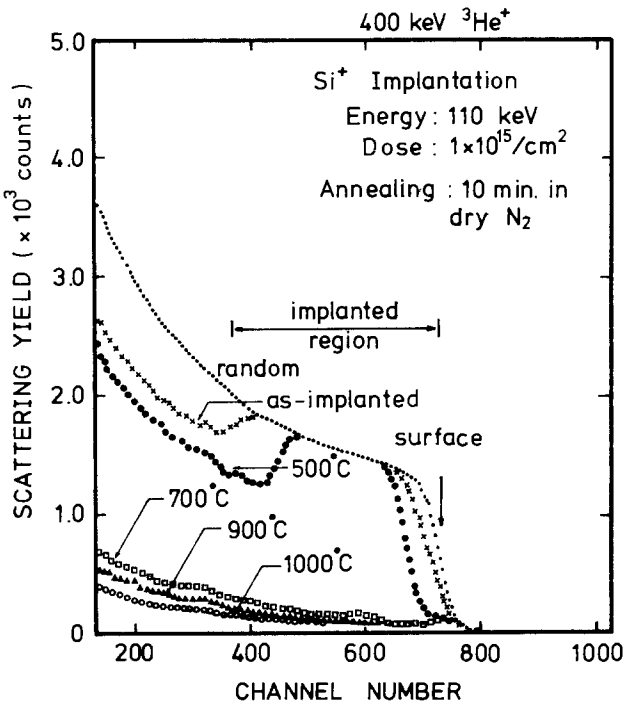

Fig. 4. RBS spectra of Si^+-implanted silicon. Silicon ions of 1×10^{15}/cm^2 were implanted with the energy of 110 keV, and annealed at 500°, 700°, 900°, and 1000°C for 10 min.

age after the annealing above 700°C cannot be determined in these spectra.

Depth profiles of the crystalline imperfection in the same samples obtained by UVRM are shown in Fig. 5. It is evident that the amorphous state is not formed by Si^+ implantation with a dose of $1 \times 10^{15}/cm^2$, and that the degree of damage in the surface region of 40 nm is less than that in the region between 40 and 240 nm. It is considered that the amorphous state was not formed in the implanted region because of increase of the substrate temperature during the ion implantation. As observed in RBS spectra, it is evident from UVRM spectra that the recrystallization proceeds from the substrate toward the surface, and that the recrystallization also takes place from the surface by the annealing at 500°C. It is clear that the damage induced by the ion implantation remains in the region between 80 and 180 nm. In the case of the annealing at higher temperature, the residual damage can be detected by UVRM. The implanted region is recrystallized mainly from the substrate toward the surface by the annealing above 700°C. After the annealing at 1000°C, the damage still remains in the surface region of 100 nm, and it is considered that the surface region is not recrystallized completely because the crystalline quality of this region, that acts as a seed for the recrystallization from the surface, is poor compared with the substrate. The annealing for a longer time is required for the complete recrystallization of the implanted region.

The depth profile of both the crystalline imperfection obtained by UVRM and the dechanneled fraction by RBS in the epitaxial film on a porous silicon layer are shown in Fig. 6. Dechanneled fractions were calculated from the ratio between the aligned yield and the random yield at the same depth, and have a correlation to the defect density. A large value of the dechanneled fraction near the interface indicates existence of a transition region from the porous structure to a uniform epitaxial film, where micropores are pinching off quickly according to the film growth. A tendency of increase of the crystalline imperfection given by UVRM is in good agreement with the distribution profile of the dechanneled fraction obtained by RBS measurement. It is revealed that UVRM is also available in the evaluation of the crystalline quality of silicon epitaxial films.

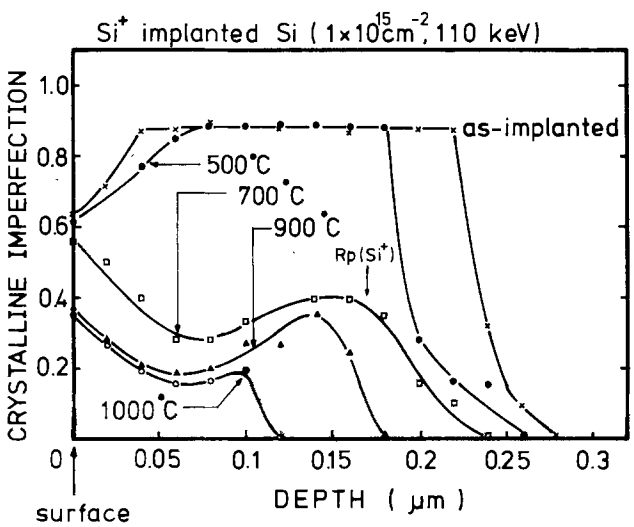

Fig. 5. UVRM spectra of Si^+-implanted silicon

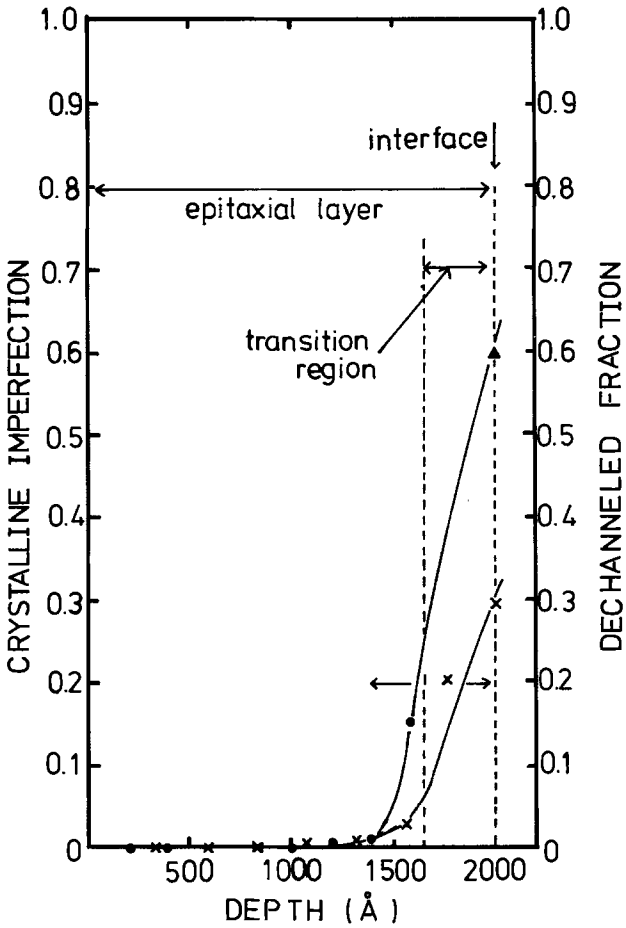

Fig. 6. Comparison between the crystalline imperfection given by UVRM and the dechanneled fraction by RBS measurement. Silicon film of 0.2 μm was grown on a porous silicon layer of 2 μm. ▲ shows the crystalline imperfection of original surface of the porous silicon layer measured before the epitaxy.

Conclusion

Ultraviolet reflectivity measurement is an excellent technique for the evaluation of the crystalline qualities of epitaxial films and damage in ion-implanted regions. Though the dependence of the optical reflectivity on the lattice damage is not well identified, it is considered that the aligned yield obtained by RBS measurement depends on the density of atoms displaced from the crystalline sites, and that the reflectivity change at 275 nm is caused by the increase and broadening of state density near the conduction band bottom to the lower energy side by the lattice damage. Accordingly, the degree of crystalline imperfection given by UVRM does not always agree with the experimental results obtained by RBS measurement, but detailed distribution profiles of the crystalline imperfection in silicon can be obtained by UVRM with successive stripping of the surface layer.

Manuscript submitted Oct. 22, 1982; revised manuscript received May 31, 1983.

REFERENCES

1. M. Miyao, T. Miyazaki, and T. Tokuyama, *Jpn. J. Appl. Phys.*, **17**, 955 (1978).
2. J. E. Fredrickson, C. N. Waddell, G. Spitzer, and G. K. Hubler, *Appl. Phys. Lett.*, **40**, 172 (1982).
3. E. A. Irene and D. W. Dong, *This Journal*, **126**, 1347 (1982).
4. T. Itoh and H. Takai, *Jpn. J. Appl. Phys.*, **22**, (1983).

The Mechanism of Orientation in Si Graphoepitaxy by Laser or Strip Heater Recrystallization

Henry I. Smith and C. V. Thompson[1]

Department of Electrical Engineering and Computer Science, Massachusetts Institute of Technology, Cambridge, Massachusetts 02139

M. W. Geis

Lincoln Laboratory, Massachusetts Institute of Technology, Lexington, Massachusetts 02173

R. A. Lemons,[2] **and M. A. Bosch**

Bell Laboratories, Holmdel, New Jersey 07733

ABSTRACT

An explanation is presented for the (100) texture and <100> orientation observed in Si graphoepitaxy by laser and strip heater recrystallization. With radiational heating, solid crystalline ribbons and islands, having a predominance of (100) texture, can coexist with molten Si. Crystallites with (100) texture and <100> parallel to the axis of a surface-relief grating are preferentially retained in partially molten regions, and these crystallites seed subsequent solidification, yielding the overall orientation.

In earlier papers (1-4), experiments on a type of graphoepitaxy in which amorphous or polycrystalline Si films were deposited over surface relief gratings in SiO_2 and then recrystallized[3] using a scanning laser beam or a strip heater oven were described. The resulting films were composed of large grains with (100) texture and a preferred orientation of <100> crystallographic axes along the grating axis. In this paper, we present an explanation for this texture and orientation [see also Ref. (4)].

The initial silicon graphoepitaxy research (1, 2) utilized a CW Ar-ion laser to recrystallize amorphous or polycrystalline silicon deposited over surface relief gratings of 3.8 μm spatial period in fused silica. A (100) texture and orientation of a <100> direction relative to the grating axis were observed only if recrystallization was carried out in an oxygen containing ambient (generally air was used). The oxygen caused an SiO_2 layer or cap, ~100 nm thick, to form over the Si. The (100) texture and <100> orientation showed angular spreads of $\sim\pm2°$ and $\sim\pm10°$, respectively (1-3). The orientation effect was reduced if the grating profile was degraded. Over a narrow range of laser power the silicon appeared to be partially molten and only under these conditions was orientation observed. (The partially molten condition was apparent in an image formed with the laser beam reflected off the sample.) If the silicon was fully melted, or if the recrystallization was carried out in an inert gas, or nitrogen, no orientation or texture was observed.

When these results were initially reported, there was considerable skepticism that a silicon film, heated by laser radiation, could exist in a partially molten configuration. However, recent work by Bösch and Lemons (5-7) and Biegelson and Hawkins (8, 9) has shown that one can indeed achieve a stable configuration of solid silicon crystallites in a pool of molten silicon, provided that the silicon is heated radiatively. This liquid-solid coexistence is stable only when the Si is contacted on both sides by an oxide. (The oxide on the top side can form in an O_2 containing ambient such as air, or be deposited.) The silicon crystallites are generally a few micrometers wide and have characteristic elongated shapes. They have been variously referred to as "filaments," "lamellae," or "worms" (5-9). However, since the solid extends through the thickness of the film, which is usually 5-10 times smaller than the width of the crystallites, we will refer to elongated crystallites as solid ribbons and to isolated segments of roughly equal length and width as solid islands. The width of the ribbons is remarkably constant, as is their spacing, if ribbons are densely packed.

Figure 1 illustrates the pattern of ribbons and islands in a film heated in air with an Ar-ion laser. As discussed below, it is believed that the <100> graphoepitaxial orientation effect is a product of the interaction of such ribbon and island crystallites with the surface relief grating.

The configuration of solid crystallites separated by molten Si is stable in that the fraction of material that is solid and the fraction that is liquid remain constant with time, for constant laser power input. Under Ar ion laser irradiation, the individual ribbons change shape with time and appear to move about. In some cases, small crystallite islands appear to break off from ribbons and move independently through the melt. Such motion is only apparent; the solid material itself is fixed relative to the substrate and cap. As material solidifies on one edge of a crystallite an equal amount tends to melt from the opposite edge, giving the appearance of motion. Careful observation has shown that ribbons and islands do not nucleate spontaneously in the melt. They are either unmelted remnants of the polycrystalline material, or they are the product of growth from unmelted crystallites.

Hawkins and Biegelson (8, 9) have presented a theoretical model to explain the dynamic stability of the partially molten configuration. This model takes into account the large increase in reflectivity of Si when it melts (a semiconductor-to-metal transition). The power density required to maintain a pool of fully molten Si, P_2, is higher than the power density required to heat solid Si up to the threshold of melting, P_1. At any power density intermediate between P_1 and P_2, the fraction of the film that is in the solid phase is intermediate between one and zero. If silicon is melted nonradiatively, such as by thermal conduction (9) or an electrical discharge (10), no ribbons or islands form.

[1] IBM Postdoctoral Fellow. Currently, Department of Materials Science and Engineering, Massachusetts Institute of Technology.
[2] Present address: Los Alamos National Laboratory, Los Alamos, New Mexico 87545.
Key words: recrystallization, graphoepitaxy, silicon, semiconductor.
[3] We use the term "recrystallization" to encompass both the traditional meaning (solid-state processes involving grain nucleation and/or growth) and melting followed by solidification, in accord with recent usage.

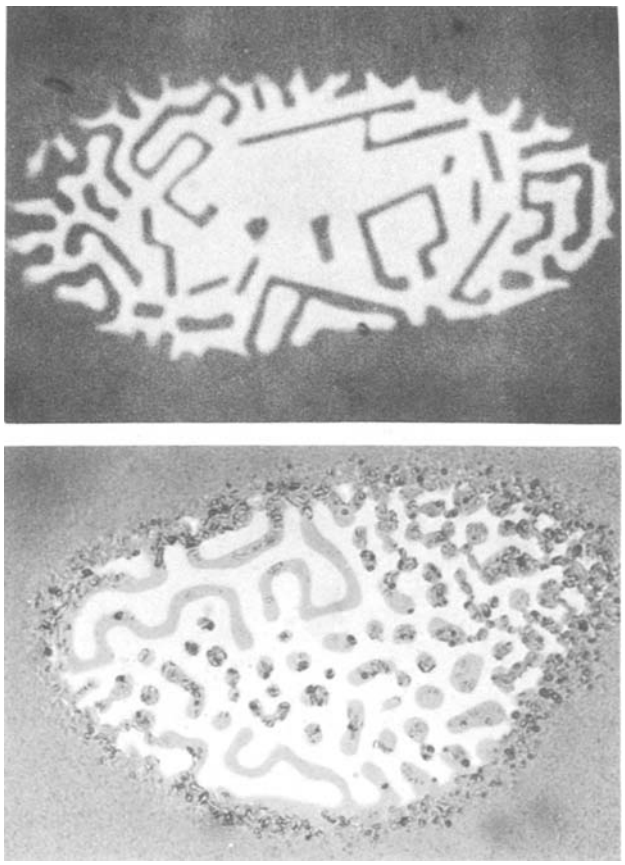

Fig. 1. Ar^+ laser irradiated area of a ~1/2 μm thick poly-Si film on fused silica. (a, top) Optical micrograph made from the back side in reflected light. Solid Si appears dark, molten Si appears bright. (b, bottom) Optical micrograph made in reflected light from the front side [a different sample than in (a)]. A thin SiO_2 encapsulation layer is formed in the air ambient. The granular appearance on the perimeter of the partially molten region probably indicates solid-state recrystallization or grain growth. Some islands in the partially molten region also have a granular appearance suggesting they have remained unmelted.

For an elliptical laser spot, such as shown in Fig. 1, ribbons extend inward from a perimeter of polycrystalline silicon. The material on the perimeter has a rough, granular appearance, as shown in Fig. 1b. This suggests that rapid solid-state recrystallization or grain growth (11) occurs in this material, which is close to the melting temperature. If so, the grain size appears to be of the order of micrometers, which is much larger than the size of polycrystalline grains away from the high temperature region ($\lesssim$ 0.1 μm). If the laser power is increased, the perimeter expands and the central region can become fully molten. As the laser power is decreased, the solid ribbons grow inward, leading eventually to complete solidification.

The solid ribbons and islands tend to be parallel-sided and take on shapes with angular features close to 90°, suggesting (100) texture (see Fig. 1). As described elsewhere (10) and below, x-ray measurements, taken after solidification of the partially melted "transition region," confirm a predominance of (100) texture. The development of (100) texture among solid ribbons and islands may be explainable by thermodynamic arguments. It is speculated that the interfacial energy between Si crystallites and the SiO_2 of the cap and substrate is lowest for crystallites with (100) texture. Although there is no direct proof that this interface is the least energetic, it is well known that it has the lowest densities of fixed oxide charge and interface electronic states (12). Also, oxidation-enhanced diffusion and the rate of growth of stacking faults are maximum for (100) Si-SiO_2 (13). We do not believe a direct calculation of the interfacial energy would be meaningful in the absence of an experimentally verified model for the Si-SiO_2 interface.

Given that Si crystallites with (100) planes parallel to the cap and substrate oxides have the lowest surface-energy contributions to their total energy, grains with (100) texture should dominate in solid-state recrystallization or grain growth immediately prior to melting. Also, (100) textured crystallites, isolated by partial melting, will have a slightly higher melting temperature ($\sim 10^{-2}$ K if one assumes a surface-energy difference of 0.01 J/m^2 for (100) Si-SiO_2, as shown in the Appendix). Since the temperature of the entire partially molten region is stabilized by the mechanism described by Hawkins *et al.* (9), even this small difference in melting temperature might lead to preferential retention of (100)-textured crystals. Regardless of whether solid-state grain enlargement or melting-temperature differential is responsible for preferential retention of (100)-textured crystallites, if a surface relief structure of square-wave cross section is present, unmelted crystallites having (100) texture and <100> directions perpendicular to (and therefore also parallel with) the grating axis should be preferentially retained (14, 15).

Recently, we studied laser recrystallization over surface relief gratings (3.8 μm period, 0.1 μm depth, square-wave cross section) in SiO_2 using an Ar-ion laser and an apparatus that permitted optical microscopy during laser irradiation (5-7). As the laser power was increased and total melting approached, the last crystallites to melt were located along the grating corners, and these tended to have oriented, square shapes (Fig. 2), suggesting <100> orientation along the grating axis. Also, ribbons tended to be parallel to the surface relief grating. When molten Si came in contact with the relief grating in SiO_2, the profile was very rapidly rounded due to plastic flow at the high temperature (1412°C). Grating profile was preserved only underneath those crystallites which had not been melted (Fig. 2). We believe such unmelted crystallites seed solidification. Since the resolidified material is oriented with <100> predominantly along the grating axis, the seeds from which it originated must also have been oriented. Thus, orientation can take place only if the seeds are located on a grating whose profile has not been degraded by plastic flow. This speculation is fully consistent with earlier observations that total melting eliminated orientation (1-4).

In the initial experiments using a stationary strip heater oven (3), larger grains were obtained than in the case of the laser and somewhat narrower angular spreads in the texture (~±0.5°) and azimuthal orientation (~±5°). The Si films were intentionally capped with ~2 μm of SiO_2, rather than a natural oxide. Recently, we investigated the mechanism of orientation for the case of strip heater Si graphoepitaxy, using substrates of thermal SiO_2 over silicon wafers. Gratings of 3.8 μm period were etched into the SiO_2 over a central 1 cm^2 region prior to deposition of 0.5 μm of Si and a cap of 2 μm SiO_2, 30 nm Si_3N_4. Using a stationary strip heater, samples were preheated to 1100°-1300°C on the lower strip and then radiation from the upper strip melted an elliptically shaped molten zone, which grew radially at 10-100 mm/sec. When the power to the upper strip was turned off, the molten zone solidified rapidly. If this resolidification took place after the elliptically shaped molten zone had grown beyond the area of the grating, (100) texture was observed, but no orientation relative to the grating. (This is consistent with the observation discussed above that total melting destroys the grating and eliminates orientation.)

After resolidification, three distinct zones are clearly discernable: zone 1, a central region that had been fully melted and resolidified, composed of large

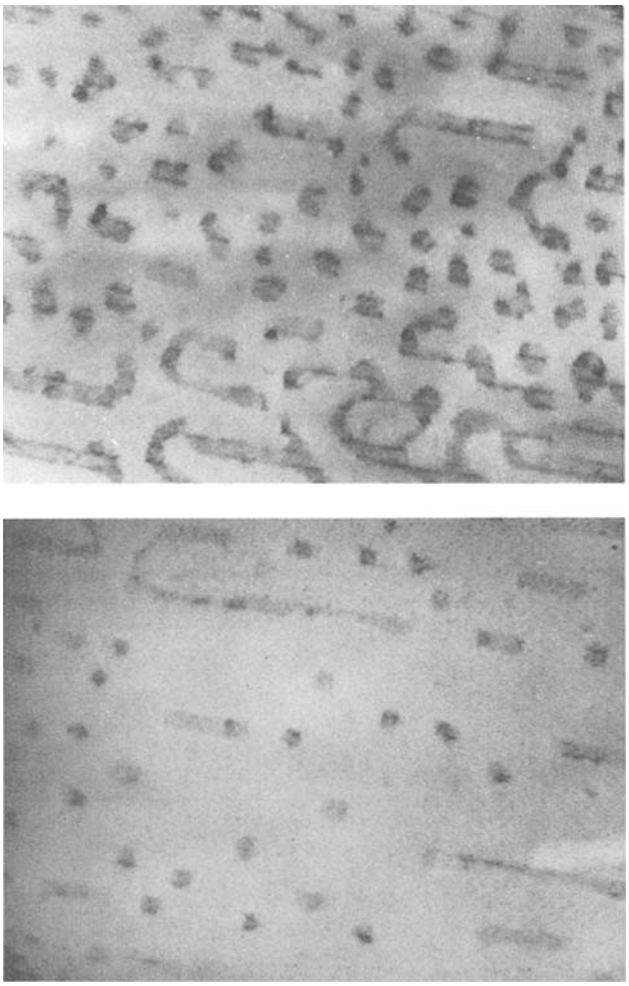

Fig. 2. Ar^+ laser irradiated area of a ~1/2 μm thick poly-Si film on a fused silica substrate in which a 3.8 μm-period surface relief grating has been etched to a depth of 0.1 μm. Photographs have been taken from a TV monitor. Corners of grating appear as dark lines at the edge of crystallites. (a, top) Note that grating profile is retained only underneath unmelted crystallites. (b, bottom) Same area after further melting.

($\gtrsim$1 mm) crystalline grains; zone 2, a narrow, annular transition region at the border of zone 1, composed of crystalline grains a few μm in diameter; and zone 3, beyond the transition region, composed of fine grain (<0.1 μm) polycrystalline silicon which had not melted or seen any significant grain growth. We believe the transition region corresponds to the condition of partial melting described above. X-ray diffraction analysis shows that there is a strong predominance of (100) texture in the transition zone, even for SiO_2 encapsulants <250 nm thick, as shown in Fig. 4 of Ref. (10). We were unable to determine if there was <100> orientation with respect to the grating within the transition region (zone 2) either during or after recrystallization. Efforts to prepare samples of transition regions for TEM analysis were invariably unsuccessful. Because of this difficulty, a "grid-of-etch-pits" technique (16) was developed to analyze grain orientation in zone 1, immediately adjacent to the transition region, zone 2. The orientation of grains in zone 1 was assumed to reflect the orientation of the smaller grains within the transition region from which they had grown. [Grains within the transition region are too small (~2 μm) to analyze by the grid-of-etch-pits technique.] Figure 3 is a histogram of the azimuthal orientation of those crystalline grains that have (100) texture and are located immediately adjacent to the transition region. Clearly, there is a preference for orientation of <100> parallel to the grating axis.

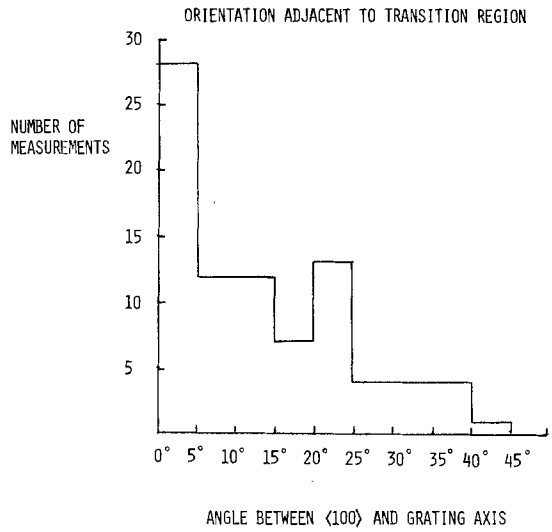

Fig. 3. Histogram of measurements of the angle between the grating axis and the <100> directions of etch pits immediately adjacent to the transition region. The etch pits were located on a square grid of 50 μm period. Measurements were taken only when the pit shape indicated (100) texture.

Histograms of grain orientation along the edges of transition regions that are not over gratings show no preferential azimuthal orientation. From these results, we conclude that orientation with respect to the surface relief grating takes place in the transition region and that crystallites in the transition region act as oriented seeds during solidification of zone 1. This is the same mechanism as is operative in laser recrystallization, discussed above: orientation takes place only in a region of partially molten silicon; (100) texture is predominant among crystallites in this partially molten region; if a surface relief grating is present, the (100)-textured crystallites have a predominant <100> orientation along the grating axis, and seed subsequent solidification. During solidification of the melt in zone 1, the grating has no further influence on orientation. The grating profile is destroyed by contact with molten Si. Moreover, even if its profile were preserved, a surface relief grating would not be expected to alter the orientation during solidification. No orientation relative to a surface relief grating was observed with a movable strip heater. In this case, orientation is along the direction of zone motion, due to directional solidification and occlusion (10, 17).

A surface relief grating does, however, change the characteristics of zone melting in one interesting way. On smooth SiO_2 surfaces, dendritic growth competes with (100)-textured growth at zone scanning speeds in excess of ~1 mm/sec (10, 17). Over surface relief gratings, the onset of dendritic growth occurred at ~3 mm/sec. We believe the surface relief structure greatly decreases the distance between interior corners of the faceted solid-liquid interface, which would support a higher rate of solidification (18). This speculation is supported by the observation that subboundaries are frequently entrained by, and run parallel to, the grating lines.

In addition to the grains having (100) texture, there are grains in the transition region, and adjacent to it, that have other textures but no specific orientation relative to the grating. These can also act as seeds during solidification of zone 1. However, as discussed in Ref. (10, 17), their growth is occluded by the growth of (100)-textured grains. The occlusion phenomenon may explain why larger grains and better texture were obtained with the stationary strip heater than with the laser (3). The analysis of orientation by x-ray pole plotting was done only in the solidified zone 1, so that grains whose texture deviated from (100) were eliminated by the occlusion effect.

The *in situ* observations of the morphology and dynamics of ribbons and islands in laser recrystallization (Fig. 1 and 2) lead us to speculate that high quality orientation (*i.e.*, much smaller angular spread in texture and orientation) with respect to artificial surface relief gratings might be realizable by laser recrystallization if one could avoid degradation of the grating profile, for example, by use of substrates with higher softening temperature. Furthermore, by oscillating the input power density, the solid ribbons and islands might be induced to settle into their lowest free-energy highly oriented configuration. However, the general view is that graphoepitaxy, especially of Si and other semiconductors, will have a far greater impact if it can be accomplished by means of low temperature processes that do not involve melting (19).

Acknowledgments

This work was sponsored by the Defense Advanced Research Projects Agency. The authors are grateful to J. M. Carter and C. L. Doherty for technical assistance, and D. A. Antoniadis, D. K. Biegelson, J. D. Plummer, F. Spaepen, W. Tiller, and many others for helpful discussions.

Manuscript submitted Jan. 14, 1983; revised manuscript received May 25, 1983.

Massachusetts Institute of Technology assisted in meeting the publication costs of this article.

APPENDIX

The Dependence of Melting Temperature on Crystallographic Texture

Consider two crystals of Si with equal cross-sectional area A and thickness t surrounded by liquid Si. We assume one of the crystals has (100) texture, that the surface energy for the interface between the crystal and an amorphous SiO_2 layer is γ_{100}, and that the other crystal has (111) texture with surface energy γ_{111}. The interfaces between the crystals and the melt also have equal area, A', and will be assigned the surface energy γ_{ls}. For the sake of simplicity, it will be assumed that γ_{ls} is isotropic. For a bulk free energy ΔG_v and atomic volume $\bar{V}$, the chemical potential for the (100) crystal is

$$\mu_{100} = (-2\gamma_{100}A - \gamma_{ls}A' + At\,\Delta G_v)/(At/\bar{V})$$

similarly

$$\mu_{111} = (-2\gamma_{111}A - \gamma_{ls}A' + At\,\Delta G_v)/(At/\bar{V})$$

The difference in chemical potential is therefore

$$\Delta\mu = \mu_{100} - \mu_{111} = \frac{2\Delta\gamma\bar{V}}{t}$$

where $\Delta\gamma = \gamma_{111} - \gamma_{100}$. Assuming a small difference in the heat capacities of the liquid and solid (20)

$$\Delta\mu = \Delta S_f\,\Delta T_m$$

where ΔS_f is the entropy of fusion per atom and ΔT_m is the difference in melting temperature [$(\Delta T_m = T_m(100) - T_m(111)]$. Thus

$$\Delta T_m = \frac{2\Delta\gamma\bar{V}}{t\Delta S_f}$$

If we assume that the average surface energy is about 0.1 Jm^{-2} and that the difference in the surface energy between (100) and (111) is about 10% (*i.e.*, $\Delta\gamma \cong 0.01$ Jm^{-2}) then for a 0.5 μm thick film, the difference in melting temperature should be 0.016°C. This effect is enhanced by larger surface-energy anisotropy and smaller film thicknesses.

REFERENCES

1. M. W. Geis, D. C. Flanders, and H. I. Smith, *Appl. Phys. Lett.*, **35**, 71 (1979).
2. M. W. Geis, D. C. Flanders, H. I. Smith, and D. A. Antoniadis, *J. Vac. Sci. Technol.*, **16**, 1640 (1979).
3. M. W. Geis, D. A. Antoniadis, D. J. Silversmith, R. W. Mountain, and H. I. Smith, *Appl. Phys. Lett.*, **37**, 454 (1980).
4. H. I. Smith and M. W. Geis, Abstract 155, p. 249, The Electrochemical Society Extended Abstracts, Vol. 82-1, Montreal, Que., Canada, May 9-14, 1982.
5. M. A. Bosch and R. A. Lemons, *Phys. Rev. Lett.*, **47**, 1151 (1981).
6. R. A. Lemons and M. A. Bosch, *Appl. Phys. Lett.*, **39**, 343 (1981).
7. R. A. Lemons and M. A. Bosch, *ibid.*, **40**, 703 (1982).
8. D. K. Biegelsen, N. M. Johnson, and M. D. Moyer, Abstract 142, p. 229, The Electrochemical Society Extended Abstracts, Vol. 82-1, Montreal, Que., Canada, May 9-14, 1982.
9. H. G. Hawkins and D. K. Biegelsen, *Appl. Phys. Lett.*, **42**, 358 (1983).
10. M. W. Geis, H. I. Smith, B-Y Tsaur, J. C. C. Fan, D. J. Silversmith, and R. W. Mountain, *This Journal*, **129**, 2812 (1982).
11. Y. Wada and S. Nishimatsu, *ibid.*, 125, 1499 (1978).
12. S. M. Sze, "Physics of Semiconductor Devices," 2nd ed., John Wiley & Sons, New York (1981).
13. S. M. Hu, *J. Appl. Phys.*, **45**, 1567 (1974).
14. D. C. Flanders, Ph.D. dissertation (M.I.T., 1978); reprinted as Lincoln Laboratory Technical Report 533 (1978).
15. H. I. Smith and D. C. Flanders, *Appl. Phys. Lett.*, **32**, 349 (1978).
16. K. A. Bezjian, H. I. Smith, J. M. Carter, and M. W. Geis, *This Journal*, **129**, 1848 (1982).
17. M. W. Geis, H. I. Smith, B-Y Tsaur, J. C. C. Fan, E. W. Maby, and D. A. Antoniadis, *Appl. Phys. Lett.*, **40**, 158 (1982).
18. M. W. Geis, H. I. Smith, D. J. Silversmith, R. W. Mountain, and C. V. Thompson, *This Journal*, **130**, 1178 (1983).
19. H. I. Smith, M. W. Geis, C. V. Thompson, and H. A. Atwater, To be published in *J. Crystal Growth*.
20. C. V. Thompson and F. Spaepen, *Acta. Metall.*, **27**, 1855 (1979).

Oxidation of Sputtered Niobium Nitride Films

P. K. Gallagher, W. R. Sinclair,* D. D. Bacon, and G. W. Kammlott

Bell Laboratories, Murray Hill, New Jersey 07974

ABSTRACT

Isothermal (440°-540°C) weight change measurements were made in 0.1% O_2 in Ar on films of cubic niobium nitride deposited on fused silica or sapphire substrates. The data were fit to various rate laws using a fraction-reacted from 0.2 to 0.9. The best fitting rate equation over these ranges of temperature and fraction-reacted was the Avrami equation, but several others fit nearly as well. The Arrhenius parameters derived from these data had an activation energy of 44.3 kcal mol^{-1} and a log pre-exponential term of 9.26 sec^{-1}. The value of the activation energy was virtually independent of the choice of the best fitting rate law. This apparent activation energy agrees well with that reported for the diffusion of oxygen in Nb_2O_3. It is suggested that the mechanism is analogous to the oxidation of niobium metal and the rate controlling step is diffusion of oxygen through a thin continuous layer of initial product. Studies of the oxidation showed no significant dependence of reaction rate on P_{O2}. The average weight gain was 25.0±0.9 (weight percent) w/o which leads to a film stoichiometry of $NbN_{0.96\pm0.06}$ based upon a stoichiometric Nb_2O_5 product. X-ray diffraction above 450°C studies indicated that the product films were the low temperature polymorph of Nb_2O_5. Below 450°C, the entire product films were amorphous or microcrystalline. In spite of the large lattice expansion associated with this oxidation, scanning electron microscopy revealed that the product films were adherent and continuous without large (>0.1 μm) cracks or pores. Matching the thermal expansion of the substrate and film does not seem important since similar results were obtained with both substrates.

Superconducting niobium nitride films are of interest as materials for Josephson junction devices (1, 2). These films have been prepared by d-c reactive magnetron sputtering of niobium in nitrogen-argon mixtures (3). The preparation of a thin continuous insulating surface layer on these films is an essential part of such devices. These surface layers are prepared by controlled oxidation of the film.

Earlier studies (4) on polycrystalline δ-$NbN_{0.9}$ prepared from bulk powder arrived at the following conclusions: (*i*) there is an enormous expansion accompanying the oxidation of δ-$NbN_{0.9}$. (*ii*) The oxidation best followed a pseudo first-order rate law. (*iii*) Both isothermal and dynamic studies gave an apparent activation energy of 50 kcal mol^{-1}. (*iv*) The product of the oxidation was Nb_2O_5 without the formation of intermediate oxynitrides or lower valent oxides of niobium.

It is the purpose of this study to determine if these conclusions are valid also for the oxidation of thin films, and if there are any significant effects induced by changing the substrate or partial pressure of oxygen.

Experimental Procedures and Results

Film preparation.—Niobium nitride films were prepared by d-c reactive magnetron sputtering in a 15% N_2-85% Ar ambient as has been recently described (3). This procedure leads to films having a T_c = 14.2 K and an average grain size of 5 nm. Sputtering was upwards from a Research Sputter Gun (5) onto substrates (1 × 2 × 0.1 cm). Substrates were either cleaned fused silica or cleaned single-crystal sapphire. After deposition of about 1 μm of film, the process was stopped, the system opened to air, and the substrates turned over for a similar deposition on the other side.

Weight change.—A Theta TG system was used to follow the isothermal weight change. An Omega Model 165 temperature controller replaced the controller packaged as part of the apparatus in order to achieve better isothermal operation. The output from a thermocouple in close proximity to the suspended sample and the output from the balance were fed to a Fluke Model 2500 data acquisition, control, and processor system. A premixed atmosphere of 0.093% O_2 in Ar or pure O_2 was flowed through the fused quartz hang down tube (1 in. diam) at 100 ml min^{-1}.

The data were least squares-fitted to those calculated for a variety of models for solid-state reactions or decompositions (6). A relatively wide range of fraction reaction (α) was used in this procedure, *i.e.*, $0.2 \leq \alpha \leq 0.9$. Of the 16 equations tested, three fit reasonably well. These were the Avrami equation (Eq. [1]), the Prout-Tompkins equation (Eq. [2]), and the simple linear equation (Eq. [3]), in which k represents the rate constant in sec^{-1}

$$[-\ln(1 - \alpha)]^{1/3} = k_1 t \quad [1]$$

$$\ln[\alpha/(1 - \alpha)] = k_2 t \quad [2]$$

$$\alpha = k_3 t \quad [3]$$

Table I presents the rate constants derived for these three equations. A plot of the data according to the Arrhenius equation (Eq. [4]

$$\log k = \log A - E/2.303RT \quad [4]$$

is shown in Fig. 1 for the Avrami and the Prout-Tompkins equations. The linear equations gave rate constants very similar to those of the Avrami equation. The lines in Fig. 1 represent the least squares fit to this equation for the data determined in 0.093% O_2 in Ar. Values of the apparent activation energy E and the log of the pre-exponential term A are given in Table I for each equation.

From the weights of the samples before and after oxidation, it is possible to make inferences with regard to the stoichiometry of the initial material, assuming that the final product is stoichiometric Nb_2O_5 and that the initial sample contained no signifi-

Table I. Rate data for the oxidation of cubic niobium nitride films in 0.1% O_2 in Ar or in pure O_2 (see Eq. [1], [2], and [3] in the text)

Temperature (K)	Substrate	k_1 (sec^{-1})	k_2 (sec^{-1})	k_3 (sec^{-1})
708.6	Sapphire	4.65 × 10^{-5}	2.27 × 10^{-4}	4.79 × 10^{-5}
708.6*	Sapphire	6.15 × 10^{-5}	3.00 × 10^{-4}	6.49 × 10^{-5}
708.8	Fused quartz	3.65 × 10^{-5}	1.78 × 10^{-4}	3.79 × 10^{-5}
723.9	Fused quartz	7.63 × 10^{-5}	3.74 × 10^{-4}	7.92 × 10^{-5}
729.7	Fused quartz	8.79 × 10^{-5}	4.30 × 10^{-4}	9.14 × 10^{-5}
733.9	Sapphire	1.43 × 10^{-4}	7.00 × 10^{-4}	1.53 × 10^{-4}
747.4	Fused Quartz	1.94 × 10^{-4}	9.54 × 10^{-4}	2.02 × 10^{-4}
754.8	Sapphire	2.10 × 10^{-4}	1.02 × 10^{-3}	2.23 × 10^{-4}
772.1	Sapphire	4.28 × 10^{-4}	2. 08× 10^{-3}	4.60 × 10^{-4}
769.0	Fused quartz	5.00 × 10^{-4}	2.45 × 10^{-3}	5.27 × 10^{-4}
773.0	Sapphire	4.94 × 10^{-4}	2.39 × 10^{-3}	5.34 × 10^{-4}
780.0*	Sapphire	6.16 × 10^{-4}	3.00 × 10^{-3}	6.41 × 10^{-4}
817.7	Fused quartz	3.15 × 10^{-3}	1.54 × 10^{-2}	3.28 × 10^{-3}
	E (kcal mol^{-1})	44.3	44.3	44.6
	log A (sec^{-1})	9.26	9.94	9.36

* Run in pure O_2. Not used for the calculation of Arrhenius parameters.

* Electrochemical Society Active Member.

Key words: kinetics, mechanisms, niobium oxide.

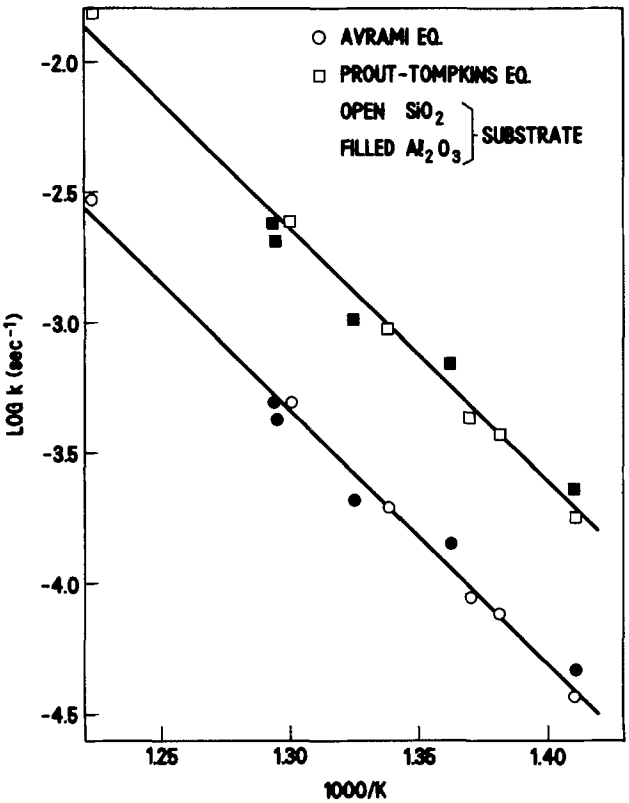

Fig. 1. Arrhenius plots for the oxidation of sputtered films of cubic niobium nitride.

cant impurities. The average weight gain of the samples oxidized to completion was 25.0 ± 0.9 w/o. This leads to a calculated initial stoichiometry of $NbN_{0.96\pm0.06}$. The nitride content is somewhat higher than $NbN_{0.9}$ observed in the previous study of the polycrystalline target material (4). This calculation neglects the contribution of carbon which is a known impurity.

Structure.—X-ray diffraction studies were made of the starting film and product films prepared at various temperatures in both 0.1% O_2 in Ar and pure O_2. The starting material was the cubic form generally referred to as δ-$NbN_{0.9}$. At the lowest temperature used for oxidation, 709 K, the product films were amorphous or microcrystalline. At higher temperatures, the same product was observed as for the oxidation of bulk polycrystalline powder (4), *i.e.*, the low temperature polymorph of Nb_2O_5.

Figure 2 presents SEM micrographs of films before and after oxidation. The product films are insulating and a covering layer of carbon has been deposited to reduce charging.

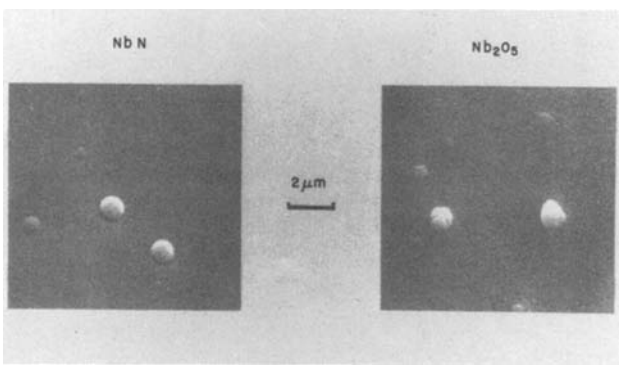

Fig. 2. Scanning electron micrographs of sputtered films of cubic niobium nitride before and after oxidation.

The change in film thickness for both amorphous and crystalline products was determined by the step height for as-deposited nitride on sapphire and after complete oxidation at 440° and 500°C. Results are presented in Table II.

Discussion

Overall weight gain and x-ray diffraction of the initial and final films indicate that the reaction under investigation is the oxidation of cubic substoichiometric niobium nitride, δ-$NbN_{0.95}$, to Nb_2O_5. In spite of the very large change in volume known to accompany this oxidation (4), see Table III, the SEM results in Fig. 2 do not indicate any blistering, cracking, or peeling of the films at this magnification. It would appear that any cracks or pores formed are less than about 0.1 μm. This is true whether the substrate is fused quartz or sapphire. Oxidation of the metal, on the other hand, requires an even greater volume change, see Table III, and the initial oxide film is protective but at greater thicknesses, blisters and cracks develop which are initially a few tenths of μm in size (7).

From the data in Table III, one would expect the product oxide film to be considerably thicker by a factor of about 2.3, depending upon its porosity, than the starting nitride film. The data in Table II indicate an increase by a factor of three in the thickness after oxidation. This does not appear to be greatly affected by the crystallinity of the product. The greater expansion would imply significant microcracks or microporosity. These pores or cracks do not arise from differences in thermal expansion of the substrate and film as substantiated by the lack of any observed difference between films deposited on fused quartz or on sapphire.

No single rate law provided consistently the best fitting oxidation rate equation. The best were those of Eq. [1], [2], and [3], and mechanistic inferences cannot be made solely from the data fitting. Substantiating evidence, generally microscopic, is necessary to confirm a particular reaction path (8). For comparison, a change from the parabolic to the linear rate law is observed for the oxidation of niobium metal once the protective nature of the oxide film has broken down by blister and crack formation. The parabolic rate is attributed to the rate being determined by diffusion of the reactant through an ever growing product layer. The linear law implies free access of the reactant and an essentially constant reaction cross section.

Examination of Fig. 1 and the Arrhenius parameters given in Table I suggests that any "reasonably" fitting rate equation will yield nearly the same value of apparent activation energy. The value of 44 kcal mol^{-1} is in good agreement with previous work on oxidation of nitride powders (4, 9) and of polycrystalline plates (9), 45-50 kcal mol.

Marker measurements for the oxidation of niobium have shown that oxide formation occurs at the metal/oxide interface (7). This is consistent with the fact that

Table II. Thickness measurements before and after oxidation

Nitride thickness (μm)	Temperature of oxidation (°C)	Oxide thickness (μm)
0.33	440	1.00
0.32	500	0.97

Table III. Molar volume of selected compounds of niobium

Compound	Molar volume (cm^3/Nb)
Nb (bcc)	10.9
$NbN_{0.9}$ (cubic)	12.8
NbN (hexagonal)	12.25
Nb_2O_5 (monoclinic)	29.15

Nb_2O_5 is an n-type semiconductor having an oxygen deficient stoichiometry. Chen and Jackson (10) have measured the oxygen diffusion constant in nearly stoichiometric Nb_2O_5 over the temperature range from 850° to 1200°C and obtained an activation energy of 49.4 ± 3.3 kcal mol. Comparison of the oxidation of the nitride herein with that of the metal (7) suggests a similar mechanism. During the very early stages or at low temperatures (<400°C), the amorphous product layer (oxide or oxynitride) is impervious and severely inhibits further growth. At higher temperatures, however, either rapid grain boundary diffusion becomes effective or microcracks or micropores are formed and the rate tends toward linearity. These pores or cracks need not be large to allow for sufficient diffusion of oxygen (11).

One would expect that the diffusion of oxygen through the continuous, amorphous, product film would be rate controlling in the low temperature regime provided that the out-diffusion of nitrogen occurs more readily. At higher temperatures where the rate law becomes more linear, one might expect the solid-state diffusion of oxygen to no longer be the rate determining step. However, the regime of constant rate does not preclude the diffusion of oxygen from being determining but merely requires the length of the path, presumably the impervious film thickness, to remain constant. Since the oxygen diffuses inward to the product/metal interface, it is suggested that the product formed at this point is the continuous, probably amorphous, phase. As the thickness increases beyond a certain value, the exterior surface becomes microporous or cracked, allowing for relatively free access of oxygen to the bulk oxide/amorphous product film interface. This transformation may be associated with strains, crystallization, or further oxidation of initial amorphous phase. The good agreement between the observed apparent activation energy for the oxidation of cubic niobium nitride during all stages of the reaction and that of the reported activation energy for the diffusion of oxygen in Nb_2O_5 (10) strongly suggests that this mechanism applies.

In the high temperature regime where linear rate behavior is approached, the values of k_3 given in Table I can be converted directly to a rate of interface motion if the motion is assumed inward and perpendicular to the surface. The film thickness for the kinetic samples was approximately 1 μm. Hence $d\alpha/dt$ of 2×10^{-4} sec^{-1} corresponds to about 2 Å/sec. Despite the great caution which should be exercised in extrapolating from the data in Table I to the low temperature regime, there is excellent agreement with recent Auger spectroscopic results obtained near room temperature (12).

Manuscript submitted Jan. 9, 1983; revised manuscript received June 24, 1983.

Bell Laboratories assisted in meeting the publication costs of this article.

REFERENCES

1. F. Shinoki, S. Takada, S. Kosaka, and H. Hayakawa, *Jpn. J. Appl. Phys.*, **19**, Suppl. **19-1**, 591 (1980).
2. R. B. Van Dover, D. D. Bacon, and W. R. Sinclair, *Appl. Phys. Lett.*, **41**, 764 (1982).
3. D. D. Bacon, A. T. English, S. Nakahara, F. G. Peters, H. Schreiber, W. R. Sinclair, and R. B. van Dover, *J. Appl. Phys.*, To be published.
4. P. K. Gallagher and W. R. Sinclair, *Isr. J. Chem.*, **22**, 222 (1982).
5. A trademark of Sputtered Films Inc., Santa Barbara, CA.
6. D. W. Johnson, Jr., and P. K. Gallagher, *J. Phys. Chem.*, **75**, 1179 (1971).
7. J. V. Cathcart, J. J. Campbell, and G. P. Smith, *This Journal*, **105**, 443 (1958).
8. P. K. Gallagher, E. M. Gyorgy, and H. E. Bair, *J. Chem. Phys.*, **71**, 830 (1979).
9. P. Lefort, J. Desmaison, and M. Billy, *Mater. Res. Bull.*, **14**, 479 (1979).
10. W. K. Chen and R. A. Jackson, *J. Chem. Phys.*, **47**, 1144 (1967).
11. E. A. Irene, *This Journal*, **129**, 413 (1982).
12. R. P. Frankenthal, D. J. Siconolfi, W. R. Sinclair, and D. D. Bacon, *ibid.*, **130**, 2056 (1983).

Thermal Oxidation of Niobium Nitride Films at Temperatures from 20°-400°C

I. The Surface Reaction

R. P. Frankenthal,* D. J. Siconolfi,* W. R. Sinclair,* and D. D. Bacon

Bell Laboratories, Murray Hill, New Jersey 07974

ABSTRACT

The air oxidation of cubic δ-NbN has been studied by Auger electron spectroscopy at temperatures from ambient to 400°C. At temperatures of 180°C or less, only the first one or two monolayers are oxidized, the reaction product being an oxynitride of niobium. Above 200°C, oxidation is not limited and obeys a linear rate law. At these higher temperatures, the reaction product initially is an oxynitride but, as the reaction proceeds, eventually becomes Nb_2O_5. The reaction proceeds by the diffusion of oxygen through the reaction product to the NbN interface. Grain boundary diffusion of oxygen into the NbN is rapid and competes with the oxidation reaction.

In some recent studies, superconducting niobium nitride has been used as the base electrode in Josephson tunnel junction devices (1-4). Several oxides, including niobium oxide, have been proposed as the barrier layer on NbN to provide tunnel diodes, and it has been shown that the air oxidation of niobium nitride at temperatures from ambient to 90°C produces suitable junctions (4). There have, however, only been a few studies of the oxidation of niobium nitride, all at temperatures above 400°C (5-7). At these temperatures, bulk oxidation is rapid, and the thin films required for a good junction cannot be formed reliably. Therefore, we have undertaken a study of the oxidation of niobium nitride thin films in air over the temperature range from 20° to 400°C.

* Electrochemical Society Active Member.
Key words: Auger electron spectroscopy, Josephson junction, oxynitride, superconductor.

Experimental

Films of cubic NbN, commonly referred to as δ-$NbN_{0.9}$, 150-550 nm in thickness, were deposited on

silicon substrates by d-c reactive magnetron sputtering of niobium in a 15% N_2-85% Ar gas mixture (4). The films have an average grain size of 5 nm and a superconducting transition temperature of 14 K. The thickness of the films was calculated from the weight gain during deposition, assuming a density of 8.4 g/cm^3 for NbN. Films of Nb_2O_5, 15-28 nm in thickness, were deposited on silicon substrates by d-c reactive magnetron sputtering of niobium in an O_2 ambient. The thickness of these films was also calculated from the weight gain, assuming a density of 4.47 g/cm^3 for Nb_2O_5.

The NbN films were oxidized in air at temperatures from ambient to 400°C for times ranging from 0.5 to 64 hr.

The oxidized films were analyzed by Auger electron spectroscopy. All spectra were obtained in the derivative mode with a Physical Electronics Industries thin film analyzer (TFA) system. Operating conditions were 5 kV electron gun voltage, 10 μA beam current, and 2 eV modulation amplitude. The spectral data were digitized with a TransEra 752 A/D converter that interfaced a Tektronix 4052 microcomputer to the TFA. Depth profiles through the films were obtained by argon ion sputter etching and measuring the intensities (peak-to-peak heights) of the Nb 167 eV, O 510 eV, and N 380 eV peaks. The argon pressure was 7 mPa (5×10^{-5} Torr). The ion beam voltage and emission current were 2 kV and 30 mA, respectively. The sputter rates, determined from the time to sputter through the films and their known thicknesses, were 5.7 ± 0.3 nm/min for the NbN films and 11 ± 1 nm/min for the Nb_2O_5 films.

Results and Discussion

Electron stimulated effects.—Initially, both the oxygen and nitrogen peaks rapidly decrease in intensity due to electron-stimulated desorption of adsorbed oxygen and nitrogen. The O peak continues to decay, but more slowly, for an additional 10-20 min before it attains its steady-state intensity. The behavior of the N peak is a function of the reaction product thickness. For very thin films about 1 monolayer in thickness (see below), *i.e.*, those formed below 100°C, the N peak also continues to decay slowly until it reaches a steady state at about the same time that the O peak does. For reaction products of intermediate or several monolayers in thicknesses, the N peak, after the initial rapid decrease, reaches a minimum and then slowly increases until it reaches a steady state. For films formed at 400°C, the N peak rapidly reaches its steady-state value with the initial desorption. It is concluded that after adsorbed oxygen and nitrogen are desorbed, some electron-stimulated decomposition of the reaction product occurs. This accounts for the slow decrease in the O intensity after the initial rapid decrease. It also explains, for the films of intermediate thickness, the increase in the N intensity after the minimum. As the film is decomposed, *i.e.*, thinned by the electron beam, the signal from the NbN substrate becomes stronger. This is not observed for the films formed at 400°C because the quantity decomposed is most likely only a fraction of a monolayer and is too little to have a measurable effect when the reaction product is reasonably thick. The continuing decrease in the N peak intensity during electron-stimulated decomposition of the films formed below 100°C indicates that the reaction product contains some N and is probably a niobium oxynitride. Additional data confirming this is given below.

Ion sputter profiles.—Nitrogen depth profiles are shown in Fig. 1 for three reaction product films of different thickness. Each profile is the intensity, I_N, of the N peak normalized against the intensity, $I_{Nb'}$, of the Nb peak from the bulk NbN film. Normalization removes the effect of any instrumental variations from one experiment to the next.

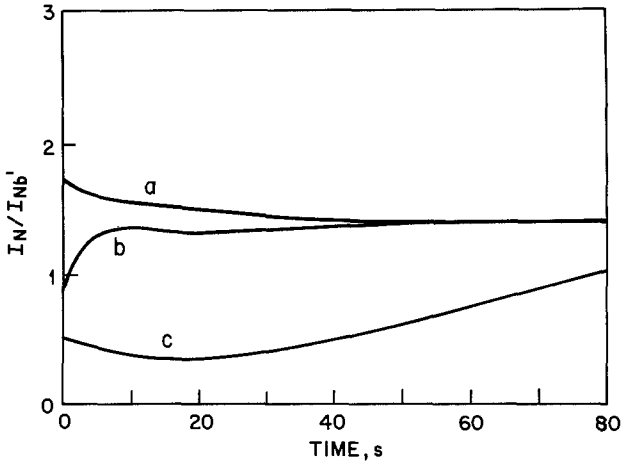

Fig. 1. Nitrogen depth profiles for oxidation at (a) 20°C for 24 hr, (b) 270°C for 16 hr, and (c) 400°C for 2 hr.

During sputter etching of the thinnest films, *i.e.*, those formed at temperatures below 100°C, the N peak decreases slowly in intensity until it reaches the steady state, corresponding to bulk NbN (Fig. 1, curve a). For films of intermediate thickness formed at 180°C, or at 270°C for oxidation times less than 20 hr, the N peak first increases in intensity, goes through a small maximum, and then decreases to the steady state (Fig. 1, curve b). For the films formed at 400°C, the N peak intensity first exhibits a small decline that is followed by a continuous increase as the reaction product is etched (Fig. 1, curve c). For the products of intermediate thickness, the initial increase in the N intensity is due to the thinning of the film with sputtering. The decrease after the maximum may be caused by some preferential sputtering of N from NbN. For the thin film, the initial decrease in the N intensity indicates that there is N associated with the outer layer of the surface. This means either that the oxidation product is discontinuous, that is, NbN is exposed at holes in the film, or that it contains both O and N. Since it is known that these films are good junctions and that they are made reproducibly (4), the film cannot be be discontinuous. Thus, it is thought that the thin reaction product is not a pure oxide but, more likely, an oxynitride. Additional confirmation for this is an observed change in shape of the N peak as the oxidation product is etched and the NbN film is exposed (Fig.2), indicating that the N-spectral peak comes from a species other than NbN.

The oxygen depth profiles are shown in Fig. 3-5 as a function of temperature and time of oxidation. Since the reaction products formed at temperatures of 180°C and below are probably oxynitrides of niobium, the sputter rate most likely lies between those for NbN and Nb_2O_5. At 20°C, the product is limited to a thickness of less than 0.5 nm, that is, to the first molecular layer (Fig. 3).[1] It does not grow thicker with further exposure to air. As noted above, the film formed at this temperature is probably an oxynitride. At 95°C, the limiting thickness is also only a monolayer of an oxynitride (Fig. 3). The initial O intensity at this temperature is greater than that observed at 20°C, which implies that the composition of the oxynitride is not fixed but is a function of the oxidation conditions. At 180°C, the steady state appears to have been reached after oxidizing for 64 hr. At this temperature, the product is 1-1.5 nm in thickness and extends into the second or, perhaps, third molecular layer (Fig. 3). The shape of

[1] For $NbN_{0.9}$, a_0 is 0.439 nm and the unit cell contains 4 molecules of NbN (8).

Fig. 2. N KLL Auger electron peaks from (a) specimen oxidized at 95°C and (b) NbN.

the N peak indicates that this film is also an oxynitride.

At 270°C, a limiting thickness for the reaction product is not observed (Fig. 4, 6). Instead the oxidation reaction appears to follow a linear rate law. The same phenomenon is observed at 400°C (Fig. 5, 7) and is consistent with the results of Gallagher *et al.* (7) who studied the oxidation of similar NbN films at temperatures above 435°C. Since, as is shown below, the reaction product at these temperatures contains Nb_2O_5, the thicknesses in Fig. 6 and 7 were calculated assuming the sputter rate for Nb_2O_5. Although at temperatures below 435°C, the oxidation reaction could not be followed by techniques that measure changes in bulk properties (5-7), Auger electron spectroscopy in conjunction with depth profiling can do so easily.

At 270°C, the presence of an oxynitride in the oxidation product is indicated by the shape of the N peak. However, it is not possible to determine whether the oxynitride is present throughout the product or only at the NbN interface. At 400°C, N is detected at low levels throughout the oxidation product (Fig. 1), the concentration at the surface being slightly higher than in the bulk of the product.

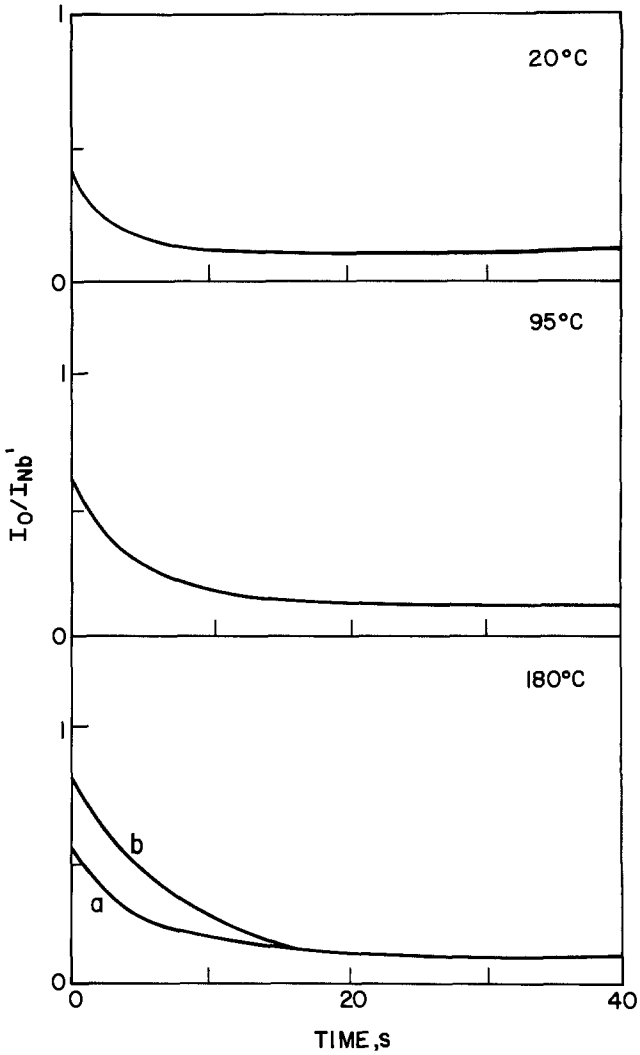

Fig. 3. Oxygen deptn profiles for oxidation at 20°C for 24 hr, 95°C for 64 hr, and 180°C for (a) 0.5 hr and (b) 64 hr.

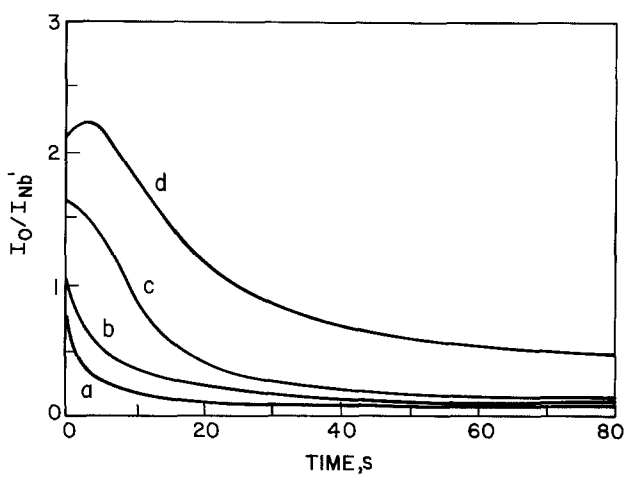

Fig. 4. Oxygen depth profiles for oxidation at 270°C for (a) 0.5 hr, (b) 16 hr, (c) 30 hr, and (d) 64 hr.

The N peak at this temperature is too small to analyze its shape. However, as the NbN substrate is approached during sputter etching, the peak corresponding to the oxynitride is observed.

To understand better the composition of the oxidation product, the shape of the MNN Nb peaks from each oxidized specimen was compared wih the shape of the peaks from the NbN substrate and from Nb_2O_5 (Fig. 9). For temperatures from 20° to 180°C and

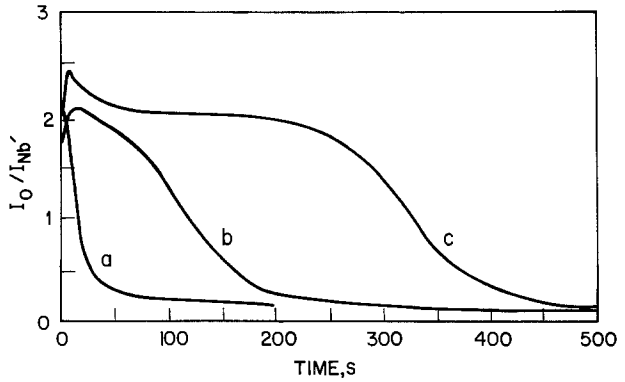

Fig. 5. Oxygen depth profiles for oxidation at 400°C for (a) 0.5 hr, (b) 2 hr, and (c) 4 hr.

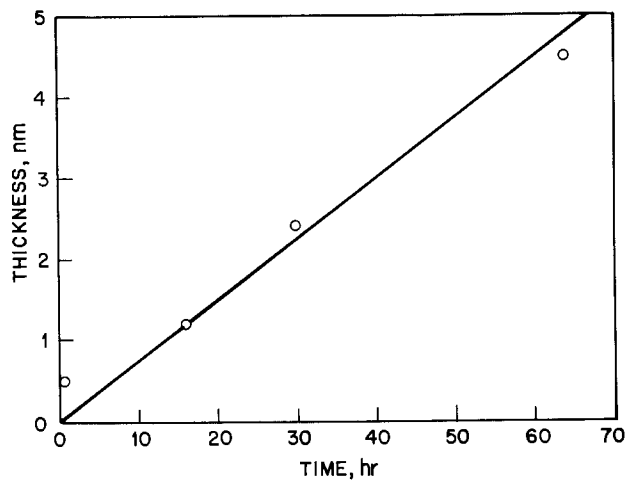

Fig. 6. Reaction product thickness vs. oxidation time at 270°C, showing apparent linear rate law.

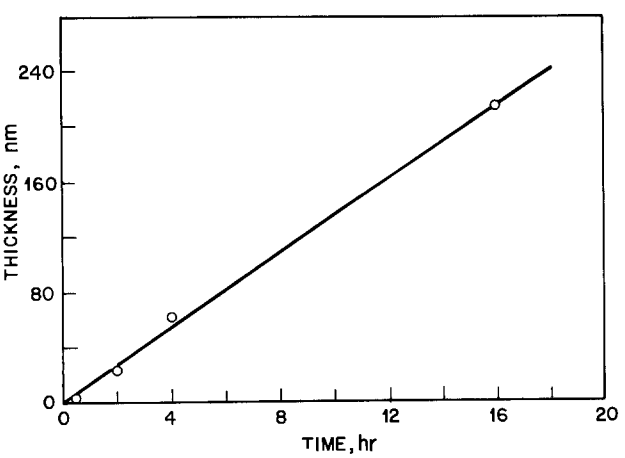

Fig. 7. Reaction product thickness vs. oxidation time at 400°C, showing apparent linear rate law.

for films less than 2 nm in thickness at the higher temperatures, Nb_2O_5 was not detected. At 270° and 400°C for reaction product films thicker than about 2 nm, the product appears to be Nb_2O_5, except at the surface, where the N concentration is greater than in the bulk (Fig. 1). There the Nb-peak shape is more like that of the oxynitrides. This suggests that, after initial formation of an oxynitride, the reaction proceeds by the inward diffusion of oxygen to the NbN interface where it reacts. In all cases, as the oxidation product is etched down to the NbN substrate, the shape of the Nb peak slowly changes to that for NbN.

The data in Ref. (7) obeyed a linear rate law

$$\alpha = kt \qquad [1]$$

in which k is the rate constant, t is the time, and α is the fraction of film reacted, *i.e.*, l/l^o in which l is the depth of NbN film of original thickness l^o that has been oxidized. Plots of the rate constant against reciprocal temperature yielded an apparent activation energy of 44.6 kcal/mol and a pre-exponential term of 2.3×10^9 sec^{-1}. Since the extent of oxidation in the present study is independent of NbN film thickness, a new rate constant k' is defined

$$k' = l^o k \qquad [2]$$

so that

$$l = k't \qquad [3]$$

To determine whether the rate constants obtained in the present study at 270° and 400°C are consistent with those reported at higher temperatures (7), k' was calculated from the data in Fig. 6 and 7 by multiplying the slopes of the linear plots by the ratio of the molar density of Nb_2O_5 (3.36×10^{-2} mol/cm^3) to that of NbN (7.86×10^{-2} mol/cm^3). These rate constants, as well as those calculated from the data in Table II of Ref. (7), are plotted against the reciprocal temperature in Fig. 8. The solid line is calculated from the activation energy and pre-exponential term in Ref. (7). The agreement between the two sets of measurements is excellent, especially when it is realized that one set was done thermogravimetrically (7), a bulk measurement, and the other was done by Auger electron spectroscopy, a surface sensitive technique. At lower temperatures, the apparent activation energy is expected to change as the mechanism shifts from one that gives a linear rate law to one that produces a limiting film thickness.

As seen in Fig. 3-5, O is found in the bulk NbN film and extends through it to the silicon substrate. It is believed that this results from the diffusion of

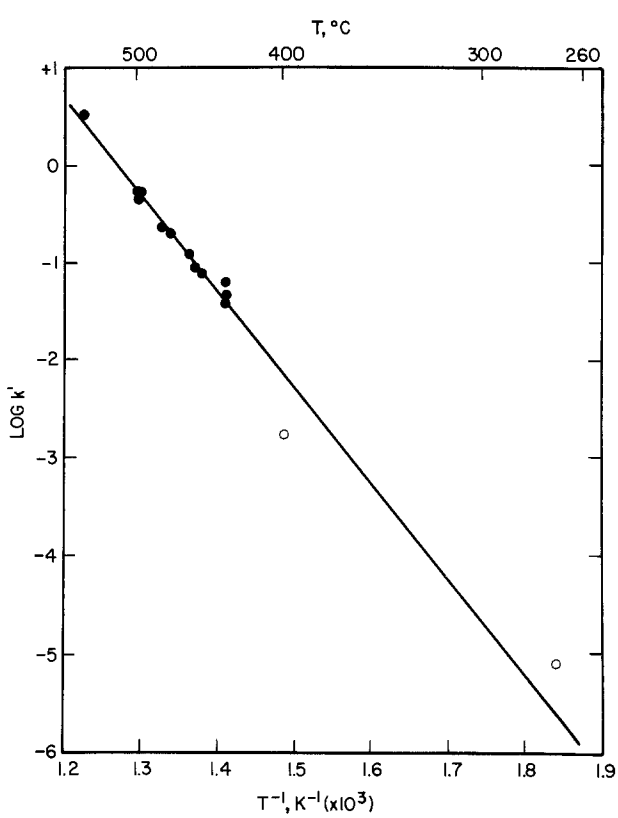

Fig. 8. Linear rate constant vs. reciprocal temperature. ●—High temperature data from Gallagher et al. (7); ○—This study. Solid line from Ref. (7).

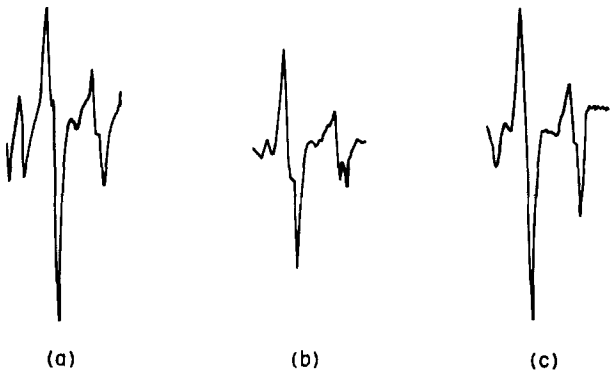

Fig. 9. Nb MNN Auger electron peaks from (a) Nb_2O_5, (b) specimen oxidized at 95°C, and (c) NbN.

oxygen down grain boundaries at a rate that must be more rapid than the rate of oxidation, at least after the first molecular layer has been oxidized. This is being studied further.

Conclusions

Based on the present data, it is concluded that at temperatures below about 200°C, surface oxidation of NbN is limited to one to two molecular layers, and the reaction product is most likely a niobium oxynitride. At higher temperatures, oxidation is not limited and follows a linear rate law. Initially, the reaction product is an oxynitride, but as the reaction proceeds, Nb_2O_5 is formed. Since the oxynitride is maintained at the surface, the reaction probably proceeds by the inward diffusion of oxygen to the product/NbN interface. Oxygen not only reacts at that interface but also diffuses through the entire NbN film, presumably along grain boundaries. It appears, therefore, that grain boundary diffusion is rapid compared to the oxidation rate, at least after the first monolayer has reacted.

Acknowledgment

The authors thank P. C. Milner for valuable discussions.

Manuscript submitted March 23, 1983; revised manuscript received May 18, 1983. This was Paper 309 presented at the Washington, DC, Meeting of the Society, Oct. 9-14, 1983.

Bell Laboratories assisted in meeting the publication costs of this article.

REFERENCES

1. F. Shinoki, S. Takada, S. Kosaka, and H. Hayakawa, *Jpn. J. Appl. Phys.*, **19**, 591 (1980).
2. S. Kosaka, F. Shinoki, S. Takada, and H. Hayakawa, *IEEE Trans. Magn.*, **mag-17**, 314 (1981).
3. A. Snoji, F. Shinoki, S. Kosaka, and H. Hayakawa, *Jpn. J. Appl. Phys.*, **20**, L587 (1981).
4. R. B. van Dover, D. D. Bacon, and W. R. Sinclair, *Appl. Phys. Lett.*, **41**, 764 (1982).
5. P. Lefort, J. Desmaison, and M. Billy, *Mater. Res. Bull.*, **14**, 479 (1979).
6. P. K. Gallagher and W. R. Sinclair, *Isr. J. Chem.*, **22**, 222 (1982).
7. P. K. Gallagher, W. R. Sinclair, D. D. Bacon, and G. W. Kammlott, *This Journal*, **130**, 2054 (1983).
8. "Gmelins Handbuch der Anorganischen Chemie," 8th ed., Nb[B1], p. 113 (1970).

The Influence of Back End Processing on the Fixed Charges Density in the Si-SiO_2 Interface

R. M. Levin*,[1]

Bell Laboratories, Murray Hill, New Jersey 07974

ABSTRACT

Variations in the density of fixed surface charges (Q_f/q) at the Si-SiO_2 interface during back end processing steps are reported. After the deposition of phosphosilicate glass (P-glass) films (LPCVD at 630°C, from TEOS, phosphine, and oxygen), Q_f/q measured on aluminum gate capacitors is in the range of $5\text{-}30\times10^{10}$ cm^{-2}. Densification of the P-glass by means of heat-treatment affects Q_f/q in a similar fashion to previously reported post thermal oxidation treatments. The effectiveness of the densification ambient in reducing Q_f/q can be ranked in the order: steam > oxygen > argon > steam + argon. After polycrystalline silicon/aluminum metallization, which involves polysilicon deposition followed by heat-treatment (doping) and aluminum deposition, Q_f/q depends very strongly on the premetallization treatment. When this metallization is applied over undensified glass, Q_f/q can be higher than 1×10^{12} cm^{-2}. It increases with increasing the doping time, the doping temperature, the glass thickness, or the phosphine to oxygen flow rate ratio during the P-glass deposition. Polysilicon/aluminum metallization applied over densified glass yields much lower Q_f/q, with the final Q_f/q value depending strongly on the densification conditions. For example, densification in steam or oxygen at 950°C for 10 min yields Q_f/q of less than 5×10^{10} cm^{-2} after the silicon/aluminum metallization. The results can be explained on a basis of oxygen deficiency in as deposited P-glass films and rearrangement of the Si-SiO_2 interface in the presence of a polysilicon cap film over the glass.

The quality of the Si-SiO_2 interface has been a subject for extensive studies during the last two decades, due to its importance in the MOS (metal-oxide-semiconductor) technology (1). In particular, charges and states in the vicinity of the Si-SiO_2 interface play a significant role in determining the electrical properties of MOSFET's. Although there is a difference of opinion concerning the origin of the surface charges and surface states, it is generally agreed that the main contribution comes from the astoichiometric nature of the interface and from bonds and structure defects in the interface (2). Most of the published works deal with the dependence of the density of the surface charges and surface states on the oxidation process and the post oxidation heat-treatments. Very little is reported on the influence of back end processing steps (after poly gate definition in a standard IC process) on the interface (3-5). In the present work, we concentrate on the influence of P-glass (phosphorus-doped SiO_2) deposition and densification, and polycrystalline sili-

* Electrochemical Society Active Member.
[1] Present address: National Semiconductor Israel Ltd., Herzliya-B, 46103, Israel.
Key words: dielectric, capacitor, glass, anneal, CVD, integrated circuits.

con/aluminum metallization process on the fixed surface charge density (Q_f).

P-glass is widely used in the integrated circuits technology to passivate the devices. The P-glass, which is applied by means of chemical vapor deposition (CVD), usually suffers from nonconformal step coverage (6-8). High temperature heat-treatment (~1050°C) is used to flow the glass in order to smooth its surface (6, 7). This treatment is intolerable in VLSI technology where very shallow p-n junctions in the source and drain are desired. Recently, it has been demonstrated that by using a P-glass deposition process in which tetraethyl orthosilicate (TEOS), phosphine, and oxygen are the reactive gases (to be referred to as P-TEOS glass), an excellent step coverage of the P-glass can be achieved, making the high temperature glass flow unnecessary (8, 9, 10). A moderate temperature (800°-950°C) heat-treatment is still necessary to densify the P-glass in order to increase its resistance to water absorption (11, 12).

A major problem of VLSI circuits, aluminum spiking through shallow p-n junctions into the Si substrate, has led to the use of polysilicon/aluminum structure for metallization (13-15). In this process, a polysilicon layer is deposited at 600°-700°C, and doped at 900°-1100°C before the aluminum metallization.

To study the influence of the three processes, P-TEOS deposition, P-TEOS densification, and polysilicon/aluminum metallization on Q_f, we carried out high frequency capacitance-voltage measurements on silicon/thermal oxide/P-TEOS/aluminum and on silicon/thermal oxide/P-TEOS/polysilicon/aluminum capacitors. We have found considerable variations of Q_f which are induced by the above treatments. The value of Q_f is affected not only by the final heat-treatment given to the sample before the aluminum evaporation, but also by previous treatments as well. The results can be explained qualitatively on the basis of oxygen deficiency in the P-TEOS glass.

Experimental Procedure

Wafers of 0.7-1.0 Ω-cm p-type single-crystal (100) silicon were thermally oxidized at 1000°C to a thickness of 1000Å, and annealed in argon for 15 min at the same temperature. P-TEOS glass was deposited at 630°C in a low pressure CVD reactor (9). The phosphorus oxide concentration in the films was determined from infrared absorption spectra as described by Levin and Adams (9). Unless otherwise noted, the phosphorus oxide concentration is 6 ± 1 mol percent (m/o), and the glass thickness is 5000 ± 500Å. The deposition samples were heat-treated at 700°-950°C in argon, oxygen, or steam ambients (densification). Polysilicon, when it was used, was then deposited by LPCVD at 625°C using SiH_4. It was phosphorus-doped at 950°C from a PBr_3 source, then dip-etched in 50:1 HF for 10 min to remove the P-glass grown on top of the polysilicon. Some samples were annealed in argon after the polysilicon deposition and the polysilicon was stripped using CF_4/O_2 plasma etching. We will refer to the heat-treatment after the polysilicon deposition (PBr_3 or argon ambient) as "polysilicon treatment." Silicon nitride was deposited on a few samples (instead of polysilicon) by LPCVD at 750°C, from SiH_2Cl_2-NH_3. The nitride was etched in hot phosphoric acid after argon annealing.

Typically, capacitors were prepared and measured at three points of the processing; after the P-TEOS deposition ("as-deposited" samples), after the densification treatment ("densified" samples), and after the polysilicon treatment. The samples were annealed in hydrogen at 450°C for 30 min. Aluminum was evaporated on all samples with only the doped polysilicon samples having polysilicon/aluminum gates, and dots of 40 mil diam were photolithographically defined and etched (aluminum in wet chemicals, polysilicon in CF_4/O_2 plasma). Every dot is surrounded by a ring electrode which is used to control the surface potential near the edge of the capacitor in order to prevent the formation of an inversion layer at the silicon surface beyond the field plate. In the presence of such an inversion layer, the capacitance-voltage characteristic is distorted (16), making it impossible to extract the dopant concentration in the silicon from the characteristic. The back surface layers were then removed and aluminum was evaporated to form the back side contact. Some small variations in the sample preparation will be mentioned later.

High frequency (1 MHz) capacitance-voltage measurements were made with a Boonton 72AD capacitance meter connected to a minicomputer-controlled measurement system. The minicomputer determined capacitance values in accumulation and inversion, computed a value for flatband capacitance, and then found the flatband voltage. This procedure was repeated for 36 devices on a wafer, so that statistics could be obtained for fixed charges, oxide thickness, etc. (The work function values used to calculate Q_f were: Al-3.35 eV; N^+-doped poly-3.25 eV; intrinsic Si-3.8 eV.) The distribution in Q_f on a wafer is typically less than ±10%.

Experimental Results

As-deposited glass.—The number of fixed surface charges measured on samples having the 1000Å thermal oxide only, is always in the low 10^{10} cm^{-2} range. After the P-TEOS deposition, the shift in the flatband voltage corresponds to surface charges density of 5-30 × 10^{10} charges/cm^2. There is no clear correlation between the surface charge density and the deposition conditions or the phosphorus oxide concentration (up to 8 m/o). A large distribution in the surface charge density after the P-glass deposition was reported previously by Drobek and Adda (17), who used P-TEOS films deposited at atmospheric pressure as well as silox glass films deposited at reduced pressure.

Densified glass.—To improve their properties, the P-glass films are usually densified by means of heat-treatment (11, 12). At 950°C, the glass is densified during the first 10 min with very small additional effects at longer heat-treatments. Table I presents the dependence of Q_f/q (where q is the electronic charge) on the densification time and the densification ambient. The densification was carried out at a temperature of 950°C in argon, oxygen, and steam. After densification treatment of 10 min, Q_f/q is highest for steam ambient (~3 × 10^{11} cm^{-2}) and lowest for argon ambient (~1.6 × 10^{11} cm^{-2}). Longer dry heat-treatment yields lower Q_f. Further reduction in Q_f/q can be achieved by a two step densification treatment in which densification in steam ambient is followed by a densification in argon (0.5 × 10^{11} cm^{-2}). This is in agreement with the results of Drobek and Adda (17).

To confirm that the charges are located at the Si-SiO_2 interface, we etched off small thicknesses of the glass and measured the shift in the flatband voltage as a function of the glass thickness. (To thin the P-glass, the field plate was stripped, some P-glass was etched, aluminum was evaporated on the sample, and dots were redefined.) We found that the shift is linearly

Table I. Number of charges per cm^2 (Q_f/q) in the Si-SiO_2 interface, after various densification treatments at 950°C (aluminum metallization).

Ambient	Densification time (min)	Q_f/q (10^{10} cm^{-2})
Argon	10	10-17
Argon	60	10
Oxygen	10	23
Oxygen	60	16
Steam	10	28
Steam	60	29
Steam + argon	10+10	9
Steam + argon	10+30	6
Steam + oxygen	10+10	17
Steam + oxygen	10+30	16

dependent on the glass thickness (*i.e.*, the calculated Q_f/q is independent of the glass thickness within 5%) for a thickness range of 0-5000Å. The same flatband shift was measured even after etching 500Å of the underneath thermally grown SiO_2. These results indicate that the charges are indeed located at the Si-SiO_2 interface. Similar measurements and results were obtained on some of the samples reported below.

Polysilicon treatment of undensified glass.—Deposition and phosphorus doping of polysilicon over undensified glass has been found to degrade the quality of the Si-SiO_2 interface. Figure 1 shows that Q_f/q increases from 1×10^{11} cm^{-2}, measured for undoped samples (poly-deposited and immediately stripped before the aluminum metallization), to 1.4×10^{12} cm^{-2} after 60 min doping at 950°C. Q_f/q increases sharply at the first few minutes of the doping and then tends to saturate. Stripping the doped polysilicon layer prior to the aluminum metallization as well as replacing the PBr_3 doping treatment by argon annealing of the samples (and then stripping the polysilicon before the aluminum metallization) do not change these results. The use of an Si_3N_4 film instead of polysilicon has no effect on the results. Doping temperatures lower than 950°C yield lower Q_f/q (Fig. 2). Doping at 700°C for 60 min does not affect the interface. Figure 3 indicates that Q_f/q is linearly dependent on the P-TEOS glass thickness in the polysilicon treatment. Extrapolation of the results to zero glass thickness yields Q_f/q of 1×10^{11} cm^{-2}, which is a typical result measured on as-deposited or argon densified samples. In contrast, Q_f/q is independent of the thickness of the thermally grown SiO_2 (in the range of 0.1-1.0μ).

The dependence of Q_f/q on the glass deposition conditions is summarized in Fig. 4 and 5. In Fig. 4, the phosphorus oxide concentration was changed by changing the phosphine flow rate, while keeping the oxygen flow rate constant. Q_f/q increases slowly with increasing phosphorus oxide concentration up to 5.5 m/o, from which it starts to increase much faster. Figure 5 shows that the important parameter is not the phosphorus oxide concentration but the phosphine to oxygen flow rate ratio during the deposition. Samples containing 3.9 and 7.0 m/o P_2O_5 have almost the same Q_f/q when the phosphine to oxygen flow rate ratio used in the deposition is the same, while samples with similar P_2O_5 concentration (4.6 and 4.7 m/o) show a large difference in Q_f/q (1.0×10^{11} and 1.6×10^{12} cm^{-2}, respectively) when the flow rate ratio is different. It is shown in Fig. 5 that Q_f/q increases with increasing the phosphine to oxygen flow rate ratio.

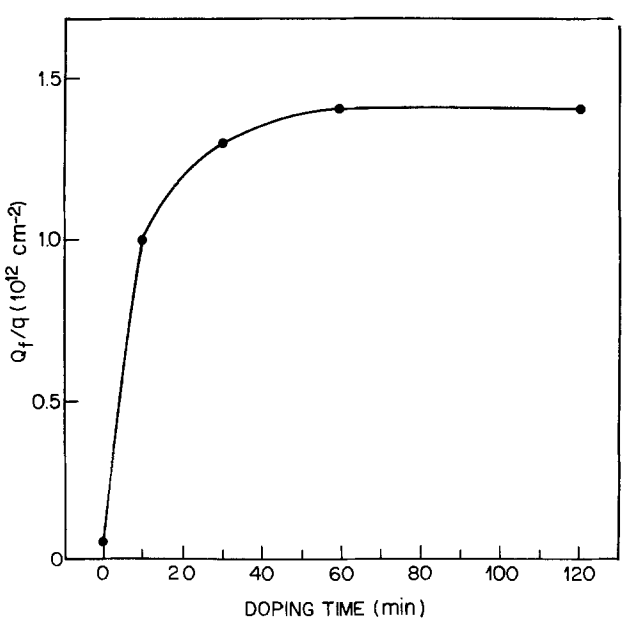

Fig. 1. Q_f/q after polysilicon treatment performed on undensified glass as a function of the polysilicon doping time. The doping temperature is 950°C.

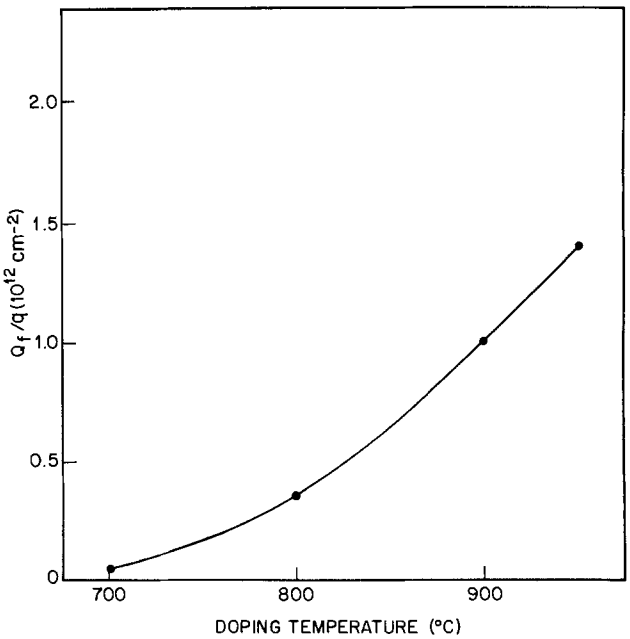

Fig. 2. Q_f/q after polysilicon treatment performed on undensified glass as a function of the doping temperature. The doping time is 60 min.

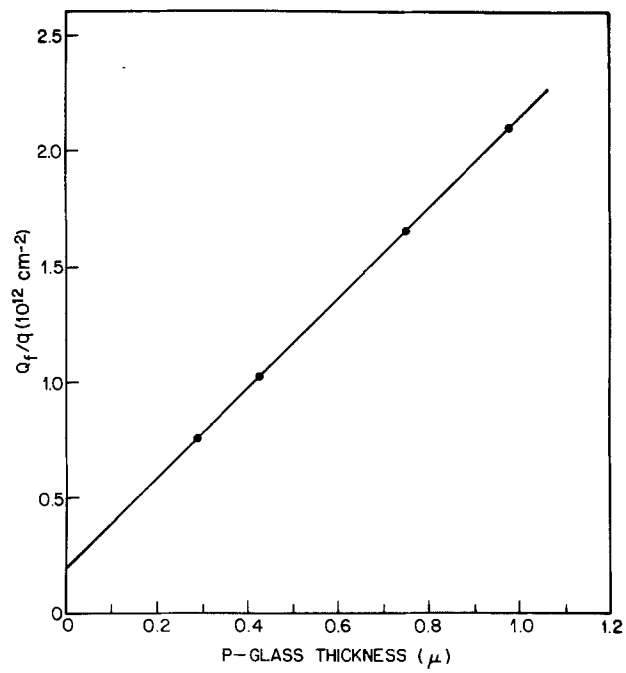

Fig. 3. Q_f/q after polysilicon treatment (950°C, 60 min) performed on an undensified glass as a function of the P-glass thickness.

It should be mentioned here that quality of the Si-SiO_2 interface can be recovered by further heat-treatments. For example, steam annealing of the samples after stripping the polysilicon layer reduces Q_f/q to the low 10^{11} cm^{-2} range.

Polysilicon treatment of densified glass.—Polysilicon treatment carried out on samples having densified P-TEOS glass yielded lower Q_f/q compared to samples having undensified glass. The dependence of Q_f/q on the densification time and the densification ambient is presented in Fig. 6. Polysilicon treatment carried out on glass which was densified in stream or oxygen ambients at 950°C for more than 10 min yielded low Q_f/q

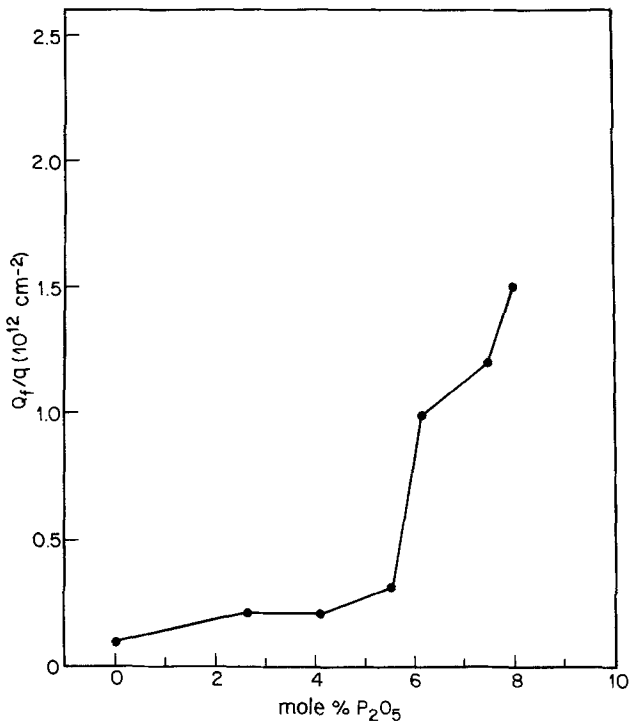

Fig. 4. Q_f/q after polysilicon treatment (950°C, 60 min) performed on an undensified glass as a function of the phosphorus oxide concentration in the glass. The phosphorus oxide concentration is varied by varying the phosphine flow rate, keeping the oxygen flow rate constant (95 cm^3/min).

(3-6 × 10^{10} cm^{-2}). This number is independent of the densification time (if it is longer than 10 min), and the original Q_f/q measured on the as-deposited glass. The influence of densification done in argon is more gradual and depends on the densification time. The dependence of Q_f/q after the poly treatment on the densification temperature is also presented in Fig. 6. It is shown that while steam densification carried out for short time at 850°C is less effective (from the point of view of Q_f/q after the polysilicon treatment) than that carried out at 950°C, they are equivalent after densification of 60 min. After 60 min, the 850°C steam densification is more effective than the 950°C argon densification.

Discussion

Before discussing the experimental results it should be mentioned that two parameters which may affect Q_f have not been monitored in this work; the presence of water molecules in the deposition and subsequent annealing ambients, and the possible presence of carbon monoxide in the glass deposition ambient. It is well known that Q_f is affected by the presence of water species in silicon dioxide (18), and therefore, it depends on the concentration of water molecules in the ambient during heat-treatments. Carbon monoxide may be one of the products in the decomposition of TEOS (8). It was proposed by Fowkes and Hess (19) that CO may remove oxygen atoms from the oxide, and as a result affect Q_f.

It is usually stated in the literature that the surface charge density in the Si-SiO_2 interface is mainly determined by the last oxidation or annealing condition (20). This also has been found to be true up to a certain degree when P-TEOS glass/SiO_2/Si structure is used without the polysilicon treatment (see Table I). Also, the dependence of Q_f on the densifying ambient, Q_f (steam) > Q_f (oxygen) > Q_f (argon) is similar to that reported in the literature (20). However, after the polysilicon treatment, Q_f depends strongly on former heat-treatments (Fig. 6).

One possible explanation for the dependence of Q_f on former heat-treatments given to the sample is that

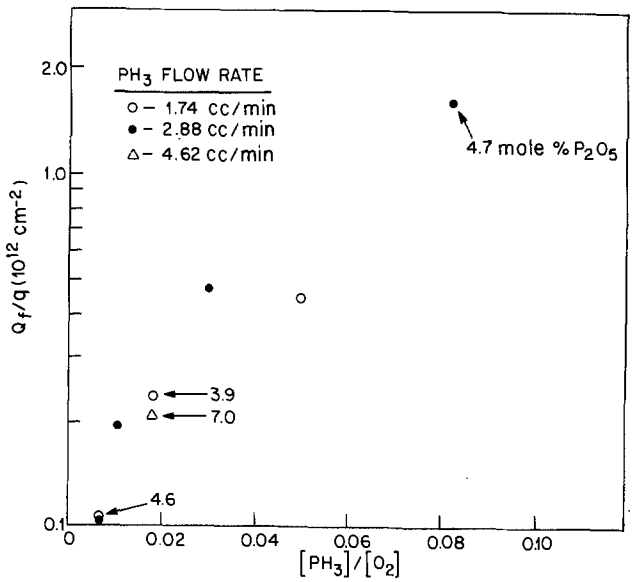

Fig. 5. Q_f/q after polysilicon treatment (950°C, 60 min) performed on an undensified glass as a function of the phosphine to oxygen flow rate ratio in the P-glass deposition.

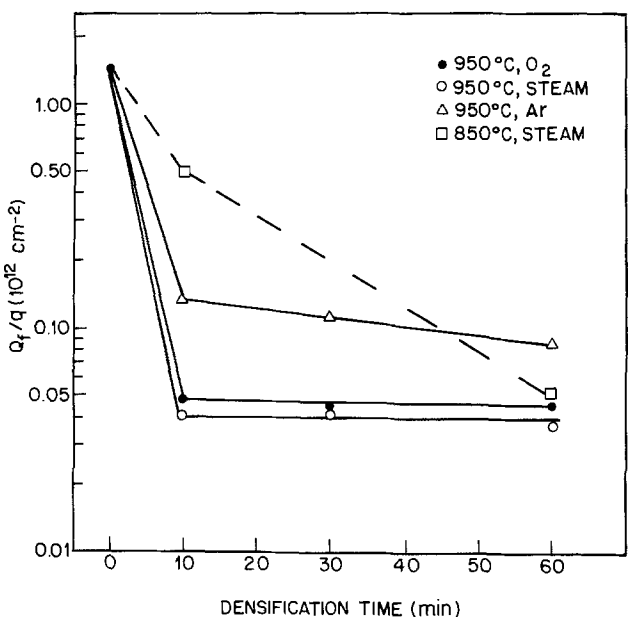

Fig. 6. Q_f/q after a polysilicon treatment (950°C, 60 min) as a function of the P-glass densification time, with densification ambient and densification temperature as parameters.

during the heat-treatment, which is a part of the polysilicon treatment, undensified glass starts to be densified. Since the glass is covered with a polysilicon film, large stresses may be introduced into the Si-SiO_2 interface, and the interface quality degrades. However, this model fails to explain the gradual effect of a prior argon densification on the Q_f/q measured after the polysilicon treatment (Fig. 6). It was reported previously (11, 12) that at 950°C the P-glass densification takes place during the first few minutes of the treatment, when oxidizing ambients as well as inert ambients are used. Also, this model does not explain the strong dependency found between the P-glass deposition conditions and Q_f/q (Fig. 4 and 5).

The increase in Q_f/q with increasing the phosphine to oxygen flow ratio in the deposition (Fig. 5), as well as the effectiveness of the densification done in oxidizing ambients in reducing the Q_f/q after the polysilicon treatment (Fig. 6), indicate that the source of the phenomenon is oxygen deficiency in the P-TEOS glass films. The deposition process of the P-TEOS glass is

described by

$$SiO_4C_8H_{20} \rightarrow SiO_2 + 4C_2H_4 + 2H_2O$$

$$2PH_3 + 4\,O_2 \rightarrow P_2O_5 + 3H_2O$$

It has been reported that if oxygen is not introduced into the system during the deposition, unoxidized phosphorus ions exist in the deposited glass (9). Thus, it is possible that even in the presence of oxygen the oxidation of phosphorus is not completed when the phosphine to oxygen ratio is too high. When the undensified glass is capped with the polysilicon layer and heat-treated, oxygen is reduced from the Si-SiO_2 interface to complete the oxidation of the phosphorus ions and the density of the fixed surface charges increases.

The experimental results presented in this paper can be explained qualitatively on the basis of oxygen deficiency in the P-glass and oxygen reduction from the interface. It is expected that the process of oxygen reduction from the interface will be slower at lower temperatures, which explains the results of Fig. 2. The linear dependence found between Q_f/q and the P-glass thickness (Fig. 3) also becomes clear, because the number of the initially unsatisfied phosphorus-oxygen bonds in the glass depends linearly on the glass thickness (assuming the glass structure is uniform). The more oxygen introduced into the deposition system the less unsatisfied phosphorus-oxygen bonds there will be in the glass, which explains the results of Fig. 4 and 5. The influence of the densification treatment is also explained. The phosphorus oxidation is completed by oxygen ions which are supplied from the ambient in the course of the densification treatment of the uncapped glass. The supply of oxygen from the ambient is slower at lower densification temperatures, and at lower partial pressure of oxidizing species (which is the case of argon treatment). As a result, the influence of the densification treatment done in steam at 850°C or in argon at 950°C on Q_f/q after the polysilicon treatment is more gradual than that of densification treatment done at 950°C in oxidizing ambients.

To further verify the proposed model of oxygen deficiency in the P-glass, oxygen ions were implanted into undensified P-glass (120 keV, 1×10^{14} cm^{-2}), and polysilicon treatment was given to the samples. Indeed, we measured Q_f/q of 1.2×10^{11} cm^{-2} for the implanted samples, as compared to 7×10^{11} cm^{-2} measured for the control unimplanted samples.

Conclusion

The influence of some back end process steps on the density of the fixed surface charges in the Si-SiO_2 interface has been studied. The results can be summarized as follows:

1. Q_f/q varies in the range 5-30 $\times$ 10^{10} cm^{-2} after the P-TEOS glass deposition (aluminum metallization).

2. Densification of the P-glass by means of heat-treatment affects the Si-SiO_2 interface. Q_f/q is a function of the densification ambient and can be ranked as Q_f (steam) > Q_f (oxygen) = Q_f (steam + oxygen) > Q_f (argon) > Q_f (steam + argon). Q_f/q decreases with increasing densification time in dry ambients (aluminum metallization).

3. Q_f/q increases sharply after polysilicon treatment when it is performed on undensified P-TEOS glass films. It increases with increasing doping time (and tends to saturate), doping temperature, glass thickness (linearly), and phosphine to oxygen flow rate ratio during the glass deposition. It is independent of the initial thermal oxide thickness.

4. By densification of the glass in oxidizing ambients prior to the polysilicon treatment, one can achieve low Q_f/q ($<5 \times 10^{10}$ cm^{-2}) after the polysilicon treatment. The effect is very fast for a densification treatment done at 950°C, but more gradual for densification done at lower temperatures.

5. An argon densification ambient (prior to the polysilicon treatment) is not as effective as oxidizing ambients in reducing Q_f/q after the polysilicon treatment.

6. Oxygen implantation into the P-glass prior to the polysilicon treatment is also effective in lowering Q_f/q after the treatment.

7. The experimental results of this work can be explained qualitatively on the basis of oxygen deficiency in the as-deposited P-TEOS glass film, and rearrangement in the Si-SiO_2 interface for capped P-TEOS glass/SiO_2/Si structure.

Acknowledgments

The author wishes to thank W. T. Lynch for his continuing interest and support, and for the suggestion to do the oxygen implantation experiment. Thanks are also expressed to L. P. Adda, J. Drobek, H. J. Levinstein, S. P. Murarka, E. H. Nicollian, and F. Vratny for valuable discussions, E. I. Povilonis for his assistance in the preparation of the samples, and P. Heimann, J. G. Barnes, and T. E. Smith for their help in the electrical measurements.

Manuscript submitted Feb. 14, 1983; revised manuscript received June 6, 1983.

National Semiconductor Corporation assisted in meeting publication costs of this article.

REFERENCES

1. For reviews of the subject see: (a) R. P. Donovan, "Integrated Silicon Devices Technology, Vol. VII, Oxidation," Technical Report No. ASD-TDR-63-316, RTI, June (1965); (b) A. Goetzberger, E. Klausman, and M. J. Schultz, *Crit. Rev. Solid State Sci.*, **6**, 1 (1976); (c) E. N. Nicollian and J. R. Brews, "MOS Physics and Technology," John Wiley & Sons, New York (1982).
2. B. E. Deal, in "Semiconducting Silicon 1977," H. Huff and E. Sirtl, Editors, p. 276, The Electrochemical Society Softbound Proceedings Series, Princeton, NJ (1977).
3. E. H. Snow and B. E. Deal, *This Journal*, **113**, 263 (1966).
4. J. M. Eldridge, R. B. Laibowitz, and P. Balk, *J. Appl. Phys.*, **40**, 1922 (1969).
5. J. M. Eldridge and D. R. Kerr, *This Journal*, **118**, 986 (1971).
6. W. Kern, *R.C.A. Rev.*, **34**, 655 (1973).
7. W. E. Armstrong and B. L. Tolliver, *This Journal*, **121**, 307 (1974).
8. K. Sugawara, Y. Yoshimi, and H. Sakai, in "5th International Conference on Chemical Vapor Deposition," J. M. Blocher, Jr., H. R. Hinterman, and L. H. Hall, Editors, p. 407, The Electrochemical Society Softbound Proceedings Series, Princeton, NJ (1975).
9. R. M. Levin and A. C. Adams, *This Journal*, To be published.
10. J. Drobek and M. K. Becker, Private communication.
11. W. Kern, *R.C.A. Rev.*, **37**, 55 (1976).
12. R. M. Levin, *This Journal*, To be published.
13. R. C. Henderson and G. Nash, Annual Report prepared for Naval Electronic Systems Command under contract N00173-76-C-0144, October (1977).
14. R. K. Wallace, A. J. Learn, and K. W. Schuette, *IEEE ISSCC Tech. Dig.*, 148 (1980).
15. T. Tsujide, N. Yasuoka, T. Tara, K. Tokushinge, N. Hirakawa, S. Matsue, and O. Kurakawi, *IEEE ISSCC Tech. Dig.*, 20 (1981).
16. E. H. Nicollian and A. Goetzberger, *IEEE Trans. Electron Devices*, **ed-12**, 108 (1965).
17. J. Drobek and L. P. Adda, Private communication.
18. E. H. Nicollian and J. R. Brews, "MOS Physics and Technology," John Wiley & Sons, New York (1982).
19. F. M. Fowkes and D. W. Hess, *Appl. Phys. Lett.*, **22**, 377 (1973).
20. B. E. Deal, M. Sklar, A. S. Grove, and E. H. Snow, *This Journal*, **114**, 266 (1967).

Comparative Study of Phosphorescence and Photostimulated Luminescence in Zinc Silicate Phosphors and Their Description by a Tunneling Model

P. Thioulouse, I. F. Chang,* and E. A. Giess

IBM Thomas J. Watson Research Center, Yorktown Heights, New York 10598

ABSTRACT

A tunneling pair recombination model has been proposed to describe the themostimulated luminescence in an earlier paper (1). Under the same concept but assuming two tunneling levels for the electron trap, a description of phosphorescence decay (PP via one tunneling level) and photostimulated luminescence (PSL via a second tunneling level) is presented. Experimental results on PP and PSL for manganese-doped silicates with and without arsenic codoping are reported. A novel method of comparing PP and PSL in the temperature and time domain leads to the determination of energy values of the tunneling states.

In an earlier paper (1) (referred to as I), we studied the thermally stimulated luminescence (TSL) of zinc silicate phosphors and applied a tunneling pair recombination model for its description. We also derived a general expression and a simplified analytical expression for TSL as a function of temperature and correlated them with experimental data obtained from manganese-doped zinc silicate single crystals with or without arsenic codoping. To obtain trap activation energies, one generally applies the so-called Hoogenstraaten method, which analyzes the shift of the TSL peaks with changes in the temperature scanning rate $\beta(T = T_o + \beta T)$. T_m being the temperature of the maximum of a TSL peak, Hoogenstraaten (7) calculated that the slope of the curve $\ln(\beta/T_m^2)$ *vs.* $1/T_m$ would give the activation energy E. In Paper I, we showed that the Hoogenstraaten method, once established assuming that electrons were thermally released into the conduction band, was still valid in the tunneling model, providing that E is defined as the energy of the trap tunneling level above trap ground state. In this paper, using the same tunneling interpretation, we develop a parallel analysis of phosphorescence decay (PP) and photostimulated luminescence (PSL) peak intensity with a two tunneling state model and describe a novel method for quantitatively determining the trap energy levels. The photostimulation effect, described elsewhere (2-4), was introduced in phosphor studies as a means of investigating deep traps. In the two-tunneling state model, we assume that the photostimulation excites the trapped electron to a higher tunneling state whereas the thermostimulation excites to a lower tunneling state as schematically shown in Fig. 1. We present the model first, then report supporting experimental results of PP and PSL measurements carried out on the same zinc silicate samples as the ones used in Ref. (1) and using the experimental setup as illustrated in Fig. 1. The numerical values for the trap energies are then derived.

Identity of Traps Involved in PP, TSL, and PSL

Connecting a coulomb meter to the output of a photomultiplier tube, we measured the total quantity of photons (with Q_{TSL1} a proportionality constant) released during a thermoglow experiment after exposing the Zn_2SiO_4:Mn sample to UV light ($\lambda = 254$ nm) for 2 min at a temperature T_{UV}. We then measured the quantity of photostimulated light Q_{PSL} released during 2 min by 633 nm photostimulation on the same sample at the same temperature T_{UV} after the same UV excitation conditions. Finally, we measured the quantity of light Q_{TSL2} released by thermoluminescence, *i.e.*, by warming the sample up at the same rate as for TSL_1, after red light was removed. For various temperatures of T_{UV} (−190°, −150°, and −100°C, selected because of high photostimulation efficiency), we obtained an invariant relation: $Q_{TSL1} = Q_{TSL2} + Q_{PSL}$. Measurements on a sample codoped with arsenic yielded the same equality. This means that the traps emptied by the photostimulation effect are the very same ones involved in thermal stimulation. Consequently, one may conclude that thermally originated phosphorescence and photostimulated luminescence involve the same distribution of traps. This very important statement emphasizes the interest of comparative measurements of PP and PSL discussed below.

Single Tunneling Level Model

Phosphorescence.—Let us recall the details of the tunneling model presented in I. Long-lived PP is accounted for by the tunneling of trapped electrons towards ionized manganese centers and their radiative recombination with captured holes. The state of the phosphor after UV excitation is characterized by a concentration (5, 6) of ionized pairs: that is pairs with an activator having captured a hole and a trap having captured an electron. This concentration p is a function of the separation R between donor and activator; $p(R, t)dR$ is the number of closest donor-activator ionized pairs which have a separation between R and $R + dR$, $p(R, t)$ may include a "nearest neighbor factor" for large impurity densities. It decays radiatively at a rate

$$\frac{dp(R,t)}{dt} = -p(R,t)W_1(R) \qquad [1]$$

where

$$W_1(R) = A_1 e^{-2R/a} f \qquad [2]$$

The parameter f is the fraction of ionized pairs whose trapping center is in a tunneling state. After UV light removal at $t = 0$, the phosphorescence intensity is given by

$$L(t) = -\frac{dp}{dt}(t) = -\int_0^\infty \frac{dp}{dt}(R,t)dR = \int_0^\infty p(R,t)W_1(R)dR \qquad [3]$$

which is a function of time. At steady temperature and with no photostimulation or excitation, and noting that $\exp - E/kT << 1$, we obtain: $f \cong \exp(-E/kT)$. Therefore, the PP intensity is

$$L_1(t,T) = A_1 e^{-E/kT} \int_0^\infty p(R,t)e^{-2R/a}dR \qquad [4]$$

* Electrochemical Society Active Member.

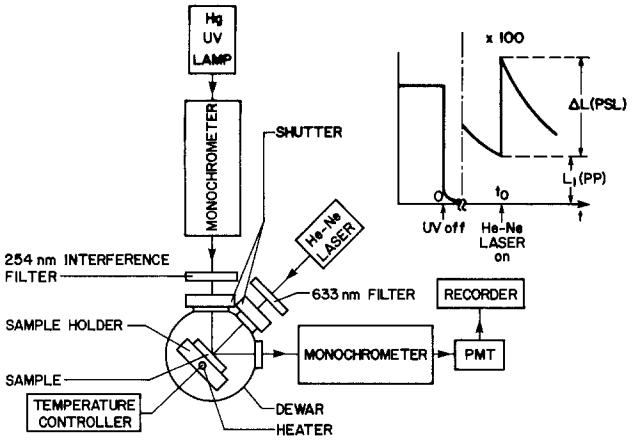

Fig. 1. Apparatus for investigation of PP and PSL

PSL peak intensity.—Let us assume as a first step that, in both thermal PP and optical PSL effects, the trapped electrons are excited to the same tunneling level located at energy E above the ground state of the trap. If, at time t_0 after UV removal, we expose the sample to visible photostimulating light, the overall luminescence is instantaneously raised to a new value L_2

$$L_2(T,I) = A_1 f(T,I) \int_0^\infty p(R,t_0) e^{-2R/a}\, dR \qquad [5]$$

where $p(R)$ is the pair concentration after a t_0 second PP decay and where $f(T,I)$ is the new value under an incident photostimulating light of intensity I. The expression for $f(T,I)$ has been found in Ref. (1) by considering that the trapped electrons are in equilibrium between the ground state and the tunneling state

$$f(T,I) \cong (\exp(-E/kT) + \alpha_1 I/C_1)/(1 + \alpha_1 I/C_1) \qquad [6]$$

In all practical cases, we have $\alpha_1 I/C_1 << 1$. Then, $f(T,I) \cong \exp(-E/kT) + \alpha_1 I/C_1$.

Taking the ratio of PSL intensity, $\Delta L(T,I) = L_2(T,I) - L_1(t,T)$ over PP intensity $L_1(t_0,T)$ at time t_0, we find

$$r = r(T,I) = \frac{f(T,I)}{f(T,0)} - 1 = (\alpha_1 I/C_1) \exp(E/kT) \qquad [7]$$

This ratio is independent of the time t_0 elapsed between UV removal and PSL excitation and can be rewritten as

$$\ln r = \frac{E}{kT} + \ln\left(\frac{\alpha_1 I}{C_1}\right) \qquad [8]$$

Therefore, measuring the ratio r at different temperatures T and plotting $\ln r$ *vs.* $1/kT$ would give a straight line with a slope E, the activation energy of the tunneling level.

The particular interest of this method arises because the ratio r of instantaneous PSL luminescence over PP intensity at the same time cancels the contribution of the pair distribution [the integral in (4) and (5)]; the analytical expression for r does not require any assumption concerning this distribution.

However, using a 633 nm He-Ne laser as PSL excitation source, we experimentally found that, at any temperature, the ratio r was dependent on the time elapsed between UV removal and the red PSL excitation, thereby invalidating our single tunneling level model for the 633 nm PSL effect. This discrepancy can be explained by the significant difference between the He-Ne laser optical energy 1.96 eV and the trap activation energy 0.7 eV as determined by the Hoogenstraaten method (7) (see the section on Experimental Results below). However, this simple single tunneling level should be valid for the PSL effect using an infrared source with optical energy close to the activation energy E. Such experiments are yet to be carried out with a tunable infrared laser.

Two Tunneling Level Model

We shall assume in this section that, although thermal activation and optical stimulation involve the same trap distribution, the PSL activated electrons are excited to a shallower and less localized tunneling state. Let us call E' the energy of the shallower tunneling level above the ground state of the trap and W_2 the corresponding tunneling rate. Let ϵ be the ground state energy of the trap measured with respect to the conduction band. Figure 2 shows the energy band diagram of this model.

PP expression.—PP is occurring from tunneling of electrons from the same trapping state (State 1 in Fig. 2) as in the single tunneling level model. Equations [1]-[4] are still valid. Here we derive a more explicit expression of $L_1(t,T)$ needed for further calculations. Starting from expression [3] for luminescence, the following calculation is very similar to Delbecq's (5) and our analysis in section II.E of I. The PP intensity is

$$L_1(t,T) = \int_0^\infty W_1(R) p(R,t)\, dR$$

$$= \int_0^\infty p_0(R) W_1(R) e^{-W_1(R)t} dR \qquad [9]$$

with

$$p(R,t) = p_0(R) e^{-W_1(R)t}$$

where $p_0(R)$ is the ionized pair concentration when UV light is just removed.

The function $g(R) = W_1(R) e^{-W_1(R)t}$ reaches its maximum at $R = R_c$, *i.e.*

$$W_1(R_c)t = 1$$

or

$$R_c(t) = \frac{a}{2} \ln(A_1 e^{-E/kT} t) \qquad [10]$$

We shall keep the same assumption, the relation [13] in section II.E. of I, that is: $A_1 \exp(E/kT) >> 1\ \text{sec}^{-1}$. Then, for t larger than 1 sec, $R_c(T)$ is much larger than a. In the same manner as in section II.E, one can demonstrate that $g(R)$ is much smaller than $g(R_c)$ outside a "narrow" region of width a around R_c. Assuming that $p_0(R)$ is varying slowly with R compared to $g(R)$, we can take the concentration function out of the integral and obtain

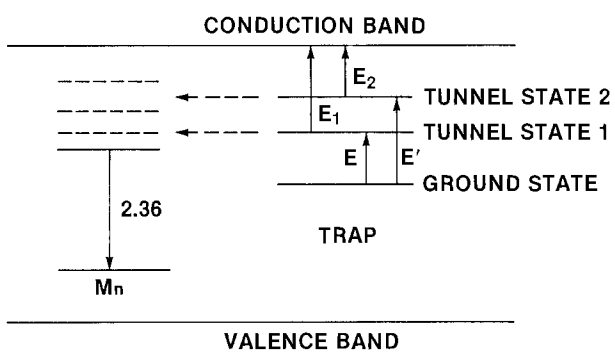

Fig. 2. Energy band diagram for manganese activated zinc silicate (with or without arsenic codoping) in the two tunneling level interpretation of phosphorescence and photostimulated luminescence. Thermally activated electrons are transferred from traps to excited Mn centers through the low energy tunneling state 1 while optically excited electrons are proceeding through the higher and thereby less localized tunneling level 2.

$$L_1(t,T) = p_0(R_c)\int_0^\infty W_1(R)e^{-W_1(R)t}dR \quad [11]$$

Employing an intermediate integration variable $v = e^{-W_1(R)t}$, and using again $A_1 \exp^{-E/kT} >> 1$ sec^{-1} and $t > 1$ sec, we get

$$L_1(t,T) = \frac{a}{2t}p_0(R_c) \quad [12]$$

where $R_c(t)$ is given by [10].

This expression is similar to that obtained by Delbecq (5), except that we keep a nonexplicit term for the pair concentration $p_0(R)$.

PSL peak intensity.—Let t_0 be the time elapsed after UV removal when we apply PSL light and ΔL be the PSL peak intensity at that time. At time t_0, the pair concentration is the one after a PP decay of t_0 sec, that is $p(R,t_0) = p_0(R)e^{-W_1(R)t_0}$. The PSL peak is due to photoexcited electrons tunneling to manganese centers from the shallower tunneling level at a rate $W_2(R)$ and can be expressed as

$$\Delta L(T,I) = \int_0^\infty P(R,t_0)W_2(R,I)dR$$
$$= \int_0^\infty p_0(R)e^{-W_1(R)t_0}W_2(R,I)dR \quad [13]$$

The rate $W_2(R,I)$ is given by

$$W_2(R,I) = A_2e^{-2R/b}f_2(T,I)$$

where b is the radius of wave function for the shallower trap tunneling level overlapping with the manganese ($b > a$) and where f_2 is the fraction of trapped electrons excited to this shallower level. This level, located high above the ground state, is likely to be only populated by photoexcited electrons; therefore

$$e^{-E'/kT} << \frac{\alpha_2 I}{c_2} << 1 \text{ and } f_2(T,I) \cong \frac{\alpha_2 I/C_2}{1+\alpha_2 I/C_2} \cong \frac{\alpha_2 I}{C_2}$$

where C_2 and α_2 are the capture cross section and photoexcitation efficiency associated with the shallower tunneling level. Similar to $g(R)$, the function $h(R) = W_2(R,I)e^{-W_1(R)t_0}$ reaches its maximum at R_d

$$R_d = \frac{a}{2}\left[\ln(t_0A_1e^{-E/kT}) + \ln\left(\frac{b}{a}\right)\right] \quad [14]$$

Assuming the relation in [13] in I as above, and noting that b/a is experimentally found to be of the order of 2, we find that R_d is almost equal to R_c and much bigger than the "width" $a + b/2$ of the function h. Following the same reasoning as in the previous section, we have

$$\Delta L(T,I) \cong A_2\frac{\alpha_2 I}{C_2}p_0(R_d)\int_0^\infty e^{-2R/b}e^{-W_1(R)t_0}dR$$

We define a new integration variable: $w = W_1(R)t_0$. Then: $dw = -\frac{2}{a}wdR$ and the integral becomes

$$G = \int_0^\infty e^{-2R/b}e^{-W_1(R)t_0}dR =$$
$$-\frac{a}{2}(A_1e^{-E/kT}t_0)^{-b/a}\int_{W_1(0)t_0}^0 w^{(a/b)-1}e^{-w}dw \quad [15]$$

where the lower integral limit is much greater than unity. Therefore, we have

$$G \cong \frac{a}{2}(A_1e^{-E/kT}t_0)\,\Gamma\left(\frac{a}{b}\right)$$

and

$$\Delta L(T,I)$$
$$\cong A_1^{-\frac{a}{b}}\frac{a}{2}A_2\Gamma\left(\frac{a}{b}\right)\frac{\alpha_2 I}{C_2}p_0(R_d)t_0^{-\frac{a}{b}}e^{+\frac{a}{b}\frac{E}{kT}} \quad [16]$$

Expression for the ratio $\Delta L/L_1$.—Comparing [10] and [14], we have

$$(R_d - R_c)/R_c$$
$$= \left(\ln\frac{b}{a}\right)\Big/\ln(t_0A_1\exp(-E/kT)) << 1$$

Thus we can assume $p_0(R_d) \cong p_0(R_c)$ and derive the expression for the ratio $r(t_0,T,I) = \Delta L(T,I)/L_1(t_0,T)$ to be

$$r(t_1,T,I) = Kt_0^{\left(1-\frac{a}{b}\right)}e^{\frac{a}{b}\frac{E}{kT}} \quad [17]$$

where $K = A_1^{-(a/b)}A_2\Gamma(a/b)\,\alpha_2 I/C_2$. One notes that, in our tunneling level model, r becomes time-dependent (comparing [17] and [7]). This time dependence is a simple power law as opposed to the case of PP (L_1) and PSL (ΔL) whose individual behavior with time is complicated by factors of $p_0(R_c(t))$ and $p_0(R_d(t))$ with unknown t-dependence.

Experimental application.—Based on the theory above, one can devise the following experimental methods to verify its validity:

Experiment 1—Keeping a steady temperature, measuring the ratio $r(t_0)$ of the PSL peak ΔL over PP intensity L_1 at a time t_0 after UV excitation removal and repeating this experiment at the same UV excitation conditions but for various values of t_0 should give us the time-dependence of r. A plot of $\log r(t_0)$ *vs.* $\log t_0$ should yield a straight line with a slope of $1 - a/b$, thereby determining the value of a/b.

Experiment 2—Repeating the same experiment for a fixed amount of time t_0, but at various temperatures, should give us the temperature dependence of r. A plot of $\ln r(t_0)$ *vs.* $1/kT$ should give a straight line with a slope of $(a/b)E$. Knowing a/b from experiment 1 we can then determine E.

We shall defer the discussion of experimental results to a later section.

A simple quantum analysis.—Let E_1 (and E_2) be the energy depth of the deeper (and shallower) tunneling level with respect to the conduction band. The constants a and b in the tunneling rate expressions are in fact the Bohr radii of the two electron excited levels in the trapping centers. Quantum theory yields that a and b are respectively proportional to $E_1^{-1/2}$ and $E_2^{-1/2}$. Therefore, we have

$$E_1/E_2 = b^2/a^2 \quad [18]$$

From [18] and $\epsilon = E + E_1 = E_2 + E'$ (see Fig. 2), we obtain

$$E_1 = (E' - E)/(1 - a^2/b^2)$$

and

$$E_2 = (E' - E)/(b^2/a^2 - 1) \quad [19]$$

Knowing the values of E and a/b from the experimental method described above and determining the energy E' of the optical excitation separately, one could then obtain the numerical values for E_1, E_2, and ϵ and get a complete and quantitative energy level relationship for the trapping centers.

Experimental Results

The experimental methods described above have been shown to be self-sufficient and to give straight forward values for E and a/b from measurements of the time and temperature dependence of the ratio $\Delta L/L_1$. However, in order to verify their accuracy, we apply the Hoogenstraaten method (validated in the tunneling process scheme in I) to get a fairly accurate value of E from TSL measurements. We then determine a/b from Experiment 1, the time dependence of r, and from Experiment 2, the temperature dependence of r, a second value of a/b which can be compared with

each other to check the validity of our two tunneling level model.

Two manganese-doped zinc silicate single crystals (8) were studied: the first one is codoped with arsenic (2228B, Mn: 0.067 w/o, As: 0.0011 w/o), the second one is arsenic-free (2159°C, Mn: 0.6 w/o). The experimental results are discussed below.

Mn-As codoped sample.—(*i*) Our thermoglow measurements show a well-defined peak at 260 K for various heating rates and the Hoogenstraaten method yields an activation energy E of 0.69 eV as shown in Fig. 3.

(*ii*) We irradiated the sample with a 254 nm Hg line for 3 min and exposed it to a 633 nm He-Ne laser beam 3 min after UV removal ($t_0 = 180$ sec). At time t_0, we measured the PP intensity L_1 (just before red light illumination) and the PSL peak intensity ΔL and calculated the ratio r. The same experiment was repeated every ten degrees from −80° to −10°C. Figure 4 gives an Arrhenius plot of L_1 (PP) and ΔL (PSL) showing their temperature dependence. An Arrhenius plot of r gave a straight line over more than two orders of magnitude as shown in Fig. 5. The slope determines that $(a/b)E = 0.46$ eV. One may point out that the experiment is limited on the high temperature side by the weakness of the PSL signal compared to PP fluctuations. The deviation of the experimental curve from the straight line on the low-temperature side can be explained in the following way: at low temperature, $\ln (t_0 A_1 \exp(-E/kT))$ can no longer be assumed to be much greater than $\ln b/a$ (or unity), R_d can no longer be considered equal to R_c and thus $p_0(R)$ may not be considered as a constant in the integral of the luminescence expression.

(*iii*) Combining the value of $(a/b)E$ found in (*ii*) with the value of E determined by the thermoglow measurements in (*i*), we obtain $a/b = 0.667$.

(*iv*) We selected the temperature −40°C in the straight part of the curve and repeated the same experiment for various times t_0. Log-log plots of PP intensity and PSL peak intensity as a function of time show two different nonlinear curves (Fig. 6). However, the ratio $r = \Delta L/L_1$ displays a power law dependence on time t_0 as $t^{0.28}$ yielding a value of 0.72 for a/b. This is in good agreement with the value (0.667) obtained from the temperature dependence measurements thus confirming the analysis in a previous section.

(*v*) The energy E' of the higher tunneling level of the traps is limited by the He-Ne laser energy which is 1.96 eV, *i.e.*, $E' \leq 1.96$ eV.

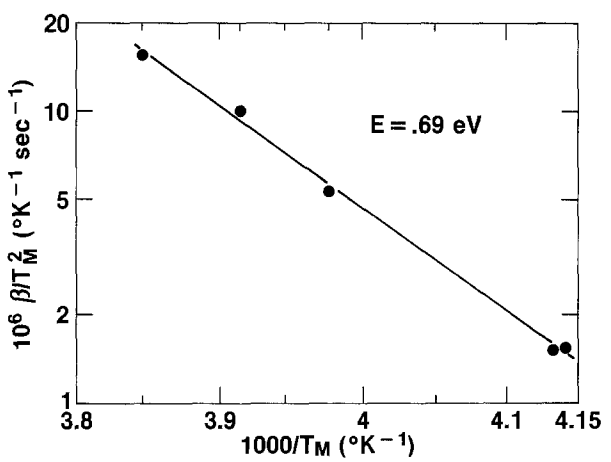

Fig. 3. A Hoogenstraaten plot for the 260 K thermoglow peak of the Zn_2SiO_4:Mn,As sample. We measured the temperature T_M of the TSL peak for various heating rates β. For all thermoglow runs, the sample was irradiated with UV light of 254 nm for 2 min at −190°C. The slope yields the activation energy: $E = 0.69$ eV.

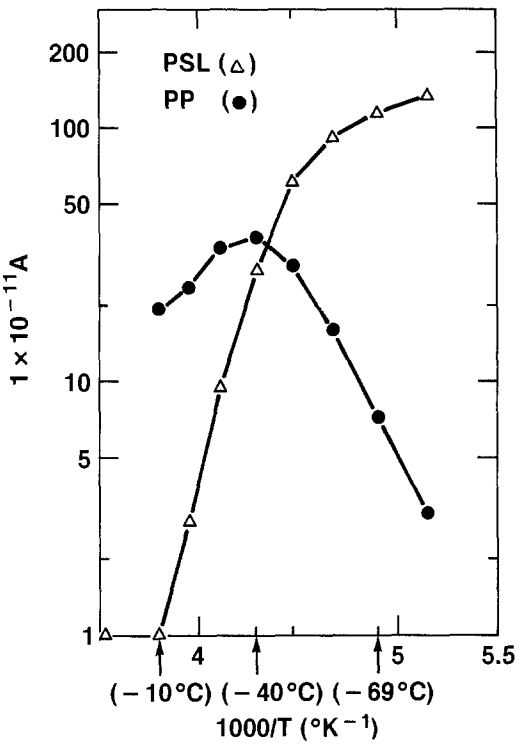

Fig. 4. Temperature dependence of the phosphorescence intensity (PP) measured 3 min after UV exposure was stopped and of the photostimulation luminescence peak intensity (PSL) induced by 633 nm He-Ne light exposure at the same time. The phosphor is Zn_2SiO_4:Mn, As. Conditions of UV exposure are 254 nm light for 3 min.

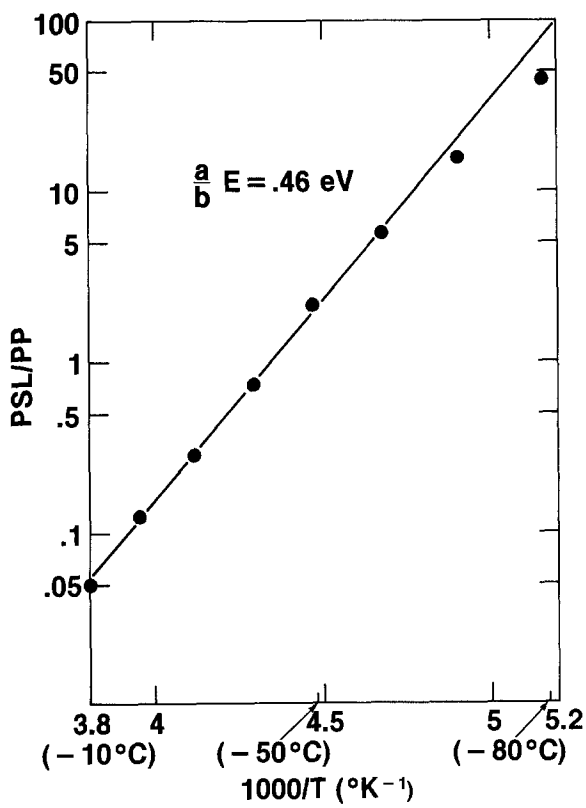

Fig. 5. Temperature dependence of the ratio $r = \Delta L/L_1$ for the Zn_2SiO_4:Mn,As sample. We used the values of ΔL (PSL) and L_1 (PP) plotted in Fig. 3. The slope yields (a/b) $E = 0.46$ eV.

From expression [19], $E = 0.69$ eV and $a/b = 0.667$, we obtain

$$E_1 \leq 2.28 \text{ eV}$$
$$E_2 \leq 1.02 \text{ eV}$$

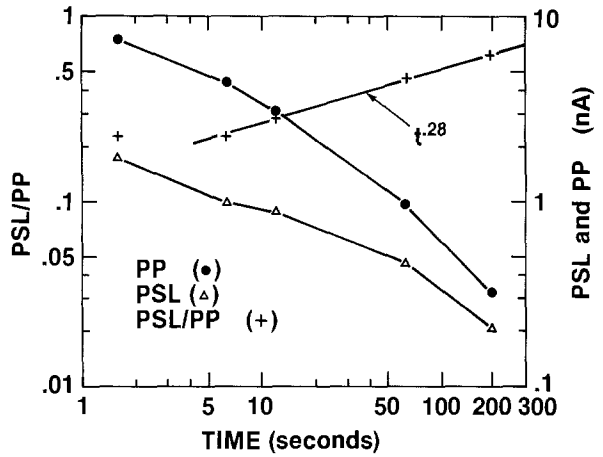

Fig. 6. Dependence of phosphorescence L_1(PP), photostimulated luminescence ΔL(PSL) and ratio $r = \Delta L/L_1$ on time elapsed after UV light is removed (temperature is at −40°C, excitation is 254 nm light for 3 min). The ratio shows a power dependence on time: $t^{0.28}$ which yields $a/b = 0.72$.

This yields a ground state energy for the trap that is equal to or less than 2.97 eV below the conduction band. The precise value of the ground state energy can be determined if one can use a high power tunable light source to determine E' precisely.

Mn doped sample.—(*i*) For this sample, thermoglow measurements show one strong peak, noted 1, at 229 K and another well separated one, noted 2, at 361 K. We did not study the first two TSL peaks (located at 140 and 179 K) because it is difficult to isolate them from the main peak. Again using the Hoogenstraaten method, we obtain an activation energy 0.68 eV for the first peak and 0.96 eV for the second one shown in Fig. 7 and Fig. 8, respectively.

(*ii*) The same experiments as for the Mn-As codoped sample were carried out. Arrhenius plots of PP intensity and PSL peak intensity (Fig. 9) at ($t_0 = 180$ sec after UV removal) show curves similar to those for Mn-As codoped samples (Fig. 7) for the low temperature region though shifted towards lower temperatures. The high temperature TSL peak introduces an additional peak in these curves. Applying the same

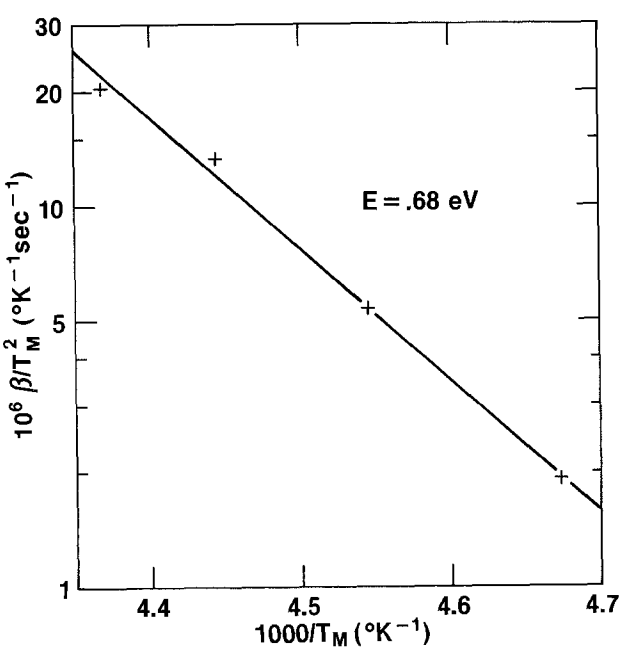

Fig. 7. A Hoogenstraaten plot for the 229 K thermoglow peak of the Zn_2SiO_4:Mn,As sample. We excited the sample with 254 nm UV light for 2 min at −190°C. The slope yields: $E = 0.68$ eV.

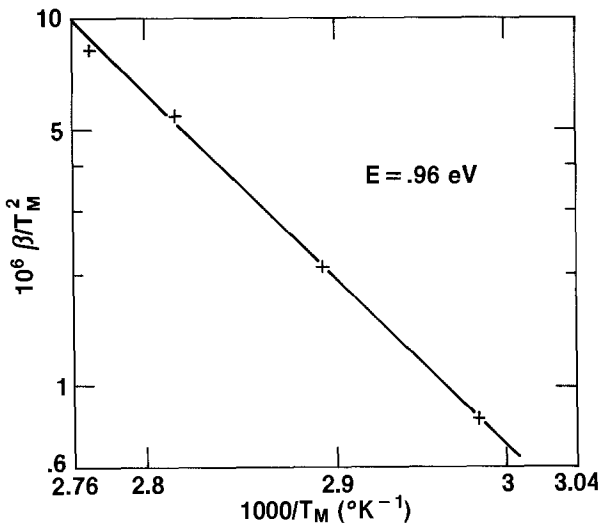

Fig. 8. A Hoogenstraaten plot for the 361 K thermoglow peak of the Zn_2SiO_4:Mn sample (we used the same TSL experiments as in Fig. 7). The activation energy found is: $E = 0.96$ eV.

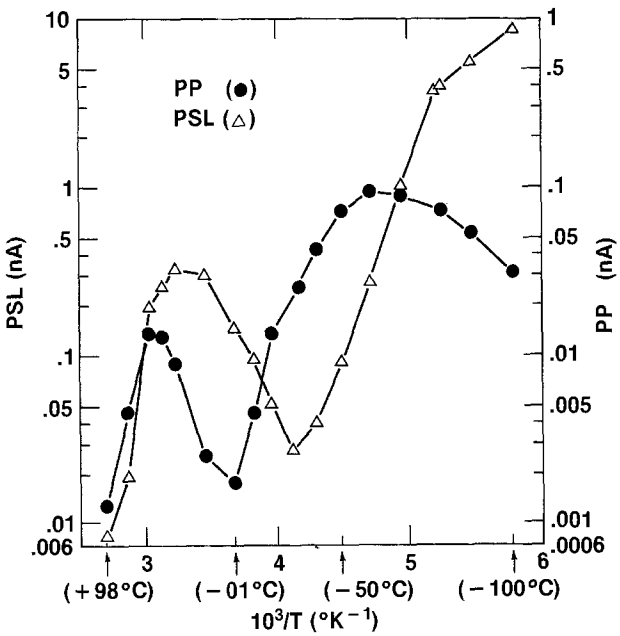

Fig. 9. Temperature dependence of L_1(PP) and ΔL(PSL) for the Zn_2SiO_4:Mn sample. The measurements were carried out in exactly the same conditions as for the sample codoped with arsenic (Fig. 4-6).

method as for the Mn-As codoped sample, the plot of $\ln r$ *vs.* $1/T$ yields a straight line over almost two orders of magnitude in the peak 1 temperature region (Fig. 10) and over one and a half orders of magnitude in the peak 2 region (Fig. 11). In Fig. 10 (peak 1), the data were limited on the low temperature side by interaction with the first two TSL peaks, on the high temperature side by involvement of the higher temperature peak in the PSL effect.

(*iii*) Analysis of peak 1. Plot of the temperature-dependence of r gives: $(a/b)E = 0.45$ eV (Fig. 10). Substituting the value of E (0.68 eV) found in the thermoglow measurements yields: $a/b = 0.662$. A plot of the time dependence of r at $T = -61$°C shows a power law behavior: $r \cong t^{0.23}$ which yields $a/b = 0.77$ (Fig. 12) which again is in good agreement with the first value calculated from the temperature dependence of r.

Similar to section above on an Mn-As codoped sample, taking the red laser energy (1.96 eV) as the

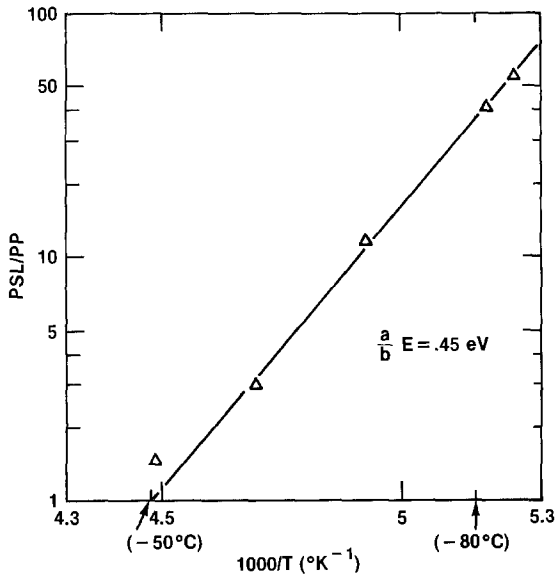

Fig. 10. Temperature dependence of ratio $\Delta L/L_1$ for the Zn_2SiO_4:Mn sample in the TSL peak 1 region. Values were computed from experimental results shown in Fig. 8. The slope determines: (a/b) $E = 0.45$ eV.

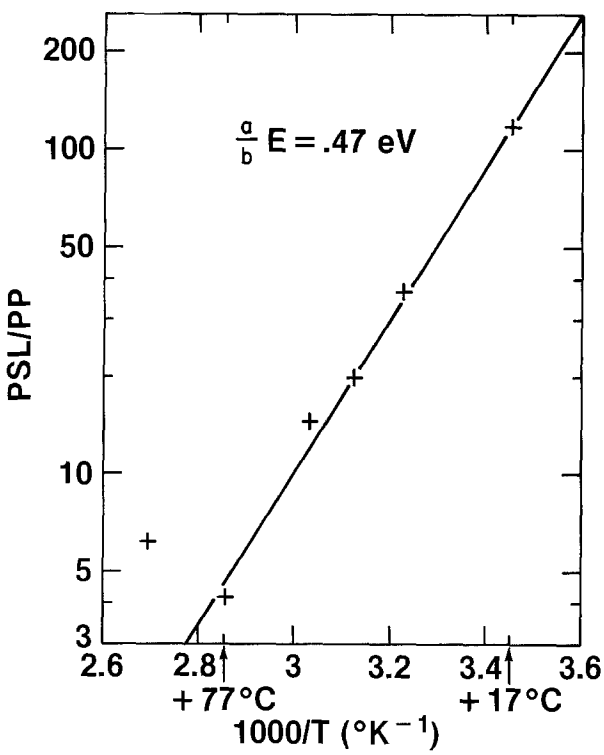

Fig. 11. Temperature dependence of ratio $\Delta L/L_1$ for the Zn_2SiO_4:Mn sample in the TSL peak 2 region. We used the data plotted in Fig. 8. The slope of this curve yields: $(a/b)E = 0.47$ eV.

maximum value for E', $E = 0.68$ eV, and $a/b = 0.662$, we obtain: $E_1 \leq 2.28$, $E_2 \leq 1$ eV, and $\epsilon \leq 2.96$ eV. One notes that these energy values are close to those determined for the Mn-As codoped sample. Moreover, for both samples, there is a similar temperature dependence of r as shown in Fig. 13. These similarities suggest that the traps responsible for PP and PSL observed (peak 1) in the Mn doped sample may be of the same nature as those in the Mn-As codoped sample. Differences in apparent PP and PSL magnitudes and their temperature dependence (compare Fig. 4 and Fig. 9) observed from one sample to the other may be due to very different pair distributions.

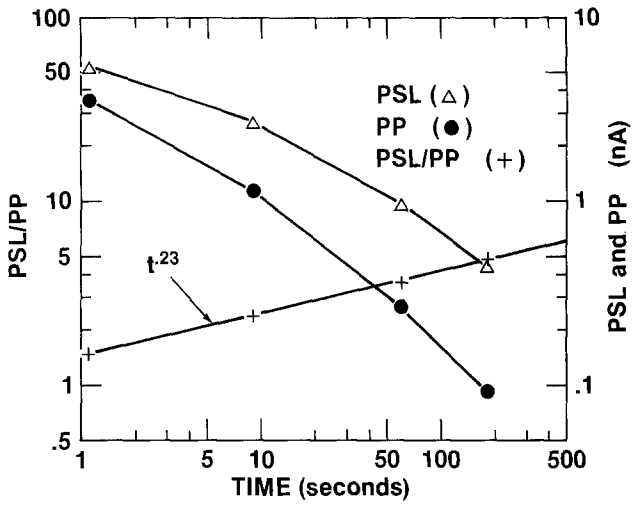

Fig. 12. Time dependence of L_1(PP), ΔL(PSL), and $r = \Delta L/L_1$ for the Zn_2SiO_4:Mn sample. Experimental conditions were similar to the ones of the Fig. 10 measurements. The temperature was at −61°C. The ratio r has a $t^{0.23}$ dependence, which yields: $a/b = 0.77$.

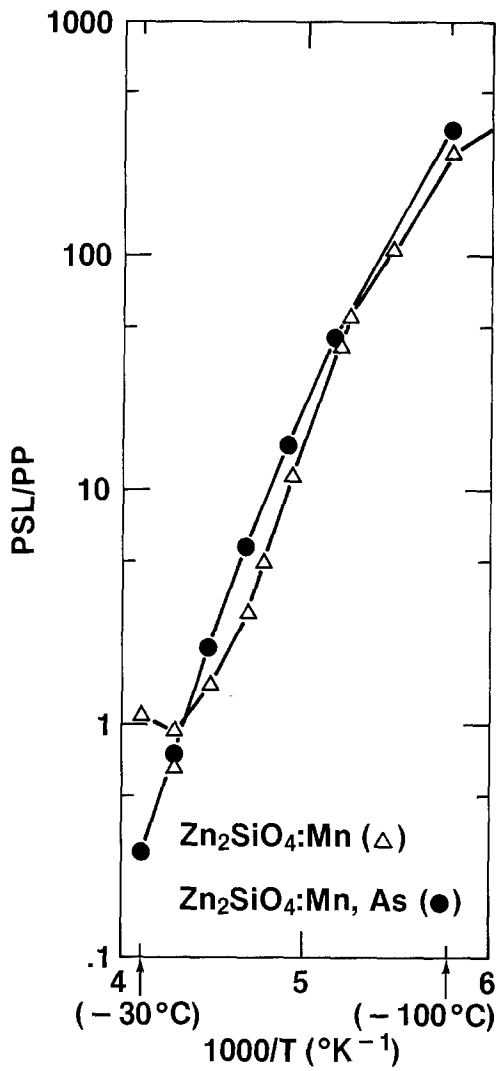

Fig. 13. Temperature dependence of the ratio $r = \Delta L/L_1$ for samples both with and without orsenic codoping. Both curves follow the same pattern over more than two orders of magnitude.

(*iv*) Analysis of peak 2. A plot of the temperature dependence of r for the peak 2 region yields $(a/b)E = 0.47$ eV (Fig. 11). Taking the Hoogenstraaten value of E as 0.96 eV, we obtain that $a/b = 0.49$. However, as

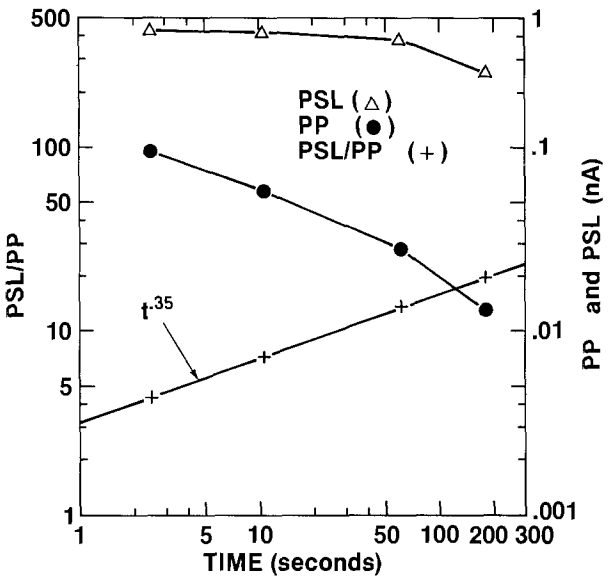

Fig. 14. Time dependence of L_1(PP), ΔL(PSL), and $r = \Delta L/L_1$ for Zn_2SiO_4: Mn sample. Experimental conditions were the same as in Fig. 6 and 12; the temperature was at +47°C. The ratio r displays a power dependence, $t^{0.35}$, leading to $a/b = 0.65$.

shown in Fig. 14, the time dependence measurement at $T = +47°C$ (Fig. 14) yields: $a/b \cong 0.65$. Thus, there is a large discrepancy between the two values ($\cong$ 30%). Furthermore, as one recalls the peculiar behavior of the TSL peak 2 to the variation of excitation conditions (see Fig. 4 and 5 of paper I), one may suggest that the charge transfer from the peak 2 set of trapping centers to luminescent centers is not limited to a tunneling process and may involve the conduction band.

Summary

Using a pair recombination model with two tunneling levels, we carried out a comparative study of PP and PSL in Mn-doped zinc silicate phosphors (with or without As) for 254 nm UV excitation and 633 nm photostimulation. Using a single tunneling level model, one predicts that the ratio r of $\Delta L(\text{PSL})/L_1(\text{PP})$ is independent of time and follows an exp $-E/kT$ temperature dependence (the activation energy E may be obtained from a Hoogenstraaten plot). However this is inconsistent with experimental data which showed a power law behavior for r *vs.* time and an exp $-\alpha E/kT$ dependence of r upon temperature with $\alpha < 1$. We presented a two tunneling level model which could account for both of these experimental t- and T-dependencies of r. Moreover, in this interpretation we could predict, in good agreement with experiment, that t- and T-dependences of r were related to each other by a common parameter a/b, that is: $r(t) = Kt(1 - a/b)$ whereas $r(T) = K' \exp - a/b\ E/kT$. Furthermore, this model yielded, through experimental determination of a/b, a complete energy level diagram of the traps responsible for PP and PSL. We determined numerical values for the depths of trap ground state and tunneling levels which are as follows. For Mn and As codoped sample, $E = 0.69$ eV, $a/b = 0.66$ by temperature dependence data and $a/b = 0.72$ by time dependence data; thus $E_1 = 2.3$ eV, $E_2 = 1.0$ eV, and $E = 3.0$ eV. For Mn-doped sample, $E = 0.68$ eV, $a/b = 0.67$ and 0.77 corresponding to the two methods. The traps present in samples both with and without arsenic are found to be of the same type but with different distribution (we exclude the high temperature set of traps of the sample without As). These results may suggest that arsenic codoping may induce a change in the trap spatial distribution rather than in the nature of the traps themselves. In the limit that the photostimulation energy is the same as the thermostimulation energy, the two tunneling level model should be reduced to a single tunneling level model which can account for the PP and PSL behavior. This should be observable if one uses a tunable light source in the infrared of sufficient intensity.

Acknowledgment

We would like to thank Ms. Sandy Macuirzynski and Ms. Evelyn Margulis for typing this manuscript. One of us (PT) would like to thank the CNET and IBM T. J. Watson Research Center for supporting this work and his one-year stay in the Phosphor Research Group at the IBM Yorktown Heights Research Center.

Manuscript submitted June 25, 1982; revised manuscript received March 15, 1983.

IBM T. J. Watson Research Center assisted in meeting the publication costs of this article.

REFERENCES

1. P. Thioulouse, E. A. Giess, and I. F. Chang, *J. Appl. Phys.*, **53**, 9015 (1982). Also see I. F. Chang and P. Thioulouse, *ibid.*, **53**, 5873 (1982).
2. I. F. Chang and G. A. Sai-Halasz, *This Journal*, **127**, 2458 (1980).
3. I. F. Chang, G. A. Sai-Halasz, and M. W. Shafer, *J. Lumin.*, **21**, 323 (1980).
4. I. F. Chang, P. Thioulouse, E. E. Mendez, E. A. Giess, D. B. Dove, and T. Takamori, Int. Lumin. Conf. Proceeding, Berlin, July 1981; *J. Lumin.*, **24/25**, 313 (1981).
5. C. J. Delbecq, Y. Toyozawa, and P. H. Yuster, *Phys. Rev.*, **B9**, 4497 (1974).
6. P. Avouris and T. N. Morgan, *J. Chem. Phys.*, **74**, 4347 (1981).
7. W. Hoogenstraaten, *Philips Res. Rep.*, **13**, 515 (1958).
8. E. A. Giess, C. F. Guerci, J. D. Kuptsis, I. F. Chang, and D. J. Robbins, *J. Cryst. Growth*, **60**, 219 (1982).

Aspects of GaAs Selective Area Growth by Molecular Beam Epitaxy with Patterning by SiO_2 Masking

A-z. Li

Shanghai Institute of Metallurgy, Shanghai, China

H. Cheng and A. G. Milnes*

Carnegie-Mellon, Institute, Pittsburgh, Pennsylvania 15213

ABSTRACT

The selective epitaxy of GaAs through windows in SiO_2 deposited on semi-insulating GaAs substrates has been studied. Etching of the (100) substrates for planar inlaid deposition may incur problems of irregular nonflat-bottomed profiles to the troughs, and problems of voids after deposition because of the SiO_2 undercutting. It is shown that flat-bottomed holes may be obtained by use of an etch of composition $1H_2SO_4$:$2.5H_2O_2$:$50H_2O$ and that this has a suitable etch rate. The problem of voids because of SiO_2 undercutting may be solved by an extra step that removes the overhangs. Many orientations of patterns were studied on the substrates to confirm the effectiveness of the recommended procedures.

Selective epitaxy is likely to become an increasingly important technology for the fabrication of monolithic gallium arsenide integrated circuits since it opens up the possibility that structures may be made that differ from those currently achieved in GaAs by ion implantation or diffusion processes.

Typically, the selective epitaxy process uses deposited SiO_2 or thermal oxide Ga_2O_3 patterned to form windows on semi-insulating (100) GaAs through which the growth takes place. The GaAs under these windows may be etched to form troughs into which epitaxial GaAs is inlaid or the GaAs may be epitaxially grown on the original substrate surface to form low profile mesa structures. The epitaxy technologies that have been considered are liquid phase epitaxy LPE (1-4), vapor phase epitaxy VPE (5-10), and molecular beam epitaxy MBE (11-20). In MBE, the growth is by impinging thermal energy beams of atoms or molecular species such as As_4 or As_2 onto the heated substrate. The result is that deposition occurs both on the exposed GaAs in the window area where the growth is epitaxial and on the insulator region SiO_2 or Ga_2O_3 where the deposit is fine grain polycrystalline GaAs that is effectively semi-insulating. If the polycrystalline GaAs is very high in resistance, it may be left in place or, if it is unwanted or lower in resistance because of doping during the growth, it may be removed after deposition.

A special feature of the MBE process is that it is a direct line of flight process and therefore in the etch-and-fill technology, epitaxy of monocrystalline GaAs takes place from the bottom of the etched trough and there is virtually no overgrowth problem at the edges of the trough. This is in contrast to LPE and VPE techniques where growth proceeds from the walls inward as well as from the bottom upward. This leads to low quality monocrystalline growth at the perimeter of the trough, facet formation, and a tendency for overgrowth of the edges with rough large grain polycrystalline GaAs. This distorts the size and shape of the effective window and the effect is orientation dependent. Hence LPE and VPE are not good processes unless overgrowth is deliberately being sought, as when burying the metal grid of a permeable base transistor or in the cleaved film process for solar cells.

However, in MBE selective epitaxy by etch-and-fill, there is need to prevent an insulator profile that arises from undercutting and results in the presence of edge voids in the refilling stage. Furthermore, for planar filling, the etched hole must be flat-bottomed. This paper discusses etching and masking procedures that accomplish these ends.

Specimen Preparation

The (100) substrates of GaAs used in the experiments were either Cr-doped or LEC semi-insulating material or conducting substrates with Si or Te doping. A normal organic solvent and acid cleaning procedure was applied and the clean polished surfaces were then coated with SiO_2 by chemical vapor deposition from SiH_4 and oxygen or by sputtering. SiO_2 thicknesses ranging from 3000 to 1000Å were used. Standard photolithographic techniques were applied and the SiO_2 in the photoresist window areas was removed by etching with buffered HF solution.[1]

After a further organic solvent treatment, the substrates on which mesas were to be grown were given an oxide removing etch of 10% HCl and rinsed in deionizing water. The substrates for the etch-and-fill experiments were etched to depths of several microns through the SiO_2 windows with a solution of $1H_2SO_4$: $2.5H_2O_2$: $50H_2O$ at room temperature (these etch proportions are discussed in the section that follows) and rinsed in DI water.

Selective Etching Studies

The surface preparation for the procedure shown in Fig. 1(a) has the aim of merely cleaning the original substrate surface of residual SiO_2, photoresist, and native oxide prior to growth and for this 10% HCl is the acid etch used. For the etch-and-fill technology of Fig. 1(b), the flatness of the bottom of the etched hole is of importance and we have studied this for a number of etch solutions.

The H_2SO_4-H_2O_2-H_2O system is the one most commonly used as a surface polishing etchant for GaAs and this is the one we have concentrated on. The proportions of this etch were found to have a considerable influence on the profile of the etched hole. Shaw (21) has reported that when using the mixture $5H_2SO_4$: $1H_2O_2$: $1H_2O$ for selective etching the bottom of the holes were very nonplanar with the greatest etching occurring near the mask edges. The etching process is considered to be as follows

$$GaAs + 4H_2O_2 = GaAsO_4 + 4H_2O$$

$$2GaAsO_4 + 3H_2SO_4 = Ga_2(SO_4)_3 + 2H_3AsO_4$$

* Electrochemical Society Active Member.

Key words: etching, orientation, semi-insulating GaAs, polycrystalline GaAs.

[1] Supplied by the Transene Company Incorporated, Rowley, Massachusetts, and consisting of a fluoride, bifluoride, and hydrofluoride acid buffer solution. U.S. Pat. 2,732,326.

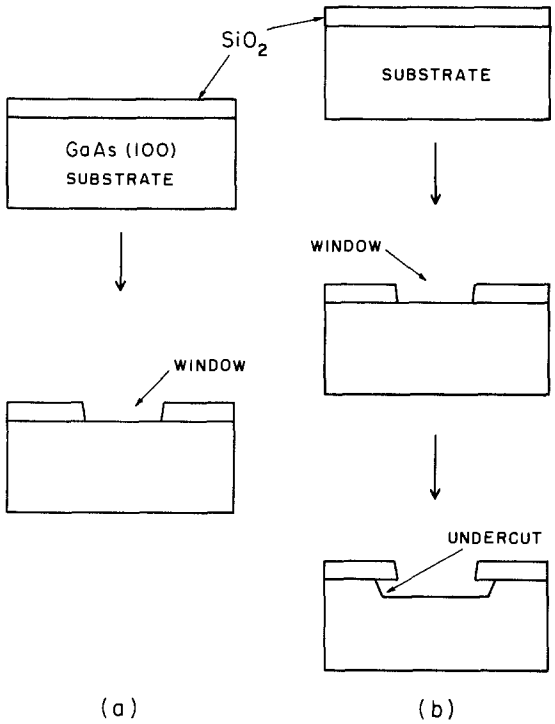

Fig. 1. Structure of specimens for selective epitaxy. (a) For growth on original substrate surface. (b) With etching of the GaAs showing the undercut effect.

These are oxidation and dissolution processes where H_2O_2 is the oxidizer and H_2SO_4 causes the dissolution. The process may be limited either by diffusion rates or chemical reaction rates. Shaw attributes the enhanced etching rates near the mask edge to the surface diffusion of adsorbed moleculars along the protective mask which effectively results in a greater flux of etchant at the mask edge. Improved results were obtained when Shaw used 0.7M H_2O_2-1M NaOH as the etchant. Other etches also have been studied (24-29).

Representative etching profiles in our work as determined by a Sloan Dektak surface profiler are shown in Fig. 2. We see preferential etching at the mask edge of a 25 μm wide window for etches of composition 6:1:1 and 3:1:1. However, for the composition $1H_2SO_4$: $2.5H_2O_2$:$50H_2O$ very flat-bottomed results are obtained, Fig. 2(c). The advantages of low H_2SO_4 solutions have been observed by Iida and Ito (22).

The etched depths *vs.* time for the various solutions are shown in Fig. 3 for (100) GaAs at 30°C. The rate for the preferred $1H_2SO_4$:$2.5H_2O_2$:$50H_2O$ solution is seen to be a convenient 0.38 μm/min and is independent of whether the GaAs is n^+ doped or semi-insulating. The other compositions are rather fast etching and exhibit deeper edges as shown by the bars and the rates are increased by ultrasonic stirring to quite unsuitable values.

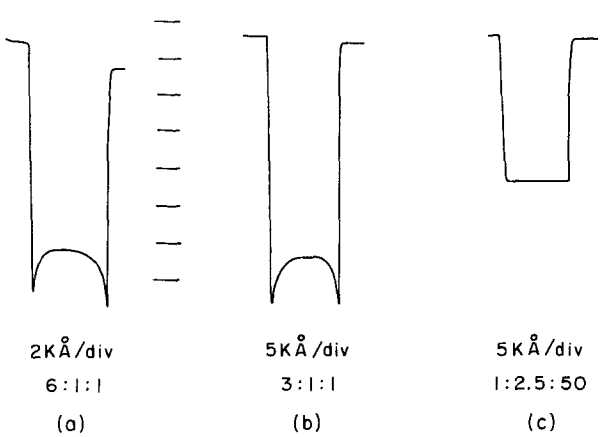

Fig. 2. The flatness of hole bottom after etching GaAs in various composition ratios of the H_2SO_4:H_2O_2:H_2O solutions. (a) 6:1:1, (b) 3:1:1, and (c) 1:2.5:50.

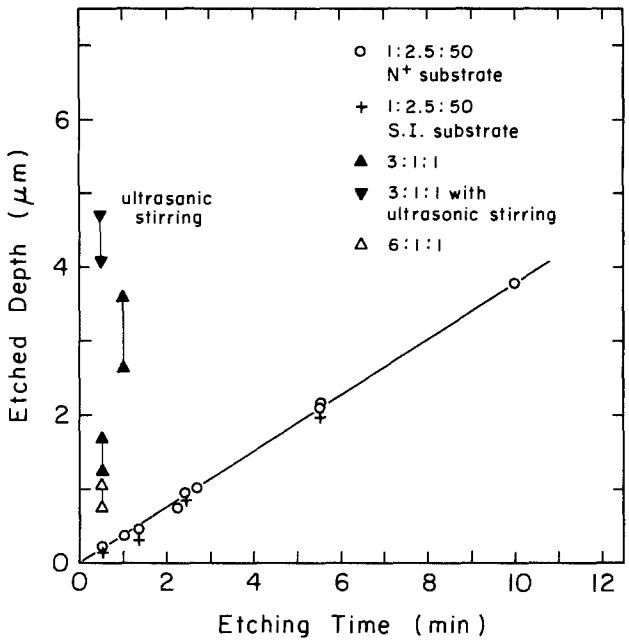

Fig. 3. Etching depth *vs.* etching time in various composition ratios of H_2SO_4:H_2O_2:H_2O and various substrates (n^+ GaAs and SI GaAs) at 30°C. (Error bar lines represent edge effect.)

The effect of temperature was explored as part of our calibration of the 1:2.5:50 etch and is shown in Fig. 4. Since this etch seemed to be a reproducible and very well-behaved one, we used it in our subsequent studies in conjunction with a mask capable of creating many orientations of rectangular windows in the SiO_2 layer.

Selective MBE Growth

The MBE system used was a Perkin Elmer Model 400 and the procedure followed that described else-

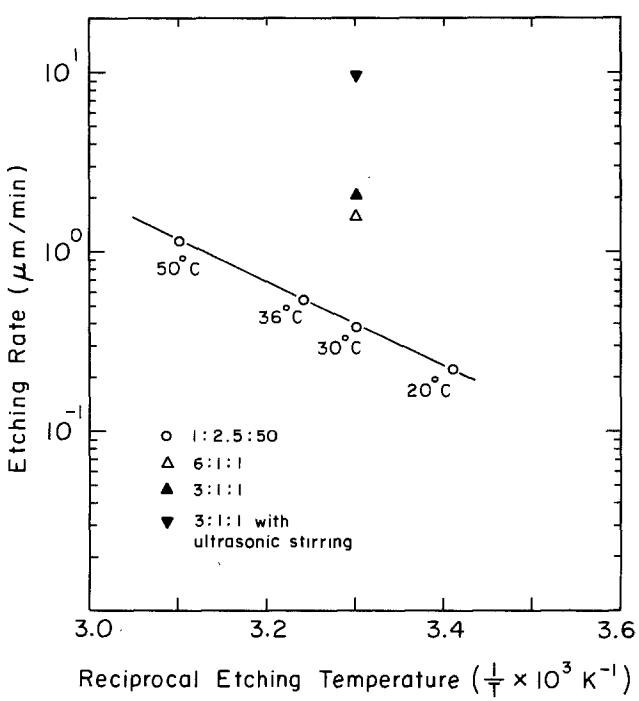

Fig. 4. Etching rate *vs.* reciprocal absolute temperature in various composition ratios of the H_2SO_4:H_2O_2:H_2O solutions.

where (23). The substrates after loading were preheated to about 610°C in the analysis chamber for 5 min to heat clean the surface and then were transferred to the growth chamber. The substrate temperature was 570°C during growth and the arsenic As_4 pressure from an arsenic effusion cell was 4.5×10^{-6} Torr. The Ga oven temperature was 1030°C and the As_4 to Ga flux ratio therefore about 5:1 with a growth rate of about 0.8 μm/hr. Ge was used as the n-type dopant and Be as the p-type dopant in some of the growths.

In one set of growths, no etching of the GaAs substrate was made except a light HCl etch to clean the original surface after the window was opened in the SiO_2 by buffered HF solution, Fig. 1(a). The GaAs ($\sim 10^{16}/cm^3$) deposited in the window was single crystal and that deposited on the SiO_2 was fine-grain polycrystalline material of high resistivity. The window edges showed no signs of faceted over-growth of large grain material unlike the effects seen with LPE and VPE. A scanning electron microscope photograph showing no distortion or overgrowth of the windows of all orientations is shown in Fig. 5.

In the second set of experiments, the GaAs in the window regions was etched with the flat-bottom etch $1H_2SO_4:2.5H_2O_2:50H_2O$ to a depth of typically 2 μm. This procedure, however, results in undercutting of the SiO_2 mask as suggested by the sketch in Fig. 1(b). The result after MBE growth is that voids are left under the overhanging SiO_2 as seen in the scanning electron microscope photograph of Fig. 6. The epitaxial GaAs layer in the window region is seen to be similar in thickness to the GaAs deposition on the SiO_2.

The GaAs undercut action and the effect of the SiO_2 overhang in creating crevasse-like perimeters between the grown epilayer in the window and the surrounding polycrystalline GaAs has been reported previously by Cho and co-workers (11-14, 16). In some applications, this is a desirable effect. For instance, Tsang and Cho point out this could be of value in the fabrication of integrated optics components such as channel optical waveguides.

In other applications such as the incorporation of refilled GaAs regions in semi-insulating substrates for monolithic circuit fabrication, the crevasses are undesirable and a complete fill is required so that metallization may cross as a planar structure. The overhang problem may be solved in principle by making the SiO_2 layer thicker than the overhang.

Removal of the overhanging SiO_2 is then possible by etching in HF (diluted to 20:1) as shown in Fig. 7(a), although this at the same time thins the complete SiO_2 layer. Since the SiO_2 overhang may be several micrometers long (depending on the depth of the etching in the GaAs window area), this procedure usually requires an excessive thickness of SiO_2 to be grown.

A better solution to the problem, we believe, is to leave the SiO_2 protected with photoresist while etching away the SiO_2 overhang from the underside as suggested by the sequence of Fig. 7(b).

We have demonstrated the practicality of this procedure using both Shipley AZ positive photoresist and Kodak negative photoresist and lateral etching with the Transene buffer HF solution. The SiO_2 etching *vs.* time for this solution at room temperature, without stirring or ultrasonic vibration, is shown in Fig. 8 and the rate is observed to be convenient.

After etching away the SiO_2 overhang to the perimeter of the GaAs trough as seen in Fig. 9, the photoresist is still in place and must be removed by solvents before the MBE growth is made. The results after MBE growth show no voids between the trough sides

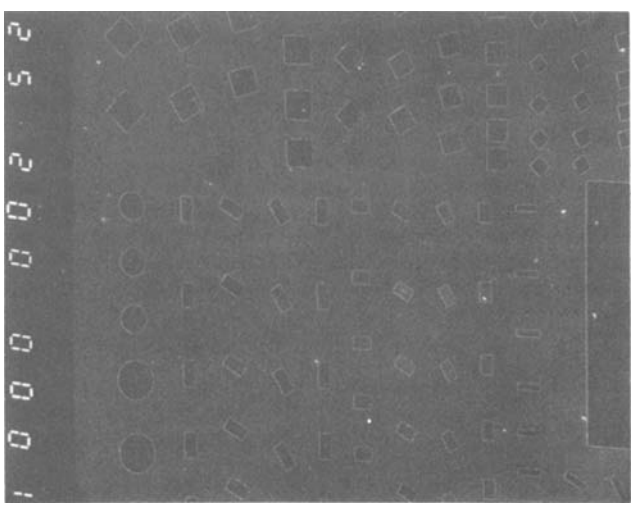

Fig. 5. An SEM photograph that shows the various window orientations in which GaAs has been grown on the original (100) substrate and the absence of any edge growth distorting the window shape.

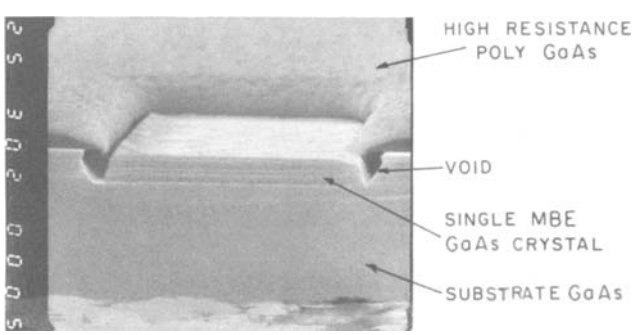

Fig. 6. An SEM photograph of an etch-and-fill growth showing the SiO_2 overhang and the resultant voids between the single crystal GaAs in the window area and the fine grain high resistance GaAs on the SiO_2.

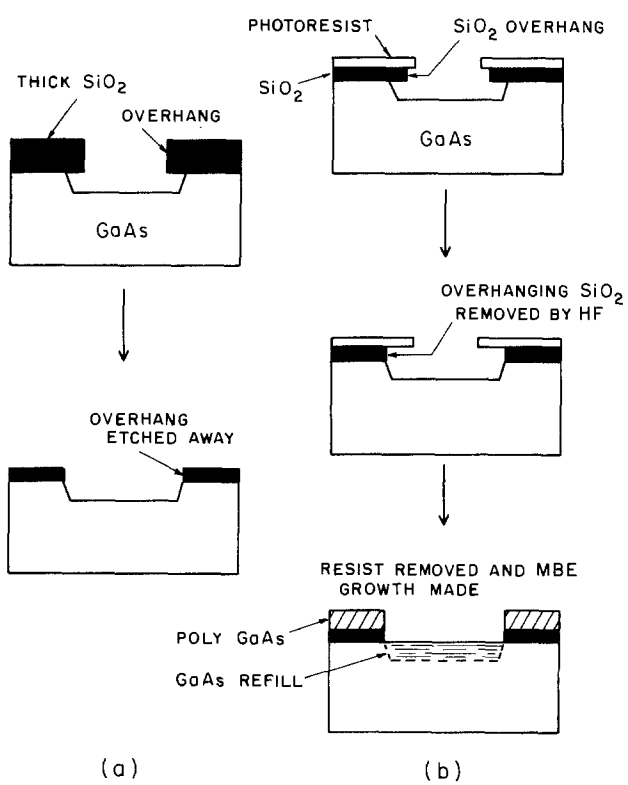

Fig. 7. Procedures for removal of SiO_2 overhang. (a) With thick SiO_2 and HF etching. (b) With thin SiO_2 protected by photoresist.

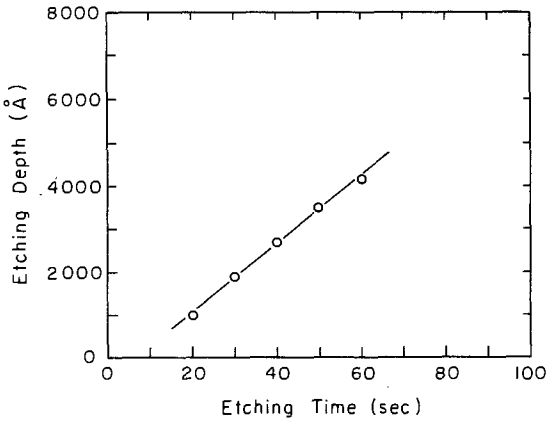

Fig. 8. Etching of SiO_2 vs. time in buffered HF solution

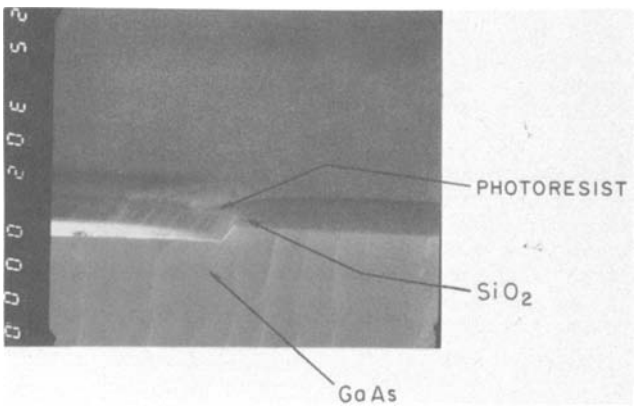

Fig. 9. GaAs trough with SiO_2 overhang etched back to the edge and the photoresist still overhanging.

and the epigrown single crystal GaAs, see Fig. 10. Also there is no sign of facet growth between the GaAs in the window and the polycrystalline GaAs on top of the SiO_2. Depending on the doping of the GaAs in the window, the polycrystalline GaAs may be high enough in resistance to leave in place in some circuit applications. In other applications, it may have to be removed.

Conclusions

The selective etching and selective deposition of GaAs has been studied on (100) substrates.

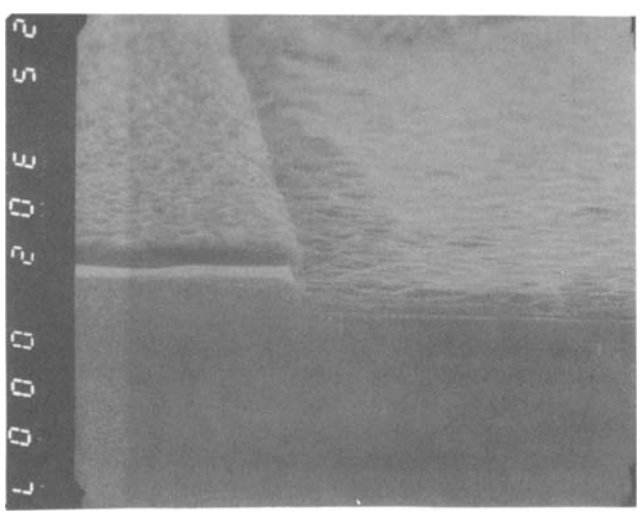

Fig. 10. The specimen of Fig. 9 after MBE growth, showing no voids at the edge between the refill GaAs and the substrate. The masking SiO_2 and the polycrystalline high resistivity GaAs deposited on it are still in place.

An etching solution with $1H_2SO_4:2.5H_2O_2:50H_2O$ composition was found that gives flat-bottomed holes, constant and suitable etching rates, and can be withstood by the photoresist.

Different shape and size patterns were used for selective MBE growth studies. Selective MBE growth does not cause overgrowth and edge distortion effects that are problems in selective LPE and VPE growth.

Etching undercutting effects can cause crevices to occur at the window edge. If these are not desired, they can be eliminated by removal of the SiO_2 overhang with buffered HF solution and the etching rates for this are given.

Acknowledgments

This work was supported in part by NSF Grant ECS 8013773. We wish to thank Shanghai Institute of Metallurgy, Chinese Academy of Sciences for supplying the mask which was used for selective orientation studies.

Manuscript submitted Dec. 4, 1982; revised manuscript received *ca.* April 15, 1983.

Carnegie-Mellon University assisted in meeting the publication costs of this article.

REFERENCES

1. M. M. Piskorski and G. D. Stareev, *Solid-State Electron.*, **18**, 859 (1975).
2. O. Ishihara, M. Otsubo, and S. Mitsui, *Jpn. J. Appl. Phys.*, **16**, 2109 (1977).
3. X. F. Yang, L. Huang, and H. C. Gatos, *This Journal*, **129**, 194 (1982).
4. A. Z. Li, J. H. Qin, and C. C. Li, Symposium on the National Conference on Microwave, Photoelectronic Devices and Compound Semiconductors, Nanjing, China (1979).
5. F. W. Tausch, Jr., and A. G. Lapierre, III, *This Journal*, **112**, 707 (1965).
6. D. W. Shaw, *ibid.*, **113**, 904 (1966).
7. Y. Ishibashi and M. Yamaguchi, *Jpn. J. Appl. Phys.*, **9**, 1007 (1970).
8. Y. Ishibashi and M. Yamaguchi, *ibid.*, **10**, 525 (1971).
9. S. Iida and K. Ito, *J. Cryst. Growth.*, **13-14**, 336 (1972).
10. F. Z. Lu and Y. C. Ding, Symposium on the National Conference on Microwave, Photoelectronic Devices and Compound Semiconductors, Nanjing, China (1979).
11. A. Y. Cho, *J. Appl. Phys.*, **46**, 783 (1975).
12. W. C. Ballamy and A. Y. Cho, *IEEE Trans. Electron Devices*, **ed-23**, 481 (1976).
13. A. Y. Cho, J. V. Dilorenzo, and G. E. Mahoney, *ibid.*, **ed-24**, 1186 (1977).
14. W. T. Tsang and A. Y. Cho, *Appl. Phys. Lett.*, **30** (6), 293 (1977).
15. W. T. Tsang and M. Ilegems, *ibid.*, **31** (4), 301 (1977).
16. W. T. Tsang and A. Y. Cho, *ibid.*, **32** (8), 491 (1978).
17. S. Hiyamizu, K. Nanbu, T. Fujii, T. Sakurai, H. Hashimoto, and O. Ryuzan, *This Journal*, **127**, 1562 (1980).
18. G. M. Metze, H. M. Levy, D. W. Woodard, C. E. C. Wood, and L. F. Eastman, *Appl. Phys. Lett.*, **37** (7), 628 (1980).
19. T. Yao, T. Minato, and S. Maekawa, *J. Appl. Phys.*, **53**, 4236 (1982).
20. P. N. Favennec, L. Henry, A. Regreny, and M. Salvi, *Electron. Lett.*, **18**, 933 (1982).
21. D. W. Shaw, *This Journal*, **113**, 958 (1966).
22. S. Iida and K. Ito, *ibid.*, **118**, 768 (1971).
23. A. Z. Li, S. H. Xin, and A. G. Milnes, *J. Electron. Mater.*, **12**, 71 (1983).
24. Y. Tarui, Y. Komiya, and Y. Harada, *This Journal*, **118**, 768 (1971).
25. J. J. Gannon and C. J. Nuese, *ibid.*, **121**, 1215 (1971).
26. J. Angilello, R. M. Potemski, and G. R. Woolhouse, *J. Appl. Phys.*, **46**, 2315 (1975).
27. W-T. Tsang and S. Wang, *Appl. Phys. Lett.*, **28**, 44 (1976).
28. Y. Mori and N. Watanabe, *This Journal*, **125**, 1510 (1978).
29. D. W. Shaw, *J. Cryst. Growth*, **47**, 509 (1979).

The Relation Between the Correction Factor and the Local Slope in Spreading Resistance

John Albers

Semiconductor Devices and Circuits Division, National Bureau of Standards, Washington, DC 20234

ABSTRACT

Dickey had proposed a technique, known as the local slope method, for the calculation of the correction factor which is used to obtain resistivity profiles from spreading resistance data. The technique is founded upon two asymptotic models for the conduction process involved in the spreading resistance measurement for the cases of (*i*) a conducting layer over an insulating substrate, and (*ii*) a high resistivity layer over a low resistivity or conducting substrate. The results of these two extreme cases are bridged by means of an assumed functional relation between the correction factor and the local slope of the spreading resistance data. This paper examines the two asymptotic models as well as the assumed functional relation between the correction factor and the local slope. It is shown that the asymptotic models adequately describe the behavior of the correction factor for a thin uniform layer over insulating or conducting boundaries. In addition, the single-valued relation between the correction factor and the local slope, which is assumed by the local slope method, is shown not to be an adequate representation of the multiple-valued relation between these two quantities found from multilayer data. For the cases considered, this distinction leads to an error in the resistivities as interpreted by the local slope method by as much as 60%. Nonetheless, the local slope results qualitatively follow the multilayer results thus making the technique a usable one for the calculation of approximate correction factors. A comparison of the two correction factor *vs.* local slope relations provides a basis for the behavior of the interpreted resistivities when they are compared with the input resistivities.

Spreading resistance measurements on bevel-sectioned materials of nonuniform resistivity provide a technique for the determination of the resistivity profiles of these materials. The relation between the spreading resistance, $R(x)$, and the resistivity, $\rho(x)$, is given by the equation

$$R(x) = \frac{\rho(x)}{2a} C(x) \qquad [1]$$

where x is the depth, a is the electrical probe radius, and $C(x)$ is the correction factor which depends upon the details of the underlying resistivity structure and the electrical probe radius. Central to the effective use of this technique is the calculation of the correction factor which provides for the extraction of the resistivity from the spreading resistance. In the calculation of the correction factor, Schumann and Gardner (1, 2) have presented a technique based upon the multilayer solution of the Laplace equation. The focal point of the multilayer Laplace equation analysis is that the correction factor may be expressed as

$$C(x) = 8\int_0^\infty A(x,\lambda)\left\{\frac{J_1(\lambda a)}{\lambda a} - \frac{J_0(\lambda S)}{2}\right\} I_\nu(\lambda a)\, a\, d\lambda \qquad [2]$$

where S is the separation between the probes, $J_0(\lambda a)$ and $J_1(\lambda S)$ are the Bessel functions of zero and first order, respectively, $A(x,\lambda)$ is the kernel of the integral and is related to the resistivity structure, $I_\nu(\lambda a)$ is the Hankel transform of the generalized probe-current density (3), and λ is the integration variable. In the analysis presented here, the origin of the coordinate system is at the substrate so that the variable x increases away from the substrate. The implementation of this technique has been greatly simplified by the recursion relation for the kernel of the correction factor integral as developed by Choo *et al.* (4). The first successful use of this method has been presented by D'Avanzo *et al.* (5, 6) who make use of the recursion relation in conjunction with a partial integral scheme for the kernel of the correction factor integral. More recently, Berkowitz and Lux (7) have greatly simplified the implementation by making use of a 22-point integration scheme.

An alternative technique for the calculation of the correction factor, known as the local slope method, has been presented by Dickey (8, 9). The focal point of this method is the investigation of the behavior of the correction factor for thin layers over insulating or conducting boundaries. By making use of parallel or series conduction models, Dickey has proposed that the correction factor may be related to the local slope of the spreading resistance data, $M(x)$, defined as

$$M(x) = \frac{d \ln R(x)}{dx} \qquad [3]$$

where the derivative is evaluated in the direction of the substrate. This analysis is based upon the asymptotic models for the cases where $M(x) \to +\infty$ and $M(x) \to -\infty$. The behavior of the correction factor as a function of the local slope between these limiting cases is provided for by an assumed single-valued relation between the correction factor and the local slope. This relation is required by construction to yield the parallel and series conduction limits as $M(x)$ becomes large and positive or large and negative. It should be noted that the philosophy of the local slope method is to bypass the integral inversion required by Eq. [2] and focus upon the spreading resistance data directly. In other words, in order to use Eq. [1] and [2], the resistivity is varied until the calculated spreading resistance agrees with the measured spreading resistance to within a given accuracy. The local slope method, on the other hand, employs the value of $M(x)$ to extract $C(x)$ by means of an assumed simple algebraic relation.

Previously, a comparison of the results of the technique of D'Avanzo *et al.* and the local slope technique for correcting model spreading resistance data has been presented (10). There it was found that the technique of D'Avanzo *et al.* gave back the resistivities used in the original model data calculation. The local slope method gave rise to resistivities which qualitatively followed the original resistivities. This agreement was particularly impressive in that the model data was constructed to take the local slope between negative and positive values. The question which naturally arose was whether the local slope equation could be derived from the more general multilayer Laplace equation. In particular, the possibility of the local slope equation being the first-order form of a more general equation relating the correction factor to the local slope was considered.

The purpose of this paper is to address this question and to show that the more general multilayer Laplace

equation does not admit to a single-valued relation between the correction factor and the local slope. In general, the multilayer equation gives rise to a multiple-valued relation between the correction factor and the local slope, which implies that the local slope is not a good variable in which to express the correction factor. Nonetheless, the local slope relation does fall in the region of the curve given by the multilayer equation. This behavior provides a basis for the understanding of why, for example, the resistivities interpreted by local slope are sometimes larger than and sometimes smaller than the original resistivities.

The Local Slope Method

The first of the asymptotic models used in the local slope derivation is that of the parallel conduction model. This is assumed to correctly describe the conduction mechanism in a thin nonuniform layer over an insulating substrate. In this model, the conduction is assumed to take place in parallel through the sublayers between the probes (akin to the model used in sheet resistance measurements). In both this model and the series conduction model, the conductivity (or resistivity) is assumed to be constant over the thickness, $\Delta x = t$, of the sublayer. The conductivity at the position x in the structure (measured from the insulating boundary) is then related to the differences between the inverses of the spreading resistances (or spreading conductances) at the positions x and $x - t$ according to

$$\sigma(x) = \frac{\ln (S/a)}{\pi t} \left\{ \frac{1}{R(x)} - \frac{1}{R(x-t)} \right\} \quad [4]$$

where $R(x)$ and $R(x - t)$ are the spreading resistances at the positions x and $x - t$, respectively. The corresponding relation between the correction factor and the local slope of the spreading resistance is

$$C(x) = K_1 M(x) \quad [5]$$

where the local slope of the spreading resistance, $M(x)$, is given by Eq. [3] and

$$K_1 = \frac{2a \ln (S/a)}{\pi} \quad [6]$$

The second asymptotic model, known as the series conduction model, is assumed to hold for the conduction mechanism in a thin nonuniform layer of high resistivity over a conducting substrate. In this model, the conduction through the high resistivity material is viewed as taking place through a cylinder of radius a until the conducting substrate is encountered where the current is shorted to the second cylinder under the second probe. For this case, the model would predict that the resistivity at the position x is related to the differences between the spreading resistances at the positions x and $x - t$ according to the relation

$$\rho(x) = \frac{\pi a^2}{2t} \{R(x) - R(x-t)\} \quad [7]$$

The corresponding relation between the correction factor and the local slope of the spreading resistance is

$$C(x) = -\frac{K_2}{M(x)} \quad [8]$$

where

$$K_2 = \frac{4}{\pi a} \quad [9]$$

and $M(x)$, the local slope, is defined by Eq. [3].

For most cases of physical interest, the resistivity structure will lie somewhere in between those used in the parallel and series conduction models. For the intermediate cases, the local slope method assumes that it is possible to express the correction factor as a single-valued function of the local slope. In particular, this single-valued function is required to reduce to Eq. [5] as $M(x) \to +\infty$ and to Eq. [8] as $M(x) \to -\infty$. The general form of the function which is proposed to satisfy these requirements is given by

$$C(x) = \frac{K_1 M(x)}{2} + \left\{ \left\{ \frac{K_1 M(x)}{2} \right\}^2 + \kappa \right\}^{1/2} \quad [10]$$

The three commonly used forms of the function, κ, include: (*i*) $\kappa = K_1 K_2$, (*ii*) $\kappa = 1$, and (*iii*) $\kappa = K_3$, where

$$K_3 = 1 + \{K_1 K_2 - 1\} \frac{2}{\pi} \tan^{-1} \left\{ \log \frac{R(x)}{R(x-a)} \right\} \quad [11]$$

where $R(x)$ is the spreading resistance of the point being considered and $R(x - a)$ is the spreading resistance one probe radius deeper into the structure. It should be obvious that the above forms of κ in the relation between the correction factor and the local slope are arbitrary, subject only to the limiting conditions where $M(x) \to +\infty$, $M(x) \to -\infty$, and $M(x) \to 0$. In particular, the first form, *i.e.*, $\kappa = K_1 K_2$, gives rise to the correct asymptotic results in the limits as $M(x) \to +\infty$, $M(x) \to -\infty$ but does not give rise to a correction factor of unity when the local slope is zero. The second form, *i.e.*, $\kappa = 1$, does not yield the asymptotic model results exactly but does reproduce a correction factor of unity for a zero value of the local slope. The third form, *i.e.*, $\kappa = K_3$, is an attempt to remedy both of these situations. However, as has been shown previously (10), this particular form has a difficulty of yielding very large resistivities (very small correction factors) in the regions where the local slope is large and negative. As indicated previously, the purpose of the present paper is to investigate the validity of Eq. [5], [8], and [10] in terms of the spreading resistance calculated from the multilayer Laplace equation.

Calculations

Test of asymptotic models.—The first set of calculations to be discussed addresses the validity of the two asymptotic models embodied in Eq. [4] and [7]. In particular, if these are adequate descriptions of the conduction processes in these two extreme cases, then their validity should be easily checked in the cases of uniform layers over insulating or conducting boundaries. For the case of a uniform layer over an insulating boundary, it is straightforward to show from Eq. [1] that Eq. [4] reduces to the form

$$\frac{2a \ln (S/a)}{\pi t} \left\{ \frac{1}{C(x)} - \frac{1}{C(x-t)} \right\} = U_{\text{ins}}(x) = 1 \quad [12]$$

Also, for the case of a uniform layer over a conducting boundary, Eq. [7] reduces to the form

$$\frac{\pi a}{4t} \{C(x) - C(x-t)\} = U_{\text{con}}(x) = 1 \quad [13]$$

In order to test Eq. [12] and [13], model spreading resistance data were generated for the cases of a uniform layer over an insulating boundary and a conducting boundary, respectively. In all cases, a probe radius of $a = 2$ μm was used. For these two situations, the kernel of the spreading resistance correction factor integral (as given by Eq. [2]) is of the form $A(\lambda x) = \coth(\lambda x)$ and $A(\lambda x) = \tanh(\lambda x)$, respectively (7). In addition to using each of these two forms of the kernel, the correction factor calculations made use of several forms of the probe-current density (3). The results of these calculations are presented in Fig. 1-4.

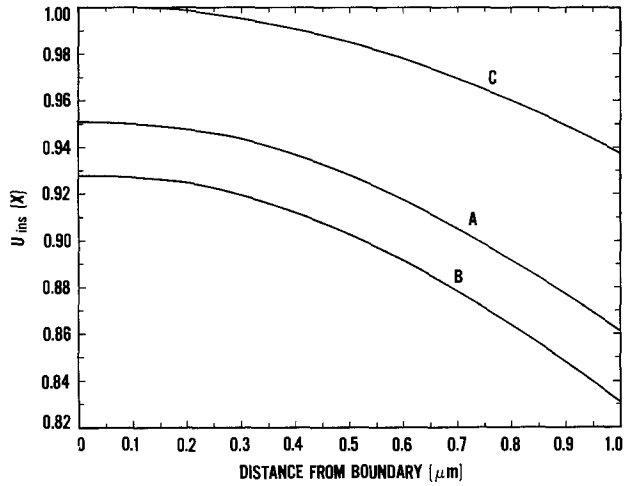

Fig. 1. Behavior of the left-hand side of Eq. [12] for the case of a uniform layer over an insulating boundary. The curves corresponding to the three current densities are as follows: Schumann and Gardner (A); Choo uniform (B); and ring delta function (C). The specific value of the probe spacing is $S = 50$ μm.

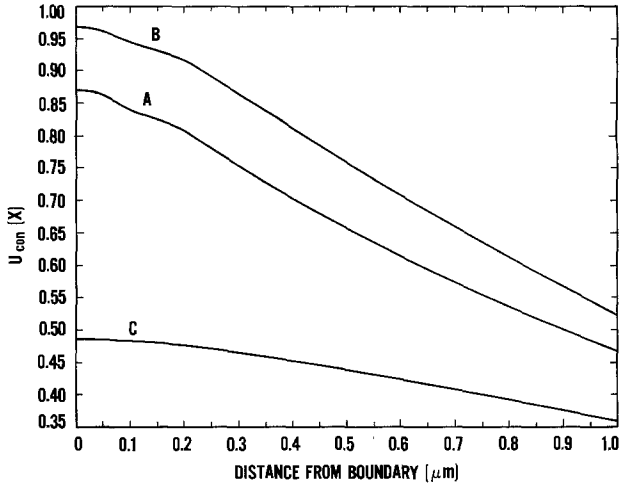

Fig. 3. Behavior of the left-hand side of Eq. [13] for the case of a uniform layer over a conducting boundary. The curves corresponding to the three current densities are as follows: Schumann and Gardner (A); Choo uniform (B); and ring delta function (C). The value of the probe separation used is $S = 50$ μm.

In Fig. 1, the left-hand side of Eq. [12] is plotted as a function of the distance from the insulating boundary for the three current densities and for a value of the probe separation, $S = 50$ μm. In particular, the three probe-current densities which were used were the Schumann and Gardner, the Choo uniform, and the ring delta function forms. These current densities and their extent of current constriction are discussed in detail elsewhere (3). These three forms of the current density gave rise to the curves denoted by A, B, and C, respectively. It is clear that the ring delta function results yield a value of unity for this situation. In Fig. 2, the ring delta function current density results are presented for several values of the probe separation. For small distances from the boundary, all values of S yield identical results. For large distances from the insulating boundary, the agreement improves with increased values of S as might be expected from the similarity of the model with the sheet resistance model. For the case of a conducting boundary, the plots presented in Fig. 3 represent the left-hand side of Eq. [13] for the three forms of the probe current density for a value of $S = 50$ μm. The Choo uniform current density clearly yields the best results. In addition, the behavior of the uniform current density results for several values of S is presented in Fig. 4. It is clear that the results are independent of S as would be expected from the nature of the conduction mechanism.

From this analysis, it can be concluded that the asymptotic models contain the correct conduction mechanisms for thin uniform layers. In addition, the two asymptotic models are in agreement with the forms of the probe current densities which would be assumed to describe the current flow pattern at the probe-material interface. The insulating boundary causes current constriction and allows current flow only at the perimeter of the probe while the conducting boundary allows current flow to be approximately uniform over the entire area of the probe-material interface.

Correction factor-local slope relation for nonuniform layers.—While the above analysis indicates that the two asymptotic models provide a good description of the conduction process for the appropriate boundary

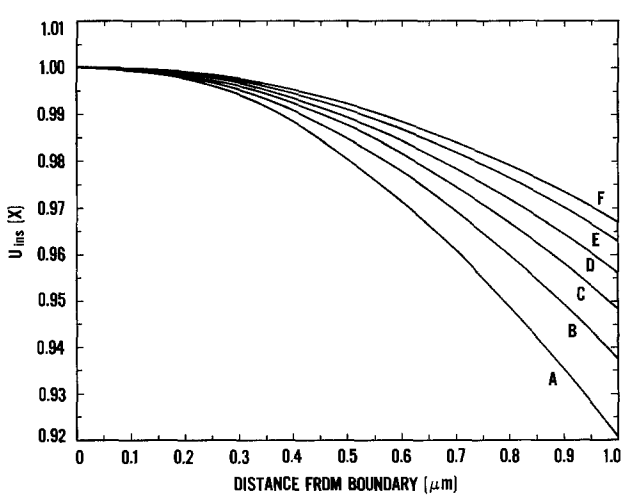

Fig. 2. This figure depicts the behavior of the left-hand side of Eq. [12] for the ring delta function current density for several values of the probe separation. The specific values of the probe separation are as follows: 25 μm (A); 50 μm (B); 100 μm (C); 200 μm (D); 500 μm (E); and 1000 μm (F).

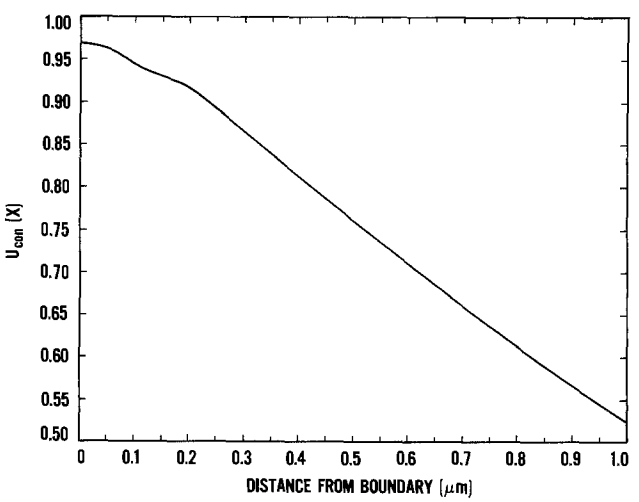

Fig. 4. This figure depicts the behavior of the results of Eq. [13] for a uniform layer over a conducting boundary for the Choo uniform current density. The curves for the values of the probe spacing used (25, 50, 100, 200, 500, and 1000 μm) all lie on top of each other. This indicates that the correction factor and, hence, the spreading resistance, is independent of the probe spacing. This is contained in the fact that the dominant contribution is the series conduction through the top layer.

conditions, the most important question focuses on the validity of the assumed single-valued relation between the correction factor and the local slope. In order to test the validity of this relation, model spreading resistance data were used. In particular, resistivity profiles typical of implant structures were employed in this investigation. The correction factor and the spreading resistance were calculated according to the Laplace multilayer equations (10) as given by Eq. [2] and [1], respectively. The local slope was then obtained from Eq. [3] and was used in Eq. [10] to obtain the corresponding local slope results. Typical resistivity results obtained for $\kappa = K_1K_2$ are contained in Fig. 5. In addition, typical results of the correction factors as a function of depth are presented in Fig. 6. It is clear from Fig. 5 that the resistivity profile obtained by the local slope method semiquantitatively agrees with the resistivity used in the multilayer method. However, there does appear to be an inconsistency in the way in which the resistivity is obtained. This is borne out by the corresponding correction factor plots presented in Fig. 6. In particular, from Fig. 5 it can be seen that there is a region up to about 0.3 μm where the local slope results are larger than the input resistivities and a region past 0.3 μm where the local slope results are smaller than the input resistivities. The reason for this nonsystematic difference can be explained by comparing the correction factor *vs.* local slope results obtained from the local slope method and from the multilayer calculations. A comparison of this type is presented in Fig. 7. The local slope results, denoted by B, are seen to be single-valued, *i.e.*, for a given value of the local slope there is only one value of the correction factor. On the other hand, the multilayer results, denoted by A, show a multiple-valued behavior, *i.e.*, for a given value of the local slope there is no unique value of the correction factor. Indeed, the feature of the multilayer curve which is most striking is that the correction factor depends upon the location along the profile. It is clear that up to about 0.3 μm, the local slope correction factor is smaller than the multilayer value, thus making the local slope resistivity larger than the input values. Beyond 0.3 μm, the local slope correction factor is larger than the multilayer value thus making the local slope resistivity smaller than the input values. In fact, the local slope curve lies in the same region of the correction factor-local slope plane as the multilayer curve. It is this fact which makes the

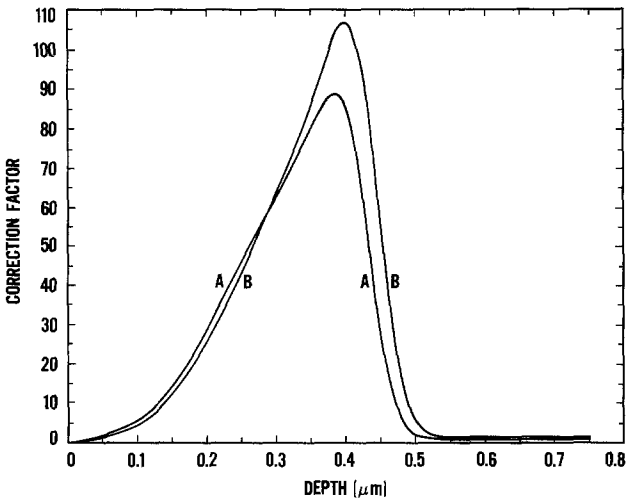

Fig. 6. This figure contains the correction factor as a function of depth as obtained from the multilayer equations (curve A) and from the K_1K_2 form of the local slope equation (curve B). The multilayer results are obtained from the input resistivities used in the multilayer equations while the local slope results are obtained from the local slope analysis of the calculated spreading resistance data. Note that the plot is not logarithmic along the y-axis. The correction factors in the region near the origin are less than unity, being on the order of 0.1.

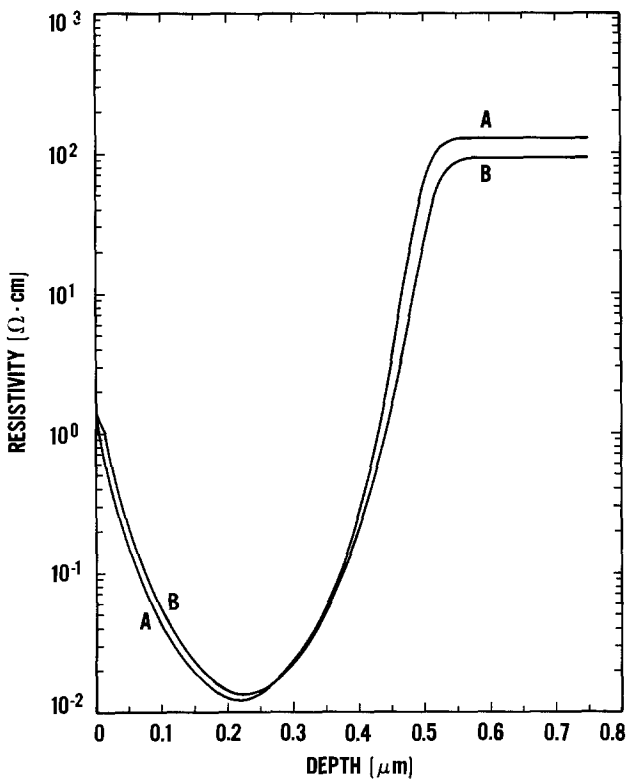

Fig. 5. This figure contains the original resistivity used to generate the model spreading resistance data (denoted by curve A) and the resistivity obtained by using the K_1K_2 form of the local slope equation on the calculated spreading resistance data. This interpreted resistivity profile is denoted by the curve B.

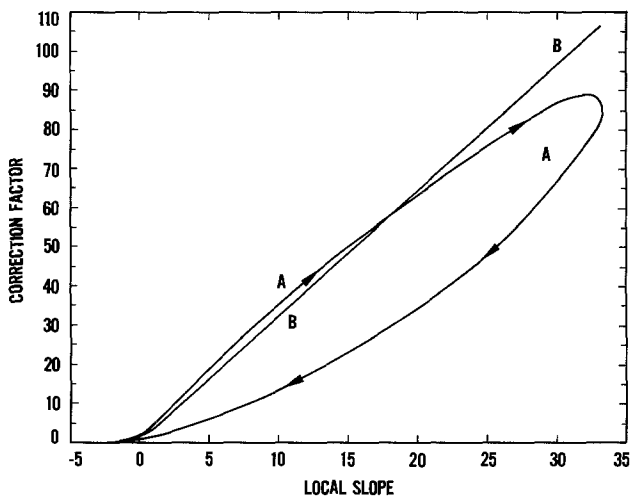

Fig. 7. These curves depict the $C_{ex}[M(x)]$ and $C_{ls}[M(x)]$ relations obtained from the multilayer and the K_1K_2 form of the local slope equation on the model spreading resistance data. The multilayer equations yield the $C(x)$ *vs.* $M(x)$ curve denoted by A while the local slope method gives rise to the $C(x)$ *vs.* $M(x)$ curve denoted by B. The arrow on the A curve indicates the path taken during the calculation from the top surface to the substrate. The path taken by the local slope method proceeds up the B curve to the maximum value and then changes direction and goes back down the B curve. The region before the crossing of the two curves is that where $C_{ex}(x) > C_{ls}(x)$ [or $\rho_{ex}(x) < \rho_{ls}(x)$]. The two correction factors are equal at the crossing point [which corresponds to the depth point at $x = 0.3$ μm of Fig. (5)]. Beyond the crossing point, $C_{ex}(x) < C_{ls}(x)$ [or $\rho_{ex}(x) > \rho_{ls}(x)$]. Similar results are obtained for the $\kappa = K3$ form and the $\kappa = 1$ form of the local slope equation.

local slope results qualitatively correct when compared with the multilayer results. It is important to emphasize that while the above results are obtained for the $\kappa = K_1K_2$ form of the local slope equation, similar results were obtained for the other two forms of κ. In particular, the $\kappa = 1$ form gave the correct substrate resistivity value and reproduced the $\kappa = K_1K_2$ form for the implant region of the structure. On the other hand, the $\kappa = K_3$ form gave rise to larger resistivities in the surface region of the implant and followed the $\kappa = K_1K_2$ form from the peak to the substrate where it went over to the correct substrate resistivity value. In all cases, the plot of the correction factor *vs.* local slope from each of these forms were very similar and did not reproduce the multiple-valued multilayer Laplace equation results. It might be argued that the square root form of the local slope equation is really double-valued. However, there is no *a priori* reason to choose one sign of the square root over another. One possible *ad hoc* way of dealing with this is to let the sign of the derivative of the local slope determine which sign to choose. This has been attempted with the present data. It was found that choosing the sign one way led to the usual local slope results while the other choice led to negative values of the correction factor, which is clearly unphysical.

Similar results were found for a number of structures. It is clear that the expansion of the correction factor in terms of the local slope is only of limited value. While the construction of a function of the form of Eq. [10] subject to the agreement with the asymptotic results as $M(x) \rightarrow +\infty$ and $M(x) \rightarrow -\infty$ appears to be a potentially useful one, there is implicit in it an assumption of single-valued behavior. However, the above analysis demonstrates that the correct relation is multiple valued. This means that the local slope is not the only variable at play in the determination of the correction factor. An alternative way of viewing this may be obtained from the expression between the spreading resistance and the correction factor as given in Eq. [1]. By taking the derivative of this equation with respect to x, it is possible to show that

$$M(x) = \frac{d \ln \rho(x)}{dx} + \frac{d \ln C(x)}{dx} \qquad [14]$$

For the case of a uniform layer, the first term on the right-hand side is zero. In this case, the resulting equation can be evaluated as

$$C(x) = C(0) \exp\left\{ \int_0^x M(x')dx' \right\} \qquad [15]$$

For this situation, the correction factor depends only upon the local slope. However, for a nonuniform resistivity case, Eq. [14] may be simply rearranged to yield

$$\frac{d \ln C(x)}{dx} = M(x) - \frac{d \ln \rho(x)}{dx} \qquad [16]$$

In this form, the equation states that the correction factor depends upon not only the local slope but also on the local variation of the resistivity. It is this additional term which gives rise to the multiple-valued behavior of the multilayer results when compared with the local slope prediction. Implicit in the use of the local slope method is the assumption that the correction factor may be obtained simply from the measured local slope. It is clear from Eq. [16] that the variation of the resistivity is neglected. In point of fact, it is not just $C(x)$ which is responsible for the specific form of $M(x)$, but it is really the product $\rho(x)C(x)$ which is mirrored in $M(x)$. This fact hinders the derivation of the local slope equations from the multilayer equations and causes the kind of behavior found in Fig. 7.

Conclusions

The asymptotic models used in the local slope method, as well as the local slope method itself, have been critically investigated. It has been shown that the asymptotic models give a good representation of the correction factor when compared with the predictions of the multilayer theory supplemented with either insulating or conducting boundary conditions. In addition, the assumption that the correction factor may be written as a single-valued function of the local slope has been addressed from the point of view of model spreading resistance data. The model data, which were calculated from the multilayer theory, show a multiple-valued relation between the correction factor and the local slope. This precludes the derivation of the local slope equations from the more general Laplace equation multilayer technique. In addition, the basic assumption implicit in the local slope method has been shown to be that the variation of the resistivity may be neglected and that the correction factor depends only upon the local slope. This assumption has been shown to be incorrect. It is the variation of the resistivity which leads to the multiple-valued relation between the correction factor and the local slope, which is obtained from the Laplace equation technique. This distinction accounts for the nonsystematic difference between the multilayer and local slope calculations exemplified in Fig. 5.

In conclusion, it is important to note that while the local slope method may not be obtained from the multilayer equations, the technique does offer qualitative and semiquantitative results which are useful in profile analysis.

Acknowledgment

This research was conducted as part of the National Bureau of Standards Semiconductor Technology Program.

Manuscript submitted Feb. 17, 1983; revised manuscript received June 9, 1983.

The National Bureau of Standards assisted in meeting publication costs of this article.

REFERENCES

1. P. A. Schumann and E. E. Gardner, *This Journal*, **116**, 87 (1969).
2. E. E. Gardner and P. A. Schumann, *Solid-State Electron.*, **12**, 371 (1969).
3. H. L. Berkowitz and R. A. Lux, *This Journal*, **126**, 1479 (1979).
4. S. C. Choo, M. S. Leong, and K. L. Kuan, *Solid-State Electron.*, **19**, 561 (1976).
5. D. C. D'Avanzo, R. D. Rung, and R. W. Dutton, Technical Report 5013-2, Stanford Electronics Laboratory, Stanford University, Stanford (1977).
6. D. C. D'Avanzo, R. D. Rung, A. Gat, and R. W. Dutton, *This Journal*, **125**, 1170 (1978).
7. H. L. Berkowitz and R. A. Lux, *ibid.*, **128**, 1137 (1981).
8. D. H. Dickey, in "Semiconductor Measurement Technology: Spreading Resistance Symposium," pp. 45-50, NBS Special Publication 400-10 (1974).
9. D. H. Dickey and J. R. Ehrstein, in "Semiconductor Measurement Technology: Spreading Resistance Analysis for Silicon Layers with Nonuniform Resistivity," pp. 15-18, NBS Special Publication 400-48 (1979).
10. J. Albers, *Solid-State Electron.*, **23**, 1197 (1980).

Growth of Single-Crystalline Epitaxial Group II Fluoride Films on InP(001) by Molecular-Beam Epitaxy

C. W. Tu, T. T. Sheng, M. H. Read, A. R. Schlier, J. G. Johnson,[1] W. D. Johnston, Jr., and W. A. Bonner

Bell Laboratories, Murray Hill, New Jersey 07974

ABSTRACT

Twin-free, single-crystalline, lattice-mismatched as well as lattice-matched, epitaxial dielectric films of group II cubic fluorides (SrF_2, CaF_2, and $Ba_xSr_{1-x}F_2$) have been grown on InP(001) substrates by molecular-beam epitaxy. The InP(001) surface was cleaned in vacuum by heating under phosphorus overpressure until a well-ordered and stoichiometric surface was obtained. The film growth of MF_2, where M is Ba, Sr, Ca, or Ba_xSr_{1-x}, was followed by reflection high energy electron diffraction (RHEED). The diffraction patterns indicate a parallel epitaxial relationship: $MF_2(001)\|[InP(001)$ and $MF_2[110]\|[InP[110]$. At low growth temperature (~250°C) and low growth rate we could obtain twin-free single-crystalline CaF_2 films. Transmission electron microscopy show the absence of any grains. At higher growth temperature (~350°C) we could obtain twin-free single-crystalline SrF_2, CaF_2, and $Ba_xSr_{1-x}F_2$ films. The latter can be lattice-matched to InP(001) at room temperature.

InP(001) has become very important in recent years because it is the substrate material for long-wavelength optical communication and high speed devices. If a dielectric film on a semiconductor substrate, such as InP(001), can be single crystalline and lattice matched to the substrate, the interface trap densities may be lowered (1). Thus, the film may be suitable for passivation and metal-insulator-semiconductor structures. Recently Harrison *et al.* showed that a CaF_2 film, E-beam evaporated on Si(111), could be a candidate as an electron resist and optical storage medium (2). Furthermore, Cho has grown epitaxial GaP on CaF_2(111) substrate by molecular-beam epitaxy (MBE) (3). Thus, there exist possibilities for epitaxial III-V semiconductor-insulator-semiconductor structures, which may be a basis for three-dimensional integration, waveguiding and device isolation in integrated optics, and other novel devices. In fact, recently we have grown the first epitaxial InP/fluoride/InP(001) double heterostructures by MBE (4). The results will be presented elsewhere.

Group II cubic fluorides are interesting for III-V compound semiconductors because they have similar crystal structure to InP and related compounds. The cubic fluorite structure consists of three interpenetrating face-centered cubic (fcc) lattices (5), whereas the zinc-blende structure of the substrate consists of two fcc lattices. Furthermore, the lattice constants of the fluorides bracket that of InP, the lattice mismatch ranging from −6.9 to +5.6% (5). Farrow *et al.* first showed epitaxial growth of BaF_2 on the (001) face of CdTe and InP at a substrate temperature of $\gtrsim$ 200°C (6). For room temperature deposition the films were polycrystalline. By modulated beam mass spectroscopy they showed that the fluoride films grow by simple nondissociative molecular sublimation and condensation (6, 7). They found film resistivities in the range of 10^{12}-10^{13} Ω/cm at room temperature. Then, Ishiwara and Asano grew epitaxial CaF_2 on Si(001) and (111) surfaces and Si/CaF_2/Si(111) at a substrate temperature of ~600°C by vacuum evaporation (8). Concurrent with the present work, Phillips *et al.* deposited epitaxial BaF_2 on Ge(111) and InP(001) also by vacuum evaporation (9). The last two groups confirmed the stoichiometry of the films by Rutherford backscattering. More recently, Sullivan *et al.* reported results on BaF_2, CaF_2, and $Ba_xCa_{1-x}F_2$ grown on InP(001) (10).

In this paper we report on the epitaxial growth of the group II cubic fluoride films, *i.e.*, CaF_2, SrF_2, BaF_2, and $Ba_xSr_{1-x}F_2$, on InP(001) by MBE. All except BaF_2 are single crystalline without twinning. We characterize the films by reflection high energy electron diffraction (RHEED), transmission electron microscopy (TEM), x-ray texture pattern, ellipsometry, and Nomarski interference-contrast microscopy.

[1] Summer employee from Cornell University, Ithaca, New York.

Key words: dielectrics, RHEED, TEM, sublimation.

Experimental Setup

The MBE system.—The MBE system, shown in Fig. 1, consists of a loadlock and an 18 in. diam Varian RHEED chamber. The loadlock has a magnetically coupled transfer rod and is pumped by an 8 liters/sec ion pump. The main chamber is pumped by a 500 liter/sec ion pump, and the wall of the chamber can be cooled by chilled water. Two Knudsen cells, surrounded by a liquid-nitrogen (LN_2) shroud, contain pieces of single-crystalline fluorides, and the third cell, also surrounded by an LN_2 shroud, contains undoped polycrystalline InP for the phosphorus source. The base pressure of the chamber could be in the mid 10^{-11} Torr (10^{-9} Pa) range, but normally between runs the base pressure was in the low 10^{-10} Torr (10^{-8} Pa) range. During film growth the pressure was ~ 2-5 × 10^{-9} Torr (~3-7 × 10^{-7} Pa). The MBE chamber contains a cylindrical mirror analyzer (CMA) with an integral electron gun for Auger analysis, a residual gas analyzer (RGA) for monitoring background gas composition and phosphorus overpressure during substrate cleaning, a 5 keV RHEED gun, a phosphorus screen, and a thin-film quartz monitor for thickness monitoring. The film thickness and refractive index were measured with an ellipsometer.

Substrate cleaning.—S-doped (10^{18} cm^{-3}) n-type InP(001) substrates were used. Many authors have shown that the surface prior to epitaxial growth is a critical factor in the quality of the grown film (11). Therefore, we shall describe our cleaning procedure in detail. The substrate was polished in Br-methanol. The final polish was done with 1% Br-methanol, rinsed with methanol, and spun dry. The quality of the polish was checked by the amount of scattering of a laser beam from the substrate. With proper polishing the Auger signals for C and O could be small [Fig. 2(a)], but the RHEED pattern was diffuse, indicating an amorphous oxide film on the surface. To produce an atomically clean surface on InP, Farrow *et al.* cleaned their surface by low energy (500 eV) Ar ion bombardment and annealing at 250°C to produce a (1 × 1) RHEED pattern (6). As in the case of GaAs (001), the (1 × 1) pattern can mean an In-rich surface (14) or the presence of carbon on the surface (11). From our own experience with ion bombardment (12) and annealing (13) of InP(001), the resulting surface, although clean, is never stoichiometric. The

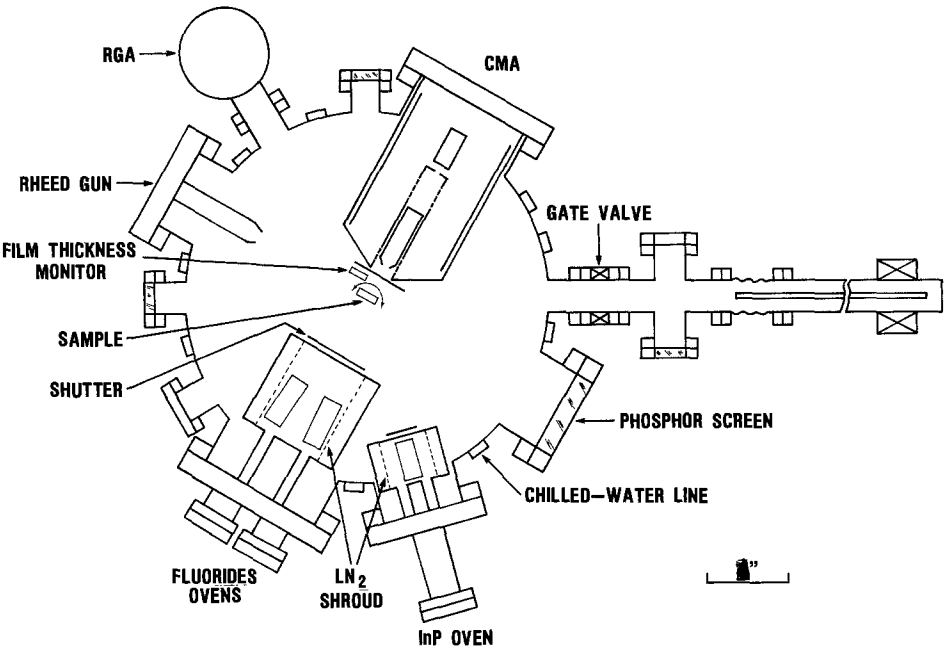

Fig. 1. A schematic diagram of the MBE system. After the initial study of cleaning procedures the CMA was removed from the chamber.

ratio of P/In as determined by x-ray photoelectron spectroscopy is about 0.9 after prolonged annealing at 300°C (13).

Our approach to cleaning the substrate is similar to that of Cheng *et al.*, who, before depositing an $In_xGa_{1-x}As$ film on InP, cleaned the InP substrate by heating it under As overpressure (15). We heated the substrate to $\lesssim$ 500°C under a P_2 beam (16) exposure from a Knudsen cell containing polycrystalline InP pieces. The total pressure as read by an ion gauge was $\gtrsim 3 \times 10^{-6}$ Torr (4×10^{-4} Pa) during exposure. The gas composition was monitored by RGA, which showed almost all phosphorus. In the beginning of the experiment the surface was monitored by Auger electron spectroscopy (AES) and electron energy-loss spectroscopy (ELS). The AES spectrum in Fig. 2(b), which is identical to that of vacuum-cleaved InP(110), shows that the surface was atomically clean and stoichiometric after being heated in phosphorus overpressure. To check further the presence of metallic In, which cannot be revealed by AES easily (12), an ELS spectrum was taken (Fig. 3). The ELS spectrum shows only the bulk and surface plasmon of InP, but not of In. Because the surface is stabilized by the phosphorus beam, the [110] and [$1\bar{1}0$] azimuth show ½- and ¼-order diffraction streaks from surface reconstruction (15) as shown in Fig. 4(a) and Fig. 8(a).

Results and Discussion

Low growth temperature (~250°C).—Once the surface was cleaned, the substrate temperature was lowered to ~250°C. Figure 4 shows RHEED patterns for different stages of BaF_2 film growth. Figure 4(a) shows the ½-order surface reconstruction along the [110] azimuth. Figure 4(b) shows the BaF_2 film at 15Å. The RHEED pattern shows some streaks but mostly spots. The streaks indicate that the growth mechanism may be two-dimensional layer growth as suggested by Farrow *et al.* (6), but the electron beam charged and roughened the surface to produce a spot pattern. The area where the electron beam impinged on the sample is clearly visible. Figure 4(c) shows single-crystal-like sharp spot patterns of a film of 950Å. The (1 × 1) pattern along the [110] azimuth indicates the parallel epitaxial relationship, $BaF_2(001)||$

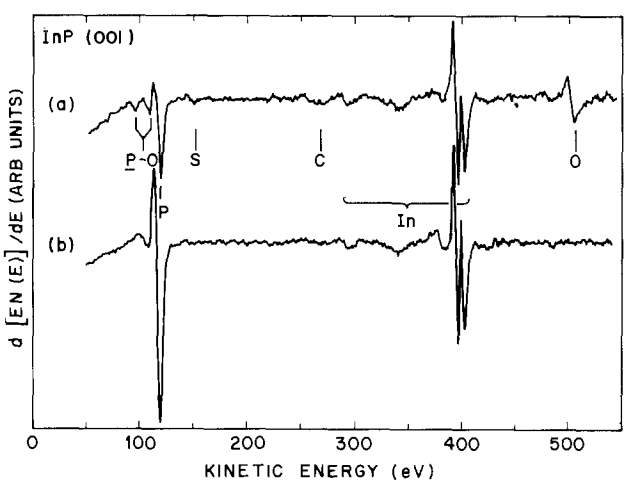

Fig. 2. (a) An AES spectrum of a freshly polished InP(001) substrate. (b) An AES spectrum of the substrate after being heated in phosphorus overpressure. The spectrum is identical to that obtained on a vacuum-cleaved InP(110) surface. The incident 3 keV electrons were normal to the surface. The peak-to-peak modulation voltage was 1.6V.

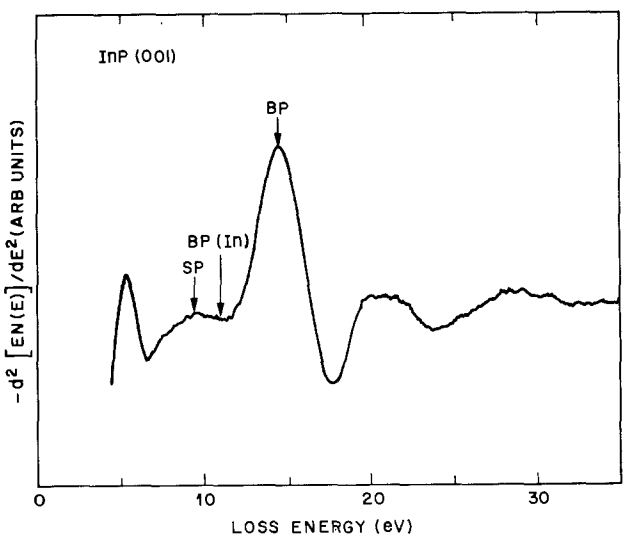

Fig. 3. An ELS spectrum of a clean InP(001) substrate. BP and SP denote bulk plasmon and surface plasmon of InP, respectively. BP(In) denotes the bulk plasmon of In. The incident 500 eV electrons were normal to the surface. The peak-to-peak modulation voltage was 1.6V.

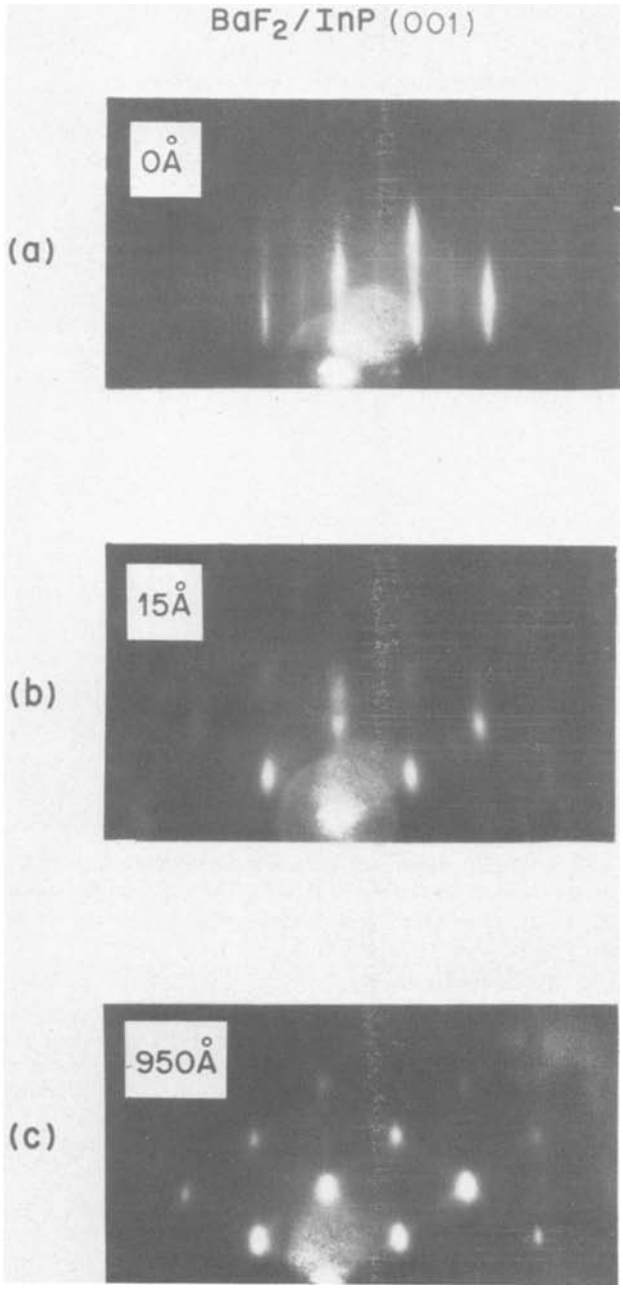

Fig. 4. RHEED patterns (5 keV) of epitaxial growth of BaF_2 on InP(001) at substrate temperature of ~250°C. (a) The initial clean surface showing the [110] azimuth-1/2 order surface reconstruction. (b) After growth of 15Å. (c) After growth of 950Å.

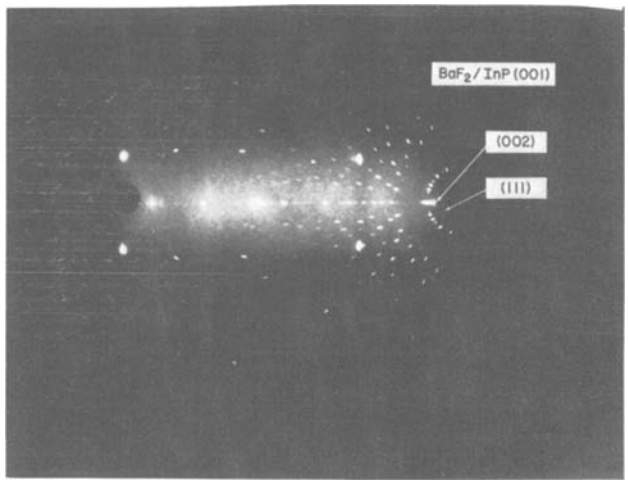

Fig. 5. An x-ray texture pattern of BaF_2 film on InP(001). Most of the spots are from the substrate. The (111) polycrystalline ring and the (002) spot from the film are indicated.

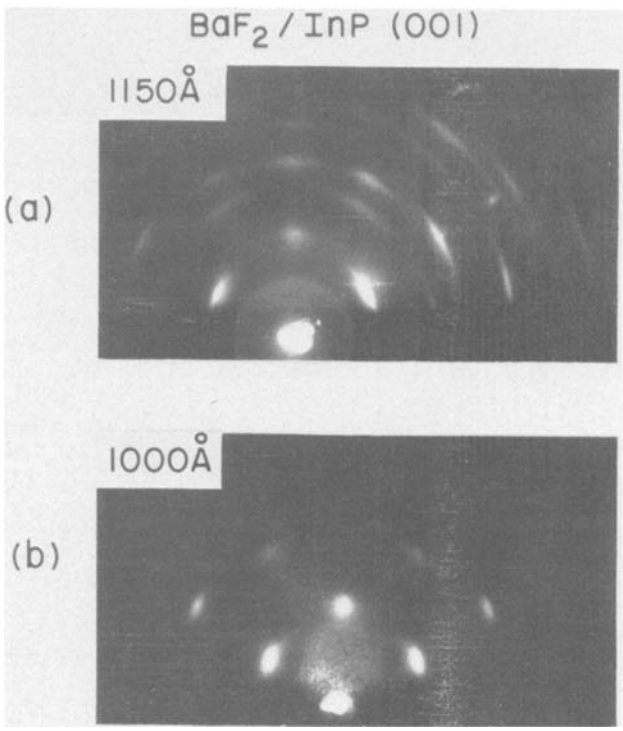

Fig. 6. RHEED patterns (5 keV) of BaF_2 films on InP(001) at (a) high growth rate (8600 Å/hr) and (b) lower than optimal growth rate (535 Å/hr).

InP(001), and BaF_2[110]||InP[110] (16). The diffraction lines connecting the spots suggest microfaceting on the {111} planes as a result of electron bombardment. Although there are no polycrystalline rings in the RHEED pattern, the film is actually a highly oriented polycrystalline film because the x-ray texture pattern (Fig. 5), taken with a Read camera (18), shows a (111) polycrystalline ring. Most of the spots are from the substrate. The strongest spot from the film is (002), confirming the parallel epitaxial relationship.

The quality of epitaxy is found to depend on the growth rate. There seems to be an optimum range in growth rate for a sharp spot pattern. Figure 6 shows the BaF_2 RHEED patterns for (a) high growth rate (8600 Å/hr) and (b) low growth rate (535 Å/hr). For the case of high growth rate the film is clearly polycrystalline with preferred (001) orientation. For the case of low growth rate the film shows a spot pattern, but the spots have a slight curvature, indicating imperfect epitaxy. The optimal growth rate of BaF_2 is ~1000 Å/hr.

Figure 7 shows RHEED patterns of SrF_2 and CaF_2 films on InP (001). Figure 7(a) shows 430Å of SrF_2 at an optimal growth rate of 430 Å/hr. Figure 7(b) shows 535Å of CaF_2 at an optimal growth rate of ~230 Å/hr. Higher growth rate results in similar patterns to Fig. 6(a).

TEM micrographs and associated transmission electron diffraction (TED) patterns show that the BaF_2 and the SrF_2 films consist of many small (~1500Å), highly oriented crystallites. However, the CaF_2 film is single crystalline as indicated by the absence of any grain boundaries. TEM results are discussed in the next section.

Nomarski interference-contrast microscopy of the films shows that they are transparent and have no visible defects, except where the electron beam impinged.

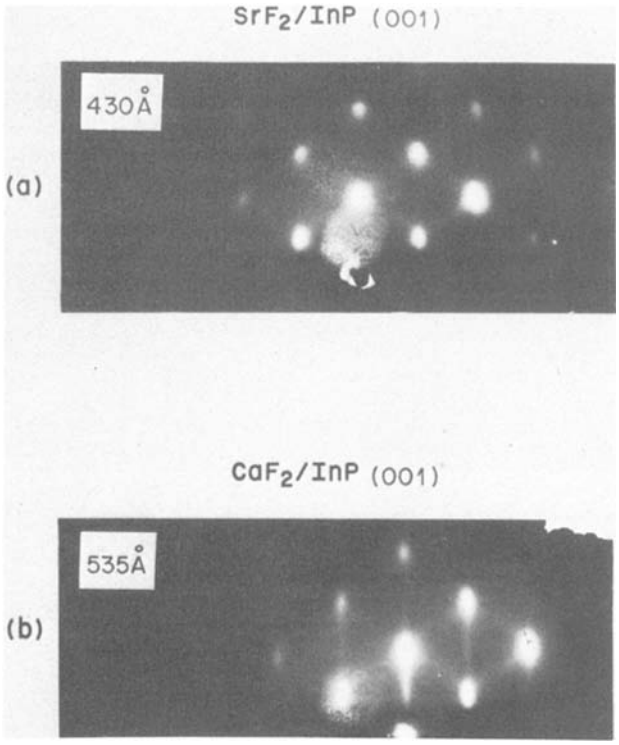

Fig. 7. RHEED pattern (5 keV) of epitaxial SrF_2 and CaF_2 on InP(001) at substrate temperature of ~250°C. (a) After growth of 430Å SrF_2 film. (b) After growth of 535Å CaF_2 film.

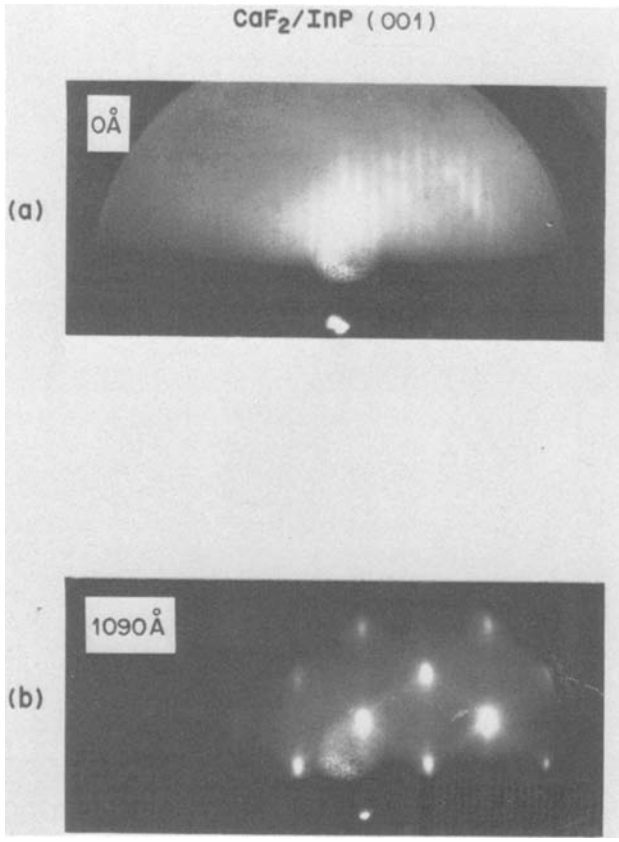

Fig. 8. RHEED pattern (5 keV) of epitaxial CaF_2 on InP(001) at substrate temperature of ~350°C. The initial surface shows the [$\bar{1}10$] azimuth-1/4 order surface reconstruction. (b) After growth of 1090Å.

High growth temperature (~350°C).—When the substrate temperature was raised to ~350°C, close to the congruent evaporation point of InP, ~365°C, (19), the growth rate could be much higher to achieve sharp spot patterns in RHEED. Figure 8 shows a CaF_2 film grown at 600 Å/hr. Figure 8(a) shows the ¼-order surface reconstruction along the [$1\bar{1}0$] direction. Figure 8(b) shows the RHEED pattern of the film with no polycrystalline rings. The BaF_2 and SrF_2 films also showed good spot RHEED patterns.

TEM analysis shows that BaF_2 films grown at higher substrate temperature are still polycrystalline and are oriented strongly along the [001] direction. However, SrF_2 films improve in quality as shown in Fig. 9. Although the TED pattern in Fig. 9(a) shows polycrystalline rings along with the spot pattern, the films are single crystalline with the inclusion of ~2000Å wide grains, as shown by the bright-field and dark-field TEM micrographs [Fig. 9(b) and (c), respectively]. Figure 10(a) shows the TED pattern of a CaF_2 film. No polycrystalline rings are present. The film appears to be single crystalline with no defects as shown in Fig. 10(b). Figure 10(b) also shows that the film broke off along <110> directions during thinning for TEM analysis.

With Nomarski interference-contrast microscopy we find that 1000Å thick CaF_2 films, but neither BaF_2 nor SrF_2 films, show crazing along the <110> directions, which was also observed by Sullivan *et al.* (10). They attributed crazing to increased lattice mismatch at room temperature compared to the growth temperature. However, thicker BaF_2 and SrF_2 films (~4000Å) also exhibit crazing as shown in Fig. 11. Since the orientation of the film is (001), the <110> directions are consistent with crazing occurring on the {111} cleavage planes of the cubic fluorides. The cause of crazing is most likely a combination of strains from large lattice mismatch ($\Delta a/a$) and from a large difference in the thermal expansion coefficients ($\Delta\alpha$). The thermal expansion coefficients of the fluorides are larger than that of InP (~20×10^{-6} *vs.* 6×10^{-6} K^{-1}). As $\Delta a/a$ becomes smaller, $\Delta\alpha$ becomes more important and crazing starts to appear at thicker film thickness. For the same film thickness, SrF_2 ($\Delta a/a = -1.2\%$) exhibits the least crazing among the three fluorides. When a mixture of fluorides ($Ba_xSr_{1-x}F_2$) was grown to achieve lattice matching to the substrate, the crazing did not appear for ~4000Å thick films, but appeared for $\gtrsim 1\mu$ thick films.

Lattice matching to InP(001).—A mixture of the fluorides, $Ba_xSr_{1-x}F_2$, was grown on InP(001) at ~350°C by adjusting the temperature of the two ovens containing BaF_2 and SrF_2. Films lattice matched to the substrate could be obtained. The lattice parameter was measured by double-crystal x-ray diffractometry. The films are also single crystalline without twinning. The TEM micrographs are similar to those of Fig. 10, but show fewer inclusions. As mentioned earlier the ~4000Å film lattice matched to the substrate shows no crazing under Nomarski interference-contrast microscope. Further studies of the lattice matched single-crystalline dielectric films are reported elsewhere (20).

Summary

We have grown epitaxial dielectric films of the group-II cubic fluorides, CaF_2, SrF_2, BaF_2, and $Ba_xSr_{1-x}F_2$, on InP(001) at relatively low substrate temperatures (~250° and ~350°C). As expected, the higher the growth temperature is, the better the epitaxy. At ~250°C, the CaF_2 film is single crystalline as shown by the absence of grains in the TEM micrograph. However, the SrF_2 and BaF_2 films consist of many highly oriented crystallites even though they show good spot RHEED patterns. At ~350°C, CaF_2, SrF_2, and $Ba_xSr_{1-x}F_2$ films are single crystalline, but BaF_2 films are not. These results show that the amount of misfit is not an important factor for epitaxy, similar to other film-substrate systems (19). The substrate

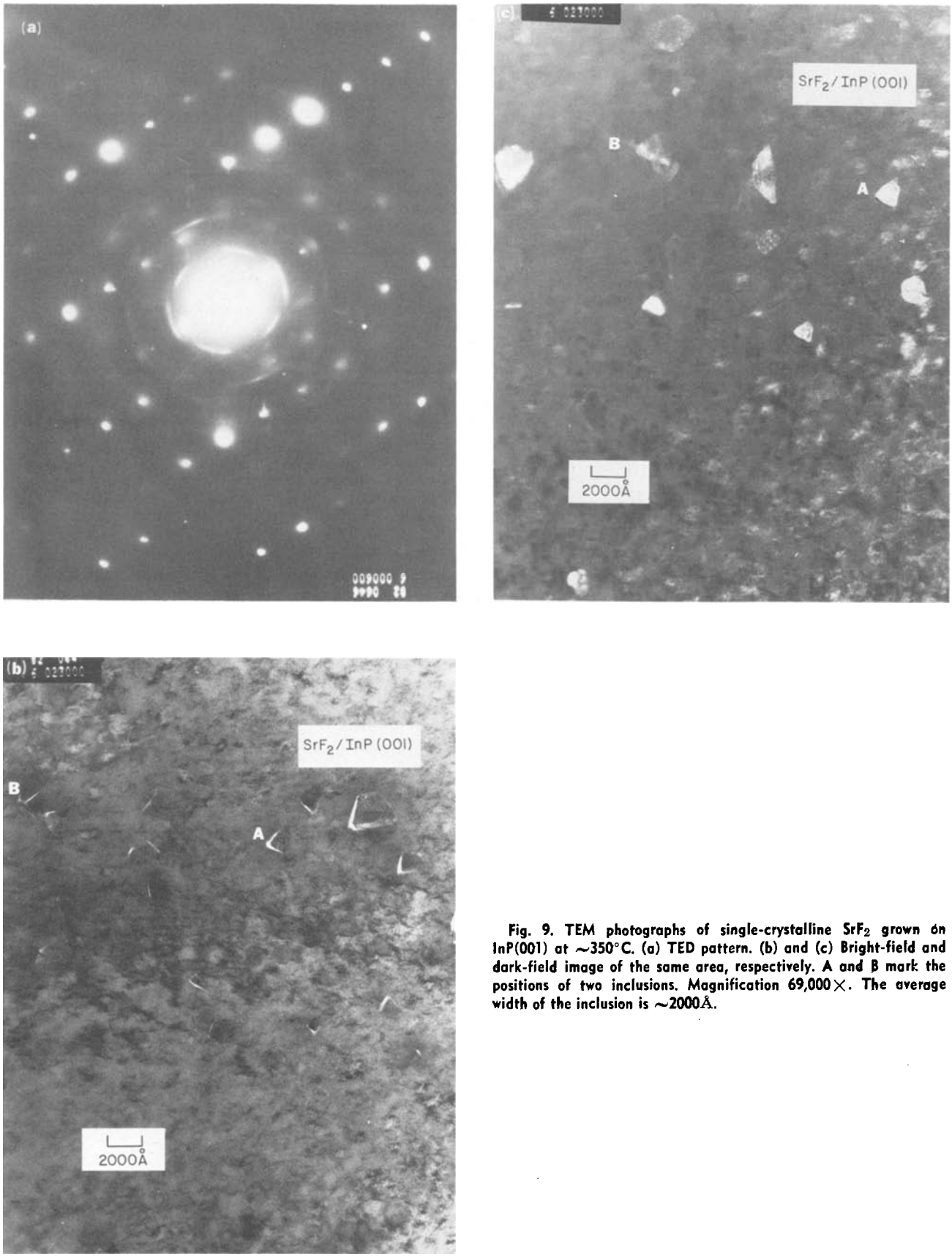

Fig. 9. TEM photographs of single-crystalline SrF_2 grown on InP(001) at ~350°C. (a) TED pattern. (b) and (c) Bright-field and dark-field image of the same area, respectively. A and B mark the positions of two inclusions. Magnification 69,000×. The average width of the inclusion is ~2000Å.

temperature and the growth rate are the crucial parameters (20) to achieve single crystallinity.

Acknowledgment

We wish to thank R. B. Marcus for his encouragement and support; T. Y. Chang, A. Y. Cho, J. C. M. Hwang, R. A. Stall, and W.-T. Tsang for helpful discussions on various aspects of MBE; S. N. G. Chu and C. M. Jodlauk for doing energy-dispersive x-ray analysis on some samples; A. T. Macrander for the measurement of lattice parameters; K. E. Strege and D. L. Mitcham for providing invaluable hints on substrate polishing; H. J. Guggenheim and G. J. Zydzik for providing the fluoride crystals; and R. H. Burton and C. L. Hollien for the use of their ellipsometer.

Manuscript submitted March 11, 1983; revised manuscript received June 6, 1983. This was Paper 337 pre-

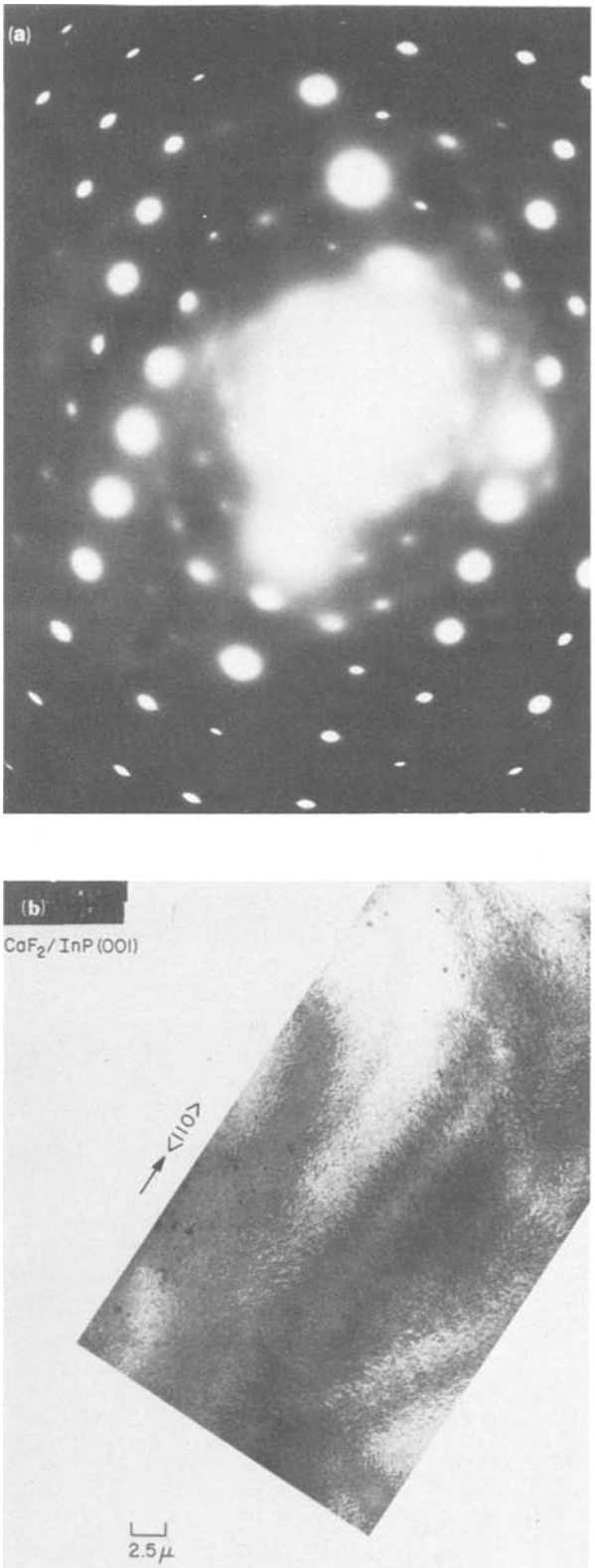

Fig. 10. TEM photographs of single-crystalline CaF_2 grown on InP(001) at ~350°C. (a) TED pattern. (b) Bright-field image. Magnification 4350×. Note the absence of any grains.

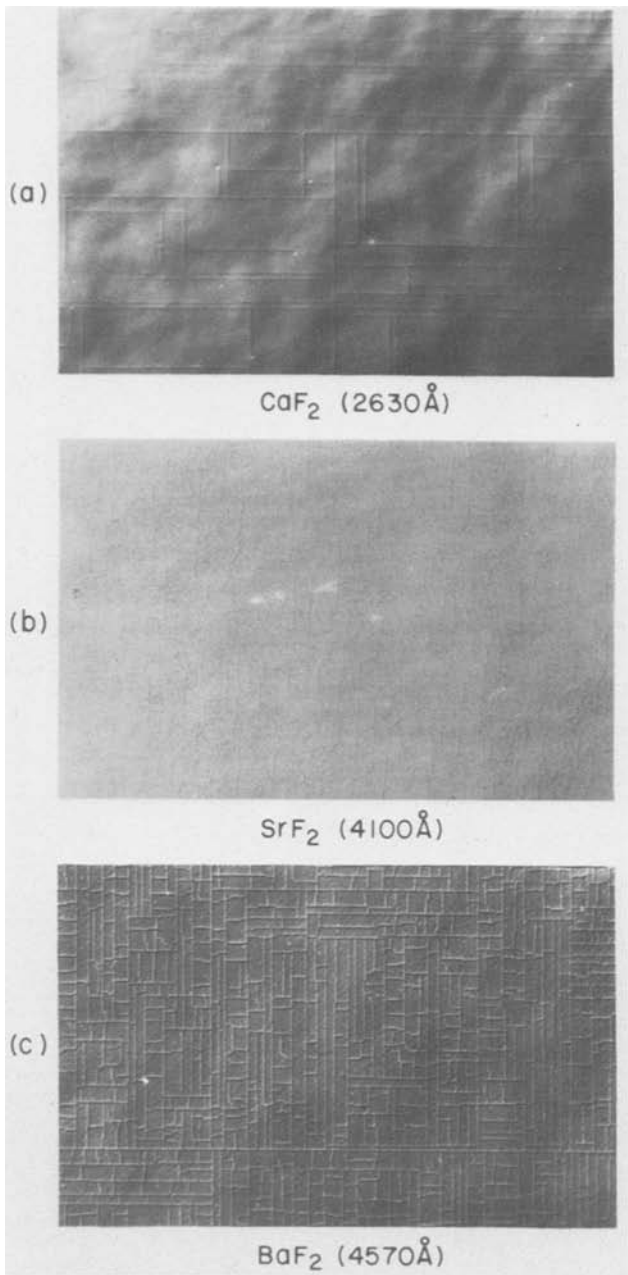

Fig. 11. A Nomarski interference-contrast micrograph of (a) 2650Å CaF_2, (b) 4100Å SrF_2, and (c) 4500Å BaF_2. The crazing is along <110> directions. Magnification 400×.

sented at the San Francisco, CA, Meeting of the Society, May 8-13, 1983.

Bell Laboratories assisted in meeting the publication costs of this article.

REFERENCES

1. J. Singh and A. Madhukar, *J. Vac. Sci. Technol.*, **19,** 437 (1981).
2. T. R. Harrison, P. M. Mankiewich, and A. H. Dayem, *Appl. Phys. Lett.*, **41,** 1102 (1982).
3. A. Y. Cho, *J. Appl. Phys.*, **41,** 782 (1970).
4. C. W. Tu, S. R. Forrest, and W. D. Johnston, Jr., *Appl. Phys. Lett.*, **43,** 569 (1983).
5. W. Hayes, in "Crystals with the Fluorite Structure," W. Hayes, Editor, Oxford University Press, Oxford (1974).
6. R. F. C. Farrow, P. W. Sullivan, G. M. Williams, G. R. Jones, and D. C. Cameron, *J. Vac. Sci. Technol.*, **19,** 415 (1981).
7. P. W. Sullivan, T. I. Cox, R. F. C. Farrow, G. R. Jones, D. B. Gasson, and C. S. Smith, *ibid.*, **20,** 731 (1982).
8. H. Ishiwara and T. Asano, *Appl. Phys. Lett.*, **40,** 66 (1982).
9. J. M. Phillips, L. C. Feldman, J. M. Gibson, and M. L. McDonald, *J. Vac. Sci. Technol.*, **81,** 246 (1983).
10. P. W. Sullivan, R. F. C. Farrow, and G. R. Jones, *J. Cryst. Growth*, **60,** 403 (1982).
11. *E.g.*, C.-A. Chang, *J. Vac. Sci. Technol.*, **21,** 663 (1982).
12. C. W. Tu and A. R. Schlier, *Appl. Surf. Sci.*, **11/12,** 335 (1982).
13. C. W. Tu, Unpublished.
14. A. Y. Cho, *J. Appl. Phys.*, **47,** 2841 (1976).

15. K. Y. Cheng, A. Y. Cho, W, R. Wagner, and W. A. Bonner, *ibid.*, **52**, 1015 (1981).
16. R. F. C. Farrow, *J. Phys. D*, **7**, 2436 (1976).
17. K. W. Andrews, D. J. Dyson, and S. R. Keown, "Interpretation of Electron Diffraction Patterns," p. 152, Plenum Press, New York (1971).
18. M. H. Read, 27th Annual Pittsburgh Diffraction Conference, Pittsburgh, PA, November 1964.
19. R. F. C. Farrow, *J. Phys. D*, **7**, L121 (1974).
20. C. W. Tu, T. T. Sheng, A. T. Macrander, J. M. Phillips, and H. J. Guggenheim, *J. Vac. Sci. Technol.*, To be published.
21. A. K. Green, J. Dancy, and E. Bauer, *J. Vac. Sci. Technol.*, **7**, 159 (1970).
22. J. H. Kahn, in "Handbook of Thin Film Technology," L. I. Maissel and R. Glang, Editors, McGraw-Hill, New York (1970).

Cerium-Activated Halophosphate Phosphors

I. Strontium Fluoroapatites

R. G. Pappalardo,* J. Walsh, and R. B. Hunt, Jr.

GTE Laboratories Incorporated, Precision Materials Technology Center, Waltham, Massachusetts 02254

ABSTRACT

In the search for alternative yellow emitting phosphors for the current commercial high brightness phosphor blends of the Lite-White type, the authors have prepared and characterized by a variety of techniques an Sr-analog of calcium fluoroapatite:Sb;Mn, with Ce replacing Sb as the sensitizer of the Mn emission. Materials with the desired emission characteristics are obtained from starting formulations containing a strong fluoride excess over the standard formulations for alkali-earth apatites. Phosphors have been obtained with emission parameters closely approaching those of Yellow Halo (YH), and only 10% lower in brightness. Lamp tests on these phosphors revealed that the efficiency of the Ce-Mn coactivated materials, as presently formulated, degrades as a result of the lamp-making process. Preliminary observations related to the mechanism of phosphor degradation are reported. Possible commercial application in lamps of the wide class of Ce-activated apatites crucially depends on identifying, and later eliminating, the degradation of phosphor efficiency during lamp fabrication.

The recent development of Lite-White blends for low pressure fluorescent lamps has signaled a marked departure from established tenets of the lighting industry. The low pressure fluorescent lamp was originally conceived as a desirable replacement for incandescent lamps, and until recently its phosphors were generally engineered so as to mimic as closely as possible the spectral-energy distribution from black-body radiators and from the sun.

In the early 1970's, Philips (1, 2) pioneered with the tricolor lamp, a novel scheme for the generation of white fields in fluorescent lamps, by the use of a combination of phosphors emitting in the spectral range of miximum sensitivity of the human eye receptors. The new lamps, incorporating both the new phosphor blends and modifications in the discharge parameters, aim at providing greater efficacies [up to 90-100 lumens per watt (lpw)] and also high color rendering. The drawback in this approach is the high cost of the rare earth phosphors required.

In 1977, GE introduced a scheme aimed at increasing the efficacy (lpw) in low pressure fluorescent lamps, at some loss in color rendering (3). The approach, embodied in the Watt-Miser II lamps and then in the Lite-White lamps, hinges on producing a high efficacy white field by a combination of narrow-band emitters in the blue, at 448 nm, and in the yellow, at 575 nm (4).

Both in the Philips and in the GE scheme, the fluorescent lamp is no longer constrained to replicate the spectral-emission distribution from incandescent sources, but its unique potentialities are now freely exercised. In terms of phosphor development this means a new set of performance objectives expected of phosphors. Materials that in the past were not competitive with the standard Sb-Mn coactivated fluoro-chloroapatites, may become superior in performance under the new set of specifications. Therefore, a renewed careful study of the spectral properties of phosphors is now required to identify those systems that can realize most efficiently the scheme of u.v.-to-visible conversion embodied in the Lite-White approach. The present report addresses the first stage of such a search, namely, the possible replacement of the yellow emitting component of the Lite-White blend.

Yellow Emitting Component for the Lite-White Blend

The requirements for a yellow emitting phosphor for the Lite-White-type blend (3, 4) are as follows: (*i*) emission peak at $\simeq$575 nm; (*ii*) narrow emission band; and (*iii*) high ($\simeq$70%) quantum efficiency. These requirements are presently well satisfied by the so-called Yellow Halo (YH) phosphor of approximate composition $Ca_5(PO_4)_3F$:Sb;Mn As for materials capable of satisfying the three aforementioned requirements, it should be pointed out that among nonlanthanide emitters, only Mn tends to exhibit relatively narrow emission bands. Also, given the nature of the Mn emitting level, as defined by a Tanabe-Sugano diagram (5), in order to have emission in the yellow, it is necessary to incorporate Mn in a site of high crystal field and relatively low distortion from cubic symmetry. In addition, Mn has to be coordinated to ionic ligands that do not promote the delocalization of the 3d-electronic cloud of Mn^{2+}.

In practice, this translates into the requirement for a fluoride matrix or a fluoride containing matrix that is also compatible with operation inside a lamp: a fluoroapatite matrix is still the best candidate to meet the aforementioned requisites. At present, the avenues open for alternatives to YH are therefore restricted to: (*a*) modifications of the basic fluoroapatite matrix; and (*b*) replacement of Sb^{3+} with a different sensitizer. Along this general direction, the authors discuss in what follows the results of the synthesis and characterization of Ce-Mn-coactivated fluoroapatite (FAP) phosphors, and specifically of SrFAP: Ce;Mn.

Synthesis of Strontium Fluoroapatites

Early attempts to prepare Sr apatites coactivated with Ce and Mn, with halide content approaching

* Electrochemical Society Active Member.

that of $Sr_5(PO_4)_3(F,Cl)$, gave materials with low brightness and deep orange emission. Yellow emitting, bright phosphors were obtained when the halide content greatly exceeded one formula unit, as for instance using the following starting formulation

$$Sr_{4.30}Ce_{0.295}Mn_{0.147}(PO_4)_{3.0}F_{1.72} \quad [1]$$

In pioneer work by Henderson and Ranby (6, 7), the fluoride excess was even greater, the phosphor materials of optimum brightness being formulated, for the purpose of comparison with [1], as

$$Sr_{4.50}Ce_{0.196}Mn_{0.245}(PO_4)_{3.0}F_{5.1} \quad [2]$$

In our preparations, the reaction components were weighed and blended in a Spex Mixer-Mill Model 8000. The blend was then loaded in shallow alumina boats ($\simeq$2.5 × 1.5 × ⅝ in.) provided with loose quartz covers, and lots of four-to-six boats were introduced into the hot zone of a quartz tube inserted in a tubular furnace. The atmosphere in the reaction zone was purged of oxygen by a preliminary pump-down, and then continually swept at 10 liter/min flow of nitrogen gas, or nitrogen gas containing 5% hydrogen. After the firing treatment at the desired temperature, the quartz tube containing the boats was allowed to cool to $\simeq$450°C, still under constant gas flow. The quartz tube was then removed and the samples extracted. The materials from this first firing were then ground, sieved (generally through a 100 mesh screen), and then refired. The second firing was carried out in inert or mildly reducing atmosphere and increased the emission efficiency of the phosphors by a few percent.

An increase in Mn content over 0.15 formula units produced marked sintering after the first firing at temperatures ranging from 950° to 1050°C. The use of a nitrogen hydrogen mixture (5% hydrogen) as firing atmosphere reduced the tendency to sintering and eliminated the pale green body color frequently observed in the nitrogen-fired phosphors. The second firing was carried out in nitrogen atmosphere at temperatures ranging from 850° to 1025°C. In some cases, a third firing of the phosphor at 850°C in "wet" forming gas (95% nitrogen/5% hydrogen) was investigated, but it resulted in a slight discoloration of the phosphor powder and in a 7% brightness loss. This approach was therefore abandoned.

The highest brightness was observed in a material formulated as

$$Sr_{4.25}Ce_{0.295}Mn_{0.245}(PO_4)_{3.0}F_{1.92} \quad [3]$$

using the reagents and firing conditions listed in Table I.

A gradient in emission brightness was observed in the doubly fired material from this run, the measured peak intensity of Mn ranging from 86.1 to 89.8% of the corresponding quantity for our internal standard (YH, GTE Sylvania Type 4381, Lot PPP 9780).

Phosphor Characterization

Phase identification.—The x-ray diffraction patterns of the powders were measured by means of a Philips vertical diffractometer, using copper radiation of 1.5405A. The source was run at 35 kV and 16 mA. The diffraction patterns were measured at a scan rate of 1°/min, using a solid-state scintillator counter and a graphite monochromator. X-ray diffraction measurements on the materials obtained from a variety of runs showed a dominant phase with hexagonal apatite lattice, isostructural with, and somewhat expanded relatively to, $Sr_2Pr_8(SiO_4)_6O_2$, the latter (8, 9) with lattice parameters: a = 9.612Å and c = 7.143Å.

A comparison of the diffraction data pertinent to $Sr_2Pr_8(SiO_4)_6O_2$ and the SrFAP:Ce;Mn material formulated according to [3] is given in Table II. Inspection of the table reveals the close agreement in the relative intensity of the diffraction lines for the two systems and the slight expansion ($\simeq$1%) of the SrFAP:Ce;Mn lattice. Four additional weak lines (with intensity of 1-2%) in the diffraction pattern suggested the presence of a minor phase ($\simeq$1%) of $CePO_4$.

Similar measurements were also performed on singly activated (Ce) and triply activated (Ce;Mn:Dy) materials briefly discussed in the text and prepared according to the data of Tables III and IV. Again the predominant phase was a hexagonal apatite, with a possible minor phase of $CePO_4$, estimated from the diffraction data as amounting to $\simeq$2% for

Table I. Reagents and phosphor formulation for optimum brightness

Starting formulation: $Sr_{4.25}Ce_{0.295}Mn_{0.245}(PO_4)_{3.0}F_{1.92}$; fired 1 hr at 950°C in 95% nitrogen/5% hydrogen; refired 1 hr in nitrogen at 1025°C

Reagents	Grams	Mol units
$SrHPO_4$ (GTE Sylvania)	8.4	3.0
$SrCO_3$ (GTE Sylvania)	1.65	0.733
$MnCO_3$ (GTE Sylvania)	0.43	0.245
CeF_3 (K&K Labs)	0.887	0.295
SrF_2 (Varacloid Chemical Company)	0.99	0.516

Table II. X-ray diffraction data for $Sr_2Pr_8(SiO_4)_6O_2$

[ASTM Ref 29-1310] (columns labeled R); and for Sr fluoroapatite:Ce;Mn (columns labeled S)

d, A		I(0)/I(1)		hkl
R	S	R	S	R
4.81		3		110
4.17	4.181	16	9.8	200
3.99		14		111
3.58	3.602	10	18.7	002
3.28	3.308	25	19.5	102
3.15	3.161	20	29.7	210
2.873	2.893	100	100	211, 112
2.774	2.788	20	29.9	300
2.711	2.729	3	4.6	202
2.310	2.320	5	7.1	310
2.278	2.206	3	4.9	221
2.191	2.150	4	6.5	302
2.135		10		113
2.081	2.091	4	2.4	400
2.067		2		203
1.994	2.007	18	18.9	222
1.939	1.950	10	13.2	312
1.910		5		320
1.900	1.913	25	22.1	213
1.845	1.855	12	6.4	321
1.817	1.825	16	16.2	410
1.798	1.808	18	11.4	402
1.786		8		004
1.641		3		204
1.573		3		420
1.553	1.567	5	6.7	214
1.509	1.516	6	7.0	502
1.502	1.500	5	4.7	304
1.490		5		323
1.462	1.471	6	7.2	332
1.369		1		115
1.355		2		404
1.304	1.313	2	3.6	324
1.301		5		215
1.273	1.283	8	5.1	414
1.270		3		305
1.249	1.257	8	6.3	522
	1.189		3.5	
	1.136		3.5	

Table III. Reagents and starting formulation for singly activated SrFAP

Starting formulation $Sr_{4.30}Ce_{0.295}Mg_{0.146}(PO_4)_{3.0}F_{1.72}$; fired in 10 liter/min nitrogen at 1000°C for 1 hr; refired 1 hr in the same atmosphere at 900°C

Reagents	Grams	Mol units
$SrHPO_4$ (GTE Sylvania)	5.6	3.0
$SrCO_3$ (GTE Sylvania)	1.32	0.879
$MgCO_3$	0.126	0.146
CeF_3 (K&K Labs)	0.59	0.295
SrF_2 (Varacloid Chemical Company)	0.533	0.417

Table IV. Reagents and starting formulation for triply activated SrFAP

Starting formulation $Sr_{4.22}Ce_{0.295}Dy_{0.04}Mn_{0.146}(PO_4)_{3.0}F_{1.70}$; fired in 10 liter/min nitrogen at 1000°C for 1 hr; refired 1 hr in the same atmosphere at 900°C

Reagents	Grams	Mol units
$SrHPO_4$ (GTE Sylvania)	5.6	3.0
$SrCO_3$ (GTE Sylvania)	1.32	0.879
$MnCO_3$	0.172	0.146
CeF_3 (K&K Labs)	0.59	0.295
DyF_3	0.09	0.04
SrF_2 (Varacloid Chemical Company)	0.44	0.344

the triply activated material and ≃1% for the two remaining materials.

Infrared properties.—The infrared absorbance spectra of the phosphor powders (2% by weight in KBr disks) were measured with a Nicolet Fourier-Transform Infrared Spectrometer MX1, Model 3600E, and were displayed on a Zeta digital plotter.

The infrared absorbance spectrum for samples of formulation [3] is given in Fig. 1, in the spectral region (420-2400 cm^{-1}) of main interest for the detection of nonapatitic orthophosphate and pyrophosphate phases. The spectrum of SrFAP:Ce;Mn is contrasted to the corresponding spectrum of the Ca-FAP:Sb;Mn material (YH) used as internal standard and known to be a bona fide apatite, containing approximately 1.4% of Ca-pyrophosphate (β-phase). The spectrum of SrFAP:Ce;Mn reproduces faithfully the main features of the spectrum of CaFAP:Sb;Mn and does not show the weak line at ≃690 cm^{-1}, commonly associated with pyrophosphate phases.

Chemical analysis.—Materials formulated as

$$Sr_{4.25}Ce_{0.295}Mn_{0.245}(PO_4)_{3.0}F_{1.92} \quad [3]$$

gave on analysis the results listed in Table V. From the chemical analysis (Table V) of the products obtained from the firing of samples of starting formulation [3], one can derive, on the assumption of three P atoms per molecule in the final product, the following phosphor composition

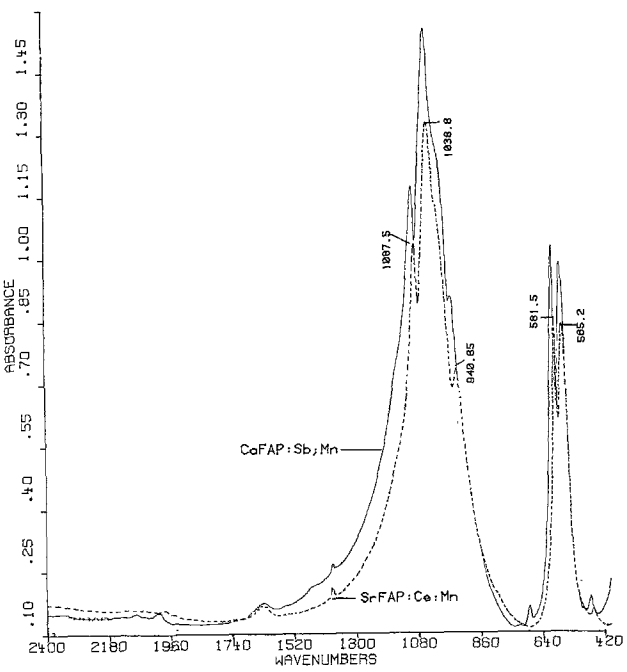

Fig. 1. Infrared absorbance of CaFAP:Sb;Mn (solid line) and of SrFAP:Ce;Mn (dashed line) in the spectral region of the main absorptions.

Table V. Results of chemical analyses on phosphors

Starting formulation: $Sr_{4.25}Ce_{0.295}Mn_{0.245}(PO_4)_{3.0}F_{1.92}$

Element	Weight percent found	Method	Error bar* (%)	Formula units†
Sr	49.5	Atom. absor.	±3	4.20
Ce	6.2	Neutron act.	±5	0.33
Mn	1.94	Atom. absor.	±5	0.26
P	12.5	Neutron act.	±3	3.0
F	2.88	Electrochem	±7	1.16

* For the quantities listed in Column 2.
† Assuming P = 3.

$$Sr_{4.20}Ce_{0.33}Mn_{0.26}(PO_x)_{3.0}F_{1.16} \quad [4]$$

namely, the fluoride content is markedly reduced in the final product, but still exceeds by ≃15% the fluoride content for a stoichiometry alkaline-earth halophosphate. Similar analytical results on the fluoride content were reported by Henderson and Ranby (6).

The total formal charge of the cations is derived from [4] as being 9.91 (assuming that all of the Ce is present as the trivalent species). The total anion charge adds up to 10.16, if one assumes that $x = 4$ in Eq. [4]. Until the chemical analyses can provide a reliable determination of both the relative content in the Ce^{3+} and Ce^{4+} species, and of the oxygen content, further discussion of the finer details of the phosphor composition and related charge compensation is of necessity in the nature of speculation.

Optical Spectroscopy of the FAP Phosphors

Experimental setup.—Spectroscopic measurements were performed both under steady-state excitation (and detection) of the phosphors and under conditions of pulse excitation of the materials. For the steady-state measurements, a modified commercial spectrophotometer, Perkin-Elmer fluorescence spectrophotometer Model MPF 44-A was utilized. The measurements on the decay kinetics of the phosphors were carried out using a nitrogen-laser-pumped dye laser Model DL12 from Molectron, and time-resolved sampling techniques in detection. The dye laser emission could be frequency-doubled, so as to have available excitation pulses of 10 nsec duration in the short u.v., at 254 nm.

Both the measurements with the spectrophotometer and with the dye laser were transferred in real time to the central computer of the GTE Labs by means of IBM Device Couplers, Model 7406. Digital pulses from TTL signal generators and pulse conditioners provided suitable master clocking for the acquisition and transfer of the measured data. An extensive software development in APL language supported various phases of data acquisition and processing. The final results were plotted on a Tektronix 4662 digital plotter.

Emission spectra.—The response of the phosphor under excitation at 254 nm are the main concern at this stage. Figure 2 contrasts, under identical excitation and detection conditions, the emission spectrum of YH and of sample RL24 of starting formulation

$$Sr_{4.25}Ce_{0.295}Mn_{0.245}(PO_4)_{3.0}F_{1.92} \quad [3]$$

The emission from YH consists of a residual Sb^{3+} emission in the blue, with peak at ≃500 nm, and of the yellow emission from Mn^{2+}, with peak at ≃575 nm. The SrFAP:Ce;Mn emission in turn comprises a Ce^{3+} emission band in the long u.v., with peak at ≃345 nm, and the Mn^{2+} emission in the yellow. The peak intensity of the Ce emission is roughly 25% that of the Mn emission in the same material. In turn the peak intensity of the Mn emission in the SrFAP sample is ≃90% the corresponding peak intensity in

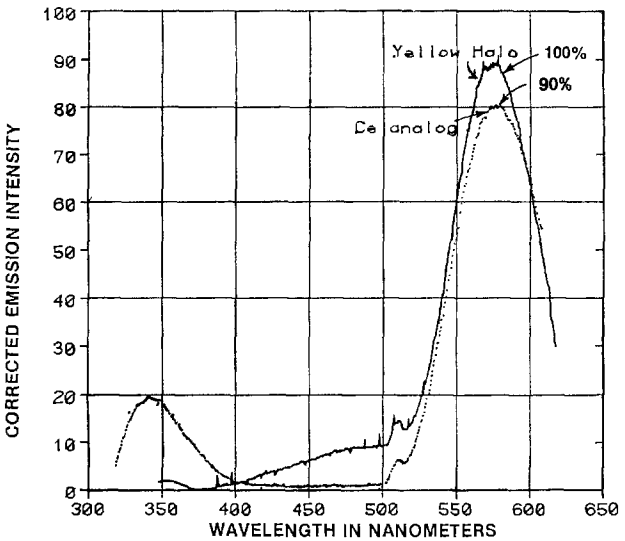

Fig. 2. Comparison of the corrected emission spectra of YH and SrFAP:Ce;Mn (sample RL24). Excitation at 254 nm. The narrow structure at 508 nm is due to scattered exciting radiation detected in second order.

YH. The emission spectra are truncated at ≃615 nm, the limiting wavelength of the corrected emission spectra directly obtainable from the MPF-44A fluorimeter.

Figure 3 shows a detailed view of the Mn emission in YH and in a somewhat less bright sample from the same SrFAP run. The emission peak is now ≃85% that of YH, and is slightly shifted to longer wavelengths, by comparison with YH. An opposite wavelength shift is found in samples with reduced Mn content, as for example in Fig. 4 for sample D7, with starting formation

$$Sr_{4.30}Ce_{0.295}Mn_{0.147}(PO_4)_{3.0}F_{1.72} \quad [5]$$

These shifts in the spectral location of the emission peak are associated with the Mn^{2+} concentration, the higher Mn content shifting the emission to longer wavelengths.

Excitation spectra.—The excitation spectra obtained on monitoring the emission at 575 nm are contrasted in Fig. 5 for the case of YH and SrFAP:Ce;Mn. In YH the absorption in the u.v. is provided by Sb^{3+} and rises rather rapidly from ≃300 nm toward shorter

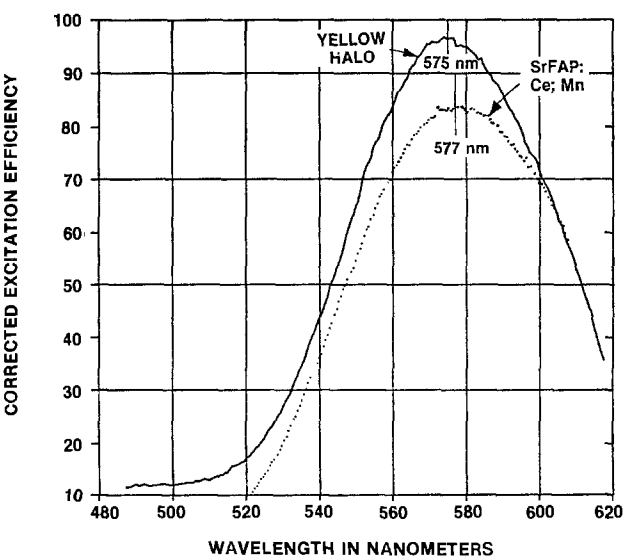

Fig. 3. Detail of the Mn emission in YH and SrFAP:Ce showing the respective peak location of the Mn emission. Excitation at 254 nm.

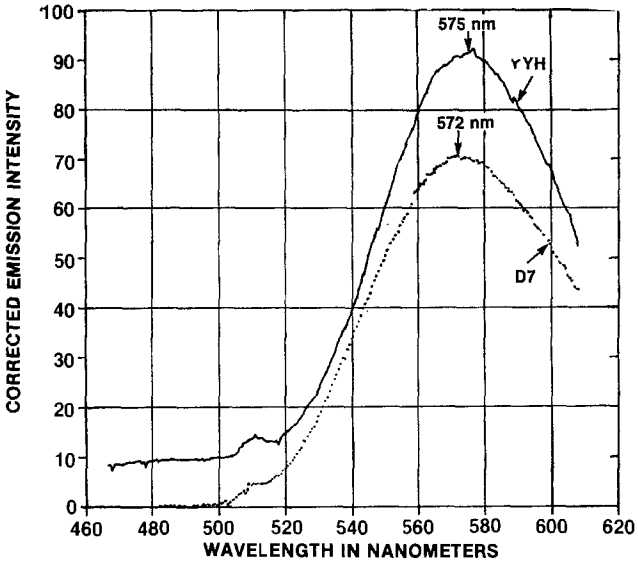

Fig. 4. Same as Fig. 3, but for an SrFAP:Ce;Mn sample with lower Mn content. The emission peak is shifted to shorter wavelengths when the Mn content is reduced.

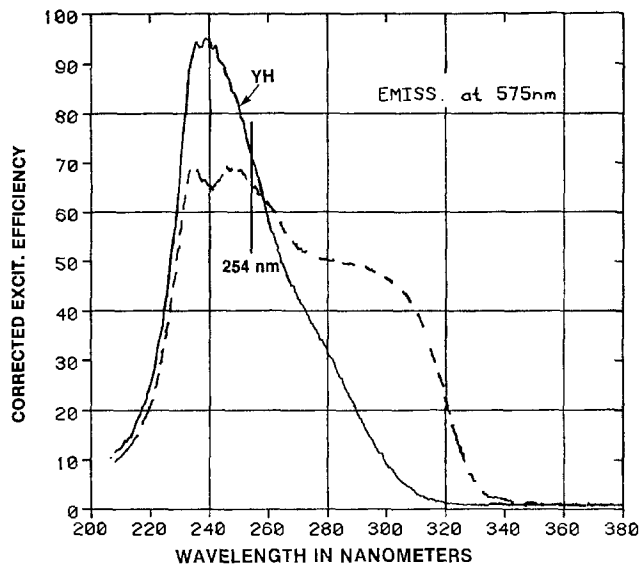

Fig. 5. Comparison of the corrected excitation efficiency (arbitrary, but same normalization) for emission monitored at 575 nm in YH and SrFAP:Ce;Mn. Note the broader excitation region for the latter.

wavelengths, peaking at 240 nm. By comparison with YH, the Ce-activated Sr fluoroapatite exhibits a broader, stronger excitation efficiency in the long u.v. and a less intense excitation efficiency at wavelengths shorter than 254 nm. The Ce^{3+} excitation peaks are located at ≃300, ≃248, and 234 nm. Excitation efficiency values at wavelengths shorter than ≃230 nm are not reliable, because of the drastic intensity drop in the exciting radiation.

Some interesting differences are noticeable in measuring the excitation spectra for Ce emission and for Mn emission in the same sample. This is exemplified in Fig. 6, again for a sample of starting formulation [3]. The excitation spectrum for Ce^{3+} emission shows a more structured level distribution and some maxima in the excitation spectra of Ce correspond to minima in the analogous excitation for Mn emission, as if the two processes were in part mutually exclusive. These differences in the two excitation spectra suggest that transfer from Ce to Mn occurs for Ce-Mn associates, the proximity of the Ce-Mn centers being indicated by the broadening of the Ce levels.

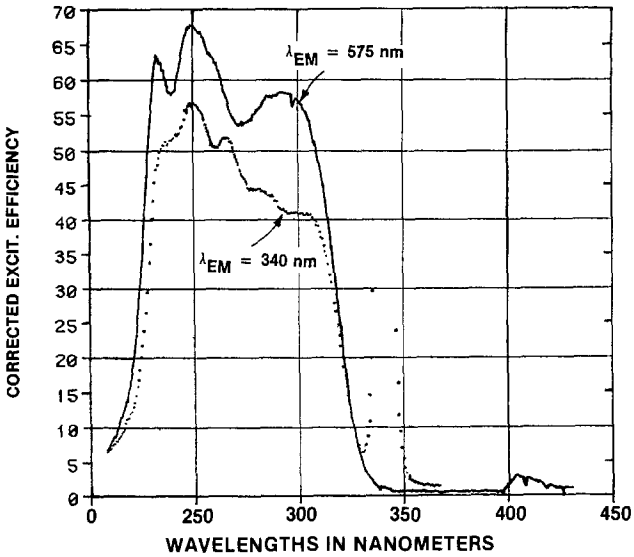

Fig. 6. Comparison of the corrected excitation efficiency in the same SrFAP:Ce;Mn material, while monitoring the emission near the peak of the Ce band in the u.v., and that of the Mn band at 575 nm. There are definite structural differences in the two excitation bands.

It can also be concluded from Fig. 6 that the absorption by Ce^{3+} at 254 nm, followed by sensitization of the Mn emission, is roughly 30 times more effective than direct absorption by Mn^{2+}, as occurring at ≃405 nm, followed by Mn emission.

A detailed view of the excitation spectra in the long u.v. and in the visible, arising from direct absorption by Mn^{2+}, is given in Fig. 7 for YH (sample RL63) and for SrFAP, sample RL68 of starting formulation [3]. The tail of the Ce excitation band in the latter partially masks the weak excitation regions of Mn^{2+} centered at 350 nm. The overall shape of the excitation spectra on the long-wavelength side of 350 nm is remarkably similar in both phosphors. The characteristic narrow peak at ≃405 nm is followed by a broader, symmetric band centered at 485 nm. The 405 nm excitation peak is actually stronger in SrFAP than in YH, suggesting a greater content

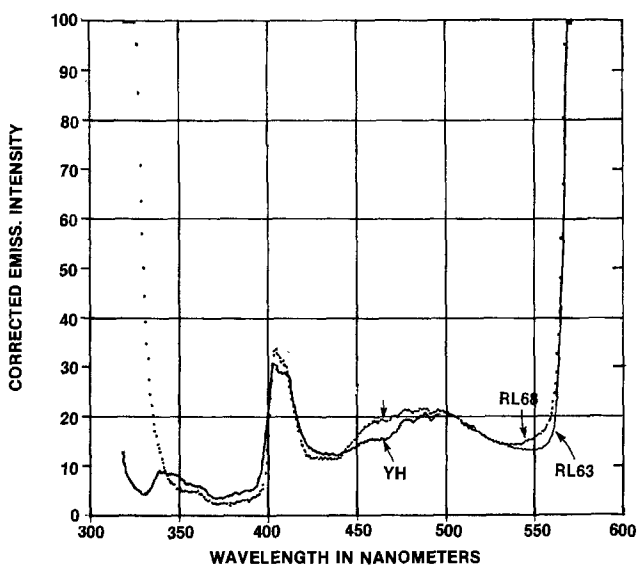

Fig. 7. Corrected excitation efficiency for YH and SrFAP:Ce;Mn (sample RL68; see text) in the spectral region of direct absorption by Mn^{2+}, while monitoring the emission at 575 nm. The marked similarity in the two excitation curves strongly suggests a similar site coordination around Mn^{2+} in both lattices, in spite of the strong fluoride excess in SrFAP.

of Mn^{2+} incorporated in the apatitic structure of the former. On the whole, the spectral measurements confirm the conclusion of the x-ray diffraction data, in the sense that despite the halide excess, the Mn^{2+} coordination in SrFAP markedly resembles that in YH.

Reflection spectra and remission spectra.—The excitation spectra detailed in the previous section map out the spectral regions that contribute to emission, after absorption of the exciting radiation, but do not provide a direct measure of the exciting radiation actually absorbed by the phosphor. Since the authors are dealing with powders, instead of measuring absorption spectra, as would be the case with transparent materials, they are restricted to measuring a complementary quantity, namely, the reflectance of the powder.

Reflectance measurements were carried out with the Perkin-Elmer spectrofluorimeter used to determine the emission and excitation properties of the phosphors. The two monochromators of the MPF-44A were set at the same wavelength, and scanned in tandem. Raw reflectance data were converted to an absolute scale by running the corresponding reflectance spectrum of a material of known properties, namely, the Eastman Kodak reflectance standard 6091. From the reflectance spectra of thick layers of powders one can derive the remission function

$$k/s = (1 - R)^2/2R \qquad [6]$$

namely, the ratio of the absorption coefficient k to the scattering coefficient s. For particles of similar morphology, and in spectral regions of intense absorption, it is justified to use the remission function as a comparative measure of the absorption of the materials considered. By deriving the remission function from the absolute reflectance data, one obtains curves that should approximate the absorption coefficient spectrum of the bulk material. An example of such remittance functions is given in Fig. 8, where we compare YH with SrFAP:Ce;Mn, sample RL68. The Ce^{3+} absorption dominates at ≃300 nm and decreases at shorter wavelengths. The Sb^{3+} absorption in YH is fairly minimal at 300 nm and rises rapidly at shorter wavelengths, peaking at 240 and at ≃222 nm. The curves for the two phosphors actually cross in the vicinity of 250 nm.

The excitation spectrum for Mn^{2+} emission from YH reproduces rather well the shape of the corre-

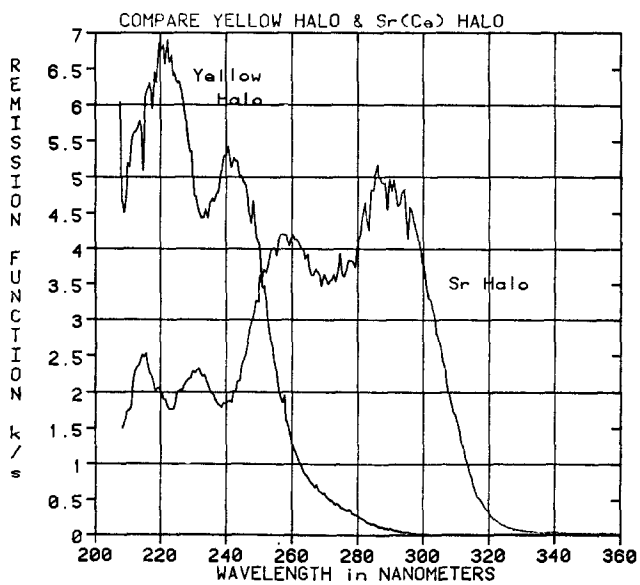

Fig. 8. Plot of the remission function k/s, namely, the ratio of the absorption coefficient to the scattering coefficient, for SrFAP: Ce;Mn (sample RL 68) and YH.

sponding remission function, up to ≃235 nm (Fig. 5 and 8). On the contrary, a comparison of the excitation spectra (with ordinates suitably scaled) and the remission spectra for sample RL68 shows that the Mn emission is more efficiently excited in the short u.v. around 250 nm than at the stronger absorption peak located at ≃290 nm (Fig. 9).

Spectral measurements at liquid-nitrogen temperatures.—A partial characterization of the spectral properties of SrFAP:Ce;Mn was performed on a sample of starting formulation [3] and with peak Mn emission at the 84% value of the YH standard. Figure 10 shows a comparison of the emission spectra at room temperature and at 77 K, for excitation at 254 nm. The Ce emission at low temperatures is split into two components located at 330 and 348 nm: this effect is due most likely to radiative transitions from a single emitting level to two J-manifolds (10) of the ^2F ground term of Ce^{3+}. Both Ce and Mn emissions increase in intensity at low temperatures, the former by almost a factor of two. The Mn emission also shifts to longer wavelengths on cooling. This can be explained on the basis of Tanabe and Sugano's diagram (5), as arising from a thermally induced increase in crystal field around Mn^{2+}. This type of long wavelength shift in the Mn^{2+} emission is also observed in YH.

Figure 11 shows the excitation spectrum at 77 K, obtained while monitoring the Mn emission at its peak. At least four excitation peaks, at 234, 250, 260, and 290 nm, are in evidence at low temperatures. Unfortunately, the corresponding excitation spectrum at room tempearture for the very same sample is not available. As an indication of the changes taking place in the shape of the excitation spectrum on cooling the phosphor, the low temperature excitation spectrum was contrasted with the room temperature excitation spectrum of Fig. 9. Cooling enhances the excitation intensity of the long wavelength portion of the excitation band, from ≃260 to ≃320 nm.

Excitation spectra at 77 K were measured in the region of direct absorption by Mn^{2+}, while monitoring the emission at 585 nm (Fig. 12). The curve of Fig. 12 should be compared with the corresponding

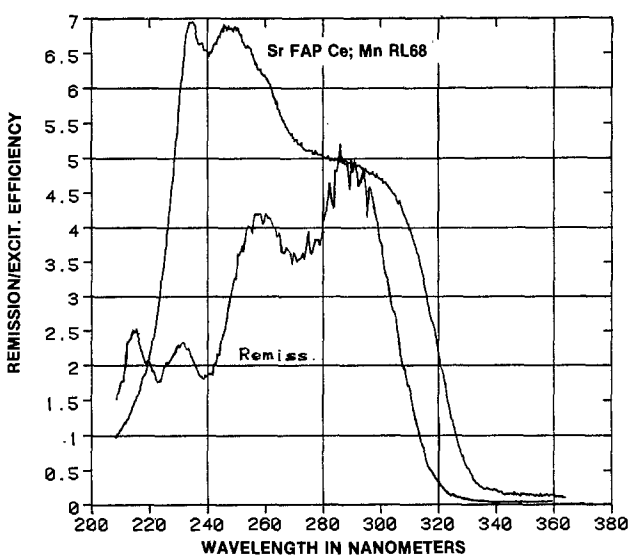

Fig. 9. Comparison of the remission function for SrFAP:Ce;Mn (sample RL68) and the excitation spectrum for Mn emission at 575 nm in the same sample. For convenience in plotting, the excitation-spectrum ordinates have been scaled down by a factor of 10.

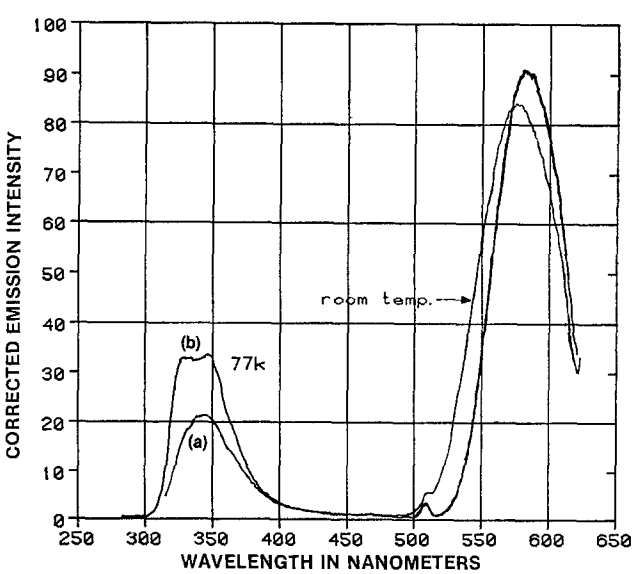

Fig. 10. Effect of temperature decrease on the emission from SrFAP:Ce;Mn. Excitation at 254 nm. (a) Room temperature, (b) at 77 K. Same excitation and detection conditions.

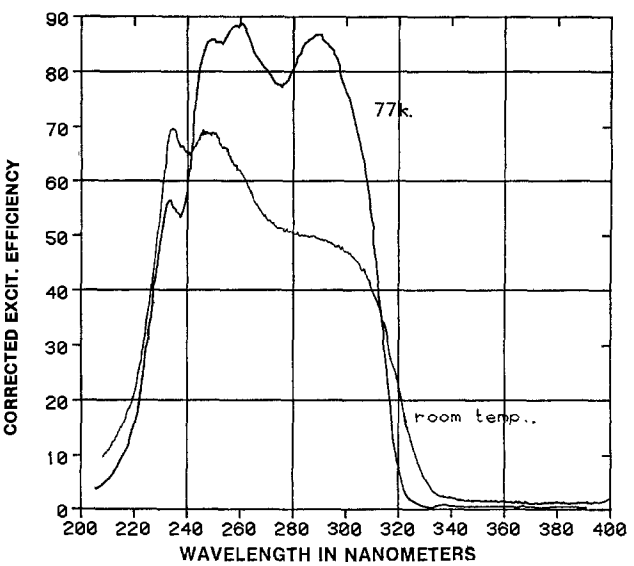

Fig. 11. Effect of the temperature decrease on the excitation spectrum for Mn emission at 575 nm in SrFAP:Ce;Mn.

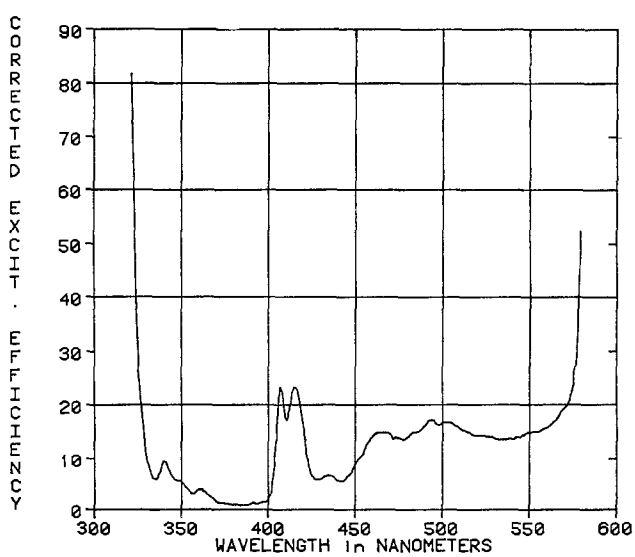

Fig. 12. Low temperature (77 K) excitation spectra for SrFAP: Ce;Mn, while monitoring the emission at 585 nm. This spectrum should be contrasted with that of Fig. 7.

curves of Fig. 7. The tail of the Ce^{3+} band is decreased in intensity at 77 K, so the Mn^{2+} group at $\simeq$350 nm becomes quite evident at low temperatures. The sharp peak at $\simeq$410 nm has now a definite doublet structure, with peaks at 406 and 415 nm. An additional weaker peak appears at 434 nm. The broader excitation region at longer wavelengths is now resolved into two components with peaks at 465 and 500 nm. Similar excitation spectra for YH have been reported by Wachtel and Ryan (11).

Emission-decay kinetics.—A useful property of phosphor activators, which is accessible to measurement and relevant to phosphor efficiency and to the sensitization process, is the decay rate of the corresponding radiative process and how it is affected by the concentration of activators and killer impurities.

The emission lifetimes for the active ions in question, Ce^{3+} and Mn^{2+}, differ by six orders of magnitude, the Ce^{3+} emission being generally of the order of 10^{-8} sec., and that of Mn^{2+} of the order of 0.01 sec. The kinetics of the emission decay from SrFAP were followed after dye laser pulsed excitation at 254 nm. In the singly activated materials (see Table III) of starting formulation

$$Sr_{4.30}Ce_{0.295}Mg_{0.146}(PO_4)_{3.0}F_{1.72} \quad [7]$$

the emission decay of Ce^{3+} for excitation at 254 nm was fairly exponential in nature, with a decay constant of $\simeq$28 nsec. The Ce decay was much faster in the presence of Mn^{2+}, because of the additional decay channel involving transfer of excitation energy from Ce^{3+} to Mn^{2+}. This is evident from an inspection of Fig. 13, where the Ce decay in the doubly activated material is almost twice as fast.

Since the decay process being measured in the case of the Ce^{3+} emission takes place during a time comparable to the excitation process, the observed emission pulse is a convolution of the exciting pulse and of the corresponding emission pulse. In order to extract the decay kinetic from the observed emission pulse, we successively convolute the excitation pulse (as measured by our detection system) with singly exponential decay processes, until a good match is obtained between synthesized and observed emission pulses. The result of one such convolution is shown in Fig. 14 for a sample doubly activated with Ce and Mn. The measured emission pulse is consistent with a decay constant for Ce of 11 nsec.

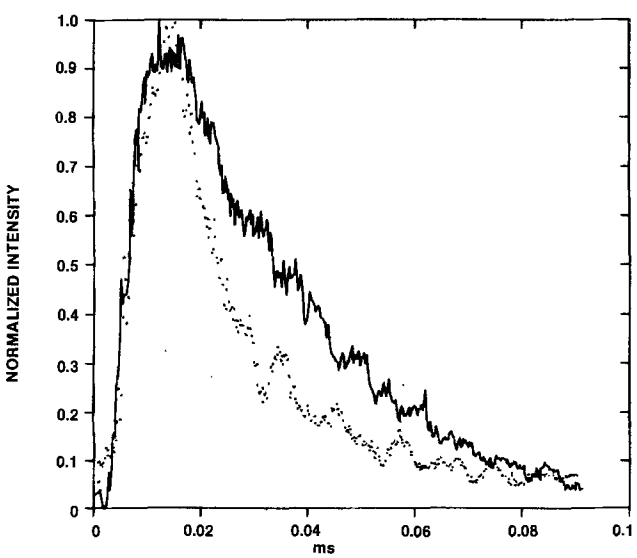

Fig. 13. Ce^{3+} emission pulse at 350 nm, following dye-laser excitation at 254 nm. Samples at room temperature. Solid line: emission from SrFAP:Ce;Mg. Dotted line: emission from SrFAP:Ce;Mn. The oscillations in the decay curves are due to rf pickup from the nitrogen-laser discharge.

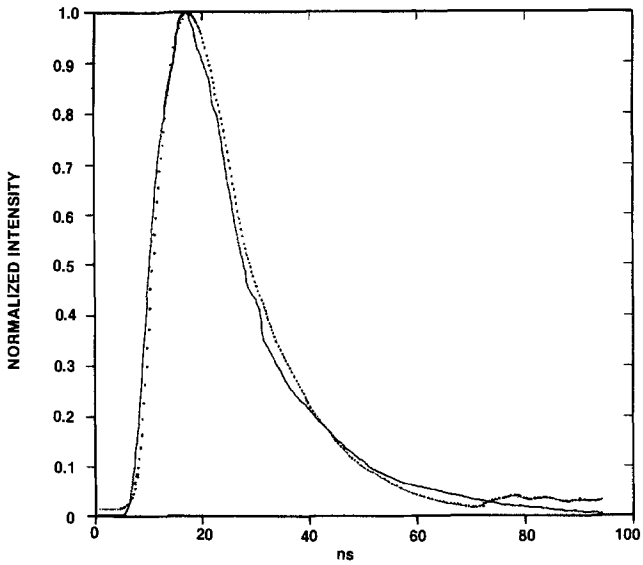

Fig. 14. Result of the convolution procedure used to extract emission decay constants from measured Ce-emission pulses. Sample of SrFAP:Ce;Mn at room temperature. The synthesized pulse (dotted curve) is the convolution of the system response function with an exponential decay of 11 nsec time constant.

The measured decay pulses of the Ce emission were not greatly affected by a decrease in sample temperature, down to $\simeq$100 K. A further decrease in sample temperature from 100 to 80 K caused the normalized emission pulse to broaden and the decay appeared to have a slower, later component (Fig. 15 and 16). Further measurements are required for a possible correlation of this abrupt change in decay characteristics with a thermally activated energy-transfer and/or sensitization process.

At room temperature the decay of the Mn emission for excitation at 254 nm is exponential (Fig. 17), with a decay constant of 14.8 msec. This value is quite close to the value measured for the Mn^{2+} emission in YH, where we find at room temperature a decay constant of 15 msec.

Singly activated strontium FAP.—Before discussing the lamp evaluation and air firing of the doubly activated SrFAP, some of the spectral properties of the

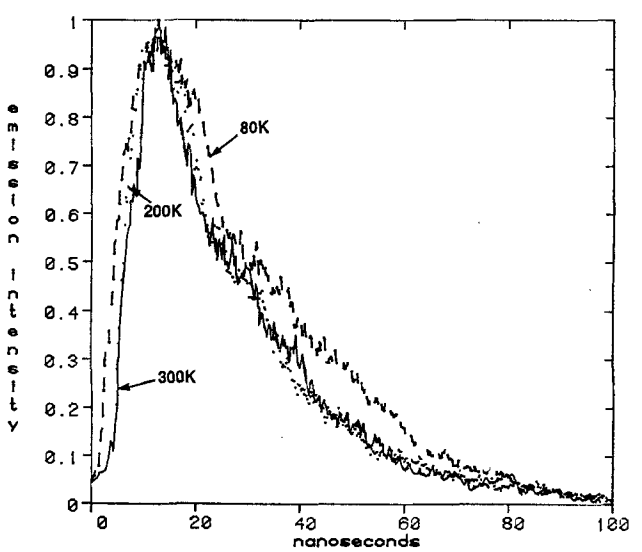

Fig. 15. Effect of decreasing temperature on the decay kinetics of Ce^{3+} emission from SrFAP:Ce;Mn. An appreciable lengthening of the decay is found at 80 K. Dye-laser excitation at 254 nm.

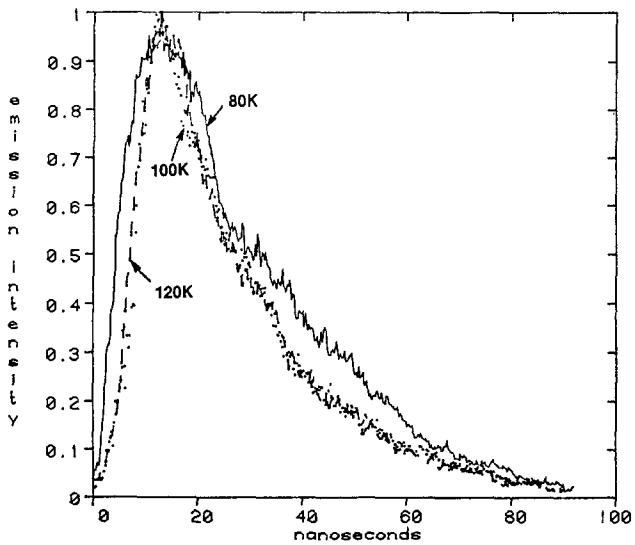

Fig. 16. Same as previous figure, but for a narrower temperature range, from 120 to 80 K. The change in the shape of the emission pulse occurs rather abruptly in going from 100 to 80 K.

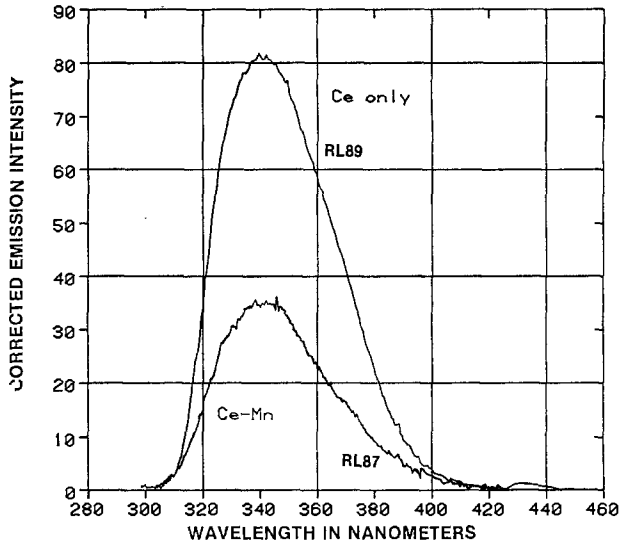

Fig. 18. Emission due to Ce^{3+} in two SrFAP:Ce phosphors, one containing both Ce and Mn, and the other with Mg replacing Mn. The Ce emission in the former is reduced by almost a factor of three, because of efficient energy transfer to the Mn^{2+} centers. The shape of the Ce^{3+} emission band is very similar in both cases.

Ce-activated SrFAP of starting formulation (7) are mentioned, since they are relevant to the lamp performance of the doubly activated phosphors. The emission from the singly activated phosphor consists of the already familiar Ce^{3+} band, with peak at $\simeq$340 nm and half-width at half-maximum of $\simeq$50 nm (Fig. 18). The Ce emission is reduced by more than half in the doubly activated sample, as seen in Fig. 18. The corresponding excitation spectra for emission at 348 nm are shown in Fig. 19. The replacement of Mg by Mn in the singly activated material produces a marked broadening of the excitation band of Ce^{3+}. This is again evidence for Ce-Mn associates in the doubly activated material.

Triple activation of SrFAP.—One of the advantages in using Ce^{3+} instead of Sb^{3+} as sensitizer in the apatite structure is the ability of Ce^{3+} to sensitize not only the emission of Mn^{2+}, but also that of trivalent rare earth ions. Sensitization of Tb^{3+} emission by Ce^{3+} in fluoroapatites has been reported by Ranby and Hobbs (12). To demonstrate the possibility of Ce-RE^{3+} sensitization even in the presence of Mn^{2+}, some preparations of SrFAP activated with Ce, Mn, and one of the rare earths were carried out

The results obtained when the rare earth ion was Dy^{3+} are given in Fig. 20. The emission consists of the now familiar Ce emission in the long u.v., of the yellow emission from Mn^{2+} and, in addition, of two line groups located at 470 and 570 nm and contributed by Dy^{3+}. In principle this combination of blue and of composite yellow emission from a single phosphor could provide the overall white field that in the Lite-White scheme is obtained using a blend of two phosphors.

A combination of Ce, Mn, and rare earth emission was also observed on activation with Tb^{3+}.

Lamp Evaluation of Doubly Activated SrFAP

Standard 40W low pressure fluorescent lamps were coated with SrFAP:Ce;Mn phosphors of starting formulation [3]. As internal standards, lamps were also fabricated with YH. The original plaque brightness of the SrFAP:Ce;Mn was approximately 85% that of

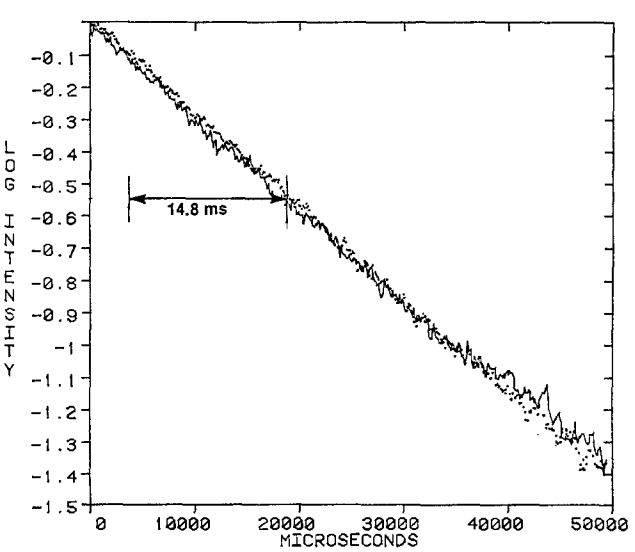

Fig. 17. Semilog plot of the emission decay at 580 nm from SrFAP:Ce;Mn as a result of dye-laser excitation at 254 nm. A decay constant of $\simeq$14.8 msec can be extracted from the straight semilog plot.

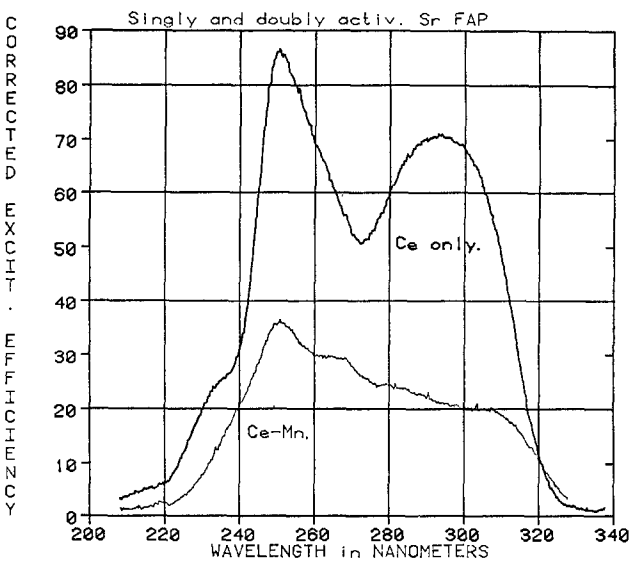

Fig. 19. Same two samples as in previous figure, but now the excitation efficiency for Ce emission at 348 nm is being monitored. The replacement of Mg with Mn markedly broadens the Ce level distribution.

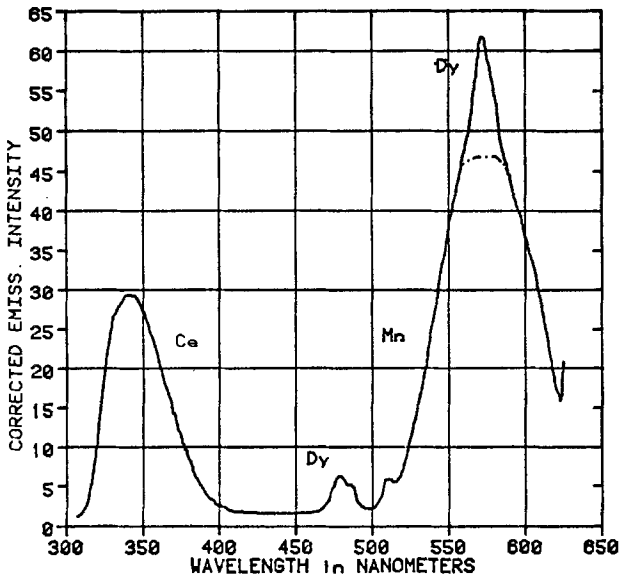

Fig. 20. Emission spectrum of a triply activated SrFAP:Ce;Mn:Dy phosphor for excitation at 254 nm. In addition to emitting in the u.v., Ce sensitizes both the Mn^{2+} emission and that of Dy^{3+}, with line groups at 470 and 570 nm.

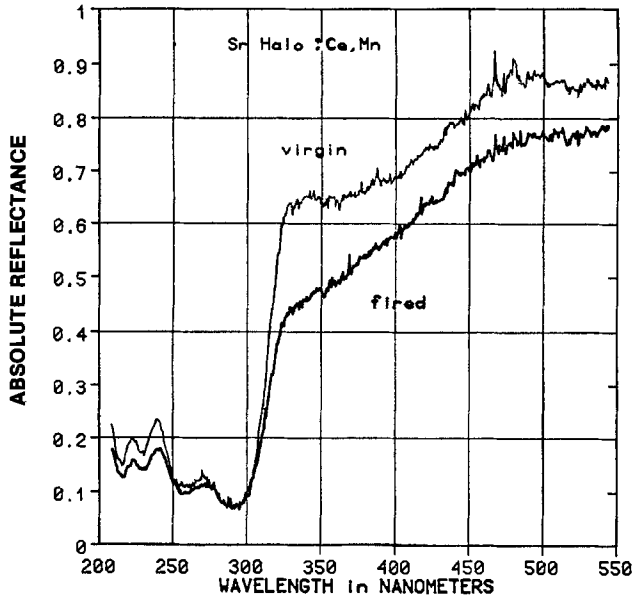

Fig. 21. Effect of air firing on the reflectivity of the SrFAP:Ce;Mn phosphors. The absorbance of the material is fairly unchanged at 254 nm, but increases from ≃310 nm to longer wavelengths.

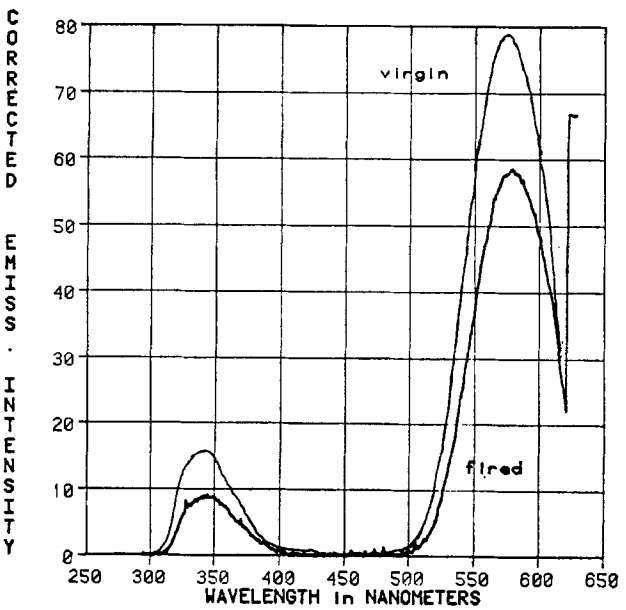

Fig. 22. Effect of air firing on the emission properties of SrFAP: Ce;Mn. Excitation at 254 nm. The emission loss is relatively higher for the u.v. emission band.

YH. At zero hour the corresponding lamp output was already down to ≃73% that of the lamp coated with YH, an indication of serious baking and short-term brightness losses. At 100 hr the output maintenance was poor, 85.4%, compared to the 97.6% maintenance for YH. It appears therefore that the phosphor, as presently formulated, although exhibiting suitable plaque brightness, is not stable to the lamp-making process.

The remainder of the present report is devoted to a preliminary inquiry into the causes of such a phosphor deterioration, namely, to determining whether the effect is associated with the matrix itself or with the oxidation of Ce^{3+} and/or of Mn^{2+}.

Effect of Air Firing on Brightness

In order to roughly simulate the conditions seen by the phosphor during baking, small amounts of the phosphor of starting formulation [3], *i.e.*, about 1g batches, were fired in air for 15 min at 640°C. This firing treatment caused a change in the body color from pale green to light tan. This effect can also be followed in the reflectance data of Fig. 21. The absorbance of the powder around 254 nm, in the region of absorption by Ce^{3+}, is barely affected by the firing treatment, while a broad continuous absorption sets in from 325 nm down into the visible region. Both in the spectral region of Ce emission and of Mn emission, the fired material is definitely more absorbing than the virgin phosphor. Therefore, it is not surprising that the increased absorbance is accompanied by serious losses in emission intensity. In effect, the emission band of Ce is decreased at the peak by almost 50%, while the Mn emission is reduced by 25% (Fig. 22). The excitation spectra for emission at 580 nm are plotted in Fig. 23 for the virgin and for the fired phosphors: the loss in excitation efficiency is highest at the shortest wavelengths (≃50% at the 235 nm excitation peak), while it is only 20% at the broad excitation peak at 290 nm.

These results on the doubly activated SrFAP should now be contrasted with the behavior of the singly activated analog of starting formulation [7]. On firing the latter, the original pale green body color of the powder veered to white. In addition, the reflectance spectra of Fig. 24 show no change in the strength of the u.v. absorption peaks of Ce^{3+}, namely, no evidence of oxidation of Ce^{3+} is seen, while there is a partial bleaching of the absorption responsible for the original green body color. As a result of the air firing, we actually register an increase in Ce^{3+} emission (Fig. 25). The preliminary conclusion is that during the air firing, and the lamp making processes, the sensitive component is not Ce^{3+} but probably Mn^{2+}, or possibly the Ce-Mn associates.

Conclusion

The first stage in the search for suitable alternatives for the yellow emitting component for the Lite-White blend has demonstrated the potentialities of Ce-Mn-coactivated fluoroapatite phosphors in providing plaque brightness approaching that of YH.

The lamp tests also revealed that the Ce-Mn Sr fluoroapatite phosphors, as presently formulated, are apparently damaged in the baking and in the lamp making process. The question of lamp compatibility is therefore central to further development and synthesis optimization of the Ce-Mn fluoroapatite phosphors. Since Ce is a more versatile sensitizer than Sb,

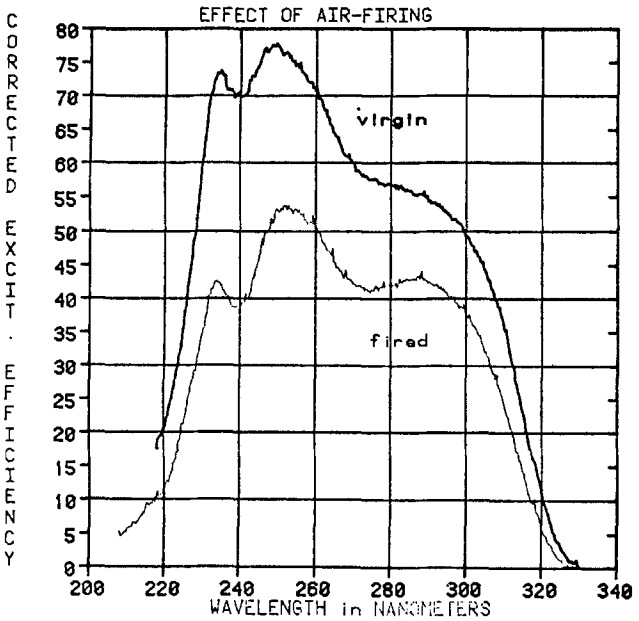

Fig. 23. Changes in the excitation spectrum for emission at 580 nm from SrFAP:Ce;Mn as a result of air firing. The efficiency loss increases toward shorter wavelengths.

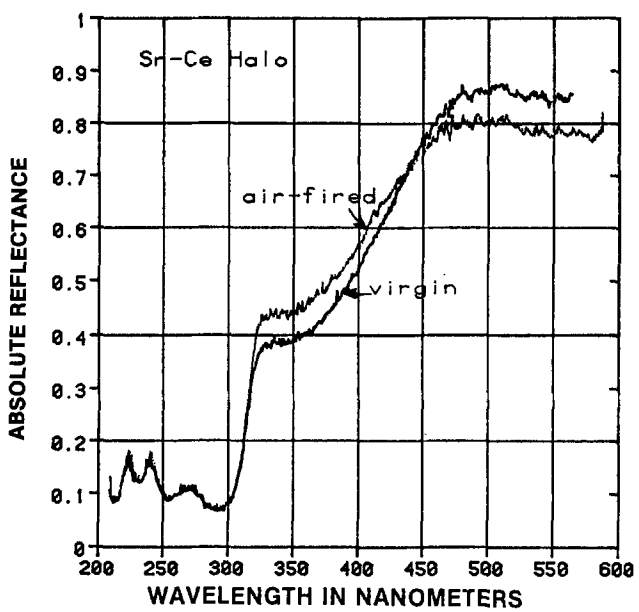

Fig. 24. Changes in the reflectance of singly activated SrFAP:Ce after air firing. No appreciable change in Ce^{3+} absorbance at 254 nm is noticeable. The absorption band centered around 350 nm, and responsible for the pale green body color, is actually decreased as a result of the air firing.

if the lamp processing losses were brought under control, a wide versatile new class of halophosphate phosphors would become available.

Acknowledgments

The writers wish to express their appreciation and thanks for the help and cooperation provided by the following GTE personnel: C. Chenot and A. Kasenga of the Towanda PMG for the preparation of those phosphor samples that were later submitted for lamp testing and for many valuable discussions on phosphor properties; J. T. Smith and J. McColl of the GTE Labs for a critical reading of the manuscript; C. Persiani and F. Durkin of the GTE Labs, and the staff of the Analytical Group of the Towanda PMG for the chemical analyses; M. Downey and G. Hamill for the x-ray powder-diffraction work; C. Miller and K. Ostreicher for the scanning electron microscopy of the samples; and P. Martakos for the infrared spectral measurements.

Manuscript submitted Feb. 8, 1982; revised manuscript received June 13, 1983. This was Paper 176 presented at the Minneapolis, Minnesota, Meeting of the Society, May 10-15, 1981.

GTE Laboratories Incorporated assisted in meeting the publication costs of this article.

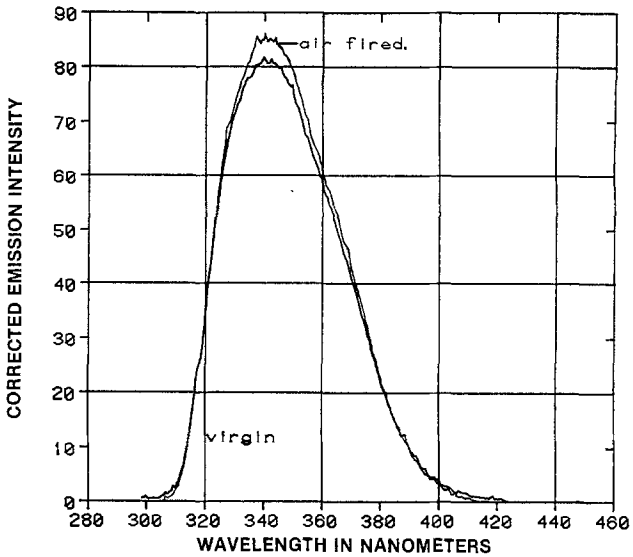

Fig. 25. Emission spectrum of the singly activated SrFAP:Ce of the previous figure, before and after air firing. The air-fired material has a stronger Ce emission, ≃6% higher at the peak.

REFERENCES

1. J. M. P. J. Verstegen, D. Radielovic, and L. E. Vrenken, *This Journal*, **121**, 427 (1974).
2. L. E. Vrenken, *Lighting Res. Technol.*, 8211 (1976).
3. W. W. Piper, J. S. Prener, and C. G. R. Gillooly, U.S. Pat. 4,075,532 (1978).
4. H. F. Ivey, *J. Opt. Soc. Am.*, **53**, 1185 (1963).
5. Y. Tanabe and S. Sugano, *J. Phys. Soc. Jpn.*, **9**, 753 (1954).
6. S. T. Henderson and P. W. Ranby, *This Journal*, **104**, 612 (1957).
7. P. W. Ranby, Br. Pat. 792,598 (1958).
8. ASTM Powder Diffraction File 29-1310.
9. C. Smith and G. McCarthy, Pennsylvania State University (1977).
10. M. A. Elyashevich, "Spectra of Rare-Earths," p. 392, State Publishing House, Moscow (1953).
11. A. Wachtel and F. A. Ryan, *This Journal*, **120**, 693 (1973).
12. P. W. Ranby and D. Y. Hobbs, Ger. Pat. 25 35 446 (1976).

Delineation of p-n Junction in Thin InGaAsP Layers Using Chemical Etching

J. A. Lourenco

Bell Laboratories, Murray Hill, New Jersey 07974

ABSTRACT

A method for the delineation of the p-n junction inside the active layers of InGaAsP/InP double heterostructures is presented. A chemical etch used with illumination on a grooved sample can accurately delineate the diffusion front of the p-dopant in quaternary layers. Using a conventional optical microscope, the technique can be used for active layers as thin as 0.1 μm. Good correlation with scanning electron microscope techniques (EBIC) is observed. The technique presented here can easily be used as a routine step during wafer characterization.

In InGaAsP/InP double heterostructures (DH) grown by liquid phase epitaxy (LPE), the p-n junction position in the nominally undoped InGaAsP active layer is formed by diffusion of the acceptor, commonly Zn, from the p-type InP confining layer. However, the Zn flux into the quaternary layer is dependent on its concentration in the confining layer and the diffusion depth can be altered by varying the time that the wafer remains at high temperature after the InGaAsP active layer has been grown. In addition, the position of the p-n junction has been found to depend on the doping level of the active layer (1, 2), and lattice mismatch, which influences the bulk properties of the epi, can also affect the Zn diffusion length (3). Consequently, the position of p-n junction can shift from run to run, and its misplacement has been a problem, particularly in very thin layers (1, 4).

An accurate way of determining the p-n junction in a double heterostructure is with the electron beam-induced current (EBIC) (5) mode of a scanning electron microscope. The EBIC method, however, is too complex to be used routinely. A simple and quick alternate method is therefore desirable. Often, chemical staining of a cleaved edge is the method of choice and it works well with thick layers (greater than 2.0 μm). It has been successfully applied to thick InGaAsP layers, although the exact procedure and the type of stain were not mentioned (2). However, when the active layer thickness is less than ~2.0 μm, the resolution of an optical microscope is limiting. Also, if the p-n junction is very close to one of the interfaces of the active layer, the junction and this interface become indistinguishable, even in a thick layer, and no information can be obtained.

In this paper, a technique is presented which can accurately reveal the position of the p-n junction inside InGaAsP layers as thin as 0.1 μm. A chemical etch is used with illumination. Coupled with the arcuic trigonometric method of calculating layer depth (6), it provides a quick and easy way of routinely determining the position of the diffusion front inside the active layer.

Experimental

A small sample (~1.5 × 3.0 mm) is cut from an LPE double heterostructure, mounted on a thin glass cover plate, and grooved using a sectioner from Philtec Instrument Company. The detailed procedure for mounting and grooving the sample has been described by McDonald and Goetzberger (7). The groove depth must be carefully controlled: it must be deep enough to completely cut through the active layer but should not go much deeper than the bottom of the layer in order to maximize the groove width-to-depth ratio. The sample is then cleaned and stained under illumination from a microscope lamp with a 15W tungsten filament bulb placed directly over the groove. The stain solution consists of 100 ml of H_2O, 8g KOH, and 0.5g $K_3Fe(CN)_6$ (8). Although the time required for staining depends strongly on dopant concentration, in most samples 5-10 sec was enough to delineate the p-n junction. Usually the surface on the p-side of the quaternary active layer becomes very rough, probably because it is more strongly attacked by the chemical etch than the n-side. After staining, the thickness of the active layer can be calculated and the exact position of the junction can be determined (6, 7). Figure 1 shows a grooved sample which has been stained for delineation of the active layer boundaries and the p-n junction position.

To evaluate the validity of this technique, several samples were analyzed using both the groove-and-stain method and the EBIC method. Figure 2 shows two scanning electron micrographs of cleaved edges of InGaAsP/InP DH light emitting diodes (LED's). The EBIC signals place the p-n junction (a) at the top of the active layer, very close to the p-InP, and (b) deep inside the active layer, closer to the n-InP. Figure 3 shows the two samples from Fig. 2, this time using the groove-and-stain technique to delineate the quaternary layer interfaces and the p-n junction. Again, the p-n junction appears (a) at the top of the active layer, and (b) closer to the bottom of the layer.

A few samples were stained without using illumination. A loss of sharpness at the p-n junction was observed and a much longer staining time was required.

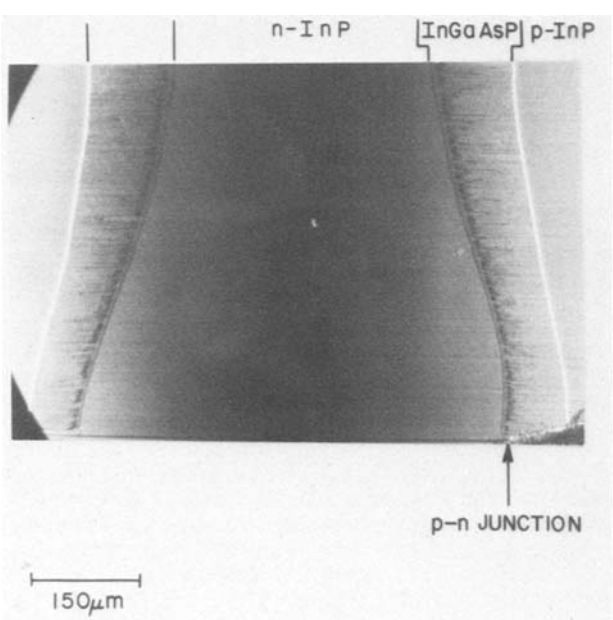

Fig. 1. Interference contrast micrograph of a grooved sample which has been stained for layer delineation and for determination of the p-n junction position.

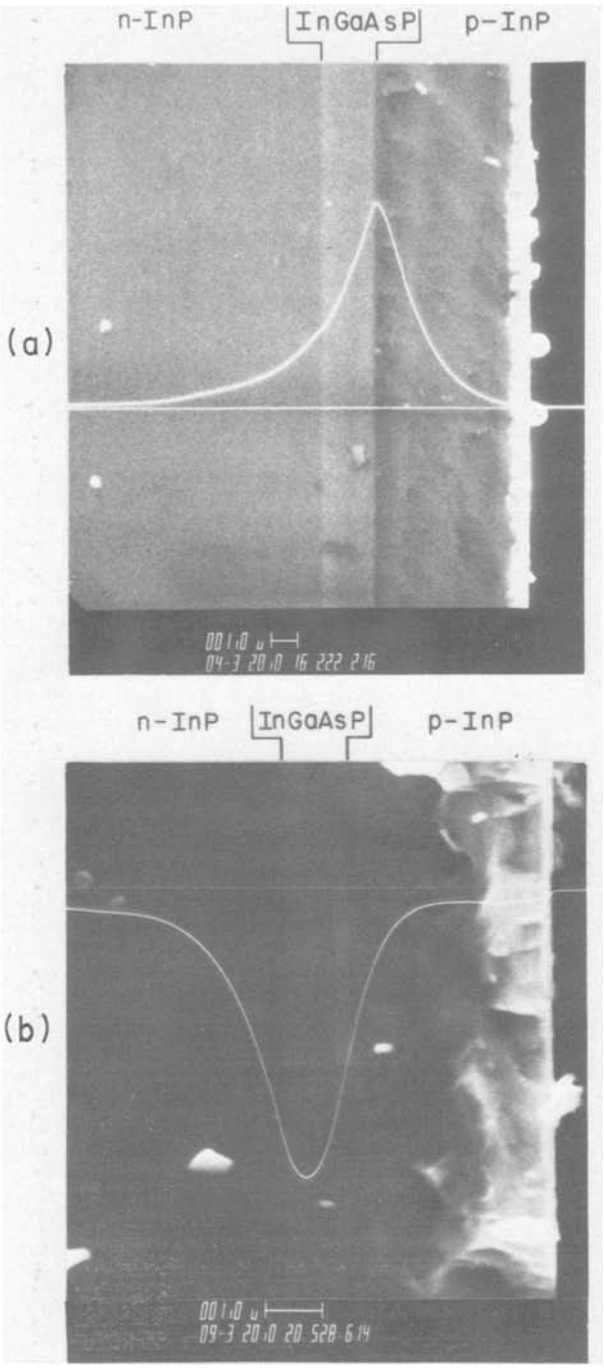

Fig. 2. Scanning electron micrograph of a cleaved edge of a InGaAsP/InP DH LED. The EBIC signal shows the p-n junction (a) at the top of the active layer, next to the InP confining layer; (b) deep inside the active layer, closer to the InP buffer layer.

This resulted in partial removal of the active layer with consequent loss of accuracy. Several stain compositions of the same components were tried, but the composition described above seemed to give the best results. In particular, compositions where the concentration of $K_3Fe(CN)_6$ is increased, like the ones usually used for quaternary layer removal (9), were too strong for staining purposes: although they delineate the p-n junction they also etch away the active layer very quickly, starting towards the center of the groove where the layer is thinnest. They are, therefore, not practical because accuracy is lost, and p-n junctions very close to the bottom of the active region cannot be detected. Delineation of the junction right at the bottom of the layer, as illustrated in Fig. 1, would be impossible if any appreciable layer removal had taken place. Other known InGaAsP etchants were

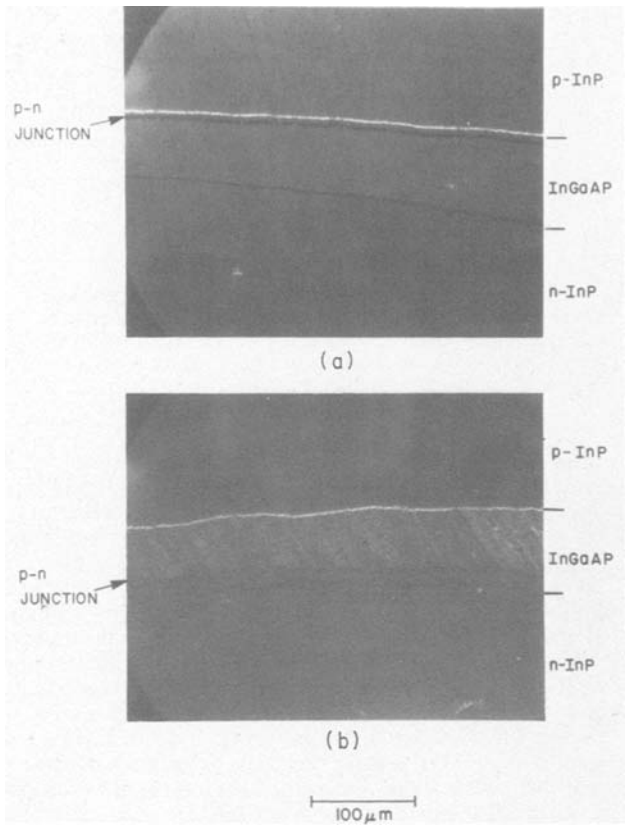

Fig. 3. Interference contrast micrograph of the same samples from Fig. 2 with the p-n junction delineated using the groove and stain method: (a) junction present at top of the active layer; (b) junction deep inside the layer.

tried, such as the AB etch (10), but these were also too fast at attacking the quaternary layer.

Most of this experimental work was done on wafers in which the active layer was nominally undoped n-InGaAsP. The p-n junction was formed by Zn diffusion from the Zn-doped InP confining layer. This technique was also successfully tried on a wafer where Cd was used as the p-dopant.

Discussion

A 100 ml solution of 8.0g potassium hydroxide and 0.5g potassium ferricyanide is strong enough to delineate th p-n junction inside a quaternary layer, but weak enough to do so without appreciable removal of InGaAsP.

Excellent correlation is observed between the EBIC and the groove-and-stain methods. However, the EBIC technique consists of a scanning electron micrograph with a superimposed EBIC signal, and the two are not always easy to align. In the groove-and-stain technique, the active layer boundaries and the p-n junction are delineated in only one step, and they are usually very sharp. Therefore, the groove-and-stain method is possibly more accurate. In this technique, illumination is necessary if sharpness of delineation and quickness are to be attained.

The major advantage of this technique is the accurate delineation of the p-n junction inside very thin layers, which is hard to do even with EBIC. Because a very shallow layer can be transformed by grooving into a width easily resolved by optical microscopes, and because the etch described above stains much faster than it etches away InGaAsP, the p-n junction can be determined in layers as thin as ≈ 0.1 μm. (See, for example, Fig. 4.) Also, junction displacement from metallurgical boundary of $\lesssim 0.1$ μm can be resolved, as illustrated in Fig. 3a. In addition, this is a quick

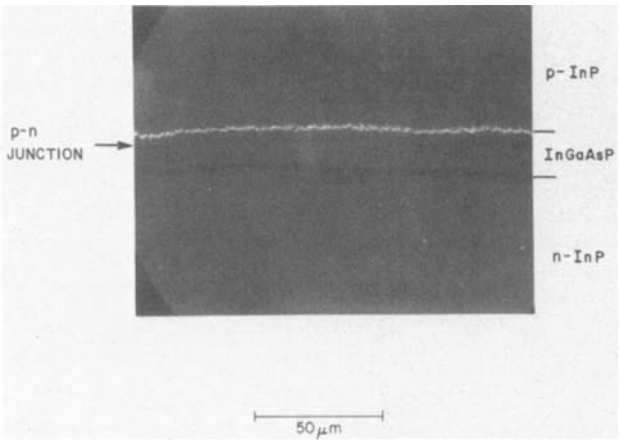

Fig. 4. Interference contrast micrograph of grooved and stained sample showing the p-n junction position inside an InGaAsP layer 0.16 μm thick.

and simple technique which can easily be used as a routine step in wafer characterization.

Acknowledgments

The author would like to thank H. Temkin and F. Ermanis for the EBIC results, A. K. Chin for useful comments, B. H. Chin for helpful guidance, and R. H. Saul for his support.

Manuscript submitted Feb. 4, 1983; revised manuscript received *ca.* May 27, 1983.

Bell Laboratories assisted in meeting publication costs of this article.

REFERENCES

1. N. Tamari, *Appl. Phys. Lett.*, **40**, 108 (1982).
2. P. D. Wright, Y. G. Chai, and G. A. Antypas, *IEEE Trans. Electron Devices*, **ed-26**, 1220 (1979).
3. M. M. Tashima, L. W. Cook, N. Tabatabaie, and G. E. Stillman, *Appl. Phys. Lett.*, **38**, 1009 (1981).
4. J. J. Coleman and F. R. Nash, *Electron Lett.*, **14**, 558 (1978).
5. L. J. Balk, E. Kubalek, and E. Menzel, *IEEE Trans. Electron Devices*, **ed-22**, 707 (1975).
6. C. L. Aley and R. S. Turner, *Semicond. Intern.*, **3**, 135 (May 1980).
7. B. McDonald and A. Goetzberger, *This Journal*, **109**, 141 (1962).
8. J. J. Hsieh, J. A. Rossi, and J. P. Donnelly, *Appl. Phys. Lett.*, **28**, 709 (1976).
9. K. L. Conway, A. G. Dentai, and J. C. Campbell, *J. Appl. Phys.*, **53**, 1836 (1982).
10. M. S. Abrahams and C. J. Buiocchi, *ibid.*, **36**, 2855 (1965).

Dependence of the Characteristics of ZnSe MBE Grown on GaAs and GaP on Thermal Treatment in a Vacuum

T. Niina, K. Yoneda, and T. Toda

Sanyo Electric Company, Limited, Research Center, 1-18-13, Hashiridani, Hirakata, Osaka, 573, Japan

ABSTRACT

The dependence of the surface morphologies, electrical and optical properties of MBE grown ZnSe layers on the surface cleanliness of both GaAs and GaP substrates after being treated by a thermal treatment procedure in a vacuum prior to growth was studied by using RHEED and AES and by measuring the Hall effect and photoluminescence. The major contaminants on the surface of both GaAs and GaP after chemical treatment are carbon and oxygen. Carbon absorbed on the surface of both GaAs and GaP can be easily decomposed by thermal treatment above 420°C. On the other hand, there is quite a difference between GaAs and GaP concerning the removal behavior of the residual oxide layers. The thermal treatment temperatures required to completely remove these oxide layers are 560°C for GaAs and 620°C for GaP. The characteristics of the MBE grown ZnSe layers depend mainly on the surface cleanliness of the substrate after the thermal removal of the residual oxide layers. In order to achieve a high quality grown layer, it is recommended that the thermal treatment be in the comparatively wide region between 560° and 630°C for the growth of ZnSe on GaAs and in the extremely narrow region between 620° and 630°C for the growth of ZnSe on GaP.

Cleaning the surface of the substrate prior to growth is an essential procedure in the preparation of a high quality epitaxial film using molecular beam epitaxy (MBE). In the case of GaAs, which has been widely used as a substrate for the MBE growth of III-V compound semiconductors, the major contaminants are oxygen and carbon. Oxygen contaminates the surface during and after chemical treatment, forming unavoidable thin oxide layers which consist of arsenic and gallium oxides (1). Arsenic and gallium oxides can be removed by thermal treatment in a vacuum, with temperatures above 370° and 570°C, respectively (2). On the other hand, carbon is easily absorbed from an ambient and a cleaning solvent (3). Ordinary carbon contaminants can be effectively decomposed by thermal treatment in a vacuum above 350°C. However, when the substrate has been exposed to an ionized beam, carbon cannot be removed by thermal treatment unless temperatures above 600°C are used (4). The presence of such residual carbon contaminants across the interface of the grown layers results in the generation of defects and affects the surface morphologies of the grown layers (5).

Key words: molecular beam epitaxy, zinc selenide, reflection high energy electron diffraction, Auger electron spectroscopy, photoluminescence, Van der Pauw method.

Recently, MBE has been extensively applied in the growth of II-VI compound semiconductor films. In particular, for the growth of ZnSe, the possibility of achieving a precisely controlled, highly conductive layer for use in blue light emitting diodes has been demonstrated (6, 7). So far GaAs has been commonly used as the substrate for the MBE growth of ZnSe because of its closed lattice match. GaP can also be used in spite of its large lattice misfit of ~ 4% (8). As in the growth of III-V compounds, the preparation of a smooth, clean, and undamaged substrate surface is also an important requirement for achieving a high quality layer in the case of ZnSe MBE growth.

In this paper, we investigated thermal treatment procedures required not only to decompose carbon contaminants but also to remove residual oxide layers

on the surface of both GaAs and GaP, and the relation between the surface cleanliness of the substrate and the characteristics of ZnSe layers grown on both GaAs and GaP. These investigations were performed by using reflection high energy electron diffraction (RHEED), Auger electron spectroscopy (AES), Hall effect measurement, and photoluminescence measurement.

Experimental Procedures

The substrates used in the present study were Cr-O doped semi-insulating GaAs (100) with a resistivity of greater than 3×10^7 Ω-cm, and also Zn-doped p-type GaP (100) with a resistivity of ~0.2 Ω-cm and a carrier concentration of $5 \sim 10 \times 10^{17}$ cm^{-3}.

After mechanical and chemical polishing, they were degreased with trichloroethylene by boiling, acetone, ethanol, and deionized water. Then, in the case of GaAs, the substrates were etched with a solution of $5H_2SO_4$-H_2O_2-H_2O for 10 min at 60°C, subsequently rinsed with deionized water, finally immersed in HCl for 10 min at 30°C in order to remove the residual oxide layer, rinsed with deionized water, and dried with dry nitrogen. In the case of GaP, the substrates were etched with a stirring solution of HCl-2HNO_3-H_2O for 10 ~ 15 min at 55°C, then rinsed with deionized water, and dried with dry nitrogen.

After these chemical treatment processes, the samples were mounted on an Mo sample block using In for adhesion, immediately inserted into a loading chamber of an MBE system, and pumped down. The MBE system used in the present study was a RIBER-MBE 1000 which was equipped with a quadrupole mass spectrometer, a 10 keV RHEED, and an AES.

After being transferred into the growth chamber, which has a base pressure less than 10^{-10} Torr, the samples were treated thermally prior to growth for 15 min at each step of the temperature regions between 300° and 670°C. All of the epitaxial films were grown on both the GaAs and the GaP substrate. 6N-Zn, Se, and Ga metal were used as source materials. For growth, the Zn cell temperature and the Se cell temperature were normally kept at ~300° and ~210°C, respectively. Under this condition, the beam flux ratio of Zn to Se was about 1. For the growth of ZnSe on GaAs, the substrates were heated either to 320°C or to 360°C. For the growth of ZnSe on GaP, the substrates were heated to 360°C to maintain a smooth surface morphology. For doping, the Ga cell temperature was fixed at ~420°C to obtain the desired carrier concentration.

At each step of the various thermal treatments, RHEED and AES observations were made to evaluate the surface cleanliness of the substrate resulting from the removal of the surface contaminations. In-depth profile measurements of AES were used to determine the transition region between the growth layer and the substrate and also to detect the impurities embedded across the interface. The electrical and optical properties of the grown layers were studied by using the Van der Pauw method and by room temperature photoluminescence excited with a 3250Å He-Cd laser, respectively.

Results and Discussion

Figure 1 shows the Auger peak heights of various elements at the substrate surfaces as functions of the thermal treatment temperatures. The Auger peak heights obtained from GaAs and GaP are shown in Fig. 1(a) and (b), respectively. The peaks retained in the Auger spectra are a 273 eV KLL transition for C, a 503 eV KLL transition for O, a 1070 eV LMM transition for Ga, a 1229 eV LMM transition for As, and a 1865 eV LMM transition for P.

Carbon contaminants absorbed on both GaAs and GaP after chemical treatment can be explicitly decomposed by thermal treatment above 420°C, which is

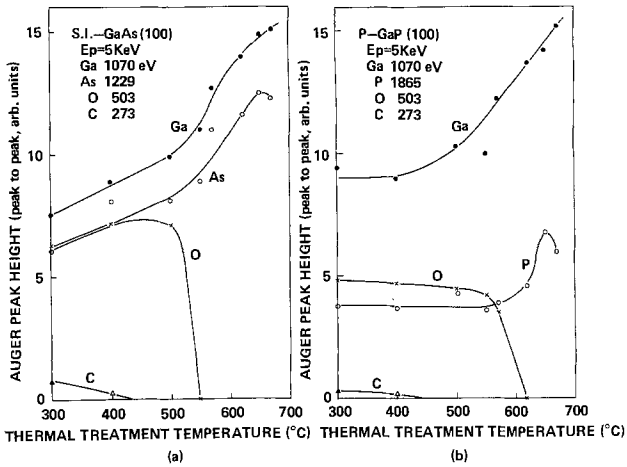

Fig. 1. Auger peak heights of various elements from different substrate surfaces of GaAs (a) and GaP (b) as a function of the thermal treatment temperatures.

slightly higher than the 350°C described by Chang *et al.* (9).

For GaAs, the oxygen peak height begins to decrease at the thermal treatment of 500°C and then disappears rapidly when a thermal treatment of 560°C is used. This corresponds to the removal behavior of an oxidation product consisting of Ga_2O_3. For GaP, the oxygen peak height decreases gradually as the thermal treatment temperature increases when thermal treatments above 500°C are used. However, this oxygen peak height will not disappear by thermal treatments unless the temperature is raised to 620°C. The above result indicates that there is quite a difference between GaAs and GaP with respect to the removal behavior of the residual oxide layers because the oxidation product on GaP is different from Ga_2O_3 on GaAs (10). With thermal treatments above 650°C, the As peak height for GaAs and the P peak height for GaP decrease as the thermal treatment temperature increases. This may be attributed to the desorption of volatile atoms from the surface due to the difficulty of maintaining a congruent evaporation.

For the growth of ZnSe on GaAs, the surface morphologies of the GaAs substrates and the subsequent epitaxial growth at the initial stage of the 1000Å thickness after different thermal treatments as observed from *in situ* RHEED patterns are shown in Fig. 2. The substrate temperature during growth was 320°C and a primary electron with a 10 keV was used along the [110] azimuth. At the thermal treatment of 550°C, the RHEED obtained from the substrate surface shows a ringed pattern due to the coverage of the oxide layer which remained after chemical treatment, as shown in Fig. 1(a). Thereafter, the RHEED obtained from the surface of the subsequent epitaxial growth at the initial stage of the 1000Å thickness also shows the ringed pattern arising from the polycrystal ZnSe growth. After thermal treatment above 560°C, the diffraction pattern obtained from the substrate surfaces changed to a spotty one. This indicates that the bare surfaces of the substrates exposed after the removal of the residual oxide layer are rough because of the congruent evaporation of Ga and As atoms from the surface. However, the surface morphologies of the subsequent ZnSe epitaxial growth with the 1000Å thickness achieve a smooth surface observed from a streak diffraction pattern, as shown by the RHEED studies.

For the growth of ZnSe on GaP, the surface morphologies of the GaP substrate, the subsequent epitaxial growth at the initial stage of the 1000Å thickness, and the total growth with a 3 μm thickness were observed from *in situ* RHEED patterns, as shown in Fig. 3. The important difference between the morphologies of GaAs and GaP after thermal treatment is a

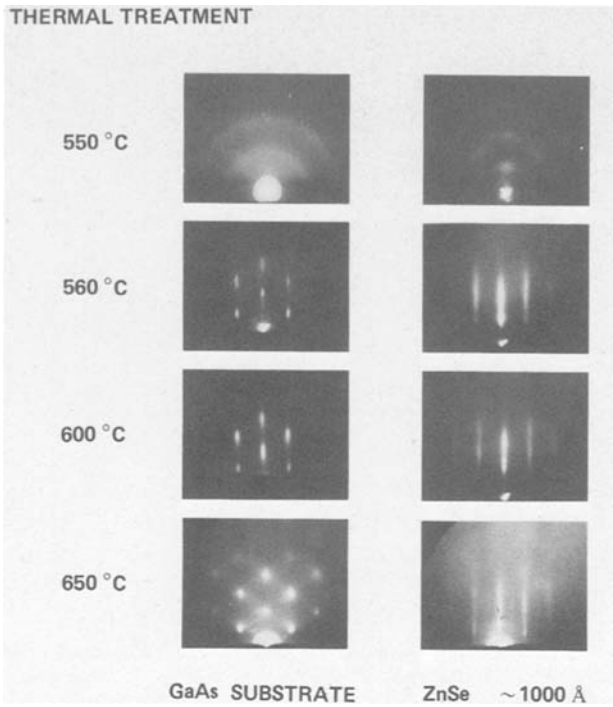

Fig. 2. RHEED patterns of the GaAs substrate prior to growth and the surface at the initial stage of the 1000Å ZnSe growth after different thermal treatments.

diffraction pattern resulting from the thermal treatment when the substrate surface is still covered with the residual oxide layers, as shown in Fig. 1. For GaP, the substrate surface exhibits a spotty pattern even at the thermal treatment temperature of 570°C. This indicates that the oxidation product on the surface of GaP is single crystalline, which is in agreement with previous work (10). The surface of the ZnSe epitaxial growth at the initial stage of the 1000Å thickness also exhibits a spotty diffraction pattern. However, the surface after the total 3 μm thickness growth changes to a streak pattern. The roughness of the growth surface at the initial stage of the 1000Å thickness may be attributed to the presence of the residual oxygen contaminations across the interface. The surface morphology after the total 3 μm thickness growth, however, could never be dominated by the detrimental oxygen contaminations. After thermal treatments above 620°C, which is the temperature required to completely remove oxide layers, as shown in Fig. 1(b), surface morphologies of the ZnSe epitaxial growth even at the initial stage of the 1000Å thickness exhibit a smooth surface observed from a streak diffraction pattern.

Figure 4 shows in-depth profiles of the Auger peak heights of various elements in the interface region between the ZnSe growth layer and the substrate at each step of the different thermal treatments for the ZnSe-GaP system and at the step of the thermal treatment of 600°C for the ZnSe-GaAs system. The substrate temperature during growth and the ZnSe growth thickness were 360°C and ~1000Å, respectively. For the ZnSe-GaP system, oxygen is embedded across the interface at the thermal treatment temperature of 570°C, as shown in Fig. 4(a). This result confirms that it is possible for oxide contaminations to dominate the surface morphology of the ZnSe growth at the initial stage. After thermal treatments above 620°C, no oxygen contaminants can be embedded across the interface, as shown in Fig. 4(b) and (c). Therefore, oxygen contaminants can arise not from the ambient during growth but from the chemical treatment. The depth of the transition region after the thermal treatment of 620°C for the ZnSe-GaP system is about 300Å, slightly wider compared to that of ~150Å after the

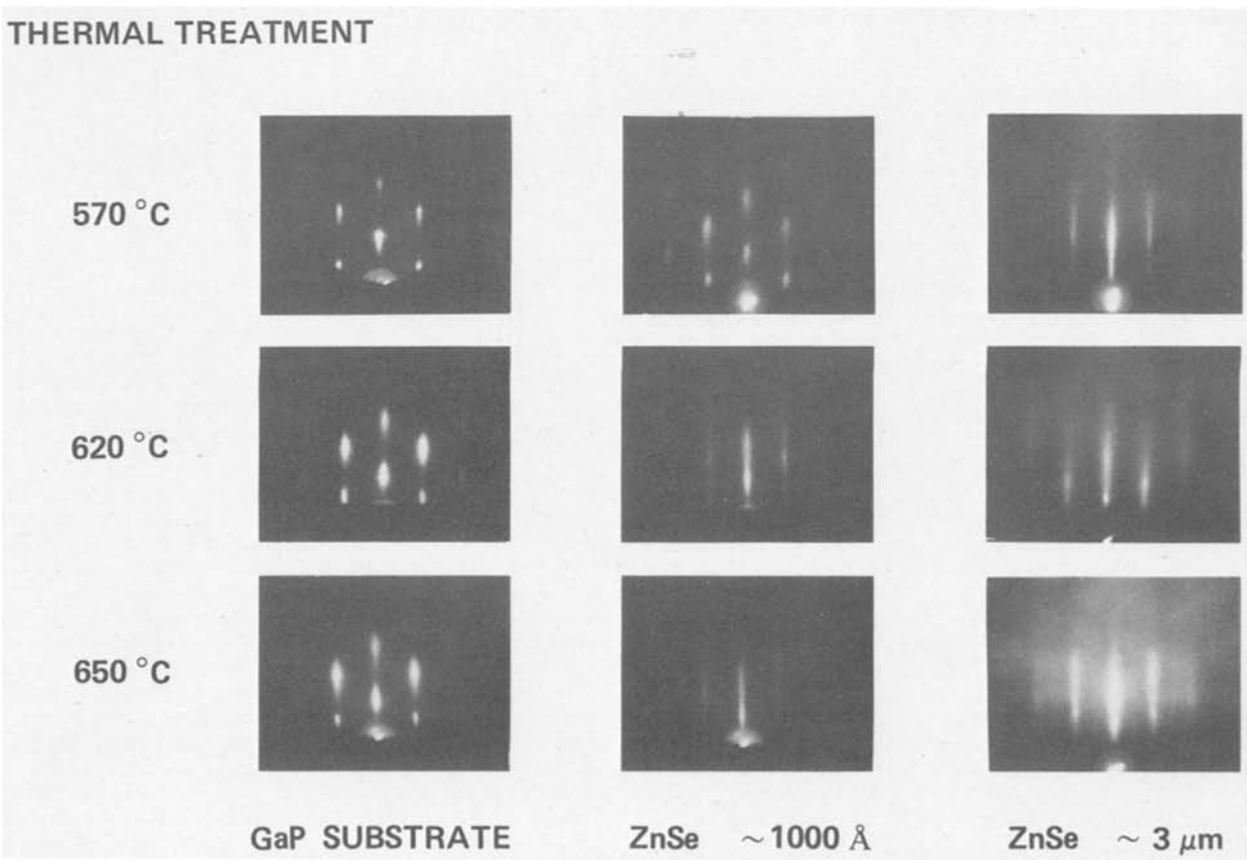

Fig. 3. RHEED patterns of the GaP substrate prior to growth and the surfaces at the initial stage of the 1000Å ZnSe growth and the sequential stage of the 3 μm growth after different thermal treatments.

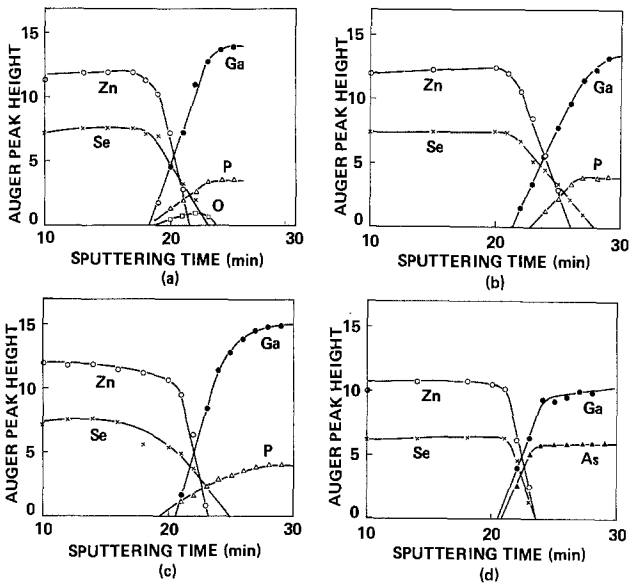

Fig. 4. In-depth profile of the Auger peak heights of various elements in the transition region between the substrate and the ZnSe grown layer after different thermal treatments of 570°C (a), 620°C (b), and 650°C (c) for the ZnSe-GaP system, and 600°C (d) for the ZnSe-GaAs system.

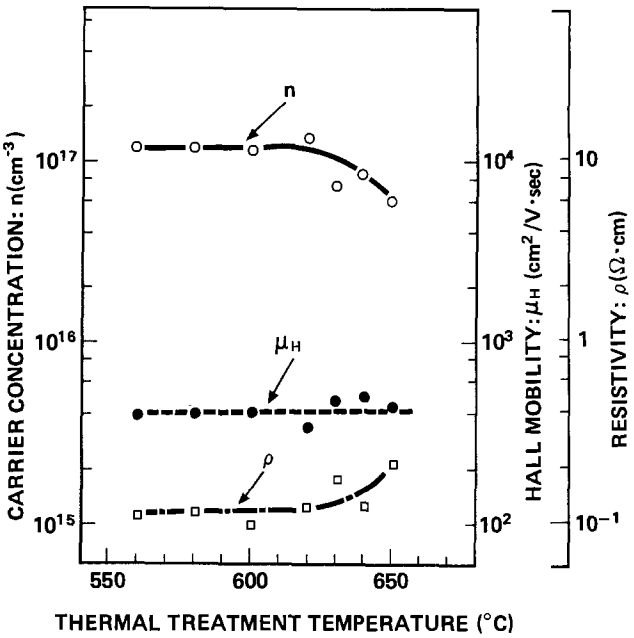

Fig. 5. The electrical properties of Ga-doped ZnSe layers grown on GaAs as a function of the thermal treatment temperatures, carrier concentration (○), Hall mobility (●), and resistivity (□).

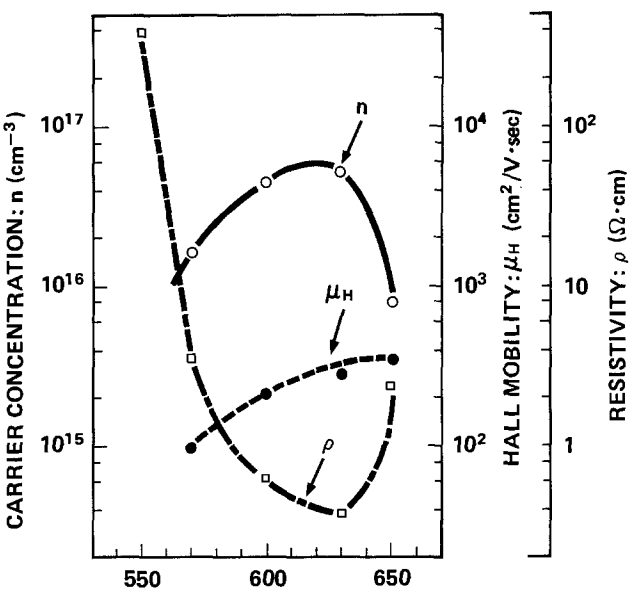

Fig. 6. The electrical properties of Ga-doped ZnSe layers grown on GaP as a function of the thermal treatment temperatures, carrier concentration (○), Hall mobility (●), and resistivity (□).

thermal treatment of 600°C for the ZnSe-GaAs system, as shown in Fig. 4(d). The difference in the depth of the transition region between the ZnSe-GaAs and ZnSe-GaP systems may be attributed to the different lattice misfit. The Auger peak height of P for the ZnSe-GaP system at the thermal treatment temperature of 650°C gradually increases toward the substrate through the interface. This is attributed to the decrease in the concentration of P atoms at the surface due to the desorption during thermal treatment.

A Van der Pauw method and a photoluminescence measurement were employed to investigate the relation between the surface cleanliness of the substrate and the electrical and optical properties of Ga-doped ZnSe growth layers. The substrate temperature during growth was 320°C for the growth of ZnSe on GaAs and 360°C for the growth of ZnSe on GaP. The Ga cell temperature was fixed at 420°C for doping. Each sample used in the present study has a ~3 μm thick ZnSe grown layer.

Figures 5 and 6 show the dependence of electrical properties of the grown layer of Ga-doped ZnSe on GaAs and GaP on the thermal treatment temperatures, respectively. For the growth of ZnSe on GaAs, the carrier concentrations and resistivities remain unaltered until the thermal treatment temperature is raised to 630°C. For thermal treatment above 630°C, however, a decrease in the carrier concentration and an increase in the resistivity begin to appear. The mobilities do not change, though, for thermal treatment between 560° and 650°C. For the growth of ZnSe on GaP, the carrier concentration increases and the resistivity decreases as the thermal treatment temperature increases when the temperatures are raised from 550° to 630°C. This indicates that when higher thermal treatment temperatures are used, more improved electrical properties are obtained in the grown layers. This is possible because the reduction in the concentration of oxygen contaminants embedded across the interface can suppress the formation of the defect complexes associated with oxygen. On the contrary, the decrease in the carrier concentrations and the increase in the resistivities begin to appear at the thermal treatment temperature of 630°C, whereas the mobilities gradually increase even when the thermal treatment is raised to 650°C. For the growth of ZnSe on both GaAs and GaP, thermal treatments higher than 630°C result in a degradation of electrical properties. This may be attributed to the following. Since it is clear from the AES and RHEED observations that the surface roughness of the substrate results from the desorption of volatile host atoms (for example As and P) at the surface by thermal treatments higher than 650°C, a certain amount of volatile atoms can possibly be dissociated from the substrate surface even after being treated at 630°C and result in roughness of the substrate surface. As the result, we speculate that the degradation of electrical properties of the ZnSe layer may be due to the generation of unavoidable defect complexes into the epitaxial layer grown on the rough surface of the substrate.

A room temperature photoluminescence spectrum of Ga-doped ZnSe grown by an MBE has a dominant

blue emission band with a peak of ~461 nm, which may be attributed to the recombination between donor electrons and free holes, and a longer wavelength broad yellow emission band with a peak of ~590 nm, which may be due to the defect complex centers associated with incorporated Ga atoms (6). Figures 7 and 8 show the relation of photoluminescence properties in the grown layer of Ga-doped ZnSe on GaAs and GaP to the thermal treatment temperatures, respectively. For the growth of ZnSe on GaAs, blue emission intensities remain unaltered until the thermal treatment of 630°C is used, whereas yellow emission intensities gradually increase as the thermal treatment temperature increases. For thermal treatment above 630°C, the reduction of both blue and yellow emission intensities begins to appear, as shown in Fig. 7. For the growth of ZnSe on GaP, the blue emission intensities monotonously increase, and the yellow emission intensities dramatically decrease as the thermal treatment temperature increases when the temperature is raised from 550° to 630°C. For thermal treatment above 630°C, however, a significant increase in yellow emission intensities begins to appear, whereas blue emission intensities slightly decrease.

From these electrical and optical data, we suggest that the degradation of characteristics in the ZnSe grown layers are probably based on the formation of defect complexes associated not only with oxygen contamination embedded across the interface during growth but also with the surface roughness arising from the desorption of volatile host atoms from the substrate surface by thermal treatments.

Summary

We have demonstrated that the surface morphologies and the electrical and optical properties of MBE grown ZnSe layers on both GaAs and GaP depend mainly on the surface cleanliness provided by a thermal treatment in a vacuum prior to growth.

After the chemical treatment procedure, the surfaces of both GaAs and GaP have carbon contaminants and residual oxide layers. Carbon contaminants left on the surface can easily be decomposed, but there is quite a difference in the removal behavior of oxidation products between GaAs and GaP. For GaAs, the thermal temperature required to explicitly remove oxidation products is around 570°C. For GaP, the removal of oxidation products begins to appear at ~550°C, and continues up to ~620°C. For GaAs, the surface shows a ringed diffraction pattern when oxidation products still remain. However, for GaP, the surface shows a spotty diffraction pattern caused by single crystalline oxidation products even though the surface is covered with the oxidation products. The important difference in the removal behavior of oxidation products between GaAs and GaP is attributed to the different oxidation products. For the growth of ZnSe on GaAs, after thermal treatment temperatures above 570°C, which is the temperature required to completely remove oxide layers, all of the surface morphologies of the growth at the initial stage of the 1000Å thickness exhibit a streak diffraction pattern. However, all of the substrate surfaces prior to growth show a spotty pattern. For the growth of ZnSe on GaP, the surface morphology of the growth at the initial stage of 1000Å thickness exhibits a spotty diffraction pattern, as does the substrate surface prior to growth, because oxidation products still remain across the interface. The surface morphology of growth at the total 3 μm thickness, however, changes to a streak diffraction pattern. After thermal treatment temperatures higher than 620°C, which is the temperature required to completely remove oxide layers, each surface morphology for growth at the initial stage of the 1000Å thickness exhibits a streak diffraction pattern.

We also investigated the relation of electrical and optical properties of the growth of ZnSe on GaAs and ZnSe on GaP to the surface cleanliness of the substrate after different thermal treatments. The electrical and optical properties of the growth of both ZnSe on GaAs and ZnSe on GaP depend mainly on the surface contaminations and morphologies of the substrate prior to growth.

In conclusion, we recommend that the most desirable thermal treatment temperature for the substrate prior to growth is in the temperature region between 560° and 630°C for the growth of ZnSe on GaAs, and between 620° and 630°C for the growth of ZnSe on GaP.

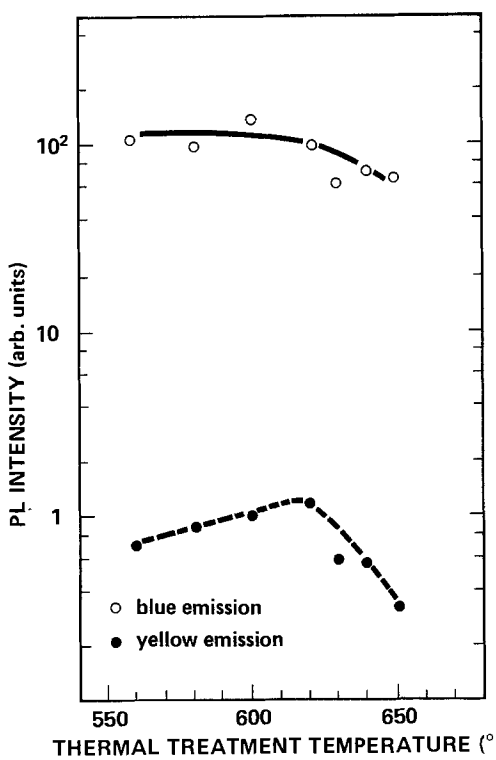

Fig. 7. The optical properties of Ga-doped ZnSe layers grown on GaAs as a function of the thermal treatment temperatures, blue emission (○) and yellow emission (●).

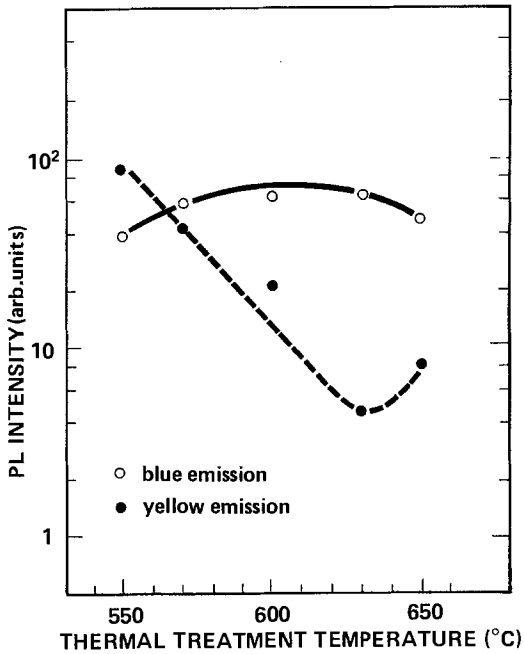

Fig. 8. The optical properties of Ga-doped ZnSe layers grown on GaP as a function of the thermal treatment temperatures, blue emission (○) and yellow emission (●).

Acknowledgments

The authors would like to thank Dr. M. Yamano and Dr. E. Komatsu of their Research Center for their guidance.

Manuscript submitted Feb. 7, 1983; revised manuscript received May 23, 1983.

Sanyo Electric Company, Limited assisted in meeting the publication costs of this article.

REFERENCES

1. C. C. Change, P. H. Citrin, and B. Schwartz, *J. Vac. Sci. Technol.*, **14**, 943 (1977).
2. A. Munoz-Yaque, J. Piqueras, and N. Fabre, *This Journal*, **128**, 149 (1981).
3. A. Trueba, E. Munoz, and J. Piqueras, *Solid State Commun.*, **15**, 199 (1974).
4. G. Laurence, F. Simondet, and P. Saget, *Appl. Phys.*, **19**, 63 (1979).
5. W. H. Koschel, R. S. Smith, and P. Hiesinger, *This Journal*, **128**, 1336 (1981).
6. T. Niina, T. Minato, and K. Yoneda, *Jpn. J. Appl. Phys.*, **21**, L387 (1982).
7. F. Kitagawa, T. Mishima, and K. Takahashi, *This Journal*, **126**, 341 (1979).
8. T. Niina, K. Yoneda, T. Toda, T. Minato, and K. Komeda, Collected papers of MBE-CST-2, 207 (1982) Tokyo.
9. C. A. Chang, *J. Vac. Sci. Technol.*, **21**, 663 (1982).
10. G. Lucovsky, *ibid.*, **20**, 761 (1982).

Hydrogen Gettering Effect of Mo_2N/Mo MOS Process

M. J. Kim* and D. M. Brown*

General Electric Company, Corporate Research and Development, Schenectady, New York 12301

ABSTRACT

Hydrogen plays a key role in maintaining the integrity of molybdenum film during high temperature processing. Hydrogen not only prevents Mo oxidation but also reduces Mo oxide, through an oxide gettering reaction at a high temperature, to produce pure molybdenum. γ-phase molybdenum nitride formed by direct reaction with ammonia can be converted to pure molybdenum after the nitride's beneficial properties have been utilized for MOS circuit fabrication. The recovery process is affected by hydrogen and the presence of an overlay layer. A recovery process for producing high conductivity Mo from Mo_2N and sputtered Mo film contaminated with oxygen was developed. This process always produces a consistent film regardless of the prior conditions to which the Mo film was subjected.

Molybdenum is receiving attention as a possible alternative to polysilicon, particularly as a VLSI interconnection, because of its high conductivity. The major problem associated with molybdenum film is its susceptibility to oxygen and moisture during the conventional semiconductor fabrication process. We have previously shown that a molybdenum nitride coating formed by direct reaction of molybdenum with ammonia improves film properties (1). This coating increased the resistance against oxidation, process chemicals, and implantation dopant penetration (2). The purpose of this study is to report the effect of hydrogen during the high temperature processing of molybdenum films. Hydrogen helps maintain the Mo film quality during the nitriding process and keeps the Mo film from oxidizing during subsequent annealing processes. It was found that Mo film resistivity which is high due to oxygen contamination is decreased by annealing in hydrogen through the reduction of the Mo oxide.

Experimental Procedure

Molybdenum films were deposited on thermally oxidized silicon wafers by using either a load-locked d-c magnetron or an S-gun sputtering system. The Mo deposition rate was 1500 Å/min with a d-c magnetron (MRC) and 720 Å/min with an S-gun (Varion). Films were sputtered at a 3 μTorr argon pressure, with the initial vacuum level about 10^{-7} Torr. The film thickness was varied from 1000 to 5000Å. (The film properties are dependent on the deposition conditions as discussed later.) Passivating Mo_2N films were made in the temperature range of 500°-750°C by direct reaction with 10% ammonia for 10 min in accordance with the method reported in Ref. (1). A submicron interconnection line could be patterned with reactive ion etch using CCl_4 and O_2. At a pressure of 250 μTorr, the etch rate of pure molybdenum was about 1000 Å/min and that of Mo_2N was 1400 Å/min.

Mo_2N was converted to pure Mo by a 1000°C annealing cycle in 10% hydrogen mixed with nitrogen. When it was necessary to retain Mo_2N, PSG or CVD SiO_2 was deposited prior to the high temperature annealing. Measurement of the sheet resistance was the most effective way to monitor the process. The thickness change of the Mo film was monitored by Sloan Dektak. All the temperature annealing processes were performed in a mixture of H_2 and N_2 gases with less than 10% of H_2. The hydrogen gettering effect was monitored by x-ray, SIMS, SEM, optical microscopy, and electrical measurements.

Experimental Results and Discussion

The qualification of Mo film for VLSI application has already been demonstrated (1, 2). Some of the features are listed in Table I. Primarily, Mo is stable in contact with SiO_2 at high temperature, with a high heat of formation [19 kcal/mol (3)] required for Mo to reduce SiO_2 to form molybdenum oxide, MoO_2. When the gettering technique is used, a highly conductive film, of better than 7.2×10^{-6} Ω-cm, can be produced. A submicron pattern can be achieved with either the RIE method or a wet etch. The patterned conductor can be passivated with Mo_2N. The film adhesion tested in accordance with ASTM D-3359-78 has been demonstrated to be excellent, with good thermal matching with silicon and SiO_2.

The Mo film properties, however, change with the deposition conditions as listed in Table II. The important properties for VLSI application, such as elec-

Table I. Qualification of Mo film for VLSI

1. Stable with SiO_2 (ΔH = 19 kcal/mol)
2. High conductivity (7.2×10^{-6} Ω-cm)
3. Easy to etch (RIE, wet)
4. Nitride passivation (Mo_2N)
5. Good adhesion (ASTM D-3359-78)
6. High melting point (2620°C)

* Electrochemical Society Active Member.

Key words: Mo films, VLSI, gettering, interconnection, conductivity.

Table II. Mo film property dependency

1. Deposition method
2. Equipment type
3. Growth rate
4. Initial vacuum
5. Residual pressure
6. Substrate temperature
7. Rotation rate
8. Deposition angle

trical and etching characteristics, are particularly sensitive to deposition conditions. Deposition methods, CVD, sputtering, and evaporation produce different structures and electrical properties. Although the films for this study were all sputtered, a film made in one type of equipment was different from that made in another. Even within a given system, the film properties vary with changes in growth rate, initial vacuum, residual pressure, substrate temperature,rotation rate, and deposition angle. Some of these parameters drastically change resistivity, while others affect etching characteristics such as etch rate and anisotropic etch. Since it is not easy to exactly control all of these parameters, films made at different times are not generally the same. A VLSI chip, on the other hand, requires consistent film properties. The following analysis shows that the hydrogen gettering process produces such consistent film characteristics, independent of deposition conditions and the past history of the film.

Mo_2N film is thermodynamically stable up to 900°C, above which temperature it dissociates into pure Mo and N_2 (4). Thus, Mo_2N can be converted to the higher conductivity Mo after the required properties of Mo_2N have been used. However, it is also possible to retain the Mo_2N film during the subsequent high temperature processing with an overlay layer such as SiO_2 or PSG deposited prior to the high temperature processing. The results with PSG and CVD SiO_2 were similar.

Figure 1 shows the change of sheet resistance of nitrided Mo films, ρ_s, with annealing time at 1000°C, with and without the PSG overlay film. The initial ρ_s is higher for samples nitrided at higher temperature, because a thicker nitride coating is formed. From our previous experiment (1), the six different temperatures would result in samples with different Mo_2N thicknesses; that is, they represent samples of 3000Å pure Mo, 220Å Mo_2N/Mo, 450Å Mo_2N/Mo, 870Å Mo_2N/Mo, 2000Å Mo_2N/Mo, and pure Mo_2N. The full curves represent the ρ_s changes of samples with the PSG overlay, and the dotted curves represent those with no PSG overlay. When the Mo_2N is exposed, the ρ_s is reduced rapidly to the lowest values, indicating the restoration to pure Mo; this is confirmed independently by x-ray diffraction analysis, which shows no trace of an Mo_2N diffraction line after annealing. It is interesting to note that the ρ_s of the nitrided samples reaches the minimum sooner than the ρ_s of the pure Mo sample. Table III shows the lattice parameter and the (110) Mo line broadening after the annealing of pure and nitrided Mo films. While no systematic change in lattice parameter was observed, there were significant line sharpenings of x-ray diffraction for the 1000°C annealed nitrided samples. The ρ_s of those samples that are covered with 5000Å PSG does not change significantly after annealing, indicating that most of the Mo_2N is still retained. In this case, the PSG presumably blocks the nitrogen escape required for the restoration.

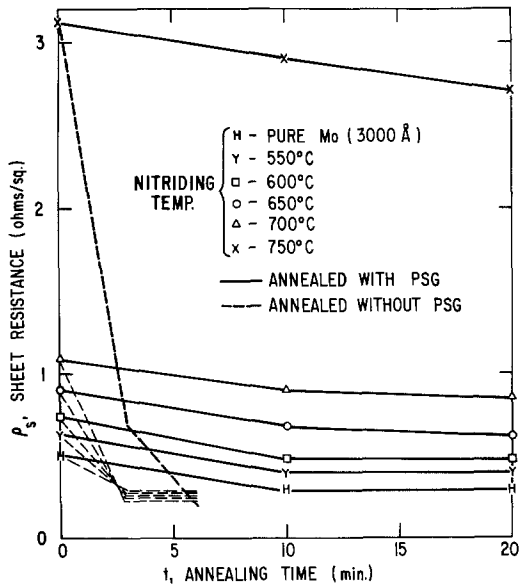

Fig. 1. Effect of annealing upon the resistance of nitrided Mo films. The annealing was performed at 1000°C in 10% H_2 + N_2, the full lines represent ρ_s changes during annealing with PSG overcoat and the dotted lines results without PSG.

Figures 2, 3, and 4 show, respectively. SEM photomicrographs of pure Mo, 650°C nitrided Mo, and 700°C nitrided Mo film with their subsequently annealed films. The pure, sputtered Mo (Fig. 2a) showed a uniform cross section, without crystal structures. When the 3000Å film was annealed for 30 min in 10% H_2 + N_2 at 1000°C, a columnar structure was developed, extending the grain boundary from the SiO_2 interface to the Mo surface, as shown in Fig. 2b. When the sample was annealed with the PSG overlay, a similar columnar structure was formed (Fig. 2c). For Fig. 3a the starting film was made by nitriding the 3000Å pure Mo film at 650°C in 10% ammonia for 10 min. This process resulted in about an 820Å Mo_2N film over the Mo but did not produce a columnar grain structure. Nor did the film shown in Fig. 4a, with 1900Å Mo_2N nitrided at 700°C, have any structural cross section. However, the annealed films with and without PSG overlays showed distinguished, large columnar grains. The only difference between these samples and the annealed pure Mo is that the grain size of the nitrided samples is not large enough to extend through 3000Å thickness for the samples shown in Fig. 3c and 4c, which are covered with PSG.

The structure of the nitrided Mo film did not show any columnar form (Fig. 3a and 4a). According to the structural analysis (1) the nitrogen atoms will not make a completely ordered structure but will randomly occupy the largest interstices. The nitriding converts the Mo β-phase to the Mo_2N γ-phase with fcc structure. According to SEM photomicrographs, the phase transformation apparently does not induce recrystallization, but, rather, maintains the partially amorphous state of the sputtered Mo film.

Table III. Lattice parameter and grain size changes observed by x-ray in Mo with different heat-treatments

Sample No.	T9-1	T9-2	T9-3	T9-4
Treatment history	No treatment (as sputtered)	1000°C anneal in (H_2 + N_2)	650°C nitriding, 1000°C anneal in (H_2 + N_2)	750°C nitriding, 1000°C anneal in (H_2 + N_2)
Lattice parameter a (angstrom)	3.144(3)	3.155(4)	3.139(2)	3.141(1)
2θ, Broadening 1/2 of (110) peak	0.442	0.369	0.255	0.270

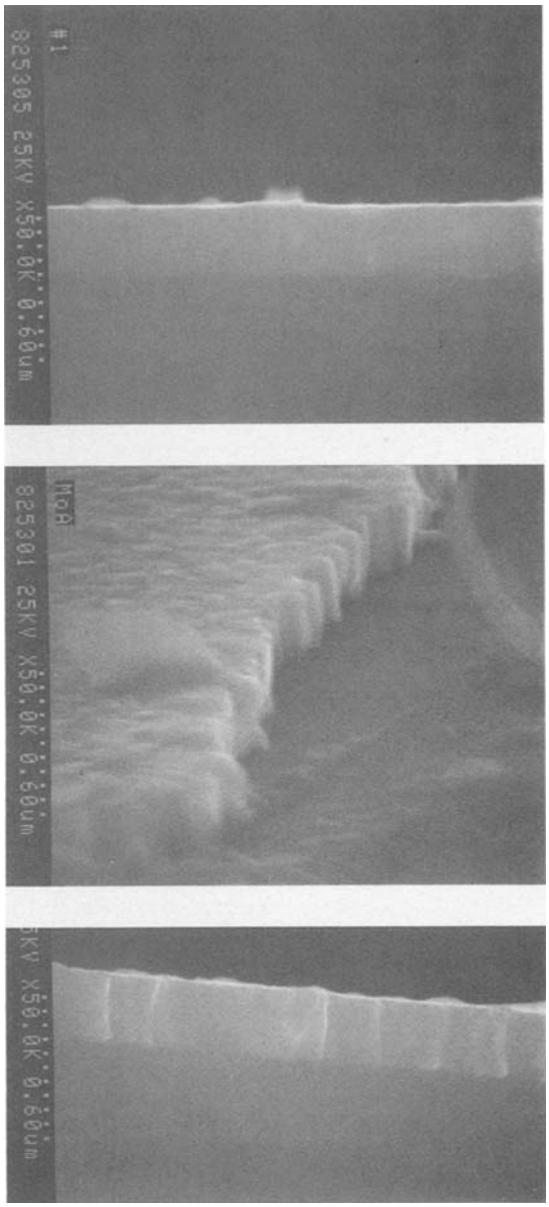

Fig. 2. SEM photomicrographs of pure Mo films of 3000Å; (a, top) as sputtered with a substrate temperature of 250°C; (b, center) annealed for 30 min in 10% H_2 + N_2 at 1000°C; (c, bottom) annealed same as (b) with PSG cover.

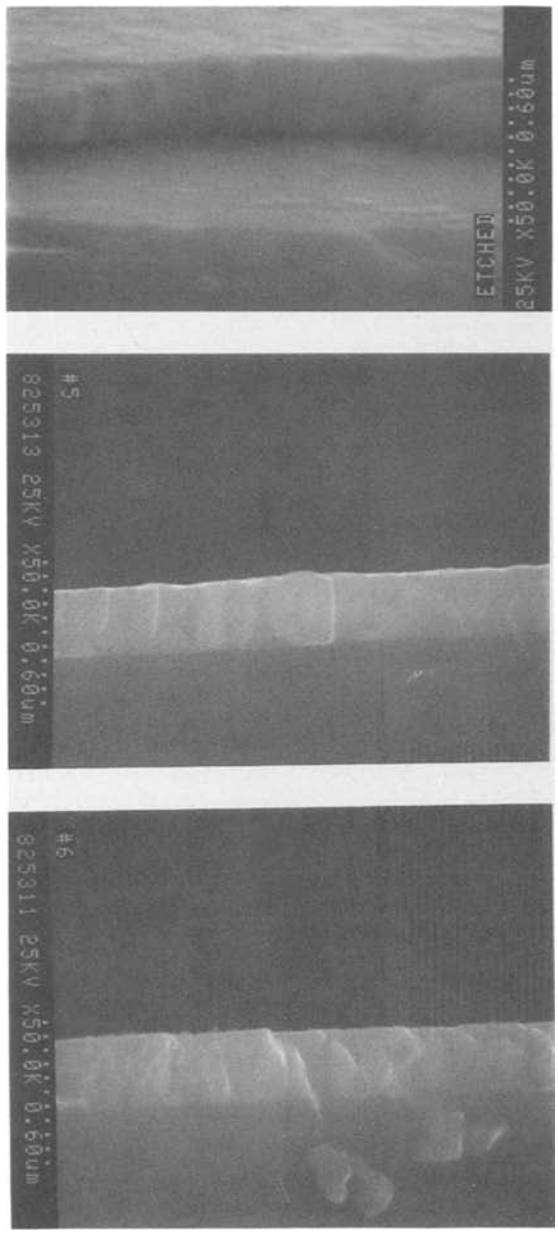

Fig. 3. SEM photomicrographs of 650°C Mo_2N/Mo film and its annealed films; (a, top) Mo_2N/Mo film made by nitriding at 650°C for 10 min to 820Å Mo_2N; (b, center) annealed for 30 min in 10% H_2 + N_2 at 1000°C; (c, bottom) annealed same as (b) with PSG cover.

Taking into account the dominance of (110) x-ray intensity in the annealed sample, the columnar direction is [110] perpendicular to the surface. As will be shown later, hydrogen annealing reduces Mo oxide near the grain boundary, and the columnar structure appears to have a tendency to increase the film tension during the annealing. A curvature measurement of the Mo film showed that the annealing increased the tension from the lower stress of the sputtered film. An original stress of 7.12×10^9 dyne/cm^2 for the sputtered film on a (100) silicon wafer at 3 μTorr Ar pressure was increased to 1.9×10^{10} dyne/cm^2 by annealing for 30 min at 1000°C. Another contributing factor to the resistivity reduction for the nitrided samples may be their larger grain size, which was observed with the line sharpening.

Figure 5 shows the ρ_s of the re-nitrided films. The pure Mo recovered from the nitride was again nitrided at the corresponding temperature for 10 min in 10% NH_3 + N_2. The nitriding reaction rate was very small in the temperature range of 500°-700°C but increased rapidly around 750°C. A resistivity peak, similar to the nitridation of sputtered Mo (1), as shown by the dotted curve, occurred at 820°C. The resistivity peak is caused by the transformation to the MoN δ-phase from the Mo_2N γ-phase. The position of the peak was shifted for the re-nitridation by a 30°C rise in temperature. The changes may also be caused by the grain size growth of Mo film during the annealing process; the growth of single crystals retards the nitrogen diffusion through the Mo, as observed in the significant reduction of the nitriding rate below 750°C. By way of contrast, corresponding heating in N_2 increased the ρ by about 30% without producing any trace of nitride.

Figure 6 shows the resistivities of S-gun-sputtered and d-c magnetron-sputtered Mo films as a function of film thickness, in their as-sputtered condition and after H_2 annealing. The substrate temperature for both cases was 250°C. The initial resistivity of the S-gun-sputtered film was more than three times that of the d-c magnetron-sputtered films and it increased rapidly below 3000Å. When the films were annealed at 1000°C in 10% H_2 + N_2, both resistivity values

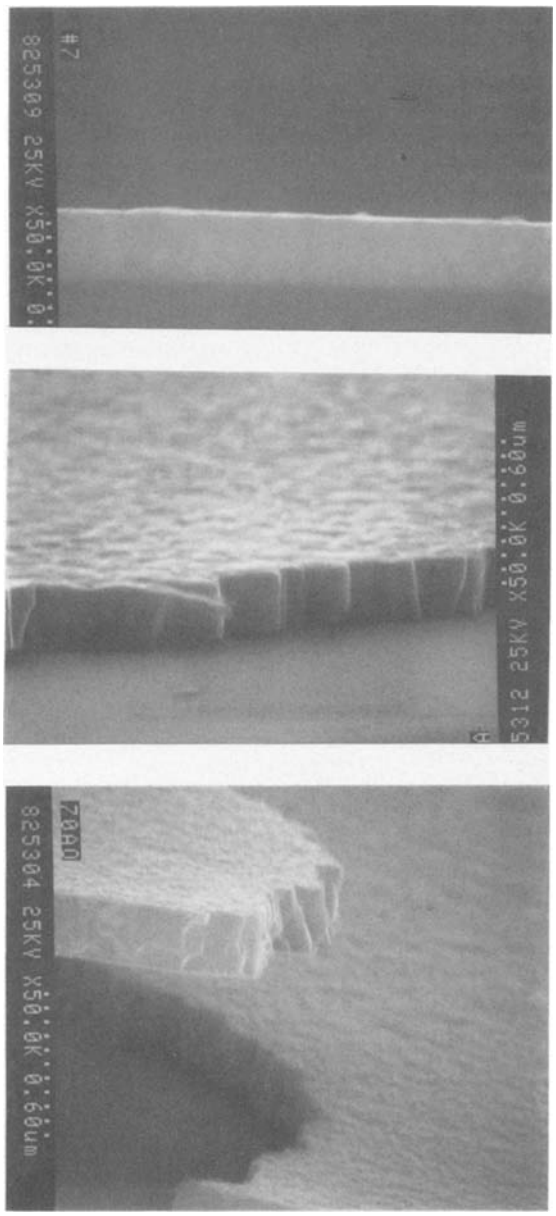

Fig. 4. SEM photomicrographs of 700°C Mo_2N/Mo film and its annealed films; (a, top) Mo_2N/Mo film made by nitriding at 700°C for 10 min to make 1900Å; (b, center) annealed for 30 min in 10% H_2 + N_2 at 1000°C; (c, bottom) annealed same as (b) with PSG cover.

converged to the same value, represented by curve C. The annealed resistivity, 7.1 $\mu\Omega$-cm was relatively independent of film thickness above 2000Å, a result that agrees well with an evaporated Mo film (5). The resistivity increase below 2000Å may be caused by columnar-like monolayer grain boundary scattering, as shown in SEM photomicrographs. The film quality recovery process was analyzed from the different origins. This behavior may be understood in terms of oxygen incorporation in the as-deposited films. In a low vacuum (5×10^{-7} Torr) the major constituent is observed to be water vapor (6), which can oxidize the Mo film grain boundary, increasing its resistivity.

The S-gun-sputtered Mo contains a larger amount of oxygen than does the magnetron-sputtered film because of its slow deposition rate. The high resistivity is correlated with the larger oxygen content for S-gun-sputtered Mo. Further, S-gun-sputtered films etch (RIE) 40% faster than do d-c magnetron films, probably due to accelerated formation of the volatile molybdenum oxychlorides as etch products (7). Hy-

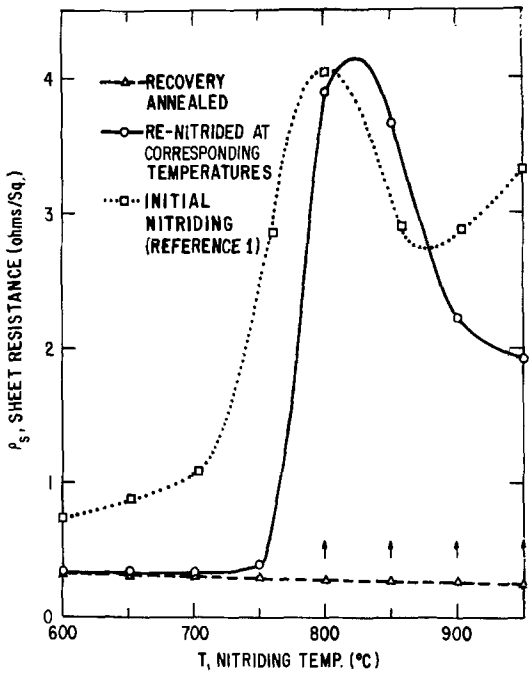

Fig. 5. Sheet resistance change as a function of re-nitriding temperature after the recovery annealing of the nitrided films at the corresponding temperature; ρ_S is compared with that of the initial nitride made from sputtered Mo.

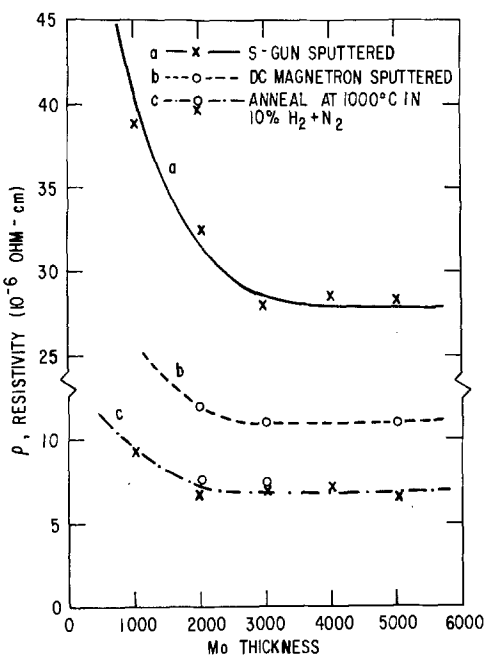

Fig. 6. Comparison of the resistivity of three different molybdenum films as a function of thickness. S-gun-sputtered Mo film (curve a) initially shows much higher resistivity than d-c magnetron-sputtered film (curve b) Mo, but both curves converge to a lower resistivity (curve c) after the annealing in H_2.

drogen annealing removes the oxygen through the formation of volatile H_2O, and both types of film exhibit the same resistivity. Direct evidence is provided by SIMS analysis.

Figure 7 shows a SIMS profile analysis of the oxygen content for 4000Å S-gun-sputtered Mo samples like those in Fig. 4. In order to increase the sensitivity to oxygen, negative cesium ions were used. Curves a, b, and c represent ion intensity before annealing for oxygen (M. 16), silicon (M. 30), and molybdenum (M. 98), respectively. Curve a' represents the oxygen ion intensity after annealing in 10% H_2 + N_2 for

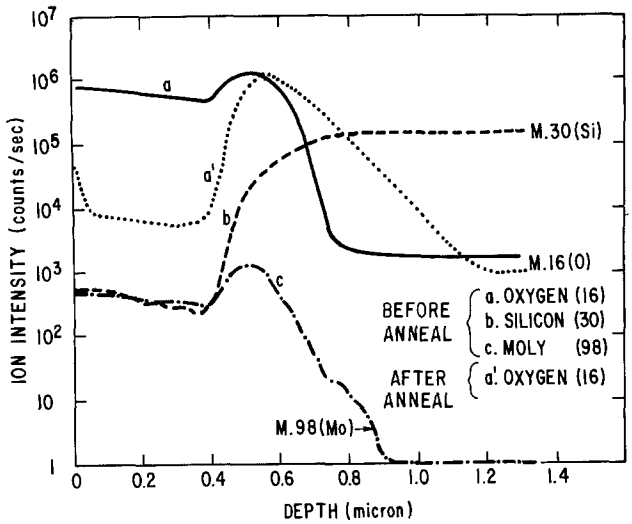

Fig. 7. SIMS depth profile of oxygen for the S-gun molybdenum film as sputtered and after the annealing. The oxygen intensity after the annealing (curve a') is two orders of magnitude lower than that before the annealing (curve a).

30 min at 1000°C. The oxygen content as measured by the intensity is reduced by two orders of magnitude by the annealing, a finding which proves that the large postannealing resistivity reduction shown in Fig. 6 is caused by the hydrogen gettering effect of the oxygen in the Mo film.

Figure 8 shows the effect of the gettering on the property of the films with different histories. The initial 3000Å film was sputtered with a d-c magnetron, and one wafer was divided into four specimens. Two of the four were nitrided at 650°C to coat with 870Å Mo_2N. A nitrided specimen and a sputtered specimen were annealed in 10% H_2 + N_2 for 30 min at 1000°C. The oxygen profiles in the four different Mo films are presented in Fig. 8. The Mo^- (M.90) and Si^- (M.30) for sputtered films are also shown as reference. Near the surface, the oxygen intensity of the sputtered specimen was about seven times higher than that of the nitrided specimen. The hydrogen by-product in the nitridation appears to partially getter the oxygen, and the nitride keeps oxygen from penetrating the Mo film afterward. The large oxygen step shift of curve b near the Mo/SiO_2 boundary is caused by the thickness expansion during the nitriding (1) When both types of film are annealed, their oxygen profiles, curves c and d, are exactly the same.

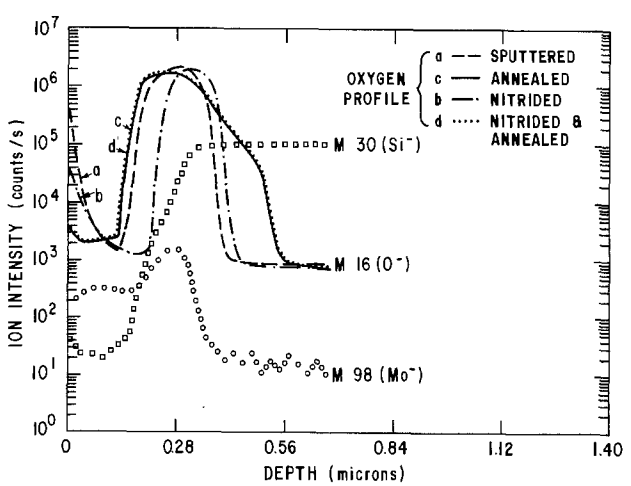

Fig. 8. Oxygen profile in d-c magnetron molybdenum films with different histories. Curve a represents a sputtered film, curve b the nitrided, curve c the annealed, and curve d the annealed after nitridation. The annealed curves have identical oxygen profiles.

Figure 9 represents the Mo film process flow required to have a unique film quality. The Mo film can either be made by a high temperature process in a large grain form or sputtered at a low temperature to produce a partially amorphous state. The H_2 + N_2 annealing at the high temperature getters impurities, oxygen in particular, and makes a <110> columnar structure, resulting in a consistent film quality as an end product.

Molybdenum films increased in resistivity upon annealing in nitrogen due, we believe, to the presence of residual O_2 or H_2O in the gas. Any trace of oxygen will, upon heating, convert Mo near the grain boundary to MoO_2. The oxidized grain boundaries increase the reflection coefficient of electrons (4) at the grain boundary, causing a resistivity increase.

In the presence of hydrogen, MoO_2 can be reduced to pure molybdenum by the following reaction

$$\tfrac{1}{2}\,Mo_2O(s) + H_2(g) = \tfrac{1}{2}\,Mo(s) + H_2O(g) \quad [1]$$

$$K = P_{H_2O}/P_{H_2}$$

where K, P_{H_2O}, and P_{H_2} are the equilibrium constant, partial pressure of H_2O, and partial pressure of H_2, respectively. Thus, when the hydrogen partial pressure is high, Mo reduction can take place at relatively low temperatures. The most accurate measurement of K useful in our range of interest was done by Gocken (8). He reports the value

$$\log K = -1298/T + 0.798 \quad [2]$$

where T is the absolute temperature. At our annealing temperature of 1000°C, K is 0.575. Since we are using much higher H_2 partial pressure than Gocken's we expect rapid MoO_2 reduction at 1000°C. Even if we assume that all the resistivity reduction of the MRC film is contributed by the grain growth, the resistivity reduction of the S-gun film is more than 10 times higher than the contributions from grain growth. Thus, the amount of sheet resistance reduction during 10% H_2 annealing (Fig. 6) is much more than the expected contribution from grain size growth shown in Fig. 2 and 3, indicating that MoO_2 reduction is the dominant factor in the improvement of conductivity, particularly for poor films.

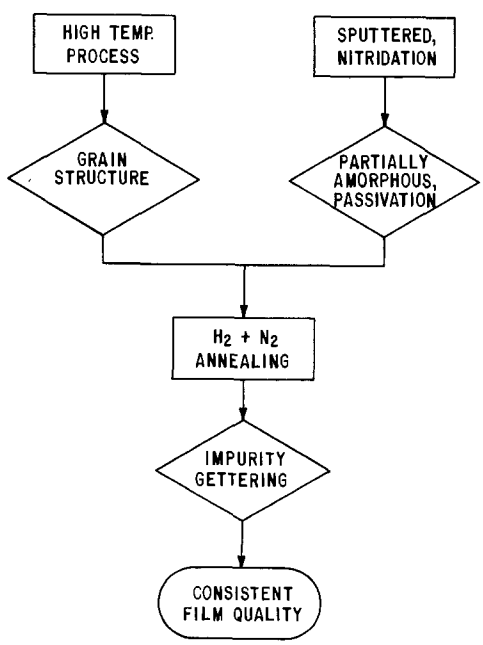

Fig. 9. Molybdenum film process flow

Conclusion

Hydrogen not only prevents oxidation of Mo but also reduces Mo oxide during high temperature annealing. Hydrogen partial pressure sufficiently in excess of the equilibrium required for reduction is easily obtained by a dilute mixture with any inert gas. For Mo nitriding in ammonia, the monatomic hydrogen dissociated from ammonia plays a key role in maintaining the integrity of the Mo underneath. Hydrogen also plays a key role in conversion to high conductivity Mo from Mo_2N by the high temperature recovery process. The high temperature gettering produces a consistent film integrity, independent of the past history of the Mo film.

Acknowledgments

The authors wish to thank M. Garfinkel, M. Ghezzo, and T. J. Soltys for their constructive advice. The authors also appreciate the processing assistance of P. A. Piacente, D. M. Skelly, and R. H. Wilson.

Manuscript submitted Jan. 25, 1983; revised manuscript received May 25, 1983.

General Electric Company assisted in meeting the publication costs of this article.

REFERENCES

1. M. J. Kim, D. M. Brown, and W. Katz, *This Journal*, **130**, 1196 (1983).
2. M. J. Kim and D. M. Brown, Extended Abstract IEDM, 560 (1982); *IEEE Trans. Electron Devices*, **ed-30**, 598 (1983).
3. G. V. Samsonov, "Handbook of High-Temperature Materials," No. 2, Plenum Press, New York (1964).
4. A. Sieverts and G. Z. Zapf, *Z. Anorg. Allg. Chem.*, **229**, 161 (1936) (.
5. K. Uda, Y. Matsushita, and S. Takasu, *J. Appl. Phys.*, **51**, 1039 (1980).
6. H. Oikawa, *J. Vac. Sci. Technol.*, **15**, 1117 (1978).
7. B. Gorowitz and R. Saia, To be published in *J. Am. Vac. Soc.*
8. N. A. Gocken, *Trans. AIME*, 1019 (1953).

The Retarded Diffusion of Arsenic in Silicon by Thermal Oxidation in Extrinsic Conditions

Y. Ishikawa, M. Tomisato, H. Honma, and S. Matsumoto

Department of Electrical Engineering, Keio University, Hiyoshi, Yokohama 223, Japan

T. Niimi

Department of Applied Physics, Tokai University, Hiratsuka 259, Japan

ABSTRACT

Arsenic diffusion in extrinsic conditions in silicon is investigated with different temperatures (950°-1100°C) and times under both oxidizing and inert atmospheres. Arsenic is prediffused into a silicon substrate from arsenic-silica film and is then subjected to a drive-in under oxidizing (dry O_2) and inert (dry N_2) atmospheres. The diffusion coefficient of arsenic is expressed by a third-order polynomial equation of arsenic concentration. This functional form is determined by fitting the arsenic concentration profile, which is calculated numerically from the diffusion equation with the functional form of diffusion coefficient assumed appropriately, to the concentration profile measured after drive-in. The diffusion coefficient is smaller under oxidizing atmosphere than under inert atmosphere at 1000°-1100°C. The degree of retarded diffusion decreases with the increase of diffusion time.

The diffusion of group III and group V elements in silicon under oxidizing atmosphere has been studied extensively. It is well known that the diffusion of boron, phosphorus, and arsenic is enhanced under oxidizing atmosphere in intrinsic conditions (1-7), and the model for this experimental result was proposed by Hu (8). The term of the intrinsic conditions means that the concentration of diffused impurity in silicon is lower than the intrinsic carrier concentration at the process temperature.

On the other hand, there are only a few works on the diffusion of boron and phosphorus under oxidizing atmosphere in extrinsic conditions, which were reported by Masetti *et al.* (9, 10) and Taniguchi *et al.* (11). Here the extrinsic conditions mean that the concentration of diffused impurity in silicon is higher than the intrinsic carrier concentration at the process temperature. There are no works on the diffusion of arsenic under oxidizing atmosphere in extrinsic conditions at present. In these cases, the diffusion coefficient depends on the concentration of impurity. This fact makes the analysis of the experimental results difficult. Both Masetti *et al.* (9, 10) and Taniguchi *et al.* (11) neglected the concentration dependence of the diffusion coefficient in their analysis. Practically, the situation that an impurity is diffused in extrinsic conditions is not uncommon for the fabrication of a device, *e.g.*, formation of drain and source wells of MOS transistor. Especially, arsenic diffusion in extrinsic conditions is important.

In this paper, the diffusion of arsenic under oxidizing atmosphere is examined with different temperatures and times in extrinsic conditions in detail. The diffusion coefficient is expressed by a third-order polynomial equation of arsenic concentration. This functional form is determined by the numerical simulation.

Key words: oxidation, diffusion, retardation, semiconductor.

Experimental

The substrates used were Czochralski-grown, p-type, dislocation-free, (100) oriented silicon wafers of resistivity 2.7-3.3 Ω-cm. Arsenic-silica film was attached on to the substrates, using a spinner. These substrates were baked at 200°C for 20 min in dry N_2. After baking, the thickness of the film was about 1500Å. Then arsenic contained in this film was prediffused into the substrates at 1100°C for 12 min. After the removal of the film, drive-in was carried out. For drive-in in dry N_2, the silicon surfaces were covered with a nondoped silicon dioxide film to avoid out-diffusion of arsenic.

Arsenic concentrations in the substrates were determined both after the prediffusion and the drive-in by the repetition of the sheet resistance measurements and anodic oxidation in phosphoric acid (H_3PO_4) solution. The average thickness of a thin layer removed by

a single run was about 100Å. Measured resistivities were converted into the concentrations of arsenic by the use of Irvin's curve (12).

In order to determine the relationship between the oxide growth rate and the oxidation time, the wafers in which arsenic was prediffused were oxidized thermally at 950°-1100°C for different times at respective temperatures in dry O_2. Silicon dioxide thickness was measured by the interference microscope.

Analysis

Under oxidizing atmosphere, the diffusion equation in silicon takes the form (13)

$$(\partial c/\partial t) = \partial/\partial x\{D(c)\ (\partial c/\partial x) + bc(dX_o/dt)\} \quad [1]$$

where t is the diffusion time, x is the depth from the silicon-silicon dioxide interface into silicon, $c(x,t)$ is the arsenic concentration in silicon, $D(c)$ is the diffusion coefficient of arsenic, which depends on arsenic concentration because arsenic concentration is higher than the intrinsic carrier concentration, $X_o(t)$ is the thickness of silicon dioxide that is growing on silicon surface, and b is the ratio of the thickness of silicon consumed by thermal oxidation to that of silicon dioxide grown on it [assumed to be 0.44 (13)].

The initial condition to solve Eq. [1] is

$$c(x,0) = c_{in} \quad [2]$$

Here, c_{in} denotes the concentration profiles measured after prediffusion. The boundary conditions are as follows

$$c(\infty,t) = 0 \quad [3]$$

$$D(c)\ (\partial c/\partial x) + c(0,t)\ (b - m)\ (dX_o/dt) = 0 \quad [4]$$

where m is the segregation coefficient of arsenic at silicon-silicon dioxide interface. The relationship

$$X_o = K\sqrt{t} \quad [5]$$

was confirmed and the proportional constant, K, was determined by thermally oxidizing the wafers in which arsenic was prediffused and by measuring the thickness of silicon dioxide. The values of K used in this work are shown in Table I.

Equation [1] was transformed into the finite-difference equation following Crank-Nicolson's implicit method. The relationship between D and c was expressed by Eq. [6]

$$D(c) = Ac^3 + Bc^2 + Cc + D \quad [6]$$

The finite-difference equation made from Eq. [1] was numerically solved by a computer simulation method with the function of $D(c)$ (Eq. [6]) assumed appropriately. The concentration profile $c(x,t)$, thus obtained, was compared with the experimental results. The function of $D(c)$ was determined so as to fit best the calculated concentration profile to the experimental concentration profile. In this simulation, a segregation coefficient m was adopted to be 0.01 irrespective of the diffusion temperature and the arsenic concentration at silicon surface. This value is the same as we used in our previous paper (16) which studied the oxidation-enhanced diffusion of arsenic and phosphorus in intrinsic conditions.

Under inert atmosphere, Fick's diffusion equation, which has a form of Eq. [1] without the second term of the right-hand side, was numerically solved like the case of oxidizing atmosphere under the blocking boundary conditions.

Table I. Values of K

Oxidation temperature (°C)	Values of K (cm/sec$^{1/2}$)
950	7.60×10^{-8}
1000	1.00×10^{-7}
1050	1.27×10^{-7}
1100	2.00×10^{-7}

Results and Discussion

Typical concentration profiles of arsenic under oxidizing and inert atmosphere are shown in Fig. 1 and 2, respectively. After the prediffusion, all samples in this work have the surface concentration of 5-7 $\times$ 10^{19} cm^{-3}. This value is much higher than the intrinsic carrier concentration at 950°-1100°C, satisfying the extrinsic conditions.

Figure 3 shows the concentration dependence of the arsenic diffusion coefficients. The diffusion coefficients of arsenic under inert atmosphere obtained by Fair and Tsai (14) and those obtained by Murota *et al.* (15) are shown together with our results. Also the intrinsic diffusion coefficients of arsenic obtained by the authors

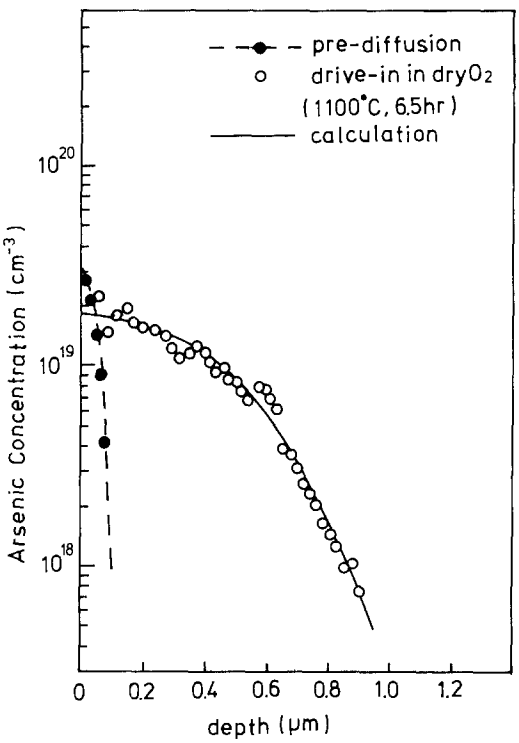

Fig. 1. Profiles of arsenic concentration (dry O_2)

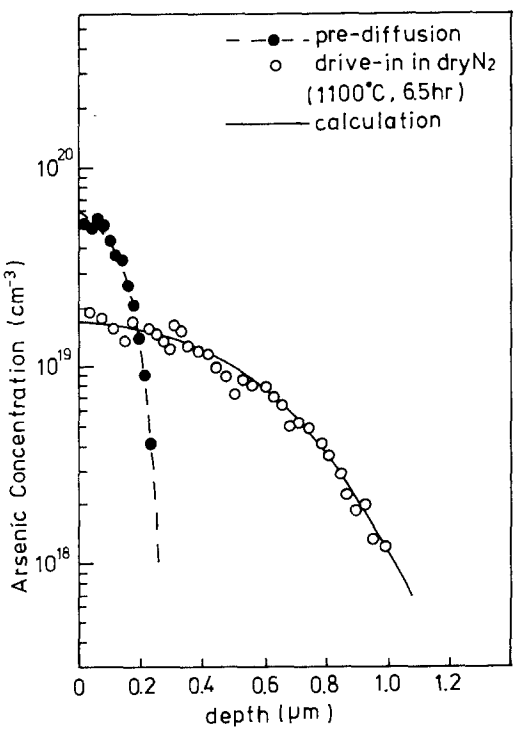

Fig. 2. Profiles of arsenic concentration (dry N_2)

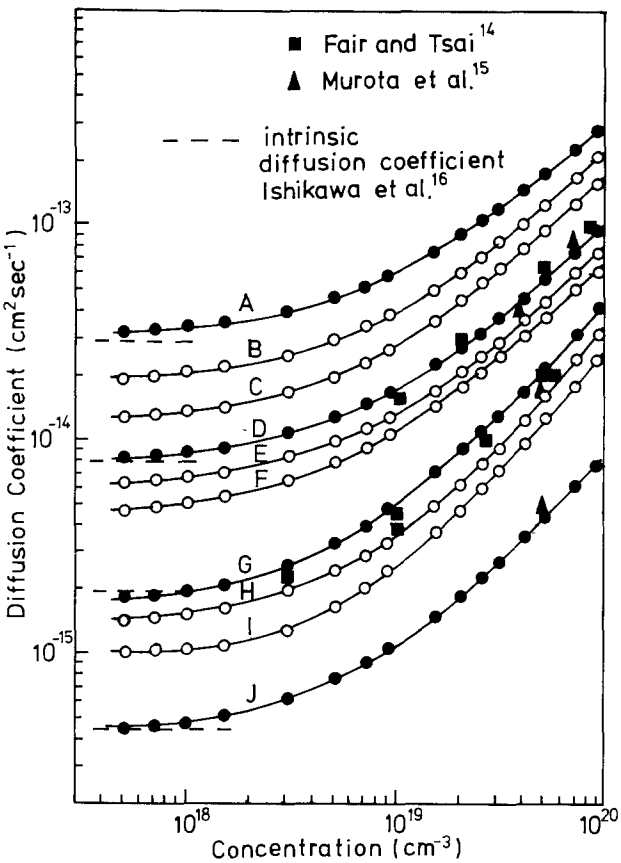

Fig. 3. Arsenic concentration dependence of diffusion coefficients. A: 1100°C 1 hr dry N_2 and 1100°C 6.5 hr dry N_2. B: 1100°C 6.5 hr dry O_2. C: 1100°C 1 hr dry O_2. D: 1050°C 6 hr dry N_2 and 1050°C 29.5 hr dry N_2. E: 1050°C 29.5 hr dry O_2. F: 1050°C 6 hr dry O_2. G: 1000°C 5.5 hr dry N_2 and 1000°C 30 hr dry N_2. H: 1000°C 30 hr dry O_2. I: 1000°C 5.5 hr dry O_2. J: 950°C 30 hr dry N_2, 950°C 54 hr dry N_2, 950°C 30 hr dry O_2, and 950°C 54 hr dry O_2.

are shown (16). A good agreement of our results under inert atmosphere with those of others supports the validity of the present procedure for the determination of the diffusion coefficient of arsenic. It is found, from Fig. 3, that the diffusion coefficients of arsenic under oxidizing atmosphere are smaller than the values under inert atmosphere all over the arsenic concentration range investigated in this work at 1000°-1100°C, that is, the retarded diffusion occurs. The degree of the retarded diffusion decreases with the increase of diffusion time. The retarded diffusion is not found at 950°C. We have already reported on oxidation-enhanced diffusion of arsenic in intrinsic conditions in Ref. (16). Our results in this work are in contrast with our previous results obtained in intrinsic conditions.

It is well known that the concentration dependence of the diffusion coefficient of arsenic under inert atmosphere in extrinsic conditions is explained by the generation of excess vacancies on the basis of the predominant contribution of the vacancy for arsenic diffusion (14, 18). Thus, we infer the present result as follows qualitatively. The concentration of vacancies is decreased by the recombination of vacancies and excess self-interstitials which are generated by thermal oxidation of silicon. Consequently, vacancy concentration becomes lower than the value under inert atmosphere, and the retarded diffusion occurs. Moreover, the diffusion coefficients under oxidizing atmosphere are smaller than the intrinsic diffusion coefficients at a relatively low concentration region at 1000°-1100°C (Fig. 3). This fact suggests that the vacancy concentration can become lower than the value under thermal equilibrium conditions at the deep region in arsenic concentration profiles.

The cause of the diffusion time dependence of the degree of the retarded diffusion may be considered briefly. The oxidation rate of silicon decreases with the increase of oxidation time. Thus, the degree of the excess in self-interstitial concentration decreases and the vacancy concentration is not decreased so much by the recombination. Therefore, the degree of the retarded diffusion decreases with the increase of diffusion time.

Conclusions

The arsenic diffusion coefficient in extrinsic conditions, which is a function of arsenic concentration, is determined under both oxidizing and inert atmospheres. It is found that the arsenic diffusion coefficient is smaller under oxidizing atmosphere than under inert atmosphere at 1000°-1100°C. The degree of this retarded diffusion decreases with the increase of diffusion time. We infer that excess silicon self-interstitials that are generated by thermal oxidation of silicon recombine with vacancies, and the concentration of vacancies becomes lower than the value under inert atmosphere, so the retarded diffusion occurs.

Manuscript submitted Feb. 3, 1983; revised manuscript received June 1, 1983.

Keio University assisted in meeting the publication costs of this article.

REFERENCES

1. G. N. Wills, *Solid-State Electron.*, **12**, 133 (1969).
2. W. G. Allen, *ibid.*, **16**, 709 (1973).
3. D. Antoniadis, A. G. Gonzales, and R. W. Dutton, *This Journal*, **125**, 813 (1978).
4. D. Antoniadis, A. M. Lin, and R. W. Dutton, *Appl. Phys. Lett.*, **33**, 1030 (1978).
5. R. Francis and P. S. Dobson, *J. Appl. Phys.*, **50**, 280 (1979).
6. A. M. Lin, D. Antoniadis, and R. W. Dutton, *This Journal*, **128**, 1131 (1981).
7. C. Hill, in "Semiconductor Silicon 1981," H. R. Huff, Y. Takeishi, and R. J. Kriegler, Editors, p. 988, The Electrochemical Society Softbound Proceedings Series, Pennington, NJ (1981).
8. S. M. Hu, *J. Appl. Phys.*, **45**, 1567 (1974).
9. G. Masetti, S. Solmi, and G. Soncini, *Philos. Mag.*, **33**, 613 (1976).
10. G. Masetti, S. Solmi, and G. Soncini, *Solid-State Electron.*, **19**, 545 (1976).
11. K. Taniguchi, K. Kurosawa, and M. Kashiwagi, *This Journal*, **127**, 2243 (1980).
12. J. C. Irvin, *Bell Syst. Tech. J.*, **41**, 387 (1962).
13. M. M. Atalla and E. Tannenbaum, *ibid.*, **39**, 933 (1960).
14. R. B. Fair and J. C. C. Tsai, *This Journal*, **122**, 1689 (1975).
15. M. Murota, E. Arai, K. Kobayashi, and K. Kudo, *J. Appl. Phys.*, **50**, 804 (1979).
16. Y. Ishikawa, Y. Sakina, H. Tanaka, S. Matsumoto, and T. Niimi, *This Journal*, **129**, 644 (1982).
17. R. B. Fair and G. R. Weber, *J. Appl. Phys.*, **44**, 273 (1973).
18. S. M. Hu and S. Schmidt, *ibid.*, **39**, 4272 (1968).

Photoelectrochemical Studies of Nearly Intrinsic Semiconductors Made Possible by Using Photoconductivity

H. Gerischer,* M. Lübke, and B. Bressel

Fritz-Haber-Institut der Max-Planck-Gesellschaft, D-1000 Berlin 33, Germany

ABSTRACT

Photocurrent generation for nearly intrinsic semiconductor electrodes has an extremely small quantum yield because the space charge layer is insufficient to promote the efficient separation of electron hole pairs when suitable biases are applied. However, if the bulk material can be made photoconductive, a space charge layer having a higher electric field strength will be created. It is demonstrated that thin platelets of GaS and CdS, although insulating in the dark, can be used as photoelectrodes if they are illuminated with light having energy less than the bandgap in addition to light having energy above the bandgap. With this arrangement, high quantum yields similar to those obtained for well-doped semiconductors are obtained. The charge distribution in a semiconductor platelet under various modes of illumination is discussed.

Photoelectrochemical studies are usually performed with adequately conducting n- or p-type materials where the doping level is high enough to keep the resistance low between the electrode/electrolyte and the ohmic contact at the rear. It is only with these materials that the bias applied creates a large enough electric field in the space charge layer underneath the semiconductor/electrolyte interface so that an efficient separation of the electron hole pairs generated by light absorption can occur (1-4). This condition, however, excludes many materials from photoelectrochemical studies because either they do not have a high enough doping level due to their formation conditions or they cannot be produced in such a state. The authors demonstrate here that many of these materials can be studied photoelectrochemically if their internal resistance can be far enough reduced by means of photoconductivity. For this purpose, one needs two light sources, one of which is only weakly absorbed and can penetrate the whole bulk of the material thus making it photoconductive. If the light from the other source is absorbed close to the interface, mainly within the diffusion length of the electronic charge carriers, photocurrents with high quantum yield can be obtained. This option was discovered during studies of GaS crystals when samples were available which were mainly of very low conductivity or were even insulating in character. Thin plates of insulating CdS crystals were used as models because the properties of this material are much better known. Some typical results are reported in order to demonstrate the principal features of this approach. A more detailed publication of these studies will follow.

Experimental

Thin slices of GaS crystals were obtained by cleaving thicker crystals received from F. Lévy, Lausanne. They were contacted with In-Hg and mounted on brass in Teflon cylinders which could be inserted into normal electrolysis cells. The edges of the crystal plates were protected with silicon rubber. The thickness of the crystal plates was in the order of 0.2-0.5 mm. Thin single-crystal plates of CdS, grown by sublimation of cadmium sulfide in a gas stream, were obtained from R. Broser of this institute. These were contacted with In and mounted in the same way described above. As electrolytes, 1M KCl for GaS and 0.5M Na_2SO_3 for CdS were used. Illumination was performed with chopped monochromatic light at different wavelengths. Continuous or pulsed light from the second lamp, which passed an interference filter or a cut-off filter cutting off all light above a fixed energy, could be superimposed. Photocurrents were measured by the lock-in technique. Voltages were measured against a saturated calomel electrode.

* Electrochemical Society Active Member.

Key words: photoconductivity, photocurrent relaxation, photoelectrochemistry, semiconductors, GaS, CdS.

Results

Figure 1 shows the absorption spectra of GaS (5) and CdS (6). The bandgaps are 2.7 eV for GaS (indirect) and 2.4 eV for CdS (direct). It turned out that the photocurrents generated by the monochromatic light source alone with a quantum energy larger than the bandgap were very small and increased linearly with increasing bias. However, after adding light from a second light source with a quantum energy cutoff below the bandgap energy, a much larger photocurrent was obtained compared to the monochromatic light source alone. The photocurrent caused by the second lamp alone was very small.

With sufficient intensity of the secondary light source (I'), the photocurrent caused by the primary light source (I) approached saturation and was thus similar

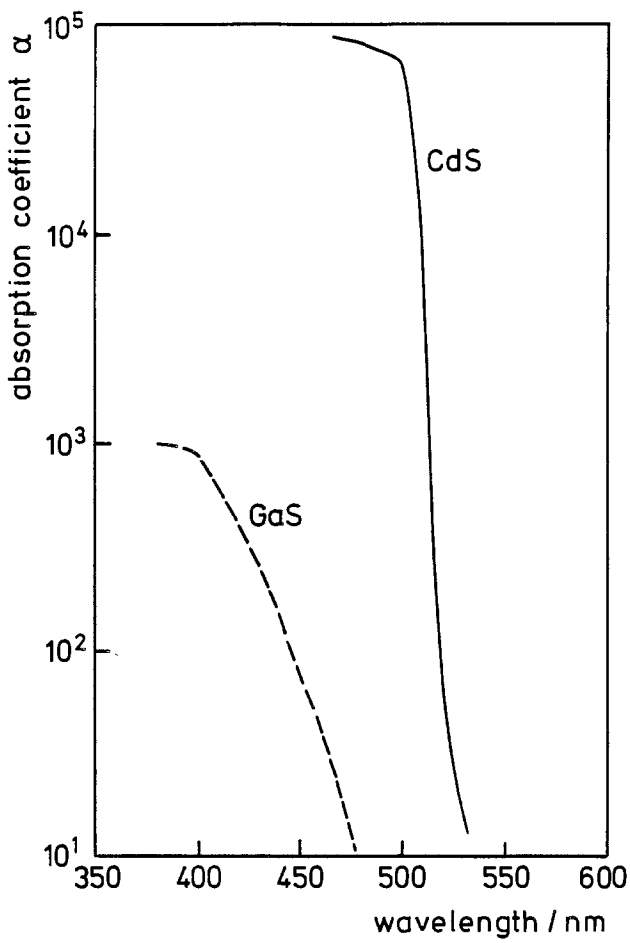

Fig. 1. Absorption coefficients of GaS (5) and CdS (6)

in behavior to that exhibited by a normally doped specimen. Figure 2 shows photocurrent voltage curves for a GaS slice with insulating character, illuminated with light of $\lambda = 360$ nm alone or with the admixture of light that had passed a cut-off filter of 495 nm. N- and p-type photoconductivity has been observed in this material depending on the method of crystal preparation (7). The GaS specimen exhibited a p-type photoconductivity. Therefore, a negative bias was applied so that the photocurrent was cathodic, resulting in hydrogen evolution because of the reduction of water by photogenerated electrons.

Analogous experiments have been performed with CdS, which is normally an n-type material. The specimen in this experiment had a doping level below 10^{13} cm^{-3} and was therefore essentially insulating. The photocurrent voltage curves for a specimen under illumination with light of $\lambda = 430$ nm alone and with admixture of light with $\lambda = 518$ nm are shown in Fig. 3. Since the CdS crystals have a much higher absorption coefficient than the GaS crystals, a saturation photocurrent was reached with a modest bias when a sufficient intensity of light from the secondary source (I') was added. The saturation current under these conditions was proportional to the intensity of the primary light source (I) as Fig. 3 indicates.

The photocurrent quantum yield obtained with one light source alone is shown as a function of wavelength in Fig. 4. This figure also shows the yield spectrum during additional illumination by the second light source with subbandgap energy. One clearly sees the enormous differences in the above bandgap energy range caused by the additional illumination.

The efficiency of the second light source is dependent on its wavelength as is demonstrated in Fig. 5 for GaS. This figure shows the additional photocurrent induced by the chopped light source with a wavelength of 400 nm (above bandgap) during a continuous illumination by the second light source. The wavelength of the latter light is varied with a monochromator. One sees

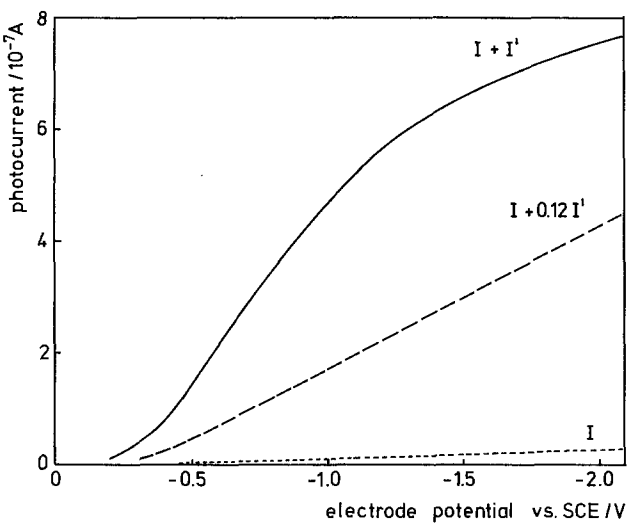

Fig. 2. Photocurrent voltage curves for a GaS crystal ($d = 0.5$ mm) in 1M KCl under illumination with 360 nm light (I) alone and with additional illumination by light with $\lambda > 495$ nm (I') at two different intensities.

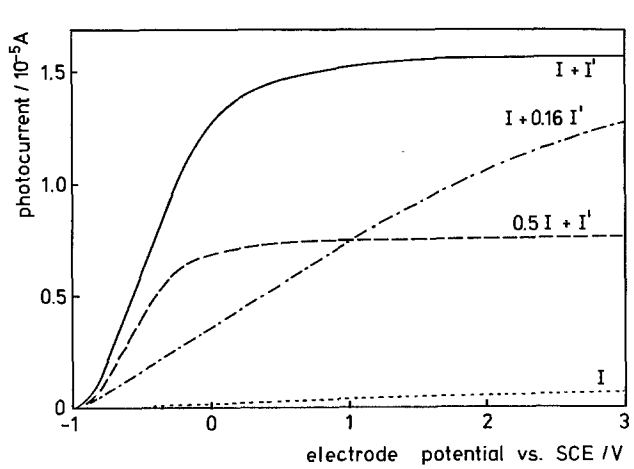

Fig. 3. Photocurrent voltage curves for a CdS crystal ($d = 0.2$ mm) in 0.5M Na_2SO_3 under illumination with 430 nm light (I) alone with additional illumination by light of $\lambda = 518$ nm (I').

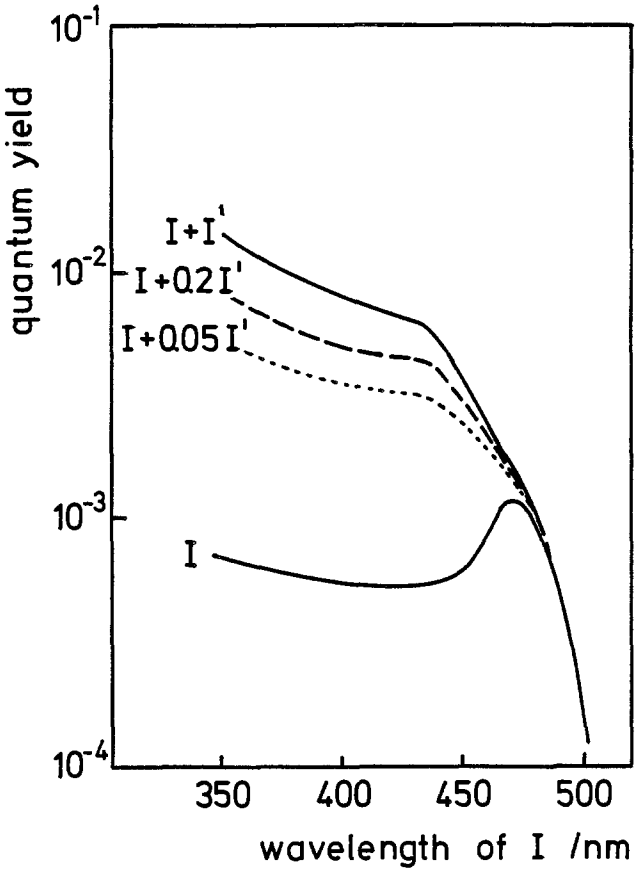

Fig. 4. Spectral dependence of the photocurrent quantum yield for chopped monochromatic light (I) alone and with additional continuous illumination by subbandgap light (I'). GaS at —1V bias vs. SCE in 1M KCl; I' ($\lambda > 495$ nm with cut-off filter).

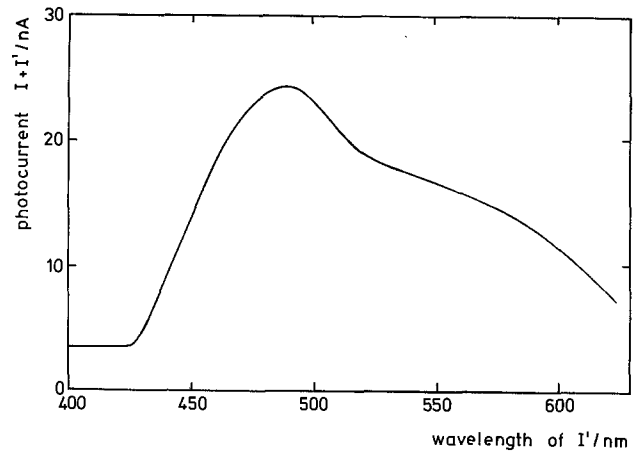

Fig. 5. Spectral dependence of the increase of the photocurrent due to chopped light at $\lambda = 400$ nm (I) by continuous illumination with a second light source (I'). GaS crystal of 0.48 mm thickness, electrolyte 1M KCl, bias —1.55V (vs. SCE).

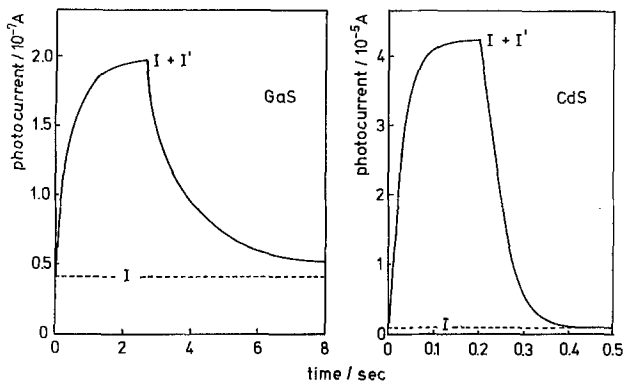

Fig. 6. Photocurrent transients during and after light pulse with subbandgap light I', added to above bandgap light I. GaS electrode as in Fig. 2 at −0.9V bias I at $\lambda = 390$ nm; I' with $\lambda > 495$ nm. CdS electrode as in Fig. 3 at +2.6V bias I at $\lambda = 440$ nm; I' with $\lambda = 518$ nm.

that there is an optimal wavelength for the effect of the second light source.

Finally, the photocurrent relaxation behavior, when a pulse of light having subbandgap energy is added, is shown in Fig. 6. The relaxation time for GaS is on the order of 1 sec and for CdS on the order of 10^{-2} sec. Such relaxation times, as shown in Fig. 6, are typical for photoconductivity (8-10). Photocurrent relaxation times for light pulses of the primary light source, maintaining constant illumination by the second light source, are much shorter.

Discussion

The very low quantum yield of the photocurrents generated by the primary light source alone is obviously caused by the high internal resistance of the semiconductor. The spectral dependence of the quantum yield with a single lamp is maximum at wavelengths where the light can penetrate the crystal to a considerable extent. This wavelength is dependent on the thickness of the crystal plate, as seen in additional experiments. The conclusion is that light absorption in the bulk reduces the internal resistance therein by photoconductivity. The increased conductivity of the bulk has the consequence that the voltage drop, caused by the applied bias, decreases in the bulk and is concentrated to a narrower region underneath the semiconductor/electrolyte contact where electron hole pairs can be separated more efficiently. Light which has wavelengths resulting in a small penetration depth compared to the thickness of the crystal cannot create considerable photocurrents because the electron hole pairs are generated in a region with a low electric field strength in the dark. Under illumination, the field in this region is to a large extent compensated or even overcompensated by an opposite field due to space charge generation. Only a very small fraction of carriers can escape recombination by diffusion or migration in the remaining electric field under these circumstances.

The situation is drastically changed if a second light source with the appropriate wavelength makes the bulk of the crystal photoconductive. The internal resistance of the crystal decreases, and the voltage applied concentrates at the interface between the crystal and the electrolyte. The existence of a maximum for the efficiency of the second light source, shown in Fig. 5 for GaS, demonstrates this photoconductivity effect. The optimum is to be expected for light which penetrates the whole crystal sufficiently well but is not too weakly absorbed. Light which is too strongly absorbed leaves the rear part of the crystal nonconductive, while light with a very small absorption coefficient induces a too low photoconductivity in the bulk.

With a higher electric field strength underneath the contact to the electrolyte, electron hole pair separation can become much more efficient for light with a high absorption coefficient. Mobile charge carriers with suitable sign, which are generated within this region of high field strength or reach it by diffusion during their lifetime, escape recombination and can at the semiconductor/electrolyte interface oxidize or reduce the redox components in solution.

Photoconductivity can have a rather long relaxation time if one of the photogenerated charge carriers is captured in deep traps which have a relatively small cross section for recombination. In the GaS samples, such traps were present for electrons but the holes remained mobile. The authors could therefore create large cathodic photocurrents. For CdS, the opposite situation existed in that holes were trapped in long-lived states (8-10) while the electrons remained mobile. If one assumes that the number of traps for electrons or holes is in the order of 10^{14}-10^{15} cm^{-3} (10), one can then easily imagine that a depletion layer similar to doped materials can be formed by such trapped charge carriers. Though a quantitative description has still to be developed, the authors can qualitatively explain their results with the above model.

The model is summarized in Fig. 7 for a thin insulating CdS specimen under anodic bias in part (a) for the run of the electric potential: (*i*) in the dark, (*ii*) under illumination by the primary light source alone (I), and (*iii*) with additional illumination by a second light source (I'). It is seen that the bias creates a kind of Schottky barrier in the photoconductive

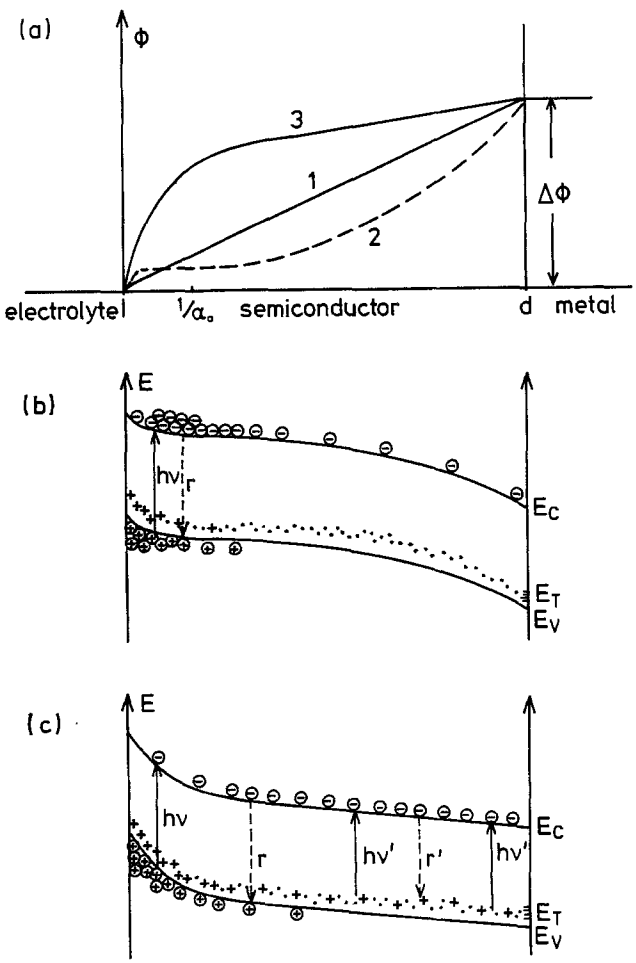

Fig. 7. (a) Run of the electric potential in a thin insulating CdS crystal with applied constant bias $\Delta\phi$. Case 1: in the dark; 2: with above bandgap illumination alone (I); 3: with additional subbandgap illumination (I + I'). (b and c): Schematic representation of the charge distribution in the energy bands and in traps for holes over the semiconductor slice in the steady state of illumination: (b) case 2; (c) case 3. r, r' = recombination.

crystal at the semiconductor/electrolyte interface and, if the illumination intensity from the second light source is intensive enough, the crystal can act like a doped material with a depletion layer at the contact to the electrolyte.

Parts b and c of Fig. 7 represent schematically the charge distribution, via an energy band diagram, under steady-state illumination for an insulating CdS crystal of thickness d at positive bias in accordance with the above model. Figure 7b shows the situation for above bandgap light alone, where electrons and holes remain concentrated at the illuminated surface and can easily recombine. Figure 7c illustrates the efficient charge separation made possible by the high electric field in the depletion layer because the trapped positive charge in the bulk (the energy position of the traps is indicated by dots) compensates the charge of the mobile electrons therein and keeps the bulk conductive.

That the quantum yield for GaS is considerably lower than for CdS can be explained by the absorption coefficient of GaS which is two orders of magnitude smaller than that of CdS at the wavelengths used in these experiments. This has the consequence that in GaS the penetration depth of the above bandgap light is much larger than the diffusion length of the holes, and it can only be expected that electron hole pairs, which are generated within a distance from the surface corresponding to the diffusion length, contribute to the photocurrents.

Acknowledgments

The authors express their gratitude to Dr. F. Lévy, Lausanne, and Dr. R. Broser for supplying the crystals of GaS and CdS, respectively. They also thank Dr. G. Scholz for his help in preparing the manuscript.

Manuscript submitted Dec. 6, 1982; revised manuscript received ca. April 1, 1983.

REFERENCES

1. H. Gerischer, in "Physical Chemistry," Vol. IX, H. Eyring, D. Henderson, and W. Jost, Editors, pp. 463-542, Academic Press, New York (1970).
2. A. J. Nozik, *Ann. Rev. Phys. Chem.*, **29**, 189 (1978).
3. R. H. Wilson, *J. Appl. Phys.*, **48**, 4292 (1977).
4. H. Reiss, *This Journal*, **125**, 937 (1978).
5. G. A. Akhundov, S. A. Musaev, A. E. Bakhyshev, N. M. Gasanly, and L. G. Musaeva, *Sov. Phys. Semicond.*, **9**, 94 (1975).
6. D. Dutton, *Phys. Rev.*, **112**, 785 (1958).
7. A. H. M. Kipperman and G. A. van der Leeden, *Solid-State Commun.*, **6**, 657 (1968).
8. I. Broser and R. Warminsky, *Ann. Physik*, **7**, 289 (1950).
9. J. Lambe, *Phys. Rev.*, **98**, 985 (1955).
10. R. H. Bube, *J. Phys. Chem. Solids*, **1**, 234 (1957).

Technical Notes

Efficient D-C Electroluminescence from ZnS:Mn and ZnS:TbF_3 Thin Films Prepared by RF Sputtering

H. Ohnishi, N. Sakuma, and K. Ieyasu

Department of Electronics Engineering, Faculty of Engineering, Ehime University, Matsuyama, Ehime 790, Japan

Y. Hamakawa

Department of Electrical Engineering, Faculty of Engineering Science, Osaka University, Toyonaka, Osaka 560, Japan

Intensive studies have been made on thin film electroluminescent (EL) devices because of their considerably higher potential in the commercial demands for a flat-type display unit. A doubly insulated ZnS:Mn a-c operated device, showing a good display performance in brightness, efficiency, and life, has approached the practical stage (1-3). The tremendous strides have been followed by the film preparation methods of molecular beam epitaxy (4), atomic layer epitaxy (5), and metal organic chemical vapor deposition (6). In contrast to a yellowish-orange emitter, more informative multicoloring devices have been fabricated by employing the rare earth fluorides as luminescent centers (7, 8). The doubly insulated ZnS:TbF_3 device, prepared usually by an electron beam evaporation, exhibits 0.1-0.2 lm/W of highest efficiency among rare earths (8, 9). Attention has been paid to the rf sputtering method because of high productivity, impurity controllability, etc. The authors have conducted a series of studies on the electroluminescence from ZnS films deposited by rf sputtering. It has been found that an efficiency beyond 0.15 lm/W is typically obtained from the system of Al-ZnS:TbF_3-$InSnO_x$ MS structure. This work presents the d-c excited characteristics of ZnS films activated with TbF_3 and Mn. The effects of impurity concentration and film thickness on the luminescence are also presented.

Key words: electroluminescence, ZnS thin films, rf sputtering.

The mixed powder of 5-nines ZnS and 3-nines TbF_3 or Mn metal was sintered at 400°-500°C for 3 hr in argon gas to exclude the absorbed gas. The mixture settled on a quartz saucer of 105 mm was used as a sputtering target. The phosphor films were deposited on an $InSnO_x$-coated glass substrate heated at 150°C under the sputtering condition of argon gas pressure = 1.45 Pa, rf power density = 1.27 W/cm^2, anode voltage = 1.5 kV. The target electrode and substrate-target space were 100 and 40 mm, respectively. The deposition rate was in a range of 150-250 Å/min. After the film preparation, heat-treatment was made at 450°-480°C in a vacuum to remove point or small defects neighboring the luminescent centers. The

Al-ZnS:TbF_3 (or Mn)-$InSnO_x$ structure was formed by depositing Al as a counterelectrode. The luminance was measured by a brightness meter, TOPCON BM-3.

The d-c electroluminescence is usually observed in a fabricated device with an Al electrode positively biased and often observed in a reversely biased case. The current-voltage and brightness-voltage relationships show nonlinear characteristics. Figure 1 shows the typical current-voltage and brightness-voltage characteristics of the both type devices. As can be seen, the voltage dependences are steeper in the ZnS:Mn device than the ZnS:TbF_3 device. The ZnS:Mn system has the threshold voltage from low to high conductance regions. The luminescent intensity increases with elevating applied voltage. The threshold field is about 1×10^6 V/cm, which is compatible with the strength reported conventionally. The ZnS:TbF_3 system, however, does not have a clear threshold and shows weaker voltage-dependence than ZnS:Mn. The reason for the steeper characteristics of the Mn device than the TbF_3 device is not understood as yet. The device sometimes suffers from damage called "burning out" beyond the voltage where the current abruptly increases. The obtainable brightness level is limited by permissible current through the device. A brightness level of 600 f-L has been obtained, but typically 200-300 f-L. Such limitation is due to the local thermal breakdown that gives rise to formation of a patch in the Al electrode. The efficiency depends on the electrical input power as shown in Fig. 2. The efficiency increases with increasing input power at low voltage because of its strong field dependence. The maximum efficiency is measured as 0.13 lm/W at 2.4×10^{-4} W/cm^2 for ZnS:Mn while it is 0.17 lm/W at 9×10^{-2} W/cm^2 for ZnS:TbF_3. As the input is further increased, the power dissipation raises the device temperature so that the efficiency decreases. One of the reasons for weak temperature quenching of the TbF_3 device can be explained on the basis that the rare earth centers have poorer

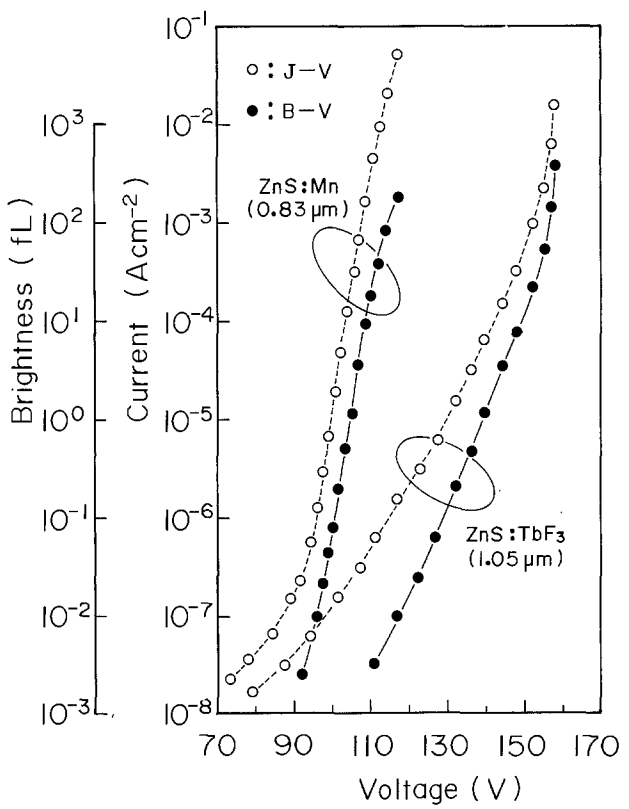

Fig. 1. Current-voltage and brightness-voltage characteristics of d-c EL devices consisting of ZnS:Mn 0.83 μm thick and ZnS:TbF_3 1.03 μm thick.

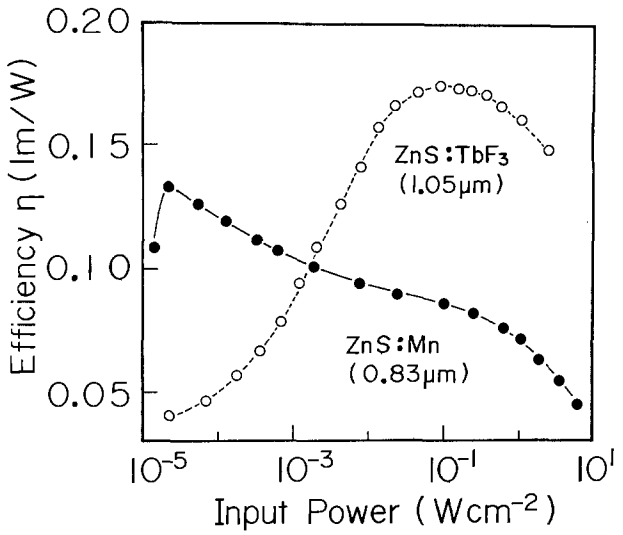

Fig. 2. Efficiency-input power relationships of ZnS:Mn and ZnS:TbF_3 d-c EL devices.

phonon impedance match with the ZnS host lattice than the Mn center.

Figure 3 shows the dependence of efficiency on the impurity concentration in sputtering target. The linear dependence at low densities is due to the increase in the number of the luminescent centers. The maximum efficiency, typically 0.15 lm/W and sometimes beyond 0.2 lm/W, is attained at 1.8 atomic percent (a/o) for ZnS:TbF_3 while it is 0.8 a/o for ZnS:Mn. An optimal density for ZnS:TbF_3 agrees with the value that Krupka *et al.* (10) have determined for the concentration in the films by x-ray fluorescence method. This agreement suggests that the rf sputtering method has a good controllability of impurity concentration. In the higher density region, the efficiency is decreased as a result of concentration quenching. This phenomenon contains two possible mechanisms: the increase of nonradiative transition, presumably due to pairing, and the decrease of electron mean free path. Figure 4 shows maximum efficiency as a function of the ZnS:TbF_3 layer thickness. Efficiency steeply increases up to 0.15 lm/W with the increase of the film thickness and saturates above 0.45 μm. Low efficiency in a thin region can be explained by the experimental results of the x-ray diffraction pattern, which has shown that the

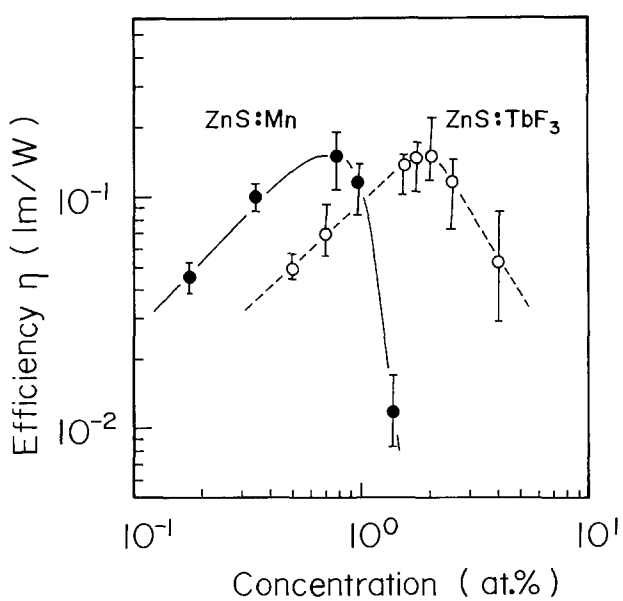

Fig. 3. Efficiency of ZnS:Mn and ZnS:TbF_3 as a function of impurity concentration.

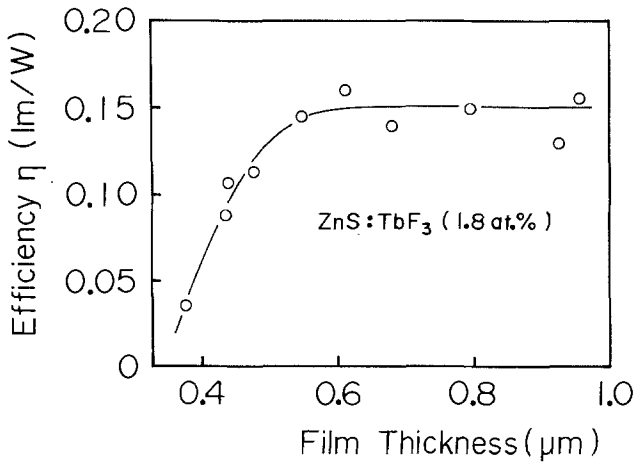

Fig. 4. Efficiency of $ZnS:TbF_3$ as a function of film thickness

crystallinity of the thin films is poorer than the thick films. The electric field is 1.5-1.8 $\times$ 10^6 V/cm at a high brightness level, which means the requirement of driving voltage is above 70V. Low voltage operation can be achieved if the crystallinity is improved in the thin region. The experimental approaches to reduce the threshold voltage and to optimize the film preparation condition are in progress.

Acknowledgments

The authors wish to express their gratitude to Drs. T. Nishino, M. Okuyama, and H. Takakura of Osaka University for their encouragement and valuable discussions throughout the course of this work. They also would like to thank H. Harada, H. Hamaguchi, H. Yoshino, and S. Takahara of Ehime University for their technical assistance during the investigation. This work is partially supported by Grant-in-Aid for Scientific Research from the Ministry of Education, Science, and Culture.

Manuscript submitted Feb. 14, 1983; revised manuscript received May 6, 1983.

REFERENCES

1. T. Inoguchi, M. Takeda, Y. Kakihara, Y. Nakata, and M. Yoshida, *SID Dig.*, 84 (1974).
2. T. Inoguchi and S. Mito, in "Electroluminescence," I. J. Pankove, Editor, Chap. 6, pp. 197-210, Springer-Verlag, Berlin (1977).
3. M. Takeda, Y. Kanatani, H. Kishishita, T. Inoguchi, and K. Okano, *SID Dig.*, 66 (1980).
4. T. Mishima, W. Quan-Kun, and K. Takahashi, *J. Appl. Phys.*, **52**, 5797 (1981).
5. T. Suntola, J. Anston, A. Pakkala, and S. Lindfors, *SID Dig.*, 108 (1980).
6. A. F. Cattell, B. Cockayne, K. Dexter, J. Kirton, and P. J. Wright, Conf. Record Inter. Display Res. Conf., p. 20 (1982).
7. E. W. Chase, R. T. Hepplewhite, D. C. Krupka, and D. Kahng, *J. Appl. Phys.*, **40**, 2512 (1969).
8. T. Suyama, N. Sawara, K. Okamoto, and Y. Hamakawa, *Jpn. J. Appl. Phys.*, **21**, Suppl. **21-1**, 383 (1982).
9. L. G. Hale, B. Garcia, R. D. Ketchpel, and T. C. Lim, *IEDM Dig.*, 719 (1980).
10. D. C. Krupka and D. M. Mahoney, *J. Appl. Phys.*, **43**, 2314 (1972).

Electrical Conduction Through Polysilicon Oxide: Interface Texture vs. Isolated Protuberances

P. A. Heimann,* P. S. D. Lin,* and T. T. Sheng

Bell Laboratories, Murray Hill, New Jersey 07974

The high electrical conductivity of oxides grown from polycrystalline silicon (poly-oxide), in comparison to the conductivity of oxides grown from single-crystal silicon, has been attributed by several workers (1-5) to asperities or protuberances at the polysilicon/poly-oxide interface. These protuberances cause a local enhancement of the electric field at the interface (3, 6) which leads to conduction through the poly-oxide by Fowler-Nordheim tunneling at a lower value of applied voltage than would be required for a smooth interface.

It has recently been found that polysilicon prepared with a smooth surface yields a marked improvement in poly-oxide dielectric properties (7), and this work was confirmed by the use of *in situ* phosphorus-doped polysilicon (8). Elevated oxidation temperature also appears to yield a smoother interface (5, 9).

The interface as seen in transmission electron micrographs (9) shows three types of textural features: a roughness due to the grain structure of the film, bumps about 0.1-0.3 μm wide due to growth anomalies during polysilicon deposition, and sharper protuberances formed during oxidation. The protuberances vary in height and surface density, with upper limits of about half the oxide thickness and about 1 $\times$ 10^7/cm^2, respectively.

The purpose of the present work was to determine whether the observed electrical currents are injected into the oxide mainly at the isolated sharp protuberances and large bumps or at the granular features and small bumps found all over the interface. Measurements were made of the current *vs.* field through samples of small areas which should contain few or no protuberances or large bumps, and of the current observed in a scanning electron microscope operated in the electron-beam-induced current (EBIC) mode.

Sample Preparation and Measurement

Low-pressure chemical vapor deposited (LPCVD) *in situ* phosphorus-doped polysilicon was deposited at 700°C onto substrates [1000Å oxide grown on 25 Ω-cm p-type (100) silicon wafers] and was oxidized at 1050°C in steam for 10 min, to yield a 1200Å thick oxide. The oxide thickness was determined from the capacitance of large-area devices, from a stylus step-height measurement after removing part of the oxide, and from TEM cross sections. All measurements agreed to within 10%. For EBIC studies, a thin ($\approx$1000Å) layer of evaporated aluminum was deposited using a shadow mask to yield 20 mil dots. For electrical measurements, 1200Å of LPCVD silicon nitride was deposited and contact windows of various areas from 7 μm^2 to 1.6 $\times$ 10^7 μm^2, were etched using CF_4/O_2 reactive ion etching. Aluminum electrodes were then deposited and patterned to yield the structure shown in Fig. 1.

Electrical conduction through the poly-oxide was measured using a home-built voltage ramp and a

* Electrochemical Society Active Member.
Key words: insulator, tunneling, capacitor, semiconductor.

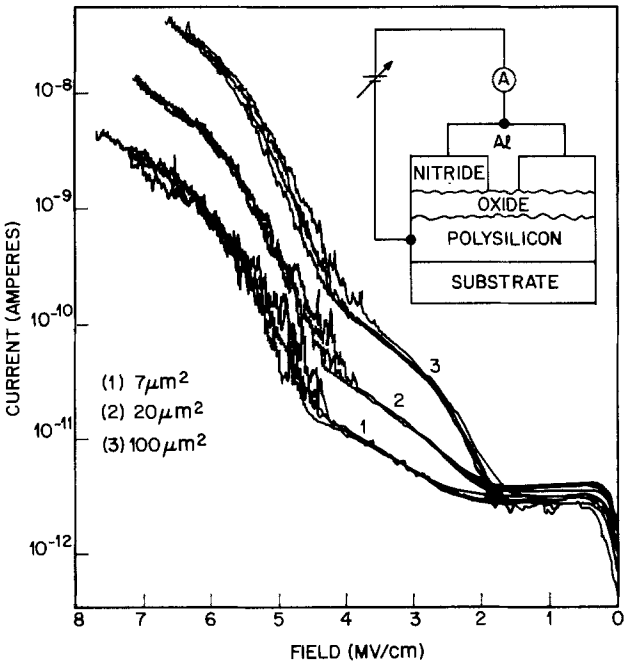

Fig. 1. Current vs. electric field for several poly-oxide samples. Note the similarity of the curves for devices of the same area.

Keithley Model 26120 logarithmic picoammeter. The details of this method have been described previously (5). If the electrical conduction arises from isolated protuberances or bumps, then the current-voltage curves for different small-area devices on a wafer should be markedly different.

The spatial variation of the electric current was also studied "directly" using a scanning electron microscope (Cambridge Stereoscan S4) in the high-field EBIC mode (10). In this technique, hot secondary electrons generated in the sample by the incident beam are injected into the poly-oxide. The injection is enhanced in regions of high local electric field, which gives rise to bright spots in the EBIC image.

Results and Discussion

The current-voltage curves for devices with areas of 7, 20, and 100 μm^2 (four devices each) are shown in Fig. 1. There is very little variation among different devices of the same area, which indicates that there must be many sites per square micron for enhanced-field injection of electrons into the poly-oxide. The same conclusion can be drawn from the EBIC image shown in Fig. 2, which shows that sites of locally enhanced current have a minimum spacing of about 0.3 μm. This is about the same spacing as that of the interface features in the TEM cross section (Fig. 3). This spacing is equivalent to about 5-25 active sites per square micron, or at least 35 active sites even in the smallest area tested for electrical conductivity.

These results show that the observed conduction through the poly-oxide arises from the enhanced electric fields at many closely spaced active sites at the polysilicon/poly-oxide interface. These sites are a property of the general texture of the interface, and one need not assume that there are large currents at isolated defect sites. These results do not pinpoint the exact nature of the active sites. They could be the high spots on the numerous bumps (see Fig. 3), since there is considerable electric field enhancement at the surface of even a moderately curved bump, as compared to the electric field at a flat interface (5). They could also be the points where the polysilicon grain boundaries meet the oxide, since the nonstoichiometry and strained bonds at these points could lower the silicon-oxide energy barrier.

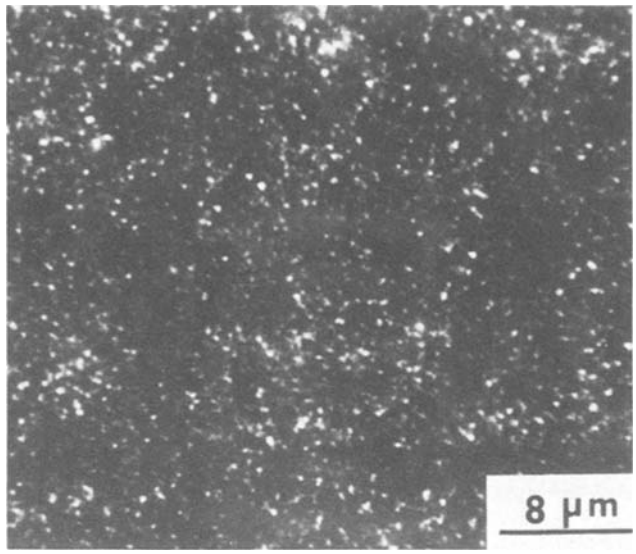

Fig. 2. EBIC image of capacitor (≈1000Å aluminum as top electrode, 1200Å of poly-oxide, +20V bias on electrode, 15 kV primary electron voltage). Bright features are interpreted as due to enhanced emission of electrons at protuberances.

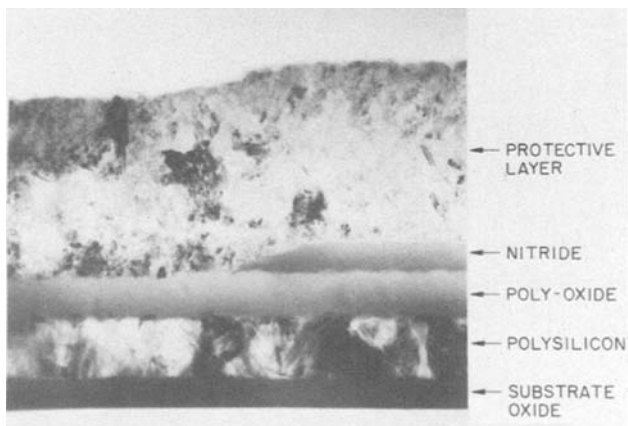

Fig. 3. TEM cross section of polysilicon/poly-oxide structure. The aluminum electrode has been replaced by a protective polysilicon layer. The substrate oxide is 1000Å thick.

Marcus *et al.* (9) have observed that the interface has nearly the same texture as that of the original polysilicon surface, which suggests that an initially smooth polysilicon surface is needed to achieve a poly-oxide with low leakage. Such oxides have recently been reported by Sternheim *et al.* (8).

Acknowledgments

We would like to thank R. A. Levy for depositing the *in situ* doped polysilicon, and R. B. Marcus and A. K. Sinha for their suggestions and encouragement.

Manuscript submitted April 5, 1983; revised manuscript received June 9, 1983. This was Paper 195 presented at the Detroit, Michigan, Meeting of the Society, Oct. 17-21, 1982.

Bell Laboratories assisted in meeting the publication costs of this article.

RERERENCES

1. D. J. DiMaria and D. R. Kerr, *Appl. Phys. Lett.*, **27**, 505 (1975).
2. R. M. Andersen and D. R. Kerr, *J. Appl. Phys.*, **48**, 4834 (1977).
3. H. S. Lee and S. P. Marin, *ibid.*, **51**, 3746 (1980).
4. H. R. Huff, R. D. Halvorson, T. L. Chiu, and D. Guterman, *This Journal*, **127**, 2482 (1980).
5. P. A. Heimann, S. P. Murarka, and T. T. Sheng,

J. Appl. Phys., **53,** 6240 (1982).
6. T. J. Lewis, *ibid.*, **26,** 1405 (1955).
7. R. B. Marcus, P. S. D. Lin, and T. T. Sheng, Private communication.
8. M. Sternheim, E. Kinsbron, J. Alspector, and P. A. Heimann, *This Journal*, **130,** 1735 (1983).
9. R. B. Marcus, T. T. Sheng, and P. S. D. Lin, *ibid.*, **129,** 1282 (1982).
10. P. S. D. Lin and H. J. Leamy, *Appl. Phys. Lett.*, **42,** 717 (1983).

JOURNAL OF THE ELECTROCHEMICAL SOCIETY

ACCELERATED

BRIEF COMMUNICATIONS

OCTOBER 1983

X-Ray Screen Performance Profile: Effect of Mechanical Energy during Phosphor

P. De Maayer* and W. Van Landeghem

Agfa-Gevaert NV, Research and Development Laboratories, Mortsel, Belgium

The effects of mechanical energy, supplied during eventual low-viscocity predispersion sandmilling, on the performance profile of x-ray intensifying screens, were studied for most phosphors in current use.

Experimental.-- Several 4 cm diameter PE-discs were rotated at 4000 rpm for varying times, in an 8 cm diameter PE-flask containing 55 w/o of 3 mm glass beads, 33 w/o of powder sample and 12 w/o of solvent-binder pre-mixture. From part of the predispersion screens were made using doctor-blade coating techniques, while the phosphor was recovered from the remainder by centrifugation and thorough appropriate solvent rinsing.

Resolution or square-wave-response $SWR(\nu) = \Delta E(\nu)/\Delta E_0$, with ΔE_0 the amplitude of intensity variation of the original signal and $\Delta E(\nu)$ that at fundamental frequency ν, was deduced from a microdensitometer scan of an imaged lead bar resolution test pattern (Funk type 36.882A), using the .027 x 1.081 mm light aperture of a Perkin Elmer PDS. The standard deviation of density fluctuations, total image noise σ_D, was also determined on a uniformly exposed film, using the .4 mm diameter aperture and measuring densities at 15,000 independant locations. For both procedures, the films were exposed to small focus, unfiltered 80 kVp tungsten radiation. The relative brightness S was evaluated by sensitometric exposure methods, described in a previous paper (1), and defined as

$$S = \log (E_s/E_{ref})$$

where E_s and E_{ref} are exposure intensities needed to cause a density 1.0 above fog on standard x-ray film for the experimental and reference Par Speed screens respectively. Agfa-Gevaert MR 4 (blind) film was used with UV-blue emitting phosphors, Kodak Ortho G film with green-emitting ones and both with 'white' emitting $Y_2O_2S:Tb^{3+}$.

Results.-- Although $CaWO_4$ and Tm^{3+} or Tb^{3+} activated LaOBr were included in our tests, table I only shows results for those screens appreciably changing their profile on milling.

$Gd_2O_2S:Tb^{3+}$ and $Y_2O_2S:Tb^{3+}$.-- Both oxysulfides show a drastic depreciation in brightness S with a concomitant increase in resolving power, after only 5 minutes milling. SWR values are given at 2 lp/mm, a frequency of direct importance to medical diagnostics, but the trend persists both at higher and lower frequencies (.5 to 5 lp/mm) (2). σ_D-changes exceed the threshold of visual perceptibility. Table I also indicates a decrease in cross-over C.O. except for the $Y_2O_2S:Tb^{3+}$-ortho film combination, for which C.O. remains virtually constant. Cross-over defines the exposure intensity from light of an x-ray screen reaching the back emulsion of a double-sided film, relative to that received by the front emulsion. No changes in physical properties could be detected for either material. Both the average equivalent spherical diameter P_{50} and the interquartile distribution width $(P_{75}-P_{25})/P_{50}$ remain constant, as confirmed by SEM and specific surface area data.

Table I : Screen performance characteristics and cross-over data.

	S	ΔS	SWR ν = 2 lp/mm	ΔSWR	σ_D D = 1.5	Δ σ_D x 10^3	C.O. %	ΔC.O.
Gd_2O_2S·Tb before	52		18		10 9		50.36	
+ ortho		−.31		.15		−.7		3.01
after (5 min)	21		33		10.2		47 35	
Y_2O_2S Tb before	47		19		11.2		48 48	
+ ortho		−.14		05		− 6		.57
after (5 min)	33		24		10.6		47 91	
Y_2O_2S. Tb before	46		22		—		45.94	
+ blind		− 18		09		—		3 34
after (5 min)	28		31		—		42.60	
BaFCl· Eu before	48		18		11 5		31.08	
+ blind		− 20		14		−9		3 25
after (60 min)	28		32		10 6		27.83	

coating weight· Gd_2O_2S. Tb & BaFCl Eu: 60 mg/cm² / Y_2O_2S. Tb 45 mg/cm²

* Electrochemical Society Active Member.

Key words : x-ray, luminescence, coatings.

An overall decrease in spectral reflectance with the appearance of characteristic absorption bands with respective maxima at 437 and 468 nm were noted for the Y- and Gd-compounds (fig. 1).

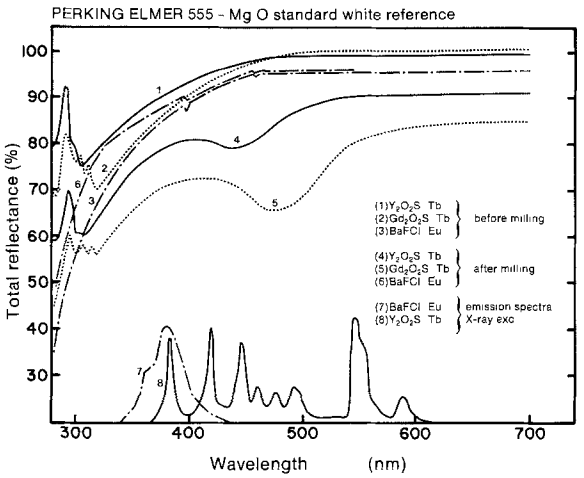

Fig.1. Total reflectance before and after milling for Y_2O_2S- and Gd-oxysulfides and BaFCl:Eu^{2+}.

Non-corrected emission spectra are also shown for BaFCl:Eu^{2+} and Y_2O_2S:Tb^{3+}. For the Gd-compound the position of the Tb^{3+} emission peaks is identical, but the UV-blue peaks are of considerably lower intensity than for Y_2O_2S.

BaFCl:Eu^{2+}.-- In contrast to the abrupt nature of the effects in case of the oxysulfides, equally large but gradual variations in S and SWR were found (fig. 2) as a function milling time. Again this trend was confirmed for a line pair frequency spectrum up to 5 lp/mm (2). P_{50} shows an equivalent monotonous decrease (fig.3), the steep initial drop in IDW indicating preferential fracturing of the larger grains along numerous cleavage planes of the tetragonal crystal structure. At the onset of milling a drastic increase in pyknometric density PD from 79 to 92 % was noted. The reflectance slightly increases in the UV-spectral range, while the C.O. and σ_D-changes are roughly equivalent to those of the oxysulfides (see table I).

Discussion and comments.-- The complexity of the optical phenomena involved in these multiphase systems do not allow as yet for a closely reasoned argumentation. Plausible but partial explanations may be given on the basis of the experimental evidence. Depreciation of oxysulfides, when heavily ball-milling or exerting large unilateral pressures, is caused by color center formation at stress induced atomically dispersed crystal defects, along with

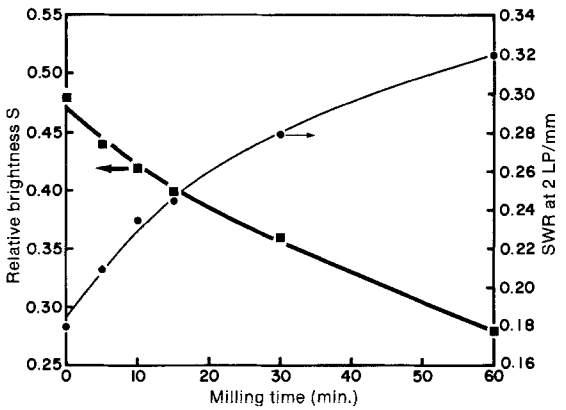

Fig.2. Brightness S and SWR (2 lp/mm) as a function of milling time for BaFCl:Eu^{2+}.

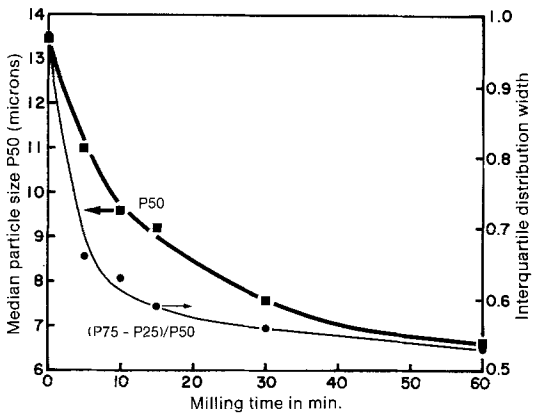

Fig.3. P_{50} and IDW as a function of milling time for BaFCl:Eu^{2+}.

particle size reduction (3,4). In our case the former effect and consequent phosphor coloring seems the only cause. The increase in sharpness is too drastic to be explained by phosphor color only, resolution being mainly scattering controlled and screens being virtually transparent to their own emission light. Stress induced changes in relative refractive index $m = n_p/n_o$ (n_p and n_o being the indices for phosphor and binder respectively) may therefore be of importance as shown by Clewell's simplified formula for the scattering coefficient $K = [(m^2-1)/(m^2+2)]/d$ at constant particle size d (5).

The variation in brightness S for BaFCl is clearly surface area controlled, as indicated by a linear relation with $1/P_{50}$ (fig.4). The scattering coefficient being inversely proportional to particle size, this plot reflects the fact that Lambert-Beer's law holds for scattering attenuation in this case. All screens were coated on highly reflective polyester base with a sharp absorption edge at 320 nm. The initial reflectance (fig. 1) is indicative of the rather transluscent character of BaFCl:Eu^{2+} screens (i.e. high transmis-

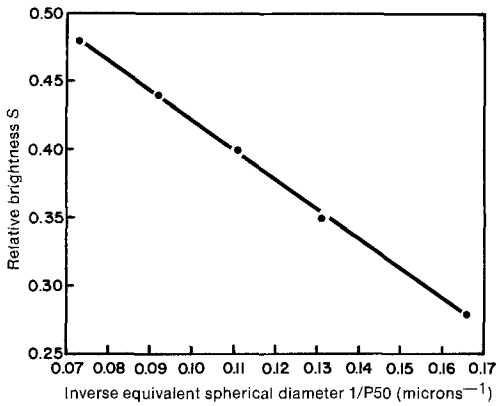

Fig. 4. S versus inverse particle size $1/P_{50}$.

sion,moderate scattering), n~1.64 being close to that of most current polymer systems used. The increase in UV reflectance on milling confirms our idea of increased internal scattering and explains part of the enhanced resolution. The large increase in packing density, with a substantial effect on physical thickness of the screens, explains for the large initial increase in SWR as a result of less geometrical unsharpness. Experiments on sieved fractions of equivalent size and distribution as samples milled for 30 minutes, showed much smaller effects (ΔS=-.07 ;ΔSWR(21p/mm) =.04). Some other milling induced factors have therfore to be of importance. These inconsistencies for both Tb-activated oxysulfides and $BaFCl:Eu^{2+}$ need further investigation, but at least two factors related to milling may be pointed out:

a) redistribution and size reduction of the void phase at roughly constant packing density may cause substantial additional internal scattering; an example is given in fig.5 for $Y_2O_2S:Tb^{3+}$.
b) decrease in cross-over unsharpness in all cases where the absorption band is situated in the range of maximum film C.O.(>420 nm for blind and between 450 and 520 nm for ortho emulsions) and as a result of the increase in UV reflectance for $BaFCl:Eu^{2+}$.

Finally, the substantial decrease in image noise σ_D implies the resolution enhanced noise perceptibility to compensate only partially the lowered quantum noise resulting from milling induced system speed reduction.

Manuscript submitted June 29, 1983; revised manuscript received Aug. 28, 1983.

Agfa-Gevaert NV assisted in meeting the publication costs of this article.

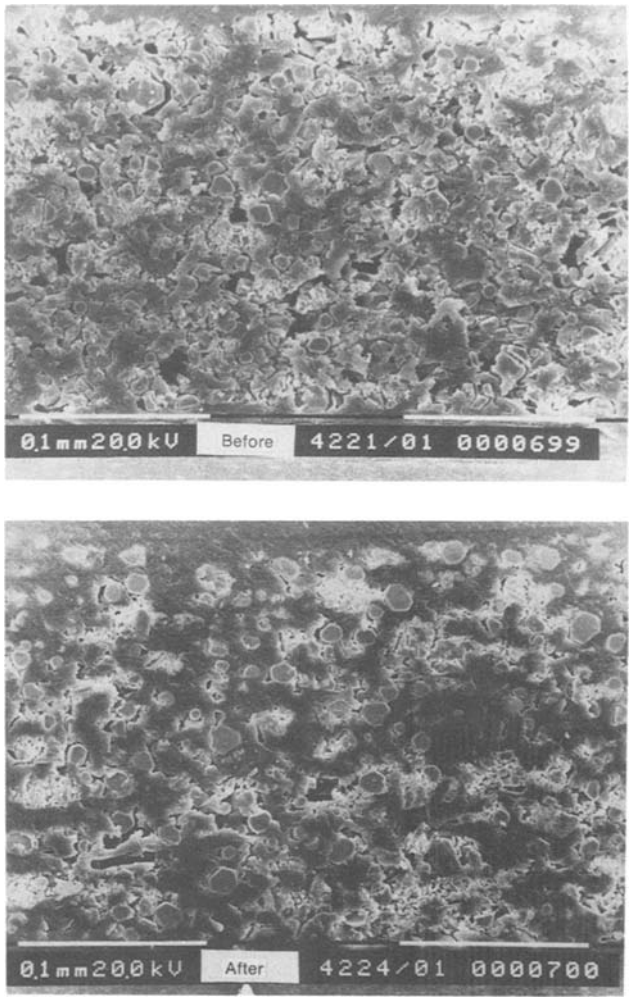

Fig. 5. SEM-cross-sectional view of $Y_2O_2S:Tb^{3+}$ screens before and after 5 minutes phosphor powder milling.

REFERENCES

1.P. De Maayer and R. Bollen, This Journal, 130, 437 (1983)
2.P. De Maayer et al,Abstract 601,905,The Electrochemical Soc. Extended Abstracts,San Francisco,California,May 8-13, 1983.
3.T. Nishimura et al,Mat.Res.Bull., 10, 747 (1975).
4.M. Tamatani et al, J. Lumin.,12/13, 935, (1976).
5.D. Clewell, J. Opt.Soc.Amer.,31,521 (1941).

This was paper 601 presented at the San Francisco, California, Meeting of the Society, May 8-13, 1983.

Characterization of Microdeformation and Crystal Defects in Silicon Wafer Surfaces

Koichi Kugimiya*

Matsushita Electronic Industry Company, Limited, Central Research Laboratory, Moriguchi, Osaka 570, Japan

Introduction: Recently increased attention has been payed to the characterization of silicon wafers and microdefects in silicon crystals in a very high degree due to the development of VLSI circuits and imaging devices with very high integration and fine performance. Intrinsic and extrinsic gettering techniques[1,2] have been intensively studied and their effectiveness has been proved in actual devices. These studies have concluded that the precise description of silicon wafers during the crystal growth is necessary for the improvements of the performance and the yield in the LSIs.

It has been also pointed out that some surface irregularities (SI's) are an indication of crystal defects beneath the wafer surfaces and that they are occasionally harmful to the device performance[3]. It is obvious that the surface defects like saw marks introduced in wafers during machining (slicing and polishing) processes are not annealed out by a heat treatment even at a high temperature, but act as a source of large crystal defects[1]. SI's are, at present, monitored in a dark-room by the naked-eye observation of the glaring surfaces or the reflected vague images of wafers[4]. This monitoring is obviously limited in sensitivity and reproducibity, and is not qualified for the VLSI specification.

To improve the image monitoring method, the author has derived a new principle combining "Makyo concept" and Schlieren apparatus, and developed a simple optical apparatus to observe directly the micro-topography of a mirror surface. As shown in Fig.1, white radiation of a W lamp is impinged on a mirror surface with a slight inclination from a normal. Reflected and scattered rays are projected on a monitor camera to form a defocussed image of a mirror surface. In this configuration, concavities and convexities are transformed to bright or dark areas on a defocussed wafer image. In term of curvature, R, which is directly related with the brightness, the apparatus is sensitive to pick up R of about 1 m and up to 100 m on a nearly perfect mirror surface. This paper describes the characteristic patterns observed in as-received and processed wafers.

Observation of surface irregularities (SI's): SI's were monitored by ZX-5100 (Matsushita Ind. Equip. Co., Ltd.) and recorded in VTR (Fig.2). It could pick up, for instance, very shallow concavities of 0.38 μm depth over about 10 mm span and 0.05 μm over about 1 mm span, corresponding to R of about 15 m and 2 m respectively. These depth profiles were measured by a surface profilometer.

Features of observed SI's on a monitor TV are shown in Figs.2 to 4. These patterns were classified to scratches, dimples, lapping (polishing) marks, saw marks and backside irregularities (Fig.2). Occasionally swirls, slips, dust crawlings, orange peels, insufficient front surface finishes and defects with a wale-like appearance were observed (Figs.3 and 4).

The SI's reflected venders wafer processing and inspection stabilities. Monitoring of wafer surfaces by the apparatus for some years has proved that the venders wafer processing characteristics were quite different from each other and even among factories of a vender. Thus their process instabilities or process changes could be readily noticiable. Number of dimples mostly reflected dust control stability. Polishing marks reflected the surface condition and quality of polishing cloths, and so on.

* Electrochemical Society Active Member
Key words: Makyo, Surface damage, Dimple, Saw mark

In-line monitoring of wafers in the IC fabrication process showed that most of these SI's persisted after annealing at high temperatures and even after the processing (Fig.4). The macroscopic surface contours and warps of wafers were also clearly observed. However SI's due to backside damages and backside scratches mostly disappeared after annealing. These facts indicated that most SI's were natural surface contours without accompanied by residual stress, therefore no crystal defect was assumed to be present beneath these SI's.

Crystal defects: Analyses of the slicing and polishing processes indicated that crystal defects might be present beneath saw marks, lapping marks and dimples. A fallowing experiment was carried out to see the presence of defects.

Slight scratches were made in a back surface of a wafer by a diamond point scriber at various loads. After breaking the wafer into 4 pieces, both sides of each piece were etched in Secco solution for 1 ∿ 10 min. Observed SI's of the wafer before and after etching are shown in Fig.5. Parallel bright lines before etching were clearly formed by the concavities made by slight stress caused by scratches in the back surface. A white spot in the figure was a dimple. After etching for 1 min, no bright line was observed but after etching for a longer time, brighter lines reappeared as shown in Fig.5b.

When scratches were made in the front surface of the wafer, dark lines were initially observed instead of bright lines and then bright lines appeared after etching as described above. These were due to (1) that etching quickly released the residual stress and thus the front surface deformation, because the etching rate was very high at scratched or damaged areas, and (2) that prolonged etching engraved the front surface along the defects which reached to the front surface from the backside scratches (or along the scratches in the front surface) and thus made concavities. This experiment showed that crystal defects and stresses were present beneath concavities if scratches were originally present in either front or back surfaces. Since crystal defects can penetrate deep into a crystal, 40 ∿ 100 μm by slicing or by scribing [5,6] and since lapping and polishing take some 10 μm off from the surface, crystal defects may be left in wafers and thus concavities may be accompanied with hidden defects.

Summary: A nondestructive optical imaging device based on a new principle to observe surface micro-topography has a very high sensitivity. It could monitor instabilities in the wafer machining process and also in the IC fabrication process.

Among the SI's, dimples and lapping (polishing) marks were most frequently observed. Most of the SI's were defect-free and thus harmless to the IC performance or to the yield. However some like saw marks, dimples and dust crawling may be accompanied with crystal defects and thus the yield may be reduced. Actually preliminary examination showed poor yield in wafers with heavy polishing marks.

This study showed that the total process management, including not only the precise specification of silicon crystals but also the wafer machining process adding to the IC fabrication process, is necessary for the improvement of the VLSI technology.

The author would like to express his thanks to Messrs. S. Tanigawa, T. Yonezawa and M. Katsuyama for designing the new apparatus and to Mr. A. Nishikawa for the cooperation in the evaluation of as-received wafers. Thanks are also due to Mr. M. Matsumoto of Matsushita Elec. Co. for the wafer and the yield evaluations in the IC production lines.

References:

1. K. Kugimiya, S. Akiyama, and S. Nakamura, Semiconductor Silicon 1981, 81-5, 294 (1981).
2. K. Inoue, K. Kotera, K. Kugimiya, and T. Yonezawa, Inst. Elect. Comm. Engr. Jpn. SSD 80-95, 13 (1981).
3. K. Kugimiya, and M. Matsumoto, Proc. 21th Symp. on Semicond. and IC Tech. (Tokyo) Electrochem. Soc. Jpn., 12 (1981).
4. S. Kato, H. Mizumaki, and R. Kawanaka, Inst. Elect. Comm. Engr. Jpn., SSD 77-81, 33 (1977).
5. H. Hirota, and K. Kugimiya, Natl. Tech. Rep., 22 (6), 753 (1976).

6. Y. Takano, H. Kozuka, N. Ogirima, and M. Maki, Semiconductor Silicon 1981, 81-5, 743 (1981).

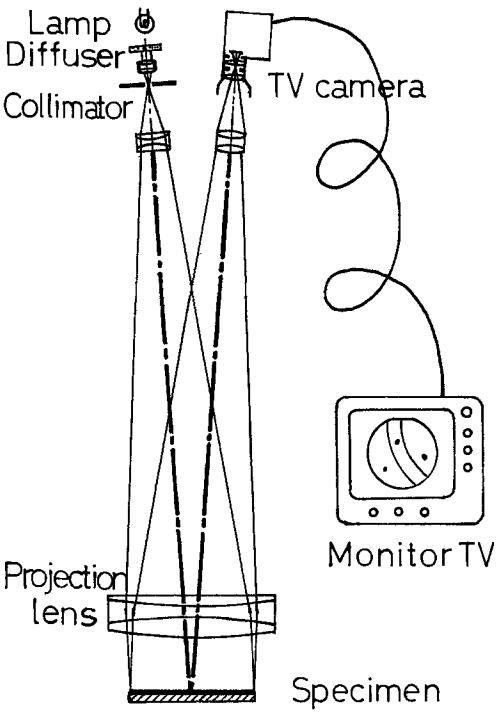

Fig.1. The simple concept of the nondestructive optical imaging apparatus.

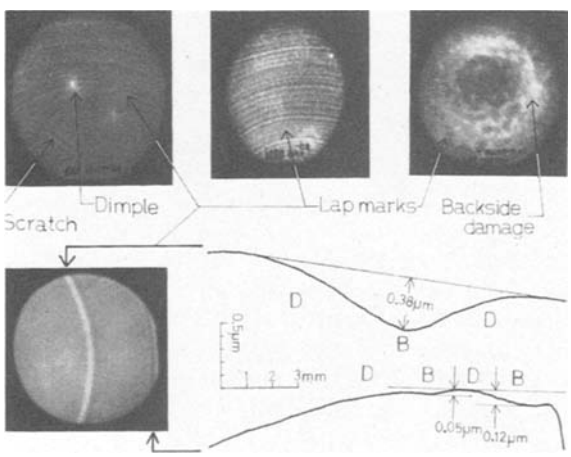

Fig.2. Representative types of microdeformation in the surface of 3" silicon wafers.

Manuscript submitted Nov. 15, 1982; revised manuscript received June 6, 1983.

Matsushita Electronic Industry Company, Limited assisted in meeting the publication costs of this article.

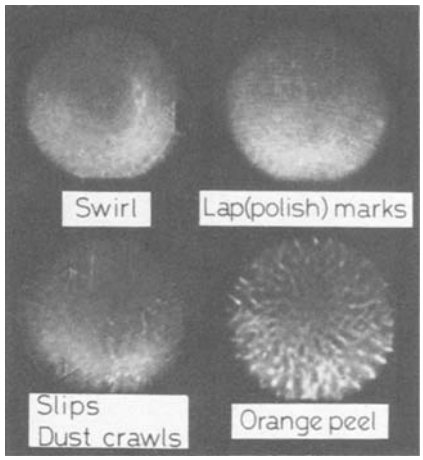

Fig.3. Examples of surface irregularities of as-received epitaxial silicon wafers.

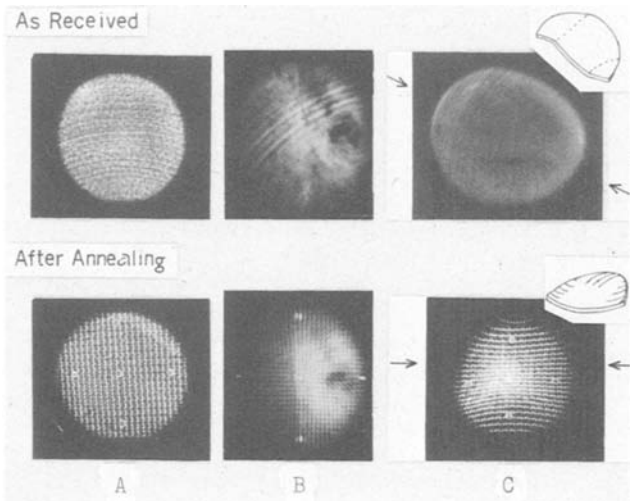

Fig.4. Warpage changes and surface irregularity preservation during the IC fabrication process.
Normal (A) and abnormal (B, C) 3" wafers.

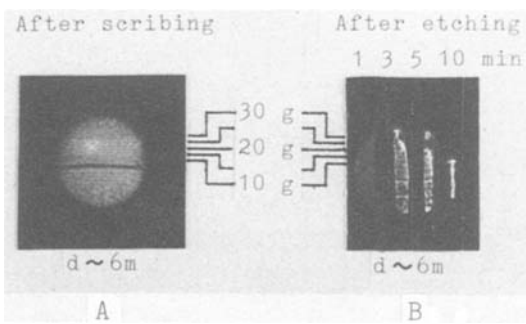

Fig.5. Microdeformation in the front surface caused by scribing the back surface of a 3" wafer.

The Incorporation of Ruthenium Oxide in Polypyrrole Films and the Subsequent Photooxidation of Water at n-GaP Photoelectrode

Rommel Noufi*

Solar Energy Research Institute, Golden, Colorado 80401

INTRODUCTION

The electrogenerated conducting polypyrrole (PP) polymer has been shown to remarkably enhance the stability of n-type photoelectrodes in photoelectrochemical cells[1-5]. In this communication, the electrogeneration of PP, the electrochemical incorporation of ruthenium oxide, and the subsequent photooxidation of H_2O at the n-GaP photoelectrode are reported. The reversible electrochemical activities of the PP polymer film, involve up-take of anions from the electrolyte upon oxidation to yield a conducting film and discharge anions upon reduction to yield an insulating film. This property allows the incorporation in the matrix of the film electroactive species or other species of interest as long as it is negatively charged. The incorporation of $Fe(CN)_6^{3-/4-}$ in PP films and its electrochemical activity as a surface attached species has been shown[1]. Here, the RuO_4^{2-} ion is incorporated electrochemically and then reduced in the matrix of the film to yield RuO_2.

EXPERIMENTAL

The procedure at a Pt electrode is explained in the following reaction scheme.

Scheme Of Incorporation of RuO_2 in Conducting Polypyrrole Film on Pt

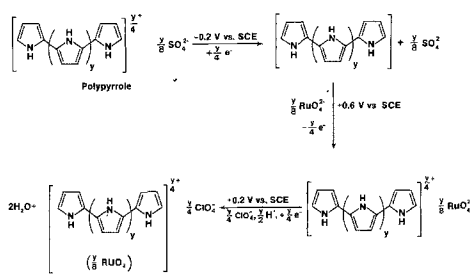

At n-GaP, the film was synthesized from an aqueous solution containing 0.1 M Na_2SO_4 and 1 M pyrrole at pH = 1. The electrode was potentiostated at 0 V versus SCE, and illuminated with 90 mW/cm^2 from a tungsten-halogen lamp. The resulting conducting film was then introduced into a solution containing only 0.1 M RuO_4^{2-} and pulsed several times between -1.1 and 0 V under illumination, terminating the pulsing at 0 V. The RuO_4^{2-} incorporated in the film is then reduced to RuO_2 by soaking for 1 hour in 0.1 M $HClO_4$ or by potentiostating the electrode in the dark at -1.15 V until the observed cathodic current decays to almost zero.

The n-GaP is single crystal S doped ($\sim 10^{17} cm^{-3}$) with <001> orientation. The crystal was etched for 5 seconds in a 1:1:3 mixture of H_2O:H_2O_2: and H_2SO_4. The electrodes were prepared as discussed in Ref. 1. The PP film thickness was about 0.1 μm. The counterelectrode was 20 cm^2 platinized Pt.

*Electrochemical Society Active Member.

RESULTS AND DISCUSSION

The incorporation scheme was first tested using a Pt electrode. The presence of RuO_4^{2-} was evident from the RuO_4^{2-} reduction wave (not shown) around +0.2 V superimposed over the film electroactivity. The films produced on Pt and n-GaP were confirmed to contain RuO_2, all through the thickness of film, by XPS, Auger, and ion microprobe. No Ru was detected above the limits of the previous techniques on the immediate surface after the removal of the PP-RuO_2 films. The quantitative results will be discussed in a following paper.

O_2 evolution from a 1 M $HClO_4$ solution on the PP-RuO_2 coated Pt-electrode occurs about 200 mV more negative compared to a bare and PP-coated Pt-electrode. However, the resulting current densities of the former were smaller. Continuous evolution of O_2 on the modified electrode resulted in the loss of the film after about two minutes.

Figure 1 shows a comparison between an n-GaP electrode modified with PP-RuO_2 film compared to one modified with PP film only. The photovoltage developed between the n-GaP and the Pt counterelectrode in 1 M $HClO_4$ is about 1.5 V. The onset of photocurrent in this solution under 100 mW cm^{-2} illumination starts about -1.2 V versus. NaSCE. This is true of the bare and the PP-modified electrodes. In the case of the bare and PP-modified electrodes, the onset shifts positive after the first scan and photocorrosion is evident. No O_2 evolution is observed in either electrodes. The PP-RuO_2 modified electrode exhibits stable photopotential for reversal scans during which O_2 evolution is clearly visible at the surface. The magnitude of the current is decreased after each scan with observable ballooning of the film in spots and the eventual bursting of the film under the pressure of O_2 trapped within the film. At this point, the current increases due to acceleration of photocorrosion. Figure 2 shows a magnification (100X) of a PP- and a PP-RuO_2-coated electrodes after 10 scans at 100 mV sec^{-1} and after the removal of the film. O_2 evolution sites (circular) are evident to the naked eye on the PP-RuO_2-coated electrode, and their appearance is the same as the pre-etched and intentionally protected sites. In between those sites, the surface is photodegraded due to the failure of intimate contact between the film and the n-GaP surface under trapped O_2 pressure. The uncatalyzed electrode (PP-coated), in comparison, shows a surface that is photodegraded compared to the pre-etched and protected surface. Electrodes catalyzed by the deposition of RuO_2 by the pyrolysis of $RuCl_3$ also exhibited immediate photodegradation of the surface.

The results, in this particular case, indicate that the presence of both the conducting film and RuO_2 is necessary for the photodissociation of H_2O. It seems that the mechanism of H_2O photooxidation is more complex than that of the semiconductor. The conducting polymer must act as a scavenger for photogenerated holes that are directed to the H_2O/O_2 redox couple sites catalyzed by the RuO_2, at a rate faster than the self-oxidation of the semiconductor.

In conclusion, a scheme was presented that incorporates RuO_2 in PP film deposited on Pt and n-GaP electrodes. Photodissociation of H_2O from 1 M $HClO_4$ was demonstrated to occur at the surface of n-GaP when modified with a film of RuO_2-catalyzed PP. The quantitative measurement of the quantum efficiency of the O_2 evolution reaction and improvement in the intimate contact between the film and the surface of the electrode are underway.

ACKNOWLEDGMENT

This work is supported by the Solar Energy Research Institute under U.S. Department of Energy contract EG-77-C-01-4042.

REFERENCES

(1) Noufi, R.; Tench, D.; Warren, L.F. J. Electrochem. Soc. 1981, 128, 2596-2599.

(2) Noufi, R.; Frank, A.J.; Nozik, A.J. J. Am. Chem. Soc. 1981, 103, 1849-1850.

(3) Cooper, G.; Noufi, R.; Frank, A.J.; Nozik, A.J. Nature (London) 1982, 295, 578-580.

(4) Fan, R.-R.F.; Wheeler, B.L.; Bard, A.J.; Noufi, R. J. Electrochem Soc. 1981, 128, 2042-2045

(5) Skotheim, T.; Lundström, I.: Prejza, J. J. Electrochem. Soc. 1981, 128, 1625-1626

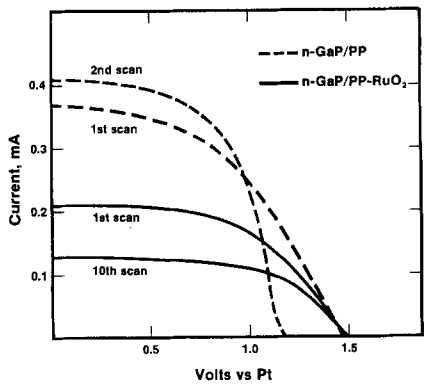

Fig. 1. Potentiostated current--voltage curves in 1 M $HClO_4$ for n-GaP/PP and n-GaP/PP-RuO_2. Scan rate = 100 mV sec^{-1}. Illumination is 100 mW/cm^{-2} from a tungsten-halogen lamp. Electrode area = 0.3 cm^2.

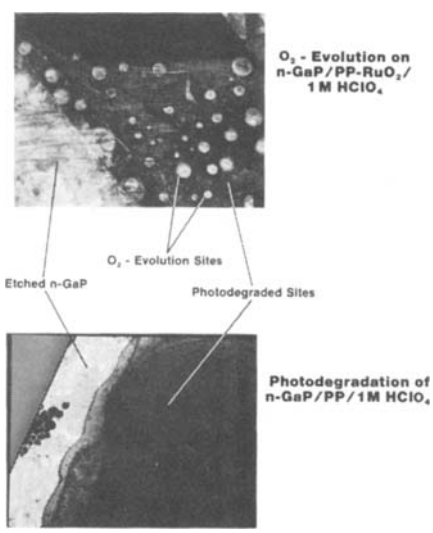

Fig. 2. Magnification (100X) of n-GaP/PP and n-GaP/pp-RuO_2 electrodes after 10 scans (100 mV sec^{-1}) and after removal of the films. Conditions are the same as in Fig. 1.

Manuscript submitted April 25, 1983; revised manuscript received July 11, 1983.

Solar Energy Research Institute assisted in meeting the publication costs of this article.

Transport of Hydrogen Through Pyrite

S. Mark Wilhelm*

Battelle Petroleum Technology Center, Houston, Texas 77073

Jose Vera,* and Norman Hackerman*

Department of Chemistry, Rice University, Houston, Texas 77001

The increased susceptibility of ferrous alloys to loss of ductility in aqueous solutions containing sulfide (sulfide stress cracking) is caused by an increase in the flux of atomic hydrogen into the metal. The increase in flux is presumably caused by an interfacial mechanism in which the sulfide participates.[1] The mechanistic details that account for the increase in hydrogen flux are not known conclusively. A prevalent "chemical" mechanism[2] is that adsorbed sulfur containing species inhibit hydrogen recombination (Tafel recombination) giving rise to an increased concentration of absorbed atomic hydrogen on the surface. Alternatively, a "solid state" mechanism[3] is that hydrogen can enter the metal via solid phase iron sulfide corrosion products on the metal surface.

As a part of investigation of the latter mechanism, measurements have been performed on the permeability of hydrogen through pyrite (FeS_2). The effort has been directed toward establishing the feasibility of hydrogen transport into a metal lattice via an iron sulfide film or precipitate on the metal surface or via iron sulfide inclusions present in the metal[4]. Pyrite is known to be a product of the corrosion of iron and iron base alloys in certain instances[5].

Of equal importance, however, is the general subject of hydrogen diffusion and solubility in crystalline sulfides and oxides. Few data exist concerning these systems. The following report offers data concerning the hydrogen/pyrite system.

The experimental technique used was essentially the same as that reported by Devanathan and Stachurski[6]. The electrochemical cell was separated into two compartments by a pyrite membrane. One side of the pyrite membrane was cathodically polarized at constant current density[7]. The other side was potentiostatically controlled such that the current for hydrogen oxidation (permeation current) could be measured.

Pyrite (FeS_2) was obtained as a naturally occurring (Ambasaquas, Spain) cubic single crystal. Microscopic examination did not reveal any visible inclusions. The particular crystal discussed (among several examined) had an edge dimension of approximately 2 cm. Specific conductivity was approximately 2 $\Omega^{-1}cm^{-1}$.

The crystal was mounted in epoxy and individual membranes were obtained by cutting parallel to the (1,0,0) crystal plane. Membrane faces were polished with alumina (0.05μ). The collection side was plated with palladium to increase collection efficiency and to prevent corrosion (background currents were less than 1μA/cm^2 on the anodic side). Solutions were 0.1M NaOH in both anodic and cathodic compartments.

A typical normalized permeation curve obtained in a galvanostatic charging experiment is shown in Figure 1. A theoretical curve was calculated using the following equation[7]:

$$\frac{i_t}{i_\infty} = 1 - 4 \sum_{o}^{\infty} \frac{(-1)^n}{\pi(2n+1)} \exp\left(\frac{-(2n+1)^2 \pi^2 \tau}{4}\right)$$

where

$\tau = D_H t/L^2$

i_∞ = steady state permeation current

i_t = permeation current at time (t)

* Electrochemical Society Active, Student, Honorary members, respectively.

Key words: pyrite, diffusion, hydrogen

L = membrane thickness

D_H = diffusivity of hydrogen

The equation assumes boundary conditions for galvanostatic charging experiments i.e., the concentration of hydrogen at the exit side is zero, and the flux of hydrogen at the entry side is constant.

Diffusivities were obtained from a plot of $1 - \ln i_t/i_\infty$ vs t, by computer fitting the experimental data to the theoretical curve and by evaluating the time lag (t_L)*.

$$t_L = L^2/2D$$

$$i_{t_L} / i_\infty = 0.629$$

Diffusivities obtained from the three methods were in general agreement.

The approximate coincidence of theoretical and experimental curves (Figure 1) suggests that hydrogen diffusion in pyrite is analogous to its diffusion in the single element metals normally analyzed by this technique. Furthermore the agreement of theoretical and experimental curves verifies the assumed galvanostatic boundary condition of a constant flux at the entry side.

The dependence of time lag on thickness (Figure 2) also indicates that hydrogen transport in pyrite is a purely diffusionary process. It should be mentioned that this conclusion is strengthened by the fact that the range of thickness (1 mm to 20 mm) over which D is independent of L is considerably greater than that which can be measured for materials of low permeability.

The mean diffusivity of the particular crystal sample examined is approximately $3.5 (\pm 1.0) \times 10^{-4}$ cm^2/sec. Measurements on different crystals exhibited a higher degree of variation (10^{-4} to 10^{-5} cm^2/sec). Subsurface solubilities[9] (C_0^H) were generally in the range 1×10^{-4} to 6×10^{-4} M/L.

Galvanastatic collection efficiencies of a 0.31 cm membrane are shown in Figure 3. The maximum hydrogen permeation flux of 18 $\mu A/cm^2$ was obtained at approximately 70 $\mu A/cm^2$ charging current density which corresponds to a 25% collection efficiency. Maximum efficiency (50 percent) was obtained at 25 $\mu A/cm^2$ charging current density. Permeation efficiency as a function of applied potential (cathodic side) is shown in Figure 4. Maximum efficiency (50 percent) occurred at approximately -0.8V.

The ambient temperature diffusivity of hydrogen in pyrite is greater in magnitude than most single element metallic materials (see Table 1). This fact coupled with a relatively large solubility makes pyrite highly permeable to hydrogen. The implications of this observation should impact several electrochemical applications in which pyrites are used as cathodes. In the present context, however, the rapid and efficient transport of hydrogen through iron disulfide supports the hypothesis of hydrogen entry into engineering materials via corrosion products or non-metallic inclusions. In some aqueous systems, the rate of hydrogen entry into a metal lattice determines the time to fracture of stressed materials.

Acknowledgement

The authors appreciate the financial support of the Robert A. Welch Foundation and Intevep (Venezuela).

REFERENCES

1. R. D. McCright, Stress Corrosion Cracking and Hydrogen Embrittlement of Iron Base Alloys, NACE, R. W. Staehle, et. al. editors, 306 (1977).

2. E. G. Daft, K. Bohnenkamp and H. J. Engell, Corrosion Science, 19, 591 (1979).

3. S. M. Wilhelm, J. Vera and N. Hackerman, to be published.

4. G. Wranglen, Corrosion Science, 9, 585 (1969).

5. D. W. Shoesmith, T. E. Rummery, M. G. Bailey and D. G. Owen, This Journal, 126, 911 (1979).

* Corrected for relaxation time[6].

6. M. A. V. Devanathan and Z. Stachurski, Proc. Roy Soc. A, 270, 90 (1962).

7. N. Boes and H. Zuchner, J of the Less Commom Metals, 49, 223 (1976)

8. J. Volkl and G. Alefeld, in Diffusion in Solids: Recent Developments, ed. by A.S. Nowick, J.J. Burton, Academic Press, New York, 231 (1975).

9. J. O'M. Bockris, Stress Corrosion Cracking and Hydrogen Embrittlement of Iron Base Alloys, NACE, R. W. Staehle, et. al. editors, 286 (1977).

TABLE 1

NOMINAL AMBIENT TEMPERATURE DIFFUSIVITIES (8)

Material	D_H^{298} (cm 2/s)
FeS_2	3.5×10^{-4}
Fe	10^{-5}
Ni	10^{-9}
Pd	10^{-7}
Nb	10^{-6}
Ta	10^{-6}

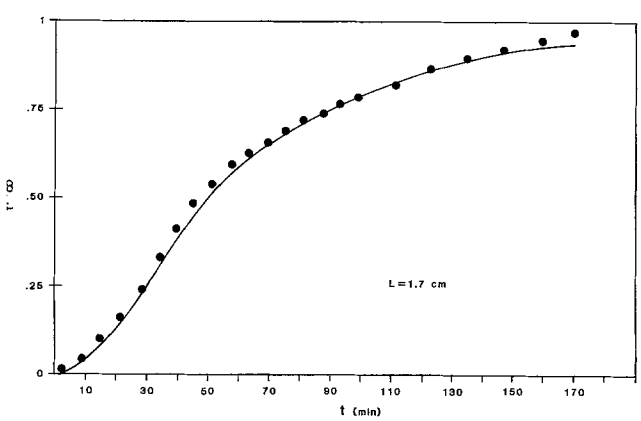

Figure 1 - PERMEATION TRANSIENT
EXPERIMENTAL POINTS
THEORETICAL CURVE

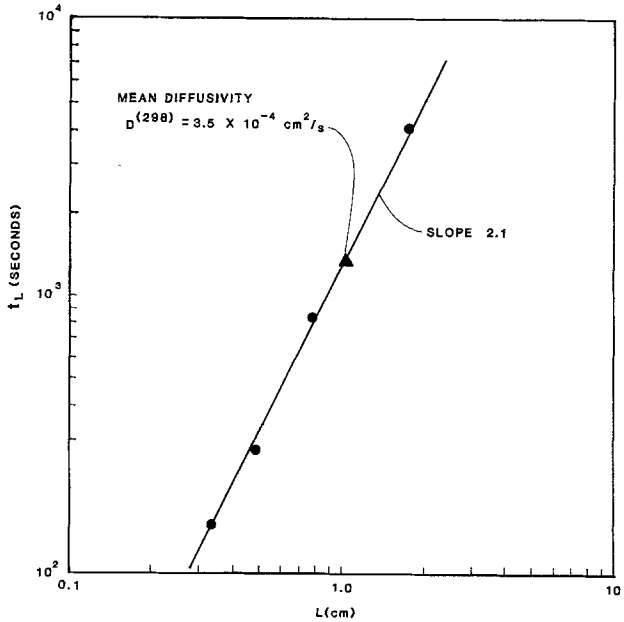

Figure 2 - TIME LAG VERSUS THICKNESS

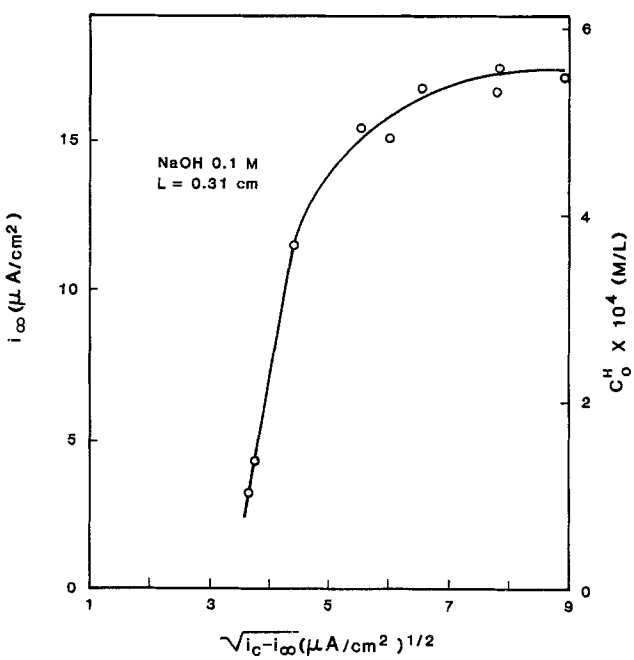

Figure 3 - PERMEATION EFFICIENCY IN GALVANOSTATIC CHARGING EXPERIMENTS

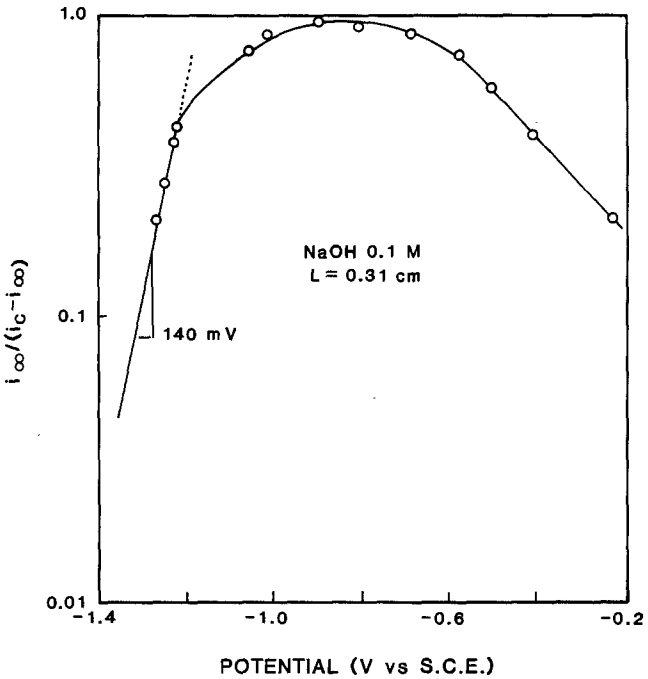

Figure 4 - PERMEATION EFFICIENCY IN POTENTIOSTATIC CHARGING EXPERIMENTS

Manuscript submitted April 14, 1983;
revised manuscript received ca. June 23, 1983.

JOURNAL OF THE ELECTROCHEMICAL SOCIETY

ELECTROCHEMICAL SCIENCE AND TECHNOLOGY

NOVEMBER 1983

Reactivity of Scratched Cadmium Electrodes in Alkaline Solutions

G. T. Burstein*

Department of Metallurgy and Materials Science, University of Cambridge, Cambridge, CB2 3QZ, England

ABSTRACT

The kinetics of reaction of scratched cadmium electrodes in alkaline solution have been measured. The anodic reaction rate of the freshly generated metal surface follows Tafel's law with a slope $\partial E/\partial \log i = 63$ mV and a reaction order $\partial \log i/\partial \log (OH^-) = 1.1$. The equilibrium parameters are defined by $E_e^\circ = 18$ mV (NHE) and $i_0 = 0.002$ A cm^{-2}. The parameters are interpreted in terms of simultaneous transfer of two electrons per cadmium atom oxidized from the bare metal surface.

The behavior of cadmium electrodes in alkaline solution is still the subject of some debate (1, 2), despite its widespread use as a reversible battery electrode material. Even in acidic sulfate and perchlorate solutions in which the metal does not equilibrate with any of its oxides (3), there is no agreement regarding its mechanism of dissolution (4-10). Lorenz (4-6) originally showed that the reaction $Cd \rightarrow Cd^{2+} + 2e$ proceeds in a single step with both electrons being transferred simultaneously; this process has been cited (7) as typifying a two-electron transfer reaction. The work was, however, criticized by Heusler and Gaiser (8) for the limited potential range over which it was studied. By extending the potential range to more positive values, Heusler and Gaiser showed that the anodic behavior deviates from the 60 mV Tafel law given by Lorenz (4-6) and gave a Tafel slope of 108 mV where the anodic current density i is between ~60 and 500 mA-cm^{-2}. The idea that both mechanisms operate in different potential ranges was supported by Hampson *et al.* (9, 10).

The mechanism of the initial stages of oxidation in alkaline solution also involves the question of whether each electron is transferred consecutively or whether both electrons are transferred simultaneously (1, 2). The former mechanism would involve the formation of a surface intermediate of Cd(I), probably as adsorbed CdOH, allowing film growth to occur by a solid-state mechanism which does not involve the formation of a dissolved intermediate, as proposed by Armstrong *et al.* (11-13). This is not in agreement with the dissolution-precipitation model (14-16) in which metal ions enter solution and are then precipitated to form the film. While there is general agreement that the steady-state film consists primarily of $Cd(OH)_2$ (2), in both the β and γ structures (17, 18), the formation of CdO, either anhydrous or hydrated, cannot be ruled out (16, 17). Indeed, it is claimed that a thin amorphous film of CdO may well exist (17) and that this film provides the passivity of the Cd electrode (16). The dissolved ion in alkaline solutions has been identified as $Cd(OH)_4^{2-}$ (11, 12) or $Cd(OH)_3^-$ (15). Species of this kind would probably result from dissolution of $Cd(OH)_2$ rather than acting as dissolved ions prior to precipitation of $Cd(OH)_2$ since it is improbable that three or four hydroxide ligands can react in one step. Thus, measurements of dissolved ion concentrations in ring disk electrode studies (12, 16) probably detect dissolution of the films. Milner and Thomas (19) have, however, mentioned that other dissolved ions such as Cd^{2+} and $CdOH^+$ may be involved as intermediates in the dissolution reaction. Detailed summaries and discussions of these investigations have been provided in the two reviews of the behavior of the Cd electrode (1, 2).

The present paper presents an analysis of the transient electrochemical behavior of freshly generated cadmium surfaces which have been created by scratching the metal with a diamond stylus while it is immersed in alkaline solution. The technique has already been used to analyze the behavior of freshly generated Al (20), Fe (21, 22), Ag (23, 24), and Cu (25) electrodes. Al (20) and Fe (21, 22) both show linear Tafel behavior in the anodic region when the maximum current density on the bare metal surface is plotted as a function of potential. This behavior has been interpreted as a measurement of the rapid first electron transfer reaction in the oxidation process. Fe (21), Ag (23), and Cu (25) all show anodic activity on the bare metal surface at potentials negative with respect to the reversible potentials for film formation, and the charge densities associated with these processes have been assigned to the formation of adsorbed oxidized products, up to coverages of one monolayer.

Earlier work on the effects of scraping cadmium electrodes (26, 27) provided measurements of the instantaneous open-circuit scrape potentials. The technique of Haggard and Chapman (26) gave scratches which were generated extremely rapidly for a period of ~1 μsec. Andersen *et al.* (27) continuously renewed the entire circular surface of their disk specimens with a period of 1.25 msec. Both authors reported that the potential acquired by the freshly generated surfaces represented the Cd/Cd(II) reversible couple. Breiter's experiments (28) provided current densities obtained by scraping a rotating cadmium cylinder circumferentially and simultaneously sweeping the electrode potential in order to obtain cyclic voltammograms. The results from a 1.0M aqueous KOH electrolyte gave a zero-current potential which, within the apparent scatter, was independent of both the scraping process and the potential sweep rate in agreement with the open-circuit work (26, 27). However, the a-c current, measured as the response to a superimposed low amplitude a-c

* Electrochemical Society Active Member.

voltage (1 kHz) applied to the electrode, showed an increase at potentials below the zero-d-c-current potential which Breiter attributed to a pseudocapacitance due to the reaction $Cd + OH^- \rightarrow Cd - OH + e^-$. The coverage of the adsorbed OH radical, its subsequent fate, and its role in metal oxidation were not discussed.

Experimental

The technique used to scratch the surface of a potentiostatically controlled rotating disk electrode has been described before (20-23). The current on a rotating disk electrode (diam 8 mm), which is held at constant potential, is allowed to reach a steady state. A diamond stylus, which is initially held away from the metal surface by an electromagnet assembly, is made to swing by pulsing the current through the electromagnet coils. It thereby strikes the rotating disk surface with a tracking weight of ~2g and creates a scratch of known dimensions. The stylus is then drawn away by the reactivated electromagnet. Current transients caused by the scratches are captured by two transient recorders (Datalab type DL 905), both triggered simultaneously by the current pulse delivered to the electromagnet. The two recorders were set to different sensitivities and different time scales in order to improve the accuracy with which the decay of each current transient could be recorded. The maximum current density which flows on the freshly generated metal surface is measured from the maximum rate at which the current increases as the scratch is being made, by the equation

$$i_s = \frac{1}{2\Pi r \omega y} \frac{dI}{dt} \qquad [1]$$

where dI is the increase in current due to scratching in time dt, ω is the electrode rotation rate, y is the scratch width, and r is the distance of the scratch from the center of rotation. For cadmium, the scratches were found to be wider than those of other metals such as Fe (21), Ag (23), and Cu (25); this is because of the relative softness of the metal. Thus y was typically 60 μm, r ~2 mm, and ω was set at 100 Hz except where otherwise stated. The maximum scratch depth was small (~4 μm) compared with the scratch width and was thus neglected.

Electrolytes were made from AR KOH and doubly distilled water to concentrations from 0.020 to 5.0M. A supporting electrolyte was not added to maintain constant ionic strength since the effects of other anions on these electrode processes are not known. Electrolytes were deaerated with purified nitrogen.

Cadmium electrodes were made from Johnson-Matthey Cd rod (99.999%) which was cut into disks and sealed into Perspex electrode holders with Araldite. These were ground to a 1200 grit finish.

A saturated calomel reference electrode was used. This was mounted outside the cell and connected to the working electrolyte via a Haber-Luggin probe which itself was filled with the same electrolyte. Potentials are presented on the normal hydrogen electrode scale and have been corrected for the liquid junction potential between the working and reference electrolytes by the formula of Henderson (29). This relationship is probably inaccurate in concentrated solutions, but the errors are considered small. The Haber-Luggin probe tip was sited vertically below the working electrode surface and ~4 cm from it. This position allows ready access for the scratching stylus. It also allows for accurate calculation of the ohmic potential drop due to the current flowing from the scratch itself since the probe tip is at an effective infinity (30). Ideally, one would mount the probe tip close to the scratch surface thereby minimizing the ohmic potential drop. This is, however, impractical since the probe tip would have to be small compared with the scratch width (60 μm) and would additionally interfere with the scratching process.

The ohmic potential drop due to the current flowing from the scratch has been calculated and is given by (30)

$$E_\Omega = I_s R_\Omega \qquad [2a]$$

where

$$R_\Omega = \frac{1}{2\Pi\sigma b} \ln\left[\frac{4b}{a}\right] \qquad [2b]$$

Here I_s is the absolute current flowing from the scratch, R_Ω is the ohmic resistance in the electrolyte, σ is the electrolyte conductivity, and b and a are respectively the half-length and half-width of the scratch. In the work presented below, both uncorrected and corrected data are shown where the ohmic resistance was calculated using published values of σ (31, 32), one of which was checked with a conductivity bridge.

Experiments were performed at 291 ± 2 K.

Results

A typical current transient arising from scratching of the metal at constant potential in alkaline solution is shown in Fig. 1. Such transients show a net anodic or a net cathodic scratch current, depending upon potential. The values of i_s are determined using Eq. [1] from the maximum slope of the rising transient and represent the maximum current density flowing from the scratch surface. As the current shown in Fig. 1 rises, some decrease in this slope occurs. This is due to formation of film on the freshly generated surface before the scratch itself is complete: the contact time, t_c, of the stylus is finite, and

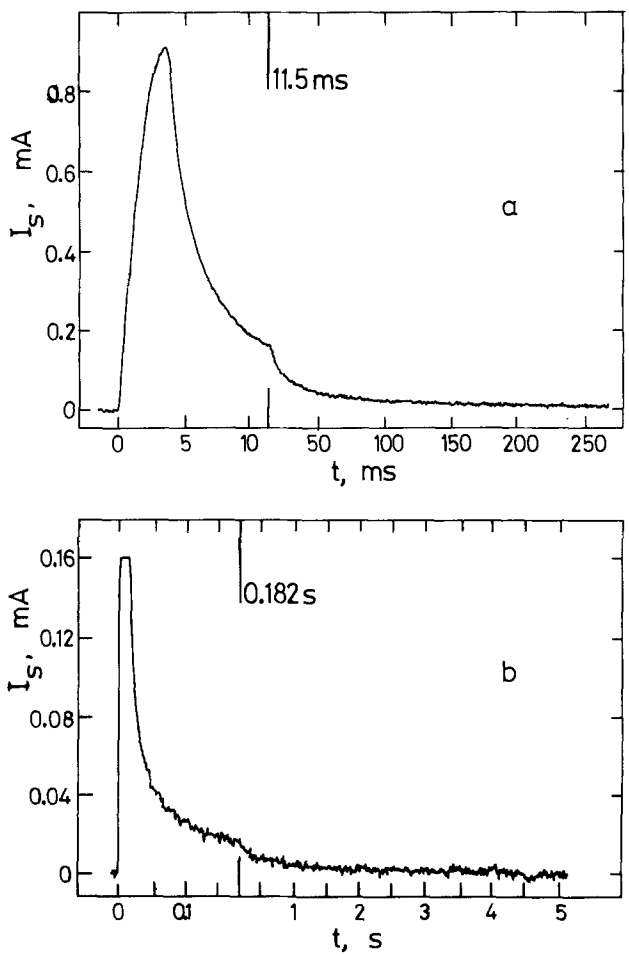

Fig. 1. Anodic current transient caused by scratching cadmium in 0.40M KOH at $E = -575$ mV (NHE) showing current decay over short (a) and long (b) times. Note changes in time scales at 11.5 msec (a) and 0.182 sec (b).

Fig. 1 shows t_c = 3.46 msec. At lower potentials, little deviation from the maximum slope occurs throughout the time t_c.

The process was investigated over a wide range of potential [from −900 to −50 mV (NHE)] in the five electrolyte solutions of concentrations from 0.020 to 5.0M KOH. For each solution, a bare surface polarization curve (log i_s *vs.* E) was plotted, and these are shown in Fig. 2-6. In each case, there is a unique potential, E_{ms}, at which the net current on the scratch is zero. For $E > E_{ms}$, i_s is anodic and the scratch surface is oxidized. For $E < E_{ms}$, i_s is cathodic. The experimental scatter in the anodic values of i_s is significant; the scatter which exists is due largely to irreproducibility in the dimensions of the scratch. For this reason, a large number of data points is presented. In the region where i_s is cathodic, the scatter of results is greater and this arises, at least in part, from the fact that the electrode as a whole is evolving gaseous hydrogen and this in itself affects the scratching process.

The anodic region for all solutions shows a potential range in which linear Tafel behavior occurs. This is observed over a current density range which varies from one decade for the dilute electrolytes to two decades for the concentrated electrolytes. Anodic Tafel slopes were calculated by linear regression and

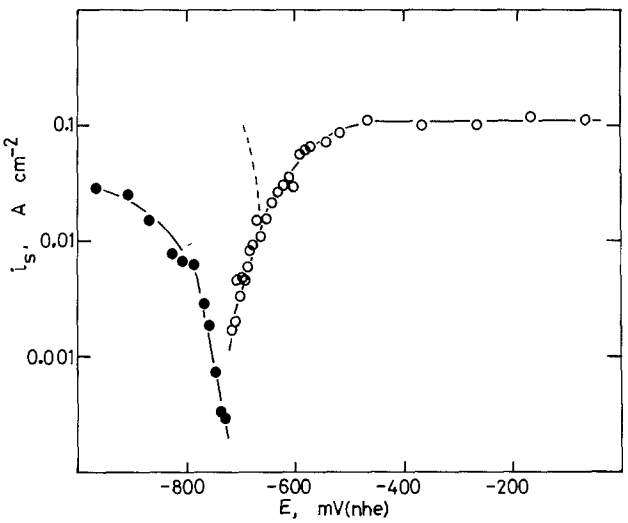

Fig. 2. Bare surface polarization curve for Cd in 0.02M KOH. ○: anodic. ●: cathodic. Broken line shows correction for ohmic potential drop (Eq. [2]).

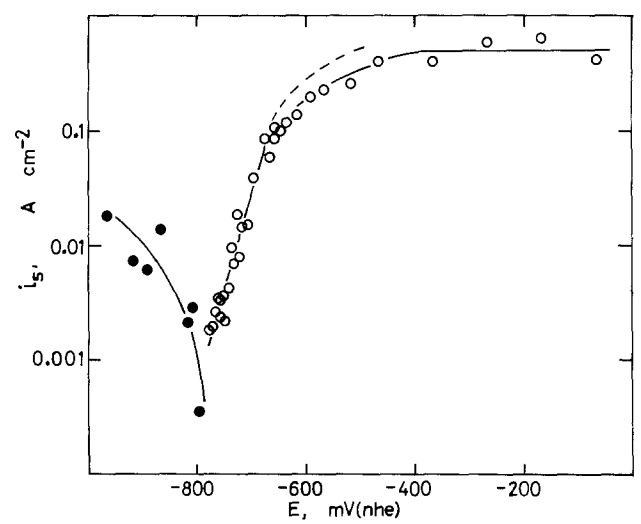

Fig. 3. Bare surface polarization curve for Cd in 0.10M KOH. ○: anodic. ●: cathodic. Broken line shows correction for ohmic potential drop (Eq. [2]).

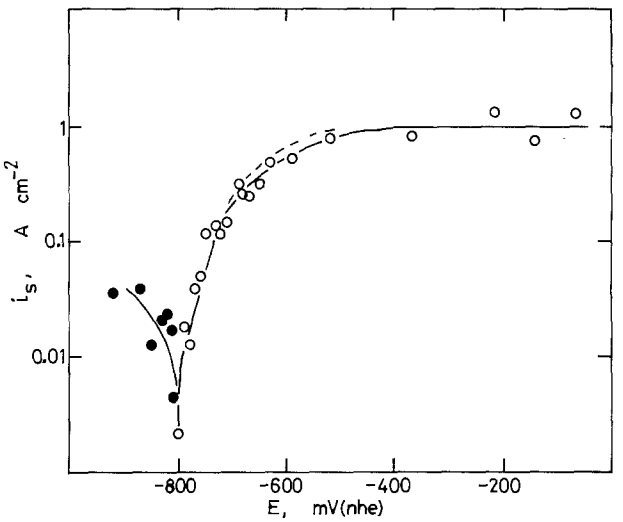

Fig. 4. Bare surface polarization curve for Cd in 0.40M KOH. ○: anodic. ●: cathodic. Broken line shows correction for ohmic potential drop (Eq. [2]).

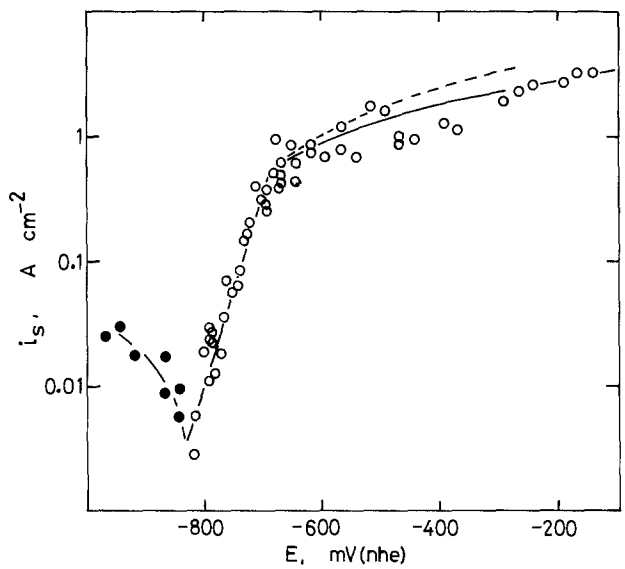

Fig. 5. Bare surface polarization curve for Cd in 1.0M KOH. ○: anodic. ●: cathodic. Broken line shows correction for ohmic potential drop (Eq. [2]).

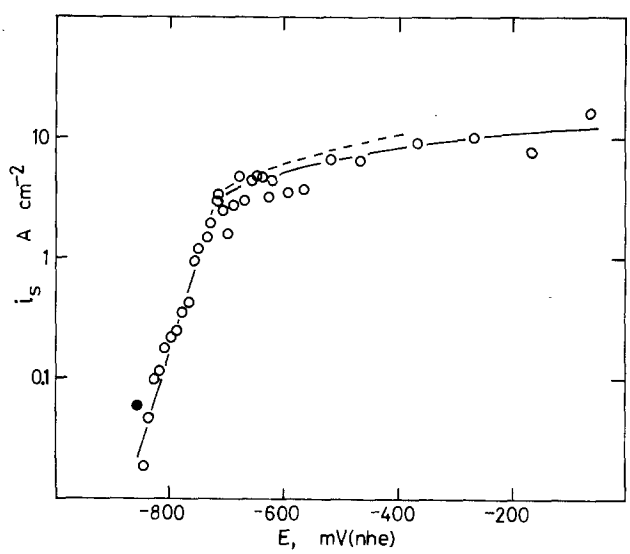

Fig. 6. Bare surface polarization curve for Cd in 5.0M KOH. ○: anodic. ●: cathodic. Broken line shows correction for ohmic potential drop (Eq. [2]).

Table I. Anodic Tafel slope and exchange current density for reaction of scratched cadmium in alkaline solution

Electrolyte	$\partial E/\partial \log i_s$ (mV)	i_o (A cm^{-2})
0.020M KOH	67	0.0012
0.010M KOH	60	0.0016
0.40M KOH	57	0.0060
1.0M KOH	66	0.0019
5.0M KOH	64	0.0025
mean	63 ± 4	0.0026 ± 0.0017

are presented in Table I: the mean value for all electrolytes gives $\partial E/\partial \log i_s = 63 \pm 4$ mV. In each case, correction for the ohmic potential drop by Eq. [2] is negligible for the linear Tafel region. The potential of −710 mV (NHE) occurs in the Tafel region of all the bare surface polarization curves (Fig. 2-6), and this was used to determine the reaction order with respect to OH^-. Figure 7 shows $\partial \log i_s/\partial \log (OH^-) = 1.1$ for $0.02M \leq (OH^-) \leq 5.0M$. Since the Tafel slopes are all similar (Table I), this hydroxide dependence is common to the entire Tafel region for all electrolytes.

As the potential increases, so the anodic bare surface polarization curves deviate from Tafel linearity and at high potential i_s tends toward potential independence. The maximum observed values of i_s (i_{smax}) are high, up to ~8 A cm^{-2}. They are plotted as a function of OH^- concentration in Fig. 7 and give $\partial \log i_{smax}/\partial \log (OH^-) = 0.97$. For current densities of this magnitude, the potential is, of course, affected considerably by the ohmic potential drop due to current flowing from the scratch itself

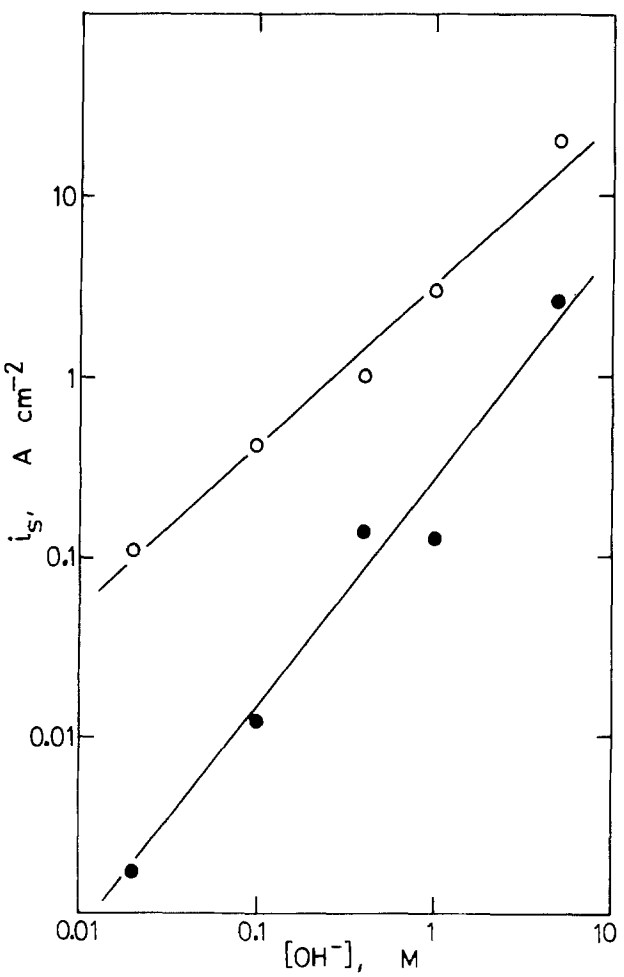

Fig. 7. Dependence of anodic reaction rate of scratched Cd on hydroxide concentration. ●: i_s at −710 mV (NHE) (Tafel region). ○: i_{smax}.

(Fig. 2-6). The region cannot, however, be controlled entirely by the onmic potential drop since for the three most dilute electrolytes (Fig. 2-4), i_s actually becomes independent of E. Pure ohmic control would show $i_s \propto E$. For the 1M and 5M electrolytes (Fig. 5, 6), the highest current regions are probably also potential independent.

The bare surface mixed potential E_{ms} is shown as a function of the OH^- concentration in Fig. 8. The data gave $\partial E_{ms}/\partial \log (OH^-) = -60$ mV. Also plotted in Fig. 8 are the equilibrium potentials E_o, for the three oxides given by Pourbaix (3). At potentials below E_{ms}, the current transients are negative (Fig. 2-6). The scatter in results is large as described above; nevertheless, within the scatter, the cathodic bare surface polarization curves show i_s to be approximately independent of the hydroxide concentration. The results give a maximum cathodic value of i_s between 0.01 and 0.1 A cm^{-2}.

Two potentials were selected for measurement of the variation of i_s with electrode rotation rate, ω. The results are shown in Fig. 9, (0.4M KOH) for a potential in the linear Tafel region and in the region where i_s is maximum. In both cases, the value of i_s is independent of ω (over some two orders of magnitude in ω) within the scatter of the data.

Discussion

For several other freshly generated pure metal surfaces (Fe, Cu, Ag), evidence has been found for the formation of oxidized monolayers which occur at an underpotential with respect to the equilibrium potentials for the metal bulk oxide reaction (21-25).

Cadmium shows no evidence of underpotential anodic activity. The bare surface mixed potentials in alkaline solutions (Fig. 8) are extremely close to the equilibrium potentials given by Pourbaix (3). The data most closely correspond to the oxide for which the standard reversible potential is $E_o^\circ = 5$ mV, referred to by Pourbaix (3) as "inactive rhombic cadmium hydroxide," although because of the proximity of the equilibrium potentials for all the oxides, the distinction is rather too fine to draw from the present results. In fact, linear regression of the data points in Fig. 8 gives E_{ms} [mV (NHE)] = 18-60 pH in excellent agreement with Pourbaix' equations for equilibrium potentials (E_o for the three cadmium (II) oxides). E_{ms} can thus be interpreted as a measure of E_o. As such, the values of the exchange current density, i_o, for the oxidation reaction may be measured

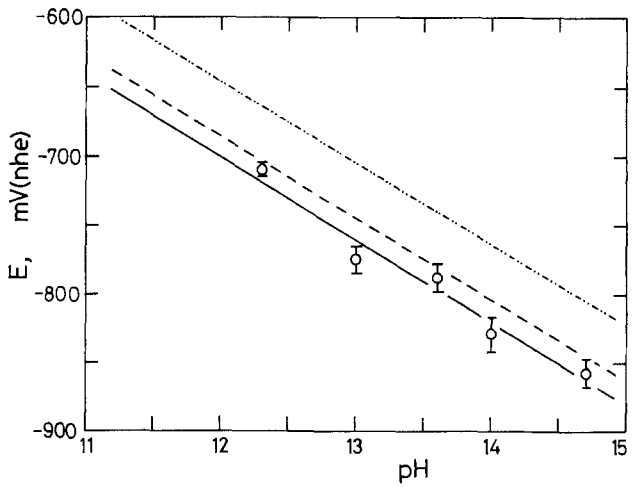

Fig. 8. Dependence of the bare surface mixed potential, E_{ms}, on pH (data points, solid line). Also shown are the equilibrium potentials for cadmium oxides given by Pourbaix (3)

———, $E_o^\circ = 5$ mV (NHE) (common with E_{ms})
------, $E_o^\circ = 23$ mV (NHE). –·–·–, $E_o^\circ = 63$ mV (NHE)

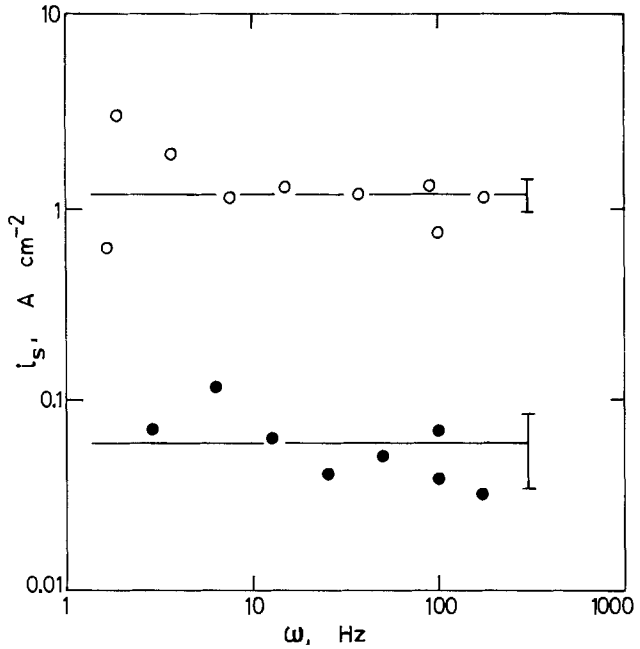

Fig. 9. Dependence of the bare surface reaction rate of Cd on electrode rotation rate, ω, in 0.40M KOH. ●: $E = -755$ mV (NHE). ○: -130 mV (NHE).

by extrapolation of the Tafel lines to E_o, and these are also given in Table I. They show that i_o is approximately independent of pH, with a mean value of 0.0026 ± 0.0017 A cm^{-2}. By allowing a surface roughness factor for the scratch of ~1.5 (23), the true value of i_o for the freshly generated surface is 0.002 A cm^{-2}. The value is high and compares with the steady-state value of i_o for the Cd/Cd^{2+} reaction in acid solutions in which the Cd^{2+} concentration is 0.01M (8). It is also important to note that the equilibrium potential for hydrogen evolution under a hydrogen pressure of 1 atm is only 5 mV more negative than that quoted above for the oxide, and so the values of E_{ms} are also representative of the potentials at which steady-state hydrogen evolution would be expected to commence. Cadmium thus shows no clear evidence of underpotential reactivity, either anodic or cathodic. As a consequence, there is no evidence for the formation of the OH radical on the scratched Cd surface as proposed by Breiter (28). It is, of course, possible that formation of OH at low potentials may be masked by the cathodic current transients. In fact, because of the extremely close proximity of E_{ms} and E_o (Fig. 8), the rate of formation of the OH radical must be small or the coverage acquired low. Even the very fast scraping experiments of Hagyard and Chapman (26) and Andersen *et al.* (27) did not reveal underpotential activity; neither did they reveal the potential of zero charge.

The anodic Tafel slope of 63 mV (Table I) for all electrolyte concentrations is consistent with two electrons being transferred simultaneously from each surface cadmium atom, and the process is first order in OH$^-$ concentration (Fig. 7). The process is, of course, not in a steady state. The method of calculating i_s from the current transients (Eq. [1]) provides the fastest detectable rate of reaction of the freshly generated surface since it is measured from the maximum rate at which the current increases as the fresh metal surface is being generated. It is also clear that the electrolyte which first reaches the new cadmium surface immediately behind the stylus as the scratch is being formed must be of bulk electrolyte composition. Because the electrolytes are all relatively dilute (compared with the concentration of water), adsorption of water must occur initially, and this is fast (33). Thus we may write

$$Cd + H_2O \rightleftarrows Cd \cdot H_2O_{ads} \quad [3]$$

The electron transfer reaction may now be written as one of the following

$$Cd \cdot H_2O_{ads} + OH^- \rightarrow CdOH^+ + H_2O + 2e^- \quad [4]$$

$$Cd \cdot H_2O_{ads} + OH^- \rightarrow Cd(OH)_2 + H^+ + 2e^- \quad [5]$$

$$Cd \cdot H_2O_{ads} + OH^- \rightarrow CdO + H_3O^+ + 2e^- \quad [6]$$

The kinetics of each of these reactions is given by

$$i_s = 2Fk(OH^-) \exp\left[\frac{2\beta FE}{RT}\right] \quad [7]$$

which gives a Tafel slope $\partial E/\partial \log i_s = 59$ mV for $\beta = 0.5$ and a reaction order $\partial \log i_s/\partial \log (OH^-) = 1$ in excellent agreement with the measured parameters. The kinetic data cannot distinguish these three mechanisms. Reactions [5] and [6] are solid-state processes in which the film is formed directly from the metal surface without prior dissolution. Reaction [4] is a dissolution-precipitation process if the CdOH$^+$ ion desorbs from the metal surface before undergoing precipitation by either of the following reactions

$$CdOH^+ + OH^- \rightarrow Cd(OH)_2 \quad [8]$$

$$CdOH^+ \rightarrow CdO + H^+ \quad [9]$$

Reactions [8] or [9] may, however, occur directly on the metal surface, in which case film formation is essentially a solid-state process. If dissolution were occurring, then one would expect that the value of i_s at high potential would be dependent on the electrode rotation rate, ω, since a degree of diffusion control would then be expected. In fact, no dependence on ω was found (Fig. 9), and there is thus no significant dissolution of Cd(II) from the bare metal surface. It is important to note, however, that the dependence on ω for a diffusion process to control i_s cannot be accurately determined from the Levich equation (34) (which gives a steady-state value of $\delta \simeq 7 \times 10^{-4}$ cm at $\omega \simeq 100$ Hz) because of the unavoidable turbulence created in the electrolyte by the scratching process itself.

It is significant that a current transient is found at all anodic overpotentials. There is thus no evidence of a steady-state film-free active metal surface as was proposed by Armstrong and West (12) to exist in 10M KOH solution. The two-electron transfer mechanism is consistent with the work of Lorenz (4-7) who proposed that dissolution of Cd as Cd^{2+} in acid solution occurs by the simultaneous loss of two electrons, and it appears, therefore, that this occurs throughout the pH range. The Tafel slope of 40 mV given by Armstrong and West (12) for dissolution in 10M KOH was measured only over a 20 mV range of potential, and its value must be regarded as suspect, although in that case, the reaction investigated was dissolution of the metal [as Cd(OH)$_3$ (19) or Cd(OH)$_4^{2-}$ (11)] from the filmed surface.

At potentials more positive than the Tafel regions of Fig. 2-6, values of i_s reach potential independence, but the maximum current density i_{smax} is still first order in hydroxide concentration (Fig. 7). Although the current densities here are high and are significantly affected by the ohmic potential drop as described above, the rates are not purely ohmically controlled since, in the three dilute electrolytes, i_s becomes independent of E. For the two more concentrated electrolytes (Fig. 5, 6), it is possible to derive an ohmic resistance by extrapolation of the linear Tafel region to higher i_s. The difference between the observed value of E and that derived from the extrapolated Tafel line is ΔE, and this is shown

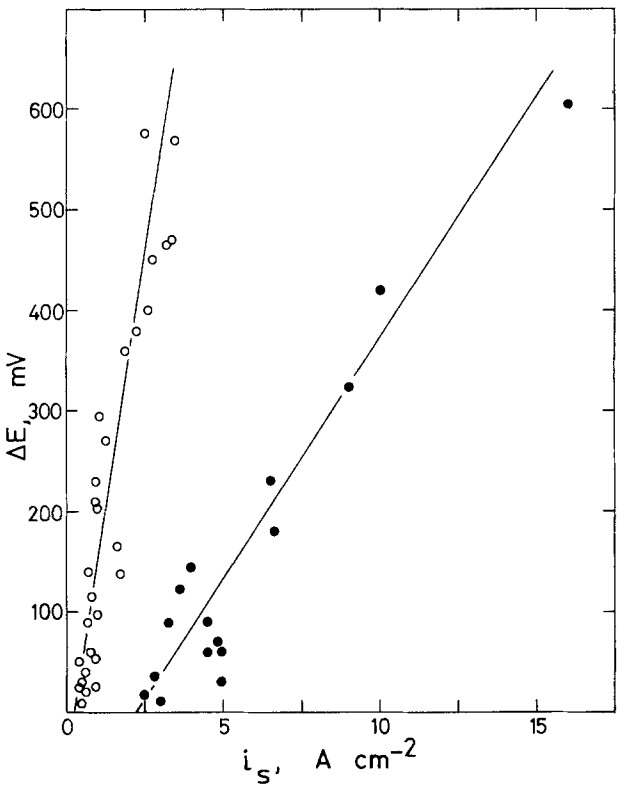

Fig. 10. Ohmic relationship between ΔE and i_s for scratched Cd in 1.0M KOH (○) and 5.0M KOH (●). ΔE is the difference between the applied potential and the potential of the extrapolated Tafel line for constant i_s (Fig. 5, 6).

plotted against i_s in Fig. 10. The scatter is large, but the graphs are approximately linear. The slope, $\partial(\Delta E)/\partial i_s$, when divided by the surface area of the scratch, gives the ohmic resistances to current flowing from the scratch in 1 and 5M KOH. These are measured as 93 and 22Ω respectively and are two to four times as large as those calculated from Eq. [2b] (25 and 9Ω, respectively). This extra resistance may be due to the presence of the stylus, or it may mean that the maximum rates in these electrolytes too are not entirely ohmically controlled, implying some curvature in Fig. 10. For the more dilute electrolyte, the ohmic plots were not linear, and alternative rate controlling factors must be important.

The maximum anodic reaction rate, i_{smax}, cannot be controlled by diffusion of OH^- to the scratch surface, since this would show that i_{smax} is dependent on ω. Figure 9 shows in fact that at high potential, i_s is independent of ω. The argument is valid even though ω controls both the diffusion rate and the rate of scratching since i_s is actually measured from the latter quantity (Eq. [1]). It is clear that since i_{smax} is first order in hydroxide concentration (Fig. 7) and is not diffusion-controlled, it must be controlled by reaction itself. This may be the transfer of OH^- or Cd^{2+} ions across such film as has already formed on the scratch scar during scratching. If the film is formed via $CdOH^+$ as an intermediate (reaction [4]) then the rate may be limited by reaction [8] in terms of nucleation of the solid phase. The region is, however, difficult to quantify because of the multiple factors contributing to rate control. It will be shown in another paper (35) that the rate of decay of the current with time depends both on the hydroxide concentration and on the electrode rotation rate. The above arguments apply only to i_s; because i_s is defined from the rate of generation of the scratch, it always contains some fraction of the surface which is still totally bare, no matter how large a value i_s has. It is also measured from the region of maximum turbulence in the electrolyte (since the contact of the stylus interrupts laminar flow over the electrode surface), and the conditions of diffusion are not very well defined.

It is worth noting that because of the close proximity of the reversible potentials for oxide growth on Cd and for hydrogen evolution, potential pulse experiments on unscratched cadmium surfaces cannot unambiguously yield the kinetics of the surface reactions since it is not possible to ensure that the electrode is initially free both of evolved hydrogen and of oxide films. Under these circumstances, a mechanical method is required to generate a surface initially free from both.

Conclusions

1. The scratched cadmium electrode shows no evidence of underpotential reactivity in alkaline solution. The bare surface mixed potential is the thermodynamic reversible potential for oxide film formation.

2. The reaction of a scratched cadmium electrode in alkaline solution involves the simultaneous loss of two electrons per cadmium atom in one reaction step. Reaction of the bare metal surface occurs with the following parameters: $\partial E/\partial \log i = 63 \pm 4$ mV, $\partial \log i/\partial \log (OH^-) = 1.1$, $i_o = 0.002$ A cm^{-2}, and $E_o^o = 18$ mV (NHE). There is no evidence of a Cd(I) intermediate.

3. The kinetics are consistent with a rate determining step represented by reactions [4], [5], or [6].

Manuscript submitted June 28, 1982; revised manuscript received Feb. 17, 1983.

REFERENCES

1. R. D. Armstrong, K. Edmondson, and G. D. West, *Chem. Soc. Specialist Report, Electrochemistry*, **4**, 18 (1974).
2. R. Barnard, *J. Appl. Electrochem.*, **11**, 217 (1981).
3. M. Pourbaix, "Atlas of Electrochemical Equilibria in Aqueous Solutions," p. 414, Pergamon, Oxford, England (1966).
4. W. Lorenz, *Naturwiss.*, **40**, 778 (1953).
5. W. Lorenz, *Z. Elektrochem.*, **58**, 912 (1954).
6. W. Lorenz, *Z. Naturf.*, **9a**, 715 (1954).
7. K. J. Vetter, "Elektrochemische Kinetik," p. **543**, Springer-Verlag, Berlin (1961).
8. K. E. Heusler and L. Gaiser, *This Journal*, **117**, 762 (1970).
9. N. A. Hampson, R. J. Latham and D. Larkin, *J. Electroanal. Chem.*, **23**, 211 (1969).
10. N. A. Hampson and R. J. Latham, *ibid.*, **32**, 175 (1971).
11. R. D. Armstrong, J. D. Milewski, W. P. Pace, and H. R. Thirsk, *ibid.*, **21**, 517 (1969).
12. R. D. Armstrong and G. T. West, *ibid.*, **30**, 385 (1971).
13. R. D. Armstrong and K. Edmondson, *ibid.*, **53**, 371 (1974).
14. K. Huber, *This Journal*, **100**, 376 (1953).
15. M. A. V. Devanathan and S. Lakshmanan, *Electrochim. Acta*, **13**, 667 (1968).
16. Y. Okinaka, *This Journal*, **117**, 289 (1970).
17. M. W. Breiter and W. Vedder, *Trans. Farad. Soc.*, **63**, 1042 (1967).
18. M. W. Breiter, *Electrochim. Acta*, **22**, 1219 (1977).
19. P. C. Milner and U. B. Thomas, in "Advances in Electrochemistry and Electrochemical Engineering," Vol. 5, C. W. Tobias, Editor, Interscience, New York (1967).
20. F. P. Ford, G. T. Burstein, and T. P. Hoar, *This Journal*, **127**, 1325 (1980).
21. G. T. Burstein and D. H. Davies, *ibid.*, **128**, 33 (1981).
22. G. T. Burstein and D. H. Davies, *Corros. Sci.*, **20**, 1143 (1980).
23. G. T. Burstein and R. C. Newman, *Electrochim. Acta*, **25**, 1009 (1980).
24. G. T. Burstein and R. C. Newman, *Electrochim. Acta*, **26**, 1143 (1981).
25. G. T. Burstein and R. C. Newman, *This Journal*,

128, 2270 (1981).
26. T. Hagyard and K. M. Chapman, *ibid.*, **113**, 961 (1966).
27. T. N. Andersen, J. L. Anderson, and H. Eyring, *J. Phys. Chem.*, **73**, 3562 (1969).
28. M. Breiter, *Electrochim. Acta*, 12, 679 (1967).
29. D. J. G. Ives and G. J. Janz, "Reference Electrodes," p. 54, Academic Press, New York (1961).
30. H. J. Pearson, G. T. Burstein, and R. C. Newman, *This Journal*, **128**, 2297 (1981).
31. D. Dobos, "Electrochemical Data," p. 45, Elsevier, Amsterdam (1975).
32. "Handbook of Chemistry and Physics," 57th ed., p. D-244, Chemical Rubber Company, Cleveland (1976).
33. T. R. Beck, *Electrochim. Acta*, **18**, 815 (1973).
34. A. C. Riddiford, in "Advances in Electrochemistry and Electrochemical Engineering," Vol. 4, P. Delahay, Editor, p. 47, Interscience, New York (1966).
35. G. T. Burstein, To be published.

Linear Potential Sweep of Lead-Acid Battery Electrodes Containing Trace Te, Sb, As, Co, and Ni

B. K. Mahato* and W. H. Tiedemann*

Johnson Controls, Incorporated, Corporate Applied Research Group, Milwaukee, Wisconsin 53201

ABSTRACT

The effect of trace Te, Sb, As, Co, and Ni ions on the linear potential sweep (LPS) of the lead-acid battery electrodes, both small size and pasted type, was investigated. This LPS technique, in general, was found to be sensitive to the presence of impurities which alter the gassing behavior of the lead and lead dioxide electrodes. The lead electrode LPS was highly sensitive to trace amounts of Te, probably because of the catalytic influence of Te on the hydrogen evolution reactions. The test results suggested that the gassing behavior of the maintenance-free lead-acid battery in the presence of Te, Sb, and As could be solely related to the lead electrode and could be related to both lead and lead dioxide electrodes in the presence of trace Ni and Co in the test system.

Linear potential sweep voltammetry (LPS) is an electrochemical technique which characterizes the potential dependent electrochemical reactions that occur on the electrode surface. Recently, this technique has been used to characterize the lead-acid battery electrode reactions, including characterization of α and β PbO_2 (1-4), corrosion behavior of battery grid alloys (5-10), and the study of the effect of organic expander on the lead electrode matrix (11-13). We have used this technique to define the influence of trace Te, Sb, As, Co, and Ni on the gassing behavior of lead and lead dioxide electrodes.

Our selection of these five elements is based upon an investigation performed by Pierson *et al.* (14). These authors studied the effect of 24 elements on the gassing behavior of the maintenance-free battery by a constant voltage overcharge test. They reported unacceptable gassing of the maintenance-free batteries in excess of 0.1 ppm Te and 1 ppm Sb, As, Co, and Ni in the cell electrolyte. This study basically serves as a screening test and does not provide any mechanistic explanation of the electrode gassing behavior in the presence of trace impurities. The purpose of the present work is to extend the work of Pierson *et al.* (14) to provide some explanation as to how these trace impurities influence the gassing behavior of the individual lead-acid battery electrodes. This we have carried out by theoretically and experimentally analyzing the effect of these trace elements on the lead and lead dioxide electrodes in the lead-acid battery operational potential range.

Theoretical

The electrochemical reactions of Te, Sb, As, Co, and Ni have been recently reviewed (15, 16). The reactions pertinent to the lead-acid battery operational potential range taken from the aforementioned references are shown in Fig. 1. The operational potential range of the lead electrode is between −1160 and −860 mV and of the lead dioxide electrode between 975 and 1425 mV, all with respect to Hg/Hg_2SO_4/1.270 sp gr H_2SO_4 reference electrode. This figure suggests various possibilities as to how these trace elements could influence the electrochemistry of lead and lead dioxide electrodes. The dominant characteristics easily observable are the following: (*i*) Te, Sb, As, Co, and Ni metal ions if present in the lead-acid battery system will reduce to elemental metal at the open-circuit potential of the lead electrode. (*ii*) Co and Ni may not influence the cathodic behavior of the lead electrode. (*iii*) On the PbO_2 electrode potential range, the electrochemical reactions of Co and Ni ions and possibly their influence on the oxygen evolution reactions appear to be more dominant than the Te, Sb, and As ions. This suggests a stronger influence of Co and Ni species on the lead dioxide electrode charging behavior than the Te, Sb, and As species in the system. (*iv*) Hydrides of Te, Sb, and As could occur during charging of the lead electrode, all prior to or during hydrogen gas evolu-

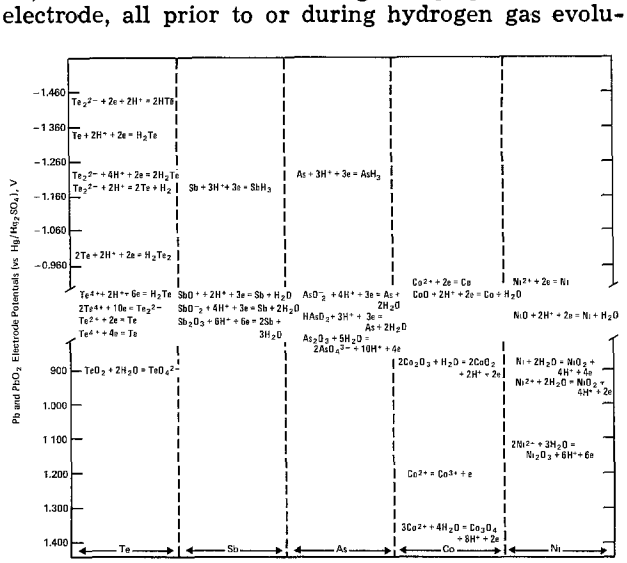

Fig. 1. Dominant reactions of Te, Sb, As, Co, and Ni in the lead-acid battery operating potential range.

* Electrochemical Society Active Member.
Key words: lead electrode, lead dioxide electrode, gas evolution overvoltage.

tion. (v) A few redox reactions of tellurium species could occur simultaneously in the lead electrode potential range. A combination of some of these reactions may offer catalytic influence of Te on the H_2 gas generation on the lead electrode (*e.g.*, $2Te + 2H^+ + 2e = H_2Te_2$; $H_2Te_2 = 2H^+ + Te_2^{2-}$; $Te_2^{2-} + 2H^+ = 2Te + H_2$).

Experimental

Two types of lead and lead dioxide electrodes were used. The small size electrode was 2 mm diam and 2 cm long wire type and the large size was the regular pasted type SLI electrode. The small size lead electrode was either a freshly prepared or an electrode potentiostatically cycled between −1160 and −860 mV (*vs.* reference) at 0.5 mV/sec scan rate. The small size lead dioxide electrode was potentiostatically cycled between 975 and 1425 mV (*vs.* reference) at 1 mV/sec scan rate. The small size electrodes were cast wire made out of 99.999% Pb (Cominco). The potentiostatically cycled electrode preparation was carried out at room temperature and in 1.250 sp gr H_2SO_4 solution unless mentioned otherwise. The sulfuric acid solution was prepared out of the AR grade acid and laboratory distilled water. The Te, As, Sb, Ni, and Co ion containing atomic absorption standard test solutions were obtained from Sargent-Welch Scientific Company.

The pasted electrodes were made out of conventional Pb-Ca grid with dimensions 14.5 cm long and 12.0 cm wide. The thickness of the pasted type lead and lead dioxide electrodes were 1.50 and 2.25 mm, respectively. These electrodes were conventionally prepared using a well-controlled quality ball mill oxide. The oxide had 30 ± 3% free lead with 0.04% Bi, 0.0006% As, and spectrographically undetectable amounts of Cu (<0.003%), Cr (<0.002%), Co (<0.003%), Fe (<0.003%), Ni (<0.003%), Ti (0.001%), Zr (<0.003%), Mn (<0.0001%), and Pt (<0.003%). The electroformation was carried out against two countergrid (Pb-Ca) electrodes in 1.250 sp gr H_2SO_4 at 0.5 A/plate for a 24 hr period.

The constant potential source was a Wenking potentiostat 70 HP 10. The voltage scan generator was PAR Model 175. The X-Y recorder was Hewlett Packard/Moseley Autograph Model 7000 AM. The reference electrode was a cracked glass type Hg/Hg_2SO_4/1.270 sp gr H_2SO_4 (12).

The test cell with small size electrode had a test electrode, a counterelectrode, and a reference electrode all dipped in 50 ml, 1.270 sp gr H_2SO_4 test solution. The pasted type electrode was tested against two grid counters with a spacer but no separator in between. The electrolyte volume varied between 700 and 850 ml. Prior to cathodic LPS of the lead electrode, it was held at −980 mV (*vs.* reference) for 5 min and then scanned at 5 mV/sec to hydrogen evolution. Similarly, at the start, the lead dioxide electrode was held at +1150 mV (*vs.* reference) for 5 min prior to anodic LPS at 5 mV/sec to oxygen evolution. Both the cathodic and anodic LPS at 1 and 5 mV/sec scan rates were found to be identical.

The effect of trace metal ions on the cathodic LPS of the small size lead electrode was carried out after addition of the metallic ions in the test electrolyte. This was repeated after a period of open-circuit stand and after potentiostatically cycling the electrode. The potentiostatic cycling of the lead and the lead dioxide electrode was carried out as stated earlier. The effect of metal ions on the anodic LPS of the lead dioxide electrode was determined by preparing the electrode in presence of metal ions and comparing the anodic LPS of the control electrode prepared in pure electrolyte. The LPS of the pasted electrodes were also carried out in a similar manner but in several cases the mode of metal ion inclusion in the test system was varied and is discussed along with the results.

Results and Discussion

Effect of Te ion on the lead electrode.—The open-circuit potential of Te metal in 1.270 sp gr H_2SO_4 was found to be −40 mV (*vs.* reference). This agrees very well with the reported oxidation potential of Te metal in acid solution (15-17) assuming 615 mV for the Hg/Hg_2SO_4 reference electrode to standard hydrogen electrode (SHE). The cathodic LPS of the Te metal in 1.270 sp gr H_2SO_4 solution is shown in Fig. 2. This figure suggests that the electrochemical behavior of Te metal in 1.270 sp gr H_2SO_4 solution is fairly stable up to −880 mV. The cathodic reaction at this metal electrode becomes visible at potentials more cathodic than −880 mV. This agrees with the dominant reactions of Te ions in the lead acid battery potential range as shown in Fig. 1. However, this does not provide enough information to predict the influence of Te on cathodic behavior of the lead-acid battery lead electrode.

Figure 3 shows the effect of Te ion in the 1.270 sp gr H_2SO_4 solution on the cathodic LPS of the lead electrode. The high hydrogen overvoltage of the lead electrode is evident from curve A. A noticeable reduction of this hydrogen overvoltage occurs in the presence of Te ion (Te^{4+}) in the test solution (curves B, C, and D). The magnitude of this reduction in hydrogen overvoltage is small immediately after addition of Te ion in the test solution (curves B and C), but highly noticeable after open-circuit rest at a moderately higher temperature (compare curve D with B). This reduction in hydrogen overpotential is apparently associated with the deposition of Te (as

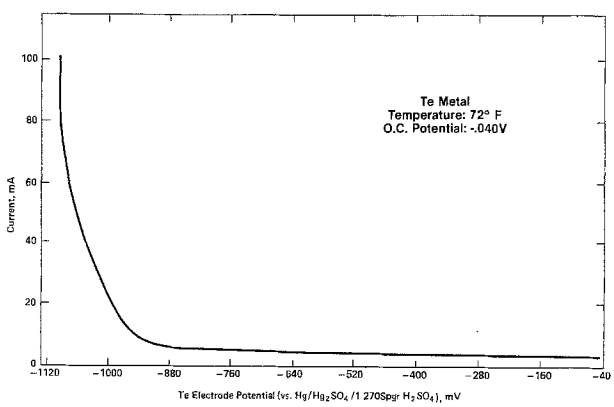

Fig. 2. Cathodic LPS of tellurium metal in 1.270 sp gr H_2SO_4 at 72°F and 5 mV/sec scan rate.

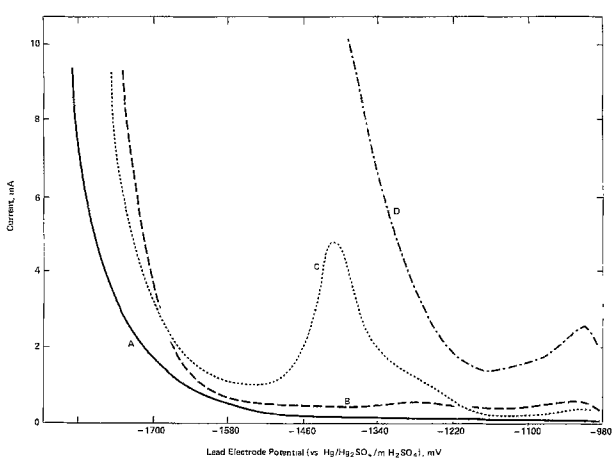

Fig. 3. Cathodic LPS of lead electrodes as a function of Te ion concentration in 1.270 sp gr H_2SO_4, temperature, and rest period: (A) no Te ion, 72°F; (B) 2 ppm Te ion, 72°F; (C) 4 ppm Te ion, 72°F; and (D) 2 ppm Te ion, 50 min rest period at 125°F. Scan rate 5 mV/sec.

well as its distribution) on the electrode surface and its subsequent reduction during follow-up cathodic LPS. The Te pickup of the lead electrode is indicated by current acceptance at the start of the sweep experiment (curves B and D). The lower initial current acceptance of curve C than curve B is probably related to the starting of the experiment rather than the Te ion concentration in the test solution. The subsequent reduction of deposited Te on the lead electrode surface initiates around −1260 mV. This reaction appears to control the gassing behavior of the electrode. The intensity of this reaction is small immediately after addition of 2 ppm Te ion (curve B). However, this reaction intensity increases with increasing Te ion concentration in the test solution (compare curves B and C) or by allowing more time to deposit Te metal on the electrode surface (compare curves B and D). The limiting current around −1400 mV observed in the lead electrode LPS immediately after addition of 4 ppm Te ion in the test solution is probably associated with the limited absorption of Te metal on the lead electrode surface and hence the reaction site for hydrogen generation. The extremely high reaction intensity of the electrode (curve D) in potential more cathodic to −1260 mV or a significant reduction in the lead electrode hydrogen overpotential suggests that Te may catalytically influence the hydrogen gas generation on the lead electrode surface.

The mechanism of trace Te ion-induced catalytic hydrogen evolution on the lead electrode is not known. The cathodic behavior of Pb-Te alloy in an acidic solution may provide a better understanding and would be a subject of worthwhile study. The available information, as summarized in Fig. 1 and 3, indicates the catalytic hydrogen evolution at the lead electrode could have resulted from reactions leading to H_2Te_2 formation ($2Te + 2H^+ + 2e = H_2Te_2$), generation of ditelluride ion ($H_2Te_2 = 2H^+ + Te_2^{2-}$), and oxidation of Te_2^{2-} to Te metal ($Te_2^{2-} + 2H^+ = 2Te + H_2$). However, the amphoteric nature of tellurium and its existence as multivalent species in a solution dictates a possibility of a number of simultaneous reactions leading to cathodic hydrogen and/or hydride generation (15). The final product of the reduction of tetravalent tellurium is elemental "Te" concluded Komandenko (20). Panson reported the feasibility of formation of telluride (Te^{2-}) or ditelluride (Te_2^{2-}) by the cathodic reduction of Te (21). Speranskaya asserted the reduction of Te^{4+} on mercury cathode in an acidic solution to Te^{2-} which catalyzes the hydrogen evolution (22).

Additional study of the effect of tellurium ion on the lead electrode was carried out from the LPS study of the pasted electrode in a test cell in which Te was introduced to the system by pretreating either the test or the counterelectrode in Te ion containing solution. The counterelectrodes were two bare grids of identical dimension. The results of this study are summarized in Fig. 4 and 5. Figure 4 demonstrates the effect of electrode treatment on the cathodic LPS of the pasted type lead electrode. Curve A is for the control electrode, B for the electrode immersed in 1 ppm Te ion containing solution for 30 min, and C for electrode cathodized at −1025 mV (*vs.* Hg/Hg_2SO_4) for 30 min. The total amount of Te ion in the treatment solution in both cases was 0.75 mg. The pasted type electrode had 70g active material with 348 cm^2 geometric surface area. The overall effect of Te ion on the cathodic LPS of the pasted electrode is close to that of the small size electrode (Fig. 3) except for some positive shift in prehydrogen evolution reaction zone (Fig. 4 and 5). These potential shifts appear to be related to the active matrix composition and system temperature. The cathodically treated plate (curve C, Fig. 4), as expected, has shown less

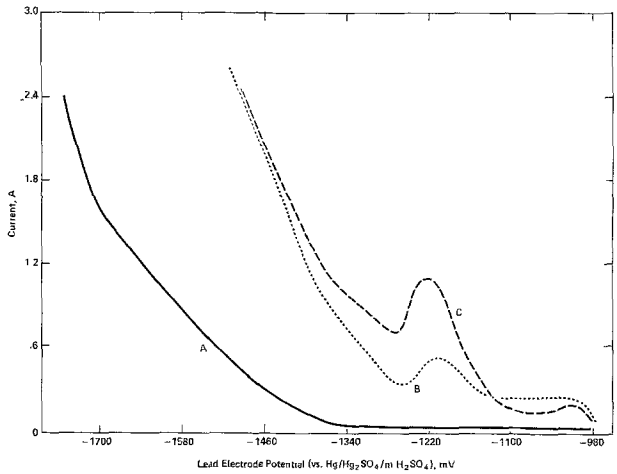

Fig. 4. Cathodic LPS of the pasted type lead electrodes in 1.270 sp gr H_2SO_4 as a function of electrode pretreatment: (A) no pretreatment; (B) 30 min immersion in 1.270 sp gr H_2SO_4 with 0.75 mg Te ion; and (C) 30 min cathodic treatment at −1025 mV (vs. $Hg/Hg_2SO_4/m\ H_2SO_4$) in 1.270 sp gr H_2SO_4 with 0.75 mg Te ion. Scan rate 5 mV/sec.

current acceptance during the early part of the LPS and a greater prehydrogen evolution peak than the immersion treated plate (curve B, Fig. 4). The amount of charge obtained from the prehydrogen evolution peaks were 17 and 26C for the immersion and cathodically treated electrodes, respectively. Assuming a four electron transfer reaction, this represents 5.6 and 6.1 mg Te equivalent material deposited on the immersion and cathodically treated surface, respectively. These figures are significantly higher than the Te ion content in the treatment solution and substantiates the feasibility of the catalytic influence of Te in generating the prehydrogen evolution reaction on the lead electrode.

We carried out another test to demonstrate the sensitivity of Te ion concentration on the LPS of the

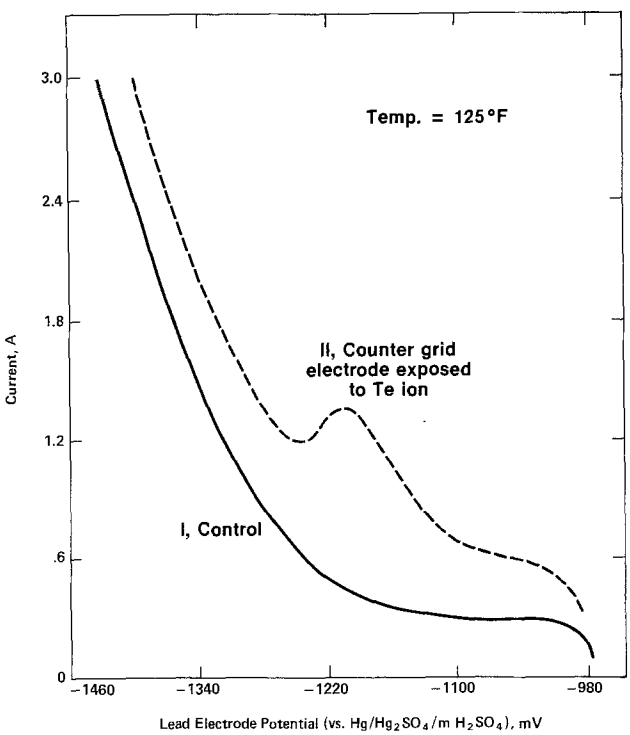

Fig. 5. Cathodic LPS of the pasted type lead electrodes in 1.270 sp gr H_2SO_4 at 125°F in the presence of countergrids without (I) and with (II) immersion treatment in 0.75 mg Te ion containing test solution followed by washing with distilled water. Scan rate 5 mV/sec.

lead electrode. This experiment was carried out in a test cell with a test electrode (pasted type) and two bare grids as counterelectrode. The experimental temperature was 125°F. We swept this electrode in pure acid (curve I, Fig. 5). Then we took the countergrids, immersed them in acid solution with 0.75 mg Te ion for 5 min, washed them with water, and placed them back in the test cell. This was followed by potential sweep of the test electrode (curve II, Fig. 5). This shows that the cathodic behavior of the lead electrode is highly sensitive to the trace Te content in the test solution. The differential pulse polarography, which uses a principle similar to the LPS technique, could detect 10 ppb tellurium in a lead matrix, as had recently been reported by Wilkinson *et al.* (23).

Effect of Sb, As, Co, and Ni on the lead electrode.— The effect of 5 ppm Sb and As ion in 1.270 sp gr H_2SO_4 on the cathodic LPS of a small size lead electrode are shown in Fig. 6 and 7. In both cases, a noticeable reduction in potential for the onset of hydrogen gas evolution was observed immediately after addition of Sb and As ion in the test solution (curve B-1, Fig. 6 and 7). This was further reduced when the electrode was on rest for a 17 hr period (curve B-2, Fig. 6 and 7). The follow up potentiostatic cycling of the test electrode in the negative electrode potential range (−860 to −1160 mV *vs.* Hg/Hg_2SO_4/m H_2SO_4 at 0.5 mV/sec scan rate) showed a further reduction in hydrogen overpotential for Sb ion containing test system but not for the test system with As ion (curve B-3, Fig. 6 and 7). The hydrogen overpotential of the potentiostatically cycled test electrode with As ion showed a more cathodic shift than the overpotential observed after a 17 hr rest period (Fig. 7).

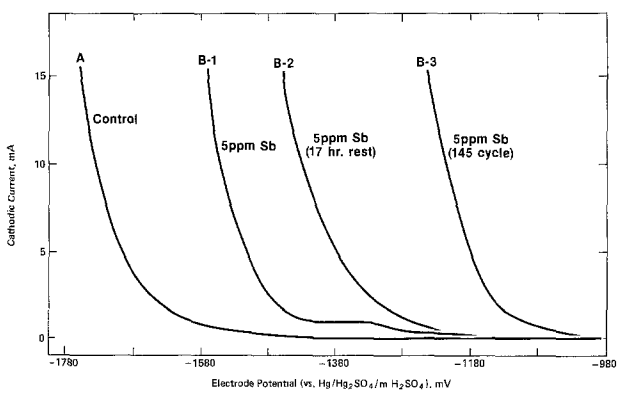

Fig. 6. Effect of 5 ppm Sb ion in 1.270 sp gr H_2SO_4 on the cathodic LPS of the lead electrodes at 72°F as a function of rest period and potentiostatic cycling: (A) without Sb ion; (B-1) with Sb ion, no rest period; (B-2) with Sb ion and 17 hr rest period; (B-3) with Sb ion and 48 hr potentiostatic cycling. Scan rate 5 mV/sec.

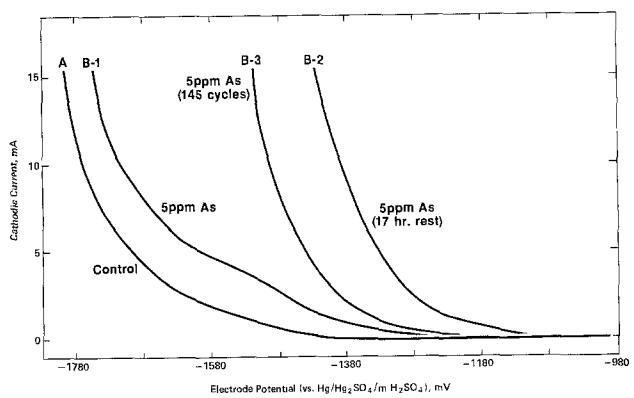

Fig. 7. Effect of 5 ppm As ion in 1.270 sp gr H_2SO_4 on the cathodic LPS of the lead electrode at 72°F as a function of rest period and potentiostatic cycling: (A) without As ion; (B-1) with As ion, no rest period; (B-2) with As ion and 17 hr rest period; (B-3) with As ion and 48 hr potentiostatic cycling. Scan rate 5 mV/sec.

The open-circuit potentials of Sb and As metal in 1.270 sp gr H_2SO_4 solution at 72°F were −406 and −230 mV (*vs.* reference), respectively. This suggested that Sb and As ion when present in the test solution could deposit on the lead electrode, which has open-circuit potential around −960 mV (*vs.* reference). The presence of a broad shoulder around −1300 mV (*vs.* reference) for the system with Sb ion in the test solution (curve B-1, Fig. 6) indicated either the change in charge state of the Sb ion in the solution or the formation of Sb hydride. Since the equilibrium potential of SbH_3 (g) formation in Sb-H_2O system at 25°C is −510 mV *vs.* SHE (−1125 mV *vs.* Hg/Hg_2SO_4), the broad shoulder in curve B-1, Fig. 6 could be associated with SbH_3 formation. The equilibrium potential of AsH_3 (g) formation in acid solution at 25°C is −608 mV SHE (−1223 mV *vs.* Hg/Hg_2SO_4). This suggests that the inflection observed in curve B-1, Fig. 7, around −1500 mV, could be associated with the AsH_3 (g) formation on the lead electrode surface.

Figures 6 and 7 also include the cathodic LPS of the lead electrode after 145 LPS cycles between −1160 and −860 mV (*vs.* reference) at 0.5 mV/sec. LPS cycling did not change the cathodic LPS of the control electrode. Presence of 5 ppm Sb in the test solution made it more anodic whereas 5 ppm As made it more cathodic. The shifts in cathodic LPS after LPS cycling may have resulted from the distributive pattern of the deposited trace element and/or the loss of the same from the system due to hydride formation during cycling. The results note the greater influence of trace Sb in reducing the lead electrode hydrogen overpotential than the trace As (Fig. 6 and 7). This is also evident from the comparison of the electrode cyclic voltammograms taken after LPS cycling (Fig. 8). The starting voltammograms of these three electrodes were identical and similar to the control. The control did not change during cycling and could be used as a reference point to note the change caused by the presence of 5 ppm Sb or As in the test system. The greater detrimental influence of the trace Sb than As on the lead electrode capacity maintenance during cycling is evident in Fig. 8. These results are in agreement with the reported influence of Sb and As ions on the capacity maintenance behavior of the lead electrode and in turn the lead-acid battery (14, 18, 19).

The effect of 4 ppm Ni and Co ion in the test 1.270 sp gr sulfuric acid solution on the cathodic LPS of the lead electrode is shown in Fig. 9. Both Co and Ni ion have increased the local cell reaction-induced self-discharge of the lead electrode as noted from the current intensity during the early part of the LPS but not significantly on the onset of the hydrogen evolution potential. The open-circuit potentials of metallic Ni and Co in 1.270 sp gr H_2SO_4 solution are −372 and −785 mV (*vs.* reference), respectively. These data suggest the possibility of deposition of Ni and Co on the lead electrode and explain the self-discharge processes observed in the lead electrode during the early part of the cathodic LPS. However, this self-discharge process of the lead electrode may not influence the gassing behavior of the maintenance-free lead acid cell in presence of Ni and Co ion as observed by Pierson *et al.* (14). This suggests that the presence of Ni and Co might influence the gas evolution behavior of the lead dioxide electrode more than the lead electrode. An experiment was carried out to substantiate this hypothesis.

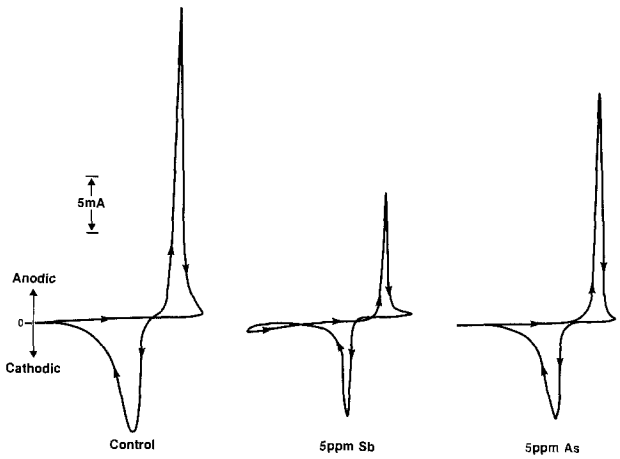

Fig. 8. Lead electrode cyclic voltammograms between −1160 and −860 mV (*vs.* Hg/Hg_2SO_4/m H_2SO_4) at 0.5 mV/sec without (control) and with 5 ppm Sb and As ions in 1.270 sp gr H_2SO_4 at 72°F after 145 cycles.

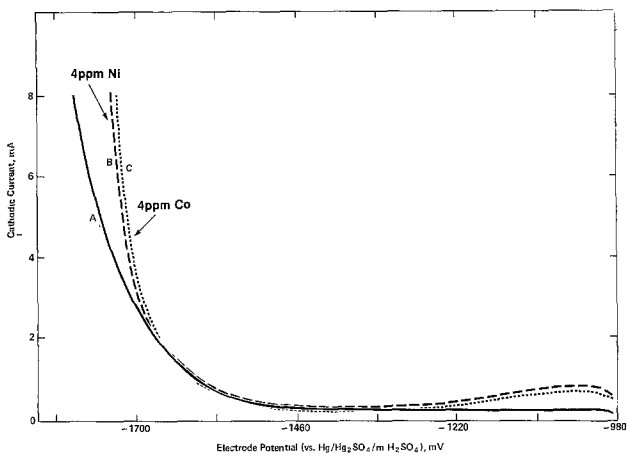

Fig. 9. Cathodic LPS of lead electrodes without (A) and with 4 ppm Ni (B) and Co (C) ions in 1.270 sp gr H_2SO_4 at 72°F. Scan rate 5 mV/sec.

Effect of Co and Ni on the lead dioxide electrode.— Figure 10 shows the effect of 5 ppm Co and Ni ion in the test 1.270 sp gr H_2SO_4 on the anodic LPS of the lead dioxide test electrode. The test electrodes were formed by LPS cycling between 975 and 1425 mV (*vs.* reference) at 1 mV/sec and tested in test solution with or without 5 ppm Ni or Co. The greater influence of 5 ppm Co in reducing the lead dioxide electrode oxygen overvoltage is evident from the figure. The oxygen gas evolution potential as determined from the intersection of base line and the tangent of the LPS curve at 20 mA current acceptance is reduced by 65 mV in presence of 5 ppm Ni and 145 mV in presence of 5 ppm Co in the test electrolyte (Fig. 10). This suggests a greater gassing of the maintenance-free lead-acid battery in presence of Co than Ni in the electrolyte in agreement with the observation of Pierson, Weinlein, and Wright (14). These authors reported the gassing of the maintenance-free lead-acid cell is five times more in presence of 5000 ppm Co than 5000 ppm Ni in the test electrolyte.

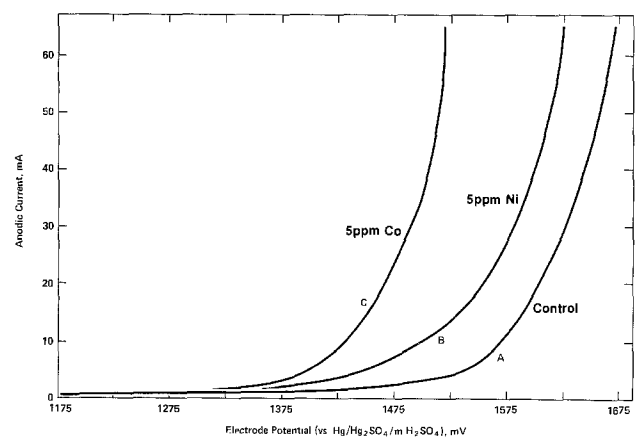

Fig. 10. Anodic LPS of lead dioxide electrodes without (A) and with 5 ppm Ni (B) and Co (C) ions in 1.270 sp gr H_2SO_4 at 72°F. Scan rate 5 mV/sec.

The effects of trace Co and Ni on the lead dioxide electrode characteristics are further elucidated from the cyclic voltammograms of these electrodes between 900 and 1500 mV at 1 mV/sec scan rate as shown in Fig. 11. The subject of interest here (Fig. 11) is the anodic behavior of the electrode which shows the conversion of $PbSO_4$ to PbO_2 around 1375 mV (*vs.* reference) followed by a reduction in charge current until it reaches a potential for oxygen evolution. The anodic oxygen evolution current at +1500 mV (*vs.* reference) could be considered as a measure of charge inefficiency. The inefficiency increases with the increasing anodic current or the oxygen gas evolution. Figure 11 shows that the charge inefficiency is maximum for the test solution with 5 ppm Co ion. This is followed by test solution with 5 ppm Ni ion and the control test solution. These electrodes were developed for a different length of time, and the electrode capacity, as shown by the cathodic portion of the voltammograms, were not solely caused by the electrolyte additives.

Conclusions

1. LPS can detect the effect of trace impurities on gassing behavior of lead-acid battery electrodes.

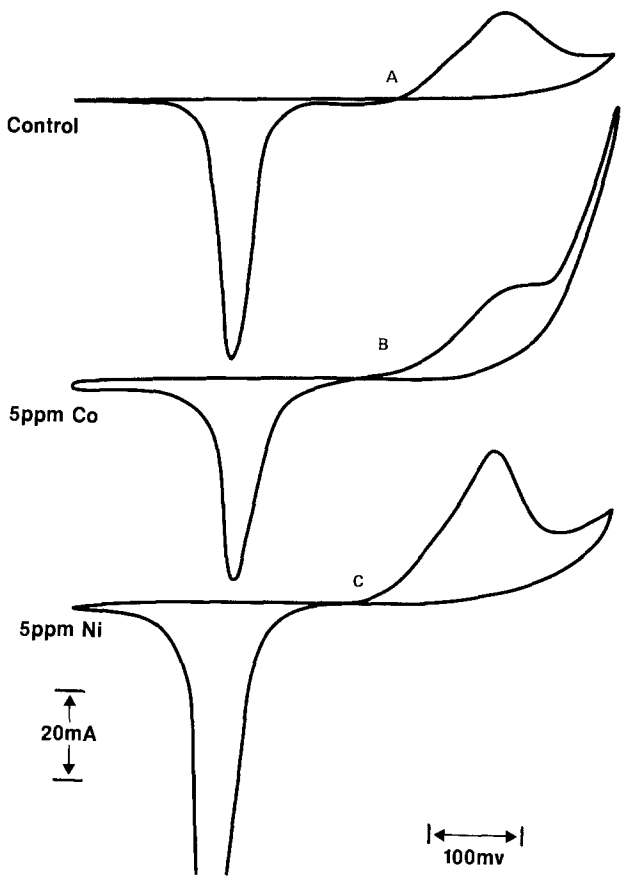

Fig. 11. Lead dioxide electrode cyclic voltammograms between 900 and 1500 mV (*vs.* Hg/Hg_2SO_4/m H_2SO_4) at 1 mV/sec without (A) and with 5 ppm Ni (C) and Co (B) ions in 1.270 sp gr H_2SO_4.

2. Trace Te in a lead-acid battery acts catalytically to generate hydrogen gas during charging.
3. Trace Sb and As increase the intensity of lead-acid battery gassing by reducing the lead electrode hydrogen overpotential. During cycling, this gassing rate is more sustained in presence of Sb than As.
4. Increased lead-acid battery gassing behavior in the presence of trace Co and Ni is more due to their role in reducing oxygen overvoltage of the lead dioxide electrode than their influence on the lead electrode hydrogen overvoltage. Presence of Co in the test solution causes more gassing in the lead-acid battery than the presence of Ni in the test solution.

Acknowledgments

The authors would like to thank Globe Battery Division of Johnson Controls, Incorporated for permission to publish this work.

Manuscript submitted June 1, 1982; revised manuscript received July 12, 1983. This was Paper 53 presented at the Denver, Colorado, Meeting of the Society, Oct. 11-16, 1981.

Johnson Controls, Incorporated assisted in meeting the publication costs of this article.

REFERENCES

1. H. S. Panesar, in "Power Sources 3," D. H. Collins, Editor, p. 79, Oriel Press, New Castle upon Tyne (1971).
2. J. P. Carr and N. A. Hampson, *This Journal*, **118**, 1262 (1971).
3. J. P. Carr and N. A. Hampson, *Chem. Rev.*, **72**, 679 (1972).
4. W. Visser, *J. Power Sources*, **1**, 257 (1976/1977).
5. J. L. Weininger, *ibid.*, **2**, 241 (1977/1978).
6. B. K. Mahato, *This Journal*, **126**, 365 (1979).
7. T. F. Sharpe, *ibid.*, **122**, 845 (1975); **124**, 168 (1977).
8. K. R. Bullock, *ibid.*, **126**, 360 (1979).
9. T. G. Chang, M. M. Wright, and E. M. L. Valerioté, in "Power Sources 6," D. H. Collins, Editor, Academic Press, London (1977).
10. S. Kelly, N. A. Hampson, and K. Peters, *J. Appl. Electrochem.*, **12**, 81 (1982).
11. M. P. J. Brennan and N. A. Hampson, *J. Electroanal. Chem. Interfacial Electrochem.*, **48**, 465, (1973); **52**, 1 (1974).
12. B. K. Mahato, *This Journal*, **127**, 1679 (1980); **128**, 1416 (1981).
13. H. Niklas and H. Jakobljevich, *J. Appl. Electrochem.*, **2**, 165 (1972).
14. J. R. Pierson, C. E. Weinlein, and C. E. Wright, in "Power Sources 5," D. H. Collins, Editor, p. 97, Academic Press, London (1975).
15. "Encyclopedia of Electrochemistry of Elements," A. J. Bard, Editor, Marcel Dekker, Inc., New York (1975); A. P. Tomilov and N. E. Chomutov, *ibid.*, Vol. II, pp. 21-52; N. Maki and N. Tanaka, *ibid.*, Vol. III, pp. 43-211; A. J. Arvia and D. Posadas, *ibid.*, Vol. III, pp. 212-422; V. Past, *ibid.*, Vol. IV, pp. 2-42; S. I. Zhdanov, *ibid.*, Vol. IV, pp. 393-445.
16. M. Pourbaix, "Atlas of Electrochemical Equilibria in Aqueous Solutions," Translated by J. A. Franklin, Pergamon Press, New York (1966).
17. S. A. Awad, *Electrochim. Acta*, **13**, 925 (1968).
18. J. Burbank, A. C. Simon, and E. Willihnganz, in "Advances in Electrochemistry and Electrochemical Engineering," Vol. 8, P. Delahay and C. W. Tobias, Editors, John Wiley & Sons, Inc., New York (1970).
19. H. Bode, "Lead-Acid Batteries," John Wiley & Sons, Inc., New York (1977).
20. V. M. Komandenko, *Zh. Prikl. Khim.*, **43**, 2480 (1970); **44**, 523 (1971).
21. A. J. Panson, *J. Phys. Chem.*, **67**, 2177 (1963).
22. E. F. Speranskaya, *Elektrokhimiya*, **3**, 1212 (1967); **3**, 1450 (1967).
23. D. F. Wilkinson, K. R. Bullock, and C. L. Wang, Abstract 52, The Electrochemical Society Extended Abstracts, Vol. 81-2, p. 135, Denver, Colorado, Oct. 11-16, 1981.

Physical Changes in Positive Active Mass during Deep Discharge-Charge Cycles of Lead-Acid Cell

Katsuhiro Takahashi, Masaharu Tsubota, Kunio Yonezu, and Koji Ando*

Japan Storage Battery Company, Limited, Lead-Acid Battery Laboratory, Corporate Research and Development Center, Kyoto, Japan

ABSTRACT

The positive active mass of a pasted-type lead-acid cell changes morphologically to a great extent during deep discharge-charge cycles. In order to reduce these changes, the effect of compression on the active mass has been studied. When compression is applied to a positive plate, expansion of the positive active mass is suppressed and the structural changes become smaller. Therefore, the cycle life of the positive plate increases remarkably. The reason why the cycle life increases by compression is due to suppression of the decrease in cohesion between PbO_2 particles.

The cycle life of a pasted-type lead-acid battery operating under deep discharge-charge cycles is generally limited by the life of the positive plate. Therefore, it is necessary to clarify the failure mechanism of the plate, particularly the process of the change in the active mass itself, in order to improve the cycle life of the battery.

The structural changes in the positive active mass have been studied with optical and scanning electron microscopes, resulting in the development of so-called coralloid structure and voids in it (1). Studies using nuclear magnetic resonance and neutron diffraction have also been carried out (2, 3). These studies have gradually revealed the changes in fine structure morphology and properties of the active mass. However, they are insufficient to make the failure mechanism of the positive plate clear.

For years we have also investigated the changes in the structure and various physical properties of the positive active mass and have found the following phenomena: (*i*) change in pore size distribution, (*ii*) decrease in cohesion between PbO_2 particles, (*iii*) decrease in reactivity of PbO_2 particles, and (*iv*) shedding of PbO_2 particles. These phenomena interact with each other and seem to relate closely to microstructural changes in the active mass resulting from the volume change, that is, its expansion and shrinkage during cycling.

* Electrochemical Society Active Member.
Key words: electrode, discharge, failure.

Accordingly, it was considered that suppression of the structural change might be effective in improving the cycle life of a pasted-type positive plate. Therefore, pasted-type positive plates were cycled under compressed conditions, and the changes in the structure and physical properties of the active mass during cycling and its cycle life performance were examined.

Experimental

Test cell.—The test cell construction is illustrated in Fig. 1. The cell consisted of three positive plates and four negative plates having higher capacity than the positives. These plates were separated by conventional glass mats and microporous rubber separators.

A stiff plastic plate, 20 mm thick, was attached to each side of the flexible container, and the assembly was tightened by bolts and nuts to maintain compression on the elements. The degree of compression was measured by a load cell. Ten cells were assembled at a pressure of 100 kg/dm^2 in the dry state, and the other ten at 20 kg/dm^2.

The structure of the tested positive plate is shown in Fig. 2. The plate is about 3.3 mm thick and lead-antimony conductors were arranged at both sides of the plate. Two probes for measuring the electrical resistance of the active mass were mounted in the upper part of the plate. The apparent density of the active mass was about 3.9 g/cm^3, and the specific gravity of electrolyte, dilute H_2SO_4, was 1.280(20°C).

Test procedures.—Cycle life testing was carried out after two cycles of the initial capacity test. The test conditions are as follows:

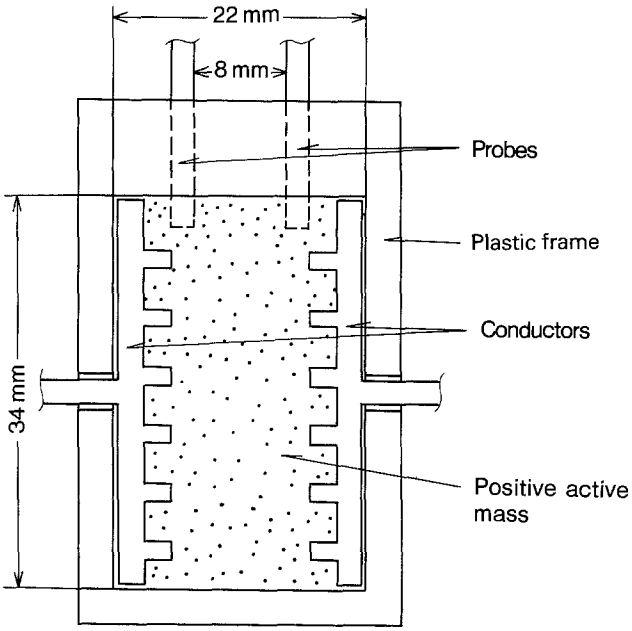

Fig. 2. Structure of positive test plate

capacity test
- discharge current: 440 mA (about 5 hr-rate)
- cut-off voltage: 1.70V
- temperature: ambient

cycle test
- discharge: 550 mA × 3 hr (depth of discharge: about 75% of 5 hr-rate capacity)
- charge: 400 mA × 5 hr
- temperature: ambient

Measurements and observation.—The following measurements and observation were made at intervals in cycling to examine the changes in the properties of the positive active mass: (*i*) electrical resistance, (*ii*) cohesion,[1] (*iii*) thickness, (*iv*) chemical composition, (*v*) porosity and pore size distribution, (*vi*) microstructure, (*vii*) size and crystallinity of PbO_2 particles, and (*viii*) surface area.

[1] Cohesion was determined by measuring the force required for a flat-head needle of 1 mm diam to pierce through the positive active mass.

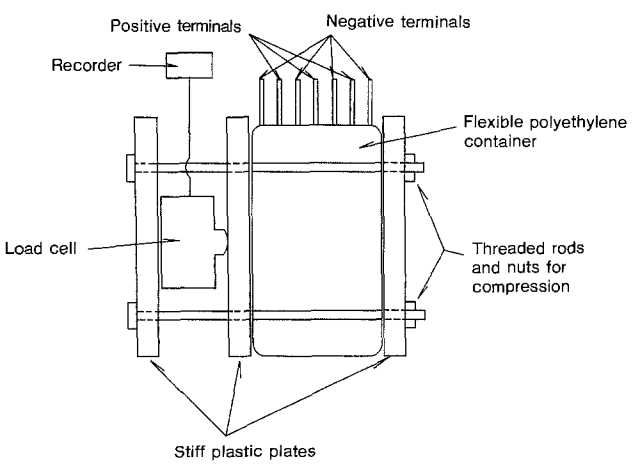

Fig. 1. Test cell construction

Results and Discussion

Changes in the properties of positive active mass during cycling.—Figure 3 shows the changes in discharge capacity and electrical resistance of the positive active mass during cycling. There is no difference in the initial capacity between cell A (compression 100 kg/dm^2) and cell B (20 kg/dm^2). However, there is an obvious difference in cycle life performance. Namely, the capacity in cell A after 536 cycles is 94% of the initial capacity, while it is 66% in the

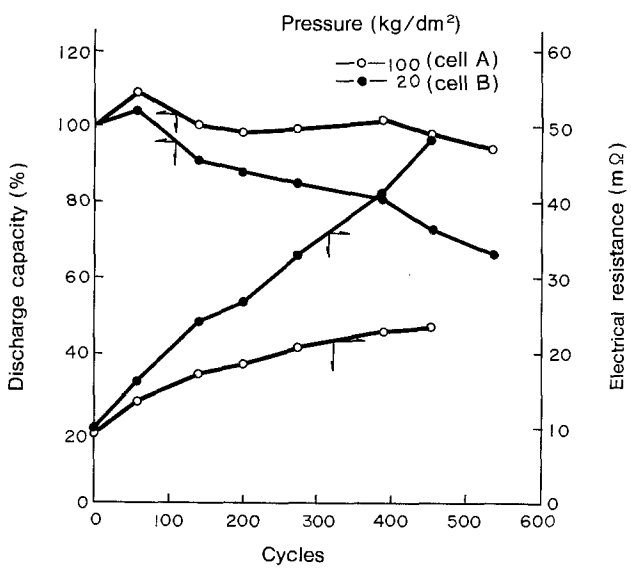

Fig. 3. Changes in electrical resistance of positive active mass and discharge capacity.

case of cell B. The difference in this cycle life performance is attributable to the positive plates, because the discharge capacity of the test cells is limited by the positive plates throughout the cycle test. Therefore, it is considered that the cycle life of the cell is improved by compression on the positive plates.

On the other hand, the electrical resistance of the active mass increases with cycling. However, the rate of increases is slower in cell A than in cell B. Such changes in electrical resistance corresponding to discharge capacity are shown in Fig. 4. The discharge capacity decreases with the increase in the electrical resistance of the active mass. This decrease is not due to mere lowering of the discharge voltage caused by the ohmic iR drop, but is related to loose cohesion between the PbO_2 particles. Namely, such particles are easy to separate from each other or to be insulated by $PbSO_4$ formed during discharge, so that the discharge capacity decreases with increasing electrical resistance. Bouet *et al.* (4) reported that capacity degradation of the positive plate occurred only as a result of increased contact resistance.

Table I shows the $PbSO_4$ and PbO_2 contents in the charged positive active mass. There is no difference in the $PbSO_4$ content during cycling between cell A and B. The amounts of sediment after 536 cycles are only 1% in cell A and 6% in cell B, respectively. These data suggest that the difference in discharge capacity and electrical resistance during cycling between cell A and B results from the difference in the characteristics of the active mass itself.

Figure 5-7 show the changes in cohesion, thickness, and porosity of the positive active mass during cycling. The cohesion decreases in both cell A and B with cycling, but the degree of decrease is less in cell A than in cell B.

The porosity increases remarkably up to the 50th cycle and thereafter does not change much in cells A and B. The degree of increase is less in cell A than in cell B. The change corresponds to the change in thickness of the active mass. The maximum discharge capacity at about the 50th cycle is attributable to the remarkable increase in porosity.

The structural change of the positive active mass is caused by the dissolution-precipitation reaction (5). The molar volume of $PbSO_4$, about 48 cm^3/mol, is twice as large as that of PbO_2, about 25 cm^3/mol

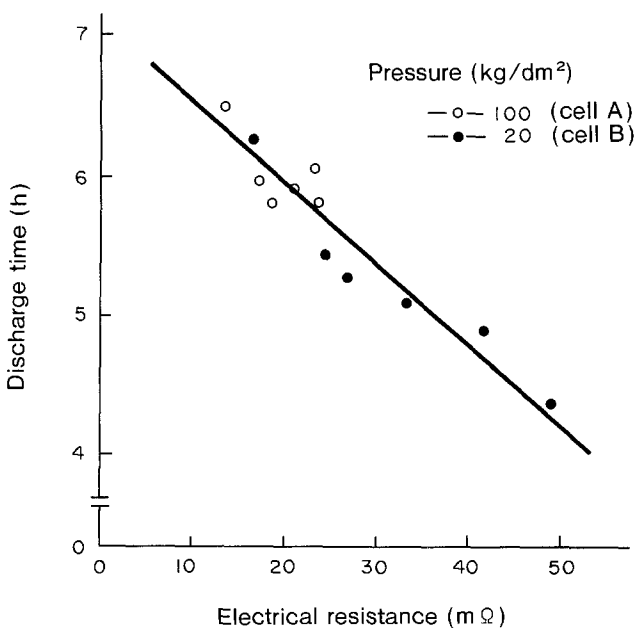

Fig. 4. Relationship between electrical resistance of positive active mass and discharge capacity.

Table I. PbO_2 and $PbSO_4$ contents in positive active mass

Cycles	PbO_2 content, (%)		$PbSO_4$ content, (%)	
	Pressure 20 kg/dm²	Pressure 100 kg/dm²	Pressure 20 kg/dm²	Pressure 100 kg/dm²
1	87	88	7.2	5.8
58	91	91	4.0	4.3
140	90	92	3.9	4.0
201	91	91	4.0	4.1
273	92	91	4.2	4.4
387	91	90	3.9	4.1
452	91	94	4.0	4.1
536	93	91	4.1	4.1

(6). The expanded volume resulting from the formation of $PbSO_4$ during discharge will not be reduced completely during charge, so that the positive active mass gradually expands with cycling. Such a volume change enlarges the pores and cracks, resulting in larger porosity and weaker cohesion, and furthermore the electrical resistance of the active mass becomes large. When compression is applied to the positive plate, expansion of the active mass is suppressed and consequently the structural change becomes smaller.

Figure 8 shows the difference in pore size distribution between cells A and B. After two cycles of the initial capacity test, the volume occupied by the pores below 1 μm in diameter is more than half of the total pore volume. With cycling, the pores below 1 μm decrease and the pores above 1 μm increase. However, the increase in the pores above 1 μm is suppressed in cell A with high compression.

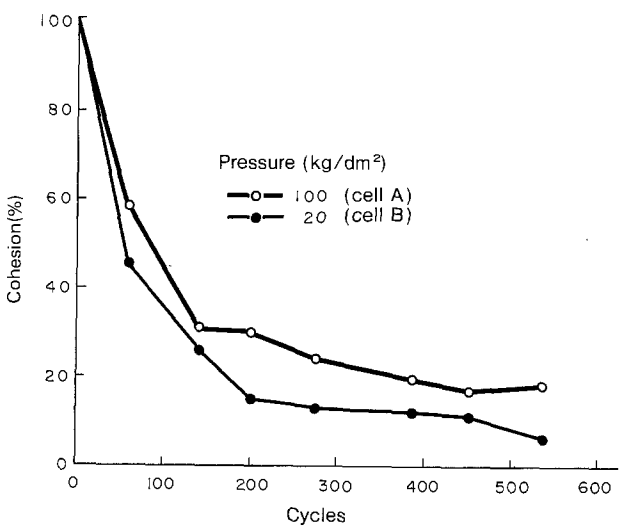

Fig. 5. Change in cohesion of positive active mass

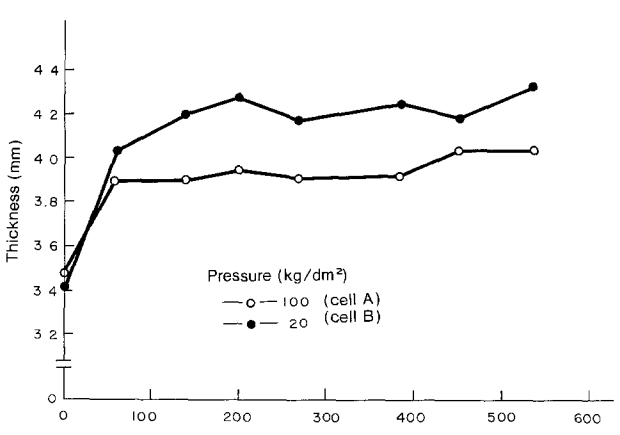

Fig. 6. Change in thickness of positive active mass

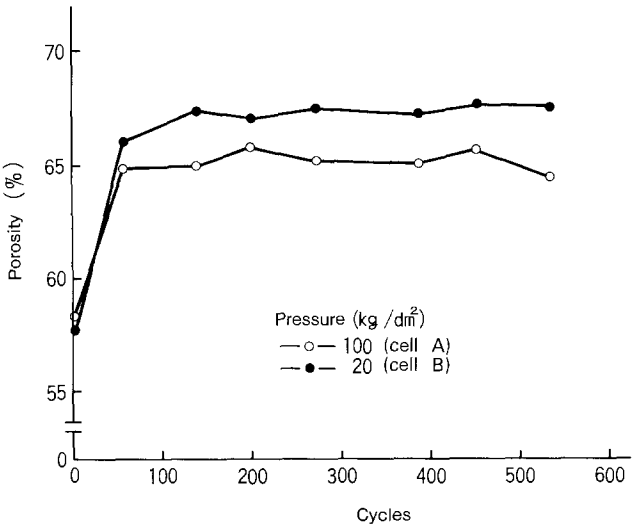

Fig. 7. Change in porosity of positive active mass

The scanning electron photomicrographs are shown in Fig. 9. In cell B, the coralloid structure observed in the early stages of cycling changes to a structure having large voids in the last stage, while in cell A the coralloid structure is maintained even after 536 cycles.

Compression also affected the crystallinity of PbO_2 particles. Figure 10 shows the changes in the half-value of the β-PbO_2 (110) diffraction pattern. The half-value becomes smaller with cycling in cells A and B. However, the decrease is less in cell A than in cell B. The half-value is related to the true particle size and the defects or strain in the crystal lattice. In order to clarify which factor affects the half-value, the surface area of the positive active mass was measured. Figure 11 shows the change in surface area during cycling. The surface area becomes smaller with cycling up to the 140th cycle and thereafter it is nearly constant. It does not depend on the degree of compression. Therefore, it

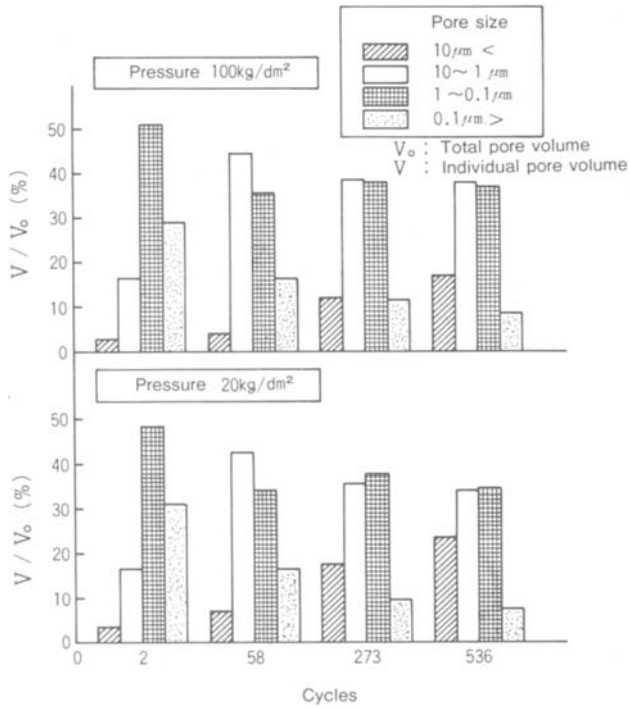

Fig. 8. Change in pore size distribution of positive active mass

seems that the difference in the half-value between cells A and B results from the defects or strain in the crystal lattice rather than the particle size.

Change in compression of test cell during cycling.— In order to examine the change in the degree of compression applied to the elements during cycling, a load cell was attached to one of the test cells A (see Fig. 1), and the pressure was continuously measured from the initial assembly to the 450th cycle.

Figure 12 shows the change in the pressure of the cell during cycling. When the cell is filled with

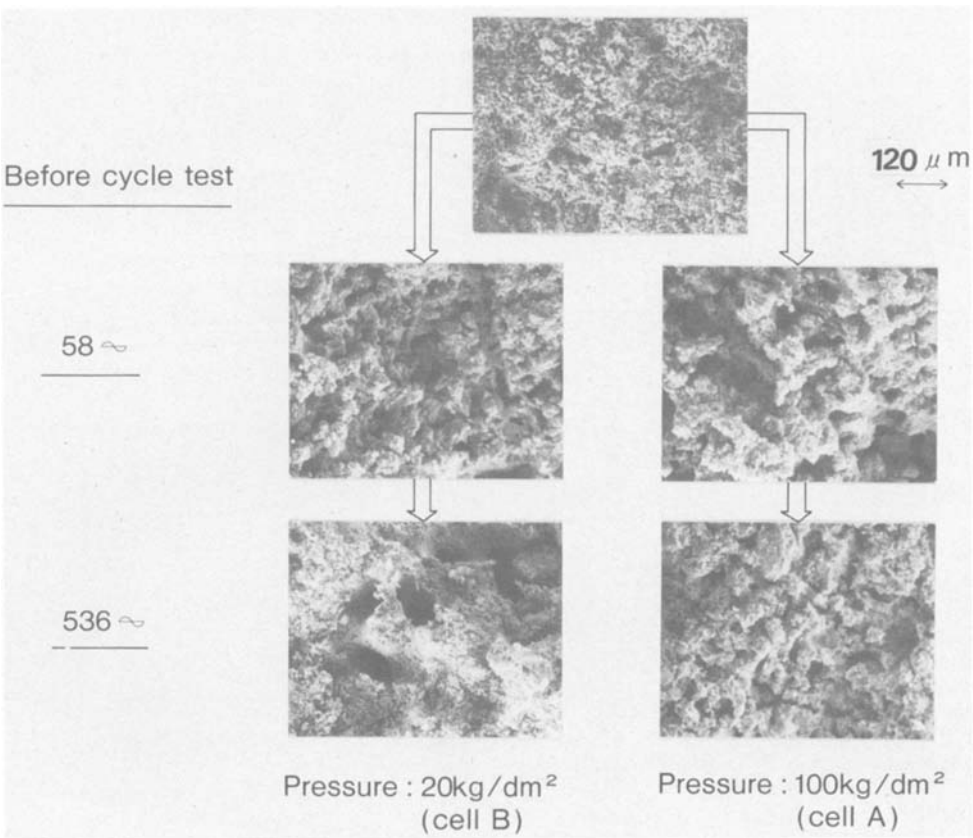

Fig. 9. Photomicrographs of positive active mass (SEM: cross section).

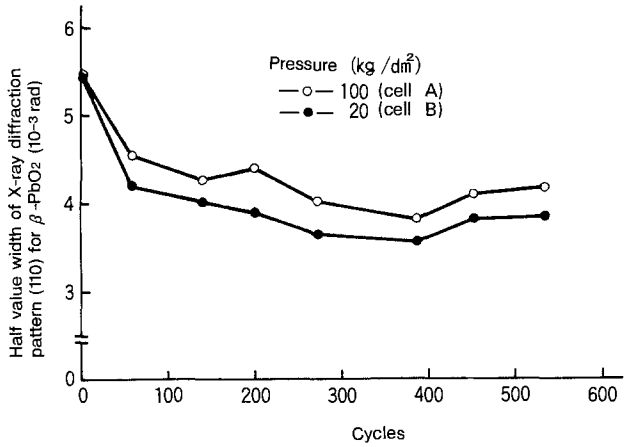

Fig. 10. Change in half-value width of x-ray diffraction pattern for positive active mass (β-PbO_2).

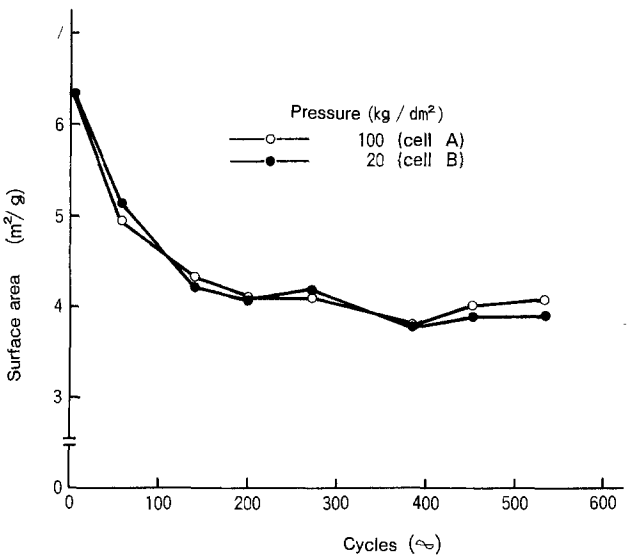

Fig. 11. Change in surface area of positive active mass

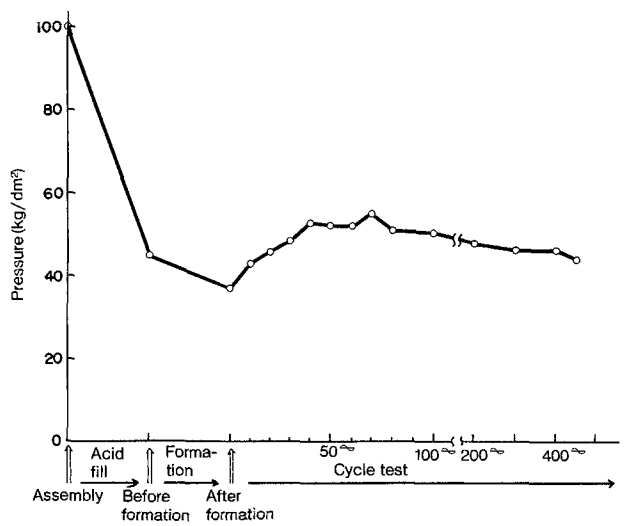

Fig. 12. Change in degree of pressure of test cell

dilute sulfuric acid, the pressure rapidly drops from 100 to 40 kg/dm². This is due to swelling of the adhesive binding glass fibers by sulfuric acid and loss of elasticity. The pressure also decreases slightly during formation. During cycling, it increases up to the 50th cycle and thereafter becomes nearly constant. This mode of the change in the pressure resembles the change in the thickness of the positive active mass. It is considered that the increase in pressure during cycling is attributable to expansion of the active mass. When the expanding force of the active mass becomes equivalent to the pressure exerted on it, the pressure will become constant and the expansion of the active mass will stop.

Figure 13 shows the changes in the pressure of the cell during charge and discharge. The pressure increases during discharge and decreases during charge. These changes correspond to the above-mentioned expansion and shrinkage of the positive active mass. The change during a charge and discharge cycle is 2-3 kg/dm² in the early stages of cycle testing, while with cycling it gradually becomes a smaller value (about 1 kg/dm² at the 300th cycle). This suggests that the structural change in the active mass in the early stages is larger than that in the later stages.

Relationship between the degree of compression and the cycle life of the cell.—Since it has been proved that compression is an important factor in improving the cycle life of the positive plate, cells with a pressure of 20, 40, 100, and 300 kg/dm² in the dry state were assembled, and the relationship between the degree of compression and the cycle life was examined. These cells consisted of eight positive and nine negative plates with lead-antimony alloy grids. These plates were separated by glass mats and microporous rubber separators. The conditions of cycle testing are as follows: discharge, 37.5A × 3 hr;[2] temperature, 30°C; charge, 27.0A × 5 hr; specific gravity of electrolyte, 1.280 (20°C). The initial discharge capacity of these cells is about 150 A-hr (5 hr-rate) and the energy density is about 45 W-hr/kg.

Figure 14 shows the change in discharge capacity during cycling. When the pressure applied to the element is increased from 20 to 40 kg/dm², the cycle life is nearly doubled. However, even though the pressure is increased further beyond 40 kg/dm², the cycle life does not increase much and there is no difference in cycle life between 100 and 300 kg/dm².

Conclusions

Studies were carried out to determine whether structural changes in the positive active mass of

[2] Depth of discharge: about 75% of 5 hr-rate capacity.

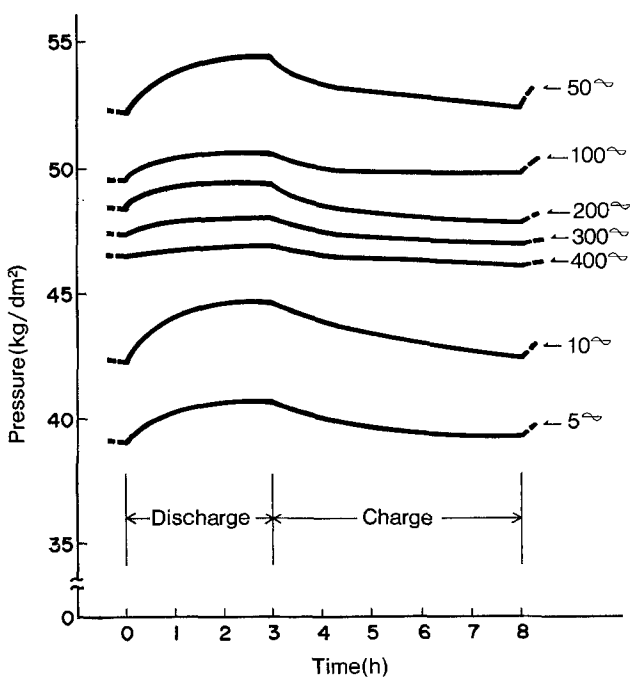

Fig. 13. Change in degree of pressure of test cell during charge and discharge.

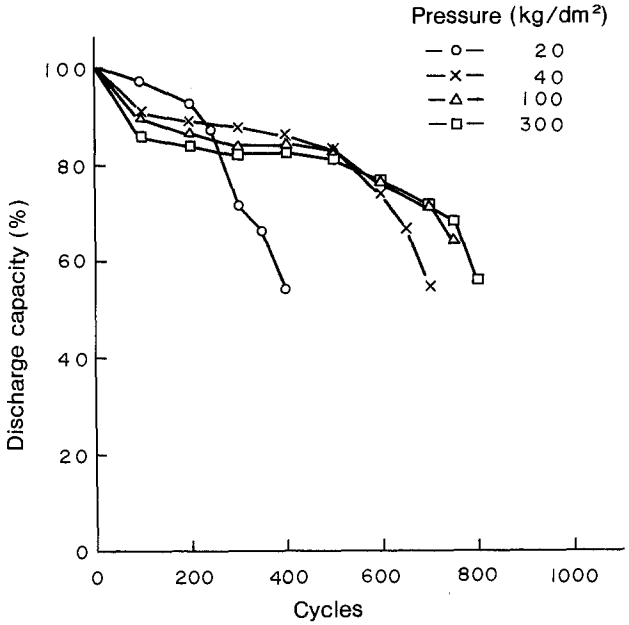

Fig. 14. Change in discharge capacity vs. cycles

a pasted-type lead-acid battery during deep charge and discharge cycles can be prevented by compression on the positive plates with glass mats. With high compression, the structural changes in the active mass become smaller and the cycle life of the cell increases remarkably.

The structural change takes place due to the stress caused mainly by the volume change of the active mass during charge and discharge cycling, and consequently the active mass gradually expands with cycling. The rate of expansion is higher in the early stages of cycle testing. Once the coralloid structure is formed, it absorbs the stress of the volume change. It is considered that the reason why the cycle life increases by compression is due to the suppression of structural changes in the positive active mass and the considerable suppression of the decrease in the cohesion between PbO_2 particles.

Manuscript submitted Nov. 29, 1982; revised manuscript received June 23, 1983. This was Paper 7 presented at the Detroit, Michigan, Meeting of the Society, Oct. 17-21, 1982.

Japan Storage Battery Company, Limited assisted in meeting the publication costs of this article.

REFERENCES

1. A. C. Simon and S. M. Caulder, in "Power Sources 5," D. H. Collins, Editor, p. 109, Academic Press, New York (1975).
2. S. M. Caulder, J. S. Murday, and A. C. Simon, *This Journal*, **120**, 1515 (1973).
3. S. M. Caulder and A. C. Simon, "Improving Vehicle Propulsion and Load Levelling Battery," ILZRO Project LE-255 (1977, 1978).
4. J. Bouet and J. P. Pompon, *Electrochim. Acta*, **26**, 1477 (1981).
5. K. J. Euler, *Bull. Schweiz. Elektrotechn. Ver.*, **61**, 1054 (1970).
6. H. Bode, "Lead-Acid Batteries," Translated by R. J. Brodd and K. V. Kordesch, p. 13, Wiley-Interscience, New York (1977).

High Speed Gold Plating: Anodic Bath Degradation and Search for Stable Low Polarization Anodes

C. G. Smith* and Y. Okinaka*

Bell Laboratories, Murray Hill, New Jersey 07974

ABSTRACT

Two kinds of anodic bath degradation occur in high speed gold plating: the oxidation of cyanoaurate(I) to cyanoaurate(III) ion resulting in a decrease in plating current efficiency, and the oxidation of citrate ion causing a loss of buffer capacity. These oxidation reactions can be minimized by replacing the conventional platinum or platinum-coated anode with a low polarization anode such as the so-called "dimensionally stable anode (DSA®)." However, the ordinary DSA with a coating consisting of RuO_2 and TiO_2 is not sufficiently stable under the conditions of this application. This paper describes results of three studies: *(i)* analysis of laboratory data for the rate of Au(III) accumulation to develop a method for predicting the concentration of Au(III) and plating current efficiency under scaled-up production conditions; *(ii)* analysis of the rate of degradation of citrate buffer capacity as a function of bath operating conditions; and *(iii)* an extensive search for a more stable low polarization anode, which led to the development of a coating consisting of IrO_2 and Ta_2O_5 with barium as the additive.

Gold plating technology has advanced significantly in recent years. Automated machines now plate gold selectively to minimize its usage, and at high speeds to maximize throughput and thus to minimize capital outlays. To maintain the process under high speed conditions, the control of plating bath characteristics becomes significantly more important. The degradation of bath characteristics occurs much more rapidly in high speed processes than in conventional low speed processes.

Two types of bath degradation have been found to take place. Both result from anodic reactions occurring at the conventional platinum or platinized titanium anodes. Oxidation of the cyanoaurate(I) ion to the cyanoaurate(III) ion leads to a decrease in current efficiency (1). The destructive oxidation of citrate buffers also occurs. Degradation products apparently do not affect the nature of the deposit (2). However, a hitherto unrecognized effect is a resultant loss of buffer capacity. As the initial capacity decreases, a point is eventually reached at which loss of control of the interfacial pH at the cathode occurs.

In the previous work (1, 3), it was shown that the rate of Au(III) formation is significantly lower at the so-called "dimensionally stable anode (DSA®)" (4). This well-known type of anode usually consists of a titanium substrate coated with a mixture of a precious metal oxide, such as RuO_2, and a valve metal oxide, typically TiO_2. The RuO_2-based anode,

* Electrochemical Society Active Member.
Key words: electrodeposition, electrode, kinetics.

however, has a limitation that its useful life is too short for practical high speed plating applications.

This paper is concerned with three aspects of high speed gold plating. (*i*) Laboratory data for the rate of Au(III) accumulation have been analyzed mathematically to derive expressions useful for extending laboratory results to scaled-up production conditions. (*ii*) The magnitude of loss of buffer capacity of citrate-based systems has been evaluated theoretically and experimentally. It is shown that citrate degradation occurs at a much lower rate on DSA than on a platinum anode. (*iii*) Mixed metal oxide coatings much more stable than the RuO_2-TiO_2 combination have been developed. It is shown that coatings consisting of IrO_2 and Ta_2O_5, particularly with barium as additive, provide electrodes with considerably extended lifetimes. Since the usefulness of these electrodes in gold plating results from their very low anodic polarizations (low oxygen overpotentials) as demonstrated in this communcation, they will be called "low polarization anodes."

Experimental

Plating apparatus and Au(III) analysis.—The rate of Au(III) accumulation during plating with various anode materials was measured for a high speed, additive-free hard gold (AFHG) bath operated at 40°C. This bath (5) consisted of a pH 7 phosphate buffer containing 100 g/liter KH_2PO_4 and 28 g/liter KOH, and 30 g/liter Au(I) added in the form of $KAu(CN)_2$. A polarographic method (6) was used to analyze the bath for total gold and Au(III). The plating apparatus has been described previously (1). The cathode was a copper cylinder rotating at 3600 rpm, and the anode a concentric cylinder 3 cm in inside diameter and 2 cm in height. The volume of the plating solution was 250 ml, and the temperature was maintained at 40°C by circulating water through a jacketed glass vessel. The bath was replenished every one-eighth turnover (a turnover defined as completed when the amount of gold initially present has been plated out and this amount of gold replenished) to limit a variation in total gold between 26 and 34 g/liter.

Measurement of citrate degradation.—The functional property of importance of a buffer is its buffer capacity, which characterizes the effectiveness with which a constant hydronium ion concentration is maintained. As the buffer capacity is proportional to the concentration of buffer, it can be expected that, in citrate-based gold plating baths, the buffer capacity will decrease as citrate ions are oxidized at the anode. In the present work, the decrease in buffer capacity, rather than the increase in degradation products, is considered as a measure of the degree of citrate degradation.

The rate of citrate buffer degradation was determined by measuring the "integral buffer capacity" as a function of electrolysis time. The integral buffer capacity, C_H, is defined as

$$C_H = C_b \int \frac{\beta}{C_{br}} dp\mathrm{H} \qquad [1]$$

where β is the buffer value (7) which is a differential ratio given by

$$\beta = \frac{db}{dp\mathrm{H}} \qquad [2]$$

where db is an increment of strong base in gram equivalents. A solution has a unit buffer value when a liter of it will take up 1g equivalent of strong alkali per unit increase in pH. Other symbols are explained in the list attached at the end of the text. Theoretically, the integral buffer capacity should be equal to the hydrogen content for the first three dissociation states of citric acid available to react with KOH and, therefore, can be calculated from the dissociation constants of citrate species. The values calculated for a total citrate concentration of 1M at different pH values are given in Table I. The integral buffer capacity for a given solution is obtained by multiplying these normalized values by the total citrate concentration. Thus, if the citrate concentration decreases due to the decomposition at the anode, the integral buffer capacity decreases proportionally. Experimentally, the integral buffer capacity as a function of electrolysis time was determined as follows. Eighty milliliters of a pH 4.5 mixture of 74 g/liter acid ($H_3C_6H_5O_7 \cdot H_2O$) and 111 g/liter base ($K_3C_6H_5O_7 \cdot H_2O$) was electrolyzed at 30°C in a 100 ml cell equipped with an anode (2 cm^2) and a large cylindrical stainless steel cathode (3 cm in diameter and 2 cm in height). Small samples were withdrawn at various times and titrated to pH 7.6 with 1M KOH.

Preparation of anodes.—Binary oxide anodes were prepared by thermal decomposition of coatings of chloride mixtures on titanium substrates (8). The chloride mixtures were prepared by mixing desired volumes of 0.06M platinum metal chlorides in 2.4M HCl and 0.06M valve metal chlorides in methanol. The titanium disks, 1.27 cm in diameter, formed at an end of titanium rods, were used as substrates for anode aging experiments. The substrates used for citrate degradation experiments were titanium sheets, 1 × 1 cm. In the Au(III) formation experiments titanium cylinders, 0.13 cm thick, measuring 3 cm in inside diameter and 2 cm in height were used. These substrates were dry honed and etched in 2.4M HCl at 70°C for 15 min immediately prior to application of coatings. Unless mentioned otherwise, oxide coatings were produced by first applying three coats of the chloride mixtures and baking at 450°C for 20 min, followed by repeating the process of chloride application and baking two additional times. The baking process converts the chlorides into oxides, and the temperature used will be called conversion temperature. The final baking was done for 1 hr. Ternary oxide anodes were prepared in the same manner with the addition of the third component in the form of either chloride or nitrate.

Anode aging experiments.—Accelerated aging tests were performed at 30°C by electrolyzing the pH 4.5 citrate buffer or the pH 7 phosphate buffer at a constant cell voltage. For convenience, four anodes were tested simultaneously in the same cell. A common, four-sided stainless steel cathode was used, and the anodes were each located with a 3 cm anode-cathode separation. Initial currents were adjusted with variable resistors in series with each anode.

Results and Discussion

Au(III) accumulation.—Rates of accumulation of Au(III) and resulting decreases in plating current efficiency are shown in Fig. 1. The anode current density used was approximately 150 mA/cm^2. These results are similar to those presented earlier (1),

Table I. Calculated integral buffer capacity of 1M citrate at various pH values

(pK values used: $pK_1 = 3.13$, $pK_2 = 4.76$, $pK_3 = 6.40$)

pH	H_3R (M)	H_2R^- (M)	HR^{-2} (M)	R^{-3} (M)	Integral buffer capacity*
4.5	0.07	0.61	0.32	0.004	1.74
5.0	0.01	0.36	0.61	0.02	1.36
5.5	0.002	0.14	0.76	0.10	1.04
7.0	0.0	0.001	0.20	0.80	0.20

* The units are mols of H per liter (per mol of citrate).

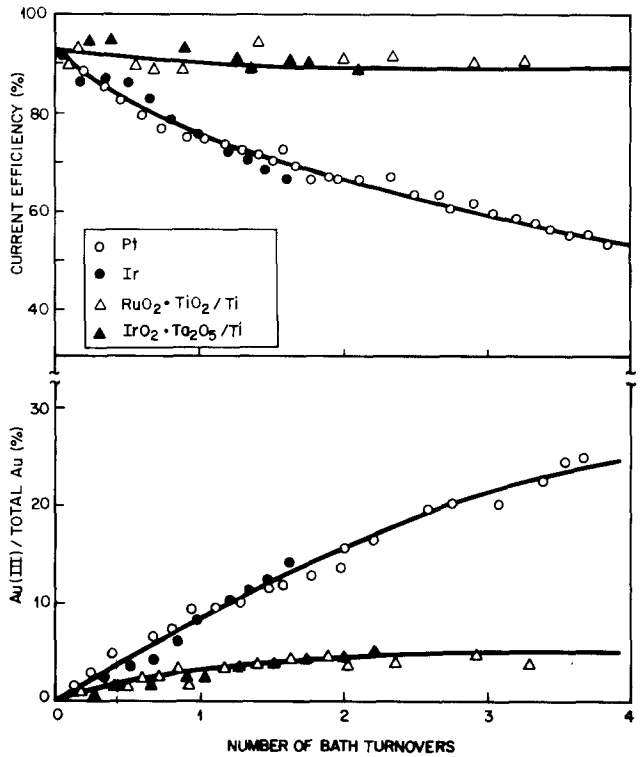

Fig. 1. Accumulation of Au(III) during gold plating from AFHG bath with various anodes and corresponding decrease in plating current efficiency. (Anode current density, 150 mA/cm².)

with additional results for a 50:50 Ir:Ta oxide coated anode and an iridium metal anode. For a fraction p of the total gold existing as Au(III), the current efficiency η is given by

$$\eta = \frac{1}{1 + 2p} \qquad [3]$$

A surprising result is that while the IrO_2-Ta_2O_5 anode gave a low Au(III) accumulation rate similar to that observed with the RuO_2-TiO_2 anode, the accumulation rate with iridium metal was identical to that with platinum. Figure 2 shows polarization curves for oxygen evolution in the citrate buffer (30°C, pH 4.5). The shift to high potentials for the iridium metal anode is possibly due to the formation of a passive surface film. These results support the interpretation proposed previously (1) that the faster accumulation of Au(III) observed with the platinum anode results from the higher potential at this anode.

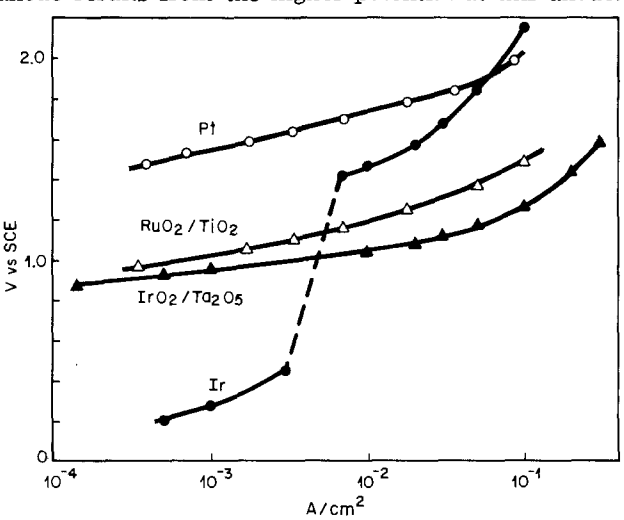

Fig. 2. Polarization curves for oxygen evolution at various anodes. (Citrate buffer, pH 4.5, 30°C, 50:50 active metal to binder metal oxides.)

The rate of Au(III) formation in grams per hour for a given plating system can be calculated from the experimental results presented in Fig. 1 by considering the differential mass balance for Au(III) in the plating system. The observation that the accumulation rate of Au(III) depends on anode potential implies that its formation rate at the anode is independent of Au(I) concentration above a certain critical concentration. With this assumption, the mass balance gives.

$$\frac{\partial(pC_{au}{}^{*}V)}{\partial t} = F_a - v_d p C_{au}{}^{*} - \frac{3600IM}{F}\frac{p}{1 + 2p} \qquad [4]$$

This equation is not valid for very low Au(I) concentrations, where p approaches unity, and the formation rate would approach zero. The second term on the right represents Au(III) lost to dragout. The last term is for the reduction of Au(III) to Au at the cathode and was derived by assuming that the reductions of Au(I) and Au(III) to Au are the only reactions that must be considered, and that Au(I) and Au(III) reduction rates are both mass transport limited. Assuming further that the total gold concentration $C_{au}{}^{*}$ is constant, the equation is nondimensionalized by using the dimensionless time T

$$T = t/\alpha_0\,; \quad \alpha_0 = \frac{C_{au}{}^{*}V}{7.35I} \qquad [5]$$

The characteristic time α_0 is the time it takes to complete one turnover of gold at 100% current efficiency. Substitution of T gives

$$\frac{dp}{dT} = C_1 - C_2 p - \frac{p}{1 + 2p} \qquad [6]$$

The constants in Eq. [6] are

$$C_1 = \frac{F_a}{7.35I}\,; \quad C_2 = \frac{v_d C_{au}{}^{*}}{7.35I} \qquad [7]$$

The constant C_2 is the dragout in fraction of the total electrolyte volume per turnover. The experimental results indicate that at large T, p approaches a steady-state value. This steady-state value, p_{ss}, can be obtained from Eq. [6]

$$p_{ss} = \frac{[C_4{}^2 + 8C_1C_2]^{1/2} - C_4}{4C_2} \qquad [8]$$

where the constant C_4 is

$$C_4 = 1 + C_2 - 2C_1 \qquad [9]$$

An approximation to Eq. [6], which should be valid for small p, is

$$\frac{dp}{dT} = C_1 - (1 + C_2)p \qquad [10]$$

With the initial condition $p = p_i$ at $T = 0$, the solution to Eq. [10] is

$$p = C_3 + (p_i - C_3)\exp(-(1 + C_2)T) \qquad [11]$$

where the constant C_3 is defined by

$$C_3 = \frac{C_1}{1 + C_2} \qquad [12]$$

Equations [11] and [12] are suitable for determining rates. For zero dragout ($v_d = 0$ and hence $C_2 = 0$ and $C_3 = 3C_1$), and with no initial Au(III) ($p_i = 0$), Eq. [11] can be rearranged to give

$$F_a = \frac{7.35Ip}{1 - e^{-T}} \qquad [13]$$

Experiments were conducted under the conditions described above for three anodes: platinum, a 35:60:5

Ir:Ta:Ba composition, and a 65:30:5 Ir:Ta:Ba composition. The anode current density was varied from 35 to 210 mA/cm². The Au(III) percentage, p, at one-half turnover was substituted into Eq. [13] to determine formation rates. The formation rate was normalized by the anode area, and these results are presented in Fig. 3. The rate varies linearly with current density for platinum between 30 and 250 mA/cm² and for the Ir-Ta-Ba anodes below 75 mA/cm².

To estimate Au(III) accumulation in a production facility, an electrolyte volume of 80 liters, an anode area of 800 cm², and total machine currents of 12 and 20A will be considered. The rate of Au(III) formation, F_a, corresponding to these conditions was calculated for various anodes using the data in Fig. 3. These results are presented in Table II.

Equation [6] was solved numerically using the Runga-Kutta-Gill algorithm (9, 10). The results for the platinum and 35% Ir oxide anodes, with a gold concentration of 30 g/liter and 5% dragout per turnover, are presented in Fig. 4. Also shown is the accumulation of Au(III) predicted by the approximate Eq. [11]. The approximate analytical solution agrees with the exact numerical solution up to one-half turnover, which validates the procedure used to determine rates. While the steady-state value predicted from Eq. [11] agrees quite well for low formation rates, characteristic of the iridium oxide anode, the value for large formation rates is a very poor approximation. Therefore, the steady-state value given by Eq. [8] should always be used. Steady state is obtained after about five turnovers. The exponential term in Eq. [11] could be used as an approximation for the time to reach steady state.

The effect of dragout in reducing Au(III) accumulation as calculated by using Eq. [6] is illustrated in Fig. 5. The difference in steady-state values for 5 and 10% dragout per turnover is relatively small. The formation of Au(III) at the anode is balanced chiefly by its reduction at the cathode.

Steady-state values of Au(III) for the platinum, 35% Ir and 65% Ir oxide anodes are presented in Table III. The difference between the 35 and 65% iridium oxide anodes is relatively minor, compared with the steady-state values for the platinum anode.

Citrate buffer degradation.—Figure 6 shows the percentage of the initial integral buffer capacity as a function of electrolysis time at an anode current density of 100 mA/cm². Under the accelerated conditions of this experiment (see Experimental section) all of the citrate was decomposed after 24 hr with the platinum anode, while no change was apparent with the IrO_2-Ta_2O_5 anode. Rate constants for the buffer degradation at the platinum anode are presented in Table IV.

For actual plating baths, changes in the citrate concentration and hence in the buffer capacity result from three factors: degradation at the anode, loss by

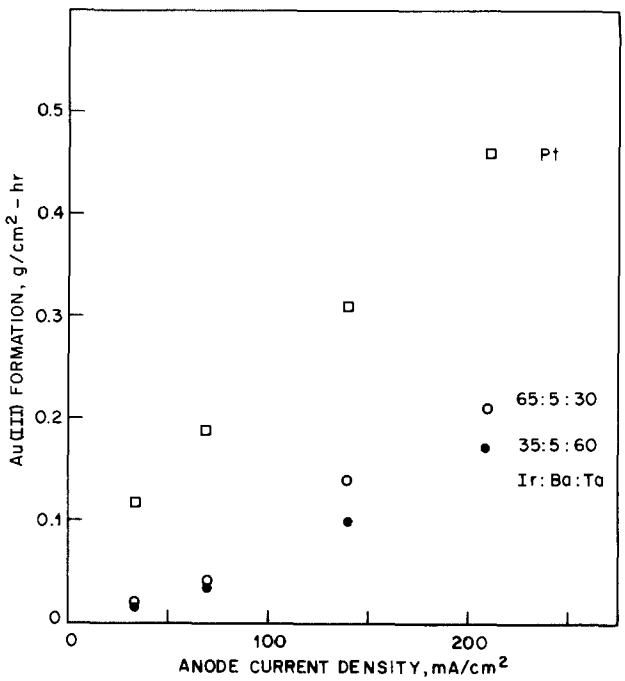

Fig. 3. Au(III) formation rates for various anodes. (AFHG bath, 30 g/liter Au, pH 7.0, 40°C.)

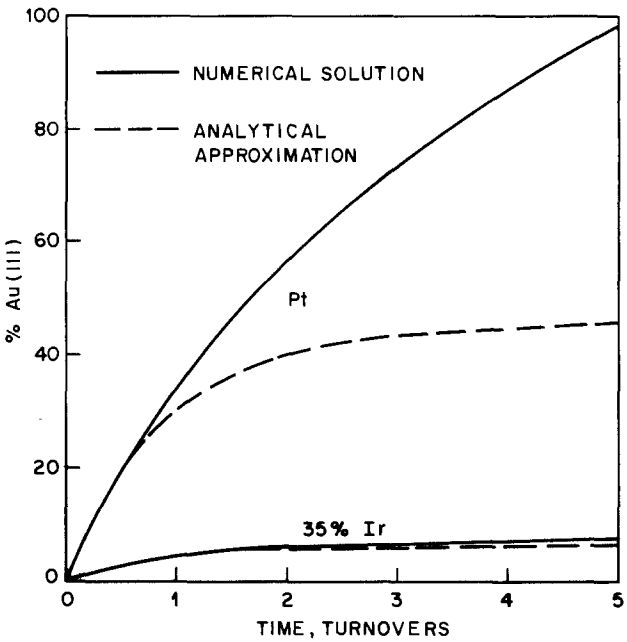

Fig. 4. Au(III) accumulation predicted from exact numerical solution to Eq. [6] and from approximate analytical solution, Eq. [11]. (Formation rate, F_a, given in Table II. Electrolyte volume 80 liters, 12A plating current, 30 g/liter Au.)

Table II. Au(III) formation rates

I (A)	Anode*	F_a (g/hr)
12	35:60:5 Ir:Ta:Ba	6.06
20	35:60:5 Ir:Ta:Ba	9.47
12	65:30:5 Ir:Ta:Ba	7.13
20	65:30:5 Ir:Ta:Ba	11.14
12	Pt	42.7
20	Pt	67.1

* Area, 800 cm².

Table III. Steady-state Au(III) percentages (p_{ss}) and plating current efficiencies (η)*

I (A)	Anode	Dragout (%)	p_{ss} (%)	η (%)
20	35% Ir	5.0	6.8	88
20		10.0	6.5	88
12		5.0	7.4	87
12		10.0	7.0	87
12	65% Ir	5.0	8.7	86
12		10.0	8.4	86
20	Pt	5.0	90.1	36
20		10.0	81.1	38
12		5.0	98.5	34
12		10.0	88.5	36

* Steady state achieved after five turnovers. Values of p_{ss} calculated using numerical solution to Eq. [6] and F_a values given in Table II. Current efficiencies calculated from Eq. [3].

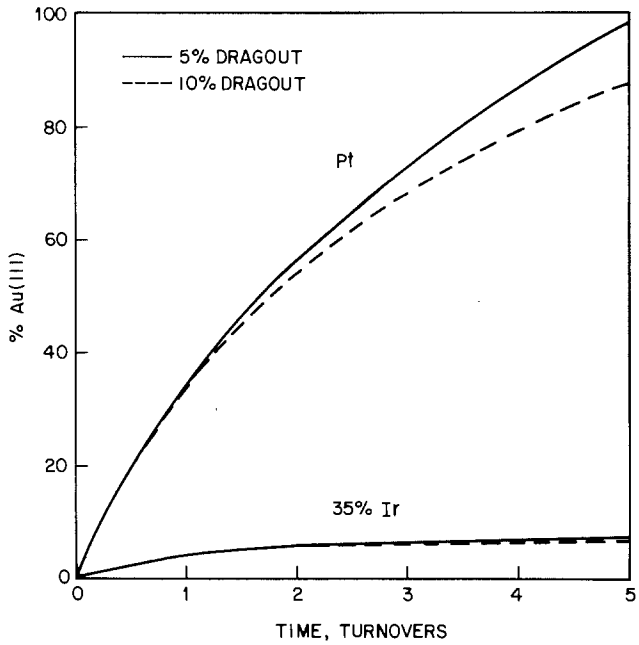

Fig. 5. Variation of Au(III) accumulation with dragout. (Solid curve, 5% per turnover; dashed curve, 10% per turnover. Electrolyte volume 80 liters, 12A plating current, 30 g/liter Au.)

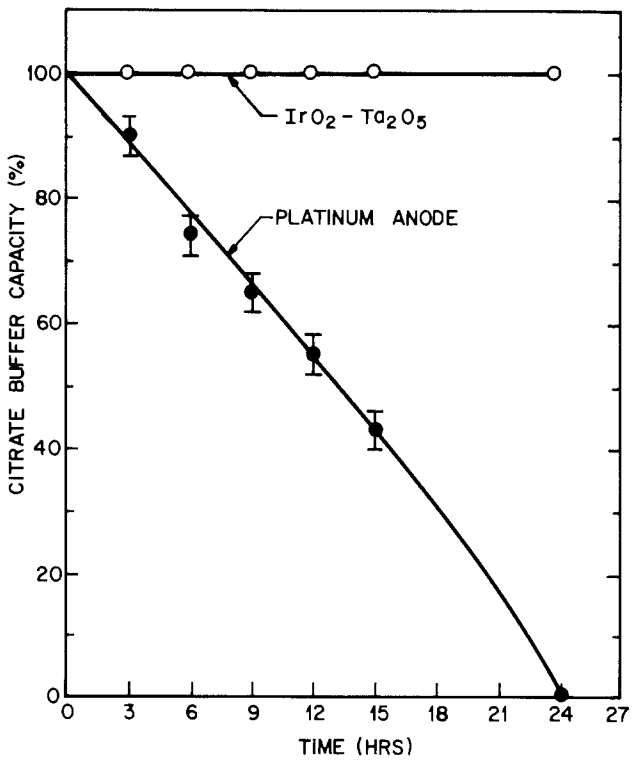

Fig. 6. Degradation of citrate during electrolysis with 50:50 Ir:Ta oxide anode. (Citrate buffer, pH 4.5, 30°C, 80 ml volume, anode current density 100 mA/cm². The ordinate is the percent of the integral buffer capacity.)

dragout of the plating solution, and addition of citric acid, which is made to maintain pH. A mass balance including these three contributions can be used to predict the change in citrate concentration with time. It should be noted that the experimentally determined rate constants presented in Table IV characterize only the anodic degradation. Dragout rates vary with the plating system and also need to be determined experimentally. The rate of citric acid addition is related to the cathodic current efficiency as shown below.

Table IV. Rate of citrate oxidation at Pt anode

i (mA/cm²)	Oxidation rate (mols/hr-cm²)	k_a* (mols/hr-A)
50	0.00023	0.0023
100	0.00048	0.0048
200	0.00142	0.0142

* K_a (Eq. [16]) $= k_a(I/A)A = k_aI$.

The cathodic current efficiency of a citrate-based, cobalt-containing gold plating bath can be as low as 35%, even in the absence of Au(III) (1). The low efficiency in this case is due to simultaneous hydrogen evolution. To estimate the rate of citric acid addition required to maintain pH, it is assumed that the only cathodic processes involved are Au(I) reduction and hydrogen evolution. The Au(III) formation and its reduction will not be considered here. The overall change in hydronium ion concentration is due to three processes: (*i*) hydrogen evolution, (*ii*) formation of HCN from CN^- liberated from the $Au(CN)_2^-$ complex, and (*iii*) acid formation accompanying oxygen evolution at the anode. The net change can be related to the current efficiency and system amperage as

$$\Delta H^+ = j_3 - j_1 - j_2 = \frac{I}{F}[1 - (1 - \eta) - 2\eta] = -\frac{\eta I}{F} \qquad [14]$$

where the subscripts 1, 2, and 3 refer to the above three processes, respectively. To balance this net loss of hydronium ions, citric acid is added. In view of the fact that citric acid has three dissociatable hydrogen atoms, the rate of citric acid addition necessary to maintain pH is given by

$$j = \frac{3600}{3F}\eta I = 0.0124\eta I \quad \text{mol/hr} \qquad [15]$$

As already mentioned, the change in total citrate concentration results from addition of citric acid, degradation at the anode, and loss by dragout. The differential mass balance for these three contributions is

$$\frac{\partial C_b V}{\partial t} = 0.0124\eta I - K_a - v_d C_b \qquad [16]$$

Substituting the dimensionless concentration θ and time T defined as

$$\theta = \frac{C_b}{C_{bo}}; \quad T = \frac{t}{\alpha} \qquad [17]$$

into Eq. [16] yields

$$\frac{\partial \theta}{\partial T} = \frac{0.0124\alpha\eta I}{C_{bo}V} - \frac{\alpha K_a}{C_{bo}V} - \frac{\alpha v_d}{V}\theta \qquad [18]$$

By defining α in turnovers of gold as in Eq. [5]

$$\alpha = \frac{C_{au}^* V}{7.35I\eta} \qquad [19]$$

Eq. [18] becomes

$$\frac{\partial \theta}{\partial T} = K_4 - K_3\theta \qquad [20]$$

The constants in Eq. [20] are

$$K_3 = \frac{C_{au}^* v_d}{7.35I\eta}; \quad K_4 = K_1 - K_2 \qquad [21a]$$

where

$$K_1 = \frac{0.0124C_{au}^*}{7.35C_{bo}}; \quad K_2 = \frac{K_a C_{au}^*}{7.35I\eta C_{bo}} \qquad [21b]$$

The solution to Eq. [20] with the initial condition $\theta(t = 0) = 1$ is

$$\theta = \frac{K_4}{K_3} + \left[1 - \frac{K_4}{K_3}\right] \exp(-K_3 T) \qquad [22a]$$

From Eq. [1] it can readily be shown that the dimensionless concentration θ is also a dimensionless integral buffer capacity. As the reference concentration C_{bo} is chosen as the initial citrate concentration, θ is the dimensionless capacity relative to the initial value. The integral buffer capacity at a given pH can be obtained by multiplying θ by the initial buffer capacity, which is the product of the normalized capacities given in Table I and the initial buffer concentration

$$C_H = \theta C_{bo} \int \frac{\beta}{C_{br}} dpH \qquad [22b]$$

Equation [22] should be useful for the application of the degradation rates given in Table IV to production conditions. For the purpose of illustration, the dragout rate is chosen to maintain a constant salt concentration in the plating bath by balancing the rate of citric acid addition with dragout

$$v_{de} C_b = 0.0124 \eta I \qquad [23a]$$

Combining Eq. [23a] with the expression for K_3 (Eq. [21a]) yields

$$K_3 = 0.0169 \frac{C_{au}^*}{C_{bo}} \qquad [23b]$$

It should be noted from a comparison of Eq. [18] and Eq. [20] that K_3 is the dragout ratio per turnover. For a gold content of 30 g/liter and an initial total citrate concentration of 1M, Eq. [23b] yields $K_3 = 0.051$, indicating that a dragout of 5.1% per turnover is required to maintain the citrate concentration constant. At smaller dragout rates, the buildup of salts would eventually cause components to precipitate out.

At current densities lower than 100 mA/cm^2, the degradation rate is linear with current density (Table IV). When the current is expressed in amperes, we may write

$$K_a = 0.0048 I \qquad [24]$$

As an approximation for greater current densities, it is assumed that a second linear region lies between 100 and 200 mA/cm^2. In this region

$$K_a = 0.0094 I - 0.00046 A \qquad [25]$$

A gold plating system is now considered with 30 g/liter Au, an initial citrate concentration of 1M, an anodic current density less than 100 mA/cm^2, and the dragout for maintaining constant citrate concentration equal to 5.1% per turnover. Equations [22] and [24] yield

$$\theta = 1 - \frac{0.39}{\eta} + \frac{0.39}{\eta} e^{-0.051 T} \qquad [26]$$

Integral buffer capacities as a function of time are presented in Fig. 7 for cathodic current efficiencies of 80, 60, and 30%. It is seen that with Pt anode the buffer capacity for efficiencies of 60 and 80% eventually reaches a greatly reduced steady-state value after approximately 60 turnovers. At 30% efficiency, the capacity rapidly drops to zero. The capacity of a plating system using IrO_2-Ta_2O_5 anodes remains constant, because citrate does not degrade at these electrodes.

Search for stable low polarization anodes.—The RuO_2-TiO_2 anode has gained wide-spread usage in the chlor-alkali industry (4, 8). In this application, the predominant anode reaction is the evolution of chlorine, and the electrode is very stable. However, when this electrode is used in electrolysis systems where the anode reaction is oxygen evolution (such as in the gold plating), the useful life of the electrode is limited because of the increase in electrical resistivity with use (8).

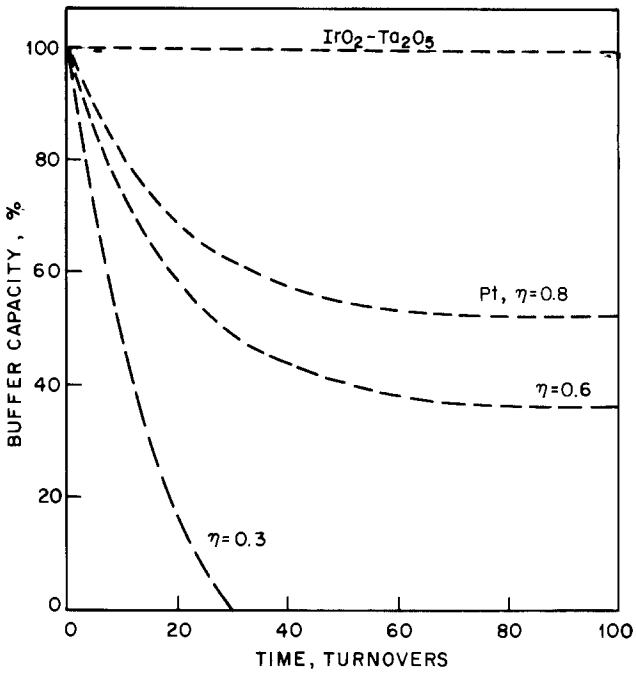

Fig. 7. Decrease in integral buffer capacity with time for various cathodic current efficiencies, η. (Initial total citrate concentration 1M, 30 g/liter Au, 5.1% per turnover dragout, anodic current density < 100 mA/cm^2.)

Two properties of the anode coatings are important. The electrode should have a low potential for oxygen evolution to minimize bath degradation. The coating should also exhibit good electrical conductivity to be useful at high current densities. Many metal oxides have multiple valence states. It is expected that the minimum potential required for oxygen evolution is the equilibrium potential of the lower oxide/higher oxide couple (11). Literature values for this potential as well as the type of conductivity of the oxides are given in Table V. The oxide couples indicated are attainable during anodic polarization. In addition, Ru(IV) is oxidized to Ru(VIII) at 1.39V, and Ir(IV) is oxidized to Ir(VI) at 2.06V (*vs.* the normal hydrogen electrode). These data indicate that Ir, Os, Ru, Ni, and Co should exhibit lower potentials for oxygen evolution than Pt, Rh, or Pd. Osmium was excluded from study because of the very low (130°C) boiling point of OsO_4. Nickel and cobalt oxides were not investigated because of their poor conductivity (11).

Binary oxides.—The four platinum group metal oxides chosen as being representative of active oxides were those of Ir, Ru, Rh, and Pt. Oxides of five valve metals, Ti, Ta, Nb, Hf, and Zr were selected as binders.

Figure 8 shows representative current-time behavior observed with various binary oxide systems. Initial current densities were adjusted to 200 mA/

Table V. Redox potentials and conductivity types of metal oxide couples

Oxide couple	E *vs.* NHE (V)*	Conductivity type
Ir_2O_3/IrO_2	0.93	Metallic**
Ru_2O_3/RuO_2	0.94	Metallic**
OsO_2/OsO_4	1.00	Metallic**
Ni_2O_3/NiO_2	1.43	Semiconductor*
Co_2O_3/CoO_2	1.45	Semiconductor*
Rh_2O_3/RhO_2	1.73	Semiconductor**
PtO_2/PtO_3	2.00	Semiconductor**
PdO_2/PdO_3	2.03	Semiconductor**

* Ref. (11).
** Ref. (12).

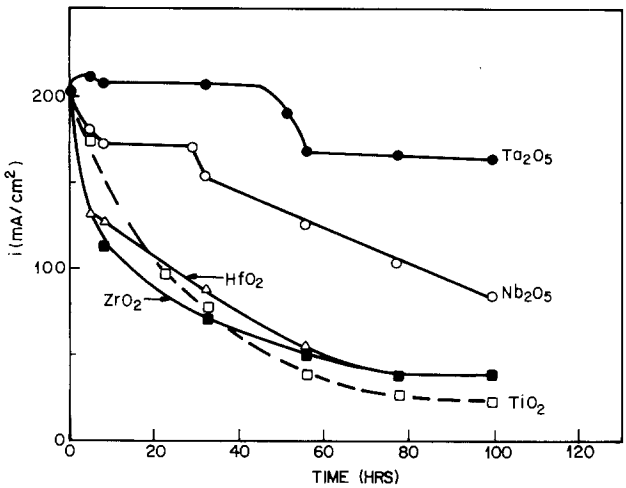

Fig. 8. Stability of iridium oxide-valve metal oxide anodes. (50 m/o IrO_2, citrate buffer, pH 4.5, 30°C.)

cm² for anodes containing Ir and Rh and 150 mA/cm² for those containing Ru and Pt. In the constant cell voltage experiments, anode degradation is indicated by a decrease in current density. Relative electrode stabilities for twenty different binary systems are given in Table VI. Iridium oxide was found to be the most stable active oxide for this application. In addition, the active metal oxide-binder metal oxide combination is extremely important. The Ir-Ta oxide system has the greatest stability under the conditions used. It should be noted that this system is also known to be highly stable in sulfuric acid (13).

For the Ir-Ta system, four factors have been found to have major effects on electrode stability: coating thickness, current density, composition of the coating, and free cyanide in the plating bath. Tests were conducted at the initial current density of 100 mA/cm² in the citrate buffer with the 50:50 Ir:Ta composition. Electrode life was defined as the time at which the current density drops to one-half of its initial value. The energy dispersive x-ray spectrometer (EDAX) attachment to the scanning electron microscope was used to characterize film thickness. The intensity of the detected signal is proportional to the amount of iridium present in the volume of the coating per unit area. The ratio of the major Ir peak to the major Ti substrate peak was selected as a measure of the coating thickness for the same coating

Table VI. Stability of binary metal oxide anodes*

Active oxide	Binder oxide	i (t = 0) (mA/cm²)	i (t = 50 hr) (mA/cm²)
IrO_2	Ta_2O_5	200	200
	Nb_2O_5	200	134
	HfO_2	200	62
	ZrO_2	200	54
	TiO_2	200	46
RhO_2	Ta_2O_5	200	147
	Nb_2O_5	200	58
	HfO_2	200	42
	ZrO_2	200	30
	TiO_2	200	30
RuO_2	HfO_2	150	82
	TiO_2	150	46
	Ta_2O_5	150	46
	Nb_2O_5	150	10
	ZrO_2	150	10
PtO_2	Nb_2O_5	150	20
	HfO_2	150	13
	Ta_2O_5	150	11
	TiO_2	150	4
	ZrO_2	150	4

* Citrate buffer (30°C, pH 4.5), 2 μm thick films, 50:50 molar ratio of active oxide to binder oxide.

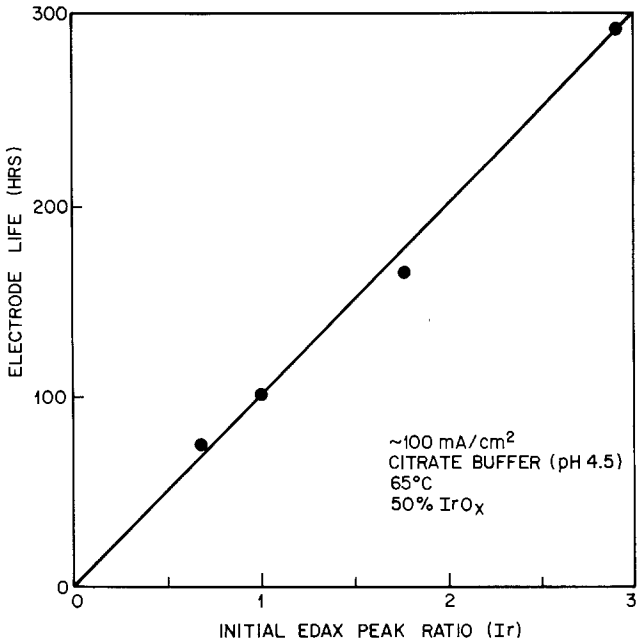

Fig. 9. Electrode life as a function of coating thickness. (50:50 Ir:Ta, citrate buffer, pH 4.5, 65°C, 100 mA/cm².) (EDAX ratio is the ratio of major Ir peak to major Ti peak, normalized by the value giving 100 hr of electrode life.)

composition, and it is plotted against the electrode life in Fig. 9, in which the initial peak ratio of 3 corresponds to 1 μm in thickness as calculated from the amount of the coating material applied and bulk densities of the oxides. At least for thin films, electrode life is directly proportional to film thickness.

A critical current density has been observed for ruthenium-based anodes (14). At electrode potentials above the potential corresponding to this critical current, RuO_2 is oxidized to higher valence species. A similar critical current density was found to exist for IrO_2. Figure 10 shows that above approximately 300 mA/cm², the Ir-Ta system is unstable. Below the critical value, electrode life is not strongly dependent on current density.

Electrode life depends greatly on the Ir:Ta ratio in the oxide mixture. Life tests were performed in the citrate buffer at 65°C and in the phosphate buffer

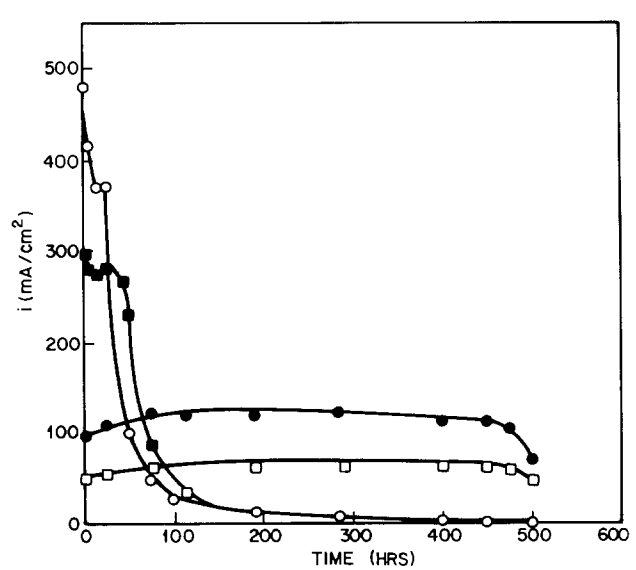

Fig. 10. Stability of Ir-Ta binary oxide anodes as a function of initial current density. (50:50 Ir:Ta, citrate buffer, pH 4.5, 65°C.)

at 40°C, and the results are shown in Table VII. The initial current density was 200 mA/cm². In the phosphate buffer a 70 mol percent (m/o) Ir composition gave the longest life, while in the citrate buffer a 40 m/o Ir composition was most durable. The amount of iridium in the coatings was normalized by dividing the major Ir peak by the major Ti substrate peak. A second normalization, which was made to allow comparison of electrode service life independent of coating thickness, was to divide the Ir/Ta ratio by the ratio for the composition giving the longest service life.

Free cyanide is liberated from the cyanoaurate(I) complex at the cathode during gold plating. This cyanide escapes relatively rapidly from the bath as HCN at *p*H 4.5, but can accumulate significantly at *p*H 7.0, especially in high speed plating conditions. Experience with a phosphate-buffered bath indicates that the concentration can build to about 0.2 g/liter CN^-. To observe the effect of free cyanide, tests were performed in the phosphate buffer with a concentration of 0.5 g/liter. These results are also presented in Table VII. It is seen that the electrode stability is greatly reduced. Ternary metal oxide systems were subsequently investigated in order to overcome this problem.

Ternary oxide systems.—To determine which ternary systems would be more resistant to free cyanide than the binary Ir-Ta system, a mol ratio of 60:40 Ir:Ta, which had the minimum stability in Table VII, was used. With a 10% additive level, this yields a 54:36:10 Ir:Ta:additive composition. As IrO_2 is the dominant active component of the film, it is necessary to find an additive which stabilizes the IrO_2 phase of the oxide mixture. A preferred class of additives would be those which form mixed metal oxides with iridium. Alkaline earth and rare earth metals (group IIa and group IIIb) are known to form iridates (7). A second class of additives would be those which form solid solutions of oxides, of which the IrO_2-SnO_2 system is an example. A third criterion used was the solubility product of the metals with OH^- anions (less soluble oxides would be more stable). Metals in groups VIb, VIIb, IIb, IIIb, and IVa, tend to form insoluble oxides.

Life tests were performed in the *p*H 7 phosphate buffer containing 0.5 g/liter CN^- at 40°C with an initial current of 150 mA/cm². Addition of oxides of other group VIII metals, Ru, Co, Ni, Rh, Pd, and Pt, gave shorter electrode lives. Furthermore, effects of the addition of Mg, Ca, Sr, Ba, Li, K, Cs, Cr, Mn, Fe, Cd, Ga, In, Tl, Ge, Sn, Bi, Sc, Y, La, and Ce were investigated. After 20 hr, only electrodes containing Ba, Ca, Cr, Sc, or Sn had current densities at least equal to the initial value of 150 mA/cm². Of these, chromium and tin were found to have a detrimental catalytic effect; the electrode potential was higher in the presence of these elements than in their absence. It was concluded that the preferred additive for the Ir-Ta system is barium. Life tests indicated that 5-20 m/o compositions of barium are useful under high speed gold plating conditions. With an approximate loading of 0.1 mg/cm² of iridium, an electrode life of 275 hr was obtained at 100 mA/cm² for a composition of 50:40:10 Ir:Ta:Ba as compared to 30 hr in the absence of barium.

Use of a conversion temperature (see Experimental section) of 450°C was found to be critical for good electrode stability, as shown in Table VIII. Samples were prepared for x-ray powder diffraction measurements by converting metal chlorides to oxides on a quartz substrate. Conversion temperatures of 450° and 350°C were used, followed by final baking at 450°C for 1 hr. Table IX presents results for the conversion temperature of 450°C and the compositions of 50:50 Ir:Ba and 50:40:10 Ir:Ta:Ba. The majority of d-spacings for the Ir-Ba samples are not found in the JCPDS listings for the distinct oxides IrO_2 or BaO, indicating that a new compound is formed, presumably $BaIrO_3$. The 50:40:10 Ir:Ta:Ba sample yielded d-spacings corresponding to IrO_2 and the tentatively identified barium iridate. When the conversion temperature of 350°C was used, no $BaIrO_3$ was observed. Distinct BaO was present in oxides containing 50:20:30 Ir:Ta:Ba as indicated by d-spacings at 3.11 and 2.77Å. The amount of BaO

Table VII. Stability of Ir-Ta oxide anodes

Mol % Ir	Bath	Ir*/Ti (EDAX ratios)	Ir**/Ti (EDAX ratios)	Life (hr)	Life*** (hr)
40	Phosphate(a)	1.34	1.08	515	477
50		1.57	1.26	350	223
60		2.35	1.88	460	245
70		1.25	1.00	725	725
40	Citrate(b)	0.11	1.00	425	425
50		0.08	1.38	262	190
60		0.12	0.92	33	36
70		0.07	1.57	29	19
40	Phosphate(c)	0.60	0.94	40	43
50		0.44	0.69	22	32
60		0.82	1.28	65	51
70		0.64	1.00	106	106
80		0.83	1.30	70	54
85		0.62	0.97	26	27
90		0.34	0.53	75	144

* Normalization for Ir content using ratio of major EDAX peaks, Ir to Ti (substrate).
** Ir/Ta ratio relative to ratio giving longest service life.
*** Normalized life obtained by dividing actual life by Ir**/Ta ratio.
(a) *p*H 7.0, no CN^-, 40°C.
(b) *p*H 4.5, no CN^-, 65°C.
(c) *p*H 7.0, 0.5 g/liter CN^-, 40°C.

Table VIII. Effect of conversion temperature on electrode stability in cyanide-containing phosphate buffer

(50 m/o Ir, 10 coats, final bake for 1 hr at 450°C, initial current 150 mA/cm², 0.5 g/liter CN^-, *p*H 7.0, 40°C.)

Mol % Ta	Mol % Ba	Conversion temperature (°C)	i (t = 50 hr) (mA/cm²)
50	0	350	55
40	10	350	39
50	0	450	85
40	10	450	124

Table IX. X-ray powder diffraction data

(Sweep rate, 1 deg/min; time constant, 40; 45 kV; 14 mA; copper K_α radiation.)

Ir:Ba 50:50		Ir:Ta:Ba 50:40:10		IrO_2*	BaO*
d (A)	I/I₁	d (A)	I/I₁	d (A)	d (A)
5.53	68	5.57	14		
4.17	39	4.21	16		
3.91	37	4.02	12		
3.39	19				
3.20	100	3.20	74	3.18	3.20
3.05	90	3.06	38		3.11
2.85	42	2.86	26		2.77**
2.59	79	2.60	100	2.58	2.59
2.49	57	2.50	24		
2.41	55	2.41	19		
2.35	73	2.35	18		
2.25	81	2.28	22	2.25	2.23
2.00	21				2.12
1.98	25				1.96**
					1.81
		1.71	29	1.70	1.68
		1.59	14	1.59	1.55
					1.50
		1.42	16	1.42	1.40
				1.35	1.33
				1.29	1.24

* d-spacings for IrO_2 and BaO taken from JCPDS files 15-870 and 26-176A (or 22-1056 as indicated by **), respectively.

formed appears dependent on the preparation conditions. The use of lower conversion temperatures and thicker metal chloride layers results in an increase in the amount of BaO and a consequent decrease in the amount of $BaIrO_3$. The observed compound formation between barium and iridium is believed to be responsible for the stabilizing effect.

Conclusions

Two types of plating bath degradation occur at significant rates on conventional platinum or platinized titanium anodes in high speed gold plating processes. The oxidation of Au(I) to Au(III) can lead to a rapid decrease in plating current efficiency. In the AFHG bath the initial value of 100% can decay to 33% after only six turnovers. In citrate-buffered baths, the oxidation of citrate ions results in a loss of buffer capacity and subsequently a loss of control of the interfacial pH at the cathode. The theoretical analysis presented indicates that the most important parameter influencing the integral buffer capacity is the cathodic current efficiency, because, in the citrate system, the cathodic hydrogen evolution is the major cause of plating inefficiency. When additives such as cobalt are used as hardening agents, the cathodic current efficiency can be as low as 35% because of preferential hydrogen evolution. With such a low cathodic efficiency, loss of control of the interfacial pH can occur very rapidly.

The rates of oxidation of both Au(I) and citrate ions are much smaller at DSA-type low polarization anodes. For the additive-free hard gold bath the steady-state percentage of Au(III) occurring in a process using these anodes is 8% with a cathodic current efficiency of 85%. At these anodes the rate of citrate degradation is essentially zero, and citrate-based baths are stable at all current efficiencies.

A low polarization anode with RuO_2 as the active oxide is unstable for high speed gold plating applications. Anodes containing IrO_2 have a much longer service life. In particular, the three-component system Ir-Ta-Ba has a superior service life. Based on x-ray diffraction studies, the effect of Ba addition is attributed to the formation of a compound between BaO and IrO_2, presumably $BaIrO_3$.

Manuscript submitted Jan. 18, 1983; revised manuscript received June 14, 1983. This was Paper 374 presented at the Hollywood, Florida, Meeting of the Society, Oct. 5-10, 1980.

Bell Laboratories assisted in meeting the publication costs of this article.

LIST OF SYMBOLS

A	anode area, cm^2
C_{au}	gold(I) concentration in mols/liter
C_{au}^*	total gold concentration in g/liter
C_b, C_{bo}	citrate concentration, mols/liter. The subscript o refers to the initial concentration
C_{br}	reference buffer concentration for integral buffer capacity definition, 1M citrate
C_H	integral buffer capacity, mols H^+/liter
$\mathbf{F}$	Faraday constant, 96,500 C/mol-equiv.
F_a	Au(III) formation rate, g/hr
f_a	Au(III) formation rate per unit anode area, g/hr-cm^2
I	total plating current, A
j	flux to electrode surface
K_a	rate of citrate degradation, mols/hr
k_a	rate of citrate degradation per unit anode area, mols/hr-cm^2
M	atomic weight of gold (= 197)
m	multiplier to v_{de}
p	fraction of total gold as Au(III)
T	dimensionless time; t/α
v_d	dragout rate, liters/hr
v_{de}	dragout rate to balance citric acid addition
V	volume of plating solution, liters
α, α_o	reference time, hr/turnover
β	buffer value, mols H^+/liter
η	cathode current efficiency for Au(I) plating
θ	dimensionless buffer concentration, C_b/C_{bo}. Also dimensionless integral buffer capacity

REFERENCES

1. Y. Okinaka and C. Wolowodiuk, *This Journal*, **128**, 28 (1981).
2. H. A. Reinheimer, *ibid.*, **121**, 490 (1974).
3. Y. Okinaka and C. Wolowodiuk, U.S. Pat. 4,067,783 (1978).
4. G. Bianchi, V. DeNora, P. Gallone, and A. Nidola, U.S. Pat. 3,616,445 (1971).
5. F. B. Koch, Y. Okinaka, C. Wolowodiuk, and D. R. Blessington, *Plating Surf. Finish.*, **67** (6), 50 (1980); **67** (7), 43 (1980).
6. Y. Okinaka and C. Wolowodiuk, *ibid.*, **66** (9), 50 (1979).
7. R. G. Bates, "Electrometric pH Determinations," p. 93, John Wiley & Sons, New York (1954).
8. F. Hine, M. Yasuda, T. Noda, T. Yoshida, and J. Okuda, *This Journal*, **126**, 1439 (1979).
9. S. Gill, *Proc. Cambridge Philos. Soc.*, **47**, 96 (1951).
10. M. J. Romanelli, "Mathematical Methods for Digital Computers," pp. 110-120, John Wiley & Sons, New York (1960).
11. A. C. C. Tseung and S. Jasem, *Electrochim. Acta*, **22**, 31 (1977).
12. V. B. Lazarev and I. S. Shaplygin, *Russ. J. Inorg. Chem.*, **23**, 163 (1978).
13. A. Nidola, P. M. Spaziante, and L. Giuffre, Abstract 481, p. 1202, The Electrochemical Society Extended Abstracts, Seattle, Washington, May 21-26, 1978.
14. R. U. Bondar and E. A. Kalinovskii, *Elektrokhimiya*, **14**, 730 (1978).

Hydrogen Production by the Electrolysis of Water

The Kinetic and Thermodynamic Framework

Rodney L. LeRoy*

Electrolyser Inc., Etobicoke, Ontario M9C 1B9, Canada

ABSTRACT

The electrical energy efficiency of commercial water electrolyzers is normally limited by internal energy losses; heat generated at economic current density levels exceeds the heat required to maintain the temperature of the electrolyte, and cooling must be used. The energy losses reflect the effects of ohmic resistance and of the electrode overvoltages. Development of activated electrode systems and of improved electrode geometries promises to reduce these losses to the point where efficiency will be limited instead by the requirement that sufficient heat be generated internally to maintain the electrolyte temperature. The limitation on electrical energy efficiency then becomes thermodynamic. This paper reviews the major thermodynamic and kinetic considerations which impact design of industrial water electrolyzers. Options indicated for development of advanced technology are considered. These are then related to the approaches being taken in major worldwide programs which are working to reduce the cost of hydrogen production from water and electricity.

The process of hydrogen production by the electrolysis of water is well-established industrially (1). It has found its economic niche in a broad range of applications and locations where high purity is required, or where merchant hydrogen and hydrogen produced from hydrocarbon feedstocks are for some reason unavailable or expensive. Typical end uses are hydrogenation of edible fats and oils, semiconductor processing, heat-treatment of specialty steels, and cooling of the casings of electric power generators. With few exceptions, plant capacities have corresponded to power inputs less than 5 MW.

Worldwide interest in this historic process has been renewed during the past decade, based on expectations that hydrogen will have a role as an energy carrier or "currency." Several applications have been identified in which hydrogen production by electrolysis is likely to find economic application on a large scale in the very near future. These are notably the production of ammonia and methanol, in areas where hydrocarbons are scarce or expensive (2). Also, the rapid expansion of nuclear-based generating capacity in some jurisdictions has led to plans for hydrogen production from off-peak electricity (3, 4). Responding to these opportunities, vigorous technology development programs are now underway, in the European Economic Community (5), Canada (6), the United States (7), Japan (8), and elsewhere.

All of these programs share a two-fold objective: to improve the energy efficiency, electricity to hydrogen; and to reduce the capital cost. These objectives are strongly interrelated, as reduced capital cost can be achieved by the use of higher current densities which, in turn, result in increased voltage and lower energy efficiency.

Most work reported has focused on the kinetic limitations of the water decomposition process, with cell voltage reductions being achieved by use of higher electrolyte temperatures, electrode activation, and modified geometries to reduce ohmic losses. As lower voltages have been achieved, however, several groups have begun to face the issues related to thermodynamic limitations of the process (9-11). This paper reviews these limitations and considers the interplay between kinetic and thermodynamic constraints.

Kinetic Constraints

The voltage of an electrolyzer cell may be viewed as the sum of several components, most of which are strong functions of current density. Principal among these are the reversible potential, corresponding to the free energy change in the reaction, the electrode overvoltages, and the voltage contribution due to the electronic and ionic resistances in the cell (12).

The reversible potential is independent of current density, having a value of 1.192V at 70°C and 1 atm pressure. It increases with increasing pressure and decreases significantly with increasing electrolyte temperature (11).

Prior to introduction of electrode activation, the traditional cathode material was mild steel, while anodes were nickel-plated mild steel. Overvoltages on these electrodes were substantial, typically 400 mV for the anode and 300 mV for the cathode (12). All major development programs have given attention to reducing these values through use of electrocatalysis.

Electrocatalysis at moderate temperatures has become widely used commercially for improving the operating efficiency of water electrolyzers. Figure 1 presents typical results obtained for anodes developed under the Electrolyser Inc. program. The upper frame shows overvoltage measurements made in small laboratory electrolyzers, while the lower frames extend these results to larger laboratory cells, and finally to 1 kA pilot electrolyzers. Details of the test arrangements have been described previously (6, 12). In each case the electrolyte was 25% w/w KOH, thermostated to a temperature of 70°C. Cathodes were unactivated mild steel. Overvoltage measurements were made with respect to mercury/mercury oxide reference electrodes. Comparison is made in each frame of the figure with voltage measurements obtained using unactivated nickel-plated steel anodes. In each case, the test current density was 134 mA/cm^2.

Figure 2 records similar results obtained for cathode catalyst systems in experiments leading from laboratory to pilot-plant cells.

When the anode and cathode electrode systems are combined, excellent levels of electrolyzer efficiency have been demonstrated over prolonged periods. The results recorded in Fig. 3 were obtained in 1 kA pilot electrolyzers. Although the electrode treatments used are proprietary to Electrolyser Inc., similar levels of performance have been achieved in other programs (6, 13). The general result is that oxygen overvoltages have been reduced to the 200-275 mV range, and hydrogen overvoltages to the 75-125 mV range. These values are relatively independent of current density over the operating range of interest, because of the logarithmic dependence of overvoltage on current.

The ohmic contribution to cell voltage, of course, increases linearly with current density. Many programs have achieved modifications in electrode de-

* Electrochemical Society Active Member.

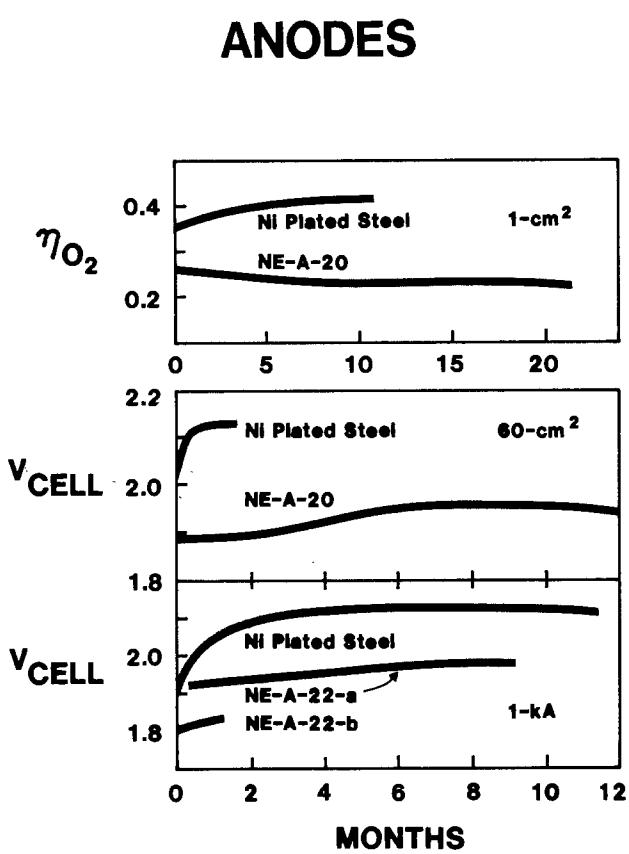

Fig. 1. Representative performance of proprietary anode systems in laboratory and pilot-plant electrolyzers, in comparison with results obtained using nickel-plated mild steel anodes. Test current density in each case was 134 mA/cm², and electrolyte was 25% KOH at 70°C. Cathodes were unactivated mild steel.

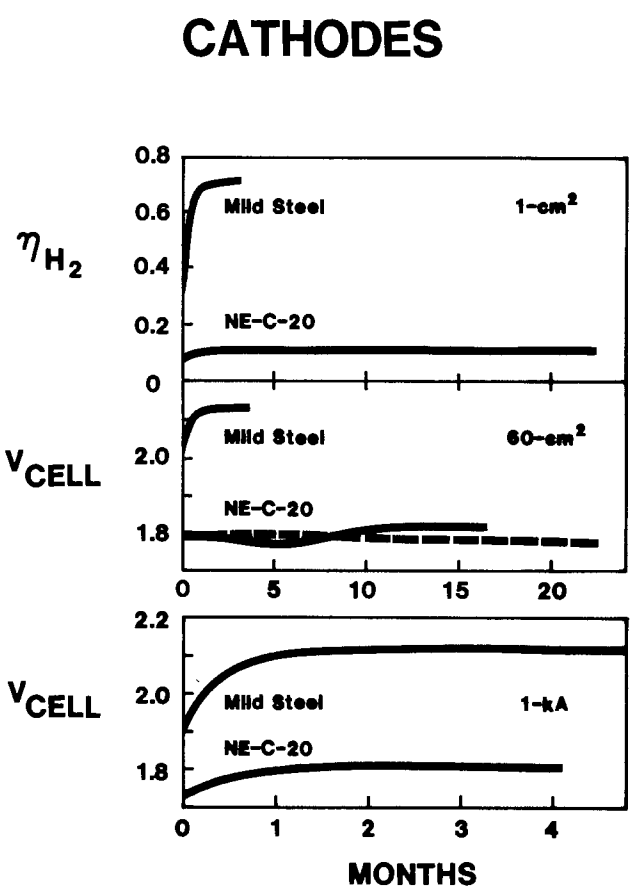

Fig. 2. Performance of proprietary cathode activation systems in laboratory and pilot-plant electrolyzers, in comparison with results obtained on unactivated mild steel. Test current density was 134 mA/cm², and electrolyte was 25% KOH at 70°C. Anodes in each case were nickel-plated mild steel.

sign and reductions in separator resistivities which have resulted in much-reduced ionic resistance and have allowed substantially increased current densities, as high as, for example, 1000 mA/cm² in most European programs (5, 14).

The resistance contribution related to the flow of electrons through current-collecting structures is relatively unimportant in the bipolar design, where the current passes through thin bipolar plates. However, careful attention must be given to control of this value in unipolar electrolyzers, where current must be removed from each individual electrode (6, 13).

Increasing electrolyte temperature benefits every component of cell voltage with the exception of the electronic resistance. The results recorded in Fig. 4 are typical. They were obtained in 1 kA unipolar electrolyzers having unactivated mild-steel cathodes and nickel-plated steel anodes. The indicated voltage benefit is approximately 4 mV per centigrade degree, similar to values recorded by other groups (15, 16). The results also suggest that increased electrolyte concentration benefits cell voltage. There is a well-known trade-off, however, as conditions of increased temperature and caustic concentration can reduce cell lifetime and necessitate the use of higher cost materials of construction.

Thermodynamic Constraints

From an alternative viewpoint, the voltage of an electrolyzer may be viewed as determined by the requirement for balance between energy inflows to and outflows from the electrolyzer. The situation is illustrated in Fig. 5. The energy input to the electrolyzer as electricity must serve several ends in addition to providing the heat content of the hydrogen and oxygen products of electrolysis. It must heat the feed-

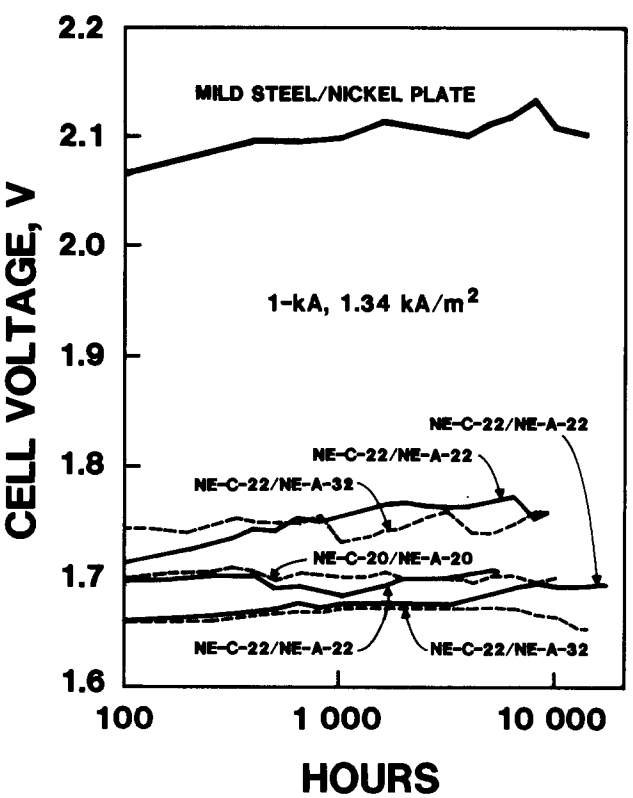

Fig. 3. Performance of combined active cathode and active anode systems in 1 kA pilot electrolyzers, in comparison with results obtained with unactivated electrodes. Electrolyte was 25% KOH at 70°C.

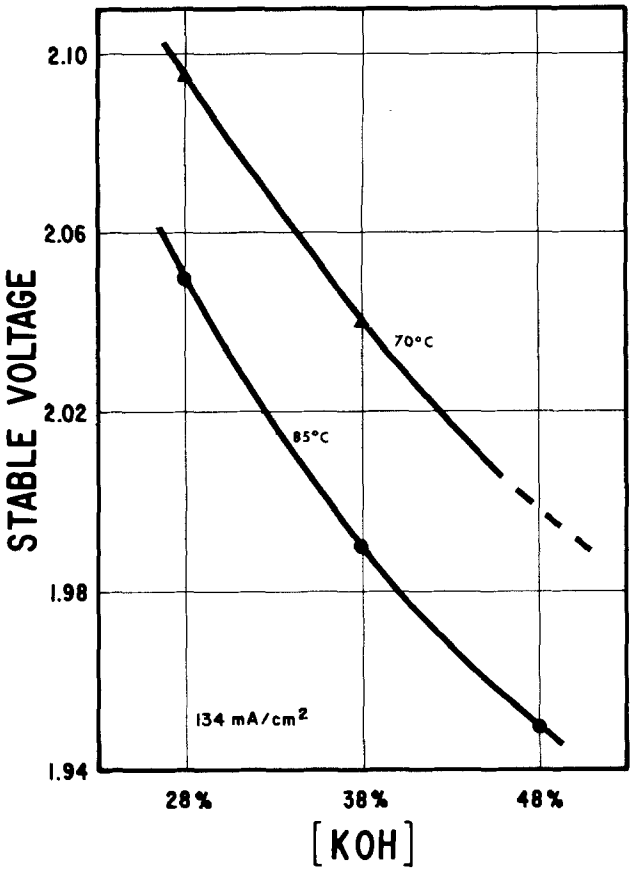

Fig. 4. Performance of 1 kA pilot electrolyzers as a function of electrolyte concentration and temperature. Cathodes were unactivated mild steel, while anodes were unactivated nickel-plated steel.

water to the temperature of the electrolyte, evaporate the water which is carried away with the product gases, and provide the heat which is lost, due to imperfect insulation, by radiation and convection. In addition, it must supply heat which is lost by conduction, normally to cooling water. The conduction term could be negative, if heat were being provided to the electrolyzer from an external source. Also, the feedwater-heating term could be negative, if hot water or steam were used.

Under stable operating conditions, the voltage of an electrolyzer will always assume a thermal-balance value which is equal to the sum of the energy outflows from the cells, expressed as a voltage. This is illustrated in Fig. 6 for the example of an electrolyzer operating at 25 atm pressure with 30% KOH electrolyte (11). Four distinct voltage parameters characterizing the water-decomposition process are indicated in the figure. These are defined as follows.

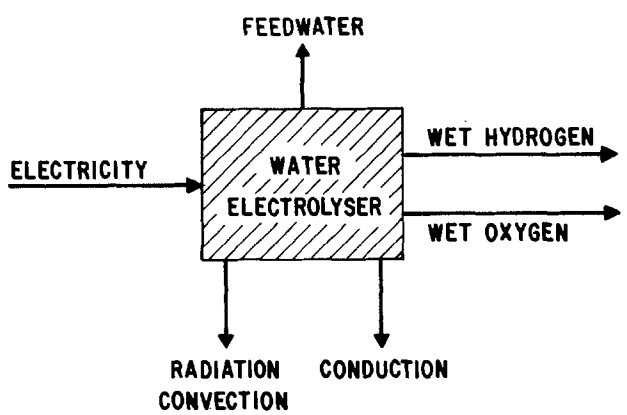

Fig. 5. Schematic representation of the energy flows to and from a water electrolyzer.

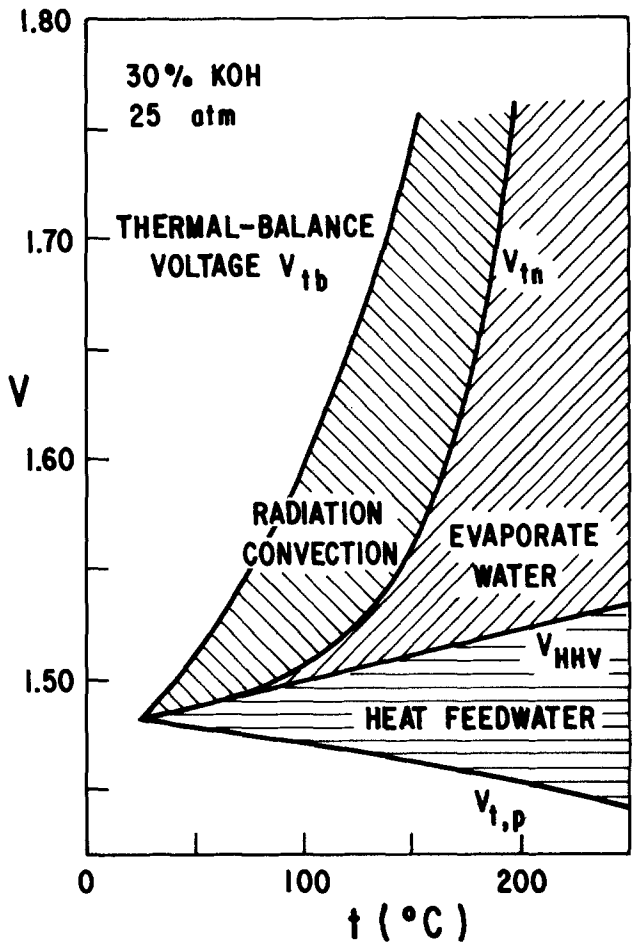

Fig. 6. Energy flows contributing to the thermal-balance voltage of a water electrolyzer, as a function of temperature. The contribution of radiation and convection to the thermal-balance voltage has been calculated assuming an electrolyzer surface area of 0.1 m^2/kA and a surface emissivity of 0.8.

The enthalpic voltage $V_{t,p}$.—The minimum thermodynamic voltage is the enthalpic voltage, corresponding to the change in enthalpy in the electrolysis process, at the temperature of the electrolyte. Its value may be calculated from (11)

$$V_{t,1\ atm} = 1.4850 - 1.490 \times 10^{-4}t - 9.84 \times 10^{-8}t^2 \quad [1]$$

where t is the electrolyte temperature in °C. Its value decreases from 1.481V at 25°C to 1.474V at 70°C and 1.460V at 150°C. This thermodynamic parameter is only a very weak function of pressure (11).

The higher heating-value voltage V_{HHV}.—The higher heating-value voltage corresponds to the heat content of the product hydrogen and oxygen gases with respect to water at 25°C. The difference between this voltage and the enthalpic voltage represents the heat required to raise the feedwater from a reference temperature of 25°C to the electrolyte temperature (cf. Fig. 6). The value of this voltage parameter may be calculated from the expression (11)

$$V_{HHV,t,1\ atm} = 1.4756 + 2.252 \times 10^{-4}t + 1.52 \times 10^{-8}t^2 \quad [2]$$

Similar to the enthalpic voltage, V_{HHV} is only a very weak function of pressure. Its value at 25°C is, by definition, equal to that of the enthalpic voltage, 1.481V. It rises to 1.491V at 70°C and 1.510V at 150°C.

Although references in the literature are not totally clear, it is likely that the higher heating-value volt-

age is the parameter which has been commonly referred to as the "isothermal" or "thermoneutral" voltage (17, 18). It is clear, however, that isothermal operation will not be possible at these voltage levels in practical industrial equipment, since significant energy losses due to water evaporation, radiation, and convection are unavoidable.

The higher heating-value voltage is useful as the reference voltage for calculation of electrical energy efficiency of a water electrolyzer. It correctly represents the enthalpy content of the product gases at the electrolyte temperature, with respect to water at 25°C. An electrolyzer operating at 100°C and 1.75V, for example, would have an energy efficiency of 1.498/1.750 = 85.6%. A cell operating at 1.40V under these same conditions would have a calculated efficiency of 107%. Heat input to this latter unit would clearly be necessary to maintain the electrolyte temperature at its design value.

The thermoneutral voltage.—The thermoneutral voltage is the voltage at which a perfectly insulated electrolyzer would operate, if there were no net inflow or outflow of heat by conduction. It is thus the sum of V_{HHV} and a voltage corresponding to the energy required for saturation of the product gases with water vapor.

The value of the thermoneutral voltage is a thermodynamic quantity, a single-valued function of the operating conditions of electrolyte temperature, electrolyte concentration, and total pressure. It may be calculated from the value of the higher heating-value voltage using the expression

$$V_{tn,t,p} = V_{HHV,t,p} + \Phi Y \quad [3]$$

Here $\Phi = 1.5\ p_w/(p - p_w)$ represents the number of mols of water evaporated for each mol of hydrogen gas produced, and p and p_w are, respectively, the total pressure and the partial pressure of water vapor over the electrolyte. An analytical expression for p_w over potassium hydroxide electrolyte is recorded in Ref. (11). Y is the molar enthalpy of water at the temperature and pressure of electrolysis, with respect to the molar enthalpy of liquid water at 25°C. In voltage terms, it may be approximated within 0.02% by (11)

$$Y = 0.2226 + 2.112 \times 10^{-4}t - 3.46 \times 10^{-7}t^2 \quad [4]$$

The representative result for V_{tn} which is plotted in Fig. 6 illustrates that, even at a total pressure of 25 atm, this voltage rises sharply above 1.7V as electrolyte temperature approaches 200°C. This implies that under these conditions an electrolyzer could not be operated at 200°C and 1.7V without input of heat from an external source.

While increasing operating pressure has no significant effect on either the enthalpic or higher heating-value voltages, it results in a sharp reduction in the thermoneutral voltage. This simply reflects the decreasing mol fraction of water vapor in the product gases as total pressure is increased, with a corresponding reduction in energy requirements for water evaporation.

The thermoneutral voltage also depends strongly on electrolyte concentration, reflecting the dependence of the vapor pressure of water over the electrolyte on this parameter. Results for the limiting case of zero electrolyte concentration are tabulated in Table I. These are the thermoneutral voltages which would apply in an electrolyzer operating with a solid polymer electrolyte. The data indicate that pressures above 10 atm are necessary to achieve high energy efficiency at operating temperatures greater than 120°C.

The thermal-balance voltage.—The true "isothermal" voltage of a practical electrolyzer is the sum of the thermoneutral voltage V_{tn} and a contribution which accounts for losses due to radiation and convection. To distinguish from earlier terminology, this is called the thermal-balance voltage. Unlike the other energy-loss parameters described above, the voltage corresponding to radiative and convective losses is not a thermodynamic quantity, and its value depends on the detailed design of the electrolyzer equipment. It can be reduced by the use of suitable insulation. The method of calculation is outlined in Ref. (11). The example of Fig. 6 is derived for an electrolyzer which has a surface area of 0.1 m²/kA of current passing through the cell.

Table I. Thermoneutral voltage with a solid polymer electrolyte

p (atm)	Thermoneutral voltage (V) 90°C	120°C	150°C
5	1.553	1.739	7.481
10	1.522	1.592	1.839
20	1.509	1.543	1.624
30	1.504	1.529	1.579

Implications for Electrolyzer Design

Figure 7 considers the consequences of the combined kinetic and thermodynamic constraints for the operation of practical electrolyzers. The example is drawn for an electrolyzer operating at 25 atm pressure with 30% KOH electrolyte. The broken curve illustrates a typical dependence of cell voltage on operating temperature. With a temperature coefficient of 4 mV/°C, it is representative of a result that could be obtained with an industrial electrolyzer as the electrolyte temperature is adjusted using an external control system. This curve would shift to higher voltages if the cell were operated at higher current loadings and, conversely, would move lower if the current density were decreased.

The superimposed solid curve in Fig. 7 is the thermal-balance voltage, taken directly from Fig. 6.

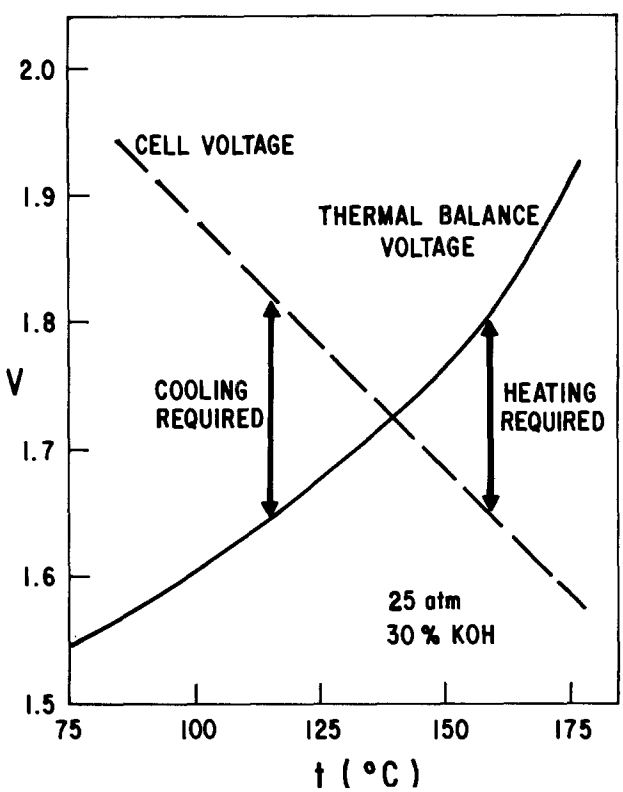

Fig. 7. Representative isothermal and thermal-balance voltages as a function of temperature at 25 atm total pressure.

An electrolyzer operating with no net input or removal of heat would gradually adjust its temperature to the crossing point of these two curves, around 140°C. At lower temperatures, the cell would have to be cooled, while at higher temperatures a net input of heat would be necessary. Note that both the temperature and voltage at which an electrolyzer would operate without heating or cooling would increase with increasing current density. The heating or cooling requirement for a particular electrolyzer design will depend on the voltage-current density characteristics, electrolyte concentration, and operating pressure, together with parameters which affect heat losses by radiation and convection.

Beginning with the work published by Srinivasan and his colleagues at Brookhaven in 1976 (19), several groups have noted the high efficiencies that can be achieved in electrolyzers operating at high pressures, and at temperatures approaching 200°C or more. At least one of the major European programs has been oriented to this type of operating condition (10). Figure 7 suggests, however, that operating temperatures much above 150°C are unlikely to be practical, for thermodynamic reasons alone. Low operating voltages would not be possible without the use of heat input from an external source, or of systems for recovering the heat content of evaporated water and returning it to the electrolyzer. Systems of this type have been described in recent patents granted to Compagnie Electromécanique of France (20), but their cost is likely to be high.

Figure 8 illustrates a similar result for operation of an electrolyzer at atmospheric pressure. In this case, the thermodynamic constraints become more stringent. Temperatures much above 90°C are impractical because of the large energy losses associated with water evaporation.

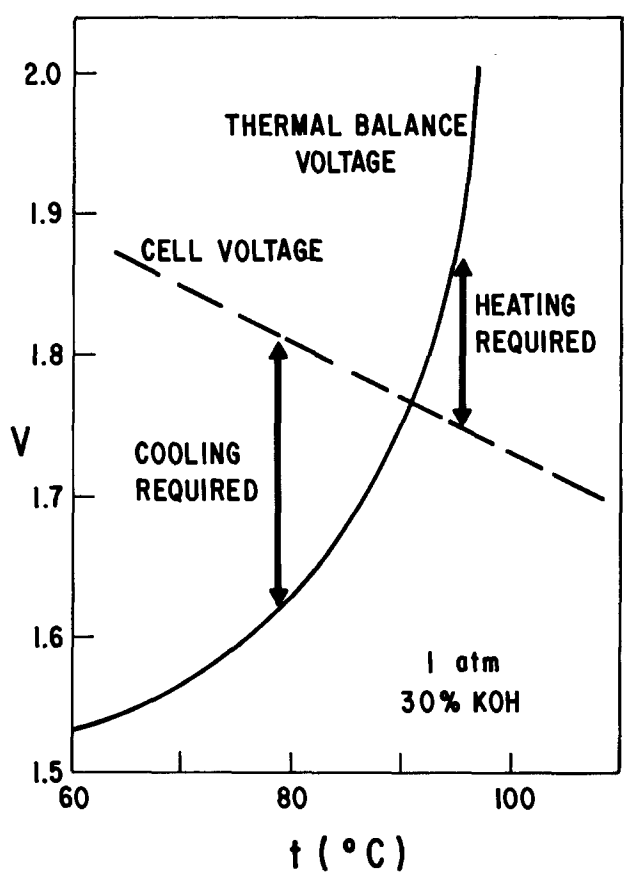

Fig. 8. Representative isothermal and thermal-balance voltages as a function of temperature at 1 atm total pressure.

Conclusion

Combined kinetic and thermodynamic considerations suggest that there are three "windows" for development of water electrolysis technology. The first of these is operation at very high temperatures, to reduce electrode overvoltages, and at high pressures to control water losses. This has been the direction of the Compagnie Electromécanique group (10, 20) and, at least initially, of the French group headed by Creusot Loire (21) and the German group at Darmstadt (22). In all of these cases, heat recovery systems would be required to achieve acceptable electrical energy efficiencies.

The second alternative is to use intermediate electrolyte temperatures, in the range of 110°-150°C, with electrode activation to achieve acceptable overvoltages. At pressures above 25 atm, cell voltages in the range of 1.6-1.7V become thermodynamically possible. This is the development window which has been selected by Teledyne Energy Systems in the United States (23), Compagnie Générale d'Electricité in France (24), SCK/CEN in Mol, Belgium (14), the Japanese advanced alkaline program (8), and the SPE programs being carried out by General Electric in the U.S. (7), Brown Boveri in Switzerland (25), and in Japan (26).

Finally, operation at atmospheric pressure is possible for electrolyte temperatures below 90°C. This is the traditional operating regime of commercial water electrolyzers (1, 27). It offers the most favorable conditions for long life of electrocatalysts and of materials of construction. Electrolyser Incorporated is apparently the only firm developing advanced electrolyzer equipment for operation under these conditions (6, 13).

Acknowledgments

I am indebted to Messrs. C. T. Bowen, A. F. Hufnagl, and D. J. LeRoy for valuable and stimulating discussions concerning the subject matter of this paper, and to Messrs. B. F. Henshaw, M. B. I. Janjua, and R. Renaud for their contribution in obtaining the data of Fig. 1-4.

Manuscript submitted Sept. 20, 1982; revised manuscript received *ca.* May 16, 1983. This was Paper 459 presented at the Montreal, Que., Canada, Meeting of the Society, May 9-14, 1982.

REFERENCES

1. P. V. Tilak, P. W. T. Lu, J. E. Colman, and S. Srinivasan, in "Comprehensive Treatise of Electrochemistry," Vol. 2, J. O'M. Bockris, B. E. Conway, E. Yeager, and R. E. White, Editors, p. 1, Plenum Press, New York (1981).
2. G. A. Crawford and A. K. Stuart, in "Hydrogen Energy Progress—IV," Vol. 4, T. N. Veziroglu, W. D. Van Vorst, and J. H. Kelley, Editors, p. 1549, Pergamon Press, Oxford (1982).
3. "Hydrogen: A Challenging Opportunity," Report of the Ontario Hydrogen Energy Task Force, Government of Ontario, September 1981.
4. R. Aureille and J. Pottier, in "Hydrogen Energy Progress—IV," Vol. 4, T. N. Veziroglu, W. D. Van Vorst, and J. H. Kelley, Editors, p. 1563, Pergamon Press, Oxford (1982).
5. G. Imarisio, *Int. J. Hydrogen Energy*, **6**, 153 (1981).
6. R. L. LeRoy and A. K. Stuart, *ibid.*, **6**, 589 (1981).
7. M. Bonner, T. Botts, J. McBreen, A. Mezzina, F. Salzano, and C. Yang, in "Hydrogen Energy Progress—IV," Vol. 1, T. N. Veziroglu, W. D. Van Vorst, and J. H. Kelley, Editors, p. 117, Pergamon Press, Oxford (1982).
8. "Japan's Sunshine Project: Summary of Hydrogen Energy R & D," Agency of Industrial Science and Technology, Ministry of International Trade and Industry (1981).
9. Anon., *Nitrogen*, **97**, 35 (1975).
10. S. Kunstreich and J. Sterlini, in "Hydrogen Energy System," Vol. 5, T. N. Veziroglu and W. Seifritz, Editors, p. 2413, Pergamon Press, Oxford (1979).

11. R. L. LeRoy, C. T. Bowen, and D. J. LeRoy, *This Journal*, **127**, 1954 (1980).
12. R. L. LeRoy, M. B. I. Janjua, R. Renaud, and U. Leuenberger, *ibid.*, **126**, 1674 (1979).
13. R. L. LeRoy and A. F. Hufnagl, Paper presented at the 4th World Hydrogen Energy Conference, Pasadena, June 14-17, 1982; *Int. J. Hydrogen Energy*, **8**, 581 (1983).
14. H. Vandenborre, R. Leysen, H. Nackaerts, and P. Van Asbroeck, in "Hydrogen Energy Progress—IV," Vol. 1, T. N. Veziroglu, W. D. Van Vorst, and J. H. Kelley, Editors, p. 107, Pergamon Press, Oxford (1982).
15. J. N. Murray and M. R. Yaffe, in "14th Intersociety Energy Conversion Engineering Conference," Proceedings Vol. 1, p. 747, American Chemical Society, Washington (1979).
16. P. J. Moran and G. E. Stoner, in "Industrial Water Electrolysis," Vol. 78-4, S. Srinivasan, F. J. Salzano, and A. R. Landgrebe, Editors, p. 169, The Electrochemical Society Softbound Proceedings Series, Princeton, NJ (1978).
17. J. Evangelista, B. Phillips, and L. Gordon, NASA Technical Memorandum TM X-71856 (December 1975).
18. D. P. Gregory, "A Hydrogen-Energy System," Report prepared for the American Gas Association, Institute of Gas Technology, Chicago (August 1972).
19. M. H. Miles, G. Kissel, P. W. T. Lu, and S. Srinivasan, *This Journal*, **123**, 332 (1976).
20. S. Kunstreich, European Pat. 4,799 (1981); J. Sterlini, European Pat. Application 7,835 (1980).
21. M. Prigent and T. Nenner, in "Hydrogen Energy Progress—IV," Vol. 1, T. N. Veziroglu, W. D. Van Vorst, and J. H. Kelley, Editors, p. 299, Pergamon Press, Oxford (1982).
22. J. Fischer, H. Hofmann, G. Luft, and H. Wendt, *AIChE. J.*, **26**, 794 (1980).
23. J. N. Murray, in "Hydrogen Energy Progress—IV," Vol. 1, T. N. Veziroglu, W. D. Van Vorst, and J. H. Kelley, Editors, p. 151, Pergamon Press, Oxford (1982).
24. Final Report, Contract No. 403-77-10 EHF, Commission of the European Communities Report EUR 6764 (1980).
25. S. Stucki, *Rev. générale de l'électricité*, **3**, 190 (1982).
26. H. Takenaka, E. Torikai, Y. Kawami, and N. Wakabayashi, *Int. J. Hydrogen Energy*, **7**, 397 (1982).
27. "Industrial Water Electrolysis," S. Srinivasan, F. J. Salzano, and A. R. Landgrebe, Editors, The Electrochemical Society Softbound Proceedings Series, Princeton, NJ (1978).

Study of Cd-Chalcogenide/Ferri-Ferrocyanide Photoelectrochemical Cells: Effect of Surface Morphology and Added Salt

R. Tenne

Department of Plastics Research, The Weizmann Institute of Science, Rehovot 76100, Israel

ABSTRACT

We carried out an investigation of the Cd-chalcogenide/ferri-ferrocyanide photoelectrochemical cells. In particular, the effect of surface morphology and the effect of added salts upon the characteristics of these cells were investigated. Successive etching with Br_2 (3%)/methanol, aqua regia, and finally photoetching increases the surface roughness of CdSe (CdS, CdTe) which has a marked effect on the cell characteristics in the ferri-ferrocyanide electrolyte (and polysulfide electrolyte as well). In contrast with polysulfide electrolyte, added salts decrease the output stability of the cell and the onset potential for the photocurrent, which can be explained by the removal of the physiosorbed ferrocyanide ions from the electrode surface by the ions of the salt. On increasing the surface roughness of the electrode, while keeping the salt concentration unchanged, the output stability and the onset potential were increased. A kinetic model is used to explain these phenomena. Thus, added salts can be used to probe the strength of the adsorption of the active electrolyte on the surface of the photoelectrode. Finally, we report on the surface morphology of CdSe and CdTe after irradiation in ferri-ferrocyanide solution and compare our findings to surface morphologies which were observed previously with the help of photoelectrochemical etching (photoetching). It is found that small rectangular crystallites, probably of cadmium ferrocyanide, deposit on the crystal surface during the photocorrosion process in addition to elemental Se(Te).

In contrast to the polysulfide ions which are chemisorbed onto the surface of Cd-chalcogenide semiconductors, ferrocyanide ions show fairly low affinity to these surfaces (1). Despite that fact, photoelectrochemical cells (PEC's) based on the CdSe(CdS)/ferrocyanide junction have demonstrated high conversion efficiencies and output stabilities of several hours (2). Our present investigation was motivated mainly by this difference in the adsorption properties which allowed us to test some of our previous concepts. The present work deals with the effect of surface morphology on the performance and stability of Cd-chalcogenide based PEC's. This effect of surface morphology upon the performance and stability of Cd-chalcogenide/polysulfide PEC's was investigated intensively in the past (3-5). It has been demonstrated that roughening of the surface improves the kinetics of hole transfer into the electrolyte thereby decreasing the amount of holes available for photocorrosion so that both photocurrent and output stability are improved. Since photogenerated holes are powerful oxidants which can tunnel over appreciable distances, it was suggested that the kinetic model presented above does not apply to chemisorbed electrolytes only, and, therefore, it is expected that roughening of the surface would improve the photocurrent and the output stability in ferrocyanide solutions as well. This view is examined in the present work.

When indifferent salts are added to the polysulfide electrolyte, they improve the output stability of Cd-chalcogenides without (6a) having appreciable effect on the photocurrent and photovoltage of these PEC's (6). It was suggested, therefore, that the indifferent salts, even at large concentrations, do not change the structure of the inner Helmholtz layer in the electrolyte (*i.e.*, the ions of the salt cannot desorb the preferentially adsorbed sulfide ions from the semiconductor surface). Rather, we speculated that the indifferent salts decrease the Debye radius of the sulfide ions thereby increasing their mobility in a depletion region which extends outside the interface (7). One way to scrutinize this concept is to add excessive amounts of salt into a solution contain-

Key words: photoetching, ionic strength, etching, physisorption, adsorption.

ing a redox couple, the components of which have weak affinity to the semiconductor surface, and to look at the changes in performance and output stability of the PEC.

Earlier, we found that a light-induced electrochemical etching process (3, 8) which modifies the morphology of the semiconductor surface enhances the activity of various PEC's [see also (9)]. The solutions used for this process are diluted chemical etchant which contain no redox species that can serve as a hole acceptor (aside from the water itself). Presumably, redox couples which stabilize the interface only partially, under illumination, can also be used as a medium for selective photoetching of semiconductor surfaces, and ferrocyanide belongs to this category. We studied the morphology of the semiconductors, after short irradiation in ferri-ferrocyanide solution by scanning electron microscopy.

Experimental

Low resistivity CdS (Cleveland), CdSe (Cleveland), and n-CdTe (W. Giriat, IVIC, Venezuela) crystals were used for the preparation of electrodes according to previously described procedures (8, 10). Electrodes were polished (5μ) and etched prior to each experiment. CdS was etched in concentrated HCl for 30 sec; CdSe in a mixture of 1 part HNO_3, 4 parts HCl (aqua regia) for 30 sec; and CdTe was etched for 15 sec in a mixture of 3 parts H_2SO_4, 7 parts saturated solution of potassium dichromate. In order to obtain CdSe with very even surface, the CdSe electrode was etched in either of two ways: (*i*) in Br_2(3%)/methanol, and (*ii*) mixture of CrO_3:H_2O and HCl in weight ratios of 6:4:10, respectively (chromic acid etch). Photoetching was carried out in diluted (five-ten times) solution of the etching agents, according to previously described procedures, for 3-5 sec. After photoetching, the electrode was immersed in polysulfide electrolyte to dissolve the top layer of elemental chalcogen. Solutions were prepared from analytical grade reagents, without any further purification, and deionized water.

Instrumentation included a homemade linear sweep generator (Voltage scanner); X-Y recorder (Houston Instruments); X-t recorder (Yokogawa); Wenking MP75 potentiostat. The light source used was a stabilized tungsten halogen lamp. A standard calomel electrode (SCE) was used as a reference electrode and a large surface area Pt mesh as counterelectrode. SEM micrographs were taken with Jeol 35JSMC scanning electron microscope.

Results

In a recent publication, Hodes *et al.* (4) demonstrated unambiguously the role of the real surface area of the photoelectrode upon the output stability of CdSe/polysulfide PEC's. A further investigation (5) into that problem demonstrated both experimentally and theoretically that as the area of the junction is increased, more sulfide ions which serve as hole acceptors can be accommodated on the surface of the electrode thereby increasing the photocurrent and the output stability. That this notion is not limited to chemisorbed sulfide ions only is demonstrated in what follows. Thus, Fig. 1 shows the photocurrent of a CdSe/ferrocyanide PEC *vs.* light intensity for photoelectrodes with different surface roughness. The Br_2(3%)/methanol etch leaves a very even surface (4) which becomes rough upon etching in aqua regia. Finally, a short photoetching creates many pits on the surface. In all cases, the photocurrent increases linearly with light intensity under weak illumination but it undergoes saturation at strong light intensities. The greater the surface roughness, the larger is the saturation value for the photocurrent. The increase in the saturation value of

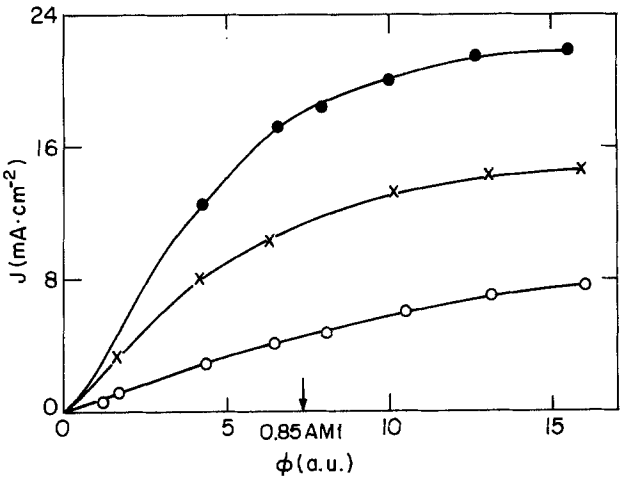

Fig. 1. Photocurrents (*J*) *vs.* light intensity (ϕ) for CdSe in aqueous solution of 0.4M $K_3[Fe(CN)_6]$ and 0.4M $K_4[Fe(CN)_6]$ at pH 13. Bias is +200 mV *vs.* SCE. Different surface morphologies were obtained with: ○, Br_2(3%)/methanol etch; x, 20% HNO_3/80% HCl (aqua regia) etch; ●, photoetching with aqua regia diluted ten times.

the photocurrent is indicative of the ratio of surface roughness which is about (1/2/3) for the etching in Br_2(3%)/methanol, aqua regia, and photoetching. Figure 2 shows the effect of surface morphology on the dark current across CdSe/ferri-ferrocyanide interface. Again, as in polysulfide solution (10), the forward dark current increases with surface roughness in a nonlinear manner. Similar behavior is observed in the case of CdTe. Figure 3 shows the open-circuit voltage of a CdSe/ferri-ferrocyanide/Pt cell *vs.* light intensity for various surface morphologies and, as expected, at a given light intensity, the open-circuit voltage decreases with increasing surface roughness (10). Finally, Fig. 4a and 4b show the output stability of CdSe (a) and CdTe (b) in ferri-ferrocyanide electrolyte. Thus, increasing the surface roughness leads to an improved stability of the cell for both chemisorbed (polysulfide) and physisorbed (ferrocyanide) electrolytes. For the CdTe, it was necessary to heat the photoetched electrode in polysulfide to 70°C in order to dissolve the Te top layer. A post-treatment in concentrated HCl was also necessary, possibly for the dissolution of a passivating

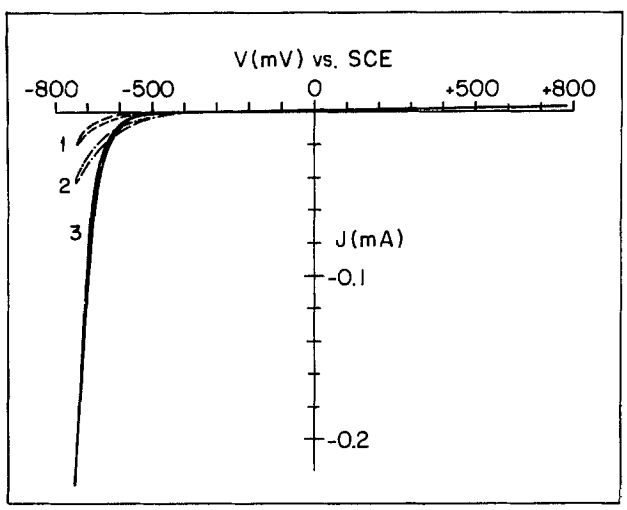

Fig. 2. Dark currents *vs.* bias for CdSe in aqueous solution of 0.1M $K_3[Fe(CN)_6]$ and 0.3M $K_4[Fe(CN)_6]$ for various surface morphologies. 1, Br_2(3%)/methanol etch; 2, aqua regia etch; 3, photoetched. Surface area of the electrode, 0.04 cm^2, scan rate 50 mV/sec.

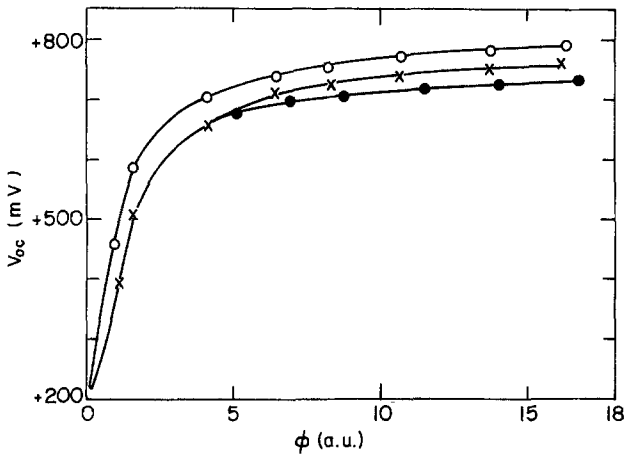

Fig. 3. Open-circuit voltage as a function of light intensity for the CdSe/ferri-ferrocyanide cell shown in Fig. 1. Symbols are as in Fig. 1.

layer which was created upon immersion in the hot polysulfide.

Figures 5a and 5b show the photocurrent *vs.* time (output stability) of etched and photoetched CdSe in an aqueous solution of ferri-ferrocyanide containing increasing concentration of NaCl. Here, the deactivation is due to a top layer of elemental Se which is formed under illumination (2b) (see, however, Fig. 9c and 10b). Table I gives the onset potential for the photocurrent of these PEC's. In contrast to the CdSe/polysulfide PEC, increasing the concentration of the indifferent salt leads to a faster deactivation of the cell and to a less negative onset potential. Furthermore, there is a remarkable difference between the etched and the photoetched electrode. The latter electrode is affected by the salt to a lesser extent so that its output stability is improved and its onset potential is more negative compared to the etched electrode at a given concentration of the salt. This result can be understood on the basis of the difference in surface roughness of the two electrodes as is elaborated in the discussion. In Fig. 6, we show the output stability of photoetched CdSe in two solutions with different $Fe^{2+}(CN)_6^{4-}$ concentrations and constant concentration of salt (0.5M) and $Fe^{3+}(CN)_6^{3-}$ (0.1M). It is noticed that the higher concentration of the ferrocyanide the onset potential is more negative and the stability is improved. The same is true for CdSe etched in Br_2/methanol and in aqua regia. Further addition of ferrocyanide has very little effect on the output stability under these particular conditions. Figure 7 show the output stability (which is determined by the rate of formation of top layer of elemental S) of CdS in the ferri-ferrocyanide electrolyte with and without NaCl. Table II gives the onset potentials for the solutions studied in Fig. 7. Again, as a result of the presence of high concentration of salt, the ferrocyanide ions are removed from the surface of the semiconductor and the cell is deactivated slowly. This is contradictory to what has been observed in the case of polysulfide electrolyte where

Table I. Onset potential for the photocurrent of CdSe in an aqueous solution of 0.1M $K_3[Fe(CN)_6]$ and 0.5M $K_4[Fe(CN)_6]$ with varying concentrations of salt

NaCl concentration (M)	Onset potential aqua regia etching (mV *vs.* SCE)	Onset potential after photoetching (mV *vs.* SCE)
3	−580	−1040
2	−800	−1040
1	−800	−1040
0	−885	−1210

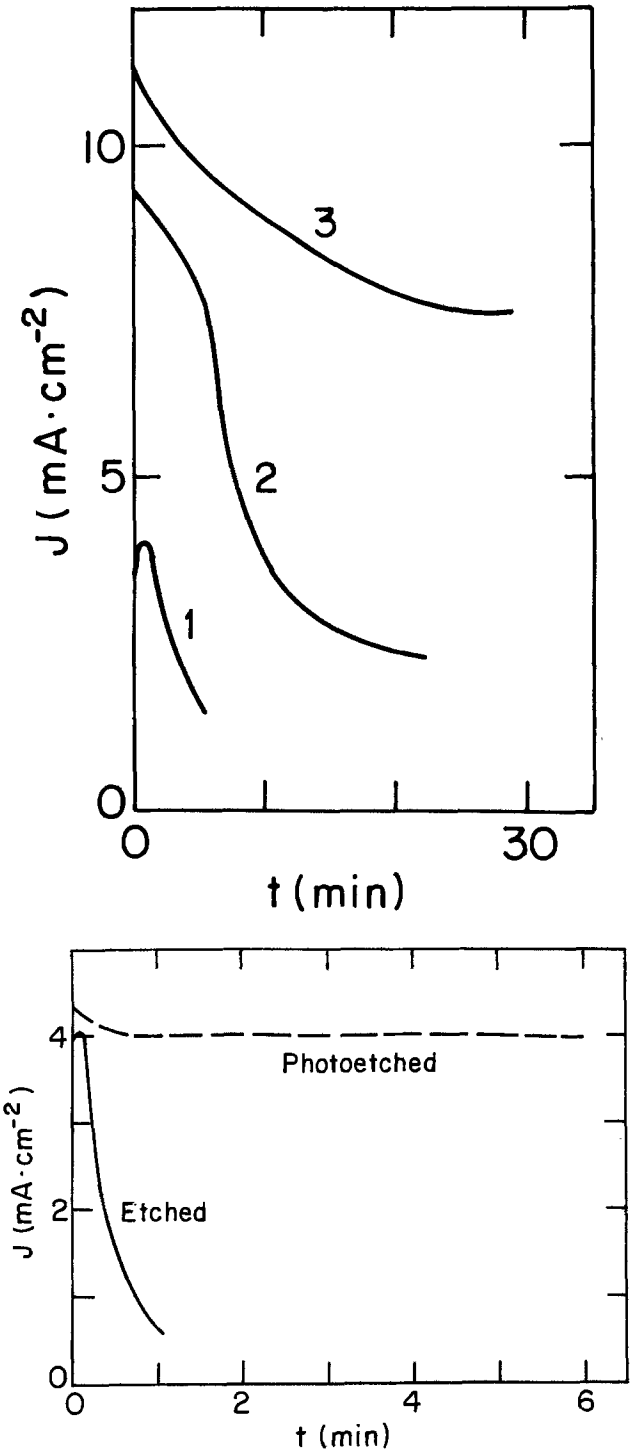

Fig. 4. (a, top) Output stability of CdSe in an aqueous solution of 0.1M $K_3[Fe(CN)_6]$ and 0.5M $K_4[Fe(CN)_6]$. 1, 2, and 3 refer to different etching techniques (see Fig. 2). Light intensity is *ca.* 0.8 AM1. (b, bottom) Output stability of CdTe prepared by etching (——) and photoetching (---). Electrolyte is 0.08M $K_3[Fe(CN)_6]$ and 0.4M $K_4[Fe(CN)_6]$. Light intensity is *ca.* 1/2 AM1.

the output stability was improved by the addition of the salt.

Wilson and Park (11) observed recently that the addition of small amounts of KCl to iron(II)-EDTA decreases the rate of CdS photodissolution, but this trend is reversed on increasing the salt concentration. Their explanation for this observation is that low concentrations of the salt improve the electrolyte conductivity (decrease of the Debye radius), leading to a slower photocorrosion. Higher concentrations of the salt hinders the approach of the electron donors to the electrode surface which leads to a higher rate

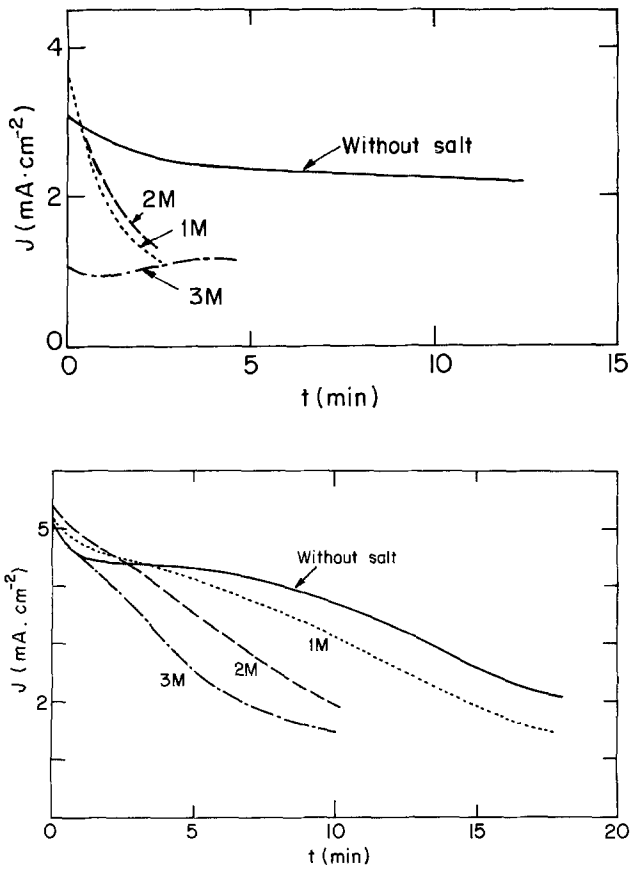

Fig. 5. Output stability of CdSe in an aqueous solution of 0.1M $K_3[Fe(CN)_6]$ and 0.5M $K_4[Fe(CN)_6]$ and various concentrations of NaCl, as indicated on each curve. Bias is −200 mV vs. SCE, light intensity ca. 1/2 AM1. (a) aqua regia etched; (b) photoetched.

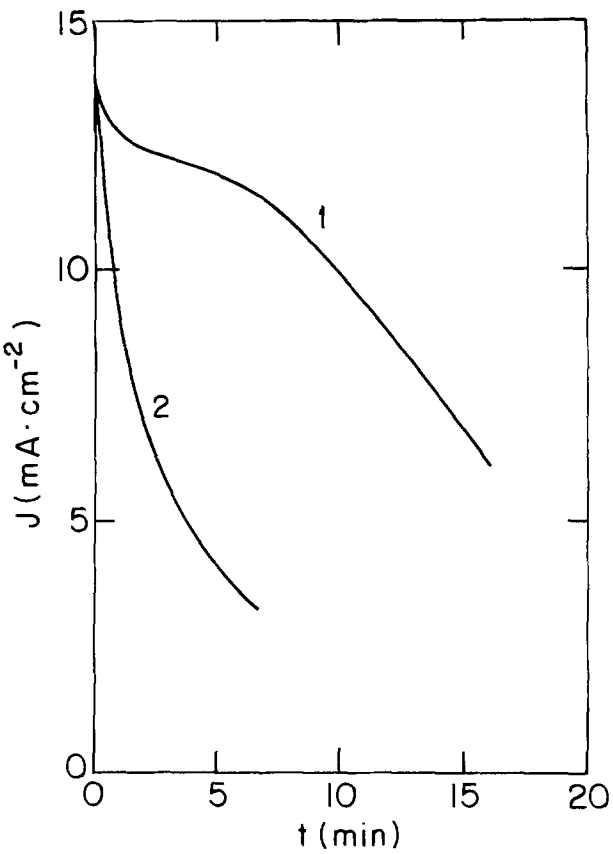

Fig. 6. Output stability of photoetched CdSe in an aqueous solution of 0.1M $K_3[Fe(CN)_6]$ and 0.5M NaCl. 1, 0.3M $K_4[Fe(CN)_6]$ (onset potential of −880 mV vs. SCE); 2, 0.1M $K_4[Fe(CN)_6]$ (onset potential of −820 mV vs. SCE). Bias is 0 mV vs. SCE.

of photocorrosion. Our observations and the model put forward (6) agree very well with the work of Wilson and Park. However, we worked with relatively large concentrations of salt but with two electrolytes which show different affinity for the surface of the electrode.

Another way to look at the effect of added salts is shown in Fig. 8a and 8b where the photocurrent is plotted as a function of light intensity for various concentrations of the salt. Thus, the photocurrent of the etched electrode (a) decreases when the salt concentration increases, whereas the photocurrent of the photoetched electrode (b) is not affected by the addition of high concentration of salt.

We therefore conclude that the addition of indifferent salts can be used as a probe to discriminate between chemisorbed and physisorbed ions by means of simple photoelectrochemical measurements.

Another subject of interest is the morphological changes on the semiconductor surface which are induced by the illumination in a solution of ferri-ferrocyanide. Since this redox couple stabilizes the surface of the semiconductor only partially, it could be expected that some kind of photoetching will result after prolonged irradiation and removal of the top oxidized chalcogen layer. Figure 9 shows the SEM micrographs of (a) aqua regia etched CdSe; (b) aqua regia etched CdSe which was further photoetched in dilute aqua regia; and (c) aqua regia etched CdSe after prolonged irradiation in ferri-ferrocyanide solution (until a maximum in the photocurrent was reached). In all three cases, the electrode received a post-treatment in polysulfide electrolyte to remove the top layer of Se. The most interesting observation here is that instead of the submicron pits which are observed on the aqua regia photoetched CdSe, small rectangular crystallites are observed on the CdSe which was irradiated in ferrocyanide solution.

Table II. Onset potential for the photocurrent of HCl-etched CdS (S face) in the solution of Table I

NaCl concentration (M)	Onset potential (mV vs. SCE)
3	−750
1	−1050
0	−1150

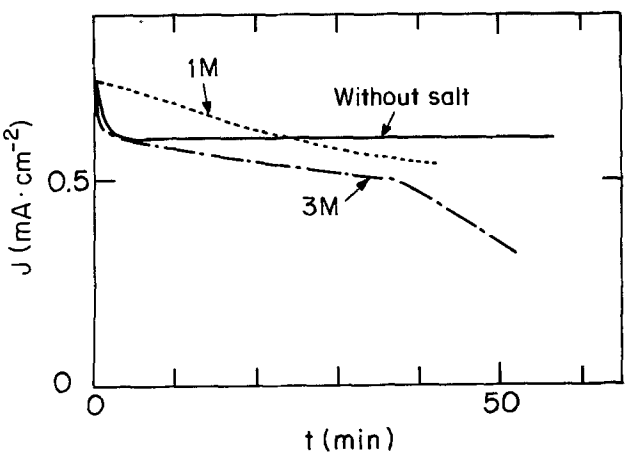

Fig. 7. Output stability of etched CdS (S face) in an aqueous solution which is 0.1M with respect to $K_3[Fe(CN)_6]$, 0.5M with respect to $K_4[Fe(CN)_6]$ and various concentrations of NaCl as indicated for each curve. Bias is 0 mV vs. SCE and light intensity is ca. 1/2 AM1.

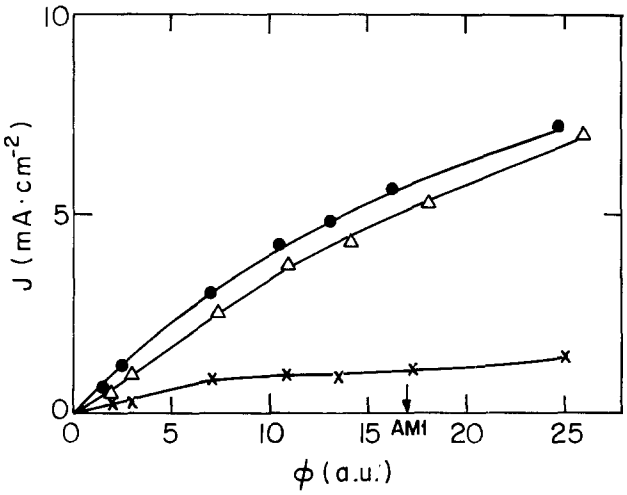

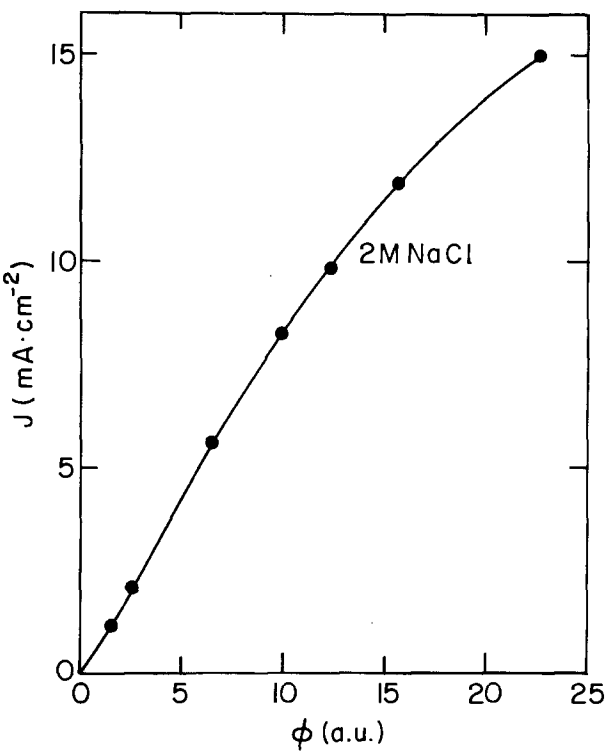

Fig. 8. (a, top) Photocurrent vs. light intensity for chromic acid-etched CdSe in an aqueous solution which is 0.1M with respect to $K_3[Fe(CN)_6]$ and $K_4[Fe(CN)_6]$. Salt concentration is indicated for each curve. Bias is −400 mV vs. SCE. ●—●, without salt; △—△, 0.5M NaCl; ×—×, 2M NaCl. (b, bottom) The same as (a), but with photoetched CdSe electrode. Same curves were obtained without salt and with 0.5M NaCl.

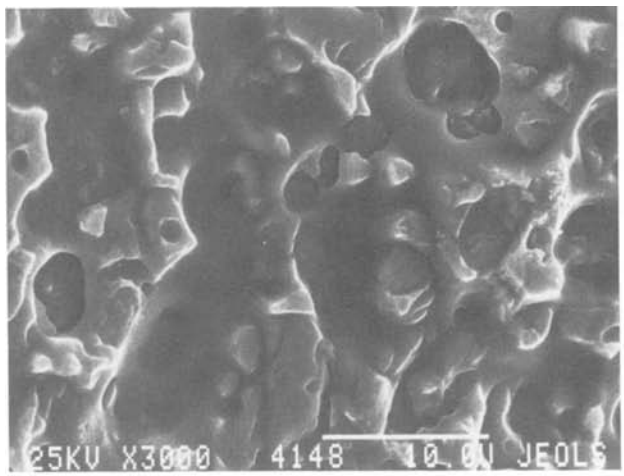

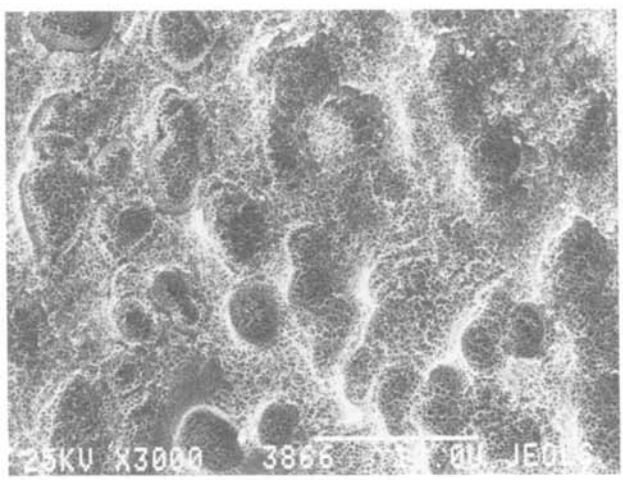

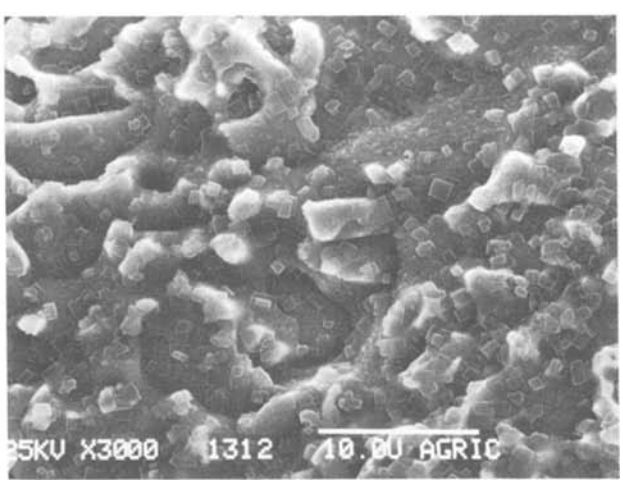

Fig. 9. Comparison (SEM micrographs) of surface morphologies of CdSe which obtained different surface treatments. (a, top) Etched CdSe. Magnification is 3000×; (b, center) photoetched CdSe (3000×). Note the dense pattern of submicron pits; (c, bottom) CdSe which was illuminated in ferri-ferrocyanide solution until deactivation.

In Fig. 10, we compare the texture of photoetched CdTe (a) and the texture of the same crystal after prolonged irradiation in a solution of ferri-ferrocyanide (b). Here also, rectangular crystallites appear on the surface of the CdTe crystal after irradiation in the ferrocyanide solution. It is suggested that in both cases (CdSe and CdTe) Cd^{2+} ions which diffuse out from the crystal during the photocorrosion process combine with ferrocyanide ions to form an insoluble salt which deposits on the crystal surface. This growth mode of photocorrosion leads to a roughening of the crystals' surface which becomes less reflective (black mat). Immersion of the deactivated CdSe and CdTe electrodes in a hot KCN solution (10%) leads to the dissolution of the passivating layer and to a regaining of the metallic color due to the complexation of the Cd ions with the cyanide. Irradiation in other partially stabilizing electrolytes (like sulfite) results in pitting of the semiconductor surface (R. Tenne and G. Hodes, to be published).

Discussion

We will now consider the effect of the presence of indifferent salt in the redox electrolyte using a rather simple model for competitive adsorption. We first assume that the hole flux (J_ϕ) arriving at the semiconductor surface under illumination is consumed in

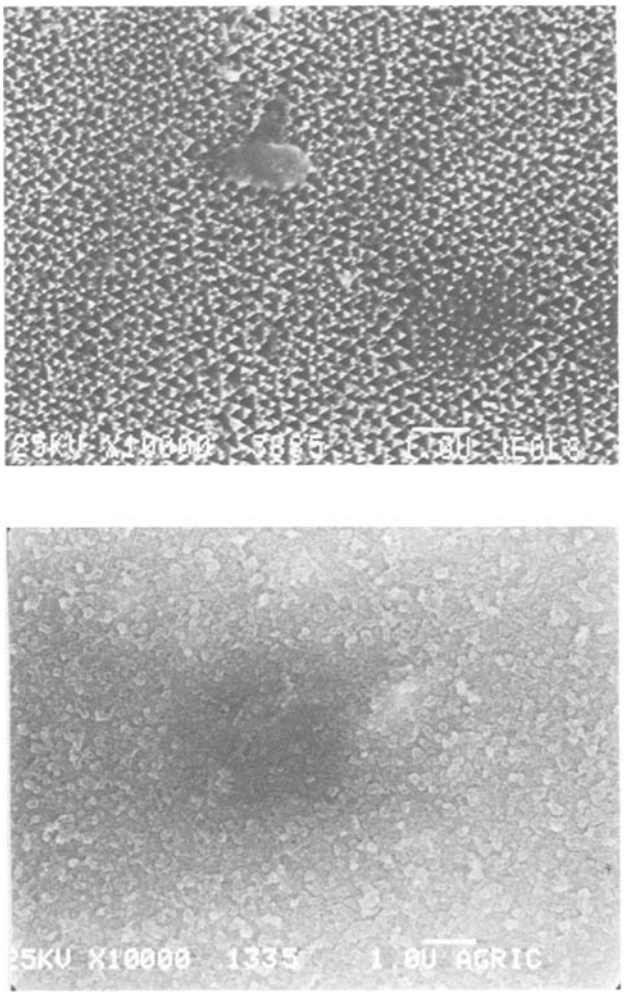

Fig. 10. Comparison (SEM micrographs) of surface morphologies of CdTe which obtained different surface treatments. (a, top) Photoetching (3000×); (b, bottom) irradiation in ferri-ferrocyanide solution until deactivation.

either of three ways: (*i*) by oxidizing the electrolyte, leading to regenerative photocurrent, J_{reg}; (*ii*) through self-oxidation of the crystal itself, *i.e.*, photocorrosion, J_{cor}. Finally, certain portion of the hole flux is consumed by (*iii*) various surface, or near surface, recombinative processes leading to a recombination current density J_{rec}. Hence we have

$$J_\phi = J_{reg} + J_{cor} + J_{rec} \quad [1]$$

To analyze our results, we consider the following scheme to describe the fate of holes at the interface

$AB \xrightarrow{J_\phi} AB + h^+ + e^-$	generation of holes	[2]
$AB + e^- + h^+ \xrightarrow{Sr} AB$	surface and near surface recombination	[3]
$AB + h^+ \xrightarrow{k_1} A^+ + B$	photocorrosion	[4]
$C_e^{2-} \underset{k_{-3}}{\overset{k_3}{\rightleftharpoons}} C_{e,ads}^{2-}$	adsorption-desorption of the electrolyte	[5]
$C_s \underset{k_{-4}}{\overset{k_4}{\rightleftharpoons}} C_{s,ads}$	adsorption-desorption of the salt	[6]
$C_{e,ads}^{2-} + h^+ \xrightarrow{k_2} C_e^-$	oxidation of the electrolyte followed by desorption	[7]

In this scheme, AB is a compound semiconductor (like Cd-chalcogenide), h^+ are holes which arrive at the surface in a flux J_ϕ, e^- are electrons which under the effect of the field migrate to the counter-electrode, Sr is the rate of recombination.

The adsorption kinetics of the reduced species of the electrolyte (redox couple) are described by Eq. [5], whereas those of the ionic constituents of the salt are given by Eq. [6]. Finally, the oxidation of the reduced species of the electrolyte is described by Eq. [7]. Although the actual mechanism for the reactions of holes at the interface is more involved than the one given above, it is possible to get some insight into the problem using this rather simplistic approach. For example, in the present model the adsorption of the ferricyanide ions is ignored. This is an oversimplification in view of the adiabatic charge transfer theories which assume that the position of the ions remains unchanged during the charge transfer process. However, the addition of another physisorbed species does not alter the consequences of our qualitative approach and makes it intuitively more complicated to understand.

As a first approximation, we invoke the quasi steady-state assumption which assumes that the reorganization of the interface after the onset of illumination is very rapid (seconds) as compared to the actual rate of deactivation (minutes). In this case, we can write for the (light-induced) excess concentration of holes at the semiconductor surface the following equation (7)

$$0 = \frac{dp_s^*}{dt} = J_\phi - S_r' p_s^* - k_2 p_s^* \theta_e - k_1 p_s^* \quad [8]$$

where $\theta_e = C_{e,ads}^{2-}/M$ is the surface density (coverage) of C_e^{2-} (redox species), and M is the number of adsorption sites. Note that in Eq. [8] we assume that the rate constant for recombination has been modified and it includes the density of electrons near the surface. Using Eq. [8] we can write for p_s^*

$$p_s^* = J_\phi/(S_r' + k_1 + k_2\theta_e) \quad [9]$$

Using the quasi steady-state assumption for θ_e and θ_s (coverage of electrolyte and salt, respectively), we also obtain

$$\theta_e = \frac{K_3(C_e^{2-})(1-\theta_s)}{1 + K_3(C_e^{2-}) + K_2 p_s^*} \quad [10]$$

where $K_3 = k_3/k_{-3}$ and $K_2 = k_2/k_{-3}$ and (C_e^{2-}) is the concentration of C_e^{2-} molecules in the electrolyte.

$$\theta_s = \frac{K_4(C_s)(1-\theta_e)}{1 + K_4(C_s)}, \quad K_4 = \frac{k_4}{k_{-4}} \quad [11]$$

Substituting Eq. [11] into Eq. [10] we obtain for θ_e

$$\theta_e = \frac{K_3(C_e^{2-})}{1 + K_3(C_e^{2-}) + K_4(C_s) + K_2 p_s^*[1 + K_4(C_s)]} \quad [10a]$$

We can now write expressions for the various light induced currents

$$J_{rec} = S_r' p_s^* = J_\phi \left(\frac{S_r'}{S_r' + k_1 + k_2\theta_e}\right) \quad [11a]$$

$$J_{cor} = k_1 p_s^* = J_\phi \left(\frac{k_1}{S_r' + k_1 + k_2\theta_e}\right) \quad [11b]$$

$$J_{reg} = k_2 p_s^* \theta_e = J_\phi \left(\frac{k_2\theta_e}{S_r' + k_1 + k_2\theta_e}\right) \quad [11c]$$

Equations [9] and [10a] are coupled and they can be solved numerically. However, we can discuss the observed phenomena in a qualitative manner with-

out resorting to a numerical analysis. We first notice that in the absence of light Eq. [10a] is a Langmuir type isotherm for two components which adsorb on the surface competitively. We can express K_3 and K_4 in terms of the (free) energy of adsorption

$$K_i = R_i \exp(-E_{ads}^i/kT), \quad i = 3, 4 \qquad [12]$$

Therefore, if the active electrolyte C_e^{2-} is chemisorbed onto the surface of the semiconductor (*i.e.*, E_{ads}^3 is a very large negative quantity), as in the case of polysulfide on CdSe, and the salt is physisorbed on the surface, then $K_3 >> K_4$ and the active electrolyte is preferentially adsorbed on the electrode surface, *i.e.*, $\theta_e \rightarrow 1$. Hence, when a salt is added to the polysulfide electrolyte (3) it does not seriously influence the interface between the semiconductor and the electrolyte. Such an addition does, however, improve the supply of the sulfide ions into the interface (which is not accounted for in the present model) since the ionic strength of the solution is increased and its series resistance decreases. On the other hand, if the active electrolyte is physisorbed, only K_3 and K_4 are of the same order of magnitude, so that by increasing the concentration of salt (C_s) θ_e decreases. It can be deduced from Eq. [11] that J_{reg} decreases while J_{rec} and J_{cor} increase. This results in a decrease in the photocurrent (Fig. 8a) and destabilizes the electrodes as is shown in Fig. 5a and 5b. If we keep C_s (salt concentration) constant and increase C_e^{2-} then θ_e is increased so that J_{reg} is improved at the expense of J_{rec} and J_{cor} as is shown in Fig. 6. If we now increase the surface area of the junction (surface roughness) by a factor s, more molecules of the two species can be accommodated on the surface so that new coverages $s\theta_e$ and $s\theta_s$ should be used. Substituting $s\theta_e$ and $s\theta_s$ into Eq. [10] and [11], we obtain for the new components of the light-induced currents (7)

$$J_{rec} = J_\phi \left(\frac{S_r'}{S_r' + k_1 + k_2 s\theta_e} \right) \qquad [13]$$

$$J_{cor} = J_\phi \left(\frac{k_1}{S_r' + k_1 + k_2 s\theta_e} \right) \qquad [14]$$

and

$$J_{reg} = J_\phi \left(\frac{sk_2\theta_e}{S_r' + k_1 + k_2 s\theta_e} \right) \qquad [15]$$

so that both J_{rec} and J_{cor} decrease while J_{reg} is increased by roughening the surface of the electrode (Fig. 5b). This also means that for a physisorbed species (like ferrocyanide) the addition of salt has a less of an adverse effect for a photoetched electrode than for an etched electrode as is actually observed.

Conclusions

We conclude that the addition of an indifferent salt can be used to discriminate between chemisorbed and physisorbed ions. However, a more sensitive probing method such as measurements with rotating ring-disk electrode is necessary for any quantitative estimation of the adsorption energy. The surface area and variation in surface roughness of the electrodes should also be determined more accurately. Measurements with photoacoustic spectroscopy (12) were not fully satisfactory. However, roughly 50% increase in the surface area does not seem an overestimation. Geometrical considerations give a similar increase in the surface roughness after photoetching.

Acknowledgment

I thank Dr. G. Hodes for some helpful discussions of the salt effect and for suggesting the explanation for the origin of the microcrystallites in Fig. 9 and 10, and Dr. D. Cahen for the careful reading of the manuscript.

Manuscript submitted Nov. 29, 1982; revised manuscript received June 13, 1983.

REFERENCES

1. H. Gerischer, *J. Electroanal. Chem.*, **58**, 236 (1975).
2. (a) H. Gerischer and J. Gobrecht, *Ber. Bunsenges.*, **80**, 327 (1976); (b) K. W. Frese Jr., *Appl. Phys. Lett.*, **40**, 275 (1982).
3. R. Tenne and G. Hodes, *ibid.*, **37**, 428 (1980).
4. G. Hodes, J. Manassen, and D. Cahen, *This Journal*, **128**, 2325 (1981).
5. R. Tenne, N. Müller, Y. Mirovsky, and D. Lando, *ibid.*, **130**, 852 (1983). R. Tenne, H. Flaisher, B. Vainas, N. Müller, G. Hodes, J. Manassen, D. Lando, Y. Mirovsky, and D. Cahen, "Photoelectrochemistry: Fundamental Processes and Measurement Techniques," W. L. Wallace, A. J. Nozik S. K. Deb, and R. H. Wilson, Editors, p. 172, The Electrochemical Society Softbound Proceedings Series, Princeton, NJ (1982); H. Flaisher and R. Tenne, *J. Phys. Chem.*, **87**, 3064 (1983).
6. (a) R. Tenne, *This Journal*, **129**, 123 (1982); (b) P. Bratin and M. Tomkiewicz, "Photoelectrochemistry: Fundamental Processes and Measurement Techniques," W. L. Wallace, A. J. Nozik, S. K. Deb, and R. H. Wilson, Editors, p. 704, The Electrochemical Society Softbound Proceedings Series, Princeton, NJ (1982).
7. A. Heller, G. P. Schwartz, R. B. Vadimsky, S. Menezes, and B. Miller, *This Journal*, **125**, 1156 (1978); R. H. Wilson, *ibid.*, **126**, 1187 (1979).
8. G. Hodes, *Nature*, **285**, 29 (1980); R. Tenne, *Appl. Phys. Lett.*, **23**, 13 (1981); N. Müller and R. Tenne, *ibid.*, **39**, 283 (1981); R. Tenne, Y. Mirovsky, Y. Greenstein, and D. Cahen, *This Journal*, **129**, 1506 (1982); R. Tenne, *Appl. Phys. Lett.*, **43**, 204 (1983).
9. A. Kirsch-De Mesmaeker, A. M. Decoster, and J. Nasielski, *Solar Ener. Mater.*, **4**, 203 (1981); R. DeWitt, A. Kirsch-De Mesmaeker, and J. Nasielski, p. 20, Book of Abstracts, 4th Inter. Conf. on Photochem. Conversion and Storage of Solar Ener., Jerusalem (1982); C. J. Liu, J. Olsen, D. R. Saunders, and J. H. Wang, *This Journal*, **128**, 1224 (1981); J. F. Reber, K. Meier, and N. Bühler, p. 252, Book of Abstracts, 4th Inter. Conf. on Photochem. Conversion and Storage of Solar Ener., Jerusalem (1982).
10. R. Tenne, *Ber. Bunsenges.*, **85**, 413 (1981).
11. J. R. Wilson and S. M. Park, *This Journal*, **129**, 149 (1982).
12. Y. Mirovsky, D. Cahen, R. Tenne, and G. Hodes, "Photoelectrochemistry: Fundamental Processes and Measurement Techniques," W. L. Wallace, A. J. Nozik, S. K. Deb, and R. H. Wilson, Editors, p. 517, The Electrochemical Society Softbound Proceedings Series, Princeton, NJ (1982).

Electrochemical Fluorination of Anthracene Derivatives. II.

J. F. Carpenter, L. H. Ekes, P. F. King, H. A. Mariani, M. Mirza Zadeh, R. F. O'Malley,* and V. J. Roman

Department of Chemistry, Boston College, Chestnut Hill, Massachusetts 02167

ABSTRACT

The controlled potential electrolyses of anthracene(I), 9-methylanthracene(II), and 9-phenylanthracene(III) in acetonitrile solutions containing $(CH_3)_4NF \cdot 2HF$ led to the formation of fluoro derivatives in the 9- and 10-positions. Yields were limited by dimer formation. The products from the electrolyses are consistent with the involvement of radical cations as intermediates.

A number of papers have appeared that describe the electrolytic fluorination of aromatic hydrocarbons in acetonitrile solutions of tetraalkylammonium fluorides (1). A controversy regarding the mechanism of this method of fluorination has arisen (2), and extensive discussions of the factors involved have appeared (3).

With this method, partial and selective fluorinations of aromatic hydrocarbons and their derivatives are deemed possible, and a fairly general applicability of the method has been assumed (1). Rozhkov *et al.* (4) reported the fluorination of naphthalene, benzene, and some of their derivatives. We have described the fluorination of 9,10-diphenylanthracene(IV), which gave the addition product (IX) (5) and benz[a]anthracene from which the 7- and 12-fluoro and 7,12-difluoro derivatives resulted (6a). Some aromatic hydrocarbons yielded only trace amounts of fluoro products, however (6b).

Results and Discussion

The anodic fluorination of anthracene and derivatives described here were usually performed at a controlled potential at or near the oxidation half-wave potential of the aromatic hydrocarbon. Anthracene(I) gave V and small quantities of VI. An extended electrolysis led to the formation of XI. The electrolysis of 9-methylanthracene(II) gave VII; 9-phenylanthracene(III) gave VIII and X

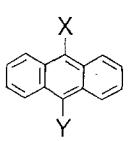

I, X = H, Y = H

II, X = CH_3, Y = H

III, X = C_6H_5, Y = H

IV, X = C_6H_5, Y = C_6H_5

V, X = H, Y = F

VI, X = F, Y = F

VII, X = CH_3, Y = F

VIII, X = C_6H_5, Y = F

Anthracene and 9- and 10- Substituted Anthracenes

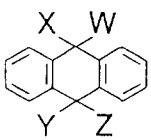

IX, W = C_6H_5, X = F, Y = C_6H_5, Z = F

X, W = C_6H_5, X = F, Y = F, Z = F

XI, W = F, X = F, Y = F, Z = F

9- and 10- Substituted 9,10-Dihydroanthracenes

The first step in the pathway of anodic fluorination of aromatic hydrocarbons in nonaqueous solvents is the formation of radical cations of the substrate: $ArH \rightarrow ArH^{+\cdot}$. It has been amply demonstrated that radical cations of polycyclic aromatic hydrocarbons are formed at the anode during electrolysis in nonaqueous solvents (7), and several reactions of radical cations have been shown to occur. At least the following are pertinent to anodic fluorination: (*i*) attack by an anionic nucleophile, $HAr^{+\cdot} + Nu^- \rightarrow HArNu^{\cdot}$; (*ii*) the formation of dications, $HAr^{+\cdot} \rightarrow HAr^{2+} + e^-$; (*iii*) attack by other nucleophiles, H_2O or CH_3CN; and (*iv*) dimerization and polymerization.

(*i*) In early reports (4, 5) it was assumed that fluorination occurred via attack by fluoride-providing anions as a nucleophile on the radical cations. When addition occurred, as in the case of IV (5), a second electron was lost, followed by attack of another fluoride ion

$$Ar^{+\cdot} \xrightarrow{F^-} ArF^{\cdot} \xrightarrow{-e^-} ArF^+ \xrightarrow{F^-} ArF_2$$

In substitution, *e.g.*, naphthalene (4), the loss of a proton occurred with the removal of the second electron

$$HAr^{+\cdot} \xrightarrow{F^-} HArF^{\cdot} \xrightarrow{-e^-} HArF^+ \xrightarrow{-H^+} ArF$$

(*ii*) Partly on theoretical grounds, the question has been raised whether radical cations can react with fluoride ions, react very slowly, or only in some cases (3). One of the arguments advanced was that the first fluorination of IV was accomplished at a potential of 1.65V *vs.* SCE (5), a potential at which the dication of IV could be formed, which was the more likely intermediate (2). Later the fluorination of IV was accomplished even at a lower potential, at which dication formation could be ruled out (8). The fluorination of benz[a]anthracene (6) occurred at or near its oxidation half-wave potential, a potential at which dication formation was unlikely.

(*iii*) Generally reactions of the radical cations with the solvent of traces of water as nucleophiles have not interfered with the fluorination described here.

(*iv*) The yields of fluoro derivatives have been limited by dimerization and/or polymerization as the principal competing reactions. For anthracene, mass spectral evidence indicated the presence of 9,9'-bianthracene(XII) and XIII, while the formation of three dimeric species, XIV, XV, and XVI, resulted from II. At higher potentials (1.24-1.50V *vs.* SCE), the photoisomer of XIV, XVII, was the principal product

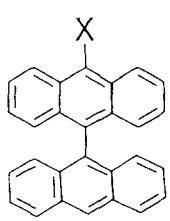

XII, X = H

XIII, X = F

9,9'-Bianthracene and 10-Fluoro-9,9'-bisanthracene

* Electrochemical Society Active Member.

Key words: anode, electrolysis, organic, synthesis.

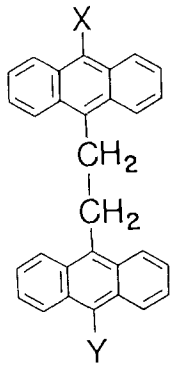

XIV, X = H, Y = H

XV, X = H, Y = F

XVI, X = F, Y = F

9,9'-(1,2-Ethanediyl)bisanthracenes

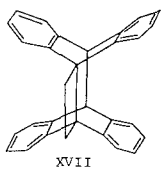

XVII

Photoisomer of 9,9'-(1,2-Ethanediyl)bisanthracene

The presence of a fluorine atom in the product of the electrolysis did not significantly change the oxidation potential; radical cations of the monofluoro derivative were formed which led to mixtures of products difficult to separate. Multiple fluorination may sometimes be advantageous, but often it is not. When geminal difluoro compounds were formed they hydrolyzed on silica gel during work-up, a reaction similar to that described by Oksenenko *et al.* (9). Hydrolysis of X gave

10-hydroxy-10-phenyl(10H)-anthracenone (XVIII) and XIX

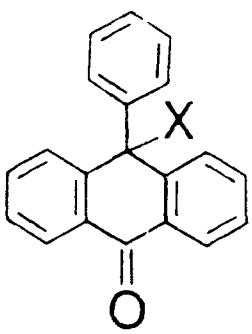

XVIII, X = OH

XIX, X = F

The need for another simple direct method of selective fluorination of aromatic hydrocarbons still exists. Fluorine substitution at specific sites in polycyclic aromatic hydrocarbons is desired for carcinogenic mechanistic studies (10), for example. In principle, the reaction of radical cations with fluoride-donating anions offers an intriguing possibility. The general applicability of the method may be limited for the reasons cited, but it provides a convenient path to the direct synthesis of some fluoro derivatives not easily obtained otherwise (6). The fluorinations described here were conducted at several potentials; the best results were obtained near the oxidation half-wave potential of the substrate. Under the conditions of the electrolyses in this work, it is unlikely that the dications were the main intermediates. The more likely mechanism involves the attack of radical cations by fluoride-donating anions, an ECEC pathway. In addition to the localization of positive charge that is assisted by the benzenoid stability of the outer rings (11), one can argue that orientation of the positive site of the cation radical away from the anode surface would facilitate adduct formation with a fluoride ion at least by electrostatic attraction. The removal of the second electron from the adduct could follow. This is essentially one of the mechanisms suggested by Eberson (12) for anodic fluorination.

Blount (13) has shown that a half-regeneration reaction occurs when the radical cations of 9,10-diphenylanthracene are attacked by nucleophiles. Such a pathway may be involved here, and the second electron transfer need not occur at the electrode, but may take place in the solution also. The designation ECE is used here as suggested by Adams (7), "for all electrochemical reactions with a chemical step interposed between two charge transfers."

A mechanism involving disproportionation of radical cations has been described (14) but the evidence seems to favor the half-regeneration pathway here.

Experimental

Electrolyses were conducted in 250 mliter resin flasks as undivided cells. Platinum anodes were used unless coating occurred, then graphite cloth (Union Carbide, Grade WCA) was used. Cathodes were platinum or stainless steel. The reference electrode was either SCE or Ag/Ag^+ (0.1M) in acetonitrile. The solvent was Burdick and Jackson acetonitrile (UV), introduced through a column of neutral alumina (activity *I*, activated at 400° for 3 hr). The supporting electrolyte was $(CH_3)_4NF \cdot 2HF$ prepared as previously described (15) or purchased from Ozark Mahoning. Additions of the salt and substrate (Aldrich) were made in a dry box. Melting points (Meltemp apparatus) are uncorrected. NMR spectra were measured with a Perkin-Elmer R-24 or a Varian FT 80A instrument, mass spectra on a Hitachi-Perkin-Elmer RMS 4 mass spectrometer, and infrared spectra on a Perkin-Elmer 137 or 421 spectrometer. The potential was controlled by a modified Lingane-Jones (16) potentiostat constructed in the Boston College Electronics Shop. An atmosphere of argon was maintained during the electrolyses. The progress of the electrolyses was followed by occasional TLC examination of the electrolyte and observation of the decrease in current. Following removal of the solvent, the residue was washed with water to remove the excess salt and separated by column chromatography on silica gel.

Anthracene.—Anthracene (1.0g) was added to 200 mliters of 0.5M $(CH_3)_4NF \cdot 2HF$ in acetonitrile and electrolyzed at 1.00V *vs.* Ag/Ag^+ (0.1M) [$E_{1/2}$ 0.84V (17)]. The current rose to 500 mA; when it had fallen to 20 mA another 1.0g of anthracene was added (a total of 11.2 mmol). Again the current rose and was allowed to fall to 10 mA. A total of 6 hr was required. A white precipitate of $(CH_3)_4NF \cdot HF$ formed near the end of the electrolysis. After removal of acetonitrile the residue was washed with water to dissolve the salt. Polymeric material was removed by chromatography on a short silica gel column by elution with petroluem ether. A medium pressure chromatographic separation on silica gel by petroleum ether elution then yielded 1 mg of 9,10-difluoroanthracene (18) and 0.338g of 9-fluoroanthracene, mp 102°-103° (19). Analysis: Calculated for $C_{14}H_9F$: C, 85.70; H, 4.62; F, 9.68. Found: C, 85.71; H, 4.73; F, 9.64. Mass spectral analysis of the remaining material gave masses of 372, 354, 195, and 177, indicating traces of dianthracene and a fluoro derivative. At 1.30V 10 mg of 9, 9, 10, 10-tetrafluoro-9,10-dihydroanthracene, mp 106° (20) was obtained. Analysis: Calculated for $C_{14}H_8F_4$: C, 66.66; H, 3.20; F, 30.13. Found: C, 67.29; H, 3.09; F, 29.58.

9-Methylanthracene.—In a manner similar to that of anthracene 1.0g of 9-methylanthracene (5.2 mmol) was electrolyzed in 200 mliters of 0.5M $(CH_3)_4NF \cdot 2HF$ in acetonitrile at 0.75V *vs.* Ag/Ag^+ (0.1M). After removal of the solvent and washing with water to remove the salt, the residue was separated on a silica

gel column by elution with petroleum ether. A light yellow solid, mp 105°-108° was identified as 9-fluoro-10-methylanthracene (21). Analysis: Calculated for $C_{15}H_{11}F$: C, 85.72; H, 5.23; F, 9.04. Found: C, 85.56, H, 5.37, F, 8.85.

Another electrolysis was run at a potential of 1.25V *vs.* SCE (equivalent to 0.95V *vs.* Ag/Ag^+ 0.1M) and in 0.1M $(CH_3)_4NF \cdot 2HF$ in acetonitrile. A white precipitate (0.601g) formed which did not melt sharply. On heating it turned yellow then brown at approximately 240° and decomposed at 310°. A mass spectral analysis had major peaks at 382, 191, and 165. Analysis: Calculated for $C_{30}H_{22}$: C, 94.20; H, 5.80. Found: C, 93.70; H, 5.99. It was reasonable to expect the formation of XIV, but it has been described as a yellow, fluorescent solid melting at 310°-315° with decomposition (22). The color and behavior on heating indicates that the white solid was in fact the photoisomer of XIV, XVII (23).

An analysis of the white solid showed the presence of 0.30% fluorine; the mass spectrum had minor peaks at 400, 418, and 209. This is evidence for the presence of trace quantities of XV and XVI. Evaporation of acetonitrile, removal of the salt with water, and chromatography on silica gel gave VII in low yield (1-2%) along with unidentified polymeric material.

9-Phenylanthracene.—In the first run 9-phenylanthracene (1.75g) was added to 200 mliters of 0.5M $(CH_3)_4NF \cdot 2HF$ in acetonitrile and electrolyzed at 2.0V *vs.* SCE. The residue remaining after evaporation of acetonitrile was extracted with ether and separated by column chromatography on silica gel with benzene-chloroform mixtures. A yellow solid (66 mg) mp 105°-105.5° was identified as X. Analysis:[1] Calculated for $C_{20}H_{13}F_3$: C, 77.42; H, 4.22; F, 18.36. Found: C, 78.40; H, 4.17; F, 17.34. A ^{19}F NMR spectrum showed two symmetrically skewed doublets at 81.3-84.4 and 107.7-110.8 ppm relative to trichlorofluoromethane. The presence of a singlet at 150.9 ppm showed the possible presence of a mono fluoro derivative.

In another run at 1.30V *vs.* SCE 2.0g of III gave 56 mg of a yellow solid, mp 180.5°-181.0°, which was identified as VIII (24). Analysis: Calculated for $C_{20}H_{13}F$: C, 88.24; H, 4.78; F, 6.98; M.W., 272. Found: C, 88.57; H, 5.01; F, 6.31; M.W., 298. A white solid mp 213°-214° identified as XVIII by its infrared spectrum was present in the products of both runs. Analysis: Calculated for $C_{20}H_{14}O_2$: C, 83.91; H, 4.90; O, 11.19. Found C, 83.06; H, 5.05; O, 11.71. In both cases most of the product could not be identified.

The best results were obtained when the electrolysis was conducted at 0.9-1.0V *vs.* Ag/Ag^+ (0.01M). After the removal of acetonitrile and extraction with water, the residue was sublimed at 100° and 20 mm. The sublimate was identified as a mixture of X, VIII, and III. Analysis:[2] Calculated for $C_{20}H_{13}F_3$: C, 77.42; H, 4.19; F, 18.39. Found: C, 79.63; H, 4.88; F, 15.33 in the mixture. TLC showed the presence of three compounds including III. Gas chromatographic examination of the sublimate on an Apiezon L-Chrom G 12-ft column at 320° confirmed the presence of III, VIII, and X as did a mass spectral examination. The elemental analysis, GC, and mass spectra were consistent with a mixture containing 74% X, 19% VIII, and 6% III. To confirm that X was hydrolyzed on the column in the early experiments, samples of VIII and X were passed through a silica gel column. Nearly all of VIII was recovered unchanged while X hydrolyzed to form XVIII.

[1] This analysis is not within the accepted limits but is sufficient to indicate the nature of the product.

[2] This is the analysis of a known mixture, not a single compound.

Acknowledgment

The assistance with mass spectral measurements by Professor G. Vogel and NMR measurements by Professor D. J. Sardella are gratefully acknowledged.

Manuscript submitted Jan. 13, 1983; revised manuscript received June 11, 1983. This was Paper 435 presented at the St. Louis, Missouri, Meeting of the Society, May 11-16, 1980.

Boston College assisted in meeting the publication costs of this article.

REFERENCES

1. I. N. Rozhkov, *Usp. Khim.*, 1222 (1976), (English Transl., p. 615).
2. L. Eberson and K. Nyberg, *Tetrahedron*, **32**, 2192 (1976).
3. L. Eberson and K. Nyberg, *Acta. Chem. Scand.*, **B32**, 235 (1978), and references therein.
4. (a) I. N. Rozhkov, A. V. Bukhtiarov, N. D. Kuleshova, and I. L. Knunyants, *Dokl. Akad. Nauk SSSR*, **193**, 1322 (1970), (English Transl., p. 618); (b) I. N. Rozhkov, A. V. Bukhtiarov, and I. R. Knunyants, *Izv. Akad. Nauk SSSR, Ser. Khim.*, 1130 (1972), (English Transl. p. 1082); (c) I. N. Rozhkov and I. Y. Alyev, *Tetrahedron*, **31**, 977 (1975).
5. C. J. Ludman, E. M. McCarron, and R. F. O'Malley, *This Journal*, **119**, 874 (1972).
6. (a) R. F. O'Malley, H. A. Mariani, A. R. Buhler, and D. M. Jerina, *J. Org. Chem.*, **46**, 2816 (1981); (b) P. F. King and R. F. O'Malley, *J. Org. Chem.*, Submitted for publication.
7. R. N. Adams, "Electrochemistry at Solid Electrodes," p. 305, Marcel Dekker, New York (1969).
8. I. N. Rozhkov, N. P. Gambaryan, and E. G. Gal'pern, *Tetrahedron Lett.*, 4819 (1976).
9. B. G. Oksenenko, M. Shakirov, and V. D. Shteingarts, *Russian J. Org. Chem.*, **12**, 1307 (1976), (Engl. Transl.,); *Zh. Org. Khim.*, **12**, 1313 (1976).
10. A. W. Wood, W. Levin, R. L. Chang, A. H. Conney, T. J. Slega, R. F. O'Malley, M. S. Newman, D. R. Buhler, and D. M. Jerina, *J. Nat. Cancer Inst.*, **69**, 725 (1982).
11. E. Clar, "The Aromatic Sextet," John Wiley & Sons, London (1972).
12. L. Eberson, Z. Blum, B. Helger, and N. Nyberg, *Tetrahedron*, **34**, 731 (1978).
13. H. N. Blount, *J. Electroanal. Chem.*, **42**, 271 (1973).
14. H. J. Shine, J. J. Silber, R. J. Bussey, and T. Okuyama, *J. Org. Chem.*, **37**, 2691 (1972), and references therein.
15. J. D. Domijan, C. J. Ludman, E. M. McCarron, R. F. O'Malley, and V. J. Roman, *Inorg. Chem.*, **8**, 1534 (1969).
16. J. J. Lingane and S. L. Jones, *Anal. Chem.*, **22**, 1169 (1950).
17. W. C. Neikam and M. M. Desmond, *J. Am. Chem. Soc.*, **86**, 4811 (1964).
18. A. L. Logothetis and G. N. Sausen, *J. Org. Chem.*, **31**, 3689 (1966).
19. J. Rigaudy, J. Barcelo, and M. Rabaud, *Bull. Soc. Chim. Fr.*, 3538 (1969).
20. W. R. Hasek, W. C. Smith, and V. A. Engelhardt, *J. Am. Chem. Soc.*, **82**, 543 (1960).
21. G. L. Anderson and L. M. Stock, *J. Org. Chem.*, **36**, 1140 (1971).
22. I. M. Roitt and W. A. Waters, *J. Chem. Soc.*, 2695 (1952).
23. R. Livingston and K. S. Wei, *J. Am. Chem. Soc.*, **89**, 3098 (1967).
24. J. Rigaudy and J. Barcelo, *Bull. Soc. Chim. Fr.*, 3783 (1968).

The Photocurrent-Voltage Characteristics of the Heterojunction Combination n-Si/SnO_2/Redox-Electrolyte

F. Decker*,[1], M. Fracastoro-Decker,[1] W. Badawy,[2] K. Doblhofer, and H. Gerischer*

Fritz-Haber-Institut der Max-Planck-Gesellschaft, Faradayweg 4-6, D-1000 Berlin 33, Germany

ABSTRACT

A model for Schottky barrier-like heterojunction photoelectrodes is presented. This model allows the calculation of the current-voltage curves for such electrodes under different conditions of illumination and electrochemical charge transfer. SnO_2-coated n-type Si electrodes in contact with the redox systems K_3/K_4 Fe $(CN)_6$ and Cl_2Cl^- show experimental photocurrent-voltage curves with the behavior predicted by the model. The effect of the charge transfer overvoltage and the expected current limitation due to photon control and/or redox ion diffusion are demonstrated. The feasibility of solar energy conversion through photoelectrolysis, by means of cells based on heterojunction photoelectrodes, is discussed.

Photocorrosion is a general problem of photoelectrochemical cells where small bandgap semiconducting electrodes are used. To avoid this problem, a range of coatings has been applied to the electrode surfaces. Thin layers of metals (1-5) or of transparent and conducting oxides (6-8) have been deposited onto the semiconductor by different techniques. The resulting electrodes can mostly be described as Schottky barrier-like heterojunctions with an electrolyte front contact.

SnO_2 is a particularly attractive material for this purpose because of its high transmittance in the visible-infrared range, its resistance against chemical attack, and because of the possibility of incorporating foreign atoms which modify both solid-state and interfacial properties in a wide range (9-12). We shall consider the following electrodes composed of n-type Si-SnO_2 heterojunctions. A schematic representation of the Si-SnO_2-electrolyte system is given in Fig. 1. The photovoltage V_j is generated at the junction Si-SnO_2, which is a device of the Schottky barrier type (13). The electrochemical reaction, on the other hand, proceeds at the SnO_2-electrolyte interface and is thus separated from the photoactive junction by the protective oxide film. This physical separation is advantageous in the definition of the current-voltage characteristics of the system since it permits first analyzing separately and then combining the concepts characterizing the photovoltaic and the electrochemical part of this photoelectrochemical cell.

In this work, we derive a mathematical model for the treatment of heterojunction photoelectrodes. Furthermore, we shall use this model to discuss the performance of illuminated Si-SnO_2 electrodes in contact with the redox systems K_3/K_4 Fe$(CN)_6$ and Cl_2/Cl^-. We disregard in our treatment the special case of such thin layers ($\lesssim$ 50Å) that can be tunneled by photogenerated minority carriers. Their protection against corrosion is not likely to last for long enough time since it is hardly possible to produce such thin layers without pinholes or larger defects. The SnO_2 layers of about 800Å thickness used in our experiments here were tight, and we could not detect any photocorrosion of the silicon after more than 30 hr of operation under solar-like illumination (14).

Theory

The equivalent circuit corresponding to the considered photoelectrochemical system is shown in Fig. 2. Note that the overvoltage occurring at the counterelectrode, η_{CE} in Fig. 2, and the solution resistance, R_E, will be disregarded in the following analysis. The usable voltage, V_{cell}, which is the driving force for photoelectrolysis in our system, is thus defined by the barrier height ($\Phi_B - \Delta\Phi$), diminished by the losses V_B, JR_S, and η (see Fig. 1 and 2)

$$|V_{cell}| = \Phi_B - \Delta\Phi - (V_B + \eta) - JR_S \qquad [1]$$

V_B is the voltage drop in the semiconductor space-charge layer between bulk and surface, JR_S the ohmic drop, and η the electrochemical overpotential at the oxide-electrolyte interface. Equation [1] may be written as

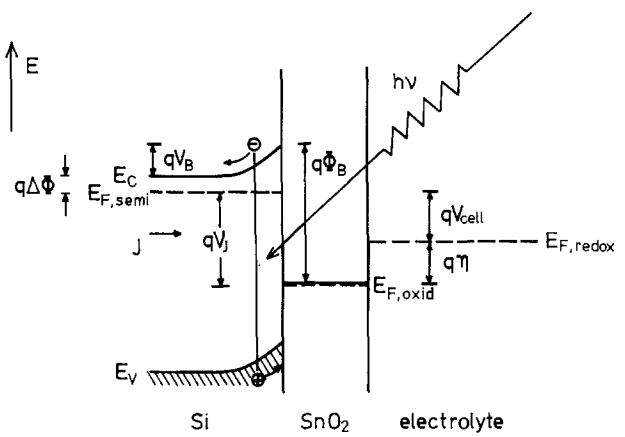

Fig. 1. Energy band diagram of the photoelectrochemical cell based on an SnO_2-coated n-Si electrode, close to its maximum output power point. The dashed lines represent the Fermi levels, E_F, of Si, SnO_2, and redox electrolyte. The arrow next to *J* shows the direction of positive current flow. η is the overvoltage of the electrochemical process. V_{cell} is the usable cell voltage. Other potentials characterized by the symbols *V* and Φ are explained in the text.

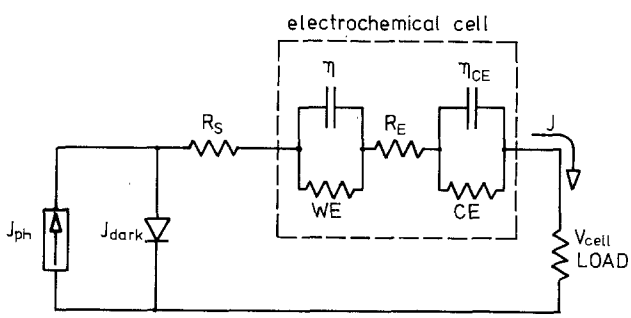

Fig. 2. Simplified equivalent circuit for the same photoelectrochemical cell described in Fig. 1. The conversion of light into electricity is here represented. *WE* corresponds to the electrochemical reaction proceeding at the SnO_2 surface with overvoltage η, *CE* is the counterelectrode.

* Electrochemical Society Active Member.
[1] Permanent address: Instituto de Fisica-UNICAMP, 13100 Campinas (S.P.), Brazil.
[2] Permanent address: Chemistry Department, Faculty of Science, Cairo University, Cairo, Egypt.
Key words: solar energy, photoelectrolysis, semiconductor, overvoltage.

$$|V_{cell}| = |V_j| - JR_S - \eta \quad [1a]$$

where V_j is the photovoltage across the heterojunction between Si and SnO_2. For convenience, we have used the absolute values of V_j and V_{cell}, because in a Schottky barrier with an n-type semiconductor the sign of the photovoltage is negative. In the following equations, we omit the vertical bars symbolizing the absolute values. The dark forward electron current of the SnO_2-Si heterojunction is given by the following equation

$$J_{dark} = J_o \left[\exp\left(\frac{qV_j}{mkT}\right) - 1 \right] \quad [2]$$

where J_o is the reverse saturation electron current density, m the diode quality factor, and q, k, and T have the usual meaning. Under illumination, we assume the superposition principle to hold for the photocurrent and the dark current

$$J = J_{ph} - J_{dark} \quad [3]$$

If carrier mobilities and lifetimes are large and interfacial recombination is negligible, as we can assume for our samples, J_{ph} is constant, and the saturation photocurrent density is defined by

$$J_{sat} = J_{ph} + J_o \simeq J_{ph} \quad [4]$$

if $J_{ph} >> J_o$ (15). In the steady state, the currents passing the Si/SnO_2 and the SnO_2/electrolyte junctions must be equal. We can therefore combine Eq. [1]-[4] and obtain a general description of the current-voltage relationship of this heterojunction photoelectrochemical device

$$J = J_{sat} - J_o \exp\left[\frac{q}{mkT}(V_{cell} + JR_S + \eta)\right] \quad [5]$$

Equation [5] may be written in the form

$$V_{cell} = \frac{mkT}{q} \ln\left(\frac{J_{sat} - J}{J_o}\right) - \eta - JR_S \quad [5a]$$

in which the first term defines $V_j(J)$.

The main source of R_S in photocells is normally the collecting front contact (16). In our cell, this is the whole SnO_2 electrode surface, where the redox reaction takes place. With this geometry, no lateral current flows in the oxide film. With oxide films which have a thickness of the order of 100 nm, one is therefore close to reality in assuming $R_S = 0$. Then Eq. [1a] simplifies to

$$V_{cell} = V_j - \eta \quad [1b]$$

which shall be used to determine V_j from the experimental V_{cell} and η data.

Two types of overvoltage (17) are relevant for the electrochemical processes at the SnO_2 surface, viz., the mass-transport overvoltage, in particular the diffusion overvoltage, η_{diff}, and the charge transfer overvoltage ,η_{CT}

$$\eta = \eta_{diff} + \eta_{CT} \quad [6]$$

The diffusion overvoltage, η_{diff}.—We consider here the situation in which the transport of the redox species is rate determining. This means, the charge transfer reaction is so fast that at the electrode surface the Nernst equilibrium is established also during current flow. The $\eta(J)$ relationship is then defined by the particular mode of mass transport to the electrode surface. For a rotating disk electrode (we used a similar geometry in this work), we have, in the presence of a high concentration of background electrolyte (18)

$$\eta(J) = \eta_{diff} = \frac{RT}{n\mathbf{F}} \ln\left(\frac{J - J_{lc}}{J_{la} - J}\right) + \frac{RT}{n\mathbf{F}} \ln\left(\frac{D_{red}}{D_{ox}}\right)^{2/3} \quad [7]$$

The limiting current densities, J_{lc} and J_{la}, are defined by (19)

$$J_{lc} = -0.62n\mathbf{F}D_{ox}^{2/3}\omega^{1/2}\nu^{-1/6}C_{ox} \quad [8a]$$

$$J_{la} = 0.62n\mathbf{F}D_{red}^{2/3}\omega^{1/2}\nu^{-1/6}C_{red} \quad [8b]$$

In Eq. [7] and [8], D_{ox} and D_{red} are the diffusion coefficients of the components of the redox system, ox and red, ω is the rotation rate of the disk electrode in rad sec^{-1}, ν is the kinematic viscosity of the electrolyte solution, and C_{ox} and C_{red} are the concentrations of the components of the redox couple. R, T, n, and $\mathbf{F}$ have their usual electrochemical significance. Since $D_{ox} \sim D_{red}$ the second term of Eq. [7] is very close to zero and shall be neglected in the following.

The charge transfer overvoltage, η_{CT}.—The charge transfer overvoltage can be related to the cell current by the Butler-Volmer equation

$$J = j_o \left[\exp\left(\frac{\alpha n\mathbf{F}\eta_{CT}}{RT}\right) - \exp\left(-\frac{(1-\alpha)n\mathbf{F}\eta_{CT}}{RT}\right) \right] \quad [9]$$

where α is the charge transfer coefficient. The exchange current density, j_o, is defined by the formal rate constant of the heterogeneous charge transfer process, k_o', and the concentration of the redox system, $C_{ox} = C_{red} = C$

$$j_o = n\mathbf{F}k_o'C \quad [10]$$

Near the equilibrium potential of the redox couple one obtains an expression for η_{CT} by linearizing Eq. [9]

$$\eta_{CT} = \frac{RT}{n\mathbf{F}j_o} J \quad [11]$$

At larger values of η, the back reaction, *i.e.*, the second term in the brackets of Eq. [9], becomes negligible and the electrochemical reaction can be described by the well-known Tafel equation (anodic)

$$\eta_{CT} = \frac{RT}{\alpha n\mathbf{F}} \ln\left(\frac{J}{j_o}\right) \quad [12]$$

These expressions may be introduced into Eq. [5a] to obtain explicit current-voltage relations of photoelectrochemical cells. With Eq. [7] and [11] we obtain

$$V_{cell} = \frac{RT}{\mathbf{F}} \left[m \ln\left(\frac{J_{sat} - J}{J_o}\right) - \frac{1}{n} \ln\left(\frac{J - J_{lc}}{J_{la} - J}\right) - \frac{J}{nj_o} \right] \quad [13]$$

When η_{CT} assumes high values, Eq. [12] will be valid, and instead of Eq. [13] we obtain

$$V_{cell} = \frac{RT}{\mathbf{F}} \left[m \ln\left(\frac{J_{sat} - J}{J_o}\right) - \frac{1}{n} \ln\left(\frac{J - J_{lc}}{J_{la} - J}\right) - \frac{1}{\alpha n} \ln\left(\frac{J}{j_o}\right) \right] \quad [14]$$

The first term in the brackets of Eq. [13] and Eq. [14] corresponds to V_j, the second to η_{diff}, and the third to η_{CT}; R_S is assumed to be zero.

Experimental

The SnO_2 films were prepared on the (100) surface of a single-crystal n-type Si ($\rho = 1\ \Omega$ cm) with the method of chemical vapor deposition. Dibutyl-tin-diacetate reacted with air and water vapor at 400°C to form the oxide. The complete film was 80 ± 5 nm thick. Details of the procedure were described previously (14). To prepare the Sb- and Ru-doped films, the combined spray/CVD method described

previously (20) was used. Thereby, *ca.* 1% Sb was incorporated by including $SbCl_5$ in the spray, and doping with *ca.* 1% Ru was achieved by adding $RuCl_3$ to the spraying solution. The analyses were made by ESCA. The SnO_2-coated Si crystals were mounted as shown in Fig. 3. A Pt wire was attached to the SnO_2 surface and connected to the brass tube of the electrode holder. The back side of the Si single crystal had an In-Ga low ohmic contact and was attached by means of a conducting epoxy to a brass cylinder. The electrode holder could then be mounted onto the rotating ring-disk device available in this laboratory, whereby the coated semiconductor electrode ("disk") could be polarized, illuminated, and rotated in the electrolyte while the potential of the SnO_2 surface could be continuously monitored via the "ring" connection of the device. Therefore, it was possible to simultaneously determine the overvoltage of the electrochemical process (η), the cell voltage (V_{cell}), and the cell current density (J) under different light intensity and mass transport conditions.

All solutions were made with pure p.a. reagents and triply distilled water. Cell electrolytes were deaerated with dry ultrapure nitrogen. Illumination was provided by means of a 150W xenon lamp coupled with an ORIEL solar simulator filter, and all experiments were performed under potentiostatic control in the three electrode configurations. η was measured by means of a high impedance microvoltmeter (Keithley 155). The solution redox potentials were +220 mV *vs.* saturated calomel electrode for a 10 mM $K_3Fe(CN)_6$ + 10 mM $K_4Fe(CN)_6$ in 0.5M KNO_3 solution (*p*H 7), and 1120 mV for the 3M NaCl/sat. Cl_2 system.

Results

The current-voltage behavior of a diffusion-controlled process on a rotated disk electrode is impressed on the photoelectrochemical cell when $J_{la} < J_{sat}$. The experiments presented in Fig. 4 demonstrate the dependence of the limiting current on $\sqrt{\omega}$. The junction $V_j(J)$ characteristics, obtained by correcting the cell voltage for the overvoltage η, (Eq. [1b]), are included for all rotation rates. The light intensity is such that the saturation photocurrent density is 14 mA cm^{-2}.

The photoelectrochemical experiments presented in Fig. 5 show the transition from diffusion control, J_{la}, to limitation of the current by the light intensity, J_{sat}. The light intensity has now been attenuated by a factor of four with respect to the conditions of Fig. 4, while the other parameters were kept constant. Still, $J_{la} < J_{sat}$ for rotation velocities of 4 and 9 sec^{-1}

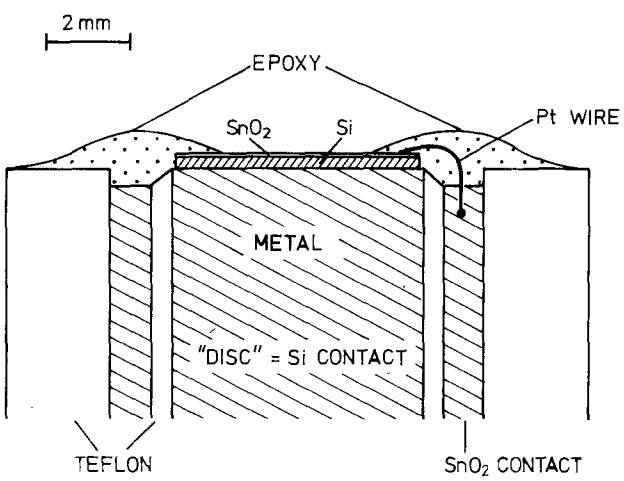

Fig. 3. The SnO_2-coated n-Si rotating photoelectrode used in this work. Note the separate contacts to the silicon and the SnO_2 surface.

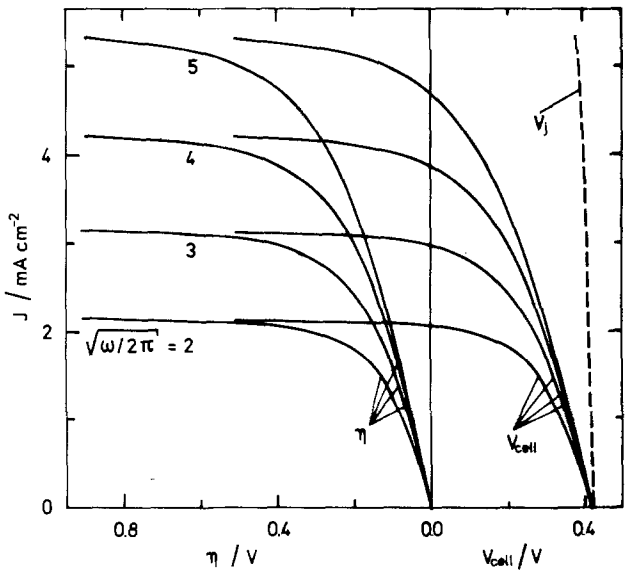

Fig. 4. Experimental $V_{cell}(J)$, $\eta(J)$, and $V_j(J)$ curves obtained with the system Si-SnO_2-$Fe(CN)_6^{3-/4-}$ (10^{-5} mol cm^{-3}). Support electrolyte $5 \cdot 10^{-4}$ mol cm^{-3} KNO_3, *p*H 7. Illumination intensity ~50 mW cm^{-2}. The electrode rotation rates are given in $sec^{-1/2}$.

and, therefore, both the $\eta(J)$ and the $V_{cell}(J)$ curves resemble those shown in Fig. 4 for the same rotation velocities. For rotation velocities of 16 and 25 sec^{-1}, $J_{la} > J_{sat}$, and the photon flux now controls the limiting photocurrent of the cell. Figure 5 is an experimental demonstration of the interplay between the electrochemical and photovoltaic parameters, as related by Eq. [13].

Figures 6 and 7 show the situation of $J_{la} > J_{sat}$. This situation can be realized experimentally with a high concentration of the redox-system and a high rate of mass transport to the electrode surface (cf. Eq. [8]). In these experiments, almost no change is observed when the electrode rotation velocity is varied. The cell current becomes limited as the saturation photocurrent is reached, this last one being linearly proportional to the light intensity at least up to solar irradiation level. The highest curve in Fig. 7 represents the cell characteristics under AM1-simulated solar irradiation (~ 100 mW/cm^2). There is a clear

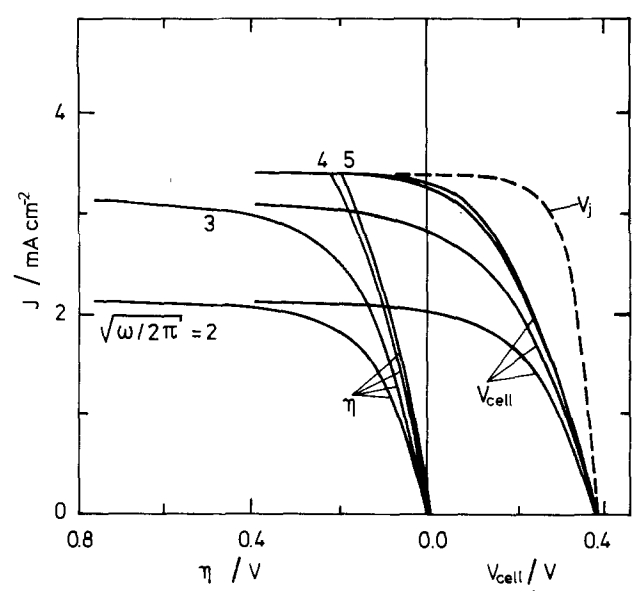

Fig. 5. Experimental $V_{cell}(J)$, $\eta(J)$, and $V_j(J)$ curves demonstrating the transition from diffusion to illumination limitation. Parameters as in Fig. 4, except for the illumination intensity of 11 mW cm^{-2}.

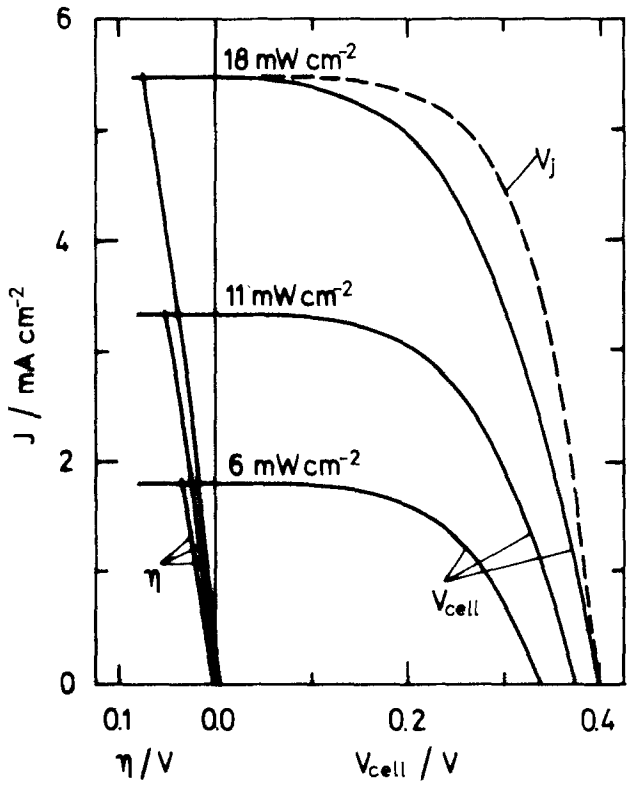

Fig. 6. Experimental photocurrent (J) vs. cell voltage (V_{cell}) curves of an Si-SnO_2-$Fe(CN)_6^{3-/4-}$ ($2.5 \cdot 10^{-4}$ mol cm^{-3}) photoelectrochemical cell under different light intensities. Support electrolyte $5 \cdot 10^{-4}$ mol cm^{-3} KNO_3, pH 7. The experimental $\eta(J)$ curves were determined with the front contact on the SnO_2 electrode. The junction voltage (V_j) was obtained by adding the values of V_{cell} and η for each value of J. Electrode rotation rate $(\omega/2\pi) = 16$ sec^{-1}.

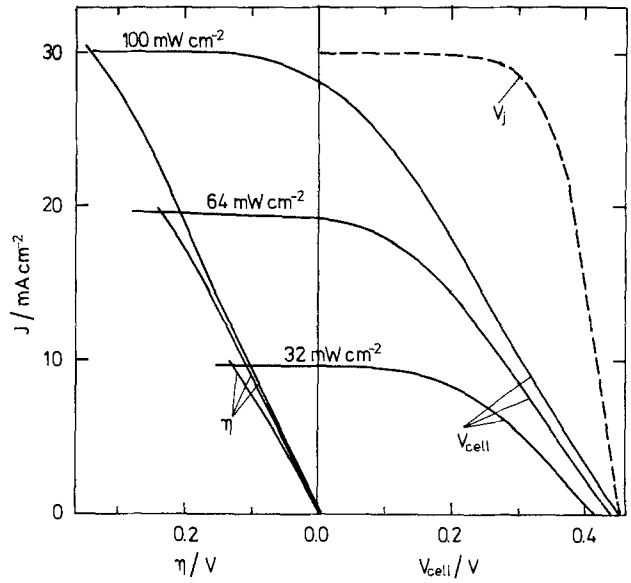

Fig. 7. Experimental $V_{cell}(J)$, $\eta(J)$, and $V_j(J)$ as in Fig. 6, but with higher light intensities. The upper curve corresponds to AM1 illumination (~100 mW cm^{-2}). The same curves are obtained with $(\omega/2\pi) = 16$ sec^{-1} and with $(\omega/2\pi) = 25$ sec^{-1}.

decrease of the actual cell fill factor with increasing light intensity, due to η_{CT}. The $\eta(J)$ curves of Fig. 6 and 7 vary somewhat with the illumination intensity. This may be due to a photoeffect at the Pt/SnO_2 contact, because the insulating epoxy (Fig. 3) allowed a small fraction of the light to be transmitted. This effect was, however, of little consequence for our analysis and was therefore not further investigated.

In Fig. 8 the current-voltage curves of the Cl_2 evolution reaction are plotted. The variation of activity of the used electrodes is due to incorporation of 1% Sb or 1% Ru into the SnO_2.

The measurements shown in Fig. 8 and 9 were made *vs.* an SCE. For consistency with the previous diagrams, the equilibrium potential of the Cl_2/Cl^- couple was taken as the zero-point of the V_{cell} scale in Fig. 9. Negative values on this scale indicate that, in addition to the photovoltage, an auxiliary voltage has to be applied to drive the cell reaction. The results of Fig. 8 and 9 were not obtained with the Pt/SnO_2 contact, Fig. 3, but with SnO_2 films prepared on glassy carbon (Fig. 8) and on Si (Fig. 9) under identical conditions.

Discussion

The interaction between light and transport control has been experimentally demonstrated in a very elegant way by Miller *et al.*, modulating both light intensity and rotation speed of an Au-coated GaAs rotating electrode (21). However, this technique did not allow the exact measurement of the potential of the coating. Simultaneous measurements of the potential of both substrate and overlayer have been reported in the literature (5, 22), but in these works the diffusion conditions of the reacting species were not precisely known and, therefore, no quantitative analysis of the electrochemical process could be applied. The technique used in this work allows both the simultaneous potential measurement of substrate and coating and a good control of the mass transport conditions by means of electrode rotation. This allows a meaningful comparison between the theory for heterojunction photoelectrodes and the experiments.

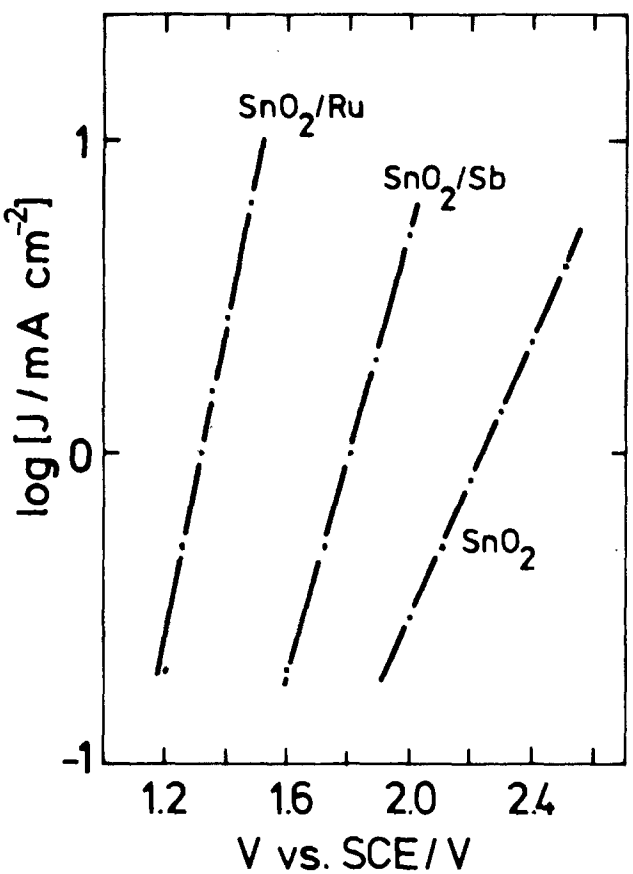

Fig. 8. Current-voltage curves obtained with undoped and doped (*ca.* 1% Sb, *ca.* 1% Ru) SnO_2 electrodes deposited on glassy carbon. The electrolyte was 3M NaCl; with SnO_2/Ru it was saturated with Cl_2. The equilibrium potential was then 1.12V *vs.* SCE.

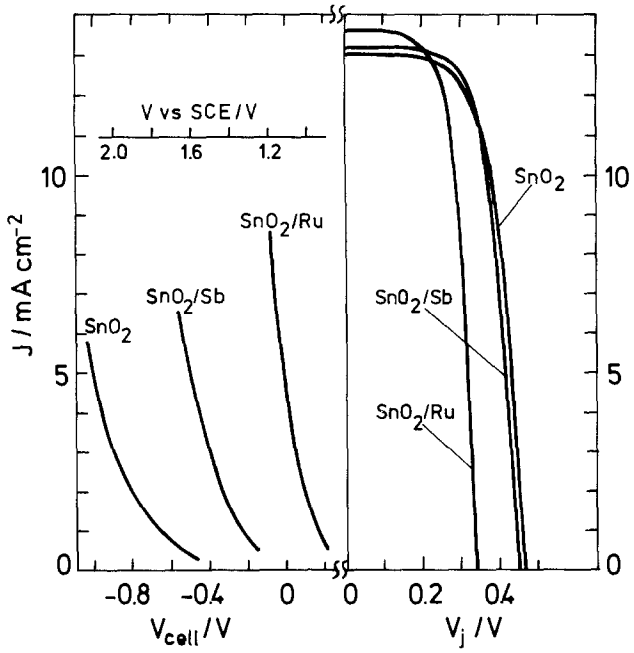

Fig. 9. Photoelectrochemical performance of the doped and undoped (as in Fig. 8) SnO_2, deposited on Si, in 3M NaCl. To determine $V_j(J)$, the $\eta(J)$ data from Fig. 8 were used. The electrochemical potential scale (V vs. SCE) is included to facilitate comparison with Fig. 8.

Current limited by the rate of diffusion, J_{la}.—Equations [13] and [14] indicate that, independent of the particular η_{CT} function, the current can neither exceed J_{sat} nor J_{la} (we assume a photocurrent driving an anodic reaction). The dependence of cell current on the electrode rotation rate according to Eq. [8b], as shown in Fig. 4, demonstrates limitation by diffusion. By increasing the rotation rate and by increasing C_{red}, the limiting current may be raised until it is larger than J_{sat}. This transition from diffusion control to photon control is shown in the experiment of Fig. 5. For an efficient energy conversion system, current limitation by J_{la} is of course undesirable. Accordingly, the experiments discussed in the following are set up such that the condition $J_{la} > J_{sat}$ is fulfilled.

Comparison of the J vs. V_j curves with theory.—In Fig. 10, $V_j(J)$ curves are shown which were derived (Eq. [1b]) from the $V_{cell}(J)$ and $\eta(J)$ curves for different light intensities shown in Fig. 6 and 7. These $V_j(J)$ curves characterize the actual solid-state junction between n-Si and SnO_2. To determine if the analysis is self-consistent, the open-circuit potentials obtained with lower light intensities were determined. At these potentials, the dark current should equal the respective J_{sat} (cf. Eq. [3] and [4]). Subtracting these values from J_{sat}°, the saturation current density at 100 mW cm^{-2}, the experimental $V_j(J)$ curve at this illumination should be obtained (23). These points are shown as circles in Fig. 10. The deviation from the experimental 100 mW $V_j(J)$ curve can be explained by a residual series resistance of 1.5Ω, which is probably due to a layer of insulating SnO_2 aqueous on the electrode surface. This explanation is consistent with recent results of sensitization experiments on SnO_2 (24), and also with the low values of α regularly found with SnO_2 electrodes (cf. Fig. 8).

The solid line in Fig. 10 represents a theoretical curve calculated with Eq. [5] and $R_S = \eta = 0$, and the parameters of the Si/SnO_2 junction $J_o = 1 \times 10^{-7}$ A cm^{-2}, $m = 1.44$, and $J_{sat}^{\circ} = 3.01 \times 10^{-2}$ A cm^{-2}. The fill factor is 0.73. The curve clearly fits the points derived with the described procedure very well. This result proves that the junction properties are satisfactory.

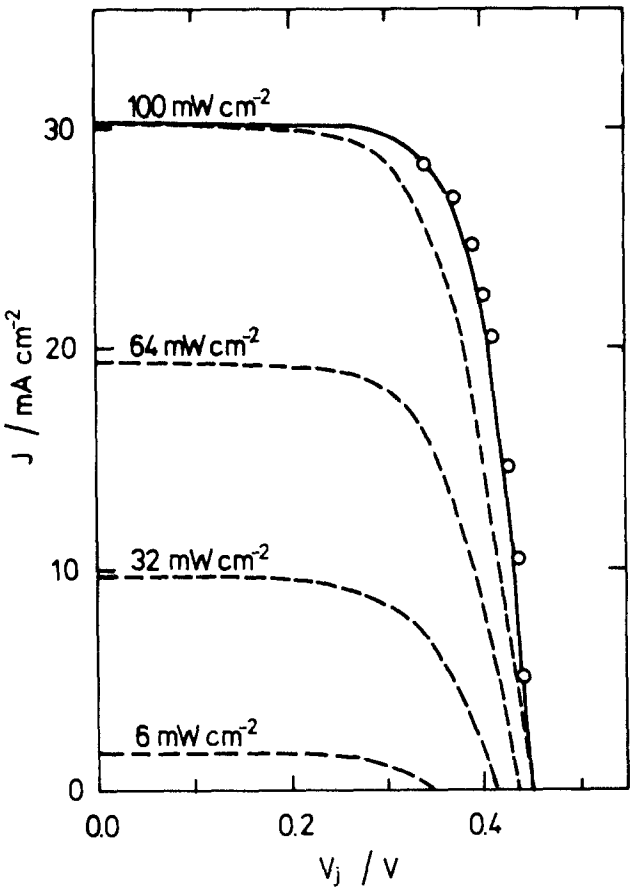

Fig. 10. J vs. V_j curves derived from Fig. 6 and 7 for different light intensities (dashed line). The dots represent the ($J^{\circ}_{sat} - J_{sat}$) vs. V_{oc} values. The solid line is calculated from Eq. [5], with $R_S = \eta = 0$.

Effect of the overvoltage on the cell performance.—The effect of η shall be analyzed using plots of V_{cell}, V_j, and η *vs.* J taken from Fig. 6 and 7. In addition to these data, Fig. 11 contains the corresponding $\eta_{diff}(J)$ curve calculated with Eq. (7), and

$$V_{cell}^{diff} = V_j - \eta_{diff} \qquad [15]$$

$V_{cell}^{diff}(J)$ would be the observed cell voltage/current function if the interfacial charge transfer were very fast (*i.e.*, $k_o' \to \infty$). Unfortunately, η_{CT}, which is the difference between η and η_{diff}, is large. This is due to a small rate constant k_o', which can be determined from the slope of the $\eta_{CT}(J)$ curve near $\eta = 0$ (cf. Eq. [11])

$$k_o' = \frac{RT}{F^2C}\left(\frac{dJ}{d\eta_{CT}}\right)_{\eta=0} \qquad [16]$$

From the data of Fig. 11, a value of $k_o' = 2.4 \times 10^{-3}$ cm sec^{-1} is obtained, which agrees well with the literature values (9). The experimental results agree thus with the expected behavior. Note that the rate constant on Pt is $k_o' = 2 \times 10^{-1}$ cm sec^{-1} (25).

Clearly, low values of k_o' correspond to low fill factors, particularly at high current densities. Thus, at the lower light intensity (19 mW cm^{-2}, Fig. 11) the fill factors are 0.67 for $V_j(J)$, 0.66 for $V_{cell}^{diff}(J)$, and 0.54 for $V_{cell}(J)$. At AM1 illumination, the corresponding fill factors are 0.64, 0.62, and 0.28. With these fill factors and the values of V_{oc} and J_{SC}, one calculates an energy conversion efficiency of 9% for the Schottky barrier at AM1 illumination, but of only 3% when the output of the photoelectrochemical cell, $V_{cell}(J)$, is considered. These results demonstrate the

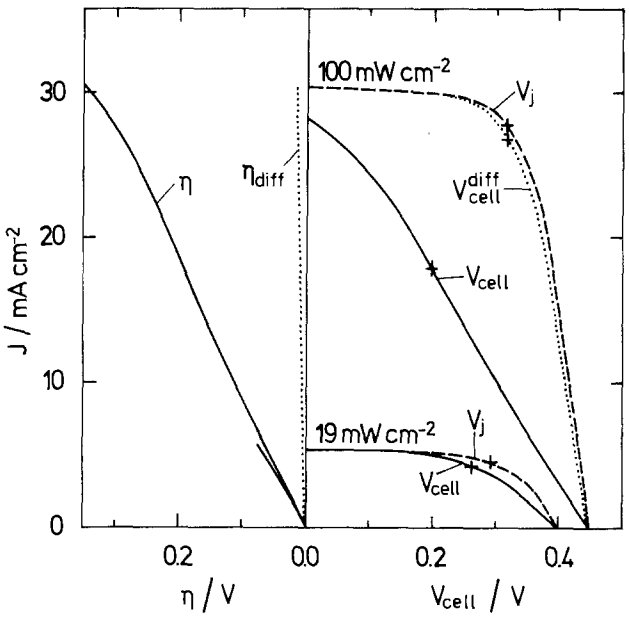

Fig. 11. Data of $V_{cell}(J)$, $V_j(J)$, and $\eta(J)$ collected from Fig. 6 and 7. The calculated (Eq. [7]) values of η_{diff} (dotted) are included as well as the corresponding V_{cell}^{diff} curves expected for a fully reversible redox system. The crosses represent the maximum power points. The corresponding fill factors are in the text.

detrimental effect of the large overvoltage on the SnO_2 film electrode and therefore the need of improving the rate of charge transfer to obtain a photoelectrochemical system which is efficient under solar irradiation.

Irreversible electrochemical reactions.—The $\eta_{CT}(J)$ curves obtained with K_3/K_4 $Fe(CN)_6$ on SnO_2 can be described in the considered current range (Fig. 11) by the linearized function Eq. [11]. This is not possible when an "irreversible" reaction, such as the chlorine evolution on SnO_2, is considered. In this case, the Tafel relation (Eq. [12]) leads to linear plots, as shown in Fig. 8. A photoelectrochemical cell with such a redox system is thus described by Eq. [14]. Such $V_{cell}(J)$ curves are shown in Fig. 9, together with the corresponding $V_j(J)$ curves obtained with $\eta(J)$ from Fig. 8.

The experiments shown in Fig. 8 and 9 were initiated to enhance the electrocatalytic activity of the SnO_2. Indeed, the improvement achieved by doping is born out by a rise of j_o and α (cf., the intercepts and the slopes of the Tafel plots). However, the $V_j(J)$ characteristics are adversely affected by this doping. Inspection of Fig. 9 indicates that V_{oc} decreases from 0.47V for the undoped SnO_2 to 0.34V for the Ru-doped SnO_2. It is not the purpose of this work to discuss these results in depth; however, they should demonstrate the value of the proposed analysis.

The band diagrams for the considered photoelectrochemical situations.—The $V_{cell}(J)$ curves of Fig. 4 and 6, varying with the light intensity and rotation rate, respectively, exhibit some apparent resemblance. Note, however, that the physical situation is quite different in the two cases. This fact is clearly shown in the corresponding band diagrams.

Knowing the value of $\Phi_B = 0.8V$ (13) and the voltage across the heterojunction, $V_j(J)$, the band diagrams can be constructed using Eq. [1] and [1a] and Fig. 1. Accordingly

$$V_B(J) = 0.8 - [V_j(J) + \Delta\Phi] \qquad [17]$$

Figure 12 shows the band diagrams corresponding to $V_{cell} = 0$ and $J \sim 3$ mA cm^{-2}. The diagram "photon control" (Fig. 12a) is deduced from data as shown

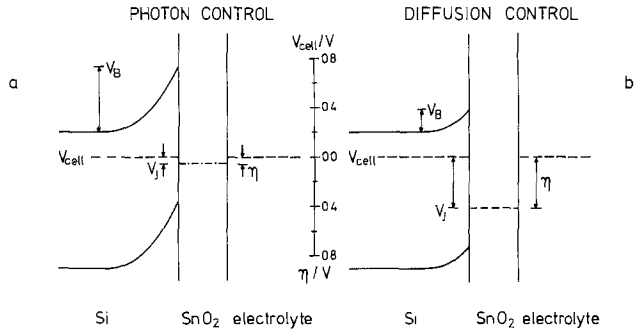

Fig. 12. Solid lines: energy band diagrams for the Si-SnO_2-$Fe(CN)_6^{3-/4-}$ photoelectrochemical cell in short circuit. (a) Photon control, from Fig. 6, 11 mW cm^{-2}; (b) diffusion control, from Fig. 4, curve 3. The resulting cell current and cell voltage are the same in (a) and (b). Dotted lines: energy band diagrams as before, except for the cell voltage = −0.1V.

in Fig. 6 at 11 mW cm^{-2} illumination. The data of Fig. 12b, "diffusion control," correspond to curve 3, Fig. 4.

In the case of current limitation by the light intensity, V_B rises in order to supply the maximum photocurrent possible according to the particular photon flux. A correspondingly small overvoltage η suffices to drive the electrochemical reaction. When, however, the cell current is limited by the diffusion rate of the electroactive species, η has to rise, while a limited amount of band bending V_B suffices to provide that much photocurrent that can be transported through the electrolyte. All the voltages described in Eq. [1] and [1a] are here represented and have been deduced from the experimental data relative to the particular photoelectrode described in this work. Photon and diffusion control are clearly identified by the different distribution of the total voltage drop of the photoelectrochemical cell among η and V_B.

Conclusions

A mathematical description of heterojunction photocells in contact with an electrochemical system was derived. Thereby, the photovoltaic characteristics as well as the mass transport and charge transfer overvoltage of the coupled electrochemical reaction are considered (Eq. [13] and [14]).

The experimental curves obtained with the heterojunction n-Si/n-SnO_2 in contact with the redox systems $Fe(CN)_6^{3-/4-}$ and Cl_2/Cl^-, comply with the derived model. The current limitation by either the photon flux or the rate of redox-ion diffusion is well characterized. A low charge transfer rate was demonstrated to have a deteriorating effect on the fill factor. The redox system $Fe(CN)_6^{3-/4-}$ was shown to have a rather low electrochemical rate constant on the SnO_2 electrode: $k_o' = 2.4 \times 10^{-3}$ cm sec^{-1}. This leads to a fill factor of 0.28 at AM1 illumination, compared with a value of 0.62 which would be obtained under the same conditions if the electrode reaction were electrochemically reversible. The solid-state part of the device, *i.e.*, the Si/SnO_2 heterojunction, was shown to meet the expectations of an efficient photovoltaic cell. Thus, to improve the cell performance it will be necessary to increase the rate of the electrochemical reaction at the SnO_2 film electrode.

Acknowledgments

The authors thank Dr. J. Melsheimer (Materialforschungslabor, FHI) for the CVD preparation of the SnO_2 films, Dipl.-Phys. S. Krause for the ESCA spectra, and S. Wasle for continued technical assistance. This work was supported by the European Community under the contract ESD-012-80 D.

Manuscript submitted Dec. 27, 1982; revised manuscript received May 20, 1983.

REFERENCES

1. S. Menezes, A. Heller, and B. Miller, *This Journal*, **127**, 1268 (1980).
2. Y. Nakato, T. Ohnishi, and H. Tsubomura, *Chem. Lett.*, 883 (1975).
3. Y. Nakato, K. Abe, and H. Tsubomura, *Ber. Bunsenges. Phys. Chem.*, **80**, 1002 (1976).
4. R. H. Wilson, L. A. Harris, and M. E. Gerstner, *This Journal*, **124**, 1233 (1977).
5. L. A. Harris, M. E. Gerstner, and R. H. Wilson, *ibid.*, **124**, 1511 (1977).
6. P. A. Kohl, S. N. Franck, and A. J. Bard, *ibid.*, **124**, 225 (1977).
7. M. Tomkiewicz and J. M. Woodall, *ibid.*, **124**, 1436 (1977).
8. H. P. Maruska and A. K. Ghosh, *Solar Energy Mater.*, **1**, 411 (1979).
9. D. Elliott, D. L. Zellmer, and H. A. Laitinen, *This Journal*, **117**, 1343 (1970).
10. J. Kane, H. P. Schweizer, and W. Kern, *ibid.*, **123**, 270 (1976).
11. F. Möllers and R. Memming, *Ber. Bunsenges. Phys. Chem.*, **76**, 469 (1972).
12. T. A. Chertykortseva, D. M. Skob, and V. I. Veselovskii, *Elektrokhimiya*, **14**, 1260 (1978).
13. A. K. Ghosh, C. Fishman, and T. Feng, *J. Appl. Phys.*, **49**, 3490 (1978).
14. F. Decker, J. Melsheimer, and H. Gerischer, *Isr. J. Chem.*, **22**, 195 (1982).
15. N. Tarr and D. Pulfrey, *IEEE Trans. Electron Devices*, **ed-27**, 771 (1980).
16. H. J. Hovel, "Semiconductor and Semimetals, Vol. 11: Solar Cells," Academic Press, New York (1975).
17. K. J. Vetter, "Elektrochemische Kinetik," Springer-Verlag, Berlin-Göttingen-Heidelberg (1961).
18. A. J. Bard and L. R. Faulkner, "Electrochemical Methods," J. Wiley & Sons, New York (1980).
19. V. G. Levich, "Physico-Chemical Hydrodynamics," Prentice-Hall, Englewood Cliffs, NJ (1962).
20. W. Badawy, F. Decker, and K. Doblhofer, *Solar Energy Mater.*, **8**, 363 (1983).
21. B. Miller, S. Menezes, and A. Heller, *This Journal*, **126**, 1483 (1979).
22. W. E. Pinson, *Nature*, **269**, 316 (1977).
23. S. J. Fonash, "Solar Cell Device Physics," Academic Press, New York (1981).
24. B. Bressel and H. Gerischer, *Ber. Bunsenges. Phys. Chem.*, In press.
25. E. L. Goldstein and M. R. Van de Mark, *Electrochim. Acta*, **27**, 1079 (1982).

Photoelectrochemical Characteristics of Semiconductor-Metal/SPE/Metal Cells

Kohei Uosaki* and Hideaki Kita

Department of Chemistry, Faculty of Science, Hokkaido University, Sapporo 060, Japan

ABSTRACT

A solid polymer electrolyte (SPE) photoelectrochemical cell, semiconductor-metal/SPE/Pt, is proposed as a new device to convert solar energy to electrical and/or chemical energy. The photoelectrochemical characteristics of TiO_2-Pt/SPE and TiO_2-Au/SPE were studied as well as those of the whole cell systems TiO_2-Pt/SPE/Pt and TiO_2-Au/SPE/Pt. By above bandgap energy illumination of the TiO_2-metal side, negative photovoltage and anodic photocurrent were observed, as reported at TiO_2 electrodes. In whole cell systems, *i.e.*, TiO_2-Pt/SPE/Pt and TiO_2-Au/SPE/Pt, the conversion of light to electricity was achieved without using electrolyte solution.

The conversion of solar energy to chemical and/or electrical energy by photoelectrochemical (1, 2) and photocatalytic (3, 4) methods has been studied very extensively. Both methods have advantages and disadvantages. In the photoelectrochemical method, the products can be obtained separately. That is particularly useful when water is decomposed photoelectrochemically. Electricity can be generated, but the presence of electrolyte is essential in this system. On the other hand, the photocatalytic method does not require electrolyte, but the products, *e.g.*, oxygen and hydrogen, are generated in the same compartment. Thus an extra separation process is required and no electricity can be obtained.

The advantages of a solid polymer electrolyte (SPE) in water electrolysis (5), organic electrochemistry (6), and fuel cells (7) have been well recognized and the application of SPE to photoelectrochemical cells should also be advantageous. Recently, Skotheim and Lundström have constructed all-solid photoelectrochemical cells using poly(ethylene oxide) as the SPE (8).

Here, we propose a new type of SPE photoelectrochemical cell that contains layers of a semiconductor as a sensitizer, a metal, an ion exchange membrane as an SPE, and a metal. We report the photoelectrochemical characteristics of TiO_2-Pt/SPE and TiO_2-Au/SPE as well as those of TiO_2-Pt/SPE/Pt and TiO_2-Au/SPE/Pt. By using this type of cell, even electrolyte-free photoelectrolysis of water may be possible, as shown in Fig. 1.

* Electrochemical Society Active Member.

Key words: energy conversion, semiconductor, photoelectrochemistry, solid polymer electrolyte.

Experimental

Nafion 315 perfluorinated cation exchange membrane was used as an SPE material. The deposition of metal on the SPE was carried out by the electroless plating method suggested by Takenaka and Torikai (9, 10). After a swelling treatment in boiling water for 30 min, the membrane was set as a separator in the cell shown in Fig. 2. The upper compartment was filled with a metal salt (H_2PtCl_6 or $HAuCl_4$) solution and the other compartment was filled with an $NaBH_4$(1M)-NaOH(1M) solution. $NaBH_4$ diffused through the membrane and reduced the metal salt to the metal on the membrane surface at the upper compartment. After several hours, the solution of the upper compartment became colorless, suggesting most of the salt was reduced, and the surface of the membrane at the upper compartment became black. The amount of metal deposited was 4-12 mg $\cdot$ cm^{-2}. Hereafter this configuration is called Pt/SPE or Au/SPE. In some cases, after washing the membrane thoroughly with distilled water, the other side of the membrane was also coated with a metal

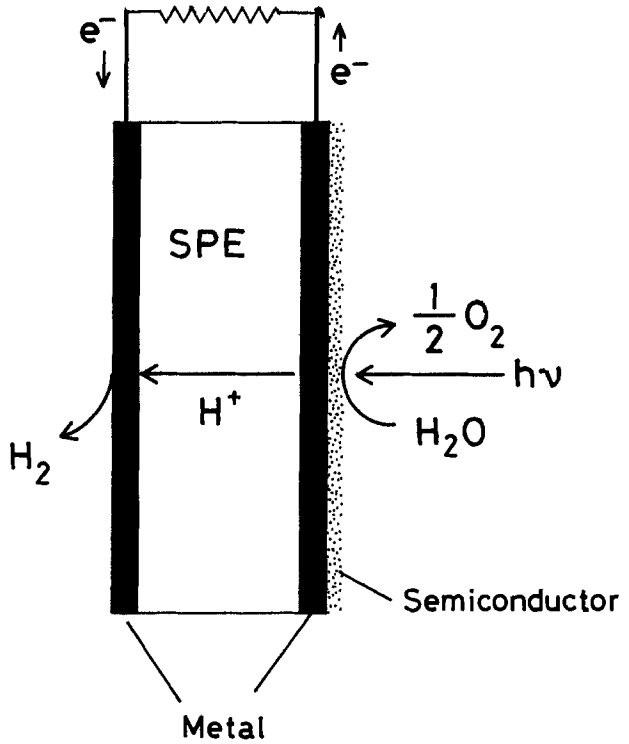

Fig. 1. Schematic diagram of proposed SPE photoelectrochemical cell.

in the same way. At laest one side of the membrane was coated with platinum. This configuration is called Pt/SPE/Pt or Au/SPE/Pt. The side coated with either Pt or Au will be called side 1 and the side always coated with Pt will be called side 2 in the rest of this paper. Side 1 was further coated with TiO_2 by drops of a TiO_2 (Merck, Anatase) powder suspension (2g TiO_2/25 cm^3 distilled water), following the method used by Davidson *et al.* for the coating of Pt wire with TiO_2 (11). The membrane was then dried in an oven at 70°C for 15-20 hr. After this treatment, most of the TiO_2 powder came off but some remained on the metal. This configuration is called TiO_2-Au/SPE, TiO_2-Pt/SPE, TiO_2-Au/SPE/Pt, or TiO_2-Pt/SPE/Pt.

The (photo)electrochemical characteristics of TiO_2-Pt/SPE and TiO_2-Au/SPE electrodes were studied in the cell shown in Fig. 3.

A potentiostat (Nikko Keisoku, NPGS-301S) was used to control the electrode potential. A platinum wire and a silver/silver chloride electrode were used as a counter and a reference electrode, respectively. The working electrode, TiO_2-Pt or TiO_2-Au, is disk shaped and 2.5 cm in diameter. A gold ring was used as a current collector.

The photoelectrochemical characteristics of whole cells, TiO_2-Pt/SPE/Pt and TiO_2-Au/SPE/Pt, were studied in a cell shown in Fig. 4.

Results

The cyclic voltammograms of Pt/SPE and TiO_2-Pt/SPE in 0.5M H_2SO_4 are shown in Fig. 5. It is clear from the figure that the electrochemical characteristics of Pt/SPE are similar to those of a Pt electrode. The real surface area of Pt was calculated as *ca.* 1125 cm^2, *i.e.*, the roughness factor was *ca.* 230, from the area of the oxide reduction peak. By comparing the

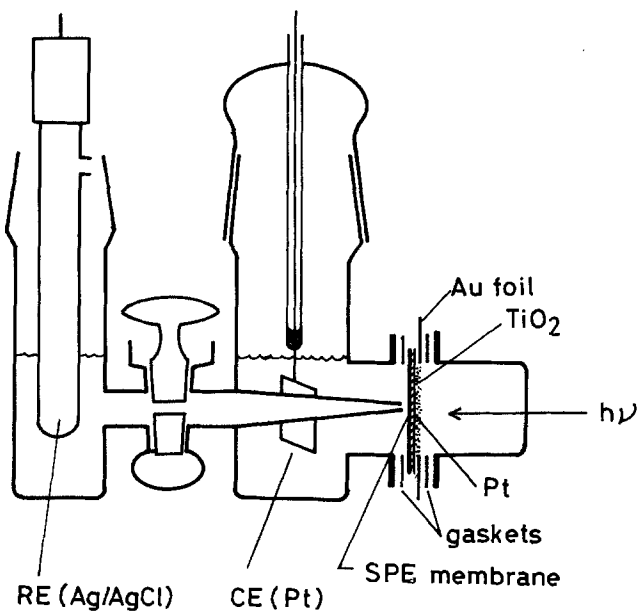

Fig. 3. A cell used for the measurements of (photo)electrochemical characteristics of TiO_2-Pt/SPE and TiO_2-Au/SPE electrodes.

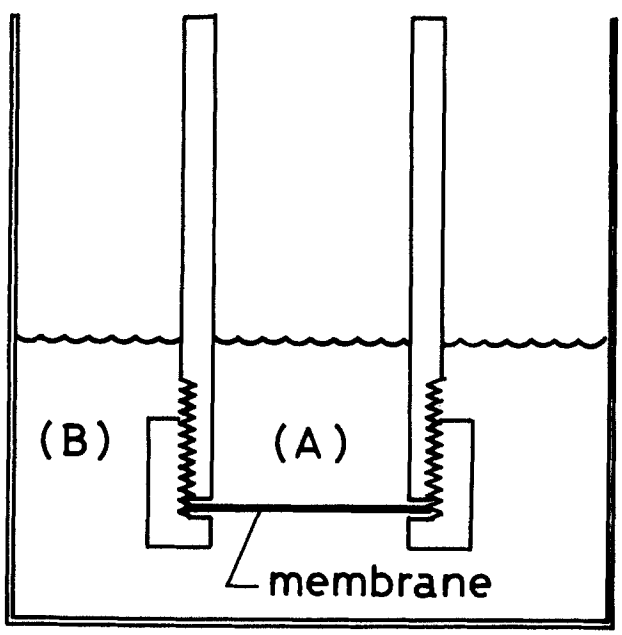

Fig. 2. Schematic diagram of the cell used for the electroless plating of SPE. Solution (A) is a metal salt solution and solution (B) is an $NaBH_4$(1M)-NaOH(1M) solution.

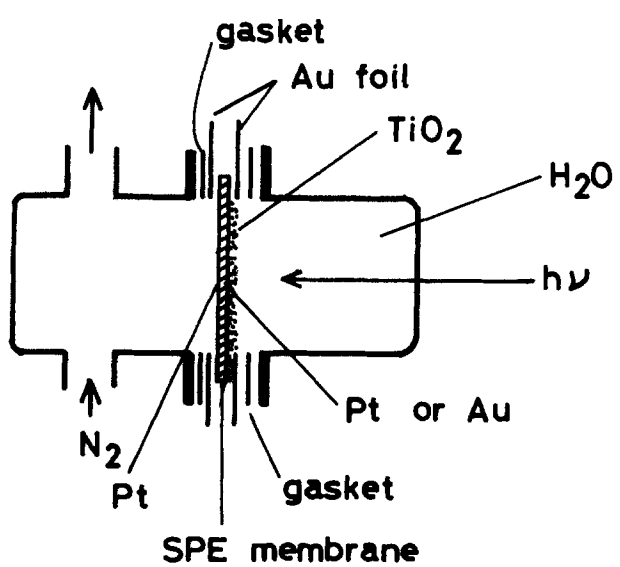

Fig. 4. A cell used for the measurements of photoelectrochemical characteristics of TiO_2-Pt/SPE/Pt and TiO_2-Au/SPE/Pt.

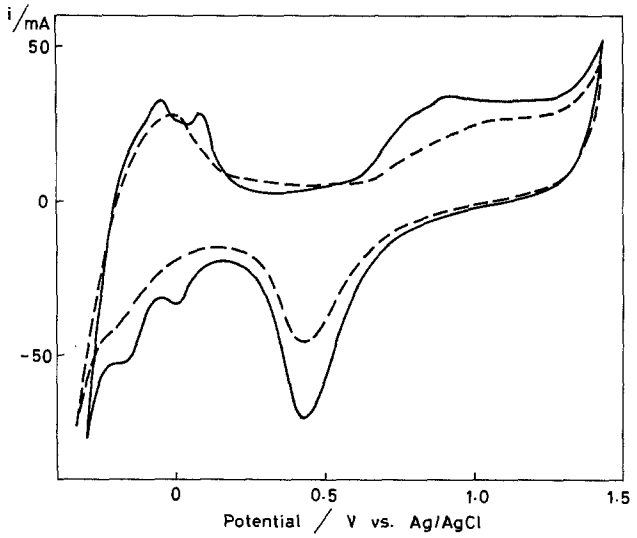

Fig. 5. Cyclic voltammograms of Pt/SPE(——) and TiO_2-Pt/SPE (---) in 0.5M H_2SO_4. Sweep rate was 30 mV · sec^{-1}.

area of the oxide reduction peak in the cyclic voltammogram of TiO_2-Pt/SPE with that of Pt/SPE, the coverage of the Pt surface by TiO_2 was calculated as *ca.* 35%, *i.e.*, a significant portion of Pt was still exposed, as observed with TiO_2-coated Pt wire. The cyclic voltammograms of TiO_2-Au/SPE in 0.5M H_2SO_4 before and after photoelectrochemical measurements are shown in Fig. 6. From the cyclic voltammogram of Au/SPE which is not shown here, the real area of Au was calculated as *ca.* 100 cm^2, *i.e.*, roughness factor was *ca.* 20. By comparing the cyclic voltammogram of Au/SPE and that of TiO_2-Au/SPE, the coverage of Au surface by TiO_2 was calculated as 75%. The cyclic voltammogram of TiO_2-Au/SPE after the photoelectrochemical measurements shows that the nature of gold on the SPE changed and indeed a change in the appearance of the membrane surface was observed. Thus a better method for depositing Au on the SPE should be developed. When the TiO_2-metal side was illuminated by a 500W Xe lamp through an infrared absorbing filter, a negative photovoltage was developed, as observed with Pt wire coated with TiO_2, and is shown in Fig. 7. The time course of photovoltage of TiO_2-Pt illuminated by 360 nm monochromatic light is also shown in Fig. 7. The photovoltage was small and the time constant was large when the electrode was illuminated with monochromatic light. The wavelength dependence of the photovoltage is shown in Fig. 8 and is similar to

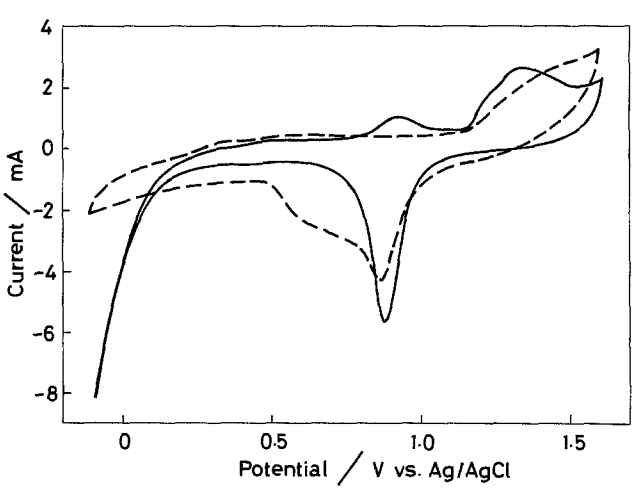

Fig. 6. Cyclic voltammograms of TiO_2-Au/SPE in 0.5M H_2SO_4 before (——) and after (---) photoelectrochemical measurements. Sweep rate was 100 mV · sec^{-1}.

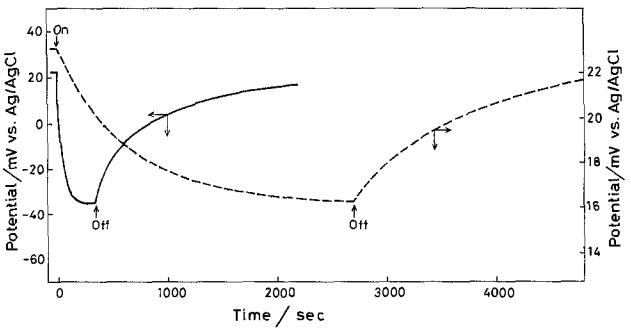

Fig. 7. Photoeffect on the potential of TiO_2-Pt on SPE in 1M NaOH illuminated by 500W Xe lamp with infrared absorbing filter (——) and by 360 nm monochromatic light (---).

that of Pt/TiO_2 powders (12). These results support the view that the photoresponse was due to absorption of light by TiO_2. Anodic photocurrents were also observed potentiostatically. A typical photocurrent-time relation at TiO_2-Pt/SPE is shown in Fig. 9.

The photocurrent-potential relations at TiO_2-Pt/SPE and TiO_2-Au/SPE are shown in Fig. 10 and are quite different from those of TiO_2 electrodes. It is clear that the photocurrents were strongly affected by the underlying metals. There are peaks in the relations and the peak potentials coincide with those at which oxides of the metals are formed.

The results reported so far are all for TiO_2-Pt/SPE and for TiO_2-Au/SPE and not those for whole cell systems, *i.e.*, TiO_2-Pt/SPE/Pt or TiO_2-Au/SPE/Pt. For the whole cell systems, both compartments of the cell shown in Fig. 4 were filled with distilled water, not an electrolyte solution, and then the water in the Pt side (side 2) of the compartment was drained off. This compartment was then filled with N_2 gas. When the TiO_2-metal side (side 1) and the Pt side (side 2) were connected by an electrometer and the TiO_2-metal side was illuminated by light, the potential of TiO_2-metal became more negative than that of Pt. When the two sides were connected with a resistor of finite resistance, a photocurrent (TiO_2-metal as an anode and Pt as a cathode) was observed. Thus the conversion of light to electricity without electrolyte solution was achieved. A typical time course of the

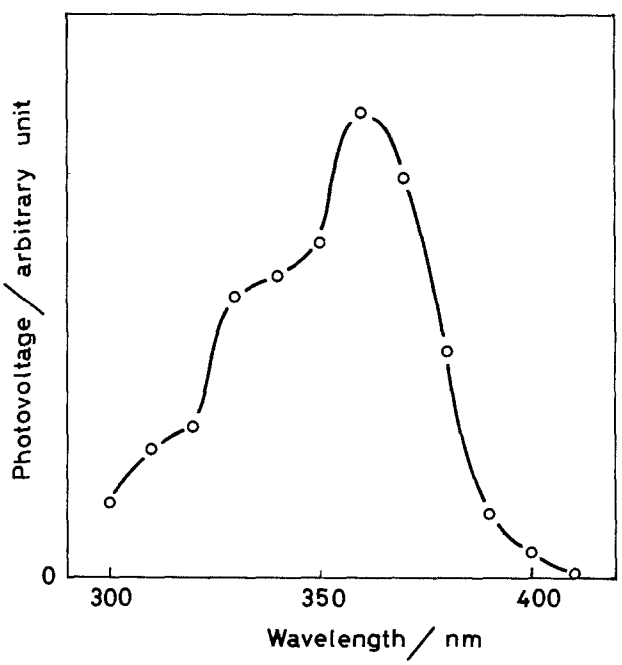

Fig. 8. Photovoltage-wavelength dependence of TiO_2-Pt/SPE in 1M NaOH. The photovoltages are not calibrated for photon numbers.

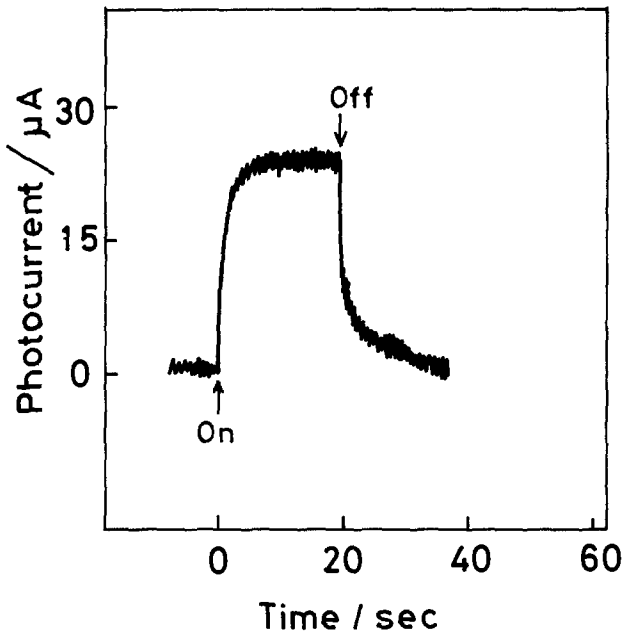

Fig. 9. A typical photocurrent-time relation of TiO_2-Pt/SPE in 1M NaOH at 0.5V (vs. Ag/AgCl).

photocurrent is shown in Fig. 11. The larger the resistance, the larger the time constant of this process. The wavelength dependence of the photocurrent, which is shown in Fig. 12, again confirms that photocurrents were due to the absorption of light by TiO_2. After the measurements, TiO_2 remained on the metal surface as shown by the reflection spectrum in Fig. 13.

The cell performance of TiO_2-Pt/SPE/Pt cell was determined by changing the resistor which connected the TiO_2-metal side to the Pt side and is shown in Fig. 14. The characteristics of the cells were relatively poor compared with those of TiO_2 electrodes (13).

The quantitative detection of the reaction product by using a membrane polarographic detector (MPD) (14) was tried but failed because of too low an efficiency.

By adding ethanol to the water of the TiO_2-metal compartment, the photocurrent increased by several times but by not as much as observed in photocatalytic systems (15, 16).

Discussion

When the TiO_2-metal side (side 1) of the TiO_2-metal/SPE was illuminated by light of greater than bandgap energy, electron-hole pairs was generated

$$h\nu \xrightarrow{TiO_2} p^+ + e^- \quad \text{(side 1)} \qquad [1]$$

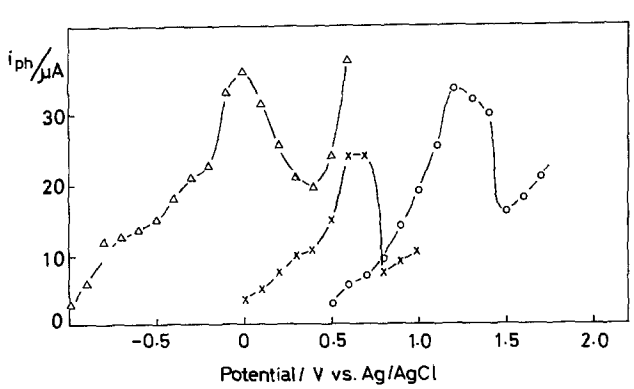

Fig. 10. Photocurrent-potential relations of TiO_2-Pt/SPE in 1M NaOH (—△—) and in 0.5M H_2SO_4 (—×—) and of TiO_2-Au/SPE in 0.5M H_2SO_4 (—○—).

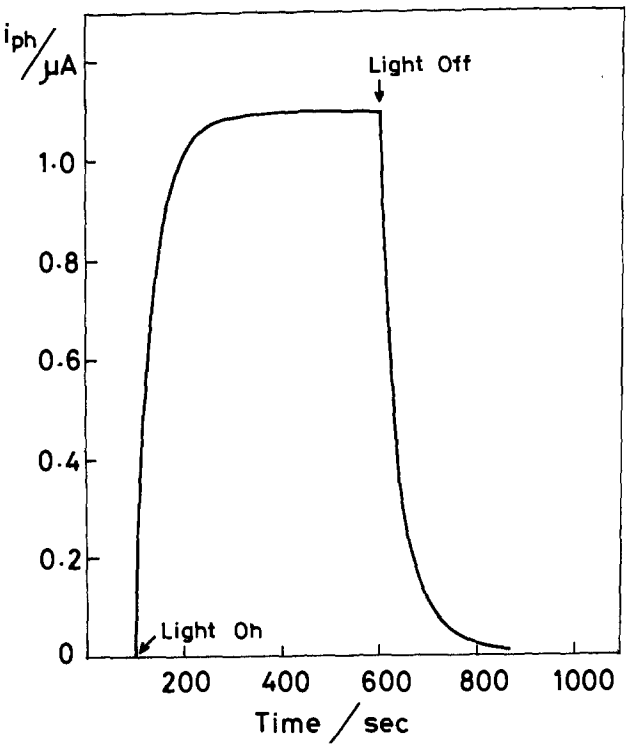

Fig. 11. A typical time course of photocurrent of H_2O/TiO_2-Pt/SPE/Pt/N_2 cell when H_2O/TiO_2-Pt side was illuminated by 360 nm monochromatic light.

where p^+ and e^- are the hole and electrons generated at side 1 by the light. In analogy to ordinary photoelectrochemical systems, the holes oxidized water

$$H_2O + 2p^+ \rightarrow \tfrac{1}{2}\,O_2 + 2H^+ \quad \text{(side 1)} \qquad [2]$$

When the circuit was open, the electrons accumulated on side 1, the Fermi level of TiO_2-metal was raised and the potential of TiO_2-metal became negative by the illumination as shown in Fig. 7. In the potentiostatic condition, electrons could be removed from TiO_2-metal through an external wire and anodic photocurrent was observed, as shown in Fig. 9. The reason for the effect of the metal substrate on the photocurrent potential is not clear, but the coincidence of photocurrent peak potential with oxide formation potential suggests that change of the po-

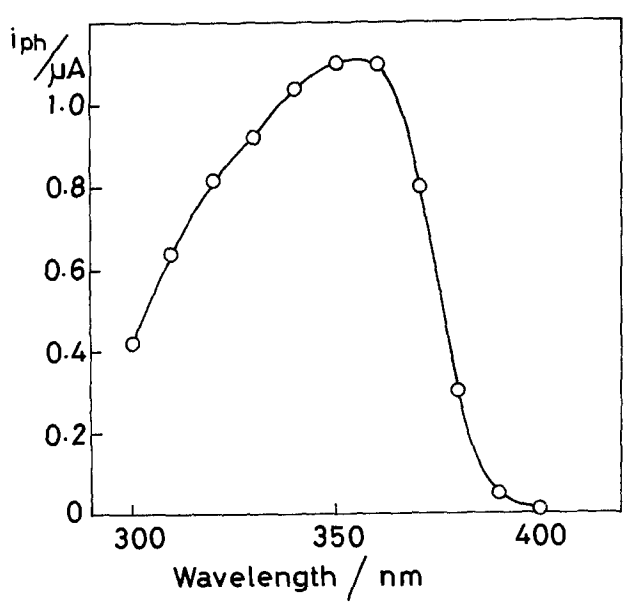

Fig. 12. Photocurrent-wavelength dependence of H_2O/TiO_2-Pt/SPE/Pt/N_2 cell.

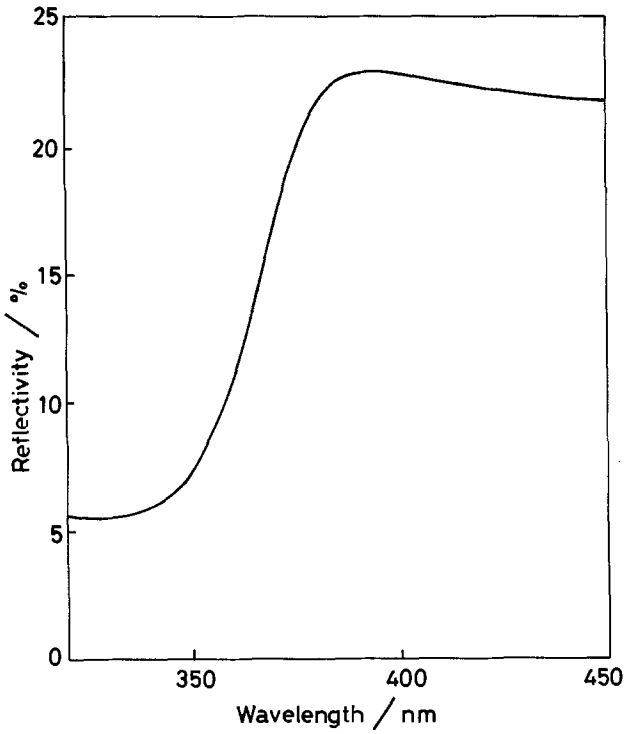

Fig. 13. Reflection spectrum of TiO_2-Pt/SPE after the photoelectrochemical measurements.

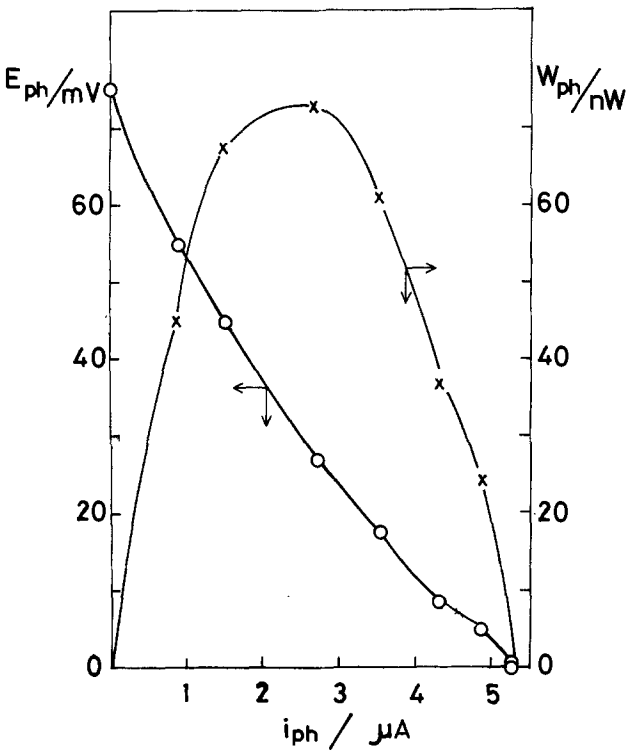

Fig. 14. Photovoltage (E_{ph})-output power (W_{ph})-photocurrent (i_{ph}) relations of H_2O/TiO_2-Pt/SPE/Pt/N_2 cell under illumination of 500W Xe lamp with infrared absorbing filter (Toshiba, IRA-20).

tential distribution at TiO_2-metal(oxide) interface has some effect on the relations. The relatively large exposure of metal substrate is a complicating factor.

In whole cell systems, *i.e.*, TiO-Au/SPE/Pt and TiO_2-Pt/SPE/Pt, reactions [1] and [2] also occurred and, at open circuit, electrons accumulated at the TiO_2-metal side (side 1) and the potential of TiO_2-metal became more negative than that of Pt (side 2). When the TiO_2-metal and Pt were connected with a resistor of finite resistance, electrons flowed through the resistance and H^+ moved through the SPE to Pt of side 2 as confirmed by anodic photocurrent. One of the possible reactions at side 2 was the hydrogen evolution reaction

$$H^+ + e^- \rightarrow \tfrac{1}{2} H_2 \quad \text{(side 2)} \qquad [3]$$

Thus a possible net reaction is photodecomposition of water

$$H_2O \xrightarrow{h\nu} H_2 + \tfrac{1}{2} O_2 \qquad [4]$$

However, in the present experimental condition, this reaction did not take place as the potential of the TiO_2-Pt side was much more positive than the reversible hydrogen electrode potential as shown in Fig. 7.

The comparison between the photovoltage generated by 500W Xe lamp illumination and the one generated by 360 nm monochromatic light suggests that the potential of TiO_2-Pt may become negative enough to proceed through reaction [4] by increasing the intensity of light. The reaction which seemed to take place at side 2 in the present experimental condition was the reduction of oxygen due to the small amount of oxygen in side 2 despite the nitrogen purge

$$\tfrac{1}{2} O_2 + 2H^+ + 2e^- \rightarrow H_2O \quad \text{(side 2)} \qquad [5]$$

The light-electricity conversion efficiency was also very low, possibly for several reasons. The short-circuit reactions at the TiO_2-metal surface (side 1), such as oxygen reduction and hydrogen evolution reactions, consumed electrons at side 1 and, thus, reduced the conversion efficiency

$$H^+ + e^- \rightarrow \tfrac{1}{2} H_2 \quad \text{(side 1)} \qquad [6]$$

$$\tfrac{1}{2} O_2 + 2H^+ + 2e^- \rightarrow H_2O \quad \text{(side 1)} \qquad [7]$$

The use of a metal which is an inactive catalyst for reactions [6] and [7] as a substrate may improve the efficiency. The rate of reaction [2] seemed to be slow and the recombination reaction [8] effectively competed with reaction [2] and reduced the conversion efficiency

$$p^+ + e^- \rightarrow \text{recombination} \quad \text{(side 1)} \qquad [8]$$

The increase of the photocurrent by the addition of ethanol supports this argument. The prevention of reactions [6], [7], and [8] and the acceleration of reaction [2] would increase not only the light-electricity conversion efficiency but also the electrochemical potential of the electron at the TiO_2-Pt side, *i.e.*, the possibility of electrolyte-free photoelectrolysis of water.

It must be noted that most of the photoelectrochemical and photocatalytic systems presently available can be constructed as SPE photoelectrochemical cells, *e.g.*, $Ru(bpy)_3Cl_2$-M/SPE/M (17) and $Ru(bpy)_3Cl_2$-$RuO_2 \cdot TiO_2$-M/SPE/M (18) where M is the metal substrate.

Conclusion

The SPE photoelectrochemical cell is proposed as a new device to convert solar energy to electrical and/or chemical energy. The conversion of light to electricity without the intervention of an electrolyte solution was achieved in TiO_2-Pt/SPE/Pt and TiO_2-Au/SPE/Pt cells. An increase of light intensity with a smaller contribution of short-circuit reactions at the TiO_2-metal surface may make electrolyte-free photoelectrolysis of water possible, although it was not attained in this work.

Acknowledgment

Dr. H. Nakajima and Mr. K. Hayashi are acknowledged for the preparation of Pt/SPE/Pt and Au/SPE/Pt. Thanks are due to Dr. A. Mills for his useful information on MPD. This work was partly supported by a Grant-in-Aid for Scientific Research, Ministry of Education, Science and Culture, 56740177.

Manuscript submitted March 29, 1983; revised manuscript received June 21, 1983. This was Paper 250 presented at the Detroit, Michigan, Meeting of the Society, Oct. 17-21, 1982.

Hokkaido University assisted in meeting the publication costs of this article.

REFERENCES

1. A. Fujishima and K. Honda, *Nature*, **238**, 37 (1972).
2. K. Rajeshwar, P. Singh, and J. Dubow, *Electrochim. Acta*, **23**, 1117 (1978), a review of work published up to early 1978.
3. T. Kawai and T. Sakata, *Chem. Phys. Lett.*, **72**, 87 (1980).
4. M. Grätzel, *Ber. Bunsenges. Phys. Chem.*, **84**, 981 (1980).
5. B. V. Tilak, P. W. T. Lu, J. E. Colman, and S. Srinivasan, in "Comprehensive Treatise of Electrochemistry," Vol. 2, J. O'M. Bockris, B. E. Conway, E. B. Yeager, and R. E. White, Editors, Chap. 1, Plenum, New York (1981).
6. A. Ogumi, K. Nishio, and S. Yoshizawa, *Electrochim. Acta*, **26**, 1779 (1981).
7. K. Kordesch, in "Comprehensive Treatise of Electrochemistry," Vol. 3, J. O'M. Bockris, B. E. Conway, E. B. Yeager, and R. E. White, Editors, Chap. 3, Plenum, New York (1981).
8. T. Skotheim and I. Lundström, *This Journal*, **129**, 894 (1982).
9. H. Takenaka and E. Torikai, Nippon Kokai (Pat.) 55-38934 (1980).
10. A. Ogumi, K. Nishio, and S. Yoshizawa, *Denki Kagaku*, **49**, 212 (1981).
11. R. S. Davidson, R. M. Slater, and R. P. Meek, *J. Chem. Soc., Faraday Trans. 1*, **75**, 2507 (1979).
12. K. Uosaki and H. Kita, *This Journal*, **129**, 1752 (1982).
13. A. Fujishima, K. Kohayakawa, and K. Honda, *Bull. Chem. Soc. Jpn.*, **48**, 1041 (1975).
14. A. Mills, A. Harriman, and G. Porter, *Anal. Chem.*, **53**, 1254 (1981).
15. T. Kawai and T. Sakata, *J. Chem. Soc., Chem. Commun.*, 694 (1980).
16. T. Kawai and T. Sakata, Proceedings of Seventh International Congress on Catalysis, Part B, 1198 (1980).
17. M. Noumann-Spallart and K. Kalyanasundaram, *Ber. Bunsenges. Phys. Chem.*, **85**, 704 (1981).
18. E. Borgarello, J. Kiwi, E. Pelizzetti, M. Visca, and M. Grätzel, *Nature*, **289**, 158 (1981).

Electrochemical Solar Cells with Layer-Type Semiconductor Anodes

Stabilization of the Semiconductor Electrode by Selective Polyindole Electrodeposition

L. Fornarini, F. Stirpe, and B. Scrosati*

Istituto di Chimica Fisica, University of Rome, Rome, Italy

ABSTRACT

The electropolymerization of indole has been investigated on platinum and molybdenum diselenide electrodes. When performed in the dark, the electropolymerization is selectively directed to the surface defects of the semiconductor. The effect of this surface treatment is investigated and discussed. The results indicate that the electropolymerization of indole effectively blocks the defect sites and produces a stable improvement on the output characteristics of photoelectrochemical cells with layer-type semiconductor anodes.

Photoelectrochemical cells based on layered semiconductors (*i.e.*, $MoSe_2$ or WSe_2) have both good solar to electrical energy conversion efficiency and stability against photocorrosion (1). However, the performance of these cells is largely influenced by the surface morphology of the semiconductor (2-5). Crystals with surface defects, such as steps between the van der Waals layers, show poor photoresponses. The unsaturated atoms at the edge of a step have dangling bonds exposed to the electrolyte, introducing new surface states close to the conduction band. These states act as recombination centers and promote, by tunneling of the majority carriers, back reactions of photogenerated redox species. Moreover, the contact of a surface parallel to the c-axis with the electrolyte creates a new electric field which drives the photogenerated carriers toward this region where they eventually recombine (2-5).

Consequently, large effort is presently devoted to the study of surface treatments capable of controlling these undesired morphological limitations (4, 6). Bard *et al.* (7) have proposed stabilizing the semiconductor surface by dark electropolymerization of o-phenylenediamine, specifically directed toward the blockage of the defective sites. Such a selective action is favored by the fact that only the surface defects of the semiconductor allow passage of appreciable current in the dark.

Following this direction, we have started a systematic study on electrocrystallization and electrodeposition processes on layered semiconductors. In a previous work (8), the feasibility of selective electrodeposition, in general, has been analyzed and discussed. In this paper, the effect of this type of surface treatment is further investigated by examining the polyindole electrodeposition on a single-crystal molybdenum diselenide photoanode.

Experimental

The molybdenum diselenide, $MoSe_2$, crystals were kindly provided by Dr. F. Lévy of the Polytechnic of Lausanne. The semiconductor crystals were attached with a conductive silver paste to a brass current collector. This was then potted and sealed with epoxy resin on a Teflon holder. The counterelectrode was a platinum wire, spirally arranged around the semiconductor photoanode.

Conventional three-electrode glass cells have been used for the electrodeposition and output characteristic studies. These studies were performed by controlling the voltage with a potentiostat driven by a function generator and recording the current-voltage curves with an X-Y recorder or a computerized acquisition data system.

A halogen lamp was used to irradiate the photoelectrodes. The illumination intensity and uniformity were controlled by a light intensity meter.

* Electrochemical Society Active Member.
Key words: photovoltaic, semiconductor, surfaces.

The electrolyte solutions were prepared with high purity chemicals and distilled solvents. A solution of indole (0.01M) with $(C_2H_5)_4N(BF_4)$ supporting electrolyte (0.1M) in acetonitrile, was used for the electropolymerization studies. For the evaluation of the performance of the photoelectrochemical cells, a KI (2M), I_2 (0.02M) aqueous solution was used.

Results and Discussion

The basic aspects of the electropolymerization of indole on platinum have been investigated by Tourillon and Garnier (9). These authors found that films deposited from acetonitrile, $(Bu)_4NClO_4$, and monomer are adherent and stable up to temperatures of 300°-400°C. Here we have extended the study, with particular concern to its implication on the stabilization of the layered semiconductor electrode.

In Fig. 1 is shown a typical current-voltage curve of a Pt electrode in acetonitrile solution, with (curve b) and without (curve a) indole. The oxidation potential of indole is observed to be ~0.9V *vs.* SCE, a value in good agreement with that reported by Tourillon and Garnier (9).

The effect of the deposition of polyindole is the formation of a nonconductive film on the electrode surface. The permeability of this film has been directly evaluated in a KI/I_2 aqueous solution, *i.e.*, the same solution which is normally used in the photoelectrochemical cell. The results are reported in Fig. 2. Curve a is the cyclic voltammetry of a Pt electrode in the KI/I_2 aqueous solution. The iodine-iodide peaks are clearly shown at a potential around 0.2V *vs.* SCE. Curve b is the voltammetric response of the same Pt electrode after electropolymerization of a polyindole film. This polymeric film was obtained by maintaining the Pt electrode at 0.95V *vs.* SCE in the acetonitrile, $(C_2H_5)_4N(BF_4)$, indole solution. From the charge passed (100 mC/cm²), the thickness of the film was evaluated as 1 μm. As indicated by the curve b of Fig. 2, the film clearly passivates the electrode since no appreciable current is observed in a potential range of 0-0.6V *vs.* SCE. This result appears more encouraging than that obtained by Bard *et al.*, who found that in the same I^-/I_3^- aqueous solution a coating of o-phenylenediamine exerted only a partial blocking effect on the Pt electrode (7). In fact, efficient passivation, as that observed here, may be critical for the effective blockage of the defect sites of the layered semiconductor.

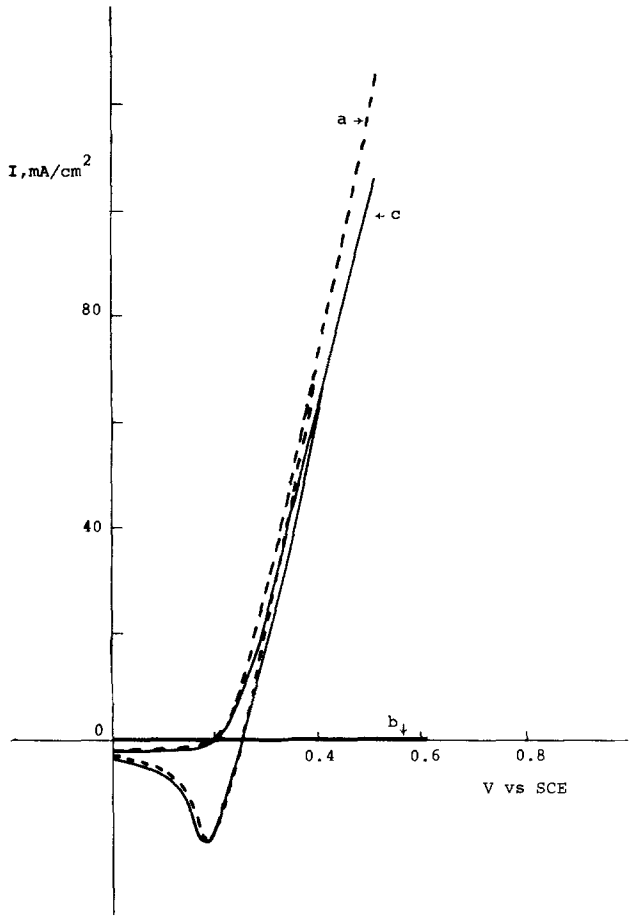

Fig. 2. Voltammogram of a Pt electrode in a KI (2M), I_2 (0.02M) aqueous solution. Curve a: untreated electrode. Curve b: after electropolymerization of a polyindole film. Curve c: after immersion in ethanol. Scan rate: 20 mV/sec.

Finally, curve c of Fig. 2 shows the voltammetric behavior of the same Pt electrode after its immersion in ethanol. The voltammogram matches that obtained with the bare electrode (see curve a); this shows that the polyindole film may be removed by dissolution in ethanol.

The investigation of the electrodeposition of the polymer was then extended to the semiconductor electrode. In Fig. 3 is shown the voltammogram response in the dark of a $MoSe_2$ electrode in the basic acetonitrile solution with (curve b) and without (curve a) indole. As already pointed out, the oxidation of indole is performed in the dark in order to direct its electrodeposition mainly onto the surface defects. Comparison

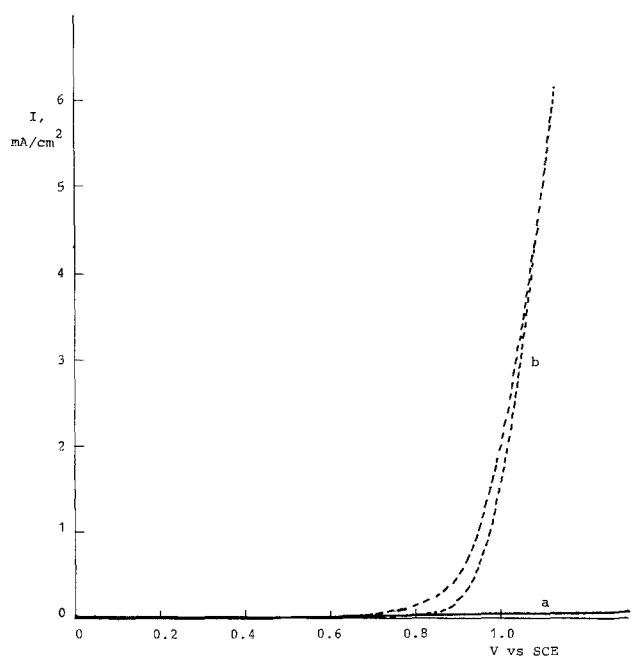

Fig. 1. Voltammogram of a Pt electrode in acetonitrile solutions. Curve a: with $(C_2H_5)_4N(BF_4)$ 0.1M supporting electrolyte. Curve b: with addition of 0.01M indole. Scan rate: 20 mV/sec.

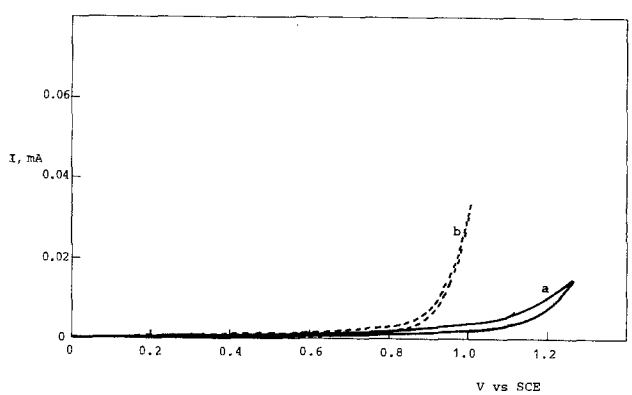

Fig. 3. Dark voltammogram of an $MoSe_2$ electrode in acetonitrile solutions. Curve a: with $(C_2H_5)_4N(BF_4)$ 0.1M supporting electrolyte. Curve b: with addition of 0.01M indole. Scan rate: 20 mV/sec.

with Fig. 1 shows that the dark behavior of $MoSe_2$ is very similar to that of platinum, as already found by Bard *et al.* in the case of the oxidation of o-phenylenediamine in WSe_2 (7).

The blocking action of the selective electrodeposition of polyindole on layered semiconductor electrodes was tested by examining their photoresponse before and after the treatment. As test sample, we selected a $MoSe_2$ crystal that had a largely defective surface morphology, as shown by its SEM photograph reported in Fig. 4. As expected, this crystal, when used as photoanode in conjunction with an I^-/I_3^- redox couple, shows a very poor photoresponse and a large dark current, as illustrated in Fig. 5 (curve a). The same electrode, after dark electrodeposition of polyindole, shows the characteristic reported as curve b in Fig. 5. The beneficial effect of the superficial treatment is clearly shown; the conversion efficiency improves about 400% and the dark current decreases substantially. Since the latter is mostly ascribable to the amount of surface defects of the layered semiconductor (10, 5), the result of Fig. 5 proves that the deposition of polyindole effectively blocks a large fraction of these defective sites from attack from the solution species.

To test the persistence of this protective action, the photoelectrochemical cell with the treated crystal was run on a 100Ω load under continuous illumination and its output characteristics determined periodically.

Fig. 4. Molybdenum diselenide crystal tested for the stabilization by indole electropolymerization.

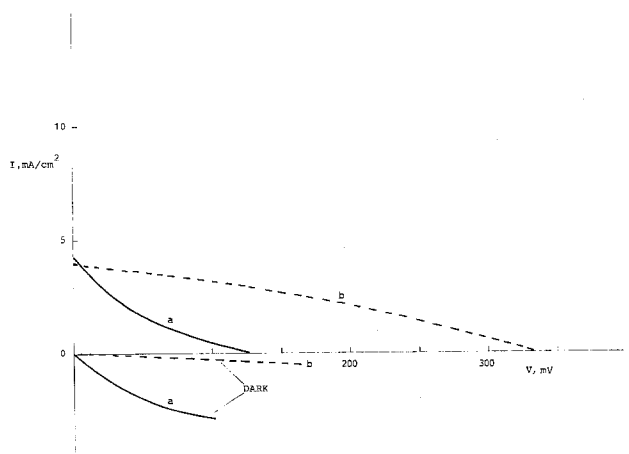

Fig. 5. Output characteristics of an $MoSe_2$/KI: (2M), I_2 (0.002M)/Pt photoelectrochemical cell before (curve a) and after dark electropolymerization of indole (curve b).

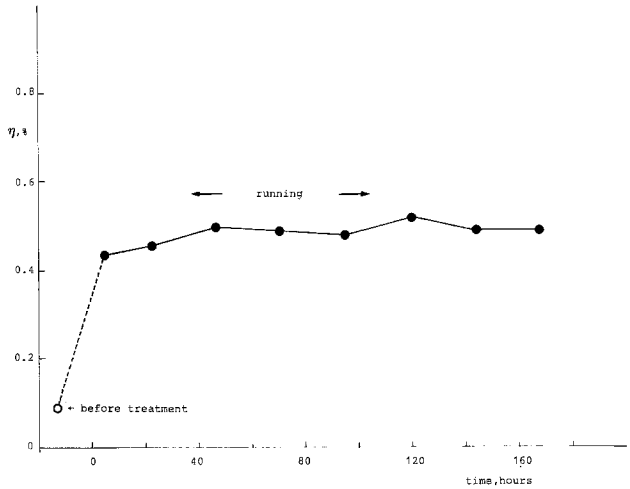

Fig. 6. Efficiency of an $MoSe_2$/KI (2M), I_2 (0.02M)/Pt photoelectrochemical cell with the $MoSe_2$ photoanode stabilized by indole electropolymerization, monitored during continuous illumination under 100Ω load. ○ refers to the efficiency obtained before indole electropolymerization.

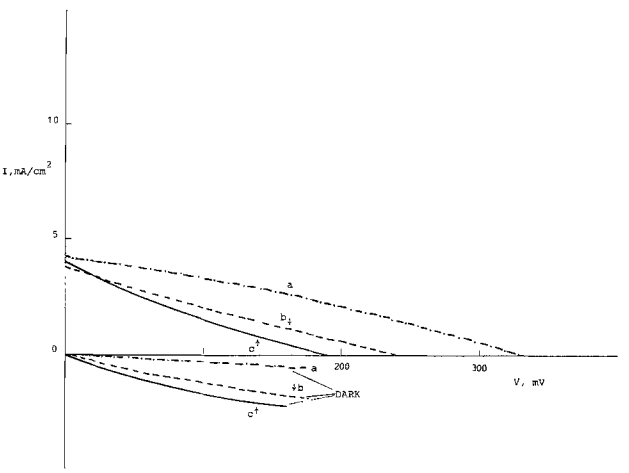

Fig 7. Output characteristics of an $MoSe_2$/KI (2M), I_2 (0.02M)/Pt photoelectrochemical cell. Curve a: with the $MoSe_2$ photoanode stabilized by indole electropolymerization and after 170 hr of illumination. Curve b: after washing the $MoSe_2$ photoanode in ethanol for 1 min. Curve c: after washing the $MoSe_2$ photoanode in ethanol for 8 min.

These characteristics, reported in Fig. 6, show that the performance of the cell did not decay after 170 hr of operation (1 week), corresponding to about 2000 C/cm².

After this prolonged illumination, a final test of the selectivity of the polymer electrodeposition and its effectiveness on the photoresponse of the layered semiconductor was performed by washing the crystal with ethanol to dissolve the polymer. The output characteristics after this treatment are illustrated in Fig. 7. The dissolution of polyindole clearly results in a progressively depressed photoresponse and increased dark current, respectively. We may, therefore, conclude that the beneficial and stable action on the performance of the layered semiconductor is indeed produced by the electrodeposition of polymer layers on the defective sites of its surface.

Acknowledgments

The authors wish to thank Dr. Lévy, of the Polytechnic of Lausanne, and Dr. G. Razzini, of the Polytechnic of Milan, for the helpful discussions.

Manuscript submitted April 20, 1983; revised manuscript received July 5, 1983. This was Paper 527 presented at the San Francisco, California, Meeting of the Society, May 8-13, 1983.

REFERENCES

1. H. Tributsch, *Ber. Bunsenges. Phys. Chem.*, **81**, 361 (1977).
2. H. J. Lowerenz, A. Heller, and F. Di Salvo, *J. Am. Chem. Soc.*, **102**, 1877 (1980).
3. W. Kautek and H. Gerischer, *Ber. Bunsenges. Phys. Chem.*, **84**, 645 (1980).
4. B. A. Parkinson, T. E. Furtak, P. Canfield, K. Kam, and G. Kline, *Faraday Discuss. Chem. Soc.*, **N.70**, 233 (1980).
5. L. Fornarini, F. Stirpe, B. Scrosati, and G. Razzini, *Solar Energy Mater.*, **5**, 107 (1981).
6. G. Razzini, L. Peraldo Bicelli, G. Pini, and B. Scrosati, *This Journal*, **128**, 2134 (1982).
7. H. S. White, H. D. Abruna, and A. J. Bard, *ibid.*, **129**, 265 (1982).
8. L. Fornarini and B. Scrosati, *Electrochim. Acta*, **28**, 667 (1983).
9. G. Tourillon and F. Garnier, *J. Electroanal. Chem.*, **135**, 173 (1982).
10. H. Tributsch, *This Journal*, **125**, 1086 (1978).

A Potential Step Study of the Influence of Metal Adatoms and Solution *p*H on the Rate of Formic Acid Oxidation at Pt Electrodes

Ines Fonseca,[1] Jiang Lin-Cai,[2] and Derek Pletcher*

Department of Chemistry, The University, Southampton S09 5NH, England

ABSTRACT

Using largely potential step techniques, the oxidation of formic acid has been studied at Pt surfaces partially covered by Bi, Cd, Pb, and Tl adatoms in 1M $HClO_4$ and in 1M ClO_4^- of *p*H 0, 1, and 2 at Pt/Pb electrodes. It is shown that for all these systems it is possible to define two time regimes. At short times the current is partly kinetically limited; the rate determining step is a chemical reaction, probably the cleavage of the C-H bond to give an adsorbed hydrogen atom and an adsorbed organic fragment. At long times, the current is close to diffusion control. The time scale for the change from kinetic to diffusion control and the extent of the kinetic control at short times vary with the adatom and the solution *p*H since these experimental parameters determine the rate constant for the chemical step. Moreover it is these differences in the rate constant together with the variation of the adatom coverages with potential that lead to apparently different "catalytic activities" in cyclic voltammetric experiments.

Since the report (1) that Hg adatoms could enhance the activity of Pt surfaces for formic acid oxidation, a number of studies have examined the influence of metal adatoms on this reaction (2-8). The past fifteen years have also seen the intensive investigation of the properties of adatoms and of monolayers of metals electrodeposited at an underpotential. The early work in this field has been summarized by Kolb (9) and particularly pertinent are later studies by Furuya and Motoo (10).

For some time, it has been our belief that a full understanding of the role of adatoms in the catalysis of formic acid oxidation has been hampered by the undue prevalence of potential sweep techniques in many investigations; in sweep experiments, several parameters, including the coverage by adatoms and the rate of several electron transfer reactions, will vary continuously, maybe with different Tafel slopes, and therefore the *I-E* response cannot be interpreted in a simple way. As a result we have sought to study the systems by potential step techniques.

An earlier paper (7) reported such a study of the oxidation of formic acid at a Pt electrode partially covered by Pb adatoms. The data obtained was compatible with the following conclusions:

1. The oxidation of formic acid occurs by the mechanism first proposed by Capon and Parsons (11), *i.e.*

$$\mathrm{HCOOH} \xrightarrow[\text{surface}]{\mathrm{Pt}} \mathrm{Pt{-}H} + \mathrm{Pt{-}COOH} \qquad [1]$$

$$\mathrm{Pt{-}H} - e \xrightarrow{\text{fast}} \mathrm{H^+} \qquad [2]$$

$$\mathrm{Pt{-}COOH} - e \xrightarrow{\text{fast}} \mathrm{H^+} + \mathrm{CO_2} \qquad [3]$$

2. The dissociative adsorption process, step [1], is relatively fast (rate constant $\simeq 10^{-2}$ cm sec^{-1}) while the oxidation of the adsorbed species is very rapid. Hence the current is determined by the rate of step [1] and/or by diffusion of formic acid to the electrode. For example, in potential step experiments, reaction [1] determines the current at short times and diffusion is the slowest step at long times. The time scale for the change in the rate determining step is found to depend on formic acid concentration and, indeed, at low formic acid concentrations (<10 mM) the reaction commonly appears to be totally diffusion controlled.

3. The role of the Pb adatoms is to prevent the formation of surface poisons by reactions such as

$$\mathrm{Pt{-}COOH} + \mathrm{HCOOH} \rightarrow \begin{matrix}\mathrm{Pt}\diagdown\\ \mathrm{Pt{-}CHO}\\ \mathrm{Pt}\diagup\end{matrix} + \mathrm{H_2O} + \mathrm{CO_2} \qquad [4]$$

which otherwise rapidly reduce the number of surface sites for the oxidation of formic acid. Whatever the exact structure of the poison, it was suggested (11) that its formation requires three or more, adjacent Pt sites on the surface. The role of the Pb adatoms is to arrange themselves over the surface so as to create a large number of sites where there are two adjacent Pt atoms available for reaction [1] to occur, but there are few sites where there are sufficient adjacent Pt atoms for the poison to form. Certainly the most active Pb/Pt electrode (4, 7) is one where $\theta_{Pb} = 0.5$, and since each Pb atom interacts with two Pt sites, this corresponds to a surface where the "average site" is 1Pb + 2Pt atoms.

Many of these concepts have been discussed in the earlier papers (1-8), but the conclusions are most clearly demonstrated and the results are made more quantitative by the use of the potential step method.

In this paper we report an investigation of the influence of *p*H on the oxidation of formic acid at Pb/Pt surfaces and the effects of changing the adatom. It is again shown that the interpretation of the results requires the separation of the kinetic

* Electrochemical Society Active Member.
[1] Permanent address: CECUL, Faculdade de Ciencias, 1200 Lisboa, Portugal.
[2] Permanent address: Department of Chemistry, The South China Teachers' University, Guangzhou, China.
Key words: electrocatalysis, anodic oxidation of formic acd, fuel cells, dissociative adsorption.

limitation from diffusion effects. Indeed it will be shown that the major effect of varying pH and the adatom is to alter the rate constant for reaction [1] and at long times the current tends to the same, diffusion-controlled value.

Experimental

The results are very adversely affected by impurities in the solution and can also depend on the history of the Pt surface. Hence the glassware was carefully cleaned by a published procedure (7) and solutions were prepared from triply distilled water and Analar perchloric acid, sodium perchlorate, formic acid, lead nitrate, cadmium sulfate, thallous carbonate, and GPR bismuth nitrate.

The electrochemical instrumentation and cells have been described elsewhere (7). In fact, two three-electrode, two-compartment cells were used in parallel. One was filled with 1M $HClO_4$ for use as part of the cleaning cycle and also for the determination of real surface areas. The other was filled with the solution under study. The Pt wire working electrode was transferred between cells as necessary and each cell used a Pt spiral counterelectrode and a normal hydrogen electrode with hydrogen generated *in situ* by electrolysis; all potentials in this paper are quoted *vs.* the NHE.

Between the series of experiments, the Pt electrode was cleaned chemically in an H_2SO_4/NHO_3 solution and then electrochemically by the application of a repetitive triangular potential sweep between +0.02 and +1.60V in 1M $HClO_4$ until a voltammogram showing the characteristic response described in the literature was obtained (12). This electrochemical cleaning was carried out regularly during experiments and was followed by the estimation of the real surface area using the procedure described below. The working electrode was then transferred to the cell containing the solution under study and held at 1.5 or 1.6V (to ensure the absence of adsorbed organics or underpotential metal deposit on the surface) until the commencement of the experimental pulse sequence. This always began with a step into the potential region 0.2-0.5V where the Pt oxide is reduced and underpotential metal deposition occurs; in experiments where the purpose is the study of formic acid oxidation, this pulse was always of sufficient length to ensure that the surface is covered by a complete monolayer of metal.

The real surface area of the Pt electrode was determined by recording a cyclic voltammogram in 1M $HClO_4$ at 0.1V sec^{-1} between the potential limits +0.05 and +0.40V and graphical integration of the area under the hydrogen desorption peaks. The adsorption potential, +0.05V, was chosen since this gives the exact number of Pt sites (10). The roughness factors were determined by dividing the hydrogen desorption charge by 210 $\mu C\ cm^{-2}$. In fact, the roughness factor was 2.0 ± 0.1 throughout this study. In this paper, currents determined by both diffusion and surface kinetics are discussed, but for clarity all current densities are reported in terms of the apparent geometric area.

The coverages of the metal adatoms as a function of potential were estimated using a procedure applied previously (7). The step sequence 1.5V → 0.3V (60 sec) → E_{ox} (2 sec) (1.2V → 0.4V (60 sec) → E_{ox} (2 sec) for Tl^+) was applied to the electrode in a solution $10^{-3}M$ M^{n+} in 1M $HClO_4$. The charges were measured during both the formation of the monolayer of the metal adatoms and its oxidation at the potential E_{ox}. The coverage at the potential E_{ox} could be calculated from the ratio of the charges corrected for the charges associated with Pt oxidation and reduction determined from the appropriate blank experiments in the absence of M^{n+}. The coverages estimated from an equivalent cyclic voltammetry procedure were the same to within 10%.

The method of Motoo (10) was used to determine the number of Pt atoms interacting with each metal adatom. This number was found from a plot of $Q_H - Q_H^M$ *vs.* Q_M/n using a solution $10^{-4}M$ M^{n+} in 1M $HClO_4$. $Q_M - Q_H^M$ and Q_M were determined in two separate experiments where the potential was stepped +1.5 V → E_D (t_D sec) then (*i*) swept from E_D to 0.05V at 10V sec^{-1} to estimate $Q_H - Q_H^M$ from the decrease in hydrogen adsorption charge caused by the presence of adatoms or (*ii*) swept from E_D in a positive direction to determine the charge for the complete oxidation of the metal adatoms on the surface, Q_M (the Pt oxidation charge was subtracted). t_D was varied in the range 1-200 sec and E_D took the values 0.5, 0.4, 0.35, and 0.50V for Bi, Pb, Cd, and Tl, respectively.

All solutions were deoxygenated with oxygen-free nitrogen (BOC Limited) for 30 min and experiments were carried out at 18° ± 2°C.

Results and Discussion

Effect of pH.—Figure 1 shows *I-E* curves resulting from linear potential sweep experiments with a Pt electrode in solutions of $NaClO_4$ + $HClO_4$ (total concentration 1M but of pH 0, 1, and 2) containing $10^{-3}M$ Pb^{2+} and 0.1M HCOOH. It can be seen that all the curves show a peak of substantial current density at a potential close to +0.6V *vs.* NHE and the peak current density can also be seen to increase with pH, the increase between pH 0 and 1 being particularly marked. The *I-E* curve for the 1M $HClO_4$ solution is identical to that reported earlier (3, 4, 7) where it was shown that the peak potential corresponds to that for $\theta_{Pb} = 0.5$ and that the current in the region +0.4 to +0.8V is far in excess of that for the oxidation of HCOOH at Pt in the absence of Pb^{2+}.

The effect of solution pH was then investigated by potential step experiments. *I-t* transients were recorded for potential steps from +0.2V to values in the range +0.5 to +0.8V for the solutions of pH 0-2 (all solutions contained $10^{-3}M$ Pb^{2+} and 0.1M HCOOH). At short times (< 1 sec) the current was found to depend strongly on pH and potential but at long times (> 10 sec) the current tended to similar values. Table I shows data taken for experiments where the potential step was to +0.6V. It suggests a kinetic limitation at short times, the extent of which varies with pH, and that the diffusion of formic acid in solution later becomes the rate determining step. This interpretation is confirmed by replotting the *I-t* transient data as *I* *vs.* $t^{-1/2}$, and such plots for the

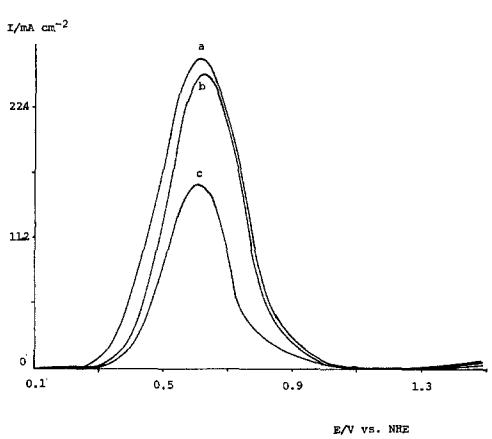

Fig. 1. Linear potential sweep voltammograms showing the effect of pH on the catalytic activity for a platinum anode covered by lead adatoms. The solutions are 0.1M HCOOH + $10^{-3}M$ Pb^{2+} in (a) 0.01M $HClO_4$ + 0.99M $NaClO_4$, (b) 0.1M $HClO_4$ + 0.90M $NaClO_4$, (c) 1M $HClO_4$. Potential sweep rate 0.1 V sec^{-1}.

Table I. Currents for the oxidation of formic acid as a function of time following a potential step from +0.2 to +0.6V. Pt electrode; solutions all 0.1M HCOOH + 10^{-3} $Pb(NO_3)_2$ + 1M ClO_4^-. Complete potential sequence 1.5V → 0.2V (60 sec) → 0.6V.

	Current mA/cm² (apparent geometric area) after			
pH	0.1 sec	1.0 sec	10 sec	80 sec
0	38	28	13.3	3.5
1	78	41	15.6	3.6
2	106	49	17.6	3.8

solutions of pH 0 and 2 are reported in Fig. 2. For the solution pH 2, deviations from linearity of the I-$t^{-1/2}$ plots are only apparent for $t < 4$ sec while at pH 0, the deviation is clear at much longer times. The value of D estimated from the slope at long times is 2×10^{-5} cm² sec^{-1}. This estimate may be high due to the contribution to mass transfer from convection at the time scales which must be used here.

The differences at short times are emphasized by a series of experiments where the charge passed during the first second of oxidation of formic acid is determined. The variation of this charge with pH and potential is shown in Fig. 3. It is again obvious that over the time scale of 1 sec, the amount of formic acid oxidized varies with pH and E and comparison of the curves for solutions containing 10^{-3}M Pb and that in the absence of Pb^{2+} again demonstrates the strong catalysis by Pb adatoms (7). The shapes of these Q-E plots mimic closely those of the I-E curves of Fig. 1, but this is not surprising since they represent experiments on similar time scales and both largely reflect the coverage of the surface by Pb adatoms. The maximum activity occurs at $\theta_{Pb} = 0.5$; above this value some of the surface is totally inactive because there are no exposed Pt atoms, while as the coverage is decreased from 0.5 the surface increasingly behaves at Pt and areas become deactivated due to the formation of poison. It is also interesting to estimate the maximum charge which could be obtained for the oxidation of formic acid in these experiments. This is obtained by integrating the Cottrell equation (13) and leads to the value of 101 mC cm^{-2} (apparent geometric area) with $D = 2 \times 10^{-5}$ cm² sec^{-1}. This

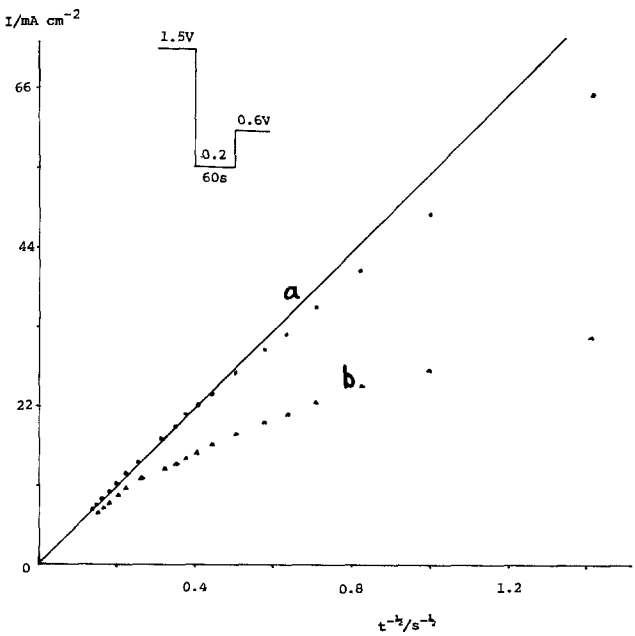

Fig. 2. Plots of I vs. $t^{-1/2}$ showing the influence of pH on the rate of oxidation of formic acid. Solutions are 0.1M HCOOH + 10^{-3}M Pb^{2+} in the media of a. 0.01M $HClO_4$ + 0.99M $NaClO_4$, b. 1M $HClO_4$.

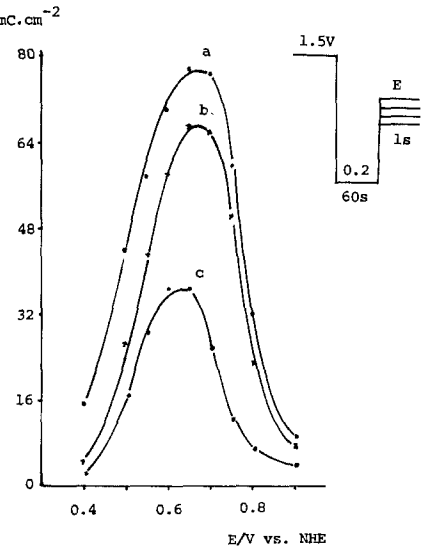

Fig. 3. Charges (1 sec) for the oxidation of formic acid as a function of oxidation potential and pH.

is only 25% above the peak value found for the solution of pH 2 confirming that with this solution the current is a large proportion of the diffusion-controlled value even over the first second of oxidation and with the high formic acid concentration.

In an earlier paper (7), equations were developed which allowed the estimation of the rate constant for the cleavage of the C-H bond in the dissociative adsorption process, step [1]. Using these equations, a value $\theta_{Pb} = 0.5$ at 0.6V (which was confirmed experimentally at all pH) and the procedure of Delahay and Oka (14), the values found for k were 0.8×10^{-2}, 2.1×10^{-2}, and 2.6×10^{-2} at pH 0, 1, and 2, respectively. Hence the rate constant clearly increases with decreasing acidity. The pH in these experiments were, however, well below the pK_A of formic acid, 3.75 (15), and it is therefore unlikely that the increase in rate constant is due to a mechanism where formate ion is an intermediate. On the other hand, it is possible that the loss of a proton from the species Pt-COOH could increase the rate of step [3], but this explanation would introduce a potential dependence to the measured rate constant; this is not observed (7). In any case the increase in rate constant is small for a 100-fold change in proton concentration and is more likely to be due to a secondary factor such as a change in solvation of the formic acid or in the extent of adsorption of perchlorate ion at the active site.

Influence of adatoms.—The cyclic voltammetric response for the oxidation of formic acid in the presence of various metal adatoms has been reported (2) and the I-E curves were quite different. The objective of this study was to define more closely the reasons for the difference in the ability of Bi, Cd, Pb, and Tl adatoms to catalyze formic acid oxidation.

Table II reports the number of platinum sites occupied by each metal adatom, the potential range where oxidation of a complete monolayer leads to a surface partially covered by adatoms, and the particular potential where half the monolayer has been oxi-

Table II. Characteristics of the underpotential layers of metals on Pt

Adatom	Number of Pt sites occupied by each M	Potential range (V) for adatom removal	$E_{\theta=0.5}$/V vs. NHE
Bi	3	0.80-0.95	0.90
Cd	2	0.45-0.65	0.54
Pb	2	0.50-0.74	0.61
Tl	3	0.90-1.05	0.95

dized. Each has been determined in these laboratories under conditions as close as possible to those used for the study of formic acid oxidation. The number of platinum sites occupied by Bi and Tl adatoms is the subject of some disagreement; our data are identical to those of Furuya and Motoo (10), but Cadle and Bruckenstein (16) and Bowles (17, 18) report that Bi and Tl interact with only two Pt sites. Indeed, our data can be seen to be different, even qualitatively, to that reported by Cadle and Bruckenstein (16), although this may be due to the presence of some nitrate ions in our system [our solutions were prepared from $Bi(NO_3)_3$]. It should also be noted that when a complete monolayer of metal is present on the surface, no hydrogen adsorption peaks are observed, *i.e.*, for all the metals, there are no Pt sites exposed between adatoms.

The oxidation of a solution of 0.1M HCOOH in 1M $HClO_4$ containing 10^{-3}M M^{n+} was studied using potential step methods. Figure 4 shows plots of the charge for the first second of oxidation of formic acid following a potential step *vs.* potential for each of the metal adatoms. The *Q-E* plots each show peaks that would again suggest that the curves might reflect the variations in the adatom coverages, θ_m, with potential. The peaks for Tl and Cd are, however, not at the potential expected on the basis of the data in Table II; the peak in the Cd curve appears at a more positive potential than expected, while that for Tl appears at a less positive potential. Indeed the peak in the Tl curve occurs at potentials where in the absence of formic acid, the surface is totally covered by a monolayer of thalium. These observations are discussed later. It can also be seen from Fig. 4 that there are large differences in the maximum charges, the catalytic activity decreasing in the order Pb > Bi > Tl > Cd.

These *Q-E* curves, and indeed cyclic voltammograms, relate to the relatively short time response and do not allow the definition of the causes of the differences between the metals. Hence *I-t* transients in response to the potential steps were again recorded over time scales between 0.1 and 100 sec. These short and long time-scale responses are illustrated by the transients in Fig. 5 and 6 (the potentials were selected to obtain maximum currents free from effects of platinum oxide). The *I-t* transients below 1 sec are quite different with the different adatoms; with Bi, Cd, and Pb ad-

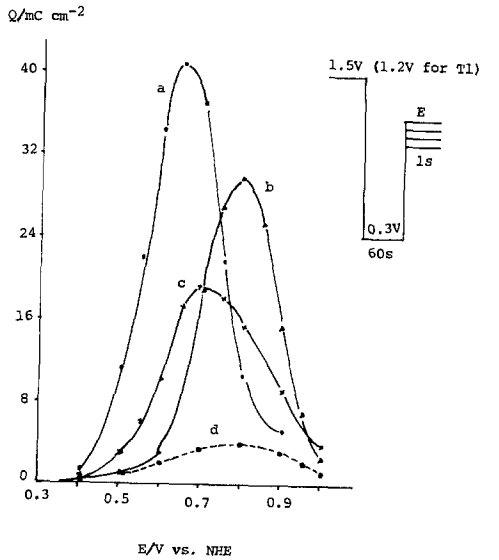

Fig. 4. Plots of charges (1 sec) for the oxidation of formic acid as a function of potential for various metal adatoms. Solutions were 0.1M HCOOH + 1M $HClO_4$ + 10^{-3}M M^{n+}. M^{n+}: (a) Pb^{2+}, (b) Bi^{3+}, (c) Tl^{+}, (d) Cd^{2+}.

atoms falling *I-t* transients are observed although the current densities are quite different, while with Cd the current is virtually independent of time. In contrast, the transients to 100 sec show that at long times, the current densities with Bi, Pb, and Tl adatoms fall to very similar values. Moreover, the current densities are very close to those calculated for a diffusion-controlled process. (The Cottrell equation gives the value 5.5 mA cm^{-2} for the diffusion-controlled current at 80 sec.) Even the current density for the electrode partially covered by Cd adatoms has remained constant and the value is a large fraction of that expected for diffusion control. Overall, the transients are compatible with a situation where the currents at short times are controlled by the rate of a chemical reaction, the rate of the reaction depending on the adatom, but at long times the reactions tend to diffusion control.

The transients were also recorded for potentials other than those shown in Fig. 5 and 6. The currents at short times are sensitive to potential, due presum-

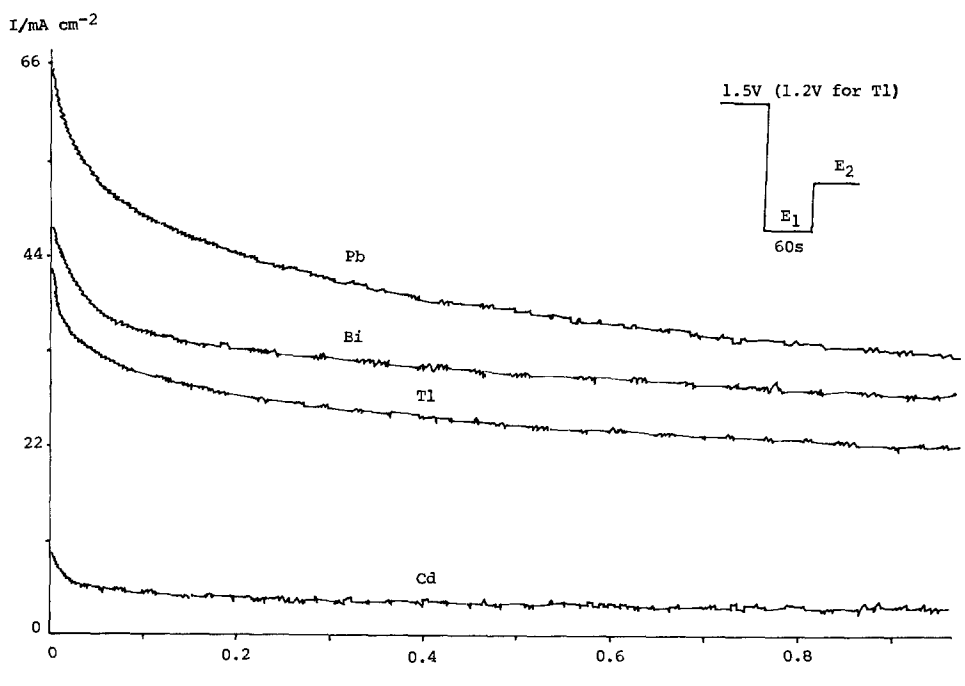

Fig. 5. The transients resulting from a potential step experiment for different metal adatoms. The solutions are as in Fig. 4. The potential profiles are shown in the figure. For Pb: E_1 0.2V; E_2 0.60V; for Bi: E_1 0.35V; E_2 0.70V; for Tl and Cd: E_1 0.2V; E_2 0.70V.

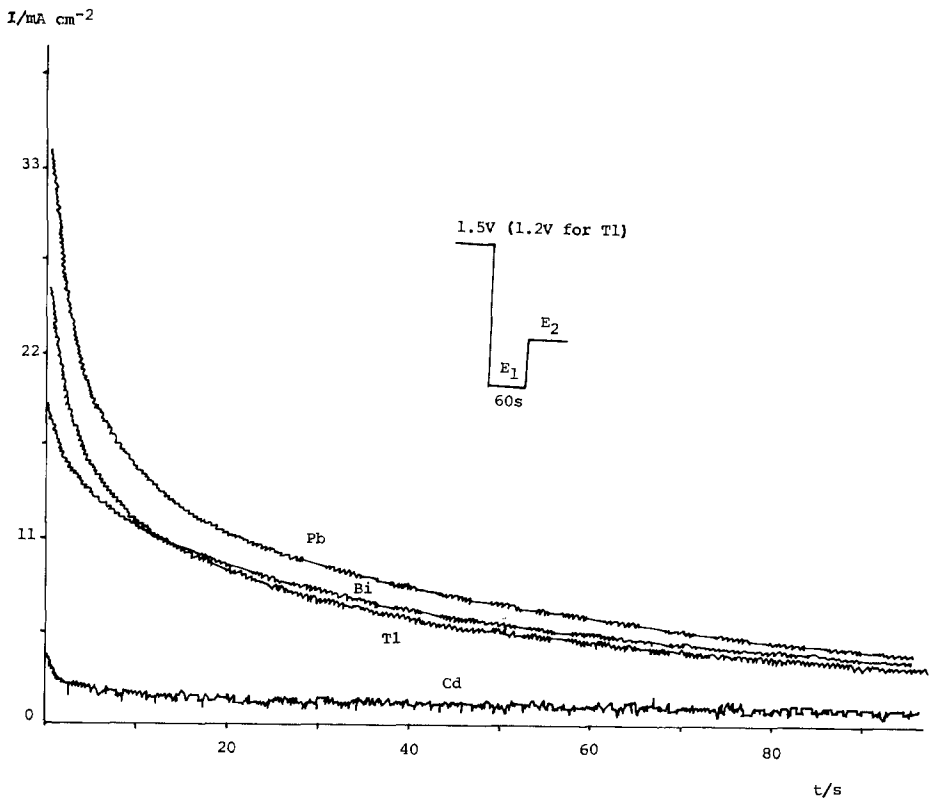

Fig. 6. The transients obtained at long times. The other conditions are as in Fig. 5.

ably to a difference in adatom coverage, but at long times, there is a range of potentials where the currents are independent of potential, see Table III. This table also reports data from transients for solutions of 0.1M HCOOH in the absence of a metal ion. The latter data confirm the strong catalysis by the metal adatoms over a range of potentials. The interpretation of the data in Table III should recognize that (*i*) at +0.5V the currents are always low and this may imply that at this potential the current is additionally limited by the rate of an electron transfer process, *e.g.*, reaction [3], and (*ii*) at +0.8V, platinum oxide is forming at free Pt sides and this could lower the activity of good catalytic surfaces but improve very poor catalysts, *e.g.*, Pt in the absence of adatoms.

Therefore, it seems that the behavior of Pt electrodes partially covered by Bi, Cd, Pb, and Tl in 1M $HClO_4$ can be fitted into a uniform pattern. The mechanism for the oxidation of formic acid at these surfaces is well described by reactions [1]-[4] where the initial step is a chemical reaction occurring at two adjacent Pt atoms and at sufficiently positive potentials, the oxidation of the adsorbed fragments is a rapid reaction. A role of the adatoms is then to divide the surface into Pt sites where reaction [1] can occur but the formation of poison, reaction [4], cannot. Moreover it is clear from the data presented above that the rate constant for the chemical step has, in most situations, a value such that, on the time scale of electrochemical experiments, mixed control by diffusion and the chemical step will be observed. Certainly in potential step experiments, the control normally changes from mixed to pure diffusion control during the time scale 0.1-100 sec. In such a reaction scheme, the response at short times reflects the coverage of the surface by metal adatoms and the maximum catalytic activity will occur when the coverage by adatoms leads to the highest number of sites for reaction [1] without creating many sites for the formation of poison [*e.g.*, $\theta_m = 0.5$ for the case of Pb (7)]. On the other hand, the diffusion-controlled current is independent of θ_m and, of course, the value of the chemical rate constant, and this leads to the similar long-term responses over a range of experimental conditions.

Table III. Currents measured 80 sec after a potential step from 0.3V to the working potential as a function of the adatom and potential. Solution is 0.1M HCOOH + 1.0M $HClO_4$ + 10^{-3}M M^{n+}. Pt electrode. Potential sequence 1.5V → 0.3V (60 sec) → E_0 (80 sec) except for thalium where the initial potential is +1.2V.

	Current mA/cm² (apparent geometric area)			
Adatom/*E vs.* NHE	0.5V	0.6V	0.7V	0.8V
Bi	—	0.87	4.7	5.4
Cd	1.1	1.1	1.1	1.2
Pb	—	4.8	5.1	4.2
Tl	2.5	4.8	4.3	4.6
None	0.06	0.08	0.10	0.44

The estimation of the rate constant for step [1] requires an estimate of the adatom coverage, θ_m, and an assumption about the way the adatoms are arranged on the surface. The calculations are not readily extended to metals which interact with three Pt atoms. Even so, it is clear that in a qualitative sense the rate constant for reaction [1] is dependent on the choice of adatom and decreases in the order Pb > Bi >Tl > Cd, and with Cd the rate constant is so low that the *I-t* response is totally kinetically controlled. The observation that the rate constant varies with adatom implies quite reasonably that the adatoms interact electronically with the surface so as to modify the properties of neighboring Pt sites.

Cyclic voltammetry and *Q vs. E* plots (taken from short pulses) will emphasize the circumstances where the electrode reaction is partially kinetically controlled. Hence the curves are peaked because they follow the θ_m *vs. E* dependence and the differences in peak currents and maximum charge result from variations in both *k* and the number of active sites (hence the number of Pt sites covered by each adatom). Such experiments, however, do not give information about the "steady state" response and the conclusion from "steady state" experiments would be quite different. The catalytic activity then appears insensitive to the choice of adatom and the coverage.

As noted above, however, the cyclic voltammetric peaks and the maximum in the Q-E plots for the systems involving Tl and Cd do not appear at the expected potentials. The data in Table II are, however, obtained from experiments involving solutions without formic acid. Therefore, it seems probable that the presence of formic acid affects the θ_m-E dependence either by complexing ions in solution or by competitive adsorption on the surface. In the case of Cd, though, such an explanation is not convincing since it would be expected to lead to a negative shift in the potential region for catalytic activity. It was, however, noted with this metal that, in the potential region 0.5-0.65V, potential step experiments with solutions containing both formic acid and cadmium ions led to a rising current during the first 1 sec. Such behavior could arise if the oxidation of the Cd adatoms was not instantaneous and it takes a period of up to a second to achieve the equilibrium coverage at the new potential. In any case, the occurrence of the rising I-t transients certainly leads to a substantial decrease in current at short times and this will lead to low responses in experiments such as cyclic voltammetry and the Q-E plots which reflect only short term activity, at least until there is an overpotential to drive the oxidation of the Cd adatoms.

Manuscript submitted Dec. 7, 1982; revised manuscript received April 12, 1983. This was Paper 707 presented at the San Francisco, California, Meeting of the Society, May 8-13, 1983.

REFERENCES

1. H. Angerstein-Kozlowska, B. MacDougall, and B. E. Conway, *This Journal*, **120**, 756 (1973).
2. R. R. Adzic, D. N. Simic, D. M. Drazic, and A. R. Despic, *J. Electroanal. Chem.*, **61**, 117 (1975).
3. R. R. Adzic, D. N. Simic, D. M. Drazic, and A. R. Despic, *ibid.*, **65**, 587 (1975).
4. R. R. Adzic, D. N. Simic, A. R. Despic, and D. M. Drazic, *ibid.*, **80**, 81 (1977).
5. R. R. Adzic, K. I. Popov, and M. A. Pamic, *Electrochim. Acta*, **23**, 1191 (1978).
6. R. R. Adzic, W. E. O'Grady, and S. Srinivasan, *This Journal*, **128**, 1913 (1981).
7. D. Pletcher and V. Solis, *J. Electroanal. Chem.*, **131**, 309 (1981).
8. S. Motoo and M. Watanabe, *ibid.*, **98**, 203 (1979).
9. D. M. Kolb, *Adv. Electrochem. Electrochem. Eng.*, **11**, 125 (1978).
10. N. Furuya and S. Motoo, *J. Electroanal. Chem.*, **98**, 189 (1979).
11. A. Capon and R. Parsons, *ibid.*, **45**, 205 (1973).
12. R. Woods, in "Electroanalytical Chemistry," Vol. 9, A. J. Bard, Editor, p. 1, Marcel Dekker, New York (1976).
13. A. J. Bard and L. R. Faulkner, "Electrochemical Methods—Fundamentals and Applications," John Wiley & Sons, Inc., New York (1981).
14. P. Delahay and S. Oka, *J. Am. Chem. Soc.*, **82**, 329 (1960).
15. "Handbook of Chemistry and Physics," The Chemical Rubber Co., Cleveland, OH (1973).
16. S. H. Cadle and S. Bruckenstein, *Anal. Chem.*, **44**, 1993 (1972).
17. B. J. Bowles, *Nature*, **212**, 1456 (1966).
18. B. J. Bowles, *Electrochim. Acta*, **15**, 737 (1970).

Establishment of an Acidity-Potential Diagram Through Use of an Electrode with a Solid Membrane Selective of Oxide Ions in Molten Alkali Metal Nitrate

E. Plumat, A. Labani, and M. Ghodsi

Université libre de Bruxelles, Chimie Industrielle et Chimie des Solides, 1050 Bruxelles, Belgium

ABSTRACT

The object of this study is to establish a practical acidity-potential diagram in molten alkali nitrates at 475°C in order to delimit the zone of acidity of a molten bath in which glass protection would be ensured against surface alterations which may occur in the course of ion exchanges.

Problems of contact between a glass surface and a molten salt have been the subject of numerous experimental studies by Stern *et al.* (1-3) and by others (4-8) aimed at determining electrochemical properties and ion transfer in glass and in molten salts. However, few authors have concerned themselves with the importance of the acid-base properties of the molten salt and with their surface degradation of the glass. Among salts which contain oxyanions, such as SO_4^{2-}, CO_3^{2-}, and NO_3, alkali metal nitrates form a particularly interesting category with respect to glass/salt ion exchange, since they have a relatively low melting point and a very low rate of decomposition below 500°C; it is precisely in nitrate systems that alterations can occur.

This study is devoted to establishing a practical diagram of acidity-potential in order to delimit the zone of acidity of a fused bath in which glass protection would be ensured against surface alteration.

To establish the acidity-potential diagram, two types of electrode were used: an electrode with a stabilized zirconia membrane indicating the O^{2-} level and an Ag^+/Ag reference electrode. Through preliminary calibration of the zirconia electrode with respect to the reference electrode, first in a basic, then in an acidic system, we were able to construct the E-$p_{O^{2-}}$ diagram.

Key words: ceramics, emf, ion exchange.

Theoretical Considerations

In the theory of ion exchange the oxoacidity reaction is not taken into account and it is assumed that the molten system containing oxyanions remains inert with respect to the glass surface. In industrial practice a degradation of the glass surface due to parasitic reactions in the course of ion exchange is often observed. This degradation occurs in acid-base reactions resulting from a difference in O^{2-} ion activity between the systems under consideration.

In molten nitrates the O^{2-} oxide ion results from the thermal dissociation of the nitrate anion according to the following equilibrium

$$2NO_3^- \rightleftharpoons 2NO_2\uparrow + \frac{1}{2}O_2\uparrow + O^{2-} \qquad [1]$$

This dissociation though very weak produces a sizable quantity of O^{2-} in solution and the resulting basicity

of the melt, through contact with a more acidic glass, would induce penetration of O^{2-} ions into the surface network according to the following equilibrium

$$(\equiv S - O - Si \equiv)_{glass} + O^{2-}{}_{solution} \rightleftharpoons 2(\equiv Si - O^-)_{glass} \quad [2]$$

Reaction [2] is shifted to the right and ends in a depolymerization of the network. However, if the molten salt is more acidic than the glass, the O^{2-} ions are removed from the vitreous mass and equilibrium [2] is shifted to the left, leading to progressive polymerization of the silicate network.

It is therefore of considerable importance for the glass industry to bring to light and control acid-base reactions in oxygenated molten salts. To that effect, it is necessary to use an electrode which indicates O^{2-} (oxide) ions. Several researchers (9, 12) have used platinum as an oxygen electrode, on the basis of the following electrochemical equilibrium

$$\frac{1}{2}O_2 + 2e^- \rightleftharpoons O^{2-} \quad [3]$$

Although Nernst's law is applicable to this electrode, Zambonin (13) and Shams El Din and El Hosary (14) have noticed anomalies in the measured values of normal potentials. The prelogarithmic factor should theoretically be equal to $RT/2F$ or to RT/F, which corresponds to

$$\frac{1}{2}O_2 + 2e^- \rightleftharpoons O^{2-} \qquad E = E°_{O_2/O^{2-}} + \frac{RT}{2F}\ln\frac{(O_2)}{(O^{2-})} \quad [4]$$

$$O_2 + e^- \rightleftharpoons O_2^- \qquad E = E°_{O_2/O_2^-} + \frac{RT}{F}\ln\frac{(O_2)}{(O_2^-)} \quad [5]$$

Equilibrium [4] shows that the stability of O^{2-} ions is based on a mechanism of two exchanged electrons whereas in equilibrium [5] only one electron is exchanged. Zambonin and Jordan (15) have studied the conditions of stability of the oxide ion. Their studies have shown that the O^{2-} anion is not the only stable form of ionic oxygen in nitrates and that one should also take O_2^{2-} and O_2^- into consideration. Moreover, redox equilibria occur between the four chemical forms of oxygen O^{2-}, O_2^{2-}, O_2^-, and molecular oxygen O_2, involving NO_3^- anions. However, Zambonin (13) has ascertained that in the presence of a Pyrex glass surface O^{2-}, O_2^{2-}, and O_2^- ions form complexes according to the following equilibrium

	ΔG at 475°C (kcal/mol)
$O^{2-} + SiO_2 \rightleftharpoons SiO_3^{2-}$	−56.59
$O_2^{2-} + SiO_2 \rightleftharpoons SiO_3^{2-} + \frac{1}{2}O_2$	−42.01
$2\,O_2^- + SiO_2 \rightleftharpoons SiO_3^{2-} + \frac{3}{2}O_2$	−50.679

[free energies are calculated at 475°C on the basis of data from thermodynamic tables (16)].

In order to avoid any interference with the measurement of the O^{2-} oxide ion, it is necessary to use an electrode the potential of which represents the O_2/O^{2-} couple.

By analogy with the glass electrode used in pH measurements, an electrode with a solid membrane solely permeable to O^{2-} ions will allow measurement of the acidity of the system, thereby avoiding the foregoing criticism. The electrode which exhibits these properties is well known. Its main component is a zirconia membrane stabilized by CaO or Y_2O_3. It has been used respectively, by Picard, Seon, and Tremillon (17) in fused chlorides at 470°C and by Flinn and Stern (18) in nitrates at 250°-400°C.

Determination of the Acidity Scale in Molten Alkaline Nitrates

The nitrate anion can undergo partial dissociation into NO_2, O_2, and O^{2-}. In view of Lux's concept (19), NO_3^- can be considered as a donor of O^{2-} and, therefore, as a base in the following dissociation equilibrium

$$2NO_3^- \rightleftharpoons 2NO_2 + \frac{1}{2}O_2 + O^{2-}$$

$$\text{base} \rightleftharpoons \text{acid} + O^{2-}$$

and as an acceptor of O^{2-} in the solvation reaction of this particle.

In view of the amphoteric character of NO_3^-, if one assumes that its chemical potential remains constant, it is possible to write

$$K = [NO_2]^2\,[O_2]^{1/2}\,[O^{2-}] \quad [6]$$

In the analysis of reactions in dilute solutions only concentrations of the dissolved species (NO_2, O_2, O^{2-}) lower than molal concentrations are taken into consideration. It is thereby possible to suppose that the thermodynamic behavior of the solution is practically ideal or that activity coefficients are constant in the dilute range. Activity can therefore be replaced by concentration and we can assume that $\mu(O^{2-}) = \mu° + RT \ln [O^{2-}]$. If we define $PO^{2-} = -\log [O^{2-}]$ and assume the solubility of NO_2 and O_2 is proportional to the pressures P_{NO_2} and P_{O_2} in accordance with Henry's law, we can write

$$[NO_2] = k'_H P_{NO_2}, \qquad [O_2] = k''_H P_{O_2}$$

$$k = k'_H{}^2 \cdot k''_H{}^{1/2}, \qquad K' = \frac{K}{k}$$

and relation [6] may be written

$$PO^{2-} = -\log K' + \log P_{NO_2}{}^2\,P_{O_2}{}^{1/2} \quad [7]$$

Given this relation we can construct a practical acidity scale. Its range will be equal to $-\log K'$ on condition that it is graduated in units of $P_O{}^{2-}$. It is possible to follow evolution of its potential in relation to a reference electrode by using an electrode which measures $P_O{}^{2-}$, *i.e.*, in this case a stabilized zirconia electrode, and by imposing acid-base conditions. The reference electrode chosen is the Ag^+/Ag couple which has frequently been used in nitrates below 500°C (11, 12).

Experimental Procedure and Results

Electrode assembly.—Zirconia membrane electrode.—This electrode shown in Fig. 1a consists of a tube of zirconia, stabilized by lime, of the Degussa type (ZrO_2 95%, CaO 5% mol). A layer of platinum, obtained by decomposition of platinum chloride, lines the inside of the tube. Electrical contact between a piece of platinum wire and the bottom of the tube is ensured by a locking system, the details of which are shown in Fig. 1b. The piece of platinum wire linked to the locking system is sheathed in an alumina capillary tube. The gas serving to maintain a constant pressure of oxygen at the triple contact, platinum-zirconia-oxygen, circulates inside the alumina tube.

Ag^+/Ag reference electrode.—A piece of pure silver wire is welded at the end of a piece of pure platinum wire sealed in a Pyrex tube. After an estimated 2g of homogeneous equimolar mixture of $(Na,K)NO_3$ with 0.1 mol/kg of $AgNO_3$ have been introduced into the tube of the electrode, the whole is fixed with quick-hardening araldite. To ensure lateral fit, a relative vacuum is created before filling the tube with an

inert gas under atmospheric pressure. The tube is then welded at point a (Fig. 2).

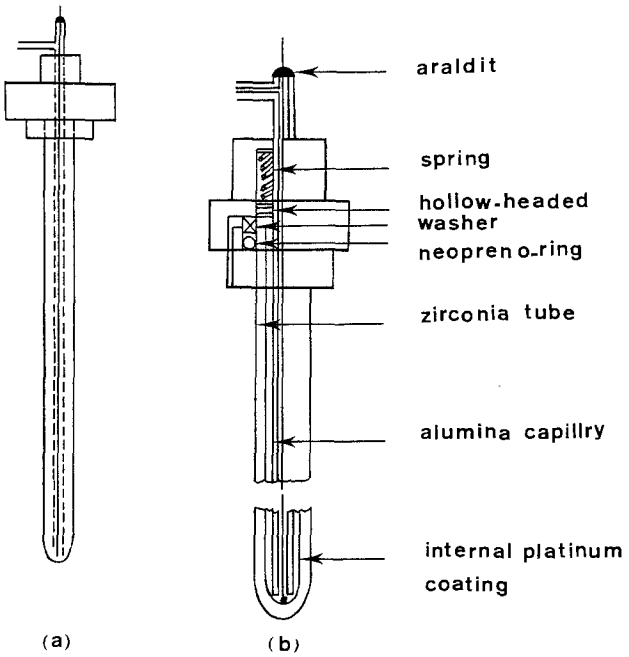

Fig. 1. Zirconia electrode

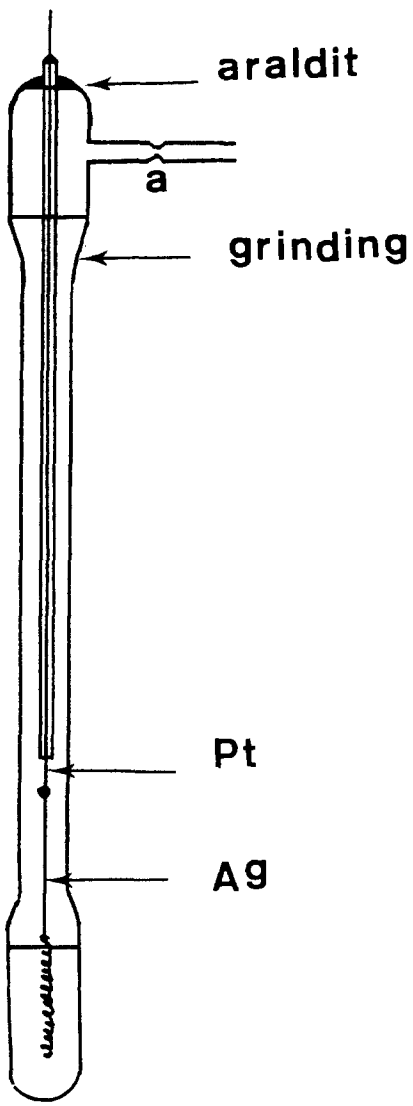

Fig. 2. Reference electrode

Experimental installation.—The experimental installation is shown in Fig. 3. It consists of a vertical cylindrical oven with its regulator, the Pyrex reactor, and a platinum crucible containing 150g of salt. The temperature was measured to a precision of ±1°C. The emf was measured with an electronic millivoltmeter (Type D Symetra) linked to a Perkin Elmer recorder, both with a high input impedance. Sodium and potassium nitrates (U.C.B.) f.a. and ultrapure sodium oxide and peroxide (Merck) f.a. were used.

Conditioning of the baths.—Preparation of basic baths.—The basic zone of the PO^{2-} scale can be reached by dissolving a strong base of known concentration in the bath. According to Flinn and Stern (18), Na_2O and Na_2O_2 at concentrations below 0.1 mol/kg are completely soluble in molten alkali nitrates. Mother mixtures with a high concentration of O^{2-} were prepared by adding 0.1 mol/kg of Na_2O and Na_2O_2 to an equimolar mixture of $(Na,K)NO_3$ dried beforehand in an oven at 120°C. The mixtures obtained are melted for 3 hr in a platinum crucible under an atmosphere of argon. After cooling the mother mixtures are finely ground and kept in a desiccator.

Preparation of acidic baths.—A high PO^{2-} is obtained by applying known partial pressures of NO_2 and O_2 corresponding to equilibrium [1]. Since the NO_2 is obtained through the reaction $NO + \frac{1}{2} O_2 \rightarrow NO_2$, the 99% pure NO with a 10 ml/min flow was mixed with pure oxygen or dry air. Condensation of NO_2 is avoided by keeping the temperature in the pipe at 80°C.

The flow of pure oxygen or air is regulated by the experimental installation shown schematically in Fig. 4. As it leaves the mixer, the gas flux is split by two micrometric gates, one of which regulates the outflow which will be bubbled through the bath (20 ml/min), while the other one drains off the surplus. Before releasing the gas into the atmosphere, the NO_2 is trapped.

Gas analysis.—Periodic samples of the gaseous mixture are analyzed by Whitnack and Milligan's method (20, 21). This method involves the absorption of NO_2, and NO if present, by concentrated sulfuric acid, followed by titration by $KMnO_4$. In the mixture with pure oxygen $p_{O_2} = 1 - p_{NO_2}$. In the mixture with dry air, O_2 content is determined by measurement of the volume of gas after absorption of NO_2. Therefore

$$\% NO_2 = \frac{\text{ml } NO_2 \text{ absorbed}}{\text{ml } NO_2 \text{ absorbed} + \text{ml water moved by the gas}}$$

Calibration of the electrode with a zirconia oxide membrane.—The primary cell is of the following type

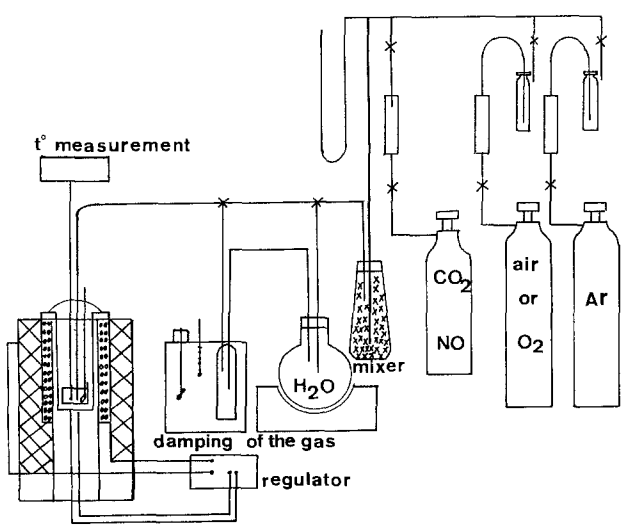

Fig. 3. Experimental installation

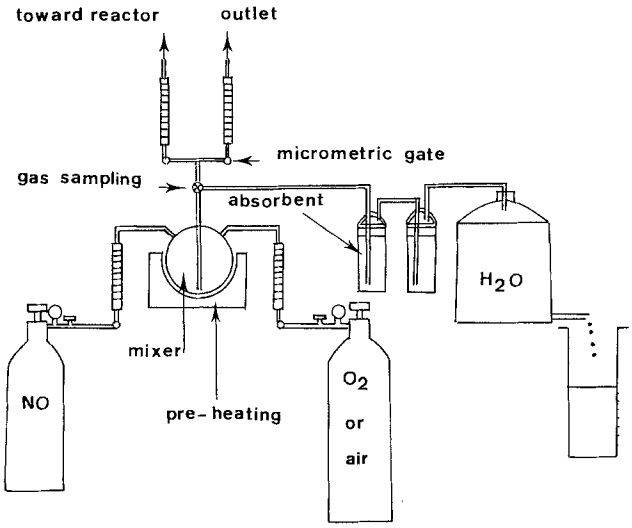

ciricuit and sampling of NO_2

Fig. 4. Circuit and sampling of NO_2

$$(-)\,p_t(\text{air})_R|ZrO_2\text{-}CaO|\,(Na,K)NO_3|Pyrex|$$
$$(Na,K)NO_3 + 0.1\ \text{mol/kg}\ AgNO_3|Ag(+)$$
$$O^{2-}, \text{gas}$$

The emf of this cell is given by Labani (22)

$$E = E^\circ + \frac{RT}{2F}\,2.302\log\frac{PO_{2(R)}{}^{1/2}}{(O^{2-})\,(Ag^+)^2} \qquad [8]$$

If we assume that this is an ideal solution and that activity can be replaced by concentration, then with an Ag^+ concentration of 0.1 mol/kg and a pressure of oxygen $p_{O2(R)}$ inside the zirconia tube of 0.21 atm at 475°C

$$E = E^{\circ\prime} - 0.074\log(O^{2-})$$
$$E = E^{\circ\prime} + 0.074\,PO^{2-} \qquad [9]$$

In a basic system.—EMF values obtained with variable concentrations of Na_2O in an equimolar mixture of $(Na,K)NO_3$ are given in Table I.

A graph of E(V) as a function of the logarithm of the concentration (Fig. 5) shows that the experimental points are all on a straight line, the slope of which corresponds to the theoretical slope 2.3 $RT/2F$ to within about 5 mV

$$E(V) = -0.600 - 0.074\log(O^{2-})_{added} \qquad [10]$$

By comparing this with [9] we can deduce

$$E^{\circ\prime} = -0.600 \pm 0.0005\ (V)$$

We shall now examine the influence of the formation of other species of oxygen such as O_2^{2-} and O_2^- on the functioning of the zirconia electrode corresponding to the O_2/O^{2-} couple. According to Ref. (18, 24) the oxide ion O^{2-} in the presence of oxygen is converted into peroxide and superoxide according to the following equilibrium

$$O^{2-} + \tfrac{1}{2}\,O_2 \rightleftharpoons O_2^{2-} \text{ at } 230°C \qquad K = 10^{16}$$
$$O_2^{2-} + O_2 \rightleftharpoons 2\,O_2^- \qquad K = 2 \times 10^6$$

Table I. Calibration of the zirconio membrane electrode in a basic system

(O^{2-}) (mol/kg) added	Log (O^{2-}) added	$E_{measured}$(V)/Ag^+/Ag
0.823×10^{-3}	−3.08	−0.372
1.924×10^{-3}	−2.71	−0.400
3.277×10^{-3}	−2.48	−0.416
10.56×10^{-3}	−1.98	−0.453
13.3×10^{-3}	−1.87	−0.461
15.5×10^{-3}	−1.8	−0.470

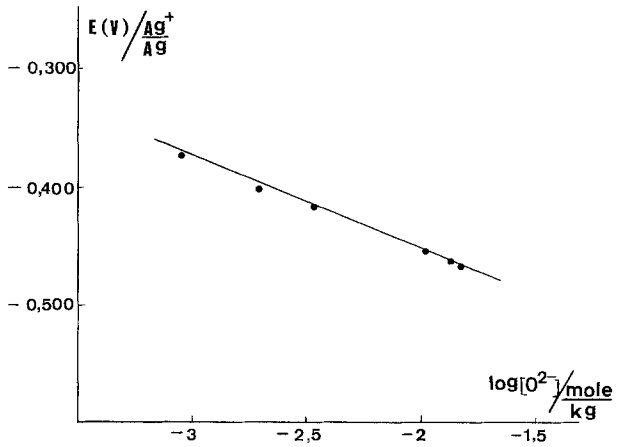

Fig. 5. Calibration of the zirconia electrode in a basic system

(the constants are expressed in molality). It can be ascertained that the formation constant of peroxide can be roughly considered to be several orders of magnitude greater than the formation constant of superoxide. Moreover, superoxide is less stable at higher temperature (18, 25, 26). One should therefore take the formation of superoxide into account when adding O^{2-}. If we assume that part of the oxide added is transformed into peroxide

$$[O^{2-}]_{added} = [O_2^{2-}] + [O^{2-}]$$

according to the equilibrium

$$O^{2-} + \frac{1}{2}\,O_2 \rightleftharpoons O_2^{2-} \qquad [11]$$

$$K_{11} = \frac{O_2^{2-}}{[O^{2-}]\,p_{O_2}{}^{1/2}_{melt}}$$

$$[O^{2-}] = \frac{[O^{2-}]_{added}}{K_{11}\,p_{O_2}{}^{1/2}_{melt}} \qquad [12]$$

If one substitutes this in [9] the expression of the emf of the zirconia electrode becomes

$$E = E^{\circ\prime} - 0.074\log\frac{[O^{2-}]_{added}}{K_{11}\,p_{O_2}{}^{1/2}_{melt} + 1} \qquad [13]$$

For any given oxygen pressure on top of the fused bath, the variation of the emf always follows Nernst's law with a slope of 0.074 mV. Only the absolute value of the emf could change if the oxide in solution disappears. It can also be noted that the form of Eq. [13], with the exception of a constant, resembles experimental behavior [10]. The linearity of Fig. 5 shows that within the interval of concentration used the activity coefficient of oxides remains constant and that the emf of the cell only depends on O^{2-} activity. Any increase in the emf (Ag more positive) depends on an increase in O^{2-} activity.

In an acidic system.—By replacing Eq. [7] in [9] we obtain

$$E = E^{\circ\prime} - 0.074\log K' + 0.074\log p_{NO_2}{}^2\,p_{O_2}{}^{1/2}$$
$$E = E^{\circ\prime\prime} + 0.074\log p_{NO_2}{}^2 p_{O_2}{}^{1/2} \qquad [14]$$

The experiments are carried out under a gaseous atmosphere containing NO_2 and O_2 under given partial pressures. It is necessary to wait for 10 hr before obtaining a state of equilibrium for the first measurement. In a state of equilibrium, when the composition of the gaseous mixture is modified, a lapse of time of 1 hr is necessary for the resulting emf to become constant to within about 5 mV. Table II gives the composition of the gaseous atmosphere and the emf of the

Table II. Calibration of zirconia membrane electrode in an acidic system

p_{O_2} (atm)	p_{NO_2} (atm)	log $(p_{O_2}/atm)^{1/2}$ $(p_{NO_2}/atm)^2$	E(V)/Ag$^+$/Ag
0.15	0.1	−2.41	−0.070
0.163	0.11	−2.31	−0.050
0.09	0.188	−1.97	−0.047
—	0.33	−0.97	−0.037
0.81	0.19	−1.48	+0.015
0.66	0.33	−1.05	+0.037
0.2	0.8	−0.54	+0.080

zirconia electrode with respect to the Ag$^+$/Ag reference electrode.

Figure 6 shows $E(V) = f(\log (p_{O_2}/atm)^{1/2} (p_{NO_2}/atm)^2)$. The experimental points are on a line with a slope of 78 mV/decade, and the regression line has the following equation

$$E(V)/Ag^+/Ag = 0.121 + 0.078 \log (PO^{2-}/atm)^{1/2} (p_{NO_2}/atm)^2$$

The variation in the emf of the zirconia electrode is typical of the O_2/O^{2-} couple, expressing as it does the exchange of two electrons per decade. This corresponds to the theoretical slope of 2.3 $RT/2F$ of about 74 mV/decade. A comparison with [14] yields: $E^{\circ\prime\prime} = 0.121$ (V).

Experimental PO^{2-} scale.—A PO^{2-} scale has been constructed on the basis of Fig. 5 and 6. Indeed the two experimental line segments (basic system and acidic system) having the same slope are the continuation of one another and form a single line (Fig. 7). This figure shows that except for a constant log $p_{O_2}{}^{1/2}$ $p_{NO_2}{}^2$ represents $PO^{2-} = -\log (O^{2-})$.

In accordance with the selective properties of stabilized zirconia we can say that, irrespective of the system (acidic or basic) and within the area studied, the potential of the zirconia electrode is solely a function of the PO^{2-} of the system. As for the redox reaction, we must assume that the potential of the zirconia electrode would become a mixed potential varying between the limits of normal potentials of the O_2/O^{2-} couple and of NO_3^-/NO_2, O_2 representing

$$\frac{1}{2} O_2 + 2e^- \rightleftharpoons O^{2-}$$

$$2NO_3^- \rightleftharpoons 2NO_2 + O_2 + 2e^-$$

$$2NO_3 \rightleftharpoons 2NO_2 + \frac{1}{2} O_2 + O^{2-}$$

The constant associated with this equilibrium is

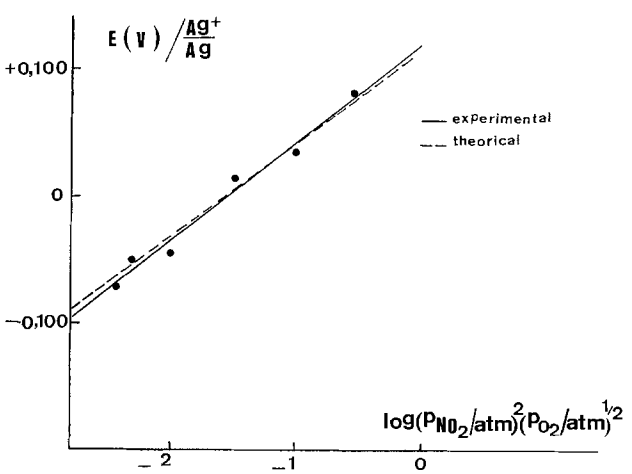

Fig. 6. Calibration of the zirconia electrode in an acidic system

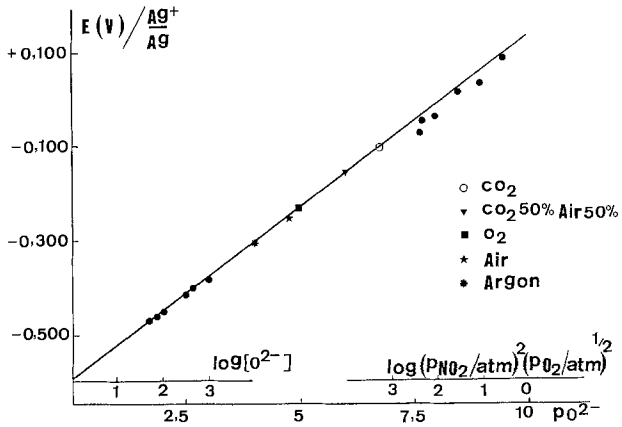

Fig. 7. PO^{2-} scale of an equimolar (Na, K)NO_3 at 475°C

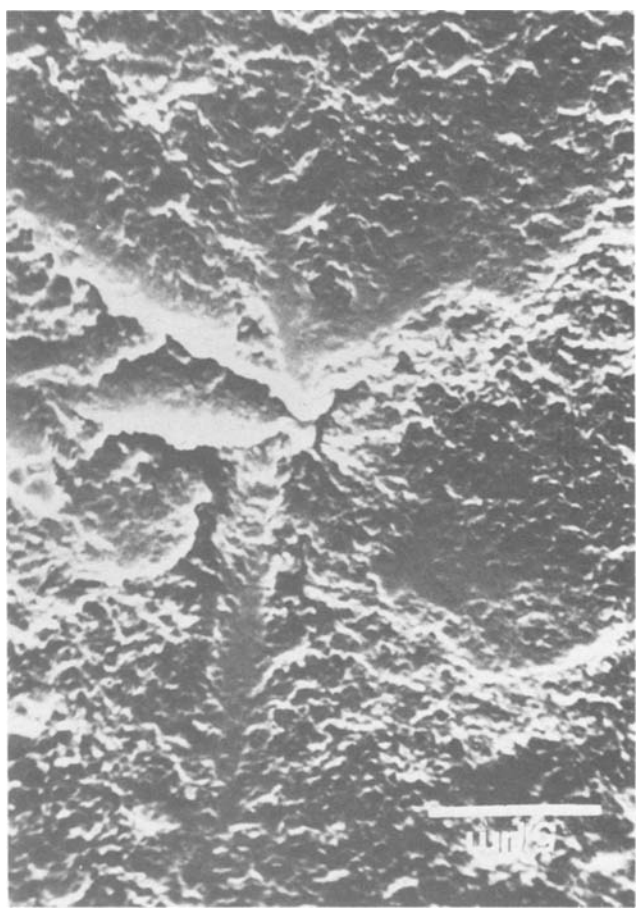

Fig. 8. Attack morphology of the glass treated in a highly basic system. $PO^{2-} = 2$, treatment 16 hr.

$$K' = \exp\left(-\frac{2F}{RT} (E^{\circ\prime\prime}\, NO_3^-/NO_2, O_2 - E^{\circ\prime}\, O_2/O^{2-})\right)$$

at 475°C; $K'/at.^{5/2} \cdot mol\, kg^{-1} = 1.92\,10^{-10}$.

When the bath is subjected to other gaseous atmospheres such as N_2, CO_2 pure or mixed with air or steam, a measurement of the potential is enough to deduce the value of PO^{2-} from Fig. 6. The general expression of the emf of the zirconia electrode is at 475°C

$$E(V)/Ag^+/Ag\ (0.1\ m) = -0.600\ (\pm 0.005) + 0.074\ PO^{2-}$$

Constant K' as obtained experimentally comprises the constant of thermodynamic dissociation of the NO_3^-

anion (K) and the solubility coefficients of NO_2 (K'_H) and O_2 (K''_H) in molten nitrates.

If constant K as given by Ref. (27) is transferred to a molality scale by means of $K_m = K_x(1000/M_S)^{\Sigma\gamma_i}$ where K_m and K_x are constants of equilibrium expressed as a function of molality and mol fraction, respectively, M_S is the average molecular mass of the solvent, and $\Sigma\gamma_i$ is the sum of stoichiometric coefficients of equilibrium $K/mol^{3/2} \cdot kg^{-3/2} = 10^{-17}$, we can see that the number obtained is not identical to K'. The difference is due to the fact that the solubility of these gases under atmospheric pressure is lower than 1 mol/kg. We have seen that $K = k_H K'$, from which we can deduce

$$k_H = k'^2_H \cdot k''^{1/2}_H = 5.2\,10^{-8}\ (mol \cdot kg^{-1} \cdot atm^{-1})^{3/2}$$

If we assume that the decomposition of the solvent is not significant on initial approximation, we can extrapolate the value of $k''_{H(O_2)}$ from Ref. (28)

$$k''_H \simeq 8 \cdot 10^{-6}\ mol \cdot kg^{-1} \cdot atm$$

$$k'_{H(NO_2)} = \sqrt{\frac{k_H}{k''^{1/2}_{H(O_2)}}} = 4.3 \cdot 10^{-3}\ mol \cdot kg^{-1} \cdot atm^{-1}$$

which is comparable to the value of k'_H at 300°C as given by Ref. (29), *i.e.*, k'_H (5 ± 3) 10^{-3} mol 1^{-1} atm (with $d = 2 g/cm^3$).

Proportioning of nitrite in solution.—When the bath is exposed to atmospheres such as N_2 and NO_2, nitrites are formed (9, 20) according to the following equilibriums

$$NO_3^- + O^{2-} \rightleftharpoons NO_2^- + O_2^{2-}$$

under neutral atmosphere

$$2NO_2 + O^{2-} \rightleftharpoons NO_2^- + NO_3^-$$

under an atmosphere of NO_2

In order to have some notion of the quantity of nitrite formed in solution, samples were obtained from the rapidly cooled molten bath. By using the method of colorimetry with formation of azoic coloring (Griess reagent) as described in Ref. (30) we determined the quantity of nitrite formed. Table III shows the concentration of NO_2^- formed.

Discussion and Conclusions

Experimental results show that the potential of the stabilized zirconia electrode varies in a basic system as a function of the equilibrium potential O_2/O^{2-}. Within the interval of (O^{2-}) concentration added (between 10^{-4} and 0.1 mol/kg) the response of the zirconia electrode is linear, with a slope approximating to within 0.005V of the theoretical slope. For concentrations of (O^{2-}) below 10^{-4} mol/kg the potential of the zirconium oxide electrode tends toward the equilibrium potential of the bath without any basic com-

Table III. Concentration of NO_2^- in solution (mol/kg)

Composition of the bath	Atmosphere	pO^{2-}	$NO_2^- \times 10^2$
(Na,K)NO_3	NO_2	8	8.4
	0.66% NO_2 + 0.33% O_2	8.5	5.9
	0.12% NO_2 + 0.16% O_2	8	5.9
	CO_2	6	1.1
	N_2	4	7.5
(Na,K)NO_3 + Na_2O	Air	1.83	9

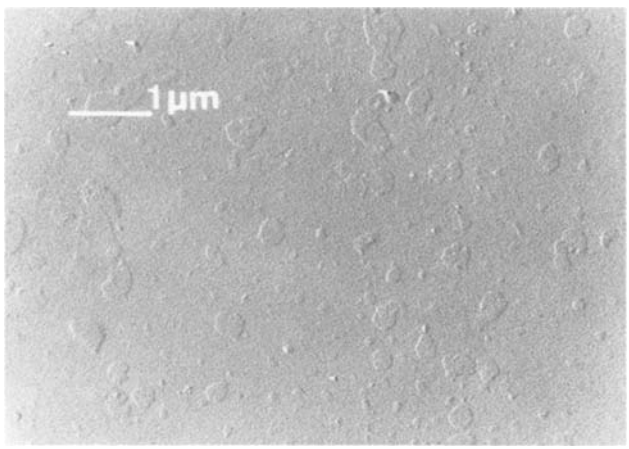

Fig. 10. Attack morphology of the glass treated in a weak acidic system. $PO^{2-} = 7$, treatment 16 hr.

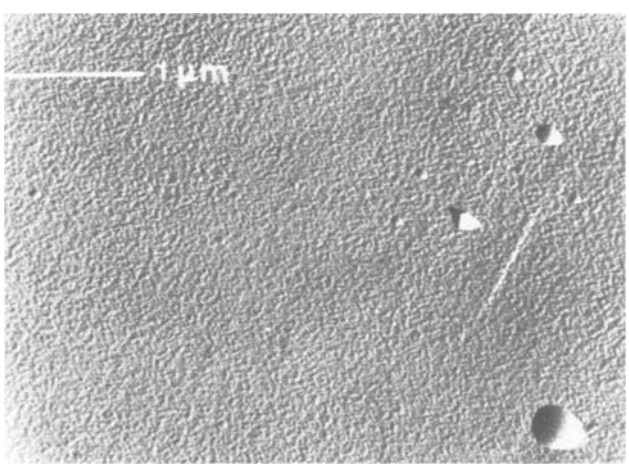

Fig. 9. Attack morphology of the glass treated in a neutral system. $PO^{2-} = 6$, treatment 16 hr.

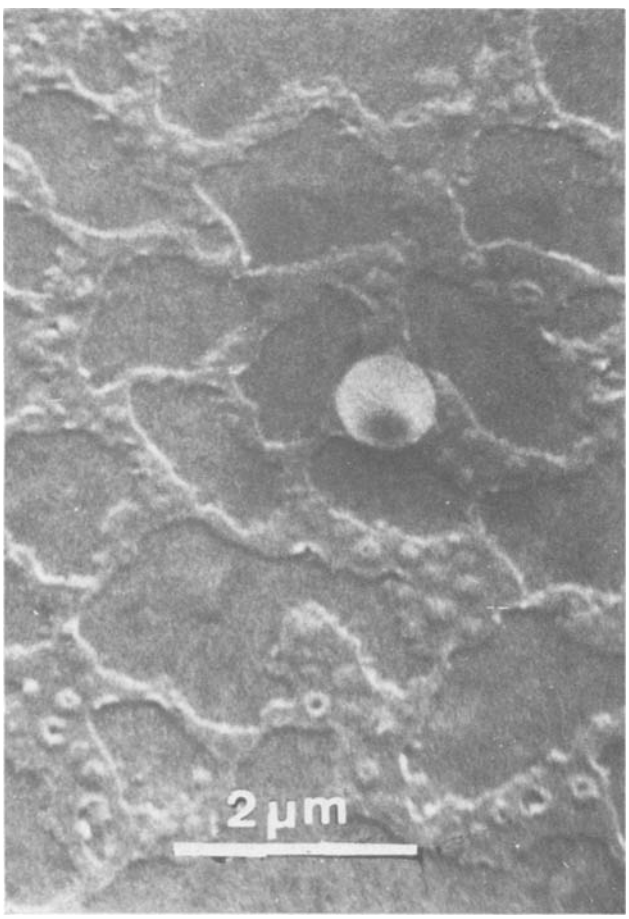

Fig. 11. Attack morphology of the glass treated in a highly acidic system. $PO^{2-} = 8$, treatment 16 hr.

pound. For concentrations of (O^{2-}) above 0.1 mol/kg, owing to deviation from ideal conditions, the linear law does not apply.

In an acidic system, the more acidic the bath the higher the value of PO^{2-} is; by replacing in Eq. [7] $p_{O_2} = 1 - p_{NO_2}$ and $\partial p_{O2-}/\partial p_{NO_2} = 0$, we obtain $p_{NO_2} = 0.8$ atm and $p_{O_2} = 0.2$ atm and $p_{O2-_{max}} = -\log K' = 10$. It follows that the experimental acidity scale of molten alkali nitrates at 475°C is of approximately 10 units of PO^{2-}.

For other gaseous atmospheres above the molten bath, a simple measurement of the potential of the zirconia electrode with respect to the Ag^+/Ag reference electrode allows us to deduce PO^{2-} by using the diagram in Fig. 7.

Manuscript submitted Dec. 9, 1982; revised manuscript received *ca.* May 17, 1983.

The Université libre de Bruxelles assisted in meeting the publication costs of this article.

APPENDIX

If one takes into account the formation of superoxide out of peroxide

$$O_2^{2-} + O_2 \rightleftharpoons 2\,O_2^- \qquad [A\text{-}1]$$

$$K_I = \frac{[O_2^-]^2}{[O_2^{2-}]p_{O_2}}$$

taking account of the disproportionate of oxide by superoxide

$$2\,O_2^- + 2\,O^{2-} \rightleftharpoons 3\,O_2^{2-} \qquad [A\text{-}2]$$

$$K_{II} = \frac{[O_2^{2-}]^3}{[O_2^-]^2\,[O^{2-}]^2}$$

By eliminating $[O_2^-]$ between the two equations

$$[O_2^{2-}] = [O^{2-}]\sqrt{K_I K_{II} p_{O_2\,melt}}$$

$$[O^{2-}]_{add} - [O^{2-}] = [O^{2-}]\sqrt{K_I K_{II} p_{O_2\,melt}}$$

$$[O^{2-}] = \frac{[O^{2-}]_{add}}{\sqrt{K_I \cdot K_{II} p_{O_2} + 1}}$$

Eq. [9] becomes

$$E = E^{\circ\prime} - 0.074 \log \frac{[O^{2-}]_{add}}{\sqrt{K_I K_{II} p_{O_2\,melt} + 1}}$$

REFERENCES

1. K. H. Stern, *J. Phys. Chem.*, **72**, 2256 (1968).
2. K. H. Stern, *ibid.*, **74**, 1323 (1970).
3. D. R. Flinn and K. H. Stern, *ibid.*, **76**, 1072 (1972).
4. J. O. Isard, *Phys. Chem. Glass*, **17**, 1 (1976).
5. J. P. Doremus, *J. Phys. Chem.*, **68**, 2212 (1964).
6. J. P. Lacharm, *C. R. Acad. Sci. Paris, Série C*, 559 (1968).
7. J. P. Lacharm, *Silicates Industriels*, **35**, 169 (1976).
8. G. Eisenman, *Biophys. J.*, **2**, Pt. 2, 259 (1962).
9. A. De Haan and H. Vanden Poorten, *Bull. Soc. Chim. France*, **11**, 2522 (1973).
10. R. F. Bartholomew, *J. Phys. Chem.*, **70**, 3442 (1966).
11. R. N. Kust, *This Journal*, **116**, 1137 (1969).
12. N. S. Wrench and D. Inman, *J. Electroanal. Chem.*, **17**, 319 (1969).
13. P. G. Zambonin, *ibid.*, **24**, 365 (1970).
14. A. M. Shams El Din and A. A. El Hosary, *ibid.*, **17**, 238 (1968).
15. P. G. Zambonin and J. Jordan, *J. Am. Chem. Soc.*, **91**, 2225 (1969).
16. D. R. Stull, Editor, "JANAF Thermochemical Tables," The Dow Chemical Co., Midland, MI (1965).
17. G. Picard, F. Seon, and B. Tremillon, *J. Electroanal. Chem.*, **39**, 63 (1979).
18. D. R. Flinn and K. H. Stern, *ibid.*, **63**, 39 (1975).
19. H. Lux, *Z. Elektrochem.*, **45**, 303 (1939).
20. C. Whitnack, J. Clifford, E. Halford, St. Clair Gantz, and G-B. L. Smith, *J. Anal. Chem.*, **23**, 464 (1951).
21. L. H. Milligan, *J. Phys. Chem.*, **28**, 544 (1924-1925).
22. A. Labani, Thèse de doctorat, Université libre de Bruxelles (1982).
23. K. H. Stern, M. L. Deanhardt, and Rm. Panayappan, *J. Phys. Chem.*, **83**, 22, 2848 (1979).
24. P. G. Zambonin, *J. Electroanal. Chem.*, **33**, 243 (1971).
25. P. G. Zambonin, *ibid.*, **24**, App. 25 (1970).
26. J. M. Schlegel and D. Priore *J. Phys. Chem.*, **20**, 2841 (1971).
27. K. H. Stern, *J. Phys. Chem.*, Ref. Data Parts 3, Nitrates and Nitrites.
28. P. G. Zambonin and J. Jordan, *J. Electroanal. Chem.*, **38**, 373 (1972).
29. L. E. Topol and R. A. Osteryoung, *J. Phys. Chem.*, **70**, 2857 (1951).
30. G. Charlot, "Les Méthodes de la chimie analytique," p. 619, Masson, Paris (1961).

Characterization of Films Formed on Tungsten Electrodes in Molten Nitrates Using Electrochemical and X-Ray Photoelectron Spectroscopic Studies

Luigia Sabbatini

Istituto di Chimica Analitica, Universita degli Studi, 70126 Bari, Italy

Peter M. A. Sherwood

Department of Inorganic Chemistry, University of Newcastle upon Tyne, Newcastle upon Tyne NE1 7RU, England

Pier G. Zambonin

Istituto di Chimica Analitica, Universita degli Studi, 70126 Bari, Italy

ABSTRACT

X-ray photoelectron spectroscopy (XPS) and electroanalytical techniques were combined to analyze the behavior of tungsten electrodes in molten nitrates. Cyclic voltammetric profiles obtained in the stability range of the given melt reveal previously unreported peaks, and XPS was performed on samples treated at the significant potential regions. The XPS analysis reveals the presence of tungsten in oxidation states IV, VI, and an intermediate one at various potentials, together with underlying tungsten metal in appropriate cases. In the studies of electrochemically oxidized samples it is found that there is electrochemical evidence for tungsten even in low oxidation states formed on the electrode, but it appears that these species are dissolved in the melt and thus not seen in XPS studies. A study of the corrosion of tungsten by the melt was also carried out.

Tungsten and its oxides are very important from a technological point of view. Particular attention has been given to the phenomenon of electrochromism (1-8) in WO_3 films because of its potential use for passive alphanumeric displays. Tungsten trioxide has been recently used as a stable semiconducting material for the photoelectrolysis of aqueous solutions (9-11) and the semiconducting properties of monocrystalline tungsten trioxide (12) or amorphous film (13) electrodes in different solutions and in the presence of different redox couples have also been studied. Studies have also been carried out on the chemistry and electrochemistry of tungsten in molten salts (14-16) in view of its possible use in high temperature alloys.

Preliminary results concerning the electrode-catalyzed chemical decomposition of ammonia have been reported (17-19) during the course of a systematic investigation of hydrogen and oxygen electrodes in molten nitrates performed at Bari. Since tungsten is a good catalyst for NH_3 decomposition (20), it may be useful as an electrode material for high temperature hydrogen electrodes. In such an application a study of its corrosion in molten nitrates may prove essential.

In this paper we report a study of films formed on a tungsten electrode surface under different experimental conditions by x-ray photoelectron spectroscopy (XPS or ESCA). This technique can identify the chemical nature of such films and give information about their thickness (21). The complete identification of the films formed on electrodes is central to a proper understanding of electrochemical systems. In addition, important information may be obtained about corrosion processes and in some cases unusual compounds, not easily prepared by other methods, may be studied. XPS has usually been applied to electrodes in aqueous systems, but has also been applied to electrodes in molten salt systems (22-24). In this paper we report a detailed study of the behavior of tungsten electrodes in molten nitrates under chemical and electrochemical treatment. In contrast to the situation in aqueous solution (25), the surface of electrodes that have been used in molten nitrates shows the presence of lower oxidation states of tungsten in addition to W(VI). The binding energies for the 4f level in tungsten and its different oxidation states [W(0), W(IV), W(V), and W(VI)] from this work are compared with those of other previously reported studies (26-31).

Key words: ESCA, surfaces, analysis.

Experimental

All the spectra were obtained using an AEI (Kratos) ES200B x-ray photoelectron spectrometer, operated in the FRR mode, using Mg $K\alpha$ x-radiation. The data were collected using an Apple II microcomputer system linked to an IBM 370/168 computer, the latter being used for most of the data analysis (32). The base pressure in the sample chamber varied from 10^{-8} to 10^{-9} Torr. Samples were etched using an Ion Tech B24 mechanically scanned Saddle Ion source. Calibration was based upon the W $4f_{7/2}$ metal peak (31.5 eV) and the carbon 1s electron peak (284.6 eV) due to residual pump oil on the sample surface.

Spectra were fitted using a nonlinear least squares method with a Gaussian/Lorentzian (33) peak shape, including the effect of nonlinear background subtraction (34) and radiation satellites.

Current-voltage curves were recorded using a triangular voltage sweep at several sweep rates (20-500 mV sec^{-1}) using a Princeton Applied Research 174A potentiostat and an Electrochemlab Amel function generator. The electrochemical cell has been described previously (35). The working electrode was a tungsten wire (1 mm diam) sealed in a glass tube, the reference electrode was an Ag^+/Ag 0.07 mol kg^{-1} and the counterelectrode was a platinum foil. When samples were examined by XPS the working electrode was a tungsten plate approximately 10^{-4} m^2 in area. In these cases the electrode was removed from the melt, without disconnecting the potentiostat, and washed in triply distilled deoxygenated water to remove the melt. In some experiments a rotating disk electrode was used (1 mm diam, with a rotation speed 600 rpm). The solvent was an equimolar mixture of sodium and potassium nitrate at 230°C. All the reagents used were RP analytical grade, and the melt was maintained under nitrogen (ultra pure grade) which was dried over mo-

lecular sieves. Ventron, Alfa Division 99.9% purity tungsten of 0.125 mm thickness was used for the experiments.

Results and Discussion

Electrochemical Studies

The main features from cyclic voltammetry measurements.—Most of the information about the tungsten-molten nitrates system could be obtained from cyclic voltammograms starting from potentials in the range 1.0-1.8V where a large oxidation current could be recorded. Figure 1 shows a typical cyclic voltammogram obtained with a tungsten microelectrode in molten nitrates under an inert atmosphere. The cyclic voltammogram can be seen to be rather complex. Only peaks H and F have been previously described (36, 37) in the literature, the other peaks being new. Peak H has been ascribed to the passivation of the electrode as a result of the formation of insoluble sodium oxide which precipitates on the electrode, according to the equation

$$NO_3^- + 2e \rightleftharpoons NO_2^- + O^= \quad [1]$$

$$2Na^+ + O^= \rightleftharpoons Na_2O(s) \quad [2]$$

and peak F to the oxidation of this oxide to superoxide anions

$$2Na_2O(s) \rightleftharpoons O_2^- + 4Na^+ + 3e \quad [3]$$

The limits A and I are due to the electro-oxidation (38-40) and electroreduction (36, 41, 42) of the solvent, respectively. The remaining peaks can probably be ascribed to the formation and reduction of tungsten oxide films on the electrode surface. In particular, at a potential corresponding to the peak at about +1.3V a species is formed which passivates the electrode up to +6.0V. If a potential scan is started from +1.3V toward less positive values (as in Fig. 1), one can see that this surface species undergoes a first reduction process at about −1.2V; and a second one giving rise to a shoulder at about −1.6V on the peak H. Then sodium oxide formation is attained according to Eq. [1] and [2].

If a potential scan is started from −2.6V toward more positive values (as in Fig. 1), then the first peak (F) results from superoxide formation, then reoxidation of the tungsten species previously reduced gives rise to peaks D and C, and then passivation of the electrode causes peak B. It is important to emphasize that peak C occurs as a single peak on decreasing the scan rate, and its profile is rather irregular as generally happens when gas evolution is involved, while peaks D and F decrease. A limiting situation showing the disappearance of peaks D and F is obtained under rotating electrode conditions (*vide infra*).

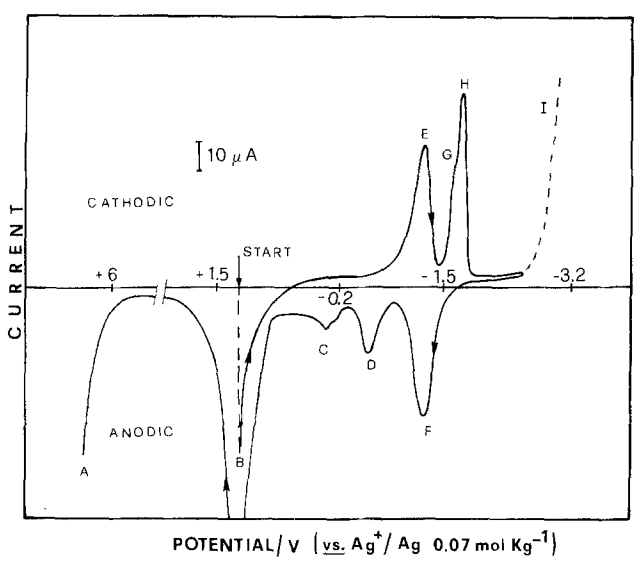

Fig. 1. Typical cyclic voltammogram obtained with a tungsten microelectrode in pure $(Na,K)NO_3$ eutectic mixture at 230°C under a dry nitrogen atmosphere. Scan rate: 200 mV sec^{-1}. Starting potential +1.3V (for peak assignment see last section).

Behavior in vicinity of cathodic passivation peak.—Figure 2 shows a peculiar feature involving the cathodic passivation peak at about −1.65V. The potential-current profiles are shown recorded at constant cathodic scan rate and variable anodic scan rate. At low anodic scan rates, on reversing the potential scan, unexpected (cathodic) currents are found. It is clear from Fig. 2 that the cathodic contribution is higher the lower is the anodic scan rate, and only for very fast scan rates can the oxidation peak be seen. The cathodic portion of the peak becomes more and more negligible when the scan is reversed at more and more cathodic potential values as shown in Fig. 3. A similar behavior is obtained, of course, if the scan is stopped at point 1 before reversing its direction. The longer the "waiting time" at this point, the more similar the current-potential profile becomes to that of curve 3. This peculiar behavior indicates (43-44) that the passive state is not very stable and that there is a competition between a passivation and a depassivation effect, that is, between the film formation and its chemical dissolution (*vide infra*).

Rotating disk electrode studies.—Figure 4 shows a typical voltammogram obtained with a tungsten rotating disk electrode starting from anodic passivation conditions. The cathodic profile is almost the same as

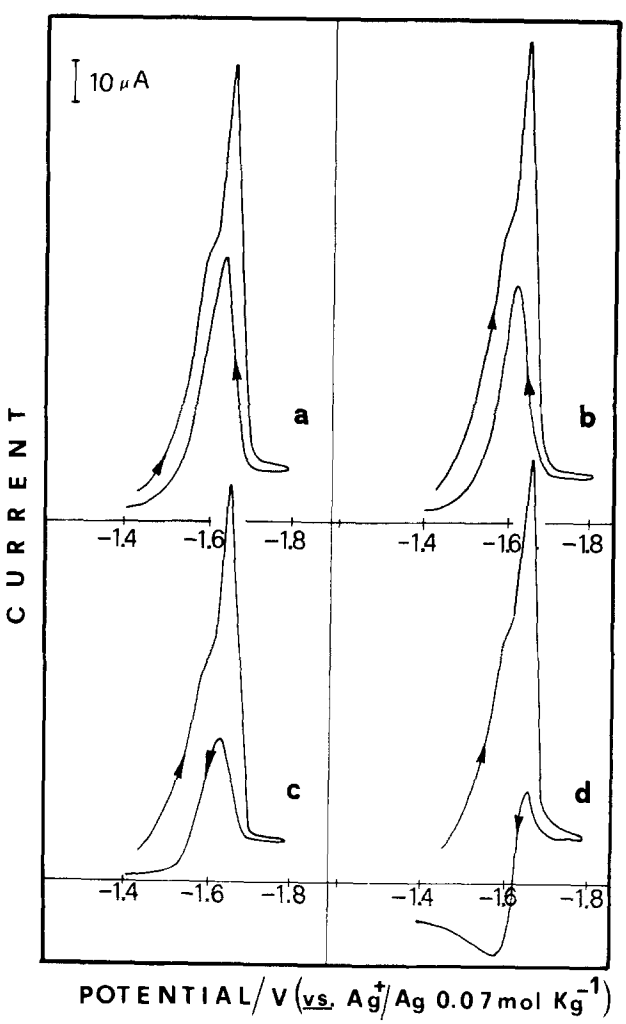

Fig. 2. Current-potential profiles obtained with a tungsten microelectrode in pure $(Na,K)NO_3$ eutectic mixture at 230°C under a dry nitrogen atmosphere. Cathodic scan rate: 100 mV sec^{-1}; anodic scan rates: (a) 20 mV sec^{-1}, (b) 50 mV sec^{-1}, (c) 100 mV sec^{-1}, (d) 500 mV sec^{-1}.

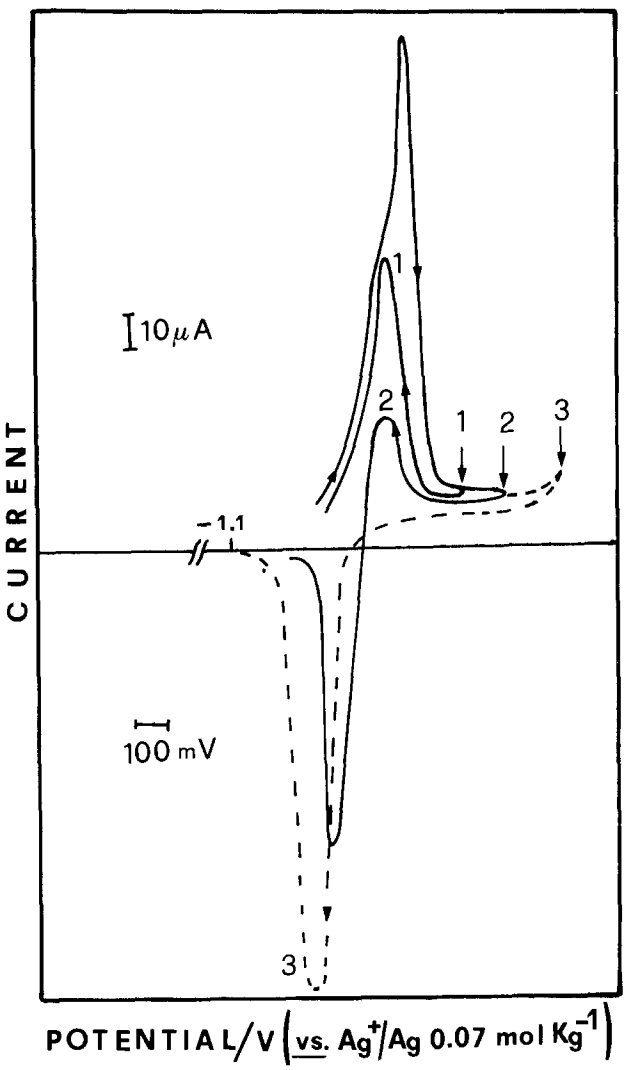

Fig. 3. Current-potential profiles obtained with a tungsten microelectrode in pure $(Na,K)NO_3$ eutectic mixture at 230°C under a dry nitrogen atmosphere. Cathodic and anodic scan rate: 100 mV sec^{-1}. The arrows show the scan reversing point for each curve.

that obtained from the cyclic voltammetry measurements at low scan rates. Thus, after recording the passivation peak at −1.65V, on reversing the scan toward less negative potential values, the previously decribed cathodic current contribution can be recorded. In the anodic region the oxidation signal at −0.5V (peak D in Fig. 1) is absent while the double peak at −0.2V (C in Fig. 1) is present as a single peak. Finally the passivation peak at +1.3V occurs.

X-ray Photoelectron Spectroscopic Studies

An attempt was made to correlate the electrochemical behavior described above with the nature of the species present on the electrode surface. A systematic XPS investigation was performed on samples polarized (cathodically or anodically) at different potentials. Table I shows the XPS data for the W4f doublet in this work and compares it with previous studies. Error limits for this work are shown as two standard deviations.

Studies of tungsten metal.—Many of the spectra obtained in this study showed peaks due to tungsten metal, in addition to tungsten oxides. Such spectra were curve fitted using parameters derived from accurately fitted metal spectra. The metal was reduced in hydrogen at 500°C and then argon ion etched to remove any residual oxide, giving the W4f spectra shown in Fig. 5(a). The small shoulder on the left (chemical

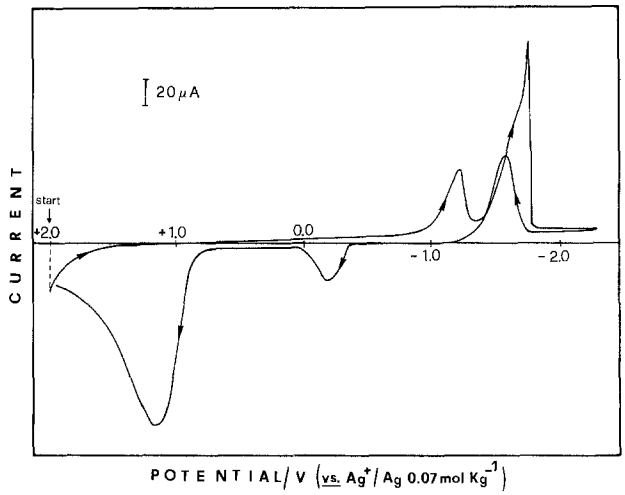

Fig. 4. Typical tungsten RDE voltammogram recorded in pure $(Na,K)NO_3$ eutectic mixture at 230°C under a dry nitrogen atmosphere. Starting potential +2.0V; rotation speed 600 rpm; scan rate 10 mV sec^{-1}.

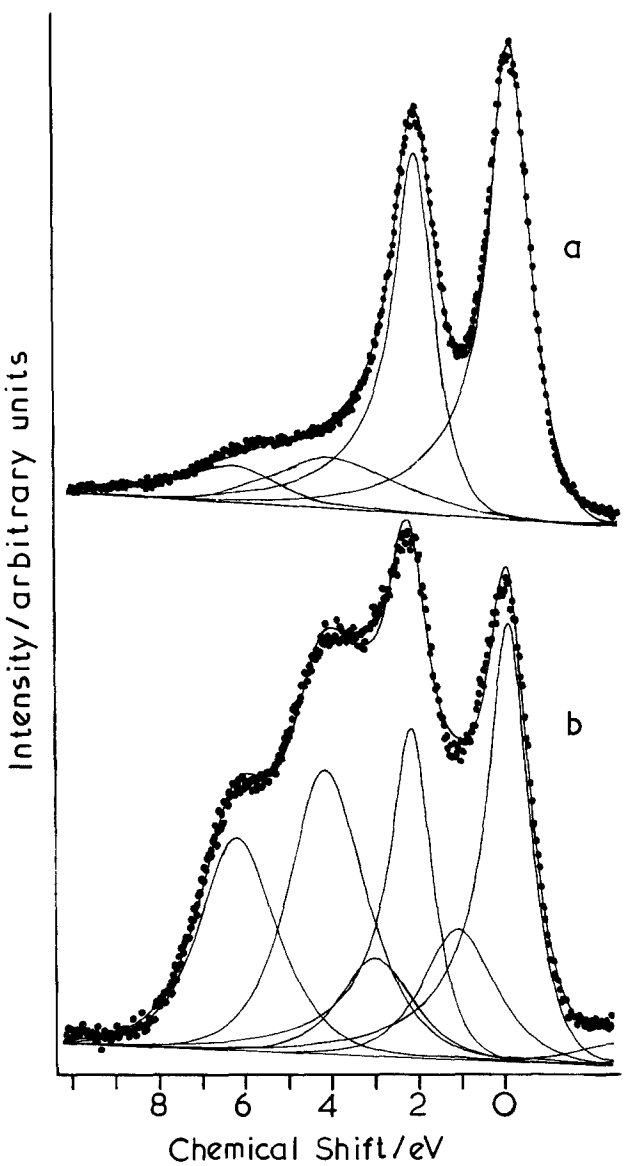

Fig. 5. Tungsten 4f ESCA spectra (chemical shift with respect to tungsten metal $4f_{7/2}$ peak). (a) Tungsten metal etched with argon ions (5 kV, 2 mA for 30 min); (b) same sample as in (a) but analyzed under a grazing angle.

Table I. ESCA spectra of W4f doublet in tungsten and its oxides in different oxidation states

Oxidation state	Binding energy, (eV) W4f7/2	Binding energy, (eV) W4f5/2	Spin-orbit splitting (eV)	FWHM 4f (eV)	Separation from W(0) (eV)	References
W(0)	31.2 ± 0.1	33.4 ± 0.1	2.18 ± 0.02			(8)
	31.2		2.20 ± 0.5'			
			2.10 ± 0.05"			(7)
	31.5	33.6	2.1			(28)
	32.5	34.5	2.0			(25)
	31.3 ± 0.4	33.5 ± 0.4	2.2 ± 0.05	0.86 ± 0.07		This work
W(II)	33.1					(28)
W(IV)	32.5 ± 0.1				1.3	(8)
	34.6	36.7	2.1		3.1	(28)
	33.6	35.7	2.1			(30)
	33.5	35.6	2.1			(27, 29, 31)
	33.0	35.1	2.1			(6)
	32.7				2.0	(26)
	33.1 ± 0.2	35.4 ± 0.2	2.3 ± 0.3	2.0 ± 0.4	1.8 ± 0.4	This work
W(V)	35.4	37.5	2.1		3.9	(28)
	35.1	37.2	2.1			(27, 29, 31)
	35.0	37.1	2.1			(6)
	35.4 ± 0.2	37.6 ± 0.2	2.1	1.5	4.1 ± 0.1	This work
W(VI)	35.5 ± 0.1	37.6 ± 0.1	2.14 ± 0.02		4.3	(8)
	35.7	37.85	2.15		4.5	(7)
	36.1	38.2	2.1		4.6	(28)
	36.8	38.8	2.0		4.3	(25)
	36.1	38.2	2.1			(27, 29)
	36.1	38.2	2.1			(31)
	35.4	37.5	2.1			(30)
	35.0		2.0		4.3	(26)
	36.0	38.1	2.1			(6)
	35.8 ± 0.5	37.8 ± 0.5	2.1 ± 0.1	1.3 ± 0.03	4.5 ± 0.1	This work

' = cubic bronzes.
" = tetragonal bronzes.

shift 4-7 eV) of the metal peaks (split by spin-orbit splitting) was found to be due to mainly W(VI) oxide, confirmed by the surface sensitive, very low take-off angle (45) experiments [Fig. 5(b)]. It should be noted that although one might expect some tungsten $5p_{3/2}$ intensity and the small shoulder can be fitted to a peak separated by 3.56 eV from the $4f_{7/2}$ peak with an area ratio ($4f_{7/2}$:$5p_{3/2}$) of 3.23:1, this ratio is much less than the value of 8.83:1 expected from Schofield's cross sections (52). Further the angle-resolved experiments show that there is considerable oxide intensity in this region. Thus any $5p_{3/2}$ contribution has been ignored as its contribution to the fitted spectra would be expected to be very small and cannot be quantified. The oxide could not be removed by argon ion etching and presumably results from knock-on effects during the etching process. The asymmetry in the metal peak shape is due to conduction band interaction effects (46-48).

Studies of chemical oxidation of tungsten metal.—Tungsten metal prepared by reduction in hydrogen at 500°C was exposed to the melt for different times. This showed the formation of tungsten in oxidation states (IV) and (VI) which must thus exist as an insoluble stable species on the metal surface. The assignment of the peaks to different oxidation states was based on XPS studies of chemically prepared powder samples of the different oxides, previous literature values (26-31), and metal to oxide peak separations in oxidized metal samples; the values chosen were W(VI) 4.5 eV, W(IV) 1.8 eV. The thickness of the oxide film increased and the composition changed with time of exposure. In most cases the substrate metal could be observed, suggesting that the oxide films were of the order of 2 nm or less. Typical curve-fitted spectra are shown in Fig. 6. In general the amount of W(VI) species tends to increase with the time of exposure, while that of W(IV) species tends to assume a constant value (around 20%) and then disappear for the longest times of contact between the sample and the melt. After prolonged exposure (several hours) the signal from the underlying metal becomes almost negligible, the surface being completely tungsten(VI). When thick oxide layers were formed a certain peeling of the film was sometimes observed.

Studies of electrochemical treatment of tungsten metal.—When a potential of +1.3V is applied to the electrode a high oxidation current is recorded (Fig. 1) which is related to the formation of a passivation species. XPS analysis was performed in order to define the nature of this species and to detect any changes in surface composition after electroreduction and reoxidation at potential values corresponding to the peaks in Fig. 1.

The XPS spectra shown in Fig. 7 indicate that when the electrode is polarized at +1.3V (or more anodic potentials) the tungsten metal is oxidized to tungsten(VI) oxide, with a film thickness that increases with time. Examples of curve-fitted spectra at important points in the cyclic voltammogram are reported in Fig. 8. Thus Fig. 8a shows a spectrum recorded after sweeping to −1.2V (where the first reduction process occurs) which exhibits tungsten metal and "tungsten(V)" (*vide infra*) species. Figure 8b is a spectrum recorded after sweeping to −1.6V (where the second reduction process occurs) and shows some tungsten(VI) with the underlying metal. One might expect to see lower oxidation state species at this point, but it is thought that such species might dissolve in the melt and are thus not seen on the electrode surface (see last section). Figure 8c shows the situation after sweeping the potential cathodically up to −2.0V and then anodically up to −0.5V which shows tungsten(IV), some tungsten(VI) together with metal [the fit is not perfect and the W(VI) peaks are somewhat wider than expected and this may be explained by the presence of a little "tungsten(V)"]. Figure 8d shows the spectrum obtained after sweeping the potential cathodically up to −2.0V and then anodically up to +0.1V which shows only tungsten(VI) together with metal [there may be some tungsten(V) as in Fig. 8c]. In all the spectra recorded after maintaining the samples for relatively long periods of time (2 min) at potentials between −1.6 and −2.0V (see for example Fig. 8b) the only detectable species on the electrode surface is W(VI), in amounts similar to that obtained when a pure tungsten metal sample is exposed to air and submitted to the washing operation.

It must be pointed out that although Fig. 8a clearly indicates the presence of "W(V)" [from the chemical shift from the metal (4.1 eV)] on the surface of elec-

trodes treated at −1.2V, the amount of this species is usually found to be less than expected on the basis of the starting quantity of W(VI) and sometimes it is not detectable at all [though some W(VI) can be seen]. These results suggest that: (*i*) "W(V)" is not a "stable" species being soluble in the melt and/or in the water used in washing, and (*ii*) only when the "W(V)" film is completely lost can the underlying metal be oxidized to W(VI).

No evidence was found in the overall XPS spectrum of the existence of sodium on the surface, thus avoiding the possibility of insoluble "bronze" formation (53).

Mechanistic Considerations

The combination of electrochemical and spectroscopic information allows the behavior of tungsten electrodes in molten nitrates to be tentatively explained. The proposed reaction paths shown below, which relate to the labeled peaks in the cyclic voltammogram in Fig. 1, are consistent with the studies above, and with the information about the stability of oxygen species in the melt (49-51). The apex "e" indicates solid species on the electrode surface, the other species being in solution

$$\text{Peak B:}\quad W^e + 3NO_3^- \rightleftharpoons WO_3^e + 3NO_2 + 3e \qquad [4]$$

is supported by XPS analysis [which detects the presence of W(VI)], the observation of yellow gas evolution, and the yellow color of the film.

$$\text{Peak E:}\quad 4WO_3^e + e \rightleftharpoons 2W_2O_5^e + O_2^- \qquad [5]$$

is supported by XPS analysis and the known super-

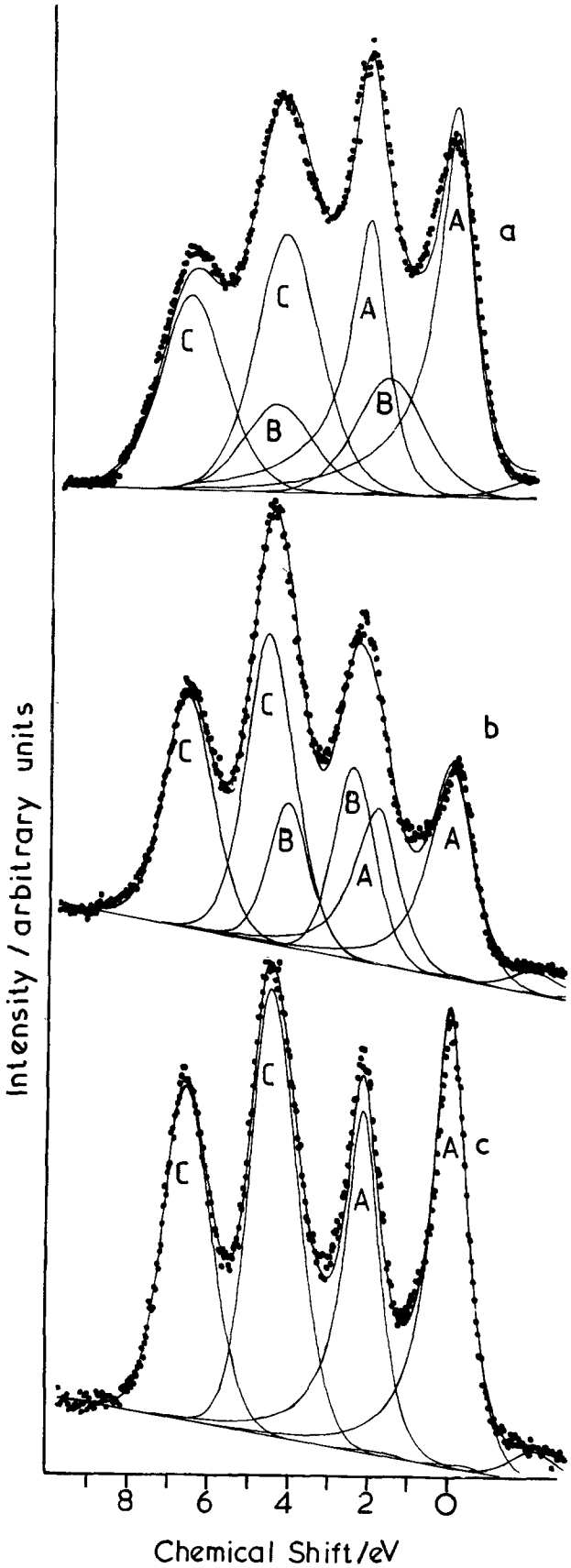

Fig. 6. Tungsten 4f ESCA spectra. Representative examples of spectra recorded on samples maintained in contact with the melt for different times shown fitted to different tungsten species: (A) tungsten(0) doublet, (B) tungsten(IV) doublet, (C) tungsten(VI) doublet. (a) 10 min, (b) 30 min, (c) 120 min.

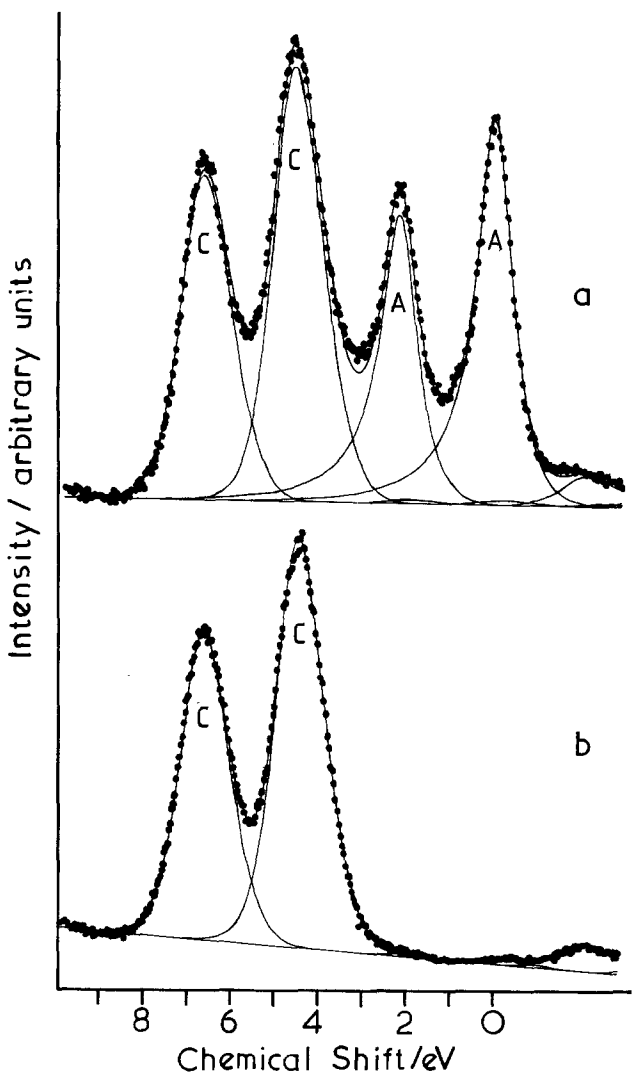

Fig. 7. Tungsten 4f ESCA spectra. Spectra from W electrodes polarized at +1.3V for different times shown fitted to different tungsten species: (A) tungsten(0) doublet, (C) tungsten(VI) doublet. (a) 1 sec, (b) 30 sec.

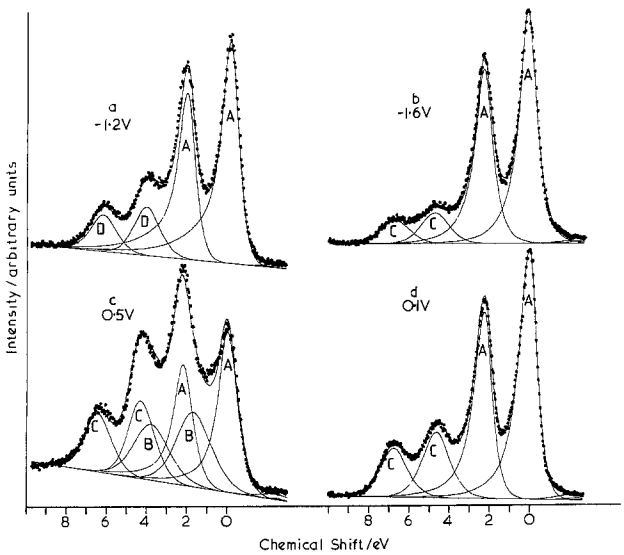

Fig. 8. Tungsten 4f ESCA spectra. Representative examples of spectra from samples polarized at different potentials (for peak assignment and experimental conditions see Fig. 7). (A) Tungsten(0) doublet, (B) tungsten(IV) doublet, (C) tungsten(VI) doublet, (D) tungsten(V) doublet.

oxide stability (49, 50) in this potential region.

$$\text{Peak G:}\quad W(V)^e + ne \rightleftharpoons W(V-n)^e \qquad [6]$$

is suggested by voltammetric measurements, but the final oxidation state is not known since XPS is unable to detect the product species due to the chemical reaction of the product with Na_2O and its subsequent dissolution, as shown below

$$\text{Peak H:}\quad \begin{cases} NO_3^- + 2e \rightleftharpoons NO_2^- + O^= & [a] \\ 2Na^+ + O^= \rightleftharpoons Na_2O^e & [b] \end{cases}$$

see Ref. (36, 37), then

$$W(V-n)^e \xrightarrow[NO_3^-]{Na_2O^e} Na_xW_yO_z \text{ (quite soluble)}$$

$$\text{Peak F:}\quad 2Na_2O(s) \rightleftharpoons O_2^- + 4Na^+ + 3e \qquad [3]$$

see Ref. (37).

$$\text{Peak D:}\quad W(V-n)^e \rightleftharpoons W(IV)^e + (n-1)e \qquad [7]$$

is supported by XPS analysis and is detectable only at high scan rates.

$$\text{Peak C:}\quad \begin{cases} W(IV)^e + NO_3^- \rightleftharpoons W(VI)^e + NO_2 + e & [8] \\ W_2O_5^e + NO_3^- \rightleftharpoons 2WO_3^e + NO_2 + e & [9] \end{cases}$$

is supported by XPS analysis and the observation of gas evolution

$$\text{Infinite tail A:}\quad NO_3^- \rightarrow NO_2 + \tfrac{1}{2}O_2 + e \qquad [10]$$

$$\text{Infinite tail I:}\quad Na^+ + e \rightleftharpoons Na^e \qquad [11]$$

see Ref. (36, 38, 40-42).

The passivating W(VI) species can be formed according to Eq. [4]. This oxide is known to be a stable noninsulating species which has some conductivity (it is a semiconductor) as long as the oxide film is not too thick. Passivation occurs when the oxide film becomes too thick. On scanning the potential in the anodic direction, the current reaches a very low and constant value until, at about +6V, the oxide film is broken and the solvent oxidation proceeds with oxygen and NO_2 evolution (Eq. [10]). On scanning the potential in the cathodic direction, the reduction of W(VI) to an oxidation state that may lie in between tungsten(VI) and tungsten(IV) occurs. We have called this "W(V)" for convenience, though a unique assignment of this species based on the direct comparison with a pure compound is impossible since the bulk W(V) oxide is not known. This species is further reduced to a lower oxidation state, but the process is inhibited by the formation of sodium oxide according to Eq. [1] and [2]. In any case, this reduced species in the presence of Na_2O^e and of the solvent anions (NO_3^-) seems to give a quite soluble product. This is in agreement with: (*i*) the competition between film formation leading to passivation and depassivation effects arising from chemical dissolution of the film as previously shown (see Fig. 2 and 3 and the discussion under the section on Behavior in vicinity of cathodic passivation peak); (*ii*) the inability to detect any $W(V-n)$ species on the electrode surface by XPS studies following treatment at these potentials.

Then the sodium oxide excess oxidizes to superoxide according to the well-known process (Eq. [3]). Peak D (Fig. 1) can be ascribed to the oxidation of $W(V-n)$ to W(IV) and peak C to the oxidation of W(IV) and W(V), respectively, to W(VI). It is not possible to record the peak at −0.5V when using low scan rates with a stationary electrode, or when using a rotating disk electrode. The reason for this behavior is that the $W(V-n)$ species is completely soluble and thus diffuses away from the electrode at low scan rates (when there is more time available for diffusion) or when diffusion is enhanced by electrode rotation. If the $W(V-n)$ species is lost into solution then the processes described by Eq. [7] and [8] cannot occur. This explains why the signal appears as a single peak at low scan rate, since there is now only one process possible (Eq. [9]). The irregular profile at low scan rate can be ascribed to NO_2 evolution.

In conclusion the study presents an overall view of the tungsten electrode in molten nitrates. While the detailed situation is complex, XPS studies show that the electrode examined is tungsten(VI) oxide rather than tungsten metal and that other tungsten oxidation states [such as tungsten(IV)] can also be seen under appropriate conditions.

Acknowledgment

The authors would like to thank Mrs. C. Kozlowski for carrying out some of the curve fitting and Miss A. G. Cavinato for performing part of the electrochemical experiments. The work was carried out with the financial assistance of the Science and Engineering Research Council (U.K.) and the Italian National Research Council (CNR).

Manuscript submitted Jan. 11, 1983; revised manuscript received May 23, 1983.

REFERENCES

1. B. W. Faughnan, R. S. Crandall, and P. M. Heyman, *RCA Rev.*, **36**, 177 (1975).
2. H. N. Hersh, W. E. Kramer, and J. H. McGee, *Appl. Phys. Lett.*, **27**, 646 (1975).
3. H. Witzke, Paper 423 presented at the Electrochemical Society Meeting, Washington, DC, May 2-7, 1976.
4. A. Di Paola, F. Di Quarto, and C. Sunseri, *This Journal*, **125**, 1344 (1978).
5. F. Di Quarto, A. Di Paola, and C. Sunseri, *ibid.*, **127**, 1016 (1980).
6. G. Hollinger, Tran Minh Duc, and A. Deneuville, *Phys. Rev. Lett.*, **37**, 1564 (1976).
7. G. K. Wertheim, M. Campagna, J. N. Chazalviel, and D. N. E. Buchanan, *Appl. Phys.*, **13**, 225 (1977).
8. R. J. Colton, A. M. Guzman, and J. W. Rabalais, *J. Appl. Phys.*, **49**, 409 (1978).
9. G. Hodes, D. Cahen, and J. Manassen, *Nature*, **260**, 312 (1976).
10. M. A. Butler, R. D. Nasby, and R. K. Quinn, *Solid*

State Commun., **19**, 1011 (1976).
11. W. A. Gerrard, *J. Electroanal. Chem.*, **86**, 421 (1978).
12. P. Lemasson, G. Peslerbe, A. M. Baticle, and P. Vennereau, *ibid.*, **86**, 395 (1978).
13. F. Di Quarto, A. Di Paola, and C. Sunseri, *Electrochim. Acta*, **26**, 1177 (1981).
14. P. G. Dudley and D. Inman, p. 196, Extended Abstracts of the International Society of Electrochemistry, Trondheim, Norway Meeting (1979).
15. A. N. Baraboshkin and V. P. Bychin, p. 199, Extended Abstracts, Meeting of the International Society of Electrochemistry (1979).
16. A. N. Baraboshkin, K. A. Kaliev, and S. M. Zacharyash, p. 202, Extended Abstracts, International Society of Electrochemistry, Trondheim, Norway (1979).
17. E. Desimoni, F. Paniccia, and P. G. Zambonin, *Anal. Chim. (Rome)*, **70**, 351 (1980).
18. E. Desimoni and P. G. Zambonin, *J. Chem. Soc., Faraday Trans. 1*, **78**, 89 (1982).
19. E. Desimoni, F. Palmisano, L. Sabbatini, and P. G. Zambonin, Paper 650, p. 1624, The Electrochemical Society Extended Abstracts, Vol. 80-2, Hollywood, FL, Oct. 5-10, 1980.
20. C. Egawa, H. Shindo, T. Onishi, and K. Tamaru, *J. Chem. Soc., Faraday Trans. 1*, **77**, 927 (1981).
21. P. M. A. Sherwood, in "Contemporary Topics in Analytical and Clinical Chemistry," Vol. 4, D. M. Hercules, M. A. Evenson, G. M. Hieftje, and L. R. Snyder, Editors, Chap. 7, pp. 205-293, Plenum Press, New York (1982).
22. L. Sabbatini, P. G. Zambonin, E. Desimoni, and B. A. De Angelis, *Chemica e Industria*, **59**, 493 (1977).
23. L. Sabbatini, F. Palmisano, P. G. Zambonin, and B. A. De Angelis, *Ann. Chim. (Rome)*, **67**, 525 (1977).
24. L. Sabbatini, B. Morelli, P. G. Zambonin, and B. A. De Angelis, *J. Chem. Soc., Faraday Trans. 1*, **75**, 2628 (1979).
25. T. A. Carlson and G. E. McGuire, *J. Electron Spectrosc.*, **1**, 161 (1972-1973).
26. K. T. Ng and D. M. Hercules, *J. Phys. Chem.*, **80**, 2094 (1976).
27. B. A. De Angelis and M. Schiavello, *Chem. Phys. Lett.*, **38**, 155 (1976).
28. J. Haber, J. Stoch, and L. Ungier, *J. Solid State Chem.*, **19**, 113 (1976).
29. B. A. De Angelis and M. J. Schiavello, *Solid State Chem.*, **21**, 67 (1977).
30. L. P. Kazansky and J. P. Launay, *Chem. Phys. Lett.*, **51**, 242 (1977).
31. B. A. De Angelis and M. Schiavello, *ibid.*, **58**, 249 (1978).
32. P. M. A. Sherwood, *J. Microsc. Spectrosc. Electron.*, **5**, 475 (1980).
33. R. O. Ansell, T. Dickinson, A. F. Povey, and P. M. A. Sherwood, *J. Electroanal. Chem.*, **98**, 79 (1979).
34. A. Proctor and P. M. A. Sherwood, *Anal. Chem.*, **54**, 13 (1982).
35. P. G. Zambonin, E. Desimoni, F. Palmisano, and L. Sabbatini, in "Ionic Liquids," D. Lovering and D. Inman, Editors, Plenum, London (1981).
36. H. S. Swofford and H. A. Laitinen, *This Journal*, **110**, 814 (1963).
37. P. G. Zambonin, *J. Electroanal. Chem.*, **24**, 365 (1970).
38. L. B. Topol, R. A. Osteryoung, and J. M. Christie, *J. Phys. Chem.*, **70**, 2857 (1966).
39. A. F. J. Goeting and J. A. A. Ketelaar, *Electrochim. Acta*, **19**, 267 (1974).
40. W. E. Triaca and A. J. Arvia, *ibid.*, **9**, 1055 (1964).
41. H. E. Bartlett and K. E. Johnson, *This Journal*, **114**, 64 (1967).
42. H. A. Laitinen, *Talanta*, **12**, 1237, Pergamon Press, Oxford (1965).
43. N. D. Tomashov and G. P. Chernova, in "Passivity and Protection of Metals against Corrosion," H. H. Uhlig, Editor, Chap. IV, Plenum (1967).
44. J. Gallego Herrera, C. E. Castellano, A. J. Calandra, and A. J. Arvia, *J. Electroanal. Chem.*, **66**, 207 (1965).
45. C. Kozlowski and P. M. A. Sherwood, Unpublished results.
46. S. Doniach and M. Sunjic, *J. Phys. Chem.*, **3**, 285 (1970).
47. S. K. Hufner and G. K. Wertheim, *Phys. Rev. B*, **11**, 678 (1975).
48. G. K. Wertheim and D. N. E. Buchanan, *Phys. Rev. B*, **16**, 2613 (1975).
49. P. G. Zambonin and J. Jordan, *J. Am. Chem. Soc.*, **91**, 2225 (1969).
50. P. G. Zambonin, *ibid.*, **97**, 4405 (1975).
51. F. Paniccia and P. G. Zambonin, *Ann. Chim. (Rome)*, **66**, 155 (1976).
52. J. H. Scofield, *J. Electron Spectrosc. Relat. Phenom.*, **8**, 129 (1976).
53. C. L. Rollinson, in "Comprehensive Inorganic Chemistry," Vol. 3, J. C. Bailor, H. J. Emeleus, R. Nyholm, and A. F. Trotman-Dickenson, Editors, Chap. 36, pp. 764-766, Pergamon Press, Oxford (1973).

Electrodeposition of Metal Particles and Films by a Reducing Redox Polymer

P. G. Pickup, K. N. Kuo, and Royce W. Murray

Kenan Laboratories of Chemistry, University of North Carolina, Chapel Hill, North Carolina 27514

ABSTRACT

The electrodeposition of copper, silver, cobalt, and nickel onto poly-[$Ru(bpy)_2$ 4-vinylpyridine$_2$]$^{2+}$-coated Pt electrodes is described. The Ru(I) and Ru(0) states of the polymer are used to mediate the metal reductions. Metal deposited directly onto the underlying Pt electrode and that deposited on the polymer can be distinguished from the cyclic voltammetry; experimental conditions promoting the latter were established. SEM and XPS confirm that metal can be deposited mainly on the outer polymer surface. The kinetics of nucleation of metal particles on the polymer were detectable. Rotated disk permeation measurements show that the deposited metal films impede the diffusion of probe molecules like ferrocene through the polymer film. The electrodeposition of copper could also be mediated by a dissolved viologen mediator which permeates the polymer film.

The deposition of metal particles and metal films onto polymers has both scientific and technological importance. Such deposition has commercial potential for the metallization or finishing of plastics as metal substitutes. Classically, the reagents which reduce the metal ions are components of a so-called electroless deposition solution contacting the polymer. In principle, however, the polymer itself might contain the reducing agent(s), either as added polymer phase solutes or as redox groups affixed to the redox polymer lattice. There are now known a number of polymers that contain sites that can be charged as reducing agents (1-27), which might be used as substrates for metal deposition. Two examples of metal reduction have in fact appeared (28, 29): Si electrodes coated with viologen polymer films containing Pt or Pd par-

ticles photoelectrocatalytically evolve hydrogen (28), and copper deposition was used to study the structure of Nafion films containing conducting crystals (29).

Aiming at a fuller understanding of metal particle nucleation, growth, and film formation on reducing polymer films, we have coated a redox polymer film on a conductor electrode (Pt), so as to permit control of the supply of electrons to the reducing sites in/on the polymer film by the potential applied to the electrode. The redox polymer used, as a model, is one of a series of transition metal monomers, $[Ru(bpy)_2(vpy)_2]^{2+}$, which (18, 21, 30) can be electropolymerized to form smooth, relatively pinhole free (31) films *ca.* 5-5000 monomer sites thick [bpy= 2,2′-bipyridine; vpy=4-vinylpyridine]. The poly-$[Ru(bpy)_2(vpy)_2]^{2+}$ films impede the direct reduction of metal ions by the Pt electrode, and when charged to the (formal) Ru(I) and Ru(0) states, can reduce Cu, Ag, Co, and Ni ions from their solutions in acetonitrile solvent

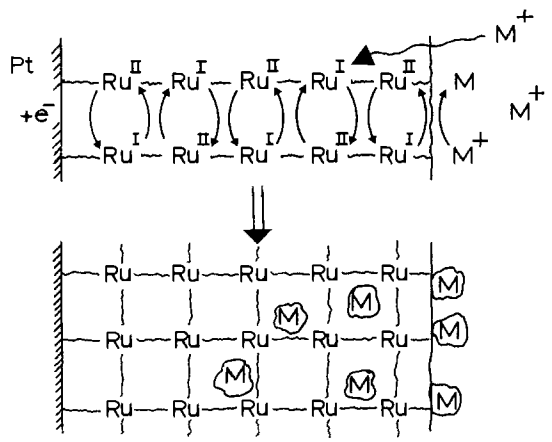

Important aspects of the electrochemical metal deposition reaction include the experimental factors controlling whether the metals are deposited onto or near the surface of the reducing polymer (as opposed to deposition at the Pt/polymer interface), how to determine where the metal did deposit, and how to follow the nucleation and growth of metal particles on the polymer surface. Interesting results on the locale of Pt and Pd deposition on a reducing viologen polymer have been described by Wrighton *et al.*, using Auger spectroscopy (28).

Besides the fundamentally interesting problem of electrodepositing metals on polymers, and the potentialities of preparing catalytically useful metal particles in this way, we see other uses for metal deposition on redox polymers. For instance, many applications of redox polymer films, in electrocatalysis (14, 32-39) and in rectifying film structures like bilayer electrodes (30, 40) depend on electrons being efficiently transported across the polymer film. Metal films deposited on redox polymer films on electrodes, sandwiching the thin (<1 μm) polymer film between the two conducting contacts, could be useful in investigating this electron conductivity (41). Another possible use could be in electrical devices made from bilayer electrodes, where it is necessary that the electrodeposited metal film not only contact the outside of the thin polymer film but additionally be porous to the solvent and electrolyte flow necessary for charging of the film. We accordingly investigated the porosity of an electrodeposited Co film by measuring the permeability of the polymer/metal film layer on a rotated Pt disk to an electroactive probe molecule, ferrocene. Finally, we also briefly studied the electrodeposition of copper mediated by a reduced viologen ion which permeated the ruthenium polymer film.

Experimental Design

The experiment's aim is to deposit metal onto or within the polymer film, but not onto the Pt electrode. The highly reducing Ru(I) and Ru(0) states in films of poly-$[Ru(bpy)_2(vpy)_2]^{n+}$ are used to mediate the metal ion reduction. These states are formed in significant concentrations at Pt electrode potentials more negative than about −1.3 and −1.5V *vs.* SSCE, respectively. Both reduced polymer states can reduce the metal ions used in this work, but also so can the Pt electrode at these potentials, should the metal ions penetrate the polymer film. The polymer film should ideally therefore exclude cations. This is expected for this polymer since it is poly-cationic, but it may nonetheless be somewhat permeable to small metal cations. The problem is to know, under a certain set of experimental conditions, where the metal will deposit. The problem has similarity to electrocatalysis at redox polymer films (38, 39, 42), where the relative rates of several reaction steps determine the locus of the electrocatalytic reaction, and the five relevant reaction steps in metal deposition can be stated in analogous fashion:

1. Diffusion of metal ions through the polymer film to the Pt electrode (*SUBS* flux).
2. Diffusion of electrons through the polymer from the Pt electrode (*e.g.*, charge transport, *CT* flux).
3. Reduction of the metal ions by the reduced polymer (including steps for nucleation and deposition of metal) (*CHEM* flux).
4. Reduction of the metal ions by the Pt surface (including nucleation there).
5. Mass transfer of metal ions from the solution to the polymer film surface (*MT* flux).

Taking a simplified model for illustration, assume that any metal ions reaching the Pt electrode are reduced immediately (step 4), and that the metal ion concentration outside the polymer is not depleted, as in rotating electrode experiments extrapolated to high rotation rates (step 5). The locus of metal deposition then depends on the relative rates of steps 1-3, as illustrated by the schematic concentration-distance profiles in Fig. 1.

Construction of the profiles of Fig. 1 follows previous reasoning (42). If diffusion of metal ions through the polymer (step 1) is fast relative to the rates of reaction of the ions with the polymer (step 3) or of electron transport in the polymer (step 2), then the metal is mainly deposited onto the Pt electrode, underneath the polymer film (Fig. 1A, B). If, on the other hand, the ions diffuse slowly through the polymer (step 1) relative to the rates of reduction of the metal ions by the polymer and of electron diffusion (step 3), then the metal will be deposited on the outside of the polymer film (Fig. 1E, F). The intermediate kinetic situation results in the metal being deposited inside the polymer film (Fig. 1C, D).

For a given polymer/metal/solvent combination, the controllable experimental variables are the polymer film thickness, the concentration of metal ions in the solution, diffusion *vs.* hydrodynamic mass transfer, and how the electrode potential is manipulated to charge the reducing sites in the polymer. To avoid metal deposition on the Pt, the above analysis suggests that the polymer film be thick and the solution concentration of metal ion be low, to slow step 1. Also, when using thick films (> 1000Å on our scale), it may not matter whether the metal deposits on the outer polymer film boundary or if the metal penetrates into the film a certain extent (< 500Å). The latter situation could in fact be advantageous to the structural properties of the film. Low solution concentrations of metal ion may, on the other hand, incur a penalty of long deposition times to produce a metal film of desired thickness. In this study we examine the effects

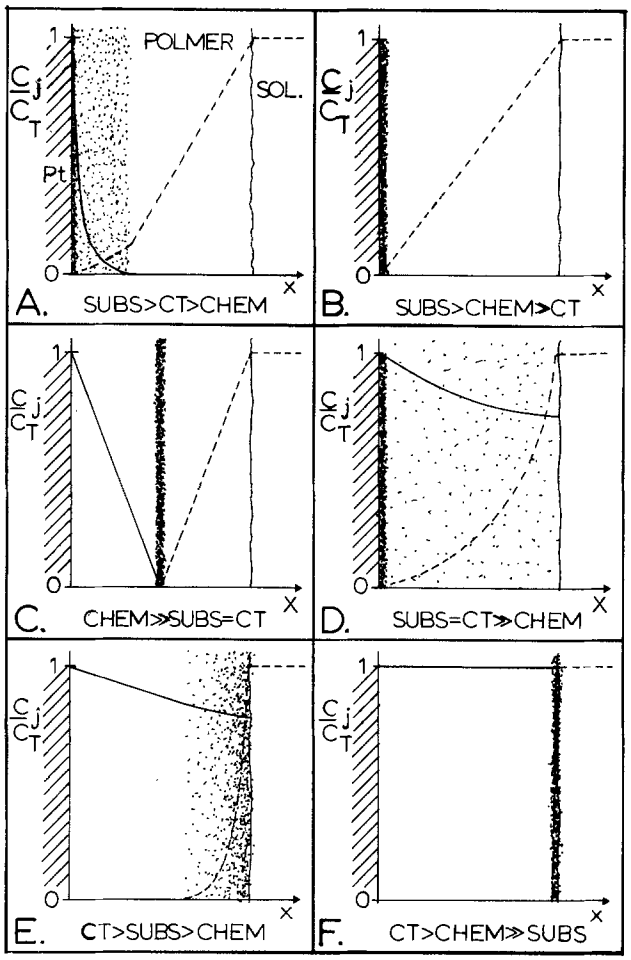

Fig. 1. Schematic concentration-distance profiles for metal deposition at a reducing polymer-coated electrode. C_j = concentration of reduced polymer sites (——) or concentration of metal ions (- - -). C_T = total concentration of polymer redox sites or bulk concentration of metal ions outside polymer. Dots represent distribution of metal particles, *SUBS* = rate of diffusion of metal ions through the polymer (step 1); *CT* = rate of charge transport through the polymer (step 2); *CHEM* = rate of reduction of metal ions by the reduced polymer sites (step 3).

of polymer film thickness, metal ion concentration, and mass transfer on the distribution of deposited metal.

The above discussion was greatly over-simplified by not stressing the probable importance of the kinetics at which metal particles are nucleated on the non-crystalline polymer. Thus, the rate of step 3 may be slow initially, before metal nucleation, but increases greatly after nuclei are formed onto which metal ions can deposit. Therefore it may be that nucleation on the Pt electrode surface occurs earlier than nucleation in/on the polymer, *e.g.*, initially the rate of step 4 > 3. However, once nucleation has occurred on the polymer, subsequent metal film growth on the polymer may be faster than that on Pt (step 3 > 4), because of the slowness of step 1. Thereafter the supply of metal ions for reduction of Pt (step 4) is starved due to the more rapid deposition on the outer part of the film (step 3). Because of these consequences of nucleation phenomena, the manner of supply of metal ion to the polymer and of controlling the polymer charging with electrode potential can be important experimental variables. One can reason, for example, that, to achieve the condition of Fig. 1F, one might first slowly supply a low concentration of metal ion from the solution to an already charged polymer surface, seeking to promote nucleation on the outer boundary of the polymer. After nucleation there, metal ion mass transfer and concentration could be increased to grow the metal film. Clearly, until the kinetic role of metal nucleation can be assessed, this discussion indicates that the quantitative analysis of the overall metal deposition kinetics is a very complex problem. We address this problem only by examining relative amounts of metal depositions which occur under different experimental situations.

Experimental

Electrochemistry.—Equipment and cells were of conventional design. All experiments were conducted in thoroughly degassed CH_3CN containing 0.1*M* Et_4NClO_4. Rotated disk electrode experiments were conducted using a Pine Instruments rotator. Electrode potentials are referenced to the NaCl-saturated SCE (SSCE).

Electrodes.—Teflon-shrouded Pt disk electrodes were mirror polished with 1 μm diamond paste (Buehler). The poly-$[Ru(bpy)_2(vpy)_2]^{2+}$ film was deposited onto the electrode surface either by continuous cyclic potential scans between −1.0 and −1.7V *vs.* SSCE or by potentiostating the electrode at −1.8V *vs.* SSCE, in a thoroughly degassed solution of 0.5 m*M* $[Ru(bpy)_2(vpy)_2](ClO_4)_2$ in 0.1*M* Et_4NClO_4/CH_3CN. Metal ions were reduced by Pt/poly-$[Ru(bpy)_2(vpy)_2]^{1+/0}$ films from dilute CH_3CN solutions of their perchlorate salts. The metal coated Pt/poly-$[Ru(bpy)_2(vpy)_2]^{2+}$ electrodes described here were stable to copious washing with either $(CH_3)_2CO$ or H_2O.

Chemicals.—$[Ru(bpy)_2(vpy)_2](ClO_4)_2$ was prepared according to the published procedure (21) and chromatographically purified. The metal perchlorate salts were G. F. Smith materials vacuum dried at 50°C overnight before use. Acetonitrile (Burdick & Jackson) was dried over 4Å molecular sieves.

Spectra.—XPS spectra were acquired with a du Pont 650B spectrometer, referencing binding energies to C 1s at 285.0 eV. SEM micrographs were taken with an EETC scanning electron microscope at 20 keV.

Results and Discussion

Cyclic voltammetry.—*Copper.*—The cyclic voltammogram of copper(II) at naked Pt (Fig. 2A) displays at $E^{o'}$ = 1.06V quasi-reversible waves for the Cu(II/I) couple, at E_p = −0.52V a cathodic wave for deposition of copper metal, and at E_p = −0.28V a sharp anodic stripping peak for stripping of copper metal from the Pt electrode.

Currents for both the Cu(II/I) and Cu(I/0) reactions are severely depressed at Pt/poly-$[Ru(bpy)_2(vpy)_2]^{2+}$ electrodes. Additionally, the potential at which the Cu(I/0) currents appear is shifted to more negative potentials, depending on the thickness of the poly-$[Ru(bpy)_2(vpy)_2]^{2+}$ film. For a thin film (3.9×10^{-9} mol/cm^2), a perceptible wave for the Cu(I/0) reaction rises at *ca.* −0.7V (Fig. 2B), and on the reverse potential scan, a hysteresis is observed in the current trace before the metal stripping peak at −0.3V. The hysteresis shows that the overpotential for Cu(0) deposition which was imposed by the polymer film, is eliminated once some Cu(0) is formed. The hysteresis implies that the polymer film acts to slow nucleation of Cu(0) (step 4) on the Pt surface.

When the poly-$[Ru(bpy)_2(vpy)_2]^{2+}$ film is thicker (1.2×10^{-8} mol/cm^2), so as to reduce the flux of Cu(II) to the Pt, the nuleation of Cu(0) on Pt is slowed so much that no Cu(I/0) wave can be seen in a potential scan (Fig. 2C) at potentials more positive than those reducing the film itself. Figure 3 shows more negative-going scans in volammograms of such a thicker (1.2×10^{-8} mol/cm^2) film without (curve A) and with (curves B and C) 3 m*M* copper present in the solution. In the cyclic voltammogram in the absence of Cu(II) (curve A), the redox polymer Ru(III/II) wave appears at $E^{o'}$ = 1.22V and the Ru(II/I) and Ru(I/0) waves at $E^{o'}$ = −1.35 and −1.56V, respectively. [The anodic spike at +1.09V and the cathodic

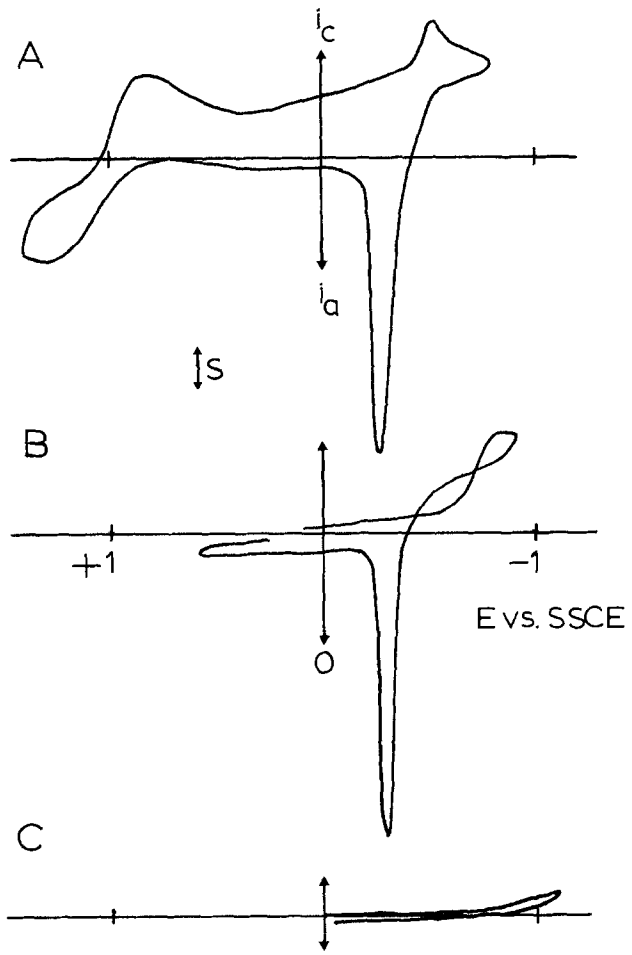

Fig. 2. Cyclic voltammogram at 200 mV/sec of *ca.* 1.3 mM $Cu(ClO_4)_2$ at naked Pt (curve A) and at Pt/poly-$[Ru(bpy)_2(vpy)_2]^{2+}$ electrodes (curve B, $\Gamma_{Ru} = 3.9 \times 10^{-9}$ mol/cm^2; curve C, $\Gamma_{Ru} = 1.2 \times 10^{-8}$ mol/cm^2). S = 147 μA/cm^2 for A, 133 μA/cm^2 for B, and 490 μA/cm^2 for C. In 0.1M Et_4NClO_4/CH_3CN as are data in all other figures.

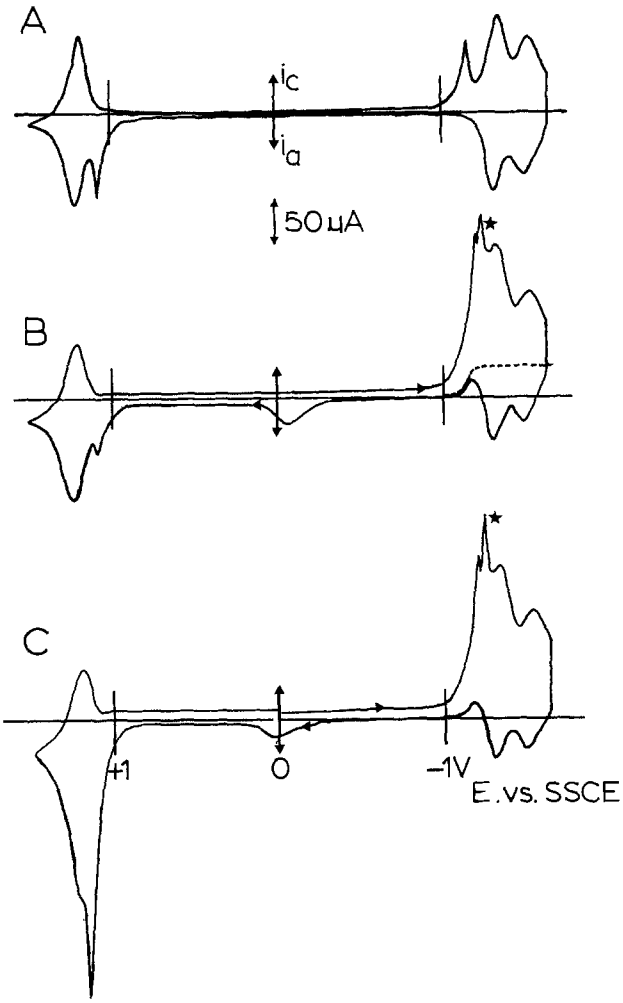

Fig. 3. Cyclic voltammogram at 100 mV/sec of a 1.2×10^{-8} mol/cm^2 Pt/poly-$[Ru(bpy)_2(vpy)_2]^{2+}$ electrode without (curve A) and with (curves B,C) 3 mM Cu(II) present in the solution. The scan was interrupted at −1.7V during recording of curve C, the potential being held at −1.7V for 10 sec before scanning positively. Electrode area 0.12 cm^2.

spike at −1.18V in curve A are host-guest mediated waves for an impurity produced in the polymer film during its preparation (21, 30).] Addition of 3 m*M* $Cu(ClO_4)_2$ changes the first-scan voltammogram of the Pt/poly-$[Ru(bpy)_2(vpy)_2]^{2+}$ electrode (curve B) in the following ways: starting in a negative scan from 0V, an additional cathodic spike (*) appears at −1.28V, both the reductive and oxidative scans of the Ru(II/I) and Ru(I/0) waves at −1.35 and −1.56V become elevated upon a plateau of cathodic current (see dashed line), a small oxidation wave appears at −0.08V, and the area under the polymer Ru(II/III) oxidation wave is increased slightly relative to the Ru(III/II) reduction wave. In a variant of the experiment (curve C), in scanning negatively from 0V the potential scan is interrupted at −1.7V, holding the potential there for 10 sec, and then scanned positively. The result is that the area under the polymer Ru(III/II) oxidation wave becomes greatly increased and includes a large anodic spike at +1.15V. Curves B and C are typical results.

We rationalize the voltammetry of copper deposition in curves B and C in Fig. 3 as follows. Any Cu(II) permeating through the film should at potentials more negative than −0.52V be reduced to Cu metal, but this reaction is suppressed both by slow Cu(II) diffusion through the polymer and by the inhibition of nucleation of Cu metal at the Pt surface by the polymer. At potentials near the Ru(II/I) wave, Ru(I) is produced and mediates Cu(II) reduction, which appears first as a burst of current (*) and then as a cathodic current plateau (curve B, dashed line) upon which the polymer waves remain superimposed until during the reverse, positive-going scan, all of the polymer is reoxidized to the Ru(II) state. The prolonged hysteresis of Fig. 2B is not seen, showing that the presence of reduced polymer [*e.g.*, Ru(I)] is necessary to sustain the deposition. Subsequently on the positive-going scan, the small wave at −0.08V is taken as representing oxidation of a small amount of Cu(0) metal which did deposit directly on the Pt electrode. The current for the Ru(II/III) oxidation wave is enhanced relative to the Ru(III/II) wave, which is taken as the Ru(III) mediated oxidation of copper deposited within and on the surface of the polymer film but not in contact with the Pt. In this way, the two forms of deposited Cu(0) are conveniently distinguished.

The quantity of Cu metal deposited directly onto the polymer in curve B, Fig. 3, as measured by the enhanced area under the Ru(II/III) wave, is 1.5×10^{-9} mol/cm^2; that deposited directly onto the Pt as measured by the area under the −0.08V Cu(0/I) wave is 6.0×10^{-9} mol/cm^2. The total charge for the two forms of copper metal stripping, 60 + 30 = 90 μC, is much less than the charge under the cathodic current plateau (dashed line curve B), 470 μC, so most of the current in the cathodic plateau must then be due to reduction of Cu(II) only to Cu(I) which diffuses away into the solution. Halting the potential scan at −1.7V as in curve C, however, drastically alters the dominant

course of the Cu(II) reduction reaction. In curve C, the amount of Cu metal deposited within or upon the polymer film [as measured by the enhancement of the Ru(II/III) oxidation wave] is increased ten-fold to 1.6×10^{-8} mol/cm², while the amount of copper deposited on Pt (measured from the stripping peak at −0.08V) remains unchanged. It appears that during the 10 sec pause at −1.7V in curve C, the primary reaction becomes no longer Cu(II) to Cu(I), but is now deposition of Cu(0) within or on the polymer film. The profile situation is as in situations E, or F, in Fig. 1, but not situation C, since the known (43) rate of electron diffusion in this polymer can support much larger currents than these. Evidently, as the potential was negatively scanned to −1.7V, sufficient copper nuclei were produced within or on the polymer film to greatly increase the rate of subsequent Cu(0) deposition there. From the Ru(II/III) wave enhancement in curve C, we conclude that Cu metal is deposited on the outside of the polymer film, or deposited in spaces extending into the film over a distance less than the film thickness (*ca.* 1500Å), or both.

It is possible using electrodes with thinner polymer films to obtain some information about the deposition distance, as in Fig. 4, where a 2.8×10^{-9} mol/cm² film (*ca.* 300Å) is examined (curves B, C) in a manner analogous to that of Fig. 3B, C, respectively. The obvious consequence in the cyclical scan experiment, curve B, is the increase in the amount of copper metal that is deposited onto the Pt electrode, 2.9×10^{-8} mol/cm², measured from the area under the copper stripping peak at −0.15V. The increase must be due to the greater flux of Cu(II) diffusing through the thinner film to the Pt electrode; this flux causes the greater cathodic current and region of hysteresis in the positive-going potential sweep in curve B. However, as with the thicker film in Fig. 3, a 10 sec pause in the potential scan at −1.7V, Fig. 4, curve C, again promotes more copper deposition within or on the polymer film, enhancing the charge under the Ru(II/III) oxidation wave in curve C. The resulting deposition of Cu(0) on copper nuclei on the outermost part of the polymer (not in electrical contact with the Pt) also starves Cu(0) deposition on Pt, seen by a decrease in the amount of copper stripped from Pt in the peak at −0.15V. This result demonstrates that in Fig. 4C, some copper nuclei must be produced within the polymer film at distances less than 300Å from its outer boundary.

According to the above discussion, if the positive potential scan in Fig. 3, curve C, were interrupted at say, +0.5V, the resulting electrode should retain the copper metal nuclei residing on the outer part of the polymer. This has been experimentally supported by reversing the positive scan at +0.5V. After the potential is again scanned negatively through the polymer reduction waves, the subsequent Cu(0/I) stripping peak at −0.08V is depressed by 2-3×. This is because Cu(0) deposition on the Pt surface is starved by Cu(0) depositing onto the polymer immediately after some of the polymer is reduced, aided by the copper nuclei remaining there. This result confirms the essential validity of our picture of deposition conditions being changed from those of Fig. 1A, B to those of Fig. 1E, F by the presence of Cu nuclei on the outer part of the polymer.

The dependency of where Cu(0) is deposited on the Cu(II) concentration is illustrated in Fig. 5 for an electrode with an intermediate thickness film (6.8×10^{-9} mol/cm²). Increasing the Cu(II) concentration causes slightly more Cu metal to be deposited onto the polymer film [from the Ru(III/II) oxidation wave enhancement], but also causes a large increase in Cu deposited onto the Pt electrode (the copper stripping wave, see data in Table I). This probably mainly reflects the increasing quantities of Cu(II) ions par-

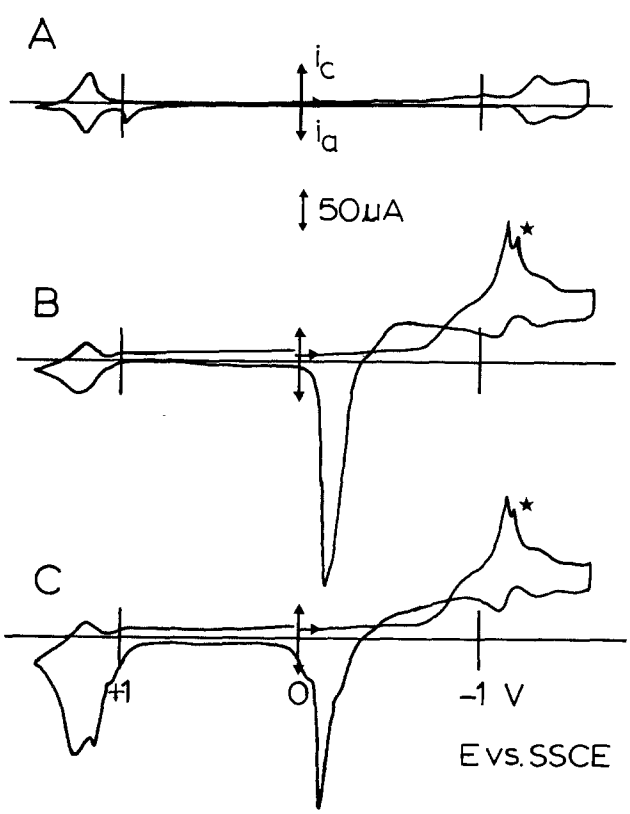

Fig. 4. Same as Fig. 3 except for a thinner polymer film (2.8×10^{-9} mol/cm²). Electrode area = 0.12 cm².

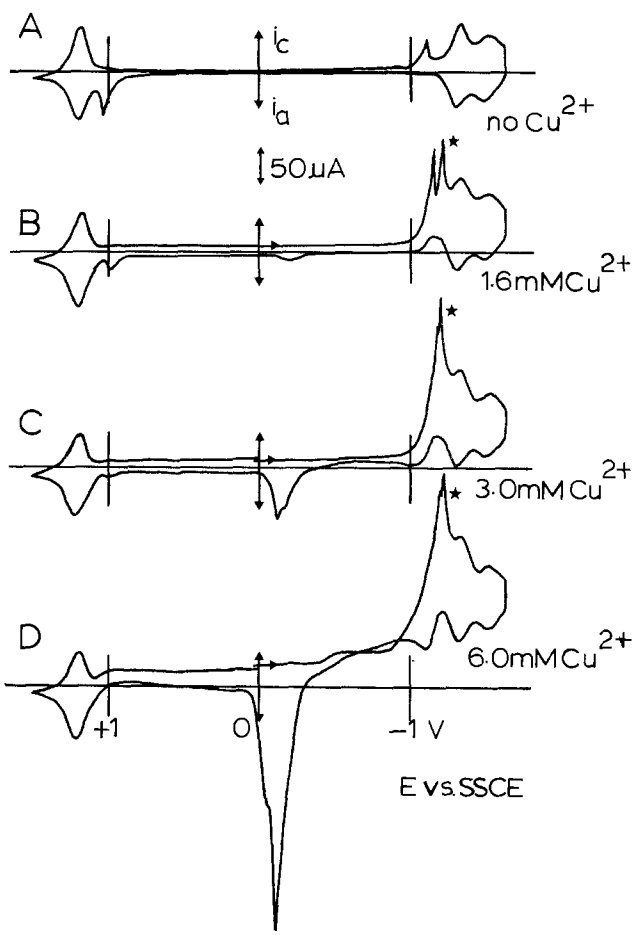

Fig. 5. Cyclic voltammogram at 100 mV/sec of a 6.8×10^{-9} mol/cm² Pt/poly-$[Ru(bpy)_2(vpy)_2]^{2+}$ electrode in the presence of indicated concentrations of $Cu(ClO_4)_2$. Electrode area = 0.12 cm².

Table I. Charge passed to oxidize copper deposited onto the polymer or the Pt electrode

Deposition is during single $0 \rightarrow -1.7$V scan in solutions containing various Cu(II) concentrations. $\Gamma_{Ru} = 6.8 \times 10^{-9}$ mol/cm² (see Fig. 5)

[Cu(II)] (m*M*)	Area under Ru(II/III) oxidation wave (μG)	Area under Cu(I/0) oxidation wave (μC)
0	110	0
1.6	110	50
3.0	100	100
6.0	140	400

titioned into the polymer film at the start of the experiment, and the increased extent to which nucleation and growth at the Pt surface is thereby favored. Clearly metal deposition on the outer region of the polymer film is better accomplished using low initial metal ion concentrations, as we reasoned at the outset.

Silver.—Cyclic voltammograms of $AgClO_4$ (1 m*M*) at naked Pt (dashed curve) and of a 8×10^{-9} mol/cm² Pt/poly-$[Ru(bpy)_2(vpy)_2]^{2+}$ electrode are shown in Fig. 6A, and of the latter electrode in the presence of 1 m*M* Ag(I) in curves B and C. The interpretation of the latter voltammograms is the same as in the case of copper for thick films and low concentration (cf. Fig. 3). The film's permeability to Ag(I) seems greater than that to Cu(II), as seen by the small flattened wave rising at about +0.2V (compare Fig. 5B). The oxidation wave at *ca.* 0.4V in Fig. 6B, C is taken as dissolution of silver that was deposited onto the Pt electrode. Since this silver stripping wave is unchanged by a 30 sec pause in the potential scan at −1.7V, curve C, it follows that during the pause silver is mainly deposited on the polymer film rather than onto the Pt electrode (as in Fig. 1E, F). Comparing Fig. 6B to Fig. 5B, more Ag than Cu deposits onto the Pt electrode under similar sets of conditions, presumably due to the film's greater permeability to Ag(I) than Cu(II). Curve C nonetheless shows that Ag metal can be deposited onto the outside of a Pt/poly-$[Ru(bpy)_2(vpy_2)]^{2+}$ film in the same way that Cu can.

Cobalt.—Voltammograms of $Co(ClO_4)_2$ (1 m*M*) at naked Pt (curve A) and at a thin film (1.3×10^{-9} mol/cm²) Pt/poly-$[Ru(bpy)_2(vpy)_2]^{2+}$ electrode (curves B, solid line, and C) are shown in Fig. 7. The electrochemistry of Co(II) in CH_3CN at naked Pt (curve A) is complex, and not very reproducible. In a continuous potential scan (solid line), a metal deposition wave appears at *ca.* −1.0V and a metal stripping wave at +0.33V. When the potential scan pauses at −1.35V for 30 sec (dashed line), the metal stripping wave at *ca.* 0.3V is attenuated and two additional oxidation waves appear at *ca.* +1.5 and +1.8V. The additional waves are enhanced by longer pauses at −1.35V, but the relative sizes of the three oxidation waves vary considerably from one experiment to the next and we attempt no interpretation of this behavior here.

The electrochemistry of Co(II) at a Pt/poly-$[Ru(bpy)_2(vpy)_2]^{2+}$ electrode (Fig. 7, curves B (solid line) and C) is in some respects similar to that of Cu(II) and Ag(I). The Co(II) reduction wave is suppressed, and an additional cathodic current spike

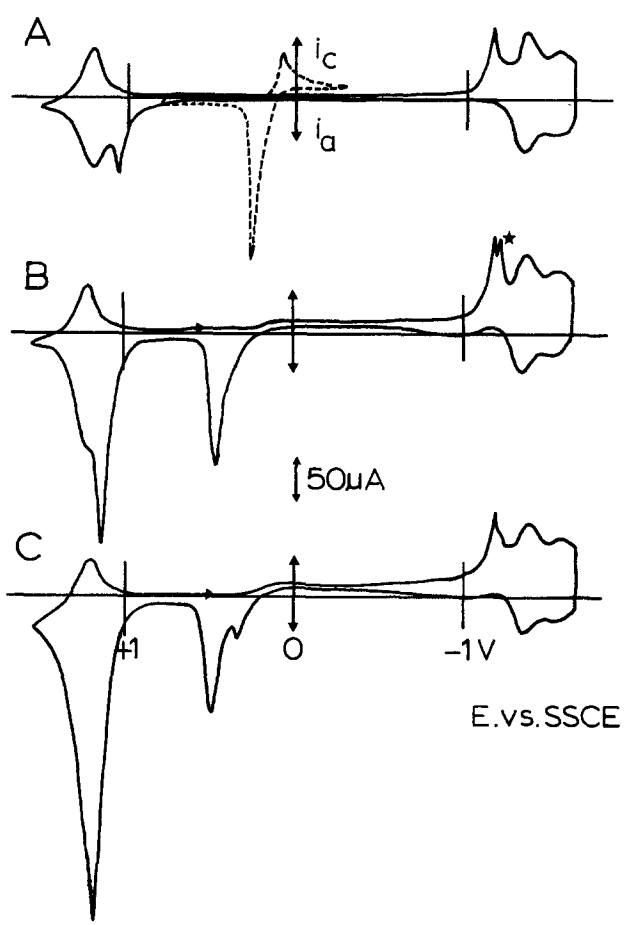

Fig. 6. Cyclic voltammogram at 100 mV/sec of: 1 m*M* $Ag(ClO_4)$ at naked Pt [curve A (- - -)] and of an 8×10^{-9} mol/cm² Pt/poly-$[Ru(bpy)_2(vpy)_2]^{2+}$ electrode [curve A (——)]; the latter electrode in the presence of a 1 m*M* $Ag(ClO_4)$ without (curve B) and with (curve C) a 30 sec pause at −1.7V. Electrode area = 0.12 cm².

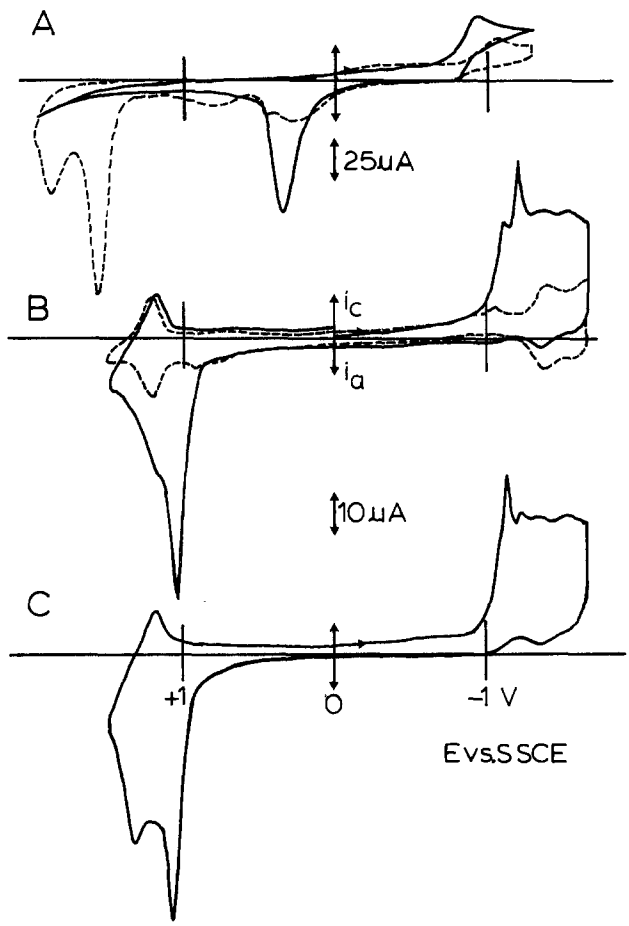

Fig. 7. Curve A: voltammogram at 100 mV/sec of 1 m*M* $Co(ClO_4)_2$ at naked Pt with (- - -) and without (——) a 30 sec pause at −1.35V; curve B: voltammograms of a 1.3×10^{-9} mol/cm² Pt/poly-$[Ru(bpy)_2(vpy)_2]^{2+}$ electrode in the absence (- - -) and presence (——) of 1 m*M* Co(II); and curve C with a 10 sec pause at −1.7V. Electrode area = 0.12 cm².

(E_p = −1.25V) and a superimposed cathodic current plateau appear in the polymer reduction region, from film-mediated reduction of the Co(II) there. A greatly enhanced Ru(II/III) oxidation wave is seen on the positive potential scan which we take as Ru(III)-mediated oxidation of Co metal. No wave due to stripping of Co from the Pt electrode is seen at *ca.* 0.3V, for which there are two possible explanations: no Co metal was deposited onto the Pt at all (unlikely given the thinness of the polymer film, 150Å), or oxidation of Co metal at this potential is inhibited by the polymer film [quite possible given the complex electrochemistry of Co(II) at naked Pt]. In either event, it is possible that the enhanced Ru(II/III) wave represents Ru(III)-mediated oxidation of both Co deposited on Pt and on the polymer film, and so these two modes of metal deposition are not as clearly separated by the electrochemistry as for Cu and Ag. XPS and SEM results, below, do show, however, that at least some and possibly all of the cobalt is deposited within or on the polymer film.

Nickel.—Voltammograms of $Ni(ClO_4)_2$ (1 m*M*) at naked Pt (curve A) and at a Pt/poly-$[Ru(bpy)_2(vpy)_2]^{2+}$ electrode (2.4×10^{-8} mol/cm^2) (curve B) are shown in Fig. 8. Reduction of Ni(II) at naked Pt is not well defined; different waves appear in the reigon 0 → −2V for each scan. The metal stripping wave at *ca.* 0.7V seems well defined, but its charge is always smaller than the quantity of reductive charge passed. A pause in the potential scan for 30 sec does not increase the size of the +0.7V wave, and this wave furthermore tends to disappear after a few cyclical, −2.0 to +1.4V scans.

The voltammogram of Ni(II) at a Pt/poly-$[Ru(bpy)_2(vpy)_2]^{2+}$ electrode (Fig. 8, curve B) is similar to that for Cu(II), Ag(I), and Co(II). It appears from the enhancement of the Ru(II) oxidation wave and the absence of the +0.7V metal stripping wave that reduction of Ni(II) has produced a metal deposit on the outside of the polymer. However, as with Co, the complex electrochemistry of Ni(II) at Pt does not permit a clean conclusion.

Determination of the quantity of deposited metal.—The quantity of metal deposited on the polymer film is, in principle, estimable from the cathodic charge used to produce the metal film. However, this could be inaccurate due to (*i*) reduction of other materials (solvent, dioxygen, trace water) electrocatalyzed by the freshly formed metal crystal surface, (*ii*) metal particles that did not adhere to the polymer, and (*iii*) reduction to soluble products [*e.g.*, Cu(II) to Cu(I)]. The charge involved in the Ru(III)-mediated oxidation of the metal film provides a better approach. For example, consider curve C in Fig. 3. The oxidation wave at *ca.* 1.2V corresponds to oxidation of the polymer film from Ru(II) to Ru(III) and of Cu(0) to Cu(II) and so its charge (Q) is related to the quantity of Cu metal in the film by

$$Q = \mathbf{F}A(\Gamma_{Ru} + 2\Gamma_{Cu}) \qquad [1]$$

where Γ_{Ru} is the surface coverage of polymer and Γ_{Cu} the surface coverage of copper. Thus, the metal film formed in Fig. 3, curve C, had 1.6×10^{-8} mol/cm^2 of copper, which corresponds to an average metal thickness of *ca.* 10Å.

Determination of the quantity of deposited metal in this way assumes a quantitative oxidation of the metal during the Ru(III) mediated wave. That this is true in Fig. 3 is shown by the Ru(II/III) oxidation wave diminishing to its original size [equal to the Ru(III/II) reduction wave] in a second potential scan through the wave. This is not always the case when large quantities of metal are deposited however. Consider for example Fig. 9, where a thick coating (>250Å) of Ag metal was deposited from 1 m*M* $AgClO_4$ by holding the potential for 20 min at −1.7V. Now, even after three scans through the Ru(II/III) oxidation wave, changes still occur, the original wave has not yet reappeared, and no Ru(III) reduction peak is seen. Clearly, metal continues to be oxidized from the polymer and, to measure its amount, constant potential coulometry would be superior to the voltammetry in this case.

Figure 9 raises incidentally the question of the kinetics of oxidation of the metal film. The maximum oxidation current observed was 0.13 mA which is much less than can be accounted for by electron diffusion-limited current (41). Accordingly the kinetics

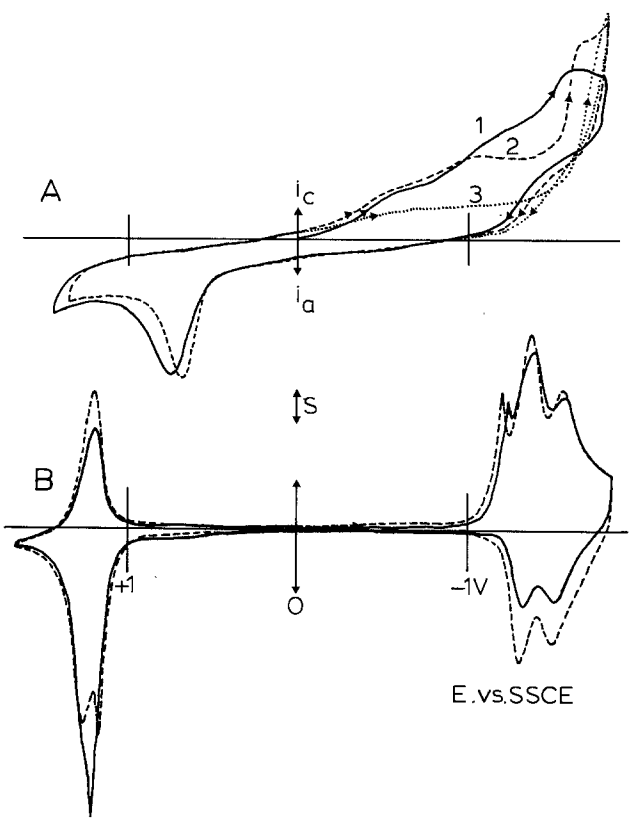

Fig. 8. Curve A: three consecutive voltammetric scans for 1 mM $Ni(ClO_4)_2$ at naked Pt; curve B: voltammograms of a 2.4×10^{-8} mol/cm^2 Pt/poly-$[Ru(bpy)_2(vpy)_2]^{2+}$ electrode in the absence (- - -) and presence (——) of 1 mM $Ni(ClO_4)_2$. Sweep rate = 200 mV/sec. S = 128 μA/cm^2 (curve A), 368 μA/cm^2 (curve B, - - -), and 490 μA/cm^2 (curve B, ——).

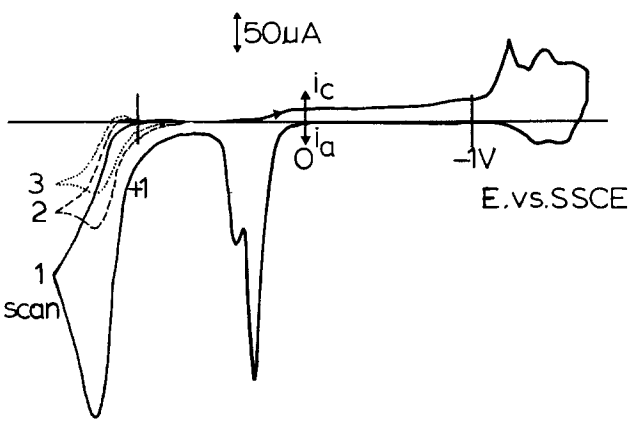

Fig. 9. Voltammogram at 100 mV/sec of an 8×10^{-9} mol/cm^2 Pt/poly-$[Ru(bpy)_2(vpy)_2]^{2+}$ electrode in the presence of 1 mM Ag(I). The potential was scanned negatively from +0.5V and held at −1.7V for 20 min. The potential was then scanned positively to +1.5V and then between +0.8 and +1.5V. Electrode area = 0.12 cm^2.

of Ru(III)-mediated oxidation of silver(0) have become limiting. We have not studied this problem further.

Film growth and structure.—The cyclic voltammetric results show for Cu and Ag that metal deposited onto the polymer film can be distinguished from metal deposited on and in contact with the Pt electrode. For Cu, the evidence further localized the deposition to within the outer few hundred angstroms of the polymer. Further insights into film structures were obtained by SEM and XPS experiments.

XPS proved quite informative for Co and Ni. Figure 10 shows spectra of a Pt/poly-$[Ru(bpy)_2(vpy)_2]^{2+}$ electrode and of a similar electrode after deposition of cobalt. The average film thickness of Co deposited, judging the amount from the enhanced charge under the Ru(III/II) wave, is very small, *ca.* 30Å, but this thickness is nevertheless large compared to the expected escape depth through Co of photoelectrons originating from the polymer. The spectrum of the cobalt-coated electrode shows a Co $2p_{3/2}$ peak (binding energy 780.9 eV), but no polymer N 1s peak or Ru $3d_{5/2}$ peaks. We conclude that most of the average 30Å thickness of the cobalt film must rest on the outer surface of the polymer so as to scatter the polymer film's photoelectrons. The Co film must still have some holes and voids, since the Ru(III/II) electroactivity remains observable, but the collective area of these defects must be only a small fraction of the cross-sectional electrode area.

Second, XPS binding energies for Co(0), Ni(0), and Cu(0) deposits on Pt/poly-$[Ru(bpy)_2(vpy)_2]^{2+}$ electrodes, shown in Table II along with values for the bulk metals (44) are uniformly shifted a considerable *ca.* 3 eV to higher binding energy relative to the bulk metals. While these shifts might in part be due to the metal layers being more aggressively air oxidized (being microparticulates) than the bulk metals, we believe they more likely reflect the well-known charging effect in photoelectron spectroscopy, where a poorly conducting sample surface becomes (via photoionization) electron deficient and positively charged. In the present case, the metal films are in poor electrical contact with the Pt electrode, being on the outside of the polymer, and can thereby become electron deficient. The similarity of behavior of Co and Ni to Cu provides additional evidence that, like Cu, the Co and Ni films are deposited on the outside of the polymer film.

Table II. XPS

	Binding energy, eV		
	Co $2p_{3/2}$	Ni $2p_{3/2}$	Cu $2p_{3/2}$
Pt/poly-$[Ru(bpy)_2(vpy)_2]^{2+}$/Co(0)	780.9		
Co metal	777.9†		
Pt/poly-$[Ru(bpy)_2(vpy)_2]^{2+}$/Ni(0)		855.8	
Ni metal		852.3†	
Pt/poly-$[Ru(bpy)_2(vpy)_2]^{2+}$/Cu(0)			935.7
Cu metal			932.4†
ΔE^* =	3.0	3.5	3.3

* Difference between bulk metal and metal electrodeposited on polymer.
† Ref. (44).

SEM micrographs were useful in examining the morphology of growth of the metal deposits and its dependency on experimental conditions.

Copper.—The strategy of exposing an already charged, reducing polymer surface to a low concentration of metal ion was explored with Cu(II). The polymer-coated electrode was potentiostated at −1.5V, producing the Ru(I) state. [The Ru(0) state was not used because it is more sensitive to trace O_2 and being neutral might show greater permeability to Cu(II).] A small crystal of $Cu(ClO_4)_2$ (*ca.* 10 mg) was added to the quiet electrolyte solution (*ca.* 2 cm^3) and allowed to dissolve slowly, thereby exposing the reducing polymer surface to a gradually increasing Cu(II) concentration. Subsequent positive potential scans showed indeed that little if any Cu was deposited on the Pt electrode under this condition, while large amounts of Cu were deposited on the outer part of the polymer film. SEM photographs of films with average thickness of *ca.* 400 and 1000Å [estimated from the Ru(III) mediated wave] are shown in Fig. 11A, B. The former Cu film, shiny dark blue in appearance, consists of a few *ca.* 2 μm particles and numerous smaller particles. The thicker film, made after much Cu(II) had dissolved and thus during a period of very

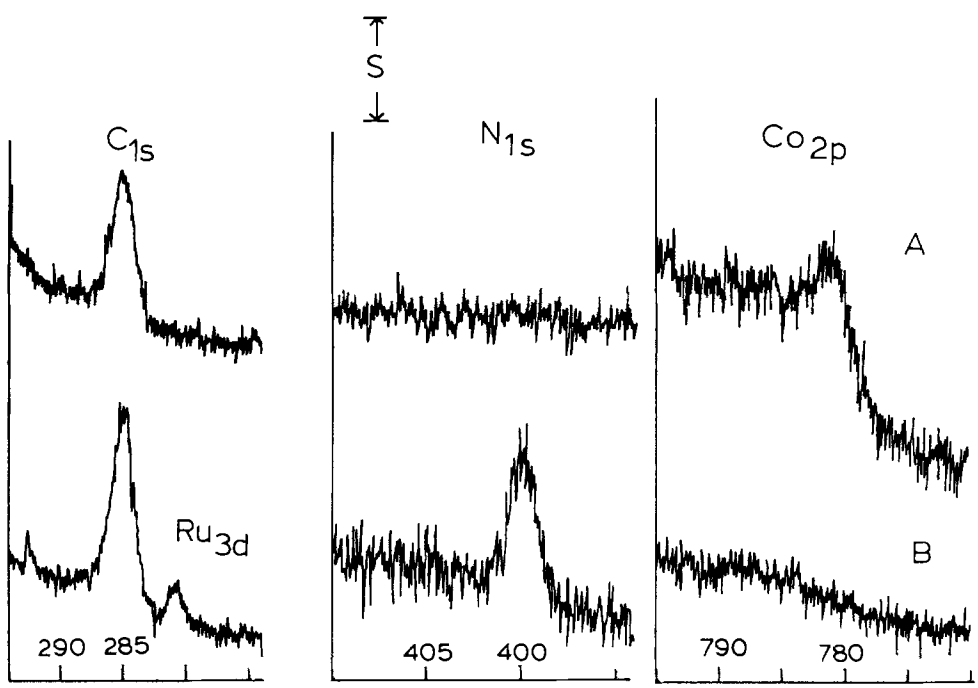

Fig. 10. XPS spectra of a Pt/poly-$[Ru(bpy)_2(vpy)_2]^{2+}$ / Co electrode (curve A) and a Pt/poly-$[Ru(bpy)_2(vpy)_2]^{2+}$ electrode (curve B). S = 1024 counts (curve A and N 1s, curve B); and 2048 counts (C 1s, Co $2p_{3/2}$, curve B).

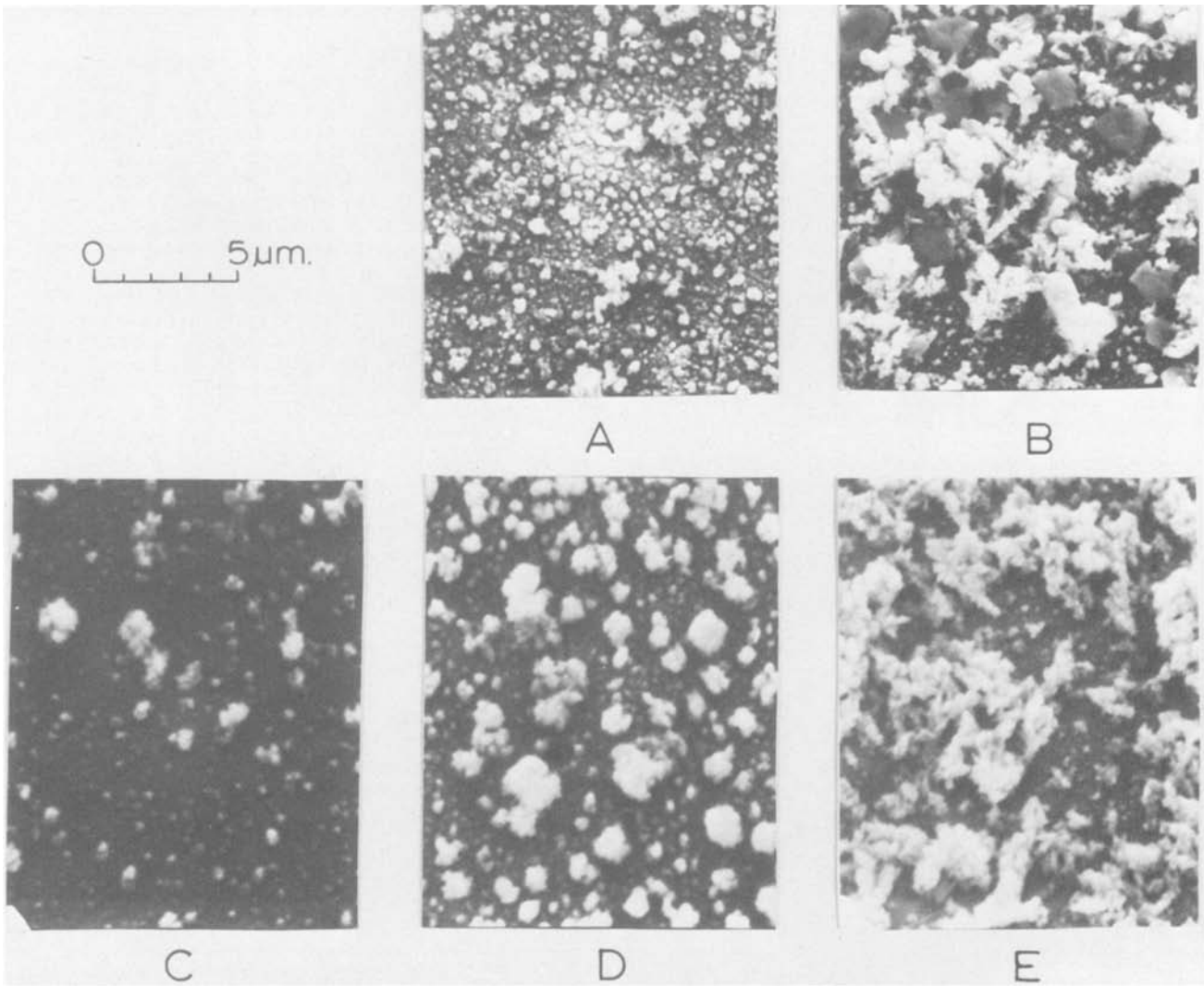

Fig. 11. SEM micrographs of Pt/poly-$[Ru(bpy)_2(vpy_2)]^{2+}$/Cu electrodes. The copper deposits shown in panels A and B were grown from still solutions containing a dissolving $Cu(ClO_4)_2$ crystal (see text). Those in panels C through E were grown at electrodes rotated at 2500 rpm in 0.4 mM $Cu(ClO_4)_2$ for 2, 4, and 8 min, respectively.

rapid film growth, is dark brown and granular in appearance, spongy, porous, with some dendrites. Neither film is continuous from the standpoint of making a suitable electrical contact to the outside of the film.

Redesigning the experiment in order to supply low but steady metal ion concentrations to the reducing polymer surface, the polymer-coated electrode was used as a rotated disk, being placed in dilute (30-640 μM) $Cu(ClO_4)_2$, quickly stepped to -1.5V, and rotated at between 900 and 4900 rpm for various times. The rotation is stopped, the potential stepped to 0V, and the electrode removed from the solution, washed, and dried. Figure 11C-E gives typical results of how metal particles grow on the polymer. Again a range of particle sizes appears during the initial growth (panel C). Throughout the range of concentrations, rotation rates, and times, the thicker Cu films remained, however, somewhat porous and spongy (panel E).

Cobalt.—Optimization for attractive cobalt deposition was more easily achieved. A Pt/poly-$[Ru(bpy)_2(vpy)_2]^{2+}$ electrode potentiostated at -1.78V *vs.* SSCE and rotated at 1600 rpm gave the best results. Figure 12A-C illustrates the result for $5.0 \times 10^{-5} M$ $Co(ClO_4)_2$ solution while rotating the electrode at 1600 rpm for 3, 20, and 60 min, respectively. Cobalt particles (light colored spots) appear in panel A with a variety of sizes (0.1-0.7 μm), on the polymer surface, distributed randomly about the polishing grooves lying underneath the poly-$[Ru(bpy)_2(vpy)_2]^{2+}$ film.

After 20 min of deposition (panel B), particles consolidated to produce a smooth cobalt film that was stable to solvent washing. After a much longer deposition time, 60 min, Fig. 12C shows that cobalt crystals appear to grow on top of the smooth film of Fig. 12B. The cobalt deposition was quite sensitive to concentration and this pattern was altered by as small a change as lowering Co(II) concentration to $3.0 \times 10^{-5} M$.

The nucleation step in electrocrystallization on metal surfaces is known (45) to follow either what is called simultaneous or progressive nucleation. In simultaneous nucleation, many nuclei are formed at nearly the same time with a typically small induction time, and these nuclei thereafter grow similarly in size. In progressive nucleation, nuclei are formed over a range of time and grow to produce metal crystals of a variety of sizes. Progressive nucleation is more likely when nucleation kinetics are inherently slow, and this appears from the range of particle sizes in Fig. 11A, C and 12A to be the case for Cu and Co deposition on Pt/poly-$[Ru(bpy)_2(vpy)_2]^{2+}$ electrodes. We know of no previous electrocrystallization data on polymer surfaces with which to compare this conclusion, but intuitively it is not surprising that the amorphous polymer surface

would not promote rapid, ordering phenomena such as nucleation. Importantly, however, we have shown that nucleation on the reducing polymer can occur, which leaves open the possibility of securing deposition conditions leading to adherent and highly reflective metal coatings with technological utility.

Permeability of a Pt/poly-$[Ru(bpy)_2(vpy)_2]^{2+}$ electrode coated with electrodeposited Co to an electroactive solute.—We have shown (31) that the permeability of electropolymerized ruthenium complex films to solution redox reagents depends on the number and length of polymerization links in the polymer and on the redox reagent size and charge. Permeability is measured by rotating disk voltammetry (46) using the equation

$$\frac{1}{i} = \frac{d}{n\mathbf{F}AD_{S,pol}PC_S} + \frac{1}{0.62\, n\mathbf{F}AD_S^{2/3}\nu^{-1/6}\omega^{1/2}C_S} \quad [2]$$

where d is polymer film thickness, C_S is the redox reagent solution concentration, P and $D_{S,pol}$ its partition and diffusion coefficient into the polymer, respectively, and ω is in rad/sec.

The deposition of metal particles such as Co onto a Pt/poly-$[Ru(bpy)_2(vpy)_2]^{2+}$ polymer surface should limit the permeation of a redox reagent through the film to the Pt electrode. This effect could provide further clues as to the structure of the Co layer, in particular its microporosity. The following, preliminary results show that the permeation limitation can be detected.

Pt/poly-$[Ru(bpy)_2(vpy)_2]^{2+}$ electrodes were coated with different amounts of Co and the permeability of the coated, rotated disk electrode to ferrocene in acetonitrile evaluated using inverse Levich plots of the above equation as in Fig. 13. Curves B and D are for electrodes with no electrodeposited Co, from whose intercepts $PD_{S,pol}$ of ferrocene in the film is evaluated as 6.7×10^{-8} and 6.1×10^{-8} cm^2/sec, respectively. Curves A and C correspond to relatively thick and thin, respectively, deposited films of Co metal. For the thin Co layer, the slope of the inverse Levich plot (inversely proportional to area, Eq. [2]), is increased by a small amount (1.6×) and the intercept by 3.4× (curve C) as compared to the same electrode before Co deposition (curve D). For the thick Co layer (curve A), there is a more definite increase in slope (6.0×), as well as an increase in intercept (2.0×), as compared to the same electrode before Co deposition (curve B).

The effects in Fig. 13 can be understood in terms of a microporous Co film resting on top of the polymer film. The effect is of two kinds. First, the Co film reduces the effective macroscopic area of the rotated electrode for which ferrocene transported from the solution encounters polymer film and a pathway to the Pt electrode. The effective macroscopic area depends on the relative spacing of the holes in the Co film and the dimension of the ferrocene diffusion layer in the solution. The effect shows up in the slope of the inverse Levich plot as predicted by models for active sites on electrodes (47-49) and microelectrode assays (50). Calculating the diffusion layer thickness for $\omega = 400$ rpm, indicates that the spacing of the holes in the Co film must exceed 0.004 cm in order to generate the slope increase in Fig. 13A for the Co film prepared with longer electrodeposition time, where SEM (Fig. 12) has indicated that particle consolidation occurs.

The second effect, appearing as increased inverse Levich plot intercepts, is related to ferrocene transport in the polymer film in between the Co film and the Pt electrode. This effect is not represented in the previous theories but is readily argued by intuition. If the rate of transport of ferrocene through the polymer is fast so that the effective ferrocene diffusional range in the polymer is large compared to the spacing between the holes in the Co film where ferrocene enters the polymer, then the apparent area of the membrane through which ferrocene diffuses will approach 100% of the cross-sectional electrode area. If, on the other hand, the ferrocene transport is slow in the above relative distance sense, the apparent membrane area (and the corresponding intercept value) becomes just the area of the holes in the Co film. (Additionally the distance of membrane diffusion must include the path length of pores in the Co film as well as of the polymer film itself.) The results in Fig. 13 suggest that ferrocene transport inside the polymer is slow but not to the limiting degree, since the apparent membrane area is lowered by 2-3× compared to the electrode macroscopic area, but the area of the holes in the Co film must be less than this.

The results in Fig. 13 are preliminary, but are very encouraging by demonstrating a way to probe the spatial character of deposits on polymer films. Bard

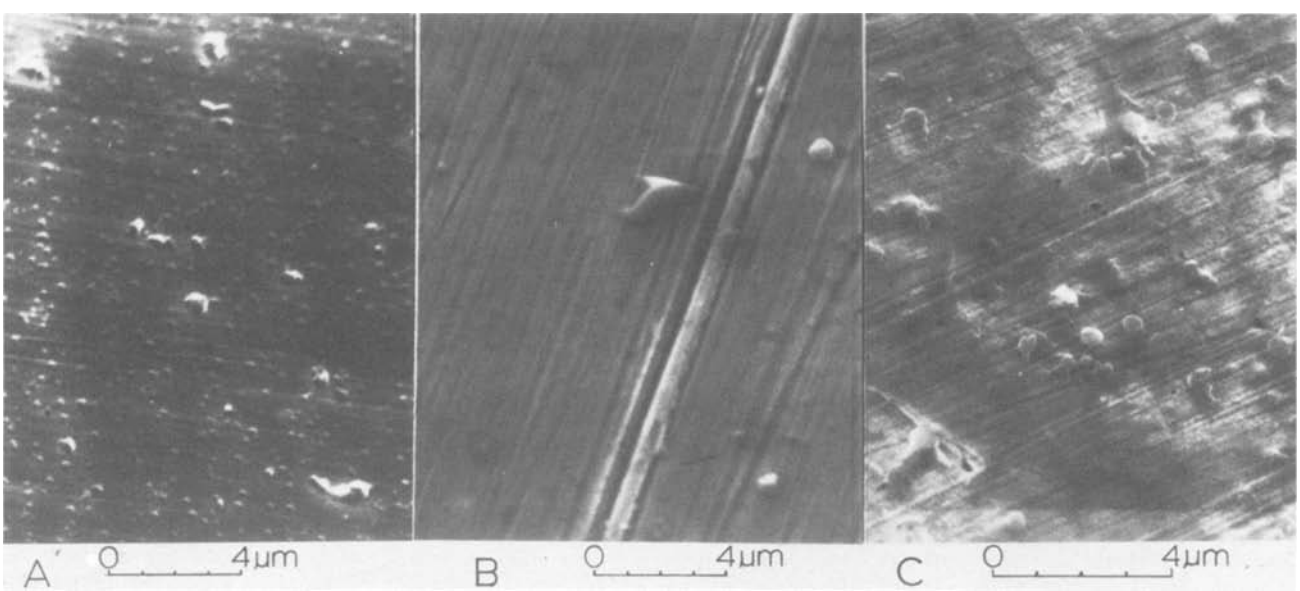

Fig. 12. SEM micrographs of Co deposits on a Pt/poly-$[Ru(bpy)_2(vpy)_2]^{2+}$ electrode. The deposits were grown for 3 min (panel A), 20 min (panel B), and 60 min (panel C) from 5.0×10^{-5}M Co(II) at 1600 rpm.

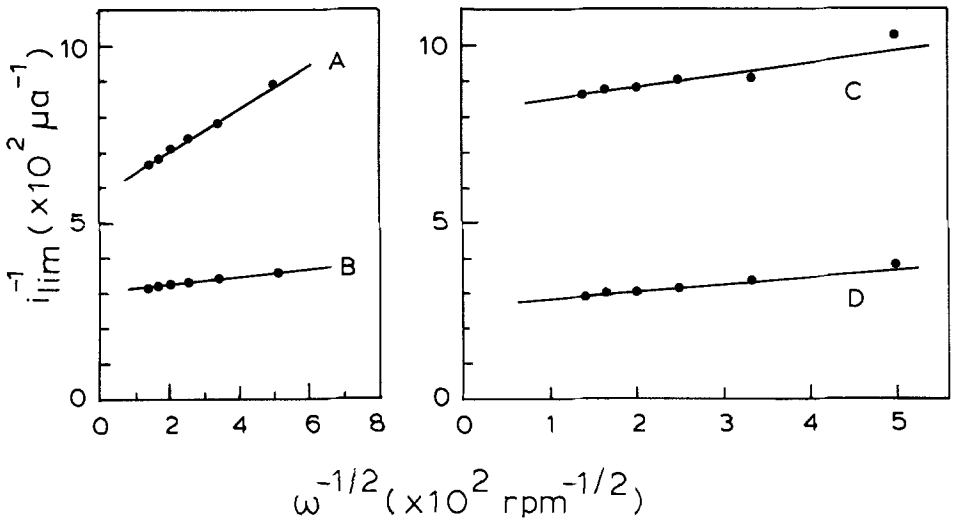

Fig. 13. Inverse Levich plots for oxidation of 1.29 mM ferrocene at Pt/poly-$[Ru(bpy)_2(vpy)_2]^{2+}$ electrodes (curves B, D) and Pt/poly-$[Ru(bpy)_2(vpy)_2]^{2+}$ / Co electrodes (curves A, C). The cobalt was deposited from 5.0 × 10^{-5}M Co(II) at 1600 rpm for 3 min (curve C) and 30 min (curve A). Γ_{Ru} = 3.0 × 10^{-8} mol/cm² (curves A, B) or 2.0 × 10^{-8} mol/cm² (curves C, D).

and co-workers (51) have also used the permeation approach to explore the film structure, which should be additionally useful for polymer films with embedded electrodes (52) and which have vapor-deposited Au films (41).

Mediation of copper deposition by an electroactive solute.—In the preceding experiments, the metal reduction reaction(s) were mediated by electron levels of the poly-$[Ru(bpy)_2(vpy)_2]^{2+}$ film itself. In principle, the reducing medium could instead be an electroactive solute which can diffuse through the film, be reduced at Pt, and diffuse outward through the film to reduce, say, Cu(II). To briefly test this scheme, we chose N,N'-ethylene-2,2'-bipyridine (diquat, DQ^{2+}), a small molecule which although dicationic has (31) measurable permeability through poly-$[Ru(vbpy)_3]^{2+}$, a related film. Figure 14 shows the voltammetry of diquat at naked Pt (curve A) and at a Pt/poly-$[Ru(bpy)_2(vpy)_2]^{2+}$ electrode (curve B). The flattened appearance of curve B reflects membrane-controlled permeation, rotated disk voltammetric measurement of which gave a value of $PD_{S,pol}$ = 3.0 × 10^{-9} cm² sec^{-1}, slightly less than that observed for the probably more cross-linked poly-$[Ru(vbpy)_3]^{2+}$ film (31).

Using a solution containing both DQ^{2+} and Cu(II), an irreversible wave appears at a poly-$[Ru(bpy)_2(vpy)_2]^{2+}$ electrode (curve C, Fig. 14) which is larger than currents given by either species alone, (curves D,E). A mixture of DQ^{2+} and Cu(I) [the Cu(I) was made by electrolytic dissolution of Cu(0) in acetonitrile], on the other hand, produced only a slight current enhancement at the DQ^{2+} potential. Since $E^{\circ\prime}$ for the $DQ^{2+/1+}$ couple (−0.38V) is much more negative than that for Cu(II/I), but is slightly positive of that for Cu(I/0), curve C in Fig. 14 can be interpreted as mainly a DQ^{+}-mediated reduction of Cu(II) to

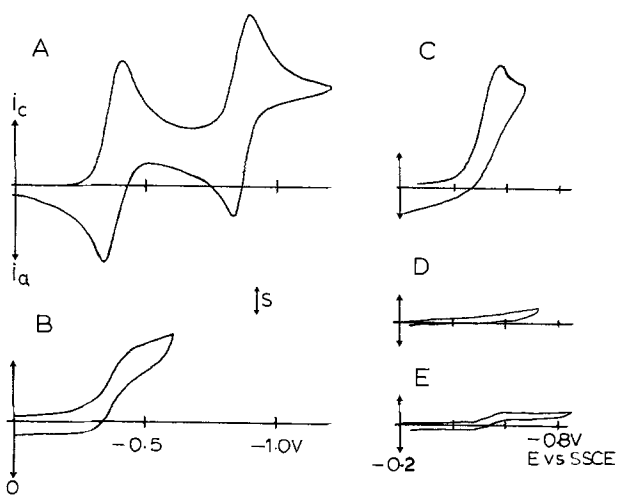

Fig. 14. Cyclic voltammogram at 100 mV/sec of (curve A) 1.1 mM diquat at naked Pt, S = 63.3 μA/cm² and (curve B) at an 8.5 × 10^{-9} mol/cm² Pt/poly-$[Ru(bpy)_2(vpy)_2]^{2+}$ electrode. S = 12.7 μA/cm²; 1.2 mM diquat plus 1.0 mM Cu(II) (curve C), 1.0 mM Cu(II) (curve D), and 1.2 mM diquat (curve E) at a 5.5 × 10^{-9} mol/cm² Pt/poly-$[Ru(bpy)_2(vpy)_2]^{2+}$ electrode, S = 47.6 μA/cm².

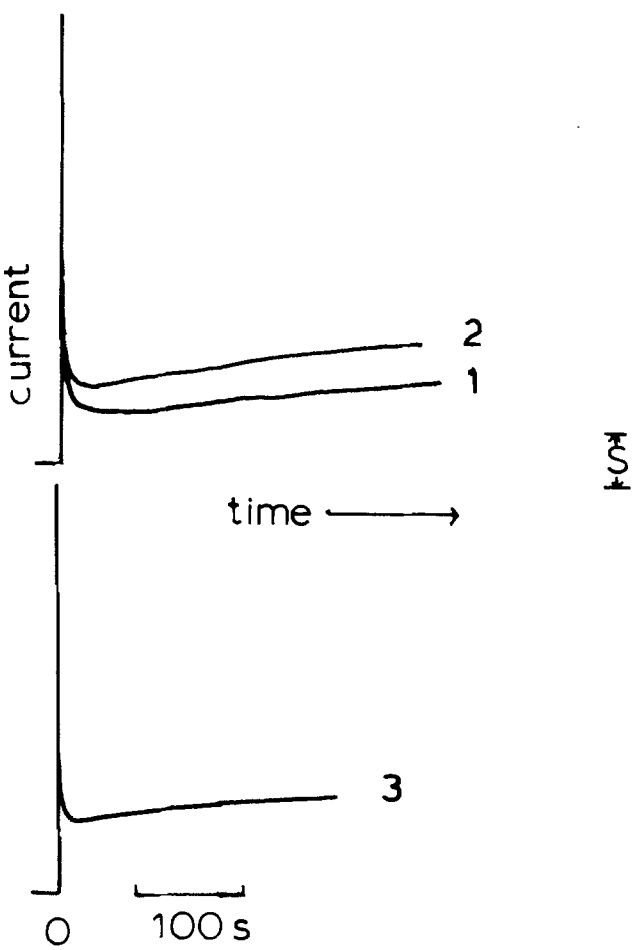

Fig. 15. Constant potential electrolysis current vs. time plots for 1.1 mM Cu(II) plus 1.2 mM diquat at a 3.2 × 10^{-9} mol/cm² Pt/poly-$[Ru(bpy)_2(vpy)_2]^{2+}$ electrode, at −0.47V vs. SSCE. Curves A, B, and C are the first three consecutive electrolyses. S = 73.5 μA/cm².

Cu(I), with little production of Cu(0) on the voltammetric time scale.

Longer periods of contact of DQ^{1+} electrogenerated in this way in the Cu(II) solution do give evidence for slow Cu(0) deposition, however. Figure 15 shows the result of potentiostating a Pt/poly-$[Ru(bpy)_2(vpy)_2]^{2+}$ electrode at −0.47V. The current initially falls as expected, then gradually rises. No Cu(0/I) stripping peak is seen in a subsequent positive potential scan. If the potential scan is stopped short of the Ru(II/III) region [which should leave in the polymer film any deposited Cu(0) not in contact with the Pt] and the potential returned to −0.47V, the same pattern results (curve B), but the rise in current occurs more promptly. A third potential step likewise accelerates the onset of current rise. The curve A-C pattern can be repeated if the electrode is scanned through the Ru(II/III) region. Our interpretation of these results is that the longer electrolysis allows a gradual formation of Cu(0) nuclei by DQ^{1+} + Cu(I) reaction, producing thereafter an increase in current due to even more rapid Cu(0) deposition in the presence of nuclei. It appears that metal deposition can be mediated by a polymer-dissolved reductant but in the present example, with a quite slow rate of nucleation.

Acknowledgments

This research was supported in part by grants from the Office of Naval Research and the National Science Foundation.

Manuscript submitted March 18, 1983; revised manuscript received June 25, 1983.

The University of North Carolina at Chapel Hill assisted in meeting the publication costs of this article.

REFERENCES

1. A. Merz and A. J. Bard, *J. Am. Chem. Soc.*, **100,** 3222 (1978).
2. L. L. Miller and M. R. Van de Mark, *J. Electroanal. Chem.*, **100,** 3223 (1978).
3. R. Nowak, F. A. Schultz, M. Umana, H. Abruna, and R. W. Murray, *ibid.*, **94,** 219 (1978).
4. M. S. Wrighton, R. G. Austin, A. B. Bocarsly, J. M. Bolts, O. Haas, K. D. Legg, L. Nadjo, and M. C. Palazzotto, *ibid.*, **87,** 429 (1978).
5. P. J. Peerce and A. J. Bard, *ibid.*, **112,** 97 (1980).
6. P. J. Peerce and A. J. Bard, *ibid.*, **114,** 89 (1980).
7. H. D. Abruna and A. J. Bard, *J. Am. Chem. Soc.*, **103,** 6898 (1981).
8. M. F. Dautartas and J. F. Evans, *J. Electroanal. Chem.*, **109,** 301 (1980).
9. O. Haas, M. Kriens, and J. G. Vos, *J. Am. Chem. Soc.*, **103,** 1318 (1981).
10. C. DeGrand and E. Laviron, *J. Electroanal. Chem.*, **117,** 283 (1981).
11. N. Oyama and F. C. Anson, *J. Am. Chem. Soc.*, **101,** 3450 (1979).
12. N. Oyama and F. C. Anson, *This Journal*, **127,** 640 (1980).
13. K. Shigehara, N. Oyama, and F. C. Anson, *J. Am. Chem. Soc.*, **103,** 2552 (1981).
14. J. B. Kerr, L. L. Miller, and M. R. Van De Mark, *ibid.*, **102,** 3383 (1980).
15. C. DeGrand and L. L. Miller, *ibid.*, **102,** 5728 (1980).
16. M. Fukui, C. DeGrand, and L. L. Miller, *ibid.*, **104,** 28 (1982).
17. P. Daum, J. R. Lenhard, D. Rolison, and R. W. Murray, *ibid.*, **102,** 4649 (1980).
18. J. M. Calvert, R. H. Schmehl, B. P. Sullivan, J. S. Facci, T. J. Meyer, and R. W. Murray, *Inorg. Chem.*, Submitted.
19. H. D. Abruna, J. M. Calvert, P. Denisevich, C. D. Ellis, T. J. Meyer, W. R. Murphy, R. W. Murray, B. P. Sullivan, and J. L. Walsh, ACS Symposium Series, Vol. 192, pp. 133, American Chemical Society, Washington, DC (1982).
20. K. W. Willman and R. W. Murray, *J. Electroanal. Chem.*, **133,** 211 (1982).
21. P. Denisevich, H. D. Abruna, C. R. Leidner, T. J. Meyer, and R. W. Murray, *Inorg. Chem.*, **21,** 2153 (1982).
22. D. C. Bookbinder, J. A. Bruce, R. N. Dominey, N. S. Lewis, and M. S. Wrighton, *Proc. Nat. Acad. Sci.*, **77,** 6280 (1980).
23. A. B. Bocarsly, E. G. Walton, and M. S. Wrighton, *J. Am. Chem. Soc.*, **102,** 3390 (1980).
24. M. S. Wrighton, M. C. Palazzotto, A. B. Bocarsly, J. M. Bolts, A. B. Fischer, and L. Nadjo, *ibid.*, **100,** 7264 (1978).
25. M. S. Wrighton, A. B. Bocarsly, J. M. Bolts, M. G. Bradley, A. B. Fischer, N. S. Lewis, M. C. Palazzotto, and E. G. Walton, *Adv. Chem. Ser.*, **184,** 295 (1980).
26. F. B. Kaufman, A. H. Schroeder, E. M. Engler, S. R. Kramer, and J. Q. Chambers, *J. Am. Chem. Soc.*, **102,** 483 (1980).
27. F. B. Kaufman and E. M. Engler, *ibid.*, **101,** 547 (1979).
28. M. S. Wrighton, ACS Symposium Series, Vol. 192, p. 99, American Chemical Society, Washington, DC (1982).
29. T. P. Henning, H. S. White, and A. J. Bard, *J. Am. Chem. Soc.*, **104,** 5862 (1982).
30. H. D. Abruna, P. Denisevich, M. Umana, T. J. Meyer, and R. W. Murray, *ibid.*, **103,** 1 (1981).
31. T. Ikeda, R. Schmehl, P. Denisevich, K. Willman, and R. W. Murray, *ibid.*, **104,** 2683 (1982).
32. N. Oyama and F. C. Anson, *Anal. Chem.*, **52,** 1192 (1980).
33. J. B. Kerr and L. L. Miller, *J. Electroanal. Chem.*, **101,** 263 (1979).
34. K. N. Kuo and R. W. Murray, *ibid.*, **131,** 37 (1982).
35. J. Facci and R. W. Murray, *Anal. Chem.*, **54,** 772 (1982).
36. C. P. Andrieux and J.-M. Saveant, *J. Electroanal. Chem.*, **93,** 163 (1978).
37. C. P. Andrieux, J. M. Dumas-Bouchiat, and J.-M. Saveant, *ibid.*, **114,** 159 (1980).
38. C. P. Andrieux, J. M. Dumas-Bouchiat, and J.-M. Saveant, *ibid.*, **123,** 171 (1981).
39. C. P. Andrieux, J. M. Dumas-Bouchiat, and J.-M. Saveant, *ibid.*, **131,** 1 (1982).
40. P. Denisevich, K. W. Willman, and R. W. Murray, *J. Am. Chem. Soc.*, **103,** 4727 (1981).
41. P. G. Pickup and R. W. Murray, *ibid.*, **105,** 4510 (1983).
42. R. D. Rocklin and R. W. Murray, *J. Phys. Chem.*, **85,** 2104 (1981).
43. W. Kutner, P. G. Pickup, and R. W. Murray, Submitted to *J. Amer. Chem. Soc.*
44. C. D. Wagner, in "Handbook of X-ray Photoelectron Spectroscopy," Perkin-Elmer Corp., Physical Electronics Division (1979).
45. H. R. Thirsk and J. A. Harrison,, "A Guide to the Study of Electrode Kinetics," Academic Press, London (1972).
46. D. A. Gough and J. K. Leypoldt, *Anal. Chem.*, **51,** 439 (1979).
47. R. Landsberg and R. Thiele, *Electrochim. Acta*, **11,** 1243 (1966).
48. F. Scheller, S. Muller, R. Landsberg, and H.-J. Spitzer, *J. Electroanal. Chem.*, **19,** 187 (1968).
49. F. Scheller, R. Landsberg, and S. Muller, *ibid.*, **20,** 375 (1969).
50. T. Gueshi, K. Tokuda, and H. Matsuda, *ibid.*, **89,** 247 (1978).
51. J. Leddy and A. J. Bard, *ibid.*, In press.
52. P. Burgmayer and R. W. Murray, *J. Am. Chem. Soc.*, **104,** 6139 (1982).

Technical Note

Oxidation of Coal Slurries in Acidified Ferric Sulfate

K. E. Anthony[1] and H. G. Linge

CSIRO Division of Mineral Chemistry, Port Melbourne, Victoria 3207, Australia

Coughlin and Farooque (1, 2) achieved a *ca.* 66% reduction in the applied cell voltage required for the electrolytic production of copper and also of hydrogen gas by depolarizing the anode with slurried coal rather than by the oxygen evolution reaction, as used in the conventional operation. They assumed that the carbon in the coal was electrochemically gasified to CO_2, *e.g.*, by oxidation reactions of the type

$$C + 2H_2O \rightarrow CO_2 + 4H^+ + 4e \qquad [1]$$

for which the standard potential is *ca.* 1V less than for oxygen evolution at the same pH.

Several independent investigations (3-5) have now shown that the anodic currents observed with coal slurries arise in fact from the oxidation of dissolved Fe(II), which is readily leached and/or exchanged from the coal surface in acidic solutions. The current actually arising from electron transfer between colliding coal particles and the anode is small, *e.g.*, less than 25 $\mu A/cm^2$ for a slurry concentration of 10 g/liter (3), and the use of coal as an anode depolarizer has therefore been questioned (4). However, this criticism overlooks that coal can be readily oxidized by Fe(III), *e.g.*, as produced anodically from the dissolved Fe(II). In practice (3, 5-7), the electrochemical gasification of coal is an indirect (mediated) electrolysis in which the overall rate is determined by the reaction between carbon and Fe(III) at the surface of the coal particle. In this paper, we present results on the stoichiometry and kinetics of this reaction and also show the current-time response for indirect coal electrolysis in ferric sulfate solution.

Ground coal (passing 100 μm) was prewashed by reflux boiling in deoxygenated 2M H_2SO_4 to eliminate interference from mineral leaching, carbonate dissolution, and thermal decarboxylation on the coal oxidation reaction. The coal was washed and stored in vacuo after drying at 50°C or as stock slurries in deoxygenated 0.1M H_2SO_4. The reaction between coal and Fe(III) was studied in magnetically stirred thermostated glass cells, fitted with appropriate electrochemical control probes. N_2 was passed through the cell during a run and the exit gas stream desaturated with a condenser to prevent evaporation of the hot cell solution.

Reaction product yields were determined by mixing Fe(III) solution and dry coal in varying proportions and following the reaction to completion. Produced CO_2 gas was concentrated on molecular sieves (type 5A) and the amount collected in a known reaction interval (G, mol) determined by infrared spectrometry after gas desorption from the sieves at 360°C. The charge passed (Q, mol) was determined from the produced Fe(II), using Eq. [2]

$$Fe(III) + e \rightarrow Fe(II) \qquad [2]$$

The concentration of Fe(II) was measured voltammetrically on a calibrated Pt microelectrode in the slurry. At the end of a run, the coal was washed, dried, and weighed to assess the extent of oxidative coal dissolution in the electrolyte.

Figures 1 and 2 show results obtained with North Dakota lignite coal. Figure 1 shows that coal and Fe(III) do react and that Eq. [2] is obeyed since the total amount of Fe(II) produced in the reaction is the same as the initial amount of Fe(III). CO_2 is also produced in the reaction, but in much smaller amounts than expected from Eq. [1]. Figure 2 demonstrates this for different experiments in the form of plots of

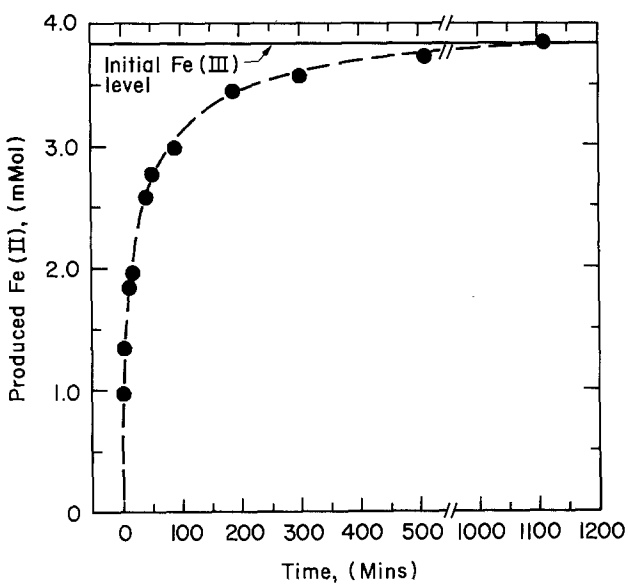

Fig. 1. Production of Fe(II) from Fe(III). [2.6g of North Dakota lignite coal slurried in 80 ml of 0.1M H_2SO_4 at 85°C, originally containing 3.85 mmol Fe(III)].

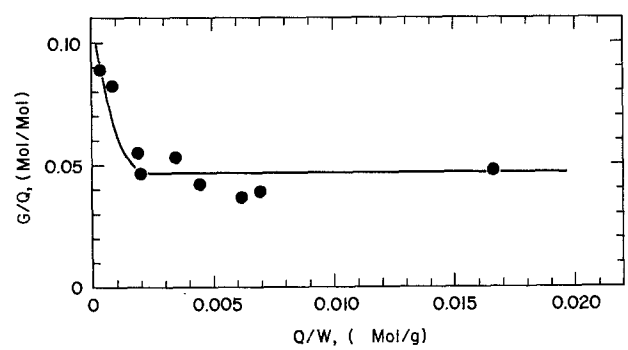

Fig. 2. Production of CO_2 gas during oxidation of North Dakota lignite coal in acidified ferric sulfate at 85°C. (Separate experiments; G = mol of CO_2 collected; Q = mol of charge passed; W = g of coal initially used).

[1] Permanent address: BHP Central Research Laboratories, Shortland, N.S.W., 2307, Australia.

Key words: coal slurry oxidation, electrochemical coal gasification, coal electrolysis.

G/Q *vs.* Q/W, the charge passed per unit initial weight of coal (W,g). For practical reasons, the duration of these experiments was limited to one week and this determined the accessible range of Q/W values for the coal. Initially, G/Q had values near 0.1, but then the values were practically constant at 0.047 ± 0.007 as the reaction progressed. Elemental analysis shows that this coal has the empirical formula $C_{100}H_{66}O_{20}N_{1.1}S_{0.3}$. The initial average oxidation state of carbon is therefore −0.3, practically independent of the assumed valences of N and S in the coal. The upper limit for G/Q values is thus (cf. Eq. [1]) 1/4.3, *i.e.*, 0.23. The current efficiency for the electrochemical gasification of this coal amounts therefore to only 20%. The partial stoichiometry for prolonged coal oxidation with Fe(III) (*e.g.*, for $Q/W = 0.02$) is

$$C_{100}H_{66}O_{20}N_{1.1}S_{0.3} - 32e \rightarrow 1.5\ CO_2 \qquad [3]$$

indicating that only 1.5% of the carbon in the coal is evolved as CO_2.

The ratio of the final and initial coal weight averaged at 1.01 ± 0.02. The major source of error in this measurement is an unavoidable loss of solids on the vessel walls. Therefore, the result probably implies that the coal weight increases slightly during the oxidation; there is certainly no significant coal dissolution. This suggests that oxidation with Fe(III) does not break up the linking bonds connecting the aromatic units in the coal structure (8). Most of the (positive) charge passed in the reaction (cf. Eq. [3]) is retained on the coal and the overall oxidation state of the residual carbon increases to approximately zero. This implies that oxygen atoms have been added to the coal during the oxidation, even though the extent of this addition is small. The reaction of coal with Fe(III) seems to be limited to a few reactive carbon sites, probably already associated with peripheral heteroatoms or unsaturated carbon bonds in the coal structure. In these reactions, new C–COOH sites are also formed and some of these decarboxylate by the standard Kolbe mechanism (9) forming the small amounts of CO_2 produced in the reaction.

Similar results have been obtained with bituminous coals, although the extent of the reaction and the CO_2 current efficiency is decreased with increasing coal rank. However, for all coals the behavior is drastically changed for oxidation at higher potentials; *e.g.*, at 1.5V (SHE), using ceric sulfate as the oxidant. Complete coal dissolution is then readily achieved. All of the lignite coal is dissolved for $Q/W = 0.15$, with a CO_2 current efficiency approaching 80%. The residual electrolyte has a yellow-brown color and contains about 50% of the coal carbon evidently in the form of aromatic carboxylic acids (10).

Indirect coal electrolysis was carried out in the anode compartment of a diaphragm cell with an acidified ferric sulfate anolyte. The cell had a high anode area/anolyte volume ratio (*ca.* 0.5 cm^{-1}) to ensure that practically all of the Fe(II) produced from the coal/Fe(III) reaction was converted immediately back to Fe(III) by anodic oxidation. Figure 3 shows a typical current-time response obtained with a 1% lignite coal slurry (10 g/liter) at 95°C. Short time currents exceed 50 mA and currents greater than 25 mA could be maintained readily for at least one day. The results show that the capacity of this slurry anode for producing, *e.g.*, cathodic hydrogen is about 10 ml/hr. In practice, dense slurries will therefore be required, *e.g.*, a 50% slurry can produce about 1/2 liter/hr. The activation energy of coal oxidation was measured by this technique with a bituminous coal as 13.6 kcal/mol. This figure is similar to the results obtained by the other workers (1, 4, 5) for lignites and anthracites and shows that for all coals, elevated temperatures must be used for any practical application of coal slurry anodes.

The reaction kinetics were measured at controlled coal surface potentials using the potentiometric titration procedure previously described (11). In these experiments, the oxidizing potential of the solution (E_h) is determined by the ratio of dissolved Fe(III) and Fe(II). The Fe(III) consumption in the reaction is compensated by titrating acidified ferric sulfate at constant E_h, using Pt sensors and a commercial pH stat. Coal oxidation rates (R) are then obtained from the slope of the recorded titrant volume-time curve at representative stages during the reaction.

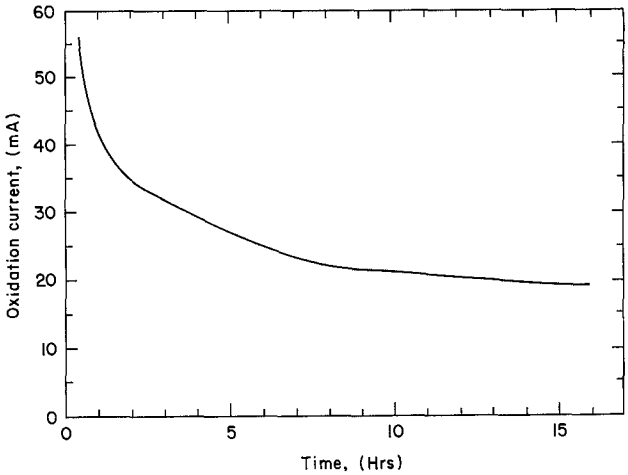

Fig. 3. Coal oxidation current in indirect electrolysis of North Dakota lignite coal (10 g/liter) at 95°C in 0.1M ferric sulfate [$(H^+) = 1M$].

Figure 4 shows a logarithmic plot of the time variation of R (expressed in mA/g of coal in the suspension) at 0.7V (SHE) for a low rank bituminous coal in 0.1M H_2SO_4 at 85°C. Reproducibility of these results was within ±15% and within these limits the overall reaction rate was proportional to the weight (and hence contact area) of coal (cf. run C7/C11 in Fig. 4). The rate decreases during the reaction and the solid line in Fig. 4 represents the kinetics adequately over at least three decades of time. The rate law is of the general form

$$R = k/t^n \qquad [4]$$

with constant k and n. The slope of the line in Fig. 4 gives $n = 0.4 \pm 0.1$ and this range of values also covers our results (7) for lignite and high rank bituminous coals. k measures intrinsic coal reactivity and its value increases with decreasing coal rank, *e.g.*, for a suite of six coals we found (7) relative reactivities ranging from about 20-500% of the levels shown in Fig. 4.

The titration of ferric sulfate at constant E_h raises the solution concentration of both Fe(III) and Fe(II) during the run, typically at least fifty-fold. These con-

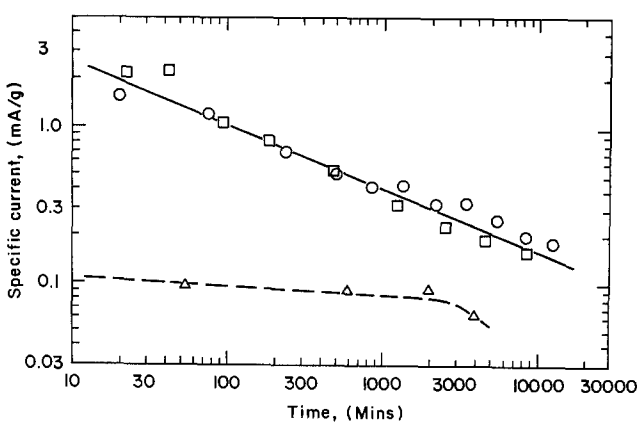

Fig. 4. Kinetics of oxidation of Lambton bituminous coal with Fe(III) in 0.1M H_2SO_4 at 0.7V (SHE) and 85°C. Rate dependence on slurry density and solution composition (○ run C7, 6 g/liter; □ run C11, 10 g/liter; △ run C8, continuation of run C7 with fresh electrolyte substituted at zero time).

centration changes have no significant effect on R, cf. test C8 (Fig. 4), in which all of the coal from the preceding run (C7) was reused with fresh electrolyte. In the new experiment, R was as low as at the end of the preceding run, showing that the coal alone is responsible for the observed decline in the rate of the reaction. Rate control by any step directly dependent on solution concentration is therefore unlikely. These steps include: Nernst-layer or pore diffusion of Fe(III) to reaction sites; Fe(III) adsorption and reduction at each site; and the equivalent steps for produced Fe(II) or any other dissolved reaction product. Repeated tests with fresh coal confirm that coal oxidation rates at a fixed E_h are independent of the actual solution concentrations of Fe(II) and Fe(III) at all stages of the reaction. However, the reaction accelerates with increasing E_h. This fact causes an apparent dependence of the observed current for indirect coal electrolysis on the ferric sulfate concentration (3, 5) and on the coal slurry stirring speed (7); and we would caution against using such results for any kinetic evaluation (5) of the coal oxidation mechanism.

Coal is a heterogeneous organic solid with a complex structure and composition (8), and modeling of Eq. [4] is therefore quite difficult. Mass transport control by some coal species, either via non-steady diffusion or via steady-state diffusion through a thickening film, gives $n = 0.5$, in Eq. [4]. Although this n value provides a close match to the observed kinetics, it is difficult to reconcile these diffusion models with the fact that coal has a polymeric character, consisting of macromolecules of different sizes with varying types and degrees of cross-linking (8). Since most of the (positive) charge passed in the reaction is retained on the coal, localization of the reaction to specific reaction sites, distributed through the coal, seems to be a more realistic approach to modeling Eq. [4]. The decline in R then results from the disappearance of these sites during the reaction, *e.g.*, by transformation of one type of carbon bond into another one. If the sites disappear by a law, perhaps first order in site concentration, R consists of a summation of terms each decaying exponentially with time at different rates, depending on the reactivity of each type of site for the reaction with Fe(III). Such a summation has prospects for modeling Eq. [4], depending on the form of the distribution function chosen for the reactivities of the sites. The detailed evaluation of this approach to modeling Eq. [4] is in progress in these laboratories.

Acknowledgments

We thank Mr. N. B. Valentine for the CO_2 assay and NERDDC for financial support of this work. Dr. K. E. Anthony wishes to thank CSIRO and BHP for financial support as a Visiting Scientist to CSIRO Division of Mineral Chemistry.

Manuscript submitted Dec. 27, 1982; revised manuscript received March 22, 1983.

CSIRO Division of Mineral Chemistry assisted in meeting the publication costs of this article.

REFERENCES

1. R. W. Coughlin and M. Farooque, *Nature*, **279**, 301 (1979).
2. R. W. Coughlin and M. Farooque, *Nature*, **280**, 666 (1979).
3. D. A. J. Swinkels, K. E. Anthony, T. Tran, and H. G. Linge, NERDDC Research Report Contract No. 80/0210, publ. BHP Central Research Laboratories, Shortland, N.S.W., July (1981).
4. G. Okada, V. Guruswamy, and J. O'M. Bockris, *This Journal*, **128**, 2097 (1981).
5. P. M. Dhooge, D. E. Stilwell, and S. M. Park, *ibid.*, **129**, 1719 (1982).
6. F. Rallo, Paper A15, Extended Abstracts, 31st Meeting of ISE, Vol. 1, Venice, (September 1980).
7. D. A. J. Swinkels, K. E. Anthony, H. G. Linge, and N. B. Valentine, NERDDC Research Report Contract No. 80/0210, publ. BHP Central Research Laboratories, Shortland, N.S.W., April (1982).
8. D. Whitehurst, in "Organic Chemistry of Coal," J. W. Larsen, Editor, Chap. 1, American Chemical Society Symposium Series 71, Washington, DC (1978).
9. L. Eberson, in "Organic Electrochemistry," M. M. Baizer, Editor, Chap. 13, Marcel Dekker Inc., New York (1973).
10. H. G. Linge and N. B. Valentine, Paper 11 presented at the 7th National Convention of RACI, Canberra, August (1982).
11. H. G. Linge, *Hydrometallurgy*, **2**, 51 (1976).

JOURNAL OF THE ELECTROCHEMICAL SOCIETY

SOLID-STATE SCIENCE AND TECHNOLOGY

NOVEMBER 1983

Preparation and Properties of the Anodic Al_2O_3 Film on InP and $In_{0.53}Ga_{0.47}As$

Nobuhiko Susa and Felix Schmitt[1]

Musashino Electrical Communication Laboratory, Nippon Telegraph and Telephone Public Corporation, Musashino-shi, Tokyo 180, Japan

ABSTRACT

Optical and electrical properties of the anodic Al_2O_3 film were measured. Leakage current was small near the breakdown voltage and ohmic conduction may be a dominant process, because of a few trap centers. The anodic Al_2O_3 film is superior with respect to leakage current to the plasma CVD Si_xN_y film, which is used for planar type photodetectors. The Nss values were 9×10^{11} and 8×10^{12} $eV^{-1} \cdot cm^{-2}$ for InP and $In_{0.53}Ga_{0.47}As$, respectively. The refractive indexes were 1.85+0.08. The oxide was found to be suitable for selective diffusion masks. The measured results indicate that the Al_2O_3 film is useful in various kinds of devices.

III-V compound semiconductors, such as InP, are attractive materials for the light emitting diode (LED), laser diode (LD), photodiode (PD), avalanche photodiode (APD), and field effect transistor (FET). This is because they have direct bandgap and larger low field electron mobilities than Si. Insulators are important for these devices, as passivation film, antireflection coating, selective diffusion mask, insulation for MIS structure, and film for selective epitaxial growth. Various kinds of films, such as CVD SiO_2 (1-3), plasma CVD Si_xN_y (4), CVD, anodic and plasma anodic Al_2O_3 (5-9), native anodic oxide (10, 11), and plasma native oxide (12) have been studied.

Recently, anodic Al_2O_3 film has been successfully employed for MIS diodes with low interface-state density (6) and MIS-FET with high electron mobility on InP (7).

In the present experiment, optical and electrical properties of the anodic Al_2O_3 film were measured for application to various kinds of devices. The film was also evaluated as a selective diffusion mask and antireflection coating.

Preparation of Anodic Al_2O_3 Film

Anodic Al_2O_3 films were formed by anodization of vacuum-deposited Al on InP and InGaAs. The Al was of 99.999% purity. In the previous work, the AGW (6) electrolyte was mixed using a 3% aqueous solution of tartaric acid and propylene glycol of 1:9 by volume; in the present work, phosphorous acid was tried in place of tartaric acid. The Al films were anodized at a constant current of 1 mA/cm² under dark condition. Figure 1 shows typical cell voltage *vs.* oxidation time. The original Al thickness was 940Å and the Al_2O_3 film formed was 1700Å thick. The offset voltage at $t = 0$ is attributed to the ohmic resistance of electrolyte and InP. When Al anodization was terminated, the voltage suddenly increased, as shown in Fig. 1, and the process was stopped at this point.

The InP substrates were washed in hot trichloroethylene, acetone, and ethanol. They were etched with $2H_2SO_4:1H_2O_2:1H_2O$ for 30 sec and in 2.5% bromine-methanol for 2 min before Al deposition. In the present experiment, the anodic Al_2O_3 film was also formed on $In_{0.53}Ga_{0.47}As$. The InGaAs layers were grown by hydride vapor phase epitaxy (13) on (100) 1° off toward <111> InP substrates with 5×10^{18} cm^{-3} carrier concentration. Ternary layer thicknesses were 4-5 μm. The n-type InGaAs layers, $7\text{-}9 \times 10^{15}$ cm^{-3}, were doped with sulfur. Lattice mismatches were less than 0.1%. The InGaAs surfaces were briefly etched with $2H_2SO_4:1H_2O_2:1H_2O$ solution for 15 sec at room temperature and rinsed with deionized water before the Al deposition.

It is important to eliminate water completely from the crystal surfaces before the Al deposition. When H_2O remains at the interface, it is decomposed into H_2 and O_2 through electrolysis. This causes bubbles and loosens the Al_2O_3 film adhesion. No preoxidation heat-treatment, as proposed by others (6), is necessary when a water-free surface is used before the Al

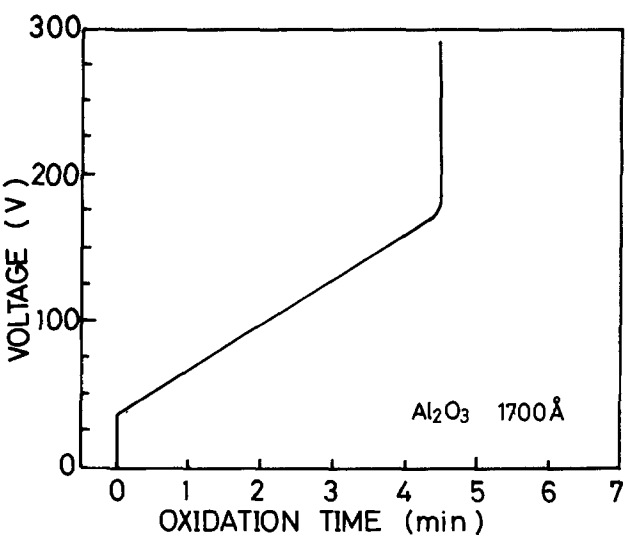

Fig. 1. Cell voltage as a function of Al oxidation time

[1] On leave from the Heinrich Hertz Institute fur Nachrichtentechnik GmbH, Einsteimifer 37, D-1000 Berlin 10, Germany.

Key words: electrical properties, optical properties, passivation film, silicon nitride.

deposition. Figures 2 (a and b) show phase-contrast photographs of oxide surfaces for water-free and -contaminated surfaces.

The relation between the thickness of Al consumed and Al_2O_3 films formed at 28°C is shown in Fig. 3. The Al_2O_3/Al thickness ratio was 1.8. The ratio was 1.9 when the film was anodized at 50°C. The etch rates in 5% HF for the Al_2O_3 formed at 28° and 50°C were 1440 and 1900 Å/min, respectively. This suggests that oxides formed at higher temperature may be more porous. This was confirmed by leakage current measurement showing larger current.

All Al_2O_3 films were uniform in thickness. The color was blue for 1500Å and changed to yellow at about 2000Å thickness.

Electrical Properties

Interface characteristics.—Interface state densities (Nss) for anodic Al_2O_3-InP and Al_2O_3-$In_{0.53}Ga_{0.47}As$ were evaluated by the Terman method (14). $In_{0.53}Ga_{0.4}As$ is a promising material for use as an FET, because of its large electron mobility. Samples measured were all n-type. The Au-Ge-Ni alloyed contact was employed as an ohmic contact. Al dots with 140 or 194 μm diam were formed by a photolithographic lift-off process. The Al film was evaporated on the oxide with a resistance heater. Capacitance was measured at room temperature by changing bias voltage at a rate of 70 mV/sec in the 10 kHz-10 MHz frequency range. Heat-treatment effects on Nss were also measured.

InP.—Figure 4 shows typical capacitance *vs.* bias voltage characteristics for an unannealed InP-Al_2O_3 MIS diode at 10 kHz, 100 kHz, and 1 MHz. Bias was applied from depletion to accumulation. The InP crystals were of (100) orientation and the carrier concentration was 5×10^{15} cm^{-3}. The Al_2O_3 was 1550Å thick. The Al electrode diameter was 140 μm. The frequency dispersion in the accumulation is less than 1% in the 10 kHz to 1 MHz range, as reported in the previous work (6). No change was observed in these characteristics after heat-treatment, which will be described later. Hysteresis, however, was observed as shown in Fig. 5 for frequencies measured. Hysteresis still exists after annealing.

Nss was estimated from the C-V measurement at 1 MHz. Figure 6 indicates the results with and without heat-treatment. In this case, samples were annealed in the H_2 gas flow at 400° and 500°C for 30 min. Nss can be reduced by the annealing process, mainly in the region between midgap and conduction band. For high temperature annealing, the Nss is reduced to 9×10^{11} $eV^{-1} \cdot cm^{-2}$, as shown in Fig. 6.

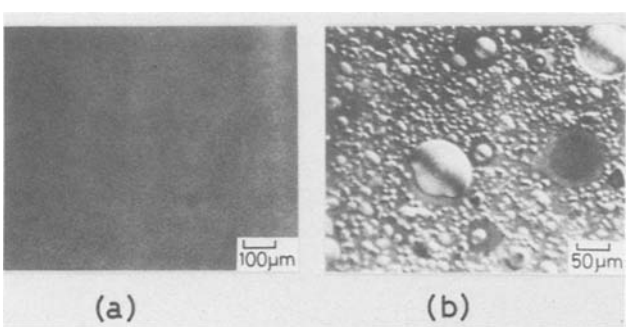

Fig. 2. Surfaces for anodic Al_2O_3 films for (a) water-free and (b) water-contaminated InP wafers before Al deposition.

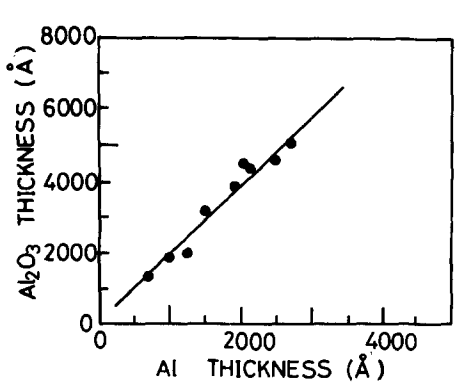

Fig. 3. The anodic Al_2O_3 thickness as a function of the Al thickness.

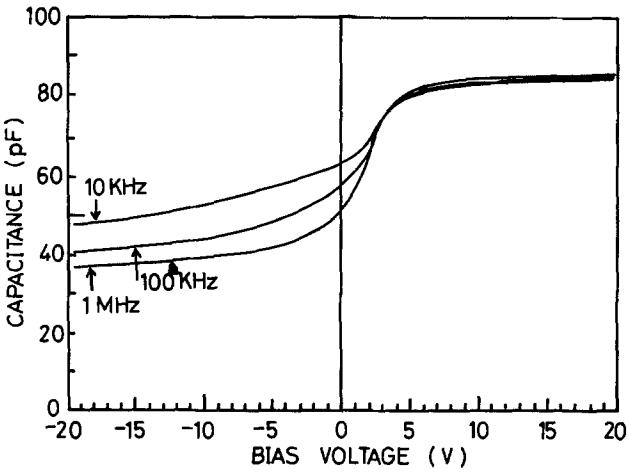

Fig. 4. Capacitance-voltage characteristics for Al_2O_3/n-InP with 5×10^{15} cm^{-3} diode measured at 10 kHz, 100 kHz, and 1 MHz.

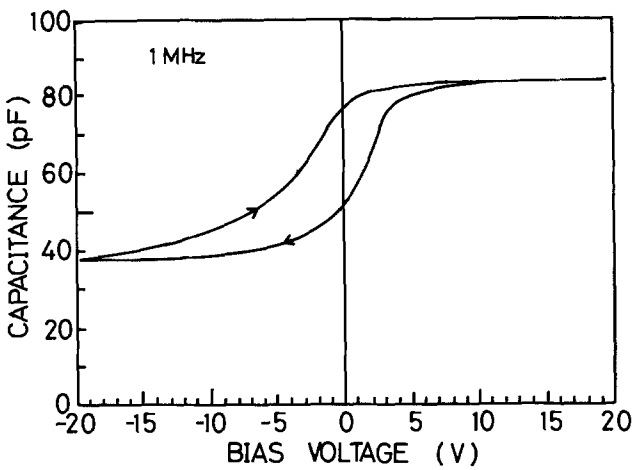

Fig. 5. Hysteresis curve of capacitance for anodic Al_2O_3/n-InP diode.

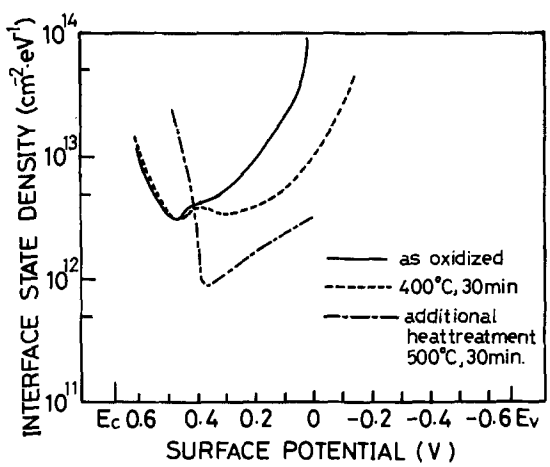

Fig. 6. Interface state densities for anodic Al_2O_3 (as oxidized and annealed)/InP diode.

$In_{0.53}Ga_{0.47}As$.—Interface properties between insulator and $In_{0.53}Ga_{0.47}As$ have been studied for plasma CVD Si_3N_4 (15), native plasma oxide (9), and CVD SiO_2 (16). Very recently anodic Al_2O_3, combined with native oxide, has been successfully applied to $In_{0.53}Ga_{0.47}As$ (8). In the present experiment, the Al_2O_3-InGaAs interface properties were measured.

Figure 7 shows the C-V characteristics measured at several frequencies. Here, the Al_2O_3 film was annealed at 300°C for 20 min in the H_2 gas flow. The Al dot diameter was 194 μm. The oxide was 1250Å thick. The C-V curves exhibited a minimum at 10 and 40 kHz frequencies, which is not observed in InP. This might be due to a faster generation-recombination rate in the inversion, caused by the smaller bandgap. These curves also exhibit hysteresis. Frequency dispersion was very small in the accumulation, as shown in Fig. 7.

The Nss value, calculated from the capacitance at 1 MHz, is shown in Fig. 8. Annealing at 300°C for 20 min in the H_2 flow reduces the value to 8×10^{12} $eV^{-1} \cdot cm^{-2}$. This value is, however, large enough to diminish effective channel mobility of an MIS-FET (17). Further improvements in the cleaning process before Al evaporation and the anodization process are required.

Leakage currents.—The characteristic of small leakage current as well as large breakdown voltage is desirable when insulator film is actually applied to devices such as the planar photodiode. Leakage currents were compared for anodic Al_2O_3 film, plasma CVD Si_xN_y, Al_2O_3 film deposited by electron beam evaporation, and native oxide of InP.

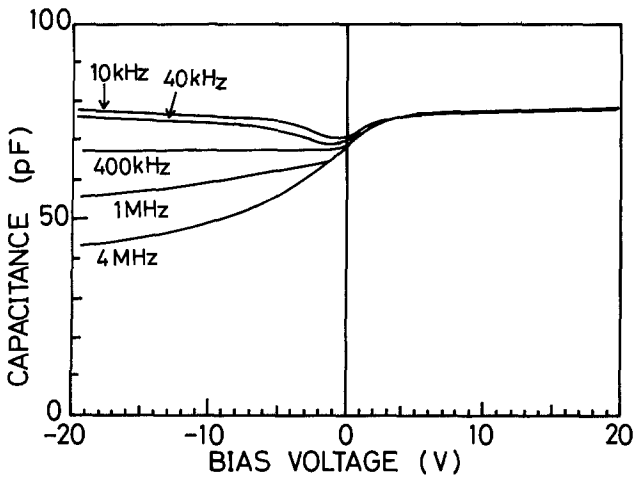

Fig. 7. Capacitance-voltage characteristics for anodic Al_2O_3/$In_{0.53}Ga_{0.47}As$ diode at several frequencies.

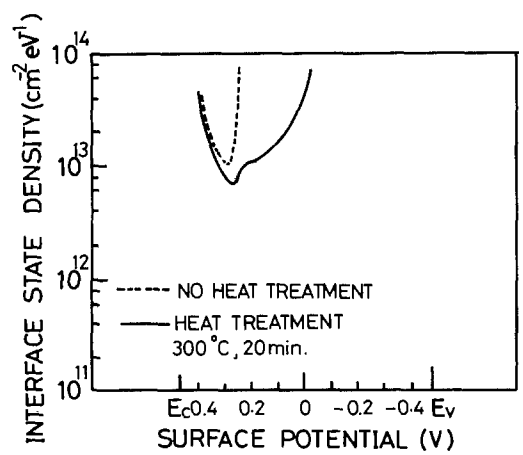

Fig. 8. Interface state densities for anodic Al_2O_3/$In_{0.53}Ga_{0.47}As$ diode, as oxidized and annealed.

The p-CVD Si_xN_y film was deposited by using the SiH_4-NH_3-N_2 gas system and mainly used for planar-type photodetectors (4). For the native oxide, InP with 5×10^{15} cm^{-3} carrier concentration was oxidized under illumination in AGW solution of 3% tartaric acid and propylene glycol with a 1:3 mixing ratio by volume. The pH value was adjusted to 7.0 using NH_4OH. The samples were prepared at a constant 0.5 mA/cm^2 current density. Thicknesses for native oxide and Al_2O_3 film deposited by electron beam were 3000 and 2800Å, respectively. Thicknesses were 3000 and 3400Å for the Si_xN_y and anodic Al_2O_3, respectively.

Leakage currents measured are shown in Fig. 9a as a function of reverse bias voltage. The Al dot diameter was 140 μm. The Al electrodes were positively biased. The electron beam-deposited Al_2O_3 film showed relatively large leakage current. Leakage current for the InP native anodic oxide film was largest. Its breakdown electric field strength was 4-5 $\times 10^5$ V/cm, lower by one order than that of the other films. The breakdown fields were 8.1×10^6 and 6.4×10^6 V/cm for the silicon nitride and the Al_2O_3 films, respectively. Although the anodic Al_2O_3 exhibits a breakdown field lower than that for the Si_xN_y, leakage current was smaller near the breakdown voltage, as shown in Fig. 9a. This is favorable for a planar-type APD, where a large electric field is applied to the insulator.

The plasma CVD Si_xN_y film exhibited steeper current increase near the breakdown. In order to examine the different leakage current dependence on bias voltage at high reverse bias voltage, conduction mechanisms were studied for the anodic Al_2O_3 and plasma CVD Si_xN_y films.

It is well known that Schottky and Poole-Frenkel emissions are dominant processes in thick insulator film. The relationships between current and electric field, calculated for both mechanism, are given by Eq. [1] and [2] (18)

$$J_s = A^*T^2 \exp\left[-q(\phi_b - \sqrt{qE/4\pi\epsilon_0\epsilon_i})/kT\right] \quad [1]$$

$$J_{pF} = C \cdot E \cdot \exp\left[-q(\phi_b - \sqrt{qE/\pi\epsilon_0\epsilon_i})/kT\right] \quad [2]$$

Here, A^* is the effective Richardson constant, ϕ_b is barrier height, ϵ_i is the relative dielectric constant of

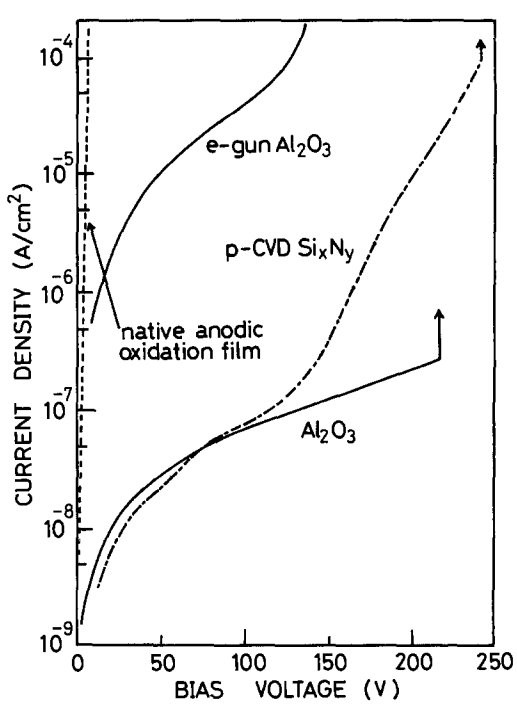

Fig. 9a. Leakage current densities vs. applied voltage for InP native oxide, plasma CVD Si_xN_y, and anodic Al_2O_3 films.

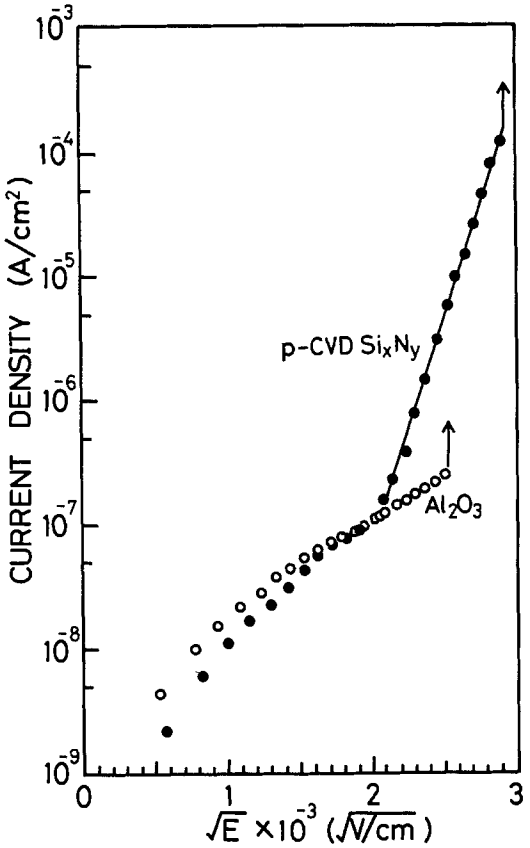

Fig. 9b. Leakage current densities vs. $\sqrt{E}$ for plasma CVD Si_xN_y and anodic Al_2O_3.

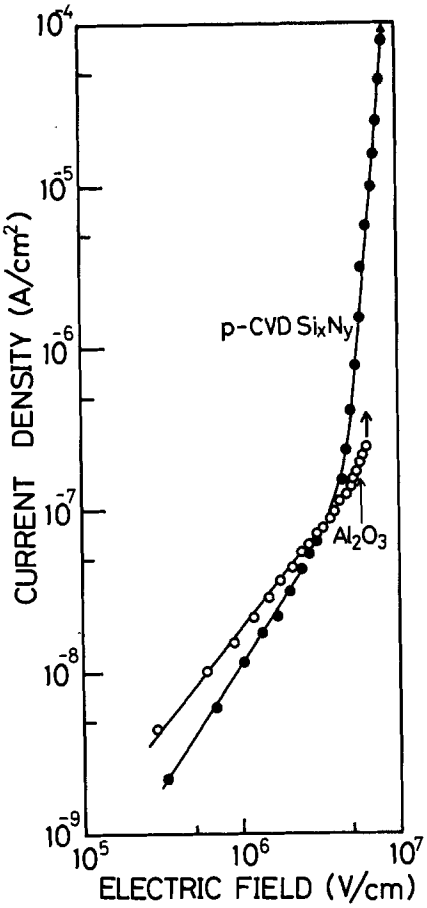

Fig. 9c. Leakage current densities vs. electric field for plasma CVD Si_xN_y and anodic Al_2O_3.

the insulator, and C is a constant, independent of field and temperature.

To determine which of these mechanisms is responsible for the strong current increase in the silicon nitride near the breakdown, log (J) *vs.* $\sqrt{E}$ is plotted as shown in Fig. 9b. The silicon nitride film gave a straight line and the dielectric constant was calculated from the slope. The values $\sqrt{\epsilon_i}$ were 3.76 under the assumption of the Poole-Frenkel mechanism and 1.88 for the Schottky emission.

Optical measurement for the Si_xN_y gives a refractive index of 1.95, similar to the value, $\sqrt{\epsilon_i}$, obtained by assuming Schottky emission. This suggests that the conduction occurs by Schottky emission in the silicon nitride, rather than by the Poole-Frenkel mechanism. The electric conduction in the present SiH_4-NH_4-N_2 film was different from that for the SiH_4-NH_3-Ar (19) and SiH_4-N_2-Ar film (20), caused by the Poole-Frenkel mechanism.

The anodic Al_2O_3 films also appeared to give a straight line in Fig. 9b. However, since dielectric constants calculated from the slope were too large compared with the value calculated from the Al_2O_3 refractive index, the conduction in the Al_2O_3 film cannot be explained by the two processes described above. The data were replotted as log (J) *vs.* log (E) in Fig. 9c. The straight line for the anodic Al_2O_3 may indicate ohmic conduction, as in the P_3N_5 insulator film for InP (21). This suggests few trap centers in the anodic Al_2O_3 film.

Electrical as well as optical properties are summarized in Table I.

Optical Properties

The refractive index is an important parameter when an insulator is applied to optical devices as an antireflection coating. Reflectance was measured for InP, whose surface was coated with anodic Al_2O_3 film. The measurement method was similar to the previous one (4). The film thickness was 1900Å. The reflectance is shown in Fig. 10, as a function of wavelength. The minimum value was 5.1% at 1.35 μm, comparable to the value for plasma CVD Si_xN_y film. This value was larger than a theoretically expected value of 0.5%, probably due to surface roughness of the InP and the film. The refractive index, calculated from the thickness and the minimum wavelength, was 1.78 at 1.35 μm. The indexes measured for several samples were

Table I. Optical and electrical properties for various kinds of insulators

	Anodic Al_2O_3 (present work)	Anodic Al_2O_3 (6)	Plasma anodic Al_2O_3 (9)	Al_2O_3 deposited by E-gun (present work)	Plasma CVD Si_xN_y (4)
Electric field strength at V_B (V/cm)	(5-8) × 10^6	2-3 × 10^6	(1.2-1.6) × 10^6	(5.3-6.0) × 10^6	~8 × 10^6
Resistivity at 1/2 V_B (Ω-cm)	(0.3-9) × 10^{14}	10^{15}	5 × 10^{10}-10^{12}	(4-13) × 10^{10}	~3 × 10^{13}
Refractive index at 1.3 μm	1.85 ± 0.08	—	1.72	1.85 ± 0.05	1.95-2.0
Relative dielectric constant (1 MHz)	8.1 ± 0.4	8.1-8.7	~7	6.8 ± 0.5	7.2 ± 0.3

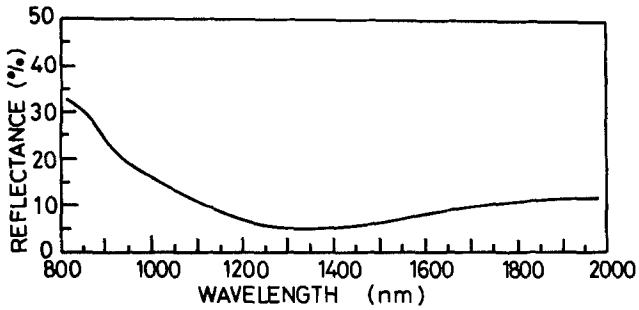

Fig. 10. Reflectance of anodic Al_2O_3/InP as a function of wavelength. The Al_2O_3 thickness is 1900Å.

1.85 ± 0.08 at about 1.3 μm. The film is suitable for antireflection coating, because the Al_2O_3 refractive index value is similar to the square root of the InP refractive index of about 3.4.

Selective Diffusion

Selective diffusion is an imperative technique for an LD and an APD with a planar structure. Some kinds of insulators resulted in an abnormal diffusion wing (4) at the p^+-n junction periphery, caused by the unusually fast lateral diffusion along the mask-InP interface, when an acceptor, such as Zn or Cd, was preferentially diffused into n-InP. Even if no wing was observed, a planar diode with a p^+-n junction sometimes showed large leakage current (4, 22). In the present experiment, the anodic Al_2O_3 was evaluated as a selective diffusion mask for InP.

Figure 11 shows the cleaved and stain-etched surface of InP diffused with Zn using anodic Al_2O_3 film as a selective diffusion mask. Diffusion was accomplished by using Zn_2P_3 at 520°C for 80 min. The 1550Å thick Al_2O_3 was etched with 5% HF aqueous solution. No diffusion wing can be seen after stain-etching with $1K_3Fe(CN)_6$:2KOH:$8H_2O$, as shown in Fig. 11.

Leakage current was measured for a photodiode with a planar structure, which was fabricated by Zn-selective diffusion at 520°C for 1 hr. The p^+-layer was 4.5 μm thick. The film thickness was 1900Å. The hole diameter for the diffusion was 140 μm. The n-InP has a 5×10^{15} cm^{-3} carrier concentration. The dark current *vs.* applied voltage is shown in Fig. 12. The diode exhibits a low dark current up to breakdown. These results reveal that the anodic Al_2O_3 film is suitable for use as a selective diffusion mask.

Conclusion

Optical and electrical properties are summarized in Table I. The data for plasma-anodic Al_2O_3 (9), Al_2O_3 deposited by electron beam, and plasma CVD Si_xN_y film (4) are also described for comparison. The anodic Al_2O_3 film is superior to the plasma CVD Si_xN_y, which is used for planar-type photodetectors, with respect to leakage current. The Al_2O_3 film shows lower leakage current near the breakdown. Ohmic conduction may be dominant in the anodic Al_2O_3, probably due to there being a few trap centers. On the other hand, leakage current for the plasma CVD silicon nitride was determined by Schottky emission, which exhibits steeper bias voltage dependence.

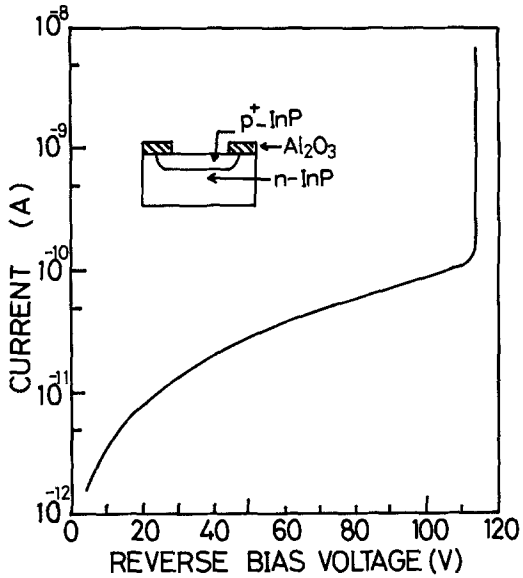

Fig. 12. Dark current *vs.* reverse bias voltage for a planar InP diode fabricated by Zn selective diffusion with anodic Al_2O_3 film.

Frequency dispersion for the Al_2O_3 MIS capacitance was less than 1% in the accumulation. The Nss for the Al_2O_3-InP was smaller than that for $In_{0.53}Ga_{0.47}As$. The Nss values can be reduced by annealing in H_2 gas flow, and 9×10^{11} and 8×10^{12} $eV^{-1} \cdot cm^{-2}$ for InP and $In_{0.53}Ga_{0.47}As$, respectively.

Refractive indexes, measured from the thickness and minimum wavelength, were 1.85 ± 0.08. The Al_2O_3 film is suitable for antireflection coating.

No abnormal diffusion wing was observed in the selective diffusion for InP using the anodized Al_2O_3 film. Dark current for a planar InP PD having the Al_2O_3 film was small. The anodic oxide can be used for a selective diffusion mask.

Thus, the anodic Al_2O_3 film is concluded to be useful for optoelectronic devices.

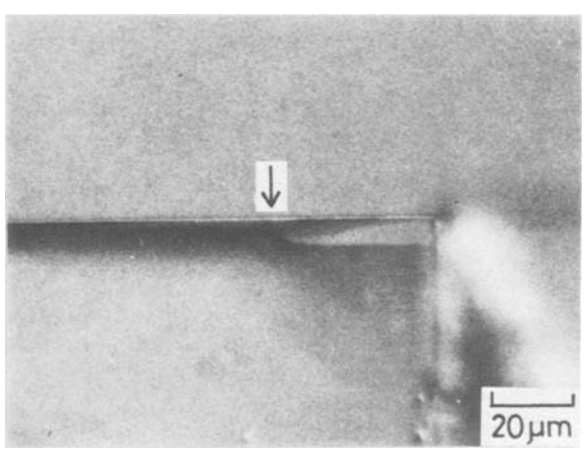

Fig. 11. Cleaved and stain-etched surface of n-InP with 5×10^{15} cm^{-3}, diffused with Zn by using anodic Al_2O_3 as selective diffusion mask.

Acknowledgments

The authors would like to express their gratitude to Dr. Tatsuya Kimura, Dr. Hiroshi Kanbe, and Dr. Osamu Mikami for helpful discussions. They are also grateful to Hiroaki Ando for assistance in the area of diffusion, Yoshiharu Yamauchi for crystal growth, and Rie Nojima for technical assistance.

Manuscript submitted Jan. 31, 1983; revised manuscript received June 29, 1983.

Nippon Telegraph and Telephone Public Corporation assisted in meeting the publication costs of this article.

REFERENCES

1. L. Meiners, D. L. Lile, and D. A. Collins, *J. Vac. Sci. Technol.*, **16**, 1458 (1979).
2. J. Stannard, *ibid.*, **16**, 1462 (1979).
3. J. D. Oberstar, B. G. Streetman, and E. A. Sammann, *Thin Solid Films*, **81**, 347 (1981).
4. N. Susa, H. Kanbe, H. Ando, and Y. Ohmachi, *Jpn. J. Appl. Phys.*, **19**, L675 (1980).
5. M. Okamura and T. Kobayashi, *ibid.*, **19**, 2143 (1980).
6. T. Sawada, K. Ishii, and H. Hasegawa, *ibid.*, Supplement 21-1, 397 (1982).

7. T. Sawada and H. Hasegawa, *Electron. Lett.*, **18,** 742 (1982).
8. K. Ishii, T. Sawada, H. Ohno, and H. Hasegawa, *ibid.*, **18,** 1034 (1982).
9. Y. Hirayama, H. M. Park, F. Koshiga, and T. Sugano, *Inst. Phys. Conf. Ser.*, **63,** 341 (1981).
10. A. Yamamoto and C. Uemura, *Electron Lett.*, **18,** 63 (1982).
11. K. P. Pande and G. G. Roberts, *J. Vac. Sci. Technol.*, **16,** 1470 (1979).
12. B. Tell, R. E. Nahory, R. F. Leheny, and J. C. DeWinter, *Appl. Phys. Lett.*, **39,** 744 (1981).
13. N. Susa, Y. Yamauchi, H. Ando, and H. Kanbe, *Jpn. J. Appl. Phys.*, **19,** L17 (1980).
14. L. M. Terman, *Solid-State Electron.*, **5,** 285 (1962).
15. A. S. H. Liao, R. F. Leheny, R. E. Nahory, and J. C. DeWinter, *IEEE ED Lett.*, **EDL-2,** 288 (1981).
16. R. Kaumanns, J. Selders, and H. Beneking, *Inst. Phys. Conf. Ser.*, **63,** 329 (1981).
17. Y. Shinoda and T. Kobayashi, *J. Appl. Phys.*, **52,** 6386 (1981).
18. S. M. Sze, "Physics of Semiconductor Devices," pp. 402-407, Wiley-Interscience, New York (1981).
19. A. K. Sinha and T. E. Smith, *J. Appl. Phys.*, **49,** 2756 (1978).
20. M. Maeda and Y. Arita, *ibid.*, **53,** 6852 (1982).
21. T. Kobayashi and Y. Hirota, *Electron. Lett.*, **18,** 180 (1982).
22. N. Susa, Y. Yamauchi, H. Ando, and H. Kanbe, *IEEE ED Lett.*, **EDL-1,** 55 (1980).

Reactive Ion Etching of Aluminum/Silicon

R. W. Light*

Sandia National Laboratories, Albuquerque, New Mexico 87185

ABSTRACT

High resolution, reproducible dry etching of Al/Si can be achieved using BCl_3 and Cl_2 mixtures in a hexagonal cathode reactive ion etching system. The etch directionality is a function of the BCl_3/Cl_2 composition, the number of wafers in the reactor, and the d-c self-bias voltage. Increases in the concentration of etching species produced by raising the percentage of Cl_2 in BCl_3 and by decreasing the wafer load increases the total etch rate while enhancing the isotropic etch rate relative to the anisotropic etch rate. The d-c self-bias voltage (or applied rf power) appears to partition the active etching species between isotropic etching and anisotropic etching without affecting the total etch rate.

Dry etching of Al and Al alloys is one of the more challenging of the techniques required for the fabrication of fine line integrated circuits. Among the problems with these processes are poor linewidth control, polymer deposition, moisture sensitivity, nonreproducibility, slow etching Al_2O_3 on the Al surface, nonuniformity, inadequate end-point detection techniques, poor photoresist integrity, toxicity and reactivity of the etch gases, and residues remaining on the etch surface (1-5). A number of these problems can be overcome by a judicious selection of process parameters. A variety of chlorinated gases including CCl_4, Cl_2, $CHCl_3$, CCl_2F_2, HCl, $SiCl_4$, BCl_3, and PCl_3 (5-19) have been used to etch Al and Al alloys. Recently interest has been shown in BCl_3 and Cl_2 etch gas mixtures (9, 11, 17, 20-22). Plasma processes using these mixtures offer several advantages over chlorocarbon-based processes including freedom from polymeric deposits and less moisture sensitivity due to the rapid reaction of BCl_3 with residual water vapor. Fine line pattern definition is affected both by the etching chemistry and the related physical plasma parameters. By etching under conditions of energetic ion bombardment, linewidth control of small dimensions can be achieved.

This work describes reactive ion etching of Al/1% Si with BCl_3 and Cl_2 mixtures using a hexagonal cathode etching apparatus. The Al/Si, photoresist, silicon, and silicon dioxide etch rates are discussed as functions of the BCl_3/Cl_2 composition, reactor loading, flow rates, d-c self-bias voltage, and pressure. The anisotropy of the etching and the rate of photoresist erosion are examined during the etch and during the overetch period. The trends established in this study are integrated to yield an efficient and effective etching process.

Experimental

Samples.—One hundred millimeter diameter silicon wafers are coated with SiO_2 by low pressure chemical vapor deposition and then with 1.0 μm of Al/1% Si by evaporative deposition. These wafers are coated with 1.5 μm of KTI 1450 positive photoresist and patterned with 2, 3, 4, and 5 μm lines and spaces. Following development the samples are baked at 90°C for 30 min. A second type of sample is prepared by deposition of 5000Å of SiO_2 on <100> orientation, 3-6 Ω-cm, phosphorus-doped silicon wafers, patterning, and wet etching to leave one-half of the wafer bare silicon and the other half SiO_2. A grid pattern of KTI 1450 photoresist is applied over the wafer. These wafers permit the measurement of the SiO_2 and Si etch rates on a single wafer.

Etching.—A Plasma Therm Incorporated, Hexetch 640 reactive ion etching system with a 3000W, 13.56 MHz rf power supply is used for this study. This reactor holds 24, 100 mm diam wafers on a central, vertically configured, hexagonal cathode enclosed in a bell jar. Rf power is applied to the cathode and can be controlled either as watts input or as the d-c self-bias voltage developed on the cathode. The greater the rf power applied, the larger (more negative) the d-c self-bias voltage becomes. The wafer holding cathode and the bell jar are temperature regulated at 45°C. SiO_2-coated wafers are placed in wafer locations not containing Al/Si wafers. This etching system contains both a cryopump to minimize residual water vapor during the initial pump down and a throttle valve controlled turbopump for use during the etching process. The system is cryopumped to below 5×10^{-5} Torr before the introduction of the etching gases. The BCl_3 and Cl_2 flows are regulated using automatic mass flow controllers. The end point is determined by observing the intensity change in the 396 nm Al emission line as the etch progresses.

Etch rates are determined from the 396 nm Al emission signal by profilometer measurements and by scanning electron microscopy (SEM) of 2 and 3 μm Al/Si lines on transversely sectioned wafer samples.

* Electrochemical Society Active Member.
Key words: metals, plasmas, integrated circuits.

Results and Discussion

Al_2O_3 removal.—Aluminum, when exposed to air, forms a thin layer of aluminum oxide, Al_2O_3, on the surface. This thin oxide surface layer can be a barrier to etching if the Al/Al_2O_3 etch rate ratio is sufficiently low and has been reported to result in nonuniform etching of the underlying Al layer (1, 5, 8, 9). The presence of the Al oxide layer produces an initiation period in which the onset of Al etching is delayed until the inhibiting layer is etched away. This is a potential problem if some method of process monitoring is not available and a timed etch is being utilized. Figure 1 is a typical end-point trace using the 396 nm Al emission signal with an induction period of 0.7 min. As illustrated in Fig. 2, the d-c bias voltage is the major factor affecting the length of the induction period. The decrease in induction time with increasing negative bias voltage suggests that the Al_2O_3 etch rate increases with the energy of ion bombardment. The induction time is insensitive to the BCl_3/Cl_2 composition from 30 to 50% Cl_2 in BCl_3 but lengthens when the Cl_2 percentage is increased to 70%. With 100% Cl_2 no etching is observed at −400V even after 20 min. These results are consistent with BCl_x (x = 0-3) species being involved with the reduction of Al_2O_3, presumably removing oxygen as boron oxide compounds (5, 9, 21). A loading effect is not observed for the etching of the Al_2O_3 layer and the data in Fig. 2 include from 1 to 24 wafers in the etching system.

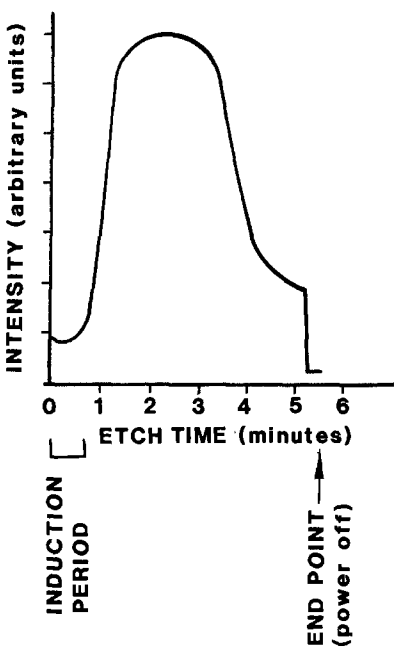

Fig. 1. 396 nm Al emission end-point trace obtained for one wafer, 70% Cl_2, −400V, 10 mTorr, and 50 sccm.

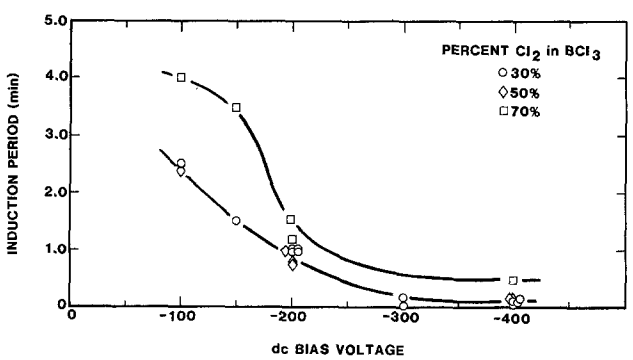

Fig. 2. The effect of d-c self-bias voltage and Cl_2 percentage on the induction time at 10 mTorr and 50 sccm.

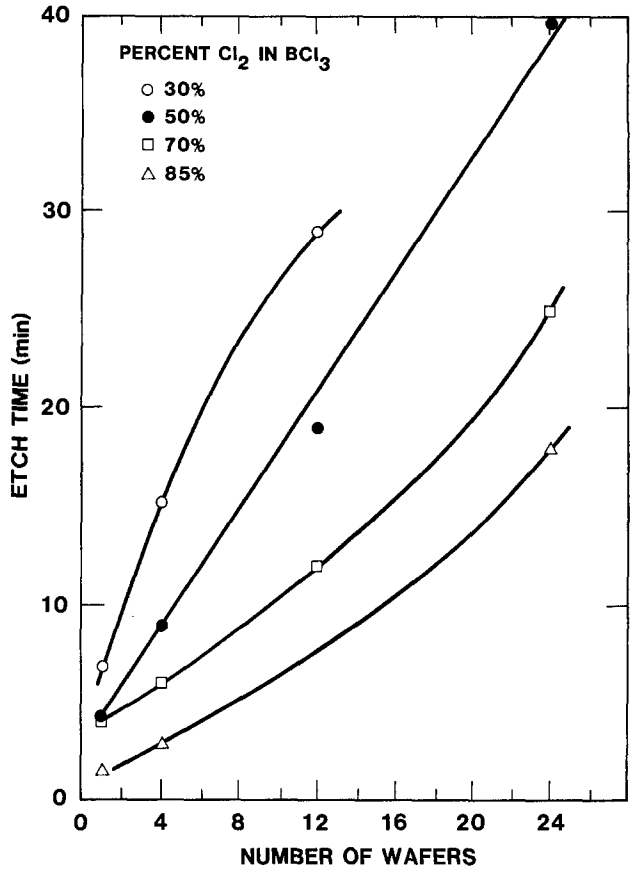

Fig. 3. The loading effect for Al/Si etching

Al/Si etch rate.—The etch rate of Al/Si as determined by monitoring the 396 nm Al emission is a function of the BCl_3/Cl_2 composition, the number of wafers in the reactor, and the total flow rate. This etch rate is independent of the d-c self-bias voltage over the range investigated in this study, −100 to −400V (250-1000W input power). As evident in Fig. 3, a typical loading effect is observed with the Al/Si etch time for a 1.0 μm film (the inverse of the etch rate) nearly linearly dependent on the number of wafers in the reactor (23). These data also demonstrate that the etch rate is higher and the loading effect less severe (lower slope) at higher Cl_2 percentages. This rate enhancing effect of Cl_2 has been previously observed with BCl_3 and may be a consequence of Cl_2 being a more efficient source of the active etching species for Al than is BCl_3 (5, 17, 21, 22). The identity

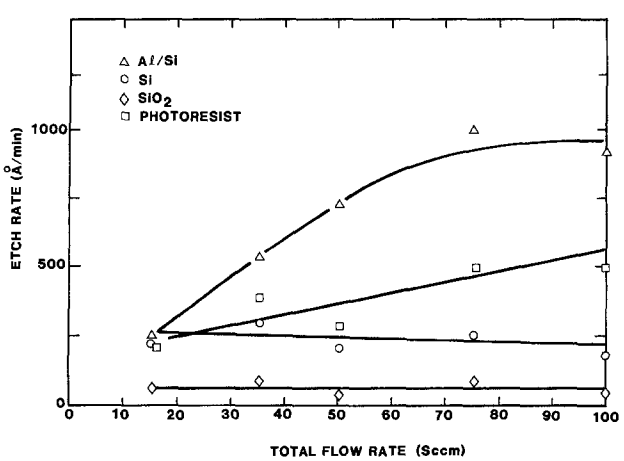

Fig. 4. The effect of flow rate on the Al/Si, Si, SiO_2, and photoresist etch rates. The experimental conditions are four wafers, 30% Cl_2, −200V, 10 mTorr, and 50% overetch.

of the active etching species is not clear but may be atomic chlorine, molecular chlorine, Cl^+, Cl_2^+, or, perhaps, a combination of these (5, 21, 24). Figure 4 illustrates the effect of total flow rate at 30% Cl_2 in BCl_3 on the etch rates of Al/Si, Si, SiO_2, and photoresist. The etch rate of Al/Si increases rapidly between 15 and 50 sccm and begins to level out between 50 and 100 sccm. The positive slope of the flow rate curve and lack of voltage (power) dependence of the Al/Si etch rate suggests that the Al/Si etch rate is flow-rate limited and not limited by the generation rate of active species or by the residence time of the gas molecules in the discharge (25, 26). Increasing the pressure from 10 to 30 mTorr does not significantly change the total etch rate but can increase the linewidth nonuniformity within a wafer. At 30 mTorr a significant bull's-eye effect occurs with the outside of the wafer etching faster than the inside. The etch rate nonuniformity combined with the isotropic nature of the etch at this pressure (other conditions: −200V d-c bias voltage, 1-4 wafers in reactor, 30-70% Cl_2 in BCl_3, and 50-100 sccm total flow) results in the lines on the outer portion of the wafer being severely undercut. This nonuniform etching also tends to obscure the emission end-point signal.

Photoresist etch rate.—The d-c self-bias voltage, the Cl_2 percentage, the number of wafers in the reactor, and the total flow rate all affect the photoresist etch rate. The photoresist etch rate is insensitive to pressure over the 10-30 mTorr range. As shown in Fig. 5, the photoresist etch rate increases as the d-c self-bias voltage becomes more negative. This is consistent with an ion-enhanced etching mechanism in which more energetic positive ion bombardment leads to higher photoresist etch rates. A loading effect is also observed for the photoresist etch rate with a strong dependence on the Cl_2 percentage. As illustrated in Fig. 6, the loading effect is not ideal with the 50% Cl_2 data showing markedly nonlinear behavior. Since the active etching species of Al/Si and the photoresist may be the same, consumption of the active species by both materials may contribute to the observed loading effects. The data in Fig. 4 show an increase in photoresist etch rate with total flow rate. As mentioned for the Al/Si etch rate, this suggests that the photoresist etch rate is flow-rate limited at this bias voltage. Although the highest Al/Si etch rate occurs at 100 sccm, a consideration of both the Al/Si etch rate and the photoresist etch rate indicates

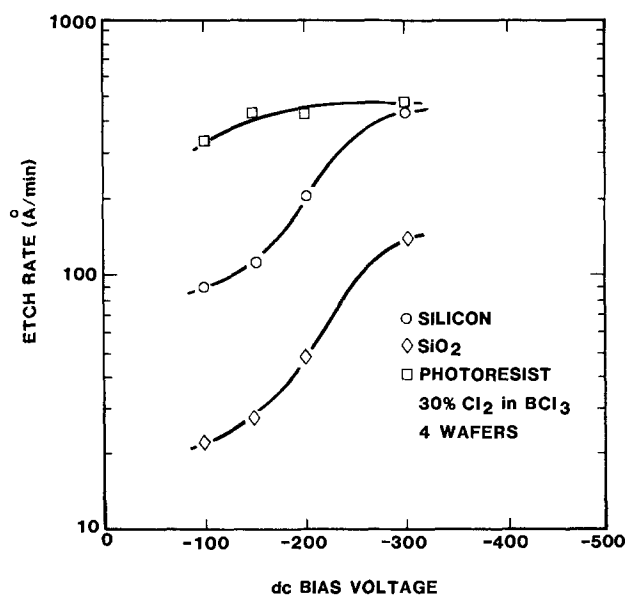

Fig. 5. The influence of the d-c bias voltage on the etch rate of photoresist, Si, and SiO_2 with four wafers, 30% Cl_2, 10 mTorr, 50 sccm, and 50% overetch.

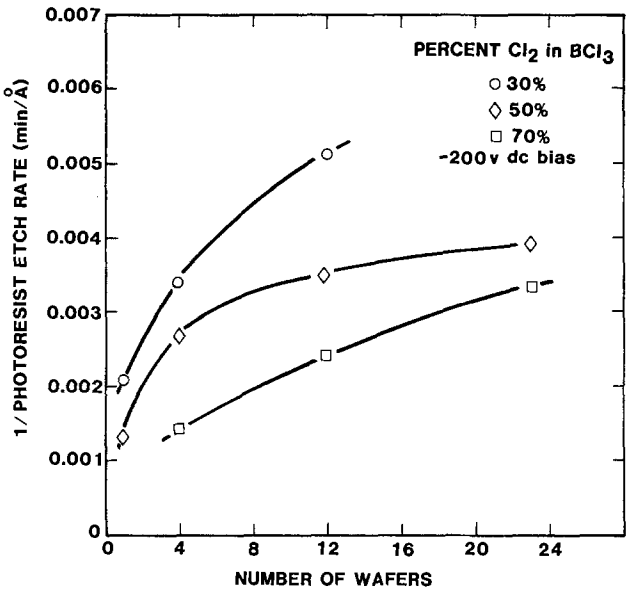

Fig. 6. The loading effect for photoresist etching at −200V, 10 mTorr, 50 sccm, and 50% overetch.

that the optimum Al/Si to photoresist etch rate ratio occurs at about 50 sccm total flow.

Si and SiO_2 etch rates.—The primary parameter affecting the etch rate of Si and SiO_2 is the d-c bias potential as shown in Fig. 5. The increase of etch rate with the d-c self-bias potential (more negative) suggests an ion-enhanced mechanism. The etch rate of Si is independent of wafer load, Cl_2 percentage, flow rate, and pressure in the −100 to −300V d-c bias range. A low d-c bias voltage would be indicated for cases in which a low Si etch rate is a primary consideration. This situation may occur if contact areas are not completely covered by photoresist and Si is exposed as the unmasked Al is cleared away. The etch rate of SiO_2 appears to depend only on the d-c self-bias voltage and remains between 30 and 50 Å/min under all conditions of Cl_2 percentage, loading, flow rate, and pressure.

Anisotropy.—In most applications of Al etching the goal is to achieve etching in the vertical direction only (anisotropic etching), thereby maximizing the cross-sectional area of the Al line. Figure 7 defines an etching model in which the vertical etch rate and the associated etch distance are composed of an isotropic etch rate component, i, and an anisotropic etch rate component, a. The lateral etch rate and associated etch distance are composed of the isotropic component only. Using this scheme, the percent anisotropy can be calculated from the following data and simple relationships: LW_{PR}, photoresist linewidth before etch, μm (base of line); LW_{Al}, Al linewidth after etch, μm (top of line); ET_{EP}, etch time to end point, min; ET_T, etch time to end point + overetch time, min; $LW_{PR} - LW_{Al} = \Delta LW$ linewidth change, μm

$$i = \frac{\Delta LW}{2(ET_T)}$$

$$i + a = 1.0\ \mu\text{m}/ET_{EP} \quad \text{for } 1.0\ \mu\text{m of Al/Si}$$

$$a = 1.0\ \mu\text{m}/ET_{EP} - i = 1.0\ \mu\text{m}/ET_{EP} - \frac{\Delta LW}{2(ET_T)}$$

$$\%\ \text{anisotropy} = \frac{a}{i + a} \times 100$$

$$\%\ \text{anisotropy} = \frac{1.0\ \mu\text{m}/ET_{EP} - \dfrac{\Delta LW}{2(ET)_T}}{1.0\ \mu\text{m}/ET_{EP}} \times 100$$

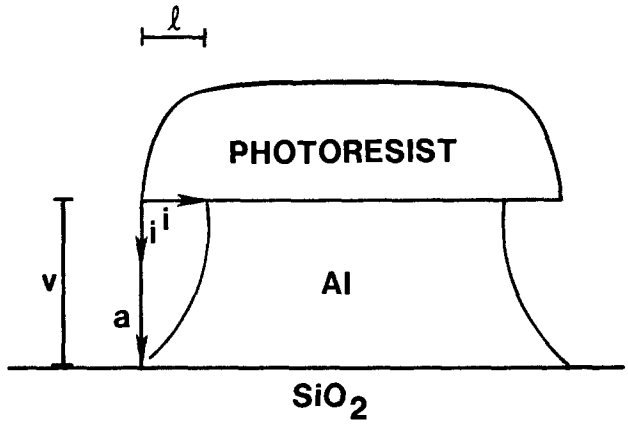

Fig. 7. The definition of the isotropic etch rate component, *i*, and the anisotropic etch rate component, *a*. *v* is the vertical etched distance and *l* the lateral etched distance.

Linewidth loss resulting from erosion of the photoresist is included in this calculation as part of the lateral etch rate and will generally limit the calculated percent anisotropy to 80-90%. Anisotropic etching is achieved by balancing the concentration of the active etching species and the d-c self-bias voltage. The steady-state concentration of the etching species as reflected in the etch time is a function of the BCl_3/Cl_2 composition and the wafer load. The isotropic etch rate appears to decrease with respect to the anisotropic etch rate as the availability of etching species becomes limited due to smaller Cl_2 percentages and/or larger wafer loads. An increase in the d-c bias voltage (more negative) at a constant Cl_2 percentage and wafer load increases the anisotropic etch rate and decreases the isotropic etch rate leaving the total etch rate or etch time constant. The total etch rate is controlled by the wafer load and the percent Cl_2 in BCl_3, and the d-c self-bias voltage serves to partition the active species between isotropic etching and anisotropic etching. These effects are illustrated in Fig. 8 where the percent anisotropy from the formula above is plotted against d-c bias voltage and etch time. In this figure, an increase in etch time implies a decrease in steady-state Cl_2 concentration. As the etch time is shortened by increasing the Cl_2 percentage and/or using smaller loads, the d-c bias voltage must be increased (more negative) to remain in the anisotropic region of the graph. Either increasing the pressure from 10 to 30 mTorr or increasing the total flow rate from 50 to 100 sccm shifts the boundary to the right, requiring higher d-c bias potentials to offset the apparent increase in active species concentration and lateral etch rate.

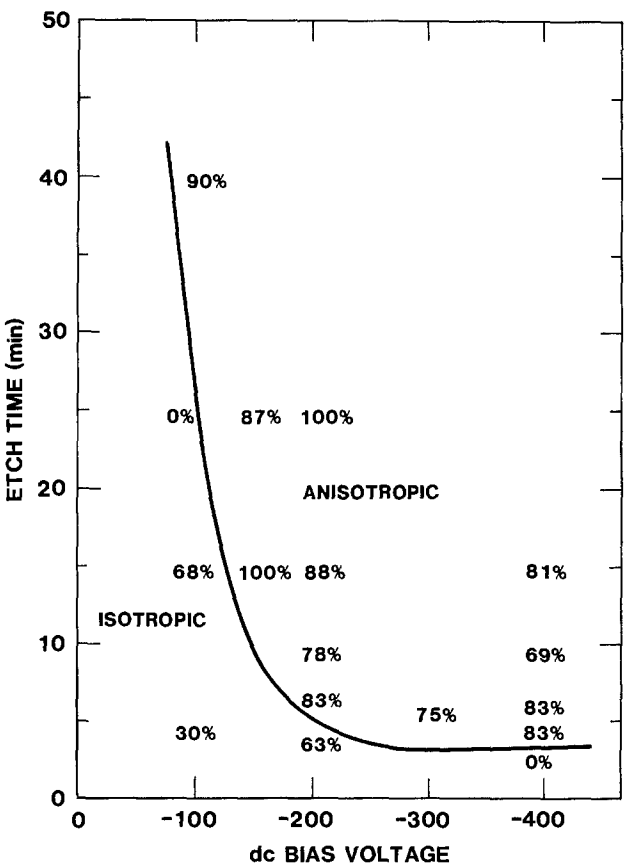

Fig. 8. The influence of etch time (to end point) and d-c bias voltage on the percent anisotropy at 10 mTorr and 50 sccm. An increase in etch time implies a decrease in the steady-state Cl_2 concentration due to an increase in the number of wafers in the reactor and/or a decrease in the Cl_2 percentage.

The largely phenomenological description of etch directionality presented above may be justified in terms of some simple etching models. Anisotropic etching is often interpreted as ion-enhanced etching on exposed surfaces perpendicular to the direction of ion bombardment with the vertical walls protected from etching by recombinants or polymer deposition (27). This model is in qualitative agreement with the data since the decrease in relative lateral etch rate with decreasing Cl_2 percentage or increasing load may be explained in terms of an increase in the relative concentration of BCl type recombinants (24). The dependence of line profile on the d-c bias voltage is consistent with ion-assisted chemistry occurring on the bombarded surfaces. Another view of directional etching emphasizes the importance of ion-neutral collisions in the plasma sheath in producing lateral etching (28, 29). Substitution of a more massive neutral, such as BCl_3, for a less massive neutral, such as Cl_2, would be expected to result in more randomization and increased lateral etching due to collisions with either Cl^+ or Cl_2^+ ions. In fact, the opposite is found to be true, the greater the fraction of BCl_3, the smaller the relative degree of lateral etching. However, this model does provide for an increase in anisotropy with increasing d-c bias voltage by indicating that the sheath electric field which is proportional to the d-c bias voltage controls the direction of ion transport to the wafer surface. Random ion transport produced by collision results in isotropic etching, and directed ion transport which increases with the sheath electric field produces anisotropic etching.

Overetch effects.—Residues of Al left in etched areas can lead to shorts between lines and can result in a major loss of yield in device production. The origins of these residues are thickness nonuniformities in the Al film surface, often called hillocks, and thickness nonuniformities produced at steps by conformal or near conformal Al films (30, 31). Because of the desired anisotropic nature of the Al etch process, overetching is required to clear the etched areas of these residues.

In the plasma etching of polysilicon films with fluorocarbon gases, the lateral etch rate is commonly observed to increase with the onset of the overetch period. As the polysilicon film is cleared away from the unmasked areas over slow etching SiO_2, the sudden decrease in film area reduces the loading, increases the availability of the active etching species, and, therefore, increases the etch rate. As demonstrated in Fig. 9, this effect is not generally observed in this study, although the 50% Cl_2, −200V data do indicate an increase in lateral etch rate with overetch. This is an unexpected result since the relative lateral etch rate is increased by a reduction in the number of wafers in the reactor at constant Cl_2 percentages, and a similar reduction of the loading produced at the end point would be anticipated to increase the lateral etch rate.

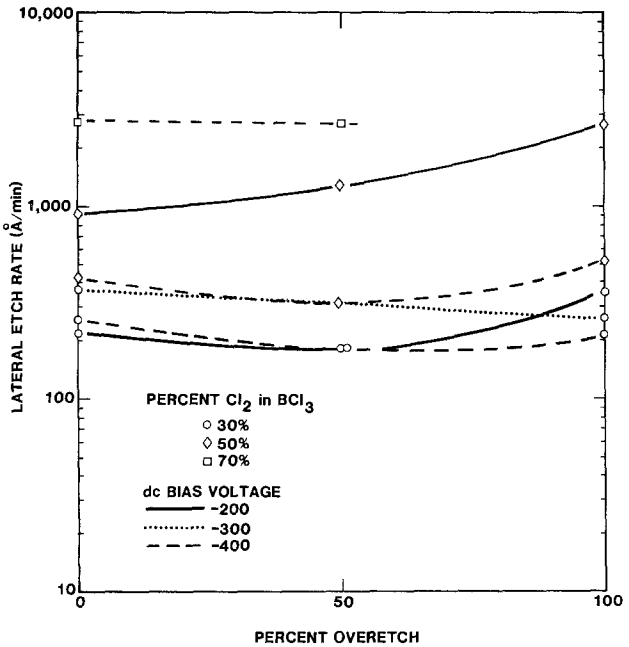

Fig. 9. The dependence of the lateral etch rate of Al/Si lines on percentage overetch with one wafer, 50 sccm, and 10 mTorr.

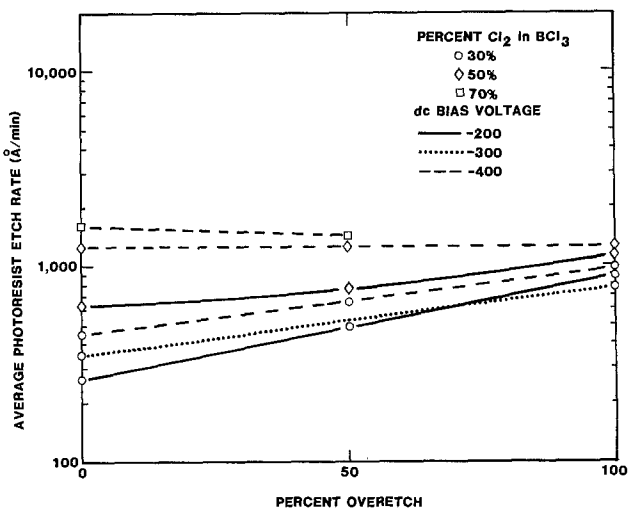

Fig. 10. The effect of percentage overetch on the etch rate of photoresist with one wafer, 50 sccm, and 10 mTorr.

While an increase in the lateral etch rate of the Al/Si lines is not observed upon overetch, the average photoresist etch rate generally does increase with overetch. The etch rate data as a function of percentage overetch are displayed in Fig. 10. The origin of the increase in photoresist etch rate may be the increased availability of a common etching species as the Al/Si is cleared from the unmasked areas. At high enough d-c bias voltages and percent Cl_2 values this effect appears to be unimportant and the photoresist etch rate is relatively constant with overetch. The anomalous behavior of the Al/Si lateral etch rate may be influenced by competition of the photoresist for the etching species on overetch.

Process considerations.—A useful reactive ion etching process for Al/Si interconnect requires a rapid etch rate, good selectivity for Al/Si over SiO_2, anisotropic etching, a reasonable photoresist etch rate, and the ability to overetch. Greater than ten to one Al/Si over SiO_2 etch rate ratios are easily achieved and the major compromises are among etch time, anisotropy, and photoresist erosion. As the etch time is decreased for a given wafer load by increasing the percent Cl_2 in BCl_3, the d-c bias potential must be increased to provide anisotropic etching. An increase in the d-c bias voltage and the percent Cl_2 results in an increase in the photoresist erosion rate. A low d-c bias potential may also be desired if a high Al/Si to Si etch rate ratio is an important consideration. Twelve to twenty-four wafers in the reactor, 70% Cl_2 in BCl_3, −200V d-c bias, 10 mTorr pressure, and 50 sccm total flow rate will give anisotropic etching with etch times ranging from 7 to 24 min depending on the wafer load and the pattern on the wafer. The Al/Si to photoresist etch rate ratio is 3:1 to 4:1, the Si etch rate is 200 Å/min, and the SiO_2 etch rate is 45 Å/min. Overetching under these conditions is unacceptable due to the increase in photoresist etch rate (from 200 to 800 Å/min for a 12 wafer load) on overetch. However, by dropping the Cl_2 percentage to 20% and leaving the other conditions constant, overetching can be performed with a photoresist etch rate of 500 Å/min. The Si and SiO_2 etch rates are approximately the same as with 70% Cl_2. At a given Cl_2 percentage and d-c bias voltage, the 396 nm Al emission line intensity during the etch increases with the number of wafers in the reactor. A comparison of the intensity of the emission following the end point of a 12 to 24 wafer load with an emission intensity *vs.* loading curve suggests that the remaining Al residue amounts to approximately the area of one patterned wafer or less. A one wafer load etched at 20% Cl_2 in BCl_3 and −200V gives an

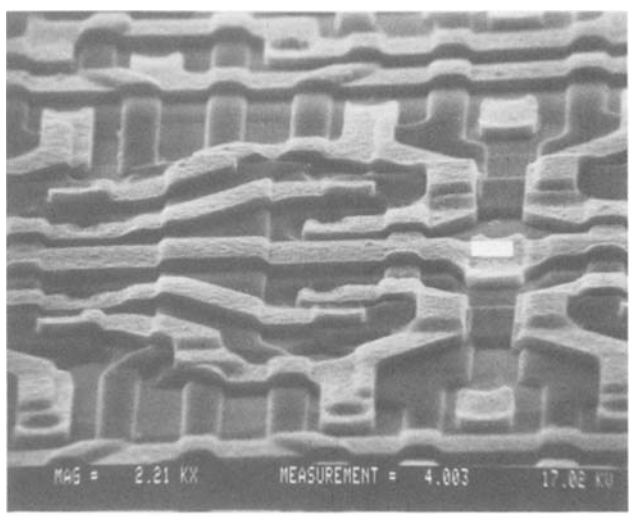

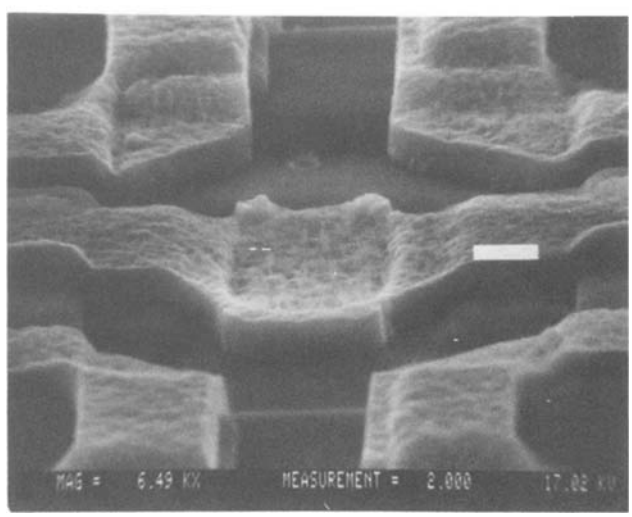

Fig. 11. An etch Al/Si pattern with the photoresist removed. Measurement units are in microns.

etch rate of 1000 Å/min. Therefore, a 10 min overetch of 12 to 24 wafers at 20% Cl_2 amounts to a 100% overetch of the wafers. Examination of Al/Si hillock residues (0.2-1.0 μm above the surface of the oxide at end point) at various stages of overetch confirms this conclusion. An initial photoresist thickness of 1.5-2.0 μm is suggested for this process. SEM photographs at high and low magnifications of an etched Al/Si pattern with a 100% overetch are shown in Fig. 11.

Conclusion

High resolution patterning of Al/Si can be achieved by reactive ion etching in a hexagonal cathode system with BCl_3 and Cl_2 mixtures. Lateral etching of the Al/Si lines is prevented by limiting the availability of active etching species and by using a sufficiently high d-c self-bias voltage. Although the lateral etch rate does not increase upon overetch, the photoresist etch rate does increase in response to the decreased Al/Si load. By decreasing the Cl_2 percentage at the end point, overetching can be performed with an acceptable photoresist etch rate. Results are reproducible, within the wafer and wafer to wafer linewidth variation is less than ±5%, and the entire process can be automated due to the sharp emission endpoint signal produced under the conditions described.

Acknowledgments

I wish to thank K. E. Rodgers for the SEM work, H. A. Macro for the measurements, and J. J. Clement, R. E. Anderson, and D. L. Weaver for reviewing this manuscript. This work was performed at Sandia National Laboratories supported by the U.S. Department of Energy under Contract No. DE-AC04-76DP00789.

Manuscript submitted March 17, 1983; revised manuscript received June 27, 1983.

Sandia National Laboratories assisted in meeting the publication costs of this article.

REFERENCES

1. B. Chapman and M. Nowak, *Semiconductor International*, 138 (November 1980).
2. W. Winkler, F. Schmidt, and N. Hoffman, in "Plasma Processing," R. G. Frieser and C. J. Mogab, Editors, p. 253, The Electrochemical Society Softbound Proceedings Series, Pennington, NJ (1981).
3. T. Tsukada, H. Mito, and M. Nagasaka, in "Plasma Processing," J. Dieleman and R. G. Frieser, Editors, p. 326, The Electrochemical Society Softbound Proceedings Series, Pennington, NJ (1982).
4. W. Lee and J. M. Eldridge, *J. Appl. Phys.*, **52**, 2994 (1981).
5. D. W. Hess, *Plasma Chem. Plasma Processing*, **2**, 141 (1982).
6. A. R. Reinberg, in "Etching for Pattern Definitions," H. G. Hughes and M. J. Rand, Editors, p. 91, The Electrochemical Society Softbound Proceedings Series, Princeton, NJ (1976).
7. P. M. Schaible, W. C. Metzger, and J. P. Anderson, *J. Vac. Sci. Technol.*, **15**, 334 (1978).
8. T. Tokunaga and D. W. Hess, *This Journal*, **127**, 928 (1980).
9. T. Tokunaga, F. C. Redeker, D. A. Danner, and D. W. Hess, *ibid.*, **128**, 851 (1981).
10. G. K. Herb, R. A. Porter, P. D. Cruzan, J. Argaz-Guerena, and R. B. Soller, Abstract 291, p. 710, The Electrochemical Society Extended Abstracts, Vol. 81-2, Denver, CO, Oct. 11-16, 1981.
11. M. Nakamura, M. Itoga, and Y. Ban, in "Plasma Processing," R. G. Frieser and C. J. Mogab, Editors, p. 225, The Electrochemical Society Softbound Proceedings Series, Pennington, NJ (1981).
12. D. K. Ranadive and D. L. Losee, in "Plasma Processing," R. G. Frieser and C. J. Mogab, Editors, p. 236, The Electrochemical Society Softbound Proceedings Series, Pennington, NJ (1981).
13. F. Schmidt and N. Hoffman, in "Plasma Processing," J. Dieleman and R. G. Frieser, Editors, p. 287, The Electrochemical Society Softbound Proceedings Series, Pennington, NJ (1982).
14. R. A. M. Wolters, in "Plasma Processing," J. Dieleman and R. G. Frieser, Editors, p. 293, The Electrochemical Society Softbound Proceedings Series, Pennington, NJ (1982).
15. L. Peccoud, Ph. Laporte, M. Chevallier, and T. Fried, in "Plasma Processing," J. Dieleman and R. G. Frieser, Editors, p. 299, The Electrochemical Society Softbound Proceedings Series, Pennington, NJ (1982).
16. K. G. Donohoe, in "Plasma Processing," J. Dieleman and R. G. Frieser, Editors, p. 306, The Electrochemical Society Softbound Proceedings Series, Pennington, NJ (1982).
17. R. H. Bruce and G. P. Malafsky, in "Plasma Processing," J. Dieleman and R. G. Frieser, Editors, p. 336, The Electrochemical Society Softbound Proceedings Series, Pennington, NJ (1982).
18. P. M. Schaible and G. C. Schwartz, *J. Vac. Sci. Technol.*, **16**, 377 (1979).
19. G. C. Schwartz and P. M. Schaible, *Solid State Technol.*, 85 (1980).
20. A. Weiss, *Semiconductor International*, 69 (October 1982).
21. D. W. Hess, *Solid State Technol.*, 189 (April 1981).
22. R. G. Poulsen, *J. Vac. Sci. Technol.*, **14**, 266 (1977).
23. C. J. Mogab, *This Journal*, **124**, 1262 (1977).
24. V. M. Donnelly and D. L. Flamm, *Solid State Technol.*, 161 (April 1981).
25. B. N. Chapman and V. J. Minkiewicz, *J. Vac. Sci. Technol.*, **15**, 329 (1978).
26. B. N. Chapman, "Glow Discharge Processes," p. 330, John Wiley & Sons, Inc., New York (1980).
27. C. J. Mogab and H. J. Levinstein, *J. Vac. Sci. Technol.*, **17**, 721 (1980).
28. C. B. Zarowin and R. S. Horwath, *This Journal*, **129**, 2541 (1982).
29. C. B. Zarowin, "Plasma Etch Anisotropy—Theory and Some Verifving Experiments Relating Ion Transport, Ion Energy, and Etch Profiles," The Perkin Elmer Corp. (October 1982).
30. S. C. P. Lim, *Solid State Technol.*, 135 (April 1982).
31. J. W. Coburn, "Plasma Etching and Reactive Ion Etching," p. 1, American Vacuum Society (1982).

Dry Etching of Polyimide in O_2-CF_4 and O_2-SF_6 Plasmas

Guy Turban and Michel Rapeaux

Laboratoire de Physique Corpusculaire, E.R.A. 924, Université de Nantes, 44072 Nantes Cedex, France

ABSTRACT

The plasma etching of the type H Kapton polyimide film has been studied in a parallel plate reactor with two different gas mixtures; O_2–CF_4 and O_2–SF_6. High etching rate (0.5–3 μm/min) has been obtained in both cases. At a pressure of 0.2 Torr an anomalous loading effect is observed which is attributed to the nitrogen released by the polyimide. The gaseous effluents from etching have been detected by mass spectrometry and indicate that both atomic oxygen and atomic fluorine are the main etchants of the polymer. A comparison with silicon etching in a SF_6–O_2 plasma is made in order to give the main channels of the reaction scheme. XPS measurements of the polyimide surface before and after etching are consistent with the mass spectrometric observations.

The use of polyimides as dielectrics has become increasingly important in different electronic applications due to their excellent thermal and chemical inertness. In integrated circuit fabrication, polyimide films are used in multilevel structures as the interlevel dielectric (1). In printed circuit, Kapton® polyimide film, type H is usually the dielectric part of the multilayer printed boards between the copper plates (2). Kapton "H"[1] (poly 4,4-oxydiphenyl pyromellitimide) is an aromatic polyimide (3) which is commercially available in thick foils (7.5-50 μm). Its behavior in oxygen-fluorinated plasmas is interesting for two applications: plasma desmearing and surface treatment. In the manufacture of multilayer printed circuit boards (either of the rigid or flexible variety), interconnecting holes are drilled through the boards and interconnecting metallic layers are plated within the drilled holes to provide an electric connection between exposed edge portions of conducting layers of the printed circuit boards (2). Plasma desmearing is a technique used in order to strip the smeared adhesives and polyimide materials that coat the sidewalls of the drilled holes which prevent proper electrical contact between inner conducting layers. In this context, the dry etching of Kapton and adhesive smears has been studied, usually in an O_2-CF_4 (70/30) mixture (4).

Wydeven (5) has studied the Kapton etching in an oxygen plasma. Pederson (6) has compared the etch rates of a variety of polymer films among which Kapton film, in CF_4-O_2 and CF_4 discharges with a barrel-type reactor.

We have studied the etching process of Kapton in O_2-CF_4 and O_2-SF_6 plasmas and we have compared the etching rates with those of epoxy and acrylic resins which are the adhesives used in printed circuit boards. The gaseous effluents of the etching reaction have been studied by mass spectrometry and some comparisons are made with the silicon etching. On the basis of these measurements, we discuss the chemistry of SF_6-O_2 discharge and the consequences of atomic oxygen and fluorine consumption upon the secondary reactions between neutral active species.

Experimental Setup and Method

The plasma reactor is of the diode type with alumina walls. Electrodes are anodized aluminum plates of 71 cm^2 with an interelectrode spacing of 5 cm. Flow rates are measured with Brooks rotameters, calibrated with a volumeter at the standard pressure. The total flow rate is adjusted to 40 sccm. The power is coupled to the reactor from an rf generator (13.56 MHz) or a broadband amplifier (15 kHz-12MHz) via a suitable impedance matching network. The power level is set at 50W and is controlled by a powermeter. The pressure is measured by means of a capacitance manometer and varied from 0.1 up to 1 Torr.

The Kapton film is adhered to a copper foil with epoxy resin and disposed on the anode.

The neutral molecules are extracted from the plasma through a 200 μm sampling orifice bored in a Macor ceramic cylinder placed on the reactor wall. The molecular beam of the products goes through a first chamber pumped down to 10^{-6} Torr and then reaches the Balzers QMG 311 spectrometer in a second chamber pumped down to 10^{-7} Torr by a diffusion pump. Neutral species are ionized by using the electron impact ionizer of the mass spectrometer set at 90 eV and mass analyzed. The apparatus is calibrated by using a standard gas mixture containing He, N_2, Ar, Kr, and Xe. For each mass, a transmission coefficient T is determined from the peak intensity i and the partial pressure p in the reactor as follows

$$T = i/p\sigma$$

where σ is the partial ionization cross section of the gas. The mass dependence of T is found to follow an empiric law

$$T = \alpha m^{-0.85}$$

Then the partial pressure of a gas appearing in the plasma (SO_2F_2 for example) is obtained from the parent peak intensity by using the transmission coefficient T and the cross section or the sensitivity of the gas relative to n-butane (7) or nitrogen (8). If a peak results from several compounds, mass interference corrections are made, based on published fragmentation patterns (7, 8).

The studied Kapton polyimide is 50 μm thick with a copper foil on one side. Etch rates are measured by weighing on a Mettler M 5 microbalance assuming a density of 1.42 g cm^{-3}.

Results and Discussion

Kapton etch rates—Loading effect.—The etching rate of Kapton H in O_2-SF_6 plasmas is quite high (0.5-3 μm/min) depending on power, pressure, and gas mixture. An increase of the etch rate is observed as a function of the treatment duration, especially for long exposure and high pressure (Fig. 1). Simultaneously, we note a rise of the electrode temperature, for example, from 20° up to 80°C in 50 min, as measured with a thermocouple probe. The variation of the etch rate appears to be related to this thermal increase. Pederson (6) observed the same behavior for several polymers.

A study of the Kapton etch rate as a function of the excitation frequency of the discharge from 15 kHz up to 13.56 MHz (Fig. 2) shows that high frequencies are more efficient than low frequencies, probably due to a greater dissociation of the etchant gas.

Figure 3 illustrates the evolution of the Kapton etch rates as a function of the input gas composition

Key words: polyimide, SF_6, plasma etching, plasma chemistry.

[1] Kapton "H"® is a trademark of E. I. du Pont de Nemours and Company.

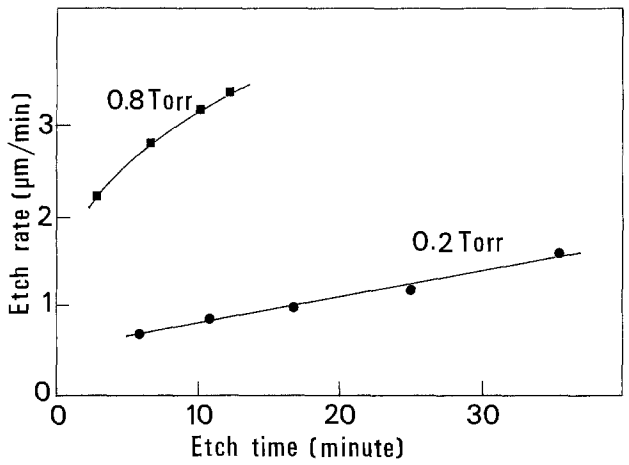

Fig. 1. Kapton etch rates as a function of the plasma treatment duration. Gas mixture = O_2-CF_4 (70/30), Kapton area = 5 cm², frequency = 13.56 MHz.

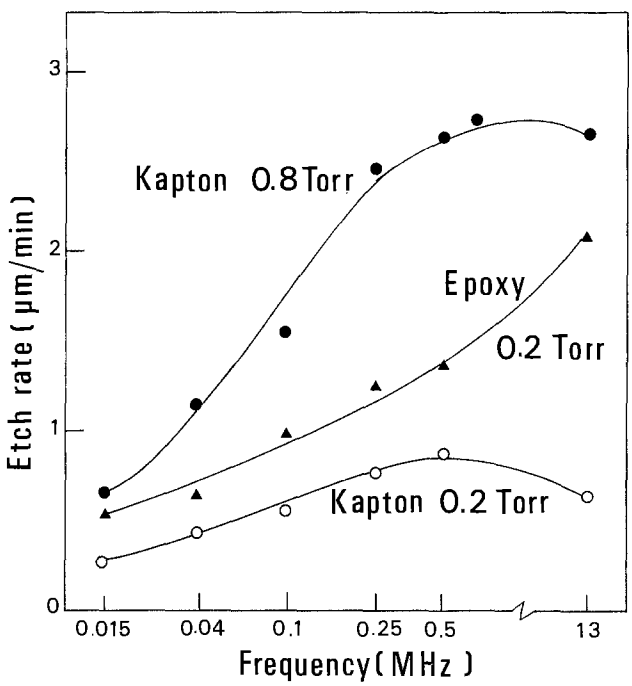

Fig. 2. Etch rates of Kapton and epoxy resin vs. excitation frequency. Gas mixture = O_2-CF_4 (70/30), sample area = 5 cm².

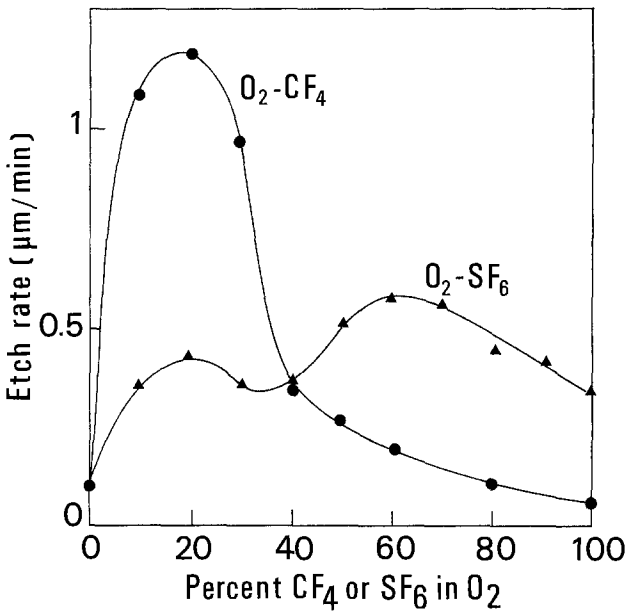

Fig. 3. Etch rates of Kapton in O_2-CF_4 and O_2-SF_6 discharges. Pressure = 0.2 Torr, sample area = 4.5 cm², frequency = 13.56 MHz.

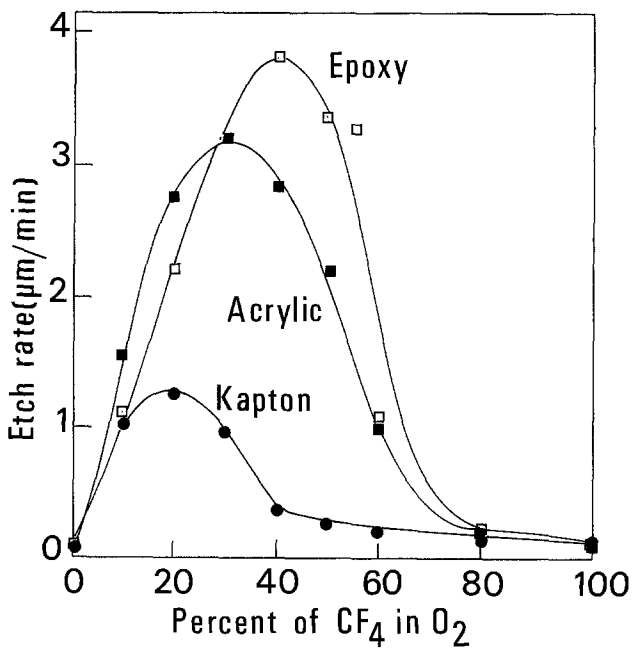

Fig. 4. Etch rates of Kapton and resins in an O_2-CF_4 plasma. Pressure = 0.2 Torr. sample area = 4.5 cm², frequency = 13.56 MHz.

for the two studied mixtures. The addition of small quantities of a fluorinated gas (10-20%) to oxygen causes an important increase of the etch rate (5-15×).

On the other hand, in the O_2-SF_6 plasma, the etch rate evolution exhibits two maximas, one in a dominant oxygen mixture, the other in a dominant SF_6 mixture, contrary to the O_2-CF_4 plasma in which only one maximum is observed. In Fig. 4, the etch rates of two resins normally used in printed circuit are compared as a function of the gas mixtures. These etch rates and the values of optima are modified by the presence of other polymer materials in the same reactor (9).

The influence of the material areas to be etched is reported in Fig. 5. While the epoxy resin shows a "classical" loading effect, the Kapton does not exhibit any loading effect at low pressure (0.2 Torr) in O_2-CF_4 or O_2-SF_6 mixtures but presents a loading effect at high pressure (1 Torr).

The addition of 1-5% of nitrogen in the O_2-CF_4 mixture causes an increase of the Kapton etch rates by a factor of 1.5-3 depending on the conditions. Without any polymer in the reactor, the introduction of some percent of nitrogen induces variations in the CO_2, COF_2, and F_2 concentrations measured by mass spectrometry (Table I).

No carbon-nitrogen compounds are detected in the gas phase. The role of nitrogen may be an additional etching of the polymer by N atoms as reported by Smolinsky *et al.* (10). However, the gas phase results, obtained without any Kapton in contact with the plasma, support another interpretation. The active nitrogen [N(4S/ and N_2*] can induce a decomposition of COF_2 and perhaps CO_2. As a result, the atomic fluorine and atomic oxygen produced by this reaction will increase the Kapton etch rate. Such a mechanism has been previously proposed by other authors (11)

$$N_2^* + COF_2 \rightarrow N_2 + CO + 2F \qquad [1]$$

In this scheme, the atomic fluorine in excess would recombine on the walls and be detected as F_2 (Table I).

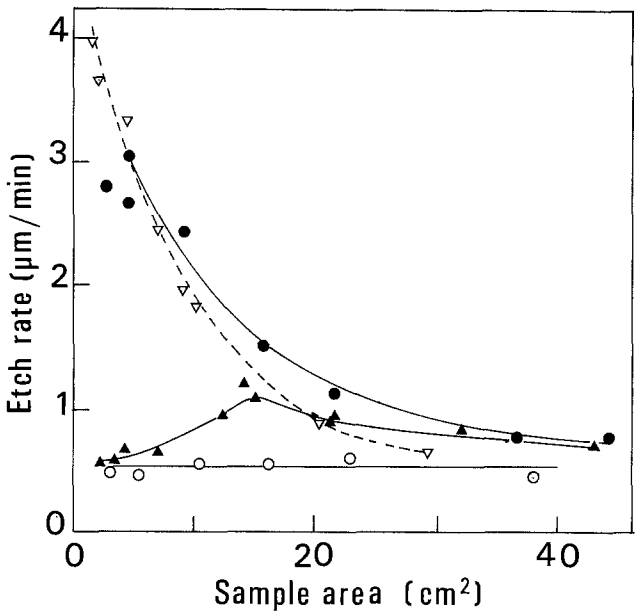

Fig. 5. Effect of load on etch rate. Frequency = 13.56 MHz. ● Kapton, O_2-CF_4, 1 Torr; ▲ Kapton, O_2-CF_4, 0.2 Torr; ▽ Epoxy resin, O_2-CF_4, 0.2 Torr; ○ Kapton, O_2-SF_6, 0.2 Torr.

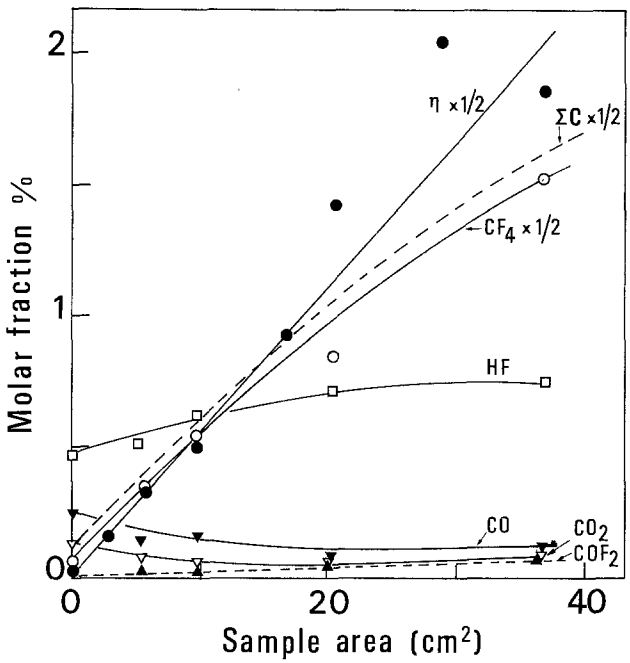

Fig. 6. Evolution of the molar fractions of gaseous effluents from Kapton etching in a pure SF_6 plasma. Pressure = 0.2 Torr, frequency = 13.56 MHz.

The absence of a loading effect at low pressure is consistent with this reaction. The content of nitrogen in Kapton is 9.09 atomic percent (a/o), so Kapton etching liberates nitrogen in the gas phase which plays a role similar to that of the added nitrogen in the above experiment, that is to compensate for the loading. At high pressures (1 Torr for example), the N_2* formation from N_2 is presumed to be less important than at low pressures, due to a difference in the electron energy of the plasma.

Mass spectrometry of gaseous effluents.—Wydeven's work (5) showed that in an oxygen plasma the gaseous effluents in Kapton etching were CO, CO_2, H_2O, H_2, and N_2. On another hand, it is known that the O_2-CF_4 discharge gives rise to identical gaseous products: CO, CO_2 (12). Several attempts have demonstrated it is impossible to discriminate in the mass spectrometric data between the variations of gas concentrations due to the Kapton etching and those due to modifications of secondary reaction rates in the gas phase, induced by the consumption of active species. So the mass spectrometric measurements reported here are only concerned with SF_6 and O_2-SF_6 plasmas in which CO and CO_2 are not by-products of the input gases. Table II gives the gaseous effluents obtained in the Kapton etching. As shown in Fig. 3, the pure SF_6 discharge etches the polymer at sizable etch rates (0.3 μm/min).

Figure 6 illustrates the evolution of effluent concentrations resulting from pure SF_6 etching.

Table I. Effect of nitrogen (5%) on the relative concentrations of CO_2, COF_2, and F_2 in the O_2-CF_4 plasma

Gas product	No nitrogen	5% Nitrogen
CO_2	1	0.86
COF_2	1	0.82
F_2	1	1.62

Table II. Main gaseous effluents from plasma etching of Kapton film

Initial gas mixture	Main effluents
O_2	CO, CO_2, H_2O
SF_6	CF_4, HF, COF_2
O_2-SF_6	CO, CO_2, H_2O COF_2, CF_4, HF

The main gaseous product is CF_4 (m/e = 69 amu). Other products are CO, CO_2, COF_2, and HF. Without Kapton in the discharge, we observe some quantity of HF which attributed to the reaction of atomic fluorine with water vapor and hydrocarbons as stated by Smolinsky and Flamm (12). The particular evolution of CO and CO_2 as a function of the Kapton area is due to deposits on the reactor walls resulting from previous runs. With small Kapton areas, the etching of these films gives more effluents than the Kapton itself. With great Kapton area, this effect is negligible. The concentration of COF_2 and HF increases when the polyimide area is increased.

The etch rate has been compared to the gaseous effluents of etching reaction by means of the η ratio defined by

$$\eta = \frac{\text{polymer etch rate (carbon atoms/sec)}}{\text{input rate of gas (molecules/sec)}} \quad [2]$$

Thus, the quantity η represents the ratio of the flow rate of carbon bearing effluent flow rate to that of the input molecules. It corresponds to an ideal molar fraction that we would obtain from etching products in the absence of secondary reactions in the plasma. So η is equivalent to a molar fraction. A good correlation between η and ΣC is obtained. The light deficit in the gaseous effluents compared with the etch rate is attributed to the solid deposits on the reactor walls coming from nonvolatile etching products, may be of aromatic nature. Indeed it is known that the vacuum pyrolysis of Kapton results in gaseous products (CO, CO_2) but also liquids and solids (including amines, phenols, phthalimides) (3).

Results from Fig. 3 and 6 support the interpretation of a direct etching of polyimide by atomic fluorine.

The etching of epoxy resin in a SF_6 plasma gives rise to the same effluents (CF_4, HF, CO, CO_2, and COF_2) but with a greater contribution of HF due to the higher content of hydrogen in resin than in Kapton.

The evolution of the relative concentration of various gaseous products with etching in an O_2-SF_6 plasma is shown in Fig. 7. These curves clearly demonstrate that with an oxygen dominant plasma (input O_2 > 50%) the gaseous compounds are mainly oxygenated, that is, CO, CO_2, COF_2, and H_2O, whereas with an

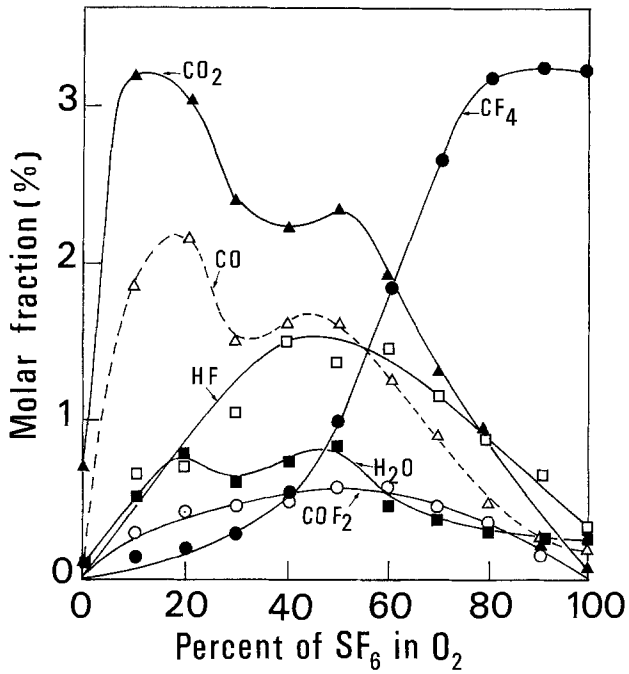

Fig. 7. Evolution of the molar fractions of gaseous products from Kapton etching in an O_2-SF_6 plasma. Pressure = 0.2 Torr, frequency = 13.56 MHz.

SF_6 dominant plasma (input $SF_6 > 50\%$) the main reaction product is CF_4. So we conclude that in the first region, atomic oxygen is the main etchant and in the second, atomic fluorine dominates. The important increase of the etch rate, when some percent of SF_6 (or CF_4) is added to an O_2 plasma, can be explained by an enhancement of the atomic oxygen concentration as shown by optical measurements (13, 14), but also by a direct reaction of F with the hydrogen of the polymer as proved by the production of HF. A good correlation between the etch rate (η ratio) and the carbon bearing products (CO, CO_2, COF_2, CF_4) noted ΣC is obtained as shown in Fig. 8. The existence of a solid deposit on the reactor walls is proved by the detection of carbon products without any Kapton in the reactor. The evolution of H_2O due to etching is

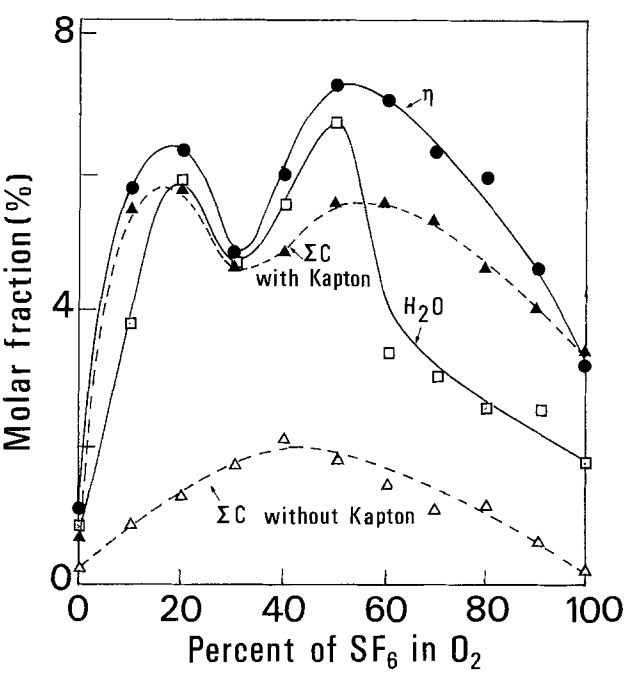

Fig. 8. Correlation between the carbon containing compounds (ΣC) and the Kapton etch rate (η).

well correlated with the etch rate except for the SF_6 dominant plasmas where the fluorine atoms in excess can destroy the water vapor. Kapton is known to have a great moisture absorption, so some desorption of H_2O cannot be ruled out.

After etching is achieved, a desorption of effluents at masses 30, 44, and 46 is observed in proportion with the previous etching rate. This desorption, not detected after polyethylene etching for example, is attributed to NO, NO_2, and N_2O formation resulting from rearrangement in the polymer after the etching reaction (15).

Secondary reactions in O_2-SF_6 plasmas.—Previous results show that polyimide consumes oxygen and fluorine atoms during the etching process. We have studied the modifications introduced in neutral radical secondary reaction rates in the plasma when both O and F atoms are depleted, compared with rates obtained during the silicon etching when only F atoms are consumed. The aim of this comparison is to gain some insights on the very complex chemistry of SF_6 and SF_6-O_2 plasmas.

Figures 9a and 9b give the evolution of molar fractions of SO_2, SOF_4, SOF_2, and SO_2F_2 as a function of the input gas mixture both without and with Kapton. In Fig. 10a, we have plotted the difference between the molar fractions of SO_2, SOF_4, SOF_2, and SO_2F_2, measured without any sample in the plasma, and the molar fractions of the same molecules, measured with a Kapton sample in the reactor. The sum $\Sigma\Delta$ represents the algebraic sum of all these concentration variations. The differences between the molar fractions emphasize the effect of F and O consumption on the various secondary reactions which produced SO_2, SOF_4, SOF_2, and SO_2F_2. Similar measurements, conducted with a silicon sample instead of Kapton, are illustrated in Fig. 10b. From this figure, we deduce that the fluorine consumption increases the formation rate of all the secondary compounds, particularly SOF_2 and SO_2F_2. On the contrary, during Kapton etching, partial pressures of SOF_4 and SO_2F_2 decrease (Fig. 10a).

These results are well rationalized on the basis of the reaction scheme given in Fig. 11.

This scheme is in agreement with the study of d'Agostino and Flamm (16). Two reactions with H_2O are added in order to explain the experimental observations. The first reaction

$$SF_4 + H_2O \rightarrow SOF_2 + 2HF \qquad [3]$$

is directly stated by a correlation observed between the concentration of SF_4 and of SOF_2 during the silicon etching (9). These reactions were previously proposed by other authors (17). With Kapton, since water vapor is a direct product of etching, such reaction rates are expected to be important. From this comparison we can conclude: (*i*) the source reactions for SOF_4 and SO_2F_2 are clearly due to atomic oxygen because its depletion during Kapton etching causes a decrease in their concentrations. (*ii*) The source reactions of SOF_2 and SO_2 are due to both O and H_2O. So the depletion of oxygen during etching has no noticeable effect because H_2O compensates the consumption of O. (*iii*) The source reactions of SOF_2, SO_2F_2, SO_2, and SF_4 are due to SF_n radicals because the silicon etching favors their formation. Other results (18) demonstrated the limitation of the recombination reactions

$$SF_n + F \rightarrow SF_{n+1} \qquad [4]$$

by the silicon etching, in agreement with the reaction scheme of Fig. 11.

ESCA measurements of Kapton.—X-ray photoelectron spectroscopy (XPS) has been employed in order to investigate the structure of Kapton H and the modification produced by the plasma treatment. ESCA spectra of the polymer are recorded on a Leybold-Heraeus EA 10 spectrometer. The atomic composition

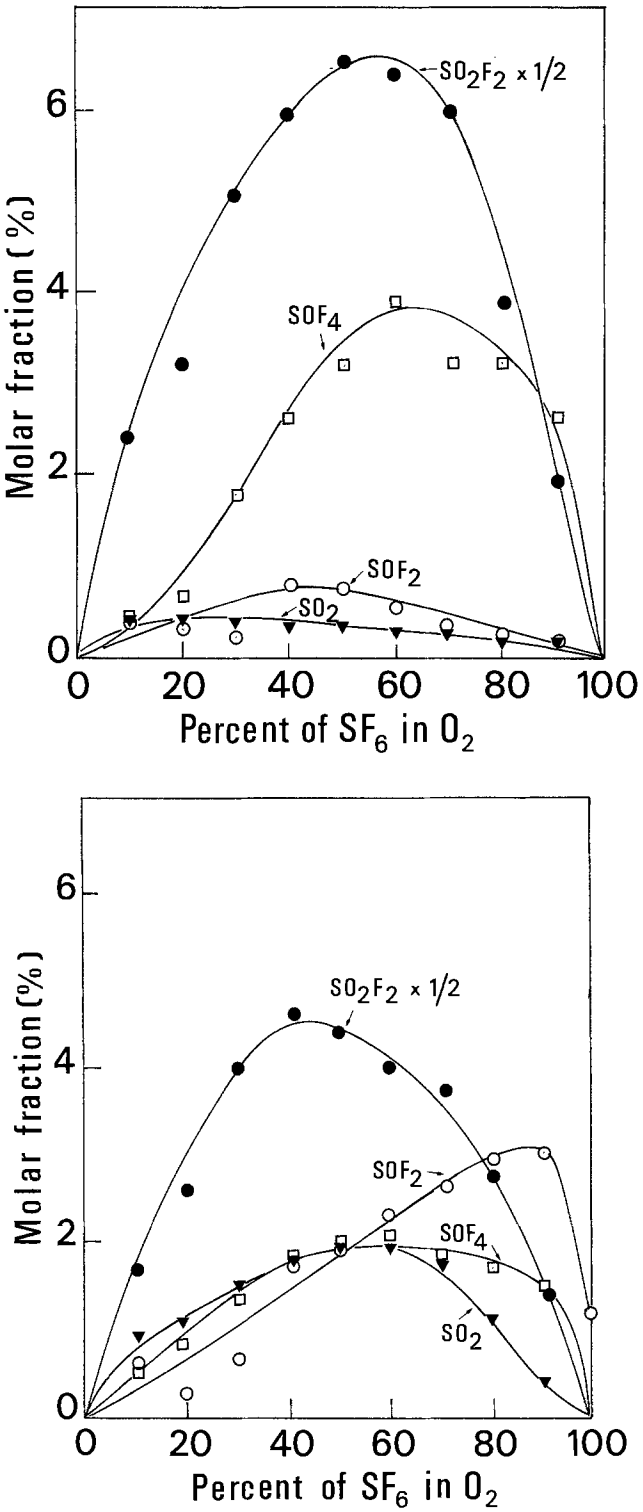

Fig. 9. Molar fractions of the main gaseous products in an O_2-SF_6 plasma. (F_2 is omitted). Pressure = 0.2 Torr. (a, top) Without sample, (b, bottom) with a Kapton sample (40 cm^2).

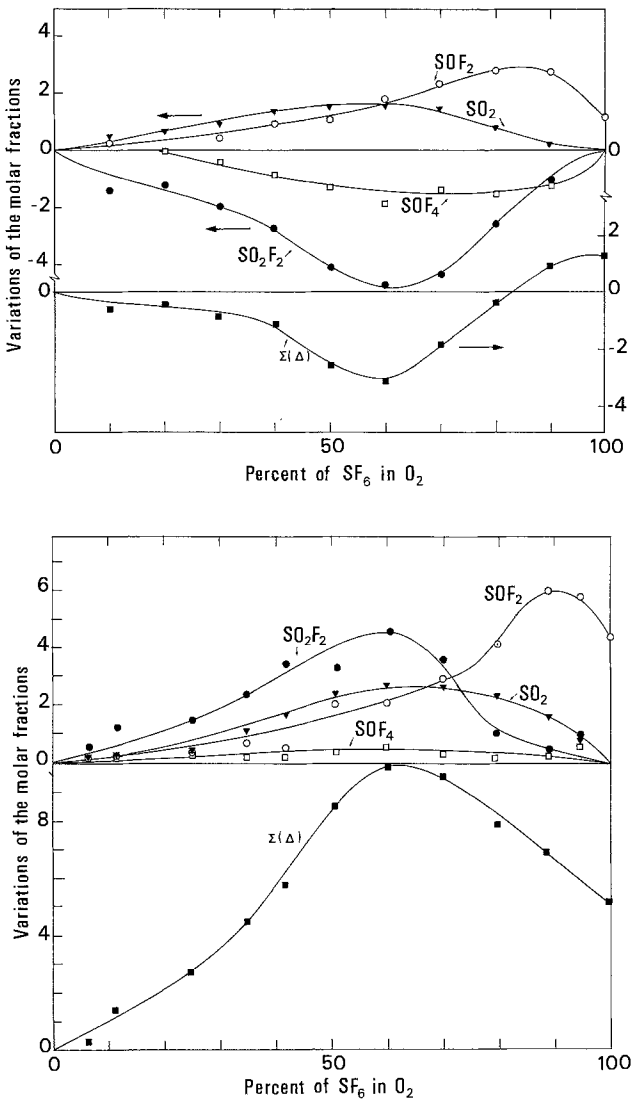

Fig. 10. Variations of the molar fractions (%) of the main gaseous products in an O_2-SF_6 plasma due to the introduction of a sample. (a, top) With a Kapton sample, (b, bottom) with a silicon sample.

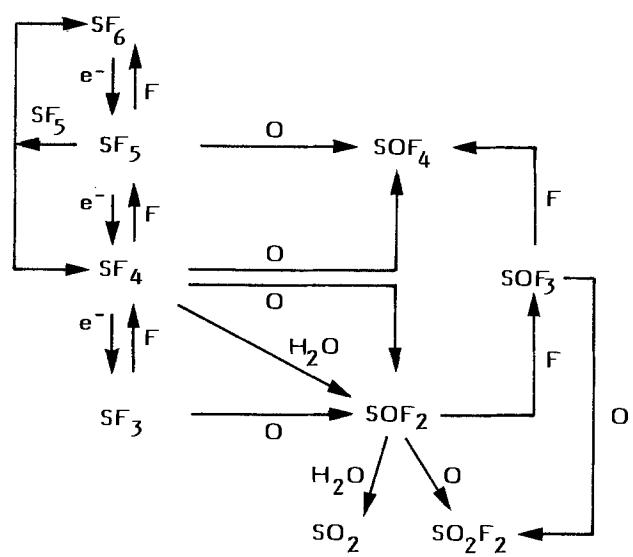

Fig. 11. Reactional scheme in an O_2-SF_6 plasma

of the Kapton surface obtained from these spectra is given in Table III. The untreated sample is nitrogen deficient compared with theoretical structure. After scraping with a knife under argon or after plasma etching, the samples exhibit a correct atomic composition. After plasma etching with an O_2-SF_6 mixture, a fluorination and a sulfurization of Kapton surface is observed contrary to some observations made by XPS in silicon etching (19) but in agreement with other authors (20).

This fluorination is in agreement with the observation of CF_4 as the main gaseous effluent of the Kapton etching and supports the conclusion that atomic fluorine is an etchant of Kapton. The XPS spectra of O1s are shown in the Fig. 12. In the case of an oxygen dominant plasma treatment, an increase of the O1s peak intensity is observed.

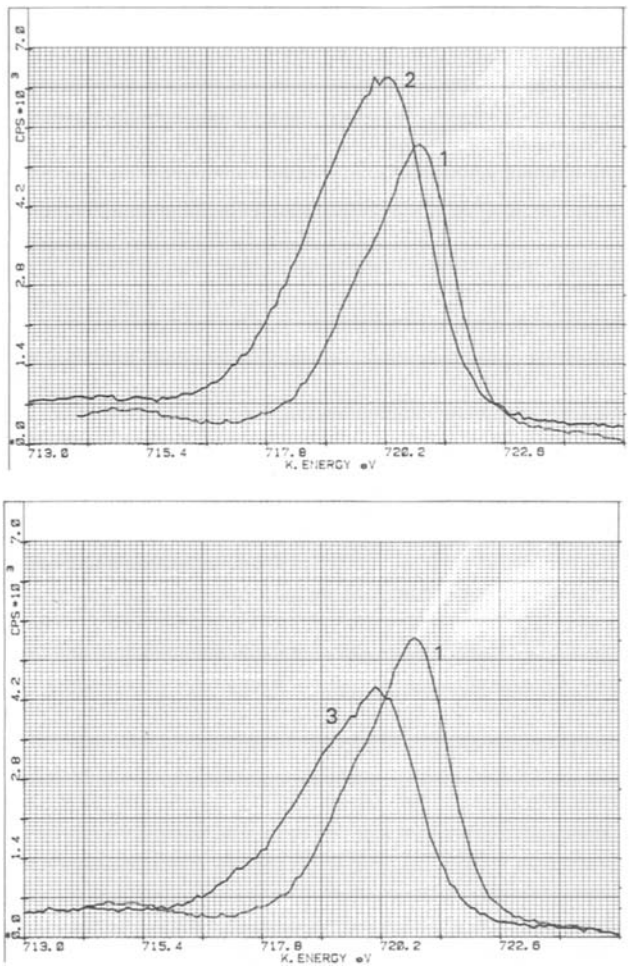

Fig. 12. ESCA spectra of Kapton samples (O1s peak). 1, after scraping with knife under argon; 2, after O_2-SF_6 80/20 plasma etching; 3, after O_2-SF_6 20/80 plasma etching.

An example of C1s and O1s peak deconvolutions is presented in Table IV. The comparison with the theoretical structure formula (3) points out significant differences.

According to Leary and Campbell (21), such discrepancies are related to a partial imidization of the surface and a curing (in N_2 to 325°C) produces a change in the O1s, C1s, and N1s spectra in agreement with the expected bulk structure.

Table III. Atomic composition of Kapton deduced from ESCA spectra

Atoms	Structural stoichiometry	Untreated samples	Samples scraped under argon	Samples etched in O_2-SF_6 plasmas (20/80)
C	100	100	100	100
O	20.9	18.5	19.5	19.5
N	9.09	5.0	8.8	8.2
F	—	—	—	26.3
S	—	—	—	0.2

Table IV. Examples of peak deconvolutions (atoms/molecule) from ESCA spectra of Kapton after scraping under argon

Peak	Energy	Theoretical value	Experimental values
C1s	285.2	10	9.36-7.26
	286.2	8	9.92-11.94
	289.1	4	2.77-2.80
O1s	532.6	1	1.36-1.39
	533.9	4	3.64-3.07

Conclusions

O_2-CF_4 and O_2-SF_6 plasmas have been used to etch Kapton "H" polyimide. The dependence of the etch rate on the reactor parameters such as mixing ratio of gas, excitation frequency, and exposed Kapton area have been investigated in a diode reactor in conjunction with mass spectrometry of effluents.

1. The rate of etching is quite high (0.5-3 μm/min) and shows no loading effect at low pressure.
2. A few percent of nitrogen increases the etching rate by a factor ~2, probably owing to the reaction of active nitrogen with COF_2. This explains the no-loading effect.
3. The products of etching are CO, CO_2, COF_2, H_2O, HF, and CF_4, showing that oxygen and fluorine atoms are the main etchants of the polymer.
4. XPS measurements confirm the role of O and F atoms in the plasma etching.
5. The effects of the consumption of F and O on the secondary neutral radical reactions rates, compared with the consumption of F atoms alone in silicon etching, bring experimental evidence of the proposed reactional channels for the formation of SOF_2, SOF_4, and SO_2F_2.

Acknowledgments

This study was supported by the Direction Générale des Télécommunications under Contract No. DAII 82 35 103.

Author's thanks are due to Dr. Berresheim from Leybold-Heraeus, Köln, Germany, who performed the ESCA measurements and interpretation.

Manuscript submitted March 30, 1983; revised manuscript received June 24, 1983. This was Paper 177 presented at the San Francisco, California, Meeting of the Society, May 8-13, 1983.

REFERENCES

1. L. B. Rothman, *This Journal*, **127**, 2216 (1980).
2. "Printed Circuits Handbook," C. F. Coombs, Jr., Editor, McGraw-Hill, New York (1978).
3. "Encyclopedia of Polymer Science and Technology," N. M. Bikales, Editor, p. 247, John Wiley and Sons, New York (1969).
4. *E.g.*, E. Phillips, U.S. Pat. 4,012,307 (1977).
5. T. Wydeven, C. C. Johnson, M. A. Colub, M. S. Hsu, and N. R. Lerner, in "Plasma Polymerization," p. 299, American Chemical Society Symposium Series (1979).
6. L. A. Pederson, *This Journal*, **129**, 205 (1982).
7. A. Cornu and R. Massot, "Compilation of Mass Spectral Data," Vol. I, Heyden and Son, London (1975).
8. W. H. Beattie, *Appl. Spectrosc.*, **29**, 334 (1975).
9. M. Rapeaux, Thèse de 3e cycle, Université de Nantes, Nantes, France (1982).
10. G. Smolinsky, E. A. Truesdale, D. N. K. Wang, and D. Maydan, *This Journal*, **129**, 1036 (1982).
11. F. H. M. Sanders and J. Dieleman, in "Proceedings of the 5th Symposium Plasma Chemistry," p. 29, Edinburgh (1981).
12. G. Smolinsky and D. L. Flamm, *J. Appl. Phys.*, **50**, 4982 (1979).
13. D. L. Flamm, *Solid State Technol.*, **22**, 109 (1979).
14. D. L. Flamm and V. M. Donnelly, *Plasma Chem. Plasma Process*, **1**, 317 (1981).
15. G. Turban and M. Rapeaux, *Le Vide Les Couches minces*, **212**, (suppl.), 79 (1982).
16. R. d'Agostino and D. L. Flamm, *J. Appl. Phys.*, **52**, 162 (1981).
17. R. Gilbert, J. Castonguay, and A. Théoret, *J. Appl. Polymer Sci.*, **24**, 125 (1979).
18. G. Turban, J. Pasquereau, M. Rapeaux, Y. Catherine, and B. Grolleau, Abstract 262, p. 636, The Electrochemical Society Extended Abstracts, Vol. 81-2, Denver, CO, Oct. 11-16, 1981.
19. K. M. Eisele, *This Journal*, **128**, 123 (1981).
20. J. J. Wagner, Ph.D. Thesis, University of Wisconsin (1980).
21. H. J. Leary, Jr., and D. S. Campbell, *Surf. and Interface Anal.*, **1**, 75 (1979).

Silicon Damage Caused by Hydrogen Containing Plasmas

R. G. Frieser,* F. J. Montillo,* N. B. Zingerman, W. K. Chu, and S. R. Mader

IBM General Technology Division, East Fishkill, Hopewell Junction, New York 12533

ABSTRACT

This study shows that the damage observed in silicon slices after exposure to reactive ion etching in a hydrogen containing plasma is caused by physical bombardment of the surface by hydrogen ions. This conclusion is based primarily on extensive measurements of retention time, Rutherford backscattering, and Auger analysis data. When the etch gas is a mixture of CF_4 and H_2, hydrogen ions are implanted into the silicon surface to an approximate depth of 200Å. Because the etch rate of silicon in CF_4/H_2 is slow, any resulting surface damage due to this plasma increases faster than can be removed by a fast silicon etch, like CF_4 alone. However, the damaged layer can readily be removed by any dry or wet etching agent. Metal oxide semiconductor (MOS) measurements of charge retention indicate that an exposure to hydrogen containing plasmas for less than 5 min does not degrade the silicon surface sufficiently to be of concern for device fabrication on VLSI. Good product yields have been fabricated with a plasma that contains hydrogen.

Reactive ion etching (RIE) is a preferred, dry process step for the fabrication of micron as well as submicron structures on VLSI circuits. A high selectivity of etching oxide to silicon is a necessity for many manufacturing steps in present and future technologies. Such selectivity can be obtained readily by the addition of hydrogen to CF_4 (1), or by the use of an etch gas containing a proton, *i.e.*, CHF_3. The addition of H_2 to a CF_4 plasma affects the etch rates of silicon significantly by the deposition of polymeric material on the silicon. It affects the etch rate of SiO_2 only moderately (2). This achieves a high etch rate ratio between oxide and silicon.

Extensive precautions were taken to eliminate inadvertent contamination of the silicon surfaces from heavy metals sputtered off the chamber walls. Such contamination on device surfaces would inevitably lead to device failures. One sensitive technique for detecting such contamination on silicon substrates is by MOS charge retention time studies (3). In addition to this technique, Auger surface analysis was used to identify and monitor metal contamination on the plasma-exposed silicon surfaces.

Early in the investigation we observed that wafers exposed to any hydrogen containing plasmas had excessive high leakage currents, thus poor retention times.

Experimental

Plasma conditions.—Silicon wafers were supported on a silicon cathode in a parallel plate reactor operated at 13.56 MHz. The uniformity of the plasma in the particular reactor (stainless steel), was assured by placing a grounded aluminum cylinder (97%) inside to avoid contamination due to sputtering off the walls. The following etch conditions were employed: power density, 0.2-0.5 W/cm^2 (which corresponded in our system to 200-500W); pressure, 35 microns; and the total flow rate was set at 24 sccm, whether the etch gas was a one- or two-component system. When hydrogen was added to the primary etch gas, CF_4, the concentration by flow was 35.5%. In special experiments hydrogen was replaced by helium or deuterium, used alone or in combination with CF_4. Some wafers were exposed to CHF_3 as well.

Retention Time Measurements

The retention time technique is a measurement of the minority carrier generation rate in silicon, which is directly related to the defect level in the silicon. This in turn affects the leakage current of the MOS devices. The wafers for retention time measurements used in this experiment were 82 mm p-type, 10 Ω-cm material. The cleaning process (4) for these wafers and the measurement technique itself is published elsewhere (5). It is essential to point out that after plasma exposure, the silicon wafers were subjected to a wet HCl oxidation process at 1000°C to provide an oxide surface approximately 5000Å thick. These wafers, too, were sintered for 60 min at 400°C in forming gas (90% N_2-10% H_2). That was part of the process forming the MOS structure.

Analytical Examination

Traditionally, retention time measurements have been used to attest to the cleanliness of reactors and their freedom from heavy metal contamination. All sources of heavy metal contaminants had been removed (*e.g.*, replacing stainless steel components with aluminum, as confirmed by Auger, x-ray, fluorescence, and neutron activation analysis). All silicon wafers exposed to a CF_4/H_2 plasma for 30 min exhibited unacceptably large leakage currents. It became obvious that our problem was not one of contamination.

Published data on MOS devices have suggested that CF_4/H_2 plasmas can cause possible damage on silicon surfaces (6). This investigation now concentrated on studying the structural changes due to plasma exposure.

Experimental Results

Our main techniques were Rutherford backscattering, secondary electron microscopy (SEM), and transmission electron microscopy (TEM), as well as some secondary ion microscopy (SIMS) profiles. Figure 1 is an SEM picture of a silicon surface reactively ion etched in CF_4/H_2 that had been oxidized (~5000A).

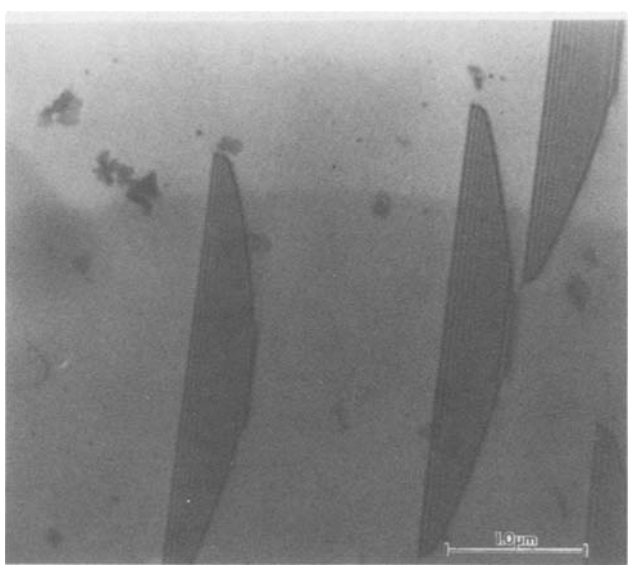

Fig. 1. Oxidized RIE silicon surfaces after oxide stripping and Wright etch.

* Electrochemical Society Active Member.

This oxide was stripped and the surface was delineated with Wright etch. SEM's taken before and after oxidation Wright etch did not show any texturing of the surface. Oxidation stacking faults are clearly evident, however, no such defects were found on a surface previously unexposed to the plasma. It is obvious that this RIE damage cannot be removed by thermal oxidation. Oxidation of the reactively ion etched surface drives the damage into the bulk of the silicon, hence forming the stacking faults. As previously mentioned, the retention time measurement technique was the method used to screen the etched wafers to define an acceptable process. Leakage currents peaking at 300 pA or less were considered acceptable. Table I is a summary of the significant experiments. The following observations can be made: CF_4 and CF_4/He are the only etch gases looked at during these experiments that do not show high leakage currents. However, when hydrogen is present in the plasma either as CF_4/H_2 or CHF_3, the leakage currents are large, unless the total time of plasma exposure of the wafer is less than 10 min. A reduction in the leakage current is noted when a CF_4/H_2 plasma is followed by a pure CF_4 plasma. Pure hydrogen or helium plasma produces huge leakage currents. Figure 2 shows that MOS device leakage, due to silicon damage, increases with etch time in CF_4/H_2 at 350W. Therefore, it is evident from Fig. 2 that etch times greater than 5 min produced large increases in MOS leakage currents. Shorter etch times resulted in leakages of 200-300 pA. The amount of surface damage, and hence leakage, also increased with power for a constant etch time of 30 min (see Fig. 3). Obviously, to enhance device performance junction leakages have to be minimized. This data indicates that high leakage currents could be the result of accumulated surface damage.

Comparing the leakage data after 30 min of etching in CF_4-deuterium, and CF_4-H_2 a clear trend can be seen to increased leakage with decreasing atomic weight of the addition to CF_4, namely, He, D, H. This is an indication of a possible role of implementation of the light species. Their ranges, and the displacement damage which they cause in the Si surface layer, increases with decreasing atomic weight. This is explored further in the Discussion section.

Structural Analysis

The analytical Rutherford backscattering technique is documented elsewhere (7). Briefly, a high energy helium ion beam is impinged on and backscattered from a silicon sample. When the direction of the incident beam is aligned with the crystalline direction, a channeling condition is fulfilled. Backscattering channeling of light ions provides the information on the amount of surface damage in the silicon. For example, Fig. 4 shows three channeling backscattering spectra of 2.3 MeV helium ions from three different samples. The incident beam is aligned with the 100 direction. This alignment reduces the backscattering probability

Table I. Comparison of retention time leakage data as a function of various cases

RIE conditions	Leakage (PA)	Damage layer equivalent* (thickness, A)
CF_4 30 min	175	7
CF_4 25 min and CF_4/H_2 5 min	375	12
CF_4/H_2 25 min and CF_4 5 min	937	
CF_4/H_2 10 min	552	
CF_4/H_2 30 min	118,000	32
CHF_3 30 min	73,010	15
CF_4-deuterium 30 min	5,993	
CF_4-helium 30 min	171	
Hydrogen 30 min	43,758	160
Helium 30 min	125,000	240

* Assume bulk density for damaged layer which is uniformly distributed, e.g., 3.5×10^{15} Si/cm^2 out of lattice sites equivalent to 7A Si 350W 35.

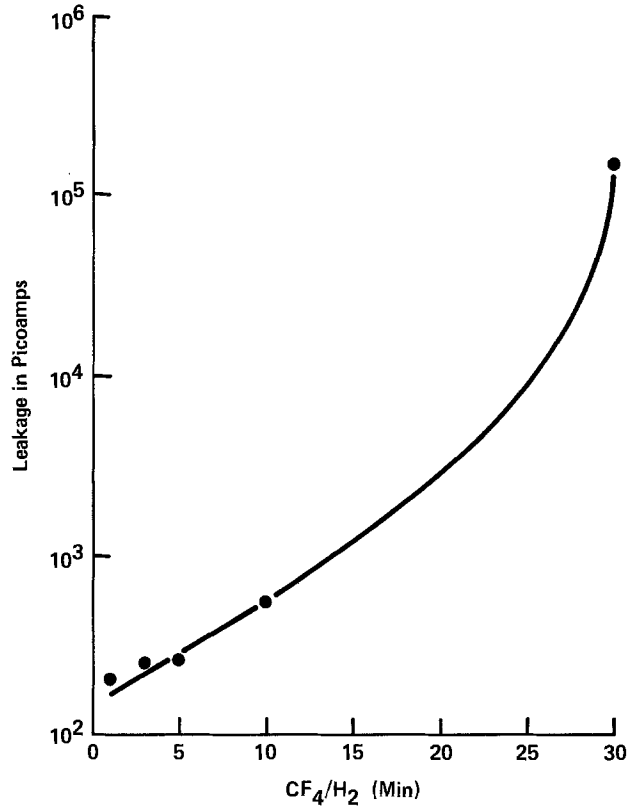

Fig. 2. MOS leakage as a function of CF_4/H_2 etch time

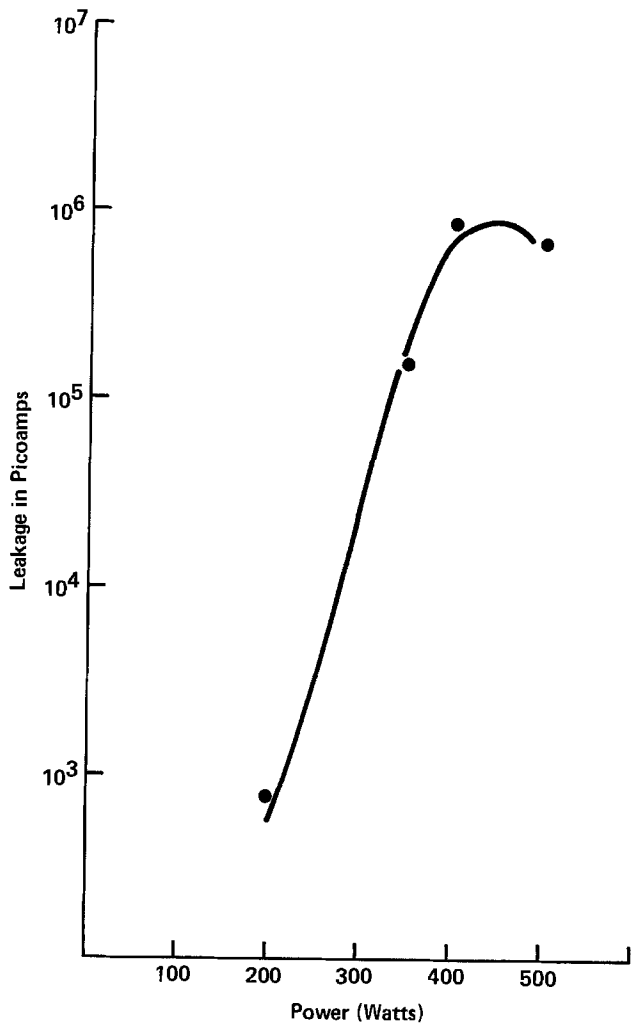

Fig. 3. MOS leakage as a function of power for a CF_4/H_2 etch time of 30 min.

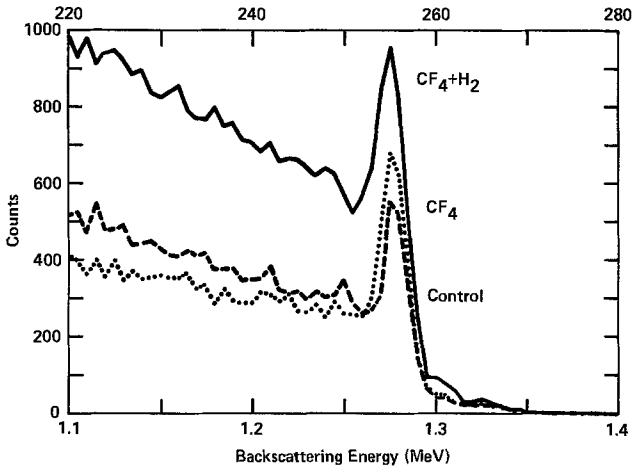

Fig. 4. Backscattering spectra of 2.3 MeV helium ions from three different silicon surfaces.

by a factor of 40 for silicon atoms on the lattice site and makes the damage peak stand out. The solid curve in Fig. 4 is the spectrum for a sample subjected to 30 min of $CF_4 + H_2$ reactively ion etched. The dotted curve is obtained after CF_4 exposure without hydrogen, the dot-dash curve is that of an unetched control sample. The surface peak on the control sample is due to the backscattering of the first monolayer of silicon atoms, plus the subsequent layer of silicon atoms not shadowed by the first layer due to thermal vibration. The total area under a surface peak is a direct measurement of the amount of silicon atoms not on the lattice site after subtraction of the background, which is obtained from the control sample. For example, Fig. 4 indicates that there are 3.5×10^{15} and 1.6×10^{16} silicon atoms per square centimeter which have been displaced from their lattice sites for CF_4 and $CF_4 + H_2$ etched samples, respectively. If it is assumed that the displaced silicon atoms were stacked into a thin layer of amorphous silicon, the number of displaced silicon atoms per square centimeter could be translated into a layer thickness. For example, Fig. 4 indicates that the number of silicon atoms displaced from their lattice sites would be equivalent to an amorphous layer of 7Å for $CF_4 + H_2$ etch sample.

Summarizing the backscattering data, Table I shows the amount of damage in angstroms of the amorphous silicon layer. This way of expressing the data is convenient because it provides a more graphic presentation of the damage. By no means are we implying that the damage is a thin amorphous layer. The damage could be distributed in the depth of a thicker layer of predominantly crystalline character as well. For further characterization, microscopic methods must be used.

Transmission Electron Microscope Analysis

TEM specimens were prepared by chemical thinning of the samples from the back side. In this way, the defect structure near the top surface is accessible to inspection.

Figure 5 shows bright field and dark field micrographs of silicon after 30 min of reactive ion etching in CF_4/H_2. Dislocation loops with up to 20 nm diam are visible. They are agglomerates of Si interstitials. The compressive nature (and hence interstitial character) of the defects is best seen from the curvature of the thin foil which causes local changes of the Bragg reflecting condition. For Fig. 5 the foil was oriented in such a way that the Bragg condition was exactly fulfilled in a vertical band in the center of the micrographs. To the left, the deviation from the exact Bragg condition was found to be negative and to the right it was positive. This leads to the curvature diagram at the bottom of Fig. 5.

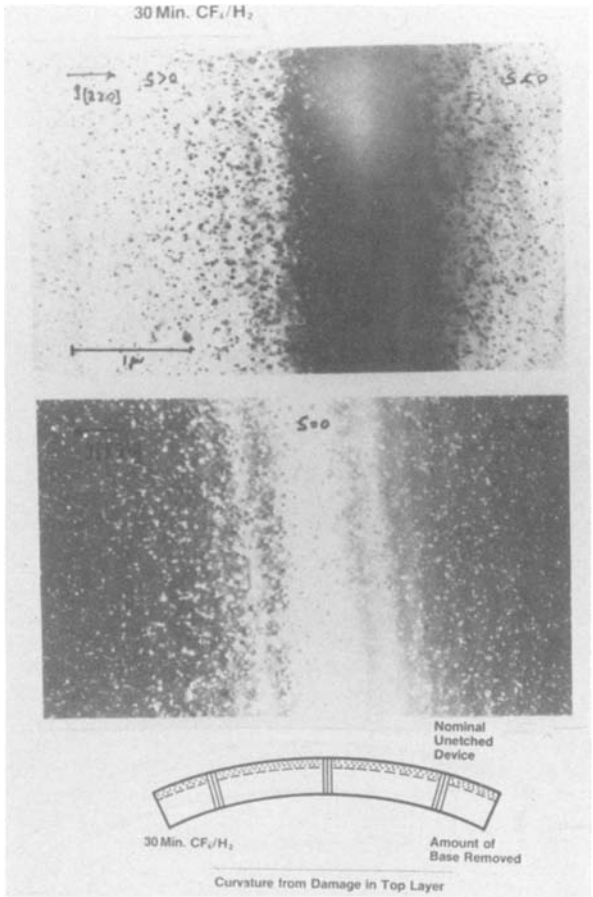

Fig. 5. Bright and dark field micrographs after 30 min RIE CF_4/H_2.

Figure 6A shows a darkfield micrograph after 5 min of reactive ion etching in CF_4/H_2. No dislocation loops are present. Figure 6B shows the same situation after exposure to CF_4 only. No dislocation loops are visible.

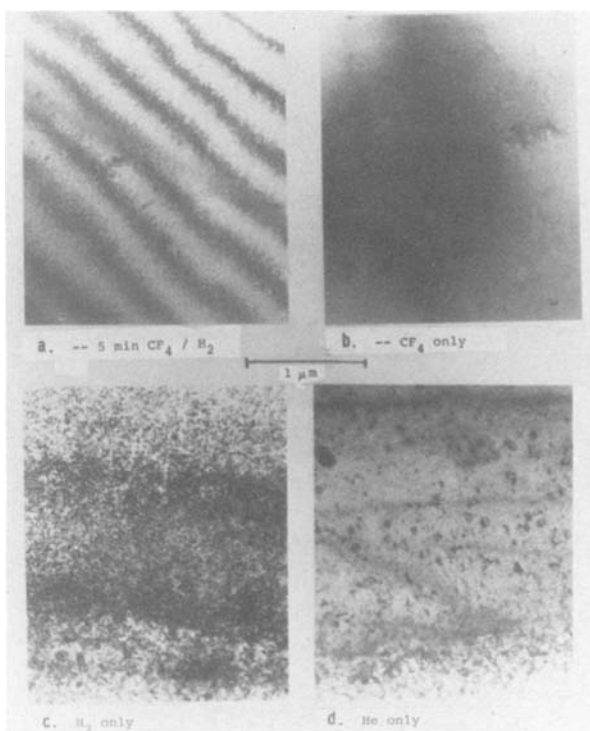

Fig. 6. Dark field micrographs of silicon surfaces RIE'd by: A, CF_4/H_2; B, CF_4; C, H_2; and D, He.

The backscattering and TEM results described so far indicate that the damage is of a physical nature (namely, consisting of Si atoms displaced from regular lattice sites and of agglomerates of Si interstitials) and that hydrogen plays a role in generating this damage. To further pursue the role of hydrogen, some wafers were exposed for 30 min to pure hydrogen and helium plasmas. Helium is another atom of small mass but different chemical properties. Backscattering-channeling results indicated large numbers of displaced Si atoms for both plasma exposures (see Table I). Similarly, TEM micrographs (Fig. 6C and D) show a dense structure of compression centers, dislocation loops, and possibly gas-filled microblisters. This structure is the same as obtained by ion implantation of H_2 (in the 100 keV range) near the end of the projectile's path (8).

It is apparent that CF_4/H_2 leaves less displacement damage in the Si surface layer than H_2 only. Under the experimental plasma conditions, a 5 min exposure is not even sufficient to produce agglomerations of interstitials that would be visible by TEM.

Impurity Profiles by Secondary Ion Mass Spectrometry (SIMS)

In order to detect any residues of H, C, and F in the wafer which had been exposed to CF_4/H_2 plasma for 30 min, a SIMS depth profile was obtained and is shown in Fig. 7.

The depth scale (in angstroms) is obtained from the calibrated sputter etch rate, while the ordinates are relative count rates. In the absence of suitable standards, these values cannot be converted to concentrations. Because there is less sensitivity for hydrogen detection in the SIMS technique, not much is inferred from it. The sensitivity is better for C and F. Figure 7 shows that C penetrated about 120Å, and F to about 350Å.

Discussion

The analytical work, in particular TEM observations, have shown that exposure of an Si wafer to hydrogen and helium containing plasmas generates a unique defect structure. It consists mainly of Si atoms that were displaced from their lattice sites, migrated several nanometers, and reorganized into interstitial dislocation loops with diameters up to 20 nm. This defect structure is quite different from the one resulting from sputtering (with, *e.g.*, Ar ions), which generates an amorphous surface layer of one to several nanometers thickness. It is also different from the damage created by low energy implantation of typical dopant ions, which consists of localized (at the end of the projectile's path) displacement cascades or amorphous zones of one or several nanometers diameter (10).

It is reasonable to assume that a wafer is bombarded during plasma exposure by all ion species that are present in the plasma. The more energetic ions can penetrate into the wafer and cause displacement damage. The question arises: is there a significant difference in the nature of displacement damages made by H and He compared to other ion projectiles? In particular, does the H and He displacement damage contain a component which can diffuse in the crystal during plasma exposure? The facts that recoiled Si atoms had reorganized themselves into dislocation loops and that C and F penetrated deeper than 10 nm indicate that some diffusion had taken place.

Ions that enter a solid with initial kinetic energy E_0 are slowed by electronic losses (which are approximately proportional to their velocity) and by nuclear collisions. The relative importance of the two mechanisms depends on the projectile mass; nuclear energy losses are more important for heavy ion masses. In a collision, a fraction of the kinetic energy of the projectile is transferred to the target atom. This fraction is the largest for equal masses of projectile and target atom and decreases with decreasing projectile mass. If the energy transferred to the target atom is above a threshold value, E_D, the target atom is displaced from its lattice position and converted into an interstitial atom. If the transferred energy is twice E_D, the primary recoil can generate a second interstitial atom. With larger transferred energies, whole cascades of displaced atoms are formed. The distances between individual displacements in a cascade are generally within one or a few interatomic distances. They transform a small volume of Si into amorphous zones which are generally stable. The source of diffusion (in the present case) is probably associated with displacement of single atoms where the special separation between recoil events is several interatomic distances (larger than 1 nm).

Model calculations for H (Fig. 8), He, C, F, and Si projectiles show that H is efficient in generating widely dispersed interstitial atoms of Si. With $E_0 = 1$ keV and $E_D = 20$ eV, one obtains about five interstitials separated by 5 nm or more. This is because the energy transfer during a collision is so inefficient that the primary recoil cannot generate a cascade. C, F, and Si, on the other hand, generate cascades or closely

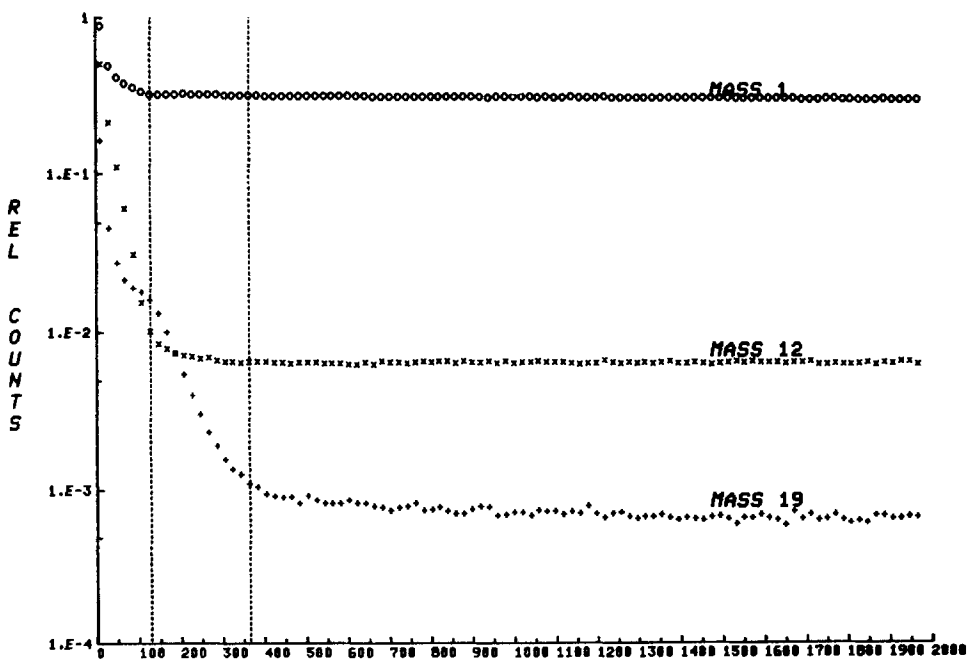

Fig. 7. RIE damage by SIMS. PC-5 front. LN2 cooled.

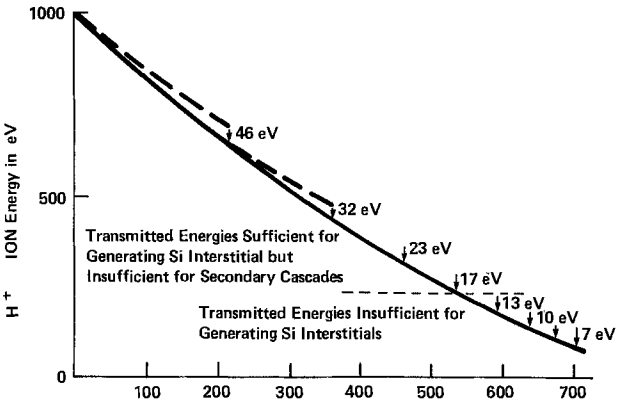

Fig. 8. Distribution of discrete nuclear collision losses along the path of hydrogen ions.

spaced interstitials within less than 1 nm of each other. He occupies an intermediate position and generates three small cascades and three recoils with separations between 1.5 and 3 nm.

The dividing line between the separation of point defects trapped in stable clusters and the separation of point defects, which are assumed to be freely mobile, is ordinarily taken to be 1 nm. A different figure, say 0.5 nm, does not change the qualitative difference between light and heavy ion projectiles. The displacement damage generated by H and He produces point defects that can diffuse during plasma exposure, while the heavier projectiles produce clusters in which most of these defects remain trapped.

These clusters are close to the surface, not deeper than about 3 nm, and they constitute what usually is considered sputtering damage. The mobile defects agglomerate to form dislocation loops at depths of up to 30 nm.

These dislocation defects are not removed by subsequent annealing and oxidation. They propagate into the silicon substrate in the form of oxidation stacking faults. It is this type of defect that would impair device yields and cause leakage in the MOS capacitors.

Silicon samples reactively ion etched by CF_4 alone have a very low defect density. Samples etched by CF_4 + He also have low defect densities. This is presumably because damage layer creation by helium plasma and layer removal by CF_4 reaches a dynamic equilibrium. In the case of $CF_4 + H_2$ reactive ion etching of silicon, the silicon etch rate is very slow and damage due to hydrogen bombardment accumulates with etch time. The longer the duration, the more the defect generation. This study indicates that a 5 min etch on silicon by $CF_4 + H_2$ produces no significant detrimental effects of the silicon surface (9).

Device Implications

A CF_4/H_2 process resulting in an SiO_2/Si etch rate ratio of about 10:1 has been practiced on bipolar devices. Electrical yield data obtained with in-process silicon probing, as well as fully metallized device wafers on split lots, has revealed no detrimental effects on low leakage yield.

Conclusions

This study indicates that the mechanism of defect formation in CF_4/H_2 RIE is not chemical. It is due to the hydrogen bombardment of the silicon surface. This damage accumulates, since the rate at which it forms is faster than the etch rate of silicon when silicon wafers are exposed to hydrogen plasmas. The damage and defect formation are very similar to that observed in hydrogen ion implantation. Similar defects have been observed with CF_4/He plasmas. Subsequent annealing and oxidation did not remove this defective layer. Propagation of defects into silicon substrates was observed in the form of stacking faults below the silicon dioxide-silicon interface during thermal oxidation.

These defects cause the lifetime degradation of MOS capacitors and the defects are caused by the ion bombardment. The degree of damage can be reduced by shortening the time the silicon surface is exposed to the hydrogen containing plasma, and good devices have been made.

Acknowledgment

The authors wish to thank a number of colleagues whose assistance and support made the work possible. Special thanks to H. S. Wildman and R. M. Strang, for the Auger analysis; R. T. Scott and D. Bouldin, for the neutron activation analysis; R. Kastl, for SIMS; and P. Smith and A. Leighton for additional TEM work. A special note of thanks is extended to R. L. Pistor, who automated the retention time test tool. The test tool provided a rapid measurement for a large number of samples. Last, but not least, the authors wish to thank G. C. Schwartz for her suggestions and initial review of this manuscript.

Manuscript submitted Feb. 15, 1983; revised manuscript received June 6, 1983. This was Paper 279 presented at the Denver, CO, Meeting of the Society, Oct. 11-16, 1981.

IBM Corporation assisted in meeting the publication costs of this article.

REFERENCES

1. R. Heinecke, U.S. Pat. 3,940,506 (1976).
2. J. W. Coburn, *J. Appl. Phys.*, **50**, 5210 (1979).
3. F. J. Montillo, M. R. Poponiak, and R. L. Pistor, 6th Symposium on Solid State Device Technology, Toulouse, France, S6.4 (1981).
4. W. Kern and D. Puotinen, *RCA Rev.*, **31**, 187 (1970).
5. M. Zerbst, *Z. Angew. Phys.*, **22**, 30 (1966).
6. K. Kurosawa, Y. Horiike, H. Okano, and K. Okumura, Proceedings of 2nd Symposium on Dry Etching, Tokyo, Japan, pp. 43-48 (1980).
7. W. R. Chu, J. W. Mayer, and M. A. Nicolet, "Backscattering Spectrometry," Academic Press, New York (1978).
8. W. R. Chu, R. A. Kastl, R. F. Lever, and S. R. Mader, in "Ion Implantation in Semiconductors," Fa Chernow *et al.*, Editors, Plenum Publishing Co., New York (1977).
9. F. J. Montillo, W. K. Chu, R. G. Frieser, and S. R. Mader, Abstract 279, p. 681, The Electrochemical Society Extended Abstracts, Denver, CO, Oct. 11-16, 1981.
10. J. F. Gibbons, *Proc. IEEE*, **60**, 1062 (1972).

Plasma Processing of Thin Chromium Films for Photomasks

B. J. Curtis,* H. R. Brunner, and M. Ebnoether

Laboratories RCA Limited, 8048 Zurich, Switzerland

ABSTRACT

The preparation of photomasks from thin chromium films on glass substrates is described using both optical and electron beam resists. Plasma processing techniques are used both for pattern definition and for a passivation step prior to either plasma or liquid etching that enables the image to be reversed, *i.e.*, to produce a negative image with a positive resist or vice versa. Plasma etching conditions, using mixtures of carbon tetrachloride and oxygen are described that allow the use of PBS resist which is much less robust than other electron beam or optical resists. Pattern reversal is achieved either by first exposing the patterned chromium to a tungsten hexafluoride plasma after which the resist is stripped and the unpassivated chromium is plasma etched, or the patterned chromium is exposed to an oxygen, argon, or sulfur hexafluoride plasma, the resist is stripped, and the chromium is liquid etched in a mixture of ceric ammonium sulfate and sulfuric acid. In the first case, passivation of the exposed chromium is achieved by the deposition of a thin tungsten layer that is resistant to plasma etching and in the second case by the deposition of material back sputtered from the substrate electrode (*e.g.*, silicon dioxide) that is insoluble in the liquid etchant.

Photomasks, in which the desired pattern is defined in a thin film of chromium that is evaporated onto a transparent substrate, have been in use in the semiconductor industry for many years (1). Chromium has the advantages of excellent adherence to glass, high scratch and wear resistance (especially important if contact printing techniques are still in use), freedom from attack by solvents, and versatile etchability with good edge definition (due to its high optical absorption, 0.08 μm Cr has absorption equivalent to 4 μm of Ag photographic emulsion). Such masks are capable of transferring patterns with dimensions at least as small as 0.15 μm; these structures may be defined in the chromium by either optical or electron beam patterning procedures.

Up to the present time, pattern transfer of a structure defined in resist that is coated upon the chromium has been accomplished largely by wet etching techniques. There are a number of reports in the literature in which chromium photomasks are prepared by plasma etching using carbon tetrachloride or chlorine mixed with oxygen (2-5) or carbon tetrafluoride mixed with oxygen (6). This report describes the application of plasma processing to the etching of chromium photomasks. It also describes methods for the reversal etching of chromium in which the exposed areas on a resist-patterned surface are passivated by a plasma treatment, the resist is stripped, and the unpassivated chromium is subsequently either liquid or plasma etched.

The main problem that is posed by the plasma etching of chromium is the high erosion rate of the resist. Fortunately, the chromium film that is used as the mask is usually no thicker than about 1000Å. If a resist layer about 3000Å thick is used, this means that a Cr:resist etch rate ratio of 0.3:1 can be tolerated. This becomes of particular importance when electron beam resists are used for pattern definition since they are much less robust under plasma etching conditions than are optical resists. The fact that the chromium film is relatively thin means that if the dimensions of the structures to be etched are no smaller than about 1.0 μm, any undercutting that may arise from an isotropic etching component has no great effect on the linewidth of the etched pattern. It is probably for this reason as much as any that the plasma etching of chromium has not received as much attention as the etching of other materials. However, as the packing density of integrated circuits increases, it is possible that considerations such as lower defect density and more etching anisotropy will increase the need for dry processing in chromium mask making.

* Electrochemical Society Active Member.

Experimental

Chemistry.—The deciding factor that determines the plasma etchability of any material is whether a suitable compound exists that is volatile enough under the etching conditions to be removed from the etched surface by the pumping system. The halides of chromium have boiling or sublimation points well above 500°C. Chromium carbonyl boils at 151°C, but a suitable etching chemistry based on this compound is not known at present. Possible volatile compounds are the oxyhalides, chromyl chloride, CrO_2Cl_2 (bp 117°C) and chromyl fluoride, CrO_2F_2 (gaseous at room temperature). In order to form either of these compounds, it is necessary to mix either the chlorine-containing or the fluorine-containing etch gas with a large proportion of oxygen; it is because of this that resist erosion is such a problem. We used gaseous mixtures of carbon tetrachloride and oxygen for all of the plasma etching experiments to be reported here. The carbon tetrachloride was contained in an aluminum vessel and was transferred to the etching chamber under its own vapor pressure via a float-type flowmeter.

Procedure and apparatus for normal etching.—The resist erosion rate is very high if reactive sputter etching of chromium (20 mTorr pressure, substrate on the powered electrode) is attempted due to the higher energies of bombarding particles which result in an unusable etch rate ratio. Thus, chromium must be etched under plasma etching conditions (pressure greater than 200 mTorr, substrate on the grounded electrode or floating in a barrel reactor).

Our etching experiments have been carried out mostly in a home-built parallel plate reactor which consisted of a borosilicate glass cylinder 30 cm in diameter and 35 cm high with stainless steel end plates and 14 cm diam stainless steel water-cooled electrodes spaced 40 mm apart run at 13.56 MHz. The gases were fed in through a side arm in the glass chamber using a calibrated float-type flowmeter for the carbon tetrachloride and mass flow controllers for the other gases. The system was evacuated through the center of the lower electrode by means of a rotary pump via a liquid nitrogen trap. The substrates were placed on the lower, grounded electrode. A few etching experiments were also carried out in a barrel reactor (International Plasma Corporation Model PM-1913).

Procedure and apparatus for reversal etching.—The observation that chromium films a few months old etch more slowly than fresh films in an aqueous solution of sulfuric acid and ceric ammonium sulfate led to the suggestion that it might be possible to passivate chromium by exposing it to an oxygen plasma such

that, after stripping the resist, those parts that had been covered by tne resist would liquid etch whereas the passivated regions would be unattacked. As we shall see later, although this procedure will enable reversal etching to be carried out, the mechanism by which it occurs is not so simple as was at first thought, since plasma processing in an inert gas such as argon also passivates chromium toward liquid etching.

A reversal plasma etching method reported by Nishioka *et al.* (5) gave us the idea that a chromium surface could be passivated to an etching plasma. In their method, chromium patterned by photoresist is etched at high power in a carbon tetrachloride/oxygen or wet air plasma. If the chromium surface is contaminated by a tungsten compound, which originates from the boat or heating spiral in the evaporation step, a reversed pattern is obtained. This occurs because tungsten compounds do not etch in a chlorine containing plasma since tungsten chlorides are involatile under those conditions. During the plasma etching, a reaction occurs between the photoresist and the underlying tungsten surface contamination. Etching is continued until all of the resist has been removed, at which point all of the tungsten contamination has reacted and also been removed. As etching continues, these now uncontaminated areas etch away and those regions that never had been covered by resist retain their contamination and do not etch, thus reversing the pattern.

A plasma pretreatment step is required for our reversal etching process. This is carried out in the sputtering mode, *i.e.*, at a pressure around 20 mTorr with the substrate resting on a powered electrode run at 13.56 MHz. The normal arrangement was to have the substrate resting on a silicon dioxide backing plate which rested on the powered copper electrode. As we shall see later, this has important implications. The home-built system that we used had a diffusion-pumped aluminum chamber, 30 cm in diameter, which served as the grounded electrode, with a powered, 15 cm diam water-cooled electrode; no counterelectrode was used. Figure 1 shows schematically the two routes that we have used for reversal etching. The pretreatment, or passivation, is done with tungsten hexafluoride for plasma reversal etching and with oxygen, argon, or sulfur hexafluoride for liquid reversal etching. The resist is stripped in a conventional solvent using ultrasonic agitation. The liquid etchant contained 28 ml of concentrated sulfuric acid and 64g of hydrated ceric ammonium sulfate per liter of water. Untreated chromium etched at about 500Å/min in this. Changes in the thickness of the resist are measured by a laser interferometer that operates through a window in the top plate of the reactor. It is important to have this facility available because the plasma passivation erodes the resist and, obviously, this treatment should be stopped before all the resist has been removed, otherwise the entire chromium surface would be passivated.

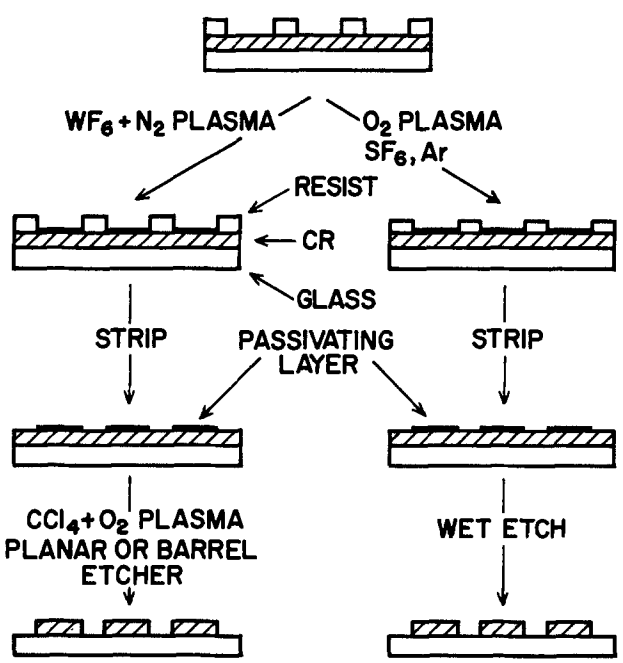

Fig. 1. Two routes for the reversal processing of chromium

Results

Conventional patterning using AZ1350 resist.—The etching characteristics of chromium and AZ1350 resist were studied as a function of gas composition, pressure, and plasma power at a constant total flow rate of 40 sccm. As the pressure was decreased to below about 250 mTorr, the plasma became increasingly unstable, eventually focusing itself into a volume of a few cubic centimeters between the electrodes. The power density in this "fireball" was much higher than in the normal discharge and it also moved around between the electrodes. Thus, the lowest pressure used for the experiments to be described in this section was 250 mTorr.

The etch rate of chromium can vary from batch to batch when either liquid or dry etching methods are used, which accounts for the differences in chromium etch rates shown in Fig. 2 and 3. This is related to its surface condition and can be taken advantage of in the reversal etching of chromium as is discussed below. The etch rates of chromium and AZ1350 as a function of pressure for a 1:1 mixture of carbon tetrachloride and oxygen are shown in Fig. 2. As the pressure is decreased, the etch rates of chromium and resist begin to increase at around 400 mTorr. Light emission also increases indicating that the plasma is much denser. The etching selectivity of chromium: photoresist goes through a maximum at about 40% carbon tetrachloride in oxygen (Fig. 3). Chromium

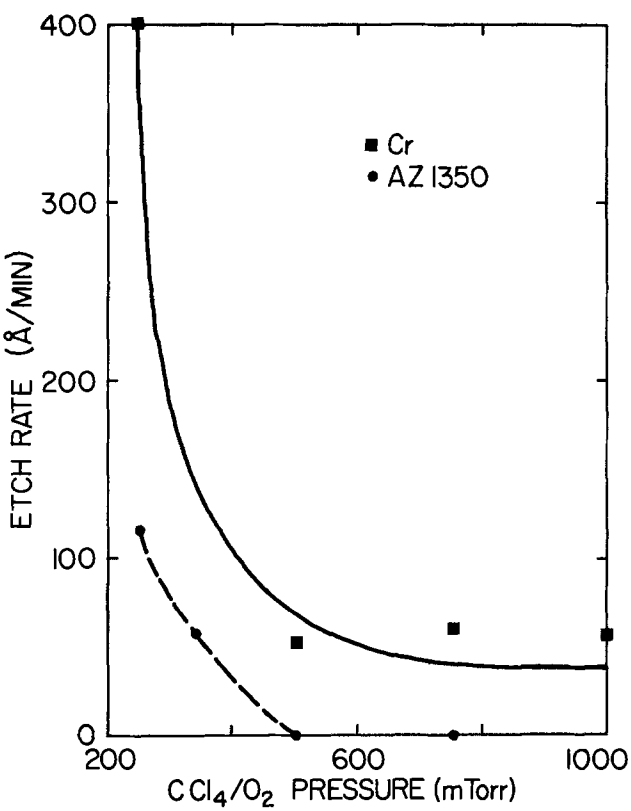

Fig. 2. Plasma etch rates of chromium and AZ1350 as a function of gas pressure for a 1:1 mixture of carbon tetrachloride and oxygen at 30W (0.17 W-cm^{-2}). ■ Cr; ● AZ1350.

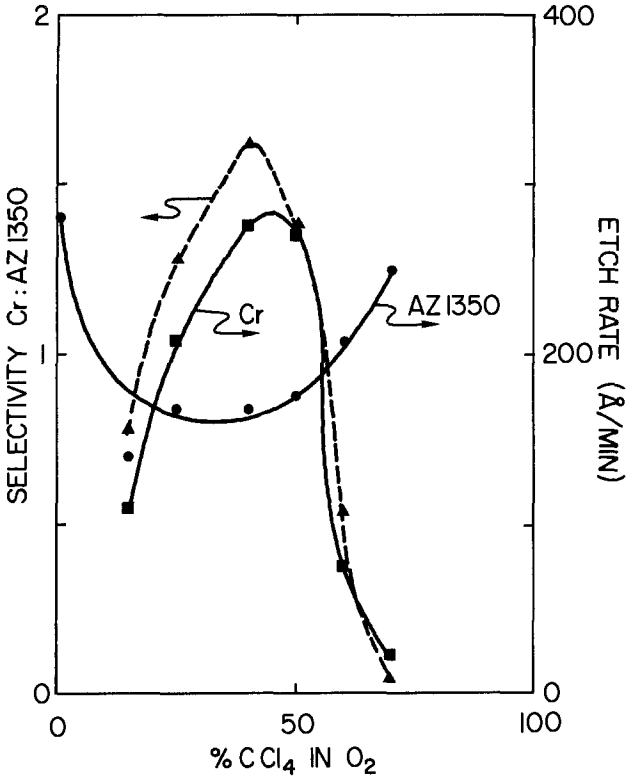

Fig. 3. Etching selectivity of chromium: AZ1350 *vs.* percentage of carbon tetrachloride in oxygen. Pressure 250 mTorr, 50W (0.28 W-cm^{-2}). Selectivity; ● AZ1350; ■ Cr.

does not etch at all in pure carbon tetrachloride due to the formation of involatile chromium chlorides at the surface. The dependence of the selectivity on the plasma power is shown in Fig. 4. For our parallel

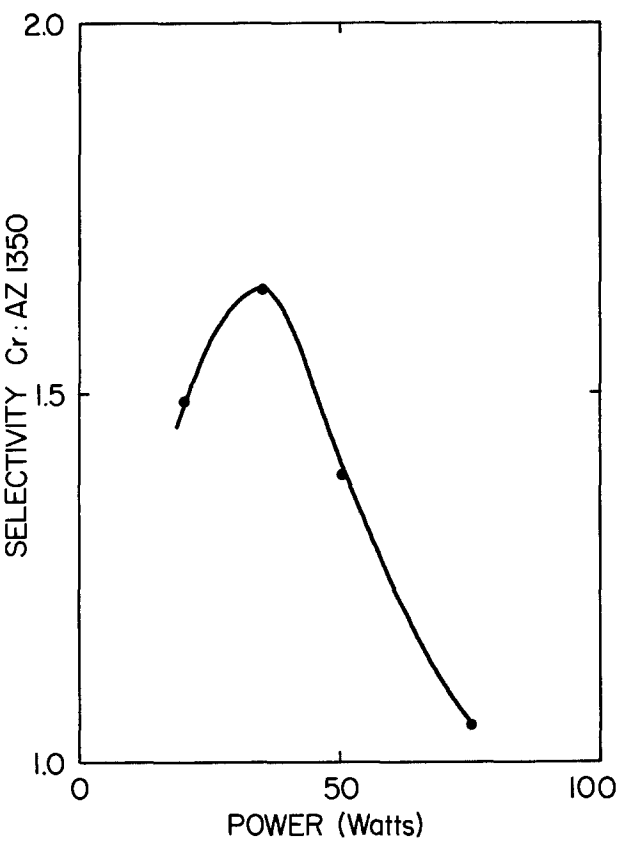

Fig. 4. Power dependence of the etching selectivity of chromium: photoresist for 50% carbon tetrachloride in oxygen at 250 mTorr.

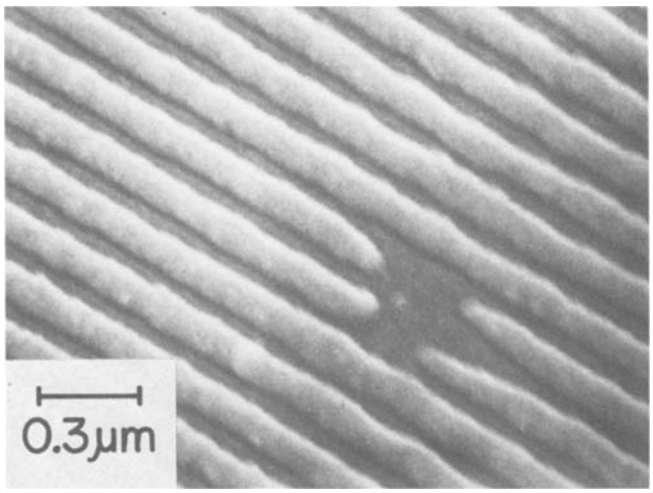

Fig. 5. 0.3 μm periodicity grating plasma etched into 300Å chromium masked with AZ1350 (resist stripped).

plate etcher, the optimum conditions for chromium etching using AZ1350 as a mask are: gas composition, 50% carbon tetrachloride in oxygen; gas pressure, 250 mTorr; total flow rate, 40 sccm; power, 35W (0.23W cm^{-2}).

A 0.3 μm periodicity grating etched into 300Å of chromium using these conditions is shown in the SEM picture of Fig. 5. The defect in the center of the picture helps to make the actual line profile more visible. The original grating in AZ1350 resist was prepared by laser interference. Apparently the line profiles are rounded; this could be due to either a rounded resist profile after the laser exposure and subsequent development or to an isotropic component in the etching step. Gratings such as this have been used successfully as etch masks or as photomasks for the contact printing of fine gratings in photoresist.

Conventional pattern definition using electron beam resists.—Electron beam resists must, by their very nature, be sensitive to electron bombardment. It is, therefore, not surprising that they have much higher erosion rates in the plasma than photoresists. Thus, it is necessary to keep the energy of the various species in the plasma as low as possible by operating at a low plasma power and a high pressure. The dependence of the etch rates of chromium, COP, and PBS resists and their etch rate ratios on pressure at 35W (0.23W cm^{-2}) is shown in Table I. As mentioned above, the plasma becomes much more dense at low pressures which is reflected in the increased etch rates of chromium and resist. PBS has much less resistance to the plasma than COP, which is unfortunate since PBS finds wider application and has the higher resolution of the two.

It can be seen from Table I that the chromium etch rate remains more or less constant in the pressure range 500-1000 mTorr but that the selectivity improves as the pressure is increased. Thus, our standard plasma etching conditions for chromium using PBS electron beam resist are: gas composition, 50% carbon tetrachloride in oxygen; gas pressure, 1000 mTorr; total flow rate, 40 sccm; power, 35W (0.23W cm^{-2}).

Table I.

Pressure	Etch rates (A/min)			Etch rate ratio	
(mTorr)	Cr	PBS	COP	Cr:PBS	Cr:COP
1000	56	33	2	1.7:1	25:1
750	60	75	2	0.8:1	25:1
500	52	104	43	0.5:1	1.2:1
250	400	2000	500	0.2:1	0.8:1

A comparison of liquid etched (spray method using a mixture of ceric sulfate and nitric acid) and plasma-etched structures that had been masked by PBS is shown in Fig. 6. The patterns were generated in an MEBES machine under conditions that would produce structures suitable for liquid etching. No difference can be seen between the liquid etched (Fig. 6b) and the plasma etched pattern (Fig. 6c); 0.5 μm lines and spaces are resolved on both. SEM photographs reveal differences in the etched profiles. The sidewalls on the liquid etched sample (Fig. 6d, the same magnification as Fig. 6e) slope at 45° as expected from an isotropic etch. The plasma etched sample (Fig. 6e), on the other hand, has sidewalls that slope at a much shallower angle due to resist erosion during the etching. Figure 6a shows that the resist profile is roughly sinusoidal and erosion of such a profile during etching will cause the etched structure to have sloping sidewalls. However, for structures with dimensions down to about 0.5 μm, these tapered walls do not seem to affect the linewidth of the mask when viewed in projection. The other difference that is noticeable is that the surface, after stripping the resist in an oxygen plasma, is clean for liquid etched chromium whereas a residue is left behind after plasma etching.

Reversal etching.—With plasma pretreatment and liquid etching.—All of our initial experiments on liquid reversal etching were done using an oxygen plasma for the passivation step; later on, the need arose to reverse etch "black" chromium, *i.e.*, chromium that had been made antireflecting by coating it with a thin film of chromium oxide. We thought at first that treatment in an oxygen plasma would not work, since an oxide film was already present on the surface. Therefore, we used a sulfur hexafluoride plasma with the hope that chromium fluoride would be formed and so render the surface passive to the liquid etch. This in fact worked but probably not for the reason that we originally thought. A comparative study showed that both bright and black chromium can be passivated toward the liquid etch in a plasma containing either oxygen, sulfur hexafluoride, or argon. This clearly indicates that an additional factor apart from a reaction between the plasma and the chromium surface plays a role in the passivation and this is discussed in what follows.

In order to judge the effectiveness of the passivation step, the clearing times for passivated and unpassivated areas were measured and the etch rate ratio was calculated. The variation of this etch rate ratio as a function of pressure, time, and plasma power is shown in Fig. 7, 8, and 9, respectively. A number of interesting points can be seen from these curves. The most striking is the difference in passivation effect between black

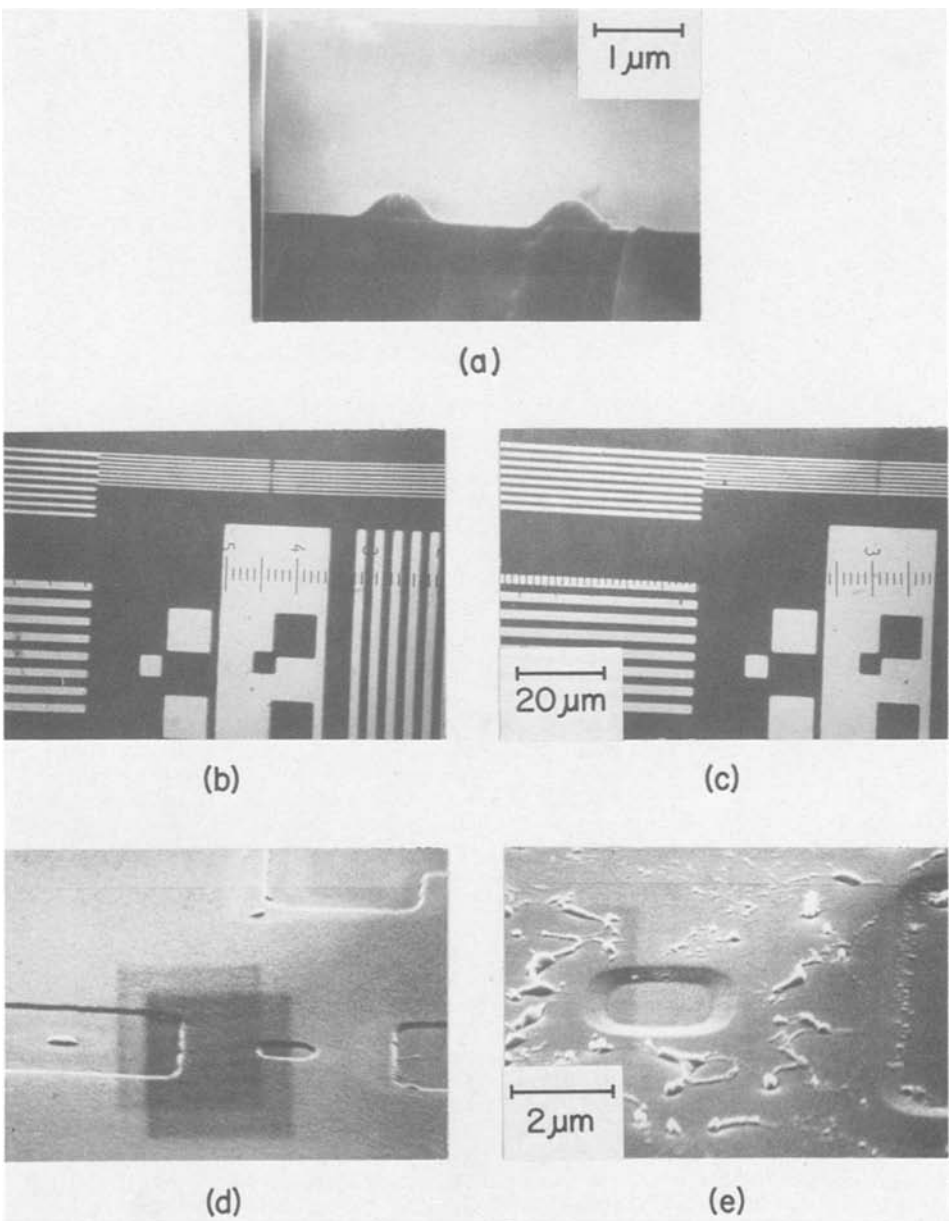

Fig. 6. Comparison of liquid-etched and plasma-etched structures masked by PBS electron beam resist. (a) Resist profile as prepared in the MEBES machine. (b) and (d) Optical and SEM micrographs, respectively, of liquid-etched chromium film. (c) and (e) Optical and SEM micrographs, respectively, of plasma-etched chromium film.

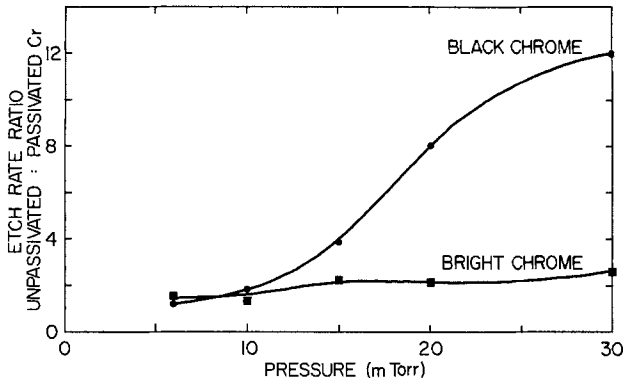

Fig. 7. Pressure dependence of the liquid etch rate ratio of unpassivated to passivated bright and black chromium. 150W (0.9 W-cm^{-2}) in argon with SiO_2 backing plate.

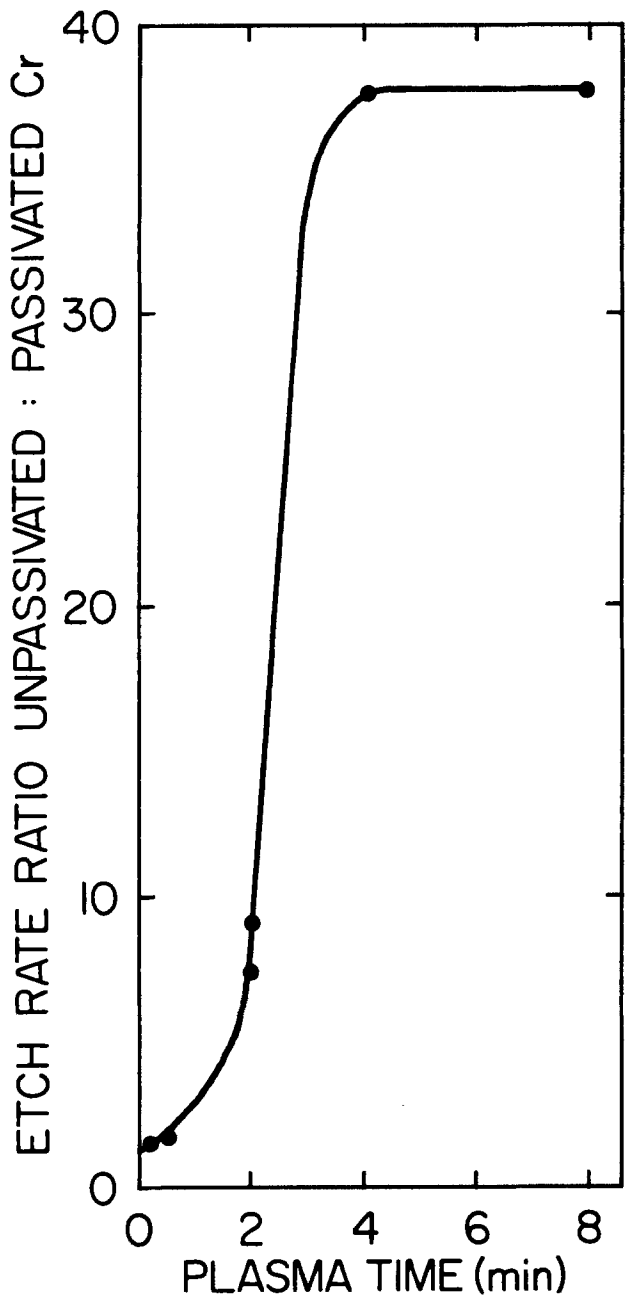

Fig. 8. Variation of the etch rate ratio of unpassivated to passivated black chromium with argon plasma treatment time. 100W (0.57 W-cm^{-2}) and 20 mTorr oxygen with an SiO_2 backing plate.

chromium and bright chromium (Fig. 9); black chromium (curve A) passivates much more efficiently

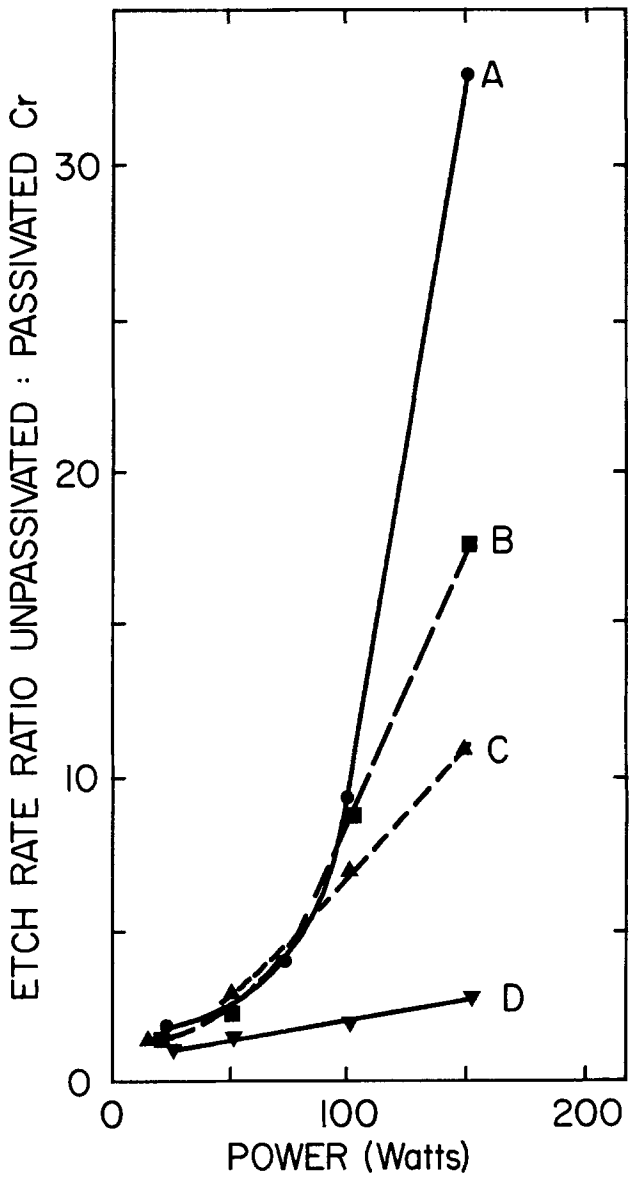

Fig. 9. Variation of the etch rate ratio of unpassivated to passivated chromium with plasma power and pattern size. Oxygen pressure 20 mTorr, 2 min treatment time. Curve A: unpatterned black chromium; curve B: black chromium, 300 μm periodicity grating; curve C: black chromium, 7 μm periodicity grating; curve D: unpatterned bright chromium.

than bright chromium (curve D). Note that these curves were both obtained from unpatterned substrates. The second point is that chromium patterned with photoresist passivates less efficiently than unpatterned chromium, with the finer pattern (curve C) having a greater influence than the coarser pattern (curve B). Also to be noted is the different pressure dependence of the passivation of black chromium and bright chromium (Fig. 7) and the rapid increase of passivation efficiency between 2 and 4 min plasma treatment time (Fig. 8). There is no difference in the plasma etching times of this passivated and unpassivated chromium, presumably because the thin passivating layer formed during the plasma treatment is just as reactive as the untreated chromium.

Figure 10 shows an SEM photograph of a reversal processed and liquid etched grating with 1500Å lines and spaces in a 400Å thick chromium film. The plasma processing conditions were: oxygen pressure, 20 mTorr; oxygen flow rate, 15 sccm; power, 100W (0.57W cm^{-2}); time, 40 sec. The resist mask was prepared in 2000Å thick AZ1350 by laser interference. It is thus

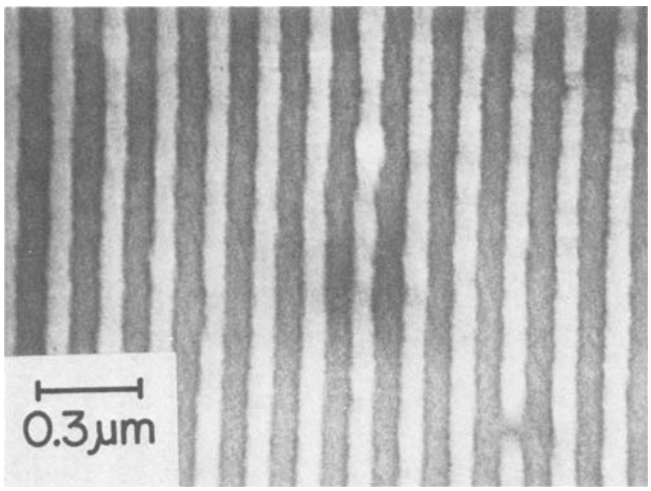

Fig. 10. Liquid reversal etched 0.3 μm periodicity grating in bright chromium after plasma passivation in oxygen using an SiO_2 backing plate.

perfectly possible to wet etch 1500Å wide lines and spaces in thin chromium films.

Since good passivation of black chromium can be achieved by treatment in an argon plasma (Fig. 7), it is clear that passivation is not due simply to the formation of a protective layer, by a gas-solid interaction, which is less soluble in the liquid etchant than an untreated surface. The results can be explained by the deposition of material sputtered from the backing plate, which is usually silicon dioxide. Since the only analytical technique readily available to us is an electron microprobe, it was not possible to analyze the chromium surface for silicon because the electron beam would penetrate into the glass substrate which, of course, contains silicon. A test experiment was therefore made using a niobium backing plate. Reversal etching with a selectivity of passivated:unpassivated black chromium of 16:1 was possible using a niobium backing plate, argon at a pressure of 20 mTorr, and a power of 150W (0.9W cm^{-2}). Microprobe analysis of such a sample before wet etching, but after resist stripping, showed that niobium was present on the regions that had been exposed to the argon plasma and absent on those areas that had been masked by the resist. Thus, it seems fairly certain the mechanism of passivation depends on material sputtered from the backing plate and deposited on the substrate.

With a tungsten hexafluoride plasma and plasma etching.—As mentioned above, a chromium film that is contaminated with a tungsten containing layer is unreactive toward a chromium etching plasma. This led us to the idea that treatment of chromium in a plasma containing a tungsten compound, such as tungsten hexafluoride, would enable exposed chromium on a patterned surface to be passivated. After stripping the resist, reversal etching should be possible. We have found that this indeed works very well, but that the plasma treatment must be done at low pressure with the substrate on the powered electrode. Apparently a certain minimum bombardment energy of the gas phase species is required for good pattern definition; if the tungsten hexafluoride treatment is done at higher pressures with the substrate on a grounded electrode, the pattern is very ill-defined and subsequent plasma etching gives a very poor result. As is shown below, the passivation functions by the deposition of a tungsten containing layer on the exposed chromium and the resist. As long as a coherent film covers the chromium this will be sufficient to protect it against the etching plasma. On the other hand, if this deposited film is too thick, it will make stripping of the resist, prior to etching, very difficult and so the thickness of this must be kept to a minimum. We have found that it is desirable to dilute the tungsten hexafluoride with nitrogen, otherwise the rate of deposition is too rapid. Suitable conditions are: gas composition, 25% tungsten hexafluoride in nitrogen; pressure, 15 mTorr; power, 100W (0.6W cm^{-2}); time, 30 sec.

After the plasma pretreatment, the resist must be solvent stripped using ultrasonic agitation; any residues will act as etch masks and introduce additional features on the mask. Since the pretreatment time is short, resist erosion is no problem and PBS can be reversal etched as well as normal photoresists. Figure 11(a) shows a grating pattern, the left side of which was reversal processed and the right side of which was normally processed. As a dark (chromium) line is followed across, the pattern reversal can be seen at the boundary of the reversal processed region. Figure 11(b) shows a reversal etched pattern defined using PBS electron beam resist. This was etched in the barrel reactor in 50% oxygen/carbon tetrachloride at 250 mTorr, 100W and shows well-defined 0.5 μm lines and spaces; the etch rate was about 120 Å/min. Chromium that has been passivated in this way will not plasma etch at all even after times longer than 1 hr. Liquid

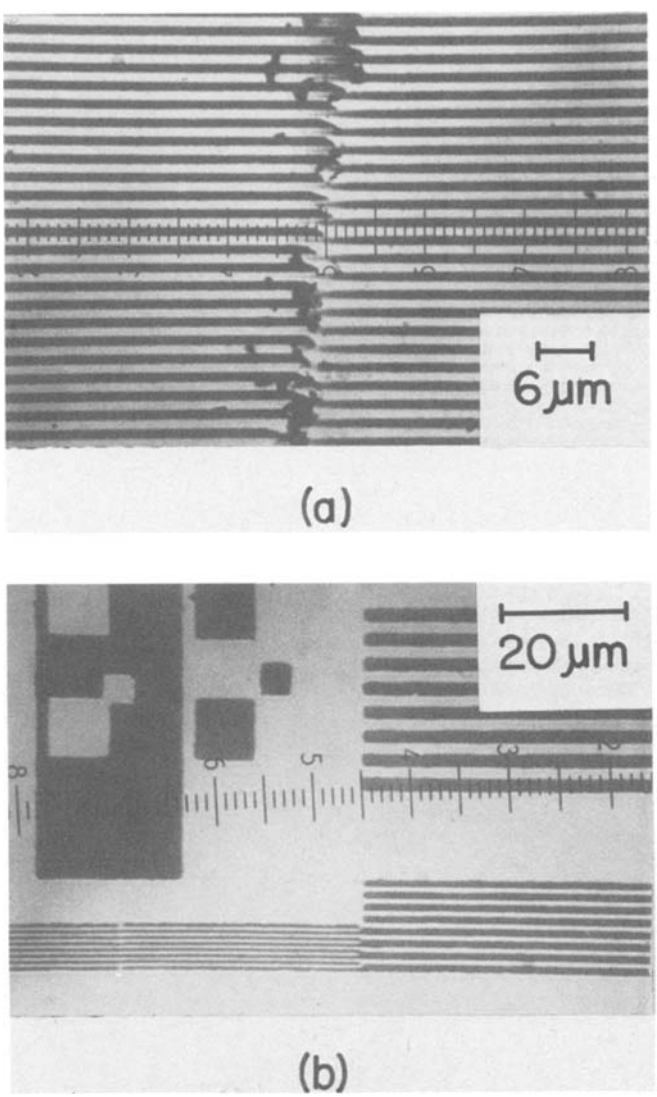

Fig. 11. Plasma passivated and reversal plasma etched bright chromium. (a) Left side reversal processed, right side normally processed. (b) Pattern defined with PBS electron beam resist and plasma etched in a barrel reactor.

etching, on the other hand, shows no selectivity whatsoever.

The mechanism of this type of reversal etching has been confirmed by electron microprobe analysis of a tungsten hexafluoride treated pattern from which the resist had been stripped. This is shown in Fig. 12. The picture itself is a secondary electron emission image in which the lighter regions have a stronger emission (indicative of a heavier element) than the darker areas. The horizontal white line is the path of a subsequently scanned electron beam used to generate x-rays from the probed surface; the intensity variation across the patterned area of the tungsten x-ray emission is shown by the other white line and it correlates well with the light colored areas.

Discussion

It is clear from the foregoing that it is much more difficult to plasma etch structures that have been defined in chromium using E-beam resists that those defined by optical resists. Optical resists, such as AZ1350, erode at much lower rates than E-beam resists, which correlates with the fact that the aromatic groups of the former would be expected to endow them with more stability toward the plasma (7). However, it is only possible to define patterns in chromium by plasma etching at all because the metal film is thin, which renders practicable the poor selectivity of Cr:resist = 1.6:1. The etching conditions that have to be used when PBS is used for pattern definition result in a rather low chromium etch rate, *i.e.*, about 50 Å/min (see Table I). This gives an etching time of about 20 min for a chromium film 1000Å thick. Although this is rather a long etching time, it would probably be acceptable in practice since the electron beam writing time would be the rate limiting step.

It is interesting to note that the erosion rate of AZ1350 *vs.* gas composition passes through a minimum at about 40% carbon tetrachloride in oxygen. The reason for this is not clear; possibly it may be associated with partial polymerization of the carbon tetrachloride protecting the resist to some extent.

Reversal etching can sometimes be used to advantage when the resist properties or processing render the fabrication of a particular structure rather difficult. We have already seen that it is possible to plasma process a pattern defined with PBS in a barrel reactor, which would be impossible using the normal plasma etching conditions. A further example is illustrated in Fig. 13. If one tries to fabricate a grating structure with a constant of, say, 0.3 μm (1500Å lines and spaces), it is very difficult to achieve this aspect ratio of 1:1. It is not easy to adjust the exposure and development times and

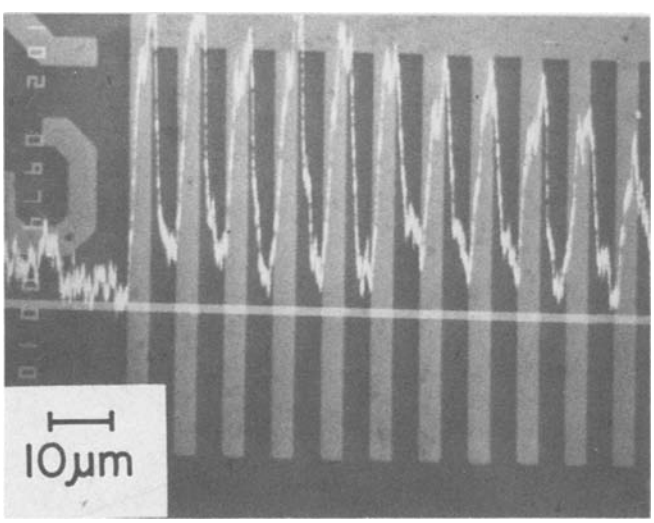

Fig. 12. Electron microprobe trace of bright chromium after plasma passivation in tungsten hexafluoride with the resist stripped.

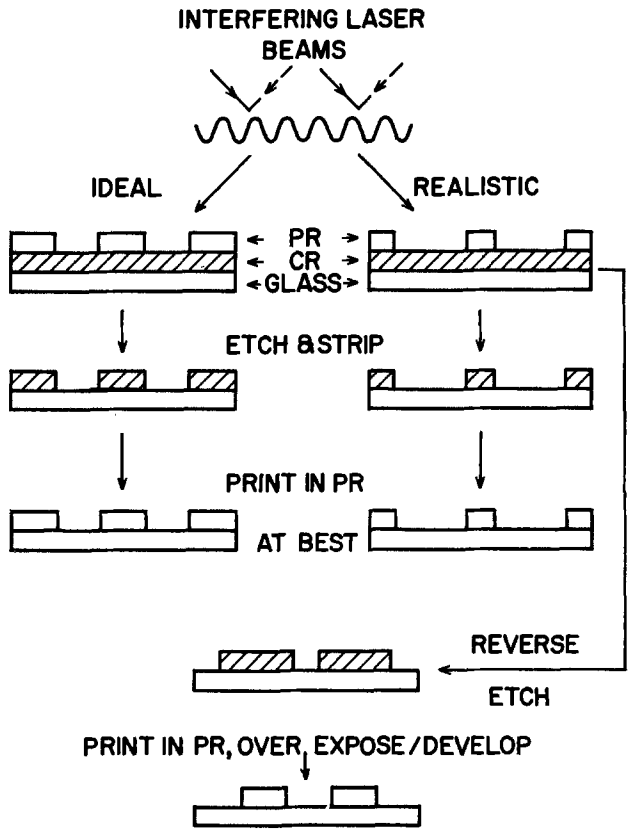

Fig. 13. The preparation of a grating with 0.3 μm periodicity and a 1:1 aspect ratio by the reversal processing of chromium.

more often than not an aspect ratio of less than 1:1 results ("realistic" in Fig. 13). However, if a chromium film with a resist grating of aspect ratio less than 1:1 on its surface is reversal processed, the resultant grating in the chromium has an aspect ratio of greater than 1:1. Then, by using this mask to prepare a grating in photoresist, it is possible to achieve a 1:1 aspect ratio by suitable overexposure and/or development.

The mechanism of reversal etching a liquid etchant fairly certainly depends on the sputtering of substrate backing plate material onto the chromium surface to be etched. In addition to the electron microprobe results, the increase in passivating effect with increasing pressure shown in Fig. 7 also supports this idea. At higher pressure (and the accompanying lower d-c self-bias) there will be increased scattering and deposition of sputtered material in a horizontal plane. Of course, for this method to be successful, sufficient area of the backing plate must be exposed to provide a source of backsputtered material for deposition on the substrate. One open question is the reason for the difference in the efficiency of passivation when bright chromium as opposed to when black chromium is used.

Acknowledgments

The authors would like to thank J. Mitchell for providing MEBES patterned chromium plates.

Manuscript submitted March 14, 1983; revised manuscript received June 15, 1983.

Laboratories RCA Limited assisted in meeting the publication costs of this article.

REFERENCES

1. R. E. Szupillo, *Solid State Technol.*, **12**, 58 (August 1969).
2. H. Abe, K. Nishioka, S. Tamura, and A. Nishimoto, Proceedings of 7th Conference on Solid State Devices, Tokyo, p. 25 (1975).
3. T. Yamazaki, Y. Suzuki, J. Uno, and H. Nakata, *Jpn.*

J. Appl. Phys., **19**, 1371 (1980).
4. H. Saeki, Y. Watakabe, H. Toyoda, H. Nakata, and T. Kashiwaggi, *J. Electron. Mater.*, **11**, 1049 (1982).
5. K. Nishioka and H. Abe, Abstract 148, p. 406, The Electrochemical Society Extended Abstracts, Vol. 77-2, Atlanta, GA, Oct. 9-14, 1977.
6. B. Hasler, German Pat. 2,738,839 (Siemens AG).
7. L. A. Pederson, *This Journal*, **129**, 205 (1982).

Belt Transport CVD Processing

Ming-Kwang Lee and Chih-Yuan Lu

Institute of Electronics, National Chiao-Tung University, Hsin-Chu, Taiwan, China

Chin-tay Shih

Electronics Research and Service Organization, ITRI, Hsin-Chu, Taiwan, China

ABSTRACT

Belt transport CVD processing, a simple but useful technique applied widely in wafer fabrication, is evaluated in this work. An empirical relation, (T_{ox}) (belt speed)$^n = K$, where T_{ox} is the oxide thickness, is established. The value of n is found to be 1.09 experimentally and 1.0 as analyzed theoretically. A simple deposition model is discussed. The effects of belt speed on film thickness and the effects of flow rate on characteristics are also studied in detail.

Chemically vapor deposited SiO_2 and doped SiO_2 are widely used in IC fabrication due to the low deposition temperature. Three applications, namely, as masking materials for diffusion and etching, as coating material for protective passivation, and as field oxide material, are frequently employed (1, 2). Therefore, it is very important to obtain stable processing conditions for the fabrication of CVD films.

There are many kinds of CVD reactors (3-6). However, two types of reactors are classified. The first is the chemical vapor transport (CVT)[1] reactor. The wafers in this type are fixed inside the furnace; the chemical vapor is conducted into the inlet and forms the solid product on the wafer surface (Fig. 1a). The solid product may also be formed in the vapor phase other than on the wafer surface, and the particulates may fall on wafer surface and result in passivation defects. Generally, CVT is applied in low pressure and/or higher temperature CVD processing.

The second is the belt transport (BT) CVD reactor. In this system, the wafers are placed on a hot plate which is traversed under a nozzle head by a moving belt (Fig. 1b). The nozzle head is cooled by chilled water; the chemical vapor flows into the nozzle head and spreads over the hot plate. The solid chemical product can be formed more dominantly on the surface of the hot area due to thermal activation. Furthermore, the particle contamination problem on the wafer surface can be minimized, and the deposition rate and uniformity are more stable.

The effects of variables on CVD processing in the BT reactor have been studied.

Theoretical Analysis

When SiH_4 is mixed with oxygen gas, chemical reactions occur to form the solid products such as SiO_2, SiO, and Si.

The following possible chemical reactions should be considered

$$SiH_{4(g)} + 2\,O_{2(g)} \xrightarrow{k} SiO_{2(s)} + 2H_2O_{(g)} \quad [1]$$

$$SiH_{4(g)} + O_{2(g)} \xrightarrow{k_1} SiO_{(s)} + 2H_2O_{(g)} \quad [2]$$

$$\xrightarrow{k_2} SiO_{2(s)} + 2H_{2(g)} \quad [3]$$

$$SiH_{4(g)} \xrightarrow{k_3} Si_{(s)} + 2H_{2(g)} \quad [4]$$

In the case of higher O_2 concentration during the oxidation of silane, reaction [1] will dominate and SiO_2 is the major component of the silox film. Conversely, the Si content will be higher due to the larger contribution of Eq. [2], if the O_2 concentration is decreased.

Consider Eq. [1], *i.e.*, high oxygen-to-silane ratio, all the silane molecules are to be reacted fully into $SiO_{2(s)}$

$$R = \rho A \left[\frac{dT_{ox}}{dt} \right] \quad [5]$$

Chemically, the rate in weight per unit time is

$$R = k \cdot P_{SiH_4} \cdot P_{O_2}{}^2 \quad [6]$$

where ρ is the density of the silox film, A is the deposition area including the whole surface under the nozzle head, k is the reaction rate constant, P_{SiH_4} is the partial pressure of SiH_4, and P_{O_2} is the partial pressure of O_2. According to Eq. [5] and [6]

$$dT_{ox} = \left[\frac{kP_{SiH_4}P_{O_2}{}^2}{A\rho} \right] dt \quad [7]$$

On integrating the time from 0 to t

$$T_{ox} = \left[\frac{kP_{SiH_4}P_{O_2}{}^2}{A\rho} \right] t \quad [8]$$

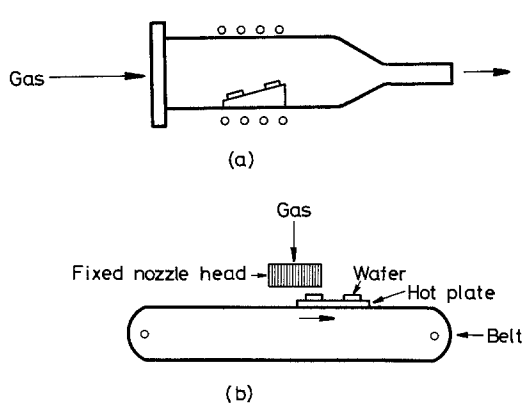

Fig. 1. (a) The CVT deposition reactor. (b) The BT deposition reactor.

Key words: belt, transfer, CVD.

[1] Not to be confused with chemical transport reactions in which deposition results from transport (usually by diffusion) between zones of different temperature in a reversible equilibrium (4).

However, in the belt transport system

$$t = \left[\frac{L}{\text{belt speed}}\right] \quad [9]$$

where L is the width of the nozzle head. Using Eq. [8] and [9], we thus obtain

$$(T_{ox})\,(\text{belt speed}) = \left[\frac{kP_{SiH_4}P_{O_2}^2}{A\rho}\right] L = K \quad [10]$$

And then, for a given apparatus (A and L constant)

$$K = K(P_{SiH_4}, P_{O_2}, \rho, T) \quad [11]$$

Therefore, K is a function of reactant partial pressure, film density, and wafer surface temperature.

However, at a high oxygen-to-silane ratio, the partial pressure of oxygen can be thought of as constant even though the O_2 gas is further increased. And therefore, at high O_2/SiH_4 ratios

$$\frac{dT_{ox}}{dt} = K'(T) \cdot P_{SiH_4} \quad [12]$$

or

$$(T_{ox})\,(\text{belt speed}) = K''(T) \cdot P_{SiH_4} \quad [13]$$

i.e., the deposition rate is linearly dependent on the partial pressure of SiH_4, where K' in Eq. [12] and K'' in Eq. [13] are temperature dependent factors. Thus, SiH_4 partial pressure and wafer surface temperature will affect the deposition rate.

Experimental

A Pacific Western System (PWS) Model 2000 CVD reactor was used in this work. The temperature of the wafer surface was measured by a Wahl International Model 392/°C thermometer. The oxide thickness was measured by a Beckman Model 26 spectrophotometer. The index of refraction was measured by a Princeton Applied Material Ellip 7610 ellipsometer. The wafers were cleaned by a standard acid/H_2O_2 process prior to depositing the CVD film. The layout of gas lines is shown in Fig. 2. O_2, SiH_4, and N_2 were conducted and controlled by Brooks Tube flowmeters. The wafer surface temperature was kept high enough so that deposition can occur.

Results and Discussion

Effect of belt speed on film thickness.—By following the specified deposition parameters, $N_2(O_2) = N_2(SiH_4) = 5900$ cm³/min; $O_2 = 640$ cm³/min; $SiH_4 = 48$ cm³/min, and the wafer surface temperature of 415° ± 5°C, it is observed that the deposit thickness varies inversely with belt speed (Fig. 3). The empirical reaction between the film thickness and belt speed was established as

$$(T_{ox})\,(\text{belt speed})^{1.09} = 6.79 \times 10^{-4}\ \text{cm}^2/\text{min}$$

This result is approximately consistent with that theoretically analyzed in Eq. [10],

Effect of oxygen-to-silane ratio on film characteristics.—The observed refractive index of CVD films depends strongly on the deposition parameters. Also, the thermal annealing of as-deposited CVD films (7) in an ambient of nitrogen gas at 1100°C changes the refractive index. Figure 4 indicates that the refractive index of as-deposited CVD films of higher oxygen-to-silane ratio (greater than 12:1) is abnormally low. However, after thermal annealing for 30 min, the refractive index becomes normal at a value of 1.45. Interestingly, the refractive index at lower oxygen-to-silane ratio changes from 1.45 to 1.50 after annealing treatment. Therefore, two phenomena are implied in accordance with the above observations, First, there may exist oxygen and/or nitrogen in as-deposited CVD films at larger oxygen-to-silane ratios, *i.e.*, faster deposition due to a higher concentration of oxygen in the gas mixture may cause oxygen and/or nitrogen to be trapped in the as-deposited CVD film. The trapped gas will be evolved on thermal annealing. Second, the CVD film exhibits a silicon-rich phenomenon at lower oxygen-to-silane ratio, *i.e.*, the silicon content of the CVD film will be higher as reaction [2] becomes more important in the formation mechanism of the film. Consequently, the deposition model described in Eq. [10] will not fit well for deposition at lower oxygen-to-silane ratios.

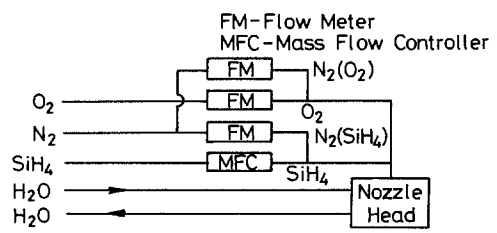

Fig. 2. The layout of gas lines in the BT CVD system

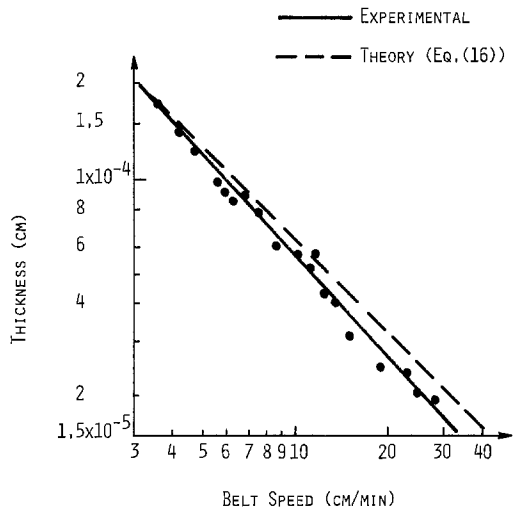

Fig. 3. The effect of belt speed on film thickness

Reaction model.—If it is assumed that the partial pressure of the i-component gas in gaseous mixture is

$$P_i = \left[\frac{r_i}{r_{total}}\right] P_{atm} \quad [14]$$

where r denotes the flow rate of gas read from the flowmeter, and r_{total} denotes the summation of flow rates of all gases during the deposition period. Then, Eq. [10] can be written as

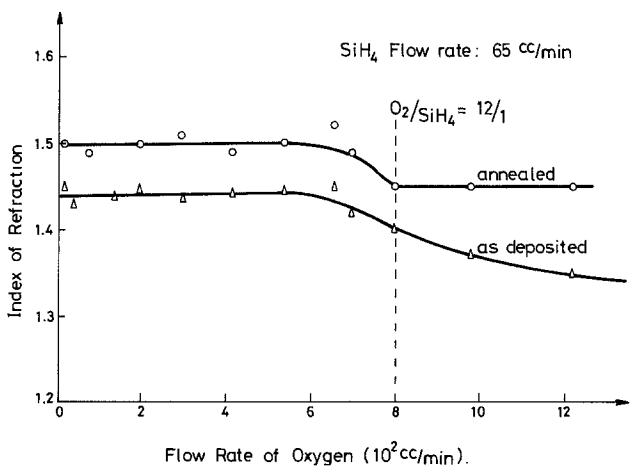

Fig. 4. The effect of thermal annealing at 1100°C in N_2 on the refractive index of CVD silicon oxide films.

$$(T_{ox})\,(\text{belt speed}) = K(T)\cdot\left[\left(\frac{r_{SiH_4}}{r_{O_2}}\right)\left(\frac{r_{O_2}}{r_{total}}\right)^3\right] \quad [15]$$

$$= K(T)\cdot S \quad [16]$$

The logarithm (T_{ox})(belt speed) is plotted *vs.* the logarithm of the S factor as shown in Fig. 5. It is obvious that the (T_{ox}) (belt speed) product varies approximately linearly with respect to the S factor, (T_{ox}) (belt speed) $= KS^{0.90}$. This fact implies that in high oxygen-to-silane ratio CVD processing, Eq. [1] dominates the deposition reaction and $SiO_{2(s)}$ is the major component in the silox film as explained previously.

Effect of gas-flow on film thickness.—At fixed parameters of belt temperature, belt speed, flow rate of cooling water, flow rate of nitrogen, etc., silox films were deposited with various flow rates of SiH_4 and O_2. The results are shown in Fig. 6 and 7. It is observed that excessive flow of O_2 reduces the film thickness. This phenomenon is similar to that reported by Kern *et al.* (8) and Baliga *et al.* (9). The reason given by Baliga *et al.* is that adsorption of oxygen on the silicon substrates retards the chemical reaction. However, Fig. 8 indicates that the value, (T_{ox}) (belt speed), is linearly decreased with the decreasing partial pressure of SiH_4 which resulted from the further increase of oxygen flow, *i.e.*, the effect is consistent with that described previously in Eq. [13].

Figure 9 shows the effect of nitrogen on film thickness. It is observed also that the decrease of partial pressure of both SiH_4 and oxygen by the further addition of nitrogen gas reduces the deposition rate. On the other hand, heat will be carried away from the wafer surface by the increased flow of oxygen and nitrogen.

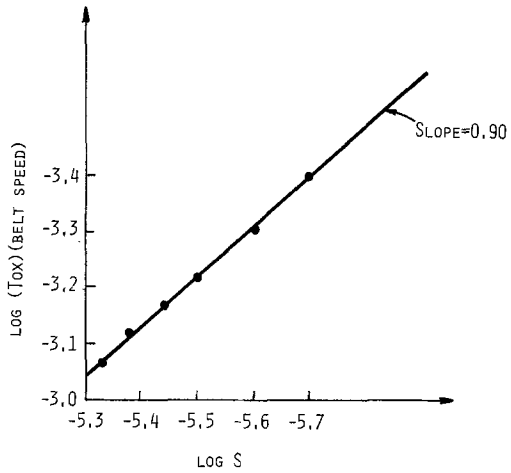

Fig. 5. The plot of log(T_{ox})(belt speed) vs. log S

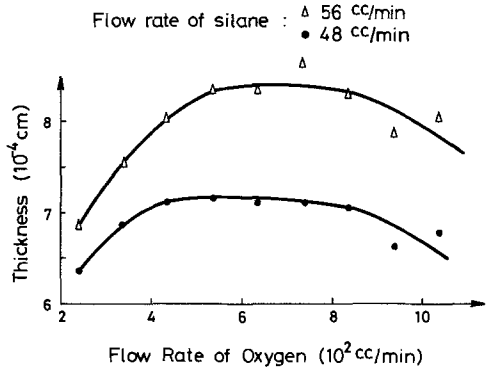

Fig. 6. The effect of oxygen flow rate on film thickness

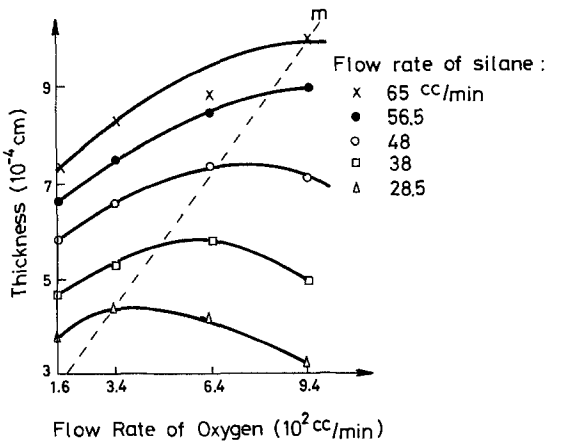

Fig. 7. The effect of oxygen flow rate on film thickness. Curve m denotes the optimum film thickness.

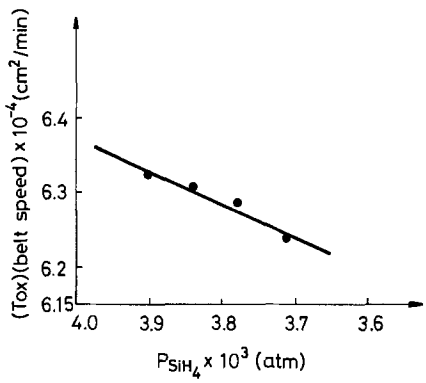

Fig. 8. The effect of further addition of oxygen on (T_{ox})(belt speed). The (T_{ox})(belt speed) factor is plotted vs. the partial pressure of silane.

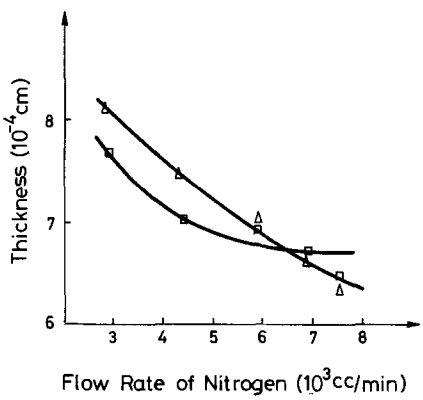

Fig. 9. The effect of nitrogen flow rate on film thickness. Δ Varied $N_2(O_2)$ with $N_2(SiH_4)$ constant at 5900 cm³/min. ⊟ Varied $N_2(SiH_4)$ with $N_2(O_2)$ constant at 5900 cm³/min.

Therefore, excessive flow of oxygen or further addition of nitrogen lowers the wafer surface temperature, *i.e.*, $K'(T)$ or $K''(T)$ will be decreased if the heating power of the CVD system is kept constant.

Conclusions

With the belt transport CVD reactor used in this work, three conclusions on CVD silox formation are summarized : (*i*) The deposition rate is proportional to (T_{ox}) (belt speed), the product of film thickness and belt speed. (*ii*) The oxygen-to-silane ratio during the deposition period is very important for CVD process control. Too large a ratio will result in deposition rate decrease; however, too small a ratio will cause the CVD film to be silicon-rich. It is recommended that a

ratio of 12/1 be employed for silox CVD processing. (*iii*) The deposition rate decrease with increased flow of nitrogen is attributed to two factors, depression of the silane partial pressure and lowering of the wafer surface temperature.

Acknowledgments

The authors wish to give their sincere thanks to Mr. Jen-Kong Chen and Mr. Jyan-Bang Chen for their help in sample preparations in these studies. Thanks are also to Mr. Fang-Churng Tseng for his support.

Manuscript submitted Dec. 17, 1982; revised manuscript received June 21, 1983.

National Chiao-Tung University assisted in meeting the publication costs of this article.

REFERENCES

1. T. L. Chu, *J. Vac. Sci. Technol.*, **6**, 25 (1969).
2. T. L. Chu and R. K. Smeltzer, *ibid.*, **10**, 1 (1973).
3. C. F. Powell, J. H. Oxley, and J. M. Blocher, "Vapor Deposition," pp. 249, 343, John Wiley & Sons, Inc., New York (1966).
4. H. Schäfer, "Chemical Transport Reactions," p. 163, Academic Press, Inc. (1964).
5. W. Kern and V. S. Ban, in "Thin Film Process," J. L. Vossen and W. Kern, Editors, pp. 278-285, Academic Press Inc. (1978).
6. M. L. Hammond, *Solid State Technol.*, p. 61 (Dec. 1979).
7. W. Kern, *RCA Rev.*, **37**, 55 (1976).
8. N. Goldsmith and W. Kern, *ibid.*, **28**, 153 (1967).
9. B. J. Baliga and S. K. Ghandhi, *J. Appl. Phys.*, **44**, 990 (1973).

Behavior of Pd/Sn and Pd Catalysts for Electroless Plating on Different Substrates Investigated by Means of Rutherford Backscattering Spectroscopy

Leo G. Svendsen

Institute of Physics, University of Aarhus, DK-8000, Aarhus C, Denmark

Tetsuya Osaka*

Department of Applied Chemistry, Waseda University, Shinjuku-ku, Tokyo, Japan

Hideo Sawai

OKI Electric Industry Company, Limited, Materials Department, Research Laboratories, Hachioji-shi, Tokyo, Japan

ABSTRACT

Two catalytic systems for electroless metal deposition have been investigated by means of Rutherford backscattering spectrometry (RBS). The well-known tin sensitizer, palladium activator, two-step catalyst had the main emphasis, but also a commercial one based on evaporated palladium was examined. The behavior of the two-step catalyst was largely dependent on the substrates used. On Al_2O_3, the Sn:Pd ratio was 1:1 with 1.3×10^{15} atoms/cm^2 each. On carbon substrates, the Sn:Pd ratio was 1:4 with 6×10^{15} tin atoms/cm^2 and 24×10^{15} palladium atoms/cm^2. Both these results violate the simple reaction mechanism described by the equation $Sn^{2+} + Pd^{2+} \rightarrow Sn^{4+} + Pd^0$. The commercial catalyst on polyimide containing 2.5×10^{15} palladium atoms/cm^2 on the surface behaved differently compared to the two-step catalyst by diffusing into the deposited layer and thereby influencing its deposition rate.

The catalyst systems used for initiating the deposits from autocatalytic Ni-P and Ni-P-W baths have been investigated by means of Rutherford backscattering spectrometry (RBS). The results thus obtained may contribute to the current discussion of this subject. This article reports on two types of catalysts, *i.e.*, the well-known two-step sensitizer-activator system containing Sn^{2+} and Pd^{2+} and a commercial method, where catalyzing takes place by means of a sparse layer of evaporated palladium atoms.

Previously, the two-step system has been investigated by Meek (1, 2) using RBS as well as the mixed catalyst system (3). Meek found results in agreement with those obtained by Cohen *et al.* (4), using Mössbauer spectroscopy; they stated that the simple reaction

$$Sn^{2+} + Pd^{2+} \rightarrow Sn^{4+} + Pd^0 \qquad [1]$$

takes place to make the surface catalytically active. These findings were actually in disagreement with those of de Minjer *et al.* (5) as well as with those from the photosensitive sensitizers based on both Sn^{2+} and Sn^{4+}, neither of which could be explained by the simple Eq. [1] only. The latter results are mainly obtained by Schlesinger *et al.* (6-9).

The RBS Method

When a surface is bombarded with swift $^4He^+$ ions, the scattered particles can yield information on the stoichiometry *vs.* depth in the surface layer. The spectra consist of the number of particles as a function of the particle energy after scattering, shown in Fig. 1. From the width of a peak, the layer thickness may be determined, while the peaks stemming from the same layer contain information on the stoichiometry. As seen in Fig. 1, this is phosphorus and nickel in the top layer and aluminum and oxygen in the substrate. After a deposition time of 40 sec, the dotted spectrum in Fig. 1 indicates that a layer of a certain thickness has been formed on the substrate. The retrograde movement of the signals stemming from oxygen, aluminum, and Pd/Sn is due to their staying in-depth, whereas the nickel and phosphorus peaks always start at the same position, indicating signals from the surface. The tail is due to an in-depth deposition on the substrate.

In Fig. 1, the insert shows the experimental setup. An area of 1×1 mm^2 of the surface is irradiated by 2 MeV $4He^+$ ions to a dose of 40 μC. The investigation

* Electrochemical Society Active Member.
Key words: electroless, Rutherford backscattering, catalysis.

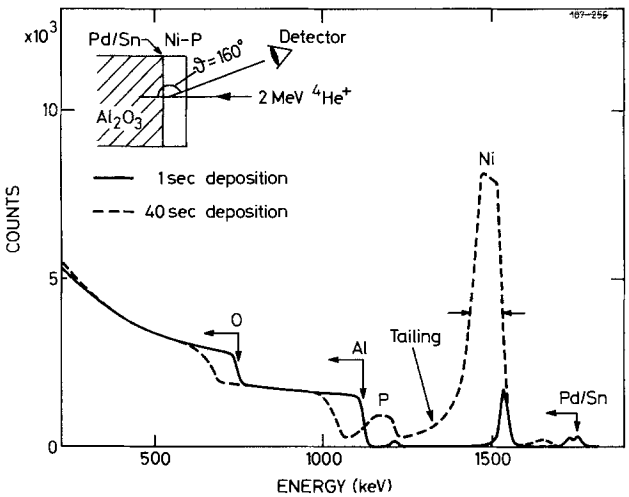

Fig. 1. RBS spectra of Ni-P(b) layers on top of sintered alumina substrates. The backward movement of some signals is indicated by "↩."

was made under a pressure below 5×10^{-7} Torr. The scattered ions are detected by a surface-barrier detector at an angle θ of 160°. A detailed description of the equipment and software used in this investigation is given in Ref. (10), and for an introduction to the RBS method, the reader is referred to Ref. (11).

Experimental

Three types of substrates were used in the investigation, *i.e.*, (*i*) alumina, a sintered 96 weight percent (w/o) α-Al_2O_3 ceramics[1] often used for hybrid IC substrate; (*ii*) carbon, as 99 w/o pure graphite containing a phenol-resin binder;[2] (*iii*) a type of polyimide[3] used for flex-print substrate. The alumina and carbon substrates were degreased with ethanol, rinsed in water, and dried prior to being made catalytic for nickel deposition. This was done in the following way: sensitization: 2 min, rinse 10 sec; activation: 2 min, rinse 10 sec; sensitization: 2 min, rinse 10 sec; activation: 2 min, rinse 10 sec. Deionized water was used for rinsing, and the solutions were made as follows: sensitizer: $SnCl_2 \cdot 2H_2O$, 1 g/liter; HCl 37%, 1 ml/liter; activator: $PdCl_2$, 0.1 g/liter; HCl 37%, 0.1 ml/liter. The repeated two-step process[4] was used because of its superior catalytic effect on alumina substrate compared to those of a mixed $PdCl_2/SnCl_2$ catalyst. To compare the results, the same procedure was applied to graphite to make the substrate catalytic. The catalyst thus made is denoted "A catalyst." The polyimide was catalytic when purchased. This has been done by evaporating palladium sites onto one side of the specimens, and this catalyst is denoted "B catalyst."

When the substrates had been made catalytic, nickel was deposited from one of the following baths: Ni-P (a): a commercial bath[5] with pH = 5.2 and hypophosphite as a reductant; Ni-P(b): pH = 9.0 and with the following composition: 0.027 M/liter $NiSO_4$, 0.068 M/liter Na_3-citrate, 0.227 M/liter $(NH_4)_2SO_4$, 0.066 M/liter NaH_2PO_2; Ni-P-W: same composition and pH as Ni-P(b) plus 0.106 M/liter Na_2WO_4.

All the baths were operated at 90°C, and the samples were dipped into the hot baths for different periods of time to find the deposition rate. The electroless Ni-P-W film has previously shown (12) some superior properties concerning the uniformity and the thermal stability of film resistance compared to a film precipitated from the Ni-P(b) bath, although the baths are differing only in that the Ni-P-W bath contains Na_2WO_4.

[1] From Nippon Tokushu Togyo Company, Limited (NGK Spark Plug Company Limited).
[2] From Nippon Carbon Company, Limited.
[3] From Tore Company, Limited, film thickness of polyimide used is 75 μm.
[4] Since alumina substrate is a difficult-to-plate substrate, the catalization carried out only by a mixed catalyst is not sufficient to form the basis for a uniform electroless nickel film. This repeated two-step process is effective for alumina. It is sometimes used for alumina substrate in practical use, *e.g.*, at the Precision Electronic Components Limited, Toronto, Ont., Canada
[5] NICKA 311 from Kaseihin-Kogyo Company, Limited.

Results

Below, descriptions are given of the results that were achieved concerning the catalysts.

Composition and content.—In Fig. 1, only palladium and tin give visible signals stemming from the A-type catalysts. Any signal from the oxygen that may be present due to a tin-oxo compound can be detected neither on alumina nor on graphite substrates because of interfering signals (on graphite, these are caused by the oxygen content in the phenol resin binder). Chlorine, on the other hand, should be easily detectable at a position 80 keV above the phosphorus peak in Fig. 1, but no peak is present in any of the spectra. This is a general result, and the investigations show that the amount of chlorine adhering to the surface must be less than 12% of the original chlorine content in $SnCl_2 \cdot 2H_2O$ and $PdCl_2$. It may therefore be concluded that after 1 sec of deposition, the amount of chloride ions following the adhering tin and palladium is insignificant.

RBS gives the following ratios and contents for Pd/Sn:

Alumina substrates: Pd/Sn ratio 1:1 within 15%. Content for both palladium and tin: $1.3 \pm 0.3 \times 10^{15}$ atoms/cm^2.

Carbon substrates: Pd/Sn ratio 4:1 within 20%. Palladium content: $24 \pm 2 \times 10^{15}$ atoms/cm^2. Tin content: $6 \pm 1 \times 10^{15}$ atoms/cm^2.

Polyimide: palladium content: $2.5 \pm 0.3 \times 10^{15}$ atoms/cm^2.

The findings were unaffected by the baths used for covering the surface with a thin, conductive Ni-P layer. Figure 2, I and II show that 1 sec in the acidic Ni-P(a) bath and 1 sec in the basic Ni-P-W bath result in the same peaks in the RBS spectra. The substrates, on the other hand, greatly affect the Pd/Sn ratio and content. A comparison between the RBS peak of Pd/Sn on alumina and on carbon given in Fig. 2 demonstrates the difference of the catalyst.

Behavior of the catalysts.—Figure 3 shows a figure series of the behavior of the two-step A catalyst on alumina and on the evaporated palladium catalyst the B catalyst. It is found that the two types of catalysts behave differently with respect to a deposited Ni-P layer from the Ni-P(b) bath. The spectra of the two-step process indicate that the catalyst gradually becomes situated in greater depth as the deposition proceeds, whereas the spectra of the evaporated catalyst show that it moves both in the precipitated layer and is present at the very surface.

The results in Fig. 4 show that catalyst A remains at the interface since the deposition rate is the same when measured at the nickel peak and at the Pd/Sn peak. This result holds for catalyst A for all baths and both substrates under investigation. The error bars in Fig. 4 include the uncertainty referring to the measuring system only (the RBS equipment), *i.e.*, the uncertainty stemming from the experimental procedure is not registered.

Influences of the catalysts.—Figure 3 shows that palladium remains at the very surface when catalyst B is used. This may be the reason for the considerable change in deposition rate in the earlier stages. On polyimide, the Ni-P(b) bath deposits at a rate of 40% only of that on alumina when the other conditions are identical, and the Ni-P-W bath has reduced its deposition rate to only 30% of that on alumina. However, until catalysts A and B have been investigated on the same type of substrate, other explanations cannot be fully excluded.

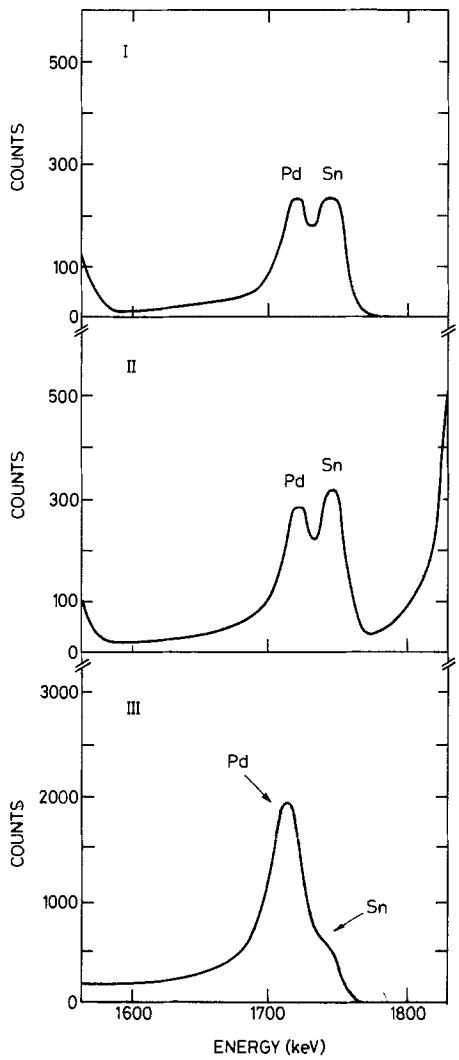

Fig. 2. RBS signals from catalyst A on Al_2O_3 (I and II) and from catalyst A on C (III). I, 1 sec deposit in Ni-P(a) bath; II, 1 sec deposit in Ni-P-W bath; III, 3 sec deposit in Ni-P(b) bath.

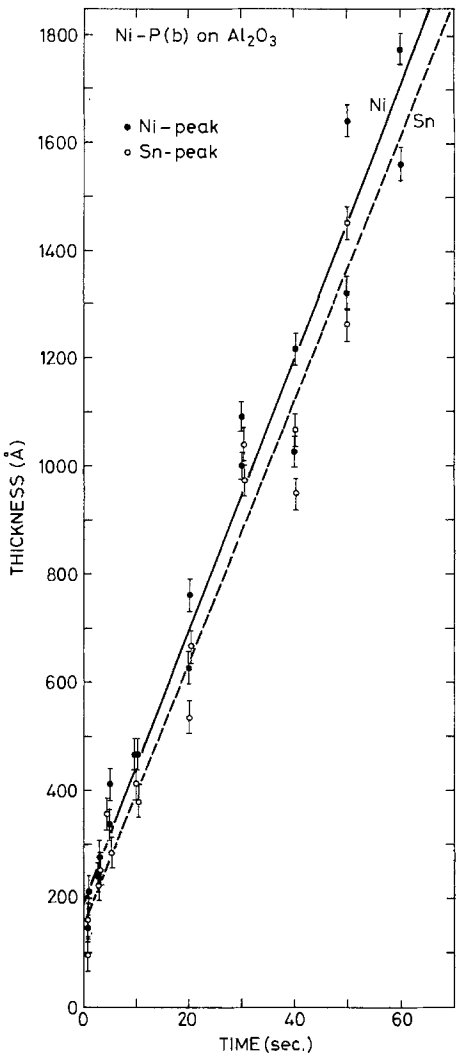

Fig 4. Relation between deposition time and the thickness of Ni-P(b) layer on Al_2O_3. The thickness is found by the width of the Ni peak and the backward movement of the Sn peak in the RBS spectra. Two linear relations are as follows: thickness (in angstroms) = 24.7 ± 1.1 × sec + 207 ± 36, and 23.6 ± 1.3 × sec + 162 ± 34.

Discussion and Conclusion

The use of RBS for obtaining information on the two-step Pd/Sn catalyst and the commercial palladium catalyst has successfully added to what we already know.

The fact that chlorine is missing on the substrate surface means that tin is present in an oxygen compound. This is in agreement with Ref. (5 and 13) and is also in agreement with Ref. (1) when the discussion in Ref. (6) is borne in mind. Here it is stated that very diluted sensitizer solutions consist mainly of oxo-compounds, whereas the more concentrated ones also contain chlorine. The sensitizer used in the present investigation must be rather dilute compared to that

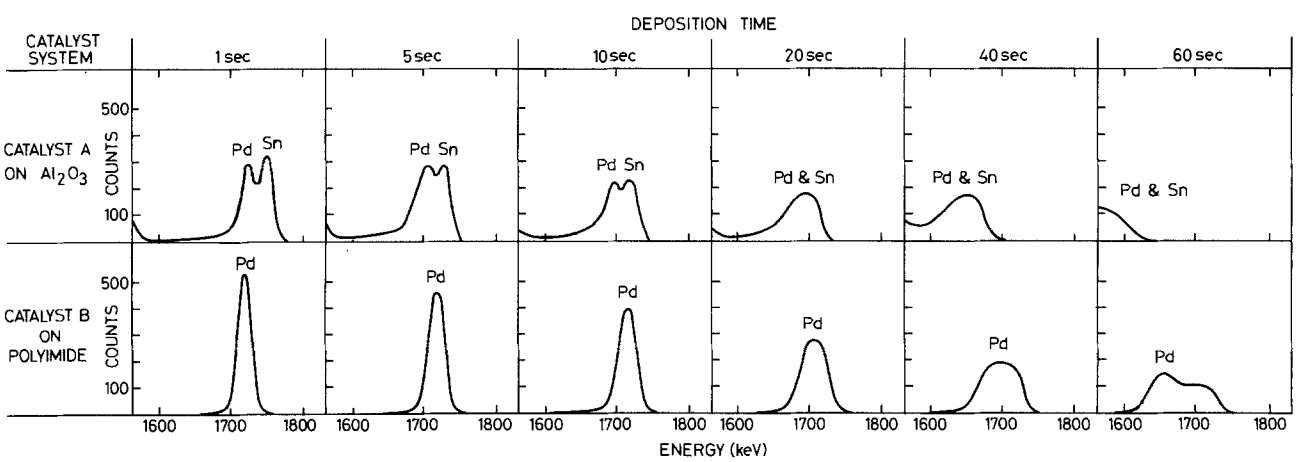

Fig. 3. RBS signals from catalysts A and B when the Ni-P(b) is deposited on the surface. As deposition proceeds, the signals from catalyst A move toward lower energies. The signals from catalyst B broaden and always start at the same position in the different spectra.

used in Ref. (1), which contains 16 g/liter $SnCl_2 \cdot 2H_2O$ and that in Ref. (6) containing 7 g/liter. In Ref. (5), the very dilute sensitizer containing only 0.1 g/liter was used. A tin concentration on graphite of 6×10^{15} atoms/cm^2 is smaller than the 11×10^{15} atoms/cm^2 on graphite found in Ref. (1), however, the difference is not so large, considering the differences of the sensitizers and the activating process. The palladium concentration of 1.3×10^{15} atoms/cm^2 found on the alumina is somewhat larger than that of 0.9×10^{15} atoms/cm^2 on glass substrate in Ref. (1). Reference (1) agrees with the catalyst remaining on the interface. However, the amount of palladium on carbon is almost ten times greater than that found in Ref. (1), and the ratios Pd:Sn of 1:1 and 4:1 on alumina and graphite both violate Eq. [1] when it is borne in mind that most of the tin must be in the form of Sn^{4+} according to Ref. (4 and 13). The result means that it is not a simple redox process. This result is not unique for alumina and carbon. Reference (14) reports similar results for polymer surfaces. The substrate species is concluded to control not only the concentration of adsorbed catalyst but also the ratio of Pd:Sn.

Two other discrepancies were found for system A. Neither a large dissolution of tin ions into the metal bath nor the migration of the catalyst into the deposits was found, as in Ref. (1). Whereas, the results on the B catalyst on polyimide showed that the migration of palladium into the deposited layer takes place.

Manuscript submitted Jan. 13, 1983; revised manuscript received June 7, 1983.

Waseda University assisted in meeting the publication costs of this article.

REFERENCES

1. R. L. Meek, *This Journal*, **122**, 1478 (1975).
2. R. L. Cohen and R. L. Meek, U.S. Pat. 4,042,730 (1977).
3. R. L. Meek, *This Journal*, **122**, 1177 (1975).
4. R. L. Cohen, J. F. D'Amico, and K. W. West, *ibid.*, **118**, 2042 (1971).
5. C. H. deMinjer and P. F. J. v. d. Boom, *ibid.*, **120**, 1645 (1973).
6. B. K. W. Baylis, C-C. Huang, and M. Schlesinger, *ibid.*, **126**, 394 (1979).
7. M. Schlesinger, *ibid.*, **121**, 667 (1974).
8. B. K. W. Baylis, A. Busuttil, N. E. Hedgecock, and M. Schlesinger, *ibid.*, **123**, 348 (1976).
9. B. K. W. Baylis, N. E. Hedgecock, M. Schlesinger, and A. van Wijngaarden, *ibid.*, **126**, 1671 (1979).
10. S. S. Eskildsen, in "Ion Implantation into Metals," V. Ashworth, W. A. Grant, and R. P. M. Procter, Editors, p. 315, Pergamon, Oxford (1982).
11. W-K. Chu, J. W. Mayer, and M-A. Nicolet, "Backscattering Spectrometry," Academic Press (1978).
12. T. Osaka, H. Sawai, and N. Kasai, *Kinzoku Hyomen Gijutsu, (J. Met. Fin. Soc. Jpn.)*, **32**, 615 (1981).
13. R. L. Cohen and K. W. West, *This Journal*, **119**, 433 (1972).
14. L. G. Svendsen and G. Sørensen, Proceedings of International Conference on Electroless Metallization on Sensitized Polymer Powders Fused onto a Polymer Surface. To appear in "Physicochemical Aspects of Polymer Surfaces," K. L. Mittal, Editor, Plenum Press, New York (1982).

Chemically Deposited Ni-P and Ni-P-W Layers Investigated by Means of Rutherford Backscattering Spectrometry

Leo G. Svendsen

Institute of Physics, University of Aarhus, DK-8000 Aarhus C, Denmark

Tetsuya Osaka* and Ichiro Koiwa

Department of Applied Chemistry, Waseda University, Shinjuku-ku, Tokyo, Japan

Hideo Sawai

OKI Electric Industry Company, Limited, Materials Department, Research Laboratories, Hachioji-shi, Tokyo, Japan

ABSTRACT

Information on the deposition of Ni-P and Ni-P-W from autocatalytic baths has been obtained by means of Rutherford backscattering spectrometry (RBS). Measurements of the kinetics during the first 60 sec of precipitation established the deposition rate to be highly dependent on the catalyst used. The Ni-P-W bath precipitates at a lower rate than do the various Ni-P baths. The investigation on the stoichiometry indicates that the codeposition of phosphorus on an average decreases from 10.0 to 3.1% when tungsten is present in the layer. For brief deposition periods (1 and 3 sec), the phosphorus content is found to be higher than the average. The phosphorus content in the first 500Å of a layer seems to be increased compared to the layer average; however, this result is on the detection limit of the RBS method.

Electroless nickel is by far one of the most utilized of all electroless-bath systems. Previously, the deposit from autocatalytic nickel baths has been investigated in a variety of ways, ranging from pure chemical methods (1) to x-ray (2) and electron beam based spectroscopy (3, 4). Rutherford backscattering spectrometry (RBS) has been applied to the examination of the kinetics of copper deposits (5, 6) and the composition of the catalysts used for electroless deposition (7-9), but so far, there have been few reports on RBS analysis of electroless nickel layers (10).

* Electrochemical Society Active Member.
Key words: electroless, Rutherford backscattering, catalysis.

The present paper discusses the results obtained by RBS as far as both the kinetics and the stoichiometry of various deposited Ni-P and Ni-P-W layers are concerned.

Analytical Method

Reference (9) gives a very brief introduction into the field of RBS. With this method, knowledge of the surface is obtained by irradiating a specimen with swift monoenergetic light ions and measuring the yield of the ions backscattered an angle θ. The method is nondestructive and yields information on stoichiometry *vs.* depth (from the surface of the specimen) down

to a depth of approximately 0.5 μm with a depth resolution in the range of 50 ~ 200Å.

For the present investigation, an area of 1 × 1 mm² of the surface is irradiated by 2 MeV $^4He^+$ to a dose of 40 μC. The scattered ions are detected by a surface-barrier detector at an angle θ of 160°. During analysis, the system is kept under a vacuum of 5×10^{-7} Torr.

Experimental

The present research is based on the same combinations of substrates and baths as described in Ref. (9), *i.e.*, alumina,[1] carbon,[2] and polyimide[3] substrates, and the baths denoted Ni-P(a), Ni-P(b), and Ni-P-W. The acidic Ni-P(a)[4] bath is merely used as a reference, whereas the basic Ni-P(b) and Ni-P-W baths prepared in the laboratory are the more important ones due to the electroless Ni-P-W film having high crystallinity and giving good results on the uniformity of film resistivity even though the only difference between the two baths is that Ni-P-W contains Na_2WO_4. Prior to precipitation, the two substrates are made catalytic using the way described in Ref. (9), carbon and alumina by a repeated two-step Sn-Pd process, and polyimide by evaporated palladium. Two or three samples of each kind are analyzed by RBS. The combinations of substrate, type of bath, and plating periods are summarized in Table I. The plating period is defined as the time from the evolution of the first hydrogen bubble on the substrate surface until the sample is removed, *i.e.*, the induction period prior to plating is not included. The induction period on alumina is around 1 sec, less on carbon but 3~5 sec on polyimide.

Results

The thickness of a layer is measured by means of RBS in units of atoms per square centimeter, but this can easily be converted into a physical depth scale, *e.g.*, angstroms, if the density of the layer is known. For the present results, the thickness is converted into angstroms, using a calculated density for either nickel-phosphorus or nickel-phosphorus-tungsten. The calculated densities are in agreement to within 1% with those quoted in Ref. (13 and 14).

Coverage of the surface.—For the same type of samples, the thickness-to-yield ratio for the nickel signal is observed to be constant as far as thin layers are concerned. There may be two reasons for the possible discrepancies in the ratios obtained: (*i*) either the layer is not covering the surface completely, or (*ii*) the thickness is estimated incorrectly. In RBS, layers thinner than three times the system resolution are normally estimated to be too wide; hence they will cause too small a ratio.

The ratios stemming from samples which have been deposited for 1 and 3 sec are too small, whereas the layers which have been deposited for longer periods have a constant ratio for the same type of specimen. It can thus be concluded that the nickel-phosphorus and the nickel-phosphorus-tungsten deposits do indeed cover the surface after a deposition time of 5 sec. This result can in addition set a lower limit to the number of catalytic sites. For the two-step Pd/Sn catalyst on carbon and alumina, the number of catalytic sites can be estimated to at least 6×10^3 sites/μm².

Kinetics.—The deposition rates of the thin layers precipitated within the first 60 sec are shown in Table II. The uncertainties given for the slopes and intercepts are the standard deviations. The correlation coefficients in the last column give an estimate of the goodness of the linear-regression analysis. They are close to one, indicating a linear relationship between time and thickness.

Two sets of slope and intercept values are given in Table II for each combination of substrate and bath, one stemming from the nickel signals and the other attached to some other signal in the particular spectra. On polyimide substrates, the oxygen signal was applied, while on alumina and carbon substrates, the position of the signals from the Pd/Sn catalyst gave the information. With two different trend lines for each system of specimen, it is possible to estimate the systematic errors introduced by using only one type of information; it is also possible to investigate whether the underlying catalyst stays at the interface.

For the different baths, the slopes are found to be Ni-P(a) > Ni-P(b) > Ni-P-W. For the alumina and carbon substrates, the Ni-P(b) and Ni-P-W baths deposit at approximately the same rate, but on polyimide, the rate is much smaller, and it is found (9) that the catalyst system used on polyimide is causing this decrease. On polyimide, the Ni-P-W and Ni-P(b) baths are depositing at a rate of only 30 and 40%, respectively, when compared to the rate on other substrates.

Figure 1 shows Ni-P(b) and Ni-P-W deposition rates on polyimide, and a linear relationship is seen. The error bars indicate the uncertainty of the RBS measurement only; the errors introduced when preparing the samples have not been taken into account.

Average composition.—Due to the mass differences between phosphorus, nickel, and tungsten, the signals

[1] 96 weight percent (w/o) α-Al_2O_3 ceramics (11) purchased from Nippon Tokushu Togyo Company, Limited (NGK Spark Plug Company, Limited).
[2] 99 w/o pure graphite containing a phenol-resin binder purchased from Nippon Carbon Company, Limited.
[3] 75 μm thickness film catalyzed by evaporated palladium purchased from Tore Company, Limited.
[4] NICKA 311 from Kaseihin-Kogyo Company, Limited.

Table I. The combination of substrate, type of bath, and plating period

Substrate	Bath type	Plating periods in sec
Alumina	Ni-P (a)	1, 3, 5, 10, 20, 30 40, 50, 60
Alumina	Ni-P (b)	1, 3, 5, 10, 20, 30 40, 50, 60
Alumina	Ni-P-W	1, 3, 5, 10, 20, 30 40, 50, 60
Carbon	Ni-P (b)	1, 3, 5, 10, 20, 40, 60
Carbon	Ni-P-W	1, 3, 5, 10, 20, 40, 60
Polyimide	Ni-P (b)	1, 3, 5, 10, 20, 40, 60
Polyimide	Ni-P-W	1, 3, 5, 10, 20, 40, 60

Table II. Slopes and intercepts for the trend lines related to the first 60 sec deposition time

Type of sample	Signal used for thickness measurement	Slope in angstrom/sec	Intercept in angstroms	Correlation coefficient
Ni-P-W on polyimide	Ni	6.6 ± 0.3	163 ± 10	0.985
Ni-P-W on polyimide	O	6.2 ± 0.4	125 ± 13	0.974
Ni-P (b) on polyimide	Ni	11.1 ± 0.5	213 ± 14	0.991
Ni-P (b) on polyimide	O	11.4 ± 0.8	167 ± 24	0.977
Ni-P(a) on Al_2O_3	Ni	81.8 ± 1.2	46 ± 37	0.998
Ni-P(a) on Al_2O_3	Pd/Sn	73.7 ± 2.3	101 ± 24	0.996
Ni-P(b) on Al_2O_3	Ni	24.7 ± 1.1	207 ± 36	0.984
Ni-P(b) on Al_2O_3	Pd/Sn	23.6 ± 1.3	162 ± 34	0.979
Ni-P-W on Al_2O_3	Ni	21.4 ± 0.7	108 ± 22	0.992
Ni-P-W on Al_2O_3	Pd/Sn	19.1 ± 0.7	109 ± 22	0.990
Ni-P(b) on carbon	Ni	29.0 ± 1.0	111 ± 28	0.994
Ni-P(b) on carbon	Pd/Sn	28.6 ± 1.3	70 ± 25	0.996
Ni-P-W on carbon	Ni	26.6 ± 1.0	53 ± 30	0.994
Ni-P-W on carbon	Pd/Sn	24.5 ± 1.2	28 ± 22	0.995

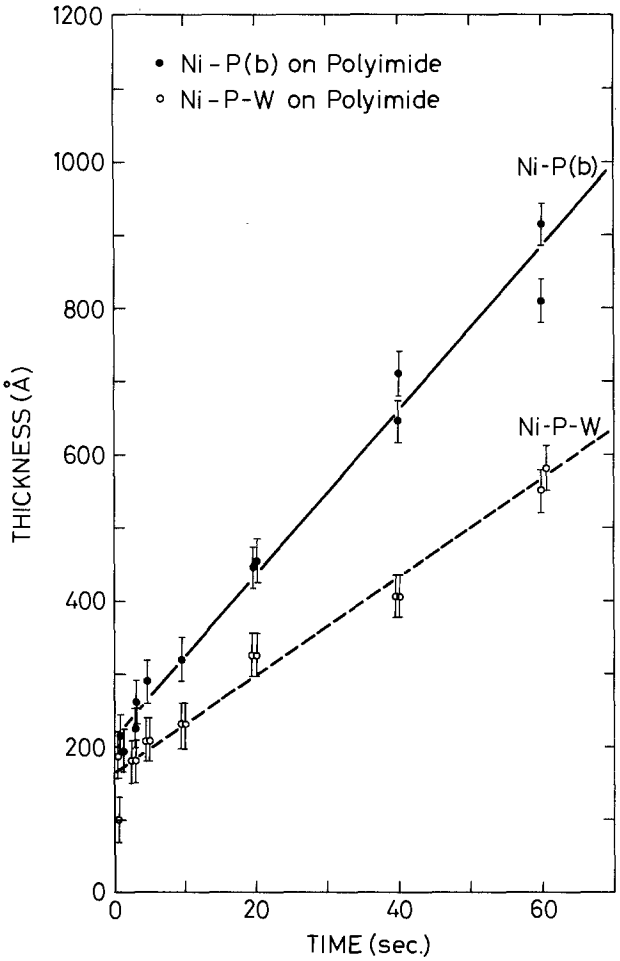

Fig. 1. Trend lines for Ni-P(b) (thickness in angstroms = 11.1 · sec + 213) and Ni-P-W (thickness in angstroms = 6.6 · sec + 163) using polyimide substrate.

stemming from each of the deposited elements will be totally separated in the RBS spectra; thus the stoichiometry is easily obtainable as shown in Table III. The uncertainties in Table III are the standard deviations. Based on the results presented in Table III, the following conclusions can be made.

1. The Ni-P(a) and Ni-P(b) baths have almost the same stoichiometry even though Ni-P(a) is an acidic and Ni-P(b) an alkaline bath [and the deposition rate of Ni-P(a) is taking place at least three times faster than for Ni-P(b)].

2. Codeposition of tungsten reduces the phosphorus content by two thirds.

3. Contrary to the deposition rates, the stoichiometry is not affected by the catalyst species.

Table III. The average stoichiometry for the different types of samples

Type of sample	Element	Composition in atomic %	Composition in weight %
Ni-P (a) on Al_2O_3	Ni	84.0 ± 1.8	90.8 ± 1.9
	P	16.1 ± 1.7	9.2 ± 1.0
Ni-P (b) on Al_2O_3	Ni	80.1 ± 1.7	88.4 ± 1.9
	P	19.9 ± 1.7	11.6 ± 1.0
Ni-P-W on Al_2O_3	Ni	93.2 ± 1.3	93.7 ± 1.3
	P	5.8 ± 1.3	3.1 ± 0.6
	W	1.0 ± 0.2	3.2 ± 0.5
Ni-P (b) on carbon	Ni	82.6 ± 1.7	90.0 ± 1.9
	P	17.4 ± 1.7	10.0 ± 1.0
Ni-P-W on carbon	Ni	92.4 ± 2.1	93.3 ± 2.1
	P	6.6 ± 1.7	3.5 ± 0.9
	W	1.0 ± 0.4	3.2 ± 1.3
Ni-P (b) on polyimide	Ni	83.7 ± 1.1	90.7 ± 1.2
	P	16.3 ± 1.1	9.3 ± 0.7
Ni-P-W on polyimide	Ni	93.2 ± 1.0	94.1 ± 1.0
	P	5.7 ± 0.3	3.0 ± 0.2
	W	0.9 ± 0.4	2.8 ± 1.2

Composition vs. deposition time.—Figure 2 illustrates the variation in stoichiometry *vs.* deposition time. The stoichiometry is in atomic percent, and the uncertainties are the same as for Table III. From the illustrated results (and similar results for alumina substrates), it can be concluded that the composition fluctuates

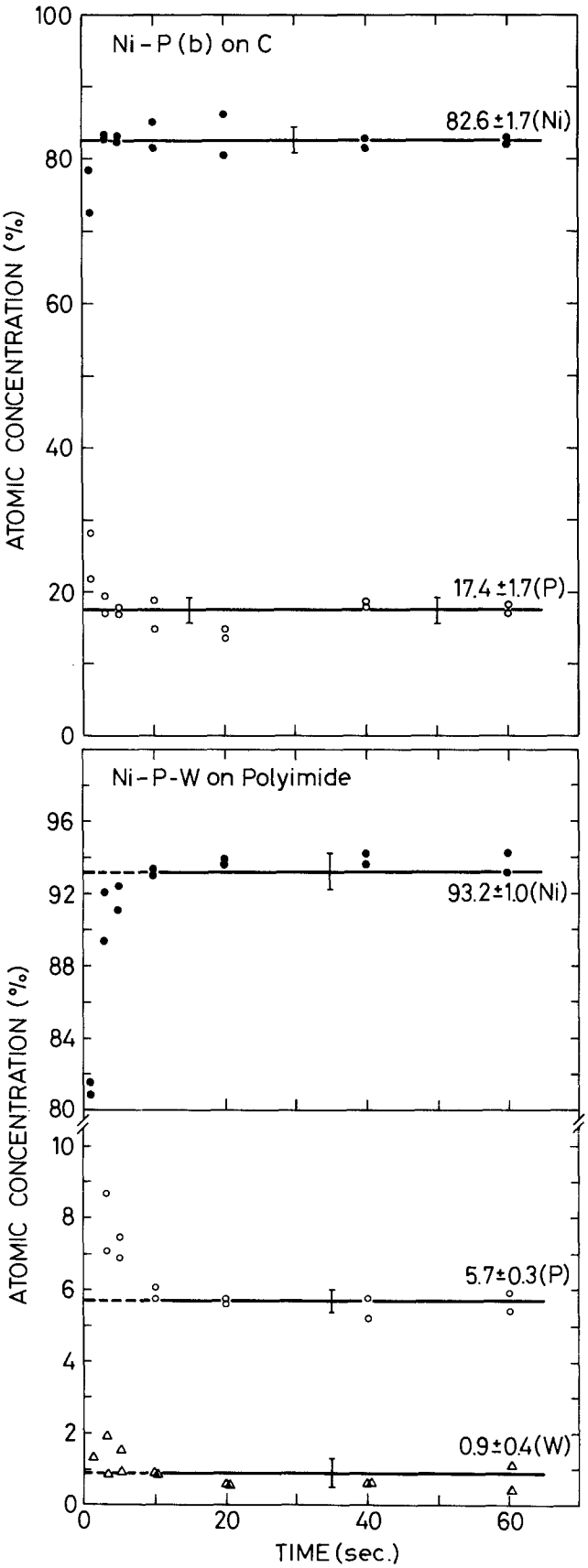

Fig. 2. Atomic concentration *vs.* deposition time for deposits of Ni-P(b) on C and Ni-P-W on polyimide.

around the mean value for deposition periods longer than 5 sec. The very thin layers, which were deposited for only 1 and 3 sec, always contain a surplus of phosphorus of up to 50% above average.

Composition of the single layers.—Figure 3 shows the stoichiometry *vs.* depth of a nickel-phosphorus layer on alumina. The result has been obtained by analyzing the spectrum step by step via the different signals. The depth scale is given in units of 10^{17} at./cm^2, equivalent to 125Å. The depth resolution is around 125Å at the surface, decreasing to 250Å at the metal-alumina interface. A structure extending less than the depth resolution must be considered as merely a statistical fluctuation.

In the nickel-phosphorus layer, the stoichiometry is correct to within 2~3%, but when aluminum and oxygen appear in the system, the uncertainty increases to 7~8%. At a depth of 16 × 10^{17} at./cm^2, the phosphorus content is below the detection limit. Thus phosphorus corresponding to the nickel content may still be present deep inside the sample.

From results similar to those presented in Fig. 3, it is possible to conclude that deposition takes place below the substrate surface when carbon or alumina is used. It means that the deposition occurs inside the pores of carbon and alumina substrate, since both substrates have a fairly open and granular structure (11). On polyimide substrates, a similar conclusion cannot be made because the decrease in nickel content at the interface (~7 × 10^{17} at./cm^2) is comparable to the depth resolution. As one can see in Fig. 4, the decay of the nickel signal is following an error function with a

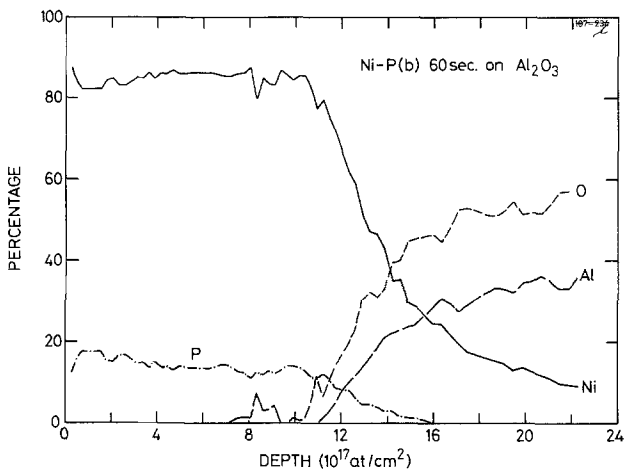

Fig. 3. Composition *vs.* depth of Ni-P(b) on alumina at 60 sec deposition time.

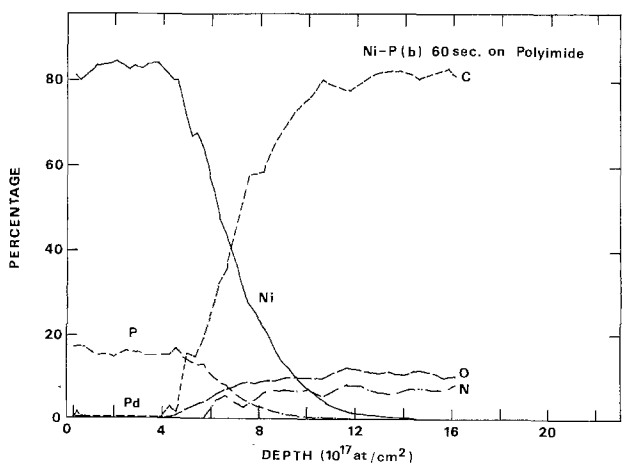

Fig. 4. Composition *vs.* depth of Ni-P(b) on polyimide at 60 sec deposition time.

standard deviation of around 1.5 × 10^{17} at./cm^2, which is the resolution to expect in this depth.

In both Fig. 3 and 4 an increment in the phosphorus content in the outermost 4 × 10^{17} at./cm^2 (~500Å) may be seen, however, the RBS method is capable of giving only a strong indication of this result.

Discussion

Considerations in the previous section on how thin layers can be measured by RBS also suggest a lower limit for the number of catalytic sites. This lower limit is found to be in agreement with the direct measurement in Ref. (15), where 10^4 sites/μm^2 were obtained for the two-step Pd/Sn activating method on glass slides.

Kinematics.—In a previous study (4, 12), the deposition rate was measured by a gravimetric method, yielding 53 Å/sec for the Ni-P(a) bath and 13.3 Å/sec each for the Ni-P(b) and Ni-P-W baths. Those results are 37% below the rates found in the present study. Neither the gravimetric nor the RBS method has systematic errors of this magnitude, and the discrepancy may be explained by two different types of deposition rates being measured. The gravimetric method yields the deposition rate integrated over 1 hr of precipitation, *i.e.*, it measures the long-time deposition rate, whereas the RBS method gives the short-time rate within the first 60 sec. The large difference in deposition rates for different catalytic systems may be seen only in the short-time rate. The gravimetric method may possibly never exhibit such a variation. Honma *et al.* (16), using a laser-analysis technique, reported that at the initial stage, an electroless nickel film deposits faster than it does later, which supports the above discussion.

Stoichiometry.—The composition of the precipitated layers has been investigated by an electron-probe microanalyzer (4), and the phosphorus content is found to be 8.9 w/o for the Ni-P(b) deposits and 3.0 w/o phosphorus and 3.3 w/o tungsten for the Ni-P-W deposits. These findings are in good agreement with the results listed in Table III. The reason for the phenomenon that the codeposition of tungsten reduces the phosphorus content in Ni-P-W deposit was already discussed (17). The decrease of phosphorus content may be caused by the depression of decomposition reaction of hypophosphite by tungstate ion at the deposit-solution interface.

The increase in phosphorus content for the very thin layers deposited for only 1 and 3 sec has not been reported previously. The larger content of phosphorus in the initial plating stage may be caused by the presence of decomposition reaction of hypophosphite due to the direct contact of palladium catalyst.

The calculations of stoichiometry as a function of depth show deposition inside the substrate in the cases of alumina and carbon, whereas this is not so for polyimide substrates. This result can be related to the adhesion of the layers, which is significantly worse for polyimide substrates than for the other types.

Conclusion

The excellent properties of the RBS analyzing method have been demonstrated for the case of the first stages of electroless nickel deposition, especially for the measurements of kinetics and stoichiometry. Principally, the results are in agreement with those found by other methods, but some of the findings concerning the stoichiometry have never been reported previously. A future examination of these items may lead to an extended understanding of the precipitation method.

Manuscript submitted Jan. 13, 1983; revised manuscript received June 7, 1983.

Waseda University assisted in meeting the publication costs of this article.

REFERENCES
1. F. Pearlstein and R. F. Weightmore, *Electrochem. Technol.*, **6**, 427 (1968).
2. G. S. Cargill, *J. Appl. Phys.*, **41**, 12 (1970).
3. A. H. Graham, R. W. Lindsay, and H. J. Read, *This Journal*, **112**, 401 (1965).
4. T. Osaka, H. Sawai, F. Otoi, and K. Nihei, *Metal. Fin.*, **80**, 31 (1982).
5. R. L. Meek, *This Journal*, **122**, 1177 (1975).
6. L. G. Svendsen and G. Sørensen, Proceedings of International Conference on Electroless Metallization on Sensitized Polymer Powders Fused onto a Polymer Surface, K. L. Mittal, Editor, To appear in "Physicochemical Aspects of Polymer Surfaces," Plenum Press, New York (1982).
7. R. L. Meek, *This Journal*, **112**, 1478 (1975).
8. B. K. W. Baylis, N. E. Hedgecock, M. Schlesinger, and A. van Wijngaarden, *ibid.*, **126**, 1671 (1979).
9. L. G. Svendsen, T. Osaka, and H. Sawai, *ibid.*, **130**, 2252 (1983).
10. A. van Wijngaarden, M. Schlesinger, N. E. Hedgecock, and B. K. W. Baylis, *ibid.*, **127**, 1124 (1980).
11. Y. Ieda and R. Kanbe, *Jitsumu Hyomen Gijutsu, (J. Met. Fin. Practice Jpn.)*, **29**, 541 (1982).
12. T. Osaka, H. Sawai, and N. Kasai, *Kinzoku Hyomen Gijutsu (J. Met. Fin. Soc. Jpn.)*, **32**, 615 (1981).
13. F. Ogburn, R. M. Shoonover, and C. E. Jonson, *Plating Surf. Finish*, **68**, 45 (1981).
14. W. M. Safranek, "The Properties of Electrodeposited Metals and Alloys," p. 466, American Elsevier Publishing Co., Inc., New York (1974).
15. J. P. Marton and M. Schlesinger, *This Journal*, **115**, 16 (1968).
16. A. Waku and H. Honma, Extended Abstract of the 64th Conference of Metal Finishing Society of Japan, p. 124 (1981).
17. T. Osaka, F. Otoi, and H. Sawai, *Kinzoku Hyomen Gijutsu*, **32**, 13 (1981).

Study on A-C Powder EL Phosphor Deterioration Factors

Katsuhiko Hirabayashi, Haruki Kozawaguchi, and Bunjiro Tsujiyama

Ibaraki Electrical Communication Laboratory, Nippon Telegraph and Telephone Public Corporation, Tokai mura, Ibaraki-ken, 319-11 Japan

ABSTRACT

It is shown that a-c powder EL deterioration is closely related to sulfur vacancy in the phosphor and the phosphor crystal quality, by measurement of ESR spectrum and x-ray diffraction pattern. The EL phosphor life is improved with a decrease in the sulfur vacancy density in the phosphor. It is further improved with a decrease in the x-ray diffraction (111) peak intensity of the phosphor.

The a-c powder EL cell has long been known to deteriorate slowly during continued operation. Many efforts have been made to improve its brightness and maintenance. Various phenomena in regard to deterioration have been investigated and various models for the deterioration mechanism have been proposed. However, the intrinsic deterioration mechanism has not yet been revealed experimentally.

From the microscopic observation of light emitting phosphor under the electric field, Fischer (1) proposed the deterioration model as follows: the tips of the copper-sulfide imperfection lines, which cause the local field, can be blunted by drift of copper ions or by attraction of copper ions from the adjacent host crystal, and EL brightness decreases as the result of local field reduction. However, this model was not confirmed by experiments. The only experimental result of changes in EL phosphor under electric field was Jaffe's report (2) that the sulfur vacancy density in the phosphor measured by thermoluminescence was increased by operation in a dry atmosphere. Lehmann (3) explained that (Zn,Cd)S:Cu,Br phosphor became extremely deterioration-resistant after being fired and refired in pure sulfur. From these results, Lehmann presumed that the EL deterioration was due to sulfur vacancy diffusion from the phosphor surface to the interior.

However, this Lehmann's hypermaintenance phosphor has been more often quoted than reproduced (4). Hahn (5) reported that no additional traps, such as sulfur vacancy, were built in aged phosphors, though he also performed the same experiment as Jaffe.

In this study, to clarify this point, the authors investigated the relation between the deterioration and the properties of the EL phosphor such as the sulfur vacancy density or the crystal quality.

First, the ESR spectrum for sulfur vacancy in ZnS phosphor powder was measured and the method of measuring relative sulfur vacancy density was established. Next, the time dependence of sulfur vacancy density during deterioration was measured. The relation between the sulfur vacancy density and the life of as grown EL phosphors was investigated. Then, as grown EL phosphors with low sulfur vacancy density were fractionated, etched, milled, or annealed, and the changes of phosphor crystal quality, brightness, and life were measured. As a result, it was clarified that the sulfur vacancy density was not increased by deterioration, but the sulfur vacancy was one factor which accelerated EL deterioration. As-grown EL phosphor with high sulfur vacancy density has a short life. It was also clarified that EL phosphor crystal quality was another factor of deterioration. The EL life is improved with a decrease in the x-ray diffraction (111) peak intensity.

Key words: electroluminescence, defects, crystallography, ESR.

Experimental Methods

ESR measurement.—The ESR spectrum for sulfur vacancy in ZnS single-crystal was measured by Schneider (6) but that in ZnS phosphor powder has not been measured. The authors measured the ESR spectrum for sulfur vacancy in ZnS:Cu,Br and ZnS:Cu,Al phosphor powder as follows. The ESR measurements were made at −150°C with a JES-PE-3X spectrometer operated at X-band (9.2 GHz) with 100 Hz magnetic field modulation. The cavity had a window to allow optical excitation of the samples. The light source used was a 150W high pressure mercury lamp, equipped with a Toshiba UV-D25 filter. The typical ESR spectrum measured for ZnS:Cu,Br phosphor is shown in Fig. 1. The spectrum can be divided into three different components; A, B, and C. A is a signal characterized by the g-factor, $g = 2.0035$, which is ascribed to the sulfur vacancy because its g-factor coincides with that of the sulfur vacancy of the ZnS single-crystal ESR signal measured by Schneider, and it is also supported by the fact that its intensity de-

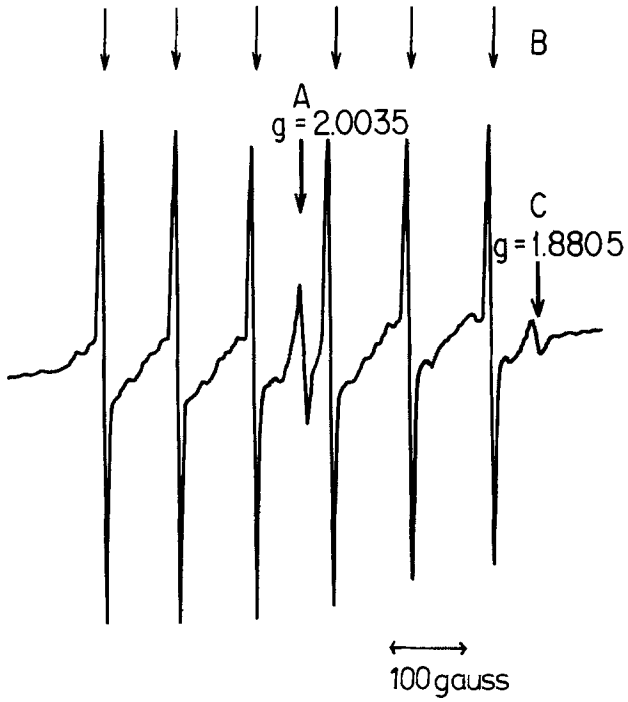

Fig. 1. Typical ESR spectrum for ZnS:Cu,Br phosphor

creases proportionally to thermoluminescence spectrum intensity of sulfur vacancy with an increase in dopants content, as will be mentioned later. The hfs satellites could not be detected in this study, since the sample was powder. B is six equal intensity signals, which are ascribed to Mn in ZnS. C is a signal characterized by a g-factor, g = 1.8805, and is ascribed to a mobile electron, because its g-factor coincides with that of a mobile electron, as measured by Muller (7).

In order to determine the relative density of sulfur vacancy, MgO was used as an internal standard. The MgO:Mn standard sample was prepared by firing MgO with Mn at 900°C in air. The MgO:Mn standard sample contained about 0.01 m/o (mole percent) Mn. The mixture of ZnS phosphor and MgO:Mn powder, weight ratio 10:1, was measured by ESR. The sulfur vacancy density for ZnS phosphor was estimated by the intensity ratio of the sulfur vacancy signal in ZnS phosphor to the Mn signal in MgO:Mn (S vacancy/Mn).

Crystal quality measurement.—The crystal quality is estimated by measuring intensity, half-width, or the diffraction angle in x-ray diffraction patterns. However, in measuring the x-ray diffraction patterns for various ZnS phosphors, their differences in the half-width could not be detected. Moreover, it is difficult to estimate the crystal quality by measuring the diffraction angle, since the diffraction angle is closely related to a lattice constant which depends on the Cu, Br content of ZnS:Cu,Br phosphor. Therefore, for estimating the crystal quality, the x-ray diffraction intensity, the (111) peak which is the strongest among all the diffraction peaks, was measured in this study.

Experimental Results and Considerations

Sulfur vacancy density change before and after deterioration.—A-c powder EL deterioration is classified into two types: one results in EL phosphor blacking and the other does not. The former kind of deterioration occurs rather rapidly, when the EL is operated in a wet atmosphere or irradiated by u.v. The latter kind of deterioration occurs slowly, when the EL cell is operated in a dry atmosphere. The sulfur vacancy density for the phosphors before and after these deteriorations were measured.

The phosphor deteriorated in the dry atmosphere was made as follows. The emission layer was made by the coating of a mixture of the phosphor and fluoro rubber binder on an iron board. The area and the thickness were 15 × 20 cm^2 and 100-200 μm, respectively. An aluminum film was deposited on the layer to form the rear electrode. After this device was operated under 500V, 10 kHz application, the Al rear electrode was removed with NaOH. The emission layer was dissolved in methylethylketone (MEK), and the deteriorated phosphor was dried at room temperature because the brightness of deteriorated phosphors was recovered by heat-treatment at 100°-200°C (8). The time dependence of the brightness and the sulfur vacancy density in the case of deterioration in the dry atmosphere are shown in Fig. 2(a) and 2(b), respectively. Though the brightness decreases, the sulfur vacancy density is almost constant during operation.

The sulfur vacancy density of the phosphor, which was blackened by u.v. irradiation, was also measured. The ESR spectra for ZnS:Cu,Br phosphor before and after u.v. irradiation are shown in Fig. 3(a) and 3(b). The sulfur vacancy density is apparently increased by u.v. radiation. The phosphor deteriorated by exposure to u.v. radiation has almost the same property as the phosphor deteriorated in a wet atmosphere. Therefore, deterioration during operation in a wet atmosphere is considered to be due to the sulfur vacancy density increase. The deterioration mechanism of EL phosphor

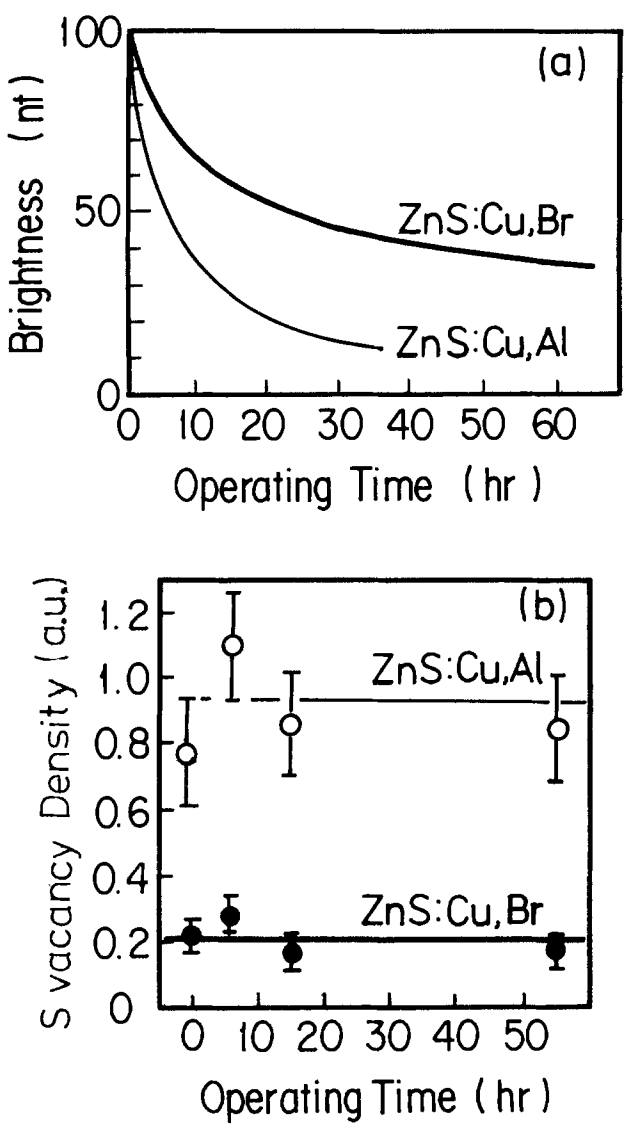

Fig. 2. Time dependence of (a) the brightness and (b) the sulfur vacancy density in the case of operation in a dry atmosphere.

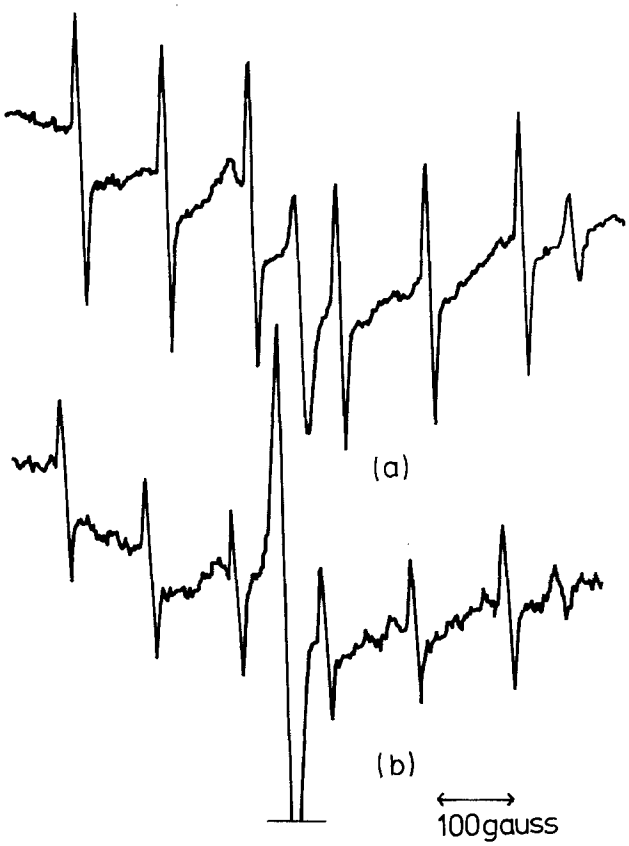

Fig. 3. ESR spectra for ZnS:Cu,Br phosphors (a) before and (b) after u.v. irradiation.

operated in a wet atmosphere, is considered to be

$$ZnS + 2H_2O \rightarrow SO_2 + Zn + 2H_2 \quad [1]$$

Sulfur escapes from the phosphor particle in the form of SO_2. As a result, sulfur vacancy and Zn, which blacken the phosphor, are left in the phosphor.

Jaffe reported that the sulfur vacancy density was increased by operation in a dry atmosphere, which is opposite to the present result. However, since his experiment time is about 1000 hr, it seems that moisture was introduced into the desiccator and this moisture made the sulfur vacancy density increase.

As mentioned above, in the case of the deterioration which blackens EL phosphor, caused by u.v. irradiation or operation in a wet atmosphere, the sulfur vacancy density increases. However, in the deterioration in a dry atmosphere the density does not increase with operating time. Therefore, the cause of EL deterioration in a dry atmosphere is not an increase in sulfur vacancy density.

On the other hand, from Fig. 2 it is noticed that ZnS:Cu,Al phosphor, which has a larger amount of sulfur vacancy density, has a shorter life than ZnS:Cu,Br phosphor having a smaller density. It is expected that EL phosphor having a large amount of sulfur vacancy has a short life. Then, the relation between the sulfur vacancy density and the life of as-grown EL phosphors was investigated in detail.

The relation between the life and the sulfur vacancy density of as-grown phosphors.—ZnS:Cu,Br phosphors were prepared by firing ZnS at 900°C for 6 hr with the addition of Cu, in the form of CuCOOH, and Br, in the form of NH_4Br. The measuring methods for brightness and life, t_c, for the phosphor in this experiment are the same as those described in a previous paper (9).

The average dopant content dependence of the brightness, the life, t_c, and the sulfur vacancy density measured by ESR are shown in Fig. 4. As the average dopant content increases, the sulfur vacancy density

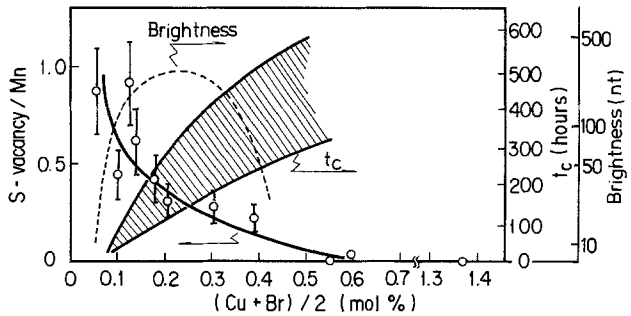

Fig. 4. Dopant content dependence of the sulfur vacancy density (S vacancy/Mn), the brightness, and life (t_c) for ZnS:Cu,Br phosphor.

decreases and the long life EL phosphor can be obtained. The brightness reaches a maximum at (Cu + Br)/2 = 0.2-0.3 m/o.

The thermoluminescence spectra for phosphors with varying dopant content were also measured. The results are shown in Fig. 5. Each spectrum has peaks at about −160°, −130°, and −40°C. The −160° and −40°C peak intensities decrease and the −130°C peak intensity increases with an increase in dopant content. From Hoogenstraaten's thermoluminescence study (10), it is considered that the −160°, −130°, and −40°C peaks are, respectively, due to sulfur vacancy, Br, and sulfur vacancy pairing. The thermoluminescence results also prove that the sulfur vacancy density decreases with the dopant content. The reason for decreasing sulfur vacancy density with an increase in dopant content is considered to be that the coactivator, Br, enters the sulfur vacancy.

The above results show that EL phosphor with a large amount of sulfur vacancy has a short life, and sulfur vacancy is considered to be one factor which accelerates EL deterioration.

The authors expected that the life could be improved by decreasing the sulfur vacancy density. However, decreasing the sulfur vacancy density by doping too much Cu and Br causes the brightness decrease. Refiring high brightness ZnS:Cu,Br phosphors having optimum dopants content, (Cu + Br)/2 ≃ 0.3 m/o, which has a small amount of sulfur vacancy, was tried.

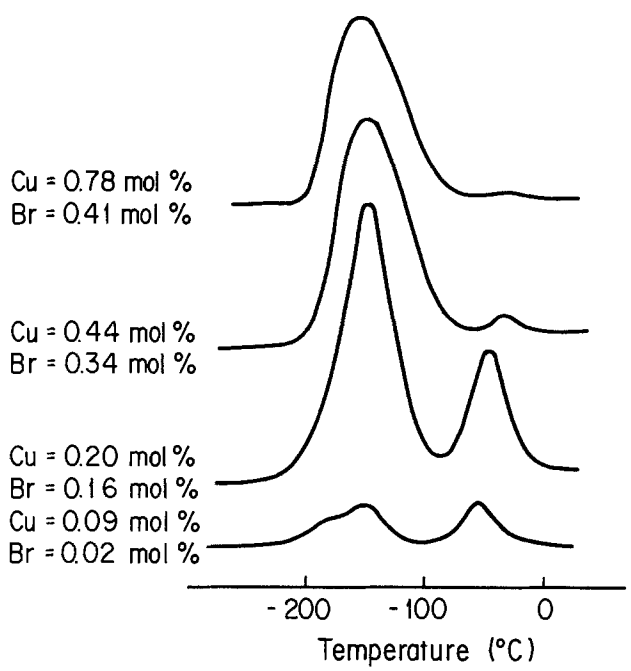

Fig. 5. Thermoluminescence spectra for ZnS:Cu,Br phosphors with varying dopant content.

Sulfur vacancy density for the phosphors refired with sulfur is smaller than for those refired with no sulfur, but their life was not improved.

The authors improved the life of ZnS:Cu,Br phosphors having optimum dopant content by fractionation, etching (11), and annealing (12). Sulfur vacancy density did not decrease by these treatments, while the life was improved .The above results indicate that sulfur vacancy is not the only factor of deterioration.

From various measurements, the authors found that the phosphor crystal quality was closely related to the life.

The relation between life and crystal quality.—Phosphors having a small amount of sulfur vacancy were fractionated, etched, milled, or annealed, and the change of the crystal quality, the brightness, and the life were measured.

The fractionated phosphor particle size dependence of the (111) peak intensity, the brightness, and the life are shown in Fig. 6. The (111) peak intensity decreases with the particle size. This relation inversely resembles the particle size dependence of the life. The etched phosphor particle size dependence of the (111) peak intensity, the brightness, and the life are shown in Fig. 7. The (111) peak intensity increases with the

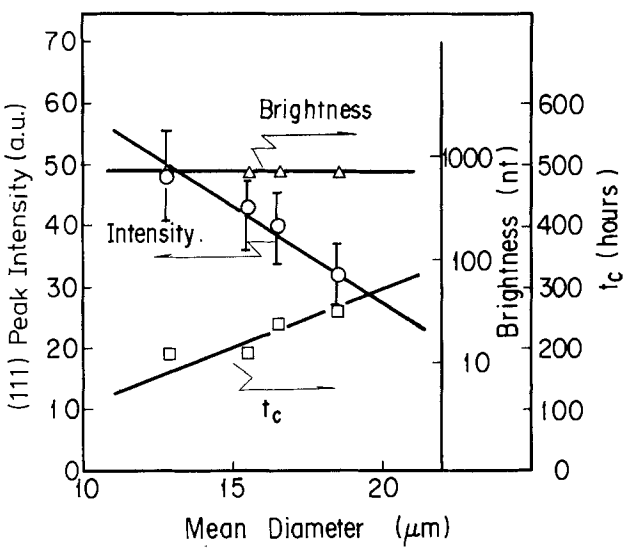

Fig. 6. Fractionated phosphor particle size dependence of the x-ray diffraction (111) peak intensity, the brightness, and the life.

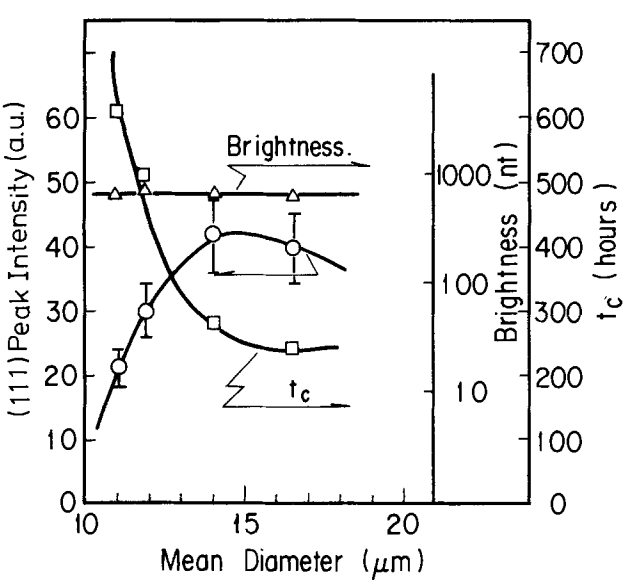

Fig. 7. Etched phosphor particle size dependence of the x-ray diffraction (111) peak intensity, the brightness, and the life.

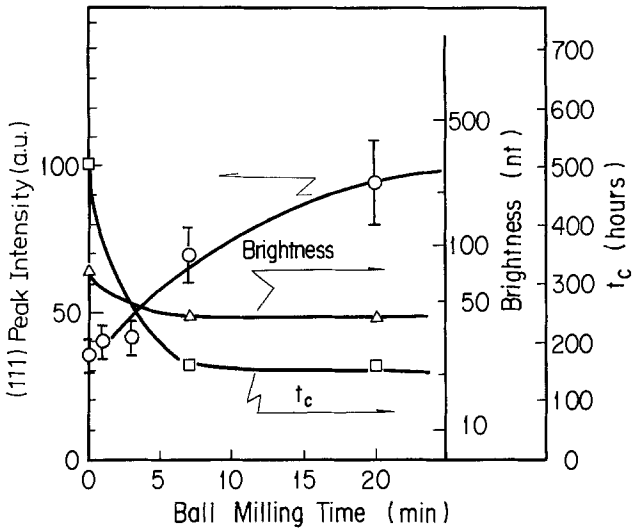

Fig. 8. Ball milling time dependence of the x-ray diffraction (111) peak intensity, the brightness, and the life.

particle size. This relation also inversely resembles the particle size dependence of the life. The milling time dependence of the (111) peak intensity, the brightness, and the life are shown in Fig. 8. The (111) peak intensity increases, while the brightness and the life decrease with milling. In the previous paper (12), the authors reported that the phosphor life was improved and the (111) peak intensity was decreased by annealing. This relation is again shown in Table I. A decrease in the (111) peak intensity is considered to be due to a change in EL phosphor crystal quality, such as formation of stacking faults. The life of EL phosphor having a small amount of sulfur vacancy is closely related to phosphor crystal quality. The long-life EL phosphor can be obtained by the fractionation, etching, or annealing of the phosphor with a small amount of sulfur vacancy.

Consideration of Deterioration Mechanism

The above mentioned results indicate that sulfur vacancy and crystal quality are major factors of the deterioration. In a previous paper (8), the authors showed that deteriorated EL cell brightness could be recovered by heat-treatment, the recovered brightness depends on the temperature and time of the heat-treatment, and the activation energy of recovery process was 0.3 eV, which coincided with that for the deterioration. Since the value of deterioration and recovery activation energy was found to be equal to the activation energy for Cu diffusion in ZnS, the authors presumed for the deterioration and recovery model that Cu ions diffuse under the electric field during operation and return to the initial position by heat-treatment.

The present experimental results can be explained by this model as follows. First, producing a large amount of sulfur vacancy makes Cu ion diffusion easy in the EL phosphor and results in short life phosphors. Second, decreasing the (111) peak intensity by a change in EL phosphor crystal quality, such as formation of stacking faults, prevents the Cu ion diffusion, so the phosphor life is improved.

In another paper (12), the authors showed that the activation energy of deterioration changed from 0.3 to

Table I. Air annealing dependence of the x-ray diffraction (111) peak intensity and EL life (900°C, 2 hr)

	X-ray diffraction (111) peak intensity (Arbitrary unit)	Half-life (hr)
Before annealing	32 + 3	≃10
After annealing	25 + 2	≃200

0.45 eV by annealing. This indicates that a change in EL phosphor crystal quality by annealing prevents Cu ion diffusion. Therefore, this study also supported the deterioration model where Cu ions diffuse in ZnS phosphor under the electric field.

Conclusion

To clarify the EL deterioration mechanism, the relation between deterioration and sulfur vacancy was investigated. The relation between deterioration and crystal quality for EL phosphor having a small amount of sulfur vacancy was also investigated. As a result, sulfur vacancy and EL phosphor crystal quality are major factors of deterioration. That is, as grown EL phosphor having a large amount of sulfur vacancy has a short life. In the case of EL phosphor having a small amount of sulfur vacancy, the life is improved with a decrease in the x-ray diffraction (111) peak intensity. The long-life phosphor can be obtained by decreasing the (111) peak intensity of the phosphors having a small amount of sulfur vacancy.

Acknowledgments

The authors wish to thank K. Murase, K. Katoh, and J. Ohwaki for their valuable discussion.

Manuscript submitted March 29, 1983.

Nippon Telegraph and Telephone Public Corporation assisted in meeting the publication costs of this article.

REFERENCES

1. A. G. Fischer, *This Journal*, **110**, 733 (1963).
2. P. M. Jaffe, *ibid.*, **108**, 711 (1961).
3. W. Lehmann, *ibid.*, **113**, 40 (1966).
4. W. E. Howard, SID Seminar Lecture Notes, Vol. 1, p. 77 (April 28 1980).
5. D. Hahn and J. Mimkes, *J. Phys. Chem. Solids*, **29**, 1287 (1968).
6. J. Schneider, in "Semiconducting Compounds," D. G. Thomas, Editor, p. 40, W. A. Benjamin, Inc., Menlo Park, CA (1967).
7. K. A. Muller, *Phys. Lett.*, **4**, 28 (1963).
8. K. Hirabayashi and Y. Itoh, *This Journal*, **129**, 362 (1982).
9. Y. Itoh, K. Hirabayashi, and K. Murase, *ibid.*, **129**, 813 (1982).
10. W. Hoogenstraaten, *Philips Res. Rep.*, **13**, 515 (1958).
11. K. Hirabayashi, Y. Itoh, and K. Murase, *This Journal*, **129**, 2059 (1982).
12. K. Hirabayashi, H. Kozawaguchi, and B. Tsujiyama, To be submitted to *This Journal*.

Surface Oxygen Chemical Potential in a Gas-Solid Reaction

Lutgard C. De Jonghe and Mei Chang

Materials and Molecular Research Division, Lawrence Berkeley Laboratory and Department of Materials Science and Mineral Engineering, University of California, Berkeley, California 94720

ABSTRACT

A method is developed defining the oxygen chemical potential on the surface of oxide on the metal phase during a gaseous reduction reaction. The method couples the gas reaction with a solid-state defect reaction. It is shown that, during this gas-solid reaction, the surface oxygen chemical potential, μ_s, is between that of the gas phase, μ_g, and that of the metal/metal oxide equilibrium, μ_e. If the adsorption-desorption step is slow, μ_s is close to μ_e; if the adsorption-desorption step is fast, μ_s is close to μ_g.

In certain gas-solid reactions, such as oxide reduction by CO/CO_2 mixtures, it may be necessary to define the surface oxygen chemical potential. This potential is an important quantity, since it provides a boundary value for solid-state transport processes that occur as part of the reduction mechanism.

In most studies of gas-solid reduction or oxidation reactions, the surface oxygen chemical potential has been considered either implicitly or explicitly. It has been common to assume that this potential is established by the gas phase through some equilibrium reaction that, for example, establishes a corresponding surface coverage (1-3). At significant reaction rates, this surface coverage is not simply related to the gas composition by some equilibrium reaction (1). Intermediate steps, such as desorption and adsorption reactions, introduce chemical potential differences between oxygen in the gas phase and oxygen in the solid surface making the adsorbed gas composition a complex function of the reaction rate (4). The kinetic parameters governing these intermediate steps need, therefore, to be taken into account explicitly when determining the surface oxygen chemical potential. This explicit consideration can show more clearly the connection between specific catalytic phenomena and surface chemical potentials of relevant species.

The significance of this surface oxygen chemical potential was recently demonstrated by Chang and De Jonghe (5) for the gaseous reduction of an ion bearing oxide, cobalt ferrite, where the oxygen chemical potential at the metal-oxide-gas triple junction, μ_s, determines the morphology of the metallic reaction product. In the case of CO/CO_2 reduction of the cobalt ferrites, metallic alloy whiskers are formed, as shown in Fig. 1a, with a diameter that is determined by the rate at which the oxygen is removed from under the whisker (metal-oxide interface) and by a surface gas-solid reaction at triple junction. The situation is shown schematically in Fig. 1b. This oxygen chemical potential is between that for the metal-oxide equilibrium, μ_e, and that for the gas phase equilibrium, μ_g. In this paper, we consider how the oxygen chemical potential, μ_s, may be defined for a reduction reaction when the oxide or the metal surface is the active reaction phase where the conversion of CO to CO_2 occurs.

Key words: surfaces, reduction, oxygen potential, adsorption, catalysis.

Kinetic and Thermodynamic Consideration

Only the simplest reaction sequence will be considered here. This will permit a clearer discussion of the procedure, without undue algebraic complexity.

During a gas-solid reaction, such as reduction of oxide MO to metal M by CO/CO_2, the oxygen chemical potential in the gas phase, μ_g, will differ from the one on the surface of the solid, μ_s, which in turn will differ from the MO/M equilibrium one, μ_e. The reduction reaction may, in its most elementary form, be described by a first-order reaction sequence

$$CO(g) + MO \underset{l_1}{\overset{k_1}{\rightleftarrows}} CO(a) + MO \qquad [1]$$

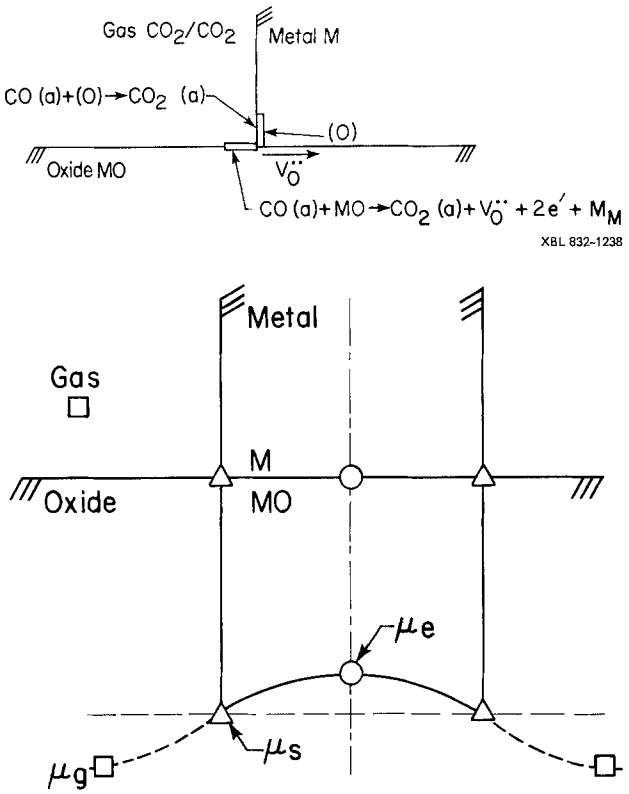

Fig. 1. (a, top) Reactions occurring on the metal or on the oxide phase near the metal-oxide-gas triple junction. Oxygen vacancies or dissolved oxygen may need to be transported along or near the metal-oxide interface when the progress of the reaction requires that oxygen is removed from that interface. (a) means "adsorbed"; (O) means "dissolved oxygen". (b, bottom) Schematic representation of the oxygen chemical potential for a reduction reaction where oxide MO is converted to metal M.

$$CO(a) + MO \underset{l_2}{\overset{k_2}{\rightleftarrows}} CO_2(a) + M \quad [2]$$

$$CO_2(a) + M \underset{l_3}{\overset{k_3}{\rightleftarrows}} CO_2(g) + M \quad [3]$$

where (g) refers to the "gas phase" and (a) refers to the "adsorbed phase." This sequence does not specify where the adsorption, exchange, or desorption reactions occur. In actuality, different parts of the reactions may well take place on different phases when both metal and oxide are present as surface phases; *e.g.*, adsorption might occur on the metal surface,

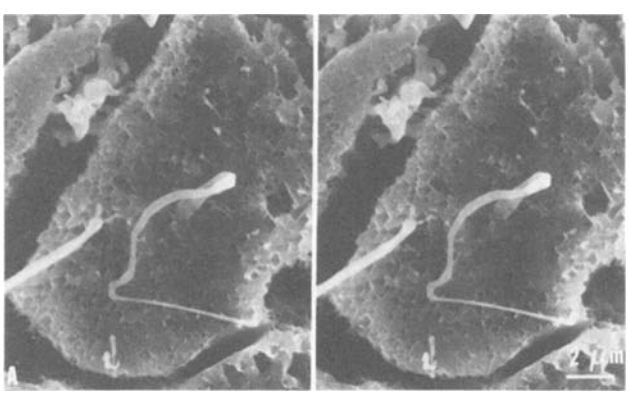

Fig. 2. Example of metal whiskers formed as a result of CO/CO_2 reduction of $CoFe_2O_4$. The oxide was reduced at 900°C, for 300 sec, at a total gas pressure of 100 Torr, with $CO/CO_2 = 11.8$.

followed by surface diffusion of the reaction product to the adjacent oxide where desorption might occur easily, similar to processes occurring on bifunctional catalysts or in spill-over processes (6, 7). These and other complications will, however, be ignored here. To define the oxygen chemical potential on the surface during reaction, we first find $R_a = [CO(a)]/[CO_2(a)]$. Equations [1]-[3] give the first-order flux equations during steady state

$$J = k_1[CO(g)] - l_1[CO(a)] \quad [4]$$

$$= k_2[CO(a)] - l_2[CO_2(a)] \quad [5]$$

$$= k_3[CO_2(a)] - l_3[CO_2(g)] \quad [6]$$

which, after some algebra, leads to

$$R_a = [R_g k_1(k_3 + l_2) + l_2 l_3]/[R_g k_1 k_2 + l_3(k_2 + l_1)] \quad [7]$$

where $R_g = [CO(g)]/[CO_2(g)]$.

One can also write

$$J = k^*[CO(g)] - l^*[CO_2(g)] \quad [8]$$

where

$$k^* = k_1 k_2 k_3/(k_2 k_3 + k_3 l_1 + l_1 l_2) \quad [9]$$

and

$$l^* = l_1 l_2 l_3/(k_2 k_3 + k_3 l_1 + l_1 l_2) \quad [10]$$

This follows from combining Eq. [4], [5], and [6] to eliminate [CO(a)] and $[CO_2(a)]$.

To find the oxygen chemical potential in the surface during reaction, a solid-state interaction must be invoked. For gaseous reduction with the relevant reactions occurring on the oxide phase, oxygen is removed from the MO lattice so that, in the simplest case, using Kröger-Vink notation (8), Eq. [2] and [3] are replaced by

$$CO(a) + MO \underset{l_4}{\overset{k_4}{\rightleftarrows}} CO_2(a) + V_O^{\cdot\cdot} + 2e' + M_M \underset{l_5}{\overset{k_5}{\rightleftarrows}} CO_2(a) + M \quad [11]$$

with the flux equations

$$J = k_4[CO(a)] - l_4[CO_2(a)](V_O^{\cdot\cdot})(e')^2 \quad [12]$$

$$= k_5[CO_2(a)](V_O^{\cdot\cdot})(e')^2 - l_5[CO_2(a)] \quad [13]$$

These two reactions can be combined to eliminate the terms containing $(V_O^{\cdot\cdot})$ and put in the same form as Eq. [5], giving a new meaning to k_2 and l_2

$$k_2 = k_4 k_5/(k_5 + l_4) \quad [14]$$

$$l_2 = l_4 l_5/(k_5 + l_4)$$

Substituting for k_2 and l_2 using Eq. [14], one obtains an expression of the same general form for R_a as given in Eq. [7]. Since the oxygen vacancies $V_O^{\cdot\cdot}$ and the electrons e' are present in the solid-state phase, local equilibrium between them may be assumed, so that

$$MO \underset{l_6}{\overset{k_6}{\rightleftarrows}} \tfrac{1}{2} O_2(g) + V_O^{\cdot\cdot} + 2e' + M_M \quad [15]$$

with

$$(V_O^{\cdot\cdot})(e')^2 = K_6/p_{O_2}^{1/2} \quad [16]$$

where $K_6 = k_6/l_6$, and where the p_{O_2} is an effective oxygen partial pressure that would have established the same nonstoichiometry in the surface as the one expressed by the reaction equation, Eq. [11]. Combination of Eq. [12] and [16] gives

$$p_{O_2}^{1/2} = \left(\frac{[CO_2(a)]}{[CO(a)]}\right)\frac{K_6}{K_4}\Big/\,(1 - J/k_4[CO(a)]) \quad [17]$$

Elimination of [CO(a)] with Eq. [7] and of J with Eq. [8] and with $K_a = k_1/l_1$, leads to

$$p_{O_2}^{1/2} = \frac{K_5}{K_4}\frac{1}{R_a} \Bigg/ \left[1 - \frac{\left(1 - \frac{R_g^\circ}{R_g}\right)}{k_4\left[K_a/k^* - \left(1 - \frac{R_a^\circ}{R_g}\right) \Big/ l_1\right]}\right] \quad [18]$$

where $R_g^\circ = l^*/k^*$ = the M/MO equilibrium $[CO(g)]/[CO_2(g)]$ ratio in Eq. [8]. At equilibrium, combination of Eq. [11] and [15] also yields

$$K_6/K_4 = R_a^\circ (p_{O_2}^\circ)^{1/2} \quad [19]$$

where R_a° and $p_{O_2}^\circ$ are the M/MO equilibrium values of R_a and p_{O_2}. The oxygen chemical potential in the surface during reaction will then be

$$\mu_s = \mu_s^\circ + kT \ln p_{O_2}^{1/2} \quad [20]$$

If we put

$$\Delta\mu_{MO} = \mu_s - \mu_e \quad [21]$$

then combination of Eq. [18]-[21] gives

$$\Delta\mu_{MO} = kT \ln \left\{ \frac{R_a^\circ}{R_a} \Bigg/ \left[1 - \frac{\left(1 - \frac{R_g^\circ}{R_g}\right)}{k_4\left[K_a/k^* - \left(1 - \frac{R_g^\circ}{R_g}\right) \Big/ l_1\right]}\right]\right\} \quad [22]$$

If the gas-solid exchange process occurs on the metal phase M in an M-MO two phase surface, a different reaction scheme can be considered. Then, Eq. [2] and [3] are replaced by

$$CO(a') + MO \underset{l_7}{\overset{k_7}{\rightleftarrows}} CO(a') + (O) + M \underset{l_8}{\overset{k_8}{\rightleftarrows}} CO_2(a') + M \quad [23]$$

where (O) is oxygen dissolved in the M surface. CO(a') and CO_2(a') are the species adsorbed on M. The (O) can again be considered to establish the surface oxygen chemical potential by

$$(O) \underset{l_9}{\overset{k_9}{\rightleftarrows}} \tfrac{1}{2} P_{O_2} \quad [24]$$

The same procedure as before, with $K_d = k_3/l_3$, then leads to

$$\Delta\mu_M = kT \ln \left\{ \frac{R_a^\circ}{R_a} \times \left[\frac{K_d\left(\frac{R_g}{R_g^\circ} - 1\right)}{l_8\left[\left(\frac{R_g}{R_g^\circ} - 1\right) \Big/ l_3 + 1/l^*\right]} + 1\right]\right\} \quad [25]$$

with k_2 and l_2 in Eq. [7], [9], and [10] now replaced by

$$k_2 = k_7 k_8/(l_7 + k_8) \quad [26]$$

$$l_2 = l_7 l_8/(l_7 + k_8) \quad [27]$$

To predict how $\Delta\mu_{MO}$ or $\Delta\mu_M$ depends on reaction conditions would require knowledge of a large number of reaction rate parameters k_i and l_i. This information is rarely, if ever, available. It is, however, useful to consider the trend of $\Delta\mu_{MO}$ or $\Delta\mu_M$ for limiting cases where the surface processes or the adsorption-desorption reactions are rate controlling. Such calculations have been performed for Fig. 3 and 4. Various values of $k_i = l_i$, indicated in the figures, have been assumed for the case where $R_g^\circ = 1$. Curve A in Fig. 3 and 4 give $\Delta\mu$ as a function of R_g/R_a°, for all $k_i = l_i = 1$. It is evident when exchange reactions are fast compared to adsorption-desorption reaction, case B in Fig. 3 and 4, that μ_s remains close to μ_e. When adsorption-desorption processes are fast compared to the surface exchange reactions, case C in Fig. 1 and 2, μ_s remains closer to μ_g. In this case, a larger driving force is available for transporting oxygen from under the metal to the face surface, as shown schematically in Fig. 1a.

Conclusions

The surface oxygen chemical potential during a gas-solid reaction, such as the reduction of an oxide by CO/CO_2 gas mixtures, can be defined by invoking a solid-state defect reaction. For the gaseous reduction of MO to M, this chemical potential is between that of the gas phase and that of the MO/M equilibrium,

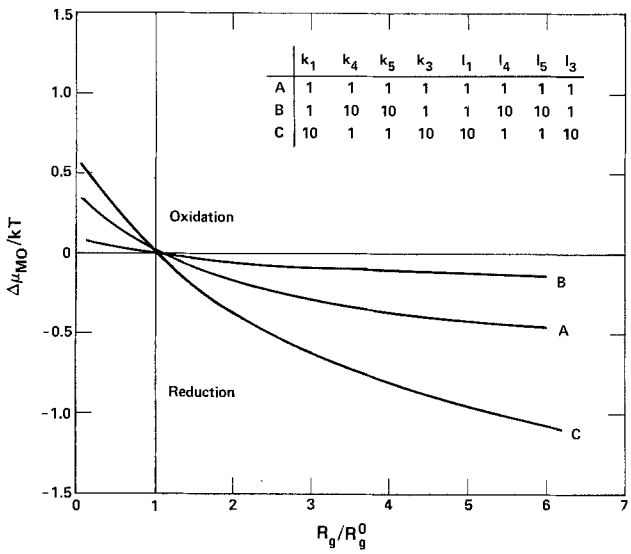

Fig. 3. $\Delta\mu_{MO}$ as a function of R_g/R_g° for various assumed values of k_i and l_i, with $R_g^\circ = 1$ and $k_i = l_i$ for all cases.

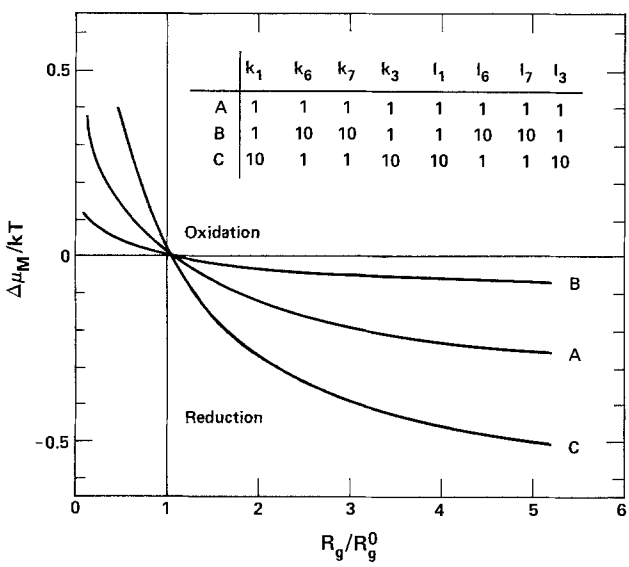

Fig. 4. $\Delta\mu_M$ as a function of R_g/R_g° for various assumed values of k_i and l_i, with $R_g^\circ = 1$ and $k_i = l_i$ for all cases.

depending on the relative rates of adsorption-desorption and surface exchange reactions

Acknowledgments

This work was supported by the Division of Materials Sciences, Office of Basic Energy Sciences of the U.S. Department of Energy, under Contract No. DE-AC03-76SF00098.

Manuscript submitted April 11, 1983; revised manuscript received June 21, 1983.

The University of California assisted in meeting the publication costs of this article.

REFERENCES

1. H.-J. Grabke, *Ber. Bunsenges.*, **69**, 48 (1965).
2. E. T. Turkdogan, W. M. McKewan, and L. Zwell, *J. Phys. Chem.*, **69**, 327 (1965).
3. H.-J. Grabke, *Ann. N. Y. Acad. Sci.*, **213**, 110 (1973).
4. W. W. Smeltzer, *Acta Metall.*, **8**, 337 (1960).
5. M. Chang and L. C. De Jonghe, LBL-15707, (March 1982).
6. G. C. Bond and P. Sermon, *J. Chem. Soc., Faraday Trans. 1*, **76**, 889 (1980).
7. G. C. Bond, L. R. Molloy, and M. J. Fuller, *J. Chem. Soc. Chem. Commun.*, 796 (1975).
8. F. A. Kröger, "The Chemistry of Imperfect Crystals," North Holland, Amsterdam (1974).

Evaluation of Dislocation Generation on Silicon Substrates by Selective Oxidation

Y. Tamaki, S. Isomae, S. Mizuo, and H. Higuchi*

Hitachi Limited, Central Research Laboratory, Kokubunji, Tokyo 185, Japan

ABSTRACT

The density of dislocations generated at Si_3N_4/SiO_2 composite film edges on a silicon substrate as a result of selective oxidation was measured, and the relation between selective oxidation conditions and dislocation generation was investigated. Results show that the dislocation density decreases markedly with increasing oxidation temperature. The transition temperature of this drop becomes low as the thickness of the SiO_2 pad increases. The results are interpreted in terms of the temperature-related characteristics of viscous SiO_2 flow. A further experiment reveals that the density of dislocations increases with an increase in the depth of Si etching before oxidation. This phenomenon is considered to be due to stress concentration resulting from the volume expansion of SiO_2 film during oxidation. The effect of oxidation pressure on dislocation generation was also investigated. The dependence of the bird's beak length on oxidation temperature and SiO_2 pad thickness was subsequently measured. The results are presented and the temperature dependence is explained using oxidation theory. Finally, suitable conditions for selective oxidation are discussed.

Selective oxidation of silicon using chemical vapor deposited (CVD) Si_3N_4 films as oxidation masks is a technique that has been widely used in the isolation of integrated circuits for silicon devices. These Si_3N_4 films on silicon substrates have a large intrinsic stress (1, 2). In addition to this kind of stress, selective oxidation produces great stress along the edge of the oxidized area, often leading to the generation of dislocations in silicon substrates (3, 4). Since these dislocations are detrimental to device characteristics, SiO_2 film has been inserted under Si_3N_4 film so as to avoid generation of dislocations. However, the SiO_2 pad causes formation of a long bird's beak at the perimeter of the silicon islands (5, 6), which in turn constitutes an insuperable barrier to improving the packing density of the integrated circuits.

Therefore, selective oxidation conditions that can prevent the generation of dislocations on a silicon substrate without extending the bird's beak have been sought. Although some papers have reported on dealing with selective oxidation conditions (6-8), there is no report which quantitatively examines the generation of dislocations with an Si_3N_4/SiO_2 mask nor of the oxidation temperature dependence of the bird's beak length.

In this paper, the relation between dislocation generation and selective oxidation conditions with both Si_3N_4 and Si_3N_4/SiO_2 masks is reported quantitatively. In particular, the effects of very thin SiO_2 pads, Si etching before oxidation, and oxidation pressure are newly investigated. The oxidation temperature dependence and SiO_2 pad thickness dependence of bird's beak length are examined. The most suitable conditions for selective oxidation are then discussed.

* Electrochemical Society Active Member.

Key words: defect density, SiO_2 pad, bird's beak, Si etching, viscosity of SiO_2.

Experimental Procedure

Sample preparation.—The samples were (001) oriented p-type, 20-50 Ω-cm, dislocation-free, 400 μm thick Czochralski-grown silicon wafers with 10 × 10 μm square masks consisting of Si_3N_4/SiO_2 composite layers. The SiO_2 pad was thermally grown at 950°C in dry O_2 atmosphere. The thickness of the film was 3-50 nm. For very thin films, 10% O_2 in an N_2 atmosphere was used to control the thickness. Si_3N_4 film 150 nm thick was deposited by reacting SiH_4 and NH_3 in N_2 at 950°C. The deposition rate was 25 nm/min, and the NH_3/SiH_4 flow rate ratio was 150.

The pattern of the Si_3N_4 film was formed by conventional H_3PO_4 etching using phosphorus-doped SiO_2 film as a mask. Next, the pad SiO_2 and phosphorus-doped SiO_2 were etched using buffered HF. The exposed silicon substrate was anisotropically etched using a KOH solution containing isopropyl alcohol. The depth of the grooves was 0.2-1.0 μm.

After the silicon etching process, the samples were oxidized so as to grow 1.8 μm thick SiO_2 at 900°-1100°C in wet O_2 under either atmospheric pressure (1 atm) or high pressure (7 atm) so as to form recessed oxide structures. Oxidation times are listed in Table I. These structures correspond to those for isolation of bipolar integrated circuits.

Measurement.—Dislocations generated on the silicon substrate were revealed by Secco etching (9) after removal of the surface films from the sample using diluted HF. Since the force acting on the Si_3N_4 film edge is very large, dislocation density depends on the perimeter length of the film edges. If the occurrence of dislocations can be represented by a Poisson distribution, the yield of patterns (the probability that a pattern has no dislocations) is given by

$$Y = e^{-\lambda l}$$

Table I. Oxidation times

Oxidation temperature (°C)	Oxidation pressure 1 atm (hr)	7 atm min
900	32	200
1000	16	100
1050	10	68
1100	7	50

where λ is the dislocation density per unit length of the film edge and l is the perimeter length of the pattern. Consequently the dislocation density can be obtained by measuring the yield of 10 × 10 μm square patterns. In this case since l is 40 μm, Y becomes 0.9 when λ is 2.5 mm^{-1}. It is difficult to measure Y correctly if Y becomes less than 0.9, because the probability of having two or more dislocations in one pattern increases. Therefore, densities over about 1 mm^{-1} cannot be measured correctly.

In order to evaluate the length of the bird's beak, cross sections of the samples after selective oxidation were observed by scanning electron microscope (SEM).

Results and Discussion

Generation of dislocations by selective oxidation.— In order to examine the effects of SiO_2 pads, the density of dislocations generated at Si_3N_4 film edges after selective oxidation was measured. Figure 1 shows the relation between SiO_2 pad thickness and the dislocation densities. In this figure the data in the upper frame indicate that dislocations are generated in every 10 × 10 μm square pattern. It can be seen that the dislocation density decreases with insertion of a thin SiO_2 pad. The degree of the decrease depends greatly on the oxidation temperature. At temperatures above 1000°C this decrease occurs with a very thin (3-10 nm) SiO_2 pad. No more decreases occur with an increase in the thickness of the SiO_2 pad. On the contrary, at a temperature of 900°C the effect of suppressing the dislocation generation by inserting an SiO_2 pad is very little.

The temperature dependence of the dislocation generation is shown in Fig. 2. A feature of this figure is that the temperature of the decreasing dislocation density decreases as the SiO_2 pad thickness increases. This phenomenon suggests that the viscosity of SiO_2 film plays an important role in dislocation generation (8). It is known that the viscosity of SiO_2 decreased rapidly with increasing temperature and that viscous flow of SiO_2 film occurs at temperatures around 950°C (10, 11). Figure 2 indicates that the stress relaxation due to the SiO_2 pad occurred at temperatures above 950°C. This figure also indicates that the difference in dislocation densities between the case for the SiO_2 pad existing and that for no SiO_2 pad becomes large at temperatures around 1000°C. Therefore, a thin SiO_2 pad less than 10 nm thick can effectively prevent dislocation generation at oxidation temperatures around 1000°C.

Next, the effect of pressure during oxidation will be looked at. From Fig. 1 it can be seen that the dislocation density at 7 atm is smaller than that at 1 atm, except when there is no SiO_2 pad. It is thought that the dislocation density increases as the oxidation time increases, because of the generation and multiplication of dislocations induced by the stress concentration due to the expansion of SiO_2 film volume during oxidation. Since the oxidation time at 7 atm is much shorter than that at 1 atm, the dislocation density decreases by using high pressure oxidation.

Looking at the effect of Si etching, etching of the Si epitaxial layer by 0.5-1 μm is needed in bipolar integrated circuits, because the epitaxial layer must be

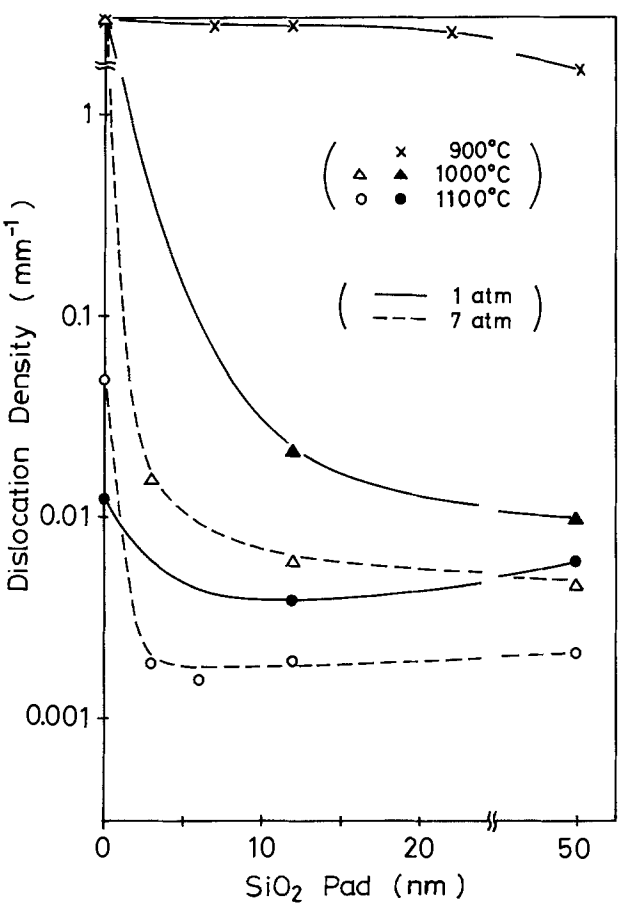

Fig. 1. Relationship between dislocation density and SiO_2 pad thickness. The marks ×, △, ○ show that oxidation temperatures were 900°, 1000°, and 1100°C, respectively. Dashed lines show the case for high pressure oxidation.

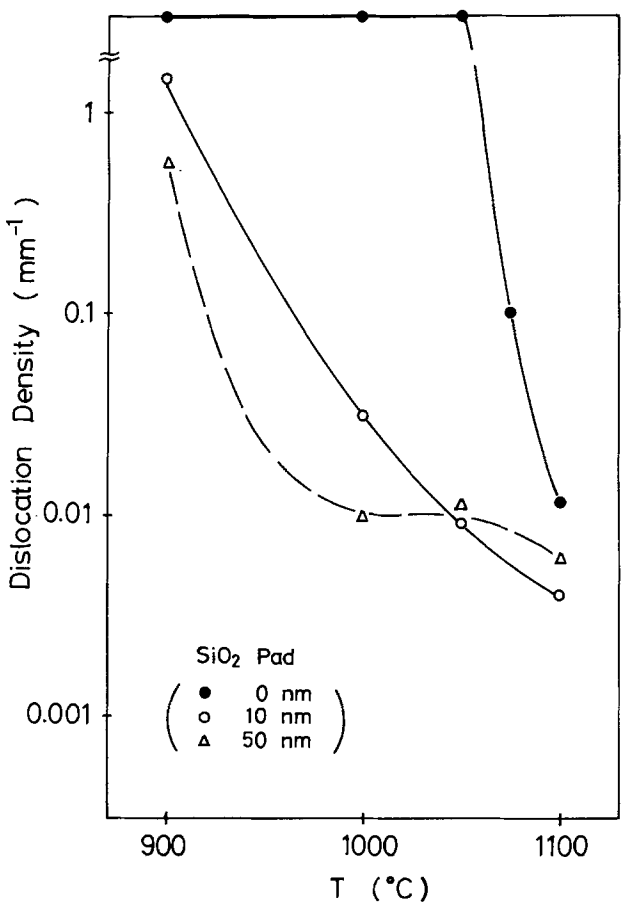

Fig. 2. Oxidation temperature dependence of dislocation densities for various pad SiO_2 thicknesses.

isolated by SiO_2 film. The Si etching depth dependence of the dislocation generation is shown in Fig. 3. For the present experiment, Si epitaxial wafers were used and selective oxidation was performed at 1000°C for 16 hr in wet O_2 under atmospheric pressure. This figure shows that the dislocation density increases as the etching depth increases. The cause of this phenomenon is considered to be stress concentration due to the expansion of SiO_2 film volume during oxidation in the groove. Since the phenomenon is very complicated, it is difficult to perform a quantitative analysis. Further investigation is necessary.

Bird's beak length.—Cross sections of the samples after selective oxidation are shown in Fig. 4 and 5. It is clear that the length of the bird's beak (this is defined as the length between the edge of the Si_3N_4 film and the top of the beak) varies as does the SiO_2 pad thickness and oxidation temperature. Figures 6 and 7 show SiO_2 pad thickness and oxidation temperature dependence of the bird's beak length, respectively. From these figures, the length of the bird's beak becomes as long as the SiO_2 pad becomes thick. However, temperature dependence with an SiO_2 pad is different from that without SiO_2 padding.

The with-padding case is explained by the lateral diffusion of the oxidant through the pad SiO_2. From the oxidation theory, the relation between oxide thickness, X, and oxidation time, T, is given by (12)

$$X^2 + AX = B\ (T + \tau)$$

Here, B is the parabolic rate constant, B/A is the linear rate constant, and τ is the time for the initial oxidation step. Half of the ratio, A, of the parabolic rate constant and linear rate constant represent the oxide thickness at which the oxidation mechanism changes

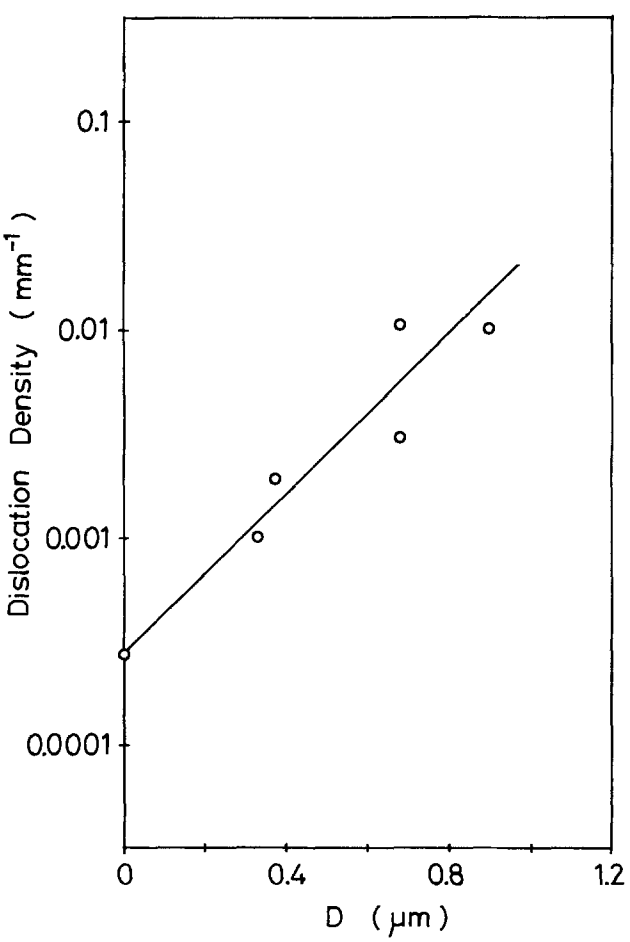

Fig. 3. Dependence of dislocation densities on Si groove depth. Si substrate is etched anisotropically and oxidized at 1000°C for 16 hr in wet O_2.

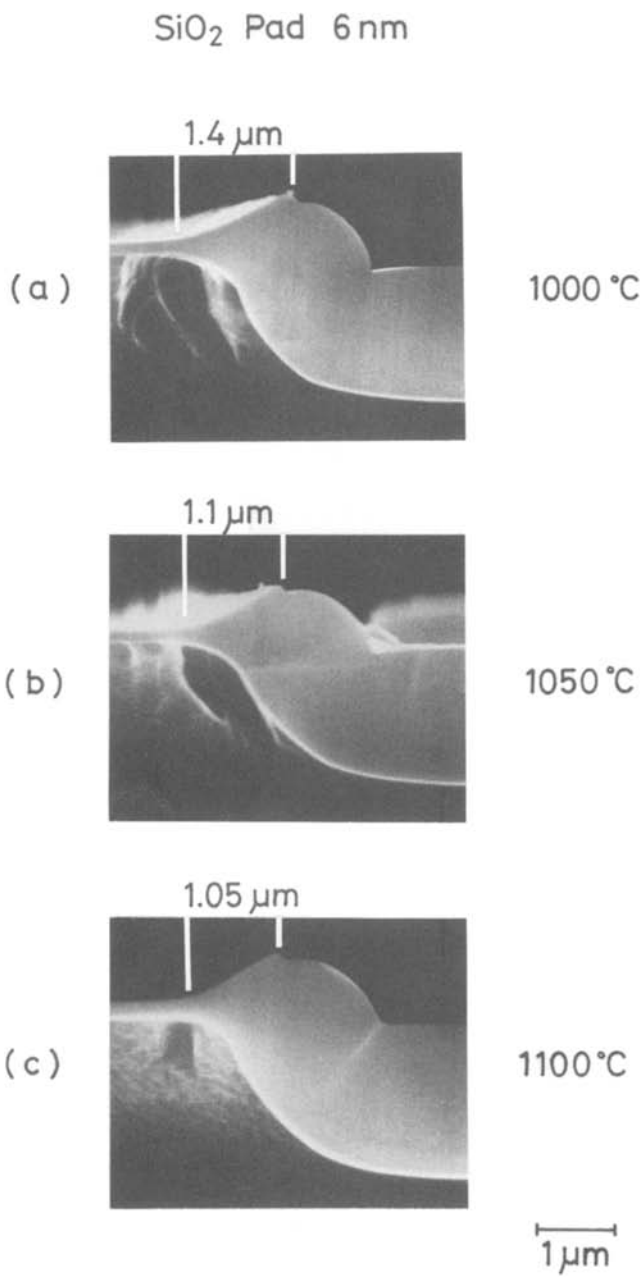

Fig. 4. SEM photographs of sample cross sections consisting of 6 nm thick SiO_2 pad.

from being reaction controlled to being diffusion controlled. This indicates that at the initial stage of the oxidation (the reaction-controlled stage) relatively large quantities of the oxidant diffuse laterally through the SiO_2 pad, because consumption of the oxidant at the Si-SiO_2 interface is limited due to the reaction of Si and the oxidant. Since the ratio, A, becomes as small as the oxidation temperature increases (13), the initial stage also becomes short as temperature increases. Therefore, the bird's beak length decreases with use of high temperature oxidation.

The no-padding case is explained not only by oxidant diffusion, but also by the stress effect of SiO_2 film grown on the Si substrate. Although it is not clear as to why the bird's beak increases in length as oxidation temperature increases, the viscosity of SiO_2 film and the adhesiveness between Si_3N_4 and Si are considered to be important factors. Since the bird's beak length when there is no SiO_2 padding becomes long, and that with the SiO_2 pad becomes short as the oxidation temperature increases, it was concluded that the influence

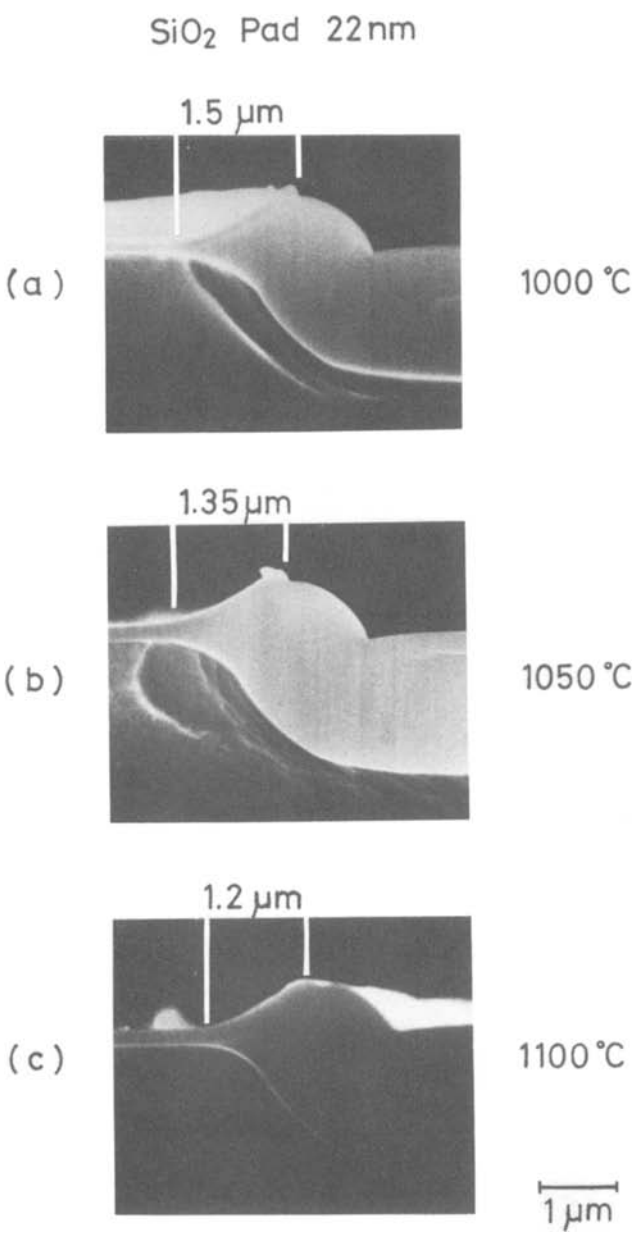

Fig. 5. SEM photographs of sample cross sections consisting of 22 nm thick SiO_2 pad.

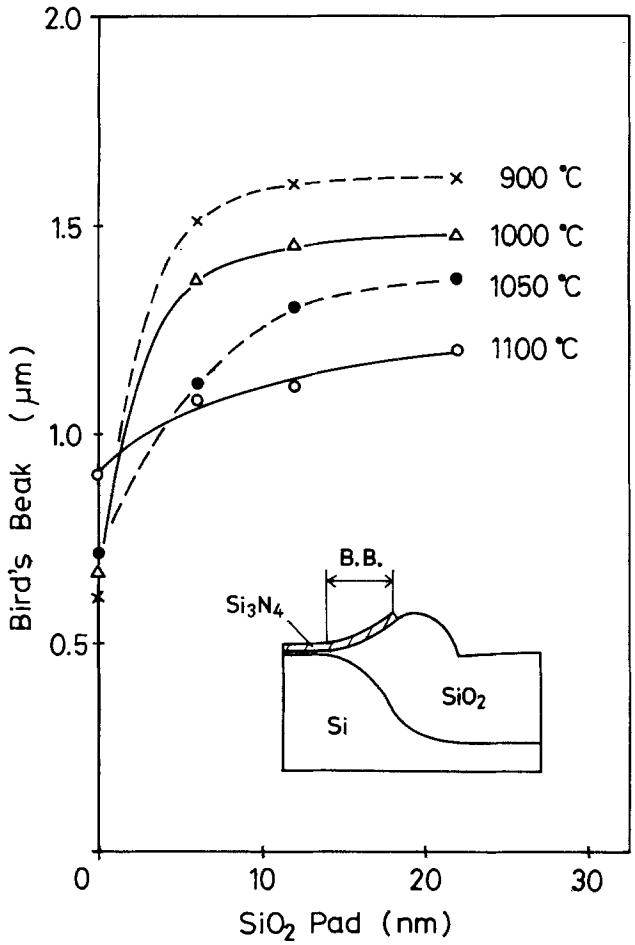

Fig. 6. Relationhip between bird's beak length and SiO_2 pad thickness.

of the SiO_2 pad on the bird's beak length decreases as the oxidation temperature increased.

Optimum conditions.—Three conditions necessary for selective oxidation are: a short bird's beak, low oxidation temperature, and low defect density. From Fig. 1, 2, 6, and 7, it is clear that there is no condition for selective oxidation that will satisfy the above three conditions. In other words, conditions that will shorten the bird's beak and those that will decrease the defect density are in opposition to each other.

However, if some restrictions are allowed, desirable conditions for selective oxidation can be arranged. If high temperature (about 1100°C) oxidation is allowed, no oxide pad is necessary. Since generation of dislocations with no SiO_2 pad increases as the oxidation pressure increases, atmospheric pressure oxidation is preferable in this case. Furthermore, redistribution of impurities introduced into the substrate (for example, channel stoppers and buried layers) due to high temperature annealing may cause problems. If high temperatures and long oxidation periods have to be avoided, some SiO_2 padding is necessary.

From Fig. 2 and 7, it is clear that the dislocation density and bird's beak length increase greatly as the oxidation temperature decreases. Therefore, an oxidation temperature of 1000°C with a thin (5-10 nm) SiO_2 pad is desirable. Looking at Fig. 1, generation of dislocation with an SiO_2 pad decreases at high oxidation pressure. Since oxidation time is inversely proportional to oxidation pressure, this time can be cut down greatly by means of high pressure oxidation.

One more important factor affecting the bird's beak and defect density is the thickness of the Si_3N_4 film. It is known that defect density drops as Si_3N_4 film thickness decreases (3, 8) .However, with the decrease in film thickness, pinholes or thin film defects are likely to generate. Furthermore, the bird's beak increases in length as the Si_3N_4 film thickness decreases (6). Therefore, the thickness of the Si_3N_4 film cannot be greatly varied. In this case, conditions for shortening the bird's beak and decreasing the defect density are opposed to each other.

In order to solve this problem some methods for suppressing the bird's beak have been proposed (14-16). Although these methods are relatively easy to put into practice, they cannot eliminate lateral oxidation under the Si_3N_4 mask. Recently, a new method called "groove isolation" was presented (17, 18). This method can almost entirely eliminate the bird's beak. Since the structure for these new methods is complicated, stress concentration on the silicon substrate is likely to occur. Further investigation of dislocation generation in the new structure is needed.

Conclusion

The results of this study lead to several conclusions.

1. Insertion of an SiO_2 pad under Si_3N_4 film causes the density of dislocations generated on the silicon

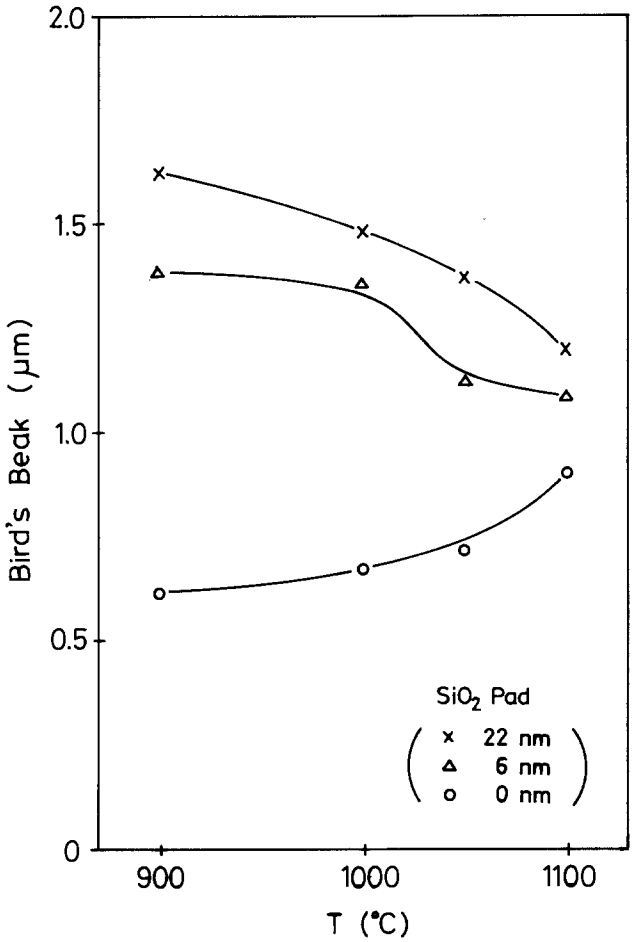

Fig. 7. Dependence of bird's beak length on oxidation temperature for various thicknesses of SiO_2 pad.

substrate due to selective oxidation to decrease. This effect is amplified as the thickness of the SiO_2 pad increases. The dislocation density decreases drastically with increasing oxidation temperature. The critical temperature for this decrease drops low as the thickness of the SiO_2 pad increases. Such phenomena are explainable by the effect of the viscous flow of SiO_2 film.

2. When Si is etched and oxidized to form a recessed oxide structure, the dislocation density increases due to the stress concentration produced by the expansion in volume of the SiO_2 film during oxidation.

3. Dislocation density decreases with increasing oxidation pressure (leading to a reduction in oxidation time) with insertion of the SiO_2 pad.

4. The length of the bird's beak shortens as the thickness of the SiO_2 pad decreases and as the oxidation temperature increases. These effects are related to the oxidation mechanism.

5. Although ideal conditions for selective oxidation have not been determined, a desirable condition is oxidation at 1000°C under high pressure steam, with an SiO_2 pad of about 10 nm thickness.

Acknowledgment

The authors wish to thank Dr. M. Ogirima for useful discussions.

Manuscript submitted Oct. 5, 1982; revised manuscript received June 13, 1983.

Hitachi Limited assisted in meeting the publication costs of this article.

REFERENCES

1. M. Tamura and H. Sunami, *Jpn. J. Appl. Phys.*, **11,** 1097 (1972).
2. E. A. Irene, *J. Electron Mater.*, **5,** 287 (1976).
3. W. A. Westdorp and G. H. Schwuttke, in "Thin Film Dielectrics," F. Vratny, Editor, p. 546, The Electrochemical Society Softbound Proceedings Series, Princeton, NJ (1969).
4. A. Bohg and A. K. Gaind, *Appl. Phys. Lett.*, **33,** 895 (1978).
5. J. A. Appels and M. M. Paffen, *Philips Res. Rep.*, **26,** 157 (1971).
6. E. Bassous, H. N. Yu, and V. Maniscalco, *This Journal*, **123,** 1729 (1976).
7. K. Shibata and K. Taniguchi, *ibid.*, **127,** 1383 (1980).
8. Y. Tamaki, S. Isomae, S. Mizuo, and H. Higuchi, *ibid.*, **128,** 644 (1981).
9. F. S. d'Arogona, *ibid.*, **119,** 948 (1972).
10. J. R. Patel and N. Kato, *J. Appl. Phys.*, **44,** 965 (1973).
11. E. P. EerNisse, *Appl. Phys. Lett.*, **35,** 8 (1979).
12. B. E. Deal and A. S. Grove, *J. Appl. Phys.*, **36,** 3770 (1965).
13. W. A. Pliskin, *IBM J.*, **10,** 198 (1966).
14. I. Magdo and A. Bohg, *This Journal*, **125,** 932 (1978).
15. D. Kahng, T. A. Shankoff, T. T. Sheng, and S. E. Haszko, *ibid.*, **127,** 2468 (1980).
16. K. Minegishi, K. Imai, K. Kiuchi, K. Hirata, and Y. Yoriume, *Jpn. J. Appl. Phys.*, **20,** Supplement 20-1, 55 (1981).
17. H. B. Pogge, Paper presented at the Electrochemical Society Meeting, Boston, MA, May 6-11, 1979.
18. Y. Tamaki, T. Kure, T. Shiba, and H. Higuchi, *Jpn. J. Appl. Phys.*, **21,** Supplement 21-1, 37 (1982).

Infrared Radiation Annealing of Ion-Implanted Polycrystalline Silicon Using a Graphite Heater

Koji Takebayashi, Toshiyuki Yokoyama, Masakatsu Yoshida, and Morio Inoue

Matsushita Electronics Corporation, Semiconductor R & D Center, Nagaokakyo, Kyoto, 617, Japan

ABSTRACT

Ion-implanted polycrystalline silicon layers were annealed using the radiation from a graphite heater. 0.4 μm thick polycrystalline silicon films implanted with 40 keV P^+ ions to a dose of $2 \times 10^{16}/cm^2$ were annealed in vacuum at 1000° – 1200°C for 10 – 60 sec. A minimum sheet resistance of 9 Ω/□ was obtained for a sample which was encapsulated with a 0.3 μm PSG film and annealed at 1200°C for 10 sec. TEM photographs show that the grain size of polycrystalline silicon grew up to around 1.0 μm in diam. The activation of the implanted phosphorus, the annealing of a damaged layer, and the increase of grain size leads to the reduction of sheet resistance of polycrystalline silicon and the increase of carrier mobility.

Polycrystalline silicon is widely used for gates and interconnections in MOS technology. Reduction of the resistance is one of the most important requirements. Recently, laser annealing of polycrystalline silicon has been investigated (1-5) in order to decrease the resistance. But laser annealing has some problems for device processing. First, because of the small spot area of the coherent light sources, the beam must be scanned over the wafer and the throughput capacity of laser annealing is somewhat low. Second, the dwell time of laser annealing is of the order of 1 msec and in typical annealing cases, the material is subjected to severe thermal shocks. Finally, the interference of the monochromatic laser radiation in dielectric layers makes it impractical to anneal device structures which have varying thicknesses of SiO_2 or Si_3N_4. Instead of laser, infrared radiation sources, such as lamps (6-8) and graphite heaters (9, 10), have been studied to improve the uniformity of the annealing temperature. Most studies to date, however, have been concerned with the activation of ion-implanted bulk single-crystal silicon, and reports on polycrystalline silicon annealing are not available. In this paper, we described the use of an incoherent light source, radiation from a graphite heater, to anneal implanted polycrystalline silicon layers.

Experimental Procedure

The polycrystalline silicon samples were obtained by low pressure chemical vapor deposition at 610°C onto 65 nm SiO_2 layer thermally grown on (100) silicon wafers. The polycrystalline layer thickness was 0.4 μm. After deposition, the wafers were ion-implanted with 40 or 80 keV P^+ ions to a dose of $2 \times 10^{16}/cm^2$ at room temperature. Prior to annealing, some samples were encapsulated with a 0.3 μm thick PSG film to prevent out-diffusion of phosphorus as well as to decrease reflection of infrared radiation during annealing. The PSG film was deposited at 420°C at atmospheric pressure. The phosphorus concentration of the glass was 4 w/o (weight percent). As capping layers, we also used a 0.3 μm thick undoped oxide and a 0.8 μm thick plasma nitride.

In our experiment, infrared radiation annealing from a graphite heater was carried out by using a Rapid Isothermal Annealing (RIA) system.[1] An individual wafer was placed in a vacuum chamber and the front wafer surface faced a planar graphite heater. The annealings were carried out in a vacuum with pressure less than 1.3×10^{-2} Pa at temperatures of 1000°-1200°C for 10-60 sec. The temperature was measured by a thermocouple placed 2 mm away from the graphite heater. The annealing time was the total exposure time of the wafer to the graphite heater. An annealing time consists of the initial raising time of 7-8 sec, and holding time of the constant highest temperature. After the exposure, the wafers were cooled to below 500C in 3 sec.

The sheet resistance was measured by a four-point probe. We used transmission electron microscopy to investigate the grain structure of P^+-implanted polycrystalline silicon after infrared radiation annealing by the RIA method. The changes in surface morphology were also investigated. The carrier mobility and the carrier concentration were measured by the van der Pauw and Hall effect methods.

Results and Discussion

Figure 1 shows the sheet resistance of annealed polycrystalline silicon as a function of annealing temperature. The annealing time was 10 sec. The sheet resistance decreases remarkably with increasing annealing temperature both with a PSG film and without one, but the sheet resistance of the polycrystalline silicon films without a PSG is about ten times higher than that of the capped polycrystalline silicon films at various temperatures.The lowest sheet resistance of 9 Ω/□ was obtained for a sample encapsulated with a PSG film at 1200°C annealing. This value is lower than that of a furnace-annealed sample (1000°C, 30 min) with a sheet resistance of 15 Ω/□.

Figure 2 shows the sheet resistance of annealed polycrystalline silicon encapsulated with a PSG film as a function of annealing time. For 10 sec annealing, the sheet resistance decreases with increasing annealing temperature. On the other hand, for more than 30 sec annealing, it tends to saturate as the annealing time increases still more and the values of less than 10 Ω/□ were consistently obtained, but slip lines, due to the extreme thermal gradients and stress, were found on the periphery of the substrate. On the contrary, for the samples without a PSG film, annealed at more than 1100°C for more than 30 sec, the outward diffusion of phosphorus is remarkable, and the sheet resistance of polycrystalline silicon increases drastically. Eventually, it cannot be measured by the four-point probe method.

The uniformity of sheet resistance over a 4 in. wafer is shown in Fig. 3. The samples were implanted with 80 keV P^+ ions to a dose of $2 \times 10^{16}/cm^2$ and were annealed at 1200°C for 10 sec. Over a 4 in. wafer area, fairly good uniformity is obtained. The standard deviation of sheet resistance was typically ±5% for the sample with a PSG film, but for the sample without a PSG film, the uniformity is not as good. Particularly, the sheet resistance of the periphery of the wafer becomes larger with increasing annealing time or temperature because of the outward diffusion of phosphorus. This implies that it is necessary to cover the wafer with a film for obtaining good uniformity. This capping effect was also obtained by using a 0.3 μm thick undoped oxide or a 0.8 μm thick plasma nitride

Key words: polycrystalline silicon, ion implantation, annealing.

[1] Varian's annealing system.

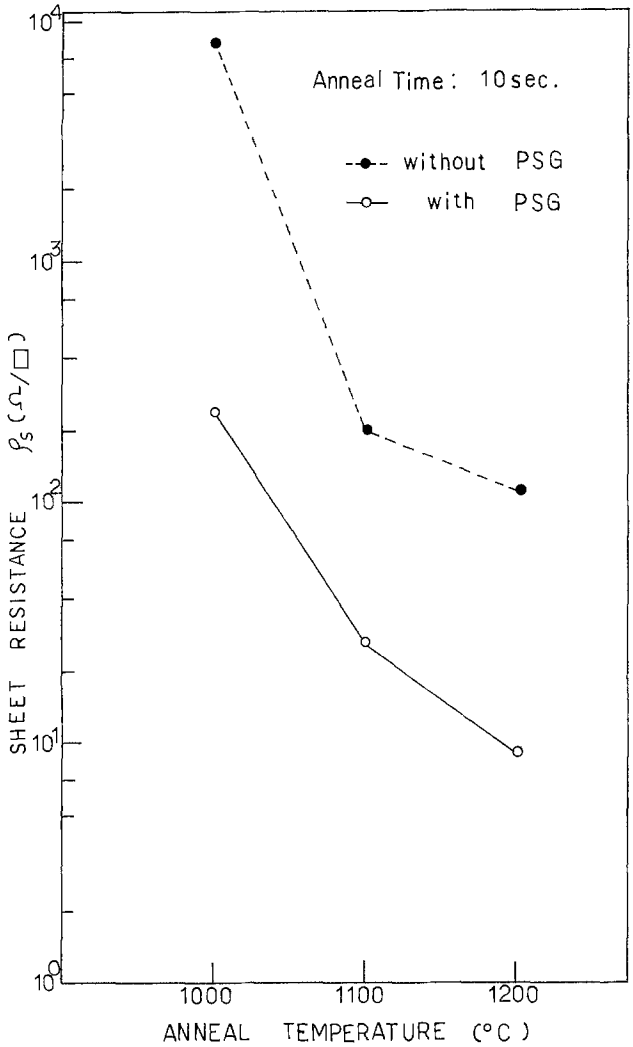

Fig. 1. The sheet resistance of annealed polycrystalline silicon by RIA as a function of annealing temperature.

film instead of PSG. As for the phosphorus incorporation from the PSG, the dopant from the PSG could not be considered because the sheet resistance did not change when the samples were covered with undoped oxide or nitride instead of PSG film.

Figure 4 shows TEM micrographs of ion-implanted and infrared annealed samples which were encapsulated with PSG. The annealing time was 10 sec. The grain size of as-deposited sample was around 0.1 μm. Up to 1100°C, the grain size increased slightly to around 0.3-0.4 μm. When the annealing temperature was increased to 1200°C, a significant increase of grain size was observed. The typical grain size was 1.0 μm. This increase of grain size contributes to the reduction of sheet resistance of polycrystalline silicon.

Figure 5 shows TEM micrographs of P^+-implanted polycrystalline silicon without a PSG film after annealing. In comparison with the sample with a PSG film, it is obvious that the grain growth is suppressed. Even at 1200°C annealing, the grain size slightly increased up to 0.2-0.3 μm. Moreover, the surface structure greatly changed for the sample which was annealed at 1200°C for 30 sec. To make it clear, we took replica electron micrographs of these samples. These results are shown in Fig. 6. The replica electron micrograph revealed that the surface was rough for the sample without a PSG which was annealed at 1200°C for 30 sec. On the contrary, the surface of the samples with a PSG were very smooth even if they were annealed at 1200°C for 30 sec. This surface roughness may be related to the mass transport of silicon when the surface is not constrained by an overlying oxide.

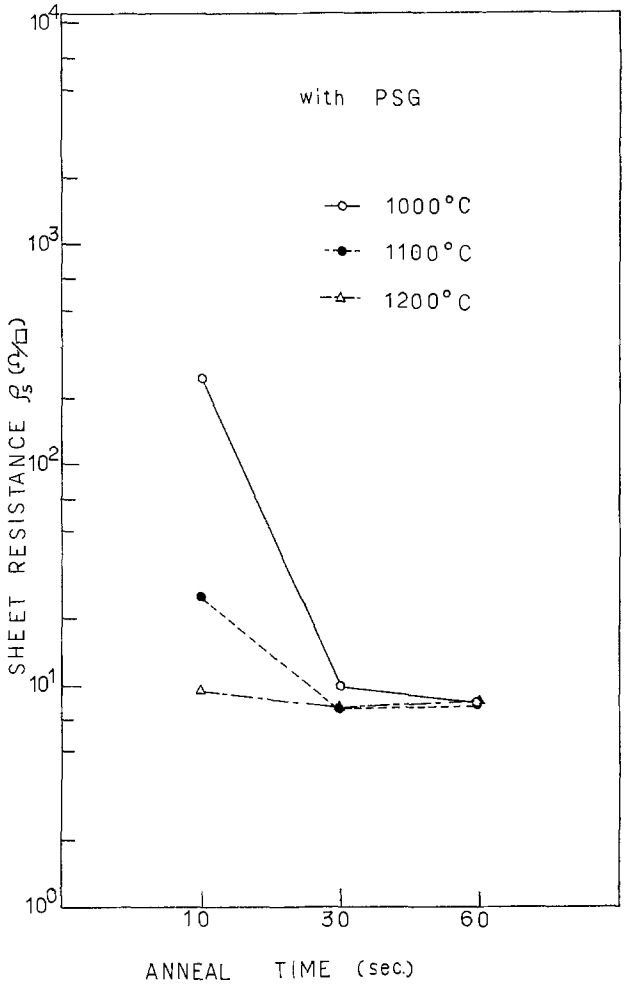

Fig. 2. The sheet resistance of annealed polycrystalline silicon by RIA with a PSG film as a function of annealing time.

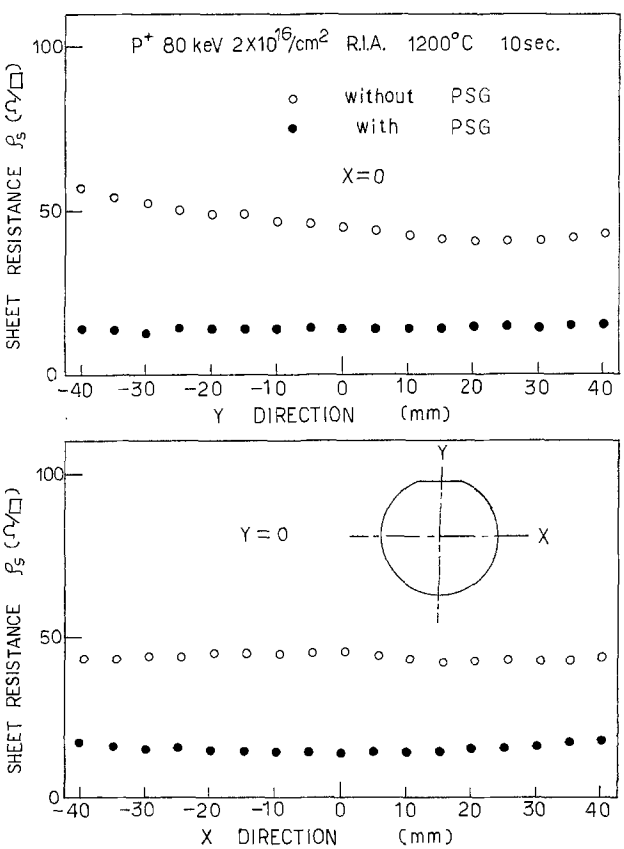

Fig. 3. Uniformity of sheet resistance in P^+-implanted polycrystalline silicon annealed by rapid infrared anneal.

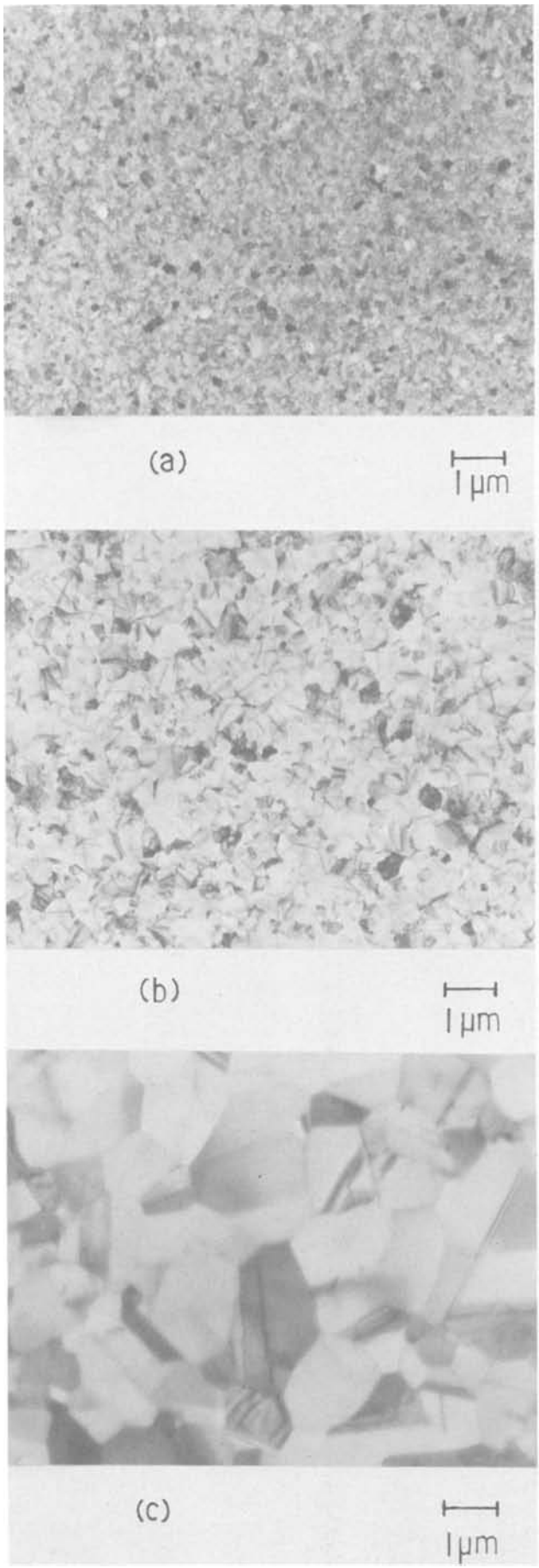

Fig. 4. TEM micrographs of P^+-implanted polycrystalline silicon after rapid infrared anneal (with PSG). (a) 1100°C, 10 sec; (b) 1100°C, 10 sec; (c) 1200°C, 10 sec.

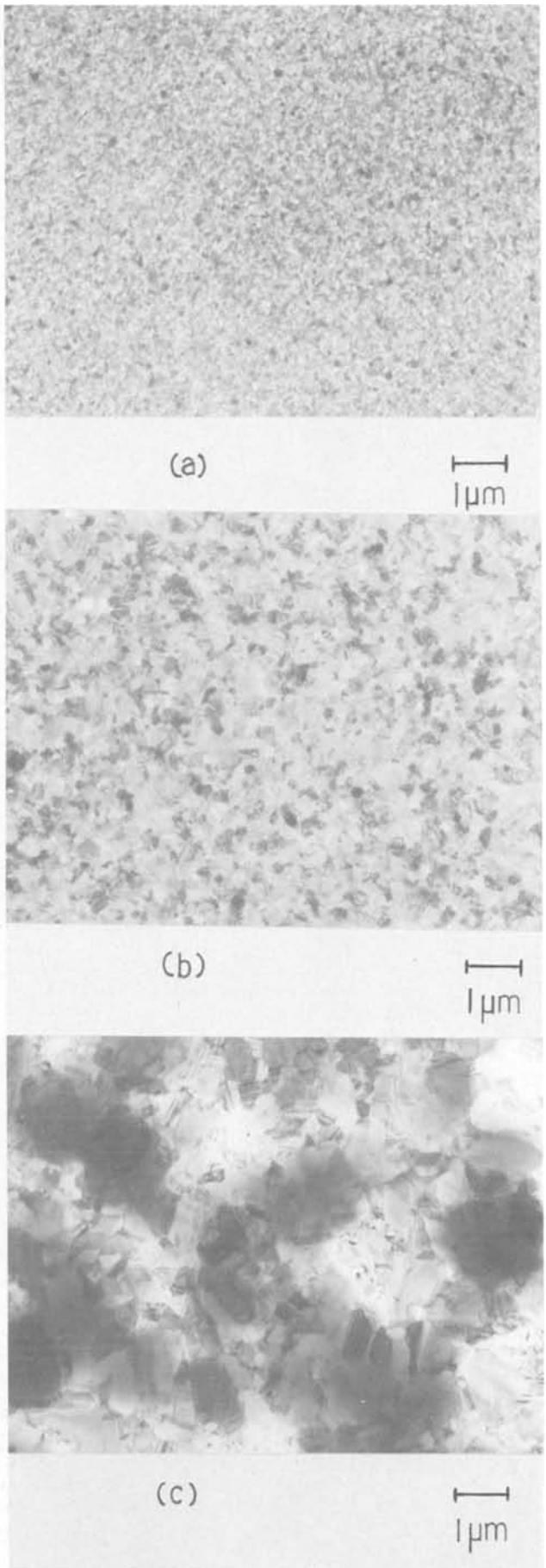

Fig. 5. TEM micrographs of P^+-implanted polycrystalline silicon after rapid infrared anneal (without PSG). (a) 1000°C, 10 sec; (b) 1200°C; 10 sec; (c) 1200°C, 30 sec.

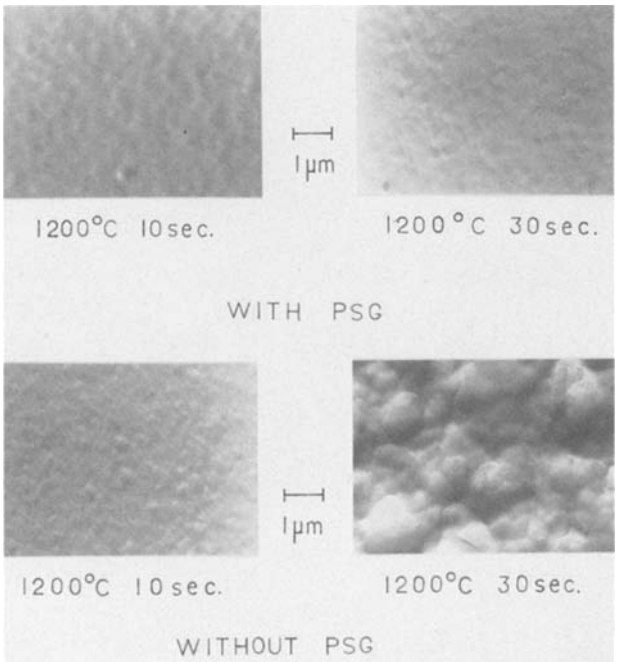

Fig. 6. Replica electron micrographs of P+-implanted polycrystalline silicon after rapid infrared anneal.

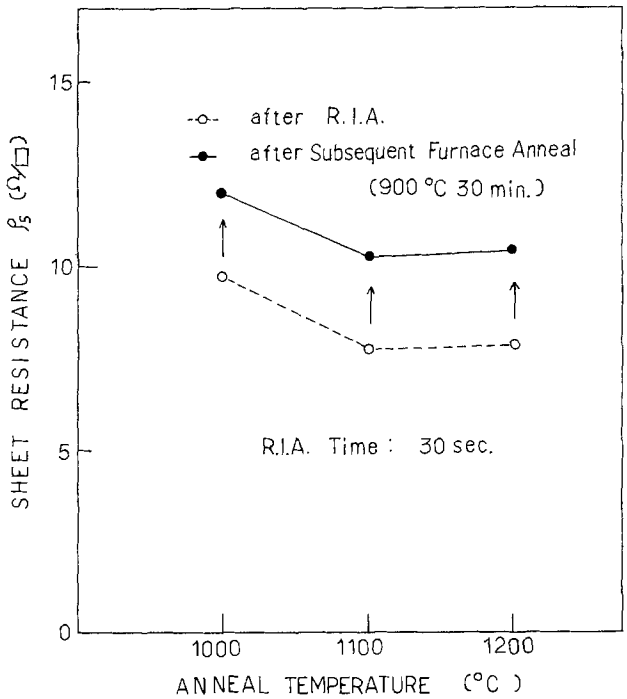

Fig. 7. Subsequent furnace anneal effect on rapid infrared anneal.

To investigate the carrier mobility and the carrier concentration of the annealed polycrystalline silicon, we experimented with van der Pauw and Hall effect measurements. The sheet carrier concentration and carrier mobility of the sample with PSG, which was annealed at 1200°C for 20 sec, were $1.0 \times 10^{16}/cm^2$ and 33 cm^2/V sec, respectively. These values were nearly equal to those of furnace annealed samples with a similar phosphorus implantation. The furnace anneal was carried out at 1000°C for 30 min in nitrogen atmosphere. The phosphorus concentration of the sample with PSG was below solid solubility [about $4 \times 10^{20}/cm^3$ at 1050°C (11)]. On the other hand, the sheet carrier concentration and carrier mobility of the sample without PSG were $3.1 \times 10^{15}/cm^2$ and 16 $cm^2/Vsec$, respectively, under the same annealing conditions. It could be understood, therefore, that the reduction in sheet resistance and the increase of mobility correlate with the out-diffusion of phosphorus and an increase of grain size.

In order to characterize thermal stability, we have studied the effects of the subsequent furnace annealing on the resistance of polycrystalline silicon. The subsequent furnace anneal condition was 900°C for 30 min in dry nitrogen. These results are shown in Fig. 7. After subsequent furnace anneal, the sheet resistance increased about 20-30%. This value is close to that for laser annealing (12). During this anneal, the grain growth could not be observed.

Conclusion

The sheet resistance reduction of polycrystalline silicon annealed using the infrared radiation from a graphite heater has been described. In order to decrease the sheet resistance, it is necessary to cover polycrystalline silicon with a passivation film, for example, PSG.

We have obtained a minimum sheet resistance 9 Ω/□ for the ion-implanted polycrystalline silicon which was encapsulated with a 0.3 μm thick PSG film and annealed at 1200°C for 10 sec. This is due to the activation of the dopant in the polycrystalline silicon, to the prevention of phosphorus out-diffusion from polycrystalline silicon surface, and to the increase of carrier mobility resulting from a large increase in grain size. It is concluded that the infrared radiation anneal from a graphite heater can provide resistivity reduction of polycrystalline silicon.

Acknowledgment

The authors would like to thank Mr. Ichikawa for the TEM observations.

Manuscript submitted Jan. 31, 1983; revised manuscript received June 28, 1983.

Matsushita Electronics Corporation assisted in meeting the publication costs of this article.

REFERENCES

1. S. A. Kokorowski, G. L. Olson, and L. D. Hess, in "Laser and Electron-Beam Solid Interactions and Materials Processing," J. F. Gibbons, L. D. Hess, and T. W. Sigmon, Editors, North Holland (1981).
2. G. L. Olson, L. D. Hess, G. Yaron, and J. Peng, in "Laser and Electron Beam Processing of Materials," C. W. White and P. S. Peercy, Editors, Academic Press, New York (1980).
3. S. Ongo, S. Kohyama, K. Shibata, Y. Nagakuba, and H. Iizuka, *Jpn. J. Appl. Phys.*, **19**, 133 (1979).
4. A. Gat, L. Gerzberg, J. F. Gibbons, T. J. Magee, J. Peng, and J. D. Hong, *Appl. Phys. Lett.*, **33**, 775 (1978).
5. S. Solmi, M. Severi, R. Angelucci, L. Baldi, and R. Bilenchi, *This Journal*, **129**, 1811 (1982).
6. K. Nishiyama, M. Arai, and N. Watanabe, *Jpn. J. Appl. Phys. Lett.*, 19L563 (1980).
7. A. Gat, *IEEE Trans. Electron Devices Lett.*, **edl-2**, 85 (1981).
8. R. A. Powell, T. O. Yep, and R. T. Fulks, *Appl. Phys. Lett.*, **39**, 150 (1981).
9. R. T. Fulks, C. J. Russo, P. R. Hanley, and T. L. Kamins, *ibid.*, **39**, 604 (1981).
10. B. Y. Tsaur, J. P. Donnelly, John C. C. Fan, and H. W. Geis, *ibid.*, **39**, 93 (1981).
111. G. Masetti, D. Nobili, and S. Solmi, in "Semiconductor Silicon 1977," H. R. Huff and E. Sirtl, Editors, p. 648, The Electrochemical Society Softbound Proceedings Series, Princeton, NJ (1977).
12. T. Shibata, H. Iizuka, S. Kohyama, and J. F. Gibbons, *Appl. Phys. Lett.*, **35**, 21 (1979).

The Effect of Stress on the Redistribution of Implanted Impurities in GaAs

J. Kasahara, Y. Kato, M. Arai, and N. Watanabe

Sony Corporation Research Center, Hodogaya-ku, Yokohama, 240 Japan

ABSTRACT

The stress introduced by the difference in thermal expansion coefficients between an encapsulant and a substrate was found to affect the redistribution of implanted impurities during annealing. Compressive stress introduced by an Si_3N_4 film on GaAs enhanced the diffusion of implanted Si, Se, and S. Diffusion constants of Si and Se increased exponentially with the increase in the film thickness in a thickness region less than 0.1 μm. The diffusion mechanism was discussed and it was concluded that the change in the jump frequency of diffusing atoms was dominant in determining the effect of stress in the damaged implantation layer. Excess of carriers was also observed in Se- and S-implanted samples, while deficit in carriers was observed in Si-implanted samples when the samples were subsequently annealed with an Si_3N_4 film.

Small logic swing is essential for achieving a GaAs logic integrated circuit, particularly in enhancement-mode logic circuits, where logic swing in Schottky barrier FET's should be 0.7V at most and that in junction FET's 1.2V to avoid appreciable gate current. Channel layers of both FET's are usually formed by ion implantation directly into a semi-insulating substrate. Variation of the carrier concentration profile in the ion-implanted channel layer over the whole wafer is a most crucial problem for uniformity and reproducibility of the devices. Precisely controlled ion-implanted layers are required to achieve GaAs integrated circuits.

Ion implantation technology is advantageous, because it can, in principle, control the profile for the channel layer only by changing the implantation energy and ion dose. The profile is predicted by the LSS range statistics (1). A damaged layer by ion implantation, however, has to be annealed at high temperature in order to remove radiation damage and to activate implanted impurities as donors or acceptors. Implanted impurities are redistributed by diffusion during post-implantation annealing at high temperature. The factors affecting the redistribution were discussed previously by Kasahara and Watanabe (2) and Yoder (3). Thermal stress during post-implantation annealing was pointed out to be one of the factors, and the example was shown in the case of Zn ion implantation into GaAs (2). The effect of the thermal stress on the redistribution of Cr in Cr-doped semi-insulating substrates was also reported (4, 5). However, it is not clear how the stress influenced the redistribution of implanted impurities in GaAs.

In this paper, the effect of the external stress on the redistribution of implanted Si, Se, and S in GaAs is investigated by using a wafer with thermal stress introduced by the difference in the thermal expansion coefficient between an encapsulant and GaAs. Following the descriptions of the experimental conditions and the results, we discuss variations in the diffusion constants of implanted Si and Se under a wide range of external stress conditions. Variations in the doping efficiency of the implanted impurities are also described briefly as a function of the thickness of the encapsulant.

Experimental

The external stress during annealing was introduced by encapsulating a GaAs substrate with a plasma-deposited Si_3N_4 film. The refractive index of the Si_3N_4 was 2.05 $\pm$ 0.01. An oxygen content in the film, which is known to be detrimental to an encapsulant, was below the detection limit ($< \sim 0.1\%$) of Auger electron spectroscopy. The difference in the thermal expansion coefficient between the encapsulant and the substrate causes stress to the substrate. The magnitude of the stress was varied by varying the film thickness from 0 to 5830Å. The film thickness was measured by the ellipsometry.

Key words: anneal, diffusion, encapsulant.

Substrates used in this experiment were (100) oriented lightly Cr-doped LEC (liquid encapsulated Czochralski) semi-insulating crystals. Substrates were specified to have Cr concentration of 0.07 wt ppm and verified to remain semi-insulating after the annealing at 850°C for 30 min in H_2 atmosphere with face-to-face configuration. After degreasing the surface with organic solvents followed by a slight etch to remove surface damage, samples were implanted with Si, Se, and S to a dose of 3×10^{12} ions/cm^2 at an energy of 70, 170, and 150 keV, respectively. The same ion dose results in the same amount of a carrier concentration for all implantation species. The implantation energies of Si and Se were chosen to give the same projected range (Rp). Samples implanted with Si or Se were annealed at 850°C for 15 min with and without Si_3N_4 films. Samples implanted with S were annealed at 900°C for 15 min also with and without the encapsulant. All the samples were annealed in palladium-purified H_2 under arsine partial pressure of 3.0 Torr. Without an encapsulant (capless annealing), the samples were annealed in the face-to-face configuration described in a previous publication (6), while, with an encapsulant (capped annealing), the samples were annealed in the face-up configuration (6).

Carrier concentration profiles were measured by the C-V technique using an Hg Schottky barrier contact. The layer removal technique using the etchant of H_3PO_4 was combined with the C-V measurement in the case of S implantation because S atoms penetrated deeply during annealing and the carrier concentration profiles were broadened. Doping efficiencies were determined by integrating the carrier concentration profiles. Hall mobility was measured by the conventional van der Pauw method. Photoluminescence measurements were made at 4.2 K by immersing samples in liquid helium. An Ar laser operating at the wavelength of 5145Å with an intensity of ~100 mW at the sample surface was used as the source of excitation. The emission spectra were analyzed by a ¾m grating spectrometer and detected with a cooled photomultiplier with an S-1 response.

Results

Carrier concentration profiles in Si-implanted samples are shown in Fig. 1. The thickness of the Si_3N_4 film ranged from 260 to 2980Å. The increase in the film thickness resulted in broadened carrier concentration profiles. In addition, the carrier concentration was depressed with the increase in the film thickness. The sample annealed by the capless method showed the highest carrier concentration and the sharpest carrier

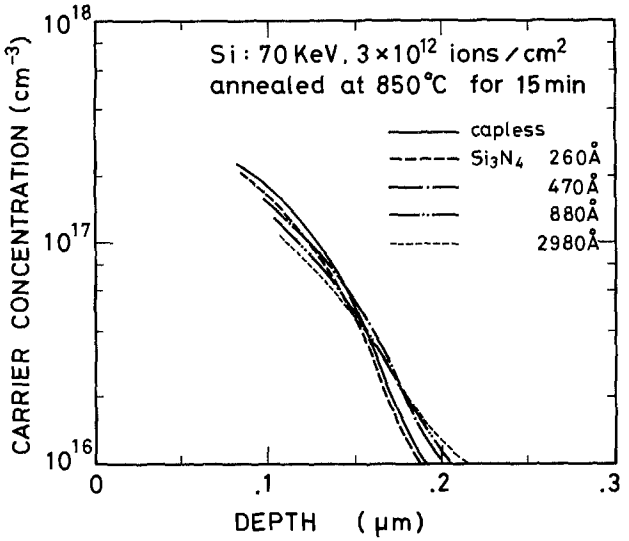

Fig. 1. Carrier concentration profiles of Si-implanted samples with different thicknesses of Si_3N_4 cap. Samples were implanted at 70 keV to a dose of 3×10^{12} ions/cm^2 with subsequent annealing at 850°C for 15 min under arsine partial pressure of 3.0 Torr. The film thickness was varied from 0 to 2980Å.

concentration profile. Similar broadening of the carrier concentration profile was observed in Se-implanted samples as is shown in Fig. 2. However, the decrease in the carrier concentration with the increase in the film thickness was not observed in Se-implanted samples in contrast with Si-implanted ones. All the profiles in Si- or Se-implanted samples were approximated as a part of the Gaussian profiles. On the other hand, the profiles were not Gaussian in the case of S implantation as is shown in Fig. 3. A similar deformed profile has often been observed for Zn in GaAs and has been explained by the interstitial-substitutional diffusion mechanism (7). Although the profiles in S-implanted samples were different from those in Si- and Se-implanted samples, the broadening of the profiles with the increase in the film thickness showed the same tendency. Redistribution and broadening of the carrier concentration profile in GaAs implanted with Zn was similar to that implanted with S as was previously reported (2). Siu and Immorlica also reported on the effect of Si_3N_4 capping on the broadening of the profiles in Se- and S-implanted GaAs wafers by comparing the profiles after capped and capless annealing (8). As well as electrical profiles, the broadening of the atomic concentration profile of implanted Zn was observed after capped annealing by SIMS analysis (9). These broadenings of the profiles in the capped annealing must be mainly due to stress during the post-implantation annealing.

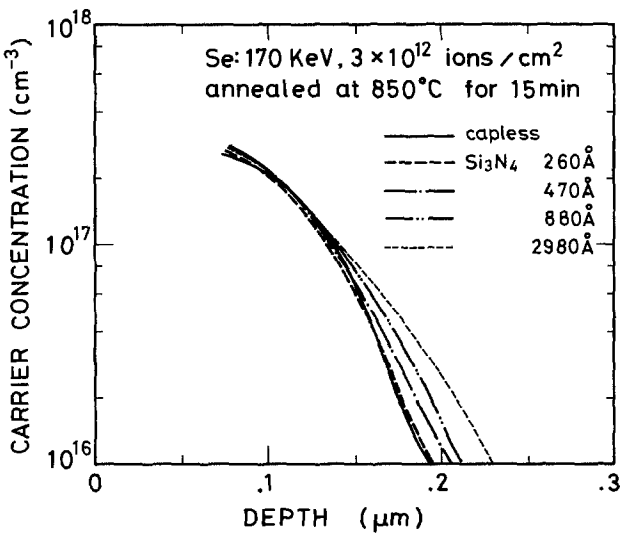

Fig. 2. Carrier concentration profiles of Se-implanted samples with different thicknesses of Si_3N_4 cap. Implantation dose was 3×10^{12} ions/cm^2 and the energy was 170 keV. Samples were annealed at 850°C for 15 min under arsine partial pressure of 3.0 Torr. The thickness of Si_3N_4 was varied from 0 to 2980Å.

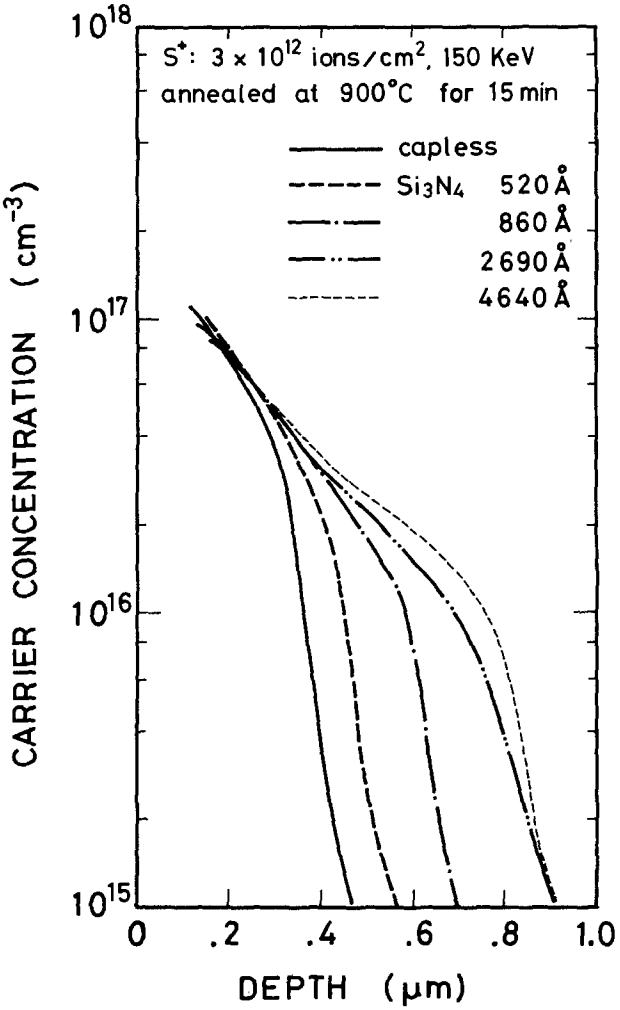

Fig. 3. Carrier concentration profiles of the samples implanted with S at 150 keV to a dose of 3×10^{12} ions/cm^2 with subsequent annealing at 900°C for 15 min under arsine partial pressure of 3.0 Torr. The thickness of the capping film was varied from 0 to 4640Å.

Doping efficiencies (the ratio of sheet carrier concentration to ion dose) determined by integrating the carrier concentration profiles are plotted in Fig. 4 as a function of the film thickness. As can be seen from the profiles, the doping efficiency of implanted Si was lowered with the increase in film thickness, whereas slight increase of the doping efficiency was observed for Se or S implantation. The doping efficiencies of Si, Se, and S were almost the same, about 90%, after the capless annealing. Discussion about the variation in the doping efficiency is given briefly in a later section.

Discussion

Calculation of stress.—Before discussing the stress dependence of the redistribution of implanted impurities, we have to calculate the external stress at the interface between the film and the substrate. The external stress calculated was assumed to be uniform through the implanted layer, because the implanted layer was quite thin close to the interface. A magnitude of the stress σ was calculated using Eq. [1] based on the analysis by Sugano and Kakemoto (10)

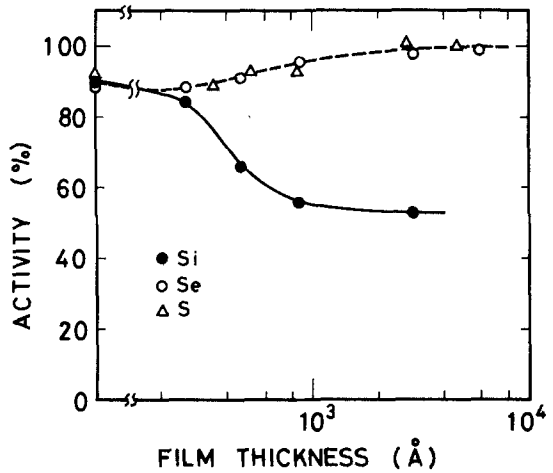

Fig. 4. Doping efficiency of the samples implanted with Si, Se, or S to a dose of 3 × 10^{12} ions/cm² as a function of the thickness of the capping film.

$$\sigma = E_s/(1-\nu_s)\,[-4(\alpha_s-\alpha_f)\,(Rt_f/t_s)\,\Delta T] \quad [1]$$

$$R = [E_f/(1-\nu_f)]/[E_s/(1-\nu_s)] \quad [2]$$

where α is the thermal expanison coefficient, deg^{-1}; t, the thickness, cm; E, Young's modulus, dyne/cm²; ν, Poisson's ratio; and ΔT, the difference between processing and deposition temperature, °C. The subscripts "s" and "f" represent substrate and film, respectively. R is the correction factor when the difference in the value of $[E/(1-\nu)]$ is large between a substrate and a film. The parameters used for this work are $\alpha_s = 7 \times 10^{-6}$ deg^{-1} (11), $\alpha_f = 3 \times 10^{-6}$ deg^{-1} (12), $[E_s/(1-\nu_s)] = 1.3 \times 10^{12}$ dyne/cm² (13), and $[E_f/(1-\nu_f)] = 3 \times 10^{12}$ dyne/cm² (14). Substrate thickness was 410 ± 10 μm. Deposition temperature of Si_3N_4 was 350°C, and $\Delta T = 500° \sim 550°C$.

Stress dependence of the diffusion constant.—Diffusion constants of implanted Si and Se under external stress field were determined by fitting calculated profiles to experimental profiles. The calculated profiles were obtained by the simple method (15) based on the LSS range statistics (1) assuming a Gaussian profile. For S implanted samples, however, diffusion constants were not determined. The analysis for the diffusion of implanted S is complicated because the diffused profiles cannot be explained by a simple vacancy mechanism or an interstitial-substitutional mechanism as can be easily understood from Fig. 3. Discussion on this complicated diffusion mechanism is beyond the scope of this paper. On the other hand, diffusion of Si and Se can be analyzed by the simple vacancy mechanism. The stress dependence of the diffusion constants are discussed only for Si and Se implantation.

Examples of fitting procedures are shown in Fig. 5 and 6 for Si and Se implantation, respectively. Experimental profiles represented by the solid and broken lines agreed well with the calculated profiles represented by dots. Thus, diffusion constants were determined and plotted in Fig. 7 as a function of the external stress introduced by the encapsulant. The stress is compressive in the configuration of Si_3N_4 on GaAs. Diffusion constants increased with the increase in the film thickness, that is, the increase in the compressive external stress both for Si and Se. In the region of smaller stress, diffusion constants increased exponentially. In the region of larger stress, however, experimentally determined diffusion constants were apart from the exponential relationship and tended to saturate or decrease slightly. Diffusion constant D is expressed by the following equation on the basis of the random walk diffusion model (16)

$$D \propto a^2 f \quad [3]$$

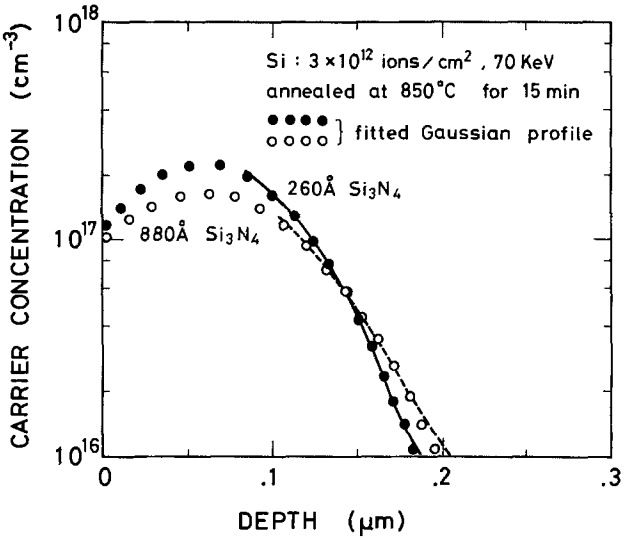

Fig. 5. Examples of the fittings of the calculated profiles (dots) to the experimental carrier concentration profiles in Si implanted and annealed samples (solid and broken lines).

where a is the lattice constant and f the probability with which an atom jumps from one lattice site to a nearest lattice site. The probability f is proportional to the exact jump frequency ω and vacancy concentration N_v. In a crystal strained by stress, lattice constant is changed to $a = a_o[1 + \sigma(1-\nu_s)/E_s]$. For a crude approximation, ω and N_v are written in the form (17)

$$\omega = \omega_o \exp(K_1\sigma) \quad [4]$$

$$N_v = N_{vo} \exp(K_2\sigma) \quad [5]$$

Subscript "o" represents each value in an unstrained crystal. Consequently in the strained crystal, the diffusion constant is rewritten as

$$D = D_o[1 + \sigma(1-\nu_s)/E_s]^2 \exp(K_1\sigma) \exp(K_2\sigma) \quad [6]$$

K_1 and K_2 are constants. So far as our experiments are concerned, the factor coming from the change in the lattice constant was negligible because the magnitude of the external stress in our experiments were of the

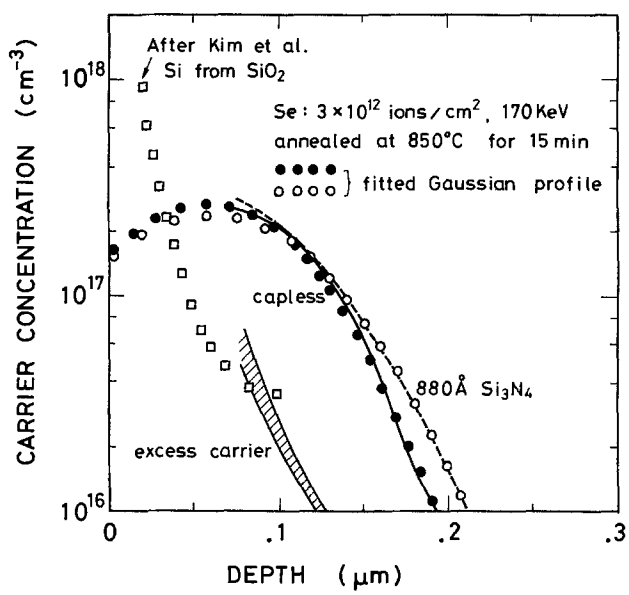

Fig. 6. Examples of the fittings of the calculated profiles (dots) to the experimental carrier concentration profiles in Se implanted and annealed samples (solid and broken lines). Also shown in the figure are the excess carriers from this work (hatched) and from Kim et al. (25) (open rectangles).

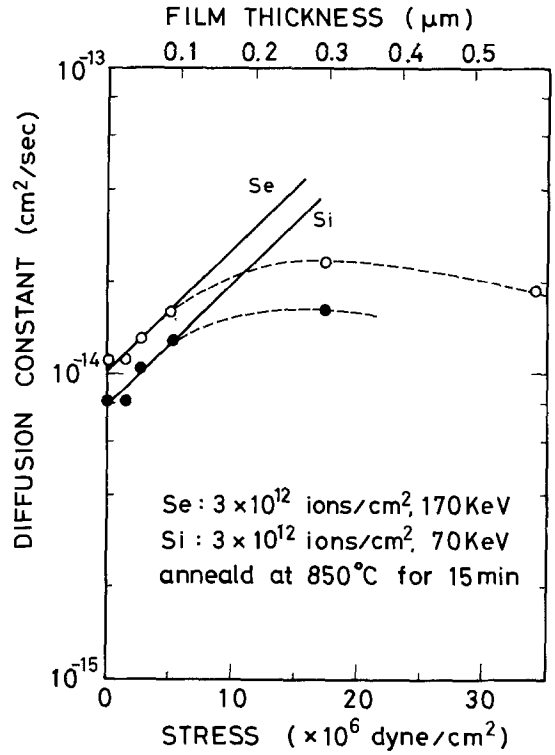

Fig. 7. Diffusion constants of Si and Se implanted to a dose of 3×10^{12} ions/cm² after annealing at 850°C for 15 min as a function of stress.

order of $10^6 \sim 10^7$ dyne/cm², and $(1 - \nu_S)/E_S$ is much smaller than unity. Therefore, Eq. [6] is again rewritten to the expression

$$D = D_0 \exp(K_1\sigma) \exp(K_2\sigma) \quad [7]$$

Equation [7] qualitatively elucidates the experimental results that the diffusion constant in the strained crystal has an exponential dependence on the stress in a smaller stress region. However, we have to consider signs of K_1 and K_2 further. The jump frequency ω and the vacancy concentration N_V are described in terms of entropy and enthalpy (18). Considering a change in enthalpy by compressive stress, we can estimate the signs of K_1 and K_2. The vacancy concentration is known to be a decreasing function of the compressive stress (19). The jump frequency is an increasing function of the compressive stress in regarding a barrier height to be overcome by a diffusing atom and to move from one lattice site to another in a strained crystal. Then, K_1 is positive and K_2 is negative. Therefore, the experimental result shown in Fig. 7 suggests that the dependence of the diffusion constant on the stress in the implanted layer is dominated by the jump frequency at least in the region of smaller stress. This should be due to the supersaturation of the vacancy concentration. It is easy to understand that the vacancy concentration exceeds its equilibrium value in an ion-implanted layer at the temperature considered. The results reported on the redistribution of Zn-implanted samples (2) support the speculation. Diffusion of Zn with an interstitial-substitutional mechanism was retarded in the implanted layer; approximately Rp (projected range) + 2ΔRp (projected standard deviation), in which the vacancy concentration would exceed its equilibrium. It is reasonable to conclude that the vacancy concentration is in the state of supersaturation and the change in the concentration depending on the stress is small in the implanted layer close to the surface. The external stress dependence of the diffusion constants of Si and Se implanted into GaAs are elucidated. Dependence of their diffusion constants on the external stress are dominated by the jump frequency of diffusing atoms in the smaller compressive stress region. However, the change in the vacancy concentration affects the diffusion constant in the larger compressive stress region.

Doping efficiency.—The authors have reported (20) that the doping efficiency of implanted impurities are lower after annealing with Si_3N_4 capping than after capless annealing. It was observed in this experiment that the doping efficiency on the capped annealing depended on the thickness of an encapsulant as is shown in Fig. 4. For Se implantation, slight excess carriers were observed. Experimental carrier concentration profiles after the capped annealing deviate from the calculated profiles near the surface as shown in Fig. 6. Excess carriers were shown by a hatched band in Fig. 6. Contrary to the case of S or Se, the doping efficiency of implanted Si decreased with the increase in the film thickness. One of the possible causes for the deficit in carriers is Mn accumulation near the surface (21, 22). However, this is not the case. Figure 8 shows photoluminescence spectra from the samples: (*i*) implanted with Si and annealed without Si_3N_4, (*ii*) implanted with Si and annealed with 470Å of Si_3N_4, (*iii*) implanted with Si and annealed with 2980Å of Si_3N_4, and (*iv*) implanted with Se and annealed with 2980Å of Si_3N_4. We observed the emission related to Mn acceptor (1.408 eV) (23) only in the sample annealed caplessly. The samples in which the deficit in carriers were observed did not show the emission at 1.408 eV. It is also difficult for Cr accumulation near the surface to explain both deficit in carriers in Si implantation and excess carriers in Se and S implantation. Another possible cause is an anti-site defect of Ga on an As-site which is thought to be an acceptor having the activation energy of 77 ~ 78 meV (24). This is not the case either, because the anti-site acceptors cannot explain excess carriers observed on S and Se implantation. Contamination by Si from Si_3N_4 film is one of the possible causes for the excess carriers. Kim *et al.* (25) reported on in-diffusion of Si from SiO_2 during SiO_2-capped annealing by analysis with SIMS measurement, and their profile of the in-diffused Si at 860°C for 20 min annealing is also plotted in Fig. 6 as a reference. Similar in-diffusion of Si from Si_3N_4 was also reported by Lidow *et al.* (26). In-diffused Si atoms would elucidate not only excess carriers in S- or Se-implanted samples but also the deficit in carriers in Si-implanted samples

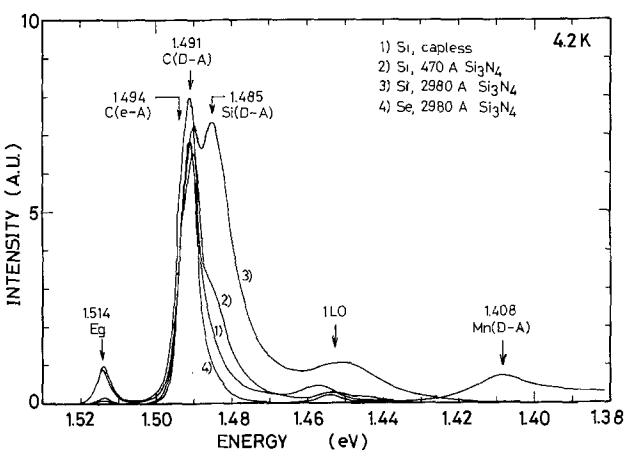

Fig. 8. Photoluminescence spectra at 4.2 K from the samples: curve 1, implanted with Si and annealed without Si_3N_4; 2, implanted with Si and annealed with 470Å of Si_3N_4; 3, implanted with Si and annealed with 2980Å of Si_3N_4; and 4, implanted with Se and annealed with 2980Å of Si_3N_4. Six emission peaks related to band-to-band transition (1.514 eV), C-acceptor (1.494 and 1.491 eV) (29), Si-acceptor (1.485 eV), phonon replica of band-to-acceptor transition (~1.45 eV), and Mn acceptor (1.408 eV) are observed.

with the assistance of a stoichiometric deviation, because Si is amphoteric in GaAs. Photoluminescence spectra in Fig. 8 support this speculation. The emission at 1.485 eV assigned as transition from donor to Si acceptor (27) increased with the increase in film thickness and was not observed in the Se-implanted sample even after annealing with 2980Å of Si_3N_4. Self-compensation between Si-donors on Ga-sites and Si-acceptors on As-sites is speculated in Si-implanted samples. The compensation ratio in the samples annealed with Si_3N_4 of 2980Å was estimated from the mobility measured at 77 K referring to the table by Walukiewicz *et al.* (28). Averaged carrier concentration at 77 K was 4.0×10^{16} and 1.3×10^{17} cm^{-3} in Si and Se implantation, respectively, assuming the thickness of the implanted layers to be 0.15 μm. The mobility was 6940 and 5920 $cm^2/V \cdot sec$ in Si and Se implantation, respectively. The compensation ratio, the ratio of acceptor concentration to donor concentration, in the Si-implanted sample was 0.40 and much higher than that in the Se-implanted sample in which the compensation ratio was 0.26. The fact demonstrates that a part of in-diffused Si from Si_3N_4 might be responsible for the variation in the doping efficiency. In-diffusion of Si might be enhanced by the stress as discussed in the section on Stress dependence of the diffusing constant. Therefore, the doping efficiency varies with the film thickness as shown in Fig. 4.

Conclusions

The stress introduced by the difference in the thermal expansion coefficient between a capping film and GaAs modifies the redistribution of ion-implanted impurities. The redistributions were enhanced by the compressive stress in Si-, Se-, and S-implanted wafers. The exponential enhancement of the diffusion constants of implanted Si and Se was thought to be due to the increase in the jump frequency of diffusing atoms in the smaller compressive stress region. In the larger stress region, however, a change in the vacancy concentration must be taken into account.

The variation in the doping efficiency of implanted impurities was also observed by varying the thickness of the encapsulant. Excess carriers were observed in the samples implanted with Se or S, group VI impurities. On the other hand, the doping efficiency was lowered in the samples implanted with Si, group IV impurity.

It is noteworthy that both the doping efficiency and the carrier concentration profile in ion-implanted GaAs are affected not only by the material for an encapsulant but by a combination of the encapsulant and an implanted species and by the thickness of the encapsulant.

Acknowledgments

The authors acknowledge Mr. M. Kamada, Mr. K. Akimoto, and Mr. K. Taira for their helpful discussions. Miss M. Ema is specially acknowledged for performing the measurements. The authors also express their appreciation to Messers. H. Sakurai and T. Suzuki for the ion implantations and Miss I. Sugawara for the Si_3N_4 depositions.

Manuscript submitted Nov. 9, 1982; revised manuscript received July 5, 1983.

Sony Corporation Research Center assisted in meeting the publication costs of this article.

REFERENCES

1. J. F. Gibbons, W. S. Johnson, and S. W. Mylroie, "Projected Range Statistics," Dowden Hutchinson and Ross, Stroudsburg, PA (1975).
2. J. Kasahara and N. Watanabe, "Semi-Insulating III-V Materials, Evian, 1982," To be published.
3. M. N. Yoder, in "Semi-Insulating III-V Materials," G. J. Rees, Editor, p. 281, Shiva Publishing Ltd., Orpington, England.
4. V. Eu, M. Feng, W. B. Henderson, H. B. Kim, and J. M. Whelan, *Appl. Phys. Lett.*, **37**, 473 (1980).
5. C. A. Evans, Jr., V. R. Deline, T. W. Sigmon, and A. Lidow, *ibid.*, **35**, 291 (1979).
6. J. Kasahara, M. Arai, and N. Watanabe, *This Journal*, **126**, 1997 (1979).
7. B. Tuck and M. A. H. Kadhim, *J. Mater. Sci.*, **7**, 581 (1972).
8. D. P. Siu and A. A. Immorlica, Jr., *J. Electron. Mater.*, **9**, 857 (1980).
9. J. Kasahara, H. Sakurai, Y. Kato, and N. Watanabe, *Jpn. J. Appl. Phys.*, **21**, L103 (1982).
10. T. Sugano and K. Kakemoto, *J. Inst. Elect. Comm. Engrs.*, (Japan), **49**, 1887 (1966).
11. Y. S. Toulouskian, R. K. Kirby, R. E. Taylor, and T. Y. R. Lee, *Thermodynamical Properties of Matter*, **13**, 747 (1977).
12. Y. Nakai and M. Watanabe, *Oyobutsuri* (in Japanese), **39**, 551 (1970).
13. N. A. Gorynova, in "The Chemistry of Diamond-Like Semiconductors," J. C. Anderson, Editor, p. 236, The MIT Press, Cambridge, MA (1965).
14. E. A. Irene, *J. Electron. Mater.*, **5**, 287 (1976).
15. T. E. Seidel and A. U. MacRae, *Trans. AIME*, **245**, 491 (1969).
16. B. Tuck, "Introduction to Diffusion in Semiconductors," p. 123, Peter Peregrinus Ltd., Herts. (1974).
17. L. A. Grifalco and H. H. Grimes, *Phys. Rev.*, **121**, 982 (1961).
18. H. C. Casey, Jr. and G. L. Pearson, in "Point Defects in Solids," Vol. 2, J. H. Crawford, Jr., and L. M. Slifkin, Editors, p. 169, Plenum Press, New York (1975).
19. G. C. Jain, B. C. Charkravarty, and A. Prasad, *Phys. Status Solidi A*, **64**, 485 (1981).
20. J. Kasahara, M. Arai, and N. Watanabe, *J. Appl. Phys.*, **50**, 8229 (1979).
21. P. B. Klein, P. E. R. Nordquist, and P. G. Siebenman, *ibid.*, **51**, 4861 (1980).
22. H. Kanber, M. Feng, and J. M. Whelan, *Appl. Phys. Lett.*, **40**, 960 (1982).
23. P. W. Yu and Y. S. Park, *J. Appl. Phys.*, **50**, 1097 (1979).
24. K. R. Elliott, D. E. Holmes, R. T. Chen, and C. G. Kirkpatrick, *Appl. Phys. Lett.*, **40**, 898 (1982).
25. H. B. Kim, J. M. Whelan, V. Eu, and W. B. Henderson, Proceedings of the Cornell Conference, p. 121 (1980).
26. A. Lidow, J. F. Gibbons, and T. J. Maggee, *Appl. Phys. Lett.*, **31**, 158 (1977).
27. D. J. Ashen, P. J. Dean, D. T. J. Hurle, J. B. Mullin, and A. M. White, *J. Phys. Chem. Solids*, **36**, 1041 (1975).
28. W. Walukiewicz, J. Lagowski, and H. C. Gatos, *J. Appl. Phys.*, **53**, 769 (1982).
29. H. Kunzel and K. Ploog, *Appl. Phys. Lett.*, **37**, 416 (1980).

An n-CdSe/SnO_2/n-Si Tandem Electrochemical Solar Cell

J. Gobrecht,*[1] R. Potter,[2] R. Nottenburg,[3] and S. Wagner*[4]

Solar Energy Research Institute, Golden, Colorado 80401

ABSTRACT

We demonstrate a new type of monolithic tandem junction solar cell. The cell is made up of a bottom (low energy gap) Schottky barrier and a top (high energy gap) semiconductor-electrolyte junction. By using silicon as the low gap and cadmium selenide as the high gap semiconductor we chose a pair of semiconductors which produces equal photocurrents when stacked on top of each other. We have observed open-circuit voltages up to 1.21V which demonstrate addition of the output voltage of the two cells. Short-circuit currents are low, reflecting the poor quality of the CdSe film.

The energy bandgap of the absorbing semiconductor chosen for a solar cell represents a compromise for high photocurrent (suggesting a small gap) and high photovoltage (suggesting a large gap) (1). Tandem- and higher multiple-junction solar cells improve this compromise by employing in series two or more absorbing semiconductors that cover a range of energy gaps (2). To maximize efficiency and to provide a single output voltage such cells are arranged in electrical series. Tandem cell configurations comprise either two physically separate cells which receive separate portions of the solar spectrum from a dichroic mirror (a spectrum-splitting filter) (3), or a monolithic structure whose top cell absorbs the short wavelength portion of sunlight and transmits the long wavelength portion to the lower cell (4).

Series connection of the two cells requires balancing of the photocurrents produced by each individual cell. This requirement makes the two energy gaps depend on each other. The use of semiconductor alloys (3) provides flexibility in the choice of energy gaps, but requires expensive fabrication technology which can be justified only for high performance concentrators.

The theoretical principles of tandem solar cells have been analyzed by several authors (5, 6). However, few experimental tests of tandem cells have been reported. It is difficult to find and to combine semiconductors with acceptable photovoltaic properties and whose bandgaps are well matched.

In this paper we demonstrate a tandem cell with CdSe ($E_g = 1.73$ eV) and Si ($E_g = 1.12$ eV). At Air Mass 1 insolation, the photon flux with $h\nu \geq 1.73$ eV is 1.3×10^{17} cm^{-2} sec^{-1} and with $h\nu \geq 1.12$ eV, 2.7×10^{17} cm^{-2} sec^{-1}. Thus the photon currents absorbed in the two partners of a monolithic CdSe/Si structure are nearly equal. Therefore, the CdSe/Si combination lies close to the point of maximum attainable efficiency for monolithic tandem cells. This semiconductor combination provides a near-ideal vehicle for a highly efficient tandem cell without the expense of alloy semiconductors. Since polycrystalline n-CdSe photoanodes have been demonstrated with promising efficiency (7), the n-CdSe/n-Si tandem photoanode is an interesting candidate for use in an efficient regenerative photoelectrochemical cell. The observed high output voltage also suggests application in a photoelectrochemical storage cell (8); the voltages developed by most photoelectrochemical cells are insufficient to drive the desired *in situ* fuel-producing reactions, for instance the splitting of water.

The principle of a tandem photoelectrode was first demonstrated with n-CdS/n-GaAs (9). Because of a substantial mismatch of energy gaps (E_g, CdS = 2.42 eV; E_g, GaAs = 1.43 eV) the photocurrent is restricted to the low value provided by CdS. In the CdS/GaAs structure, the diode with CdS is set up by contact with the electrolyte, and the diode with GaAs by contact with CdS. The barrier height of the latter depends on a fortuitous combination of work functions and interface charge due to lattice mismatch and possibly interface contamination. In the present study, we set up a separate junction for Si which does not depend on its contact properties with the top semiconductor. We selected the SnO_2/n-Si junction which has been demonstrated as an efficient solar cell (10). The SnO_2/n-Si structure is a semiconductor-insulator-semiconductor cell (11). Like the CdSe layer, the SnO_2 film can be prepared by thin film techniques at relatively low processing temperature. The separated junctions provide greater flexibility in device fabrication and permit the isolation of the constituent photodiodes which proved quite useful in subsequent device analysis. Results on a photoanode based on a similar structure (a CdSe film grown on a p^+n silicon solar cell) were published recently (12). This configuration requires a tunnel junction between the p^+-Si and the n-CdSe and thus is less flexible and more difficult to fabricate.

In this publication, we describe the preparation of the electrolyte/n-CdSe/SnO_2/n-Si tandem solar cell, its photovoltaic performance, and an analysis of this performance. The device model, including the effects of series resistance and partial shunting, as well as the cell response to different wavelengths, was discussed in a separate paper (13).

Experimental

Fabrication of tandem photoanodes.—Approximately 1×2 cm^2 n-type 1.2 Ω-cm silicon pieces were cut from [100] oriented polished wafers. After routine cleaning the silicon was etched in concentrated HF for 30 sec, rinsed in deionized water, and dried. The substrates were then spray-coated with a ~100 nm SiO_2 film at a substrate temperature of 400°C (10). The spray solution was electronic grade $SnCl_4$ in spectroscopic grade ethyl acetate. The CdSe layer was prepared using this SnO_2/Si diode in turn as a substrate. CdSe was evaporated from a single source, using a baffled tungsten boat, at a background pressure $<10^{-4}$ Pa ($<7.5 \times 10^{-4}$ microns of mercury), a substrate temperature of 400°C, and a deposition rate of ~3 nm sec^{-1}. The starting material was optical grade 99.999% CdSe.

Two other methods of CdSe deposition were studied: electrolytic codeposition of Cd and Se from heated solution (14) and spraying of a solution of $CdCl_2$ and N,N'-dimethylselenourea onto the heated substrate (15). The electrodeposited films were smooth and adhered well. For good photoresponse they had to be annealed in an inert atmosphere at temperatures above

* Electrochemical Society Active Member.
[1] Present address: Brown Boveri Forschungszentrum, 5405 Baden-Daettwil, Switzerland.
[2] Present address: Department of Physics, Colorado State University, Fort Collins, Colorado 80523.
[3] Present address: Institut Interdepartemental de Microelectronique, Ecole Polytechnique Federale, 1015 Lausanne, Switzerland.
[4] Present address: Department of Electrical Engineering and Computer Science, Princeton University, Princeton, New Jersey 08544.
Key words: semiconductor-electrolyte junction.

500°C for at least 10 min. Such annealing severely degraded the performance of the SnO_2/Si junction. The sprayed photoanodes never reached the performance of the evaporated layers.

After the CdSe film deposition the edges of the samples were cleaved off to ensure that the front SnO_2 and CdSe layers were not shorted to the back (Si) contact. The thickness of the CdSe films was determined at cleaved faces by optical microscopy. The back contact to the silicon was made, after scratching the Si with a diamond scriber, with a Ga-In eutectic alloy or by evaporation of about 200 nm of Al. A wire was attached to the back contact, and the entire electrode except for the front CdSe face was insulated with epoxy resin or black wax.

Measurements.—Electrochemical characterization of cells with the tandem electrode was carried out with a triangular voltage ramp generator, a PAR 175 potentiostat, and a two-channel X-Y recorder. For general electrochemical measurements the potentiostat was operated in a three-electrode mode using a standard calomel reference electrode. These experiments were carried out in glass beakers. Photoelectrochemical cell current-voltage curves were recorded in a two-electrode mode. We used carbon or platinum counterelectrodes. The aqueous polysulfide electrolyte consisted of 1M KOH + 1M Na_2S + 1M S + 0.05M Se. This electrolyte is known to stabilize CdSe against photocorrosion (16). The photoelectrochemical cell (Fig. 1) had an optically flat glass window. An Oriel AM1 solar simulator served as a light source whose intensity as measured with an NASA-Lewis standard silicon cell.

The sealed two-electrode cell for outdoor measurement in sunlight is shown in Fig. 1. This solar cell sandwich is held together with metal clips.

Experimental Results

The current-voltage characteristics of the three-electrode tandem cell in the dark and under illumination are shown in Fig. 2. The tandem photoanode is in contact with the polysulfide electrolyte. Potentiostatic conditions prevent polarization at the counterelectrode. The voltage is not plotted *vs.* that of the calomel reference electrode but the equilibrium potential of the counterelectrode. The highest open-circuit voltage (V_{oc}) observed was 1.21V. The short-circuit current density (J_{sc}) is 5.5 mA cm^{-2} and the fill factor 0.40. The sluggish onset of the dark current under forward (cathodic) bias indicates a high series resistance of the cell and possibly charge transfer polarization.

Solar cell (two-electrode) operation of a carbon/electrolyte/n-CdSe/SnO_2/n-Si device is shown in Fig. 3. Here, the curve fill factor is 0.39, although fill factors as high as 0.7 (comparable to those of all solid-state devices) have been demonstrated for other photoelectrochemical devices (17). Due to the low fill factor and short-circuit current the AM1 power conversion efficiency is only 2.5%.

To understand the device performance we measured the separate diodes, *i.e.*, the SnO_2/n-Si solid-state device and the electrolyte/n-CdSe/SnO_2 structure. In the latter device a good sheet conductivity of the back-contact oxide is required for adequate current collection. Therefore, we employed commercial indium tin oxide (ITO)-on-glass substrates for the CdSe films instead of sprayed SnO_2 on glass. The ITO substrates were vacuum-coated with CdSe films in the same way as the SnO_2/Si cells.

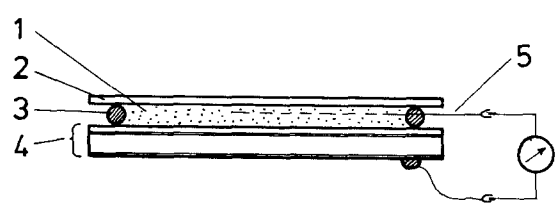

Fig. 1. Schematic cross section of the sealed two-electrode solar cell, denoting the polysulfide electrolyte, 1; the glass window, 2; the O-ring; 3, the n-CdSe/SnO_2/n-Si photoelectrode, 4; and the platinum counterelectrode, 5.

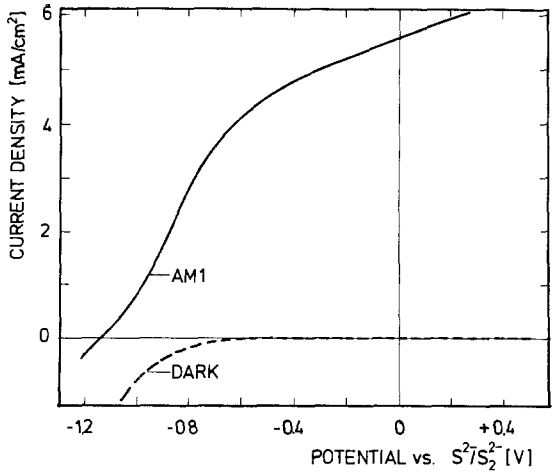

Fig. 2. Potentiodynamic I-V plots of an n-CdSe/SnO_2/n-Si electrode in the polysulfide electrolyte. Three electrodes, 100 mV sec^{-1} scan rate.

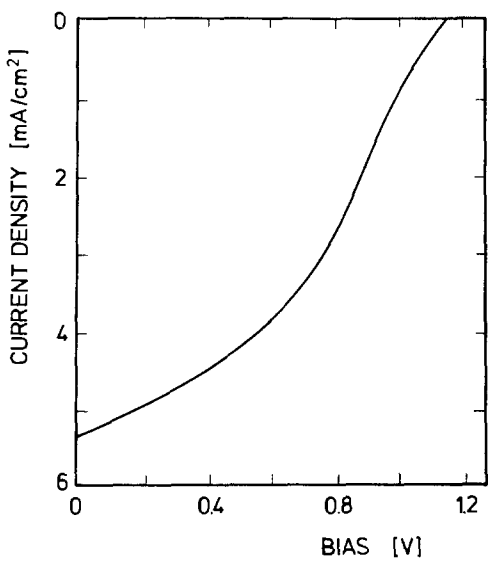

Fig. 3. Photovoltaic I-V curve of a carbon/electrolyte/n-CdSe/SnO_2/n-Si cell. Two electrodes, AM1 illumination.

I-V curves for an SnO_2/n-Si cell are shown in Fig. 4. The device had an active area of 3 cm^2 and a simple grid with 0.5 cm spacing. The dashed curve represents AM1 illumination. The fill factor is low due to the high sheet resistivity ($\geqq$ 150 $\Omega/\square$) of the SnO_2 film. The solid line is for the same device but illuminated with an AM1 spectrum filtered through the half-cell, glass/electrolyte/CdSe/ITO/glass. Due to absorption in the CdSe, which reduces the attainable photocurrent in Si by 50%, and infrared absorption by the ITO, the Si photocurrent is smaller. Simultaneously, the fill factor has improved. We should point out that in the tandem structure the photocurrent flows across the SnO_2 layer so that its low sheet conductance is of little consequence.

In the dark, the Pt/electrolyte/CdSe/ITO cell exhibits good blocking behavior under reverse bias (dashed curve of Fig. 5) in agreement with an earlier report (18). Illumination (solid curve) reveals the poor performance of the CdSe film. The low photocurrent density suggests a low minority carrier lifetime

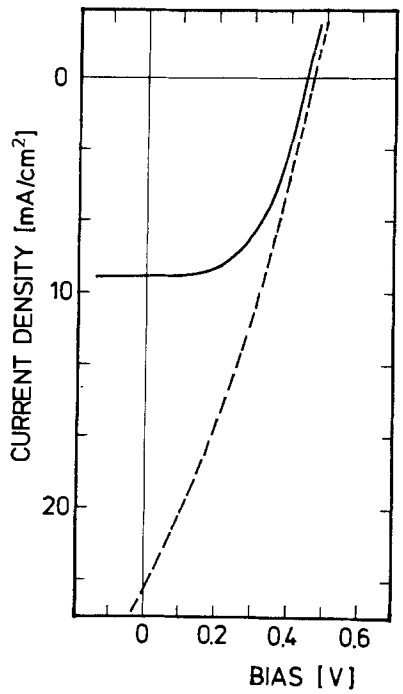

Fig. 4. I-V curves of the SnO_2/n-Si diode under AM1 illumination. Dashed curve: total AM1 spectrum; solid curve: AM1 spectrum filtered through a glass/electrolyte/CdSe/ITO/glass sandwich.

in the film and a high surface recombination velocity. The short-circuit current can be raised by ~30% by photoetching (7). However, this process increased the density of pinholes in the ~1 μm films. The open-circuit voltage varied from sample to sample. We attribute this variation to pinholes in the film. With sufficiently thick (~5 μm) films reproducible V_{oc} was obtained, but at the expense of the fill factor which dropped because of the high series resistance of the CdSe film.

The effect of high series resistance of the CdSe film was demonstrated with the following experiment. The CdSe film on part of a tandem device was removed to expose the SnO_2 which was then contacted. The contact and the exposed SnO_2 were sealed, and the electrode was employed in the usual I-V setup. With this device the potential difference between the SnO_2 and the Si, $\Delta\phi_{SnO_2/Si}$, could be monitored during I-V runs. The result is the solid line in Fig. 6a which shows that under illumination $\Delta\phi_{SnO_2/Si}$ is almost independent of the cell voltage. The value of ~0.3V indicates that the SnO_2/Si junction operates near the maximum power point (see Fig. 4). In the absence of illumination $\Delta\phi_{SnO_2/Si}$ does vary with the total cell voltage, but less than the voltage drop across the electrolyte/CdSe junction. Near equilibrium potential (−0.1 to +0.3V), all change in the cell potential is allocated to the electrolyte/CdSe junction.

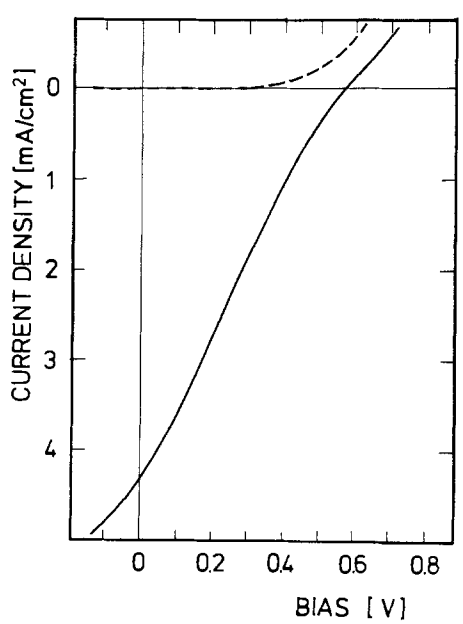

Fig. 5. I-V curves of Pt/electrolyte/CdSe/ITO/glass partial cell in the dark (dashed) and under illumination (solid).

Discussion

The main result of our study is the demonstration of photovoltage addition which proves the concept of the CdSe/Si tandem photoanode. A schematic band diagram of the tandem cell is given in Fig. 7. Analysis of the dark and light I-V characteristics of the tandem electrode and of the separate devices shows that the principal detractor from good cell performance is the CdSe film. The high film resistivity (see Fig. 6a and b) brings in a high cell series resistance and necessitates very thin films which in turn are prone to pinhole formation. The minority carrier lifetime in the CdSe is too short (Fig. 5). The inadequate quality of the film not necessarily is a consequence of the preparation method. CdSe photoanodes prepared by single source evaporation (19) and coevaporation (20) onto glass substrates have exhibited high quantum yields and good photovoltaic efficiency. We can exclude thermal expansion mismatch as being responsible for the low photocurrent because CdSe/ITO/glass showed the same performance as CdSe/SnO_2/Si. We believe that the most likely cause for the poor carrier lifetime in CdSe is contamination in the starting material (19) or in the vacuum system.

A proper course for improving the CdSe/Si tandem electrode therefore would first address the purity and

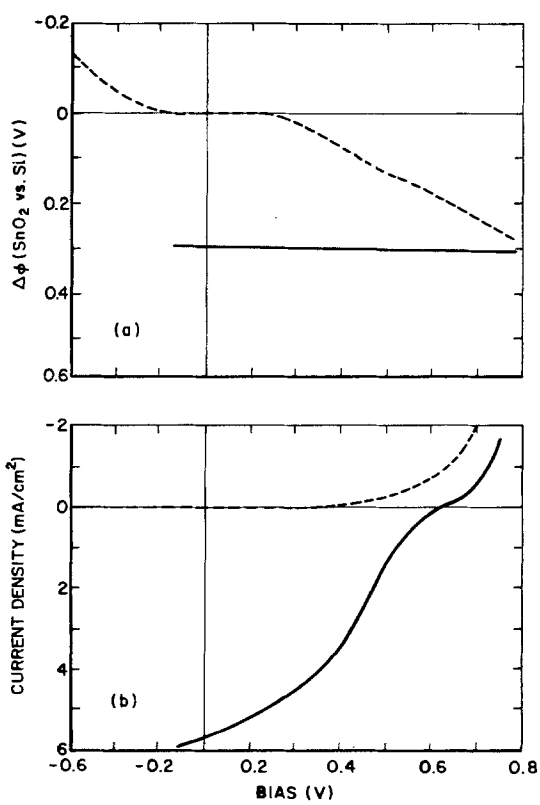

Fig. 6. (a) Potential difference between the SnO_2 layer and the Si back contact as a function of bias applied to the entire cell, in the dark (dashed) and under illumination (solid). (b) Dark (dashed) and light (solid) I-V characteristics of the tandem cell.

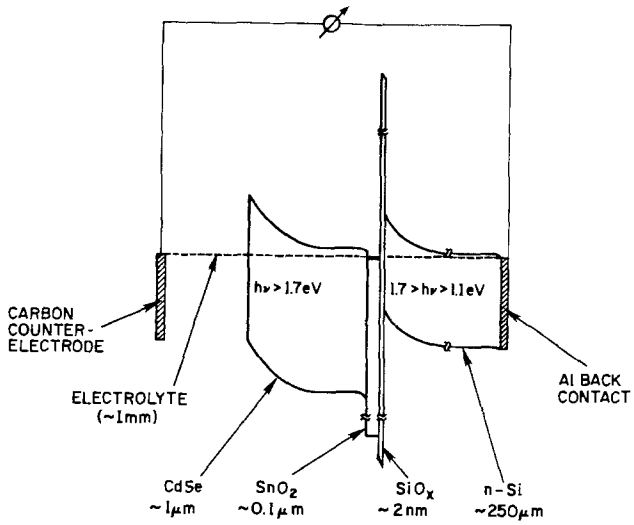

Fig. 7. Schematic band diagram of the tandem photoelectrochemical cell indicating approximate thicknesses.

doping of the CdSe film. Next, attention will have to be paid to the susceptibility of the SnO_2/n-Si diode to the processing temperature during deposition of the CdSe film. Finally, one may consider an all-solid-state device where the electrolyte and counterelectrode have been substituted by a Schottky barrier metal (19) or a large bandgap semiconductor. This would obviate the need for the polysulfide electrolyte which absorbs strongly at wavelengths below ~500 nm, and of course would remove concern about long-term degradation of the surface of the photoanode.

Manuscript submitted Nov. 28, 1982; revised manuscript received June 13, 1983.

REFERENCES

1. J. J. Loferski, *J. Appl. Phys.*, **27**, 777 (1956).
2. L. W. James and R. L. Moon, *Appl. Phys. Lett.*, **26**, 467 (1975).
3. R. L. Moon, L. W. James, H. A. Vander Plas, T. O. Yep, G. A. Antypas, and Y. Chai, Proc. 13th IEEE Photovoltaic Spec. Conf., p. 859, IEEE, New York (1978).
4. S. M. Bedair, *IEEE Trans. Electron Devices*, **ed-28**, 1231 (1981).
5. A. DeVos, *J. Phys. D, Appl. Phys.*, **13**, 839 (1980).
6. N. A. Gokcen and J. J. Loferski, *Solar Energy Mater.*, **1**, 271 (1979).
7. R. Tenne and G. Hodes, *Appl. Phys. Lett.*, **37**, 428 (1980).
8. J. Manassen, G. Hodes, and D. Cahen, *This Journal*, **124**, 532 (1977).
9. S. Wagner and J. L. Shay, *Appl. Phys. Lett.*, **31**, 446 (1977).
10. T. Feng, A. K. Ghosh, and C. Fishman, *ibid.*, **35**, 226 (1979).
11. R. Singh, M. A. Green, and K. Rajkanan, *Solar Cells*, **3**, 95 (1981).
12. W. E. Pinson, *Appl. Phys. Lett.*, **40**, 970 (1982).
13. R. R. Potter, J. R. Sites, and S. Wagner, *J. Appl. Phys.*, **53**, 5269 (1982).
14. M. Skyllas Kazacos and B. Miller, *This Journal*, **127**, 2378 (1980).
15. C.-H. J. Liu and J. H. Wang, *Appl. Phys. Lett.*, **36**, 852 (1980).
16. A. Heller, G. P. Schwarz, R. G. Vadimsky, S. Menezes, and B. Miller, *This Journal*, **125**, 1156 (1978).
17. J. Gobrecht, H. Tributsch, and H. Gerischer, *ibid.*, **125**, 1085 (1978).
18. K. C. Chang, A. Heller, B. Schwartz, S. Menezes, and B. Miller, *Science*, **196**, 1097 (1977).
19. D. Bonnet, Proc. 14th IEEE Photovoltaic Spec. Conf., p. 629, IEEE, New York (1980).
20. M. A. Russak, J. Reichman, C. Crester, and J. Decarlo, Technical Report SERI/CP-613-985, p. 65, Solar Energy Research Institute, Golden, CO (1980).

Electrochemical Properties of $WO_3 \cdot x(H_2O)$

I. The Influences of Water Adsorption and Hydroxylation

Nobuyuki Yoshiike and Shigeo Kondo

Matsushita Electric Industrial Company, Limited, Central Research Laboratory, Moriguchi, Osaka, 570 Japan

ABSTRACT

Electrochemcial properties of evaporated amorphous WO_3 films on conductive glass substrates have been studied in organic electrolytes in order to clarify the influence of water in the films on electrochromism. Compositions of water in the film have been analyzed by using FT-IR spectra and 1H-NMR. We conclude that the water adsorbed in the film during the evaporation and from ambient air not only leads to a fast electrochromic reaction at first, but also reacts gradually with WO_3 by hydroxylation and/or hydrolysis to shift the potential of the cathodic reaction to the negative side and that the hydroxylated film layer loses the electrochromic coloration density.

WO_3 is one of the most useful materials for electrochromic displays (ECD) (1-6). Electrochromism on WO_3 films was first reported by Deb (1). He proposed that the coloration occurred as a result of the formation of F or F^+ color centers in oxygen vacancies. Since then, many workers have been studying the coloration mechanism of the film. At present a model for coloration explained by Faughnan *et al.* (3) is reasonable, whereby the double injection of electrons and protons into the film forms tungsten bronze, as follows

$$WO_3 + xH^+ + xe \rightleftharpoons H_xWO_3 \qquad [1]$$

Key words: electrochromic, displays, tungsten oxide, hydroxylation.

In this hypothesis the phenomenon of coloration is explained as an intervalence electron transfer between W^{5+} (A) and W^{6+} (B). Tungsten bronzes have a stable memory effect and can be switched back into the original colorless state by reversing the current.

Recent studies (7-13) have confirmed that water in the film and electrolytes plays an important role in the coloration mechanism. Reichman and Bard (7) have reported that the kinetics of the electrochromic process for WO_3 films depend on the quantity of water in the film and its porosity. Hurditch (9) has also studied the dependence of the coloration phenomenon on the water content in the film. He suggested $WO_3 \cdot aq$ as an intermediate between a fractionally hydrated form of tung-

sten oxide and a polytungstic acid. Pickelman *et al.* (10) have reported that the electrochromic property of the film is caused by the water partial pressure P_{H_2O} in the vacuum chamber during the evaporation process. Zeller and co-workers (11) concluded that the crystal water not only provided a high ionic conductivity which is a condition for a fast electrochromic reaction, but also stabilized electrocatalytically active surface sites.

Although all the authors have recognized the importance of the presence of water, the relationship between states of water adsorbed in the WO_3 film and electrochemical properties of the film is still not clear. On the other hand, it is known that, even in the atmosphere, metal oxides usually chemisorb water molecules to form surface hydroxyl groups on which further water molecules are physically adsorbed through hydrogen bonding. The adsorbed states of water on metal oxides have been investigated by many authors (14-20), and they have reported that properties such as a sensitivity and a catalytic effect of metal oxides greatly depends on the adsorbed state of water.

In this paper, we report the structural and electrochemical properties of $WO_3 \cdot x(H_2O)$ films which were prepared by various evaporation methods and stored under several different conditions. In particular, we elucidate a difference between the influence of free water from physisorption and that of chemisorbed hydroxyl groups on the electrochemical properties of the film.

Experimental

Preparation of WO_3 films.—WO_3 films were deposited by an electron beam evaporation method. WO_3 targets (99.99%) were supplied by Fuluuchi Kagaku Company, Limited. The deposition rate was 4-5 Å/sec, the deposition angle was varied within ±40° with a planetary rotation, and the substrate temperature was usually maintained at 80°C after preheating at 110°C for 5 min. The substrates were In_2O_3-coated glass (20 Ω/cm^2) used for electrochemical measurements and electron diffraction analyses, silicon wafers (200 μm thickness) used for infrared spectra, and Al films (10 μm thickness) used for the NMR experiments.

Compositions of the residual gas in the chamber during the evaporation process were monitored by a mass-spectrometer ANAVAC-2 (VG-Gas Analysis Limited, England) and partial pressures of H_2O, O_2, and N_2 were controlled by an individual gas-introduction method.

For the purpose of investigating the influence of humidity on the evaporated WO_3 films, the films were stored in air at constant relative humidity (RH) of 50% and constant temperature of 25°C.

Electrochemical measurements.—The electrochemical measurements, especially cyclic voltammetry measurements, were performed with a potentiostat (Hokuto Denko Company, Limited, Model HA-301) which was supplied with voltage from a function generator (same company, Model HB-104). The WO_3 film thickness and area were 3000Å and 0.3 cm^2, respectively. The counter-electrode was a Pt plate. The reference electrode was a saturated calomel electrode (SCE). A salt bridge was used for an intermediate between the SCE and the electrolytes. The electrolytes were propylene carbonate (PC) solutions containing 0.3*M* $LiClO_4$ and 0.03*M* $LiBF_4$. PC (the first grade, Wako Junyaku) was freshly distilled under vacuum, $LiClO_4$ (purity > 99%, Mitsuwa Kagaku) and $LiBF_4$ (purity > 93%, Morita Kagakukogyo) were used. Ar gas was bubbled for more than 5 min before measurements. The H_2O contents in the electrolytes were checked in each case by an Aquacounter (Hiranuma Seisakusho, Model AQ-3B), and these concentrations were typically 0.03-0.05*M*. For the purpose of comparison, 1*M* H_2SO_4 aqueous solutions were also used for electrolytes.

Analyses of WO_3 films.—Infrared spectra were taken with an FT-IR spectrometer (Nihon Denshi, Model JIR-40D). For these measurements, the WO_3 film thickness on an Si wafer was 16,000Å which was thicker than those used for electrochemical measurements in order to obtain high analytical sensitivity. Resolution was 8 cm^{-1} and the number of spectra for one measurement was 400 cycles.

^1H-NMR was measured with an NMR spectrometer (Nihon Denshi, Model FX 90Q) by a conventional FT-NMR method at 28°C and in a dry atmosphere. The sample was WO_3 (16,000Å) deposited on both sides of the Al film (10 μm) and the film, flat in configuration, was packed in a 10 mmϕ glass tube. Measurement frequency and width was 89.55 MHz and 20 kHz, respectively. The 45° pulses (15.5 μsec) were given 10,000 times at 3 sec intervals.

Results and Discussion

Water adsorption during the evaporation process.—We prepared WO_3 films on In_2O_3 electrodes under different conditions of water partial pressure (P_{H_2O}) in the chamber during the evaporation process. For the purpose of determining the dependence of P_{H_2O}, the total gas pressure (P_{total}) and the oxygen partial pressure (P_{O_2}) were controlled to be practically constant because P_{total} influences the film packing density which affects the electrochromic sensitivity. P_{O_2} may also influence the composition of WO_x. Two typical examples of the conditions are shown in Table I.

Deposited WO_3 films which were prepared under the conditions shown in Table I and confirmed by electron diffraction observations were typically amorphous; packing density of the films calculated from the film thickness and weight was 5.38 g/cm^3, and the reflection index, evaluated from the interference patterns of visible absorption spectra and film thickness, was 1.85.

Cyclic voltammograms of the film (3000Å) were taken and are shown in Fig. 1, in which the films were set in an electrochemical measurement cell just after deposition and cooling in the chamber.

The cathodic current which starts at +450 mV *vs.* SCE is associated with coloration of the film and the anodic current is associated with bleaching.

In Fig. 1, the cathodic curves were similar to each other, whereas the anodic current peak of the film prepared under the condition of high water partial pressure was located at a more negative potential (about 400 mV) and was larger than that of the film prepared under the condition of low water partial pressure. The same result was obtained from other samples which were prepared with various conditions of P_{H_2O}: 6.5×10^{-6}-2.1×10^{-5} Torr. This is shown in Fig. 2a, in which the bleaching response was evaluated for convenience from anodic current values at +400 mV *vs.* SCE of cyclic voltammograms which started at +1V and returned at −200 mV with 200 mV/sec scan rate. The faster bleaching speed corresponds to the smaller anodic current values at +400 mV, since the increase of P_{H_2O} during the evaporation makes the fast bleaching reaction. On the other hand, the cathodic curves were similar to each other in spite of different water pressure conditions, that is, the water

Table I. Two examples of evaporation conditions for WO_3 films. P_{total} were measured by an ionization gauge, P_{H_2O} P_{N_2}, and P_{O_2} measured by a mass-spectrometer (ANAVAC-2)

	Pressure in the chamber (10^{-5} Torr)				Deposition rate (Å sec)	Sub. temp. (°C)
	P_{total}	P_{H_2O}	P_{N_2}	P_{O_2}		
1	4.0 ~ 5.0	2.4 ~ 2.5	0.16	0.12	4.4	78
2	3.7 ~ 5.0	1.4 ~ 0.9	1.6	0.15	4.2	80

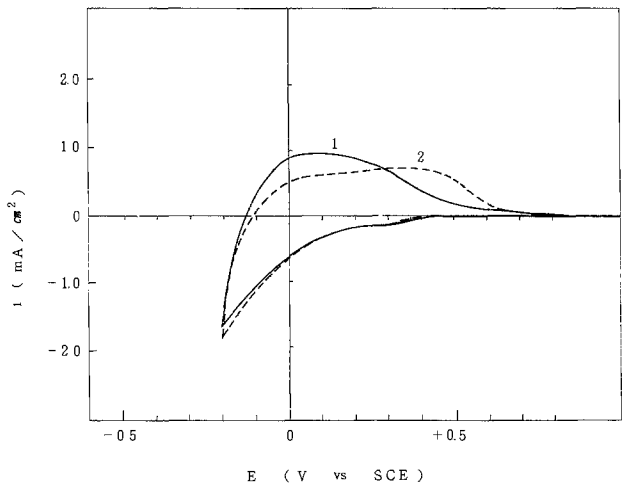

Fig. 1. Cyclic voltammograms at 0.2 V/sec scan rate for as-deposited WO_3 films in PC electrolytes. 1, WO_3 evaporated under the No. 1 condition in Table I and 2, under that of No. 2.

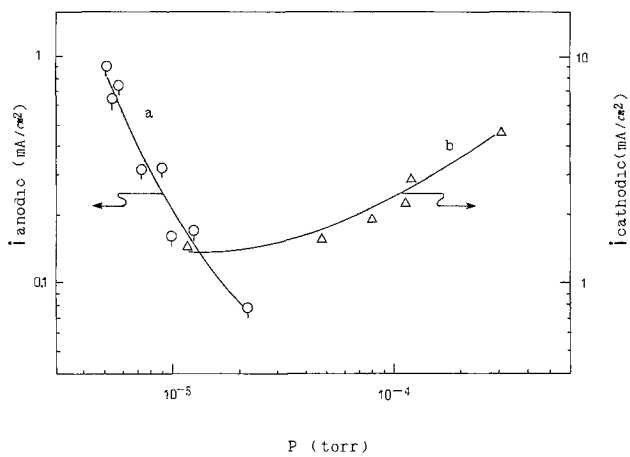

Fig. 2. Plots of anodic current values at +400 mV *vs.* SCE of the cyclic voltammograms for WO_3 films in PC electrolytes (scan rate: 0.2 V/sec); (a) and (b) as a function of P_{H_2O} and P_{total} in the chamber during the evaporation, respectively.

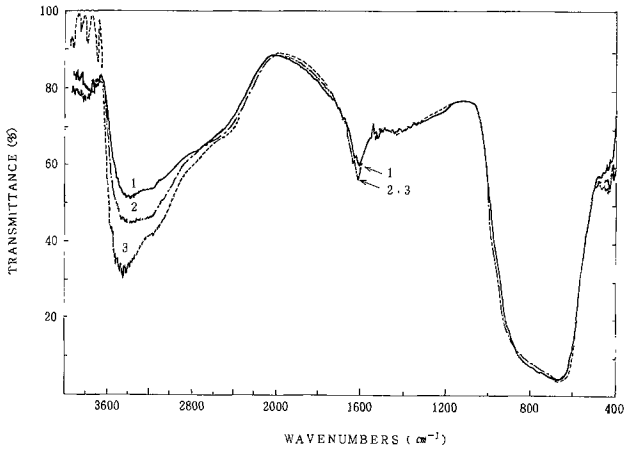

Fig. 3. FT-IR spectra of WO_3 films. 1, as-deposited, 2, stored in air at 25°C and 50% RH for 24 hr, and 3, for 1080 hr.

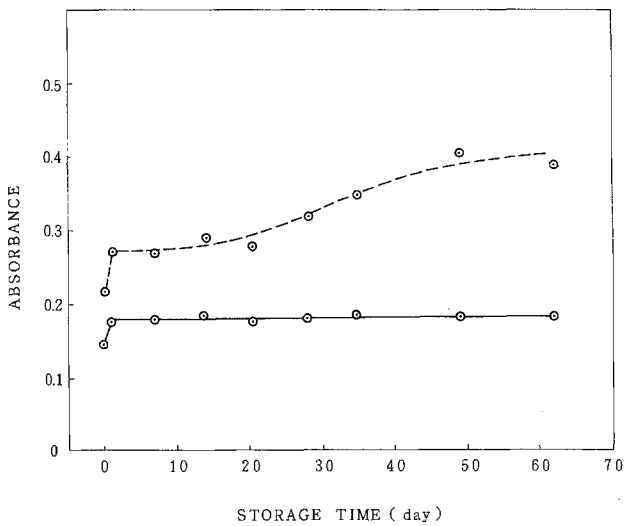

Fig. 4. Plots of FT-IR absorbance of WO_3 films, as a function of storage time in air at 25°C and 50% RH. Solid line is absorbance at 1600 cm^{-1} and dashed line is at 3400 cm^{-1}.

pressure during the evaporation may affect the bleaching reaction of the film rather than the coloration reaction.

Cyclic voltammograms of WO_3 films prepared under different conditions of total pressure in the chamber during the evaporation process were measured, in which P_{total} was controlled by N_2 gas introductions, and the cathodic current values at −200 mV *vs.* SCE of the cyclic voltammograms as a function of P_{total} are shown in Fig. 2b. The cathodic current increases with an increase of P_{total}. The packing density (PD) of the film decreases with an increase of P_{total}: for example, we confirmed that PD = 5.7 g/cm³ when $P_{total} = 1.2 \times 10^{-5}$ Torr and PD = 4.9 g/cm³ when $P_{total} = 1 \times 10^{-4}$ Torr. We assume that the random packing of substoichiometric tungsten oxide clusters leads to a large surface area and a system of communicating voids, so that the cathodic current increases apparently with increase in P_{total} rather than P_{H_2O}.

Water adsorption and chemical reaction during storage.—Infrared spectra of the films stored in air at 25°C and 50% (RH) are shown in Fig. 3. The broad peak at 3400 cm^{-1} is assigned to —O—H stretching and the sharp peak at 1600 cm^{-1} to the H—O—H deformation. The two peaks at 1600 and 3400 cm^{-1} change with time. The changes of the peaks are shown more in detail in Fig. 4 using absorbance values as a function of the film storage time, in which the peak at 1600 cm^{-1} increases remarkably, by about 25% with a storage of 24 hr but scarcely changes upon longer storage. On the other hand, the peak at 3400 cm^{-1} continues to increase with time after a remarkable increase of about 23% for 24 hr storage. From these results, we would say that physisorbed water content in the film increases with the storage in air at 25°C and 50% (RH), it comes to equilibrium within 24 hr, and that, besides OH groups of physisorbed water, the amount of chemisorbed OH groups continues to increase gradually with time.

^1H-NMR spectrum of the WO_3 film stored in air at 25°C and 50% (RH) for about 8 weeks and measured by the conventional FT-NMR (90 MHz) method is shown in Fig. 5A. For background data, the spectrum of the Al substrate film is shown in Fig. 5B indicating that the ^1H signal of the $Al(OH)_x$ and/or H_2O adsorbed on the glass tube are negligibly small. In Fig. 5A, two compositions of a small sharp peak and a large broad one were observed, and the chemical shift of the former small sharp peak (a) was assigned to be 5 ppm from TMS and the peak of the latter large broad spectrum (b) was located at 1.3 ppm on the lower frequency side than the sharp peak (a).

It is reasonable that the sharp peak (a) is associated with ^1H of free water such as the physisorbed water in the WO_3 layer and the broad peak is associated with ^1H of hydroxyl groups of the chemisorbed water such as $W(OH)_x$.

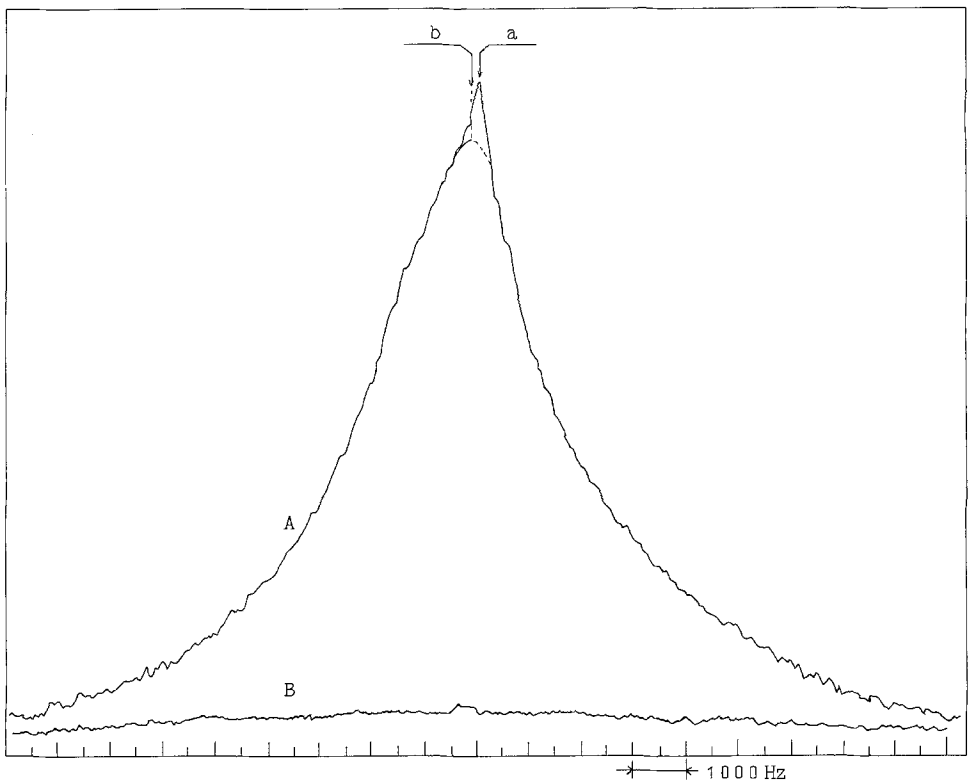

Fig. 5. ^{1}H-NMR data for WO_3 films (16,000Å on both sides of Al films). A: WO_3 data and B: Al film-data (background). The WO_3 films were stored in air for 8 weeks. The chemical shift of the small sharp peak (a) is 5 ppm from TMS, and the large broad peak (b) locates at 1.3 ppm lower frequency side than the sharp peak.

Therefore, we can also assume that from ^{1}H-NMR measurements, the WO_3 film stored in air for a long time includes large amounts of chemisorbed hydroxyl groups, besides a small amount of free water.

Cyclic voltammograms of the films stored under the same conditions as the infrared samples are shown in Fig. 6. In order to obtain a good comparison of the electrochemical properties to the infrared analyses, several initial coloration-bleaching cycles were used because the properties of the films are changed by a continuous potential cycling. The V-I curve of the film after the 24 hr storage showed a fast cathodic and anodic reaction [Fig. 6a, curve 2] which is associated with the increase of physisorbed water content in the film as shown in the infrared data, whereas cyclic voltammograms of the films stored in dry air atmosphere rarely changed and behaved similarly to as-deposited films. This phenomenon resembles the effect of water content in the films reported by Reichman and Bard (7), in which the current value increases with an increase in water content, but the potential of the cathodic reactions rarely shifts to the negative side. Therefore, physisorbed water during the storage contributes to a fast electrochemical coloration reaction, but not to the potential shift of the cathodic reaction.

The V-I curves of the films after longer term storage are shifted to more negative potential with time as shown in Fig. 6a, curves 3-6. The same effect of the V-I curve shift was observed with other various packing density samples (PD: 4.9-5.7 g/cm^3) prepared under the conditions of P_{total}: 1.6×10^{-4}-1.2×10^{-5} Torr, in which the potential (E_c) of the cathodic reactions of all virgin samples was almost +450 mV *vs.* SCE. E_c is used for convenience as the potential at which the cathodic reaction current begins to flow.

The E_c of the films shifted remarkably to the negative side by about 300 mV after 7 days' storage and gradually shifted by about an additional 100 mV after 77 days' storage as shown in Fig. 7. The E_c was independent of the potential scan rate of the measurements between 10 and 200 mV/sec; E_c of the films stored in dry air for long term did not shift with storage time. The potential shift values were not directly proportional to the increase of OH peak with infrared experiments, however, it is assumed that E_c shift phe-

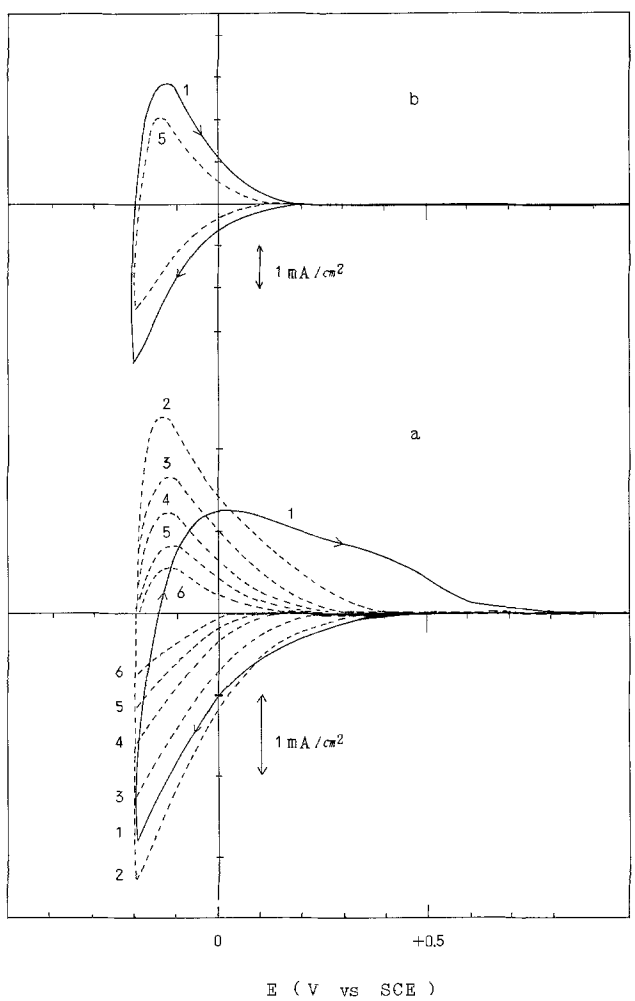

Fig. 6. Cyclic voltammograms at 0.2 V/sec for WO_3 films, (a) in PC electrolytes and (b) in 1M H_2SO_4 aqueous solutions. 1, as-deposited; 2, stored in air at 25°C and 50% RH for 24 hr; 3, for 72 hr; 4, for 144 hr; 5, for 384 hr; and 6, for 1854 hr.

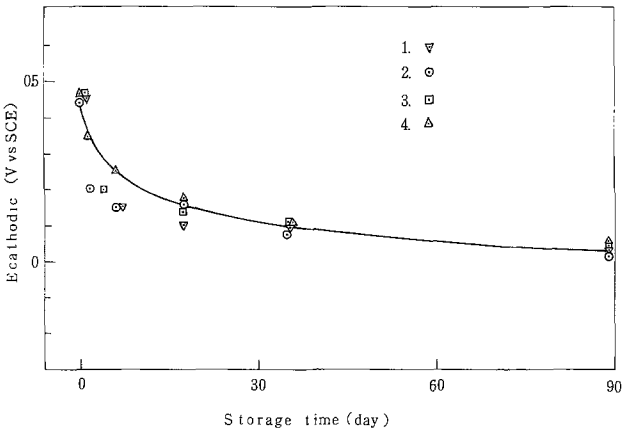

Fig. 7. Plot of starting potentials of the cathodic reactions at 0.2 V/sec scan rate for WO_3 films in PC electrolytes as a function of storage time. 1, P_{total} during the WO_3 evaporation was 1.15×10^{-4} Torr; 2, 4.3×10^{-5} Torr; 3, 3.5×10^{-5} Torr; and 4, 1.6×10^{-5} Torr.

nomenon would be attributed to the effect of the hydroxylated surface layer and is probably not based on the change of a composition of WO_x to WO_y.

As described above, PC electrolytes were used for the electrochemical measurements, because if aqueous electrolytes are used for these measurements, the large amount of water and protons in the electrolyte would obscure the observation of the behavior of H_2O and/or OH groups initially contained in the film. Moreover, it is not unexpected that the WO_3 film is easily hydroxylated by exposure in aqueous solutions. In fact, the potential (E_c) of cathodic reaction of the as-deposited films in a 1*M* H_2SO_4 aqueous solution was +200 mV *vs.* SCE and it corresponds to the potential of 250 mV more negative than that in the PC electrolyte, but the E_c of the film stored in air at 25°C and 50% RH for 384 hr was similar to that in the PC electrolyte. These relationships of V-I curves are shown in Fig. 6, in the case of measurements in aqueous electrolytes (Fig. 6b), the potential negative shift was only 100 mV with 384 hr storage in humid air and is a very small value compared with the result (350 mV) in PC electrolytes. Therefore, by using PC electrolytes for these measurements, the behavior of chemisorbed OH groups seems to be clearly separated from that of physisorbed water.

Consequently, we would say that OH groups are increased by hydroxylation and/or hydrolysis in air containing humidity as follows, as in the case of other metal oxides (14, 16, 17, 20)

$$\text{—O—W=O} + H_2O \rightarrow \text{—O—W(OH)—OH} \quad [2]$$

$$\text{—O—W—O—W—O—} + H_2O \rightarrow \text{—O—W—OH} + \text{HO—W—O—} \quad [3]$$

and that the hydroxylated surface layer causes the shift in the potential of the cathodic coloration reaction. Therefore, the hydroxylated tungsten oxide film loses the electrochromic coloration density under the same applied voltage for virgin tungsten oxide film. In order to prepare ECD cells having constant electrochromic properties, they must have controlled conditions of storage time and humidity.

Conclusion

The WO_3 film prepared under high water partial pressure in the chamber during evaporation has the fast anodic bleaching reaction, and the faster cathodic coloration reaction is caused by the high total residual gas pressure during the evaporation rather than the water partial pressure.

The water adsorbed from ambient air after film removal from the vacuum chamber contributes to fast cathodic and anodic reaction. However, the adsorbed water reacts gradually with WO_3 by hydroxylation and/or hydrolysis and then the hydroxylated film has a negative shift in the potential of the cathodic reaction, so that the electrochromic coloration density of the hydroxylated film is lost gradually with storage time.

Acknowledgments

We are grateful to Dr. M. Fukai, the director of the Material Research Laboratory for permission to publish the paper and for encouragement. We thank Dr. T. Morimoto and M. Kamikawaji, members of Techno-Research Department, for performing the infrared observations, and we also thank Dr. K. Matsushita, a member of Technical and Engineering Division of Nihon Denshi Company Limited, for performing the NMR observations and for helpful discussions.

Manuscript submitted Dec. 3, 1982; revised manuscript received *ca.* June 20, 1983.

Matsushita Electric Industrial Company, Limited assisted in meeting the publication costs of this article.

REFERENCES

1. S. K. Deb, *Appl. Opt. Suppl.*, **3**, 192 (1969).
2. C. J. Schoot, J. J. Ponjee, H. T. Van Dam, R. A. Van Doorn, and P. T. Bolwijn, *Appl. Phys. Lett.*, **23**, 64 (1973).
3. B. W. Faughnan, R. S. Crandall, and P. M. Heyman, *RCA Rev.*, **36**, 177 (1975).
4. J. D. E. McIntyre, G. Beni, and J. L. Shay, Abstract of the 20th EMC (Santa Barbara, 1978).
5. M. M. Nicholson and R. V. Galiardi, *SID 1978 Digest*, p. 24.
6. N. Yoshiike, S. Kondo, and M. Fukai, *This Journal*, **127**, 1496 (1980).
7. B. Reichman and A. J. Bard, *ibid.*, **126**, 583 (1979).
8. Y. Hajimoto, M. Matsushita, and S. Ogura, *J. Electron. Mater.*, **8**, 301 (1979).
9. R. Hurditch, *Electron. Lett.*, **11**, 142 (1975).
10. L. Pickelmann and P. Schlotter, Euro Display 81, Sept. 16-18, 1981, Proceeding of the first European display research conference (Munich, 1981).
11. H. R. Zeller and H. V. Beyeller, *Appl. Phys.*, **13**, 231 (1977).
12. T. C. Arnoldussen, *This Journal*, **128**, 117 (1981).
13. A. Deneuville, P. Gerard, and P. Billat, *Thin Solid Film*, **70**, 203 (1980).
14. M. Egashira, M. Nakashima, S. Kawasumi, and T. Seiyama, *J. Phys. Chem.*, **85**, 4125 (1981).
15. M. Nagao, *ibid.*, **75**, 3822 (1971).
16. E. De Pauw and J. Marien, *ibid.*, **85**, 3550 (1981).
17. M. Primet, P. Pichat, and M. V. Mathieu, *ibid.*, **75**, 1216, 1221 (1971).
18. T. Morimoto and H. Naono, *Bull. Chem. Soc. Jpn.*, **46**, 2000 (1973). T. Morimoto, M. Nagao, and F. Tokuda, *ibid.*, **41**, 1533 (1968).
19. H. P. Boehm, *Discuss. Faraday Soc.*, **52**, 264 (1971).
20. M. Egashira, S. Kawasumi, S. Kagawa, and T. Seiyama, *Bull. Chem. Soc. Jpn.*, **51**, 3144 (1978).

The Photoelectrochemical Oxidation of (100), (111), and ($\bar{1}\bar{1}\bar{1}$) n-InP and n-GaAs

P. A. Kohl,* C. Wolowodiuk, and F. W. Ostermayer, Jr.

Bell Laboratories, Murray Hill, New Jersey 07974

ABSTRACT

The photoelectrochemical oxidation of (100), (111), and ($\bar{1}\bar{1}\bar{1}$) n-InP and n-GaAs in several acidic solutions has been investigated. Specific interactions between the single crystal semiconductors and solvent selectively reveal crystal faces other than those originally exposed to the solvent. The relative stability of the n-InP faces is (111) > (100) > ($\bar{1}\bar{1}\bar{1}$). The first case of electron injection during the photoanodic dissolution of III-V compound semiconductors has been observed with (100) and ($\bar{1}\bar{1}\bar{1}$) n-InP. Nucleophilic attack by Cl^- or Br^- produce intermediates whose potential and kinetics allow electron injection into the semiconductor conduction band reducing the number of photons required for the reaction from six to four. The conditions for selectively etching smooth surfaces on (100) n-InP are discussed in detail along with the conditions for maintaining polished surfaces on n-InP(111) or A-face, which is difficult with conventional chemical polishes.

The mechanism, rate, and suppression of n-type III-V semiconductor oxidation plays a critical role in several scientific areas. Chemical oxidation of semiconductors is a well-known method of polishing and removing damage from III-V surfaces (1) and electrochemical etching (2-4) has been used to study crystal defects. The characterization (5-8) of the GaAs and InP semiconductor/aqueous solution interface and study of its photo-oxidation (9-14) has led to the design of stable photovoltaic cells for the conversion of optical power into chemical and/or electrical power (15-18).

More recently, the advent of solid-state devices based on III-V materials for use in optical communication and high speed electronic systems has created new interest in the etching and selective etching (19-22) of the semiconductors. For example, the photoelectrochemical etching of n-InP and n-GaAs has been used to: form integral lenses on 1.3 μm InP/InGaAsP LED's (23), separate LED's and photodetectors into individual devices from wafer form (24), produce long wavelength annular p-i-n photodetectors (25), and etch millimeter wave electron oscillators (26).

In such cases where the decomposition of the semiconductor is desirable, it is necessary to control the rate of etching and surface topography. In this report, the photo-oxidation of (111), (100), and ($\bar{1}\bar{1}\bar{1}$) n-InP and n-GaAs is explored in several acidic solutions. It has previously been found that etching is initiated by a hole at the surface and nucleophilic attack by the solvent (9-12), with all subsequent electron transfer steps also requiring holes except for Ge. It has been found in most cases that reactive intermediates capable of injecting electrons into the InP conduction band selectively expose crystal planes other than those initially exposed. Thus, smooth surfaces can only be etched when the reactivity of the various faces and the dissolution of both species of the compound semiconductor are nearly equal. The conditions for producing maximum smoothness are examined.

Experimental

The single crystals of GaAs and InP were obtained from Atomergic Chemicals (Long Island, New York) and chemically/mechanically polished. The (100) and ($\bar{1}\bar{1}\bar{1}$), or B-face which has phosphorus or arsenic atoms on the surface, were polished in a Br_2/methanol solution. The (111), or A-face which has only indium or gallium atoms on the surface was chemically/mechanically syton polished. The GaAs samples were Te doped except for the (100) sample which was Si doped. The InP samples were primarily doped with Sn, however, S and undoped n-InP(100) material were used for comparison. The doping density was less than $2 \times 10^{17}/cm^3$ except for the (100) n-InP(S) and n-InP (undoped) which were $1\text{-}2 \times 10^{18}/cm^3$ and $5\text{-}8 \times 10^{15}$, respectively.

Ohmic contacts were made to the crystals with a Ga/In alloy and the semiconductors were then mounted as electrodes. Silver paint was used to make electrical contact and the sides and back of the crystal were insulated with glycol phthalate wax.

The electrochemical measurements were made with a PAR (Princeton Applied Research, Princeton, N.J.) 173 potentiostat, 179 coulometer, and 175 programmer. The surface roughness was measured with a surface profiler.

An He-Ne laser was used in conjunction with an EG&G 450-1 radiometer and neutral density filters to obtain a known photon flux. The measurements were corrected for the reflective losses from the cell and the surface of the semiconductor to determine the photons absorbed. The absolute error is <10%. A tungsten-halogen lamp was used as the illumination source to uniformly etch large area electrodes for surface smoothness studies. The intensity was varied with neutral density filters.

Results

The current-voltage (I-V) behavior of the (100), (111), and ($\bar{1}\bar{1}\bar{1}$) faces of n-InP and n-GaAs were examined in several different acidic solutions under a variety of illumination conditions. Figures 1 and 2 show typical I-V curves for InP and GaAs, respectively. Only a small fraction of the electrode was illuminated by the laser in Fig. 1 and 2 and the total radiant power in μwatts is shown for each electrode.

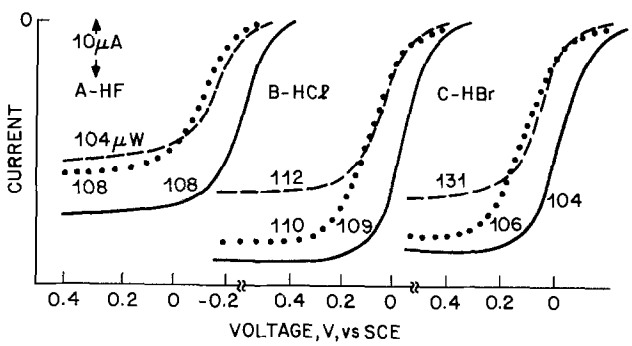

Fig. 1. Voltammogram of (———) n-InP(100), (– – –) n-InP(111), and (●●●●) n-InP($\bar{1}\bar{1}\bar{1}$) in (A) 2*N* HF, 0.5*N* KOH, (B) 2*N* HCl, and (C) 2*N* HBr. The radiant power (μwatt) of the He-Ne laser corrected for reflective losses is shown for each curve. The scan rate was 20 mV/sec.

* Electrochemical Society Active Member.
Key words: semiconductor, etching, photoetching.

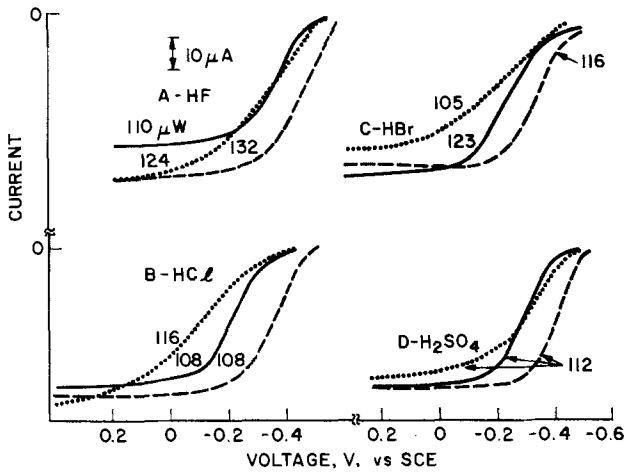

Fig. 2. Voltammogram of (———) n-GaAs(100), (– – –) n-GaAs(111) and (● ● ● ●) n-GaAs($\bar{1}\bar{1}\bar{1}$) in (A) 2*N* HF, 0.5*N* KOH, (B) 2*N* HCl, (C) 2*N* HBr, and (D) 1*N* H_2SO_4. The radiant power (μwatt) of the He-Ne corrected for reflective losses is shown for each curve. The scan rate was 20 mV/sec.

In buffered HF, the I-V curves were shifted to potentials more negative than the other acids because of the *p*H dependence of V_{FB} (8, 15). The I-V curve for n-InP (100) was consistently shifted to more negative potentials than the (111) and ($\bar{1}\bar{1}\bar{1}$) presumably because of changes in the flatband potential of the semiconductor arising from differences in the Helmholtz layer. Undoped n-InP ($N_D \sim 10^{16}$) behaved the same as high sulfur-doped n-InP ($N_D \sim 2 \times 10^{18}$).

A slightly more complicated trend was observed with GaAs. The (111) face was consistently shifted to more negative potentials than the (100) or ($\bar{1}\bar{1}\bar{1}$), and the relative shape of the ($\bar{1}\bar{1}\bar{1}$) curves varied. Also there is a greater change in onset potential with GaAs than that expected from changes in *p*H. The onset potential in H_2SO_4 is more negative than in HCl or HBr in spite of the similar *p*H. At potentials on the photocurrent plateau the current was directly proportional to radiant intensity over wide ranges. In HCl, the current range exceeded 100 mA/cm² whereas in HF and HBr only about 80 and 30 mA/cm², respectively, could be obtained before the rate of dissolution of the reaction products limited the current density. These current density limits were also dependent on agitation and electrolyte concentration.

The two most striking differences in the photooxidation of the various faces are the changes in the plateau current for the various faces and the topography differences of the semiconductor upon prolonged etching. Although all the currents in Fig. 1 and 2 were directly proportional to light intensity, the observed current was significantly different for the various InP faces in the solvents. The origin of the photocurrent can be summarized in Eq. [1] and [2]

$$\text{n-III-V (face A)} + x\text{hv} \rightarrow \text{n-III-V (face A)} + xh^+ + xe^- \quad [1]$$

$$\text{n-III-V (face A)} + xh^+ \xrightarrow{\text{solvent}} \text{n-III-V (face B)} + III^{3+} + V^{3+} + ye^- \quad [2]$$

Minority carrier holes, h^+, and electrons, e^-, are photogenerated in Eq. [1] and at potentials positive of V_{FB} they are forced to the semiconductor/solution interface where they participate in the photodissolution of the semiconductor, Eq. [2]. The number of photons participating in the oxidation of one III-V molecule is given by x, however, the total number of electrons transferred through the external circuit is $x + y$, where y is the number of nonphotogenerated electrons involved.

Electrons can be injected directly into the conduction band by reaction intermediates whose reduction potential is more negative than the conduction band-edge. The only previously reported electron injection has been for Ge (11, 12). The total number of electrons involved per molecule $x + y$ was measured to be 5.8 and 5.4 for n-InP(100) in HCl and HF, respectively. This is within experimental error of 6 electrons/InP previously reported (14). These values were independent of potential for voltages from 0.1 to 0.9V *vs.* SCE and currents from 10 to 20 mA/cm². Table I gives the number of photons per molecule of InP and GaAs assuming a six-electron process. The number of electrons ($x + y$) measured in the external circuit exceeded the number of photons absorbed by the n-InP (100) and ($\bar{1}\bar{1}\bar{1}$). Thus, the deviations in plateau currents observed in Fig. 1 are due to electron injection into the conduction band which does not require light.

In HCl and HBr, the etching of n-InP(100) and ($\bar{1}\bar{1}\bar{1}$) required only about 4 photons/InP and thus 2 electrons were injected. Less injection was observed in HF. The InP(111) required about 6 photons assuming a small fraction of the light was lost to recombination from photons absorbed outside the space charge region and surfaces defects. These values were consistent for laser intensities from 0.1 to 1.5 mW. The number of photons required for GaAs dissolution was relatively consistent for the different solvents and is reasonably close to the expected value of 6. The current decayed slightly with time during the GaAs dissolution process increasing the apparent number of photons required.

There was a definite correlation between the surface topography of the InP after etching ~20 C/cm² and the amount of electron injection as shown in Table I. The InP(100) and ($\bar{1}\bar{1}\bar{1}$) in HCl and HBr were significantly rougher than those etched in HF where the amount of electron injection was less.

A scanning electron micrograph of the InP(100), (111), and ($\bar{1}\bar{1}\bar{1}$) surfaces in HCl and HF are shown in Fig. 3. The two roughest surfaces gave the most electron injection; n-InP(111) and (100) in HCl as shown in Fig. 3A and B, respectively. They both appear velvety black to the eye. Figure 4A shows a cross section of the n-InP(100) shown in Fig. 3B cleaved along the (011) plane. There is 35°-40° angle between the planes exposed in Fig. 4A and the original surface. This strongly suggests that (110) planes are revealed (Fig. 4A) upon etching n-InP(100) in HCl. Upon prolonged etching of n-InP(100), >50 μm etched, very deep pits

Table I. Maximum number of photons/molecule for photodissolution of n-III-V, corrected for reflective losses

Crystal	Face	Solvent	Photons[a]	Roughness (μm)[b]
InP	100	HCl	4.1	0.5
InP	100	HF	5.2	0.04
InP	100	HBr	4.1	—
InP	111	HCl	6.3	0.1
InP	111	HF	6.9	0.04
InP	111	HBr	6.2	—
InP	$\bar{1}\bar{1}\bar{1}$	HCl	4.3	1
InP	$\bar{1}\bar{1}\bar{1}$	HF	6.4	0.25
InP	$\bar{1}\bar{1}\bar{1}$	HBr	4.2	—
GaAs	100	HCl	7.0	0.5
GaAs	100	HF	6.6	4
GaAs	100	HBr	7.0	—
GaAs	100	H_2SO_4	6.7	—
GaAs	111	HCl	7.2	3
GaAs	111	HF	7.1	1
GaAs	111	HBr	6.8	—
GaAs	111	H_2SO_4	7.2	—
GaAs	$\bar{1}\bar{1}\bar{1}$	HCl	7.2	0.5
GaAs	$\bar{1}\bar{1}\bar{1}$	HF	6.9	1
GaAs	$\bar{1}\bar{1}\bar{1}$	HBr	7.1	—
GaAs	$\bar{1}\bar{1}\bar{1}$	H_2SO_4	7.2	—

[a] Measured with He-Ne laser of 50 to 1500 μW.
[b] Minimum roughness after etching 30 C/cm² at a current density of ~15 mA/cm² with a white light source.

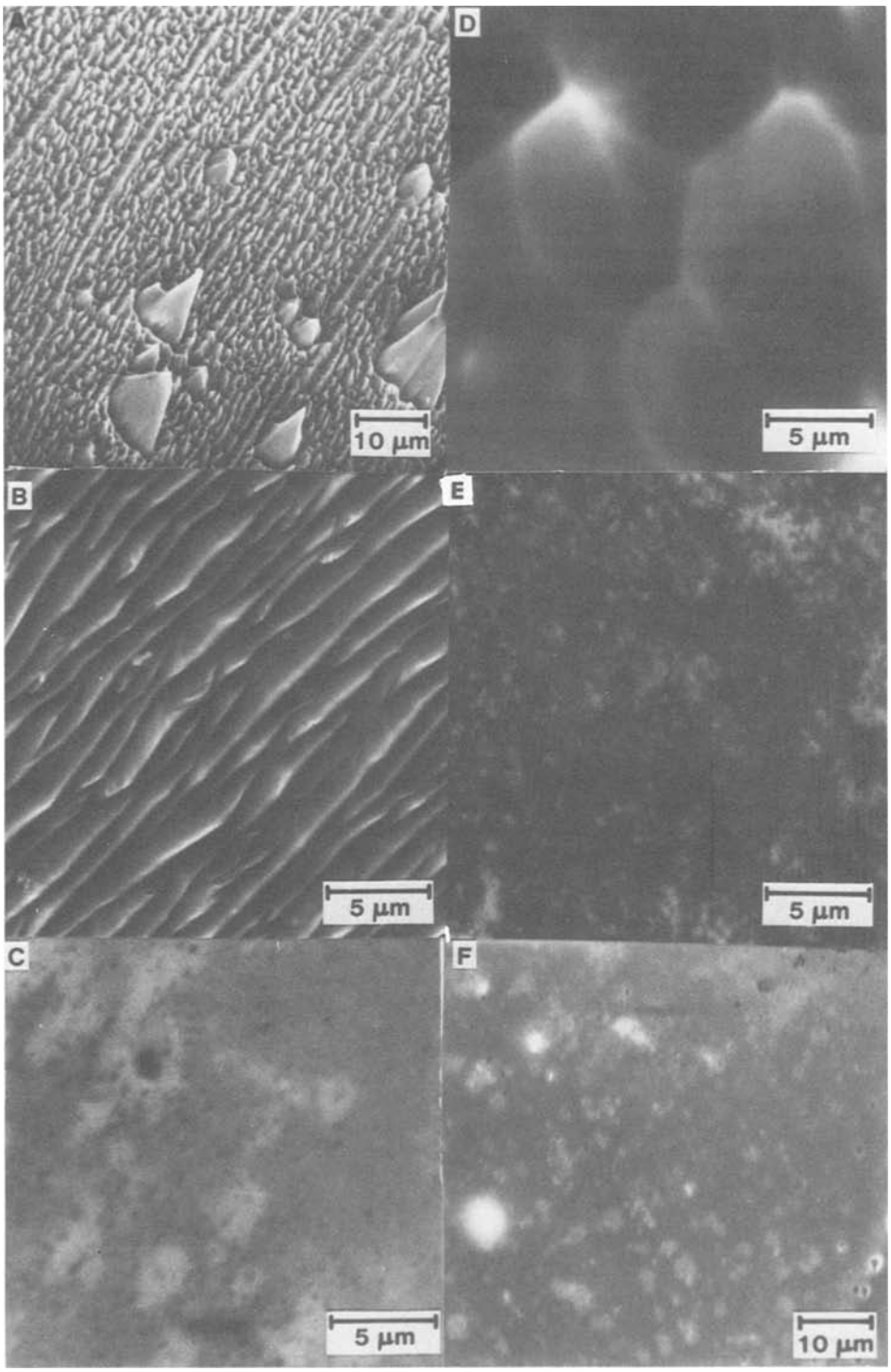

Fig. 3. Scanning electron micrograph of n-InP crystals etched ~30 C/cm² (A) ($\bar{1}\bar{1}\bar{1}$) in 2*N* HCl, (B) (100) in 2*N* HCl, (C) (111) in 2*N* HCl, (D) ($1\bar{1}\bar{1}$) in 2*N* HF, 0.5*N* KOH, (E) (100) in 2*N* HF, 0.5*N* KOH, and (F) ($\bar{1}\bar{1}\bar{1}$) in 2*N* HF, 0.5*N* KOH.

are formed as shown in Fig. 4B. Although it may appear that the peaks in Fig. 4B are not etching, there is no measurable decrease in the current density upon etching showing that the light is utilized as efficiently as when the etching started.

Crystal facets with a 52°-60° angle were observed upon etching n-InP($\bar{1}\bar{1}\bar{1}$) in HCl when cleaved along the (110) plane. This suggests that the ($1\bar{1}\bar{1}$) face is preferentially exposed. When the (111) is etched, Fig. 3C, the original surface is preserved. This indicates that no crystal plane is exposed preferential to the (111).

In HF, there is much less electron injection and very little preferential featuring of the crystal surface as shown in Fig. 3D, E, and F. The surfaces are quite smooth and the electrical current exceeded the photon flux only with the (100) surface of InP. The n-InP ($\bar{1}\bar{1}\bar{1}$) shows the only crystallographic featuring, Fig. 3D. In general, there was much less of a tendency to expose alternate crystal planes in HF as compared to HCl or HBr. Chemically, the important difference in the two types of solvents is the ability of Cl^- and Br^- to participate in In dissolution whereas F^- does not. This aspect will be discussed in greater detail in the next section.

The surface topography of the n-InP etched in HF is a function of the solution condition and etch rate. The n-InP(100) sulfur-doped ($N_D \sim 10^{18}$) was examined in detail because of its low defect density and hence device applications. Table II shows that the smoothest etched surfaces were produced at the lower current densities. The larger surface features in Table II were

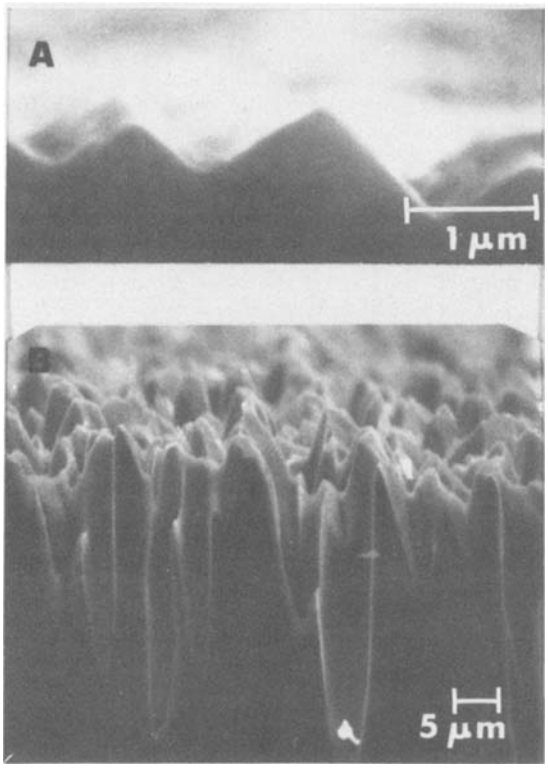

Fig. 4. Cross section of n-InP(100) etched in 2N HCl for (A) 30 C/cm² and (B) 200 C/cm².

generally from damage or defects and the small roughness value was indicative of a more ideal surface. This indicates that the smoothness is not dependent on the formation of insoluble surface films as in electropolishing which limit the rate of dissolution. The slow rate of oxidation allows adequate time for dissolution and solvation of the reaction products. As the current density increases, a rougher surface is observed as the limiting rate of dissolution is approached until finally a precipitate is observed on the InP surface for current densities >100 mA/cm². The current density is then no longer a linear function of light intensity.

Although the etch rate or current density is directly proportional to intensity on the limiting current plateau, nonlinear relationships have been found at other potentials on the rising portion of the I-V curve. At these potentials the semiconductor space charge region is thinner than the absorption depth of the incident radiation and only of a fraction of the photogenerated carriers migrate to the semiconductor-solution interface.

Figures 5 and 6 show the collection efficiency of the light as a function of intensity for InP in HF and HCl, respectively. The 100% value is that observed on the limiting plateau. At lower intensities the relative efficiency of the etching is greater than at high intensities. This nonlinearity is discussed in the next section. Knowledge of this behavior is of particular importance when specific profiles are to be etched into semiconductor surfaces (24).

Table II. Effect of current density on surface topography using n-InP(100) S-doped at 10^{18}/cm³ in 1.5N HF/0.5N KOH

Current density (mA/cm²)	Potential vs. SCE	Charge (C/cm²)	Roughness (μm)
101.4	+0.2	30.2	2
53.4	+0.2	30.0	2
37.5	+0.2	22.6	0.5
21.5	+0.2	29.8	0.4
11.5	+0.1	29.9	0.08
11.3	+0.2	30.0	0.10
5.0	+0.2	31.3	0.07

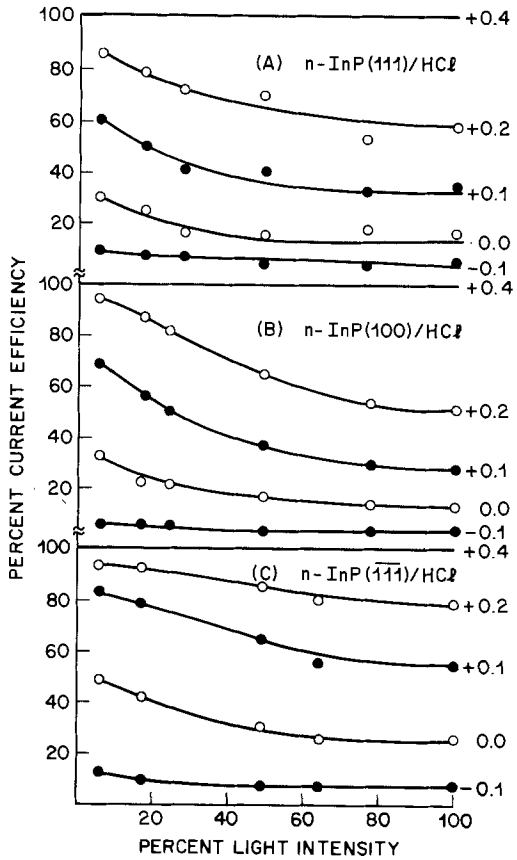

Fig. 5. Current efficiency (fraction of the plateau current) vs. light intensity at various potentials in 2N HCl for n-InP (A) (111), (B) (100), and (C) ($\bar{1}\bar{1}\bar{1}$). The maximum current density was (A) 131 mA/cm². (B) 120 mA/cm², and (C) 111 mA/cm² with the white light source used.

Discussion

The energetics of the semiconductor/solution interface have been extensively discussed and many specific solid-solvent interactions have been described which dramatically affect the junction (15). Small variations in the nature of the surface can affect the adsorption of ions on molecules and change the potential drop across the Helmholtz layer in solution. This change will shift the potential of zero charge in the semiconductor (V_{FB}). The negative shift of all GaAs electrodes in H_2SO_4 and the *p*H dependence of the electrodes are examples of changes in the Helmholtz layer.

The solid/solvent interaction takes on a more dynamic role as photo-oxidation occurs. The six-electron transfer reactions and accompanying chemical reactions, Eq. [2], are initiated by a photogenerated hole and nucleophilic attack (9-12).

$$A\text{-}B + h^+ + X^- \rightarrow A\text{-}X + B \qquad [3]$$

The more electropositive species A of the compound semiconductor A-B forms an intermediate species with the ligand X^- specific to the particular solvent system. Each of the six-electron transfer reactions is characterized by a free energy. The free energy of the overall reaction, Eq. [2], is composed of the individual potentials and thermodynamics of the chemical reactions. The importance of this overall reduction potential to the stabilization of liquid junction solar cells has been discussed elsewhere (16, 17).

The reduction potential of the reactant and products in Eq. [3] is strongly tied to the nucleophilic attack of X^-. It has been found that the dissolution of In^{+3} from In or In(Hg) electrodes in Cl^-, Br^-, I^-, or SCN^- solutions is via a ligand bridge intermediate (27-29). However, because F^- is nonpolarizable, it only forms solution complexes such as InF^{2+} and does not partici-

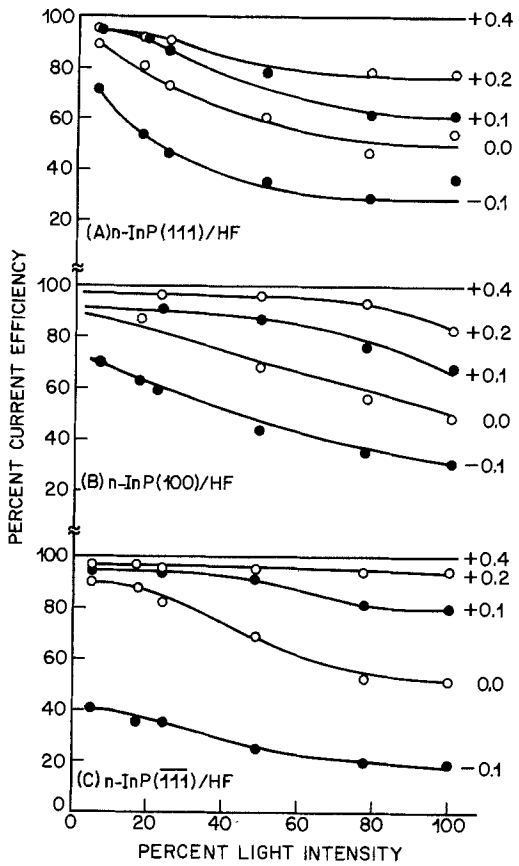

Fig. 6. Current efficiency (fraction of the plateau current) vs. light intensity at various potentials in 2*N* HF/0.5*N* KOH for n-InP (A) (111), (B) (100), and (C) (111). The maximum current density was (A) 100 mA/cm², (B) 89 mA/cm², and (C) 88 mA/cm² with the white light source used.

pate in the dissolution intermediate. A similar effect appears to be responsible for the electron injection and resulting roughness with n-InP. The P-rich face, n-InP (111), is the most susceptible to attack and dissolution by halogenated solvents (1). The surface In has the least number of bonds to the lattice and an In-rich (111) surface is exposed upon etching (111) in Cl^- or Br^-. Also, electron injection in these solvents shows that the reduction potential of the intermediate is stabilized or shifted to more negative voltages. The absence of nucleophilic attack by F^- makes the In on the (100) and (111) faces similar in dissolution rate and hence less electron injection and less preferential exposure of a different crystal face is observed.

When the n-InP(100) face is exposed to the solvent, the (110) crystallographic face is preferred in HCl. The large amount of electron injection (two of the six electrons in Eq. [2]), again indicates the relative stability of the intermediate in Cl^- and Br^-. Upon etching the In-rich (111) face no electron injection or crystallographic exposure of other faces is observed. The order of reactivity in Cl^- or Br^- is the same as that found in chemical etches: (111) > (100) > (111).

The absence of electron injection with GaAs and all other semiconductors studied thus far, except Ge, is possibly because of the more negative potential of the conduction bandedge and probability of forming intermediates such as In(I). Specular surfaces are maintained upon etching InP when the rates of dissolution of both species in the compound semiconductor are comparable and the relative stability of the faces is nearly equal. Buffered HF appears to meet these requirements and yet maintain oxide dissolution. Thus, the hole initiated etching of (100) and (111) InP maintains smooth surfaces. This is in contrast to chemical etchants which cannot polish (111) InP.

The rate of etching is directly proportional to the hole concentration at the surface, Eq. [2], even when electron injection occurs for intermediate species. However, potentially nondesirable deviations from linearity occur on the rising portion of the I-V curve. The collection efficiency decreases for several reasons. First, any uncompensated *IR* drops in the electrode or electrolyte make the actual electrode potential more negative than that applied. In this situation, the field within the semiconductor is reduced and the space charge region is thinner. Second, photogenerated carriers increase the net free carriers within the space charge region and decrease its depth relative to the absorption length of light. Thus, a greater percent of the carriers will be generated outside the space charge region at higher intensities. Third, any recombinations which are dependent on the concentration of electrons and holes consume a greater fraction of the carriers at higher intensities because of their increased concentration.

The differences in solid/solvent interaction can be of particular significance with polycrystalline materials where many faces are exposed simultaneously. The collection efficiency of light, stability, and reaction energetics are nonuniform across the surfaces. Further, it points out the importance of grain boundaries because this is the location where perturbations in the solid merge.

Conclusions

The mechanism and energetics of the n-GaAs and n-InP photoinitiated oxidation is dependent on the hole concentration at the semiconductor/solution interface and specific interactions with the solvent. Smooth profiles can be etched into n-type III-V single crystal surfaces if the rate of dissolution of the two species and reactivity of the faces is similar. Specular surfaces can be etched on n-GaAs and n-InP crystals including the (100) and (111) or A-face which is difficult to do by other chemical means. Crystal faces other than those originally used can be selectively exhibited. This is accompanied by electron injection into the conduction band of the semiconductor because ligand bridging by Cl^- and Br^- forms intermediate species whose potential is more negative than the potential of the conduction bandedge.

Acknowledgments

The authors gratefully acknowledge R. H. Burton and S. Nakahara for their many helpful discussions. The support of R. R. Buckley, D. K. Hindermann, and D. E. Koontz is also gratefully recognized.

Manuscript submitted Dec. 17, 1982; revised manuscript received June 15, 1983.

Bell Laboratories assisted in meeting the publication costs of this article.

REFERENCES

1. B. Tuck, *J. Mater. Sci.*, **10**, 321 (1975).
2. M. M. Faktor and J. L. Stevenson, *This Journal*, **125**, 621 (1978).
3. C. R. Elliott and J. C. Regnault, *ibid.*, **128**, 113 (1981).
4. A. Yamamoto, S. Tohno, and C. Uemura, *ibid.*, **128**, 1095 (1981).
5. T. Ambridge and M. M. Faktor, *J. Appl. Electrochem.*, **4**, 135 (1974).
6. R. L. Van Meirhaeghe, F. Cardon, and W. P. Gomes, *Ber. Bunsenges. Phys. Chem.*, **83**, 236 (1979).
7. F. El Guibaly, K. Colbow, and B. L. Funt, *J. Appl. Phys.*, **52**, 3480 (1981).
8. A. M. Van Wezemael, W. H. LaFlere, F. Cardon, and W. P. Gomes, *J. Electroanal. Chem.*, **87**, 105 (1978).
9. H. Gerischer, *Ber. Bunsenges. Phys. Chem.*, **69**, 578 (1965).

10. H. Gerischer, *This Journal*, **113**, 1174 (1966).
11. H. Gerischer and W. Mindt, *Electrochim. Acta*, **13**, 1329 (1968).
12. H. Gerischer, *Surf. Sci.*, **13**, 265 (1969).
13. A. Yamamoto and S. Yano, *This Journal*, **122**, 260 (1975).
14. I. G. Erusalimchik and D. M. Levin, *Elektrokhimiya*, **16**, 1854 (1980).
15. S. R. Morrison, "Electrochemistry at Semiconductor and Oxidized Metal Electrodes," Plenum Press, New York, (1980) and references therein.
16. A. J. Bard and M. S. Wrighton, *This Journal*, **124**, 1706 (1977).
17. H. Gerischer, *J. Electroanal. Chem.*, **82**, 133 (1977).
18. S. M. Park and M. E. Barber, *ibid.*, **99**, 67 (1979).
19. F. Kuhn-Kuhnenfeld, *This Journal*, **119**, 1063 (1972).
20. R. W. Haisty, *ibid.*, **108**, 790 (1961).
21. R. M. Osgood, Jr., A. Sanchez-Rubio, D. J. Ehrlich, and V. Daneu, *Appl. Phys. Lett.*, **40**, 391 (1982).
22. D. J. Ehrlich, R. M. Osgood, Jr., and T. F. Deutsch, *ibid.*, **36**, 698 (1980).
23. F. W. Ostermayer, Jr., P. A. Kohl, and R. H. Burton, *ibid.*, **43**, 642 (1983).
24. P. A. Kohl, R. H. Burton, F. W. Ostermayer, Jr., and C. Wolowodiuk, *IEEE Electron Device Lett.* (In preparation).
25. S. R. Forrest, P. A. Kohl, R. Panock, E. Yanowski, J. C. DeWinter, and R. E. Nahory, *ibid.*, **edl-3**, 415 (1982).
26. D. Lubzens, *Electron Lett.*, **13**, 171 (1977).
27. L. Popisil and R. DeLevie, *J. Electroanal. Chem.*, **25**, 245 (1970).
28. A. M. Bond, *This Journal*, **119**, 1503 (1972).
29. V. V. Losev and A. I. Molodov, in "Encyclopedia of Electrochemistry of the Elements," Vol. VI, Chap. 1, A. J. Bard, Editor, Marcel Dekker, New York (1976).

Technical Note

Contact Hole Formation in Integrated Circuits Using Ion Beam Nitriding

Jayant K. Bhagat and John R. Troxell

General Motors Research Laboratories, Electronics Department, Warren, Michigan 48090-9055

A method of opening contact holes through phosphosilicate glass (PSG) and thermally grown silicon dioxide to the underlying diffused source-drain regions and diffused polysilicon gates of MOSFETs (metal oxide semiconductor field effect transistor) which minimizes the problem of contact blooming and resultant gate to source or drain shorts is described.

In the fabrication of MOSFET integrated circuits, making contact holes to the source, drain, and gate is the last step prior to metallization. Improper contact holes can cause either an open circuit or a short circuit between adjacent circuit elements in an otherwise properly processed device or circuit. Due to this fact, contact holes are opened carefully and elaborate processing techniques are used in the industry. We have found that the presently available techniques are neither simple nor completely reliable. In this note, an alternative technique for opening the contact holes is presented.

The problem in opening the contact holes lies with the differential etch rate of the phosphosilicate glass (PSG) and the thin thermal silicon dioxide (SiO_2) layers lying over the diffused region of interest. To visualize the situation, consider the basic MOSFET structure shown in Fig. 1. A thin layer of SiO_2 grows in the contact regions during the source-drain junction formation. Subsequently, ~1 μm of PSG is deposited and densified on top of this SiO_2 layer. In order to make electrical contact to the device, vias must be opened through both of these insulating layers. Conventionally, this is accomplished using a patterned photoresist layer and a hydrofluoric (HF) acid-based etchant. In such etchants, the etch rate of PSG is typically 10-15 times faster than that of thermally grown SiO_2 (1). Consequently, after etching PSG, the etchant not only etches the thermally grown oxide, but severely undercuts the photoresist. Two problems can be identified due to this: (*i*) shorts between source and gate or drain and gate, and (*ii*) discontinuities in the metal interconnection layer over the PSG. The former problem can be aggravated due to alignment error of the contact opening photomask relative to the polysilicon gate. In the latter case, the overetched PSG can cause discontinuity in the overlying lines, depending upon the severity of etching. Also, metal lines which are continuous can be subsequently attacked by metal etchant entrapped between the metal and the overetched PSG.

To alleviate this situation, we realized that it is best not to have to etch the PSG and the thin thermal SiO_2 simultaneously for opening the contact holes. In our modified process, the PSG layer is etched first, and then the thin thermal SiO_2 layer is removed by ion beam sputtering and replaced by a thin silicon nitride layer in the contact windows. The entire contact opening process is performed with a single photolithography step.

The process sequence is to deposit 1 μm of PSG over the entire wafer after source-drain and polygate diffusions, and then densify (1) it at 900°C for 20 min in a nitrogen ambient. After the required photolithography step using negative photoresist, the PSG layer is etched with buffered hydrofluoric (BHF) acid. The etch rate of PSG is critically dependent upon the phosphorus content in the PSG (1); with about 6% phosphorus in the PSG, a 1 min etch in BHF can remove about 1 μm of PSG. No attempt is made to etch through the thermal SiO_2 at this step.

A collimated nitrogen ion beam from a Kaufman-type ion source is then employed to erode the remain-

Key words: ion beam nitriding, contact hole opening, reflow oxidation, MOSFET.

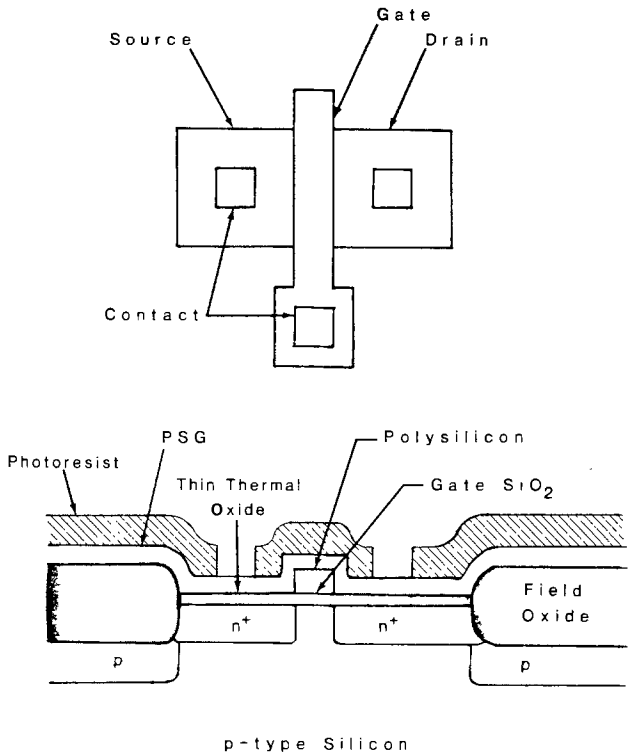

Fig. 1. Plan view of the MOSFET (top). Cross section of the MOSFET. Note that the contact of the polysilicon gate is not shown in the cross section (bottom).

ing thermal SiO_2 layer and to subsequently form a thin (~10 nm) layer of silicon nitride in the opened contact regions. The 15 cm diam, 2.1 keV, 1 mA cm^{-2} ion beam removes about 60 nm of SiO_2 per min, while the erosion rate of silicon is only about 25 nm per min (Fig. 2). During this process, the PSG is protected by the layer of photoresist which was used to pattern the PSG layer. The selectivity in the sputtering rates results from the fact that the nitrogen can chemically bond to the silicon (2, 3), but apparently does not replace oxygen in the silicon-oxygen bonds of the oxide layer. Thus, when the ion beam penetrates through the oxide layer, it generates a silicon nitride layer in the surface of the underlying silicon (4-6). This silicon nitride layer then acts as an oxidation mask for the contact regions during the subsequent PSG reflow operation in a wet oxygen ambient.

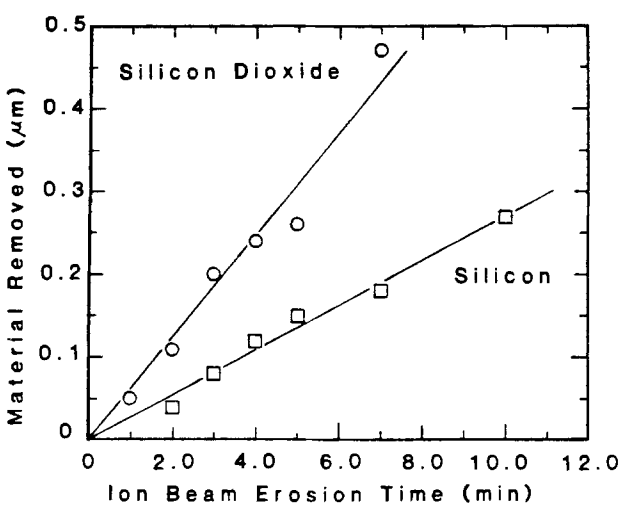

Fig. 2. Nitrogen ion beam sputtering rates for silicon and silicon dioxide. Incident ion beam; 2.1 keV, 2 mA cm^{-2}, neutralized by a hot wire filament.

It should be noted that in order to produce the silicon nitride layer, significant heating of the sample wafers is unavoidable. A typical process employs a 2 min exposure to the 2.1 keV, 1 mA cm^{-2} neutralized ion beam, yielding an incident flux of ~8×10^{17} nitrogen atoms per unit area. This flux is sufficient to produce a silicon nitride film after milling through a thermal SiO_2 layer ~60 nm thick (4, 6). In addition, however, this process generates more than 180W in a 7.6 cm diam wafer. Even with a water cooled sample holder, this can result in severe deterioration of positive photoresists such as AZ 1350J[1] and AZ 111H[1]. Negative photoresist (Kodak 747[2]) shows much less susceptibility to heat damage and, thus, was employed in these studies. Also, in many cases it is not necessary to keep the photoresist in place during the nitridation process (the nitrogen ion beam would only remove ~200 nm of PSG in those regions, which could be compensated for by a thicker initial PSG deposition). In the future, though, it will be necessary to develop techniques to allow for the use of both negative and positive photoresist in this contact opening process.

Following the ion beam nitridation process, the wafers are slowly pushed into the furnace (temperature ~1050°C) in a wet O_2 ambient for 10-20 min for PSG reflow. During the reflow process, the sharp edges

[1] Shipley Company, 2300 Washington St., Newton, MA 02162.
[2] KTI Chemicals, Inc., 1170 Sonora Court, Sunnyvale, CA 94086.

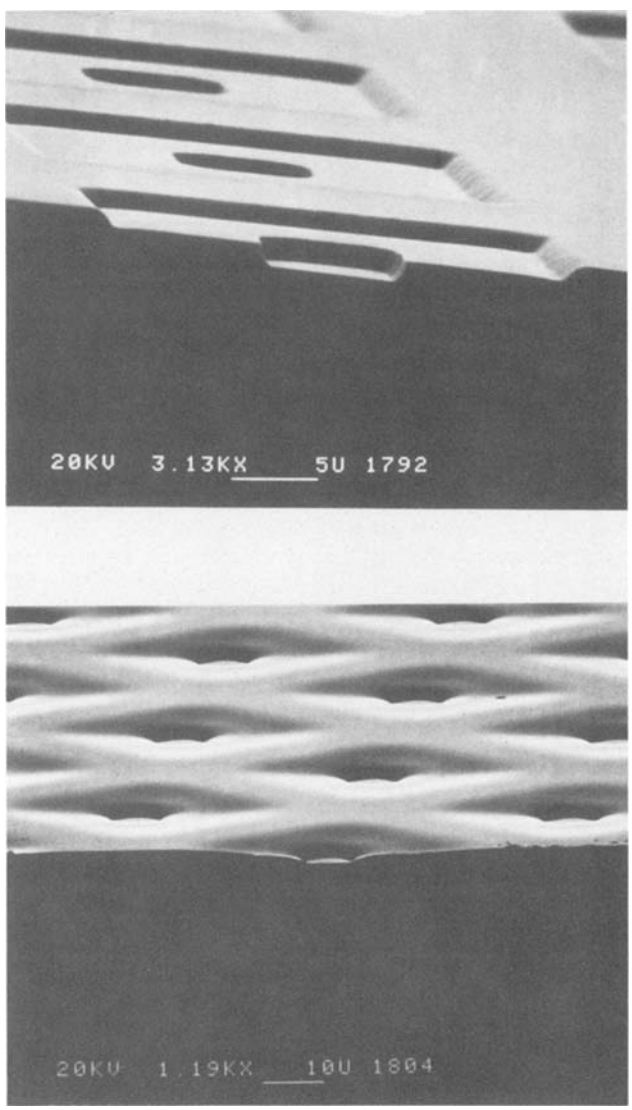

Fig 3. VDMOS device electromicrograph (mag. 3.13 KX) after etching densified PSG (top). VDMOS device electromicrograph (mag. 1.19 KX) after PSG reflow (bottom).

of the PSG are rounded off. Additionally, in the case of considerable mask misalignment, a silicon dioxide layer (~200 nm) grows over the polysilicon sidewalls, further reducing the chance of interelement metallization shorts. The silicon nitride layer is then removed, prior to metallization, by etching for 30 sec in a CF_4 plasma. (Alternatively, an H_3PO_4 etch can be used.)

The reliability of this contact opening technique has been demonstrated by its successful use in the fabrication of vertical double-diffused metal oxide semiconductor (VDMOS) power MOSFET devices, each of which requires up to 5000 individual contact hole openings. The quality of the contacts on these devices can be seen in the electron micrographs of Fig. 3. Figure 3a shows the cross section after etching densified PSG, while Fig. 3b shows the same region after PSG reflow. The smooth contouring of PSG edges which prevents metal line breakup is clearly visible.

Summary

A new technique for opening contact holes during integrated circuit fabrication is described. This method requires only a single photolithography step to etch the contact holes. Following chemical etching of the PSG, a high current density nitrogen ion beam is employed to sputter off the remaining thermal silicon dioxide layer and to implant a thin silicon nitride layer in the contact regions. This silicon nitride layer acts as an oxidation mask during the PSG reflow step and is removed prior to metallization in a brief (30 sec) CF_4 plasma etch. The resulting devices have minimal undercutting and as a result no metallization discontinuities. In addition, during the PSG reflow operation, any exposed silicon surface such as the polysilicon gate sidewalls are oxidized, thereby reducing the possibility of interelement metallization shorts. This method has been used successfully to make VDMOS power transistors with up to 5000 contact hole openings.

Manuscript submitted June 6, 1983; revised manuscript received *ca.* July 12, 1983.

General Motors Research Laboratories assisted in meeting the publication costs of this article.

REFERENCES

1. W. Kern, *RCA Rev.*, **37**, 55 (1976).
2. N. Lieske and R. Hezel, *Thin Solid Films*, **85**, 7 (1981).
3. R. Hezel and N. Lieske, *This Journal*, **129**, 379 (1982).
4. M. Ramin, H. Ryssel, and H. Kranz, *Appl. Phys.*, **22**, 393 (1980).
5. T. Y. Chiu, H. Bernt, and I. Ruge, *This Journal*, **129**, 408 (1982).
6. J. C. Hui, T. Y. Chiu, S. S. Wong, and W. G. Oldham, *IEEE Trans. Electron Dev.*, **ed-29**, 554 (1982).

JOURNAL OF THE ELECTROCHEMICAL SOCIETY

ACCELERATED

—BRIEF COMMUNICATIONS—

NOVEMBER 1983

DCEL Thin Films of ZnS:Mn with Amorphous Chalcogenide Control Layers

M. S. Waite,* J. Williams, and J. Siddle

School of Materials Science and Physics, Thames Polytechnic, London, SE18 6PF, England

Current research in electroluminescent display systems favours thin films in order to reduce the slow degradation found in powder based systems containing mobile copper (1,2). Hot electron excitation of Mn in breakdown fields (about 10^8 V m^{-1}) is responsible for the luminescence in ZnS:Mn thin films and in DC excited devices the avalanche current is controlled by an accompanying layer where the field is lower than in the ZnS film. In this role, cermets(3), ZnSe(4), GaAs(5), Cu-coated ZnS powder(6) and the oxides MnO_2(7) and Ta_2O_5(8) have been used. We describe below the characteristics observed when various chalcogenide glasses are used to control the avalanche current in ZnS:Mn thin films(9).

EXPERIMENTAL

Experimental cells, Fig. 1, were prepared by sequential e-beam deposition of Mn doped ZnS films (0.5 ⟶ 1.0 μm) and amorphous chalcogenide films (1 ⟶ 2 μm) onto tin oxide coated glass substrates. The ZnS films were deposited at 150°C, annealed at 450°C, and contained 0.33 ± 0.03 m/o Mn. The chalcogenide films were deposited at room temperature.

The chalcogenides chosen covered a range of compositions and included the following: $Cu_8As_{42}Se_{50}$ (G1), $Ge_{33}As_{12}Se_{55}$ (G2), $Ge_{13}As_{10}Sb_{10}Se_{67}$(G3) and $Ge_{20}Sb_{30}Se_{50}$ (G4). In addition, films were evaporated from a mixture of G3 + 10% w/w Sb, (G5). The chalcogenides were synthesised prior to evaporation by melting the constituents in evacuated ampoules in a rocking furnace at 900°C and quenching in air. All formed glassy boules except G4. EDAX analysis of the evaporated films revealed no trace of Cu in G1 films, whilst a general feature was a lower Se content than in the bulk sample (Table 1).

Brightness/voltage and current/voltage characteristics obtained using the test circuit in Fig. 1 are shown in Figs. 2 and 3. Current/voltage curves for ZnS:Mn alone are not shown since these films invariably break down at or below the threshold for electroluminescence. The presence of a chalcogenide layer inhibits catastrophic breakdown above the electroluminescence threshold. For an arbitrary luminescent brightness of 10^{-3} Ft.L. the threshold field was found to be in the region 1.0 ⟶ 1.4 x 10^8 V m^{-1}.

Figure 2 and Table 1 demonstrate that the chalcogenide films can tolerate fields of at least 4 x 10^7 V m^{-1} before avalanching or catastrophic breakdown (indicated by loss of the chalcogenide and overlying electrode). Samples containing both As and Sb (particularly G5) showed the highest ultimate conductivity before breakdown. Switching from a high to low resistivity state was only encountered once (in a G3 sample) in over 200 devices. Generally, a smooth but non-linear increase in current with applied voltage was observed, with significant photoconductivity in G5. Under white light illumination of 60 Lux photocurrent gains of up to 20 were observed, the gain disappearing as the breakdown field is approached (Fig. 3).

DC excitation of ZnS:Mn films backed with the chalcogenide layers produced typical Mn emission at 580 nm. The brightness/voltage and current/voltage plots for three of the chalcogenide backed panels are given in Fig. 3.

---

* Electrochemical Society Active Member.

Key words: Electroluminescence, ZnS:Mn, Amorphous, Chalcogenide.

In general, stable electroluminescence was found in a voltage interval between the luminescence threshold (corresponding approximately to the ZnS breakdown field) and ultimate breakdown of the device. Maximum efficiencies of 2 x 10^{-4} w/w have so far been observed, with G2, G3 and G5 glasses. These efficiencies are comparable to those reported for other DC thin film devices incorporating evaporated ZnS(4). The brightness increases linearly with current up to current densities of about 100 A m^{-2}. The level of brightness which can be obtained in practice depends upon the current sustained without catastrophic breakdown. Consequently, the chalcogenides which show the greatest super-linear increase in current and the highest ultimate breakdown strength are required. Of the materials examined, G2 and G5 appear the most promising. Co evaporation of the Sb modifier element with G3 was found to give higher current densities before breakdown than G3 glass melted and equilibrated with the additional Sb before evaporation. Ovshinsky and colleagues report similarly that chalcogenide glasses co-sputtered with Ni show higher conductivity than glasses containing dissolved Ni(10).

A comparison of the current/voltage characteristics of G2 and G5 with and without ZnS indicates that the breakdown strength of the glasses is not apparently affected by the presence of ZnS. However, G1 and G4 glasses tended to breakdown prematurely with loss of material when combined with the ZnS film. These glasses were less stable in the presence of the noise and hot electron injection associated with the avalanching ZnS. An additional advantage of the use of these chalcogenides is the increased contrast obtained compared to that observed with d.c. powder el panels. The fundamental absorption edge is at $\sim$ 650 nm for these glasses and is even further into the red than the As_2S_3 insulating films used in the Sigmatron ACEL device(11).

The high field conduction processes in the chalcogenide films, the effect of photoconductivity and the stability of the electroluminescent devices will be reported later.

We are grateful to the Science and Engineering Council (UK) for financial support for this project, and to British Technology Group for assisting with the Patent Application.

REFERENCES

1. J. Kirton, Handbook of Semiconductors. Vol. 4, C. Hilsum (ed). North Holland (1980) Review.

2. R. Mach, G.O. Muller, Phys.Stat. (a) 69, 11 (1982) (Review).

3. J.J. Hanak, Japn.J.Appl.Phys.Supp. 2, pt. 1, 809 (1974).

4. J. Doi, H. Ohnishi, I.T. Leyashu, Y.Hamakawa. J.Appl.Phys. 51, 4555 (1980).

5. H. Ohnishi, Y. Hamakawa, Japn.J.Appl.Phys. 17, 1275 (1978).

6. C.J. Alder, A.F. Fray, C. Hilsum, P.Lloyd. Displays, 151, (1980).

7. A.F. Cattell, B. Cockayne, F. Dexter, J. Kirton, P.J. Wright, Proc. 1982 Intern. Display Conf. (IEEE), P.25 (1982).

8. R. Tornquist, T.O. Tuomi, J.Lumin. 24/25, 901 (1981).

9. M.S. Waite, J.L. Williams, J. Siddle, UK Patent Application No. 8,235,221 (10th December, 1982).

10. R. Elasch, M. Izu, K. Sapru, T.Anderson, S.R. Ovshinsky, H. Fritsche, Proc. 7th Intern.Conf. Amorphous and Liquid Semiconductors (1977) p.524. W. Spear (ed). Edinburgh (1977).

11. G. Steele, E. Soxman. U.S.Pat. 3,560,783, February (1971).

Manuscript submitted May 23, 1983.

Thames Polytechnic assisted in meeting the publication costs of this article.

Table 1. Characteristics of the chalcogenide films

Chalcogenide	Composition of Evaporated Films	Mean Breakdown Field (10^8v m^{-1})
G1	$As_{60}Se_{40}$	0.8
G2	$Ge_{37}As_{12}Se_{51}$	0.6 ⟶ 1.3 Depending on thickness
G3	$Ge_7As_{16}Sb_7Se_{70}$	0.6
G4	$Ge_{24}Sb_{30}Se_{46}$	0.4 ⟶ 0.6
G5	$Ge_9As_{16}Sb_{15}Se_{60}$	0.8

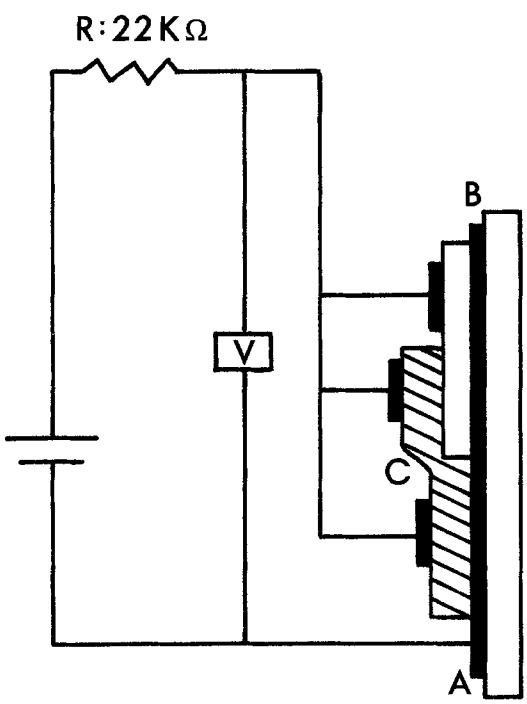

Fig.1. Electroluminescent test cells with Al back electrodes : 10^{-5} m^2 areas
A : Tin oxide electrode
B : ZnS:Mn
C : Chalcogenide
V : High impedance DVM

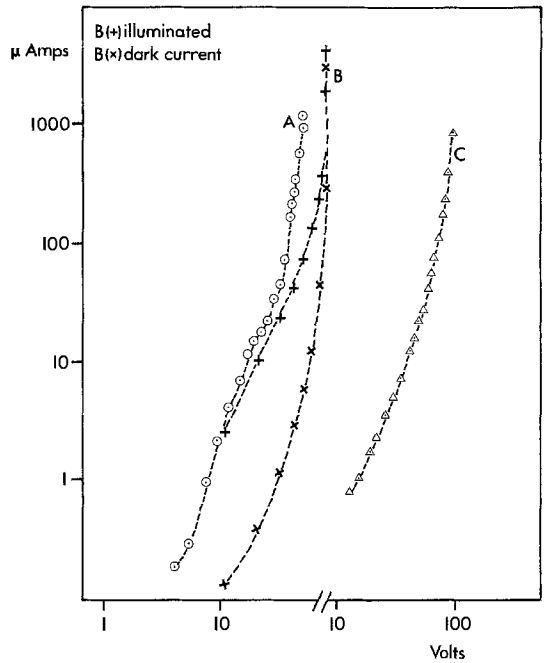

Fig.2. Current/voltage characteristics for various chalcogenides
A : TF 203 : G4 (1.2 μ m)
B : TF 189 : G5 (1.0 μ m)
C : TF 114 : G2 (1.0 μ m)

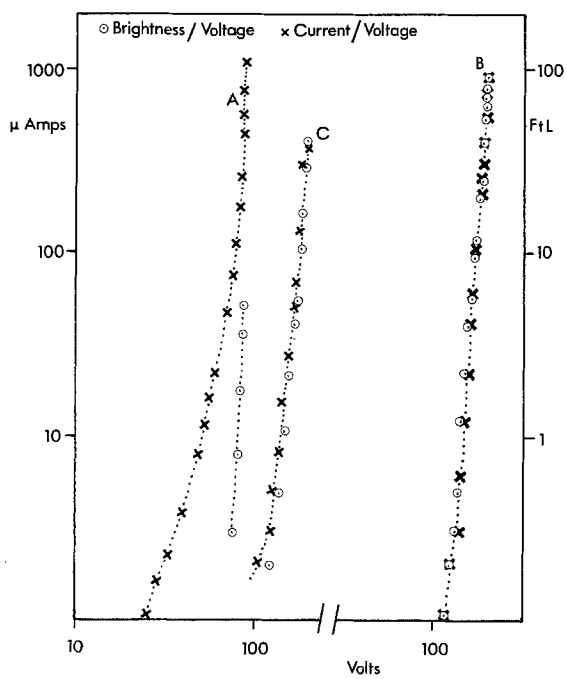

Fig.3. Brightness/voltage, current/voltage characteristics for ZnS:chalcogenide cells
A : TF 203, G4 + ZnS:Mn (0.5 μ m)
B : TF 189, G5 + ZnS:Mn (0.8 μ m)
C : TF 114, G2 + ZnS:Mn (0.9 μ m).

Importance of Interatomic Spacing in Catalytic Reduction of Oxygen in Phosphoric Acid

V. Jalan* and E. J. Taylor*

Giner, Incorporated, Waltham, Massachusetts 02154

INTRODUCTION

General trends between geometrical-electronic properties and electrocatalyst activity have been the subject of many papers and review articles (1-4). In fact, much of the interest may be traced to the "volcano relationship" between the logarithm of the reaction rate and the free energy of adsorption, ΔG_{ads}, derived from electrochemical principles for the hydrogen evolution reaction (5,6). Assuming that ΔS_{ads} remains constant, many workers have observed the "volcano type" behavior between the logarithm of the reaction rate and various quantities which may be rationalized to be proportional to ΔH_{ads}. This assumption should be viewed with some caution however, as a "compensation" effect has been observed (7) between ΔS_{ads} and ΔH_{ads} which tends to negate the beneficial effects of optimizing ΔH_{ads}. Volcano relationships have been reported when the percent d-band character has been used to estimate the relative value of ΔH_{ads} (8,9), where the percent d-band character is calculated from a relationship given by Pauling (10). It is interesting to note that the single bond radius of the metal (a parameter relating to geometrical factors) is used to calculate the percent d-band character, an electronic characteristic. The importance of the geometric characteristic interatomic spacing has been demonstrated for the hydrogen evolution reaction (11) and for several bimolecular reactions (12), with a maximum reaction rate occuring at an optimum interatomic distance. However, it is never clear if a correlation based on interatomic spacing means that this property is the underlying cause of the catalytic effect, or if it is related to some other property which is itself the cause.

We believe that geometric considerations (specifically, the nearest-neighbor distance) play a major role in the oxygen reduction reaction and propose an explanation based on reaction models compatible with the experimental data. The kinetic parameters of the oxygen reduction reaction in hot, concentrated phosphoric acid on highly dispersed platinum have been rationalized in terms of the rate determining step being the rupture of the O-O bond via various dual site mechanisms (13,14). Clearly, if any of these mechanisms is operative, the spacing between the sites at which the O-O bond rupture is occuring would play a critical role in the overall reaction rate and an optimum spacing should exist. At larger then optimum spacings, dissociation would have to occur prior to adsorption and at smaller than optimum spacings repulsive forces would retard dual site adsorption. We propose that the distance between nearest-neighbor platinum atoms on the surface of a supported catalyst is not ideal for dual site adsorption of O_2 or "HO_2" and that the introduction of foreign atoms which reduce the platinum nearest-neighbor spacing would result in higher oxygen reduction activity. Following the work of Turovskii (15), one may be able to determine from quantum chemical calculations the critical O-O bond interatomic distance and hence the optimum Pt-Pt separation for bond rupture.

To test the plausibility of the nearest-neighbor distance/activity correlation required by the dual site mechanisms, we have plotted the activation energies for O_2 reduction on various metal surfaces in H_3PO_4 measured by Appleby (3) versus the logarithm of the nearest-neighbor distances of the electrocatalysts (16). The results are shown in Figure 1, and a good linear correlation is apparent. It is noteworthy that Au and Ag, not members of the platinum group metals, follow the trend so well.

*Electrochemical Society Active Member.

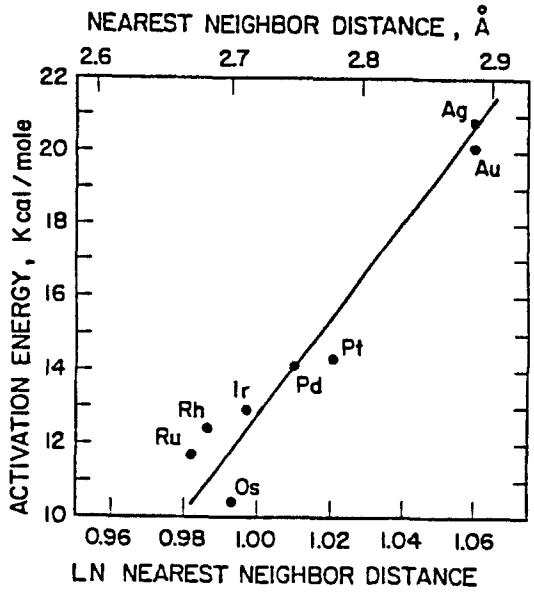

Fig. 1. Activation Energy for Oxygen Reduction Versus Electrocatalyst Near-Neighbor Distance

From these considerations, the catalyst to be sought is one with, among its other properties, a comparatively lower interatomic distance. Presumably, platinum has the necessary "other properties" and the effect of interatomic distance should be apparent in platinum rich alloys in which the platinum character is maintained and interatomic spacing varies.

EXPERIMENTAL

Various platinum alloy electrocatalysts supported on carbon were prepared as described earlier (17-20). The general technique was to precipitate an oxide or hydroxide of the alloying component onto platinum supported on carbon black which had been dispersed in water. The material was then heated to 900°C under inert or reducing atmosphere, to effect alloying via the following reaction;

$$Pt + MO_X + (X/2)C \rightarrow Pt\text{-}M + (X/2)\ CO_2 \quad [1]$$

The platinum carbide electrocatalyst was prepared (21,22) by heat treating the 10% platinum on carbon material under flowing carbon monoxide at 350°C for twenty minutes, followed by one hour under flowing nitrogen at 900°C, and then an additional twenty minutes under flowing carbon monoxide at 350°C.

All the platinum alloy electrocatalysts were fabricated into gas diffusion electrodes of about 0.5 mg platinum per cm^2 and 40% Teflon sintered at 350°C. The particle sizes/surface areas of the materials were determined from transmission electron microscopy (TEM), cyclic voltammetry (CV), and x-ray diffraction (XRD). The XRD analysis was also used used for structure and lattice parameter determination. The oxygen reduction activity in 100% H_3PO_4 at 200°C of the various electrocatalysts was determined using the floating half cell technique and the dynamic hydrogen reference electrode.

RESULTS AND DISCUSSION

The XRD analysis indicated that all the electrocatalysts maintained the fcc structure of the platinum precursor and the (111), (200), and (220) diffraction peaks were used to determine the lattice parameters and the nearest-neighbor distances of the electrocatalysts. Recently, Ross (23,24) reported enhanced oxygen reduction activity in phosphoric acid for various Pt-Group IVB and VB intermetallics (Pt_3V, Pt_5Ta, Pt_4Zr, and Pt_4Hf) with an ordered fcc structure of the $AuCu_3$ type. Since there were no superlattice lines in our XRD patterns, we must conclude that the alloy electrocatalysts reported here are solid solutions and not intermetallic compounds. The particle sizes and surface areas determined from TEM, CV, and XRD of all the electrocatalysts were in good agreement. The specific surface area of the platinum standard was 135 m^2/g and that of the platinum alloy electrocatalysts ranged from 70-90 m^2/g. The specific activity for oxygen reduction measured as current density at 900 mV was used to compare the performance of the electrocatalysts.

In Figure 2, a plot of specific activity for oxygen reduction versus the nearest-neighbor distance determined from x-ray diffraction for the various platinum alloy catalysts is presented. A linear relationship is in fact observed--the Pt-Cr alloy electrocatalyst exhibited the highest electrochemical activity for oxygen reduction and the smallest nearest-neighbor distance. The obvious question

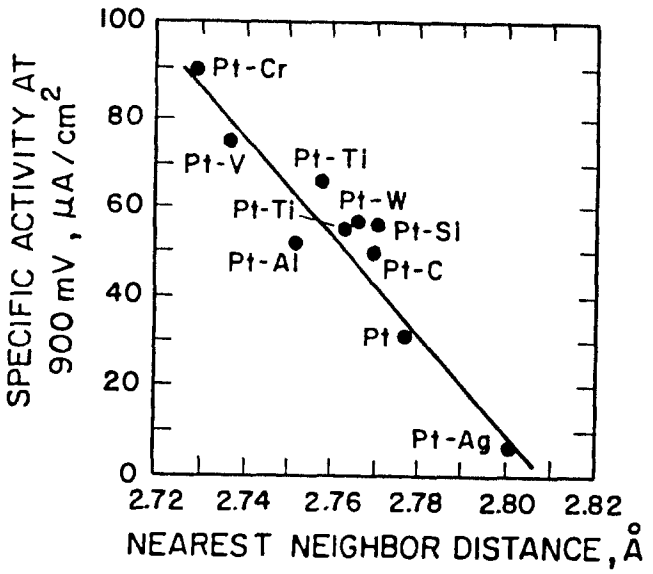

Fig. 2. Specific Activity for Oxygen Reduction vs. Electrocatalyst Nearest-Neighbor Distance.

is how much additional activity may be achieved by further decreasing the nearest-neighbor distance before the curve turns down? The other interesting point is the listing of Pt-C as an alloy, with higher electrocatalytic activity than platinum. Previously, Jalan (21,22) had reported increased activity and stability of CO treated supported platinum and postulated the formation of Pt-C alloy but without any evidence. We have now demonstrated the existence of platinum carbide in the fine particle form as evident from the XRD analysis which revealed a contraction in the lattice parameter of the CO treated platinum to 3.909 Å (compared to 3.918Å for untreated platinum). Although Pt-C is not reported to exist in bulk form, Konig (25) had similarly observed Pt-C in a thin film and very recently researchers at Univ. of California have demonstrated the existence of platinum carbide (26).

In this communication, a correlation between the nearest-neighbor distance and the oxygen reduction activity of various platinum alloys is reported. A composite analysis shows that our data on supported platinum alloys are consistent with Appleby's data on bulk metals with respect to specific activity, activation energy, preexponential factor and percent d-band character. The relationship of these factors will be discussed in detail in a complete paper to follow. We recognize that factors such as changes in surface structure, surface free energy, oxidation potential and oxygen interaction with the alloying material may alter the electrochemical characteristics of platinum upon alloying. Notwithstanding the above, the nearest-neighbor distance correlation for the platinum alloys presented here has demonstrated the importance of interatomic spacing in oxygen reduction in hot concentrated phosphoric acid. Furthermore, this correlation is theoretically consistent and provides a guideline for selection of candidate platinum alloy catalysts for future research. Specifically, based on lattice parameter information (27) the next best platinum alloy catalyst to prepare will be Pt-Ni, Pt-Co and combinations thereof. Further work is required to determine the optimum Pt-Pt distance and to ascertain the effect of intermetallic compound formation on the oxygen reduction reaction.

ACKNOWLEDGEMENT

The authors gratefully acknowledge the experimental assistance of B. Morriseau. This work is being supported by NASA under Contract Number DEN3-294.

REFERENCES

1. P. Delahay, "Double Layer and Electrode Kinetics", pp. 242-268 Interscience, New York, (1965).
2. J. O'M. Bockris and H. Wroblowa, J. Electroanal. Chem. 7, 428(1964).
3. A.J. Appleby, Catalysis Reviews 4, 221(1970).
4. P. Stonehart and P. Ross, Catal. Rev. Sci. Eng., 12(1), 1-35(1975).
5. R. Parsons, Trans. Faraday Soc. 54, 1053-63(1957).
6. B.E. Conway and J. O'M. Bockris, J. Chem. Phys. 26, 532(1956).
7. A.J. Appleby, Proc. Workshop Electrocatalysis of Fuel Cell Reactions, Electrochem. Soc. PV 79-2, Brookhaven National Lab, May 15-16,(1978).
8. A.J. Appleby, This Journal 117, 1157 (1970).
9. A. Kuhn, H. Wroblowa, and J. O'M. Bockris, Trans. Faraday Soc., 63, 1958(1967).
10. L. Pauling, "The Nature of the Chemical Bond", p. 420 Cornell Univ. Press, 3rd edition, New York, (1973).

11. H. Leidheiser, J. Am. Chem. Soc., 71, 3634-36 (1949).
12. J. O'M. Bockris and S. Srinivasan, "Fuel Cells: Their Electrochemistry", p. 314 McGraw-Hill, New York, (1969).
13. E. Yeager, EPRI Report EM-505 (1977).
14. W. Vogel and J. Baris, Electrochem. Acta., 22, 1259(1977).
15. A.A. Turovskii, R.V. Kucher and N.A. Turovskii, Theor. Eksp. Khim., 12, 606(1976).
16. J. Anderson, "Structure of Metallic Catalysts", p. 446 Academic Press, London, (1975).
17. V. Jalan and D. Landsman, U.S. Patent 4,186,110, Jan. 29, 1980.
18. V. Jalan, D. Landsman and J. Lee, U.S. Patent 4,192,907, March 11, 1980.
19. V. Jalan, U.S. Patent 4,202,934, May 13, 1980.
20. D. Landsman and F. Luczak, U.S. Patent 4,316,944, Feb. 23, 1982.
21. V. Jalan, Extended Abstract #356, Montreal Electrochem. Soc. Meeting.
22. V. Jalan and C. Bushnell, U.S. Patent 4,137,373, Jan. 30, 1979.
23. P.N. Ross, National Fuel Cell Seminar, San Diego, CA, July 14-16, 1980.
24. P.N. Ross, EPRI Final Report for Contract RP 1200-5, March 5, 1980.
25. H. Konig. Naturierss. 38, 154(1951).
26. M. J. Whitcomb, U. Dahmen, and K. H. Westmacott, Acta Met., 31 743(1983).
27. W.B. Pearson, "Handbook of Lattice Spacings and Structures of Metals," Vol. 1, p. 821, Pergamon Press, New York (1958).

Manuscript submitted May 9, 1983; revised manuscript received ca. Sept. 19, 1983.

Giner, Incorporated assisted in meeting the publication costs of this article.

JOURNAL OF THE ELECTROCHEMICAL SOCIETY

ELECTROCHEMICAL SCIENCE AND TECHNOLOGY

DECEMBER 1983

Accelerated Testing of Additives in Zinc Plates of Nickel Zinc Cells

C. Biegler, R. L. Deutscher, S. Fletcher,* S. Hua,[1] and R. Woods

CSIRO, Institute of Energy and Earth Resources, Division of Mineral Chemistry, Port Melbourne, Victoria 3207, Australia

ABSTRACT

An accelerated test for zinc plates in nickel/zinc cells has been developed. Using the test, a large number of additives have been screened to see if they improve zinc utilization over 100 deep discharge cycles of the zinc plate. Three additives have yielded statistically significant results. These are Bi_2O_3, CdO, and acetylene black. The mechanism of capacity loss of zinc plates was investigated by scanning electron microscopy. It was found that the major mechanism of capacity loss was a decrease in the porosity of active material.

For the last 15 years there has been a major effort around the world to develop nickel/zinc batteries for electric vehicles. Much of this work is summarized in reports (1-9), research papers (10-27), and patents (28-58). The United States Department of Energy has described the specifications which need to be met by electric vehicle batteries, and these are (*i*) a selling price $\leq$ \$70 (kw-hr)$^{-1}$ (1981 U.S. dollars), (*ii*) a specific energy $\geq$ 56 W-hr · kg^{-1}, (*iii*) a specific power $\geq$ 104 Wkg^{-1}, and (*iv*) a cycle life $\geq$ 800 cycles at 80% depth of discharge (59). Unfortunately, nickel/zinc batteries do not meet the cycle life specification, mainly because zinc plates lose capacity when they are cycled under deep discharge conditions. A detailed mechanism for this capacity loss has not been established. However, some correlation has been suggested between plate failure and shape change of the active mass of the plate material (1-16).

The need to improve zinc plates in nickel/zinc batteries has led many researchers to consider whether the incorporation of organic and inorganic additives might help. Some additives that have recently been patented include lead, cadmium and tin salts (28-33), hydroxyalkylcelluloses (29), cadmium metal (30), carbon fibers (34), cobalt hydroxide (35), tin metal (36), inorganic titanates (37), calcium oxide (38), bismuth oxide (38), and polytetrafluoroethylene (39). However, the role of these additives is by no means certain, even their efficacy has been questioned (60), and in some cases the patent literature describes experiments in which samples of data were obviously too small for valid conclusions to be drawn.

Recognition of this problem led us to develop an accelerated test procedure to screen additives. This provided enough data for proper statistical methods to be applied. Of course, there are always difficulties in predicting cell performance from accelerated tests because conditions must be used that are not encountered in practical applications (27, 61, 62). Nevertheless, we found that our test, which concentrated on zinc electrode behavior, was sufficient for the "relative efficacy" of additives to be determined. We describe this test in the present work. We also show that the additives Bi_2O_3, CdO, and acetylene black significantly enhanced zinc utilization under the conditions of the test.

* Electrochemical Society Active Member.

[1] On leave from: Department of Chemistry, Shandong University, Jinan, Shandong, China.

Key words: battery, energy storage, additives, reliability.

Experimental

Chemicals.—The ZnO and KOH were AR grade; additives were reagent grade.

Nickel electrodes.—Commercial paste-type nickel electrodes were obtained from Eagle-Picher Industries (USA) and Yardney Electric Corporation (USA). Pocket-type electrodes were supplied by Chloride Batteries (Australia). All electrodes were fitted with nickel wire leads by spot-welding.

Separators.—Separator materials were obtained from Celanese Plastics Corporation (USA). Most cells were constructed using 3 or 6 layers of Celgard 3401 microporous polypropylene film having a nominal thickness of 25 μm and a porosity of 38% with a 0.02 μm effective pore size. However, some tests were conducted with Celgard K317, a nickel-coated separator, which was used between two layers of Celgard 3401.

Electrolyte absorber.—A non-woven polypropylene felt (Webril M-1450, The Kendal Corporation, USA) with a thickness of 0.13 mm and porosity approx. 60% was used as an electrolyte absorber.

Cell specifications and assembly.—An exploded view of the cell is shown in Fig. 1. The cell case consisted of

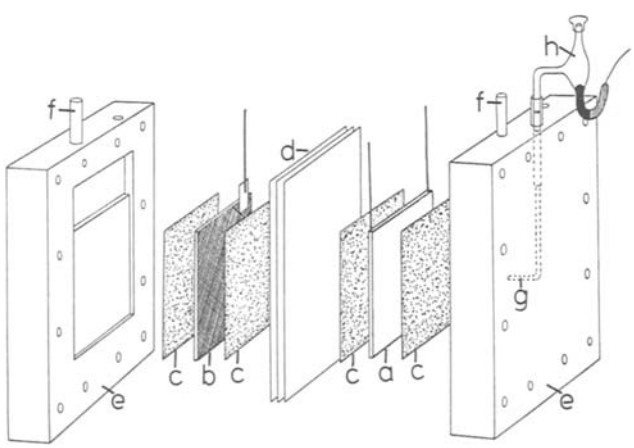

Fig. 1. Exploded view of cell. (a) Zinc electrode (5 × 5 cm), (b) nickel electrode, (c) polypropylene felt, (d) separator layers, (e) acrylic cell housing, (f) vents, (g) Luggin capillary, (h) Hg/HgO reference electrode.

two 1.6 cm thick acrylic plates. The zinc electrode (25 cm^2) was housed in a 0.8 mm deep recess and the nickel electrode in a 2.5 mm deep recess. Both cell compartments were fitted with vents which led via glass bulbs to a common air-lock.

Hg/HgO reference electrodes were connected via a Luggin capillary to the back faces of zinc electrodes. The narrow horizontal portion of the capillary was tightly packed with polypropylene felt to prevent penetration by gas bubbles.

Zinc electrodes were prepared *in situ* as follows: a thick aqueous paste of ZnO and additives was spread evenly onto a current collector (silver-plated expanded copper mesh) which was placed on a sheet of polypropylene felt in the cell recess. Another layer of felt was laid over the paste and the electrode was lightly compressed and dried under vacuum over silica gel. The electrode loading was 0.13 ± 0.03g cm^{-2} with a theoretical capacity of 86 ± 20 mA-hr cm^{-2}.

Some experiments were carried out with commercial zinc electrodes removed from nickel/zinc batteries (Eagle-Picher Type NZS-30); these were placed in the cell recess between two layers of polypropylene felt.

Nickel electrodes were sandwiched between polypropylene felt sheets. Occasionally, polyethylene sheets were used as packing at the back of these to ensure they were tightly compressed when the 12 bolts holding the cell together were tightened. In assembled cells the separator layers were sealed between the two cell halves with a thin layer of epoxy resin.

The electrolyte.—The electrolyte was 6.9M KOH with no added zincate. It was prepared by diluting a concentrated stock solution which had been standardized with HCl using a pH meter. The volume of electrolyte that was added to each cell was ~5 ml.

Equipment and cycling procedures.—Cells were charged and discharged at 20 mA cm^{-2} constant current using Amel Model 565 galvanostat-electrometers (Amel, Italy). The electrometers were connected across the zinc and reference electrodes so that the potential of zinc electrodes could be cycled between −1.46 and −1.15V *vs.* Hg/HgO. Zinc potentials, together with cell voltages, were recorded on YEW 3066 pen recorders. All cells were filled with electrolyte at least 8 hr before cycling, and all were cycled in water baths at 25°C.

A recurrent problem in nickel/zinc research has been the occurrence of dendrites at high cathodic overpotentials on zinc plates. In most cases we were able to avoid these by setting the cathodic switching potential below −1.46V. However, much lower potentials could not be used because the nucleation peak in the charging curve (see Fig. 7) meant that premature switching of our electronics occurred. In the case of plates made of pure zinc oxide, we found that dendrites grew even below −1.46V, which meant they were virtually unavoidable using our charging regime.

Results and Discussion

Accelerated testing.—Previous workers have accelerated battery tests by using higher-than-normal temperatures and higher-than-normal charge and discharge rates (61, 62). However, we did not use these methods because of the risk of introducing failure modes not evident under normal battery operation, thermal degradation, for example. Instead we devised a new test based on the known properties of nickel/zinc cells.

Nickel/zinc cells are designed with an excess of zinc oxide on their zinc plates, so that their cell capacities are initially limited by the capacities of the nickel plates, *i.e.*, they are nickel-limited. Consequently, they only become zinc-limited after about 100 deep discharge cycles. However, we knew that if zinc plates could be deep discharged on every cycle then cell collapse would be accelerated. So to speed things up we cycled cells not between specified cell voltages, as is usual, but between specified zinc potentials instead. This had the advantage that zinc plates were discharged to 100% depth on every cycle, and also differences in nickel plate performance between experiments were minimized.

Relationship between capacity and cycle number.—Figures 2 and 3 show how the measured capacities of nickel/zinc cells varied when they were cycled at constant current between (A) specified zinc electrode potentials and (B) specified cell potentials. It can be seen that similar relationships were observed for both commercially manufactured zinc plates (Eagle-Picher) and those pasted in our own laboratories. As expected, in the early stages the zinc plate capacities were lower for cycling according to regime (B) than (A), and this resulted in extended cycle lives. This was because of the nickel limitation discussed above.

In the accelerated tests, in which zinc electrodes were cycled between specific potentials, it was found that plate capacities decreased linearly with the logarithm of the cycle number (Fig. 2A and 3A). This relationship was found in most cases, except for a small minority of plates which had capacities that stayed constant for 6-12 cycles before decreasing logarithmically in the usual way. Eventually, after 100 cycles, all cells exhibited roughly constant residual capacities but these were too low to be useful. For example, even for the best zinc plates the residual capacities were typically less than 13% of those recorded on the first cycle.

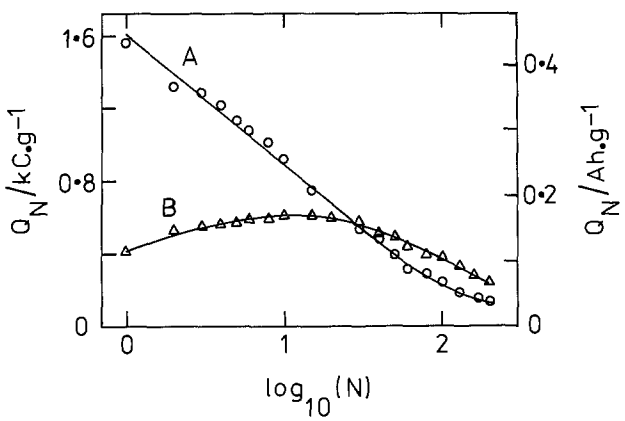

Fig. 2. Graphs of capacity *vs.* log (cycle number) for commercial ZnO electrodes cycled galvanostatically at 20 mA cm^{-2}. (A) Electrode cycled between potential limits −1.46 and −1.15V *vs.* Hg/HgO. (B) Cell cycled between voltage limits of 2.0 and 1.2V.

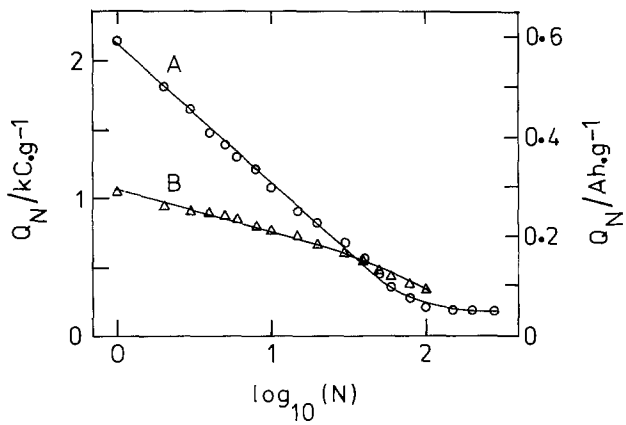

Fig. 3. Graphs of capacity *vs.* log (cycle number) for laboratory-pasted ZnO electrodes, without additives, cycled galvanostatically at 20 mA cm^{-2}. (A) Electrode cycled between potential limits of −1.46 and −1.15V *vs.* Hg/HgO. (B) Cell cycled between voltage limits of 2.0 and 1.2V.

Measurement of plate performance.—In order to investigate the effects of different additives on zinc utilization we defined a "cumulative capacity," expressed by the formula

$$\text{Cumulative capacity} = \sum_{N=1}^{N=n} Q_N \qquad [1]$$

Where N was the cycle number, Q_N was the capacity recorded on cycle N, and n was the total number of cycles considered. Q_N was always normalized with respect to the initial plate loading of ZnO, measured in grams. We usually truncated the sum in Eq. [1] at $n = 100$, which was felt to be a natural choice given the form of the Q_N *vs.* log N functions (Fig. 2A and 3A). However, for a few special purposes (discussed later on) we truncated the sum at $n = 10$.

Effect of additives on plate performance.—The cumulative capacities of zinc plates, in those cells which did not fail by dendritic shorting before 100 cycles, are listed in order of decreasing rank in Table I. Note that mercuric oxide was generally added to zinc plates to inhibit self-discharge. It was included in many, though not all, of our cells. Three types of nickel plate were used but these showed no significant effects on zinc plate cumulative capacity. It can be seen from Table I that the additives bismuth oxide and acetylene black were dominant at the top of the list. Most other additives appeared at scattered locations throughout the list because of large variations in cumulative capacity even for formally identical zinc plate compositions.

The scatter of experimental data in Table I meant that statistical analysis was needed to determine if the effects of additives were significant. We therefore applied t-tests to the data (63), to see how the effects of various additives compared with those of a control group consisting of those additives that showed no significant beneficial effect. The results are presented in Table II. In order to simplify comparisons, variations in the levels of additives were ignored. Only three additives showed statistically significant beneficial effects; bismuth oxide, cadmium oxide, and acetylene black. Differences between these additives were not statistically significant when they were considered at the 0.05 probability level.

It would have been of interest to compare cumulative capacities of plates containing various additives with cumulative capacities of a control group containing pure zinc oxide. Unfortunately, cells containing pure zinc oxide plates failed rapidly because of dendrite penetration of separators. In fact, only one cell containing pure zinc oxide lasted over 100 cycles, and therefore it could not reasonably be claimed to be representative. However, it turned out that t-tests could be applied if cumulative capacities were evaluated after 10 cycles rather than 100, because in that case seven cells containing pure zinc oxide survived. The results are presented in Table III. Now only two additives are identified as beneficial, bismuth oxide and acetylene black. In addition, plates which included CMC in the zinc oxide paste and/or the electrolyte are seen to have a significantly "lower" cumulative capacity. CMC was added to gel the electrolyte to slow down the transport of zincate, but overall we found that deleterious effects, such as increased cell resistance, outweighed any beneficial effects. The additives piperonaldehyde, dextrin, and cellulose acetate were also tested, because they are used as leveling agents or brighteners in zinc electroplating (64, 65), however we found no significant effects on cumulative capacities.

Commercial (Eagle-Picher) plates were significantly lower in cumulative capacity after 10 cycles than pure pasted ZnO plates. However, this result may be biased because the commercial plates had a considerably higher loading of ZnO than ours (0.20g cm^{-2} *vs.* 0.13g cm^{-2}).

Cadmium oxide was not identified as a significantly beneficial additive from cumulative capacity data over the first ten cycles, although it had been when 100 cy-

Table I. Cells ranked in order of cumulative capacity over 100 cycles

Rank	$\sum_{1}^{100} Q_N$	2% HgO?	Other additives	Ni electrode[a]
1	20.1	Yes	10% Bi_2O_3	EP
2	18.9	No	6% acetylene black	Y
3	18.6	Yes	5% acetylene black, 1% PTFE, 1% CMC	Y
4	18.4	Yes	5% SnO_2, 5% CdO	EP
5	16.7	Yes	10% Bi_2O_3	Ch
6	16.5	Yes	10% CdO	EP
7	16.4	Yes	10% CdO	Ch
8	16.2	Yes	5% acetylene black, 1% PTFE, 1% CMC	Ch
9	16.2	No	5% CdO, 5% TiO_2	Ch
10	16.0	No	None	EP
11	15.8	No	4% acetylene black	Y
12	15.6	No	2% PTFE	Ch
13	15.5	No	4% acetylene black	Y
14	15.3	Yes	10% PbO	EP
15	14.9	No	10% Bi_2O_3	Y
16	14.6	No	10% Bi_2O_3	Y
17	14.5	Yes	10% CdO	EP
18	14.4	Yes	10% CdO	EP
19	14.1	Yes	10% CdO	EP
20	14.1	Yes	16% Bi_2O_3	Y
21	13.8	Yes	10% PbO	EP
22	13.6	Yes	10% CdO	EP
23	13.4	Yes	4% Bi_2O_3	Y
24	13.2	Yes	10% CdO, 2% PTFE, 1% CMC, gel[b]	Ch
25	13.1	Yes	5% CdO, 3% CMC, gel	Ch
26	13.1	No	1% piperonaldehyde	Ch
27	12.5	No	2% dextrin, 1% CMC, 1% PTFE	Ch
28	11.9	Yes	5% CdO, 5% PbO	EP
29	11.9	Yes	10% CdO	Ch
30	11.9	Yes	10% TiO_2	EP
31	11.3	Yes	10% V_6O_{13}	EP
32	11.2	Yes	10% SnO_2	Ch
33	11.2	Yes	10% CeO_2	Ch
34	10.8	Yes	None	Y
35	10.8	No	1% CMC	EP
36	10.7	Yes	8% Bi_2O_3	Y
37	10.7	No	2% dextrin	Ch
38	10.0	No	2% cellulose acetate, 2% PTFE	Ch
39	9.91	Yes	10% TiO_2	Ch
40	9.85	No	1% piperonaldehyde, 2% PTFE	Ch
41	9.52	No	2% CMC, 2% PTFE	Ch
42	9.43	Yes	10% TiO_2	Ch
43	8.81	Yes	10% V_6O_{13}	Ch
44	8.59	Yes	10% SnO_2	EP
45	6.73	Yes	10% PbO	EP
46	5.99	Yes	1% CMC, 2% PTFE	Y
47	5.63	No	10% PbO	EP

[a] Ch = Chloride pocket-type Ni electrode; EP = Eagle-Picher paste-type Ni electrode; Y = Yardney paste-type Ni electrode.
[b] Gel means that the electrolyte was gelled with 5% CMC.

Table II. *t* tests of additive effects on 100 cycle cumulative capacity

Additive	$\sum_{1}^{100} Q_N$/A-hr · g^{-1} Mean	Standard deviation	Number	*t*	Significant?[a]
All	13.0	3.4	47	—	—
Bi_2O_3[b]	14.9	2.9	7	2.8	Yes
Acetylene black	16.7	1.9	3	3.0	Yes
CdO[b]	14.5	1.6	7	2.7	Yes
PbO[b]	11.9	4.6	3	0.3	No
CdO + CMC[b]	13.1	0.1	3	1.1	No
Control[c]	11.2	3.0	17	—	—
TiO_2	11.9	2.5	3	0.4	No

[a] Test if mean of $\sum_{1}^{100} Q_N$ is significantly different from the mean of control group at 0.05 confidence level.
[b] Includes plates containing 2% HgO.
[c] Control group consisted of three cells containing PbO + HgO, two cells containing TiO_2 + HgO, two cells containing SnO_2 + HgO, two cells containing V_6O_{13} + HgO, and one each of cells containing PTFE, dextrin, piperonaldehyde, PbO, HgO, no additive, CeO_2 + HgO, and piperonaldehyde + PTFE mixture. Other mixtures listed in Table I were excluded.

Table III. t tests of additive effects on 10 cycle cumulative capacity

Additive	$\sum_{1}^{10} Q_N$/A-hr · g^{-1} Mean	Standard deviation	Number	t	Significant?[a]
Bi_2O_3[b]	4.1	0.6	10	2.8	Yes
Acetylene black	4.2	0.8	5	2.4	Yes
CdO[b]	3.7	0.6	11	1.6	No
CMC	2.5	0.6	10	2.8	Yes
PbO[b]	2.4	0.9	4	2.2	No
SnO_2[b]	3.7	0.8	4	1.1	No
TiO_2[b]	3.3	0.9	3	0	No
CeO_2[b]	3.3	0.9	3	0	No
Pure	3.3	0.4	7	—	—
CdO/CMC[b]	2.9	0.3	3	1.5	No
Eagle-Picher	2.3	0.6	6	3.6	Yes

[a] Test if mean $\sum_{1}^{10} Q_N$ is significantly different from the mean for pure ZnO at the 0.05 confidence level.
[b] Includes plates containing 2% HgO.

cles were considered (Table II). The reason for this difference becomes apparent when the dependence of capacity on cycle number is examined. Figures 4, 5, and 6 show how the capacities of plates containing CdO, Bi_2O_3, and acetylene black compared with the mean values of all plates. It can be seen that the influence of CdO occurs predominantly in the later cycles (Fig. 5) whereas that of Bi_2O_3 (Fig. 4) and acetylene black (Fig. 6) is manifested in the early cycles.

Prediction of $\sum_{N=1}^{N=100} Q_N$ *from results on initial cycles.*—A greater acceleration of cell testing would have been possible if the performance over 100 cycles had been predictable from the results over the first few cycles. To test this idea we plotted cumulative capacities after n cycles *vs.* cumulative capacities after 100 cycles, for a series of cells, and then used linear regression (63) to obtain a best-fit straight line. However, an adequate prediction of cumulative capacity for 100 cycles, or more, could not be obtained unless at least 75 cycles were recorded, so this approach was rejected.

A second way of predicting long-term plate performance was to fit polynomials of arbitrary order to cumulative capacity data up to n cycles, and then extrapolate the curves to $n > 100$ cycles. Again, at least 75 cycles were needed to be certain of an acceptable extrapolation, so this approach was rejected too.

Phenomenology of zinc plates containing bismuth.—Because we cycled zinc battery plates between potentials measured *vs.* Hg/HgO reference electrodes, it was possible to record their potential/time curves directly. One such curve is shown in Fig. 7, which illustrates the behavior of the zinc electrode potential during the first few galvanostatic charge and discharge cycles, for a zinc plate initially containing 10% Bi_2O_3. (In this experiment the copper grid was also bismuth-plated prior to use.) The main features of the curves are easily identified and they are indicated on the figure. On the first cycle it is interesting to observe the deposition of bismuth metal. This occurs at high overpotentials as measured *vs.* the Bi/Bi_2O_3 open-circuit potential, which is about −600 mV in this solution.

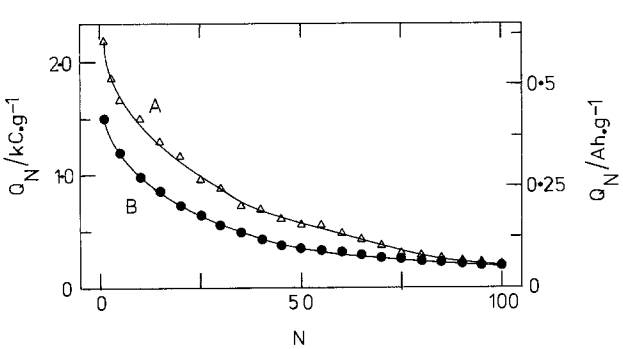

Fig. 4. Graphs of capacity *vs.* cycle number for zinc electrodes cycled galvanostatically at 20 mA cm^{-2}, between potential limits of −1.46 and −1.15V *vs.* Hg/HgO. (A) ZnO paste with additives 10% Bi_2O_3 and 2% HgO (electrode ranked no. 1). (B) Mean of all cells tested that lasted >100 cycles.

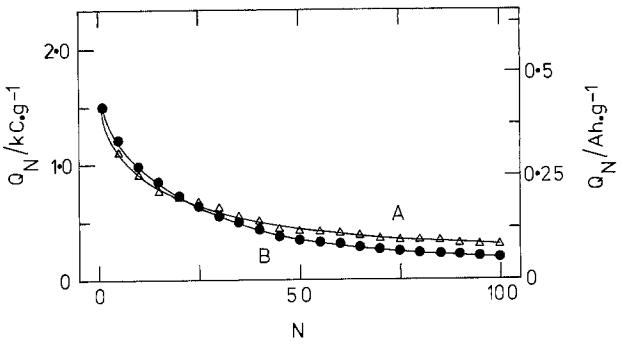

Fig. 5. Graphs of capacity *vs.* cycle number for zinc electrodes cycled galvanostatically at 20 mA cm^{-2}, between potential limits of −1.46 and −1.15V *vs.* Hg/HgO. (A) ZnO paste with additives 10% CdO and 2% HgO (electrode ranked no. 17). (B) Mean of all cells tested that lasted >100 cycles.

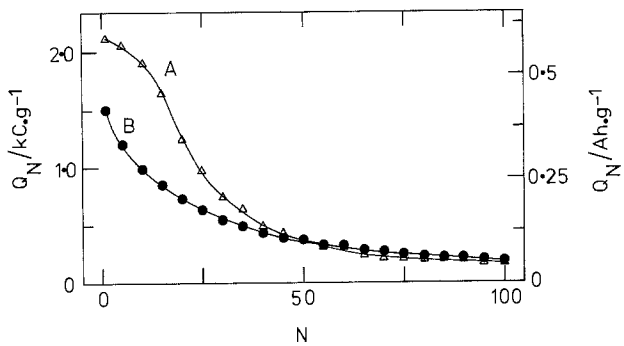

Fig. 6. Graphs of capacity *vs.* cycle number for zinc electrodes cycled galvanostatically at 20 mA cm^{-2}, between potential limits of −1.46 and −1.15V *vs.* Hg/HgO. (A) ZnO paste with additives 5% acetylene black, 1% PTFE, 1% CMC, and 2% HgO (electrode ranked no. 3). (B) Mean of all cells tested that lasted >100 cycles.

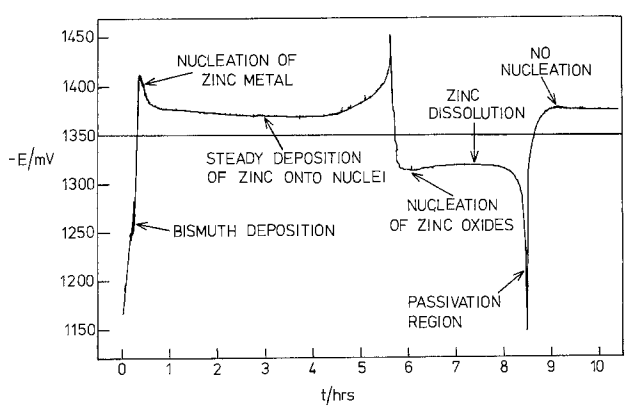

Fig. 7. Potential of ZnO electrode during galvanostatic cycling at 20 mA cm^{-2}, between potential limits of −1.45 and −1.15V *vs.* Hg/HgO. Additives were 10% Bi_2O_3 and 2% HgO; the grid was bismuth-plated.

The deposition of bismuth is followed by the nucleation of zinc metal onto the bismuth substrate and after that the steady deposition of zinc from zinc oxide can be seen, possibly via soluble zincate in the electrolyte. When the zinc oxide is finally depleted, the electrical potential of the zinc plate rises until the cell is automatically switched to discharge. On discharge the nucleation of zinc oxides is evident, as well as the dissolution of zincate and the passivation of zinc.

At the start of the second charge no nucleation peak is resolved because pre-existing metallic zinc eliminates the need for new nuclei, and all the electrical current is sustained via reaction on existing zinc. This explains why some areas of grid become stripped of zinc in the later stages of cycling, a phenomenon generally termed "shape change" (1-9). Thus, when an element of grid loses its coverage of zinc via dissolution on a discharge cycle, then that element of grid will not renucleate zinc on subsequent charges unless it is supplied with the required nucleation overvoltage. As can be seen from Fig. 7, at 20 mA cm^{-2} on the grid, this overvoltage amounts to nearly 40 mV over and above that required to sustain steady zinc deposition.

Mechanism of capacity loss.—The occurrence of shape change on a macroscopic scale is visible evidence that changes occur in zinc plates during cycling. Indeed, it is a widely held view that the control of shape change is a key step in improving the cycle life of nickel/zinc cells. However, we found that shape change was not the major cause of capacity loss. A simple proof was that, after 100 deep discharge cycles, zinc plates were typically found to retain 70% coverage by active material, whereas they always had less than 13% of their original capacity. Thus it was clear that the most important changes were not taking place on the macroscopic level of shape change but at some microscopic level below optical resolution. For this reason we undertook a scanning electron microscopy study of the changes taking place during deep discharge of zinc plates.

A representative micrograph of a cross section through a bismuth-containing zinc plate after an initial charge cycle is shown in Fig. 8(a). The principal features were identified by microprobe; these are the rectangular copper grid support, the bismuth plating on its outer edges, and the porous active mass of zinc metal surrounding the grid. The area of most interest, however, is the zinc metal itself. This is shown at higher magnification in Fig. 8(b). Comparison of this photograph with representative photographs obtained from later cycles, such as those in Fig. 8(c) and 8(d), shows that as plates were cycled and their capacities decreased, the active mass of zinc metal decreased in porosity. This general result was found for all the samples that we tested.

Why does a decrease in porosity correlate with a decrease in plate capacity? The most likely explanation is that, on discharge, zinc dissolution only proceeds for

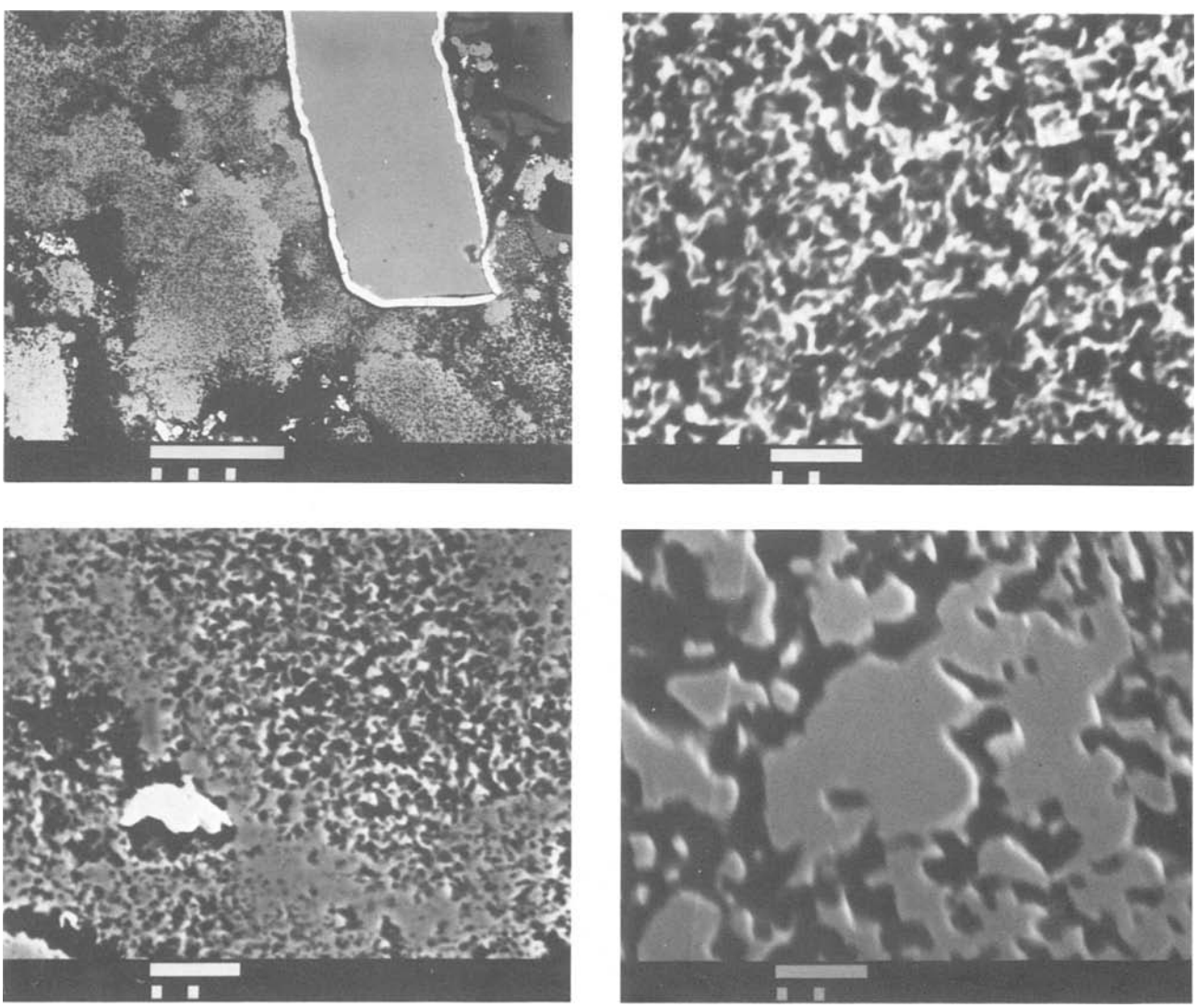

Fig. 8. Scanning electron micrographs showing cross sections through zinc plates having 10% Bi_2O_3 originally in their active mass, and bismuth-plated grids. (a, top left) Bar = 100 μm, photograph after 1st charge. (b, top right) Bar = 10 μm, photograph after 1st charge. (c, bottom left) Bar = 10 μm, photograph after 15th charge. (d, bottom right) Bar = 10 μm, photograph after 105th charge.

a finite "penetration" depth into the plate before the onset of a passivation reaction (13). Thus pores would increase the penetration depth, and hence the capacity, whereas their absence would decrease it.

We were unable to identify the precise mechanisms by which Bi_2O_3, CdO, and acetylene black improved zinc electrode performance. However, we knew that Bi_2O_3 and acetylene black improved active material utilization mainly in the early cycles (Fig. 4 and 6), which suggested the existence of a conducting matrix of bismuth or carbon which did not survive very long. On the other hand, cadmium oxide slowed down the rate of capacity loss in later cycles (Fig. 5), and here it is possible that the cadmium influenced zinc morphology in such a way that plate porosity was maintained. Unfortunately, conclusive evidence for such an effect has not yet been obtained.

In the literature much work has been directed at identifying electrolyte additives which decrease zinc solubility, the idea being to minimize the transport of zinc ions involved in the solution side of the shape change process. However, if the major mechanism of capacity loss is a decrease of plate porosity, as we suggest, then additives of this type would be counterproductive. This is because a decrease in zinc solubility would promote passivation and hence decrease plate capacity. Indeed, an electrolyte which maximized zinc solubility would be more useful, or the addition of an aggressive anion to help prevent passivation (43). It is worth pointing out that some nickel/zinc cells have been developed in which passivation is prevented by having an excess of electrolyte and vibrating the zinc plate (4). These cells do indeed improve the cycle life of zinc plates, albeit at the cost of decreasing the energy density to an unacceptable level. Nevertheless, the principle that improving zinc solubility improves plate capacity is consistent with our observations.

Conclusions

An accelerated test procedure for deep discharging zinc plates in nickel/zinc cells was devised. It was shown that Bi_2O_3, CdO, and acetylene black individually enhanced zinc utilization over 100 deep discharge cycles. However, further work is needed to identify the optimum levels of these additives, and to determine to what extent they improve the cycle life of Ni/Zn cells under practical conditions.

Besides screening additives we also discussed the phenomenology of zinc plates and the mechanism of their capacity loss. We found that capacity loss was caused by a decrease in plate porosity.

Acknowledgments

This work was sponsored by the International Lead-Zinc Research Organization (ILZRO), project ZE-295, and the Australian National Energy, Research Development and Demonstration Council (NERDDC). Their financial support is gratefully acknowledged. One of us, S.H., thanks China for a fellowship.

Manuscript submitted March 16, 1983; revised manuscript received July 1, 1983.

CSIRO assisted in meeting the publication costs of this article.

REFERENCES

1. G. Adzic, D-T. Chin, M. G. Chu, E. Gannon, J. McBreen, and R. Sethi, Report, Brookhaven National Laboratory, Upton, NY, Code No. BNL 51370 (1980).
2. M-B. Liu, G. M. Cook, and N. P. Yao, Report, Argonne National Laboratory, Argonne, IL, Code No. ANL/OEPM-80-1 (1980).
3. O. C. Wagner, Report, U.S. Army Electronics Research and Development Command, Fort Monmouth, NJ, Code No. PSD-4C Report No. 4 (1981).
4. Exide Management and Technology Company, Report, Argonne National Laboratory, Argonne, IL, Code No. ANL/OEPM-81-12 (1980).
5. Energy Research Corporation, Report, Argonne National Laboratory, Argonne, IL, Code No. ANL/OEPM-80-13 (1981).
6. D. Dappert, Report, U.S. Air Force Systems Command, Wright-Patterson Air Force Base, OH, Code No. AFWAL-TR-80-2050 (1980).
7. T. Katan and P. J. Bergeron, Report, U.S. Dept. of Energy, Washington, DC, Code No. LMSC-D-681417 (1979).
8. R. L. Deutscher, S. Fletcher, C. S. Halliday, C. Harvey, S-N. Hua, S. Phang, and R. Woods, Report, CSIRO Institute of Energy and Earth Resources, Melbourne (Vic.) Australia, Code No. MCC 408 Report No. 4 (1982).
9. A. Charkey, Report, Lawrence Berkeley Laboratory, University of California, Berkeley, CA, Code No. LBL-14674 (1982).
10. J. McBreen and E. J. Cairns, in "Advances in Electrochemistry and Electrochemical Engineering," Vol. II, H. Gerischer and C. W. Tobias, Editors, pp. 273-352, John Wiley and Sons, New York (1978).
11. O. C. Wagner, A. Almerini, and R. L. Smith, in "Proceedings of the 29th Power Sources Conference, pp. 237-240, The Electrochemical Society Inc., Pennington, NJ (1980).
12. W. G. Sunu and D. N. Bennion, *This Journal*, **127**, 2007 (1980).
13. M-B. Liu, G. M. Cook, and N. P. Yao, *ibid.*, **129**, 239 (1982).
14. G. Kawamura and Y. Maki, *Denki Kagaku*, **48**, 592 (1980).
15. L. Binder, W. Odar, and K. Kordesch, *J. Power Sources*, **6**, 271 (1981).
16. P. Reasbeck, *Phil. Trans. R. Soc. Lond.*, **A302**, 351 (1981).
17. G. P. Litovka, Yu. M. Loshkarev, V. V. Trofimenko, V. E. Kazarinov, and N. B. Grigor'ev, Soviet Electrochem., **15**, 1064 (1979).
18. V. I. Lubyanova and E. F. Zavgorodnyaya, *ibid.*, **15**, 918 (1979).
19. L. A. Reznikova, D. P. Aleksandrova, and B. N. Kabanov, *ibid.*, **16**, 489 (1980).
20. L. A. Reznikova, D. P. Aleksandrova, and B. N. Kabanov, *ibid.*, **17**, 445 (1981).
21. E. F. Zavgorodnyaya, V. I. Lubanova, and Z. E. Degtyareva, *J. Appl. Chem. (USSR)*, **52**, 2445 (1979).
22. Yu. L. Gun'ko, M. G. Mikhalenko, and V. N. Flerov, *ibid.*, **54**, 68 (1981).
23. M. G. Chu, J. McBreen, and G. Adzic, *This Journal*, **128**, 2281, 2287 (1981).
24. T. P. Dirkse, *ibid.*, **127**, 1452 (1980).
25. I. Epelboin, M. Ksouri, and R. Wiart, *ibid.*, **122**, 1207 (1975).
26. S. Kang, K. Matsuda, and R. Tamamushi, *Coll. Czech. Chem. Comm.*, **47**, 1433 (1982).
27. N. J. Maskalick, *This Journal*, **122**, 19 (1975).
28. Yardney Electric Corp., UK Pat. (Application) GB 2,006,512A, Oct. 13, 1977 (May 2, 1979).
29. Yardney Electric Corp., UK Pat. (Application) GB 2,007,420A, Oct. 31, 1977 (May 16, 1979).
30. Energy Research Corp., UK Pat. 1,558,725, Jan. 13, 1977 (Jan. 9, 1980).
31. Yardney Electric Corp., US Pat. 4,118,551, Oct. 31, 1977 (Oct. 3, 1978).
32. United States, Secretary of the Navy, US Pat. 4,084,047, Nov. 29, 1976 (April 11, 1978).
33. Energy Research Corp., US Pat. 4,022,953, Aug. 22, 1975 (May 10, 1977).
34. Michelin et Cie., UK Pat. (Application) GB 2,027,-260A, July 25, 1978 (Feb. 13, 1980).
35. Israel, Ministry of Industry, Commerce and Tourism, National Physical Laboratory of Israel, and Scientific Research Foundation, US Pat. 4,152,-224, Aug. 24, 1976 (May 1, 1979).
36. Varta Batterie AG., German Pat. (Offenlegungsschrift) 2,748,992, Nov. 2, 1977 (May 3, 1979).
37. Yardney Electric Corp., British Pat. 1,533,698, July 27, 1976 (Nov. 27, 1978).
38. Tokyo Shibaura Electric Co. Ltd., British Pat. 1,530,961, Jan. 20, 1975 (Nov. 1, 1978).
39. Energy Research Corp., British Pat. 1,476,550, March 18, 1975 (June 16, 1977).

40. Hebrew University, National Laboratory of Israel, UK Pat. (Application) GB 2,028,569A, Aug. 23, 1978 (March 5, 1980).
41. EL-Chem Corp., UK Pat. (Application) GB 2,026,-763A, July 25, 1978 (Feb. 6, 1980).
42. Varta Batterie AG, UK Pat. (Application) GB 2,007,421A, Nov. 2, 1977 (May 16, 1979).
43. Varta Batterie AG., UK Pat. (Application) GB 2,015,242A, Feb. 22, 1978 (Sept. 5, 1979).
44. Yardney Electric Corp., UK Pat. 1,557,775, July 27, 1976 (Dec. 12, 1979).
45. Gould Inc., UK Pat. (Application) 2,005,290A, Sept. 30, 1977 (April 19, 1979).
46. Matsushita Electric Industrial Co., Ltd., US Pat. 3,976,502, Dec. 17, 1974 (Aug. 24, 1976).
47. Gould Inc., UK Pat. (Application) 2,005,289A, Sept. 30, 1977 (April 19, 1979).
48. Yardney Electric Corp., UK Pat. 1,555,586, July 27, 1976 (Nov. 14, 1979).
49. United States, Secretary of the Navy, US Pat. 4,192,908, June 15, 1979 (March 11, 1980).
50. Yardney International Corp., Brit. Pat. 1,442,556, March 11, 1974 (July 14, 1976).
51. US Administrator of the National Aeronautics and Space Administration, US Pat. 3,972,727, Aug. 13, 1975 (Aug. 3, 1976).
52. Gould Inc., Brit. Pat. (Application) 2,000,899A, July 8, 1977 (Jan. 17, 1979).
53. Yardney Electric Corp., UK Pat. (Application), GB 2,019,674A, April 25, 1978 (Oct. 31, 1979).
54. Firma Deutsche Automobilgesellschaft GmbH., US Pat. 4,145,482, June 30, 1972 (March 20, 1979).
55. Aktiebolaget Tudor., US Pat. 4,015,053, Dec. 1, 1975 (March 29, 1977).
56. McGraw-Edison Co., US Pat. 3,970,472, July 8, 1975 (July 20, 1976).
57. Yardney Electric Corp., UK Pat. (Application) GB 2,020,221A, May 1, 1978 (Nov. 14, 1979).
58. P. R. Mallory, and Co. Inc., US Pat. 4,195,120, Nov. 3, 1978 (March 25, 1980).
59. J. F. Miller, J. B. Rajan, F. Hornstra, C. C. Christianson, and N. P. Yao, Abstract 1, p. 1. The Electrochemical Society Extended Abstracts, Fall Meeting, Detroit, MI, Oct. 17-21, 1982.
60. A. Himy, in "Proceedings of the 16th Intersociety Energy Conversion Engineering Conference," pp. 645-647, The American Society of Mechanical Engineers, New York (1981).
61. J. E. Clifford and R. E. Thomas, Report, Sandia National Laboratories, Albuquerque, NM, Code No. SAND82-7049 (1982).
62. J. McCallum, R. E. Thomas, and J. H. Waite, Report, Columbus Laboratories of the National Aeronautics and Space Administration, Code No. NASA Sp-323 (1973).
63. "C.R.C. Handbook of Tables for Probability and Statistics," 2nd ed., W. H. Beyer, Editor, The Chemical Rubber Co., Cleveland, OH (1968).
64. K. Boto, *Electrodeposition Surf. Treat.*, **3**, 77 (1975).
65. "Metal Finishing Guidebook Directory," 42nd ed. N. Hall, Editor, Metals and Plastics Publications Inc., Hackensack, NJ (1974).

Rechargeability of the Ambient Temperature Cell Li/2Me-THF, $LiAsF_6/Cr_{0.5}V_{0.5}S_2$

K. M. Abraham,* P. B. Harris, and D. L. Natwig

EIC Laboratories, Incorporated, Newton, Massachusetts 02158

ABSTRACT

Practical usefulness of $Cr_{0.5}V_{0.5}S_2$ as a rechargeable positive electrode for ambient temperature Li cells has been assessed. The rate-capacity behavior of the $Cr_{0.5}V_{0.5}S_2$ cathode has been evaluated as a function of carbon content, electrolyte, and temperature. Rechargeability of the disulfide has been investigated by extended cycling of Li cells utilizing 2Me-THF/$LiAsF_6$. Cells with cathode capacities as large as 10 Ahr have been constructed and tested. Many cells have exceeded 200 deep discharge-charge cycles. A scheme of studies useful for assessing the practicality of potential solid cathodes for ambient temperature rechargeable Li cells is presented.

Among the numerous potentially useful positive electrodes identified for ambient temperature rechargeable Li cells, solid-state materials that undergo intercalation or insertion reactions offer the greatest promise for immediate practical applications (1, 2). The layered dichalcogenides, typified by TiS_2 (3), and the three-dimensional network oxides, exemplified by V_6O_{13} (4, 5), are some of the prominent members of insertion electrodes.

The excellent rechargeability and the high rate-capability of TiS_2 has been demonstrated by many investigators (6-8). It is by far the most developed of all rechargeable positive electrodes. Its major disadvantage is its modest specific energy. Recently we have explored the practical usefulness of V_6O_{13} (5). We have shown that the very high energy densities forecasted (4) for V_6O_{13}-containing cells, on the basis of data from small laboratory cells, cannot be achieved in practical cells. This is because V_6O_{13} electrodes require a relatively large amount of carbon in order to permit cell discharges resulting in useful capacities over a wide range of current density. We have also shown that data from development studies are required for a full assessment of the practical utility of a positive electrode material.

The potential usefulness of the layered mixed metal disulfides. $Cr_nV_{1-n}S_2$, as rechargeable positive electrodes for ambient temperautre Li cells was originally demonstrated by Murphy and co-workers (9). These authors studied $Cr_{0.75}V_{0.25}S_2$ and found a reversible capacity of ~0.60 Li per mol of the disulfide. They did not report, however, on the long-term cycling characteristics of the dichalcogenide. Subsequent to Murphy *et al.*'s paper, some preliminary work was carried out at EIC with $Cr_{0.5}V_{0.5}S_2$ (10). Those early results indicated that $Cr_{0.5}V_{0.5}S_2$ might be superior to $Cr_{0.75}V_{0.25}S_2$ in both capacity and rechargeability. We have now completed a more thorough study of $Cr_{0.5}V_{0.5}S_2$. Practical energy density and specific energy of Li/$Cr_{0.5}V_{0.5}S_2$ cells have been assessed. Rechargeability of the Li/$Cr_{0.5}V_{0.5}S_2$ system has been evaluated by extended cycling of cells which utilize 2Me-THF/$LiAsF_6$ (11). We have already demonstrated the desirability of using 2Me-THF/$LiAsF_6$ in state-of-the-art ambient temperature rechargeable Li cells (3, 5, 8, 16). Other recent publications dealing with intercalation chemistry of $Cr_{0.5}V_{0.5}S_2$ or materials related to it can be found in Ref. (12-15).

* Electrochemical Society Active Member.
Key words: Li anode, insertion cathode, battery.

Experimental

General.—All experiments were carried out in the absence of air and moisture under an Ar atmosphere in a Vacuum-Atmospheres Corporation dry box equipped with a Model He-493 Dri-Train.

Materials.—2,Methyl-tetrahydrofuran (2Me-THF), obtained from Aldrich Chemical Company, was distilled off CaH_2 under Ar from a Perkin-Elmer Model 251 Auto Anular Still. The reflux ratio was 5:1 and the middle 70% fraction was collected. The distilled 2Me-THF typically contained ~0.2% 2,methyl-furan, as determined from GC analysis. Tetrahydrofuran (THF) was obtained from Burdick and Jackson Laboratories, Michigan. Lithium hexafluoroarsenate ($LiAsF_6$) (U.S. Steel Agri-Chemicals, electrochemical grade) was used as received. Lithium foil, sealed under Ar, was obtained from Foote Mineral Company.

The electrolytes, 2Me-THF/$LiAsF_6$(1.3M), THF/$LiAsF_6$(1.5M), and the blended solution, 50:50 THF:2Me-THF/$LiAsF_6$(1.5M), were prepared as we have described previously (5, 8, 11).

The resistivities of pressed pellets were measured using a four-point probe method (16).

Li/$Cr_{0.5}V_{0.5}S_2$ Cells

Synthesis of $Cr_{0.5}V_{0.5}S_2$.—In a preparation, a well ground mixture consisting of 9.5g (0.052 mol) V_2O_5, 7.9g (0.052 mol) Cr_2O_3, and 7.7g (0.104 mol) Li_2CO_3, was placed in a graphite boat, which in turn was introduced into a quartz tube. While maintaining an H_2S flow (~25 cm³/min) over the oxide mixture, the quartz tube was heated at 700°C for ~16 hr. The air-sensitive $LiCr_{0.5}V_{0.5}S_2$ was obtained as a black powder. The material was delithiated by treatment with an excess of 0.4*N* I_2/CH_3CN solution for 24 hr. The delithiated product was washed several times with CH_3CN and dried in vacuum initially at 25°C and then at 160°C. Both $LiCr_{0.5}V_{0.5}S_2$ and $Cr_{0.5}V_{0.5}S_2$ were characterized from their Debye-Sherrer x-ray patterns.

Cathode preparation.—Cathodes for laboratory test cells were prepared as pressed powder electrodes. An intimate mixture consisting of $Cr_{0.5}V_{0.5}S_2$, C (Shawinigan 50% compressed), and Teflon, taken in desired weight proportions, was prepared in a blender. The mixed powder then was pressed on either side of an expanded Ni screen (Exmet Corporation, 5Ni 7-4/0) at a pressure of ~1000 psi. The electrode thickness varied from 1-1.5 mm. The 70 weight percent (w/o) $Cr_{0.5}V_{0.5}S_2$, 20 w/o C, 10 w/o Teflon electrodes, used in most laboratory cell studies, had a thickness of ~1.3 mm.

Cathodes for the 10 Ahr cells were prepared by a pasting technique. A slurry of the cathode mix was prepared in decane. It was then pasted on either side of a 1 mil thick pierced Ni foil. The decane was removed by prolonged pumping in vacuum until the electrode attained constant weight.

Cells.—In laboratory test cells, the electrode package comprised one cathode flanked on either side by an Li electrode. Each cathode was wrapped in two layers of Celgard 2400(TM) (Celanese Corporation) polypropylene separators and the latter was heat-sealed in the periphery of the electrode. The total cathode area per cell was ~20 cm². The Li electrode was fabricated usually from a 15 mil thick Li foil by pressing the foil on the cathode-facing side of an expanded Ni screen. Each Li electrode was ~10 cm². The electrode package was introduced into a D-cell can (Ni-plated cold-rolled steel), and compression was applied to the package by Teflon hemi-cylinders. The cell was filled with ~9 ml of the electrolyte. The cell was either soft-sealed (16), or hermetically sealed by Tig-welding (8).

The large hermetically sealed rectangular cells were constructed with electrodes having an area of 9.95 cm × 9.25 cm = 92 cm²/side. The cells were assembled in a commercially available steel can. A readily available can off-the-shelf was chosen because of the limited number of cells being produced. The cans were significantly heavier than would be used in an optimized cell. The cell contained 10 cathodes and 11 anodes. The theoretical capacity of the cell, based on $1e^-/Cr_{0.5}V_{0.5}S_2$, was 11 Ahr. The electrolyte was 2Me-THF:$LiAsF_6$ (1.4M). Further details of cell construction are given in Ref. (16).

Cells were cycled galvanostatically with the aid of standard cycling equipment. The potential limits, unless otherwise mentioned, were 1.6V for discharge and 3.1V for recharge. Data collection and retrieval were done with a Bascom-Turner 8000 Recorder equipped with microprocessor accessories.

Results and Discussion

Characterization of $Cr_{0.5}V_{0.5}S_2$.—Scanning electron micrographs (16) have revealed that $Cr_{0.5}V_{0.5}S_2$ is a crystalline substance with particle sizes of the order of 1-2 μm. This extremely small particle size is achieved in the delithiation step, prior to which the particle size of $LiCr_{0.5}V_{0.5}S_2$ is 15-20 μm.

The Debye-Sherrer x-ray pattern of $Cr_{0.5}V_{0.5}S_2$ is given in Table I. The data are consistent with a hexagonal layered 1T CdI_2-type structure with a_o = 3.2Å and C_o = 5.71Å. The x-ray patterns of the lithiated compounds strongly support the contention that lithiation, both chemical and electrochemical, involves an intercalation process. In this context we draw attention to a prior report on the structure and electrochemical properties of the Na-intercalates of $Cr_{0.5}V_{0.5}S_2$ (12).

The data listed in Table II show that there is very little change of electronic conductivity in $Li_xCr_{0.5}V_{0.5}S_2$ for $0 < x < 1$. The magnitude of the resistivities appears to be small enough to permit electrochemical cycling of cathodes without a conductivity enhancing additive such as carbon in the electrode. However, our experimental results indicate that addition of carbon to the electrode is extremely beneficial; it substantially increases both the rate-capability and the rechargeability of the electrode. The reasons for the beneficial effects due to carbon are discussed later in this paper.

Table I. Debye-Sherrer x-ray patterns of $Cr_{0.5}V_{0.5}S_2$ and its Li compounds

$Cr_{0.5}V_{0.5}S_2$		$Li_{0.77}Cr_{0.5}V_{0.5}S_2$*		$LiCr_{0.5}V_{0.5}S_2$**	
d,Å	$I_{(obs)}$	d, Å	$I_{(obs)}$	d,Å	$I_{(obs)}$
5.71	70	6.04	90	6.06	100
2.78	8	2.98	8	2.98	10
2.49	100	2.65	100	2.65	80
2.00	90	2.13	90	2.11	70
1.58	30	1.73	40	1.73	50
1.35	20	1.67	40	1.67	50
1.26	20	1.45	5		
1.12	10	1.34	5		
		1.20	5		

* Electrochemically prepared sample.
** High temperature material.

Table II. Electronic conductivity data for $Cr_{0.5}V_{0.5}S_2$ and typical electrode compositions

Sample	Resistivity (Ω-cm)	Specific conductivity $(\Omega\text{-cm})^{-1}$
$Cr_{0.5}V_{0.5}S_2$ (CVS)	0.094	10.64
90 w/o CVS, 10 w/o Teflon (T)	0.134	7.46
80 w/o, CVS, 10 w/o C, 10 w/o T	0.291	3.44
70 w/o CVS, 20 w/o C, 10 w/o T	0.357	2.80
60 w/o CVS, 30 w/o C, 10 w/o T	0.338	2.96
90 w/o $Li_{0.77}Cr_{0.5}V_{0.5}S_2$, 10 w/o T	0.642	1.56
$LiCr_{0.5}V_{0.5}S_2$	0.175	5.71

Discharge-charge behavior of $C_{0.5}V_{0.5}S_2$.—Typical galvanostatic cycles for an Li/$Cr_{0.5}V_{0.5}S_2$ cell, obtained at the relatively low current density of 0.5 mA/cm², are shown in Fig. 1. The mid-discharge voltage is 2.30V. The discharge shows a downward sloping potential profile with a clear, and relatively sharp, potential drop to the cut-off voltage of 1.6V, when a capacity of ~0.8e^-/$Cr_{0.5}V_{0.5}S_2$ has been achieved. The recharge at the same rate is nearly 100% efficient. The mid-charge voltage is 2.5V. The open-circuit voltage (OCV) of a cell discharged by 0.5e^-/$Cr_{0.5}V_{0.5}S_2$ was found to be 2.4V. The deviation of the mid-discharge and mid-charge voltages from this OCV reflects resistive polarizations in the cell. When cycling is continued at this low rate, usually only very small decreases in utilization are observed. However, we found that both the utilization of the cathode and its cycling behavior, especially at higher current densities, strongly depend on the amount of carbon in the electrode. The 10 w/o carbon in this electrode was initially chosen on an arbitrary basis.

Effect of carbon on cathode performance.—In Fig. 2, we compare the performance of electrodes with 0.0, 10, 20, and 30 w/o carbon. The data represent discharge capacities at current densities between 0.5 and 4 mA/cm². All cells utilize 2Me-THF/1.3M $LiAsF_6$. The relevant data were obtained by discharging each cell successively at 0.5, 1, 2, 3, and 4 mA/cm², with each discharge followed by a charge at 0.5 mA/cm². The discharge curves for a typical case are given in Fig. 3.

The lowest material utilization is found in electrodes that do not contain any carbon. For example, even at 0.5 mA/cm², the capacity exhibited by such an electrode is only ~0.6e^-/$Cr_{0.5}V_{0.5}S_2$. By adding ~10 w/o carbon, capacities approaching the theoretical 1e^-/

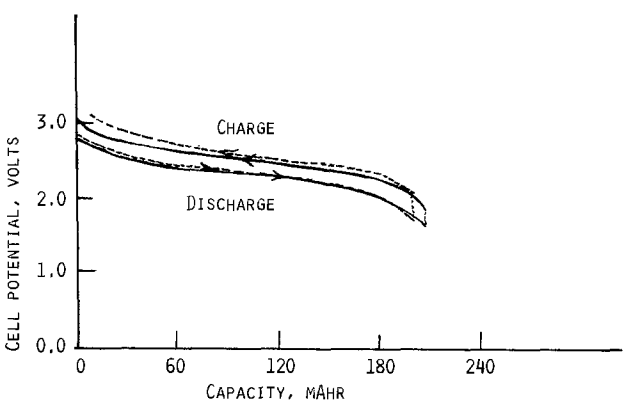

Fig. 1. Typical cycles of an Li/$Cr_{0.5}V_{0.5}S_2$ cell with 2Me-THF/$LiAsF_6$ (1.3M). Cathode has ~10 w/o carbon. Current density = 0.5 mA/cm². Voltage limits; 1.6-3.1V. Theoretical cathode capacity = 250 mAhr. —— Cycle 1, ---- Cycle 5.

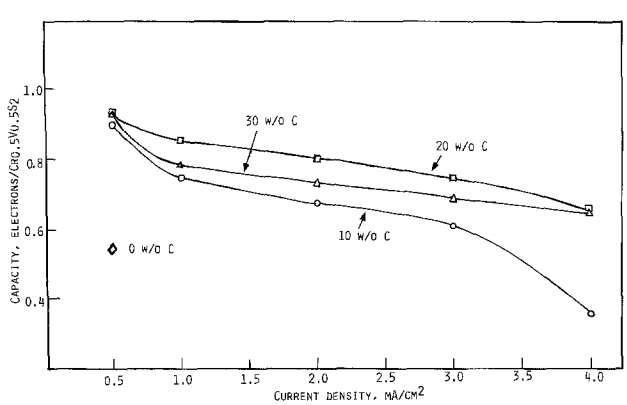

Fig. 2. Effect of carbon on the capacity of Li/$Cr_{0.5}V_{0.5}S_2$ cells at various current densities.

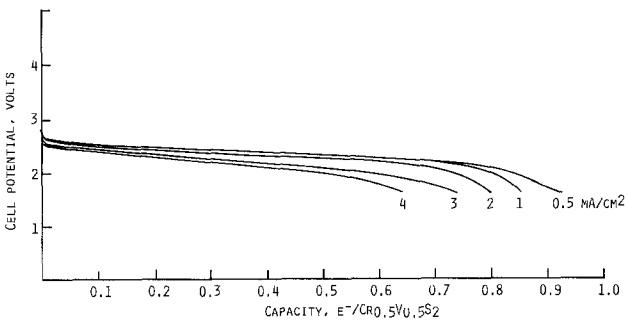

Fig. 3. Discharges of the Li/$Cr_{0.5}V_{0.5}S_2$ cell with 20 w/o carbon in the cathode.

$Cr_{0.5}V_{0.5}S_2$ are obtained, provided the current densities are kept low; say, ≤0.5 mA/cm². For current densities ≧1 mA/cm², even larger amounts of carbon are required for the best performance of the electrode. The cathodes with 20 w/o carbon appear to exhibit the optimal behavior.

The data presented in Table II indicate that the cathode composition with 20 w/o carbon actually has a slightly higher resistivity than that of $Cr_{0.5}V_{0.5}S_2$ itself. The observed trend of slightly increasing electrode resistivity with added carbon is in accordance with the formation of increased pellet porosities and/or larger grain boundaries. It is apparent that the beneficial effect of carbon on cathode utilization is not related to the electronic conductivity of the electrode. Rather, it appears that the carbon ensures greater electrode porosity and better particle-to-particle contacts. The latter advantage seems to negate the adverse effects of expansion and contraction experienced by the insertion electrode during Li uptake and expulsion. The crystallographic expansion of $Cr_{0.5}V_{0.5}S_2$ resulting from a full intercalation with Li to form $LiCr_{0.5}V_{0.5}S_2$ is ~7%.

Based on the above results, we have chosen electrodes with 20 w/o carbon for all further studies. It should, however, be noted that the optimal amount of carbon required practically would depend on the type of carbon, and the rates at which the cell is required to operate. The data in Fig. 4 illustrate the manner in which the carbon content of the electrode would affect the volumetric energy density of the cell. The data, calculated for an electrode package consisting of the appropriate cathode, Celgard 2400(TM) separators, and Li anodes having five times the capacity density of the cathode, are given to exemplify the relative changes in energy density with carbon content; they do not represent the energy densities of finished cells.

Cell performance at low temperatures.—Some pertinent data are given in Fig. 5. The discharge capacities of two cells, one with 2Me-THF/1.3M $LiAsF_6$ and the other with 50:50 2Me-THF:THF/1.5M $LiAsF_6$,

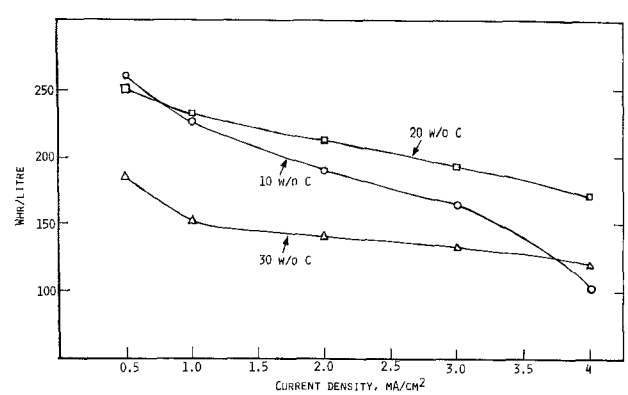

Fig. 4. Effect of carbon on volumetric energy density

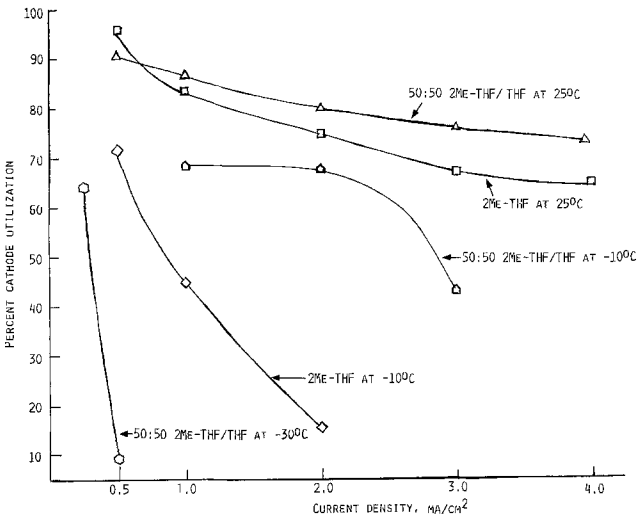

Fig. 5. Cathode utilization vs. current density at various temperatures.

are compared at 25°, −10°, and −30°C. The conductivity of the 2Me-THF/1.3M $LiAsF_6$ solution at 25°C is 0.35 × 10^{-2} $(\Omega\text{-cm})^{-1}$, and that of the mixed solution at 25°C is 1 × 10^{-2} $(\Omega\text{-cm})^{-1}$.

At 25°C, both of the cells exhibit fairly similar discharge behavior for current densities up to 4 mA/cm². The slightly higher capacities exhibited by the cell with the mixed solution at current densities ≥2 mA/cm² may be reflective of its higher conductivity.

The data for −10° and −30°C clearly indicate that the rate capability of the cell at these temperatures is largely determined by the electrolyte; $Cr_{0.5}V_{0.5}S_2$ itself appears to be capable of discharges at useful rates down to −30°C. In a prior paper we have attributed the limited low temperature capability of 2Me-THF/$LiAsF_6$ solutions to poor solubilities of the $LiAsF_6(2Me\text{-}THF)_n$ complexes, which crystallize out of solution, resulting in considerably reduced conductivities (8). In the 50:50 THF:2Me-THF/$LiAsF_6$ solution, although there is an apparent increase in viscosity, the salt-solvent complexes do not seem to crystallize even at −30°C. A similar behavior has been exhibited also by Li/TiS_2 cells utilizing these same two electrolytes (19).

Rechargeability of the Li/$Cr_{0.5}V_{0.5}S_2$ cell.—Any discussion of rechargeability of an Li cell must deal with two major issues; the rechargeability of the Li anode, and the rechargeability of the positive electrode. As we have discussed in a recent review (3), the rechargeability of the Li anode is electrolyte dependent. In two prior papers (5, 8) we have reported Li electrode cycling efficiencies between 96 and 97.5% in Li/TiS_2 (8) and Li/V_6O_{13} (5) cells, both utilizing 2Me-THF/$LiAsF_6$. These efficiencies correspond to figures of merit (FOM_{Li}) of 25-40. A rather broad range of Li cycling efficiency reflects its dependence on current density. All our experience to date indicates that $Cr_{0.5}V_{0.5}S_2$ does not in any way interfere with the cycling of the Li electrode. Indeed, in 2Me-THF/$LiAsF_6$, $Cr_{0.5}V_{0.5}S_2$ appears to behave in a way very similar to TiS_2. In addition, all of the cells being discussed in this paper contain sufficient Li to afford >200 deep discharge/charge cycles based on the aforementioned efficiencies. Therefore, in the following discussion, we deal with the rechargeability of the positive electrode; its chemical reversibility, and effects due to electrode structure, current density, and voltage limits.

Electrochemical reversibility of $Cr_{0.5}V_{0.5}S_2$ has been assessed from the results of long-term cycle tests and x-ray analysis of cycled cathodes. Several laboratory cells, each having a cathode capacity of ~225 mAhr, based $1e^-/Cr_{0.5}V_{0.5}S_2$, exceeded more than 200 deep discharge-charge cycles. The cycling was performed at constant currents ranging from 0.5 to 2 mA/cm². While the average cathode utilization depended on current density, x-ray analysis of extensively cycled cathodes indicated no discernible chemical changes of the disulfide. However, we found small amounts of LiF in the cathodes from cells utilizing a 50:50 THF:2Me-THF/$LiAsF_6$ solution. In addition, both $Cr_{0.5}V_{0.5}S_2$ and $Li_xCr_{0.5}V_{0.5}S_2$ were identified in many cathodes, irrespective of the electrolyte and despite a final full recharge of the cell at a relatively low current density. The LiF apparently comes from the reduction of $LiAsF_6$. The presence of $Li_xCr_{0.5}V_{0.5}S_2$ in a fully recharged cathode subsequent to extensive cycling implies physical isolation of some of the material from the bulk. The latter effect, in our opinion, is a major cause of the gradual capacity loss that is frequently seen in continued cycling of these cells. The presence of carbon in the cathode minimizes the extent of this loss.

A plot displaying discharge capacity *vs.* cycle number usually shows two major features: an initial region featuring a relatively rapid rate of loss of capacity; and a second region showing a more gradual rate of loss of capacity. This is exemplified by the data displayed in Fig. 6 for a cell having a theoretical cathode capacity of 240 mAhr or 12 mAhr/cm². The capacity loss in the first 10 cycles is ~2% per cycle. In the next 50 cycles, however, the rate of decrease in capacity is ~0.2% per cycle. Subsequently it is even lower. In the 177th cycle, we reduced the current density to 0.5 mA/cm² and, as a result, the capacity increased to nearly 60% of the theoretical. The latter is the same as the capacity in the 10th cycle. Cycling data obtained from cells constructed with various amounts of carbon and tested at various current densities between 0.5 and 3 mA/cm² indicate that the major loss seen in the initial 10-20 cycles can be minimized by an optimal carbon content, thinner electrodes, application of compression to the electrode package, and cell testing at lower current densities.

The major cause of capacity loss in the second region appears to be the inefficiency of recharge. However, this inefficiency does not appear to be chemically derived. It can be minimized by use of low charge current densities of the order of 0.5 mA/cm². This indicates its strong association with electrode structural factors.

The significance of a low charge current density on cathode rechargeability may be illustrated further with the data for a cell which was initially cycled at 3 mA/cm² for both discharge and charge between 1.6-3.2V. The initial capacity of ~$0.75e^-/Cr_{0.5}V_{0.5}S_2$ decreased to ~$0.2e^-/Cr_{0.5}V_{0.5}S_2$ by the 15th cycle. There was no further capacity change until the 20th cycle. The recharge current density was then reduced to 1

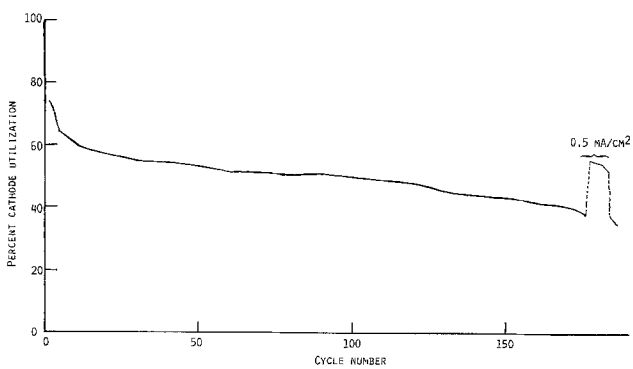

Fig. 6. Cathode utilization vs. cycle number for a Li/$Cr_{0.5}V_{0.5}S_2$ cell. Electrolyte, 50:50 THF:2Me-THF/$LiAsF_6$(1.5M). Current density; $id = ic = 2$ mA/cm², except where noted. Voltage limits; 1.6-3.1V.

mA/cm² with the result that the discharge capacity at 3 mA/cm² increased to ~0.6e^-/$Cr_{0.5}V_{0.5}S_2$. The latter capacity remained steady for the next 20 cycles, after which the test was ended.

The behavior of cells cycled to depth of discharges (DOD) of either 30% or 60% did not differ much from that discussed above.

Limitations at the Li electrode also contribute to some of the capacity loss during later stages in cell cycling. Dendritic Li continues to accumulate on the anode surface and this Li reacts with the electrolyte. The result is a gradual loss of electrolyte and a slow increase in cell resistance.

Figure 7 depicts the cycling behavior of a cell with a theoretical capacity of ~11 Ahr. The cell was cycled at 1.0A constant current, corresponding to a C/10 rate. Some typical cycles of the cell are depicted in Fig. 8. The excellent behavior of the cell, showing a rather low capacity fade rate with cycling, is largely attributed to the thinner electrodes. Although cycling at a C/10 rate, the current density is a relatively low 0.54 mA/cm². The eventual cell failure is believed to be caused by resistance rises due to Li-electrolyte reactions and not by cathode failure. The failure modes of rechargeable Li cells with 2Me-THF/$LiAsF_6$ will be the subject of a separate future paper (18).

Effects of voltage limits on the rechargeability of the cell have been investigated with laboratory cells (16). Charge limits up to 4V could be used for many cycles without any immediate consequences on cell performance. Spectroscopic analyses, however, revealed organic products indicative of solvent degradation. A safe upper voltage limit for constant current cycling would be 3.2V. A safe lower limit appears to be 1.5V, below which some electrolyte reduction seems to occur. Cells showed practically no rechargeability after a discharge to ~1V. X-ray analysis revealed that such overdischarged cathodes contain LiF, presumably resulting from the reduction of $LiAsF_6$. The sulfide remained as $LiCr_{0.5}V_{0.5}S_2$. The irreversibility of overdischarged cathodes appears to be caused by excessive LiF deposition.

Comparison of $Cr_{0.75}V_{0.25}S_2$ and $Cr_{0.5}V_{0.5}S_2$.—The data of Murphy *et al.* (9) indicate a reversible capacity of ~0.6e^-/mol of $Cr_{0.7}V_{0.5}S_2$ with a mid-discharge voltage of ~2.65V. However, no data beyond five cycles are given in that paper. We have confirmed the results of Murphy *el al.* However, we found the capacity of $Cr_{0.75}V_{0.25}S_2$ to fade significantly by ~10 cycles even when the cathode had ~20 w/o carbon. Therefore, we prefer $Cr_{0.5}V_{0.5}S_2$ for long cycle-life cells. An advantage of $Cr_{0.75}V_{0.25}S_2$, of course, is its higher voltages, indicating potential special uses.

Conclusions

The capacity and rechargeability of the $Cr_{0.5}V_{0.5}S_2$ cathode have been shown to depend on the composition of the cathode, and are determined by the relative amounts of the disulfide, carbon, and the binder. The higher capacities shown, over a wide range of current densitites, by electrodes optimized with respect to their carbon contents are not the result of higher electronic conductivities of those electrodes; rather, those advantages appear to be due to the higher porosities and better particle-to-particle contacts in such electrodes. Because of the relatively larger amounts of carbon in optimized $Cr_{0.5}V_{0.5}S_2$ electrodes, the specific energy and energy densities achieved in practical cells have been lower than what we have obtained in comparable Li/TiS_2 cells (17) (see Table III). However, $Cr_{0.5}V_{0.5}S_2$ provides higher cell voltages (the mid-discharge voltage of Li/TiS_2 cells is ~2.1V and that of Li/$Cr_{0.5}V_{0.5}S_2$ cells is ~2.3V), which combined with its excellent rechargeability may make this material desirable for many applications. We have also demonstrated that the rechargeability of $Cr_{0.5}V_{0.5}S_2$ is superior to that of $Cr_{0.7}V_{0.25}S_2$.

The scheme of studies discussed in this paper appears to be useful for the evaluation of potential positive electrodes for ambient temperature Li cells. We believe that such studies are essential for making claims about the energy density and specific energy achievable in practical cells.

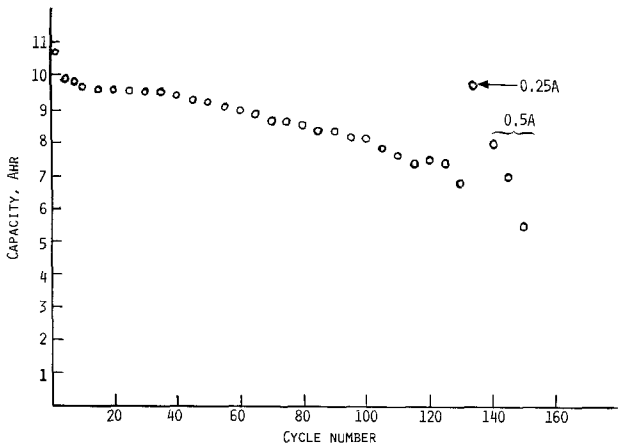

Fig. 7. Capacity vs. cycle number in a 10 Ahr Li/$Cr_{0.5}V_{0.5}S_2$ cell. Electrolyte; 2Me-THF/$LiAsF_6$(1.4M). Current; 1A, except where noted.

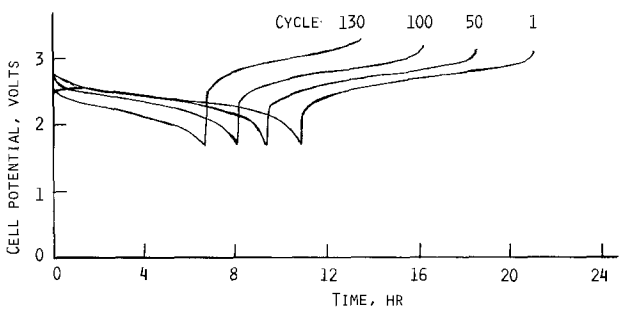

Fig. 8. Typical cycles of the cell shown in Fig. 7. Current; 1A. Voltage limits; 1.6-3.1V.

Table III. Energy densities in Li/TiS_2 and Li/$Cr_{0.5}V_{0.5}S_2$ cells with 2Me-THF/$LiAsF_6$

Cell type	Cathode composition	Volumetric energy density, W-hr/liter			Specific energy,* W-hr/kg		
		Cycle 1	Cycle 50	Cycle 100	Cycle 1	Cycle 50	Cycle 100
Li/TiS_2**	84 w/o TiS_2 8 w/o C 8 w/o Teflon	166	125	108	90 (160)	68 (120)	60 (103)
Li/$Cr_{0.5}V_{0.5}S_2$	70 w/o $Cr_{0.5}V_{0.5}S_2$ 20 w/o C 10 w/o Teflon	110	88	76	63 (117)	51 (93)	44 (83)

* The numbers in parentheses represent values excluding the weights of can and cover.
** Data to be published.

Acknowledgment

This work was supported by the U.S. Army Electronics Research and Development Command under Contract DAAK20-81-C-0378.

Manuscript submitted March 18, 1983; revised manuscript received *ca.* July 19, 1983.

REFERENCES

1. K. M. Abraham, *J. Power Sources*, **7**, 1 (1981/2).
2. M. S. Whittingham, *Prog. Solid State Chem.*, **12**, 41 (1978).
3. K. M. Abraham and S. B. Brummer, in *"Lithium Batteries,"* J. P. Gabano, Editor, Chap. 14, Academic Press, London (1938).
4. D. W. Murphy and P. A. Christian, *Science*, **205**, 651 (1979).
5. K. M. Abraham, J. L. Goldman, and M. D. Dempsey, *This Journal*, **128**, 2493 (1981).
6. G. L. Holleck and J. R. Driscoll, *Electrochim. Acta*, **22**, 644 (1977).
7. G. H. Newman, in "Proceedings of the Workshop on Lithium Non-Aqueous Battery Electrochemistry," E. B. Yeager, B. Schumm, G. Blomgren, D. R. Blankenship, V. Leger, and J. Akridge, Editors, p. 143, The Electrochemical Society Softbound Proceedings Series, Pennington, NJ (1980).
8. K. M. Abraham, J. L. Goldman, and D. L. Natwig, *This Journal*, **129**, 2409 (1982).
9. D. W. Murphy, J. N. Carides, F. J. DiSalvo, and J. V. Waszczak, *Mater. Res. Bull.*, **12**, 825 (1977).
10. J. R. Driscoll and G. L. Holleck, EIC Corporation, Newton, MA, unpublished results.
11. J. L. Goldman, R. M. Mank, J. H. Young, and V. R. Koch, *This Journal*, **127**, 1461 (1980).
12. K. M. Abraham and L. Pitts, *ibid.*, **128**, 2574 (1981).
13. R. V. Moshtev, V. Manev, A. Nassalevska, G. Pistoia, and M. Icovi, *ibid.*, **128**, 1399 (1981).
14. D. W. Murphy, F. J. DiSalvo, and J. N. Carides, *J. Solid State Chem.*, **29**, 339 (1979).
15. R. Rizzo, in "Lithium Batteries," H. V. Venkatasetty, Editor, p. 223, The Electrochemical Society Softbound Proceedings Series, Pennington, NJ (1981).
16. K. M. Abraham, D. L. Natwig, P. B. Harris and J. W. Avery, Final Report, No. DELET-TR-81-0378-F, on ERADCOM Contract DAAK20-81-C-0378 (1982).
17. K. M. Abraham, J. L. Goldman, P. B. Harris, J. Avery and S. B. Brummer, Paper 314 presented at The Electrochemical Society Meeting, Detroit, MI, Oct. 17-21, 1982.
18. K. M. Abraham, To be published.
19. K. M. Abraham and J. L. Goldman, *J. Power Sources*, **9**, 239 (1983).

Corrosion Behavior of β and Martensitic Al Brasses

J. P. Celis, J. R. Roos,* F. Terwinghe

Departement Metaalkunde, Katholieke Universiteit Leuven, B-3030 Heverlee, Belgium

ABSTRACT

Shape memory alloys are characterized by either a thermally or mechanically induced phase transformation. Such alloys are, *e.g.*, ternary Cu-Zn-Al alloys in which a $\beta \rightleftarrows$ martensite (β') phase transformation can be induced. In the present study, the influence of the phase structure on the dezincification behavior of Al brasses was investigated using accelerated tests, field tests, and electrochemical measurements. From these tests, the unsuitability of accelerated tests based on weight losses is demonstrated as well as the large dependence of dezincification on phase transformation temperature.

The phenomenon and the name "shape memory effect" have become well-known since the discovery of this property in a nickel-titanium alloy, called Nitinol. But in fact, many years before the development of Nitinol, a shape memory effect has been found in Cu-Zn, Au-Cd alloys, and also ternary bcc aluminum brasses. These copper-zinc-aluminum alloys with either beta phase or martensitic structure exhibit several unusual properties such as shape memory effect and superelasticity (1).

The basic mechanism governing the properties of shape memory alloys is a transformation in atomic structure. On cooling, an austenitic structure (β) transforms over a small temperature range ($\pm 10°C$) into a martensitic structure (β') and reverts to the austenitic structure when heated up again. The temperature at which the transformation austenite $\rightarrow$ martensite starts cooling is called the M_s temperature; the temperature at which the transformation stops is called M_f. For the reverse transformation, these temperatures are called A_s and A_f, respectively. The principle of the shape memory effect is illustrated in Fig. 1. Let us consider a martensitic material which has been previously deformed at a temperature below A_s (for instance, compressed from an initial length l_1, to a final length l_2). By simply heating up the material above A_f it regains its original shape (length l_1). By cooling below M_f, the length again becomes l_2 (two-way memory effect). For simplification, the effect of common thermal expansion is neglected.

Superelasticity is best demonstrated by a stress-strain curve as shown in Fig. 2. If a shape memory material is stressed at a temperature above A_f, the slope of the stress-strain curve decreases abruptly when a critical stress is reached. The elongation is composed of a "classical" elastic deformation of the original austenitic matrix phase and of an elongation

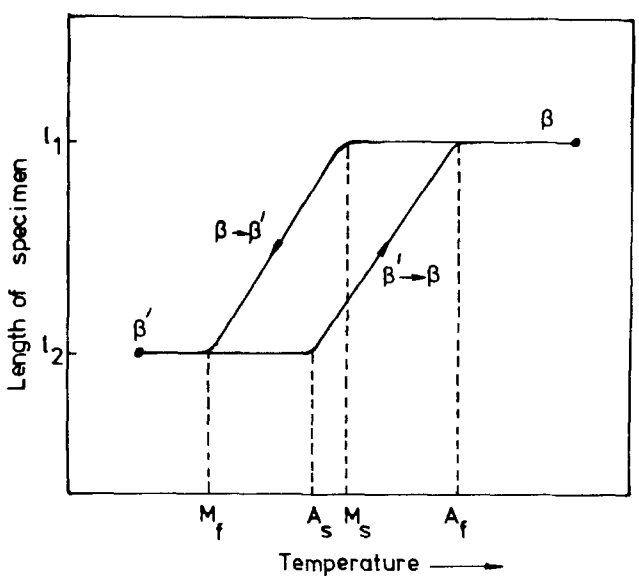

Fig. 1. Illustration of the shape memory effect

* Electrochemical Society Active Member.
Key words: corrosion, alloys, phase transformation.

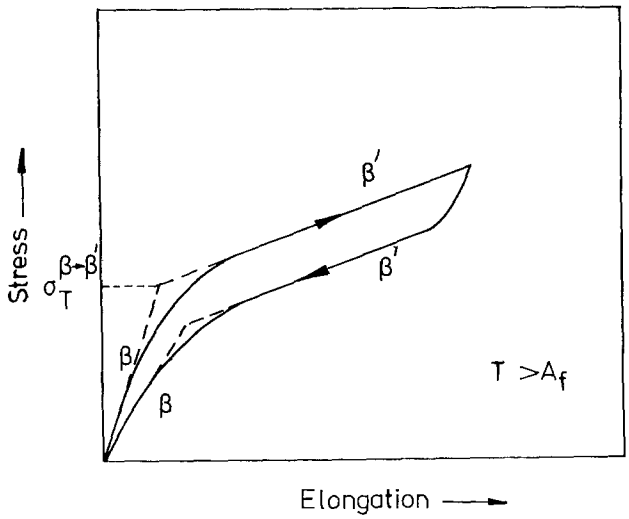

Fig. 2. Illustration of superelasticity. $\sigma_T^{\beta\to\beta'}$ is the theoretical stress level for the $\beta\to\beta'$ transformation at temperature T.

due to the stress-assisted transformation of the austenite (β) into martensite (β'). When the applied stress is released the martensite transforms back to the original β matrix and the elongation reverts to zero. It can thus be stated that the M_s temperature determines in which temperature range a shape memory alloy can be used. The value of this M_s temperature depends upon the chemical composition of the shape memory alloy. In the case of the Cu-Zn-Al shape memory alloys, the M_s temperature can vary from about −100° up to 250°C (Fig. 3) (2). From mechanical and physical considerations, the zinc content of shape memory aluminum brasses can only vary between 10 and 25 weight percent (w/o), the aluminum content between 3 and 10 w/o.

The shape memory effect of these Cu-Zn-Al alloys can be put to use among many other applications in heat sensors like, *e.g.*, the PROTEUS® heat sensor, already successfully tested in electrolysis plants. This heat sensor (Fig. 4) is composed of a metallic holder in which a Cu-Zn-Al spring is located. The heat sensor is connected to the object to be monitored, *e.g.*, fitted on the cathode bus bars in an electrolytic cell. Any rise in temperature of the cathode due, *e.g.*, to short circuits between electrodes is transferred to the spring which at a predetermined temperature, starts expanding and lifts a plastic cap, thereby exposing a brightly colored and highly visible part of the heat sensor (Fig. 5). Other applications are being developed in the field of thermal and mechanical energy transducers, temperature regulating systems, self-activating fasteners, etc.

The corrosion behavior of brasses has been studied extensively for many years. The corrosion problem of these alloys is mainly the dezincification of the base material. Work has been concentrated mainly on α Cu-Zn alloys but also upon duplex α plus β, and β Cu-Zn alloys (3-5). The major results can be summarized as follows: (*i*) α Cu-Zn is suffering from dezincification only when the alloy contains more than 15 w/o Zn; (*ii*) α Cu-Zn is less susceptible to dezincifi-

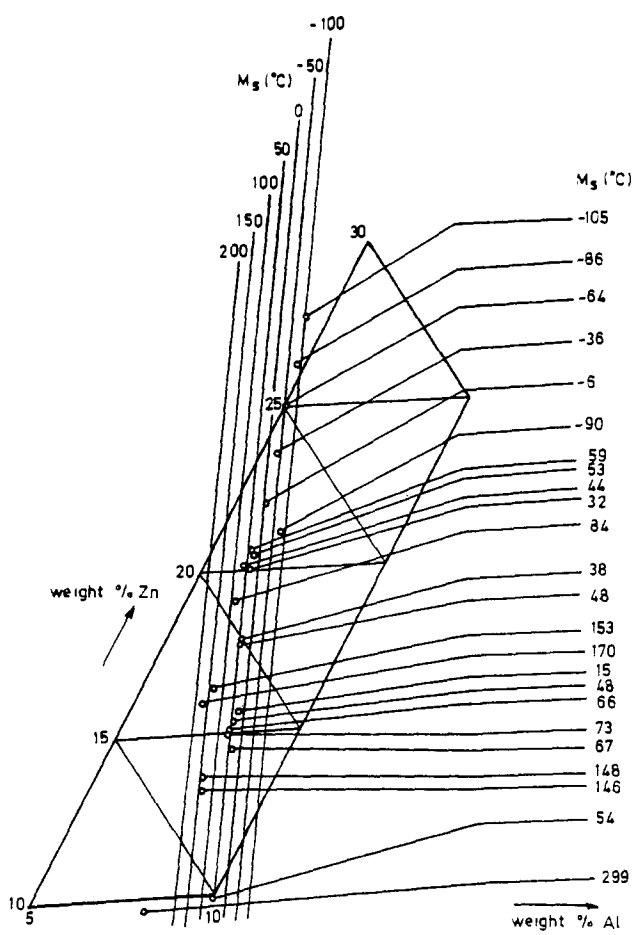

Fig. 3. Relation between composition and transformation temperature in ternary Cu-Zn-Al alloys (2).

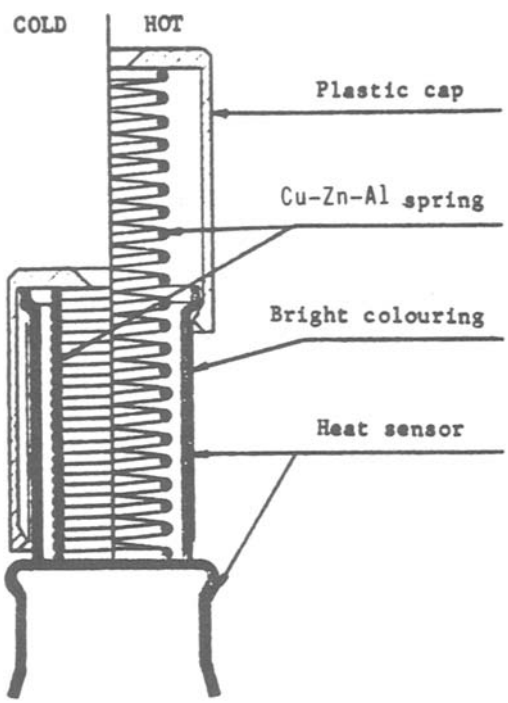

Fig. 4. Schematic representation of the heat sensor at low and high temperature.

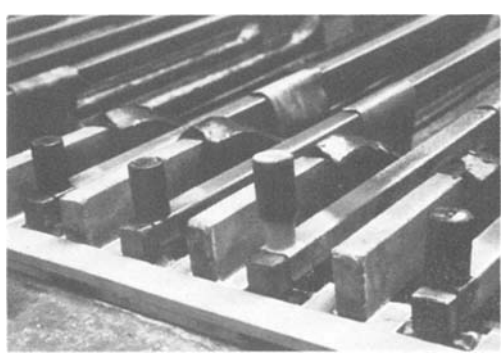

Fig. 5. Temperature sensor mounted on an electrolysis cell

cation than duplex α plus β Cu-Zn and β Cu-Zn alloys; and (*iii*) in the case of duplex α plus β brass, the zinc-rich β phase undergoes preferential dezincification.

To explain dezincification of these brasses, two basic theories are generally proposed (6, 7). The first one points out that there is a selective dissolution of zinc atoms whereby a porous copper layer remains. The second theory claims that zinc and copper atoms go into solution followed by a redeposition of copper and a further dissolution of zinc. Lucey (6) studied the phenomenon of copper redeposition. He performed dezincification tests upon α and β brasses in oxygen-free copper chloride/zinc chloride solution. In this solution, copper can be redeposited by reduction of Cu^+ at potentials below -0.65V *vs.* SCE while Cu^{2+}, after the disproportionation of $CuCl_2$, can be reduced below -0.40V *vs.* SCE. He determined also the potential of film-free β brass (-0.80V *vs.* SCE) and of α brass (-0.62V *vs.* SCE). He demonstrated that on α brass, only Cu^{2+} ions can be reduced although on β brass, both Cu^{2+} and Cu^+ ions can be reduced. Further, he showed that the disproportionation of $CuCl_2$ is prohibited by the addition of a very small amount of arsenic acting through the following pair of reactions

$$3Cu^{2+} + As \rightarrow 3Cu^+ + As^{3+} \quad [1]$$

$$3Cu + As^{3+} \rightarrow 3Cu^+ + As \quad [2]$$

Lucey found that 0.02% As already prevents dezincification of α brass. For β brass, on the contrary, the addition of As did not have any effect. Lucey's conclusion was that the theory of copper redeposition is the right one because by adding arsenicum, Cu^{2+} ions are no longer formed and only Cu^+ ions can still be reduced, and since these ions can only be reduced on β brass, the direct relation between deposition of copper and dezincification was proven. Heidersbach and Verink (7) carried out a set of experiments on α and β brass in an oxygen-free 5*N* HCl solution. In their study, x-ray diffraction, electron microscopic, metallographic, atomic absorption, and electrochemical techniques were used. The general conclusion of their investigation was that both dezincification mechanisms can be operative depending on conditions of potential and pH for both α and β brasses. It should be recognized that neither Lucey nor Heidersbach and Verink performed tests under real life conditions. They both studied the dezincification problem in very aggressive, highly concentrated chloride solutions.

In recent years, a number of studies on the dezincification of α aluminum brasses have been published (8-11). These alloys containing up to 2 w/o Al are commonly used in condenser tubes. Shreir (10) concludes that addition of aluminum decreases the dezincification of such ternary α brasses in comparison to α Cu-Zn alloys with similar zinc content. Here the presence of As, even in trace amounts (As $>$ 0.006 w/o), markedly ameliorates the corrosion resistance of the aluminum brass (9). It has been shown that surface conditions play a decisive role in the corrosion process of these alloys (11). About β and β' Cu-Zn-Al alloys, no information has appeared in the literature as far as we know. In the present paper, a corrosion investigation of these alloys is reported. Tests on α Cu-Zn and α plus β Cu-Zn were also performed for the purpose of comparison. The study of the corrosion behavior of shape memory aluminum brasses under an applied load or under thermal cycling is out of the scope of this work and is the aim of a future investigation.

Experimental

The alloys were produced by melting and ingot casting of weighed amounts of pure Cu, Zn, and Al. The mechanical processing consisted either of hot extrusion into rods of ϕ 12 mm or hot rolling to plates of 1.5 mm thickness. In the hot rolled condition, the mean grain size of these alloys is rather large and ranged around 1 mm. Typical microstructures of β and β' Cu-Zn-Al alloys tested are shown in Fig. 6 and 7, respectively. The β microstructure consists of large grains. Differences in grain growth orientation causes a difference in light reflectivity between different grains. The β' microstructure also contains large grains (in fact the original β grains) in which fine martensite plates of different orientations are visible.

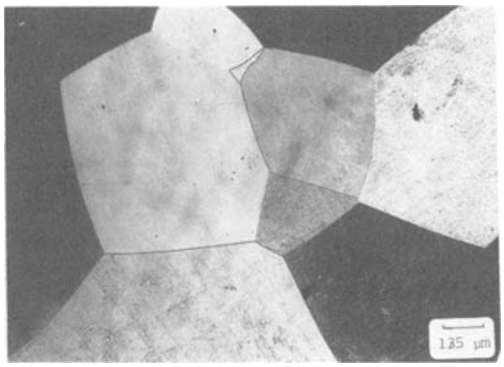

Fig. 6. Microstructure of a β Cu-Zn-Al alloy

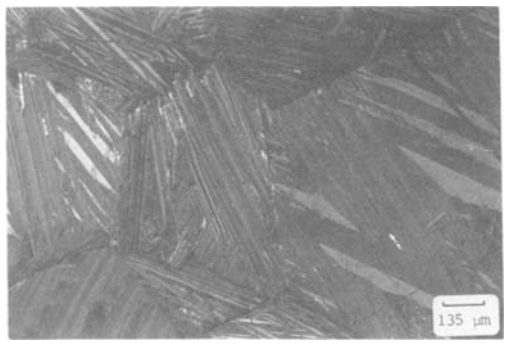

Fig. 7. Microstructure of a β' Cu-Zn-Al alloy

The susceptibility to dezincification of the different alloys has been studied using accelerated tests, field tests, and electrochemical measurements. Chemical analysis, M_s temperature, and metallographic structure of the materials tested are given in Table I. Depending on the experimental testing technique, different procedures for the specimen preparation were used, namely, sand blasting of hot rolled plates for outdoor tests, sand blasting of hot extruded rods for accelerated tests and immersion tests in tap water. Specimens for electrochemical measurements were prepared by grinding hot rolled plates on 1200 grit paper followed by rinsing with ethanol.

Electrochemical measurements were done in a three-electrode glass cell with saturated calomel ref-

Table I. Characteristics of materials tested

Reference	Chemical analysis Cu	Zn	Al	Approximate M_s temp. (°C)	Metallographic structure
(1)	90.03	9.97	—		α
(2)	75.30	24.90	—		$\alpha + \beta$
(3)	71.14	25.38	3.52	+200	$\alpha + \beta$ after extrusion β' after heat-treatment
(4)	70.14	25.32	4.57	+35	β'
(5)	69.56	25.40	5.07	−50	β
(6)	76.10	17.81	6.26	+200	β'
(7)	75.25	17.75	7.22	+35	β'
(8)	74.35	17.99	7.67	−50	β
(9)	79.86	11.84	8.74	+200	β'
(10)	78.93	11.94	9.44	+35	β'
(11)	78.35	11.49	10.57	−50	β

erence electrode and platinum counterelectrode connected to a PAR 173 potentiostat and a PAR 175 function generator. For the outdoor field tests, test specimens (10 × 15 cm, thickness 1.5 mm) were fixed on a painted frame through plexi holders. The specimens were mounted on a 30° slope. After testing, either the weight loss of corroded specimens was determined or the corrosion depth was measured with a Leitz MeF light microscope on polished cross sections after mounting the specimens in nonconductive resins. The procedure used for the determination of the dezincification depth is the one described by Mattsson (12) which consists of an examination of the entire cross section, viewing field by field, one measurement being made at a fixed point in each field. In order to ensure the highest possible accuracy, the greatest possible degree of magnification and the largest number of measured viewing fields were selected. SEM analysis was done with a Cambridge 600 scanning electron microscope equipped with EDX facilities for elemental analysis.

Results and Discussion

The most convenient method to test the corrosion behavior of materials is the use of standard tests. In connection with brasses, it seems from the literature that the most reliable results for dezincification are obtained by using the Swedish Standard test SMS 3226 (12). This test consists of an immersion of the specimens in a 10 g/liter $CuCl_2$ solution at 75° ± 3°C for 24 hr using a solution volume of 250 ml per cm^2 exposed specimen area. Besides this industrially well accepted testing technique, another standard test for determining the susceptibility of alloys to dezincification is sometimes used, namely, the Australian standard test AS C316-1970 (13). This test procedure consists of an immersion during 14 days at 80°C into a solution containing 13.5 g/liter hydrated ferric chloride, 18.7 g/liter hydrated copper sulfate, and 1.5 ml/liter hydrochloric acid. The evaluation of the susceptibility to dezincification is in both tests based on the determination of the depth of dezincification as described earlier.

Taking into account the $\beta' \rightarrow \beta$ phase transformation (see Fig. 1) which will occur on heating up Cu-Zn-Al alloys having an M_s temperature between room temperature and 75°C, a modification of this standard test procedure for testing the susceptibility to dezincification of β' Cu-Zn-Al alloys became necessary. The phase structure should remain constant during testing for a correct evaluation of the susceptibility to dealloying. Therefore, the procedures mentioned in both the Swedish Standard test SMS 3226 and the Australian Standard test AS C316-1970 have been performed at a controlled testing temperature of 20°C. In this way, modified standard tests caused a dezincification and dealuminization of β and β' Cu-Zn-Al alloys sufficiently large for the study of the susceptibility to dealloying. Dezincification depths from the modified Swedish Standard test SMS 3226 are shown in Fig. 8 for the different Cu-Zn and Cu-Zn-Al alloys mentioned in Table I. As can be seen from Table I, three groups of Cu-Zn-Al alloys were selected with a constant zinc content of 25, 18, and 12 w/o, respectively. For each group, the aluminum content was selected in such a way that M_s temperatures of +200°, +35°, and −50°C were obtained. From Fig. 8 it can be deduced that, using the modified Swedish Standard test: (*i*) β and β' Cu-Zn-Al alloys are much more sensitive to dezincification than α and $\alpha + \beta$ Cu-Zn alloys with a comparable zinc content; (*ii*) at constant zinc content, β' Cu-Zn-Al alloys are more sensitive to dezincification than β Cu-Zn-Al; (*iii*) β' Cu-Zn-Al alloys with comparable zinc content have a larger tendency to dezincification at increasing M_s temperature, corresponding to a lower aluminum

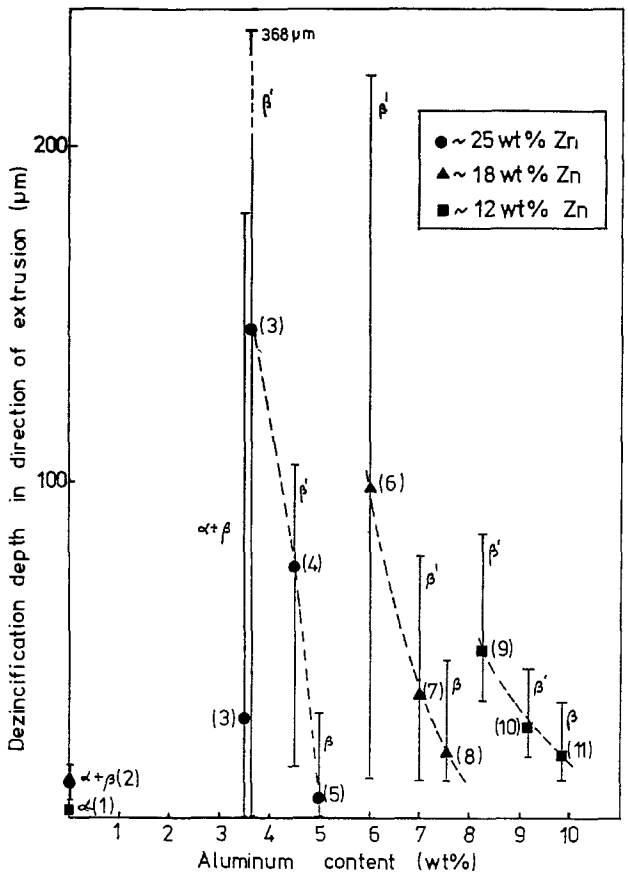

Fig. 8. Dezincification depth determined after a Swedish test SMS 3226 at 20°C for 24 hr.

content. From the modified Australian Standard test, a much larger dezincification depth was determined in comparison to the one obtained by the modified Swedish Standard test. However, the conclusions which can be drawn from the modified Australian Standard test are identical to those mentioned earlier for the modified Swedish Standard test.

In order to check the validity of these accelerated tests, prolonged field tests in running tap water at room temperature and outdoor field tests in a marine, industrial, and rural location were performed. Outdoor field tests were evaluated on the basis of the maximum dezincification depth which was measured on a polished cross section. Some typical polished metallographic cross sections of β and β' Cu-Zn-Al alloys after 4 months outdoor exposure are shown in Fig. 9 and 10, respectively. In martensitic Cu-Zn-Al alloys, it seems that the dealloying occurs along the

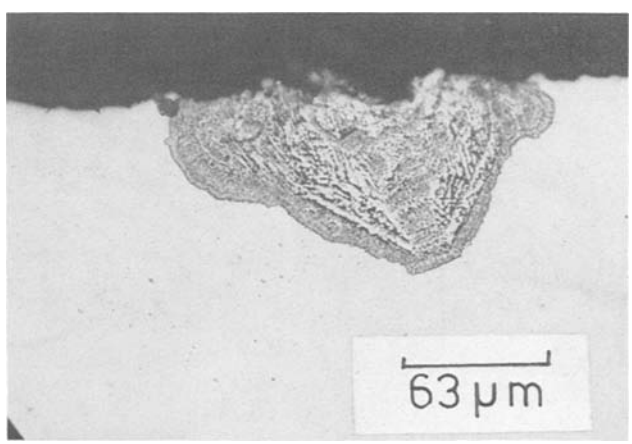

Fig. 9. β Cu-27Zn-4Al structure after an outdoor field test in a marine environment for 4 months.

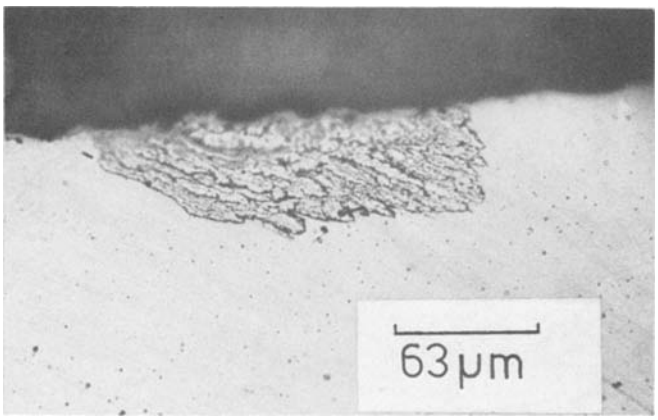

Fig. 10. β' Cu-15Zn-8Al structure after an outdoor field test in an industrial environment for 4 months.

martensite plate boundaries. Metallographic examination of polished cross sections showed that in contrast to Cu-Zn alloys in which dezincification is spread out over the entire exposed surface, dezincification in β and β' Cu-Zn-Al alloys is limited to a few locations, most frequently where crevice corrosion is likely to occur. At these locations, dezincification progresses very deeply into the material. Such a localized dezincification in a β' Cu-Zn-Al spring, tested for 100 days in a marine environment, is shown in Fig. 11. As can be seen from this figure, dezincification occurs preferentially along grain boundaries. Results obtained after 2 yr atmospheric exposure testing (see Table II) gave the following series from low to high dezincification: α Cu-20Zn-3Al < α Cu-30Zn < β Cu-27Zn-4Al < β' Cu-15Zn-8Al. This series is in accordance with the results obtained from the modified Swedish Standard test. The small differences among results obtained at different locations are in accordance with the expected relative aggressivity of these environments (largest for the marine environment, lowest for the rural environment).

Extensive scanning electron microscopy including energy dispersive analysis on polished cross sections of corroded specimen from an outdoor field test was also performed. Typical results obtained for a β Cu-27Zn-4Al alloy and β' Cu-25Zn-8Al tested in a rural and in an industrial environment, respectively, for a period of 1 yr are shown in Fig. 12 and 13. Zn and Al profiles across noncorroded and corroded areas are

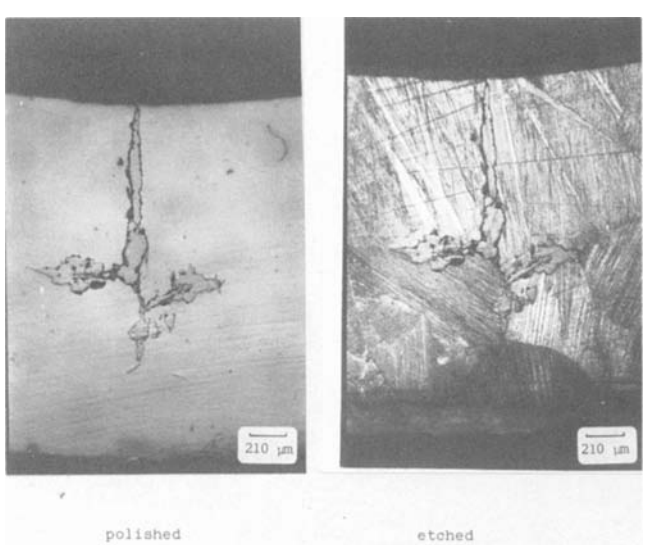

Fig. 11. Dezincification path in a β' Cu-Zn-Al alloy being tested for 100 days in a marine environment.

Table II. Maximum dezincification depth measured in different brasses

	Outdoor field tests (exposure time 2 yr) Max. dezincification (μm)		
	Rural area	Industrial area	Marine area
α Cu-20Zn-3Al	<2	12.2	20.4
α Cu-30Zn	28.5	30.6	24.5
β' Cu-15Zn-8Al	46.9	48.9	187.7
β Cu-27Zn-4Al	55.1	89.1	192.0

shown. These analyses show that in the corroded area zinc is no longer present; aluminum, however, is still present but confined along certain bands. Using modified standard tests, similar results on dealloying were obtained. In Fig. 14, *e.g.*, EDX analysis results for a β' Cu-16Zn-7Al alloy tested according to the modified Australian Standard test AS C316-1970 procedure are shown. Figure 14 shows relative intensities for different elements measured at three different locations across the noncorroded to the corroded transition area. The local aluminum concentration reaches at well-defined bands much larger values than in the bulk of the uncorroded alloy. Thus, during dealloying, the aluminum seems to concentrate at the frontier between virgin material and dealloyed material, while the zinc

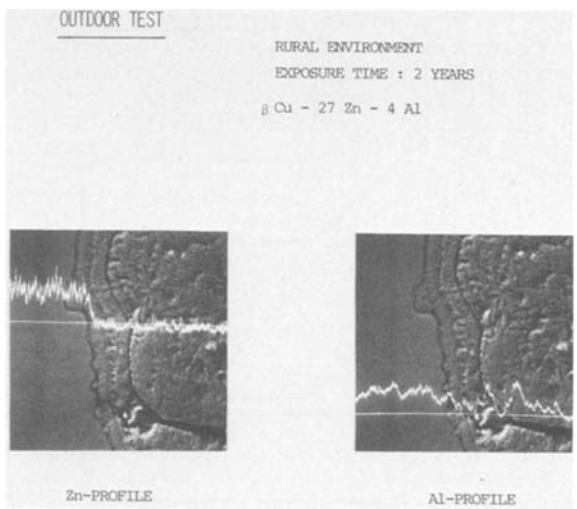

Fig. 12. SEM microstructures and EDS analyses of corroded material.

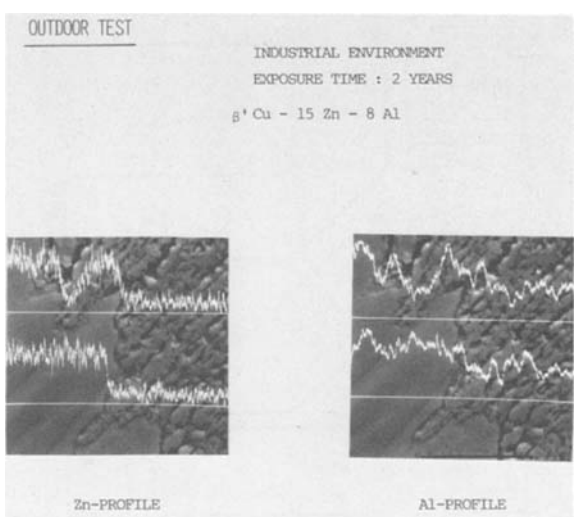

Fig. 13. SEM microstructures and EDS analyses of corroded material.

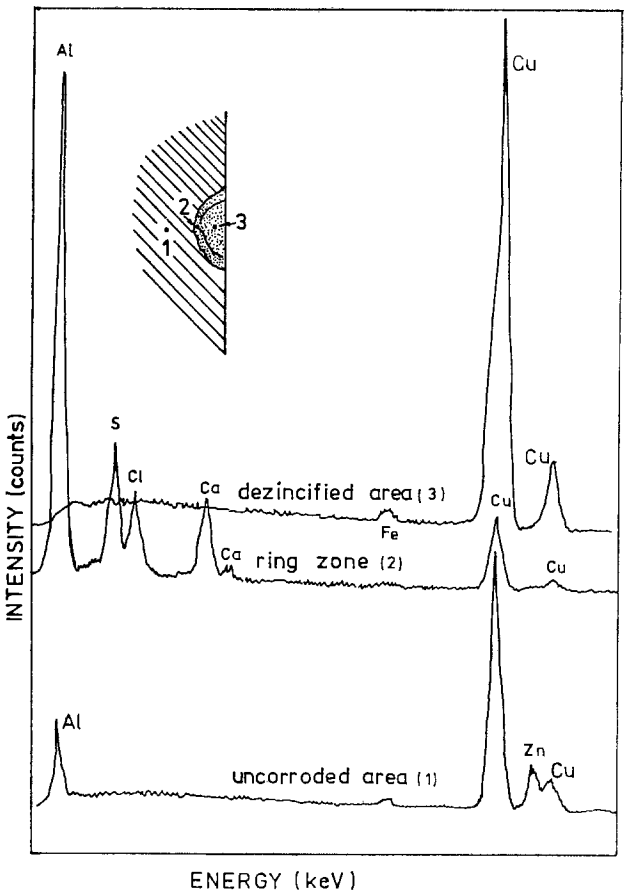

Fig. 14. EDX analyses determined on a β' Cu-16Zn-7Al alloy after an Australian test C316-1970 at 20°C.

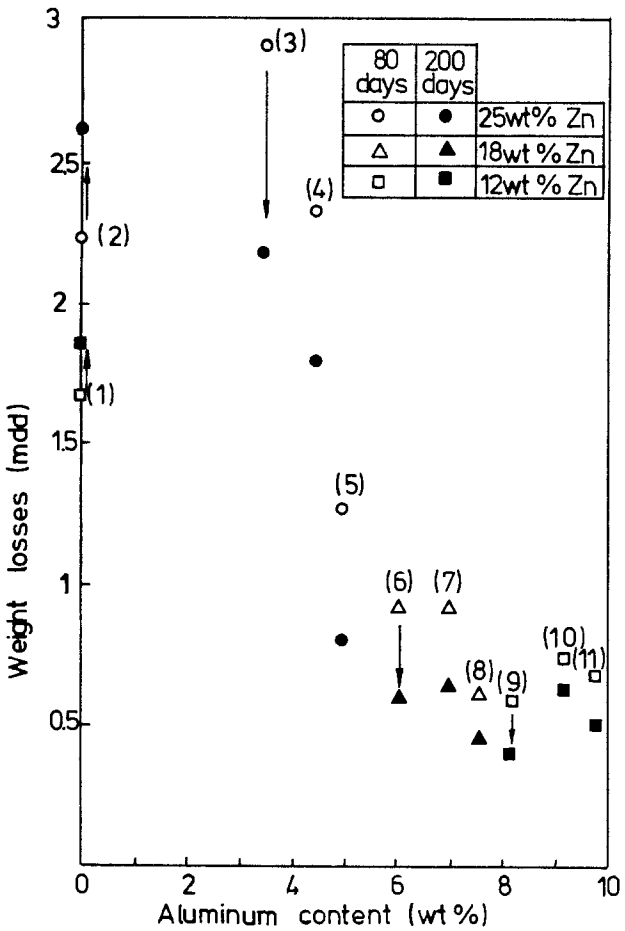

Fig. 15. Weight loss determined after a field test in flowing tap water at room temperature.

is leached out towards the surrounding environment. Concerning the mechanism of dealloying, this increased aluminum content in between dezincified and non-dezincified areas supports the hypothesis of an anodic dissolution of the brass matrix followed by a redeposition of copper (in a porous form) from the solution. Redeposition of aluminum ions is thermodynamically impossible at the rest potential in tap water of Al brasses (14).

Corrosion progress during immersion tests in running tap water was based on weight loss expressed in mg/day/dm^2. The weight loss determined after 80 and 200 days immersion in running tap water is given in Fig. 15. The numbers in Fig. 15 refer to materials mentioned in Table I. These results appear to be in contradiction with the results from the accelerated tests, in that, *e.g.*: (*i*) β and β' Cu-Zn-Al alloys do not show higher weight losses than Cu-Zn alloys with a comparable zinc content; (*ii*) For β and β' Cu-Zn-Al alloys, no dependence on the M_s temperature can be deduced, but that an exponential decrease of the weight loss occurs at increasing aluminum content between 3 and 10 w/o. The important role of the pile-up of aluminum along the dezincification front can be shown based on results of field tests in tap water given in Fig. 15. At increasing test duration and in contrast to Cu-Zn alloys, β and β' Cu-Zn-Al alloys show a decreasing weight loss. This decrease can be attributed to the formation of an aluminum barrier acting as a passivation layer. Some electrochemical support for this passivating behavior is given in Fig. 16. Potentiokinetic curves were recorded for three β' Cu-Zn-Al alloys with comparable M_s temperature but different aluminum content in tap water at room temperature. In the anodic part, a passivation effect appears at increasing aluminum content. Taking into account the results of Fig. 9, this passivation effect seems to be more effective in lowering dezincification sensitivity

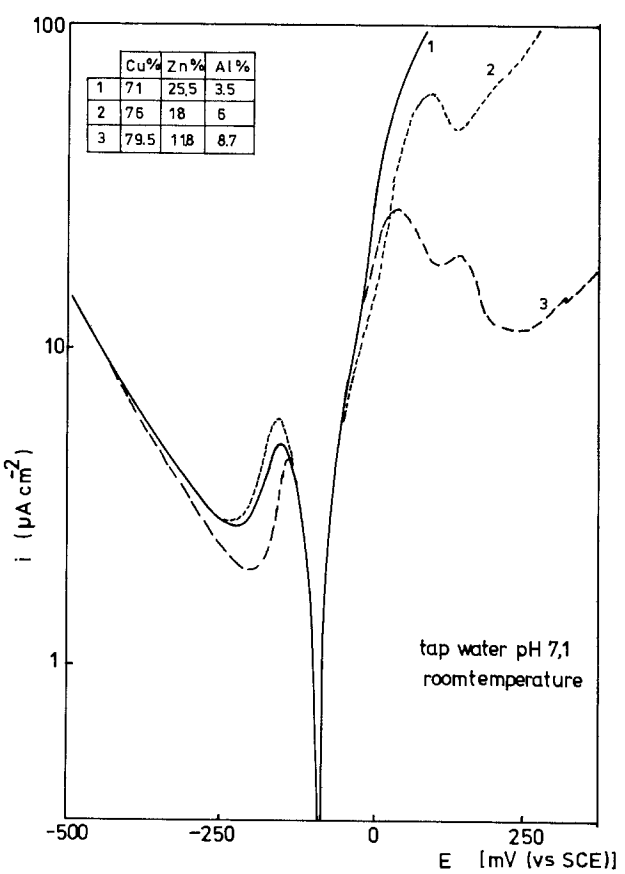

Fig. 16. Potentiokinetic polarization curves of different β'

in β Cu-Zn-Al alloys than in β' Cu-Zn-Al alloys. The reason for this is far from fully understood, but different diffusion rates in β and β' Cu-Zn-Al alloys could be partly responsible for it.

Conclusion

In order to test the corrosion behavior of recently developed β and β' Cu-Zn-Al alloys, accelerated standard tests as the Swedish Standard tests C316-1970 are found suitable if a modified test temperature of 20°C instead of 75° and 80°C, respectively, is used. Good agreement between these standard tests and field tests is obtained if comparisons are made on the basis of dealloying depth, rather than on the basis of weight loss. In comparison with conventional α and $\alpha + \beta$ Cu-Zn alloys and with α Cu-Zn-Al alloys which are successfully used as material for heat exchanger tubes in marine environments, β and β' Cu-Zn-Al alloys show a larger, more localized, dezincification susceptibility. This localized dezincification, which extends preferentially along grain boundaries into the bulk of the material, explains the unsuitability of tests based on weight loss measurements.

With increasing aluminum content, a decreasing dezincification was determined which could be due to a pile up of aluminum along the frontier between virgin material and dezincified area. Besides the effect of the aluminum content, the results clearly indicate a dependency on the atomic structure. At comparable zinc and aluminum content, the β structure is less sensitive to dezincification than the β' structure. Experimental evidence supports a dezincification mechanism based on an anodic dissolution of the brass followed by a redeposition of copper in a porous form from the solution.

Manuscript submitted March 5, 1982; revised manuscript received *ca.* July 18, 1983.

REFERENCES

1. L. Delaey, E. Aernoudt, and J. Roos, *Metall.* **31,** 1325 (1977).
2. M. Jaenen, Engineering Thesis, Katholieke Universiteit Leuven, Heverlee, Belgium (1977).
3. H. Leidheiser, in "The Corrosion of Copper, Tin and their Alloys," Chap. 6, John Wiley & Sons, New York (1971).
4. H. Logan, in "The Stress Corrosion of Metals," Chap. I, John Wiley & Sons, New York (1966).
5. H. Uhlig, in "Corrosion Handbook," John Wiley & Sons, New York (1963).
6. V. Lucey, *Br. Corros. J.*, **1,** 10 (1965); **1,** 53 (1965).
7. R. Heidersbach and E. Verink, *Corrosion,* **28,** (11), 397 (1972).
8. R. Muller, in "Proceedings of the 8th International Congress Metallic Corrosion," p. 1470, Mainz (1981).
9. F. Mazzia and S. Torchio, in "Proceedings of the 8th International Congress Metallic Corrosion," p. 199, Mainz (1981).
10. L. Shreir, in "Corrosion," Vol. 1, Chap. 4.2, G. Newnes Ltd., London (1965).
11. G. Gusmano, R. Cigna, L. Giuliani, and R. Loreti, *Br. Corros. J.*, **15,** 222 (1980).
12. E. Mattsson and M. Linder, Proceedings of Eurocor 1977, p. 445, London (1977).
13. B. Dillon, *Met. Forum,* **1,** 71 (1978).
14. M. Pourbaix, in "Atlas of Electrochemical Equilibria in Aqueous Solutions," NACE, Houston (1974).

Molecular Generality of Surface-Enhanced Raman Spectroscopy: Application to the Study of Surface Resonance Raman-Enhanced Complexes of Iron (II) with 1,10-Phenanthroline on Silver and Iron

R. P. Van Duyne and M. Janik-Czachor[1]

Department of Chemistry, Northwestern University, Evanston, Illinois 60201

ABSTRACT

RR and SERR spectra of adsorbed complexes of 1,10 phenantroline with Fe(II) (*viz.*, $Fe(phen)_3^{+2}$) on silver from highly dilute solution (*viz.*, 5×10^{-6}M) are presented. The first attempt to combine SERS and RRS in order to investigate the surface spectra of $Fe(phen)_3^{+2}$ on an iron substrate is also reported. The results are encouraging with regard to possible application of SERS and RRS to studies of wet metallic corrosion, *in situ*.

Surface-enhanced Raman spectroscopy (SERS) has become a useful *in situ* technique for the molecular characterization of the metal-solution interface (1-8). Surface Raman spectra have been observed for more than 50 different molecules and ions adsorbed on silver. The monolayer detection sensitivity of SERS is made possible through a 10^6-fold enhancement of the effective Raman scattering cross section for the adsorbed species relative to that for the same molecule in bulk (1, 4). Surface-enhanced Raman spectra have also been observed on Cu and Au substrates with enhancement factors in the 10^5 range. It is generally accepted that an enhancement factor of at least 10^3 is required to observe Raman scattering from molecular monolayers (1, 9, 10). These findings are in agreement with the predictions of the Image Field Enhancement Model (IFE) of SERS (1, 9). This model predicts that the enhancement factor (e) is critically dependent on the optical properties of the substrate. The nature of the metal enters into the electromagnetic theory through its dielectric constant. Studies of carefully chosen alloys whose dielectric constant can be changed in a controlled way (*viz.*, Ag_{1-x} Pd_x) can be used to test this concept (11).

The IFE model predicts also that such metals as Li and Hg should be strong SERS enhancers (12). The recent results for adsorbates on Li (13) seem to confirm this prediction although the results on Hg have now been retracted (14). Unfortunately, many important metals are expected to yield enhancements below the critical value (9).

The unconfirmed reports of SERS for Ni, Pt (15) and Cd (16) are not pertinent, since no efforts have been made to check whether the Raman bands that have been observed actually exhibit all the characteristic features of surface-enhanced signals. However, it is possible that low enhancement metals can be probed

[1] On leave from the Institute of Physical Chemistry, Polish Academy of Sciences, Warsaw, Poland.

Key words: complex, iron, phenanthroline, raman spectroscopy.

through a combination of resonance Raman spectroscopy (RRS) and surface-enhanced effects which would bring the total enhancement factor above 10^3 (1, 4, 17). Previous studies of adsorbates on silver have shown that a total enhancement of 10^{10} can be observed by superimposing these effects (1, 4, 18).

In this paper, we will consider the RR and SERR spectra of adsorbed complexes of 1,10-phenanthroline with Fe(II), (*viz.*, $Fe(phen)_3^{2+}$). This complex is characterized by a small dissociation constant ($K = 5 \times 10^{-22}$) (19) and an intense electronic absorption spectrum in the visible region ($\epsilon_{510nm} = 1150$ dm^3 M^{-1} cm^{-1}) (20). The solution RRS of $Fe(phen)_3^{2+}$ has already been reported (21). In addition, we have studied the adsorption of $Fe(phen)_3^{2+}$ on an Ag electrode, from a 5×10^{-6}M $[Fe(phen)_3](ClO_4)_2$ solution, in a manner similar to that reported earlier (18). We also attempted to combine SERS and RRS to investigate the surface spectra of Fe $(phen)_3^{2+}$ on an iron substrate, where the SERS enhancement for Fe is probably $< 10^3$ (9).

Iron was chosen as a substrate material because of its technological importance. In particular, one is interested in the ability of RRS or SERS to probe, *in situ*, the surface chemical processes associated with corrosion and passivation.

Experimental

All Raman spectra were obtained using the 514.5 nm line of a Coherent Radiation Laboratories Model CR-3 argon ion laser. Descriptions of the Raman detection system and spectroelectrochemical cell have appeared previously (1, 4).

The following systems were investigated:

$Ag/[Fe(phen)_3(ClO)_4]_2$;

$C = 5 \times 10^{-6}$ M/Borate buffer/H_2O

$pH = 8.4$

Fe/phen; $C = 5 \times 10^{-3}$ M/Borate buffer/H_2O

$pH = 8.4$

The first one served as a reference system for the second.

All solutions were prepared with deionized water (Milli-Q, Millipore Corporation) and were thoroughly deoxygenated with prepurified nitrogen prior to the immersion of an electrode. 1,10-phenanthroline (Aldrich Chemical Company, Incorporated) was recrystallized twice from a mixture of CH_3OH and H_2O (1:10). $[Fe(phen)_3](ClO_4)_2$ (G. Federick Smith Chemical Company) was recrystallized three times from CH_3OH. Polycrystalline silver electrodes were electrochemically roughened by a single double potential step ($E_1 = -0.6$V *vs.* SCE and $E_2 = +0.2$V *vs.* SCE) anodization pulse passing 20 mC/cm^2. Polycrystalline iron electrodes were mechanically roughened with grade 800 emery paper.

Results and Discussion

Ag/Fe(phen)$_3^{+2}$.—Figure 1(a) shows the surface Raman spectrum of $Fe(phen)_3^{2+}$ adsorbed on an anodized Ag electrode from a 5×10^{-6}M solution. At this concentration, the bulk RR scattering is expected to be negligible. To confirm that the spectrum in Fig. 1(a) is a true surface enhanced RR spectrum, both the potential dependence and depolarization ratios were investigated. The standard model of the electrochemical double layer predicts that cationic complexes such as $Fe(phen)_3^{+2}$ would be most strongly adsorbed at potentials negative to the point of zero charge (pzc), which for silver is approximately −0.7V *vs.* SCE (1). The coverage should decrease at potentials positive to the pzc. This behavior was observed for the Ag/$Fe(phen)_3^{+2}$. The intense SERS signals found at −0.8V (Fig. 1(a)) practically disappear below the noise level at 0.0V *vs.* SCE (Fig. 1(b)) where the surface coverage is reduced. Depolarization ratios for the most intense peaks, given in Table I, were found to be above 0.7. In comparison, the corresponding bulk $Fe(phen)_3^{2+}$ depolarization ratios are much lower (Table I).

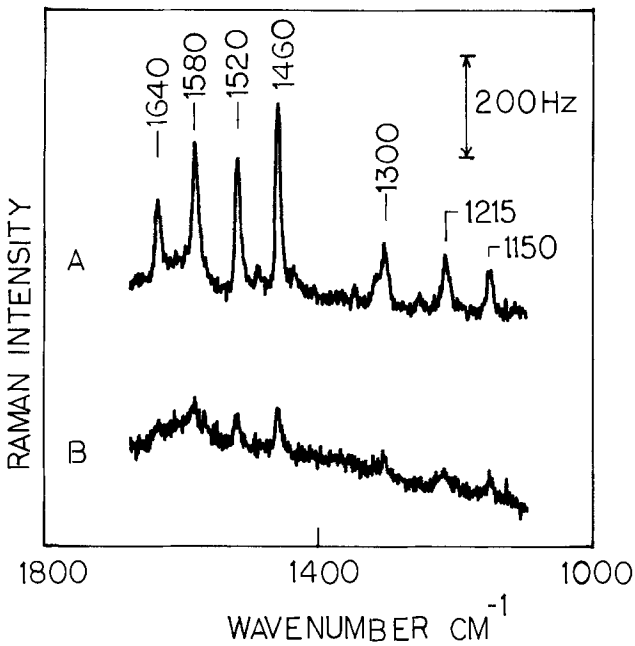

Fig. 1. Effect of potential on the SERS spectrum of $[Fe(phen)_3^{2+}]$ on silver (a) −0.8V (b) 0V. Laser power 60 mW, slits 2 cm^{-1}, solution concentration of $Fe(phen)_3(ClO_4)_2$ 5×10^{-6}M. Laser wavelength 514.5 nm.

In Fig. 2, Raman spectra of $Fe(phen)_3(ClO_4)_2$ in solution, on a silver electrode, and in the solid state are compared. The relative intensities of the bands in the surface spectrum are similar to those of the solid state but differ from those of the bulk solution.

Fe/phenanthroline.—The Image Field Enhancement Model (IFE) of SERS predicts that an enhancement factor of only *ca.* 10^2 can be expected on transition metal substrates (1, 9). This value is below the minimum enhancement required to observe a surface-enhanced Raman spectrum while using a conventional cw laser/double monochromator system. However, by superimposing an enhancement due to RRS on the SERS enhancement, one might expect to increase the overall enhancement factor enough so that signal from the adsorbed species can be detected (see (17, 18)). We anticipated that in a 1,10 phenanthroline containing solution, the $Fe(phen)_3^{2+}$ complexes can be formed only within the potential region where Fe^{+2} is the dissolution product (*viz.* active metal dissolution at low anodic potentials). It was of interest to find out if the dissolution of Fe in the presence of 1,10 phenanthroline takes place through the forma-

Table I. Resonance Raman spectra of $[Fe(phen)_3]^{2+}$ depolarization ratios for the most prominent modes

$\Delta\nu$/cm^{-1}	a $\rho_{solution}$	b $\rho_{surf,\ Ag}$	c $\rho_{surf,\ Fe}$
1150	0.42	0.8	0.6
1215	0.35	0.75	0.55
1300	0.34	0.75	0.54
1460	0.30	0.80	0.46
1520	0.38	0.80	0.5
1580	0.40	0.70	0.5
1640	0.26	0.80	0.55

[a] See R. J. H. Clark *et al.*, Ref. (21).
[b] Measured at −0.8V *vs.* SCE.
[c] Measured at −0.5V *vs.* SCE.

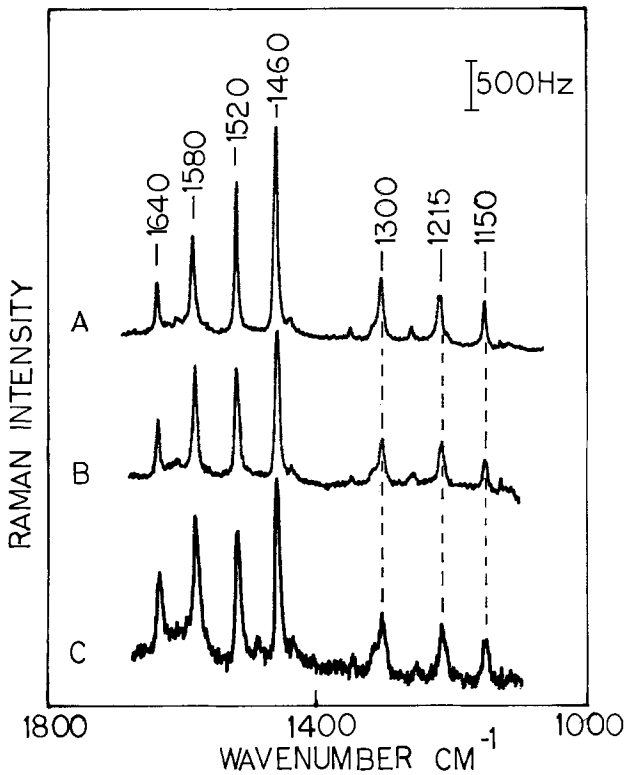

Fig. 2. Comparison of the Raman spectra of $Fe(phen)_3^{2+}$ in various environments: (a) 5×10^{-3}M aqueous solution, (b) solid $Fe(phen)_3(ClO_4)_2$, (c) adsorbed on Ag electrode, as in Fig. 1a (4× expanded). Laser power 60 mW, slits 2 cm^{-1}, laser wavelength 514.5 nm.

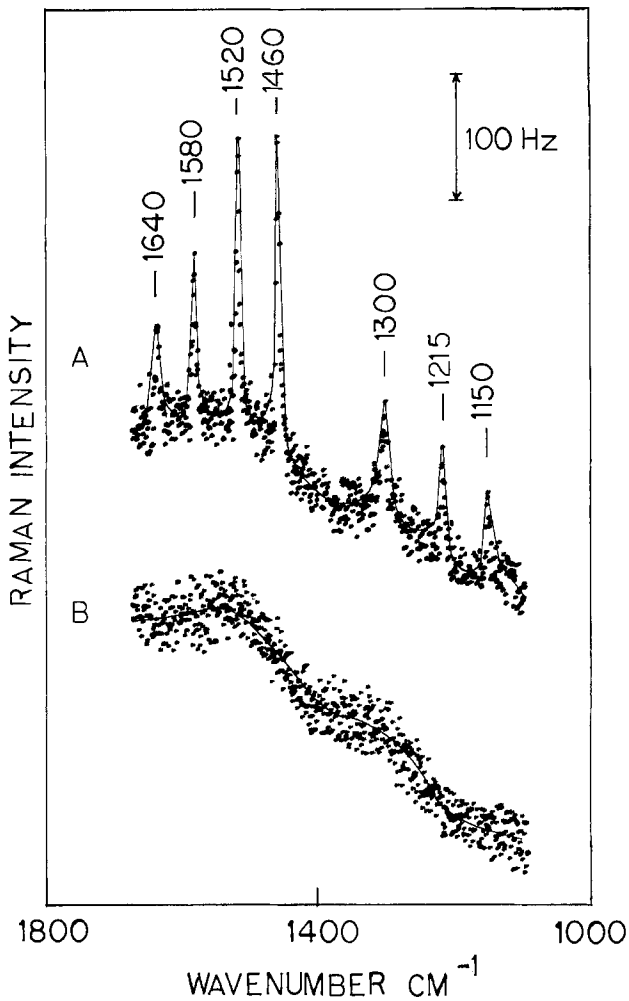

Fig. 3. Effect of potential on the SERS spectrum of $[Fe(phen)_3^{2+}]$ on Fe electrode, in 5×10^{-3}M 1,10-phenanathroline solution. (a) −0.5V (b) +1V. Laser power 200 mW, slits 2 cm^{-1}, laser wavelength 514.5 nm.

tion of surface complexes of $Fe(phen)_3^{2+}$, and whether we can observe surface spectra of these complexes.

In Fig. 3a, a Raman spectrum is shown for $[Fe(phen)_3^{2+}]$ formed during the anodic dissolution of Fe electrode at −0.5V in a borate buffer solution containing 0.005M 1,10 phenanthroline. Since there is a continuous flux of Fe^{+2} into the solution and, therefore, continuous formation of $[Fe(phen)_3^{2+}]$, one might expect the overall Raman spectrum to arise from scattering off both adsorbed and bulk species. The depolarization ratios for the various peaks in Fig. 3a lie between those for the corresponding bands of the complex in solution and on a silver electrode. This behavior might be expected for spectra having contributions from both bulk and adsorbed species.[2] In order to verify this hypothesis, the effect of potential on the peak intensities was investigated. Figure 3b shows an example of the spectrum at +1V. At this high anodic potential in the passive region, iron is dissolved as Fe^{+3} so that $Fe(phen)_3^{2+}$ complexes are not formed. Consequently, all the RR lines characteristic for this complex disappear.

1,10 phenanthroline is an inhibitor of iron dissolution (22). Fischer and Yamaoka (22) have speculated, on the basis of their kinetic and capacitive measurements, that the metal dissolution of iron goes via surface ligand complexes with phenanthroline. This changes the potential distribution within the double layer and results in an inhibitive effect. In the present paper, we were able to show, at least for Fe/borate buffer system, that the $[Fe(phen)_3^{+2}]$ complexes are indeed present at the iron surface during its anodic dissolution. This finding suggests that the combination of SERS and RRS can be successfully applied in investigations of some corrosion inhibitors for transition metals.

[2] However, a more precise distinction between the part of the signal due to surface and due to bulk species has not yet been done.

Ogura and Hackerman (23) have studied the anodic behavior of iron in borate buffer containing 1,10 phenanthroline. They have concluded that the light blue complex $[Fe(phen)]_3^{+3}$ is formed within the passive region instead of the red $[Fe(phen)]_3^{+2}$, which is formed within the active dissolution region. This is a natural consequence of Fe^{+3} production within the passive region, and Fe^{+2} production within the anodic active dissolution region. The effect of potential on the $[Fe(phen)]_3^{+2}$ spectrum, presented in Fig. 3a, is most probably a result of this behavior, which obviously is not changed by the presence of the inhibitor. Unfortunately it was not possible to obtain the surface spectrum of $[Fe(phen)]_3^{+3}$, due to lack of sensitivity. We have found that the molar extinction coefficient of $[Fe(phen)]_3^{+3}$ is only $\sim 10^2$, in contrast to the value of $\sim 10^4$ for the $[Fe(phen)]_3^{+2}$, *i.e.*, that the absorbance of the green light by $[Fe(phen)]_8^{+3}$ is several times lower than that of the Fe(II) complex (20).

In conclusion, the data presented are encouraging with regard to possible application of SERS + RRS to studies of metallic corrosion and dissolution. In the present investigation, the $Fe(phen)_3^{+2}$ complexes were produced during the anodic dissolution of an iron electrode at low anodic potentials. We were able to detect, *in situ*, the surface signals from these complexes. This is indicative of the formation of these complexes as intermediates in an adsorbed state during the dissolution reaction. This type of structural information is not available from conventional electrochemical experiments. Thus, the combination of

SERS and RRS technique may prove to be a sensitive probe of the mechanism of wet corrosion.

Furthermore, surface enhanced RR spectra on Ag electrode were obtained for highly dilute solutions of the $Fe(phen)_3^{2+}$ complexes, confirming that SERS has potential for detecting RR scattering from extremely small amounts of the adsorbed species from solution.

Acknowledgments

We gratefully acknowledge the financial support of the Office of Naval Research (Contract N00014-79-C-0369), and the National Science Foundation (Grant CHE-7824866).

Manuscript submitted Sept. 7, 1982; revised manuscript received July 18, 1983.

Northwestern University assisted in meeting the publication costs of this article.

REFERENCES

1. R. P. Van Duyne, in "Chemical and Biochemical Applications of Lasers," Vol. 4, C. B. Moore, Editor, pp. 101-185, Academic Press, New York (1979).
2. M. Fleischmann, P. J. Hendra, and A. J. McQuillan, *J. Chem. Soc., Chem. Commun.*, 80, (1973).
3. M. Fleischmann, P. J. Hendra, and A. J. McQuillan, *Chem. Phys. Lett.*, **26**, 163 (1974).
4. D. L. Jeanmaire and R. P. Van Duyne, *J. Electroanal. Chem.*, **84**, 163 (1974).
5. R. P. Van Duyne, *J. Physique*, **38**, C5-239 (1977).
6. M. G. Albrecht and J. A. Creighton, *J. Am. Chem. Soc.*, **99**, 5115 (1977).
7. V. V. Marinyuk and R. M. Lazorenko-Manevich, *Elektrokhimiya*, **14**, 452 (1978). V. V. Marinuyk, R. M. Lazorenko-Manevich, and Ya. M. Kolotyrkin, *ibid.*, **14**, 1019 (1978).
8. B. Pettinger and U. Wenning, *Chem. Phys. Lett.*, **56**, 253 (1978).
9. G. C. Schatz and R. P. Van Duyne, *Surf. Sci.*, **101**, 425 (1980).
10. S. G. Schultz, M. Janik-Czachor, and R. P. Van Duyne, *ibid.*, **104**, 413 (1981).
11. T. E. Furtak and J. Kester, *Phys. Rev. Lett.*, **45**, 1652 (1980).
12. G. C. Schatz, in "Surface Enhanced Raman Scattering," p. 39, Plenum Press, New York (1982).
13. M. Moskovitz and D. P. Dilella, *ibid.*, p. 263.
14. R. Naaman, S. J. Buelow, O. Chesnovsky, and D. R. Herschbach, *J. Phys. Chem.*, **84**, 2692 (1980); L. A. Sanchez, L. R. Burke, and J. R. Lombardi, *Chem. Phys. Lett.*, **79**, 219 (1981); R. L. Burke, J. R. Lombardi, and L. A. Sanchez, *Adv. in Chemistry*, **201**, 69 (1982).
15. H. Yamada and Y. Yamamoto, *Chem. Phys. Lett.*, **77**, 520 (1981).
16. B. H. Loo, *J. Chem. Phys.*, **76**, 5955 (1981).
17. G. Hagen, B. Simic-Glavaski, and E. Yeager, *J. Electroanal. Chem.*, **88**, 269 (1978).
18. T. M. Cotton, S. G. Schultz, and R. P. Van Duyne, *J. Am. Chem. Soc.*, **102**, 7960 (1980).
19. T. S. Lee, J. M. Kolthoff, and D. L. Leussing, *ibid.*, **70**, 2348 and 3596 (1948).
20. A. E. Harvey, J. A. Smart, and E. G. Amis, *Anal. Chem.*, **27**, 26 (1955).
21. R. J. H. Clark, P. C. Turtle, D. P. Strommen, B. Striesand, J. Kincaid, and K. Nakamoto, *Inorg. Chem.*, **16**, 84 (1977).
22. H. Fischer and E. Yamaoka, *Electrochim. Acta*, **10**, 679 (1965).
23. H. Ogura and N. Hackerman, *This Journal*, **121**, 1013 (1974).

Analysis of Passive Films on Austeno-Ferritic Stainless Steel by Microscopic Ellipsometry

Katsuhisa Sugimoto* and Shiro Matsuda

Department of Metallurgy, Faculty of Engineering, Tohoku University, Sendai 980, Japan

ABSTRACT

An ellipsometer which provides the determination of optical properties of a thin film on the microscopic area of a specimen has been developed. Using this ellipsometer the thickness and optical constants of passive films on individual grains in the microstructure of a 22Cr-10Ni austeno-ferritic stainless steel have been measured *in situ* in pH 6.0, 1 kmol · m^{-3} Na_2SO_4 under potentiostatic control. It has been found that the films on α grains are thicker than those on γ-grains in both the passivity and the transpassivity regions. The variation in film thickness from grain to grain has also been measured. Significant differences in film thickness exist at α/γ phase boundaries. The film thickness varies even among grains of the same phase. Passive films on γ-grains are found to be thinner but more corrosion resistant than those on α grains.

Austeno-ferritic, or duplex, stainless steels have been celebrated for their good resistance to dangerous localized corrosion, such as pitting corrosion, crevice corrosion, intergranular corrosion, and stress-corrosion cracking (1-3). Owing to these superior characteristics, the demand for the steels as the material for equipment used in chloride media, for example, seawater heat exchanger tubes, continues to expand (4).

It is important, however, to note that the corrosion resistance of the steels depends on the volume ratio of ferrite (α) to austenite (γ) in the steel. The change in the structure of the steel caused by inadequate heat-treatment or welding, which accompanies the change in the ratio, deteriorates the corrosion resistance of the steels (2, 5). This means the corrosion resistance of the steels is controlled by that of each phase in the steels. It is important, therefore, to know the properties of the passive film on each phase, which determine the corrosion resistance, for getting a better understanding about the corrosion characteristics of the steels.

Ellipsometry has been known as an effective method for *in situ* analysis of passive films and used extensively in the determination of the thickness and optical properties of the films on Fe-Cr (6), Fe-Cr-Ni (7-11), and Fe-Cr-Ni-Mo (12-15) alloys. There is no report, however, about the application of ellipsometry on the analysis of films on austeno-ferritic stainless steels. This is because an ordinary ellipsometer needs a fairly large measurement area, more than a few square millimeters, and simply gives total information about a film on the area containing many α and γ grains.

The purpose of present investigation is to determine the thickness and optical constants of passive

* Electrochemical Society Active Member.

Key words: microscopic ellipsometry, passive film, austeno-ferritic stainless steel.

films on individual grains of α and γ in an austeno-ferritic stainless steel. To realize this purpose, a microscopic ellipsometer which provides the measurement of a film on an area of *ca.* 10 μm in diameter has been developed. Using this ellipsometer, passive films on individual grains of a 22Cr-10Ni austeno-ferritic stainless steel were measured *in situ* at various potentials in a neutral Na_2SO_4 solution. The thickness, potential-dependent growth rates, and optical constants of the films on α- and γ-grains were then determined. Finally, the relationship between the properties of the film and the corrosion resistance of each phase is discussed.

Experimental

Microscopic ellipsometer.—Figure 1 shows the schematic of the microscopic ellipsometer developed in this study. Although the fundamental optical arrangement is close to an ordinary null method ellipsometer, this ellipsometer equips two groups of lenses behind the analyzer for magnifying the polarized reflection image of the specimen. A MICRO-NIKKOR-f3.5-55 mm lens was used as the primary magnifying lens and a NIKKOR-f3.5-20 mm lens the secondary magnifying lens. This combination of lenses can provide a maximum magnification of *ca.* 600 times and a long working distance of *ca.* 40.6 mm. As a result, it was possible to measure a region of *ca.* 10 μm in diameter on the specimen surface by using this ellipsometer.

The enlarged polarized reflection image from the magnifying lenses was projected on the screen of observing apparatus. The iris was stopped at the position of the image of the grain desired and narrowed down to pass the light only from the grain.

Monochromatic light of wavelength 546.1 nm from a diffraction grating monochromator coupled to a xenon arc source was used for the measurement. The angle of incidence of the monochromatic light was 59.65°. The compensator was fixed at an angle of −45°. Two optical parameters, the relative phase retardation Δ and the relative amplitude reduction Ψ, were obtained from the angles P and A of the polarizer and the analyzer at the extinction positions.

Cell.—The cell was made of Pyrex glass and had two optically flat windows of synthetic quartz. It was also equipped for electrochemical measurements.

Specimens.—A cold-rolled sheet of 2 mm thickness of 22Cr-10Ni austeno-ferritic stainless steel with chemical composition given in Table I was used. Coupons 20 × 30 mm were cut from the sheet, heated at 1350°C under vacuum for 30 min, and then water-quenched. After this heat-treatment, the α/γ volume ratio in the sheet was *ca.* 1, and the grain size was tens of μm. The mean composition for α- and γ-grains

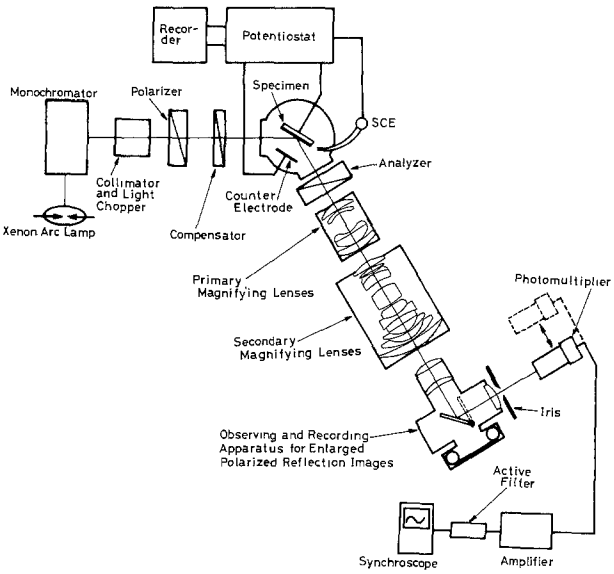

Fig. 1. Schematic illustration of microscopic ellipsometer

in the steel determined by electron probe microanalysis (EPMA) are shown on the lines for α- and γ-phase in Table I, respectively. The mean composition of α was 25% Cr and 8.6% Ni and that of γ was 21% Cr and 12% Ni, that is, Cr enriched in α and Ni in γ.

The two types of alloys shown in Table I as the α- or the γ-phase simulated alloys were made to have just the same average composition as the α- or the γ-phase in the steel. Regular octagonal plates with edges of length 8 mm were cut from cold-rolled sheets of 2 mm thickness of these alloys, heated at 1050°C under vacuum for 30 min, and then water-quenched to get a homogeneous structure. The specimens from the alloys were used to get approximate values of optical constant for film-free surfaces of α- and γ-grains in the steel and also approximate anodic polarization curves of them.

The surfaces of all the specimens were ground with emery paper up to no. 1500, and then finished with diamond paste. After polishing, they were degreased in ultrasonic baths of acetone and absolute ethyl alcohol.

Solution.—The solution used for most of the electrochemical experiments was 1 kmol · m^{-3} Na_2SO_4 adjusted to *p*H 6.0. Deaeration was achieved by bubbling purified N_2 through the solution for 4 hr. All experiments were carried out in an N_2 atmosphere at 20° ± 0.5°C under stationary condition.

Table I. Chemical composition of specimen (mass %)

Specimen	Cr	Ni	C	S	P	Si	Mn	Mo	Cu
Fe-22Cr-10Ni	22.3	10.4	0.0045	0.0093	0.004	0.028	0.0008	0.0022	0.0160
→ α-phase*	25.0	8.6							
→ γ-phase*	20.8	12.0							
α-phase simulated alloy	24.9	8.8	0.0018	0.0114	0.004	0.028	0.0019	0.0020	0.0078
γ-phase simulated alloy	20.6	11.9	0.0024	0.0110	0.004	0.027	0.0015	0.0020	0.0149

* analyzed by EPMA

Measurement of the film-free surface.—In our previous study (10), it was confirmed that the film-free surface of 18-8 stainless steel, which was obtained by the film removal treatment in a 0.5% bromine-methanol solution, could be kept stably in deaerated dehydrated methanol, with which the bromine-methanol solution was replaced immediately after the treatment. The treatment using the bromine-methanol solution, however, causes surface roughening, which affects ellipsometer readings and sometimes results in a serious error in the evaluation of optical constant of the film-free surface. Therefore, in order to avoid this, the technique of triboellipsometry (16) in nonaqueous environment was applied to get the optical constants of film-free surfaces of the alloys. The cell used for triboellipsometry is shown in Fig. 2. It was equipped with a polisher with $\phi 0.3$ μm Al_2O_3 powder containing silicon rubber as the polishing material and two optical windows with an angle of incidence of 60.00°. The surface of the alloy specimen attached on the PTFE holder was gently polished in dehydrated deaerated methyl alcohol. Polishing was paused sometimes, and ellipsometric parameters of the polished surface were measured immediately without changing the environment. The measurement was continued until the ellipsometer readings on the surface became constant and independent of polishing time. The ellipsometric parameters thus obtained were used for the calculation of optical constants of the film-free surfaces of specimens.

Electrochemical polarization.—The passivation of the specimens was accomplished under potentiostatic control. In the case of measurement of the change in specimen surface with increasing potential, the potential was changed from the corrosion potential in the noble direction at intervals of 100 mV and held for 1 hr at each setting potential after which the current and ellipsometric parameters were noted. A saturated calomel electrode was used as the reference electrode and the potentials reported here are referred to this base.

Procedure for microscopic ellipsometry.—The pretreatment of specimen for microscopic ellipsometry is shown in Fig. 3. First, the specimen was elctrochemically etched in 10 mass% oxalic acid to reveal crystallographic microstructure. Desired grains of α or γ with adequate dimensions for measurement were marked by a Micro-Vickers hardness tester [Fig. 3(a)]. Then, in order to avoid the effect of surface roughness on ellipsometric parameters, the etching structure on the surface was erased by polishing slightly with diamond paste [Fig. 3(b)]. The specimen

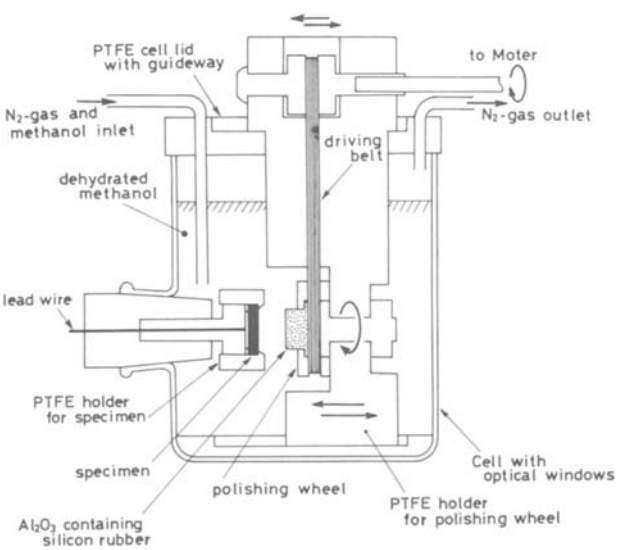

Fig. 2. Schematic illustration of the cell used for triboellipsometry

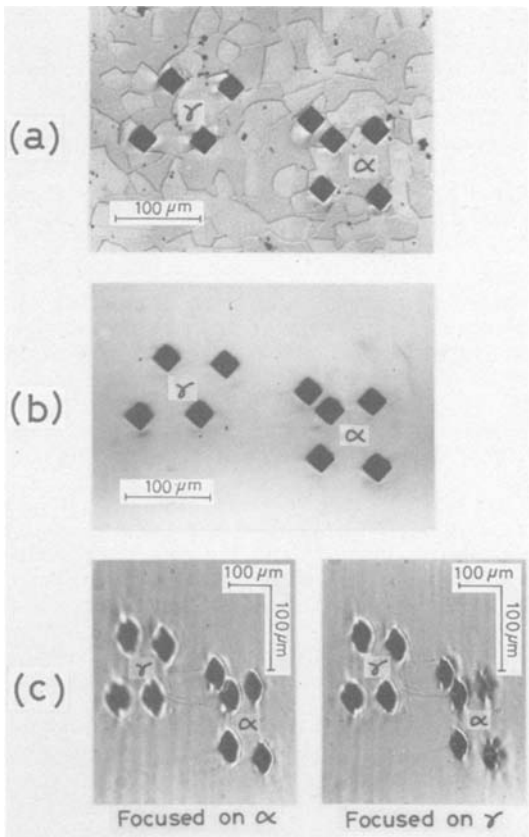

Fig. 3. Surface preparation for microscopic ellipsometry. (a) Etched and marked microstructure, (b) after polishing (a), (c) observation of (b) with microscopic ellipsometer.

in this condition was used for microscopic ellipsometric measurement. The figure of the specimen observed with the microscopic ellipsometer is shown in Fig. 3(c). Since the specimen was set at an angle of 60° against the axis of magnifying lenses, the enlargement ratio of the figure became larger longitudinally than horizontally. Only a single area surrounded by the markers was subjected to a single measurement by microscopic ellipsometry. The ordinary macroscopic ellipsometric measurement, however, was also performed on an area including many α- and γ-grains in order to know mean properties of the surface of the steel.

Interpretation of ellipsometric data.—The thickness and the complex refractive indexes of passive and transpassive films were determined using the theoretical Δ *vs.* Ψ curve which fits the experimental Δ *vs.* Ψ curve with minimal error. The theoretical Δ *vs.* Ψ curves were obtained by solving Drude's exact equations with the aid of an Acos-600 computer assuming that parallel sided isotropic homogeneous films with various complex refractive indexes $n_2 - k_2 i$ in the ranges $1.5 \leq n_2 \leq 3.0$ and $0.0 \leq k_2 \leq 0.8$ grown from 0 to 10 nm in thickness. These ranges for n_2 and k_2 almost cover the complex refractive indexes of oxide and hydroxide films on iron, chromium, nickel, and their alloys (6, 10). Other values used in the calculations were 1.356 for the refractive index of the 1 kmol $\cdot$ m^{-3} Na_2SO_4 solution, 546.1 nm for the wavelength of the light, 59.60° for the incident angle of the light and the optical constants for the film-free surfaces of the α- and the γ-phase simulated alloys determined in this work.

Results and Discussion

Optical constants for film-free surfaces of the α- and the γ-phase simulated alloys.—The optical constants $N_3 = n_3 - k_3 i$ for the film-free surfaces of the α-phase simulated alloy (Fe-25Cr-9Ni alloy) and the γ-phase

simulated alloy (Fe-21Cr-12Ni alloy) were calculated from the ellipsometric parameters measured immediately after polishing in dehydrated deaerated methyl alcohol. The refractive index of methyl alcohol $n_1 = 1.334$ was also used for the calculations. The errors resulting from surface roughening by polishing and from the birefringence of the cell windows were corrected in accordance with the procedure given in a previous paper (10). The values of N_3 thus determined are $2.68 - 3.91i$ for the α-phase simulated alloy and $2.56 - 3.77i$ for the γ-phase simulated alloy.

Change in surface film on each phase with increasing potential.—Experimental Δ *vs.* Ψ curves were obtained for individual grains of each phase after 1 hr oxidation at various potentials in pH 6.0, 1 kmol · m^{-3} Na_2SO_2. The theoretical Δ *vs.* Ψ curves were fitted to the experimental curves by the computer. Figure 4 illustrates the typical results for an α-grain (a) and a γ-grain (b).

In the case of the α-grain, the passivity region extends from —0.2-0.8V, and the experimental curve in this region coincides with the theoretical curve calculated for a film with an optical constant of $2.5 - 0.4i$. It can be read in this theoretical curve that the thickness of the passive film increases from 1.5 nm at —0.2V to 3.2 nm at 0.8V with increasing potential.

Transpassive dissolution started above 0.8V and was accompanied by characteristic changes in the ellipsometer readings. It has been found previously that surface roughening caused by transpassive dissolution does not have a serious effect on the ellipsometer readings, especially in a neutral solution (10). Therefore the change in Δ and Ψ in the potential range above 0.8V can be attributed to the change in the surface film. The experimental curve in the potential range 1.2-1.3V coincides with the theoretical curve for a film with an optical constant of $3.0 - 0.5i$ and the thickness of the transpassive film thus ranges from 3.7 nm at 1.2V to 4.0 nm at 1.3V. There is a transition region between 0.8 and 1.2V. The experimental curve in this region does not give a straight line corresponding to the growth of a film with a fixed optical constant. This suggests that the transformation of the passive film into the transpassive film takes place in this potential range.

For the γ-grain, it is evident that the experimetal curve in the passivity region between —0.2 and 0.8V coincides with the theoretical curve for a film with an optical constant of $2.3 - 0.4i$, while that for the transpassivity region between 0.9 and 1.3V corresponds to a film with an optical constant of $3.0 - 0.4i$. The film thickness in the passivity region increases from 0.5 nm at —0.2V to 2.1 nm at 0.8V and that in the transpassivity region does from 1.8 nm at 0.9V to 2.9 nm at 1.3V. A transition region in which the passive film transforms into the transpassive film exists in the potential range 0.8-0.9V.

The ordinary macroscopic ellipsometric measurement was performed on an area of the specimen containing many α- and γ-grains. The result is shown in Fig. 5. This figure seems to illustrate that the passive film with the optical constant of $2.4 - 0.4i$ grows from 1.1 nm at —0.2V to 2.8 nm at 0.8V and the transpassive film with the optical constant of $3.0 - 0.4i$ does from 3.0 nm at 1.1V to 3.6 nm at 1.3V on the area.

Figure 6 summarizes the film thickness as a function of potential for the individual grains of α and γ and the macroscopic area above mentioned. The film thickness for the α-grain is larger than that for the γ-grain at any potential measured. The thickness and the growth rate with potential for the transpassive film are always larger than those for the passive film on both the phases. The apparent film thickness on the macroscopic area determined by macroscopic ellipsometry is intermediate between the film thickness for the α-grain and that for the γ-grain.

Line analysis of film thickness.—In order to know the variation in the film thickness from grain to grain, a linear analysis was performed on the area including several grains of α and γ. Figure 7 shows the microstructure of the area analyzed. Three α-grains designated α-1, α-2, and α-3 and three γ-grains designated γ-1, γ-2, and γ-3 were selected for the analysis and marked in the same way as stated in the section on procedure for microscopic ellipsometry. Chemical composition of these grains were determined by EPMA between the points A and B and listed in Table II. The grains of the same phase have approximately the same composition and no remarkable fluctuations in Cr and Ni contents can be seen among them.

Figure 8 shows the values of Δ and Ψ obtained for the α- and γ-grains held for 1 hr at 0.5 and 1.1V, which are in the passivity and in the transpassivity regions, respectively. Theoretical Δ *vs.* Ψ curves with the same optical constants as those of the curves shown in Fig. 4 are also given in this figure. The thickness of film on each grain can be read from the position of a point for a pair of experimental Δ and Ψ values on the theoretical curves.

The film thickness thus determined for each grain is shown in Fig. 9 as a function of the distance from

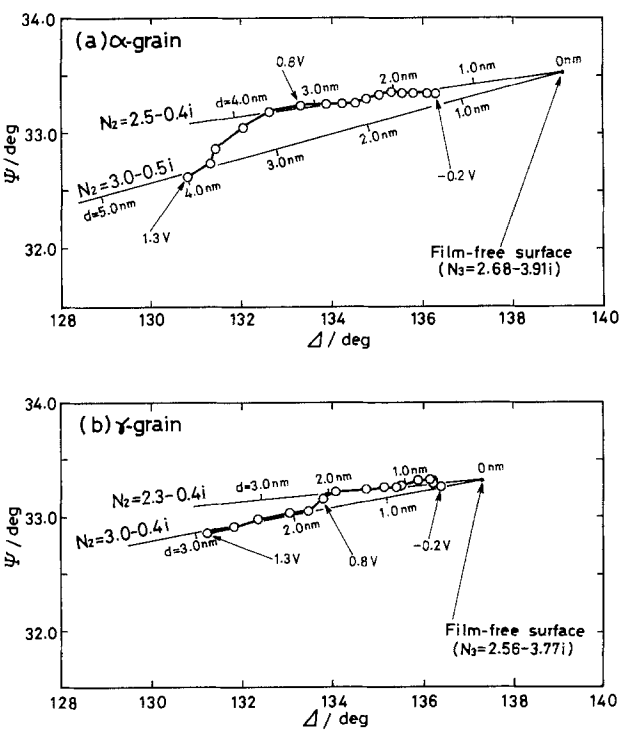

Fig. 4. Δ — Ψ loci for an α-grain (a) and for a γ-grain (b) under anodic polarization in pH 6.0, 1 kmol · m^{-3} Na_2SO_4 at 20°C.

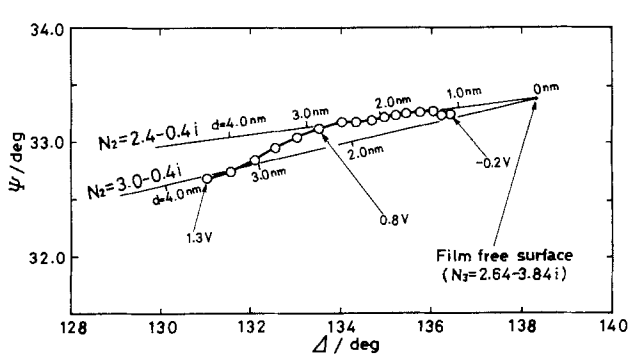

Fig. 5. Δ — Ψ locus for a macroscopic area containing many α- and γ-grains under anodic polarization in pH 6.0, 1 kmol · m^{-3} Na_2SO_4 at 20°C.

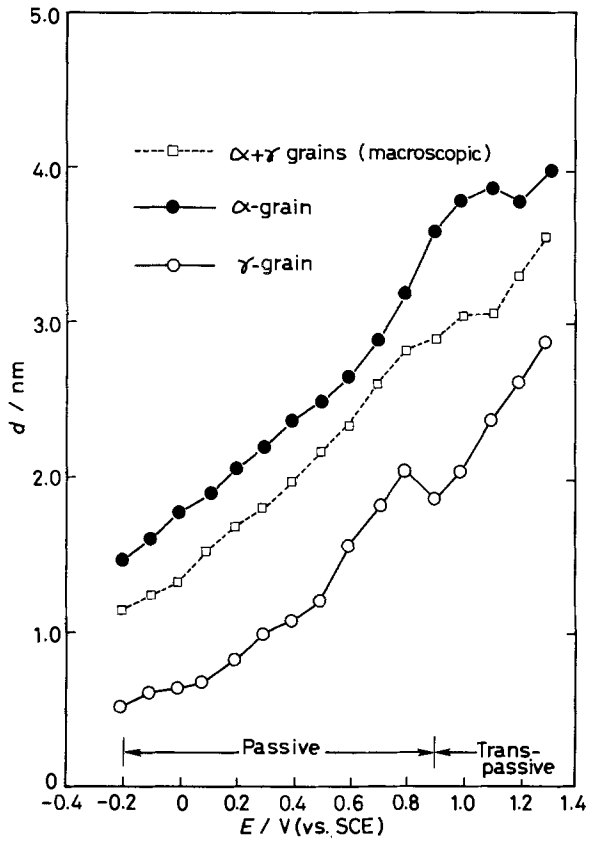

Fig. 6. Thickness d of the passive and transpassive films as a function of potential E for individual grains of α and γ and for a macroscopic area containing many α- and γ-grains.

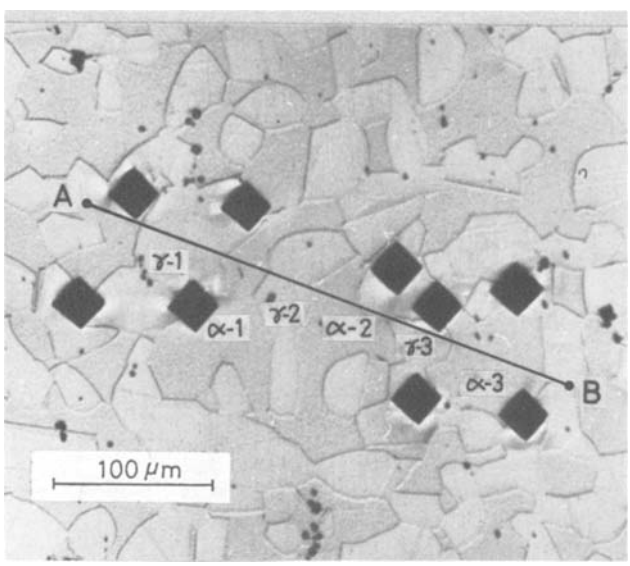

Fig. 7. Microstructure of the area subjected to the line analysis of film thickness.

the point A. In the upper part of the figure a sketch of the microstructure taken from Fig. 7 is also given. The variation in the thickness from grain to grain can be seen on both the passive and transpassive films. The thickness of the films differs even on fellow grains of the same phase. This should be due to the difference

Table II. EPMA analysis of the grains labeled in Fig. 7

Grain	γ-1	α-1	γ-2	α-2	γ-3	α-3
Cr (mass%)	21.0	25.3	20.8	25.2	20.9	25.1
Ni (mass%)	11.9	8.7	11.9	8.5	11.7	8.5

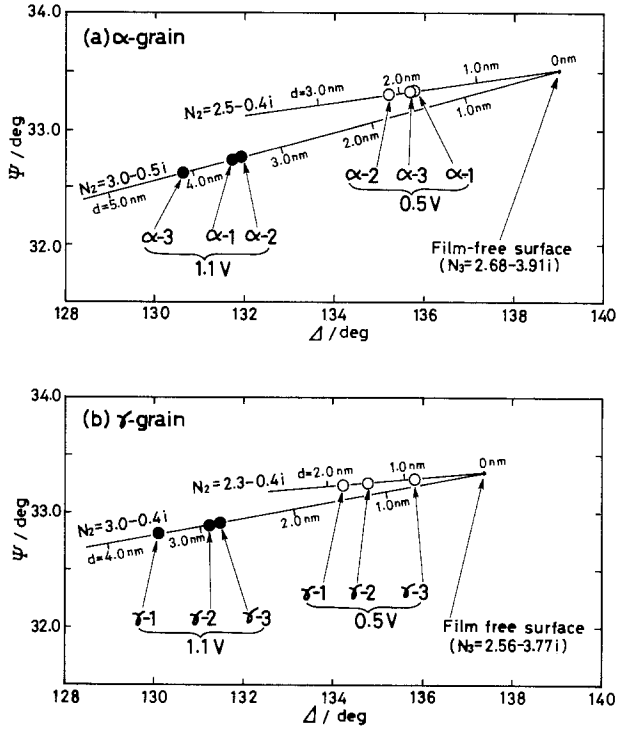

Fig. 8. Δ — Ψ plots for α-grains (a) and for γ-grains (b) oxidized anodically at 0.5 and 1.1V in pH 6.0. 1 kmol · m^{-3} Na_2SO_4 at 20°C.

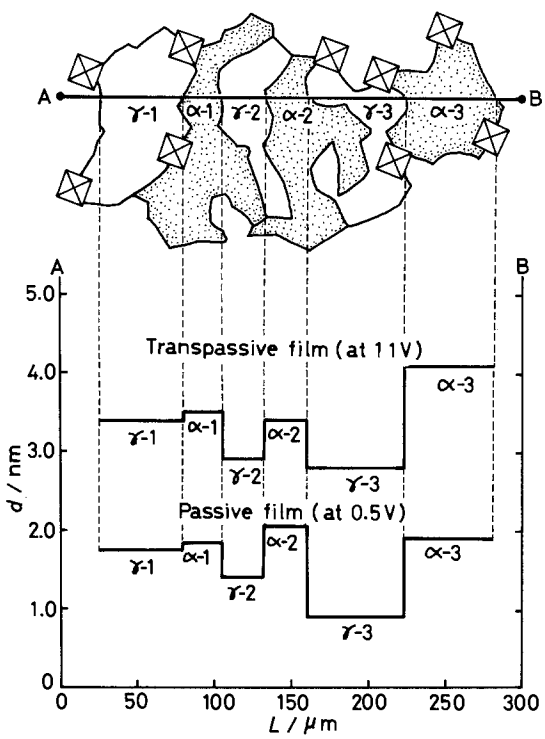

Fig 9. Thickness d of the passive and transpassive films as a function of distance L from the point A to the point B in the microstructure shown in the upper part.

in grain orientation because the fluctuations in chemical compositions among grains of the same phase are very small (see Table II). Large differences in the film thickness exist between adjoining α- and γ-grains, especially between the grains α-3 and γ-3. Such a large difference in film thickness should occasionally make a misfit at an α/γ phase boundary, which acts as a weak point for corrosion. Duquette *et al.* reported that pits initiate at the α/γ phase boundaries in the

welded steel 304L (17) and the transformed steel 308L (18) in chloride media.

Anodic polarization behavior of α- and γ-phases.—In order to enable a comparison with the anodic behavior of individual phases in the 22Cr-10Ni stainless steel, anodic polarization curves for the α- and the γ-phase simulated alloys were measured.

Figure 10 shows the anodic polarization curves for the alloys in pH 6.0, 1 kmol · m^{-3} Na_2SO_4 at 20°C measured at the same potential ascending rate as that used in the ellipsometric measurements. Although the difference in the current densities between these curves is small, the current density in the passivity region for the α-phase alloy is estimated to be larger than that for the γ-phase alloy.

To get a clearer difference in the anodic polarization characteristics of the alloys, the measurement of the curves was performed under more severe conditions. The result obtained in pH 0.2, 0.5 kmol · m^{-3} H_2SO_4 at 50°C is given in Fig. 11. It is clear that the anodic dissolution rate of the α-phase alloy is larger than that of the γ-phase alloy in both the active and the passive regions.

From these facts it can be presumed that the corrosion resistance of α-phase in the 22Cr-10Ni stainless steel is a little lower than that of γ-phase in the steel in the passivity region. Therefore, it could be concluded that the passive film on the γ-phase in the steel is thinner but has higher protection ability compared to the film on the α-phase in the steel.

Conclusions

1. A microscopic ellipsometer which can provide the measurement of passive film on a single grain in an austeno-ferritic stainless steel has been constructed.

2. Optical constants for the film-free surfaces of α- and γ-phases of 22Cr-10Ni stainless steel were simulated by those for the alloys having similar compositions as that of the α- and the γ-phases in the steel.

3. The thickness and optical constants of passive and transpassive films on individual grains of α and γ of 22Cr-10Ni stainless steel were determined *in situ* in a pH 6.0, 1 kmol · m^{-3} Na_2SO_4 solution. The thickness of the films on α-grains is larger than that of the films on γ-grains.

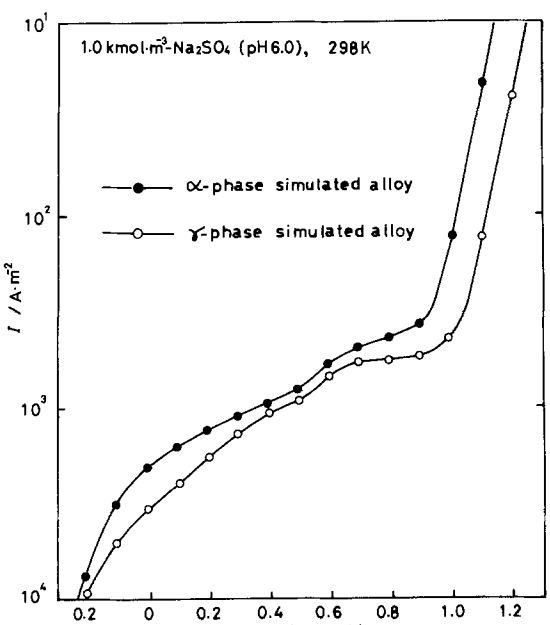

Fig. 10. Anodic polarization curves for the α- and the γ-phase simulated alloys in pH 6.0, 1 kmol · m^{-3} Na_2SO_4 at 20°C, measured in ascending steps of 100 mV after holding for 1 hr at each potential.

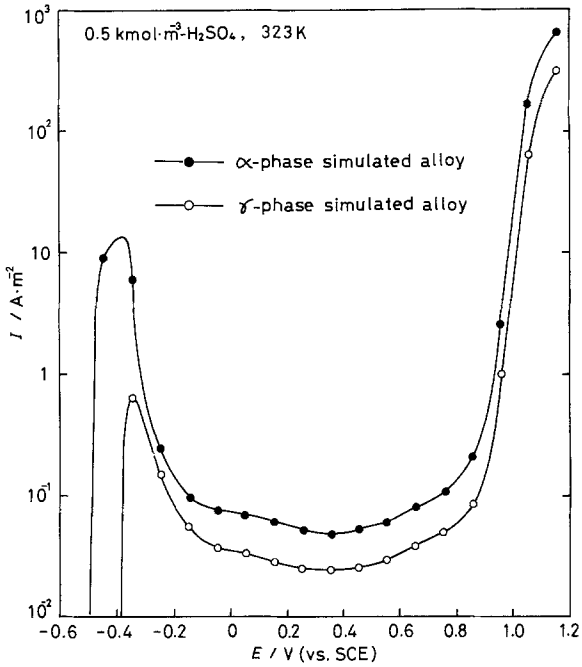

Fig. 11. Anodic polarization curves for the α- and the γ-phase simulated alloys in pH 0.2, 0.5 kmol · m^{-3} H_2SO_4 at 50°C, measured in the potential scanning rate of 22 mV · min^{-1}.

4. The variation in film thickness from grain to grain was measured. Significant differences in film thickness were found to exist at α/γ phase boundaries in the steel. The film thickness varies even among grains of the same phase.

5. The corrosion resistance of γ-grains was presumed to be higher than that of α-grains at potentials in the passivity region. The passive films on γ-grains, therefore, should provide more corrosion protection than those on α-grains, although their thickness is smaller.

Acknowledgment

The authors would like to thank A. Kasamatsu and K. Otani for their help with the experimental work.

Manuscript submitted Feb. 3, 1983; revised manuscript received *ca.* July 26, 1983.

Tohoku University assisted in meeting the publication costs of this article.

REFERENCES

1. J. Hochmann, A. Desestret, P. Jolly, and R. Mayoud, in "Stress Corrosion Cracking and Hydrogen Embrittlement of Iron Base Alloys," J. Hochmann and R. W. Staehle, Editors, p. 956, National Association of Corrosion Engineers, Houston, Texas (1973).
2. K. Harada, *Corros. Eng.* (*Boshoku Gijutsu*), **26,** 721 (1977).
3. M. Kowaka, *Bull. Jpn. Inst. Metals,* **17,** 657 (1978).
4. M. Mizuno, *Corros. Eng.* (*Boshoku Gijutsu*), **27,** 291 (1978).
5. H. Nagano and M. Kowaka, *Tetsu-to-Hagané,* **66,** 1150 (1980).
6. K. Sugimoto and S. Matsuda, *Mater. Sci. Eng.,* **42,** 181 (1980).
7. V. V. Andreeva, *Corrosion,* **20,** 35 (1964).
8. G. Okamoto and T. Shibata, *Corros. Sci.,* **10,** 37 (1970).
9. K. N. Goswami and R. W. Staehle, *Electrochim. Acta.,* **16,** 1895 (1971).
10. S. Matsuda, K. Sugimoto, and Y. Sawada, *J. Jpn. Inst. Metals,* **39,** 848 (1975); *Trans. Jpn. Inst. Metals,* **18,** 66 (1977).
11. S. Matsuda, K. Sugimoto, and Y. Sawada, in "Passivity of Metals," R. P. Frankenthal and J. Kruger, Editors, p. 699, The Electrochemical Society, Inc., Princeton, NJ (1978).
12. G. M. Bulman and A. C. C. Tseung, *Corros. Sci.,* **13,** 531 (1973).

13. K. Sugimoto and Y. Sawada, *ibid.*, **17**, 425 (1977).
14. S. Matsuda, K. Hamano, K. Sugimoto, and Y. Sawada, *J. Jpn. Inst. Metals*, **42**, 808 (1978).
15. S. Matsuda and K. Sugimoto, *Corros. Eng. (Boshoku Gijutsu)*, **29**, 19 (1980).
16. J. R. Ambrose and J. Kruger, *Corrosion*, **28**, 30 (1972).
17. P. E. Manning, C. E. Lyman, and D. J. Duquette, *ibid.*, **36**, 246 (1980).
18. P. Hronsky and D. J. Duquette, *ibid.*, **38**, 63 (1982).

Tafel Constants and Changes in Hydrogen Coverage during Corrosion of Fe18Cr

Murray Rosen* and Jonathan G. Harris

U.S. Department of the Interior, Bureau of Mines, Avondale Research Center, Avondale, Maryland 20782

ABSTRACT

Cathodic Tafel constants associated with the hydrogen reaction at Fe18Cr in H_2-saturated 1*N* H_2SO_4 were determined by computer analysis of the potential decay following current interruption at fixed starting potentials positive to the corrosion potential. The values of $b = -2.3\ RT/\alpha\mathbf{F}$ were evaluated from the general current-interruptive equation, $E = E_i + b \cdot \log [1 + t/\tau]$, from its linear log form, and from a modification of the general equation that was derived to analyze multiple Tafel regions. For starting potentials of 0, −0.05, −0.075, and −0.2V (RHE), the number of Tafel regions was 3, 3, 2, and 1, respectively. The amount of hydrogen associated with the electrode at the fixed potentials and during decay was determined from anodic charging pulses. Results indicated that the bonding strength between metal sites and hydrogen varies with decay and starting potential. The first Tafel region from 0, −0.05, and −0.075V was under combination control, $2H \rightarrow H_2$. The decay from −0.2V was controlled by the electrochemical-desorption step, $H^+ + e + H \rightarrow H_2$.

For a metal at some potential other than its steady state, open-circuit corrosion potential (E_c), some process must occur in order for that metal to reach its E_c. To describe that period of open-circuit transient behavior that leads to steady-state corrosion at E_c, we have selected the term "corrosion onset." The controlling cathodic processes in highly purified O_2-free solutions usually involve hydrogen evolution (HER) and/or hydrogen atom permeation into the metal, and it is expected that one (or both) of these processes should be operative during corrosion onset.

The HER is generally comprised of the following: discharge, $H^+ + e^- \rightarrow H$; followed by combination, $2H = H_2$; and/or electrochemical discharge, $H^+ + e^- + H \rightarrow H_2$, with one step of the sequence being slow and the other at equilibrium. Also, the discharge step may be followed by both the combination and electrochemical discharge occurring in parallel. It is also possible to consider "coupled" reactions (1) when the discharge is slow, the second reaction is not in equilibrium, and the rates of the reactions are comparable. Tafel constants associated with the HER are listed in Table I (2).

At the same time that these evolution reactions are occurring, a fraction of the adsorbed surface hydrogen may enter the metal lattice, *i.e.*, "dissolve." Kinetic constants for hydrogen entry into the metal are also shown in Table I. These constants are theoretical slopes corresponding to $\partial\eta/\partial \log (J_\infty)$ where J_∞ is the steady-state permeation current density (2). One of the assumptions made (2) is that J_∞ is proportional to θ, the fraction of the surface available for hydrogen adsorption that is covered with hydrogen so that $\partial\eta/\partial \log \theta \propto \partial\eta/\partial \log J_\infty$. To use these diagnostic criteria in the present study, Tafel constants were determined from potential decays from potentials positive to E_c, and information on hydrogen coverage with potential was obtained from anodic charging pulses.

The general current-interruptive equation by which potential decay curves can yield kinetic information is based upon the early work of Gurney (3), Armstrong and Butler (4), and Busing and Kauzman (5)

$$E = E_i + b \cdot \log [1 + t/\tau] \qquad [1]$$

Here E_i is the applied starting potential, and b is the cathodic Tafel constant and is related to the exponential terms in the Butler/Volmer equation as $b/2.3 = -RT/\alpha\mathbf{F}$, where α is the cathodic transfer coefficient. In Eq. [1], τ is equal to $-bC/2.3i_r$, where C is the double layer capacitance, assumed independent of potential, and i_r is the initial cathodic discharge current density equal in magnitude to the anodic current density at interruption. The terms R, T, and $\mathbf{F}$ have their usual meaning. By identifying b as the cathodic Tafel constant, it is assumed that the decay process is under cathodic control and that changes in potential back to E_c are not controlled by the anodic reaction. Evidence interpreted in the Discussion section will support this position.

For graphical presentation of the decay, Eq. [1] can be rewritten as

$$E = E_s + b \cdot \log [t + \tau] \qquad [2]$$

where $E_s = E_i - b \cdot \log \tau$. At times where $t >> \tau$, the decay potential can be plotted as

$$E = E_s + b \cdot \log [t] \qquad [3]$$

and b will be the $\partial E/\partial \log [t]$ slope. In the present work, most of the potential decay data plotted by Eq.

Table I. Diagnostic criteria for H.E.R.

	$-\partial\eta/\partial \log$ (i) Langmuir[1]	Temkin Non-Act.	Temkin Act.	$-\partial\eta/\partial \log$ (J) Langmuir[1]	Temkin Non-Act.	Temkin Act.
DC	2A			0	0	0
DE			A			
DC	A/2			A		
DE	2A/3					
c DC		5A/2	3A	4A	5A/2	3A/2
c DE	2A			0	0	0

[1] Assumes $\theta < 0.1$.
A = 2.3 $RT/\mathbf{F}$ = 59.1 mV at 25°C.
D: discharge; C: combination; E: electrochemical; c: coupled.
_ rate determining step.

* Electrochemical Society Active Member.
Key words: cathode, discharge, potential, adsorption.

[3] exhibited multiple linear regions. The appearance of more than one linear region was interpreted as an indication that there was a change in the rate-controlling step for the decay process. To determine the subsequent Tafel constants, a modification of Eq. [1] was used. Brystrov and Krishtalik (6) derived an analytical expression for the voltage as a function of time for a second Tafel region, which was separated from the first by a region of "discontinuity" that reflected similar discontinuity in the steady-state polarization curve. Using methods similar to those of Brystrov and Krishtalik (6), a simpler equation is derived below that can be used even when the Tafel regions are separated by a smooth, nonfaradaic discharge region.

This simpler equation can be obtained by following the same steps used for the derivation of Eq. [1]. Assuming the cathodic discharge of the double layer capacitance proceeds through a faradaic impedance, the application of Kirchoff's law for a current loop (4) yields the differential equation

$$C \cdot \frac{d\eta}{dt} - i_0 \cdot \exp\left[\frac{-\alpha\eta\mathbf{F}}{RT}\right] = 0 \qquad [4]$$

whose solution is

$$\frac{RT}{\alpha\mathbf{F}} \cdot \exp\left[(\alpha\mathbf{F}/RT)\eta\right] = \frac{i_0}{C}t + \text{const.} \qquad [5]$$

where i_0 is the exchange current density and η is the overvoltage for the process.

The first Tafel region, when there are multiple regions, would be described by Eq. [1] or [3]. When there is a second Tafel region beginning at $t = t^*$, the Tafel constant for this region, $b_2/2.3$, equals $-RT/\alpha_2\mathbf{F}$ and $i_{o,2} = -i^*_{r,2} \cdot \exp[-\eta/b_2]$, where $i^*_{r,2}$ is the current density at t^*. Utilizing the procedure for deriving Eq. [1] from Eq. [5], one arrives at a similar expression for the second decay region by integrating Eq. [4] between t and t^*

$$E = E^* + b_2 \cdot \log\left[(t - t^*)/\tau_2 + 1\right] \qquad [6]$$

where E^* is the potential at t^* and τ_2 is $-b_2C/2.3i^*_{r,2}$. Equation [6] is the simpler equation used to determine the b values of the multiple decay regions.

The data presented in the present paper have been analyzed by Eq. [1], [3], and [6]. As will be shown, the data yield, at least for the initial decay, Tafel constants associated with the mechanisms attributed to hydrogen evolution where simple Langmuir adsorption is operative. It was also assumed that the capacitance was not potential dependent.

Experimental

The all-glass enclosed cell systems, reference and counter platinum electrodes, water and gas purification systems, and cleanup procedures have been described (7) and have been employed previously for platinum (8) and gold (9) electrodes. The Fe18Cr wires were prepared by the Albany (Oregon) Research Center from stocks of 99.94 and 99.5 weight percent (w/o) Fe and Cr, respectively. Details of the fabrication, heat-treatment, and electropolishing can be found in (7). For this work, the Fe18Cr wires were sealed into the glass holder by a shrinkable Teflon[1]/polyethylene seal. Two wires in two separate cells were studied with the majority of the study done on one of the electrodes. Measurements were made in 1N H_2SO_4 solutions that were vigorously stirred by H_2 flow. Potentials were measured using a platinum reference electrode and are reported *vs.* the reversible hydrogen electrode potential in the same solution.

[1] Reference to specific trade names is made for identification only and does not imply endorsement by the Bureau of Mines.

Figure 1 shows the schematic arrangement of the various electronic components. An Fe18Cr wire electrode is potentiostated to a fixed d-c potential with respect to the platinum reference electrode, r_s. Once steady-state current is reached (1-6 hr), the digital delay generator (DDG) provides a square pulse to "open" the switch. The latter is a diode-bridge-type analogue switch that has a current leakage on the order of 2 nA in the open position. The decay in potential is measured with respect to another platinum reference electrode, r_t, and is digitally recorded on a Nicolet Explorer III Waveform recorder equipped with a floppy-disk drive for data storage. The recorder is interfaced to a Hewlett Packard 85 Laboratory Computer for analysis of the decay curves. For measuring hydrogen accumulated during decay, the pulse generator is turned on by a trigger pulse from the DDG at times (1-30 sec) corresponding to the settings of the delay generator to interrupt the decay process with an anodic current pulse. Measurements of hydrogen were also made at steady-state potentials prior to current interruption. No correction was made for double layer charging.

Results

Representative examples of potential decay of Fe18Cr from steady-state potentials of 0, −0.05, −0.075, and −0.2V are shown in Fig. 2 as E *vs.* log [t] plots. In comparing the four curves, it is interesting to note that the potential decay goes negative to the corrosion potential, and that the number of linear regions increases as the starting potential becomes less negative between −0.2 and −0.05V. Also, for decay from −0.075V, an initial, rapid-decay region precedes the Tafel region found for the other

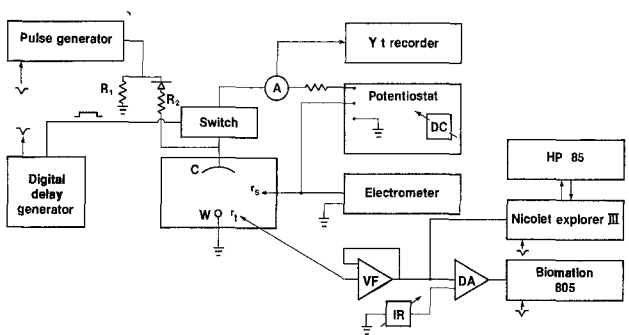

Fig. 1. Schematic of the current-interruption and anodic charging circuits and the data acquisition instrumentation.

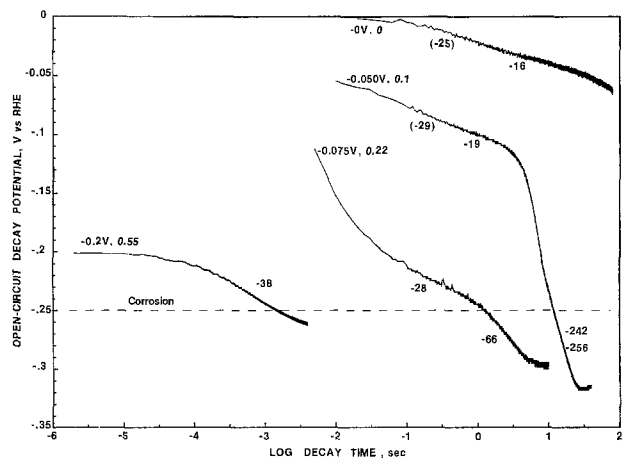

Fig. 2. Decay plots following current interruption. Numbers next to starting potential are effective H atom concentrations expressed as fraction found at −0.25V. Numbers near curves are average cathodic Tafel constants, mV, determined by LINFIT and AUTFIT using Eq. [3] and [1], respectively.

decay cases. Included next to the potential value for each curve in Fig. 2 is a corresponding value of θ', defined as the total amount of H, (H), found at steady state at that potential divided by, $(H)_c$, the amount found at steady state at E_c, −0.25V. (No distinction is made at this point as to the chemical form of H or its location on or in the metal.) The other numbers shown near different portions of each curve are the averaged Tafel constants in millivolts determined by a mathematical treatment of the data using Eq. [3] and [1], as explained below. Values obtained by use of Eq. [1] appear in the parentheses.

An example of potential decay from −0.05V is shown in greater detail in Fig. 3 and 4. Figure 3 shows the two linear regions observed in the first 80 mV of decay from −0.05V. For this particular decay curve, the numbers −26.0 and −22.3 mV are the Tafel constants determined using Eq. [3], and the numbers in parentheses correspond to the Tafel constants determined using Eq. [1]. Figure 4 shows the latter portion of the decay curve occurring from −0.05V. The linear portion passes through −0.25V after approximately 14 sec of the decay. At longer times, approaching 4 to 6 hr, the potential returns to −0.25V, which is the steady-state, open-circuit corrosion potential. The Tafel value from Eq. [3] is −223 mV, and −260 and −201* mV are the Tafel values determined using Eq. [1] and [6], respectively, where $t^* = 10$ sec was selected.

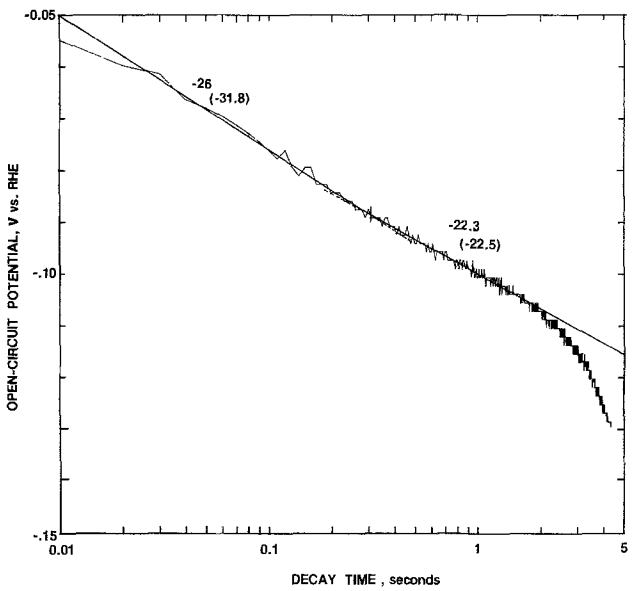

Fig. 3. Decay plot following current interruption at −0.05V showing first two Tafel regions. Numbers are Tafel constants, mW, determined by LINFIT and AUTFIT.

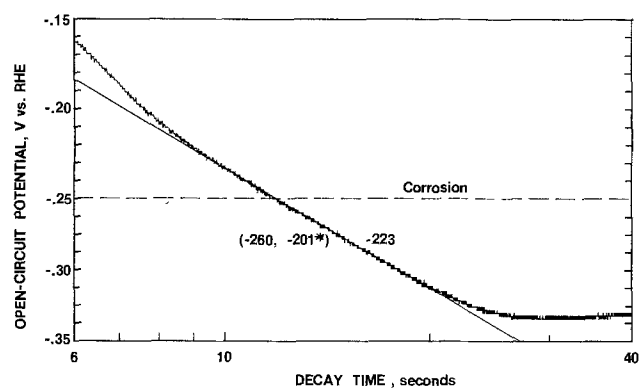

Fig. 4. Decay plot following current interruption at −0.05V showing 3rd Tafel region. Numbers are Tafel constants, mV, determined by LINFIT, AUTFIT, and AUTFIT*.

The amount of hydrogen atoms (H) either at steady state or during potential decay was determined from the length of the H-oxidation region in the response curve to an anodic charging pulse. The results shown in Fig. 5 are for Fe18Cr at 0, −0.05, and −0.25V steady state and −0.27V during decay from −0.05V. The measurement taken at open-circuit corrosion, −0.25V, was for the second electrode; the other three were for the first electrode. Points a and b represent the end of the H-oxidation for the open-circuit and −0.27V case, respectively. These points were determined graphically by drawing intersecting lines through the portion of the response curve where hydrogen is oxidized. The values of (H) were then divided by the electrode's appropriate value for $(H)_c$ to give θ'. Plots of log θ' *vs.* potential for open-circuit decay from −0.05V for the two electrodes are shown in Fig. 6. The numbers in the figure are the slopes $(\partial\eta/\partial \log \theta')$ calculated over potentials that correspond to the third decay region.

Decay Curve Analysis

Tafel constants were determined by fitting Eq. [1], [3], and [6] to appropriate linear portions of the E *vs.* log $[t]$ decay plots. Mathematical analysis was accomplished by a program, written in BASIC to run on a Hewlett Packard HP 85, containing three fitting

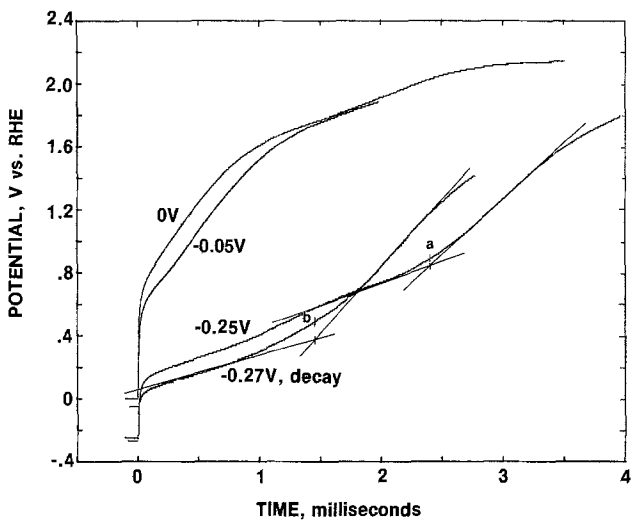

Fig. 5. Response to anodic charging pulses applied at 0 and −0.05V, before decay, −0.25V open-circuit corrosion, and at −0.27V during decay from −0.05V. "a" and "b" are respective ends of H oxidation regions.

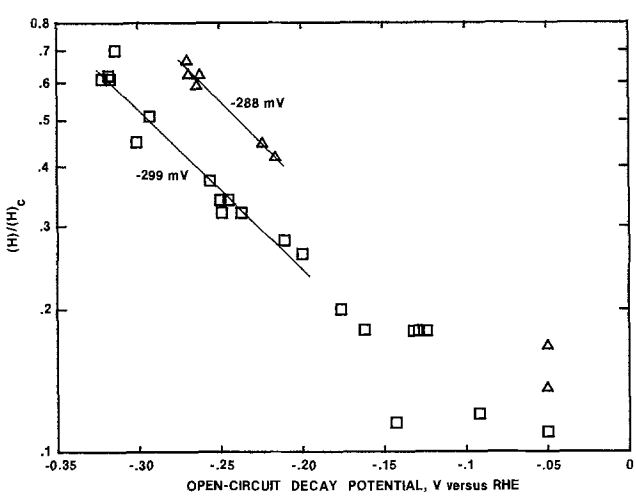

Fig. 6. Accumulation of H atoms during potential decay following current interruption at −0.05V. Numbers are the reciprocals of the slopes. Symbols represent the two electrodes.

routines and a statistical routine. The Tafel constant of Eq. [3] was determined by the linear least squares routine LINFIT. In order to utilize Eq. [1] or [6] over any portion of the decay curve, and not just when $t >> \tau$, two nonlinear least squares routines, AUTFIT and AUTFIT*, respectively, were used. Program strategy is given in Appendix A. Table II summarizes the averaged constants (at the 95% confidence levels) determined by the three methods.

Except for the latter portion of decay from −0.05V, the Tafel constants determined by the same method (AUTFIT, AUTFIT*, or LINFIT) in corresponding regions for the two electrodes could be combined and averaged. Because of this difference between the two electrodes in the −0.05V case, the averaged LINFIT value for each electrode is shown for the third region in Fig. 2. Values for the two electrodes were averaged together in the other regions. The decision not to combine the data for this third region was based on the statistical "t" test that showed that there were significant differences between the data at the 95% confidence level.

The comparison of the LINFIT, AUTFIT, and AUTFIT* shows that, with the exception of the regions at the beginning of the decay, the linear approximation of the Tafel equation provided an adequate model for determining the Tafel constant of the decay process. The linear method has the advantage of its simplicity and speed. Additional comparisons of the methods can be found in Appendix B.

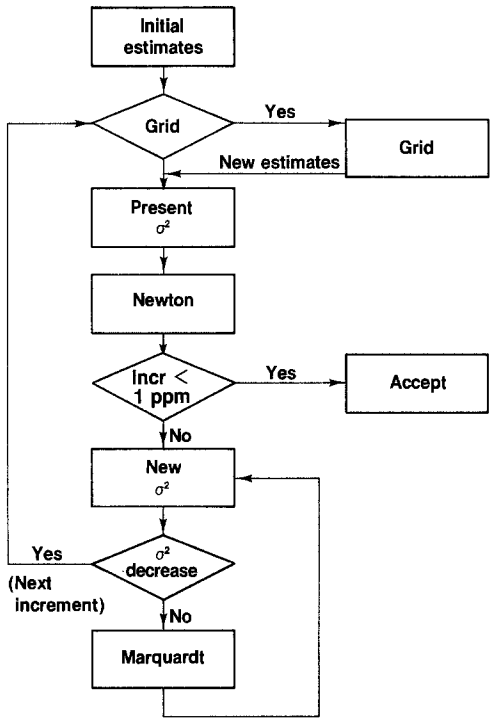

Fig. 7. Schematic flow chart of AUTFIT

Discussion

As was stated in the Background section, "corrosion onset" is viewed here as being rate controlled by the parallel cathodic paths of HER and permeation of adsorbed surface hydrogen. This dependency is demonstrated in Fig. 2 by the fact that, in all cases, the overall decay rate decreases as the starting potential is made more positive. This trend is opposite to anodic-controlled decay which would have faster decay with more posiitive starting potentials. The initial rapid-decay region for the −0.075V case was unexpected. The fast drop in potential indicates there is a path that can initially discharge the double layer more easily than the cathodic reactions at the other starting potentials. Assuming a double layer of 40 $\mu F/cm^2$, the charge required for the approximately 0.125V potential change is about 5 $\mu C/cm^2$, which can be the result of almost any process; a fast hydrogen reaction and/or some adsorption process or even anodic dissolution.

The influence of the paths on the open-circuit potential decay can be seen in the curves of Fig. 2. Most notable are the number of Tafel regions and the degree of overshoot beyond E_c. To relate these observations to the two paths, certain assumptions about the distribution of hydrogen are necessary. It will be assumed that the amount of hydrogen (H), at any point before and during decay, is the sum of the surface hydrogen (H_s*) from the HER and the dermasorbed[2] hydrogen (H_d* and H_d) from the permeation reaction. (The asterisk represents "active" sites responsible for the potential.) It is assumed that all the surface hydrogen is initially involved in determining the potential. Previous work suggests (7) that the likely chemical form of the dermasorbed hydrogen is CrH_4. As is stated in the definition of θ for active sites, there is at any time during the decay a certain fraction of the total available potential-determining sites that are filled. From the definition of (H), θ is the ratio of $(H_s^*)/(Cr^*)$, where the total number of available active sites is represented by (Cr^*). The cathodic active sites will either be Cr or CrH_4.

Using decay from −0.05V as an example, the occurrence of an overshoot in the curves of Fig. 2 can be interpreted now in terms of H distribution. In the first two regions where (H) is small and relatively constant (Fig. 6), decay is thought to be primarily determined by the HER. In the third region, where the bulk of the H is accumulated, it is concluded that the influence of the permeation reaction becomes more pronounced. This influence results in H_s* not only producing H_2, but, also H_s* being dermasorbed, and at a rate that increases Cr* so that the ratio of $(H_s^*)/(Cr^*)$, or θ, remains quite small. Since (H_s^*) is also increasing, but not as fast, the potential continues

[2] Hydrogen atoms beneath the "skin" of the metal. Term introduced (10) to describe H dissolved in Pt.

Table II. Summary of cathodic Tafel constants, mV

Decay regions	1st		2nd		3rd	
Starting potential, V	LINFIT[1]	AUTFIT	LINFIT	AUTFIT	LINFIT	AUTFIT
0.0	−21 ± 1	−25 ± 2[2]	−16 ± 2	−16 ± 2 −14 ± 3[*,3]	[4]	[4]
−0.05	−24 ± 1	−29 ± 1	−20 ± 1	−20 ± 1	−242 ± 10 −256 ± 22	−308 ± 10 −186 ± 29[*,3] −355 ± 48 −248 ± 47[*]
−0.075	−28 ± 1	−28 ± 2	−66 ± 14	−66 ± 14 −69 ± 22[*]	Only 1 region	Only 2 regions
−0.2	−38 ± 4	−46 ± 2				

[1] LINFIT Eq. [3]
[2] AUTFIT Eq. [1]
[3] AUTFIT* Eq. [6]
[4] No measurements made of 3rd region.

to decrease. Eventually, a potential will be reached that corresponds to the appropriate (Cr*) for the alloy under these transient corrosion conditions. From this point on, the ratio of $(H_s^*)/(Cr^*)$ becomes larger as (H_s^*) increases, and (Cr*) remains essentially constant. Normally, (H_s^*) would reach a nearly constant value that would cause the potential to level off as the remaining H is accumulated to occupy nonactive sites either on the surface or dermasorbed beneath the surface. However, since this is a corroding metal, loss of either Fe or Cr sites could lower the local cell current such that the transient potential conditions near −0.3V would not be supported any further, and the potential would rise. There also could be additional metallurgical reactions that favor $H_s^* \rightarrow H_d$ without forming additional H_d^*, resulting in an increase in potential to E_c.

Even though explicit identification cannot be made as to which type of metal site (grain boundary, crystal dislocation, imperfection, etc.) is active or which type of metallurgical reaction is occurring, it can be seen from Fig. 2 that their participation during decay is dependent on the initial steady-state potential. As the initial potential (0, −0.05, and −0.075V) is set closer to −0.25V, it would be expected that the initial ratio of $(H_s^*)/(Cr^*)$ would become greater. This may account for the overshoot in potential past −0.25V becoming less, and the number of Tafel regions going from 3 to 2 to 1. Moreover, these trends suggest that once corrosion onset begins from a given starting potential, the metal sites that supply electrons and offer adsorption will continue to do so on a preferred basis throughout most of the decay. Otherwise, over the same potential range, decay from −0.05V would be the same as decay from −0.075V, etc. Thus, when decay begins at −0.2V, more of the sites associated with open-circuit corrosion are already participating as compared to the −0.05V case. The establishment of steady-state corrosion from more positive potentials would then involve bringing more sites up to their active levels.

Applying the criteria of Table I to identify which hydrogen reaction mechanism is operative during decay requires discussion of the hydrogen measured in the anodic charging curves. The choice to express the measured hydrogen in the charging curves as θ' based upon (H) at E_c rather than as θ based upon (H) at 0V was an operational one. It was used because θ normally requires adsorption isotherms based on reversible equilibrium behavior, and these Fe18Cr electrodes did not exhibit reversible behavior for the H^+/H_2 exchange, as have previous Fe18Cr electrodes (7). Moreover, it was not known explicitly which chemical form of H is represented in the oxidation regions of the charging curves. Even if a surface hydrogen oxidation region could be identified, it would not be known if all or part of the surface hydrogen was responsible for the potential.

Evidence that not all of the (H) is critical for the exchange has been shown for H_2 evolution on Rh (11) and Pt (12) and for H accumulation on Pt (8). In these cases, less than 10% of the total (H) present at 0V was shown to be responsible for the exchange reaction, even though six H oxidation regions were found and coverage was slightly greater than one monolayer. The interpretation given is that there are metal sites of varying activity resulting in Pt-H bonds of varying strength, with some of the H dermasorbed beneath the surface (8, 10). In contrast to H associated with a lower potential oxidation region, H in an upper potential region is more strongly bound to the metal site.

For Fe18Cr, the charging curves show that there were at least two observable oxidation regions for hydrogen. The occurrence of one region or the other, or both regions, was dependent on starting-potential and decay time. For instance, from steady state at −0.05 and −0.075V, one region was observed, and it occurred at the more positive potentials. From steady state at −0.2V and E_c, two oxidation regions were observed, with the possibility that also some H was oxidized in the transition region adjoining the two obvious regions. From 0V steady state, no oxidation region was observed. The charging curves taken during decay from −0.05V indicate that the bonding between H and Cr is different during decay when $\theta' \rightarrow 0.7$ near −0.32V, because the accumulated H is oxidized in the lower region of the charging curve and not just in the upper region (Fig. 5). Moreover, this lower region was occurring at potentials more negative (less strongly held) than the lower region for the −0.25V steady-state case. The conclusions then are that H accumulated during decay from a steady potential at which $(H) \rightarrow 0$ is weakly bound and that once steady-state, open-circuit corrosion is established, two degrees of metal-H bonding are found, both of which are stronger than the one during H accumulation. However, it cannot be said at this time whether the weakly bound H represents H_s^* or not. Based upon results of the Pt metals and the previous discussion of the overshoot, the fraction of the total H present that controls the potential during decay is thought to be small. Using θ' rather than θ to express H coverage is useful because it can be assumed that there is a proportionality constant linking θ' to θ that would drop out when determining the $\partial\eta/\partial \log \theta$ slopes of Table I. Ideally, dividing each (H) measurement by the appropriate $(H)_c$ should normalize the data so that in Fig. 6 both sets of points would fall on the same line. Although this did not happen, the lines are nearly parallel. Small differences in actual Cr concentration or other factors could contribute to slightly different values of $(H)_c$. The Tafel constants determined in the third region for decay from −0.05V already indicate that there were slight differences in these electrodes. Also, it has been shown on Pt (13) that full coverage of the Pt by hydrogen will vary even for the same electrode.

The values of θ' for steady-state starting potentials and the Tafel constants for the first decay region (Fig. 2 and Tables I and II), together indicate that the onset of corrosion from 0, −0.05, and −0.075V is initially controlled by the combination step and from −0.2V by the electrochemical-desorption step. These conclusions hold for $\theta < 0.1$ and for moderate θ values if nonactivated Temkin adsorption is assumed. Once decay proceeds past the initial regions of 0, −0.05, and −0.075V, interpretation as to the mechanism becomes difficult because there is increased variation in the average b value, and the values are not those generally associated with the simple hydrogen evolution sequences. Even when considering Temkin-type adsorption, specific mechanistic interpretation is still difficult. For instance, for the second region of the −0.075V case, based on a nearly −60 mV average slope, one cannot distinguish between any one of reactions becoming rate controlling after the combination step which was rate controlling for the first region. Parsons (1) showed that only a coupled discharge mechanism can follow combination control, but slopes for this possibility are all greater than −60 mV.

For the −0.05V case, where there are three Tafel regions, the third one is characterized by b values that ranged from less than −200 to −400 mV. These Tafel b values are not those commonly found for the HER, yet in this region the majority of the hydrogen is accumulated. The slopes of Fig. 6, for the uptake of hydrogen by the metal, could indicate a coupled discharge-recombination, but this assumes an Langmuir isotherm with $\theta \rightarrow 0$. The only way that θ could be small when there are large amounts of H present ($\theta' \rightarrow 0.7$) is if on corroding metals at potentials more

negative than < -0.2V, active sites are mostly unoccupied. This is the same as the conclusion from the overshoot results. Another explanation for these Tafel values is that Eq. [1] does not hold in this region, possibly due to complications involving capacitive adsorption that is potential dependent on critical metallurgical features of each electrode.

Manuscript submitted Feb. 17, 1983; revised manuscript received July 13, 1983. This was Paper 138 presented at the Denver, Colorado, Meeting of the Society, Oct. 11-16, 1981.

The U.S. Department of the Interior, Bureau of Mines assisted in meeting the publication costs of this article.

APPENDIX A

Program strategy.—The nonlinear routines of AUTFIT and AUTFIT* (Fig. 7) used Newton's method (14, 15) with the gradient expansion algorithm of Marquardt (16) to minimize, with respect to the parameters b and τ, the least squares function

$$\phi = \Sigma[f(t_i) - Y_i]^2 \qquad [A\text{-}1]$$

where $f(t)$ is described by Eq. [1] or [6] and the Y_i's are the measured potentials at times t_i's. The first and second partial derivatives used in calculating the increments of the parameters were evaluated from the analytical expressions derived from Eq. [1] or [6] for AUTFIT and AUTFIT*, respectively. Generally, the Marquardt algorithm was needed to force the search to move in the right direction in the beginning, but was not used once the increments became small and the search appeared to be converging toward a minimum. When the estimators of b and τ obtained from each successive iteration failed to converge toward reasonable values (*e.g.*, $0>b>2$V or $\tau>0$), a grid search algorithm (17, 18) was employed to supply better initial values for Newton's method. The grid search sought the minimum by improving the estimates for each parameter while holding the other constant. The estimates of the linear parameter (b) were improved by linear regression, and the estimates of the nonlinear parameter (τ) were improved by an interpolation formula using three equally spaced points surrounding the minimum located by a stepwise search in the direction of decreasing ϕ.

To assure convergence when Newton's method was used, the procedure was continued until the increments were less than 1 part per million for each parameter. Once the estimates were within about 1% of each parameter from the minimum, the estimates usually converged very rapidly and the increments with each successive iteration decreased by at least a factor of 10 and often by a factor of greater than 100. It was found that computing time was saved by initially performing the estimation procedure using only 50 or fewer points and using these estimates as the initial guesses when the procedure was followed using all of the points. The program also calculated the variance of the estimates ($\sigma^2 = \Sigma[Y_i - f(t)_i]^2/[N\text{-}2]$). It then plotted the standardized residuals, residuals/σ, *vs.* $f(t_i)$. The variance and the plot were used to judge individual fits and to compare analysis methods.

APPENDIX B

Method comparison.—Since the three fit routines gave essentially identical b values for decay from -0.2 and -0.075 and 0V, the remaining discussion of the data treatment will deal with the three regions of decay from -0.05V. For the first region in Fig. 3, all the data from $t = 0$ to 0.31 sec was used in AUTFIT, but only from $t = 0.03$ to $t = 0.31$ sec for LINFIT. In the second region, the time ranges were the same, 0.31 to 1 sec. For the first decay region, the values for b by the two methods are statistically different. In the second region, the agreement between all three equations or methods was very good. In the third region, AUTFIT* and LINFIT values were in better agreement than AUTFIT values were with the other two.

The goodness of fit of the linear approximation dependency on time can be seen from the slope, E *vs.* log $[t]$, from Eq. [6] where

$$dE/d\log[t] = bt/(t + \tau - t^*) =$$

$$b - b(\tau - t^*)/t + \ldots \qquad [B\text{-}1]$$

The linear approximation produces a good fit as long as $t >> (\tau - t^*)$. In the case of region one, the Tafel behavior extends to the beginning of the decay curve. Here τ becomes significant in Eq. [B-1]. Thus, the slopes of the linear fits are smaller than b. In the later regions of the decay curves, the ratio $(\tau - t^*)/t$, is smaller, and the effect of the scatter in the data becomes larger than the error due to the approximation to the linear function.

When using AUTFIT* and Eq. [6], an initial point (t^*, E^*) must be selected. For region one, the obvious choice is to pick $t^* = 0$ and $E^* = E_0$, the actual starting potential. This choice amounts to using AUTFIT and Eq. [1]. For other regions, any initial point is appropriate as long as the calculated curve fits the desired portion of the experimental decay curve. However, since τ describes the conditions at the initial point and its definition depends on it being part of a Tafel region, τ has physical significance only if the initial point is part of the desired Tafel region in the experimental curve. Thus, when using AUTFIT*, t^* and E^* were selected at a time and potential data point that was in the center of the scatter at the beginning of the desired Tafel region. It was found that if a bad point were chosen, then the fitting process would fail to converge or would do so to an equation that poorly fitted the data. In region two, AUTFIT, AUTFIT*, and LINFIT yielded essentially the same values for b, and their respective equations all fitted the data equally well.

In region three, it was found that when the parameters obtained using AUTFIT were used in Eq. [1], the resultant curves fitted the data less accurately than the curves obtained from AUTFIT* and LINFIT. This judgment was based on the standard deviation of the estimates and the standardized residual plots. Those plotted from the fitted equations used in AUTFIT showed more significant curvature and skewness.

REFERENCES

1. R. Parsons, *J. Chim. Phys.*, **49**, 1 (1952).
2. J. McBreed and M. A. Genshaw, in Proceedings of Conference Fundamental Aspects of and Stress Corrosion Cracking, Columbus, Ohio, 1967.
3. R. W. Gurney, *Proc. Roy. Soc.* **134A**, 137 (1931).
4. G. Armstrong and J. A. V. Butler, *Trans. Faraday Soc.* **29**, 1261 (1933).
5. W. R. Busing and W. J. Kauzman, *Chem. Phy.*, **20** (7), 1129 (1952).
6. I. Brystrov and L. I. Krishtalik, *Elektrokhimiya*, **5** (4), 392 (1969).
7. M. Rosen, Bureau of Mines Report of Investigations, 1980, RI 8425.
8. M. Rosen and S. Schuldiner, *This Journal*, **117**, 35 (1970).
9. M. Rosen and S. Schuldiner, *Electrochim. Acta*, **18**, 686 (1973).
10. T. B. Warner and S. Schuldiner, *This Journal*, **112**, 853 (1965).
11. S. Schuldiner, *ibid.*, **107**, 452 (1960).
12. S. Schuldiner, *ibid.*, **106**, 891 (1959).
13. M. Rosen, S. Schuldiner, and D. R. Flinn, *ibid.*, **119**, 412 (1972).
14. Y. Bard, "Non-Linear Parameter Estimation," pp. 81-91, Academic Press, New York (1974).
15. P. Bevington, "Data Reduction and Error Analysis," pp. 204-208, McGraw Hill, New York (1969).
16. P. Bevington, "Data Reduction and Error Analysis," pp.235-236, McGraw Hill, New York (1969).
17. P. Bevington, "Data Reduction and Error Analysis," pp. 208-215, McGraw-Hill, New York (1969).
18. W. Hubin, "Basic Programming for Scientist and Engineers," pp. 82-87, Prentice-Hall Inc., Englewood Cliffs, NJ (1978).

Electrochemical Reactions in a Pure Na_2SO_4 Melt

W. C. Fang* and R. A. Rapp*

Department of Metallurgical Engineering, The Ohio State University, Columbus, Ohio 43210

ABSTRACT

Cyclic voltammetry and chronopotentiometry were used to study the electrochemical reduction reactions of SO_3 gas, O_2^- and SO_4^{2-} ions in a Na_2SO_4 melt at 900°C. The reduction reaction of SO_3 follows a ce mechanism: SO_3 first reacts chemically with SO_4^{2-} to form $S_2O_7^{2-}$ and then proceeds via a one-electron electrochemical reduction reaction to form SO_3^-. The reduction of peroxide O_2^- ions forms either O^{2-} or both O^{2-} and superoxide O_2^{2-} ions. Sulfate ions are subjected to decomposition at either very positive or very negative potentials. At very high positive potentials, sulfate ions decompose to evolve SO_2 and O_2 gases, in addition superoxide ions are also formed. At very negative potentials, sulfate ions decompose to form sulfide and peroxide.

In general, the attack of metals by a salt film in an oxidizing gas, which is called "hot corrosion" (1), becomes virulent only when the salt is molten. In this circumstance the alloy is physically separated from the gas phase by the molten salt so that the mechanism of corrosion must involve mainly electrochemical reactions. Obviously, an electrochemical study should be the most promising approach to investigate hot corrosion and might eventually explain the reaction mechanisms.

Electrochemical studies have been confined mostly to alkali halide melts where a voluminous literature can be found(2). Sulfate melts, on the other hand, have received little study because of their limited practical importance except for their deleterious effect in the hot corrosion of metals. Na_2SO_4, because of its high thermodynamic stability, is the constituent most commonly found in the salt film deposited by the combustion of fossil fuels; knowledge about the electrochemical reactions taking place in this melt is essential to the understanding of the Na_2SO_4-induced hot corrosion mechanism. Electrochemical reduction of SO_4^{2-} ions has been studied by several investigators. Liu (3) found sulfite and sulfide, but little or no sulfur, as the reduction products of a Li_2SO_4-K_2SO_4 melt electrolyzed between platinum electrodes at 625°C. Johnson and Laitinen (4) however reported that a eutectic Li_2SO_4-Na_2SO_4-K_2SO_4 melt electrolyzed at 550°C formed either sulfur or a metallic sulfide. In prolonged cathodic electrolysis of a $LiSO_4$-K_2SO_4 melt at 625°C, Burrows and Hills (5) observed the formation of elementary sulfur, oxide ions, and SO_2. Reduction reactions for the dissolved gaseous species O_2, SO_2, and SO_3 in the Li_2SO_4-K_2SO_4 eutectic melt were studied using cyclic voltammetry by Burrows and Hills (5). They found no cathodic reduction of dissolved oxygen but there were reduction waves for dissolved SO_3 and SO_2; nonetheless, no reduction reaction mechanism for SO_3 and SO_2 was given. Shores and Fang (6) suggested that the reduction of SO_3 in a pure Na_2SO_4 melt at 900°C actually proceeded through the reduction of the pyrosulfate ion ($S_2O_7^{2-}$) which was the reaction product from reacting SO_3 with SO_4^{2-}. The present study concerns the electrochemical reactions of dissolved SO_3, oxide ions, and sulfate ions (SO_4^{2-}) in a pure Na_2SO_4 melt at 900°C in O_2, and in O_2 environments containing SO_2 and SO_3. The results will be compared with those from previous studies.

Experimental Procedures

Cyclic voltammetry, chronopotentiometry, and potentiostatic chronocoulometry were used in this study. A three-electrode system was used for all electrochemical measurements. The reference electrode was a silver wire dipped into a 10 m/o Ag_2SO_4/Na_2SO_4 melt contained in a 0.6 cm ID mullite ($3Al_2O_3 \cdot 2SiO_2$) tube[2] as the electrolyte. A glassy grain boundary phase is known to provide predominant Na^+ conduction (7). The counterelectrode was a circular strip of platinum foil about 0.5 cm width and 7.0 cm circumference centered about the working electrode; this electrode provided a uniform current to the working electrode. The working electrode had a variety of shapes. In cyclic voltammetry studies, the working electrodes were 0.05 diam platinum wires sealed in alumina tubes with alumina cement to expose about 1-2 cm length of wire. The exposed area of the Pt electrode was totally immersed in the fused salt. In other studies, fully immersed square platinum foils of 0.5 × 0.5 cm were used. These electrodes were spot-welded to the platinum wire (0.05 cm diam) sealed in alumina tubes. The platinum electrodes were cleaned by flame polishing in a torch burning a mixture of natural gas and oxygen.

The cell assembly and electrodes are shown diagrammatically in Fig. 1. The cell consisted of a 4.5 cm OD, closed-end mullite tube (45 cm long) with a 304 stainless steel flange at the top. Epoxy was used to join the bottom flange to the mullite. The flange and the joint were cooled by a blower and a water-cooled jacket. The top and the bottom flanges were sealed with a Teflon O-ring which resisted attack by the $SO_2/SO_3/O_2$ gas mixtures. The electrodes were immersed in fused Na_2SO_4 in an alumina crucible of 2.5 cm OD and 4.0 cm height. All the measuring leads were platinum wire protected by alumina tubes.

The cell assembly was heated in a tubular furnace powered and controlled by a proportional-type temperature controller (Leeds and Northrup Electromax III). The constant temperature zone in the furnace was about 3.5 cm, and the temperature was kept constant within ±0.5°C at the experimental temperature of 900°C.

Reagent grade Na_2SO_4 (99.9% pure) was used without further purification. Known amounts of salt were charged into the crucible to give a melted salt thickness from 0.3 to 1.0 cm. The cell was first heated at 400°C under vacuum for 1-2 hr to remove moisture, then heated further to the operating temperature of 900°C. Most of the experiments were conducted in controlled SO_2-SO_3-O_2 gas mixtures. The desired gas compositions were obtained by mixing SO_2 and O_2 through two calibrated flow 'meters (Matheson No. 610). Gases containing SO_2 were passed through a bed of platinum gauze at the experimental temperature to ensure that equilibrium among SO_2, SO_3, and O_2 was achieved.

In the cyclic voltammetry experiment, the voltammetric scans were performed with an Aardvark Model V potentiostat coupled with a Bioanalytical Systems

* Electrochemical Society Active Member.
[1] Present address: Bell Laboratories, Murray Hill, New Jersey 07974.

Key words: hot corrosion, sodium sulfate, cyclic voltammetry, chronopotentiometry, a-c impedance.

[2] McDaniel MV-30.

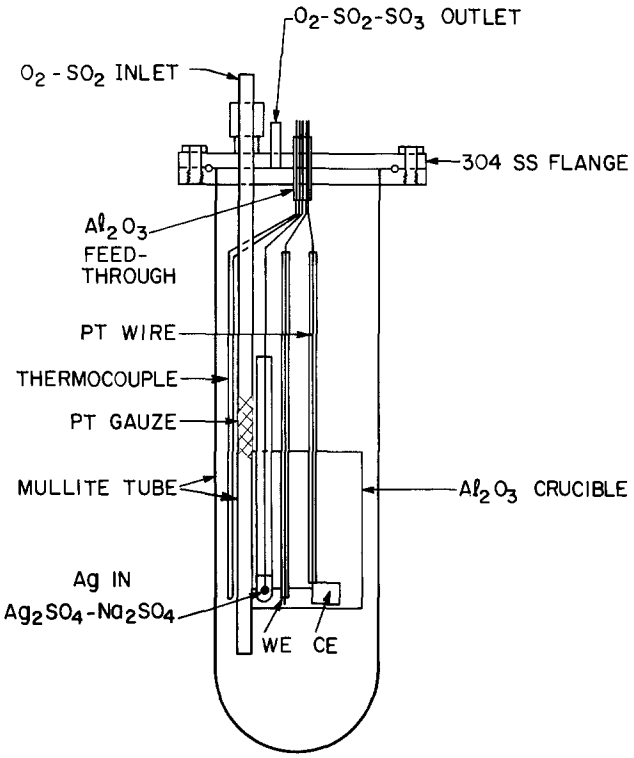

Fig. 1. Schematic assembly for electrochemical studies

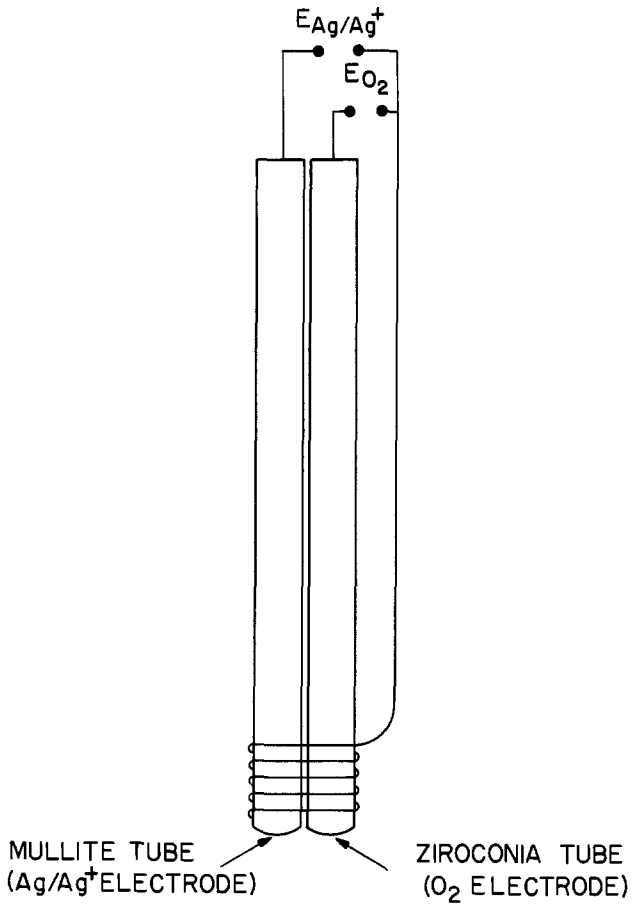

Fig. 2. A combination of two probes used to measure SO_2 and SO_3 in the atmosphere.

Model CV-1B-120 cyclic voltammetry unit; this unit was capable of generating scan rates from 0.01 to 10 V/sec. The current-potential curves were recorded on a Houston Model 2000 X-Y recorder. The voltammetric scan was started after the cell potential reached a steady value (after about 2 hr). The scan was normally begun from the open-circuit rest potential; however, in some cases the scan was started from other values of potential fixed by a biasing potentiostat. After completing a cycle, the cell potential was permitted to return to the original value before the next scan was started. Scan rates in the range of 0.05-3 V/sec were used.

A PAR (Princeton Applied Research) Model 174 potentiostat/galvanostat was used for chronopotentiometry and current reversal chronopotentiometry. The current could be reversed manually at any time. The potential-time curves were recorded on an HP 7101BM strip-chart recorder which had a maximum chart speed of 5 cm/sec. Occasionally *E-t* curves were recorded on a Tektronix oscilloscope with memory and photographed with a Polaroid camera.

For a given solute concentration, only a very narrow experimental range of current could be applied to detect the transition times. For too small currents the transition time was too long and could not be observed because of interference by convection; for too large currents the transition times were too short to be easily detected. In practice, trial and error preliminary experiments were used to choose currents suitable to observe the transition time.

In a potentiostatic coulometry experiment in pure Na_2SO_4, gases such as SO_2 and SO_3 could be formed as reaction products. Measurements of potential changes of a Ag/Ag^+ electrode and an oxygen electrode were used to detect the formation of these gases (7). Figure 2 shows the arrangement of the two electrodes which were held above the melt; a platinum wire, wrapped around the two electrodes, was used as the indicating electrode in the gas phase. This wire provided large contact areas with the electrodes. The portions of the tubes wrapped with the platinum wire were sprayed with a thin layer of Na_2SO_4 salt. The oxygen electrode was a closed-end 0.6 cm OD zirconia (3.5 w/o CaO) tube. The inside bottom portion of the zirconia tube was platinized; a platinum gauze spot-welded to a platinum wire made contact with the platinized bottom of the tube region and served as the electrode lead. The change of SO_3 partial pressure in the atmosphere could be monitored by suspending these electrodes just above the melt and measuring the potential of the Ag/Ag^+ electrode and the O_2 electrode, both with respect to the platinum indicating electrode.

In a-c impedance measurements, a Wenking potentiostat in series with a digital frequency response analyzer (Schlumberger-Solartron 1172) provided the constant d-c potential and the a-c potential. An a-c potential of 10 mV amplitude peak to peak was used. Data were collected through an Apple II microcomputer connected to the Solartron. The Apple computer was also used to control the operation of the Solartron automatically. The frequencies used were between 0.01 Hz and 10 kHz.

Results and Discussion

SO_3 reduction reaction.—A typical chronopotentiogram for a platinum electrode in a deep Na_2SO_4 melt (about 0.5 cm deep) in a 1% SO_2 + O_2 environment is shown in Fig. 3. Two transition times were found for the forward cathodic current and for the reversed anodic current. The first transition time (τ_1^c) must correspond to the reduction of the $S_2O_7^{2-}$ ion (6) while the second transition time (τ_2^c) must correspond to the reduction of the product formed in the first reduction, namely, the product from the $S_2O_7^{2-}$ reduction. This second conclusion is drawn because no other species in the melt has a concentration high enough to account otherwise for the observed long transition time (τ_2^c). For example, the next most abundant species besides $S_2O_7^{2-}$ under

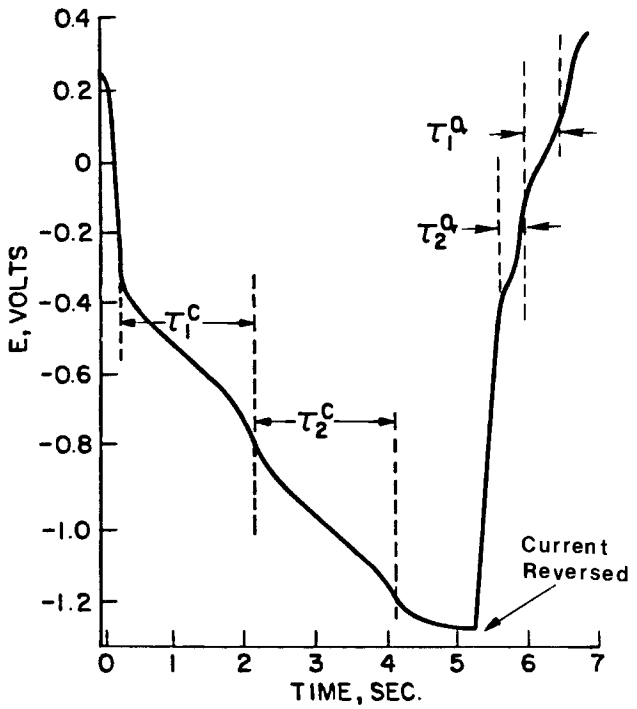

Fig. 3. Chronopotentiometry curve for Na_2SO_4 in O_2 + 1.0% (SO_2 + SO_3) gas at 900°C, i = 8 mA/cm².

the experimental conditions should be dissolved O_2 (8), and the calculated diffusivity based on the transition time measured from Fig. 3, assuming $n = 4$ would be 0.35 cm²/sec, which is obviously unreasonably high (6). The appearance of the second transition time was neither reproducible nor well defined. Therefore only the first transition reaction is further analyzed here to elucidate the reaction mechanism.

For a reversible reaction involving a soluble species, the potential at any time t in a chronopotentiogram is given by the relationship (9)

$$E = E_{\tau/4} - (RT/n\mathbf{F}) \ln [(\tau^{1/2} - t^{1/2})/t^{1/2}] \quad [1]$$

where $E_{\tau/4}$ is the quarter-wave potential ($E_{\tau/4}$ is equivalent to $E_{1/2}$ in cyclic voltammetry), τ is the transition time, n is the number of electrons, and R, T, and $\mathbf{F}$ have their conventional electrochemical meanings. A plot of the potential E *vs.* $\ln [(\tau^{1/2} - t^{1/2})/t^{1/2}]$ gives a straight line of slope $-RT/n\mathbf{F}$. The number of electrons involved in the reaction can therefore be obtained from the slope. Such a plot for the first forward reduction wave of Fig. 3 is given in Fig. 4. The slope obtained from Fig. 4 has a value of 0.109 which is very close to the theoretical value of 0.101 for a reaction with $n = 1$. Therefore the number of electrons is unity for the reduction of $S_2O_7^{2-}$. For a simple electrochemical reaction, the value of $i\tau^{1/2}$ should be independent of the applied current (9). However, a plot of $i\tau^{1/2}$ *vs.* i for the first reduction reaction in pure Na_2SO_4 shows a decrease in $i\tau^{1/2}$ with increasing i (Fig. 5). This signifies that the electrochemical reaction (e) has a preceding homogeneous chemical reaction (c); thus the first reduction obeys a ce mechanism (9). An a-c impedance complex plot for pure Na_2SO_4 melts as a function of SO_2 pressure is shown in Fig. 6. The curve for pure O_2 (Fig. 6) shows a slow electron exchange reaction. But as the amount of SO_2 in O_2 increases, and therefore SO_3 increases accordingly, the rate of charge transfer increases as depicted from the reduction in the radius of the semicircle at high frequencies (10) in Fig. 6.

According to Smith (11), a plot of cot ϕ *vs.* $\omega^{1/2}$ (ϕ = phase angle, ω = frequency) can be used for mechanistic diagnosis. For example at low frequencies, if the chemical reaction is in equilibrium, then an electrochemical reaction coupled with either a preceding first-order chemical reaction (ce) or a following first-order chemical reaction (ec) will show a maximum in a plot of cot ϕ *vs.* $\omega^{1/2}$, while a catalytic reaction (ec') will give cot $\phi \to \infty$ as $\omega \to 0$ where c' is the catalytic reaction. At high frequencies, all the plots of cot ϕ *vs.* $\omega^{1/2}$ for ce, ec, and ec' mechanisms will show a straight line which is determined by charge-transfer kinetics.

But if the electrochemical reaction is in equilibrium at low frequencies, which is the case for the reaction of SO_3 in Na_2SO_4 (6), the reaction becomes diffusion controlled. Then the plots of cot ϕ *vs.* $\omega^{1/2}$ for e, ec, ce, and ec' mechanisms would resemble those shown in Fig. 7 for a finite diffusion layer. Although a-c impedance data do not unequivocally reveal the

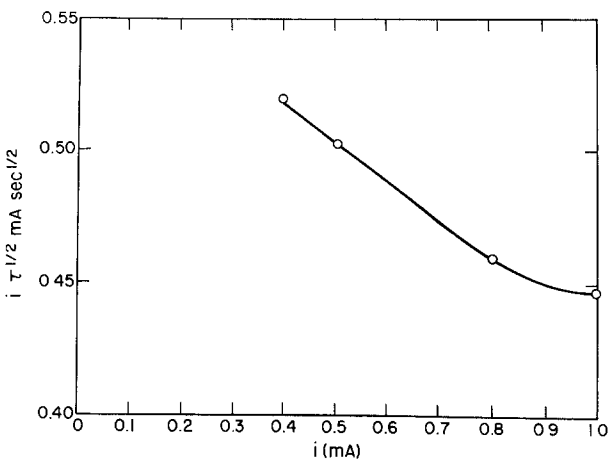

Fig. 5. Dependence of $i\tau^{1/2}$ on current for pure Na_2SO_4, O_2 + 1.0% (SO_2 + SO_3) at 900°C.

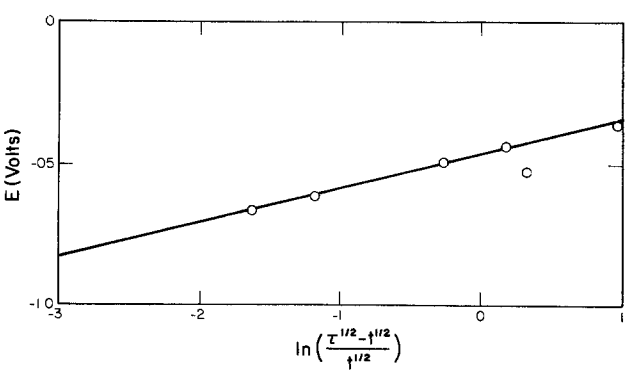

Fig. 4. Plot of chronopotentiometric data according to Eq. [1]

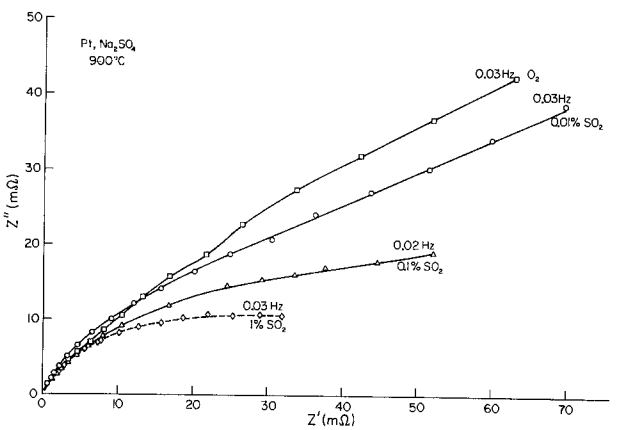

Fig. 6. A-C impedance diagram at open-circuit potentials as a function of P_{SO_2} in the atmosphere, Na_2SO_4, 900°C.

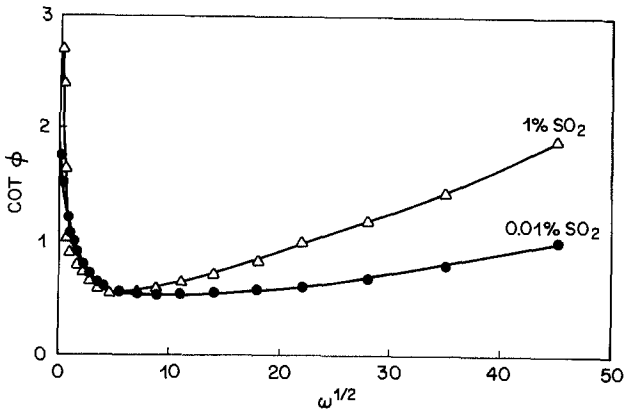

Fig. 7. Frequency dependence of phase angle of Na_2SO_4 in different P_{SO_2} atmospheres.

exact reaction mechanism for the SO_3 reaction in Na_2SO_4, they are not inconsistent with the conclusion from the chronopotentiometry experiment. Based on these inferences for a ce mechanism and the result that $n = 1$, the following reaction scheme for the SO_3 reduction reaction is proposed.

$$SO_3 + SO_4^{2-} \underset{k_b}{\overset{k_f}{\rightleftharpoons}} S_2O_7^{2-} \qquad c \qquad [2]$$

$$S_2O_7^{2-} + e^- = SO_4^{2-} + SO_3^- \qquad e \qquad [3]$$

followed by the chemical combination reaction

$$SO_3^- + SO_3^- = S_2O_6^{2-} \qquad [4]$$

or followed by a further electrochemical reaction

$$SO_3^- + e^- = SO_3^{2-} \qquad [5]$$

Since the species $S_2O_6^{2-}$ and SO_3^{2-} may not be stable under the experimental conditions (acidic melt), further chemical reactions would probably take place to form SO_2, O^{2-}, O_2^-, etc., *e.g.*

$$S_2O_6^{2-} \rightarrow 2SO_2 + O_2^{2-} \qquad [4a]$$

or

$$SO_3^{2-} \rightarrow SO_2 + O^{2-} \qquad [5a]$$

Reaction [5] could correspond to the second transition reaction observed in the chronopotentiogram; the instability of SO_3^- may explain why the second transition is not reproducible. Reaction [4] must be very slow; otherwise a cec mechanism would be observed instead of a ce mechanism. Shores and Fang (6) proposed the following cathodic reaction of SO_3 based on the limiting cathodic current density observed in polarization experiments

$$S_2O_7^{2-} + 8e^- = SO_4^{2-} + S^{2-} + 3\,O^{2-} \qquad [6]$$

These reduction products were suggested without experimental substantiation, and apparently Eq. [6] is not correct. The present chronopotentiometry results establish the n value as one for $S_2O_7^{2-}$ reaction according to reaction [3]. Wrench and Inman (12) studied the dissociation of Na_2SO_4 in a NaCl-KCl melt at 750°C by adding a very strong acid (*e.g.*, $NaPO_3$) to the melt, and proposed an electrochemical reaction scheme for SO_3 similar to reaction [3].

Reaction rate constants of k_f and k_b in reaction [2] can be calculated from Fig. 5. by using the following equation derived by Delahay and Berzins (13)

$$i\tau^{1/2} = \frac{1}{2} nFAC^b\sqrt{\pi D} - \frac{i}{2K}\left(\frac{\pi}{k_f + k_b}\right)^{1/2} \operatorname{erf}\left[(k_f + k_b)\tau\right]^{1/2} \qquad [7]$$

where $K = k_f/k_b$, erf [ ] the error function, A the electrode area, and C^b is the bulk concentration.

At low currents, Eq. [7] reduces to the following form

$$i\tau^{1/2} = \frac{1}{2} nFAC^b\sqrt{\pi D} - \frac{i}{2K}\left(\frac{\pi}{k_f + k_b}\right)^{1/2} \qquad [8]$$

A plot of $i\tau^{1/2}$ *vs.* i gives a straight line and the value of $\frac{1}{2K}\left(\frac{\pi}{k_f + k_b}\right)^{1/2}$ is readily obtainable from the slope. At high currents, Eq. [7] can be written as follows

$$i\tau^{1/2} = \frac{nFAC^b\sqrt{\pi D}}{2(1 + 1/K)} \qquad [9]$$

Equation [9] indicates that the product $i\tau^{1/2}$ is independent of the current at high currents. K can be readily calculated from Eq. [9] if the limit of $i\tau^{1/2}$ is observed in the experiment. Figure 5 shows a reasonably straight line at low currents and a limiting value for $i\tau^{1/2}$ at high currents; k_f, k_b, and K were obtained by this method and have the following values: $k_f = 2.72 \times 10^{-2}$ sec^{-1}, $k_b = 8.36 \times 10^{-3}$ sec^{-1}, and $K = 3.26$.

The diffusion coefficient for $S_2O_7^{2-}$ in Na_2SO_4 can be obtained from an extrapolation to $i = 0$ in Fig. 5 according to Eq. [7]

$$(i_o\tau^{1/2})_{i\to 0} = \tfrac{1}{2}(\pi^{1/2}FAnC^bD^{1/2}) \qquad [10]$$

where i_o is the current density, and D is the diffusion coefficient. The diffusion coefficient was calculated to be 2.67×10^{-4} cm^2/sec, which seems rather high compared to that for ions in molten salts. However Wrench and Inman (12) have obtained a similar diffusion coefficient for SO_3 in a NaCl-KCl melt at 750°C.

Oxide ion reduction and reaction of its related species.—The redox reaction of the oxide ion and its related species was studied by adding known amounts of Na_2O_2 to Na_2O_4 followed by cyclic voltammetry and chronopotentiometry experiments. Figure 8 shows the cyclic voltammogram for Na_2SO_4 containing 5 m/o Na_2O_2. One pair of peaks (A_1, A_2) is observed which represents a redox reaction involving the peroxide ion (O_2^-) as explained later.

In the chronopotentiometry study, no transition time was found for an initial anodic applied current. However, one transition time was found for the cathodic current, and subsequent current reversals gave two distinct transitions as shown in Fig. 9. Table I lists all the possible reduction reactions among the species O_2^-, O_2^{2-}, and O^{2-}. Reactions involving O_2 and O reduction are ruled out because no redox peaks in cyclic voltammetry and no transition times in chronopotentiometry were found for pure Na_2SO_4 in an O_2 gas environment. Furthermore the chemical decomposition of Na_2O_2 to form O^{2-} according to $O_2^{2-} = O^{2-} + \frac{1}{2}O_2$ could not go to completion; otherwise no reduction transition would be observed in a Na_2SO_4

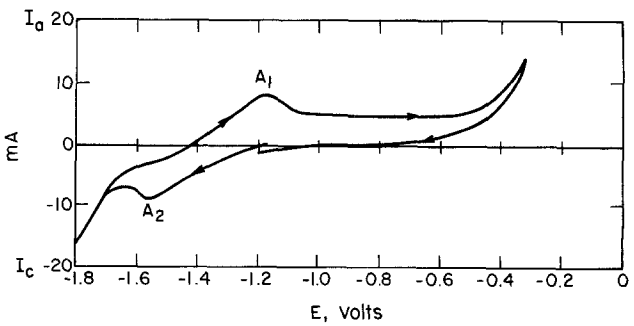

Fig. 8. Cyclic voltammogram for 5 m/o Na_2O_2 in Na_2SO_4, scan rate = 1.0 V/sec, air atmosphere, 900°C.

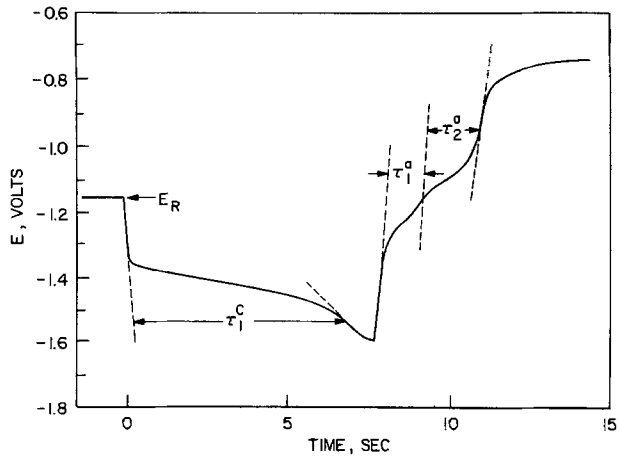

Fig. 9. Chronopotentiometry curve for Na_2SO_4 + 5 m/o Na_2O_2, i = 0.2 A/cm², air atmosphere, 900°C.

melt containing Na_2O_2, because O^{2-} could not be reduced further.

To assist in determining the reduction reaction mechanism for the oxygen species, an n value for the cathodic reduction reaction observed in a chronopotentiogram is obtained from the slope in a plot of E *vs.* ln $[(\tau^{1/2} - t^{1/2})/t^{1/2}]$ according to Eq. [1] as shown in Fig. 10. A slope of 30 mV is obtained for the cathodic reaction which is in good agreement with theoretical value of 33 mV for $n = 3$. However, in other runs, $n = 4$ (for 24 mV) was also obtained; therefore the n value for the cathodic reduction reaction can be either 3 or 4. This may be caused by a competition between reactions $n = 3$ and $n = 4$. The potential-time relationship (14) for the reverse portion of the chronopotentiometry curve is described by the equation

$$E = E_{\tau/4} + \frac{RT}{n\mathbf{F}} \ln \left[\left(\frac{\tau^{1/2}}{(\tau + t')^{1/2} - 2t'^{1/2}} \right) - 1 \right] \quad [11]$$

where t' is the time after current reversal. A plot of E *vs.* the logarithmic term in Eq. [11] should yield a straight line whose slope is $RT/n\mathbf{F}$. However, the values of the bracketed term in Eq. [11] for the data presented in Fig. 9 are mostly negative, so that no information can be obtained. However, if the forward current was held for a sufficient time to let the potential reach a steady value before the current was reversed, Eq. [1] should be applicable because the cathodic reaction is brought to completion before the reversal; in fact, a linear fit to Eq. [1] is observed as shown in Fig. 10 for the anodic waves.

The first reverse wave has a slope of 49 mV which is close to the theoretical value of 51 mV for $n = 2$. The second wave shows a slope of 77 mV which is in fair agreement with the theoretical value of 101 mV for $n = 1$.

Based on these n values and the reactions listed in Table I, two reaction pathways can be postulated: (*i*) a consecutive reoxidation of the products for the reduction reaction with $n = 3$

$$O_2^{2-} + O_2 = 2\,O_2^- \qquad \text{Chemical equilibrium} \qquad [12]$$

$$O_2^- + 3e^- = 2\,O^{2-} \qquad E_{\tau/4} = -1.39\text{V red'n} \qquad [13]$$

$$2\,O^{2-} = O_2^{2-} + 2e^- \qquad E_{\tau/4} = -1.35\text{V oxid'n 1} \qquad [14]$$

$$O_2^{2-} = O_2^- + e^- \qquad E_{\tau/4} = -1.22\text{V oxid'n 2} \qquad [15]$$

Table I. Possible reduction reactions of oxygen and its related species

(a) $O_2^{2-} + 2e^- = 2\,O^{2-}$
(b) $O_2^- + 3e^- = 2\,O^{2-}$
(c) $O_2^- + e^- = O_2^{2-}$

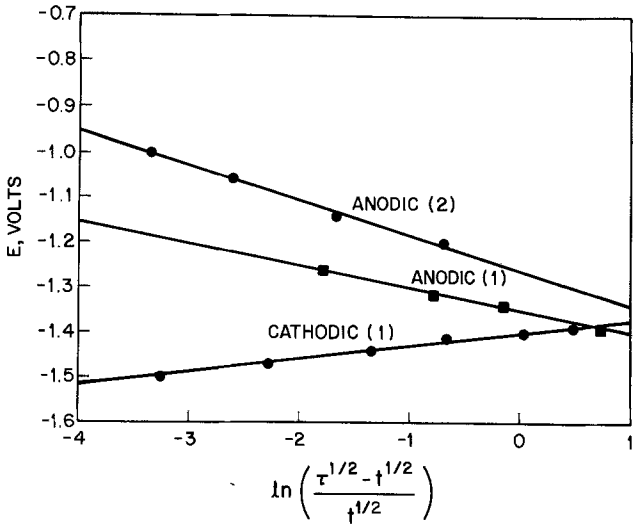

Fig. 10. Semilogarithmic plot of chronopotentiometric data according to Eq. [1].

(*ii*) parallel reoxidation reactions for the products from the reduction reaction with $n = 4$

$$O_2^{2-} + O_2 = 2\,O_2^- \qquad \text{Chemical equilibrium} \qquad [12]$$

$$2\,O_2^- + 4e^- = 2\,O^{2-} + O_2^{2-} \qquad E_{\tau/4} = -1.39\text{V red'n} \qquad [16]$$

$$2\,O^{2-} = O_2^{2-} + 2e^- \qquad E_{\tau/4} = -1.35\text{V oxid'n 1} \qquad [17]$$

$$O_2^{2-} = O_2^- + e^- \qquad E_{\tau/4} = -1.22\text{V oxid'n 2} \qquad [18]$$

where $E_{\tau/4}$ are the quarter-wave potentials whose values were obtained from the intercepts in the plot of E *vs.* ln $[(\tau^{1/2} - t^{1/2})/t^{1/2}]$ given as Fig. 10. The quarter-wave potential for reaction [13] and reaction [16] is −1.39V, which is close to the value of −1.37 obtained from the cyclic voltammetry result shown in Fig. 8.

The mechanisms proposed above show that superoxide ions (O_2^-) are reduced in the Na_2SO_4 melt. This disagrees with the previous assumptions that when adding Na_2O_2 to a Na_2SO_4 melt the decomposition of Na_2O_2 to form O^{2-} and O_2 proceeds to completion (24). In that case, no cathodic transition should be observed because O^{2-} could not be reduced further. No previous similar study for the reduction of oxygen-related species in sulfate melts is available for comparison; however numerous studies have reported O_2^- and/or O_2^{2-} ions in alkali halide (15-19) and nitrate melts (20-22).

Sulfate oxidation reaction.—A typical cyclic voltammogram for a pure Na_2SO_4 melt is shown in Fig. 11. The anodic reaction has a prewave (A_1) before the current rises rapidly. This prewave which is very insensitive to the gas environment above the melt can probably be attributed to the formation of sulfite ions ($S_5O_{16}^{2-}$ and $S_6O_{19}^{2-}$). This is supported by the x-ray analysis (Table II) of the frozen melt deposited on the platinum foil which has been held at the potential of 1.52V with respect to the Ag/Ag^+ reference electrode for 3 min. The platinum foil electrode was withdrawn from the melt with the potential maintained at 1.52V. Na_8PtO_6 was also found in the deposit. The evolution of a couple ppm to several hundred ppm SO_2 gas (depending on applied current) was detected by the electrodes of Ag/Ag^+ (mullite electrolyte) and O_2 (stabilized zirconia electrolyte) suspended just above the melt. A second oxidation peak could not be observed in the cyclic voltammogram in Fig. 11 because 2.0V was the upper voltage limit obtainable for the equipment used in this study. But the large oxidation current above 2V must re-

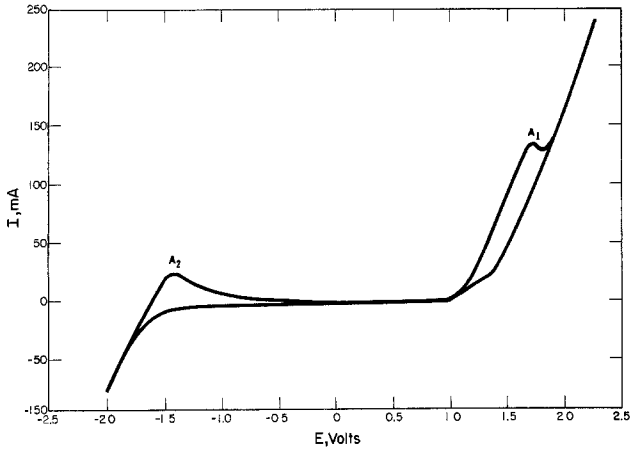

Fig. 11. Cyclic voltammetry for Na_2SO_4 in O_2 + 0.1% (SO_2 + SO_3) atmosphere at 900°C.

sult from SO_4^{2-} oxidation because no other species in the melt under the experimental conditions could provide such large currents.

In view of the cyclic voltammetry, x-ray diffraction, and the detection of SO_2, the following parallel oxidation reactions for sulfate ions are proposed

$$SO_4^{2-} = SO_3 + \tfrac{1}{2}\,O_2 + 2e^- \quad [19]$$

$$5SO_4^{2-} = S_5O_{16}^{2-} + 2\,O_2^{+} + 6e^- \quad [20]$$

$$12SO_4^{2-} = 2S_6O_{19}^{2-} + 5\,O_2^{-} + 15e^- \quad [21]$$

$$2\,O^{2-} = O_2^{-} + 3e^- \quad [22]$$

and a Pt or PtO_2 dissolution reaction

$$Pt + 8\,O_2^{-} = PtO_6^{8-} + 5\,O_2 \quad [23]$$

$$PtO_2 + 4\,O^{2-} = PtO_6^{8-} \quad [24]$$

Based on the x-ray analyses (Table II) and the results for oxygen-related species described in the previous section, the formation of O_2^- is favored. Reactions [19], [20], and [21] are highly irreversible and no corresponding cathodic peaks are observed in the cyclic voltammogram (Fig. 11).

There is very little information on the limiting anodic reaction in sulfate melts. As mentioned earlier, Johnson and Laitinen (4) studied the electrolysis of the melt Li_2SO_4-Na_2SO_4-K_2SO_4, by determining the potential and current characteristics on platinum microelectrodes in an argon atmosphere. Without analysis of the anode products, the following sulfate oxidation reaction was proposed

$$SO_4^{2-} = SO_3 + \tfrac{1}{2}\,O_2 + 2e^- \quad [25]$$

Delimarskii and Markov (23) studied the oxidation of the sulfate ion in a fused NaCl + KCl melt by measuring the discharge potential. The reaction for sulfate ion discharge was given, again without analysis of the product, as

$$SO_4^{2-} = SO_3 + 2e^- \quad [26]$$

In the present study, as shown earlier, Ag/Ag^+ and O_2 probes were used to detect any change of O_2 and SO_2 concentrations in the argon atmosphere above the melt during the potentiostatic chronocoulometry experiment. Results indicated that both SO_2 and O_2 increased upon the oxidation of sulfate ions, which provides evidence for reaction [25]. In addition, the x-ray analyses revealed that sulfites and peroxide ions are also formed as the products from the oxidation of sulfate ions.

Table II. X-ray diffraction analysis of deposits on Pt electrode in pure Na_2SO_4 melt

Potential applied (3 min)	Compounds found
1.52V	Na_2SO_4, NaO_2, Na_2O, $Na_2S_5O_{16}$, $Na_2S_6O_{19}$, Na_2PtO_6
−2.00V	Na_2SO_4, Na_2O_2, Na_2O, $Na_2S \cdot 5H_2O$, PtS, PtS_2

Sulfate reduction reaction.—The cyclic voltammogram shown in Fig. 11 indicates that a reduction reaction must take place at a potential more negative than −1.5V (again, the peak could not be observed due to equipment limitation). This reaction must involve the reduction of sulfate ions because of the extremely large current for $E < -2.0$V. However, the conjugate anodic peak A_2 (Fig. 11) indicates some reversibility for the sulfate reduction reaction. X-ray analysis (Table II) supports either of the following reactions for sulfate reduction

$$SO_4^{2-} + 4e^- = S^{2-} + 2\,O_2^{2-} \quad [27]$$

$$O_2 + 2e^- = O_2^{2-} \quad [28]$$

and

$$Pt^{4+} + 2S^{2-} = PtS \quad [29]$$

The Pt^{4+} ion becomes stable in a high oxidizing and acid melt at high positive potentials.

There have been several studies of the reduction reactions in sulfate melts. Liu (3) found sulfite and sulfide but little or no sulfur in the cathode compartment of a Li_2SO_4-K_2SO_4 melt electrolyzed between platinum electrodes at 625°C. Johnson and Laitinen (4) reported that a eutectic Li_2SO_4-Na_2SO_4-K_2SO_4 melt at 550°C formed either sulfur or a metallic sulfide. The present results show that at $E = -2.0$V with respect to a Ag/Ag^+ reference electrode, the products resulting from the cathodic reduction of sulfate ions are sulfide and peroxide with no sulfur or sulfite formation; this agrees partially with the previous results from Liu and from Johnson and Laitinen. Obviously differences between these results can be caused by the different potentials, temperatures, and compositions used in the electrolysis experiments.

Conclusions

In a pure Na_2SO_4 melt, a variety of electrochemical reactions can take place. The extent to which a particular reaction can occur depends on the gas composition, the electrode potential, the electrode material, and the salt thickness.

In atmospheres containing SO_2 and SO_3, the primary electrochemical reactions involving gas species at an immersed platinum electrode are the reduction of pyrosulfate ions according to: $S_2O_7^{2-} + e^- = SO_4^{2-} + SO_3^-$ followed by a chemical combination reaction, or else by a further electrochemical reaction. Besides the pyrosulfate reduction reaction, a reduction reaction for dissolved oxygen could also occur, but to a much lesser extent because of the very low solubility for oxygen in Na_2SO_4 (8). At equilibrium with an atmosphere containing 0.15% SO_2 in O_2, about 87% of the cathodic limiting current results from the pyrosulfate reduction reaction and 13% from oxygen reduction (6). As the SO_2 concentration of the gas phase is increased, the percentage of the reduction reaction contributed by oxygen is reduced.

In a basic Na_2SO_4 melt, such as the melt in an argon or oxygen atmosphere, or the melt in the vicinity of a cathodic reaction which generates O^{2-} ions, reactions involving oxide ions or its related species can occur. Two different reduction reactions are possible when Na_2O_2 is added to Na_2SO_4 in an air atmosphere: $O_2^- + 3e^- = 2\,O^{2-}$ or $2\,O_2^- + 4e^- = 2\,O^{2-} + O_2^{2-}$.

Under very extreme conditions, *e.g.*, under a very high anodic or cathodic overpotential, decomposition of pure Na_2SO_4 may occur. This is possible for highly reducing conditions for the corrosion of a reactive metal covered by a deep melt, or where the salt may be trapped in the pore within the oxide scale and thereby decomposes. In this case, sulfate ions

can decompose electrochemically either anodically to form SO_3, O_2, O_2^- and sulfites or cathodically to form S^{2-} and O_2^{2-}.

Overall, in the corrosion of metals beneath a thin fused sulfate film in a SO_2-containing atmosphere, the primary cathodic reduction reaction at the salt/oxide interface should be the reduction of pyrosulfate ions with oxygen reduction to a lesser extent, if the oxide scale is compact and impervious to the salt. However, if the oxide scale is porous or has cracks, so that the salt can penetrate to the metal, then the reduction of sulfate ions to form sulfide ions according to reaction [27] could be possible. The sulfide ions can react with metal or metal oxide to form metal sulfide which provides rapid cation diffusion and accelerates the rate of attack. The rate of reaction [27] is very fast as indicated in the cyclic voltammetry experiment by an extremely large peak current for the reduciton of sulfate ions. As a result, corrosion could become catastrophic.

Acknowledgments

This research was sponsored by the National Science Foundation, Metallurgy Program of the Division of Material Research under grant DMR 791190. The advice of Professor D. D. Macdonald is greatly appreciated.

Manuscript submitted Nov. 29, 1982; revised manuscript received July 26, 1983.

The Ohio State University assisted in meeting the publication costs of this article.

REFERENCES

1. J. Stringer, *Ann. Rev. Mater. Sci.*, **7**, 477 (1977).
2. Y. K. Delimarskii and B. F. Markov, "Electrochemistry of Fused Salts," Sigma Press (1961).
3. C. H. Liu, *J. Am. Chem. Soc.*, **66**, 164 (1962).
4. K. E. Johnson and H. A. Laitinen, *This Journal*, **110**, 314 (1963).
5. B. W. Burrow and G. J. Hills, *Electrochim. Acta.*, **15**, 446 (1970).
6. D. A. Shores and W. C. Fang, *This Journal*, **128**, 346 (1981).
7. D. A. Shores and R. C. John, *J. Appl. Electrochem.*, **10**, 275 (1980).
8. R. Andersen, *This Journal*, **126**, 328 (1979).
9. P. Delahay, "New Instrumental Methods in Electrochemistry," Interscience Publ. Inc., New York (1954).
10. M. Sluyters-Rehbach and J. H. Sluyters, in "Electroanalytical Chemistry," Vol. 4, A. J. Bard, Editor, p. 1, Dekker Publ., New York (1970).
11. D. E. Smith, *Anal. Chem.*, **35**, 602 (1963).
12. D. M. Wrench and D. Inman, *Electrochim. Acta.*, **12**, 160 (1960).
13. P. Delahay and T. Berzins, *J. Am. Chem. Soc.*, **75**, 2486 (1953).
14. T. Berzins and P. Delahay, *ibid.*, **75**, 4205 (1953).
15. F. L. Whiting, G. Mamantov, and J. P. Young, *J. Inorg. Nucl. Chem.*, **34**, 2475 (1972).
16. D. L. Manning and G. Mamantov, *This Journal*, **124**, 480 (1977).
17. F. L. Whiting, G. Mamantov, G. M. Begun, and J. P. Young, *Inorg. Chem. Acta.*, **5**, 260 (1971).
18. D. L. Manning and G. Wilkinson, "Advanced Inorganic Chemistry," 3rd ed., p. 417, Interscience, New York (1972).
19. M. L. Dearnhardt and K. H. Stern, *This Journal*, **110**, 314 (1963).
20. D. R. Flinn and K. H. Stern, *J. Electroanal. Chem.*, **63**, 39 (1975).
21. P. G. Zambonin and A. Cavaggioni, *J. Am. Chem. Soc.*, **93**, 2845 (1971).
22. P. G. Zambonin, *J. Electroanal. Chem.*, **24**, 365 (1970).
23. Y. K. Delimarskii and B. F. Markov, "Electrochemistry of Fused Salts," Metallurgizdat, Moscow (1960).
24. D. K. Guta and R. A. Rapp, *This Journal*, **127**, 2194 (1980).

Structural Studies of Electroless Thin Ni-P Films Grown in an Alkaline Environment

R. O. Cortijo and M. Schlesinger

Department of Physics, University of Windsor, Windsor, Ontario, Canada N9B 3P4

ABSTRACT

A comparative study of the microstructure of electroless Ni-P thin films grown from an alkaline metallizing bath with different pH values was performed. Using radial distribution function (RDF) analysis of electron diffraction patterns, it was concluded that the films differ mainly by the size of their component crystallites.

Chemically (electrolessly) deposited nickel films are a binary system of nickel and phosphorous. The initial structure of as-deposited Ni-P films is metastable. Heat-treatment will transform it to a more stable two-phase state of fcc nickel and tetragonal Ni_3P. This state of affairs is quite well established for nickel deposited from acidic metallizing baths. Films obtained using alkaline solutions in the as-deposited state exhibit crystallinity depending on their phosphorous content. This in turn can be controlled by varying the pH of the metallizing solution (1).

In the present study we employ electron micrographs, electron diffraction, and reduced radial distribution curves to elucidate the crystalline state of as-deposited alkaline produced Ni-P films. It is concluded that the pH of the metallizing bath (*i.e.*, the phosphorous content) determines the crystallite sizes, but that the crystallites are of the same character regardless of size.

Experimental

Samples.—Thin electrolessly deposited Ni-P films were the object of the present study. The films were grown on Formvar-coated glass slides. The metallized Formvar was floated off the slide and placed in the sample holder of a JEOL Model JEM-100CX electron microscope.

The sensitizing and metallizing procedures were as given in Ref. (1, 2). The pH was controlled by adding NaOH to the metallizing bath. Films were grown from the same solution with different pH values and the metallizing bath temperature was kept constant at 43°C.

The electron microscope was operated at 100 kV, and both electromicrographs and diffraction patterns (focal length of 236 mm) were recorded photographically.

In all of these samples, care was taken to have the films examined in the electron microscope on the

same day they were grown. Also, the beam width and intensity were such that no heating effects were introduced, so one could view the films as being in the as-deposited state.

Calculations.—The diffraction patterns were scanned by a standard microdensitometer whose output was fed into an ADC of a PDP 11/03 minicomputer. The computer stored the diffraction patterns digitally in a fashion such that each diffraction graph consisted of 1024 points. Before embarking on the derivation of radial distribution functions, a number of corrections had to be made to account for systematic errors. Those arise from (*i*) nonlinear photographic film response, (*ii*) improper normalization of the diffraction pattern, (*iii*) termination effects, (*iv*) effects due to nonelastic electron scattering.

For a detailed discussion of these errors and procedures to correct for them see Ref. (3). We have employed similar correction methods in our work. This is discussed in detail in Ref. (4).

Details of the derivation of the expressions for the radial distribution function may be found in several excellent papers and review articles (5). Here we present the essentials. For a one-component material, the observable elastic scattering function is given by

$$I(s) = Nf^2(s)\left[1 + \frac{2}{s}\int_0^\infty r[\rho(r) - \rho_0]\sin 2\pi sr\,dr\right] \quad [1]$$

where N is the number of scattering atoms, $f(s)$ is the atomic scattering factor, $\rho(r)$ is the atomic density distribution function, ρ_0 is the average atomic density and s is the scattering parameter ($s = 2\sin\theta/\lambda$). Equation [1] can be rearranged to read

$$s\left[\frac{I(s)}{Nf^2(s)} - 1\right] = 2\int_0^\infty r[\rho(r) - \rho_0]\sin 2\pi sr\,dr \quad [2]$$

The reduced interference function, $i(s)$ is defined as

$$i(s) = s\left[\frac{I(s)}{Nf^2(s)} - 1\right] \quad [3]$$

such that

$$i(s) = 2\int_0^\infty r[\rho(r) - \rho_0]\sin 2\pi sr\,dr \quad [3a]$$

which has the form of a Fourier transform with the inversion formula

$$r[\rho(r) - \rho_0] = \int_{-\infty}^{\infty} i(s)\sin 2\pi sr\,ds \quad [4]$$

Therefore, the reduced distribution function known as

$$G(r) = 4\pi r[\rho(r) - \rho_0] \quad [5]$$

is given by

$$G(r) = 8\pi\int_0^\infty i(s)\sin 2\pi sr\,ds \quad [6]$$

and finally the radial distribution function (RDF)

$$RDF(r) = 4\pi r^2\rho(r) = 4\pi r^2\rho_0 + 8\pi r\int_0^\infty i(s)\sin 2\pi sr\,ds \quad [7]$$

It is the reduced RDF Eq. [6], $G(r)$ that we present in the next section. Clearly, it depicts the average atomic distribution around a lattice atom as a function of r, the distance from that atom. The first peak in such a curve, for instance, represents the average near neighbor distance. In a purely crystalline material this and subsequent peaks are expected to be sharp and well defined; otherwise, the peaks will possess a finite width and some might appear to fuse together. The resolution in our $G(r)$ curves is 0.13Å, and only peaks closer than that would appear as one. In our $G(r)$ calculations, we used the "one component only" version. This is justified for films grown in metallizing baths of *p*H 9 and up. The reason for this is that the phosphorous content of such films is less than two percent (6). In order to determine $G(r)$ for films grown in baths of *p*H lower than 9, a two-specie calculation has to be made.

The computer software was developed in our laboratory and was based on existing algorithms for the performance of FFT, such as Sande-Tuckey (7). Typically, the digitalization of one diffraction pattern takes 1-2 min, and the production of the $G(r)$ curve takes an additional 60 sec.

Results

In Fig. 1, we present a series of electron micrographs of thin Ni-P grown at different *p*H values of the metallizing bath (from *p*H about 8 through *p*H about 12). Based on electron transmittivity, we judge our films to have grown to about the same thickness each. We did not attempt to determine their thicknesses in any accurate fashion, but we estimated them to be about 500Å. It can readily be seen from the figure that the higher the *p*H value, the larger and more sparsely distributed on the surface the metal islands are. Figure 2 presents the microdensitometer output curves of the diffraction patterns obtained from the films corresponding to Fig. 1. Note the sharpening and better resolution of the different peaks as one proceeds from lower to higher *p*H values. Figure 3 depicts the $G(r)$ curves for the films grown at *p*H 9.0 and 12.3. Note the relatively well-resolved sharp peaks in all of these curves.

Discussion

The electron micrographs show the usual picture of a discontinuous film consisting of individual islands. Those are presumably the result of Sn-Pd nucleation centers present on the surface (1) after activation and before metallizing started. In our samples, the islands are almost touching, *i.e.*, the films are nearly continuous. It is noted that as the *p*H increases, the rate of deposition and with it the island sizes increase, and the islands are less densely distributed. Also in this connection, we observe that each film has a nearly uniform island size. We attribute these to the following. First, the effect of raising the *p*H on hypophosphite is to increase its reduction potential (8), thus enhancing film growth rate. Second, it has been observed (8) that some time in the alkaline metallizing bath is necessary before the material present on the substrate after Sn(II)-Pd(II) sensitization-activation is capable of catalyzing Cu plating. This is expected (also in our case) to result in less active nucleation centers available the higher the *p*H, simply because the time spent in the metallizing bath is shorter.

The tentative models for the Ni-P alloys grown in alkaline environment (1) are those of a solid solution of phosphorous in crystalline fcc nickel structure. The smearing out of the diffraction pattern (Fig. 2) for lower *p*H values can be initially attributed to one or more of the following: (*i*) partial crystallinity, (*ii*) small crystallite size, (*iii*) internal strains.

It is known (9) that the size contribution to the width of the Bragg diffraction peak Δs is related to the crystallite size, D, normal to the diffracting plane by the expression

$$\Delta s = \frac{C}{D} \quad [8]$$

C is a quantity which depends on the Miller indexes of reflection and the shape of the crystallites. For iso-

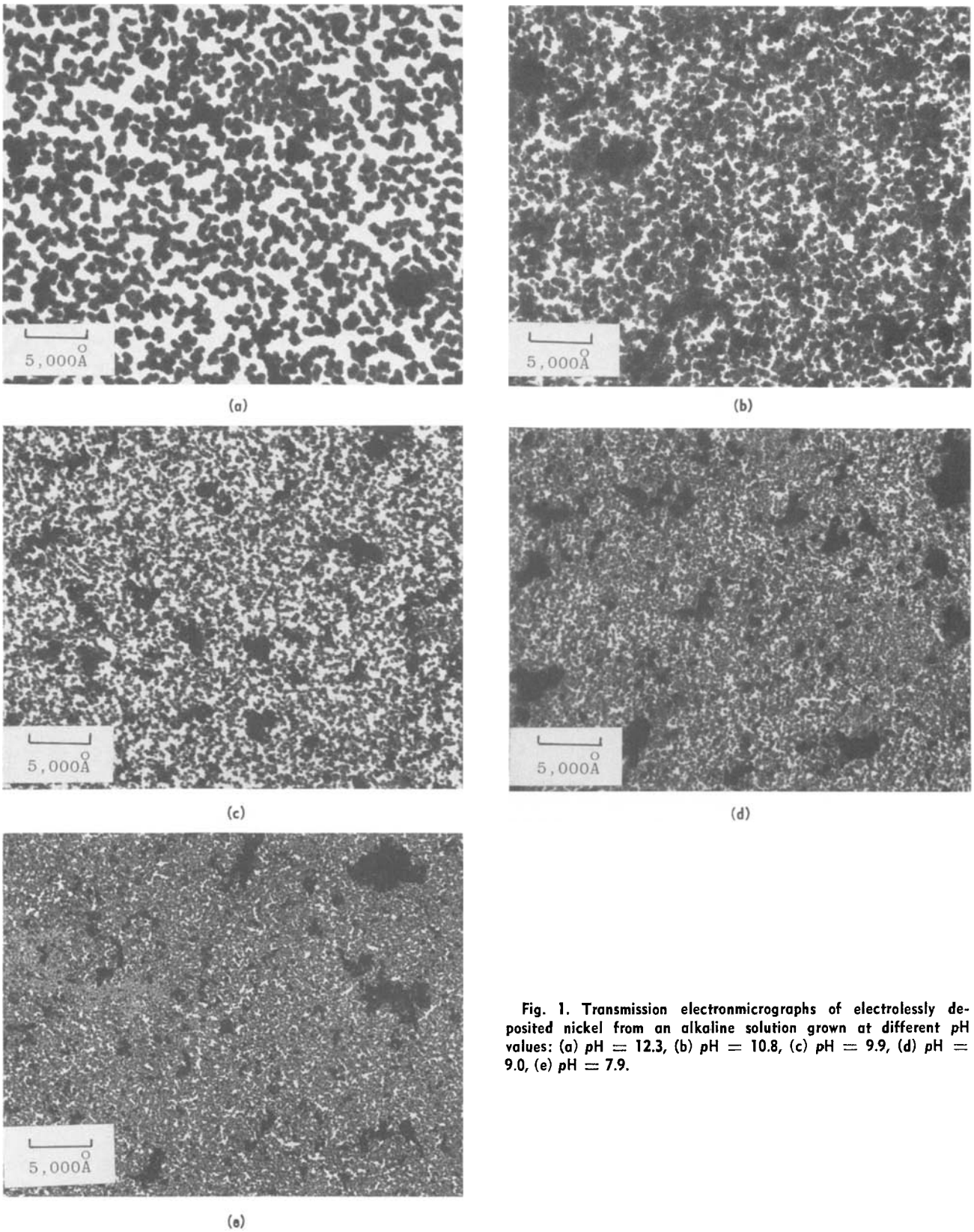

Fig. 1. Transmission electronmicrographs of electrolessly deposited nickel from an alkaline solution grown at different pH values: (a) pH = 12.3, (b) pH = 10.8, (c) pH = 9.9, (d) pH = 9.0, (e) pH = 7.9.

tropic crystallites, however, it is about unit for all reflections.

As the size of crystallite decreases, all peaks are expected to broaden equally. This is observed to be the case as one passes from the diffraction pattern curves corresponding to pH 8 through pH 12 (see Fig. 2). The crystallite sizes as determined from [8] vary from about 10Å for the former to 20Å for the latter. This seems to be in agreement with previously made estimates (1, 10). This agreement points to the fact that the broadening of peaks in the diffraction patterns is probably entirely due to effect (*ii*). The $G(r)$ curves presented in Fig. 3 lend further support to this line of thought. The curves represent an fcc structure with nearest and next to nearest, etc. neighbor distances possessing values different from bulk, but independent of pH (see Table I); thus ruling out effects of strains, etc. A careful study of the curves further showed that, at least as far as the first ten peaks are concerned, their width is also nearly pH independent. This indicates that while the crystal sizes change they are not only strain free,

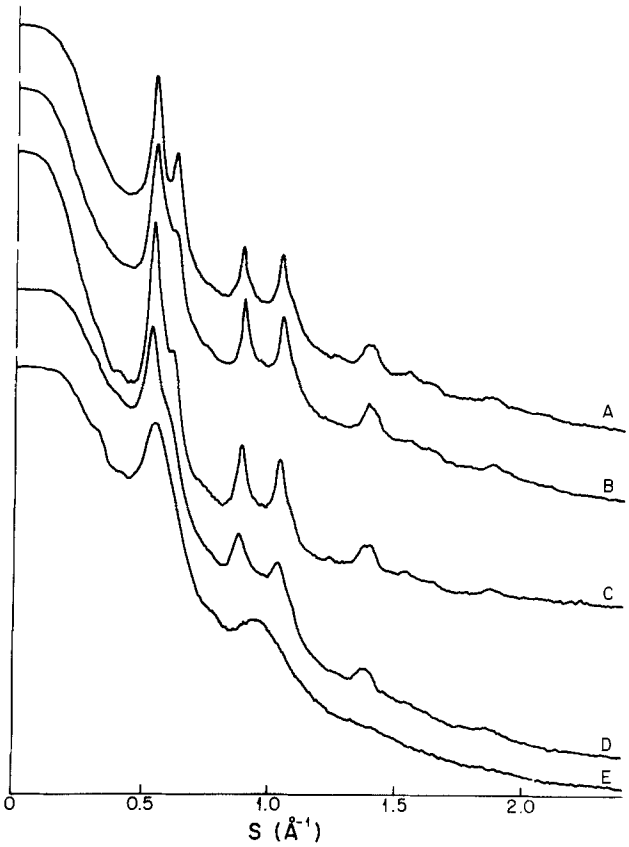

Fig. 2. Electron diffraction pattern curves corresponding to the films shown in Fig. 1.

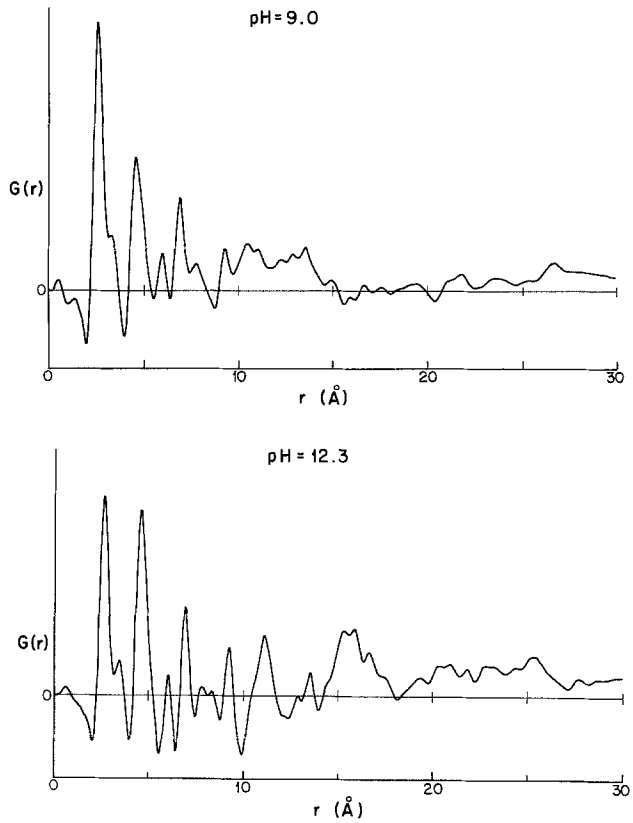

Fig. 3. Reduced radial distribution functions (G(r)): (a) for a film grown at pH 9.0, (b) for a film grown at pH 12.3.

but also that their degree of crystallinity does not vary. Because it is impossible to entirely correct for the systematic errors referred to in the Experimental section, one is unable to derive quantitative information from peaks above about the tenth. However, a general observation is possible. That is that within the crystallites there seems to exist a "long" range order of about 15Å. The farther peaks tend to smear out, indicating, perhaps, the lack of longer range order, or that these distances represent points usually beyond a given crystallite.

Acknowledgment

The present work constitutes part of a thesis submitted by R.O.C. to the graduate faculty at the University of Windsor in partial fulfillment of the requirements for the M.Sc. degree.

Manuscript submitted Jan. 28, 1983; revised manuscript received May 23, 1983. This was Paper 136 presented at the Detroit, Michigan, Meeting of the Society, Oct. 17-21, 1982.

The University of Windsor assisted in meeting the publication costs of this article.

Table I. Displacement values (in Å) for the first ten peaks in the G(r) curves presented in Fig. 3

Peak No. 1*	Peak No. 2	Peak No. 3	Peak No. 4	Peak No. 5
2.60	3.50	4.60	6.00	6.90
Peak No. 6	Peak No. 7	Peak No. 8	Peak No. 9	Peak No. 10
7.70	8.20	9.10	10.40	11.00

* N.N. distance Bulk (pure) Ni = 2.49A.

REFERENCES

1. J. L. Chow, N. E. Hedgecock, M. Schlesinger, and J. Rezek, *This Journal*, **119**, 1614 (1972).
2. J. P. Marton and M. Schlesinger, *This Journal*, **115**, 16 (1968).
3. R. Kaplow, S. L. Strong, and B. J. Averbach, *Phys. Rev.*, **138**, 1336 (1965).
4. R. O. Cortijo, M.Sc. Thesis, University of Windsor (1983).
5. D. B. Dove, "Physics of Thin Films," Vol. 7, p. 1, Academic Press, New York (1973).
6. J. P. Marton, Ph.D. Thesis, University of Western Ontario (1969).
7. E. Oran Brigham, in "The Fast Fourier Transform," Prentice-Hall, Englewood Cliffs, NJ (1974).
8. I. Kiflawi and M. Schlesinger, *This Journal*, **130**, 872 (1983).
9. B. E. Warren, *J. Appl. Phys.*, **12**, 375 (1941).
10. S. T. Pai, J. P. Marton, and J. Brown, *J. Appl. Phys.*, **43**, 282 (1972).
11. G. S. Cargill, *J. Appl. Phys.*, **41**, 12 (1970).

Lithium Insertion in Wadsley-Roth Phases Based on Niobium Oxide

R. J. Cava, D. W. Murphy, and S. M. Zahurak

Bell Laboratories, Murray Hill, New Jersey 07974

ABSTRACT

We have found the Wadsley-Roth class of crystallographic shear structures in chemical systems based on Nb_2O_5 to undergo lithium insertion reactions at ambient temperature to stoichiometries of 0.4 to 1.4 Li per host metal on reaction with n-BuLi. For the general case of structures with intersecting shear planes, minimal structural distortion occurs on lithiation even for compounds with the largest ReO_3-like block sizes. We report crystal-chemical data for 14 lithium insertion compounds of this type, and the behavior of selected host compounds mixed with carbon as the positive electrodes in small lithium secondary test cells.

Compounds which can reversibly incorporate lithium atoms into their crystal structures are of interest for use as positive insertion electrodes in ambient temperature secondary batteries. Lithium insertion reactions of ReO_3 and vanadium oxide based crystallographic shear structures derived from it have been reported (1-3). The framework of the ReO_3 host consists exclusively of corner-shared ReO_6 octahedra, which twist about their shared corners on lithium insertion to form $LiReO_3$ and Li_2ReO_3 (4). This distortion in ReO_3, which changes the oxygen array from one that is 3/4 CCP to complete HCP, severely impedes the lithium diffusion, and thus accounts for the slow kinetics and large activation energy of the insertion reaction. The crystallographically sheared FeV_3O_8 host structure, however, (of the VO_2(B) type) is extensively edge shared, and the large perovskite-like cavities do not collapse on Li insertion (5). Crystallographic shear introduces edge sharing into the corner shared ReO_3 framework and stabilizes the host structures against severe distortion on lithium insertion; thus enhancing kinetics and reducing hysteresis. While minimizing structural distortion during insertion, crystallographic shear also reduces the number of available sites for lithium, and hence the maximum insertion capacity of the compounds. The present study was undertaken to determine the minimum amount of crystallographic shear necessary to stabilize $MO_{3-\delta}$, ReO_3-like structures against such distortion on lithium insertion, so that both good diffusion rates and high capacity might be obtained. The class of compounds known as Wadsley-Roth phases affords a large number of chemically similar compounds with different types and amounts of crystallographic shear. We have found many compounds of this class to undergo lithium insertion reactions, and that little crystallographic shear is necessary to stabilize the geometry of the host structure during insertion. Results on tungsten vanadium oxides have been communicated (6). This paper describes the synthesis, characterization, and crystal chemistry of the lithium inserted Wadsley-Roth phases, and their performance in secondary lithium cells.

Experimental

Fourteen structurally or chemically distinct Wadsley-Roth phases were synthesized in the stoichiometry range $MO_{2.3}$-$MO_{2.7}$. Powders of the host compounds were prepared by standard solid-state synthesis techniques as described in the literature (7-12) and in accordance with the phase equilibria diagrams. They were prepared in air, at temperatures between 750°-1300°C, in covered alumina crucibles, with the exception of the tungsten vanadium oxides, whose synthesis has been described elsewhere (6). Nb_3O_7F was prepared according to the procedure of Andersson and Astrom (8). The products were carefully characterized during each step in the synthesis by powder x-ray diffraction, and all compounds were single phase powders with good crystallinity before they were used in the insertion reactions. Heating times were generally 1-3 days, with 1-2 intermediate grindings.

Lithium was inserted chemically into the Wadsley-Roth phases by reaction with n-butyllithium in hexane. The activity of lithium in n-BuLi is about 1V less than lithium metal. Reaction mixtures containing approximately 250 mg of host material and n-BuLi, 10% excess of a 1*N* solution, were sealed in Pyrex ampuls under He and were stirred for 4 days at room temperature. The amount of lithium consumed in the reactions was determined by acid-base titration of the excess n-BuLi. In the case of Nb_3O_7F, reactions were also performed with Li-benzophenone (Li activity about 1.5V lower than Li metal). Delithiation reactions were carried out on the lithium insertion compounds with iodine in acetonitrile. This reagent chemically mimics potentiometric charging at 2.8V *vs.* Li/Li^+. The quantity of iodine consumed in the delithiation reactions was determined by titration of the excess with a standard thiosulfate solution.

The lithium-inserted Wadsley-Roth phases were characterized by powder x-ray diffraction. Patterns were recorded between 5° and 60° 2θ, at 1°/min, with $CuK\alpha$ radiation. The powder patterns thus obtained are generally complex, but good fits to the observed reflections can be obtained in all cases for unit cells similar to those of the unlithiated materials, with the exception of Li-inserted Nb_3O_7F. Observed peak positions for all samples were calibrated against an internal silicon standard. The thermal stability of the inserted phases was determined by differential scanning calorimetry. Samples were heated at 10°C/min in sealed He-filled Al capsules, to maximum temperatures of approximately 625°C. X-ray diffraction patterns were also recorded for each compound after the iodine delithiation reaction, and compared to those of the original host materials to check for irreversible structural changes due to the lithium insertion. Small electrochemical test cells (13) were fabricated using the host Wadsley-Roth phases mixed with 50 weight percent (w/o) graphite as positive electrodes, with Li metal negative electrodes and 1*M* $LiClO_4$/PC electrolyte.

Results

Wadsley-Roth phases (14) generally occur at stoichiometries between MO_3 and MO_2, and are built primarily of edge- and corner-shared MO_6 octahedra. As the stoichiometry is varied from MO_3 to MO_2, the component octahedra cannot exclusively share corners, and an increasing number of edge-shared octahedra are introduced. Compounds within that stoichiometry range mix corner- and edge-shared octahedra and still display open-tunnel-like regions in their structures, generally bound by regions of extensive edge sharing. Structures are built of $n \times m \times \infty$ ReO_3-type blocks (where n and m are the length and width of the blocks, respectively, in numbers of octahedra) joined to adjacent blocks either through edge sharing or a combination of edge sharing and tetrahedrally coordinated metal atoms at the block corners. Stoichiometries are described by the formula $M_{nmp+1}O_{3nmp-(n+m)p+4}$; where p is the number of blocks at the same level joined by edge sharing. Structures with n and m be-

tween 2 and 5 and some $n \times \infty \times \infty$ have been observed, and more than one type of block may be present. Wadsley-Roth phases occur extensively in the chemical systems Nb_2O_5-WO_3, Nb_2O_5-NbO_2, Nb_2O_5-TiO_2, and Nb_2O_5-NbO_2F. Small differences in stoichiometry result in different amounts of edge sharing; and many distinct, but similar, crystal structures are observed. Different crystallographic phases at the same stoichiometry can be formed through differences in chemical and/or thermal synthesis conditions. Figure 1 presents the structures of ReO_3 and H-Nb_2O_5 for comparison. The H-Nb_2O_5 structure contains both $3 \times 4 \times \infty$ and $3 \times 5 \times \infty$ ReO_3-type blocks, joined to each other both through edge sharing octahedra along their perimeters, and corner sharing involving MO_4 tetrahedra.

We have investigated lithium insertion reactions in Wadsley-Roth phases based on compounds of niobium oxide with oxides of titanium, vanadium, tungsten, germanium, and lithium; and tungsten vanadium oxides. The structural and chemical characteristics of these compounds are summarized in Table I. For the sake of discussion, compounds are distinguished by chemistry, stoichiometry, block size, and characteristic block joining. The latter is the manner in which blocks at the same level are joined. Distinctions are: T—tetrahedral metal at block corner, E—edge sharing at block corner, and M—mixture of both. The two entries "H" and "N" Nb_2O_5 are different crystal structures of Nb_2O_5, the latter apparently stabilized by very small quantities of fluorine (8). The N-Nb_2O_5 structure can also be stabilized by small amounts of lithium (7) and we have synthesized it at the composition $LiNb_{13}O_{33}$. Details of the nonstoichiometry are not known. The $3 \times \infty \times \infty$ E-type structure of Nb_3O_7F is similar to that of V_2O_5, with one extra plane of MX_6 octahedra (10). The compounds VNb_9O_{25} and $GeNb_{18}O_{47}$ have been reported to have the same $3 \times 3 \times \infty$ T-type structure (15), with the details of the apparent nonstoichiometry again not known. The $3 \times 3 \times \infty$ T-type structure of VNb_9O_{25} is presented in Fig. 2. The known $n \times m \times \infty$ T structures with $n = m$ are similar to this except for the block size. The $3 \times 3 \times \infty$ E-type structure of $TiNb_2O_7$ is also presented in Fig. 2. H-Nb_2O_5 (Fig. 1) is an M-type structure. $WV_2O_{7.5}$ has the M-Nb_2O_5 structure (16).

All of the niobium oxide based Wadsley-Roth phases reacted with n-BuLi to form insertion compounds ranging from 0.4 to 1.4 Li per transition metal in the host structure. Compounds were generally pure single-phase materials by x-ray diffraction, with the exception of $Li_{1.2}TiNb_2O_7$ and $Li_{6.4}Ti_2Nb_{10}O_{29}$, which both have one peak in their diffraction pattern near

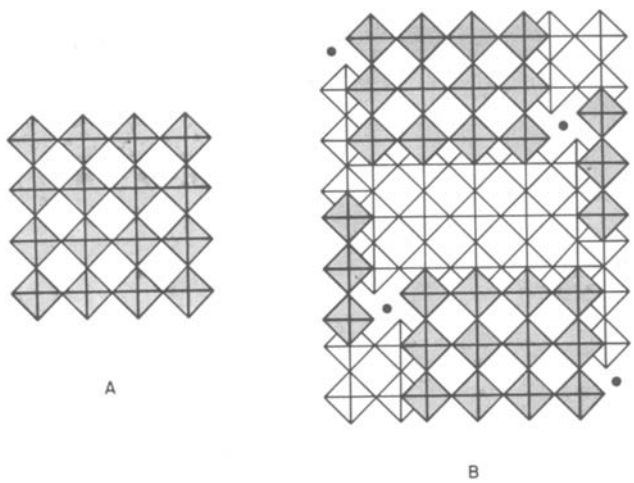

Fig. 1. A) Corner-shared structure of ReO_3 represented by MO_6 octahedra. B) Crystallographic shear structure of H-Nb_2O_5. Shaded octahedra at same level. Solid circles are tetrahedrally coordinated niobium atoms.

Table I. Wadsley-Roth phases investigated for Li insertion reactions

Compound	Stoichiometry x in MO_x	Block size in number of octahedra $n \times m \times \infty$	Type of block joining†
H-Nb_2O_5	2.500	3×4, 3×5	T
N-Nb_2O_5	2.500	4×4	M
$LiNb_{13}O_{33}$	2.357*	4×4	M
Nb_3O_7F	2.667	$3 \times \infty$	E
VNb_9O_{25}	2.500	3×3	T
$GeNb_{18}O_{47}$	2.474‡	3×3	T
$TiNb_2O_7$	2.333	3×3	E
$Ti_2Nb_{10}O_{29}$	2.417	3×4	E
$TiNb_{24}O_{62}$	2.480	3×4	M
$WNb_{12}O_{33}$	2.538	3×4	T
$W_3Nb_{14}O_{44}$	2.588	4×4	T
$W_5Nb_{18}O_{69}$	2.654	5×5	T
$WV_2O_{7.5}$	2.500	4×4	E
$W_{0.2}V_{2.8}O_7$	2.333	3×3	E

* $LiNb_{13}O_{33}$ is a lithium-stabilized N-Nb_2O_5 structure. The details of the lithium positions and the nonstoichiometry are unknown. It can be considered as an $MO_{2.5}$ structure.

‡ $GeNb_{18}O_{47}$ has the PNb_9O_{25} structure, as does VNb_9O_{25}. The details of the nonstoichiometry are presently unknown, and it also can be considered an $MO_{2.5}$ structure.

† Adjacent $n \times m \times \infty$ blocks in these structures are shifted by ½ octahedron parallel to the ∞ block direction and share edges at their border. The entries in this column distinguish how blocks at the same level are joined, which occurs at the corners of the blocks. They are either joined by the presence of a tetrahedral niobium atom at the corner (T), the sharing of edges of several octahedra near the corner (E), or mixtures of both (M). In this classification scheme, V_2O_5 (R-Nb_2O_5) and V_6O_{13} are $2 \times \infty \times \infty$ E and $2 \times 3 \times \infty$ E structure types, respectively.

Table II. Insertion compounds prepared by reaction of Wadsley-Roth phases with n-butyllithium

Host	F.U./cell	Insertion compound	Li/host metal	Decomposition temp, °C, DSC*	Equivalents of I reaction/host metal
H-Nb_2O_5	14	$Li_{1.9}Nb_2O_5$	1.0	400,575	0.8
N-Nb_2O_5	16	$Li_{1.7}Nb_2O_5$	0.9	350,575	0.8
$LiNb_{13}O_{33}$	2.42	$Li_{11}LiNb_{13}O_{33}$	0.5	320,520	0.5
Nb_3O_7F	2	$Li_{1.0}Nb_3O_7F$	0.5	350	0.6
VNb_9O_{25}	2	$Li_{11.4}VNb_9O_{25}$	1.1	400	1.2
$GeNb_{18}O_{47}$	1	$Li_{17.0}GeNb_{18}O_{47}$	0.9	380,550	1.0
$TiNb_2O_7$	6	$Li_{1.2}TiNb_2O_7$	0.4	590	0.5
$Ti_2Nb_{10}O_{29}$	4	$Li_{6.4}Ti_2Nb_{10}O_{29}$	0.5	380,590	0.3
$TiNb_{24}O_{62}$	2	$Li_{15.7}TiNb_{24}O_{62}$	0.6	480,590	0.8
$WNb_{12}O_{33}$	2	$Li_{10.7}WNb_{12}O_{33}$	0.8	225,375	0.9
$W_3Nb_{14}O_{44}$	2	$Li_{16.8}W_3Nb_{14}O_{44}$	1.0	225,400	0.9
$W_5Nb_{10}O_{69}$	2	$Li_{22.0}W_5Nb_{18}O_{69}$	0.9	225	1.0
$WV_2O_{7.5}$	10.67†	$Li_{4.3}WV_2O_{7.5}$	1.4	150	1.2
$W_{0.2}V_{2.8}O_7$	6	$Li_{3.6}W_{0.2}V_{2.8}O_7$	1.2	50	0.9

* Temperatures obtained at heating rates of 10°C/min by DSC. Decomposition may occur in some cases by long-time heating at lower temperatures.

† 16 M_2O_5 formula units per cell.

22.2°, of about 15% maximum intensity, which cannot be indexed by the unit cells of the host or lithiated materials. We do not know whether $Li_{1.5}Nb_3O_7F$ is single phase, as we could not index the x-ray pattern. Minor side reactions may occur on lithiation which yield products such as Li_2O which are not observable by x-ray diffraction. In all cases, delithiation reactions with iodine yielded materials having x-ray diffraction patterns identical to those of the starting materials, indicating that the reaction with lithium may be reversed at room temperature. In Table II, we present the stoichiometry of the insertion compounds obtained by reaction with n-BuLi, the number of equivalents of iodine reacting with the insertion compounds, and the decomposition temperature(s) as determined by DSC. Note that for $Ti_2Nb_{10}O_{29}$, the stoichiometry of the iodine reaction with the insertion compound is significantly less than the stoichiometry of the n-BuLi reaction. For $W_8Nb_{18}O_{69}$ and $TiNb_{24}O_{62}$, where, obviously, more Li cannot be removed than was inserted, some reaction of the host compound or side reaction product with I_2 may be occurring. The "decomposition" tem-

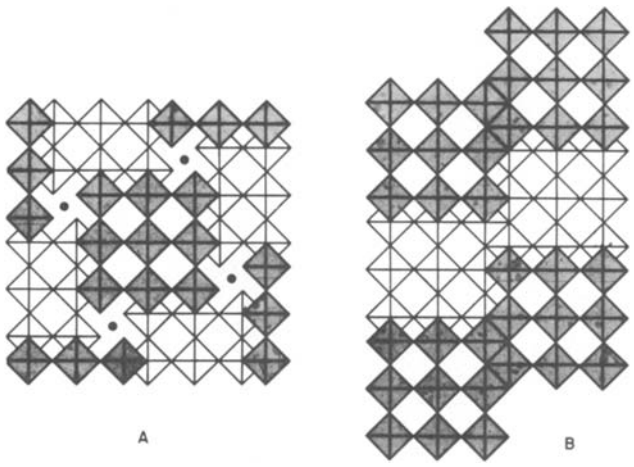

Fig. 2. Two examples of 3 × 3 × ∞ Wadsley-Roth phases. A) VNb_9O_{25}, circles are tetrahedrally coordinated metal atoms. B) $TiNb_2O_7$. Shaded octahedra at same level.

peratures reported by DSC are irreversible and exothermic and may be due to either strain relief, as previously observed for Li-inserted anatase (17), or a true "decomposition" via a transition to one or more thermodynamically stable phases. We include these temperatures as a rough guide to the thermal stability range of the insertion compounds.

Lattice parameters for the lithium insertion compounds were obtained by least squares fits to the powder diffraction patterns for all materials except $Li_{1.5}Nb_3O_7F$. The cell parameters are compared to those of the unlithiated host materials in Table III. We cannot distinguish subtle differences in the space-group symmetry via the powder x-ray diffraction method, but no apparent changes in the space-group-derived systematic absences of the host materials were observed on insertion. Table IV presents observed and least squares fit calculated d values for the powder patterns from which the lattice parameters for the lithium-inserted Wadsley-Roth phases have been determined. We note that for a large, low symmetry cell such as that of N-niobia, the indexing of every line on the powder diagram is not unambiguous, even where, as in the unlithiated case, single crystal intensity data has been employed to assist the indexing. The relative intensities of the lines for the lithium-inserted Wadsley-Roth phases are similar to those reported in the powder diffraction file or the literature for the host materials. Due to the large unit cell sizes, reflections other than those included in the least squares fits and in Table IV are observed for some of the compounds. The powder pattern for $Li_{1.6}Nb_3O_7F$ prepared by reaction of Nb_3O_7F with Li-benzophenone is presented in Table V. Powder patterns for $Li_{3.5}WV_2O_{7.5}$ and $Li_{3.7}W_{0.2}V_{2.8}O_7$ have been presented elsewhere (6).

Stoichiometries observed in electrochemical cells are generally in good agreement with those obtained chemically. Only half the expected capacity was observed for H-Nb_2O_5, whereas the capacity was double the chemical value for $TiNb_2O_7$. The low capacity of H-Nb_2O_5 may result from the fact that cells were only discharged to 1.4V *vs.* lithium because of irreversible reaction with carbon at lower potentials, whereas n-BuLi is more reducing (~1V *vs.* lithium). The higher stoichiometries in cells for $TiNb_2O_7$ and $Ti_2Nb_{10}O_{29}$ may result from a blockage of insertion because of a small amount of second phase formed in the n-BuLi reaction.

The shape of the discharge-charge curves of the cells reveals some differing behavior. Virtually all of the materials showed a sharp, multistepped drop in voltage during the first 20-30% of discharge followed by a nearly constant plateau. Several compounds showed good reversibility of this curve on charge. The curves for H-Nb_2O_5 are shown in Fig. 3. The difference between the charge and discharge curves increases on cycling, indicating an increasing cell resistance, which is likely responsible for the fade in capacity on cycling.

Table III. Crystallographic unit cell parameters for lithium insertion compounds compared to host compounds

Compound	a	b	c	β	Volume (A³)	Symmetry
H-Nb_2O_5	21.08	3.823	19.33	119.80	1351.8	Mon.
$Li_{1.9}Nb_2O_5$	20.78(1)	4.139(2)	19.150(8)	119.62(3)	1431.8	
Change (%)	−1.4	+8.3	−0.90		+5.9	
N-Nb_2O_5	28.51	3.830	17.48	120.80	1639.5	Mon.
$Li_{1.7}Nb_2O_5$	28.49(2)	4.106(2)	17.47(2)	125.55(10)	1662.7	
Change (%)	−0.07	+7.2	−0.05		+1.4	
$LiNb_{13}O_{33}$	28.511	3.831	17.544	125.22	1565.5	Mon.
$Li_{11}LiNb_{13}O_{33}$	28.51(2)	4.115(2)	17.47(2)	125.40(8)	1670.7	
Change (%)	0.0	+7.4	−0.42		+6.7	
VNb_9O_{25}	15.72		3.821		944.24	Tet.
$Li_{11.4}VNb_9O_{25}$	15.54(1)		4.207(3)		1016.0	
Change (%)	−1.1		+10.1		+7.6	
$GeNb_{18}O_{47}$	15.70		3.817		940.85	Tet.
$Li_{17}GeNb_{18}O_{47}$	15.570(8)		4.180(2)		1013.3	
Change (%)	−0.83		+9.5		+7.7	
$TiNb_2O_7$	11.93	3.81	20.44	120.17	803.21	Mon.
$Li_{1.2}TiNb_2O_7$	11.96(1)	3.935(5)	20.61(2)	120.90(8)	832.29	
Change (%)	+0.25	+3.2	+0.83		+3.6	
$Ti_2Nb_{10}O_{29}$	28.50	3.805	20.51		2224.2	Orth.
$Li_{6.4}Ti_2Nb_{10}O_{29}$	28.31(4)	4.031(4)	20.69(2)		2361.1	
Change (%)	−0.67	+5.9	+0.88		+6.2	
$TiNb_{24}O_{62}$	29.78	3.821	21.12	94.90	2394.4	Mon.
$Li_{15.7}TiNb_{24}O_{62}$	29.51(4)	4.103(4)	20.94(2)	94.77(18)	2526.6	
Change (%)	−0.91	+7.4	−0.85		+5.5	
$WNb_{12}O_{33}$	22.37	3.825	17.87	123.60	1273.6	Mon.
$Li_{10.7}WNb_{12}O_{33}$	21.98(3)	4.140(3)	17.51(2)	123.06(6)	1335.4	
Change (%)	−1.7	+8.2	−2.0		+4.9	
$W_3Nb_{14}O_{44}$	21.02		3.824		1689.6	Tet.
$Li_{16.8}W_3Nb_{14}O_{44}$	20.894(7)		4.112(4)		1795.1	
Change (%)	−0.60		+7.5		+6.2	
$W_8Nb_{18}O_{69}$	26.270		3.814		2632.1	Tet.
$Li_{22}W_8Nb_{18}O_{69}$	26.354(7)		4.046(2)		2810.1	
Change (%)	+0.32		+6.1		+6.8	
$WV_2O_{7.5}$	19.50		3.70		1406.9	Tet.
$Li_{3.5}WV_2O_{7.5}$	20.016(5)		4.059(4)		1626.2	
Change (%)	+2.6		+9.7		+15.6	
$W_{0.2}V_{2.8}O_7$	14.01		3.72		730.2	Tet.
$Li_{3.7}W_{0.2}V_{2.8}O_7$	14.414(6)		4.049(3)		841.2	
Change (%)	+2.9		+8.8		+15.2	

Table IV. Observed and calculated *d* values for lithium—inserted Wadsley-Roth phases corresponding to lattice parameters in Table III

$Li_{1.6}Nb_2O_5$ (H)

h	*k*	*l*	*d* calc	*d* obs	I/I_0
2	0	−1	10.372	10.390	40
1	0	−2	9.568	9.581	10
2	0	0	9.030	9.071	25
0	0	2	8.324	8.337	10
2	0	1	6.675	6.676	5
1	0	−3	6.240	6.232	40
4	0	−2	5.186	5.182	10
4	0	−1	5.030	5.036	95
1	0	−4	4.581	5.582	95
1	1	−1	4.024	4.020	100
1	0	−5	3.608	3.605	90
3	1	−1	3.542	3.540	20
5	0	−5	3.437	3.432	90
5	0	−6	3.044	3.046	20
5	1	−2	2.929	2.931	80
5	1	−1	2.860	2.862	55
2	1	−5	2.796	2.790	40
4	1	−6	2.512	2.514	30
7	0	−7	2.455	2.457	10
6	1	−6	2.355	2.356	70
0	2	0	2.069	2.069	45
−10	0	6	2.044	2.042	95
−2	0	9	2.019	2.018	95

$Li_{1.7}Nb_2O_5$ (N)

h	*k*	*l*	*d* calc	*d* obs	I/I_0
0	0	1	14.214	14.347	20
−2	0	1	13.689	13.810	10
0	0	2	7.107	7.103	30
−4	0	1	6.965	6.981	15
−6	0	2	4.743	4.745	100
1	1	0	4.043	4.054	65
−3	1	1	3.768	3.774	15
0	0	4	3.553	3.556	95
−8	0	3	3.558	3.556	
−7	1	2	2.875	2.880	50
−7	1	3	2.875	2.880	
−10	0	4	2.838	2.833	20
7	1	1	2.355	2.355	40
−7	1	6	2.354	2.355	
0	2	0	2.053	2.049	20
−14	0	5	2.034	2.034	55
−3	1	7	2.022	2.021	60
2	2	0	2.021	2.021	

$Li_{11.4}VNb_9O_{25}$

h	*k*	*l*	*d* calc	*d* obs	I/I_0
3	1	0	4.914	4.925	100
1	0	1	4.060	4.067	40
4	0	0	3.885	3.887	10
3	3	0	3.663	3.658	10
2	1	1	3.599	3.601	10
4	2	0	3.474	3.479	80
5	1	0	3.048	3.043	15
3	2	1	3.010	3.014	35
4	1	1	2.807	2.807	30
5	2	1	2.379	2.379	35
0	0	2	2.103	2.102	25
7	3	0	2.040	2.038	80

$Li_{11}LiNb_{18}O_{55}$

h	*k*	*l*	*d* calc	*d* obs	I/I_0
−6	0	2	4.747	4.747	100
1	1	0	4.052	4.062	45
−3	1	1	3.775	3.782	15
−8	0	3	3.560	3.556	95
0	0	4	3.560	3.556	
−7	1	2	2.880	2.882	40
−7	1	3	2.879	2.882	
8	0	1	2.569	2.575	10
7	1	1	2.362	2.357	25
−7	1	6	2.355	2.357	
0	2	0	2.057	2.056	20
−14	0	5	2.038	2.035	45
−3	1	7	2.025	2.205	65
2	2	0	2.026	2.025	

$Li_{17}GeNb_{18}O_{47}$

h	*k*	*l*	*d* calc	*d* obs	I/I_0
1	1	0	11.010	11.078	10
3	1	0	4.923	4.938	100
1	0	1	4.037	4.043	70
3	3	0	3.669	3.667	15
2	1	1	3.583	3.585	20
4	2	0	3.481	3.486	90
3	2	1	3.003	3.003	50
4	1	1	2.802	2.801	60
5	3	0	2.670	2.672	10
6	2	0	2.461	2.459	10
5	2	1	2.377	2.378	55
0	0	2	2.090	2.089	45
7	3	0	2.044	2.041	90

$Li_{1.3}TiNb_2O_7$

h	*k*	*l*	*d* calc	*d* obs	I/I_0
1	0	0	10.261	10.245	15
−1	0	2	9.548	9.581	10
2	0	0	5.130	5.143	90
−1	0	4	5.128	5.143	
0	1	1	3.841	3.838	30
1	0	4	3.465	3.465	25
3	0	0	3.420	3.421	100
−2	0	6	3.426	3.421	
2	1	1	2.922	2.922	15
−2	1	5	2.818	2.822	35
3	0	2	2.758	2.748	15
−3	1	1	2.708	2.706	15
4	0	0	2.565	2.560	10
1	0	6	2.511	2.508	15
1	1	5	2.342	2.345	20
−4	1	5	2.335	2.333	15
5	0	0	2.052	2.056	45
2	1	5	2.045	2.044	35

$Li_{5.4}Ti_2Nb_{10}O_{29}$

h	*k*	*l*	*d* calc	*d* obs	I/I_0
2	0	0	14.152	14.301	15
1	0	2	9.715	9.847	15
4	0	0	7.076	7.092	45
0	0	4	5.171	5.188	60
1	0	4	5.087	5.105	20
6	0	0	4.717	4.720	100
0	1	1	3.957	3.963	40
1	1	1	3.919	3.913	15
8	0	0	3.538	3.532	80
0	0	6	3.447	3.447	50
1	0	6	3.422	3.430	30
1	1	5	2.872	2.881	30
7	1	1	2.828	2.826	25
7	0	6	2.624	2.620	15
7	1	5	2.349	2.351	30
0	0	10	2.068	2.063	25
0	2	0	2.015	2.014	70

$Li_{25.7}TiNb_{24}O_{69}$

h	*k*	*l*	*d* calc	*d* obs	I/I_0
0	0	2	10.432	10.513	15
4	0	1	6.759	6.778	10
−2	0	4	5.050	5.076	100
6	0	1	4.685	4.690	80
−6	0	2	4.584	4.587	45
−1	1	1	3.997	4.004	50
−3	1	2	3.595	3.604	45
8	0	1	3.569	3.570	60
−2	0	6	3.449	3.458	85
−1	1	5	2.928	2.926	35
−3	1	5	2.849	2.852	25
7	1	2	2.783	2.778	20
−4	0	8	2.525	2.519	20
−9	1	4	2.356	2.356	45
−4	0	10	2.052	2.051	85
0	2	0	2.051	2.051	
2	2	1	2.020	2.019	75

These data are in qualitative agreement with electrodes obtained by oxidizing niobium metal (18). Other materials which showed this kind of reversibility are N-Nb_2O_5, $TiNb_{10}O_{27}$, and $TiNb_{24}O_{62}$. Another type of behavior is exhibited by VNb_9O_{25}, $GeNb_{18}O_{47}$, $WNb_{12}O_{33}$, and $TiNb_2O_7$ with the data for VNb_9O_{25} shown in Fig. 4. The steeply dropping initial part of the discharge is not rechargeable in the cell. This must be a kinetic problem, since iodine removes all the lithium at room temperature. The remainder of the mixed metal nio-

Table IV (continued)

$Li_{10.7}WNb_{12}O_{33}$

h	k	l	d calc	d obs	I/I_0
−4	0	3	4.968	4.991	100
2	0	2	4.637	4.646	100
1	1	0	4.039	4.049	75
−1	1	1	4.019	4.020	75
2	0	3	3.585	3.588	90
−6	0	4	3.460	2.467	80
−5	1	3	2.971	2.970	35
1	1	3	2.946	2.948	30
−5	1	4	2.821	2.818	40
3	1	2	2.798	2.798	30
−4	0	7	2.486	2.486	25
−7	1	1	2.363	2.362	75
−3	1	6	2.361	2.362	
0	2	0	2.070	2.069	30
−10	0	7	2.042	2.040	75
4	0	5	2.024	2.022	80
−3	1	6	2.361	2.362	
0	2	0	2.070	2.069	30
−10	0	7	2.042	2.040	75
4	0	5	2.024	2.022	80

$Li_{23}W_8Nb_{18}O_{69}$

h	k	l	d calc	d obs	I/I_0
5	3	0	4.520	4.529	25
1	0	1	3.999	4.004	65
2	1	1	3.827	3.826	15
6	4	0	3.654	3.655	100
8	2	0	3.195	3.200	10
9	1	0	2.910	2.908	20
5	4	1	2.885	2.884	45
6	3	1	2.818	2.815	50
9	3	0	2.777	2.778	15
10	2	0	2.584	2.583	25
9	2	1	2.334	2.334	45
11	7	0	2.021	2.020	100

$Li_{16.3}W_3Nb_{14}O_{44}$

h	k	l	d calc	d obs	I/I_0
2	2	0	7.387	7.399	15
3	1	0	6.607	6.632	15
4	2	0	4.672	4.680	100
1	0	1	4.034	4.040	75
2	1	1	3.764	3.760	20
5	3	0	3.583	3.585	90
3	2	1	3.353	3.354	10
6	2	0	3.303	3.305	10
5	0	1	2.931	2.930	50
5	5	0	2.955	2.954	15
5	2	1	2.822	2.818	60
7	3	0	2.743	2.742	15
8	2	0	2.533	2.532	15
7	2	1	2.353	2.352	50
10	2	0	2.048	2.051	35
9	5	0	2.029	2.027	80

bium oxides show behavior intermediate to these extremes showing partial rechargeability of the initial steep drop. Nb_3O_7F shows an unusually large voltage difference between discharge and charge (Fig. 5) indicative of the larger structure change on insertion which has prevented us from indexing its diffraction pattern. Charge discharge curves for cells made with $WV_2O_{7.5}$ and $W_{0.2}V_{2.8}O_7$ positive electrodes are smooth and continuous over the full insertion range, and are presented in Ref. (6).

Discussion and Conclusions

The Wadsley-Roth phases based on niobium oxide generally show reversible lithium insertion reactions at reasonable rates at room temperature, to stoichiometries of 0.4 Li/metal or greater on reaction with n-BuLi. The shear in orthogonal directions delineating the $n \times m \times \infty$ blocks stabilizes the structures against twisting to a more closely packed oxygen array, even for the largest ($5 \times 5 \times \infty$, $W_8Nb_{18}O_{69}$) block size, as is apparent from the small changes in the lattice parameters after insertion. The stability maintains acceptable lithium diffusion rates during the insertion process. Interstitial sites of the geometry appropriate to accommodate inserted lithium atoms to stoichiometries greater than 0.4 Li/host metal are present.

Of the compounds studied, only lithium-inserted Nb_3O_7F apparently undergoes significant structural distortion during insertion. The powder pattern of $Li_{1.6}Nb_3O_7F$ is similar to that of the host material, but shows shifts of the strong lines as well as the appearance of additional lines. Nb_3O_7F is unique among the materials studied in that its $3 \times \infty \times \infty$ structure does not contain orthogonal shear planes defining finite block sizes in two directions. The structure may, therefore, have sufficient freedom to twist about shared corners to accommodate inserted lithium.

The lattice parameter shifts of the host compounds indicate a general expansion on insertion along the infinite block direction, and a small contraction or expansion of about 1% parallel to the finite block directions. The net change in cell volume is always positive. The largest changes (between 3 and 10%) in the cell dimensions occur parallel to the b (monoclinic or orthorhombic) or c (tetragonal) cell directions, indicating an expansion of the heights of the framework octahedra from the characteristic 3.8Å in the unlithiated phases to ~4.0-4.15Å in the lithiated phases. Lat-

Table V. X-ray powder diffraction pattern for $Li_{1.6}Nb_3O_7F$ prepared by reaction with Li-benzophenone

d (Angstroms)	I/I_0	d (Angstroms)	I/I_0
10.037	15	2.892	30
4.961	30	2.747	25
3.832	100	2.569	40
3.746	80	2.339	5
3.641	15	2.280	10
3.587	15	2.231	15
3.520	5	1.978	15
3.431	5	1.895	10
3.302	60	1.861	10
2.950	25		

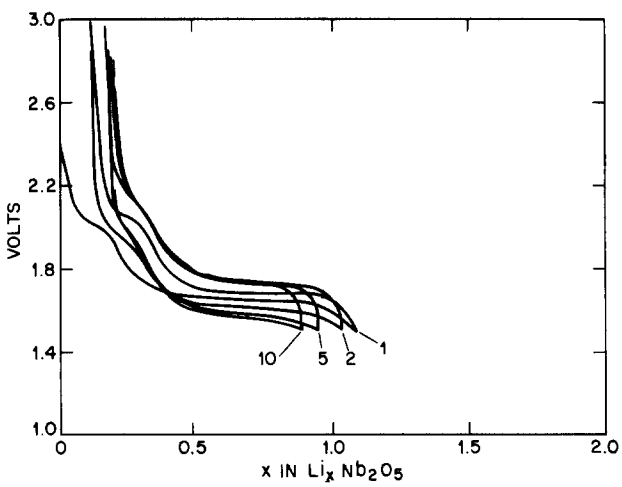

Fig. 3. The first 10 cycles of an H-Nb_2O_5 (carbon)/$LiClO_4$, PC/Li cell containing 5.45 mg Nb_2O_5. The first cycle is at a current of 50 μA. Subsequent cycles at 100 μA.

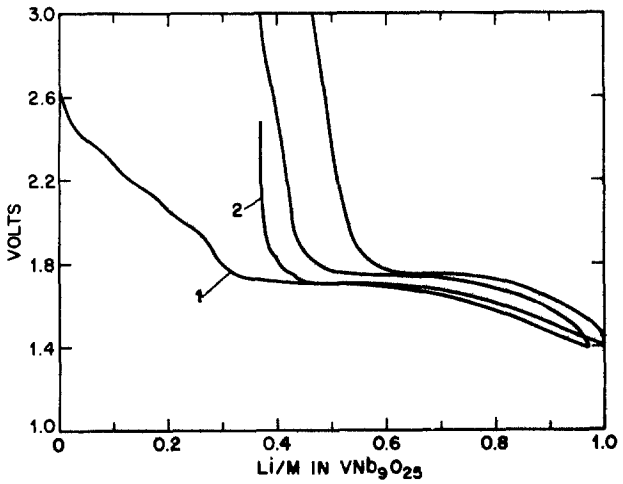

Fig. 4. Two cycles of a VNb_9O_{25} (carbon)/$LiClO_4$, PC/Li cell containing 5.25 mg VNb_9O_{25} at 100 μA.

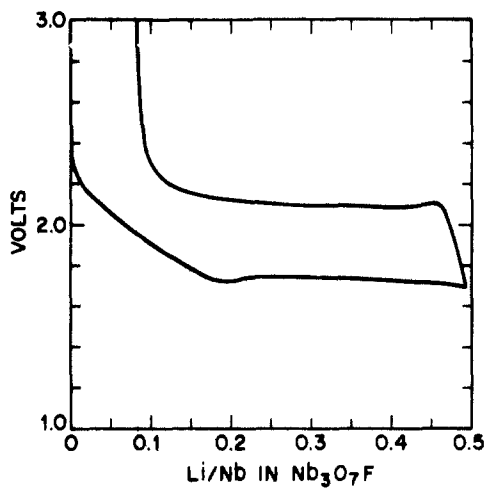

Fig. 5. The first discharge and charge of an Nb_3O_7F (carbon)/$LiClO_4$, PC/Li cell containing 10.3 mg Nb_3O_7F at a current of 20 μA.

tice parameters of 4.0 ~ 4.15Å are commonly found parallel to the infinite block directions in oxide bronze structures, and similar changes in cell size have been observed in lithium-inserted VO_2(B), FeV_3O_8, and V_6O_{13}(19).

Five types of cavities occur in Wadsley-Roth phases based on niobium oxide. These are illustrated in Fig. 6, and the number of each type for each of the structure types studied is presented in Table VI. The type I cavity is the basic ReO_3 cavity with a 12 coordinate center. In Nb_3O_7F this cavity is modified to become singly capped providing 5 coordinate sites of the type found occupied by Li in $Li_2FeV_3O_8$ (5). The type II cavity occurs where edge sharing between blocks displaced by 1/2 an octahedron occurs, and is singly capped, containing one possible 5-coordinate site for lithium. I and II occur in Wadsley-Roth phase structures with all types of block joining, and increase in number as the size of the blocks increases. Cavities of type IV and VI occur only in compounds in which blocks at the same level are joined by edge sharing (*i.e.*, $p \neq 0$). Both are bicapped cavities with two available 5-coordinate sites for Li, a minimum of approximately 2.3Å apart, an allowable Li-Li separation (5). Cavities of types III and V occur only in compounds where tetrahedral host lattice cations are present. The type V cavities are tetrahedrally coordinated and are separated from tetrahedrally coordinated host metal atoms by 1/2 the *b* monoclinic (and orthorhombic, or *c* tetragonal) cell axes, 2.0-2.1Å. This close separation may preclude occupancy of Li in sites of this type. Inserted lithium has been found to occupy 5-coordinate sites of the type abundant in the Wadsley-Roth phases (5). In WO_3 and ReO_3, it occupies 12-coordinate ReO_3 (type I) cavities, but its actual coordination is square planar (20). Based on these known coordinations (octahedral sites are not present), type I and II cavities might accommodate at least one Li atom; types III, IV, and V, two Li atoms; and type VI, no Li atoms. Approximate stoichiometries obtained by counting sites provide useful structural bases for comparison of stoichiometries obtained by experiment. These are listed in Table VII, presented in terms of number of available sites per host cation.

The number of equivalents of reducible host lattice ions per host lattice ion are also presented in Table VII. Li and Ge are not reducible under the present conditions. Results reported here and elsewhere (2, 3, 17, 21) indicate that $Nb^{5+} \rightarrow Nb^{4+}$, $V^{5+} \rightarrow V^{4+} \rightarrow V^{3+}$ (two equivalents), $W^{6+} \rightarrow W^{5+}$, and $Ti^{4+} \rightarrow Ti^{3+}$ may occur in structures of this type. Also included in Table VII are the numbers of lithium per cavity for each phase at the stoichiometry attained in the n-BuLi reaction.

The most general conclusion that can be reached by inspection of the entries in Table VII is that site counting and reducible ion counting yield expected inserted Li stoichiometries that are quite similar, and close to those actually observed in the n-BuLi reactions. This results, in general, in the accommodation of 1-2 inserted Li per cavity and does not allow a distinction between chemical and structural influences on the insertion stoichiometry.

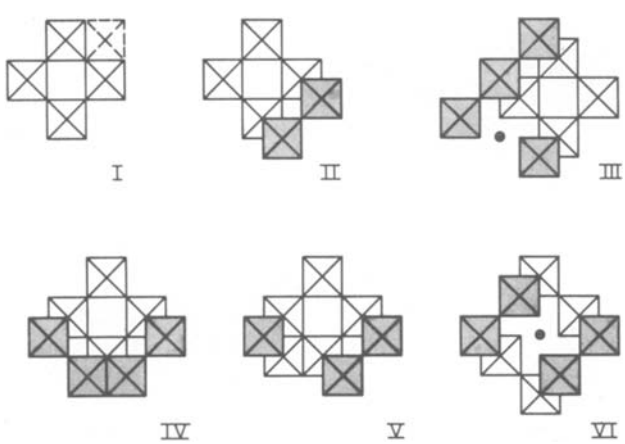

Fig. 6. The six cavity types in Wadsley-Roth crystallographic shear structures. I) Basic ReO_3 type cavity. II) Singly-capped ReO_3 type cavity. III-V) Variations of doubly capped cavities. VI) Tetrahedral site cavity. For type I, dotted ocathedron is sometimes present.

Table VI. Characterization of Wadsley-Roth phases by cavity type

Compound	* Cavity type, and number per unit cell					
	I	II	III	IV	V	VI
$H\text{-}Nb_2O_5$	0	6	4	2	2	1
$N\text{-}Nb_2O_5$	2	8	0	4	4	0
$LiNb_{13}O_{33}$	2	8	0	4	4	0
Nb_3O_7F	4	0	0	0	0	0
VNb_9O_{25}	0	0	8	0	0	2
$GeNb_{18}O_{47}$	0	0	8	0	0	2
$TiNb_2O_7$	0	0	0	4	4	0
$Ti_2Nb_{10}O_{29}$	0	8	0	8	8	0
$TiNb_{24}O_{62}$	0	8	8	4	4	2
$WNb_{12}O_{33}$	0	4	8	0	0	2
$W_3Nb_{14}O_{44}$	2	8	8	0	0	2
$W_3Nb_{18}O_{69}$	8	16	8	0	0	2
$WV_2O_{7.5}$	2	8	0	8	0	0
$W_{0.2}V_{2.8}O_7$	0	0	0	8	0	0

* I. ReO_3 type.
II. Singly capped ReO_3 type.
III. Bicapped ReO_3 type, tetrahedral atom in proximity.
IV. Bicapped ReO_3 type.
V. Double cavity, bicapped ReO_3 type.
VI. Tetrahedral cavity.
Cavity types are illustrated in Fig. 6.

Table VII. Comparison of observed insertion stoichiometries with those approximated by cavity and reducible ion counting

Host	Potential Li sites/ host metal*	Reducible ion† equivalents/ host metal	Experimental n-BuLi Li/host metal	Li/cavity**
H-Nb_2O_5	0.79	1.0	0.95	1.9
N-Nb_2O_5	0.81	1.0	0.85	1.5
$LiNb_{13}O_{33}$	0.81	0.93	0.80	1.5
Nb_3O_7F	0.67	1.0	0.53	0.8
VNb_9O_{25}	0.80	1.1	1.1	2.9
$GeNb_{18}O_{47}$	0.84	0.95	0.89	2.1
$TiNb_2O_7$	0.89	1.0	0.40	0.9
$Ti_2Nb_{10}O_{29}$	0.83	1.0	0.53	1.1
$TiNb_{24}O_{62}$	0.80	1.0	0.63	1.3
$WNb_{12}O_{33}$	0.77	1.0	0.82	1.8
$W_3Nb_{14}O_{44}$	0.76	1.0	0.96	1.8
$W_8Nb_{18}O_{69}$	0.77	1.0	0.85	1.4
$WV_2O_{7.5}$	0.81	1.33	1.4	2.5
$W_{0.2}V_{2.8}O_7$	0.89	1.5	1.2	2.8

* Cavities of I and II types counted as one possible site; cavities of III, IV, and V types counted as two possible sites; cavities of VI type not considered as containing possible sites.

** Strictly, the number of Li determined in the n-butyllithium reaction at room temperature divided by the number of cavities, excluding cavities of type VI.

† Li and Ge are not considered as reducible ions. Reducible ions are: $Nb^{5+} \rightarrow Nb^{4+}$, $V^{5+} \rightarrow V^{4+} \rightarrow V^{3+}$, $W^{6+} \rightarrow W^{5+}$, and $Ti^{4+} \rightarrow Ti^{3+}$.

Several distinctions and similarities of interest are brought out, however, in the entries in Table VII. The lithium insertion stoichiometries in the tungsten niobates are similar for the three different block sizes ($3 \times 4 \times \infty$, $4 \times 4 \times \infty$, and $5 \times 5 \times \infty$) and are intermediate to those predictable by simple site counting and reducible ion counting. Both tungsten and niobium are likely to be reduced at the observed stoichiometries. The compounds VNb_9O_{25} and $GeNb_{18}O_{47}$ ($3 \times 3 \times \infty$ block size) are members of the same subclass of Wadsley-Roth phases (here called "T" phases) as the tungsten niobates. The insertion stoichiometry of $GeNb_{18}O_{47}$ is quite similar to those of the tungsten niobates, but the stoichiometry of the lithium-inserted VNb_9O_{25} is quite different, due to the presence of the easily reducible V^{5+} ion. The observed stoichiometry is consistent with the reduction of all V^{5+} to V^{3+} and all Nb^{5+} to Nb^{4+}, resulting in the largest average number of inserted Li/cavity of the Wadsley-Roth phase structures, 2.9, and suggests that lithium occupies sites in the cavities in VNb_9O_{25} of different geometry from those previously structurally characterized, perhaps in the type VI cavities. Approximately one third of the Li in VNb_9O_{25} has slow insertion kinetics. $Li_{3.6}W_{0.2}V_{2.8}O_7$ and $Li_{4.3}WV_2O_{7.5}$ contain approximately 2.8 and 2.5 Li/cavity, respectively, implying again that some previously uncharacterized type of Li coordination may be occurring.

The class of shear structures known as Wadsley-Roth phases undergo lithium insertion reactions to significant lithium stoichiometries, and at reasonable rates, at room temperature. The nature of the crystallographic cavities and chemical reducibility of the host ions in such structures based on Nb_2O_5 are both important factors in the good quality of the insertion reactions. We have shown that even for the largest block size, $5 \times 5 \times \infty$ ($W_8Nb_{18}O_{69}$), the edge sharing in orthogonal directions of the type found in Wadsley-Roth phases is sufficient to stabilize the structures to the insertion of significant quantities of lithium. Structural and/or chemical distinctions in the behavior of the compounds within the class are not great, but suggest that the structures with a smaller proportion of edge sharing and compounds which contain a larger fraction of easily reducible ions will have the highest lithium-accommodation stoichiometries. The low conductivities of the host compounds containing metal atoms in their highest oxidation states exclusively makes the addition of a significant amount of graphite to positive cell electrodes necessary for reasonable cell performance. The small test cells we have fabricated reveal in many cases the formation of several distinct phases during Li insertion in the Nb_2O_5-based Wadsley-Roth phases. The performances of the compounds $WV_2O_{7.5}$ and $W_{0.2}V_{2.8}O_7$ in secondary test cells are comparable to those of V_6O_{13} and TiS_2. A description of the results of those investigations has been published elsewhere (6).

Acknowledgment

We are thankful for the generous assistance of Robert S. Roth in providing information on the synthesis and structures of the Wadsley-Roth phases employed in this investigation.

Manuscript submitted Jan. 9, 1983; revised manuscript received *ca.* June 30, 1983.

Bell Laboratories assisted in meeting the publication costs of this article.

REFERENCES

1. M. S. Whittingham, *Prog. Solid State Chem.*, **12,** 1 (1978).
2. D. W. Murphy and P. A. Christian, *Science,* **205,** 651 (1979).
3. D. W. Murphy, P. A. Christian, F. J. DiSalvo, and J. N. Carides, *This Journal,* **126,** 497 (1979).
4. R. J. Cava, A. Santoro, D. W. Murphy, S. Zahurak, and R. S. Roth, *J. Solid State Chem.,* **42,** 251 (1982).
5. R. J. Cava, A. Santoro, D. W. Murphy, S. Zahurak, and R. S. Roth, *Solid State Ionics,* **5,** 323 (1981).
6. R. J. Cava, D. W. Murphy, and S. M. Zahurak, *This Journal,* **130,** 243 (1983).
7. R. S. Roth, *Prog. Solid State Chem.,* **13,** 159 (1980).
8. S. Andersson and A. Astrom, *Acta. Chem. Scand.,* **19,** 2136 (1965).
9. R. S. Roth and A. D. Wadsley, *Acta Crystallogr.,* **19,** 26 (1965).
10. S. Andersson, *Acta Chem. Scand.,* **18,** 2339 (1964).
11. J. L. Waring and R. S. Roth, *Acta Crystallogr.,* **17,** 455 (1964).
12. S. Andersson and A. Astrom, *Acta Chem. Scand.,* **18,** 2233 (1964).
13. D. W. Murphy, J. N. Carides, F. J. DiSalvo, C. Cros, and J. V. Waszczak, *Mater. Res. Bull.,* **12,** 825 (1977).
14. A. D. Wadsley and S. Andersson, in "Perspectives in Structural Chemistry," Vol. 3, Dunitz and Ibers, Editors, p. 1, John Wiley and Sons, New York (1970).
15. R. S. Roth, A. D. Wadsley, and S. Andersson, *Acta. Crystallogr.,* **18,** 643 (1965).
16. S. Launay-Mondet, *Rev. Chim. Miner.,* **8,** 391 (1971).
17. D. W. Murphy, M. Greenblatt, S. M. Zahurak, R. J. Cava, J. V. Waszczak, G. Hull, and R. S. Hutton, *Rev. Chim. Miner.,* **19,** 441 (1982).
18. B. Reichman and A. J. Bard, *This Journal,* **128,** 344 (1981).
19. D. W. Murphy, M. Greenblatt, R. J. Cava, and S. M. Zahurak, *Solid State Ionics,* **5,** 327 (1981).
20. P. J. Wiseman and P. G. Dickens, *J. Solid State Chem.,* **17,** 91 (1976).
21. K. H. Cheng and M. S. Whittingham, *Solid State Ionics,* **1,** 151 (1980).

Detailed Analysis of a Redox Stabilized Liquid Junction Solar Cell

Application to the n-GaAs/(Se^{2-}/Se_2^{2-}) Cell

P. Allongue and H. Cachet

G. R. 4 du CNRS "Physique des Liquides et Electrochimie," associé à l'Université Pierre et Marie Curie, 75230 Paris Cedex 05, France

G. Horowitz

CNRS, Laboratoire de Photochimie Solaire, 94320 Thiais, France

ABSTRACT

The factors determining the response of a stabilized liquid junction solar cell are obtained by simultaneous current and impedance measurements, in dark and under illumination. Impedance data give the energy diagram of the junction (bandedges, surface states...). A model is developed that describes the kinetics of charge transfer and the mass transport effect under various working conditions. Moreover a simple method to estimate the reorganization energy λ of the redox couple in solution is presented. In the case of the n-GaAs / 1M KOH + 1M (Se^{2-}/Se_2^{2-}) cell a high surface-state density (~10^{13} cm^{-2}), located at 0.4 eV below the conduction band, is found. It is connected with a shift of the flatband potential under illumination. As a result the maximum theoretical open-circuit voltage is reduced, and it appears that the performances of the cell are limited by this shift and by charge transfer kinetics at the semiconductor-electrolyte interface.

Several models have been reported to describe the photocurrent-voltage characteristics of a photoelectrochemical (PEC) cell. One of the earliest is the one discussed by Gärtner in 1959 (1). Various improvements have been made on this model. Wilson (2) included the interface transfer kinetics and surface recombinations. Reichman's model (3) took into account the majority carrier current and carrier recombinations in the space charge region (SCR). In recent papers (4), El Guibaly *et al.* gave expressions of the dark and photocurrent that included surface and SCR recombinations.

On the other hand, impedance analysis has been proved to be a valuable tool to provide information about most of the parameters involved in the photoresponse of a PEC cell: bandedge position (5, 6), surface-state distribution (5, 7-9), mass transport effect (10). Furthermore, experimental results have shown a shift of the flatband potential under illumination (11-13).

The model presented in this paper includes all these effects and develops a complete description of charge transfer processes across the electrolyte-semiconductor interface. As an illustration of the model, simultaneous impedance and photocurrent measurements have been carried out on the n-GaAs/1M KOH + 1M (Se^{2-}/Se_2^{2-})/Pt cell which is known to be among the best PEC devices for solar energy conversion (14, 15).

Experimental

Undoped n-type (1-2 $\times$ 10^{16} cm^{-3}; <100> orientation) and Zn-doped p-type (1.3 $\times$ 10^{17} cm^{-3}; <111> orientation) GaAs single crystals were purchased from MCP-Limited. Before each experiment, the electrode surface was chemically etched in an $H_2SO_4|H_2O_2|H_2O$ (1,1,1) mixture. All measurements were made in a classical three-electrode electrochemical cell with a saturated calomel (SCE) reference electrode and a Pt counterelectrode, under controlled atmosphere to prevent the oxidation of the selenide electrolyte. Solutions were prepared either by neutralizing a KOH solution with H_2Se, or by the electrochemical reduction of selenium on a mercury cathode (15).

A 450W xenon arc lamp or a 100W tungsten-halogen lamp was used for illumination. Light intensity was changed by means of neutral filters and measured with a MACAM TR 3010 radiometer. Stationary I-V curves and impedance measurements were performed under potentiostatic conditions. Impedances were determined in the frequency range 1 Hz-5 $\times$ 10^5 Hz by using a 1174 SOLARTRON Frequency response analyzer equipped with a data management system. Impedance data were analyzed by means of a nonlinear least squares method (8).

Key words: impedance measurements, semiconductor electrodes, surface states, photocurrent model, photoelectrochemistry.

Models

Semiconductor/redox couple charge transfer.—At an n-type semiconductor-electrolyte interface under illumination, the transfer reaction with a redox couple is

$$\mathrm{Red} + h^+ \underset{k_b}{\overset{k_f}{\rightleftarrows}} \mathrm{Ox} \qquad [1]$$

where h^+ is a hole arriving at the semiconductor surface, with an energy equal to that of the top of the valence band, Red and Ox the reduced and the oxidized species, k_f and k_b the forward and the backward rate constants of the reaction. k_f and k_b may change when the electrode is illuminated. Assuming a first order kinetics for all the reactants, the hole transfer current J_p, under illumination, is given by

$$J_p = k^*_f c_r p_s - k^*_b c_{Ox} N_v \qquad [2]$$

where N_v is the density of states at the top of the valence band, p_s the surface hole concentration, c_r and c_{Ox} the concentrations of Red and Ox at the surface of the electrode, k^*_f and k^*_b values of k_f and k_b under illumination.

At equilibrium, in dark $J_p = 0$, and we have

$$k_f c_r^o p_s^o = k_b c_{Ox}^o N_v \qquad [3]$$

where c_r^o, c_{Ox}^o, and p_s^o are the equilibrium values of c_r, c_{Ox}, and p_s.

The rate constants in reaction [1] are a function of the overlap between the top of the valence band and the reduced and the oxidized state density of the redox couple. If we assume that these latter are given by Gerisher's model (5), we have in dark (16)

$$k_f = \langle q\sigma v d \rangle \left(\frac{kT}{\pi\lambda_{Red}} \right)^{1/2} \exp - \frac{(E_v^s - E_{Red})^2}{4\lambda_{Red} kT} \qquad [4a]$$

$$k_b = \langle q\sigma v d \rangle \left(\frac{kT}{\pi\lambda_{Ox}} \right)^{1/2} \exp - \frac{(E_v^s - E_{Ox})^2}{4\lambda_{Ox} kT} \qquad [4b]$$

where σ is the capture cross section of an ion in solu-

tion, v the thermal velocity of holes, d a distance of reaction between the solid and liquid phases [<30Å (17)], E_v^s the energy of the top of the valence band at the electrode surface in dark, $E_{Red}(E_{Ox})$ the most probable electron energy at a reduced (oxidized) ion and $\lambda_{Red}(\lambda_{Ox})$ the rearrangement energies of the solvation layer for the reduced (oxidized) species. If the bandedges are shifted under illumination E_v^s is changed into E_v^{s*}

$$E_v^{s*} = E_v^s - \Delta E_F \quad [5]$$

$$\Delta E_F = -q\Delta V_{FB} = E_F^* - E_F \quad [6]$$

where E_F and E_F^* are related to the flatband potentials in dark and under illumination.

Taking into account Eq. [3]-[6] and assuming $\lambda_{Red} = \lambda_{Ox} = \lambda$, Eq. [2] becomes

$$J_p = k^*_f c_r^o p_s^o \left(\frac{p_s}{p_s^o} \frac{c_r}{c_r^o} - \exp - \frac{q\Delta V_{FB}}{kT} \right) \quad [7]$$

It is shown in the Appendix that even when λ_{Ox} and λ_{Red} are very different the final result (Eq. [7]) is not significantly changed.

In Eq. [7] the factor c_r/c_r^o accounts for a possible mass transport effect of the reduced species (It is assumed that this effect does not exist for the oxidized species: $c_{Ox} = c_{Ox}^o$). Equation [7] can be rewritten as

$$J_p = J_p^{o*} \left(\frac{p_s}{p_s^{o*}} \frac{c_r}{c_r^o} - 1 \right) \quad [8]$$

where

$$J_p^{o*} = k_f^* c_r^o p_s^{o*} \quad [8a]$$

and

$$p_s^{o*} = p_s^o \exp - \frac{q\Delta V_{FB}}{kT} \quad [9]$$

p_s^o can be expressed as

$$p_s^o = p_o \exp \frac{qV_b^o}{kT} \quad [10]$$

where p_o is the hole concentration in the bulk of the semiconductor and $V_b^o = V_{Redox} - V_{FB}$ the band bending at equilibrium (Fig. 1). From Eq. [9] and [10] we have

$$p_s^{o*} = p_o \exp \frac{qV_b^{o*}}{kT} \quad [11]$$

where $V_b^{o*} = V_b^o - \Delta V_{FB}$ (Fig. 1) represents the maximum available open-circuit voltage. p_s^{o*}, V_b^{o*}, and J_p^{o*} play the same role as p_s^o, V_b^o, and J_p^o in the model of Reichman (3). The stared parameters account for the shift of the bandedges at the semiconductor surface under illumination. Consequently we can define them as pseudoequilibrium surface hole concentration, pseudoequilibrium band bending, and pseudoexchange current.

Similarly n_s^{o*} is defined as

$$n_s^{o*} = N_D \exp - \frac{qV_b^{o*}}{kT} \quad [12]$$

It can be easily shown that the electron transfer current is thus

$$J_n = J_n^{o*} \left(\frac{n_s}{n_s^{o*}} - 1 \right) \quad [13]$$

where n_s is the surface electron concentration. The total current through the interface is then: $J = J_p - J_n$. It must be pointed out that, because of the shift of the flatband potential, the electron currents in dark and under illumination have no reason to be equal.

Mass transport effect.—If a constant gradient of concentration of Red is assumed over a distance δ from the electrode surface, the first Fick's law and

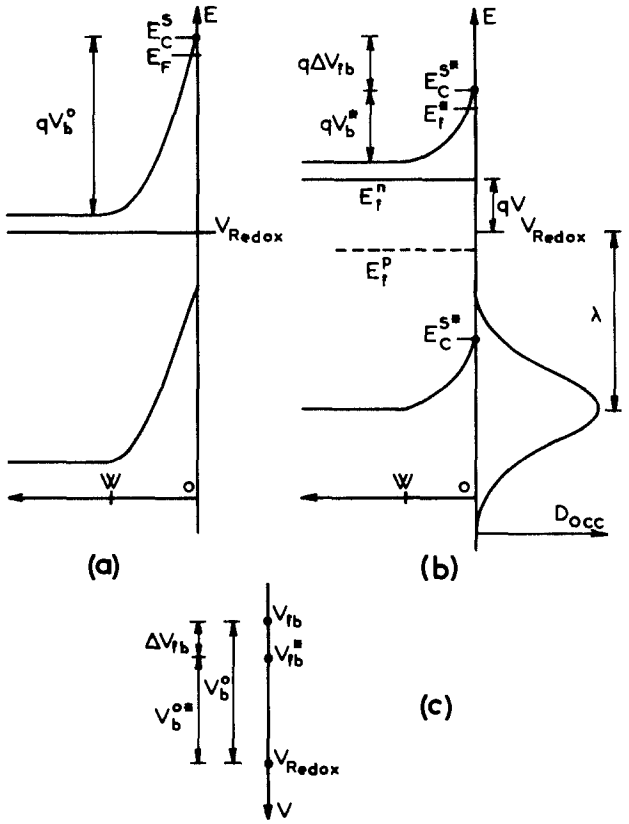

Fig. 1. Energy diagram of a semiconductor-electrolyte junction: (a) junction at equilibrium, (b) junction under illumination with an applied voltage with respect to the redox potential. E_f^n and E_f^p are the electron and hole quasi-Fermi levels. (c) V_b^o band bending at equilibrium, V_b^{o*} maximum theoretical open-circuit available under illumination.

Eq. [8] give (10)

$$\frac{c_r}{c_r^o} = \frac{1+\beta}{1+\beta \dfrac{p_s}{p_s^{o*}}} \quad [14]$$

where β is defined as

$$\beta = \frac{\delta k_f^* p_s^{o*}}{zqD} \quad [15]$$

z being the number of electrons exchanged per mol of Red and D the diffusion coefficient of Red in the solution. It appears that β is independent of the applied voltage and is a constant depending on the junction and the cell geometry. β will be determined by impedance measurements (generally $\beta << 1$).

Photocurrent.—The total current at the electrode surface is the sum of several contributions that will be now dealt with.

Diffusion current in the neutral region.—This current is given by the resolution of the diffusion equation for holes

$$J_w = -J_o \left(\frac{p_w}{p_o} - 1 \right) + qI_o \frac{\alpha L}{1+\alpha L} \exp(-\alpha w) \quad [16]$$

where $J_o = qDp_o/L$ is the reverse saturation current density, p_w the hole density at $x = w$, $w = (2\epsilon\epsilon_o/qN_D)^{1/2} \sqrt{V_b^*}$ the SCR width, V_b^* the band bending (Fig. 1), I_o the incident photon flux, α the absorption coefficient, and L the hole diffusion length. As $p_s = p_w \exp qV_b^*/kT$ we have, using Eq. [11]

$$\frac{p_w}{p_o} = \frac{p_s}{p_s^{o*}} \exp \frac{q}{kT} (V_b^{o*} - V_b^*) \quad [17]$$

Current due to generation in the SCR.—This current is given by (1)

$$J^{G}_{SCR} = qI_o\,(1 - \exp - \alpha w) \qquad [18]$$

From Eq. [16] and [18], the total generated current at the electrode surface is then

$$J^{G}_{tot} = J_g - J_o \frac{p_s}{p_s{}^{o*}} \exp \frac{qV}{kT} \qquad [19]$$

where $V = V_b{}^{o*} - V_b{}^*$ is the voltage applied to the junction and J_g the Gärtner's current: $J_g = J_o + qI_o\,[1 - \exp\,(-\alpha w)/(1 + \alpha L)]$.

Recombination currents.—Recombinations can take place in the SCR and at the electrode surface. The corresponding currents can be derived from the recombination rate given by Sah, Noyce, and Schockley (18). The SCR recombination current is (19)

$$J^{R}_{SCR} = \frac{\pi kT}{4\tau V_b{}^*}\, w\,(np)^{1/2} \qquad [20]$$

where τ is the hole lifetime. In the quasi-equilibrium hypothesis, the quasi-Fermi levels for holes and electrons are supposed to be flat over the SCR, *i.e.*, $np = n_s p_s$. Taking into account Eq. [11] and [12] and $n_s = N_D \exp -qV_b{}^*/kT$, J^{R}_{SCR} yields

$$J^{R}_{SCR} = \frac{\pi kT}{4\tau V_b{}^*}\, w n_i{}^2 \exp \frac{qV}{2kT} \cdot \left(\frac{p_s}{p_s{}^{o*}}\right)^{1/2} \qquad [21]$$

where n_i is the intrinsic electron density.

The current $J_S{}^R$ due to hole surface recombinations is given by

$$J_S{}^R = \int_{E_v{}^{s*}}^{E_c{}^{s*}} q\sigma_{ss} v N_{ss}(E)\, \frac{n_s p_s - n_i{}^2}{n_s + p_s + 2n_i \cosh\,((E_i{}^{s*} - E)/kT)}\, dE \qquad [22]$$

where $E_i{}^{s*}$ is the surface midgap energy under illumination. The interface states are characterized by their capture cross section σ_{ss}, their energy level E, and their surface density $N_{ss}(E)$. Interface states are states located within the bandgap at the semiconductor surface. They can be either intrinsic surface states of the semiconductor electrode or interface states that appear when the electrode is put into contact with an electrolyte. The distribution $N_{ss}(E)$ can be determined by impedance measurements. We rewrite Eq. [22] as

$$J_S{}^R = \int_{E_v{}^{s*}}^{E_c{}^{s*}} q\sigma_{ss} v n_i{}^2 N_{ss}(E)\, \frac{\left(\frac{p_s}{p_s{}^{o*}} \exp \frac{qV}{2kT} - 1\right)}{n_s + 2n_i \cosh \frac{E_i{}^{s*} - E}{kT} + p_s{}^{o*}\left(\frac{p_s}{p_s{}^{o*}}\right)}\, dE \qquad [23]$$

If there is a discrete distribution of interface states, $J_S{}^R$ is the sum of rational fractions in $p_s/p_s{}^{o*}$.

The total hole current transferred to the solution is given by the total generated current minus the recombination currents

$$J^{G}_{tot} - J^{R}_{SCR} - J_S{}^R = J_p \qquad [24]$$

From Eq. [14], [19], [21], and [23] it can be seen that the hole current at a given V is only determined by $p_s/p_s{}^{o*}$. A numerical calculation of J_p can be achieved by first equating Eq. [8] and [24] and solving it to get $p_s/p_s{}^{o*}$, and then reporting the obtained value in Eq. [8]. Equation [24] simplifies to an equation of the fourth degree in $(p_s/p_s{}^{o*})^{1/2}$ if surface recombinations are neglected. With a single surface state, one gets an equation of the sixth degree. Moreover, for large band bending (>0.6V), calculation shows that the photocurrent is equal to J_g, the Gärtner's current.

Our model improves the model of Reichman on several points: it includes both bulk and surface recombinations and takes into account mass transport effect ($c_r \neq c_r{}^o$). More importantly it also accounts for the shift of the flatband potential under illumination by replacing $p_s{}^o$, V_{FB}, $V_b{}^o$, and $J_p{}^o$ by their pseudovalues $p_s{}^{o*}$, $V_{FB}{}^*$, $V_b{}^{o*}$, and $J_p{}^{o*}$. The pseudoexchange current $J_p{}^{o*}$ plays a major role in the computation of the photocurrent. Equations [4a] and [8a] show that it can be fully determined if λ and $k_f{}^*$ are known. An estimation of these last parameters will be dealt with in the following section.

Estimation of λ and $k_f{}^*$.—Reaction [1]: Red + $h^+ \rightleftarrows$ Ox, that occurs at an n-type semiconductor-electrolyte interface under illumination also takes place, in dark, at a p-type semiconductor surface under anodic bias. It is possible to take advantage of this feature to estimate λ and $k_f{}^*$. Under forward bias, the hole current at a p-type electrode in dark is given by

$$J_p = k_f{}^p c_r{}^o p_s{}^o \left(\exp \frac{qV}{kT} - 1\right) \qquad [25]$$

A plot of log J_p *vs.* V should be a straight line when $V > 3kT/q$, and the intercept of this line at $V = 0$ gives $k_f{}^p c_r{}^o p_s{}^o$. As $c_r{}^o$ and $p_s{}^o$ can be calculated from the measurements of the redox potential and the flatband potential, through Eq. [10] for the latter, one gets then an estimation of the rate constant $k_f{}^p$.

$k_f{}^p$ is given by Eq. [4a]. We can assume that the factor $<q\sigma v d>$ is the same for n- and p-type. With $\sigma = 10^{-15}$ cm^2 and $d = 10$Å (17) we have $<q\sigma v d> = 2.7 \times 10^{-34}$ A · cm^4. From $k_f{}^p$, λ can be calculated and its value used to estimate $k_f{}^*$ for an n-type semiconductor. Measurements of the direct current on a p-type electrode give then a check of the value of the pseudoexchange current $J_p{}^{o*}$, that can be also estimated from the onset of the photocurrent on an n-type electrode.

Equivalent circuit and diffusion impedance.—The equivalent circuit of the junction is given in Fig. 2 (5, 8). It is a classical scheme for a Schottky barrier. A faradaic impedance Z_F has been added to account for the diffusion of the electroactive species in solution.

The expression of Z_f is the result of the second Fick's law for a small sinusoidal perturbation of the potential (20). In the frame of the Nernst hypothesis and for a semiconductor electrode current $J = J_p - J_n$, the faradaic impedance is (10)

$$Z_f = R_f \left(1 + \frac{(1 + \beta)c_r{}^o - c_r}{c_r} \cdot \frac{th\sqrt{j\omega\tau_D}}{\sqrt{j\omega\tau_D}}\right) \qquad [26]$$

where ω is the pulsation of the perturbation, τ_D the diffusion time constant, and R_f the parallel combination of the faradaic resistances corresponding to the anodic and cathodic components of the current. When $\omega = 0$, Eq. [26] becomes

$$\lim_{\omega \to 0} Z_f = R_p = R_f(1 + \beta)\frac{c_r{}^o}{c_r} \simeq R_f \frac{c_r{}^o}{c_r} \qquad [27]$$

where R_p is the polarization resistance. This is a very important relation which shows that the ratio $c_r/c_r{}^o$

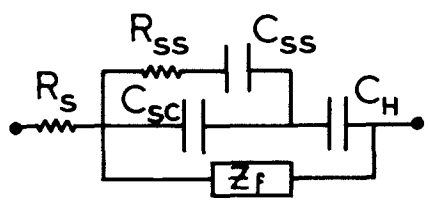

Fig. 2. Electrical equivalent circuit of a semiconductor electrolyte junction. R_S is the series resistance ($\simeq 2\Omega \times$ cm^2); see text for other symbols.

can be determined, experimentally, by impedance measurements ($\beta << 1$). Generally $\tau_D >> 1$ sec and if $\omega\tau_D >> 1$ Z_f is almost a pure resistance R_f, the so-called faradaic resistance. The high frequency response of the impedance is then interpreted as has been reported in a previous paper (8). The impedance response presents two main loops: a high frequency loop, mainly determined by the SCR capacitance C_{sc} and the faradaic resistance R_f, and a low frequency loop, characteristic of the diffusion (Fig. 3).

A frequency independent value of C_{sc} is obtained by an analysis of the high frequency loop. Mott-Schottky plots C_{sc}^{-2}-V provide then a determination of the flatband potential. This approach is able to reveal the shift of the bandedges under illumination (Fig. 4). The dispersion capacitance C_{ss} can be attributed to charges trapped in surface states. $C_{ss}(V)$ and the surface state distribution $N_{ss}(E)$ are connected through the relation (5)

$$C_{ss}(V) = \frac{q^2}{kT}\int_{E_v^{s*}}^{E_c^{s*}} N_{ss}(E)\frac{df}{dV}dE \qquad [28]$$

f being the occupation rate of electrons at the energy E. This factor will be discussed in a following section. At some potentials it was necessary, to get a good representation of the high frequency impedance loop, to introduce several time constants $R_{ss}{}^iC_{ss}{}^i$: in other words, the branch $R_{ss}C_{ss}$ was replaced by parallel series circuits $R_{ss}{}^iC_{ss}{}^i$ (21). This can be justified if there is a distribution of states. The capacitance $C_{ss}(V)$ used in Eq. [28] is then the sum of all the $C_{ss}{}^i$ (21)

$$C_{ss} = \sum_i C_{ss}{}^i \qquad [29]$$

The time constant $\tau_{ss} = R_{ss}C_{ss}$ gives information on the surface-state capture cross section σ_{ss}. For a single surface state, the simple relation holds

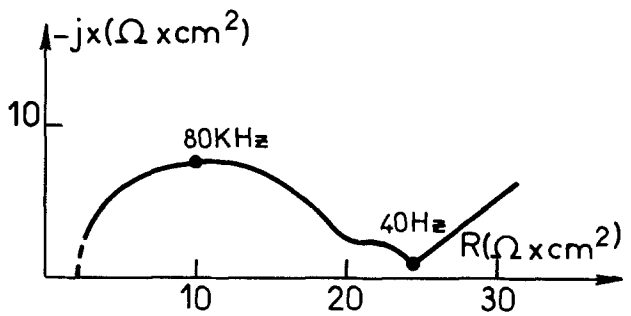

Fig. 3. Typical impedance diagram of an illuminated n-GaAs/selenide liquid junction corresponding to the point −1.4 V/SCE of the *I-V* characteristic in Fig. 6.

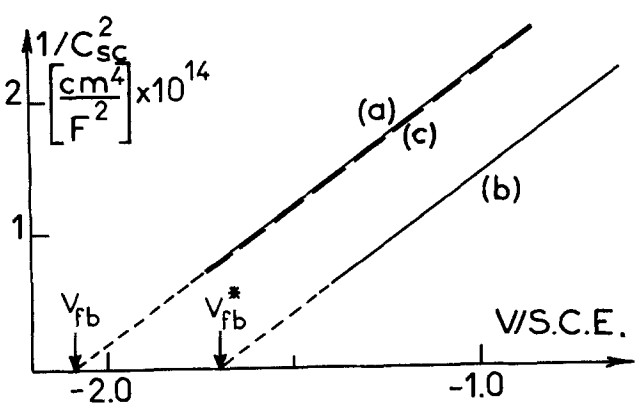

Fig. 4. Mott-Schottky plots for the same n-GaAs/selenide junction. (a) In the dark, (b) under 20 mW/cm² illumination, (c) back again in the dark.

$$\sigma_{ss} \simeq \frac{1}{\tau_{ss} v p_s} \qquad [30]$$

Finally the Helmholtz layer capacitance C_H is supposed to be independent of the potential (17). C_H cannot be clearly reached by impedance measurements. In fact, at some potentials a value of a few μF/cm² is either much greater than the other capacitances of the equivalent circuit or comparable with the value of the surface-state capacitance C_{ss}. In the last case the series combination of C_H and C_{ss} is measured. For C_H ranging from 4 to 20 μF/cm² (17), C_{ss} is divided by 2 but C_{sc} and R_f are not significantly modified.

Results and Discussion

This section is devoted to the application of our model to the n-GaAs/(Se^{2-}/Se_2^{2-}) PEC cell. The redox reaction considered is

$$2Se^{2-} + 2h^+ \rightleftarrows Se_2^{2-}$$

the redox potential of which is

$$V_{Redox} = V_o - \frac{kT}{2q}\ln\frac{[Se^{2-}]^2}{[Se_2^{2-}]}$$

where $[Se^{2-}] = c_r$, $[Se^{2-}] + 2[Se_2^{2-}] = 1M$, and $V_o = -0.95$ V/SCE.

Determination of λ_{Red}.—In Fig. 5, the extrapolation of the Tafel plot for p-GaAs to the redox potential gives $k_r{}^p c_r{}^o p_s{}^o = 2.5$ μA/cm². In a polyselenide electrolyte, dark measurements for n <111> GaAs electrode give $V_{FB} = -1.82 \pm 0.06$ V/SCE. If we assume that the bandedges have the same position for n- and p-type electrodes, we obtain $V_{FB}{}^p = -0.56 \pm 0.06$ V/SCE for the p-type, which is in good agreement with the literature (22). Taking this value and $\langle q\sigma vd\rangle = 2.7\ 10^{-34}$ A · cm⁴, we get $\lambda = (1.2 \pm 0.2)$ eV.

Figure 6 presents the *I-V* characteristics of an n-GaAs/(Se^{2-}/Se_2^{2-}) junction under 20 mW/cm² illumination. We analyzed this curve with negligible surface recombination and diffusion. These simplifications will be shown to be justified. The only adjustable parameter is $J_p{}^{o*}$, and a good fit between calculated and experimental curves was obtained with a value of (0.0012 ± 0.0005) mA/cm², leading to $\lambda_{Red} = (1.0 \pm 0.05)$ eV with $\langle q\sigma vd\rangle = 2.7\ 10^{-34}$ A · cm⁴.

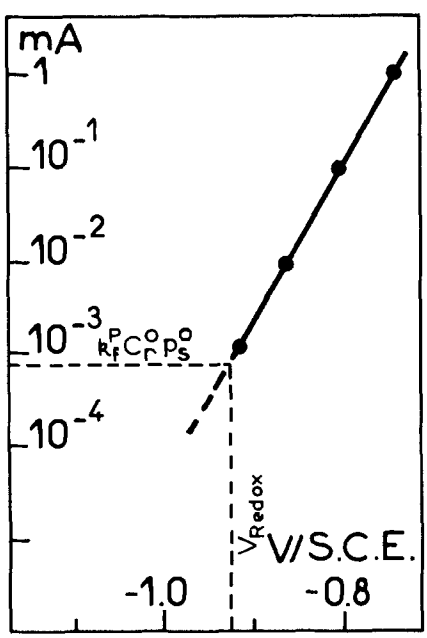

Fig. 5. Tafel plot of a p-type GaAs electrode in 1M (Se^{2-}/Se_2^{2-}) electrolyte under anodic bias. For $V_{Redox} = -0.925$ V/SCE one gets $k_f{}^p c_r{}^o p_s{}^o = 2.5$ μA/cm². Electrode area: 0.25 cm².

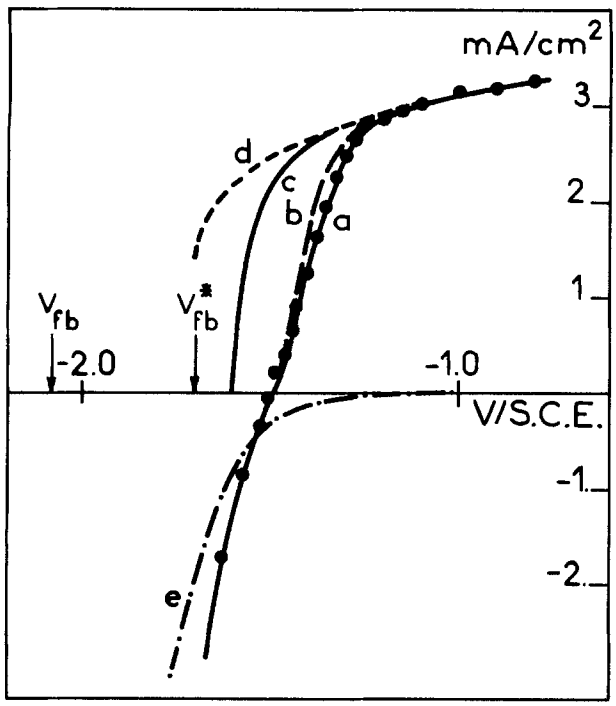

Fig. 6. Comparison between calculated *I-V* curves, in different hypothesis, and the experimental characteristic of the n-GaAs/selenide solar cell under 20 mW/cm². (●) Experimental data. (a) Calculated curve according to the complete model $\alpha = 26000$, $L = 0.13$ μm, $\tau = 6\ 10^{-11}$s, $N_D = 2.3\ 10^{16}$ cm^{-3}, $V^*_{FB} = -1.7$ V/SCE, $J_p{}^{o*} = 0.0012$ mA/cm², $J_n{}^{o*} = 1.5\ 10^{-4}$ mA/cm², $\beta = 3.5\ 10^{-4}$. (b) Same as (a) but without diffusion ($\beta = 0$). (c) Same as (b) but without SCR recombinations ($J^R_{SCR} = 0$). (d) Gärtner current. (e) Dark current. This current is quite different from the cathodic branch of the *I-V* curve (a) under illumination.

This fit is very good and the corresponding uncertainty on λ_{Red} is smaller than for p-type measurements because of the scattering in the flatband potential determination. It seems reasonable to take a value of $\lambda_{Red} = 1.0$ eV which is in the range of the usual values given for the rearrangement energy (23, 24).

Surface-state density.—Impedance measurements under illumination were analyzed according to the circuit in Fig. 2. Figure 7 shows that $C_{ss}(V)$ presents a peak that extends over about 100 mV and is centered at 0.4 eV below the bottom of the conduction band (*i.e.*, near the photocurrent onset). The corresponding surface-state density is $\sim 10^{13}$ cm^{-2} and its capture cross section $\sigma_{ss} \simeq 10^{-18}$ cm². This peak does not occur in dark. This does not mean that the surface states are induced by illumination. Rather, we think that in the dark their occupation rate f (appearing in Eq. [28]) is constant because they are filled by electrons coming from the reduced species in solution. On the other hand, holes created by illumination can be trapped by the surface state, leading to a variation of the surface charge. A complete model describing this phenomenon will be reported in a further paper (26). The bases of this model are very similar to the one developed by Kelly and Memming (11). From this model Eq. [22] and [23] should be modified in order to account for the exchange current between surface state and reduced species. However, the low value of σ_{ss} leads to a negligible surface recombination current.

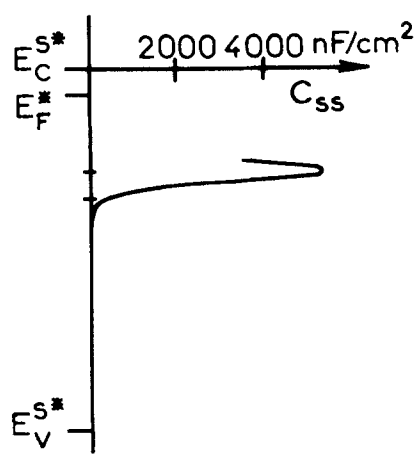

Fig. 7. Distribution of the surface-state capacitance of an illuminated n-GaAs/selenide liquid junction with $C_H = 5$ μF/cm².

Flatband potential determination.—Figure 4 presents Mott-Schottky plots in dark and under illumination. In all cases we obtain good straight lines, and the doping level corresponding to the slope is in good agreement with the value given by the supplier. Under illumination, the slope is unchanged but the flatband potential is shifted toward positive potentials ($\Delta V_{FB} \simeq 350$ mV). Furthermore we observe that this shift is reversible. If an illuminated electrode is put back again in dark, the flatband potential returns to its previous value. We must point out that this shift is much greater than the ohmic drop of the cell which is always smaller than 10 mV. The good linearity of the Mott-Schottky plots justifies our analysis of the impedance according to the circuit given in Fig. 2, and reinforces the hypothesis that attributes the capacitance dispersion to charges localized at the surface.

The flatband potential shift ΔV_{FB} can be explained from the previous subsection. Whereas the surface states are filled in the dark, they are emptied by holes under illumination for a band bending $\gtrsim 300$ mV. Consequently an additional voltage drop is induced in the Helmholtz layer. The shift should be then given by $\Delta V_{FB} = qN_{ss}/C_H$. With $N_{ss} = 10^{13}$ cm^{-2} and $C_H = 5$ μF/cm² we have $\Delta V_{FB} = 320$ mV which is in fair agreement with our results: $V_{FB} = (-2.08 \pm 0.03)$ V/SCE and $V_{FB}{}^* = (-1.70 \pm 0.03)$ V/SCE.

Under illumination the photocurrent onset takes place at about 200 mV anodic from $V_{FB}{}^*$. As already discussed, this difference is not due to surface recombination. Rather we attribute it to a limitation due to transfer kinetics. This limitation appears in Eq. [8]. It must be noticed that the bandedges shift under illumination changes the value of $J_p{}^{o*}$ by two or three orders of magnitude. Similarly, the majority carrier current J_n is modified under illumination by the bandedge shift. This modification was accounted for by a fit of Eq. [13] to the experimental cathodic current. This description of the majority carrier current is purely phenomenological, and does not assume any precise transfer mechanism. This transfer could take place directly from the conduction band, and/or via surface states, as suggested by Parkinson *et al.* (25).

Influence of diffusion.—Diffusion is characterized by the parameter β. The measurement of the polarization resistance R_p (given by the *I-V* curve) and the faradaic resistance R_f calculated by impedance analysis allowed us to get experimental values for $R_f(V)/R_p(V)$ (Fig. 8). Moreover at a given value of β we were able to calculate the theoretical curves *I-V* and $R_f(V)/R_p(V)$. The comparison of the experimental and theoretical curves R_f/R_p determines β. The method is very accurate and the error on β is less than 10%.

Figure 6 clearly shows that diffusion only affects the photocurrent rise. The plateau region is well represented by Gärtner's model. This shows that the performances of a PEC cell are influenced by its geometry, for limitations due to mass transport in solution tend to reduce the fill factor.

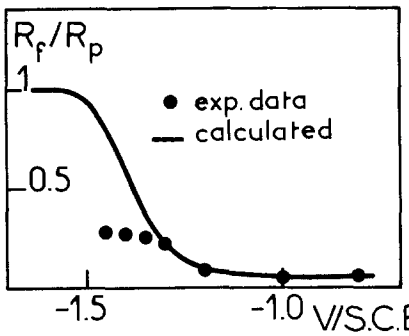

Fig. 8. Ratio R_f/R_p vs. potential corresponding to the *I-V* curve of Fig. 6.

Conclusions

Our model is able to simulate the *I-V* curves of n-GaAs/selenide liquid junction under different working conditions. It must be pointed out that every parameter involved in the model is determined experimentally from impedance data except for the semiconductor characteristics and the rearrangement energy λ_{Red} which is known from current measurements. Furthermore, the assumption of a first order kinetics for the transfer reaction is found to be very adequate. Particularly, the equilibrium condition (see Eq. [3]) is well verified. Within the energetic conditions under illumination, *i.e.*, taking into account the bandedge shift, we put forward a photocurrent onset controlled by kinetics, mass transport, and SCR recombinations.

We have evidenced a surface-state distribution characterized by a sharp peak located at 0.4 eV below the conduction band. It is responsible for a shift of the bandedges under illumination, which reduces the maximum theoretical open-circuit voltage ($V_{Redox} - V_{FB} = 1.1V$) by an amount of 300-400 mV. Work is in progress in order to get a better description of surface states and their influence on the flatband potential shift under illumination.

Acknowledgments

The authors wish to thank Dr. A. Bourrasse (C.E.A.-CEN Cadarache 13115 St-Paul-lez-Durance, France) for supplying selenide solutions and for very useful discussions.

Manuscript submitted Jan. 31, 1983; revised manuscript received June 2, 1983.

CNRS assisted in meeting the publication costs of this article.

APPENDIX

If we assume $\lambda_{Ox} \neq \lambda_{Red}$, the term $- q\Delta V_{FB}/kT$ in Eq. [7] becomes

$$- q\frac{\Delta V_{FB}}{kT}\left[1+\left(\frac{E_{Redox}-E_v^s}{2}-q\frac{\Delta V_{FB}}{4}\right)\left(\frac{1}{\lambda_{Ox}}-\frac{1}{\lambda_{Red}}\right)\right]$$

In the case of the n-GaAs/polyselenide junction we have $E_{Redox} - E_v^s \simeq 0.25$ eV, $q\Delta V_{FB} \simeq 0.3$ eV, and $\lambda_{Red} \simeq 1$ eV. Even if λ_{Ox} is two times smaller than λ_{Red} the correction in ΔV_{FB} is about 5%. This correction becomes 2.5% if λ_{Ox} is two times greater than λ_{Red}.

REFERENCES

1. W. Gärtner, *Phys. Rev.*, **116**, 84 (1959).
2. R. Wilson, *J. Appl. Phys.*, **48**, 4292 (1977).
3. J. Reichman, *Appl. Phys. Lett.*, **36**, 574 (1980).
4. F. El Guibaly, K. Colbow, and B. L. Funt, *J. Appl. Phys.*, **52**, 3480 (1981); F. El Guibaly and K. Colbow, *ibid.*, **53**, 1737 (1982).
5. H. Gerischer, in "Physical Chemistry," Vol. IXA, H. Eyring, D. Henderson, and W. Jost, Editors, Chap. 5, Academic Press, New York (1970).
6. J. F. Dewald, *Bell Syst. Tech. J.*, **39**, 615 (1960).
7. W. Siripala and M. Tomkiewicz, *This Journal*, **129**, 1240 (1982).
8. P. Allongue and H. Cachet, *J. Electroanal. Chem.*, **119**, 371 (1981).
9. G. Horowitz, Thesis, University Paris VII (1981).
10. P. Allongue and H. Cachet, Ext. Abstr., 33rd Meeting of the International Society of Electrochemistry, p. 819, Lyon (1982).
11. J. J. Kelly and R. Memming, *This Journal*, **129**, 730 (1982).
12. Y. Nakato, A. Tsumura, and H. Tsubomura, *ibid.*, **127**, 1502 (1980).
13. R. Schumacher, D. M. Teschner, and A. B. Heinzel, *Ber. Bunsenges. Phys. Chem.*, **86**, 1153 (1982).
14. A. Heller and B. Miller, *Electrochim. Acta*, **25**, 29 (1980).
15. A. Bourrasse, H. Cachet, G. Horowitz, and S. Le Crom, *Revue Phys. Appl.*, **17**, 801 (1982).
16. S. R. Morrison, "The Chemical Physics of Surfaces," Chap. 2, Plenum, New York (1977).
17. S. R. Morrison, "Electrochemistry at Semiconductor and Oxidized Metal Electrodes," Plenum, New York (1980).
18. C. T. Sah, R. N. Noyce, and W. Schockley, *Proc. IRE*, **45**, 1228 (1957).
19. C. H. Henry, R. A. Logan, and F. R. Merritt, *J. Appl. Phys.*, **44**, 3530 (1978).
20. I. Epelboin and M. Keddam, *This Journal*, **117**, 1052 (1970).
21. E. H. Nicollian and A. Goetzberger, *Bell Syst. Tech. J.*, **46**, 1055 (1967).
22. W. P. Gomes and F. Cardon, in "Semiconductor Liquid Junction Solar Cells," A. Heller, Editor, p. 120, The Electrochemical Society Softbound Proceedings Series, PV 77-3, Princeton, NJ (1977).
23. K. W. Frese, Jr., M. J. Madou, and S. R. Morrison, *This Journal*, **128**, 1527 (1981).
24. K. W. Frese, Jr., *J. Phys. Chem.*, **85**, 3911 (1981).
25. B. A. Parkinson, A. Heller, and B. Miller, *This Journal*, **126**, 954 (1979).
26. P. Allongue and H. Cachet, To be published.

Localized Photoelectrochemical Measurements of Passive Films on Titanium

M. A. Butler*

Sandia National Laboratories, Albuquerque, New Mexico 87185

ABSTRACT

Using a focused laser and a digitally controlled x-y stage, localized photoelectrochemical measurements have been made on 100Å thick passive films on polycrystalline titanium. The photocurrent dependence on potential is semiquantitatively explained by a model considering trap dominated electronic charge transport in the passive film. Variations in the measured electronic properties are observed which correlate with the underlying metal grain structure. The data suggest extremely high trap densities in the passivating film.

The corrosion resistant metals are stable because of the growth of passivating films on the metal surface. For such metals the initiation of corrosion involves breakdown of the protective film. Since in practical applications these metals are polycrystalline in nature, it would not be surprising to find that the passivating film is inhomogeneous in nature. Ideally then to study the corrosion initiation process due to breakdown of the passive film requires a local probe. Techniques which measure the average properties of the film cannot be expected to give a detailed insight into the mechanism for local breakdown of the film. For this reason we have applied an optical probe to study locally the photoelectrochemical response of the passivating film on titanium. Titanium was chosen because it and related alloys form a class of corrosion resistant materials of current practical interest (1). Furthermore, the passivating layer is known to be TiO_2 (1), a semiconducting material which has been extensively studied in its bulk form. In particular, many photoelectrochemical measurements have been made on TiO_2 (2).

* Electrochemical Society Active Member.
Key words: semiconductor, electrode, photoconductivity, passivity.

Experimental Results

The spatial resolution is obtained by using the laser scanning system shown in Fig. 1. Light from the kypton laser at one of the wavelengths listed is chopped at 15.6 Hz, then passes through the beam splitter. This is a quartz plate which deflects a few percent of the beam to serve as a reference. The light is then focused on the electrochemical cell with a spot size limited by diffraction effects. While less than 1 micron is theoretically possible, the best we have observed, in keeping with the limits imposed by the optics used, is about 3 microns. The photoelectrochemical cell uses a quartz window with a thin (3 mm) electrolyte layer to minimize distortions of the laser beam. A conventional saturated calomel reference electrode is used. The cell is mounted on a numerically controlled x-y

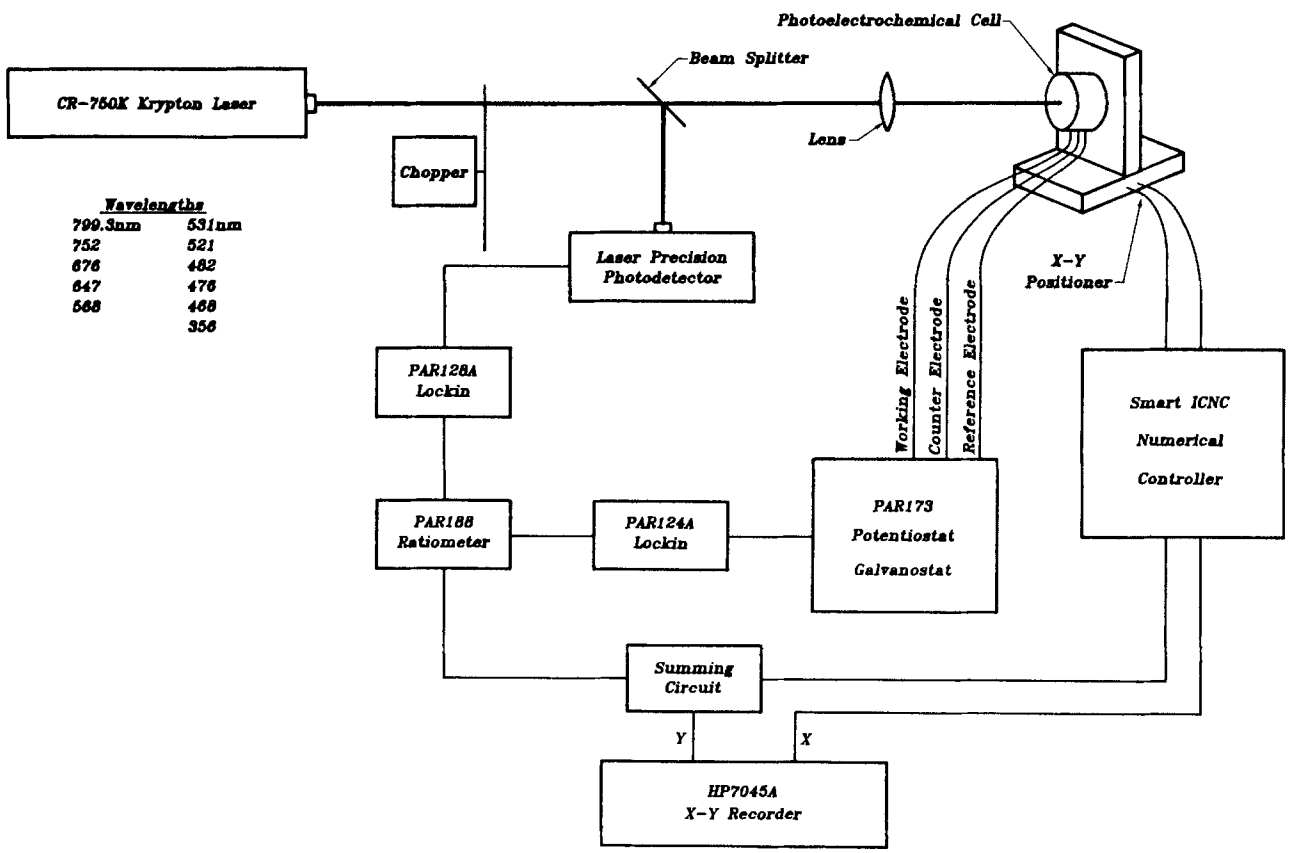

Fig. 1. Schematic of laser scanning system. The beam splitter is used to monitor beam intensity and the ratiometer corrects for fluctuations in beam intensity.

stage which can be stepped in half-micron steps. The cell is operated under potentiostatic control with lock-in detection of the photocurrents. The photocurrent is divided by the reference laser intensity to remove possible effects due to fluctuations in laser intensity. The resulting signal is added to the y axis position signal to produce a photoelectrochemical map of the surface as shown in Fig. 2.

The sample used was CP Ti which had the surface mechanically polished and then lightly etched in HF to bring out the grain structure. The sample was then polarized at +2V (SCE) in 0.2N Na_2SO_4 to grow the surface oxide. Sufficient time was allowed for the current due to the growing oxide to decay away. The average thickness of the oxide layer was estimated from capacitance measurements using optical measurements as a calibration (3). The oxide thickness for the data taken in Fig. 2 is about 100Å. The accuracy of this number is probably about a factor of 2. This is caused by two factors. The film is inhomogeneous, and this is thus an average number. The capacitance has a complex dependence on potential and it is difficult to decide which value of capacitance to use. This dependence of capacitance on potential also suggests a complex electronic structure for the oxide. It is not simply a pure insulator or uniform semiconductor.

The photoelectrochemical map shown in Fig. 2 may be compared to the photograph of the surface in Fig. 3. The photograph clearly shows the polycrystalline nature of the titanium and the inhomogeneous nature of the overlying oxide film. It is interesting to note that variations in the oxide film correspond to the underlying grain structure. This may be due to variation in oxide layer growth rate and therefore thickness depending upon the exposed crystallographic face of the underlying metal or to variations in the electronic properties such as doping concentration or trap concentration.

Referring to Fig. 2 we clearly see a disk-shaped region of no photocurrent corresponding to the dot of black epoxy. In addition there is considerable other structure corresponding to variations in the oxide layer properties with underlying grain structure. This can be clearly seen by comparing the numbered regions in Fig. 2 and 3. Thus both the photoelectrochemical measurements and the photograph show the inhomogeneous nature of the passivating oxide layer on titanium.

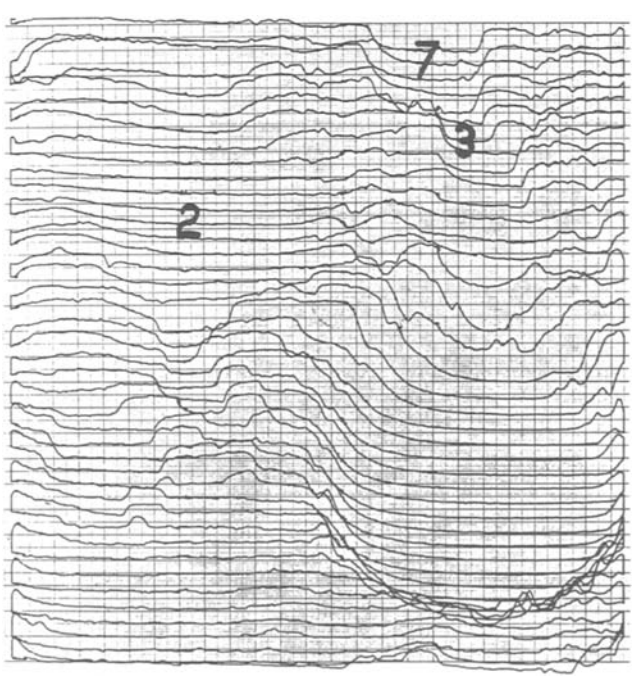

Fig. 2. Photoelectrochemical map of polycrystalline Ti surface at 2.0V (SCE) in 0.2N Na_2SO_4 and laser photon energy of 3.5 eV. The scan is 2 mm wide with each line stepped 50 microns in the y direction. The numbers correspond to grains identified in Fig. 3.

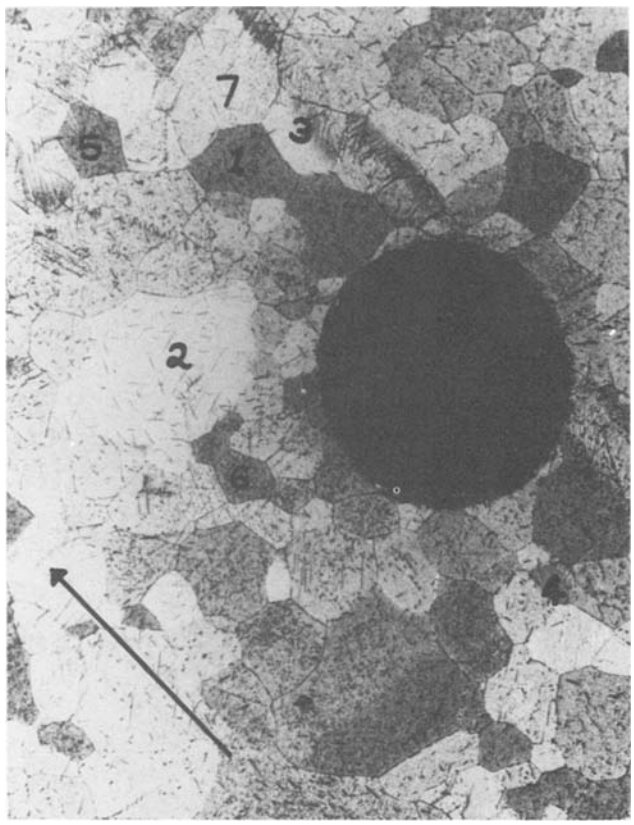

Fig. 3. Photograph of the surface of the polycrystalline Ti sample. The black spot is a dot of epoxy approximately 1 mm in diameter to provide a reference marker and scale factor. The arrow defines the up direction in the photoelectrochemical maps and the numbers identify the grains which correspond to structure observed in the photoelectrochemical maps.

Figure 4 shows schematically the structure of the metal-oxide-electrolyte interface. The oxide is shown as insulating with a uniform electric field throughout. We know already from capacitance measurements that this is not the case. The field is expected to vary throughout the oxide layer due to trapped charge. The layer is optically thin, so it is a good approximation to assume uniform excitation of electron-hole pairs by photons with energy larger than the bandgap. Photoelectrochemical measurements of the spectral response of such films suggest a bandgap of about 3.0 eV in keeping with the crystalline rutile form of TiO_2. The bandgap of anatase has been reported as

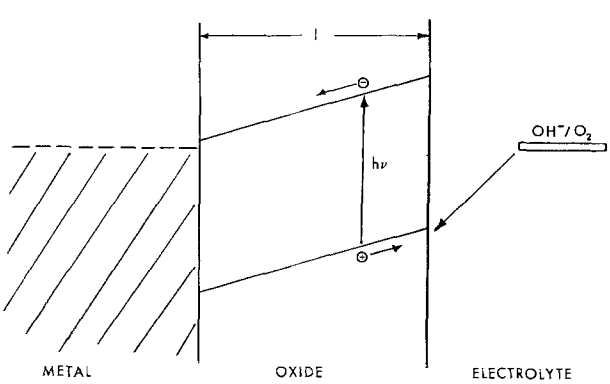

Fig. 4. Schematic representation of the metal-oxide-electrolyte interface. The oxide thickness l is much smaller than the optical absorption depth, α^{-1}.

~3.2 eV (4) and even larger values for the bandgap are found in amorphous films (5). So excitation of electron-hole pairs by photons with energy larger than the bandgap gives photocurrents with some oxidative reaction occurring at the oxide-electrolyte interface, probably oxygen evolution. Variations in photocurrent correspond to variations in the oxide properties including thickness and carrier recombination rate due to traps.

Similar photoelectrochemical maps can be made with photons of energy below the bandgap. Previous experiments in bulk TiO_2 have shown sub-bandgap photocurrents related to deep traps in the bandgap (6). Such a photocurrent map is shown in Fig. 5. Because of the much weaker signal, the data are considerably noisier. However, one can clearly see the circular depression of no photocurrent corresponding to the black epoxy dot on the surface. As in the above bandgap case there are other variations in photocurrent corresponding to the underlying grain structure. This can be clearly seen by comparing the numbered regions in Fig. 5 with the corresponding numbered regions in Fig. 3. However, we can tell that the regions of increased sub-bandgap photocurrent occur in regions where the above bandgap photoelectrochemical map shows no structure. Therefore, we are safe in interpreting these grains as regions of increased trap density rather than regions where the oxide is thicker. One might expect that increases in trap density would result in more carrier recombination and a decrease in above bandgap photocurrent. Apparently the traps observed in the below bandgap photoelectrochemical map do not contribute significantly to the recombination rate.

Discussion

These results are very qualitative in nature, and we would like to use this technique to obtain quantitative information about different regions of the passivating film. In order to do this we need a quantitative theory of transport of photoexcited carriers in the thin oxide layer. Such a theory for a semiconductor with noninjecting contacts has been developed by Goodman and Rose to explain the behavior of the photoconductor in television vidicons (7). The model quantitatively predicts the behavior of photocurrent *vs.* voltage across the photoconductor for uniform excitation of electron-hole pairs and noninjecting contacts. These conditions are met in our case by the passivating layer being optically thin and for positive potentials applied to the titanium (*i.e.*, the situation shown in Fig. 4). The general features of the model are: photocurrent proportional to voltage for low voltages, photocurrent proportional to the square root of the voltage at higher voltages and eventual saturation of the photocurrent. The linear and square root regions are clearly visible in our data shown in Fig. 6. These four sets of data are taken from the four locations identified in Fig. 3. This is another example of the advantages of the laser scanning system and its ability to make localized measurements. While the total incident power is relatively small the power density is quite large since the light is focused to a spot about 15 microns diameter. Since the film was grown at an applied potential of 2V, the measurements are not taken at significantly more positive potentials to preclude additional film growth. This is the reason we are unable to observe saturation of the photocurrent.

The flatband potential (8) is that applied potential at which no potential drop exists across the passivating layer. This may be easily obtained by extrapolating the linear portion of the photocurrent *vs.* applied potential curve. The values obtained for these four regions are shown in Table I. Measurements for regions 1 and 2 were taken at one time while the measurements for regions 3 and 4 were taken at a separate

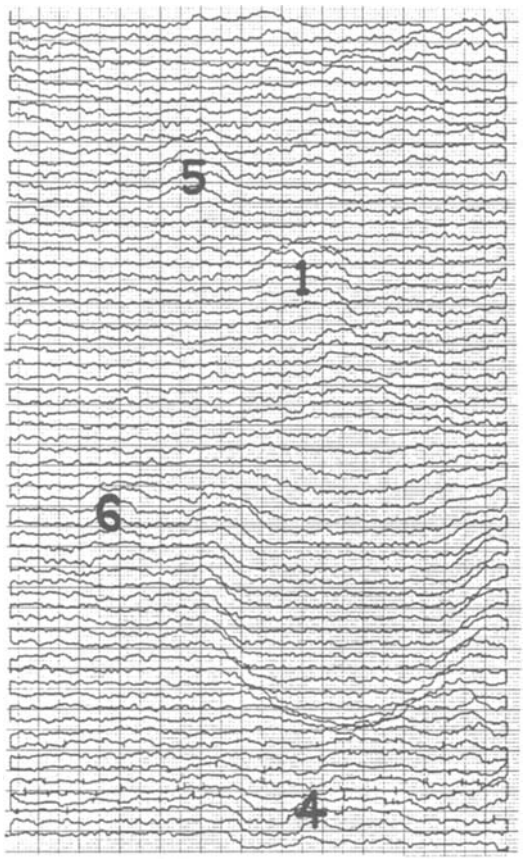

Fig. 5. Photoelectrochemical map of polycrystalline Ti surface at 2.0V (SCE) in 0.2*N* Na_2SO_4 and laser photon energy of 2.6 eV. The scan is 2 mm wide and each line stepped 50 microns in the y direction. A TiO_2 window is used to remove spurious u.v. light effects. The numbers correspond to grains identified in Fig. 3.

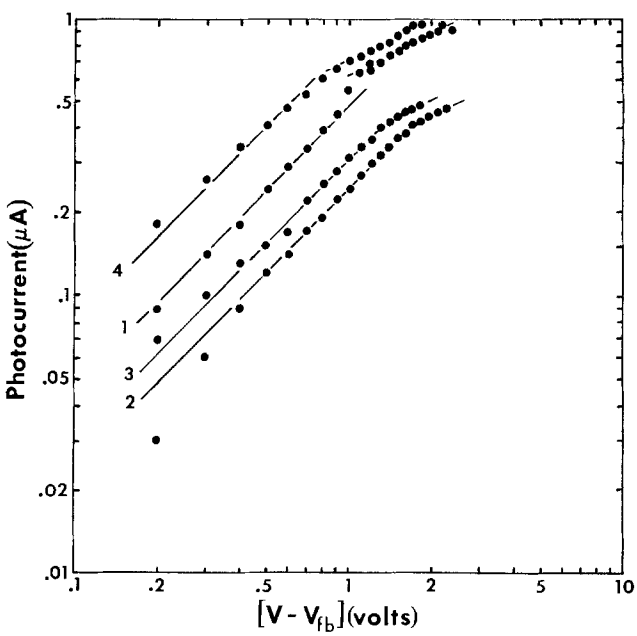

Fig. 6. Log photocurrent *vs.* log applied potential across the passivating layer for TiO_2 film approximately 100Å thick. Incident light is ~250 μW at 3.5 eV. The four sets of data are measured at the four locations identified in Fig. 3. The straight lines at low potentials have a slope of 1 and at higher potentials a slope of 1/2.

time. Thus it appears that the differences in flatband potential are due to different treatments of the sample on these two occasions rather than variations from one region of the film to another. The cause of these un-

usually large flatband shifts is not known. Illumination for a long enough time to reach steady-state conditions should insure identical charging of the passive film from measurement to measurement. Thus this should not be a cause for the shifts. We have observed optically induced changes in the film properties at high light intensities which might account for the shifts. Another possibility is changes in surface charge due to compositional variation in the electrolyte.

These localized flatband measurements should be compared to the bulk, reduced TiO_2 value at the measured *p*H for the 0.2*N* Na_2SO_4 electrolyte of 6.7, which is −0.5V (SCE) (9). Some of this difference undoubtedly comes from the lack of free carriers in the passivating layer and the high density of traps, which would move the Fermi level further below the conduction band in the TiO_2. It should be pointed out that regions 1 and 4 correspond to regions with large sub-bandgap photoresponses shown in the photoelectrochemical map in Fig. 5, and regions 2 and 3 correspond to regions of low above bandgap photocurrents shown in Fig. 2.

In order to explore the capabilities of the Goodman-Rose model more quantitatively, we have determined from the data the slope of the linear part of the I_{ph}-v curve, S_L, the slope of the quadratic part of the I_{qh}-V curve, S_Q, and the potential where the break occurs between these two regions, V_b, defined as the potential at which the linear and quadratic terms are equal. These values are shown in Table I. The Goodman-Rose model predicts that the photocurrent has the following forms (7)

$$j = \frac{(1+b)\{-b+[b^2+4(1-b)(1+b^2)v/(1+b)^2]^{1/2}\}}{2(1-b)} \quad [1]$$

where both j and v are normalized to the saturation photocurrent J_o and the potential at which saturation occurs v_o, respectively, and b is a parameter depending on the electron and hole transport properties. Thus

$$j = J/J_o \quad [2]$$

$$v = V/V_o \quad [3]$$

$$J_o = e(2\alpha l) \quad [4]$$

and

$$V_o = (1+b^2)l^2/\mu_n\tau_n(1+b)^2 \quad [5]$$

The saturation photocurrent J_o is just the electron charge e times the total number of excited electron-hole pairs. This is approximately twice the optical absorption coefficient, α, because of reflection at the metal-oxide interface, times the thickness l. The parameter b is defined as

$$b \equiv \frac{\mu_n\tau_n}{\mu_p\tau_p} \quad [6]$$

the ratio of the mobility-lifetime products for electrons and holes. From Eq. [1] we can determine expressions for the linear and quadratic slopes and the break point. These are

$$S_L = \frac{J_o}{V_o}\left[\frac{1+b^2}{b(1+b)}\right] \quad [7]$$

$$S_Q = \frac{J_o}{V_o^{1/2}}\left[\frac{1+b^2}{1-b}\right]^{1/2} \quad [8]$$

and

$$V_b = V_o\frac{b^2(1+b)^2}{2(1-b)(1+b^2)} \quad [9]$$

Notice that in the linear region the photocurrent $J = S_L V$ has an l^{-1} dependence on thickness of the oxide layer because of the combined effects of J_o and V_o. In the quadratic region the slope is independent of l but the photocurrent increases linearly with l because of a potential independent term

$$J = \frac{-b(1+b)}{2(1-b)}J_o + S_Q V^{1/2} \quad [10]$$

Furthermore, V_b has an l^2 dependence through V_o. All of this suggests that it would be interesting to explore the thickness dependence of the photocurrent in various potential regimes .Finally Eq. [7], [8], and [9] can be combined to provide a relationship between S_L, S_Q, and V_b

$$\frac{S_Q}{S_L\sqrt{V_b}} = \sqrt{2} \quad [11]$$

The experimental values for this quantity for the four regions measured are shown in Table I. The agreement is reasonable within the uncertainty inherent in the determinations of S_L, S_Q, and V_b.

Using the above expressions we can now try to determine a value for the electron and hole $\mu\tau$ products which give a reasonable fit to the data with the Goodman-Rose model. Taking our film thickness as 100Å, 250 μW of 3.5 eV photons incident on the sample and the optical absorption coefficient at this energy (10) of 10^4 cm^{-1} we calculate using Eq. [4] a saturation current $J_o = 1.4$ μA. Extrapolation of curves 2 or 3 in Fig. 6 to this current gives a $V_o \sim 15$V. Taking the breakpoint as 1.5V gives a value for b from Eq. [9] of about 0.3. Using these values of b, J_o, and V_o, we then calculate using Eq. [7] and [8] linear and quadratic slopes of 0.33 μA/V and 0.45 μA/V$^{1/2}$ in reasonable agreement with the experimental values for regions 2 and 3 given in Table I. These estimates are rather crude, but there really is no point in trying to make more accurate comparisons between theory and experiment because of the uncertainties in the passivating layer thickness and carrier generation rate.

Now using Eq. [5] we can obtain the $\mu\tau$ products shown in Table II. In bulk TiO_2 the Hall mobility at room temperature has been measured as ~0.25 cm^2/V-sec (11). Thus the electron lifetime is approximately 2×10^{-13} sec. This indicates a very large density of electron traps in the oxide layer. Unfortunately there are no measurements of the hole mobility in TiO_2 so we cannot estimate accurately the hole lifetimes.

A similar analysis can be made for regions 1 and 4 assuming that the film thickness is the same. The extrapolation of the data in Fig. 6 to the saturation current gives $V_o \sim 5$V. Taking the break point as 1.0V gives a value for b from Eq. [9] of ~0.4. Using these values of b, J_o, and V_o we can calculate using Eq. [7] and [8] linear and quadratic slopes of 0.58 μA/V and 0.87 μA/V$^{1/2}$ in reasonable agreement with the measured values shown in Table I for regions 1 and 4. As before we now use Eq. [5] to obtain the $\mu\tau$ products shown in Table II. Here we find about a factor

Table I. Characteristics of photocurrent-voltage curves

Region	V_{FB} (SCE)	Linear slope (μA/V)	Quadratic slope (μA/$\sqrt{V}$)	Breakpoint (V−V_{BF})	$S_Q/S_L\sqrt{V_b}$
1	−0.2	0.55	0.70	1.1	1.2
2	−0.2	0.27	0.38	1.6	1.1
3	+0.2	0.31	0.44	1.3	1.2
4	+0.2	0.7	0.82	0.8	1.3

Table II. Electron-hole transport properties

Region	$\mu_n\tau_n$ (cm^2/V)	$\mu_p\tau_p$ (cm^2/V)	τ_n (sec)
2 + 3	4×10^{-14}	1.4×10^{-13}	1.7×10^{-13}
1 + 4	1.1×10^{-13}	3×10^{-13}	4×10^{-13}

of two or three increase in both electron and hole lifetimes which implies a corresponding decrease in trap densities. It is this increase which accounts for the change in V_0 and thus the linear and quadratic slopes. This shows that the increased state density observed at 2.6 eV in regions 1 and 4 does not correspond to the states responsible for trapping in this oxide layer.

Another feature of the Goodman-Rose model is a linear dependence of photocurrent on light intensity as long as space charge limiting effects are not important. Indeed, we only observe a linear dependence of photocurrent on light intensity. Thus it seems that the Goodman-Rose theory quantitatively describes the transport of photoexcited carriers in passivating oxide layers on titanium metal. However, Hughes and Sokel (12) have pointed out the limitations of the G-R model. These are the lack of diffusion effects and not explicitly including recombination with trapped charge. Furthermore, Hughes and Sokel have numerically solved the transport problem including these two effects and applied their computer code to PbO (12). They find $\mu\tau$ products an order of magnitude larger than obtained from the G-R model for PbO. Another limitation of the G-R model is that it describes steady-state behavior when considerable time dependence exists in the approach to these steady-state values. Quantitative modeling of this time behavior provides a further check on our understanding of the processes going on. Application of the Hughes-Sokel computer code to the transient and steady-state behavior of the photocurrent in oxide layers on titanium will be published elsewhere (13).

Conclusions

In this paper we demonstrated that localized photoelectrochemical measurements can be made on 100Å thick passivating layers on titanium. Since passivating films on other metals have a semiconducting character, it is believed that these techniques should be extendable to all passivating films. The only limitation would be if the bandgap of the passivating layer becomes too large for the laser photons. These kinds of measurements probe the electronic transport properties of the passivating layer. Significant variations in these properties are observed across the film and these variations correspond to the underlying grain structure in the metal substrate. This variation demonstrates the need for local probes to study passivating layers since corrosion initiation is a local phenomena dependent on the local properties. The dependence of steady-state photocurrent on voltage across the passivating film is semiquantitatively described by a model (7) proposed by Goodman and Rose involving trap dominated electronic transport.

These results are a first step in exploring microscopically the behavior of passivating films on corrosion resistant metals. This localized photoelectrochemical technique will enable correlations between local electronic properties of the passivating layer and pit initiation to be explored. The role of alloying in corrosion resistance and its effect on the electronic transport properties of the passivating layer may be explored. The localized probe may also be used to explore the role of the underlying metal crystallographic face in determining the electronic properties of the passivating layer.

Acknowledgments

The author is deeply indebted to W. H. Smyrl for providing the samples and numerous invaluable discussions concerning pitting corrosion and to R. C. Hughes for an understanding of trap-dominated electronic transport. This work was performed at Sandia National Laboratories supported by the U.S. Department of Energy under Contract Number DE-AC04-76DP00789.

Manuscript submitted April 7, 1983; revised manuscript received July 1, 1983. This was Paper 7 presented at the Montreal, Quebec, Canada, Meeting of the Society, May 9-14, 1982.

Sandia National Laboratories assisted in meeting the publication costs of this article.

REFERENCES

1. E. J. Kelly, in "Modern Aspects of Electrochemistry," No. 14, J. O'M. Bockris, B. E. Conway, and R. E. White, Editors, Chap. 5, Plenum, New York (1982).
2. A. J. Nozik, *Ann. Rev. Phys. Chem.*, **29**, 189 (1978).
3. D. Laser, M. Yaniv, and S. Gottesfeld, *This Journal*, **125**, 358 (1978).
4. V. B. Gusev, L. M. Lenev, and I. I. Kalinichenko, *Zh. Prikl. Spektrosk.*, **35**, 939 (1981).
5. W. D. Brown, Ph.D. Thesis, University of New Mexico, Albuquerque, NM (1975).
6. M. A. Butler, M. Abramovich, F. Decker, and J. F. Juliao, *This Journal*, **128**, 200 (1981).
7. A. M. Goodman and A. Rose, *J. Appl. Phys.*, **42**, 2823 (1971).
8. M. A. Butler and D. S. Ginley, *J. Mater. Sci.*, **15**, 1 (1980).
9. A. J. Nozik, *Ann. Rev. Phys. Chem.*, **29**, 189 (1978).
10. F. Mollers, H. J. Tolle, and R. Memming, *This Journal*, **121**, 1160 (1974).
11. C. H. Seager, *Solid State Commun.*, **20**, 539 (1976).
12. R. C. Hughes and R. J. Sokel, *J. Appl. Phys.*, **52**, 6743 (1981).
13. M. A. Butler and R. C. Hughes, Unpublished.

Effect of Concentration on Ion Transport in Donnan Dialysis

Patrick K. Ng* and Dexter D. Snyder*

General Motors Research Laboratories, Electrochemistry Department, Warren, Michigan 48090/9055

ABSTRACT

The transfer rate of ions across a cation selective membrane depends on membrane properties, solution concentration, and hydrodynamic environments outside the membrane. This work examined the effects of concentration and solution flow rate on the ion transport across a perfluorosulfonic acid tubular membrane. Experiments were conducted using copper sulfate as the feed solution and sulfuric acid as the stripping agent. Conditions under which either membrane or boundary layer resistance dominates were identified. Mass transfer correlations and membrane interdiffusion coefficient were obtained to characterize these two resistances.

Donnan dialysis which employs the properties of ion-selective membranes is considered to be promising as a separation and purification process with relatively low energy cost. The recently available tubular ion selective membranes make it possible to design shell-and-tube type dialyzers that can provide a large surface area for ion transport. Eisenmann (1) used such a design to recover nickel from a dilute rinsing water, and Law (2) illustrated the feasibility of prolonging the life of a gold plating solution by using tubular membranes.

Figure 1 shows the barriers metal ions may encounter while being transported from the waste to stripping stream. They are the waste stream boundary-layer resistance, the membrane resistance, and the stripping stream boundary-layer resistance. The last resistance usually can be minimized by using a high concentration in the stripping stream, *e.g.*, 0.5M H_2SO_4. The relative importance of the other two resistances depends on membrane properties, the waste stream concentration, and hydrodynamic environment.

We investigated (3) the hydrodynamic effect on transport flux in a dilute nickel sulfate (100 ppm in nickel) system, using perfluorosulfonic acid membranes in a shell-and-tube type dialyzer. At such a low ion concentration, the boundary-layer film was found to be dominant and the transport flux depended strongly on flow rate. In the present work, we studied the concentration effect on transport flux at different flow rate, and we also shift to a copper solution to expand the applicability of the process.

Experimental

The shell-and-tube type dialyzer was similar to the one used in previous work (3). It consisted of a perfluorosulfonic acid membrane (designation 810) with OD of 0.312 cm and ID of 0.238 cm. The outer shell was fabricated from acrylic tubing with ID of 0.635 cm and length of 17.15 cm.

Copper sulfate solution (100-5000 ppm in Cu) was circulated through the membrane tube side while 0.5M H_2SO_4 stripping solution was pumped through the shell side. Each stream contained initially 500 ml solution, and its flow rate was controlled by a tubing pump and monitored with a flowmeter. The flow rate in the tube side spanned the range of 28-3000 ml/min. Samples were taken from each reservoir at time intervals and were analyzed for pH and copper.

Results and Discussion

Rate constant measurements.—During each experiment, the copper concentration in the tube-side (waste stream) reservoir was found to decrease exponentially with time, consistent with the results in our previous work (1). Figure 2 illustrates this with an initial copper concentration of about 1000 ppm. The reservoir can thus be regarded as a reactor with a first-order rate constant, m (min^{-1}), given by the equation

$$C_i = C_i^o \exp(mt) \qquad [1]$$

where C_i is the reservoir copper concentration (mol/

* Electrochemical Society Active Member.
Key words: membrane, mass transport, ion exchange, dialysis.

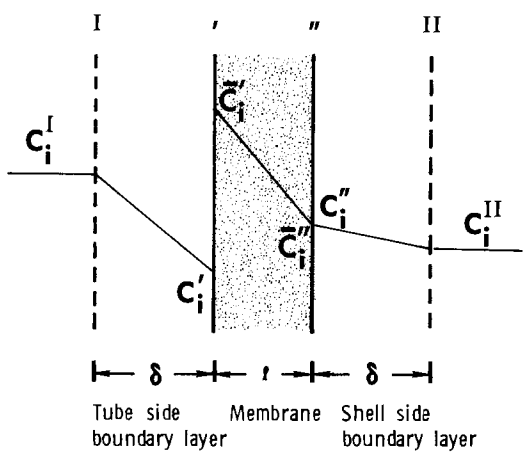

Fig. 1. Ion transport across a membrane

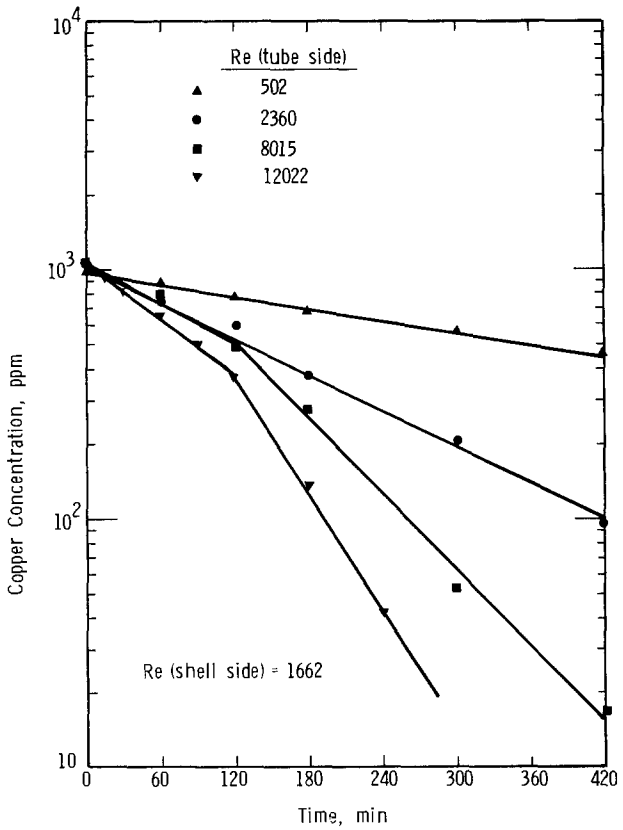

Fig. 2. Transient variation of copper concentration in the reservoir

ml) at time t (min), and C^o_i is the initial concentration. The copper flux (mol/cm^2 · min) can be calculated by

$$J_{Cu} = -\frac{mV_R}{A}C_i \qquad [2]$$

where V_R is the reservoir volume in milliliter and A is the membrane surface area in cm^2. In some of the experiments, the value of m tends to change when the reservoir copper concentration (C_i) has decreased to about 300-500 ppm. This suggests a change in transport mechanism which depends on concentration.

The effect of stripping stream (shell-side) flow rate on rate constants was also studied and the results are shown in Fig. 3. Our previous work (3) also indicated that the concentration of stripping solution (H_2SO_4) has less effect on the transport flux.

Boundary-layer and membrane resistances.—As the copper ions start moving through the membranes, they have first to overcome the boundary-layer resistance on the tube side. A concentration gradient usually exists in this film, whose thickness depends on the hydrodynamic conditions. A higher flow rate means a thinner film and a higher copper flux toward the membrane. As a result, if the boundary-layer film is the major barrier to transport, the copper flux should be proportional to flow rate. On the other hand, when the membrane is responsible for the copper transfer, the copper flux becomes independent of flow rate and tube-side concentration.

Figures 4 and 5 illustrate the change of flux *vs.* flow rate and initial copper concentration, respectively. For the 810 membrane, there exists a maximum copper flux of about 4.5 × 10^{-6} mol/cm^2 · min.

At low copper concentration, such as 100 ppm, Fig. 4 clearly indicates that the boundary layer is the main limiting factor. The transport flux of copper depends strongly on flow rate. A very high Reynolds number (about 10^5 in Fig. 4) is needed to create enough turbulence to eliminate the boundary-layer effect.

With increasing copper concentration, the span of flow rate in which the boundary layer is limiting becomes smaller. For example, at 2000 ppm, the boundary layer is controlling only at a Reynolds number less than 10^3. The membrane resistance becomes progressively more important at higher flow rate. Eventually, a Reynolds number is reached at which the membrane resistance completely controls the ion transport through the membrane, and a maximum flux is observed. It is apparent from Fig. 4 and 5 that both flow rate and waste stream concentration have to be specified to locate the transition region.

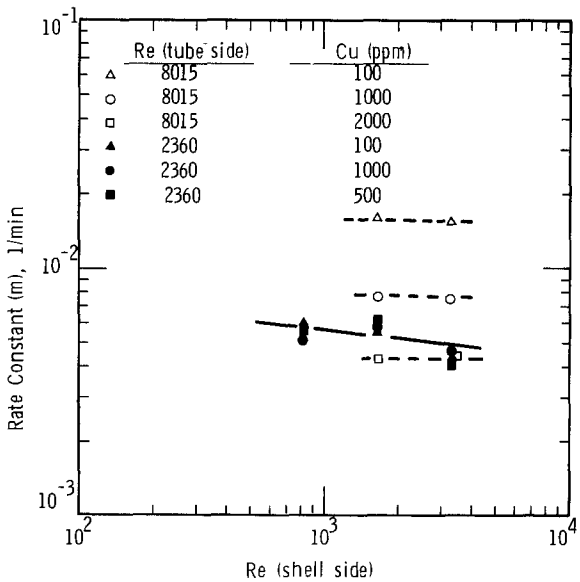

Fig. 3. Effect of shell-side flow rate on rate constant

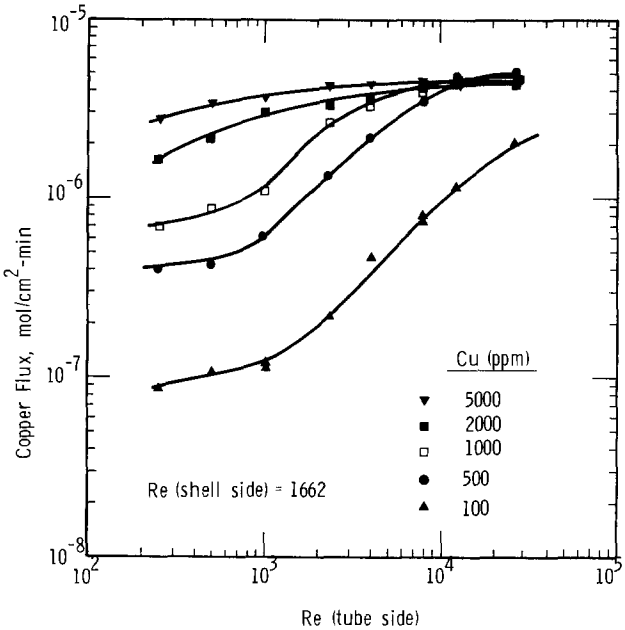

Fig. 4. Effect of flow rate on flux

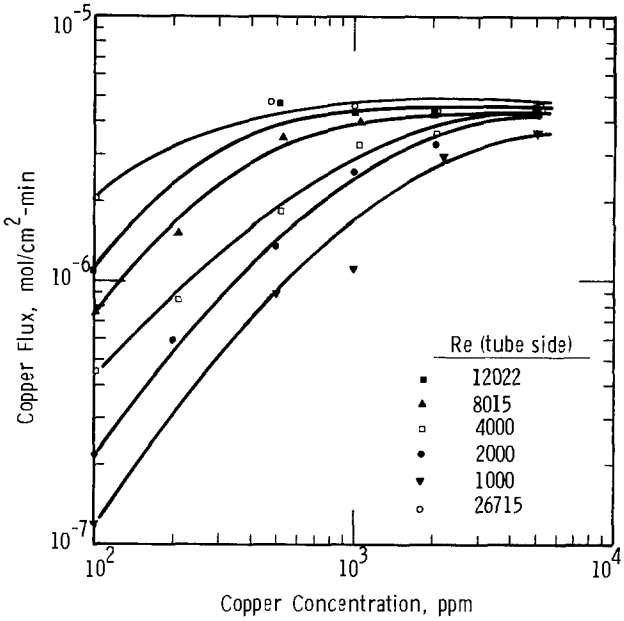

Fig. 5. Effect of concentration on flux

The boundary-layer film can be characterized by a mass transfer coefficient (K_{BL}) calculated by a previously developed model (3). The model assumed that the tube-side solution is well mixed and its concentration is uniform and equal to the outlet concentration. K_{BL} can be defined by the mass balance equation for copper in the tube side of the dialyzer as

$$Q(C_i - C_o) = K_{BL}AC_o \qquad [3]$$

in which C_o is the outlet concentration from the dialyzer and Q is the volumetric flow rate (ml/min). This assumption is reasonable at low copper concentration where boundary layer controls the copper transfer. At 100 ppm, the calculation (3) showed that the membrane surface concentration is less than 5% of the bulk concentration. By combining Eq. [1], [3], and a mass balance equation for the reservoir, K_{BL} can be written in terms of measurable parameters as

$$K_{BL} = \frac{-mV_R}{A\left(1 + \frac{mV_R}{Q}\right)} \quad [4]$$

The calculated K_{BL} can usually be written in dimensionless form as the Sherwood number ($Sh = K_{BL}d/D$). Figure 6 shows the variation of $Sh \cdot Sc^{-1/3}$ with Reynolds number ($Re = vd/\nu$), and the results can be represented by the following correlations

$$Sh \cdot Sc^{-1/3} = 0.0157\,Re^{0.796} \quad 1000 < Re < 26{,}700 \quad [5]$$

$$Sh \cdot Sc^{-1/3} = 0.48\,Re^{0.28} \quad Re < 1000 \quad [6]$$

The kinematic viscosity of water and the $CuSO_4$ diffusion coefficient at infinite dilution (8.7×10^{-6} cm^2/sec) were used in calculating the Schmidt number (Sc). Equation [6] fits the data at copper concentration up to 2000 ppm, whereas Eq. [5] applies only to 100 and 500 ppm. At high Reynolds number and high copper concentration, membrane resistance is dominant and mass transfer correlations become meaningless.

Considering the swelling nature of membranes, the exponents of Re in Eq. [5] and [6] agree reasonably well with those frequently cited in literature for turbulent flow (0.8) and for laminar flow (1/3 by Leveque calculation). These improved correlations over those in the nickel sulfate system (3) can serve as the first approximation in designing practical dialyzers.

When the membrane controls the ion transport (high concentration and high flow rate), it is desirable to measure the membrane mass transfer coefficient (K_m) from which the interdiffusion coefficient (D) can be calculated. K_m is obtained by the following equation (see Fig. 1)

$$J_{Cu} = K_m(\bar{C}'_{Cu} - \bar{C}''_{Cu}) \quad [7]$$

where the membrane concentrations, $\bar{C}'_{Cu}$ and $\bar{C}''_{Cu}$, are calculated by assuming a uniform concentration profile in the two flowing streams. By extrapolating the value $1/K_m$ to infinite flow rate ($1/Re = 0$), one obtains a K_m from which $\bar{D}_{Cu\text{-}H}$ can be calculated by

$$\bar{D}_{Cu\text{-}H} = (K_m)_{Re \to \infty} \cdot l \quad [8]$$

where l is the membrane thickness (0.0368 cm). Figure 7 shows the extrapolations for concentrations 1000, 2000, and 5000 ppm, and the r^2 values for the corresponding linear fits. The intercepts ($1/K_m$) for the three lines ranged from 6190 to 6812 sec/cm, and yielded an average K_m of 1.56×10^{-4} cm/sec. The interdiffusion coefficient was calculated by Eq. [8] to be 5.73×10^{-6} cm^2/sec.

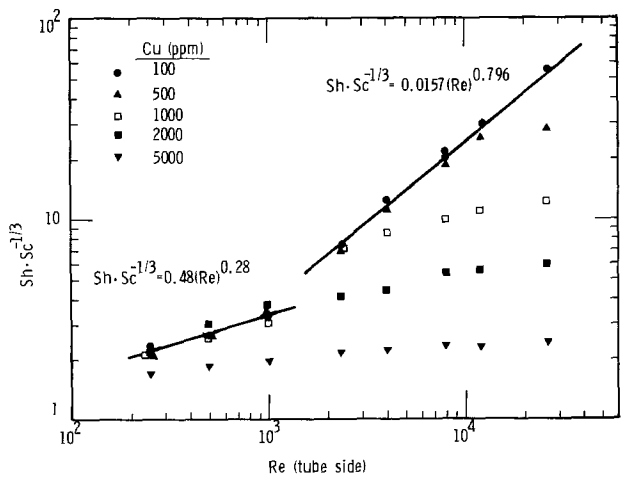

Fig. 6. Mass transfer correlations

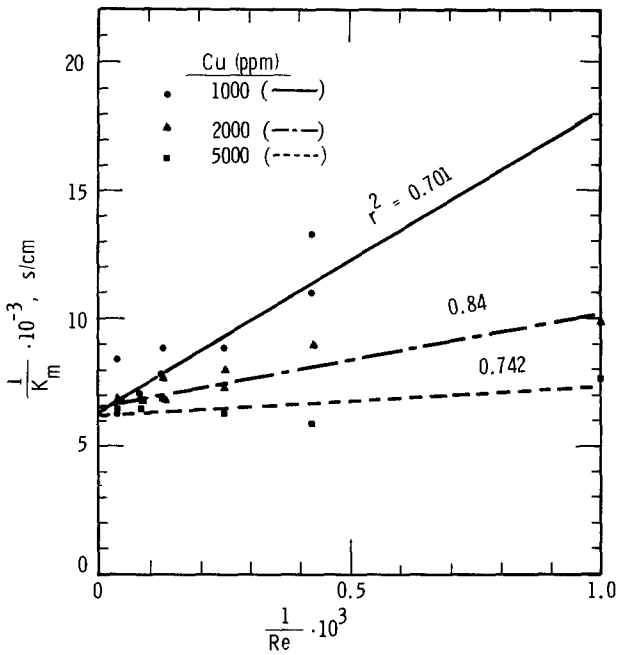

Fig. 7. Extrapolation of membrane resistance

Many factors influence the interdiffusion coefficient, such as membrane properties (*e.g.*, ion exchange capacity and water content) and the charge of diffusing ions. Values reported in literature (4-9) range in magnitude from 10^{-6} to 10^{-8} cm^2/sec, depending on membrane and electrolyte system. As pointed out by Lake and Melsheimer (4), the extrapolation technique yields more accurate results at high concentrations. This may explain the insensitivity of $\bar{D}_{Cu\text{-}H}$ to concentration in this work as compared to our previous work (3) that showed the dependence of $\bar{D}_{Ni\text{-}H}$ on concentration. Graydon and co-workers (5-7) indicated that the interdiffusion coefficient is independent of solution concentration since the concentration gradient in the membrane is relatively insensitive to external solution concentration when the membrane controls the ion diffusion process.

Acknowledgment

The authors thank Robert Paluch of the Electrochemistry Department for conducting the experiments and for analyzing the samples.

Manuscript submitted Oct. 19, 1982; revised manuscript received *ca.* May 6, 1983.

General Motors Research Laboratories assisted in meeting the publication costs of this article.

REFERENCES

1. J. L. Eisenmann, 2nd Conf. Adv. Pollution Control Metal Finish. Ind., Florida, p. 99, 1979.
2. H. H. Law, *Plating Surf. Finish.*, **69**, 72 (1982).
3. P. K. Ng and D. D. Snyder, *This Journal*, **128**, 1714 (1981).
4. M. A. Lake and S. S. Melsheimer, *J. AIChE*, **24**, 130 (1978).
5. R. J. Stewart and W. F. Graydon, *J. Phys. Chem.*, **60**, 750 (1956).
6. A. S. Tombalakian, C. Y. Yeh, and W. F. Graydon, *Can. J. Chem. Eng.*, **42**, 61 (1964).
7. A. S. Tombalakian, C. Y. Yeh, and W. F. Graydon, *J. Phys. Chem.*, **71**, 435 (1967).
8. M. A. Peterson and H. P. Gregor, *This Journal*, **106**, 1051 (1959)
9. T. C. Huang and P. H. Lian, *Ind. Eng. Chem. Fundam.*, **18**, 221 (1979).

Composition Gradients in Electrolyzed LiCl-KCl Eutectic Melts

C. E. Vallet,* D. E. Heatherly, and J. Braunstein*

Chemistry Division, Oak Ridge National Laboratory, Oak Ridge, Tennessee 37830

ABSTRACT

Analysis of transport in a mixed electrolyte has previously predicted significant composition gradients in the LiCl-KCl electrolyte of high temperature Li/S batteries. Composition gradients in quenched electrolyzed LiCl-KCl eutectic contained in yttria felt are measured with high distance resolution by scanning electron microscopy with energy dispersive x-ray spectroscopy. The reported results include composition profiles of LiCl-KCl contained in porous Y_2O_3 and electrolyzed in three cells, two with solid Li-Al electrodes and one with a porous Li-Al anode.

Despite the importance of the distribution of reactants and products in an operating battery, and although current-induced composition gradients have been demonstrated in mixed molten salt electrolytes, there has been a dearth of related measurements for batteries with molten salt electrolytes (1-4). Gradients have been measured in $AgNO_3$-$NaNO_3$ melts electrolyzed between silver electrodes (1), and predicted in mixed molten salt battery electrolytes (2-4). Computations predicted LiCl precipitation at the negative electrode and KCl precipitation or enhanced J-phase formation at the positive electrode (3). Examples of observed deleterious effects include: (*i*) Reduced energy utilization in the negative electrode of experimental cells, attributed to freezing of the electrolyte (6). (*ii*) Freezing of electrolyte in the Li-Si negative electrode of a thermal battery with LiCl-KCl, cited as an end-of-life mechanism of the cell (7). (*iii*) Precipitation of KCl in the pores of the FeS electrode, reported to decrease the discharge rate of LiAl/FeS cells (8). Other evidence for solid precipitation in molten salt cells also has been reported (5, 9-11). These effects would be reduced by the use of an all lithium electrolyte (12), but would not all be eliminated, because electromigrational composition gradients still are expected (2, 13).

In situ measurements of composition are desirable. Although valuable information can be obtained from analysis of discharged cells (5, 14), diffusional and other relaxations occurring after discharge alter the reactant and product distributions established during cell operation. A closer approach to *in situ* measurements is provided by analysis of systems in which the compositions during current flow have been frozen in by quenching the cell (1). For such experiments, a small laboratory cell with identical electrodes is more convenient for the isolation and measurement of current-induced component separation than a complete battery.

This paper presents the first measurements of the shape of the composition profile in LiCl-KCl eutectic melt produced by electrolysis between Li-Al electrodes. The measured profiles in the cell separators are compared to the profiles numerically calculated (3) with the binary diffusion coefficient corrected for the porosity of the yttria matrix (1, 4) and with composition dependent transference number of K relative to Cl (15). Results of measurement of the electrolyte composition changes in the anolyte within porous Li-Al electrodes will be presented in a subsequent paper.

Experimental

The battery electrolyte (LiCl-KCl eutectic) was electrolyzed between two Li-Al electrodes. Li^+ is produced by the faradaic process at the anode and an equivalent quantity is removed at the cathode. The ion flows in such an electrolysis experiment are similar to those in an Li/S battery, except that in the battery Li^+ is precipitated at the FeS_x electrode as a sulfide (1). After electrolysis the assembly was quenched rapidly, and then sampled for chemical analysis of the composition gradient established between the electrodes. Atomic absorption spectroscopy (AA) of Li^+ and K^+ in noncontiguous sections cut parallel to the electrode faces, and scanning electron microscopy with x-ray fluorescence (SEM/EDX) measurement of K/Cl ratios in small areas on a section cut perpendicular to the electrode faces were used to obtain the composition gradient.

Cell.—In the cell, shown in Fig. 1, the LiCl-KCl eutectic melt (polarographic grade, Anderson Physics Laboratories) is contained in porous yttria (Y_2O_3) felts.[1] The spring loaded upper electrode holder provides electrode-electrolyte contact. For studies of the composition gradients in the porous alloy electrodes, the cell also can accommodate, as upper electrode, a

[1] Zircar Company, Florida, New York.

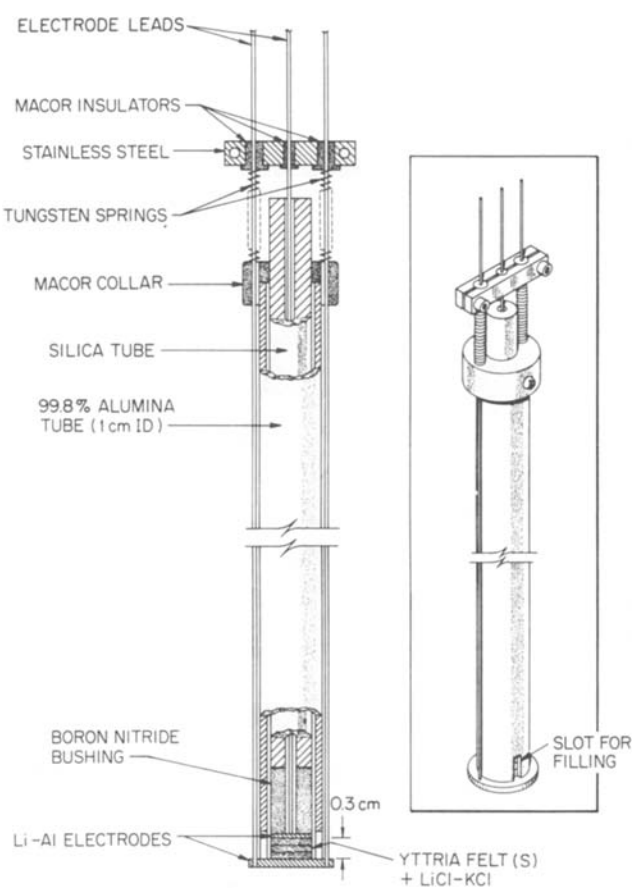

Fig. 1. Cell assembly for electrolysis-quench experiments with Li-Al electrodes and LiCl-KCl electrolyte in Y_2O_3 felt matrix. The assembly is immersed to the level of the upper electrode in LiCl-KCl eutectic in a Al_2O_3 tube.

* Electrochemical Society Active Member.
Key words: battery, electrolyte, fused salts, SEM.

powdered alloy. The powder (βLiAl, 51% Li) is retained by a stainless steel mesh with a stainless steel current collector at the top. The cell is heated in an electric furnace in a controlled atmosphere helium glove box excluding water, oxygen, and nitrogen. Electrolysis, quenching, and cutting of the sample are carried out in the same glove box; samples are transferred to the electron microscope in a desiccator.

The salt content of the yttria felts was ascertained by aqueous extraction of the salt from the felt and weighing, as for the previously reported $AgNO_3$-$NaNO_3$ mixtures (1). The average measured porosity, summarized in Table I, is 0.85 ± 0.04, compared with the value 0.90 ± 0.02 found for similar yttria felts filled with nitrate mixtures (1), which wet the yttria more easily than does LiCl-KCl.

Electrolysis and sampling for analysis.—Three quenched electrolyzed samples of LiCl-KCl eutectic were prepared using either two solid two-phase (α + β) Li-Al electrodes or a solid (α + β) cathode and powdered βLi-Al porous anode. The solid two-phase Li-Al electrodes were prepared by catholysis of an aluminum electrode in LiCl-KCl melt at low current density (1 mA cm^{-2}), and had overall compositions ranging from 15 to 40 a/o Li. Before assembly, the potential of these 2-phase electrodes *vs.* a cast solid (α + β) reference electrode was less than 1 mV. Conditions of electrolysis for the three cells for which we report composition profiles are summarized in Table II. At the end of electrolysis, the assembly was quenched by immersion in cold silicone oil in less than 1 sec after cessation of current. The sampling for profile analysis by SEM/EDX and by AA has been described previously (1).

SEM/EDX analysis.—Scanning electron microscopy with x-ray fluorescence spectroscopy of quenched samples gives the distance resolution necessary in the analysis of the composition gradients extending over distances of the order of 2-3 mm. The 21 kV electron beam causes ionization and fluorescence to depths of the order of 1 μm, thus providing local bulk analysis. The position relative to the electrodes of a scanned area was measured from the electron micrograph within 3 μm, and the composition is related to the ratio of the x-ray lines of potassium to chlorine. The two lines at 2.62 keV for chlorine and at 3.31 keV for potassium are well separated. Lithium cannot be observed with the Si(Li) detector (ORTEC) with a beryllium window.

Calibration.—Although SEM/EDX is a very sensitive method for detecting small quantities of elements, quantitative analysis in a three-phase composite matrix of mixed particles remains difficult (16). Calibration standards of weighed-in composition were prepared and handled by identical procedures, except for current flow, to those for the electrolyzed samples in order to provide a particle size distribution in these standards very close to that in the cells. The standards were examined by SEM/EDX with scanned areas of varying size in order to ascertain the matching of the spatial resolution with the homogeneity of the samples. The K/Cl ratios did not vary significantly when areas as small as 10^{-6}-10^{-5} cm^2 were scanned (17), hence subsequent measurements were made in this range. The calibration curve shown in Fig. 2 was measured from seven standards ranging from 0.25 to 0.6 mol fraction KCl. EDX determinations were made by scanning areas of about 5 × 10^{-6} cm^2 for 300 sec at 10-15 different locations, and the tilt angle was fixed at 32°.

Comparison with ZAF correction.—In order to test whether calibration could be based on the theoretical ZAF equation (18) and measurement on a single pure KCl standard, K/Cl count ratios were measured on a KCl single crystal (optical grade) and also on a sample melted and quenched in yttria. The K/Cl count ratio was 0.721 ± 0.003 for the crystal and a little higher, 0.783 ± 0.01, in the yttria matrix, which leads to a mean elemental intensity ratio I°_K/I°_{Cl} of 0.82 in pure KCl. If this ratio were used with the ZAF corrections (19) computed from the atomic properties of the elements, the calculated calibration curve would lie systematically above the measurements in the standards. Since the composition of pure KCl is far from the composition range of interest in this study, a least squares adjusted value, I°_K/I°_{Cl} = 0.67, was used to represent the calibration curve in Fig. 2. This value was determined from the measurements in the seven standards, using the composition dependent ZAF coefficients calculated with the FRAME program (19), and gives a standard deviation of 0.03 in the K/Cl count ratio. The difference between the values of I°_K/I°_{Cl} obtained from measurements with pure KCl and with mixtures in the Y_2O_3 matrix is of the same order (20%) as the difference we reported in $NaNO_3$-$AgNO_3$ mixtures (1). Discrepancies up to 30% between different matrices are not uncommon in the EDX literature (16), and may be attributed to uncertainties in the penetration of the electron beam assumed in the FRAME program (20). The calibration samples are more representative of those to be analyzed than is pure KCl, therefore the experimental calibration curve has been used for the subsequent measurements.

Accuracy.—The dispersion of the count ratio at different locations in a sample was smallest, 0.003, for the single crystal sample. For quenched pure KCl in yttria the observed dispersion was 0.01. This increased dispersion may be attributable to a rougher surface for the KCl-yttria sample than for the single crystal. The average dispersion observed with the standard LiCl-KCl mixtures in yttria is 0.027, which is significantly higher than with pure KCl in yttria. The larger dis-

Table I. Measured porosities of yttria matrix filled with quenched LiCl-KCl melts

Melt composition (mol fraction)	Sampled volume (cm^3)	Porosity
0.6 KCl-0.4 LiCl	0.1171	0.78
0.45 KCl-0.55 LiCl	0.1114	0.88
Eutectic	0.0648	0.86
Eutectic (electrolyzed)	0.0258	0.87

Table II. Electrolysis conditions of LiCl-KCl eutectic

Cell	Temp. (°C)	Electrode separation (cm)	Time of electrolysis (sec)	Current density (A cm^{-2})	Polarity of top electrode
1	425	0.326	152.0	0.202	−
2	425	0.416	242.0	0.254	+
3 (porous anode)	425	0.350	240.0	0.252	+

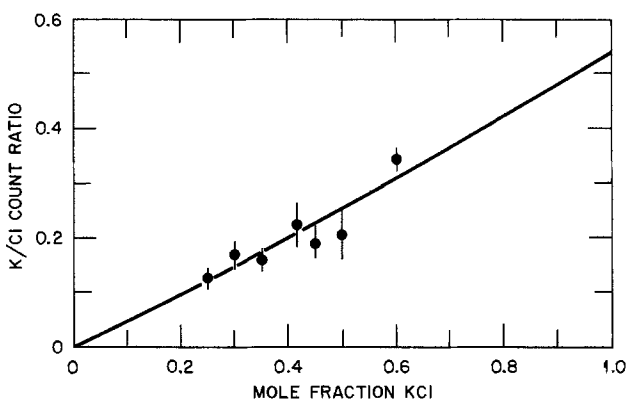

Fig. 2. EDX calibration for LiCl-KCl melts quenched in yttria. ϕ Data and observed dispersion for 15-20 determinations in different locations within the standard. —— Least squares fitted calibration curve.

Table III. Atomic absorption results in cell No. 1 and cell No. 2

Section	Distance of center from anode (cm)	Weight of salt extracted (g)	Mol fraction KCl				
			From Li analysis	From K analysis	From Li & K analysis combined	Predicted and deviation ( )	
Cell No. 1							
1	0.0567	0.04420	0.411	0.399	0.406	0.393	(3.3%)
2	0.1104	0.02219	0.416	0.403	0.410	0.410	(0%)
3	0.1658	0.04714	0.402	0.406	0.404	0.415	(2.6%)
4	0.2222	0.02754	0.417	0.414	0.416	0.421	(1.2%)
Cell No. 2							
1	0.0343	0.00616	0.414	0.274	0.337	0.349	(3.4%)
2	0.1003	0.02513	0.415	0.377	0.397	0.385	(3.1%)
3	0.1714	0.01232	0.489	0.321	0.410	0.407	(0.7%)
4	0.2448	0.01693	0.414	0.409	0.411	0.419	(1.9%)
5	0.3146	0.02195	0.406	0.420	0.412	0.437	(5.7%)
6	0.3756	0.02104	0.459	0.431	0.447	0.476	(6%)

persion in the mixtures may result from additional inhomogeneity in the distribution of crystallites of LiCl and of KCl. However, the calibration curve, obtained by sampling several locations in each of the seven standards, gives the composition within an uncertainty of the order of 8%.

Results

Analysis of sections by atomic absorption.—The AA data obtained with cells No. 1 and No. 2 are summarized in Table III.

Except for sections 1 and 3 in cell No. 2, where the weight of extracted salt was less than half the average weight in the other sections, the results obtained from the Li analysis and from the K analysis (in columns 4 and 5, respectively) agree, on average, within 3-4%, indicating that the weight loss after extraction is correctly known in most of the cases. Column 6 shows the composition based on the combined Li and K analyses, which is thus independent of weight loss after extraction. The last column indicates the predicted average composition in each section and (in parentheses) the deviations between the predicted compositions and the measured values listed in column 6. The deviations are less than 6% and are of the order expected from the accuracy of AA. One disadvantage of this method is that the compositions are for noncontiguous portions of the separator because of the thickness of the saw blade. The major disadvantage is the low distance resolution of these measurements, limited by the impossibility of obtaining coherent sections thinner than 0.03-0.04 cm, which prevents measurement of the composition gradient close to the electrodes.

SEM/EDX measurements.—Measurements of composition profiles with high distance resolution were obtained by SEM/EDX on cross sections from these two cells. The areas scanned were typically 6 μm squares randomly chosen over a region of quenched electrolyte 0.5 mm wide located near the axis of the cylindrical cell. The composition changes measured as a function of distance from the anode in cell No. 2 are shown in the upper part of Fig. 3 along with the predicted composition profile, and demonstrate a 50% gradient across the separator. The vertical bar indicates the standard deviation of measurements of a typical standard. The lower portion of the figure, a deviation plot showing the differences between the measured and predicted compositions, shows little systematic trend. Because of inhomogeneity of the electrolyte matrix and of the current distribution, the apparent distance resolution is lower than that nominally attainable with the magnification used. Some form of smoothing is therefore required to generate an average one dimensional profile. In order to ascertain the accuracy with which the shape of a profile can be determined, the data were analyzed by several methods.

Composition profile in separator.—First, to smooth the data without the bias of a function of given form (*e.g.*, a predicted profile), the measurements in cells 1 and 2 were averaged in a "moving window" of width $\pm 0.05 \times$ the reduced distance. This running average is shown by the solid horizontal bars in Fig. 4. The small loss of resolution resulting from this smoothing is much less than that resulting from the AA analysis of sections that were about 0.4 mm thick and not contiguous. The bars represent overlapping groups of points spanning less than 0.15 mm. The dashed line is the predicted profile calculated numerically. The moving window smoothing is model independent, and demonstrates the current-induced composition gradients and general shape of the profile.

Second, in order to obtain a smooth curve to represent the data, again without introducing the bias of a theoretical equation, a least squares fit to the data was done with a simple empirical function (quadratic) which represents a profile passing through the initial composition midway between the electrodes, *i.e.*, at a

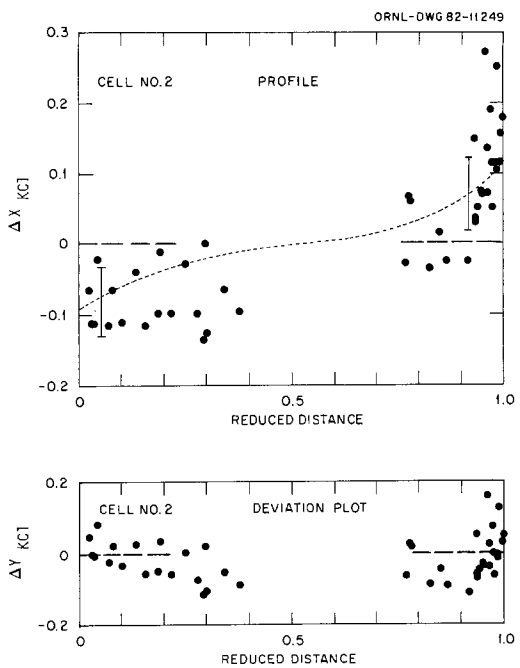

Fig. 3. Profiles of composition change (ΔX_{KCl}) from initial composition, and of difference between measured and predicted compositions (ΔY_{KCl}). Upper: measured composition change by EDX in cell No. 2. Anode at left. ● Data; --- predicted profile; I Typical dispersion in standard. Lower: difference between measured and predicted compositions.

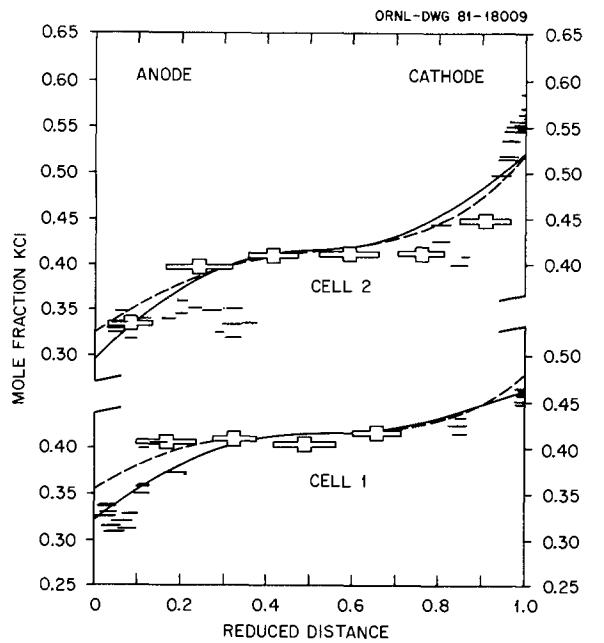

Fig. 4. Measured and predicted composition profiles in yttria separator in cells No. 1 and No. 2, with solid Li-Al electrodes. ⊏⊐ Atomic absorption and width of section. — EDX and width of window (≤0.018 cm). ——— Least squares fit to EDX and AA data with quadratic functions. ---- Predicted profiles.

reduced distance, $u = 0.5$

$$X_{KCl} - 0.415 = A(u - 0.5)^2 \text{ for } u > 0.5;$$
$$X_{KCl} - 0.415 = -B(u - 0.5)^2 \text{ for } u < 0.5 \quad [1]$$

Values of A and B are given in Table IV for the fit to the predicted profiles and to the experimental data in cells No. 1 and No. 2. The use of Eq. [1] to fit the predicted profile calculated from the initial composition, current, and electrolysis time, gives an agreement factor of 4×10^{-3} mol fraction KCl. Application of Eq. [1] to the data gave an agreement factor of 4-5 $\times 10^{-2}$ mol fraction KCl. Figure 4 shows the quadratic fits to the raw data for cells No. 1 and No. 2 as solid lines, and the predicted composition profiles as dashed lines. The compositions calculated from the fit of Eq. [1] to the data are within about 6% of the predicted composition profile.

Electrolyte in porous anode.—For cell 3, with a porous anode, the smoothing was done during the measurements by scanning a 8×10^{-3} cm strip (parallel to the interface) that was 2×10^{-3} cm wide, and then displacing the beam by half this width for successive scans. This procedure reduces markedly the fluctuations between successive measurements, with little loss in distance resolution. The SEM/EDX results in the separator of cell 3 are shown on the right side of Fig. 5. The bars are averages over overlapping moving windows of 50 μm width. Although the compositions measured in the Y_2O_3 separator near the anode were very close to LiCl saturation at the experimental temperature (0.30 mol fraction KCl), precipitation of LiCl in the separator was not detected. None of the scanned areas showed spectra free of potassium; also there was no significant increase of fluctuation in Li/K ratios found in scans of neighboring areas. On the left side

Table IV. Coefficients in quadratic fits of predicted and measured composition profiles

Cell	Predicted A	Predicted B	Experimental A	Experimental B
1	0.217	0.217	0.195	0.376
2	0.401	0.367	0.439	0.477

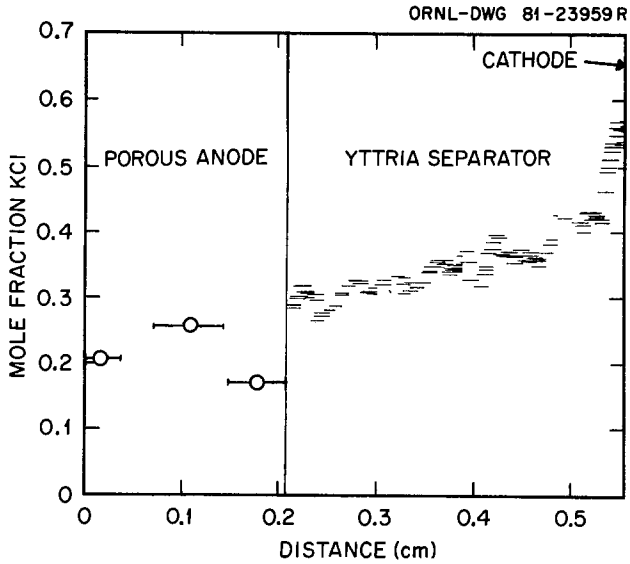

Fig. 5. EDX measured composition profile in the LiCl-KCl electrolyte of cell No. 3, with porous Li-Al anode on the left and the yttria separator on the right. —Average of 5-6 determinations through overlapping windows 50 microns wide in the separator. —○— Data, with width of scanned area, in the porous anode.

of Fig. 5, preliminary measurements in the porous anode indicate lower K/Cl mol ratio than in the separator, and suggest LiCl precipitation. Subsequent, more detailed, measurements in the porous anode showed that LiCl precipitation had occurred in the front part of the electrode, and will be presented in a later paper.

Conclusions

Composition gradients induced by current in mixed electrolytes of Li/S batteries have been isolated by quenching of LiCl-KCl eutectic melt electrolyzed between two Li-Al electrodes.

Composition profiles were measured by atomic absorption and by SEM/EDX. The results obtained in the three cells demonstrate the composition gradients in the Y_2O_3 separator resulting from current flow. Results obtained by AA and by SEM/EDX are consistent, indicating no artifact caused by the small size of the volume sampled by EDX. The SEM/EDX composition profiles in quenched Y_2O_3-LiCl-KCl were obtained with a distance resolution better than 50 μm and a relative accuracy of better than 10%.

Relatively low counts of K and Cl in portions of the felts close to the upper electrode (cathode in cell No. 1 and anode in cell No. 2), probably resulting from voids in that region of the felt, contribute to the dispersion; the dispersion also is larger for measurements made at the junction of two felt disks because of the roughness of the scanned surface and the absence of salt in that region.

Current-induced gradients in Li/K ratio of 40-50% across the electrolyte were measured. The lithium chloride concentrations near the anode approached saturation. Preliminary measurements in a porous anode suggested LiCl precipitation.

Refinements in the scanning procedure should lead to better accuracy in the EDX measurements, probably to the order of 5%. The method can be used in the analysis of the distribution of products and reactants in high temperature molten salt batteries.

Acknowledgments

The authors are pleased to acknowledge the interest and helpful suggestions of Dr. L. D. Hulett, Analytical Chemistry Division, regarding the SEM/EDX measurements.

This work was sponsored by the Division of Energy Storage Systems, U.S. Department of Energy, under

contract W-7405-eng-26 with the Union Carbide Corporation through Memorandum Request LBL 4506210 from Lawrence Berkeley Laboratory.

Manuscript submitted Dec. 20, 1982; revised manuscript received July 18, 1983. This was Paper 437 presented at the Montreal, Quebec, Canada, Meeting of the Society, May 9-14, 1982.

Oak Ridge National Laboratory assisted in meeting the publication costs of this article.

REFERENCES

1. C. E. Vallet, D. E. Heatherly, R. L. Sherman and J. Braunstein, *This Journal*, **129**, 49 (1982); C. E. Vallet, L. M. Kidd, D. E. Heatherly, R. L. Sherman, and J. Braunstein, *ibid.*, **129**, 931 (1982); J. Braunstein, S. Cantor, and C. E. Vallet, Proceedings of the 16th Intersociety Energy Conversion Engineering Conference, The American Society of Mechanical Engineers, Vol. 1, p. 759, New York (1981).
2. J. Braunstein and C. E. Vallet, *This Journal*, **126**, 960 (1979).
3. C. E. Vallet and J. Braunstein, *ibid.*, **125**, 1193 (1978).
4. R. Pollard and J. Newman, *ibid.*, **128**, 491 (1981).
5. Z. Tomczuk, S. K. Preto, and M. F. Roche, *ibid.*, **128**, 760 (1981).
6. M. J. Willars, J. G. Smith, and R. W. Glazebrook, *J. Appl. Electrochem.*, **11**, 335 (1981).
7. J. W. Searcy and J. R. Armijo, Sandia National Laboratory Report SAND 82-0565 (June 1982).
8. W. Borger, W. Kappus, and H. S. Panesar, Proceedings of the 17th Intersociety Energy Conversion Engineering Conference, The American Society of Mechanical Engineers, Vol. 2, p. 544 (1982).
9. G. L. Holleck and J. Giner, *This Journal*, **119**, 1161 (1972).
10. B. A. Askew and R. Holland, Abstract 56, p. 138, The Electrochemical Society Extended Abstracts, Fall Meeting, Boston, MA, Oct. 7-11, 1973.
11. L. Redey, I. Poruksky, and I. Molnar, in Power Sources 5, Proceedings of the 9th International Symposium, Brighton, Sept. 1974, D. H. Collins, Editor, p. 559, Academic Press, London (1975).
12. D. L. Barney *et al.*, Argonne National Laboratory ANL-81-65 (1982).
13. C. E. Vallet and J. Braunstein, *This Journal*, **126**, 527 (1979).
14. B. J. Burrow, K. W. Nebesny, N. R. Armstrong, R. K. Quinn, and D. E. Zurawski, *ibid.*, **128**, 1919 (1981).
15. C. T. Moynihan and R. W. Laity, *J. Phys. Chem.*, **68**, 3312 (1964).
16. R. L. Myklebust, J. A. Small, and D. E. Newbury, Scanning Electron Microscopy/1981/I, p. 477, SEM Inc., AFM O'Hare, Chicago.
17. C. E. Vallet, D. E. Heatherly, R. L. Sherman, and J. Braunstein, Abstract 186, p. 492, The Electrochemical Society Extended Abstracts, Fall Meeting, Los Angeles, CA, Oct. 14-19, 1979.
18. K. F. J. Heinrich, in "X-ray Spectroscopy," H. K. Herglotz and L. S. Birks, Editors, Chap. 7, Marcel Dekker, Inc., New York (1978).
19. H. Yakowitz, R. L. Myklebust, and K. F. J. Heinrich, NBS Technical Note 796, Government Printing Office, Washington, D.C. (1976).
20. L. D. Hulett, Private communication.

Electrolytic LiCl Precipitation from LiCl-KCl Melt in Porous Li-Al Anodes

C. E. Vallet,* D. E. Heatherly, L. Heatherly, Jr., and J. Braunstein*

Chemistry Division and Metals and Ceramics Division, Oak Ridge National Laboratory, Oak Ridge, Tennessee 37830

ABSTRACT

Composition gradients such as those predicted to occur during discharge of porous Li-Al negative electrodes of Li/S batteries with LiCl-KCl eutectic electrolyte were generated and measured in the LiCl-KCl anolyte of an electrolysis cell with Li-Al electrodes. Precipitation of lithium chloride during electrolysis was observed by two-dimensional scanning of electrolyte composition in the front part of quenched porous Li-Al anode sections using SEM/EDX. The distribution of sites of increased or decreased LiCl concentration, LiCl saturation and precipitation was mapped. Cathodic regions were observed near the cell walls. Preliminary results of analysis by Auger spectroscopy confirm LiCl precipitation in the porous anode.

We have previously reported SEM/EDX measurements of current-induced composition profiles in LiCl-KCl contained in yttria matrices and electrolyzed between solid Li-Al ($\alpha + \beta$) electrodes (1). This paper presents the results of SEM/EDX and Auger analysis of the anolyte composition in powdered electrodes following electrolysis and quenching. Since the primary driving force for component separation in a mixed electrolyte is the electrode reaction (2, 3), the electrolyte composition shift is larger in the porous electrode (3) than in the separator. Precipitation of lithium chloride is observed.

Experimental

The cell and the SEM/EDX procedure have been described previously (1). The Li-Al powder of the porous anode was 51 a/o lithium (β phase), with grain sizes of the order of 0.3-0.4 mm. Figure 1 shows (a) an electron micrograph of a filled yttria matrix with a porous Li-Al electrode and stainless steel screen together with the elemental mappings for: (b) yttrium, (c) chlorine, and (d) potassium in a nonelectrolyzed cell. The elemental mappings demonstrate the filling of the assembly by melt. Figure 1(b) shows the yttria substrate in the separator; the few bright spots in the electrode probably result from smearing during cutting, and represent background in the electrode. Both chlorine and potassium mappings show a large number of areas filled with salt and uniformly dispersed in the porous electrode, as shown by the brightness well above background.

A nonelectrolyzed porous electrode filled with LiCl-KCl eutectic (0.42 mol fraction KCl) was examined by SEM/EDX in order to test whether the calibration curve established for LiCl-KCl in an yttria matrix (1) could be used for measurements in the Li-Al matrix. Some 300 EDX spectra from scanned areas (8×10^{-3} cm $\times$ 2×10^{-3} cm) distributed along three different paths perpendicular to the Al_2O_3 walls and extending from one wall to the other gave a K/Cl count ratio of 0.182 ± 0.021. This value of the K/Cl count ratio in

* Electrochemical Society Active Member.

Key words: battery, electrolyte, fused salts, SEM, AES, porous electrode.

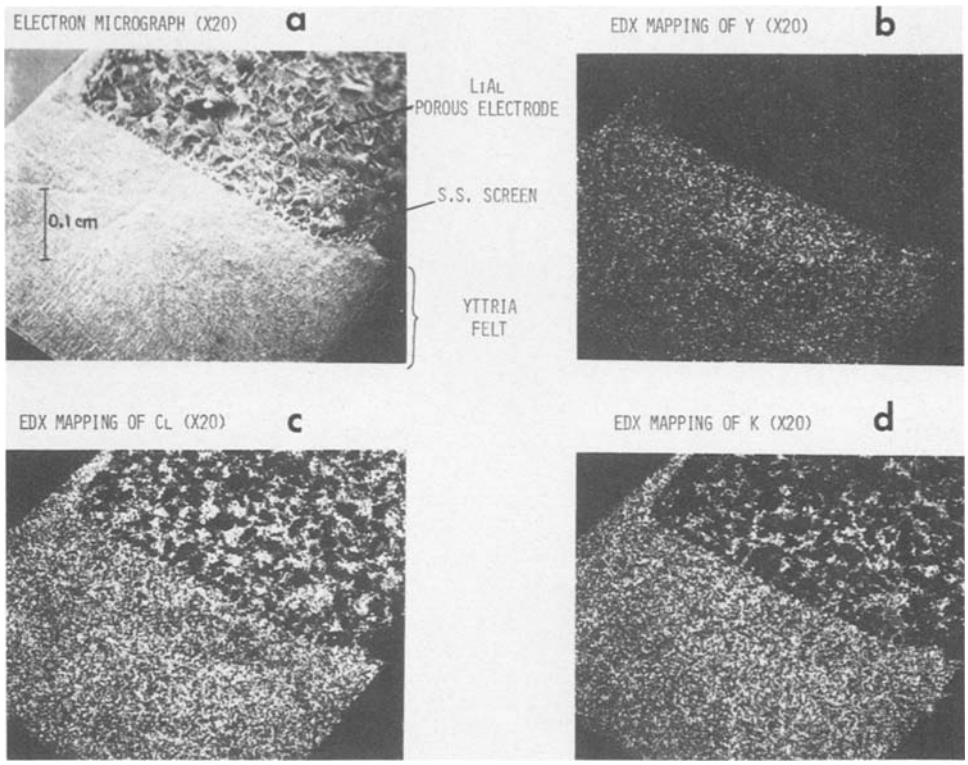

Fig. 1. Electron micrograph (a) and EDX elemental mappings of (b) Y, (c) Cl, and (d) K in quenched cell with Li-Al porous electrode.

the Li-Al matrix agrees with the value 0.21 ± 0.04 obtained previously in an yttria matrix and with the value 0.20 ± 0.03 calculated with the least squares fitted calibration curve (1). The dispersion is of the same order as in an yttria matrix, and no difference was observed between data from the center of the cell and from regions close to the Al_2O_3 walls. Quenching of the melt in yttria or in Li-Al does not produce significant inhomogeneities of concentration. The calibration curve obtained previously in yttria matrices was used to obtain the anolyte compositions in Li-Al electrodes.

Results

SEM/EDX measurements.—The porous Li-Al electrode of a cell, whose electrolyte composition profile in the separator was reported previously (1), was examined along a path close to the cell axis. This cell, with a porous Li-Al electrode 0.21 cm thick and electrode separation 0.35 cm, had been electrolyzed 4 min at 0.252 A cm^{-2}; the electrolyte composition in the portion of the separator adjacent to the anode was close to LiCl saturation (0.30 mol fraction KCl) at the electrolysis temperature of 425°C (1).

Composition gradient at the electrode/electrolyte interface.—The front part of the electrode was first analyzed for a distance of up to 0.5 mm into the electrode by scanning strips 6×10^{-3} cm wide and displacing them by half this width in successive scans. These results are shown in Fig. 2 together with those obtained in the separator over a similar distance from the interface. Measured compositions in the anode near the anode/yttria separator interface showed a decrease of KCl mol fraction from the initial value of 0.42 to values between 0.08 and 0.21. These concentrations are all lower than those in the yttria separator, 0.26-0.37 mol fraction KCl, at similar distances from the geometric interface. The concentration of KCl in the electrolyte drops very sharply across the geometric interface, from 0.26 in the separator to 0.2 in the anode within a distance of 0.003 cm. At about 0.01 cm from the interface the measured concentrations level off at 0.1 mol fraction KCl. Those measurements are consistent with the value of 0.17 mol fraction KCl obtained by scanning a large strip (0.06 cm thick) extending from the interface into the electrode. While the K/Cl ratios in the yttria are close to the liquidus composition (0.30 mol fraction KCl), those in the front part of the anode are well below and therefore indicate LiCl precipitation.

In order to measure the overall variation of electrolyte composition along this axial path in the electrode, scans were made of three adjacent strips about 0.5 mm wide. The strip adjacent to the interface has the lowest KCl concentration (0.17 mol fraction KCl), while the concentration in the middle and in the back of the electrode is 0.2-0.26 mol fraction KCl.

Lithium chloride precipitates.—The front part of the anode, where LiCl precipitation had occurred, was studied in detail for local composition changes. Figure 3 is a 200 magnification micrograph of a portion of the anode and separator; the interface is shown by the dashed line. Scans of 6-7 μm squares (4×10^{-7} cm^2) covered a larger region of about 2×10^{-4} cm^2 in which large count numbers for chlorine were measured, but very few counts for potassium. Two such regions, which appear lighter in the micrograph, are shown in Fig. 3 along with a typical EDX spectrum from one of the scans. In measurements on unelectrolyzed standards (4), the scan areas had to be below

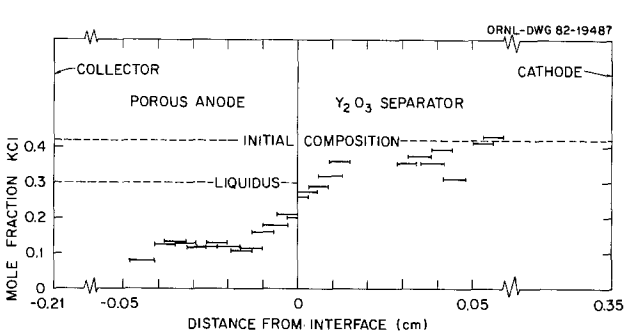

Fig. 2. EDX measured electrolyte concentrations near the electrode/electrolyte interface in the porous anode and in the Y_2O_3 separator. The horizontal bars indicate the position and the width of the scanned area.

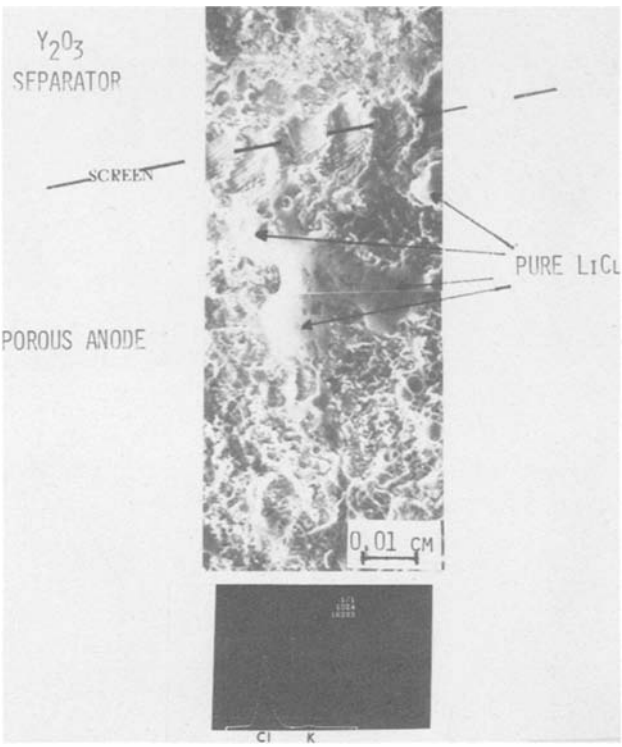

Fig. 3. LiCl precipitation in porous Li-Al anode. Top: Electron micrograph with regions of LiCl precipitation indicated by arrows. Bottom: Typical EDX spectrum in an indicated region.

10^{-9} cm^2 in order to find some without the K line in the spectrum. The EDX measurements in the porous anode thus confirm that the LiCl precipitation in the anolyte occurred during electrolysis. The regions where pure LiCl is found are not continuous along the anode/yttria interface, and therefore one-dimensional composition profiles along different paths vary considerably. This probably accounts for much of the fluctuation observed in one-dimensional composition profiles (1).

Distribution of electrolyte composition in porous anode.—In a second cell, electrolysis time and electrode separation were chosen in order to produce a composition gradient leading unequivocally to LiCl prepicipitation in the separator, near the anode. The electrode separation was 0.25 cm and the porous anode was 0.42 cm thick; this cell was electrolyzed for 7 min at 0.337A cm^{-2}. For a cell with two solid electrodes, with 0.25 cm separation, the calculated (2) composition at the anode at the end of electrolysis is 0.279 mol fraction KCl, well below the liquidus composition of 0.30 mol fraction KCl. Since measurements in the first porous anode cell had indicated that a one-dimensional compositional profile cannot represent the composition in the anolyte, SEM/EDX measurements of composition were made along seven nearly equally spaced paths perpendicular to the Y_2O_3 separator/anode interface. Four hundred and sixty areas were scanned in the front of the electrode. These areas were uniformly distributed over the paths, as shown on the electron micrograph in Fig. 4, and covered about a quarter of the electrode thickness. The size of a typical scanned strip was 8×10^{-3} cm $\times$ 2×10^{-3} cm, and on each path the scanned strips were overlapped by half their thickness.

The postelectrolysis distribution of K/Cl ratios in the front part of the anode is shown in Fig. 5a. The composition surface was calculated from the measurements on the planar electrode section, and the composition contours are projected on the base. A more detailed view is shown in Fig. 5b, where the front-to-back distance scale has been expanded by a factor of ten. Most of the front of the anode (region with front-to-back shading) shows an increase of more than 10% in the LiCl mol fraction, as expected from the anodic reaction. Included in this region are the smaller but significant regions (dark) in which the increase was sufficient to exceed LiCl solubility, and LiCl precipitates were observed in these regions. The unshaded regions correspond to composition changes less than 10%. The regions of unchanged composition are mostly located around the cell axis, and surround the regions of enrichment and precipitation of LiCl. This suggests a blockage of pores by solid precipitate, which would be analogous to the mechanism predicted (5) and verified (6) in porous silver electrodes with sparingly soluble reactant. The side-to-side shaded and dotted regions, primarily at the left edge and towards the rear, indicate increases in KCl concentration of greater than 10 and 20%, respectively. Since the composition changes are greater than the experimental uncertainty (~8%), the increase may result from local cathodic reaction within the anode caused by nonuniform current distribution. Calculations with a one-dimensional model also predicted cathodic reaction at the collector in the back of the electrode (7). The measurements suggest that peripheral portions of the stainless steel mesh enclosing the Li-Al powder may have acted as current collector during the electrolysis. Nonuniform current distribution could also be attributed to resistances caused by poor electrode-current collector contact, by unfilled pores resulting from poor wetting, and by precipitates of LiCl.

Anodic and cathodic regions.—The contour projection shows that the areas with appreciable composition change tend to be not randomly distributed, and they form regions of significant size. This distribution is illustrated in Table I and Fig. 6. The entries in the table are the percentages of scanned areas in successive distance increments of 0.02 cm, along the paths shown in Fig. 6a, which fell in different ranges of composition. Figures 6b, 6c, and 6d show the fraction of measurements with LiCl concentrations larger (b) than the initial composition, the fraction showing pure LiCl (c) and the fraction with LiCl concentration lower (d) than the initial composition. Figure 6b shows clearly that the anodic reaction, leading to larger concentra-

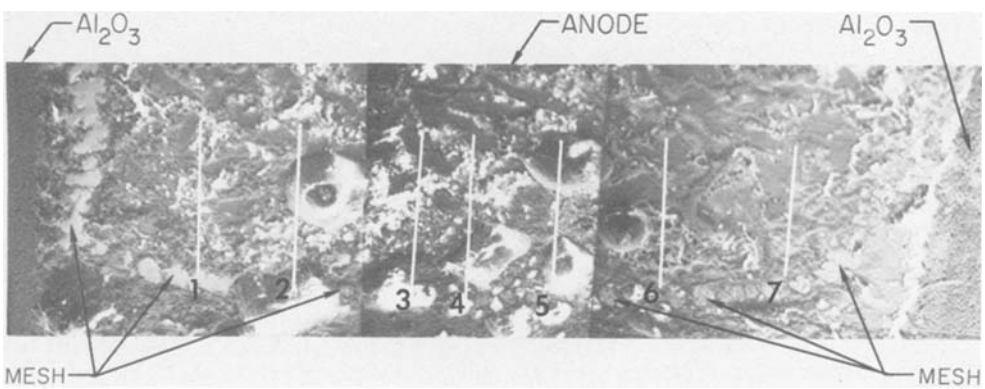

Fig. 4. Electron micrograph of the front part of quenched anode and paths scanned for EDX analysis.

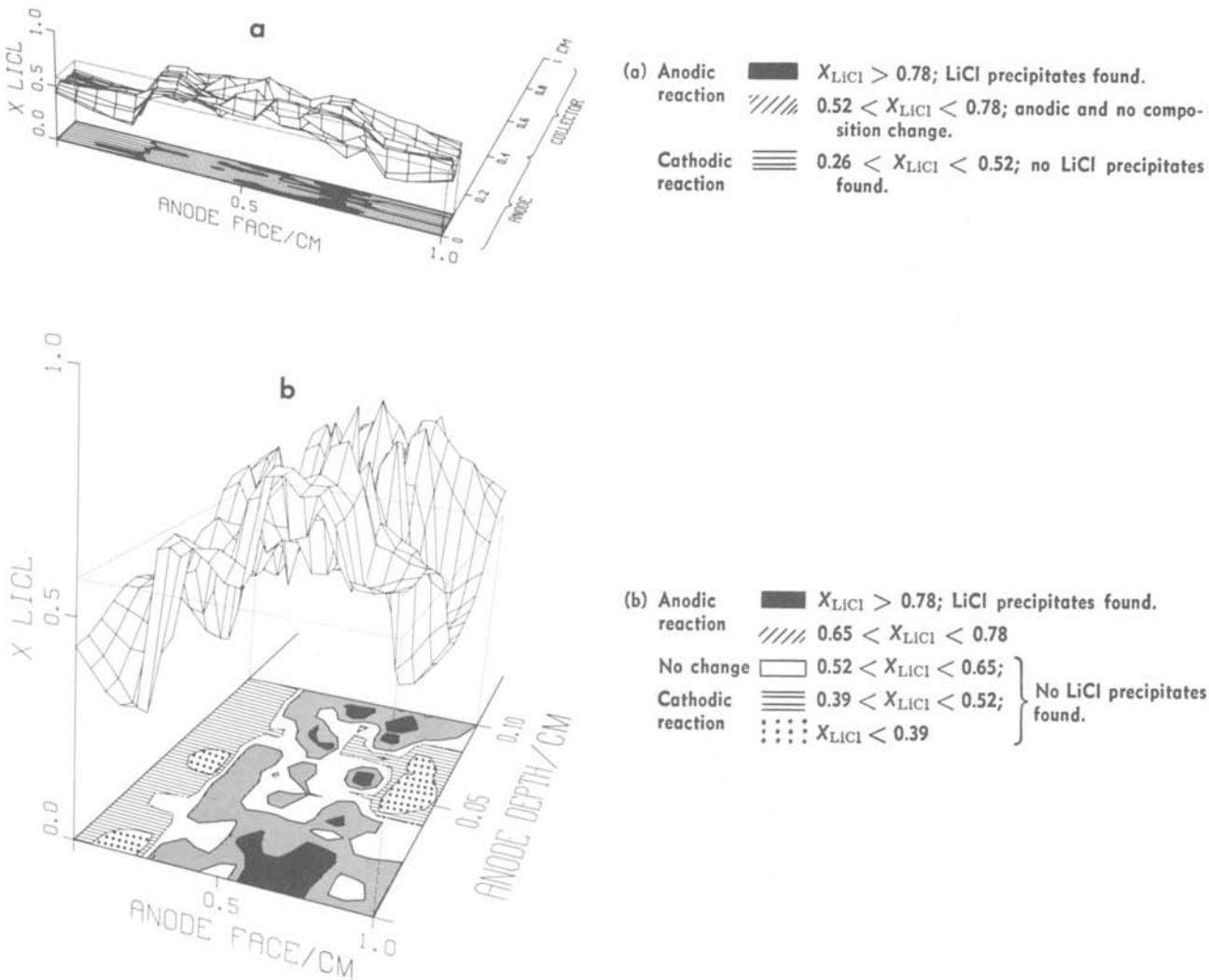

Fig. 5. Measured anolyte composition in the front part of an Li-Al porous electrode and projected composition isopleths. Shadings indicate areas of the LiCl precipitation, of anodic reaction, of no composition change, and of cathodic reaction.

tions of LiCl than in the initial melt, was predominant (>75%) along paths 2-7 over a distance of 0.04 cm from the interface. Lithium chloride precipitates (Fig. 6c) are found on paths 4-6, and account for nearly 40% of the measurements close to the cell axis and within 0.02 cm of the interface. The size of this region is

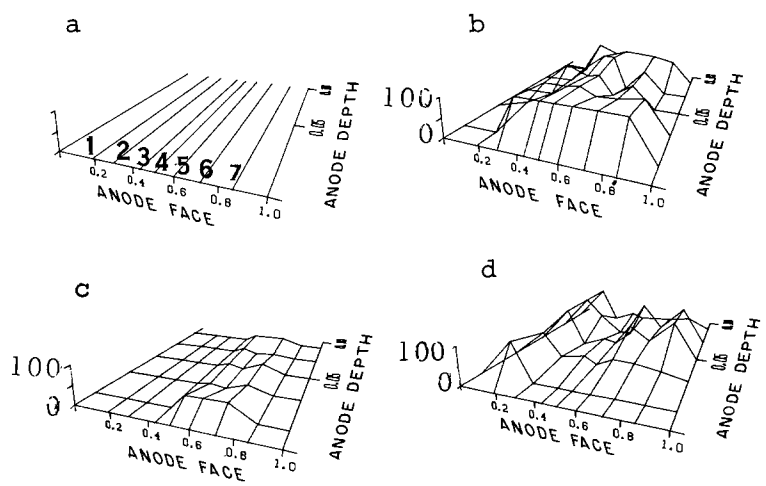

Fig. 6. Spatial distribution of measured anolyte composition: (a) paths scanned by EDX with 8×10^{-3} cm $\times$ 2×10^{-3} cm overlapping areas, (b) relative number of measurements with LiCl mol fraction larger than the initial composition (anodic reaction), (c) relative number of measurements with pure LiCl, (d) relative number of measurements with LiCl mol fraction smaller than the initial composition (cathodic reaction).

Table I. Distribution of the measured composition along scanned paths

Distance from interface (cm)	Composition* \ Path	Scanned areas (percent)** 1	2	3	4	5	6	7
0-0.02	b	0	100	100	100	100	100	100
	c	0	0	0	37.5	37.5	38.9	0
	d	100	0	0	0	0	0	0
0.02-0.04	b	25	87.5	87.5	94	73	75	86
	c	0	0	0	5.9	0	18.8	0
	d	75	12.5	12.5	6	27	25	14
0.04-0.06	b	0	100	75	82	25	63	0
	c	0	0	0	11.8	0	25	0
	d	100	0	25	18	75	37	100
0.06-0.08	b	0	50	100	100	0	65	0
	c	0	0	0	12.5	0	5.9	0
	d	100	50	0	0	100	35	100
0.08-1	b	0	100	75	88		81	67
	c	0	0	0	17.6		19	0
	d	100	0	25	12		19	33

* Composition range (b) $X_{LiCl} > X_{LiCl}$ (initial); (c) $X_{LiCl} = 1$; (d) $X_{LiCl} < X_{LiCl}$ (initial).
** Entries are the percent of measurements falling in the above composition range.

similar to that observed at the interface of the first cell. Concentrations of LiCl lower than the initial composition, which suggest cathodic reaction, are found primarily on paths near the Al_2O_3 cell walls where the effect of nonuniform current distribution is likely to be most pronounced. The percentages, listed in Table I, tend to be either large (>70%) or small (<30%). Random fluctuations in the compositions measured in neighboring locations would lead to values around 50%. Therefore, the inhomogeneities in the measured concentrations must be attributed to current flow.

Auger spectroscopy.—Since SEM/EDX is unable to detect lithium directly, Auger spectroscopy was initiated in order to check the possibility of simultaneous analysis of LiCl and KCl in the salt as well as Li metal in the electrode. Auger spectroscopy has been used in studies of compositional changes in an Li-Si/LiCl-KCl/FeS_2 cell (8). Difficulties in Auger measurements arise from the low penetration of Auger electrons, however, and the results may not reflect the bulk composition. Previous Auger investigation of lithium metal (9) has shown a characteristic line at 50 eV when the 510 eV oxygen line is barely detectable. An oxygen pressure of 5×10^{-6} Torr in the vacuum chamber results in the disappearance of the Li line at 50 eV and the appearance of a line at 40 eV attributed to lithium oxide. The line at 40 eV has also been observed in LiH (10) and LiF (11). This large chemical shift could be useful to distinguish between lithium metal and LiCl in an Li-Al porous anode, but only in the absence of oxygen.

Li-Al metal.—Figure 7 gives typical first derivative energy distribution spectra obtained under low pressure (10^{-10} Torr) with a 3 keV beam in the quenched anode of the second of the cells previously studied by SEM/EDX. Spectra (a) and (b) correspond to an Li-Al metal particle since the lines for chlorine (181 eV) and potassium (252 eV) are very weak. Spectrum (b), obtained after a 1½ hr argon sputtering with grazing incidence (15°) and with sputtering during the analysis, shows a marked decrease of oxygen and the appearance of the strong line for aluminum metal at 68 eV and the weak one at 84 eV. However, the absence of a lithium metal line indicates coverage by a lithium oxide layer. The calculated (11) atomic fractions are lithium 0.35, aluminum 0.58, chlorine 0.003, potassium 0.029, and oxygen 0.038 and give Li/Al ratio of about the bulk composition. Sputtering under normal incidence followed by analysis was not efficient, probably because oxygen diffuses rapidly back to the surface (9), and we observed an increase in the oxygen line with increasing sputtering time. A similar observation was reported with an Li-Si electrode (8).

LiCl-KCl salt.—The intense chlorine lines in spectra (c) and (d), obtained after sputtering (1½ hr) under grazing incidence, show that the areas contained salt. The area analyzed in spectrum (d) is nearly pure KCl with calculated atomic fractions potassium 0.41, chlorine 0.47, lithium 0.074, aluminum 0.019, and oxygen 0.027. Spectrum (c), in an area at the interface with the yttria separator, showed calculated atomic fractions of lithium 0.68, chlorine 0.19, aluminum 0.09, potassium 0.005, and oxygen 0.032. This analysis indicates that the area contains both salt and Li-Al. The observed lithium line has a contribution from lithium oxide on the metal surface and from lithium chloride. The relatively high Li/Al ratio found in spectrum c with 3.2% of oxygen is more likely attributable to the displacement and loss of chlorine during sputtering rather than to the enrichment in lithium of the LiAl metallic particles since spectrum (b) of Li-Al with a comparable oxygen concentration gives the bulk composition. Decreasing intensity of chlorine was observed and is illustrated in Fig. 6 by the comparison of spectra (a) and (b) recorded after differing sputtering times. It is very likely that spectrum (c) corresponds to an area containing nearly pure lithium chloride. The Auger determination confirms, by simultaneous observation of lithium and potassium, lithium chloride precipitation from electrolysis observed by SEM/EDX in this anode.

Quantitative analyses.—The Auger results presented above are semiquantitative; quantitative analysis in this system would be difficult for several reasons. Auger spectroscopy samples only few atomic layers and analysis may include composition changes produced during sectioning. In addition, first, the low oxygen level required for distinguishing between lithium in Li-Al and lithium as chloride necessitates extensive argon sputtering which can induce changes in the surface composition by displacing K^+ and Cl^- whose sizes are comparable to that of argon. Thus, the peak to peak chlorine intensity is a poor reference in the salt analysis since it varies markedly with sputtering time (12).

Conclusions

Although current-induced precipitation in the electrolyte of porous electrodes may adversely affect the utilization of reactants and overall battery performance (2, 3, 13-16), there has been no direct measurement of the effect in a molten salt battery. In this study, composition shifts such as those which could occur during discharge in the Li-Al negative electrode of an Li/S battery with an LiCl-KCl eutectic electrolyte were observed and measured in the LiCl-KCl anolyte of an electrolysis cell with Li-Al electrodes.

The SEM/EDX analysis of anolyte composition shows regions in the front part of the electrode where pure lithium chloride precipitated during electrolysis.

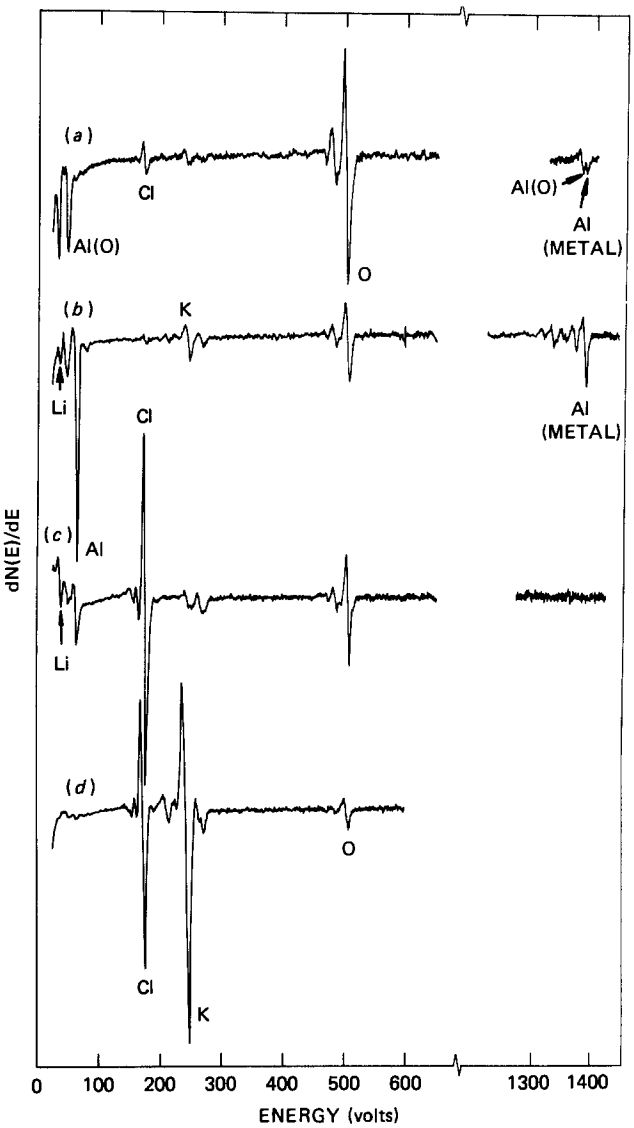

Fig. 7. Auger electron spectra in porous Li-Al anode. (a) Li-Al metal particle after 17 min normal argon sputtering and no sputtering during the recording. (b) Same Li-Al metal particle as in (a) after 1½ hr grazing argon sputtering and sputtering during the recording. (c) Salt mixture of high LiCl concentration and Li-Al metal after 1½ hr grazing sputtering and sputtering during recording. (d) Nearly pure KCl after 1½ hr grazing sputtering with no sputtering during recording.

Solid precipitation accentuates the nonuniformity of current distribution, as shown by adjacent regions with no composition change. Cathodic reaction, indicated by increased KCl concentration, was observed, primarily near the cell walls. Similar inhomogeneities could have considerable effect on swelling, ohmic resistance, and other properties of battery cells, and could lead to certain failure modes.

Measurements of electrolyte composition by the methods demonstrated in this study, together with analysis of the alloy phases in the Li-Al negative electrode, would provide more detailed understanding of the distribution of reactants and products. Similar studies should be extended to Li-Si electrodes and to porous iron sulfide positive electrode.

Acknowledgments

The authors gratefully acknowledge Dr. R. E. Clausing, Metals and Ceramics Division, for his interest and helpful suggestions regarding the Auger spectroscopy and H. W. Dunn, Analytical Chemistry Division, for his help with the SEM/EDX elemental mappings.

This work was sponsored by the Division of Energy Storage Systems, U.S. Department of Energy under contract W-7405-eng-26 with the Union Carbide Corporation through Memorandum Request LBL 4506210 from Lawrence Berkeley Laboratory.

Manuscript submitted Dec. 22, 1982; revised manuscript received July 18, 1983. This was Paper 768 presented at the San Francisco, CA, Meeting of the Society, May 8-13, 1983.

Oak Ridge National Laboratory assisted in meeting the publication costs of this article.

REFERENCES

1. C. E. Vallet, D. E. Heatherly, and J. Braunstein in "Transport Processes in Electrochemical Systems," R. A. Yao, T. Katan, and D.-T. Chin, Editors, p. 122, The Electrochemical Society Softbound Proceedings Series, Pennington, NJ (1982); Oak Ridge National Laboratory Report ORNL/TM-8489 (October 1982); *This Journal*, **130**, 2366 (1983).
2. C. E. Vallet and J. Braunstein, *This Journal*, **125**, 1193 (1978).
3. R. Pollard and J. Newman, *ibid.*, **128**, 491 (1981); *ibid.*, **128**, 503 (1981).
4. C. E. Vallet, D. E. Heatherly, R. L. Sherman, and J. Braunstein, Abstract 186, p. 492, The Electrochemical Society Extended Abstracts, Fall Meeting, Los Angeles, CA, Oct. 14-19, 1979.
5. J. S. Dunning, D. N. Bennion, and J. Newman, *This Journal*, **118**, 1251 (1971); J. S. Dunning, D. N. Bennion, and J. Newman, *ibid.*, **120**, 906 (1973); H. Gu, D. N. Bennion, and J. Newman, *ibid.*, **123**, 1364 (1976).
6. T. Katan, H. Gu, and D. N. Bennion, *ibid.*, **123**, 1370 (1976).
7. R. Pollard and J. Newman, "Applied Battery and Electrochemical Research Program for Fiscal Year 1980," LBL-12514, E. Cairns, Editor, p. 48.
8. B. J. Burrow, K. W. Nebesny, N. R. Armstrong, R. K. Quinn, and D. E. Zurawski, *This Journal*, **128**, 1919 (1981).
9. R. E. Clausing, D. S. Easton, and G. L. Powell, *Surf. Sci.*, **36**, 377 (1973).
10. G. L. Powell, G. E. McGuire, D. S. Easton, and R. E. Clausing, *ibid.*, **46**, 345 (1974).
11. L. E. Davis, N. C. MacDonald, P. W. Palmberg, G. E. Riach, and R. E. Weber, "Handbook of Auger Electron Spectroscopy," 2nd ed., Physical Electronics Industries, Inc., Eden Prairie (1976).
12. R. E. Clausing, Personal communication.
13. M. J. Willars, J. G. Smith, and R. W. Glazebrook, *J. Appl. Electrochem.*, **11**, 335 (1981).
14. Z. Tomczuk, S. K. Preto, and M. F. Roche, *This Journal*, **128**, 760 (1981).
15. J. W. Searcy and J. R. Armijo, Sandia National Laboratories Report SAND 82-0565 (June 1982).
16. W. Borger, D. Kunze, and H. S. Panesar, Proceedings of the Second Contractors Meeting on Advanced Batteries and Fuel Cells, Kelkheim, Germany, April 1982, EUR 8078 EN, p. 18-20.

The Coupling Between Transport of Electric Charge and Chemical Reaction

K. S. Førland

Laboratory of Inorganic Chemistry, The Norwegian Institute of Technology, N 7034 Trondheim - NTH, Norway

T. Førland

Laboratory of Physical Chemistry, The Norwegian Institute of Technology, N 7034 Trondheim - NTH, Norway

A. A. Makange

Department of Chemical Engineering, University of Dar es Salaam, Dar es Salaam, Tanzania

S. K. Ratkje

Laboratory of Physical Chemistry, The Norwegian Institute of Technology, N 7034 Trondheim - NTH, Norway

ABSTRACT

A type of electrochemical cell was investigated in which chemical reactions take place in compartments between membranes. A theoretical treatment of the cells is presented whereby the Gibbs energy of reaction is avoided in the basic flux equation and in the equation for entropy production. Experimental data and theoretical calculations are presented for a cell of the above type.

Many processes in physical chemistry involve coupling of transport and a chemical reaction. A very simple example is the isothermal cell

$$(Pt)\,H_2(g)\,|HCl(aq)\,|Cl_2(g)\,(Pt)$$

where the chemical reaction

$$\tfrac{1}{2}\,H_2(g) + \tfrac{1}{2}\,Cl_2(g) = HCl(aq) \qquad [1]$$

causes transport of charge across the cell. When a small charge is transferred under near equilibrium conditions, the emf, $\Delta\phi$, in dimensions $J\mathbf{F}^{-1}$ (the electric work per faraday) is related to the Gibbs energy of reaction by the Nernst equation

$$\Delta G + \Delta\phi = 0 \qquad [2]$$

For this cell the electric work and the vectorial ion fluxes are coupled to the scalar function ΔG in a simple way. For more complex cells, where chemical reactions take place in compartments between membranes, the above kind of correlation between Gibbs energy of reaction and electric work may not be valid. In the cells dealt with in this paper, only part of the Gibbs energy of reaction is converted to electric work. To calculate the local loss of energy, we will use the formalism of irreversible thermodynamics. Thus we do not limit the calculations to cases where the current is zero.

The irreversible thermodynamic calculations are based on the assumption of local equilibrium. We will limit the number of components to that required by the phase rule. As a consequence the scalar function ΔG of reaction does not enter our flux equations, and we avoid the problem of scalar-vector coupling. The components are neutral compounds or elements (see Ref. [1] and [2]). Unmeasurable quantities such as single ion chemical potentials and local gradients in electric potential do not appear in our equations. The method permits an analysis of approximations introduced at any step of the calculations. Furthermore, local losses can be expressed by measurable quantities. We will first demonstrate the method of calculation for the above simple cell.

Reformulation of the Nernst Equation

The system in the above cell has three components in accordance with the phase rule. They are, *e.g.*, H_2, HCl, and H_2O. The chemical potential, μ, of each one of these species can be varied independently. The fourth species, Cl_2, is not an independent component as its chemical potential is given by the species HCl and H_2. When there is local equilibrium in the system, we have

$$\tfrac{1}{2}\,\mu_{Cl_2} = \mu_{HCl} - \tfrac{1}{2}\,\mu_{H_2} \qquad [3]$$

When a positive charge of $1\mathbf{F}$ is passed through the cell from left to right, ½ mol of Cl_2 and ½ mol of H_2 are removed from the cell at the left- and right-hand side electrode, respectively. Since Cl_2 is not chosen to be a component, the removal of ½ mol Cl_2 is described as a removal of 1 mol HCl and a simultaneous supply of ½ mol H_2. That is, ½ mol H_2 is transported across the cell from a chemical potential $\mu^\circ_{H_2(g)}$ at the left-hand side electrode where there is $H_2(g)$ at 1 atm pressure, to a chemical potential of

$$\mu_{H_2(g)} = 2\mu_{HCl(aq)} - \mu^\circ_{Cl_2(g)}$$

at the right-hand side electrode where there is $Cl_2(g)$ at 1 atm pressure.

The chemical potential of HCl is the same at both electrodes, and thus HCl is transported over a zero gradient in chemical potential. The emf of the cell can be related to the transfer of neutral components by the equation [see Ref. (2)]

$$\Delta\phi = -\int_1^2 \sum_i t_i d\mu_i \qquad [4]$$

where t_i is the number of mols of the neutral component i transferred per faraday. The left- and right-hand side electrodes are indicated by 1 and 2, respectively. For the present system with the two components H_2 and HCl, Eq. [4] gives

$$\Delta\phi = -\int_1^2 (t_{H_2} d\mu_{H_2} + t_{HCl} d\mu_{HCl}) = -\int_1^2 t_{H_2} d\mu_{H_2} \qquad [5]$$

where t_{H_2} is the number of mols of H_2 transferred per faraday. Since ½ mol H_2 is transferred per faraday, $t_{H_2} = \tfrac{1}{2}$.

Thus

$$\Delta\phi = -\int_1^2 \tfrac{1}{2}\, d\mu_{H_2} = -\tfrac{1}{2}\,(\mu_{H_2(g)} - \mu^\circ_{H_2(g)}) \qquad [6]$$

which is equivalent to Eq. [2]. The more complex cells described below, demonstrate the advantage of the method.

Cells with Cation and Anion Conducting Membranes

A cell of this type is shown in Fig. 1. It was investigated by Makange (3). The theoretical treatment of this cell is based on the postulates of irreversible thermodynamics. Again, the number of components used to describe the system is the minimum required by the phase rule.

The cell has a number of compartments separated by cation selective membranes, C, and anion selective membranes, A. The region of the cell denoted "repeating unit," extending from the middle of compartment I to the middle of compartment V, can be repeated several times. The electrodes are Ag/AgCl electrodes. Electric potential gradients, $\nabla\phi$, can be measured by introducing small Ag/AgCl test electrodes anywhere in the system (in order to obtain defined electric potentials in compartments III and IV, very small quantities of KCl must be added). In order to increase the conductivity in compartment III, an electrolyte HA (or KCl) is added. The ion A^- is very large, and thus the permeability of the anion-conducting membrane to A^- is very low.

By the transfer of **1F**, the cell reaction in a "repeating unit" is

$$HCl + KOH = KCl + H_2O \qquad [7]$$

We choose the following set of components

KCl, HCl, H_2O, and HA

They are given the numbers 1-4. KOH is not considered a component. It can be expressed by the others

$$KOH = KCl + H_2O - HCl$$

Local Entropy Production and Flux Equations

Transference numbers for neutral components are used [compare Ref. (2)]. They are defined as

$$t_i = \frac{J_i}{I} \qquad i = 1 \ldots 4 \qquad [8]$$

for $\nabla\mu_1 = \nabla\mu_2 = \nabla\mu_3 = \nabla\mu_4 = 0$

where J_i is the flux of the component i in dimensions mol m^{-2} sec^{-1}, and I is the current density in dimensions Fm^{-2} sec^{-1}.

The local entropy production per unit volume per unit time, θ, is given by the equation [see Ref. (1)]

$$T\theta = \sum_{i=1}^{4} J_i(-\nabla\mu_i) + I(-\nabla\phi) \qquad [9]$$

The unit of $\nabla\phi$ is JF^{-1} m^{-1} and the unit of I is $Fsec^{-1}$ m^{-2}.

The flux of charge, or current density, is given by

$$I = -\sum_{i=1}^{4} L_{5i}\nabla\mu_i - L_{55}\nabla\phi \qquad [10]$$

where L_{55} is related to the conductivity, κ; $L_{55} = -\kappa/F^2$. Rearrangement gives

$$\nabla\phi = -\sum_{i=1}^{4} \frac{L_{5i}}{L_{55}}\nabla\mu_i - \frac{I}{L_{55}} \qquad [11]$$

where L with a subscript is a phenomenological coefficient used in the linear theory of irreversible thermodynamics.

Further

$$\frac{L_{5i}}{L_{55}} = \frac{J_i}{I} = t_i \qquad [12]$$

for $\nabla\mu_1 = \nabla\mu_2 = \nabla\mu_3 = \nabla\mu_4 = 0$.

Equations [9]-[12] do not contain the scalar function ΔG of reaction.

The emf is obtained by integrating Eq. [11] for $I \approx 0$

$$\Delta\phi = -\int_I^V (t_{HCl}d\mu_{HCl} + t_{KCl}d\mu_{KCl} + t_{H_2O}d\mu_{H_2O} + t_{HA}d\mu_{HA}) \qquad [13]$$

For zero current there will be no gradient in concentration of HA in compartment III. Further, we have $d\mu_{H_2O} \approx 0$ over the whole system since all electrolytes are dilute. This means that the two last terms may be neglected.

The component transference numbers are related to the ionic transference numbers [see Ref. (3)]. For the cell given in Fig. 1 with perfectly selective cation and anion membranes (the anion A^- is too large to diffuse through the membrane), we will have the following changes when one faraday passes through the cell from left to right. One mol of Cl^- ions is produced at the right-hand electrode. This is compensated for by a transfer of K^+ through the cation membrane from compartment IV to V, $t_{K^+} = 1$. Further, OH^- is transferred from compartment IV to III through the anion membrane, $t_{OH^-} = 1$. Again H^+ is transferred from compartment II to III through the cation membrane, $t_{H^+} = 1$. Finally Cl^- is transferred from compartment II to I, $t_{Cl^-} = 1$, and in compartment I, one mol of Cl^- ions is removed.

From stoichiometric relations we have $n_{KCl} = n_{K^+}$ and $n_{HCl} = n_{Cl^-} - n_{K^+}$. The transference number for KCl is equal to the transference number for K^+

$$t_{KCl} = t_{K^+} \qquad [14]$$

The transfer of Cl^- from left to right is equal to the quantity reacted at the electrodes minus the quantity migrated from right to left through the electrolyte, $1 - t_{Cl^-}$. This gives for t_{HCl}

$$t_{HCl} = (1 - t_{Cl^-}) - t_{K^+} \qquad [15]$$

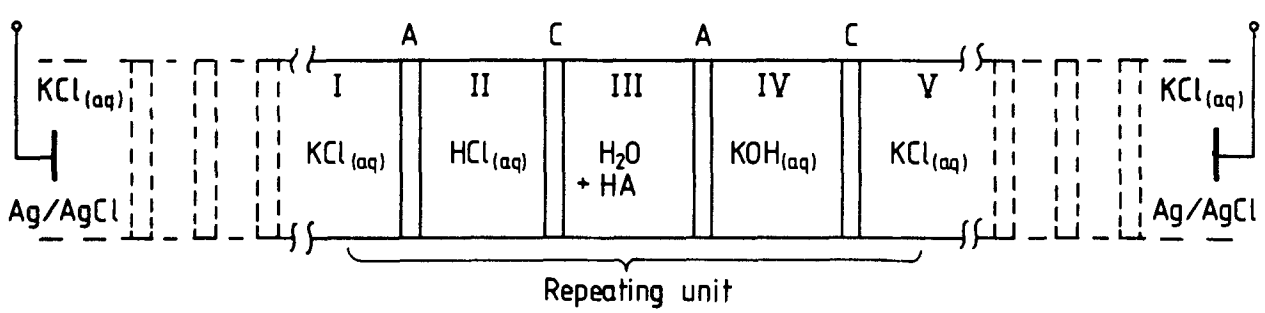

Fig. 1. Acid-base reaction in an electrochemical cell. A and C are anion and cation selective membranes, respectively. HA is an electrolyte, the main purpose of which is to increase the conductivity of compartment III. The anion A^- is too large to diffuse through the membrane.

Since the sum of all ionic transference numbers is equal to unity we have

$$t_{HCl} = 1 - t_{Cl^-} - t_{K^+} = t_{H^+} + t_{OH^-} + t_{A^-} \quad [16]$$

In the cell we thus have t_{KCl} equal to unity from compartment IV to V and equal to zero elsewhere, while t_{HCl} is equal to unity irom compartment II to IV and equal to zero elsewhere. When these relations are introduced in Eq. [13], one obtains

$$\Delta\phi = -\int_{II}^{IV} d\mu_{HCl} - \int_{IV}^{V} d\mu_{KCl} \quad [17]$$

or

$$\Delta\phi = -(\mu_{HCl\,IV} - \mu_{HCl\,II} + \mu_{KCl\,V} - \mu_{KCl\,IV}) \quad [18]$$

The chemical potential $\mu_{HCl\,IV}$ can be expressed as

$$\mu_{HCl\,IV} = \mu_{KCl\,IV} + \mu_{H_2O\,IV} - \mu_{KOH\,IV} \quad [19]$$

With the choice of components that we made, any transfer of an ion containing oxygen represents a transfer of H_2O since this is the only component containing oxygen (KOH is not a component). Thus the transfer of OH^- from compartment IV to III corresponds to a transfer of H_2O. This transfer of H_2O may be introduced together with Eq. [19] in Eq. [18] (even though transfer of H_2O does not contribute to $\Delta\phi$). Electro-osmotic water transfer is neglected. Then Eq. [18] takes the form

$$\Delta\phi = -(\mu_{KCl\,V} + \mu_{H_2O\,III} - \mu_{HCl\,II} - \mu_{KOH\,IV}) \quad [20]$$

or

$$\Delta\phi = -\Delta G = -(\Delta G^\circ - RT \ln (c_{H^+\,II} \times c_{OH^-\,IV})) \quad [21]$$

where ΔG° is the standard Gibbs energy of reaction, see Eq. [7], (units of c are mol dm^{-3}, activity coefficients have been omitted). Thus, under the conditions of perfectly selective membranes and no impurities in compartment III, we arrive at the Nernst equation through equations that express $\Delta\phi$ by means of "gradients" in chemical potentials of neutral components only (compare Eq. [11]). As will be shown below, the method allows us to calculate local energy losses under other conditions.

Calculations of Loss of Energy in the Cell

By the energy loss in an electrochemical cell we understand the difference between the maximum emf obtainable and the actual measured value. The maximum value of $\Delta\phi$, calculated from ΔG (omitting activity coefficients) is 0.71V. The measured value having pure water in compartment III (no HA is added) was 0.52 (3). The membranes are not 100% selective (99% for cation selective membranes and 96% for anion selective membranes). The above difference, however, is too large to be explained by membrane imperfection. One may understand the cause of the difference by inspecting Eq. [13]-[16]. The main cause of loss in $\Delta\phi$ must be small quantities of impurities in compartment III, making $t_{H^+} + t_{OH^-} < 1$. In order to investigate this loss in electric potential further, two sets of experiments were performed.

In the first set of experiments known quantities of KCl were added to the water in compartment III (no HA is added). The main contribution to the emf is the integral $-\int_{II}^{IV} t_{HCl} d\mu_{HCl}$ over compartment III and the two neighboring membranes. The maximum contribution is for $t_{HCl} = 1$. Lower values of t_{HCl} means lower coupling between transfer of HCl and transfer of charge. Contribution to the emf by the integral $\int t_{KCl} d\mu_{KCl}$ over compartment III is very small and is neglected. The loss in emf can be expressed as (compare Eq. [16])

$$\text{Loss} = -\int_{II}^{IV} (1 - t_{HCl})\, d\mu_{HCl} = -\int_{II}^{IV} (t_{K^+} + t_{Cl^-})\, d\mu_{HCl} \quad [22]$$

Since the transference number of an ion, t_i, is proportional to the ion mobility, u_i, and to the ion concentration, c_i, we have

$$t_i = \frac{u_i c_i}{\sum_j u_j c_j} \quad [23]$$

and

$$t_{K^+} + t_{Cl^-} = \frac{u_{K^+}c_{K^+} + u_{Cl^-}c_{Cl^-}}{u_{H^+}c_{H^+} + u_{OH^-}c_{OH^-} + u_{K^+}c_{K^+} + u_{Cl^-}c_{Cl^-}} \quad [24]$$

With known concentration profiles one can use Eq. [22] and [24] to calculate the loss in emf as a function of the KCl concentration.

When compartment III is filled with a KCl solution of concentration c, there will be an interdiffusion of positive ions across the cation membrane on the left-hand side and an interdiffusion of negative ions across the anion membrane on the right-hand side. In a short time the H^+ will have replaced most of the K^+ adjacent to the cation membrane while similarly OH^- will have replaced Cl^- adjacent to the anion membrane. Further, a nonstationary diffusion will take place across the compartment whereby H^+ and OH^- will meet and combine.

We will consider two extreme models for the concentration profiles.

A. Early in the diffusion process, we assume constant concentration of Cl^- in the left-hand part of the compartment and constant concentration of K^+ in the right-hand part.

B. We assume that the concentration of Cl^- and of K^+ adjacent to the cation membrane and the anion membrane, respectively, will keep equal to c until the concentration of each has attained ½ c at the neutral point ($c_{H^+} = c_{OH^-} = 10^{-7}$). By assuming linear gradients, the loss in emf can be calculated.

The calculated loss for the two cases A and B are shown in Fig. 2 together with observed losses. (Corrections for nonideal solutions would give slightly better agreement with experiments.) Measurements of emf

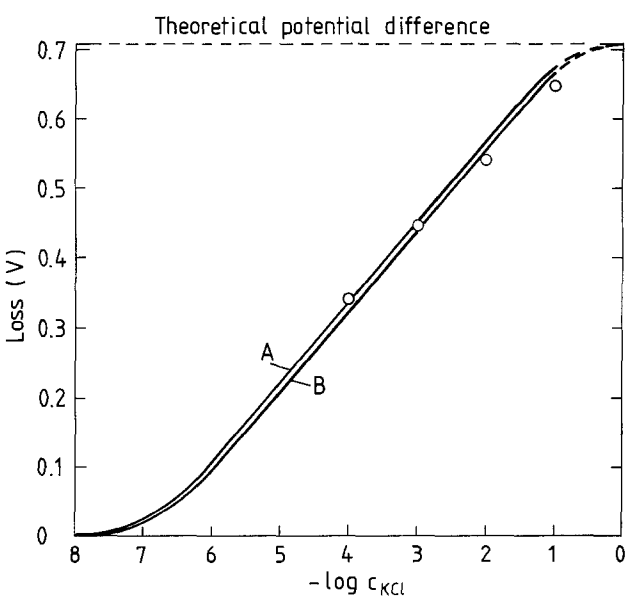

Fig. 2. Loss in emf as a function of concentration (mol dm^{-3}) of KCl in compartment III. A, Calculated loss at an early stage of diffusion process. B, Calculated loss at a later stage of diffusion process. O, Experimental points.

were carried out for concentrations of KCl sufficiently high to predominate over impurities.

From the above calculations and measurements one can see that KCl should not be used to improve conductivity in compartment III, since KCl gives large losses in emf. One can also see how small quantities of impurities in the experiment with water in compartment III give significant reduction of the emf.

In the second set of experiments, different types of organic acids/bases were tested as the component HA. In this case the transference number of HCl is given by Eq. [16], and A^- as well as H^+ and OH^- contribute to t_{HCl}.

With electric current passing through the cell (in positive direction) HA will accumulate on the left-hand side of compartment III, and the last term of the integral in Eq. [13] will be different from zero.

The additional contribution to the emf is

$$-\int t_{HA} d\mu_{HA} = -\int (-t_{A^-}) d\mu_{HA} \qquad [25]$$

since $t_{HA} = -t_{A^-}$

The contribution is negative, *i.e.*, there is a loss in emf. For a current density of 100 mA cm^{-2}, a concentration $c_{HA} = 0.1$ mol dm^{-3} and a length of compartment III of 1 mm, the calculated loss in emf due to this term is only about 0.3 mV.

The effect of different types of HA on the cell emf is shown in Table I [see Ref. (3) for further details]. One of the components in Table I, aminonaphthalene disulfonic acid, is capable of restoring the emf to 94% of the theoretical value. This molecule contributes to t_{HCl} both as a positive and as a negative ion.

In the above calculations local changes are expressed by locally defined forces only. The method permits us to locate energy losses, and to predict means of minimizing the losses. The addition of HA improves electric conductivity in compartment III without reducing the coupling between electric energy and Gibbs energy of reaction. Additions of KCl, however, will destroy the coupling, see Eq. [16].

Cells Containing Reciprocal Salt Pairs

With the present efforts in many laboratories to develop high temperature ion selective membranes for batteries, one may consider a high temperature cell of the type shown in Fig. 3. Here one set of membranes is selective for Li^+ ions, the other set for K^+ ions. By transfer of 1**F**, the cell reaction in a "repeating unit" is

$$LiBr + KCl = LiCl + KBr \qquad [26]$$

In fused salt chemistry it is common practice to describe this kind of system by three components. We may choose the following components, LiCl, LiBr, and KCl. In mixtures of fused salts it is unsuitable to use a single ion chemical potential (4), so we continue using the chemical potential of neutral salts and the transference numbers of neutral salts.

For $I = 0$ the emf per "repeating unit" is (compare Eq. [13])

Table I. Variation of cell emf E by addition of components HA (10^{-2} mol dm^{-3}) to compartment III of the cell in Fig. 1. The theoretical maximum value of emf is $E_T = 0.71$ V and η is the efficiency of the cell. The temperature is 25°C.

HA	E volt	$\eta = E/E_T$
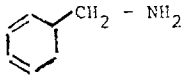 Benzylamine	0.42	0.59
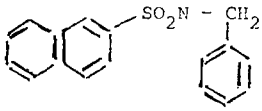 N-phenylmethyl Naphthalenesulfonamid	0.46	0.65
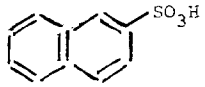 Naphthalenesulfonic acid	0.52	0.73
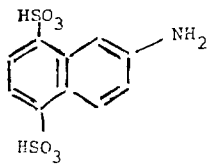 Aminonaphthalene disulfonic acid	0.67	0.94
KCl, 10^{-2} mol dm^{-3}	0.17	0.24

$$\Delta\phi = -\int (t_{LiCl} d\mu_{LiCl} + t_{LiBr} d\mu_{LiBr} + t_{KCl} d\mu_{KCl}) \qquad [27]$$

From stoichiometric relations ($n_{KCl} = n_{K^+}$, $n_{LiBr} = n_{Br^-}$, and $n_{LiCl} = n_{Li^+} - n_{Br^-}$) the transference numbers of neutral salts can be identified

$$t_{KCl} = t_{K^+}; \quad t_{LiBr} = -t_{Br^-} = 0$$

and

$$t_{LiCl} = t_{Li^+} + t_{Br^-} = t_{Li^+} \qquad [28]$$

The transference number $t_{Br^-} = 0$ since all membranes are cation selective. Thus

$$\Delta\phi = -\int (t_{Li^+} d\mu_{LiCl} + t_{K^+} d\mu_{KCl}) \qquad [29]$$

and for perfectly ion selective membranes

$$\Delta\phi = -\int_{II}^{III} d\mu_{LiCl} - \int_{I}^{II} d\mu_{KCl} \qquad [30]$$

or

$$\Delta\phi = -(\mu_{LiCl\ III} - \mu_{LiCl\ II}) - (\mu_{KCl\ II} - \mu_{KCl\ I}) \qquad [31]$$

In compartment II the chemical potential of KCl may be expressed as

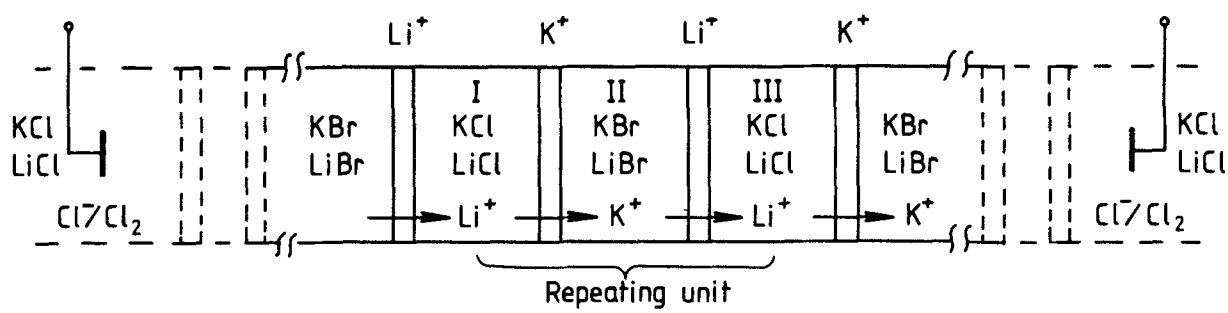

Fig. 3. Reciprocal salt pair reaction in an electrochemical cell. The cell contains cation conducting membranes, one set selective for K^+ ions and one set selective for Li^+ ions. Electrolytes are fused salts.

$$\mu_{KCl} = \mu_{KBr} + \mu_{LiCl} - \mu_{LiBr} \quad [32]$$

This gives the anticipated result

$$\Delta\phi = -(\mu_{LiCl\ III} + \mu_{KBr\ II} - \mu_{KCl\ I} - \mu_{LiBr\ II}) \quad [33]$$

The derivation [27]-[31] shows the validity conditions for Eq. [33]

Thus if the cell unit starts in the state

$$\ldots LiBr \,||\, KCl \,||\, LiBr \,||\, KCl \ldots$$

then, through the transfer of charge we will end up with

$$\ldots KBr \,||\, LiCl \,||\, KBr \,||\, LiCl \ldots$$

or a complete reaction of the reciprocal salt pair.

Discussion and Conclusions

The description of transport pheomena given in this paper has several advantages.

Only measurable quantities are used to describe the transport phenomena. Thus any approximation introduced in the derivations can be checked by measurements.

The choice of components is in accordance with the phase rule which gives independent forces and fluxes when the formalism of irreversible thermodynamics is applied. In systems where chemical reactions take place under local equilibrium conditions, this permits a simple way of describing the transport phenomena, since the problem of scalar-vector coupling is avoided. This way of dealing with chemical reactions is new.

The description is independent of the structure of the system. Thus a calculation of transport processes can be done without any assumption of structural units like ionic groups. Local energy losses can be analyzed in terms of measurable quantities.

The commonly used equation for electric potential changes in a solution is

$$\mathbf{F}d\phi_s = -\Sigma(t_i/z_i)\,d\mu_i \quad [34]$$

where $\mathbf{F}$ is Faraday's constant; ϕ_s is the solution potential; t_i, z_i, and μ_i the transference number, charge, and chemical potential of the ion i; and the sum is over all ionic species present. The equation contains local electric potential gradients, which are unmeasurable, and gradients in single ion chemical potentials, also unmeasurable. One integrates this equation and adds to it the unmeasurable single electrode potentials. The unmeasurable quantities add up to give measurable quantities, and the emf of the cell can be calculated.

Our treatment has a different purpose. We ask the question: Where do we find the local Gibbs energy changes responsible for the external emf (or electric work per unit charge)? This question can be answered in detail for local changes as expressed by measurable and well-defined quantities.

We believe that this operational approach may be useful for electrochemists. Models of the system and assumptions about ionic species can always be introduced at a later stage in the analysis of the properties of a system.

The present way of treating the coupling between chemical reaction and electric work may be profitable in the search for new types of batteries.

Manuscript submitted Dec. 3, 1982; revised manuscript received July 18, 1983. This was Paper 740 presented at the San Francisco, California, Meeting of the Society, May 8-13, 1983.

The Norwegian Institute of Technology assisted in meeting the publication costs of this article.

REFERENCES

1. T. Førland and S. K. Ratkje, *Electrochim. Acta*, **25**, 157 (1980).
2. K. S. Førland, T. Førland, and S. K. Ratkje, *Acta Chem. Scand.*, **A31**, 47 (1977).
3. A. Makange, *ibid.*, **A35**, 255 (1981).
4. T. Førland and K. Grjotheim, *Met. Trans.*, **9B**, 45 (1978).

The Electrochemistry of Ferrophosphorus in Strong Aqueous Acid

Pamela J. Peerce-Landers*,[1] and Raymond J. Jasinski*

Occidental Research Corporation, Irvine, California 92714

ABSTRACT

The electrochemistry of ferrophosphorus in 1*N* aqueous acid was investigated and compared to that of iron. The effects of chloride and dissolved oxygen were also studied. Ferrophosphorus was found to be much more resistant to anodic oxidation than iron in strong acid. Chloride did not change the potential at which ferrophosphorus oxidized. Dissolved oxygen assisted in the passivation of ferrophosphorus. Anodic oxidation of ferrophosphorus resulted in the formation of an adherent protective film of ferric phosphate on the electrode surface. Ferric and orthophosphate ions were also released into the solution. Reduction of both soluble Fe^{+3} and adsorbed ferric phosphate were observed following anodic oxidation of ferrophosphorus.

Ferrophosphorus is a commercial mixture of iron phosphide (FeP) and diiron phosphide (Fe_2P) and typically contains approximately 22-25% phosphorus, less than 1% silicon dioxide, and the balance iron (1). Because of its corrosion resistance in aqueous media, ferrophosphorus has been used in corrosion protection coatings (2). It has also been considered for use as an inexpensive corrosion resistant anode in electroorganic chemistry (3, 4). Nevertheless, a complete description of its electrochemical behavior in aqueous solution has not yet appeared in the literature. The results of our study in strong aqueous acid are reported herein.

* Electrochemical Society Active Member.
[1] Present address: Betz Laboratories, Inc., The Woodlands, Texas 77380.
Key words: alloy, refractories, ferrophosphorus, voltammetry.

Experimental

Materials.—Ferrophosphorus ingots were obtained from Hooker Chemical Company (Columbia, Tennessee). The elemental analysis was consistent with a ratio of Fe_2P to FeP of 6.5. Iron wire was obtained from Alfa-Ventron (99.9%). The epoxy in which the polished ferrophosphorus disks were imbedded was comprised of Araldite 506 Resin and Araldite 956 Hardener (4 parts resin: 1 part hardener by weight). The epoxy does not dissolve or soften in aqueous solutions below 100°C. The mold release agent was Buehler Release Agent. The epoxy and release agent were obtained from Symplastics, Incorporated (Montrose, California). All solutions were prepared by dissolving reagent grade chemicals in distilled water.

Electrode fabrication, ferrophosphorus.—Several disks 1/2 in. in diameter and 1/4 in. thick were cut from a ferrophosphorus ingot. Each disk was placed in separate cylindrical glass molds 1 in. in diameter coated with Buehler release agent. The molds were then filled with Araldite epoxy and allowed to cure overnight at room temperature. The casts were removed from the molds and the exposed face of each ferrophosphorus disk was mechanically polished with increasingly finer grades of silicon carbide grit and finally with 0.3μ diamond paste until the exposed surface was shiny. The casts were then placed on a hot plate for a few minutes to soften the Araldite epoxy, and the epoxy was cut away from the ferrophosphorus disks. Electrodes were constructed from these disks.

Silver paint was used to make an ohmic contact between the back side of the ferrophosphorus disk and a length of copper wire. (The copper wire had been threaded through some 1/4 in. OD glass tubing.) After the silver paint had dried, the contact was secured with a few drops of 5 min epoxy. The electrode assembly was then centered within a length of 3/4 in. ID glass tubing resting on a piece of plate glass which had been wiped with Buehler release agent. This glass mold was filled with Araldite epoxy and allowed to cure overnight at 40°C. (The Araldite epoxy masked all but the polished face of the ferrophosphorus disk and protected the electrical contact.) All traces of Araldite epoxy and Buehler release agent were then removed from the polished face of the finished electrode.

The area of the ferrophosphorus electrodes, as measured by chronoamperometry, was 1.26 cm^2.

Apparatus.—Cyclic voltammograms were obtained using a Princeton Applied Research 175 Universal Programmer in conjunction with a Princeton Applied Research 173 Potentiostat and a Princeton Applied Research 179 Digital Coulometer. The electrochemical cell was a standard three-compartment cell which isolated the working and auxiliary electrodes with provision for degassing the solution in the working electrode compartment. A platinum wire served as the auxiliary electrode. Potentials were measured and are reported with respect to an aqueous saturated calomel electrode (SCE) (situated in the working electrode compartment).

Procedure.—Immediately before each use, the ferrophosphorus and iron electrodes were polished with 0.05μ alumina powder on moist felt, rinsed thoroughly with distilled water, and then dried with a Kimwipe. Electrolyte degassing was accomplished by bubbling prepurified nitrogen through the solution for 10-15 min. The nitrogen flow was then diverted over the solution to prevent the reabsorption of oxygen. All measurements were performed at the laboratory temperature, 25° ± 2°C. In the cyclic voltammograms, reductive currents are positive and negative potentials are to the right.

Results and Discussion

The cyclic voltammetric behavior of ferrophosphorus in aqueous acid was examined and compared with that of iron. The effects of chloride and dissolved oxygen on the electrochemistry of ferrophosphorus were also studied.

Cyclic voltammograms for ferrophosphorus and iron in air-saturated 1*N* H_2SO_4 are shown in Fig. 1 and 2, respectively. The large anodic wave at +1.3 in Fig. 1 represents the anodic oxidation of ferrophosphorus. Significant anodic current was observed at potentials positive of +0.6V. By contrast, anodic oxidation of iron occurred at potentials positive of −0.5V (Fig. 2). Soluble products were formed.

The electrochemistry of ferrophosphorus in 1*N* HCl (Fig. 3) was very similar to that observed in 1*N* H_2SO_4 (Fig. 1). The only significant difference was that in 1*N* HCl the first cathodic wave shifted somewhat positive. Since the behavior of ferrophosphorus in these two

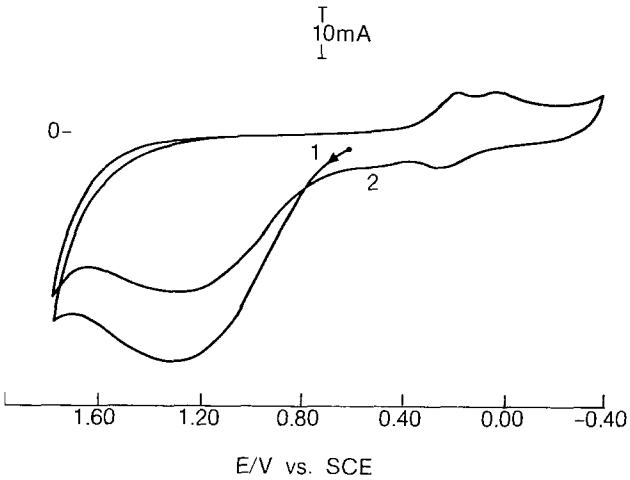

Fig. 1. Cyclic voltammetry of ferrophosphorus in air-saturated 1*N* H_2SO_4. Initial scan direction: positive. Scan rate: 0.1 V/sec.

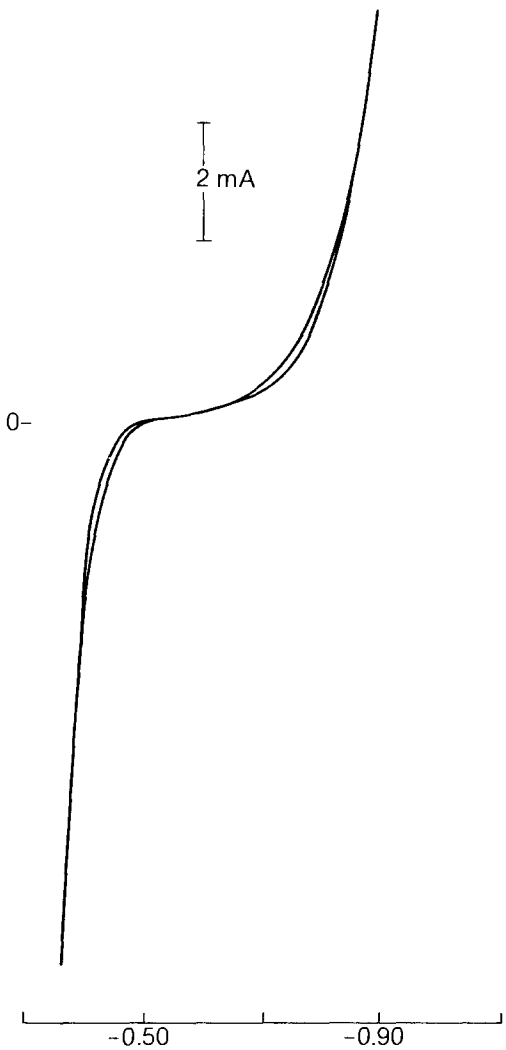

Fig. 2. Cyclic voltammetry of iron in air-saturated 1*N* H_2SO_4. Initial scan direction: positive. Scan rate: 0.1 V/sec.

acids was virtually identical, there was no basis of preference in subsequent experiments.

The effect of dissolved oxygen on the electrochemical behavior of ferrophosphorus is illustrated in Fig. 4. The initial scans were negative. In the presence of oxygen (Fig. 4A), the open-circuit potential was *ca.* 160 mV more positive, and less current was observed for the oxidation of ferrophosphorus on the first anodic scan

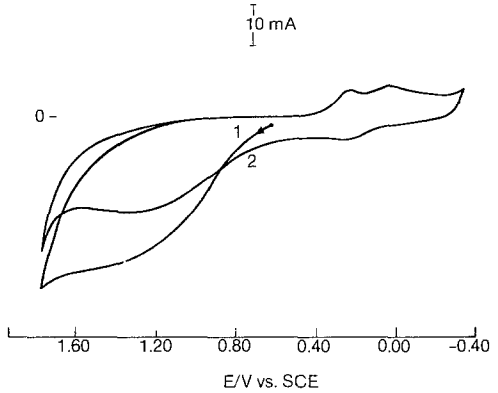

Fig. 3. Effect of chloride. Cyclic voltammetry of ferrophosphorus in 1N HCl. Initial scan direction: positive. Scan rate: 0.1 V/sec.

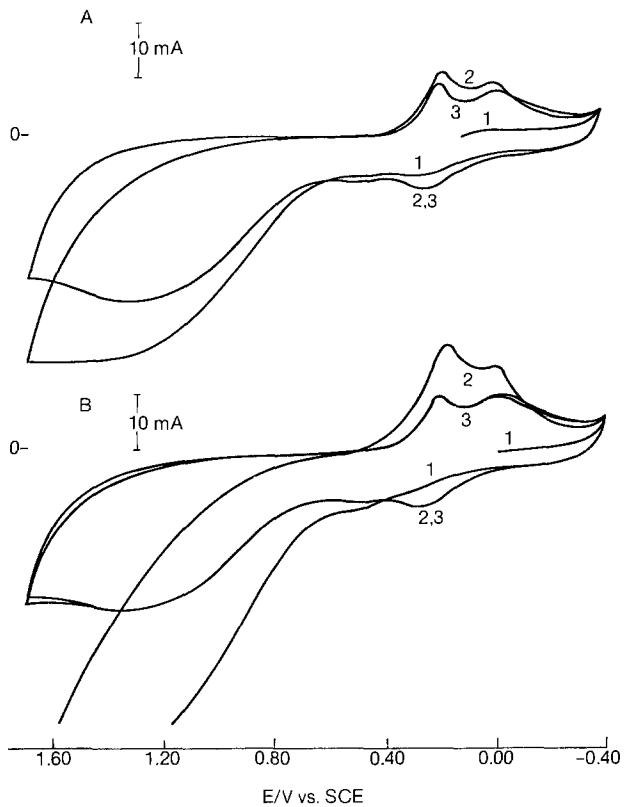

Fig. 4. Effect of dissolved oxygen. Cyclic voltammetry of ferrophosphorus in 1N HCl. Initial scan direction: negative. Scan rate: 0.1 V/sec. Part A: air-saturated. Part B: deaerated.

[cf. Fig. 4A (oxygenated) and 4B (deoxygenated)]. After the second anodic scan, the two voltammograms were essentially indistinguishable. Apparently, in the presence of oxygen, ferrophosphorus passivates more readily. Although a separate wave attributable to oxygen reduction was not observed, the peak current expected was less than 1 mA. Therefore, the oxygen wave may simply be unresolved.

Figure 4 also suggests that the species responsible for the cathodic waves at *ca.* +0.2 and 0 V arise from the oxidation of ferrophosphorus. These waves were absent during the first cathodic scan but appeared after the potential had been swept positive to +1.7V. (The same results were obtained in 1*N* H_2SO_4.) The larger cathodic currents observed after the first anodic sweep in the absence of oxygen also support this conclusion. Subsequent experiments showed that these two pairs of waves could not both be explained by soluble iron species. The evidence and reasoning for this statement are described below.

Wood (4) reported that when iron phosphide (FeP) and diiron phosphide (Fe_2P) (the constituents of ferrophosphorus) were anodically oxidized in 1*N* acid, ferric and orthophosphate ions were released into the solution. Ferrous ions were not observed because the potentials required for the oxidation of FeP and Fe_2P are considerably more positive than the standard potential of the Fe^{+3}/Fe^{+2} couple. The net anodic oxidation of FeP and Fe_2P may therefore be described by the following equations

$$FeP + 4H_2O \rightarrow Fe^{+3} + H_3PO_4 + 5H^+ + 8e^- \quad [1]$$

$$Fe_2P + 4H_2O \rightarrow 2Fe^{+3} + H_3PO_4 + 5H^+ + 11e^- \quad [2]$$

Since the ratio of Fe_2P to FeP in the ferrophosphorus ingots used in this work was 6.5, the overall equation for the observed oxidation of ferrophosphorus is

$$0.13\ FeP + 0.87\ Fe_2P + 4H_2O \rightarrow 1.87\ Fe^{+3} + H_3PO_4 + 5H^+ + 10.6e^- \quad [3]$$

It is well known that the phosphate complexes iron (5, 6). Consequently, the potential of the Fe^{+3}/Fe^{+2} couple is more negative in phosphoric acid than in either hydrochloric or sulfuric acid (7). Given the stoichiometry in Eq. [3], it is tempting to assign the two pairs of waves observed between −0.6 and +0.2V to the reduction and subsequent reoxidation of soluble Fe^{+3} uncomplexed by phosphate and soluble Fe^{+3} complexed by phosphate. However, only a single pair of waves were observed at platinum when increasing amounts of H_3PO_4 were added to a solution of 0.05*M* $FeCl_3$ in 1*M* HCl. The reduction potential shifted negative as the total concentration of H_3PO_4 was gradually increased to 0.23*M*, but the waves did not split. (Above 0.23*M* H_3PO_4, no further shift in the reduction potential was observed.) Consequently, the two pairs of waves observed at ferrophosphorus cannot both be attributable to soluble Fe^{+3}/Fe^{+2}. Moreover, the Fe^{+2}/Fe° couple cannot be involved because the standard potential for Fe^{+2}/Fe° is −0.65V *vs.* SCE. Therefore, one of these pairs of waves is peculiar to ferrophosphorus.

When ferrophosphorus was anodized at +1.2V in 1*M* HCl for a few minutes, the oxidation current gradually decayed from 30 mA to a steady-state value of *ca.* 4 mA. Inspection of the freshly anodized electrode surface revealed the presence of a very adherent white film. No such film was observed on prolonged anodization of the iron electrode at −0.35V in 1*M* HCl. However, when the iron electrode was anodized in 1*M* HCl containing 0.2*M* H_3PO_4 at −0.33V *vs.* SCE for 5 min, a similar white film also formed on its surface. This film protected the iron from further oxidation.

This behavior of iron in the presence of phosphate is not new. It is well documented that phosphate inhibits the corrosion of iron (8, 9). Passivation is attributed to the formation of a film of ferrous phosphate on the exposed metal surface (8-10). Work by Florianovich, Kolotyrkin, and Kononova has shown that ferrous phosphate does not precipitate on the iron surface, but rather is formed in a direct electrochemical reaction between iron metal and phosphate (11). Since the oxidation of ferrophosphorus produces phosphate, it is likely that a similar mechanism is operative here. This would explain why no film formation was observed in the experiments conducted at platinum (see above). Experiments described later confirm this similarity in mechanism.

Anodic oxidation of ferrophosphorus occurs at potentials which are *ca.* 1.5V positive of those at which iron is oxidized. Therefore, the protective film formed on ferrophosphorus is probably ferric phosphate rather than ferrous phosphate. Although ferric phosphate is moderately soluble in strong acid (the conditional solubility product at *p*H 0 is 2×10^{-2}), the following experiments demonstrate that the film persisted sufficiently long on the cyclic voltammetric time scale to undergo subsequent reduction. Soluble iron species were also observed.

A freshly polished ferrophosphorus electrode was first repeatedly cycled between +1.7 and −0.4V in 1*N* H_2SO_4 until the steady-state response was obtained (*ca.* five cycles). The solution was then stirred and cycling continued. The more positive pair of waves diminished on stirring, whereas the more negative couple was relatively unaffected by stirring (Fig. 5A). This result suggests that the more positive couple is due to dissolved Fe^{+3}/Fe^{+2} and the more negative couple to Fe^{+3}/Fe^{+2} phosphate on the electrode surface. Moreover, the more positive couple was much more sensitive to changes in the anodic switching potential.

Following the experiments shown in Fig. 5A, stirring was discontinued but potential cycling was continued while the solution became quiescent (*ca.* 60 sec). The anodic switching potential was then successively set to +0.7, +1.3, and +1.7V. The results are shown in Fig. 5B. The more positive cathodic wave was barely discernible at the lowest switching potential (+0.7V). It increased in height and shifted negative as the anodic switching potential was increased. The more negative cathodic wave was less sensitive to variations in the anodic switching potential.

The behavior exhibited by the first couple is consistent with its assignment to soluble Fe^{+3}/Fe^{+2}. Assuming the first couple represents reduction and reoxidation of a mixed sulfate-phosphate ferric complex, one would expect its potential to shift negative as the phosphate concentration increased, *i.e.*, as the anodic switching potential was increased. Moreover, since the oxidation of ferrophosphorus is the only source of Fe^{+3}, one would expect the height of this wave to increase as more time was permitted for the oxidation of ferrophosphorus, *i.e.*, as the anodic switching potential was increased. Conversely, once formed, the attached or bound film of ferric phosphate should be less sensitive to changes in the anodic switching potential as was observed. The slight diminution in the height of the second cathodic wave with a decrease in the anodic switching potential reflects the gradual dissolution of

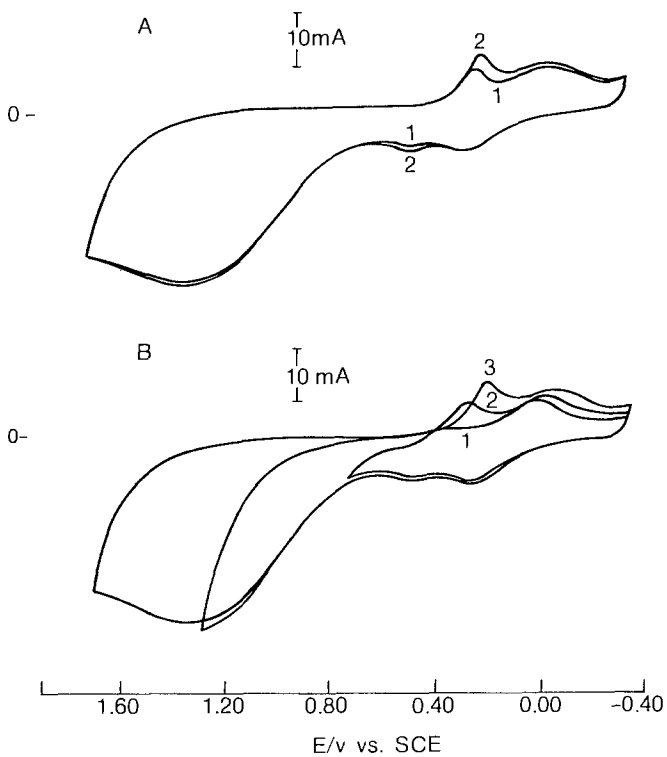

Fig. 5. Cyclic voltammetry of ferrophosphorus in air-saturated 1*N* H_2SO_4. Scan rate: 0.1 V/sec. Part A: Effect of stirring (curve 1, stirred; curve 2, not stirred). Part B: Effect of anodic switching potential (curve 1, E_λ = 0.7V, curve 2, E_λ = 1.3V; curve 3, E_λ = 1.7V.

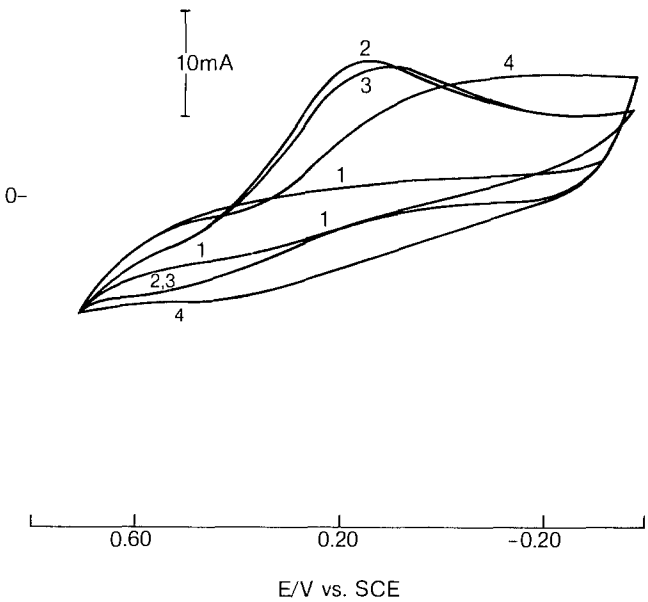

Fig. 6. Cyclic voltammetry of Fe^{+3} at a freshly polished ferrophosphorus surface in air-saturated 1*N* H_2SO_4. Curve 1, no added Fe^{+3}; curve 2, 0.05*M* $Fe_2(SO_4)_3$; curve 3, 0.05*M* $Fe_2(SO_4)_3$ + 0.027*M* H_3PO_4; curve 4, 0.05*M* $Fe_2(SO_4)_3$ + 0.3*M* H_3PO_4.

the ferric phosphate film in the strong acid medium. The validity of this assignment was confirmed by the following experiment.

A freshly polished ferrophosphorus electrode was first cycled between +0.7 and −0.3V in 1*N* H_2SO_4 (curve 1, Fig. 6). (This positive potential is insufficient to substantially oxidize the ferrophosphorus surface.) An amount of $Fe_2(SO_4)_3$ sufficient to yield a 0.05*M* solution was then added and curve 2 (Fig. 6) was obtained. The observed peak potentials for soluble Fe^{+3}/Fe^{+2} closely correspond to those observed for the more positive couple in Fig. 1. The solution was then made 0.027*M* in H_3PO_4 to mimic the stoichiometry in Eq. [3]. As shown by curve 3 (Fig. 6), the cathodic peak potential shifted *ca.* 40 mV negative, but was still well positive of that observed for the more negative couple (*cf.* Fig. 1). The waves did not split. Therefore, the second pair of waves shown in Fig. 1 cannot be due to soluble, phosphate-complexed Fe^{+3}/Fe^{+2}. Only when this solution was 0.3*M* in H_3PO_4 (curve 4, Fig. 6) did the cathodic peak potential shift sufficiently negative to correspond to that of the second reduction peak observed at oxidized ferrophosphorus in 1*N* H_2SO_4 (Fig. 1). Splitting of the Fe^{+3}/Fe^{+2} waves was never observed. These results and those described above support the assignment of the first pair of waves to soluble Fe^{+3}/Fe^{+2} and the second pair to adsorbed iron phosphate. Furthermore, the iron phosphate film forms directly on the ferrophosphorus surface during anodization rather than by precipitation from solution. This behavior is analogous to that reported when iron is oxidized in phosphate solution (10).

Manuscript submitted March 25, 1983; revised manuscript received July 20, 1983.

Occidental Research Corporation assisted in meeting the publication costs of this article.

REFERENCES

1. "Mellor's Comprehensive Treatise on Inorganic and Theoretical Chemistry," Vol. VIII, Supp. III, pp. 322-330, Wiley-Interscience, New York (1971); "Ferrophos®," Material Safety Data Sheet, Hooker Chemicals & Plastics Corp., Niagara Falls, NY (1979).
2. E. Leon and J. A. Pawlak, U.S. Pat. 3,562,124 (1971); N. D. Blair, U.S. Pat. 3,884,705 (1975).
3. D. W. Wood, Ph.D. Thesis, University of Illinois, IL (1953); *Dissert. Abstr.*, **13**, 362 (1953).

4. M. Williams and N. C. Fawcett, Paper 49 presented at the 181st National American Chemical Society Meeting, Atlanta, GA, March 29-April 3, 1981.
5. L. G. Sillen and A. E. Martell, "Stability Constants of Metal Ion Complexes," Spec. Publ. No. 17, p. 185, The Chemical Society, London (1964).
6. A. Ram, A. K. Bose, and S. Kumar, *J. Sci. Ind. Res.*, **15B**, 78 (1956).
7. "Handbook of Chemistry and Physics," 59th ed., p. D-193, CRC Press, Inc., West Palm Beach, FL (1978).
8. T. Kodama, *Boshoku Gijutsu*, **23**, 545 (1974).
9. N. Sato, K. Kudo, and T. Noda, *Z. Physik. Chem. N. F.*, **98**, 271 (1975).
10. G. M. Florianovich, Ya. M. Kolotyrkin, and M. D. Kononova, in "Proceedings of the 4th International Congress on Metal Corrosion," p. 694, National Association of Corrosion Engineers, 1972.

A Mechanistic Study of Oxygen Evolution on $NiCo_2O_4$

II. Electrochemical Kinetics

P. Rasiyah* and A. C. C. Tseung**

Department of Chemistry, The City University, Northampton Square, London, England EC1V 0HB

ABSTRACT

Oxygen evolution studies were carried out on pre-anodized, Teflon-bonded $NiCo_2O_4$ electrodes in KOH electrolytes of eight different concentrations ranging from 0.1 to 5.0 mol dm^{-3}. Oxygen evolution was found to be governed by two Tafel regions, 0.04V per decade at lower overpotentials and 0.12V per decade at higher overpotentials, in KOH electrolytes of concentration of 1.2 mol dm^{-3} and greater. In KOH electrolytes of concentration less than 1.2 mol dm^{-3}, the Tafel slope of 0.04V per decade was not observed. The two Tafel regions have been discussed in relation to the activity of divalent and trivalent sites of $NiCo_2O_4$ toward oxygen evolution.

The production of hydrogen is an important process, as it can be used as a nonpolluting fuel. A simple way of producing hydrogen is by the electrolysis of water. At present, alkaline water electrolyzers have a low energy efficiency due to the high activation overvoltage of oxygen evolving anodes such as nickel, nickel-plated iron, and ferrous nickel alloys (1). Recently, much effort has been directed to the study of transition metal oxides as oxygen evolving anodes in alkaline media (2-7), in an attempt to lower the oxygen overvoltage. Of such oxides reported in literature, the mixed spinel $NiCo_2O_4$ is a promising material, due to its favorable properties of low intrinsic electrical resistivity and fairly low oxygen overvoltage, and corrosion stability in alkaline media. Although many workers (7-12) have studied oxygen evolution on $NiCo_2O_4$ and its stability as an anode on a long-term basis, no definite mechanism has yet been put forward that involves the identification of the active sites of the mixed spinel. Such studies not only help in understanding the complicated process of oxygen evolution, but also help in developing better oxygen evolution electrocatalysts.

Tseung and Jasem (6) put forward guidelines for the choice of semiconducting oxides for the oxygen evolution reaction. They emphasized the role of the metal/metal oxide couple or the lower metal oxide/higher metal oxide couple in determining the minimum voltage of oxygen evolution. This consideration, as well as other essential requirements such as electrical resistivity and corrosion resistance, suggested that $NiCo_2O_4$ should be a good oxygen evolution electrocatalyst. This was confirmed experimentally; Teflon-bonded $NiCo_2O_4$ electrodes gave oxygen evolution currents of 1 A cm^{-2} at 1.6V *vs.* the dynamic hydrogen electrode at 70°C in 5*N* KOH. Tseung *et al.* (9) carried out long-term endurance tests by evolving oxygen on Teflon-bonded $NiCo_2O_4$ electrodes at a current density of 1 A cm^{-2} at 85°C in 45% KOH for 3000 hr with less than 50 mV increase in overpotential. Vandenbore and Leysen (8) reported that the performance of $NiCo_2O_4$ was the best out of four electrocatalysts studied and to have stable overvoltages for over 2000 hr of operation at a current density of 1 A cm^{-2} at 85°C in 50% KOH. The $NiCo_2O_4$ electrodes studied by these workers were prepared by thermal decomposition of nickel and cobalt nitrates on perforated nickel plates. Singh *et al.* (7) investigated oxygen evolution on $NiCo_2O_4$ obtained by thermal decomposition of nickel and cobalt salts on metal substrates, and found a Tafel slope of 0.045V per decade. However, Efremov and Zhukov (11) reported oxygen evolution on $NiCo_2O_4$ to be controlled by two Tafel slopes, a slope of 0.05V per decade at low potentials increasing to a slope of 0.09V per decade at higher potentials. Jasem and Tseung (12) carried out potentiostatic pulse studies on Teflon-bonded $NiCo_2O_4$ electrodes and found oxygen evolution to be also controlled by two Tafel regions, the value of the slopes depending on the initial pulsing potential. In a previous paper (12), we reported coulometry studies carried out on $NiCo_2O_4$ at potentials before oxygen evolution and found that the nickel and cobalt (A) cation sites on the surface of the polycrystalline $NiCo_2O_4$ undergoes oxidation state transitions $A^{2+} \rightarrow A^{3+} \rightarrow A^{4+}$; thus attaining highest oxidation state before oxygen is evolved. In this paper we report the investigation carried out to elucidate the oxygen evolution mechanism on $NiCo_2O_4$ and postulate a role for the different surface sites on $NiCo_2O_4$ during the oxygen evolution process.

Experimental

The $NiCo_2O_4$ for this study was obtained by freeze drying (13) a solution of nickel and cobalt nitrate. The mixed, dried nitrates were vacuum decomposed and thermally treated in air at 400°C for 10 hr to obtain the spinel. X-ray characterization confirmed complete spinel phase formation. The room temperature electrical resistivity of the oxide was measured using a Teflon die and was found to be less than 10 Ω-cm. The BET specific surface area of the oxide was found to be 43 $m^2\ g^{-1}$.

Teflon-bonded electrodes of $NiCo_2O_4$ were fabricated (14) using 100 mesh Ni screen as current collector. Before actual measurements were taken, the $NiCo_2O_4$ electrode under study was pre-anodized for ~200 hr at a current density of 1 A cm^{-2} at 70°C, to reduce the

*Electrochemical Society Student Member.
** Electrochemical Society Active Member.
Key words: oxygen evolution, nickel cobalt oxide, active sites.

oxygen bubble size and to obtain a stable and reproducible electrode surface. Oxygen evolution current-potential measurements were obtained on the pre-anodized $NiCo_2O_4$ electrode in KOH solutions of concentration 0.1, 0.2, 0.4, 0.6, 1.2, 2.2, 4 and 5, mol/dm^{-3} at 25°C using a 3A Chemical Electronics Potentiostat in a galvanostatic mode. A three-compartment glass cell was used for this study. A piece of 100 mesh Ni screen was used as the secondary electrode. All potentials were measured against the dynamic hydrogen electrode (DHE). The DHE was calibrated against the reversible hydrogen electrode in the same electrolyte, for the different electrolytes, at 25°C and was found to vary between −18 mV to −21 mV. All electrolytes were pre-electrolyzed *in situ* by passing a 2 mA current between two pieces of 3 cm × 3 cm platinum mesh electrodes placed at the working electrode compartment and at the secondary electrode compartment, with continuous N_2 purging for ~12 hr. The interrupter technique was used to measure the ohmic drop (15) between the Luggin capillary and the working electrode.

Results and Discussion

Figure 1 shows the current-potential oxygen evolution performance on pre-anodized, Teflon bonded $NiCo_2O_4$ in KOH solutions of concentration 0.1, 0.2, 0.4, 0.6, and 1.2 mol/dm^{-3}. As shown in Fig. 1, oxygen evolution in KOH electrolyte of concentration 1.2 mol/dm^{-3} shows two Tafel slopes. The slope at lower potentials is ~0.04V per decade, and the slope at higher potentials is ~0.12V per decade. Similar slopes were also obtained in KOH electrolyte of concentration 2.2, 4, and 5 mol/dm^{-3}. However, it is to be noted that the Tafel plots in KOH concentration less than 0.4 mol/dm^{-3} did not show a decrease of the slope at lower potentials. Furthermore, the oxygen evolution performance remained constant in electrolyte of KOH concentration greater than 2.2 mol/dm^{-3}.

To explain the slope of 0.12V per decade, the first two mechanistic steps during oxygen evolution on a divalent nickel or cobalt site (M) on the $NiCo_2O_4$ surface can be written as

$$M + OH^- \rightarrow MOH + e \quad [1]$$

$$MOH + OH^- \rightarrow MO + H_2O + e \quad [2]$$

It is to be noted that the oxidation state of the cations of the species formed in Eq. [2] is +4, and no further electronic transitions can take place before oxygen is evolved (12). Oxygen evolution will take place chemically by

$$2MO \rightarrow 2M + O_2 \quad [3]$$

The slope of 0.12V per decade may be due to Eq. [1] being rate determining at low coverage of MOH, *i.e.*, $\theta_{MOH} \rightarrow 0$, or due to Eq. [2] being rate determining at high coverage of MOH, $\theta_{MOH} \rightarrow 1$. Equation [1] is the preferred rate determining step. A further confirmation of the rate determining step from the electrochemical reaction order parameters is not possible, since both reactions when rate determining give similar rate equations. Thus, the rate equation for the slope of 0.12V per decade is

$$i = nFkC_{OH^-} \exp\left(\frac{\beta EF}{RT}\right) \quad [4]$$

where i is the current density, E is the potential, C_{OH^-} is activity of the OH^- in the electrolyte, β is the symmetry factor, and n, F, R, and T have the usual meanings. To confirm the validity of the rate equation, reaction order parameters $(\partial \log i/\partial \log C_{OH^-})_{E,T}$ and $(\partial \log i/\partial \log C_{OH^-})_{\eta,T}$ were obtained experimentally as shown in Fig. 2 and 3 and are found to be 0.96 and 0.6, respectively. The latter parameter has a theoretical value of $(1 - \beta)$ which could be obtained from the rate equation and Eq. [5] and [6]

$$E = E_e + \eta \quad [5]$$

$$E_e = E_e - \frac{2.303\,RT}{F} \log C_{OH^-} \quad [6]$$

where, E, E_e and η are the equilibrium potential, standard equilibrium potential, and activation overpotential, respectively, for oxygen evolution. The former reaction order parameter has a value of 1 from Eq. [4]. Table I compares the theoretically predicted and the experimentally obtained kinetics parameters for the slope of 0.12V per decade, and shows a good correlation.

The Tafel slope of 0.04V per decade at lower potentials (*e.g.*, 10^{-3} A cm^{-2} at potentials 1.52V *vs.* the DHE in 1.2 mol/dm^{-3} KOH at 25°C, 10^{-2}A cm^{-2} at potentials 1.56V *vs.* the DHE in 5 mol/dm^{-3} KOH at 25°C) could be related to Eq. [2] being rate determining at low MOH coverage, *i.e.*, $\theta_{MOH} \rightarrow 0$. However, according to the oxygen evolution mechanism given in Eq. [1], [2], and [3], the trivalent sites of Ni and Co have no role to play. This is because if trivalent sites evolve oxygen by this mechanism, Eq. [2] will form a pentavalent species, which is contrary to our previous findings (12).

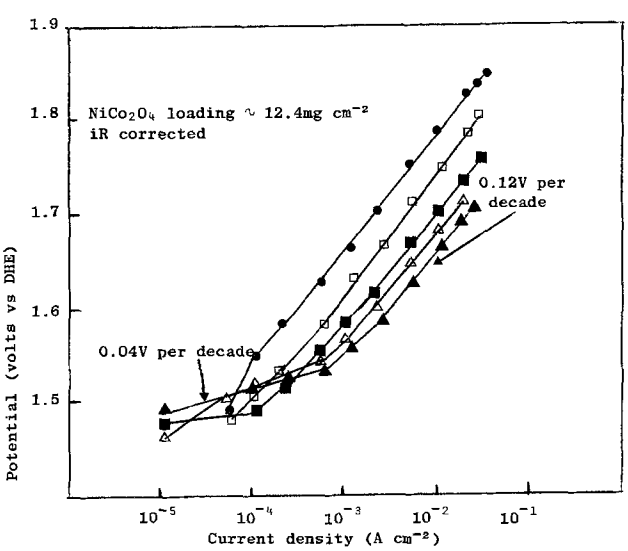

Fig. 1. Oxygen evolution on preanodized Teflon-bonded $NiCo_2O_4$ in KOH concentrations of 0.1 (●), 0.2 (□), 0.4 (■), 0.6 (△), and 1.2 (▲), mol/dm^{-3} at 25°C.

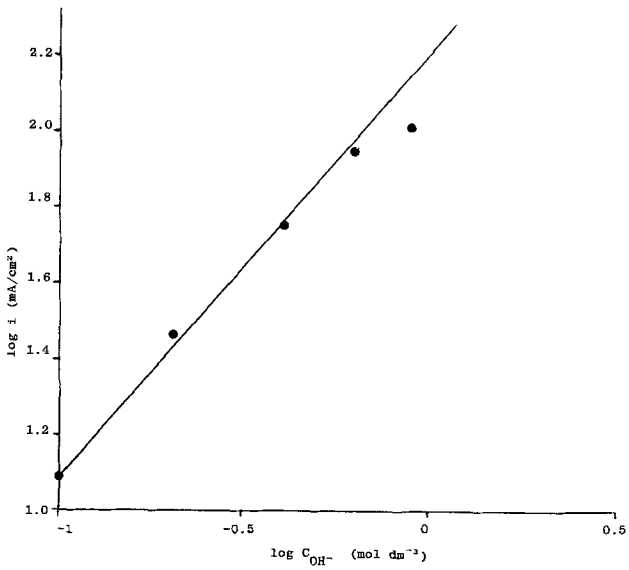

Fig. 2. KOH concentration dependence of current density on preanodized Teflon-bonded $NiCo_2O_4$ at an oxygen evolution potential of 1.20V (*vs.* the standard hydrogen electrode) at 25°C.

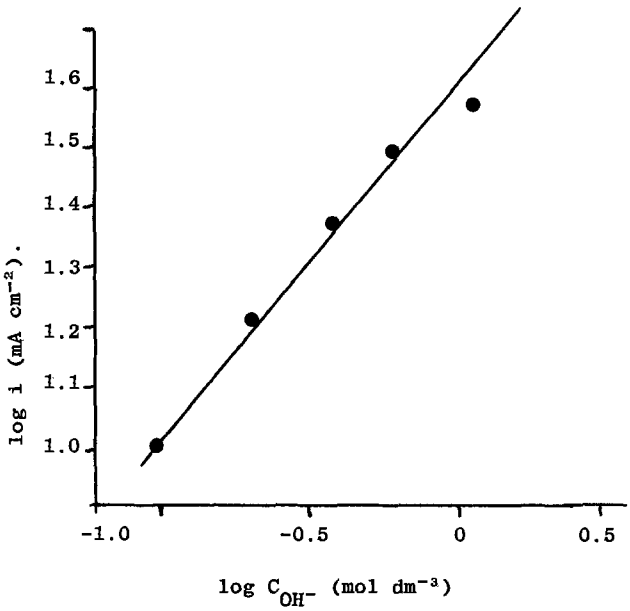

Fig. 3. KOH concentration dependence of current density on preanodized Teflon-bonded $NiCo_2O_4$ electrode at a constant overpotential of 0.42V at 25°C.

The lower Tafel is related to oxygen evolution taking place on trivalent cation sites of $NiCo_2O_4$. The cation distribution of $NiCo_2O_4$ at rest (16) is $Co_{0.9}^{2+}Co_{0.1}^{2+}(Ni_{0.9}^{2+}Ni_{0.1}^{3+}Co^{3+})\ O_{3.2}^{2-}O_{0.8}$ where the cations inside the parenthesis are in octahedral environment and those outside are in tetrahedral sites. According to this formula, 2/5 of the cations are trivalent and the rest divalent. A possible mechanistic sequence on trivalent sites (T) is

$$T + OH^- \rightarrow TOH + e \quad [7]$$

$$TOH + OH^- \rightarrow TO^- + HO \quad [8]$$

$$TO^- + M \rightarrow T\begin{matrix}O\\ \diagup\ \diagdown\\ \end{matrix}M + e \quad [9]$$

$$2T\begin{matrix}O\\ \diagup\ \diagdown\\ \end{matrix}M \rightarrow 2T + 2M + O \quad [10]$$

where M in this reaction sequence is divalent or trivalent. A Tafel slope of 0.04V per decade could be due to Eq. [9] being rate determining at low TOH coverage *i.e.*, $\theta_{TOH} \rightarrow 0$. A low coverage condition in this case is justifiable. since T sites are minority sites. The trivalent sites, which are postulated to evolve oxygen at lower potentials than the divalent sites, do not interfere with the kinetics of the divalent sites, because of their lower surface concentration and their requirement of four sites at sufficiently close vicinity to evolve oxygen.

Conclusions

This study suggests that trivalent nickel and cobalt ions evolve oxygen at lower potentials than divalent nickel and cobalt ions. Further studies of oxygen evolution carried out on Li-doped Co_3O_4 where the trivalent ions can be increased to a maximum of 78% confirm this suggestion (17, 18).

Table I. The theoretically predicted and experimentally obtained kinetic parameters for the higher Tafel region of oxygen evolution on preanodized Teflon-bonded $NiCo_2O_4$

Kinetic indicator	Theoretical	Experimental
$(\partial E/\partial \log i)_{T,C_{OH^-}}$	$2.303RT/\beta F$	~0.12V
$(\partial \log i/\partial \log C_{OH^-})_{T,E}$	=0.118V	
	1	0.96
$(\partial \log i/\partial \log C_{OH^-})_{T,\eta}$	$(1-\beta)$	
	= 0.5	0.6

Acknowledgment

This work was supported by UK Science Research Council.

Manuscript submitted July 19, 1982; revised manuscript received April 19, 1983. This was Paper 530 presented at the Minneapolis, Minnesota, Meeting of the Society, May 10-15, 1981.

REFERENCES

1. T. Ohta, in "Solar-Hydrogen Systems," T. Ohta Editor, p. 40, Pergamon Press, Oxford (1979).
2. H. Tamura, C. Iwakura, and M. Morita, *Kagaku*, **33**, 407 (1978).
3. G. Fiori, E. Mandelli, C. M. Mari, and P. V. Scolori, in "Hydrogen Energy Systems," Vol. 1, T. N. Viziroglu and S. Scifritz, Editors, p. 193, Pergamon Press, Oxford (1978).
4. C. Iwakura, K. Fukunda, and T. Tamura, *Electrochim. Acta*, **21**, 501 (1976).
5. S. Trasatti, in "International Society of Electrochemistry 31st Meeting," E. Vecchi, Editor, p. 115 (1980).
6. A. C. C. Tseung and S. Jasem, *Electrochim Acta*, **22**, 31 (1977).
7. G. Singh, M. H. Miles, and S. Srinivasan, in "Electrocatalysis on Non-Metallic Surfaces," National Bureau of Standards Special Publication 455, p. 289 (1975).
8. H. Vandenbore and R. Leysen, in "International Society of Electrochemistry 31st Meeting," E. Vecchi, Editor, p. 319 (1980).
9. A. C. C. Tseung, P. Rasiyah, M. C. M. Mann, and K. L. K. Yeung, "Hydrogen as an Energy Vector," Commission of European Communities, 199 (1978).
10. S. M. Jasem and A. C. C. Tseung, *This Journal*, **126**, 1352 (1978).
11. B. N. Efremov and S. R. Zhukov, in "All-Union Conference on Electrocatalysis (Abstracts)," p. 39, Moscow (1978).
12. P. Rasiyah, A. C. C. Tseung, and D. B. Hibbert, *This Journal*, **129**, 1724 (1982).
13. A. C. C. Tseung and H. L. Bevan, *J. Mater. Sci.*, **5**, 604 (1970).
14. A. C. C. Tseung, S. Jasem, and M. N. Mahmood, in "Hydrogen Energy Systems," Vol. 1, T. N. Viziroglu and W. Seifritz, Editors, p. 214 Pergamon Press, Oxford (1978).
15. K. R. Williams, "An Introduction to Fuel Cells," p. 58, Elsevier, Amsterdam (1966).
16. W. J. King and A. C. C. Tseung, *Electrochim. Acta*, **19**, 492 (1974).
17. P. Rasiyah and A. C. C. Tseung, *This Journal*, **130**, 365 (1983).
18. A. C. C. Tseung, P. Rasiyah, and D. B. Hibbert, Provisional Brit. Pat. Application, 804483 (1980).

Electrolytic Reduction of Bicarbonate Ion at a Mercury Electrode

Yoshio Hori and Shin Suzuki

Department of Synthetic Chemistry, Faculty of Engineering, Chiba University, Yayoi-cho, Chiba 260, Japan

ABSTRACT

Electrolytic reduction of HCO_3^- at Hg was conducted in aqueous solutions of $NaHCO_3$ (0.5-1.0 mol · kg^{-1})-Na_2CO_3 (0.025-0.1 mol · kg^{-1}) mixtures. $HCOO^-$ is formed as the product; this agrees with the results obtained in the cathodic reduction of CO_2. The following reaction mechanism is proposed: The dissociation of HCO_3^- takes place in the electrolyte solution and forms CO_2, which diffuses through the reaction layer and is cathodically reduced at the electrode. The diffusion equation and Tafel equation for the electrode kinetics are combined and mathematically treated. The partial current of $HCOO^-$ formation, i_C, is related to the electrode potential and the concentration of the components in the solution. The analysis shows that the experimental data obey the relationship derived in accordance with the model. The rate constant of HCO_3^- dissociation is compared with literature values.

Carbon dioxide has been suggested to be feasible as an energy storage medium by Russell *et al.* (1) and Williams *et al.* (2). Carbon dioxide is electrolytically reduced to methanol or formic acid, which in turn can be fed to a fuel cell or a decomposer to generate hydrogen. This process is superior to the hydrogen energy system, since the transport and storage of these liquid fuels are more convenient and less expensive than hydrogen. In addition to the advantage of energy storage, this process will help to prevent increases in atmospheric concentrations of carbon dioxide.

Cathodic reduction of carbon dioxide in aqueous solutions has been studied by many workers; the CO_2 molecule has been regarded as the electroactive species on the basis of voltammetric studies (3, 4). However, because the solubility of CO_2 in water is low, the limiting currents are as low as 10 mA/cm^2 under 1 atm of CO_2. If HCO_3^- can be utilized as an electroactive species, the cathodic reduction of CO_2 will proceed more efficiently, since solubility of HCO_3^- is much higher than CO_2 in aqueous solutions. Iwahara *et al.* (5) recently reported that HCO_3^- is electrolytically reduced at Hg electrode. Other previous authors (6, 7) also have suggested that HCO_3^- is electrolytically reduced. The present study attempts to elucidate the mechanism of the cathodic reduction of HCO_3^- in an aqueous solution in order to develop a better process of CO_2 utilization.

Experimental

The details of the apparatus and the procedures are found elsewhere (8). The electrolytic solutions were buffer solutions of $NaHCO_3$-Na_2CO_3, prepared from commercial reagent-grade chemicals without further purification. Commercial nitrogen was purified by a column of activated copper and wash bottles containing aqueous NaOH solution. Both the potentiostatic and galvanostatic electrolysis experiments were conducted at 25°C with purified mercury as the cathode. The potential of the cathode was measured with respect to an Ag/AgCl reference electrode at 25°C, which was introduced to the catholyte via a Pyrex Luggin tube. Nitrogen was introduced into the cell, bubbling moderately through the solution during most of the electrolytic experiments, although some experiments were carried out with nitrogen flowing above the solution after removal of the dissolved oxygen. Sample solutions were taken out for analysis immediately after electrolysis, with the mercury electrode kept cathodic in order to prevent interference by the amalgam.

The product resulting from the electrolysis was qualitatively tested by the following methods: (*i*) the formaldehyde and formic acid by chromotropic acid test (9) and (*ii*) the oxalic acid by thiobarbituric acid test (9). The solutions in the cell were quantitatively analyzed for their reducible substances by the permanganate titration technique.

Key words: carbon dioxide, bicarbonate, cathodic reduction, electrochemical kinetics.

Results

Reaction products.—The reaction product was confirmed to be $HCOO^-$; formaldehyde and oxalic acid were not detected. This is in agreement with the cathodic reduction of CO_2. Amalgam formation and hydrogen evolution were seen to proceed in parallel with HCO_3^- reduction.

Partial current of $HCOO^-$ formation.—The steady-state electrolysis experiments were conducted for 15-120 min. The electrode potential changed by *ca.* 60 mV during the galvanostatic electrolysis due to Na amalgam formation. The electrode potentials were then averaged for the period of electrolysis. The total current decreased down to 1/4-1/5 during the potentiostatic electrolysis. The partial current of $HCOO^-$ formation, i_C, was calculated from the results of the permanganate titration. The experimental data obtained in the galvanostatic and potentiostatic experiments were compatible with each other, therefore no distinction between the two was made in this study. Each partial current, i_C, may include an error of up to 5% due to the inaccuracy of the titration technique. The experimental error due to the IR drop between Luggin capillary tip and the cathode was always less than 6 mV.

The partial current, i_C, is shown in Fig. 1 as a function of the electrode potential for a mixed electrolytic solution of $NaHCO_3$ (m = 1.0 mol/kg)[1] and Na_2CO_3

[1] m is the concentration in terms of molality.

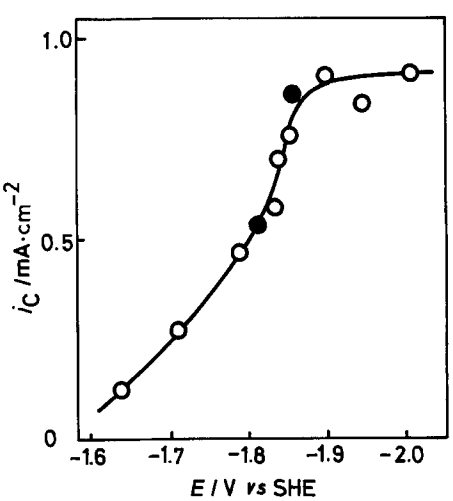

Fig. 1. Partial current of $HCOO^-$ formation with (○) and without (●) N_2 bubbled plotted against the electrode potential. Electrolyte: $NaHCO_3$ (m = 1.0 mol · kg^{-1})-Na_2CO_3 (m = 0.05 mol · kg^{-1}).

(m = 0.05 mol/kg). The pH of this solution ranged between 8.58 and 8.63. The fraction of the total charge going to the formation of $HCOO^-$ varied from 66% at −1.637V (*vs.* SHE) to 15.2% at −2.008V (*vs.* SHE). Since various concentrations of electrolyte solutions were employed in the present study, the electrode potential was corrected for the variation of the potential of outer Helmholtz plane ϕ_2 with reference to 1-1 electrolyte solution (arbitrarily chosen m = 0.274 mol/kg).[2] Figure 1 shows a limiting current in a more negative region of potential. Iwahara *et al.* conducted electrolysis in $KHCO_3$ solution and also pointed out the appearance of the limiting current (5). Figure 1 contains experimental data which were taken from electrolysis experiments with nitrogen flowing just above the unstirred solution. The data obtained without stirring fall along the same curve as the data obtained with N_2 stirring. Therefore, moderate convective motion of the solution does not affect the transport process of the reactant species. This will be discussed later in terms of a reaction layer thickness.

Dependence of i_C on HCO_3^- concentration and pH.— Figure 2 shows i_C plotted against the HCO_3^- concentration, where the concentration ratio $[CO_3^{2-}]/[HCO_3^-]$ is kept constant at 0.05; the electrode potential is −1.813V *vs.* SHE. i_C apparently depends linearly upon the HCO_3^- concentration, which suggests that HCO_3^- is involved in the reaction. The pH increased during electrolysis. Therefore, HCO_3^- is electrolytically reduced to form $HCOO^-$ and OH^- according to the electrode reaction

$$HCO_3^- + H_2O + 2e^- \rightarrow HCOO^- + 2\,OH^- \qquad [1]$$

The pH of the solutions ranged between 8.5 and 9.2. i_C was seen to decrease significantly in accordance with pH when the electrode potential and HCO_3^- concentration were kept constant.

Discussion

Dissociation of HCO_3^- and transport of resulting CO_2.—As shown above, i_C is proportional to the concentration of HCO_3^-, and the electrode reaction is presumed to be Eq. [1]. However, if HCO_3^- is reduced at the cathode as the electroactive species, the limiting current would be *ca.* 10^2 times greater than the value shown in Fig. 1, since the concentration of HCO_3^- is 1 mol/kg.

i_C is insensitive to the convective motion of the electrolyte, even when i_C is nearly equal to the limiting current. Accordingly, the limiting current is not controlled by the diffusion of reactant species (*e.g.* CO_2) from the bulk of the solution.

The pH of the solution significantly changes i_C.

These experimental facts suggest that the dissociation of HCO_3^- takes place as a preceding homogeneous chemical reaction in close vicinity to the electrode

$$HCO_3^- \underset{k_r}{\overset{k_d}{\rightleftharpoons}} CO_2 + OH^- \qquad [2]$$

$$HCO_3^- + OH^- \rightleftharpoons CO_3^{2-} + H_2O \qquad [3]$$

The rate of CO_2 formation is assumed to be relatively slow; the concentration of HCO_3^- is constant throughout the entire electrolyte solution, *i.e.* from bulk to electrode surface. CO_2 thus formed diffuses within a reaction layer to the surface of the electrode and is electrolytically reduced at the cathode

$$CO_2 + H_2O + 2e^- \rightarrow HCOO^- + OH^- \qquad [4]$$

The thickness of the reaction layer is assumed to be smaller than that of the adhering stagnant layer (diffusion layer). The present reaction model can be treated in accordance with the theory developed by Gerischer and Vetter (10).

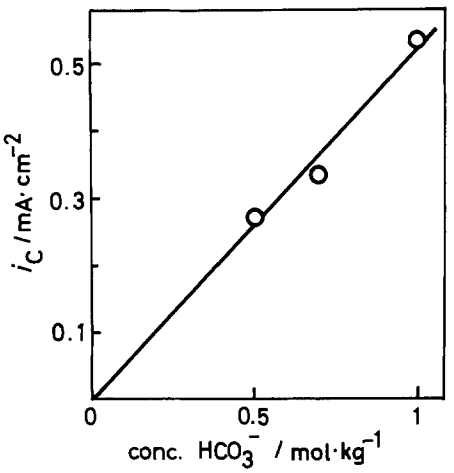

Fig. 2. Plot of i_C *vs.* HCO_3^- concentration. The concentration ratio $[CO_3^{2-}]/[HCO_3^-]$ is kept constant at 0.05. The electrode potential is −1.813V *vs.* SHE.

The rate of formation of CO_2 in reaction [2] is

$$V = k_d \cdot C(HCO_3^-) - k_r \cdot C(CO_2) \cdot C(OH^-) \qquad [5]$$

where k_d and k_r are the rate constants for the forward and backward reaction [2]; $C(HCO_3^-)$, $C(CO_2)$, and $C(OH^-)$ are the concentrations of the respective species. Reaction [2] is at equilibrium in the bulk of the solution

$$V = 0, \quad C(CO)_2 = C_b(CO_2) = \bar{C}(CO_2) \qquad [6]$$

where $C_b(CO_2)$ and $\bar{C}(CO_2)$ represent the bulk concentration and the equilibrium concentration of CO_2, respectively. Then Eq. [5] becomes

$$k_d \cdot C(HCO_3^-) - k_r \cdot \bar{C}(CO_2) \cdot C(OH^-) = 0 \qquad [7]$$

The rate of reaction [3] is assumed to be fast enough to keep reaction [3] at equilibrium. Eliminating $k_r \cdot C(OH^-)$ from Eq. [5] and Eq. [7], one obtains the reaction rate

$$V = k_d \cdot C(HCO_3^-) \cdot \left(1 - \frac{C(CO_2)}{\bar{C}(CO_2)}\right) = V_0 \cdot \left(1 - \frac{C(CO_2)}{\bar{C}(CO_2)}\right) \qquad [8]$$

where

$$V_0 = k_d \cdot C(HCO_3^-) \qquad [9]$$

The extended Fick's second law

$$\frac{\partial C(CO_2)}{\partial t} = D \cdot \frac{\partial^2 C(CO_2)}{\partial x^2} + V \qquad [10]$$

is applied to the present model, where x is the distance from the electrode surface and D the diffusion coefficient of CO_2 in the solution. Equation [10] is solved for the steady state, $\partial C(CO_2)/\partial t = 0$. The boundary conditions are $(C[CO_2]/\bar{C}[CO_2])_{x\rightarrow\infty} = 1$ and $(\partial C[CO_2]/\partial x)_{x\rightarrow\infty} = 0$. Thus one obtains from Eq. [8] and [10]

$$\frac{dC(CO_2)}{dx} = \left(\frac{V_0 \cdot \bar{C}(CO_2)}{D}\right)^{1/2} \cdot \left(1 - \frac{C(CO_2)}{\bar{C}(CO_2)}\right) \qquad [11]$$

Both Faraday's law and Fick's first law hold at the electrode surface, $x = 0$; $n\mathbf{F} \cdot D(dC(CO_2)/dx)_{x=0} = i$. Hence the partial current, i_C, for the reduction of CO_2 resulting from HCO_3^- is

[2] The corrections of ϕ_2 were made on the basis of the Gouy-Chapman equation for the diffuse double layer. The details are found in the previous report (8). The amount of corrections in the present study ranges between 18 and 38 mV.

$$i_C = nF \cdot D\left(\frac{dC(CO_2)}{dx}\right)_{x=0}$$
$$= nF(V_0 \cdot \bar{C}[CO_2] \cdot D)^{1/2}\left(1 - \frac{C_s(CO_2)}{\bar{C}(CO_2)}\right) \quad [12]$$

where $C_s(CO_2)$ denotes the concentration of CO_2 at the surface of the electrode. If Eq. [12] is solved for $C_s(CO_2)$, it can be rewritten as

$$C_s(CO_2) = \bar{C}(CO_2)\left[1 - \frac{i_C}{nF} \cdot (V_0 \cdot \bar{C}(CO_2) \cdot D)^{-1/2}\right] \quad [13]$$

Tafel relationship obtained from cathodic reduction of gaseous CO_2.—Gerischer and Vetter studied the electrode reaction with a rate determining homogeneous reaction, and have mathematically described the system (10). They treated the problem with the condition that the other component steps of the overall reaction are not rate determining. The charge transfer process is essentially at equilibrium, even during the flow of current, and the concentrations of the components of the overall electrode reaction (HCO_3^- in the present case) remain essentially constant throughout the electrolyte. The present authors extend Gerischer and Vetter's theory to the case where the rate of charge transfer is comparable with that of preceding chemical reaction.

The charge transfer process involved in the cathodic reduction of CO_2 can be studied by bubbling gaseous CO_2 in solution. The concentration of CO_2 dissolved in solution and at equilibrium with gaseous CO_2 is much greater than that in the present HCO_3^--CO_3^{2-} solutions. Paik *et al.* (11) and the present authors (8) studied this reaction with mercury as the cathode. Paik *et al.* revealed the following experimental facts. The current efficiency of CO_2 reduction is 100% within the experimental error. The current of CO_2 reduction, i_C', is not affected by stirring of the electrolyte. i_C' is proportional to $P(CO_2)$, the partial pressure of CO_2, at relatively high current densities.[3] A Tafel relationship holds between i_C' and electrode potential E. Thus,

$$i_C' \propto P(CO_2) \cdot \exp\left(-\frac{\alpha FE}{RT}\right) \quad [14]$$

where α is the transfer coefficient.

The Tafel relationship is written in terms of E in the present paper instead of using overvoltage and exchange current. Henry's law is expected to be valid for CO_2 in the bulk of the solution

$$C_b(CO_2) = \bar{C}(CO_2) = h \cdot P(CO_2) \quad [15]$$

where h is a constant. Then, Eq. [14] can be written as

$$i_C' = nF \cdot k \cdot C_b(CO_2) \cdot \exp\left(-\frac{\alpha FE}{RT}\right) \quad [16]$$

where k is a rate constant that incorporates h, the Henry law constant. Paik *et al.* obtained experimental data in the region where mass transfer resistance can be neglected and i_C' is expressed by Tafel's equation. Thus, $C_s(CO_2)$ is approximately equal to C_b in the experiment carried out by Paik *et al.*

$$C_s(CO_2) = C_b(CO_2) \quad [17]$$

Equation [17] is substituted into Eq. [16] in order to obtain the following equations

$$i_C' = nF \cdot k \cdot C_s(CO_2) \cdot \exp\left(-\frac{\alpha FE}{RT}\right)$$
$$= nF \cdot C_s(CO_2) \cdot r \quad [18]$$

[3] The present measurements were conducted in this region of current density.

$$r = k \cdot \exp\left(-\frac{\alpha FE}{RT}\right) \quad [19]$$

According to the authors' previous report, the following values are obtained (8): $i_C' = 5 \times 10^{-4}$ A · cm^{-2} for $P(CO_2) = 1$ atm and $E = -1.487$V *vs.* SHE, $\alpha = 0.278$, and $T = 298$ K. These values are in good agreement with the values obtained by Paik *et al.* (11). The constant h is given as (12)

$$h = \frac{C_b(CO_2)}{P(CO_2)} = 3.38 \times 10^{-5}\ \text{mol} \cdot \text{cm}^{-3} \cdot \text{atm}^{-1}$$

Substituting these values into Eq. [16] gives

$$k = 7.80 \times 10^{-12}\ \text{cm} \cdot \text{sec}^{-1}$$

Hence

$$r = 7.80 \times 10^{-12} \exp(-10.83E)\ \text{cm} \cdot \text{sec}^{-1} \quad [20]$$

Cathodic reduction of CO_2 resulting from dissociation of HCO_3^-.—As shown in Eq. [12], the cathodic reduction of CO_2, stemming from the dissociation of HCO_3^-, is controlled by the rates of formation and diffusion of CO_2. At the same time, the cathodic reduction of CO_2 obeys a Tafel relationship Eq. [18]. i_C in Eq. [12] must be equal to i_C' in Eq. [18] in the steady-state condition.

Substituting Eq. [13] into Eq. [18] yields

$$i_C = nF(V_0 \cdot \bar{C}(CO_2) \cdot D)^{1/2} \cdot \frac{r}{r + \left(\frac{V_0 \cdot D}{\bar{C}(CO_2)}\right)^{1/2}} \quad [21]$$

When reaction [2] is at equilibrium, the following reactions are also at equilibrium

$$CO_2 + H_2O \rightleftharpoons H^+ + HCO_3^- \quad [22]$$
$$-[H_2O \rightleftharpoons H^+ + OH^-]$$
$$CO_2 + OH^- \rightleftharpoons HCO_3^-$$

The equilibrium concentration of CO_2 is

$$\bar{C}(CO_2) = \frac{1}{K_a} \cdot \frac{\gamma(H^+) \cdot \gamma(HCO_3^-)}{\gamma(CO_2)} \cdot C(H^+) \cdot C(HCO_3^-) \quad [23]$$

where K_a is the equilibrium constant of reaction [22], and γ's are the activity coefficients of the respective species. Substitution of Eq. [9] into Eq. [21], followed by the substitution of Eq. [23] into Eq. [21] yields

$$\frac{r}{i_C} \cdot nF \cdot \frac{\gamma(H^+) \cdot \gamma(HCO_3^-)}{\gamma(CO_2)} \cdot C(H^+) \cdot C(HCO_3^-)$$
$$= \left(\frac{K_a}{k_d \cdot D}\right)^{1/2} \cdot \left(\frac{\gamma(H^+) \cdot \gamma(HCO_3^-)}{\gamma(CO_2)}\right)^{1/2} \cdot C(H^+)^{1/2} \cdot r + K_a \quad [24]$$

Equation [24] can be rewritten as

$$\frac{r}{i_C} \cdot nF \cdot a(H^+) \cdot a(HCO_3^-) = \left(\frac{K_a}{k_d \cdot D}\right)^{1/2} \cdot (\gamma(HCO_3^-) \cdot \gamma(CO_2))^{1/2} \cdot a(H^+)^{1/2} \cdot r + K_a \quad [25]$$

Numerical values obtained from the analysis of the model.—The activity of HCO_3^- was estimated from the concentration of the solution and the activity coefficient reported by Han and Bernardin (13). The other variables in Eq. [25] are readily calculated from the experimental data. The compositions of the electrolyte were as follows; 1.0-0.1, 1.0-0.05, 1.0-0.025, 0.7-0.07, 0.7-0.035, 0.5-0.1. 0.5-0.05, and 0.5-0.025.[4] A comparison of

[4] The compositions are shown in an abbreviated form, *e.g.*, 1.0-0.1, which indicates a solution containing $NaHCO_3$ (m = 1.0 mol · kg^{-1}) and Na_2CO_3 (m = 0.1 mol · kg^{-1}).

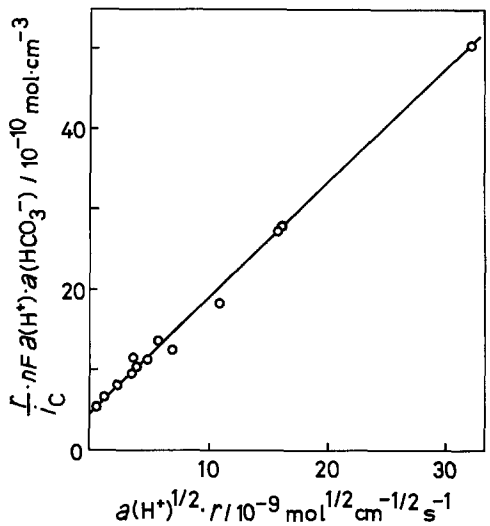

Fig. 3. Model confirmation. Plot of Eq. [24]

Eq. [25] with the experimental data is shown in Fig. 3. K_a is determined from the intercept to the ordinate

$$K_a, \text{experimental} = 4.8 \times 10^{-10}\ \text{mol} \cdot \text{cm}^{-3}$$

The theoretical value of K_a is easily calculated on the basis of tabulated thermochemical data (14)

$$K_a, \text{theoretical} = 4.50 \times 10^{-10}\ \text{mol} \cdot \text{cm}^{-3}$$

The good agreement of the two values confirms the validity of the present model.

The slope of the straight line shown in Fig. 3 readily yields the value k_d if the following numerical constants are employed: $D = 1.9 \times 10^{-5}\ \text{cm}^2 \cdot \text{sec}^{-1}$ (15), $\gamma(HCO_3^-) = 0.56$ on the average (13), and $\gamma(CO_2)$ is assumed to be unity

$$k_d = 6.8 \times 10^{-4}\ \text{sec}^{-1}$$

The thickness of the reaction layer δ is defined by the linear extrapolation of the concentration gradient at $x = 0$ (electrode surface) to $C(CO_2) = \overline{C}(CO_2)$, and is

$$\delta = \left[\frac{\overline{C}(CO_2) \cdot D}{V_0}\right]^{1/2} \qquad [26]$$

The numerical value δ is readily calculated for the solution $NaHCO_3^-$ ($m = 1.0\ \text{mol} \cdot \text{kg}^{-1}$)-$Na_2CO_3$ ($m = 0.05\ \text{mol} \cdot \text{kg}^{-1}$)

$$\delta = 0.008\ \text{cm}$$

The solutions were moderately stirred by nitrogen sparging. Since the stagnant boundary layer thickness will not be less than 0.01 cm under the present conditions, the reaction layer is obviously within the diffusion layer, as assumed before. Thus it is natural that i_C is not affected by convective motion of electrolyte caused by nitrogen bubbling.

Rate constant k_d.—The rate constant k_d has been measured by various techniques (16-22). The values are scattered, but they appear to converge to approximately $2 \times 10^{-4}\ \text{sec}^{-1}$ in very dilute solutions. This value is less than 1/3 the value obtained in the present study. The discrepancy could stem from a dependence of k_d on the ionic strength. Pinsent *et al.* (16, 17) reported that k_r increases at high ionic strengths. k_d is related to k_r as derived from Eq. [7]; $k_d/k_r = K_b$, where K_b is the equilibrium constant for reaction [2]. Thus k_d naturally increases at high ionic strengths. Koefoed and Engel (20) have reported a value for k_r in 0.75M $NaHCO_3$ at 0°C that is about 5 times higher than those values obtained in very dilute solutions.

Contribution from HCO_3^- dissociation to the cathodic reduction of CO_2.—When the electrolytic reduction of CO_2 is conducted with CO_2 bubbling in an HCO_3^- aqueous solution, CO_2 is supplied to the electrode in two ways. One is the diffusion of CO_2 dissolved from the gas phase. Another is the dissociation of HCO_3^-.

The limiting current controlled by the diffusion of CO_2 from the gas phase at 1 atm can be estimated with use of the values of h and D as given above. The calculated current density is $1.2 \times 10^{-2}\ \text{A} \cdot \text{cm}^{-2}$ for a diffusion layer thickness of 0.01 cm.

The limiting current, controlled by the dissociation of HCO_3^-, is evaluated on the basis of Eq. [25] with r increasing infinitely. The activity of HCO_3^- is $0.520 \times 10^{-3}\ \text{mol} \cdot \text{cm}^{-3}$ in a solution of $NaHCO_3$ ($m = 1.0$), and pH is 7.54 under 1 atm of CO_2. The limiting current is estimated to be $3.9 \times 10^{-3}\ \text{A} \cdot \text{cm}^{-2}$. Thus, the electrolytic reduction of HCO_3^- is a very slow process, due to the slow dissociation of HCO_3^-. If appropriate catalyses or electrolytes are found to raise the rate of dissociation of HCO_3^-, the limiting current will consequently be enhanced.

Acknowledgments

The authors would like to thank Mr. Mikio Yoshimiya for his assistance in part of experiments.

Manuscript received Aug. 17, 1982; revised manuscript received *ca.* June 28, 1983.

Chiba University assisted in meeting the publication costs of this article.

REFERENCES

1. P. G. Russell, N. Kovac, S. Srinivasan, and M. Steinberg, *This Journal*, **124**, 1329 (1977).
2. R. Williams, R. S. Crandall, and A. Bloom, *Appl. Phys. Lett.*, **33**, 381 (1978).
3. T. E. Teeter and P. Van Rysselberghe, *J. Chem. Phys.*, **22**, 759 (1954).
4. S. Meshitsuka, M. Ichikawa, and K. Tamaru, *J. Chem. Soc., Chem. Commun.*, 158 (1974).
5. H. Iwahara, H. Uchida, and M. Kishigami, Paper presented at 48th Meeting of the Electrochemical Society of Japan, Yokohama (1981).
6. K. S. Udupa, G. S. Subramanian, and H. V. K. Udupa, *Electrochim. Acta*, **16**, 1953 (1971).
7. A. Lieben, *Monatsh. Chem.*, **16**, 211 (1895).
8. Y. Hori and S. Suzuki, *Bull. Chem. Soc. Jpn.*, **55**, 660 (1982).
9. F. Feigl, "Spot Test in Organic Analysis," 6th ed., Elsevier, New York (1960).
10. K. J. Vetter, "Electrochemical Kinetics," Academic Press, New York (1967). Originally published in H. Gerisher and K. J. Vetter, *Z. Physik. Chem.*, **197**, 92 (1951).
11. W. Paik, T. N. Andersen, and H. Eyring, *Electrochim. Acta*, **14**, 1217 (1969).
12. J. A. Dean, "Lange's Handbook of Chemistry," 12th ed., McGraw-Hill (1979).
13. S. T. Han and L. J. Bernardin, *T.A.P.P.I.* (Technical Association of the Pulp and Paper Industry, New York), **41**, 540 (1958).
14. D. D. Wagman, W. H. Evans, V. B. Parker, I. Halow, S. M. Bailey, and R. H. Schumm, NBS Technical Note 270 (1968).
15. D. M. Himmelblau, *Chem. Rev.*, **64**, 527 (1964).
16. B. R. W. Pinsent and F. J. W. Roughton, *Trans. Faraday Soc.*, **47**, 263 (1951).
17. B. R. W. Pinsent, L. Pearson, and F. J. W. Roughton, *ibid.*, **52**, 1512 (1956).
18. J. A. Sirs, *ibid.*, **54**, 207 (1958).
19. D. M. Himmelblau and A. L. Babb, *AIChE J.*, **4**, 143 (1958).
20. J. Koefoed and K. Engel, *Acta Chem. Scand.*, **15**, 1319 (1961).
21. F. Goodridge and M. D. Taylor, *Trans. Faraday Soc.*, **59**, 2868 (1963).
22. D. J. Poulton and H. W. Baldwin, *Can. J. Chem.*, **45**, 1045 (1967).

Technical Notes

The Behavior of the Polythiazyl, $(SN)_x$, Paste Electrode in Aqueous Media

Kumuda P. Shenoy, Kevin J. Mulligan, and Harry B. Mark, Jr.*

Department of Chemistry, University of Cincinnati, Cincinnati, Ohio 45221

Electrodes constructed of single crystals (1-7), films (8, 9), and composites (10) of the polymeric conductor polythiazyl, $(SN)_x$, have been studied in aqueous (1-10) and nonaqueous (11, 12) media. These construction procedures are often tedious and unreliable, and, generally, these electrodes exhibit large background currents. In addition, the surfaces of these electrodes cannot be renewed. Recently, the fabrication of a polythiazyl, $(SN)_x$, paste electrode, prepared in a similar manner as carbon paste electrodes (13, 14), and its behavior in nonaqueous media have been reported (15). These electrodes had renewable surfaces and low background currents. However, these $(SN)_x$ paste electrodes exhibited very poor properties in aqueous media (16).

We report the conditions necessary to treat the $(SN)_x$ paste electrode in order to obtain normal electrochemical response in aqueous media, and some typical experimental results. The $(SN)_x$ paste electrodes have substantially lower background currents as compared to single crystal $(SN)_x$ electrodes, and the electrode surface can be renewed.

Experimental

The $(SN)_x$ crystals were prepared by a method based on that of MacDiarmid and co-workers (17), with slight modification (8). The $(SN)_x$ paste electrodes were prepared by a modified procedure of Nowak *et al.* (15), as follows: Dry clean $(SN)_x$ crystals were ground in a mortar and pestle, and the separated fibers formed (Fig. 1) were then mixed with Apiezon^R M grease in a ratio approximately 2:1 (polythiazyl: grease). This paste was compacted into the end of a glass tube (outside diameter of 3 mm and length of 5 cm) and ohmic contact was made with a silver wire. These electrodes were stored in a dessicator prior to use. Single crystal $(SN)_x$ electrodes were prepared as previously described (1-3).

Cyclic voltammetric experiments were carried out using a system made up of a Bioanalytical Systems CV-1B potentiostat, a Keithley 179A TRMS multimeter, and a Hewlett-Packard 136A X-Y recorder. All solutions were deaerated with argon. In addition to the $(SN)_x$ paste [or $(SN)_x$ crystal] working electrode, the electrochemical cell contained a platinum wire auxiliary electrode and a saturated calomel reference electrode.

All solutions were prepared using distilled water passed through a carbon and demineralization cartridge, and all chemicals, except that specified below, were reagent grade. The N,N-dimethylformamide (DMF) was Matheson, Coleman and Bell spectroquality grade.

Results and Discussion

The behavior of the $(SN)_x$ paste electrodes, prepared in the manner described above, was studied in both DMF and acetonitrile media with different supporting electrolytes (16) and it was found that they had identical characteristics with respect to breakdown potentials and background currents as those reported by Nowak *et al.* (15). The direct use of these electrodes in aqueous media resulted in current behavior that resembled an almost totally passive electrode surface. No defined redox waves were observed for the cyclic voltammetry study of ferricyanide regardless of supporting electrode and *p*H value employed. Paste electrodes prepared in the exact manner as those of Nowak *et al.* had the same poor behavior. Attempts to activate these electrodes by repeated cycling at various potential limits were also unsuccessful.

It was found, however, on brief dipping (~30 sec) the $(SN)_x$ paste electrode in a pure DMF solution, the behavior changed dramatically from almost passive to essentially ideal response as described below. First, as shown in Fig. 2, background currents in aqueous media for the $(SN)_x$ paste electrodes were very low and showed no significant surface faradaic waves in contrast to that observed for a mounted parallel single crystal $(SN)_x$ electrode in the same media as shown in Fig. 2 (perpendicular single crystal $(SN)_x$ electrodes behaved the same as the parallel electrode). In addition, the anodic breakdown potential shifted from about +0.50 to about +0.80V *vs.* SCE for the $(SN)_x$ paste electrode. On normalizing the geometric surface area of the paste and single crystal electrodes, the background current densities for the paste electrodes are about 10^{-3} of that for the single crystal electrodes.

The ferro/ferricvanide couple was used to assess the behavior of the $(SN)_x$ paste electrodes using the experimental conditions employed in the previous study of single crystal and film $(SN)_x$ electrodes in aqueous

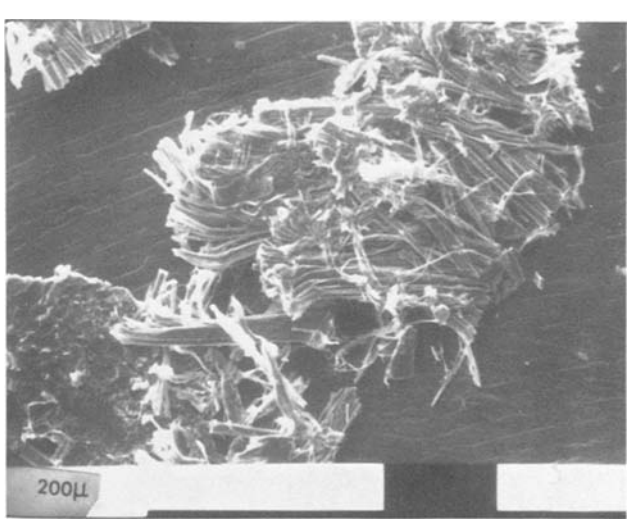

Fig. 1. Scanning electron micrograph of shredded $(SN)_x$ crystals prior to the preparation of the paste.

* Electrochemical Society Active Member.

Key words: polythiazyl paste electrodes, aqueous media, polymeric conductor, background and currents, ferro/ferricyanide.

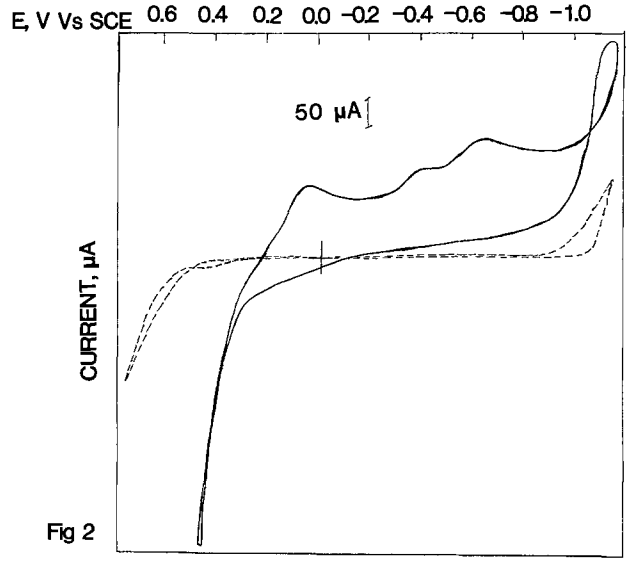

Fig. 2. Background currents at $(SN)_x$ paste electrode (----); and at $(SN)_x$ parallel single crystal electrode (——) in 0.1*N* KCl; ν = 200 mV/sec paste electrode, surface area 2.3 × 10^{-2} cm^2 crystal = 5 × 10^{-3} cm^2.

media (1, 9). Well-defined oxidation and reduction waves are observed at the potentials expected and a typical cyclic voltammagram is shown in Fig. 3a. Figure 3b shows a typical cyclic voltammogram using an untreated paste electrode for comparison. Peak separations were about 130 mV (compared to the theoretical value of 59 mV), while those found for single crystal electrodes were 80-100 mV (1) and much less than the 2-300 mV peak separations observed for $(SN)_x$ film electrodes (9). Values for the ratio of i_{pc}/i_{pa} ranged from 1.10 to 1.0, again indicating essentially reversible behavior at the $(SN)_x$ paste electrode.

Experiments were carried out to determine the life time of the DMF-dipped $(SN)_x$ paste electrode in aqueous media. In one case, the electrode was left in the electrolysis cell containing 1 × 10^{-3}M ferricyanide, and 0.1M KCl and cyclic voltammograms were taken periodically over a time span of several days. The cyclic voltammograms taken during the first 4-6 hr were essentially identical, and only after about 24 hr

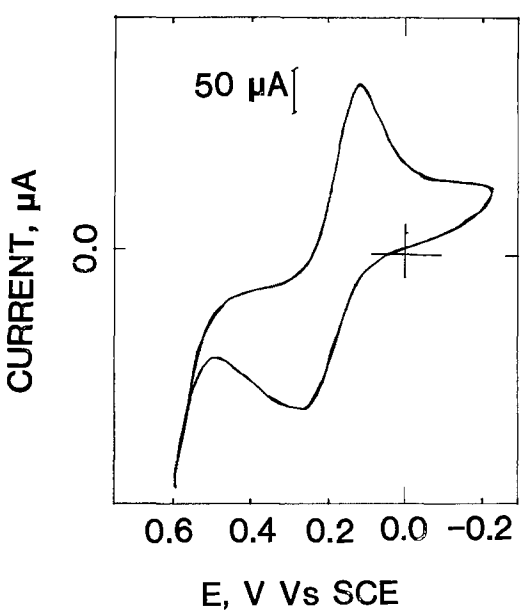

Fig. 3a. Cyclic voltammogram of the ferri/ferrocyanide couple at a DMF-treated $(SN)_x$ paste electrode; the solution is 1 mM potassium ferricyanide, 0.1M KCl; ν = 200 mV/sec; electrode surface area = 2.3 × 10^{-2} cm^2.

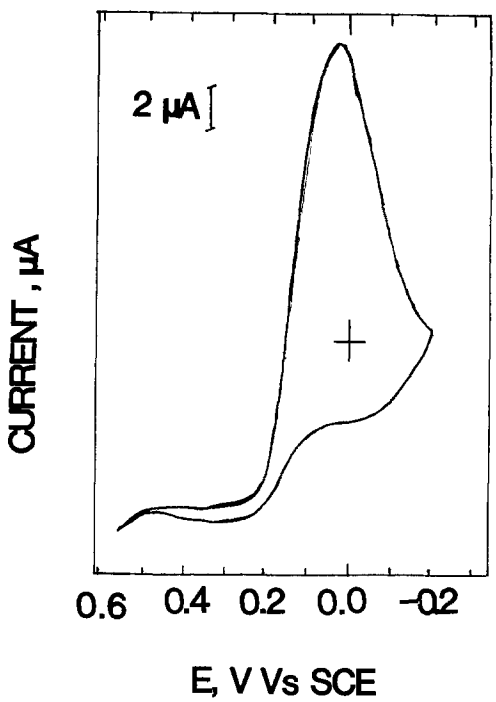

Fig. 3b. Cyclic voltammogram of ferri/ferrocyanide couple at an untreated $(SN)_x$ paste electrode. Experimental condition the same as for Fig. 3a.

were any significant peak width broadening or change in i_p values observed. In the second case, the electrodes were removed from the cell and stored in water between measurements. Again, degradation of the electrode response appeared after about 20-24 hr. In both cases, retreating the $(SN)_x$ paste in DMF again restored the ferro/ferricyanide cyclic voltammograms back to the original shape. This surface renewal could be repeated indefinitely.

It had previously been shown that parallel and perpendicular oriented single crystal $(SN)_x$ electrodes exhibited very different cyclic voltammetric behavior for the $Pb^{+2}/Pb°$ couple (3). The electrodeposition/dissolution peaks on the perpendicular surface were essentially reversible and diffusion controlled. However, on the parallel surface the waves were ill defined and resembled those obtained on other electrode surfaces where slow nucleation was the rate-limiting step in the electrodeposition (3). The $(SN)_x$ paste electrodes were used with the $Pb^{+2}/Pb°$ couple to determine if chain end or fiber axis orientations of the $(SN)_x$ in the paste predominated. Figure 4 shows a typical $Pb^{+2}/Pb°$ couple cyclic voltammogram. Although there is

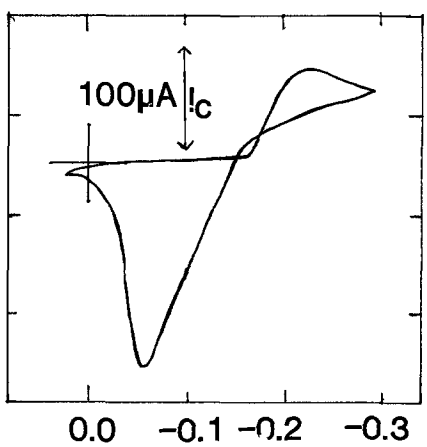

Fig. 4. Cyclic voltammogram obtained with $(SN)_x$ paste electrode for 1 mM $Pb(NO_3)_2$, 0.1M KNO_3 solution; scan rate = 200 mV/sec, electrode surface area = 2.3 × 10^{-2} cm^2.

some hysteresis observed on potential reversal, which is pronounced for the parallel single crystal electrodes, the overall characteristics of the peaks more closely resemble that of perpendicular $(SN)_x$ surface.

Dipping newly prepared $(SN)_x$ paste electrodes in acetonitrile produces similar results to DMF dipping. However, it does not seem to be quite as effective as DMF, as ferro/ferricyanide cyclic voltammograms are not quite as well defined, and the electrodes degrade somewhat faster.

Conclusions

The $(SN)_x$ paste electrodes appear to have a thin film of some component of the Apiezon^R M grease on the fiber surfaces initially, which insulates them with respect to electron transfer. The dipping in DMF probably dissolves this film and activates the $(SN)_x$ surface. This film reforms only slowly on the electrode, but the active surface can be renewed on redipping. In general, the $(SN)_x$ paste electrode is superior to the single crystal and film $(SN)_x$ electrodes with respect to background currents, reproducibility of preparation and response, and surface renewal. It is also easier to make and does not exhibit the pronounced anisotropic behavior of single crystal electrodes with different orientations.

Acknowledgments

The authors gratefully acknowledge financial assistance received through the National Science Foundation, grant number NSF CHE 8205873.

Manuscript submitted May 2, 1983; revised manuscript received July 25, 1983. This was Paper 627 presented at the San Francisco, California, Meeting of the Society, May 8-13, 1983.

The University of Cincinnati assisted in meeting the publication costs of this article.

REFERENCES

1. R. J. Nowak, W. Kutner, H. B. Mark, Jr., and A. G. MacDiarmid, *This Journal*, **125**, 232 (1979).
2. R. J. Nowak, W. Kutner, J. F. Rubinson, A. N. Voulgaropoulos, H. B. Mark, Jr., and A. G. MacDiarmid, *ibid.*, **128**, 1927 (1981).
3. R. J. Nowak, H. B. Mark, Jr., A. G. MacDiarmid, and D. C. Weber, *J. Chem. Soc., Chem. Commun.*, 9 (1977).
4. A. N. Voulgaropoulos, R. J. Nowak, W. Kutner, and H. B. Mark, Jr., *ibid.*, 244 (1978).
5. H. B. Mark, Jr., A. N. Voulgaropoulos, and C. A. Meyer, *ibid.*, 1021 (1981).
6. A. Czerwinski, A. N. Voulgaropoulos, J. F. Johnson, and H. B. Mark, Jr., *Anal. Lett.*, **12**, 1084 (1979).
7. A. N. Voulgaropoulos and H. B. Mark, Jr., *ibid.*, **13**, 959 (1980).
8. J. F. Rubinson, T. D. Behymer, and H. B. Mark, Jr., *J. Am. Chem. Soc.*, **104**, 1224 (1982).
9. J. F. Rubinson, T. D. Behymer, H. B. Mark, Jr., and R. J. Nowak, *This Journal*, **130**, 121 (1983).
10. S. Beaudoin, C. Bernard, R. Vallot, G. Robert, and Liang Tse Yu, *Comte Rend. Acad. Sci., Paris*, **286C**, 217 (1978).
11. C. Bernard, C. Tarby, and G. Robert, *Electrochim. Acta*, **25**, 435 (1980).
12. C. Tarby, C. Bernard, and G. Robert, *ibid.*, **26**, 663 (1981).
13. R. N. Adams, *Anal. Chem.*, **30**, 1576 (1958).
14. L. S. Marcous, K. B. Prater, B. G. Prater, and R. N. Adams, *ibid.*, **37**, 1446 (1966).
15. R. J. Nowak, C. L. Joyal, and D. C. Weber, *J. Electroanal. Chem.*, **143**, 413 (1983).
16. R. J. Nowak, Personal communication (1982).
17. C. M. Mikulski, P. J. Russo, M. J. Saran, A. G. MacDiarmid, A. F. Garito, and A. J. Heegar, *J. Am. Chem. Soc.*, **97**, 6358 (1975).
18. K. P. Shenoy, M.S. Thesis, University of Cincinnati (1983).

Electrogenerative Oxidation of Sulfur Dioxide in the Presence of Oxygen

Robert M. Spotnitz,*,[1] José Colucci,* and Stanley H. Langer*

Department of Chemical Engineering, University of Wisconsin-Madison, Madison, Wisconsin 53706

The production of sulfuric acid from sulfur dioxide and oxygen in a cell with concomitant d-c electrical energy generation has been shown to be an attractive possibility; with efficacious porous electrodes and reactor designs, significant current densities have been obtained albeit at low cell voltages (1). The net electrode reactions are

Anode:

$$SO_2 + 2H_2O \rightarrow SO_4^{2-} + 4H^+ + 2e^- \quad [1]$$

Cathode:

$$0.5\,O_2 + 2H^+ + 2e^- \rightarrow H_2O \quad [2]$$

which give rise to a standard cell potential of 1.06V. In some suggested applications of the process, the sulfur dioxide reactant would be obtained from roasting a sulfide ore or burning sulfur. In either case, if present technology [*e.g.*, Ref. (2)] were used, the SO_2 stream could contain significant oxygen. The question naturally arises then, whether or not sulfur dioxide may be galvanically oxidized in the presence of oxygen? In earlier electrogenerative work, the need for separation of reactants was noted (3). Katagiri, Takehara, and Yoshizawa (4) studied the anodic oxidation of dilute sulfur dioxide (2% or less) on smooth platinum in the presence of oxygen using the potentiostatic method. They found that the presence of oxygen influenced the anodic polarization behavior only at potentials near the rest potential. At 30 mV anodic of the rest potential, the anodic oxidation rate of sulfur dioxide was little affected by the presence of oxygen. The experiments reported here with mixtures of 18% sulfur dioxide and air indicate that the presence of oxygen at a porous platinum anode has only a slightly deleterious effect on generated current in the galvanic oxidation of sulfur dioxide.

Experimental

The electrogenerative reactor used in this study was a divided flowing electrolyte type. Figure 1 shows a schematic of gas and electrolyte flows. Electrolyte flows by gravity from a reservoir (not shown) into the bottom of the catholyte chamber, to sweep and exit through the top of the catholyte chamber, from where it is conducted outside the cell by a polytetrafluoroethylene pipe, to reenter the cell at the bottom of the anolyte chamber. Finally, the electrolyte exits from the cell at the top of the anolyte chamber where a flow rate control valve is located. The free electrolyte anolyte and catholyte chambers (each chamber was 6 mm thick) were separated by an ion exchange mem-

* Electrochemical Society Active Member.
[1] Present address: W. R. Grace & Company, Washington Research Center, Columbia, Maryland 21044.
Key words: fuel cell, porous electrodes, synthesis.

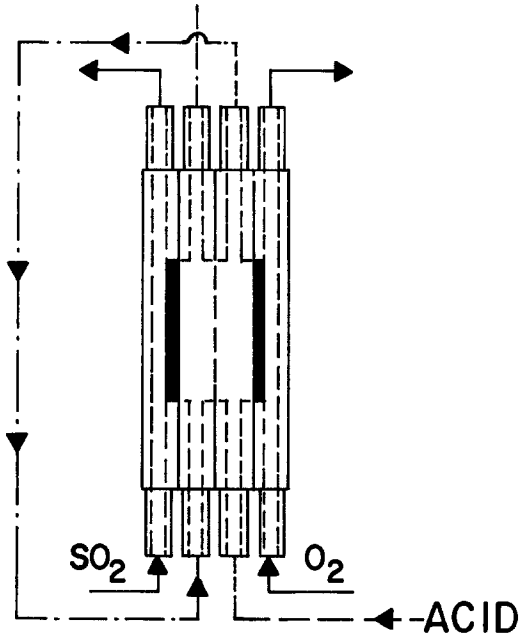

Fig. 1. Schematic representation of divided flowing electrolyte reactor. Gas chambers constructed of KEL-F, electrolyte chambers of polytetrafluoroethylene.

brane (R4010, RAI Research, Incorporated) which permits the passage of cations. The R4010 membrane is a sulfonated styrene graft on a preformed 2 mm fluorinated polymer film. The membrane resistance is about 0.03Ω based on cell resistance measurements made with and without the membrane in place. This membrane has been recommended earlier as an effective diffusion barrier for SO_2 in SO_2/H_2 electrolyzers by workers at Westinghouse (5). Porous polymer-bonded Teflon-backed electrolyte impermeable fuel cell electrodes containing 10 mg/cm^2 of platinum black (United Technologies Corporation) were used at both the anode and cathode. These circular electrodes had an area of 5.1 cm^2.

During polarization runs, a commercially available saturated calomel reference electrode (SCE) (American Scientific Products) was immersed in the electrolyte reservoir (see above) so that the potential of the working oxygen electrode could be monitored relative to the SCE with the electrolyte serving as a bridging solution.

Pure oxygen (Chemetron) was fed to the cathode. SO_2/N_2 and SO_2/air mixtures were prepared by mixing (in a tube containing glass beads) pure SO_2 (Matheson) with nitrogen (prepurified, Badger Welding Supply, Incorporated) or compressed air (Badger Welding Supply, Incorporated), respectively. Inlet gas flow rates were monitored with rotameters (Matheson, Model 7651T). The rotameters were calibrated with nitrogen; for use with sulfur dioxide, the rotameter reading was multiplied by 1.53 and the calibration curve for nitrogen used. The factor 1.53 is the square root of the ratio of the specific gravity of SO_2 to that of N_2 (6). For measuring air flow rates, the calibration curve for nitrogen was used directly. Sulfuric acid solutions (4.5M) were prepared from reagent grade sulfuric acid and distilled water. The electrolyte flow rate steadily decreased during the experiment as the head of the reservoir decreased.

Before an experiment, the electrodes were electrolytically pretreated in 4.5M sulfuric acid by applying a constant current of 50 mA, with reversal every 2 min, for a total of 12 min. A polarization curve was obtained first with an SO_2/N_2 mixture fed to the anode. Next, without pretreating the electrodes again, an SO_2/air mixture was substituted for the SO_2/N_2 mixture. The new gas mixture flowed across the anode for 30 min, while at open circuit, to ensure adequate purging before obtaining a polarization curve.

Polarization curves were obtained by stepwise discharge of the cell through an external variable resistance (1). Steady state was assumed when the cell voltage was constant within 2 mV for 5 min. Cell resistance was determined as described earlier (1). The average cell resistance (based on four separate measurements) was 0.43 ± 0.01Ω. With the use of the well-characterized hydrogen-oxygen fuel cell, the effective resistance between the oxygen electrode and the reference electrode was estimated to be 0.06Ω. This hydrogen-oxygen cell was operated in the same reactor under the same conditions to obtain this value. All experiments were performed at ambient temperature (23° ± 2°C).

Results

Figure 2 shows the results of typical experiments with pure sulfur dioxide, sulfur dioxide-nitrogen mixtures, and sulfur dioxide-air mixtures at the anode. Dilution of sulfur dioxide with air instead of nitrogen reduces the cell voltage (corrected for *IR*-drop) at particular current densities by 30-50 mV. Using the results illustrated by Fig. 3, we find this voltage reduction occurs mainly at the anode. The polarization behavior at the cathode (see Fig. 3) in all runs (including one with a hydrogen anode not shown in Fig. 3) established that this electrode was not affected by sulfur dioxide at the anode and that the cation exchange membrane was an effective SO_2 diffusion barrier. This is in good agreement with the results of Lu *et al.* (5). Part of the voltage loss can be attributed to some electrode deactivation which occurs with aging; a second consecutive polarization curve taken without changing gas compositions often lies about 20 mV below the first. Thus, the presence of oxygen in the simulated sulfur dioxide stream only slightly diminishes cell performance. This finding is encouraging for the pursuit of the suggested applications of the electrogenerative oxidation of sulfur dioxide. It is also consistent with the recent report of Matveeva *et al.* (7) wherein the effectiveness of SO_2 as a poison for oxygen electroreduction at platinum electrodes is demonstrated. Some of the deleterious effect of oxygen also may be due to

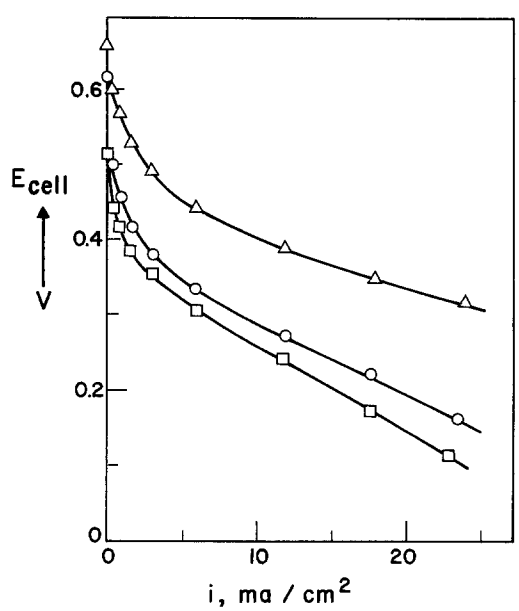

Fig. 2. *IR*-corrected cell voltage vs. current density for the cell of this study. △, pure SO_2 anode gas; ○, anode gas [18.5 volume percent (v/o) SO_2, remainder N_2, total flow rate 102 ml/min]; □, anode gas (18.5 v/o SO_2, 17.1% O_2, plus N_2, flow rate 104 ml/min). Pure oxygen as cathode gas with 4.5M sulfuric acid electrolyte (electrolyte flow rate varied from 7.9 ml/min initially to 7.2 ml/min at end of experiment).

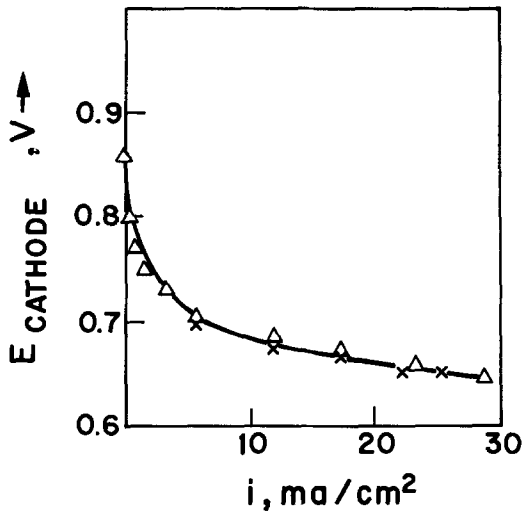

Fig. 3. The cathode voltage (*IR*-corrected relative to SCE) vs. current density for the cell of this study. △, anode gas is 18.5 v/o SO_2, remainder N_2, total flow rate 102 ml/min; ×, anode gas is 18.5 v/o SO_2, 17.1% O_2, plus N_2 at a flow rate of 104 ml/min. Oxygen is used at the cathode. The flow rate of the 4.5M sulfuric acid electrolyte varied from 7.9 to 7.2 ml/min.

the type of localized cell activity suggested earlier (4) wherein oxygen is initally electrochemically reduced to hydrogen peroxide. This reacts with sulfur dioxide, *i.e.*

$$O_2 + 2H^+ + 2e^- \rightarrow H_2O_2 \quad [3]$$

$$H_2O_2 + SO_2 \rightarrow SO_4^{2-} + 2H^+ \quad [4]$$

Reaction [1] above completes the local cell.

The concentration of oxygen in the sulfur dioxide stream could be reduced substantially if more concentrated SO_2 streams were needed or desirable. The tolerance for high levels of oxygen at the SO_2 electrode indicates that other practical applications of the electrogenerative reactor might be feasible (*e.g.*, a means of oxidizing and lowering sulfur dioxide concentrations in effluent air streams).

Acknowledgment

The authors thank the University of Wisconsin and the National Science Foundation for the support of this work and United Technologies Corporation for the gift of the porous electrodes.

Manuscript received June 6, 1983.

REFERENCES

1. R. M. Spotnitz, C. E. Loeffler, II, and S. H. Langer, *J. Appl. Electrochem.*, **11**, 403 (1981).
2. T. S. Harrer, in "Kirk-Othmer's Encyclopedia of Chemical Technology," Vol. 19, 2nd ed., p. 441, Wiley, New York (1969).
3. S. H. Langer, A. D. Miller, and S. Pietsch, *J. Appl. Chem. Biotechnol.*, **27**, 176 (1977).
4. A. Katagiri, S. Takehara, and S. Yoshizawa, *Denki Kagaku*, **41**, 430 (1973).
5. P. W. T. Lu, R. L. Ammon, and G. H. Parker, Westinghouse Advanced Energy Systems Division, Sulfur Cycle Hydrogen Process, Final Report, Contract No. 955380, Pittsburgh, PA (1980).
6. A. S. Foust, L. A. Wenzel, C. W. Clump, L. Mans, and L. B. Andersen, "Principles of Unit Operations," p. 411, Wiley, New York (1960).
7. E. S. Matveeva, V. A. Shepelin, and E. V. Kasatkin, *Elektrokhimiya*, **17**, 617 (1981).

Electron Energy Loss Spectroscopy of a Barrier-Type Film Formed on Aluminum in Oxalate Solution

Y. Xu, G. E. Thompson, and G. C. Wood

Corrosion and Protection Centre, University of Manchester, Institute of Science and Technology, Manchester M60 1QD, England

Transmission electron microscopy of ultramicrotomed sections of barrier-type anodic films on aluminum has been employed to determine film thickness and uniformity over the macroscopic metal surface (1). Upon initial examination in the electron microscope the generally amorphous film material appears relatively featureless, although telling changes in texture are apparent after more prolonged exposure to the electron beam (2). Generally, the inner regions of the film, adjacent to the metal/film interface, crystallize more rapidly than the outer regions of the film. CTEM/STEM/EDX analysis of films formed in appropriate electrolytes has confirmed directly that the outer region, showing a slower response to crystallization, contains species incorporated from the anodizing electrolyte, *e.g.*, phosphate (3), tungstate (4), or their dissociation products. Allied with ion implantation of inert marker layers, *i.e.*, xenon, which may be observed and analyzed directly in the film section (5), analytical transmission electron microscopy is a powerful technique for assessing rapidly and relatively precisely contributions to solid film growth at the metal/film and film/solution interfaces both generally over the macroscopic metal surface and locally at flaws, the relative mobilities of Al^{3+} ions outwards, O^{2-} or OH^- inwards, and the mobilities, or otherwise (6), of other incorporated anions.

A problem arising with EDX analysis is the inability to detect light elements of interest which may be incorporated into anodic films, *e.g.*, carbon incorporated within films formed in oxalate solution, and oxygen. Potentially this problem of light element analysis has been alleviated by electron energy loss spectrometry (EELS) (7) where the incident electrons interact with electrons from an inner shell of an atom, losing a significant amount of energy by inelastic scattering. The energy loss, or characteristic edge, resulting from the ionization of an atom (uniquely characteristic of that element) may be measured and calibrated to give an elemental analysis spectrum (7). This communication presents preliminary data of such analysis from anodic films formed on aluminum in oxalate solution.

Suitable specimens were prepared by anodizing electropolished superpure aluminum at constant current density (300 A m^{-2}) to 100V in near-neutral 0.1M oxalate solution at 293 K, without subsequent current decay. Ultramicrotomed sections were prepared in the usual manner (1), where final sectioning with a diamond knife produced electron transparent sections

Key words: films, anode, transmittance, analysis.

of anodic film, attached to the aluminum substrate, about 50 nm thickness. Since controlled specimen thickness is critical for inelastic scattering events it was assumed that this thickness approached sufficiently the mean free path for such events from the inner electron shells of carbon, which has been reported previously to be of the order of 600[7]-1000 nm[8]. The sections were examined directly and analyzed in a Philips EM 400T electron microscope fitted with STEM/EDX/EELS facilities; a Gatan electron energy loss spectrometer was employed for this study.

The ultramicrotomed section of the aluminum substrate and its barrier-type anodic film is shown in Fig. 1; the film is about 100 nm thick, with a nm V^{-1} forming ratio of approximately 1.0, and appears relatively featureless in texture upon initial examination. Parallel studies involving Auger analysis and electron beam induced crystallization have suggested that the outer two-thirds of the film contain incorporated oxalate or its dissociation products and the inner one-third of the film, adjacent to the metal/film interface is relatively pure alumina (9). This is shown in the corresponding schematic diagram of Fig. 2. For EELS analysis five regions within the section, including the aluminum substrate, the complete film section, and various regions within the film, were selected for analysis. The electron beam was contained within the particular regions of interest and the electron energy loss spectrum determined with the focused spectrometer. Typical portions of the spectra generated from the regions of interest are illustrated in Fig. 3, with the cursor identifying the energy at which a carbon K-edge would be observed, if detected. Qualitatively, direct interpretation of the spectra suggests that carbon is detected, within the detection limits of the technique (the minimum detectable mass of carbon in silicon has been estimated at about 5×10^{-17}g), in the film material (Fig. 3b), with no carbon yield evident for probe positions within the aluminum substrate (Fig. 3a).

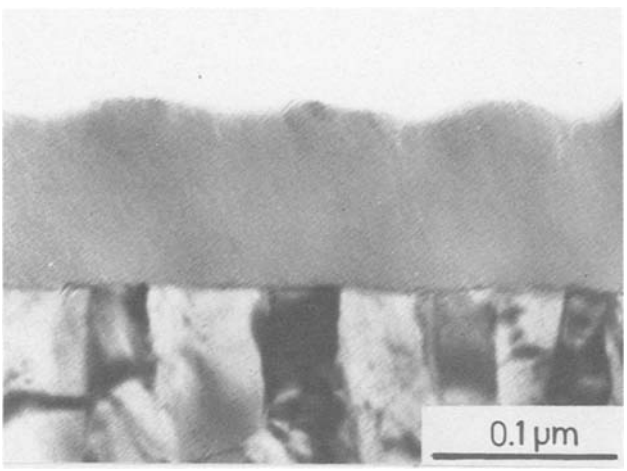

Fig. 1. Transmission electron micrograph of an ultramicrotomed section of the barrier-type anodic film formed on aluminum at a constant current density of 300 A m^{-2} to 100V in near neutral 0.1M oxalate solution at 293 K, without current decay.

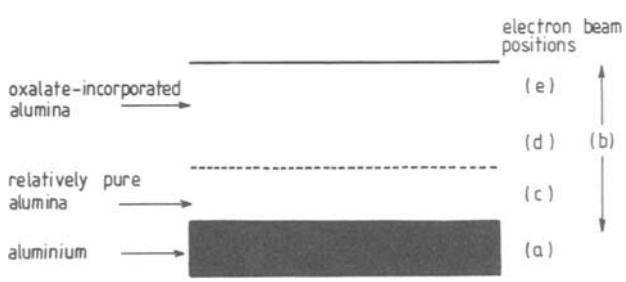

Fig. 2. Schematic diagram of the aluminum substrate and the film, formed under the conditions of Fig. 1, showing the relatively pure alumina region adjacent to metal/film interface and the outer carbon-containing alumina region.

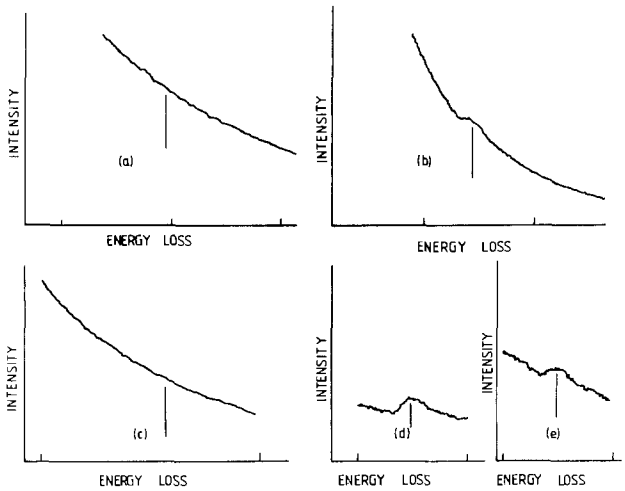

Fig. 3. Electron energy loss spectra derived from film regions identified in the schematic diagram of Fig. 2 (the full-scale width of the portion of the spectra is about 100 eV, and the position of the carbon K-edge, at 283 eV, is marked): (a) metal substrate; (b) film section; (c) inner region of relatively pure alumina; (d) outer region of carbon-containing film material adjacent to (c); (e) outer region of film material near the film/solution interface.

Reduction of the electron beam spot size, to an effective diameter of about 30 nm, so that it was confined to the inner region of relatively pure alumina and two areas within the outer film regions, one adjacent to the inner region of film and the other nearer the film/solution interface, generated the spectra shown in Fig. 3c-e. Here, carbon is not detected in the inner region of film, probably relatively pure alumina, but is evident for both probe positions within the outer, carbon-incorporated film material.

The data presented here show that direct analysis in the transmission electron microscope, of suitably prepared film sections, may be extended to light elements, not detected by EDX techniques, by use of EELS. Thus, knowledge of film composition and detection of appropriate species may be furthered by direct study. The present qualitative information revealed about the location of carbon, derived from oxalate, within the film is in good agreement with Auger analysis and electron beam induced crystallization of similar films (9). Presently the amount of incorporated oxalate is not known from this preliminary examination, but gravimetric analysis of porous anodic films formed in oxalate acid has shown about 2.4 w/o oxalate in these latter relatively thick films (11). However, progress in the quantification of EELS analysis is being made progressively, in addition to the possibility of determining further information from the initial electron energy loss spectrum, *e.g.*, chemical nature of the element of interest and local atomic arrangements. It is this kind of information which is of prime importance for further understanding of anion-incorporated anodic films on aluminum which have been assumed to be amorphous, composed of fine microcrystallites of alumina, or even glassy.

In summary, the application of ultramicrotomy allows the aluminum substrate and its film to be examined directly, with control of specimen thickness. It is also of interest that the technique may be applied to other metals/alloys (12), *e.g.*, magnesium, titanium, stainless steels, etc. and their films, thus extending further the possibility of analytical transmission electron microscopy.

Acknowledgments

The authors are indebted to the Chinese Ministry of Education and the British Council for the award of a studentship to Y. Xu. The authors also thank Dr. G. W. Lorimer, of the joint U.M.I.S.T./University of Manchester Department of Metallurgy, for provision of time on the Philips EM 400T with STEM and EDX facilities, and Philips Instruments for use of the electron energy loss spectrometer.

Manuscript submitted April 21, 1982; revised manuscript received April 5, 1983.

REFERENCES

1. R. C. Furneaux, G. E. Thompson, and G. C. Wood, *Corros. Sci.*, **18**, 853 (1978).
2. K. Shimizu, G. E. Thompson, and G. C. Wood, *Thin Solid Films*, **77**, 313 (1981).
3. G. E. Thompson, K. Shimizu, and G. C. Wood, *Electrochim. Acta*, **26**, 951 (1981).
4. K. Shimizu, G. E. Thompson, and G. C. Wood, *Thin Solid Films*, **81**, 39 (1981).
5. K. Shimizu, G. E. Thompson, G. C. Wood, and Y. Xu, *ibid.*, **88**, 255 (1982).
6. K. Shimizu, G. E. Thompson, and G. C. Wood, *ibid.*, **85**, 53 (1982).
7. D. C. Joy, in "Introduction to Analytical Electron Microscopy," J. J. Hren, J. I. Goldstein, and D. C. Joy, Editors, p. 223, Plenum Press, New York (1979).
8. W. Brunger and W. Menz, *Z. Phys.*, **184**, 271 (1965).
9. Y. Xu, G. E. Thompson, and G. C. Wood, To be published.
10. D. M. Maher, in "Introduction to Analytical Electron Microscopy," J. J. Hren, J. I. Goldstein, and D. C. Joy, Editors, p. 285, Plenum Press, New York (1979).
11. C. E. Alvey, Ph.D. Thesis, University of Manchester (1974).
12. K. Shimizu, G. E. Thompson, and G. C. Wood, Unpublished work.

JOURNAL OF THE ELECTROCHEMICAL SOCIETY

SOLID-STATE SCIENCE
—AND TECHNOLOGY

DECEMBER
1983

Morphological Study of Thermal Decomposition of InP Surfaces

S. N. G. Chu, C. M. Jodlauk, and W. D. Johnston, Jr.

Bell Laboratories, Murray Hill, New Jersey 07974

ABSTRACT

The morphological evolutions of the (100), (111), and (110) InP surfaces decomposed at typical VPE and LPE growth temperatures in hydrogen are examined under the microscope using a hot stage. The detailed surface morphology resolved by SEM indicates that the development of the decomposition pits on InP surfaces begins with the nucleation of indium droplets of a few thousand angstroms in diameter. The subsequent etching of the InP surface in contact with the indium droplet initiates the decomposition pits. The nucleation temperature of indium droplets decreases with increasing hydrogen flow. The evolution of the decomposition pits are recorded on video tape. Detailed growth mechanisms and geometries of the pits on each orientation are described. The effects of misorientation and hydrogen flow rate on the decomposition morphology are discussed. The results suggest that the hydrogen flow over the substrate surface prior to VPE growth should be held to a minimum in order to minimize the thermal decomposition.

The rapid incongruent vaporization of In and P from a polished InP substrate surface, prepared for device fabrication, at VPE and LPE growth temperatures poses a major problem for the reproducible preparation of high quality InP buffer layers (1). The indium metal left on the surface tends to be trapped at the interface as growth commences and causes interfacial problems. The influence of thermal decomposition of the substrate surface on the quality of the epilayer has been discussed by Temkin *et al.* (1). The understanding of the nature of thermal decomposition of InP, therefore, has considerable technological importance in view of the recent increase in demand for optoelectronic devices prepared from this material.

The decomposition of InP in vacuum has been studied by various authors (2-5). Bayliss *et al.* (3, 4) showed that the restructuring of the (100) InP surface due to incongruent vaporization of In and P readily occurred at temperatures above 300°C. Gallagher *et al.* (5), using the kinetic parameters obtained from powder samples, estimated a decomposition rate of 9 monolayers per sec on the (100) InP surface at a typical VPE growth temperature (700°C).

The decomposition of InP in ambient gases has been investigated for LPE growth conditions (6-12). The presence of the ambient gases generally alters the decomposition kinetics and hence the decomposition morphology. Various ways for increasing the phosphorus partial pressure (6, 9, 11, 12) have been proposed to suppress the decomposition. However, none of them has been shown to suppress the decomposition completely. The decomposed surface has been characterized in detail by using LEED (4), photoluminescence, Auger analysis, and SEM (6), yet no study of the detailed evolution of the decomposition morphology has been reported. This work concentrates on the mechanisms of initiation and evolution of the decomposition morphology on (100), (111), and (110) InP surfaces decomposed at typical VPE and LPE growth temperatures in a hydrogen ambient. The nucleation of indium droplets and the initiation and growth of the decomposition pits are discussed in detail. The effects of hydrogen flow rate and misorientation from the (100) surface are also presented.

Experimental Method

S-doped (10^{18-19} cm^{-3}) (100) and Sn-doped (10^{18} cm^{-3}) (111) InP substrate wafers were used in this study. These wafers were cut from crystal boules grown in (100) and (111) orientations, respectively, by the LEC technique. The wafers with 3° misorientation towards (110) direction were obtained from the Sumitomo Electric Company. Samples with 6° misorientation were prepared by angle lapping from the 3° misoriented wafer. The wafers were chemi-mechanically polished in 2% Br-methanol solution to remove the saw damage. The as-polished surfaces were highly specular. Samples 4 mm × 4 mm in size, cleaved from regions with dislocation density less than 1000 per cm^2, were subjected to a second quick polishing immediately before the decomposition experiment.

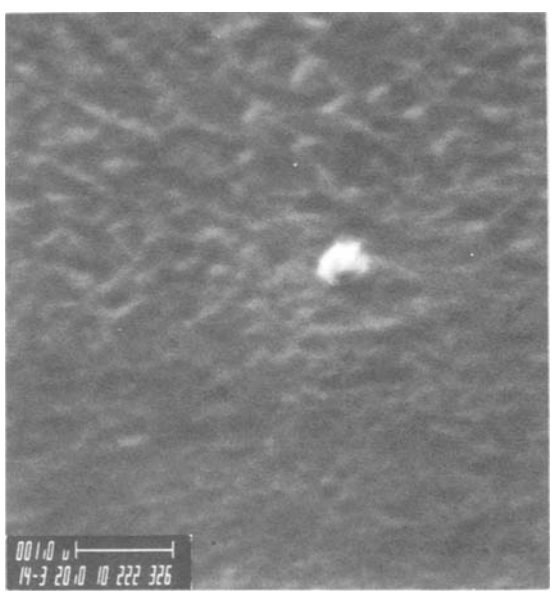

Fig. 1. SEM micrograph of indium nucleus developed on (100) InP surface at 630° under a hydrogen flow rate of 300 cm^3/min.

Thermal decomposition of InP was conducted under a hydrogen atmosphere. The real time evolution of the decomposition morphology was monitored under a Zeiss Ultraphot microscope equipped with a Leitz Model 1350 heating stage and video recording facilities. A d-c power supply was used to supply the current to the heating stage, and the temperature of the sample was recorded. The nucleation temperatures of the indium droplets were determined as the temperature where visible nuclei first appeared under the microscope at 200× magnification. The detailed structure of the surface morphology was examined using the SEM and Nomarski interference microscopy. The crystallographic facets which bounded the decomposition pits were determined by measuring the relative angles of the facet with respect to the substrate orientation on the (110) cross section cleaved through the facet.

The study of the effect of hydrogen flow rate on the decomposition morphology was done inside a quartz tube furnace under a constant flow of hydrogen gas. The inner diameter of the furnace tube was 10 mm, and hydrogen flow rates ranged from 0 to 600 cm³ per min. The sample was placed inside a quartz sample tube which inserted into the furnace tube. The corresponding linear gas flow velocity ranges from 0 to 1.5m per sec.

Results and Discussion

Nucleation of indium droplets and initiation of decomposition pits.—Although incongruent vaporization of the (100) InP surface in vacuum starts at temperatures above 300°C, initiation of decomposition pits in hydrogen did not occur until the temperature reached 600°C. High-magnification (SEM) microscopy indicated that the decomposition pits initiated from indium droplets, which were expected to nucleate as the amount of indium accumulated on the surface reached a critical value. Shown in Fig. 1 is an example of the indium droplet nucleated on the (100) InP surface at 630°C under a hydrogen flow of 300 cm³ per min. The typical size is about a few thousand angstroms in diameter. The nucleation temperature of the indium droplet, as shown in Fig. 2 for a (100) surface, is strongly dependent on the hydrogen flow rate. The nucleation temperature indicated by the arrows in Fig. 2, decreases by 80°C for an increase in hydrogen flow rate from 20 cm³ per min to 600 cm³ per min. The slight variation in the heating rate is due to the difference in the amount of heat carried away by the hydrogen at different flow rates. At the same hydrogen flow rate, the effect of heating rate on the nucleation temperature is negligible, see R = 300.

Nucleation of indium droplets on (111) surfaces is basically similar to that on the (100) surface, except that the nucleation temperatures, shown in Fig. 3, are generally higher as compared to the (100) surface at the same hydrogen flow rate. The (111) In face is chemically stable, as compared to the (111) P face which has two unpaired bonds associated with each P

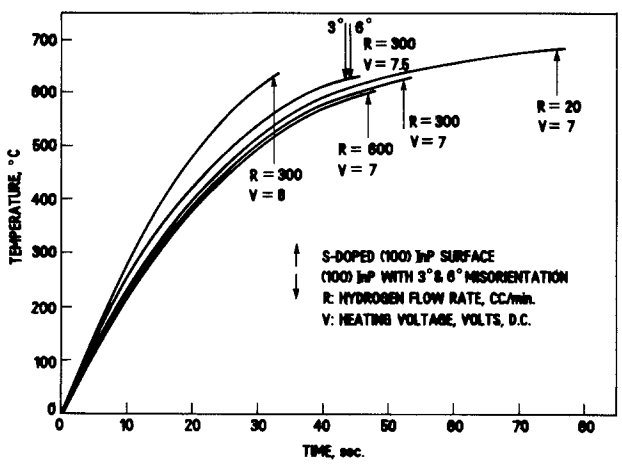

Fig. 2. Nucleation temperatures of indium droplets, indicated by the arrows, caught along the heating curve for (100) and 3°- and 6°-misoriented (100) InP surfaces at different hydrogen flow rates and heating rates.

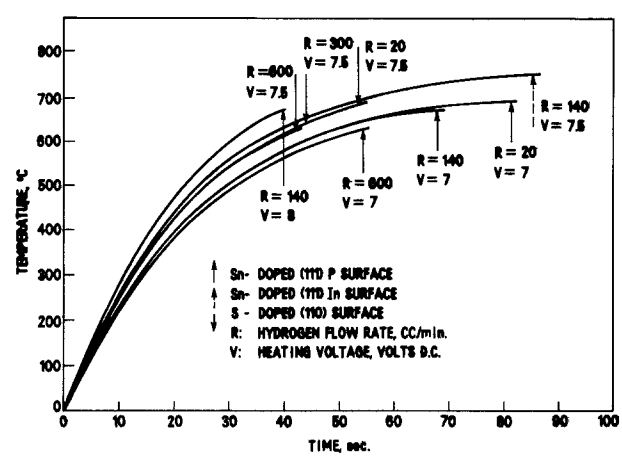

Fig. 3. Nucleation temperatures of indium droplets, indicated by the arrows, caught along the heating curve on (111) P, (111) In, and (110) In surfaces at different hydrogen flow rates and heating rates.

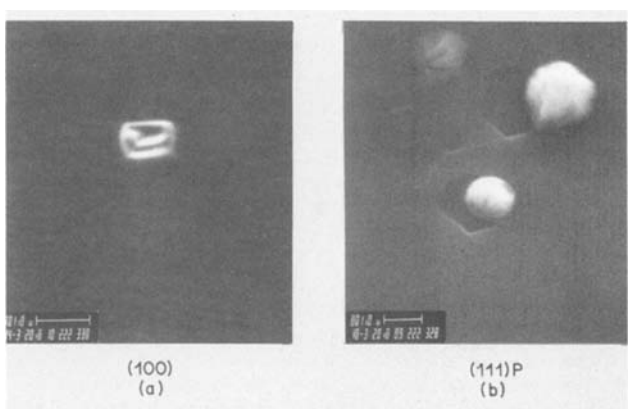

Fig. 4. Initiation of decomposition pits on (a) (100) InP surface, and (b) (111) P InP surface. The edges of the pits are all aligned along the <110> direction.

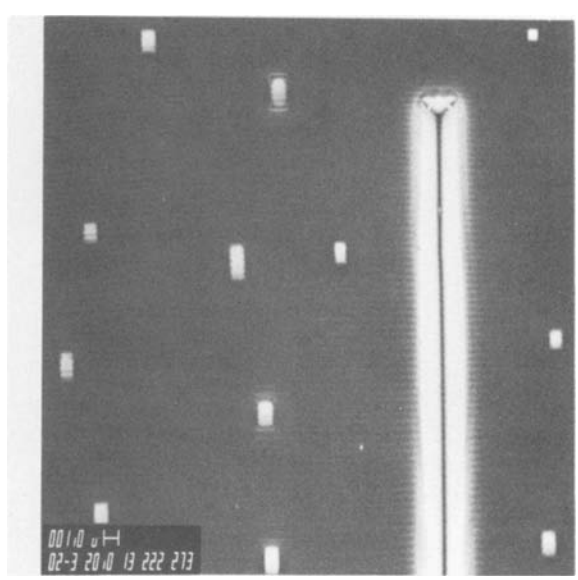

Fig. 5. Well-developed decomposition pits on the (100) InP surface. The pits are filled with large indium droplets. Bright spots are small indium droplets.

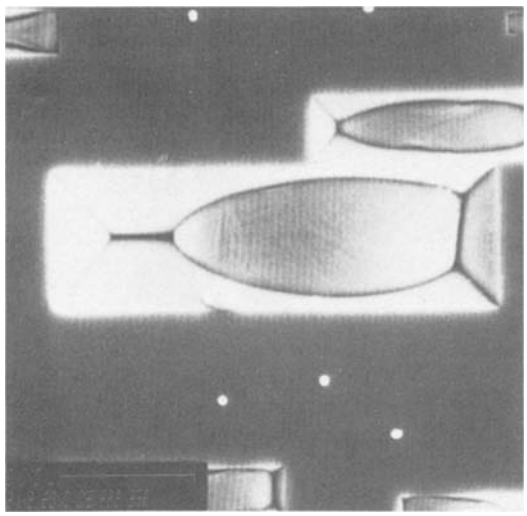

Fig. 6. Decomposition tips develop from secondary nucleation of indium droplets. The large pit develops from the first nucleation.

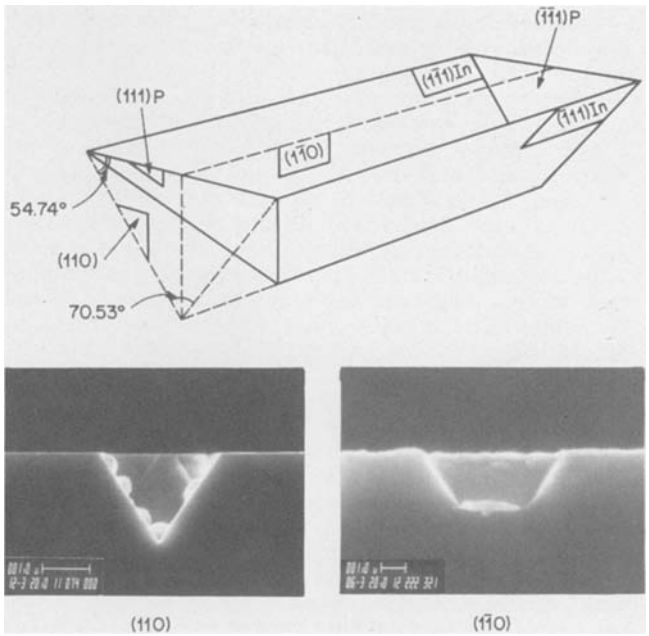

Fig. 7. Determination of crystallographic facets which bound the decomposition pits on the (100) InP surface. The SEM micrographs show the relative angles of the facets with respect to the (100) surface as determined on (110) and (1$\bar{1}$0) surfaces cleaved through the pit.

atom. Accordingly, the stability of the surfaces was expected to be in the order of (111) In, (111) P and (100), and the nucleation temperatures to decrease in that order as well. This is observed and shown in Fig. 3 at a hydrogen flow rate of 140 cm^3 per min. The effect of heating rate on the nucleation temperature is again negligible. The nucleation temperatures for the (110) surface are close to those of the (111) P surface.

The formation of decomposition pits follows immediately after indium droplets are nucleated. The mechanism is believed to be melt-back or enhanced decomposition of the InP surface in contact with the indium droplets. The typical initial stage of the decomposition pits developed on the (100) and (111) P faces are shown in Fig. 4a and 4b. The edges of the rectangular pits on the (100) surface and of the hexagonal impressions on (111) P surface are all parallel to the <110> directions.

As the decomposition proceeds, second nucleation always occurs in the region surrounding the existing decomposition pits. Shown in Fig. 5 is an example. The small decomposition pits are developed from a second nucleation of the indium droplets shortly after the pits from the first nucleation begin to grow.

Growth of the decomposition pits.—The continuous monitoring of the growth of decomposition pits using video recording revealed the following growth mechanisms on (100), (111), and (110) surfaces.

(100) surface.—The decomposition pits, initiated by the melt back or enhanced decomposition of the InP surface in contact with the indium droplets on the 100 surface, grow rapidly along a unique [110] direction. The indium droplets trapped inside the pits run back and forth along the rapid-growth direction. The cause of the agitation of the molten indium droplets is believed to be due to the formation of P_2 gases as a result of the decomposition of the surface of the pit. The growth rate along the rapid-growth direction is greatly enhanced for those pits with indium droplets trapped at the ends, which is additional direct evidence of the enhancement of decomposition of the InP surface in contact with the molten indium. As the rectangular pits grow in width, the molten indium spreads out evenly and settles at the bottom of the pit. The growth rate along the rapid-growth direction usually falls off

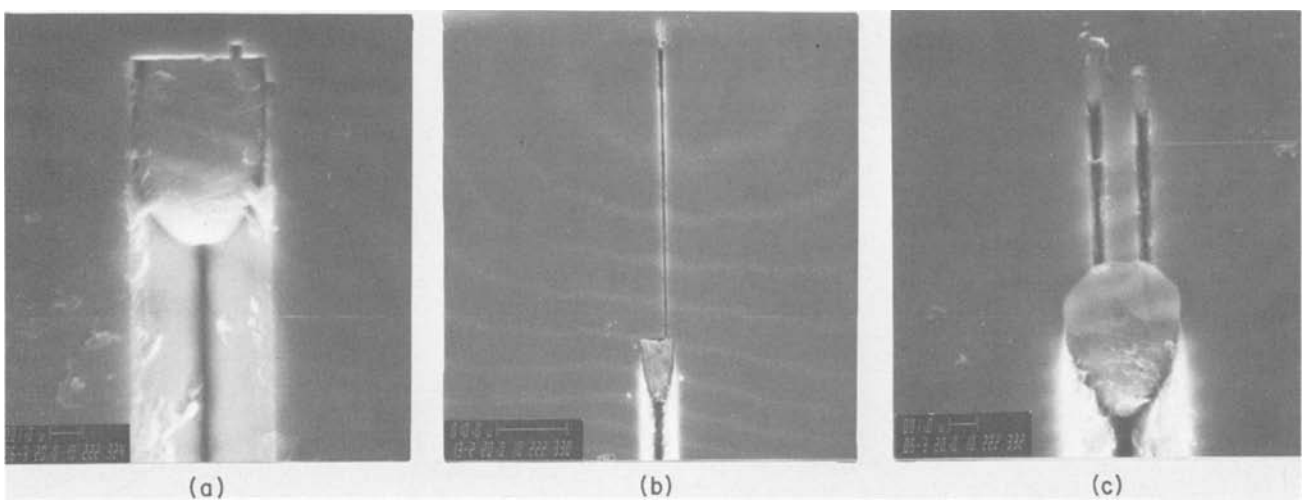

Fig. 8. Growth of new pits at the ends of growing pits: (a) the initiation of the new pits; (b) the rapid growth of the new pit at the end of the growing parent pit; (c) multiple pit nucleation.

drastically at this point. Occasionally the indium melt is agitated by P_2 gases bubbling through.

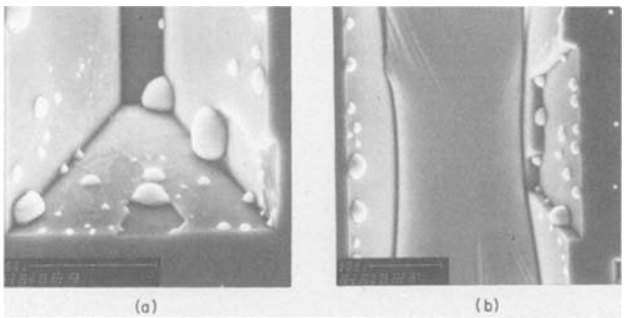

Fig. 9. The detailed decomposition morphology on (a) the fast moving (111)P facet, and (b) the slow moving (111) In facet. The growth rate of the pit controlled by the decomposition rate.

A typical decomposition pit is shown in Fig. 6. A large drop of indium is trapped inside a rectangular pit bounded by crystallographic facets. The small bright spots are also indium droplets. The orientation of the facets was determined by measuring the angles of the plane with respect to the (100) surface on the (110) cross section cleaved through the pits. The results are shown in Fig. 7. The rectangular pit is bound by four (111) planes, consistent with Lum's observation (6). The fast moving facets are believed to be the (111) P-planes, and the slow moving facets to be the (111) In planes.

In some cases, nucleation of new pits occurs at the ends of the growing pits (see Fig. 8a). These newly nucleated pits grow at a more rapid rate than the parent pits (Fig. 8b). Sometimes more than one pit may be nucleated (Fig. 8c). However, this phenomenon occurs only at those pits in which the indium droplet becomes trapped at one end.

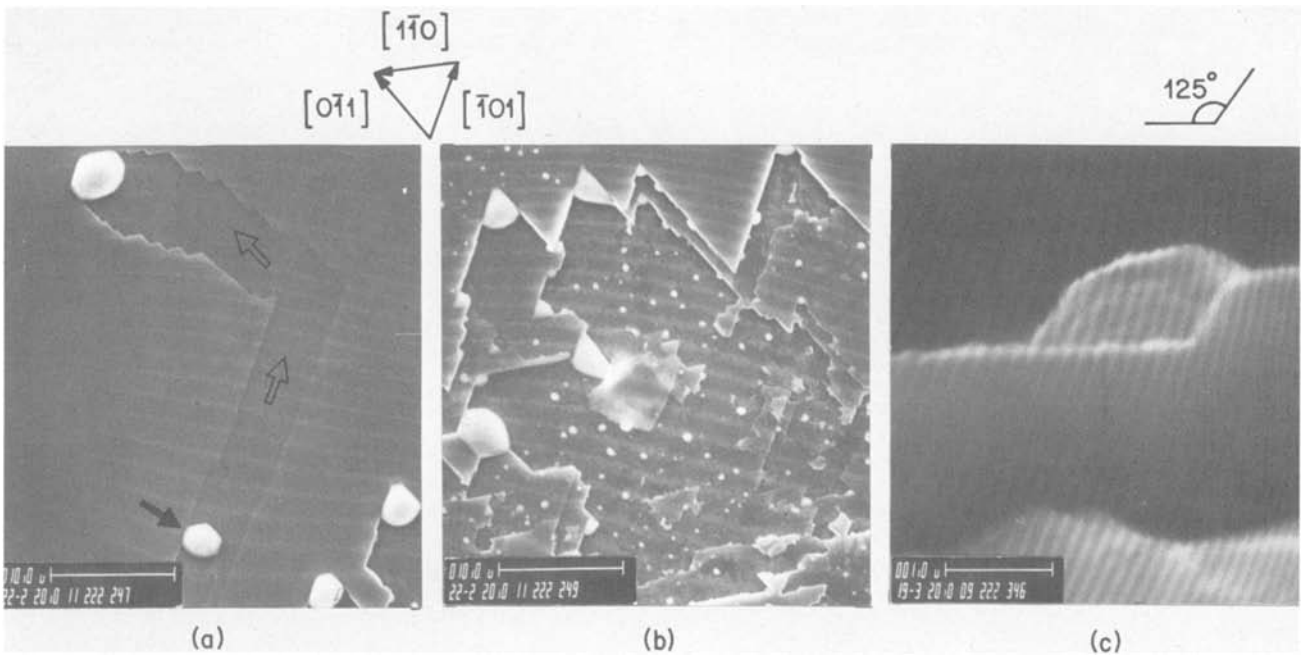

Fig. 10. The detailed decomposition mechanisms of the (111) P InP surface: (a) indium droplets move around in all three <110> directions and "dig tracks" on the surface as they pass by. The hollow arrows show the directions of motion of the indium droplets. The solid arrow shows a second indium droplet nucleated and forming a track inside the track of the previous indium droplet; (b) the layer structure of a decomposed (111) P surface; (c) the cross-section view on the (110) plane cleaved through the fast moving facet shows the facet to be a (100) plane.

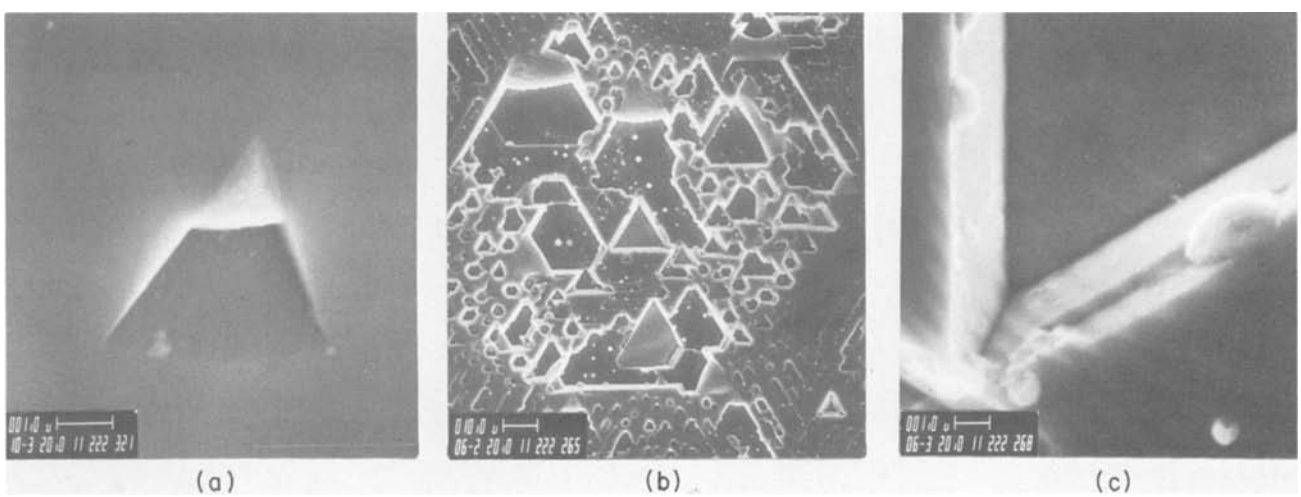

Fig. 11. Decomposition morphology on (111) In surface: (a) initiation of triangular decomposition pits; (b) a well-decomposed surface; (c) the detailed decomposition morphology on(111) P facet.

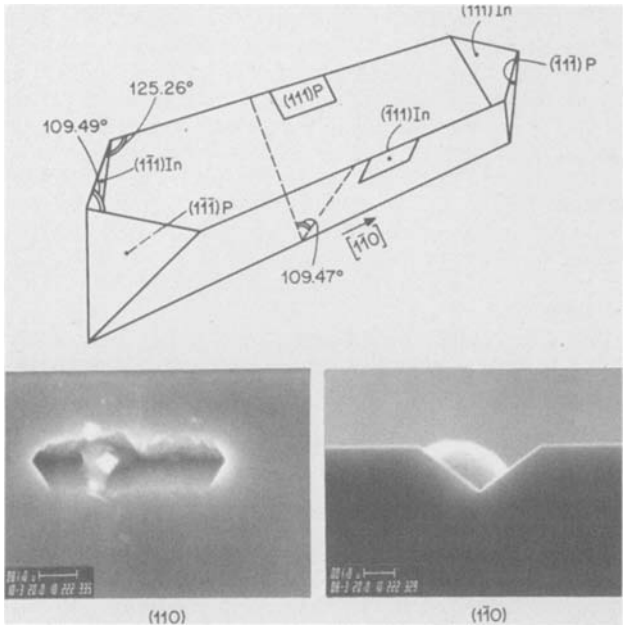

Fig. 12. The geometry of all the observed (111) facets which bound the decomposition pits on the (110) InP surface.

Since the facets which form the decomposition pits on the (100) surface are (111) planes, the growth rate of the pits is expected to be rate controlled by the decomposition of the (111) surfaces. Shown in Fig. 9 is a high magnification of the (111) P and (111) In facets. The decomposition of the facet leaves large indium droplets. Steps and tracks form on the surface of the facets as the indium droplets move around. A detailed

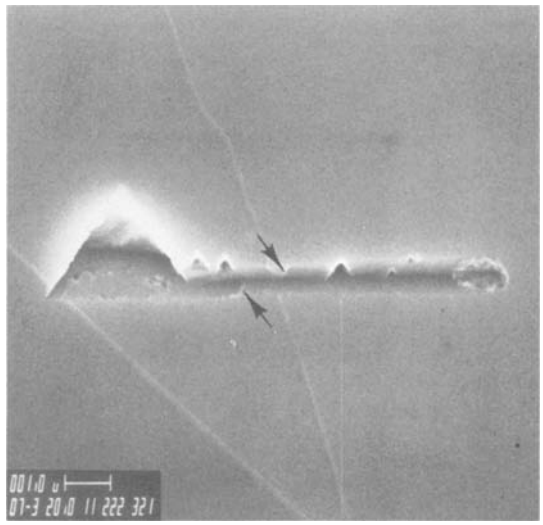

Fig. 14. The development of a linear pit from the triangular pit. The arrows show the trace of the (111) P facets. Small triangular pits are also developed on the (111) P facet of the linear pit.

decomposition mechanism on (111) surfaces will be discussed in the following sections.

(111) surface.—The evolution of decomposition pits on the (111) P surface is different from that on the (100) surface. The indium nuclei on the (111) P face are observed to move in any one of the three equivalent <110> directions, and indeed may "jump" from one such direction to another as they are moving. An example is show in Fig. 10a. The hollow arrows indicate the directions of movement of the indium droplet. As the indium droplet passes by, a track is formed on

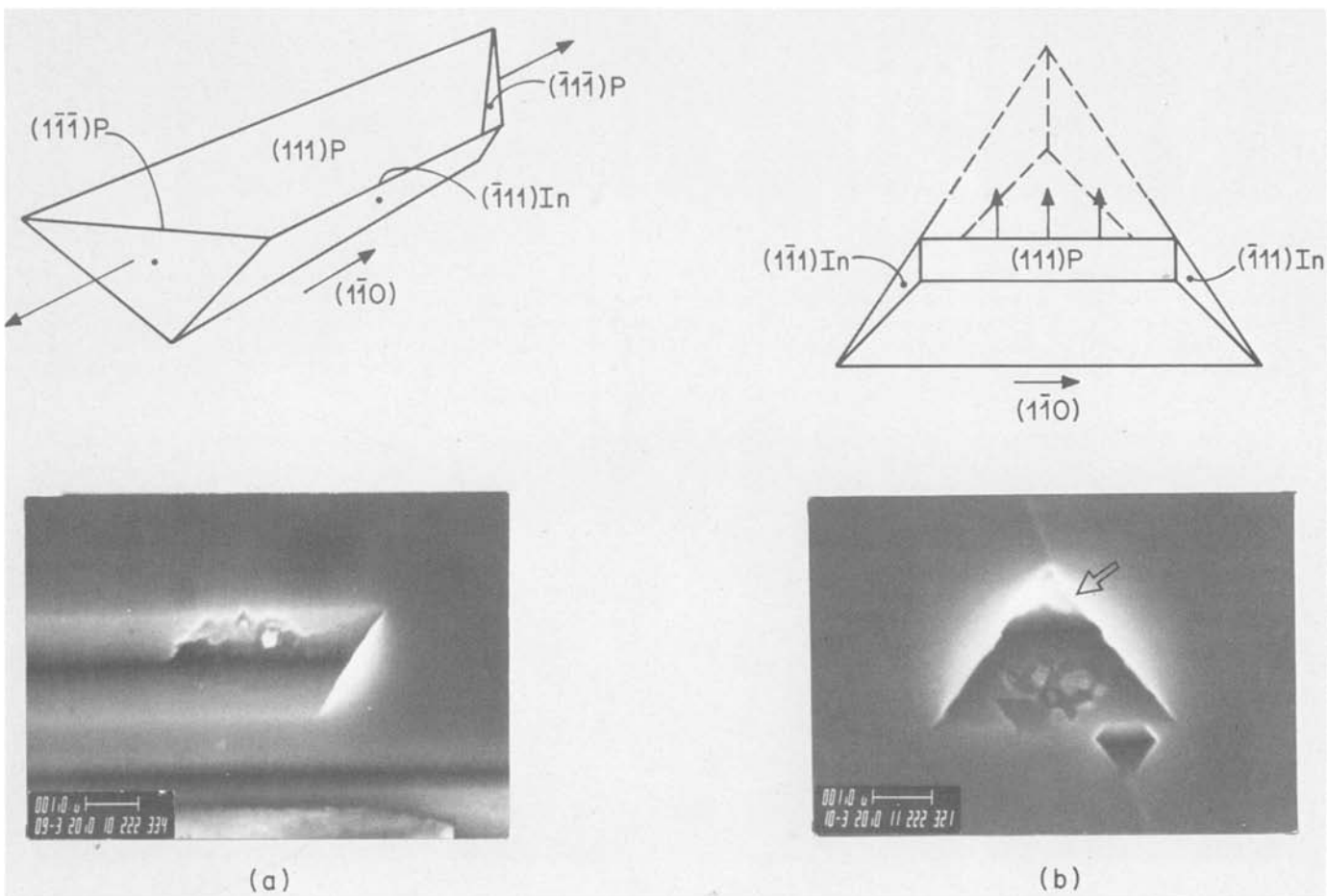

Fig. 13. Schematics showing the mechanisms of formation of (a) the fast growing linear pits and (b) the triangular pits. The arrow indicates an indium droplet.

the surface as the result of enhanced decomposition or melt back of the surface. Nucleation of an indium droplet inside the track also occurs, as marked by the solid arrow, and a second track may form inside the original track. As a result, the material on the (111) P surface decomposes in a layered fashion. The typical layer structure resulting is shown in Fig. 10b. The facets which bound the track intersect the (111) P surface along <110> directions. The orientation of the fast moving facet determined on the cross section cleaved through the indium droplet is found to be the (100) planes (see Fig. 10c). Occasionally, the (111) In plane is observed, which is believed to be the slow moving facet.

(111) In surface.—The indium droplets nucleated on the (111) In face do not move around in the way described for the (111) P face. They stay more or less still and develop triangular pits (Fig. 11a). An extensively decomposed surface is shown in Fig. 11b. A high magnification of the decomposition structure of the facets (shown in Fig. 11c) reveals triangular steps, indicating that the orientation of the walls are (111) P faces. However, in extensively decomposed samples (100) facets are also observed.

(110) surface.—The decomposition pits observed on the (110) surface have shapes which depend on the initial formation of the end facets. The orientation of the observed facets were determined to be the (111) planes. The pit which reveals all the facets is sketched and shown in Fig. 12, and the two most commonly observed shapes are shown in Fig. 13. The well-developed decomposition pits usually take the form of linear pits elongated in one of the (110) directions. The end facets (as shown in Fig. 13a) were found to be the (111) P planes. With an indium droplet trapped at one end, these linear pits lengthened rapidly. If the initial formations of the end facets were (111) In planes, the relatively slow moving indium facets bound the ends of the (111) P facet. These eventually developed into triangular pits, as sketched and shown in Fig. 13b. The indium droplet moving along with the (111) P facet finally becomes trapped in a corner, as indicated by the arrow. Other evidence supporting the above growth mechanism is shown in Fig. 14. A linear pit was observed to grow out of the original triangular pits as soon as a (111) P facet was formed at the lower right corner of the triangular pit. The traces of the (111) P facet are indicated by the arrows.

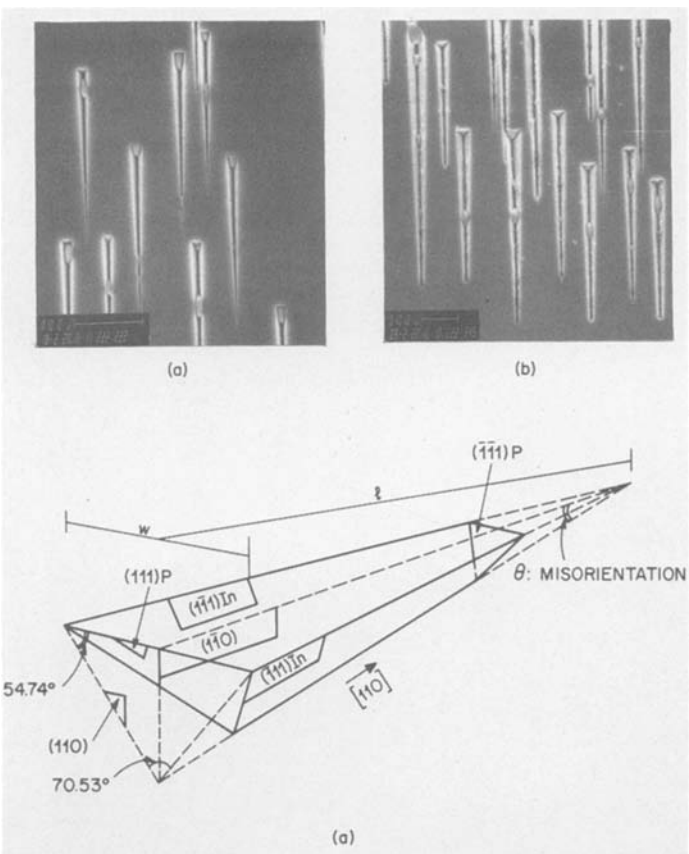

Fig. 15. Decomposition morphology on misoriented (100) surface: (a) the decomposition pits developed on a surface with 3° misorientation towards the (110) direction; (b) the sharp tips become truncated as the pits grow in size; (c) the geometry and facets of the tapered pits determined from the (110) cross sections using SEM.

The effect of misorientation on the decomposition of (100) InP surface.—The decomposition pits developed on a (100) InP surface with a 3° misorientation toward the rapid growth (110) direction are shown in Fig. 15a. The pits become tapered along the (110) direction. The facets bounding the pits are found to be the same as shown in Fig. 7 for the (100) surface. The geometry of the taper pits is sketched in Fig. 15c. By measuring the length l and base width w of the pits, the misorientation angle can be calculated from the equation $\theta = \arctan(1.4\ l/w)$. The taper pits initially formed have sharp tips. As they grow in size, (111) P facets start to develop and the tips become truncated, as shown in Fig. 15b.

No significant dependence of misorientation was observed for the critical nucleation temperature of indium droplets on (100) surface. In Fig. 2, the nucleation temperatures for 3°- and 6°-misoriented (100) surface are also presented.

The growth rate of the pits following initial nucleation on the misoriented surfaces was found to be greater than that for the (100) surface. Continuous monitoring of the growth process indicated that liquid indium is always trapped at the tapered end of the pits, and the rapid advancement of this tapered end caused the fast growth.

The effect of hydrogen flow rate on the decomposition of (100) InP surfaces.—The effect of hydrogen flow rate on the decomposition morphology was studied using a quartz tube furnace. The results shown in Fig. 16 and Fig. 17 are for 0°- and 3°-misoriented surfaces at 618° and 718°C. The three hydrogen flow rates chosen were near zero, 300, and 600 cm³ per min. At 618°C, the decomposition pits on (100) surfaces show large differences in size between near-zero flow and 300 cm³ per min of hydrogen (Fig. 16). This indicates that the rate of decomposition is greatly enhanced in the presence of hydrogen flow. However, the difference in the pit size between 300 cm³/min and 600 cm³/min of hydrogen flow is not as large as was expected. The decomposition of (100) surface at 718°C is much more severe than at 618°C. The size of the pits also depends strongly on the hydrogen flow rate. At 600 cm³ per min of hydrogen flow, the surface becomes covered with large decomposition pits (as shown in Fig. 16c).

A similar situation can be observed on a misoriented surface, except that in most cases the density of the pits is lower. Shown in Fig. 17 is an example of a 3°-misoriented (100) surface. The difference in the size of pits developed at 718° and 618°C, and the strong dependence on the hydrogen flow rate are striking.

Conclusion

The deterioration of surface morphology of decomposing InP at VPE and LPE growth temperatures in hydrogen ambient begins with the nucleation of indium droplets. The subsequent melt-back or enhanced surface decomposition of the InP surface in contact with the liquid indium droplets initiate characteristic decomposition pits. The critical nucleation temperature for indium droplets depends strongly on the

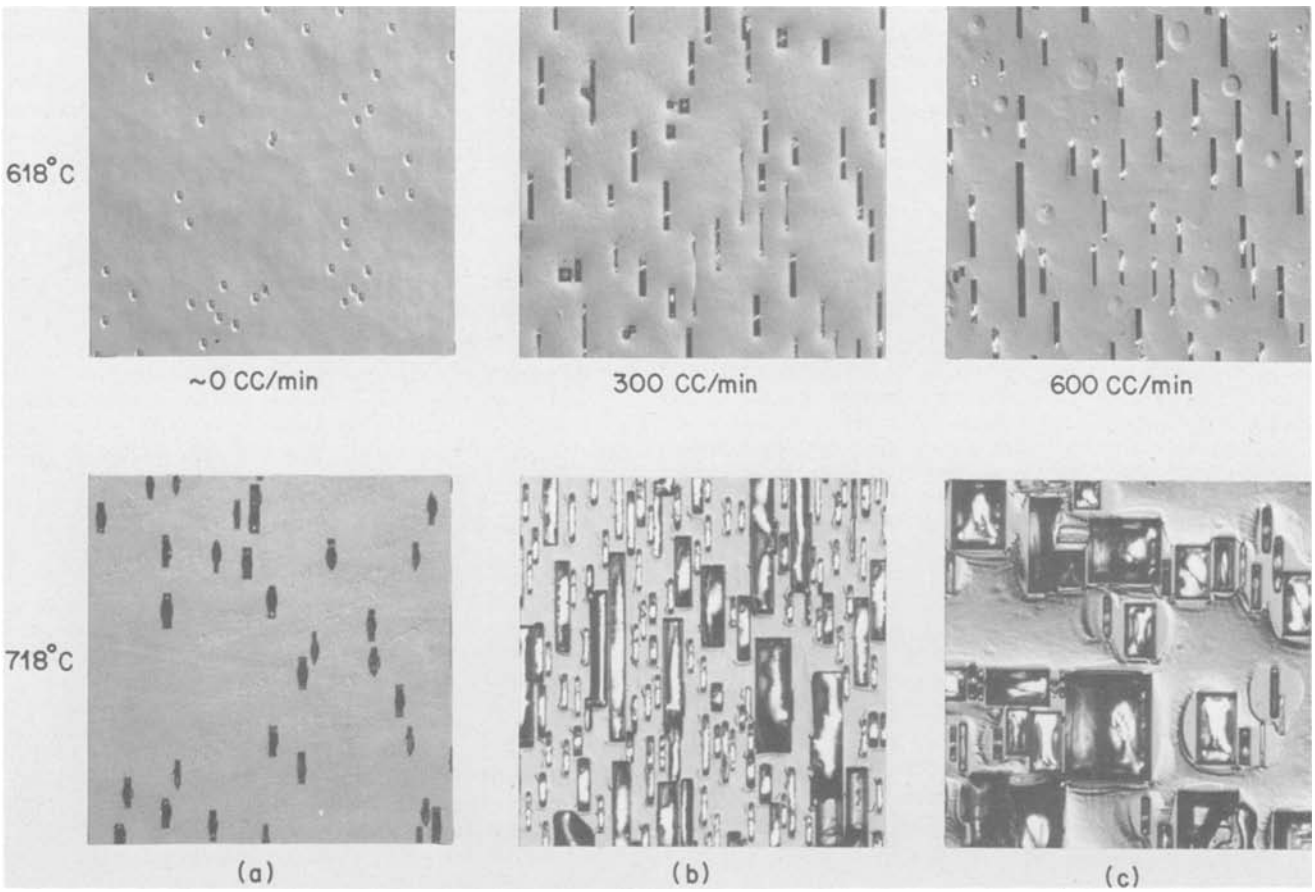

Fig. 16. The effects of hydrogen flow rate on the decomposition morphology of (100) InP surfaces decomposed at 618°C and 718°C. Hydrogen flow rates: (a) ~0 cm^3/min; (b) 300 cm^3/min; (c) 600 cm^3/min.

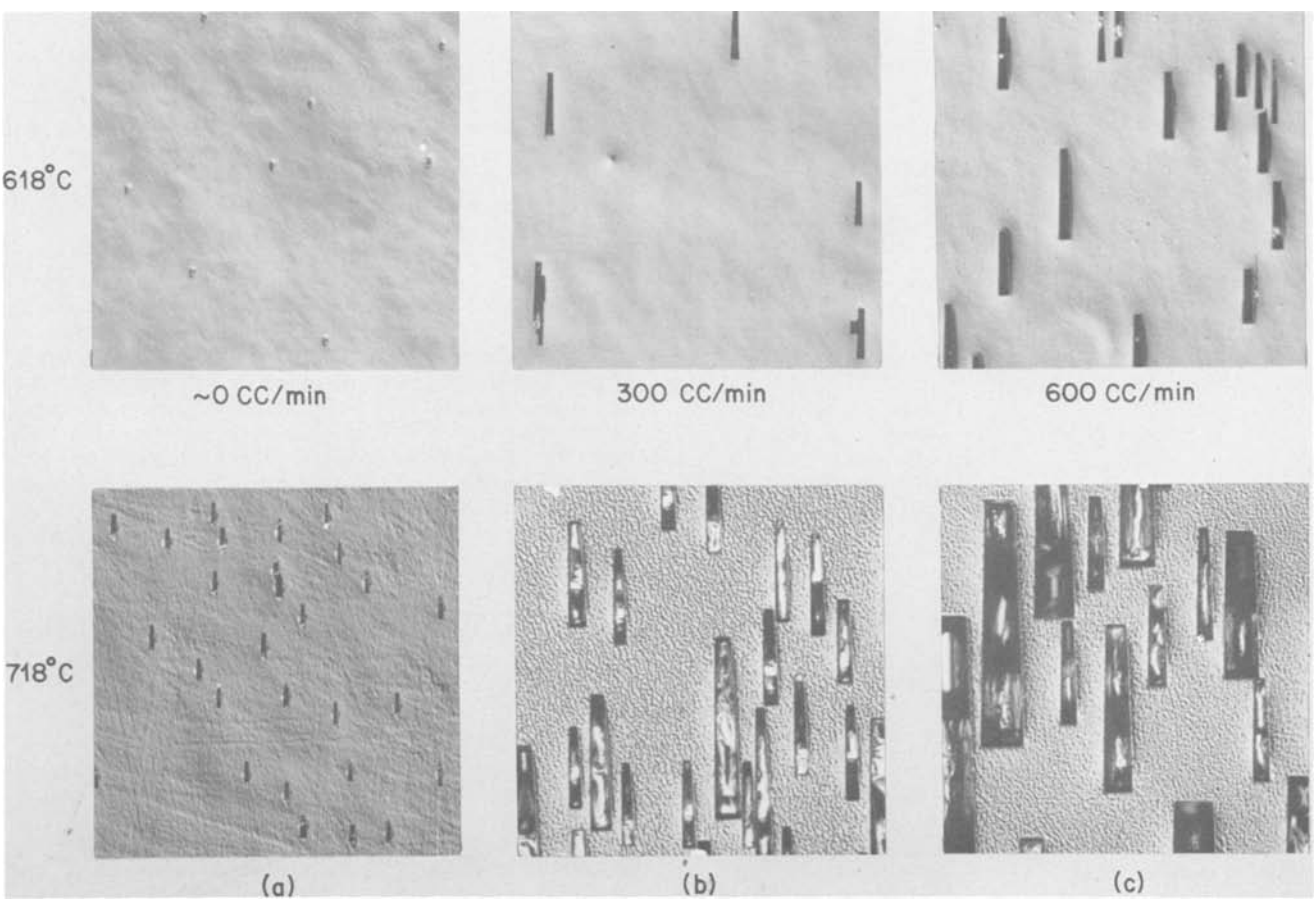

Fig. 17. The effect of hydrogen flow rate on the decomposition morphology for 3°-misoriented (100) InP surfaces decomposed at 618°C and 718°C. Hydrogen flow rates: (a) ~0 cm^3/min; (b) 300 cm^3/min; (c) 600 cm^3/min.

hydrogen flow rate, and decreases with increasing hydrogen flow. At the same hydrogen flow rate, the nucleation temperatures of indium droplet on the different crystallographic planes are found to have the following order

$$T_{(111)In} > T_{(111)P} \sim T_{(110)} > T_{(100)} \quad [1]$$

The decomposition pits are bounded by crystallographic facets. These are {111} racets for pits on the {100} and {110} surfaces, and {111} and {100} facets for pits on the {111} surfaces. These results are consistent with the observations of Lum *et al.* The (111) P face, which contains two unpaired bonds associated with each P atom, is known to be more chemically active than the (111) In face, which contains no unpaired bonds. Hence, the (111) P face is expected to decompose more easily than the (111) In face, and thus constitute the fast moving facets. The shape of the decomposition pits is thus determined by the facets initially formed. As demonstrated on the (110) surface, decomposition pits can either be linear or triangular in shape, depending upon the initial orientation of the end facets.

The growth of the decomposition pits depends on the decomposition of the facets. It is observed that the growth rate of the facets is greatly enhanced when in contact with the liquid indium. On the {100} and {110} surfaces, indium droplets trapped inside the linear pits jiggle back and forth along the rapid growth direction bounded by {111} P facets. An advance of the {111}'P facets is visually apparent under the microscope each time an indium droplet rests on a facet. On the {111} P surface, the rapidly moving {100} facets are always attached to an indium droplet. This indicates that the decomposition of InP is enhanced by direct contact with the indium droplet.

There is no significant effect of misorientation of the (100) surface on the nucleation temperature for indium droplets. However, taper pits developed on the misoriented surface tend to trap the indium droplet in the sharp end. This leads to more rapid growth in that direction.

A strong effect of hydrogen flow rate on the decomposition morphology on (100) InP surface can be obtained. A practical expedient to minimize thermal decomposition in epitaxial growth is, thus, to hold the hydrogen flow over substrate surfaces to a minimum.

Acknowledgment

The authors would like to thank R. B. Marcus for the use of his video recorder.

Manuscript received March 11, 1983.

Bell Laboratories assisted in meeting the publication costs of this article.

REFERENCES

1. H. Temkin, V. G. Keramidas, and S. Mahajan, *This Journal*, **128**, 1088 (1981).
2. R. F. C. Farrow, *J. Phys. D*, **7**, 2436 (1974).
3. C. R. Bayliss and D. L. Kirk, *Thin Solid Films*, **20**, 2997 (1975).
4. C. R. Bayliss and D. L. Kirk, *J. Phys. D*, **9**, 233 (1976).
5. P. K. Gallagher and S. N. G. Chu, *J. Phys. Chem.*, **86**, 3246 (1982).
6. W. Y. Lum and A. R. Clawson, *J. Appl. Phys.*, **50**, 5296 (1979).
7. A. R. Clawson, W. Y. Lum, and G. E. McWilliams, *J. Cryst. Growth*, **46**, 300 (1979).
8. K. Pak and T. Nishinaga, *Jpn. J. Appl. Phys.*, **18**, 1859 (1979).
9. K. Pak, T. Nishinaga, and S. Uchiyama, *Jpn. J. Appl. Phys.*, **14**, 1613 (1975).
10. J. A. Lourenco, BTL, TM: 81-52342-32.
11. G. A. Antypas, *Appl. Phys. Lett.*, **37**, 64 (1980).
12. Y. Yamauchi and N. Susa, *This Journal*, **128**, 210 (1981).

Early Stages of the Oxidation of Chromium in H_2-H_2O-H_2S Gas Mixtures

M. LaBranche, A. Garratt-Reed, and G. J. Yurek

The H. H. Uhlig Corrosion Laboratory, Department of Materials Science and Engineering, Massachusetts Institute of Technology, Cambridge, Massachusetts 02139

ABSTRACT

The oxidation of (100) and (110) orientations of Cr in H_2-H_2O-H_2S gas mixtures was studied at 900°C with $P_{O_2} = 10^{-19}$ atm and $P_{S_2} = 10^{-14}$, 10^{-10}, $10^{-7.5}$ and $10^{-6.5}$ atm. Specimens were analyzed primarily by SEM, TEM, and STEM. No sulfides were detected after one hour with $P_{S_2} = 10^{-14}$ or 10^{-10} atm. Sulfides were detected at the Cr/scale interface with $P_{S_2} = 10^{-7.5}$ atm. Two-phase scales comprising Cr_2O_3 and $Cr_{1-x}S$ formed at $P_{S_2} = 10^{-6.5}$ atm. Preoxidation for two hours with $P_{O_2} = 10^{-19}$ atm was successful in preventing sulfur penetration for 20 hr. After 111 hr, however, the initial protective oxide was lost and the scale consisted of a mixture of Cr_2O_3 and $Cr_{1-x}S$ partially overgrown by Cr_2O_3.

Structural alloys that are employed for high temperature service in environments that contain oxygen- and sulfur-bearing gaseous, liquid, or solid phases typically contain about 15-50 weight percent (w/o) Cr. Chromium is present in these alloys to form a surface scale of Cr_2O_3 that is supposed to inhibit high-temperature corrosion. In many cases, however, Cr_2O_3 scales eventually break down because sulfides form both at the alloy/Cr_2O_3 and at the Cr_2O_3/environment interfaces (1-5).

The mechanisms of the breakdown of Cr_2O_3 scales in sulfur-bearing environments are not understood. It is clear that the dissolution of Mn, Fe, Ni, etc. from the alloy into the Cr_2O_3 scales and the subsequent diffusion of these elements through Cr_2O_3 play a role in the breakdown process (2, 3, 5). It is not clear, however, whether dissolution and diffusion of these elements in Cr_2O_3 are affected by the presence of sulfur. The mechanisms of the penetration of Cr_2O_3 scales by sulfur are also not understood.

In order to elucidate the mechanisms of the breakdown of Cr_2O_3 scales on alloys in sulfur-bearing environments, it seems axiomatic that an understanding of the mechanisms of the growth and breakdown of Cr_2O_3 scales on pure Cr in sulfur-bearing environments be developed. The object of this paper is to present the results of an investigation of the early stages of the oxidation of pure Cr in H_2-H_2O-H_2S gas mixtures. This investigation is part of a larger pro-

Key words: sulfidation, surfaces, transport.

Table I. Solid source mass spectrometric analysis of chromium (ppm atomic). Numbers are accurate within a factor of 2-3.

4	B	0.2	K	0.2	Zr
60	C	0.4	Ca	0.1	Nb
24	N	0.3	Ti	0.1	Mo
48	O	4	V	0.07	Cd
0.2	Na	18	Fe	0.7	Sb
0.07	Mg	3	Ni	0.1	Ba
12	Si	8	Cu	0.2	Th
1	S	0.2	As	70	W
0.06	Cl	0.5	Y		

gram that is directed to determining the mechanisms of the formation, growth, and breakdown of protective scales in sulfur-bearing environments.

Experimental

Specimen preparation.—Single crystals of Cr employed in this program were produced at the Ames Laboratory (Ames, Iowa) by directional solidification of iodide Cr in a water-cooled copper mold. The composition of the Cr is listed in Table I. The single-crystalline boules were oriented using Laue back-reflection and subsequently cut to produce approximately disk-shaped specimens, (~1 cm diameter) with (110) or (100) orientations.

The specimens were ground through 600 grit SiC paper, polished through 1 μm diamond paste, and finally polished with a slurry of 0.3 μm alumina in water. The specimens were subsequently electropolished in a solution of acetic acid-5% perchloric acid to remove the deformed metal produced by mechanical grinding and polishing (~15 μm of Cr were removed by electropolishing). The orientations of the electropolished specimens, which were checked using Laue diffraction, were within two degrees of the (100) or (110) orientations. Immediately after electropolishing, the specimens were etched in a solution of 11% HCl in water for 4 min, rinsed in distilled water, dried in air, and stored in a desiccator. Before oxidation, the specimens were rinsed first in methanol and then in ethanol.

Gas mixtures.—The oxidation experiments were conducted at 900°C in H_2-H_2O-H_2S gas mixtures with $P_{O_2} = 10^{-19}$ atm (~4.2 volume percent [v/o] H_2O) and $P_{S_2} = 10^{-14}$, 10^{-10}, $10^{-7.5}$, or $10^{-6.5}$, atm (2.6×10^{-4}, 2.6×10^{-2}, 4.6×10^{-1}, or 1.4 v/o H_2S). The sulfur and oxygen partial pressures employed are indicated by the four points on the Cr-S-O stability diagram (6) in Fig. 1, which demonstrates that Cr_2O_3 was the equilibrium solid phase for all of the experimental conditions.

The H_2-H_2O-H_2S gas mixtures were prepared by mixing H_2-H_2O and H_2-H_2S gas mixtures (each at a known flow rate controlled by a constant-head capillary flowmeter) in a glass column which was packed with glass beads. The H_2-H_2O gas mixtures were prepared by bubbling high-purity H_2 gas (99.999% H_2, Matheson Gas Products) at a controlled flow rate, first through a flask containing heated distilled water (presaturator), and then through a column of distilled water (saturator) at a temperature held constant to within ±0.04°C by a constant temperature bath. The temperature of the saturator determined the vapor pressure of the water, and so the H_2O content of the H_2 gas stream. All of the gas lines after the saturator were heated by electrical resistance heating tape to prevent condensation of water. The actual H_2O contents in the H_2 gas streams were determined by absorbing the water vapor in preweighed U-tubes containing P_2O_5. The amounts of water vapor absorbed from the gas streams were within 6% of the values expected from the vapor pressure of water (7) at the temperatures in the saturator.

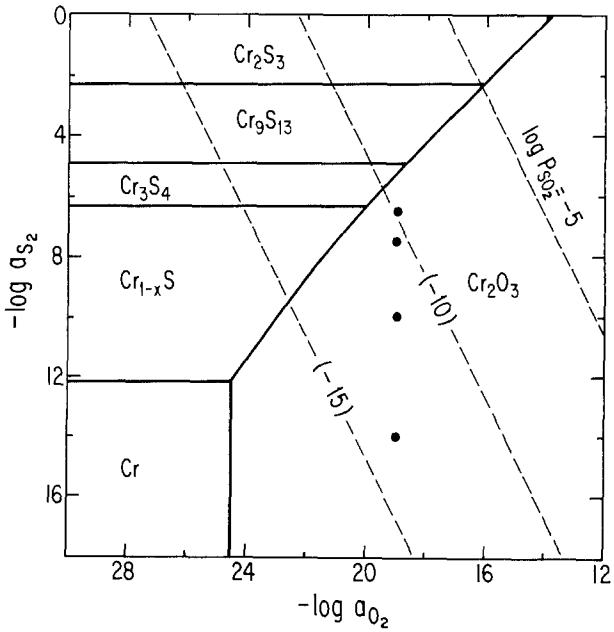

Fig. 1. Stability diagram for the Cr-S-O system at 900°C. The filled circles indicate the gas compositions used in this investigation ($a_i \equiv P_i/P_i^\circ$, $P_i^\circ \equiv 1$ atm). Thermochemical data for the Cr-S system were obtained from Ref. (6).

The H_2-H_2S gas mixtures were obtained as premixed and analyzed compressed gas mixtures from Matheson Gas Products. In the present work, three gas mixtures, H_2-12.7 v/o H_2S, H_2-800 ppm H_2S, and H_2-9 ppm H_2S, were employed. The flow rates of the gases employed to produce the H_2-H_2O-H_2S mixtures are listed in Table II.

The flowmeter for the H_2 was calibrated by measuring the time required for the gas to push a soap bubble through a tube of known volume. The flowmeter for the H_2-H_2S gas mixtures was calibrated in the same way using pure H_2 and subsequently applying Poiseuille's equation (8) to account for the small change in the viscosity of the gas caused by the presence of H_2S.

Reaction chamber.—The reaction chamber comprised an alumina refractory tube that was held in a verticle tube furnace heated by counter-wound Kanthal wire. Some of the earlier experiments were conducted using a mullite tube, which caused no apparent difference in the results. The linear flow rates of the gases in the alumina (3.18 cm ID) and mullite (3.81 cm ID) tubes were 0.66 and 0.45 cm/sec, respectively. The temperature

Table II. Conditions employed to obtain equilibrium partial pressures of O_2 and S_2 at 900°C and 1 atm total pressure

Concentration of H_2S in premixed H_2-H_2S*	Saturator temperature, °C	Vapor pressure of water, mm Hg	Room temperature flow rates, cm³/min		Equilibrium partial pressures, atm	
			H_2	H_2-H_2S	P_{O_2}	P_{S_2}
0	29.94	31.72	287	0	10^{-19}	0
9 ppm	36.00	44.56	199	88.2	10^{-19}	10^{-14}
800 ppm	37.20	47.58	188	100	10^{-19}	10^{-10}
12.7%	30.51	32.76	277	11	10^{-19}	$10^{-7.5}$
12.7%	31.84	35.35	253	34.5	10^{-19}	$10^{-6.5}$

* Gases supplied and analyzed by Matheson Gas Products.

of the furnace was held constant to within ±1°C by a proportional controller. A Pt/Pt-10%Rh thermocouple, which had been calibrated against a standard thermocouple, was enclosed in an alumina protection tube and located adjacent to the specimen to measure its temperature.

The gas mixtures were admitted to the bottom of the reaction tube, the lower portion of which was packed with alumina beads to minimize thermal diffusion and to heat and equilibrate the gas mixtures. Platinum gauze was placed on top of the beads to further ensure equilibration of the gases. During an experiment, the Cr specimens were suspended by means of a Pt wire in the hot zone of the furnace just above the Pt gauze, which was never more than 5°C cooler than the Cr specimens.

Oxidation experiments.—At the beginning of an experiment, the desired gas mixture was passed through the furnace while the specimen was held in the cold zone above the furnace. After flushing the reaction tube with the gas mixtures for about 20 min, the specimen was lowered quickly into the hot zone. The times of exposure were 2.5, 12.5, and 60 min. At the end of an experiment, the specimen was quenched in the H_2-H_2O-H_2S gas mixture by raising it quickly to the cold zone.

Characterization of scales.—The topology, morphology, and chemistry of the scales were characterized using scanning electron microscopy (SEM), transmission and scanning transmission electron microscopy (TEM and STEM), and Auger electron spectroscopy (AES). These techniques complemented each other, allowing characterization over the complete range from macroscopic to microscopic detail.

Prior to examination in the SEM, oxide specimens were lightly coated with copper by evaporation to prevent charging and to enhance contrast. The SEM provided information on topography and, using the energy-dispersive x-ray detector (EDX), the Cr/S ratios of the larger features. The Cr/S ratios reported are simply ratios of the integrated Cr-Kα and S-Kα peaks; corrrections for absorption, fluorescence, and the atomic number effect were not made.

TEM and STEM were used to study the microstructures of the scales. Sections of scale parallel to the metal/scale interface were prepared by the following method. Three millimeter-diameter disks were cut from oxidized specimens by spark-machining. These disks were thinned from one side by grinding on silicon-carbide paper, followed by jet electropolishing in a 10:1 solution of methanol:perchloric acid maintained at −50°C. The electropolishing exposed a section of the scale at the metal/scale interface. The top side of the scale was protected by a coating of Crystalbond wax (Aremco Products, Inc.) during electropolishing. The Crystalbond was subsequently dissolved in acetone, after which ion-milling was employed to thin the scale for observation. By milling from one or both sides of the scale, specimens were prepared at the metal/scale or scale/gas interfaces, or at the center. Scales were coated by evaporation with a thin layer of carbon to prevent charging.

STEM was capable of chemical analysis at resolutions <0.01 μm using its EDX system. In the present work, no attempt was made to perform more than a semiquantitative analysis. Specimens studied by AES were placed directly in the instrument with no prior treatment.

Results

Oxidation of Cr in H_2/H_2O gas mixtures.—The oxidation of pure Cr in H_2-H_2O gas mixtures ($10^{-22} < P_{O_2} < 10^{-15}$ atm) at 900°C will be discussed in detail elsewhere (9). The Cr_2O_3 scales formed on pure Cr at 900°C and $P_{O_2} = 10^{-19}$ atm did not lift or buckle at the reaction temperature or during cooling, regardless of the orientation of the Cr; however, small patches of the scale spalled during cooling as shown in Fig. 2a. In the latter case, the stresses generated in the scales by oxide formation were apparently small, which was attributed to predominant cation diffusion in the scales at the lower oxygen partial pressures (9-11). The localized spallation that occurred on cooling was apparently caused by stresses in the scales that were generated during cooling because of the 30% difference in the coefficients of thermal expansion of Cr and Cr_2O_3.

The grains comprising the Cr_2O_3 scales were very small. Grain diameters measured in planes parallel to the Cr/Cr_2O_3 interface using TEM were less than 0.5 μm for reaction times $\lesssim$ 20 hr. An electron micrograph of the Cr_2O_3 scales near the center of the scale after 120 min at 900°C with $P_{O_2} = 10^{-19}$ atm is shown in Fig. 2b. Although cavities were observed in some of the oxide grains, they apparently did not form a continuous network in the scale. Microcracks, which would be potential paths for transport of gaseous species through the scales, were not observed. Because the scales formed at $P_{O_2} = 10^{-19}$ atm were coherent and adherent to the Cr, this P_{O_2} was chosen for ex-

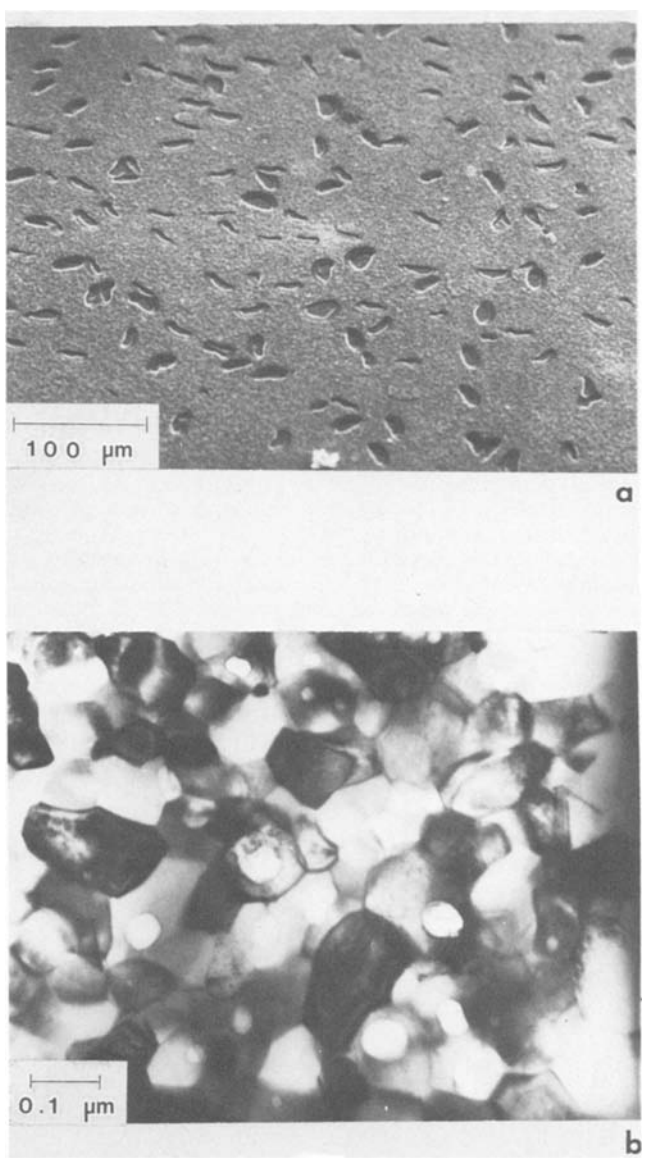

Fig. 2. (100) Cr oxidized in a H_2-H_2O gas mixture for 120 min at 900°C with $P_{O_2} = 10^{-19}$ atm; (a) SEM image of the scale/gas interface; (b) TEM bright field image of a section in the center of the scale parallel to Cr/Cr_2O_3 interface.

periments in which Cr was oxidized in H_2-H_2O-H_2S gas mixtures.

Direct exposure of Cr to H_2-H_2O-H_2S gas mixtures.—Additions of 0.026, 0.46, or 1.4% H_2S ($P_{O_2} = 10^{-10}$, $10^{-7.5}$, and $10^{-6.5}$ atm) to H_2-H_2O gas mixtures with $P_{O_2} = 10^{-19}$ atm at 900°C caused considerable changes in the morphologies of the Cr_2O_3 scales compared with those formed in the absence of H_2S. The morphologies of the scales are described in the following sections.

$P_{S_2} = 10^{-14}$ atm (2.6×10^{-4} v/o H_2S, $P_{O_2} = 10^{-19}$ atm, 900°C).—The scales exhibited the same topology as those formed in the absence of H_2S (see Fig. 2a). Only trace amounts of sulfur could be detected by AES after partial ion milling of the scale.

$P_{S_2} = 10^{-10}$ atm (0.026 v/o H_2S, $P_{O_2} = 10^{-19}$ atm, 900°C).—The scales formed up to 60 min had a topology similar to those formed in the absence of H_2S, although localized spallation was not observed. Some spallation occurred, however, after 120 min. After oxidation for 60 min, the Cr_2O_3 scales contained only trace amounts of dissolved sulfur according to EDX analyses of the scales in a STEM. Sulfide precipitates were not detected in the scale by STEM, nor at the Cr/Cr_2O_3 interface by SEM.

$P_{S_2} = 10^{-7.5}$ atm (0.46 v/o H_2S, $P_{O_2} = 10^{-19}$ atm, 900°C).—An example of the topology of the scale formed at $P_{S_2} = 10^{-7.5}$ atm after 60 min of oxidation of a (100) Cr single crystal is shown in Fig. 3a. The topologies and the microstructures of the scales formed on (110) and (100) orientations of Cr were the same. In general, the scales buckled and spalled on cooling (see Fig. 3a). Sometimes, however, the scales separated, approximately in half, along a plane parallel to the metal/scale interface, in which case the outer layer of the delaminated scale buckled and curled considerably.

When the scales spalled, small particles could be seen in contact with the metal at the Cr/Cr_2O_3 interface, as shown in Fig. 3b. When the scales did not spall naturally, they were spalled by scratching the surface with a needle to expose the underlying metal. The Cr/S ratio of the particles varied between 15/1 and 12/1, as determined from the ratio of the Cr-Kα and the S-Kα peaks generated by EDX analysis in an SEM. The actual Cr/S ratio for these particles is expected to be much lower, but during EDX analysis the Cr matrix adjacent to the particles was excited by broadening of the electron beam. Only trace amounts of sulfur could be detected by EDX analysis of the Cr adjacent to the particles. The low concentration of sulfur that was detected was probably due to fluorescence of the S-Kα transition caused by x-rays generated by the electron beam striking the Cr. It is concluded that the particles are sulfides of Cr, which must be $Cr_{1-x}S$ according to Fig. 1.

The particles of $Cr_{1-x}S$ at the Cr/Cr_2O_3 interface increased in size as the time of oxidation increased. This is demonstrated in Fig. 3b and 4, which show that the particles at the Cr/Cr_2O_3 interface are larger by about a factor of two after 60 min (Fig. 3b) compared with those formed after 2.5 min (Fig. 4). In both cases, 9-10% of the Cr surface was covered by $Cr_{1-x}S$ precipitates, as determined with the aid of an Image Analyzer. More specimens must be examined to determine precisely the size and amount of sulfides as a function of time.

A SEM image of the back side of a fragment of spalled scale (*i.e.*, at the Cr/Cr_2O_3 interface) is presented in Fig. 5a, which demonstrates that some sulfides detached from the metal and remained in contact with the scale. Figure 5b is a higher magnification image of a portion of the scale shown in Fig. 5a, which illustrates once again the very fine grain size of the oxide.

A section of a scale formed after 60 min was examined in a STEM. The section was parallel to the

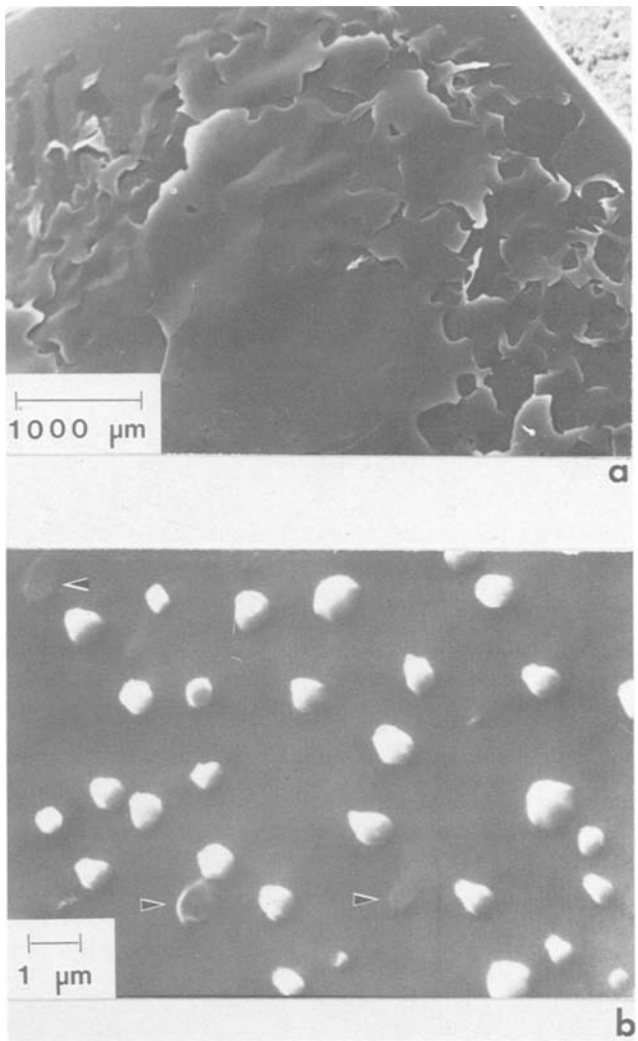

Fig. 3. (100) Cr oxidized in a H_2-H_2O-H_2S gas mixture for 60 min at 900°C with $P_{O_2} = 10^{-7.5}$ atm; (a) SEM image of the scale/gas interface; (b) SEM image of the metal surface in a region where the oxide layer spalled (the white particles are sulfide precipitates). Arrows indicate several regions where the sulfides detached from the metal.

Cr/Cr_2O_3 interface and near the center of the scale. Sulfides could not be detected in the oxide layer. Low concentrations of sulfur dissolved in the oxide were

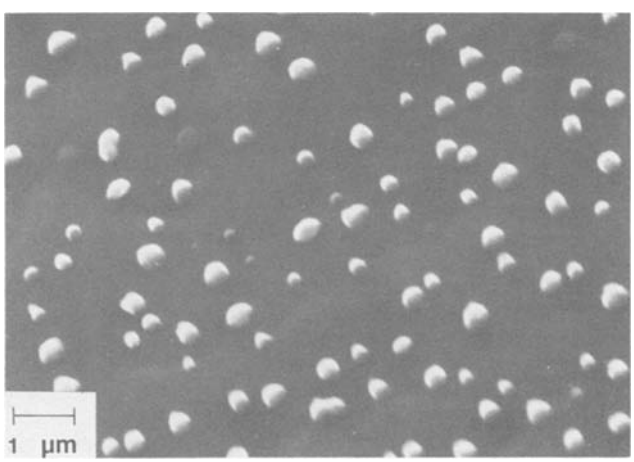

Fig. 4. (100) Cr oxidized in a H_2-H_2O-H_2S gas mixture for 2.5 min at 900°C with $P_{O_2} = 10^{-19}$ and $P_{S_2} = 10^{-7.5}$ atm. SEM image of the metal surface in a region where the oxide scale spalled. The white particles are sulfide precipitates.

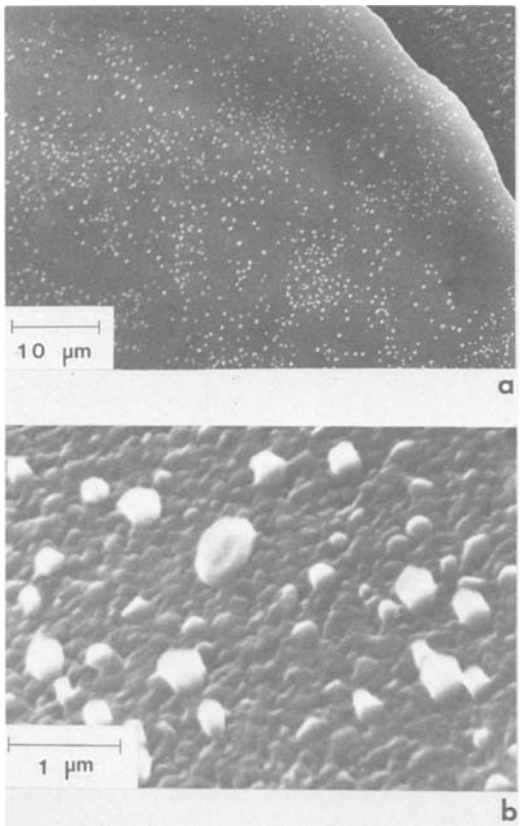

Fig. 5. (100) Cr oxidized in a H_2-H_2O-H_2S gas mixture for 2.5 min at 900°C with $P_{O_2} = 10^{-19}$ and $P_{S_2} = 10^{-7.5}$ atm; (a) SEM image of the back side of a spalled scale showing sulfide precipitates that remained in contact with the scale; (b) a higher magnification of (a).

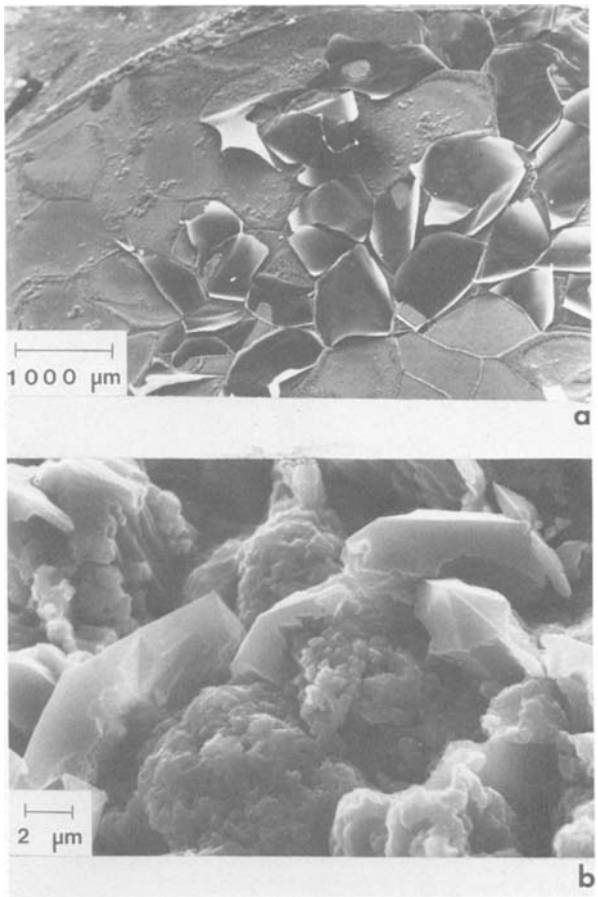

Fig. 6. (100) Cr oxidized in a H_2-H_2O-H_2S gas mixture for 2.5 min at 900°C with $P_{O_2} = 10^{-19}$ and $P_{S_2} = 10^{-6.5}$ atm; (a) SEM image of the scale/gas interface (the edge of the specimen can be seen in the upper left-hand corner); (b) a high magnification image of one of the ridges in (a). The large crystals are sulfides.

detected by EDX analysis, but a quantitative determination of the sulfur concentration was not made.

No significant differences between the scales formed on (110) and (100) orientations of Cr were observed. One specimen of Cr, however, which had one large (100) grain and two other smaller grains of random orientation, exhibited a much greater concentration of sulfide particles in contact with one of the randomly oriented grains compared with the (100) grain.

$P_{S_2} = 10^{-6.5}$ atm (1.4 v/o H_2S, $P_{O_2} = 10^{-19}$ atm, 900°C).—The topology of the scale formed after 2.5 min of exposure to a gas mixture with $P_{S_2} = 10^{-6.5}$ atm is shown in Fig. 6a. The outer portion of the scale lifted and buckled. The ridges and mounds in Fig. 6a comprised sulfide crystals, some of which were ~10 μm in width (Fig. 6b), having a Cr/S ratio of ~0.67 by EDX analysis. A $Cr_{1-x}S$ standard which was formed in a H_2-H_2S gas mixture at 900°C with $P_{S_2} = 10^{-8}$ yielded a Cr/S ratio of ~0.47, although the orientation of the individual sulfide crystals to the electron beam influenced that value considerably (variations of 0.41-0.83 were measured; corrections for absorption, fluorescence, and the atomic number affect were not made). The Cr/S weight ratio in stoichiometric CrS is 1.6. It is assumed that the large crystals in Fig. 6b are $Cr_{1-x}S$. The large crystals were covered partially by a fine-grained material that increased in amount after 12.5 min of oxidation. After 60 min, the sulfides were covered completely by the fine-grained material.

Conversion of the $Cr_{1-x}S$ crystals to Cr_2O_3 is expected to occur eventually because Cr_2O_3 is the stable condensed phase in the gas mixture employed. Thus, the fine-grained material was thought initially to be Cr_2O_3. Examination in a STEM of the outer portions of the scales formed after 60 min demonstrated that the scales actually comprised a two-phase mixture of oxides and sulfides, as shown in Fig. 7. Figure 7a is a STEM bright field image of a small portion of the scale. It was always more difficult to produce sharp images of scales that contained mixtures of oxide and sulfide compared to scales that comprised only oxide because the specimens varied in thickness owing to the slower rate of milling of the sulfide phase. Figure 7b is a sulfur map of the area shown in Fig. 7a, indicating the presence of a sulfur-rich grain overlapped partially by oxide grains. Figure 7c is presented to indicate more clearly the positions of grain boundaries in the specimen imaged in Fig. 7a.

The sulfur-rich areas had a Cr/S ratio of ~1.4 by weight according to EDX analysis, and are presumably $Cr_{1-x}S$. The sizes of the sulfide and oxide grains ranged from 0.1 to 0.5 μm. Large areas in the center of the scale were analyzed with EDX, indicating an average Cr/S ratio of approximately 12, which corresponds to ~14% CrS by volume in the scale. It was not determined whether the sulfide phase was continuous.

Preoxidation experiments.—Specimens of Cr single crystals [(100) and (110) orientations] were preoxidized in a H_2-H_2O gas mixture for 2 hr at 900°C with $P_{O_2} = 10^{-19}$ atm to produce flat, adherent scales. Then, while maintaining the specimens at temperature, H_2S was admitted into the reaction chamber to form a gas mixture with $P_{O_2} = 10^{-19}$ and $P_{S_2} = 10^{-6.5}$ atm. Prior to each experiment, pure oxygen was passed through the hot reaction chamber for two days to desulfurize it, in an attempt to avoid contamination of the specimen with sulfur during the preoxidation step.

The times of exposure to the sulfur-bearing gas mixture after preoxidation were 2, 20, and 111 hr. No sulfides were detected in any part of the scale by SEM

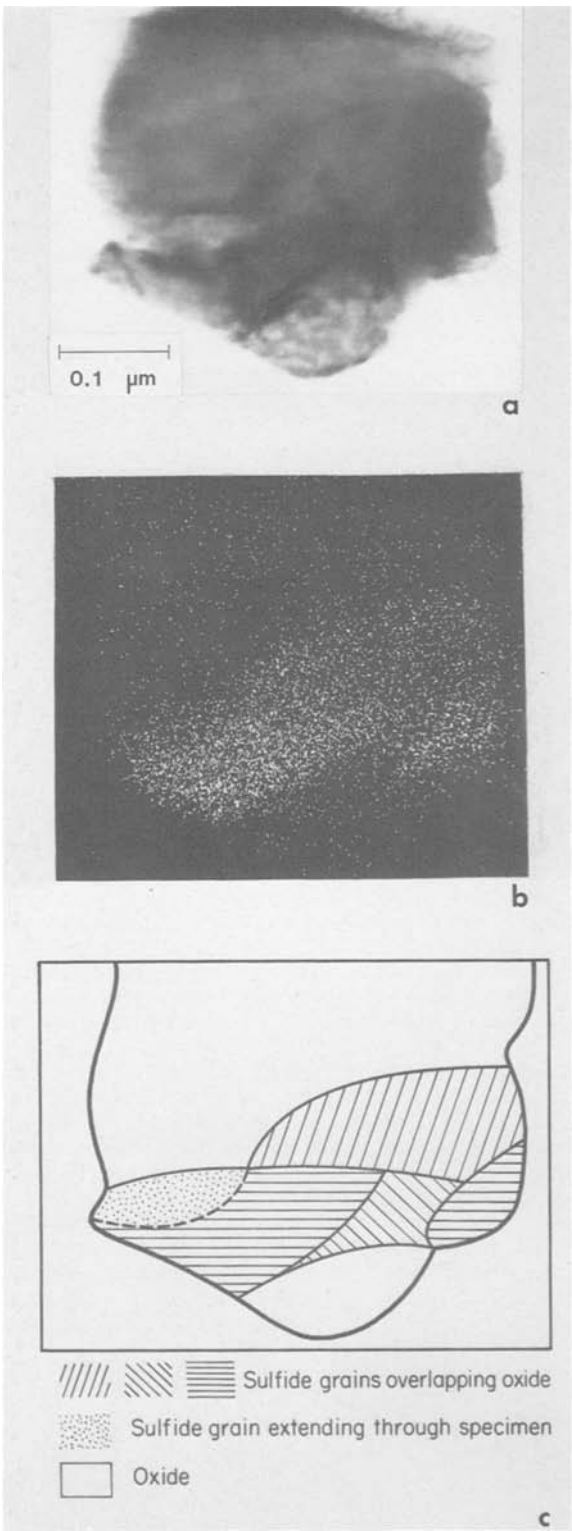

Fig. 7. (100) Cr oxidized in a H_2-H_2O-H_2S gas mixture for 60 min at 900°C with $P_{O_2} = 10^{-19}$ and $P_{S_2} = 10^{-6.5}$ atm; (a) STEM bright field image of the scale at the scale/gas interface; (b) a sulfur x-ray map of the region shown in (a); (c) a drawing showing the grain boundaries and the location of the sulfide grain in the image shown in (a).

or by STEM after 2 or 20 hr of exposure. Whiskers were observed at the scale/gas interface after the 2 hr preoxidation and after the 2 and 20 hr subsequent exposures to the sulfur-bearing gas mixtures (Fig. 8). The Cr/S ratio in the scale at the scale/gas interface after 20 hr was 1000:1-500:1 as determined in the STEM, which corresponds to ~0.07 to 0.14 w/o S in Cr_2O_3.

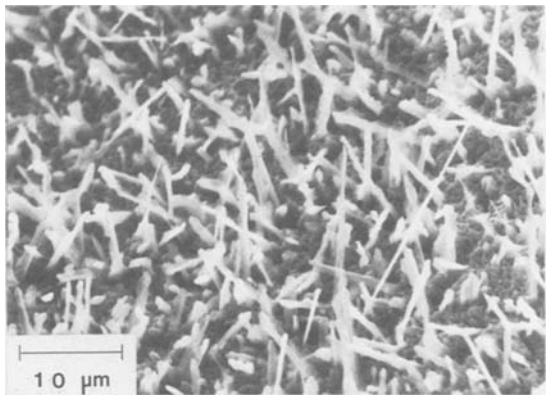

Fig. 8. A SEM image of the surface of a (100) Cr specimen preoxidized in a H_2-H_2O-H_2S mixture for 2 hr at 900°C with $P_{O_2} = 10^{-19}$ atm and subsequently exposed to a H_2-H_2O-H_2S gas mixture for 20 hr at 900°C with $P_{O_2} = 10^{-19}$ and $P_{S_2} = 10^{-6.5}$ atm. Whiskers are present after the initial oxidation step and continue to form upon exposure to the sulfur-bearing gas.

The scales formed on specimens exposed for 111 hr contained both oxide and sulfide. Figure 9a shows the scale grown on a (100) Cr specimen. The outer scale was spalled partially by scratching with a needle, and thereby revealing large crystals of $Cr_{1-x}S$ (1-5 μm in width) in contact with the metal (Fig. 9b). The outer surfaces of the scale showed protrusions (Fig. 9c) that were relatively rich in sulfur (Cr:S = 50:1, SEM/EDX), indicating regions where sulfides had been overgrown by oxide. Other areas of the surface exhibited features (Fig. 9d) with even higher sulfur contents (Cr:S = 7:1, SEM/EDX), which indicate that sulfides were in contact with the gas. The presence of sulfides at the scale/gas interface was confirmed by STEM.

Discussion

An unsettled issue in the area of high temperature oxidation is the mechanisms whereby sulfides form under conditions in which oxides are the only stable condensed phases in equilibrium with the gas mixture (*e.g.*, the conditions indicated by the points in Fig. 1). It is not generally recognized that the mechanisms of oxidation may differ when the gas mixture has a very low equilibrium P_{O_2} (*e.g.*, H_2-H_2O-H_2S) instead of a high equilibrium P_{O_2} (*e.g.*, gas mixtures containing significant quantities of SO_2). The difference in mechanisms that may be observed are discussed in this section. The conditions necessary for initial formation of a two-phase (oxide/sulfide) scale are pointed out and the conditions required for continued growth of a two-phase scale in H_2-H_2O-H_2S gas mixtures are discussed.

$P_{S_2} = 10^{-14}$ atm (2.6 × 10^{-4} v/o H_2S, $P_{O_2} = 10^{-19}$ atm, 900°C).—Sulfides were detected neither at the Cr/Cr_2O_3 interface nor within the scale. Trace amounts of sulfur could be detected at the Cr_2O_3/gas interface, but not beneath the surface of the scale. This is attributed to adsorption of sulfur on the specimen when it was cooled to room temperature in the H_2-H_2O-H_2S gas mixture.

It was not possible for sulfides to form on the bare Cr surface upon first exposure to the gas mixture because the partial pressure of sulfur in the gas phase, $P_{S_2}^g$, was less than $P_{S_2}(Cr/Cr_{1-x}S)$. Although cracks might develop in the oxide scale after reaction times longer than one hour, sulfides could form neither in the cracks nor at the Cr/Cr_2O_3 interface in the H_2-H_2O-H_2S gas mixture used in this experiment (12). When a metal or alloy is exposed to such a gas mixture, the maximum partial pressure of sulfur in the reaction system metal/oxide/gas is in the bulk gas phase and is determined by the equilibrium between H_2 and H_2S

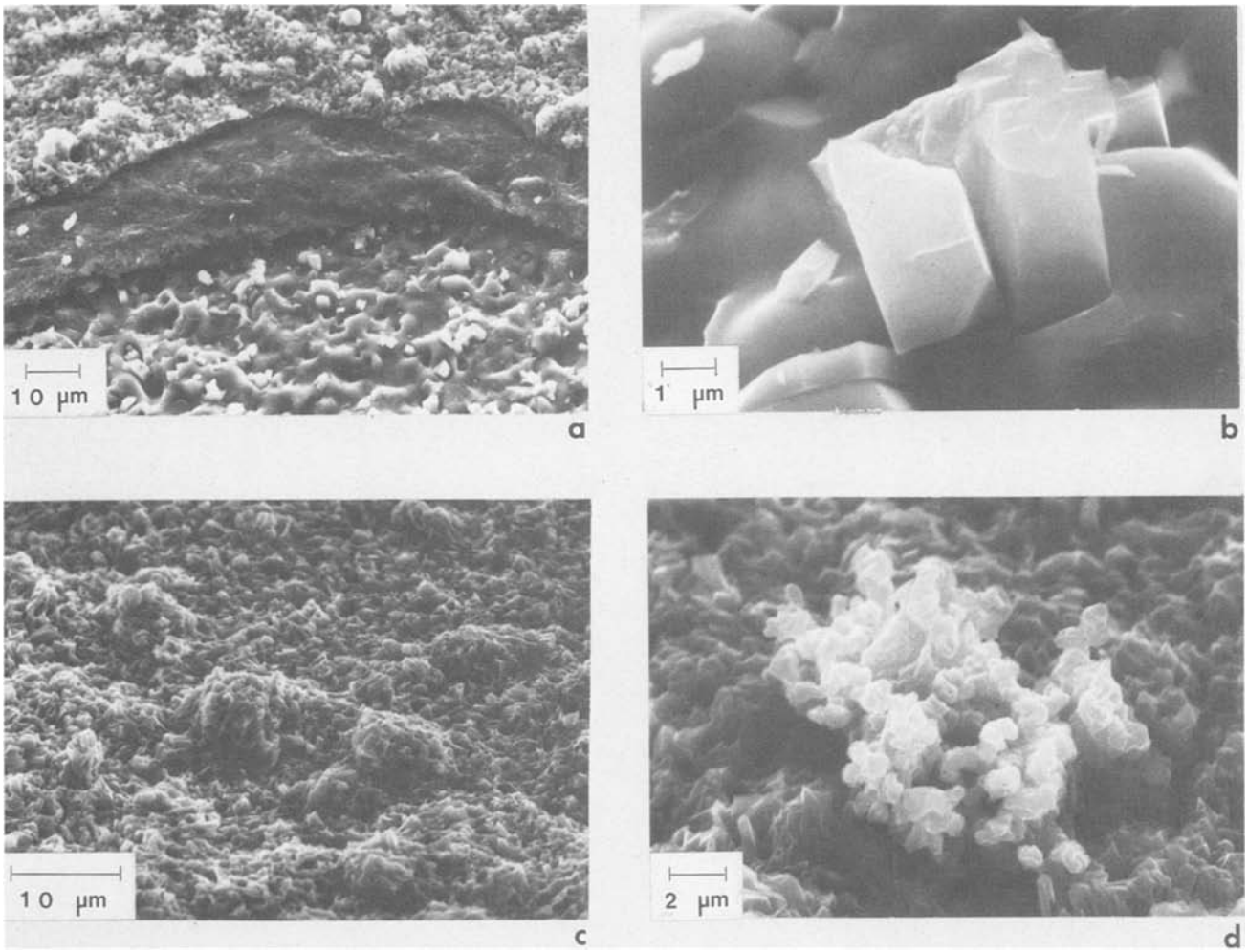

Fig. 9. SEM images of a (100) Cr specimen preoxidized in a H_2-H_2O mixture for 2 hr at 900°C with $P_{O_2} = 10^{-19}$ atm and subsequently exposed to a H_2-H_2O-H_2S mixture for 111 hr at 900°C with $P_{O_2} = 10^{-19}$ and $P_{S_2} = 10^{-6.5}$ atm: (a) a region where the scale was spalled to reveal the underlying metal; (b) sulfide crystals on the metal surface; (c) examples of protrusions at the scale/ gas interface that were rich in sulfur compared with surrounding regions; (d) an example of one of the features at the scale/gas interface that contained high concentrations of sulfur (Cr:S ≅ 7:1), indicating the presence of sulfides at the scale/gas interface.

(12, 13). If this maximum P_{S_2} is less than P_{S_2} for equilibrium between the metal and its lowest sulfide, then sulfides cannot form.

This is unlike the situation that may occur when a metal is exposed to a gas mixture that contains a significant quantity of bioxidant molecules (*e.g.*, SO_2 or COS). In the latter case, the sulfur partial pressure in a crack or pore in an oxide scale can increase from the scale/gas to the metal/scale interface. Sulfides can form in or beneath an oxide scale under these conditions even though the partial pressure of sulfur in the gas phase is less than that for equilibrium between the metal and its lowest sulfide.

The latter model, which was first delineated by Birks (14) to explain the formation of sulfides beneath oxide scales exposed to SO_2-bearing gases, has been employed in various forms by a number of investigators (15-20). Application of the model should be restricted, however, to oxidation of metals in SO_2-bearing bases in which the oxygen content is low (*e.g.*, pure SO_2, SO_2-Ar mixtures, etc.), or to cases wherein the transport of O_2 molecules through the physical defects is greatly restricted, *i.e.*, when the pores or cracks are very narrow. Otherwise, the oxygen activity in the crack would be approximately constant, in which case the sulfur activity in the crack would have a constant and low value.

$P_{S_2} = 10^{-10}$ atm (0.026 v/o H_2S, $P_{O_2} = 10^{-19}$ atm, 900°C).—No sulfides could be detected in or beneath the Cr_2O_3 scales that formed under these conditions. Because $P_{S_2}{}^{g} > P_{S_2}$ ($Cr/Cr_{1-x}S$), $Cr_{1-x}S$ could have nucleated on the Cr during the initial stage of reaction. Assuming that the relative amount of sulfide formed initially depends on the relative rates of adsorption of H_2O and H_2S on Cr (12), one calculates that $\lesssim 1\%$ of the initially formed scale would be sulfide (see Table III). Thus, it is not surprising that sulfides were not detected.

Although a sulfide-free Cr_2O_3 scale formed early in the reaction, sulfides could have formed in or beneath the scale by solid state or gaseous diffusion of sulfur or H_2S through the scale because $P_{S_2}{}^{g} > P_{S_2}$ ($Cr/Cr_{1-x}S$). The scales formed after 60 min were still free of sulfides, indicating that little, if any, sulfur penetrated the scale. Scales formed under these conditions could develop cracks after longer periods of oxidation, owing to the buildup of stresses in the oxide. Sulfides could form in such cracks as long as they were sufficiently narrow to insure that the local oxygen partial pressure in the crack was determined by the local equilibrium oxygen activity in the ad-

Table III. Area fraction of sulfide, A_S, formed on initial oxidation of pure Cr as a function of H_2O and H_2S concentrations (12)

P_{H_2O}	P_{H_2S}	P_{H_2O}/P_{H_2S}	A_s
0.042	2.6×10^{-4}	160.0	0.008
0.042	0.0046	9.0	0.13
0.041	0.014	2.8	0.31

jacent oxide phase (12). Otherwise, the composition of the gas phase in the cracks would be the same as that in the bulk gas phase, in which case the oxidation product would be Cr_2O_3.

$P_{S_2} = 10^{-7.5}$ atm (0.46 v/o H_2S, $P_{O_2} = 10^{-19}$ atm, 900°C).—Sulfides that nucleated on the Cr in the initial stage of reaction were overgrown rapidly by Cr_2O_3. Sulfide particles were observed at the Cr/Cr_2O_3 interface after the Cr_2O_3 was intentionally spalled by scratching the surface with a needle (Fig. 3 and 4). The fraction of the metal surface covered by sulfide particles after 2.5 min was 9-10%, which agrees reasonably well with a value of ~13% (see Table III), calculated by assuming that the amount of sulfide formed initially depends only on the relative rates of adsorption of H_2S and H_2O on Cr. Although the latter calculation yielded reasonable agreement with measured quantities of oxidation of (100) and (110) orientations of Cr, a randomly oriented grain of Cr exhibited a higher area fraction of sulfide than a (100) orientation exposed under the same conditions. Thus, the orientation of Cr appears to be an important factor in determining the amount of sulfide formed initially. Such a result is not surprising considering that Bardolle and Bénard (21) observed that the number of oxide nuclei formed on Fe varied with crystallographic orientation of the metal by as much as 100×. The calculation presented previously (12), may be considered to yield a rough estimate of the effect of gas composition on the relative amount of sulfide formed initially.

Although both oxide and sulfide formed in the initial stage of reaction, only oxide could be detected in the scale away from the Cr/scale interface after 60 min of oxidation. Continued growth of a two-phase scale can occur if the rate of scale growth is controlled at least partially by a phase boundary reaction or by diffusion in the gas phase (14, 22, 23). Under these conditions, the activity of Cr at the scale/gas interface may remain greater than a_{Cr} (minimum). The latter quantity is the minimum activity of Cr needed to form $Cr_{1-x}S$ at a particular temperature and P_{S_2} in the gas phase. In addition, however, the simultaneous formation of oxide and sulfide requires that the rates of supply of sulfur and oxygen to the scale/gas interface not be significantly different (12). As noted previously (12), a H_2O/H_2S ratio of at least nine is necessary to avoid growth of two-phase (oxide/sulfide) scales during oxidation of Cr in H_2-H_2O-H_2S at 900°C, although some sulfide may form on initial exposure. With $H_2O/H_2S > 9$, it appears that two-phase scales are quickly overgrown by single-phase oxide scales because the rate of supply of oxygen (H_2O) is much greater than the rate of supply of sulfur (H_2S) to the scale surface. Much higher values of the H_2O/H_2S ratio are required to avoid sulfide formation during the entire course of reaction.

The sulfides that formed initially in the gas mixture with $P_{O_2} = 10^{-19}$ and $P_{S_2} = 10^{-7.5}$ atm remained at the Cr/Cr_2O_3 interface during subsequent oxidation. Preliminary results indicate that the area fraction of sulfides remained the same (~9-10%) from 2.5 to 60 min; however, the number of particles decreased and their diameter approximately doubled. Since the height of the sulfide particles also increased by about a factor of two (compare Fig. 3 and 4), it is concluded that the total volume of $Cr_{1-x}S$ increased by about a factor of two. Thus, the change in size and number of the particles was caused not only by Ostwald ripening, but also by an ingress of sulfur. The latter may have occurred, in principle, by solid-state diffusion of sulfur through the oxide or by diffusion of H_2S through cracks or pores.

If a H_2-H_2O-H_2S gas mixture diffused through physical defects in the Cr_2O_3 scale, and if the gas phase in the defects were in local equilibrium with the oxide, then sulfide could have formed in the defects and at the Cr/Cr_2O_3 interface as described in a previous paper (12). Indeed, for the present gas mixture, only the outer 10% of the scale would be free of sulfide (12). Sulfides were not detected in the center of the scale by STEM. Of course, the gas mixture may have diffused inward through a few widely spaced microcracks that were not included in the specimen examined in the STEM. In that case, however, the growth of sulfide particles at the Cr/scale interface would have been confined primarily to regions adjacent to the intersection of the cracks with the metal/scale interface. The sulfide particles increased in size uniformly along the entire interface. Thus, it appears that sulfur diffused inward uniformly by lattice or grain-boundary diffusion through the oxide scale. The fine grain size of the oxide (see Fig. 5) supports a possible mechanism of grain boundary diffusion.

$P_{S_2} = 10^{-6.5}$ atm (1.4 v/o H_2S, $P_{O_2} = 10^{-19}$ atm, 900°C).—After 2.5 min, the scale comprised a mixture of oxide and sulfide. The sulfide was present in the form of relatively large crystals (Fig. 6b) and small grains intermixed with the oxide phase. According to Table III, 31% of the surface of Cr could be converted to sulfide if adsorption of H_2S and H_2O controlled the relative amounts of oxide and sulfide formed upon exposure of the metal to the gas mixture. Thus, the large amount of sulfide observed is not surprising. It is not understood why some of the large sulfide crystals were present in the form of interconnected ridges. (Fig. 6a).

After 60 min, the scale in contact with the gas comprised a mixture of oxide and sulfide (Fig. 7), which indicates that the activity of Cr at the scale/gas interface was greater than a_{Cr} (minimum) and that the rate of supply of oxygen to the surface of the scale was not significantly different from the rate of supply of sulfur. Although oxidation kinetics were not measured, it is clear that the rate of oxidation up to 60 min was controlled, at least partially, by diffusion in the gas phase or by a chemical reaction at the scale/gas interface. It is not possible, based on the present results, to determine which step was rate controlling.

Because $P_{S_2}{}^g > P_{S_2}(Cr/Cr_{1-x}S)$ in the present case, sulfides could form in narrow cracks or pores in the scales. Indeed, only the outer 5% of the scale adjacent to cracks or pores would be free of sulfide (12). If large cracks formed in the scale or the scale spalled to allow direct access of the gas mixture to the metal surface, a two-phase scale would form such as that developed on the bare metal initially. Thus, it is unlikely that pure Cr can oxidize in a protective fashion under these conditions, and it is not surprising that Cr-bearing alloys also do not perform well in similar environments.

Preoxidation experiments.—These experiments were performed to determine the resistance of a preformed Cr_2O_3 layer on Cr to degradation in a H_2S-bearing gas mixture. An adherent layer of Cr_2O_3 was formed at 900°C after two hours in a H_2-H_2O gas mixture with $P_{O_2}{}^g = 10^{-19}$ atm. Subsequent exposure to a H_2-H_2O-H_2S mixture with $P_{S_2}{}^g = 10^{-6.5}$ atm ($P_{O_2}{}^g = 10^{-19}$ atm) for 2 or 20 hr did not yield sulfide formation in or beneath the Cr_2O_3 scale. After 111 hr of exposure to the sulfur-bearing gas, the scale comprised a mixture of oxide and sulfide (Fig. 9). Sulfides existed, in fact, at the scale/gas interface.

After 20 hr of exposure to the H_2-H_2O-H_2S mixture, 0.07 to 0.14 w/o S was dissolved in the Cr_2O_3 near the Cr_2O_3/gas interface. Hence, the equilibrium concentration of sulfur dissolved in Cr_2O_3 under the stated conditions of temperature and gas composition is apparently ~0.1 w/o. Only trace amounts of sulfur were detected closer to the Cr/Cr_2O_3 interface. Thus, very little sulfur diffused into the preformed oxide layer

by solid-state diffusion in 20 hr. Because sulfides were not detected, H_2S did not penetrate the scale by diffusion in pores or cracks.

It is clear that between 20 and 111 hr the protective properties of the preformed oxide layer were lost. Because sulfides were found throughout the scale, including at the scale/gas interface, the mostly likely explanation for the loss of protection is that large cracks formed in the Cr_2O_3, or the Cr_2O_3 spalled, thereby exposing bare Cr to the bulk gas mixture. As noted above, a two-phase scale can form on Cr under these conditions. Evidence that the preformed scale spalled completely sometime after 20 hr of exposure to the sulfur-bearing gas mixture comes from the observation that whiskers covered the surface of the scale after preoxidation and after 20 hr of subsequent exposure, but not after 111 hr (*cf.* Fig. 8 and 9). The presence of sulfides at the scale/gas interface indicates that equilibrium had not yet been reached at that interface. Thermogravimetric experiments may help to clarify the mechanism. In any case, the present experiments confirm the conclusion that Cr would oxidize in an unprotective fashion under these conditions, even if it were preoxidized.

Conclusions

1. Scale morphologies depend on the relative amounts of H_2O and H_2S in the gas. At 900°C with $P_{O_2} = 10^{-19}$ atm, sulfides were not detected with $P_{S_2} = 10^{-10}$ and 10^{-14} atm, but sulfides were observed at the metal/scale interface with $P_{S_2} = 10^{-7.5}$ atm and a duplex oxide/sulfide structure formed at $P_{S_2} = 10^{-6.5}$ atm.

2. A two-hour preoxidation of Cr with $P_{O_2} = 10^{-19}$ atm was successful in preventing sulfur penetration for at least 20 hr of subsequent exposure to H_2-H_2O-H_2S gas mixtures ($P_{O_2} = 10^{-19}$, $P_{S_2} = 10^{-6.5}$ atm). However, after 111 hr of subsequent exposure, the initial oxide scale was completely lost, and the resulting scale consisted of a duplex oxide/sulfide mixture.

3. Differences exist between scaling of pure metals in SO_2-bearing gases and in H_2-H_2O-H_2S gas mixtures. In the former case, P_{S_2} depends on P_{O_2}, so that sulfides can form even if $P_{S_2}{}^g$ is less than P_{S_2} for equilibrium between the metal and its lowest sulfide. The sulfur activity in H_2-H_2O-H_2S gas mixtures is fixed when P_{O_2} is low and depends on the initial H_2/H_2S ratio in the bulk gas. Sulfides can form only if $P_{S_2}{}^g$ is greater than P_{S_2} for equilibrium between the metal and its lowest sulfide.

4. Only small amounts of sulfur dissolve in Cr_2O_3; *i.e.*, approximately 0.1% by weight at 900°C with $P_{O_2} = 10^{-19}$ and $P_{S_2} = 10^{-6.5}$ atm. It is unclear to what extent sulfur diffusion in Cr_2O_3 is significant in the scaling of Cr in H_2-H_2O-H_2S mixtures. Sulfur diffusion, however, may play a role in the growth of sulfide particles at the Cr/scale interface with $P_{O_2} = 10^{-19}$ and $P_{S_2} = 10^{-7.5}$ atm.

Acknowledgments

The authors would like to thank W. Worrell for his careful reading of the manuscript, and M. Graham, who had the analysis of the Cr done at the National Research Council of Canada. This research was supported by the Division of Basic Energy Sciences, under DOE contract no. DE-ACO2-79ER10507.

Manuscript submitted Feb. 7, 1983; revised manuscript received June 6, 1983.

REFERENCES

1. F. S. Pettit, J. A. Goebel, and G. W. Goward, *Corr. Sci.*, **9**, 903 (1969).
2. R. A. Perkins, in "Proceedings of the Corrosion/Erosion of Coal Conversion Systems Materials Conference," A. V. Levy, Editor, p. 351, NACE, Houston (1979).
3. C. S. Giggins and F. S. Pettit, *Oxid. Met.*, **14**, 363 (1980).
4. A. S. Nagelberg and R. W. Bradshaw, *This Journal*, **128**, 2655 (1981).
5. H. Hindam and D. P. Whittle, *Corrosion*, **38**, 32 (1982).
6. G. J. Yurek, *Metall. Trans. B*, To be published.
7. "CRC Handbook of Chemistry and Physics," 61st ed., R. C. Weast and M. J. Astle, Editors, p. D-196, CRC Press, Inc., Boca Raton, Florida (1980).
8. W. J. Moore, "Physical Chemistry," 4th ed., p. 154, Prentice-Hall, Englewood Cliffs, NJ (1972).
9. M. LaBranche and G. J. Yurek, Massachusetts Institute of Technology, Cambridge, MA, unpublished research (1983).
10. K. P. Lillerud and P. Kofstad, *This Journal*, **127**, 2397 (1980).
11. P. Kofstad and K. P. Lillerud, *ibid.*, **127**, 2410 (1980).
12. G. J. Yurek and M. LaBranche, in "Proceedings of the Corrosion-Erosion-Wear of Materials in Emerging Fossil Energy Systems," A. V. Levy, Editor, p. 933, NACE, Houston (1982).
13. G. J. Yurek and M. LaBranche, Paper presented at the International Conference on High-Temperature Corrosion, San Diego, March 2-6, 1981.
14. N. Birks, "High Temperature Gas-Metal Reactions in Mixed Environments," S. A. Jansson and Z. A. Foroulis, Editors, p. 322, TMS/AIME, Boston (1972).
15. P. Singh and N. Birks, *Oxid. Met.*, **12**, 23 (1978).
16. M. C. Pope and N. Birks, *ibid.*, **12**, 173 (1978).
17. P. Kofstad and G. Åkesson, *ibid.*, **12**, 503 (1978).
18. K. L. Luthra and W. L. Worrell, *Met. Trans.*, **9A**, 1055 (1978).
19. K. L. Luthra and W. L. Worrell, *ibid.*, **10A**, 621 (1979).
20. F. Gesmundo, C. de Asmundis, and C. Bottino, *Oxid. Met.*, **14**, 15 (1980).
21. J. Bardolle and J. Benard, *Rev. Met.*, **49**, 613 (1952).
22. T. K. Ross, *Corros. Sci.*, **5**, 327 (1965).
23. T. Flatley and N. Birks, *J. Iron Steel Inst.*, **209**, 523 (1971).

Leakage-Current Increase in Amorphous Ta_2O_5 Films Due to Pinhole Growth during Annealing Below 600°C

Shin-ichiro Kimura, Yasushiro Nishioka, Akira Shintani, and Kiichiro Mukai

Central Research Laboratory, Hitachi, Limited, Kokubunji, Tokyo, 185, Japan

ABSTRACT

Effects of high temperature annealing over the range 400°-1000°C on the leakage current of tantalum pentoxide (Ta_2O_5) films deposited by reactive sputtering are investigated. Leakage current of polycrystalline Ta_2O_5 film (annealed above 700°C) is about 10^7-10^8 times larger than that of as-deposited amorphous film. However, it is found that leakage current in Ta_2O_5 film annealed at 600°C increases drastically as well, even though the films have not yet recrystallized. TEM observation reveals that pinholes ranging from 5 nm to 15 nm in diameter are formed near the bottom of the depressions in Ta_2O_5 film annealed even at 600°C. Electrical properties of the Ta_2O_5 films are discussed in terms of crystallographic properties such as pinhole growth and grain boundaries.

For many years, Ta_2O_5 films have been widely used as a capacitor insulator in hybrid IC's (1). Innovative attempts (2, 3) to apply Ta_2O_5 film as the storage capacitor in highly integrated dynamic MOS random-access memories (MOS-dRAM's) in order to form a large capacitance have also been reported. Ta_2O_5 film is a promising material for providing large capacitance in forthcoming VLSI's. This is because Ta_2O_5 film has several outstanding characteristics, such as a high capacitance-to-area ratio and relatively high dielectric-breakdown strength. However, the conventional MOSRAM fabrication process requires high temperature annealing near 1000°C after dielectric film formation. Therefore, it is necessary to investigate the effects of annealing and crystallographic structure on the electrical properties of Ta_2O_5 film.

Several papers have already reported on the electrical properties of amorphous Ta_2O_5 films grown by anodization (4, 5, 6), thermal oxidation (7), or reactive sputtering (8). The influence of low temperature annealing around 200°C on electrical properties has also been investigated (6, 9). In addition, Ta_2O_5 film is known to become polycrystalline when annealed above 700°C (10). However, the effects of high temperature annealing on electrical properties have not been extensively investigated yet in conjunction with structural parameters.

In this paper, the relation between high temperature annealing and leakage current in Ta_2O_5 film is studied. This is an important issue because an extremely low leakage current is essential for any dielectric material used as a storage capacitor insulator in MOS-dRAM's.

Ta_2O_5 films have generally been grown by anodic oxidation of Ta film in a wet solution. However, the anodic oxidation has a drawback; possible impurities in the solution are incorporated in oxides and degrade the LSI's reliability. In this work, Ta_2O_5 films were grown using reactive sputtering. Through this experiment, it was found that the leakage current in annealed Ta_2O_5 film increases drastically, even though the Ta_2O_5 film has not yet recrystallized. A measurement of optical properties and transmission electron microscope (TEM) observation were also employed to investigate the reasons for large leakage current in noncrystalline Ta_2O_5 film.

Experimental

Ta_2O_5 films were grown using reactive sputtering of a metallic Ta target with 99.9% purity. Total gas pressure (Ar and O_2) in the sputtering chamber was held to 0.68 Pa (5×10^{-3} Torr). Presputtering of the target was carried out for 20 min to remove surface contamination from the target. Both p-type and n-type silicon wafers with (100) orientation were used as substrates. The deposited films were annealed in a quartz tube for 1 hr in nitrogen or oxygen ambient. The crystal structure of the annealed Ta_2O_5 films were investigated by both x-ray and electron diffractions. Ta_2O_5 films 100 nm thick were used for the x-ray diffraction. The films for TEM observation were deposited on a self-supporting Si_3N_4 film placed over a small hole through a silicon substrate, as shown in Fig. 1 (12). The refractive index of the Ta_2O_5 film was measured using an ellipsometer. The wavelength of the incident light was 546.1 nm. The absorption coefficient of the film was also obtained using Hitachi 340 spectrophotometer.

Metal-oxide-semiconductor (MOS) diodes with an Al/Ta_2O_5/Si structure were fabricated to measure the leakage current. The area of the Al electrode was 2×10^{-3} cm^2. The Al was deposited after annealing of the Ta_2O_5 film to avoid any reaction between the Ta_2O_5 film and the Al during annealing. Leakage current was measured with a Keithley picoammeter Model 26000 in an optically and electrically shielded box by applying a ramp bias (0.1 V/sec) to the MOS diodes.

Results and Discussion

Sputtering condition and physical properties of Ta_2O_5 film.—The dependence of film-deposition rate and Ta concentration in the deposited film on oxygen partial pressure (P_{O_2}) are shown in Fig. 2. The Ta concentration was measured by Inductively Coupled Plasma Spectroscopy (ICPS). The deposition rate steeply decreased for P_{O_2} between 0.04 Pa and 0.005 Pa. On the other hand, the Ta concentration in the deposited film gradually decreased in accordance with the P_{O_2} increase, and finally became saturated when P_{O_2} exceeded 0.05 Pa. Although the Ta concentration in compositionally saturated films is a little different from that in stoichiometric Ta_2O_5 (broken line), this difference seems to be caused by the insufficient accuracy of ICPS. The surfaces of deposited films grown at P_{O_2} below 0.04 Pa looked metallic. However, the electric resistivity of these films was high (500 $\mu\Omega \cdot$ cm) compared with that of bulk Ta (12 $\mu\Omega \cdot$ cm) because of the large oxygen content (Fig. 2). Films grown at P_{O_2} above 0.05 Pa looked transparent. It is this transparent film that we considered to be Ta_2O_5 film (13). All of the Ta_2O_5 films used to investigate the electrical properties were deposited at a P_{O_2} of 0.1 Pa.

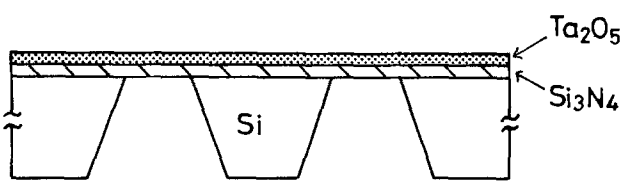

Fig. 1. Schematic cross section of the specimen used for TEM observation. Thickness of Si_3N_4 film and Ta_2O_5 film are 50 nm and 40 nm, respectively.

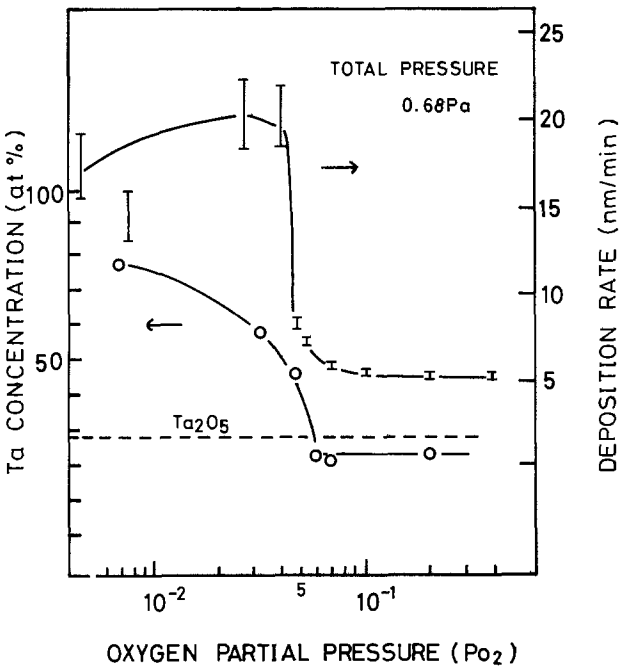

Fig. 2. Deposition rate and tantalum concentration in the deposited film as a function of oxygen partial pressure. Broken line shows the tantalum concentration of stoichiometric Ta_2O_5.

Crystallization and leakage current in Ta_2O_5 film.— Figure 3 shows the x-ray diffraction spectrum for Ta_2O_5 film annealed at 800°C in nitrogen ambient for 1 hr. Similar diffraction spectra were observed in all specimens annealed above 700°C. The height of the two peaks near 22.9° and 28.7°, which correspond to the diffraction from (001) and (200), respectively, are plotted as a function of annealing temperature in Fig. 4. Ta_2O_5 films annealed below 600°C do not show any notable peak in spectrum. Therefore, the crystallization temperature of Ta_2O_5 film grown by reactive sputtering lies between 650°C and 700°C. The crystallization temperature obtained in this work is consistent with previous results (10, 14) for anodically or thermally grown Ta_2O_5 film. It is concluded that the crystallization temperature of Ta_2O_5 film does not depend on the method by which the film is grown.

Leakage current through MOS diodes as a function of applied electric field is shown in Fig. 5. The thickness of the Ta_2O_5 film was about 100 nm, and n-type (0.01 Ω · cm) Si was used as the substrate. Forward-bias voltage was applied, *i.e.*, the Al electrode was biased positively to form the accumulation layer on the Si surface. The open circles in the figure show the leakage current of as-deposited Ta_2O_5 film.

The logarithm of the highest applicable electric field (HAEF) *vs.* annealing temperature is plotted in Fig. 6.

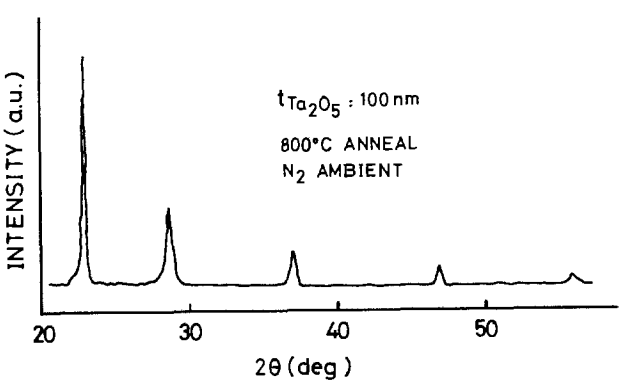

Fig. 3. X-ray diffraction spectrum of crystallized Ta_2O_5 film annealed at 800°C in nitrogen ambient.

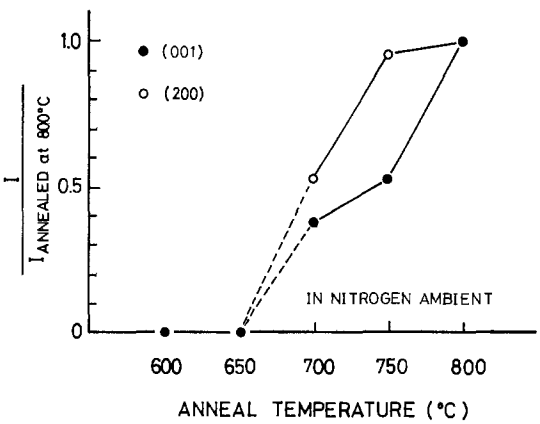

Fig. 4. Intensity of two peaks from (001) and (200) of crystallized Ta_2O_5 films as a function of annealing temperature. Each intensity is normalized to that of Ta_2O_5 film annealed at 800°C.

The HAEF is defined as the electric field at which leakage current becomes 10^{-6} A/cm². The HAEF obtained for Ta_2O_5 films annealed in oxygen ambient is also plotted in this figure (closed circles). The HAEF of as-deposited Ta_2O_5 film was about 5 MV/cm, and it increased to about 6 MV/cm after annealing at 400°C. The HAEF of Ta_2O_5 films annealed above 600°C was smaller than that of as-deposited Ta_2O_5 film. Also, it was shown that the HAEF of Ta_2O_5 film annealed at 600°C depends on the annealing ambient. The small HAEF increase observed in Ta_2O_5 film annealed at 1000°C in oxygen ambient can be attributed to silicon-dioxide formation along the interface of the Ta_2O_5 film and the Si substrate. This speculation is made sufficiently valid by the fact that the capacitance of a MOS diode annealed at 1000°C decreased.

It is shown that the area of the charge storage capacitor will be less than 10 μm² (10^{-7} cm²) in a million-bit-class MOS-dRAM(15). This indicates that the thickness of Ta_2O_5 film would have to be 20-30 nm to store sufficient charge (around 300 fC) for memory operation. (In this calculation, dielectric constant of Ta_2O_5 film is assumed to be 20.) Since 5V is expected

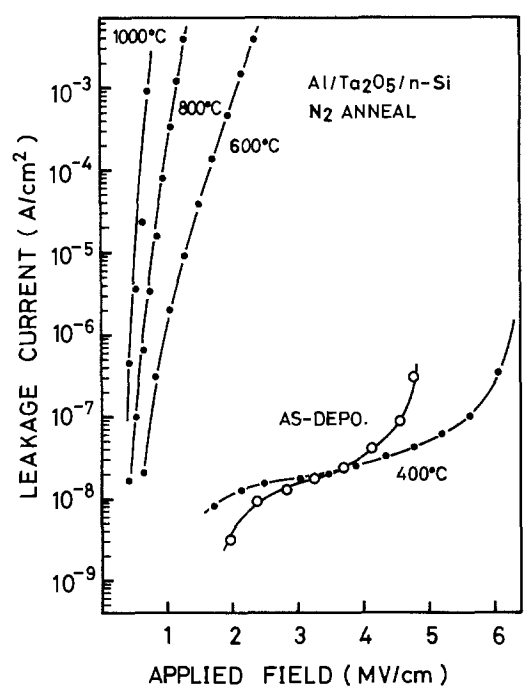

Fig. 5. Leakage current of MOS diodes consisting of Al/Ta_2O_5/Si structure *vs.* applied electric field. Ta_2O_5 film was deposited on n-type (0.01 Ω · cm) Si to a thickness of 100 nm. Ramp bias (0.1 V/sec) was applied. Open circles show the leakage current of as-deposited Ta_2O_5 film.

to be applied to the capacitor, leakage current less than 10^{-6} A/cm^2 at about 2-3 MV/cm is essential for the capacitor insulators. It is evident from Fig. 5 that Ta_2O_5 film annealed below 400°C has the potential to be applied to a million-bit-class MOS-dRAM.

From the results shown in Fig. 4 and 6, it is concluded that the drastic decrease of HAEF (*i.e.*, the increased leakage current) of Ta_2O_5 film annealed above 800°C is probably due to polycrystallization of the Ta_2O_5 film. Also, grain boundaries of polycrystallized Ta_2O_5 films probably become paths for leakage current. However, it was also observed that the leakage current in Ta_2O_5 film annealed at 600°C became larger than that of as-deposited Ta_2O_5 film, even though the annealed film had not yet polycrystallized as shown in Fig. 4.

Young (6) suggested that the increase of leakage current in annealed Ta_2O_5 film (200°C) was related to the water desorption, which gave rise to the structural changes such as oxygen deficiency or suboxide formation. In order to investigate the evidence of water desorption from the film, optical absorption of the annealed film was measured as follows.

Optical absorption property of annealed Ta_2O_5 film.—It is well known that the absorption coefficient (α) observed near the fundamental absorption edge of materials is exponentially proportional to photon energy as follows

$$\alpha = A \cdot \exp(\Gamma h\nu)$$

where A and Γ are constant.

This exponential part of the absorption edge is considered to be evidence of energy levels introduced by structural disorder in the forbidden energy gap of the materials. Nakamura *et al.* (16) investigated the absorption spectrum of annealed tungsten-oxide film (200°C) formed by vacuum deposition, and clarified that the α of the annealed tungsten-oxide film became smaller compared with that of as-deposited film. They concluded that the decrease of α is related to the structural disorder associated with water desorption from the film.

Figure 7 shows the absorption coefficient of as-deposited and annealed Ta_2O_5 films. The specimen was a 2 μm-thick Ta_2O_5 film deposited on quartz plate and annealed in nitrogen ambient for 1 hr. It was shown that annealing at 600°C (open circle) did not give rise

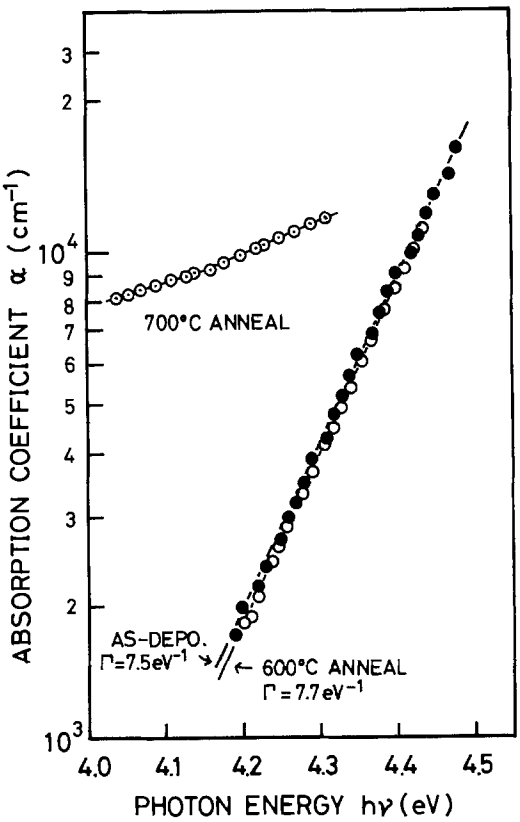

Fig. 7. Absorption coefficient of Ta_2O_5 film. Specimens were 2 μm-thick film deposited on transparent quartz plate. α is exponentially proportional to photon energy.

to any change of absorption coefficient. On the contrary, the absorption coefficient of crystallized film (annealed at 700°C) was quite large. Since the crystallized film became opaque, it is speculated that the decrease of transmissibility is related to the increased absorption coefficient. The structural change associated with water desorption probably did not occur in the film used in this experiment. Therefore, the increase of leakage current may be due to the structural defects such as flaws.

Refractive index of annealed Ta_2O_5 films.— The refractive index of Ta_2O_5 films as a function of annealing temperature is shown in Fig. 8. In Fig. 8, the vertical axis shows the percentage of change in refractive in-

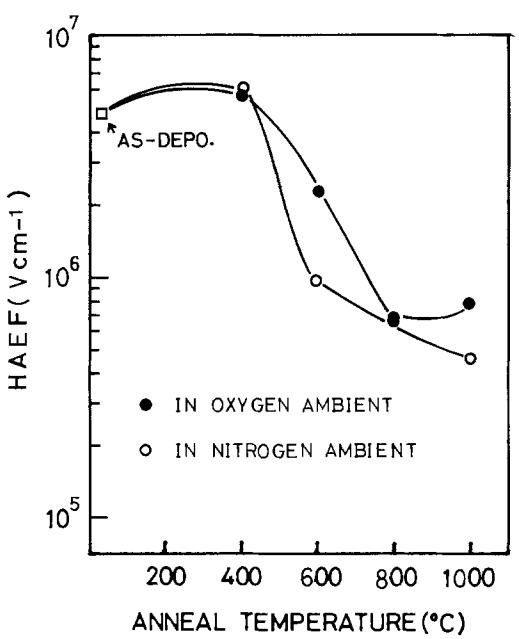

Fig. 6. Highest applicable electric field (HAEF) vs. annealing temperature. HAEF is defined as the electric field where leakage current is 10^{-6} A/cm^2. Open circle: Ta_2O_5 film annealed in N_2 ambient; closed circle: in O_2 ambient; square: as-deposited film.

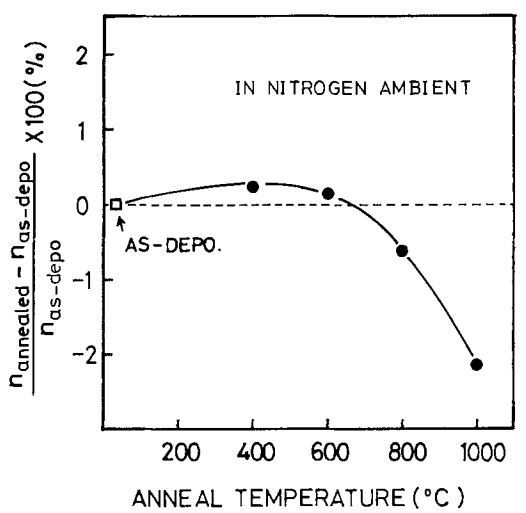

Fig. 8. Refractive index of annealed Ta_2O_5 film vs. annealing temperature. Vertical axis shows the percentage of the refractive index increase from that of as-deposited Ta_2O_5 film. Square is the refractive index of as-deposited Ta_2O_5 film.

dex. The refractive index of as-deposited Ta_2O_5 film is 2.1.

The refractive index of a thin film is known to be closely related to the porosity of that film (17). Also, any increase in the refractive index is equivalent to densification of the film. In Fig. 8, the refractive indexes of Ta_2O_5 films annealed at 400°C and 600°C are a little larger than that of as-deposited Ta_2O_5 film. This indicates that annealing at 400°C or 600°C makes Ta_2O_5 films denser. Therefore, it is assumed that the HAEF increase in Ta_2O_5 film annealed at 400°C is related to this densification of the film. However, the HAEF of Ta_2O_5 film annealed at 600°C became smaller, though the refractive index still increases. This result

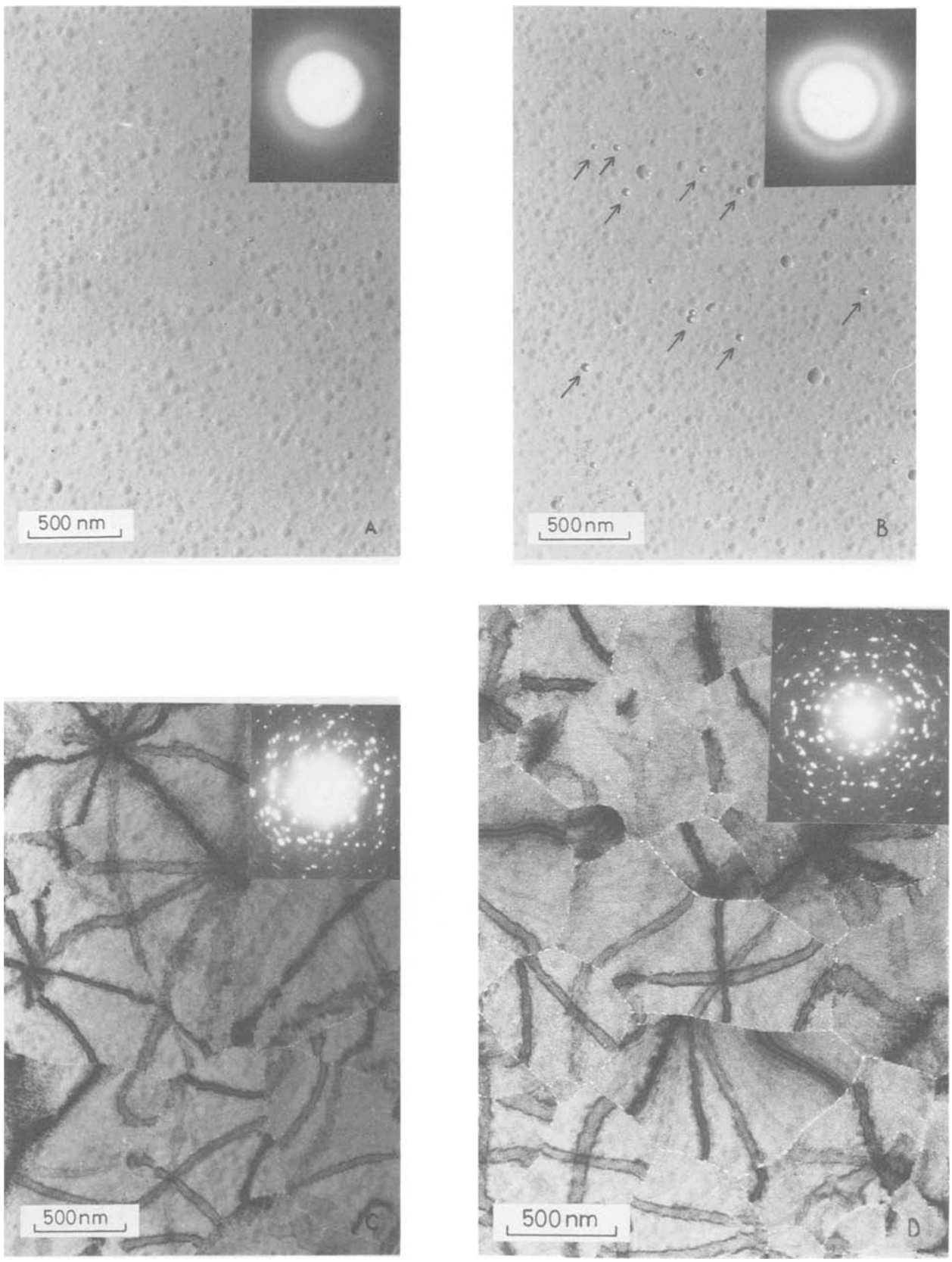

Fig. 9. Bright field images and electron diffraction patterns of annealed Ta_2O_5 films. Ta_2O_5 film was deposited in the thickness of 40 nm on the self-supporting Si_3N_4 film (50 nm) on a Si substrate which had a small hole. Arrows in B indicate pinholes. A: as-deposited; B-D: annealed at 600°C, 800°C, 1000°C, respectively.

implies that densification of the film by annealing near 600°C may give rise to micro-defect formation or growth in Ta_2O_5 film.

A large decrease in refractive index was observed (Fig. 8) when crystallized Ta_2O_5 film was measured. This decrease is due to the surface roughness caused by polycrystallization of the film, as was suggested by Fenstermaker *et al.* (18).

TEM observation.—Figure 9 shows bright-field images of annealed Ta_2O_5 films and their electron-diffraction patterns. Many depressions are observed in the noncrystalline Ta_2O_5 films (Fig. 9a and Fig. 9b). Since this kind of depression is not observed in the Si_3N_4 film supporting the Ta_2O_5 film, Ta_2O_5 films probably have such depressions. From the diffraction pattern in Fig. 9b, it is reconfirmed that Ta_2O_5 film annealed at 600°C is amorphous, which is consistent with the results shown in Fig. 4. In Fig. 9b, there are some white spots ranging from 5 nm to 15 nm in diameter near the bottom of the depressions. These are indicated by arrows. These spots seem to indicate pinholes near the bottoms of the depressions. These pinholes play roles as paths for leakage current in Ta_2O_5 films annealed at 600°C.

A few workers directly observed the flaws in anodically formed Ta_2O_5 film (19, 20). They concluded that the flaws are produced by carbides and by geometrical irregularities on the base-metal surface. However, in our experiment, since mirror-polished Si wafers for LSI fabrication were used, it is unlikely that the contaminants or irregularities exist on the substrate surface. Therefore, we conclude that the pinholes grow during annealing. The mechanism of pinhole growth could be as follows.

As-deposited Ta_2O_5 film has small pinholes, as shown in Fig. 9a. However, the density of the pinhole is so small that the pinhole cannot become an effective path for leakage current. (In this work, it is not clear whether the white spot in Fig. 9a is a pinhole through the film or a void in the film (21, 22, 23, 24).) Annealing near 600°C causes densification of the film. Since the densification of the film does not occur uniformly, stress originating in this densification induces pinhole growth near the bottom of the depression because stress concentration occurs nearby. Accelerated annihilation of excess vacancies at the pre-existing pinholes by annealing is another probable mechanism of pinhole growth.

In Fig. 9c and 9d, bright field images and diffraction patterns of polycrystallized Ta_2O_5 films are shown. Not only grain boundaries but also many pinholes along the grain boundaries are observed. It is probable that these pinholes become a path for leakage current.

Conclusion

The influence of annealing on crystallization and leakage current in Ta_2O_5 films grown by reactive sputtering have been investigated by x-ray diffraction, optical property measurement, and TEM observation. It is concluded that the crystallization temperature of Ta_2O_5 film lies between 650°C and 700°C. Also, the large leakage current in polycrystallized Ta_2O_5 film originates in the grain boundaries. On the other hand, Ta_2O_5 film annealed at 600°C also shows large leakage current, though the film has not yet polycrystallized. TEM observation reveals that pinholes are formed at the weakest points in the film, such as at the bottom of the depressions. These pinholes become paths for leakage current. The mechanism for pinhole growth is as follows.

Annealing at 600°C increases Ta_2O_5 film density. However, stress originating in this densification induces pinholes near the bottom of depressions. Therefore, to eliminate leakage current increase, it is necessary to make the thickness of the film uniform. Furthermore, it is necessary to have a low temperature process for Ta_2O_5 film to be applied to LSI as a dielectric material.

Acknowledgment

The authors wish to thank T. Ishiba for x-ray diffraction measurement and H. Kakibayashi for TEM observation. Dr. K. Hinode is also acknowledged for providing the Si_3N_4 film used as a substrate of TEM observation. Dr. Sunami and Dr. Alwitt are thanked for their critical reading of the manuscript.

Manuscript submitted March 24, 1983; revised manuscript received July 22, 1983.

Hitachi, Limited assisted in meeting the publication costs of this article.

REFERENCES

1. D. A. McLean, N. Schwartz, and E. D. Tidd, *Proc. IEEE*, **52**, 1450 (1964).
2. M. Koyanagi, H. Sunami, and N. Hashimoto, *Jpn. J. Appl. Phys.*, **18-1**, 135 (1978).
3. K. Ohta, K. Yamada, K. Shimizu, and Y. Tarui, *IEEE Trans. Electron Devices*, **ed-29**, 368 (1982).
4. Y. Sasaki, *J. Phys. Chem. Solids*, **13**, 177 (1960).
5. P. L. Young, *J. Appl. Phys.*, **47**, 235 (1976).
6. P. L. Young, *ibid.*, **47**, 242 (1976).
7. D. J. Smith and L. Young, *IEEE Trans. Electron Devices*, **ed-28**, 22 (1981).
8. D. M. Hughes and M. W. Jones, *J. Phys. D*, **7**, 2081 (1974).
9. S. M. Gubanski and D. M. Hughes, *Thin Solid Films*, **52**, 119 (1978)
10. D. A. Vermilyea, *Acta Metall.*, **1**, 282 (1953).
11. D. M. Smyth, G. A. Shirn, and T. B. Tripp, *This Journal*, **110**, 1264 (1963).
12. K. Hinode, Personal communication.
13. E. Kirkorian and R. J. Sneed, *J. Appl. Phys.*, **37**, 3674 (1966).
14. J. Harvey and H. Wilmon, *Acta Crystallogr.*, **14**, 1278 (1961).
15. K. Itoh and H. Sunami, *IEE Proc.*, **130**, 127 (1983).
16. A. Nakamura, T. Kawauchi, K. Urabe, M. Kitao, and S. Yamada, *J. Vac. Soc. Jpn.*, **24**, 471 (1981).
17. O. S. Heavens and S. D. Smith, *J. Opt. Soc. Am.*, **47**, 469 (1957).
18. C. A. Fenstermaker and F. L. McCrackin, *Surf. Sci.*, **16**, 85 (1969).
19. D. A. Vermilyea, *This Journal*, **110**, 250 (1963).
20. K. Huber, *ibid.*, **110**, 1236 (1963).
21. R. Andrew and U. Krasevec, *Philos. Mag.*, **31**, 1295 (1975).
22. J. R. Lloyd and S. Nakahara, *J. Vac. Sci. Technol.*, **14**, 655 (1977).
23. S. K. Sharma and J. Spitz, *Philos. Mag.*, **41**, 209 (1980).
24. S. K. Sharma and J. Spitz, *Thin Solid Films*, **67**, 109 (1980).

Characterization of Plasma Silicon Nitride Layers

W. A. P. Claassen, W. G. J. N. Valkenburg, F. H. P. M. Habraken,[1] and Y. Tamminga

Philips Research Laboratories, 5600 JA Eindhoven, The Netherlands

ABSTRACT

The authors have studied deposition of plasma silicon nitride layers as a function of gas-phase composition for the SiH_4-NH_3-x system, where x is N_2, Ar, or H_2. Most of the depositions were performed at 300°C and at an operating frequency of 50 kHz. The deposited layers were characterized with Anger electron spectroscopy in combination with ion-bombardment, Rutherford backscattering, and infrared spectroscopy. It is shown that the ratio of the amount of atomic hydrogen atoms bonded to silicon and nitrogen atoms is only a function of the silicon-nitrogen ratio of the deposited layers. It is further shown that the etch rate of plasma silicon nitride layers in buffered HF depends primarily on the silicon-nitrogen ratio and the density of the deposited material.

Silicon nitride layers prepared by plasma CVD can be used as final passivation for IC's because they act as barriers against the diffusion of impurity ions (1). Also, a PECVD (plasma-enhanced CVD) silicon nitride layer can be used as an insulator in double layer structures. The structural and electrical properties of plasma silicon nitride layers depend greatly on the consumption of the layers and, therefore, on the deposition conditions. Samuelson and Mar (2) measured the Si/N and the Si-H/N-H ratio for plasma silicon nitride layers deposited under different conditions, and concluded that the Si-H/N-H ratio is directly correlated to the refractive index of the deposited layer, whereas the Si/N ratio does not have a simple correlation with the refractive index. Chow *et al.* (3) compared plasma silicon nitride layers from different commercially available reactors and concluded that the etch rate of plasma nitride layers in buffered-HF solution (BHF) is a function of the total amount of hydrogen incorporated in the layer.

This paper reports on a study of the composition of plasma silicon nitride layers (Si/N ratio, Si-H/N-H ratio, total amount of hydrogen) as a function of the deposition conditions, and correlates these data with refractive index and etch-rate measurements in BHF.

Experimental

A low-pressure, radial-flow parallel-plate reactor operating at 50 kHz was used for the experiments. Experimental details can be found in the literature (4). Plasma silicon nitride layers were deposited onto silicon substrates at a temperature of 300°C, a total pressure of 3.3×10^{-4} bar, an RF power of 200W, and a total gas flow of about 1200 cm². Plasma silicon nitride layers with different compositions were grown by varying the flows of the input gases silane (SiH_4), ammonia (NH_3), and nitrogen (N_2). Layers were also grown with hydrogen (H_2) or argon (Ar) instead of nitrogen as diluent. The gas-phase composition was changed by varying the ratio of the input gases of NH_3 and x, where x is N_2, Ar, or H_2, while the $NH_3 + x$ flow was kept constant. To characterize the as-deposited layers, we used an ellipsometer for refractive index measurements ($\lambda = 632.8$ nm), Auger depth profiling, and Rutherford backscattering spectroscopy (RBS) for Si/N measurements, and infrared spectroscopy for [H] determination. A detailed description of these techniques can be found elsewhere (5, 6). Talystep measurements were made across an etched step to determine the thickness of the deposited layer. The density of the layers was calculated from the thickness of the deposited layer and the weight increase upon deposition. Etch rates in BHF (1:7) at room temperature were measured by timing the removal of the complete layer with known thickness (Talystep). The stress in the layers was measured and calculated from the curvature of the substrate.

[1] Present address: Lab. for Exp. Physics, University of Utrecht, P.O. Box 80.000, 3508 TA Utrecht, The Netherlands.

Key words: plasma, silicon nitride, characterization.

Experimental Results and Discussion

In Fig. 1 the refractive index (n) of plasma silicon nitride layers is plotted as a function of the gas-phase composition for layers deposited at 200W, at 300°C, and a total pressure of 3.3×10^{-4} bar. The refractive index of the deposited silicon nitride layers varies with the NH_3/N_2 ratio in the gas phase, particularly at the highest silane flow. As will be discussed below, a high refractive index indicates a nitrogen-poor layer. The variation with the NH_3/N_2 ratio is ascribed to the higher dissociation energy of N_2 compared to that of NH_3. With argon or hydrogen instead of nitrogen, the variation in refractive index is even larger.

Typical AES in-depth profiles, obtained by combining AES with sputter removal of the film by ion bombardment (2 keV, Ar^+), are given in the Fig. 2 and 3 for plasma silicon nitride layers with different thicknesses. Figure 2 shows the AES in-depth profile of a plasma silicon-nitride layer with a thickness of 60 nm as measured by ellipsometry. It can be seen that oxygen is present at the surface and at the interface between silicon and silicon nitride. At the surface silicon oxide is present with an equivalent thickness of about 1.0 nm. due to the fact that plasma silicon nitride lay-

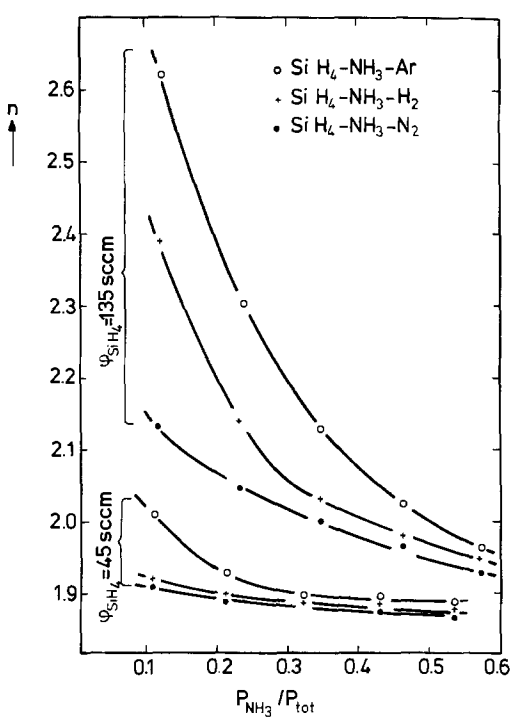

Fig. 1. The refractive index of plasma silicon nitride layers deposited at 300°C, a total pressure of 3.3×10^{-4} bar and an RF power of 200W, as a function of the NH_3 partial pressure for the SiH_4-NH_3-x system (x = Ar, N_2, H_2): $Q_{NH_3+x} = 1115$ cm².

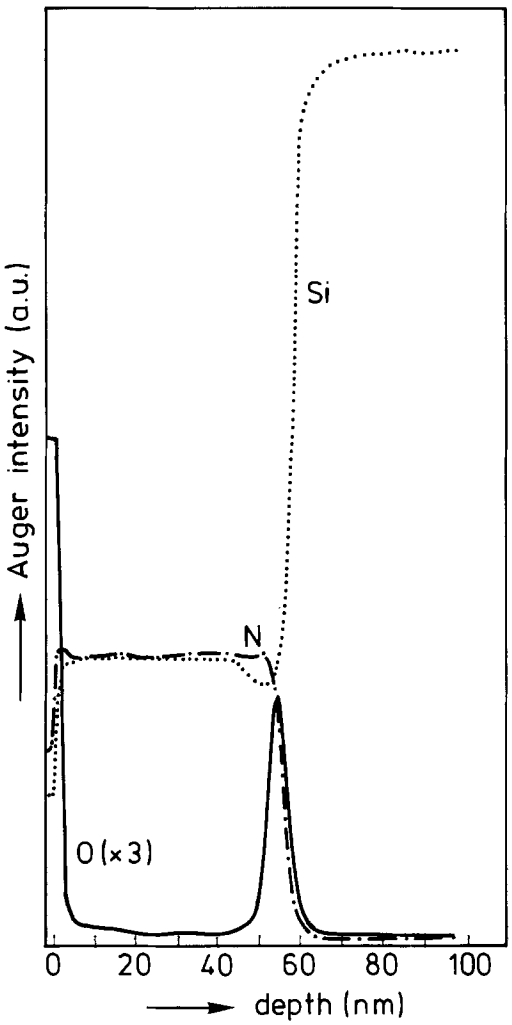

Fig. 2. An Auger in-depth profile of a 60 nm-thick plasma silicon nitride layer on a silicon substrate (sputter rate = 0.5 nm/min).

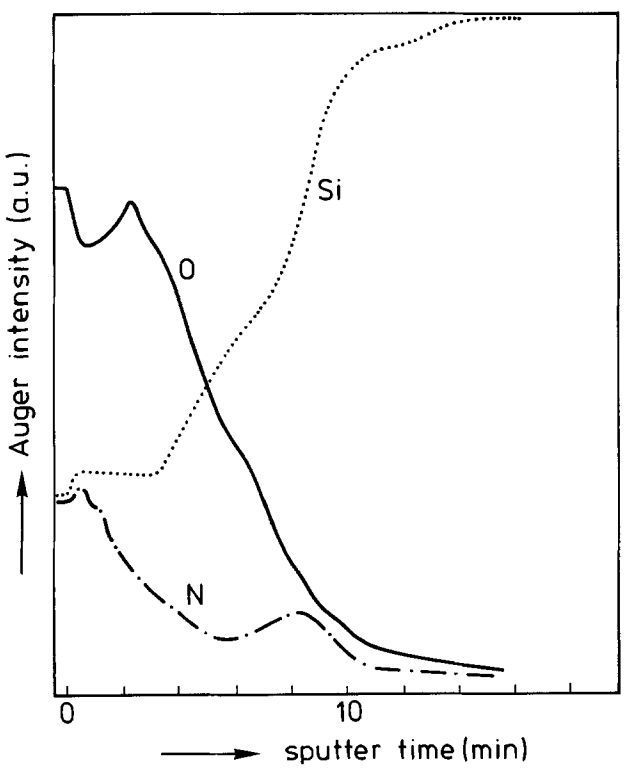

Fig. 3. Auger in-depth profile of a plasma nitride film grown in 0.1 min.

ers slightly oxidize when they are unloaded from the reactor. At the interface between silicon and silicon nitride an oxygen-containing layer of about 10 nm thickness is present, equivalent to ~1.5 nm SiO_2 and being the thickness of a native oxide layer at the silicon surface before plasma deposition (5). The width of the oxygen-containing region at the interface is between two and three times as large as measured under equal Ar-ion sputter conditions with LPCVD Si_3N_4 layers of comparable thickness. The widening of the oxygen pile-up at the interface is possibly due to ion bombardment in the early stage of plasma deposition. The oxygen content in the bulk of the silicon nitride is typically 0.5 atomic percent (a/o) (almost independent of the gas phase composition), indicating that the presence of oxygen in the bulk of the layer is due to the background pressure of oxygen or water vapor in the reactor. It can further be observed that the Si/N ratio in the bulk of the plasma silicon nitride layer is fairly constant in depth. Figure 3 gives the AES in-depth profile of a very thin plasma nitride layer (~1 nm) on top of a silicon substrate covered with a native oxide. The oxygen and nitrogen atoms are almost completely mixed in this sample. One can also see the presence of a nitrogen pile-up at the SiO_2/Si interface. An almost equal nitrogen profile was obtained when a thin thermal-oxide layer on top of a silicon substrate was exposed to NH_3 plasma at 300°C. We conclude that the native oxide is converted to an oxy-nitride after which the actual deposition starts. A significant smaller Si/N ratio was also found during the initial stages of deposition by RBS measurements of layers deposited at various deposition times (7). The native oxide can be removed by a fluorine-containing plasma prior to deposition (7). The layers deposited in the SiH_4-NH_3-Ar system also contain argon, ranging from 0.4 a/o for the lowest argon flux (440 sccm) to 1.5 a/o for the highest argon flux (980 sccm). For absolute Si/N ratio determination, the RBS technique (5) was used. In Fig. 4 Si/N ratios as measured by RBS are given as a function of the refractive index for plasma silicon nitride layers in the thickness range of 40-100 nm. The RBS data are corrected for the presence of SiO_2 in the layer. The refractive index values vary linearly with the composition of the layers and can be expressed in the experimental regime under discussion as

$$n = 0.70 \frac{\text{Si}}{\text{N}} + 1.39 \qquad [1]$$

The scatter in the experimental data is possibly due to small differences in densities of the deposited layers, as will be given below.

We see from Fig. 4 that a plasma silicon-nitride layer deposited at 300°C has a refractive index around 1.9

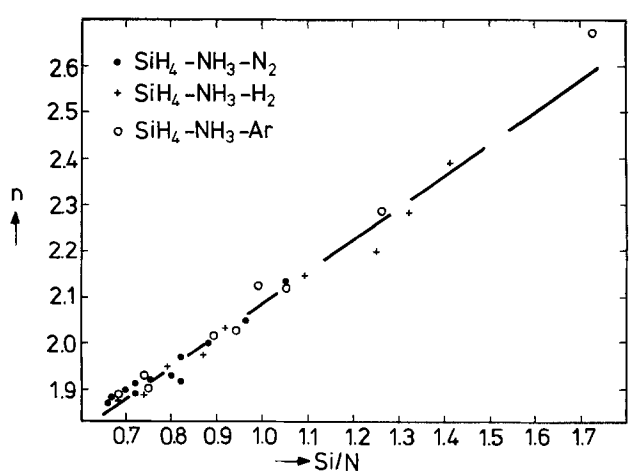

Fig. 4. The refractive index of plasma silicon nitride layers deposited at 300°C as a function of the Si/N ratio as measured by RBS.

for a Si/N ratio of 0.75, compared to a refractive index of 2.00 for a high temperature silicon nitride with the same Si/N ratio. This difference is due to the large amount of hydrogen atoms incorporated in the plasma nitride layers. The amount of hydrogen atoms incorporated in the layer can be calculated using a hydrogen profiling technique using a resonant nuclear reaction ($^1H[^{15}N, \alpha, \gamma]^{12}C$). Using this reaction, we observed that the concentration of hydrogen atoms is fairly constant in the bulk of the layer. Under these circumstances, infrared absorption spectroscopy can also be used in order to measure the amount of hydrogen in the layer, using the method described by Lanford and Rand (6). In Fig. 5 the concentration of hydrogen *vs.* the Si/N ratio of the plasma silicon nitride layers (layer thickness ~0.5 μm) is given for the three systems mentioned above. These data are calculated from the number of hydrogen bonds per cm^3, the Si/N ratio (by using refractive index measurements and the expression as given by Eq. [1]), the thickness of the layer (as measured by Talystep), and the density of the layer as given below. In a first approximation the concentration of hydrogen atoms is independent of the Si/N ratio of the nitride layers and of the gas system used, although there is some scatter in the data, notably in the SiH_4-NH_3-H_2 system. According to Chow *et al.* (3), who measured the concentration of atomic hydrogen via the ^{15}N-hydrogen profiling technique, the concentration of hydrogen atoms incorporated in the layer varies with deposition temperature. At a deposition temperature of 300°C they found 23.7% H for a SiH_4/NH_3 system, which is in good agreement with the data given in Fig. 5. We measured the hydrogen content of layers deposited at 300°C using a SiH_4-N_2 mixture. In the present system, only uniform layers, as far as thickness spread and refractive index are concerned, can be deposited at a deposition rate of 5 nm/min. Layers deposited under these circumstances contain about 11 a/o hydrogen. In conclusion, it can be said that the amount of hydrogen incorporated in the layer is determined in a first approximation by the deposition temperature if ammonia is present in the gas system.

In the regime investigated, the ratio of the ammonia flux and the silane flux was varied between 1 and 15. Without ammonia, silane is the only supplier of hydrogen, and the amount of hydrogen in the as-grown layer is much lower than with ammonia. As infrared absorption spectra exhibit peaks at 2180 cm^{-1} and 3340 cm^{-1}, which can be assigned to Si-H and N-H stretching modes, respectively, the number of Si-H and N-H bonds per cm^3 can be calculated from these spectra. Figure 6 gives the fraction of Si-H bonds as a function of the Si/N ratio of the plasma nitride layers for the gas systems given before. At high Si/N ratios almost all the hydrogen atoms are bonded to silicon. At Si/N ratios smaller than 0.75 the number of N-H bonds is larger than the number of Si-H bonds. In Fig. 7 the Si-H/N-H ratio *vs.* the refractive index is dotted. A linear relationship between u and the Si-H/N-H ratio was found which can be expressed under the present deposition conditions as

$$n = 0.059\ (\text{Si-H/N-H}) \text{ at } 1.88 \qquad [2]$$

A comparison of Fig. 4 and 6 (or the expressions as given by Eq. [1] and [2]) shows a linear relationship between the refractive index and the Si/N ratio, as well as with the Si-H/N-H ratio. Combination of the expressions as given by Eq. [1] and [2] leads to

$$\text{Si/N} = 0.084\ (\text{Si-H/N-H}) + 0.70 \qquad [3]$$

This empirical relation suggests that the Si-H/N-H

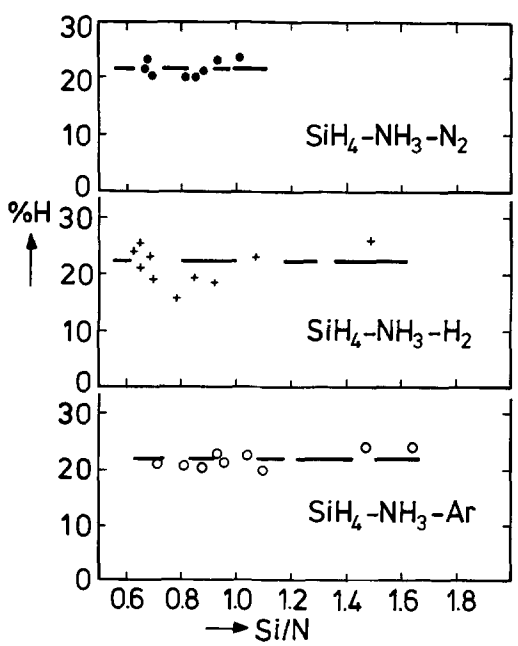

Fig. 5. The hydrogen content as a function of the Si/N ratio of the plasma silicon nitride layer.

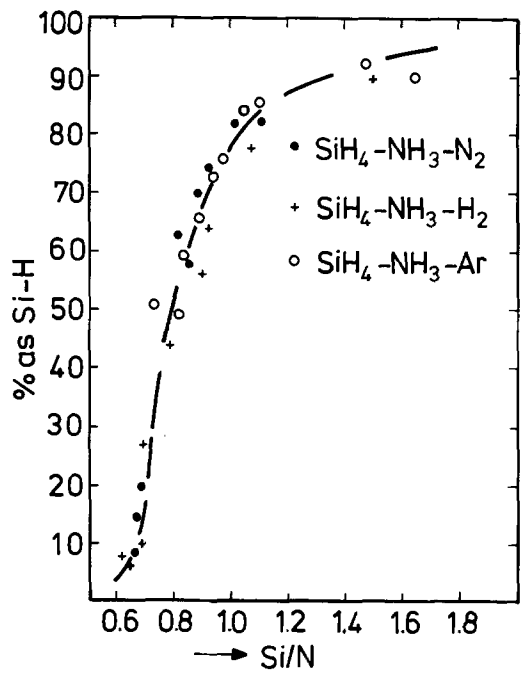

Fig. 6. The fraction of hydrogen atoms bonded to silicon atoms in plasma silicon nitride layers *vs.* Si/N.

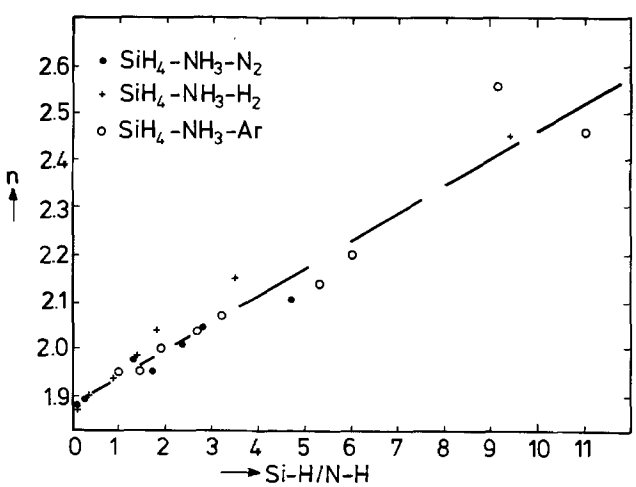

Fig. 7. Correlation between the refractive index and the Si-H/N-H ratio.

ratio is only a function of the Si/N ratio of the as-deposited layers. In order to prove this, we performed a series of deposition runs at 300°C, in the reactor described before and in a furnace-type parallel-plate reactor. In the radial-flow, parallel-plate reactor depositions were also performed at operating frequencies of 10 and 110 kHz, using SiH_4-NH_3-N_2 gas mixtures; and at 50 kHz using two SiH_4-N_2 gas mixtures. Some experiments were done in a home-built furnace-type parallel-plate reactor at operating frequencies of 400 kHz and 3 MHz at 300° and 500°C. The corresponding Si/N and Si-H/N-H values are plotted in Fig. 8, in which Eq. [3] is also depicted. It can be concluded that in a wide range of deposition conditions the expression as given by Eq. [3] is a good fit.

In Fig. 9 and 10, the etch rate (R) in BHF (1:7) at room temperature, and the density (ρ) of plasma silicon nitride layers are given, respectively, as a function of the Si/N ratio of the plasma silicon nitride layers. These figures give data for 135 sccm SiH_4 in NH_3/H_2, NH_3/N_2, and NH_3/Ar mixtures, and for 45 sccm SiH_4 in a NH_3/H_2 mixture. The data given in Fig. 8 and 9 are for ~0.5 μm-thick plasma silicon nitride layers, deposited under the deposition conditions given in Fig. 1. It can be observed that R in BHF is a function of the Si/N ratio and also of the gas phase composition. The

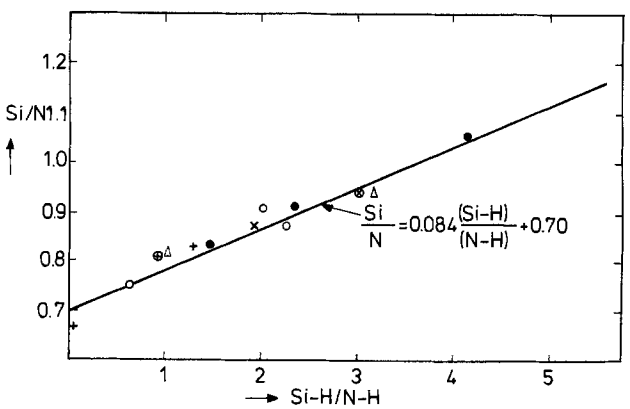

Fig. 8. Si/N ratio vs. Si-H/N-H ratio: ●, ○, △ radial flow reactor (●—10 kHz, ○—110 kHz, △—50 kHz [SiH_4-N_2]) parallel plate furnace reactor: +—400 kHz 300°, ⊕—400 kHz 500°C, ×—3 MHz 300°C, ⊗—3 MHz 500°C).

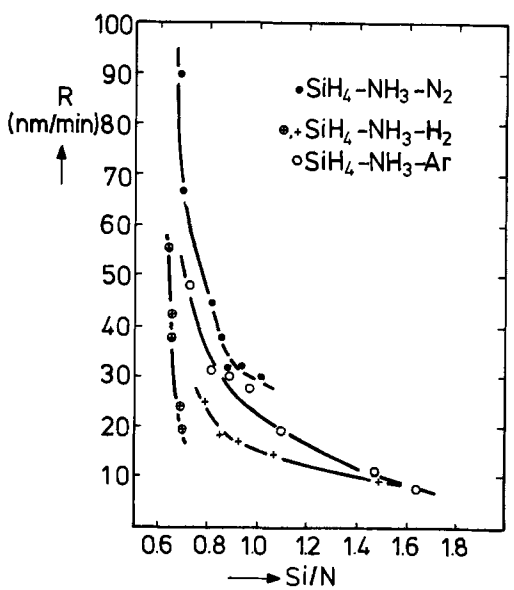

Fig. 9. The etch rate of plasma silicon nitride layers in BHF (1:7, *RT*) *vs.* Si/N for the SiH_4-NH_3-N_2, the SiH_4-NH_3-H_2, and the SiH_4-NH_3-Ar systems (●, +, ○ SiH_4 = 135 sccm, ⊕ SiH_4 = 45 sccm).

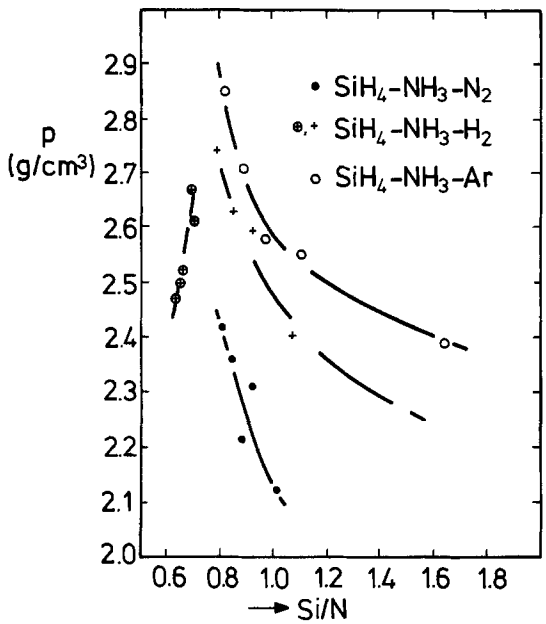

Fig. 10. The density of the deposited plasma silicon nitride layers deposited at 300°C as a function of the Si/N ratio (symbols as in Fig. 9).

general picture is that R increases with decreasing Si/N ratio, notably below Si/N = 0.75. The etch rates of layers deposited in the SiH_4-NH_3-N_2 system are higher than for layers deposited in the SiH_4-NH_3-Ar system and much higher than for layers deposited in the SiH_4-NH_3-H_2 system. It can further be observed that the experimental etch rates for the SiH_4-NH_3-H_2 system cannot be fitted by one curve: the input pressure of silane has an influence on the etch rate. The differences in etch rates between the four series as given in Fig. 9 can be correlated with the density and the deposition rate of the plasma silicon nitride layers. According to Fig. 10, the density of plasma silicon nitride layers increases with decreasing Si/N ratios up to Si/N = 0.75, whereas at lower Si/N ratios the opposite is the case. It can be seen that at Si/N ratios above 0.75 the density of the deposited plasma silicon nitride layer is higher when argon or hydrogen is used as a dilution gas. This is due to the relatively low deposition rate in argon and hydrogen. At high deposition rates layers are formed with a low density. They can be etched relatively fast. However, low deposition rates give a denser material and, therefore, a slower etch rate. According to Chow *et al.* (3), the etch rate of plasma silicon nitride layers in BHF is determined by the concentration of hydrogen atoms in the layers. We, therefore, combined the experimental data as given in Fig. 5 and 8, and plotted in Fig. 11 the etch rate in BHF *vs.* the amount of hydrogen incorporated in the layers. It should be noted that all these layers were deposited at 300°C. From Fig. 11 we concluded that there is no simple relationship between the etch rate in BHF and the concentration of hydrogen atoms in the layer. We note that the vertical variation in the etch rate is due to a variation in the Si/N ratio of the layers under investigation. The conclusion can therefore be drawn that the etch rate of plasma silicon nitride layers depends both on the Si/N ratio and the density of the deposited layer. The stress in ~0.5 μm-thick plasma nitride layers on monocrystalline silicon deposited under the experimental conditions given above was measured and calculated from the curvature of the substrate. Layers deposited in the SiH_4-NH_3-Ar system and the SiH_4-NH_3-H_2 system have a compressive stress somewhat higher than layers deposited in the SiH_4-NH_3-N_2 system (4-6 × 10^8 N/m^2 for H_2 and Ar, and 2-4 × 10^8 N/m^2 for N_2). These differences can also be explained by the differences in deposition rate or the density of deposited material.

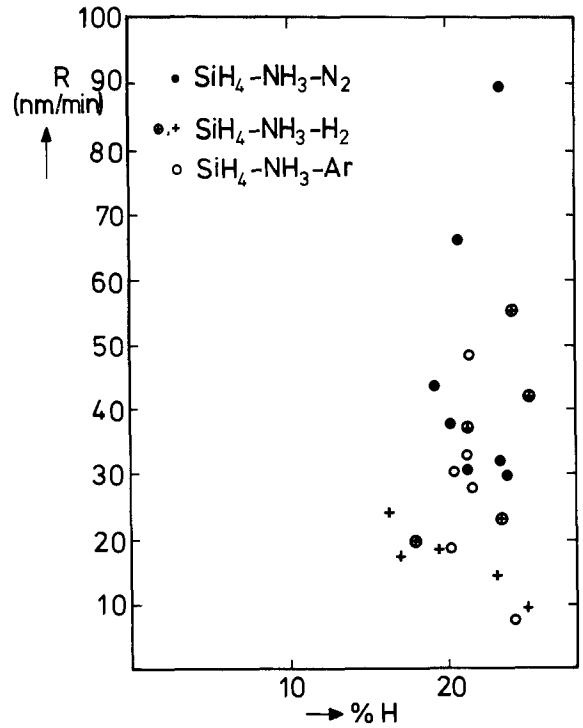

Fig. 11. The etch rate of plasma silicon nitride layers in BHF (1:7, RT) vs. the hydrogen concentration in the layers (symbols as in Fig. 9).

Conclusion

Our study of the composition of plasma silicon nitride layers deposited at 300°C under different deposition conditions shows that the silicon nitrogen ratio of the plasma silicon nitride layers strongly depends on gas-phase composition. AES depth profiles of silicon nitride layers on monocrystalline silicon show the presence of oxygen at the interface between silicon and silicon nitride and at the surface. Using RBS, we measured Si/N ratios between 0.6 and 1.7 in the experimental range investigated, and it was shown that in this regime the refractive index varies linearly with the Si/N ratio of the plasma silicon nitride layers. The total amount of hydrogen bonded to silicon and nitrogen is about 2×10^{22} (cm^{-3}) or ~20 a/o, almost independent of the gas-phase composition as measured by infrared absorption spectroscopy. It is further shown that the Si-H/N-H ratio is also linearly correlated with the refractive index. The Si-H/N-H ratio appeared to be only a function of the Si/N ratio of the as-deposited layer for a large variety of deposition conditions.

The etch rate of plasma silicon nitride deposited at 300°C in BHF depends on the Si/N ratio and the density of the plasma silicon nitride layers.

Acknowledgment

The authors wish to thank M. Willemsen for the RBS measurements and Professor J. Bloem and Dr. A. E. T. Kuiper for valuable discussions.

Manuscript submitted Jan. 17, 1983; revised manuscript received July 11, 1983.

Philips Research Laboratories assisted in meeting the publication costs of this article.

REFERENCES

1. A. K. Sinha, H. J. Levinstein, T. E. Smith, G. Quintana, and S. E. Haszko, *This Journal*, **125**, 601 (1978).
2. G. M. Samuelson and K. M. Mar, *ibid.*, **129**, 1773 (1982).
3. R. Chow, W. A. Lanford, W. Ke-Ming, and R. S. Rosler, *J. Appl. Phys.*, **53**, 5630 (1982).
4. R. S. Rosler, W. C. Benzing, and J. Baldo, *Solid State Technol.*, **19**, 45 (1976).
5. F. H. P. M. Habraken, A. E. T. Kuiper, A. v. Oostrom, Y. Tamminga, and J. B. Theeten, *J. Appl. Phys.*, **53**, 404 (1982).
6. W. A. Lanford and M. J. Rand, *ibid.*, **49**, 2472 (1978).
7. W. A. P. Claassen, W. G. J. N. Valkenbrug, A. E. T. Kuiper, and Y. Tamminga, in "Proceedings of the Fourth European Conference on Chemical Vapour Deposition," Eindhoven, The Netherlands, May 31-June 2, 1983.

The Structural and Compositional Characterization of Bismuth Sulfide Films Grown by Cathodic Deposition

Andrzej S. Baranski,* W. Ronald Fawcett,* and Claude M. Gilbert*

Guelph-Waterloo Centre for Graduate Work in Chemistry, Department of Chemistry, University of Guelph, Guelph, Ontario, Canada N1G 2W1

ABSTRACT

The structure and composition of Bi_2S_3 films grown by cathodic electrodeposition from a diethylene glycol solution containing $BiCl_3$, NH_4Cl, and elemental sulfur have been studied. Elemental analysis showed that the films contain 6 atomic percent (a/o) of chloride ion as an impurity. On the basis of x-ray analysis, it was found that the films are amorphous when grown below 100°C, and crystalline when grown above 100°C. The crystalline material had an orthorhombic structure and was highly oriented. Electron micrographs show that the deposit is very uniform and free from cracks. The amorphous material which is photosensitive was tested in a photoelectrochemical cell to determine its efficiency in converting light to electrical energy.

A variety of techniques for electrodepositing metal chalcogenides have been described in the literature (1-7), including anodic oxidation of the parent metal in an aqueous solution containing the chalcogenides ion (1-3), coreduction of the appropriate metal ion and an oxyanion containing the chalcogen in a higher oxidation state (4, 5), and coreduction of the metal ion and elemental chalcogen in a nonaqueous medium in which the latter is soluble (6, 7). The last technique can be used to deposit a variety of metal chalcogenides (6) but has been developed chiefly with respect to CdS (7, 8) and CdSe (9).

Bismuth sulfide (Bi_2S_3) is an n-type semiconductor which has received relatively little attention as a potential component in solar energy conversion devices in spite of the fact that it has a nearly ideal bandgap (1.3 eV). Two previous studies relating to the electro-

* Electrochemical Society Active Member.

deposition of this material have appeared in the literature (1, 3). Miller and Heller (1) reported the anodic formation of Bi_2S_3 on Bi and demonstrated the n-type behavior of the resulting film in a photoelectrochemical cell (PEC). Peter (3) studied Bi_2S_3 films grown in the same way and showed that this material exhibited a photocurrent quantum yield close to unity over a wide spectral range. He also showed that the electrodeposited material had two transitions on interaction with light, an indirect one at 1.25 eV, and a direct one at 1.7 eV. The latter is particularly interesting since satisfactory adsorption of visible light via a direct transition can be obtained with films a few microns in thickness. In a preliminary study (6), it was demonstrated that Bi_2S_3 could also be deposited cathodically from a dimethylsulfoxide (DMSO) solution containing $BiCl_3$, and elemental sulfur; these films also had an n-type semiconductor behavior under illumination in a PEC. The purpose of the present study was to determine the conditions for cathodic deposition of Bi_2S_3 in more detail, and to determine the composition and structure of the resulting films.

Experimental

The cell used for the electrodeposition was similar to that described earlier (7). The Bi_2S_3 films were most often deposited on high purity platinum foil with an exposed area of 1.3 cm^2; other substrates used were high purity molybdenum foil, high purity nickel foil, and platinum sputtered on glass. The counterelectrode was graphite and the electrolysis was carried out without a reference electrode. The electrolyte solution contained 0.032M $BiCl_3$, 8×10^{-4}M S_8 (6.4×10^{-3} g-atom S), and 0.93M NH_4Cl, and the solvent was reagent grade diethylene glycol (DEG). During electrolysis, the solution was held in a hot oil bath whose temperature was controlled. Unless stated otherwise, deposition was carried out with a constant current of 2.0 mA cm^{-2}. The solution was stirred continuously at the same time. The Pt substrate was prepared by cleaning it in concentrated nitric acid, rinsing with distilled water, and finally heating it in a flame until the metal was "red hot." The Mo foil was etched in a mixture of concentrated HCl and 30% H_2O_2, and rinsed with distilled water followed by acetone. The Ni foil was etched in concentrated sulfuric acid, washed with distilled water, and then dried. After the deposit had been formed on the substrate, the electrode was removed immediately from the solution and rinsed with acetone.

The structural properties of the films were investigated using scanning electron microscopy (SEM) and x-ray diffraction with a cobalt target as described earlier (7).

Compositional analysis was performed on large area samples (5-8 cm^2) grown on a Mo substrate for $\sim$ 20 hr. The deposit was removed from the substrate, washed with acetone to remove residual DEG, and dried; 0.05g of deposit was dissolved in concentrated HNO_3, and the resulting solution diluted with distilled water to obtain a final solution with an acid concentration of 0.5M. The concentrations of Bi (III) and Cl^- in this solution were determined by normal pulse polarography. Determination of sulfur was based on a procedure described by Vogel (10). A known weight of deposit was oxidized using concentrated HNO_3 in the presence of a 2:3 volume ratio mixture of Br_2 and CCl_4 in order to convert the sulfide ions to sulfate. The bismuth ion was removed by precipitating it as $Bi(OH)_3$ then, sulfate was precipitated as $BaSO_4$ and determined gravimetrically. The reliability of procedure was established using pure commercial Bi_2S_3.

The role of the supporting electrolyte in determining film properties was estimated by using NaCl and KCl instead of NH_4Cl. The concentration of Na^+ or K^+ in the 0.5M HNO_3 solution referred to above was determined by flame emission using a Perkin Elmer atomic adsorption spectrophotometer (Model 2380).

The conductivity of the Bi_2S_3 films was determined by first removing them from the substrate, making ohmic contacts using indium-gallium alloy, and finally measuring the resistance between these contacts. The technique for removing the films involved pressing the exposed face of the deposit on epoxy glue spread on a glass slide, being certain to avoid air bubbles between the glue and the deposit. After the glue had set, the metal backing was peeled off, with the electrodeposited material remaining on the surface of the epoxy glue. The thickness of the samples was estimated using SEM.

The performance of the semiconducting film was also evaluated in a photoelectrochemical cell (PEC). The electrolyte solution contained 1M Na_2S, 0.125M S_8, and 1M NaOH in water; the counter and reference electrodes were both graphite. The Bi_2S_3 film was illuminated with a 600W tungsten lamp, and at the same time, the photocurrent was recorded while the potential across the cell was varied. The cell was designed so that absorption of light by the solution would be minimized.

Results and Discussion

Examination of films deposited at different temperatures revealed that two types of films were formed. Below 98°C, the deposit was glossy and metallic blue in color with a mirror-like surface. Samples grown above 102°C were darker and nonglossy. The two types had exactly the same chemical composition corresponding to 38 atomic percent (a/o) Bi, 55 a/o S, 6 a/o Cl, and 0.6 a/o M, where M^+ is NH_4^+, Na^+, or K^+, indicating that a significant amount of chloride anion is incorporated in this material. The efficiency of the process with respect to bismuth content in the resulting films assuming the overall electrode process

$$2Bi^{+3} + \frac{3}{8}S_8 + 6e \rightarrow Bi_2S_3 \qquad [1]$$

was 90% with a fresh electrolyte solution; the efficiency decreased somewhat with use of the electrodeposition solution. The efficiency for Bi_2S_3 formation is greater than that observed earlier for CdS (7); this result may reflect the use of DEG as solvent instead of DMSO. The decrease in efficiency with the amount of Bi_2S_3 deposited from a given solution can be attributed to a corresponding decrease in Bi(III) and S_8 concentrations and increase in the concentrations of products of side reactions which also can react at the cathode. The source of Cl^- ion in the film was determined by replacing the NH_4Cl used as electrolyte by a perchlorate salt. The elemental analysis of the resulting films was exactly the same as above, suggesting that the source of Cl^- ion in the film is complex ions in which Cl^- is complexed to Bi(III), the source of Cl^- ion in solution being $BiCl_3$ itself.

X-ray structural analysis of the electrodeposited films revealed that those deposited at temperatures below 98°C were amorphous, the diffractograms of samples with thicknesses between 1 and 3 μm being featureless between $2\theta = 2°$ and 100°. On the other hand, films grown above 102°C were strongly oriented with an orthorhombic crystal structure (Fig. 1). The diffractogram of a sample deposited to a thickness of 30 μm on sputtered Pt showed a very large peak at $2\theta = 53.7°$ corresponding to an interplanar distance of 0.198 nm. According to the literature (11), the (002) planes of bismuth sulfide are separated by a distance of 0.199 nm, so that it is probable that reflections from this plane give rise to the large peak. However, this reflection is not one of the most intense for randomly oriented polycrystalline Bi_2S_3. In this case, intense lines are observed for reflections from the (230) and (211) planes ($d = 0.312$ nm), and from the (130) ($d = 0.357$ nm) and (310) planes ($d = 0.353$ nm) (11). In addition, the

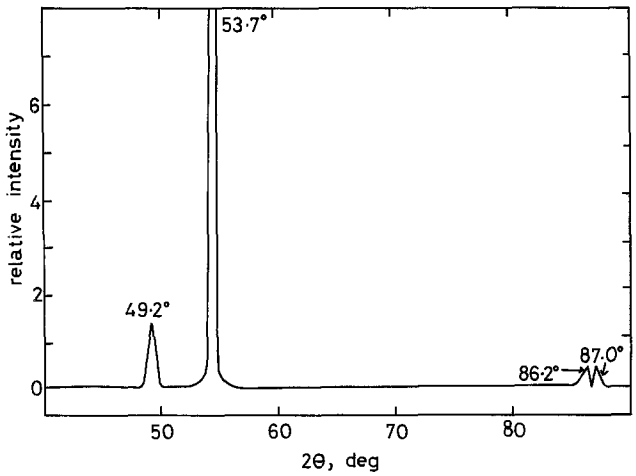

Fig. 1. X-ray diffractogram of a Bi_2S_3 deposit grown at 110°C on Pt sputtered on gloss with a current density of 2.0 mA cm^{-2} for 18,000 sec (thickness ~30 μm) using a cobalt $K_{\alpha 1}$ line, λ = 0.178890 nm.

intensity of the reflection from the (002) planes is only 18% of that from the (130) planes. This difference suggests that the structure of the electrodeposited material is very different from that of the randomly oriented material.

From the work of Black *et al.* (12), orthorhombic crystals of Bi_2S_3 [space group = D_{2h}^{16} (Pbnm)] have four formulas per unit cell, each bismuth atom having three nearest neighbor sulfur atoms at a distance approximately equal to the sum of the covalent radii. Beyond these atoms, there are three or four additional neighbors at not much larger distances. This gives a unit cell with dimensions a = 1.113 nm, b = 1.127 nm, and c = 0.397 nm (12). The crystal can be considered to be composed of puckered sheets of stoichiometric composition running parallel to the c-axis (perpendicular to the interface), with the same angle in the [010] direction. The binding between these sheets is considerably weaker than that among atoms in a sheet. This suggested to Black *et al.* (12) that cleavage would take place on (010) planes and crystal growth in the [001] direction, that is, perpendicular to the substrate surface in the present case. The present x-ray data confirm that crystal growth occurs in the [001] direction. The fact that the peak corresponding to reflection from the (002) planes is so strong suggests that the sheets described above are perfectly parallel to one another and separated by 0.198 nm. The orientation of the Bi_2S_3 films is similar to that observed earlier for CdS grown by a similar technique (7); however, Bi_2S_3 is characterized by a layered structure with strong bonding in two dimensions whereas CdS is characterized by a structure with three dimensional bonding.

It was also observed that the strongly oriented crystalline form of Bi_2S_3 is not present in very thin films grown at higher temperatures. Films grown from various chloride solutions at 110°C appeared to be amorphous for deposition up to 600 sec at a current density of 2 mA cm^{-2} (thickness <1 μm), being glassy and blue in color. In addition, these films were photosensitive whereas those grown for longer periods at 110°C were not. The crystalline form develops slowly after this initial period. At first, the crystalline material was not strongly oriented. For example, a sample grown in DEG solution with NH_4Cl as supporting electrolyte for 800 sec had an x-ray diffractogram composed of three small peaks of equal intensity with interplanar distances equal to 0.343, 0.302, and 0.196 nm corresponding to reflections from the (310), (230) or (211), and (002) planes, respectively. The strong orientation described above was reached only after deposition for a longer time. Experiments on Ni and Mo substrates confirmed that the structural properties of the deposits were independent of the nature of the substrate.

The above experiments demonstrate that one may deposit crystalline Bi_2S_3 on the amorphous form; however, it was not possible to do the reverse. For example, in an additional experiment, an amorphous film was deposited at 100°C for 1800 sec and then the temperature of the bath was rapidly increased to 95°C without interrupting the deposition. Deposition at the lower temperature was continued for a further 4.5 hr. Examination of this sample by x-ray diffraction revealed a very high peak at 2θ = 54° similar to that found for a sample grown at a constant high temperature. These observations suggest that once the crystalline form is nucleated, further growth involves deposition of new crystalline material. Apparently, nuclei of crystalline Bi_2S_3 do not form below 98°C during the time scale of the present experiments.

The structural differences between the amorphous and crystalline forms can also be discerned by SEM. Micrographs of two thick samples (~30 μm) grown at 90° and 110°C for 5 hr on sputtered Pt are shown in Fig. 2. The sample grown at the lower temperature appears similar to ordinary glass, especially when viewed along a fissure produced by bending or scratching the deposit. The deposit is completely uniform in depth and the surface is quite smooth except for a few protuberances of spherical shape and low height. A very different structure is apparent for the sample grown at the higher temperature. The glassy appearance characteristic of the amorphous sample is not seen but instead, the surface is slightly rough with a structure characteristic of a collection of crystallites which have grown to different thicknesses. The crystallites appeared to have diameters of the order of 1 and 2 μm. The thickness of the sample is very uniform and no cracks were apparent as was the case for CdS samples grown from DMSO solutions (7).

Micrographs of Bi_2S_3 films grown on Mo and Ni foils are shown in Fig. 3 and 4. The characteristics of these deposits are qualitatively similar to those grown on sputtered Pt with some differences in the appearance of the surfaces. In the case of the amorphous films grown at 90°C, those on Mo foil had many more surface features than those on Pt or Ni; specifically, a larger number of spherical protuberances were apparent on these samples. Although the number of protuberances could be reduced by not etching the Mo substrate, it was clear that Bi_2S_3 films grown on this substrate were always rougher than those on Pt or Ni. Furthermore, the crystalline sample grown on Ni is somewhat rougher than that grown on Mo, and the nonuniform growth of the crystallites appears to have created pores in some areas. This result is probably a reflection of the fact that the film on Ni is thicker, having been grown for a longer time. The differences ob-

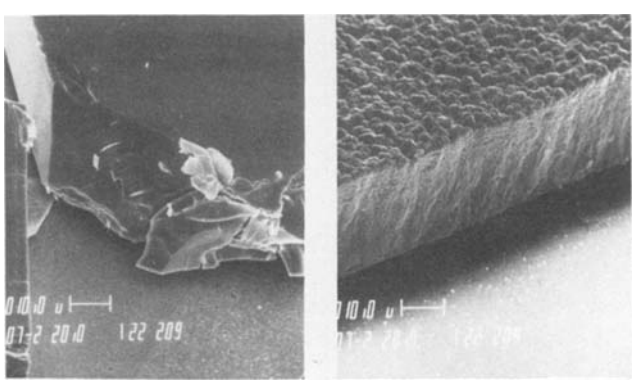

Fig. 2. Electron micrographs of Bi_2S_3 grown on sputtered Pt at 90° (a, left) and 110°C (b, right) with a current density of 2.0 mA cm^{-2} for 18,000 sec (thickness ~30 μm). Magnification is 700×; tilt = 45°.

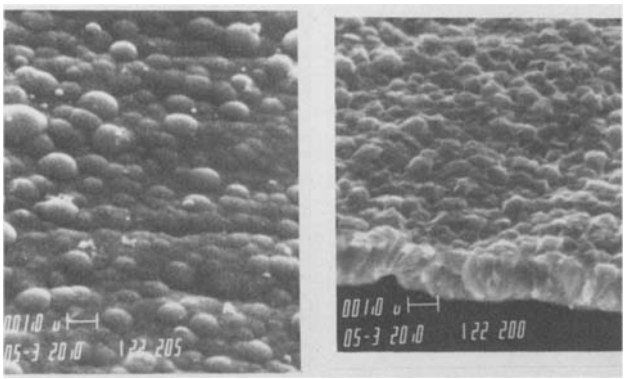

Fig. 3. Electron micrographs of Bi_2S_3 grown on etched Mo foil at 90° (a, left) and 110°C (b, right) with a current density of 2.0 mA cm^{-2} for 1500 sec (thickness ~1.5 μm). Magnification is 5000×; tilt = 45°.

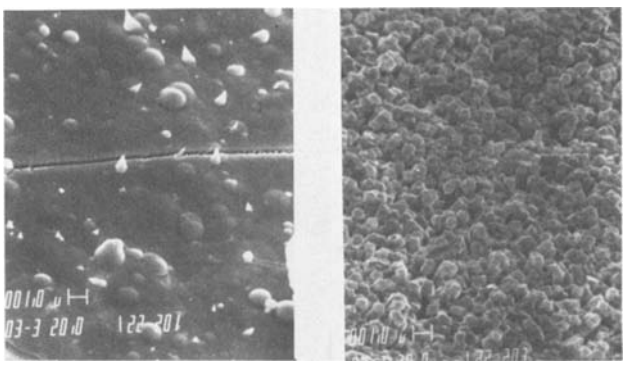

Fig. 4. Electron micrographs of Bi_2S_3 grown on etched Ni foil at 90° (a, left) and 110°C (b, right) with a current density of 2.0 mA cm^{-2} for 3600 sec (thickness ~2.0 μm), magnification is 3000×; tilt = 45°.

served in samples grown on these substrates are undoubtedly due to the varying roughnesses of the substrates and the resulting different rates of nucleation for crystalline samples. The role of substrate roughness in determining the nature and number of protuberances on amorphous samples is not clear but it could be related to nonuniformity of the current density at a rough surface.

The resistivity of the deposit determined from films stripped from Ni substrates was the same for both amorphous and crystalline samples and equal to (1.0 ± 0.2) × 10^{-3} Ωcm. Thus, the Bi_2S_3 material has a conductivity approaching that of metals. As a result, films of considerable thickness and uniformity can be obtained by electrodeposition. It is probable that the high Cl^- ion content of the film contributes significantly to the conductivity, and that the semiconductor is degenerate as a result.

Tests of the films as photoanodes in a PEC revealed that only the amorphous material was photosensitive. The photocurrent against photovoltage curve obtained in a polysulfide electrolyte is shown in Fig. 5. The open-circuit voltage obtained with this sample is some what less than that reported by Miller and Heller (1) for Bi_2S_3 films grown anodically on Bi (0.32V), and by Battacharya and Pramanik (13) for chemically deposited films (0.39V). This result probably reflects the degenerate nature of the Bi_2S_3 material. The power efficiency was estimated using the relationship

$$\eta = \frac{fI_{sc}V_{oc}}{P_o} \qquad [2]$$

where f is the fill factor, I_{sc}, the short-circuit circuit, V_{oc}, the open-circuit voltage, and P_o, the incident light intensity. In the present case, using an estimated fill factor of 0.38, $\eta = 2 \times 10^{-4}$; this efficiency is considerably less than that obtained with the chemically deposited material (1.2×10^{-3}) (13). A significant dark current was also obtained with the electrodeposited material (Fig. 5). Undoubtedly, the poor performance of these films in the PEC is due to the high concentration of chloride ion impurities.

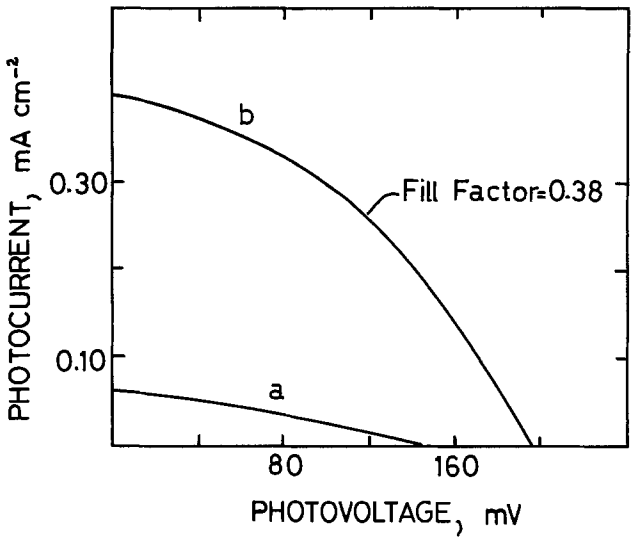

Fig. 5. Current against voltage curve for a PEC with the configuration Pt/Bi_2S_3/1.0M Na_2S, 1.0M S, and 1.0M NaOH in H_2O/C (a) without illumination and (b) illuminated with a tungsten lamp (1700W m^{-2}). The Bi_2S_3 film was grown at 85°C with a current density of 2.0 mA cm^{-2} for 600 sec (thickness ~1 μm).

In conclusion, the present electrodeposition technique produces very uniform Bi_2S_3 deposits with either an amorphous or oriented crystalline structure. Although the amorphous material is photosensitive, its properties do not lead to an efficient conversion of light to electrical energy in a PEC. It is highly probable that the electrical characteristics of the material would improve significantly if chloride impurities in the deposit could be avoided. This would necessitate finding a soluble form of Bi(III) in DEG which is not complexed with Cl^-. In this regard, preliminary experiments have shown that Bi_2S_3 films can be grown from DEG solutions containing the perchlorate salt. Studies are also underway to determine the mechanism of film formation. This work should help to elucidate the means by which anionic impurities are incorporated, and to optimize electrolyte bath composition so that films of high quality with respect to both structural and electrical properties can be grown. The results of this work will be discussed in future papers.

Acknowledgments

The financial support of the Natural Sciences and Engineering Research Council, Canada (NSERC, Strategic Energy Programme) and of the Technology Development Corporation, Canada, through operating grants is gratefully acknowledged. C. M. Gilbert also acknowledges the receipt of a NSERC graduate student scholarship as well as a Quebec-Ontario scholarship from le fonds F.C.A.C. pour l'aide et le soutien à la recherche (Quebec, Canada).

Manuscript submitted March 4, 1983; revised manuscript received July 25, 1983.

REFERENCES

1. B. Miller and A. Heller, *Nature*, **262**, 680 (1976).
2. L. M. Peter, *Electrochim. Acta*, **23**, 165 (1978).
3. L. M. Peter, *J. Electroanal. Chem.*, **98**, 49 (1979).
4. G. Hodes, J. Manassen, and D. Cahan, *Nature*, **261**, 403 (1976).
5. M. P. R. Panicker, M. Knaster, and F. A. Kroger, *This Journal*, **125**, 566 (1978).
6. A. S. Baranski and W. R. Fawcett, *ibid.*, **127**, 766 (1980).

7. A. S. Baranski, W. R. Fawcett, A. C. McDonald, R. M. de Nobriga, and J. R. MacDonald, *ibid.*, **128**, 963 (1981).
8. A. S. Baranski, W. R. Fawcett, and A. C. McDonald, *J. Electroanal. Chem.*, In press.
9. A. S. Baranski, W. R. Fawcett, K. Gatner, A. C. McDonald, J. R. MacDonald, and M. Selen, *This Journal*, **130**, 579 (1983).
10. A. I. Vogel, "Textbook of Quantitative Inorganic Analysis," p. 466, Longmans, London (1961).
11. H. E. Swanson, H. F. McMurdie, M. C. Morris, and E. H. Evans, "Standard X-Ray Diffraction Powder Patterns," Monograph 25, Section 5, p. 13, National Bureau of Standards (U.S.) (1967).
12. J. Black, E. M. Conwell, L. Seigle, and C. W. Spenser, *J. Phys. Chem. Solids*, **2**, 240 (1957).
13. R. N. Bhattacharya and P. Pramanik, *This Journal*, **129**, 332 (1982).

Chemical Etching Characteristics of (001)GaAs

Sadao Adachi and Kunishige Oe

Nippon Telegraph and Telephone Public Corporation, Musashino Electrical Communication Laboratory, Musashino-shi, Tokyo 180, Japan

ABSTRACT

The chemical etching characteristics of (001)GaAs are studied through an SiO_2 (or AZ-1350J photoresist) mask in the solutions of various etching systems: *(i)* HCl, *(ii)* HNO_3, *(iii)* $HCl:HNO_3$, *(iv)* HBr, *(v)* H_3PO_4, *(vi)* H_2SO_4, *(vii)* HF, *(viii)* $Br_2:CH_3OH$, *(ix)* NaOCl, and *(x)* alkaline system. The etching profiles are examined by cleaving the wafer in orthogonal directions along the (110) and ($\bar{1}$10) planes. Various etching profiles, such as ordinary-mesa shaped, reverse-mesa shaped structures, and nearly vertical walls, are formed by stripes being etched on the (001) planes. The indexes of the etch-revealed planes are identified by making a comparison with the calculated angle between the (001) surface and etch-side planes. The utility of these etching solutions is also discussed in detail for a variety of GaAs device applications.

Chemical polishing and etching of semiconductors play an essential role in electron device technology and are, therefore, widely employed in the fabrication of many device systems. Chemical etching is used for removing the damage layer of material close to the surface, for producing a high-purity shiny flat surface, and for shaping semiconductor devices, as well as for characterizing structural and compositional features. The electrical and optical properties of semiconductors strongly depend on the dislocation structure in these materials. Certain chemical etchants provide the effect of producing surface features on the semiconductor which can be related to the defects in the crystal. This is essentially true of dislocations, which often form etch pits at their points of intersection with a surface, thus providing a simple way of estimating dislocation densities. A great many techniques have also been described to stain or delineate electrical (pn-junctions) or material interfaces (heterojunctions) of semiconductors by means of chemical etching. Reviews have been published describing some of them (1).

Of the compound semiconductors, GaAs is of great interest because of recent requirements of high-speed transistors, and light sources and detectors for optical fiber communication. From an aspect of device technology, important factors determining the choice of an etchant are in general the etching rate for the material in question (in this case for GaAs), the degree of surface quality and undercutting, the solution chemical aggressiveness toward photoresist masks, and the desired etching profile for the relevant purpose. The most commonly used etchants are various compositions of $Br_2:CH_3OH$, $H_2SO_4:H_2O_2:H_2O$, $NaOH:H_2O_2:H_2O$, and $NH_4OH:H_2O_2:H_2O$ mixtures. Tarui *et al.* (2) have reported preferential etching characteristics of GaAs in the $Br_2:CH_3OH$ system and have discussed a few examples of practical applications of preferential etching for the device-structure design and fabrication (Gunn-effect devices, field-effect devices, and luminescent devices). Selective etching of GaAs in the $H_2SO_4:H_2O_2:H_2O$ system has been studied in detail (3, 4). The etching solutions, $NH_4OH:H_2O_2:H_2O$ (5) and $H_3PO_4:H_2O_2:H_2O$ (6) have also been developed for use in preferential etching of GaAs and the utility of these solutions has been discussed by their application to the fabrication of field effect and bipolar transistors. However, there have been a few reports on device shaping for GaAs by preferential etching. This is a motivation of the present work.

In the present paper, we report the preferential etching characteristics of the (001) surface of GaAs in the solutions of various systems: (*i*) HCl, (*ii*) HNO_3, (*iii*) $HCl:HNO_3$, (*iv*) HBr, (*v*) H_3PO_4, (*vi*) H_2SO_4, (*vii*) HF, (*viii*) $Br_2:CH_3OH$, (*ix*) NaOCl, and (*x*) alkaline system. The etching profiles are examined by cleaving the (001)GaAs wafer in orthogonal directions along the (110) and ($\bar{1}$10) planes and are discussed in detail from a crystallographic aspect. The profiles applicable to device-structure design and fabrication are also discussed in detail.

Key words: GaAs, chemical etching, etching profile.

Experimental

Sample.—The GaAs single crystals employed were Si-doped, n-type with carrier densities in the region of 10^{18} cm^{-3}. All wafers used were of (001) surface orientation with an uncertainty of 1° or less. After being mirror-like finished, degreased, and rinsed in deionized water, they were chemically etched in a $H_2SO_4:H_2O_2:H_2O = 3:1:1$ solution for 30 sec at 80°C. The thickness of these wafers was about 100 μm to permit cleavage for the observation of etching profiles.

Masking pattern.—Etching studies were performed for the etching-selected regions of (001) surface GaAs through windows in an SiO_2 mask (see Fig. 1). The SiO_2 masks used were approximately 2000Å thick and were prepared with conventional sputtering equipment. The desired geometries, in this case the window width of 28 μm wide, were defined by standard photolithography technique using AZ-1350J and an SiO_2 etchant of the $HF:NH_4F:H_2O$ system. Only the HF system, studied in the present work, dissolves the SiO_2 masking pattern. Thus, for this case we used AZ-1350J as a mask of the preferential etching study.

Etching solution.—The etching solutions employed can be classified, for convenience, into the following ten groups: (*i*) HCl system ($HCl:CH_3COOH:H_2O_2$, $HCl:H_3PO_4:H_2O_2$, etc.) (*ii*) HNO_3 system ($HNO_3:H_2O_2$, $HNO_3:CH_3COOH$, etc.), (*iii*) $HCl:HNO_3$ system ($HCl:HNO_3$, $(HCl:HNO_3):H_2O$, etc.), (*iv*) HBr system ($HBr:HNO_3$, $HBr:HNO_3:H_2O$, etc.), (*v*) H_3PO_4 system

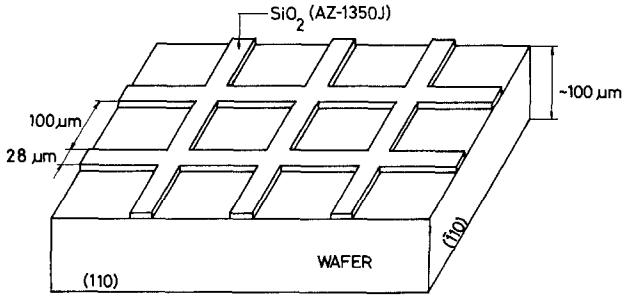

Fig. 1. An SiO_2 (or AZ-1350J) masking pattern on (001)GaAs wafer for chemical etching. The etching profiles are obtained by cleaving the wafer in orthogonal directions along the (110) and (1̄10) planes.

(H_3PO_4:H_2O_2:H_2O, H_3PO_4:CH_3COOH:H_2O_2, etc.), (*vi*) H_2SO_4 system (H_2SO_4:H_2O_2:H_2O, H_2SO_4:CH_3COOH:H_2O, etc.), (*vii*) HF system (HF:HNO_3:H_2O, HF:HNO_3:H_2O_2, etc.), (*viii*) Br_2:CH_3OH system (Br_2:CH_3OH, Br_2:CH_3OH:CH_3COOH, etc.), (*ix*) NaOCl system (NaOCl and NaOCl:HCl), and (*x*) alkaline system (NaOH:H_2O_2:H_2O, NaOH:H_2O_2:H_2O:NH_4OH, etc.). The chemicals used were all of reagent grade. They were as follows: HCl (12*N*), CH_3COOH (17*N*), H_2O_2 (30%), H_3PO_4 (15*N*), $K_2Cr_2O_7$ (purity ≧ 99.8%), HNO_3 (14.5*N*), HBr (9*N*), C_2H_5OH (purity 99.5%), H_2SO_4 (36*N*), HF (50%), Br_2 (purity ≧ 99%), CH_3OH (purity 99.5%), NaOCl aqueous solution (active chlorine min. 5%), NaOH (purity ≧ 96%), NH_4OH (29%), KOH (purity ≧ 86%), and H_2O (deionized water). A large quantity of solution was prepared to prevent the etching temperature from rising and the etch-solution composition from varying during the experiments. Etching was carried out in a temperature-controlled water vessel without illumination. The etchant was freshly mixed prior to each experiment. All etching experiments were done at room temperature without stirring.

Etched depth and etching profile.—After etching, removing the SiO_2 (or AZ-1350J) mask, and rinsing in deionized water, the {110} plane perpendicular to the etched one was cleaved with a razor blade and the etched depths of samples were measured with a calibrated optical microscope. The etched depths were also measured from a step height between the etched and unetched surfaces using an interference microscope. Etching profiles were observed on the (110) and (1̄10) cleavage planes perpendicular to the wafer surface under an optical microscope.

Etching Profile

HCl system.—The etching profiles of (001)GaAs etched in the solutions of the HCl system are shown in Fig. 2: (a) 1HCl:1CH_3COOH:1H_2O_2 (2 min), (b) 1HCl:1H_3PO_4:1H_2O_2 (2 min), (c) 1HCl:1CH_3COOH:1(1*N*-$K_2Cr_2O_7$) (5 min), and (d) 1HCl:1H_3PO_4:1(1*N*-$K_2Cr_2O_7$) (8 min). Note that etchants containing CH_3COOH and H_2O_2 will explode when heated. The cross sections are obtained by cleaving the wafers in orthogonal directions along the (110) and (1̄10) planes (see Fig. 1). The determination of crystallographic directions was made by means of the etch-figure test, where the etch figures were developed on the (001) plane of GaAs by etching in the Br_2:CH_3OH solution through pin-hole windows in an SiO_2 mask (7). The bars drawn in the top of the figure correspond to the masking-pattern length (28 μm).

It is clear from the figure that the etching profiles change in shape with a crystallographic rotation of 90° about the <001> axis and that they exhibit clear crystal habits. The profiles of the (110) cleavage planes [Fig. 2(a), (b), and (c)] exhibit the reverse-mesa shaped planes forming an angle of about 110° with

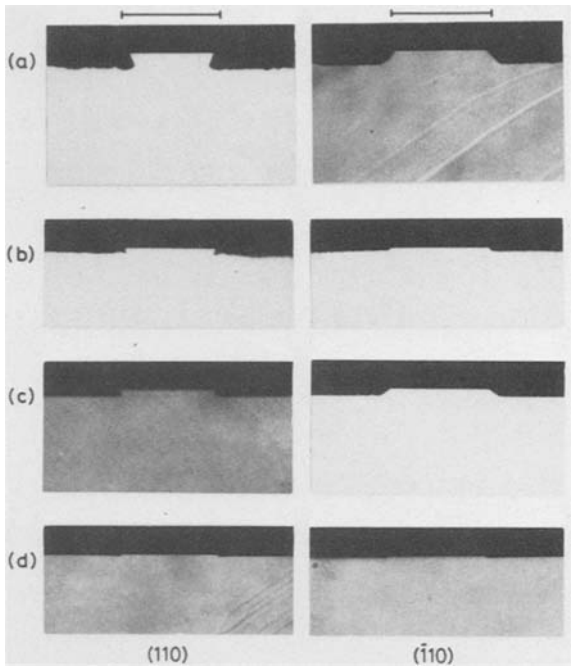

Fig. 2. Etching profiles of (001)GaAs etched in the solutions of the HCl system: (a) 1HCl:1CH_3COOH:1H_2O_2 (2 min), (b) 1HCl:1H_3PO_4:1H_2O_2 (2 min), (c) 1HCl:1CH_3COOH 1(1*N*-$K_2Cr_2O_7$) (5 min), and (d) 1HCl:1H_3PO_4:1(1*N*-$K_2Cr_2O_7$) (8 min). The bars drawn in the top of the figure correspond to the masking pattern length (28 μm).

respect to the (001) surface planes. The profiles of the (1̄10) cleavage planes [Fig. 2(a), (b), and (c)] indicate the inclined planes whose sides form an angle of about 55° [Fig. 2(a) and (b)] or 45° [Fig. 2(c)] with respect to the (001) surface planes. The 1HCl:1H_3PO_4:1(1*N*-$K_2Cr_2O_7$) solution did not provide etch depth for an accurate etching-profile observation. One can, however, barely find from Fig. 2(d) that the etchant produces the ordinary-mesa shaped planes for both the (110) and (1̄10) cleavage planes. The 1HCl:1CH_3COOH:1H_2O_2 [Fig. 2(a)] and 1HCl:1H_3PO_4:1H_2O_2 solution [Fig. 2(b)] exhibit that the side-etch speed (undercutting rate) of the (110) cleavage planes is much faster than that of the (1̄10) cleavage planes. It was also found that the HCl:CH_3COOH (or H_3PO_4) solution does not etch GaAs but addition of H_2O_2 to the solution enables the etching of this material. As may be clearly seen in Fig. 2(a) and (b), the solutions produce a microscopic roughness on the etched-bottom surfaces of GaAs. The 1HCl:1CH_3COOH:1(1*N*-$K_2Cr_2O_7$) [Fig. 2(c)] and 1HCl:1H_3PO_4:1(1*N*-$K_2Cr_2O_7$) solution [Fig. 2(d)], on the other hand, provide high quality etched surfaces without any undesirable roughness or etch pits.

There have been a few reports on the etching characteristics of GaAs with HCl-based etchants [HCl:Fe^{+++} (8) and HCl:H_2O_2:H_2O (9)]. The HCl:CH_3COOH:(1*N*-$K_2Cr_2O_7$) solution does not erode photoresists such as AZ-1350J and gives high quality surfaces. This new solution can, thus, be used as an etchant of GaAs for producing a shiny flat surface as well as for shaping the samples. Details of this solution will be presented in the near future.

HNO_3 system.—It is known that the Ga{111} plane of GaAs etches unsatisfactorily in most etchants. The Ga{111} plane can, however, be polish-etched like the As{111} surface with the HNO_3:H_3PO_4 solution at 60°C (10). The HNO_3:H_2O solution can also be utilized as a stain etchant to delineate the pn-junction position (11). The etching profiles of (001)GaAs etched in the solutions of the HNO_3 system are shown in Fig. 3: (a)

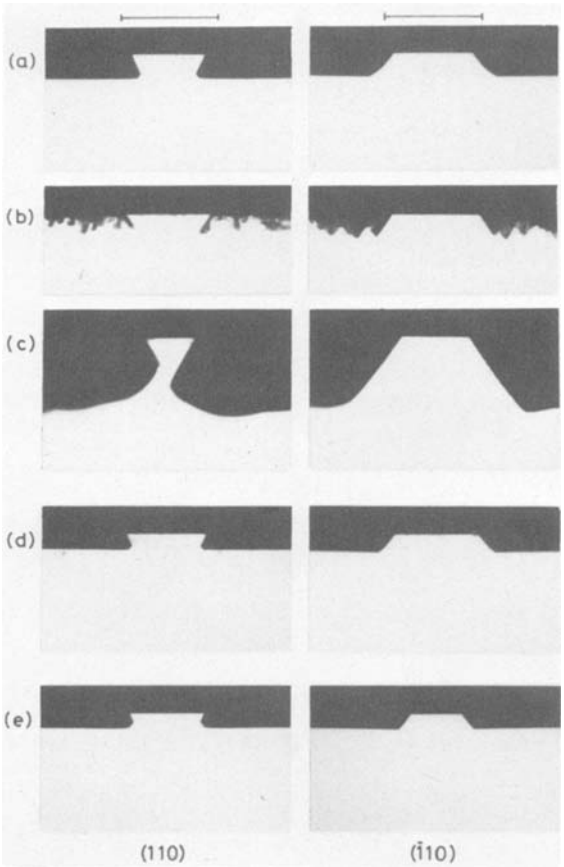

Fig. 3. Etching profiles of (001)GaAs etched in the solutions of the HNO_3 system: (a) $1HNO_3:1H_2O_2$ (1 min), (b) $1HNO_3:1CH_3COOH$ (2 min), (c) $1HNO_3:1H_3PO_4$ (2 min), (d) $1HNO_3:1CH_3COOH:1H_2O_2$ (1 min), and (e) $1HNO_3:1H_3PO_4:1H_2O_2$ (1 min). The bars drawn in the top of the figure correspond to the masking pattern length (28 μm).

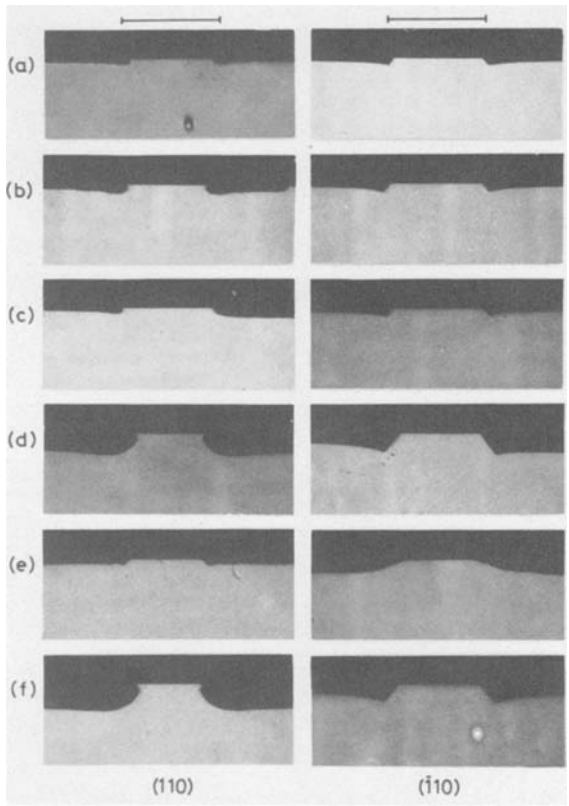

Fig. 4. Etching profiles of (001)GaAs etched in the solutions of the $HCl:HNO_3$ system: (a) $1HCl:1HNO_3$ (2 min), (b) $1HCl:2HNO_3$ (2 min), (c) $2HCl:1HNO_3$ (4 min), (d) $1(1HCl:1HNO_3):1H_2O$ (6 min), (e) $1(1HCl:1HNO_3):1H_2O_2$ (2 min), and (f) $1(1HCl:1HNO_3):1CH_3COOH$ (4 min). The bars drawn in the top of the figure correspond to the masking pattern length (28 μm).

$1HNO_3:1H_2O_2$ (1 min), (b) $1HNO_3:1CH_3COOH$ (2 min), (c) $1HNO_3:1H_3PO_4$ (2 min), (d) $1HNO_3:1CH_3COOH:1H_2O_2$ (1 min), and (e) $1HNO_3:1H_3PO_4:1H_2O_2$ (1 min). In the case of the (110) cleavage planes, the etching profiles of Fig. 3(a), (d), and (e) exhibit two individual etch-revealed planes, *i.e.*, reverse-mesa shaped planes forming an angle of about 115° and ordinary-mesa shaped planes forming an angle of 55° with respect to the (001) surface planes, followed by the flat-bottomed surface planes. The profiles shown in Fig. 3(b) and (c), on the other hand, indicate only the crystal-habit planes forming an angle of about 120° with respect to the (001) surface planes. In the case of the ($\bar{1}10$) cleavage planes, the profiles [Fig. 3(a)-(e)] indicate the ordinary-mesa shaped planes whose sides form an angle of 55° with respect to the (001) surface planes. The etch-revealed planes of Fig. 3(b), (c), and (e) [($\bar{1}10$ cleavage planes] indicate clear crystal habits. The $1HNO_3:1H_2O_2$ (a), $1HNO_3:1CH_3COOH:1H_2O_2$ (d), and $1HNO_3:1H_3PO_4:1H_2O_2$ solution (e) provide high quality etched surfaces with well-defined profiles and flat etched bottoms. The $1HNO_3:1CH_3COOH$ (b) and $1HNO_3:1H_3PO_4$ solution (c), on the other hand, provide conspicuous roughness on the etched-bottom surfaces.

HCl:HNO₃ system.—The etching profiles of (001)GaAs etched in the solutions of the $HCl:HNO_3$ system are shown in Fig. 4: (a) $1HCl:1HNO_3$ (2 min), (b) $1HCl:2HNO_3$ (2 min), (c) $2HCl:1HNO_3$ (4 min), (d) $1(1HCl:1HNO_3):1H_2O$ (6 min), (e) $1(1HCl:1HNO_3):1H_2O_2$ (2 min), and (f) $1(1HCl:1HNO_3):1CH_3COOH$ (4 min). The etching profiles of the (110) cleavage planes [Fig. 4(a)-(d) and (f)] exhibit the reverse-mesa shaped structures with roundish tails at the etched bottoms, where the reverse-mesa walls form an angle of about 110° with respect to the (001) surface planes. The profiles of the ($\bar{1}10$) cleavage planes [Fig. 4(a)-(d) and (f)] indicate the inclined planes forming an angle of 55° with respect to the (001) surface planes, similar to those of the HNO_3 system (see Fig. 3). The etching profiles of Fig. 4(e), on the other hand, do not exhibit clear crystal habit for both the (110) and ($\bar{1}10$) cleavage planes. It is clear from Fig. 4 that the degree of undercutting for the direction along the [$\bar{1}10$] axis is larger than for the direction along the [110] axis. The optical microscope images indicate that the $HCl:HNO_3$ system, except $1(1HCl:1HNO_3):1H_2O$, produces microscopic roughness on the etched-bottom surfaces. Only the $1(1HCl:1HNO_3):1H_2O$ solution [Fig. 4(d)] results in an etch-pit free, high quality surface.

HBr system.—The etching profiles of (001)GaAs etched in the solutions of the HBr system are shown in Fig. 5: (a) $1HBr:1HNO_3$ (2 min), (b) $1HBr:1HNO_3:1H_2O$ (3 min), (c) $1HBr:1CH_3COOH:1(1N\text{-}K_2Cr_2O_7)$ (1 min), and (d) $1HBr:1H_3PO_4:1(1N\text{-}K_2Cr_2O_7)$ (2 min). The etching profiles of the (110) cleavage planes [Fig. 5(a), (c), and (d)] indicate the etch-revealed planes which are nearly perpendicular to the (001) surface planes with roundish tails at the etched bottoms. The profiles of the ($\bar{1}10$) cleavage planes [Fig. 5(a), (c), and (d)] indicate the ordinary-mesa shaped, inclined planes forming an angle of about 55° with respect to the (001) surface planes. The HBr system, such as HBr, $1HBr:1HCl$, and $1HBr:1H_3PO_4$, does not etch the GaAs sample. The $1HBr:1HNO_3$ [Fig. 5(a)] and $1HBr:1HNO_3:1H_2O$ solution [Fig. 5(b)] produce rugged surfaces on the etched bottoms. The solutions, $1HBr:1CH_3COOH:1(1N\text{-}K_2Cr_2O_7)$ [Fig. 5(c)] and $1HBr:1H_3PO_4:1(1N\text{-}K_2Cr_2O_7)$ [Fig. 5(d)], on the other

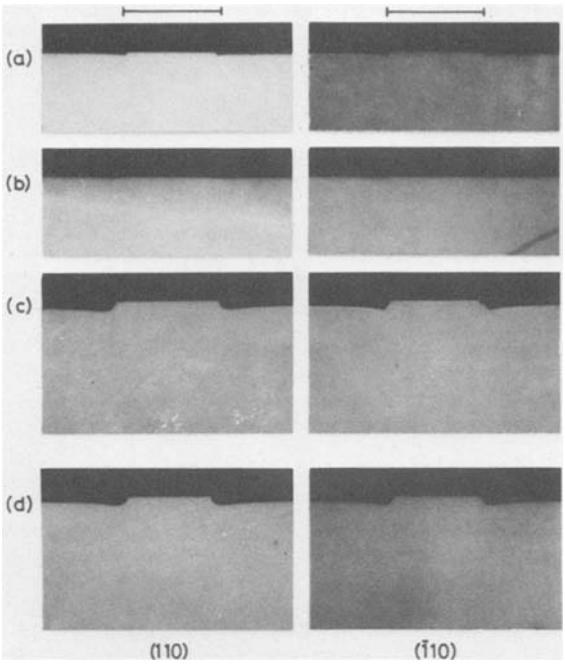

Fig. 5. Etching profiles of (001)GaAs etched in the solutions of the HBr system: (a) 1HBr:1HNO_3 (2 min), (b) 1HBr:1HNO_3:1H_2O (3 min), (c) 1HBr:1CH_3COOH:1(1*N*-$K_2Cr_2O_7$) (1 min), and (d) 1HBr:1H_3PO_4:1(1*N*-$K_2Cr_2O_7$) (2 min). The bars drawn in the top of the figure correspond to the masking pattern length (28 μm).

hand, provide relatively smooth etched surfaces without any undesirable etch pits.

Recently, we reported a new chemical solution composed of HBr, CH_3COOH (or H_3PO_4), and a $K_2Cr_2O_7$ aqueous solution for use in etching of InP (12, 13). It was found that this etchant provides high quality etched surfaces without any undesirable roughness or etch pits. The etchant does not erode photoresists such as AZ-1350J, and provides a desirable mesa-shaped structure on the InP and InGaAsP/InP DH (double-heterostructure) wafers with good photoresist-pattern definition. The etching characteristics obtained in the present study are similar to those reported in (12). The HBr:CH_3COOH(or H_3PO_4):$K_2Cr_2O_7$ solution may, thus, be suitable for use in etching of not only the InP but also the GaAs samples.

H_3PO_4 system.—Figure 6 shows the etching profiles of (001)GaAs etched in the solutions of the H_3PO_4 system: (a) 1H_3PO_4:1H_2O_2:1H_2O (2 min), (b) 1H_3PO_4:1CH_3COOH:1H_2O_2 (3 min), (c) 1H_3PO_4:1CH_3OH:1H_2O_2 (2 min), and (d) 1H_3PO_4:1C_2H_5OH:1H_2O_2 (2 min). As can be clearly seen in the figure, the H_3PO_4 system develops the etching profiles which exhibit clear crystal habits. In the case of the (110) cleavage planes, the profiles [Fig. 6(a)-(d)] indicate the reverse-mesa and ordinary-mesa shaped structures, following by the flat-bottomed surfaces. The reverse-mesa and ordinary-mesa planes form angles of about 115° and 55°, respectively, with respect to the (001) surface planes. The etching profiles of the (1̄10) cleavage planes [Fig. 6(a)-(d)], on the other hand, exhibit only the inclined sides that slope downward away from the SiO_2 masks. The etch-revealed planes form an angle of about 55° with respect to the (001) surface planes.

A few papers have been published on the etching characteristics of GaAs in the H_3PO_4-based chemical solutions (6, 14). As is shown in this subsection, the H_3PO_4 system provides high quality etched surfaces with well-defined profiles and shiny flat etched bottoms. This system may, thus, be applicable to a wide variety of the device-structure design and fabrication.

H_2SO_4 system.—The H_2SO_4:H_2O_2:H_2O system is known to be one of the most commonly employed etch-

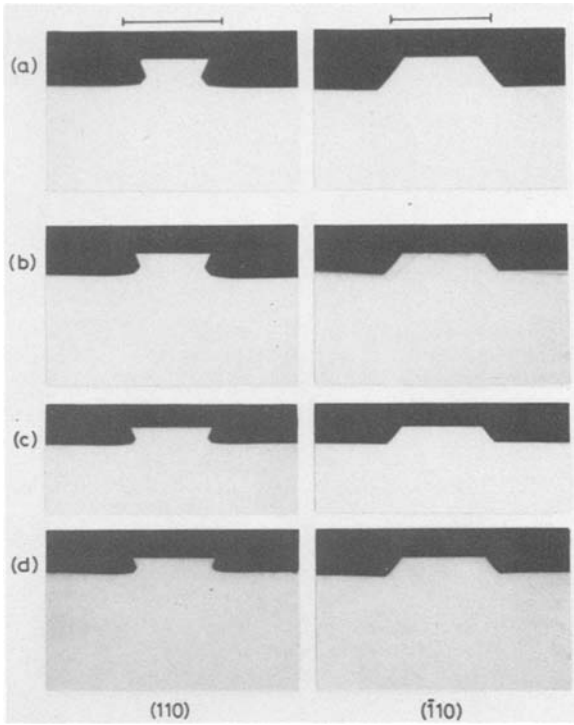

Fig. 6. Etching profiles of (001)GaAs etched in the solutions of the H_3PO_4 system: (a) 1H_3PO_4:1H_2O_2:1H_2O (2 min), (b) 1H_3PO_4:1CH_3COOH:1H_2O_2 (3 min), (c) 1H_3PO_4:1CH_3OH:1H_2O_2 (2 min), and (d) 1H_3PO_4:1C_2H_5OH:1H_2O_2 (2 min). The bars drawn in the top of the figure correspond to the masking pattern length (28 μm).

ants for GaAs (3, 4). Chemical polishing by use of this system also gives high quality GaAs surfaces of low index orientations except for the Ga{111} surface. The etching profiles of (001)GaAs etched in the solutions of the H_2SO_4 system are shown in Fig. 7: (a) 1H_2SO_4:1H_2O_2:1H_2O (1 min), (b) 1H_2SO_4:1CH_3COOH:1H_2O (1 min), (c) 1H_2SO_4:1H_3PO_4:1H_2O (1 min), and (d)

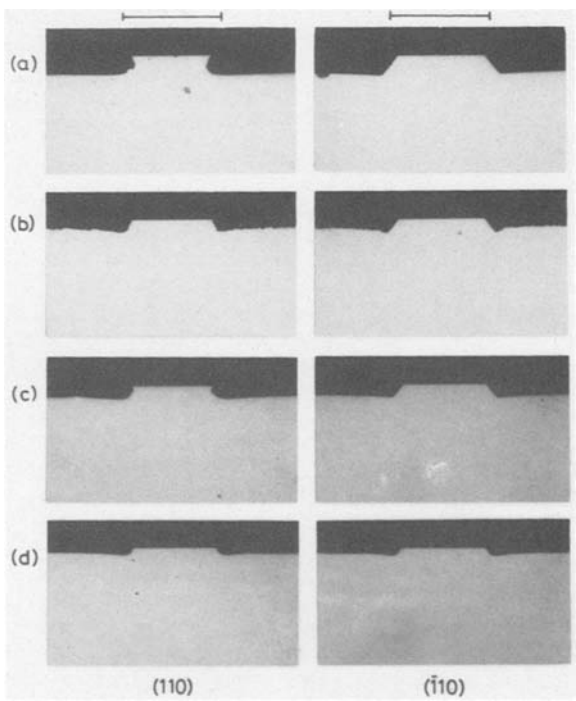

Fig. 7. Etching profiles of (001)GaAs etched in the solutions of the H_2SO_4 system: (a) 1H_2SO_4:1H_2O_2:1H_2O (1 min), (b) 1H_2SO_4:1CH_3COOH:1H_2O (1 min), (c) 1H_2SO_4:1H_3PO_4:1H_2O (1 min), and (d) 1H_2SO_4:1HCl:1(1*N*-$K_2Cr_2O_7$) (2 min). The bars drawn in the top of the figure correspond to the masking pattern length (28 μm).

$1H_2SO_4:1HCl:1(1N\text{-}K_2Cr_2O_7)$ (2 min). The $1H_2SO_4:1H_2O_2:1H_2O$ solution for the (110) cleavage plane provides the etch-revealed wall which is composed of two individual reverse-mesa and ordinary-mesa shaped planes. The reverse-mesa and ordinary-mesa planes form angles of about 110° and 55°, respectively, with respect to the (110) surface plane. This solution gives the ordinary-mesa shaped profile for the (110) cleavage plane forming an angle of 55° with respect to the (001) surface plane. The $1H_2SO_4:1H_3PO_4:1H_2O$ solution for the (110) cleavage plane provides the reverse-mesa plane with roundish tail at the etched bottom. The reverse-mesa shaped plane forms an angle of about 110° with respect to the (001) surface plane. The solution gives the ordinary-mesa shaped profile for the $(\bar{1}10)$ cleavage plane forming an angle of 55° with respect to the (001) surface plane. The $1H_2SO_4:1H_2O_2:1H_2O$ and $1H_2SO_4:1H_3PO_4:1H_2O$ solutions provide relatively high quality etched surfaces on the (001)GaAs samples. The $1H_2SO_4:1HCl:1(1N\text{-}K_2Cr_2O_7)$ solution gives the nearly vertical and inclined planes for the (110) and $(\bar{1}10)$ cleavage planes, respectively, with roundish tails at the etched bottoms. This solution also provides relatively high quality etched surface on the (001)GaAs sample. Details of this etching solution can be found in (15).

HF system.—The HF system rigorously attacks the GaAs sample and, as a result, behaves like a fast-speed etchant for this material (16-19). The etching profiles of (001)GaAs etched in the solutions of the HF system are shown in Fig. 8: (a) $1HF:1HNO_3:1H_2O$ (1 min), (b) $1HF:1HNO_3:1H_2O_2$ (15 sec), (c) $1HF:1HNO_3:1CH_3COOH$ (5 sec), (d) $1HF:1HNO_3:1H_3PO_4$ (5 sec), and (e) $1HF:1H_2SO_4:1H_2O_2$ (10 sec). The $1HF:1HNO_3:1H_2O$ [Fig. 8(a)] and $1HF:1HNO_3:1H_3PO_4$ solution [Fig. 8(d)] provide roundish profiles for both the (110) and $(\bar{1}10)$ cleavage planes. The etching profiles of the $1HF:1HNO_3:1CH_3COOH$ solution [Fig. 8(c)] exhibit the roundish and inclined planes for the (110) and $(\bar{1}10)$ cleavage planes, respectively. This inclined plane forms an angle of about 55° with respect to the (001) surface plane. The $1HF:1HNO_3:1H_2O_2$ and $1HF:1H_2SO_4:1H_2O_2$ solutions provide the etching profiles indicating no clear crystal habit [see Fig. 8(b) and (e)].

Br_2:CH_3OH system.—It is known that the $Br_2:CH_3OH$ system gives good results for preferential etching of GaAs (3). The etching rates can be easily controlled by varying the Br_2 concentrations in CH_3OH. Figure 9 shows the etching profiles of (001)GaAs etched in the solutions of the $Br_2:CH_3OH$ system: (a) 4% by volume $Br_2:CH_3OH$ (1 min), (b) 1% by volume $Br_2:CH_3OH$ (3 min), (c) 1(1% by volume $Br_2:CH_3OH$):$1CH_3COOH$ (5 min), and (d) 1(1% by volume $Br_2:CH_3OH$):$1H_3PO_4$ (10 min). The Br_2CH_3OH solutions [Fig. 9(a) and (b)] provide that the profiles of the (110) cleavage planes indicate the reverse-mesa shaped structure forming an angle of about 120° with respect to the (001) surface planes while those of the $(\bar{1}10)$ cleavage planes indicate the ordinary-mesa shaped structure forming an angle of 55° with respect to the (001) surface planes. The 1(1% $Br_2:CH_3OH$):$1CH_3COOH$ solution [Fig. 9(c)] provides the same etching profiles as the $Br_2:CH_3OH$ solutions. Such profiles are the same as those of (001)InP etched with the $Br_2:CH_3OH$ system (7). In the case of the 1(1% $Br_2:CH_3OH$):$1H_3PO_4$ solution [Fig. 9(d)], the etching profiles exhibit the inclined planes for both the (110) and $(\bar{1}10)$ cleavage planes. The ($Br_2:CH_3OH$):CH_3COOH and ($Br_2:CH_3OH$):H_3PO_4 solutions also provide relatively good etched surfaces on GaAs. These solutions may, thus, be used as the slow speed etchants for GaAs.

NaOCl system.—Nonpreferential polishing to obtain high quality GaAs surfaces has been achieved by employing the $NaOCl:H_2O$ solution (20). Figure 10 shows

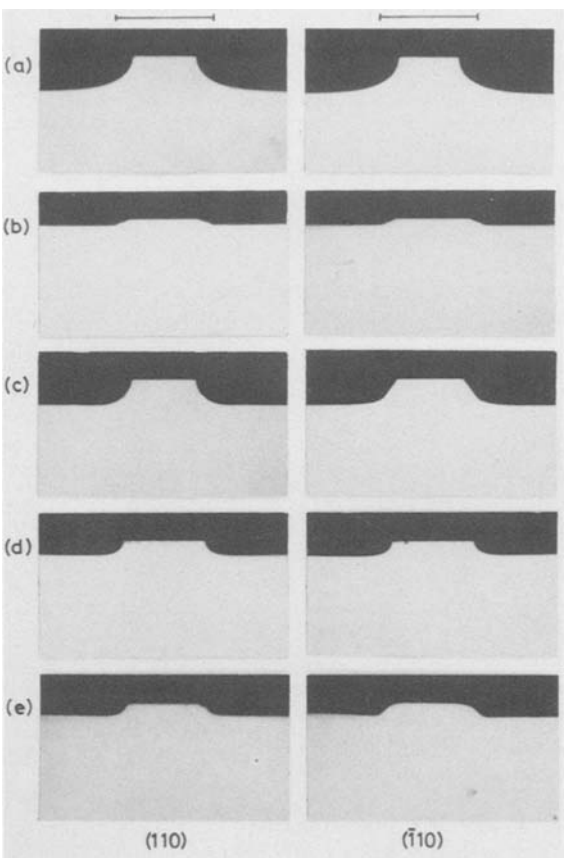

Fig. 8. Etching profiles of (001)GaAs etched in the solutions of the HF system: (a) $1HF:1HNO_3:1H_2O$ (1 min), (b) $1HF:1HNO_3:1H_2O_2$ (15 sec), (c) $1HF:1HNO_3:1CH_3COOH$ (5 sec), (d) $1HF:1HNO_3:1H_3PO_4$ (5 sec), and (e) $1HF:1H_2SO_4:1H_2O_2$ (10 sec). The bars drawn in the top of the figure correspond to the masking pattern length (28 μm).

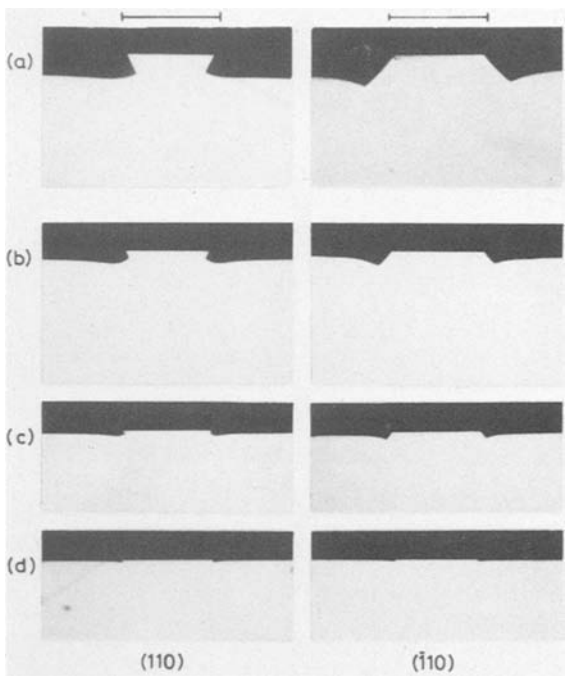

Fig. 9. Etching profiles of (001)GaAs etched in the solutions of the $Br_2:CH_3OH$ system: (a) 4% by volume $Br_2:CH_3OH$ (1 min), (b) 1% by volume $Br_2:CH_3OH$ (3 min), (c) 1(1% by volume $Br_2:CH_3OH$):$1CH_3COOH$ (5 min), and (d) 1(1% by volume $Br_2:CH_3OH$):$1H_3PO_4$ (10 min). The bars drawn in the top of the figure correspond to the masking pattern length (28 μm).

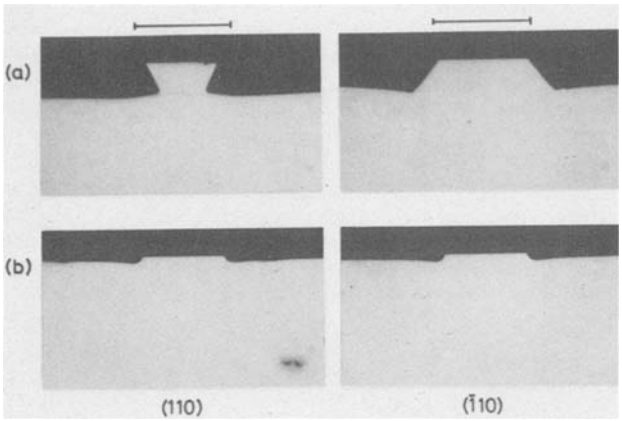

Fig. 10. Etching profiles of (001)GaAs etched in the solutions of the NaOCl system: (a) NaOCl (5 min) and (b) 5NaOCl:1HCl (2 min). The bars in the top of the figure correspond to the masking pattern length (28 μm).

the etching profiles of (001)GaAs etched in the solutions of the NaOCl system: (a) NaOCl (5 min) and (b) 5NaOCl:1HCl (2 min). The etching profile of the (110) cleavage plane [Fig. 10(a)] indicates the reverse-mesa shaped plane forming an angle of about 115° with respect to the (001) surface plane. The profile of the ($\bar{1}$10) cleavage plane [Fig. 10(a)], on the other hand, exhibits the ordinary-mesa shaped plane forming an angle of 55° with respect to the (001) surface plane. Such profiles are the same as those in Fig. 2(a), (c), and Fig. 3(a). The etching profiles of the sample etched with the 5NaOCl:1HCl solution [Fig. 10(b)] indicate the planes which are nearly perpendicular to the (001) surface planes for both the (110) and ($\bar{1}$10) cleavage planes, followed by the roundish tails at the etched bottoms. These profiles are very similar to those in Fig. 8(a) and (d).

Alkaline system.—The alkaline solutions, such as NaOH:H_2O_2:H_2O (21-25) and NH_4OH:H_2O_2:H_2O (5, 26) are the commonly employed etchants for GaAs. The profiles of (001)GaAs etched in the solutions of the alkaline system are shown in Fig. 11: (a) 1(1*N*-NaOH):1H_2O_2:10H_2O (4 min), (b) 5(1*N*-NaOH):1H_2O_2:1NH_4OH (4 min), (c) 1NH_4OH:1H_2O_2:5H_2O (4 min), (d) 1(1*N*-KOH):1H_2O_2:10H_2O (4 min), and (e) 5(1*N*-KOH):1H_2O_2:1NH_4OH (4 min). The etching profiles of the (110) cleavage planes [Fig. 11(a)-(c) and (e)] indicate the reverse-mesa shaped planes forming an angle of about 110° with respect to the (001) surface planes. The profiles of the ($\bar{1}$10) cleavage planes [Fig. 11(a)-(c) and (e)] indicate the ordinary-mesa shaped, inclined planes whose sides form an angle of about 55° with respect to the (001) surface planes. The alkaline solutions, except 1NH_4OH:1H_2O_2:5H_2O, result rough sandpaper textures on the etched bottom surfaces, but the 1NH_4OH:1H_2O_2:5H_2O provides a high quality etched surface.

Crystallographic Aspect and Proposed Device Application

In this section, we discuss the etching profiles of (001)GaAs demonstrated in Fig. 2-11 from an aspect of crystallography. The utility of these etching solutions is also discussed for a variety of GaAs device applications.

From a view point of crystallography, we can classify the etching profiles obtained in Fig. 2-11 into the six individual groups, as demonstrated in Fig. 12. The etch-revealed planes forming angles of 110°-115° with respect to the (001) surface planes, observed on the (110) cleavage planes in the solutions of the HCl (Fig. 2) and alkaline system (Fig. 11), correspond to the Ga{2$\bar{2}\bar{1}$} crystallographic planes [see Fig. 12(a)]. The

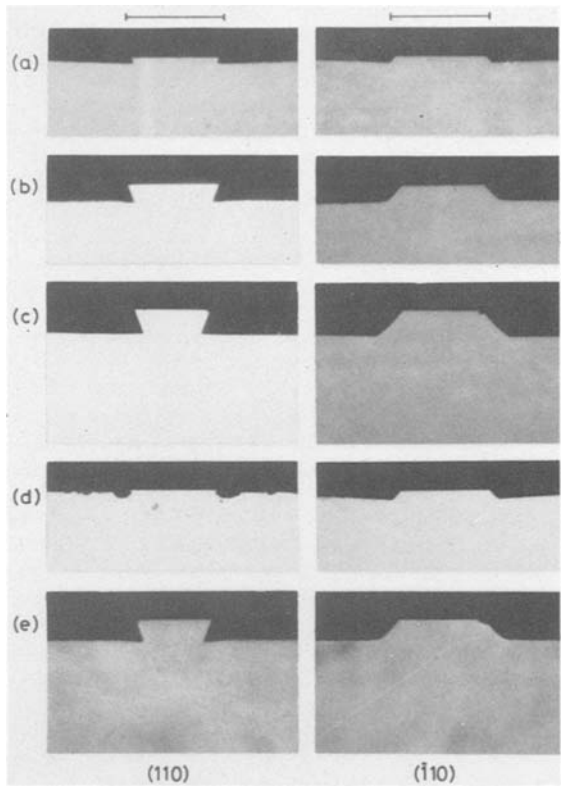

Fig. 11. Etching profiles of (001)GaAs etched in the solutions of the alkaline system: (a) 1(1*N*-NaOH):1H_2O_2:10H_2O (4 min), (b) 5(1*N*-NaOH):1H_2O_2:1NH_4OH (4 min), (c) 1NH_4OH:1H_2O_2:5H_2O (4 min), (d) 1(1*N*-KOH):1H_2O_2:10H_2O (4 min), and (e) 5(1*N*-KOH):1H_2O_2:1NH_4OH (4 min). The bars drawn in the top of the figure correspond to the masking pattern length (28 μm).

Ga{2$\bar{2}\bar{1}$} crystallographic plane, in principle, forms an angle of 109.5° with respect to the (001) surface plane. The inclined planes forming an angle of about 55° with respect to the (001) surface planes, observed on the (110) cleavage planes in the 1HCl:1CH_3COOH:1H_2O_2 [Fig. 2(a)] and 1(1% Br_2:CH_3OH):1H_3PO_4 solution [Fig. 9(d)], correspond to the Ga{1$\bar{1}$1} or As{1$\bar{1}$1} crystallographic planes [see Fig. 12(b)]. The {1$\bar{1}$1} crystallographic plane, in principle, forms an angle of 54.7° with respect to the (001) surface plane. The etching profile quite similar to Fig. 12(b) was observed on (001)InP etched in the solutions of the HBr system [HBr and HBr:H_3PO_4] (7). The inclined planes forming an angle of about 55° with respect to the (001) surface planes, observed on the ($\bar{1}$10) cleavage planes in the solutions of the various etchant systems [see, *e.g.*, Fig. 11(a)], correspond to the Ga{$\bar{1}\bar{1}$1} crystallographic planes which in principle form an angle of 54.7° with respect to the (001) surface planes. The ordinary-mesa shaped plane forming an inclined angle of about 45°, observed on the ($\bar{1}$10) cleavage plane in the 1HCl:1CH_3COOH:1(1*N*-$K_2Cr_2O_7$) solution [Fig. 2(c)], may correspond to the {0$\bar{1}$1} crystallographic plane. The plane, in principle, forms an angle of 45° with respect to the (001) surface plane. This plane is a novel one observed on the ($\bar{1}$10) cleavage planes of (001)GaAs. The {0$\bar{1}$1} crystallographic plane was also produced on (001)InP etched in the HBr:H_3PO_4 solution (7).

The etching profile of the (110) cleavage plane, shown in Fig. 12(c), is composed of two individual planes forming angles of 109.5° and 54.7° with respect to the (001) surface plane, while that of the ($\bar{1}$10) cleavage plane exhibits only the mesa-shaped structure forming an angle of 54.7° with respect to the (001) surface plane. These crystallographic planes corre-

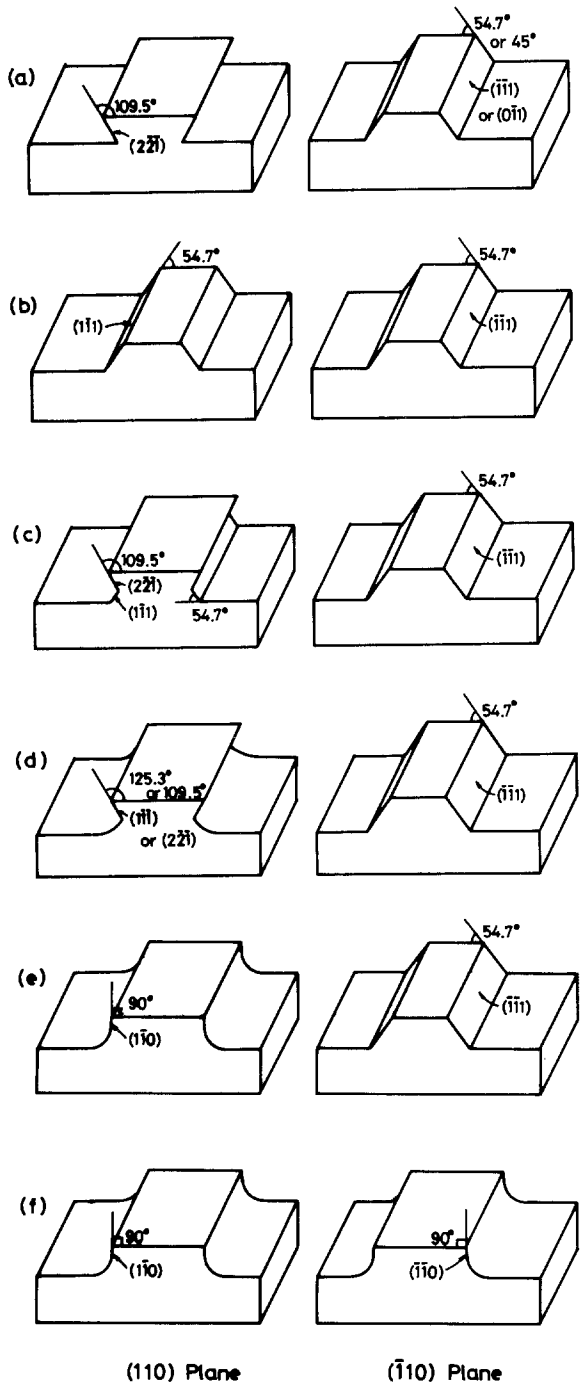

Fig. 12. Schematic diagrams of the etching profiles produced in the (001) planes of GaAs by the various etching solutions (see text).

spond to the Ga{2$\bar{2}\bar{1}$} and Ga{1$\bar{1}$1} or As{1$\bar{1}$1} planes for the (110) cleavage plane and to the Ga{$\bar{1}\bar{1}$1} plane for the ($\bar{1}$10) cleavage plane, respectively. The etchants, HNO_3 [Fig. 3(a), (d), and (e)], H_3PO_4 [Fig. 6(a)-(d)], H_2SO_4 [Fig. 7(a)], and NaOCl system [Fig. 10(a)], provide the etching profiles same as that illustrated in Fig. 12(c). The reverse-mesa and ordinary-mesa shaped structures can be produced on the (110) and ($\bar{1}$10) cleavage planes, respectively, with etchants such as the HNO_3 [Fig. 3(c)] and Br_2: CH_3OH system [Fig. 9(a)-(c)]. These etch-revealed planes form angles of about 120° (reverse-mesa shaped structure) and 55° (ordinary-mesa shaped structure) with respect to the (001) surface planes. The planes can, thus, be identified to be the Ga{111} crystallographic planes. The etching proceeds up to the Ga{111} planes, because the As{111} planes are very active compared with the Ga{111} planes. Consequently, as shown in Fig. 12(d), the Ga{$\bar{1}$1$\bar{1}$} reverse-mesa and Ga{$\bar{1}$1$\bar{1}$} ordinary-mesa shaped planes are produced on the (110) and ($\bar{1}$10) cleavage planes, respectively, whose sides in principle form angles of 125.3° (reverse mesa) and 54.7° (ordinary mesa) with respect to the (001) surface planes. The etchants, HCl:HNO_3 [Fig. 4(a)-(d) and (f)] and H_2SO_4 system [Fig. 7(c)], also provide the reverse-mesa and ordinary-mesa shaped profiles for the (110) and ($\bar{1}$10) cleavage planes, respectively. In this case, the reverse-mesa shaped profiles are defined predominantly by the Ga{2$\bar{2}\bar{1}$} slow etching rate faces [see Fig. 12(d)].

The etch-revealed walls perpendicular to the (001) surface planes, obtained on the (110) cleavage planes in the solutions of the HBr [Fig. 5(a), (c), and (d)], H_2SO_4 [Fig. 7(d)], and HF system [Fig. 8(c)], correspond to the {1$\bar{1}$0} crystallographic planes [see Fig. 12(e)]. The etching profiles of the ($\bar{1}$10) cleavage planes revealed by these systems exhibit the ordinary-mesa structures which are defined by the Ga{$\bar{1}\bar{1}$1} crystallographic planes. Some etchants, such as the HF [Fig. 8(a) and (d)] and NaOCl system [Fig. 10(b)], provide the nearly perpendicular walls with respect to the (001) surface planes for both the (110) and ($\bar{1}$10) cleavage planes, followed by the roundish tails at the etched bottoms [see Fig. 12(f)]. This fact clearly suggests that the solutions act isotropically in etching behavior [*i.e.*, they etch the (001) GaAs samples non-preferentially].

The dissolution process under consideration is far too complex and the available information rather limited to allow a quantitative development of the dissolution mechanism. Moreover, it is difficult to obtain a complete explanation of the difference in the etching profiles with various etching solutions. However, we suggest that this difference is due to the differences of the etching rates in the various crystallographic planes. The etch-revealed planes identified are summarized in Table I along with the etching time and etched depth.

The etching profiles obtained in the present study should be very useful for the design and fabrication of electron devices, such as transistors and Gunn-effect devices. A series of the device-fabrication steps of such devices require various kinds of etchants in accordance with each purpose, *e.g.*, surface cleaning, mesa fabrication, electrical isolation, etc. The etchants mentioned in this paper are, thus, thought to be attractive for a variety of the device-fabrication steps.

Investigations on the subject of ballistic electron transport in submicron semiconductor devices have recently been carried out extensively (27, 28). The ballistic electron transport in semiconductors leads to the realization of low power, high speed switches and high frequency transistors (ballistic Tr's). The realistic ballistic Tr's may have a structure of n^+-n^--n^+ or n^+-p^--n^+ junction diodes, where n^- (or p^-) is the active layer of submicron dimension and n^+ is the source and drain layers. Relevant device technology is, however, very complicated and the gate contact is thought to be difficult to fabricate (27). This problem can be overcome by use of chemical etching. The reverse-mesa shaped profile enables the use of a self-aligned metal evaporation and, therefore, it is possible to fabricate the gate (Schottky) contact on the active layer. The etchants, such as the HCl [Fig. 2(c)], H_3PO_4 [Fig. 6(a)-(d)], H_2SO_4 [Fig. 7(a)], and alkaline system [Fig. 11(c)], are suitable for this use.

A laterally confined structure is required and important in a variety of electro-optic devices, *i.e.*, waveguides, directional couplers, and optical switches, fabricated from GaAs crystals. The etchants, such as the HCl:CH_3COOH:(1*N*-$K_2Cr_2O_7$) [Fig. 2(c)] and HBr:CH_3COOH:(1*N*-$K_2Cr_2O_7$) solution [Fig. 5(c)], are

Table I. The composition of the etchants in parts by volume, etching time, etched depth, and identified crystallographic planes revealed by etching

Etchant	Etching time	Etched depth (μm)	Identified planes (110)	Identified planes ($\bar{1}10$)
1HCl:1CH_3COOH:1H_2O_2	2 min	4.0	{$2\bar{2}1$}	{$\bar{1}\bar{1}1$}
1HCl:1H_3PO_4:1H_2O_2	2 min	1.5	{$2\bar{2}1$}	{$\bar{1}\bar{1}1$}
1HCl:1CH_3COOH:1(1*N*-$K_2Cr_2O_7$)	5 min	2.0	{$2\bar{2}1$}	{$0\bar{1}1$}
1HCl:1H_3PO_4:1(1*N*-$K_2Cr_2O_7$)	8 min	0.3	{$1\bar{1}1$}	{$\bar{1}\bar{1}1$}
1HNO_3:1H_2O_2	1 min	7	{$2\bar{2}1$}, {$1\bar{1}1$}	{$\bar{1}\bar{1}1$}
1HNO_3:1CH_3COOH	2 min		{$1\bar{1}\bar{1}$}	{$\bar{1}\bar{1}1$}
1HNO_3:1H_3PO_4	2 min	20	{$1\bar{1}\bar{1}$}	{$\bar{1}\bar{1}1$}
1HNO_3:1CH_3COOH:1H_2O_2	1 min	4.5	{$2\bar{2}1$}, {$1\bar{1}1$}	{$\bar{1}\bar{1}1$}
1HNO_3:1H_3PO_4:1H_2O_2	1 min	3.5	{$2\bar{2}1$}, {$1\bar{1}1$}	{$\bar{1}\bar{1}1$}
1HCl:1HNO_3	2 min	1.0	{$2\bar{2}1$}	{$\bar{1}\bar{1}1$}
1HCl:2HNO_3	2 min	1.5	{$2\bar{2}1$}	{$\bar{1}\bar{1}1$}
2HCl:1HNO_3	4 min	1.0	{$2\bar{2}1$}	{$\bar{1}\bar{1}1$}
1(1HCl:1HNO_3):1H_2O	6 min	5.0	{$2\bar{2}1$}	{$\bar{1}\bar{1}1$}
1(1HCl:1HNO_3):1H_2O_2	2 min	2.0	•	•
1(1HCl:1HNO_3):1CH_3COOH	4 min	5.0	{$2\bar{2}1$}	{$\bar{1}\bar{1}1$}
1HBr:1HNO_3	2 min	0.5	{$1\bar{1}0$}	{$\bar{1}\bar{1}1$}
1HBr:1HNO_3:1H_2O	3 min	0.15		
1HBr:1CH_3COOH:1(1*N*-$K_2Cr_2O_7$)	1 min	1.5	{$1\bar{1}0$}	{$\bar{1}\bar{1}1$}
1HBr:1H_3PO_4:1(1*N*-$K_2Cr_2O_7$)	2 min	2.0	{$1\bar{1}0$}	{$\bar{1}\bar{1}1$}
1H_3PO_4:1H_2O_2:1H_2O	2 min	8	{$2\bar{2}1$}, {$1\bar{1}1$}	{$\bar{1}\bar{1}1$}
1H_3PO_4:1CH_3COOH:1H_2O_2	3 min	6	{$2\bar{2}1$}, {$1\bar{1}1$}	{$\bar{1}\bar{1}1$}
1H_3PO_4:1CH_3OH:1H_2O_2	2 min	5.0	{$2\bar{2}1$}, {$1\bar{1}1$}	{$\bar{1}\bar{1}1$}
1H_3PO_4:1C_2H_5OH:1H_2O_2	2 min	4.0	{$2\bar{2}1$}, {$1\bar{1}1$}	{$\bar{1}\bar{1}1$}
1H_2SO_4:1H_2O_2:1H_2O	1 min	5.0	{$2\bar{2}1$}, {$1\bar{1}1$}	{$\bar{1}\bar{1}1$}
1H_2SO_4:1CH_3COOH:1H_2O	1 min	2.5	•	{$\bar{1}\bar{1}1$}
1H_2SO_4:1H_3PO_4:1H_2O	1 min	3.0	{$2\bar{2}1$}	{$\bar{1}\bar{1}1$}
1H_2SO_4:1HCl:1(1*N*-$K_2Cr_2O_7$)	2 min	1.5	{$1\bar{1}0$}	{$\bar{1}\bar{1}1$}
1HF:1HNO_3:1H_2O	1 min	10	{$1\bar{1}0$}	{$\bar{1}\bar{1}0$}
1HF:1HNO_3:1H_2O_2	15 sec	2.0	•	•
1HF:1HNO_3:1CH_3COOH	5 sec	7	{$1\bar{1}0$}	{$\bar{1}\bar{1}1$}
1HF:1HNO_3:1H_3PO_4	5 sec	4.0	{$1\bar{1}0$}	{$\bar{1}\bar{1}0$}
1HF:1H_2SO_4:1H_2O_2	10 sec	3.5	•	•
4% Br_2:CH_3OH	1 min	6	{$1\bar{1}\bar{1}$}	{$\bar{1}\bar{1}1$}
1% Br_2:CH_3OH	3 min	2.0	{$1\bar{1}\bar{1}$}	{$\bar{1}\bar{1}1$}
1(1% Br_2:CH_3OH):1CH_3COOH	5 min	1.0	{$1\bar{1}\bar{1}$}	{$\bar{1}\bar{1}1$}
1(1% Br_2:CH_3OH):1H_3PO_4	10 min	0.2	{$1\bar{1}1$}	{$\bar{1}\bar{1}1$}
NaOCl	5 min	9	{$2\bar{2}1$}, {$1\bar{1}1$}	{$\bar{1}\bar{1}1$}
5NaOCl:1HCl	2 min	1.5	{$1\bar{1}0$}	{$\bar{1}\bar{1}0$}
1(1*N*-NaOH):1H_2O_2:10H_2O	4 min	1.5	{$2\bar{2}1$}	{$\bar{1}\bar{1}1$}
5(1*N*-NaOH):1H_2O_2:1NH_4OH	4 min	4.5	{$2\bar{2}1$}	{$\bar{1}\bar{1}1$}
1NH_4OH:1H_2O_2:5H_2O	4 min	7	{$2\bar{2}1$}	{$\bar{1}\bar{1}1$}
1(1*N*-KOH):1H_2O_2:10H_2O	4 min	2.0	•	{$\bar{1}\bar{1}1$}
5(1*N*-KOH):1H_2O_2:1NH_4OH	4 min	5.5	{$2\bar{2}1$}	{$\bar{1}\bar{1}1$}

• Etching profile does not exhibit clear crystal habits.

thought to be useful for the fabrication of laterally confined electro-optic devices because these solutions provide high quality etched surfaces with good resist-pattern definition. A laterally confined structure is also required especially in a variety of GaAs semiconductor lasers. The lateral confinement structure not only improves laser operation characteristics such as threshold current, stable fundamental transverse mode, and high temperature operation, but also linear light-current characteristics, narrow beam divergence, and high power output. The results presented in this paper show that one can easily obtain various types of laterally confined channels by properly choosing the etching mixtures, its component proportion, channel width, and etching time.

Realization of a monolithic integrated optical circuit is a current topic in the field of injection laser technology. To fabricate the high quality etched mirrors, it is desirable to employ etching solution which provides vertical mirror walls on the etching profile (13). The etching solutions, HBr [Fig. 5(c) and (d)], H_2SO_4 [Fig. 7(d)], HF [Fig. 8(a), (c), and (d)], and NaOCl system [Fig. 10(b)], provide the nearly vertical mirror walls for the (110) cleavage planes and are, thus, thought to be suitable for use in the etched mirror definitions. The etchants may also be widely used in GaAs devices to obtain desirable mesa-shaped structure or to isolate individual device component on one wafer.

Conclusion

We have studied chemical etching characteristics of (001) GaAs in the solutions of various systems: (*i*) HCl, (*ii*) HNO_3, (*iii*) HCl:HNO_3, (*iv*) HBr, (*v*) H_3PO_4, (*vi*) H_2SO_4, (*vii*) HF, (*viii*) Br_2:CH_3OH, (*ix*) NaOCl, and (*x*) alkaline system. The etching profiles exhibiting crystal habits, *e.g.*, ordinary-mesa shaped, reverse-mesa shaped structures, and nearly vertical walls, have been found to be formed by stripes parallel to the <110> and <$\bar{1}$10> directions being etched on the (001) planes. The indexes of the etch-revealed planes have been identified by making a comparison with the calculated angle between the (001) surface and etch-side planes. The etching profiles applicable to the device-structure design and fabrication have also been discussed in detail.

Acknowledgment

The authors wish to thank K. Kumabe, S. Hashimoto, and N. Kuroyanagi for their continual encouragement.

Manuscript submitted Feb. 18, 1983; revised manuscript received July 8, 1983.

Nippon Telegraph and Telephone Public Corporation assisted in meeting the publication costs of this article.

REFERENCES

1. B. Tuck, *J. Mater. Sci.*, **10,** 321 (1975); W. Kern, *RCA Rev.*, **39,** 278 (1978).
2. Y. Tarui, Y. Komiya, and Y. Harada, *This Journal*, **118,** 118 (1971).
3. S. Iida and K. Ito, *ibid.*, **118,** 768 (1971).
4. D. W. Shaw, *ibid.*, **128,** 874 (1981).
5. J. J. Gannon and C. J. Nuese, *ibid.*, **121,** 1215 (1974).
6. Y. Mori and N. Watanabe, *ibid.*, **125,** 1510 (1978).
7. S. Adachi and H. Kawaguchi, *ibid.*, **128,** 1342 (1981).
8. H. C. Gatos and M. C. Lavine, *ibid.*, **107,** 427 (1960).
9. E. Biedermann and K. Brack, *ibid.*, **113,** 1088 (1966).
10. J. G. Grabmaier and C. B. Watson, *Phys. Status Solidi*, **32,** K13 (1969).
11. T. H. Yeh and A. E. Blakeslee, *This Journal*, **110,** 1018 (1963).
12. S. Adachi, *ibid.*, **129,** 610 (1982).
13. S. Adachi, Y. Noguchi, and H. Kawaguchi, *ibid.*, **129,** 1524 (1982).
14. J. L. Merz and R. A. Logan, *J. Appl. Phys.*, **47,** 3503 (1976).
15. S. Adachi, H. Kawaguchi, and G. Iwane, *J. Mater. Sci.*, **16,** 2449 (1981).
16. J. L. Richard and A. J. Crocker, *J. Appl. Phys.*, **31,** 611 (1960).
17. B. Tuck, J. S. M. Mills, and A. J. Hartwill, *J. Mater. Sci.*, **11,** 847 (1976).
18. D. J. Stirland, *ibid.*, **9,** 969 (1974).
19. F. K-Kuhnenfeld, Inst. Phys. Conf. Ser. No. 33a, 158 (1977).
20. V. L. Rideout, *This Journal*, **119,** 1778 (1972).
21. D. W. Shaw, *ibid.*, **113,** 958 (1966).
22. I. Shiota, K. Motoya, T. Ohmi, N. Miyamoto, and J. Nishizawa, *ibid.*, **124,** 155 (1977).
23. T. Kobayashi and K. Sugiyama, *Jpn. J. Appl. Phys.*, **12,** 619 (1973).
24. M. M. Fakter, D. G. Fiddyment, and M. R. Taylor, *This Journal*, **122,** 1566 (1975).
25. C. J. Nuese and J. J. Gannon, *ibid.*, **117,** 1094 (1970).
26. J. C. Dyment and G. A. Rozgonyi, *ibid.*, **118,** 1346 (1971).
27. L. F. Eastman, R. Stall, D. Woodard, N. Dandekar, C. E. C. Wood, M. R. Shur, and K. Board, *Electron. Lett.*, **13,** 525 (1980).
28. S. Adachi, M. Kawashima, K. Kumabe, K. Yokoyama, and M. Tomizawa, *IEEE Electron Dev. Lett.*, **edl-3,** 409 (1982).

On the Structural and Luminescent Properties of the M′ $LnTaO_4$ Rare Earth Tantalates

L. H. Brixner and H.-y. Chen

E. I. du Pont de Nemours and Company, Central Research and Development Department, Experimental Station, Wilmington, Delaware 19898

ABSTRACT

The structure of M′ $YTaO_4$ has been redetermined and was refined to an R value of 0.034. M′ $YTaO_4$ crystallizes in P2/a symmetry with a = 5.298(1), b = 5.451(1), c = 5.111(1) Å, β = 96.45 deg. At temperatures >1450°C, M′ $YTaO_4$ will convert by way of a reconstructive transformation into the $I4_1/a$ symmetry of scheelite, and, upon cooling, a second-order ferroelastic transition (4/mF2/m) to M (fergusonite) $YTaO_4$ occurs. There are significant structural differences between M and M′ $YTaO_4$ which are discussed. M′ $LnTaO_4$ compounds exist from Ln = Sm to Lu. As a host for luminescent ions, M′ $YTaO_4$ is superior to the M modification, as well as all other compounds in the Y_2O_3/Ta_2O_5 phase diagram.

Structure

Contrary to the $LnNbO_4$-type rare earth niobates (1), which exhibit only one structural type (fergusonite) at room temperature, the tantalates crystallize in three different structures: the $P2_1/n$ type for La, Ce, and Pr (2); the fergusonite or M type (1) for Nd, Sm, Eu, Gd, Tb, Dy, Ho, and Er; and the M′ type (3) of Tm, Yb, and Lu. The latter type (M′) is the true equilibrium phase at room temperature, and all of the M-type tantalates (except Nd) also crystallize in this structure if prepared under appropriate conditions. In addition to these three structures, all $LnTaO_4$ tantalates convert to the $I4_1/a$ structure type (scheelite) at temperatures generally >1400°C.

Historically, Ferguson (4) in 1957 was first to describe both natural fergusonite (an yttrium-niobium-tantalate) as well as synthetic $YTaO_4$ correctly as crystallizing in monoclinic symmetry with the probable space group I2/a. This corrected the previous assumption originating with the morphological description by Haidinger (5) that fergusonite would be tetragonal and of scheelite type, which was also held by Barth (6) and Komkov (7). The first comprehensive listing of parameters for most $LnTaO_4$-type rare earth tantalates was given by Keller (1) in 1962. Keller could not characterize La, Ce, and $PrTaO_4$, as well as Tm, Yb, and $LuTaO_4$. The structure of the first three tantalates was reported by Wolten and Chase (2) to be $P2_1/n$, and the latter three tantalates could be structurally identified when Wolten (3) described yet another modification of $YTaO_4$ in the space group P2/a. Although Wolten (3) stated that this modification also exists for the tantalates of Sm to Yb, he did not report lattice parameters. Some of these (Er, Tm, Yb) appeared in the literature in form of ASTM file cards by McIlvried and McCarthy (8), who also described M′ $LuTaO_4$. The high temperature tetragonal ($I4_1/a$) modification of Nd, Sm, Gd, Tb, and $HoTaO_4$ was described by Stubican (9). In addition to the M′ structure of $YTaO_4$, we report here the cell dimensions of all $LnTaO_4$ compounds, both for the M and M′ forms, wherever they exist.

Key words: inorganic, crystallography, x-rays, luminescence.

Luminescence

While the luminescence of $CaWO_4$ was studied as early as 1897 (10), fluorescence properties of the rare earth tantalates were not mentioned in the literature until 1964 (11). Later on, extensive luminescence studies with the M (fergusonite) type rare earth tantalates (where Ln = Gd, Y, and Lu) were carried out by Blasse and Bril (12). These authors were primarily concerned with the energy and charge transfer processes of excitation via u.v. as well as electrons, and they recognized the NbO_4 group to be an efficient luminescent center in the fergusonite $YTaO_4$ host, where tetrahedral local site symmetry was assumed.

The dual purpose of the present paper was to confirm or correct Wolten's (3) structure for M′ $YTaO_4$, which was only refined to R = 15%, and to study the efficiency of some luminescing rare earths as well as

Nb^{+5} in this particular structure, specifically under x-ray excitation.

Experimental

Materials preparation

The phosphors described in this paper were prepared from the constituent components Ln_2O_3 and Ta_2O_5 or Nb_2O_5. The rare earth oxides were generally of 99.9+% purity. They were obtained from Research Chemicals Corporation and were always prefired in air at 1000°-1100°C to eliminate any absorbed moisture or CO_2. Ta_2O_5 and Nb_2O_5 were of "optical" quality from Kawecki/Berylco. These components were also prefired at 1000°C. For all phosphors, stoichiometric quantities were mixed for ½ hr with a spex mill or a paint shaker (depending on size of preparation, varying from 10g to 1000g), and fired in recrystallized Al_2O_3 containers in air at 1200°C for 8-10 hr. The reaction product was then milled in a urethane lined vessel on a Sweco mill, using Freon®-TF[1] solvent as grinding medium, for about 6 hr. After removal of the liquid, the phosphor was refired—either by itself or in the presence of 50 weight percent (w/o) Li_2SO_4—at 1250°C for another 10-14 hr. In the cases where flux was used, it was leached with water, followed by methanol rinsing, and drying at 130°C. After this procedure, single phase, well-crystallized products were obtained. For the M′ $YTaO_4$ single crystal studies, a special slow cool (5°C/hr) run using LiCl flux was carried out in a sealed Pt tube, starting at 1300°C.

X-ray studies

Powder examination.—The x-ray powder diffraction patterns of all reported compounds were obtained with a Guinier Hägg-type focusing camera (radius = 40 mm). The radiation was monochromatic $CuK_{\alpha 1}$ (λ = 1.5404Å), and Si (a = 5.4305Å) was used as an internal standard. Line positions on the film were determined to ±5 μm with a David Mann film reader (a precision screw, split-image comparator). Intensities were estimated by oscilloscopic comparison of film density with the strongest line of the pattern. Refined cell dimensions were obtained by a least squares procedure (local computer program).

Single-crystal studies.—All the crystals examined were twinned in such a way that the two parts of the crystal were the mirror image of each other across the bc-plane, and the angle between the two a-axes was about 12.1°. The diffraction patterns clearly showed that the crystal was twinned and could be separated into two parts except for the zone (okl) with h = 0, where there was a complete superposition. Intensity data suitable for structure refinements were obtained from such twinned crystals.

Intensity data were obtained on a crystal, approximately 0.05 × 0.05 × 0.027 mm, with a Picker FACS-I diffractometer. To reduce absorption problems, AgK_α radiation was used. (λ = 0.05608Å and μ = 319.2 cm^{-1} for $YTaO_4$.) The crystal was mounted with the a*-axis on the spindle. Using nine strong reflections with 2θ between 8° and 25°, the orientation matrix of the crystal was refined, and the corresponding parameters for the monoclinic cell were as follows: a = 5.291 (9), b = 5.431(8), c = 5.098(8)Å, and β = 96.11° in excellent agreement with the powder data in Table I. The extinction condition, hol: h = 2n + 1, confirmed the space group assignment by Wolten (*loc. cit.*). A total of 617 reflections from the hemisphere (±h,k,±1) were collected for $2\theta \leq 40°$. The intensities were measured by scanning in the $2\theta/\omega$ mode at a 4°/min scan rate and a scan range of $\Delta\theta = 1.20 + 0.02 \tan\theta$. Background was obtained by stationary counting at the scan extremes for 40 sec each. After the completion of the data collection, a mirror symmetry operation was applied to the orientation matrix, and without further refinement the reflections of the counter part of the twinned crystal were also collected.[2] This data set, however, was not used in the structure analysis.

[1] Freon® — TF, trichlorotrifluoroethane.

Table I. Cell edges of the $LnTaO_4$-type rare earth tantalates including the M′ polymorphs

Ln	a, A	b, A	c, A	β, deg	V, A^3	ρ, g/ml^{-1}	Type
La	15.008	5.596	3.905	93.4	327.4	7.78	$P2_1/n$
Ce	15.015	5.500	3.873	93.3	319.3	8.00	$P2_1/n$
Pr	15.016	5.495	3.867	94.2	318.2	8.08	$P2_1/n$
Nd	5.512	11.234	5.113	95.7	157.5	8.21	M
Sm	5.458	11.139	5.092	95.7	154.0	8.52	M
	5.385	5.546	5.196	96.7	154.1	8.51	M′
Eu	5.429	11.098	5.088	95.7	152.5	8.64	M
	5.368	5.525	5.181	96.7	152.6	8.63	M′
Gd	5.406	11.065	5.084	95.6	151.3	8.83	M
	5.356	5.509	5.168	96.7	151.5	8.81	M′
Tb	5.382	11.016	5.066	95.7	149.4	8.97	M
	5.338	5.489	5.142	96.6	149.7	8.96	M′
Dy	5.349	10.970	5.061	95.6	147.8	9.41	M
	5.318	5.471	5.130	96.6	148.3	9.12	M′
Ho	5.330	10.937	5.055	95.5	146.6	9.28	M
	5.302	5.453	5.115	96.5	146.9	9.26	M′
Er	5.307	10.900	5.047	95.5	145.3	9.42	M
	5.286	5.440	5.101	96.4	145.8	9.39	M′
Tm	5.290	10.861	5.035	95.5	144.0	9.54	M
	5.272	5.432	5.080	96.4	144.6	9.50	M′
Yb	5.278	10.831	5.034	95.2	143.2	9.69	M
	5.254	5.423	5.071	96.2	143.6	9.57	M′
Lu	5.253	10.815	5.024	95.4	142.1	9.81	M
	5.239	5.425	5.060	96.1	143.0	9.75	M′

Because of the high absorption coefficient of $YTaO_4$, absorption corrections to the intensities were essential. These were carried out by using the ACACA program with the ϕ-scan data of the (200) reflection at χ = 270°. The grid size was 4 × 6 × 8, and there were totally 288 grid points in a 5 × 10^{-8} cm^3 volume of the crystal, which was treated as a single crystal in the calculation of the transmission coefficient. The calculated transmission coefficient ranged from 0.26 to 0.55. The second set of data was not corrected for absorption.

Excluding the entire (okl) zone, the data were averaged to yield a data set of 274 unique reflections of which 242 had $I > 2\sigma(F)$. For the refinement, the 1972 x-ray programs compiled by Stewart (13) were used, and all the reflections assumed unit weight. Starting with the parameter reported by Wolten, the refinement converged very rapidly to R = 0.034 and R_w = 0.056 with 29 variables including anisotropical thermal parameters for Ta and Y atoms. The thermal parameters of the O atoms were refined isotropically and are reported with the interatomic distances in Tables II and III.

Optical studies

All u.v.-excited fluorescent emission spectra were run with a Perkin-Elmer MPF spectrophotometer. Raman spectra were recorded on a J-Y laser Raman microprobe. Spectral slit widths were 3-4 cm^{-1}, and the 5145Å line from an argon ion laser was used. Detection was made with an RCA C31034 phototube operated in the photon counting mode. The x-ray excited spectra were generally obtained with 30 kVp Mo radiation from a GE XRD-5 generator modified as shown in Fig. 1.

Results and Discussion

Structural Data

The structure of M′ $YTaO_4$ presented by Wolten (3) is basically correct, particularly in the positioning of the metal atoms. With a final R factor of 0.146, his Y atoms were off by less than 0.02Å while O atoms only are off by 0.15-0.20Å. With the atoms more accurately positioned in the present study, a more detailed analysis of the interatomic distances and the coordination numbers can be attempted. The Y atoms (Fig. 2) are 8-coordinated. Looking along the b-axis, the eight O atoms resemble a distorted cube, but the coordination can be best described as a distorted square anti-

[2] The successful data collection after the transformation supported the proposed twinning mechanism.

Table II. Positional and thermal parameters

Atom	Pt. sym	x	y	z	B(11) or Bo	B(22)	B(33)	B(12)	B(13)	B(23)
Ta		0.25	0.3056(2)	0.5	0.06(6)	0.17(6)	0.25(6)	0	0.00(3)	0
Y		0.25	0.7658(5)	0	0.34(9)	0.21(9)	0.48(10)	0	0.00(6)	0
O(1)	1	0.489(2)	0.434(2)	0.268(2)	0.3(2)					
O(2)	1	0.102(2)	0.084(2)	0.252(2)	0.4(2)					

Table III. Interatomic distances

Ta-O				Y-O			
		This study	Wolten			This study	Wolten
O(2)	2x	1.857(13)	1.94	O(2)	2x	2.295(13)	2.25
O(1)	2x	1.950(13)	2.03	O(1)	2x	2.315(13)	2.34
O(1)	2x	2.226(13)	2.14	O(2)	2x	2.339(13)	2.40
				O(1)	2x	2.472(13)	2.42
Average:		1.98		Average:		2.355(80)	

Table IV. High temperature x-ray data for M' $YTaO_4$

	1375°C	25°C
a	= 5.302Å	5.298Å
b	= 5.554Å	5.451Å
c	= 5.115Å	5.111Å
β	= 96.45 deg	96.45 deg
V	= 149.6 $Å^3$	146.7 $Å^3$

prism with the unique direction along the c-axis. The two distorted squares projected on the ab-plane twist over 30°, as compared with 45° expected for a square antiprism. The average Y-O distance is 2.355Å, in very good agreement with the predicted value of 2.37Å by Shannon and Prewitt (14). The Ta atoms (Fig. 2) are in a distorted octahedral coordination, with four shorter Ta-O bonds at 1.86 and 1.95Å and two 0.4Å longer at 2.23Å. The former, however, do not form a regular tetrahedron, since three of them are essentially coplanar. As a result, it would need TaO_6 rather than TaO_4 to complete the coordination description. An overall view of the structure is shown in Fig. 3.

The coordinations of Y and Ta in the M'-phase differ from those of the scheelite and the fergusonite phases. The most significant difference is in the coordination of the Ta atoms. In scheelite as well as in fergusonite, the Ta atoms are essentially tetrahedrally coordinated with a second, relatively larger tetrahedron at the immediate surrounding, forming a distorted cube. A similar appearance is also present in the M'-phase, but the two tetrahedra transform into an octahedron, allowing two O atoms to move further away. The difference between the M and M' structures arises from a stacking in different sequence of similar building blocks, and the transformation requires a motion of large blocks *in toto*, as suggested by Wolten. Such a transformation will only happen at elevated temperatures, and is definitely of the first-order type and disruptive.

Efforts were made to directly observe this disruptive transformation in a Rigaku high-temperature diffractometer. Unfortunately, equipment limitation to 1375°C did not allow conversion to the $I4_1/a$ scheelite type. The data are shown in Table IV, and it is obvious that β did not change at all, contrary to the smooth, reversible second-order change of fergusonite (M) to scheelite (T), where β gradually goes to 90°, as shown by Stubican (9). We did, however, run rapid quenching experiments with $YTaO_4$, and could approximate the transition temperature to between 1450°C and 1460°C, as indicated in Table V. These data suggest that all M' $YTaO_4$ preparations have to be made below 1450°C, and, furthermore, that M' is really the true equilibrium phase at room temperature with the M modification existing in the metastable state. Phase transition temperatures for other M' $LnTaO_4$ tantalates, where Ln = Nd, Sm, Gd, Tb, and Ho have been reported by Stubican (9). We grew a single crystal of $NdTaO_4$ at 1980° ± 10°C in the scheelite structure, and could observe the two prerequisite domain walls for the Aizu (15) trans-

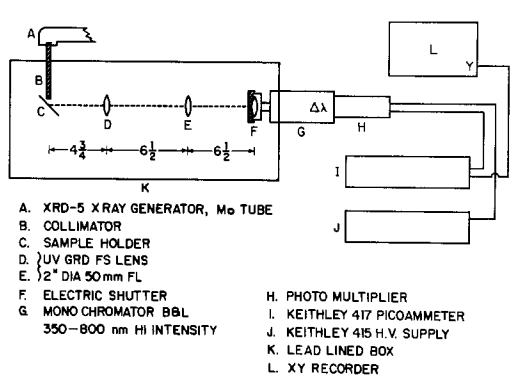

Fig. 1. Schematic showing phosphor examination under x-ray excitation.

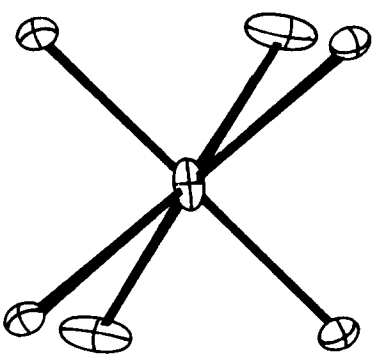

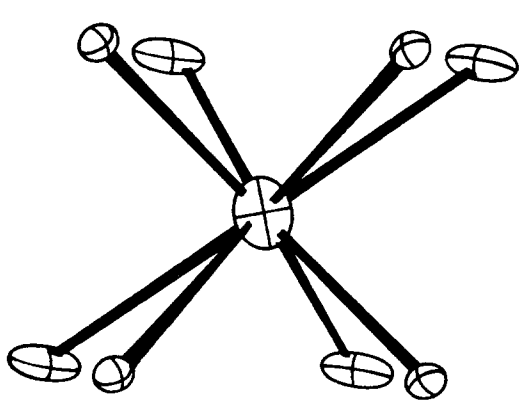

Fig. 2. Y (top) and Ta (bottom) coordination in M' $YTaO_4$

Table V. $YTaO_4$ cell dimensions after quenching to room temperature

T, °C	Time, hr	a, A	b, A	c, A	β, deg	V, A³	Structure
1450	14	5.298 ±1	5.451 ± 1	5.111 ± 1	96.4	146.6	M'
1480	14	5.329 ± 1	10.929 ± 2	5.056 ± 1	95.6	293.1 (146.5)	M

formation 4/mF2/m. This is further evidence for the centric structure of fergusonite.

It was also suggested by Sleight (16) that the M' structure could be viewed as related or identical to the P2/c symmetry of wolframites such as $InTaO_4$ or $NiWO_4$. The fact that this is tempting is illustrated in Table VI, where, after appropriate conversion of P2/a to P2/c, $NiWO_4$ and $YTaO_4$ are compared. $InTaO_4$ is actually the wolframite with the largest A ion and the greatest cell volume. We, therefore, attempted to prepare solid solutions with it and the smallest known M' composition, which is $LuTaO_4$. The data are summarized in Table VII, and it is obvious that while some solid solubility occurs in the wolframite structure, there is essentially none in the M' structure. A plot of r^3 *vs.* cell volume as shown in Fig. 4 further illustrates the point that the M' structure of $YTaO_4$ has truly unique symmetry and is also not related to the M structure. This is contrary to what Wolten (3) indicated by stating that the powder patterns of the M and M' modification of $YTaO_4$ are "difficult to distinguish." To show the distinctive differences of powder data for the two forms, we report the first 20 lines of each structure in Tables VIII and IX. It is worth noting that for each compound, all lines were indexed. To a *d*-value of about 1.3Å, there are typically 40 reflections for the M' and 48 for the M structure. The major difference is seen in $\Sigma(hkl)^2$, which is even for M and mixed for M'. The differences can also easily be seen in diffractometer patterns or Guinier films. To further support the difference in local site symmetry, we show two Raman spectra in Fig. 5, without giving any detailed vibrational frequency assignments. Much has been made of the difference between the M and M' structure, but this is quite important since it is the sole basis for the superior luminescent efficiency which is nearly two times greater for pure M' $YTaO_4$ than it is for M $YTaO_4$. This will be discussed in more detail in the luminescence section.

In addition to our extensive studies on M' $YTaO_4$, we prepared all other M' rare earth tantalates where they exist and summarize the cell constants together with those for the M modifications in Table I. For completeness, we have included the $P2_1/n$ compounds of La, Ce, and Pr. In Fig. 6, we have chosen to halve the cell volumes of the M modifications to show that the two volume lines appear to converge at $NdTaO_4$, for which no M' modification appears to exist. This would put an upper limit of about 1.11Å on the ionic radius of Ln^{+3} for the existence of M'. At the lower end, we find that the cell volume difference is largest for M and M' $LuTaO_4$. Since the densities of the M structure are generally slightly higher (see Table I), this suggests that pressure should help in preparing this modification. In fact, we could not prepare pure M compounds of Tm, Yb, and $LuTaO_4$ without pressure at 1600°C, and, therefore, we prepared them at 60 kbars and 1400°C. In general, the M cell dimensions agree well with those given by Keller (1), and the M' numbers are in fair agreement with those which were reported by McIlvried and McCarthy (8), except for $TmTaO_4$, where those authors find a larger volume for the M modification, which cannot be correct.

Table VI. Comparison of wolframite-type $NiWO_4$ and M' $YTaO_4$ in P2/c symmetry

	$NiWO_4$	$YTaO_4$(M')	$InTaO_4$
a	4.600Å	5.110Å	5.160
b	5.665Å	5.451Å	5.778
c	4.912Å	5.292Å	4.829
B	90.1°	96.4°	91.4
Ax	0.5	0.5	
Ay	0.653	0.769	
Az	0.25	0.25	
Mx	0.0	0.0	
My	0.18	0.306	
Mz	0.25	0.25	
O_1x	0.22	0.242	
O_1y	0.11	0.93	
O_1z	0.96	0.92	
O_2x	0.26	0.23	
O_2y	0.38	0.54	
O_2z	0.39	0.51	

Since Nb^{+5} had never been incorporated into M' $YTaO_4$, it was of interest to study the M' structure as a function of Nb-concentration in $YTa_{1-x}Nb_xO_4$ particularly since no rare earth niobates of the M' structure are known. This information is summarized in Table X, and the most striking result is the fact that the M' structure cannot support more than 15 m/o Nb^{+5}, despite the fact that it is essentially identical (0.64Å for VI coordination) in size to Ta^{+5} according to Shannon (14). From 30 m/o Nb^{+5} on, all compounds crystallize in the fergusonite structure. No pure rare earth niobate is known to exist in the M' structure, and this may have to do with what Gingerich (18) reported—that M → T transition temperatures for these compounds are between 300° and 800°C. Even hydrothermal techniques at relatively low temperatures failed to produce M' $YNbO_4$. This is a rare case where a specific structure (M') is exclusively restricted to tan-

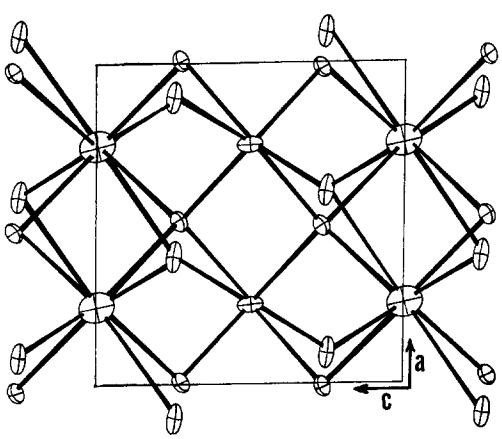

Fig. 3. b-axis projection of M' $YTaO_4$ structure

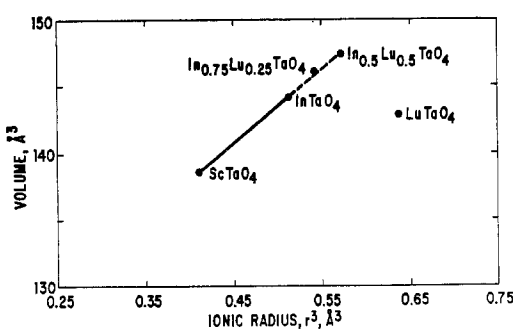

Fig. 4. Cell volumes *vs.* r^3 for 6 coordination of some wolframites and for M' $LuTaO_4$.

Table VII. Cell dimensions of some $Lu_{1-x}In_xTaO_4$ solid solutions

x	Composition	Type	a, A	b, A	c, A	β, deg	V, A³	Comment
0	$LuTaO_4$	M'	5.238	5.425	5.060	96.1	146.2	—
0.25	$Lu_{0.75}In_{0.25}TaO_4$	—	—	—	—	—	—	2 phase
0.5	$Lu_{0.5}In_{0.5}TaO_4$	W	4.889	5.811	5.189	93.0	147.3	—
0.75	$Lu_{0.25}In_{0.75}TaO_4$	W	4.988	5.644	5.203	93.9	146.2	—
1.0	$InTaO_4$	W	4.828	5.779	5.158	94.4	143.8	—

Table VIII. Observed and calculated *d*-values for the first 20 lines of M-type $LuTaO_4$

Line No.	I	h	k	l	$d_{(obs)}$	$d_{(calc)}$
1	10	0	2	0	5.401	5.407
2	10	1	1	0	4.705	4.708
3	5	0	1	1	4.538	4.540
4	100	−1	2	1	3.107	3.107
5	15	1	3	0	2.968	2.968
6	85	1	2	1	2.913	2.912
7	50	0	4	0	2.703	2.703
8	60	2	0	0	2.615	2.615
9	55	0	0	2	2.501	2.501
10	5	2	1	1	2.187	2.187
11	15	1	4	1	2.129	2.129
12	5	−2	3	1	2.005	2.004
13	5	1	5	0	1.999	1.998
14	15	0	5	1	1.985	1.985
15	5	−1	3	2	1.964	1.964
16	60	2	3	1	1.898	1.898
17	65	2	4	0	1.879	1.879
18	10	1	3	2	1.864	1.864
19	60	0	4	2	1.836	1.836
20	5	0	6	0	1.802	1.802

Table IX. Observed and calculated *d*-values for the first 20 lines of M'-type $LuTaO_4$

Line No.	I	h	k	l	$d_{(obs)}$
1	10	0	1	0	5.436
2	35	0	1	1	3.692
3	100	−1	1	1	3.130
5	90	1	1	1	2.908
6	60	0	2	0	2.713
7	65	2	0	0	2.605
9	55	0	0	2	2.516
10	35	1	2	0	2.406
11	5	0	1	2	2.282
12	5	−2	1	1	2.211
13	20	1	2	1	2.130
14	15	2	1	1	2.053
15	60	12	0	2	1.913
16	65	2	2	0	1.878
17	60	0	2	2	1.844
19	5	−2	2	1	1.807
20	20	−1	2	2	1.782

Table X. Cell dimensions for the $YTa_{1-x}Nb_xO_4$ system

Composition	a, A ± 3	b, A ± 3	c, A ± 3	β, deg	V, A³	ρ, g/ml⁻¹
$YNbO_4$	5.2989	10.9488	5.0717	94.569	293.31	5.56_7
$YNb_{0.8}Ta_{0.2}O_4$	5.3045	10.9412	5.0668	94.813	293.05	5.96_9
$YNb_{0.6}Ta_{0.4}O_4$	5.3108	10.9394	5.0628	95.027	293.00	6.36_9
$YNb_{0.4}Ta_{0.6}O_4$	5.3156	10.9349	5.0583	95.214	292.78	6.77_4
$YNb_{0.3}Ta_{0.7}O_4$	5.3207	10.9339	5.0572	95.320	292.94	6.97_0
$YNb_{0.25}Ta_{0.75}O_4$	2-phase		M' + M			—
$YNb_{0.2}Ta_{0.8}O_4$	2-phase		about 50% each		M' + M	—
$YNb_{0.15}Ta_{0.85}O_4$	5.2991	5.4471	5.1109	96.425	146.60	7.26_8
$YNb_{0.1}Ta_{0.9}O_4$	5.2989	5.4469	5.1107	96.430	146.58	6.36_1
$YNb_{0.05}Ta_{0.95}O_4$	5.2975	5.4486	5.1103	96.453	146.57	7.46_8

talates. In almost all other known structures niobates and tantalates are always isomorphous.

Luminescence

$YTaO_4$ as host.—X-ray excitation.—Since the ultimately intended practical utilization of these tantalate-based phosphors is in x-ray intensifying screens, the x-ray excited data will be discussed first.

To have near-optimum efficiency of a phosphor, whether for color TV, fluorescent lamps, electroluminescence, or x-ray screens, one should have well-crystallized, preferably polyhedral particles of approximately 3-10 μm diameter. Larger sizes would cause difficulty in screen making, and efficiency losses are experienced via internal scatter as the particle size gets much below ~3μ. It was, therefore, a primary objective to obtain M' $YTaO_4$ in a form approximating the indicated dimensions. Since $YTaO_4$ is an extraordinarily refractory material, with a melting point near 2000°C, high reaction temperatures are needed. Only Li_2SO_4 as a flux produced the phosphor shown in Fig. 7.

One of the key advantages of M' $YTaO_4$ over $CaWO_4$ is the higher density of 7.56 g/ml⁻¹ *vs.* 6.06 g/ml⁻¹, combined with the fact that Y, with a K_α absorption

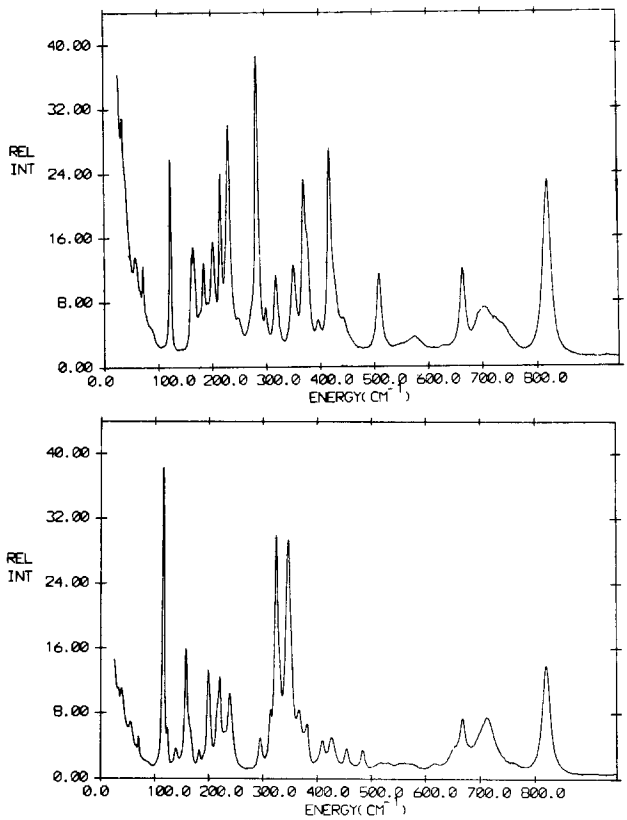

Fig. 5. Raman spectra of M' (top) and M $YTaO_4$

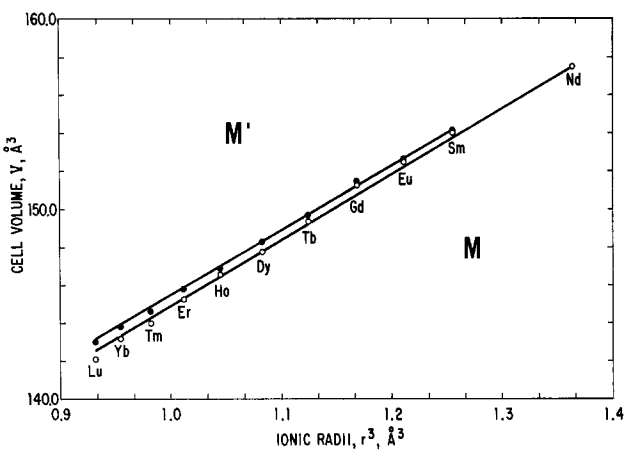

Fig. 6. Cell volumes *vs.* r^3 for both the M' (solid circles) and M (open circles) modifications of the $LnTaO_4$ rare earth tantalates.

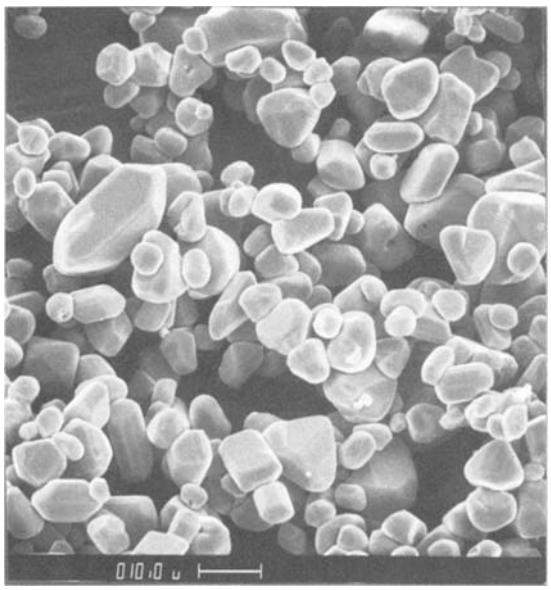

Fig. 7. Typical morphology of M' $YNb_{0.02}TaO_{0.98}O_4$ phosphor. Note bar length = 10 μm.

edge at 17.04 keV contributes to the x-ray absorption process, particularly if soft radiation such as Mo is used. This fact is best illustrated in Fig. 8, which shows x-ray absorption as a function of keV.

Next to absorption, intensity of emission is of great importance. Undoped M' $YTaO_4$ emits at 337 nm and is

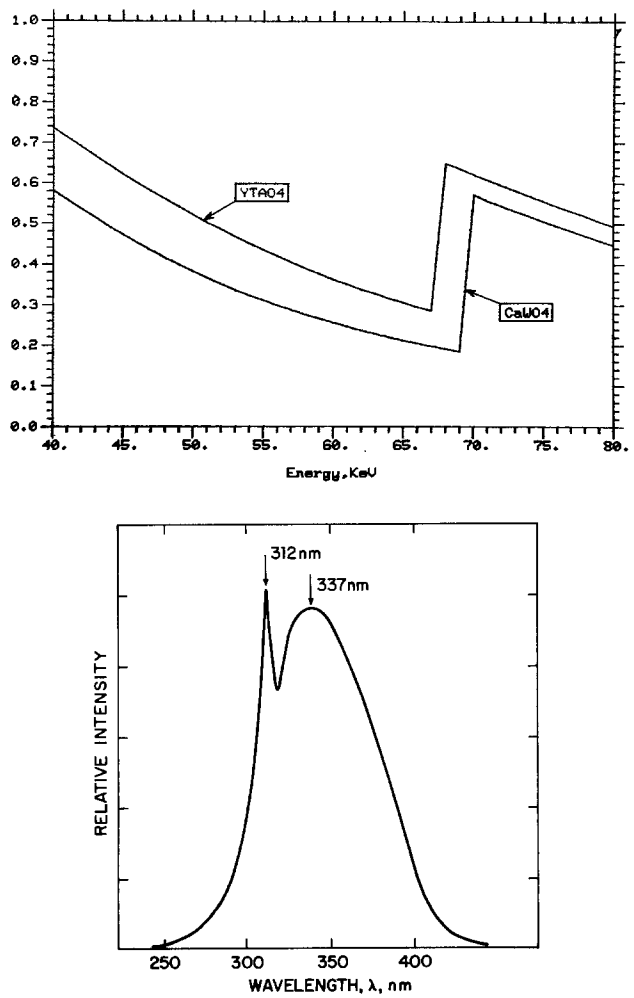

Fig. 8 (Top) Relative x-ray absorption of $YTaO_4$ and $CaWO_4$ (Bottom) 30 kVp (Mo) x-ray-excited fluorescent emission spectrum of M' $YTaO_4$.

superior to $CaWO_4$ in speed. A comparsion of these speeds is made in Table XI, and Fig. 8a shows the x-ray excited fluorescent emission of $YTaO_4$. The sharp line at 312 nm is no artifact, but rather emission stemming from inadvertent impurities of Gd^{+3} in Y_2O_3. The higher energy emission relative to $CaWO_4$ (which peaks at 440 nm) is actually desirable in combination with blue film, which is more sensitive in that region. There also is very little, if any, "crossover" of light to the other side of the double emulsion film. This yields exceptional sharpness for this phosphor. The emission at 337 nm is ascribed to the TaO_4^* luminescent center being excited via a charge-transfer process (12). For TaO_4, this charge transfer transition requires considerably higher energy than for the NbO_4 case, which is the reason why $YTaO_4$ cannot be excited with 2537Å u.v. Blasse's (12) reported emission of ~330 nm for M $YTaO_4$ via 229 nm excitation is very close to the emission observed under x-ray excitation. The speed difference for the M and M' $YTaO_4$ structures as reported in Table XI is, therefore, ascribed to a more efficient charge-transfer process for the M' structure, where the average Ta-O distances are closer than in the M structure (see Table II).

If Nb is substituted for Ta in M' YTaO, even more efficient emission is observed. This is ascribed to energy transfer from the absorbing TaO_4 group, similar to the situation described by Blasse (19) for the $CaW_{1-x}Mo_xO_4$ system. Speeds as a function of Nb-concentration are represented in Fig. 9, where the M' and M region are separated by the shaded two-phase area. One can assume the overall efficiency curve to be composed of two individual curves for the M and M' structure, with peak emissions occurring at different concentrations. Although the peak for the M' composition is relatively narrow, $YTa_{0.98}Nb_{0.02}O_4$ can be considered to be the best composition for optimum speed. A direct comparison of the emission characteristics of this phosphor with Cronex®[3] Hi Plus-type $CaWO_4$ is made in Fig. 10 for equivalent thickness screens. The superior overall efficiency (area under the curve) combined with the higher energy emission is clearly evident.

Actual performance data under 80 kVp excitation of the new phosphor in a series of varying thickness screens are illustrated in Fig. 11.

At equivalent coating weight, the resolution of M' $YNb_{0.03}Ta_{0.97}O_4$ is also at least two line/pairs/mm greater than for $CaWO_4$, as seen in Fig. 12.

In addition to Nb substitution into the Ta site, we also substituted some of the fluorescing rare earth ions into the Y site of M' $YTaO_4$. This type of fluorescence has been discussed extensively for Eu^{+3} and Tb^{+3} in M $YTaO_4$ by Blasse (12), and is quite similar, although it is somewhat more efficient in M' $YTaO_4$. The x-ray excited spectra of $Y_{0.9}Eu_{0.1}TaO_4$ and $Y_{0.998}Tb_{0.002}TaO_4$ are shown in Fig. 13 and Fig. 14.

UV excitation.—As already stated, M' $YTaO_4$ by itself could not be excited with 2537Å u.v. As soon as even trace quantities of Nb^{+5} (0.001 mols or less) are introduced into M' $YtaO_4$, strong u.v.-excitable Nb fluorescence can be observed. Undoubtedly, the blue emission observed under 2537Å u.v. by Brixner (11) earlier was due to Nb^{+5} impurities in Ta_2O_5. When Nb^{+5} is introduced into M' $YTaO_4$. both excitation and emission move to lower energies, as shown in Fig. 15. The large Stokes shift of 14,062 cm^{-1} is similar (although slightly

[3] Cronex® Hi-Plus, $CaWO_4$. intensifying screen.

Table XI. Intensity of luminescence of M and M' $YTaO_4$

Modification	After °C	Relative speed (Hi-Plus = 1.0)
M	1500	0.63
M'	1200	1.16

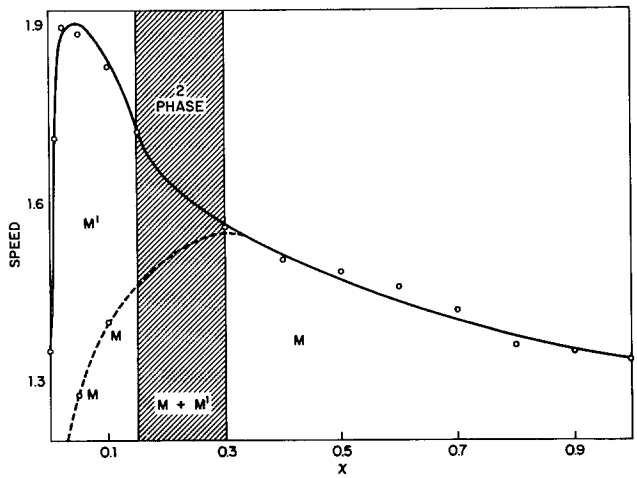

Fig. 9. Speed as a function of Nb^{+5} concentration x in $YTa_{1-x}Nb_xO_4$.

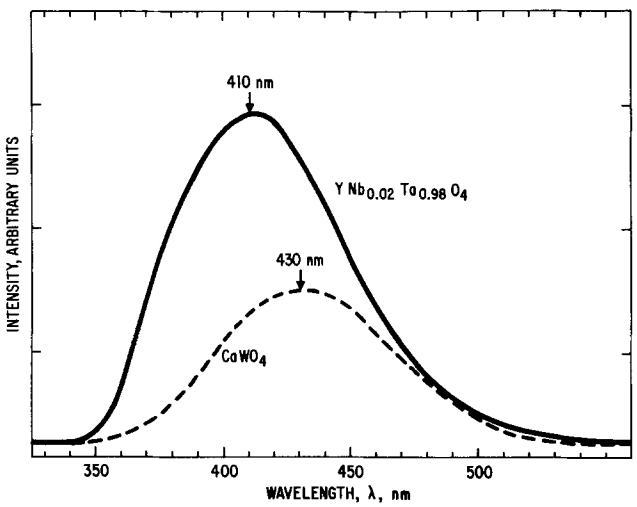

Fig. 10. 30 kVp (Mo) x-ray-excited fluorescent emission spectra of M' $YNb_{0.02}Ta_{0.98}O_4$ and $CaWO_4$.

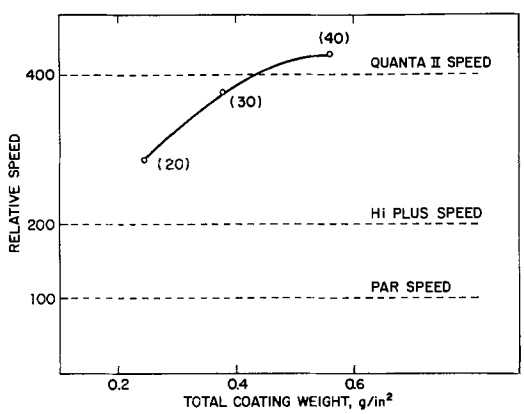

Fig. 11. Speed as a function of screen thickness for M' $YNb_{0.02}Ta_{0.98}O_4$ phosphor.

smaller) to that for $CaWO_4$, and is the reason for the relatively high thermal quenching temperature of >250°C for this phosphor.

$GdTaO_4$ as Host

Since the title compound also occurs in the M' modification, it was of interest to study its luminescent properties, particularly under x-ray excitation. With an x-ray K_α absorption edge of 50.2 keV, Gd also contributes significantly to the absorption process of typical medical (100 kVp) exposures, peaking near 60 keV. This is best illustrated in Fig. 16, where the $GdTaO_4$ absorption is compared to both $CaWO_4$ and Gd_2O_2S, another extensively used host for x-ray phosphors. Both below the Gd edge and above the W edge, $GdTaO_4$ is superior to the other phosphors. Additionally, M' $GdTaO_4$ has a density of 8.55 g/ml^{-1}, compared to (7.13 g/ml^{-1} and 6.06 g/ml^{-1} for Gd_2O_2S and

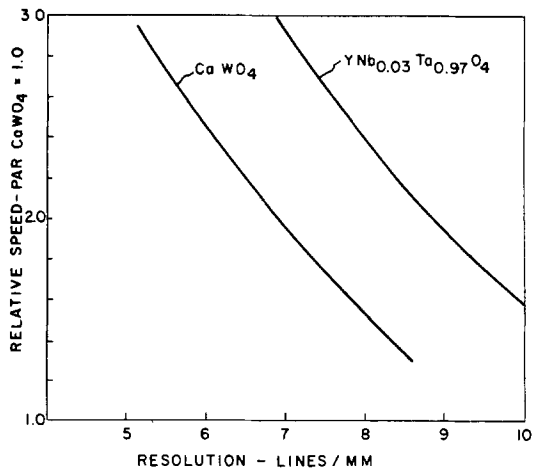

Fig. 12. Speed vs. resolution for equivalent thickness screens of M' $YNb_{0.03}Ta_{0.97}O_4$ and $CaWO_4$.

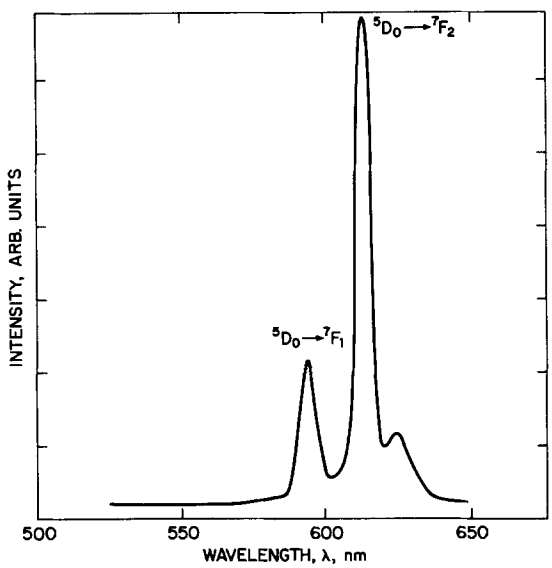

Fig. 13. 30 kVp (Mo) x-ray-excited fluorescent emission spectrum of $Y_{0.9}Eu_{0.1}TaO_4$.

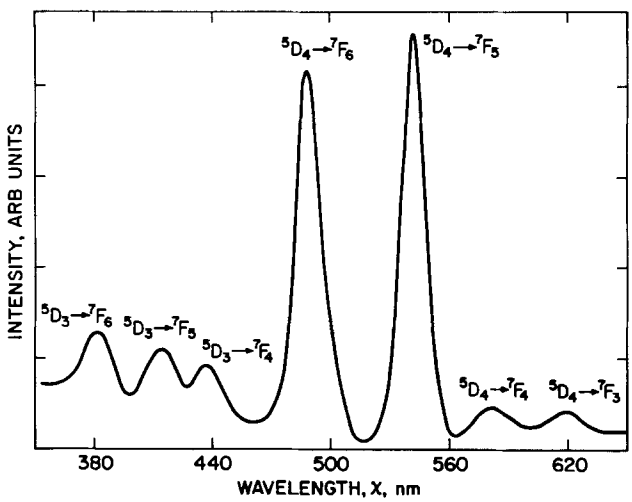

Fig. 14. 30 kVp (Mo) x-ray-excited fluorescent emission spectrum of $Y_{0.998}Tb_{0.002}TaO_4$.

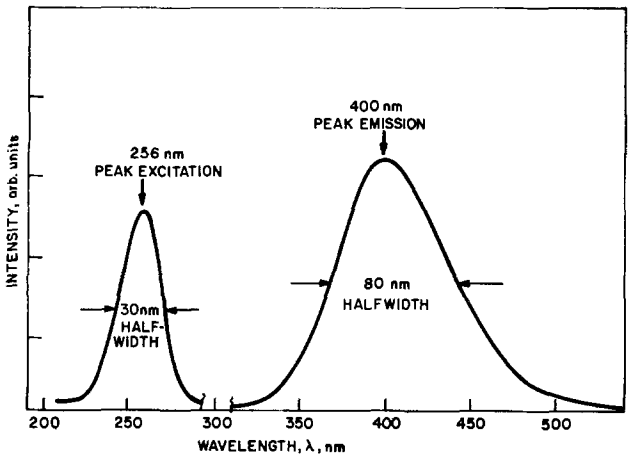

Fig. 15. UV excitation and emission spectra of $YNb_{0.05}Ta_{0.98}O_4$

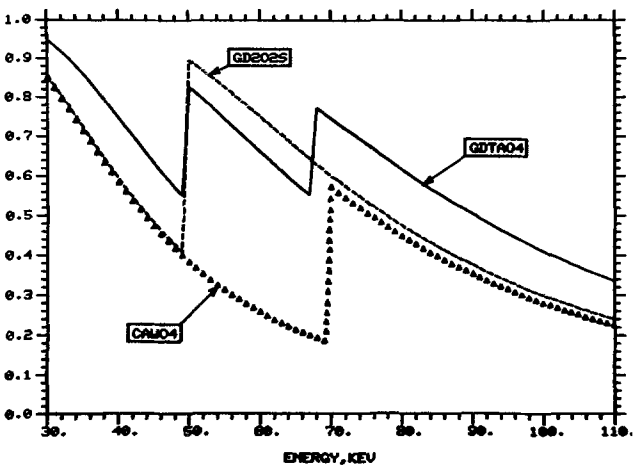

Fig. 16. Relative x-ray absorption of M' $GdTaO_4$, Gd_2O_2S, and $CaWO_4$.

$CaWO_4$, respectively. This further increases x-ray absorption per unit volume of phosphor. Absorption, however, is only one part of the overall x-ray-to-light conversion process. As far as luminescence is concerned, the situation with M' $GdTaO_4$ is quite different from that with M' $YTaO_4$, because we now have a rare earth with 7f electrons, allowing f → f emission from extremely low Gd^{+3} concentrations. This emission is rapidly concentration quenched, so that $GdTaO_4$ by itself does not emit. Nb^{+5} also is not an activator, since energy transfer to Gd^{+3} occurs and the emission is quenched. One can, however, introduce Tb^{+3} into M' $GdTaO_4$ and obtain efficient luminescence for both the $^5D_4 \rightarrow {}^7F_j$ and the higher energy $^5D_3 \rightarrow {}^7F_j$ transitions. At very low concentrations, a significant part of the spectrum is due to the $^5D_3 \rightarrow {}^7F_j$ emission, while at higher concentrations this emission is essentially quenched, as can be seen in Fig. 17 and Fig. 18. Neither phosphor is as efficient as the well-known green emitter Gd_2O_2S:Tb.

Finally, we looked at $LuTaO_4$, which has a density of 9.75 g/ml^{-1} and is one of the densest white materials known. Because of the extraordinary cost of Lu_2O_3 (~$2,000/pound), $LuTaO_4$ could, of course, never be considered as a realistic practical candidate. We examined only Nb^{+5} doping and found that, unlike $GdTaO_4$, it will yield efficient Nb^{+5} emission, quite similar to M' $YTaO_4$. While $YTaO_4$ has no f electrons at all, $LuTaO_4$ has a completely filled shell with 14. The u.v. excitation and emission spectra are shown in Fig. 19. One can see that peak fluorescence occurs at slightly higher energy than in $YTaO_4$:Nb. This yields a somewhat smaller Stokes shift of 12,360 cm^{-1}.

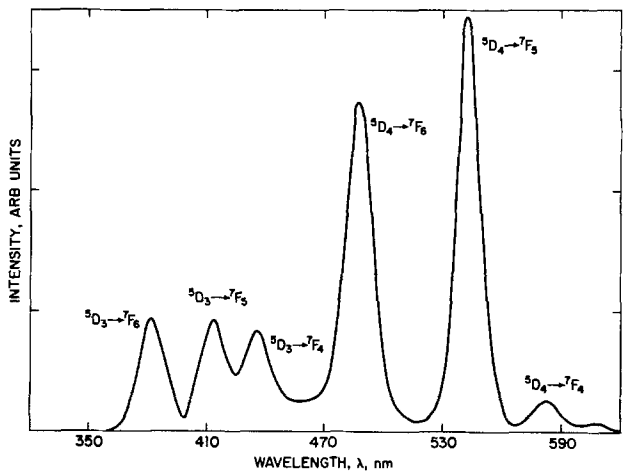

Fig. 17. 30 kVp (Mo) x-ray-excited fluorescent emission spectrum of $Gd_{0.998}Tb_{0.002}TaO_4$.

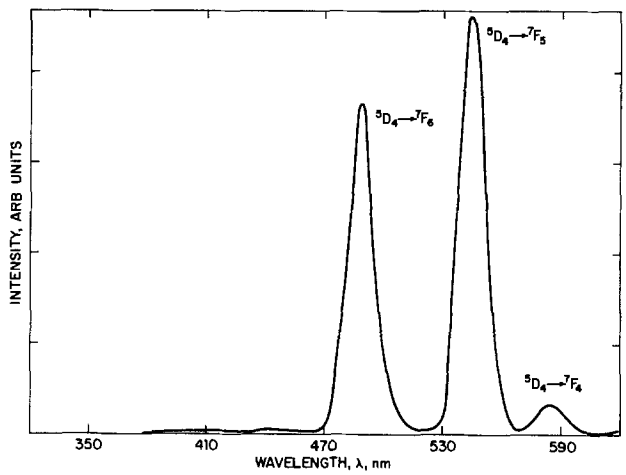

Fig. 18. 30 kVp x-ray-excited fluorescent emission spectrum of $Gd_{0.95}Tb_{0.05}TaO_4$.

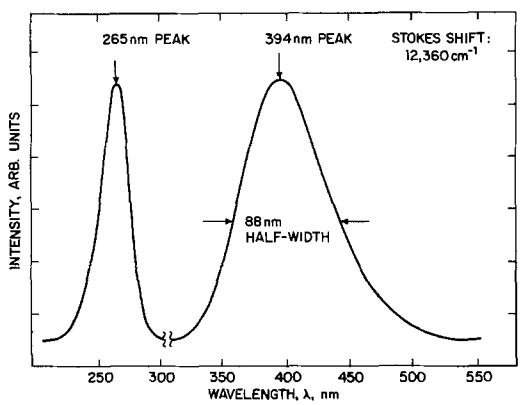

Fig. 19. UV excitation and emission spectra of M' $LuNb_{0.05}Ta_{0.95}O_4$

Conclusions

In summary, we can state that the M' rare earth tantalates show interesting luminescent behavior. This sets them apart from the fergusonite-type compositions because of the unique structural features of the M' structure. More detailed low temperature spectroscopy, life-time measurements, and Raman spectra evaluations certainly seem to be challenging objectives for further research.

Acknowledgments

The authors would like to thank Mrs. E. Matthews for running the u.v.-excited spectra, Dr. B. Chase for obtaining the Raman data, and Mr. J. W. Rooney for technical assistance.

Manuscript received June 1, 1983. This was Paper 508 presented at the Montreal, Quebec, Canada, Meeting of the Society, May 9-14, 1982.

E. I. du Pont de Nemours and Company assisted in meeting the publication costs of this article.

REFERENCES

1. C. Keller, *Z. Anorg. Allg. Chem.*, **318**, 89 (1962).
2. G. M. Wolten, *Inorg. Chem.*, **5**, 484 (1966).
3. G. M. Wolten, *Acta Crystallogr.*, **23**, 939 (1967).
4. R. B. Ferguson, *Can. Mineral.*, **6**, 72 (1957).
5. W. Haidinger, *Trans. R. Soc. Edinburgh*, **9**, 23 (1926).
6. T. F. W. Barth, *Nor. Geol. Tidsskr.*, **9**, 23 (1926).
7. A. I. Komkow, *Dokl. Akad. Nauk SSSR*, **126**, 853 (1959).
8. J. McIlvried and G. McCarthy, JCPDS, ASTM, 24-1339 (1974).
9. V. S. Stubican, *J. Am. Ceram. Soc.*, **47**, 55 (1964).
10. M. Pupin, "Radiologic Science for Technologists," p. 8, C. V. Mosby Company, St. Louis (1975).
11. L. H. Brixner, *This Journal*, **111**, 690 (1964).
12. G. Blasse and A. Bril, *J. Lumin.*, **3**, 109 (1970).
13. J. Stewart, Tech. Rep. TR-192, University of Maryland (1972).
14. R. D. Shannon and C. T. Prewitt, *Acta Crystallogr.*, **B25**, 925 (1969).
15. K. Aizu, *Phys. Rev.*, **B2**, 754 (1970).
16. A. W. Sleight, Private communication.
17. K. A. Gingerich and H. E. Baiv, *Adv. X-Ray Anal.*, **7**, 22 (1964).
18. G. Blasse and A. Bril, *J. Chem. Phys.*, **45**, 2350 (1966).

Photoluminescence of Zinc Silicate Doped with Al and Ti

H. Hess, A. Heim, and M. Scala

Institut für Festkörperphysik, Technische Universität, A-8010 Graz, Austria

ABSTRACT

Photoluminescence of sintered zinc orthosilicate doped with Al or Ti has been measured in the temperature range between 20 and 650 K, peak emissions being noted at 407 and 400 nm, respectively. The corresponding excitation spectra show peaks at 218 and 236 nm for Zn_2SiO_4:Al and at 218 and 232 nm for Zn_2SiO_4:Ti. The 218 nm peak must be assigned to the excitation of the undoped zinc silicate where doping with Al as well as Ti effects an enhancement of this band. The two phosphors have different decay times at room temperature (Zn_2SiO_4:Al,$t \approx 10$ sec; Zn_2SiO_4:Ti,$t \approx 10^{-3}$ sec). We observed the greatest quantum efficiency for the u.v.-blue emission approximately at activator concentrations of 1 mol percent (m/o) Al or 0.6 m/o Ti. Deviations from the linear dependence of the luminescence intensity on the photoexcitation intensity are observed above 400 K.

In a recent paper (1), we found that unactivated Zn_2SiO_4 has (300 K) emission and excitation bands at 385 and 218 nm with a decay time of 0.5 sec; a second emission band peaks at 285 nm, on excitation at 216 nm, decay time being $t \approx 10^{-2}$ sec. The latter emission is faint at room temperature increasing to low temperatures. Kröger (2) found no luminescence for unactivated Zn_2SiO_4 but a u.v.-blue cathodoluminescence emission for Zn_2SiO_4 activated by 1 mol percent (m/o) Ti which he attributes to tetravalent Ti^{4+}. Both Uehara *et al.* (3) and Leverenz (4) reported that the u.v.-blue cathodoluminescence emission of undoped Zn_2SiO_4 is greatly improved by the addition of TiO_2.

An efficiency enhancement of the conventional green emitting P1 phosphor (Zn_2SiO_4:Mn) by $AlPO_4$ addition was found by Chang *et al.* (5) to be of great practical interest because of its application to fluorescent lamps and screens in electronic devices. We have examined Al- and Ti-doped Zn_2SiO_4 in greater detail.

Experimental

The experimental setup and preparation of the phosphors are described in detail in an earlier work (1). Materials were synthesized by reacting 99% ZnO, 99.9% SiO_2 with 99.6% Al_2O_3 or 99.95% TiO_2 at 1200°C. After additional milling, pellets were pressed and sintered at 1200°-1480°C in air. The reflectance spectra were recorded at room temperature by the reference-beam technique of diffuse reflectance spectroscopy with a Beckman DK-2A spectroreflectometer. $BaSO_4$ was used as the standard. The absorbance has been determined from reflectance measurements using the relation $\alpha = 1 - \rho$. The measured excitation and emission spectra were corrected for the spectral distribution of the xenon lamp emission, the transmission of the monochromators, and the spectral sensitivity of the detector.

Key words: zinc silicate, aluminum, titanium, excitation, emission.

Results

Figure 1 shows the excitation and emission spectra of unactivated (curve 1) and Al_2O_3 activated (curve 2-4) zinc orthosilicate at room temperature. Besides the 218 nm excitation band of the undoped material, a new excitation band with a maximum at 234 nm arises with increasing Al_2O_3 content. The u.v.-emission band (285 nm) with an excitation maximum at 216 nm, which exists in the undoped zinc silicate only at low temperatures (1), disappears with increasing Al_2O_3 content so that an emission at 285 nm could not be measured at 20 K when 1 m/o Al_2O_3 was added to the "pure" material. Practically identical excitation and emission spectra were found by using Al_2O_3 or $AlPO_4$ as an initial ingredient for the introduction of Al as an activator. The excitation spectra of u.v.-blue luminescence of Zn_2SiO_4:Al are therefore composed of two bands: one located near the fundamental absorption

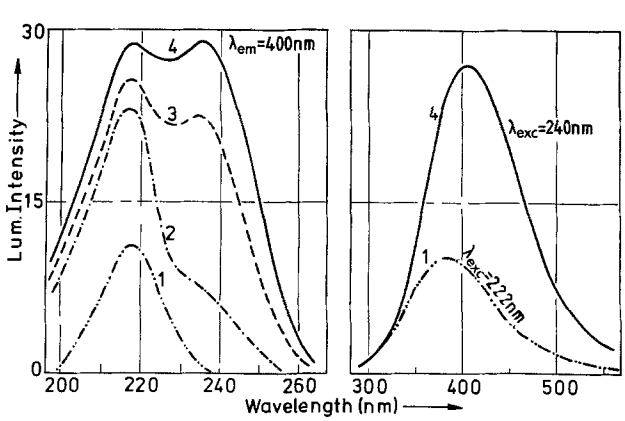

Fig. 1. Spectral characteristics of Zn_2SiO_4 doped with (1) 0 (2) 0, 1% (3) 0, 3% and (4) 2% Al_2O_3.

edge at about 216 to 219 nm, and the other located in a region 231 to 236 nm, which is characteristic of the luminescence center caused by doping with Al.

The emission of the Al-doped Zn_2SiO_4 exhibits a large maximum at about 407 nm at excitation with 240 nm with a tail extending into the green region (Fig. 1, curve 4). For excitation with 220 nm, the emission spectrum is shifted somewhat to a lower wavelength (λ_{max} = 400 nm). Cooling down to 20 K causes a shift of the emission spectra excited at 240 nm of about 5 nm to greater wavelengths (λ_{max} = 412 nm). None of the recorded spectra show any vibrational structural features. As we can see in Fig. 1, the half-width of the emission band of the Al-doped Zn_2SiO_4 is a little greater than that of the undoped material. It is therefore supposed that the broad emission band of Zn_2SiO_4:Al results from a close overlap of the emission band of the undoped Zn_2SiO_4 with a second emission band originating from Al doping. Evidence was found by measuring the decay curves at different wavelengths of the Al-doped Zn_2SiO_4 emission band.

The results of the decay measurements for several wavelengths of the u.v.-blue emission are shown in Fig. 2a for constant excitation intensity. The decay rate becomes greater as the excitation intensity is increased, indicating that a bimolecular process is responsible for the decay of luminescence. If the decay process of luminescence is governed by bimolecular kinetics, the equation $I = I_0/(1 + at)^p$ holds (6). In this case however, the curves cannot all be fit by the same a and p values. Thus Fig. 2a shows that decay curves are nearly equal for emission wavelengths $\lambda > 520$ nm. In the wavelength range $\lambda < 520$ nm, the decay of luminescence becomes faster with decreasing wavelengths. From the set on nonnormalized decay curves, we have determined the time-resolved emission spectra shown in Fig. 2b. The red shift of the u.v.-blue emission band from 407 to 425 nm (Fig. 2b) during the decay time $0 < t < 0.5$ min is associated with the growth of the long wavelength part of the emission band. For decay times $t > 0.5$ min, no essential change of the phosphorescence spectra takes place after turning off continuous excitation. Therefore, it is possible to explain the decay process of the luminescence of the Al-activated Zn_2SiO_4 by the superposition of several emission bands with different decay times.

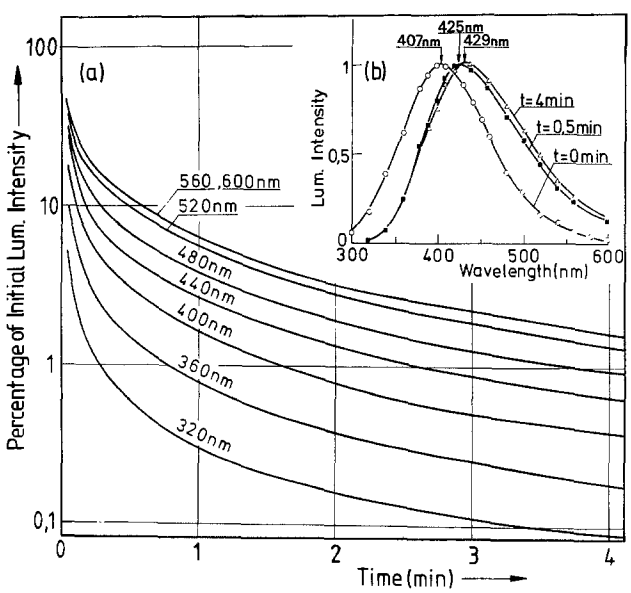

Fig. 2. (a) Decay curves for the u.v.-blue luminescence of Zn_2SiO_4:Al (2%) phosphor at 300 K for different emission wavelengths, excited 4 min at 240 nm. (b) Normalized time-resolved emission spectra determined from the set of nonnormalized decay curves. The delay times after turning off the continuous excitation are specified in the figure (0, 0.5, and 4 min).

In Fig. 3, one can see the composition of the u.v.-blue emission band of Zn_2SiO_4:Al (2%) (curve a) by two sub-bands by using the emission band of the "pure" Zn_2SiO_4 (curve b). The difference of the two curves $a(\lambda)$-$b(\lambda)$ yields a spectra distribution $c(\lambda)$ which closely coincides with the spectral distribution of the long afterglow (curve c in Fig. 3 is equivalent to the curve at t = 4 min in Fig. 2b). These facts may reasonably lead to the conclusion that the broad u.v.-blue emission band of Zn_2SiO_4:Al may be due to a superposition of the emission band of the undoped zinc silicate, peaked at about 390 nm with a decay time of about 0.5 sec (curve b, Fig. 3) and a second emission band, peaked at 429 nm with a long afterglow of about 10 sec (Fig. 3, curve c), which mainly originates from Al activation. The long wave tail ($\lambda > 500$ nm) of the emission band c is caused by a third sub-band due to traces of manganese. This green Mn emission band of the Zn_2SiO_4:Al has a very long afterglow as can be seen from the decay curves in Fig. 2a. The different decay of the blue and green luminescence can be observed distinctly for zinc silicate which is doped with 2 m/o Al_2O_3 and 0.1 m/o $MnCO_3$. At this activator ratio, the green Mn emission accompanies the u.v.-blue emission. After turning off the continuous excitation (254 nm), the visible light blue afterglow changes into a long persistent green phosphorescence after about 3 sec.

Further evidence for emission band superposition is derived from the temperature dependence of the short wavelength and long wavelength emission of the Al-activated zinc silicate. These temperature dependent curves were obtained by varying the temperature of the sample at constant exciting intensity. The efficiency scale is now fixed in such a manner that at the level where the luminescence intensity reaches a maximum, the efficiency is assumed to be one. In the short wavelength range, where the emission bands overlap a little, one should find mainly the temperature dependence of the emission band of the undoped zinc silicate. In fact, the temperature dependence of Zn_2SiO_4:Al at an emission wavelength of 340 nm (Fig. 4, curve 2) nearly corresponds with the temperature dependence of the undoped zinc silicate (Fig. 4, curve 1), while at an emission wavelength of 480 nm, one gets mainly the temperature dependence of the luminescence depending on Al doping (Fig. 4, curve 3).

The dependence of the emission intensity on the excitation intensity for Zn_2SiO_4:Al is found to be nonlinear and similar to nonactivated zinc silicate (1). For an excitation wavelength of 240 nm, the emission intensity increases linearly at temperatures 20 K $< T <$ 410 K and superlinearly at temperatures $T >$ 410 K

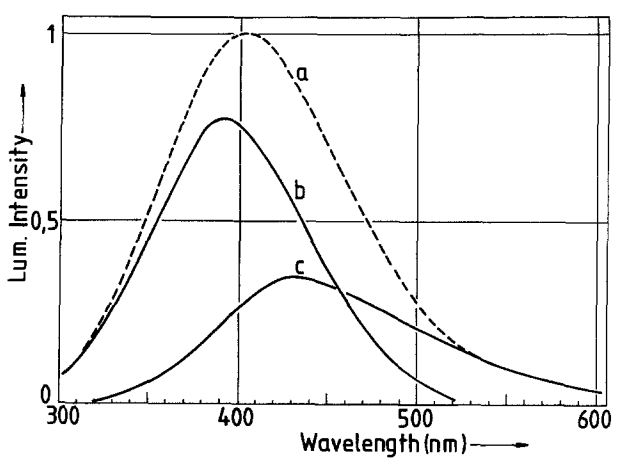

Fig. 3. Superposition of emission spectra of the luminescence at continuous excitation for Zn_2SiO_4:Al (2%) at room temperature. (a) Emission spectrum of Zn_2SiO_4:Al (2%), (b) emission spectrum of undoped Zn_2SiO_4, (c) emission spectrum of the luminescence in consequence of Al doping (c = a − b).

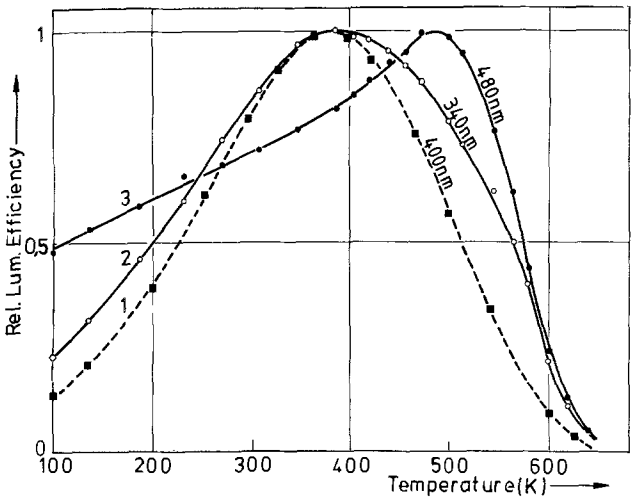

Fig. 4. Dependence of the relative luminescence efficiency on temperature of Zn_2SiO_4 doped with (1) 0 and (2), (3) 1% Al_2O_3. $\lambda_{exc} = 220$ nm.

with exciting intensity (7). This means that the range of temperature quenching itself is dependent on the intensity of excitation. As will be shown in Fig. 5, an increase of the intensity of the excitation from 1 to 50 causes a shift of the quenching range of about 60 K towards higher temperatures.

In the case of Al-activated zinc silicate, the nature of the final states reached in absorption is indicated by the occurrence of n-type photoconductivity (8) and proved by means of Dember effect measurement, phosphorescence, and the nonlinear response correlated with the luminescence. All these phenomena indicate that electrons have been liberated from energy states somewhat above the valence band. Therefore, it is reasonable to determine the thermal activation energy E_{Al} (distance of the level from the top of the valence band) for the luminescence center using the well-known relation for temperature quenching of the luminescence of inorganic phosphors $I/I_0 = [1 + \exp(-E_{Al}/kT)]^{-1}$ from the temperature dependence of the relative luminescence efficiency I/I_0 of Fig. 5 for high excitation energy to avoid nonlinear effects (9). Thereby, one gets $E_{Al} = 0.81$ eV.

Figure 6 shows typical excitation and emission spectra for TiO_2-doped zinc silicate (curves 2-4). With increasing Ti content in Zn_2SiO_4, a new excitation band with a maximum at about 232 nm arises similar to Al-doped zinc silicate. The half-width value of this excitation band is smaller than that of Zn_2SiO_4:Al so that in contrast to the Al-doped material, Zn_2SiO_4:Ti could not be excited by 254 nm. As we can see from Fig. 6, curves 1 and 3, Ti doping causes a considerable enhancement of the excitation band at 218 nm of the undoped zinc silicate, which cannot only be explained by overlapping of the two excitation bands. The u.v. emission band (285 nm) of the undoped zinc silicate (1) disappears with increasing TiO_2 content similar to

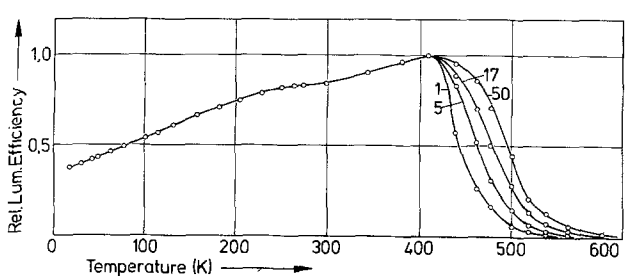

Fig. 5. Dependence of the normalized luminescence efficiency on temperature of Zn_2SiO_4:Al (2%) at different excitation intensities (1:5:17:50). $\lambda_{em} = 400$ nm, $\lambda_{exc} = 250$ nm.

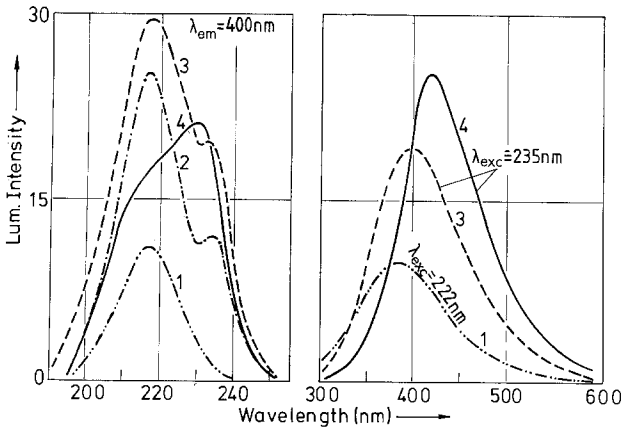

Fig. 6. Spectral characteristics of Zn_2SiO_4 doped with (1) 0, (2) 0.2, (3) 0.6, and (4) 1% TiO_2.

Zn_2SiO_4:Al. Compared to the emission of the undoped zinc silicate, the u.v.-blue emission of Zn_2SiO_4:Ti with a maximum at 400 nm is shifted somewhat to longer wavelengths (Fig. 6, curves 1 and 3). The change of the excitation and emission spectrum after doping with 1 m/o TiO_2 (Fig. 6, curve 4) is caused by undissolved TiO_2 which absorbs the exciting and emitting radiation, as one can see from a comparison of the absorption spectra of TiO_2 (Fig. 7, curve 1) with the emission spectrum of Zn_2SiO_4:TiO_2 (1%) in Fig. 6, curve 4. The decay of the luminescence of Zn_2SiO_4:Ti is short ($t \approx 10^{-3}$ sec) compared to the luminescence of the "pure" Zn_2SiO_4 ($t \approx 0.5$ sec) or Zn_2SiO_4: Al ($t \approx 10$ sec).

The relative quantum efficiency of the u.v.-blue luminescence of Zn_2SiO_4:Al and Zn_2SiO_4:Ti excited by 220 nm (Fig. 8) depends on the activator concentration in the usual way: in the region of low concentration it increases to reach a maximum and decreases again towards higher concentrations. The decrease of the efficiency at higher concentrations of added Al_2O_3 or TiO_2 is partially caused by absorption (besides the quenching due to high activator concentrations) of the exciting and emitting radiation by compounds as $Zn(AlO_2)_2$ and TiO_2 or Zn_2TiO_4, detected by x-ray diffraction and optical reflectance spectra as separate phases.

X-ray diffraction spectra of some Zn_2SiO_4:Al_2O_3 samples sintered for 1 hr at 1370°C show separate lines in addition to the lines of the willemite lattice of Zn_2SiO_4, which correspond to the cubic face-centered lattice of $Zn(AlO_2)_2$. These lines are visible at Al_2O_3 concentrations greater than 2 m/o. As one can see from the absorption spectrum (Fig. 7, curve 3), $Zn(AlO_2)_2$ behaves like a filter substance for the exciting radiation ($\lambda < 300$ nm) of the u.v.-blue emission of Zn_2SiO_4:

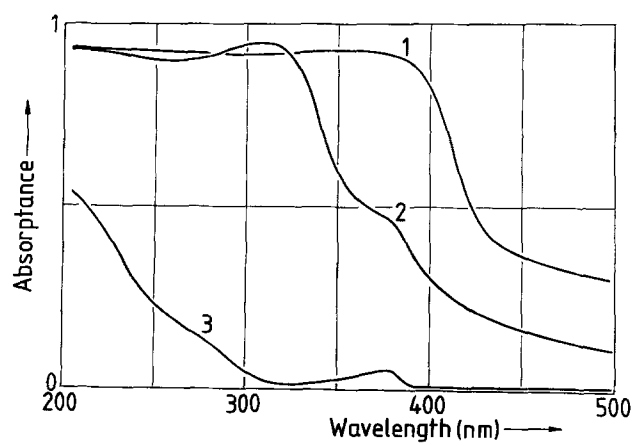

Fig. 7. Absorption spectra obtained from diffuse reflection spectra ($\alpha = 1 - \rho$) of (1) TiO_2, (2) Zn_2TiO_4 + ZnO in excess, (3) $Zn(AlO_2)_2$.

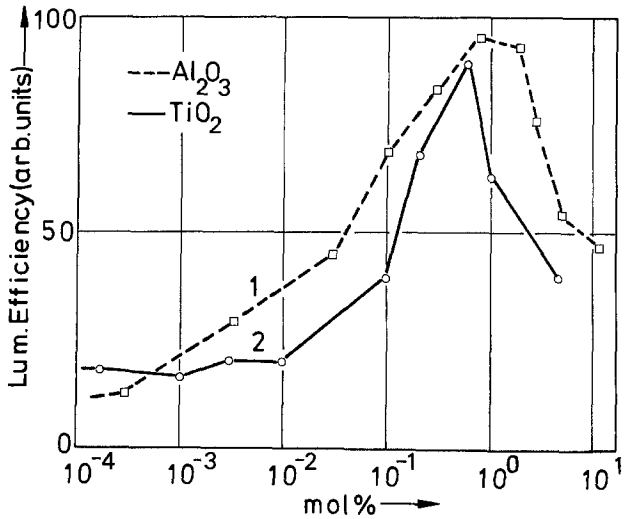

Fig. 8. Relative efficiency of the u.v.-blue luminescence of Zn_2SiO_4 doped with different (1) Al_2O_3 and (2) TiO_2 concentrations. λ_{em} = 400 nm, λ_{exc} = 220 nm.

Al. While the u.v.-blue emission intensity of undoped Zn_2SiO_4 increases with increasing sintering temperatures until the melting point (Fig. 9, curve 1), Al-doped zinc silicate shows a decrease of the luminescence intensity at sintering temperatures above 1300°C (Fig. 9, curve 3). This behavior can be explained by enhanced formation of $Zn(AlO_2)_2$ from ZnO and Al_2O_3 at elevated temperatures. According to Gmelin (10), the velocity of the reaction $ZnO + Al_2O_3 \rightarrow Zn(AlO_2)_2$ is very small, below 1100°C. Only at about 1400°C does a complete reaction take place in a relatively short time, in agreement with the phase diagram of the ternary system $ZnO-Al_2O_3-SiO_2$ (11). In a similar way, the strong drop of the luminescence efficiency of Zn_2SiO_4:TiO_2 (0.6%) at sintering temperatures above 1420°C (Fig. 9, curve 2) may be caused by the favored formation of $ZnO-TiO_2$ compounds with a strong absorption for wavelengths below 450 nm (Fig. 7, curves 1 and 2). The occurrence of a separate phase besides Zn_2SiO_4 with a short wavelength absorption is clearly visible at the slightly yellow body color of the samples sintered at temperatures above 1420°C.

Fig. 10 shows characteristic glow curves of undoped Ti- and Al-doped zinc silicate obtained after irradiation with 220 nm at 20 K. By measuring the glow curves at different wavelengths of emission in the range of 300 nm $< \lambda <$ 480 nm; it is possible to determine the spectral distribution at temperatures of the glow peaks, which coincide approximately with the spectral distribution at continuous excitation. Therefore, the glow emission of the undoped zinc silicate samples show a peak at about 385 nm while Al- and Ti-doped specimens have the greatest glow emission at about 400-407 nm. The total stored light sum depends on sintering time, sintering temperature, and the concentration of the TiO_2 and Al_2O_3 additions. A small specimen dependence of the position of the glow peaks was found for Zn_2SiO_4 and Zn_2SiO_4:Ti for temperatures > 280 K. As one can see from Fig. 10 (curves 1 and 2), the glow curves of the undoped Zn_2SiO_4 and the Zn_2SiO_4:Ti show distinct peaks at different temperatures. No distinct glow peaks could be measured not even at small heating rates (10 K/min) for Zn_2SiO_4:Al; a superposition of several glow curves with separate peaks close together is assumed. The long and bright afterglow at 20 K indicates that in the crystal lattice a great number of sites are present where electrons and holes with low energy of activation are trapped. The shallowest traps marked by dotted lines could not be measured, because they are already emptied by the radiation of the surroundings (12) before the glow curve measurements began.

Discussion and Conclusion

A comparison of Fig. 1 with Fig. 6 shows that the incorporation of Al as well as Ti in zinc silicate effects the excitation spectrum of the undoped zinc silicate in two ways. Firstly, a new excitation band occurs at 235 and 232 nm for increasing amounts of Al_2O_3 or TiO_2 added to the undoped Zn_2SiO_4. Secondly, the incorporation of Al as well as Ti enhances the original excitation band of the undoped Zn_2SiO_4 at 218 nm. In these cases, the incorporation of two different elements as Al and Ti produces an intensification of the u.v.-blue emission of the undoped Zn_2SiO_4 in the same way, namely, by introducing a new excitation band in the wavelength region 230 nm $< \lambda <$ 236 nm and by enhancement of the excitation band of the undoped material. Preliminary evidence obtained in our laboratory indicates that gallium incorporated in Zn_2SiO_4 affects the excitation and emission spectrum of pure zinc silicate in a similar way as Al and Ti. Therefore,

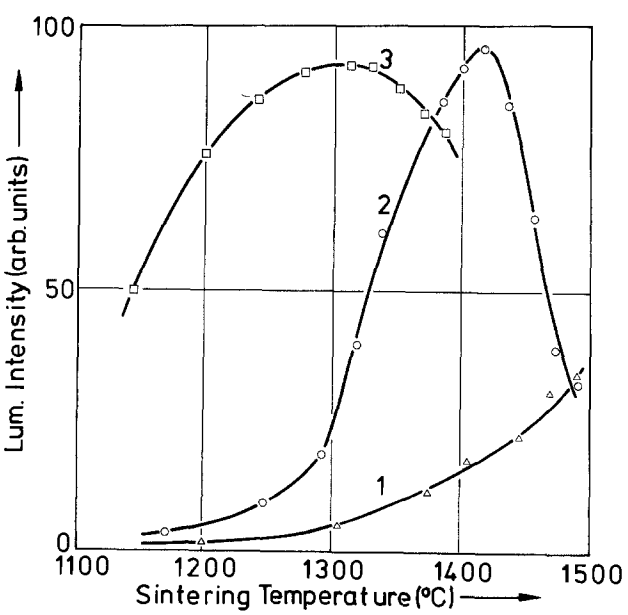

Fig. 9. Relative efficiency of the u.v.-blue luminescence of Zn_2SiO_4 doped with (1) 0, (2) 0.6% TiO_2, and (3) 0.8% Al_2O_3 at different sintering temperatures. λ_{em} = 400 nm, λ_{exc} = 220 nm.

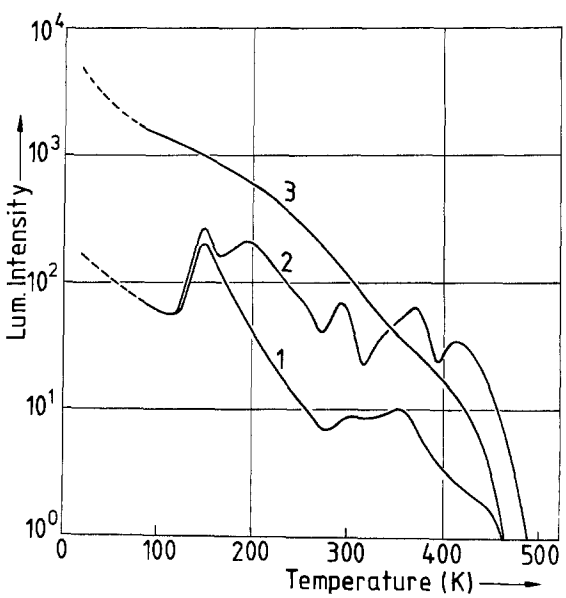

Fig. 10. Thermal glow curves of Zn_2SiO_4 doped with (1) 0, (2) 0.6% TiO_2, and (3) 1% Al_2O_3 after excitation with 220 nm for 4 min. λ_{em} = 400 nm, heating rate 15 K/min.

we think that the dependence of the luminescence on the presence of the atoms Al, Ga, or Ti is primarily indirect. These metallic impurities may produce a reduction in the degree of stoichiometry of the Zn_2SiO_4 samples by creating additional lattice imperfections which act as luminescence centers. Further, it could be possible that the primary action of the activator atoms Al, Ga, or Ti is to disturb the crystal field and to influence the host crystal selection rules in the vicinity of the emitting atom or atomic group of the host crystal. These notions are confirmed by a similar observation of Leverenz (4). He found that several silicate phosphors, *e.g.*, $ThSiO_4$, $CdSiO_3$, Mg_2SiO_4, $CaSiO_3$, and $(Zn, Be)_2SiO_4$, have very similar cathodoluminescence emission bands compared with undoped Zn_2SiO_4. The efficiency of some of these phosphors is greatly improved by incorporation of TiO_2. It is also known that different quartz glasses and crystals show characteristic emission bands with maxima at 280 and 396 nm excited by radiation $\lambda < 253$ nm (13) similar to the luminescence of undoped zinc silicate (1). However, the assumption of assigning the luminescence of undoped or doped zinc silicate to a separate phase of SiO_2 besides Zn_2SiO_4 does not seem to be correct, because no essential change of the intensity of the u.v.-blue emission of undoped and Al-, Ga-, or Ti-doped Zn_2SiO_4, prepared with an excess of 0.05 mol, 0.1 mol, or 0.2 mol SiO_2, has been found. Because of these facts, we propose that the luminescence of undoped as well as Al-, Ga-, and Ti-doped Zn_2SiO_4 is due to the $[SiO_4]$ unit of the zinc silicate. The characteristic luminescence of quartz glass with maxima at 396 nm was associated with oxygen vacancies situated in the glass lattice in a microregion with structure of cristobalite type (13, 14). How far the u.v.-blue luminescence bands of the undoped or Al-, Ga-, and Ti-doped Zn_2SiO_4 are associated with oxygen vacancies of the SiO_4-tetrahedra of the willemite lattice, has to be proved by later experiments.

The superlinear dependence of the luminescence on the excitation intensity or what amounts to the same, the dependence of the temperature quenching on the exciting intensity, is found at undoped (1) as well as Al- (Fig. 5) and Ti-doped zinc silicate at temperatures above 400 K. Zinc silicate activated with a high concentration of manganese shows a superlinear behavior likewise (15). Commonly, superlinearity is explained by hole migration (16-19). If luminescence centers with energy states somewhat above the valence band are only excited with low intensity, then the holes originated in the valence band can migrate to neighboring deep traps, whose energy levels lie higher than those of the luminescence centers, and will there recombine with trapped electrons nonradiatively. At higher excitation intensities and low temperatures, these processes are no longer dominant and energy losses via deep traps become unimportant. Because of the fact that undoped as well as doped zinc silicate show a similar superlinear behavior, it is supposed that the origin of the superlinearity, namely, deep traps, could be mainly attributed to lattice imperfections of the zinc silicate itself. Al doping of Zn_2SiO_4 causes an increase of the glow emission (Fig. 10, curve 3) in connection with a long decay time of the luminescence (Fig. 2a) and an increase of n-type photoconductivity (1) in comparison to the undoped zinc silicate. Furthermore, in context with the glow emission, a thermally stimulated conductivity is found. Similar results were noted for Ga-doped zinc silicate. All these experimental results indicate an increase in the concentration of electron trapping centers as a consequence of Al or Ga doping.

The willemite lattice of zinc orthosilicate consists of corner-joined tetrahedral groups of $[ZnO_4]$ and $[SiO_4]$. In the crystals, the $[ZnO_4]$-tetrahedra are all interconnected, whereas the $[SiO_4]$-tetrahedra with strong Si-O bonds are isolated from each other. From the feldspars (20) and the color centers in smoky quartz (21), it is known that aluminum can form tetrahedral bonds by accepting an extra electron, so that $[SiO_4]$-tetrahedra could be substituted by $[AlO_4]$-tetrahedra. Thus it seems reasonable that small quantities of aluminum or gallium atoms should replace silicon atoms in the willemite lattice of zinc orthosilicate. Since the substitutional aluminum or gallium requires an extra electron to complete all four tetrahedral bonds, these centers may act as a trap for electrons.

Acknowledgment

The authors wish to thank Professor E. Krautz for useful discussions and for making his low temperature equipment available for these investigations. We thank Professor H. Kahlert for critically reading the manuscript. We are also grateful to the Fonds zur Förderung der wissenschaftlichen Forschung for financial support under the project No. 4507.

Manuscript submitted March 24, 1983; revised manuscript received *ca.* July 5, 1983.

REFERENCES

1. H. Hess, E. Krautz, and M. Scala, *Acta Phys. Austr.*, **54**, 265 (1982).
2. F. A. Kröger, "Some Aspects of the Luminescence of Solids," Elsevier, Amsterdam (1948).
3. I. Uehara and U. Umekawa, *J. Chem. Soc. Jpn.*, **61**, 907 (1940).
4. W. Leverenz, "An Introduction to Luminescence of Solids," Dover Publications, New York (1968).
5. I. F. Chang and M. W. Shafer, *J. Appl. Phys. Lett.*, **35**, 229 (1979).
6. E. J. Adirowitsch, "Einige Fragen zur Theorie der Lumineszenz," Berlin Akademie-Verlag, Berlin (1953).
7. A. Heim, Thesis, Technische Universität Graz, Austria (1981).
8. H. Hess and E. Krautz, *J. Lumin.*, **24/25**, 321 (1981).
9. H. Witzmann and J. Buhrow, in "Zur Physik und Chemie der Kristallphosphore," Berlin Akademie-Verlag, Berlin (1966).
10. "Gemlins Handbuch der Anorganischen Chemie," Bd. 35, p. 608, Verlag Chemie (1956).
11. E. M. Levin, C. R. Robbins, and H. F. McMurdie, "Phase Diagrams for Ceramists," The American Ceramic Society, Columbus, OH (1964).
12. N. Riehl, G. Bauer, and L. Mader, *Z. Naturforsch.*, **24a**, 1296 (1969).
13. A. V. Amosov *et al.*, *Zh. Prikl. Spektrosk.*, **25**, 817 (1976).
14. D. L. Griscom, in "The Physics of SiO_2 and its Interfaces," S. T. Pantelides, Editor, pp. 232-252, Pergamon Press, Elmsford, NY (1978).
15. W. Hoogenstraaten and F. A. Kröger, *Physica*, **15**, 541 (1949).
16. M. Schön, *Tech. Wiss. Abh. Osram-Ges.*, **6**, 49 (1953).
17. A. Rose, *Phys. Rev.*, **97**, 322 (1955).
18. I. Broser and R. Broser-Warminsky, *Ann. Phys.*, **16**, 361 (1955).
19. H. A. Klasens, *J. Phys. Chem. Solids*, **7**, 175 (1958).
20. W. Hinz, "Silikate," Vol. 1, VEB Verlag für Bauwesen, Berlin (1970).
21. M. C. M. O'Brien, *Proc. R. Soc. London, Ser. A*, **231**, 404 (1955).

AC Powder Electroluminescence Maintenance Improvement

Katsuhiko Hirabayashi, Haruki Kozawaguchi, and Bunjiro Tsujiyama

Nippon Telegraph and Telephone Public Corporation, Ibaraki Electrical Communication Laboratory, Tokai Mura, Ibaraki-ken, 319-11, Japan

ABSTRACT

The effects of annealing and quenching EL phosphors on their maintenance are investigated. Annealing at a temperature from 700° to 1000°C for more than 1 hr in NH_3 or air, and quenching are most efficient for EL life improvement. For example, EL phosphor annealed in air at 900°C for 2 hr and quenched has a half-life of more than 3000 hr (initial brightness = 100 nt). Sulfur vacancy density, dopant content, and phosphor particle size are not changed appreciably by annealing, but the x-ray diffraction peak intensity changes, and the activation energy of deterioration increases from 0.3 to 0.45 eV by annealing. These results suggest that the crystal quality is changed by annealing and quenching.

AC powder EL cells have long been known to deteriorate slowly during continuous operation. Many efforts have been made to improve their brightness and maintenance. Thornton (1) improved their brightness and life by investigating dopant content and phosphor particle size effects on ZnS:Cu,Cl phosphor. Jaffe (2) improved life by the replacement of chlorine by bromine. The authors have investigated dopant content, fractionation, and etching effect on ZnS:Cu,Br phosphor brightness and life, and measured sulfur vacancy density and crystal quality dependence of life to study the deterioration mechanism by electron spin resonance (ESR) and x-ray diffraction. It has been reported that brightness has a maximum at (Cu + Br)/2 = 0.2 – 0.3 mol percent (m/o), and life is improved by optimization of dopant content, fractionated phosphor particle size, and by etching (3-4). It is also clear that life is improved with a decrease in sulfur vacancy density and x-ray diffraction (111) peak intensity (5).

On the other hand, for improvement of EL phosphor maintenance, annealing and quenching is well known to be effective. Aven (6) reported that EL life was improved by annealing at a relative low temperature in an atmosphere selected from the group consisting of neutral and oxidizing atmosphere. Thornton (7) stated that EL life improves by a factor of roughly 2-10 by air annealing and quenching. Lehmann (8) observed that (Zn,Cd)S:Cu,Br phosphor became extremely deterioration-resistant after refiring and quenching in pure sulfur. Recently, Lehmann (9) reported that annealing in sulfur atmosphere is not important, but quenching is essential for life improvement. However, we have discovered that there is a more effective means of improving EL phosphor life which does involve quenching. Why quenching is important is not yet clear.

In this paper, the authors investigated the most efficient annealing condition (atmosphere, annealing time, and annealing temperature), and also measured the changes in EL phosphor characteristics produced by the annealing treatment.

Experimental

ZnS:Cu,Br phosphor was first prepared in accordance with the conventional techniques mentioned in the previous paper (3). ZnS with approximately 0.5 weight percent (w/o) copper in the form of CuCOOH and 2.0 w/o bromine in the form of NH_4Br was fired at 900°C for 6 hr in H_2S + Ar atmosphere. These fired products were then washed by NaCN to remove surface contaminants. These products contained about 0.3 m/o copper and 0.3 m/o bromine. The mean particle diameter was 17-20 μm. Next, these products were annealed in N_2, sulfur, NH_3, or air. Annealing in sulfur atmosphere means to fire the products in H_2S + Ar with 10, 20, or 40 w/o sulfur addition. Annealing was done as follows. The phosphor in the boat was placed in the firing vessel. After the firing vessel was evacuated by a rotary pump, each gas was introduced into the vessel to assure a good exchange. The firing vessel was then placed in a preheated furnace and was fired in each gas. Then, the vessel was withdrawn and allowed to cool to room temperature. The brightness and life-measurement methods were the same as those mentioned in the previous paper (3).

Key words: electroluminescence, annealing, life improvement, phosphors.

Results

Dependence of phosphor performance on annealing conditions.—The voltage dependence of the brightness at 10 kHz operation for EL cells incorporating each phosphor annealed for 2 hr at 900°C is shown in Fig. 1. The time dependence of the brightness is shown in Fig. 2. The brightnesses for the phosphors annealed in sulfur, N_2, air, and NH_3 atmosphere are reduced to about 3/4, 1/2, 1/3, and 1/3 of that for the phosphor before annealing, respectively. The half-life for phosphors

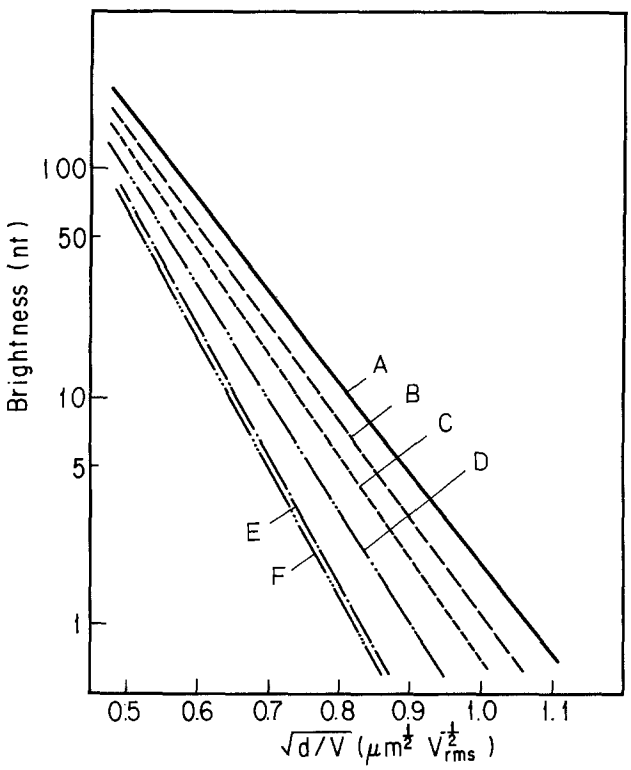

Fig. 1

Fig. 1. Voltage dependence of brightness for EL cells incorporating annealed phosphors. Binder is silicon grease (dielectric constant is about 3). Emission layer thickness is 100 μm. A; before annealing, B; annealed in sulfur atmosphere (10 or 20 w/o sulfur addition), C; annealed in sulfur atmosphere (40 w/o sulfur addition), D; annealed in N_2 atmosphere, E; annealed in air, F; annealed in NH_3 atmosphere.

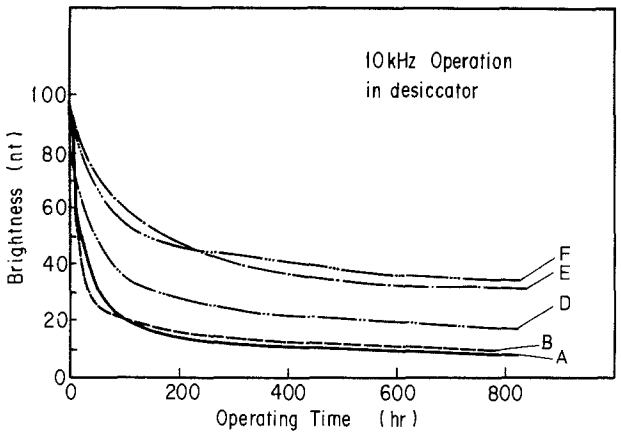

Fig. 2. Time dependence of brightness for EL cells incorporating annealed phosphors. Binder is an organic material, fluoro rubber (dielectric constant is about 10). Emission layer thickness is 30 ~ 40 μm. A; before annealing, B; annealed in sulfur atmosphere (10, 20, or 40 w/o addition), D; annealed in N_2 atmosphere, E; annealed in air, F; annealed in NH_3 atmosphere.

annealed in sulfur, N_2, air, and NH_3 atmosphere is improved about 1-, 3-, 8-, and 10-fold, respectively, compared to that for unannealed phosphor. From these results, it can be concluded that annealing in air or NH_3 atmosphere is most effective with respect to improving maintenance.

The effect on maintenance of the cooling rate after annealing was investigated for annealing in air. After the phosphors were taken out of the firing vessel, they were cooled by the following three methods; without forced cooling, by ventilating, and by casting into water. The time dependences of the brightness for EL cells incorporating phosphors cooled by the above methods are shown in Fig. 3. The life of the phosphor cooled by casting into water is impaired, and the lives of phosphors cooled without forced cooling and by ventilating were improved, compared with phosphor which was allowed to cool slowly in the firing vessel. From these results, it can be seen that cooling at an appropriate speed, about 1000°C/hr, is effective for improving EL life.

In order to find the optimum annealing condition, the annealing time and temperature dependence of brightness and life were investigated for annealing in air. The phosphor was taken out and was allowed to cool without forced cooling. Figures 4a and 4b show EL cell initial brightness *vs.* annealing temperature and time, respectively. As shown in these figures, the initial brightness decreases with annealing temperature and decreases with annealing time, up to 30 min, after

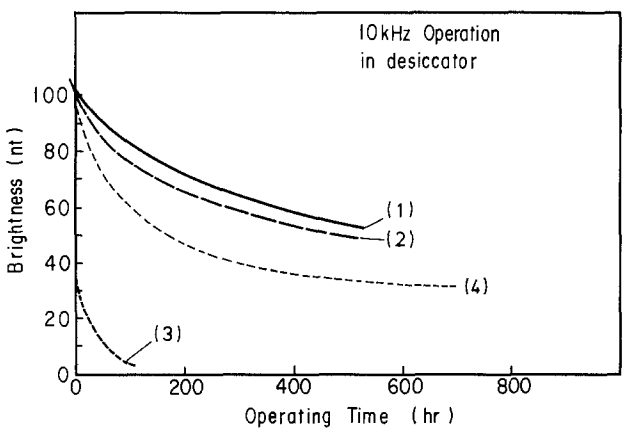

Fig. 3. Time dependence of brightness for EL cells incorporating phosphor quenched after air annealing. (1) cooled without forced cooling; (2) cooled by ventilating; (3) cooled by casting into water; (4) cooled slowly in firing vessel.

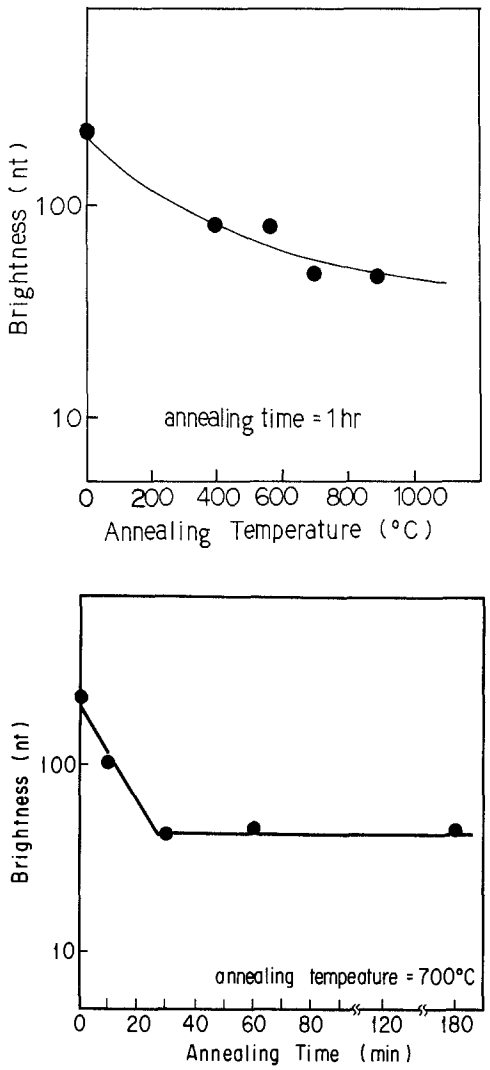

Fig. 4. EL cell initial brightness *vs.* annealing temperature (a) and time (b).

which it is constant. Figures 5a and 5b show half-life *vs.* annealing temperature and time, respectively, in the case that the initial brightness is 100 nt. Below 400°C, half-life diminishes. Above 450°C, half-life improves. Half-life increases with annealing time. When annealing at a temperature above 700°C for more than 1 hr is performed, these phosphors perform better, because half-life increases by 20-40 times, though the initial brightness decreases to 1/3 or 1/4 of that for unannealed phosphor. The typical time dependence of the brightness at 2 kHz operation for the phosphor annealed in the optimum condition (900°C, 2 hr) is shown in Fig. 6, where half-life is indicated to be above 3000 hr.

Characterization of annealed phosphors.—To study the reason why annealed phosphor has a long life, sulfur vacancy density, dopant content, particle size, the component covering the phosphor particle surface, activation energy of deterioration, and crystal quality for unannealed and annealed phosphors, which are major factors of the EL life, were measured.

The changes in sulfur vacancy density caused by air annealing are measured by ESR and thermoluminescence. The sulfur vacancy density by ESR measurement for phosphor before and after annealing in air is shown in Table I. It was found by ESR that the sulfur vacancy density was not changed appreciably by annealing in air. The thermoluminescence spectra for phosphors before and after annealing in air are shown in Fig. 7. The right-hand and left-hand peak are considered to be due to sulfur vacancy pairs and to Br,

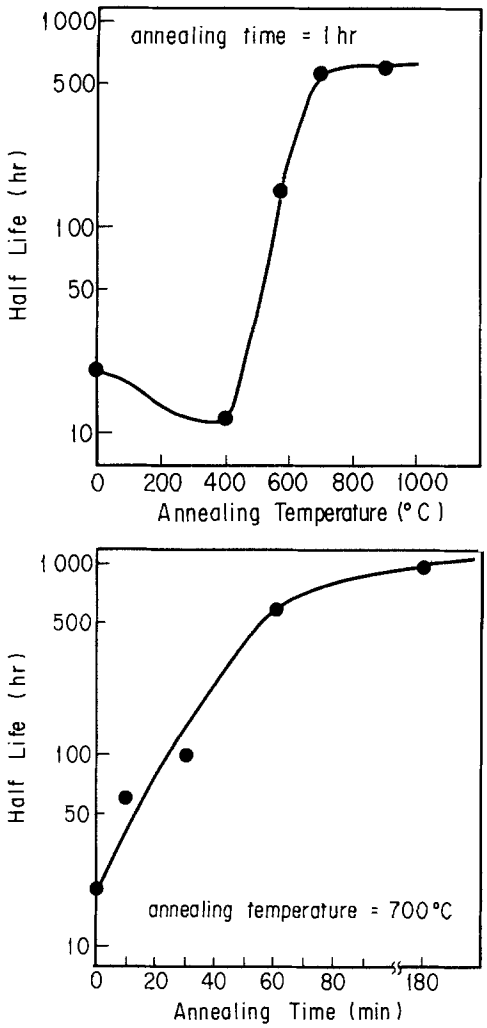

Fig. 5. Time required to decrease to 50% of the initial brightness (= 100 nt) vs. annealing temperature (a) and time (b).

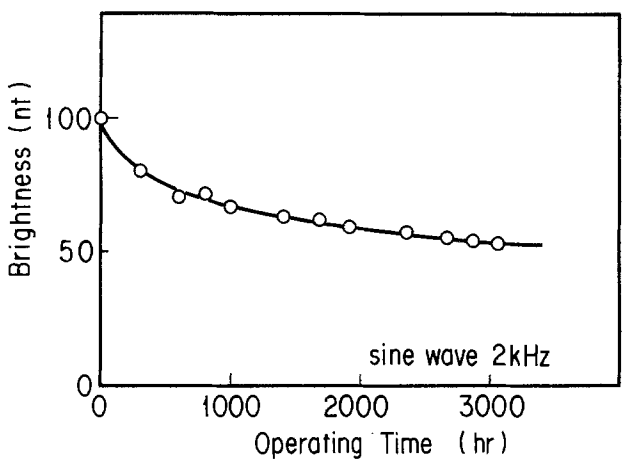

Fig. 6. Time dependence of brightness for phosphors annealed under optimum conditions (900°C, 2 hr in air).

respectively. This result also indicates that sulfur vacancy density is not changed by annealing in air.

The variations in dopant content and particle size caused by annealing in air were measured, and these results are shown in Table II. The Cu content tends to increase and the Br content tends to decrease a little, but these variations are small. Particle size does not change.

It was found that the EL phosphor particle surface is changed by reaction with the annealing atmosphere. In the case of air annealing, a greater amount of zinc

Table I. Sulfur vacancy densities for phosphors before and after annealing in air. S vacancy/Mn means the ESR signal intensity ratio of sulfur vacancy in ZnS and Mn in the internal standard, MgO:Mn.

	Sample number	S vacancy/Mn
Before annealing	1	0.074
	2	0.076
After annealing	1a	0.065
	2a	0.078

Phosphors 1a and 2a were produced from phosphors 1 and 2 by annealing under the condition of 900°C, 2 hr.

Table II. Dopant content and mean particle diameter for phosphors before and after annealing in air

	Sample number	Cu content (m/o)	Br content (m/o)	Mean particle diameter (μm)
Before annealing	1	0.33 ± 0.005	0.35 ± 0.005	20 ± 1
	2	0.285 ± 0.005	0.30 ± 0.005	19 ± 1
After annealing	1a	0.36 ± 0.005	0.35 ± 0.005	19 ± 1
	2a	0.285 ± 0.005	0.26 ± 0.005	19 ± 1

oxide is formed on the surface of the phosphor particles. In the x-ray diffraction spectra of the phosphor annealed in air, three peaks due to zinc oxide appear as shown in Fig. 8.

The SEM picture of the phosphor annealed in air is shown in Fig. 9. The many fine particles precipitated on the phosphor surface are probably zinc oxide. The authors expected that the reason that annealing improves EL life is that zinc oxide covers the phosphor particle surface, and made an attempt to remove zinc oxide by etching for 10 min with acetic acid (80°C) and for 2 hr with 6*N* HCl (80°C). Most of the zinc oxide was removed by these etchings, as shown in Fig. 10. The time dependences of the brightness of this phosphors before and after etching are shown in Fig. 11. Contrary to expectations life is improved by these treatments. Therefore, it is concluded that the life improvement produced by annealing is not due to zinc oxide covering the phosphor particle surface.

Activation energy was measured for ZnS:Cu,Br phosphor annealed in air. The measuring method of the activation energy was the same as that of the previous paper (10). The time dependence of EL

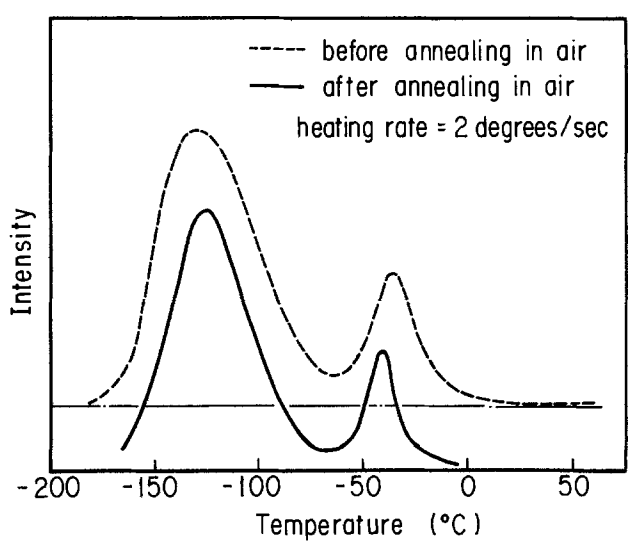

Fig. 7. Thermoluminescence of phosphors before and after annealing in air.

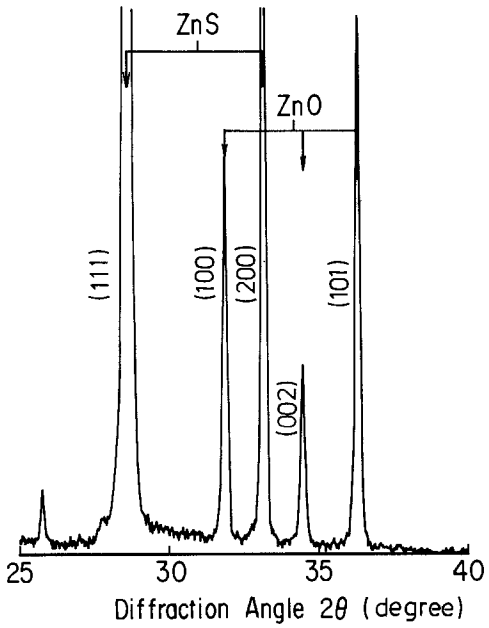

Fig. 8. X-ray diffraction pattern for phosphors annealed in air

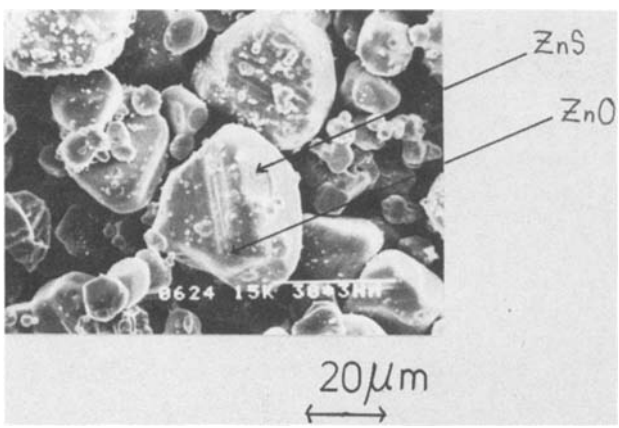

Fig. 9. SEM picture of phosphor annealed in air

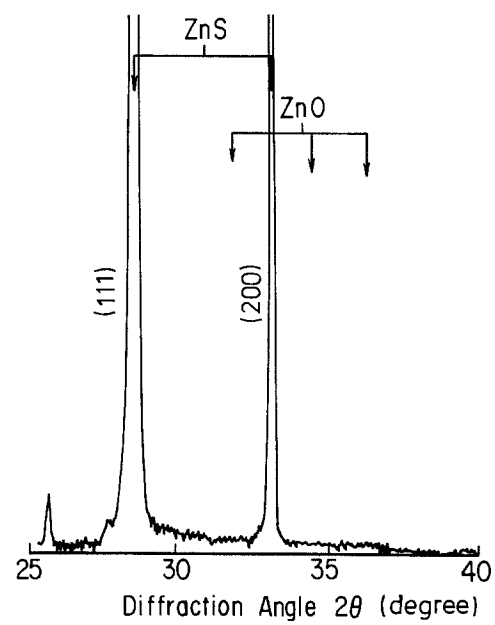

Fig. 10. X-ray diffraction pattern for etched phosphor

brightness can closely be described by $B = B_o/(1 + t/t_c)$, where B_o is the initial brightness. Arrhenius plots of t_c for deterioration of the phosphors, before and after annealing in air, are shown in Fig. 12. From their slopes, it was found that the activation energies were varied from about 0.3 to 0.45 eV by annealing in air.

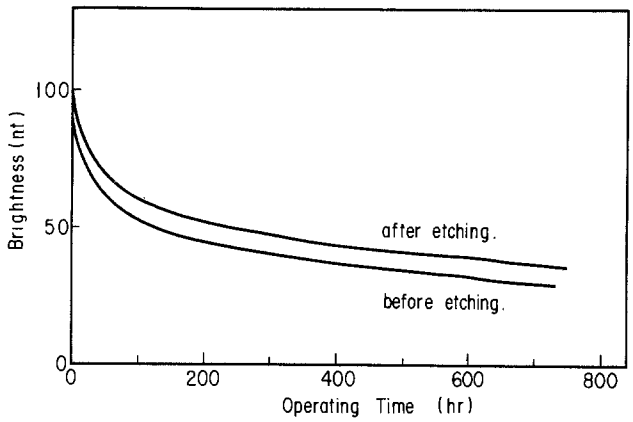

Fig. 11. Time dependence of brightness for etched and unetched phosphors annealed in air.

X-ray diffraction was measured for the phosphors before and after annealing in air. Figure 13 shows annealing temperature dependence of the (111) peak intensity, which is the strongest x-ray diffraction peak. This graph inversely resembles the annealing temperature dependence of the life shown in Fig. 5a. EL phosphor life improvement correlates with a decrease in the (111) peak intensity.

Discussion

At the beginning in this experiment, the following were suggested as possible reasons for improving life by annealing: (*i*) a material covers the phosphor particle surface; (*ii*) trap density, for example, sulfur vacancy, decreases; (*iii*) the dopant content and particle size, which are the factors of EL phosphor life,

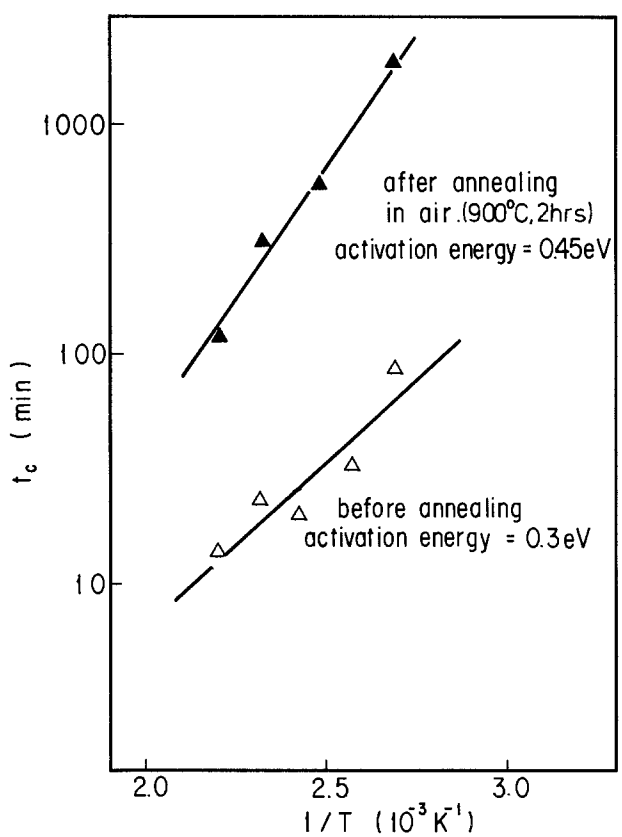

Fig. 12. Arrhenius plots of t_c for deterioration of the phosphor before and after annealing in air.

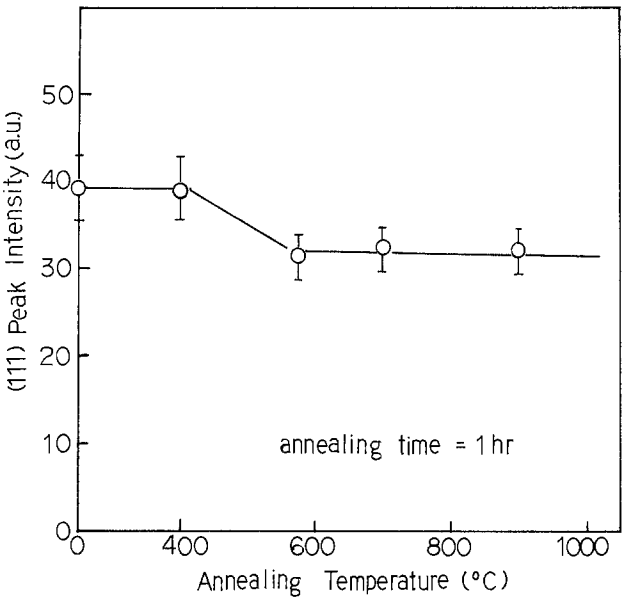

Fig. 13. Annealing temperature dependence of the (111) peak intensity.

are changed by annealing; (*iv*) several elements of the annealing atmosphere are introduced into the phosphor. However, these models were rejected for the following reasons.

Removing zinc oxide on the phosphor surface by etching does not impair life. ESR and thermoluminescence measurements indicate that the trap density (sulfur vacancy density) is not varied by annealing in air. Variations in Cu and Br content and the particle size by annealing in air are small. Various atmospheres are efficient for improving life.

Therefore, the reason for improvement in life by annealing is considered to be not the above facts (*i*)-(*iv*), but structural changes in the EL phosphor particles.

Upon annealing, the x-ray diffraction (111) peak intensity decreases, and deterioration activation energy increases from 0.3 to 0.45 eV. Reference (5) reports that the (111) peak intensity of x-ray diffraction is closely related to EL maintenance. Life tends to improve with a decrease in the (111) peak intensity in the case of fractionation, etching, and ball milling. This suggests phosphor crystal quality is closely related to life.

On the other hand, Ref. (10) reports that the deterioration activation energy of unannealed ZnS:Cu, Br phosphors is about 0.3 eV, which is equal to the activation energy of Cu diffusion in ZnS.

From these results, the reason why the annealed phosphor has a long life may be considered to be that the crystal quality is changed by annealing, which prevents Cu diffusion. In addition, it appears that quenching after annealing accelerates the change of phosphor crystal quality.

On the other hand, the reason why air and NH_3 atmospheres are more effective than N_2 or sulfur atmospheres for EL life improvement cannot be explained by the authors.

Summary

Annealing EL phosphor at temperatures from 700° to 1000°C for more than 1 hr in NH_3 or air and quenching was found to be most effective for life improvement. For example, phosphor annealed in air at 900°C for 2 hr had a half-life of more than 3000 hr (initial brightness = 100 nt). Variations in sulfur vacancy density, dopant content, and phosphor particle size by annealing are small, but x-ray diffraction peak intensity was changed, and the activation energy of deterioration was increased from 0.3 to 0.45 eV by annealing. The reason the annealed and quenched phosphor has a long life may be that the crystal quality is changed.

Acknowledgment

The authors wish to thank Mr. K. Murase, Mr. K. Katoh, and Mr. J. Ohwaki for their valuable discussion.

Manuscript submitted Jan. 17, 1983; revised manuscript received *ca.* July 5, 1983.

Ibaraki Electrical Communication Laboratory assisted in meeting the publication costs of this article.

REFERENCES

1. W. A. Thornton, *This Journal*, **107**, 895 (1960).
2. P. M. Jaffe, *ibid.*, **110**, 759 (1963).
3. Y. Itoh, K. Hirabayashi, and K. Murase, *ibid.*, **129**, 813 (1982).
4. K. Hirabayashi, Y. Itoh, and K. Murase, *ibid.*, **129**, 2059 (1982).
5. K. Hirabayashi, H. Kozawaguchi, and B. Tsujiyama, *ibid.*, **130**, 2259 (1983).
6. M. Aven, U.S. Pat. 3,080,325.
7. W. A. Thornton, U.S. Pat. 3,082,344.
8. W. Lehmann, *This Journal*, **113**, 40 (1966).
9. W. Lehmann, *J. Electron. Mater*, **11**, 341 (1982).
10. K. Hirabayashi and Y. Itoh, *This Journal*, **129**, 362 (1982).

Surface Charging Effects during Photoanodic Dissolution of n-GaAs Electrodes

J. J. Kelly and P. H. L. Notten

Philips Research Laboratories, 5600 JA Eindhoven, The Netherlands

ABSTRACT

The photoanodic dissolution of n-GaAs was investigated in an electrolyte, 0.1M EDTA solution at pH 5, in which oxide formation can occur at higher light intensity. The effect of illumination and film formation on the charge and potential distribution of the electrode was studied by means of impedance measurements. A model involving positively charged states at the semiconductor/oxide interface is developed to account for the buildup of a high surface charge density during illumination. The importance of surface oxide and interface charge for photoanodic reactions is considered in terms of this model.

Two factors are mainly responsible for the current interest in the dissolution of III-V materials: etching is an important step in the fabrication of many semiconductor devices (1, 2) while corrosion of n-type electrodes constitutes a serious problem in photoelectrochemical solar cells (3). It has been suggested that

Key words: semiconductor, interfaces, impedance, photoconductivity.

charge localization in surface or interface states may be important in the dissolution of semiconductor electrodes (4-7). Such states may act as intermediates in the dissolution reaction and may, when electrically charged, influence the potential distribution at the electrode/electrolyte interface. The effect of interface states is expected to be modified by the formation of a surface film, which often accompanies dissolution (8).

In the present study of the photoanodic dissolution of n-GaAs, we chose an electrolyte, 0.1M EDTA solution at *p*H 5, which is known to give rise to oxide formation under illumination (9). Using steady-state and transient impedance measurements, we have observed characteristic surface charging effects during dissolution. On the basis of the influence of light intensity and film formation on the charge and potential distribution of the GaAs electrode, we suggest a model to describe charge localization at the illuminated semiconductor/electrolyte interface and we consider the consequence of surface charging for the photoanodic dissolution reaction.

Experimental

The n-type single-crystal wafers, with {100} orientation and a carrier density in the range 10^{17}-10^{18}/cm^3, were obtained from MCP Electronics, England. Mechanochemically polished electrodes with a diameter of 3 mm, were etched at room temperature in H_2SO_4 (98%)/H_2O_2 (30%)/H_2O (3/1/1) solution and dipped in concentrated HCl solution prior to use.

Impedance was measured under potentiostatic control in a conventional electrochemical cell using either a General Radio Company 1615 A capacitance bridge or a Solartron 1172 Frequency Response Analyzer with an rms signal of 10 mV. In order to normalize the experimental impedance results with respect to unit area, a conversion factor of 7.1×10^{-2} (cm^2) must be used. In the mathematical treatment, the corresponding values are given in normalized form. Potentials are quoted with respect to the reference saturated calomel electrode (SCE) in all cases.

For illumination, a Spectra-Physics 1 mW 133 He-Ne laser was used in combination with a light cable. Absolute light intensities were not determined but the limiting photocurrent of an n-GaAs electrode in 1*N* H_2SO_4 was used as a measure of the photon density. An intensity N_{ph} with arbitrary unit (a.u.) = 1 corresponds to a limiting photocurrent density of 0.1 mA/cm^2. Neutral filters were used to vary the intensity.

The electrolyte solutions, prepared from reagent grade chemicals, were not stirred during the measurements, which were performed at room temperature. EDTA refers to ethylenediamine tetraacetic acid; its disodium salt, designated Na_2 EDTA, was used in the present work.

Results and Discussion

Film formation: photocurrent results.—The shape of the photocurrent-potential curve of an n-GaAs electrode in 0.1M Na_2 EDTA, 0.1M $NaClO_4$ solution at *p*H 5 was similar to that found in $NaClO_4$ solution without EDTA: in both cases the onset potential for photocurrent flow was −0.8V and the current reached its limiting value at approximately −0.6V. Although the limiting photocurrent was potential independent in both electrolytes, the presence of EDTA in the solution had a considerable influence on the magnitude of this current. This effect is illustrated in Fig. 1 and 2.

At low light intensity, the anodic photocurrent i_{ph}, measured at +0.50V in 0.1M Na_2 EDTA, 0.1M $NaClO_4$ solution at *p*H 5, was constant in time [curve (a), Fig. 1] and its magnitude was directly proportional to the photon density N_{ph}, as shown in the lower part of curve (a), Fig. 2. At higher light intensity, the photocurrent observed initially was the same as that found

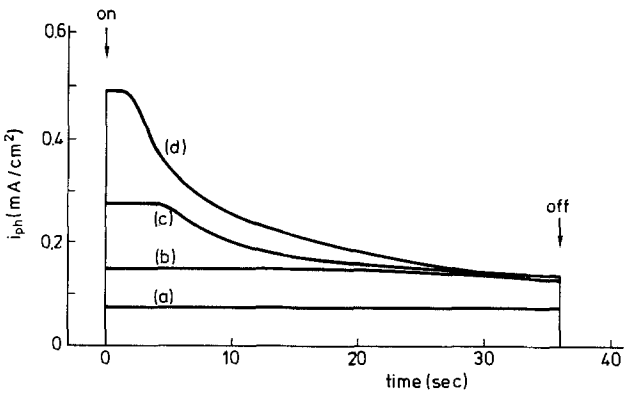

Fig. 1. Photocurrent transients for n-GaAs at +0.50V (SCE) in 0.1M Na_2 EDTA, 0.1M $NaClO_4$, *p*H 5 at photon densities N_{ph} = 0.75 [curve (a)]; 1.5 [curve (b)]; 2.8 [curve (c)], and 4.9 a.u. [curve (d)].

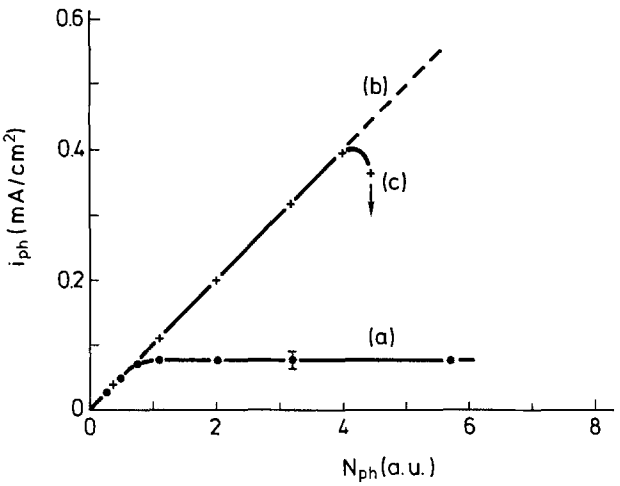

Fig. 2. Steady-state photocurrent of n-GaAs at +0.50V (SCE) as a function of photon density (a) 0.1M Na_2 EDTA, 0.1M $NaClO_4$, pH 5; (b) as (a) but without Na_2 EDTA; (c) as (a) but with 0.1M Fe^{II} EDTA added.

in 0.1M $NaClO_4$ alone [dashed line (b), Fig. 2]. This current, however, decayed after an induction period [curves (b)-(d), Fig. 1]. The induction time decreased as the light intensity was increased. In this case, the steady-state photocurrent was essentially independent of photon density [curve (a), Fig. 2]. The inhibition of the anodic photocurrent could be prevented by adding to the electrolyte a reducing agent (0.1M Fe^{II} EDTA) capable of competing with the GaAs dissolution (3) [curve (c), Fig. 2]. At higher light intensity, the competition was incomplete and photocurrent decay was eventually observed.

Such results, found in various electrolytes containing EDTA at *p*H 5, strongly suggest the formation of a solid film on the electrode. Similar effects were observed by Elliott and Regnault at much higher potentials which gave rise to considerably thicker anodic films (9). Since the original photocurrent transient could be reproduced after film formation by maintaining the electrode at the same potential in the dark (see Fig. 3), it is clear that the surface film dissolves chemically in the electrolyte. Under steady-state conditions, the rate of chemical dissolution determines the magnitude of the photocurrent. This explains why the current in the limiting photocurrent range is independent of light intensity and applied potential. On the basis of this constant photocurrent and the time required to dissolve the surface film in the dark, and assuming a molecular weight and density typical of a

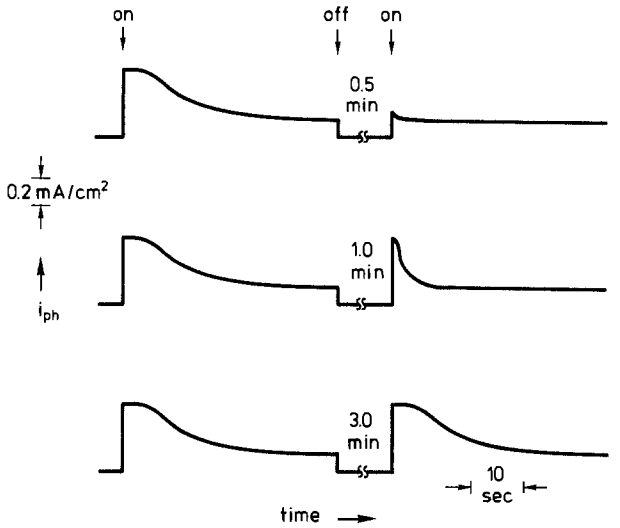

Fig. 3. Recovery of the photocurrent after film formation at +0.50V (SCE). The photocurrent transient was recorded until a steady-state current was attained. The light was switched off and the electrode kept at +0.50V in the dark for the time shown, before illumination was recommended (N_{ph} = 5 a.u.).

GaAs oxide, a thickness of the order of 1.5-5 nm was calculated for the various films described in this work.

Influence of illumination and film formation on the electrode impedance.—The Mott-Schottky plot for an n-GaAs electrode measured in the dark in EDTA solution at *p*H 5 [curve (a), Fig. 4] was identical to that found in a citrate/NaOH buffer solution of the same *p*H; C_S is the equivalent series capacitance of the electrode measured, in this case, at 10 kHz. In the dark, a surface oxide, if present on the GaAs electrode, is expected to be very thin. Since the capacitance of the Helmholtz layer is much greater than that of the depletion layer, the change in the externally applied potential V is concentrated in the space-charge region of the semiconductor, and the electrode behaves as a Schottky barrier.

When the electrode was exposed to a low light intensity, a linear plot was again observed [curve (b)] but displaced with respect to the dark [curve (a)]. An increase in light intensity, to a value still not sufficient to cause film formation, gave a further shift in the curve [curve (c)]. Such a parallel displacement of the Mott-Schottky plots would be consistent with hole trapping at the electrode surface (4, 5). The potential across the Helmholtz layer changes by an amount corresponding to ΔV_{FB}, the displacement of the flat-band (FB) potential.

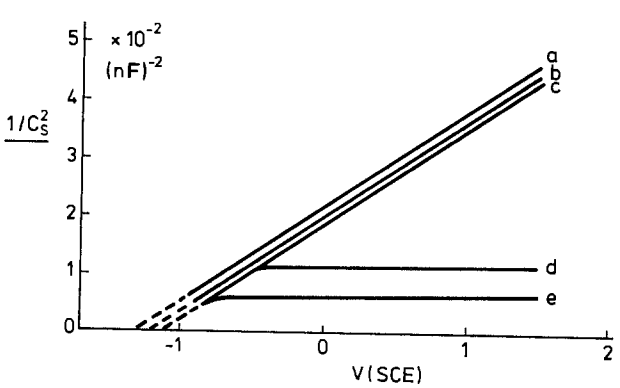

Fig. 4. Mott-Schottky curves (10 kHz) for n-GaAs in 0.1M Na_2 EDTA, 0.1M $NaClO_4$, *p*H 5 in the dark (curve a) and with illumination: N_{ph} = 0.35 [curve (b)]; 0.65 [curve (c)]; 2.0 [curve (d)]; and 3.2 a.u. [curve (e)].

The presence of the surface film had a dramatic effect on the impedance of the illuminated electrode. This is shown in curve (d) of Fig. 4 for a photon density capable of maintaining a stable film. The steady-state C_S value at 10 kHz became almost independent of the applied potential in a wide range. C_S increased with increasing photon density as shown in curve (e). That these effects are connected with the presence of the surface film can be deduced from transient measurements at 10 kHz (Fig. 5). During the induction period of film formation [see curve (a)], C_S increased somewhat with respect to its dark value [curve (b)]. This change corresponds to the parallel shift in the Mott-Schottky curve of Fig. 4. The capacitance, however, increased markedly as the photocurrent decayed to its steady-state value. A corresponding change was also observed in the equivalent series resistance R_S [curve (c)]. Similar behavior was found at other light intensities, with C_S and R_S following the photocurrent changes closely. It should be noted that, although the surface film dissolved only slowly in the dark (Fig. 3), both C_S and R_S relaxed "rapidly" when the light was switched off (Fig. 5).

Further evidence that the anodic film formed in EDTA solution is responsible for the impedance results in curves (d) and (e) of Fig. 4 is provided by measurements in an EDTA-free electrolyte at *p*H 5. As already mentioned, the photocurrent in the absence of EDTA was stable and directly proportional to light intensity up to the highest values used (Fig. 2). In this case, illumination also gave a shift in the Mott-Schottky curve similar to that shown in curves (b) and (c) of Fig. 4. However, the displaced curve remained parallel to the dark curve even up to the highest photon densities; the change in FB potential tended to a limiting value ($\Delta V_{FB} \approx 0.22$V) at higher light intensity.

If the capacitance of the film-covered electrode, measured under illumination, is due mainly to the

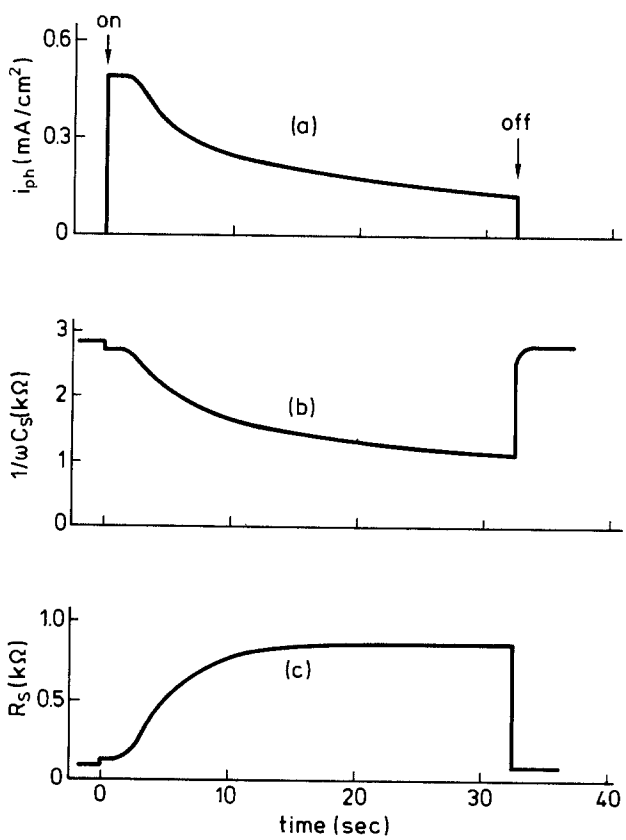

Fig. 5. The influence of light (N_{ph} = 5) on the current and impedance (10 kHz) of n-GaAs at +0.50V (SCE) in 0.1M Na_2 EDTA, 0.1M $NaClO_4$, *p*H 5.

space-charge layer of the semiconductor, then the potential independent C_S values in curves (d) and (e) of Fig. 4 imply a considerably reduced but almost fixed band bending. Such an apparent pinning of the Fermi level could result from a buildup of charge at the GaAs-oxide interface. A fast decay of this interface charge would account for the rapid relaxation of the electrode impedance when the light is switched off.

The results reported above therefore suggest that charge is stored at the GaAs surface during photoanodic dissolution. It is obvious that the model of a Schottky barrier, which describes the electrode under depletion conditions in the dark and at low light intensity, does not hold for an illuminated electrode with surface film. Before further considering the effect of illumination on the charge and potential distribution at the interface, we first examine a model for the film-covered electrode. We then use the results to discuss the nature of the interface charge and its role in the dissolution reaction.

Model for the film-covered electrode under illumination.—The behavior of the electrode with photoanodic film, described in the previous section, resembles, in certain respects, that of the illuminated MOS transistor (10-12). In order to treat our results, we shall therefore use an analogous electrolyte oxide semiconductor (EOS) model [Fig. 6(a)], with additional features involving a "leaky" insulator and hole trapping in interface states. A similar approach has been used qualitatively by Morrison and co-workers (8, 13) for photoanodic reactions at n-type Si electrodes.

The equivalent circuit for such a model is shown in Fig. 6b. In the theory describing the illuminated MOS transistor (11), the depletion layer capacitance C_{sc} is the high frequency limit, characterized by the fact that minority carriers cannot respond to the small a-c measuring signal; the low frequency semiconductor capacitance C_{if} describes the storage capacity of the minority carriers in the interface region, for the case in which the carriers are in quasi-equilibrium; R_L takes into account the generation/recombination resistance between the two bands and gives information on the path through which minority carriers are supplied to the surface region; C_{ox} and R_e refer, respectively, to the film capacitance and the solution plus bulk semiconductor resistance.

In the present case, a small d.c. flows during illumination. This means that the space charge and surface film capacitances must be shunted by a large (nonlinear) faraday resistance. This resistance, which could be deduced from measurements at low frequency, had a value in excess of $5 \times 10^5 \Omega$. For simplicity, it has been omitted from Fig. 6b as it is not important for the impedance measurements at higher frequency discussed here.

In order to test the applicability of such a model for the present EOS case, we measured the frequency dependence of the electrode impedance at various light intensities. The real and imaginary components, Z_{re} ($= R_S$) and Z_{im} ($= 1/\omega C_S$), are plotted in Fig. 7

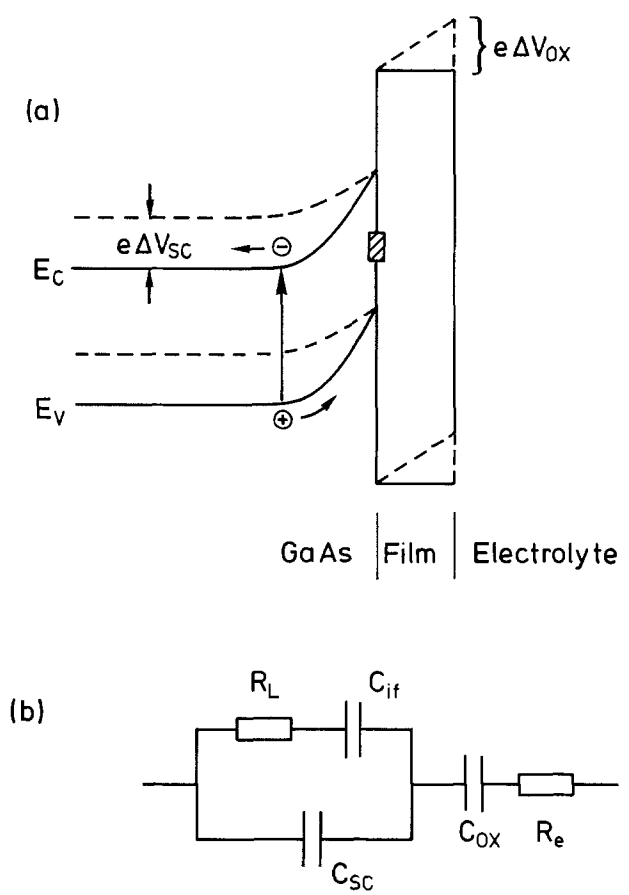

Fig. 6a. EOS model for illuminated n-GaAs. E_c and E_v (solid lines) refer to conduction and valence bands in the dark. As a result of illumination, a positive charge density Q_{if} is built up at the GaAs/film interface. The semiconductor band bending is reduced by ΔV_{sc} and a corresponding potential ΔV_{ox} appears over the surface film (dashed lines).

Fig. 6b. Equivalent circuit for an illuminated n-GaAs electrode with surface film.

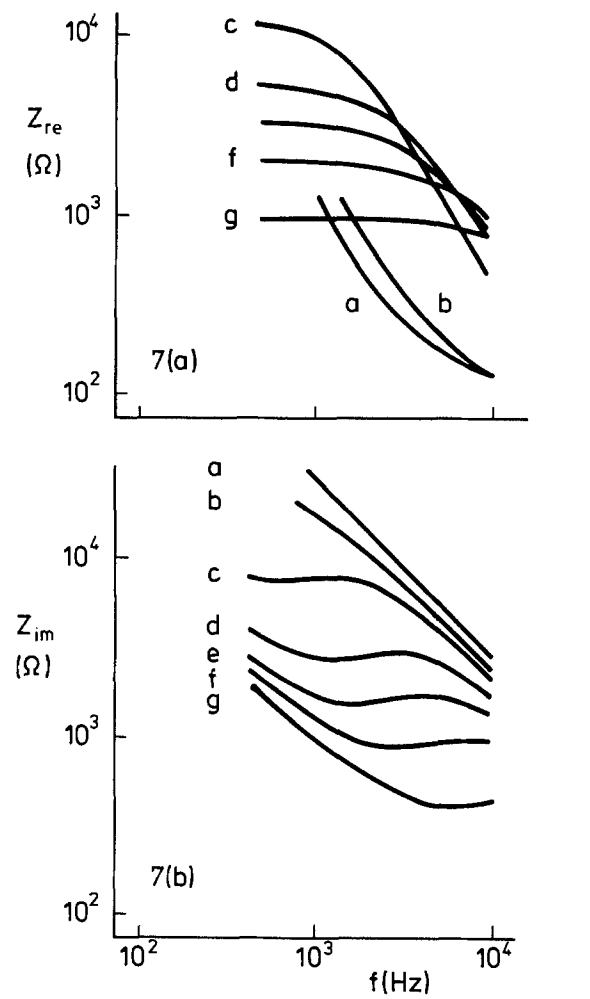

Fig. 7. The frequency dependence of the real (Z_{re}) and imaginary (Z_{im}) components of the impedance of n-GaAs at +0.50V (SCE) in 0.1M Na_2 EDTA, 0.1M $NaClO_4$, pH 5 in the dark [curve (a)]. Remaining curves (b)-(g) refer to illuminated electrode at increasing light intensity. N_{ph} values are given in Table I.

in the frequency range 500 Hz-10 kHz, for an electrode without a surface film in the dark and at low light intensity [curves (a) and (b), respectively], and at increasing light intensity for an electrode with an anodic film [curves (c)-(g)]. The light intensity clearly has a significant effect on the impedance of the film-covered electrode.

An analysis of the equivalent circuit yields the following equations

$$\frac{1}{Z_{re} - R_e} = (R_L C_{sc}^2)\omega^2 + \frac{(C_{if} + C_{sc})^2}{R_L C_{if}^2} \quad [1]$$

$$\frac{\omega Z_{im}}{Z_{re} - R_e} = \left\{ \frac{R_L C_{sc}(C_{sc} + C_{ox})}{C_{ox}} \right\} \omega^2 + \frac{(C_{if} + C_{sc})(C_{if} + C_{sc} + C_{ox})}{R_L C_{ox} C_{if}^2} \quad [2]$$

R_e can be obtained from the high frequency limit of Z_{re} in the dark. It follows from these equations that plots of $1/Z_{re} - R_e$ and $\omega Z_{im}/Z_{re} - R_e$ as a function of ω^2 should give straight lines. In Fig. 8, the second of these functions is plotted for a film-covered electrode at a photon density $N_{ph} = 2$ a.u. Excellent linearity is observed over a range of two orders of magnitude. This was also the case for Eq. [1]. Some deviation from such ideal behavior was found at lower frequency (< 2 kHz) at the highest light intensities.

It was not possible to obtain the four unknown circuit elements directly from Eq. [1] and [2]. In order to get an estimate of the various capacitances, we assumed that the oxide thickness is directly proportional to the potential drop across the oxide (15). Using a proportionality constant for the potential dependence of the film thickness in the range 1.5-4.0 nm/V, as expected for anodic films on GaAs (15), we showed that $C_{ss} >> C_{sc}$. This latter condition was subsequently used to calculate a self-consistent set of impedance parameters. The intercept and slope of the plot of Eq. [1] yield R_L and C_{sc}, and C_{ox} can then be obtained from Eq. [2]. The most striking aspect of this analysis is the very significant decrease in R_L and the gradual increase in C_{sc} with increasing photon density (Table I). The latter result supports the suggestion made in the previous section that illumination decreased the band bending. This is also found with the illuminated MOS device (10). We further note a dependence of R_L on light intensity

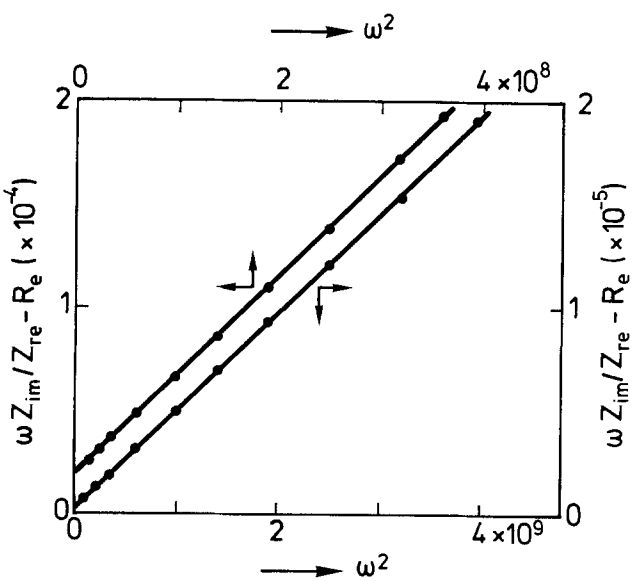

Fig. 8. The results shown in curve (d) of Fig. 7 plotted according to Eq. [2], as described in the text.

Table I. Influence of photon density N_{ph} on the parameters R_L, C_{sc}, and ΔV_{sc} ($= -\Delta V_{ox}$) measured at +0.50V (SCE)

Case	N_{ph} (a.u.)	R_L (kΩ)	C_{sc} (nF)	ΔV_{sc} ($= -\Delta V_{ox}$)
a	dark	≧500.0	5.8	—
b	0.35	400.0	6.0	(0.10)[1]
c	1.1	10.8	8.1	0.88
d	2.0	4.8	9.2	1.08
e	3.2	2.7	10.1	1.21
f	5.7	1.6	10.7	1.27
g	11.4	0.8	11.1	1.31

[1] An anodic film is not formed ($\Delta V_{sc} = -\Delta V_H$).

$$R_L \propto N^n{}_{ph} \quad \text{with} \quad n \approx -1.1$$

similar to that found for the MOS transistor (11, 12). In the MOS case, this dependence has been accounted for theoretically by the Shockley-Read recombination model (11).

Table II shows that, at constant light intensity, C_{sc} and R_L change only slightly with applied potential in the limiting photocurrent range. The film capacitance C_{ox} decreases with increasing potential; this indicates an increase in film thickness, as might be expected for electric field dependent film growth (14). Except at low potential, C_{ox} is approximately an order of magnitude smaller than the generally accepted values of the Helmholtz capacitance; omitting C_H from the circuit of Fig. 6 involves, however, some error in the C_{ox} determination. If we assume a dielectric constant of 8 for the surface film (15), the measured C_{ox} values indicate a film thickness ranging from 1.5 to 4 nm, in reasonable agreement with those already estimated.

For electrolytes without EDTA, the impedance spectra of the electrode illuminated up to high intensity resembled those of the EDTA system in the dark or at very low light intensity [Fig. 7, curves (a) and (b)]. The Z_{im}-f plots were linear between 1 and 10 kHz with a slope of −1. The equivalent R_L term was very large and decreased only slightly on illumination, in contrast to the very considerable decrease in the EDTA case (Table I). In the absence of an anodic film, recombination is not important as hole transfer to the solution remains effective even at high photon density.

Potential and charge distribution.—By using the results of the impedance analysis from the previous section and following a procedure very similar to that adapted by Frese and Morrison (15), information can be obtained concerning the potential and charge distribution at the semiconductor/film interface. If we denote the charge density in the depletion region of the semiconductor by Q_{sc} and that at the interface by Q_{if} without, for the moment, considering whether this is located in an inversion layer or in interface states, then

$$Q_{sc} + Q_{if} = Q_{ox} \quad [3]$$

where Q_{ox} is the charge density on the outer surface of the oxide. The potentiostatically fixed potential difference V between the GaAs and the reference electrode is given by

$$V = V_{sc} + V_{ox} + V_H + V' \quad [4]$$

where V_{sc}, V_{ox}, and V_H refer to the potential drop across the space charge region, the surface film, and the Helmholtz layer, respectively, and V' allows for

Table II. Influence of electrode potential on impedance parameters measured at $N_{ph} = 11$ a.u.

V (SCE)	0.00	0.50	1.00
R_L (Ω)	7.6×10^2	7.7×10^2	7.5×10^2
C_{sc} (nF)	11.1	11.1	11.0
C_{ox} (nF)	3.2×10^2	1.9×10^2	1.4×10^2

the potential difference associated with the reference electrode. If V_{FB} is defined as the value of V at which $V_{sc} = V_{ox} = 0$, then V_{FB} is the measured value of V for an extremely thin film at FB condition and

$$V_{ox} = V - V_{FB} - V_{sc} \quad [5]$$

Introducing the linear film capacitance $C_{ox} = Q_{ox}/V_{ox}$ we obtain

$$C_{ox}(V - V_{FB} - V_{sc}) = Q_{sc} + Q_{if} \quad [6]$$

The potential drop across the depletion layer V_{sc} can be calculated from the measured value of C_{sc} (see Table I) via the Mott-Schottky relation (15)

$$C_{sc} = \left(\frac{\epsilon\epsilon_0 N_D e}{2}\right)^{1/2} \left(V_{sc} - \frac{kT}{e}\right)^{-1/2} \quad [7]$$

in which ϵ is the dielectric constant and N_D the donor density of the semiconductor. Using Eq. [5], V_{ox} can now be calculated as a function of light intensity. Values for the change in band bending ΔV_{sc}, which results from illumination, are given in Table I and confirm the trend already discussed. The decrease in V_{sc} is, of course, compensated by an increase in V_{ox} ($-\Delta V_{sc} = \Delta V_{ox}$) as shown schematically in Fig. 6. Since the depletion layer charge Q_{sc} can be estimated for a given value of V_{sc} from an integrated form of Eq. [7] and since C_{ox} and V_{ox} are known, the charge density Q_{if}, stored at the interface, can be calculated. The values of Q_{if}/e range from approximately $5 \times 10^{12}/cm^2$ to $3 \times 10^{13}/cm^2$ at the highest light intensity for the film-covered electrode.

We can deal with the lower light intensity case involving a very thin surface film ($C_{ox} > C_H$) in a similar manner. The capacitance measured at high frequency is almost identical to the depletion layer capacitance ($C_{sc} << C_H$). Consequently, the change in V_{sc} and Q_{sc}, caused by illumination, can be calculated directly from the measured C_S values of the Mott-Schottky plots [*e.g.*, curves (a)-(c) of Fig. 4]. Since the applied potential is fixed, a change in V_{sc} must, in this case, be compensated by a change in the Helmholtz potential ($\Delta V_H = -\Delta V_{sc}$). In order to obtain the corresponding interface change density

$$C_H \Delta V_H = \Delta Q_{sc} + Q_{if} \quad [8]$$

we assume, by analogy with other electrodes under comparable conditions, a value of 20 $\mu F/cm^2$ for C_H; this is necessary since the Helmholtz capacitance cannot be measured directly in this case. It is clear from curves (a)-(c) of Fig. 4 that Q_{if} increases with increasing light intensity. The limiting value of Q_{if}/e, for a photon density just below that required to form an anodic film, was of the order of $3 \times 10^{13}/cm^2$.

Mechanism of surface charging.—During photoanodic dissolution, holes generated by light move under influence of the electric field in the space-charge region of the semiconductor to the surface where bond breaking occurs (6, 16). In the previous section, we have shown that a considerable charge accumulates at the interface during dissolution and the potential distribution changes significantly. In the absence of a thick surface film, as at low light intensity, excess holes are readily removed from the surface region by the dissolution reaction ($i_{ph} \propto N_{ph}$), a deep depletion condition is observed [curves (b) and (c), Fig. 4] and the change in the Helmholtz potential can be attributed to positive charge in surface or interface states. Such states do not seem unlikely since anodic dissolution of a semiconductor involves the rupture of many surface bonds and the formation of radical- and ion radical-like intermediates (4, 6, 16, 17).

The presence of an anodic film, as formed at higher light intensity, can have two important effects: dissolution is inhibited so that holes created by light cannot escape to solution at a sufficient rate; and as C_{ox} is considerably smaller than C_H, the surface film can accommodate a more substantial rearrangement of the surface potential ($-\Delta V_{sc} = \Delta V_{ox} \approx Q_{if}/C_{ox}$) for a given value of Q_{if}. We shall return to these points later. Although the interface charge could, in this case, be located in an inversion layer, various indications seem to favor an interface state interpretation here also. The interface charge densities found when a surface film was present are quite similar to those for a film-free electrode at slightly lower intensity. The same intermediate states are expected in both cases. In the latter case, a deep depletion and not an inversion condition is found to prevail. In addition, apparent Fermi level pinning sets in at low values of the band bending [curves (d) and (e) of Fig. 4] at which the surface majority carrier concentration is still very high; this makes an explanation based on inversion unlikely and leads us to conclude that interface states dominate over inversion. On the other hand, inversion is important in determining the capacitance of the illuminated MOS transistor (11, 12). However, the interface state density for the MOS device is reported to be more than two orders of magnitude lower than that indicated in the present work (20). Another significant difference is, of course, that the oxide thickness is not constant in this work but increases with applied potential, even up to high potentials (9).

In the above discussion we have suggested, as other workers have also done (5, 6, 16), that the interface states can act as intermediates in the dissolution reaction. It is therefore of interest to examine the experimental impedance results in terms of the kinetics of the charging of such states, in order to obtain information on the importance of surface charging for the dissolution reaction. Although the light-induced change in V_{sc}, and thus in V_H or V_{ox} as shown in Fig. 6, is expected to be a complex function of minority carrier generation, trapping, recombination, and faraday rates, we can use a simple reaction scheme to illustrate the possible effect of these parameters. This scheme is suggested by analogy with models already described in the literature (3, 4, 18); in the present case, the intermediate is considered to be positively charged

$$h\nu \rightarrow e^- + h^+ \qquad \text{step 1. generation}$$

$$h^+ + S \underset{k_r}{\overset{k_p}{\rightleftharpoons}} S^+ \qquad \text{step 2. hole trapping}$$

$$S^+ + e^- \overset{k_n}{\rightarrow} S \qquad \text{step 3. recombination}$$

$$S^+ + h^+ \xrightarrow[(x^-)]{k_f} \text{Products} \qquad \text{step 4. dissolution}$$

We assume that all holes, generated by light at a rate g in step 1, reach the semiconductor surface where they may be trapped at states S. These states very likely involve surface imperfections such as steps or dislocations. The hole trapping reaction is considered to be reversible. The charged states can be discharged by electrons in step 3. Reaction of a charged intermediate S^+ in step 4 with a second hole and the nucleophilic reagent X^- from solution is followed by the dissolution of a GaAs entity.

Such a scheme can be described by the following equations (19)

$$\frac{dp_s}{dt} = g - k_p p_s N(1 - f) + k_r N f - k_f p_s N f \quad [9]$$

$$N\frac{df}{dt} = k_p p_s N(1 - f) - k_r N f - k_f p_s N f - k_n n_s N f \quad [10]$$

$$n_s = n_0 \exp(-eV_{sc}/kT) \quad [11]$$

in which n_s and p_s are the surface concentrations of electrons and holes, n_0 is the bulk electron concentration, N is the interface state density, f is the fraction of states occupied by a hole, and the k terms refer to the various rate constants. Since the applied potential may be located in the space-charge layer and in the Helmholtz layer, it follows that the band bending under illumination V_{sc} is given by

$$V_{sc} = V - V_{FB} - \Delta V_H \quad [12a]$$

with

$$\Delta V_H \approx eNf/C_H \quad (\Delta Q_{sc} < Q_{if}) \quad [12b]$$

In these expressions, C_H and V_H must be replaced by C_{ox} and V_{ox} when the surface film becomes dominant ($C_{ox} < C_H$). Equations [9]-[12] yield under steady-state conditions

$$\Delta V_H = (V - V_{FB}) + \frac{kT}{e} \ln\left(\frac{g - j_F}{k_n n_0 N f}\right) \quad [13]$$

For a chosen value of f, ΔV_H can be calculated from Eq. [12b], and the faraday flux j_F ($= 2k_f p_s N f$) can be obtained using p_s from Eq. [9]. Inserting these values into Eq. [13], we obtain the corresponding value of $V - V_{FB}$. In this way, ΔV_H or V_{sc} (see Eq. [12a]) can be calculated as a function of the applied potential $V - V_{FB}$ for a given set of kinetic parameters. On inserting the value for V_{sc} from Eq. [12] into Eq. [7], we get the modified Mott-Schottky expression for the illuminated case

$$\frac{1}{C_{sc}^2} = \left(\frac{2}{\epsilon\epsilon_0 N_D e}\right)\left(V - V_{FB} - \frac{eNf}{C_H} - \frac{kT}{e}\right) \quad [14]$$

In Fig. 9 the band bending under illumination, calculated using an arbitrary set of rate constants for the dissolution reaction and for electron and hole capture (19), is plotted as a function of applied potential. When $V - V_{FB}$ is small, the degree of occupation of the interface states is limited, ΔV_H is negligible, and V_{sc} increases linearly with applied potential. At low interface state density or at very low light intensity, this continues to high values of $V - V_{fb}$ [curve (a), Fig. 9]; the holes are removed by the dissolution reaction. The Mott-Schottky curve measured under illumination does not differ from the dark case ($eNf/C_H \approx 0$ in Eq. [14]). In previous work (4), we found this to be essentially the case for photoanodic dissolution of n-GaAs in H_2SO_4 solution.

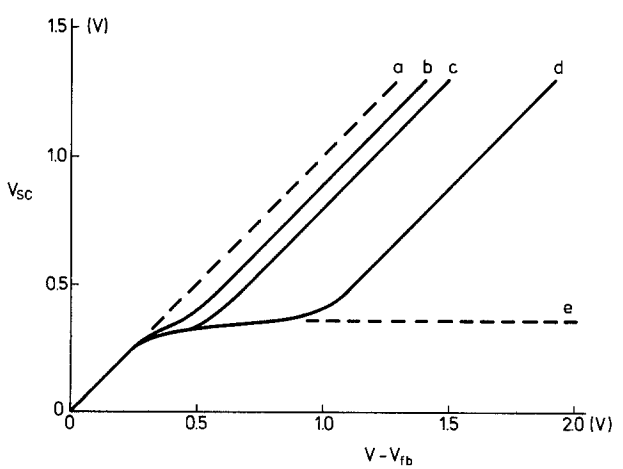

Fig. 9. Calculated band bending V_{sc} as a function of applied potential $V - V_{FB}$. $n_0 = 10^{17}/cm^3$, $N = 5 \times 10^{13}/cm^2$, $k_p = 10^{-7}$ cm^3/sec, $k_n = 10^{-9}$ cm^3/sec, $k_f = 10^{-9}$ cm^3/sec, $k_r = 10^4$/sec. Curve (a) refers to electrode in the dark or at very low light intensity. Curves (b), (d), (e): $g = 10^{15}/cm^2$ sec; curve (c): $g = 5 \times 10^{15}/cm^2$ sec. Curves (b), (c): $C_H = 20$ μF/cm^2; curve (d): $C_H = 3.5$ μF/cm^2. For curve (e), see the text.

At higher light intensity, the interface states begin to fill as V_{sc} increases and the electron concentration at the surface is reduced. If the value of N is appreciable ($> 10^{13}/cm^2$ in this case), the potential in the Helmholtz layer increases and V_{sc} tends to level off [curve (b), Fig. 9]. When the steady-state occupancy is attained, characteristic of the particular photon density, V_H remains constant, V_{sc} again increases, and deep depletion may result. At higher light intensity, a larger steady-state f value is expected and a correspondingly larger ΔV_H shift is calculated [curve (c), Fig. 9]. From Eq. [14], it follows that the parallel shift in the V_{sc} plots, caused by illumination, must lead to an equivalent displacement of the Mott-Schottky curves; this is indeed found with the EDTA system at low intensity (Fig. 4) and with the EDTA-free electrolyte in the complete intensity range. Nakato *et al.* (17) report similar effects with n-GaP electrodes, while we have made similar observations with n-GaP and n-CdS (4).

The value of C_H, used in the examples so far, was typical of that for a normal Helmholtz layer. The effect of an increased capacitance, as for the case when a surface film is present on the electrode ($C_{ox} < C_H$), is clear from curve (d). The film is about 2 nm thick, in this case, and we have again assumed that dissolution is not kinetically inhibited. The surface barrier height is held almost constant over a much wider potential range ($\approx$ 0.6V) as the potential across the surface film builds up. For the EDTA case at higher light intensity, the limiting photocurrent is independent of photon density as a result of film formation [curve (a), Fig. 2]. In addition, the film thickness increases with increasing potential and the film capacitance decreases. This tends to accentuate the effect shown in curve (d), and the apparent pinning of the Fermi level is expected to extend over an even wider potential range. In order to get a rough estimate of the band bending in this case [curve (e)], we again assumed the oxide thickness to be directly proportional to V_{ox} ($d_{ox} = \alpha V_{ox}$ with $\alpha = 2.5$ nm/V). This allows us to calculate Q_{ox}, and by taking this value to be (approximately) equal to (eNf), f can be calculated and consequently, V_{sc}. The constant value of V_{sc} suggested in curve (e) implies a C_{sc} value which is independent of applied potential.

Conclusions

In this paper, evidence is presented to show that a relatively high charge density is localized at the n-GaAs/EDTA-electrolyte interface during photoanodic dissolution. An EOS model, involving the formation of positively charged interface states during illumination, is proposed for this system. The model can account for the parallel displacement of the Mott-Schottky plots at lower light intensity and the drastic changes in the electrode impedance when thicker oxide films are formed at higher photon densities.

It is clear that measurements of the type described in this work may be useful in obtaining information on the mechanism of photoanodic dissolution. For example, if the reverse reaction in the hole trapping step 2 is disregarded, then it can be shown that the parallel displacement of the Mott-Schottky curves becomes independent of light intensity. If, on the other hand, a second hole is not involved in the dissolution step 4, then the displacement should be a linear function of the light intensity. Neither of these observations is in agreement with the experimental results. A study of the relaxation of the interface charge, which is very likely responsible for the fast changes in C_S and R_S when the light is switched off, may give information on the nature of the surface states. The simple reaction scheme, proposed here, emphasizes again the importance of surface charge trapping (4) and recombination (18) for the kinetics of photoanodic reactions,

especially in the low quantum efficiency-potential range.

The role of oxide films may be considerable, even when they are not thick enough to act as a tunnel barrier for holes. Such films may serve to stabilize surface intermediates by shielding them from solution; the reason why charging effects are less pronounced in H_2SO_4 solution might be due to a higher oxide solubility at low pH. We have seen that the film may significantly influence the potential distribution when charge is stored at the interface [compare curves (b) and (d) of Fig. 9]. Finally, the considerable surface charging observed in the present work implies, of course, a shift in the semiconductor bandedges with respect to the solution. This aspect has important consequences for the stabilization of n-type electrodes by means of competitive oxidation of reducing agents, as discussed by Madou *et al.* for n-type Si (8, 13).

Acknowledgment

The authors wish to thank Dr. R. Memming of Philips Forschungslabor, Hamburg, Mr. J. E. A. M. van den Meerakker, and Prof. Dr. J. F. Verwey for helpful discussions.

Manuscript submitted Feb. 18, 1983; revised manuscript received June 30, 1983.

Philips Research Laboratories assisted in meeting the publication costs of this article.

REFERENCES

1. M. M. Faktor, T. Ambridge, C. R. Elliott, and J. C. Regnault, *Curr. Top. Mater. Sci.*, **6**, 1 (1980).
2. R. P. Tijburg and T. van Dongen, *This Journal*, **123**, 687 (1976).
3. K. W. Frese, M. J. Madou, and S. R. Morrison, *J. Phys. Chem.*, **84**, 3172 (1980).
4. R. Memming and J. J. Kelly, in "Photochemical Conversion and Storage of Solar Energy," J. S. Connolly, Editor, Chap. 9, Academic Press, New York (1981).
5. Y. Nakato, A. Tsumura, and H. Tsubomura, *This Journal*, **128**, 1300 (1981).
6. H. Gerischer, *Faraday Spec. Discuss. Chem. Soc. No. 70*, 137/258 (1980).
7. J. J. Kelly and P. H. L. Notten, Extended Abstract No. IV C 12, 33rd ISE Meeting, Lyon, Sept. (1982).
8. B. H. Loo, K. W. Frese, and S. R. Morrison, *Surf. Sci.*, **109**, 75 (1981).
9. C. R. Elliott and J. C. Regnault, *This Journal*, **127**, 1557 (1980).
10. J. Crosvalet and C. Jund, *IEEE Trans. Electron Devices*, **ed-14**, 777 (1967).
11. R. F. Pierret and C. T. Sah, *Solid-State Electron.*, **13**, 269 (1970).
12. R. F. Pierret and C. T. Sah, *ibid.*, **13**, 289 (1970).
13. M. J. Madou, K. W. Frese, and S. R. Morrison, *J. Phys. Chem.*, **84**, 3423 (1980).
14. J. J. Kelly, *Electrochim. Acta*, **24**, 1273 (1979).
15. K. W. Frese and S. R. Morrison, *This Journal*, **126**, 1235 (1979).
16. R. Memming, *Electrochim. Acta*, **25**, 77 (1980).
17. Y. Nakato, A. Tsumura, and H. Tsubomura, in "Photoeffects at Semiconductor-Electrolyte Interfaces," A. J. Nozik, Editor, p. 145, American Chemical Society Symposium, Houston, TX (1980).
18. D. Vanmaekelbergh, W. P. Gomes, and F. Cardon, *This Journal*, **129**, 546 (1982).
19. J. J. Kelly and R. Memming, *ibid.*, **129**, 730 (1982).
20. A. S. Grove, B. E. Deal, E. H. Snow, and C. T. Sah, *Solid-State Electron.*, **8**, 145 (1965).

Application of EPR Spectroscopy to Oxidative Removal of Organic Materials

J. M. Cook and Brent W. Benson[1]

Bell Laboratories, Allentown, Pennsylvania 18103

ABSTRACT

Oxidative species produced in a microwave discharge ($^3P_{2,1}$ O and $^1\Delta$ O_2) have been detected, and some of their reactions with organic solids characterized using a gas phase electron paramagnetic resonance (EPR) spectrometer assembled for that purpose. It has been shown that O atoms rather than excited-state oxygen molecules are the primary reactive species responsible for removal. Also, the O atom oxidation of phenolformaldehyde polymers and graphite has been investigated. The recombination kinetics of O atoms in this flow system can be described by an exponential decay equation involving both wall- and gas-phase collisional recombinations. This allows the signal observed downstream of the reaction to be interpreted as an indication of the gas-solid reaction rate and thus allows the determination of the activation energies of removal of photoresist (0.5 eV) and graphite (0.45 eV). These experiments have established EPR as a useful analytical tool in the development of gaseous cleaning and other, analogous processes, such as etching.

Reactive species produced in a gas-phase discharge readily attack many materials and may be used to etch or clean surfaces in integrated circuit processing (1-2). The major long-lived and potentially reactive species produced in a molecular oxygen discharge are oxygen atoms (ground state) and $^1\Delta$ excited-state molecular oxygen. These, along with the parent ground-state molecular oxygen, can be detected quantitatively using electron paramagnetic resonance (EPR) spectroscopy.

We have assembled and characterized a gas-phase EPR spectrometer and used it to study the production and reactions of oxygen discharge products with organic materials. Interpretation of the EPR data, which are taken downstream from the production and reaction sites, requires an understanding of how the signal varies as a function of the distance downstream. This, in turn, requires a verification of the recombination kinetics of O atoms, both homogeneous (gaseous collisions) and heterogeneous (wall collisions). In these ways we have established EPR as an analytical technique for the study of oxidation (or etching) reactions and have obtained useful information for the development of gaseous cleaning techniques for hybrid integrated circuit processing. This work has been done to show the usefulness of EPR as an analytical tool for the study of cleaning and etching processes.

Experimental

Our EPR spectrometer is a typical balanced-bridge design, operating at 9.6 GHz and using 100 kHz mag-

[1] Visiting Scientist. Permanent address: Physics Bldg. 16, Lehigh University, Bethlehem, Pennsylvania 18015.

Key words: integrated circuits, etching, discharge, oxidation.

netic field modulation with phase-sensitive detection, yielding the recorded first derivative of the absorption. The concentration of the species present in the EPR cavity can be shown to be directly related to the integrated intensity of the signal (3-5). It is thus possible to obtain relative concentration measurements for a given species by measuring the area of its absorption signal. In addition, the absolute concentration of a transient species can be determined by using a stable, paramagnetic gas to calibrate the spectrometer (3). Furthermore, the EPR technique is electronic state-selective and nonperturbing and can detect several species in a reasonably short time.

The basic components of the oxygen discharge, reaction, and detection apparatus are shown in Fig. 1. Oxygen (>99%) flow through the Air Products flowmeter is controlled by a stainless steel needle valve. The discharge is excited in a 25 mm OD quartz tube using a standard Evenson-type microwave cavity (6). The microwave power can be varied between 0 and 200W, although only 75W (<3 reflected) were normally used. The discharge cavity can be moved along the quartz tube to vary the time between production and detection. Certain discharge cavity orientations and positions relative to the EPR cavity caused considerable noise in the EPR signal. This noise depended somewhat on the pressure in the tube. Paramagnetic species produced by the discharge were detected with the EPR system described above. The pumping rate was controlled by a throttling valve before the vacuum pump. Gas pressure at both ends of the reaction tube was measured by an MKS Baratron capacitance manometer.

For the reaction studies, samples were held in a Teflon carrier, as shown in cross section in Fig. 2. The small vertical glass tube was centered with a Teflon bushing and held in an Ultra Torr fitting. The fine tip, containing a thermocouple junction, was then pressed against the sample surface. Temperatures were displayed on a Fluke digital thermometer and simultaneously on an HP dual strip chart recorder, along with the EPR signal.

Samples were heated using a focused infrared lamp positioned below the reaction tube as shown in Fig. 2, with the most intense portion of the beam covering roughly 80% of the sample. A Variac was used to control the lamp supply voltage and thereby the sample temperature.

Phenolformaldehyde polymer sample preparation consisted of spraying the material, as a photoresist, (7) onto ceramic substrates, which had been previously laser scribed, to a thickness of about 10 microns. The substrates were then snapped into 14 mm squares (area $\simeq$ 2 cm^2). Nonreproducibility in preliminary experiments suggested that volatile components were being driven from the photoresist and reacting with the oxygen atoms. Therefore, subsequent photoresist samples were baked at 140°C for 40 min in a nitrogen atmosphere. These samples gave results more consistent with a single reaction of O atoms with the photoresist. Sample weights were determined in a conventional microgram balance.

Square graphite samples (>99.99% pure) roughly 14 mm on a side by 1 mm thick were cut from thin sheets. Gravimetric determinations were not done, as handling produced erosion of random amounts comparable to that removed by reaction.

Before the removal-rate experiments, the quartz reaction tube was cleaned by etching with 48% HF for 40 min. In the absence of cleaning, O atom recombination was sufficiently large in the "as-delivered" tube to prevent any EPR detection. Typical EPR signal intensities decreased during the photoresist experiments, but were improved by recleaning as above. Although the tube was generally left closed between experiments, it was opened for sample insertion and to position sequentially each of the six samples in the reaction position over the IR lamp. This resulted in some signal degradation as well.

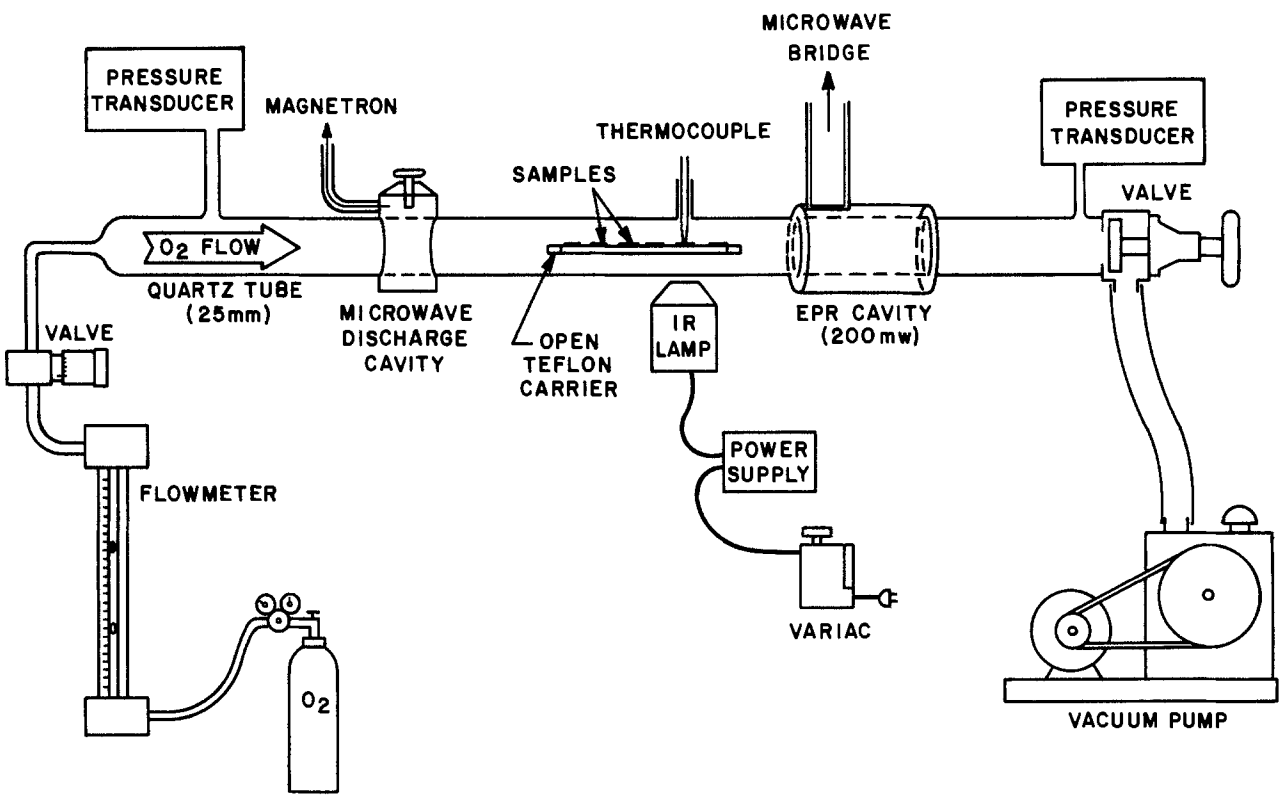

OXYGEN DISCHARGE AND REACTION APPARATUS

Fig. 1. Schematic of gas flow system

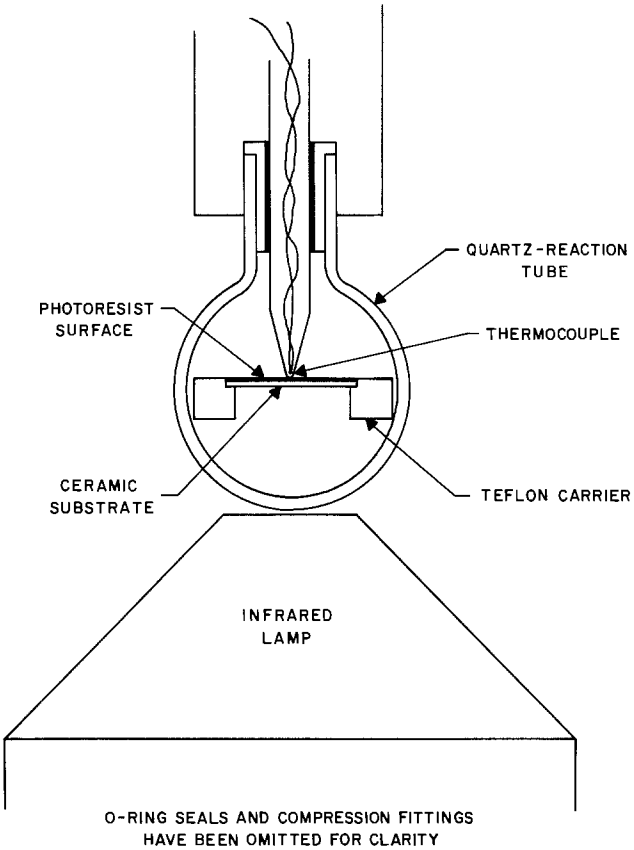

Fig. 2. Cross section of flow tube with Teflon holder in place

EPR-Detected Species

EPR can detect only species having a magnetic moment resulting from net angular momentum (spin, orbital, etc.). Both ground-state O_2 and the metastable singlet state have been observed (8-11). The ground-state lines can be used to determine the absolute concentrations of short-lived species, such as the singlet molecular state or the ^3P, atomic ground state. This work used only relative concentrations, however, so the height of the observed line was sufficient as an indicator of the concentration (providing the pressure was constant for all measurements).

Oxygen atom spectra are presented in Fig. 3. At low pressures all six lines (12-13) may be seen (Fig. 3a), whereas at the pressures used in most of this work, the middle four lines coalesce into one, as shown in Fig. 3b.

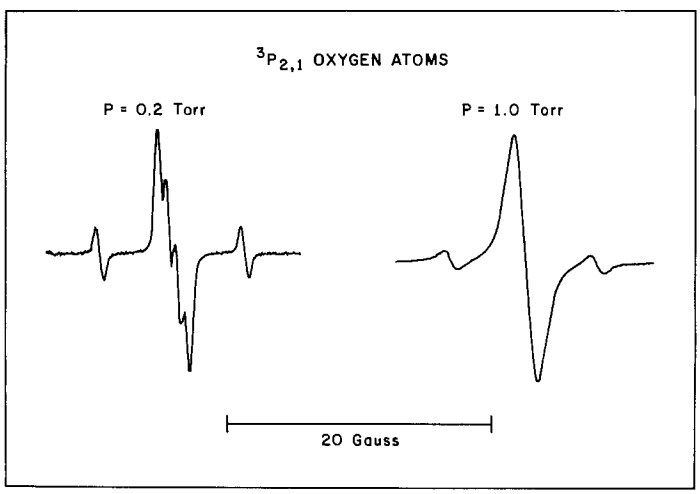

Fig. 3. O atom ($^3P_{2,1}$) spectra at different pressures showing resolved structure at low pressure.

Production and Recombination

Oxidation of organic materials by a gaseous discharge can be effected using several different discharge configurations. In gaseous cleaning they are generally of two types: those that contain the sample within the confines of the discharge (one site), and those where the sample is located remotely, requiring transport of the active species (downstream). Both types have their advantages and disadvantages.

Because of the numerous types of specimens which must be cleaned, and the sensitivity of some to heat and radiation, we have chosen the "remote" or downstream systems for our work. The environment to which the specimen is subjected, with respect to heating and incident radiation and particles, can be well-controlled, something that is far more difficult, although not impossible, in the one-site type of system.

To use the EPR apparatus successfully requires an understanding of how the oxygen atom concentration varies between the discharge exit and the detector cavity. This allows the effects of loss mechanisms (other than reaction with the organic material) to be accounted for, so that signal variation reflects only this reaction.

Previous work in similar systems showed that the principal loss mechanisms were hetero- and homogeneous recombination (14). The homogeneous, or volume recombination, processes produce molecular oxygen by direct recombination of the oxygen atoms or through an ozone intermediate (13-14). The heterogeneous process involves recombination on the walls of the flow tube. In this work, $[O] << [O_2]$ so that the ozone process is the more important and the direct process can be neglected. A rate expression containing these processes can be written, using pure O_2 as the feed gas, as: (13)

$$[O] = [O]_o \exp\{-(2k_1[O_2]^2 + k_2)\ (d/v)\} \quad [1]$$

where $[O]_o$ is the atom concentration at the discharge exit, k_1 and k_2 rate constants for the homo- and heterogeneous processes, respectively, d the distance from the discharge to the detector, and v the linear velocity of the atoms down the tube, typically 5-10 meters/sec at 1 Torr. We found k_1 and k_2 to be about 3×10^{-34} cm^6 molec^{-2} sec^{-1} and 0.2 sec^{-1}, respectively. These values agree well with other determinations (13). Considerations of viscous pressure drop and diffusion show them to be unimportant for our case. We are thus able to use signal variation as a probe for understanding the oxidation and removal of organic materials and how they are affected by heat, incident radiation, and variation in gas mixture.

Reactive Species

Reactions of the various oxygen species with various organic materials may be observed as a decrease in the species' EPR signal (*i.e.*, their concentration) at the EPR cavity. It is possible to follow the reaction closely by holding the magnetic field on the signal peak (actually the maximum slope of the absorption as the signal is displayed as a first derivative) and continuously monitoring intensity as a function of time. In Fig. 4a, the O atom decrease is quite marked. The signal approaches the baseline, indicating that within the limits of sensitivity of the instrument (about 10^{11} atoms cm^{-3}), all O atoms are removed by the reaction. Figure 4b shows that ground-state O_2 does not appreciably participate in the reaction. It was found that the singlet molecular signal was likewise unaffected.

Loss of photoresist can be visually observed if the reaction is allowed to continue. Later experiments make use of weight loss as a measurement technique to be compared to EPR signal changes. The resist is removed at a rate of a few thousand angstroms/min, and if the reaction is allowed to proceed long enough, all photoresist is removed and the O atom signal returns to its original value. Other experiments with

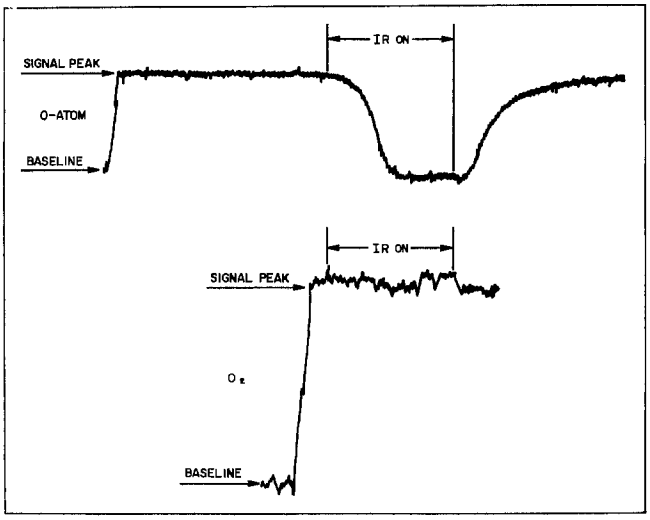

Fig. 4. a) Spectrometer sitting on O atom peak while IR lamp turned on and off, b) same procedure for $^3\Sigma_g^-$ O_2.

uncoated ceramic showed also that heating the ceramic produced no observable O atom signal loss.

Removal Kinetics and Reactions

The study of the removal of the organic material in these experiments requires a knowledge of at least five parameters: gas pressure, flow, relative species' concentration, sample temperature, and sample weight lost. To determine profiles for all parameters completely would have been extremely laborious and probably unnecessary. Instead, general features were studied for selected values of the parameters by using five or six samples mounted consecutively on the Teflon carrier and sequentially moved into position.

Figure 5 shows the O atom signal (upper trace) and sample temperature (lower trace) as functions of time for a sample having a final temperature of ≈130°C.

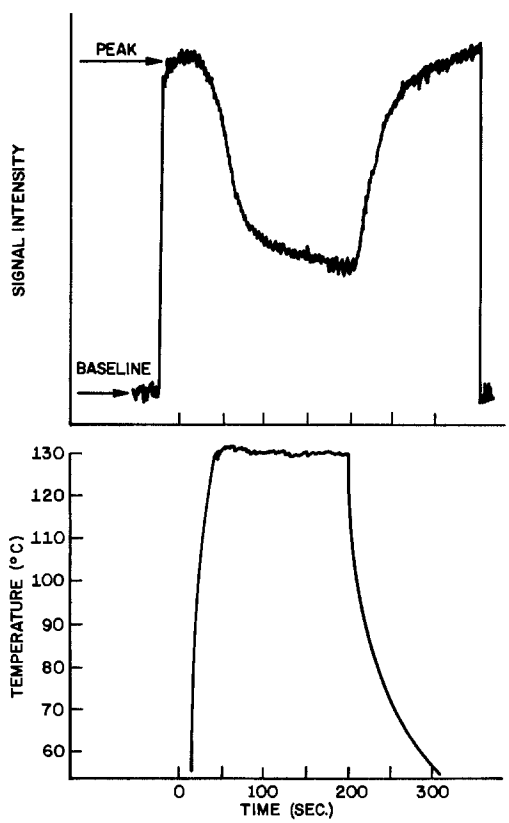

Fig. 5. O atom loss (upper) as a function of temperature (lower) for maximum temperature of ≈130°C.

For a given flow rate and pressure, the number of atoms delivered to the sample per unit time is constant, so that the amount by which the signal decreases is proportional to the reaction rate. These proportionalities, as a function of temperature, have been fitted to the familiar Arrhenius expression

$$\text{rate} = A \exp(-E_{act}/RT) \quad [2]$$

to yield an effective activation energy for the removal process. The fraction of the signal lost is plotted as ln(rate) *vs.* $^1/T$ in Fig. 6, along with the least squares fitted line. Also plotted are weight loss data. These show the excellent agreement between them and the EPR signal loss values. The data were actually fitted to the exponential rather than linearized form of the equation, since the absolute errors are equal for all points. Table I lists several activation energies determined for photoresist removal under various conditions. Although there is great uncertainty in the individual determinations, the average agrees reasonably well with the value found gravimetrically (0.56 eV). A similar, though perhaps fortuitous, value has been obtained for a different resist using a shielded stripper (0.5 eV) (15).

For a constant flow rate (both volume and velocity), the EPR signal intensity is proportional to an atom flux across the tube cross section. Thus, the integral of the signal over time represents the total number of atoms observed. Hence, a quantity proportional to the total number of atoms reacted can be determined from the integral of the signal lost over the time of the reaction. If weight loss is proportional to the number of atoms reacted, as one would expect, a plot of one of these quantities *vs.* the other should yield a straight line. This is shown in Fig. 7. If the number of atoms is made absolute rather than relative, the slope of the line determined from this plot gives the stoichiometry of the reaction under these conditions.

Of interest is the fact that at higher sample temperatures virtually all O atoms react, at least to the limits of our sensitivity, even though the näive view might be that one-half of them pass by the uncoated side of the ceramic. An elementary kinetic theory calculation shows that for typical flow rates and pressures, a given O atom undergoes approximately a 3 cm random-walk displacement from its original position in the moving gas during the time it takes the flowing gas to move roughly 2 cm. The flow tube is 2.5 cm in diameter and the sample 1.4 cm on a side, so perhaps it is reasonable to assume some of the atoms passing beneath the substrates can react with the photoresist surface, even though at first consideration this seems unlikely. Also, diffusion of atoms flowing over a perfect sink might well contribute.

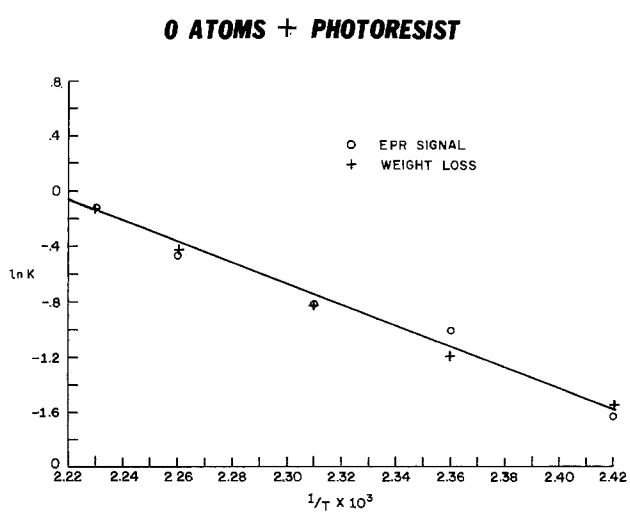

Fig. 6. Plot of ln *k* *vs.* 1/*T* for O atoms + photoresist with weight loss data also plotted for comparison.

Table I. O_2 flow rate = 101 cm^3/min NTP

Pressure (Torr)	E_{act} (kcal/mol^{-1})
1	14.7
2	11.2*
3	10.4*
	11.6 Avg
	(0.50 eV)

* Average of two runs.

Another mechanism that might better account for some or the entire loss would be the downstream reaction of O atoms with volatile, intermediate species produced by the initial O-atoms reactions on the material. Our data are taken further downstream and do not clearly distinguish between the two possibilities, although it is possible to design experiments with the apparatus to differentiate between them.

Graphite Reactions

Oxygen atoms react with heated graphite in a fashion similar to the photoresist reactions described earlier. However, unlike photoresist, room temperature graphite reduces the concentration of $^1\Delta$ O_2 such that the EPR signal all but disappears. It was not possible to follow weight loss, as in the case discussed above, owing to sample erosion during handling.

O atom loss (reaction rate) as a function of temperature is shown in Fig. 8. The graphite wafer was placed on top of a base ceramic square which was heated, as shown in Fig. 2. The temperature was measured by placing the thermocouple on the surface as before. The ceramic was used so that the lamp would heat in a similar fashion to the experiments using photoresist and the temperature measured would be that of the surface reacting with the atoms. The data yield an activation energy of 10.4 kcal/mol^{-1} (0.45 eV), which agrees well with published values of 8.8-10.0 kcal/mol^{-1} (0.38-0.43 eV) (16).

Discussion

Since oxidative cleaning is effectively a combustion process, it involves many reactions (1) that complicate its understanding. However, some insight into particular processes of interest has been gained.

Understanding the loss of reactive species between production and detection to processes other than reaction with the organic material is important. Without this understanding, design of downstream cleaning systems becomes difficult, since it is desirable to keep recombination and deactivation loss of reactive species to a minimum. Moreover, an understanding of the removal kinetics is made possible by this knowledge.

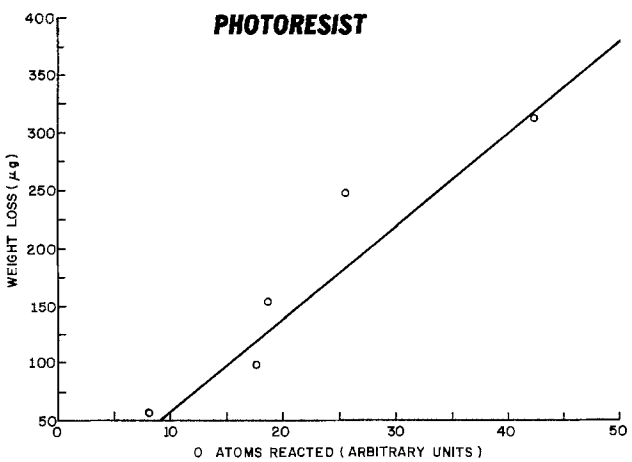

Fig. 7. Correlation of weight loss vs. signal proportional to fraction of atoms reacted.

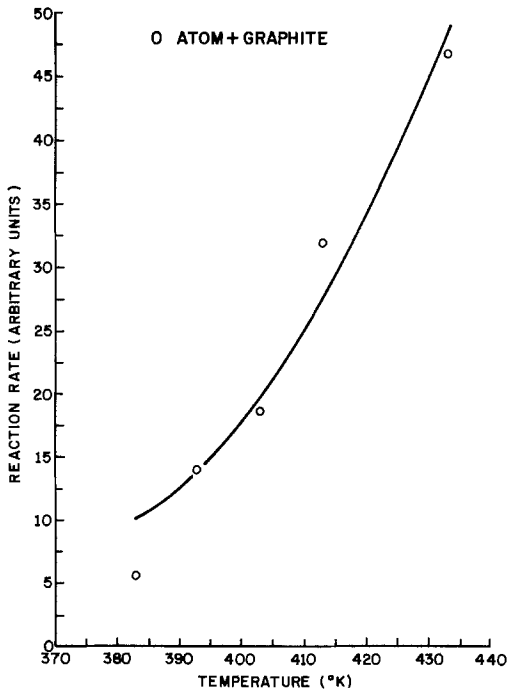

Fig. 8. Reaction rate vs. temperature for graphite. Superimposed is least squares fitted curve. Pressure is 1 Torr.

The results of this work indicate that in systems of this sort, maximum pressures of about 1 Torr or less should be utilized to maximize delivery of atoms to the samples. Quartz surfaces do not greatly decrease the reactive species' concentrations, as long as they are cleaned by etching.

O atoms have long been considered the reactive species. For photoresist, this has been confirmed. As ^3P O and $^1\Delta$ O_2 are present in comparable amounts, roughly 10^{15} cm^{-3} at 0.8 Torr, the total lack of $^1\Delta$ signal modulation on sample heating excludes $^1\Delta$ O_2 as a significant species. However, ground-state O_2 is present in much higher concentration. The lack of observable signal modulation on heating could be ascribed to lack of relative sensitivity in determining a very small change in the total ground-state O_2 concentration. However, the lack of observable material loss in the absence of a discharge, and the inactivity of the more reactive singlet state, shows that ground-state O_2 is not a significant reactant.

Understanding graphite reactions presents more of a problem, since both the O atom and $^1\Delta$ O_2 signals are affected. $^1\Delta$ O_2 reacts far less extensively with saturated compounds than with unsaturated ones (17-18). Graphite, being somewhat aromatic in character, may possibly be reacting with $^1\Delta$ O_2 to produce cyclic peroxides, or it may serve simply as a site for deexcitation.

The activation energies of this work for oxidation of photoresist and graphite agree reasonably well with other determinations. The EPR method lends itself well to such determinations if proper care is taken. Spectrometer operating conditions must be reproducible from point to point, and the sample temperature measured must represent the reacting surface of the material. Furthermore, the decay processes that further reduce the reactive species' concentration after reaction must be understood in order that the data reflect conditions immediately after reaction.

There are many avenues to be explored in future work, including determination of the relationships between ease of removal and contaminant structure, some of which have been listed already (19). Also, more materials should be examined with the aim of attaining a good predictive ability about what materials can be removed and under what conditions. The use of other gases mixed with O_2 before discharge

should be investigated for the gases' ability to enhance O atom concentration. The reaction order and the stoichiometry should also be determined, the former by the dependence on [O] of the signal fraction lost. To determine the stoichiometry requires that absolute concentration measurements of the reactive species be made, which can be done by calibration of the spectrometer, as mentioned above. This might further elucidate the relationships between structure and ease of removal.

Finally, while EPR has proven to be a powerful tool, even in these preliminary experiments, it is necessary to point out a limitation. Species such as $^1\Sigma$ O_2 and ^1A O_3 have no magnetic moment and so cannot be seen via EPR. They are both probable constituents of the discharge effluent and while their effects are probably small, their possible role in the removal process must not be completely overlooked. This could be accomplished by selectively removing the other constituents, *i.e.*, the atoms and singlet O_2, and measuring the amount of any material removed.

Conclusion

This work has demonstrated both the feasibility and the utility of EPR spectroscopy as an analytical tool in understanding gas-solid reactions used in integrated circuit manufacture. We have demonstrated its ability to monitor reaction rates and to identify reactive species. From the rates and measured temperatures, we can calculate activation energies of removal. We have discussed also the way in which both relative and absolute concentrations can be measured and how the latter may be used to determine stoichiometries of removal.

The ability to use EPR to make such measurements, combined with its ability to detect other paramagnetic species such as F atoms, indicates its general utility for studying gas-solid reactions other than oxidation. A very important class of such reactions involves the etching of semiconductors using fluorine containing gases in some sort of discharge. EPR should be able to complement already-used techniques, such as mass and emission spectroscopy in elucidating mechanisms and reactive species.

These initial results have been very encouraging and suggest a number of further experiments to better understand oxidation and removal of organic material. Some of these experiments are currently underway in particular the studies of how a few percent of added Freon™ enhance the oxidation rate, and the use of other gases to increase the number of oxygen atoms produced in the discharge.

Acknowledgment

The authors thank T. A. Miller and B. R. Zegarski for helpful discussions and technical assistance.

Manuscript submitted Dec. 3, 1982; revised manuscript received June 1, 1983.

Bell Laboratories assisted in meeting the publication costs of this article.

REFERENCES

1. R. H. Hansen, J. V. Pascale, T. De Benedictis, and P. M. Rentzepis, *J. Polym. Sci.*, **A3**, 2205 (1965).
2. D. L. Flamm and V. M. Donnelly, *Plasma Chem. Plasma Processing*, **4**, 317 (1981).
3. S. Krongelb and M. W. P. Strandberg, *J. Chem. Phys.*, **31**, 1196 (1959).
4. K. Halbach, *Phys. Rev.*, **119**, 1230 (1960).
5. A. A. Westenberg and N. de Haas, *J. Chem. Phys.*, **40**, 3087 (1964).
6. F. C. Fehsenfeld, K. M. Evenson, and H. P. Broida, *Rev. Sci. Instrum.*, **36**, 294 (1965).
7. AZ 1350J, Shipley Co., Newton, MA 02162.
8. M. Tinkham and M. W. P. Strandberg, *Phys. Rev.*, **97**, 951 (1955).
9. I. B. Goldberg and H. O. Laeger, *J. Phys. Chem.*, **84**, 3040 (1980).
10. A. M. Falick, B. H. Mahan, and R. J. Myers, *J. Chem. Phys.*, **42**, 1837 (1965).
11. A. M. Falick and B. H. Mahan, *ibid.*, **47**, 4778 (1967).
12. H. E. Radford and V. W. Hughes, *Phys. Rev.*, **114**, 1274 (1959).
13. P. D. Francis, *Brit. J. Appl. Phys.*, **2**, 1717 (1969).
14. For review, see: F. Kaufman, "Progress in Reaction Kinetics," Vol. 1, Pergamon Press, New York (1961).
15. H. Kalter and E. P. G. T. Van de Ven, Abstract 125, p. 335, The Electrochemical Society Extended Abstracts, Vol. 1976-1, Washington, D.C., May 2-7, 1976.
16. H. Marsh, T. E. O'Hair, and Lord Wynne-Jones, *Carbon* **7**, 555 (1969).
17. D. R. Kearns, *Chem. Rev.*, **71**, 395 (1971).
18. A. K. Breck, C. L. Taylor, K. E. Russell, and J. K. S. Wan, *J. Polym. Sci.*, **12**, 1505 (1974).
19. G. N. Taylor and T. M. Wolf, Technical Paper number 174 presented at Reg. Tech. Conf.—Soc. Plast. Eng., 1979.

Solubility of Implanted Dopants in Polysilicon: Phosphorus and Arsenic

N. Lifshitz

Bell Laboratories, Murray Hill, New Jersey 07974

ABSTRACT

A new method of determining the active dopant solubility limit (ADSL) of implanted dopants in polysilicon is described. ADSL is defined as the concentration of a dopant such that a further increase of the dopant content does not lead to an increase in mobile carrier concentration. The method is based on the idea that the implanted dopant in excess of ADSL does not contribute to the conduction process. The method is simple to employ and is used in the present experiments to determine the ADSL concentration of arsenic and phosphorus implanted in polysilicon.

It is known that in heavily doped crystalline silicon, some fraction of impurities does not contribute mobile carriers into electrical conduction. There exists a concentration level, called the active dopant solubility limit (ADSL), where further increase of the dopant content will not lead to an increase of free carrier concentration (1, 2).

An analogous parameter can be defined for polysilicon. There is a difference, however; polysilicon is a rather more complex structure than crystalline Si

Key words: polycrystalline silicon, solubility limit, arsenic and phosphorus, doping by ion implantation.

in that it is a conglomerate of single crystal grains. There, grain boundaries may act as a sink for dopant. It has been established, for example, that arsenic and to a lesser degree phosphorus tend to segregate to the boundaries and become in-activated (3, 4, 5).

It is believed that the concentrations exceeding ADSL cannot be achieved by a quasi-equilibrium process of diffusion. However, such concentrations can be obtained by a nonequilibrium process of ion implantation.

This work describes a method of determination of ADSL of dopants in polysilicon. The method is based on the idea that the dopant in excess of the critical concentration does not contribute to conduction. In these experiments, polysilicon layers of various thicknesses are doped by ion implantation of a certain fixed dose of arsenic or phosphorus. When the concentration of the dopant in the films is equal to or exceeds the ADSL concentration, the dependence of sheet resistance on the layer thickness obeys an inverse proportionality law (*i.e.*, for a constant dopant concentration the sheet conductance is proportional to the film thickness). As soon as the thickness of polysilicon reaches a certain limit (the critical thickness) where the fixed implant dose is not sufficient to provide the ADSL concentration, the dependence of sheet resistance on the layer thickness begins to deviate from the inverse proportionality and, in fact, becomes constant because the maximum number of active dopant atoms available are all contributing to conductivity. The solubility limit N_p can be found from the critical thickness, assuming one knows the exact implant dose.

Experimental

Polysilicon films of thicknesses varying from 900 to 6000Å were deposited by the LPCVD method at 625°C onto thermally oxidized silicon wafers. The thickness of the oxide was 1000Å. Measurements of the film thicknesses were made after polysilicon deposition, with a Nanospec/AFT interferometer. The interferometer was calibrated against a Dektak II surface profilometer by matching reading for thicker samples (4000-6000Å). Arsenic and phosphorus were implanted into the films at energies of 60 and 30 keV, respectively, which were low enough to ensure that even in the case of the thinnest films more than 95% of implanted dopant was placed into polysilicon. The films were capped with CVD oxide (1200Å) to prevent the out-diffusion of the dopant. The samples were annealed at 900°, 950°, and 1000°C for 16, 4, and 2 hr, respectively, in a dry nitrogen ambient. These times were found to be sufficient for all resistivity changes to reach equilibrium. After the protecting oxide was stripped in buffered hydrofluoric acid, the sheet resistivity was measured by the four-point probe method.

Results

Results were obtained in a form shown in Fig. 1 and 2. Here the sheet resistivity of polysilicon films implanted with As and P and annealed at 950°C is plotted as a function of film thickness. Similar plots were obtained for films annealed at 900° and 1000°C.

One can distinguish two regions on the plots: (*i*) for thin layers, $d < d_0$, the sheet resistance is inversely proportional to the thickness; (*ii*) for layers thicker than d_0, the sheet resistance is essentially constant independent of thickness.

Thus, d_0 is identified as the critical thickness where the sample ceased being saturated with the dopant. In the first (saturated) regime, the sheet resistivity obeys the relation $\rho_S = \rho/d$, where ρ is the saturated resistivity Further increase of d beyond d_0 results in no further change in conductivity because all available dopant atoms (fixed dopant dose) are participating in conductivity. For comparison we include in Fig. 2 data obtained by phosphorus diffusion at 950°C. The diffusion and implant data coincide for $d < d_0$, but for $d > d_0$ a distinct difference becomes apparent. The sheet resistance of diffused samples continues to decrease according to the inverse proportionality law because diffused layers are always saturated.

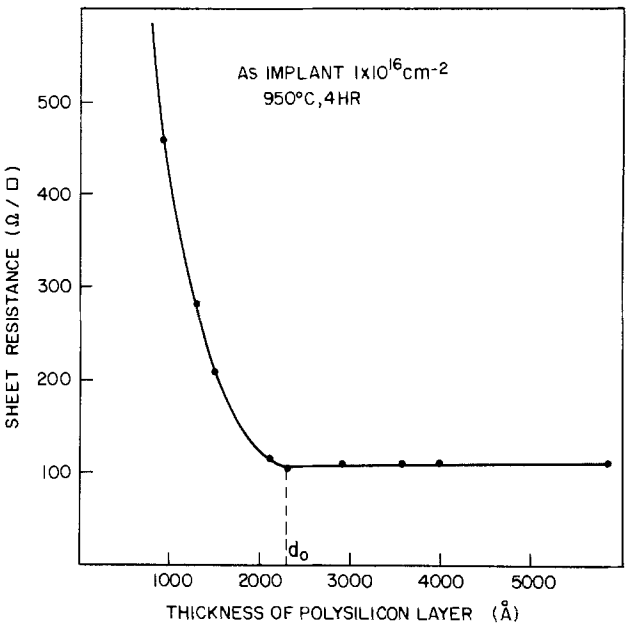

Fig. 1. Sheet resistance as a function of thickness of polysilicon films doped with As by ion implantation (1×10^{16} cm^{-2} dose) and subsequent anneal at 950°C.

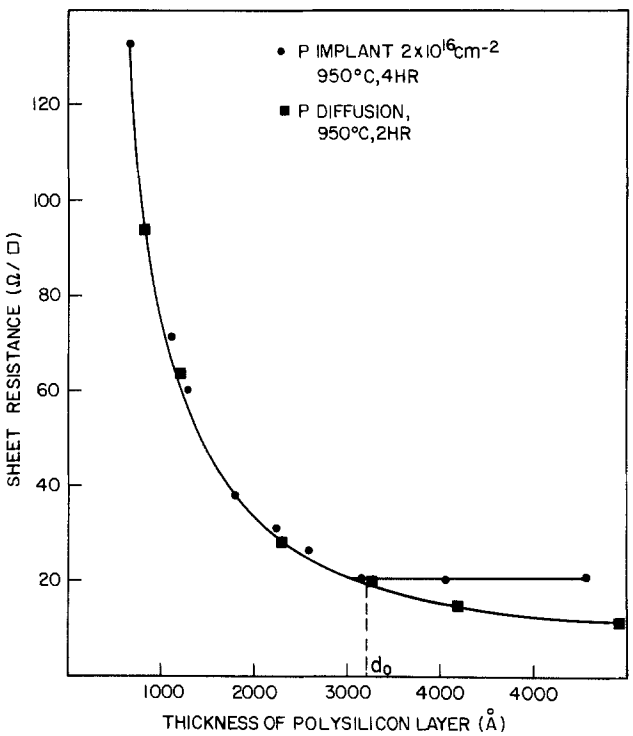

Fig. 2. Sheet resistance of polysilicon films doped with phosphorus as a function of the film thickness. Doping was achieved in two ways: (*i*) by ion implantation (2×10^{16} cm^{-2} dose) with subsequent anneal at 950°C; and (*ii*) by phosphorus diffusion at the same temperature.

In Fig. 3 and 4, results of the measurements on implanted samples are presented in a different form. Here the sheet conductance is plotted as a function of film thickness for three different anneal temperatures. The hyperbolic part of the resistance curves in Fig. 1 and 2 has transformed into a straight line having slope

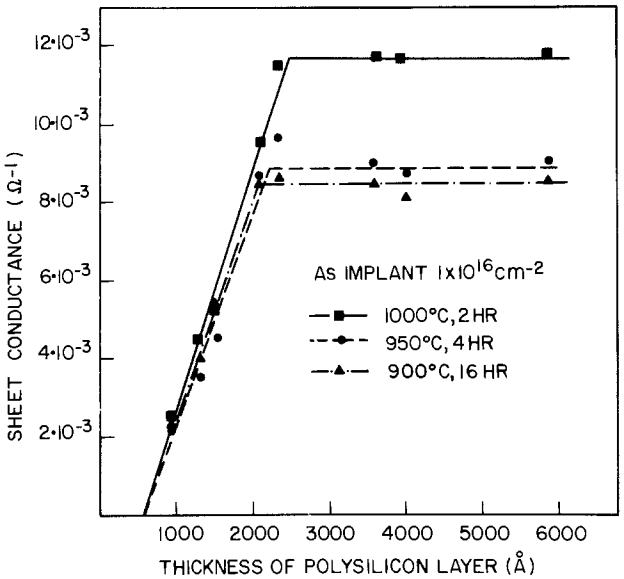

Fig. 3. Sheet conductance of arsenic-doped samples with different anneal temperatures plotted as a function of polysilicon film thickness.

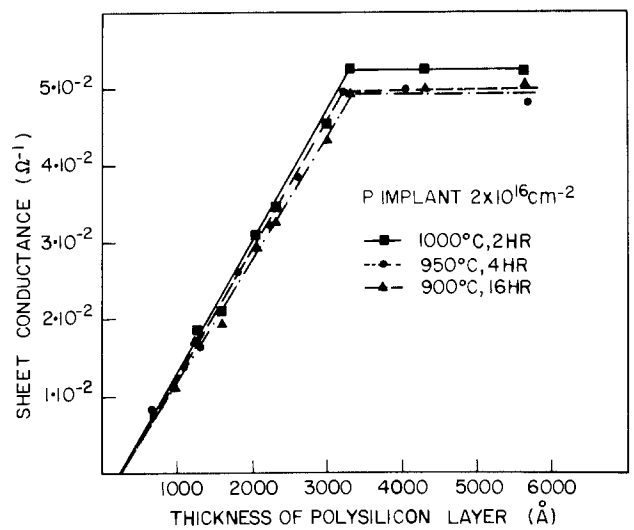

Fig. 4. Sheet conductance of phosphorus-doped samples with different anneal temperatures plotted as a function of polysilicon film thickness.

proportional to the conductivity of the polysilicon doped to the critical concentration. The onset of constant conductivity marking the critical thickness d_0 is even more sharply delineated in this kind of plot.

Additional results showing the effect of different doses of As implant are plotted in Fig. 5. The samples were annealed at 950°C. It may be noted that the two sets of samples having different implant doses, 1×10^{16} and 1.4×10^{16} cm^{-2}, exhibit identical resistivities, *i.e.* a common slope, as the implant concentration exceeds ADSL, However, the breaks occur at two widely separated values of d_0. This reflects the different implant doses.

A peculiar feature of the plots in Fig. 3, 4, and 5 is that they intercept the abscissa axis at some positive value d'. This value does not depend on anneal temperature and is equal to 600Å for As and 250Å for P-doped poly. This effect will be discussed later in this paper.

Discussion

Solubility limits of As and P in polysilicon.—The ADSL of As and P in polysilicon can be found from the data in Fig. 3 and 4 as a ratio of the implant dose to the critical thickness corresponding to this dose and

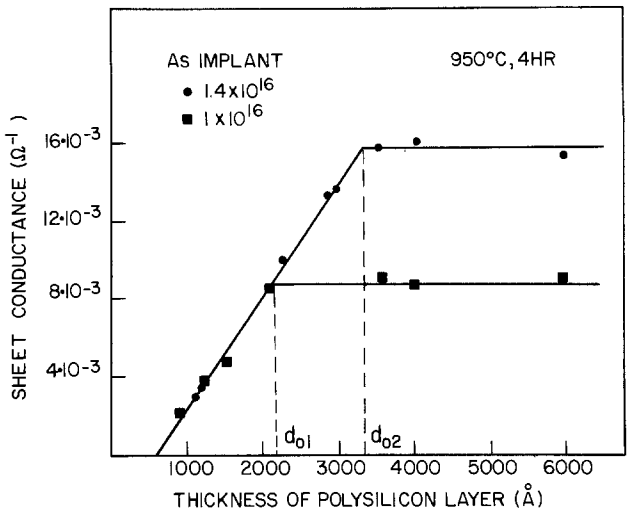

Fig. 5. Sheet conductance of polysilicon films implanted with two different doses of arsenic (1×10^{16} and 1.4×10^{16} cm^{-2}) and annealed at 950°C, plotted as a function of film thickness.

given anneal temperature. The results and parameters of calculations are tabulated in Table I. Generally, the solubility limit N_p depends upon anneal temperature. This dependence can be due to several factors, such as grain growth (6, 7, 8), variation in the surface concentration of segregated dopant in the grain boundaries with temperature (3), and increase in the solubility level of the dopants in the grains (*i.e.*, the solubility limit N_{Si} in crystalline silicon) at elevated temperatures.

It is interesting to compare our results for N_p with data from the literature for N_{Si} gathered in the rightmost column of Table I. For As, the solubility limit in polysilicon was found to vary from 4.8×10^{20} to 4.1×10^{20} cm^{-3}, corresponding to anneal temperatures of 900°-1000°C. These values are higher than N_{Si}, the difference being more pronounced at lower annealing temperatures. This difference is a direct measure of inactivated As dopant trapped at the grain boundaries.

For P, the solubility limit in polysilicon was found to be 6.2×10^{20} cm^{-3}, independently of the anneal temperature. A comparison with N_{Si} is not straightforward because of conflicting values for N_{Si} in the literature (*cf.* Table I).

On the possible influence of the polysilicon/SiO_2 interface.—It was pointed out earlier that the plots in Fig. 3, 4, and 5 intercept the abscissa axis not at the origin of coordinates but rather at some positive value d'. This value does not depend on anneal temperature and implant dose and is equal to 600Å for As and 250Å for P-doped polysilicon. It is tempting to speculate on the basis of this behavior that there might exist poorly conducting regions within the polysilicon layer.

There is additional evidence from Fig. 5 that this might be the case. In Table II we list from Fig. 5 the critical thickness d_0 and corresponding values of sheet conductance G_s (also listed are the intercepts d'). The critical thickness d should be proportional to the im-

Table I.

	Implant dose (cm^{-2})	T(°C)	d_0(A)	N_p (10^{20} cm^{-3})	N_{Si} (10^{20} cm^{-3})		
As	1×10^{16}	900	2100	4.8	2.1[11]	2.3[2]	
		950	2250	4.5	2.5	2.6	
		1000	2450	4.1	3.0	3.3	
P	2×10^{16}	900	3250	6.2	4.0[8]	5[9]	3.1[10]
		950	3250	6.2	6.0	7.4	
		1000	3250	6.2	8.0	8.8	3.5[10]

Table II.

Implant dose I (cm^{-2})	d_0 (Å)	G_s (mho)	d' (Å)	d_{01}/d_{02}	I_1/I_2	$\frac{d_{01}-d'}{d_{02}-d'}$	G_{s1}/G_{s2}
1×10^{16}	2200	8.9×10^{-3}	600	0.67	0.71	0.59	0.56
1.4×10^{16}	3300	15.8×10^{-3}	600				

plant dose I (if the samples are doped uniformly), but the value of the sheet conductance G_s at the break point $d = d_0$ should be proportional to the active thickness $d_0 - d'$ of the samples. As a test it is instructive to compare ratios of these various quantities (last four columns of Table II).

First, the ratio of sheet conductances G_{s1}/G_{s2} is closer to the ratio $(d_{01} - d')/(d_{02} - d')$ than to the ratio of the critical thicknesses d_{01}/d_{02}, suggesting that a part of the total film thickness is nonconductive. Since the films may be only one grain thick (due to grain growth during annealing), poorly conductive regions are most likely to exist at the interface with SiO_2 and be similar in nature to the grain boundaries. Swaminathan *et al.* (12) observed similar regions, about 100Å thick, at As-doped polysilicon/SiO_2 interface. Since in the present experiments the polysilicon films were bounded with SiO_2 from both sides, it is assumed that the low conductive regions occur at both interfaces. Hence, d_0 represents the total thickness of two such regions. Then, for arsenic-doped poly, this region is about 300Å thick, which is much higher than estimated in (12), and for phosphorus doping the thickness is about 120-130Å.

Second, the fact that the ratio of critical thicknesses d_{01}/d_{02} (0.67) is close to the ratio of implant doses I_1/I_2 (0.71), suggests that the dopant concentration throughout the layer is uniform and that no apparent pile-ups of arsenic are present at poly/SiO_2 interfaces. Such pile-ups have been observed at the interfaces when the arsenic concentration was below solubility limit, whereas there is no evidence of pile-up when the dopant concentration was close or above ADSL (12, 13). The latter was explained by the saturation of sites at the interface to which the arsenic atoms tend to segregate (12). Possibly this is taking place in the present experiment, where the samples are doped close to or above the ADSL level.

Final remark.—The bulk conductivity of As- and P-doped polysilicon layers can be determined from the slopes in Fig. 3, 4, and 5, the values of which are listed in Table III. Also listed in Table III are electron concentrations and Hall mobilities of samples doped to the ADSL level ($d \approx d_0$) and annealed at 950°C. The conductivity for P-doped poly exceeds by several times the conductivity of As-doped poly because of higher electron concentration and mobility. Results of Solmi *et al.* (6) on As- and P-doped polysilicon give slightly higher values of n, μ, and σ, possibly due to the higher anneal temperatures (1050°C) and thicker films (4400Å) used in their experiments.

Table III.

	$\sigma(\Omega^{-1}\ cm^{-1})$			$\mu(cm^2\ V^{-1}\ sec^{-1})$	$n(cm^{-3})$
Dopant	900°C	900°C	1000°C	950°C	950°C
As	5.6×10^2	5.8×10^2	6.3×10^2	21	1.8×10^{20}
P	1.65×10^3	1.65×10^3	1.65×10^3	30	3.5×10^{20}

Conclusions

1. A new approach to determining the active dopant solubility limit (ADSL) of implanted dopants in polysilicon is described. ADSL is defined as the concentration of dopant such that a further increase of the dopant content does not lead to an increase in mobile carrier concentration. The new approach is used in the present work to determine ADSL concentrations of arsenic and phosphorus implanted in polysilicon.

2. The solubility limit of As in polysilicon was found to depend on anneal temperature, decreasing from 4.5 $\times$ 10^{20} to 4.1 $\times$ 10^{20} cm^{-3} in the temperature range from 900°-1000°C. These numbers are higher than similar data quoted for single crystal silicon. The difference in ADSL for two materials is a direct measure of the dopant segregated to the grain boundaries. The solubility limit of P was found to be 6.2 $\times$ 10^{20} cm^{-3}, independent of anneal temperature.

3. From some results of the present work, the presence of a poorly conducting region within a polysilicon layer might be interred, possibly at the interface with SiO_2. Conceivably, the poorly conducting regions are similar in nature to the grain boundaries.

Manuscript submitted Dec. 16, 1982; revised manuscript received July 5, 1983.

Bell Laboratories assisted in meeting the publication costs of this article.

REFERENCES

1. M. Y. Tzai, F. F. Morehead, and J. E. E. Baglin, *J. Appl. Phys.*, **51**, 3230 (1980).
2. A. Lietoila, J. F. Gibbons, and T. W. Sigmon, *Appl. Phys. Lett.*, **36**, 765 (1980).
3. M. M. Mandurah, K. C. Saraswat, C. R. Helms, and T. I. Kamins, *J. Appl. Phys.*, **51**, 5755 (1980).
4. L. Mei and R. W. Dutton, *IEEE Trans. Electron Devices*, **ed-29**, 1726 (1982).
5. N. C. C. Lu, L. Gerzberg, C. Y. Lu, and J. D. Meindl, *ibid.*, **ed-28**, 818 (1981).
6. S. Solmi, M. Severi, R. Angelucci, L. Baldi, and R. Bolenchi, *This Journal*, **129**, 1811 (1982).
7. L. Mei, M. River, Y. Kwark, and R. W. Dutton, *ibid.*, **129**, 1791 (1982).
8. J. Murota and T. Sawai, *J. Appl. Phys.*, **53**, 3702 (1982).
9. R. B. Fair and J. C. C. Tsai, *This Journal*, **124**, 1107 (1977).
10. Y. Wada and S. Nishimatsu, *ibid.*, **125**, 1499 (1978).
11. G. Masetti, D. Nobili, and S. Solmi, in "Semiconductor Silicon 1977," H. R. Huff and E. Sirtl, Editors, p. 648, The Electrochemical Society Softbound Proceedings Series, Princeton, NJ (1977).
12. B. Swaminathan, E. Demoulin, T. W. Sigmon, R. W. Dutton, and R. Reif, *This Journal*, **127**, 2227 (1980).
13. E. Kinsbron, Unpublished results.

Effect of n- and p-Type Doping on the Microhardness of GaAs, (Al,Ga)As and Ga(As,Sb) Active Layers in 0.82 and 0.87 μm Injection Lasers

V. Swaminathan,* W. R. Wagner, and P. J. Anthony*

Bell Laboratories, Murray Hill, New Jersey 07974

ABSTRACT

The effect of n- and p-type doping on the microhardness of the active layers used in the GaAs injection lasers operating at 0.82 and 0.87 μm, was investigated with the objective to alleviate the dark line degradation problem, particularly in the 0.87 μm lasers. Consistent with the results in bulk melt grown crystals, n-type doping was found to increase the hardness relative to p-type doping of the (Al,Ga)As (0.82 μm) and GaAs and Ga(As,Sb) (0.87 μm) active layers grown by liquid phase epitaxy. In addition, for n-type crystals, Ga(As,Sb) was harder than (Al,Ga)As which in turn was harder than GaAs. The n-type doping effect on hardness did not persist under optical carrier injection conditions. The growth of the plastic zone around the microhardness indentation region, examined by photoluminescence and x-ray topography, was not in any way less for the harder n-type Ga(As,Sb) or (GaAs) compared to p-type material indicating that n-type doping alone of the 0.87 μm active layers will not be effective in reducing degradation by dark line defects.

The 0.82 and 0.87 μm injection lasers required for optical communication systems are being fabricated from (Al,Ga)As-GaAs double heterostructures (1). The lasing active layer contains typically 8% Al (1) for the 0.82 μm laser while the 0.87 μm laser can be made with either GaAs or GaAs containing Sb (2) or In (3). The GaAs active layer lasers historically have had lower reliability (4) compared to that of 0.82 μm lasers, with one of the limiting factors being the degradation of the GaAs devices due to crystal defects referred to in the literature as "dark line defects" (5). Improvements in the reliability of the 0.87 μm laser have been achieved by the addition of Sb ($\lesssim$1%) to the GaAs active layer. Also, Wolf *et al.* (6) have reported for oxide stripe GaAs active layer lasers high temperature aging characteristics comparable to those of high quality 0.82 μm lasers. These improvements can be lost, however, if careful attention is not paid to all the steps involved in the fabrication of the laser. For example, the improvement in the lifetime of the 0.87 μm laser achieved by the addition of Sb to the active layer was lost when the epitaxial layers were grown on high dislocation density substrates (7).

The purpose of this work is, therefore, to explore whether any other simple composition change of the GaAs active layer besides the addition of Sb could provide additional safeguards against the formation of dark line defects. In this regard we investigated the possibility of n-type doping of the lasing active layer since for bulk GaAs single crystals the addition of n-type dopants like Si or Te increases the activation energy for dislocation glide and hence the hardness of the crystals (8, 9). Of the two kinds of dark line defects, which are actually networks of dislocations (10), the one which propagates along the <110> direction has been shown to be caused by carrier injection enhanced (11) dislocation glide (12). On the other hand, for the formation of <100> dark line defect, which is the most common variety, both pure dislocation climb (10, 13) and a combination of dislocation glide and climb (14) have been proposed. If we accept the tenet that dislocation glide plays some role in the development of either <110> or <100> dark line defect and if the n-type doping effect on dislocation velocity also prevails for the epitaxial GaAs, then an n-type active layer should be beneficial for the 0.87 μm lasers.

To study the effects of doping we measured the microhardness of thick ($\sim$10 μm) epitaxial layers of Te (n-type) or Ge (p-type) doped GaAs, (Al,Ga)As, and Ga(As,Sb), all with typical active layer compositions. Consistent with the results on bulk crystals, we observed that n-type epitaxial layers were harder than p-type for each active layer composition and that n-type Ga(As,Sb) was the hardest material of them all. This advantage of increased hardness for n-type doping was eliminated by the observation that under optical injection conditions the recombination enhanced dislocation glide was not in any sense less for the harder n-type material in comparison with the softer p-type material. In other words, the initial hardness of the crystal did not seem to have any bearing on defect motion under injection conditions.

Experimental

The effect of doping on the hardness of a crystal is generally measured by changes in its yield stress (9). This measurement requires large size (typically 5 $\times$ 5 $\times$ 10 mm) crystals and obviously cannot be made on thin epitaxial material. We therefore measured the microhardness of the epitaxial layers to determine the doping effect. Since the hardness measurement does not represent a uniaxial stress state for the crystal under which yield stresses are measured and since it depends on both the yield and strain hardening characteristics of the material (15), the hardness number is not adequate for quantitative comparisons but is sufficient to provide qualitative comparisons between materials grown under similar conditions.

Thick epitaxial layers ($\sim$10 μm) of n- and p-type GaAs, $Al_xGa_{1-x}As$ ($x \sim 0.057$-0.079) and $GaAs_{1-y}Sb_y$ ($y \sim 0.007$) were grown on (100) n-type GaAs substrates by the liquid phase technique (16). The growth temperature was 780°C and the ambient was He + 11% H_2. Te and Ge were used as the n- and p-type dopants, respectively. The amounts of the dopants were such that they would yield carrier concentrations typical of the normal active layer in the laser structure.

The microhardness measurements were made at room temperature using a Kentron microhardness tester which had a Knoop diamond indenter and a calibrated eyepiece. The indentations were made under a 50g load and the hardness numbers were obtained by measuring the indentation lengths at a magnification of $\times$500. Since previous microhardness measurements on InP have indicated hardness anisotropy on (100) planes (17, 18) care was exercised in keeping the indenter

* Electrochemical Society Active Member.

Key words: topography, photoluminescence, x-ray, recombination-enhanced-motion.

aligned along the same [110] direction on the (100) plane for all the samples.

To find the effect of carrier injection on defect motion that would prevail under actual lasing conditions, we monitored the strain contrast around the hardness indentation region before and after irradiating these regions with 6471Å line of a Kr laser at a power density of 1.2 kW/cm^2 (equivalent to $\sim 10^{18}$ electron-hole pairs for a carrier lifetime of 10 nsec) for 30 min using photoluminescence and x-ray topography. The photoluminescence topography was done by imaging the luminescence from the sample obtained at $\sim$200 W/cm^2 on to an infrared sensitive vidicon camera. For x-ray topography, the Berg-Barrett reflection technique using Cu-Kα_1 radiation and {422} reflecting planes was adopted.

Results and Discussion

The composition and doping level of the samples are listed in Table I. The indicated room temperature carrier concentrations are determined for the given atom fraction of dopant in the liquid using previous Hall measurements (19-21). The microhardness numbers are also given in Table I for each composition. The hardness numbers are the average of six measurements each, on two sets of samples for each composition grown at two different times in the same furnace.

Two conclusions can be drawn from Table I. First, for each active layer composition the hardness of the n-type sample is greater than that of the p-type sample. Second, while all the p-type samples have about the same hardness values, for the n-type samples, Ga(As,Sb) is harder than (Al,Ga)As which in turn is harder than GaAs.[1]

The hardening of the present samples with n-type doping is in complete agreement with the previous results in bulk melt-grown GaAs where n-type dopants were found to increase the yield stress (8, 9) and decrease the dislocation velocity (22). In the case of n-type Si-doped GaAs, Swaminathan and Copley (23) proposed that the hardening was due to the interaction of moving dislocations (both edge and screw) with static defect complexes having asymmetrical strain fields and the specific defect complex was suggested to be (Si_{Ga}-V_{Ga}) pairs (23, 24). It is therefore reasonable to suggest that the hardening of the epitaxial samples with n-type doping, observed for any one active layer composition, is due to the presence of asymmetrical impurity-defect complexes in them.

While the hardening in n-type samples is consistent with previous investigations, the additional hardening observed in n-type Al and Sb containing active layers (Table I) is rather unexpected. The increased hardness in these samples cannot be attributed to differences in doping levels since the amounts of the n-type dopant in the melts and the carrier concentrations for all the three active layer compositions are similar. The observation that the addition of Sb increases the hardness of GaAs finds support in some recent observations that Sb in small amounts (1-5 a/o) helps to reduce the dislocation density in Czochralski grown GaAs crystals (25). Since dislocations in such crystals are predominantly generated when the thermal stresses exceed the critical resolved shear stress for dislocation motion (26), the addition of Sb must have increased the critical resolved shear stress, consistent with the hardening observed in the present study. Also, a high pinning stress on the dislocation is calculated from considering only a simple elastic interaction (27) between the dislocation and the impurity (Sb) in Ga(As,Sb) (28). However, the hardening effect due to Al which we observe and that due to S in InP (29) would not have been expected from the simple elastic interaction model. The sources of increased hardening in n-type GaAs by the addition of Al and Sb are not clear at present.[2]

In order to find whether the hardening observed with the addition of n-type dopant and Sb to the GaAs active layer would retard the dislocation motion under lasing conditions we examined the growth of the strain region around the hardness indentation after carrier injection by optical means. Figures 1a and 2a show active layer photoluminescence topographs under 200 W/cm^2 from respectively n-type and p-type Ga(As,Sb). It can be seen that the hardness indentation region in each sample is characterized by a dark lobe perpendicular to the long dimension of the indentation. Since under the tip of the indenter, some limited plastic deformation is expected to occur locally due to the point loading (15), the dark regions in the photoluminescence topographs are due to dislocations which act as nonradiative centers. The plastic deformation zone around the indentation was also examined by x-ray topography for these samples. Figures 3a and 4a show the strain contrast around the microhardness indentations as white lobes of negligible diffracted intensity (30). In both the photoluminescence and x-ray topographs, the strained regions appear circular perhaps indicating that several {111} <110> slip systems are activated as in the case of InP (18). Qualitatively similar results were obtained for (Al,Ga)As and GaAs.

The indentation regions observed after irradiation with the 6471 line of a Kr laser at a power density of 1.2 kW/cm^2 for 30 min are shown in the photoluminescence topographs (Fig. 1b and 2b) and in the x-ray topographs (Fig. 3b and 4b) for respectively n- and p-type Ga(As,Sb) samples. It is readily seen that the strain regions have grown in size or smeared suggesting that some recombination enhanced dislocation motion has occurred at the higher excitation intensity. Similar growth of the strain regions was observed in GaAs. The rate of recombination enhanced motion is determined by both the injected carrier density and the activation energy for defect motion (11). Maeda and Takeuchi (31) measured the dislocation velocity in GaAs under electron beam excitation and observed a decrease in the activation energy for dislocation motion

[1] It may appear that the differences in hardness numbers between the n-type samples in Table I are not large enough to be significant in changing dislocation velocity. A previous study on the mechanical properties of GaAs single crystals (V. Swaminathan, Ph D. thesis, University of Southern California, 1975, unpublished) has shown that a 10% change in hardness (which is the case for the n-type samples in the present study) corresponds to a 60% change in the yield stress. This is a substantial change which will affect the dislocation dynamics.

[2] The increased hardening in n-type (Al,Ga)As and Ga(As,Sb) may not need to be attributed to Al and Sb at all since no hardening is observed in p-type samples. For example, the concentration of point defects may have been altered by the addition of these elements in n-type material only, thus affecting the hardness.

Table I. Doping, carrier concentration at 300 K and the microhardness number of the samples used in the study

Sample	Doping and amount in the melt	Type and carrier density (cm^{-3}) at 300 K	Knoop microhardness number on (100) plane at 50g and 300 K
Ga(As,Sb)	Te 2.73×10^{-5}	n 5×10^{17}	687 ± 10
	Ge 2.88×10^{-3}	p 5.7×10^{17}	598 ± 7
(Al,Ga)As	Te 5.46×10^{-5}	n 10^{18}	669 ± 7
	Ge 4.32×10^{-3}	p 5.7×10^{17}	601 ± 15
GaAs	Te 2.73×10^{-5}	n 5×10^{17}	640 ± 14
	Ge 2.88×10^{-3}	p 5.7×10^{17}	598 ± 10

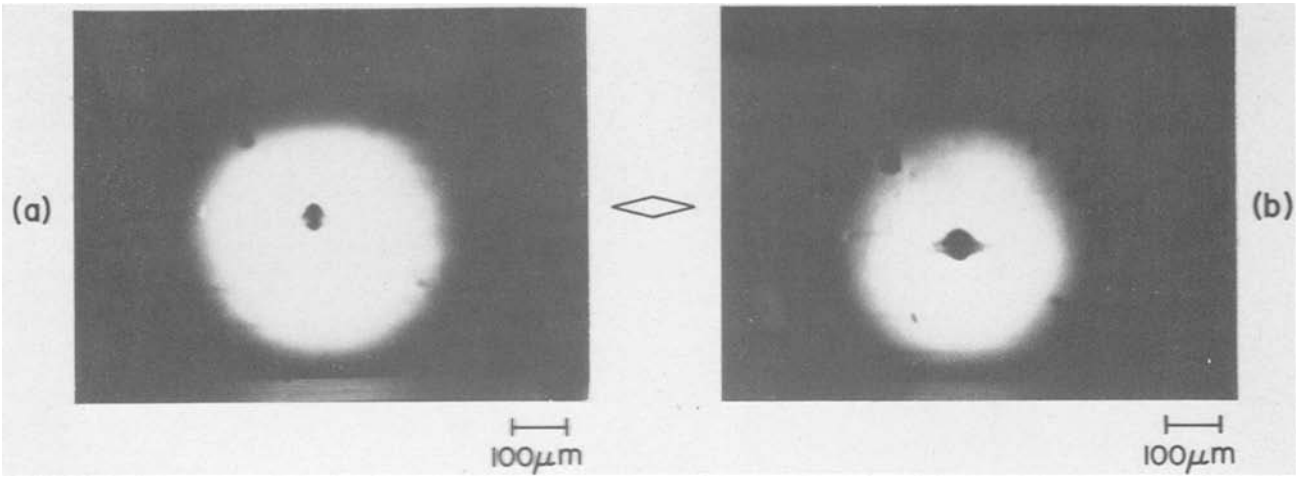

Fig. 1. Photoluminescence topographs of n-type Ga(As,Sb) showing the regions around microhardness indentations before (a) and after (b) irradiation with the 6471Å line of a Kr laser at 1.2 kW/cm² for 30 min. The topographs were taken at a power level of 200 W/cm² and the duration of excitation was not more than 2 min. The orientation of the indentation is also shown. The dark contrast around the indentation is due to nonradiative centers (see text).

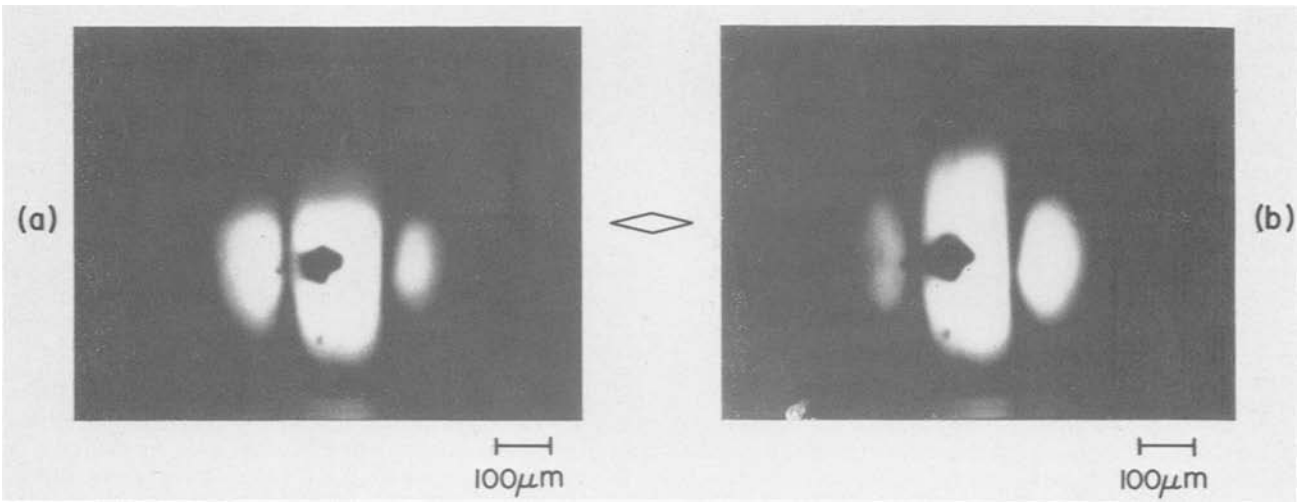

Fig. 2. Photoluminescence topographs of p-type Ga(As,Sb) showing the regions around microhardness indentations before (a) and after (b) irradiation with the 6471Å line of a Kr laser at 1.2 kW/cm² for 30 min. The topographs were taken at a power level of 200 W/cm² and the duration of excitation was not more than 2 min. The orientation of the indentation is also shown. The dark contrast around the indentation is due to nonradiative centers (see text).

from 0.95 to 0.24 eV. This difference of 0.7 eV is presumably related to the recombination energy at some dislocation level. If one assumes[3] that the recombination energy is about the same for all three compositions then one would expect that the differences between the samples observed in the absence of injection would prevail under injection conditions. But our results indicate that the harder n-type Ga(As,Sb) or GaAs are not in any way less susceptible to dislocation motion under injection conditions than p-type material. Also the (Al,Ga)As active layers showed very little or reduced growth of the strain regions around the indentation. This suggests that the injected carrier density and its distribution around the excitation volume should be different for the various samples. We conjecture that the carrier density should have been higher in Ga(As,Sb) and GaAs than in (Al,Ga)As under our experimental conditions. Our study shows that the initial hardness of the sample or the resistance to dislocation motion would have very little bearing on migration of dark line defects under the lasing conditions[4] and further that n-type doping alone of the active layer for 0.87 μm lasers would not necessarily eliminate the dark line problem.

[3] This is a valid assumption since the bandgaps for the three compositions are not different by more than 0.1 eV.

[4] Although all the p-type samples have about the same hardness numbers (Table I) it is known that only (Al,Ga)As is less susceptible to degradation by dark line defects. This observation further supports our conclusion that the initial hardness of the sample is not relevant.

Summary

We investigated the effect of n- and p-type doping on the microhardness of the active layers used in GaAs injection lasers operating at 0.82 and 0.87 μm with the objective to alleviate the degradation by dark line defects, particularly in the 0.87 μm lasers. Consistent with the results in bulk crystals we find that n-doping (Te) increases the hardness relative to p-type doping (Ge) for (Al,Ga)As (0.82 μm) and GaAs and Ga(As,Sb) (0.87 μm) active layers. In addition, for n-type crystals, addition of Sb and Al increases the hardness relative to GaAs, with Ga(As,Sb) being the hardest. To check the doping effect on hardness under injection conditions, we examined the plastic zone around the microhardness indentation by photoluminescence and x-ray topography, following irradiation with the 6471Å line of a Kr laser at 1.2 kW/cm² for 30 min. In both GaAs and Ga(As,Sb) for either doping but not in (Al,Ga)As, the plastic zone expanded after irradiation indicating recombination enhanced dislocation motion. We conclude, therefore, that n-type doping of the 0.87 μm active layers alone will not be effective in reducing degradation by dark line defects in spite of the increased hardness of the layers under dark conditions.

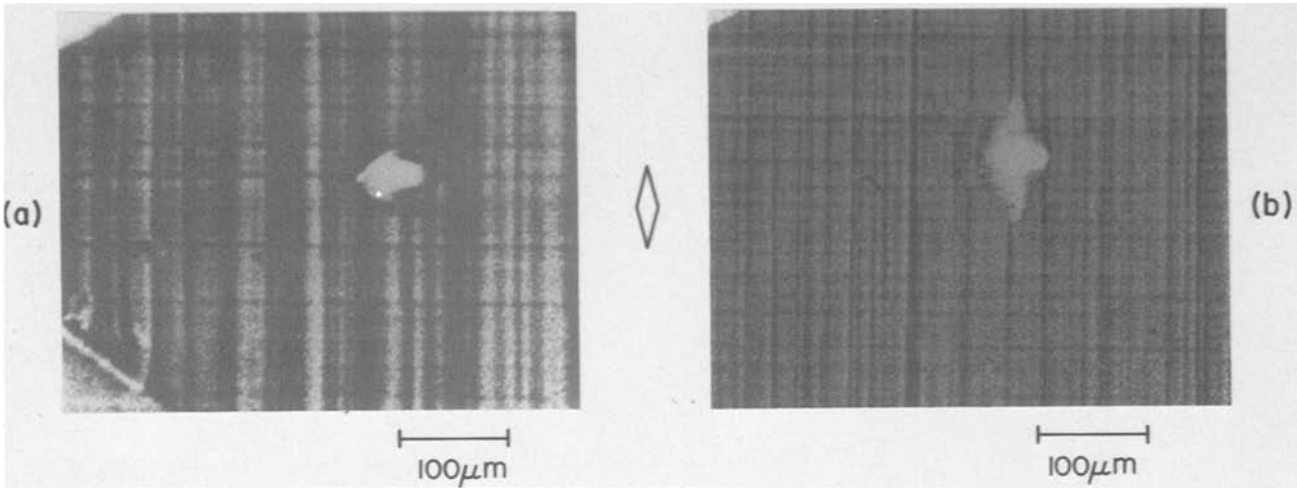

Fig. 3. X-ray topographs of n-type Ga(As,Sb) showing the regions around microhardness indentations before (a) and after (b) irradiation with the 6471Å line of a Kr laser at 1.2 kW/cm^2 for 30 min. The topographs were taken with $\{42\bar{2}\}$ reflecting planes. The orientation of the indentation is shown. The white lobe around the indentation represents negligible diffraction intensity around the strain regions (see text).

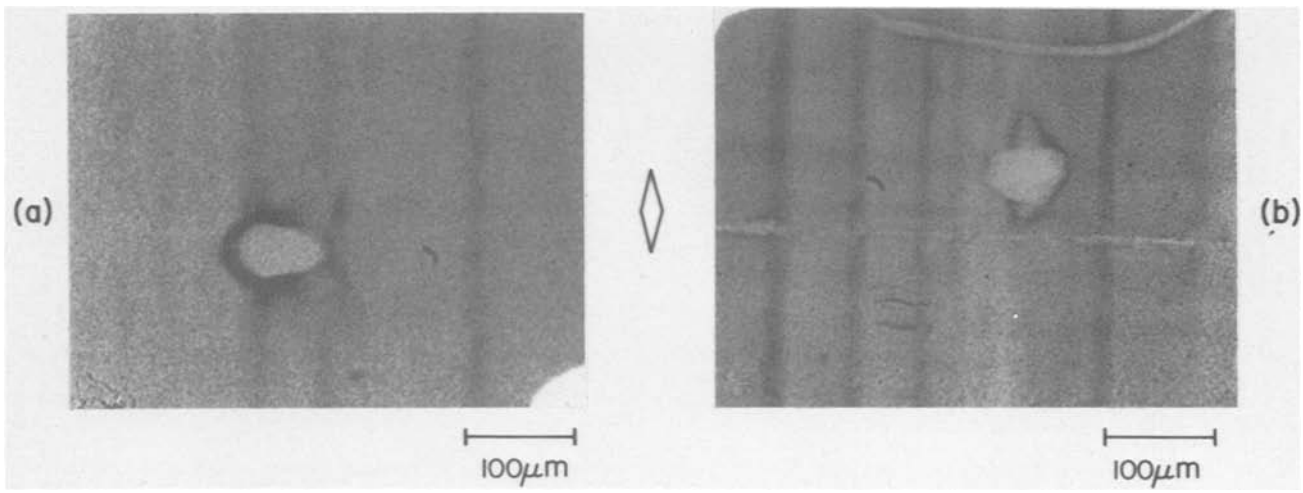

Fig. 4. X-ray topographs of p-type Ga(As,Sb) (e) showing the regions around microhardness indentations before (a) and after (b) irradiation with the 6471Å line of a Kr laser at 1.2 kW/cm^2 for 30 min. The topographs were taken with $\{42\bar{2}\}$ reflecting planes. The orientation of the indentation is shown. The white lobe around the indentation represents negligible diffraction intensity around the strain regions (see text).

Finally, the absence of growth of the plastic zone in (Al,Ga)As active layer after irradiation is in agreement with the earlier observation (32) that addition of Al suppresses the degradation by the dark line defects.

Acknowledgment

The authors are grateful to D. Van Haren for growing the epitaxial samples used in this study and to V. G. Lambrecht, Jr., for lending his microhardness equipment. They would also like to thank D. Brasen for his helpful hints regarding the microhardness measurements and S. Mahajan, F. R. Nash, and N. E. Schumaker for their comments on the manuscript.

Manuscript submitted March 2, 1983; revised manuscript received July 5, 1983.

Bell Laboratories assisted in meeting the publication costs of this article.

REFERENCES

1. R. W. Dixon, *Bell. Syst. Tech. J.*, **59,** 669 (1980).
2. P. J. Anthony, J. L. Zilko, R. L. Hartman, N. E. Schumaker, V. Swaminathan, and W. R. Wagner, *IEEE Electron Device Lett.*, **edl-2,** 50 (1981).
3. W. T. Tsang, *Appl. Phys. Lett.*, **38,** 661 (1981).
4. A. Thompson, *IEEE J. Quantum Electron.*, **qe-15,** 11 (1979).
5. M. Ettenberg and H. Kressel, *ibid.*, **qe-16,** 186 (1980).
6. H. D. Wolf, K. Mettler, and K. H. Zschauer, *Jpn. J. Appl. Phys.*, **20,** L693 (1981).
7. P. J. Anthony, R. L. Hartman, N. E. Schumaker, and W. R. Wagner, *J. Appl. Phys.*, **53,** 756 (1982).
8. D. Laister and G. M. Jenkins, *J. Mater. Sci.*, **8,** 1218 (1973).
9. V. Swaminathan and S. M. Copley, *J. Am. Ceram. Soc.*, **58,** 482 (1975).
10. P. M. Petroff and R. L. Hartman, *J. Appl. Phys.*, **45,** 3899 (1974).
11. L. C. Kimerling, *Solid-State Electron.*, **21,** 1391 (1978).
12. T. Kamejima, K. Ishida, and J. Matsui, *Jpn. J. Appl. Phys.*, **16,** 233 (1977).
13. P. W. Hutchinson and P. S. Dobson, *Phil. Mag.*, **32,** 745 (1975).
14. J. Matsui, K. Ishida, and Y. Nannichi, *Jpn. J. Appl. Phys.*, **14,** 1555 (1975).
15. "The Science of Hardness Testing and its Research Applications," J. H. Westbrook and H. Conrad, Editors, American Society for Metals, Ohio (1973).
16. H. C. Casey, Jr. and M. B. Panish, "Heterostructure Lasers," Part B, Academic Press, New York (1978).
17. D. Brasen, *J. Mater. Sci.*, **11,** 791 (1976).
18. D. Brasen, *ibid.*, **13,** 1776 (1978).

19. K. K. Shih and G. D. Pettit, *J. Electron. Mater.*, **3**, 391 (1974).
20. A. J. Spring Thorpe, F. D. King, and A. Becke, *ibid.*, **4**, 101 (1975).
21. V. Swaminathan and P. J. Anthony, Unpublished.
22. S. K. Choi, M. Mihara, and T. Ninomiya, *Jpn. J. Appl. Phys.*, **16**, 737 (1977).
23. V. Swaminathan and S. M. Copley, *J. Appl. Phys.*, **47**, 4405 (1975).
24. R. T. Chen and W. G. Spitzer, *J. Electron. Mater.*, **10**, 1085 (1981).
25. M. G. Milvidsky, V. B. Osvensky, and S. S. Shifrin, *J. Cryst. Growth*, **52**, 396 (1981).
26. A. S. Jordan, R. Caruso, and A. R. Von Neidea, *Bell Syst. Tech. J.*, **59**, 593 (1980).
27. For a review of strengthening mechanisms in solids see W. D. Nix and R. A. Menzes, *Ann. Rev. Mater. Sci.*, **1**, 313 (1971).
28. P. A. Kirby, *IEEE J. Quantum Electron.*, **qe-11**, 562 (1975).
29. S. Mahajan and A. K. Chin, *J. Cryst. Growth*, **54**, 138 (1981).
30. K. C. Yoo, B. Roessler, R. W. Armstrong, and M. Kuriyama, *Scr. Metall.*, **15**, 1245 (1981).
31. K. Maeda and S. Takeuchi, *Jpn. J. Appl. Phys.*, **20**, L165 (1981).
32. T. Hayakawa, S. Yamamoto, T. Sakurai, and T. Higikata, *J. Appl. Phys.*, **52**, 6068 (1981).

Structure of Chemically Deposited Ni/Si Contacts

P. A. Dan and G. Popovici

I. P. R. S. Bancasa, Bucharest 72996, Romania

D. Dascalu and Gh. Brezeanu

Electronics Department, Polytechnical Institute, Bucharest 77748, Romania

Al. Popa

I. F. T. A. R., Bucharest, Romania

ABSTRACT

Although widely used in the semiconductor industry, the Ni/Si contact is studied less often in literature than other contact systems. This paper presents results of experiments on the structure and electrical properties of the chemically deposited Ni/Si contact. The particular electroless Ni plating method used by the authors consists of catalytic reduction of Ni in an acid solution containing a hypophosphite as reducing agent. Phosphorus in addition to nickel deposition occurs. The silicon surface is prepared by using Pd activation centers, just prior to Ni deposition. A Ni silicide is formed by heat-treatment at 400° - 800°C in $N_2 + H_2$ (or N_2) atmosphere. The results of electrical measurements suggest the presence of an n-type surface layer (presumably doped with P atoms) near the silicide-silicon interface. This layer reduces the effective barrier and the contact resistance on n-type silicon substrates. The formation of a P-doped surface layer is confirmed by SEM, microprobe analysis and AES. The structure and electrical properties of the silicide-silicon transition layer depend upon the temperature and atmosphere used for heat-treatment. The higher this temperature, the stronger the P-doping effect. The presence of H_2 in the heat-treatment ambient favors P penetration into Si. This cheap but basically nonuniform metallization is suitable especially for large-area power devices.

The Ni/Si contact obtained through chemical deposition of Ni on Si is widely used for power semiconductor devices. Although some chemical deposition methods have been known for more than two decades (1), detailed data for this type of contact are almost absent from literature. Recently, the vacuum-deposited Ni/Si contact was intensively studied (2-8). However, the results are only in part applicable to the chemically deposited contact. We shall demonstrate, in fact, that additional elements (such as P and Pd) present in the chemical process may have a decisive influence upon the properties of the final contact.

The Ni/Si system is characterized by formation of silicides through a solid-solid metallurgical reaction above certain temperatures (9). The following silicides are known from the phase diagram (10): Ni_3Si, Ni_5Si_2, Ni_2Si, Ni_3Si_2, NiSi, and $NiSi_2$. Only those formed below the eutectic point (11) are usually important in semiconductor device fabrication, in this case Ni_2Si, NiSi, and $NiSi_2$. For vacuum-deposited Ni/Si metallization systems, the following changes take place during the heat-treatment as the temperature and duration increase: Ni/Si → $Ni/Ni_2Si/Si$ → Ni_2Si/Si → $NiSi/Ni_2Si/Si$ → NiSi/Si (3).The monosilicide begins to form only after the whole pure metal disappears in reaction. Above 750°C, the $NiSi_2$ phase occurs through disilicide nucleation in NiSi (3).

As the silicide grows, the impurities (C, O, etc.) are swept out. Therefore, the silicide purity is higher than that of the initial metal (12). For example, the chemical bonds between Ni and Si atoms are much more favorable from the energetic point of view than the bond between Ni and O (13). However, a large amount of impurities may have undesirable effects; such as changes in the reaction kinetics, phase distribution modifications, occurrence of chemical compounds, etc. For example, the presence of oxygen during the formation of nickel silicide may lead to the occurrence of Ni_2SiO_4, a compound which inhibits silicide growth (13). Recent results (8) concerning the effect of oxygen as impurity in Ni indicate the formation of initial silicon suboxides, followed by development of a thin SiO_2 layer which prevents Ni diffusion towards the Ni_2Si/Si interface and inhibits Ni_2Si formation. Therefore, the formation of NiSi begins before the amount of pure Ni is exhausted.

Impurity redistribution within the silicide and/or silicon substrate occurs during silicide growth (14, 15). According to the so-called "snowplow" effect, this may result in an accumulation of dopant atoms near the silicide-silicon interface. The semiconductor becomes

Key words: interfaces, contacts, electroless, phase transformation.

highly doped near this interface. The impurities may also be present in the silicide near its outer surface.

Most of the silicides have metallic properties (4). Therefore, the transition layer (silicide) formed during the postmetallization heat-treatment acts as an effective metallic electrode. The contact interface is located below the original metal-semiconductor interface and is almost free of defects. Therefore, the silicide-silicon interface may be considered an intimate contact, without contaminants, oxides, and so on (16). Therefore, the silicide-silicon system is closer to the ideal metal-semiconductor contact (4) than a direct metal-semiconductor contact.

The measured barrier heights for silicide-silicon systems strongly depend upon eutectic temperatures, and so the silicide-silicon interface plays a role in determining contact characteristics (17). An intermediate layer (5-7, 11, 18-22) is assumed to occur. In this "buffer" layer, a transition takes place between the covalent-type bonds in Si and metallic-type bonds in silicide. This intermediate layer may be 20Å thick for Ni/Si contacts (21). However, the nature of silicide-silicon interfaces is still a matter of debate (23).

If the metal-silicon interaction is nonuniform, as in industry-made devices, the Si substrate may be found at the same time in contact with different phases (metal or silicides). Such a situation should be modeled by means of several parallel contacts (24).

Chemically deposited Ni/Si contacts have properties considerably different from vacuum-deposited contacts. The electroless metal deposition implies a considerable amount of co-deposited impurities. These impurities interact with both the metal and the semiconductor. For example, in the case of chemical Ni deposition, by using a hypophosphite as reducing agent, the amount of P in the Ni layer may be 3-15 weight percent (w/o) (25). At temperatures above 400°C, P reacts with Ni, and the Ni_3P phosphide occurs (25). However, as shown in this paper, a certain amount of P penetrates below the silicide-silicon interface, and acts as a donor-type impurity. The electroless Ni deposition is basically nonuniform although it is quite satisfactory for power devices. Only qualitative results were obtained at this stage of investigation.

Experimental

The method of chemical deposition of Ni on Si used by the authors resembles that reported by Sullivan and Eigler (1); it is a simple and inexpensive method. Proper surface preparation before deposition is essential for obtaining desired contact properties. We used a chemical preparation beginning with removal of the native oxide layer on Si by using a mixture of HF and NH_4F. A rough silicon surface promotes good adherence of the Ni layer.

In the present investigation the test samples were fabricated by using the planar technology, and the "mirror-like" surface of the silicon wafer was asperized by using chemical methods. The surface was activated by using Pd activation centers. These centers were deposited from a mixture of $PdCl_2$, HCl, HF, and deionized water. This treatment both activates the Si surface and removes (by the action of HF acid) the native SiO_2 layer. This remnant oxide is extremely nonuniform. Therefore, oxide etching also increases the surface roughness.

The nickel deposition method consists of catalytic reduction of Ni in an acid solution, by also liberating H_2. The standard deposition solution contains (1): $NiCl_2$, NaH_2PO_2, $(NH_4)_2HC_6H_5O_7$, and NH_4Cl. The last two components play no role in the chemical reaction itself. They constitute a buffer mixture which maintains the solution pH and avoids Ni precipitation in $Ni(OH)_2$. The bath temperature is 90°-100°C.

The chemical reaction is

$$Ni^{2+} + 2H_2PO_2^- + 2H_2O \rightarrow Ni\downarrow + H_2\uparrow + 4H^+ + 2HPO_3^{2-} \quad [1]$$

Also, PH_3, P, and H_2 may form during Ni plating. Although the formation of PH_3 is thermodynamically possible, its decomposition takes place more quickly. Therefore, during plating, the Ni deposit contains P. H_2 is also liberated.

The test structures prepared for the present investigation have a number of circular contacts of various diameters. The circular metallization windows are defined by etching the silicon dioxide grown on the entire silicon wafer as in the standard planar process. During metallization, the nickel plating takes place only in the circular windows, since Ni does not adhere on the oxide.

The surface silicide layer (see above) is formed by heat-treatment (400°-800°C) in $N_2 + H_2$ (or N_2) atmosphere. The plating process is repeated and a new layer of Ni is deposited. No heat-treatment follows this deposition step. The second Ni layer is useful for a proper soldering of practical power devices, since it has good wetting and electrical properties. This Ni layer could be protected against further chemical processing by depositing a supplementary Au film. Some wafers, prepared for microphysical investigations, have no second Ni layer.

The wafer was broken into chips containing contacts of the following diameters: 10, 15, 25, 40, 65, 100, 150, and 250 μm. Two identical contacts exist for diameters ranging between 25 and 150 μm. The test samples were mounted in standard IC packages (plastic). Similar structures were used by the authors for a previous study of Al/Si contacts (16, 26). The measurement of electrical resistance of contacts of various diameters was necessary in order to separate the contact resistance itself (usually very small) from the spreading resistance of the semiconductor bulk (27).

Both Ni/Si-p and Ni/Si-n contacts were measured. The p-type samples were obtained on uniformly doped <111> Si wafers (30 mm diameter, 250 μm thickness, mechanically and chemically polished). Wafers of various resistivities were used; the range was between 0.01 and 0.72 Ωcm. The heat-treatment was performed at 500°-700°C, for 12 min in $N_2 + H_2$ atmosphere. The cooling was relatively quick (12 min at the end of the furnace tube). A 1 μm gold layer was electrochemically plated on the Ni layer. The metallization windows were contacted with a 25 μm diameter Au wire (ball-bonding). Since this contacting procedure was not applicable for small contact diameters, the 10-25 μm contacts were not used in this investigation.

The Ni/Si-n structures were processed starting from low resistivity (Sb- or As-doped) <111> Si wafers (51 mm diameter, 280 μm thickness). 10 μm-thick epitaxial layers were grown for samples with resistivities above 0.02 Ωcm. The whole resistivity range examined was from 0.001 to 2 Ωcm. The heat-treatment takes place at several different temperatures in the 400°-800°C range (15 min in $N_2 + H_2$ or N_2, followed by slow cooling). A different contacting procedure was used: the Au (or Al) wire was bonded on an Al metallization pad obtained through photolithographical techniques from an Al film evaporated on the entire wafer. The Al film was sintered for 7 min at 400°C in $N_2 + H_2$ atmosphere. This postmetallization treatment provides a good adherence of Al. The results published in Ref. (28) indicate that the interactions between Al and the silicide should be negligible for the heat-treatment used in our investigation. Moreover, the Ni layer grown on silicide during the second Ni deposition provides a supplementary protection, even if some Al_3Ni or Al_3Ni_2 may form at this temperature (29). It was verified by scanning electron microscopy (SEM) that no interactions occur between Al and the analyzed nickel silicide. On the other hand, the effect of Al sintering

conditions on the silicide-silicon system may be neglected, since the latter was generally formed at (much) higher temperatures. Therefore, we concluded that the silicide-silicon contact was almost unchanged, at least for our qualitative conclusions.

Electrical Characteristics

The Ni/Si-p contacts exhibit rectifying current-voltage characteristics. Since the I-V characteristics are nonlinear, the electrical resistance (R) will be evaluated in origin, *i.e.*

$$\frac{1}{R} = \frac{dI}{dV}\bigg|_{I=0} \qquad [2]$$

The total resistance (which was relatively high) may be considered in this particular case to be practically equal to the contact resistance (R_c), the resistive contribution from the Si bulk being negligible; therefore

$$R = R_c = \frac{4r_c}{\pi D^2} \qquad [3]$$

where r_c is the specific contact resistance (measured in Ωcm^2) and D the contact diameter.

The $R \propto D^{-2}$ dependence was verified experimentally for contacts with diameters from 65 to 250 μm. The agreement is relatively poor because of contact nonuniformities. These will be discussed later. However, even in this case, the above data lead to the following "order-of-magnitude" results.

Figure 1 shows the specific contact resistance (determined as shown above) *vs.* semiconductor doping (N_A) for a few temperatures of the postmetallization heat-treatment. The theoretical $r_c = r_c\ (N_A)$ dependence is also shown. This is obtained by using a computer program which takes into account the tunneling probability at the metal semiconductor Thomas-Fermi barrier. The height of the hole barrier ($c\phi_{Bp}$) at the contact is taken as a parameter (Fig. 1). The strong $r_c - N_A$ dependence predicted by theory is indeed verified experimentally. Because at very high semiconductor doping the contact barrier becomes very thin and is penetrated by tunneling, contact resistance becomes very low.

In the discussion which follows, we shall consider that the value of $e\phi_{Bp}$ for the theoretical curve which matches the experimental one is an "effective" barrier which describes a certain real contact. If the temperature of the postmetallization heat-treatment is low (500°C), then the effective hole barrier will correspond (Fig. 1) to the values reported for the Ni/Si contacts evaporated in vacuum and treated at similar temperatures, namely 0.4-0.45 eV (3). This is the barrier between the silicide and the silicon (3).

At higher treatment temperatures (600°-700°C) the effective hole barrier increases. When this temperature increases from 500° to 600°C, the specific contact resistance (r_c) increases with about two orders of magnitude ($e\phi_{Bp} = 0.55$ eV). A further increase from 600° to 700°C has much less effect ($e\phi_{Bp} = 0.56 \ldots 0.58$ eV).

The above results may be explained by assuming that at higher treatment temperatures certain donor impurities diffuse from the surface into the bulk. These impurities may be the phosphorus atoms which occur in the chemical deposition process, as mentioned above. They form a very thin n^+ layer in the semiconductor, at the silicide-silicon interface. The phosphorus deposit on the surface is limited, and this is a good explanation of the experimental results; the main increase in r_c occurs as the temperature increases up to 600°C. Perhaps the majority of P atoms diffuse into the bulk. A similar effect of increasing $c\phi_{Pp}$ at the Ni/Si contacts was obtained by ionic implantation of Sb in silicon, thus giving rise to an n^+-type surface layer (30).

The results obtained for Ni/Si-n contacts will be now discussed. Two types of I-V characteristics were

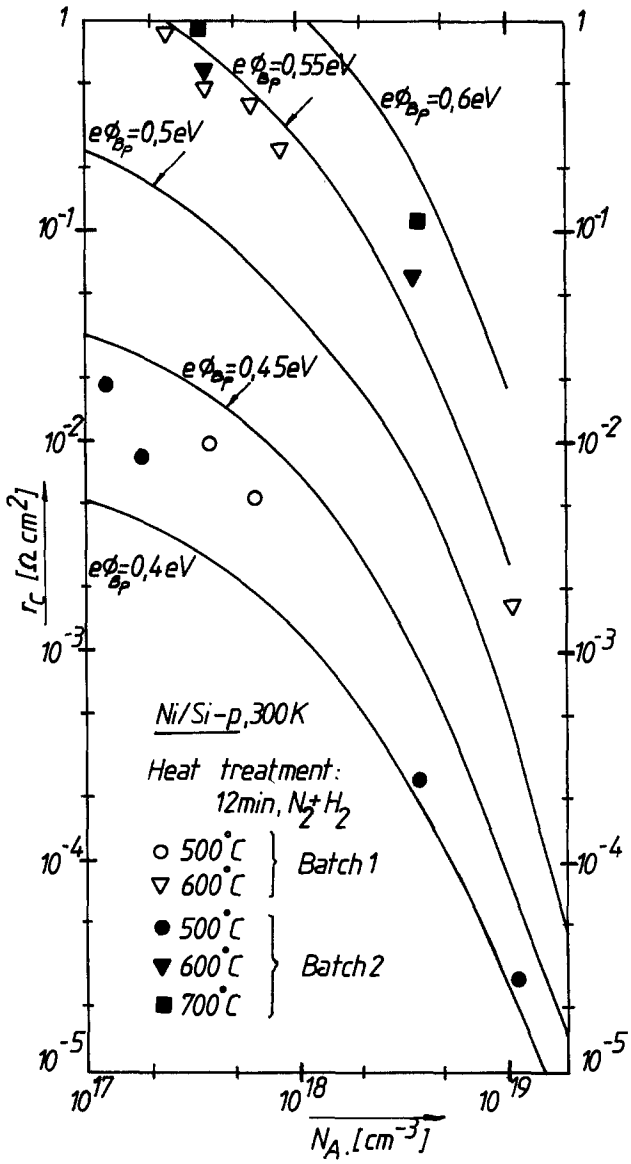

Fig. 1. The specific contact resistance (r_c) of Ni/Si-p contacts *vs.* semiconductor doping (N_A). The points are experimental results obtained for samples subjected to heat-treatment at temperatures shown. The lines indicate results of theoretical calculations, with the effective hole barrier, $e\phi_{Bp}$, as parameter.

found: (*i*) symmetrical and linear characteristics for samples of relatively low semiconductor resistivity and treated at sufficiently high temperatures; (*ii*) asymmetrical and nonlinear characteristics for high resistivity samples treated at low temperatures.

In the first case, the dispersion is quite low (a few percent) for samples treated in $N_2 + H_2$ atmosphere. Therefore, an accurate processing of experimental data is suitable. In the second case, a strong dispersion of contact resistance (more than an order of magnitude) occurs from sample to sample, especially for lower contact diameters. It is more pronounced when H_2 is absent from the atmosphere of the postmetallization heat-treatment. This dispersion suggests a strong nonuniformity of the metallization area, a hypothesis confirmed by the microscopic analysis (see below).

We shall use as a theoretical expression of the total (measured) resistance the following formula

$$R = R_c + R_s + R_p \cong \frac{4r_c}{\pi D^2} + \frac{\rho}{\pi D}\arctan\left(\frac{4H}{D}\right) + R_p \qquad [4]$$

where R_s is the spreading resistance of the semiconductor layer (of resistivity ρ and thickness H) and R_p

is the parasitic series resistance. The parameter H stands either for the total wafer thickness, or for the epitaxial layer thickness when such a layer exists (see Experimental section).

The experimental points of the $R = R(D)$ dependence are used in a computer program and r_c, ρ, and R_p are determined numerically by the least squares method. The value of the total (measured) resistance (R) is an average on a few contacts of the same diameter (D). The values of ρ and R_p are compared with the results previously obtained from independent measurements. This is a "plausibility check" for the selection of experimental points; some data were rejected by using this check. A similar method was previously used by the authors for Al/Si contacts (27). In spite of nonuniformities, a qualitative picture may be drawn up.

Figure 2 shows the specific contact resistance (r_c) obtained from Eq. [4] *vs.* the donor density (N_D) for a few postmetallization heat-treatments. The results of theoretical calculations are also shown. They were obtained for a 0.70 eV barrier, a value which is suitable for the heat-treated Ni/Si contact (3, 4). The full lines are reproduced from Ref. (31). The parameter $N_D{}^+$ is the doping of an n^+ surface layer. Such a layer doped with P is assumed to exist for chemically prepared Ni/Si contacts, as shown above Figure 2 also shows (dotted line) the $r_c = r_c(N_D)$ dependence for a uniformly doped semiconductor. This curve was obtained by interpolation from the results published in Ref. (32). The model described in Ref. (31) is no longer valid, as N_D increases and becomes comparable with $N_D{}^+$. Therefore, the full lines (31) cannot be extrapolated up to the dotted line (32).

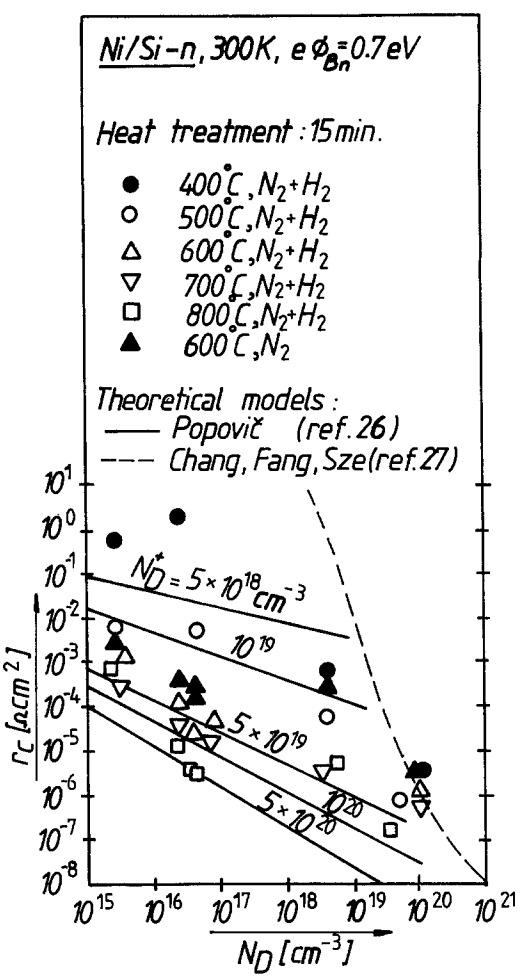

Fig. 2. The specific contact resistance (r_c) of Ni/Si-n contacts *vs.* semiconductor doping (N_D). The points are experimental data on samples subjected to various postmetallization heat-treatments. The curves are theoretical.

The experimental points in Fig. 2 show that r_c decreases by as much as four orders of magnitude as the heat-treatment temperature increases from 400° to 800°C. For low resistivity samples, the variation is lower (only two orders of magnitude). This variation is qualitatively explained by the occurrence of the n^+ surface layer doped with P. The concentration of P atoms may be roughly estimated from Fig. 2. The results are shown in Table I. The surface-layer thickness (still unknown) is assumed to be larger than the depletion-layer thickness characteristic of its doping (31).

By increasing the treatment temperature to above 600°C, the decrease in r_c is relatively small (see also the results on Ni/Si-p samples). By removing H_2 (Table I and Fig. 2), the contact resistance of 600°C samples increases by as much as an order of magnitude.

The effect of "bulk" semiconductor doping is as follows. At $N_D = 10^{20}$ cm^{-3}, the effect of the P-doped surface layer should be small; r_c is little affected by changes in the postmetallization heat-treatment. At lower semiconductor dopings, the postmetallization treatment has a significant effect and its parameters (temperature and ambient) are important.

It is worth noting that the contact resistance of Ni/Si-n samples is much lower than that of Ni/Si-p, although $\phi_{Bn} > \phi_{Bp}$ for nickel silicide-silicon contacts. This is a strong argument favoring the hypothesis of the n^+-surface layer.

The scatter of electrical data is quite large at low treatment temperatures and/or with no H_2 in the ambient. We suggest that the contact area is nonuniform and, moreover, only a fraction of the total area benefits from the surface doping mechanism discussed above. This hypothesis will be later supported by the results of SEM and microprobe analysis. The smaller diameter metallization windows exhibit a stronger probability to be inefficiently contacted. Therefore, the dispersion of electrical parameters should be larger, as is indeed observed experimentally. The nonuniformity of the metallization area should decrease as the treatment temperature increases, which is again in agreement with experimental results. Perhaps the parallel contacts model (24) may explain these more or less scattered results.

Microphysical Analysis

The results of SEM and microprobe analysis will be presented first. Figure 3 shows the SEM micrograph of a metallization window after the first nickel plating, followed by a 600°C heat-treatment (12 min, in $N_2 + H_2$). The silicon surface is rough and nonuniform, although the initial surface was polished (mirror-like). Figure 4 shows a similar contact subjected to the same treatment, except for the ambient, which is now N_2 only (the furnace and the purity of the N_2 gas were, however, the same). The absence of H_2 seems to lead to a strongly nonuniform contact, with unwanted chemical deposits.

At higher treatment temperatures, the contact uniformity improves and the surface smoothness is better.

Table I. Approximate doping of the n^+ surface layer

Heat-treatment				
Temp. (°C)	Duration (min)	Rate of gas flow (liter/min) N_2	Rate of gas flow (liter/min) H_2	$N_D{}^+$ (cm^{-3}) estimated from Fig. 2
400	15	2.5	0.7	$< 5 \times 10^{18}$
500	15	2.5	0.7	$\cong 10^{19}$
600	15	2.5	0.7	$\cong 2 \times 10^{19} \ldots 5 \times 10^{19}$
700	15	2.5	0.7	$\cong 5 \times 10^{19} \ldots 10^{20}$
800	15	2.5	0.7	$\cong 5 \times 10^{19} \ldots 5 \times 10^{20}$
900	15	2.5	—	$\cong 10^{19} \ldots 2 \times 10^{19}$

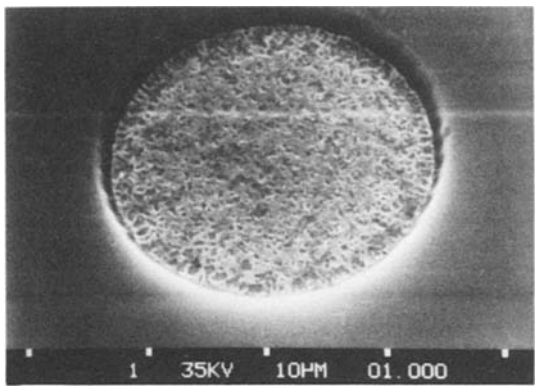

Fig. 3. SEM micrograph of a metallization window after the first nickel plating, followed by a 600°C heat-treatment (12 min, in $N_2 + H_2$). The divisions at the bottom are 10 μm.

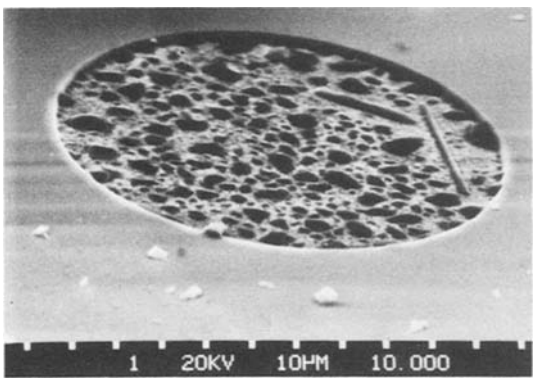

Fig. 4. The same as Fig. 3 except H_2 is missing

This fact may be seen in Fig. 5a, which shows a detail of a contact treated at 790°C, for 12 min, in $N_2 + H_2$. The microprobe analysis of the same contact identifies Ni (Fig. 5b) and Pd (Fig. 5c) in an apparent uniform quantity over the entire contact surface. It was not possible to identify phosphorus because of the resolution limits of the microprobe apparatus, although its presence was detected before the heat-treatment.

Auger electron spectroscopy (AES) was also used for samples subjected to the first nickel plating and the subsequent heat-treatment. The results are given below. Because AES analysis is a semiquantitative method, the concentration profiles obtained are at different (and arbitrary) scales for different elements (33).

Figure 6 shows the concentration profiles of the elements present in the transition layer Ni/Si as a function of the duration of the Ar ion bombardment used to remove successive layers of the probe subjected to analysis. The total thickness of the removed layer was computed as a function of the duration of the ion bombardment and the sputtering rate of the semiconductor surface. Figure 6a corresponds to a Ni/Si-n contact on an n-type wafer ($N_D = 10^{14}$ cm^{-3}), treated in $N_2 + H_2$, at 600°C (10 min, slow cooling). Figure 6b represents a similar contact, except for the fact that the ambient during the heat-treatment was only N_2.

The findings are as follows:

1. The transition silicide-silicon seems to be gradual, on a distance of the order of 10^3Å, which is much longer than that mentioned above. However, the results shown are an average on a quite large area of the investigated surface, and this area is nonuniform. We recall the rough surface of the metallized area (Fig. 3-5). The nonuniformities of the surface seem to have dimensions one order of magnitude lower than the oxide thickness (which is 1-1.2 μm). On the other hand, matrix effects and preferential sputtering with a compound target like the discussed silicide layer may produce similar results in AES. Therefore, conclusions about the actual transition-layer thickness and interface smoothness cannot be drawn from the present data.

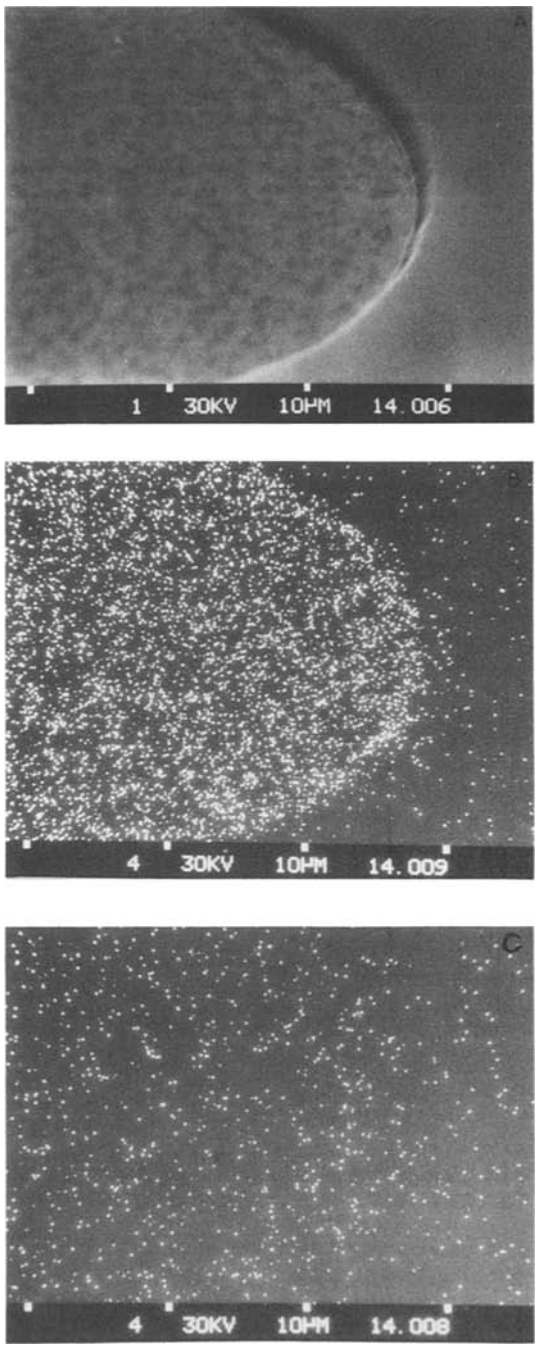

Fig. 5. (a, top) SEM micrograph of a Ni/Si contact treated at 790°C, for 12 min, in $N_2 + H_2$; (b, middle) microprobe analysis identifies Ni for the same detail of the contact; (c, bottom) microprobe analysis identifies Pd in the metallization window.

2. Auger profiles reproduced in Fig. 6 indicate the presence of P. The largest P concentration occurs at the surface, even though the treatment temperature is quite high (600°C). The presence of H_2 (Fig. 6a) seems to have a favorable effect upon the P distribution; the bulk concentration of phosphorus atoms increases at the expense of the surface concentration.[1]

[1] The lower P concentration at the surface may be also explained by the liberation of the phosphine (PH_3) as a result of chemical reaction between H_2 and P during the heat-treatment.

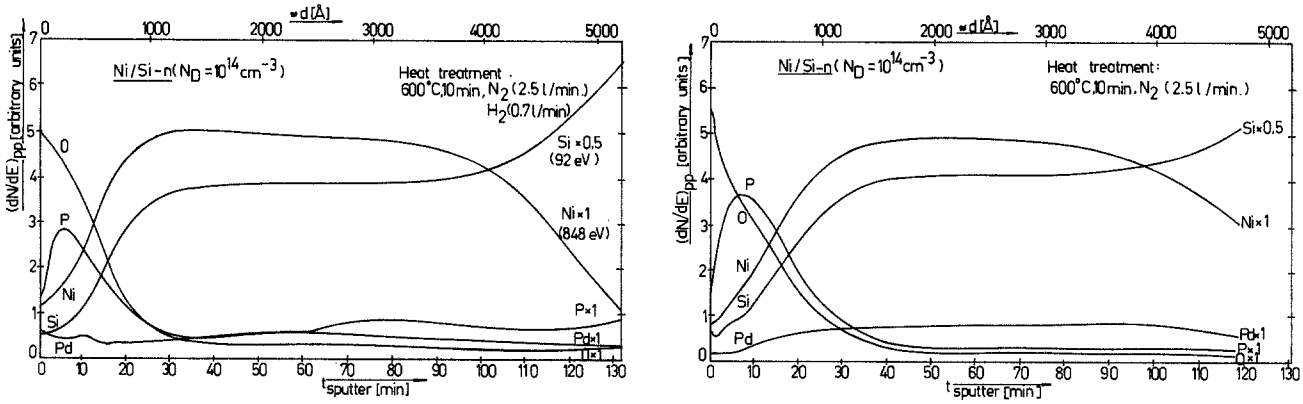

Fig. 6. Auger profiles for Ni/Si contacts treated at 600°C in $N_2 + H_2$ atmosphere (a, left) and in N_2 only (b, right). The sample surface is at the left.

This may explain the importance of H_2 in the ambient of the heat-treatment for providing a good ohmic contact on n-type silicon. Moreover, Fig. 6a shows an increase of P concentration towards the silicide-silicon interface, suggesting that the silicide "pushes" P into Si. Therefore, the $N_2 + H_2$ ambient favors the kinetics of the process of silicide formation accompanied by P penetration in Si.

3. Figure 6 also shows that Pd (used before nickel plating for surface activation) is present.

4. The oxygen (Fig. 6) detected by AES analysis shows that the silicide surface is oxidized. The oxide thickness can hardly be evaluated, since its apparent thickness of 10^3Å (Fig. 6) is of the order of surface nonuniformities (Fig. 3 and 4). The oxygen found in the silicide layer could be either the result of silicide porosity or a trace of the remnant silicon oxide present on silicon surface during plating. In fact, the "zone-refining" effect pushes oxygen to the outer surface and would not result in oxygen distributed within the silicide.

Summary and Conclusions

Based on the above results, the authors suggest the following qualitative model of the Ni/Si contact fabricated by electroless deposition and subsequent heat-treatment (34). The main results on contact structure are based on AES analysis performed on samples subjected to a 600°C/$N_2 + H_2$ ambient treatment, a process which is taken as reference.

The silicon surface is first activated by Pd atoms. It is also asperized. During the nickel plating, P deposits on the semiconductor surface also occur. The post-metallization heat-treatment leads to the formation of a silicide layer. A nickel phosphide may also be present (25, 35).

The transition layer between silicide and pure silicon contains P and Pd. An increase of P concentration towards the silicide-silicon interface was noted (600°C treatment in $N_2 + H_2$ ambient). However, the largest P concentration still occurs at the surface (at least at 600°C). The transition layer may be a Ni-Si-Pd-P complex with properties which differ from that of an ordinary silicide. The authors do not know the properties of this hypothetical complex.

The results of electrical measurements are essential. Heat-treatment produces a considerable modification of the specific contact resistance. As the treatment temperature increases, the resistance of Ni/Si-p probes increases and rectifying contacts are obtained. The contacts on Ni/Si-n samples become ohmic. The electrical behavior of these contacts is very different from that of vacuum deposited Ni/Si contacts, for which is known that $\phi_{Bn} > \phi_{Bp}$ (4). The difference can be explained by using the hypothesis of a P-doped n^+ layer occurring just under the interface between silicide (which acts as a metallic electrode) and silicon. The hypothesis of P doping was first suggested by Sullivan and Eigler (1). It is worthy to note that a similar hypothesis exists for the PtSi/Si contact obtained by chemical vapor deposition (CVD) of a Pt film following Pt $(PF_3)_4$ pyrolysis (36).

A fundamental question is that of P penetration into silicon. By extrapolating the diffusion coefficient of P in Si at low temperatures, we obtain (for the temperatures and time intervals involved in our investigation) diffusion depths from a few Å to hundreds of Å. This amount is too small to explain P penetration in silicon, since the silicide-silicon interface moves much longer distances into the silicon bulk (see Fig. 6). Therefore, a simple model of P diffusion alone in silicon cannot quantitatively explain our results. It may be assumed that other physical-metallurgical mechanisms are involved. Perhaps an impurity redistribution mechanism similar to that reported in Ref. (14, 15) is responsible for the strong accumulation of P atoms beneath the silicide and near the outer silicide surface. Further work is needed for getting a more exact insight into this electroless-deposited Ni/Si contact.

From the engineering point of view, the surface doping occurring at the silicide-silicon interface modifies the electrical characteristics as shown in Fig. 1 and 2. This change in electrical properties is controlled by the heat-treatment. The entire metallization process leads to a more or less nonuniform contact area. This is particularly dangerous for small-area devices. The nonuniformities are acceptable, however, for large-area power devices where the silicon surface may not be very smooth, and where the contact area is large and cheap metallizations are required. Certain information was obtained about the role of H_2 in the ambient during the heat-treatment. The presence of H_2 and the utilization of higher treatment temperatures improve the contact uniformity.

Manuscript submitted Dec. 20, 1982; revised manuscript received June 21, 1983.

REFERENCES

1. M. V. Sullivan and J. H. Eigler, *This Journal*, **104**, 226 (1957).
2. J. M. Andrews and F. B. Koch, *Solid-State Electron.*, **14**, 901 (1971).
3. D. J. Coe and E. H. Rhoderick, *J. Phys. D*, **19**, 965 (1976).
4. E. H. Rhoderick, "Metal-Semiconductor Contacts," Clarendon Press, Oxford (1978).
5. G. Ottaviani, *J. Vac. Sci. Technol.*, **16**, 1112 (1979).
6. P. J. Grunthaner, F. J. Grunthaner, and J. W. Mayer, *ibid.*, **17**, 924 (1980).
7. N. W. Cheung, P. J. Grunthaner, F. J. Grunthaner, J. W. Mayer, and B. M. Ullrich, *ibid.*, **18**, 917 (1981).
8. P. J. Grunthaner, F. J. Grunthaner, D. M. Scott, M. A. Nicolet, and J. W. Mayer, *ibid.*, **19**, 641 (1981).
9. J. M. A. Andrews, *ibid.*, **11**, 972 (1974).

10. M. Hansen, "Constitution of Binary Alloys," McGraw-Hill, New York (1958).
11. J. F. Ziegler, J. W. Mayer, C. J. Kircher, and K. N. Tu, *J. Appl. Phys.*, **44**, 3851 (1973).
12. J. A. Roth and C. R. Crowell, *J. Vac. Sci. Technol.*, **15**, 1317 (1978).
13. W. J. Schaffer, R. W. Bene, and R. M. Walser, *ibid.*, **15**, 1325 (1978).
14. M. Wittmer and T. E. Seidel, *J. Appl. Phys.*, **49**, 5827 (1978).
15. I. Odhomari, K. N. Tu, K. Sugaro, M. Akiyama, I. Kimura, and K. Yoneda, *Appl. Phys. Lett.*, **38**, 1015 (1981).
16. D. Dascălu, G. Brezeanu, P. A. Dan, and C. Dima, *Solid-State Electron.*, **24**, 897 (1981).
17. G. Ottaviani, K. N. Tu, and K. W. Mayer, *Phys. Rev. Lett.*, **44**, 284 (1980).
18. R. W. Bene, R. M. Walser, and J. C. Hu, in "Proc. 14th Int. Conf. Phys. Semic., 1978," p. 773, Inst. of Phys., London (1979).
19. R. W. Bene, R. M. Walser, G. S. Lee, and K. C. Chen, *J. Vac. Sci. Technol.*, **17**, 911 (1980).
20. G. Ottaviani, *ibid.*, **18**, 924 (1981).
21. B. Y. Tsaur, S. S. Lau, J. W. Mayer, and M. A. Nicolet, *Appl. Phys. Lett.*, **38**, 922 (1981).
22. J. L. Freeouf, *J. Vac. Sci. Technol.*, **18**, 910 (1981).
23. P. S. Ho and G. W. Rubloff, *Thin Solid Films*, **84**, 433 (1982).
24. I. Odhomari and K. N. Tu, *J. Appl. Phys.*, **51**, 3735 (1980).
25. F. Pearlstein, in "Modern Electroplating," F. A. Lowenheim, Editor, Chap. 31, John Wiley & Sons, New York (1974).
26. D. Dascălu, G. Brezeanu, P. A. Dan, and C. Dima, *Electrotehn. Electron. Aut.*, **24**, 5 (1980).
27. D. Dascălu, G. Brezeanu, and P. A. Dan, *Appl. Phys. Lett.*, **37**, 215 (1980).
28. E. Hökelek and G. Y. Robinson, *Thin Solid Films*, **53**, 135 (1978).
29. J. E. E. Baglin and J. M. Poate, in "Thin Films—Interdiffusion and Reactions," J. M. Poate, K. N. Tu, and J. W. Mayer, Editors, Chap. 9, The Electrochemical Society Monograph Series, John Wiley & Sons, New York (1978).
30. J. M. Shannon, *Appl. Phys. Lett.*, **25**, 75 (1974).
31. R. S. Popovic, *Solid-State Electron.*, **21**, 1133 (1978).
32. C. Y. Chang, Y. K. Fang, and S. M. Sze, *ibid.*, **14**, 541 (1971).
33. "Methods of Surface Analysis," A. W. Czánderna, Editor, Elsevier Sci. Publ. Co., Oxford (1975).
34. P. A. Dan, G. Popovici, G. Brezeanu, and A. Popa, *Electrotehn. Electron. Aut.*, To be published.
35. G. A. Walker and C. C. Goldsmith, *Thin Solid Films*, **53**, 217 (1978).
36. M. J. Rand, *This Journal*, **122**, 811 (1975).

Characteristics of $TaSi_2$/Poly-Si Films Oxidized in Steam for VLSI Applications

J. M. DeBlasi,[1] R. R. Razouk, and M. E. Thomas

Fairchild Advanced Research and Development Laboratory
Palo Alto, California 94304

ABSTRACT

The oxidation kinetics of tantalum disilicide/polycrystalline silicon composite structures in pyrogenic steam over the temperature range of 800° -1000°C have been investigated. The oxide formation over the tantalum silicide film has been found to proceed in a linear-parabolic manner similar to that observed for oxide formation over single crystal silicon. The parabolic rate constant is similar to that observed for single crystal silicon, while the linear rate constant is higher than that of lightly doped single crystal and polycrystalline silicon. The electrical properties of oxides formed over the silicide as well as oxides under the silicide/polycrystalline silicon composite layer (gate oxides) have been investigated. Gate oxide integrity has been found to degrade dramatically when, due to oxidation, the average remaining underlying polysilicon thickness is reduced to less than 2000Å at the gate electrode.

Recent advances in VLSI-circuit fabrication clearly show that interconnects with resistivities lower than those of heavily doped polycrystalline silicon are required for advanced circuit development. Improved lithographic resolution, anisotropic etching, and vertical scaling have all resulted in a substantial increase in packing density. This increase in packing density and the associated reduction in interconnect line width leads to RC delays due to the contribution of the high sheet resistance of heavily doped polycrystalline silicon lines. These delays interfere with, or cancel, the speed advantage gained by short channel devices. Refractory metal silicides/polycrystalline silicon structures, because of their low sheet resistance, are now under evaluation as possible replacements to heavily doped polysilicon, with an emphasis on the establishment of overall process compatibility.

Recent efforts have concentrated on the investigation of $MoSi_2$, WSi_2, $TaSi_2$, and $TiSi_2$ as gate interconnects. Published results indicate that the most effective use of metal silicides in integrated circuits requires the use of polycrystalline silicon/metal silicide composite structures (1-4). The advantages of the composite structure are threefold: (*i*) during oxidation, the polycrystalline layer provides the required silicon for the formation of SiO_2 over the silicide layer (this is thought to occur by diffusion of the silicon through the silicide layer); (*ii*) the presence of the polycrystalline layer prevents interaction between the silicide layer and the underlying gate SiO_2 layer (such interactions have been observed and are thought to be the cause of gate oxide degradation which in turn leads to device failure); (*iii*) the composite structure allows the retention of the advantageous polycrystalline silicon gate properties while gaining the conductivity advantages of silicides.

In this investigation, we examine $TaSi_2$ on poly-Si as a gate electrode and interconnect. Several authors have already published overviews of $TaSi_2$/poly-Si metallization schemes (1, 2) and have shown that, by using $TaSi_2$/poly-Si composite structures, low sheet resistance can be achieved while the advantages of silicon-gate properties and technology are maintained. $TaSi_2$/poly-Si, formed by sintering a tantalum film on doped polysilicon, was initially reported to have a very low oxidation rate in dry oxygen (4). This was attributed to the presence of excess Ta at the silicide-SiO_2 interface, which interfered with silicon diffusion by substitution on the $TaSi_2$ lattice. The rate limiting step was postulated to be silicon diffusion by exchange,

Key words: dielectric breakdown, oxidation rate constants, refractory metal silicide.

[1] Present address: Philips Research Laboratories, Sunnyvale, Signetics Corporation, Sunnyvale, CA 94086.

which would favor a high activation energy. In the case of steam oxidations (4), SiO_2 was readily formed, and it was postulated that Ta and Si are both initially oxidized and produce a silicon-rich silicide at the silicide-SiO_2 interface, thereby allowing silicon diffusion to occur and oxidation to continue (4).

More recently, it has been reported that co-sputtered and co-evaporated $TaSi_2$/poly-Si films oxidize in a dry ambient at a rate higher than that for lightly doped or undoped poly-Si and (100) silicon. There was no Ta in the SiO_2 layer detected by Auger electron spectroscopy (AES) in either the dry (5, 6) or steam oxides (5).

The rate limiting step in the dry oxidation of $TaSi_2$/poly-Si appears to be the diffusion of oxygen through the oxide, rather than the diffusion of the silicon from the underlying substrate (6). It should be emphasized that although no Ta was detected by AES in oxides formed on co-sputtered $TaSi_2$/poly-Si films, both AES and Rutherford backscattering spectrometry (RBS) indicated the presence of Ta in oxides grown on silicides formed by sintering a Ta film on poly-Si. However, the dry oxidation growth rates in both cases were found to be identical (6), and the tantalum did not appear to play an inhibiting role.

The purpose of the work reported here is to further clarify the oxidation kinetics of the $TaSi_2$/poly-Si structure in steam over the temperature range of 800°-1000°C. In addition, the possibility of gate oxide-integrity degradation as the poly-Si pad thickness is oxidized away, in a manner similar to that described for $MoSi_2$/poly-Si and WSi_2/poly-Si gates (3), is investigated, as it is of paramount importance in the potential use of $TaSi_2$/poly-Si in integrated circuit fabrication.

Experimental Procedure

P-type (100) silicon wafers of 11-18 Ω-cm resistivity were cleaned and thermally oxidized in a pyrogenic steam +3% HCl ambient at 800°C to grow a 250Å gate oxide. Polysilicon 3600Å thick was deposited at 630°C in a standard LPCVD reactor. After this step, the poly-Si and gate oxide were removed from the back side of the wafers, and a phosphorus predeposition was performed using $POCl_3$ for 5 min at 950°C. The poly-Si resistivity was approximately 10^{-2} Ω-cm after doping. The phosphosilicate glass was removed and another cleaning step was performed. Tantalum and silicon were S-gun co-sputtered 2600±200Å thick (atomic ratio 1.5/1 of Si/Ta) at 360°C.

Silicide reaction was performed in high purity hydrogen for 30 min at 950°C, forming approximately 2500±200Å of $TaSi_2$ with a sheet resistance of 2.4±1 Ω/□ (~60 μ Ω-cm). The poly-Si thickness was roughly 3100±200Å at this stage (see Fig. 1). The wafers were rapidly pushed into the oxidizing ambient of pyrogenic steam (no HCl) at 800°, 900°, and 1000°C for 0.2, 0.5, 1.0, 2.0, and 5.0 hr. A 15 min post-oxidation anneal in N_2 and a 5 min N_2-pull from the furnace was performed. Oxides grown on the $TaSi_2$/poly-Si structure were measured using a Gaertner automatic ellipsometer (6), using a measured substrate refractive index of 3.56±0.1 and an extinction coefficient of −2.26±0.01, for structures oxidized at 800° and 900°C. At 1000°C, the substrate index of refraction measured was 3.79±0.15, with an extinction coefficient of −2.18 ±0.1. These readings closely agreed with profilometer measurements of oxide steps made on wafers with buffered-HF etch. After the oxide thickness on $TaSi_2$ was determined, the wafers were split into two groups: those for gate oxide integrity testing (group 1), and those for testing the oxide grown on the $TaSi_2$/poly-Si (group 2) films.

The wafers from group 1 had the oxide on $TaSi_2$ removed in a buffered-HF solution. Capacitors 30 mils in diameter (0.0045 cm^2) were defined by photolithography. The $TaSi_2$/poly-Si layer was plasma etched in a barrel reactor in CF_4/4% O_2 down to the gate oxide.

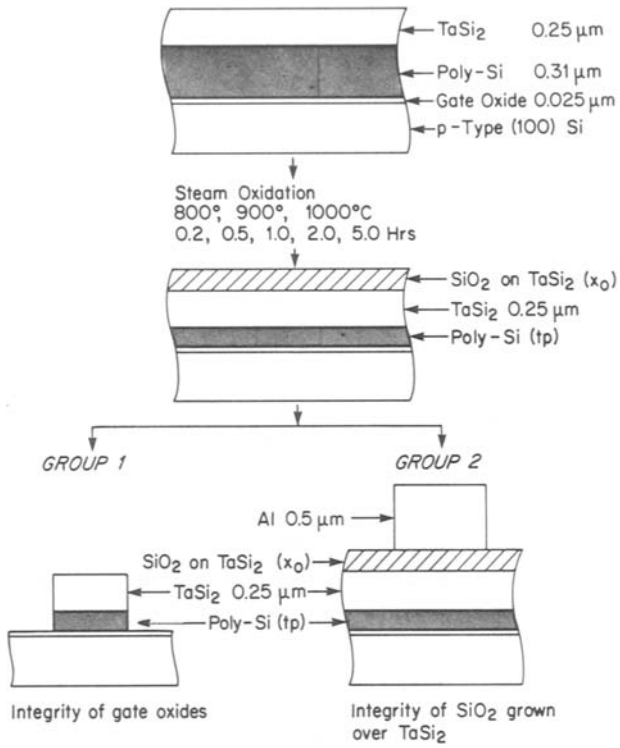

Fig. 1. $TaSi_2$/poly-Si structures fabricated for the determination of oxidation kinetics, testing the integrity of gate oxides (group 1) and the integrity of SiO_2 grown on the tantalum disilicide (group 2).

The wafers from group 2 had 5000Å of Al deposited on the SiO_2 grown over the silicide. Capacitors 30 mils in diameter were defined by photolithography. The Al was chemically etched, and the wafers were alloyed in forming gas for 20 min at 450°C.

Results and Discussion

Oxidation data.—Oxide-thickness *vs.* oxidation-time data for the $TaSi_2$/poly-Si structures oxidized at 800°, 900°, and 1000°C are shown in Fig. 2. At 900° and 1000°C, the oxide thickness curves for $TaSi_2$/poly-Si approach those of single crystal (111) silicon. This indicates that the parabolic rate constant which is

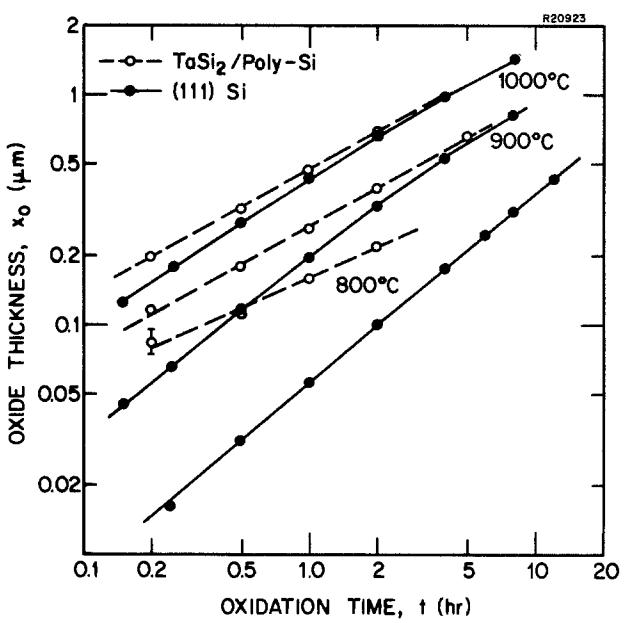

Fig. 2. Oxide thickness *vs.* oxidation time for $TaSi_2$/poly-Si structures and (111) single crystal silicon oxidized in steam at 800°, 900°, and 1000°C.

dominant at high temperature and/or for long oxidation time is nearly the same for $TaSi_2$/poly-Si and single crystal (111) silicon. The increased oxide thickness formed over the $TaSi_2$/poly-Si at small oxidation times is indicative of an increase in the linear rate constant.

Figure 3 shows a comparison at 900°C between the data obtained in this study and the data published by Pawlik *et al.* (5). Although the latter data cover a comparatively small time range, the agreement is excellent. Also shown are the results of Murarka *et al.* (4), which indicate a substantially lower oxidation rate. The slope of the oxide thickness *vs.* time curve indicates close to parabolic oxide growth, as noted by Murarka *et al.*; however, it indicates a substantially reduced parabolic rate constant.

Control wafers with the same lightly doped polycrystalline films only were oxidized simultaneously with the $TaSi_2$/poly-Si structures. The results, also shown in Fig. 3, are quite close to (111) silicon, indicating that the phosphorus concentration in the polycrystalline silicon is not sufficient to enhance the oxidation rate. The similarity to (111) silicon results is expected from consideration of the dominant grain orientation (110) in the poly-Si films (7).

Oxidation rate constants.—The oxidation rate constants were determined using the Deal-Grove (8) general relationship for silicon oxidation in steam

$$x_0^2 + Ax_0 = Bt \qquad [1]$$

where x_0 is the oxide thickness, B the parabolic rate constant, B/A the linear rate constant, and t the oxidation time. Calculated values of B and B/A are shown in Fig. 4 and 5, respectively. In Fig. 4, previously reported values of the parabolic rate constant from the oxidation of single crystal (111) and (100) silicon are shown (9), along with the results obtained in this study for $TaSi_2$/poly-Si structures. A small decrease is noted in our data, while a strong decrease is observed from the results of Murarka *et al.* (4). Interestingly, the activation energy in all cases appears to be the same at temperatures below 950°C. This could indicate that the rate limiting process is the same, *i.e.*, the diffusion of a water-related species through the oxide. The observed decrease in B is attributed entirely to a change in the pre-exponential constant, which is representative of the diffusion coefficient of water in SiO_2. Typically, this pre-exponential constant

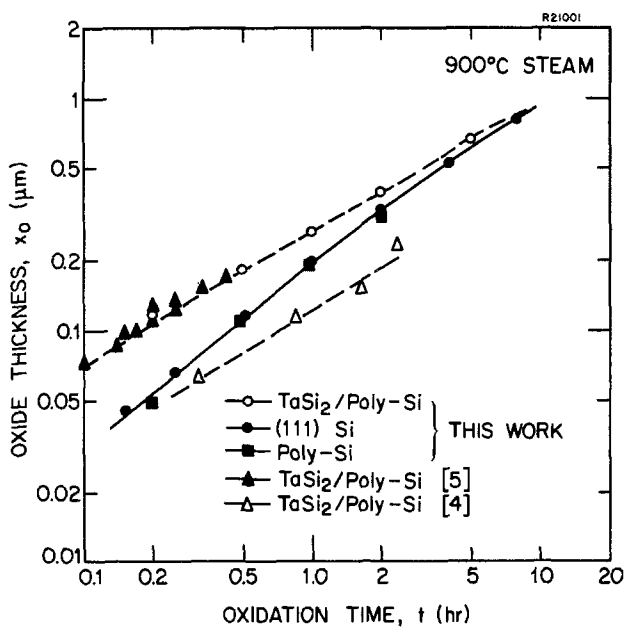

Fig. 3. Oxide thickness *vs.* oxidation time for $TaSi_2$/poly-Si, lightly doped poly-Si, and (111) silicon oxidized in steam at 900°C.

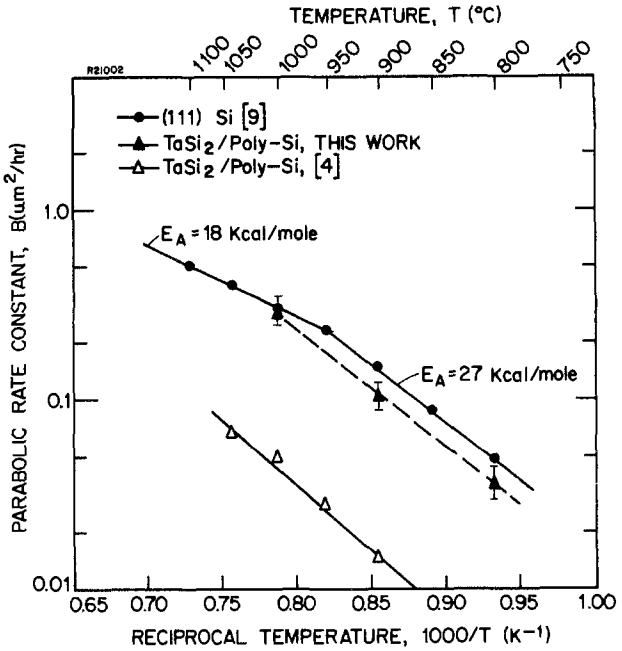

Fig. 4. Parabolic rate constant *B* *vs.* reciprocal temperature for $TaSi_2$/poly-Si and single crystal silicon oxidized in steam.

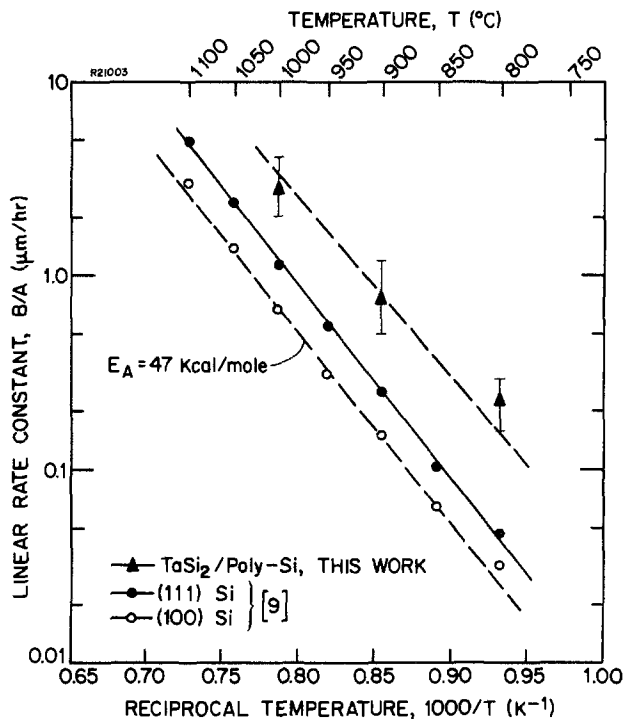

Fig. 5. Linear rate constant *B/A* *vs.* temperature for $TaSi_2$/poly-Si, single crystal (111), and (100) silicon oxidized in steam.

can be affected by the jump frequency of the diffusing species, the jump distance (a geometrical factor indicative of the structure), and the activation entropy of the diffusion process. It is plausible that small differences in the composition of the grown oxide, possibly resulting from the incorporation of tantalum, can be responsible for the factor-of-seven difference in the pre-exponential part of the parabolic rate constant observed between the data presented here and that presented elsewhere (4).

The linear rate constants calculated from the data of Fig. 2 are shown in Fig. 5. The activation energy is similar to that obtained in the oxidation of single or polycrystalline silicon. This activation energy has been previously associated with the breaking of Si-Si bonds and is likely to remain unchanged. The increase in the

magnitude of the rate constant is again related to the pre-exponential factor. It is important to recall at this time that in the case of $TaSi_2$/poly-Si oxidation in dry O_2 ambients, the linear rate constant increased to such a degree that the oxidation was dominated by the parabolic regime from the start (6). It was postulated that the diffusion of silicon through the $TaSi_2$ layer was very rapid, resulting in an abundant supply of silicon at the oxidizing interface, and a rate of oxidation enhanced so that the rate limiting step in the oxidation was related to the diffusion of oxygen through the growing oxide at all times. In the case of steam oxidation, the same behavior is expected, with one difference: the surface reaction rate in the steam ambient is higher than that in dry O_2, and although the supply of silicon through the silicide layer is similar, the oxidation is not enhanced to the point where it is limited by the diffusion of the oxidant through the oxide for thin oxides. In both the dry O_2 and steam cases, however, the enhanced oxidation rate is thought to be related to the rapid diffusivity of silicon through the silicide layer. Therefore, it is quite possible that the silicide layer is playing a catalyst-like role in the oxidation of $TaSi_2$/poly-Si composite structures. This may result in an enhanced oxidation rate at the start of the oxidation, followed by a conventional diffusion-limited oxidation. The latter is characterized by the same rates observed in the oxidation of both single crystal and polycrystalline silicon.

Transmission electron microscopy.—TEM micrographs were employed to observe changes in the $TaSi_2$/poly-Si structure as the oxidation proceeded. Figure 6a shows the TEM cross section of such a structure following a 1-hr oxidation at 900°C. The roughnesses of both the SiO_2 surface and the $TaSi_2/SiO_2$ and poly-Si/$TaSi_2$ interfaces are evident. As the oxidation proceeds and the poly-Si is consumed, the $TaSi_2$ layer contacts the gate SiO_2 layer at some locations, as shown in Fig. 6b. This direct interaction is thought to play a critical role in the integrity of the underlying gate oxide. This will be discussed in the next section.

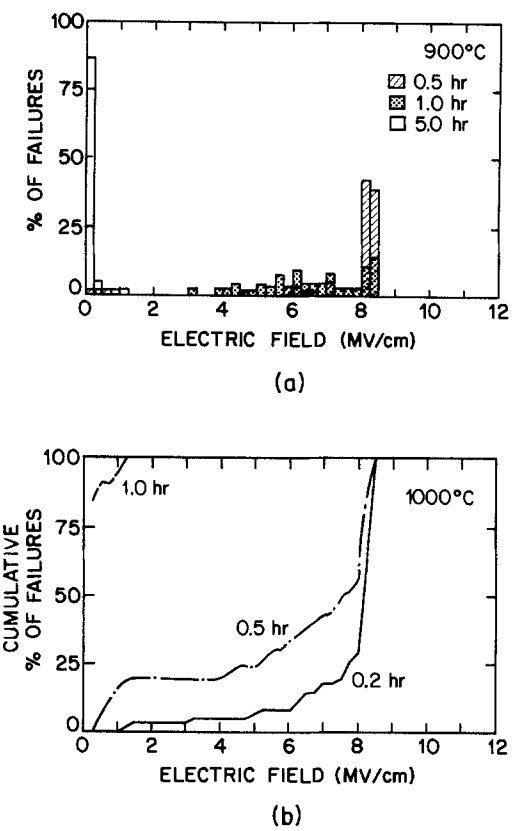

Fig. 6. (a) Percentage of gate oxide breakdowns vs. applied electric field for $TaSi_2$/poly-Si structures oxidized in steam at 900°C for 0.5, 1.0, and 5.0 hr. (b) Cumulative percentage of gate oxide breakdowns vs. applied electric field for $TaSi_2$/poly-Si structures oxidized in steam at 1000°C for 0.2, 0.5, and 1.0 hr.

Gate oxide integrity.—The current-voltage characteristics of the 250Å gate oxides were obtained by using a stepped voltage technique. The voltage was stepped in increments of 0.5V, corresponding to a field of 0.2 MV/cm, and the current measured until a value of 10^{-5} A/cm^2 was recorded. The voltage value at that current was then used to prepare histograms similar to that shown in Fig. 6a. All measurements shown here were carried out with the silicon surface in accumulation. Figure 6a shows a composite of three histograms obtained from $TaSi_2$/poly-Si structures oxidized at 900°C for 0.5, 1.0, and 5 hr. The effect of increased oxidation time is striking, and indicates almost total shorting for structures oxidized for 5 hr. The TEM cross section shown in Fig. 7b for that particular oxidation condition shows that the $TaSi_2$ layer is in contact with the gate oxide in some areas. The degradation in the oxide properties observed at this and even shorter oxidation times is probably due to a reduction of the thermal SiO_2 layer.

The gradual-failure mode observed at 900°C has also been observed at 1000°C. Cumulative percentage-breakdown data shown in Fig. 6b clearly indicate similar behavior with substantial degradation noted for oxidation times as short as 30 min.

A summary of the oxide integrity data gathered from oxidations at 800°, 900°, and 1000°C is shown in Fig. 8. The field required for 75% cumulative failure of the gate oxides is plotted *vs.* the remaining poly-Si thickness following the oxidation of the $TaSi_2$/poly-Si structures. There is a dramatic decrease in the integrity of the gate oxide as the average poly-Si thickness remaining after oxidation is reduced to under 2000Å. This finding correlates well with the percentage of effectively shorted devices *vs.* underlying poly-Si pad thickness reported for $MoSi_2$/poly-Si and WSi_2/poly-Si structures (3). It should be noted that the roughness apparent in the TEM micrographs in Fig. 7b suggests that the $TaSi_2$ layer may have come into contact with the gate oxide through preferential localized depletion of the underlying silicon.

Integrity of oxide grown on $TaSi_2$/poly-Si.—Dielectric strength of the oxide grown on silicide/poly-Si

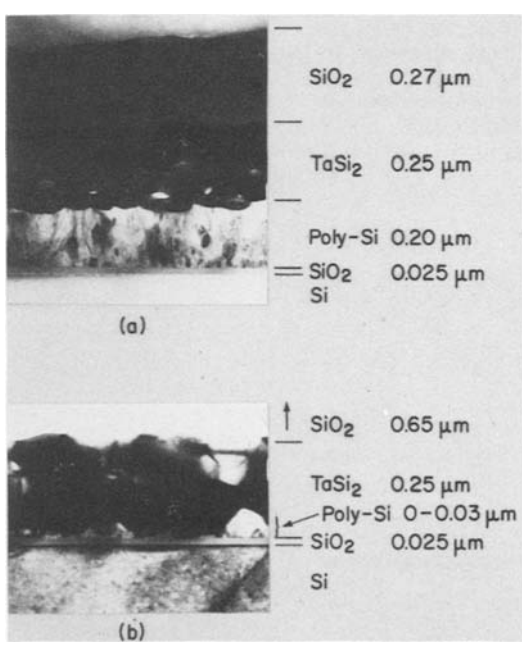

Fig. 7. TEM cross sections, bright field, of $TaSi_2$/poly-Si structures following steam oxidation at 900°C, (a) for 1 hr, and (b) for 5 hr.

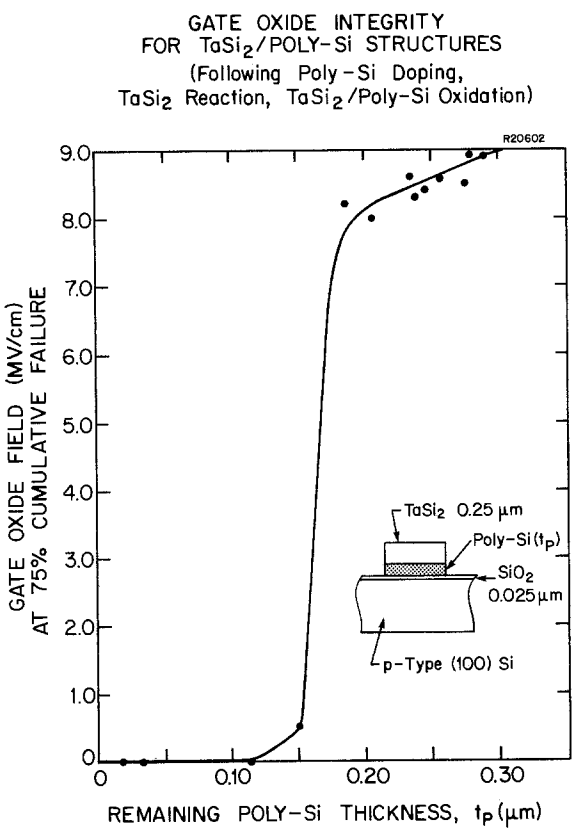

Fig. 8. Field required for 75% cumulative failure of gate oxides vs. remaining poly-Si thickness following the oxidation of $TaSi_2$/poly-Si structures in steam at 800°, 900°, and 1000°C.

structures oxidized in steam has been reported to be about 2.5-3.9 MV/cm for WSi_2/poly-Si oxidized at 1000°C (3), and to be equivalent to that of steam oxides grown on poly-Si for $TaSi_2$/poly-Si structures (4). In this work, breakdown measurements were carried out for SiO_2 grown over $TaSi_2$/poly-Si at 800°, 900°, and 1000°C in steam. The results are plotted in Fig. 9. For thin oxides (around 1000Å) over $TaSi_2$, the capacitor structures yielded predominantly shorts. This could be due to a number of factors: (*i*) a very high defect density in the growing oxide; (*ii*) the inclusion of Ta in the growing oxide in the initial phase of growth; or (*iii*) the surface roughness of the $TaSi_2$ layer and/or a nonuniform oxide growth. At intermediate thicknesses, the integrity of the oxide is seen to increase dramatically with oxide thickness and oxidation time up to a maximum of 4 MV/cm. As the thickness of the underlying poly-Si decreases to under 2000Å, a reduction in oxide integrity is noted with the breakdown field dropping to under 2 MV/cm. This again could be due to the nonuniformities in the supply of silicon from the poly-Si layer resulting in nonuniform oxide growth, or to a larger density of defects in the forming oxide.

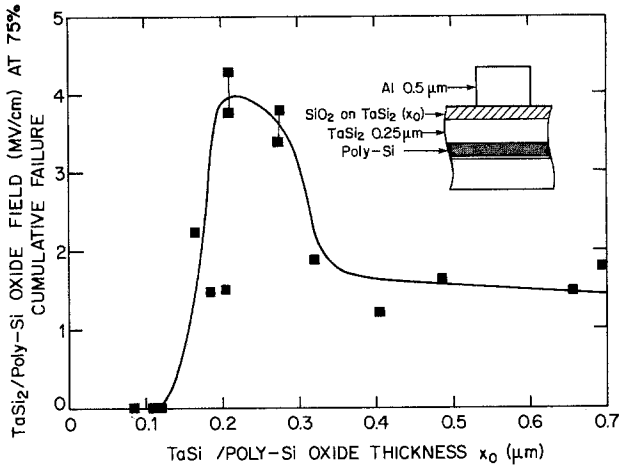

Fig. 9. Field required for 75% cumulative failure of oxides grown on $TaSi_2$/poly-Si vs. thickness of the oxide.

Summary and Conclusions

The kinetics for the steam oxidation of $TaSi_2$/poly-Si structures over the temperature range of 800°-1000°C have been presented. The diffusion of oxygen through the SiO_2 layer over $TaSi_2$ is seen as the rate limiting step for long time/high temperature oxidations. The presence of the $TaSi_2$ is seen as playing a critical role in increasing the surface-reaction rate constant, possibly by means of a catalytic-like reaction during this process. Finally, it was found that the integrity of the gate oxide under the $TaSi_2$/poly-Si gate degraded severely when the underlying poly-Si layer was reduced to an average thickness of less than 2000Å.

Acknowledgment

The authors would like to acknowledge B. Lear for performing various parts of the experimental work.

Manuscript submitted March 23, 1983; revised manuscript received Aug. 8, 1983.

Fairchild Advanced Research and Development Laboratory assisted in meeting the publication costs of this article.

REFERENCES

1. S. P. Murarka, D. B. Fraser, A. K. Sinha, and H. J. Levinstein, *IEEE Trans. Electron Devices*, **ed-27,** 1409 (1980).
2. A. K. Sinha, W. S. Lindenberger, D. B. Fraser, S. P. Murarka, and E. N. Fuls, *ibid.*, **ed-27,** 1425 (1980).
3. H. J. Geipel, Jr., N. Nsieh, M. H. Ishag, C. W. Koburger, and F. R. White, *ibid.*, **ed-27,** 1417 (1980).
4. S. P. Murarka, D. B. Fraser, W. S. Lindenberger, and A. K. Sinha, *J. Appl. Phys.*, **51,** 3241 (1980).
5. D. Pawlik, E. Doering, and H. Oppolzer, Abstract 195, p. 310, The Electrochemical Society Extended Abstracts, Vol. 1982-1, Montreal, Que., Canada, May 9-14, 1982.
6. R. R. Razouk, M. E. Thomas, and S. L. Pressacco, *J. Appl. Phys.*, **53,** 5342 (1982).
7. T. I. Kamins, *This Journal*, **126,** 838 (1979).
8. B. E. Deal and A. S. Grove, *J. Appl. Phys.*, **36,** 3770 (1965).
9. R. R. Razouk, L. N. Lie, and B. E. Deal, *This Journal*, **128,** 2214 (1981).

Cooperative Precipitation of Sulfides as a Mode of Internal Sulfidation of Nickel-Aluminum Alloys

V. S. Bhide and W. W. Smeltzer*

Department of Metallurgy and Materials Science, McMaster University, Hamilton, Ontario, Canada, L8S 4M1

ABSTRACT

Growth of three morphologically distinct layers of sulfidation products occurs during linear steady-state sulfidation of γ-phase Ni-Al alloys at 700°C in H_2S-H_2 atmospheres at sulfur pressures $10^{-8} \leq p_{S_2} \leq 10^{-2}$ atm. A scale composed of NiS or Ni_3S_2 grows by outward diffusion of nickel. The subscale, which grows by inward sulfur migration, is composed of an Al_2S_3 + Ni_3S_2 lamellar layer and an innermost Al-Ni-S liquid layer. The lamellae advance into the liquid layer by a cooperative precipitation mode. A model is advanced for internal sulfidation in which the spacing of the lamellae adjusts to the propagation of the lamellar front which is dependent on the magnitude of the linear reaction kinetics governing the overall sulfidation reaction.

The classical description of binary alloy internal oxidation is based upon general precipitation of the oxide of the selectively oxidized alloying element as small particles at a volume fraction small enough not to interfere with diffusion. It is recognized, however, that several other precipitation modes may compete and even completely suppress general precipitation. One mode encompasses discontinuous precipitation in which an oxygen-saturated alloy decomposes to lamellar oxide precipitates in the solute-depleted but structurally identical solvent-alloy phase. In discontinuous precipitation, lateral segregation of the alloying element occurs along a boundary in the metallic phase between the oxide lamellae at their growth front. Precipitation of MoS_x plates as internal sulfides upon sulfidizing a Ni-29 atomic percent (a/o) Mo alloy illustrates this behavior (1).

High temperature oxidation of γ-phase Ni-Al alloys can be cited as an example of internal oxidation proceeding by cellular precipitation (2). Oxidation of alloys containing from 3 to 13 a/o Al at temperatures in the range 800°-1200°C leads to growth of an external scale containing layers of NiO and NiO + Ni_2AlO_4 and an aluminum-depleted alloy layer containing $NiAl_2O_4$-Al_2O_3 cylindrical rods which extend right across the internal oxidation zone (2, 3). In these cases, the scale and subscale grow by parabolic kinetics, and a boundary does not appear to exist in the metal between the oxide lamellae at their growth front.

We previously published an investigation on the sulfidation properties of Ni-Al alloys exposed in H_2S-H_2 atmospheres at 700°C (4). These alloys contain 3-13 a/o Al sulfidized by linear kinetics, and the reaction products were confined to three regions: a NiS or Ni_3S_2 scale and a subscale containing an Al_2S_3 + Ni_3S_2 lamellar layer and an innermost (Ni-Al-S) liquid layer. This research was undertaken to obtain results for formulation of a model to describe the internal sulfidation processes leading to growth of sulfide lamellae into the liquid of ternary composition. We seek to describe, accordingly, a mode of internal sulfidation (oxidation) involving the liquid decomposition $(Ni\text{-}Al\text{-}S)_l \rightarrow (Al_2S_3)_\alpha + (Ni_3S_2)_\beta$ by cooperative precipitation of the two solid sulfides as parallel lamellae into this innermost liquid layer.

Experimental Methods and Results

The preparation of alloys, the thermogravimetric sulfidation assembly, and phase identification techniques are described in previous papers (4, 5). Typical features of scales and internal sulfidation zones resulting from sulfidation of γ-phase Ni-Al alloys containing from 3 to 13 a/o Al in H_2S-H_2 atmospheres, $10^{-8} \leq p_{S_2} \leq 10^{-2}$ atm, are illustrated in Fig. 1. The scales were composed of NiS at $p_{S_2} > 10^{-4}$ atm and of Ni_3S_2 at lower sulfur pressures. The subscale in all instances was composed of two distinct layers involving solid Al_2S_3 + Ni_3S_2 lamellae and the innermost liquid Ni-Al-S layer. The amount of liquid phase

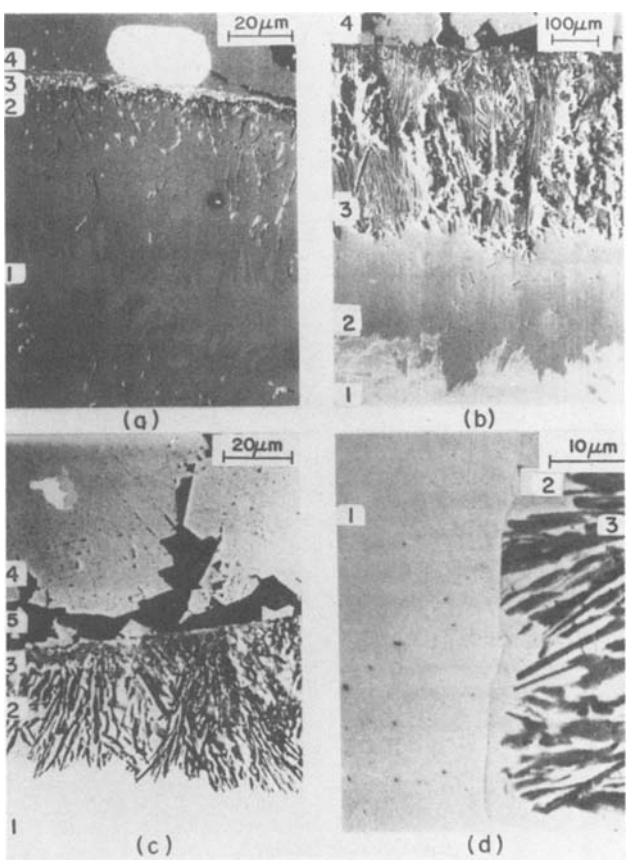

Fig. 1. Cross sections of the sulfide layers formed on the Ni-Al alloys upon sulfidation. Regions 1, 2, 3, 4 refer to bulk alloy, liquid Al-Ni-S layer, lamellar Al_2S_3 + Ni_3S_2 layer, Ni_3S_2 external scale, respectively, and the black areas 5 refer to penetrated plastic mounting material. (a) Ni-6 a/o Al specimen sulfidized at $p_{S_2} = 10^{-5}$ atm for 75 min illustrating Pt marker positioned between external scale and subscale. (b) Ni-10 a/o Al specimen sulfidized at $p_{S_2} = 10^{-7}$ atm for 49 hr. (c) Ni-13 a/o Al specimen sulfidized at $p_{S_2} = 10^{-8}$ atm for 34 hr. (d) Closeup of liquid/alloy interface in cross section (c). In lamellar region 2, Ni_3S_2 is bright phase and Al_2S_3 is gray-colored phase.

* Electrochemical Society Active Member.

Key words: Ni-Al alloys, sulfidation, lamellar subscale.

decreased with increasing aluminum alloy content. A taper cross section of a lamellar layer, Fig. 2, confirms that the two sulfide phases occur as plates and not as cylindrical rods. The crystal structures of Ni_3S_2 and Al_2S_3 belong to the hexagonal system, and this crystallographic restraint possibly abets the growth of plates.

Techniques of quantitative microscopy were used to measure the dimensions of the lamellae and the inward propagation of the different sulfide layers. Optical microscopy was used to measure lamellar spacings larger than 2 μm, since a minimum distance of 0.05 μm was measurable at 2000× magnification using an oil immersion lens. Scanning electron microscopy (SEM) was used to examine finer lamellae at a magnification of 6000×. Because of the polishing damage, many lamellae were broken or pulled from a cross section. Only those lamellae which appeared as a group of three or more were taken into account and at least 200 observations on each specimen were carried out. Because of the initial nonuniform growth of the external scale, and the fact that the subscale grew only beneath this scale, subscale penetration varied across the alloy surface (4). In order to determine the inward migration velocity of the lamellae and the liquid layer, the assumption was made that the largest penetration depth of each layer corresponded to nucleation at zero time. It is emphasized, nevertheless, that growth velocities calculated by dividing the maximum observed penetration depth by the total sulfidation time is a crude approximation, because polishing procedures may lead to cutting and distance reduction of the lamellae and liquid fronts. The measured lamellar spacings and velocities of the layer fronts are presented in Table I. A large statistical variation, ~25%, was observed in the individual plate measurements. This is common to this method of quantitative microscopy on metallographic cross sections.

Fig. 2. Typical taper section of a two-phase lamellar layer demonstrating that the lamellae are plates and not cylindrically shaped rods.

Table I. Microscopy measurements of maximum observed propagation velocities of the nickel sulfide scale (v_1), of the lamellar $Ni_3S_2 + Al_2S_3$ front (v_2) and of the liquid/alloy interface (v_3). The corresponding interlamellar spacing $\xi = \xi_\alpha + \xi_\beta$ is also given where $\alpha \equiv Al_2S_3$ and $\beta \equiv Ni_3S_2$.

Alloy	p_{H_2S}/p_{H_2}	Maximum observed propagation velocities (μm/min) v_1	v_2	v_3	Corresponding interlamellar spacing ξ (μm)	$v_2\xi^2$ (μm^3/min)
Ni-10 a/o Al	0.03	0.54	0.20	0.20	—	—
	0.05	0.64	0.29	0.29	—	—
	0.10	0.69	0.60	0.73	4.26 ± 1.83	10.9
	0.10	0.94	0.60	0.68	4.63 ± 2.62	12.9
	0.11	1.48	0.64	1.27	3.15 ± 1.08	6.4
	0.20	2.25	1.08	0.67	2.9 ± 1.36	9.1
	0.35	3.80	1.68	2.35	1.62 ± 0.63	4.4
	0.64	3.30	1.30	2.55	2.77 ± 1.37	10.0
	0.78	3.90	2.10	2.73	1.64 ± 0.52	5.6
Ni-3 a/o Al	26.20*	1.50	1.50	1.50	0.76 ± 0.34	0.87
	0.60	2.00	1.47	1.47	0.92 ± 0.36	1.24
	0.24	4.10	1.00	1.00	1.02 ± 0.42	1.04

* External scale is NiS.

A convincing indication was obtained by the following experiment that internal sulfidation corresponded to a cooperative type of liquid decomposition and precipitation mode. An alloy specimen was initially sulfidized at 700°C in a 50% H_2S-H_2 atmosphere to obtain steady-state linear kinetics. The gas composition was then changed to 10% H_2S-H_2. Linear sulfidation, accordingly, continued at a reduced rate, which led to a slower inward propagation of the lamellar layer front. As illustrated in Fig. 3, this reduction of sulfur pressure corresponding to a reduction in the reaction rate gave rise to a visibly coarse spacing of the sulfide lamellae.

Knowledge of the Ni-Al-S phase diagram at 700°C is essential in order to understand development of the reaction product layers. A tentative diagram shown in Fig. 4 was constructed in light of the following results. Pure nickel dissolves up to 0.1 a/o S (6) and a slight increase of sulfur solubility with Al addition would result from its greater affinity for sulfur. Sulfur solubilities in the alloy and intermetallic phases are assumed to be small because sulfur content in sulfidized alloys, Ni_3Al and NiAl, were less than the electron probe microanalysis (EPMA) detection limit of 1 a/o S. Al_2S_3 has negligible binary phase extent

Fig. 3. Cross section of lamellar layer formed in a Ni-10 a/o Al specimen at 700°C. The alloy was sulfidized initially in a 50% H_2S-H_2 atmosphere, which was abruptly changed to a 10% H_2S-H_2 atmosphere. Note that the fine lamellar structure (upper section of micrograph) produced at high sulfur pressure is followed by a coarser structure formed at low sulfur pressure.

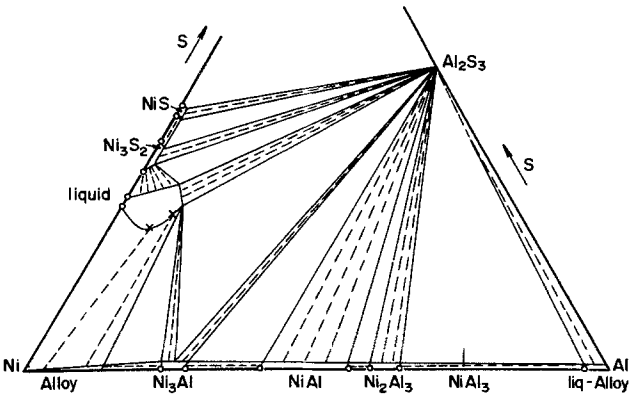

Fig. 4. A schematic version of the Ni-Al-S ternary isotherm at 700°C. Open circles correspond to values from binary phase diagrams. x corresponds to average composition of liquid sulfide in equilibrium with two different alloy compositions.

at 700°C (6). Electron probe microanalyses of two-phase ternary diffusion couples annealed at 700°C consisting of Al_2S_3, a Ni-rich alloy phase, Ni_3S_2, or NiS demonstrated that Al_2S_3 has negligible ternary phase extent. These experiments also showed that Al solubilities in Ni_3S_2 and NiS were of the order of 1 a/o. Compositional determinations of the Ni-Al-S liquid layers formed on the alloys were presented in our previous paper (4); they were used to estimate the ternary liquid-phase extent in the diagram.

Discussion

A sketch representing the morphologies of the sulfidation products on the alloys is shown in Fig. 5. During sulfidation, the external scale composed of NiS or Ni_3S_2 grew outward at velocity v_1 by metal diffusion. The subscale layers grew inward by sulfur migration: relative to the unreacted center of the specimen, the two lamellar phases Al_2S_3 (α) and Ni_3S_2 (β) penetrated into the liquid Ni-Al-S phase (l) at velocity v_2 and the liquid/alloy (γ) front propagated inward at velocity v_3. All layers grew at constant rates because of their coupling to growth of the external scale, which was confined to a constant rate by reaction steps at the scale/gas interface (4). The growth

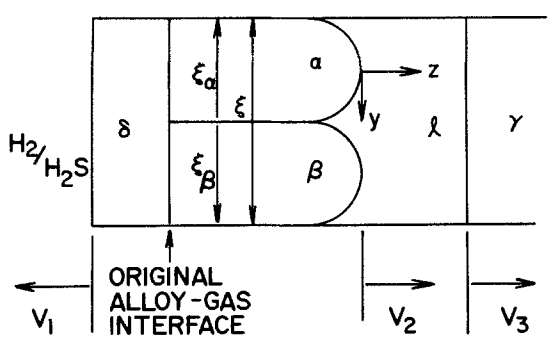

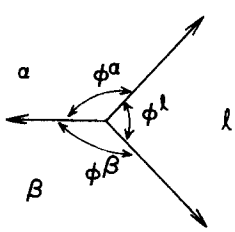

Fig. 5. A sketch of the cooperative internal sulfidation of the Ni-Al γ-solid solution alloys. v_1, v_2, v_3 refer to the velocities of the scale/gas, lamellar layer/liquid layer, and liquid/alloy interfaces, respectively. $\alpha \equiv Al_2S_3$, $\beta \equiv Ni_3S_2$, l $\equiv$ liquid and $\gamma \equiv$ Ni-Al alloy.

velocities of these layers and the spacing dimensions $\xi = \xi_\alpha + \xi_\beta$ of the lamellar layers are given in Table I.

Growth of Ni_3S_2 plates caused aluminum rejection into the liquid, and its lateral diffusion caused simultaneous growth of the Al_2S_3 plates. Consequently, steady-state propagation of the $Ni_3S_2 + Al_2S_3$ lamellar layers was attained by adjustment of the lamellar spacing, $\xi = \xi_\alpha + \xi_\beta$, such that the rate of aluminum enrichment in front of Ni_3S_2 was balanced exactly by its lateral flux to maintain the growth of Al_2S_3 plates. If local equilibrium prevails along the (α/l) and (β/l) interfaces, a relationship can be formulated for the dependence of lamellar spacing on the growth velocity. The approximate calculation of the spacing-velocity relationship by dimensional analysis outlined in the discussion is parallel to the approach developed by Zener (7) for eutectoid reaction in steels. A more accurate calculation of reactant fluxes after Hillert and co-workers (8, 9) incurs some loss of generality.

This mode of internal sulfidation involving precipitation of two sulfide compounds as lamellae from the ternary liquid can be readily interpreted by referring to the $\alpha + \beta + l$ three-phase region in Fig. 4 and by the expanded depiction in Fig. 6. The tip-composition of a Ni_3S_2 plate during its growth would correspond to a composition such as D', which lies on the metastable extension of the Ni_3S_2 phase boundary. Liquid composition at this lamellae front is given by point D on the metastable extension of the liquid-phase boundary. By this construction, Ni_3S_2 is in metastable equilibrium with liquid along the metastable tie-line $D'D$. In a similar fashion, the metastable composition of the liquid at the tips of Al_2S_3 is given by E, and E' is the metastable composition of Al_2S_3 plate tips. The driving chemical potentials for this cooperative type of lamellar growth are estimated from the concentration differences between points D and E. Thus, ΔC°_{Ni} and ΔC°_{Al} represent the enrichment of nickel and aluminum in the liquid in front of the Al_2S_3 and Ni_3S_2 plates, respectively. Curvatures of the plate tips due to capillarity causes the liquid-phase boundaries to move to reduce the supersaturations ΔC°_{Al} and ΔC°_{Ni}, as shown by the dotted lines in Fig. 6. These concentration differences disappear at a critical curvature of the lamellae. The front of solid sulfides then cannot advance into the liquid phase, because the solid lamellae of critical radii and interlamellar spacing exist in equilibrium with the ternary liquid.

These conclusions can be further clarified by referring to the phase diagram presentation in Fig. 7. Here, liquid compositions at the lamellar tips are given by the metastable extension of the ternary liquid to A and B. The metastable increase in aluminum composition is given by ΔC°_{Al}, which corresponds to a sulfur activity difference $a_S{}^B - a_S{}^E$. Thus, to a first approximation

$$\Delta C^\circ_{Al} = w(a_S{}^B - a_S{}^E) \qquad [1]$$

where w is a proportionality constant.

An expression can be obtained for the critical lamellar spacing ($\xi_c = \xi_\alpha + \xi_\beta$) to be found at equilibrium.

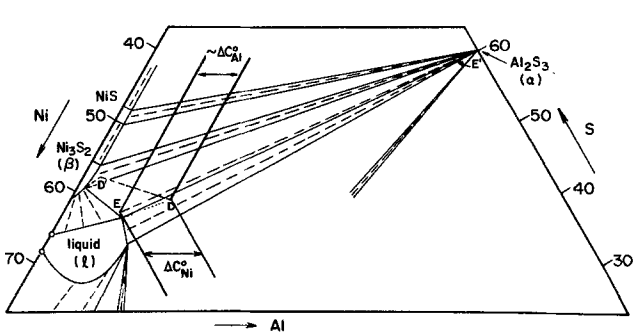

Fig. 6. Isolated view of α-β-l equilibrium region of Fig. 4

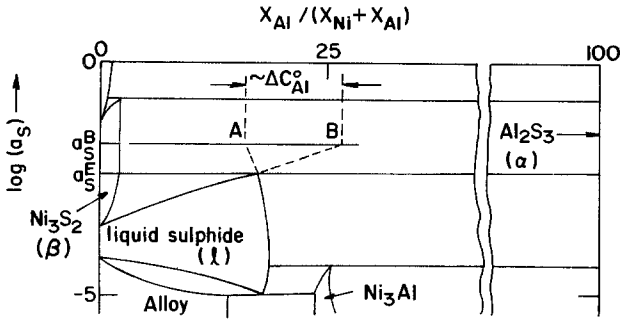

Fig. 7. Isolated view of α-β-l equilibrium region where the coordinates are the sulfur activity $(p_{S_2})^{1/2}$ and the metal molar fractions of the phases present in the system.

The free energy change for transforming unit volume of liquid to $\alpha + \beta$ at spacing ξ is

$$\Delta G_V(\xi) = \Delta G_V(\infty) + \frac{\sigma_{\alpha\beta}A_{\alpha\beta}}{V} \quad [2]$$

where $\Delta G_V(\xi)$ is a volume free energy change, $\sigma_{\alpha\beta}$ is the surface tension and $A_{\alpha\beta}/V$ is the area of α/β interface per unit volume, which is equal to $2/\xi$. $\Delta G_V(\infty)$ is the free energy change for formation of lamellae with a spacing so large that the second term in Eq. [2] is negligible. Thus, at equilibrium, $\Delta G_V(\xi_c) = 0$ and

$$\frac{1}{\xi_c} = \frac{-\Delta G_V(\infty)}{2\sigma_{\alpha\beta}} \quad [3]$$

Furthermore, $\Delta G_V(\xi)$ is a function of supersaturation $(a_S^B - a_S^E)$ and for small supersaturations

$$\Delta G_V(\infty) = w'(a_S^B - a_S^E) \quad [4]$$

Upon substitution of Eq. [4] into Eq. [3]

$$\frac{1}{\xi_c} = w''(a_S^B - a_S^E) \quad [5]$$

where w' and w'' are proportionality constants.

A relationship determining the lamellar spacing as a function of growth velocity is obtained by calculating the concentration difference between the tips of the lamellae, since the compositional gradient parallel to the growth front is predominately responsible for aluminum transport. The aluminum flux due to its rejection at the tip of Ni_3S_2 is $(C_{Al}^{\beta} - C(\infty)^l)v_2$ where C_{Al}^{β} and $C_{Al}(\infty)^l$ are the aluminum concentrations in the tips of Ni_3S_2 plates and in the liquid far away from the lamellar front, respectively. The lateral gradient of aluminum is given approximately by $\Delta C_{Al}/n\frac{\xi}{2}$ where n is a shape factor. Accordingly, steady-state diffusion is given by

$$v_2(C_{Al}^{B} - C_{Al}^{E}(\infty)) \simeq 2D_{Al}^{l}\Delta c_{Al}/n\xi \quad [6]$$

where D_{Al}^{l} is the aluminum diffusion coefficient of the liquid phase. ΔC_{Al}, which supports lateral aluminum diffusion, drops to zero as the curvature at the α/γ or β/γ interface is increased corresponding to a critical spacing ξ_c. Thus ΔC_{Al} can be described by an equation of the form

$$\Delta C_{Al} = \Delta C^{\circ}_{Al}\left(1 - \frac{\xi_c}{\xi}\right) \quad [7]$$

Substitution of [7] into [6] yields

$$v_2 = \frac{2D_{Al}^{l}\Delta C^{\circ}_{Al}}{n(C_{Al}^{\beta} - C_{Al}^{l}(\infty))\xi}\left(1 - \frac{\xi_c}{\xi}\right) \quad [8]$$

If one neglects volume change accompanying the formation of lamellae, conservation of aluminum requires

$$\xi_\alpha(C_{Al}^{l}(\infty) - C_{Al}^{\alpha}) = \xi_\beta(C_{Al}^{\beta} - C_{Al}^{l}(\infty)) = \frac{\xi_\alpha\xi_\beta}{\xi}(C_{Al}^{\beta} - C_{Al}^{\alpha}) \quad [9]$$

Upon combining [8] and [9]

$$v_2 = \frac{2D_{Al}^{l}\Delta C^{\circ}_{Al}}{n(C_{Al}^{\beta} - C_{Al}^{\alpha})}\cdot\frac{\xi_\beta}{\xi_\alpha}\cdot\frac{1}{\xi}\left(1 - \frac{\xi_c}{\xi}\right) \quad [10]$$

Equation [10] predicts two values of spacing for a given growth velocity. Investigators, accordingly, have removed this degree of freedom by assuming a variational principle to predict the actual spacing of ξ, such as optimization of the maximum growth rate (10, 11), maximum rate of decrease in free energy (12), or maximum rate of entropy production (13). These considerations predict that the steady-state spacing is a multiple of the critical spacing $\xi = \zeta\xi_c$ where ζ is a constant ranging from 2 to 3, dependent upon choice of the optimization principle. From Eq. [1], [2], and [10] with $\xi = \zeta\xi_c$, one obtains the following expression for the migration rate of the lamellar front

$$v_2\xi^2 = \frac{D_l(1 - \zeta)}{w''\zeta n(C_{Al}^{\beta} - C_{Al}^{\alpha})} = \text{constant} \quad [11]$$

Despite a lack of diffusion and thermodynamic results, it is possible to check the validity of the expression in Eq. [11] by two methods. According to Eq. [11], a plot of log ξ *vs.* log v_2 should be a linear plot of slope $-\frac{1}{2}$. This relationship is shown to be valid by the plot in Fig. 8 of results for the Ni-10 a/o Al alloys given in Table I. Evaluations of $v_2\xi^2$ are also given in Table I. A statistical t test (14) of these evaluations implies that the determined largest and smallest values of $v_2\xi^2$ are equal within the observed large variance and thus constant, as predicted by the theoretical analysis.

Summary

The sulfidation kinetics of Ni-rich Ni-Al γ-solid solution alloys in H_2S-H_2 atmospheres at 700°C exhibit a rate curve which is linear at long times. The corrosion product consists of three layers. The outer scale consists of NiS when $p_{S_2} > 10^{-4}$ atm. It consists of Ni_3S_2 otherwise. The scale/subscale boundary corresponds to the original alloy/gas interface. The scale

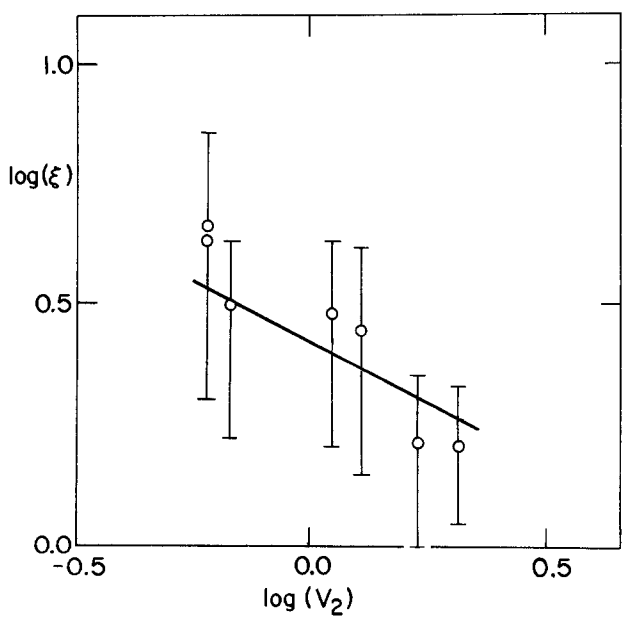

Fig. 8. Graphical verification of Eq. [11] using data for the Ni-10 Al alloy given in Table I. A straight line of slope −1/2 can be drawn through the data points.

grows by outward diffusion of nickel, and the subscale penetrates into the alloy by sulfur diffusion. A subscale layer in contact with the outer scale is composed of Ni_3S_2 + Al_2S_3 lamellae, and it propagates into the (Ni-Al-S) liquid layer in contact with the alloy.

It has been demonstrated, first, that the lamellar layer penetrates into the liquid layer by a mechanism of cooperative precipitation of Ni_3S_2 and Al_2S_3 plates and, second, that the constant propagation velocities of reaction product layers are dependent upon a rate controlling reaction step at the scale/gas interface in H_2S-H_2 atmospheres.

Acknowledgments

This research was carried out under the auspices of the Natural Sciences and Engineering Research Council of Canada. V. S. Bhide wishes to express his appreciation for awards of Noranda and Stelco Research Fellowships to carry out this research as part of his Ph.D. studies program at McMaster University. The authors are indebted to M. Hillert and G. R. Purdy for helpful discussions.

Manuscript submitted March 3, 1983; revised manuscript received July 7, 1983.

McMaster University assisted in meeting the publication costs of this article.

REFERENCES

1. D. J. Young, J. S. Kirkaldy, and W. W. Smeltzer, *This Journal*, **123**, 1758 (1976).
2. H. Hindam and W. W. Smeltzer, *ibid.*, **127**, 1622 (1980).
3. F. A. Elrefaie and W. W. Smeltzer, *Oxid. Met.*, **17**, 407, (1982).
4. V. S. Bhide and W. W. Smeltzer, *This Journal*, **128**, 902 (1981).
5. G. Romeo, W. W. Smeltzer, and J. S. Kirkaldy, *ibid.*, **118**, 841 (1971).
6. M. Hansen, "Constitution of Binary Alloys," McGraw Hill, New York (1958).
7. C. Zener, *Trans. A.I.M.E.*, **167**, 550 (1946).
8. M. Hillert, "The Mechanism of Phase Transformation in Crystalline Solids," p. 231, Institute of Metals, London (1969).
9. J. Fridberg and M. Hillert, *Acta Metall.*, **25**, 19 (1977).
10. W. H. Brandt, *J. Appl. Phys.*, **16**, 139 (1945).
11. W. H. Brandt, *Trans. A.I.M.E.*, **167**, 405 (1946).
12. J. W. Cahn, *Acta Metall.*, **7**, 18 (1959).
13. J. S. Kirkaldy, *Scr. Metall.*, **2**, 565 (1968).
14. A. J. Duncan, "Quality Control and Industrial Statistics," R. D. Irwin, Chicago (1952).

Solid Solution and Phase Transformation in the System ZnS-MnS under Hydrothermal Conditions

Shoji Kaneko, Hideo Aoki, Isao Nonaka, and Fumio Imoto

Department of Industrial Chemistry, Faculty of Engineering, Shizuoka University, Johoku, Hamamatsu 432, Japan

Koichi Matsumoto

Research Institute of Electronics, Shizuoka University, Johoku, Hamamatsu 432, Japan

ABSTRACT

The thermal behavior of the system ZnS-MnS was investigated under hydrothermal conditions. The solid solubility of MnS in ZnS was *ca.* 50 mole percent (m/o) almost independent of temperature, whereas ZnS was not dissolved into MnS at all. The transformation temperature of zinc blende (ZB) to wurtzite (WZ) in ZnS was largely lowered by the formation of the solid solution with MnS in addition to the hydrothermal effect. The phase transformations of MnS were also accelerated by means of the hydrothermal treatment; the transformation temperatures of ZB type to WZ type and WZ type to rock-salt type were lowered by more than 50°C and *ca.* 125°C, respectively, compared with those in the dry process.

Cu- or Ag-activated ZnS has been used as blue or green phosphors for television tubes and electroluminescent panels, and Mn-activated ZnS as yellow or orange phosphors. ZnS has two crystal structures, the cubic zinc-blende and hexagonal wurtzite types. The former is stable below 1020°C and the latter above that temperature (1). However, this transformation is diversely affected by the addition of copper, silver, etc., and the luminescent properties of the dimorphs differ from one another (2-9).

The phase transformation and/or solid solution in the system ZnS-MnS have to some extent been investigated in the various preparation methods of coprecipitation (10, 11), chemical transport (12), and solid-state reaction in He (9) or with KCl (13).

In the previous papers dealing with the reactions of oxides under hydrothermal conditions (14-16), it was shown that the crystallization, phase transformation, and synthesis of different materials were achieved at considerably lower temperatures compared with the dry process in air ("hydrothermal effect" attributed to pressure and dissolving power). We have also reported that the cubic-hexagonal transformation and crystallization of CdS, an isomorph of ZnS, was markedly enhanced through the hydrothermal treatment (17). Thus, a hydrothermal reaction seems to be suitable for the preparation of useful inorganic powders containing a volatile component. The purpose of the present work is to explain the solid solution and phase transformation in the system ZnS-MnS caused under hydrothermal conditions, as compared with a dry process.

Key words: inorganic, crystallography, solubility.

Experimental

Zinc sulfide powder of luminescent grade (Dai Nippon Painting Company, Limited) was used as a starting material. MnS powder was obtained as follows: the precipitate formed by bubbling H_2S into $Mn(CH_3COO)_2$ solution was washed by decantation with H_2S-saturated water and was filtered, followed by further washing with ethyl alcohol and ethyl ether. Then it was evaporated to dryness *in vacuo* at room

temperature. After mixing the two powders with methyl alcohol, the mixture was dried in an oven, and then was sealed together with a proper amount of water in a test-tube type autoclave (*ca.* 8 cm^3 volume). The autoclave was heated in an electric furnace controlled with an electronic temperature controller. The experimental conditions were as follows: molar ratios of the mixture over the entire range (0.1 interval), temperatures 500° and 600°C, pressure 500 atm [water charge was determined according to the Kennedy's method (18)], time 24 hr. After the treatment, the autoclave was instantly taken out from the furnace and promptly quenched in ice water. A dry process was also carried out by using the same autoclave without water.

The phase change and the solid solution were confirmed from x-ray diffraction patterns by using a Rigaku Geigerflex Model D-2 with Ni-filtered CuKα radiation. Highly pure Si was used as an internal standard.

Results and Discussion

Polymorphism of MnS.—Manganese sulfide prepared from $Mn(CH_3COO)_2$ showed the zinc-blende type structure (ZB) at the beginning. MnS also exists in the wurtzite type (WZ) and rock-salt type (RS) structures (19). However, the temperature ranges in which the three types of MnS are stable have not been established as yet. We investigated first the phase transformation of MnS in both dry and hydrothermal processes; as-prepared MnS was heat-treated at temperatures from 200° to 600°C for 2 hr or was treated hydrothermally at 150°-600°C, 500 atm, and for 24 hr. The determination of the crystal structure was by x-ray diffractometry. Figure 1 shows the representative x-ray diffraction patterns of MnS in the present work. Only WZ was detected just below 200°C, WZ and RS between 200° and 400°C, and RS alone at 400°C or above in the dry process. On the other hand, in the hydrothermal process only WZ was detected below 150°C, WZ and RS between 150° and 250°C, and RS alone at 250°C or above. Accordingly, the differences of the two phase-transformation temperatures in both processes were more than 50°C for ZB to WZ and *ca.* 125°C for WZ to RS, respectively. In addition, the samples which were hydrothermally treated all showed higher crystallinity than those heat-treated at the same temperatures in the dry process. These results are similar to those of CdS (17).

Solid solution and phase transformation in the system ZnS-MnS.—The crystal structure of as-received ZnS was zinc blende (ZB). The mixtures of ZnS and MnS of various molar ratios were hydrothermally treated at 500° or 600°C, 500 atm, and 24 hr. The crystalline phases appearing depended on the molar ratio of the mixture, as shown in Table I. In the hydrothermal treatment at 500°C, ZB-ZnS solid solution (ss) was only formed at the molar ratio of 8:2 and above. At this ratio the formation of WZ-ZnS ss was also found. Only the second solid solution was present between 7:3 and 5:5, and between 4:6 and 1:9 WZ-ZnS ss

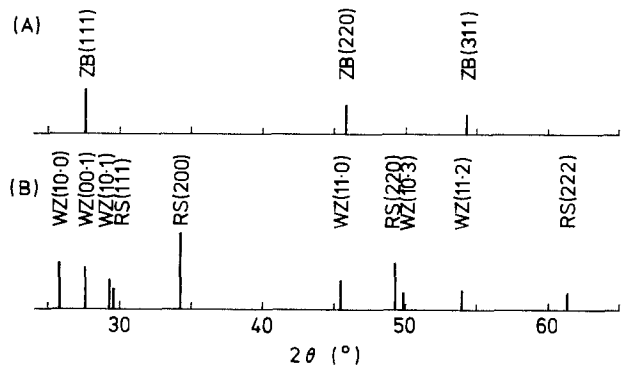

Fig. 1. The representative x-ray diffraction patterns of MnS. (A) As-received, (B) treated hydrothermally at 175°C.

appeared together with RS-MnS, which did not form any solid solution with ZnS. It is noteworthy that on account of the solution of more than 10 m/o MnS zinc blende transformed to wurtzite even at 500°C. This is much lower than 1020°C for ZnS in the dry process (1) and 860°-880°C in the growth of single crystals of the system ZnS-MnS (12). Hydrothermal treatment at 600°C further enhanced the phase transformation of ZB to WZ in ZnS ss. The formation of WZ-ZnS ss was found at the molar ratio of 9:1, and the solubility of this solid solution increased slightly with an increase in temperature. The hydrothermal treatment was compared with the normal heat-treatment at the same temperature of 600°C, and the amount of MnS dissolved into WZ-ZnS was increased by *ca.* 10 m/o.

The lattice constants of these solid solutions described above were calculated from the diffraction angles with Cohen's least squares method (20) (Fig. 2). The lattice constant (a) of ZB-ZnS ss increased in proportion to MnS content up to 10 m/o, and those (a and c) of WZ-ZnS ss also increased to *ca.* 50 m/o. On the other hand, the lattice constant (a) of MnS did not vary in the molar ratios between 5:5 and 0:10, implying that this compound did not form any solid solution with ZnS. This is in agreement with the results reported by Sato *et al.* (9) and Kröger (13) that the formation of solid solutions in the system ZnS-MnS is limited to the ZnS phase. Cook (21) reported in the system CdS-MnS that the solubilities of MnS into CdS and of CdS into MnS were 49 and 11.5 m/o, respectively, at 800°C in the dry process. The difference in these two solubilities was explained in terms of the differences of the ionic radii and electronic structures of Cd(II) and Mn(II) by Wiedemeier *et al.* (22), who also reported 50 and 13.5 m/o at the same conditions, respectively. Although the solid solubility of CdS in MnS was greater than 10 m/o, ZnS was not dissolved at all. This finding may be related to the fact that CdS has the same rock-salt structure as MnS under high pressures (23), while ZnS does not. From a simple hard sphere model, for an ionic crystal to be

Table I. The crystalline phases found in the system ZnS-MnS

Molar ratio (ZnS:MnS)	Hydrothermal treatment at 500°C	Hydrothermal treatment at 600°C	Heat-treatment at 600°C
10:0	ZB-ZnS	ZB-ZnS	ZB-ZnS
9:1	ZB-ZnS ss*	ZB-ZnS ss + WZ-ZnS ss	ZB-ZnS ss + WZ-ZnS ss
8:2	ZB-ZnS ss + WZ-ZnS ss	WZ-ZnS ss	WZ-ZnS ss
7:3	WZ-ZnS ss	WZ-ZnS ss	WZ-ZnS ss
6:4	WZ-ZnS ss	WZ-ZnS ss	WZ-ZnS ss + RS-MnS
5:5	WZ-ZnS ss + RS-MnS	WZ-ZnS ss + RS-MnS	WZ-ZnS ss + RS-MnS
4:6	WZ-ZnS ss + RS-MnS	WZ-ZnS ss + RS-MnS	WZ-ZnS ss + RS-MnS
3:7	WZ-ZnS ss + RS-MnS	WZ-ZnS ss + RS-MnS	WZ-ZnS ss + RS-MnS
2:8	WZ-ZnS ss + RS-MnS	WZ-ZnS ss + RS-MnS	WZ-ZnS ss + RS-MnS
1:9	WZ-ZnS ss + RS-MnS	WZ-ZnS ss + RS-MnS	WZ-ZnS ss + RS-MnS
0:10	RS-MnS	RS-MnS	RS-MnS

* ss: solid solution.

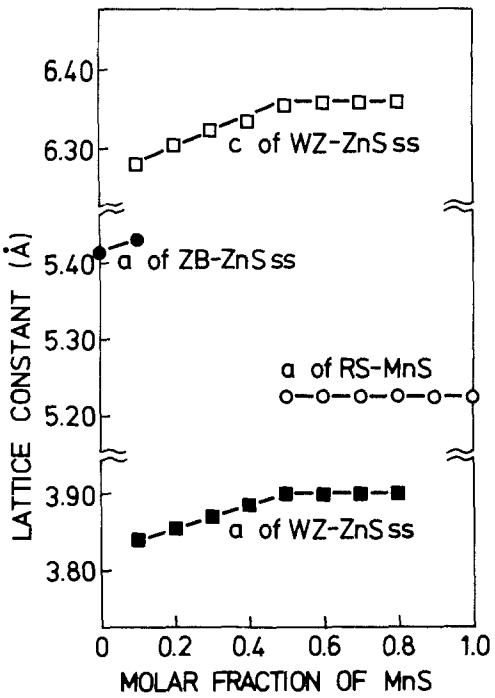

Fig. 2. The relationship between the lattice constants and the molar ratios in the compounds of the system ZnS-MnS treated hydrothermally at 600°C.

stable as an octahedrally coordinated rock-salt structure, it is necessary that the radius ratio of a cation to an anion lie between 0.414 and 0.732 (23). The Zn/S ratio is 0.40 in contrast to 0.53 for Cd/S (24), and on this basis it is less likely to show the rock-salt structure and be dissolved into MnS (radius ratio = 0.43). MnS is considered to be dissolved into ZnS to a certain extent because they have the same structure and the radii are similar.

Summary

The phase transformation temperatures of ZB type to WZ type and WZ type to RS type in MnS under hydrothermal conditions were lowered by more than 50°C and *ca.* 125°C, respectively, compared with those in the dry process. The crystallinity of the samples which were hydrothermally treated was higher than those heat-treated at the same temperatures in the dry process. The phase-transformation temperature of ZB to WZ in ZnS was lowered by the formation of solid solution with MnS and hydrothermal treatment. The solid solubility of MnS into ZnS was *ca.* 50 m/o almost without temperature dependence, whereas ZnS was not incorporated into MnS at all.

Manuscript submitted Dec. 10, 1982; revised manuscript received March 22, 1983.

REFERENCES

1. F. A. Kröger, *Z. Kristallogr.*, **120,** 136 (1939).
2. M. Aven and J. A. Parodi, *J. Phys. Chem. Solids,* **13,** 56 (1960).
3. J. Nickerson, P. Goldberg, and D. H. Baird, *This Journal,* **110,** 1228 (1963).
4. H. Gobrecht, H. Nelkowski, J. W. Baars, and G. Brandt, in "Proc. of the Inter. Conf. on Luminescence 1966," G. Szigeti, Editor, p. 1086, Akádemiai Kiadó, Budapest (1968).
5. G. Gashurov and E. Banks, *This Journal,* **114,** 1143 (1967).
6. K. Takagi and Y. Onoda, *Bull. Res. Inst. Electronics, Shizuoka Univ.,* **2,** 89 (1967).
7. T. Bansagi. E. A. Secco, O. K. Srivastava, and R. R. Martin, *Can. J. Chem.,* **46,** 2881 (1968).
8. M. Sakaguchi, M. Ohta, M. Satoh, and T. Hirabayashi, *This Journal,* **124,** 550 (1977).
9. M. Sato and M. Sakaguchi, *Denki Kagaku,* **47,** 544 (1979).
10. H. Schnaase, *Z. Phys. Chem.,* **B20,** 89 (1933).
11. R. Juza. A. Rabenau, and G. Pascher, *Z. Anorg. Allg. Chem.,* **286,** 61 (1956).
12. R. Nitsche. H. U. Bölsterli, and M. Lichtensteiger, *J. Phys. Chem. Solids,* **21,** 199 (1961).
13. F. A. Kröger, *Z. Kristallogr.,* **100,** 543 (1939).
14. F. Imoto and S. Kaneko, *Kogyo Kagaku Zasshi,* **74,** 591 (1971).
15. S. Kaneko and F. Imoto, *Nippon Kagaku Kaishi,* **1975,** 985.
16. S. Kaneko and F. Imoto, *Bull. Chem. Soc. Jpn.,* **51,** 1739 (1978).
17. S. Kaneko, K. Matsumoto, T. Sugiyama, and F. Imoto, in "Abstr. Inter. Symp. Hydrothermal Reactions," No. 68, Yokohama. Japan (1982).
18. G. C. Kennedy, *Am. J. Sci.,* **248,** 540 (1950).
19. R. D. W. Kemmitt, in "Comprehensive Inorganic Chemistry," Vol. 3, J. C. Bailar, Jr., *et al.*, Editors, p. 813, Pergamon Press, Oxford (1973).
20. H. P. Klug and L. E. Alexander, "X-ray Diffraction Procedures for Polycrystalline and Amorphous Materials," 2nd ed., p. 597, John Wiley & Sons, Inc., New York (1974).
21. W. R. Cook, Jr., *J. Am. Ceram. Soc.,* **51,** 518 (1968).
22. H. Wiedemeier and A. Khan, *Trans. Metal. Soc. AIME,* **242,** 1969 (1968).
23. W. L. Roth, in "Physics and Chemistry of II-VI Compounds," M. Aven and J. S. Prener, Editors, p. 134, North-Holland Publishing Co., Amsterdam (1967).
24. L. Pauling, "The Nature of the Chemical Bond," 3rd ed., p. 514 and p. 518, Cornell University Press, Ithaca, NY (1960).

Thermodynamic Properties of Na Ions in β- and β''-Al_2O_3 Through Thermoelectric Power Data

Alberto Schiraldi, Primo Baldini, and Paola Rossi

Istituto di Chimica Fisica e di Elettrochimica dell'Università di Pavia, 27100 Pavia, Italy

ABSTRACT

Thermoelectric power determinations allow one to evaluate some thermodynamic properties of ionic mobile species of solid electrolytes, provided that suitable reversible electrodes are employed in assembling the thermocell (1). The experimental data reported in literature (2) for β- and β''-Al_2O_3 have been employed here to evaluate the partial pressure of Na(v) in equilibrium with these solid electrolytes in the T ranges 300-500 K and 340-580 K, respectively, and the Na entropy difference between β- and β''-Al_2O_3 in the T range 340-500 K. The latter depends on T in such a way as to suggest that a second order transition would occur in β''-Al_2O_3 at about 450 K.

In a previous paper (1), we showed that determinations of the thermoelectric power of solid electrolytes should primarily concern the thermodynamic properties of the mobile species instead of its heat of transport, since, for such materials, the latter may be safely identified with the conductivity activation energy.

Here we show the results of such an approach to β- and β''-Al_2O_3 on the ground of the experimental results reported in a recent paper by Kuwamoto and Sato (2).

These authors followed the "traditional" way (3) of fitting the thermopower, ϵ, *vs.* $1/T$ with a straight line and of comparing the slope, viz., the so-called heat of transport, Q, with the value of the conductivity activation energy, E, reported in the literature.

Apart from the general objections to this procedure (1), the above comparison between Q and E is somewhat ambiguous in the case of β''-Al_2O_3, which has a non-Arrhenian conductivity.

Nevertheless, the paper by Kuwamoto and Sato is extremely interesting because of the proper choice of the thermocell electrodes, prepared with Na_2O and thence able to exchange Na ions at the interface with the solid electrolyte.

This peculiar feature gives the theoretical ground to the present work, where the Na vapor partial pressure, in equilibrium with β- and β''-Al_2O_3, and the entropy of Na ions in these solid electrolytes have been evaluated.

General Considerations

Due to the proper electrode-electrolyte pair, the thermoelectric power of the thermocell

$$Na_2O \,/\, \underset{T}{\beta\text{-}Al_2O_3} \,/\, \underset{T+\Delta T}{Na_2O}$$

may be described through the expression (4)

$$F\epsilon = S(Na, Na_2O) - S(Na, \beta\text{-}Al_2O_3) - Q_{Na}/T \quad [1]$$

where $F\epsilon$ is the thermopower expressed in entropic units, $S(Na, Na_2O)$ and $S(Na, \beta\text{-}Al_2O_3)$ are the partial ionic entropies of the Na ions in Na_2O and in β-Al_2O_3, respectively, and Q_{Na} is the heat of transport of the Na ions in the electrolyte. Analogous expression holds for the thermopower of β''-Al_2O_3, ϵ''.

Accordingly

$$F(\epsilon - \epsilon'') = S(Na, \beta''\text{-}Al_2O_3) - S(Na, \beta\text{-}Al_2O_3) - \frac{Q_{Na} - Q_{Na}''}{T} \quad [2]$$

and with the assumption [1]

$$Q_{Na} = E \quad \text{and} \quad Q_{Na}'' = E''$$

where E and E'' are the corresponding conductivity activation energies

$$F(\epsilon - \epsilon'') + \frac{E - E''}{T} = S(Na, \beta''\text{-}Al_2O_3) - S(Na, \beta\text{-}Al_2O_3) \quad [3]$$

Furthermore, if one puts [1]

$$S(Na, \beta\text{-}Al_2O_3) = S(Na, \beta\text{-}Al_2O_3, vib) + S(Na, \beta\text{-}Al_2O_3, conf)$$

i.e., splits the ionic entropy into vibrational and configurational contributions, and[1]

$$S(Na, \beta\text{-}Al_2O_3, vib) \simeq S(Na, \beta''\text{-}Al_2O_3, vib) \simeq S(Na, Na_2O, vib)$$

Eq. [1] gives

$$F\epsilon + \frac{E}{T} = R \ln \frac{P(Na, \beta\text{-}Al_2O_3)}{P(Na, Na_2O)} + RT \frac{d}{dT}\left[\ln \frac{P(Na, \beta\text{-}Al_2O_3)}{P(Na, Na_2O)}\right] \quad [4]$$

and Eq. [2] gives

$$F(\epsilon - \epsilon'') + \frac{E - E''}{T} = R \ln \frac{P(Na, \beta\text{-}Al_2O_3)}{P(Na, \beta''\text{-}Al_2O_3)} + RT \frac{d}{dT}\left[\ln \frac{P(Na, \beta\text{-})}{P(Na, \beta''\text{-})}\right] \quad [5]$$

where Na activity (entering the configurational entropy terms) has been replaced by the corresponding fugacity (symbol P) in the ratios under "ln" and R is the gas constant.

In the present case, fugacities may be safely identified with the corresponding partial pressure of Na vapor in equilibrium with the electrolyte.

Results and Discussion

Thermopower data by Kuwamoto and Sato (2) have been fitted as

$$F\epsilon = -\frac{23{,}100}{T} + 69.01 - 5.52\ 10^{-2}T \text{ J mol}^{-1} \text{ K}^{-1} \quad (300 < T < 500)$$

$$F\epsilon'' = -\frac{8172}{T} - 13.21 - 5.06\ 10^{-2}T \text{ mol}^{-1} \text{ K}^{-1} \quad (340 < T < 580)$$

The heats of transport employed are

$$Q_{Na} = 15{,}800 \text{ J mol}^{-1} \quad (5)$$

$$Q_{Na}'' = 40{,}638 - 110T + 9.11\ 10^{-2}T^2 \text{ J mol}^{-1}$$

[1] This assumption may not be exhaustively justified; however, it does not seem unreasonable. The overall degrees of freedom expected per single Na ion in beta alumina should be, in average, three or quite close to three in the T range considered here; in fact, these ions, although forced into a layered structure, do not move or oscillate independently of one another.

[from data of Ref. (6)]. Data concerning β-Al_2O_3 give

$$\frac{1}{2.3R}\left(F\epsilon + \frac{E}{T}\right) = \frac{-382}{T} + 3.61 - 2.88\ 10^{-3}T \quad [6]$$

which may be safely replaced by the mean constant value 1.48 throughout the T range considered here. The dependence of the vapor partial pressure *vs.* T is expected to be of the usual form[2]

$$\log P_i = \alpha_i/T + \gamma_i$$

so that

$$\log P_i + T\frac{d}{dT}(\log P_i) = \gamma_i = \text{constant}$$

Accordingly, from Eq. [4] through Eq. [6] one has

$$\log \frac{P(\text{Na}, \beta\text{-}Al_2O_3)}{P(\text{Na}, Na_2O)} + T\frac{d}{dT}\left[\log \frac{P(\text{Na}, \beta\text{-}Al_2O_3)}{P(\text{Na}, Na_2O)}\right] = \gamma(\text{Na}, \beta\text{-}Al_2O_3) - \gamma(\text{Na}, Na_2O) \simeq 1.48$$

$\gamma(\text{Na}, Na_2O)$ may be easily evaluated from literature data (7, 8) which allows one to recognize that

$$\log P(\text{Na}, Na_2O) = -\frac{15{,}700}{T} + 7.87 \quad [7]$$

(P is in atm); thence

$$\gamma(\text{Na}, \beta\text{-}Al_2O_3) = 9.35$$

To obtain an expression for $\log P(\text{Na}, \beta\text{-}Al_2O_3)$ it is necessary to know either the Na enthalpy variation accompanying the equilibrium $\text{Na}(\beta\text{-}Al_2O_3) \rightleftharpoons \text{Na}(Na_2O)$, or the temperature at which $P(\text{Na}, \beta\text{-}Al_2O_3)$ assumes a given value.

Literature data (7-9) allows one to establish that $P(\text{Na}, \beta\text{-}Al_2O_3) = 1$ atm somewhere within the T range 2400-2500 K. With this uncertainty one has

$$\log P(\text{Na}, \beta\text{-}Al_2O_3) = -\frac{23{,}000}{T} + 9.35 \quad [8]$$

which is in reasonable agreement with previous evaluations of the partial pressure of Na vapor in equilibrium with β-Al_2O_3 at higher temperatures (9, 10). Figure 1 allows us to realize this comparison.

Data concerning β''-Al_2O_3 give

$$\frac{1}{2.3R}\left(F\epsilon'' + \frac{E''}{T}\right) = \frac{1697}{T} - 6.44 + 7.40\ 10^{-3}T \quad [9]$$

Equation [9] may not be approximated to any mean constant value; however, the results obtained for β-Al_2O_3 may be employed to attain, also in this case, an expression for the partial pressure of Na vapor in equilibrium with β''-Al_2O_3.

Integration of Eq. [3] between $T_0 = 340$ K (the lowest T considered here) and T gives

$$\log\left[\frac{P(\text{Na}, \beta''\text{-}Al_2O_3)}{P(\text{Na}, \beta\text{-}Al_2O_3)}\right]_T - \log\left[\frac{P(\text{Na}, \beta''\text{-}Al_2O_3)}{P(\text{Na}, \beta\text{-}Al_2O_3)}\right]_{T_0} = \log\frac{P(\text{Na}, \beta''\text{-}Al_2O_3)_T}{P(\text{Na}, \beta''\text{-}Al_2O_3)_{T_0}} - \log\frac{P(\text{Na}, \beta\text{-}Al_2O_3)_T}{P(\text{Na}, \beta\text{-}Al_2O_3)_{T_0}} = -1697\frac{\ln T}{T} - 3.7\ 10^{-3}T - 14.51$$

which allows

$$T\frac{d}{dT}[\log P(\text{Na}, \beta''\text{-}Al_2O_3)] = \frac{23{,}000 + 1697(\ln T - 1)}{T} - 3.7\ 10^{-3}T \simeq 0.614 + \frac{30{,}167}{T}$$

[2] α_i = evaporation enthalpy/gas constant
γ_i = integration constant of the Clausius Clapeyron equation.

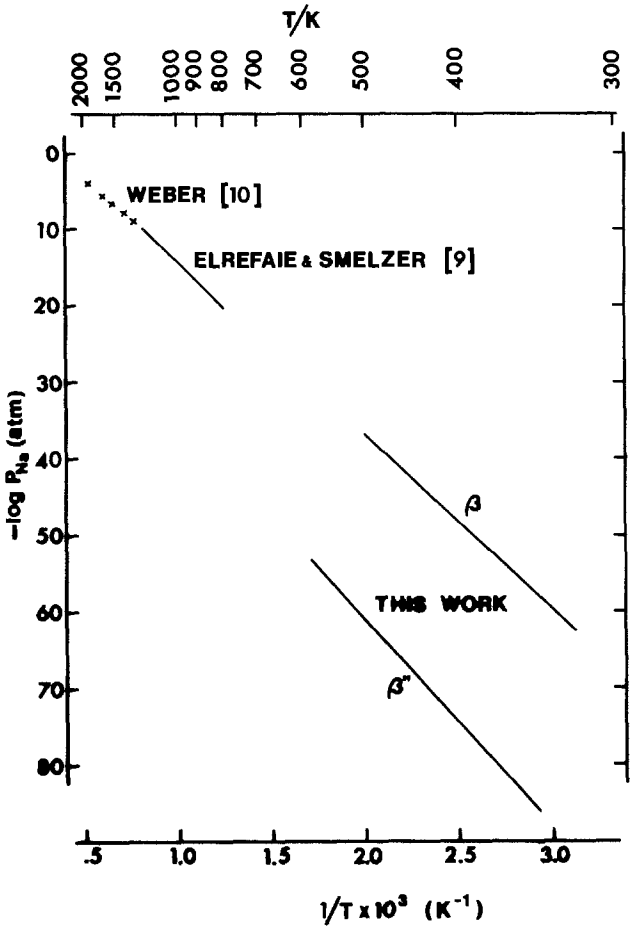

Fig. 1. Partial pressure of Na vapor in equilibrium with β-Al_2O_3 and β''-Al_2O_3 at $P(O_2) = 0.21$ atm.

and

$$\log P(\text{Na}, \beta''\text{-}Al_2O_3) = \gamma(\text{Na}, \beta''\text{-}Al_2O_3) - 0.614 - \frac{30{,}167}{T}$$

$\gamma(\text{Na}, \beta''\text{-}Al_2O_3)$ has been evaluated by adding $\gamma(\text{Na}, Na_2O)$, viz., 7.87, to Eq. [9]; thus

$$\log P(\text{Na}, \beta''\text{-}Al_2O_3) = -\frac{27{,}430}{T} - 5.95 \quad [10]$$

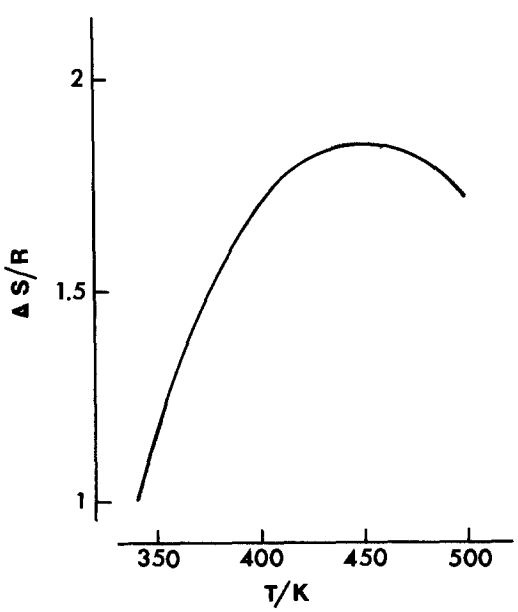

Fig. 2. Na entropy difference between β''- and β-Al_2O_3, as obtained from thermoelectric power data at various T.

where the linearization *vs.* $1/T$ is supported by a correlating factor undistinguishable from unity. The corresponding plot is reported in Fig. 1 to allow the comparison with β-Al_2O_3.

Both series of data allow employing Eq. [3] to evaluate $S(Na, \beta''\text{-}Al_2O_3) - S(Na, \beta\text{-}Al_2O_3) = \Delta S$ in the range 300-500 K (see Fig. 2).

Any comment about the trend of ΔS *vs.* T is strongly limited by the small extension of the T range considered. However, (*i*) the fact that $\Delta S > 0$ might correspond to a larger configurational entropy of the Na ions in β''-Al_2O_3; (*ii*) the fact that ΔS shows a maximum about 450 K might suggest that the state of the Na ions in β''-Al_2O_3 undergoes a modification at about this temperature; (*iii*) due to the satisfactory linearity found for both plots log $P(Na)$ *vs.* $1/T$, such a modification would occur without any heat delivery, thence looking like a second order transition (11, 12).

Manuscript submitted June 14, 1982; revised manuscript received Jan. 18, 1983.

Departimento di Chimica Fisica dell' Universita di Pavia assisted in meeting the publication costs of this article.

REFERENCES

1. A. Schiraldi, E. Pezzati, and P. Rossi, To be published.
2. H. Kuwamoto and H. Sato, *Solid State Ionics*, **5**, 187 (1981).
3. K. Shahi, *Phys. Status Solidi A*, **41**, 11 (1977).
4. K. Pitzer, *J. Phys. Chem.*, **65**, 147 (1961).
5. M. S. Whittingam and R. A. Huggins, *J. Chem. Phys.*, **54**, 414 (1971).
6. B. Dunn, R. M. Ostrom, R. Seevers, and G. C. Farrington, *Solid State Ionics*, **5**, 203 (1981).
7. G. B. Alcock and G. P. Stavropoulos, *Can. Met. Quart.*, **10**, 257 (1971).
8. JANAF, Thermochemical Tables, 2nd ed. (1971).
9. F. A. Elrefaie and W. W. Smeltzer, *This Journal*, **128**, 1443 (1981).
10. J. T. Kummer, *Prog. Solid State Chem.*, **7**, 141 (1972).
11. J. L. Briant and G. C. Farrington, *J. Solid State Chem.*, **33**, 385 (1980).
12. W. L. Roth, R. E. Benenson, V. K. Tikku, J. L. Briant, and B. Dunn, *Solid State Ionics*, **5**, 163 (1981).

Concentration Profile of Cu^{2+} Ion near a Plane Vertical Cathode in Electrolytes Containing $CuSO_4$ and an Excess of H_2SO_4 as a Supporting Electrolyte

Y. Fukunaka, K. Denpo, M. Iwata, K. Maruoka, and Y. Kondo*

Department of Metallurgy, Kyoto University, Sakyo-ku, Kyoto 606 Japan

ABSTRACT

The concentration profile of Cu^{2+} ion was measured near a plane vertical cathode placed in aqueous solution containing $CuSO_4$ and an excess of H_2SO_4 as a supporting electrolyte. It is known that the absorption bands of cupric ion near the infrared region and hydrogen ion in the ultraviolet region are widely separated. The distribution of absorbance of electrolyte at a wavelength of about 800 nm was measured near the cathode surface by an image sensor with a resolution power of 4.4 μm. The experimental results coincided well with the theoretical calculation. Under the presumption of an excess of supporting electrolyte and a uniform distribution of current density, a factor

$$f \equiv \left(\frac{\alpha_1 - \gamma\sigma^2\alpha_2}{\alpha_1'}\right)\left(\frac{1 - {}^*t_1}{1 - {}^*t_1'}\right)\Big/\left(\frac{k_1}{k_1'}\right)^2\left(\frac{\nu}{\nu'}\right) = \frac{Ra_x^*}{Ra_x^{*\prime}}$$

was proposed to explain the effect of migration due to the accumulated H^+ ion, and the variation of transport properties, on the natural convection along the cathode surface. This factor can be used for the conversion of correlations established in aqueous $CuSO_4$ solution to the correlations in $CuSO_4$-H_2SO_4 solution, as long as the similarity of velocity and concentration profiles is maintained in these solutions. The usefulness of this factor is demonstrated in the prediction of the interfacial concentration differences of Cu^{2+} and H^+ ions.

Numerous works (1-6) have been published on the ionic mass transfer associated with natural convection along a plane vertical cathode installed in an unstirred $CuSO_4$-H_2SO_4 electrolyte. The essential interest in the present study is to understand the effects of the supporting electrolyte on the rate of mass transfer of Cu^{2+} ion toward the cathode surface. Much effort has been concentrated to estimate the effects of supporting electrolyte on natural convection (1-4). The most conventional experimental technique was to employ the limiting current density where virtually zero concentration of the reacting cation is realized on the cathode surface (1-3).

Wagner (1) proposed a procedure to estimate the limiting current density in the presence of an excess of supporting electrolyte from the transport equations of ions and the equation of electroneutrality. The von Kármán-Pohlhausen integral method was applied, and the ratio of thickness of diffusion layers of H^+ ion and Cu^{2+} ion was obtained. The dependence of limiting current density on the vertical distance from the leading edge of cathode and on the bulk concentration of Cu^{2+} ion was clarified. The experimental result obtained with 0.1M $CuSO_4$-1.0M H_2SO_4 aqueous solution was in good agreement with the calculated distribution of the limiting current density.

Wilke *et al.* (2) studied the limiting current density in 0.01-0.74M $CuSO_4$ and 1.38-1.57M H_2SO_4 aqueous solutions. Under the experimental condition of relatively low cupric ion concentration, they assumed that the effective diffusivity of cupric ion was equal to that of $CuSO_4$, since sulfate ion was the only anion present and hydrogen and sulfate ions were to diffuse as sulfuric acid. They applied directly the analogy with heat transfer under the condition of constant wall temperature to this ionic transport phenomenon, assuming that the ratio of mass transfer coefficients of $CuSO_4$

* Electrochemical Society Active Member.
Key words: mass transfer, natural convection, effect of supporting electrolyte, image sensor, absorption distribution.

to H_2SO_4 is equal to the ¾th power of the ratio of the diffusivities. A very good correlation was shown between Sh and Ra numbers.

Newman (3), on the other hand, derived ionic transport equations for the dilute solution and solved them with a technique of similarity transformation. Ionic diffusivities were estimated from the limiting ionic mobilities at infinite dilution. He pointed out that migration could affect the resultant velocity profile of natural convection through the induced change in the density profile, and that the direct application of the heat transfer analogy to ionic transport in electrolytes containing H_2SO_4 could introduce an appreciable error in the estimation of the limiting current density.

Ibl *et al.* (4) studied natural convection for a condition of uniform distribution of current density in the vertical direction over the cathode surface, which is realized below current densities less than half of the limiting value. Using procedure similar to Wagner's (1), they calculated the ratio of the thickness of boundary layers of nonreactive hydrogen ion to reactive cupric ion and the interfacial concentration of both ions for various values of hydrogen transference number. They compared their calculations with the experimental results obtained by Brenner (7).

A holographic interferometry technique was introduced by Awakura *et al.* (5) to measure the profile of refractive index near the cathode surface. They reported that at lower current densities the difference of refractive index between the cathode surface and bulk electrolyte is proportional to the 4/5th power of the current density and to the 1/5th power of the vertical distance from the leading edge of natural convection. At the limiting current density they obtained the concentration difference of H_2SO_4 between cathode surface and the bulk electrolyte. They also measured the velocity profile of natural convection in an electrolyte of 0.6M $CuSO_4$-1.5M H_2SO_4 and found that the upward natural convection is depressed by the accumulated H^+ ion near the cathode surface (6). As mentioned above, the previous studies have been made to estimate the interfacial concentration of Cu^{2+} and H^+ ions, but insufficient experimental data exist to prove the theory, except for Brenner's data (7), which were obtained by freezing the electrolyte near a cylindrical cathode surface.

An experimental technique of measuring the concentration profile of cupric ion by using an image sensor is proposed in the present work. Based on the experimental results, a brief discussion is made on the effect of migration on the driving force of cathodic natural convection and on a prediction of the rate of ionic mass transfer in electrolytes containing $CuSO_4$ and an excess of H_2SO_4 under the condition of uniform current-density distribution.

Mathematical Formulation of Ionic Transfer Associated with Natural Convection

Electrochemical equations.—The ionic flux of species i toward the cathode surface in a dilute electrolyte is expressed as

$$\frac{dn_i}{dt} = \frac{s_i \cdot i}{\mathbf{F}} = k_i\left(\frac{\partial c_i}{\partial y}\right)_{y=0} + \left(\frac{k_i}{RT}\right) z_i \mathbf{F}\left(c_i \frac{\partial \psi}{\partial y}\right)_{y=0} \quad [1]$$

where s_i denotes the number of mols of ion i consumed in the cathodic reaction per unit Faraday (1). Combining these expressions for each ion by using the electroneutrality principle of

$$\Sigma z_i c_i = 0 \quad [2]$$

to eliminate an expression of the potential gradient, we have the concentration gradient of species j at the cathode surface as

$$\left(\frac{\partial c_j}{\partial y}\right)_{y=0} = \frac{i}{\mathbf{F}}\left[\frac{s_j}{k_j} - z_j c_j \frac{\Sigma(z_i s_i/k_i)}{\Sigma z_i^2 c_i}\right]_{y=0} \quad [3]$$

It is known that bisulfate ion is not completely dissociated except at extreme dilution, and four ionic species, Cu^{2+}, H^+, HSO_4^-, and SO_4^{2-}, should be taken into consideration in the aqueous $CuSO_4$-H_2SO_4 solution. Assigning the subscript to each of these ions as

$$s_1 = \tfrac{1}{2}, \quad s_2 = s_3 = s_4 = 0$$
$$z_1 = 2, \quad z_2 = 1, \quad z_3 = -1, \quad z_4 = -2 \quad [4]$$

and denoting the concentration of $CuSO_4$ and H_2SO_4 in the solution as m_1 and m_2 (mol/liter), respectively, and the degree of dissociation of bisulfate ion as a, the following expressions are derived

$$c_1 = m_1$$
$$c_2 = (1 + a)m_2$$
$$c_3 = \frac{1 - a}{1 + a} c_2$$
$$c_4 = c_1 + \frac{a}{1 + a} c_2 \quad [5]$$

These implicitly satisfy the electroneutrality principle. Substitution of Eq. [5] into Eq. [3] yields

$$\left(\frac{\partial c_2}{\partial y}\right)_{y=0} = -\gamma\left(\frac{\partial c_1}{\partial y}\right)_{y=0} \quad [6]$$

where

$$\gamma \equiv \gamma(c_1^s, c_2^s, a) = \frac{(1 + a)c_2^s}{2(1 + a)c_1^s + (1 + 2a)c_2^s}$$
$$\left(\simeq \frac{1 + a}{1 + 2a} \text{ for } c_1^s << c_2^s\right)$$

Under the experimental conditions of an excess of supporting electrolyte and the degree of dissociation at 0.31 (3), the γ value is approximated as 0.809.

In aqueous $CuSO_4$ solution, on the other hand, Eq. [3] for cupric ion is

$$\left(\frac{\partial c_1}{\partial y}\right)_{y=0} = \frac{i^* t_4}{D_1 z_1 \mathbf{F}} = \frac{i(1 - {}^*t_1)}{D_1 z_1 \mathbf{F}} \quad [7]$$

where

$${}^*t_4 = \frac{U_4 z_4}{U_4 z_4 - U_1 z_1} \quad [8]$$

and

$$D_1 = \frac{U_4 z_4 k_1 - U_1 z_1 k_4}{U_4 z_4 - U_1 z_1} \quad [9]$$

Since the concentration gradient of cupric ion is determined by the combined effect between diffusivities of cation and anion, as seen in Eq. [7], [8], and [9], it is reasonable to deduce that D_1 corresponds to the diffusivity of $CuSO_4$, and the concentration distribution of cupric ion is governed by the same equation as that for a nonelectrolyte even in the presence of an electrolytic current. This is due to the requirement of electroneutrality (8).

It is expected that the ionic transfer process in aqueous $CuSO_4$ solution with uniform distribution of current density is similar to the natural convection, due to heat transfer or nonelectrolyte mass transfer with uniform flux, as long as the heat or mass flux at the boundary is rewritten in terms of current density.

Hydrodynamic equations.—Fundamental equations describing laminar natural convection along the cathode surface in an electrolyte containing $CuSO_4$ and an excess of H_2SO_4 are given as

$$\frac{d}{dx}\int_0^{\delta_u(x)} u^2 dy = -\nu \frac{\partial u}{\partial y}\bigg|_{y=0} + \alpha_1 g \int_0^{\delta_u} \theta_1 dy + \alpha_2 g \int_0^{\delta_u} \theta_2 dy \quad [10]$$

$$\frac{d}{dx}\int_0^{\delta_u} u\theta_1 dy = \frac{i(1-{}^*t_1)}{z_1 F} \quad [11]$$

$$\frac{d}{dx}\int_0^{\delta_u} u\theta_2 dy = -\frac{i^* t_2}{z_2 F} \quad [12]$$

$$k_1 \frac{d\theta_1}{dy}\bigg|_{y=0} \doteq \frac{i(1-{}^*t_1)}{z_1 F} \quad [13]$$

$$-k_2 \frac{d\theta_2}{dy}\bigg|_{y=0} \doteq \frac{i^* t_2}{z_2 F} \quad [14]$$

These equations are solved with the predetermined profiles of velocity and concentration according to the von Kármán-Pohlhausen integral method. They are

$$u = \frac{u_m}{\lambda - 1}\left\{ \lambda\left(\frac{y}{\tau}\right) - \left(\frac{y}{\tau}\right)^{\lambda} \right\} \qquad 0 \leqq y \leqq \tau \quad [15]$$

$$u = u_m\left(1 - \frac{y-\tau}{\epsilon\tau}\right) \qquad \tau \leqq y \leqq (\epsilon+1)\tau \quad [16]$$

$$\theta_1 = \theta_1\left(1 - \frac{y}{\eta\tau}\right)^{\omega} \qquad 0 \leqq y \leqq \delta_1 (=\eta\tau) \quad [17]$$

$$\theta_2 = \theta_2\left(1 - \frac{y}{\sigma\eta\tau}\right)^{\omega} \qquad 0 \leqq y \leqq \delta_2 (=\sigma\delta_1) \quad [18]$$

The resultant equations under the condition of uniform current density are

$$u_m = \left(\frac{\omega\eta}{\phi_1{}^3(\omega+1)^2}\right)^{1/5} \cdot \left\{ \frac{1}{\frac{7}{5}\cdot\frac{\Lambda\omega}{\phi_1\eta}\cdot\frac{1}{Sc} + \frac{\lambda}{\lambda-1}} \right\}^{2/5} \cdot \left(\frac{(\alpha_1 - \gamma\sigma^2\alpha_2) g (1-{}^*t_1)}{z_1 F}\right)^{2/5} \cdot k_1{}^{1/5} \cdot i^{2/5} \cdot x^{3/5} \cdot \nu^{-2/5} \quad [19]$$

$$\tau = \left(\frac{\omega^2(\omega+1)}{\phi_1\eta^3}\right)^{1/5} \cdot \left(\frac{7}{5}\cdot\frac{\Lambda\omega}{\phi_1\eta}\cdot\frac{1}{Sc} + \frac{\lambda}{\lambda-1}\right)^{1/5} \cdot \left(\frac{z_1 F}{(\alpha_1 - \gamma\sigma^2\alpha_2) g (1-{}^*t_1)}\right)^{1/5} \cdot k_1{}^{2/5} \cdot i^{-1/5} \cdot x^{1/5} \cdot \nu^{1/5} \quad [20]$$

$$\theta_1 = \left(\frac{\eta^2(\omega+1)}{\omega^3\phi_1}\right)^{1/5} \cdot \left(\frac{7}{5}\cdot\frac{\Lambda\omega}{\phi_1\eta}\cdot\frac{1}{Sc} + \frac{\lambda}{\lambda-1}\right)^{1/5} \cdot \left(\frac{1-{}^*t_1}{z_1 F}\right) \cdot \left(\frac{z_1 F}{(\alpha_1 - \gamma\sigma^2\alpha_2) g (1-{}^*t_1)}\right)^{1/5} \cdot k_1{}^{-3/5} \cdot i^{4/5} \cdot x^{1/5} \cdot \nu^{1/5} \quad [21]$$

$$\theta_2 = -\gamma\sigma\theta_1 \quad [22]$$

The ratio of thickness of boundary layers of hydrogen ion and cupric ion is calculated by the following equations derived from mass balance equations

$$F(\sigma) = \gamma\sigma\frac{\phi(\sigma\eta)}{\phi(\eta)} = \frac{{}^*t_2}{1-{}^*t_1}\cdot\frac{z_1}{z_2} \quad [23]$$

$$\phi(\eta) = \frac{\lambda(\eta-1)^{\omega+2}}{(\lambda-1)\cdot\eta^{\omega}\cdot(\omega+1)(\omega+2)} \cdot \left\{ \left(\frac{\eta}{\eta-1}\right)^{\omega+2} - \frac{\lambda-1}{\lambda\epsilon} - \frac{\omega+2}{\lambda(\eta-1)} - 1 \right\} - \frac{\eta^{\lambda+1}}{\lambda-1}\cdot B_{1/\eta}(\lambda+1, \omega+1) \quad [24]$$

$$B_a(b,c) = \int_0^a x^{b-1}(1-x)^{c-1} dx \quad [25]$$

The σ-value is calculated from the predetermined transference numbers and the appropriate parameters of velocity and concentration profiles. The natural convection along the cathode surface in an electrolyte containing $CuSO_4$ and H_2SO_4 are described by Eq. [19]-[22].

An example of the corresponding equations for the aqueous $CuSO_4$ solution is

$$\theta_1' = \left(\frac{\eta'^2(\omega'+1)}{\omega'^3\phi_1'}\right)^{1/5} \cdot \left(\frac{7}{5}\cdot\frac{\Lambda'\omega'}{\phi_1'\eta'}\cdot\frac{1}{Sc'} + \frac{\lambda'}{\lambda'-1}\right)^{1/5} \cdot \left(\frac{1-{}^*t_1'}{z_1 F}\right) \cdot \left(\frac{z_1 F}{\alpha_1' g (1-{}^*t_1')}\right)^{1/5} \cdot k_1{}'^{-3/5} \cdot i^{4/5} \cdot x^{1/5} \cdot \nu'^{-1/5} \quad [26]$$

The only different term between Eq. [21] and [26] is the densification coefficient other than the different physical property constants and numerical parameters for the profiles.[1] The expression on densification coefficient $(\alpha_1 - \gamma\sigma^2\alpha_2)$ for aqueous $CuSO_4$-H_2SO_4 solution represents the fact that hydrogen ion is accumulated due to migration in the cathodic concentration boundary layer, and the development of natural convection is depressed.

It is convenient to rewrite Eq. [19]-[21] into the respective dimensionless expressions of

$$\frac{u_m x}{k_1} = \left(\frac{\omega\eta}{\phi_1{}^3(\omega+1)^2}\right)^{1/5} \cdot \left[\frac{1}{\frac{7}{5}\cdot\frac{\Lambda\omega}{\phi_1\eta}\cdot\frac{1}{Sc} + \frac{\lambda}{\lambda-1}} \right]^{2/5} \cdot (Sc'\cdot Gr_x^{*\prime}\cdot f)^{1/5} \quad [27]$$

$$\frac{\tau}{x} = \left(\frac{\omega^2(\omega+1)}{\phi_1\eta^3}\right)^{1/5} \cdot \left(\frac{7}{5}\cdot\frac{\Lambda\omega}{\phi_1\eta}\cdot\frac{1}{Sc} + \frac{\lambda}{\lambda-1}\right)^{1/5} \cdot Sc'\cdot Gr_x^{*\prime}\cdot f)^{-1/5} \quad [28]$$

$$Sh_x = \frac{i(1-{}^*t_1)x}{z_1 F k_1 \theta_1} = \left(\frac{\omega^3\phi_1}{\eta^2(\omega+1)}\right)^{1/5} \cdot \left[\frac{1}{\frac{7}{5}\cdot\frac{\Lambda\omega}{\phi_1\eta}\cdot\frac{1}{Sc} + \frac{\lambda}{\lambda-1}} \right]^{1/5} \cdot (Sc'\cdot Gr_x^{*\prime}\cdot f)^{1/5} \quad [29]$$

where

$$f \equiv \left(\frac{\alpha_1 - \gamma\sigma^2\alpha_2}{\alpha_1'}\right) \cdot \left(\frac{1-{}^*t_1}{1-{}^*t_1'}\right) \Big/ \left(\frac{k_1}{k_1'}\right)^2 \cdot \left(\frac{\nu}{\nu'}\right) \quad [30]$$

[1] Quantities specified with prime are defined for aqueous $CuSO_4$ solution.

On the other hand,

$$Sh_x' = \frac{i(1 - {}^*t_1')x}{z_1 F k_1' \theta_1'} = \left(\frac{\omega'^3\phi_1'}{\eta'^2(\omega' + 1)}\right)^{1/5} \cdot \left[\frac{1}{\frac{7}{5}\cdot\frac{\Lambda'\omega'}{\phi_1'\eta}\cdot\frac{1}{Sc'} + \frac{\lambda'}{\lambda' - 1}}\right]^{1/5} \cdot (Sc' \cdot Gr_x^{*\prime})^{1/5}$$

$$= \left(\frac{\omega'^3\phi_1'}{\eta'^2(\omega' + 1)}\right)^{1/5} \cdot \left[\frac{1}{\frac{7}{5}\cdot\frac{\Lambda'\omega'}{\phi_1'\eta}\cdot\frac{1}{Sc'} + \frac{\lambda'}{\lambda' - 1}}\right]^{1/5} \cdot (Ra_x^{*\prime})^{1/5} \quad [29']$$

for aqueous $CuSO_4$ solution.

Assuming that no virtual difference in the shapes of the concentration and velocity profiles is observed between aqueous $CuSO_4$ and $CuSO_4$-H_2SO_4 solution,[2] the difference caused by migration appears only in the factor f, as the Schmidt number is very large in aqueous solutions. This factor f was introduced as the ratio of the Rayleigh numbers (Ra_x^*) in aqueous $CuSO_4$-H_2SO_4 and $CuSO_4$ solutions. As Ra_x^* expresses the ratio of the rate of convective mass transfer due to natural convection to the rate of diffusional mass transfer, f is thought to represent the contribution of migration to the rate of convective mass transfer due to the change of density distribution of electrolytes caused by the combined concentration profiles of cupric and hydrogen ions and the increased conductivity of the electrolytes. Taking the above-mentioned explanation of f into account, the following expressions are thought to be helpful to relate natural convection in the solution containing $CuSO_4$ and an excess of H_2SO_4 to that in the aqueous $CuSO_4$ solution or to the natural convection due to heat transfer with uniform distribution of the flux

$$Sh_x/Sh_x' = (Ra_x^*/Ra_x^{*\prime})^{1/5} = f^{1/5} \quad [31]$$

$$(u_m x/k_1)/(u_m x/k_1)' = f^{2/5} \quad [32]$$

$$(\tau/x)/(\tau/x)' = f^{-1/5} \quad [33]$$

$$\delta_1/\delta_1' = (\eta\tau)/(\eta\tau)' \quad [34]$$

Similarly

$$\theta_1/\theta_1' = f^{-1/5} \cdot \left(\frac{1 - {}^*t_1}{1 - {}^*t_1'}\right) \cdot \left(\frac{k_1'}{k_1}\right) \quad [35]$$

Experimental Arrangement and Procedure

Principle.—The peak of absorption spectrum of Cu^{2+} ion is located at about 800 nm, which is due to the electron transition of $[Cu(H_2O)_6]^{2+}$ complex ion. The absorption band of H^+ ion is at about 200 nm. Thus, the absorption peaks of both ions are widely separated. Beer-Lambert's law is given by

$$E(c) = \log (I_0/I) = \epsilon_1 c_1 S \quad [36]$$

From the measurement of the distribution of absorbance by using a multi-channel-photo-detector (MCPD) image sensor, together with an appropriate interference filter, the concentration profile of Cu^{2+} ion near the electrode is obtained.

The optical arrangement is illustrated in Fig. 1. An iodine lamp (12V, 100W) with a stabilized power supply was used, and the light was collimated by a lens L_1 (f = 195 mm) to pass through the cathodic diffusion layer. An SMC PENTAX lens (f = 50 mm, F 1.7) was used as another adjusting lens L_2. An image of the cathode was focused on the MCPD, and the distribution of light intensity was processed and observed on a monitoring scope. The MCPD is a one-dimensional photodiode array composed of 512 elements within a

[2] The validity of this assumption is being further studied by the present authors.

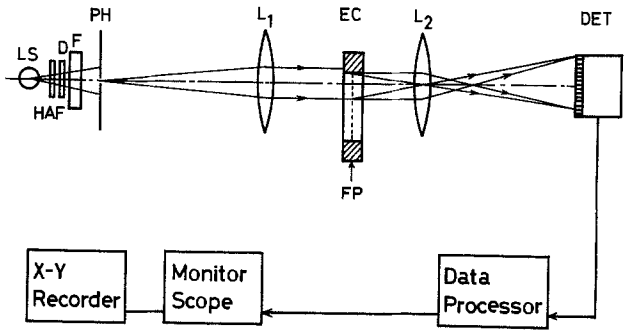

Fig. 1. Schematic illustration of experimental arrangement. LS: Light source; HAF: Heat-absorbing filter; D: Diffuser; F: Filter; PH: Pinnole; L_1,L_2: Lenses; EC; Electrolytic cell; FP: Focal plane; DET: Detector.

detector window 14.4 mm wide. The adjacent two elements were connected to form 256 pairs of photodiodes, each of which was operated under the mode of charge accumulation. The spatial resolution power of this MCPD combined with the SMC PENTAX lens is about 4.4 μm, which is extremely small compared to the thickness of the concentration boundary layer (a few hundred microns).

An interference filter (HOYA filter U330, 0.5 mm thickness) and 0.15M $CuSO_4$ solution filter of 8 mm thickness were used, and their transmittancy spectra are shown in Fig. 2. As seen in Fig. 1, the present technique of measuring the absorbance distribution is a single-beam type. It is necessary to obtain a relationship between Cu^{2+} concentration and absorbance beforehand. No virtual difference was found in this relationship between aqueous $CuSO_4$ solution and $CuSO_4$-1.85M H_2SO_4 solution under the present experimental conditions. It is reasonable to presume that the measured absorbance distribution is only due to the concentration distribution of Cu^{2+} ion.

Experimental conditions.—Figure 3 is a schematic diagram of the electrolytic cell. The copper rod electrodes used were 0.5 cm square, and the effective electrode area was 0.5 × 9.0 cm^2. The distance between both electrodes was maintained at 10 cm. A screw micrometer mechanism for rotating the electrode was used to install the cathode surface parallel to the incident beam. A portion of electrolyte remains in a space of 1 mm thickness between both sides of electrode and the cell wall. The effect of this portion of electrolyte

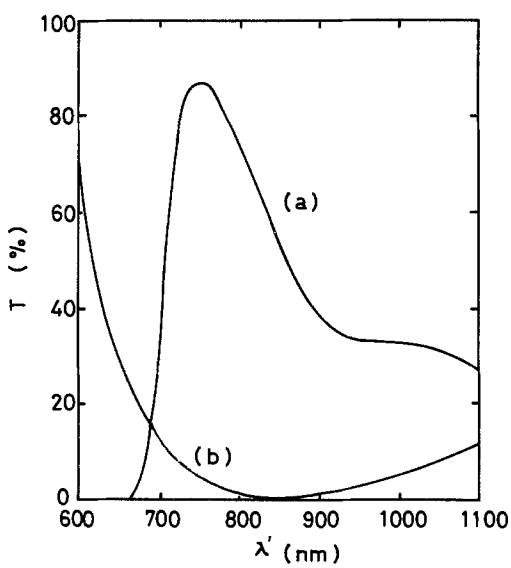

Fig. 2. Transmittancy spectra of the HOYA filter U.330 of 0.5 mm thickness [curve (a)] and 0.15M $CuSO_4$ solution filter of 8 mm thickness [curve (b)].

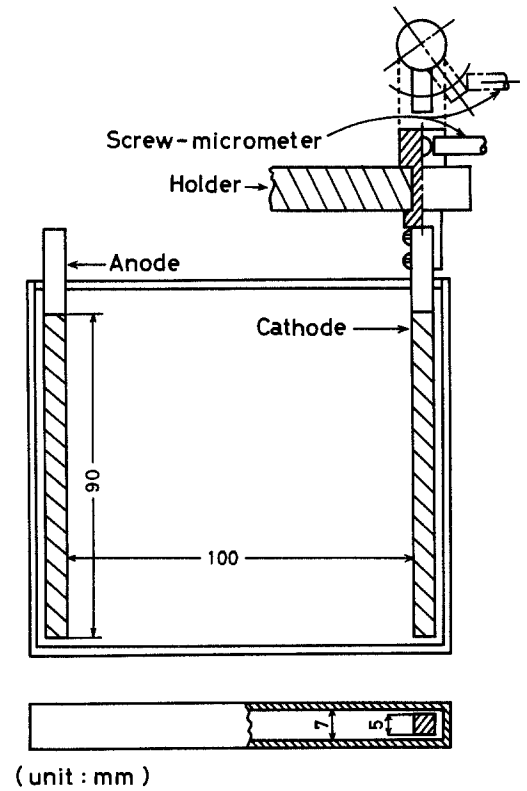

Fig. 3. Electrolytic cell

on the absorbance was taken into account by reducing the thickness of solution, S, of Eq. [36] from 7 to 5 mm. Other experimental conditions are summarized in Table I.

Experimental procedure.—After focusing on a fine nylon thread stretched on the center line of the cathode surface, the cathode rod was rotated to a position where its enlarged silhouette recedes farthest in the monitoring scope. This procedure, which assured that the cathode surface would be parallel to the incident beam, induced a difficulty due to diffraction shown in Fig. 4. By applying the fundamental theory of diffraction phenomenon on an ideal slit (see Appendix A), the geometrical position of the cathode surface was determined. The measured absorbance curve in the diffusion layer was extrapolated toward this position of the cathode surface over a distance of 50-80 μm, and the whole distribution of absorbance was obtained. A 0.15M $CuSO_4$ solution filter having no virtual contribution to the absorbance was also used to evaluate the effect of diffraction pattern on the concentration distribution of Cu^{2+} ion. The absorbance distributions with the HOYA filter U330 and with the solution filter were recorded on the data processor to try to cancel the diffraction effect.

Experimental Results and Discussion

As mentioned earlier, ionic mass transfer near the cathode surface in aqueous $CuSO_4$ solution is described

Table I. Experimental conditions

(A) Composition of electrolyte		0.05M $CuSO_4$
Distance from lower edge of cathode	(cm)	4
Average cathodic current density	(mA/cm²)	0.946, 1.84, 3.65, 4.60*
(B) Composition of electrolyte		0.05M $CuSO_4$-1.85M H_2SO_4
Distance from lower edge of cathode	(cm)	2, 4, 8
Average cathodic current density	(mA/cm²)	0.473, 0.946, 1.420, 1.960*

* Cathodic limiting current density.

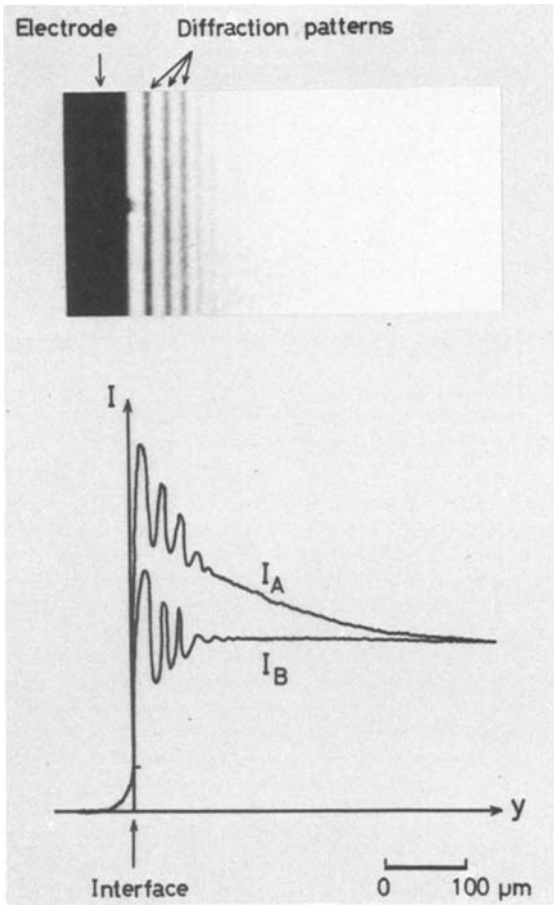

Fig. 4. Schematic illustration of intensity distribution. I_B: before electrolysis; I_A: during steady-state electrolysis.

by using the diffusivity of $CuSO_4$ shown in Eq. [9]. The governing equations of natural convection along the cathode surface are the same as the equations for nonelectrolyte mass transfer and for heat transfer. The similarity solution of natural convection presuming a uniform heat flux along the heated plate (9) is

$$Nu_x = 0.63(Pr \cdot Gr_{xH}^*)^{1/5} \text{ for } Pr > 2000 \quad [37]$$

This equation is very similar to the experimental correlation of

$$Sh_x' = 0.672(Sc' \cdot Gr_x^{*\prime})^{1/5} \quad [38]$$

for the electrolysis of aqueous $CuSO_4$ solution, in which the profile of the refractive index of solution was measured by holographic interferometry (10). It is emphasized that the essential feature of natural convection occurring near the cathode surface in aqueous $CuSO_4$ solution is predictable from heat transfer theory.

As shown in Fig. 5, the agreement was excellent between the concentration profiles of Cu^{2+} ion in aqueous 0.05M $CuSO_4$ solution measured by the present technique and measured by holographic interferometry. This shows that the above-mentioned extrapolation of the curve of concentration profile to the cathode surface was adequate (Appendix B).

The concentration profile of Cu^{2+} ion at various current densities in aqueous 0.05M $CuSO_4$-1.85M H_2SO_4 solution is shown in Fig. 6. Both the concentration difference between cathode surface and bulk electrolyte and the concentration gradient at the cathode surface are larger in this solution than in the aqueous $CuSO_4$ solution. These differences in the concentration profile of Cu^{2+} ion are caused by the higher conductivity of electrolytes containing an excess of H_2SO_4. The migration term of the ionic transport equation is reduced due to higher conductivity of the electrolyte, and it is compensated for at a constant current density by an increase in the diffusion term.

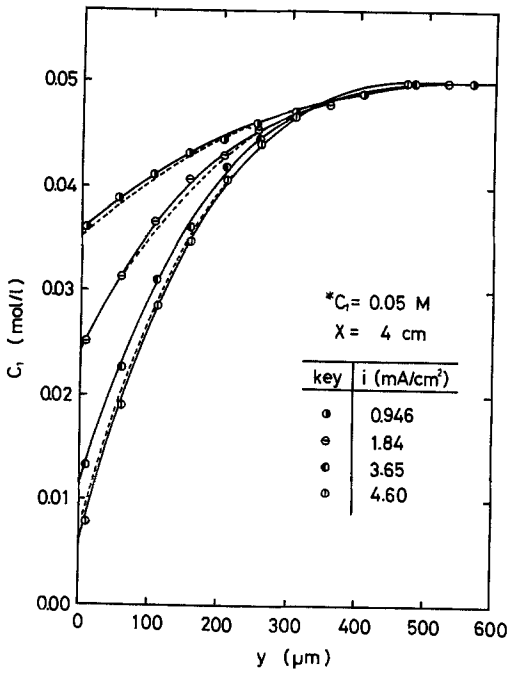

Fig. 5. Concentration profile of Cu^{2+} ion in the cathodic diffusion layer of aqueous 0.05M $CuSO_4$ solution ($x = 4$ cm). Broken lines are profiles measured by holographic interferometry (10).

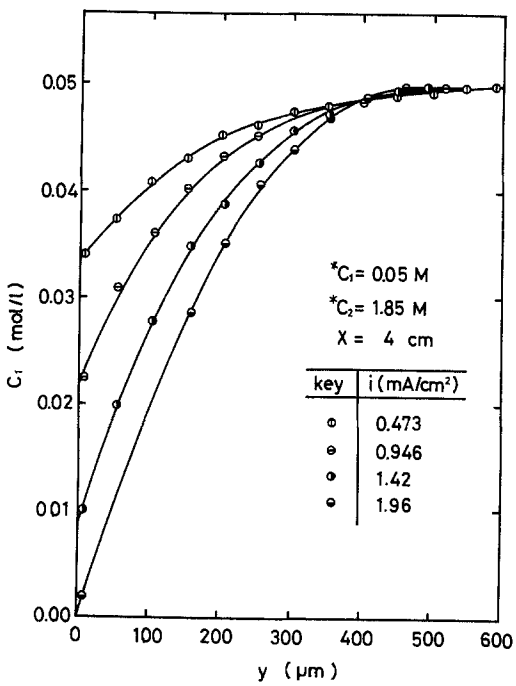

Fig. 6. Concentration profile of Cu^{2+} ion in the cathodic diffusion layer of aqueous 0.05M $CuSO_4$-1.85M H_2SO_4 solution ($x = 4$ cm).

It is also interesting to note that the interfacial concentration of Cu^{2+} ion reaches zero at a current density of 1.96 mA/cm^2, which was found to be the cathodic limiting current density from the measurement of the current-potential relationship. Furthermore, the parameter ω in Eq. [17] was determined from the slope of a plot of log (θ_1/Θ_1) *vs.* log $(1 - y/\delta_1)$, and a numerical value of 2.3 was obtained, which is very close to the 2.39 obtained in aqueous $CuSO_4$ solution (10). It can be said that the addition of an excess of supporting electrolyte yields no virtual change in the shape of the concentration profile of Cu^{2+} ion within the accuracy of the present experimental technique.

The change in the interfacial concentration difference of Cu^{2+} ion due to the applied current density is shown in Fig. 7. It is seen that the slope is 4/5. This was predicted using Eq. [21] in a region of current density below one-half of the limiting value (11). At higher current densities this relationship starts to deviate, and the dependence on the distance x from the leading edge of natural convection disappears. This phenomenon is clearly demonstrated in Fig. 8, in which the experimental relationship between log Θ_1 and log x is shown.

Based on the experimental results obtained in the present work, the effect of migration on the interfacial concentration difference was further considered. First, the ratio of thickness of concentration boundary layers of Cu^{2+} ion and H^+ ion was calculated by using Eq. [23] under conventional electrolytic conditions. Several numerical parameters of ω, η, and a reported in the literature (6) were used. As shown in Fig. 9, the relative variation of the calculated σ-value was less than a few percent within the range of the above-

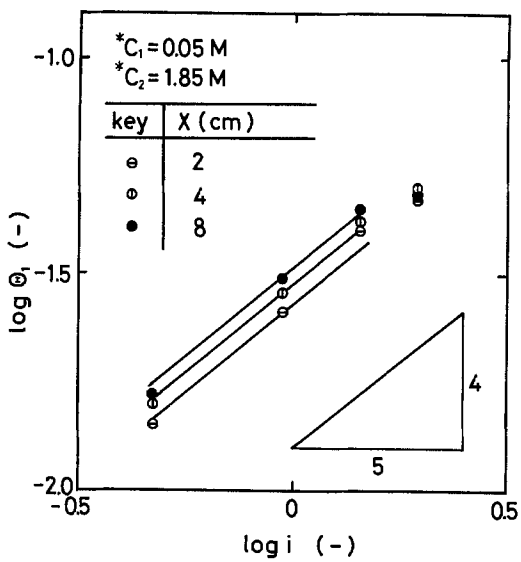

Fig. 7. Relationship between concentration difference and average cathodic current density (0.05M $CuSO_4$-1.85M H_2SO_4).

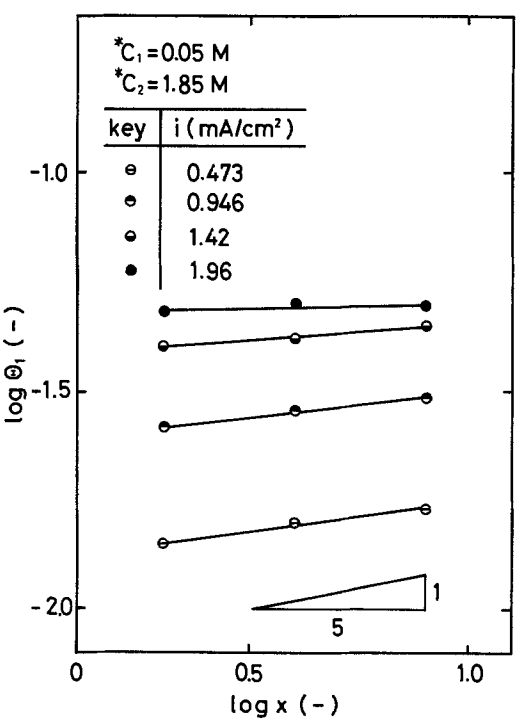

Fig. 8. Relationship between concentration difference and height from lower edge of cathode (0.05M $CuSO_4$-1.85M H_2SO_4).

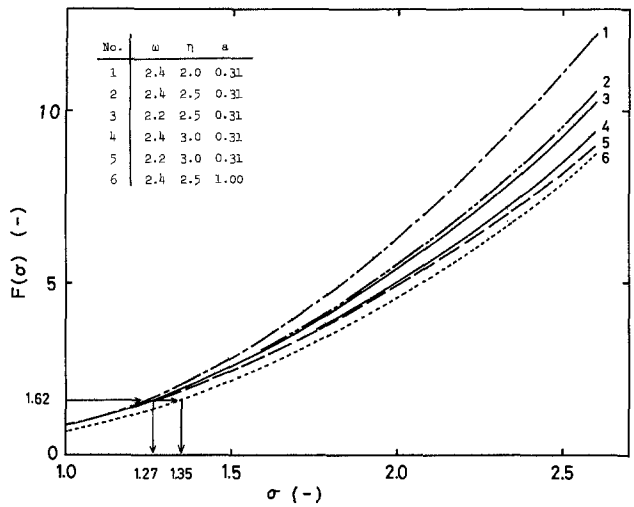

Fig. 9. Relationship between the ratio of boundary layer thickness of H^+ ion to Cu^{2+} ion and the transference number of H^+ ion.

mentioned numerical parameters. It is also seen that the lower degree of dissociation yields smaller σ-value: it varies from 1.35 for complete dissociation to 1.27 for a degree of dissociation of 0.31 when $*t_2$ is assumed to be 0.81. Wagner (1) obtained σ-value of 1.41 at the limiting current density, and Ibl *et al.* (2) reported a numerical value of 1.5 under the same electrolytic conditions as the present work. However, Ibl assumed the thickness of concentration boundary layer of H^+ ion to be equal to the hydrodynamic boundary layer and the dissociation of bisulfate ion to be complete. The calculated σ-value in the present work is slightly smaller.

The factor f defined in Eq. [30] was calculated by substituting the obtained σ-value together with the property constants summarized in Table II. It was assumed in this calculation that the shape of concentration and velocity profiles do not change by the addition of an excess of supporting electrolyte. The numerical value of f was determined as 1.19 using the diffusivity of $CuSO_4$ in both solutions in place of the ionic diffusivity shown in Eq. [30]. The ratio of the interfacial concentration difference of Cu^{2+} ion (θ_1/θ_1') was calculated to be 1.69 from Eq. [35]. This calculated value is compared with the measurement shown in Table III. In Table III, the measured θ_1'-values are referred to the measurement of holographic interferometry (10). The calculated and the measured values of θ_1/θ_1' coincide fairly well with each other below one-half of the limiting current density.

The ratio of interfacial concentration differences of H^+ ion to Cu^{2+} ion in aqueous $CuSO_4$-H_2SO_4 solution is summarized in Table IV. The interfacial concentration difference of H^+ ion was calculated from the previous measurement of the profile of refractive index (5). The theoretical value of θ_2/θ_1 is -1.03. Again, the calculated and measured values coincide fairly well with each other at current densities below one-half of the limiting value. Above this value of the current density, the uniform distribution of current density is not realized (11), which is one of the important assumptions for deriving Eq. [31]-[35].

Table II. Property constants of aqueous 0.05M $CuSO_4$ and 0.05M $CuSO_4$-1.85M H_2SO_4 solution

z_1	(—)	2
z_3	(—)	1
k_1	(cm^2/sec)	5.7×10^{-6}
k_1'	(cm^2/sec)	6.5×10^{-6}
ν	(cm^2/sec)	1.148×10^{-2}
ν'	(cm^2/sec)	1.043×10^{-2}
α_1	(cm^3/mol)	125
α_1'	(cm^3/mol)	151
α_2	(cm^3/mol)	22
$*t_1$	(—)	0.0033
$*t_1'$	(—)	0.357
$*t_2$	(—)	0.81
a	(—)	0.31

Table III. Experimental values of θ_1/θ_1' (calculated $\theta_1/\theta_1' = 1.69$)

Current density \ Distance	x = 2 (cm)	4 (cm)	8 (cm)
i = 0.473 (mA/cm^2)	1.72	1.82	1.66
0.946	1.99	1.89	1.71
1.42	2.26	2.01	1.92

Limiting current density = 1.96 mA/cm^2.

Summary

An experimental technique for measuring the concentration distribution of Cu^{2+} ion in aqueous solutions containing $CuSO_4$ and H_2SO_4 was developed. An image sensor of one-dimensional photodiode array was used, and the distribution of light absorbance was measured in the cathodic boundary layer. Significant noise due to light diffraction was superimposed on the output signal of absorbance distribution within a horizontal distance of 50 μm from the cathode surface. The measuring error caused by this noise was partly overcome by reducing the coherency of the incident beam and by extrapolating the obtained absorbance profile toward the geometrical position of the cathode surface that was predicted from the fundamental theory of Fresnel diffraction. The measured concentration profile of Cu^{2+} ion in aqueous $CuSO_4$ solution was in good agreement with the result obtained by the holographic interferometry. From the establishd experimental and theoretical analogy of natural convection due to electrolysis in aqueous $CuSO_4$ solution and due to heat transfer, the essential nature of the cathodic natural convection in aqueous $CuSO_4$ solution under a uniform distribution of current density is fully understood.

The above-mentioned experimental technique was used to measure the concentration distribution of Cu^{2+} ion in aqueous solution containing $CuSO_4$ and an excess of H_2SO_4. The variations of the observed concentration profile of Cu^{2+} ion due to the applied current density and to the vertical distance were in good agreement with the theory that was developed on the assumptions that the distribution of current density is uniform and that the solution contains an excess of supporting electrolyte. From the ratio of the thickness of concentration boundary layers of H^+ and Cu^{2+}, a new factor f was proposed. It is defined as the ratio of the Rayleigh numbers in aqueous $CuSO_4$-H_2SO_4 solution and in $CuSO_4$ solution. This factor f involves the effect of migration, which is caused by the change of transference number and the accumulation of supporting electrolytes in the concentration boundary layer in the aqueous $CuSO_4$-H_2SO_4 solution. The factor f was found to be effective in the theoretical calculations of the ratio of the interfacial concentration difference of Cu^{2+} ion in aqueous $CuSO_4$-H_2SO_4 and $CuSO_4$ solu-

Table IV. Experimental values of θ_2/θ_1 (calculated $\theta_2/\theta_1 = -1.03$)

Current density (mA/cm^2) \ Interfacial concentration difference	θ_1 (mol/liter)	θ_2 (mol/liter)	θ_2/θ_1
0.473	1.60×10^{-2}	-1.49×10^{-2}	−0.94
0.946	2.85	−2.94	−1.03
1.42	4.17	−5.18	−1.24
1.96	4.99	−5.66	−1.13

$\theta_2 = -\gamma\sigma\theta_1$
$\gamma\sigma = 1.03$.

tions, and the ratio of the interfacial concentration difference of H^+ ion and Cu^{2+} ion in the aqueous $CuSO_4$-H_2SO_4 solution at current densities below one-half of the limiting value.

Acknowledgments

The authors wish to thank Professor J. Tsujiuchi, Drs. S. Ueha and T. Honda, Tokyo Institute of Technology, and Professor R. Nagata and Dr. K. Iwata, University of Osaka Prefecture, for their valuable discussion on the optical measurements. Their thanks also extend to Dr. Y. Awakura and Mr. T. Nagamura for their suggestions. Part of this work was performed under the financial aid given to one of the authors (Y.F.) by the Kurata Foundation, to which he is grateful. Finally, they are very thankful to Professor J. M. Toguri, Department of Metallurgy and Materials Science, University of Toronto, for his kind advice and correction of English.

Manuscript submitted Dec. 14, 1982; revised manuscript received July 1, 1983.

Kyoto University assisted in meeting the publication costs of this article.

APPENDIX A

Diffraction Pattern

When a knife edge was attached to the front side of the cathode as a simulation of an ideal slit, the Fresnel diffraction was observed in the same plane as the MCPD was focused, despite the incoherency of the light source. The position s and the intensity A^2 of the first few extreme values of this pattern were examined, and were compared with the theoretical value of an ideal slit (12, 13). The results are shown in Table AI. These two sets of values are very similar to each other. It was suggested that the partial coherency for the present light source was realized due to the very small value of the ratio of a diameter of the pinhole to the focal length of the lens L_1. Furthermore, the diffraction pattern on the cathode surface was fairly similar to those for an ideal slit and for the knife edge. It is reasonable to suppose that the observed diffraction pattern in Fig. 3 was caused by a partial coherency due to the incident beam's being parallel. The following two trials were made. One was to install a diffuser as shown in Fig. 1 to decrease the coherency of the light. Another trial was to increase the ratio of the pinhole diameter to the focal length of the lens L_1, which determined how parallel the incident beam was up to 0.005. By applying these two methods, the horizontal distance of the diffraction was decreased, though the first two peaks still remained in the region of 50-80

Table AI. Comparison of Fresnel diffraction pattern, knife edge pattern, and electrode pattern.

		Ideal slit	Knife edge pattern	Electrode pattern
1st max. point	x (μm)	31.9 (s = 1.217)	35.0	29.0
	A^2 (−)	1.37	1.28	1.69
1st min. point	x (μm)	49.1 (s = 1.873)	57.5	45.5
	A^2 (−)	0.78	0.90	0.88
2nd max. point	x (μm)	61.4 (s = 2.345)	72.5	55.5
	A^2 (−)	1.20	1.05	1.19
2nd min. point	x (μm)	71.8 (s = 2.739)	85.0	66.0
	A^2 (−)	0.84	0.98	0.92

$s = \sqrt{2/b\lambda'} \cdot x \qquad b = 2.5$ mm $\qquad \lambda' = 550$ nm

$A^2 = B^2 + C^2 \qquad C = \int_s^\infty \cos\left(\frac{\pi}{2}u^2\right)du = \frac{1}{2} - \int_0^s \cos\left(\frac{\pi}{2}u^2\right)du$

$$B = \frac{1}{2} - \int_0^s \sin\left(\frac{\pi}{2}u^2\right)du$$

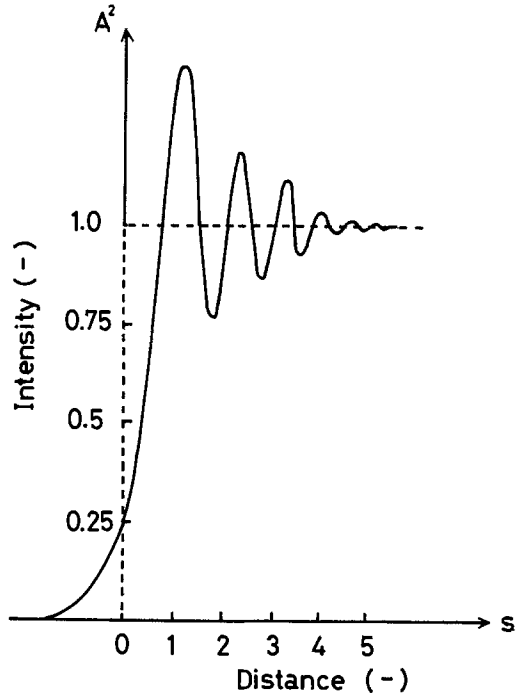

Fig. A1. Intensity pattern of Fresnel diffraction by coherent light (12, 13).

μm from the cathode surface. Then, it was decided to extrapolate the absorbance curve towards the cathode surface.

According to the diffraction theory (12, 13), the geometrical position of the ideal slit with the coherent light source corresponds to the position of 25% of the light intensity, as shown in Fig. A1. It is 50% with the incoherent light source. From the comparison of the image of cathode in the monitoring scope with the photograph of cathode taken by a camera placed at the same position as the MCPD, a value of 45% of the light intensity was determined as the position of the cathode surface from seven repetitions of the measurement.

APPENDIX B

Correction of Light Deflection

The obtained concentration profile is still affected by the light deflection effect due to the refractive index gradient, which was measured by holographic interferometry (5). According to the previous calculations (5, 14-20) for compensation for this effect, the trajectory of the incident light beam at $y = y_i$ to the electrolytic cell was calculated. This incident beam leaves the cell at $y = y_i + \Delta y$, where Δy is the function of y_i. The absorbance of this exit beam is equivalent to the imaginary light beam that passes straight to the cathode surface at $y = y_i + 1/3\,\Delta y$. Therefore, it is necessary to obtain the Δy value, which is given by

$$\Delta y(y_i) = \{n(y_o) - n(y_i)\} \Big/ \left(\frac{dn(y)}{dy}\right)_{y=y_i} \qquad \text{[B-1]}$$

$$n(y_o) - n(y_i) = n_\infty + \left(\frac{dn(y)}{dy}\right)_{y=y_i} \cdot d - \sqrt{n_\infty\left\{n_\infty + 2\left(\frac{dn(y)}{dy}\right)_{y=y_i} \cdot d\right\}} \qquad \text{[B-2]}$$

The measured concentration profile was shifted by $1/3\,\Delta y$ at the position of y_i.

LIST OF SYMBOLS

a	degree of dissociation
A^2	intensity
b	distance between a knife edge and a screen, cm
c_1	concentration of Cu^{2+} ion, mol/liter
c_2	concentration of H^+ ion, mol/liter
c_3	concentration of HSO_4^- ion, mol/liter
c_4	concentration of SO_4^{2-} ion, mol/liter

$^*c_1$ concentration of Cu^{2+} ion in bulk electrolyte, mol/liter
$^*c_2$ concentration of H^+ ion in bulk electrolyte, mol/liter
c_1^s concentration of Cu^{2+} ion at cathode surface, mol/liter
c_2^s concentration of H^+ ion at cathode surface, mol/liter
d width of cathode, cm
D_1 diffusivity of $CuSO_4$, cm^2/sec
e charge of proton, $= 1.602 \times 10^{-19}$ C
$E(c)$ absorbance
$\mathbf{F}$ Faraday constant, = 96,500 C/g-equiv.
g gravitational acceleration, = 980 cm/sec^2
i current density, A/cm^2
I intensity, erg/cm^2
I_A intensity measured after eleetrolysis is started, erg/cm^2
I_B intensity measured before electrolysis is started, erg/cm^2
I_o intensity of incident light, erg/cm^2
k Boltzmann constant, $= 1.381 \times 10^{-23}$ J/mol · K
k_i diffusivity of ion i, cm^2/sec
m_1 concentration of $CuSO_4$, mol/liter
m_2 concentration of H_2SO_4, mol/liter
n_i number of mols of ion i, mol/cm^2
R gas constant, J/K · mol
S thickness of solution, cm
s_i number of mols of ion i which reacts on cathode surface, mol/g-equiv.
T temperature, K
$^*t_1$ transference number of Cu^{2+} ion in the bulk electrolyte
$^*t_2$ transference number of H^+ ion in the bulk electrolyte
$^*t_4$ transference number of SO_4^{2-} ion in the bulk electrolyte
t time, sec
u velocity of natural convective flow, cm/sec
u_m maximal velocity of natural convective flow, cm/sec
U_i mobility of ion $(= ki/RT)$, cm^2 · mol/J · sec
x height from the lower edge of cathode, cm or horizontal distance from a knife edge, cm
y horizontal distance from cathode surface, cm
y_i distance between incident point of beam and cathode surface, cm
y_o distance between exit point of beam and cathode surface, cm
Δy $= (y_o - y_i)$, cm
z_1 valency of Cu^{2+} ion, = 2g-equiv./mol
z_2 valency of H^+ ion, = 1g-equiv./mol
z_3 valency of HSO_4^- ion, = 1g-equiv./mol
z_4 valency of SO_4^{2-} ion, = 2g-equiv./mol

Greek letters

α_1 densification coefficient of $CuSO_4$, cm^3/mol
α_2 densification coefficient of H_2SO_4, cm^3/mol
δ_1 thickness of diffusion layer of Cu^{2+} ion, cm
δ_2 thickness of diffusion layer of H^+ ion, cm
δ_u thickness of velocity boundary layer, cm
ϵ numerical parameter
ϵ_i molar extinction coefficient, mol/cm^3
η numerical parameter
θ_1 $= (^*c_1 - c_1^s)$, mol/liter
θ_2 $= (^*c_2 - c_2^s)$, mol/liter
θ_1 $= (^*c_1 - c_1)$, mol/liter
θ_2 $= (^*c_2 - c_2)$, mol/liter
Λ $= \left\{ \frac{\lambda^2}{3} - \frac{2\lambda}{\lambda+2} + \frac{1}{2\lambda+1} + \frac{\epsilon}{3}(\lambda-1)^2 \right\} \Big/ (\lambda-1)^2$
λ numerical parameter
λ' wavelength, cm
ν kinematic viscosity, cm^2/sec
σ ratio of δ_2 to δ_1
τ distance between cathode surface and the position of the maximal velocity of natural convection, cm
ψ potential, V/cm
ω numerical parameter

Nondimensional numbers

Gr_x^* modified Grashof number $= \dfrac{g\alpha i(1 - {}^*t_1)x^4}{z_1\mathbf{F}\nu^2 D_1}$
Gr_{xH}^* modified Grashof number $= \dfrac{g\beta q_w x^4}{\nu^2\lambda''}$
Nu_x Nusselt number $= \dfrac{hx}{\lambda''}$
Pr Prandtl number $= \dfrac{\nu}{(\lambda''/C_p\rho)}$
Ra_x^* Rayleigh number $= Pr \cdot Gr_{xH}^*$ or $Sc \cdot Gr_x^*$
Sc Schmidt number $= \dfrac{\nu}{k_1}$
Sh_x Sherwood number $= \dfrac{i(1 - {}^*t_1)x}{z_1\mathbf{F}k_1\theta_1}$

where

C_p heat capacity, cal/g · K
h heat transfer coefficient, cal/cm^2 · sec · K
q_w heat flux, cal/cm^2 · sec
α α_1' or $(\alpha_1 - \gamma\sigma^2\alpha_2)$, cm^3/mol
β densification coefficient $= \dfrac{1}{\rho}\dfrac{\partial\rho}{\partial T}$, 1/K
λ'' thermal conductivity, cal/cm · sec · K
ρ density, g/cm^3

REFERENCES

1. C. Wagner, *Trans. Electrochem. Soc.*, **95**, 161 (1949).
2. C. R. Wilke, M. Eisenberg, and C. W. Tobias, *This Journal*, **100**, 513 (1953).
3. J. R. Selman and J. Newman, *ibid.*, **118**, 1070 (1971).
4. N. Ibl and U. Braun, *Chimica*, **21**, 395 (1967).
5. Y. Awakura, M. Okada, and Y. Kondo, *This Journal*, **124**, 1050 (1977).
6. Y. Awakura, Y. Takenaka, and Y. Kondo, *Electrochim. Acta*, **21**, 789 (1976).
7. A. Brenner, *Proc. Am. Electroplat. Soc.*, **27**, 95 (1940); *ibid.*, **28**, 28 (1941).
8. J. Newman, "Electrochemical Systems," p. 223, Prentice-Hall, Inc., Englewood Cliffs, NJ (1973).
9. S. W. Churchill and H. Ozoe, *Trans. ASME*, Ser. C, **95**, 540 (1973).
10. Y. Awakura and Y. Kondo, *This Journal*, **123**, 1185 (1976).
11. Y. Awakura, A. Ebata, and Y. Kondo, *ibid.*, **126**, 23 (1979).
12. M. Born and E. Wolf, "Principles of Optics," 6th ed., p. 434, Pergamon Press, Oxford (1980).
13. H. Kubota, "Ohyo Kagaku [Applied Optics]," p. 106, Iwanami, Tokyo (1977).
14. R. H. Müller, in "Advances in Electrochemistry and Electrochemical Engineering," Vol. 9, P. Delahay and C. W. Tobias, Editors, p. 281, John Wiley & Sons, New York (1973).
15. K. W. Beach, R. H. Müller, and C. W. Tobias, *J. Opt. Soc. Am.*, **63**, 559 (1973).
16. F. R. McLarnon, R. H. Müller, and C. W. Tobias, *Appl. Opt.*, **14**, 2468 (1975).
17. F. R. McLarnon, R. H. Müller, and C. W. Tobias, *J. Opt. Soc. Am.*, **65**, 1011 (1975).
18. F. Mayinger and W. Panknin, *Verfahrenstechnik*, **12**, 582 (1978).
19. W. Hauf and U. Grigull, "Advances in Heat Transfer," Vol. VI, p. 133, Academic Press, New York (1970).
20. W. Panknin, Dr.-Ing. Dissertation, Technischen Universität, Hannover (1977).

Sheet Resistance and Junction Depth Relationships in Implanted Species Diffusion

S. Aronowitz and L. Mei*

Fairchild Camera and Instrument Corporation, Advanced Research and Development Laboratory, Palo Alto, California 94304

As a result of the rapid progress of CMOS technology, there is a great deal of interest in predicting the n-well and p-well junction depths after high temperature and long period drive-ins. The purpose of this communication is to propose a simple model which permits sheet resistance as well as junction depths to be accurately and relatively easily evaluated. The model is specifically applied to boron and phosphorus. It is interesting that work with arsenic displays behavior that is describable by the approach adopted in this work. We will begin the discussion, therefore, with arsenic even though our interest is the behavior of boron and phosphorus.

The properties of implanted arsenic layers after annealing have been reported by Liu and Oldham (1). The physical principles implicit in their work suggest that boron and phosphorus will exhibit patterns similar to arsenic with regard to sheet resistance and junction depth. Other recent work has shown that arsenic sheet resistance-junction depths, for various combinations of annealing times and temperatures, are essentially independent of the implant energy (2, 3) over the range examined (45-100 keV). Consequently, we infer that there should be conditions which will yield the same relative independence of the junction depth-sheet resistance relationships from the implant energy for boron and phosphorus.

Computer simulations using a version of SUPREM II (3) predict that if evaporation is negligible and if the ratio of the projected range, R_p, to the final junction depth, X_{jf}, equals

$$R_p/X_{jf} < 0.2 \qquad [1]$$

the diffusion can be treated as though the dopant is initially confined to a thin film on the surface of the silicon. A series of experiments with phosphorus and boron was initiated in order to verify the actual behavior as opposed to the predicted one.

Phosphorus was implanted in (100) p-type Si wafers (14-20 Ω-cm) at three energies: 60, 120, and 180 keV. Two dose levels were used: 3×10^{13} P^+/cm^2, 1×10^{15} P^+/cm^2. Annealing times and temperatures also were varied. Sets of each combination of dose and implant energy were annealed for either 30 or 120 min at either 1000° or 1200°C (four combinations of time and temperature). The matrix with boron was similar [(100) n-type wafers (14-20 Ω-cm)]; however, only two implant energies (60 and 120 keV) were used while the anneal times were lengthened to 90 and 360 min. All wafers then were capped with 2000Å of LPCVD Si_3N_4 during annealing to prevent dopant evaporation from the silicon surface. Figure 1 displays spreading resistance profiles for phosphorus annealed at 1200°C. The profiles are relatively independent with respect to implant energies as was reported for arsenic (2). Dose levels of arsenic in Ref. (2) ranged from 3×10^{15} to 9×10^{15} As^+/cm^2. Implantation energies ranged from 45 to 100 keV; two anneal temperatures, 950° or 1000°C, were used in combination with dose, time, and implant energy. Figure 2 displays the spreading resistance profiles obtained when boron is annealed at 1200°C. Again, the relative independence of the final profiles with respect to the implant energies is clear.

The close agreement between profiles implanted at different energies translates into close agreement between sheet resistance and junction depth measurements. R_s (Ω/□) and X_j values obtained for boron and phosphorus are displayed in Table I. The values in the table are the average over the range of implant energies. The numbers in parentheses, alongside the mean value of R_s or X_j, are the average relative deviation from the mean value. The relative deviation, not

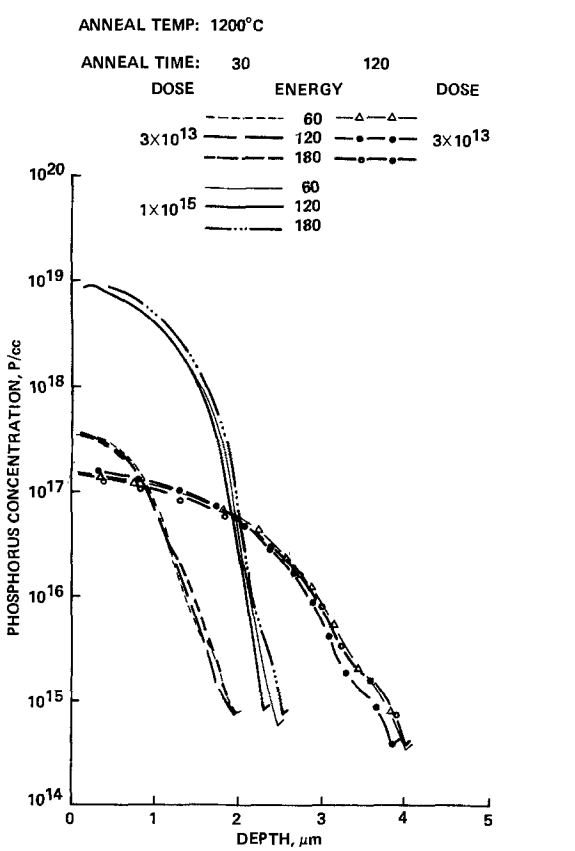

Fig. 1. Experimental phosphorus profiles from spreading resistance measurements as functions of dose, implant energy, and annealing time.

* Electrochemical Society Active Member.

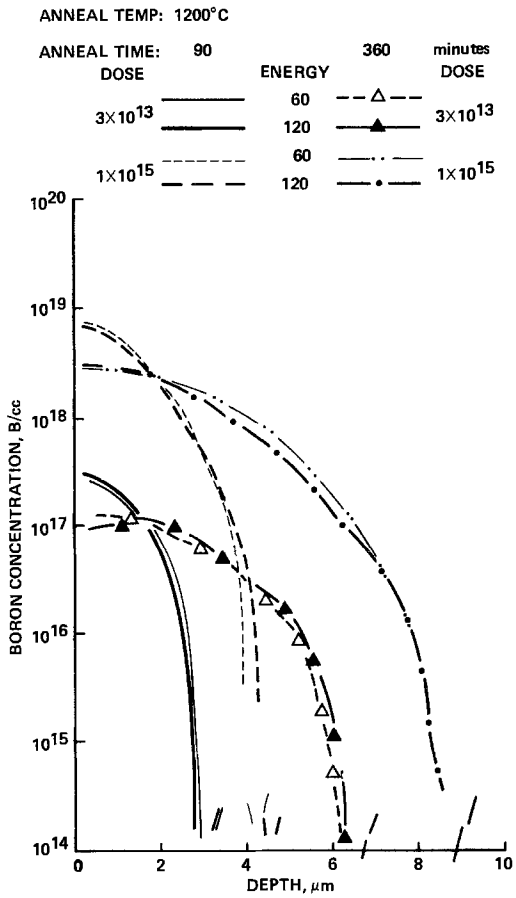

Fig. 2. Experimental boron profiles from spreading resistance measurements as functions of dose, implant energy, and annealing time.

surprisingly, decreases sharply at the higher annealing temperature; this occurs because the final junction depths are at least an order of magnitude deeper than the initial projected range. Therefore, the approximation of treating the initial distribution as a surface source becomes more realistic. As a consequence, at low and moderately high concentrations ($\leq 10^{19}$ atoms/cm^3), the concentration can be closely approximated by a Gaussian function. An empirical equation, which relates the sheet resistance to the dose and annealing temperature (assuming equal annealing times), has been derived from the experimental data and equals

$$(R_S)_A/(R_S)_B \doteq \left(\frac{T_B K}{T_A K}\right)^4 \left[\frac{(\text{Dose})_B}{(\text{Dose})_A}\right]^\alpha \qquad [2]$$

Table I. Experimental sheet resistance and junction depths for boron and phosphorus implants

Boron

Anneal temperature (°C):		1000	1200	
Dose ($\times 10^{-12}$)	Anneal time (min)	Avg. sheet resistance ($\Omega/\square$)	Avg. sheet resistance ($\Omega/\square$)	Avg. junction depth $\bar{X}_j$ (μm)
30	90	NM*	668.7 (0.02)	3.28 (0.02)
30	360	1010.7 (0.11)	583.9 (0.03)	6.66 (0.00)
1000	90	NM*	61.6 (0.03)	4.35 (0.01)
1000	360	87.1 (0.06)	49.3 (0.02)	8.91 (0.04)

Phosphorus

Anneal temperature (°C):		1000	1200	
Dose ($\times 10^{-12}$)	Anneal time (min)	Avg. sheet resistance ($\Omega/\square$)	Avg. sheet resistance ($\Omega/\square$)	Avg. junction depth $\bar{X}_j$ (μm)
30	30	672.2 (0.20)	367.9 (0.01)	1.91 (0.02)
30	120	614.3 (0.16)	303.6 (0.01)	3.92 (0.03)
1000	30	77.0 (0.10)	51.8 (0.01)	2.41 (0.06)
1000	120	72.7 (0.02)	(38.7)†	NM*

* Not measured.
† Measurement made at only one implant energy (180 keV).

where α equals 0.7 for boron and 0.6 for phosphorus. Both A and B processes must satisfy Eq. [1] if Eq. [2] is to be valid.

In conclusion, boron and phosphorus exhibit the same general features and relationships with regard to implant energy and, consequently, to the behavior of sheet resistance and junction depth. These quantities are essentially independent of implant energy; they are functions of dose, annealing time, and temperature. The concentration can be represented by Gaussians when Eq. [1] is satisfied, while the sheet resistance can be described by an empirical form (Eq. [2]) common to both elements. Aside from detailed differences arising at large concentrations ($\geq 10^{20}$ atoms/cm^3) (4), the diffusion pattern is essentially independent of the specific species for the range of dose, annealing times, and temperatures considered in this communication.

REFERENCES

1. T. M. Liu and W. G. Oldham, *IEEE Electron Dev. Lett.*, **edl-2**, 275 (1981).
2. Y. Liu, J. Sheu, and S. Aronowitz, Paper 750 RNP presented at The Electrochemical Society Meeting, Montreal, Que., Canada, May 9-14, 1982.
3. S. Aronowitz, Fairchild Technical Report 623 (1982).
4. R. B. Fair, *This Journal*, **125**, 323 (1978).

Study of Impurity Profiles in Silicon

G. Eranna and D. Kakati[1]

Centre for Systems and Devices, Indian Institute of Technology, Madras-600 036, India

Simple theories of impurity diffusion in semiconductors, assuming a constant diffusivity, yield either complementary error function profiles or Gaussian profiles. However, in most cases, strong deviations of the experimental impurity profiles from the theories do occur. For process control, an accurate knowledge of the diffusion profiles and the prediction of the diffusion depth from the knowledge of the diffusion and chip parameters is a necessity. In the present paper, we are pointing out the possible combination of anodic oxidation and chemical polishing in studying the impurity profiles up to the junction point.

The electrical characteristics of semiconductor devices are primarily determined by the impurities in-

[1] Present address: Department of Electrical Engineering, Kuwait University, Kuwait City, Kuwait.
Key words: profile estimation, boron, phosphorus, anodic oxidation, chemical polishing.

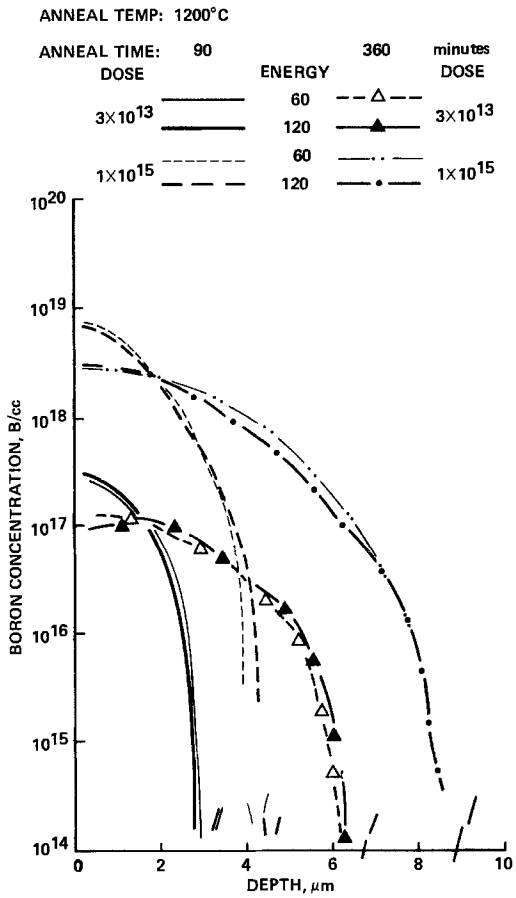

Fig. 2. Experimental boron profiles from spreading resistance measurements as functions of dose, implant energy, and annealing time.

surprisingly, decreases sharply at the higher annealing temperature; this occurs because the final junction depths are at least an order of magnitude deeper than the initial projected range. Therefore, the approximation of treating the initial distribution as a surface source becomes more realistic. As a consequence, at low and moderately high concentrations ($\leq 10^{19}$ atoms/cm^3), the concentration can be closely approximated by a Gaussian function. An empirical equation, which relates the sheet resistance to the dose and annealing temperature (assuming equal annealing times), has been derived from the experimental data and equals

$$(R_S)_A/(R_S)_B \doteq \left(\frac{T_B K}{T_A K}\right)^4 \left[\frac{(\text{Dose})_B}{(\text{Dose})_A}\right]^\alpha \qquad [2]$$

Table I. Experimental sheet resistance and junction depths for boron and phosphorus implants

Boron

Anneal temperature (°C):		1000	1200	
Dose ($\times 10^{-12}$)	Anneal time (min)	Avg. sheet resistance ($\Omega/\square$)	Avg. sheet resistance ($\Omega/\square$)	Avg. junction depth $\bar{X}_j$ (μm)
30	90	NM*	668.7 (0.02)	3.28 (0.02)
30	360	1010.7 (0.11)	583.9 (0.03)	6.66 (0.00)
1000	90	NM*	61.6 (0.03)	4.35 (0.01)
1000	360	87.1 (0.06)	49.3 (0.02)	8.91 (0.04)

Phosphorus

Anneal temperature (°C):		1000	1200	
Dose ($\times 10^{-12}$)	Anneal time (min)	Avg. sheet resistance ($\Omega/\square$)	Avg. sheet resistance ($\Omega/\square$)	Avg. junction depth $\bar{X}_j$ (μm)
30	30	672.2 (0.20)	367.9 (0.01)	1.91 (0.02)
30	120	614.3 (0.16)	303.6 (0.01)	3.92 (0.03)
1000	30	77.0 (0.10)	51.8 (0.01)	2.41 (0.06)
1000	120	72.7 (0.02)	(38.7)†	NM*

* Not measured.
† Measurement made at only one implant energy (180 keV).

where α equals 0.7 for boron and 0.6 for phosphorus. Both A and B processes must satisfy Eq. [1] if Eq. [2] is to be valid.

In conclusion, boron and phosphorus exhibit the same general features and relationships with regard to implant energy and, consequently, to the behavior of sheet resistance and junction depth. These quantities are essentially independent of implant energy; they are functions of dose, annealing time, and temperature. The concentration can be represented by Gaussians when Eq. [1] is satisfied, while the sheet resistance can be described by an empirical form (Eq. [2]) common to both elements. Aside from detailed differences arising at large concentrations ($\geq 10^{20}$ atoms/cm^3) (4), the diffusion pattern is essentially independent of the specific species for the range of dose, annealing times, and temperatures considered in this communication.

REFERENCES

1. T. M. Liu and W. G. Oldham, *IEEE Electron Dev. Lett.*, **edl-2**, 275 (1981).
2. Y. Liu, J. Sheu, and S. Aronowitz, Paper 750 RNP presented at The Electrochemical Society Meeting, Montreal, Que., Canada, May 9-14, 1982.
3. S. Aronowitz, Fairchild Technical Report 623 (1982).
4. R. B. Fair, *This Journal*, **125**, 323 (1978).

Study of Impurity Profiles in Silicon

G. Eranna and D. Kakati[1]

Centre for Systems and Devices, Indian Institute of Technology, Madras-600 036, India

Simple theories of impurity diffusion in semiconductors, assuming a constant diffusivity, yield either complementary error function profiles or Gaussian profiles. However, in most cases, strong deviations of the experimental impurity profiles from the theories do occur. For process control, an accurate knowledge of the diffusion profiles and the prediction of the diffusion depth from the knowledge of the diffusion and chip parameters is a necessity. In the present paper, we are pointing out the possible combination of anodic oxidation and chemical polishing in studying the impurity profiles up to the junction point.

The electrical characteristics of semiconductor devices are primarily determined by the impurities in-

[1] Present address: Department of Electrical Engineering, Kuwait University, Kuwait City, Kuwait.
Key words: profile estimation, boron, phosphorus, anodic oxidation, chemical polishing.

corporated into the body of the semiconductor and their spacial distribution. Three basic methods are available to determine the impurity profiles; spreading resistance, C-V measurements, and stripping or sectioning techniques. Three basic techniques for sectioning exist: mechanical polishing, using fine abrasive powder or chemical polishing which controls the fine rate of attack on the surface of the semiconductor; chemical etching; and oxidation followed by etching of the oxide. Anodic oxidation followed by etching of oxide for profile measurements is a frequently used technique. A nonaqueous solution such as ethylene glycol for anodization of silicon allows higher forming voltages, causes less contamination, and gives denser oxides (1) than acid or borate solution (2). Ethylene glycol, containing 0.04N KNO_3 and small amounts of water with trace amounts of $Al(NO_3)_3,9H_2O$ which suppresses the fluoride ion attack on growing oxide film, is suitable.

In planar diffusion technology, boron and phosphorus are the most common p-, n-type dopants for silicon. But the understanding of boron and phosphorus profiles appears to be anomalous and, in particular, phosphorus profiles are much more complicated. To understand the profiles, we have analyzed boron drive-in profiles, and phosphorus diffusion profiles by using the present technique, anodic oxidation and chemical polishing. In the case of the boron drive-in profile, finely polished silicon wafers with 5 kΩ-cm resistivity n-type with crystallographic orientation (111) were selected. Diffusion was carried out in an open tube furnace at 1100°C for 1 hr in nitrogen ambient by using B_2O_3 as the source. The drive-in step was carried out at 1200°C with oxygen ambient by a dry-wet-dry cycle for 1 hr (3). For phosphorus diffusion, finely polished silicon wafers with 1 kΩ-cm resistivity p-type with the same crystallographic orientation were selected, and the diffusion was carried out at 1100°C for 1 hr in nitrogen ambient by using P_2O_5 as the impurity source (4).

Anodization was carried out at room temperature under normal laboratory illumination. It was found that variation of cell voltage with time will not follow as it was in the beginning, and in the subsequent anodization stages, it will be impossible to get good and uniform oxide films (3). It is felt that the presence of a p-n junction will affect the oxide formation and hence, the anodization process. In order to overcome this difficulty, we selected chemical polishing over anodic oxidation to strip the silicon wafer. For this process, we selected the solution of $CuSO_4$ and NH_4F (50 and 11g in 250 cm^3 deionized water) to get fine polishing for a short duration of time (of the order of 30-45 sec) so that the removed silicon will be nearly

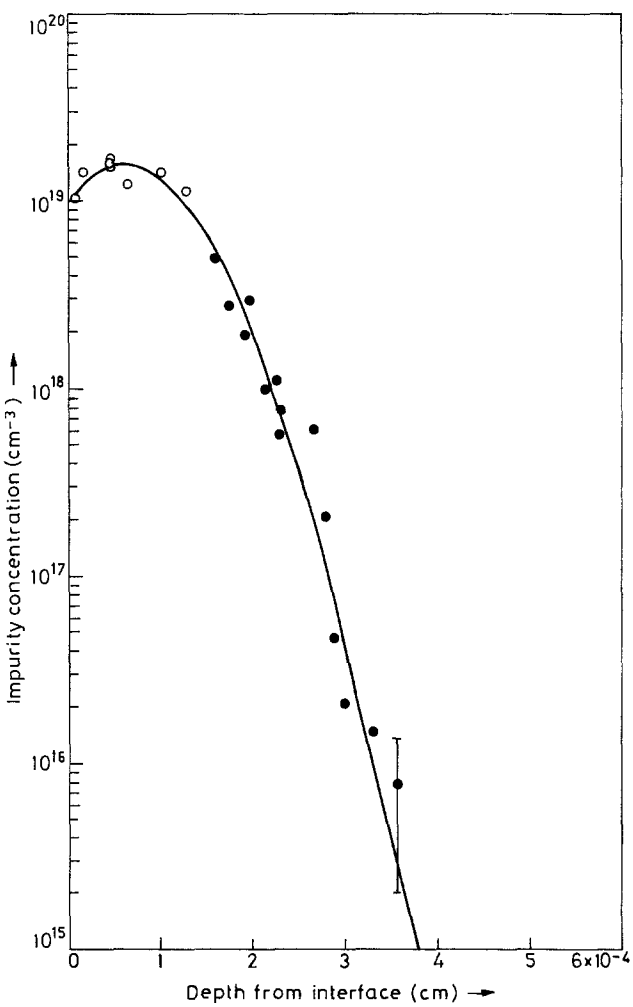

Fig. 1. Measured impurity profile of boron after 1 hr drive-in at 1200°C. Prior to drive-in, diffusion was carried out at 1100°C for 1 hr using B_2O_3 as the source [3]. The open circles (○) by anodic oxidation and filled circles (●) by chemical polishing.

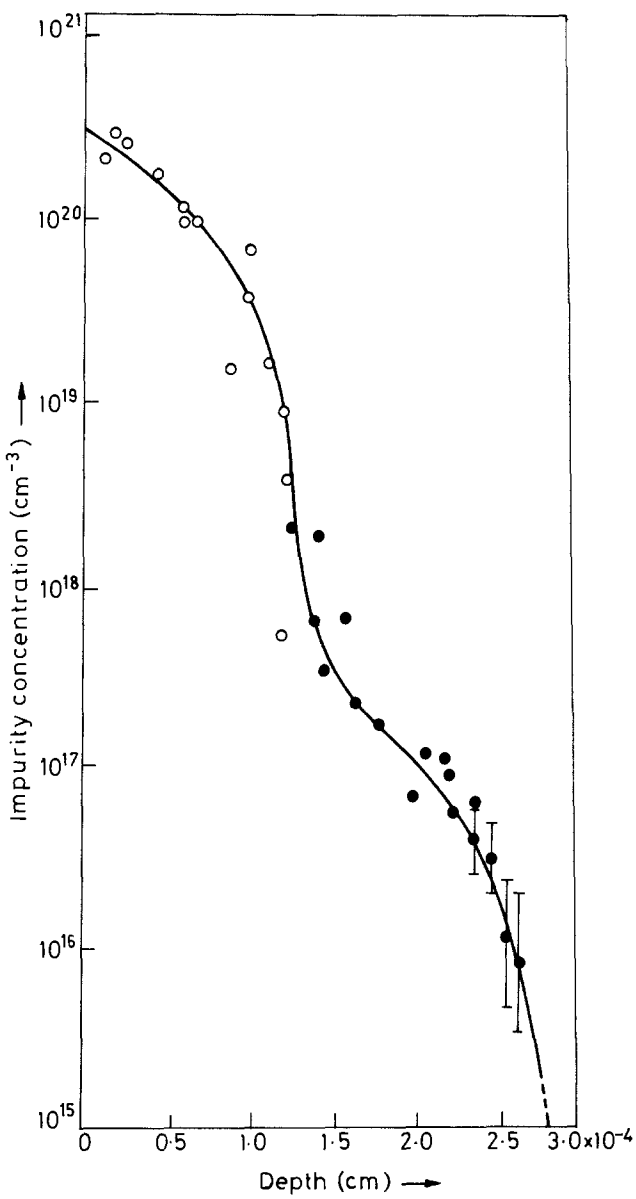

Fig. 2. Measured phosphorus diffusion profile after 1 hr diffusion at 1100°C by using P_2O_5 as the source. The smooth curve drawn to the experimental points shows kink and tail structure. The open circles (○) by anodic oxidation and filled circles (●) by chemical polishing.

equal to the removal of silicon by anodic oxidation. Care has been taken to see that the solution will polish uniformly and the polishing cloth is free from the dried solution. After polishing, the wafers were cleaned with conc. HNO_3 to free the surface from metallic ions. After each removal, the sheet resistivity was measured by the four-point probe technique, taking the precaution suggested by the authors in Ref. (5) and by Huang and Ladbrooke (6).

The conductivity of the removed silicon layer can be calculated from the relation

$$\sigma(W)\,\delta W = \frac{1}{4.532}\left(\frac{I_1}{V_1} - \frac{I_2}{V_2}\right) \qquad [1]$$

where $\sigma(W)$ is the conductivity of the removed silicon layer of thickness δW and V_1, I_1 and V_2, I_2 are probe voltages and currents of the two successive measurements on the silicon surface.

By repeating the process of removing layers of silicon, the variation of conductivity with depth $\sigma(Z)$ can be plotted. This is related to the variation in hole concentration by the relation

$$\sigma = q\mu_p P \qquad [2]$$

where μ_p is the mobility. Using the empirical relations given by Caughey and Thomas (7), as modified by Plunkett *et al.* (8), the value of P can be calculated.

From the measured values of I_1, I_2 and V_1, V_2, the concentration of impurity was calculated. Figure 1 shows the measured boron redistribution profile and Fig. 2 shows the phosphorus diffusion profile. The open circles (○) indicate the value obtained by the process of anodic oxidation and the filled circles (●) by chemical polishing. In the impurity concentration less than 1.0×10^{17} cm^{-3}, it is difficult to observe appreciable current in the four-point probe resistivity measurements for an accurate value of impurity concentration. In addition to that, in Eq. [1], one has to subtract substantial values to get the conductivity of the removed layer, which will cause appreciable error in the impurity estimation. To overcome this difficulty, both forward and reverse current directions were tried and average values are given.

Acknowledgment

This research was carried out under the sponsored programs of the R and T Scheme of Defense Research and Development Organization, Ministry of Defense, Government of India.

Manuscript submitted March 2, 1983; revised manuscript received July 18, 1983.

REFERENCES

1. E. F. Duffek, E. A. Benjamini, and C. Mylroie, *Electrochem. Technol.*, **3**, 75 (1965).
2. H. D. Barber, H. B. Lo, and J. E. Jones, *This Journal*, **123**, 1404 (1976).
3. G. Eranna, K. Prasad, A. K. Diwakar, and D. Kakati, Submitted to *Solid-State Electron.*
4. G. Eranna and D. Kakati, *J. Appl. Phys.*, Accepted for publication.
5. G. Eranna and D. Kakati, *Solid-State Electron.*, **25**, 611 (1982).
6. R. S. Huang and P. H. Ladbrooke, *ibid.*, **21**, 1123 (1978).
7. D. M. Caughey and R. F. Thomas, *Proc. IEEE*, **55**, 2192 (1967).
8. J. C. Plunkett, J. C. Stone, and A. Leu, *Solid-State Electron.*, **20**, 447 (1977).

JOURNAL OF THE ELECTROCHEMICAL SOCIETY

ACCELERATED

—BRIEF COMMUNICATIONS—

DECEMBER 1983

Reactive Ion Etching of Tantalum Pentoxide

Shunji Seki, Takashi Unagami, and Bunjiro Tsujiyama

Nippon Telegraph and Telephone Public Corporation, Ibaraki Electrical Communication Laboratory, Tokai, Ibaraki, 319-11, Japan

In recent years, tantalum pentoxide (Ta_2O_5) films have received particular interest for use in electronic devices. The higher dielectric constant of Ta_2O_5 films, compared with the dielectric constant for SiO_2, makes them attractive as storage capacitors in monolithic integrated circuits. For these applications, Ta_2O_5 films have mainly been prepared by anodic or thermal oxidation of a deposited Ta film. In these monolithic integrated circuits, capacitor structures were selectively fabricated using a micro-fabrication technique for a Ta base electrode prior to oxidation (1). More recently, it has been indicated that high-quality Ta_2O_5 films (low leakage current and high breakdown voltage) can be obtained by RF-magnetron sputtering (2). As the requirement for high-quality Ta_2O_5 films increases in those electronic devices, micro-fabrication techniques for Ta_2O_5 have become necessary, in addition to increasing the quality of the Ta_2O_5 film itself. Dry-etching techniques for Ta_2O_5 itself, which are appicable to silicon device fabrication processes, have not been reported so far. Wet chemical etching of Ta_2O_5 films was reported by Pringle (3). He showed that the anodic tantalum oxide could be etched by concentrated HF almost saturated with NH_4F. However, the etch rate for high-quality, sputtered Ta_2O_5 films with that etchant is too small. Moreover, that etchant containing a high HF concentration is not suitable for silicon microelectronic device fabrication processes. Therefore, Ta_2O_5 etching techniques, which are applicable to high-quality, sputtered Ta_2O_5 films and are suitable for the device fabrication processes, become increasingly important. The present work explores plasma etching of Ta_2O_5, and initially shows that Ta_2O_5 can be dry-etched using a reactive ion etching system.

Key words: reactive ion etching, magnetron sputtering, tantalum pentoxide.

Etching experiments were performed usin a parallel plate, RF reactive ion etchin (RIE) system (ANELVA DEM-451M) with a 13.5 MHz RF power supply. The 250 mm diamete electrodes with cathode coupled configuratio are separated by 89 mm. The wafers are mounted on the water-cooled cathode during etching. The following fluorocarbon gases were used as etch gases: CF_4, CF_4/H_2 (partial pressure ratio of CF_4/H_2 = 80/20) and CF_4/O_2 (partial pressure ratio of CF_4/O_2 = 95/5). The system pressure during etching was controlled to between 10 mTorr and 100 mTorr. Ta_2O_5 films were fabricated using an RF magnetron sputtering system. The Ta_2O_5 target, which was 10 cm in diameter and 5mm thick, was used in the sputtering experiments. The sputtering gas consisted of mixtures of argon and oxygen (partial pressure ratio of Ar/O_2 = 80/20). The wafers were patterned using Shipley AZ 1350 positive photoresist. Thickness measurements were performed with a Taylor-Hobson surface profilimeter. Etch rates for Ta_2O_5, SiO_2, single-crystalline silicon (⟨100⟩ oriented, p-type and 1.2 to 1.8 ohm-cm) and Shipley AZ 1350 positive photoresist, and individual etch rate ratios were studied.

Figure 1 shows etch rate variations for Ta_2O_5, SiO_2, Si and AZ 1350 photoresist with different etching pressures. In those cases, the experimental ranges for the etch gas flow rate and the power density were 50 sccm and 0.20 W/cm^2, respectively, and CF_4/H_2 was used as the reactive gas. As shown in Fig. 1, the etch rates for sputtered Ta_2O_5 and thermally grown SiO_2 have a similar pressure dependence, showing an increase in the etch rate with lowering pressure. At a pressure of 20 mTorr, the Ta_2O_5 etch rate has increased up to 210 Å/min. On the other hand, the etch rate for Si is independent of the system pressure, showing a constant value in the pressure range studied. The etch rate variation for AZ 1350 shows a maximum value around at 30 mTorr. As a result, the etch rate ratio of 3/1 for Ta_2O_5/Si and the etch

rate ratio of 2/1 for Ta_2O_5/AZ 1350 could be obtained at a pressure of 20 mTorr. These results have indicated that reactive ion etching using CF_4/H_2 as the etch gas is capable of etching sputtered Ta_2O_5 films and is applicable to silicon device fabrication processes.

The pressure dependence of Ta_2O_5 etch rate mentioned above implies the etching mechanism of Ta_2O_5. Although the system pressure effects are complicated, one of these effects is a variation in the self-bias voltage for the cathode; that is, the lower pressure induces an increase in the self-bias voltage. In the pressure range studied, the self-bias voltage increases from 0.37 kV to 0.7 kV as the etching pressure lowers. Under higher self-bias voltage conditions, the ionized particles have more kinetic energies. Therefore, the results shown in Fig. 1 suggest that an ion enhanced mechanism may play an important role in the etching phenomena of Ta_2O_5.

Table I shows an etch rate comparison between different reactive gas compositions: CF_4, CF_4/H_2 and CF_4/O_2. The experimental ranges for power density, etch gas flow rate and pressure were 0.2 W/cm^2, 50 sccm and 30 mTorr, respectively. Under those conditions, the self-bias voltage for the cathode is equal to 0.52 kV for each reactive gas. As shown in Table I, each reactive gas principally containing CF_4 is capable of Ta_2O_5 dry etching. A slight difference has been observed in the Ta_2O_5 etch rate depending on the addition species to the etch gas. While, the etch rate variations become more prominent for Si and AZ 1350 by addition of hydrogen and oxygen. These results indicate that addtion of hydrogen improves the etch rate ratios for Ta_2O_5/Si and Ta_2O_5/AZ 1350.

In summary, it has initially been indicated that Ta_2O_5 can be etched in the RIE mode, principally using CF_4 as a reactive gas. That etching technique is capable of etching high-quality, sputtered Ta_2O_5 films and is also applicable to silicon device fabrication processes. The etch rate of 210 Å/min for sputtered Ta_2O_5 films has been achieved at 0.20 W/cm^2 applied power density, CF_4/H_2 flow rate of 50 sccm and a pressure of 20 mTorr. The etch rate variations using CF_4, CF_4/H_2 and CF_4/O_2 as reactive gases were also studied. Those results have indicated that the addition of hydrogen to the etch gas improves the etch rate ratio for Ta_2O_5/Si and that for Ta_2O_5/AZ 1350. It has also been suggested, from the pressure effects on the etch rate, that an ion enhanced mechanism may play an important role in the plasma etching phenomena of Ta_2O_5.

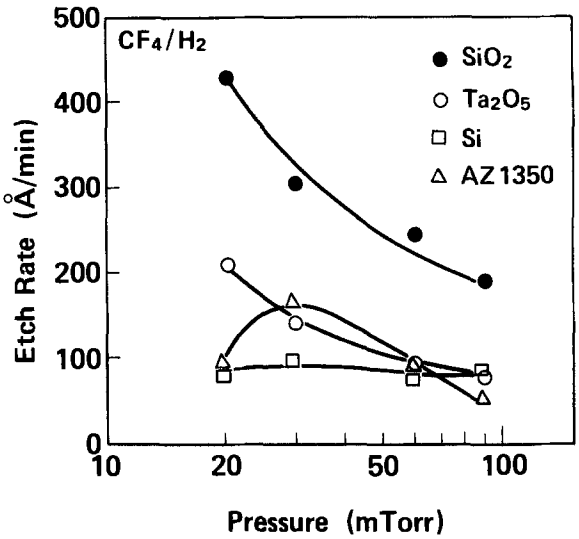

Fig. 1. Pressure effects on Ta_2O_5, SiO_2, Si and AZ 1350 photoresist etch rates.

Table I. Etch-rate comparison for different reactive gas compositions

Materials / Etch Gas	Ta_2O_5	SiO_2	Si	AZ1350
CF_4	190	330	270	360
CF_4/H_2	140	300	100	160
CF_4/O_2	200	380	300	430

etch rate(Å/min)

ACKNOWLEDGEMENTS

The authors would like to thank K.Murase for his encouragement during the course of this work.

REFERENCES

(1) K.Ohta, K.Yamada, K.Shimizu, and Y.Tarui, IEEE Trans. Electron Devices, ED-29, 368(1982).
(2) S.Seki, T.Unagami, and B.Tsujiyama, J. Vac. Sci. Technol., to be submitted.
(3) J.P.S.Pringle, This Journal, 119, 482(1972).

Manuscript received July 18, 1983.

Nippon Telegraph and Telephone Public Corporation assisted in meeting the publication costs of this article.

New Uses of Nafion® Membranes in Electro-Organic Synthesis and In Organic Acids Separations

Helena Li Chum,* Alan K. Hauser, and David W. Sopher

Thermochemical and Electrochemical Research Branch, Solar Energy Research Institute, Golden, CO 80401

INTRODUCTION

Nafion® perfluorosulfonate ion exchange membranes and chemically similar analogs are being widely used in electrolytic processes because of their excellent chemical and thermal stability, high conductivity, and permselectivity, and suitability of mechanical properties (1). In this communication we report new uses of Nafion®, applicable to other cation-exchange membranes in organic electrosynthesis and in the separation of carboxylic acids.

RESULTS AND DISCUSSION

As part of our studies on the electrochemistry of biomass-derived compounds (2) to produce chemicals of high energy content we investigated the electrochemical reduction of levulinic acid, the major product of controlled acid degradation (3) of hexose sugars at moderate temperatures (by-products of wood acid hydrolysis plants). Such studies aim to pair the cathodic reduction of levulinic acid with the Hofer-Moest (pH 7) anodic oxidation of valeric acid to gaseous butenes, butanols, and butylpentanoate (immiscible with water). This paired synthesis would require a separator capable of withstanding a pH gradient and a means of allowing protons formed at the anode to migrate to the cathode compartment, where they would maintain a necessary low pH for the reduction of levulinic to valeric acid.

We now report results on the first part of this scheme, i.e., the reduction of levulinic acid and the behavior of the Nafion® separator. Preparative constant current electrolyses (50-200 mA/cm^2) of levulinic acid (1-3 M) in sulfuric acid (0.1-1.0 M) in a modified parallel-plate flow cell (Electroprep from ECO Instruments) were carried out on a lead cathode with continuous recirculation of the catholyte, separated from the anolyte by a Nafion® membrane (type 125 reinforced or unreinforced). The anolyte underwent gravity recirculation. High current efficiencies (90%) at up to 30% conversion were obtained. We found, to our surprise, that the system has a built-in capacity for separating the valeric acid formed in the catholyte to the anolyte. For instance, for an electrolysis carried out at 200 mA/cm^2, starting with a solution of 3.6 M levulinic acid in the catholyte, after 30% conversion of that acid into valeric acid, we found none of the valeric acid in the catholyte (within the experimental error) but a 1 M solution of valeric acid in the anolyte. A small amount (about .15 M) of levulinic acid was also present in the anolyte. In these experiments there was a pressure gradient between the catholyte and anolyte of about 10-20 psi. Similar separations were also observed in electrolyses performed at other current densities.

In order to verify these findings and test the diffusion of carboxylic acids (and other organic substrates) through Nafion®, a series of experiments were carried out as a function of pH gradient, temperature, and pressure. Valeric acid, initially 0.3 M on one side, diffused through Nafion-125 so that the concentrations were the same on each side of the membrane after 20 hours (see Table I). When the sulfuric acid was omitted (pH = 2.8) the rate of diffusion was found to be the same. A valeric acid solution adjusted to pH 4.0 was found to diffuse slightly more slowly. With pH 6.0 buffer on both sides of the cell the rate of migration decreased by an order of magnitude; however, by increasing the pH of the solution to which diffusion was occurring, a slightly improved rate of transport was observed from the pH 6.0 buffer. A similar pH dependence of the rate of diffusion through Nafion has been observed for both alkali metal and transition metal cations (4), which implies that valeric acid is migrating through the membrane in a cationic form. Carboxylic acids, in solvents of high dielectric constant, such as water, are known

*Electrochemical Society Member.

Key words: cation-exchange membranes, separations, Nafion®.

Table I. Diffusion of valeric acid[a] through Nafion®-125; expressed as % acid diffused in 20 hours (% D, 20 h) and initial diffusion rate (I.D.R., Mh^{-1}). Geometric area of the membrane: 7.1 cm^2; total volume: 42 ml

Conditions	%D, 20h	I.D.R.
Valeric acid (0.3M) in H_2SO_4 (1M) to H_2SO_4 (1M)	50	0.015
Valeric acid (0.3M) in water to water	50	0.015
Valeric acid (0.3M) in pH 6 buffer to pH 6 buffer	10	0.0015
Valeric acid (0.3M) in pH 6 buffer to pH 9 buffer	15	0.002
Valeric acid (0.3M) in water at pH 4 to water	40	0.011
Valeric acid (0.1M) in water to water	40	0.003
Valeric acid (0.3M) in water to water with 0.1 psi pressure drop across membrane	--	0.019

[a]Concentrations measured by UV-VIS absorption spectrophotometry.

to exist as monomers, hydrogen-bonded to one or two solvent molecules (5). At low pH values the carboxyl group may interact with a hydroxonium ion forming a species with an overall positive charge which would then migrate by the normal cationic mechanism. Creating a pressure drop across the membrane of only 0.1 psi (ca. 700 Nm^{-2}) resulted in a 40% increase in the rate of diffusion of valeric acid. Under these conditions water was transported through the Nafion at 0.2 mlh^{-1}.

Two lower molecular weight aliphatic acids (propionic and butyric acids) were found to migrate through the membrane at essentially the same rate as valeric acid (Table II) which suggests that the diffusion rate is related to chemical functionality rather than molecular weight. In fact, carboxylic acids substituted with a second functional group (levulinic acid, C=O; lactic acid, OH; succinic acid, COOH) were all found to diffuse at a slower rate than simple aliphatic acids (Table II). This difference could be due to the occurrence of an interaction between the second functional group and the sulfonic acid functions in the membrane matrix, which would tend to retard the motion of the molecule/ion through the material. Glucose diffuses extremely slowly through Nafion probably because of the size of the molecule.

The effect of temperature on the diffusion of valeric acid through Nation® -117 is shown in Fig. 1. Apparent diffusion coefficients (6) for valeric acid are 5.5×10^{-6} cm^2s^{-1} (at 308 K) to 1.6×10^{-5} cm^2s^{-1} (at 338 K), with an activation energy of 30 kJ mol^{-1}. This activation energy is identical within the error to that observed for the self-diffusion of sodium ions on Nafion® 120 (7).

These results suggest that Nafion materials could have wider applications in organic electrolytic processes. The removal or addition of compounds could be used to synthetic advantage. In separations science, these materials could play a more important role, e.g., as column material for high performance liquid chromatography and in industrial organic separation processes. For instance, these very stable membranes could perform a variety of difficult separations of polyfunctional carboxylic acids such as complex saccharinic acids from the kraft pulping of wood and industrial separations of simple carboxylic acids in complex mixtures.

ACKNOWLEDGEMENTS

This work was supported by the Biomass Energy Systems Division of the Department of Energy under Contract No. EG-77-4042-01 (WPA 434). The authors are indebted to F. Posey for her cooperation on some analytical aspects of this work. E. I. DuPont de Nemours graciously provided the samples of Nafion used in this work.

REFERENCES

1. R. S. Yeo, This Journal, 130, 533 (1983), and references therein.
2. H. L. Chum, editor, "Electrochemistry Applied to Biomass," SERI/PR-622-1321 (1982); H. L. Chum and R. A. Osteryoung, "Survey of the Electrochemistry of Some Biomass-Derived Compounds," SERI/TR-332-417 (1982), Solar Energy Research Institute, Golden, CO.
3. R. H. Leonard, Ind. Eng. Chem., 48, 1331 (1956).

Table II. Diffusion of organic compounds[a] through Nafion®-125 expressed as % of compound diffused in 20 hours (%D, 20h) and initial diffusion rate (I.D.R.; Mh^{-1}) at different compound initial concentrations. Geometric area: 7.1 cm^2; total volume: 42 ml.

	INITIAL CONCENTRATION DIFFUSION					
	0.1 M		0.3 M		1.0 M	
COMPOUND	%D, 20h	I.D.R.	%D, 20h	I.D.R.	%D, 20h	I.D.R.
Propionic acid[b]	40	0.003	--	--	--	--
Butyric acid[b]	40	0.003	--	--	--	--
Valeric acid[b]	40	0.003	50	0.015	--	--
Levulinic acid	--	--	30	0.0065	--	--
Succinic acid	--	--	25	0.0040	--	--
Lactic acid	--	--	25	0.0030	--	--
Glucose	--	--	--	--	5	0.006

[a]Concentrations measured by gas chromatography or UV-VIS absorption spectrophotometry.
[b]Acids all present in the same solution.

4. C. Heitner-Wirguin, in "Ion Exchange: Transport and Interfacial Properties," R. S. Yeo and R. P. Buck, Editors, Pennington, NJ, The Electrohemical Society Softbound Proceedings Series, (1981).
5. G. C. Pimentel and A. L. McClellan, "The Hydrogen Bond," W. H. Freeman and Co., San Francisco (1960); L. J. Bellamy, "The Infra-Red Spectra of Complex Organic Molecules," p. 183, Chapman and Hall, London (1975).
6. M. Suhara and Y. Oda, in "Ion Exchange Transport and Interfacial Properties," p. 290, R. S. Yeo and R. P. Buck, Editors, Pennington, NJ, The Electrochemical Society Softbound Proceedings Series (1981).
7. H. L. Yeager and A. Steck, Ibidem, p. 257, (1981).

Manuscript received Aug. 8, 1983.
The Solar Energy Research Laboratory assited in meeting the publication costs of this article.

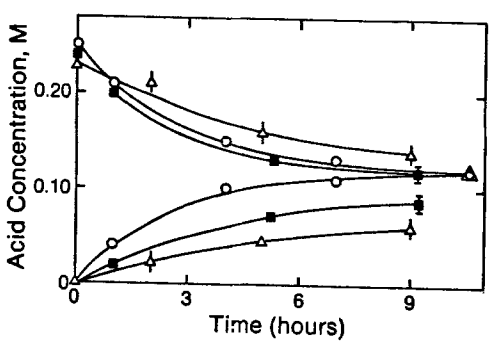

Figure 1. Results from diffusion experiments carried out on two glass half-cells with flanges (clamped by a Teflon collar, with the Nafion membrane in between) as a function of temperature (Δ, 30°C; □, 45°C; o, 60°C) [Nafion pieces (cut from the same sheet of unreinforced type 117) were pretreated by boiling in deionized water for ca. 20 minutes, followed by wiping the surfaces dry.]

In Situ FT-IR Spectroscopic Study of Electrochemical Adsorption of Phosphoric Acid on Platinum

M. A. Habib* and J. O'M. Bockris*

Department of Chemistry, Texas A&M University, College Station, Texas 77843

Variation of the rate of the reduction of oxygen in various acids used as fuel cell electrolytes, provokes questions of the adsorption of these acids on platinum catalysts (1). Since the behavior of individual crystal planes differ markedly in most cases as a result of the difference of the potential of zero charge and of the chemical nature of the surface, it is evident that accounting for the adsorption properties of a polycrystalline electrode remains difficult and complex (2). Although infrared reflectance spectroscopy has been used to detect organic radicals and carbon containing species as electrochemical reaction products in nonaqueous solvents (3-6), due to high IR adsorption by water, the applicability of this method for the study of electrochemical phenomenon in aqueous solutions remains limited (3,7,8). However, a fast Fourier transform IR spectrometer with high energy throughput in combination with a highly polished electrode surface having a thin film of solution ($\simeq 1\mu$thick) between the electrode surface and IR transparent window, brings new promise to the field of electrochemical adsorption study. We report here the electrochemical adsorption of phosphoric acid on Pt from an aqueous solution, as measured by the use of a Fourier transform infrared spectrometer system.

The working electrode used was a highly polished Pt disc attached to a teflon coated copper rod. The electrode surface was placed very close to an IR-transparent ZnSe cell window and thus had a very thin film of solution ($\simeq 1\mu$thick) in front of the electrode. The electrode surface was irradiated with the incident IR beam in the sample compartment of a Digilab FTS-20E spectrometer system equipped with a Data General Nova 4 computer and IR spectra were recorded after electrochemical polarization of the electrode surface. Phosphoric acid solution in 1 mol.dm^{-3} $HClO_4$ was used. A versatile reflection attachment (Harrick model VRA-S5D) with retromirror accessory (RMA-4DG) was used to guide the incident IR beam to the electrode surface and to guide the reflected beam back to the detector was used. The number of averaged spectra was 1000 at a resolution of 4cm^{-1}. Polarization of the reflected beam was selected by means of an infrared grid polarizer. The IR was polarized parellel to the plane of incidence (9).

The electrode was polarized potentiostatically in the range of 0V (NHE) to 1.2V (NHE) at an interval of 200 mV. The spectra reported here are the difference between the spectra at a given anodic potential and that at 0V where no phosphoric acid molecule is expected to adsorb.

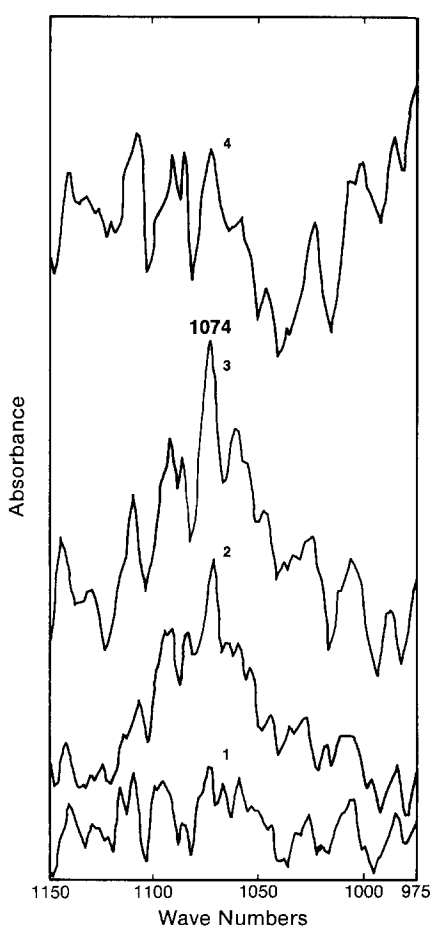

Fig.1 IR spectra of Pt surface at various values of the potential (VS NHE) in 6.6 x 10^{-3} mol.dm^{-3} H_3PO_4 + 1 mol. $dm^{-3}HClO_4$ solution: 1) 200 mV, 2) 400 mV, 3) 800 mV, and 4) 1200 mV

In figure 1, differential spectra of electrode surface at 200, 400, 800 and 1200 mV/NHE are shown. The absorbance peak at 1074 cm^{-1} is merely visible at 200 mV, but increases with potential and reaches a maximum at 800 mV. This peak again decreases with further increase of potential. The peaks in close proximity of 1074 cm^{-1} behaves the same way as that at 1074 cm^{-1} and hence are of same origin as the main one at 1074 cm^{-1}.

The peak at 1074 cm^{-1} is due to the P-O stretching vibration of the adsorbed H_3PO_4 on Pt (10). The adsorption peaks as a function of potential are plotted in Fig. 2a. The adsorption of H_3PO_4 increases with potential, passes through a maximum and decreases again at higher potentials. This result is in good agreement with those obtained for the adsorption of H_3PO_4 on Pt by radiotracer method by Horanyi, et. al. (11) and also obtained in this lab.(12) (Fig. 2b). The discrepancy at potentials <800mv may be due to the difference in the strength of H_3PO_4 - Pt interaction with potential, as pointed out by Pons (13) and Bewick (8).

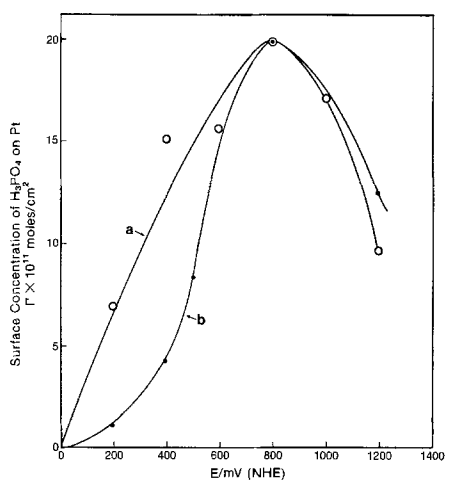

Fig. 2 Surface concentration, Γ, of H_3PO_4 as a function of potential: (a) Γ as normalized area of IR peak at 1074 cm^{-1}. The highest peak area is assumed to be Γ_{max} as obtained from (b) radio tracer measurements.

*Electrochemical Society Active Members

Key Words: Adsorption, Phosphoric acid, In-situ FT-IR, Platinum.

Confirmation that the peaks originate in H_3PO_4 was obtained by carrying out the same set of experiments without H_3PO_4 in solution. None of the peaks mentioned above, appeared. When the above experiments were performed with the orientation of the light polarizer changed to one perpendicular to the plane of incidence, none of the peaks showed up and this is considered to the proof of the fact that the peaks are related to only adsorbed H_3PO_4 molecules, because reflected light when polarized perpendicular to the plane of incidence, does not carry information about the adsorbed layer (9). With change of potential, no shift was observed in the position of the peaks, meaning that no change in the bond strength of IR absorbing molecules occurred. The area of the peaks did not increase with time at the same electrode potential.

In-situ Fourier-Transform Spectroscopy method, thus, provides direct evidence for the presence of H_3PO_4 on the electrode surface at anodic potential and hence, can be used for the measurement of electrochemical adsorption of IR active entities on solid surfaces.

ACKNOWLEDGEMENTS

We acknowledge Dr. S. Pons, Department of Chemistry, University of Utah, Salt Lake City Utah, for helpful dicussion. Partial financial support from the Electric Power Research Institute and the National Foundation for Cancer Research are acknowledged.

REFERENCES

1. P. N. Ross, Jr., J. Electrochem Soc. 130 (1983) 882
2. R. Parsons, Surface Science, 101 (1980) 316
3. A. Bewick, M. Fleischman and J. Robinson, DECHEMA - Monogr. 1981, 90 (1851 - 1870, Elektrochem Elektron)
4. T. Davidson, S. Pons, A. Bewick and P. P. Schmidt, J. Electroanal. Chem 125 (1981) 237
5. A. Bewick, K. Kunimatsu, and S. Pons, Electrochem. Acta, 25 (1980) 465
6. K. Kunimatsu, J. Electroanal. Chem. 140 (1982) 205-210
7. K. Kunimatsu, J. Electroanal. Chem. 145 (1983) 219-224
8. A. Bewick and J. W. Russell, J. Electroanal. Chem. 132 (1982) 329-344
9. A. E. Dowrey and C. Marcott, Applied Spectroscopy, July (1982) 329-344

10. K. Nakamoto, Infrared and Raman Spectra of Inorganic and Co-ordination Compounds, Third Edition, J. Wiley and Sons, New York, 1978
11. G. Horanyi, E. M. Rizmayer and G. Inzelt, J. Electroanal. Chem. 93 (1978) 183
12. M. A. Habib, J. O'M. Bockris and J. Carbajal, to be submitted, Aug. 1983
13. S. Pons, Private Communication, Aug., 1983, Department of Chemistry, University of Utah, Salt Lake City, Utah 84112, U.S.A.

Manuscript submitted Sept. 2, 1983.

Texas A&M University assisted in meeting the publication costs of this article.